European Community on Computational Methods in Applied Sciences

ECCOMAS Thematic Conference

# COMPDYN 2023

*9th International Conference on Computational Methods in Structural Dynamics and Earthquake Engineering*

# PROCEEDINGS

## Volume II

M. Papadrakakis, M. Fragiadakis (Eds.)

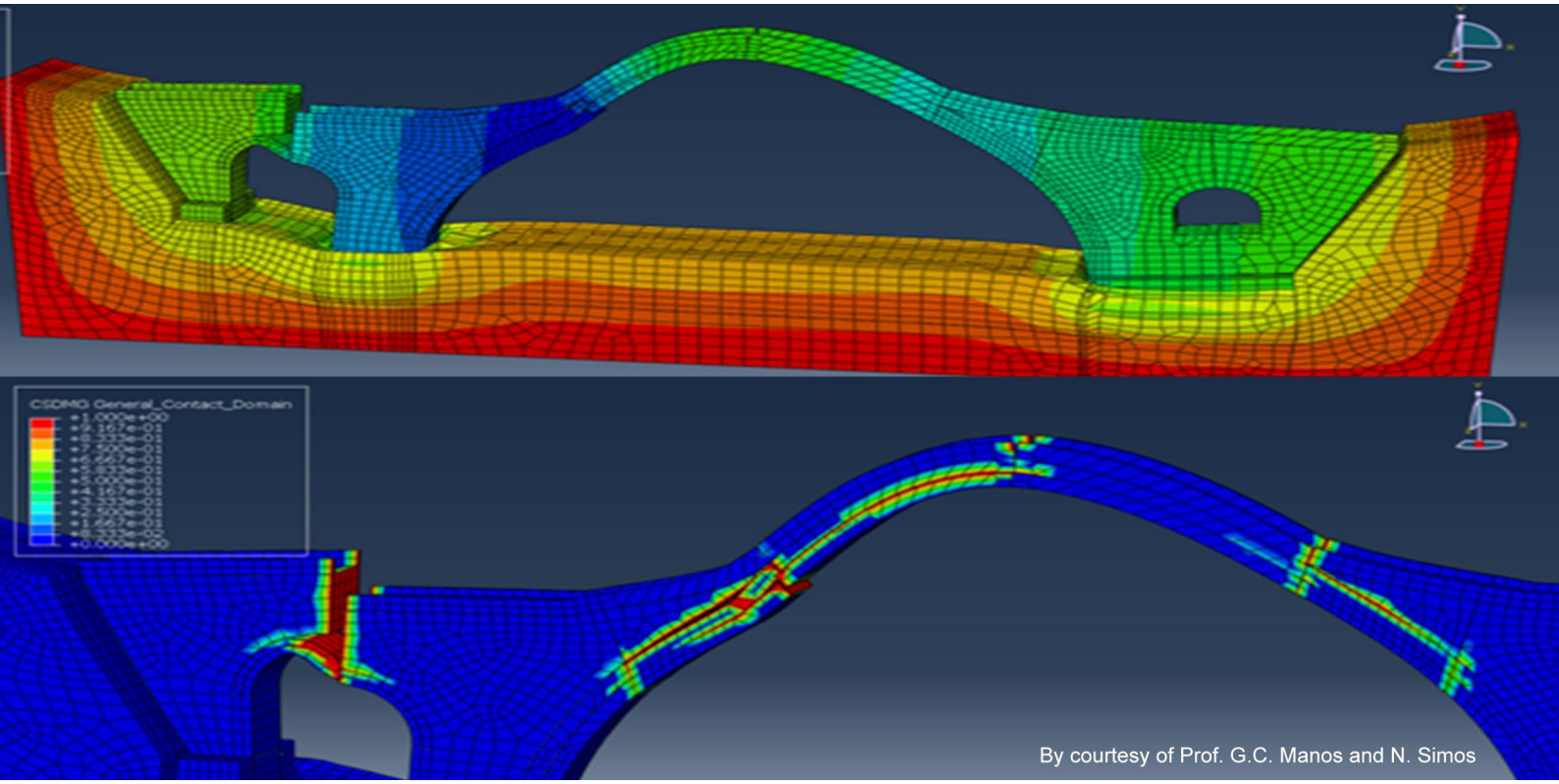


An IACM Special Interest Conference

**COMPDYN 2023**

**Computational Methods in Structural Dynamics and Earthquake Engineering**

Proceedings of the 9th International Conference on Computational
Methods in Structural Dynamics and Earthquake Engineering
Held in Athens, Greece
12-14 June 2023

Edited by:

**M. Papadrakakis**
National Technical University of Athens, Greece

**M. Fragiadakis**
National Technical University of Athens, Greece

**A publication of:**

Institute of Structural Analysis and Antiseismic Research
School of Civil Engineering
National Technical University of Athens (NTUA)
Greece

**COMPDYN 2023**
**Computational Methods in Structural Dynamics and Earthquake Engineering**
M. Papadrakakis, M. Fragiadakis (Eds.)

First Edition, October 2023

© The authors

ISBN (set): **978-618-5827-01-4**
ISBN (vol II): **978-618-5827-00-7**

## PREFACE

This volume contains the full-length papers presented in the 9th International Conference on Computational Methods in Structural Dynamics and Earthquake Engineering (COMPDYN 2023) that was held in Athens, Greece on June 12-14, 2023.

COMPDYN 2023 is one of the 32 Thematic Conferences of the European Community on Computational Methods in Applied Sciences (ECCOMAS) which were held in 2023, and is also a Special Interest Conference of the International Association for Computational Mechanics (IACM). The purpose of this Conference series is to bring together the scientific communities of Computational Mechanics, Structural Dynamics and Earthquake Engineering, to act as a forum for exchanging ideas in topics of mutual interests and to enhance the links between research groups with complementary activities. We believe that the communities of Structural Dynamics and Earthquake Engineering will benefit from their exposure to advanced computational methods and software tools which can highly assist in tackling complex problems in dynamic and seismic analysis and design of structures, while also giving the opportunity to the Computational Mechanics community to be exposed to very important engineering problems of great social interest.

The COMPDYN 2023 Conference is supported by the National Technical University of Athens (NTUA), the European Association for Structural Dynamics (EASD), the European Association for Earthquake Engineering (EAEE), the Greek Association for Computational Mechanics (GRACM).

The editors of this volume would like to thank all authors for their contributions. Special thanks go to the colleagues who contributed to the organization of the Minisymposia and to the reviewers who, with their work, contributed to the scientific quality of this e-book.

### Editors

**M. Papadrakakis**
National Technical University of Athens, Greece

**M. Fragiadakis**
National Technical University of Athens, Greece

**ACKNOWLEDGEMENTS**

The conference organizers acknowledge the support towards the organization of the "9th International Conference on Computational Methods in Structural Dynamics and Earthquake Engineering", to the following organizations:

- European Community on Computational Methods in Applied Sciences (ECCOMAS)
- International Association for Computational Mechanics (IACM)
- European Association for Structural Dynamics (EASD)
- European Association for Earthquake Engineering (EAEE)
- Greek Association for Computational Mechanics (GRACM)
- Hellenic Society for Earthquake Engineering (HSEE)
- School of Civil Engineering, National University of Athens (NTUA)

## Plenary Speakers and Invited Session Organizers

We would also like to thank the Plenary and Semi-Plenary Speakers and the Minisymposia Organizers for their help in the setting up of a high standard Scientific Programme.

**Plenary and Semi-Plenary Speakers:** Sondipon Adhikari, Siu-Kui Au, Jack Baker, Peter Betsch, Javier Bonet, Michael Brun, Eleni Chatzi, Hauke Gravenkamp, Johann Guilleminot, Muneo Hori, George Karniadakis, Paulo B. Lourenço, Ludovic Noels, Jamie Padgett, Paris Perdikaris, Alessandro Reali, Michael Shields, Daniel Straub, Bruno Sudret, Enrico Tubaldi, Haim Waisman

**MS Organizers:** Daniela Addessi, Hamid Ahmadi, Omar Alshawa, Giulia Angelucci, Eftychia Apostolidi, António Arêde, Yongtao Bai, Nikolaos P. Bakas, Rui Carneiro Barros, Michael Beer, Michele Betti, Sifeng Bi, Nicoletta Bianchini, Manuel Braz-César, Bruno Briseghella, Matteo Broggi, Eleonora Bruschi, Chiara Calderini, Paolo Calvi, Paulo Candeias, Claudia Casapulla, Paolo Castaldo, Serena Cattari, Nicola Cavalagli, A. Charalampakis, Eleni Chatzi, Francesco Clementi, Mario D'Aniello, Tommaso D'Antino, Silvia De Angeli, Dario De Domenico, Maria Teresa de Risi, Carlo Del Gaudio, Ciro Del Vecchio, Pedro Delgado, Fabio Di Carlo, Raffaele Di Laora, Marco Di Ludovico, Marco Domaneschi, Marco Donà, Usama Ebead, Matthias Faes, Giuseppe Failla, Davide Forcellini, Antonio Formisano, Pascal Fossat, Massimo Fragiacomo, Michalis Fragiadakis, Francesco Franco, Marco Furinghetti, André Furtado, G. Gabbianelli, Carmine Galasso, Manolis Georgioudakis, Ramin Ghiasi, Kyriakos Giannakoglou, Agathoklis Giaralis, Linda Giresini, Dan Givoli, Jose Gonzalez, George Goumas, Vagelis Harmandaris, Thomas JR Hughes, Antonino Iannuzzo, Mohamed Ichchou, Alper Ilki, Maria Iovino, Konstantinos A. Kapasakalis, Shaghayegh Karimzadeh, N. Kassotakis, Konstantinos Katakalos, Jin-Gyun Kim, Radek Kolman, Massimo Latour, Daniele Losanno, Paulo Lourenço, Giuseppe Maddaloni, Abdollah Malekjafarian, D. Malomo, George C. Manos, George Markou, A. Mehrotra, Nuno Mendes, Andrea Miano, Gabriele Milani, Stergios Aristoteles Mitoulis, Michela Monaco, Simone Morganti, Lukas Moschen, Mohammad Noori, Ehsan Noroozinejad, Vissarion Papadopoulos, K .C. Park, Alberto Pavese, Carlo Pettorruso, Vagelis Plevris, B. Pulatsu, Virginio Quaglini, Giuseppe Quaranta, Laura Ragni, Alessandro Reali, Stephan Rinderknecht, Xavier Romao, Emmanouil Rovithis, Antonio Sandoli, Evangelos J. Sapountzakis, Martina Sciomenta, Anastasios Sextos, Stefania Sica, Castorina Silva Vieira, Marco Simoncelli, Flavio Stochino, Alfred Strauss, Francesca Taddei, Izuru Takewaki, Diego Alejandro Talledo, Marco Tanganelli, Roberto Tartaglia, Valentina Tomei, G. Tsiatas, Grigorios Tsinidis, Yiannis Tsompanakis, P. Tsopelas, Enrico Tubaldi, N. Vaiana, Marcos Valdebenito, Gerardo Mario Verderame, Stefania Viti, Haim Waisman, Tadesse G. Wakjira, Yan Xu, Marco Zucca

## SUMMARY

**Preface**..... iii

**Acknowledgements**..... iv

**Contents**..... x

## VOLUME I

**Minisymposia**

**MS 1: NOVEL TECHNIQUES AND APPROACHES FOR SEISMIC PROTECTION OF STRUCTURES WITH ISOLATION AND/OR ENERGY DISSIPATION DEVICES** ..... 1
*Organized by Enrico Tubaldi, Laura Ragni, Dario De Domenico, Daniele Losanno and Hamid Ahmadi*

**MS 2: ADVANCES IN THE DYNAMIC RESPONSE ANALYSIS, MONITORING, AND MITIGATION OF WIND TURBINES** ..... 143
*Organized by Agathoklis Giaralis and Giuseppe Failla*

**MS 3: PROTECTION OF MUSEUM'S COLLECTIONS COMPUTATIONAL APPROACHES AND INNOVATIVE INTERVENTIONS** ..... 218
*Organized by Stefania Viti and Marco Tanganelli*

**MS 5: REPAIR AND RETROFIT OF STRUCTURES** ..... 316
*Organized by Ciro Del Vecchio, Marco Di Ludovico and Alper Ilki*

**MS 6: EXPERIMENTAL MEASUREMENTS AND NUMERICAL SIMULATION IN THE FIELD OF EARTHQUAKE ENGINEERING AND STRUCTURAL DYNAMICS – NEW STRUCTURES AND STRUCTURAL RETROFITTING** ..... 457
*Organized by George C. Manos and Konstantinos Katakalos*

**MS 7: SUSTAINABLE STRENGTHENING INTERVENTIONS TO PREVENT FAILURE IN UNREINFORCED MASONRY STRUCTURES AND INFRASTRUCTURES** ..... 770
*Organized by Claudia Casapulla, Linda Giresini, Omar Alshawa, Francesca Taddei and Ehsan Noroozinejad*

**MS 8: RECENT ADVANCES AND CHALLENGES IN GEOTECHNICAL EARTHQUAKE ENGINEERING** ..... 882
*Organized by Castorina Silva Vieira and Yiannis Tsompanakis*

**MS 9: SEISMIC SAFETY ASSESSMENT OF STRUCTURES** ..... 949
*Organized by Pedro Delgado and António Arêde*

**MS 10: RECENT ADVANCES IN SEISMIC ISOLATION OF STRUCTURES WITH NOVEL VIBRATION CONTROL APPROACHES** ..... 994
*Organized by Evangelos J. Sapountzakis and Konstantinos A. Kapasakalis*

**MS 11: THE ROLE OF THE STRUCTURAL MONITORING TO PREDICT THE PRIOR DAMAGE OR THE FACTUAL DEGRADATION PATTERN IN ORDER TO UPDATE THE SEISMIC VULNERABILITY OF EXISTING BUILDINGS** ..... 1071
*Organized by Carlo Del Gaudio, Andrea Miano, Fabio Di Carlo and Diego Alejandro Talledo*

**MS 12: ARTIFICIAL INTELLIGENCE & MACHINE LEARNING IN DESIGN AND ASSESSMENT OF STRUCTURES** ..... 1138
*Organized by George Markou, Nikolaos P. Bakas and Vagelis Harmandaris*

**MS 13: MONITORING AND LIFE CYCLE PERFORMANCE OF RAILWAY BRIDGES** ..... 1288
*Organized by Eftychia Apostolidi, Eleni Chatzi and Alfred Strauss*

**MS 14: ADVANCES IN OPTIMIZATION AND CONTROL OF STRUCTURES UNDER DYNAMIC LOADS** ..... 1350
*Organized by Giulia Angelucci, Giuseppe Quaranta, Bruno Briseghella and Izuru Takewaki*

**MS 17: STEEL JOINTS BEHAVIOR UNDER SEISMIC, FATIGUE AND ROBUSTNESS ACTIONS** ..... 1392
*Organized by Roberto Tartaglia, Mario D'Aniello and Massimo Latour*

**MS 19: RECENT ADVANCES AND CHALLENGES FOR THE PRESERVATION OF MASONRY STRUCTURES AND INFRASTRUCTURES AGAINST NATURAL AND ANTHROPIC RISKS** ..... 1556
*Organized by Daniela Addessi, Michele Betti, Nicola Cavalagli, Francesco Clementi, Antonio Formisano and Gabriele Milani*

**MS 20: ADVANCED NUMERICAL METHODS IN DYNAMICS, COMPUTATIONAL INTERFACE MECHANICS AND COUPLED PROBLEMS** ..... 1947
*Organized by Jose Gonzalez, Jin-Gyun Kim, Radek Kolman and K .C. Park*

**MS 22: HYSTERESIS PHENOMENA IN STRUCTURAL DYNAMICS AND EARTHQUAKE ENGINEERING: EXPERIMENTS, MODELING, AND DESIGN** ..... 1996
*Organized by N. Vaiana, A. Charalampakis, G. Tsiatas and P. Tsopelas*

**MS 24: ADVANCES IN SEISMIC ASSESSMENT AND INTEGRATED RETROFITTING FOR ENVELOPES OF RC** ..... 2070
*Organized by André Furtado, Marco Donà and Maria Teresa de Risi*

**MS 25: TOWARDS SEISMIC RESILIENCE: STRATEGIES AND TECHNOLOGICAL INNOVATION FOR SEISMIC RISK REDUCTION OF EXISTING STRUCTURES** ..... 2168
*Organized by Virginio Quaglini, Paolo Calvi, Tommaso D'Antino, Eleonora Bruschi and Carlo Pettorruso*

**MS 26: NON-DETERMINISTIC MODEL UPDATING AND HEALTH MONITORING WITH UNCERTAINTY TREATMENT** ..... 2335
*Organized by Sifeng Bi, Matthias Faes, Marcos Valdebenito, Yongtao Bai, Matteo Broggi and Michael Beer*

**MS 28: MONITORING, DAMAGE MODELLING AND SOIL-STRUCTURE-INTERACTION IN CULTURAL HERITAGE CONSTRUCTIONS** ..... 2380
*Organized by Giuseppe Maddaloni, Stefania Sica, Antonino Iannuzzo and Michela Monaco*

**MS 29: SOFT COMPUTING AND ARTIFICIAL INTELLIGENCE TECHNIQUES IN STRUCTURAL ENGINEERING** ..... 2520
*Organized by Vagelis Plevris, Usama Ebead and Tadesse G. Wakjira*

**MS 30: THE ASSESSMENT OF RESILIENCE WITH APPROACHES BASED ON NUMERICAL SIMULATIONS** ..... 2540
*Organized by Davide Forcellini*

**MS 31: BEYOND DISCONTINUUM-BASED ANALYSIS: NOVEL APPROACHES FOR DISCRETE ELEMENT STRUCTURAL MODELLING OF COMPOSITE MATERIALS** ..... 2618
*Organized by D. Malomo, A. Mehrotra, N. Kassotakis, G. Gabbianelli and B. Pulatsu*

## VOLUME II

**Minisymposia**

**MS 32: MULTI-HAZARD RISK MANAGEMENT OF THE BUILT ENVIRONMENT: RECENT ADVANCES AND OPEN CHALLENGES** ..... 2677
*Organized by Serena Cattari, Silvia De Angeli, Carmine Galasso and Xavier Romao*

**MS 33: INSIGHT IN SEISMIC PERFORMANCE OF RETROFITTED BUILDINGS: FEASIBILITY AND EFFECTIVENESS OF INTERVENTION IN RC BUILDINGS** ..... 2819
*Organized by Maria Teresa De Risi, Carlo Del Gaudio and Gerardo Mario Verderame*

**MS 34: INSIGHTS AND DEVELOPMENTS IN DYNAMIC SOIL-FOUNDATION-STRUCTURE INTERACTION** ..... 2894
*Organized by Maria Iovino, Raffaele Di Laora and Emmanouil Rovithis*

**MS 35: RECENT ADVANCES IN GROUND- AND STRUCTURE-BORNE NOISE AND VIBRATION ASSESSMENT & PREDICTION** ..... 2972
*Organized by Lukas Moschen, Anastasios Sextos and Grigorios Tsinidis*

**MS 36: EXPERIMENTAL TESTING ON SEISMIC ISOLATION AND ENERGY DISSIPATION DEVICES** ..... 3017
*Organized by Marco Furinghetti, Alberto Pavese and Paolo Castaldo*

**MS 37: DESIGN OF STRUCTURES UNDER EXTREME LOADS** ..... 3091
*Organized by Marco Simoncelli, Flavio Stochino and Marco Zucca*

**MS 38: TIMBER-BASED SYSTEMS FOR NEW AND EXISTING STRUCTURES IN SEISMIC AREA: RECENT DEVELOPMENTS AND FUTURE TRENDS** ..... 3187
*Organized by Antonio Sandoli, Valentina Tomei, Martina Sciomenta and Massimo Fragiacomo*

**MS 39: SHM FOR TRANSPORT INFRASTRUCTURE RESILIENCE** ..... 3331
*Organized by Marco Domaneschi, Eleni Chatzi, Yan Xu and Stergios Aristoteles Mitoulis*

**MS 40: APPLICATION OF DEEP LEARNING AND IOT IN NUMERICAL MODELLING AND HEALTH MONITORING OF STRUCTURES/INFRASTRUCTURES** ..... 3357
*Organized by Ramin Ghiasi, Abdollah Malekjafarian, Mohammad Noori and Eleni Chatzi*

**MS 42: COMPUTATIONAL METHODS FOR INVERSE PROBLEMS IN STRUCTURES AND GEOPHYSICS** .... 3379
*Organized by Dan Givoli and Haim Waisman*

**MS 45: STRUCTURAL DYNAMICS, SEISMIC SAFETY AND RISK ASSESSMENT OF SPECIAL STRUCTURES** ..... 3415
*Organized by Rui Carneiro Barros and Manuel Braz-César*

**MS 48: RECENT ADVANCES IN GROUND MOTION SELECTION AND SCALING TECHNIQUES** ..... 3507
*Organized by Shaghayegh Karimzadeh, Manolis Georgioudakis and Michalis Fragiadakis*

**MS 49: SEISMIC RESPONSE OF MASONRY CROSS VAULTS: SHAKING TABLE TESTS AND NUMERICAL VALIDATIONS** ..... 3580
*Organized by Chiara Calderini, Paulo Lourenço, Nuno Mendes, Nicoletta Bianchini and Paulo Candeias*

## Thematic Sessions

**TS 2: ALGORITHMS FOR STRUCTURAL HEALTH MONITORING** .....3620

**TS 3: BRIDGE DYNAMICS** .....3732

**TS 4: CONSTITUTIVE MODELLING** .....3856

**TS 5: DYNAMICS OF CONCRETE AND MASONRY STRUCTURES** .....3908

**TS 9: GEOTECHNICAL ENGINEERING** .....4044

**TS 10: IMPACT DYNAMICS** .....4206

**TS 11: INVERSE PROBLEMS IN STRUCTURAL DYNAMICS** .....4217

**TS 13: NONLINEAR DYNAMICS** .....4265

**TS 14: NUMERICAL SIMULATION METHODS FOR DYNAMIC PROBLEMS** .....4339

**TS 15: OPTIMUM DESIGN AND CONTROL** .....4550

**TS 17: PERFORMANCE-BASED EARTHQUAKE ENGINEERING** .....4641

**TS 19: REPAIR AND RETROFIT OF STRUCTURES** .....4727

**TS 20: SEISMIC ISOLATION** .....4817

**TS 24: SOIL-STRUCTURE INTERACTION** .....4870

**TS 25: SOLUTION STRATEGIES FOR DYNAMIC PROBLEMS** .....4948

**TS 26: SOUND AND VIBRATION** .....4997

**TS 27: STEEL STRUCTURES** .....5041

**TS 28: STOCHASTIC DYNAMICS** .....5131

**TS 30: WAVE PROPAGATION** .....5155

**TS 31: SEISMIC RISK AND DAMAGE ASSESSMENT** .....5179

**TS 32: SEISMIC RELIABILITY ANALYSIS** .....5376

# CONTENTS

## VOLUME I

### Minisymposia

#### MS 1: NOVEL TECHNIQUES AND APPROACHES FOR SEISMIC PROTECTION OF STRUCTURES WITH ISOLATION AND/OR ENERGY DISSIPATION DEVICES


SEISMIC ISOLATION OF COMPOSITE BRIDGE WITH SKEWED DECK ..... 1
*Mohammad Mahdi Mohammadi Dehnavi, Alessandra De Angelis, M.R. Pecce*

SEISMIC PROTECTION OF SUBSTANDARD RC FRAMES THROUGH SELF-CENTERING DISSIPATIVE BRACES ..... 9
*Dario De Domenico, Luca Facconi, Emanuele Gandelli, Alberto Gioitta, Paolo Longo, Natale Maugeri*

FINITE ELEMENT MODELING OF THE ROLLING BEHAVIOR OF A POLYURETHANE SPHERE FOR LOW-COST SEISMIC ISOLATION APPLICATIONS ..... 24
*Sergio I. Reyes, Michalis F. Vassiliou, Konstantinos Agathos, Dimitrios Konstantinidis*

OPTIMUM DESIGN OF ROCKING WALL COUPLED WITH BUILDING UNDER STOCHASTIC SEISMIC GROUND MOTION ..... 33
*Michela De Angelis, Giuseppe Quaranta, Giulia Angelucci, Stefano Pampanin, Fabrizio Mollaioli*

NUMERICAL MODELLING OF MASONRY-INFILLED RC FRAMES WITH RUBBER JOINTS ..... 45
*Prateek Kumar Dhir, Enrico Tubaldi, Hamid Ahmadi, Bartolomeo Panto*

FINITE ELEMENT MODELING OF THE SHAKE-TABLE RESPONSE OF A BRIDGE-LIKE MODEL COMPRISING ROCKING COLUMNS ..... 56
*Antonios A. Katsamakas, Michalis F. Vassiliou*

SEISMIC RETROFIT OF INDUSTRIAL V BRACED STEEL STRUCTURES THROUGH ASYMMETRIC RE-CENTERING DISSIPATIVE DEVICES ..... 66
*Agnese Natali, Francesco Morelli*

INFLUENCE OF DESIGN PARAMETERS ON THE SEISMIC RELIABILITY OF BASE ISOLATED SYSTEMS ..... 77
*Fabio Micozzi, Fabrizio Scozzese, Laura Ragni, Andrea Dall'Asta*

BUILDING BACK BETTER: THE CASE STUDY OF THE FAZZINI COLLEGE ..... 89
*Laura Gioiella, Fabio Micozzi, Laura Ragni, Andrea Dall'Asta*

DEVELOPMENT OF A TUNED LIQUID PARTICLE DAMPER WITH OPTIMISED DAMPING CHARACTERISTICS ..... 97
*Sebastian Völkel, Kersten Latz*

SEISMIC RETROFITTING OF PRECAST INDUSTRIAL BUILDINGS THROUGH ENERGY DISSIPATION DEVICES ..... 112
*Davide Bellotti, Francesco Cavalieri, Roberto Nascimbene*

A GLANCE AT OPTIMAL CONFIGURATIONS OF LARGE MASS TUNED MASS DAMPERS IN SOIL-STRUCTURE SYSTEMS ..... 127
*Pasquale Roberto Marrazzo, Davide Noè Gorini, Elide Nastri, Rosario Montuori*

RETROFITTING OF R.C. FRAME BUILDINGS WITH DOUBLE CON-CAVE CURVED SURFACE ISOLATOR SLIDERS CHARACTERIZED BY OVER-STROKE DISPLACEMENT CAPACITY ..... 135
*Felice Carlo Ponzo, Antonio Di Cesare, Nicla Lamarucciola*

**MS 2: ADVANCES IN THE DYNAMIC RESPONSE ANALYSIS, MONITORING, AND MITIGATION OF WIND TURBINES**

REDESIGNING THE TRANSITION PIECE FOR MITIGATING THE SEISMIC RESPONSE OF OFFSHORE WIND TURBINES ..... 143
*Rohollah Rostami, Alessandro Tombari*

MONITORING MOORING(MONIMOOR) LINES OF FLOATING STRUCTURES USING DEEP LEARNING BASED APPROACHES ..... 158
*Smriti Sharma, Vincenzo Nava, Nicolas Gorostidi*

AN IMPLEMENTATION OF MULTI-SUPPORT SEISMIC INPUT MOTION INTO OPENFAST FOR THE EARTHQUAKE ANALYSIS OF OFFSHORE WIND TURBINES ..... 172
*Carlos Romero-Sánchez, Luis A. Padrón*

DESIGN AND PERFORMANCE OF A PASSIVE VIBRATION CONTROL DEVICE FOR HAWT ..... 186
*Ettore Sorge, Carlos Riascos, Nicola Caterino, Cristoforo Demartino, Christos Thomas Georgakis*

SEISMIC PERFORMANCE ASSESSMENT OF FLOATING OFFSHORE WIND TURBINES SUPPORTED BY TENSION LEG PLATFORMS ..... 196
*Sadra Amani, Athul Prabhakaran, Subhamoy Bhattacharya*

**MS 3: PROTECTION OF MUSEUM'S COLLECTIONS COMPUTATIONAL APPROACHES AND INNOVATIVE INTERVENTIONS**

SEISMIC VULNERABILITY OF MUSEUMS' COLLECTIONS: A CASE-STUDY ..... 218
*Silvia Lelli, Maria Gatto, Marco Tanganelli, Stefania Viti*

ARBITRARY LAGRANGIAN EULERIAN ANALYSIS OF THE NEPTUNE FOUNTAIN IN FLORENCE SUBJECTED TO BLAST LOADS ..... 229
*Piermatteo Cicolini, Marco Domaneschi, Marco Tanganelli*

SAN NICCOLO'S TOWER-GATE, FLORENCE – ITALY: MASONRY CHARCTERISATION AND STRUCTURAL ANALYSIS .. 239
*Massimo Coli, Giorgio Lacanna, Paola Vannucchi, Emanuele Marchetti, Marco Tanganelli, Francesco Trovatelli, P. Papeschi, Anna Livia Ciuffreda, Giorgio Caselli, Costanza Stramaccioni*

CONTINUOUS SEISMOMETRIC MONITORING OF THE NATIONAL ARCHAEOLOGICAL MUSEUM "GAIO CILNIO MECENATE" IN AREZZO, ITALY ..... 249
*Riccardo Mario Azzara, Martina Occhipinti, Angelo D'Ambrisi, Marco Tanganelli, Francesco Trovatelli, Nicoletta Vettori*

ROCKING RESPONSE AND VULNERABILITY OF THE PULPIT BY GIOVANNI PISANO IN PISTOIA (ITALY) …… 259
*Gianni Bartoli, Michele Betti, Luca Facchini, Silvia Monchetti*

HUMAN-INDUCED VIBRATIONS ON MUSEUM ARTEFACTS: LITERATURE REVIEW AND CALCULATION EXAMPLE …271
*Elena Sara Saeed, Linda Giresini, Olimpia Niglio, Francesco Graziotti*

SEISMIC PROTECTION OF CULTURAL HERITAGE BUILDING CONTENTS BY KINEMATIC ISOLATION DEVICES …… 285
*Gabriele Guerrini, Francesco Graziotti, Maria Rota, Andrea Penna*

THE STUDY OF DONATELLO'S SCULPTURE OF SAN MARCO IN ORSANMICHELE (FLORENCE), THROUGH A THREE-DIMENSIONAL DIGITAL RECONSTRUCTION IN VISIBLE AND UV LIGHT …… 296
*Michelangelo Micheloni, Anna Livia Ciuffreda, Gabriela Simoni, Mattia Faiulo*

STRUCTURE FROM MOTION SURVEY OF STATUE FOR FINITE ELEMENT MODELLING …… 308
*Maria Aurora Vincenti, Michele Arturo Caponero, Miriam Lamonaca, Giuseppe Occhipinti, Omar AlShawa, Luigi Sorrentino*

**MS 5: REPAIR AND RETROFIT OF STRUCTURES**

REVIEW OF RETROFIT AND STRENGTHENING STRATEGIES USED IN BUILDINGS IN MEXICO CITY AFTER STRONG EARTHQUAKES …… 316
*Arturo Tena-Colunga, Héctor Hernández-Ramírez, Eber A. Godínez-Domínguez*

SIMPLIFIED ANALYTICAL/MECHANICAL PROCEDURE FOR THE RESIDUAL CAPACITY ASSESSMENT OF EARTHQUAKE-DAMAGED REINFORCED CONCRETE FRAMES …… 392
*Michele Matteoni, Livio Pedone, Simone D'Amore, Stefano Pampanin*

CONTRIBUTION OF FLAX-TRM SYSTEMS TO THE SHEAR RESISTANCE OF RETROFITTED MASONRY WALLS …… 414
*Niki Trochoutsou, Kypros Pilakoutas, Maurizio Guadagnini*

COMPUTER AIDED DESIGN OF FRP STRENGTHENING FOR EXISTING RC BEAM-COLUMN JOINTS …… 422
*Ciro Del Vecchio, Marco Di Ludovico, Alberto Balsamo, Andrea Prota*

ALTERNATIVE RETROFIT STRATEGIES FOR SEISMIC RISK-REDUCTION: STUDYING THE EFFECTIVENESS OF LOW-DAMAGE EXTERNAL EXOSKELETONS …… 432
*Simone D'Amore, Livio Pedone, Stefano Pampanin*

**MS 6: EXPERIMENTAL MEASUREMENTS AND NUMERICAL SIMULATION IN THE FIELD OF EARTHQUAKE ENGINEERING AND STRUCTURAL DYNAMICS – NEW STRUCTURES AND STRUCTURAL RETROFITTING**

STRUCTURAL HEALTH MONITORING OF THE FATIGUE BEHAVIOR OF FRP STRENGTHENED RC BEAMS …… 457
*Barbara Charalambidi, Konstantinos Providakis, Konstantinos Katakalos, Alexandros Charalampidis*

C-FRP ROPES AS EXTERNAL STRENGTHENING REINFORCEMENT OF RC COLUMNS …… 468
*Emmanouil Golias, Grigorios E. Manoukas, Constantin E. Chalioris, Chris C. Karayannis*

DYNAMIC ANALYSIS AND EXPERIMENTAL VERIFICATION OF THE MECHANICAL CHARACTERISTICS OF VARIABLE CROSS-SECTION INDUSTRIAL PYLONS ..... 477
*Konstantinos Katakalos, George D. Manolis, George C. Manos, Lazaros Melidis, Georgios Dadoulis, Vasil Kavardzikov, Georgi Stoilov*

SHEAR RETROFITTING OF REINFORCED CONCRETE T-BEAMS USING CARBON FIBER-REINFORCED POLYMER (FRP) ROPES AND U-SHAPED SHEETS - TESTS AND FRP DEBONDING FAILURE IDENTIFICATION ..... 497
*Adamantis G. Zapris, Violetta K. Kytinou, George M. Sapidis, Constantin E. Chalioris, Chris G. Karayannis*

SHAKING TABLE TESTS ON SCALED TWO-FLOOR STEEL FRAMED STRUCTURES – DESIGN AND PRELIMINARY NUMERICAL INVESTIGATIONS ..... 511
*Georgios Balaskas, Cristian Vulcu, Benno Hoffmeister, Christoph Butenweg*

EXPERIMENTAL AND NUMERICAL INVESTIGATION OF THE SEISMIC RESPONSE OF CONFINED MASONRY WALLS .....528
*Nemanja Krtinić, Matija Gams, Marko Marinković*

ASSESSING THE PERFORMANCE OF EXISTING RC BEAM-COLUMN JOINTS ..... 544
*Emmanouil Golias, Demitrios Cotsovos*

STUDYING THE PERFORMANCE OF STONE MASONRY ARCH BRIDGES EMPLOYING IN-SITU MEASUREMENTS AND NUMERICAL PREDICTIONS ..... 560
*George C. Manos, Konstantinos Katakalos, Lampros Kotoulas, Lazaros Melidis*

EARTHQUAKE RETROFITTING OF “SOFT-STORY” RC BUILDINGS ..... 581
*George C. Manos, Konstantinos Katakalos, Vassilios Soulis, Lazaros Melidis*

LIMIT-STATE RESPONSE OF STONE MASONRY USED IN THE CONSTRUCTION OF CULTURAL HERITAGE IN GREECE ..... 592
*George C. Manos, Konstantinos Katakalos, Lampros Kotoulas, Lazaros Melidis*

REINFORCED MASONRY PIERS BUILT WITH A NOVEL CLAY MASONRY UNITS UNDER SEISMIC-TYPE LOADS ..... 618
*George C. Manos, Lazaros Melidis, Konstantinos Katakalos*

TESTING OF CONCRETE OR METAL HOLLOW POLES EMPLOYING PSEUDO-DYNAMIC OR FATIGUE LOADS ..... 628
*George C. Manos, Dimitris Mpoufidis, Lazaros Melidis, Konstantinos Katakalos*

OUT OF PLANE BEHAVIOR OF THERMAL INSULATED MASONRY WALLS AS PART OF BUILDING RETROFITTING ..... 640
*George C. Manos, Konstantinos Katakalos, Lazaros Melidis, Anthimos Anastasiadis*

THE SEISMIC PERFORMANCE OF THE DAMAGED BELL TOWER OF KOUROUKLATA IN KEFALONIA, GREECE DURING THE 2014 EARTHQUAKE SEQUENCE – A PROPOSAL FOR RETROFITTING ..... 648
*George C. Manos, Lampros Kotoulas, Lazaros Melidis, Konstantinos Katakalos*

PRELIMINARY EXPERIMENTAL TESTS ON STEEL-CONCRETE HYBRID COUPLED WALL SUBCOMPONENTS ..... 677
*Francesco Morelli, Agnese Natali, Fabrizio Scozzese, Nicola Ceccolini, Alessandro Zona*

EXPERIMENTAL STUDY ON THE INFLUENCE OF LARGE LONGITUDINAL REBAR RATIOS ON THE CRACKING CHARACTERISTICS OF R/C ELEMENTS …… 686
*Theodoros A. Chrysanidis*

NUMERICAL INVESTIGATION OF R/C COLUMNS BEFORE AND AFTER FRP STRENGTHENING UNDER SEISMIC TYPE LOADINGS UTILIZING A NOVEL ANCHORING SYSTEM …… 696
*Georgia Kotanidou, Lazaros Melidis, Konstantinos Katakalos*

EXPERIMENTAL AND NUMERICAL STUDY OF THE PERFORMANCE OF EXISTING PRESTRESSED CYLINDRICAL CONCRETE PIPES STRENGTHENED WITH REINFORCED CONCRETE OR CARBON-REINFORCED FIBER POLYMER JACKETS …… 705
*George C. Manos, Lazaros Melidis, Vassilios Soulis, Konstantinos Katakalos*

GEOMETRY OPTIMIZATION OF ARCHED STONE STRUCTURES UNDER GRAVITY AND SEISMIC TYPE LOADINGS …… 715
*Alexandros G. Chortis, Lazaros N. Melidis, Konstantinos V. Katakalos, Amaryllis G. Iliadi Manou*

STRUCTURAL HEALTH MONITORING(SHM) OF POLYFYTOS BRIDGE AND EVALUATION OF ITS DYNAMIC PROPERTIES …… 741
*Alexandros G. Chortis, Ioannis G. Ramandanis, Georgios I. Dadoulis, Lazaros N. Melidis, George C. Manos, Konstantinos V. Katakalos*

EFFECT OF THE SLAB ON THE INELASTC RESPONSE OF REINFORCED CONCRETE BEAM-COLUMN JOINTS: A NUMERICAL INVESTIGATION …… 759
*Charoula D. Zaki, Vassilis K. Papanikolaou*

**MS 7: SUSTAINABLE STRENGTHENING INTERVENTIONS TO PREVENT FAILURE IN UNREINFORCED MASONRY STRUCTURES AND INFRASTRUCTURES**

FRAGILITY ASSESSMENT OF RC BUILDINGS IN SOUTHERN SPAIN BASED ON NEURAL NETWORK PREDICTIONS …. 770
*Jaime de Miguel-Rodríguez, María Victoria Requena-García-Cruz, Emilio Romero-Sánchez, Antonio Morales-Esteban*

FRAGILITY CURVES FOR ROCKING MASONRY FAÇADES OF CHURCHES: A SENSITIVITY STUDY OF VULNERABILITY PARAMETERS …… 784
*Luca Umberto Argiento, Claudia Casapulla, Francesca Ceroni*

EQUIVALENCE OF DAMPING PROPERTIES OF DISSIPATIVE DEVICES FOR MITIGATING THE SEISMIC RISK OF RIGID BLOCKS …… 798
*Linda Giresini, Omar AlShawa, Luca Umberto Argiento, Claudia Casapulla*

ISO-CLASS CURVES FOR THE ASSESSMENT OF SEISMIC/ENERGY RETROFITTING OF AN EXISTING MASONRY BUILDING THROUGH A TIMBER FRAME SYSTEM …… 816
*Linda Giresini, Francesca Corona, Gabriele Guerrini, Francesco Graziotti*

TWO-BODIES VERTICAL SPANNING WALL RESTRAINED BY AN ELASTIC TIE ROD …… 837
*Giacomo Destro Bisol, Sanjeev Prajapati, Omar AlShawa, Luigi Sorrentino*

NUMERICAL DYNAMIC ANALYSIS OF A MASONRY TRIUMPHAL ARCH: COMPARISON OF DIFFERENT STRENGTHENING CONFIGURATIONS ..... 844
*Vieri Cardinali, Barbara Pintucchi, Marco Tanganelli, Francesco Trovatelli*

EXPERIMENTAL PULL-OUT BEHAVIOR OF HELICOIDAL STEEL BARS IN MASONRY ..... 854
*Manuela Scamardo, Sara Cattaneo, Pietro Crespi*

OUT-OF-PLANE RESPONSE OF MASONRY CHURCH FACADES INCLUDING P-DELTA EFFECTS ..... 862
*Valeria Cusmano, Bartolomeo Pantò, Claudia Casapulla, Ivo Caliò*

A TWO-STEP APPROACH FOR THE SEISMIC ASSESSMENT OF MASONRY STRUCTURES ACCOUNTING FOR THE ACTUAL MASONRY PATTERN ..... 872
*Simon Szabò, Marco F. Funari, Antonio Maria D'Altri, Stefano de Miranda, Paulo B. Lourenço*

**MS 8: RECENT ADVANCES AND CHALLENGES IN GEOTECHNICAL EARTHQUAKE ENGINEERING**

A COMPARISON STUDY BETWEEN 1D AND 3D SITE RESPONSE ANALYSES BASED ON OBSERVED EARTHQUAKE ACCELERATION RECORDS ..... 882
*Shima Sadeghzadeh, Atilla Ansal*

GEOTECHNICAL CONSIDERATIONS AND VIBRATION RESPONSE DURING ROTARY PILING FOR CONSTRUCTING BRIDGES ..... 889
*Rajeev Kumar Garg, Seema Garg, Ganesh Kumar Sahu, Jitendra K. Goyal, K.N. Ghosh*

PREDICAMENT OF THE 1D ASSUMPTION IN SITE RESPONSE ANALYSIS AND IMPLICATION ON VERTICAL GROUND MOTION ASSESSMENT ..... 900
*Junfei Huang, David McCallen*

1D HARMONIC RESPONSE OF INHOMOGENEOUS SOIL DEPOSITS WITH EXPONENTIALLY VARYING STIFFNESS: EXACT & APPROXIMATE SOLUTIONS ..... 925
*Haralambos Parashakis, Emmanouil Rovithis, George Mylonakis*

SEMI-ANALYTICAL SOLUTIONS FOR EVALUATING THE FIM FOR PILE FOUNDATIONS ..... 939
*Stefano Stacul, Nunziante Squeglia*

**MS 9: SEISMIC SAFETY ASSESSMENT OF STRUCTURES**

CONTINUOUS STRAIN FIELD ESTIMATION FOR CAST-IN-SITU REINFORCED CONCRETE SANDWICH WALLS UNDER CYCLIC LATERAL IN-PLANE LOADING ..... 949
*Carlos Andrés Riascos González, Paolino Cassese, Antonio Occhiuzzi, Carlo Rainieri*

THREE-DIMENSIONAL FRAME ANALYSIS OF Q–Δ RESONANCE OF CENTER-CORE BIAXIALLY SYMMETRICAL HIGH-RISE BUILDING UNDER LONG-PERIOD EARTHQUAKE MOTION ..... 961
*Masayuki Kohiyama, Shiori Maki*

EXPERIMENT AND SIMULATION OF Q–Δ RESONANCE USING FOUR-LAYER BENDING-SHEAR TYPE SPECIMEN …… 971
*Ryohei Kai, Masayuki Kohiyama*

NUMERICAL MODELLING AND STRUT-AND-TIE CONCEPTS FOR SEISMIC DESIGN AND ASSESSMENT OF PRE-CAST TWO-COLUMN BENTS …… 982
*Lucas Carvalho, Mário Pimentel, Pedro Delgado, António Arêde, Nelson Vila Pouca, José Rui Pinto*

**MS 10: RECENT ADVANCES IN SEISMIC ISOLATION OF STRUCTURES WITH NOVEL VIBRATION CONTROL APPROACHES**

EXPERIMENTAL STUDY OF PHONONIC STRUCTURES WITH DDA ENHANCED UNIT-CELLS …….. 994
*Moris Kalderon, Antonios Mantakas, Kyriakos Alexandros Chondrogiannis, Ioannis A. Antoniadis*

3D NUMERICAL INVESTIGATION OF AN EXTENDED KDAMPER ABSORBER FOR SEISMIC RETROFITTING OF LOW-RISE BUILDINGS …… 1005
*Antonios Mantakas, Konstantinos Kapasakalis, Moris Kalderon, Maria Antoniou, Ioannis A. Antoniadis, Evangelos Sapountzakis*

ON THE VIBRATION ATTENUATION PERFORMANCE OF A GEOMETRICALLY NONLINEAR DEVICE MOUNTED TO A MULTI-STOREY STRUCTURE …… 1016
*Kyriakos Alexandros Chondrogiannis, Vasilis Dertimanis, Eleni Chatzi*

PERFORMANCE EVALUATION OF NEGATIVE STIFFNESS-BASED VIBRATION CONTROL DEVICES FOR SEISMIC PROTECTION OF BUILDING STRUCTURES …… 1031
*Konstantinos Kapasakalis, Antonios Mantakas, Moris Kalderon, Maria Antoniou, Evangelos Sapountzakis*

EVALUATION OF THE INTER-STORY ISOLATION SYSTEM APPLIED TO AN EXISTING MASONRY SCHOOL BUILDING …… 1043
*Enrico Bernardi, Marco Donà, Sergio Sut, Elisa Saler, Amedeo Caprino, Francesca da Porto*

EVALUATION OF THE INTER-STORY ISOLATION SYSTEM APPLIED TO AN EXISTING RC SCHOOL BUILDING …… 1057
*Enrico Bernardi, Marco Donà, Marco Ceresara, Marco Gaspari, Francesca da Porto*

**MS 11: THE ROLE OF THE STRUCTURAL MONITORING TO PREDICT THE PRIOR DAMAGE OR THE FACTUAL DEGRADATION PATTERN IN ORDER TO UPDATE THE SEISMIC VULNERABILITY OF EXISTING BUILDINGS**

TYPOLOGICAL SEISMIC LOSSES ASSESSMENT BY DAMAGED MASONRY BUILDINGS AFTER L'AQUILA 2009 AND EMILIA 2012 EARTHQUAKES …… 1071
*Matteo Tatangelo, Lorenzo Audisio, Michele D'Amato, Rosario Gigliotti*

DAMAGE EVALUATION IN MASONRY INFILLED RC BUILDINGS FROM SHM DATA …… 1084
*Alessandro Lubrano Lobianco, Marta Del Zoppo, Marco Di Ludovico*

URBAN SETTLEMENTS MONITORING USING EGMS DATA THROUGH ADAFINDER TOOL …… 1091
*Annalisa Mele, Michele Crosetto, Andrea Miano, Andrea Prota*

FRAGILITY CURVES ASSESSMENT OF AN EXISTING TYPOLOGICAL RC BUILDING SUBJECTED TO THE COMBINED ACTION OF SLOW-MOVING SETTLEMENTS AND EARTHQUAKE ..... 1104
*Andrea Miano, Annalisa Mele, Carlo Del Gaudio, Gerardo Mario Verderame, Andrea Prota*

ESTIMATION OF THE COMBINED SEISMIC-FIRE RISK: A CRITICAL REVIEW AND FUTURE RESEARCH AGENDA ..... 1116
*Donatella de Silva, Andrea Miano, Andrea Prota, Emidio Nigro*

A METHODOLOGY FOR THE EVALUATION OF MORPHOLOGY-BASED CONSTITUTIVE LAWS OF CORRODED STEEL REBARS ..... 1126
*Fabio Di Carlo, Diego Alejandro Talledo, Luisa Berto, Paolo Isabella, Alberto Meda, Zila Rinaldi, Irene Rocca, Anna Saetta*

**MS 12: ARTIFICIAL INTELLIGENCE & MACHINE LEARNING IN DESIGN AND ASSESSMENT OF STRUCTURES**

WHICH SIGNIFICANT DURATION OF GROUND MOTIONS TO USE? INVESTIGATIONS ON ARTIFICIAL NEURAL NETWORKS PREDICTING BUILDING SEISMIC COLLAPSE ..... 1138
*Konstantinos Theodoros Tsalouchidis, Christoph Adam*

AUTOMATIC IDENTIFICATION OF BUILDING FEATURES FOR SEISMIC DAMAGE ASSESSMENT ON A LARGE SCALE .....1157
*Pietro Carpanese, Marco Donà, Francesca da Porto*

SURROGATE MODELING OF THE RESPONSE OF A BEARING DEVICE FOR PASSIVE SEISMIC ISOLATION ..... 1169
*Todor Zhelyazov*

DEVELOPMENT OF FORMULAE FOR THE SECTION ROTATIONS DUE TO BENDING OF CURVED STEEL I-BEAMS THROUGH AI AND ML ALGORITHMS ..... 1177
*Victor T. Chibaya, George Markou, Nikolaos Bakas*

DEVELOPING FUNDAMENTAL PERIOD FORMULAE FOR STEEL FRAMED STRUCTURES THROUGH MACHINE LEARNING AND AUTOMATED ALGORITHMS ..... 1188
*Duan Calitz, George Markou, Nikolaos Bakas, Manolis Papadrakakis*

DEVELOPING AN ARTIFICIAL NEURAL NETWORK MODEL THAT PREDICTS THE FUNDAMENTAL PERIOD OF STEEL STRUCTURES USING A LARGE DATASET ..... 1206
*Ashley Megan van der Westhuizen, Nikolaos Bakas, George Markou*

SMART METHOD RECOMMENDATIONS FOR THE DETECTION OF POST-EARTHQUAKE DAMAGES IN RC BUILDINGS ..... 1214
*Gamze Doğan, Musa Hakan Arslan, Alper Ilki*

SEISMIC RESPONSE REDUCTION USING AN ACTIVE TUNED MASS DAMPER DRIVEN BY AN ARTIFICAL NEURAL NETWORK CONTROLLER ..... 1227
*Nour Elhouda Ghanemi, Mahdi Abdeddaim, Abdelhafid Ounis*

MACHINE LEARNING-BASED IDENTIFICATION OF VULNERABILITY FACTORS FOR MASONRY BUILDINGS IN AGGREGATE: THE HISTORICAL CENTRE OF CASENTINO HIT BY THE 2009 L'AQUILA EARTHQUAKE ..... 1236
*Silvia Pinasco, Sergio Lagomarsino, Caterina Carocci, Andrea Coraddu, Luca Oneto, Serena Cattari*

DERIVING COARSE-GRAINED MODELS OF MOLECULAR SYSTEMS BY APPROXIMATING THE FREE ENERGY SURFACE WITH MACHINE LEARNING ALGORITHMS ..... 1249
*Nikolaos P. Bakas, Antonis Chazirakis, Eleftherios Christofi, Vangelis Harmandaris*

PREDICTION OF REINFORCED CONCRETE COLUMNS LIMIT STATES USING MACHINE LEARNING ALGORITHM .....1255
*Anthos I. Ioannou, Nikolaos Bakas, George Markou, Ashley Megan van der Westhuizen, Stavroula J. Pantazopoulou, Michael F. Petrou, Dimos C. Charmpis*

A BIBLIOMETRIC OVERVIEW OF OPEN SCIENCE RESEARCH ..... 1266
*Nikolaos P. Bakas, Andreas Athenodorou, Nana Anastasopoulou, Katerina Kyprianou, George Katsikatsos, George Markou*

A PROBABILISTIC BASED ADAPTIVE REFINEMENT FOR RELIABILITY ASSESMENT USING KRIGING METAMODEL .. 1276
*Ioannis A. Prentzas, Michalis M. Fragiadakis*

**MS 13: MONITORING AND LIFE CYCLE PERFORMANCE OF RAILWAY BRIDGES**

INDIRECT MONITORING OF RAILWAY BRIDGES USING THE CONTINUOUS TRACK MONITORING SYSTEM CTM2.0 ..... 1288
*Steven Robert Lorenzen, Klaus Ulrich Wolter, Maximilian Michael Rupp, Günther Grunert, Eftychia Apostolidi, Jens Schneider*

A MACHINE LEARNING LEVERAGED AND MINIMAL HARDWARE-BASED TRAIN AND LOAD RECOGNITION SYSTEM ..... 1303
*Jascha Brötzmann, Christian-Dominik Thiele, Maximilian Rupp, Mingchen Xing, Uwe Rüppel*

CASE STUDY: IMPACT OF ROUTE SPECIFIC LOAD MODELS AND NUMERICAL MODEL CALIBRATION ON FATIGUE LIFETIME ASSESSMENT OF AN EXISTING RAILWAY BRIDGE ..... 1321
*Stefan Lachinger, Sebastian Pissermayr, Marian Ralbovsky, Alois Vorwagner*

MONITORING OF A RAILWAY BRIDGE RECURRING TO COSTUMIZED SENSORS ..... 1337
*Chanalisa Salvi, Carlos Moutinho, Borja Conde, Manuel Cabaleiro, Elsa Caetano*

**MS 14: ADVANCES IN OPTIMIZATION AND CONTROL OF STRUCTURES UNDER DYNAMIC LOADS**

ANALYTICAL INVESTIGATION OF THE INFLUENCE OF SEISMICITY ON THE CONSTRUCTION COST OF THE R/C LOAD-BEARING STRUCTURE OF A 5-STOREY BUILDING WITH SPRING SUPPORTS ..... 1350
*Aggelos H. Michalitsianos, Diogenis I. Rogkogkos, Theodoros A. Chrysanidis*

OPTIMAL TOPOLOGICAL DESIGN OF STRUCTURES SUBJECTED TO NON-STATIONARY STOCHASTIC EXCITATIONS ..... 1364
*Giulia Angelucci, Giuseppe Quaranta, Fabrizio Mollaioli*

PERFORMANCE ASSESSMENT OF PINNED ROCKING CORE WALLS IN STEEL MULTI-STORY BUILDINGS SUBJECTED TO STRONG SEISMIC GROUND MOTIONS ..... 1380
*Michela De Angelis, Giulia Angelucci, Giuseppe Quaranta, Fabrizio Mollaioli*

**MS 17: STEEL JOINTS BEHAVIOR UNDER SEISMIC, FATIGUE AND ROBUSTNESS ACTIONS**

PREDICTION OF THE STATIC AND FATIGUE PERFORMANCE OF PITTED STEEL WIRE ROPES ..... 1392
*Aldo Milone*

CYCLIC PERFORMANCE OF HOT-DRIVEN RIVETED CONNECTIONS ..... 1400
*Aldo Milone*

SEISMIC ASSESSMENT OF THE STEEL MOMENT RESISTING FRAME EQUIPPED WITH FRICTION BEAM-TO-COLUMN JOINTS ..... 1407
*Arash Poursadrollah*

PROBABILISTIC ANALYSIS OF THE MR-FRAMES EQUIPPED WITH FREEDAM DAMPERS ..... 1415
*Maria Maglio, Rosario Montuori, Elide Nastri, Vincenzo Piluso, Alessandro Pisapia*

SEISMIC STRENGTHENING OF AN EXISTING RC FRAME BUILDING DESIGNED FOR GRAVITY LOADS ..... 1426
*Alessandro Prota, Gianmaria Di Lorenzo*

STRENGTH OF CONNECTIONS BETWEEN SHS COLUMNS AND THROUGH PLATES ..... 1434
*Atsushi Sato, Massimo Latour, Amparo de la Peña, Sabatino Di Benedetto, Antonella Bianca Francavilla, Gianvittorio Rizzano*

FATIGUE STRENGTH EVALUATION OF RIVETED SHEAR SPLICES ..... 1445
*Annarosa Lettieri*

STEEL BRACING SYSTEMS TO REDUCE THE SEISMIC VULNERABILITY OF LWS SUSPENDED CEILINGS: EXPERIMENTAL CHARACTERISATION ..... 1456
*Alessandro Prota, Amirhossein Nikpour*

EXPERIMENTAL RESPONSE OF A LARGE-SCALE STEEL STRUCTURE EQUIPPED WITH INNOVATIVE COLUMN BASES ..... 1464
*Elena Elettore, Fabio Freddi, Massimo Latour, Vincenzo Piluso, Gianvittorio Rizzano*

RETROFITTING OF AN EXISTING BUILDING WITH CONCRETE WALLS AND STEEL FRAMES FOR GRAVITY LOADS AND PROGRESSIVE COLLAPSE RESISTANCE ..... 1473
*Florea Dinu, Calin Neagu, Dan Dubina, Constantin Stanciu*

SINGLE AND MULTI-HAZARD ROBUSTNESS ASSESSMENT OF MULTI-STORY STEEL FRAME BUILDINGS ..... 1485
*Florea Dinu, Calin Neagu, Dan Dubina*

DESIGN FOR ROBUSTNESS OF A PILOT BUILDING EQUIPPED WITH DISSIPATIVE FREE FROM DAMAGE STEEL CONNECTIONS .....1499
*Tudor Golea, Roberto Tartaglia, Massimo Latour, Mario D'Aniello, Jean-François Demonceau, Raffaele Landolfo,Vincenzo Piluso*

THEORETICAL AND EXPERIMENTAL EVALUATION OF SEISMIC BEHAVIOUR OF CFS WALL WITH UHS STEEL BRACING ..... 1512
*Alessia Campiche*

EFFECT OF CONSTRUCTION DETAILS ON THE IN-PLANE SEISMIC RESPONSE OF DRYWALL FAÇADES ..... 1525
*Alessia Campiche*

ON THE INFLUENCE OF SEMIRIGID JOINTS ON THE SEISMIC RESPONSE OF ONE STOREY STEEL BUILDINGS ..... 1537
*Greta Agata Venneri, Gianfranco De Matteis, Giuseppe Brando*

BEAHVIOUR OF JOINTS WITH FRICTION DAMPERS UNDER COLUMN LOSS SCENARIO ..... 1546
*Roberto Tartaglia, Mario D'Aniello, Roberto Carlevaris, Raffaele Landolfo*

**MS 19: RECENT ADVANCES AND CHALLENGES FOR THE PRESERVATION OF MASONRY STRUCTURES AND INFRASTRUCTURES AGAINST NATURAL AND ANTHROPIC RISKS**

COMPRESSIVE BEHAVIOUR OF A CIRCULAR UNBONDED FIBER-REINFORCED ELASTOMERIC ISOLATOR (UFREI) 1556
*Gaetano Pianese, Gabriele Milani, Antonio Formisano*

FINITE ELEMENT ANALYSIS OF HIGH DAMPING UNBONDED FIBER REINFORCED ELASTOMERIC ISOLATORS (UFREIS) OF DIFFERENT SHAPE FACTORS ..... 1563
*Gaetano Pianese, Gabriele Milani, Antonio Formisano*

APPLICATION OF A GENERAL PURPOSE DISTINCT ELEMENT MODEL (DEM) FOR THE SEISMIC VULNERABILITY PREDICTION OF MASONRY AGGREGATES ..... 1571
*Peixuan Wang, Gabriele Milani*

LIMIT ANALYSIS MODEL FOR A FAST EVALUATION OF CHINESE MASONRY PAGODAS VULNERABILITY ..... 1581
*Peixuan Wang, Gabriele Milani, Shengcai Li*

FINITE ELEMENT MODEL FOR RUBBER SEISMIC ISOLATION WITH AND WITHOUT S-SHAPED STEEL DAMPERS ... 1592
*Kai Guo, Gaetano Pianese, Gabriele Milani*

HETEROGENEOUS LIMIT ANALYSIS FOR MASONRY ARCH BRIDGES WITH FULL MODELING OF BACKFILL ..... 1605
*Yiwei Hua, Gabriele Milani*

MECHANICAL-BASED SEISMIC FRAGILITY ASSESSMENT AND RETROFIT INTERVENTION OF CLUSTERED BUILDINGS ..... 1615
*Giovanna Longobardi, Antonio Formisano*

FINITE ELEMENT MODELING OF AN ITALIAN MASONRY ARCH BRIDGE DETECTING DAMAGE UNDER SEISMIC EXCITATIONS ..... 1633
*Daniela Addessi, Domenico Liberatore, Andrea Battisti*

SEISMIC VULNERABILITY ASSESSMENT OF VAULTED MAYA CONCRETE TEMPLES IN BONAMPAK, CHIAPAS, MÉXICO ..... 1644
*Humfrey M. Kimanya, Anna M. Remus, Omar Hamad, Justin W. Sennyondo, Dung T. Nguyen, Selman Tezcan, Renato L. Perucchio*

PREDICTING THE UNIAXIAL COMPRESSIVE CAPACITY OF NON-STRENGTHENED AND FRP-STRENGTHENED MASONRY COLUMNS USING A FAST NUMERICAL APPROACH ..... 1660
*Luis Carlos da Silva, Gabriele Milani, Ernesto Grande*

SEISMIC RESPONSE OF HISTORICAL MASONRY CHURCHES: THE CASE OF THE BANAT ROMANIAN REGION ..... 1669
*Anna Lo Monaco, Nicola Grillanda, Iasmina Onescu, Mihai Fofiu, Francesco Clementi, Michele D'Amato, Antonio Formisano, Gabriele Milani, Marius Mosoarca*

LONG-TERM MONITORING OF A MASONRY TOWER WITH WIRELESS ACCELEROMETERS ..... 1687
*Giacomo Zini, Francesca Marafini, Silvia Monchetti, Michele Betti, Luca Facchini, Gianni Bartoli, Maria Girardi, Gianmarco Gurioli, Cristina Padovani, Daniele Pellegrini*

GENERATIVE MODELLING AND SEISMIC ASSESSMENT OF ANCIENT TEMPLES: THE TEMPLE OF VESTA (TIVOLI) ..1697
*Annalaura Vuoto, Marco Francesco Funari, Shaghayegh Karimzadeh, Paulo B. Lourenço*

NONLINEAR BEHAVIOR OF EXISTING MASONRY STRUCTURES: AN APPLICATION TO A CASE STUDY WITH DIFFERENT STRUCTURAL CONFIGURATIONS ..... 1707
*Roselena Sulla, Michele D'Amato, Rosario Gigliotti, Domenico Liberatore*

SEISMIC VULNERABILITY ANALYSIS OF S. SEBASTIANO CHURCH DAMAGED DURING THE 2016 CENTRAL ITALY SEISMIC SEQUENCE ..... 1719
*Michol Rampado, Elvis Cescatti, Francesco Rossetto, Francesca da Porto, Claudio Modena*

EFFECTS OF AGING AND DETERIORATION ON THE SEISMIC FRAGILITY OF MASONRY ARCH BRIDGES ..... 1731
*Giovanni Tecchio, Sara Barbisan, Elisa Saler, Francesca da Porto*

ON THE IN-PLANE FLEXURAL RESPONSE OF CANTILEVER UNREINFORCED CLAY BRICKWORK MASONRY WALL PANELS ..... 1744
*Hisham Tariq, Mohammad Amir Najafgholipour, Vasilis Sarhosis, Gabriele Milani*

MULTI-SCALE TOPOLOGY OPTIMIZATION FOR INNOVATIVE 3D-PRINTED WALLS AND SHELL STRUCTURES ..... 1758
*Andrea Chiozzi, Andrea Nale*

A TYPOLOGICAL-MECHANICAL APPROACH TO ASSESS LARGE-SCALE SEISMIC FRAGILITY OF MASONRY BUILDINGS IN HISTORICAL CENTRES ..... 1766
*Chiara Tosto, Valeria Leggieri, Sergio Ruggieri, Giuseppina Uva*

SEISMIC FRAGILITY EVALUATION OF TYPOLOGICAL MASONRY AGGREGATES ACCOUNTING FOR LOCAL COLLAPSE MECHANISMS ..... 1779
*Valeria Leggieri, Francesco Salvatore Liguori, Sergio Ruggieri, Antonio Bilotta, Antonio Madeo, Siro Casolo, Giuseppina Uva*

DIFFERENT MODELING APPROACHES APPLIED TO A RESILIENT MASONRY STRUCTURE ..... 1792
*Matti Schiavoni, Ersilia Giordano, Francesca Roscini, Francesco Clementi*

NUMERICAL INVESTIGATION ON THE FLANGE EFFECT IN UNREINFORCED MASONRY WALL SYSTEMS THROUGH NONLINEAR FINITE ELEMENT MODELLING ..... 1801
*Elia Acconcia, Valentina Buonocunto, Fulvio Parisi*

STATICALLY ADMISSIBLE SHELL INTERNAL FORCES FOR THE STABILITY ANALYSIS OF THE DOME OF PISA CATHEDRAL LOADED BY VERTICAL AND HORIZONTAL LOADS ..... 1810
*Francesco Barsi, Riccardo Barsotti, Stefano Bennati*

MODELLING THE IN-PLANE BEHAVIOUR OF MASONRY FAÇADES VIA A MULTI-UNIT DISCRETIZATION WITH SIMPLIFIED INTERFACE LAYOUT ..... 1823
*Ylenia Di Lallo, Davide Rapone, Maria Giovanna Masciotta, Giuseppe Brando*

AN APPROACH FOR DERIVING FRAGILITY CURVES OF MASONRY BUILDINGS IN AGGREGATES ..... 1835
*Valentina Cima, Valentina Tomei, Ernesto Grande, Maura Imbimbo*

SIMULATION OF IN PLANE REINFORCED MASONRY WALLS BEHAVIOUR BY MEANS OF SIMPLIFIED METHOD .... 1848
*Riccardo Piazzon, Paolo Zampieri, Carlo Pellegrino*

PROPOSAL OF A GENERAL METHODOLOGICAL APPROACH FOR THE SEISMIC ASSESSMENT OF HISTORICAL MASONRY AGGREGATES ..... 1855
*Maurizio Acito, Martina Buzzetti, Giuseppe Alfredo Cundari, Gabriele Milani*

'HYBRID' FULL MODELS FOR SEISMIC ASSESSMENT OF MASONRY AGGREGATES THROUGH PUSHOVER ANALYSIS ..... 1871
*Maurizio Acito, Martina Buzzetti, Giuseppe Alfredo Cundari, Gabriele Milani*

COMPARISON OF THE RECORDED SEISMIC SIGNALS FOR THE 2012 EMILIA AND 2016 CENTRAL ITALY SEISMIC SEQUENCES WITH THE DESIGN EARTHQUAKES BASED ON THE PSHA APPROACH ..... 1881
*Maurizio Acito, Martina Buzzetti, Claudio Chesi, Gabriele Milani*

SEISMIC RESPONSE OF DIFFERENT MASONRY BUILDING AGGREGATE CONFIGURATIONS BY A REFINED FE MICROMODEL ..... 1894
*Marilisa Di Benedetto, Fabio Di Trapani, Sofia Villar, Massimo Petracca, Guido Camata*

INVESTIGATING THE SEISMIC RESPONSE OF URM WALLS WITH IRREGULAR OPENING LAYOUT THROUGH DIFFERENT MODELING APPROACHES ..... 1906
*F. Parisse, V. Buonocunto, C. Cantagallo, A. Di Primio, E. Di Domenico, N. Lo Presti, E. Acconcia, F. Cannizzaro, G. Castellazzi, A. M. D'Altri, S. Liseni, C. F. Manzini, R. Marques, G. Occhipinti, G. Pacella, M. Petracca, L. C. Silva, G. Brandonisio, B. Calderoni, I. Caliò, G. Camata, P. B. Lourenço, G. Milani, S. de Miranda F. Parisi, G. Magenes, S. Cattari*

DAMAGE PATTERN ANALYSIS OF THE BASILICA DI COLLEMAGGIO USING AEM MICRO-MODELING ..... 1921
*Cosimo Pellecchia, Alessandro Cardoni, Gian Paolo Cimellaro, Ahmed Amir Khalil*

A PROCEDURE FOR THE PROBABILISTIC ASSESSMENT OF MASONRY STRUCTURES UNDER TSUNAMI ..... 1932
*Panagiotis G. Asteris, Marco F. Ferrotto, Liborio Cavaleri*

**MS 20: ADVANCED NUMERICAL METHODS IN DYNAMICS, COMPUTATIONAL INTERFACE MECHANICS AND COUPLED PROBLEMS**

ASYNCHRONOUSLY IN TIME INTEGRATED INTERFACE DYNAMICS PROBLEM WHILE MAINTAINING ZERO INTERFACE ENERGY ..... 1947
*Radim Dvořák, Radek Kolman, Ondřej Jiroušek, Jose Angel Gonzalez Perez, K.C. Park*

FINITE ELEMENT TECHNOLOGY-BASED SELECTIVE MASS SCALING FOR SHEAR DEFORMABLE STRUCTURAL ELEMENT FORMULATIONS ..... 1965
*Bastian Oesterle, Anton Tkachuk, Manfred Bischoff*

FINITE ELEMENT TECHNOLOGY-BASED SELECTIVE MASS SCALING FOR EXPLICIT DYNAMIC ANALYSES OF THIN-WALLED STRUCTURES USING SOLID ELEMENTS ..... 1974
*Moritz Hoffmann, Anton Tkachuk, Manfred Bischoff, Bastian Oesterle*

PERSITALTIC DRIVEN FLOWS IN PIEZOELECTRIC POROUS DYNAMIC METAMATERIALS - HOMOGENIZATION BASED MODELLING ..... 1983
*Eduard Rohan, Vladimír Lukeš*

**MS 22: HYSTERESIS PHENOMENA IN STRUCTURAL DYNAMICS AND EARTHQUAKE ENGINEERING: EXPERIMENTS, MODELING, AND DESIGN**

CLASSIFICATION AND PHENOMENOLOGICAL MODELING OF HYSTERESIS PHENOMENA IN ENERGY DISSIPATION DEVICES ..... 1996
*Ciro Napolitano, Nicolò Vaiana, Luciano Rosati*

ON THE RESPONSE OF SDOF RATE-INDEPENDENT HYSTERETIC MECHANICAL SYSTEMS SUBJECTED TO SHOCK EXCITATION ..... 2009
*Diego Francisco Ledezma-Ramirez, Pablo Ernesto Tapia-Gonzalez, Nicolò Vaiana*

SIMPLIFIED-MICRO MODELLING OF UNREINFORCED AND JOINT REPOINTED BRICK MASONRY ..... 2017
*Maja Gosheva, Sergey Churilov, Elena Dumova-Jovanoska, Veronika Shendova, Lidija Krstevska*

WORK AND ENERGY COMPONENTS IN MECHANICAL SYSTEMS WITH COMPLEX HYSTERETIC BEHAVIOR ..... 2038
*Raffaele Capuano, Nicolò Vaiana, Luciano Rosati*

NONLINEAR DYNAMIC ANALYSIS OF RIGID BODIES SUPPORTED BY RATE-INDEPENDENT HYSTERETIC ELEMENTS ..... 2050
*Nicolò Vaiana, Luciano Rosati*

SIMULATION OF THE HYSTERETIC BEHAVIOR OF TIMBER CONNECTIONS BY THE VAIANA-ROSATI MODEL: PRELIMINARY RESULTS ..... 2062
*Agnese Spedicato, Nicolò Vaiana, Luciano Rosati*

**MS 24: ADVANCES IN SEISMIC ASSESSMENT AND INTEGRATED RETROFITTING FOR ENVELOPES OF RC**

ON THE INFLUENCE OF CLIMATE AND SEISMIC HAZARD CONDITIONS IN THE IDENTIFICATION OF OPTIMAL RETROFITTING STRATEGIES FOR RC BUILDINGS ..... 2070
*Rita Couto, Gianrocco Mucedero, Rita Bento, Ricardo Monteiro*

INVESTIGATION OF SEISMIC BEHAVIOUR OF EXISTING MASONRY INFILLS THROUGH COMBINED CYCLIC IN-PLANE AND DYNAMIC OUT-OF-PLANE TESTS ..... 2085
*Maithree Kurukulasuriya, Riccardo Milanesi, Guido Magenes, Davide Bolognini, Luca Grottoli, Filippo Dacarro, Paolo Morandi*

DEVELOPING STOREY LOSS FUNCTIONS FOR EVALUATION OF SEISMIC RISK IN ITALIAN RESIDENTIAL BUILDING TYPOLOGIES ..... 2098
*Gianrocco Mucedero, Daniele Perrone, Ricardo Monteiro*

SIMPLIFIED ASSESSMENT OF COMBINED INTERVENTION FOR THE SEISMIC AND ENERGETIC RETROFIT OF A SCHOOL BUILDING IN PADUA (ITALY) ..... 2111
*Giacomo Piredda, Enrico Prataviera, Laura Carnieletto, Michele de Carli, Francesca da Porto*

RC FRAMES WITH MASONRY INFILLS WITH AND WITHOUT OPENINGS: EXPERIMENTAL AND NUMERICAL RESULTS ..... 2127
*Aleksa Milijaš, Bogdan Šakić, Marko Marinković, Christoph Butenweg, Matija Gams, Sven Klinkel*

ANALYTICAL MODEL FOR PREDICTING OOP LATERAL BEHAVIOR OF MASONRY INFILL WALLS ..... 2144
*Marco Gaspari, Sara Mozzon, Marco Donà, Nicolò Verlato, Francesca da Porto*

EXPERIMENTAL CALIBRATION OF THE IP BEHAVIOR OF STRENGTHENED INFILL WALLS AND SEISMIC ANALYSIS INCLUDING IP/OOP EFFECTS ..... 2155
*Marco Gaspari, Marco Donà, Francesca da Porto*

**MS 25: TOWARDS SEISMIC RESILIENCE: STRATEGIES AND TECHNOLOGICAL INNOVATION FOR SEISMIC RISK REDUCTION OF EXISTING STRUCTURES**

FRAGILITY FUNCTION UNCERTAINTY QUANTIFICATION IN INFILLED RC FRAME BUILDINGS ..... 2168
*Al Mouayed Bellah Nafeh, Gerard J. O'Reilly*

EVALUATION OF THE EFFECT OF MASONRY INFILLS ON RESPONSE OF RC BULDINGS EQUIPPED WITH FPS DEVICES: A CASE STUDY ..... 2182
*Diego Gino, Elena Miceli, Adolfo Ricioppo, Guglielmo Amendola, Luca Giordano, Paolo Castaldo*

OPTIMAL PROPERTIES OF SINGLE CONCAVE FRICTION PENDULUM BEARINGS FOR THE ISOLATION OF BRIDGES SUBJECTED TO FAR FIELD RECORDS ..... 2194
*Elena Miceli, Diego Gino, Adolfo Ricioppo, Gugliemo Amendola, Luca Giordano, Paolo Castaldo*

VARIABLE ORIFICE DAMPER IMPLEMENTATION FOR SEISMIC SEMI-ACTIVE CONTROL OF CIVIL STRUCTURES .... 2204
*Andrea Troise, Eleonora Bruschi, Marco Martino Rosso, Angelo Alosio, Alessandro Rizzo, Nikos D. Lagaros, Virginio Quaglini, Giuseppe Carlo Marano*

FULL-SCALE SHAKE TABLE TESTS OF A R.C. BUILDING EQUIPPED WITH AN ACTIVE MASS DAMPER: EXPERIMENTAL RESULTS AND NUMERICAL SIMULATIONS ..... 2217
*Giovanni Rebecchi, Fabio Menardo, Matteo Rosti, Alberto Bussini, Paolo Martino Calvi*

DESIGN, TESTING AND MODELLING OF A NOVEL FRICTION DAMPER WITH ENHANCED RESISTANCE TO REPEATED SEISMIC LOADS ..... 2229
*Virginio Quaglini, Eleonora Bruschi, Carlo Pettorruso, Mauro Sartori*

DISPLACEMENT-BASED DESIGN OF HYSTERETIC DAMPERS FOR SEISMIC RETROFIT OF FRAMES ..... 2238
*Eleonora Bruschi, Virginio Quaglini, Luca Zoccolini*

ADVANCED MODELLING AND RISK ANALYSIS OF RC BUILDING EQUIPPED WITH ENERGY DISSIPATION DEVICES DESIGNED BY THE ITALIAN SEISMIC CODE ..... 2249
*Eleonora Bruschi, Virginio Quaglini, Marco Furinghetti, Alberto Pavese*

SEISMIC RETROFITTING OF FRAMED STRUCTURES BY DAMPED BRACES CONSIDERING THE OUT-OF-PLANE RESPONSE OF MASONRY INFILLS ..... 2261
*Fabio Mazza, Rodolfo Labernarda*

LOSS-BASED SEISMIC PRIORITISATION OF EXISTING RC GIRDER BRIDGES ..... 2271
*Andrea Nettis, Giuseppina Uva*

EFFECT OF CYCLIC LOAD ON THE TENSILE BEHAVIOR OF A PBO FRCM COMPOSITE ..... 2286
*Angelo Savio Calabrese, Alessandro Cagnoni, Veronica Bertolli, Tommaso D'Antino, Pierluigi Colombi, Carlo Poggi*

SHEAR DEFICIENT RC BEAMS RETROFITTED WITH INORGANIC-MATRIX COMPOSITES ..... 2296
*Dario De Domenico, Natale Maugeri, Paolo Longo, Matteo Mazzeo, Giuseppe Ricciardi, Antonino Quattrocchi, Roberto Montanini, Luigi Calabrese*

NUMERICAL MODELING OF A NOVEL STEEL-CONCRETE COMPOSITE BEAM-COLUMN JOINT SOLUTION ..... 2315
*William D. Galik, Paolo M. Calvi*

DIRECT LOSS-BASED SEISMIC DESIGN: STATE OF THE ART AND CURRENT CHALLENGES ..... 2325
*Roberto Gentile*

**MS 26: NON-DETERMINISTIC MODEL UPDATING AND HEALTH MONITORING WITH UNCERTAINTY TREATMENT**

BAYESIAN UPDATING OF WOODEN STRUCTURAL PARAMETERS AND SEISMIC DAMAGE CLASSIFIER USING NEURAL NETWORK ..... 2335
*Rikuto Mizobuchi, Masayuki Kohiyama, Takuzo Yamashita*

A COMPARISON OF SAMPLING-BASED BAYESIAN MODEL UPDATING APPROACHES APPLIED UPON A NEW BENCHMARK AEROSPACE TESTBED ..... 2348
*Ewan B. Smith, Kui He, Sifeng Bi*

UNCERTAINTY QUANTIFICATION IN THE CONSTITUTIVE BEHAVIOR OF HDRBS ..... 2369
*José A. Gallardo, Juan C. de la Llera, Katrin Beyer*

**MS 28: MONITORING, DAMAGE MODELLING AND SOIL-STRUCTURE-INTERACTION IN CULTURAL HERITAGE CONSTRUCTIONS**

STRENGTHENING OF MASONRY ARCHES: THE "SANTA MARIA DELLE GRAZIE" CHURCH ..... 2380
*Luigi Massaro, Luciana Di Gennaro, Mariateresa Guadagnuolo, Giorgio Frunzio*

NUMERICAL AND OPERATIONAL MODAL ANALYSES OF A MASONRY BELL-TOWER INSERTED IN A BUILDING AGGREGATE ..... 2394
*Alessandra De Angelis, Giuseppe Maddaloni, Maria Rosaria Pecce*

THE DOME OF THE SAN FRANCESCO DI PAOLA BASIL: A REAL GEOMETRY BASED ASSESSMENT ..... 2406
*Claudia Cennamo, Conceta Cusano, Arsenio Cutolo, Federico Guarracino, Ida Mascolo*

THE ROLE OF FRICTION IN THE DYNAMIC BEHAVIOUR OF FREESTANDING MARBLE OBJECTS ..... 2416
*Ester Sallicandro, Michela Monaco*

THE ROLE OF UNDERGROUND ARCHAELOGICAL REMAINS ON THE SEISMIC RESPONSE OF A HISTORIC SITE ..... 2424
*Antonella Ambrosino, Enza Zeolla, Alessandra De Angelis, Stefania Sica*

INFLUENCE OF THE DISPLACEMENT OF THE SUPPORTS ON THE COLLAPSE BEHAVIOR OF MASONRY SEMI-CIRCULAR ARCHES ..... 2434
*Simona Coccia, Fabio Di Carlo*

EVALUATION OF THE SEISMIC STABILITY OF UNDERGROUND CAVITIES IN NAPLES ..... 2444
*Filomena de Silva, Stefania Fabozzi, Emilio Bilotta, Alessandro Flora*

A NOVEL FE MODEL FOR THE TOWER OF PISA ..... 2452
*Dionis Butuc, Anna De Falco, Carlo Resta, Nunziante Squeglia, Laura Vignali*

SEISMIC VULNERABILITY ASSESSMENT OF AN ITALIAN ANCIENT CHURCH ACCORDING TO CONVENTIONAL APPROACHES ..... 2465
*Stefania Imperatore, Gian Piero Lignola, Barbara Ferracuti*

3D EXPLORATION OF INTERNAL STRESSES DUE TO LATERAL LOADS AND FOUNDATION MOVEMENTS IN A SEMICIRCULAR ARCH ..... 2476
*Antonino Iannuzzo, Antonio Gesualdo, Carlo Olivieri, Andrea Montanino*

APPLICATION OF THE CONTINUOUS AIRY-BASED FOR STRESS SINGULARITIES (CASS) TO THE LOAD BEARING CAPACITY OF MASONRY STRUCTURES UNDER SEISMIC LOADS ..... 2492
*Andrea Montanino, Francesca Linda Perelli, Daniela De Gregorio, Giulio Zuccaro*

AN HYBRID METHODOLOGY FOR THE DEFINITION OF LOCALIZED COLLAPSE CURVES FOR UNREINFORCED MASONRY STRUCTURES ..... 2505
*Daniela De Gregorio, Francesca Linda Perelli, Carlo Olivieri, Petros Christou*

**MS 29: SOFT COMPUTING AND ARTIFICIAL INTELLIGENCE TECHNIQUES IN STRUCTURAL ENGINEERING**

A NEW DEEP LEARNING ACCELERATED BLAST LOADING EFFECT ANALYSIS OF FRP RETROFITTED CONCRETE SLAB ..... 2520
*Arya Prakash Padhi, Vaibhav Bhandari, Anupam Chakrabarti, Rajib Chowdhury*

CLASSIFICATION OF WALL DEFECTS FOR MAINTENANCE PURPOSES USING IMAGE PROCESSING ..... 2529
*Waqas Qayyum, Rana Ehtisham, Vagelis Plevris, Junaid Mir, Afaq Ahmad*

**MS 30: THE ASSESSMENT OF RESILIENCE WITH APPROACHES BASED ON NUMERICAL SIMULATIONS**

SUPPLEMENTARY DAMPING DEVICES TO MITIGATE THE NEAR-FAULT SEISMIC EFFECTS ON THE UFREI-ISOLATED STRUCTURES ..... 2540
*Shiv Prakash, Radhey Shyam Jangid*

SAFE DESIGN OF SUBSEA PIPELINES TO COMBINED SEISMIC AND THERMAL LOADING ..... 2554
*Daniele Mina, Hassan Karampour, Davide Forcellini*

SEISMIC POUNDING OF TYPICAL REINFORCED CONCRETE BUILDINGS SUBJECT TO SOIL STRUCTURE INTERACTION EFFECTS ..... 2566
*İbrahim Öz, Kaan Kaatsiz*

EXPERIMENTAL TESTING OF INNOVATIVE, BIOMIMETIC SEISMIC METAISOLATORS ..... 2581
*Valentina Adinolfi, Saeedh Qaderi, Giovanni Germano, Julia de Castro Motta, Gianmario Benzoni, Ada Amendola, Massimo Ruzzene, Fernando Fraternali*

3D NUMERICAL SIMULATIONS OF MULTI-LAYERED ELASTOMERIC BEARINGS (EB) SUBJECTED TO COMBINED VERTICAL AND HORIZONTAL LOADS ..... 2587
*Davide Forcellini, Kostantinos Kalfas*

THE VULNERABILITY OF HIGHLY POPULATED BUILDINGS IN THE FACE OF EARTHQUAKE AND TSUNAMI HAZARDS ..... 2597
*Behnam Beheshtian, Javad Hashemi, Hing-Ho Tsang*

EFFECT OF NON-LINEAR SOIL STRUCTURE INTERACTION IN SEISMIC RESPONSE OF ASYMMETRIC STRUCTURES 2609
*Vivek Balachandra Kartha, Raj Mukeshbhai Patel*

**MS 31: BEYOND DISCONTINUUM-BASED ANALYSIS: NOVEL APPROACHES FOR DISCRETE ELEMENT STRUCTURAL MODELLING OF COMPOSITE MATERIALS**

IN-PLANE RESPONSE OF A MODULAR RETROFIT SYSTEM FOR URM WALLS USING DEM ..... 2618
*Nicolò Damiani, Matthew J. DeJong, Luca Albanesi, Guido Magenes, Andrea Penna, Paolo Morandi*

NONLINEAR ANALYSIS OF A LARGE RC CANTILEVER GRANDSTAND OF SAN SIRO MEAZZA STADIUM IN MILAN USING THE APPLIED ELEMENT METHOD ..... 2628
*Nicola Scattarreggia, Martina Cogliano, Gian Michele Calvi, Matteo Moratti*

SENSITIVITY ANALYSIS OF DRY-JOINT STONE MASONRY WALLS USING DISCRETE ELEMENT METHOD ..... 2640
*Ciro Canditone, Fulvio Parisi*

THREE-DIMENSIONAL DISCRETE ELEMENT MODELLING OF RUBBLE MASONRY STRUCTURES FROM GEOSPATIAL DATA ..... 2656
*Nicko Kassotakis, Vasilis Sarhosis, Ajit Pillai, Lars Johanning*

## VOLUME II

### Minisymposia

**MS 32: MULTI-HAZARD RISK MANAGEMENT OF THE BUILT ENVIRONMENT: RECENT ADVANCES AND OPEN CHALLENGES**

EMPIRICAL MULTI-VARIABLE TSUNAMI DAMAGE MODELS BASED ON THE 2011 GREAT EAST JAPAN DATASET: ANALYSIS OF THE PERFORMANCES AT DIFFERENT SPATIAL SCALES ..... 2677
*Mario Di Bacco, Anna Rita Scorzini, Anawat Suppasri*

APPLICATION OF HAZARD RISK METHDOLOGY ON HISTORICAL BUILT ENVIRONMENT IN TIMISOARA ..... 2687
*Iasmina Onescu, Eugen Onescu, Marius Mosoarca*

A MULTI-RISK FRAMEWORK FOR ASSESSING AND RANKING SEISMIC AND FLOOD RISKS: AN APPLICATION IN ITALY-SLOVENIA TRANSBOUNDARY REGION ..... 2698
*Maria Polese, Gabriella Tocchi, Matjaz Dolsek, Anze Babič, Marta Faravelli, Barbara Borzi, Nicola Rebora, Daria Ottonelli, Matjaz Mikos, Davide Quaroni, Rocco Masi, Andrea Prota*

DEFINITION OF MULTI-HAZARD VULNERABILITY INDICATORS FOR CULTURAL HERITAGE BUILDINGS ..... 2709
*Marco Lazzati, Silvia De Angeli, Giorgio Boni, Serena Cattari, Xavier Romão*

MULTI-RISK ASSESSMENT OF A BASE ISOLATED STRUCTURE ..... 2725
*Donatella de Silva, Antonio Bilotta, Romeo Tomeo, Emidio Nigro*

A BUILDING CLASSIFICATION SYSTEM FOR MULTI-HAZARD RISK ASSESSMENT OF HISTORICAL RELIGIOUS BUILDINGS ..... 2741
*Federica Del Carlo, Silvia Caprili, Tiago Miguel Ferreira, Pere Roca, Marco Uzielli*

MULTI SCALE URBAN MODELLING TO IMPROVE THE RECOVERABILITY OF CITIES EXPOSED TO MULTIPLE NATURAL HAZARDS ..... 2752
*Soheil Mohammadi, Giorgio Boni, Francesca Pirlone, Serena Cattari, Silvia De Angeli*

LARGE-SCALE VULNERABILITY ANALYSIS OF HISTORICAL MASONRY BUILDINGS ..... 2762
*Valentina Buonocunto, Giorgio Serino, Fulvio Parisi*

IMPULSIVE ACTIONS DUE TO SEISMIC JERK AND DESIGN OF REINFORCEMENTS TO COUNTERACT THEIR EFFECTS IN MASONRY BUILDINGS ..... 2777
*Massimo Mariani, Francesco Pugi*

RESILIENCE ASSESSMENT OF ROAD BRIDGES IN MULTI-HAZARD ENVIRONMENT ..... 2806
*Olga Markogiannaki, Anna Karatzetzou, Sotiria Stefanidou, Grigorios Tsinidis*

**MS 33: INSIGHT IN SEISMIC PERFORMANCE OF RETROFITTED BUILDINGS: FEASIBILITY AND EFFECTIVENESS OF INTERVENTION IN RC BUILDINGS**

INFLUENCE OF CLADDING PANELS RETROFIT ON THE SEISMIC RISK OF AN EXISTING PRECAST BUILDING ..... 2819
*Marius Eteme Minkada, Marco Bosio, Andrea Belleri, Paolo Riva*

NUMERICAL MODEL CALIBRATION OF A LOW IMPACT STRENGTHENING TECHNIQUE BASED ON BED-JOINTS SLIDING IN SEISMIC RETROFITTING OF MASONRY INFILLS ..... 2828
*Marco Vailati, Amedeo Gregori, Federico Morelli, Giorgio Monti, Edoardo Ciuffetelli, Alfredo Peditto*

PRELIMINARY RESULTS OF A SHAKING-TABLE DYNAMIC TEST ON A REPAIRED AND ENHANCED REINFORCED CONCRETE INFILLED STRUCTURE ..... 2841
*Riccardo R. Milanesi, Gabriele Guerrini, Davide Bolognini, Luca Grottoli, Filippo Dacarro, Paolo Morandi*

COLD FORMED STEEL PANELS FOR THE SEISMIC STRENGHTENING OF EXISTING RC BUILDINGS ..... 2857
*Simone Labò, Andrea Belleri, Michelle Gualdi, Atsushi Sato*

IMPROVEMENT OF SEISMIC SAFETY BY LOCAL STRENGHTNING IN ITALIAN PRE-70 RESIDENTIAL RC BUILDINGS DESIGNED FOR GRAVITY LOADS ..... 2867
*Santa Anna Scala, Maria Teresa De Risi, Carlo Del Gaudio, Gerardo Mario Verderame*

IINFILL-FRAME INTERACTION: REFINED MODELLING FOR THE ANALYSIS AND THE ESTIMATION OF THE INTERNAL FORCES IN SEISMIC ASSESSMENT OF RC BUILDING STRUCTURES ..... 2882
*Fabio Di Trapani, Marilisa Di Benedetto, Massimo Petracca, Guido Camata*

**MS 34: INSIGHTS AND DEVELOPMENTS IN DYNAMIC SOIL-FOUNDATION-STRUCTURE INTERACTION**

SOIL-FOUNDATION-STRUCTURE PROBLEMS RELATED TO TRAIN-INDUCED VIBRATIONS – THE KINEMATIC INTERACTION OF TUNNEL EXCITED PILE FOUNDATIONS AND THE INERTIAL INTERACTION OF HIGH-RISE BUILDINGS ..... 2894
*Lutz Auersch*

NUMERICAL BACK-ANALYSIS OF DYNAMIC CENTRIFUGE TESTS ON THE SEISMIC BEHAVIOUR OF CAISSON FOUNDATIONS SUPPORTING BRIDGE PIERS ..... 2908
*Domenico Gaudio, Fabrizio Murillo*

A PHYSICS INFORMED NEURAL NETWORK (PINN) APPROACH FOR SOIL-PILE INTERACTION ..... 2917
*Michail Madianos, Panagiotis Lykourgias, Dimitrios Loupas, Maria Papanikolaou, Stijn François, George Anoyatis, Aggelos Tsikas*

FILTERING EFFECT FOR A PILE IN TWO-LAYER SOIL ..... 2929
*Raffaele Cesaro, Raffaele Di Laora*

ON THE SSI PERIOD AND DAMPING FOR BRIDGE PIERS ON CAISSON FOUNDATIONS …… 2938
*Riccardo Conti, Emmanouil Rovithis, Raffaele Di Laora*

ASSESSMENT OF MACRO-ELEMENTS IN THE PREDICTION OF THE RESPONSE OF OFFSHORE WIND TURBINES … 2946
*Olgu Orakci, Nunzia Letizia, Stijn François, Shiaohuey Chow, Yinghui Tian, George Anoyatis*

DIMENSIONLESS FACTORS GOVERNING THE LATERAL DISCONNECTION EFFECTIVENESS …… 2963
*Fausto Somma, Alessandro Flora*

**MS 35: RECENT ADVANCES IN GROUND- AND STRUCTURE-BORNE NOISE AND VIBRATION ASSESSMENT & PREDICTION**

CONCRETING UNDER TRAFFIC: IN-DEPTH INVESTIGATION OF THE EFFECTS OF VIBRATIONS ON YOUNG CONCRETE …… 2972
*Christian Gasser, Soufiane El Yassini, Alfred Lechner, Lukas Hausner, Alois Vorwagner*

EFFECT OF THE LENGTH OF SEISMIC METASURFACES ON VIBRATION MITIGATION PERFORMANCE …… 2983
*David Carneiro, Pieter Reumers, Geert Lombaert, Geert Degrande*

LOW-COST HYBRID DESIGN STRATEGIES: LARGE-SCALE SHAKING TABLE TESTS AND CHALLENGES OF IMPLEMENTATION …… 2996
*Anastasios Tsiavos, Anastasios Sextos*

DYNAMIC ANALYSIS OF RAILWAY BRIDGES CONSIDERING THE NONLINEAR AMPLITUDE-DEPENDENT SYSTEM BEHAVIOUR - SIMULATION AND IN-SITU TESTS …… 3004
*Michael Reiterer, Andrei Firus*

**MS 36: EXPERIMENTAL TESTING ON SEISMIC ISOLATION AND ENERGY DISSIPATION DEVICES**

STATIC AND DYNAMIC EXPERIMENTAL VALIDATIONS OF THE LATERAL IMPACT RESILIENT DOUBLE CONCAVE FRICTION PENDULUM (LIR-DCFP) BEARING …… 3017
*Gaspar Auad, Paolo Castaldo, José L. Almazán, Diego Quizanga*

SHAKE-TABLE TESTING OF LOW-COST, HIGH-PERFORMANCE SEISMIC ISOLATORS BASED ON ROLLING RUBBER SPHERES …… 3028
*Antonios A. Katsamakas, Michalis F. Vassiliou*

BEHAVIOR OF COMPLEX CURVED SURFACE SLIDER IN DESIGN AND EXPERIMENTAL SITUATION …… 3041
*Frederik Bomholt, Toshihisa Mano*

EXPERIMENTAL TESTS OF VARIOUS TYPES OF SEISMIC ISOLATION SYSTEMS …… 3052
*Mohammed S. Mohammed, Scott C. Darling, Ahmed F. Ibrahim, Ahmed O. Atiek*

ANALYSIS OF THE FORCE RESPONSE OF BEARING DEVICES FOR BRIDGE STRUCTURES …… 3064
*Marco Furinghetti, Simone Reale, Matt J. Fox, Yuan Fan, Chiara Casarotti, Alberto Pavese*

EXPERIMENTAL AND FINITE ELEMENT ANALYSIS OF THE CYCLIC BEHAVIOUR OF LINEAR DISSIPATIVE DEVICES .. 3077
*Salvatore Pagnotta, Muhammad Ahmed, Piero Colajanni*

**MS 37: DESIGN OF STRUCTURES UNDER EXTREME LOADS**

ROBUSTNESS OF RC FRAMES UNDER EARTHQUAKE AND BLAST CHAINED SCENARIOS ..... 3091
*Mattia Francioli, Juliano Ferreira Martins, Francesco Petrini, Franco Bontempi*

EQUIVALENT DAMPING RATIO EVALUATION FOR HISTORICAL CHURCH REINFORCED BY CROSS LAM ROOF STRUCTURE FOR IMPROVING THE SEISMIC RESPONSE ..... 3105
*Nicola Longarini, Pietro Crespi, Marco Zucca*

EVALUATION OF MAINTENANCES INTERVENTION PERIOD ON STOCK OF EXISTING RC BRIDGES SUBJECT TO DAMAGE PHENOMENA ..... 3122
*Marco Zucca, Pietro Crespi, Flavio Stochino, Mario Lucio Puppio, Fausto Mistretta, Nicola Longarini, Mauro Sassu*

STRUCTURAL BEHAVIOUR OF STEEL STORAGE RACKS UNDER DIFFERENT FIRE SCENARIOS ..... 3135
*Marco Simoncelli, Marco Zucca, Flavio Stochino, Livia Bhardi*

A NUMERICAL STUDY ON FIRE RESISTANCE OF BLAST DAMAGED REINFORCED CONCRETE COLUMNS ..... 3145
*Ravi Mudragada, Ankit Agrawal, Pradeep Bhargava*

THE INFLUENCE OF DAMPING ON PROGRESSIVE COLLAPSE ANALYSIS ..... 3157
*Alex Sixie Cao, Andrea Frangi*

FRAGILITY CURVES FOR STEEL INDUSTRIAL SILOS ACCOUNTING FOR FILLING LEVEL OF GRANULAR-LIKE MATERIAL ..... 3173
*Mohammad Khalil, Sergio Ruggieri, Vito Tateo, Giuseppina Uva*

**MS 38: TIMBER-BASED SYSTEMS FOR NEW AND EXISTING STRUCTURES IN SEISMIC AREA: RECENT DEVELOPMENTS AND FUTURE TRENDS**

EFFECT OF THE STRUCTURAL INTERACTIONS IN MULTI-STOREY CLT SHEAR WALLS ..... 3187
*Elisabetta Maria Ruggeri, Giuseppe D'Arenzo, Marinella Fossetti*

TIMBER CARPENTRY WITHOUT STEEL CONNECTORS ..... 3203
*Luigi Massaro, Roberto Serpieri, Giorgio Frunzio, Luciana Di Gennaro*

EXPERIMENTAL AND NUMERICAL ASSESSMENT OF AN IMPROVED PLYWOOD-BASED IN-PLANE RETROFITTING METHOD FOR TIMBER FLOORS IN HIGHLY SEISMIC AREAS ..... 3213
*Michele Mirra, Andrea Gerardini*

LIGHT TIMBER FRAME WALLS WITH CLADDING– NUMERICAL INVESTIGATION OF THE SEISMIC PERFORMANCE OF A MULTI-STORY BUILDING BASED ON TEST RESULTS ..... 3228
*Lukas Rauber, Cristian Vulcu, Vera Wilden, Georgios Balaskas, Benno Hoffmeister*

AN INSIGHT ON THE ROLE OF THE DESIGN PROCEDURES ON DAMAGE TOLERANCE AND COST OF CLT BUILDINGS IN SEISMIC AREAS ..... 3246
*Antonio Sandoli, Bruno Calderoni, Carla Ceraldi, Giovanni Fabbrocino*

SEISMIC FRAGILITY ANALYSIS TO ASSESS THE IMPACT OF TIMBER VERTICAL ADDITIONS ON EXISTING RC BUILDINGS: A CASE STUDY ..... 3261
*Andrea Bartolotti, Michele Sartori, Ivan Giongo*

A PARAMETRIC STUDY ON THE CYCLIC RESPONSE OF POST-TENSIONED LOW DAMAGE TIMBER WALLS WITH DISSIPATIVE DEVICES ..... 3271
*Valentina Tomei, Maria Zucconi, H. Monsef, Barbara Ferracuti*

THE USE OF STRUCTURAL TIMBER IN EUROPE: AN OVERVIEW ON RECENT DEVELOPMENTS ..... 3280
*Valentina Tomei, Martina Sciomenta, Antonio Sandoli*

CYCLIC BEHAVOIR OF AN INNOVATIVE JOINT PROTOTYPE FOR CLT PANELS ..... 3300
*Antonio Tancredi, Italo Marchionni, M.G. Masciotta, Giuseppe Brando*

DEVELOPMENT OF A HOLISTIC PARAMETRIC FRAMEWORK FOR MULTI-PERFORMANCE LIFE-CYCLE EVALUATION OF POST-TENSIONED TIMBER BUILDINGS ..... 3310
*Giada Formichetti, Michele Matteoni, Stefano Pampanin*

**MS 39: SHM FOR TRANSPORT INFRASTRUCTURE RESILIENCE**

SYSTEM IDENTIFICATION OF LONG-SPAN BRIDGES VIA SYNCHRO-SQUEEZED ADAPTIVE WAVELET TRANSFORM BASED OPTIMIZED MULTIPLE ANALYTICAL MODE DECOMPOSITION ..... 3331
*Hongya Qu, Mwenda Lomthundzi, Yan Xu, An Chang*

RESTORATION OF A LANDMARK BALANCED CANTILEVER BRIDGE CONSIDERING DIFFERENT RESILIENCE AND SUSTAINABILITY STRATEGIES ..... 3339
*Marco Domaneschi, Stergios Aristoteles Mitoulis, Raffaele Cucuzza, Valentina Villa, Roberta Di Bari, Gopika Siva*

**MS 40: APPLICATION OF DEEP LEARNING AND IOT IN NUMERICAL MODELLING AND HEALTH MONITORING OF STRUCTURES/INFRASTRUCTURES**

DEEP LEARNING-BASED CRACK, LOCATION AND AREA IDENTIFICATION FOR A PIPELINE BY THE CONVOLUTIONAL NEURAL NETWORK BASED ON CRACK CONTOUR NETWORK METHOD ..... 3357
*Wael A. Altabey, Mohammad Noori, Zhishen Wu*

EFFECTIVE TECHNIQUE FOR STRUCTURES DAMAGE DETECTION BASED ON THE STRUCTURAL FREQUENCY MAPS ..... 3369
*Wael A. Altabey, Mohammad Noori, Zhishen Wu, Ahmad Silik, Nabeel S. D. Farhan*

**MS 42: COMPUTATIONAL METHODS FOR INVERSE PROBLEMS IN STRUCTURES AND GEOPHYSICS**

INVERSE IDENTIFICATION OF CABLE FORCES USING ITS MODAL BEHAVIOR BY DIRECT AND NON-CONTACT VIBRATION MEASUREMENTS ..... 3379
*Max Johannes Alois Fritzsche, Maximilian Michael Rupp, Steven R. Lorenzen, Lucia Hofmann, Lia Birmele, Jens Schneider*

STRUCTURAL DEFORMATION RECONSTRUCTION USING THE HYBRID SHELL-BEAM INVERSE FINITE ELEMENT METHOD: THEORY & NUMERICAL RESULTS ..... 3394
*Rinto Roy, Marco Esposito, Marco Gherlone, Cecilia Surace*

STRUCTURAL DEFORMATION RECONSTRUCTION USING THE HYBRID SHELL-BEAM INVERSE FINITE ELEMENT METHOD: EXPERIMENTAL APPLICATION ON A THIN-WALLED STIFFENED PANEL ..... 3404
*Marco Esposito, Rinto Roy, Marco Gherlone, Cecilia Surace*

**MS 45: STRUCTURAL DYNAMICS, SEISMIC SAFETY AND RISK ASSESSMENT OF SPECIAL STRUCTURES**

EXPERIMENTAL AND NUMERICAL DYNAMIC EVALUATION OF PROFILED STEEL DECKING SLAB IN A CONTAINER HOUSE USING MEMS ..... 3415
*Henrique Tavares Lima, Luis Ernesto de Medeiros Alas, Mateus Narcizo de Almeida Nunes, Iálysson da Silva Medeiros, Douglas Mateus de Lima*

MACHINE LEARNING APPROACH FOR PREDICTING FLEXURAL BEHAVIOR VARIATIONS OF I-SHAPED STEEL BEAMS DUE TO MANUFACTURING TOLERANCES ..... 3433
*Cyrus Eshaghi, Arefeh Mazarei, Rui Carneiro de Barros, Xavier Romão, José Miguel Castro*

RESPONSE OF A SMALL WIND TURBINE TOWER UNDER EARTHQUAKE LOADS ..... 3445
*Anelise Dick, Rui Carneiro de Barros, Manuel Braz-César*

COMPARATIVE STUDY OF OPTIMUM FORMULATIONS FOR TUNED MASS DAMPERS IN SMALL WIND TURBINE TOWERS ..... 3454
*Anelise Dick, Rui Carneiro de Barros, Manuel Braz-César*

MODELLING STRATEGIES OF INFILL MASONRY WALLS FOR SEISMIC ANALYSIS OF BUILDING STRUCTURES ..... 3466
*Pedro P. Folhento, Rui Carneiro de Barros, Manuel Braz-César*

SEISMIC COLLAPSE RISK OF A ISOLATED TRANSMISSION TOWER AND A TRANSMISSION LINE SYSTEM IN NORTHERN PORTUGAL ..... 3483
*Fabio M. Paiva, Rui Carneiro de Barros*

STUDY OF THE SEISMIC VULNERABILITY OF A REMODELLED REINFORCED CONCRETE BUILDING IN LISBON ..... 3496
*Raquel C. Pedreiras, Rui Carneiro de Barros*

**MS 48: RECENT ADVANCES IN GROUND MOTION SELECTION AND SCALING TECHNIQUES**

SEISMIC ASSESSMENT OF TYPOLOGICAL MASONRY BUILDINGS USING SIMULATED GROUND MOTION RECORDS: A CASE STUDY FOR AZORES, PORTUGAL ..... 3507
*Shaghayegh Karimzadeh, Vasco Bernardo, Sayed Mohammad Sajad Hussaini, Daniel Caicedo, Alexandra Carvalho, Paulo B. Lourenço*

EVALUATION OF SIMULATED GROUND MOTIONS FOR SEISMIC ASSESSMENT OF A STEEL FRAME STRUCTURE USING MULTI-CRITERIA SELECTION AND SCALING APPROACH BASED ON EVOLUTIONARY ALGORITHMS ..... 3520
*Manolis Georgioudakis, Shaghayegh Karimzadeh, Michalis Fragiadakis, Paulo B. Lourenço*

QUAKEMANAGER: A COMPREHENSIVE SOFTWARE TOOL FOR GROUND MOTION SELECTION, MODIFICATION AND ANALYSIS ..... 3532
*Mahmoud M. Hachem, Bashar M. Abdo, Hamza A. Al-Jundi, Sohaib A. Al-Jundi, Bahaa T. Tayba, Bahaa S. Ghieh, Yousra A. Hachem, Khaled A. Chandab*

SCALING GROUND MOTION RECORDS BY CONSIDERING THE INELASTIC RESPONSE OF SOILS ..... 3548
*Yeudy F. Vargas-Alzate, Ana M. Zapata-Franco, Rodolfo J. Tirado, Ramón Gonzalez-Drigo, Jean Vaunat*

SELECTION AND SCALING VALIDATION OF GROUND MOTIONS ACCORDING TO TBEC-2018 FOR THE SEISMIC ASSESSMENT OF MASONRY STRUCTURES ..... 3559
*Marco F. Funari, Shaghayegh Karimzadeh, Daniel Caicedo, Sayed M. S. Hussaini, Aysegul Askan, Paulo B. Lourenço*

PERMANENT DISPLACEMENT DATABASE OF STRONG EARTHQUAKES IN TURKEY, AND AN ADJUSTED PREDICTIVE MODEL ..... 3570
*Emrecan Adanır, Gülüm Tanırcan*

**MS 49: SEISMIC RESPONSE OF MASONRY CROSS VAULTS: SHAKING TABLE TESTS AND NUMERICAL VALIDATIONS**

NUMERICAL PREDICTION OF THE SEISMIC BEHAVIOUR OF A MASONRY VAULT MOCK-UP USING THE NOSA-ITACA CODE ..... 3580
*Daniele Pellegrini*

BLIND PREDICTION OF SHAKE TABLE TESTS ON A FULL-SCALE UNSTRENGTHENED MASONRY CROSS VAULT: COMBINED FINITE-DISCRETE ELEMENT MODEL ..... 3589
*Omar AlShawa, Domenico Liberatore, Luigi Sorrentino*

NUMERICAL INVESTIGATION ON THE SEISMIC RESPONSE OF A MASONRY CROSS VAULT BASED ON THE DISCRETE MACRO-ELEMENT METHOD ..... 3596
*César Chácara, Bartolomeo Pantò, Francesco Cannizzaro, Davide Rapicavoli, Ivo Caliò*

SIMPLIFIED EVALUATION FOR THE SERA-TA BLIND PREDICTION: SEISMIC BEHAVIOR OF MASONRY CROSS VAULTS ..... 3610
*Giancarlo Ramaglia, Gian Piero Lignola, Andrea Prota*

## Thematic Sessions

### TS 2: ALGORITHMS FOR STRUCTURAL HEALTH MONITORING

COMPRESSION AND RECONSTRUCTION OF AUTOCOVARIANCE FUNCTIONS FOR DAMAGE DETECTION AND LOCALIZATION UNDER VARIABLE ENVIRONMENTAL CONDITIONS ..... 3620
*Jyrki Kullaa*

KURTOSIS AND SKEWNESS BASED COMPARISON OF HERMITE POLYNOMIAL AND JOHNSON TRANSFORMATIONS ..... 3636
*Ayşe Su Giz, Ata Mugan*

FEASIBILITY STUDY OF MICROTREMOR SIGNALS FOR STRUCTURAL HEALTH MONITORING ON REAL STEEL BUILDING STRUCTURES ..... 3647
*Chih-chun Ou, Jun Iyama*

SEVEN YEARS OF CONTINUOUS DYNAMIC MONITORING OF BAIXO SABOR DAM ..... 3660
*Sérgio Pereira, Filipe Magalhães, Jorge Gomes, Álvaro Cunha, José V. Lemos*

EVOLUTION OF THE MODAL PARAMETERS DUE PROGRESSIVE DEGRADATION OF AN RC BEAM-COLUMN JOINT ..... 3668
*Angelo Aloisio, Amedeo Gregori, Lorenzo Bizzarri, Caterina D'Agostino, Riccardo Cirella, Rocco Alaggio*

PROPAGATION OF EPISTEMIC UNCERTAINTY IN MODAL PARAMETERS AND ITS INFLUENCE ON DAMAGE ..... 3677
*Saranika Das, Koushik Roy*

LASER SCANNING OF JUMA MACHIT'S COURTYARD AND DETAILED NUMERICAL STUDY ACCOUNTING FOR ROOF MEMBERS COMPROMISED BY TERMITE INFESTATION ..... 3691
*Shakhzod M. Takhirov, Bakhodir S. Rakhmonov, Ravshanbek Nafasov, Abbos Samandarov, Sevara Sultanova, Sultan Kudratov, Mirzokhid M. Akhmedov, Ravshan A. Shamansurov*

DYNAMIC IDENTIFICATION OF A HISTORICAL MASONRY BUILDING: THE CASE STUDY OF PALAZZO ROSCIANO .. 3700
*Raffaele Tarantini, Alessandro Cardoni, Gian Paolo Cimellaro, Marco Domaneschi, Enrico Pribaz, Gianluca Rupolo*

APPLICATION OF THE WAVELET TRANSFORM INVERSE ANALYSIS FOR MODAL IDENTIFICATION AND DAMAGE DETECTION ..... 3708
*Pierre Argoul, Michalis Fragiadakis*

### TS 3: BRIDGE DYNAMICS

ASSESSMENT OF THE SEISMIC VULNERABILITY AND MODELLING OF EXISTING BRIDGE WITH DIFFERENT LEVELS OF ACCURACY: STRENGTHS AND WEAKNESSES ..... 3732
*Carlo Pettorruso, Virginio Quaglini*

STOCHASTIC MODEL UPDATING OF A RC TIED-ARCH BRIDGE ..... 3742
*Andrea Gennaro, Amedeo Caprino, Valentina Pernechele, Filippo Lorenzoni, Francesca da Porto*

THE EFFECT OF GROUND MOTION INCIDENCE ANGLE FOR SCOURED HIGHWAY BRIDGES ..... 3754
*Serenay Ateş, Özgür Avşar*

OPTIMIZED DYNAMIC DESIGN RULES FOR HIGH-SPEED BRIDGES BY USING DIGITAL TWIN ..... 3770
*Vincent Mathouraparsad, Muriel Ragueneau, Huyen Nguyen*

EXTENDED MODIFIED BRIDGE SYSTEM METHOD FOR VEHICLE-BRIDGE INTERACTION: TREATMENT OF ROTATIONAL DEGREES OF FREEDOM ..... 3784
*Hossein Homaei, Elias G. Dimitrakopoulos*

AN INTERFACE FOR CHECKING DYNAMIC COMPATIBILITY OF ROLLING STOCK WITH EXISTING RAILWAY BRIDGES ..... 3798
*Muriel Ragueneau, Huyen Nguyen, Vincent Mathouraparsad*

DYNAMIC AMPLIFICATION OF TRAFFIC LOADS ON ROAD BRIDGES EVALUATED USING PROBABILISTIC TRAFFIC SIMULATIONS ..... 3808
*Marian Ralbovsky, Maciej Kwapisz, Alois Vorwagner, Stefan Lachinger*

IMPROVING RELIABILITY OF UZBEKISTAN'S TRANSPORT INFRASTRUCTURE FACILITIES UNDER IMPACT OF NATURAL HAZARDS BY ANALYSIS OF ITS VULNERABILITY, MONITORING AND MODELING ..... 3817
*Ulugbek Z. Shermukhamedov, Zukhritdin Z. Ergashev, Shakhzod M. Takhirov, Abdurakhim A. Abdullaev*

DESIGNING A LOW-COST WIRELESS SENSING SYSTEM FOR REAL TIME DAMAGE ASSESSMENT OF R/C BRIDGES ..... 3831
*Vassilis K. Papanikolaou, Konstantinos Mixios, Sotiria Stefanidou, Olga Markogiannaki*

A DAMAGE DETECTION APPROACH TO ASSESS THE PERFORMANCE LEVEL OF R/C BRIDGES USING VIBRATIONAL RESPONSE MEASUREMENTS ..... 3842
*Konstantinos Mixios, Olga Markogiannaki, Sotiria Stefanidou, Vassilis K. Papanikolaou*

**TS 4: CONSTITUTIVE MODELLING**

A 3D FRACTURE ENERGY-BASED SMEARED CRACK APPROACH FOR THE NONLINEAR BEHAVIOR OF REINFORCED CONCRETE STRUCTURES ..... 3856
*Christos Mourlas, George Markou, Manolis Papadrakakis*

MODELING THE INFLUENCE OF STRAIN-RATE IN SUPERELASTIC SHAPE MEMORY ALLOYS ..... 3869
*Maria I. Ntina*

MODELLING OF THE FULL-RANGE RESPONSE OF ABUTMENT-BACKFILL SYSTEMS ..... 3881
*Ioannis G. Mikes, Andreas J. Kappos*

ON THE CALIBRATION OF UBCSAND CONSTITUTIVE MODEL AGAINST MONOTONIC & CYCLIC TRIAXIAL COMPRESSION DATA FOR BALLAST AGGREGATES ..... 3893
*Tadahiro Kishida, Rusul Falah Aldulaimi, George Mylonakis*

**TS 5: DYNAMICS OF CONCRETE AND MASONRY STRUCTURES**

INVESTIGATION OF FAILURE OCCURRENCE MECHANISM OF HISTORIC MASONRY BUILDINGS AND PERFORMANCE OF REINFORCEMENT MEASURES USING DEM ..... 3908
*Junji Kiyono, Aiko Furukawa*

PERFORMANCE COMPARISON OF MASONRY WALLS WITH RECTANGULAR BRICKS AND INTERLOCKING BRICKS – STATIC LOADING TEST AND DYNAMIC ANALYSIS USING DEM - ..... 3916
*Aiko Furukawa, Junji Kiyono*

VULNERABILITY ASSESSMENT OF BUILDINGS BASED ON THE PSEUDO-DYNAMIC TESTING METHOD WITH SUB-STRUCTURING: APPLICATION TO PROGRESSIVE COLLAPSE ..... 3926
*Jean-Baptiste Charrié, David Bertrand, Cédric Desprez, Stéphane Grange*

MODELING OF FRAMES WITH HYBRIDFEM, A PSEUDO-DISCRETE-FINITE MODEL INCLUDING NONLINEAR GEOMETRIC EFFECTS AND NONLINEAR MATERIALS ..... 3936
*Igor Bouckaert, Michele Godio, João Pacheco de Almeida*

ADVANCES IN 3D NUMERICAL SIMULATION OF SEISMIC RESPONSE OF SAFETY-RELATED NUCLEAR STRUCTURES ..... 3948
*Fernando Rastellini, Junior Ramirez, José Manuel Gonzalez, Alex H. Barbat, Cuauhtémoc Escudero, Yeudi F. Vargas, Luis G. Pujades*

ENERGY LOSS MECHANISMS OF ROCKING BLOCKS: EXPERIMENTAL OBSERVATIONS ..... 3960
*Georgios Vlachakis, Carla Colombo, Anastasios I. Giouvanidis, Nuno Mendes, Nathanaël Savalle, Paulo B. Lourenço*

DYNAMIC BEHAVIOUR OF A STRENGTHENED POINTED ARCH TESTED ON A SHAKING TABLE ..... 3972
*Paulo Šćulac, Nina Čeh, Matei Cukarić*

MATERIAL TESTING OF MICRO-CONCRETE AND 3D-PRINTED REINFORCEMENT FOR USE IN SMALL-SCALE SEISMIC TESTING OF RC STRUCTURES ..... 3983
*Medhat Elmorsy, Rafal Wrobel, Christian Leinenbach, Michalis F. Vassiliou*

VERIFICATION OF MATERIAL MODELS FOR MASONRY WALLS IN NONLINEAR PUSHOVER ANALYSIS ..... 3994
*Huan He, Sander J. H. Meijers*

STRUCTURAL PERFORMANCE AND HUMAN COMFORT ASSESSMENT OF RC CANTILEVER GRANDSTANDS: THE CASE OF THE SECOND RING OF SAN SIRO MEAZZA STADIUM IN MILAN ..... 4004
*Martina Cogliano, Nicola Scattarreggia, Matteo Moratti, Gian Michele Calvi*

NUMERICAL MODELLING OF POORLY DETAILED EXISTING RC BEAM-COLUMN JOINTS ..... 4017
*Michele Angiolilli, Amedeo Gregori, Lorenzo Bizzarri, Caterina D'Agostino, Edoardo Ciuffetelli, Alfredo Peditto, Pasqualino Gualtieri*

DYNAMIC CHARACTERIZATION OF THE CIRCUS MAXIMUS ARCHEOLOGICAL SITE ..... 4030
*Amir Reza Elahi, Alessandro Cardoni, Cosimo Pellecchia, Marialetizia Buonfiglio, Federica Michela Rossi, Elena Federico, Fabio Pacciani, Gian Paolo Cimellaro*

**TS 9: GEOTECHNICAL ENGINEERING**

SENSITIVITY ANALYSIS FOR DERIVATION OF 1D VS PROFILES USING INVERSE QUARTER-WAVELENGTH THEORY ..... 4044
*Mehmet Ozışın, Zehra Cagnan*

EFFECT OF THE SOIL PILE STRUCTURE INTERACTION IN A DYNAMIC ANALYSIS CONSIDERING A LINEAR BEHAVIOR ..... 4055
*Amar Alyaman, Fernando Lopez Caballero, Daniel Dias, Hussein Mroueh, Marwan Sadek, Eric Antoinet*

INVESTIGATING THE SOIL STRESS LEVELS FOR DIFFERENT PILE GEOMETRIES UNDER DIFFERENT LOADING CONFIGURATIONS ..... 4066
*Daniel Rademan, George Markou*

FRAGILITY CURVES FOR BRIDGES SUBJECTED TO THREE-DIMENSIONAL SEISMIC ENVIRONMENTS ..... 4095
*Jimena Rosas, Juan Manuel Mayoral, Mauricio Anaya*

EVALUATION OF SEISMIC SITE EFFECTS IN A REAL SLOPE THROUGH 2D FE NUMERICAL ANALYSES ..... 4110
*Annamaria di Lernia, Carmela Buono, Gaetano Elia*

MODELLING OF RIGID INCLUSIONS REINFORCED FOUNDATIONS TO INVESTIGATE THE FAILURE ENVELOPE IN THE V-M-H SPACE ..... 4125
*Ramon Alcala-Ochoa, Zheng Li, Panagiotis Kotronis, Giulio Sciarra*

FRAGILITY CURVES FOR A SMALL ZONED EARTH DAM ..... 4133
*Mariagrazia Tretola, Stefania Sica*

EFFECT OF SOIL-STRUCTURE INTERACTION ON THE DYNAMIC IDENTIFICATION OF A PRESTRESSED CONCRETE BRIDGE ..... 4144
*Antonella Ambrosino, Alessandra De Angelis, Maria Rosaria Pecce, Stefania Sica*

SHEAR RATE EFFECT ON GRAIN CRUSHING OF SANDS. A LABORATORY STUDY BY THE BROOMHEAD APPARATUS ..... 4156
*Petros Sidiropoulos, Constantinos A. Stamatopoulos, Vassilis P. Panoskaltsis*

MULTISCALE MODELING OF COUPLED THERMO-HYDRO-MECHANICAL ANALYSIS OF HETEROGENEOUS POROUS MEDIA WITH MICRO-DYNAMIC EFFECTS ..... 4174
*Amir R. Khoei, Saeed Saeedmonir*

MODEL CALIBRATION AND NONLINEAR SITE RESPONSE ANALYSIS FOR MEDIUM COMPACTED SATURATED VOLCANIC SAND ..... 4189
*Seyed Javad Fattahi, Yaser Jafarian, Maria Konstadinou, Elin asta Olafsdottir, Sigurdur Erlingsson, Bjarni Bessason, Rajesh Rupakhety*

PRELIMINARY STUDY FOR SEISMIC ASSESSMENT OF THE UNDERGROUND FACILITIES AT POINT 5 OF THE LARGE HADRON COLLIDER (LHC) AT CERN ..... 4197
*Ugo Carmando, Ahmed Mubarak, Antonio Bilotta, Emilio Bilotta, Jonathan Knappett, Saverio La Mendola, Martin Gastal, Pieter Mattelaer, Luca Sironi, Davide Merlini, Matteo Falanesca, Gianluca Bella, Filippo Gianelli, Marco Andreini*

**TS 10: IMPACT DYNAMICS**

DYNAMIC RESPONSE OF TREES SUBJECT TO A LANDSLIDE-INDUCED AIR BLAST: IMPLICATIONS FOR AIR BLAST RISK ASSESSMENTS ..... 4206
*Yu Zhuang, Perry Bartelt, Aiguo Xing, Alexander Bast*

**TS 11: INVERSE PROBLEMS IN STRUCTURAL DYNAMICS**

A NEW PHYSICS-GUIDED DATA ASSIMILATION FRAMEWORK FOR ONLINE STRUCTURAL MONITORING: APPLICATION TO SHAKING-TABLE TESTS ..... 4217
*Matthieu Diaz, Pierre-Etienne Charbonnel, Ludovic Chamoin*

OPTIMISED STRUCTURAL MODELLING FOR INVERSE ANALYSIS PARAMETER IDENTIFICATION RELYING ON DYNAMIC MEASUREMENTS ..... 4234
*Aram Cornaggia, Tomasz Garbowski, Giuseppe Cocchetti, Rosalba Ferrari, Egidio Rizzi*

INVERSE ANALYSIS INVESTIGATION BY GAUSSIAN PROCESSES OPTIMISATION OF A HISTORICAL CONCRETE BRIDGE RELYING ON DYNAMIC MODAL MEASUREMENTS ..... 4249
*Tomasz Garbowski, Giuseppe Cocchetti, Aram Cornaggia, Rosalba Ferrari, Egidio Rizzi*

**TS 13: NONLINEAR DYNAMICS**

SENSITIVITY TO DAMPING IN NONLINEAR DYNAMIC ANALYSIS ..... 4265
*Terje Haukaas*

GROUND MOTION PROCESSING IN ROCKING STRUCTURES ..... 4286
*Medhat Elmorsy, Michalis F. Vassiliou*

EQUAL DISPLACEMENT CONCEPT FOR INELASTIC ANALYSIS OF STRUCTURES ..... 4299
*Johnn P. Judd*

STEADY-STATE RESPONSE OF A HIGH-STRENGTH MOMENT-RESISTING STEEL FRAME-SELF-CENTERING STEEL PLATE SHEAR WALL SYSTEM ..... 4306
*Chuandong Xie, Xiantie Wang, George Vasdravellis*

THE SEISMIC RESPONSE OF MIXED REINFORCED CONCRETE–STEEL LOW-RISE BUILDINGS UNDER NEAR-FAULT EARTHQUAKES ..... 4319
*Paraskevi K. Askouni, George A. Papagiannopoulos*

INVESTIGATION OF THE SEISMIC BEHAVIOR OF BUILDINGS WITH U-BOOT SLABS ..... 4329
*Denise-Penelope N. Kontoni, Ali Ghamari, Mojtaba Noorollahi*

**TS 14: NUMERICAL SIMULATION METHODS FOR DYNAMIC PROBLEMS**

A NEW MULTISCALE STEEL-CONCRETE BOND MODEL FOR STRUCTURAL DYNAMICS APPLICATIONS …… 4339
*Maryam Trad, Ibrahim Bitar, Stéphane Grange, Benjamin Richard*

WAVE FINITE ELEMENT METHOD FOR THE DYNAMICS OF STRUCTURES WITH CYCLIC SYMMETRY …… 4353
*Tien Hoang, Denis Duhamel, Gilles Foret, Le-Hung Tran*

COMPUTATION OF THE RESPONSE OF DAMAGED RAILWAY TRACKS SUBJECTED TO CONSTANT MOVING LOADS: NUMERICAL RESULTS OBTAINED WITH THE WAVE FINITE ELEMENT METHOD AND AN ANALYTICAL RESULTS …. 4362
*Benjamin Claudet, Denis Duhamel, Gilles Foret, Tien Hoang, Francis Sabatier, Bertrand Findinier, Hervé Lenglin*

TEST OF AN IDEA FOR SETTING THE NONLINEARITY TOLERANCE IN NONLINEAR RESPONSE HISTORY ANALYSES ACCORDING TO PROCEDURES ORIGINATED IN THE SEISMIC CODE OF NEW ZEALAND NZS 1170.5:2004 …… 4375
*Aram Soroushian*

ML-BASED PUNCHING STRENGTH ESTIMATIONS OF FLAT SLABS WITHOUT TRANSVERSE REINFORCEMENT UNDER LATERAL LOADING …… 4391
*Hadi Panahi, Aikaterini Genikomsou*

SEMI-ANALYTICAL CHARACTERIZATION OF A SLOSHING FLUID MASS WITH THE SMOOTHED PARTICLE HYDRODYNAMIC BASED METHOD …… 4402
*Giorgia C. Goursand-Parente, Bonaventura Tagliafierro, Salvatore Capasso, Alejandro Crespo, Giacomo Viccione*

SEISMIC NUMERICAL MODELLING OF ELECTRICAL CABINETS …… 4416
*Derek Rodriguez, Simone Peloso, Emanuele Brunesi, Daniele Perrone, Andre Filiatrault*

INVESTIGATING THE IMPACT OF POROSITY DISTRIBUTION AND GRADING PARAMETER ON THE FREE VIBRATION OF FUNCTIONALLY GRADED BEAMS …… 4427
*Lazreg Hadji, Vagelis Plevris, Royal Madan*

RAILWAY TRACK STRUCTURAL DYNAMICS VIA PERIODIC APPROACHES …… 4439
*Angie C. Lamprea-Pineda, Alexandre Castanheira-Pinto, Pedro Alves Costa, Peter K. Woodward, Mohammed F.M. Hussein, David P. Connolly*

NUMERICAL INVESTIGATION ON STABILITY OF COLUMNS UNDER DYNAMIC LOADS WITH TWO FREQUENCIES …4451
*Jian Deng*

THE EVAULATION OF THE OPTIMAL COLLISION CONDITIONS BETWEEN FOLDED PAPER STRUCTURES …… 4463
*Gyehee Lee*

A NOVEL FINITE ELEMENT FORMULATION FOR THE DYNAMIC ANALYSIS OF DAMPED EULER-BERNOULLI BEAMS UNDER MOVING LOADS …… 4471
*Hugo A.F.A. Santos*

EXPLORATION OF DYNAMIC LOADING STRUCTURAL TOPOLOGY OPTIMIZATION AND APPLICATION TO BUILDING LATERAL LOAD RESISTING FRAME ..... 4484
*Arya Prakash Padhi, Vaibhav Bhandari, Anupam Chakrabarti, Rajib Chowdhury*

COMPARISON OF POD-UDEIM AND POD-ECSW MODEL ORDER REDUCTION IN THE CASE OF DAMAGING RC STRUCTURES SUBJECTED TO EARTHQUAKES ..... 4492
*Bastien Bodnar, Walid Larbi, Magdalini Titirla, Jean-François Deü, Fabrice Gatuingt, Frédéric Ragueneau*

FINITE ELEMENT MODELLING OF SUSPENDED CEILING SYSTEMS BASED ON EXTENSIVE COMPONENT TESTING AND MODEL EVALUATION VIA SHAKING TABLE TESTS: POP RIVET AND SEISMIC CLIP PERIMETER CONNECTIONS ..... 4511
*Shakhzod M. Takhirov, Yelena Straight*

PARAMETRIC ANALYSIS AND REDUCED ORDER MODEL OF RESULTING WIND LOADING ON STRUCTURAL COMPONENTS THROUGH CFD SIMULATIONS ..... 4523
*Sotiria Stefanidou, Olga Markogiannaki, Elias Paraskevopoulos*

DAMAGE ASSESSMENT OF CLASSICAL MONUMENTS USING NONLINEAR DYNAMIC SIMULATIONS ..... 4532
*Konstantina Mastrodimou, Vasliki Kalogerakou, Vicky Dimakopoulou, Michalis Fragiadakis*

**TS 15: OPTIMUM DESIGN AND CONTROL**

SEISMIC PROTECTION OF NON-STRUCTURAL ELEMENTS IN RC BUILDINGS ..... 4550
*Saraswati Setia, Gurkirat Singh*

CONTROL OF STRUCTURES SUBJECTED TO DYNAMIC LOADS USING MAGNETORHEOLOGICAL DAMPERS ..... 4560
*Verónica Valencia-Valencia, Mariana Castro-Osorio, Daniela Vallejo-Paniagua, Sebastián Echavarría-Montaña, Luis A. Lara-Valencia*

CONTROL OF THE STRUCTURAL RESPONSE OF A HIGH-RISE BUILDING UNDER WIND LOAD USING A TUNED MASS DAMPER INERTER (TMDI) ..... 4575
*Daniela Vallejo-Paniagua, Mariana Castro-Osorio, Verónica Valencia-Valencia, Luis A. Lara-Valencia, John J. Blandón-Valencia*

OPTIMAL DESIGN OF A TUNED MASS DAMPER INERTER USING A WHALE OPTIMIZATION ALGORITHM FOR THE CONTROL OF BUILDINGS SUBJECTED TO GROUND ACCELERATION ..... 4590
*Mariana Castro-Osorio, Daniela Vallejo-Paniagua, Verónica Valencia-Valencia, Luis A. Lara-Valencia, John J. Blandón-Valencia*

VARIATION STUDY OF THE CONSTRUCTION COST OF A 15-STORY R/C BUILDING BASED ON THE SEISMIC RISK ZONE ..... 4608
*Maria N. Kalaitzi, Theodoros A. Chrysanidis*

OPTIMAL PLACEMENT METHOD OF OUTRIGGER WITH BRB IN A CORE WALL SYSTEM STRUCTURE ..... 4624
*Hamid Nikzad, Shinta Yoshitomi*

INDOOR TRACKING USING UNMANNED AERIAL VEHICLES ..... 4632
*Alessandro Cardoni, Raffaele Tarantini, Gian Paolo Cimellaro*

**TS 17: PERFORMANCE-BASED EARTHQUAKE ENGINEERING**

NUMERICAL INVESTIGATIONS ON DYNAMIC BEHAVIOUR OF LUMPED MASS MODEL OF NON-STRUCTURAL ELEMENTS AND 3D RC BUILDINGS ..... 4641
*S. Saranya, Palissery Sunitha*

INVESTIGATING THE EFFICIENCY AND THE SUFFICIENCY OF IMS FOR THE PROBABILISTIC SEISMIC ASSESSMENT OF THE POUNDING EFFECT BETWEEN ADJACENT RC STRUCTURES ..... 4655
*Maria G. Flenga, Maria J. Favvata*

INFLUENCE OF BOND-SLIP ON NUMERICAL FRAGILITY CURVES AND STRUCTURAL RELIABILITY OF RC STRUCTURAL INTERNAL BEAM-COLUMN SUB-ASSEMBLY ..... 4673
*Lorenzo Audisio, Michele D'Amato, Rosario Gigliotti*

NUMERICAL SEISMIC PERFORMANCE INVESTIGATION OF AAC INFILL WALLS WITH FLAT-TRUSS BED-JOINT REINFORCEMENT ..... 4683
*Ömer Faruk Halici, Alper Ilki*

DAMPING ASSESSMENT OF BRIDGES FOR PERFORMANCE BASE DESIGN ..... 4693
*Juan Manuel Mayoral, Mauricio Pérez*

IMPACT OF EARTHQUAKES VS. HEAT WAVES ON THE SOCIO-ECONOMIC LOSSES OF BUILDINGS ..... 4706
*Simona Bianchi, Jonathan Ciurlanti, Alessandra Luna Navarro, Eleonora Brembilla*

PROBABILISTIC SEISMIC DEMAND MODELS FOR THE ASSESSMENT OF UNDERGROUND STRUCTURES ..... 4719
*Grigorios Tsinidis, Anna Karatzetzou, Sotiria Stefanidou*

**TS 19: REPAIR AND RETROFIT OF STRUCTURES**

INELASTIC TIME-HISTORY ANALYSES OF FRP-RETROFITTED BRIDGE COLUMNS SUBJECTED TO NEAR-FIELD GROUND MOTIONS ..... 4727
*Konstantinos G. Megalooikonomou*

NUMERICAL INVESTIGATION OF RETROFITTING WAFFLE SLABS WITH CARBON FIBRE REINFORCED POLYMER PLATES ..... 4738
*Michael Jung, George Markou*

SEISMIC RESPONSE ASSESSMENT OF AN EXISTING RC STRUCTURE RETROFITTED WITH STEEL EXOSKELETONS ...4748
*Francesco Nigro, Gaetano Della Corte, Enzo Martinelli*

SEISMIC ASSESSMENT AND STRENGTHENING OF THE REMAINING BEIRUT PORT SILOS DAMAGED AFTER THE 2020 AUGUST BLAST- A CASE STUDY ..... 4761
*Sahar Ismail, Wassim Raphael, Fouad Kaddah*

THE CHURCH OF SANTA MARIA DELLE GRAZIE AL CALCINAIO: FROM DIAGNOSTIC STUDIES TO ARCHITECTURAL AND STRUCTURAL REHABILITATION PROJECT ..... 4772
*Michelangelo Micheloni, Anna Livia Ciuffreda, Gabriela Simoni, Federico Salvini*

SEISMIC UPGRADING OF TELECOMMUNICATION CENTER IN SKOPJE, NORTH MACEDONIA ..... 4788
*Veronika Shendova, Aleksandar Zurovski, A. Zlateski, E. Delova, G. Jekic, Roberta Apostolska, Z. Bozinovski*

SYNTHETIC DATA GENERATION FOR THE CREATION OF BRIDGE DIGITAL TWINS WHAT-IF SCENARIOS ..... 4801
*Alejandro Jiménez Rios, Vagelis Plevris, Maria Nogal*

RETROFITTING DAMAGED BUILDINGS UNDER SEISMIC MAINSHOCK-AFTERSHOCK SEQUENCE ..... 4810
*Benyamin Mohebi, Farzin Kazemi, Neda Asgarkhani*

**TS 20: SEISMIC ISOLATION**

VARIANTS OF VIBRO-ISOLATION IN TRAM TRACKS AND EVALUATION OF THEIR EFFECTIVENESS ENGINEERING 4817
*Filip Pachla, Piotr Stecz, Tadeusz Tatara*

DEVELOPMENT OF A COMPLIANT MECHANISM TO ISOLATE THE BASE VIBRATIONS AND MINIMIZE THE SHOCK RESPONSE USING AN OPTIMIZED DYNAMIC MATHEMATICAL MODEL ..... 4825
*Kazım Yüksel, Ata Muğan*

NONLINEAR FINITE ELEMENT MODELING OF PRESTRESSED LEAD EXTRUSION DAMPERS ..... 4839
*Furkan Çalım, Ahmet Güllü, Cihan Soydan, Ercan Yüksel*

EFFECTS OF FAR FAULT EARTHQUAKES IN RETROFITTED SEISMICALLY ISOLATED BUILDING ..... 4847
*Antonello Salvatori*

**TS 24: SOIL-STRUCTURE INTERACTION**

THE LATERAL CAPACITY OF CONCRETE PILES IN STIFF CLAY TO DENSE SAND ..... 4870
*Mina Mikaeel, Andrew G. Gouda*

SEISMIC ANALYSIS FOR BUILDING STRUCTURES UNDER DYNAMIC SOIL-PILE INTERACTION USING SIMPLIFIED MODELS ..... 4888
*Jun-Yang Shi*

COUPLING OF THE ANALYTICAL SOLUTION FOR THE TIMOSHENKO BEAM WITH A FULLY SATURATED HALFSPACE BY APPLICATION OF THE WAVE BASED METHOD ..... 4896
*Mirjam Lainer, Gerhard Müller*

A 2D MACRO-ELEMENT FOR EFFICIENT NONLINEAR ANALYSIS OF PILE FOUNDATIONS UNDER SEISMIC LOADING ..... 4909
*Thomas Lhermitte, Florent Prunier, David Bertrand, Stéphane Grange, Pierre Wyniecki, Evan Monroig, Thomas Jochyms*

CROSS INTERACTION FOR A SMALL GROUP OF SHALLOW FOUNDATIONS ..... 4922
*Enza Zeolla, Filomena de Silva, Stefania Sica*

APPLICABILITY OF GYRO-LUMPED PARAMETER MODEL IN IDENTIFYING HORIZONTAL IMPEDANCE FUNCTIONS OF PILE GROUPS ..... 4930
*Masato Saitoh*

SCALING AND MODELING OF AN IMPACT PILE DRIVING 1G LABORATORY SCALE TEST ..... 4940
*Tamara Wehbe, George Anoyatis, Hadrien Rattez, Stijn François*

**TS 25: SOLUTION STRATEGIES FOR DYNAMIC PROBLEMS**

OPERATIONAL MODAL ANALYSIS OF NON-REDUNDANT WOOD FRAME BUILDING ..... 4948
*Dipendra Gautam, Simon Olafsson, Rajesh Rupakhety*

MODULAR DEPLOYMENT OF MICROPROCESSOR-CONTROLLED DATA ACQUISITION AND CONTROL WITHIN A DIGITAL TWIN ..... 4960
*Matthew Bonney, Matthew Tipuric, David Wagg, Ian Stothers*

THE DYNAMIC PROBLEM OF AN ELASTICALLY SUPPORTED BEAM ANALYSIS USING NEURAL ARCHITECTURE SEARCH WITH AUTOMATIC DIFFERENTIATION ..... 4972
*Konstantinos S. Demertzis, Konstantinos E. Morfidis, Konstantinos G. Kostinakis, Lazaros S. Iliadis*

MATRIX EQUATIONS MODELS FOR SOLVING THE DYNAMIC RESPONSE OF INELASTIC CANTILEVER STRUCTURES ..... 4987
*Assaf Shmerling*

**TS 26: SOUND AND VIBRATION**

ACTIVE NOISE CONTROL OF AIR CONDITIONING SYSTEM NOISE ..... 4997
*Orhun Okcu, Kanghyun An, Sang-Kwon Lee*

EFFECT OF DEEP FOUNDATION ELEMENTS ON TRANSFER MOBILITIES FOR GROUND-BORNE VIBRATIONS IN URBAN RAILWAY TUNNELS ..... 5003
*Theodora Makrypidi, Charisis Chatzigogos, Stefania Gobbi, Pierre-Alain Nazé*

CASE STUDY APPLICATIONS OF PERFECTLY MATCHED LAYERS IMPLEMENTED IN THE ANALYSIS OF VIBRATIONS INDUCED BY TRAIN PASSING ..... 5017
*Aleksandar Zhelyazkov, Hanno Töll, Dieter Pichler*

MODAL CHARACTERIZATION AND ROAD ROUGHNESS RECONSTRUCTION USING DYNAMIC VEHICLE ACCELERATIONS AND ANNS ..... 5034
*Kais Douier, Mohammed F. M. Hussein, Jamil Renno*

**TS 27: STEEL STRUCTURES**

MECHANICAL-BASED SEISMIC VULNERABILITY ANALYSIS OF INDUSTRIAL STEEL STRUCTURES WITH MASONRY INFILLS ..... 5041
*Francesco Salvatore Liguori, Antonio Madeo, Antonio Formisano*

NUMERICAL ANALYSIS ON A REVERSIBLE CONNECTION FOR STEEL MODULAR BUILDINGS ..... 5056
*Annarita Palmiotta, Michele D'Amato, Rosario Gigliotti*

SEISMIC EFFECT ON THE MICADO STRUCTURAL SOLUTION. A NUMERICAL ANALYSIS ..... 5066
*Ali Dalalbashi, Jorge Pinto, Cristina Reis, F. Pimenta, N. Oliveira Ferreira, N. Bento Pereira*

SEISMIC PERFORMANCE OF SPECIAL STEEL MOMENT FRAMES USING DETAILED VS SIMPLE HYSTERIC CURVES ..... 5074
*Emilia Clavijo, Jorge Molina, Nicolas Coello, Xavier Vintimilla, Francisco Flores, Pablo Quinde*

INELASTIC TORSIONAL BUCKLING OF A SYMMETRIC THREE-DIMENSIONAL MOMENT-RESISTING FRAME SUBJECTED TO HORIZONTAL FORCE IN THE DIAGONAL DIRECTION ..... 5089
*Iori Fukuda, Kohju Ikago, Takahito Maeda, Atsushi Nishimoto, Yoshikazu Araki*

ADVANCED OPTIMIZATION PROCESSES FOR THE DESIGN OF 3D-PRINTED METAL DAMPERS ..... 5102
*Francesca Romana Andreacola, Giuseppe Brando*

IMPROVING THE PERFORMANCE OF I-SHAPED DAMPERS USING STIFFENERS ..... 5110
*Ahmad Jabbar Hussain Alshimmeri, Denise-Penelope N. Kontoni, Ali Ghamari*

DEVELOPMENT OF A SIMPLIFIED BEAM MODEL FOR TUBULAR JOINTS IN JACKET STRUCTURES ..... 5120
*Antonio Sindoni, Amirali Sadeqi, Jens Henrik Nielsen, Evangelos Katsanos*

**TS 28: STOCHASTIC DYNAMICS**

ESTIMATION OF THE DYNAMIC SEISMIC RESPONSE OF BUILDINGS THROUGH TRANSFER FUNCTIONS. A PROBABILISTIC APPROACH ..... 5131
*Rodolfo Javier Tirado-Gutiérrez, Yeudy Felipe Vargas-Alzate, Ramón González-Drigo, Ana Maria Zapata-Franco*

STOCHASTIC GENERATION OF ARTIFICIAL ACCELEROGRAMS USING THE CONTINUOUS WAVELET TRANSFORM METHOD ..... 5143
*Hera Yanni, Michalis Fragiadakis, Ioannis P. Mitseas*

**TS 30: WAVE PROPAGATION**

EFFECT OF DEBONDING ON GUIDED WAVE PROPAGATION IN STIFFENED COMPOSITE PLATE UNDER OPERATIONAL LOADING AND HYGROTHERMAL ENVIRONMENT ..... 5155
*Akshay Prakash Kalgutkar, Sauvik Banerjee*

**TS 31: SEISMIC RISK AND DAMAGE ASSESSMENT**

A MODEL FOR THE STRUCTURAL AND SEISMIC ASSESSMENT OF THE MOSQUE-CATHEDRAL OF CORDOBA ..... 5179
*Maria-Victoria Requena-Garcia-Cruz, Emilio Romero-Sánchez, Antonio Morales-Esteban, N. Fernández-Pérez*

SEISMIC ASSESSMENT OF HISTORICAL COMPLEX TOWERS. THE CASE STUDY OF THE GIRALDA TOWER ..... 5191
*Emilio Romero-Sánchez, María-Victoria Requena-Garcia-Cruz, Antonio Morales-Esteban*

ESTIMATION OF SEISMIC DESIGN FACTORS FOR RC-SMRF BUILDINGS IN SEISMIC RISK FRAMEWORK ..... 5202
*Suman Banerjee, Devendra Singh, Saurabh Shiradhonkar*

SEISMIC VULNERABILITY ASSESSMENT OF CONCRETE BLOCK CONFIGURATIONS FOR RADIATION SHIELDING .... 5218
*Luca Sironi, Marco Andreini, Ziran Zhou, José Andrade, Pierino Lestuzzi, Edward Andò, Frédéric Dubois, Filippo Dacarro, Davide Bolognini*

SEISMIC FRAGILITY AND EXPECTED DAMAGE OF MASONRY SCHOOL BUILDINGS IN ITALY ..... 5229
*Elisa Saler, Francesca da Porto*

TYPOLOGICAL FRAGILITY ASSESSMENT OF PRESTRESSED CONCRETE GIRDER BRIDGES SUBJECTED TO TRAFFIC LOADS AFFECTED BY CORROSION ..... 5242
*Alessandro Nettis, Andrea Nettis, Sergio Ruggieri, Giuseppina Uva*

REDUCED ORDER MODELS TO ESTIMATE SEISMIC RISK OF UNREINFORCED MASONRY DWELLINGS ..... 5258
*Ana Maria Zapata-Franco, Yeudy Felipe Vargas-Alzate, José Ramón Gonzalez-Drigo, Rodolfo Javier Tirado-Gutiérrez*

THE CHALLENGES AND ADVANTAGES OF MACRO MODELING IN ANSYS SOFTWARE FOR SEISMIC VULNERABILITY ASSESSMENT OF HISTORIC MASONRY STRUCTURES ..... 5273
*Hatice Ayşegül Deir, Kutay Yücetürk, Engin Aktaş, Mine Hamamcıoğlu-Turan*

PERFORMANCE EVALUATION OF A MASONRY ARCH BRIDGE UNDER COMBINED SCOUR AND TRAFFIC LOADING ..... 5288
*Prateek Kumar Dhir, Daniele Losanno, Fabrizio Scozzese, Enrico Tubaldi, Fulvio Parisi*

EARTHQUAKE NATECH RISK: NUMERICAL ANALYSIS OF FLOATING ROOF AND SEALING SYSTEM IN CYLINDRICAL STORAGE TANKS ..... 5300
*Michela Salimbeni, Maurizio De Angelis, Mariano Ciucci*

ANALYTICAL ASSESSMENT OF SEISMIC DAMAGE AND USABILITY OF RC RESIDENTIAL BUILDINGS BY PERIOD ELONGATION ..... 5314
*Mariano Di Domenico, Paolo Ricci, Gerardo M. Verderame*

METRICS FOR EVALUATING THE SEISMIC VULNERABILITY OF TELECOMMUNICATION NETWORKS ..... 5324
*Alessandro Cardoni, Gian Paolo Cimellaro*

A CAT BOND-BASED SOLUTION FOR SEISMIC RISK TRANSFER IN ITALY ..... 5334
*Lorenzo Hofer, Mariano Angelo Zanini, Paolo Gardoni*

SEISMIC RISK ANALSYSIS OF DISTRIBUTION LINEAR INFRASTRUCTURES ..... 5345

*Mariano Angelo Zanini, Chiara Vianello, Flora Faleschini, Lorenzo Hofer, Carlo Pellegrino, Giuseppe Maschio*

SEISMIC VULNERABILITY ASSESSMENT OF AN URBAN NATURAL GAS NETWORK …… 5354
*Alessandro Cardoni, Sebastiano Marasco, Gian Paolo Cimellaro*

A NEW METHODOLOGY FOR COMBINED SEISMIC AND ENERGY ASSESSMENT OF BUILDINGS …… 5362
*Sotiria Stefanidou, Olga Markogiannaki, Anna Karatzetzou, Charoula Zaki, Anna Diamanti*

**TS 32: SEISMIC RELIABILITY ANALYSIS**

RELIABILITY ANALYSIS OF EMBEDDED BASE CONNECTIONS …… 5376
*Pablo Torres-Rodas, Fernando Gomez*

COMPDYN 2023
9th ECCOMAS Thematic Conference on
Computational Methods in Structural Dynamics and Earthquake Engineering
M. Papadrakakis, M. Fragiadakis (eds.)
Athens, Greece, 12-14 June 2023

# EMPIRICAL MULTI-VARIABLE TSUNAMI DAMAGE MODELS BASED ON THE 2011 GREAT EAST JAPAN DATASET: ANALYSIS OF THE PERFORMANCES AT DIFFERENT SPATIAL SCALES

**Mario Di Bacco[1,2], Anna Rita Scorzini[1], and Anawat Suppasri[3]**

[1] Department of Civil, Environmental and Architectural Engineering, University of L'Aquila, L'Aquila, Via G. Gronchi, 18, 67100 L'Aquila, Italy
annarita.scorzini@univaq.it

[2] Department of Civil and Environmental Engineering, University of Florence, Florence, Via S. Marta 3, 50139 Florence, Italy
mario.dibacco@unifi.it

[3] International Research Institute of Disaster Science, Tōhoku University
468-1 Aoba, Aramaki, Aoba-ku, Sendai, Miyagi, Japan
suppasri@irides.tohoku.ac.jp

## Abstract

*By implementing data-driven models for the 2011 Great East Japan earthquake and tsunami, the present study aims at investigating the effect of the level of spatial aggregation of the data on model's predictive ability and at identifying the possible existence of regional-dependent patterns affecting model's accuracy and feature importance. An extended version of the dataset compiled by the Japanese Ministry of Land, Infrastructure and Transportation (MLIT) after the 2011 event in the Tōhoku region was used to generate sub datasets at different spatial scales, ranging from individual cities of different sizes to clusters at regional and multi-regional levels. The results indicate a high variance in the accuracy for the models trained on the different subsets, with relative hit rates ranging from 0.68 to 0.89 and exhibiting a positive correlation with the cardinality of the sets, as well as some regional patterns in the prediction errors. The cluster-averaged feature importance is observed to be stable for all selections and reflects the results obtained from the models trained on the whole dataset, thus allowing a more informed identification of the most significant influencing factors for tsunami damage modelling.*

**Keywords:** Tsunami damage, Building vulnerability, Feature importance, Machine learning, Tōhoku tsunami.

# 1 INTRODUCTION

Fragility curves, expressing the probability of exceeding a certain damage state as a function of the features describing the hazard source and the vulnerability of the exposed objects, are the standard tools used for tsunami risk assessment. While the hazard component is generally represented by inundation depth and flow velocity (or a combination of the two), building vulnerability depends on several factors, including not only the structural and geometrical properties of the individual buildings, but also the characteristics of the surrounding environment. In particular, as regards the last aspect, coastal topography and the mutual interactions among neighboring buildings have been described to have a relevant influence on the damage mechanisms, thus making vulnerability modelling a rather complex task [1-3].

Although machine learning, data-driven models could be considered as a suitable option for tackling such complexity [4], the first applications of these approaches for empirical tsunami damage modelling are only very recent, as shown in Saengtabtim et al. [5], who developed tree-based algorithms, with only inundation depth and flow velocity as descriptive features, to study tsunami damage data for a portion (18.000 buildings in Ishinomaki city) of the dataset (containing about 250.000 damage observations) published by the Japanese Ministry of Land, Infrastructure and Transportation after the 2011 Great East Japan event in the Tōhoku region (MLIT [6]). Even more recently, Di Bacco et al. [7] integrated the MLIT dataset with additional features by including explanatory variables that are usually neglected in traditional tsunami damage models. These include building-related (i.e., shape factors) or site-related geometric parameters, calculated as a function of building position and orientation with respect to the coastline, and accounting also for the effect of the reciprocal interaction between buildings and/or singular structures, in terms of two possible opposite mechanisms: (i) a "shielding effect" generated by interacting buildings or barriers (e.g., seawalls), which may reduce water impact, and a (ii) "debris generation effect" caused by collapsed buildings that can act as an additional source of hazard.

In addition, by testing the performances of machine learning models trained with different combinations of input features, Di Bacco et al. [7] pointed out the importance of considering these mutual interactions among buildings and they suggested the implementation of more specific local models to avoid a drop in accuracy when transferring models from a region to another. By implementing data-driven ensemble decision trees on subsets of the enhanced MLIT database at different spatial scales, ranging from individual cities of different sizes to clusters at regional and multi-regional levels, this study then aims at investigating:

- the effect of the level of spatial aggregation (i.e., the cardinality of the dataset) on model's predictive ability and
- the possible existence of regional-dependent patterns in model's accuracy on unseen data and in the ranking of the feature importance on tsunami damage.

# 2 MATERIALS AND METHODS

## 2.1 The extended MLIT dataset

The present study leveraged the spatial database compiled by the Japanese Ministry of Land, Infrastructure and Transportation (MLIT [6]) for about 250.000 buildings affected by the 2011 Tōhoku tsunami. In its original form, this dataset consisted of a polygon shapefile containing building scale information on observed damage ((Damage) distinguished in 7 classes: from "no damage" (class 1) to "washed away" (class 7)) and on other associated hazard and vulnerability factors, as follows: inundation depth at the building location (h) and other possible concurrent hazard factors (OthHaz) (e.g., earthquake, fire, liquefaction), structural

type (BS) (i.e., construction material) and number of floors (NF) of the building, its intended use (Use), and year of construction (Year) [8-11]. Di Bacco et al. [7] enriched this dataset by adding other variables, calculated by means of a geospatial analysis, to account for other possible damage explicative factors, which included:

- Building geometry, in terms of extension and shape: footprint area (FA) and compactness of building shape (DegComp);
- Coast-related parameters, indicating the distance between the building and the shoreline (Distance), the direction of tsunami wave attack (WDir) and a binary factor (CoastType) for distinguishing between plain and ria types of coast over the impacted region;
- Synthetic parameters describing the shielding (ShArea, ShVol, SW) and debris generation (DIArea, DIVol) mechanisms of potentially interacting elements (i.e., buildings and/or seawalls) within defined buffer areas created around each building. Di Bacco et al. [7], while recognizing the importance of including such factors in tsunami damage predictions, demonstrated that the choice between the two proposed buffer geometries (denoted as "large" (L) and "narrow" (N) in the original study) implied only slight differences in the prediction accuracy. Moreover, proposed areal and volumetric parameters were characterized by a high cross-correlation and therefore, for the sake of conciseness, in the present study, we considered only the volumetric ones calculated on "large" buffers (i.e., LShVol, LDIVol and LSW).

## 2.2 Data handling: spatial clustering and implemented machine-learning algorithm

In this study, the subsets of the extended MLIT database were generated by selecting eight of the most impacted cities (with more than 8.000 damaged buildings in each city) or by dividing the whole dataset into 3, 5, 7, and 9 clusters, identified by using K-means spatial clustering [12] based only on geographical coordinates of the data points (i.e., geographical clustering). Figure 1 shows the identified regions and cities considered in the analysis, with indication (in brackets) of the cardinality of each sub-dataset. Within each clusterization scheme (i.e., maximum number of considered clusters), the different sub-regions are numbered with decreasing cardinality.

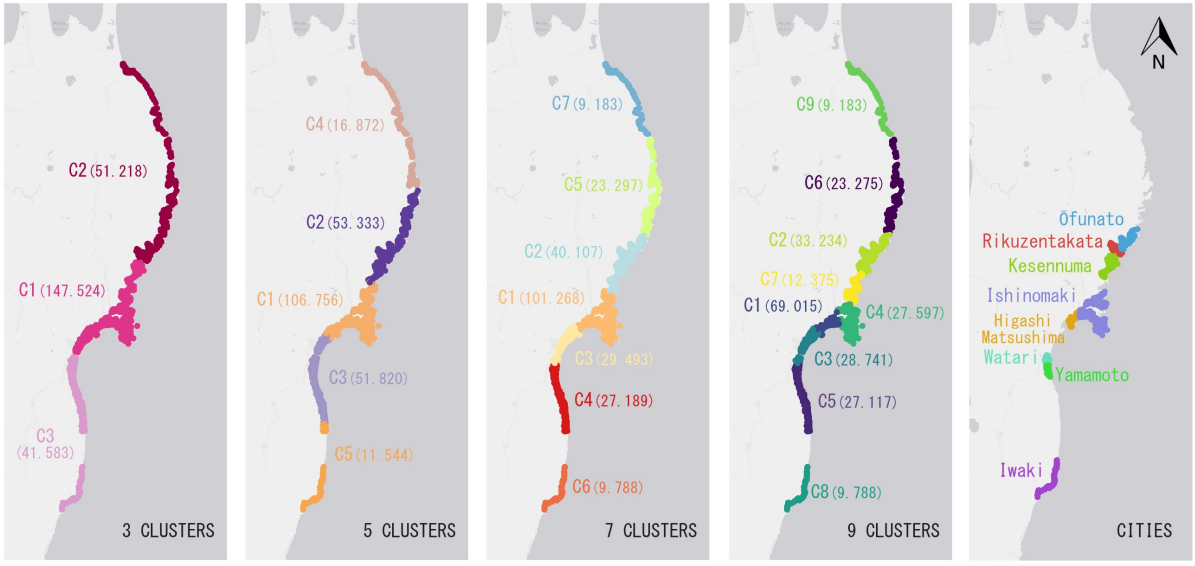


Figure 1: Identified clusters (the cardinality of the subsets is indicated in brackets) and selected cities over the impacted Tōhoku region.

For each sub-cluster, a tree-based ensemble model was set up to analyze the predictive accuracy and variable importance on tsunami damage across the different spatial domains. Among existing data-driven methods, Extremely Randomized Trees (or "Extra-Trees") [13] were chosen in this study because on the full extended MLIT dataset, they showed, as demonstrated in Di Bacco et al. [7], better performances compared to multi-layer perceptron networks, random forest and extreme gradient boosting algorithms. The rationale behind the Extra-Trees algorithm is to create a number of unpruned decision trees by randomizing attribute and splitting value selection, while a majority vote is used to combine the predictions of all trees to determine the final prediction, thus ensuring an excellent variance reduction effect.

Similarly to [7], the number of trees was here fixed at 130 and the splitting process was carried out by evaluating the drop in Gini impurity on random subsets containing 60% of the training items. The entries for each cluster dataset (Figure 1), with Damage as target output and all variables described in Section 1 as input features, were split into training and test sets in the proportion 95-5. The relative hit rate (HR), or the proportion of correct predictions over the total, was chosen as the metric for measuring the accuracy of the model; this metric was combined with the calculation of a normalized confusion matrix in order to have a deeper understanding of the error patterns.

Moreover, a permutation feature importance analysis was carried out to gain a deeper understanding on the possible variability of the feature importance on damage predictions across the different spatial clusters. This procedure consisted in assessing the mean decrease in model's accuracy when a single feature value is randomly shuffled [14], thus providing an indication of the drop in the predictive ability of the model when excluding each variable.

## 3 RESULTS AND DISCUSSION

### 3.1 Model's accuracy at different levels of spatial aggregation

Figure 2 reports the overall predictive accuracies (in terms of relative hit rate) obtained with the locally trained Extra-Trees algorithms for the different spatial clusters and cities displayed in Figure 1. The results indicate a high variance in the accuracy for the models trained on the different subsets of each selection, with hit rates ranging from 0.68 to 0.89 and exhibiting a positive correlation with the cardinality of the sets. Figure 2 also indicates that the subdivision of the dataset into a smaller number of clusters (i.e., larger size of the sub-datasets) tends to reduce the differences in the accuracies observed among the identified regions within each sub-group (the difference between maximum and minimum relative hit rate gradually increases from 0.06, 0.17, 0.18 and 0.20 when moving from a 3- to 9-clusterization).

Furthermore, a geographical pattern can be recognized for the models providing the worst relative hit rates (<0.75): in particular, these zones appear to be located at the northern (5.C4, 7.C7 and 9.C9) and southern (5.C5, 7.C6, 9.C8, with the last two almost overlapping with the Iwaki subset) extremes of the impacted region (Figures 1 and 2). The small differences (~1%) in the accuracy obtained for the couples 7.C7-9.C9 and 7.C6-9.C8, which contain exactly the same data, can be explained by the intrinsic randomization of the training process and shuffling of the dataset at the base of the implemented algorithm.

The abovementioned results are confirmed by the normalized confusion matrices represented in Figure 3, indicating the relative hit and misclassification rates among the different damage classes, obtained with the Extra-Trees models trained on the different clusters. For the sake of completeness, Figure 3 also shows, as a comparison means, the confusion matrix (displayed in larger size in the legend box) obtained by Di Bacco et al. [7] with the same model trained with the whole extended MLIT dataset (with an associated overall hit rate of 0.84).

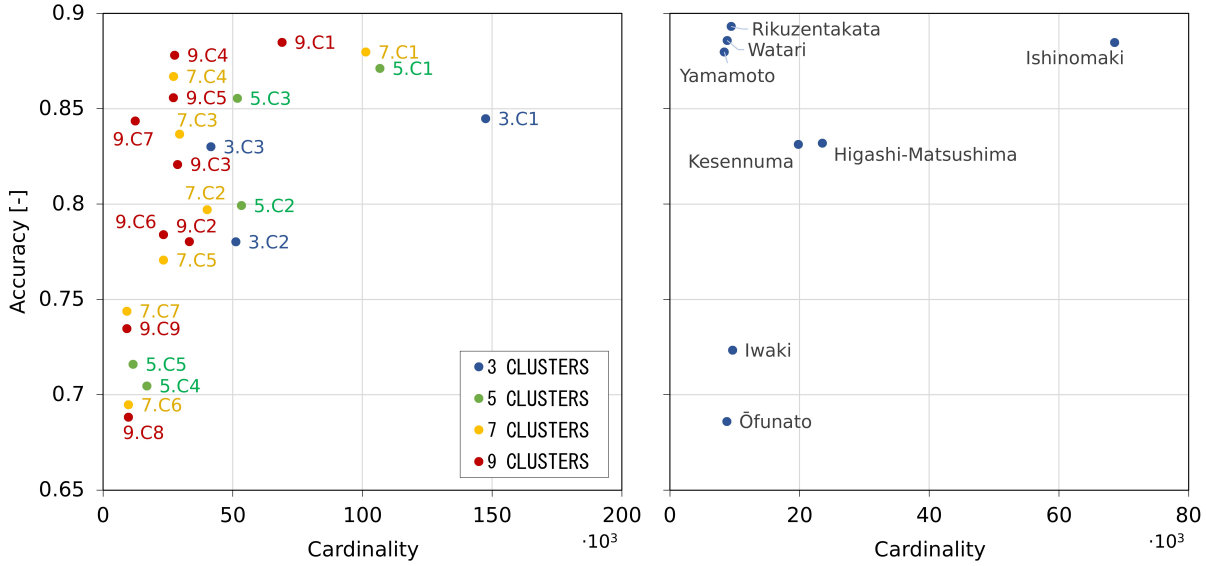


Figure 2: Models' accuracies (i.e., relative hit rate) for the models trained on the different clusters (Figure 1).

The matrices (ordered top-down with decreasing cardinality), while still revealing a dependency of models' performance on the size of the sub-sets, seem again to suggest the existence of local specificities that may significantly affect the predictive accuracy.

These local peculiarities may originate from uneven distributions of the damage classes within the sub-sets and/or from particular local relationships between damage and explicative factors that can make the predictions more complex, thus increasing the probability for misclassification. This clearly appears with a more in depth analysis of Figure 3 in combination with the empirical distributions of damage classes and inundation depth (recognized as the most important damage predictor in [7]) within the sub-sets, reported in Figure 4 for the "Cities" and "9" cluster areas as explicative cases.

For instance, if focusing on the confusion matrices for the discussed sub-sets of Iwaki (C.C4) and the northern 9.C8, it can be seen that most of the prediction error is due to a frequent misclassification of the intermediate damage levels 4 ("major damage"), 5 ("complete damage") and 6 ("collapse"). As clearly visible from the empirical distributions in Figure 4, both of these zones are almost totally covered by shallow water depths, which inherently bring larger uncertainty in damage estimation, because of the significant importance, in such conditions, of local vulnerability and hazard factors that may exacerbate damage variability [15-17]. Watari (C.C6) is also characterized by a large share of low water depths, but the model still provides one of the best accuracies (0.88), with most of the damage levels correctly predicted, if excluding only class 5 (represented in less than 1% of the C.C6 sub-set (Figure 4)), which is always mispredicted as class 6. The reason for these different behaviors can be attributed to other additional input features ("Distance" in the specific case of Watari) that can locally play an important role in reducing uncertainty at the scale of individual clusters.

Particular is the case of the model for Rikuzentakata (C.C5), which exhibits the best overall hit rate (0.89, Figure 2), while the related confusion matrix in Figure 2 depicts a very scattered pattern, with correct guesses almost only for "Washed away" (Class 7) buildings. Such a possible result is, however, well explained by the damage distribution for this city (Figure 4), where buildings in Class 7 practically represent the exclusive reported cases, thus making the weight of the recognized scatter on other classes negligible on overall accuracy.

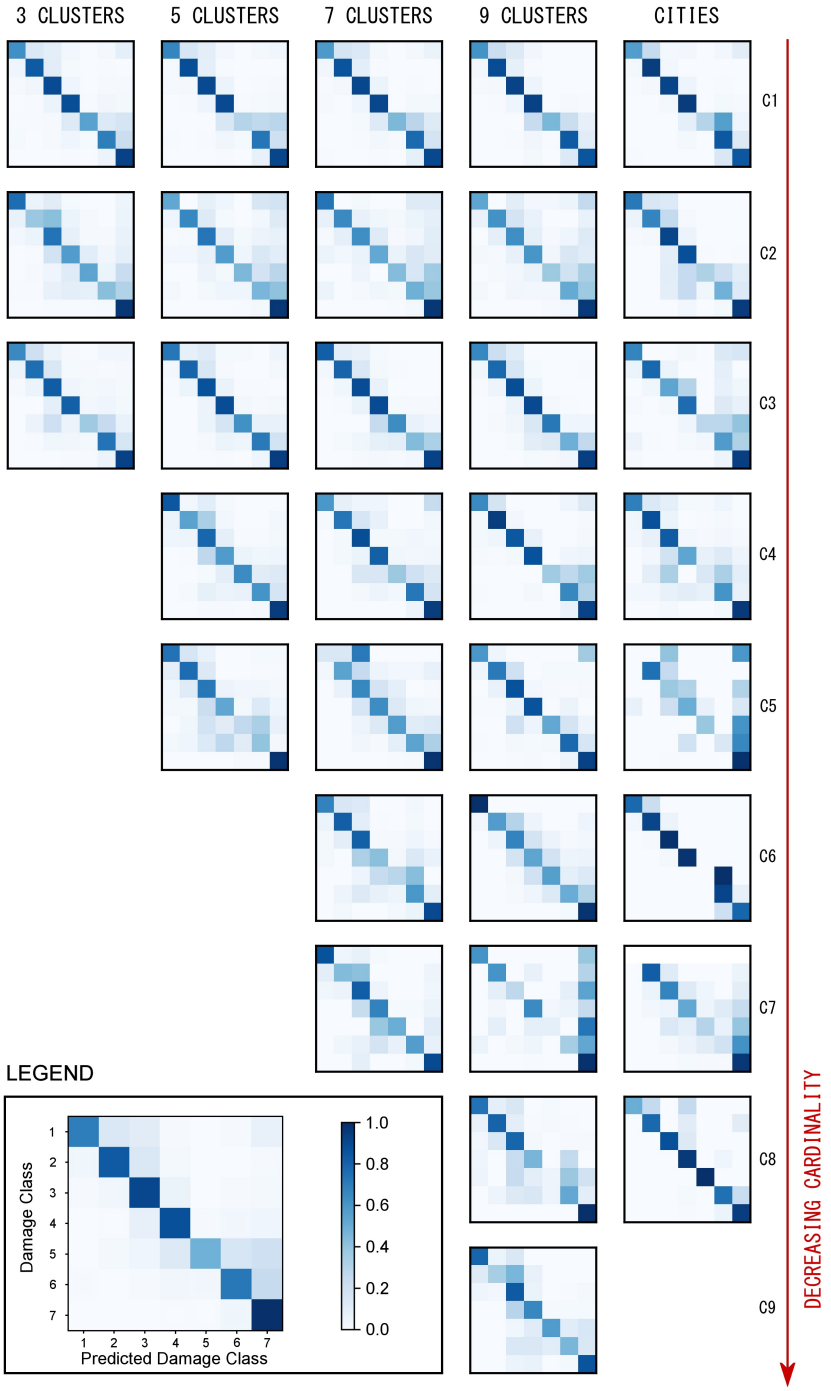


Figure 3: Normalized confusion matrices for the models trained on the different clusters (Figure 1). The matrices related to the "Cities" group are displayed in the following order (top-down): Ishinomaki (C.C1), Higashi-Matsushima (C.C2), Kesennuma (C.C3), Iwaki (C.C4), Rikuzentakata (C.C5), Watari (C.C6), Ōfunato (C.C7) and Yamamoto (C.C8).

In general, also in datasets with high cardinality, the presence of unbalanced shares of data within the different classes is mainly the obvious cause for most of the misclassification error, as evident, for instance, in Ishinomaki (C.C1), 9.C1 and 9.C4 models (Figures 3 and 4), as wells as for the whole extended MLIT-based model [7].

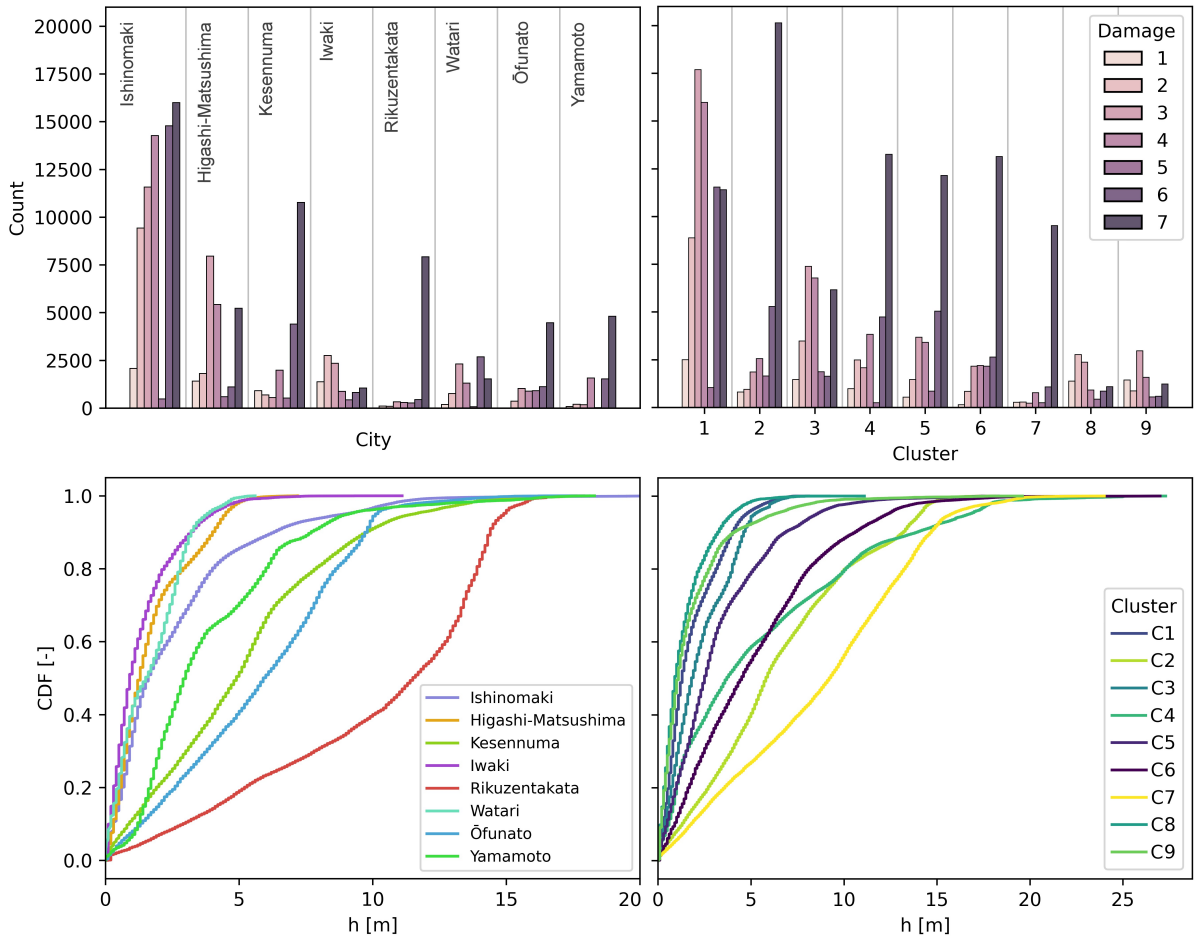


Figure 4: Empirical distributions for Damage (top) and Inundation depth (bottom) data for the "City" (left column) and "9" clusters (right column).

## 3.2 Regional variability of the feature importance at different levels of spatial aggregation

Figure 5 shows the results of the cluster-averaged feature importance and variability in terms of mean decrease accuracy obtained when the individual input features are randomly shuffled. It appears that the importance of the different predictors is stable for all selections and in good agreement with the results obtained from the models trained on the whole extended MLIT dataset [7].

In detail, out of the obvious inundation depth (highly correlated with the distance from the shoreline, which explains the share of the importance in Figure 5), other parameters recognized as important in tsunami damage modelling, almost irrespective of the clusterization method and geographical location of the impacted area, are the following: the direction of tsunami wave attack (WDir) and the indicators proposed by Di Bacco et al. [7] for accounting for the shielding and debris generation effects created by interacting buildings (LShVol and LDIVol).

Typical predictors considered in tsunami damage modelling, as the structural type (BS) and the number of floors of the building (NF), appear only after the mentioned ones, with a more pronounced local importance variability in smaller cluster datasets (e.g., for clusterization into 7 and 9 areas). Other ancillary building characteristics (related to its geometrical/shape features as well as its intended use and year of construction) have, instead, only a

marginal impact on the predictive accuracy and, therefore, they may even be neglected in damage modelling.

Figure 5 also confirms that information on coastal morphology (CoastType) is another key factor for tsunami damage predictions in Japan, because of the amplifying effects occurring in ria coasts [8, 9, 11]. The importance of this variable is only negligible for models developed for cluster areas characterized by the same (or with a large share of the same) coastal type: for example, the large variability in the mean decrease accuracy for CoastType observed in the "5 clusters" plot (Figure 5) is the result of a limited effect of this variable on clusters 5.C2, 5.C3 and 5.C5, as opposed to the more heterogeneous cluster 5.C4.

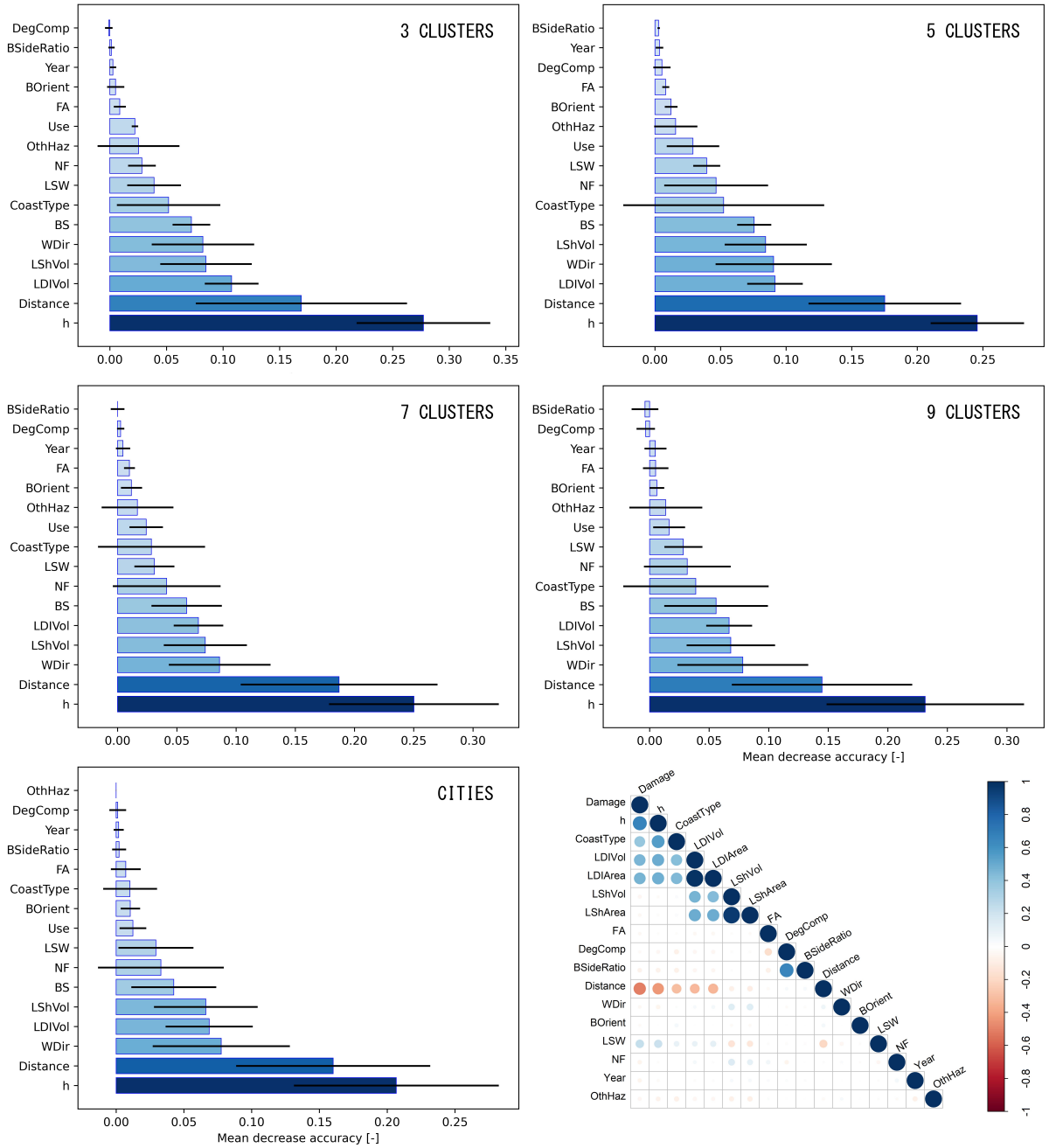


Figure 5: Results of the feature importance analysis for the different clusterization methods. The bars indicates the cluster-averaged mean decrease accuracy and the error bars the corresponding (±) standard deviation. A correlation matrix is also included (bottom right) to highlight the relationships between the variables.

Although with a generally smaller weight, similar considerations apply to OthHaz (the parameter accounting for possible concurrent hazard factors), which only in some specific cases, as in 3.C3 and 7.C4, may become significant for improving damage estimation accuracy. These findings should be interpreted while considering the relatively small portion of buildings characterized by the presence of an additional concurrent hazard factor. Specifically, these buildings accounted for only 2% of the whole MLIT dataset, with the vast majority of them (78%) concentrated within cluster 3.C3. A more in-depth analysis of this subset revealed inland flooding as the most frequent additional hazard factor, which worsened the situation for the buildings located in internal areas and in close proximity to watercourses. The nature of this concurrent hazard factor, which itself contributes to an increase in water depth, also implies that the actual importance of the OthHaz parameter may be partly masked within other features.

## 4 CONCLUSIONS

By implementing Extra-Trees models based on observed damage data for the 2011 earthquake and tsunami in the Tōhoku region (Japan), this study investigated the effect of data spatial aggregation on damage predictive ability of the models and analyzed the possible existence of regional-dependent features that may affect model accuracy.

The results showed high variance in the accuracy of models trained on data classified in spatial clusters with different cardinality. The worst performances were observed in the northern and southern extreme impacted areas and they could be attributed to the hazard features experienced in such regions, inundated by relatively shallow water depths, which emphasize the importance of local vulnerability and additional hazard factors that increase damage variability and then the probability of damage prediction errors. Such observation also explains the results found by Di Bacco et al. [7] in their analysis for the spatial transferability of the model developed with the whole extended MLIT dataset, which exhibited low accuracies for the cities of Iwaizumi and Hashikami (hit rates in the range ~0.5-0.6), both located in northern clusters, or in the more central, but still affected by shallow waters, Rifu and Matsushima.

Furthermore, the division of the dataset into clusters with a larger sample size was observed to reduce the differences in the accuracies detected among the identified regions within each sub-group. The importance of the different predictors appeared to be stable for all selections and in good agreement with the results obtained for total MLIT dataset, thus allowing the definition of a ranking for the most useful predictors for tsunami damage modelling, which include factors for taking into account the mechanisms of shielding and debris generation created by interacting buildings in inundated areas.

## REFERENCES

[1] C. Tarbotton, F. Dall'Osso, D. Dominey-Howes, J. Goff. The use of empirical vulnerability functions to assess the response of buildings to tsunami impact: comparative review and summary of best practice. *Earth-Science Reviews*, **142**, 120-134, 2015.

[2] I. Charvet, A. Suppasri, H. Kimura, D. Sugawara, F. Imamura, A multivariate generalized linear tsunami fragility model for Kesennuma City based on maximum flow depths, velocities and debris impact, with evaluation of predictive accuracy. *Natural Hazards*, **79**(3), 2073-2099, 2015.

[3] I. Charvet, J. Macabuag, T. Rossetto, Estimating tsunami-induced building damage through fragility functions: critical review and research needs. *Frontiers in Built Environment*, **3**, 36, 1-22, 2017.

[4] K. Gibert, J. Izquierdo, M. Sànchez-Marrè, S.H. Hamilton, I. Rodríguez-Roda, G. Holmes, Which method to use? An assessment of data mining methods in Environmental Data Science. *Environmental Modelling & Software*, **110**, 3-27, 2018.

[5] K. Saengtabtim, N. Leelawat, J. Tang, W. Treeranurat, N. Wisittiwong, A. Suppasri, K. Pakoksung, F. Imamura, N. Takahashi, I. Charvet, Predictive analysis of the building damage from the 2011 Great East Japan Tsunami using decision tree classification related algorithms. *IEEE Access*, **9**, 31065-31077, 2021.

[6] Ministry of Land, Infrastructure, and Transportation of Japan (MLIT). Survey of Tsunami Damage condition, http://www.mlit.go.jp/toshi/toshi-hukkou-arkaibu.html, 2012.

[7] M. Di Bacco, P. Rotello, A. Suppasri, A.R. Scorzini, Leveraging data driven approaches for enhanced tsunami damage modelling: insights from the 2011 Great East Japan event. *Environmental Modelling & Software*, **160**, 105604, 2023.

[8] A. Suppasri, E. Mas, I. Charvet, R. Gunasekera, K. Imai, Y. Fukutani, Y. Abe, F. Imamura, Building damage characteristics based on surveyed data and fragility curves of the 2011 Great East Japan tsunami. *Natural Hazards*, **66**(2), 319-341, 2013.

[9] A. Suppasri, I. Charvet, K. Imai, F. Imamura, Fragility curves based on data from the 2011 Tohoku-Oki tsunami in Ishinomaki city, with discussion of parameters influencing building damage. *Earthquake Spectra*, **31**(2), 841-868, 2015.

[10] I. Charvet, A. Suppasri, F. Imamura, Empirical fragility analysis of building damage caused by the 2011 Great East Japan tsunami in Ishinomaki city using ordinal regression, and influence of key geographical features. *Stochastic Environmental Research and Risk Assessment*, **28**(7), 1853-1867, 2014.

[11] N. Leelawat, A. Suppasri, I. Charvet, F. Imamura, Building damage from the 2011 Great East Japan tsunami: quantitative assessment of influential factors. *Natural Hazards*, **73**(2), 449-471, 2014.

[12] D. Steinley, K-means clustering: a half-century synthesis. *British Journal of Mathematical and Statistical Psychology*, **59**(1), 1-34, 2006.

[13] P. Geurts, D. Ernst, L. Wehenkel, Extremely randomized trees. *Machine learning*, **63**(1), 3-42, 2006.

[14] L. Breiman, Random forests. *Machine learning*, **45**, 5-32, 2001.

[15] B. Jongman, H. Kreibich, H. Apel, J.I. Barredo, P.D. Bates, L. Feyen, A. Gericke, J. Neal, J.C.J.H. Aerts, P.J. Ward, Comparative flood damage model assessment: towards a European approach. *Natural Hazards and Earth System Sciences*, **12**(12), 3733-3752, 2012.

[16] M. Amadio, A.R. Scorzini, F. Carisi, A.H. Essenfelder, A. Domeneghetti, J. Mysiak, A. Castellarin, Testing empirical and synthetic flood damage models: the case of Italy. *Natural Hazards and Earth System Sciences*, **19**(3), 661-678, 2019.

[17] A.R. Scorzini, B. Dewals, D. Rodriguez Castro, P. Archambeau, P., D. Molinari, INSYDE-BE: adaptation of the INSYDE model to the Walloon region (Belgium). *Natural Hazards and Earth System Sciences*, **22**(5), 1743-1761, 2022.

COMPDYN 2023
9th ECCOMAS Thematic Conference on
Computational Methods in Structural Dynamics and Earthquake Engineering
M. Papadrakakis, M. Fragiadakis (eds.)
Athens, Greece, 12-14 June 2023

# APPLICATION OF HAZARD RISK METHDOLOGY ON HISTORICAL BUILT ENVIRONMENT IN TIMISOARA

**I. Onescu[1]; E. Onescu[2]; M. Mosoarca[3];**

[1] Lecturer, Habil. Ph.D. Arch., Urban Planning and Architecture Research Center, Politehnica University of Timisoara, and Academy of Romanian Scientists, Ilfov 3, 050044, Bucharest, Romania
iasmina.onescu@upt.ro

[2] Ph.D. Stud. Arch., Politehnica University of Timisoara
eugen.eugen@student.upt.ro

[3] Full Professor, Habil. Ph.D. Eng., Urban Planning and Architecture Research Center, Politehnica University of Timisoara
marius.mosoarca@upt.ro

## Abstract

*The multi-hazard risk assessment of the built environment, especially in historical urban areas, represents a common topic nowadays, with many challenges in the management process. Timisoara, which will be the European Capital of Culture in 2023, has several historical areas which present various vulnerabilities to hazards, especially to earthquakes. Heritage buildings in Art Nouveau, Baroque, Secession architectural style present a poor state of conservation, without recent consolidation work and also without a specific knowledge of their expected damage state in case of an earthquake. Considering the fact that Timisoara is located in Banat seismic area, which is characterized by shallow earthquakes of crustal type, the opportunity of investigating the vulnerability of the most important districts of the city is highlighted.*
*The paper presents a multi-disciplinary empirical vulnerability assessment made on a historical area of Timisoara city, which investigated the structural, architectural-artistic, urbanistic and socio-economic vulnerability of the case-study area, in a simplified and efficient way. The assessment methodology represents a complex, holistic methodology that was proposed by the same authors recently, which aims to consider the cultural value of the heritage buildings in the process of multi-hazard risk management of the built environment.*

**Keywords:** masonry, hazard, vulnerability assessment, heritage buildings, risk management

## 1 INTRODUCTION

Historical buildings and historical cities represent one of the most valuable assets of the local communities, as the base of their authenticity. Due to their age and building materials and technology, implemented before the existence of any design codes, historical buildings are more vulnerable to damage or collapse during an earthquake, so their susceptibility to this hazard should be determined, to be able to ensure the preservation and safety.

For historical districts that are located in areas with seismic hazard, vulnerability is a concern for many structures in the city. For increasing their resilience, it is important to be aware of the vulnerability level, possible seismic scenarios and possible losses, to take the necessary measures to minimize the damage and to ensure the safety of the inhabitants.

Seismic vulnerability assessment of heritage buildings is one of the most important tools in the process of ensuring structural stability and preservation in case of an earthquake.

This paper aims to look at a small aggregate in Timisoara city, which has a rich historical heritage, but which is also a seismic area. The aim of the paper is to highlight the importance of conducting vulnerability assessment on those buildings, as a first step in the process of preserving the cultural heritage of the city. The assessment methodology takes into consideration more than just the structural features, so its findings are expected to contribute to the development of strategy for the seismic risk management in Timisoara.

## 1 CASE STUDY AREA

The paper focuses on one aggregate in one of the most important historical districts of Timisoara city. The name of the district is Iosefin and is located in the western part of the city, on the left bank of the Bega river, as presented in Figure 1 [1]. The district is well-known for its valuable architectural value, with many buildings in Art Nouveau and Eclectic style [2]. The district was built in the 18$^{th}$ and 19$^{th}$ Century and was settled by nobility and wealthy merchants. The most important districts palaces and mansions were built at the beginning of the 20$^{th}$ Century and are well preserved even nowadays. In the context of Timisoara European Capital of Culture 2023, a large number of historical palaces and urban areas in Iosefin district are activated to host several cultural events and festivals [3], [4]

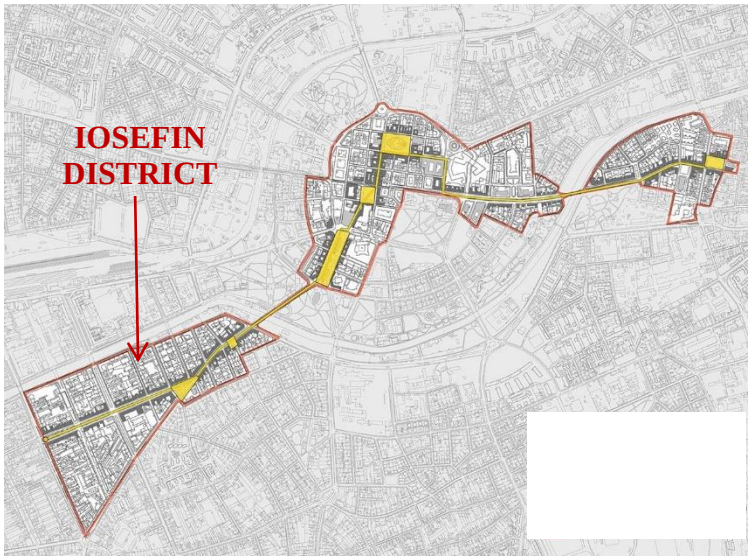


Figure 1: Main historical districts of Timisoara city [1].

The specific aggregate that represents the case study of this paper is one of the most important ones in Iosefin district, as it represents the first buildings that are seen coming from the city center, the visual connection between Iosefin and Cetate districts. The aggregate is located in the eastern extremity of the district, as shown in Figure 2a. An aerial view of the buildings within this aggregate is presented in Figure 2b.

a)  b) 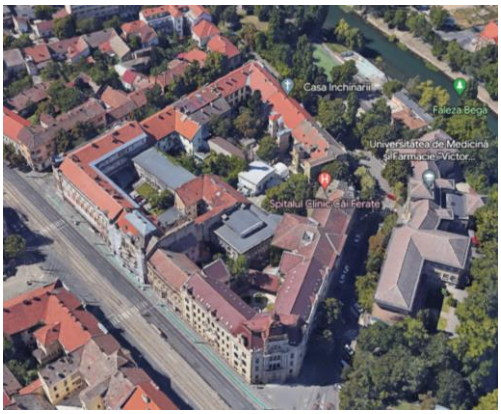


Figure 2: Case study aggregate: a) position within the Iosefin district; b) aerial view.

The buildings in the investigated aggregate are all with historical and cultural value, built in the years of 1900, in Art Nouveau principal architectural style and Eclectic secondary architectural style, with decorated facades and several architectural-artistic assets, as illustrated in Figure 3. The buildings are all made in burnt clay brick masonry with lime, with thick perimetral masonry walls and thin transversal masonry walls, with masonry vaults above basement and wooden floors [5] (in some cases concrete slabs as a retrofitting modern intervention), with rigid wooden frameworks in German style [6].



Figure 3: The historical buildings within the case study aggregate.

## 2 SEISMICITY OF THE AREA

Timisoara is located in Banat seismic area, which represents the second most important seismic region of Romania. The seismicity of Banat area is a moderate one, with earthquakes of crustal type [7]. The magnitudes in the area are between $M_W = 0.2 \div 5.6$ [8], as presented in Table 1 [9], and according to the Romanian Design Code, the peak ground acceleration for Timisoara is PGA = 0.20g [10]. Following the considered PGA, there was determined the most

probable macroseismic intensity, based on Equation 1 [5], which is IX EMS-98, as presented in Figure 4 [11].

| Seismic intensity | V | VI | VII | VII-VIII |
|---|---|---|---|---|
| Year | 1889 | 1973 | 1859 | 1879 |
| | 1896 | | 1879 | 1915 |
| | 1902 | | 1900 | 1991 |
| | 1907 | | 1941 | |
| | 1950 | | 1959 | |

Table 1: The most important seismic events in Banat area (MSK intensity scale) [9].

$$\ln(PGA) = 0.24 \times I_{EMS-98} - 3.9 \quad (1)$$

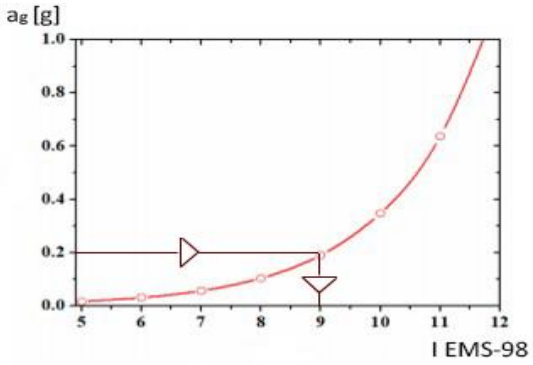


Figure 4: Correlation between the PGA and the expected macroseismic intensity EMS-98 [11].

## 3 VULNERABILITY ASSESSMENT

The vulnerability assessment of the investigated aggregate in Iosefin district was performed following a methodology that was previously developed by the authors [12], that considers also the importance and the impact of the cultural value in the process of vulnerability assessment [13]. The aim of this procedure is to be able to calibrate the seismic vulnerability based on the level of cultural importance of the building. This aspect could allow the local authorities to prioritize the rehabilitation works not only based on the highest structural vulnerability, but also based on the highest cultural value of the buildings. The preservation of the most important architectural heritage of the city, is in accordance with the European guidelines for the preservation of the cultural heritage assets [14] and also with the UNESCO program for the cultural landscape [15].

### 3.1 Methodology

The methodology is an empirical ones, based on the visual inspection of the investigated aggregate, appropriate for investigations of large urban areas, quick and simplified. It considers four categories of parameters, such as structural, architectural-artistic, urbanistic and socio-economic ones. Each category influences the vulnerability score in a smaller or higher percentage, from 70% for the structural features to 5% for the social economic ones. The

investigation form contains a total number of 42 parameters, from which the first 15 parameters refers to the structural category.

This first category, the structural one, represents actually a well-known vulnerability assessment methodology that was first proposed by profs. Bendetti and Petrini [16] for the first 10 parameters and developed by profs. Mazzolani and Formisano for the other 5 parameters that considers the interaction within the aggregate [17].

The other three categories were proposed by the authors of this paper, following several research and Romanian codes [12], [18], [19]. Those parameters are based on a personal appreciation of the architectural-artistic, urbanistic and socio-economic value of each aspect, following recommendations and guidelines from Romanian code for monument consideration and several research contracts in the field. The weights of each parameter were calibrated following the application of the form on more than 100 historical buildings.

The vulnerability index is obtained by fulfilling the final investigation form, which is presented in Table 2, as the sum of each individual score of each parameter multiplied by a corresponding weight, as in Equation 2 [20].

| % | Criteria | No. | Element | Class | | | | Weight |
|---|---|---|---|---|---|---|---|---|
| | | | | A | B | C | D | |
| 70 % | STRUCTURAL | 1 | Vertical structure organization | 0 | 5 | 20 | 45 | 1.00 |
| | | 2 | Vertical structure nature | 0 | 5 | 25 | 45 | 0.25 |
| | | 3 | Type of foundation and location/soil | 0 | 5 | 25 | 45 | 0.75 |
| | | 4 | Distribution of structural elements in plan | 0 | 5 | 25 | 45 | 1.50 |
| | | 5 | Regularity in plan | 0 | 5 | 25 | 45 | 0.50 |
| | | 6 | Regularity in elevation | 0 | 5 | 25 | 45 | 1.00 |
| | | 7 | Floor type | 0 | 5 | 15 | 45 | 0.75 |
| | | 8 | Roofing | 0 | 15 | 25 | 45 | 0.75 |
| | | 9 | Other details | 0 | 0 | 25 | 45 | 0.25 |
| | | 10 | Conservation state | 0 | 5 | 25 | 45 | 1.00 |
| | | 11 | Presence of adjacent buildings with different height | -20 | 0 | 15 | 45 | 1 |
| | | 12 | Position of the building in the aggregate | -45 | -25 | -15 | 0 | 1.5 |
| | | 13 | Presence and number of staggered floors | 0 | 15 | 25 | 45 | 0.5 |
| | | 14 | Effect of either structural or typological heterogeneity among adjacent structural unit | -15 | -10 | 0 | 45 | 1.2 |
| | | 15 | Percentage difference of opening area among adjacent façade | -20 | 0 | 25 | 45 | 1 |
| 15 % | ARCHITECTURAL ARTISTIC | 16 | Representative architectural style for the area | 0 | 10 | 15 | 25 | 1.50 |
| | | 17 | Age, importance of the build époque | 0 | 10 | 15 | 25 | 1.20 |
| | | 18 | Original woodwork/joinery | 0 | 10 | 15 | 25 | 1.00 |
| | | 19 | Original stucco, brick, floors or ceilings | 0 | 10 | 15 | 25 | 1.00 |
| | | 20 | Original statues or bass-reliefs | 0 | 10 | 15 | 25 | 1.00 |
| | | 21 | Original gable/fronton | 0 | 10 | 15 | 25 | 1.00 |
| | | 22 | Original balconies and railings | 0 | 10 | 15 | 25 | 1.00 |
| | | 23 | Original mosaics or stonework | 0 | 10 | 15 | 25 | 1.00 |
| | | 24 | Original paintings or frescoes | 0 | 10 | 15 | 25 | 1.00 |
| | | 25 | Degradation state of artistic assets | -5 | 10 | 15 | 25 | 1.00 |
| | | 26 | Authenticity/ originality (global, elements) | 0 | 10 | 15 | 25 | 1.00 |
| | | 27 | Official monument (national, regional, local, protected area) status | 0 | 10 | 15 | 25 | 1.50 |
| | | 28 | Particular construction techniques/materials | 0 | 10 | 15 | 25 | 0.50 |
| | | 29 | Conservation state of original materials | -5 | 10 | 15 | 25 | 0.50 |
| | | 30 | Representative historical events | 0 | 10 | 15 | 25 | 0.50 |
| | | 31 | Archaeological site | 0 | 10 | 15 | 25 | 1.50 |
| | | 32 | Representative/ original wooden framework | 0 | 10 | 15 | 25 | 1.00 |
| | | 33 | Past restoration work | -5 | 10 | 15 | 25 | 1.00 |
| 10 % | URBANISTIC | 34 | Importance in contouring the street profile | -5 | 10 | 15 | 25 | 1.50 |
| | | 35 | Importance in contouring the urban silhouette | -5 | 10 | 15 | 25 | 1.50 |
| | | 36 | Annexes, relation with the urban pattern | 0 | 10 | 15 | 25 | 1.00 |
| | | 37 | Location (central area, touristic area) | 0 | 10 | 15 | 25 | 1.50 |
| | | 38 | Representative/particular shape of the roof | 0 | 10 | 15 | 25 | 1.00 |
| | SOCIAL | 39 | Public/social functions | 0 | 10 | 15 | 25 | 1.50 |

| | | | | | | | | |
|---|---|---|---|---|---|---|---|---|
| 5 % | ECONOMIC | 40 | Importance for the local community memory | -5 | 10 | 15 | 25 | 1.00 |
| | | 41 | Economic value | 0 | 10 | 15 | 25 | 1.50 |
| | | 42 | Cultural functions | 0 | 10 | 15 | 25 | 1.50 |
| | | | | | | $I_{V\,CULT}$ | | |

Table 2: The investigation form that considers also the cultural value [9].

$$I_{V\,CULT} = 0.70 \times \sum_{i=1}^{10} s_i \times w_i + 0.15 \times \sum_{i=11}^{28} s_i \times w_i + 0.10 \times \sum_{i=29}^{33} s_i \times w_i + 0.05 \times \sum_{i=34}^{37} s_i \times w_i \quad (2)$$

Following the seismic vulnerability index influenced by the cultural value, there is obtained a normalized vulnerability index $V_{CULT}$, based on Equation 3 . Later on, the mean damage is obtained following Equation 4, which was previously calibrated for Banat seismic area by the authors and the most probable damage state for each building, for the considered seismic scenario, is obtained [5].

$$V_{CULT} = \frac{I_{VCULT} - I_{VCULT\,MIN}}{I_{VCULT\,MAX} + I_{VCULT\,MIN}} \quad (3)$$

$$\mu_D = 2.5\left[1 + tanh\left(\frac{I + 12.50 \times V_{CULT} - 13.1}{\Phi}\right)\right] \quad (4)$$

, where Φ is considered 2.3 because the residential predominant function of the investigated buildings [21].

### 3.2 Results

The seismic vulnerability influenced by the cultural value, for each individual investigated building, is illustrated in Figure 5 and shows expected damages states from D2 to D4, which indicates possible damages from only to non-structural elements till consistent damages to structural elements. The individual damage state, correlated with several other parameters, are illustrated in Table 3.

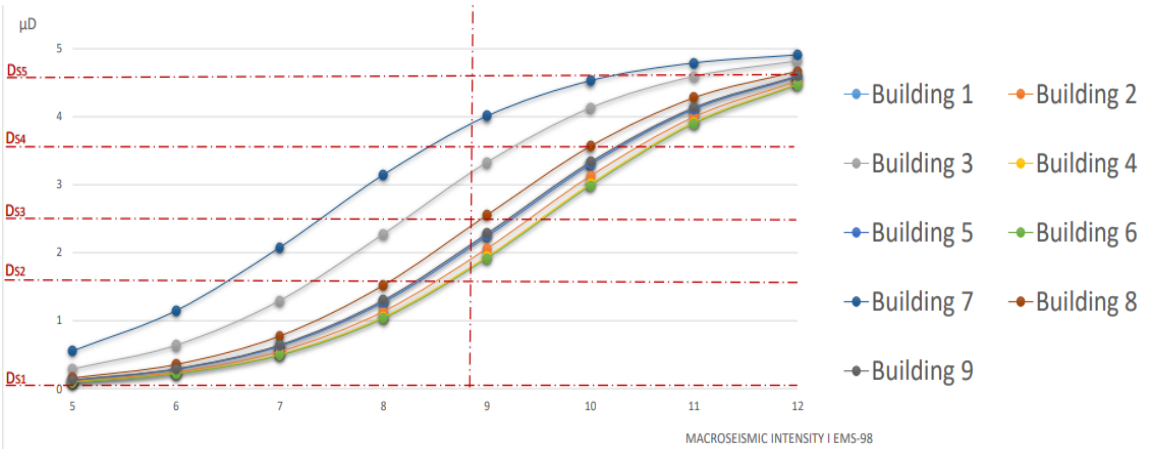


Figure 5: Seismic vulnerability curves influenced by the cultural value for each individual investigated buildings.

| No. | Street | Picture | Position | Ground floor (square meters) | Floor no. (with basement) | $I_{V\,CULT}$ | Expected damage state |
|---|---|---|---|---|---|---|---|

| | | | | | | | |
|---|---|---|---|---|---|---|---|
| 1 | 16th December |  | Corner | 1069.32 | 4 | 103.05 | DS3 |
| 2 | Tudor Vladimirescu |  | End | 389.23 | 3 | 92.9 | DS2 |
| 3 | Tudor Vladimirescu |  | Line | 356.47 | 3 | 133.85 | DS3 |
| 4 | Miron Costin |  | Corner | 770.88 | 3 | 87.175 | DS2 |
| 5 | Miron Costin |  | Line | 439.23 | 3 | 98.675 | DS2 |
| 6 | Miron Costin |  | Line | 349.55 | 3 | 87.925 | DS2 |
| 7 | 16th December |  | Corner | 1375 | 4 | 163.175 | DS4 |
| 8 | 16th December |  | Line | 342.35 | 4 | 111.225 | DS3 |
| 9 | 16th December |  | Line | 349.79 | 3 | 100.025 | DS3 |

Table 3: Correlation of each individual building to the expected damage state.

The mean vulnerability curve of the entire aggregate is presented in Figure 6, highlighting a medium seismic vulnerability influenced by the cultural value, with a general D3 expected damage state.

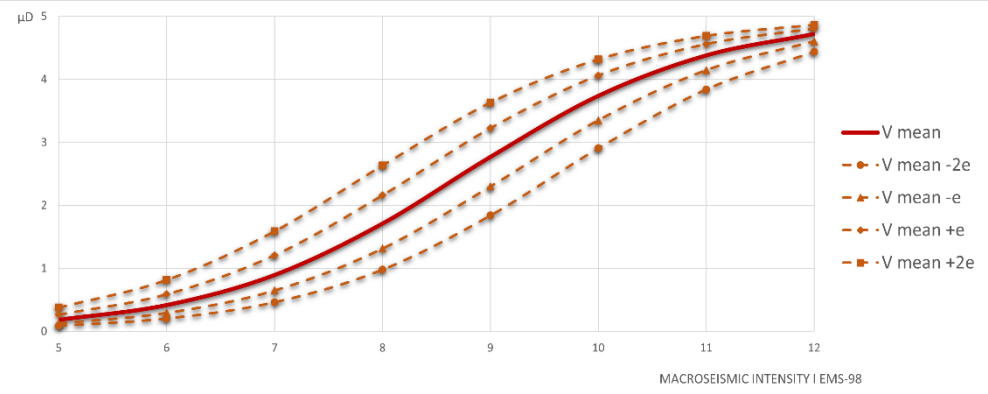


Figure 6: Mean seismic vulnerability curves influenced by the cultural value for the entire aggregate.

Moreover, there was investigated the relations between the vulnerability index for the investigated buildings, with focus on the buildings that are on a corner position (Figure 7) or with the most number of levels (Figure 8). After this correlation, there can be said that in general, with some exceptions, the most vulnerable buildings are the ones that are the tallest and in corner position.

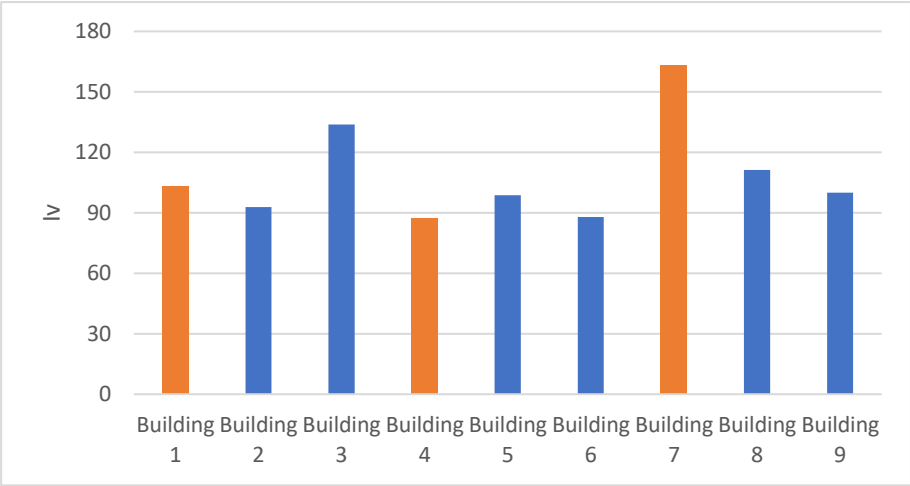


Figure 7: Vulnerability index for all buildings, with highlight on the buildings located in a corner position in the aggregate.

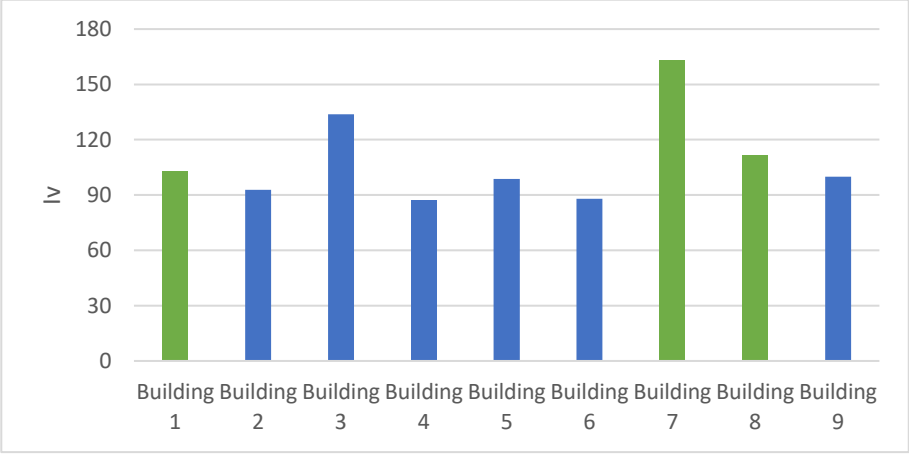


Figure 8: Vulnerability index for all buildings, with highlight on the highest buildings within the aggregate.

In the end, there was investigated the vulnerability index without the consideration of the architectural-artistic, urbanistic and socio-economic parameters, to observe how much the cultural value could influence the mean vulnerability of the case study buildings. The comparison between the vulnerability curves with and without cultural value is presented in Figure 9, showing that the consideration of the parameters that are not related only with the structural system lead to the increase of the mean vulnerability with 6%, without changing the expected mean damage state.

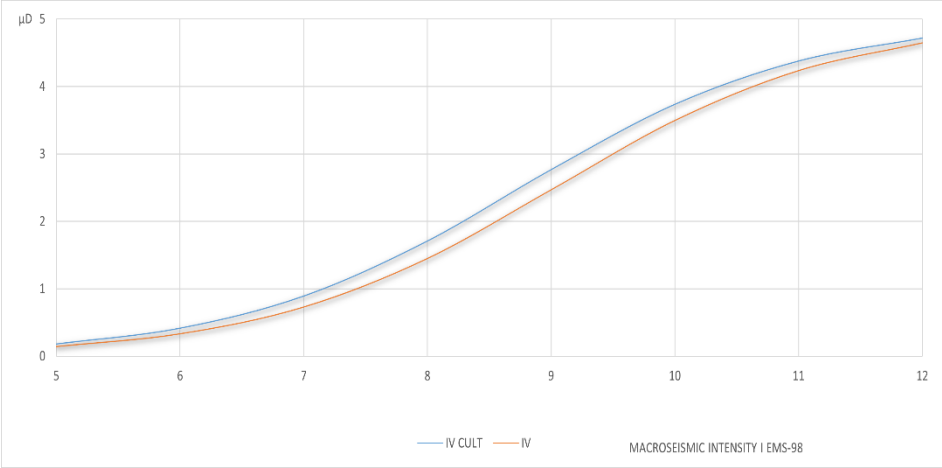


Figure 9: Comparison between mean vulnerability curves with and without the cultural value considered.

## 4 CONCLUSIONS

The case study building in Timisoara were investigated not only from a structural point of view, but also from a cultural perspective, by considering some supplementary investigations parameters that evaluates the architectural-artistic, urbanistic and socio-economic value of the heritage buildings. The results of the assessment are concluded bellow, as follows:

- The investigated historical masonry buildings in Iosefin district, Timisoara, present a medium cultural value, which influences the seismic vulnerability.
- The investigated buildings present a medium seismic vulnerability for the specific seismic scenario (macroseismic intensity IX EMS-98).
- The less vulnerable building is expected to be in the D2 damage state, meaning only non-structural damages, while the most vulnerable buildings is expected to reach D4 damage state, meaning also extensive damages to structural elements.
- The general expected damage state for the entire aggregate is D3, which means significant damage to non-structural elements and minor damage to the structural ones.
- Despite the D3 damage state for the aggregate, which isn't dangerous for structural safety, a lot of architectural-artistic assets could be damaged in case of an earthquake.
- The most vulnerable buildings are in general the ones that are the tallest and in corner positions, but some exceptions occur due to the different levels of decay between buildings.

## REFERENCES


[1] M. Mosoarca, I. Onescu, E. Onescu, B. Azap, N. Chieffo, and M. Szitar-Sirbu, "Seismic vulnerability assessment for the historical areas of the Timisoara city, Romania," *Eng Fail Anal*, vol. 101, pp. 86–112, Jul. 2019, doi: 10.1016/J.ENGFAILANAL.2019.03.013.

[2] M. Opris, *Timisoara - mica monografie urbanistica*, In Romania. Bucuresti: Editura Tehnica, 1987.

[3] "Info Centrul Turistic Timisoara, in Romanian | Iosefin and Elisabetin Districts." http://www.timisoara-info.ro/en/sightseeing/historical-quarters/iosefin/places.html (accessed Jan. 08, 2019).

[4] Timisoara Cityhall administration, "Characteristics of prioritary areas in Timisoara city, districts of Cetate, Iosefin and Fabric." Accessed: Jul. 03, 2019. [Online]. Available: https://www.primariatm.ro/uploads/files/concept/C.pdf

[5] M. Mosoarca, I. Onescu, E. Onescu, and A. Anastasiadis, "Seismic vulnerability assessment methodology for historic masonry buildings in the near-field areas," *Eng Fail Anal*, 2020.

[6] E. Onescu, I. Onescu, and M. Mosoarca, "The impact of timber roof framework over historical masonry structures," in *IOP Conference Series: Materials Science and Engineering*, 2019.

[7] National Institute for Earth Physics, "Romania seismic zones, available at https://www.infp.ro/ro/zonele-seismice-din-romania."

[8] E. Oros, M. Popa, and I. A. Moldovan, "Seismological database for banat seismic region (Romania)-part 1: the parametric earthquake catalogue," 2008. Accessed: Jan. 08, 2019. [Online]. Available: www.storing.ingv.it/es_web

[9] I. Apostol, M. Mosoarca, and V. Stoian, "Modern Consolidation Solutions for Buildings with Historical Value . Part I : Reinforced Concrete Structures," in *Modern Technologies for the 3rd Millennium*, 2017, pp. 406–413.

[10] Ministry of regional development public administration and european funds, "Romanian Design Code P100-1/2013, in Romanian," 2013. Accessed: Jan. 28, 2019. [Online]. Available: http://www.mdrap.ro/userfiles/reglementari/Domeniul_I/I_22_P100_1_2013.pdf

[11] N. Chieffo and A. Formisano, "The Influence of Geo-Hazard Effects on the Physical Vulnerability Assessment of the Built Heritage: An Application in a District of Naples," *Buildings*, vol. 9, no. 1, p. 26, 2019, doi: 10.3390/buildings9010026.

[12] I. Apostol, "Seismic vulnerability assessment of historical urban centres," Ph.D., Politehnica Timisoara.

[13] I. Onescu, E. Onescu, and M. Mosoarca, "The impact of the cultural value to the seismic vulnerability of a historical building," in *IOP Conference Series: Materials Science and Engineering*.

[14] S. Lagomarsino, and S. Cattari, "PERPETUATE guidelines for seismic performance-based assessment of cultural heritage masonry structures", *Bulletin of Earthquake Engineering*, Vol. 13, pp. 13-47, 2015, doi: 10.1007/s10518-014-9674-1.

[15] M. Rössler, "World Heritage cultural landscapes: A UNESCO flagship programme 1992 – 2006," *Landsc Res*, vol. 31, no. 4, pp. 333–353, Oct. 2006, doi: 10.1080/01426390601004210.

[16] D. Benedetti and V. Petrini, "On the seismic vulnerability of masonry buildings: an evaluation method (in Italian)," *L'Industria delle Costruzioni*, vol. 149, pp. 66–74, 1984.

[17] A. Formisano, R. Landolfo, F. Mazzolani, and G. Florio, "A quick methodology for seismic vulnerability assessement of historical masonry aggregates," *COST Action C26:*

*Urban Habitat Constructions under Catastrophic Events*, no. September, 2010, doi: 10.13140/2.1.1706.3686.

[18] R. C. Petrovici, M. Mironescu, and E. All., "P 100-8/2018: Evaluation and intervention code for structures with cultural value," 2018.

[19] Ministerul Culturii, "Strategia pentru cultură și patrimoniu național," 2016.

[20] E. Onescu, I. Onescu, and A. M. Mosoarca, "SEISMIC VULNERABILITY ASSESSMENT METHODOLOGY FOR HISTORICAL BUILDINGS WITH CULTURAL VALUE."

[21] M. Munari, M. R. Valluzzi, G. Cardani, A. Anzani, L. Binda, and C. Modena, "Seismic vulnerability analyses of masonry aggregate buildings in the historical centre of Sulmona (Italy)," in *13th International Conference SFR*, 2010.

COMPDYN 2023
9th ECCOMAS Thematic Conference on
Computational Methods in Structural Dynamics and Earthquake Engineering
M. Papadrakakis, M. Fragiadakis (eds.)
Athens, Greece, 12-14 June 2023

# A MULTI-RISK FRAMEWORK FOR ASSESSING AND RANKING SEISMIC AND FLOOD RISKS: AN APPLICATION IN ITALY-SLOVENIA TRANSBOUNDARY REGION

**Maria Polese[1], Gabriella Tocchi[1], Matjaz Dolsek[2], Anze Babič[2], Marta Faravelli[3], Barbara Borzi[3], Nicola Rebora[4], Daria Ottonelli[4], Matjaz Mikos[2] Davide Quaroni[3], Rocco Masi[3], Andrea Prota[1]**

[1] University of Naples Federico II, Department of Structures for Engineering and Architecture, via Claudio 21, 80125 Naples, Italy

e-mail: maria.polese@unina.it

[2] University of Ljubljana, Faculty of Civil and Geodetic Engineering, Jamova cesta 2, 1000 Ljubljana, Slovenia

[3] Eucentre Foundation - European Centre for Training and Research in Earthquake Engineering, Via Adolfo Ferrata 1, 27100 Pavia, Italy

[4] CIMA Research Foundation, Via A. Magliotto 2, 17100 Savona - Italy

## Abstract

*To formulate suitable prevention and mitigation policies, risk assessment is the primary tool adopted by decision makers to understand and quantify the potential impacts resulting from hazardous events. In areas exposed to multiple hazards a joint analysis for quantifying and comparing all risks that potentially affect the territory is crucial. However, the evaluation of possible interactions among risks and their comparison could be a complex task. This paper illustrates the methodology for multi-risk assessment proposed within BORIS project (Cross BOrder RISk assessment for increased prevention and preparedness in Europe), focusing on the assessment of seismic and flood risk in the Eastern Alps cross-border area between Italy, Slovenia and Austria. Adopting a multi-layer single risk approach, the risk evaluation related to the investigated hazards is performed by independent analyses and the expected losses are compared and ranked through risk curves. To ensure the comparability of the risks, the same boundary conditions for the analysis (common area, time frame of analysis and metric to represent the risk) as well as the same methodological approach to compute the probabilistic risk curves are defined. The harmonized methodology proposed is applied to a pilot transboundary region at the Italy-Slovenia border, including 27 municipalities in Italy and 6 in Slovenia. The municipal scale is selected as a scale to represent and compare the risks and the metric to evaluate impacts is measured in terms of direct economic losses. Results in terms of Expected Annual Losses (EAL) show in which municipality the overall risk is significantly high and in which town one risk could be more relevant than the other.*

**Keywords:** multi-risk, cross-border risk assessment, risk curves.

# 1 INTRODUCTION

The analysis of risks deriving from natural hazards helps stakeholders involved in risk management to investigate disaster risk reduction issues for more resilient communities and to enhance disaster preparedness for effective response. As many regions of the world are exposed to multiple hazards, a joint analysis of risks originated from different sources potentially affecting the same area is crucial. In fact, analysis of single hazards that may hit a given area gives no indication about their relative importance or possible effects amplification due to hazards interaction and/or cascading effects. Usually, different methodologies and spatial/temporal resolutions are adopted in the quantification of single risk. The metrics adopted to measure risk could vary as well. This makes the outcomes of risk analysis related to different hazards hardly comparable.

The BORIS project (Cross BOrder RISk assessment for increased prevention and preparedness in Europe) was a project funded by Directorate-General for European Civil Protection and Humanitarian Aid Operations (DG ECHO). The objective of this project, finalized in December 2022, was the development of a shared methodology aiming to improve the knowledge and understanding of disaster risk towards the most effective prevention and preparedness to flood and seismic events in transboundary regions. Addressing also issues related to effective cross-border single risk harmonization, within the project a shared framework to compare and rank the single risks in multi-risk perspectives was also proposed. In this paper, the multi-risk approach proposed in BORIS will be presented. Cross-border multi-risk assessment developed was also tested in two pilot sites in Italy-Slovenia and Slovenia-Austria transboundary areas. Herein, the outcomes of the pilot application in the cross-border area between Italy and Slovenia will be presented and discussed.

# 2 SHARED FRAMEWORK FOR MULTI-RISK COMPARISON AND RANKING

## 2.1 Multi-risk issues

In order to perform a sound comparison and ranking of different risks potentially hitting the same area, a complete Multi Risk Assessment (MRA) should be performed. In its complete acceptation, MRA entails the adoption of innovative approaches that allow risk comparison and should account for all the possible risk interactions, i.e., at the level of hazard and of vulnerability [1]. Considering interactions among the threats would allow to also evaluate the potential increase of risk with respect to the level estimated by considering each risk source as independent from one another. However, the path to a complete MRA accounting for these aspects is quite complex, and there is still the need to reinforce each single step towards the full MRA. As observed in [2], the risk evaluation related to different sources is generally done through independent analyses, adopting disparate procedures and time–space resolutions. Each hazard may be characterized by different return periods, intensity and impacts. Metrics adopted to measure risk may be very different as well. Such differences make risks hardly directly comparable, independently of the presence of possible hazard/vulnerability interactions. Therefore, [3] suggests adopting as first step towards a full MRA, the so-called multi-layer single-hazard/risk assessment approach, ignoring the interactions but harmonizing and standardizing the assessment procedures among the different perils. In other words, each risk can be assessed through independent analysis, but common time frame of analysis and common metrics for risk evaluation have to be established a priori. To represent and compare the outcomes of such individual analysis, [3] suggests the adoption of standardization schemes, such as risk matrices, i.e., table-graphs illustrating the hazard likelihood on one axis and its potential impact on the other, or risk curves, i.e., curves relating the yearly probability of occur-

rence of an earthquake with the related expected impacts. Examples or risk curves or risk matrices can be found in [4], [5], and [6].

In the BORIS project multi-layer single risk analyses are performed. Therefore, independent risk analyses are performed both for seismic and flood risks without considering any hazard or vulnerability interaction but defining a shared framework by adopting the same boundary conditions and the same methodological approach for the analysis of both hazards. Residential buildings and the population are the assets at risk considered in the analysis. Direct economic losses and population affected (e.g., victims, injured, displaced) are selected as impact indicators to evaluate each risk and risk curves are selected as standardization tool to represent and visualize results. In the following section, the procedure proposed to harmonize seismic and flood risk for the implementation of a multi-layer single risk assessment is described.

### 2.2 The BORIS approach

In performing multi-layer single risk assessment, the harmonization of procedure for the evaluation of seismic and flood risk is required to allow useful comparison towards risk ranking. Relevant issues for multi-risk harmonization mostly concern the spatial scale of analysis (the two risks are usually assessed at different scales as an extension of area impacted by diverse hazards can greatly vary), the type of analysis to perform, i.e., time-based or scenario-based, and the metrics used to evaluate impacts. As a matter of fact, the two risks are usually assessed at different scales. This is mostly due to the different extension of area potentially impacted: while seismic risk can be assessed at a large scale (e.g., regional, municipal), the scale required for flood analysis is generally much smaller as flood hazard may vary spatially much more significantly than seismic hazard. As a harmonized spatial scale is strictly required to present and compare the consequences of different hazards, such harmonization can be based on the principle of the common denominator. In other words, the scales adopted in the single risk assessments can differ, but they should allow the aggregation of the consequences to the same spatial units. Thus, the municipality scale is proposed to represent risk results, which is also the lowest level at which administrative decisions are taken. Seismic risk will be evaluated adopting such a scale of analysis, while flood risk results will be first estimated at a lower scale and then aggregated at the municipal level for risk comparison and ranking.

The type of analysis depends on the main aim of the assessment. Usually, a detailed scenario-based assessment of expected damage and impact distribution at a territorial scale is adopted in response-oriented applications, i.e., studies for emergency planning. The BORIS project focuses particularly on the development of cross-border risk analyses having the aim to improve the understanding of the disaster risk, i.e., to enhance the prevention and the preparedness of local communities. Therefore, a probabilistic framework for risk assessment is adopted. More specifically, analyses are performed considering the hazard curves related to the site or equally hazard maps with given probabilities of exceedance in 50 years (i.e., given return periods) as input. For each risk, the evaluation of potential impacts involves the combination of the risk component of hazard, vulnerability and exposure. As no hazard or vulnerability interaction is considered, different models can be used for the two risks. However, to obtain consistent single risk analysis results in a cross-border area, the same models for hazard, vulnerability and exposure should be employed in the confining countries. As also noted in [7], the models used in different nations to perform national risk assessment are different. As example, comparing the models for Italy ([8]) and Slovenia ([9]), it can be noted that they employ non-homogeneous hazard models, different criteria for buildings classification and methods to build fragility curves and variable granularity for building exposure assessment.

Therefore, the models for transboundary single risk assessment need to be harmonized before comparing relative results through risk curves. For instance, the 2020 Euro-Mediterranean Seismic Hazard Model (ESHM2020, [10], [11]) is adopted as the seismic hazard model, as it encompasses all cross-border countries involved in the project and allows to overcome issues related to differences in seismic hazard models of each country. Still, towards vulnerability harmonization, it is proposed to tackle this issue by using a heuristic approach in which a linear combination of vulnerability models is adopted in cross-border countries, as shown in [12] and [13]. Concerning flood risk, a procedure to generate flood hazard maps in cross-border catchments is proposed to harmonize flood hazard and generate maps for common and predefined return periods, while a common vulnerability model is adopted for evaluating flood vulnerability of residential buildings (HAZUS, [14]).

Impacts of single risks are expressed in terms of direct economic losses and affected population. For seismic risk, direct economic losses are usually associated with the physical damage of structures and calculated by defining damage-to-impact conversion criteria. Thus, for each damage level of the adopted damage scale, a cost ratio, i.e., a ratio of the reconstruction cost, is defined. Analogously, people affected by earthquakes can be calculated as a function of buildings' damage. For example, the number of displaced population could be calculated as the number of inhabitants in buildings that reach severe damage and are therefore considered long-term or short-term unusable, while the number of expected deaths can be estimated as a rate of occupants in collapsed or very heavily damaged buildings ([15]; [8]). Direct economic losses due to floods are usually expressed as physical damage to buildings and consequent repair costs as well ([16]; [17]). The counting of people possibly affected by floods should account for all people living in the flooded area. Thus, it also includes the residents of undamaged buildings who are evacuated due to warning issues or lose physical access to the property because of flooded roadways. Moreover, mortality in a flooded area could also increase due to social factors (e.g., age) and flood characteristics (e.g., flood velocity) ([18]; [19]). Therefore, a comparison between seismic and flood risk is performed only in terms of direct economic losses. Specifically, consequence functions for evaluating such losses are harmonized adopting the same replacement cost or reconstruction cost of buildings for both risks. In this way, the expected direct economic losses obtained can be represented and compared using the risk curves.

## 3 APPLICATION AT ITALY-SLOVENIA BORDER

An application of the proposed methodology for harmonized cross-border multi-risk assessment in the transboundary regions between Italy and Slovenia is presented herein. The area selected for this pilot application includes 27 Italian municipalities and 6 Slovenian municipalities, located close to the cities of Gorizia and Nova Gorica (Figure 1). Despite the different number of municipalities selected, the surface area covered by them is quite similar on both sides of the border.

The ESHM20 is adopted as the seismic hazard model. It provides peak ground acceleration (PGA) for six yearly exceedance probabilities corresponding to the return periods of 50, 101, 476, 976, 2500 and 5000 years. As the analyses are performed at the municipal scale, PGA values at the municipal centroid are extrapolated, starting with values at grid points considered by the model and adopting the distance-weighted average principle. Because the ESHM2020 model provides seismic hazard for rock-equivalent outcrop motion, the effects of local soil and other effects on ground motion intensity are taken into account by supplement models. Specifically, local maps with Vs30 values are used to account for the soil effects on the cross-border area analyzed. For the Italian side, the Vs30 map proposed by [20] is used. On the Slovenian side, soil classes and related Vs30 values are estimated at all locations of

buildings based on the known geological characteristics and past studies ([21];[22];[9]); such values are then used to calculate the % of municipality area classified in the 5 soil classes of EC8. Based on the Vs30 values, the amplification factors are determined by considering the guidelines from the draft version of the new EC8 ([23]).

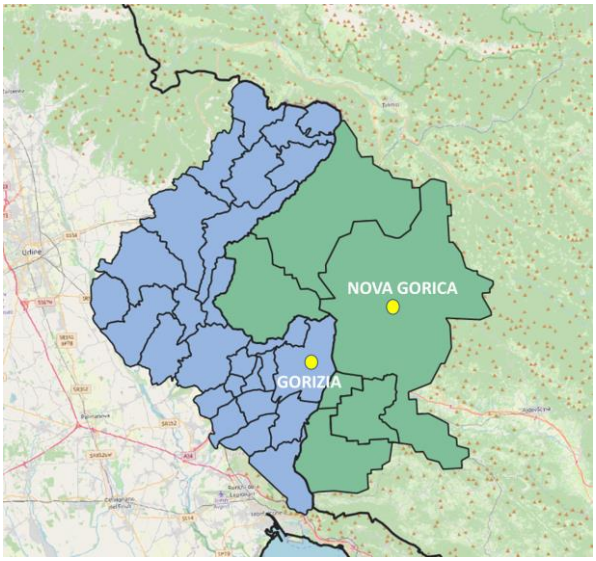


Figure 1. Italian and Slovenian municipalities included in the pilot application.

Transboundary harmonization of seismic vulnerability models is performed by adopting the heuristic approach proposed in [11]. A typology-based building classification is adopted. Six typological building classes for masonry buildings and six typological classes for RC (reinforced concrete) are considered, defined by a combination of period of construction (<1965, 1965-1982, >1982) and number of storeys (1-3, >4). Specifically, the intervals of periods of construction are defined in order to take into account the evolution of the seismic regulations in both countries. Exposure information at the municipal level is derived from census data in Italy (ISTAT, [24]) and from Real Estate Register in Slovenia. For buildings classified as "other" material are not very widespread in Italy and no vulnerability model is officially available in the Italian national risk assessment for these kinds of structures. Therefore, they are considered only in terms of exposure. This means that for each municipality buildings classified as "other" are distributed into the other building classes (i.e., masonry and RC) according to classification rules defined based on their typological features (i.e., age of construction and number of storeys) and the occurrence percentages of masonry and RC typoloties in the municipality. To develop a harmonized vulnerability model also a common damage scale for describing the damage attained by buildings needs to be established. The EMS-98 scale ([25]) is commonly used as a reference in Europe and therefore is adopted in the project. As the Slovenian model used the HAZUS scale ([26]) for describing buildings' vulnerability, conversion rules to convert the 4 damage levels of the HAZUS scale into the 5 grades of the EMS-98 one proposed in [27] are adopted. Finally, harmonized cross-border fragility functions are derived by applying the heuristic approach. It consists of the linear combination of the national typological-based fragility curves of the two countries, aimed at obtaining a set of curves for the specific cross-border context. The coefficients used in the aggregation are calibrated based on (1) differences between building typologies on a given side of the border with respect to typologies widespread in both countries nationwide (that characterized national vulnerability models) and (2) differences in methodologies used for vulnerability assessment in both countries ([12]; [13]). For the evaluation of economic losses,

harmonized earthquake-consequence functions are proposed as well. More specifically, the following percentages of cost of repair or replacement are associated with the 5 damage grades of the EMS-98 scale: 0.02, 0.1, 0.3, 0.6 and 1 of the replacement cost, respectively for damage grades from D1 to D5. It is worth mentioning that the same replacement cost is used both for seismic and flood analysis, in order to allow the comparison of the results. However, it is not possible to define a unique value of such reconstruction cost for the whole pilot area, as it is obviously country-dependent. Therefore, a replacement cost of 1350 €/$m^2$ and of 1250 €/$m^2$ is adopted for the Italian and the Slovenian side of the border, respectively. It is worth mentioning that this value in Slovenia significantly increased in the last couple of years (for about 30%).

In the flood modelling process, the proposed cross-border harmonization of flood hazard maps provided by the two countries allows to generate flood hazard maps for 20, 50, 100, 200, 300 and 500 years return periods flood scenarios. In addition to the flood extension, such maps also provide the expected flood water depth for each scenario. The latter is estimated using the FwDET algorithm ([28];[29]), a GIS (geographic information system) based tool specifically developed for evaluating the water depth using only the extension of inundated surface and the DEM (digital elevation model) ([30]). As mentioned before, for a correct evaluation flood's impact, it is necessary to consider a fine spatial resolution. Thus, detailed building-level flood exposure modelling is adopted, extrapolating buildings' footprint and their spatial distribution through a GIS software and available sources (e.g., OpenStreetMap). HAZUS vulnerability curves ([14]) are adopted for flood analysis. The curves provide the structural damage ratio (i.e., the percentage of maximum damage attainable for structures) as a function of water depth, considering as input characteristics the building type (residential and not-residential) and number of storeys. For the vulnerability characterization of exposed buildings, a logic tree approach is implemented ([30]). Starting by buildings footprint, procedure proposed in [31] is adopted to associate a building usage (residential and not residential) to each building; then, local data aggregated at municipality level for the number of storeys is adopted to associate the building's height (1 storey, 2 storeys, 3 or more storeys). After this process, in the RASOR Platform ([32]), each building is associated to a specific set of vulnerability curves and water depth value to deal with the impact assessment, obtained through the product among the damage ratio (%) (from the vulnerability curves), the replacement cost (€/$m^2$) and the area of the footprint ($m^2$) multiplied for the number of storeys.

By calculating losses for different levels of hazard intensities, risk curves can be assembled. Each point on a risk curve connects the probability of exceedance of an event (e.g., a flood or an earthquake) with the expected losses from that event. A separate risk curve is generated for each considered risk and each point of the analysis (e.g., each municipality). By comparing the risk curves of different risks for the same municipality, it is possible to compare the economic losses expected at events with the same return periods. Further, by calculating the area under a risk curve, the corresponding EAL (Expected Annual Loss) can be obtained. The EAL represents the losses expected on average each year. It accounts for all return periods and is, therefore, a better point of comparison between different risks than losses at an arbitrarily selected return period. For this reason, the ranking of risks in a municipality is performed comparing EALs. However, another useful piece of information is the total EAL, which communicates the loss expected yearly due to the combined effect of all considered risks. By neglecting the potential complex interdependencies between different risks (e.g., domino effects), the total EAL can be calculated as the sum of all single risk EALs.

Figure 2 shows the risk curves obtained for the two cities of Nova Gorica and Gorizia. EAL due to earthquakes is about 844000 € for the town of Gorizia and about 984000 for Nova Gorica, with similar values also of economic losses per square meters (0.54 €/$m^2$ and 0.57

€/m$^2$, respectively). On the contrary, greater differences can be observed in the EALs due to floods: about 1138800 € for Gorizia and 394150 € for Nova Gorica (0.73 €/m$^2$ and 0.21 €/m$^2$, respectively). This means that a possible river flooding would be more relevant for the Italian municipality than for the Slovenian one. Moreover, in Gorizia flood's losses are also higher than the seismic ones, with a EAL ratio (EAL flood over EAL seismic) equal to 1.35. In other words, economic impacts due to a flood event are potentially heavier than the impacts associated with a possible earthquake for this city.

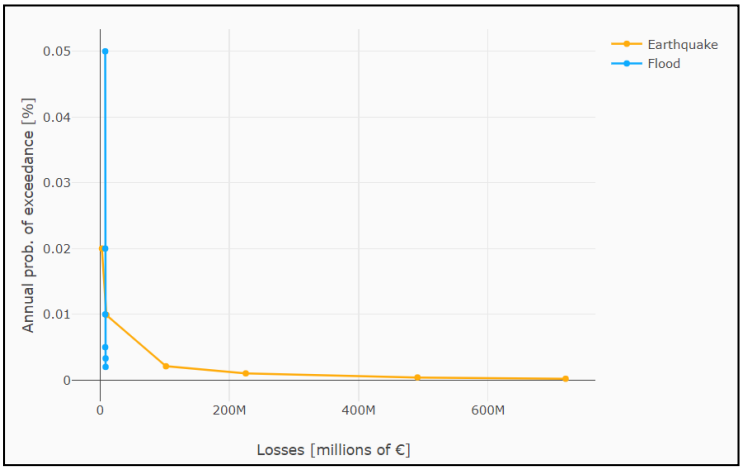


(a)

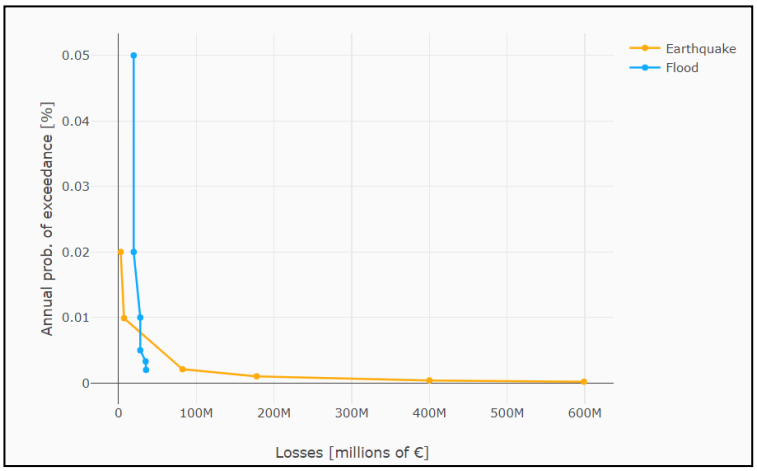


(b)

Figure 2. Risk curves for the two risks analysed for the cities of Nova Gorica (a) and Gorizia (b).

Within the project, a web GIS platform was also developed for viewing data and analysis results (https://boris.eucentre.it). The platform allows to visualize results of single and multi-risk assessment performed in BORIS, as well as input data used. For instance, it is possible to visualize models and data related to exposure modelling (e.g., number of buildings belonging to each building class at municipal level) or to vulnerability modelling (e.g., fragility curves and vulnerability curves adopted). In addition, the platform shows the results of single risk assessments, in terms of economic losses or people affected, and results of multi-risk analysis. The latter are shown both through risk curves and maps. Multi-risk maps show for each municipality in the pilot areas the values of overall EAL (as the sum of seismic and flood EALs). Also, for a better identification of the criticality of one risk over another, the ratio between the

EALs (EAL flood over EAL seismic) are also mapped. Figure 3 shows the map of such ratios as visualized in the platform.

## 4 CONCLUSIONS

This paper presents the results of the application of the methodology for multi-risk assessment presented in the BORIS project in the cross-border area between Italy and Slovenia. Seismic risk and flood risk are analyzed in the framework of multi-layer single risk assessment. Thus, individual analyses are performed for each risk, neglecting possible risk interactions, but harmonizing the procedure for the assessment. Proposals for the standardization of single risk assessment processes mostly concern the type of analysis, the scale of analysis and the metrics used for expressing risks. Risk curves were selected as a tool to show and compare risk results. The application presented here demonstrates that the BORIS approach allows to easily compare and rank different risks that could potentially affect the same area. The use of risk curves also allows a quantitative evaluation of risks, through the calculation of EALs. Also, the evaluation of ratios between the EALs of the two risks analyzed (flood/seismic) for each municipality in the pilot allows to identify the areas where one risk is more relevant with respect to the other. Although the application was demonstrated for the countries of Italy and Slovenia, the approach proposed can be easily adaptable to other contexts in Europe and worldwide. However, additional efforts are needed to harmonize the earthquake-based and flood-based consequence functions.

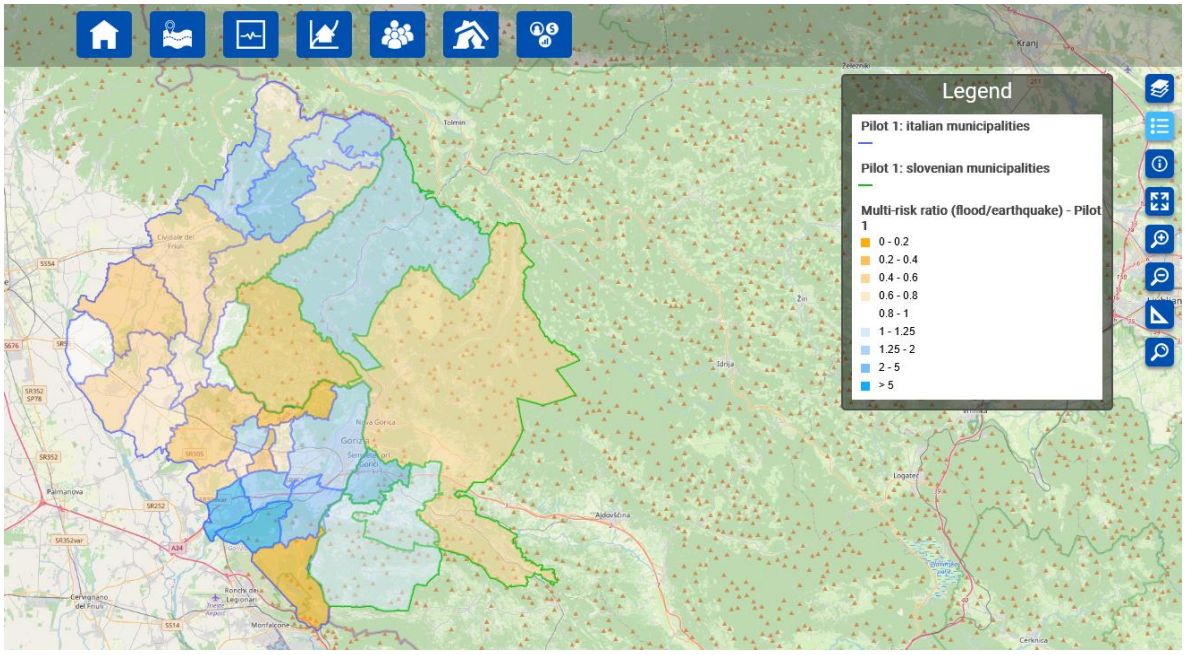


Figure 3. Maps of multi-risk ratios (EAL flood/EAL seismic) for each municipality involved in the application. Source: BORIS web platform (https://boris.eucentre.it).

## ACKNOWLEDGEMENTS

This study was performed in the framework of EU project “BORIS - Cross BOrder RISk assessment for increased prevention and preparedness in Europe” funded by UCPM-2020-PP-AG with grant n. 101004882.

## REFERENCES


[1] W. Marzocchi, A. Garcia-Aristizabal, P. Gasparini, M.L. Mastellone, A. Di Ruocco, Basic principles of multi-risk assessment: a case study in Italy. *Natural hazards*, 62(2), 551-573, 2012.

[2] K. Poljanšek, A. Casajus Valles, M. Marin Ferrer, A. De Jager, F. Dottori, L. Galbusera, B. Garcia Puerta, G. Giannopoulos, S. Girgin, M. Hernandez Ceballos, G. Iurlaro, V. Karlos, E. Krausmann, M. Larcher, A. Lequarre, M. Theocharidou, M. Montero Prieto, G. Naumann, A. Necci, P. Salamon, M. Sangiorgi, M.L. Sousa, C. Trueba Alonso, G. Tsionis, J. Vogt, M. Wood. Recommendations for National Risk Assessment for Disaster Risk Management in EU, EUR 29557 EN, P*ublications Office of the European Union, Luxembourg*, 2019, ISBN 978-92-79-98366-5 (online), doi:10.2760/084707 (online), JRC114650. 2019.

[3] J. Zschau. Where are we with multihazards, multirisks assessment capacities? *drmkc.jrc.ec.europa.eu*. 2017

[4] G. Grünthal, A.H. Thieken, J. Schwarz, K.S. Radtke, A. Smolka, B. Merz. Comparative risk assessments for the city of Cologne–storms, floods, earthquakes. *Natural Hazards*, 38(1), 21-44. 2006.

[5] N.J. Duijm. Recommendations on the use and design of risk matrices. *Safety science*, 76, 21-31. 2015.

[6] K. Fleming, S. Parolai, A. Garcia-Aristizabal, S. Tyagunov, S. Vorogushyn, H. Kreibich, H. Mahlke, Harmonising and comparing single-type natural hazard risk estimations. *Annals of Geophysics* 59(2), So216. 2016.

[7] BORIS. Deliverable 2.1: Comparison of NRA. BORIS project (GA. 101004882; UCPM-2020-PP-AG), http://www.borisproject.eu/wp-content/uploads/2022/06/BORIS-Deliverable-D2.1.pdf. 2022.

[8] M. Dolce, A. Prota, B. Borzi, F. da Porto, S. Lagomarsino, G. Magenes, C. Moroni, A. Penna, M. Polese, E. Speranza, G.M. Verderame, G. Zuccaro. Seismic risk assessment of residential buildings in Italy. *Bulletin of Earthquake Engineering*, 19, 2999–3032, https://doi.org/10.1007/s10518-020-01009-5. 2021.

[9] M. Dolšek, J. Žižmond, A. Babič, N. Lazar Sinković, A. Jamšek, M. Gams, T. Isaković,. Seismic stress test of building stock in the Republic of Slovenia (2020-2050) (in Slovenian). University of Ljubljana, Faculty of Civil and Geodetic Engineering, Institute of Structural Engineering, *Earthquake Engineering and Construction* IT: Ljubljana, Slovenija. 2020.

[10] G.A. Weatherill, S.R. Kotha, F. Cotton, L. Danciu. Innocations in ground motion characterization for the 2020 European seismic hazard model (ESHM2020). *7th World Conference on Earthquake Engineering, Sendai, Japan, September 2020*. 2020.

[11] L. Danciu, S. Nandan, C.G. Reyes, R. Basili, G. Weatherill, C. Beauval, A. Rovida, S. Vilanova, K. Sesetyan, P.Y. Bard, F. Cotton, S. Wiemer, D. Giardini. The 2020 update of the European Seismic Hazard Model - ESHM20: Model Overview. EFEHR Technical Report 001, https://doi.org/10.12686/A15. 2016.

[12] BORIS. Deliverable 4.1: Guidelines for cross-border risk assessment: Shared framework for single and multi-risk assessment at cross-border sites. BORIS project (GA.

101004882; UCPM-2020-PP-AG), http://www.borisproject.eu/wp-content/uploads/2022/06/BORIS-Deliverable-D4.1.pdf. 2022.

[13] M. Polese, G. Tocchi, M. Dolsek, A. Babic, M. Faravelli, D. Quaroni, B. Borzi, A. Prota. Seismic risk assessment in transboundary areas: the case study on the border between Italy and Slovenia. *XIX ANIDIS Conference, Seismic Engineering in Italy*, September 2022, Turin, Italy. 2022.

[14] FEMA. HAZUS-MR4 Technical manual. *Federal Emergency Management Agency (FEMA)*. 2009.

[15] G. Zuccaro, F. Cacace. Seismic casualty evaluation: the Italian model, an application to the L'Aquila 2009 event. In: Spence R, So E, Scawthorn C (eds) Human casualties in earthquakes. Advances in natural and technological hazards research. *Springer, Netherlands*, pp 171–184. 2011.

[16] J. Huizinga, H. Moel, W. Szewczyk, W. Global flood depth-damage functions. Methodology and the database with guidelines. *EUR 28552 EN*. doi: 10.2760/16510. 2017.

[17] O.M. Nofal, J.W. van de Lindt, T.Q. Do. Multi-variate and Single-Variable Flood Fragility and Loss Approaches for Buildings. *Reliab. Eng. Syst. Saf*. 2020.

[18] M.L. DeKay, G.H. McClelland. Predicting loss of life in cases of dam failure and flash flood. Risk Anal., 13, 193–205. 1993.

[19] S. Jonkman, M. Boˇckarjova, M. Kok, P. Bernardini. Integrated hydrodynamic and economic modelling of flood damage in The Netherlands. *Ecol. Econ.* 66 (1) (2008) 77-90. 2008.

[20] F. Mori, A. Mendicelli, M. Moscatelli, G. Romagnoli, E. Peronace, G. Naso G. A new Vs30 map for Italy based on the seismic microzonation dataset, *Engineering Geology*, Volume 275, https://doi.org/10.1016/j.enggeo.2020.105745. 2020.

[21] M. Ferlan, U. Herlec. Digital geological map in GIS, Geographic information systems in Slovenia 1999-2000. *Proceedings of the symposium, Ljubljana*, 26. September 2000: 209-225 (in Slovenian). 200.

[22] M. Ferlan, U. Herlec, U. Conceptual model of GIS for geology, Geographic information systems in Slovenia 2001-2002. *Proceedings of the symposium*, Ljubljana, 23. September 2002: 87-95 (in Slovenian). 2002.

[23] CEN. prEN 1998-1-1:2021 – Eurocode 8: Earthquake resistance design of structures, Working draft, CEN/TC 250/SC 8 N 1141. 2022.

[24] ISTAT (National Institute of Statistics). 15° Censimento generale della popolazione—Dati sulle caratteristiche strutturale della popolazione, delle abitazioni e variabili. http://www.istat.it/it/archivio/104317. 2011 (in Italian)

[25] G. Grünthal. European Macroseismic Scale, *Chaiers du Centre Européen de Géodynamique et de Séismologie*, vol. 15 Luxembourg. 1998.

[26] FEMA. HAZUS MH 2.1, Technical Manual, Multi-Hazard Loss Assessment Methodology. Federal Emergency Management Agency, Washington, D.C., USA. 2015.

[27] S. Lagomarsino, S. Giovinazzi. Macroseismic and mechanical models for the vulnerability and damage assessment of current buildings, Bulletin of Earthquake Engineering 4:415–443. 2006.

[28] S. Cohen, A. Raney, D. Munasinghe, J.D. Loftis J, A. Molthan, J. Bell, L. Rogers, J. Galantowicz, G.R. Brakenridge7, A.J. Kettner, Y. Huang, Y. Tsang. The Floodwater Depth Estimation Tool (FwDET v2.0) for Improved Remote Sensing Analysis of Coastal Flooding. *Natural Hazards and Earth System Sciences*, 19, 2053–2065. 2019.

[29] B. Peter, S. Cohen, R. Lucey, D. Munasinghe, A. Raney. A Google Earth Engine implementation of the Floodwater Depth Estimation Tool (FwDET-GEE), https://doi.org/10.7910/DVN/JQ4BCN, *Harvard Dataverse*, V5. 2020.

[30] BORIS. Deliverable 5.1: Seismic risk, flood risk and multi-risk assessment at pilot cross-border sites. BORIS project (GA. 101004882; UCPM-2020-PP-AG), http://www.borisproject.eu/wp-content/uploads/2022/06/BORIS-Deliverable-D5.1.pdf. 2022.

[31] M. Pesaresi, P. Politis. GHS built-up surface grid, derived from Sentinel2 composite and Landsat, multitemporal (1975-2030). European Commission, Joint Research Centre (JRC). doi:10.2905/D07D81B4-7680-4D28-B896-583745C27085. 2022.

[32] C. Arrighi, L. Rossi, E. Trasforini, R. Rudari, L. Ferraris, M. Brugioni, S. Franceschini, F. Castelli. Quantification of flood risk mitigation benefits: A building-scale damage assessment through the RASOR platform, Journal of Environmental Management, Volume 207, 2018, Pages 92-104, ISSN 0301-4797, https://doi.org/10.1016/j.jenvman.2017.11.017. 2018.

COMPDYN 2023
9th ECCOMAS Thematic Conference on
Computational Methods in Structural Dynamics and Earthquake Engineering
M. Papadrakakis, M. Fragiadakis (eds.)
Athens, Greece, 12-14 June 2023

# DEFINITION OF MULTI-HAZARD VULNERABILITY INDICATORS FOR CULTURAL HERITAGE BUILDINGS

**M. Lazzati[1], S. De Angeli[2], G. Boni[2], S. Cattari[2], and X. Romão[3]**

[1] Dept of. Electrical, Electronics and Telecommunication Engineering and Naval Architecture, University of Genoa
Via All'Opera Pia 11, Genoa, Italy
e-mail: marco.lazzati9@gmail.com

[2] Dept. of Civil, Chemical and Environmental Engineering, University of Genoa
Via Montallegro 1, Genoa, Italy
e-mail: {silvia.deangeli, giorgio.boni, serena.cattari}@unige.it

[3] CONSTRUCT-LESE, Faculty of Engineering, University of Porto
Rua Dr. Roberto Frias, 4200-465, Porto, Portugal
e-mail: xnr@fe.up.pt

## Abstract

*The Sendai Framework for Disaster Risk Reduction recognizes the importance of cultural heritage for society and emphasize the need to assess their vulnerability from multiple hazards. Developing adequate multi-hazard vulnerability assessment processes is fundamental to this end. Still, given the large number of cultural heritage assets that can be exposed to different hazards in a region, the development of simplified multi-hazard approaches that can provide an initial risk screening of multiple assets to identify the need for more detailed analyses plays a central role for prioritization.*

*In this context, we propose an index-based multi-hazard vulnerability assessment methodology for churches, able to consider vulnerability from earthquakes, floods, and fire. The proposed multi-hazard index has been obtained by combining a series of indicators, defined by performing a literature review. The indicators were selected due to their relevance for the vulnerability classification of the assets but also their ability to be easily scored from remotely sensed data or fast in situ screening. The presented research describes in detail each indicator and provides insights on how they should be scored and integrated to obtain the overall multi-hazard vulnerability index for churches. The vulnerability indicators constitute the primary component of a five-step, multi-hazard vulnerability assessment methodology that can be flexibly applied as a prioritization method to rapidly screen multiple assets and identify the most vulnerable churches that may require a more detailed assessment. The methodology is tested on a series of case study applications in Portugal and Italy.*

**Keywords:** Cultural Heritage, Churches, Multi-hazard Taxonomy, Earthquake Flood, Fire.

## 1 INTRODUCTION

The Sendai Framework for Disaster Risk Reduction [1] recognizes the importance of cultural heritage for society, thus emphasizing the need to assess the impact that potential hazards may have on the built cultural heritage. Developing adequate multi-hazard vulnerability assessment and risk management processes is fundamental to this end. Still, given the large number of cultural heritage assets that are exposed to different hazards, the development of simplified multi-hazard approaches that can provide an initial risk screening of multiple assets plays a central role in prioritization, allowing the decision maker to identify the assets where to further invest in more detailed risk analyses [2].

Internationally, in the last decade, there has been an increasing attention for multi-hazard and multi-risk, and for the impacts resulting from compound and consecutive disasters [3]–[6]. Many regions of the world are prone to multiple types of potentially interacting and overlapping natural hazards and only through an analysis of all the relevant threats, an effective risk reduction can be carried out [7]. Moreover, the risk of consecutive disasters will increase due to growing exposure, the interconnectedness of human society, and the increased frequency and intensity of nontectonic hazards [8]. The adverse impacts on lives and livelihoods, and regional and local economies are felt more and more. Losses to both tangible and intangible cultural heritage during these disasters are increasing as well. These losses include those to sites, structures and artifacts of cultural significance, as well as impacts to cultural tourism and the financial resources these sites introduce to local communities [9].

There have been various multi-hazard vulnerability assessment studies published in literature, each with their own unique perspectives and applications. Papathoma-Köhle et al. [10] created an index for dynamic flooding in mountain areas demonstrating the transferability of vulnerability assessment approaches between hazard types, reducing the amount of required data and offering a tool that can be used in areas where empirical data are not available. Kappes et al. [11] adapted the indicator-based tsunami vulnerability assessment indicator PTVA by Papathoma [12] to be applicable in a multi-hazard context. In their case study the vulnerability of buildings to debris flows, shallow landslides, and river flooding for emergency planning and for general risk reduction purposes is assessed. The implementation of the methodology leads to reasonable results indicating the vulnerable buildings and supporting the priority setting of different end-users according to their objectives. The study of Gentile et. al [13] focus on scoring, selecting, and developing physical fragility and multi-hazard vulnerability models for assets of interest, with particular emphasis on buildings. The approach is demonstrated for the buildings of the virtual urban testbed 'Tomorrowville', considering earthquakes, floods, and debris flows as case-study hazards. Moreover, the exposure and vulnerability assessment of different assets from a multi-hazard perspective is the main goal behind the development of the global exposure database for all (GED4ALL [14]). It covers several assets, including buildings, roads, railways, and lifelines, and it was developed considering earthquakes, volcanoes, floods, tsunamis, storms, cyclones, and drought.

Despite the increasing attention to this topic, the literature on cultural heritage multi-hazard vulnerability assessment, and specifically churches, is limited. Several authors addressed this topic from a single hazard perspective focusing on earthquake [15]–[22], flood [23], [24], fire [9], [25], [26], and windstorm [27], among others. However only few authors investigated the topic from a multi-hazard point of view. Sevieri et al. [28] introduced a multi-hazard risk prioritization framework specifically developed for cultural heritage assets. The proposed framework relies on a multilevel rapid-visual-survey (RVS) form for the multi-hazard exposure data collection and risk prioritization of case-study assets. The collected data are used for the computation of seismic- and wind-risk prioritization indices, specifically calibrated for

cultural heritage assets with various structural and non-structural features. Julià and Ferreira [29] contributed to paving the way towards the establishment of future multi-hazard vulnerability and risk assessment methodologies for Historic Urban Areas by offering a comprehensive review of some of the most relevant methodologies proposed to date in this research area.

In Europe, a significant portion of cultural heritage structures are churches [30]. Assessing the vulnerability of churches under a multi-hazard perspective is crucial for the preservation of cultural heritage buildings and the safety of the people who use them. Churches are not only religious and historical landmarks but also cultural and social assets that hold a significant place in the community. By identifying vulnerabilities and developing appropriate strategies to reduce multiple risks, the community can protect these valuable assets and ensure their continuity for future generations. However, there is a noticeable lack of attention from the scientific community towards this topic. This gap in knowledge and research motivated to delve into this area and try to develop an indicator-based methodology for the multi-hazard vulnerability assessment of churches.

The focus of this paper is on the multi-hazard vulnerability assessment of churches, which is achieved through the development of an indicator-based methodology. The proposed methodology can contribute towards the assessment of the impact of multiple hazards (fires, earthquakes, and floods) on cultural heritage buildings, and establish a first basis for further research in this field. Furthermore, the methodology can be a flexible prioritization method that can be applied as a basis for the fast screening of multiple assets.

The research is presented as follows. Section 2 focuses on the selection of churches vulnerability indicators for fires, earthquakes, and floods and details the review process that informed the selection. Section 3 outlines the vulnerability assessment methodology and provides a step-by-step guide for its application. Section 4 introduces two case study areas in Marche Region, Italy, and in the city of Porto, Portugal, where the methodology has been tested. Section 5 presents the results of the case study applications. In conclusion, Section 6 synthesizes the findings presented throughout the paper and offers an open discussion on the potential field of application of this methodology and its future developments.

## 2 MULTI-HAZARD VULNERABILITY INDICATORS FOR CHURCHES

In this section, the selected churches vulnerability indicators for each of the considered hazards are introduced. Fire, earthquake, and flood have been selected as a first set of hazards to investigate, because of the following two reasons:

1. Authors expertise encompasses earthquake, flood and fire risk assessment and management.
2. Most of the available literature on cultural heritage vulnerability assessment focuses on these three hazards.

Nevertheless, the proposed approach can be easily expanded in the future to cover other hazards, such as windstorms or landslides.

The choice of indicators is a key element for the development of the overall methodology (Section 3) and must be designed to align with the overall methodological aim: they should be easily obtainable and provide a comprehensive view of the building's vulnerability from different hazards. For each hazard, a subset of those usually adopted to perform the vulnerability assessment from a single hazard perspective has been selected since the procedure does not intend to replace them but instead outline a multi-risk prioritizing procedure. The source of the data (remote assessment or in-situ survey) is also a key factor, as it impacts the speed of the screening process, and therefore, the overall rapidity of the assessment. The final list of the selected vulnerability indicators for earthquake, flood and fire are reported in Table 1.

| ID | Indicator name | Source | Diff. level | References |
|---|---|---|---|---|
| | *Earthquake indicators* | | | |
| **EQ.1** | Height of the surrounding buildings - interaction with adjacent buildings | Remote and in-situ | 1 | [11], [19], [29], [31] |
| **EQ.2** | Height of the church | Remote and in-situ | 1 | [11], [15], [19] |
| **EQ.3** | Quality of the masonry | In-situ survey | 2 | [11], [15], [18], [19] |
| **EQ.4** | Roof condition | In-situ survey | 2 | [15]–[17], [19], [29] |
| **EQ.5** | Predominance of in-plane or out-of-plane mech. | In-situ survey | 2 | [19], [32] |
| **EQ.6** | Openings of wall façade | In-situ survey | 1 | [19], [31] |
| **EQ.7** | Type of soil | In-situ survey | 2 | [19] |
| **EQ.8** | Site morphology | In-situ survey | 2 | [18], [19] |
| **EQ.9** | General external state of conservation | In-situ survey | 1 | [19] |
| **EQ.10** | Bell tower presence | Remote and in-situ | 1 | [19], [33] |
| | *Flood indicators* | | | |
| **FL.1** | Number of floors | In-situ survey | 1 | [11], [23], [34] |
| **FL.2** | Dry feature of the masonry | In-situ survey | 2 | |
| **FL.3** | Opening of wall facade on the first floor | Remote and in-situ | 1 | |
| **FL.4** | Quality of the drainage system | Remote and in-situ | 2 | |
| **FL.5** | Number of exposed facades | Remote and in-situ | 1 | |
| **FL.6** | Protection by vegetation | Remote and in-situ | 1 | [11] |
| **FL.7** | Type of soil | In-situ survey | 2 | |
| **FL.8** | Slope of the ground | Remote and in-situ | 1 | |
| | *Fire indicators* | | | |
| **FI.1** | Electric Installations | In-situ survey | 2 | [26] |
| **FI.2** | Gas installations | In-situ survey | 2 | [26] |
| **FI.3** | Distance of the surrounding buildings | Remote and in-situ | 1 | |
| **FI.4** | Exterior hydrants | Remote and in-situ | 1 | [26] |
| **FI.5** | Automatic extinguish system | In-situ survey | 1 | [26] |
| **FI.6** | Active suppression system | In-situ survey | 1 | [26] |
| **FI.7** | Presence of vegetation | Remote and in-situ | 1 | [26] |
| **FI.8** | Security cameras for intentional fires | In-situ survey | 1 | |
| **FI.9** | Average occupancy | Remote and in-situ | 1 | . |
| **FI.10** | Building content | Remote and in-situ | 1 | [26] |
| **FI.11** | Open flames | Remote and in-situ | 1 | |

Table 1: List of the selected churches vulnerability indicators for earthquake, flood, and fire

For each indicator, together with the ID, name, and references, the following fields have been added:

- 'Source', that indicates the different sources of information that can be used to assess the considered indicator, including remote assessments or in-situ surveys.
- 'Diff. level', that indicates the level of difficulty in compiling and elaborating such information. Value '1' means that non experts can easily assess the indicator, while value '2' refers to the case where only experts can reliably assess the indicator.

Each indicator can assume a discrete vulnerability level, ranging from zero to three. Zero represents the best case, where the indicator has no influence on the vulnerability of the church. Three represents the worst case, where the element under evaluation is in poor conditions and can significantly increase the church vulnerability. The characterization of the different levels was informed by hazard-specific literature. As an example, a selection of vulnerability indicators and the description of the different levels they can assume is reported in Table 2.

| Indicator | Vuln. level | Description |
|---|---|---|
| **EQ.1** Height of the surrounding buildings - interaction with adjacent buildings | 0 | No one buildings are close enough and tall enough to potentially collapse on the church. The interaction with adjacent/connected buildings is considered negligible in altering the seismic response of church. |
| | 1 | At least one side of the church can be damaged by the collapse of a neighbourhood building. The interaction with adjacent/connected buildings is considered small to moderate in negatively altering the seismic response of church. |
| | 2 | At least two sides of the church can be damaged by the collapse of a neighbourhood building. The interaction with adjacent/connected buildings is considered moderate to high in negatively altering the seismic response of church. |
| | 3 | At least three sides of the church can be damaged by the collapse of a neighbourhood building. The interaction with adjacent/connected buildings is considered very high in negatively altering the seismic response of church. |
| **EQ.10** Bell tower presence | 0 | The bell tower is not present |
| | 3 | The bell tower is present |
| **FL.6** Protection by vegetation | 0 | The building is surrounded from vegetations that, in case of flood, will decrease the velocity of the water and block the transported materials |
| | 1 | No presence of vegetation around the building / the building is surrounded from an irrelevant density of vegetation |
| | 2 | The building is surrounded by low vegetation/bushes that, in case of flood, can be carried together with the flow slightly increasing the damage to the building |
| | 3 | The building is surrounded by tall vegetation that, in case of flood, can be carried together with the flow significantly increasing the damage to the building |
| **FI.10** Building content | 0 | The content is not flammable |
| | 3 | The content is flammable |

Table 2: Examples of earthquake, flood and fire vulnerability indicators and description of the different levels, from zero to three, that they can assume

Most indicators were assigned four vulnerability levels, with some exceptions. As also shown in Table 2, there are some indicators, such as 'EQ.10 Bell tower presence', which

require a binary evaluation, such as 'present'/'not present'. Therefore, only two levels of vulnerability are needed.

A detailed description of each vulnerability indicator provided in Table 1, and all the values that can assume, similarly to what has been reported as a sample in Table 2, is available at: https://github.com/silviadeangeli/Churches_MultiHazard_Vulnerability.

## 3 A MULTI-HAZARD VULNERABILITY ASSESSMENT METHODOLOGY FOR CHURCHES

The vulnerability indicators for churches, as described in Section 2, constitute the primary component of a five-step, multi-hazard vulnerability assessment methodology, as illustrated in Figure 1. This methodology can be flexibly applied as a prioritization method to rapidly screen multiple assets and identify the most vulnerable churches that may require a more detailed assessment from a multi-hazard perspective. In this section, the methodology is introduced, together with a step-by-step guide for its application.




Figure 1: The five steps of the multi-hazard vulnerability assessment methodology for churches

### 3.1 Step 1. Identification of the study area and the relevant hazards

The first step in conducting a cultural heritage assessment is to determine the localization and extent of the area to be investigated, which significantly impacts the time and effort required to complete the assessment. This aspect is closely related to the study's ultimate goal. Cultural heritage assessment and prioritization can be commissioned on different administrative units or specific areas within administrative boundaries, spanning municipal, regional, or national scales.

Once the relevant administrative units have been identified based on the study's objective, all potential hazards must be identified using historical records or existing hazard analyses. It is crucial to consider the increasing frequency of disasters in areas previously not considered at risk due to climate change.

### 3.2 Step 2. Selection of churches inside the study area

Once the extent of the study area has been determined (Step 1), all the cultural heritage buildings located within it need to be identified and geolocated. The methodology presented in this study has been specifically developed for masonry churches, so these buildings must be selected accordingly. However, this approach can be generalized in the future to include other cultural heritage buildings, such as museums or religious buildings other than churches.

Geolocating the churches allows you to determine the potential hazards that each of them face by interpolating available hazard maps and analyzing past hazard events (see Step 1). It

also allows to identify the physical and social context in which the church is situated, such as whether it is in an urban or rural area, a densely populated area, or a tourist area.

This information represents the basis to prioritize the churches based on their level of exposure and vulnerability to natural hazards, as well as their cultural and historical significance, to determine which buildings require more urgent protection and conservation measures.

Overall, geolocating cultural heritage buildings such as churches is a crucial step in the process of assessing their vulnerability to natural hazards and developing effective risk mitigation strategies to preserve these important assets for future generations.

### 3.3 Step 3. Assessment of the vulnerability indicators

In Step 3 of the methodology, a multi-hazard index-based vulnerability assessment is conducted for each identified church (see Step 2). Vulnerability levels ranging from zero to three are assigned to each hazard indicator listed in Table 1. The vulnerability sheet can be compiled using information obtained remotely or through on-site surveys by both experts and non-experts. This step represents the core of the overall methodology.

The level of uncertainty associated with the final vulnerability assessment depends heavily on the experience of the compiler. In the case of an expert compiler, vulnerability levels can be assigned with a high degree of confidence, and only one level out of the four possibilities can be chosen assigning it a 100% probability. This is referred to as a 'deterministic' assessment.

However, if the compiler is not sufficiently expert or the survey does not allow to have sufficient confidence in the assessment of the vulnerability level, it is reasonable to introduce uncertainty into the methodology by assigning a certain probability to each vulnerability level. This is referred to as a 'probabilistic' assessment.

The 'deterministic' assessment can then be seen as a special case of the more general 'probabilistic' assessment, where 100% probability is assigned to only one level for all considered indicators. The effect of uncertainty on the vulnerability assessment has been tested in case studies presented in Section 4.

### 3.4 Step 4. Weighting and combination of the indicators in a multi-hazard vulnerability index

The global multi-hazard vulnerability index $I_{MH}$ for each church can be generically computed according to eq. (1):

$$I_{MH} = \sum_{h=1}^{n}(I_h \cdot w_h) \quad (1)$$

Where: $h$ is the considered hazards, $n$ is the number of hazards considered, $I_h$ is the single hazard vulnerability indicator, and $w_h$ is the weight attributed to each hazard with $\sum_{h=1}^{n} w_h = 1$.

Each single hazard vulnerability indicator $I_h$ is computed as a weighted sum of the values assumed by every single indicator, according to eq. (2)

$$I_h = \sum_{i=1}^{m}(w_i * \sum_{v \in L_i}(v * P_V^i(v))) \quad (1)$$

Where: $i$ is each of the considered hazard indicators for hazard $h$, $m$ is the number of indicators considered for hazard $h$, $w_i$ is the weight attributed to each indicator $i$ with $\sum_{i=1}^{m} w_i = 1$, $L_i$ is the vector of the different discrete vulnerability levels $v$ for the indicator $i$, $P_V^i(v)$ is the Probability Mass Function of the vulnerability levels $v$.

In this current stage of development of the methodology we focused on three specific hazards ($n=3$: earthquake, flood, and fire) and we assumed to assign the same importance to each

of them. Therefore, eq. (1) and (2) can be further simplified, assuming the final formulations expressed respectively by eq. (3) and (4a), (4b), (4c):

$$I_{MH} = \frac{I_{EQ}+I_{FL}+I_{FI}}{3} \tag{3}$$

Where $I_{EQ}$ is the earthquake vulnerability index, $I_{FL}$ the flood vulnerability index, and $I_{FI}$ the fire vulnerability index, calculated as:

$$I_{EQ} = \sum_{i=1}^{10}(w_{EQ_i} * \sum_{v \in L_i}(v * P_V^{EQ_i}(v))) \tag{4a}$$

$$I_{FL} = \sum_{i=1}^{8}(w_{FL_i} * \sum_{v \in L_i}(v * P_V^{FL_i}(v))) \tag{4b}$$

$$I_{FI} = \sum_{i=1}^{11}(w_{FI_i} * \sum_{v \in L_i}(v * P_V^{FI_i}(v))) \tag{4c}$$

The weights associated with each indicator, as reported in Table 3, have been assigned on an expert judgment informed by the analyzed vulnerability literature.

| ID | Indicator name | Weight |
|---|---|---|
| **EQ.1** | Height of the surrounding buildings | 0,15 |
| **EQ.2** | Height of the church | 0,15 |
| **EQ.3** | Quality of the masonry | 0,1 |
| **EQ.4** | Roof condition | 0,1 |
| **EQ.5** | Predominance of in-plane or out-of-plane mechanisms | 0,1 |
| **EQ.6** | Openings of wall façade | 0,05 |
| **EQ.7** | Type of soil | 0,05 |
| **EQ.8** | Site morphology | 0,1 |
| **EQ.9** | General external state conservation | 0,1 |
| **EQ.10** | Bell tower presence | 0,1 |
| **FL.1** | Number of floors | 0,18 |
| **FL.2** | Dry feature of the masonry | 0,09 |
| **FL.3** | Opening of wall facade on the first floor | 0,14 |
| **FL.4** | Quality of the drainage system | 0,09 |
| **FL.5** | Number of exposed facades | 0,09 |
| **FL.6** | Protection by vegetation | 0,09 |
| **FL.7** | Type of soil | 0,14 |
| **FL.8** | Slope of the ground | 0,18 |
| **FI.1** | Electric Installations | 0,1 |
| **FI.2** | Gas installations | 0,1 |
| **FI.3** | Distance of the surrounded building | 0,05 |
| **FI.4** | Exterior hydrants | 0,1 |
| **FI.5** | Automatic extinguish system | 0,1 |
| **FI.6** | Active suppression system | 0,15 |
| **FI.7** | Presence of vegetation | 0,05 |
| **FI.8** | Security cameras for intentional fires | 0,05 |
| **FI.9** | Building content | 0,01 |
| **FI.10** | Open flames | 0,15 |
| **FI.11** | Average occupancy | 0,05 |

Table 3: List of the vulnerability indicators for earthquake, flood, and fire and their corresponding weights

### 3.5 Step 5. Analysis and interpretation of the results

The result of this methodology is a multi-hazard vulnerability index $I_{MH}$, representing the average vulnerability of the building based on the hazards considered. While this value can

provide a general idea of the building's overall vulnerability, it can be difficult to directly use its absolute value as a criterion for prioritization. In other words, it would be quite challenging to identify a vulnerability threshold above which we can consider a church as vulnerable, and therefore needing a deeper assessment.

Nevertheless, the multi-hazard vulnerability index $I_{MH}$ can be used to rank the assets from the most to the least vulnerable, identifying the first set of buildings that would require a deeper assessment. As a second step, it is then possible to evaluate which hazard contribute most to the overall vulnerability of each church analyzing the global multi-hazard vulnerability index $I_{MH}$ in comparison with the single hazard indices $I_{EQ}, I_{FL}$ and $I_{FI}$. By examining the specific hazard indicators, the expert will have a clear understanding of which hazard poses the greatest threat, providing valuable information for decision-making.

## 4 ITALY AND PORTUGAL CASE STUDIES

In this section, two case studies will be presented to demonstrate the applicability of the proposed methodology in different geographic contexts. The first case study includes two churches located in Porto, Portugal, while the second examines three churches in the Marche region, Italy. These two areas have been selected due to their high exposure to booth flood and seismic hazards. Additionally, these two case studies are representative of two different urban and social contexts, since the churches in Porto are in densely populated touristic areas, while in the Marche case study churches are in rural villages or not densely urbanized areas.

Applying the methodology described in Section 3, the overall multi-hazard vulnerability of all these five churches has been evaluated. The vulnerability sheets have been compiled using information obtained by on-site visits simulating the compiling of both experts and non-experts, i.e., performing both a 'deterministic' and ‘probabilistic’ assessment (see Section 3.3). In such a way, it has been possible to evaluate the effect of the uncertainty in the estimation of the different vulnerability indices on the overall vulnerability assessment.

### 4.1 Porto case study

Porto region is highly susceptible to flood hazard [35], [36], and around 50% of all occurrences are concentrated in the Porto Metropolitan Area, mainly the Porto city center and nearby riverside areas of the Douro River [37].

The two churches selected in the case study area, the Capela das Almas, and the Igreja de Santo Ildefonso, are depicted in Figure 2. Both churches are situated in high-density urban areas. The Capela das Almas is located on the busy commercial street of Rua de Santa Catarina, while the larger Igreja de Santo Ildefonso is situated in an elevated part of the city. These two churches serve active functions inside the urban context of the city of Porto. The Capela das Almas is a popular attraction for both locals and visitors, offering services that can be attended without any charge. Santo Ildefonso is also active for services but requires a fee for visiting and houses a museum within the church. Both churches attract people throughout the year and possess valuable content within their walls. Santo Ildefonso is adorned with ornate gold and wood furnishings, while Capela das Almas has its own unique character, with significant wood furnishings.

Despite being Porto a city frequently affected by floods, these churches did not sustain any damage during the devastating flood event of January 2023. This allowed for a thorough analysis of both the interior and exterior of the buildings.

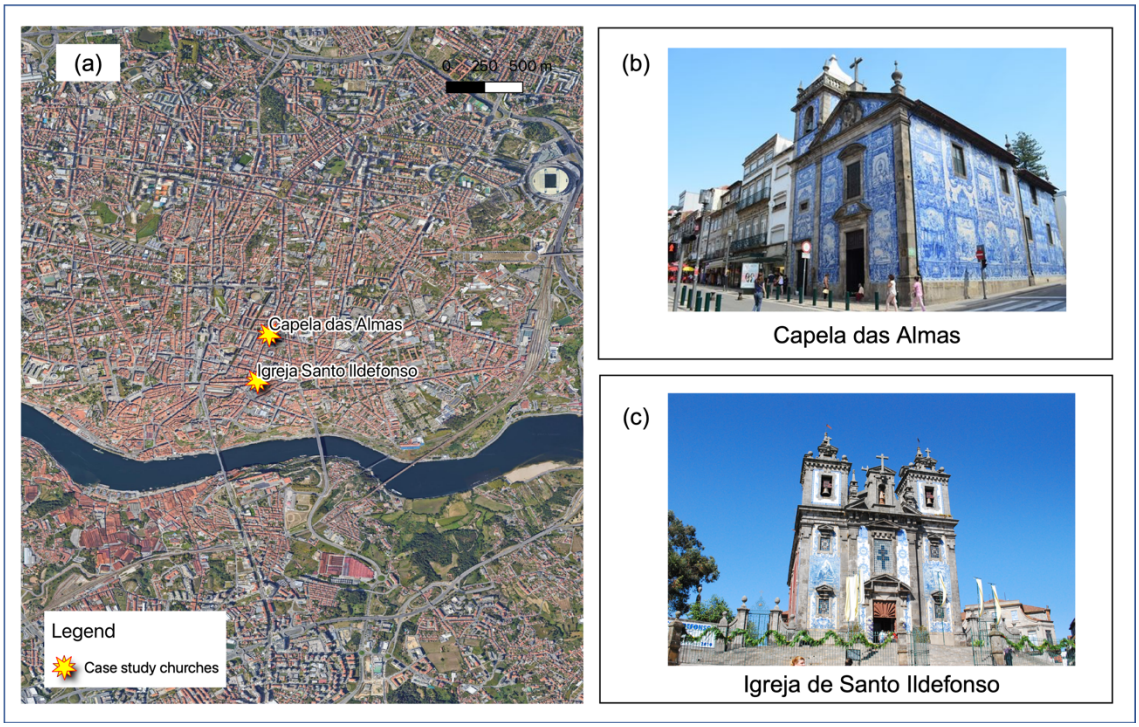


Figure 2: Case study churches located in the city of Porto, Portugal: (a) geolocation of the two churches; (b) exteriors of Capela das Almas; (c) exteriors of Igreja de Santo Ildefonso.

## 4.2 Marche region case study

On September 15th, 2022, the region was hit by a storm system that originated on the Tyrrhenian side of the peninsula. Initially, the phenomena affected the central-northern mountainous and high-hill areas of the region. Later in the afternoon, a self-regenerating and stationary system formed, affecting not only the inland areas but also the hilly and coastal part of the province of Ancona. Heavy rainfall caused a rapid rise in the hydrometric levels of several basins, including Candigliano, Cesano, Misa, and Sentino, leading to exceeding the alarm threshold levels in different sections and widespread flooding [38]. Among others, the city of Senigallia, where one of the case study churches is located, was flooded, causing severe damages.

On November 9th at 7:07 a.m., an earthquake of magnitude Ml 5.7 (Mw 5.5) was recorded by the Italian Seismic Network. The epicenter was in the sea, about 30 km from the Marche coast in the province of Pesaro Urbino. The churches in the earthquake-affected area sustained physical damage both inside and outside.

The three churches selected in the case study area are depicted in Figure 3. The Church of SS. Vincenzo and Anastasio in Roncosambaccio (Figure 3, panel (b.1)) is in the internal part of the Marche's region and it has been externally damaged by the earthquake, as illustrated in Figure 3, panel (b.2). The church, located on a hill, has suffered from seismic waves amplification. Although it was impossible to access the interior of the church, a local team of experts was able to enter a few days after the earthquake, and a video inspection has been available to support the assessment of some of the vulnerability indicators from remote.

The Sanctuary of Santa Maria Goretti in Coronado (Figure 3, panel (c.1)), is located on the top of a hill. The church show significant damages on the external masonry and signs of humidity are presents on the bottom of the building. Moreover, the church is connected with another building on one side, as shown in Figure 3, panel (c.2). This structural layout can play

an important role in case of earthquake due to pushing actions that may arise in consequence to bad connections between the two elements.

The Senigallia Cathedral (Duomo di Senigallia, in Italian; Figure 3, panel (d)) is in Senigallia city center, close to the Misa River. The church has been impacted by booth flood and earthquake events. During the field-survey conducted in January 2023, the church showed a significant presence of humidity in the bottom part of the building. Moreover, the church showed some cracks on the outside of the building.

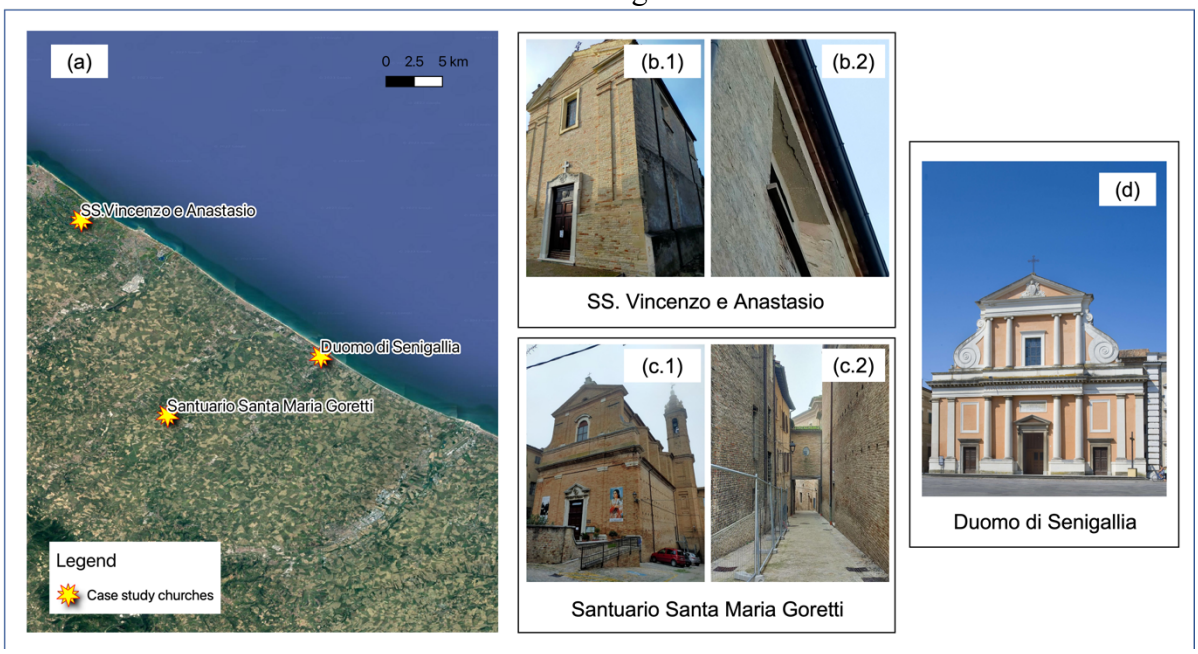


Figure 3: Case study churches located in Marche region, Italy: (a) geolocation of the three churches; (b.1-2) exteriors of SS. Vincenzo e Anastasio; (c.1-2) exteriors of Santuario di Santa Maria Goretti; (d) exteriors of Duomo di Senigallia.

## 5 RESULTS AND DISCUSSION

Using the methodology described in Section 3, we conducted an overall multi-hazard vulnerability assessment of the five churches introduced in Section 4. We compiled vulnerability sheets by gathering information from on-site surveys simulating the compiling of both experts and non-experts, i.e., performing both a 'deterministic' and 'probabilistic' assessment. The results of the assessment are summarized in this section, and some examples are given below.

Figure 4 shows the resulting fire vulnerability index $I_{FI}$ (deterministic) for two of the case studies, 'Duomo di Senigallia' and 'Capela das Almas'. Although the index is similar for the two churches in absolute value, the use of multiple indicators with different weights (see eq. (2)) allows for a distinction among the main vulnerability factors that concurred to obtain the overall fire vulnerability value. For example, the presence of exterior hydrants (FI.4) and security cameras (FI.8) plays a role in the fire vulnerability of 'Capela das Almas', while they are completely not relevant in the case of 'Duomo di Senigallia'. This information can help in targeting mitigation efforts in resource-limited situations.

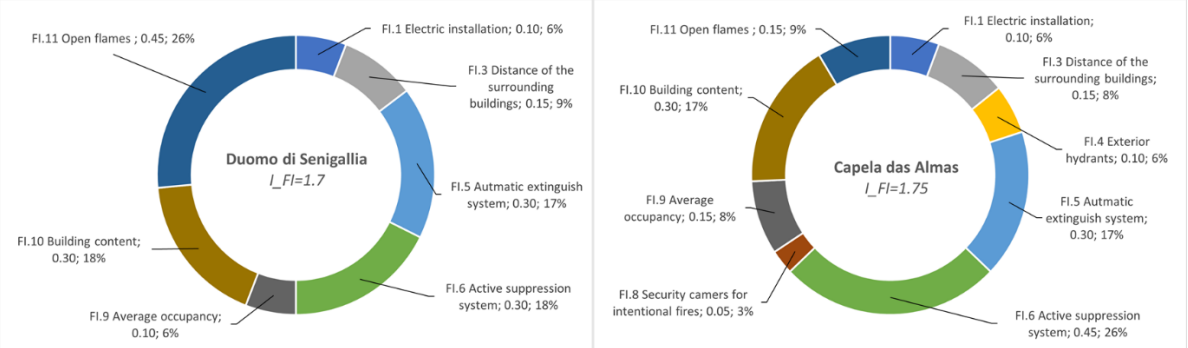


Figure 4: Comparison between the deterministic fire vulnerability index $I_{FI}$ for 'Duomo di Senigallia' and 'Capela das Almas'. The figure shows how the methodology can highlight different sources of vulnerability by investigating the role of different indicators.

The spider diagram depicted in Figure 5 compares the overall values of the deterministic multi-hazard vulnerability index $I_{MH}$ with the individual hazard indices ($I_{EQ}, I_{FL}, I_{FI}$) that compose them for all the five case study churches.

Noteworthy is the comparison between 'Duomo di Senigallia' and 'SS. Vincenzo ed Anastasio': although the two deterministic $I_{MH}$ values are not so different (1.52 and 1.22 respectively), the contribution of the different hazards is significantly different. In the first case, the church is homogeneously exposed to the three considered hazards, and there is no evidence of a dominant hazard, on which it would possibly be a priority to intervene to significantly reduce the vulnerability. In the second case, the fire vulnerability index $I_{FI}$ turns out to be decidedly dominant. In case a decision maker wanted to intervene to significantly reduce the overall vulnerability, the analysis suggests acting on the fire hazard as a priority. An action to reduce flood vulnerability, which is already low, for example, would have a limited impact on the overall vulnerability of that church.

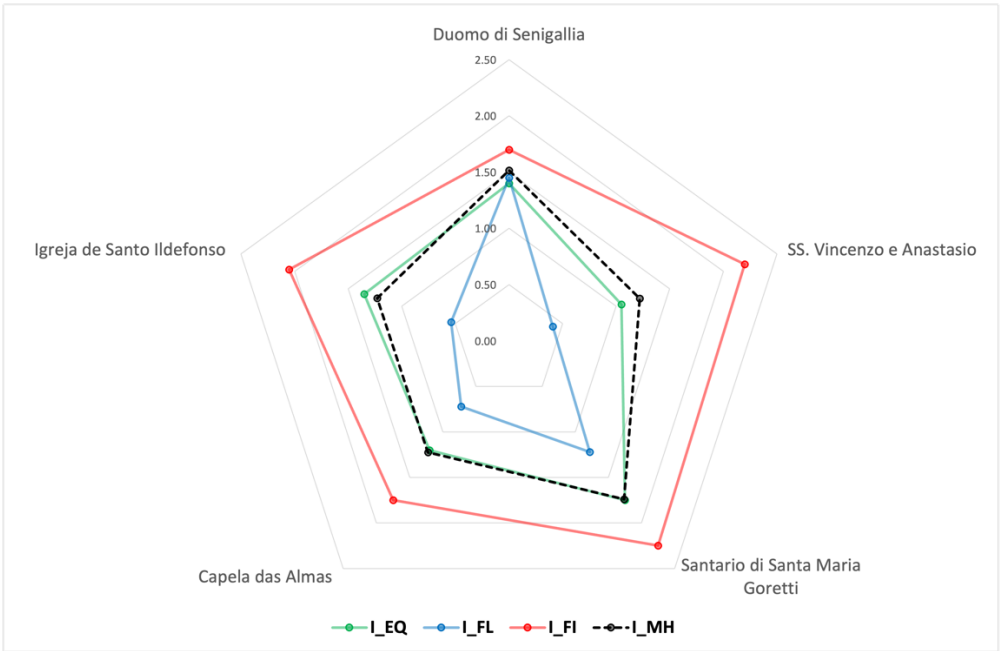


Figure 5: Spider diagram showing the values of the deterministic multi-hazard vulnerability index $I_{MH}$ and the individual hazard indices $I_{EQ}, I_{FL}, I_{FI}$ for all the five case study churches. The figure makes it possible to compare the relative importance of the different hazards in forming the overall index.

Finally, a comparison of $I_{MH}$ estimates by deterministic and probabilistic approaches is shown in Figure 6. The figure shows that the methodology is sufficiently robust even to possible uncertainties in the evaluation of the different indicators, highlighting its potential to be widely used also by non-experts. In fact, variations in $I_{MH}$ are small and are not such as to upset the ranking among the vulnerabilities of the different exposed elements considered. This turns out to be an extremely important feature of the methodology in the case of using the indices to hierarchize vulnerability mitigation interventions.

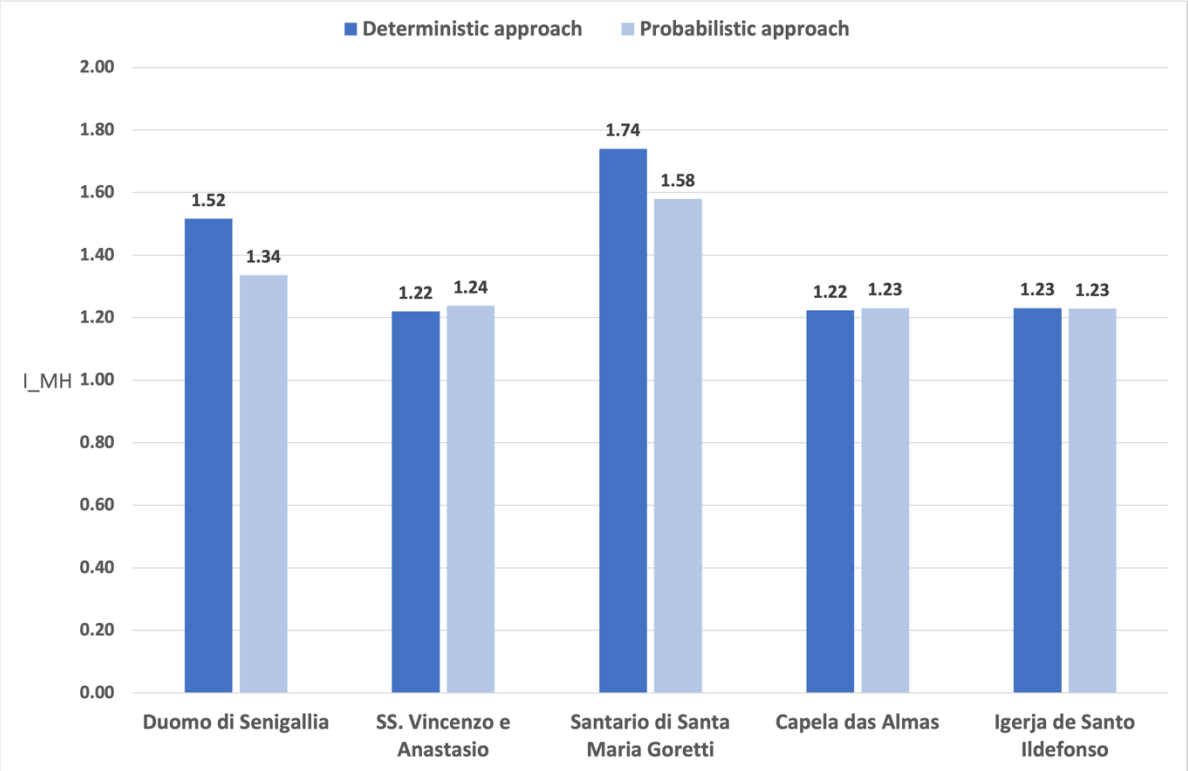


Figure 6: Comparison of the multi-hazard vulnerability indices $I_{MH}$ for different case studies evaluated using deterministic (dak blue) and probabilistic (light blue) approaches.

## 6 CONCLUSIONS

Assessing the vulnerability of churches under a multi-hazard perspective is crucial for their preservation and the safety of the people who use them. Churches are not only important religious and historical landmarks, but they are also significant cultural and social assets within the communities. Despite the large number of cultural heritage sites exposed to different hazards all over the world, in the literature there is a lack of multi-hazard approaches specifically developed for cultural heritage buildings.

To address this need, we proposed an indicator-based methodology for the multi-hazard vulnerability assessment of churches which currently considers the vulnerability from earthquakes, floods, and fire. Our approach combines a series of indicators that have been selected based on their relevance to the vulnerability classification of the assets and their ability to be easily scored using remotely sensed data or through fast in situ screening. The vulnerability assessment is robust enough to be performed by both experts and non-experts, without introducing much uncertainty in the overall vulnerability assessment.

The applicability of the methodology has been tested on five churches located in two different geographic contexts (Italy and Portugal), highlighting its validity at least in the Mediterranean area.

Further developments would include: (i) other hazards, such as windstorm or landslides; (ii) other cultural heritage buildings, such as museums or religious buildings other than churches, (iii) case studies in other countries. Of course, if highlighted by those wider applications, possible refinements of the list of selected indicators will be carried out as well.

By introducing this methodology, this work aims to contribute towards the assessment of the impact of multiple hazards on cultural heritage buildings and establish a foundation for further research in this field. Furthermore, the methodology aspires to become a valuable and practical tool for the scientific community, by providing a flexible prioritization method that can be applied as a basis for the fast screening of multiple assets.

## REFERENCES

[1] UNISDR, 'Sendai Framework for Disaster Risk Reduction 2015–2030', in *World Conference on Disaster Risk Reduction, 14 -18 March 2015, Sendai, Japan*, 2015. Accessed: Sep. 19, 2022. [Online]. Available: https://www.preventionweb.net/files/43291_sendaiframeworkfordrren.pdf

[2] X. Romão and C. Bertolin, 'Risk protection for cultural heritage and historic centres: Current knowledge and further research needs', *Int. J. Disaster Risk Reduct.*, vol. 67, p. 102652, Jan. 2022, doi: 10.1016/j.ijdrr.2021.102652.

[3] UNEP, 'AGENDA 21. Technical report.', in *United Nations Conference on Environment & Development, 3 to 14 June 1992*, Rio de Janerio , Brazil, 1992.

[4] UNISDR, 'Hyogo Framework for Action 2005-2015 : Building the Resilience of Nations and Communities to Disasters', in *World Conference on Disaster Reduction 18-22 January 2005*, Kobe, Hyogo, Japan, 2005.

[5] J. McGlade *et al.*, *Global assessment report on disaster risk reduction 2019*. UN Office for Disaster Risk Reduction, 2019. [Online]. Available: https://gar.undrr.org/sites/default/files/reports/2019-05/full_gar_report.pdf

[6] P. J. Ward *et al.*, 'Invited perspectives: A research agenda towards disaster risk management pathways in multi-(hazard-)risk assessment', *Nat Hazards Earth Syst Sci*, vol. 22, no. 4, pp. 1487–1497, Apr. 2022, doi: 10.5194/nhess-22-1487-2022.

[7] S. De Angeli, B. D. Malamud, L. Rossi, F. E. Taylor, E. Trasforini, and R. Rudari, 'A multi-hazard framework for spatial-temporal impact analysis', *Int. J. Disaster Risk Reduct.*, vol. 73, p. 102829, Apr. 2022, doi: 10.1016/j.ijdrr.2022.102829.

[8] M. C. de Ruiter, A. Couasnon, M. J. C. van den Homberg, J. E. Daniell, J. C. Gill, and P. J. Ward, 'Why We Can No Longer Ignore Consecutive Disasters', *Earths Future*, vol. 8, no. 3, p. e2019EF001425, 2020, doi: https://doi.org/10.1029/2019EF001425.

[9] C. E. Marrion, 'More effectively addressing fire/disaster challenges to protect our cultural heritage', *J. Cult. Herit.*, vol. 20, pp. 746–749, 2016.

[10] M. Papathoma-Köhle, M. Schlögl, and S. Fuchs, 'Vulnerability indicators for natural hazards: an innovative selection and weighting approach', *Sci. Rep.*, vol. 9, no. 1, Art. no. 1, Oct. 2019, doi: 10.1038/s41598-019-50257-2.

[11] M. S. Kappes, M. Papathoma-Köhle, and M. Keiler, 'Assessing physical vulnerability for multi-hazards using an indicator-based methodology', *Appl. Geogr.*, vol. 32, no. 2, pp. 577–590, Mar. 2012, doi: 10.1016/j.apgeog.2011.07.002.

[12] M. Papathoma, 'Tsunami vulnerability assessment using a geographical information system with special reference to Greece', PhD Thesis, Coventry University, 2003.
[13] R. Gentile *et al.*, 'Scoring, selecting, and developing physical impact models for multi-hazard risk assessment', *Int. J. Disaster Risk Reduct.*, vol. 82, p. 103365, Nov. 2022, doi: 10.1016/j.ijdrr.2022.103365.
[14] V. Silva, S. Brzev, C. Scawthorn, C. Yepes, J. Dabbeek, and H. Crowley, 'A Building Classification System for Multi-hazard Risk Assessment', *Int. J. Disaster Risk Sci.*, vol. 13, no. 2, pp. 161–177, Apr. 2022, doi: 10.1007/s13753-022-00400-x.
[15] T. M. Ferreira, R. Vicente, J. A. R. Mendes da Silva, H. Varum, and A. Costa, 'Seismic vulnerability assessment of historical urban centres: case study of the old city centre in Seixal, Portugal', *Bull. Earthq. Eng.*, vol. 11, no. 5, pp. 1753–1773, Oct. 2013, doi: 10.1007/s10518-013-9447-2.
[16] D. Rapone, G. Brando, E. Spacone, and G. De Matteis, 'Seismic vulnerability assessment of historic centers: description of a predictive method and application to the case study of scanno (Abruzzi, Italy)', *Int. J. Archit. Herit.*, vol. 12, no. 7–8, pp. 1171–1195, Nov. 2018, doi: 10.1080/15583058.2018.1503373.
[17] P. Salzano, C. Casapulla, F. Ceroni, and A. Prota, 'Seismic Vulnerability and Simplified Safety Assessments of Masonry Churches in the Ischia Island (Italy) after the 2017 Earthquake', *Int. J. Archit. Herit.*, vol. 16, no. 1, pp. 136–162, Jan. 2022, doi: 10.1080/15583058.2020.1759732.
[18] S. Lagomarsino, 'On the vulnerability assessment of monumental buildings', *Bull. Earthq. Eng.*, vol. 4, no. 4, pp. 445–463, Nov. 2006, doi: 10.1007/s10518-006-9025-y.
[19] S. Lagomarsino and S. Podestà, 'Seismic Vulnerability of Ancient Churches: II. Statistical Analysis of Surveyed Data and Methods for Risk Analysis', *Earthq. Spectra*, vol. 20, no. 2, pp. 395–412, May 2004, doi: 10.1193/1.1737736.
[20] F. Ceroni, C. Casapulla, E. Cescatti, V. Follador, A. Prota, and F. da Porto, 'Damage assessment in single-nave churches and analysis of the most recurring mechanisms after the 2016–2017 central Italy earthquakes', *Bull. Earthq. Eng.*, vol. 20, no. 15, pp. 8031–8059, Dec. 2022, doi: 10.1007/s10518-022-01507-8.
[21] S. Lagomarsino, S. Cattari, D. Ottonelli, and S. Giovinazzi, 'Earthquake damage assessment of masonry churches: proposal for rapid and detailed forms and derivation of empirical vulnerability curves', *Bull. Earthq. Eng.*, vol. 17, no. 6, pp. 3327–3364, Jun. 2019, doi: 10.1007/s10518-018-00542-8.
[22] A. Marotta, D. Liberatore, and L. Sorrentino, 'Development of parametric seismic fragility curves for historical churches', *Bull. Earthq. Eng.*, vol. 19, no. 13, pp. 5609–5641, Oct. 2021, doi: 10.1007/s10518-021-01174-1.
[23] R. Figueiredo, X. Romão, and E. Paupério, 'Component-based flood vulnerability modelling for cultural heritage buildings', *Int. J. Disaster Risk Reduct.*, vol. 61, p. 102323, Jul. 2021, doi: 10.1016/j.ijdrr.2021.102323.
[24] D. D'Ayala *et al.*, 'Flood vulnerability and risk assessment of urban traditional buildings in a heritage district of Kuala Lumpur, Malaysia', *Nat. Hazards Earth Syst. Sci.*, vol. 20, no. 8, pp. 2221–2241, Aug. 2020, doi: 10.5194/nhess-20-2221-2020.
[25] S. Kincaid, 'Fire prevention in historic buildings – approaches for safe practice', *Hist. Environ. Policy Pract.*, vol. 13, no. 3, pp. 361–380, Jul. 2022, doi: 10.1080/17567505.2022.2098633.
[26] L. G. F. Salazar, X. Romão, and E. Paupério, 'Review of vulnerability indicators for fire risk assessment in cultural heritage', *Int. J. Disaster Risk Reduct.*, vol. 60, p. 102286, Jun. 2021, doi: 10.1016/j.ijdrr.2021.102286.

[27] N. Chettri, G. Dhaurali, T. Neopaney, T. Cheki, and D. Gautam, 'Wind vulnerability and strengthening of Bhutanese vernacular roofs', *Geomat. Nat. Hazards Risk*, vol. 13, no. 1, pp. 1511–1534, Dec. 2022, doi: 10.1080/19475705.2022.2086830.
[28] G. Sevieri *et al.*, 'A multi-hazard risk prioritisation framework for cultural heritage assets', *Nat. Hazards Earth Syst. Sci.*, vol. 20, no. 5, pp. 1391–1414, May 2020, doi: 10.5194/nhess-20-1391-2020.
[29] P. B. Julià and T. M. Ferreira, 'From single- to multi-hazard vulnerability and risk in Historic Urban Areas: a literature review', *Nat. Hazards*, vol. 108, no. 1, pp. 93–128, Aug. 2021, doi: 10.1007/s11069-021-04734-5.
[30] V. Despotaki, V. Silva, S. Lagomarsino, I. Pavlova, and J. Torres, 'Evaluation of Seismic Risk on UNESCO Cultural Heritage sites in Europe', *Int. J. Archit. Herit.*, vol. 12, no. 7–8, pp. 1231–1244, Nov. 2018, doi: 10.1080/15583058.2018.1503374.
[31] X. Romão, E. Paupério, and N. Pereira, 'Metodologia para avaliação expedita do risco sísmico em bens culturais imóveis', Instituto da Construção, Faculdade de Engenharia da Universidade do Porto, 2015.
[32] S. Cattari, S. Degli Abbati, D. Ferretti, S. Lagomarsino, D. Ottonelli, and A. Tralli, 'Damage assessment of fortresses after the 2012 Emilia earthquake (Italy)', *Bull. Earthq. Eng.*, vol. 12, no. 5, pp. 2333–2365, Oct. 2014, doi: 10.1007/s10518-013-9520-x.
[33] S. Degli Abbati *et al.*, 'Seismic assessment of interacting structural units in complex historic masonry constructions by nonlinear static analyses', *Comput. Struct.*, vol. 213, pp. 51–71, Mar. 2019, doi: 10.1016/j.compstruc.2018.12.001.
[34] R. Figueiredo, X. Romão, and E. Paupério, 'Flood risk assessment of cultural heritage at large spatial scales: Framework and application to mainland Portugal', *J. Cult. Herit.*, vol. 43, pp. 163–174, May 2020, doi: 10.1016/j.culher.2019.11.007.
[35] S. Ferrari, S. Oliveira, G. Pautasso, and J. L. Zêzere, 'Territorial Resilience and Flood Vulnerability. Case Studies at Urban Scale in Torino (Italy) and Porto/Vila Nova de Gaia (Portugal)', in *Urban Resilience for Risk and Adaptation Governance: Theory and Practice*, G. Brunetta, O. Caldarice, N. Tollin, M. Rosas-Casals, and J. Morató, Eds. Cham: Springer International Publishing, 2019, pp. 147–174. doi: 10.1007/978-3-319-76944-8_10.
[36] W. Weber de Melo *et al.*, 'Flood Risk Assessment at the Douro River Estuary', in *Climate Change and Water Security*, Singapore, 2022, pp. 37–49. doi: 10.1007/978-981-16-5501-2_4.
[37] M. Santos, M. Fragoso, and J. A. Santos, 'Damaging flood severity assessment in Northern Portugal over more than 150 years (1865–2016)', *Nat. Hazards*, vol. 91, no. 3, pp. 983–1002, Apr. 2018, doi: 10.1007/s11069-017-3166-y.
[38] Centro Funzionale Regionale Regione Marche, 'Rapporto di Evento preliminare Maltempo 15, 16 e 17 settembre 2022 (in italian)'. Accessed: Mar. 01, 2023. [Online]. Available: https://www.regione.marche.it/portals/0/Protezione_Civile/Manuali%20e%20Studi/Rapporto_Evento_preliminare_20220915.pdf

COMPDYN 2023
9th ECCOMAS Thematic Conference on
Computational Methods in Structural Dynamics and Earthquake Engineering
M. Papadrakakis, M. Fragiadakis (eds.)
Athens, Greece, 12-14 June 2023

# MULTI-RISK ASSESSMENT OF A BASE ISOLATED STRUCTURE

**D.de Silva, A. Bilotta, R. Tomeo, E. Nigro**

Dep. of Structures for Enginerring and Architecture - University of Naples Federico II, Italy
e-mail: {donatella.desilva, antonio.bilotta, romeo.tomeo, emidio.nigro}@unina.it

## Abstract

*Seismic isolation is a design strategy adopted for the protection of both new and existing structures, based on the assumption that it is possible to uncouple a structure from the ground and thereby protect it from the damaging effects of earthquakes. The most common isolators are the elastomeric ones, which consist of alternating rubber layers and reinforcing metal sheets, connected by vulcanization of the elastomeric compound, and a lead central core. In case of a fire, this compound can suffer permanent damage which can seriously compromise the functionality of the isolation system. This study is focused on the assessment of the fire effect on the elastomeric isolators and the quantification of their loss of efficiency after a fire event.*

*At this purpose, a case study of an existing r.c. structure with multi-storey frames was analysed, for which, after a seismic vulnerability assessment, two possible interventions with seismic isolation were designed. The evaluation of the isolator thermal response for 30 and 60 minutes of exposure to the ISO 834 standard fire curve was used for quantify the damage induced by the fire in terms of degradation of vertical and horizontal stiffness and vertical load-bearing of the isolators. This damage level was defined starting from the thermomechanical properties of the elastomeric layer damaged by fire which, in particular, reached temperatures greater than a critical temperature threshold (70, 200 and 320°C). The estimated degradation was used to evaluate the seismic performance of both isolators and structure in different design configurations, also in a multi-risk scenario that foresee the occurrence of a seismic event after a fire. Finally, in order to mitigate the fire effect on the elastomeric isolators, the effectiveness of a passive fire protection system consisting of plasterboard gypsum boxes was evaluated, ensuring that the critical temperature of 70°C on the outer surface of the isolator was not exceeded even after 60 minutes of exposure to standard fire.*

**Keywords:** Fire Risk, Seismic Risk, fire after earthquake, isolated r.c. structures

# 1 INTRODUCTION

Earthquakes are among the most dangerous natural disasters, with loss of human lives, a large number of structural damages and socio-economic costs. As it is not possible to prevent earthquakes from occurring, designers have to focus on mitigating their consequences. This goal can be achieved by both increasing the structural capacity and ductility or decreasing the seismic demand of the structure. This latter solution can be reached by using the base isolation, reducing seismic induced damage. Indeed, the design of seismic isolation is a topic of great interest and it is considered a consolidated technique in the field of seismic protection of structures. However, during the nominal life of the structure, it is important to also consider the possibility that an extreme event like fire, as consequence of a main seismic event, can occur, compromising the seismic isolation system functionality and making it more vulnerable to the seismic action of an after-shock. Nowadays, the more widely used seismic isolators are the steel reinforced elastomeric ones, that are devices composed by alternate layers of elastomer and steel, connected through the vulcanization of the elastomeric compound [1]. Because of the high temperatures that can be reached during a fire event, the elastomer can suffer not reversible damages, with a decay of the mechanical properties of isolators.

In scientific literature, only few studies concerning the evaluation of fire induced damage of seismic isolators and the estimation of their mechanical properties degradation are available. In [2], the authors deal with the analysis of the thermo-mechanical behaviour of polychloroprene elastomeric isolators during a fire, proponing a model able to reproduce the behaviour of the elastomer. Based on test results, the authors set at the temperature of 320°C the onset of degradation with a significant decrease of density and, consequently, by the loss of structural integrity of the material. The model is validated comparing the results of an experimental test carried out on a specimen of elastomeric isolator with the results of a numerical simulation analysis. The study shows a good agreement between the results. In [3], the authors tested eight seismic elastomeric isolators, both in natural rubber (NRB) and with a lead core (LRB), with and without fire protection. The isolators are exposed to the standard fire curve ISO834 in order to evaluate the effects of the vertical load and fire duration on their collapse mechanisms and residual mechanical properties. In particular, the experimental results show that (i) the duration of fire exposure has an important effect on the decay of the mechanical properties of the isolators; (ii) the vertical load does not affect the residual mechanical properties and the fire resistance; (iii) the proposed passive protection system prevents an important decay of the mechanical properties of elastomeric isolators in case of fire. After 30 min of fire exposure, the mechanical properties of LRB and NRB isolators have a decay lower than 10%, while after 60 min the vertical stiffness of LRB isolators and their mechanical properties dependent by the lead core (yielding stress and cyclic energy dissipation) do not have significant variations. A more significant variation can be observed on the mechanical properties dependent by the rubber. A decrease of about 36% of the post-elastic stiffness, an increase of 20% of the equivalent damping ratio and a decrease of about 20% of the equivalent lateral stiffness are observed. For NRB isolators, the vertical and lateral stiffness decrease of 27% and 62%, respectively. With fire protection, the seismic isolators do not suffer significant changes, even after 3 hours of fire exposure, with a reduction of the mechanical properties lower than 8%. In [4], the authors evaluate the degradation of the mechanical properties of HDLRB (High-Damping-Laminated-Rubber Bearings) and LRB (Lead-Rubber Bearings) isolators based on the temperature distribution inside them, obtained with numerical analyses. As in the method of isotherm 500°C, proposed by EN1992-1-2 [5] for the evaluation of the residual properties of reinforced concrete cross sections damaged by fire, the authors propose the method of isotherm 200°C, to evaluate the reduction of the mechanical properties of the isolators damaged by fire. In this method, the residual cross section of HDLRB and LRB isolators is obtained, neglecting the elastomer with temperatures higher than the vulcanization threshold.

All the studies proposed in literature are mainly focused on the behavior of the single isolator, neglecting the behavior of the whole base-isolated structure. Furthermore, the topic of the residual seismic capacity of isolators after a fire event is very important, but a lack of knowledge and uncertainties exist. Therefore, the paper aims at evaluating the behavior of elastomeric isolators before and after a fire event and the consequences that their damage can have on the whole structural behavior.

## 2 EVALUATION OF SEISMIC AND FIRE ACTIONS

In this section, the methodology used to evaluate the seismic risk occurring after a fire event of existing seismically isolated buildings was introduced. In particular, (i) the methodology used for the evaluation of the seismic vulnerability of the structure, (ii) the criteria used for the design of the seismic isolation system and (iii) the methodology used to take into account the fire risk is shown.

### 2.1 Design of the seismic isolation system

To design the seismic isolation system for an existing structure, the first step is the assessment of its seismic vulnerability. In this paper, the evaluation of the seismic vulnerability is performed through response spectrum linear dynamic analyses. The response spectrum used is related to a life-safety limit state (SLV according to Italian Technical Code for Constructions - NTC2018 [6],[7]), with reference to the specific site conditions, reduced by a behavior factor q=1.5 (cautionary value, typical for existing structures designed for vertical loads only). NTC2018 provides response spectra and a seismic design approach very similar to EN1998 [8], but considering the specific seismic hazard of Italy. The results of the seismic vulnerability assessment are necessary for the design of seismic strengthening interventions, that, in general, could include: a) reinforced concrete jacketing of beams and columns under the seismic isolation interface, b) installation of elastomeric seismic isolators and sliding supports (multi-directional structural bearings with confined elastomeric disc) on the top of the columns, under the isolation interface. The installation of seismic isolators and sliding supports can be realized following the operative phases shown in [9]. The seismic isolation system is designed considering the elastic response spectrum corresponding to the Collapse Prevention Limit State with a viscous equivalent damping of 15% for periods (T) greater than 0.8 $T_{iso}$, with Tiso equal to the fundamental vibration period of the seismically isolated structure [6]. So, knowing the total mass of the structure $M_{tot}$ and assuming a "target" design period of the seismically isolated structure (defined on basis of the seismic vulnerability assessment and on the desired reduction of spectral acceleration), from the equation:

$$T_{iso} = 2\pi \sqrt{\frac{M_{tot}}{K_{tot,iso}}} \tag{1}$$

it is possible to calculate the "target" stiffness of the whole isolation system, as:

$$K_{tot,iso} = \frac{4\pi^2 M_{tot}}{T_{iso}^2} \tag{2}$$

and the "target" stiffness related to the single isolator, as:

$$K_{iso,i} = \frac{K_{tot,iso}}{n_{iso}} \tag{3}$$

in which $n_{iso}$ is the number of isolators.

The layout in the plan of seismic isolators and sliding supports is defined trying to minimize as much as possible the eccentricity between the effective stiffness and mass centers at the isolation interface (e.g. 3% of the plan dimensions of the building in the two directions [6]). Once the isolation system is designed, a further evaluation of the structural seismic per-

formances is performed, to check the safety of the seismic isolators in terms of loads, stresses, displacements, and deformability (see [7]).

### 2.2 Assessment of fire damage

To quantify the fire damage of seismic isolators, the degradation of mechanical properties, such as horizontal stiffness $K_H$, vertical stiffness $K_V$ and load-bearing capacity have to be evaluated. This evaluation can be conducted using a methodology similar to the one proposed in the EN1992-1-2 [5], for verifying the fire resistance of reinforced concrete elements, named "500°C isotherm method". In particular, the methodology considers a reduced cross-section in the calculation of load bearing capacity, neglecting all the concrete that has reached temperatures greater than 500ºC. The remaining concrete cross-section maintains its initial strength and stiffness values. Imagining to "adapt" this approach to elastomeric seismic isolators, the first problem is to establish a unique critical temperature threshold, since few and different information are provided in scientific literature. This temperature seems to be related to chemical phenomena that occur inside the elastomeric compound when it is exposed to elevated temperatures, so it could be obtained only by experimental tests. At this purpose Traxl et al. [2] stated that the temperature of 320 °C can be considered as an upper bound for the estimation of the residual material stiffness, since, above that temperature, the degradation process starts, with a significant decrease of density and integrity of the material. Mazza [4] suggested a more conservative temperature threshold of 200 °C, equal to the temperature of vulcanization between rubber layers and steel plates. The rubber aging behavior must be investigated by performing accelerated aging, according to ISO 18[9] , conditioning the sample at 70°C for a certain period linked to the compound type. Therefore also 70°C was chosen as temperature threshold value[10]. In conclusion, in this study, the assessment of fire damage of seismic elastomeric isolators is conducted with reference to critical temperature thresholds of 70, 200 and 320 ºC. The behaviour of elastomeric isolators is characterized by two main geometric parameters, defined as following (see Figure 1):

- $S_1 = A'/L = D'/4t_i$, called primary shape factor, defined as the ratio between the surface $A'$ in common between the single layer of the elastomer and the steel sheet, and the free lateral surface $L$ of the single layer of elastomer;
- $S_2 = D'/t_e$, called secondary shape factor, defined as the ratio between the plan dimension $D'$ of the single steel plate and the total thickness of the elastomer layers $t_e$.

The first one ($S_1$) affects the vertical stiffness $K_v$ of the isolator (controlling the rubber confinement), while the second one ($S_2$) is related to the possible occurrence of instability phenomena. For the calculation of $K_v$, only the area of the steel plate layer is considered (A') because the outer lateral layer of unconfined elastomer provides a negligible contribution to the bearing capacity against vertical loads.

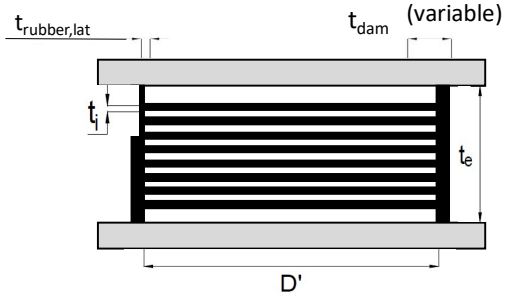


Figure 1. – Geometry of isolators.

Given the vertical stiffness of the elastomer single layer:

$$K_{Vi} = \frac{E_c * A'}{t_i} \tag{4}$$

the vertical stiffness $K_v$ of the isolator can be calculated considering each single layer in series, as:

$$K_V = \frac{1}{\sum \frac{1}{K_{pi}}} \tag{5}$$

The axial compressibility modulus $E_c$ depends on the type of elastomeric compound (dynamic shear modulus of the elastomer $G_{din}$) and the primary shape factor $S_1$, and it can be evaluated [7]:

$$E_c = \left(\frac{1}{6*G_{din}*S_1^2} + \frac{4}{3*E_b}\right)^{-1} \tag{6}$$

where $E_b$ is the volumetric modulus of the rubber, which can be assumed equal to 2000 MPa if a direct measure is not available [7].
The horizontal stiffness of the isolator can be obtained from:

$$K_H = \frac{G_{din} * A}{t_e} \tag{7}$$

where $G_{din}$, $A$ and $t_e$ are the equivalent dynamic shear modulus, the gross cross-section and the total thickness of the elastomer, respectively. All these illustrated aspects were considered in this work for evaluation of the isolator mechanical properties degradation (horizontal $K_H$ and vertical $K_V$ stiffnesses) induced by the fire. In particular, this degradation depends on two main parameters such as the critical temperature threshold $\theta$crit and the time of exposure to fire, t. In the equation (7) there is a direct dependence of the stiffness $K_H$ on the cross-section A and so on the diameter D. Therefore, assuming that the mechanical properties of the rubber ($G_{din}$, $E_b$) and the geometric characteristics of the isolator ($t_e$, $t_i$) do not change due to fire, an effective area reduced by the fire can be evaluated on the basis of thermal damage.

For the residual horizontal stiffness calculation, a diameter Dfinal,i was considered:

$$D_{final,i}(\theta_{crit}, t) = D - 2 * t_{dam,i} \tag{8}$$

In (8) $t_{dam,i}$ is the fire damaged isolator portion, variable with the thermal field induced by fire in the isolator, corresponding to the external portion of isolator with temeperature greater the fixed threshold ($\theta > \theta$ crit) . For the calculation of the residual vertical stiffness, a diameter D'final,i was considered:

$$\begin{aligned} D'_{final,i}(\theta_{crit}, t) &= D' - 2 * \left(t_{dam,i} - t_{rubber\ lat.}\right) && if\ t_{dam} \geq t_{rubber\ lat.} \\ D'_{final,i}(\theta_{crit}, t) &= D' && if\ t_{dam} < t_{rubber\ lat.} \end{aligned} \tag{9}$$

where $t_{dam}$($\theta$crit, t) is the damaged portion and trubber lat represents the rubber lateral layer which has a thickness of 10 mm and is inserted for protecting the layer of elastomer and steel plates (see Figure 1). The second equation of (9) is verified if the damaged portion $t_{dam}$ is less than the outer lateral layer of unconfined elastomer ($t_{rubber\ lat}$), which, as also said before, is not considered for the vertical stiffness calculation. So, in this case the vertical stiffness is not affected by fire damage. Since the value D'$_{final}$ affect the calculation of $S_1$ and $E_c$ , in case of fire, each layer "i" has a different value of $S_1$ and $E_c$, according to the damage state of the layer. Therefore, the post-fire stiffness $K_H$ ($\theta$crit, t) can be obtained from the equation (10), replacing "A" with "$A_{effective}$", obtained as the mean of the effective area of each elastomeric layer Aeffective,i with a diameter $D_{final}$. While A' has to be replaced with A'$_{effective,i}$ in the equation (7) for calculating the vertical post-fire stiffness of the single layer $K_{Vi}$ ($\theta_{crit}$, t). Finally, the equations of the reduction factors for horizontal ($\alpha_{kh}$) and vertical ($\alpha_{kv}$) stiffnesses, for the three critical temperature thresholds, can be expressed as following:

$$\alpha_{kh}(\theta_{crit}, t) = \frac{K_H(\theta_{crit}, t)}{K_{H,0}} \tag{10}$$

$$\alpha_{kv}(\theta_{crit}, t) = \frac{K_V(\theta_{crit}, t)}{K_{V,0}} \tag{11}$$

where $K_H(\theta_{crit,\,t})$ and $K_V(\theta_{crit,\,t})$ are the post-fire stiffnesses obtained for a certain critical temperature threshold at the time t of fire exposure, while $K_{H,0}$ and $K_{V,0}$ are the initial stiffnesses at t=0 min. Considering the load-bearing capacity of the isolators $F_{zd}$ at the ULS, the residual load-bearing capacity $F_{zd}(\theta crit,t)$ due to the effect of fire can be estimated as:

$$F_{zd}(\theta_{crit}, t) = F_{zd} * a_{eff}(\theta_{crit}, t) \tag{12}$$

where $a_{eff}(\theta_{crit}, t)$ is the effective area obtained as:

$$a_{eff}(\theta_{crit}, t) = \frac{A_{eff}(\theta_{crit}, t)}{A} \tag{13}$$

To use the reduction factors of the ULS conditions is a precautionary choice, indeed in case of fire these factors are considered equal to one [9].

## 3 APPLICATION TO A CASE STUDY

The methodology shown in the previous sections was applied to a reinforced concrete existing building. In particular, the results of the seismic vulnerability assessment and the seismic strengthening intervention are described in detail. Moreover, the effect of the fire on the seismic isolation intervention is considered, proposing possible design measures that could be used in practice to consider seismic and fire risk in a combined approach.

### 3.1 Case study description

The case study refers to an existing building made of reinforced concrete frames. The structure, built in 50s, has one underground floor and four floors above ground (total height of 19.80 m) and has a rectangular shape plan with dimensions 30 m x 12 m.

The building, designed for vertical loads only and without seismic requirements, has main frames in the direction of the longer side of the plan; the slabs, made in reinforced brick concrete, are mainly oriented in the direction of the shorter side of the building. There are not connecting beams between the main frames, except for the basement floor. In Figure 2, a typical floor carpentry of the building is represented.

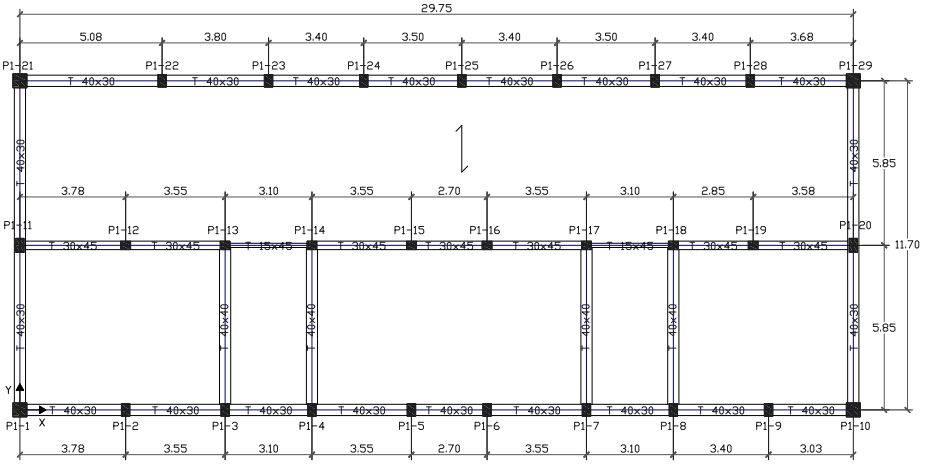


Figure 2 – Typical floor with numbering of columns and dimension of beams

The dimensions of the beams cross section are the following:

- 50x40 cm, 40x40 cm and 25x40 cm for the basement floor;
- 45x30 cm, 40x40 cm and 20x50 cm for the first floor;

- 40x30 cm, 40x40 cm, 30x50 cm and 15x45 cm for intermediate floors;
- 40x45 cm, 40x40 cm, 30x40 cm and 15x35 cm at the last floor.

The dimensions of the columns cross sections are shown in Table 1 and each column is indicated as Px-y, where x indicates the floor number, while y the number of the column (see Figure 2). The mechanical properties of the materials were defined based on the results of some destructive and non-destructive tests performed on the structural members, which allowed defining the following mean resistances: $f_{cm}$ = 27 MPa and $f_{ym}$ = 337 MPa for concrete and rebar steel respectively.

### 3.2 Seismic vulnerability analysis for existing structure

A seismic vulnerability analysis of the case study building was performed, following the approach previously described in section 2.1. The numerical analyses were carried out with the software SAP2000 [12]. The structure was modelled through "frame" elements, while the infinitely rigid behaviour of the floors was modelled through the introduction of "diaphragms" constraints. Figure 3 shows a 3D view of the numerical model.

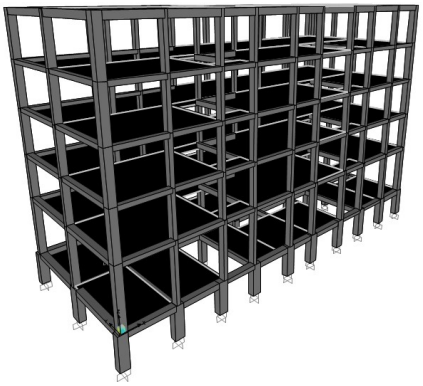

Figure 3 – Structural model of the building.

Table 1 – Cross sections of columns

| Floor | Column | B [cm] | H [cm] |
|---|---|---|---|
| Basement | 1,10,21,29 | 65 | 50 |
| | 2,3,4,5,6,7,8,9,22,23,24,25,26,27,28 | 70 | 50 |
| | 11,20 | 50 | 85 |
| | 12,13,14,15,16,17,18,19 | 50 | 50 |
| Ground floor | 1,10,21,29 | 50 | 50 |
| | 2,3,4,5,6,7,8,9,22,23,24,25,26,27,28 | 30 | 50 |
| | 11,20 | 30 | 50 |
| | 12,13,14,15,16,17,18,19 | 40 | 40 |
| Floors 1,2,3 | 1,10,21,29 | 50 | 50 |
| | 2,3,4,5,6,7,8,9,22,23,24,25,26,27,28 | 30 | 45 |
| | 11,20 | 30 | 50 |
| | 12,13,14,15,16,17,18,19 | 35 | 30 |
| Fourth floor | 1,10,21,29 | 50 | 50 |
| | 2,3,4,5,6,7,8,9,22,23,24,25,26,27,28 | 30 | 45 |
| | 11,20 | 30 | 50 |
| | 12,13,14,15,16,17,18,19 | 30 | 30 |

Based on the internal forces obtained through the numerical analyses, the safety checks of structural elements were conducted. Table 2 shows the maximum values of the ratio Demand/Capacity (D/C) obtained for beams and columns. The design strength of the materials are defined on the basis of the average values and assuming a Full Knowledge Level (LC3 according to [6], confidence factor CF=1.0), also thanks to the availability of the original design drawings and the large number of in-situ inspections performed on the structure. For shear safety checks (brittle failures) the resistances of the materials were also divided by the partial safety coefficients ($\gamma_c$ = 1.5 for concrete and $\gamma_s$ = 1.15 for rebar steel).

Table 2 – Current state: safety checks of beams and columns

| Check | Combination | $(D/C)_{max}$ |
|---|---|---|
| Beams Bending | ULS | 1.72 |
| | Seismic | 3.55 |
| Beams Shear | ULS | 0.74 |
| | Seismic | 0.94 |
| Columns Combined Axial Load/Bending | ULS | 0.93 |
| | Seismic | 3.14 |
| Columns Shear | ULS | 0.59 |
| | Seismic | 1.70 |

Based on the results of the seismic vulnerability evaluation of the structure in its current configuration, a seismic strengthening intervention, which consists of a seismic isolation sys-

tem and the reinforced concrete jacketing of some beams and columns, was designed. More details on the intervention are shown in the following sections.

### 3.3 Seismic strengthening of the structure

The intervention of seismic isolation includes also the realization, under the isolation interface, of stiffening connecting beams with cross section 40x40 cm (second span in the short direction of the building, see Figure 2). These beams, that connect the columns of the central frame (columns 12, 13, 14, 16, 17, 18, 19) and those of one of the external frames (columns 22, 23, 24, 25, 26, 27 and 28), are intended to provide a greater stiffness of the isolation interface in its own plane. The reinforced concrete jacketing of the beams leads to the increasing of the section dimensions, in particular the sections 50x40 become 60x60, the sections 25x40 become 35x60 and the ones 40x40 increase up to 50x60. Furthermore, it provides the addition of 2-3 bars of diameter 16 or 20 mm, for both positive and negative bending. The reinforced concrete jacketing of the columns at the first level provides a thickness of 10 cm of concrete class C40/50 on all the sides of the existing cross section, in order to guarantee an adequate cover for new rebars (diameter 16 mm). Concerning the stirrups, rebars of 10 mm diameter spaced of 10 cm are provided, based on the prescriptions of Italian NTC2018 [6] for DC "B" (low ductility class). In particular, the existing columns of cross section 65x50 become 85x70, the ones 50x85 become 70x105, the ones 70x50 become 90x70 and, finally, those 50x50 become 70x70. The cross sections of the jacketed columns were modelled discerning the constitutive laws of existing concrete ($f_{cm}$ = 27 MPa) and new one ($f_{ck}$ = 40 MPa, $f_{cd}$ = 23 MPa) as well as the constitutive laws of existing bars ($f_{ym}$ = 337 MPa) and new ones ($f_{yk}$ = 450 MPa, $f_{yd}$ = 391 MPa). For concrete a parable-rectangle constitutive law was used (with ultimate deformation equal to 3.5‰), while for steel an elasto-plastic constitutive law was considered. The Figure 4 shows elastic response spectra at the Collapse Limit State (SLC according to [6]) in terms of acceleration and displacement. In the figure, the fundamental vibration periods of the structure with and without seismic isolation are also shown: $T_1$ refers to the fundamental period of the existing structure, while $T_{iso}$ is the target period used for the design of the seismic isolation system. In Table 3, the values of spectral accelerations and displacements corresponding to the periods $T_1$ e $T_{iso}$ are listed. The isolation system, designed to obtain an increase of the fundamental period from 1.49s to 3.0s, is able to decrease the elastic demand in terms of acceleration of 77% and increase that in terms of displacement of 4% (at the SLC).

Table 3 – Spectral accelerations and displacements at the SLC before and after seismic isolation

| Existing structure | | "Isolated" structure | |
|---|---|---|---|
| $\xi$ | 5 % | $\xi_{iso}$ | 15 % |
| $T_1$ | 1.49 s | $T_{iso}$ | 3.0 s |
| $S_{a,el}(T_1)$ | 0.13 g | $S_{a,el}(T_{iso})$ | 0.03 g |
| $S_{d,el}(T_1)$ | 7.41 cm | $S_{d,el}(T_{iso})$ | 7.74 cm |

Assuming a target period of the isolated structure equal to 3.0s, given the total mass of the building $M_{tot}$ = 1843.95 ton, the global stiffness of the isolation system was obtained:

$$K_{tot,iso} = \frac{4\pi^2 M_{tot}}{T_{iso}^2} = \frac{4\pi^2 1843.95}{3.0^2} = 8088\ kN/m \qquad (14)$$

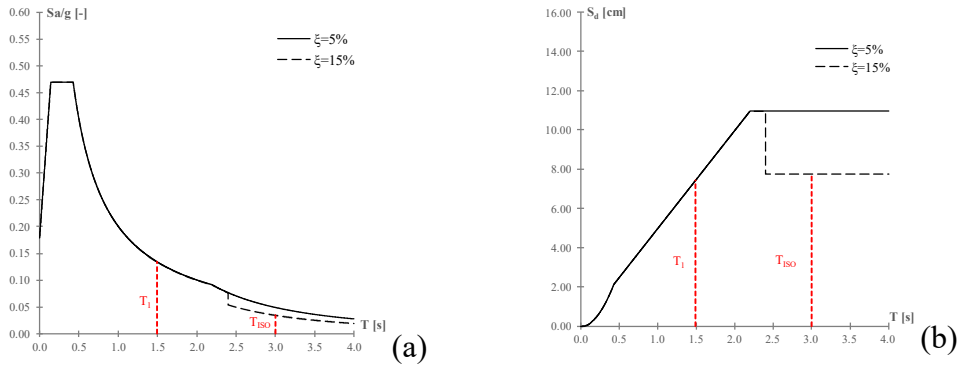


Figure 4 – Elastic spectra at SLC: acceleration (a) and displacement (b)

Assuming two different design solutions that provide the installation of 10 or 20 elastomeric isolators, the horizontal stiffness of each isolator will be equal to 0.81 kN/mm or 0.41 kN/mm, respectively. Table 4 shows the characteristics of the isolators (see Figure 5 for the symbols meaning) for the two different solutions, labelled as "solution 10" and "solution 20", respectively. Once defined the isolator typology, these were modelled in SAP2000 [13] through two nodes links with a linear behaviour. The vertical and horizontal stiffness of the links are those of the isolator, declared by the producer. The sliding supports, placed on the columns where there are not isolators, are multi-directional confined elastomeric disc structural bearings with a vertical capacity of 1500 kN and displacement capacity of 200 mm. They were also modelled with two nodes links characterized by a vertical stiffness only. The link element allows the relative displacement between the two nodes, simulating the presence of a sliding support.

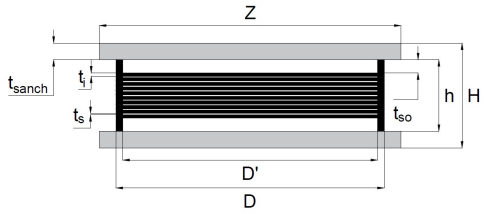


Figure 5. – Seismic isolator ($t_{sanch}$ is the thickness of anchor plates and $t_{SO}$ is the thickness of vulcanized steel plates).

| | Solution 10 | Solution 20 | |
|---|---|---|---|
| **V** | 1150 kN | 490 kN | Vertical capacity in seismic conditions (CLS) |
| **$F_{z,Ed}$** | 4680 kN | 2000 kN | Vertical capacity at ULS |
| **$K_e$** | 1.01 kN/mm | 0.51 kN/mm | Equivalent horizontal stiffness |
| **$K_v$** | 1246 kN/mm | 519 kN/mm | Vertical stiffness |
| **D** | 400 mm | 350 mm | Diameter of the isolator |
| **$t_e$** | 50 mm | 75 mm | Total thickness of rubber |
| **h** | 108 mm | 143 mm | Height of the isolator neglecting steel plates |
| **H** | 158 mm | 193 mm | Height of the isolator including steel plates |
| **Z** | 450 mm | 400 mm | Dimension of the anchor plates |
| **W** | 140 kg | 118 kg | Weight of the isolator |
| **$d_{cap}$** | 100 mm | 150 mm | Displacement capacity |
| **$G_{dyn}$** | 0.4 MPa | 0.4 MPa | Dynamic shear modulus of rubber (soft compound) |

Table 4 – Properties of the seismic isolators

The Figure 6 shows the layout in plan of seismic isolators and sliding supports for the two design hypotheses. The eccentricities between mass centre and effective stiffness centre at the isolation interface is equal to 9 cm in the direction of the long side of the building and 3 cm in the direction of the short side for "solution 10", while it is equal to 3 cm in both directions for "solution 20". For both the design hypotheses, 3 modes are sufficient to activate more than 85% of the total mass of the building. The three modes have the following periods: 2.97s, 2.82 s and 1.78s for "solution 10" and 2.96s, 2.81s and 1.61 for "solution 20", respectively. The isolators are steel reinforced elastomeric ones [14], having a low horizontal stiffness (in order to guarantee the decoupling of the horizontal motion of the structure from the ground one), a very high vertical stiffness (in order to sustain vertical loads without settlements). The geometrical properties of the isolators (global dimensions, thickness of the layers…), as well as the mechanical properties of the elastomer, are the main factors for the definition of verti-

cal and horizontal stiffness. The isolators used in this study are identified through the abbreviations SI-S 400/50 (maximum horizontal displacement of 100 mm), used in "solution 10", and SI-S 350/75 (maximum horizontal displacement of 150 mm), used in "solution 20". The elastomeric isolators SI-S 400/50 and SI-S 350/75 have a circular plan shape with diameter equal to 400 and 350 mmm, respectively, and they are realized with soft elastomeric compound (equivalent dynamic shear modulus $G_{din}$ = 0,4 MPa). The total thickness of elastomeric layers, $t_e$, is equal to 50 mm for SI-S 400/50 and 75 mm for SI-S 350/75, respectively. In Table 5 the geometrical dimensions of the two isolators are shown.

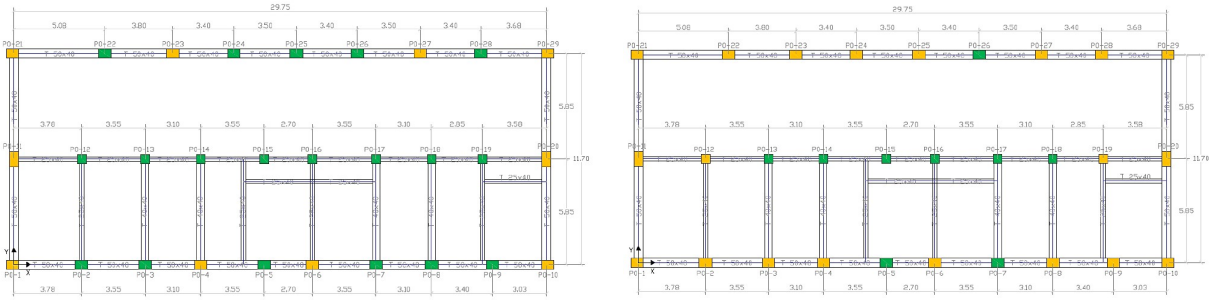

(a) (b)

Figure 6 – Plan disposition of seismic isolators and sliding support for: a) solution 10 and b) solution 20 (isolators in yellow, sliding supports in green)

Table 5 – Geometrical dimensions of the isolators

| GEOMETRICAL DIMENSION | | SI-S 400/50 | | SI-S 350/75 | |
|---|---|---|---|---|---|
| Diameter | D | 400 | mm | 350 | mm |
| Effective diameter | D' | 380 | mm | 330 | mm |
| Thickness of the single elastomeric layer | $t_i$ | 5 | mm | 5 | mm |
| Number of elastomeric layers | n | 10 | | 15 | |
| Thickness of steel layers | $t_s$ | 2 | mm | 2 | mm |
| Thickness of vulcanized steel plates (sup/inf) | $t_{so}$ | 20 | mm | 20 | mm |
| Thickness of anchor plates | $t_{sanch}$ | 25 | mm | 25 | mm |
| Height of the isolator neglecting anchor plates | h | 108 | mm | 143 | mm |
| Total height of the isolator | H | 158 | mm | 193 | mm |
| Dimension of anchor plates (sup/inf) | Z | 450 | mm | 400 | mm |

Table 6 shows the results of the safety checks of structural elements (beams and columns), that were performed for the Life Safety Limit State (SLV) assuming a behaviour factor q=1.5 (as suggested in [6]). With reference to the maximum ratios D/C it can be observed that: the safety checks of the beams are satisfied for the fundamental combination at ULS and for seismic combinations; the safety checks of the columns are all satisfied for vertical loads combined at the ULS (maximum D/C equal to 0.88 for combined axial load-bending and 0.61 for shear) and for seismic combinations (maximum D/C equal to 0.69 for ductile mechanisms and 0.59 for brittle mechanisms). Table 7 shows the results of the safety checks for seismic isolated building considering the two proposed solutions. For the safety check of the maximum displacement, the capacity values suggested by the producer are considered.

Table 6 – Strengthened structure: safety checks of beams and columns

| Check | Combination | Solution 10 $(D/C)_{max}$ | Solution 20 $(D/C)_{max}$ |
|---|---|---|---|
| Beams | ULS | **0.98** | **1.00** |
| Bending | Seism | **0.82** | **0.84** |
| Beams | ULS | **0.69** | **0.68** |
| Shear | Seism | **0.59** | **0.59** |
| Columns | ULS | **0.86** | **0.88** |
| Axial load - Bending | Seism | **0.91** | **0.93** |
| Columns | ULS | **0.59** | **0.61** |
| Shear | Seism | **0.57** | **0.59** |

Table 7 – Strengthened structure: safety checks of seismic isolators (sec. C.11.9.7 Circ. NTC2018)

| Check | Solution 10 $(D/C)_{max}$ | Solution 20 $(D/C)_{max}$ |
|---|---|---|
| Check of the maximum stress in steel plates | 0.19 | 0.26 |
| Check of the total shear strain | 0.72 | 0.86 |
| Check of the buckling load | 0.33 | 0.90 |
| Check of the maximum displacement | 0.74 | 0.49 |

### 3.4 Evaluation of the fire vulnerability of the structure

The thermal response of the elastomeric isolators was evaluated with reference to the standard IS0 834 fire curve, using the finite element software SAFIR [15]. In particular, the isolator with a portion of concrete column below and above (70 cm width and 20 cm height), was modelled in order to best reproduce the heat conduction phenomena. Indeed, the portion of the columns below the isolators is bigger, in order to give to the substructure greater strength and stiffness. These reinforced concrete jacketings dimension varied from 70 cm to 105 cm and the most critical case, from the heating transmission point of view, is related to the minimum dimension of column's side. The thermal properties of steel and concrete are considered variable with temperature, according to EN1991-1-2 [12]. The rubber was modelled as a user defined material, with the following thermal properties: thermal conductivity $\lambda$ = 0,27 W/Mk; specific heat cp = 1400 J/kgK; density $\rho$ = 1270 kg/m$^3$. These values were obtained from experimental tests on elastomeric isolators [14] and they are assumed constant with temperature. The entire model (isolator and portions of column) was heated on the lateral side by the standard ISO834 fire curve for 60 min. Figure 7 shows the trend of temperatures during 60 min of fire exposure, in some points placed at half height of each isolator.

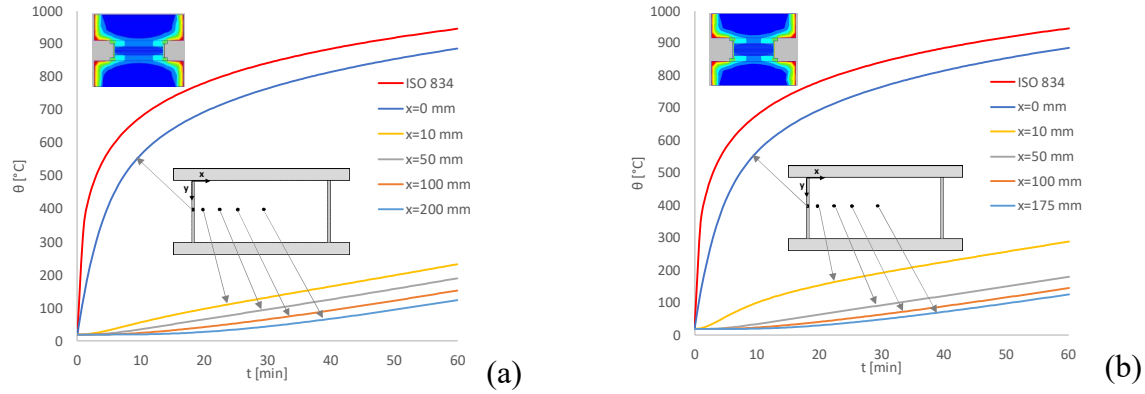


Figure 7 - Temperatures at half isolator height: (a)SI-S 400/50; (b) SI-S 350/75

The outer rubber layer (10 mm thick) that covers the alternating rubber-steel layers acts as a fire protection; indeed, a significant temperature difference between the point at x=0 mm (outer surface of the isolator) and the point at x=10 mm is obtained. The graphs show that in all the points considered the temperature exceeds 100 ºC after 60 min of fire exposure.

Figure 8 shows that the temperatures reached in the middle height of the isolator are the lowest, while moving away from the isolator centre, the temperatures increase due to the presence of the steel end plates. Therefore, relating the isolator damage to the temperature distribution, the damage it is not uniform and it is greater near to the rubber-layers at the steel vulcanized end plates. In this work, the fire assessment of damage isolators is carried out with the standard ISO834 fire curve.

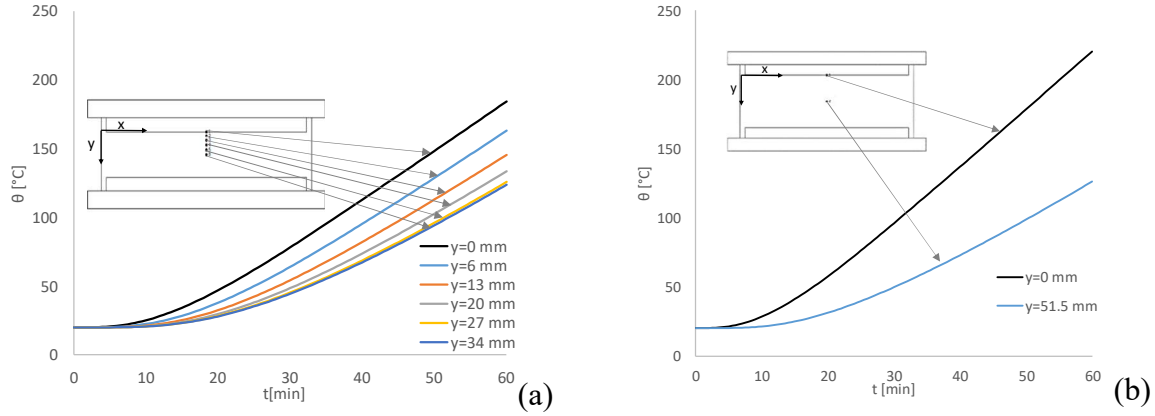


Figure 8 – Temperature evolution along central vertical axis (x = D/2):(a)SI-S 400/50 and (b) SI-S 350/75.

In particular, based on the performed thermal analyses, the thickness of the fire damaged isolator was defined using thermal fields at 30 and 60 min of fire exposure. The damaged zone is defined by the portion of isolator that reaches temperatures above a certain critical temperature threshold (or critical isotherm) at a certain time of fire exposure. In order to associate the isolator damage to the exceeding of the critical temperature threshold, each layer of elastomer has to be investigated, since the temperature distribution in the isolator is not uniform. Therefore, starting from the thermal fields at 30 and 60 min of fire exposure, for each isolator and for each critical temperature threshold, the damaged portion "$t_{dam}$" of the single layer has been defined as the portion of elastomer characterized by temperatures $\theta > \theta_{crit}$. Figure 9 shows, for the three thresholds of critical temperature (70°C, 200 °C and 320 °C), the reduction factors of horizontal $\alpha_{kh}$ and vertical $\alpha_{kv}$ stiffnesses at 30 and 60 min of exposure to standard fire.

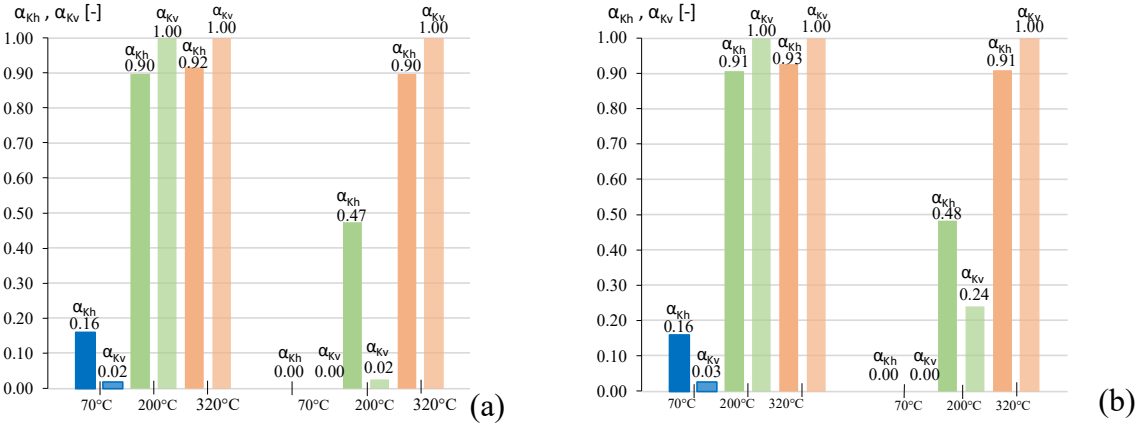


Figure 9 – Reduction factor of horizontal $\alpha_{kh}$ and vertical $\alpha_{kv}$ stiffness for (a) SI-S 350/75 and (b) SI-S 400/50 elastomeric isolators.

Furthermore, Figure 9 shows that the critical temperature equal to 70°C is particularly restrictive, indeed it causes a significant reduction of both horizontal stiffness (-79% for SI-S 400/50 isolator and -84% for SI-S 350/75 isolator) and vertical one (-97% for SI-S 400/50 isolator and -98% for SI-S 350/75 isolator) after only 30 min of exposure to the standard fire curve. In this case, in order to design an adequate passive fire protection system, depending on the fire resistance requirement, the temperature has to be maintained below 70°C. Considering a critical threshold temperature of 320°C, a minimum reduction (-10%) in horizontal stiffness is observed after 60 min of exposure to the standard fire curve for both the isolators, while no reduction of the vertical stiffness is observed, because the temperature threshold is exceeded only in the lateral rubber layer. An intermediate situation occurs with a critical tem-

perature threshold of 200 ºC, in which there is no much degradation of mechanical properties after 30 min of fire exposure. On the contrary, after 60 min the horizontal stiffness of SI-S 350/75 isolator is halved, causing a significant damage of it. Therefore, also in this case, to design a passive fire protection system is necessary, in order to guarantee, after 60 min of fire exposure, that the temperature inside the isolator remains below 200ºC.

### 3.5 Assessment of load bearing capacity after fire

In order to verify the residual load bearing capacity of the isolators, a comparison with the loads acting on them, derived from the superstructure, was necessary. Therefore, the ULS axial forces acting on the isolators were derived from the SAP2000 model, updating for each case of ($\theta_{crit,\,t}$) the stiffness parameters of the elastomeric isolators damaged by fire; the maximum axial force is considered for the isolator safety check. The tables with the results of the safety checks performed for both the isolators are reported below. The results are expressed in terms of ratio between the demand, D, and the capacity, C. In particular, Table 8 refers to the case in which the full stiffness of sliding supports is considered, while Table 9 contains the results obtained assuming a reduction of the vertical stiffness of sliding supports equal to that assumed for elastomeric isolators. In case of θcrit = 320 °C and θcrit =200 °C, both the isolators don't exhibit load bearing capacity problems, indeed the resistance Fzd is greater than the acting vertical force, NSLU. If the critical temperature is equal to 70°C, after 30 minutes of exposure to the standard fire curve, the isolator SI-S 350/75 is unable to bear the vertical loads from the structure, requiring fire protection.

Table 8 – SLU load-bearing capacity safety check

| | | **Sliding support with stiffness degradation** | | | | | | **Sliding support without stiffness degradation** | | | | | |
|---|---|---|---|---|---|---|---|---|---|---|---|---|---|
| | | **SI-S 400/50** | | | **SI-S 350/75** | | | **SI-S 400/50** | | | **SI-S 350/75** | | |
| $\theta_{crit}$ [°C] | t [min] | $F_{zd}$ ( C ) [KN] | $N_{SLU}$ ( D ) [KN] | D/C [-] | $F_{zd}$ ( C ) [KN] | $N_{SLU}$ ( D ) [KN] | D/C [-] | $F_{zd}$ ( C ) [KN] | $N_{SLU}$ ( D ) [KN] | D/C [-] | $F_{zd}$ ( C ) KN] | $N_{SLU}$ ( D ) [KN] | D/C [-] |
| 70 | 0 | 4680 | 1297 | 0.28 | 2000 | 1332 | 0.67 | 4680 | 1297 | 0.28 | 2000 | 1332 | 0.67 |
| | 30 | 1091 | 574 | 0.53 | 359 | 849 | 2.37 | 1091 | 1193 | 1.09 | 359 | 1174 | 3.27 |
| | 60 | - | - | - | - | - | - | - | - | - | - | - | - |
| 200 | 0 | 4680 | 1297 | 0.28 | 2000 | 1332 | 0.67 | 4680 | 1297 | 0.28 | 2000 | 1332 | 0.67 |
| | 30 | 4680 | 1297 | 0.28 | 2000 | 1332 | 0.67 | 4680 | 1297 | 0.28 | 2000 | 1332 | 0.67 |
| | 60 | 2505 | 1162 | 0.46 | 1063 | 909 | 0.86 | 2505 | 1279 | 0.51 | 1063 | 1170 | 1.10 |
| 320 | 0 | 4680 | 1297 | 0.28 | 2000 | 1332 | 0.67 | 4680 | 1297 | 0.28 | 2000 | 1332 | 0.67 |
| | 30 | 4680 | 1297 | 0.28 | 2000 | 1332 | 0.67 | 4680 | 1297 | 0.28 | 2000 | 1332 | 0.67 |
| | 60 | 4680 | 1297 | 0.28 | 2000 | 1332 | 0.67 | 4680 | 1297 | 0.28 | 2000 | 1332 | 0.67 |

### 3.6 Fire protection system for seismic isolators

The assessment of the fire effects on seismic protection systems is a relevant topic for different aspects and problems. For example, a localised fire involving a limited number of elastomeric isolators, may causes problems for vertical loads due to differential displacements of the isolation system generated by vertical stiffness degradation. In addition, the horizontal stiffness degradation can lead to not satisfying the designing assumption in which the centre of mass and stiffness must be, as far as possible, coincident. Furthermore, a localized degradation could cause a displacement of the stiffness centre, generating an eccentricity that can cause additional torsional effects on structural elements. Since it is difficult to experimentally characterize the thermo-mechanical properties of the seismic isolators, the conservative assumption of θcrit =70°C was adopted in this work and a fire protection system of the isolators was considered to reduce the fire induced damages. In particular, a protective box of 25 mm thick gypsum plasterboards with a variable thermal conductivity (see Table 10) was considered (see Figure 10).

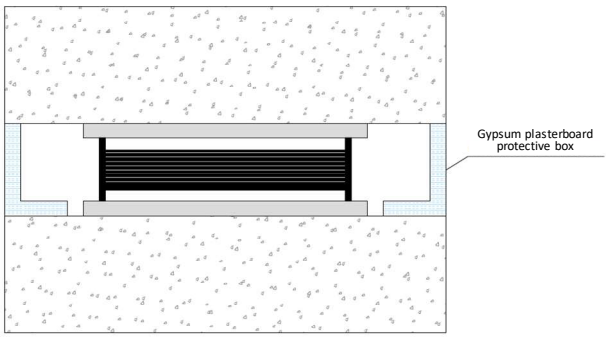


Figure 10 – Protective box installation.

Table 9 – thermal properties of gypsum plasterboard

| [°C] | λ [W/MK] | c [J/kg°C] | ρ [kg/m$^3$] |
|---|---|---|---|
| 20 | 0.20 | 800 | 800 |
| 65 | 0.80 | 800 | 800 |
| 70 | 0.80 | 5000 | 800 |
| 100 | 0.35 | 5000 | 800 |
| 102 | 0.35 | 5500 | 800 |
| 126 | 0.35 | 10000 | 800 |
| 140 | 0.12 | 10000 | 800 |
| 150 | 0.12 | 3050 | 800 |
| 370 | 0.12 | 3050 | 800 |
| 600 | 0.20 | 3050 | 800 |
| 1200 | 0.20 | 3050 | 800 |

The designed fire protection system ensures that the critical temperature of 70 ºC on the outer surface of the isolator is not exceeded after 60 min of fire exposure to the standard fire curve. Therefore, the isolators do not suffer any reduction in mechanical properties and the isolation system maintains its effectiveness

## 4 CONCLUSIONS

The paper shows the methodology to assess the seismic vulnerability after fire of buildings seismically isolated at the base. The methodology was applied to an existing multi-storey reinforced concrete building by considering two retrofit interventions with seismic base isolation. The thermal field in seismic isolators after 30 and 60 minutes of exposure to the standard fire curve ISO834 was assessed to estimate the degradation of vertical and horizontal stiffness and load bearing capacity of the isolators. This degradation was estimated based on the thermomechanical properties of the elastomer layer damaged by fire, considering the portion of isolator that achieve temperatures higher than a certain threshold (70, 200 or 320 ºC).

The results of the analyses show that:

- the experimental characterization of the behaviour of the elastomer at high temperatures would allow to evaluate with greater accuracy the need for a passive fire protection system, that should guarantee, according to the fire resistance requirement, that the critical temperature threshold θcrit is not exceeded;
- for both the cases $\theta_{crit}$ = 320 °C and $\theta_{crit}$ = 200 °C, the isolators do not show any problem in terms of load-bearing capacity;
- the case $\theta_{crit}$ = 70 °C is the most severe, since after 30 min of exposure to fire the isolator SI-S 350/75 is not able to sustain the vertical loads due to the superstructure, and requires a fire protection system.
- a passive fire protection system consisting of a protective box made of plasterboards panels, with an “L” section, guarantees that the critical temperature of 70 ºC is not exceeded on the external surface of the isolator after 60 minutes of exposure to the standard ISO834 fire curve and, therefore, that isolators do not suffer any reduction of mechanical properties.

The stiffness degradation is uniform due to the assumption of generalized fire. Is likely that localized degradation in case of localized fire change the position of the stiffness centre and this can cause additional torsional effects, which we did not consider. Moreover, in order to evaluate the static and seismic behaviour after fire of base isolated structures, in which the isolation system typically consists of both isolators and sliding supports, also the thermal degradation of the sliding supports must be considered. The ratios between the vertical loads on isolators and sliding supports before and after fire, varying the critical temperature threshold and taking into account or not the degradation of the sliding supports, show that:

- the vertical loads on the isolators reduce and consequently those in the sliding supports increase;
- the redistribution of the vertical loads on isolators and sliding supports is greater when the stiffness degradation of the sliding supports is not considered;
- assuming an equal degradation of all the seismic isolators, the more numerous are the isolators with respect to the sliding supports, the more the redistribution of vertical loads is high;
- the solution with more sliding supports is more efficient after a fire event.

The approach herein shown could be extended, in future, to fire scenarios with temperature curves different from the nominal standard curve. Moreover, localized fire scenarios could be considered, in order to take into account the effects of differential displacements that may occur when the degradation of seismic isolation devices is not homogeneous.

## REFERENCES

[1] Yasser M. Al-Anany, Michael J. Tai (2017) - Fiber reinforced elastomeric isolators for the seismic isolation of bridges – Composite Structures 160 (2017) 300-311 https://doi.org/10.1016/j.compstruct.2016.10.008

[2] Traxl R, Maier M, Bauer S, Schaur A, Zeiml M, Lackner R. (2018) - Thermochemical assessment of the load-bearing capacity of steel-reinforced elastomeric bearings subjected to fire loading - Engineering Structures 160 (2018) 12-23

[3] Fulin Z, Bo W, Ping T, Chaoyong S, Liwei H, Wu B. (2011) - Experimental study on fire resistance of building seismic rubber bearings – J. Struct. Eng. (2011) 137(12): 1593-1602

[4] Mazza F. (2017) – Residual seismic load capacity of fire-damaged rubber bearings of reinforced concrete base-isolated buildings- Engineering Failure Analysis 79 (2017) 951-970

[5] EN1992-1-2 (2004): Eurocode 2: design of concrete structures, part 1-2: general rules – structural fire design, Brussels (Belgium).

[6] D.M.II.TT. 17-01-2018: “Aggiornamento delle Norme tecniche per le costruzioni” (G.U. n. 42 del 20 febbraio 2018). (in italian)

[7] Circolare Ministero delle Infrastrutture e dei Trasporti del 21/01/2019 n. 7: Istruzioni per l’applicazione dell’aggiornamento delle “Norme Tecniche per le Costruzioni” di cui al D.M. 17/01/2018. (in italian)

[8] EN 1998-1 (2004): Eurocode 8: Design of structures for earthquake resistance – Part 1: General rules, seismic actions and rules for buildings [Authority: The European Union Per Regulation 305/2011, Directive 98/34/EC, Directive 2004/18/EC]

[9] ISO 188 Rubber, vulcanized or thermoplastic — Accelerated ageing and heat resistance tests, Int. Stand. (2007) 13.

[10] Losanno, D., Palumbo, F., Calabrese, A., Barrasso, T., Vaiana, N., Preliminary Investigation of Aging Effects on Recycled Rubber Fiber Reinforced Bearings (RR-FRBs), Journal of Earthquake Engineering, 2022, 26(10), pp. 5407–5424, DOI 10.1080/13632469.2021.1871683

[11] Trombetta P.L, Castellano M.G, Cocchio D. (2013) - Adeguamento Sismico di Edifici mediante Isolamento Sismico – In Atti del XV Convegno ANIDIS (Associazione Nazionale Italiana di Ingegneria Sismica), Padova (PD), 30 June / 4 July 2013 (in italian)

[12] EN 1991-1-2, 2002: EUROCODE 1: "Action on structures - Part 1-2: General actions-Actions on structures exposed to fire"

[13] SAP2000 (Version Ultimate 21.0.2) – Computers and Structures, Inc.

[14] Catalogo FIP INDUSTRIALE- Leading technologies. Isolatori elastomerici serie S1 (in italian)

[15] FRANSSEN J.M., "User's Manual for SAFIR2016c – a computer program for analysis of structures subjected to fire." University of Liege, Belgium 2016.

COMPDYN 2023
9th ECCOMAS Thematic Conference on
Computational Methods in Structural Dynamics and Earthquake Engineering
M. Papadrakakis, M. Fragiadakis (eds.)
Athens, Greece, 12-–14 June 2023

# A BUILDING CLASSIFICATION SYSTEM FOR MULTI-HAZARD RISK ASSESSMENT OF HISTORICAL RELIGIOUS BUILDINGS

**Federica Del Carlo[1], Silvia Caprili[1], Tiago Miguel Ferreira[2], Pere Roca[3] and Marco Uzielli[4]**

[1]University of Pisa
Largo L. Lazzarino 1, 56122 Pisa, Italy
e-mail: federica.delcarlo@phd.unipi.it, silvia.caprili@ing.unipi.it

[2] University of the West of England
Frenchay Campus, Coldharbour Lane, Bristol BS16 1QY, United Kingdom
e-mail: tiago.ferreira@uwe.ac.uk

[3]Technical University of Catalonia
Jordi Girona 1-3, 08034 Barcelona, Spain
e-mail: pere.roca.fabregat@upc.edu

[4]University of Florence
Via di Santa Marta 3, 50139, Florence, Italy
e-mail: marco.uzielli@unifi.it

**Abstract.** *UnReinforced Masonry (URM) religious buildings have proven to require special attention in the context of natural hazards risk assessment due to their high vulnerability – connected to aging and types of construction — and to their strong links with communities from both an economic and historical – cultural perspective. However, the study of this building type is extraordinarily complex, especially when the analysis is conducted on a territorial scale and involves a large number of elements. In the Italian context, following the extensive damage caused by recent major earthquakes (e.g., L'Aquila 2009, Emilia 2012, and Central Italy 2016), damage detection survey forms for the post-emergency phase, both for ordinary and religious buildings, have been developed. Nevertheless, proper classification of URM religious buildings considering attributes related to vulnerability to non-seismic hazards, and worthwhile as a tool of prevention rather than damage relief, is still lacking. This paper focuses on the development of a new structural classification system for URM religious buildings based on the identification and categorization of a set of attributes related to vulnerability to landslides, earthquakes, and geological hazards (e.g., type of load-bearing wall, building height, soil type, etc.). The classification system is then validated on an initial portfolio of thirty-eight samples, located in a specific area of the Tuscany region (Italy), to classify religious buildings into distinct structural types.*

**Keywords:** Disaster risk, Multi-hazard, Taxonomy, Vulnerability.

## 1 INTRODUCTION

Risk assessment procedures are usually based on the characterization of the hazards affecting the region of interest (in terms of expected frequency and intensity), the definition of the vulnerability of the assets exposed to the hazards, and the assessment of the assets' exposure. In a large-scale assessment, developing a model for each building identified is hardly feasible, as well as economically prohibitive. The need, therefore, arises to identify a methodology to classify buildings into typologies according to a given set of relevant attributes, which may effectively serve as seismic vulnerability attributes. The practice of categorising buildings based on building type, i.e., of defining a proper building taxonomy, has found increasing use in recent years to describe the seismic performance of existing structures. For example, in the United States, ATC-13 [1], FEMA 154 [2], and HAZUS [3] provide a building classification system based on local design and construction practices. Building taxonomies have also been developed In Europe over the years. The European Macroseismic Scale (EMS-98) [4], the RISK-EU project [5], and the Syner-G taxonomy [6], [7], are examples of classification systems developed for European buildings. Even on a global scale, attempts have been made to codify the built heritage. The Earthquake Engineering Research Institute (EERI) and the International Association for Earthquake Engineering (IAEE) have taken a big step forward in understanding and summarizing worldwide construction types in a unique building inventory, the World Housing Encyclopedia (WHE) project [8], [9]. Moving from the international to the Italian national context, the first-level AeDES form for post-earthquake damage assessment, the AeDES form [10], exploits buildings division into constructional typology to expeditiously survey the damage and usability of residential buildings, in the post-earthquake emergency phase. Another extremely valuable system for cataloguing buildings of historical and architectural interest is the ICCD standard for architectural heritage (Istituto Centrale per il Catalogo e la Documentazione). The Institute's purpose is to document and catalogue the archaeological, architectural-landscape, historical-artistic, and ethno-anthropological Italian cultural heritage. Although not directly related to the assessment of hazard vulnerability, this classification system is one of the few that accounts for the distinctive features of historical religious buildings. Indeed, despite the usefulness of all available classification systems, their thorough study has revealed inadequacy when it comes to historical religious buildings. Most of the existing taxonomies are limited to a list of ordinary building classes, and therefore lack adequate flexibility to characterize religious buildings. This type of building often requires a more in-depth analysis aimed at acquiring knowledge regarding the historical-constructive attributes (typological and dimensional data, analysis of the masonry, state of conservation, etc.), the study of macro-elements, and collapse mechanisms among others. As evidence of this, to classify earthquake damage, the Italian Civil Protection established an ad-hoc seismic detection survey form for monumental buildings and buildings of historical interest [11] (models A-DC for churches and B-DP for buildings, cf.DPCM 23-2-2006, G.U. n°55 of 7-3-2006). Furthermore, existing taxonomies usually refer solely to seismic risk, and very few of them account for multiple natural hazards [12]. Conversely, based on the multi-hazard risk assessment, great attention should be paid to combining building vulnerability-related information for each of the hazards considered.

Based on past efforts, the paper proposes a novel simplified classification system, developed specifically for masonry religious buildings. Through this new classification system, predominant building typologies, within the Tuscany region (Italy), are identified. This study is part of a broader research work whose objective is to develop a multi-hazard, spatial-oriented approach for the analysis of existing religious buildings. The approach proposed a quantitative risk analy-

sis framework, performed on a territorial scale, where the consequence of the identified hazards on a set of religious buildings can be estimated as the product of the hazard's probability of occurrence, building typologies vulnerability, and exposure. In this context, vulnerability is obtained by performing sensitivity analysis on each identified typology to assess which attributes have a greater impact, with respect to the structural performance towards the identified sources of risk. Whereas the exposure is estimated considering both the artistic value of elements at risk and the rate of occurrence with which the religious buildings are used. Indeed, for effective prevention, a territorial scale risk analysis is of the utmost importance for taking rational decisions on how to mitigate the effect of potentially disastrous natural events and for planning adequate maintenance operations, as well as monitoring measures. Section 2 presents the methodology and objectives of the work in its entirety; Section 3 illustrated the outcome of data collection regarding the main hazards affecting the area of interest; Section 4 presents the criteria for the selection of case studies and on-site Rapid Visual Form; Section 5 illustrates and comments the results of the on-site surveys.

## 2 METHODOLOGY AND OBJECTIVES

The aim of the broader research, of which the work presented here is the initial phase, is to develop and apply a multi-hazard, spatial-oriented approach for the analysis of the existing masonry churches in a selected area of the Tuscany region, with the purpose of reaching beyond a sectorial, and therefore limited, notion of risks. With reference to the risk assessment process provided by the [13], the following main phases of the work may be identified:

1. **Context definition** - at the initial stage, external and internal context are considered. In terms of the internal context, the aim of the research is delineate as the determination of the risk potential of a sample of religious buildings located into a limited geographical area. As previously stated, the risk potential is quantitative estimated as the product of the hazard's probability of occurrence, building typologies vulnerability, and building's exposure. Crucial to this phase is the correct definition of risk criteria or damage threshold. As regard the definition of the external context, cultural, historical, and geographical factors of the area of interest are carefully studied;

2. **Risk identification** - in this phase the main hazards that are expected to affect the churches are identified, together with the factors most likely to influence risk assessment (e.g. the limitation of knowledge, the impossibility of performing invasive tests, the need to carry out expeditious on-site survey, etc.). This phase resulted in the definition of the main attributes to be accounted for in the categorisation of recurrent structural typologies and to the consequently definition of a Rapid Visual Survey form (hereinafter called RVS form) specifically designed to allow expeditious, non-invasive on-site surveying;

3. **Risk analysis** - the purpose of this phase is to assess the level of risk of the churches investigated. A Bayesian approach is used to describe the occurrence probability of hazards involved, whereas the churches exposure is established in correlation with significance (i.e., main or secondary parish church) and artistic value (e.g., presence of artefacts of historical-artistic interest). For what concern the vulnerability assessment, parametric numerical models are developed for each typology identified. In order understand the relevance of selected attributes on the structure vulnerability, sensitivity analysis are performed by varying both external actions (e.g., ground motion) and internal parameters (e.g., geometry in plan and elevation);

4. **Risk evaluation** - as the final phase, the analysis outputs are compared with the risk criteria in order to match each building with a Class of Risk, allowing for straightaway identification of buildings requiring more attention, facilitating the understanding of whether and how additional action is required;

5. **GIS model** - the development of a GIS spatial model that integrates all the data collected and elaborated (risk class, hazards, churches typologies, etc.). The purpose is to create a tool which is able to quickly visualise, through Risk Classes, buildings that most require intervention or that, depending on their position/type/etc. require to be closely monitored.

This article is going to discuss in detail only the external context definition, risk identification, and RVS form structure and first application. Other phases and subsequent developments will be dealt with separately.

## 3 CONTEXT DEFINITION AND RISK IDENTIFICATION

The area selected for the present study is located in the Northern part of the Tuscany region (Italy), more specifically within the Lucca district and ranging from the Lunigiana-Garfagnana area, which covers a part of the Northern Apennines, to the River Serchio middle valley. It is a hilly and mountainous area, characterized by major centres and industrial areas connected by the main road network, and small settlements reached by the secondary road network. Earthquakes and slope instabilities can be considered the two main hazards of the selected area. From the seismic point of view, the Lunigiana-Garfagnana area is characterised by earthquakes average magnitude Mw of 5.0 [14]; the 1920 earthquake, with a magnitude Mw=6.5, which caused extensive damage throughout the upper part of the Serchio Valley represents a significant exception. The area has proven to be also prone to slope instability phenomena, due to both the geological and geomorphological characteristics, and climatic characteristics of the Serchio basin [15]. In addition to the National seismic zonation [16], and slope instability inventories available at the regional level [17], the study also involved the collection and analysis of existing seismic micro-zonation studies, which provide useful information regarding the patterns of ground motion amplification, liquefaction, surface fault ruptures, and earthquake-induced slope instability.
Following the identification of the main hazards to which the area is subjected, the churches to be investigated were selected. The Garfagnana area and Middle Serchio Valley are endowed with a large number of Romanesque churches, mostly dating back to Roman times. Together with monasteries and hospitals, these served as shelter and support for travellers who passed through these places both for necessity and for pilgrimage. In fact, the *Via Francigena*, a route from Canterbury to Rome which was one of the most important European communication routes in medieval times, together with other religious and commercial routes, such as the ancient transfer routes that the shepherds and their flocks took seasonally, still winds through these localities. An accurate list of all the religious buildings located in the area was available thank to previous research conducted in the same area [18] and include approximately four hundred religious building (Figure 1a). Considering both the characteristics of the site and the location of the churches, a first set of samples was selected by superimposing the National seismic hazard map and the inventory of Tuscan landslide phenomena to the map of the listed historical religious buildings, by means of the QGIS software. The selected buildings resulted in approximately half of the total number of churches analysed, but were instrumental in the preliminary calibration of the developed RVS form. All selected buildings present unreinforced masonry

structures and are referable to the Romanesque architectural style (Figure 1b). During the sample selection, preference was awarded to churches not plastered, so that the wall texture was visible, not excessively damaged or completely abandoned, to be able to access safely. Finally, churches part of monasteries or other religious complexes were avoided, as well as those incorporated in the urban aggregate, as it would become impossible to assess their vulnerability regardless of the context.

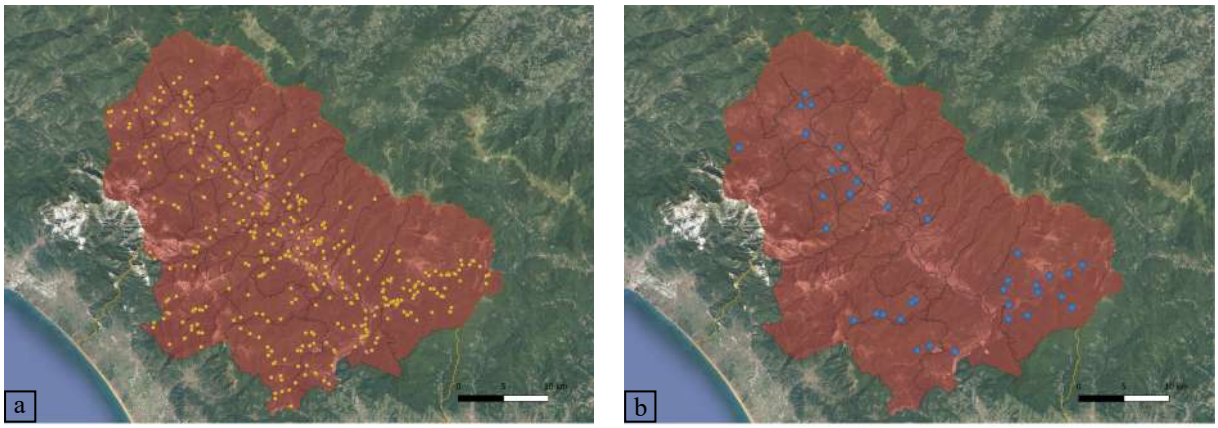


Figure 1: a) Identification of churches located in the selected area; b) Set of churches identified as samples.

## 4 BUILDING TYPOLOGY CLASSIFICATION

As previously mentioned, a review of existing literature and classification system was carried out initially. Although the authors were unable to evaluate all existing systems, this first step was crucial in understanding which attributes are recurrent in the various taxonomies [19–22], which are more relevant in defining the vulnerability to the various hazards [23–27], and how data are typically collected at the territorial scale in the context of the project [28–32]. The following section identifies building attributes adopted for the classification of historical-religious buildings into building typologies, focusing particularly on those attributes relevant in defining the vulnerability to earthquakes and slope movements, since, as mentioned, these hazards have been responsible for most of the economic and human losses in the area of interest. In this phase, the identified parameters are not ranked in terms of their influence on the structural response to the mentioned hazards.

### 4.1 Definition of the main attributes

The novel building classification was developed to identify predominant building classes among religious buildings. The chosen attributes must be compatible with a fast screening of a considerable number of churches and as mentioned, meaningful for the foreseen multi-hazard vulnerability assessment. In detail, the building taxonomy developed includes three main sections and nine sub-sections used to describe the material of construction, the lateral load-resisting system, the roof type, and the conservation state among other features. A more in-depth description of the attributes used is given in Table 1.

The three sections presented are reported on a Rapid Visual Survey Form which was used during the visual inspection of the selected churches. An example of a compiled RVS form is

| Attribute | Description | Hazard addressed |
|---|---|---|
| **General Data** | | |
| *Survey data* | day, month, year | hazard independent |
| *Loci Information* | province, municipality, sub-municipality (e.g., the Italian ”Provincia”, ”Comune”, and ”Frazione”) | hazard independent |
| *Geographic Information* | road type providing access to the building, position within the building context (e.g., isolated, attached to other buildings, at the corner of a block of buildings), GPS coordinates | relevant to both earthquakes and slope instabilities hazards |
| *Building ID* | type (e.g,. parish, cathedral etc.), name, diocese, occupancy rate (e.g. continuously, occasionally, no longer in use, etc.) | hazard independent |
| *Vertical bearing structure* | vertical and lateral load resisting system, construction material, quality and maintenance level | mainly relevant to earthquakes |
| *Roof structure* | roof shape, material, structural system, quality and maintenance level | mainly relevant to earthquakes |
| *Internal ceiling* | ceiling shape, material and structural system, quality and maintenance level | mainly relevant to earthquakes |
| *Intervention* | relevant interventions that various components of the church may have undergone (i.e., vaults reconstruction, re-covering, etc.) | relevant to both earthquakes and slope instabilities hazards |
| **Building Layout** | | |
| | plan geometry and dimensions (i.e. one nave, three naves, Greek plan, etc.), ground floor level and height above grade, presence of valuable decorative elements, orientation of the building | relevant to both earthquakes and slope instabilities hazards |
| **Facade Layout** | | |
| | facade type, quality and maintenance level, presence or absence of a bell tower, construction material of the exterior walls | mainly relevant to earthquakes |

Table 1: Church attributes relevant for multi-hazard risk assessment.

presented in Figure 2.

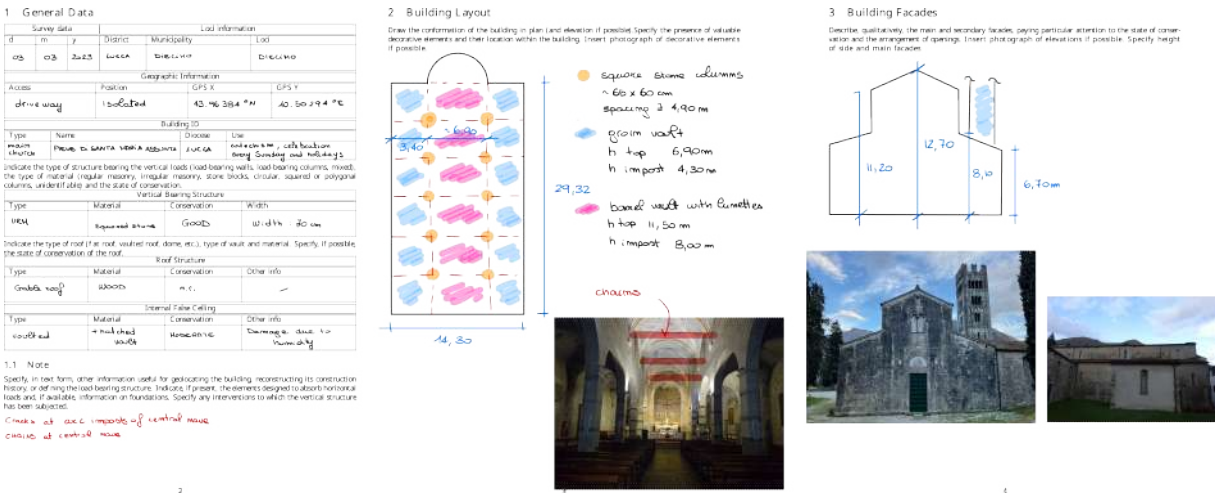


Figure 2: Example of RVS.

In comparison to more popular and well-known classification examples, the attributes chosen are fewer in number. However, this feature has proven to be valuable in the fast screening of a large number of buildings. To this purpose, the limited number of information gathered proved to be critical for categorizing buildings into major types.

## 4.2 On-site surveys

To validate the applicability of the proposed system, inspections were performed in the first thirty-eight churches selected as case studies. In addition to the compilation of RVS forms introduced above, the crack pattern of each church was observed and reported. No detailed maps were produced since the aim of the work is not to analyse extensively each church. In this framework, the damage surveys will be used as a means of the effectiveness of the result of the subsequent stages (vulnerability and risk analysis). Attention was also given to the surroundings of each building, to detect any possible evidence of ground movement, damage due to past earthquakes, or the presence of buildings that would interfere with the church itself. According to the plan layout, three recurring types of churches were identified during the first thirty-eight surveys (Figure 3): one-nave, three-nave, and Latin cross. Relevant variations in plan can be distinguished within these three types, owing primarily to the presence or lack of an apse and its shape, whether circular or rectangular. For the purpose of simplifying the subsequent stage of vulnerability analysis, however, the variations related to the apse are to be considered as variations within the same typology.

Other collected data show that the thickness of the load-bearing masonry ranges between 60 and 100 cm, while the height of the perimeter walls ranges between 6 and 10 m. The roof structure was always found to be made of wood. Where interior false ceiling was not present, wooden trusses were detected, in all others, it was not possible to identify through surveying alone whether the roof structure was pitched roofs or truss. The vaults that serve as the interior false ceiling are almost always barrel vaults with lunettes or cross vaults, either thatched or made of light material, usually local tuff. Only in two cases, related to more exposed churches, ribbed vaults were found and, in one case, a dome. In the case of three-nave churches, the

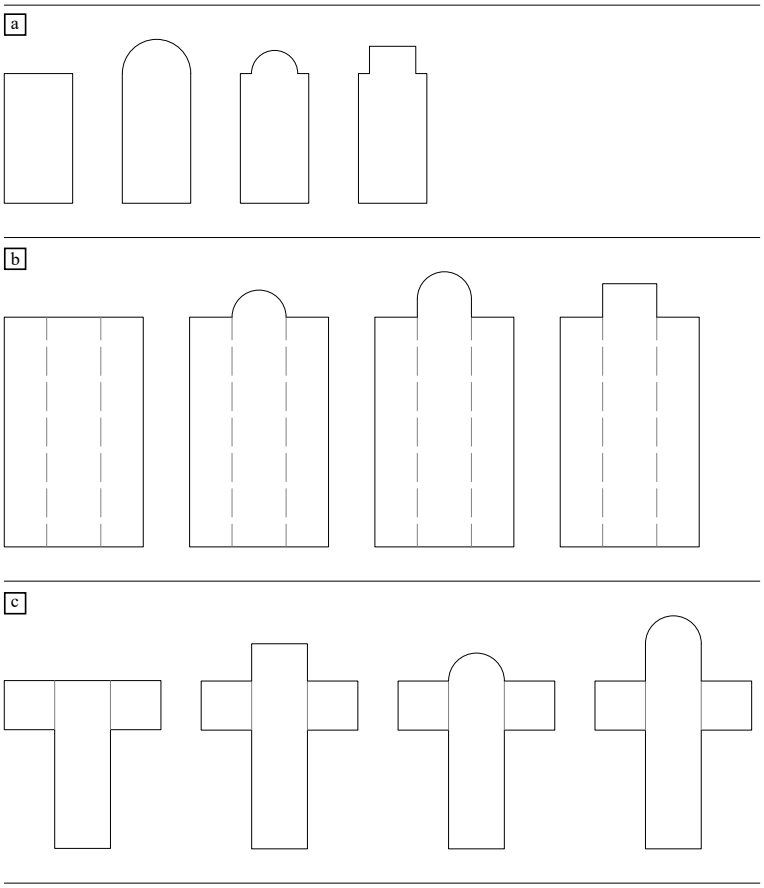


Figure 3: a) Type one: one-nave church; b) Type two: three-nave church; c) Type three: Latin cross

central and the secondary naves resulted to be separated by circular or squared columns, with spacing varying from 3 to 5 m. Moreover, as predictable considering the relevant seismicity of the area, all of the churches surveyed were found to have at least chains at the top of the central nave, in some cases also between the arches separating the main nave from the secondary ones. In some cases, surveyed churches are located on gently declining slopes, whose kinematisms are reflected by the crack pattern of the churches themselves and, if present, of the surrounding buildings.

## 5 CONCLUSIONS

Starting from existing taxonomies and vulnerability attributes, a simple structural classification system for the historical religious buildings was developed. The system was initially applied to a first sample of thirty-eight churches located in a selected area of the Tuscany Region in order to test its effectiveness within an expeditious screening project of a considerable number of historical religious buildings. The results obtained demonstrate that, despite being based on a limited number of attributes in comparison to more complex taxonomies, the proposed system effectively leads to the categorisation of buildings into three recurring main types: one-nave, three-nave, and Latin cross. This allowed the rapid visual screening of the entire portfolio of seventy-one churches and the progression to the next stage of vulnerability assessment.

## 6 ACKNOWLEDGMENTS

We are grateful to the graduating student Giacomo Bianchini for his support in data acquisition and survey.

## REFERENCES

[1] ATC (Applied Technology Council). 1985. Earthquake damage evaluation data for California. ATC-13. Redwood City, CA: Applied Technology Council.

[2] FEMA (Federal Emergency Management Agency). 1988. *Rapid visual screening of buildings for potential seismic hazards: A handbook*. FEMA 154. Washington, DC: FEMA.

[3] FEMA (Federal Emergency Management Agency). 2003. *HAZUS-MH MR4 technical manual*. Washington, DC: FEMA.

[4] G. Grünthal, European macroseismic scale 1998 (EMS-98). *Cahiers du Centre Européen de Géodynamique et de Séismologie 15*, Centre Européen de Géodynamique et de Séismologie, Luxembourg, 1998.

[5] Mouroux, P, E. Bertrands, M. Bour, B. Le Brun, S. Depinois, and P. Masure. 2004 The European Risk-Eu project: An advanced approach to the earthquake risk scenarios. In *Proceedings of the 13th World Conference on Earthquake Engineering*, 1-6 August 2004, Vancouver, Canada, paper no. 3329.

[6] Crowley H., Colombi M., Silva V., Ahmad N., Fardis M., Tsionis G., Karatoni T., Lyrantazaki F., Taucer F., Hancilar U., Yakut A., Erberik MA (2011b) D3.2 Fragility functions for common masonry building types in Europe, *SYNER-G Deliverable 3.2*. Available from URL: http://www.vce.at/SYNER-G/files/dissemination/deliverables.html

[7] H Crowley, S Özcebe, R Spence, R Foulser-Piggott, M Erdik, K Alten, Development of a European Building Inventory Database. In *Proceedings of the 15th World Conference on Earthquake Engineering*, 24-28 September 2012, Lisbon, Portugal.

[8] Brzev S., Scawthorn C., Charleson A., Jaiswal, K, and Silva V. (2013). GEM building taxonomy (Version 2.0). *GEM Technical Report 2013-02 V1.0.0.*. Pavia, Italy: GEM Foundation.

[9] Moroni, O., and Ghomez, C. World Housing Encyclopedia Report. *International Association of Earthquake Engineering*, 2002.

[10] Baggio, C., Bernardini, A., Colozza, R., Corazza, L., Della Bella, M., Di Pasquale, G., ... and Zuccaro, G. (2007). Field manual for post-earthquake damage and safety assessment and short term countermeasures (AeDES). *European Commission—Joint Research Centre—Institute for the Protection and Security of the Citizen, EUR, 22868*.

[11] Presidency of Ministers Council, Department of the Civil Protection S. Papa, G. Di Pasquale (Eds.), Manual for Compilation of the Form for Survey of the Damage to Cultural Heritage, Churches, MODEL A-DC (in Italian) (2013)

[12] Silva, V., Yepes-Estrada, C., Dabbeek, J., Martins, L., and Brzev, S. (2018). GED4ALL-Global exposure database for multi-hazard risk analysis–multi-hazard exposure taxonomy. *Global Earthquake Model Foundation: Pavia, Italy*.

[13] Standard, B., & Standard, N. Z. (2009). Risk management-Principles and guidelines. *BS ISO, 31000*, 2009.

[14] Rovida A., Locati M., Camassi R., Lolli, B., Gasperini P., Antonucci A., 2022. Catalogo Parametrico dei Terremoti Italiani (CPTI15), versione 4.0. *Istituto Nazionale di Geofisica e Vulcanologia (INGV)*. https://doi.org/10.13127/CPTI/CPTI15.4

[15] D'Amato Avanzi, G., Puccinelli, A., Trivellini, M. (1993). Slope stability maps in areas of particular seismic interest: a short report on the researches in Garfagnana and Lunigiana (Tuscany).

[16] Ordinanza del Presidente del Consiglio dei Ministri n. 3519 del 28 aprile 2006, Criteri per l'individuazione delle zone sismiche e per l'aggiormento degli elenchi delle medesime zone - n. 108. Gazzetta Ufficiale n. 108 del 11-5-2006

[17] Database Geomorfologico Della Regione Toscana
http://www502.regione.toscana.it/geoscopio/geomorfologia.html

[18] Pozzobon, E. (2019); Religious architectural heritage losing its functions. Strategies to mitigate the problem and provide new value through territorial context analysis.

[19] Dewett, D. T., Pigott, J. D., Marfurt, K. J. (2021). A review of seismic attribute taxonomies, discussion of their historical use, and presentation of a seismic attribute communication framework using data analysis concepts. *Interpretation*, 9(3), B39-B64.

[20] Porter, K. A. (2005). A taxonomy of building components for performance-based earthquake engineering. *Pacific Earthquake Engineering Research Center*.

[21] Lourenço, P. B., Oliveira, D. V., Leite, J. C., Ingham, J. M., Modena, C., Da Porto, F. (2013). Simplified indexes for the seismic assessment of masonry buildings: International database and validation. *Engineering Failure Analysis*, 34, 585-605.

[22] Ortega, J., Vasconcelos, G., Rodrigues, H., Correia, M. (2019). A vulnerability index formulation for the seismic vulnerability assessment of vernacular architecture. *Engineering Structures*, 197, 109381.

[23] Dabbeek, J., Silva, V. (2020). Modeling the residential building stock in the Middle East for multi-hazard risk assessment. *Natural Hazards*, 100(2), 781-810.

[24] Silva, V., Brzev, S., Scawthorn, C., Yepes, C., Dabbeek, J., Crowley, H. (2022). A building classification system for multi-hazard risk assessment. *International Journal of Disaster Risk Science*, 13(2), 161-177.

[25] Julià, P. B., Ferreira, T. M. (2021). From single-to multi-hazard vulnerability and risk in Historic Urban Areas: a literature review. *Natural Hazards*, 108(1), 93-128.

[26] Lagomarsino, S. (2006) On the vulnerability assessment of monumental buildings. *Bulletin of Earthquake Engineerin* 4, 445–463.

[27] Sevieri, G., Galasso, C., D'Ayala, D., De Jesus, R., Oreta, A., Grio, M. E. D. A., Ibabao, R. (2020). A multi-hazard risk prioritisation framework for cultural heritage assets. *Natural Hazards and Earth System Sciences*, 20(5), 1391-1414.

[28] Bosher, L., Kim, D., Okubo, T., Chmutina, K., Jigyasu, R. (2020). Dealing with multiple hazards and threats on cultural heritage sites: an assessment of 80 case studies. *Disaster Prevention and Management: An International Journal*, 29(1), 109-128.

[29] Gentile, R., Galasso, C., Idris, Y., Rusydy, I., Meilianda, E. (2019). From rapid visual survey to multi-hazard risk prioritisation and numerical fragility of school buildings. *Natural Hazards and Earth System Sciences*, 19(7), 1365-1386.

[30] Gentile, R., Cremen, G., Galasso, C., Jenkins, L. T., Manandhar, V., Menteşe, E. Y., ... McCloskey, J. (2022). Scoring, selecting, and developing physical impact models for multi-hazard risk assessment. *International Journal of Disaster Risk Reduction*, 82, 103365.

[31] Lagomarsino, S., Podestà, S. (2004). Seismic vulnerability of ancient churches: I. Damage assessment and emergency planning. *Earthquake spectra*, 20(2), 377-394.

[32] Santos, C., Ferreira, T. M., Vicente, R., da Silva, J. R. M. (2013). Building typologies identification to support risk mitigation at the urban scale–Case study of the old city centre of Seixal, Portugal. *Journal of Cultural Heritage*, 14(6), 449-463.

COMPDYN 2023
9th ECCOMAS Thematic Conference on
Computational Methods in Structural Dynamics and Earthquake Engineering
M. Papadrakakis, M. Fragiadakis (eds.)
Athens, Greece, 12-14 June 2023

# MULTI SCALE URBAN MODELLING TO IMPROVE THE RECOVERABILITY OF CITIES EXPOSED TO MULTIPLE NATURAL HAZARDS

**S. Mohammadi[1], G. Boni[1], F. Pirlone[1], S. Cattari[1] and S. De Angeli[1]**

[1] University of Genoa, Department of Civil, Chemical and Environmental Engineering
Via Montallegro 1, 16145, Genova
e-mail: soheil.mohammadi@edu.unige.it, {giorgio.boni, francesca.pirlone, serena.cattari, silvia.deangeli}@unige.it

## Abstract

*A resilient urban system should be able to recover from a disaster as quickly and effectively as possible. The optimal time to begin planning and implementing recovery investments to improve the urban system's recoverability is before the disaster. Considering that usually there are insufficient resources to invest in all urban facilities and infrastructures, in this research, the concept of Minimum Urban System that assures the Safeguarding of the Settlement is developed. This concept refers to the "subset of assets" of the urban system to be preserved to ensure continuing recovery efforts after a disaster and must be determined in accordance with some defined criteria that indicate the relative socio-economic worth of the various assets and the significance of their contribution to the urban system's performance. When the urban system is exposed to multiple and potentially interacting (such as cascading, consecutive, compound, etc.) risks, the assets' contribution to the system's ability to deal with these complex multi-risk conditions needs to be considered and integrated into the minimum urban system determination.*

*In light of this, the goal of this work is to establish a methodological framework in three spatial scales (macro, meso and micro) to model the urban system, and identify its most crucial components - and their interdependencies - as the minimum urban system.*

**Keywords:** Minimum Urban System, Safeguarding of the Settlement, Multi-risk, Disaster Recovery.

## 1 INTRODUCTION

Recovery is defined by UNDRR [1] as "the restoring or improving of livelihoods and health, as well as economic, physical, social, cultural, and environmental assets, systems and activities, of a disaster-affected community or society, aligning with the principles of sustainable development and 'build back better', to avoid or reduce future disaster risk". In line with this concept, several researchers indicated that to improve urban recoverability it is not only required to prepare recovery plans before the occurrence of the disaster but also to take some actions in pre-disaster time to make the system go through the recovery process in easier faster and efficient way [2]–[4].

Certain measures, like strengthening crucial infrastructures and structures, can make the system more recoverable from two perspectives. On the one hand, it would lessen the severity of the system's failure right after the disaster occurred, increasing the system's resistance. On the other hand, it would lead to the preservation of crucial structures that can help the recovery and emergency process after an event [5].

The Italian Civil Protection Department (CPD) has established certain Limit Conditions (LC) for urban areas, which serve as specific targets for disaster management planning [6]. These LCs are conceptual thresholds that relate various degrees of physical and functional damage to the urban system and its components, focusing on the seismic risk. The urban system may lose some degrees of functionality if any of these thresholds are surpassed as a result of a disaster.

While for the emergency limit condition (ELC) the CDP already proposed a well-defined procedure for assessing the functionality of some essential components of the urban system ( [6], [7]), for other limit conditions these standardized procedures are not yet available. The definition of the 'Limit Condition for Safeguarding the Existence of the Settlement' (hereinafter as SLC) following the occurrence of a disaster is the main focus of this paper. A first attempt to outline an operational procedure to quantitively assess the SLC condition considering the seismic risk has been proposed in [8].

SLC pertains to the limit condition that allows an urban system to:

1. provide emergency management services in the aftermath of the disaster;
2. initiate the recovery process using its own primary functions, i.e., the system should have the capacity to leverage its existing infrastructure and resources to restore critical services and infrastructure in the affected areas;
3. restore other important urban functions in an efficient manner.

In general, fulfillment of the SLC requirement presupposes satisfaction of the ELC. It indicates that surpassing ELC, the vital physical assets necessary for providing emergency management services, have already been functional. Nevertheless, the connection amongst ELC and SLC assets has to be taken into account.

Considering the length of the recovery process, which might take years or decades [9], [10], SLC definition cannot disregard socio-economic issues. Otherwise, the recovery process would finally create a settlement that is not resilient, with social fragmentation and unusable living circumstances, even though the settlement would be physically rebuilt at the end of the recovery [11], [12]. In this context, it could be claimed that characterizing the SLC necessitates multidisciplinary analysis and evaluation of a community's economic, social, cultural, and identity aspects.

Because of the limited resources to invest in all urban facilities and infrastructures, a minimum urban system must be preserved to ensure the SLC after a disaster. This research aims to contribute to the identification of physical elements in an urban system that after a disaster, can ensure meeting the SLC condition. These elements are identified considering: (i)

multiple **functions** (e.g., economic, education, health, etc.); (ii) the potential interactions and **interdependencies** among them as well as the overall **functionality** of the system; (iii) a multi-hazard risk perspective.

In the interests of improving the recoverability of the urban system in multi-risk conditions, we explicitly provide here a multi-scale urban modeling framework that can become the basis for an optimization model for investing in these crucial physical elements.

## 2 THE MINIMUM URBAN SYSTEM IN A MULTI RISK ENVIRONMENT

In the work illustrated in [8], the physical elements that in an urban system can ensure continuing recovery efforts after a disaster and therefore meeting the SLC represent the so-called 'Minimum Urban System that assures the Safeguarding of the Settlement' ($SLC_{MIN}$). According to [8], the $SLC_{MIN}$ must be determined in accordance with some defined criteria that indicate the relative socio-economic worth of the various assets and the significance of their contribution to the urban system's performance and probable damage that might imposed on the system as consequence of natural hazard event.

As aforementioned, the $SLC_{MIN}$ introduced in [12] focuses only on seismic risk. Nevertheless, when the urban system is exposed to multiple risks, the circumstance will become more complicated. In this condition the physical assets' contribution to the system's ability to deal with multi-risk situations of any kind (such as cascading, consecutive, compound, etc.) is a critical aspect that should be considered in the minimum urban system determination.

Based on the hazards that pose a threat, certain physical elements and assets can be vital across all phases of the risk management cycle, from prevention and preparedness to emergency and recovery. However, the present research primarily emphasizes on enhancing the recoverability of urban systems. Therefore, identifying the relevant hazard scenarios and theirs impact can aid in determining critical physical components that can facilitate the recovery process while simultaneously strengthening community resilience against potential multi-risk scenarios that may occur during recovery [13]. In this study, the two primary hazards considered for multi-risk condition analysis are earthquake and flood. The study also emphasizes buildings and urban forms (here and after called as 'strategic physical assets') in urban areas. Thus, even though there are other primary elements, including lifeline infrastructure, that can contribute to the $SLC_{MIN}$, examining them is outside the scope of the current study.

The recognition of the $SLC_{MIN}$ from a multi-hazard perspective is performed applying the procedure described in Fig.1 In order to identify the strategic physical assets to ensure the urban system's functionality and socioeconomic livelihood, the following actions should be performed:

- Modelling of the urban system functions and physical assets.
- Identification of the strategic physical assets and recognition of their importance.
- Definition of multi-hazard disaster scenarios to test the performances of the different components and the overall system.
- Implementation of a multi-criteria optimisation to identify the subset of components belonging to the $SLC_{MIN,}$ as a set of urban assets to invest on to improve the overall urban recoverability after disasters.

Hence, as a first stage, a thorough three-scale urban system modeling must be conducted with the goal of identifying the importance of the strategic physical assets in the urban area and measuring their importance in safeguarding the settlement. This step, which will be

explored more in detail in Section 3, must be conducted with perspective on the role that each asset can play during the recovery time. More explicitly, to assess the significance of strategic physical assets, it is essential to consider their importance not only ex-ante (i.e., before a disaster occurs), but also in terms of expediting and enhancing the recovery process ex-post (i.e., in the aftermath of a disaster). As an example of these assets, we mention the open spaces, that are potential places for temporary shelters during the recovery.

The next stage is to conduct a multi-hazard risk impact assessment to understand how the various multi-hazard disaster scenarios will affect the identified strategic physical assets and the urban system. The relevant multi-hazard disaster scenarios should be selected considering the different hazards that can occur in the study area and their potential interaction mechanism, either at the hazard or at the impact level [14]. Different multi-hazard disaster scenarios can be relevant: those generated by multi-hazard events that coincide in time and space, such as a strong windstorm and coastal flooding caused by the same adverse weather; those that happen in a cascade, such as an earthquake triggering a landslide or a tsunami; or even independent hazard events happening in a sequence, as in the case of an earthquake and then a flood affecting the same urban area that is still recovering from the damage caused by the previous hazards. This last case is the most interesting from the recovery perspective, since it highlights the need for integrated multi-hazard recovery planning and ex-ante strengthening interventions, able to reduce potential asynergies between earthquake and flood disaster risk reduction actions.

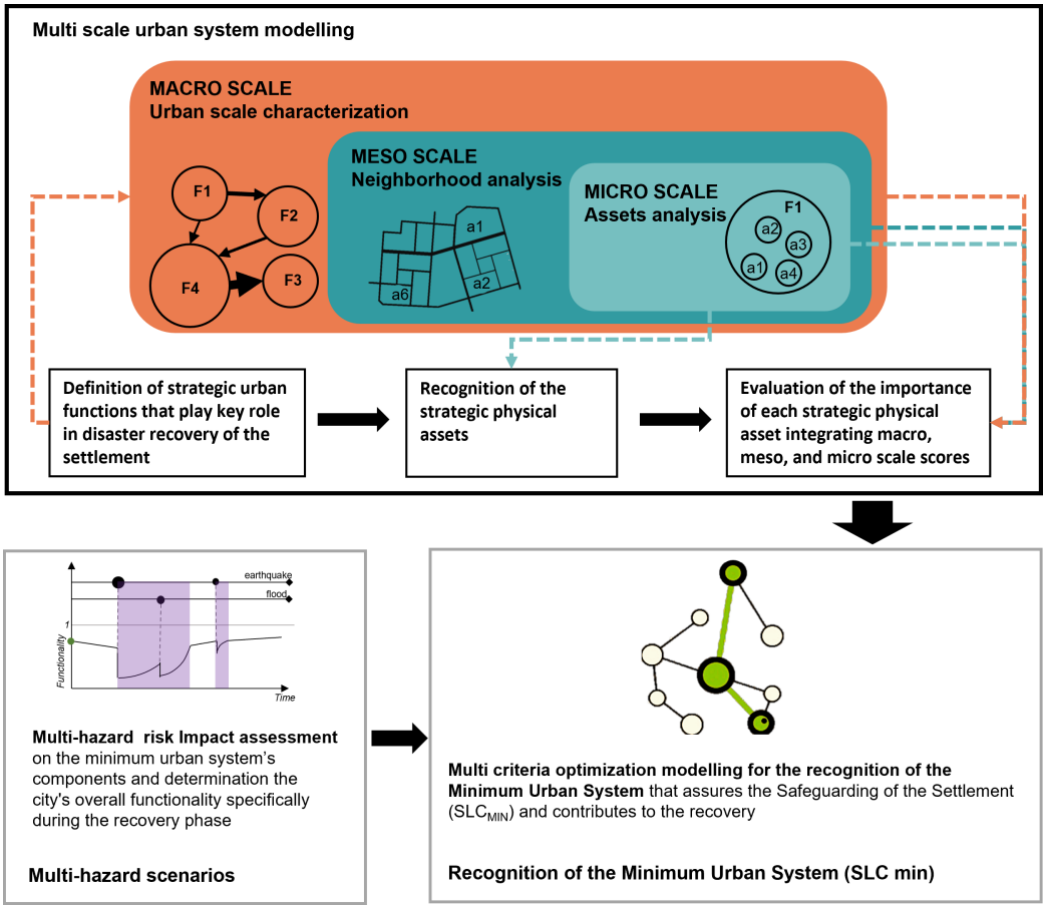


Figure 1: Overview of procedure for recognition of the Minimum Urban System that assures the Safeguarding of the Settlement in area exposed to multi hazard risk

As a main outcome from the multi-hazard risk impact assessment, the direct and indirect functional loss to each strategic physical asset and, consequently, to the overall urban system, will be obtained, also considering the effects of incremental damages and changes in the vulnerability of the damaged assets imposed by the multi-hazard risk scenarios.

Finally, the output of the multi scale urban system modelling and the multi hazard risk scenario assessment would be integrated in the last part of the procedure. The main aim of this last stage, denoted as 'Recognition of the $SLC_{MIN}$' in Figure 1, is to perform a multi criteria optimization model for deciding about direction investment on strengthening of the urban system. In other words, the strategic physical assets that worth more for the investments would be recognized according to their contribution to the $SLC_{MIN}$ and their mutual impact on and of multi risk scenarios.

## 3 MULTI SCALE URBAN SYSTEM MODELLING

As mentioned in previous section as the first step of the procedure the system modeling must be conducted. For assessing the importance of different functions and their corresponded assets in the urban system a multi-scale methodological framework is presented in this section. The importance assessment of different urban system's physical elements should be assessed in different spatial scales for the following reasons:

**1)** ***As a socio-ecological system, the urban system is a system of systems*** **[15], [16]** ***where each lower-scale component could be viewed as a system in itself, made up of finer-scale components.*** Additionally, the urban system itself interacts with other systems at the same or higher scales, such as other cities or the state/region. This research ought to focus on the **micro-scale assets**, by taking into account their corresponded **functions** within the larger urban system. Nevertheless, without considering the role of each asset inside the systems and subsystems to which it belongs, the determination of its **function** and **importance** in the urban system would be inaccurate and inadequate [17].

**2)** ***Data for describing and characterizing the urban system and its subsystems are provided at various scales.*** For instance, **demographic data** is usually presented at the city scale. This information could be essential for determining the population's needs and requirements and, as a result, for identifying the **functions** and **assets** that are fulfilling those demands. On the other hand, for example a **school's enrollment statistics** are an **asset** scale data that may be crucial for assessing the significance of the institutions and furthermore of the overall local education system.

**3)** ***Urban assets and forms at various scales contribute to the urban area's recoverability.*** For example, open spaces, that are neighborhood scale features of the urban system, are important throughout the recovery process since they can be used as potential temporary housing place [18], [19].

As a result, the urban system modeling should be carried out at three different scales: **macro, meso,** and **micro**, using the indicators that characterize the city at each of these scales [20]**,** [21]. In order to effectively assess the relative importance of diverse assets in urban settings, a comprehensive analysis must be conducted across these three distinct scales, with the aim of integrating the results to achieve a holistic understanding of their importance. The schematic diagram depicted in Figure 2 illustrates the overarching framework and the interrelationship between the scales, as well as the outcomes from the analyses conducted at each scale.

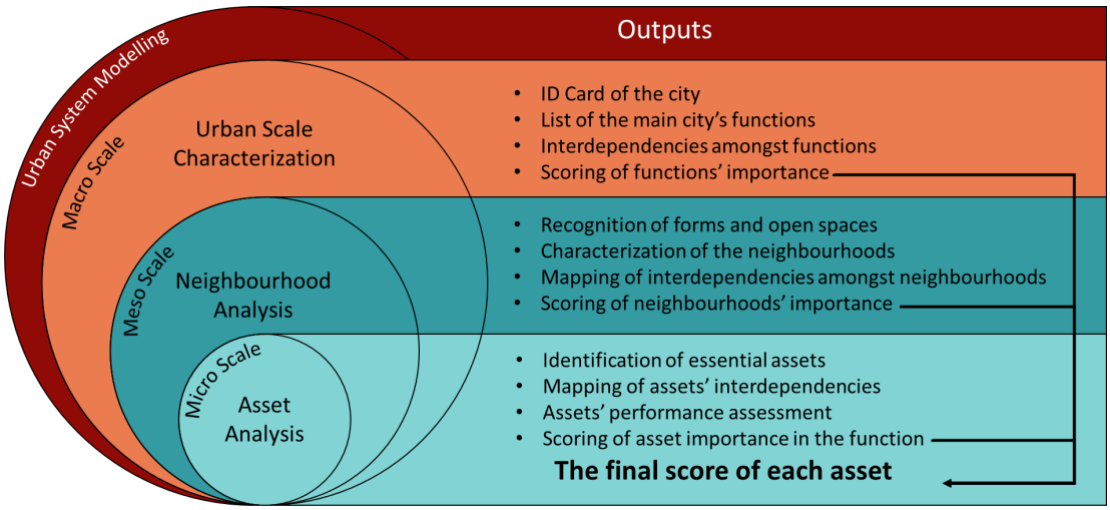


Figure 2: Overview of the proposed urban system modelling framework

The purpose of **macro scale** analysis is to characterize urban areas, which vary in their features based on capacities, shortages, settled population, and background. Different cities may have different functions and assets that are important to them, depending on their character. For example, some cities are primarily tourist destinations, while others are known for their religious or agricultural significance. Therefore, for instance the accommodation facilities might not have equal importance in these two types of cities. Accordingly, the role and importance of the different function and asset might differ in these different cities. As a result of macro scale analysis, the most important urban functions would be identified.

The primary goal at **meso scale** is to cluster urban areas into uniform districts that share the same characteristics and score them according to their importance in the recovery process. Different types of information, such as demography and socioeconomic dominant activities, should be considered in this clustering in addition to the physical data that have been gathered through the **macro** scale study. **Neighborhoods** may be the ideal unit to consider for this classification, although it should be noted that the final area selected may not correspond to neighborhood borders shown on administrative urban maps. In this research, the **neighborhood unit refers to the geographic region with a common physical and socioeconomic texture**.

Finally, the **micro scale** modelling aims at identifying the **essential assets** which contribute to the urban functions selected as a result of the **macro scale analysis**, mapping their interdependencies, evaluate their performances, and finally assign the score accordingly. For instance, after determining that schools are an essential asset in the education function, which has previously been defined as an important function as result of macro scale analysis, two schools would be compared, and each would receive a different score based on how many people they served, the size of their buildings, or any other metric that demonstrates how well they performed in the education system.

A **final score** is assigned to each urban asset as a combination of the scores it receives from the analyses performed at the micro, meso and macro scale, which encompasses:

1) The importance of the **function** it serves, obtained from the **macro scale**.
2) The **neighborhood** where the asset is located in, obtained from the **meso scale**.
3) The degree of **performance** and importance in the function the asset has attained from the **micro scale** analysis.

# 4 DATA SOURCES

## 4.1 Input data for the urban system modelling

In order to conduct an effective analysis within the context of the explained framework and specially in the section of multi-scale urban system modelling (upper box in Fig. 1), data must be collected from a variety of sources, including:

a) **Local stakeholders' knowledge**. Engaging with stakeholders, such as community members, local businesses, and city officials, can provide valuable insight into the urban system and help identify key factors and issues that should be considered in the analysis. This information can be collected through **interviews, surveys, and focus groups**. The involvement of stakeholders is crucial for both macro and micro-scale analyses.

b) **Accessibile quantitative and qualitative dataste**. This can be obtained from official databases run by statistic administration and local authorities. This data can include **demographic information, land use, economic, transportation, and environmental data**, that can be available at different geographic scales (i.e., regional, municipal, sub-municipal) and might refer to different time periods. Geographic Information System (GIS) can be used to elaborate some of these data and develop maps that can help in visualizing and analysing the urban system. This can include maps of land use, transportation infrastructure, and environmental factors such as air quality and water resources.

c) **Cadastral maps and areal-imagery**. The analysis of available cadastral maps and areal-imagery (e.g., satellite optical imagery) can support in the **recognition of the urban forms and open spaces,** and in the clustering of the different forms at the neighbourhood (i.e., meso) scale.

Macro and micro-scale analyses are performed integrating local stakeholders' knowledge with quantitative and qualitative datasets.

The meso-scale analysis is primarily conducted through the processing of data and maps collected at the micro and macro scales. Data collected at the micro and macro scales are processed and projected in a map form, providing a clearer spatial representation of the urban assets. This spatial representation enables more informed decision-making regarding the importance and location of various urban assets.

## 4.2 Data sources for the multi-hazard risk assessment

The second main step of the framework, i.e. the 'Multi-hazard risk assessments' (lower-left box in Fig. 1) requires a comprehensive and large-scale analysis, making it advisable to employ proper multi-hazard exposure and physical vulnerability models.

Generally, the framework is compatible with multi-hazard analysis of any kind, but with current research's focus on enhancing the urban system's recoverability, cascading and independent consecutive events are prioritized. In cases where two or more hazards are examined, it is essential to consider their interaction at the vulnerability level, and selecting the most appropriate multi-hazard vulnerability models [22]. Specifically, multi-variate vulnerability functions can be applied to properly evaluate the effect of compound hazards acting on the same asset. While stage-state functions are preferable when it is required to evaluate incremental impacts of consecutive events on the functionality of urban system components.

To enable the application of multiple vulnerability functions, the components of the territorial system require to be characterized by applying a proper multi-hazard exposure taxonomy, such as the GED4ALL Global Exposure Taxonomy[23].

To perform the multi-hazard impact (or risk) assessment, the loss of functionality of various assets is evaluated combining the exposure and vulnerability models with a series of hazard scenarios, which properly describe the evolution of the different hazards in space and time [14], including information about hazard intensity. These hazard scenarios can be obtained either by applying hazard models or exploiting available hazard maps.

## 5 CONCLUSIONS

The main aim of the presented procedure is the selection of a subset of assets and functions that contribute to the recoverability of the urban system after the occurrence of a disaster, improving and enlarging the definition of the 'Minimum Urban System that assures the Safeguarding of the Settlement' from a multi risk perspective.

Stakeholders are the individuals who utilize, shape, and develop the facilities and buildings that are part of an urban system. therefor as developers and final users of the urban system their ideas can play crucial role in decision making process [24], [25] to make sure that the selections outcome is going towards benefit of the settled population in urban system.

Moreover, in selecting the main assets and evaluating the performance of certain urban assets in the selected functions, or demonstration of the interdependencies amongst functions and assets, specialized knowledge may be required. However, it may not be feasible for a research team to include experts in all domains related to the active function in the urban system. To benefit from the knowledge and expertise of various professionals across different realms, it is necessary to involve them in the decision-making process as required. Therefore, it is essential to set a participation mechanism and integrate their knowledge and preferences into the modelling of the urban system.

## REFERENCES

[1] UNDRR, "Terminology." United Nations Office for Disaster Risk Reduction Geneva, Switzerland, 2020.

[2] R. Der Sarkissian, C. Abdallah, J.-M. Zaninetti, and S. Najem, "Modelling intra-dependencies to assess road network resilience to natural hazards," *Nat Hazards*, vol. 103, no. 1, pp. 121–137, Aug. 2020, doi: 10.1007/s11069-020-03962-5.

[3] L. Du and S. Peeta, "A Stochastic Optimization Model to Reduce Expected Post-Disaster Response Time Through Pre-Disaster Investment Decisions," *Netw Spat Econ*, vol. 14, no. 2, pp. 271–295, Jun. 2014, doi: 10.1007/s11067-013-9219-1.

[4] V. Rosato, A. Pietro, P. Kotzanikolaou, G. Stergiopoulos, and G. Smedile, "Integrating Resilience in Time-based Dependency Analysis: A Large-Scale Case Study for Urban Critical Infrastructures," 2021. doi: 10.5772/intechopen.97809.

[5] N. Ghorbani-Renani, A. D. González, K. Barker, and N. Morshedlou, "Protection-interdiction-restoration: Tri-level optimization for enhancing interdependent network resilience," *Reliability Engineering & System Safety*, vol. 199, p. 106907, Jul. 2020, doi: 10.1016/j.ress.2020.106907.

[6] M. Dolce, F. Bramerini, S. Castenetto, and G. Naso, "The Italian policy for Seismic Microzonation," in *Earthquake Geotechnical Engineering for Protection and Development of Environment and Constructions*, CRC Press, 2019, pp. 925–937.

[7] L. Di Ludovico and D. Di Ludovico, "Limit condition for the intermunicipal emergency," *TeMA Journal of Land Use, Mobility and Environment*, vol. 11, no. 3, Art. no. 3, Dec. 2018, doi: 10/1/Di%20ludovico.pdf.
[8] S. Cattari, D. Ottonelli, F. Franco, T. Buschiazzo, A. Guardiani, and V. Vivaldi, "TOWARDS AN IMPROVED URBAN SEISMIC RESILIENCE: THE PILOT CASE STUDY OF SANREMO MUNICIPALITY," presented at the 17th World Conference on Earthquake Engineering, 17 WCEE, Sendai, Japan, Sep. 2020.
[9] M. Dunford and L. Li, "Earthquake reconstruction in Wenchuan: Assessing the state overall plan and addressing the 'forgotten phase,'" *Applied Geography*, vol. 31, no. 3, pp. 998–1009, 2011.
[10] R. B. Olshansky, "Planning after hurricane Katrina," *Journal of the American Planning Association*, vol. 72, no. 2, pp. 147–153, 2006.
[11] D. E. Alexander, "The L'Aquila earthquake of 6 April 2009 and Italian Government policy on disaster response," *Journal of Natural Resources Policy Research*, vol. 2, no. 4, pp. 325–342, 2010.
[12] A. Özerdem and G. Rufini, "L'Aquila's reconstruction challenges: has Italy learned from its previous earthquake disasters?," *Disasters*, vol. 37, no. 1, pp. 119–143, 2013.
[13] W. Marzocchi, A. Garcia-Aristizabal, P. Gasparini, M. L. Mastellone, and A. Di Ruocco, "Basic principles of multi-risk assessment: a case study in Italy," *Nat Hazards*, vol. 62, no. 2, pp. 551–573, Jun. 2012, doi: 10.1007/s11069-012-0092-x.
[14] S. De Angeli, B. D. Malamud, L. Rossi, F. E. Taylor, E. Trasforini, and R. Rudari, "A multi-hazard framework for spatial-temporal impact analysis," *International Journal of Disaster Risk Reduction*, vol. 73, p. 102829, Apr. 2022, doi: 10.1016/j.ijdrr.2022.102829.
[15] P. Dicken, *Global Shift: Mapping the Changing Contours of the World Economy*. SAGE Publications Ltd, 2007.
[16] S. Meerow, J. P. Newell, and M. Stults, "Defining urban resilience: A review," *Landscape and Urban Planning*, vol. 147, pp. 38–49, Mar. 2016, doi: 10.1016/j.landurbplan.2015.11.011.
[17] A. Sharifi and Y. Yamagata, "Resilient Urban Form: A Conceptual Framework," in *Resilience-Oriented Urban Planning: Theoretical and Empirical Insights*, Y. Yamagata and A. Sharifi, Eds., in Lecture Notes in Energy. Cham: Springer International Publishing, 2018, pp. 167–179. doi: 10.1007/978-3-319-75798-8_9.
[18] P. Allan and M. Bryant, "The critical role of open space in earthquake recovery: a case study," in *EN: Proceedings of the 2010 NZSEE Conference (2010, Nueva Zelandia)*, 2010, pp. 1–10.
[19] D. Brand and H. Nicholson, "Public space and recovery: learning from post-earthquake Christchurch," *Journal of Urban Design*, vol. 21, no. 2, pp. 159–176, Mar. 2016, doi: 10.1080/13574809.2015.1133231.
[20] A. Sharifi, "Resilient urban forms: A macro-scale analysis," *Cities*, vol. 85, pp. 1–14, Feb. 2019, doi: 10.1016/j.cities.2018.11.023.
[21] A. Sharifi, "Urban form resilience: A meso-scale analysis," *Cities*, vol. 93, pp. 238–252, Oct. 2019, doi: 10.1016/j.cities.2019.05.010.
[22] R. Gentile *et al.*, "Scoring, selecting, and developing physical impact models for multi-hazard risk assessment," *International Journal of Disaster Risk Reduction*, vol. 82, p. 103365, Nov. 2022, doi: 10.1016/j.ijdrr.2022.103365.
[23] V. Silva, S. Brzev, C. Scawthorn, C. Yepes, J. Dabbeek, and H. Crowley, "A Building Classification System for Multi-hazard Risk Assessment," *Int J Disaster Risk Sci*, vol. 13, no. 2, pp. 161–177, Apr. 2022, doi: 10.1007/s13753-022-00400-x.

[24] D. Chandrasekhar, Y. Zhang, and Y. Xiao, “Nontraditional participation in disaster recovery planning: Cases from China, India, and the United States,” *Journal of the American Planning Association*, vol. 80, no. 4, pp. 373–384, 2014.
[25] J.-C. Gaillard and J. Mercer, “From knowledge to action: Bridging gaps in disaster risk reduction,” *Progress in human geography*, vol. 37, no. 1, pp. 93–114, 2013.

COMPDYN 2023
9th ECCOMAS Thematic Conference on
Computational Methods in Structural Dynamics and Earthquake Engineering
M. Papadrakakis, M. Fragiadakis (eds.)
Athens, Greece, 12-14 June 2023

# LARGE-SCALE VULNERABILITY ANALYSIS OF HISTORICAL MASONRY BUILDINGS

**Valentina Buonocunto**[1], **Giorgio Serino**[1], **and Fulvio Parisi**[1]

[1] Department of Structures for Engineering and Architecture, University of Naples Federico II
Via Claudio 21, 80125 Naples, Italy
{valentina.buonocunto, serino, fulvio.parisi}@unina.it

## Abstract

*Masonry structures represent a large amount of the built heritage all around the world. Many of those buildings have significant historical and cultural value but they are characterized by high levels of vulnerability to multiple hazards. Although the vulnerability of masonry buildings to earthquakes has been largely investigated in previous studies, there are still major knowledge gaps on vulnerability to other hazards such as soil settlements and environmental degradation.*

*In this study, a new methodology for multi-hazard vulnerability assessment of historic masonry buildings is proposed. Aiming at supporting nation-wide disaster risk prioritization, a large-scale probabilistic approach is delineated. The Italian built heritage was considered for the implementation of the methodology. A huge data set on historical masonry buildings was collected and processed to define realistic building archetypes, with special focus on residential buildings built before 1920. Statistical data on some properties of the building archetypes are compared to empirical relationships available in past treatises and rules of thumb.*

*A multi-scale structural modeling procedure was used, looking to both global behaviour via equivalent frame modeling of the structure and local behaviour of individual elements and sub-systems. Furthermore, the most influential structural parameters were identified through a sensitivity analysis. Analysis results show the different impact of such parameters depending on the type of hazard under consideration.*

**Keywords:** Historical masonry buildings, analytical vulnerability assessment, methodology, archetypes, system-scale structural models, sub-system-scale structural models.

## 1 INTRODUCTION

Italy is home to numerous historical masonry buildings that testify to the country's rich and varied architectural heritage. [1,2] Approximately 61% of the buildings on our territory are made of masonry [3,4]. These buildings, which date back to different historical periods, were built with traditional materials such as stone, brick and terracotta and were designed to last for many generations. Until the large-scale introduction of reinforced concrete, stone had always been the material most used by man, proving to be structurally reliable over the years. Despite the passage of time and difficult climatic conditions, many of these buildings are still standing and represent a valuable cultural heritage for the country.

The study of these structures and their structural behavior should not be considered a purely historical or artistic aspect, but a fundamental condition for the development of seismic risk prevention and reduction strategies.

From the point of view of seismic risk mitigation, an in-depth vulnerability analysis is necessary for existing buildings.[5] This must be carried out for entire territorial areas with different levels of detail depending on the quality and quantity of information available for the buildings. The complexity of this type of analysis is due to the multiplicity of factors that affect the vulnerability of historic buildings such as: the variability of structural forms, the different quality and type of materials used, and the various structural modifications carried out over the years.

The following study concerns the structural behavior of historical masonry buildings on the national territory. This work was carried out by integrating the study on the design criteria of existing masonry with the data obtained from the "Cartis" database [6,7], which was developed in the DPC-ReLUIS 2014-2016 project. In particular, the aim of the following work was to identify a methodology to assess the vulnerability of historical masonry buildings on a large scale.

We started from the characteristics of the existing masonry structures when certain features vary (e.g., type of masonry, age of construction, number of floors, etc.) and determined a building archetype that could represent a family of masonry buildings present on the national territory.

This archetype was subsequently modelled with the aid of MATLAB programming software using the equivalent frame modelling criterion (EFM) [8] with vertical and horizontal elements simulating pier and spandrel panels, respectively [2,9], which in addition to being suggested by various normative codes, is the most widespread method for the analysis of masonry structures to date.

Furthermore, in order to take into account, the influence of arches and/or vaults on structural performance, ARCO software [10] was used. Therein, the masonry arch is assessed based on the static theorem of limit analysis, allowing the computation of both vertical actions and thrust forces that the arch transfer to its supporting masonry walls and/or columns.

Subsequently, to evaluate a level of safety that could be extended to the plurality of the historic masonry buildings, an analysis was firstly carried out on the model of the archetype by means of gravitational loads, then a non-linear static analysis under displacement control (pushover).

In conclusion, a sensitivity analysis was conducted on the most influential parameters during the analysis and in the model in order to evaluate the results and arrive at possible conclusions and improvements of these structures.

## 2 METHODOLOGY

The conservation of historic masonry buildings is a complex and challenging task that requires a comprehensive approach to understanding their vulnerability. This work deals with the development and the implementation of a new methodology in order to assess the large-scale vulnerability of historic masonry buildings, based on statistical data from a database (e.g., Cartis). This methodology uses a combination of statistical data and design information from the period, through a multilevel modelling and through a identification of the most influential parameters to assess the current state of the buildings and identify their vulnerabilities, as illustrated in the flowchart in Fig. 1.

This methodology is able to provide a more accurate and reliable assessment of building vulnerability through the use of data from a comprehensive database; this lead to effective and targeted conservation interventions so as to ensure the preservation of historic masonry buildings for future generations.

### 2.1 Identification of historical building archetype

CARTIS is a database that provides mechanical and geometrical characteristics of masonry buildings in Italy [5]. It is a valuable tool for engineers and researchers who are studying the vulnerability of these historic structures.

The data collected in the CARTIS database are based on a comprehensive survey of masonry buildings in Italy, which includes information about the building's age, construction materials, size, and layout, as well as its structural features such as walls, arches, and vaults. This data is then used to create statistical models that can be used to assess the vulnerability of these buildings in the case of natural disasters such as earthquake.

The data in the CARTIS database can also be used to inform the design of new masonry buildings and to support the development of new building codes and standards. By providing a comprehensive overview of the mechanical and geometrical characteristics of masonry buildings in Italy, CARTIS helps to ensure that these structures are safe and resilient in the face of future hazards.

The evaluation strategy adopted in this study was applied to an archetype masonry building representative of the majority of masonry buildings fabricated in Italy before 1920, i.e., prior to the use of reinforced concrete [13].

The building archetype was generated from information extracted from the Cartis database. First of all, the information was filtered by age of construction in order to filter and take into account only pre-1920 buildings. Then the masonry types were investigated, and the respective geometric-structural characteristics were investigated in order to completely define the building. The relevant properties considered for the construction of the case study were:

- Number of storeys
- Presence and type of vaults
- Type of floors
- Average floor area
- Average wall thickness
- Average spacing between walls
- Average storey height
- Average ground storey height.

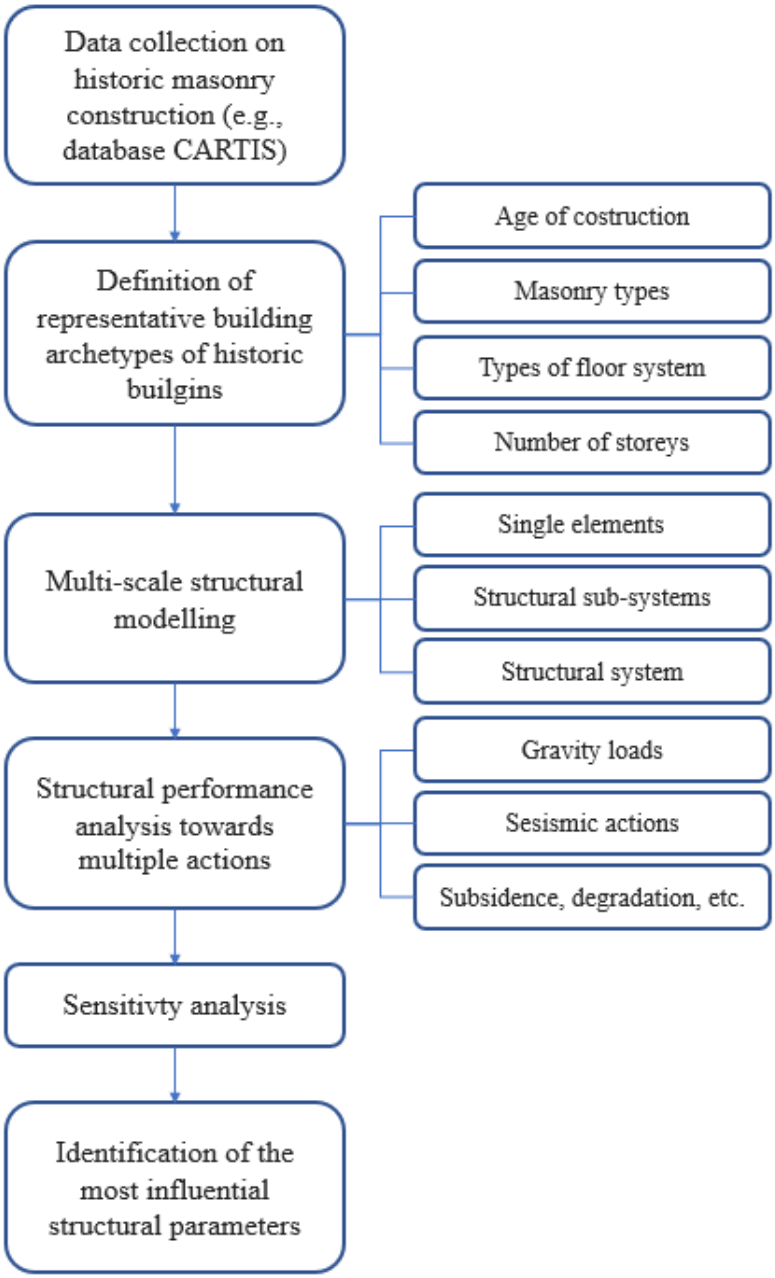


Figure 1. Flowchart methodology.

A statistical analysis was carried out on the extrapolated data, leading to the conclusion that the most recurring masonry types in the country for pre-1920 masonry buildings are: (i) irregular rough stone masonry (A2) covering the 53% of cases, (ii) regular solid brick masonry (C2) which is found in 26% and (iii) regular square stone masonry (C1) which is found in 10% of cases, as shown in Fig. 2. Based on this data, the A2 masonry type was chosen.

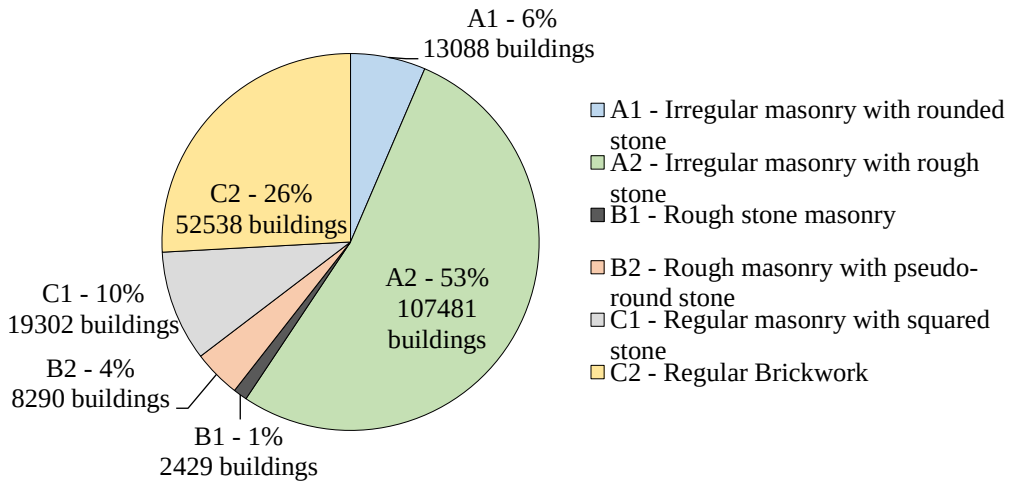


Figure 2. Types of masonry in Cartis database.

Subsequently, as already discussed, the other geometric data were extracted to generate the building and an Italian pre-1860 building archetype was identified. Its geometric characteristics are shown in Table 1. Concerning the mechanical characteristics, the "A2: irregular masonry with rough stone" under study was regarded as "rough stone masonry with parameters of uneven thickness" according to the Italian building code, i.e., NTC 2018 [11]. The mean values of mechanical properties assumed were set to the average of those provided by the Italian building code commentary, i.e., Circular n° 7/2019 [12], shown in Table 2.

| | |
|---|---|
| Age of construction | <1860 |
| Type of masonry | Irregular rough stone masonry (A2) |
| Number of storeys | 3 |
| Presence of vaults | Yes |
| Type of vaults | Barrel vaults at 1$^{st}$ floor |
| Type of floors | Timber floors at 2$^{nd}$ and 3$^{rd}$ floors |
| Average floor area | 150 m$^2$ |
| Average wall thickness | 0.75 m |
| Average wall spacing | 5 m |
| Average height of storeys | 3.50 m and 4 m at the ground floor |

Table 1. Properties of the building archetype.

| **f** | **$\tau_0$** | **$f_{v0}$** | **E** | **G** | **w** |
|---|---|---|---|---|---|
| [MPa] | [MPa] | [MPa] | [MPa] | [MPa] | [kN/m$^3$] |
| - | min - max | - | min - max | min - max | - |
| 2 | 0.035 - 0.051 | - | 1020 - 1440 | 340 - 480 | 20 |

Table 2. Mechanical properties of A2 masonry type.

Figure 3 shows the ground floor plan, typical plan and orthogonal vertical sections AA' and BB' of the selected building archetype.

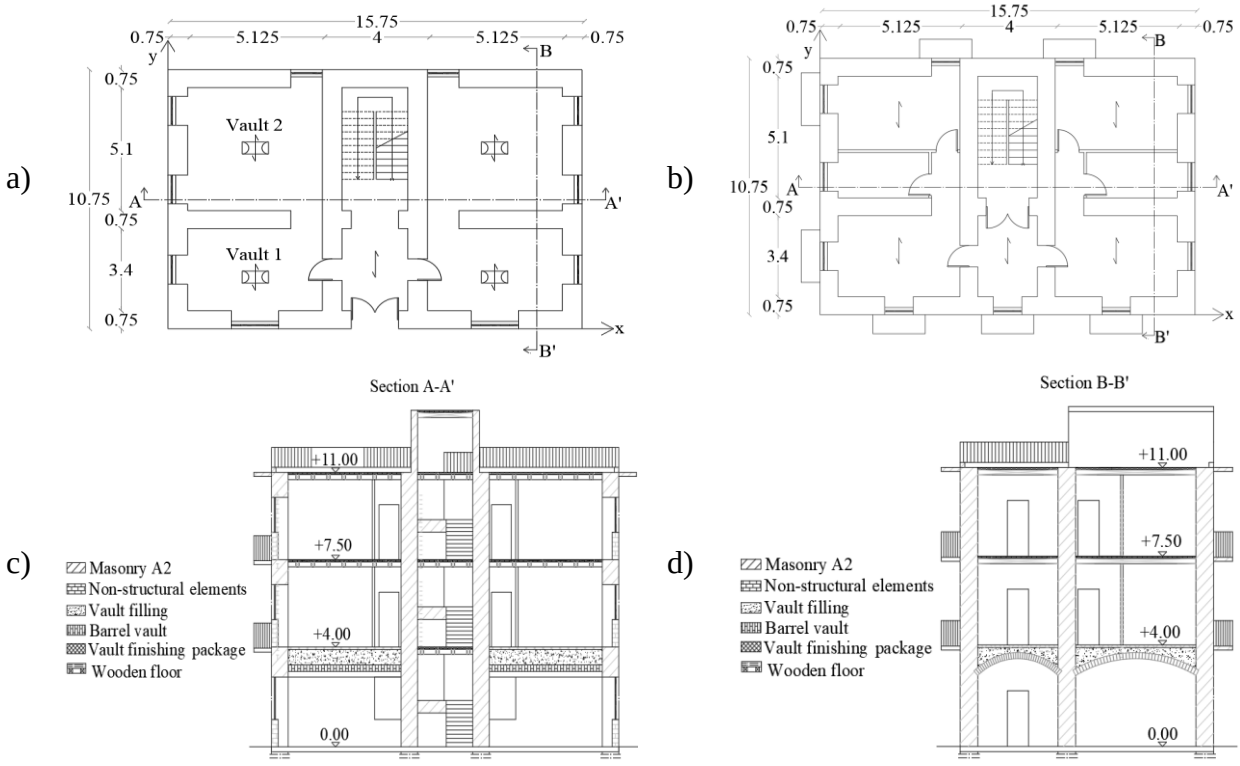


Figure 3. Archetype building: (a) ground floor plan; (b) typical floor plan; (c) section AA'; d) section BB'.

## 2.2 Structural modelling of historical building archetype

After the geometrical definition of the building archetype and after the modeling of the uncertainties related to the materials, it was generated through the use of an automatic procedure implemented in MATLAB. The building was generated according to the hypothesis of a rectangular plan and with an equivalent frame model. The last one was characterized by macro-elements assimilated to beam elements connected by rigid offsets suitably sized to consider the greater or lesser deformability of the nodes, (Figure 5).

Specifically, the effective height of the piers panels was calculated using the criterion proposed by Lagomarsino et al. [13], for both external and internal piers panels.

The floor systems were modeled through equivalent diagonal trusses with equivalent diagonal roofs with appropriate stiffness depending on the timber floor and/or vault.

The vault was first resorted to an equivalent plate modeling [14] and then the equivalent plate was modeled with diagonal connecting rods [15] with a suitable equivalent stiffness. The vault was then studied through ARCO software [10] by assimilating it to an arch and obtaining the reactions to the kidneys that could be implemented in the MATLAB program. The arch schematization of the barrel vault 2 and the values of the reactions for the vaults 1 and 2 (Figure 3a) are respectively shown in Figure 4 and Table 3.

| Vault | *H* [kN] | *V* [kN] |
|---|---|---|
| 1 | 114.7 | 61.8 |
| 2 | 52.1 | 40.8 |

Table 3. Constraint reactions of barrel vaults.

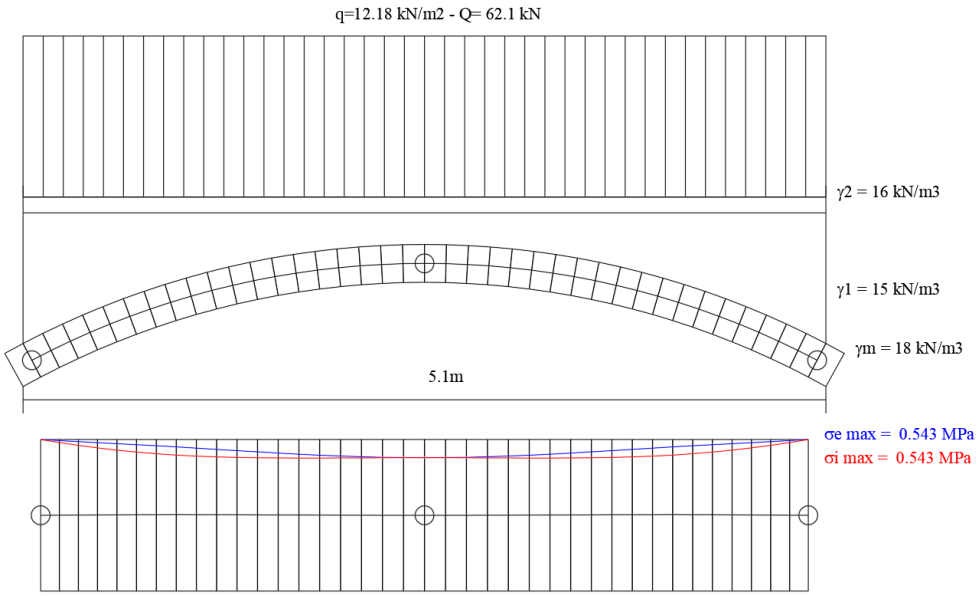


Figure 4. Arch schematization of the barrel vault 2 through the ARCO software

a) b)

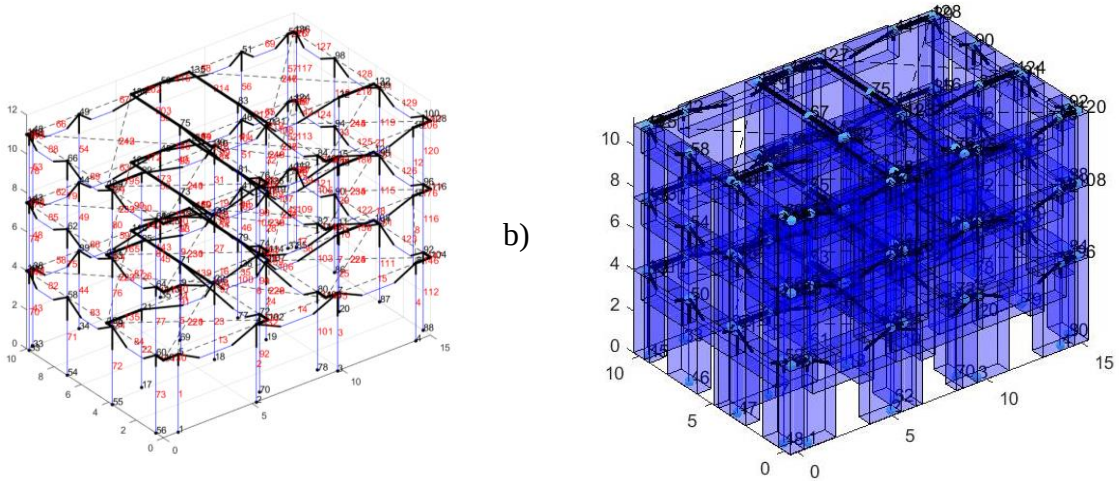

Figure 5. Structural system of archetype building: (a) equivalent frame view; (b) solid view.

## 3 MULTI-SCALE ANALYSIS OF BUILDING ARCHETYPE

Two kinds of analyses were carried out: a gravitational analysis and a non-linear static analysis.

The gravitational analysis was performed by analysing individual walls. The checks were found to be satisfied, and the ratio of the acting normal stress to the ultimate normal stress was assessed. More specifically, the $\zeta_{V,i}$ was evaluated, i.e. the ratio between the maximum value of the vertical load capacity by the i-th pier panel of the wall under investigation and the value of the acting vertical overload.

Figure 6 shows the results of this coefficient. The calculations for the three most loaded walls (those in the x direction) are shown. The value of this coefficient for the walls in the y direction is always between 3 and 16. To better understand the numbering of piers panels,

wall 1 was shown as an example in Figure 7. The numbering has been formulated as *(i,j,k)* with *i* equals the piers, *j* the spandrels and *k* the wall under consideration.

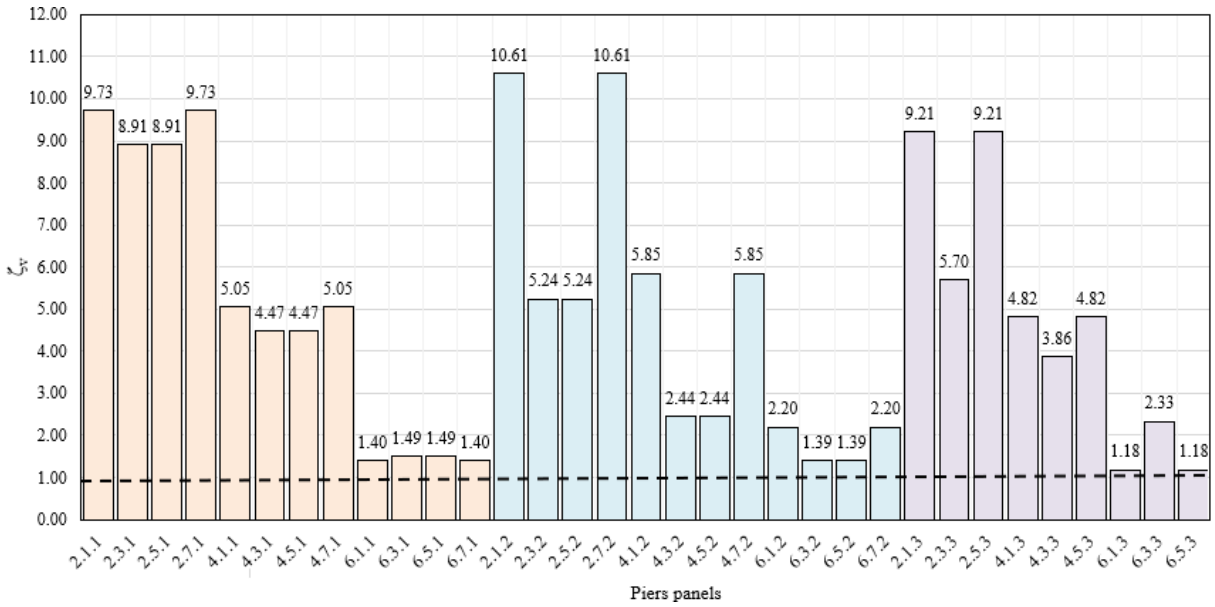


Figure 6. Demand-to-capacity ratio of pier panels under gravity loads.

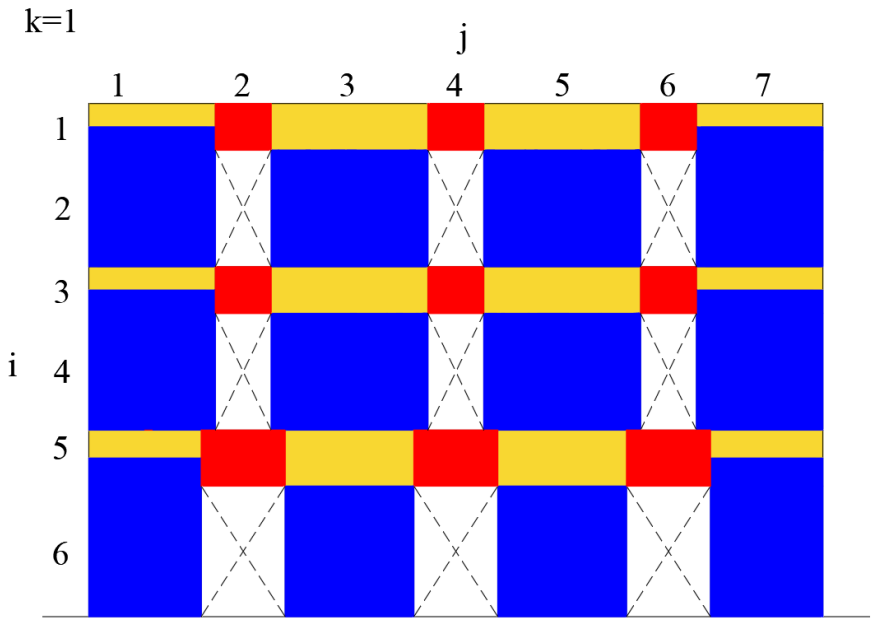


Figure 7. Macro-element modelling of wall 1.

The piers panels 6.1.1, 6.3.1, 6.5.1, 6.7.1, 6.3.2, 6.5.2, 6.1.3, and 6.5.3 has a lower slenderness ratio compared to the other panels. This was due to the unloading of the horizontal thrust caused by the presence of the barrel vault.

One solution for those piers panels was to limit the use of the i-th portion to the maximum load bearing capacity, or to introduce chains to reduce the thrust acting on the piers panels.

Subsequently, a non-linear static analysis was performed on the building archetype considering the average values of the mechanical properties, Figure 8.

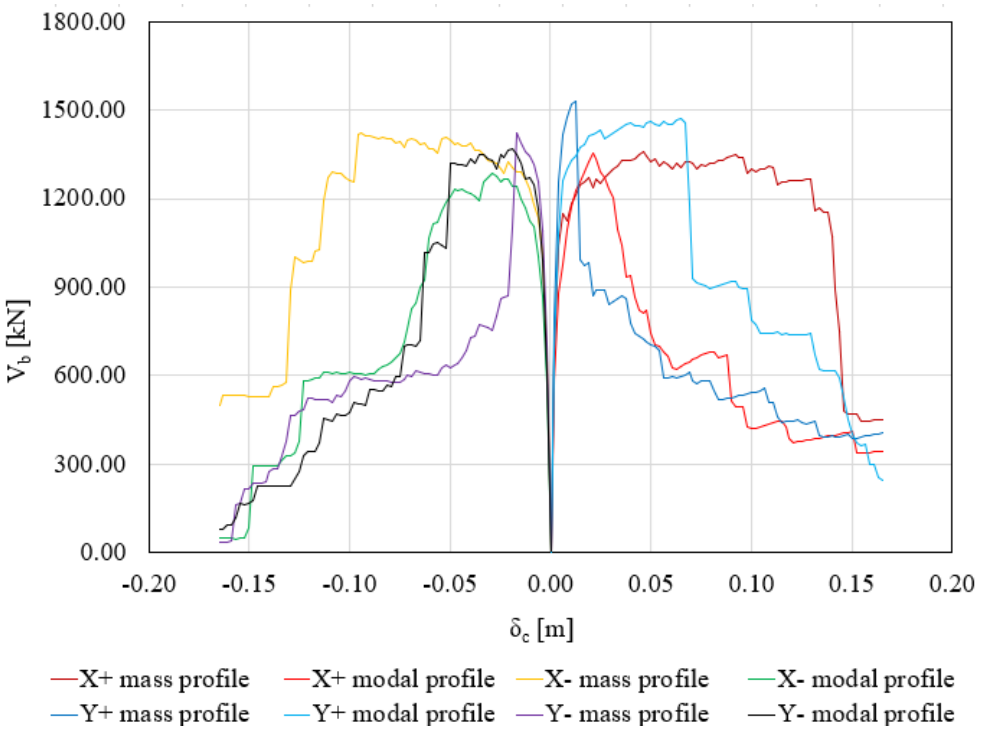


Figure 8. Pushover capacity curves of case-study building.

The results of the analysis outline that the building archetype had a greater shear resistance at the base along the y-direction than the x-direction; the latter one offered a greater ability to redistribute stresses because it is also the direction with greater wall length and less thin piers panels. The shear failure mechanism governed the analyses along the y-direction.

It was observed that once the maximum bearable shear was reached at the base, more than one panel reached the shear failure mechanism, in addition to shear crises in the other panels, this led to a drastic reduction of the load-bearing capacity of the wall.

Figure 9 shows the building during the analysis along the y-direction with a profile of perhaps proportional to the masses (blue curve in Figure 8) during the step at maximum shear and immediately afterwards. Specifically, the blue panels are panels that have not suffered damage, the red panels are panels that have suffered a buckling failure and the green panels are panels that have suffered a shear failure.

a) b)

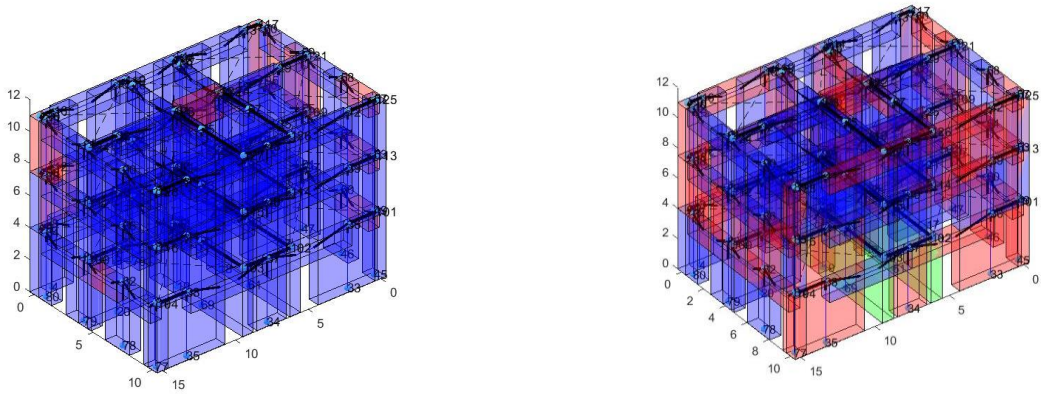

Figure 9. Identification of failure modes during seismic analysis: (a) maximum base shear (b) last step.

In addition to the numerous spandrel and piers panels in failure due to pressure deflection, it was found that in the step following the maximum shear at the base, the simultaneous failure of two piers panels due to shear is evident. These two panels, central and very large, are the panels carrying the weight of the central staircase. To this aim the curve showed a rapid reduction in bearable shear (change of -43%).

On all pushover capacity curves, five damage states were identified as:

- DS1 at 70% of the maximum base shear ($V_{b,max}$) on the increasing branch of the capacity curves.
- DS2 at $V_{b,max}$.
- DS3 at 20% degradation of $V_{b,max}$.
- DS4 at 50% degradation of $V_{b,max}$.
- DS5 when the ultimate displacement is reached.

The damage states considered are depicted in Figure 10 where they are identified on a significant global pushover curve of a building.

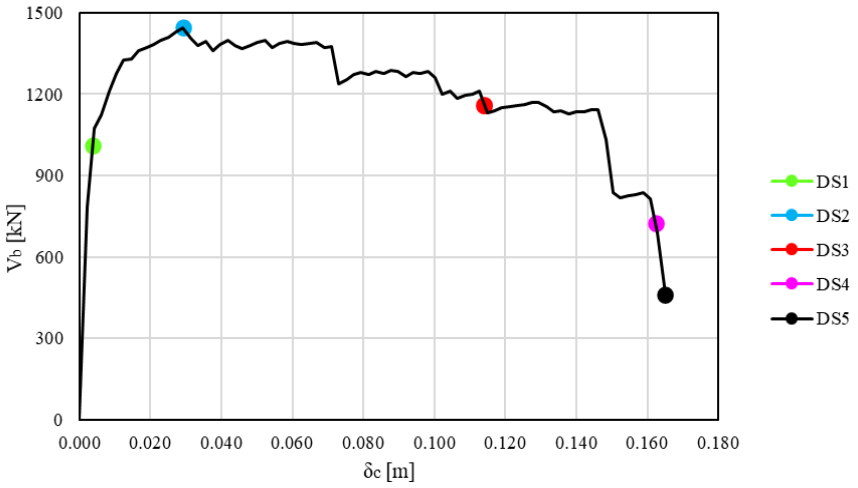


Figure 10. Definition of damage states on pushover curve.

Table 4 and 5 show the difference between the two distributions of forces in term of damage states (DSs).

| Damage state | Force profile | $V_b$ [kN] | $\Delta V_b$ [%] | $\delta_c$ [m] | $\Delta\delta_c$ [%] |
|---|---|---|---|---|---|
| DS1 | Mass | 950.32 | 0 | 0.00364 | +56% |
| DS1 | Modal | 949.13 | | 0.00566 | |
| DS2 | Mass | 1357.6 | 0 | 0.04595 | -55% |
| DS2 | Modal | 1355.90 | | 0.02089 | |
| DS3 | Mass | 1086.08 | 0 | 0.13953 | -76% |
| DS3 | Modal | 1084.72 | | 0.03383 | |
| DS4 | Mass | 678.8 | 0 | 0.14465 | -61% |
| DS4 | Modal | 677.95 | | 0.05647 | |
| DS5 | Mass | 449.7 | +24% | 0.16500 | 0 |
| DS5 | Modal | 343.40 | | 0.16500 | |

Table 4. Difference in displacement and shear for different DS for the two force profiles in the X direction.

| Damage state | Force profile | $V_b$ [kN] | $\Delta V_b$ [%] | $\delta_c$ [m] | $\Delta\delta_c$ [%] |
|---|---|---|---|---|---|
| DS1 | Mass | 1069.81 | -4% | 0.00332 | +17% |
| DS1 | Modal | 1030.05 | | 0.00388 | |
| DS2 | Mass | 1528.3 | -4% | 0.01253 | +417% |
| DS2 | Modal | 1471.50 | | 0.06475 | |
| DS3 | Mass | 1222.64 | -4% | 0.01373 | -402% |
| DS3 | Modal | 1177.20 | | 0.06889 | |
| DS4 | Mass | 764.15 | -4% | 0.04051 | -220% |
| DS4 | Modal | 735.75 | | 0.12967 | |
| DS5 | Mass | 406 | -40% | 0.16500 | 0 |
| DS5 | Modal | 245.00 | | 0.16500 | |

Table 5. Difference in displacement and shear for different DS for the two force profiles in the Y direction.

## 4 SENSITIVITY OF SEISMIC CAPACITY TO MECHANICAL PARAMETERS

After performing the non-linear static analyses considering the average characteristics in Table 2, a sensitivity analysis was carried out by varying the mechanical parameters. Specifically, the shear strength $\tau_0$ and the elastic moduli $E$ and $G$, varying them simultaneously in their range considering the minimum and maximum values.

Figure 11 shows the capacity curves for the two directions (X and Y) and the two force profiles (proportional to masses and proportional to the first mode of vibration).

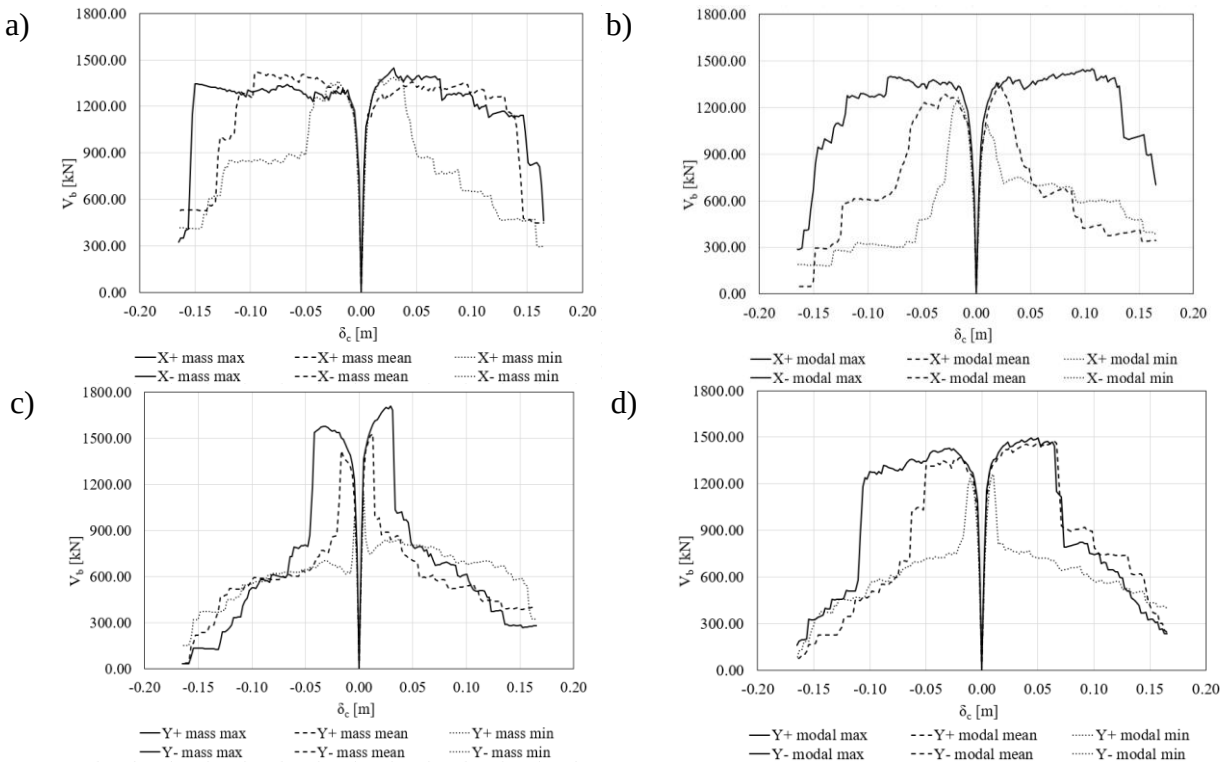


Figure 11. Pushover curves of case-study building: (a) X direction and mass profile; (b) X direction and modal profile; (c) Y direction and mass profile; (d) Y direction and modal profile.

The results outline that the variation of the mechanical parameters changed the behaviour of the building. Considering the minimum parameters in Table 2, the curves, for both directions and for both force profiles, show a sudden drop in capacity immediately after the maximum shear is reached. This is due to the reduction of the shear resistance to the minimum values.

The building, as shown in a similar condition before, had several panels experiencing a shear failure at the same time.

Tables 6 and 7 show the percentage changes in base shear, displacement and stiffness for different damage states. As regard the maximum mechanical properties the following conclusions can be drawn: (i) the change in shear with respect to the average properties is always an increase of approximately 10%, (ii) the change in displacement is always an increase in the X direction but always a decrease in the Y direction due to the numerous shear crises in the piers panels and (iii) in terms of stiffness, there is an increase in both directions but this is a consequence of the increase in the elastic modulus E.

On the other hand, in the case of the minimum mechanical properties, it was found a negative change in base shear except for the X direction with a force profile proportional to the masses; in terms of displacement there was almost always a decrease as well as in terms of stiffness. These results led to the conclusion that the structure had a better behaviour when the maximum mechanical characteristics were considered.

| | | X direction | | | | | | | | | | | |
|---|---|---|---|---|---|---|---|---|---|---|---|---|---|
| | | Mass profile | | | | | | Modal profile | | | | | |
| DS | | $V_b$ [kN] | $\Delta V_b$ [%] | $\delta_c$ [m] | $\Delta\delta_c$ [%] | k [kN/m] | $\Delta$k [%] | $V_b$ [kN] | $\Delta V_b$ [%] | $\delta_c$ [m] | $\Delta\delta_c$ [%] | k [kN/m] | $\Delta$k [%] |
| DS1 | max | 1011.6 | 6% | 0.004 | 3% | 270669 | 3% | 1016.1 | 7% | 0.005 | -12% | 201485 | 17% |
| | mean | 950.3 | | 0.004 | | 261358 | | 949.1 | | 0.006 | | 167620 | |
| | mean | 950.3 | 2% | 0.004 | 20% | 261358 | -15% | 949.1 | -19% | 0.006 | -32% | 167620 | 19% |
| | min | 970.5 | | 0.004 | | 222326 | | 764.1 | | 0.004 | | 199770 | |
| DS2 | max | 1445.1 | 6% | 0.029 | -57% | 49421 | 40% | 1451.6 | 7% | 0.107 | 80% | 13628 | -376% |
| | mean | 1357.6 | | 0.046 | | 29546 | | 1355.9 | | 0.021 | | 64919 | |
| | mean | 1357.6 | 2% | 0.046 | -36% | 29546 | 60% | 1355.9 | -19% | 0.021 | -50% | 64919 | 61% |
| | min | 1386.4 | | 0.029 | | 47414 | | 1091.5 | | 0.010 | | 104519 | |
| DS3 | max | 1156.1 | 6% | 0.114 | -22% | 10124 | 23% | 1161.3 | 7% | 0.134 | 75% | 8654 | -270% |
| | mean | 1086.1 | | 0.140 | | 7784 | | 1084.7 | | 0.034 | | 32061 | |
| | mean | 1086.1 | 2% | 0.140 | -69% | 7784 | 226% | 1084.7 | -19% | 0.034 | -45% | 32061 | 46% |
| | min | 1109.1 | | 0.044 | | 25374 | | 873.2 | | 0.019 | | 46888 | |
| DS4 | max | 722.6 | 6% | 0.162 | 11% | 4451 | -5% | 725.8 | 7% | 0.165 | 66% | 4412 | -172% |
| | mean | 678.8 | | 0.145 | | 4693 | | 678.0 | | 0.056 | | 12005 | |
| | mean | 678.8 | 2% | 0.145 | -38% | 4693 | 65% | 678.0 | -19% | 0.056 | 139% | 12005 | -66% |
| | min | 693.2 | | 0.089 | | 7748 | | 545.8 | | 0.135 | | 4039 | |
| DS5 | max | 462.7 | 3% | 0.165 | 0% | 2804 | 3% | 700.5 | 51% | 0.165 | 0% | 4245 | 51% |
| | mean | 449.7 | | 0.165 | | 2725 | | 343.4 | | 0.165 | | 2081 | |
| | mean | 449.7 | -34% | 0.165 | 0% | 2725 | -34% | 343.4 | 12% | 0.165 | 0% | 2081 | 12% |
| | min | 295.6 | | 0.165 | | 1792 | | 383.6 | | 0.165 | | 2325 | |

Table 6. Displacement and shear difference for different DS for the two force profiles in the X-direction considering maximum, mean and minimum mechanical properties.

| DS | | Y direction | | | | | | | | | | | |
|---|---|---|---|---|---|---|---|---|---|---|---|---|---|
| | | Mass profile | | | | | | Modal profile | | | | | |
| | | $V_b$ [kN] | $\Delta V_b$ [%] | $\delta_c$ [m] | $\Delta\delta_c$ [%] | k [kN/m] | $\Delta$k [%] | $V_b$ [kN] | $\Delta V_b$ [%] | $\delta_c$ [m] | $\Delta\delta_c$ [%] | k [kN/m] | $\Delta$k |
| DS1 | max | 1196.7 | 11% | 0.003 | 3% | 347941 | 7% | 1047.3 | 2% | 0.004 | -7% | 290217 | 8% |
| | mean | 1069.8 | | 0.003 | | 321933 | | 1030.1 | | 0.004 | | 265685 | |
| | mean | 1069.8 | -26% | 0.003 | -27% | 321933 | 1% | 1030.1 | -14% | 0.004 | -3% | 265685 | -12% |
| | min | 792.1 | | 0.002 | | 324780 | | 883.2 | | 0.004 | | 234460 | |
| DS2 | max | 1709.5 | 11% | 0.029 | 57% | 58463 | -109% | 1496.2 | 2% | 0.050 | -29% | 29848 | 24% |
| | mean | 1528.3 | | 0.013 | | 121955 | | 1471.5 | | 0.065 | | 22727 | |
| | mean | 1528.3 | -26% | 0.013 | -67% | 121955 | 122% | 1471.5 | -14% | 0.065 | -84% | 22727 | 432% |
| | min | 1131.6 | | 0.004 | | 270898 | | 1261.7 | | 0.010 | | 120817 | |
| DS3 | max | 1367.6 | 11% | 0.032 | 58% | 42274 | -111% | 1197.0 | 2% | 0.067 | -4% | 17996 | 5% |
| | mean | 1222.6 | | 0.014 | | 89077 | | 1177.2 | | 0.069 | | 17088 | |
| | mean | 1222.6 | -26% | 0.014 | -58% | 89077 | 75% | 1177.2 | -14% | 0.069 | -82% | 17088 | 367% |
| | min | 905.3 | | 0.006 | | 155510 | | 1009.4 | | 0.013 | | 79748 | |
| DS4 | max | 854.8 | 11% | 0.048 | 15% | 17978 | -5% | 748.1 | 2% | 0.097 | -33% | 7677 | 26% |
| | mean | 764.2 | | 0.041 | | 18865 | | 735.8 | | 0.130 | | 5674 | |
| | mean | 764.2 | -26% | 0.041 | 279% | 18865 | -80% | 735.8 | -14% | 0.130 | -31% | 5674 | 25% |
| | min | 565.8 | | 0.154 | | 3681 | | 630.9 | | 0.089 | | 7069 | |
| DS5 | max | 281.3 | -44% | 0.165 | 0% | 1705 | -44% | 234.9 | -4% | 0.165 | 0% | 1424 | -4% |
| | mean | 406.0 | | 0.165 | | 2461 | | 245.0 | | 0.165 | | 1485 | |
| | mean | 406.0 | -22% | 0.165 | 0% | 2461 | -22% | 245.0 | 63% | 0.165 | 0% | 1485 | 63% |
| | min | 315.1 | | 0.165 | | 1910 | | 399.7 | | 0.165 | | 2422 | |

Table 7. Displacement and shear difference for different DS for the two force profiles in the X-direction considering maximum, mean and minimum mechanical properties.

## 5 CONCLUSIONS

This study focused on the formulation of a methodology that, starting from data collection of data, allows large-scale probabilistic vulnerability analysis of historical masonry buildings.

The first part of the study was aimed at delineating a URM masonry building archetype that can be representative of typical historical buildings located in Italy. Geometric data sets on such buildings were collected from CARTIS database, deriving statistics for probabilistic simulation at territorial scale. Such an information was then implemented in MATLAB software to generate structural models via equivalent frame modelling. Seismic performance of the selected building archetype was evaluated through nonlinear static analysis, using the mean values of the mechanical properties provided by the Italian Building Code Commentary, i.e., Circular n°7/2019 [12]. As expected, the highest levels of earthquake resistance were found in the longitudinal direction of the building plan, where load-bearing walls have the greatest number of piers and sectional area.

A sensitivity analysis was also conducted under varying mechanical properties, evaluating variations in nonlinear response of the structure and corresponding capacity curves.

This showed that the archetype has a higher capacity and greater stiffness considering the mechanical properties with their maximum values. The redistributive capacity improves in the building panels and higher base shear are achieved.

Future developments of this study will involve consideration of other masonry types (e.g., clay brick masonry that is the second most common category in Italy) and building archetypes, taking into account the influence of the age of construction and number of floor levels.

Another future development will be to use this methodology by considering additional types of actions, such as subsidence and masonry degradation.

## ACKNOWLEDGEMENTS

This study was developed in the framework of PON "Ricerca e Innovazione" 2014-2020 research programme funded by the Italian Ministry of University and Research.

## REFERENCES

[1] F. Parisi, N. Augenti, Earthquake damages to cultural heritage constructions and simplified assessment of artworks. *Engineering Failure Analysis*, **34**, 735-760, 2013.

[2] N. Augenti, F. Parisi, *Teoria e Tecnica delle Strutture in Muratura*. Hoepli, 2019.

[3] D. Benedetti, G. Benzoni, M.A. Parisi, Seismic vulnerability risk evaluation for old urban nuclei. *Earthquake Engineering and Structural Dynamics*, **16**, 183–201, 1988.

[4] ISTAT (Italian National Institute of Statistics), *15° censimento della popolazione e delle abitazioni*. Roma, Italy, 2011.

[5] R. Vicent, D. D'Ayala, T.M. Ferreira, H. Varum, A. Costa, J.A.R. Silva, S. Lagomarsino, Seismic vulnerability and risk assessment of historic masonry buildings. *Structural Rehabilitation of Old Buildings, Building Pathology and Rehabilitation, Vol II. Springer, Berlin, Heidelberg*. 307– 348, 2014.

[6] G. Brando, G. Cianchino, D. Rapone, E. Spacone, S. Biondi, A CARTIS-base method for the rapid seismic vulnerability assessment of minor Italian historical centres. *International Journal of Disaster Risk Reduction*, **63**, 102478, 2021.

[7] G. Zuccaro, M. Dolce, D. De Gregorio, E. Speranza, C. Moroni, La scheda CARTIS per la caratterizzazione tipologico- strutturale dei comparti urbani costituiti da edifici ordinari. Valutazione dell'esposizione in analisi di rischio sismico. *34th National Conference GNGTS*, Trieste, Italy, November 17-19, 2015.

[8] F. Parisi, E. Acconcia, Formulation and experimental validation of distributed plasticity macroelement for unreinforced masonry walls. J. Kubica, A. Kwiecień, Ł. Bednarz, eds. *Brick and Block Masonry – From Historical to Sustainable Masonry, Proceedings of the 17th International Brick/Block Masonry Conference*, Kraków, Poland, July 5-8, 2020.

[9] F. Parisi, Seismic design of box-type unreinforced masonry buildings through direct displacement-based approach. *The Open Construction & Building Technology Journal*, **10** (Suppl 2: M9), 293-311, 2016.

[10] P. Gelfi, Arco. Available at <http://civserv.ing.unibs.it/utenti/gelfi/arco.htm>.

[11] NTC 2018. D.M. 17/01/2018: *Norme tecniche per le costruzioni*. Italian Ministry of Infrastructure and Transportation, Rome, 2018.

[12] CS.LL.PP. 21/01/2019 n.7: Istruzioni per l'applicazione dell'«Aggiornamento delle "Norme tecniche per le costruzioni"» di cui al decreto ministeriale 17 gennaio 2018. Ministry of Infrastructure and Transportation, 2019.

[13] S. Lagomarsino, A. Penna, A. Galasco, S. Cattari, TREMURI program: an Equivalent Frame Model for the nonlinear seismic analysis of masonry buildings. *Engineering Structures*, **56**, 1787–1799, 2013.

[14] S. Lagomarsino, S. Cattari, M. Angiolilli, S. Bracchi, M. Rota, A. Penna, Modelling and seismic response analysis of existing URM structures – Part 2: Archetypes of Italian Historical Buildings, *Journal of Earthquake Engineering*, 1-26, 2022.

[15] P.S. Marseglia, F. Micelli, M. A. Aiello, Analysis of equivalent diaphragm vault structures in masonry construction under horizontal forces. *Heritage*, **3**, 989-1017, 2020.

[16] S. Lagomarsino, S. Cattari, S. Resemini, Modelling of vaults as equivalent diaphragms in 3D seismic analysis of masonry buildings, D'Ayala, Fodde (eds) *Structural analysis of historic construction*. Taylor & Francis, London, 517-524, 2008.

COMPDYN 2023
9th ECCOMAS Thematic Conference on
Computational Methods in Structural Dynamics and Earthquake Engineering
M. Papadrakakis, M. Fragiadakis (eds.)
Athens, Greece, 12-14 June 2023

# IMPULSIVE ACTIONS DUE TO SEISMIC JERK AND DESIGN OF REINFORCEMENTS TO COUNTERACT THEIR EFFECTS IN MASONRY BUILDINGS

**Massimo Mariani**[1] **and Francesco Pugi**[2]

[1] Studio Ricerche Applicate
06123 Perugia, Italy
ricercheapplicate@libero.it

[2] Aedes Software: Ricerca e Sviluppo
56028 San Miniato, Pisa, Italy
info@aedes.it

## Abstract

*Studies on the impulsive content of seismic acceleration have highlighted the close correlation between damages caused by jerk and local failures with eventual trigger of chaotic collapses. The impulsive hammering actions can in fact generate stress concentration and consequently disaggregation. This study investigates the potential causes of structural node failures and identifies the interventions able to counteract the effects of jerk, particularly in the case of rubble stone masonry with low-quality mortar. Containment of masonry and placement of tensile-resistant elements designed to absorb the impulsive stresses proved necessary. Placement of additional transversal elements constitutes a natural extension of reinforced plaster interventions, both with traditional and modern techniques such as FRCM. Through additional bent elements, the continuity of the reinforced plaster at the structural connections can be ensured. This aspect is often overlooked particularly in the connections between load-bearing walls and internal floor slabs. The interruption of reinforced plaster at the extrados and intrados of floor slabs constitutes, in fact, an important cause of local vulnerability.*

**Keywords:** existing buildings, masonry structures, seismic motion, seismic jerk, impulsive forces, floor-to-wall connection, strengthening interventions

## 1 INTRODUCTION

Recent works [1, 2] highlighted the role of seismic jerk, defined as the variation of acceleration and expression of its impulsive content. Seismic events even very distant in time and space, confirm, in addition to the spatial nature of the seismic motion, the great relevance of the impulsive actions.

Seismic records of 2023 Turkey-Syria mainshock (MW 7.8, 06.02.2023) show very high peaks of accelerations and jerk. Station TK.3138, located near the seismic fault, recorded a horizontal PGA of 0.907 g and a vertical PGA of 1.309 g (30% higher than gravity acceleration)[1], with peak ground jerk of 67.91 g/s (horizontal) and 88.42 g/s (vertical)[2]: these are exceptional values, in particular for the vertical component, which was far beyond the structural damage threshold [3].

*Sources: [1] ESM, Engineering Strong-Motion Database; [2] elaborations with Seismic3D software, developed by Francesco Pugi and tested with Massimo Mariani.*

Starting from the scientific works produced on this subject, the study of jerk was deepened by elaborating all the available records of the most important seismic events occurred in Italy from 1976 to 2016, for a total of 447 seismic records. Then, through a statistic approach, the main characteristic parameters of jerk were defined: amplitude, frequency and duration, for the three spatial components.

Later, attention was paid to the effects of jerk on structures. The impulsive content of acceleration plays a fundamental role in the local damages, particularly in existing buildings where quality of masonry, constraints and connections between structural elements may not guarantee the strength required by stress concentrations generated by acceleration variations.

There is a close relationship between damages caused by jerk and local crises with potential trigger of chaotic collapses, typical of structures with insufficient robustness. This phenomenology provides an effective path to interpret the damages caused by recent seismic events on existing masonry buildings: collapses caused by disruptive processes where a fundamental role was played by impulsive hammering actions.

Following these considerations, two fundamental aspects have been highlighted:

- formulation of impulsive actions in terms of forces, which generate instantaneous increases in stress with potential failure due to lack of resistance.
- evaluation of jerk frequencies in relation to fundamental periods of structures: resonance amplifies the dynamic effects.

Based on the considered seismic events, a statistical analysis of jerk frequencies was conducted, finding that in vertical direction the jerk mean period is very close to the fundamental periods of structures [2].

In this work, the attention is focused on floor-to-wall connections. Experience indicates that under dynamic seismic action floors hardly collapse due to insufficient strength or excessive deformation: their collapse is more frequently due to failure in the supporting masonry walls.

The portion of masonry walls at the connection with floors is included in the so-called “rigid zone” geometrically defined by the intersection between piers and spandrels, located at the bottom and at the top of masonry piers. Normally, this part of masonry is not considered in the safety verifications, nevertheless, it is site of local phenomena which can play a fundamental role for equilibrium, particularly in relation to impulsive actions.

The mass associated to the floor-to-wall node is considered affected by an impulsive force due to jerk, which acts in combination with the state of stress due to static and seismic inertial actions. The impulsive action may be entrusted to dedicated resisting elements, in order to define integrative strengthening interventions.

The impulsive effects are particularly important for rubble stone masonry with poor quality mortar. In these cases disaggregation must be prevented and, although the additional strengthening measure are designed according to the expected seismic event, it is always advisable to intervene with the improvement of constraints and masonry quality.

Masonry typologies with higher mechanical characteristics, such as solid bricks with good quality mortars, may absorb the local impulsive effects without the need of additional strengthening elements on top of those eventually required according to common static and seismic verifications. However, beyond the numerical evaluation, at each state of the project particular attention must be paid to connections between structural elements and to discontinuities of various origins. In fact, in these areas of the construction, concentration of stress due to impulsive effects could, in any case, weaken the structural capacity.

Ultimately, a strengthening intervention must ensure the proper connections between floors and load-bearing walls, as well as guarantee the equilibrium of the constraints inserting where necessary integrative tensile resistant elements, aimed at preventing local failures under impulsive effects.

## 2 OVERVIEW OF JERK FUNDAMENTAL ASPECTS

The chaotic nature of the seismic motion is highlighted by the three-dimensional representation of the accelerograms, that is, the 3D path outlined by the acceleration vector (applied in the origin of the system) with its sharp variation in magnitude and direction.

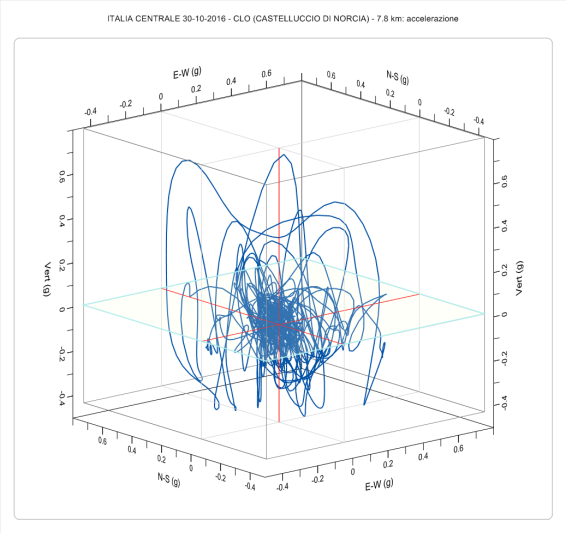


Figure 1. 3D Accelerogram at Castelluccio di Norcia (CLO) during 30.10.2016 Norcia mainshock

The 3D accelerograms indicate a new perspective in the study of the shape of the curves and their evolution throughout the duration of the seismic event. The continuous alterations of the acceleration vector in terms of magnitude and direction suggest to further investigate on the variation of acceleration [1].

The seismic ground acceleration determines structural accelerations which are strictly related to stress and deformation in the resistant elements. From the complexity of the seismic motion the following consideration arises: the safety verification applied in terms of resistance and deformation under inertial forces, may not be enough to fully describe the structural response. The assessment of the structural capacity of the resistant element cannot ignore verifications in terms of impulsive effects, that are the forces appearing in short time intervals in which the state of stress changes: increases, decreases or changes sign.

Studying the variation of acceleration means studying the time derivative of acceleration (TDoA), that is the velocity of acceleration or the third derivative of displacement, referred to as jerk and associated to the symbol $j$.

In Seismic Engineering, displacement, velocity, and acceleration are the motion parameters always used to characterize the seismic event and its effects on structures. The seismic jerk, that only in recent years has been object of attention, had so far little or no application neither in the design of new structures nor in the assessment of existing buildings and the design of strengthening interventions. Tong et al. (2005) [3] investigated on seismic jerk starting from the need of obtaining quantitative understanding about its amplitude, duration, and frequency content. The study is based on records from the 1999 Chi-Chi Earthquake in Taiwan ($M_W$ 7.6, 17:47, 20.09.1999) and one of its aftershocks ($M_W$ 6.2, 00:14, 22.09.1999). At that time, jerk sensors were not widely available; therefore, jerk time series were obtained from ground acceleration records via numerical methods. Accelerometers provide seismic acceleration as a discrete signal; therefore, seismic jerk can be calculated by the following mid-point differentiation formula:

$$j(t_i) = \frac{a(t_{i+1}) - a(t_{i-1})}{2\Delta t} (i = 2, \dots, N-1) \quad (1)$$

where: $a(t_i)$ is the acceleration at instant $t_i$; $N$ is the number of samples; $\Delta t$ is the sampling period. The formula is applied separately for each of the three components of the jerk vector $j = \frac{d\boldsymbol{a}}{dt}$.

The variation of jerk can be represented both as time series of its three components and as 3D path outlined by the jerk vector in space (like the ones shown for acceleration). In the 3D path outlined by acceleration vector it is worth noticing that jerk vector is tangent to the path in each point.

In order to understand the relationship between acceleration and jerk let us consider the ground acceleration records at station CLO (Castelluccio di Norcia) during 30.10.2016 Norcia earthquake in Central Italy (mainshock). In particular, let us consider the vertical acceleration time series focusing on a small time interval between 19.3 s and 19.8 s (0.5 s) in which both PGA and PGJ occur.

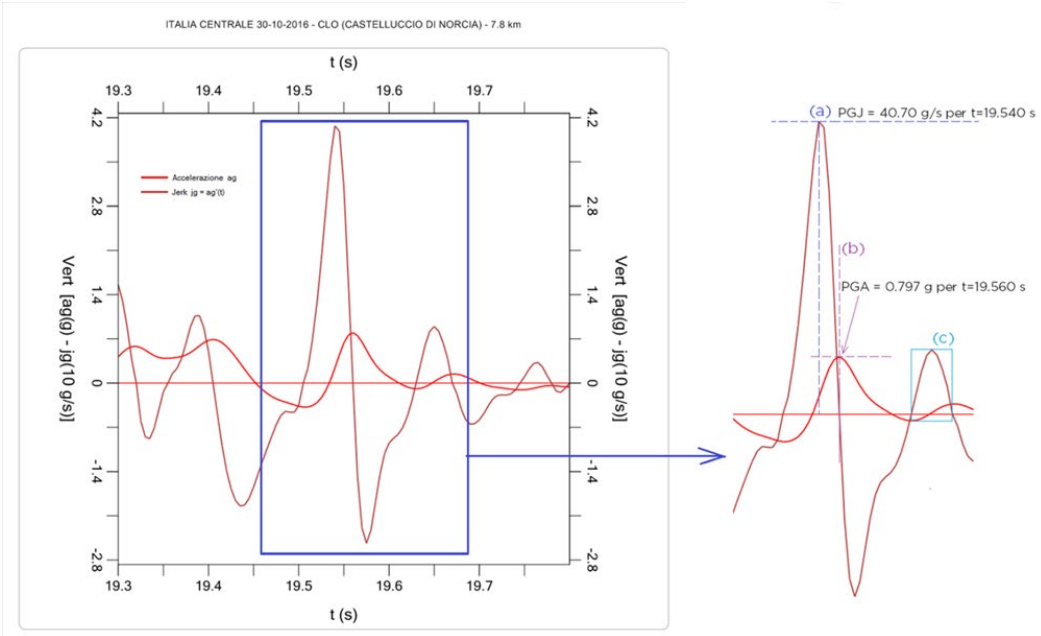


Figure 2. Comparison between acceleration and jerk time series. The detail on the right shows how the points where jerk is zero correspond to local maximum or minimum of acceleration.

Since jerk is the first derivative of acceleration it is equal to zero when acceleration shows a local maximum or minimum.

The detail in Figure 2 highlights (a) the absolute maximum of jerk (PGJ); (b) the absolute maximum of acceleration correspondent (like other local maximum) to zero in jerk; (c) the sector between two consecutive zeros of jerk correspondent to local minimum and maximum of acceleration.

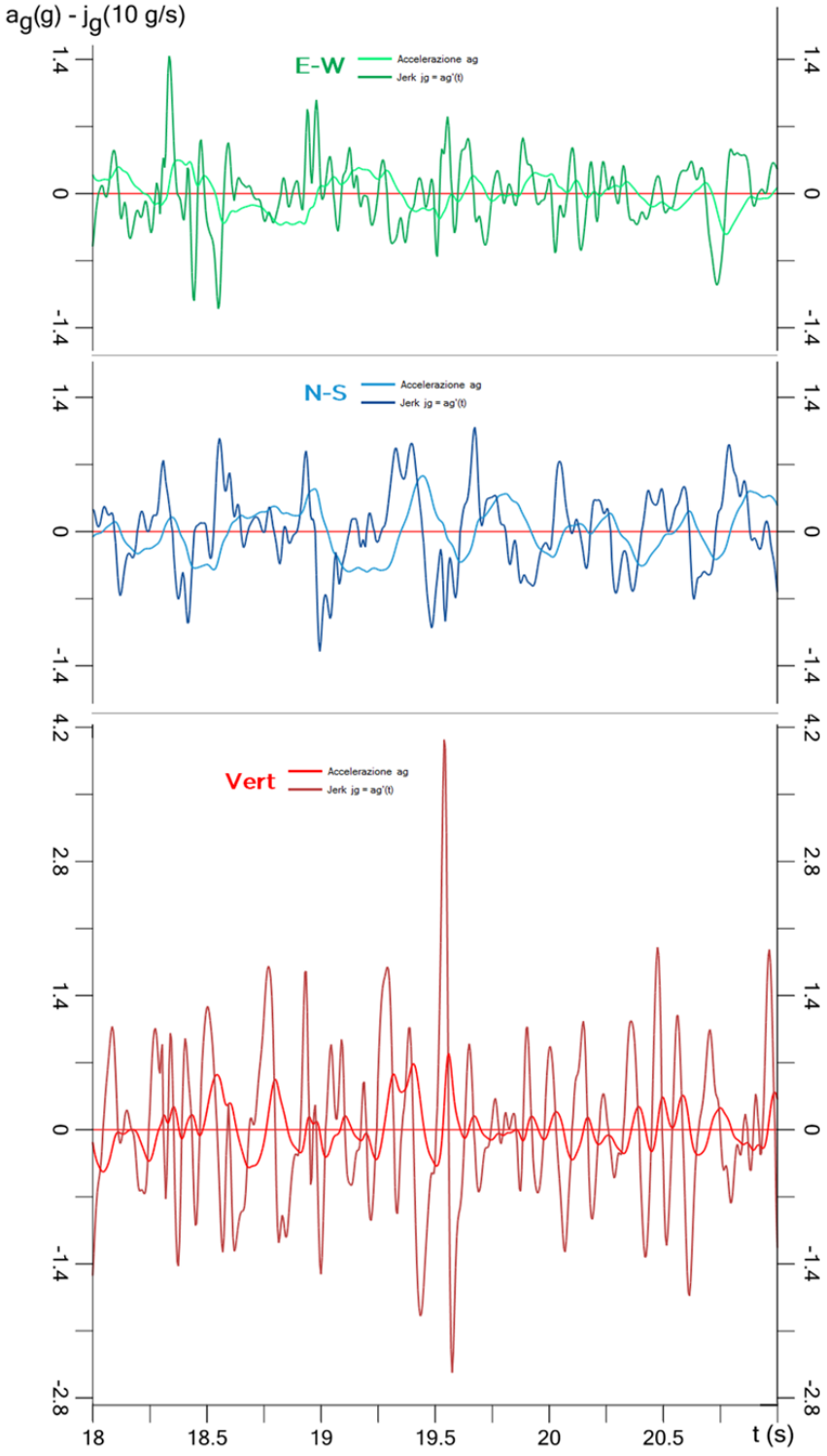


Figure 3. Acceleration and jerk time series for the three components (EW, NS, Vert)

Figure 3 shows the time series of acceleration and jerk for the three components in the time span between *18.0 s* and *21.0 s*. Jerk time series feature a higher number of fluctuations between positive and negative values: this is even more evident from the detail in Figure 4. Throughout the seismic event, the secondary fluctuation of acceleration corresponds to significant jerk peaks of alternate sign. The operation of derivation generates a "jerky" function characterized by denser peaks, that is, in strict terms, by higher frequencies.

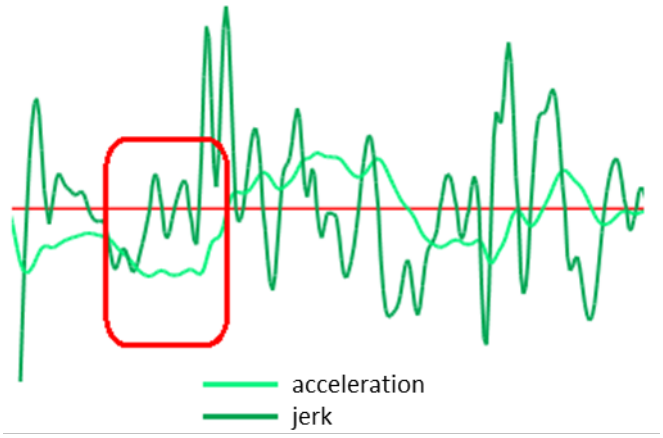


Figure 4. Secondary fluctuation of acceleration correspondent to jerk peaks

The 3D paths outlined by the jerk vector are similar to those already seen for acceleration. Comparison between acceleration and jerk paths is given in Figure 5.

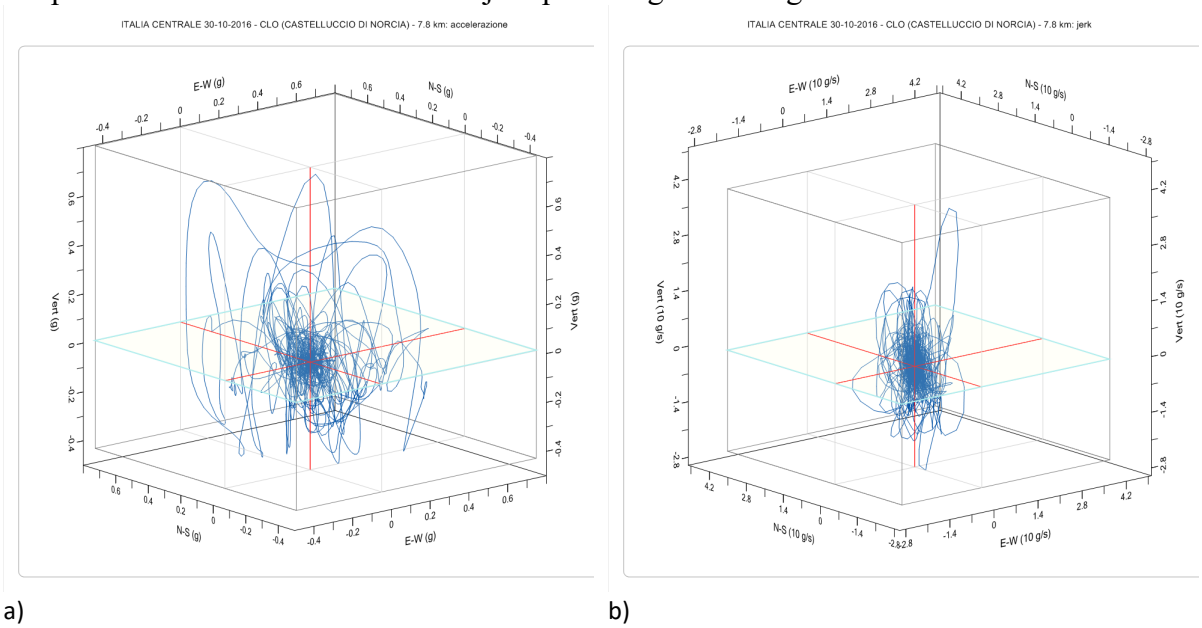


a) b)

Figure 5. Comparison between (a) acceleration and (b) jerk paths: 3D view

Figure 6 shows the comparison between acceleration and jerk 3D paths projected on a vertical plane. The jerk tangle appears stretched in the vertical direction and this points out the importance of the vertical seismic component [4, 5].

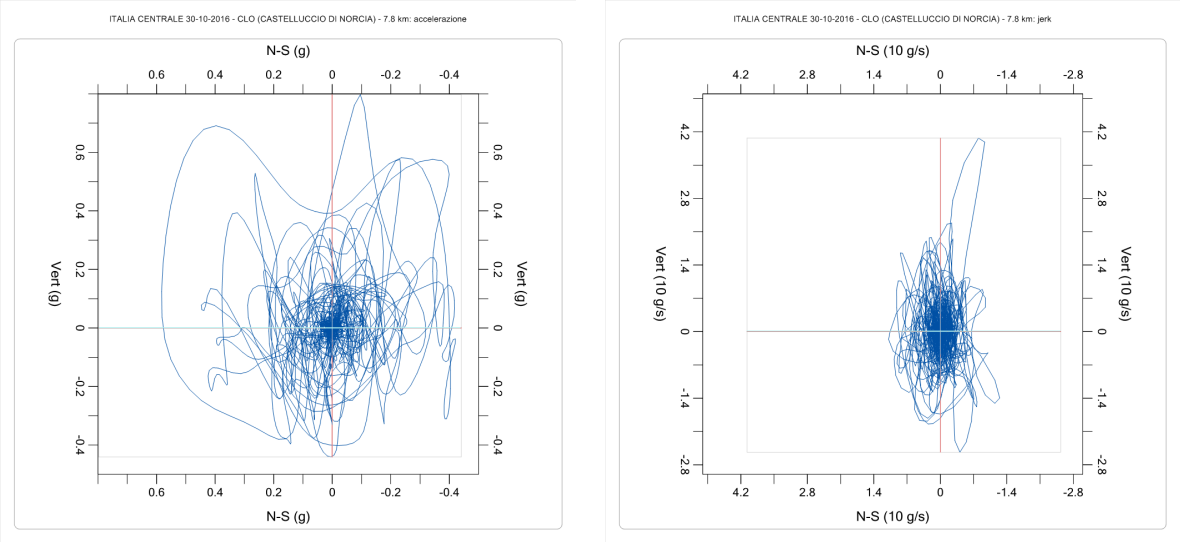


Figure 6. Comparison between (a) acceleration and (b) jerk paths: projection on vertical plane NS-Vert

During a seismic event, ground acceleration varies quickly, and the correspondent inertial forces also fluctuate in short time intervals of the order of few milliseconds. This sharp variation causes "jolts", that is, impulsive forces that act very briefly. Therefore, for jerk to become a useful parameter in structural analysis, it should be considered along with the corresponding impulsive forces. A new approach is introduced below.

Impulsive forces due to seismic jerk are distinct from inertial forces due to acceleration. The former are generated by the variation of acceleration and may be much higher than the latter. Their influence on a structure depends on the frequency content of the jerk and the dynamic properties of the structure itself.

The integral of jerk is, by its own definition, an acceleration. Since acceleration, according to Newton's Second Law, is force per unit mass, the definite integral of jerk in the interval between two consecutive zeros may be referred to as "impulsive force per unit mass" ($F_{imp}/m$). Two consecutive zeros of jerk correspond to a maximum and a minimum of acceleration, or vice-versa. The signed area bounded by the jerk function in that interval corresponds to the impulse of acceleration or deceleration. Therefore, considering the interval between instants $t_1$ and $t_2$, the impulsive force per unit mass is given by:

$$\frac{F_{imp}}{m} = \int_{t_1}^{t_2} j(t)\, dt \tag{2}$$

This expression can be applied to any of the three jerk components, each one characterized by its own sequence of zeros.

Figure 7 illustrates the definition of impulsive force per unit mass as the area bounded by the jerk function $j(t)$ between two consecutive zeros. Yellow color indicates the positive impulsive force corresponding to an interval where acceleration increases: $a(t)$ goes from a minimum to a maximum. Instead, green color indicates a negative impulsive force corresponding to the interval where acceleration decreases going from a maximum to a minimum. Therefore, the impulsive force in the interval $(t_0, t_1)$ and the one in the interval $(t_1, t_2)$ act in opposite direction.

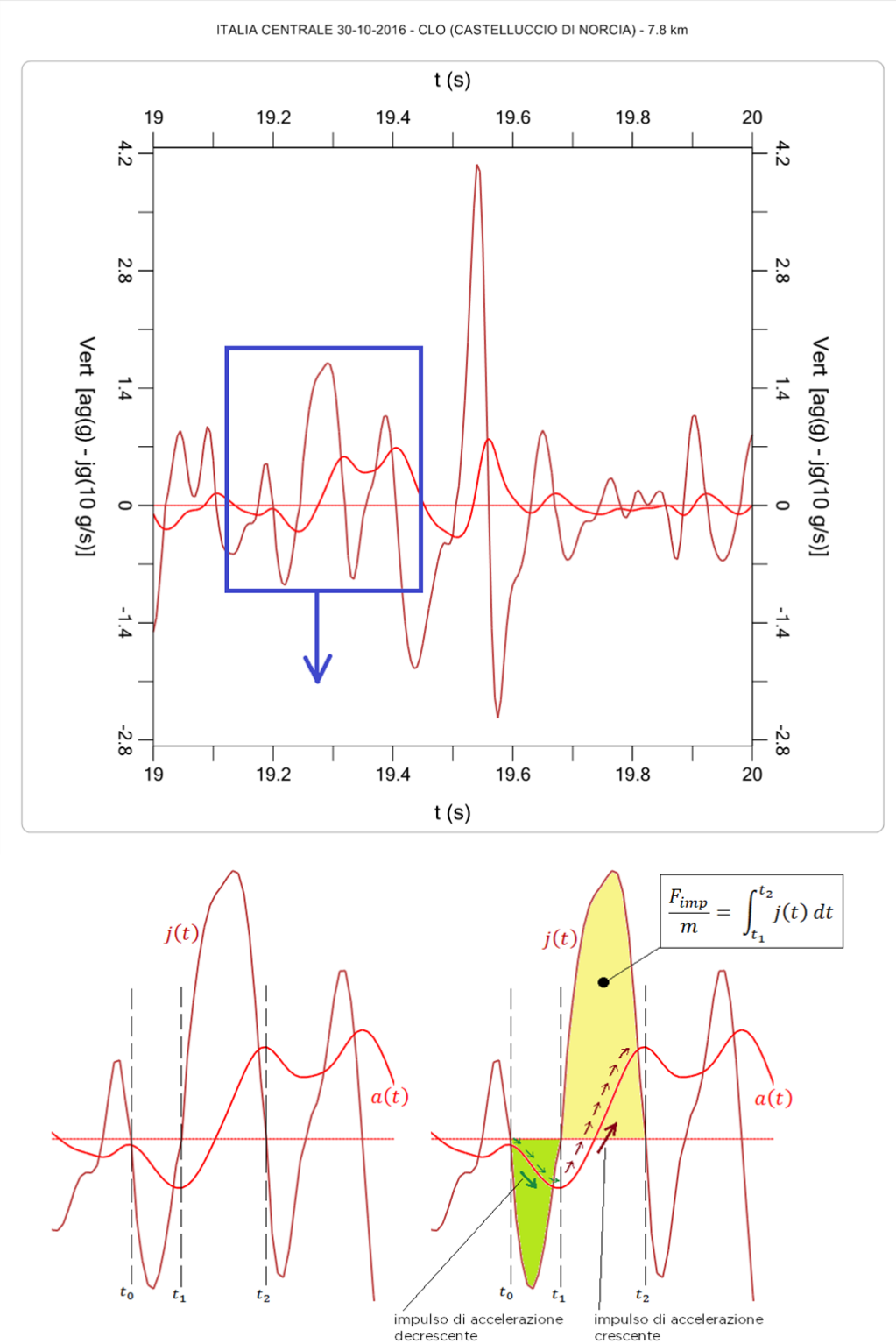


Figure 7. Impulsive force per unit mass, defined as the integral of jerk between two consecutive zeros.

Figure 7 refers to the vertical component of the ground motion recorded at station CLO (Castelluccio di Norcia) during 30.10.2016 Norcia mainshock in the time interval (19.000 – 20.000 s).

It is worth noticing the very short duration of the impulsive forces. The considered jerk zeros correspond to the following instants in the record: $t_0$ = 19.200 s, $t_1$ = 19.245 s, $t_2$ = 19.320 s.

The negative impulsive force corresponding to decreasing acceleration lasts 45 ms while the following positive impulsive force lasts 75 ms.

Thus, impulsive force may be calculated throughout the record for each time interval between two consecutive jerk zeros. The result is a step function that represents the time series of impulsive force per unit mass.

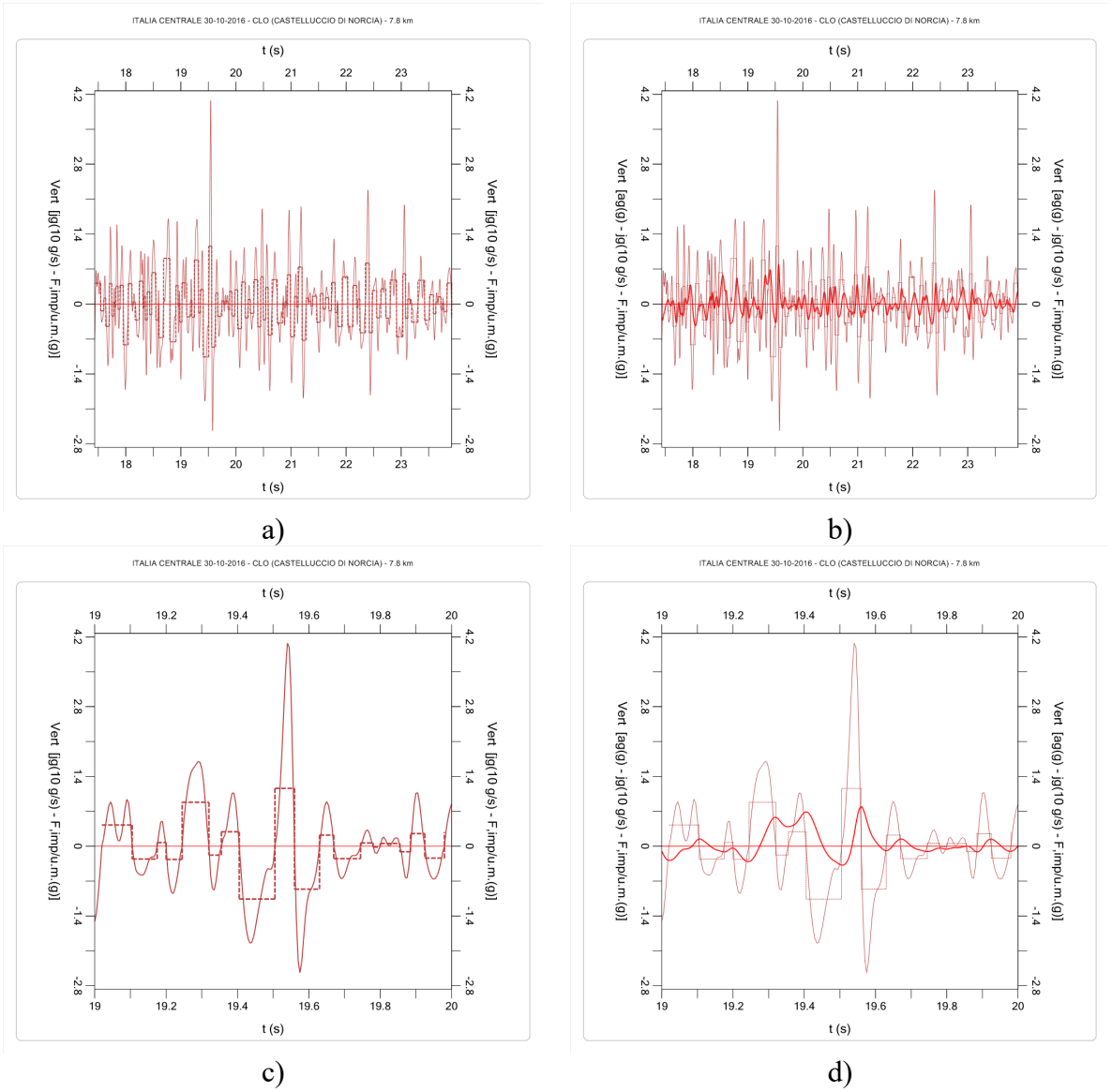


Figure 8. Jerk and impulsive forces per unit mass for the vertical seismic component.
CLO – 30.10.2016 Norcia mainshock

Figure 8 shows the jerk time series (solid line) and the step function of impulsive forces per unit mass (dashed line) for the vertical component of the reference seismic motion. The graphs on the right (b, d) also display the correspondent acceleration time series. The graphs at the top (a, b) refer to the time span between first and last acceleration peak exceeding 0.250 g, while the graphs at the bottom (c, d) refer to a shorter time interval (19.000 – 20.000 s).

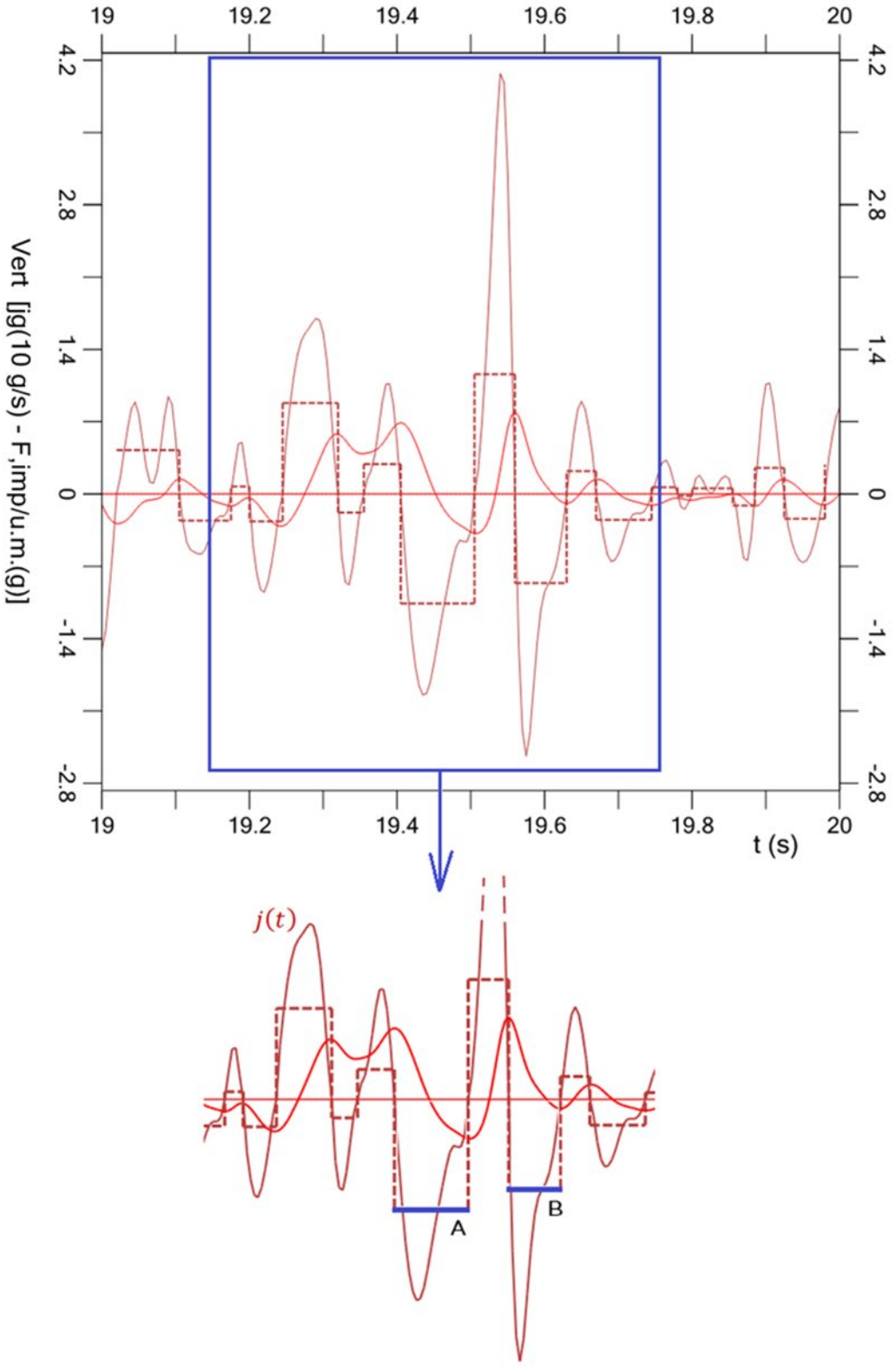


Figure 9. Peaks of jerk and correspondent impulsive forces

The detail shown in Figure 9 highlights an important aspect: the peak of jerk does not always correspond to the peak of impulsive force. This is because the impulsive force does not depend

only on the jerk value but also on the length of the time interval between two consecutive zeros. Therefore, lower jerk peaks with longer duration may yield higher impulsive forces than higher jerk peaks with shorter duration (cf. Impulsive forces A and B in Figure 9).

This behavior has general validity, it applies to all the components of seismic motion and different seismic events: the maximum values of jerk and impulsive force do not occur at the same time. The same happens between peaks of acceleration and peaks of jerk. Therefore, we get to the following property: *PGA, PGJ* and $F_{imp,max}$ are not simultaneous and there is not a direct relationship between them. However, a correlation may be pursuit from a statistical perspective.

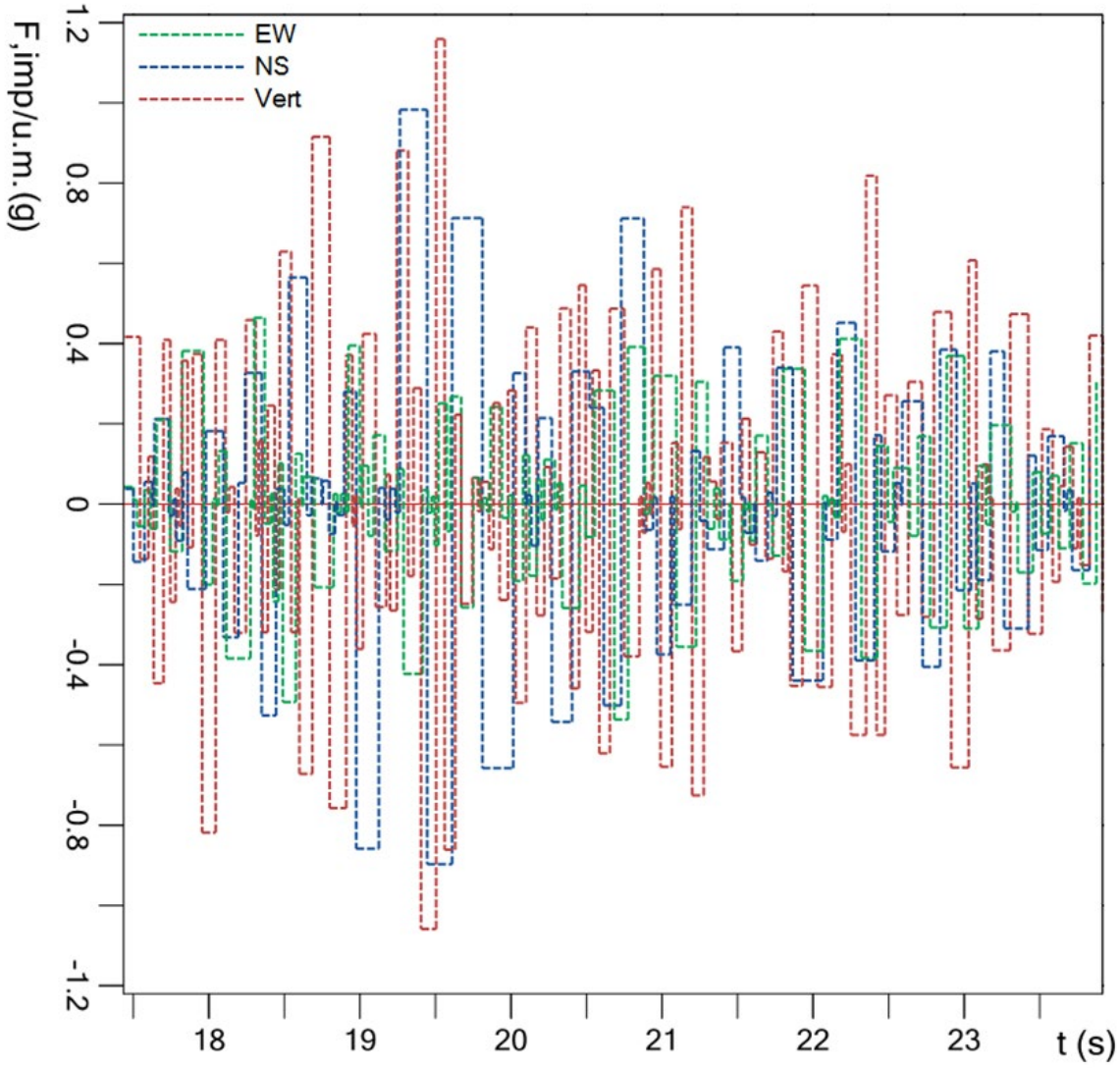


Figure 10. Time series of impulsive force per unit mass. Three components overlaid.

Figure 10 shows the time series of the three components of impulsive forces overlaid in the same graph.

Thus, considering jerk, the dynamic nature of the seismic action is expressed by a series of consecutive impulses which determine vibrations.

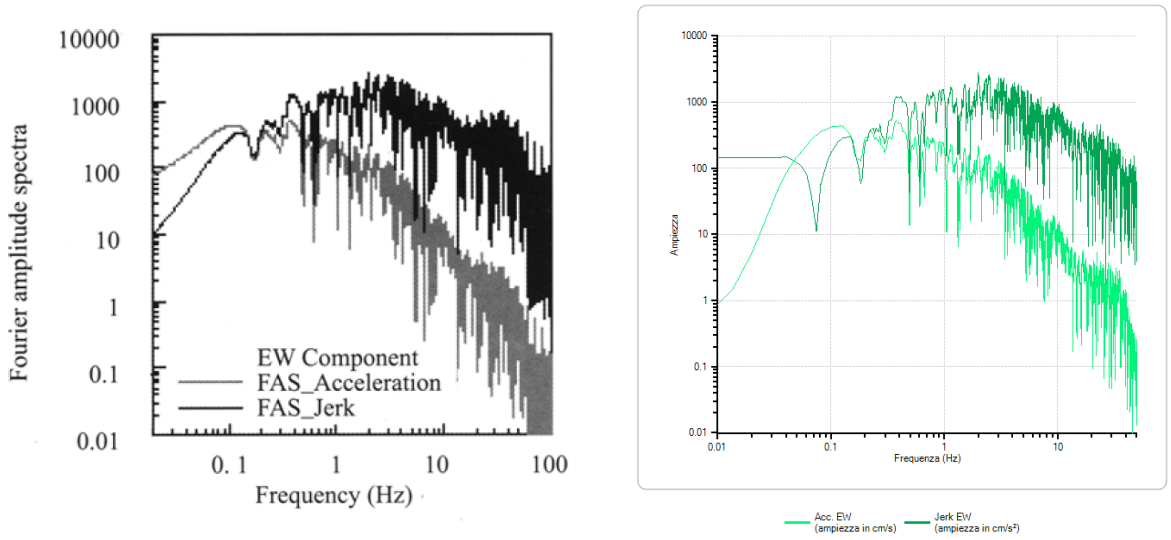


a) b)

Figure 11. Acceleration and Jerk Fourier amplitude spectra (Chi-Chi 20.9.1999, TCU068, EW component): (a) Tong et al. [3]; (b) Mariani and Pugi [1]

Tong et al. (2005) [3], in their study on the 1999 Chi-Chi earthquake in Taiwan, provided Fourier amplitude spectra both for acceleration and jerk (Figure 11). The dominant frequency contents of acceleration and jerk time series are between 1 and 10 Hz; however, jerk distributes in a much wider frequency band and its higher frequency contents are prominent: the region of significant frequencies for jerk extends at least up to 30 Hz.

This characteristic, observed for the first time in this seismic event in Taiwan, is confirmed for all seismic events in the Italian territory [1]: the jerk Fourier spectrum features a window of dominant frequency wider than the acceleration one. The jerk higher frequency content appears more important.

The identification of the dominant frequency of the seismic motion is crucial for the comparison with the natural frequencies of structures. According to Rathje et al. [14] the parameter that better characterize the frequency content is the mean period $T_m$, defined as the average of periods in the Fourier spectrum, each weighted by the square of its Fourier amplitude.

$$T_m = \frac{\sum_i c_i^2 \cdot \left(\frac{1}{f_i}\right)}{\sum_i c_i^2} \qquad \text{with } 0.25 \text{ Hz} \leq f_i \leq 20 \text{ Hz} \tag{3}$$

A first example of Fourier analysis with determination of the mean period has been performed on the seismic records from station CLO (Castelluccio di Norcia) during 30.10.2016 Norcia earthquake. Table 1 gives the mean period of acceleration and jerk for the three components of the seismic motion (EW, NS, Vert), while Figure 12 shows the Fourier amplitude spectra of acceleration and jerk for the vertical component.

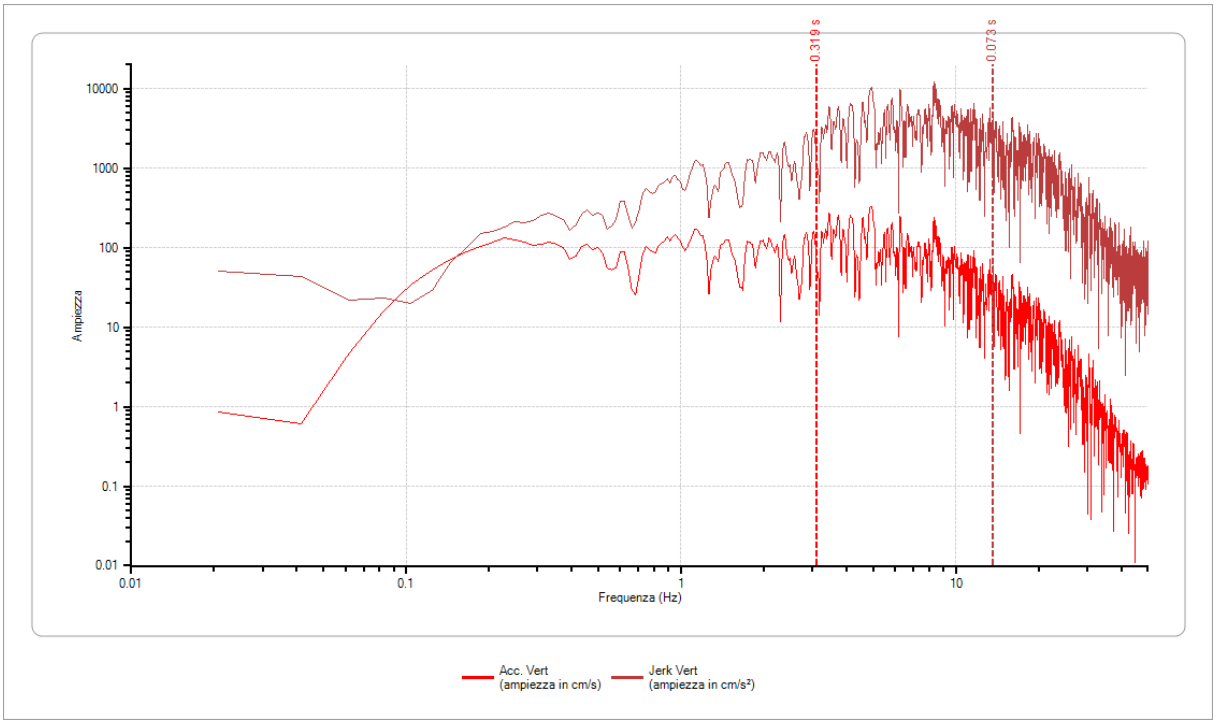


Figure 12. CLO, 2016 Norcia earthquake:
acceleration and jerk Fourier amplitude spectra for vertical component

| $T_m$(s) | EW | NS | Vert. |
|---|---|---|---|
| Acceleration | 0.657 | 0.540 | 0.319 |
| Jerk | 0.107 | 0.137 | 0.073 |

Table 1. Mean period of acceleration and jerk. CLO, 2016 Norcia earthquake

Table 1 highlights an important aspect: the impulsive nature of the vertical component. The main frequencies of the vertical component are significantly higher than the horizontal ones. It is also evident that jerk mean periods are very close to common fundamental periods of rigid structures like masonry buildings. This points out the potential issues caused by impulsive action on structural elements.

Given the chaotic nature of the seismic phenomena, to find a correlation between PGA, PGJ and the maximum Impulsive force a statistical elaboration of the seismic records was carried out.

Eight of the most recent seismic events in the Italian territory were considered: 30.10.2016 Norcia; 24.08.2016 Accumuli; 29.05.2012 Emilia; 06.04.2009 L'Aquila; 26.09.1997 Umbria-Marche; 23.11.1980 Irpinia; 19.09.1979 Valnerina; 06.05.1976 Friuli. For each of these events numerous seismic records provided by ITACA (ITalian ACcelerometric Archive) were analyzed, for a total of 447 station records.

## 3 CORRELATION BETWEEN JERK CHARACTERISTICS AND STRUCTURAL DESIGN PARAMETERS

For each analyzed record the following parameters have been calculated:

1. peak ground acceleration (*PGA*)
2. peak ground jerk (*PGJ*)

3. maximum value of impulsive force per unit mass ($F_{imp}$)
4. mean period ($T_m$) of acceleration and jerk, calculated through Fourier spectra

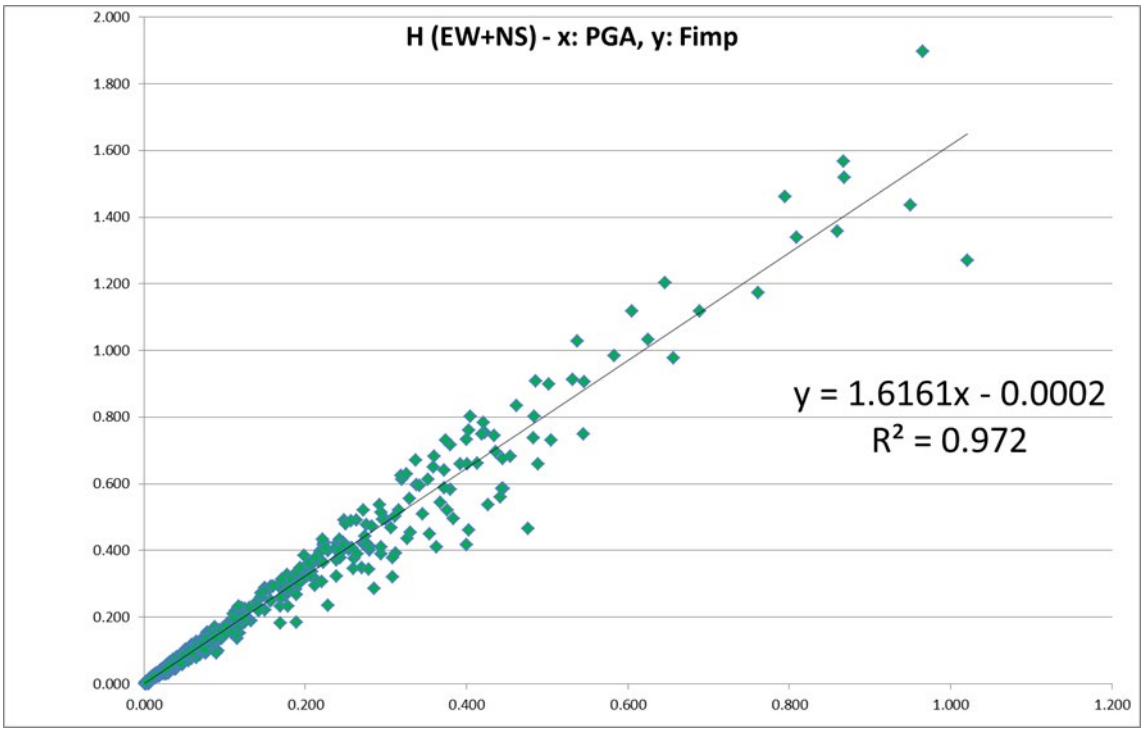


Figure 13. Correlation *PGA-Fi*$_{mp}$ for horizontal components

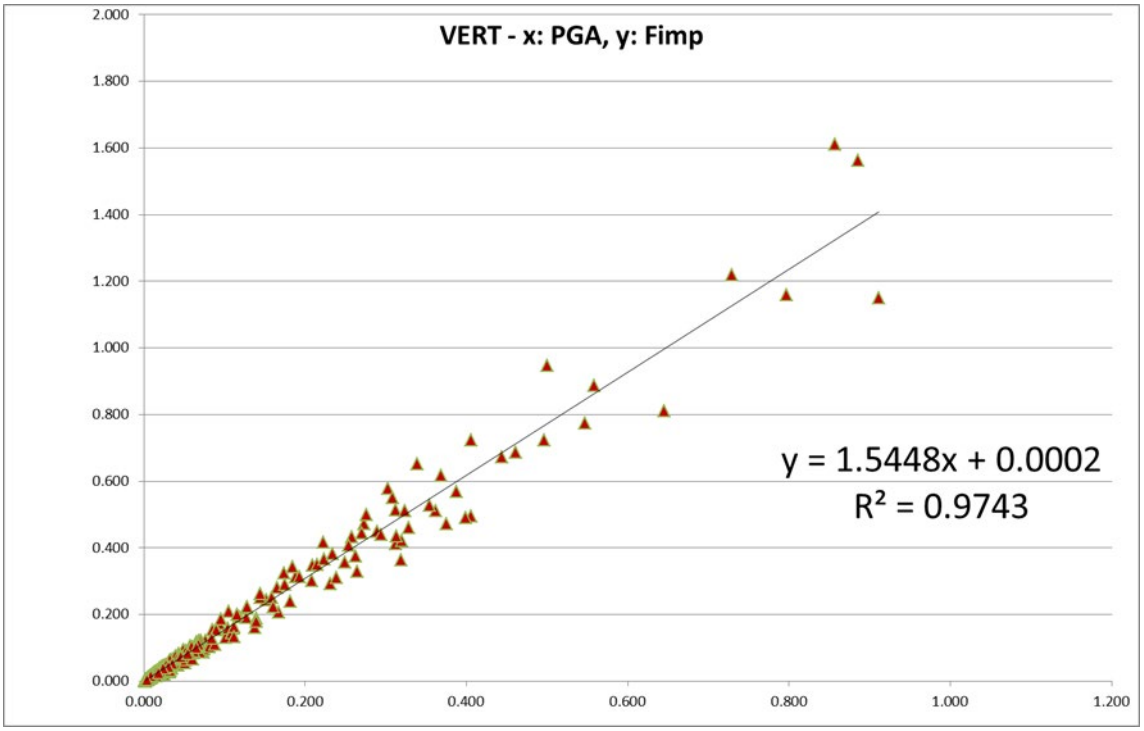


Figure 14. Correlation *PGA-F*$_{imp}$ for vertical component

Figures 13-14 show the correlation between *PGA* and maximum impulsive force for unit of mass $F_{imp}$ for horizontal and vertical components.

The correlation between *PGA* and impulsive forces, obtained through elaboration of the main seismic events in Italy, is an intrinsic property of the events themselves. The fact that the correlation has a coefficient of determination very close to 1 represents an excellent support for estimating the impulsive actions based on ground acceleration data.

The correlation obtained through statistical analysis between *PGA* and maximum impulsive force per unit mass $F_{imp,max,}$ (both expressed in g) are summed up in the following expressions (where: H stand for horizontal component, V stands for vertical component):

$$F_{imp,max,H} = 1.616\ PGA_H \tag{4}$$

$$F_{imp,max,V} = 1.545\ PGA_V \tag{5}$$

Regarding the frequency analysis, the mean period $T_m$ calculated from Fourier spectra has no relations with peak ground acceleration, peak ground jerk or maximum impulsive forces. In fact, in the single harmonic waves that constitute the signal, amplitude and frequency are mutually independent.

Investigating on the mean periods by direct comparison of the $T_m$ obtained from the 447 station records, a representative value was found in the median value, which compared to the mean value is not skewed by a small proportion of extremely large or small values, and therefore provides a better representation of the center.

Figure 15 shows for the vertical component of jerk the following information:

- a graph showing the mean period $T_m$ for each station considered. The graphs also include the mean value (black line) and the median value (red line) which in all the cases is lower than the mean.
- the frequency distribution with discretization of the periods in intervals of *0.025 s*

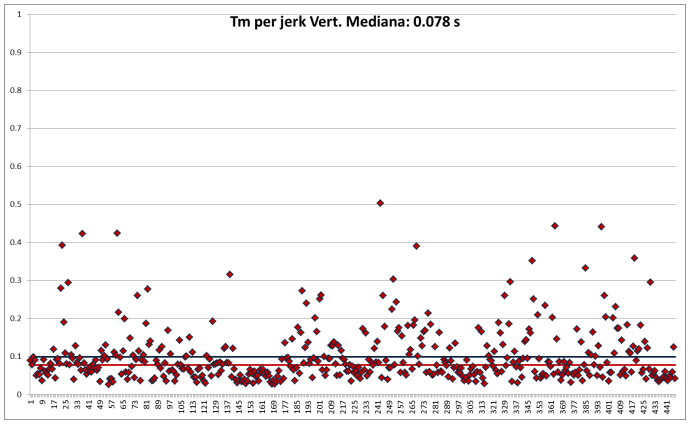


| Classe | Frequenza | |
|---|---|---|
| 0.025 | 0.00% | 0 |
| 0.05 | 21.48% | 96 |
| 0.075 | 27.52% | 123 |
| 0.1 | 19.69% | 88 |
| 0.125 | 8.50% | 38 |
| 0.15 | 6.71% | 30 |
| 0.175 | 4.25% | 19 |
| 0.2 | 3.58% | 16 |
| 0.225 | 1.79% | 8 |
| 0.25 | 0.89% | 4 |
| 0.275 | 1.79% | 8 |
| 0.3 | 1.12% | 5 |
| Altro | 2.68% | 12 |

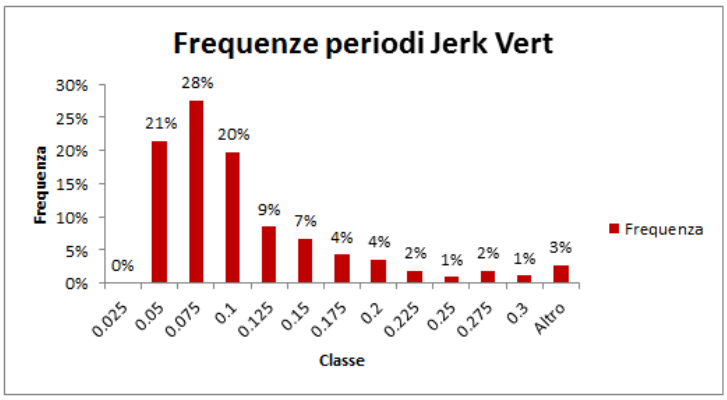


Figure 15. Statistical elaboration on the mean period $T_m$ of vertical jerk

Table 2 sums up the representative values of the mean periods and the main contribution to the distribution, both for acceleration and jerk, for each of the three components:

| | $T_m$(s) and main contribution to the distribution | |
|---|---|---|
| Component | Acceleration | Jerk |
| EW | 0.508 (19% for 0.500) | 0.102 (23% for 0.100) |
| NS | 0.509 (19% for 0.500) | 0.101 (22% for 0.100) |
| Vert. | 0.506 (15% for 0.300) | 0.078 (28% for 0.075) |

Table 2. Representative $T_m$ for acceleration and jerk

The frequency content of vertical jerk is characterized by very high frequencies. The representative value of the mean period $T_m$ is about 0.075 s, which is very close to the vertical fundamental period of many structures characterized by high vertical stiffness. Among them, existing masonry buildings shall be given special attention as they often feature weak connections which may be extremely vulnerable under the effects of impulsive forces.

*It is important to notice that other structural typologies may also show local vulnerabilities under impulsive actions. International studies (see references in [1]) take into consideration micro-scale damage of structures where discontinuities are represented by the connections between different structural elements, as in reinforced concrete or steel joints, and not by the constitutive heterogeneity of the material (like in masonry).*

To be more specific about the amplification of the structural response in terms of displacements and internal actions, considering that seismic input is a combination of many harmonic excitations, we can refer to the theory of driven harmonic oscillators with viscous damping.

Study of the simple oscillator leads to an amplification factor $C_{ampl}$ given by the following expression:

$$C_{ampl} = \frac{1}{\sqrt{\left(1-\frac{T_1^2}{T^2}\right)^2 + 4\,\xi_{eq}^2\,\frac{T_1^2}{T^2}}} \tag{6}$$

where: $T_1$ is the fundamental period of the structure; $T$ is the period of the applied force (in this case coincident with the mean period of vertical jerk component); $\xi_{eq}$ is the equivalent viscous damping coefficient.

The frequency distribution given in Figure 15, obtained from the statistical elaboration of the 447 examined seismic records, clearly shows a log-normal trend.

The jerk mean period of the seismic event that is expected to strike the building is not known and does not depend on the values of *PGA* and *PGJ*. Table 3 shows an extract from the list of the 447 examined records with the correspondent value of *PGA (g)* and jerk $T_m$ *(s)* with respect to the vertical component, ordered by the value of $T_m$. For instance, a value of $T_m$ equal to 0.034 s was correspond to many different values of *PGA*, ranging from 0.071 g to 0.645 g: there is no correlation between $T_m$ and *PGA* and there are no known studies which identify a possible design value of jerk mean period in a determined site.

Therefore, in the context of design, while *PGA* assumes precise values given the site of the structure, the same cannot be said for the jerk period. However, it is possible to correlate the jerk mean period to the fundamental periods of the structure using the frequency distribution from a probabilistic perspective.

| Evento-Stazione | | | |
|---|---|---|---|
| | PGA VERT | Tm jerk Vert | |
| 06042009_IT_AQA | 0.444 | 0.026 | |
| 29052012_TV_MIR04 | 0.263 | 0.028 | |
| 29052012_TV_MIR02 | 0.461 | 0.028 | |
| 29052012_IV_T0813 | 0.175 | 0.029 | |
| 30102016_IT_ACT | 0.254 | 0.029 | |
| 29052012_IT_SMS0 | 0.104 | 0.03 | |
| 29052012_IV_T0818 | 0.209 | 0.03 | |
| 29052012_IV_T0800 | 0.320 | 0.031 | |
| 30102016_IT_CNE | 0.547 | 0.031 | |
| 30102016_IT_NCR | 0.057 | 0.032 | |
| 29052012_IT_MRN | 0.857 | 0.032 | |
| 29052012_TV_MIR01 | 0.369 | 0.033 | |
| 06042009_IT_AQV | 0.496 | 0.033 | |
| 29052012_IV_T0805 | 0.071 | 0.034 | EMILIA SECOND SHOCK 29-05-2012 - IV_T0805 - 22.0 km - Lat. 44.9187° - Long. 11.3226° - Elev. 5 m |
| 30102016_3A_MZ63 | 0.112 | 0.034 | ITALIA CENTRALE 30-10-2016 - 3A_MZ63 - 28.4 km - Lat. 42.62981° - Long. 13.32345° - Elev. 1071 m |
| 30102016_IT_CIT | 0.138 | 0.034 | ITALIA CENTRALE 30-10-2016 - IT_CIT - 26.8 km - Lat. 42.5942° - Long. 13.1632° - Elev. 873 m |
| 29052012_TV_MIR05 | 0.152 | 0.034 | EMILIA SECOND SHOCK 29-05-2012 - TV_MIR05 - 15.8 km - Lat. 44.9808° - Long. 11.10719° - Elev. 0 m |
| 29052012_TV_MIR08 | 0.313 | 0.034 | EMILIA SECOND SHOCK 29-05-2012 - TV_MIR08 - 8.6 km - Lat. 44.9169° - Long. 11.0895° - Elev. 0 m |
| 26091997_IT_NCR | 0.406 | 0.034 | UMBRIA/MARCHE 26-09-1997 - IT_NCR - 10.9 km - Lat. 43.11158° - Long. 12.78467° - Elev. 492 m |
| 30102016_IV_T1214 | 0.645 | 0.034 | ITALIA CENTRALE 30-10-2016 - IV_T1214 - 11.4 km - Lat. 42.75954° - Long. 13.2087° - Elev. 1490 m |

Table 3. Lack of correlation between $PGA$ and $T_m$

Given the fundamental period of the structure, expression (6) provides the range of jerk mean periods corresponding to a significant amplification factor (e.g. $C_{ampl} \geq 2$). Then, the frequency distribution allows to calculate the correspondent probability of occurrence. This quantitative information constitutes an index of vulnerability of the structure with respect to impulsive actions. In this respect, strengthening interventions determining a reduction of this probability will increase robustness of the structure, that is, its capacity to avoid local damages caused by stress concentration due to jerk.

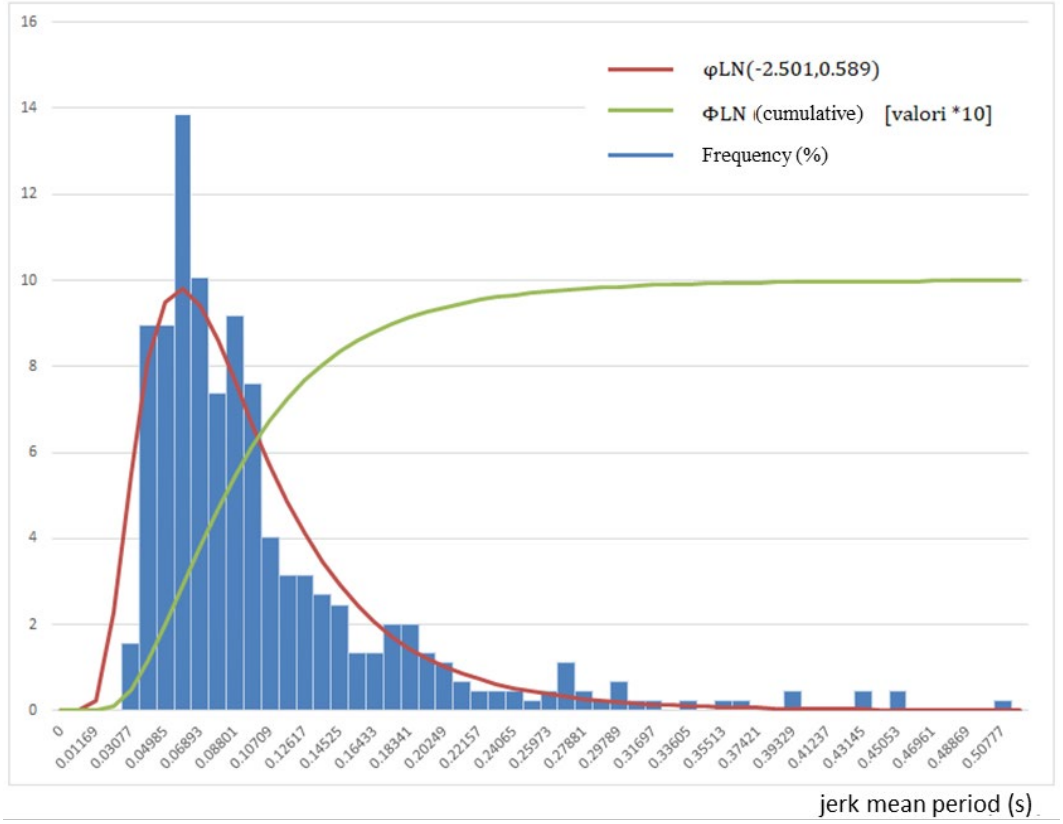


Figure 16. Frequency distribution of vertical jerk mean period

In the graph shown in Figure 16 the X-axis represents the vertical jerk mean period. The histogram represents the frequency distribution calculated for the 447 examined seismic records. The red line is the correspondent log-normal probability distribution of vertical jerk mean period ($\varphi LN$). For a structure with given vertical natural period $T_1$, through expression (6) we can identify the interval of jerk mean periods $(T_{jerk,min}, T_{jerk,max})$ for which $C_{ampl} > 1$. These are the jerk frequencies that produce resonance, thus significant amplification of the structural impulsive forces. The green line in the graph is the cumulative probability distribution ($\Phi LN$). The probability that a structure with natural period $T_1$ enters in resonance with jerk is given by:

$$\Phi LN(T_{jerk,max}) - \Phi LN(T_{jerk,min})$$

For example, let us consider a building characterized by $T_1 = 0.058\ s$ and $\xi_{eq} = 5\%$. Through expression (6) we find that the jerk mean periods corresponding to $C_{ampl} \geq 2$ are those in the interval (0.048 s, 0.082 s). Using the cumulative probability distribution, we find that the probability of significant amplification of the impulsive actions is:

$$\Phi LN(0.082) - \Phi LN(0.048) = 0.319 = 32\%$$

If the seismic jerk striking this building had mean period equal to the building natural period (0.058 s), the amplification factor would be $C_{ampl} = 10$. Assuming instead $\xi_{eq} = 10\%$ the amplification factor would be $C_{ampl} = 5$: the higher the viscous damping the lower the amplification effect, although it is still quite significant. These considerations will be resumed in the example given in the next section.

Another application of expression (6) is the following. Given a seismic event with known jerk mean period, we can find the interval of building natural periods corresponding to significant amplification of the impulsive actions.

For example, let us consider the aforementioned seismic event 30.10.2016 Norcia, CLO. The calculated jerk mean period is $T = 0.073\ s$. Considering $\xi_{eq} = 5\%$, from expression (6) we find that the natural periods corresponding to $C_{ampl} \geq 2$ are those in the interval (0.053 s, 0.113 s). Since the natural period of buildings often falls in this interval, it is reasonable to assume that a substantial number of buildings was affected by amplified impulsive actions.

## 4 IMPULSIVE ACTIONS IN STRUCTURAL JOINTS: DESIGN OF LOCAL STRENGTHENING MEASURES

The previous section described the characteristics of jerk with particular attention to corresponding impulsive forces and frequency (mean period).

International studies conducted on jerk [2, 3, 7, 8] show that vibrational wave propagation is directly related to stress concentrations and local damages. In this work, particular attention is given to existing masonry buildings where internal connections are often not totally effective: it is, therefore, necessary to investigate on the relation between impulsive actions and local damages, such as masonry disaggregation and connections failure.

Strengthening interventions that confine masonry and absorb local stress concentration improve the structural response to jerk. Considering the very brief duration of impulsive action and the rigid-brittle behavior of masonry, such interventions may be designed in terms of strength.

Let us consider a floor undergoing a conservative intervention as one of the strengthening measures designed for the building. The strengthening is achieved through a lightweight concrete slab built on top of the floor, collaborating with it through a system of connectors. At the constraints, steel bars properly anchored through masonry ensure the connection between floor and perimetral walls (see Figure 17). The usual safety verifications carried out for the floor in

terms of strength and deformability under vertical design actions (permanent, variable, and seismic loading) provide quantification of the improvement achieved.

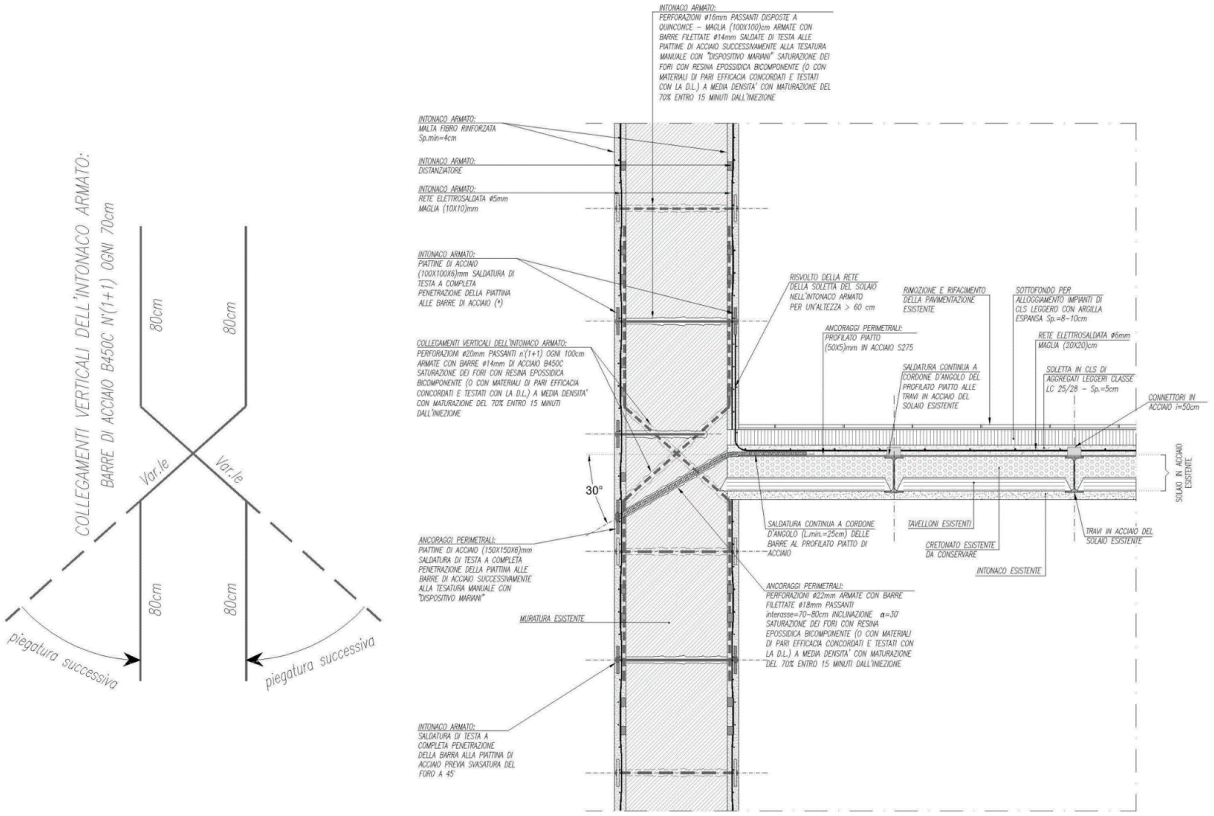


Figure 17. Floor-to-external-wall connection [1] in presence of reinforced mortar either traditional or innovative (e.g. CRM)

The masonry wall is supposed to be consolidated through traditional or innovative (e.g. CRM) reinforced plaster. The result is an increment of mechanical properties in terms of compressive and shear strength. This aspect is captured through flexure and diagonal cracking shear verifications of masonry panels under static and seismic actions. For example, in seismic analysis carried out with the pushover method, these safety verifications take into account strength and deformation capacity of masonry considering its elastic-plastic behavior.

In this kind of modelling, however, the structural joints, that is, the wall portions at the intersection between piers and spandrels or between piers and floors, are qualified as rigid zones and affect the structural response only because they reduce the effective length of masonry piers and spandrel.

In reality, as highlighted by recent studies [9], structural joints are affected by local phenomena which may play a crucial role for the equilibrium of the wall in terms of resistance and deformation, both in-plane and out-of-plane.

The study of jerk effects and impulsive nature of seismic action, suggests to pay particular attention towards floor-to-wall connections. As noted above, under impulsive actions, the areas characterized by structural discontinuity or by heterogeneity of materials (as in ruble stone masonry with poor quality mortar) are affected by stress concentration, thus it is necessary to assess the dynamic behavior of the involved local masses in order to counteract potential disaggregation. These effects are not addressed in the safety verifications normally applied in the context of seismic analysis.

Under inertial forces, safety verifications carried out according to current technical Standards, prove that traditional or innovative reinforced plaster, with transversal connections and eventual grout injections (considered in the analysis through increment of masonry mechanical properties) is effective. Under impulsive forces, however, additional reinforcement may be required in order to counteract their effect.

## 4.1 JERK-RESISTANT TRANSVERSAL TENSILE ELEMENTS

A first design hypothesis consists in the insertion of additional transversal tensile elements able to confine the structural joint during impulsive action. This intervention constitutes a local enhancement of the reinforced plaster intervention which already by regulation is complemented by transversal connections in order to ensure solidarity with the wall core.

The local mass involved in the impulsive action is subjected to a vertical force, that is, a uniaxial stress which, for the sake of simplicity, we consider concentrated on the central axis of the wall (Figure 18).

Physically, when vertical jerk compresses the local mass, masonry expands transversally, and the transversal reinforcement undergo tension generating a horizontal compressive stress on the wall in order to contain the deformation. Therefore, the stress state becomes biaxial and this involves an increase in strength if compared to the uniaxial stress state; the main effect is to prevent the joint from breaking up.

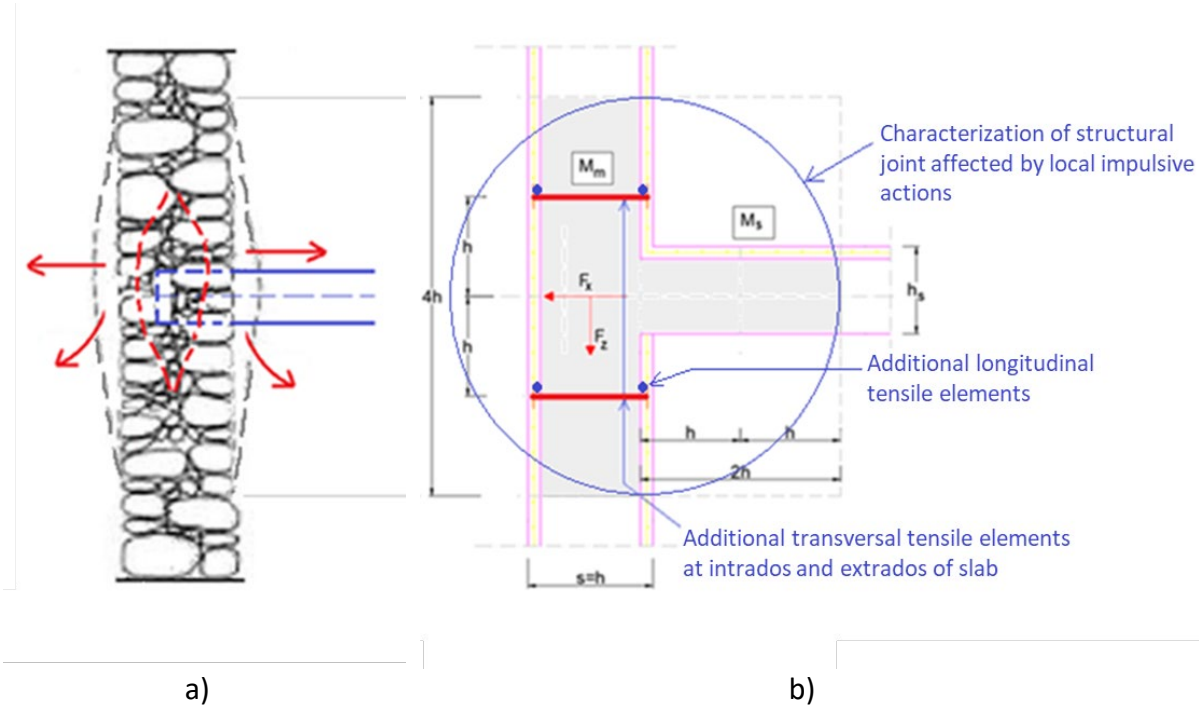


Figure 18. Impulsive actions on floor-to-wall joint: (a) sketch of the collapse mechanism; (b) reinforcement through additional tensile elements

In an elastic solid, vertical compression generates vertical contraction and transversal expansion. Under the instantaneous action of jerk, masonry tends to have a rigid behavior, corresponding to a high but unknown modulus of elasticity: on the other hand, we are not interested in quantifying the deformation (which by the way would be conventional due to the heterogeneity of masonry material), instead, we need to evaluate the transversal tension generated by the compressive stress and counteracted by the transversal tensile elements.

To this end, Poisson's ratio ν is used to determine the transversal (horizontal) stress.

Figure 18 shows the local mass *M* involved by jerk impulsive action, consisting in the masonry mass $M_m$ and the slab mass $M_s$. The longitudinal dimension b, along Y direction, can be determined considering both the spacing between load-bearing elements and the dimensions of the intersection between piers and spandrels. The thickness of the wall s and the height *4h* (with *h* equal to the thickness *s*) provide the dimensions of the mass in transversal X and vertical Z direction respectively. As a working hypothesis, the slab portion corresponding to mass $M_s$ is assigned the length *2h*.

*The choice of these dimensions, in particular the height 4h of masonry mass and the width 2h of slab mass, come from the experience gained by the authors in the observation of crack patterns after significant seismic events. From a design point of view, the dimension h is linked both to the thickness of masonry and to the space required to place the transversal tensile elements.*

Forces $F_X$ and $F_Z$ forces are the horizontal and vertical impulsive actions produced by jerk. The choice of direction is conventional; in this example $F_X$ is oriented outwards and $F_Z$ downwards.

The jerk actions relevant to the local mass M are defined by the relations linking impulsive force per unit mass to *PGA*, expressed, as already illustrated in the previous sections, by:

$$F_{imp,max,H} = 1.616\, PGA_H \tag{7}$$

$$F_{imp,max,V} = 1.545\, PGA_V \tag{8}$$

Based on typical dynamic characteristics of masonry buildings, the horizontal mean period of jerk is not very close to the horizontal natural periods of the building, while this is not the case for the vertical direction. This suggests that resonance phenomena may occur in the vertical direction.

Since the jerk mean frequency of the seismic event expected to strike the building is unknown, resonance condition is assumed for safety. Based on currently available data, in the definition of the impulsive forces we assume that jerk propagates through the building without modifications with respect to the ground.

*This is reasonable for the vertical direction. For the horizontal direction, instead, Tong et al. [3] indicate that jerk undergoes at floor level an amplification similarly to what occur for acceleration; however, these indications still need to be verified in relation to various structural typologies. On these aspects, Research shall provide further results, identifying more precisely the propagation of jerk through buildings. As a matter of fact, studies on jerk response spectra are currently in progress [10].*

According to the hypothesis, the impulsive forces in vertical direction are amplified by a factor $C_{ampl} = 5$. This amplification corresponds to resonance condition between structure and jerk assuming the equivalent viscous damping coefficient $\xi_{eq} = 10\%$, higher than what is normally considered (5%). In fact, we consider that masonry may already be cracked at the beginning of the seismic excitation, for example due to its non-cohesive nature or due to previous damages. During the expected seismic event, the development of progressive cracking would increase damping and reduce the amplifications due to resonance. However, the damages caused by impulsive actions are typically brittle and caused by instantaneous overcoming of resistance, and this can happen even at the beginning of the phenomenon. Moreover, it should

be considered that the highest vertical impulses frequently occur in the first phase of the event. For all these reasons, we assume that the equivalent viscous damping coefficient should not be higher than 10%.

Ultimately, the impulsive forces corresponding to mass M are calculated as follows:

$$F_X = 1.616\, PGA_H \cdot M \tag{9}$$

$$F_Z = 1.545\, PGA_V \cdot C_{ampl} \cdot M \tag{10}$$

Regarding the spatial simultaneity of jerk peaks, the available data (obtained processing records of the main seismic events in the Italian territory [1]) show that the phenomenon is continuously spatial and the jerk peaks in the three directions occur randomly. Precisely because of this randomness, it is not possible to exclude that significant peaks may occur simultaneously; therefore, in the safety verifications it is advisable to consider all three components of the impulsive actions. In this way under no circumstances the designed resistant elements would be insufficient.

With reference to Figure 18, the effects of $F_Y$ force, orthogonal to the section plane, are distributed within the joint and absorbed by 4 longitudinal tensile elements placed in correspondence of the transversal reinforcements. These elements are necessary to achieve longitudinal continuity of the reinforcement also considering the shear effects generated by lateral expansion of masonry. In the section plane, forces $F_Y$ and $F_Z$ both contribute to the impulsive stresses.

Force $F_Z$ generates the following vertical tension:

$$\sigma_Z = F_Z / bs \tag{11}$$

Being $E$ the modulus of elasticity of masonry, vertical contraction $\varepsilon_Z$, transversal expansion $\varepsilon_X$ and transversal tension $\sigma_X$ are given by:

$$\varepsilon_Z = \sigma_Z / E\,,\ \varepsilon_X = -\nu\, \varepsilon_Z = -\nu\ \sigma_Z / E\,,\quad \sigma_X = -\nu\, \sigma_Z \tag{12}$$

The transversal tensile elements must counteract the transversal tension $\sigma_X$ acting on the lateral faces of the node, plus the transversal impulsive force $F_X$. Therefore, the tensile force that the elements must resist is given by:

$$T = \nu\, \sigma_Z \cdot 4h \cdot b + F_X \tag{13}$$

Regarding masonry Poisson's ratio, current Italian technical Standards consider $\nu = 0.5$ (calculated from $E$ and $G$ values given in NTC18, Tab. C8.5.I), thus this is the value used in the proposed formulation. A greater value would increase the transversal tension produced by the vertical force, but as far as observed it correspond to more cracked masonry which in turn is characterized by greater $\xi_{eq}$ damping coefficient with consequent decrease of the resonance amplification factor; therefore, the two aspects compensate each other.

## 4.2 JERK-RESISTANT TRANSVERSAL AND BENT ELEMENTS

A second hypothesis of integrative elements aimed to counteract jerk effects consists in the use of bent tensile elements in addition to the transversal ones. In this case, the design can be carried out without considering the transversal behavior of masonry, thus disregarding the relation between vertical compressive and transversal tensile stress. This is achieved by considering that jerk impulsive forces are resisted by a truss-type structure where some elements resist tension and some other compression. Tensile stresses are used to design the additional transversal and bent elements, while the compressive stress acting on the struts must be compared with the compressive strength of masonry.

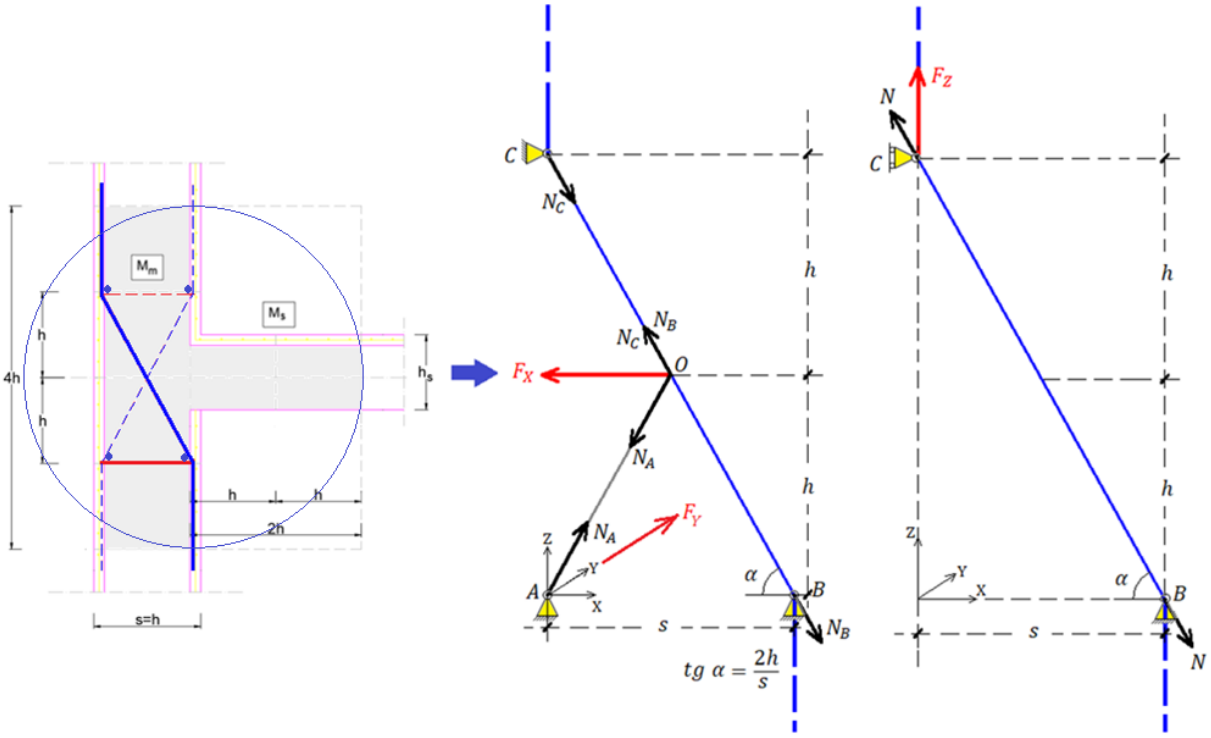


Figure 19. Additional truss-type elements to counteract impulsive actions.

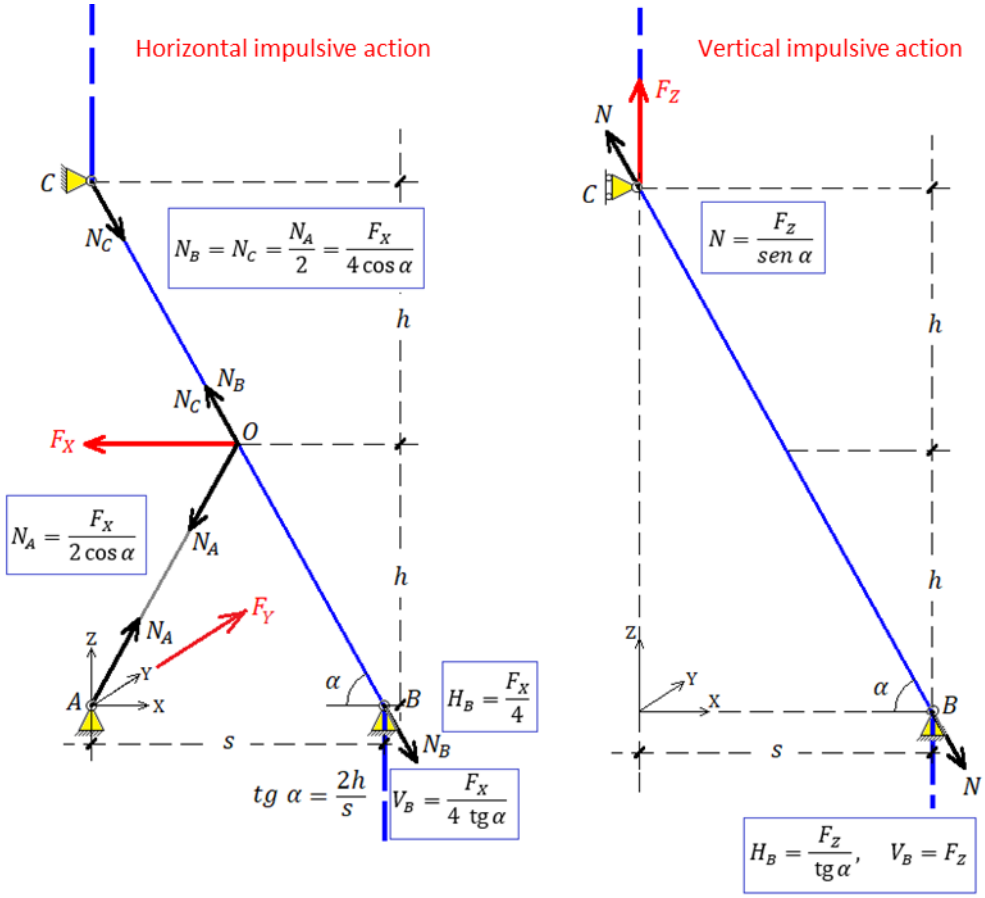


Figure 20. Internal actions in truss elements and joint reactions

Static scheme with horizontal impulsive action:

- axial forces:

$$N_A = \frac{F_X}{2\cos\alpha}, \quad N_B = N_C = \frac{N_A}{2} = \frac{F_X}{4\cos\alpha} \tag{14}$$

- joint reactions:

$$H_B = \frac{F_X}{4}, \quad V_B = \frac{F_X}{4\ \mathrm{tg}\,\alpha} \tag{15}$$

Static scheme with horizontal impulsive action:

- axial forces:

$$N = \frac{F_Z}{\mathrm{sen}\,\alpha} \tag{16}$$

- joint reactions:

$$H_B = \frac{F_Z}{\mathrm{tg}\,\alpha}, \quad V_B = F_Z \tag{17}$$

Ultimately, bent element verification is applied considering the following tensile force:

$$N_{bent} = \frac{F_X}{4\cos\alpha} + \frac{F_Z}{\mathrm{sen}\,\alpha} \tag{18}$$

While for the tensile verification of the transversal elements:

$$N_{trans} = \frac{F_X}{4} + \frac{F_Z}{\mathrm{tg}\,\alpha} \tag{19}$$

Proper anchorage of the bent elements is ensured selecting an adequate length of the vertical segments.

The additional compressive stress due to jerk is considered applied in the compressed strut having section $A_p$. Assuming $\sigma_V$ as the vertical compressive stress in the wall due to the acting loads (static and seismic), and $f_d$ as the design compressive strength of masonry, the maximum bearable compressive stress due to jerk impulsive action is given by:

$$\sigma_{j,max} = f_d - \sigma_V \tag{20}$$

This must be compared with the actual stress caused by jerk, which considering the inclination of the strut is expressed by:

$$\sigma_j = \left(N_A/A_p\right) \cdot \mathrm{sen}\alpha = \frac{F_X\,\mathrm{tg}\alpha}{2 \cdot\ A_p} \tag{21}$$

## 4.3 APPLICATION EXAMPLE

The following example refers to a masonry building located near Perugia (Italy). The design seismic action at the Ultimate Limit State of Significant Damage is characterized by: (i) in horizontal direction $a_g = 0.186g$ and $S = 1.2$, thus $PGA_H = 0.223g$; (ii) in vertical direction $a_{gV} = 0.186g$ and $S = 1.0$, thus $PGA_V = 0.186g$.

The building consists of two stories (ground floor and first floor) and its load bearing walls are made of ruble stone masonry with specific weight $w = 19\ kN/m^3$. The fundamental period of vibration in horizontal direction is equal to 0.378 *sec*, while in vertical direction it is equal to *0.058 sec*.

Considering the representative mean periods of acceleration and jerk given in Table 2, it can be observed that the jerk mean period in horizontal direction (about 0.100 sec) is far from the fundamental period of the building (0.378 sec); while in the vertical direction the two periods

are very close *(0.078 sec for jerk, 0.058 sec for the building).* Therefore, as noted above, resonance phenomena may occur in vertical direction.

Let us consider a floor-to-wall connection with the following dimensions (see Figure 18): s = 400 mm, h = s = 400 m, b = 1000 mm. The masonry mass involved in the local impulsive phenomena corresponds to the following weight:

$$P_m = wsb \cdot 4h = 19.00 \cdot 0.40 \cdot 1.00 \cdot 4 \cdot 0.40 = 12.16\ kN \tag{22}$$

The floor is characterized by 2.50 kN/m$^2$ permanent load and 2.00 kN/m$^2$ vertical load with seismic combination coefficient $\psi_2 = 0.3$; therefore, the slab mass $M_S$ corresponds to distributed load of 3.1 kN/m$^2$ and its total weight is given by:

$$P_s = (g + \psi_2 q) \cdot 2h \cdot b = 3.10 \cdot 0.8 \cdot 1.00 = 2.48\ kN \tag{23}$$

The total node weight and the corresponding impulsive forces are the following:

$$P = 12.16 + 2.48 = 14.64\ kN \tag{24}$$

$$F_X = 1.616 \cdot\ 0.223 \cdot 14.64 = 5.28\ kN \tag{25}$$

$$F_Z = 1.545 \cdot\ 0.186 \cdot 5 \cdot 14.64 = 21.03\ kN \tag{26}$$

**STRENGTHENING THROUGH TRANSVERSAL ELEMENTS**

The transversal tensile force resisted by the additional transversal elements (cf. section 3.1) is given by the following expressions:

$$\sigma_Z = 21030\ /\ (1000 \cdot 400) =\ 0.053\ \ N/mm^2 \tag{27}$$

$$T = 0.5 \cdot\ 0.053 \cdot\ 1600 \cdot\ 1000 +\ 5280 =\ 47680\ N \tag{28}$$

Considering the insertion of 2 steel bars type B450C φ12 (section 113 mm$^2$) at the intrados and extrados of the floor with longitudinal spacing of 1.00 m, the total resistant cross section is 226 mm$^2$.

Considering a partial safety factor $\gamma_S = 1.15$, the design yield strength is given by 450/1.15 = 391 N/mm$^2$. Moreover, considering a confidence factor CF = 1.20 corresponding to knowledge level KL2, the safety verification is given by:

$$\sigma_S = \frac{47680}{226} = 211 < \frac{391}{1.20} = 325\ \frac{N}{mm^2} \tag{29}$$

Expression (29) yields a safety factor equal to 1.54. This value can be considered satisfactory considering the actual ground acceleration registered in previous seismic events. Therefore, robustness is ensured even with respect of peak ground acceleration and jerk higher that those considered as design values.

For the longitudinal Y direction, we consider the insertion of 4 longitudinal bars φ10 (total cross section 314 mm$^2$) in correspondence of the ends of the transversal elements. Therefore:

$$F_Y = F_X = 5.28\ kN\ \Rightarrow\ \sigma_S = \frac{5280}{314} = 17\,\frac{N}{mm^2} \tag{30}$$

$$F = \sqrt{F_X^2 + F_Z^2} = \sqrt{21.03^2 + 5.28^2}\ kN = 21.68\ kN\ \Rightarrow\ \tau_S = \frac{21680}{314} = 69\ \frac{N}{mm^2} \tag{31}$$

$$\sigma_S^2 + 3\,\tau_S^2 = 17^2 + 3 \cdot 69^2 = 14572\ < 325^2 = 105625 \tag{32}$$

Although the proposed elements turn out to be oversized, their contribution, as already noted, is necessary to achieve longitudinal continuity of the reinforcement also considering the shear effects generated by lateral expansion of masonry.

The influence of masonry typology on the impulsive action effects can be evaluated by considering the behavior of the structural node without consolidation. In this example, the additional transversal elements have been entrusted with a total tensile force T = 47680 N. In the absence of reinforcements, masonry would increase the possibility to develop cracks perpendicular to the tensile stress, that is, in the hypothesis of centered axial force, vertical cracks. The tensile strength can be assumed, as a first approximation, equal to the shear strength ($f_{td} \cong \tau_{0d}$); therefore, the acting stress is given by:

$$\tau = T/(b \cdot 4h) = 47680/(1000 \cdot 1600) = 0.030\ N/mm^2 \tag{33}$$

According to strength values suggested by Italian technical standard with respect to knowledge level KL2 (CF = 1.2), ruble stone masonry is characterized by $\tau_{0d}$ = 0.025 / 1.2 = 0.021 N/mm$^2$. Therefore, under the hypothesis of this example, masonry alone without reinforcement would not satisfy the safety verification.

Considering nodes with the same geometry as the one in the example, it is interesting to determine for various masonry typologies the limit value of PGA beyond which the jerk effects, in the case of maximum amplification, would generate local damages.

Table 4 reports those limit values for various masonry typologies. The results were obtained, based on what illustrated above, by applying expression (13) and considering knowledge level KL2:

$$T = \nu \frac{F_Z}{bs} \cdot 4h \cdot b + F_X = 0.5 \frac{(1.545 PGA_V \cdot 5 \cdot P)}{bs} \cdot 4h \cdot b + 1.616\, PGA_H \cdot P \tag{34}$$

$$P = w\, s\, b \cdot 4h + (g + \psi_2 q) \cdot 2h \cdot b$$

The limit value of ground acceleration $a_g$ was obtained considering:

$$PGA_V = a_{gV} = a_g, \quad PGA_H = 1.2 \cdot a_g, \quad T = b \cdot 4h \cdot \tau_{od}$$

| **Masonry typology** | $\tau_{od}$ **(N/mm$^2$)** | $w$ **(kN/m$^3$)** | $a_g$ **(g)** |
|---|---|---|---|
| Rubble stone | 0.021 | 19 | 0.132 |
| Roughly hewn stone | 0.036 | 20 | 0.217 |
| Split stone | 0.054 | 21 | 0.312 |
| Irregular soft stone (tuff, calcarenite, etc.) | 0.029 | 16 | 0.209 |
| Regular soft stone (tuff, calcarenite, etc.) | 0.050 | 16 | 0.362 |
| Ashlar stone | 0.0875 | 22 | 0.486 |
| Solid bricks and lime mortar | 0.075 | 18 | 0.493 |
| Semi solid bricks and cement mortar | 0.104 | 15 | 0.792 |

Table 4. Limit ground acceleration with respect to various masonry typologies

As shown in Table 4, masonry typologies of better quality can withstand impulsive actions corresponding to higher ground accelerations. In case of rubble stone masonry local damage in the structural node can occur for ground acceleration higher than 0.132 g. Instead, in case of ashlar masonry o brick masonry this type of failure is unlikely to occur since very high ground accelerations would be required (around 0.490 g).

Rubble, roughly hewn or split stone are the masonry typologies that require particular attention as far as regard the strengthening of structural nodes. After all, these are also the masonry typologies that most frequently need interventions, such as grout injections and/or reinforced plaster. Therefore, the additional strengthening elements proposed in the present work would be mainly applied to these types of masonry.

**STRENGTHENING THROUGH TRANSVERSAL AND BENT ELEMENTS**

For the intervention with bent elements along with transversal elements we refer to the formulation given in section 3.2. On top of the data already given for the example, let us consider: α = 63.43°, sen α = 0.894, cos α = 0.447, tg α = 2 (Figure 19).

The tensile force verification in the bent bar is expressed by:

$$A_{min} = \frac{\frac{F_X}{4\cos\alpha}+\frac{F_Z}{\text{sen}\,\alpha}}{f_{yd}} = \frac{\frac{5280}{4\cdot 0.447}+\frac{21030}{0.894}}{391} = \frac{2953+23523}{391} = \frac{26476}{391} = 68\ mm^2 \quad (35)$$

Let us consider the placement of φ14 bent rebars (section *154 mm²*) with spacing between elements with same bending direction equal to *1400 mm*. The effective section must be corrected by the factor *1000/1400=0.7*. Ultimately the tensile stress due to impulsive actions is given by:

$$\sigma = \frac{26476}{154\cdot 0.7} = 246\ N/mm^2 \quad (36)$$

Thus, the safety verification is satisfied with a safety factor equal to 391/246 = 1.59.

Consider insertion of φ14 transversal rebars placed according to a quincunx layout with spacing equal to 1000 mm. The tensile stress they should resist is given by:

$$N = \frac{F_X}{4} + \frac{F_Z}{\text{tg}\,\alpha} = \frac{5280}{4} + \frac{21030}{2} = 11835\ N \quad (37)$$

$$\sigma = \frac{11835}{(1000\cdot 1600)/(1000\cdot 1000)\cdot 154} = 48\ N/mm^2 \quad (38)$$

Therefore, the transversal tensile elements are subjected to a significant lower stress compared to the case without bent elements (211 N/mm$^2$).

A remark about the different structural behavior achieved through the two proposed interventions is required. The transversal elements by themselves can counteract the jerk impulsive actions. However, the bent elements may ensure structural continuity of reinforced plaster in correspondence of the floor-to-wall connection, an aspect which is generally neglected, particularly in the connection between floors and load-bearing internal walls. The discontinuity of the reinforced plaster at the intrados and extrados of floors may in fact be the cause of local vulnerability.

Ultimately, as far as regards the compression verification of masonry strengthened through reinforced plaster, the compressive strength is evaluated according to technical Standards (NTC2018) applying an amplification factor equal to 2.5: $f_m = 2.5\cdot 1.5 = 3.75$ N/mm$^2$, then, considering a confidence factor CF = 1.2, $f_d = 3.75/1.2 = 3.125$ N/mm$^2$.

In the case under examination, the local mass affected by local impulsive actions is assumed to have a depth of 1000 mm. However, conservatively we consider that the strut will form in correspondence of the truss. Its cross section is assumed to be equal to b · μs, with coefficient of thickness reduction μ that can be assumed equal to 0.2. Therefore, the strut cross section is equal to $A_p = 1000 \cdot 0.2 \cdot 400 = 80000$ mm$^2$. Thus, the compressive stress in the strut is given by:

$$\sigma_j = \frac{\frac{F_X}{2\cos\alpha}}{A_p} = \frac{\frac{5280}{2\cdot 0.447}}{80000} = 0.07\ N/mm^2 \quad (39)$$

It corresponds to a small fraction of masonry compressive strength (0.07 / 3.125 = 2%); therefore, it is reasonable to assume that masonry can act as strut in the truss-type behavior. This proves that, under the effects of impulsive forces, masonry itself, strengthened with

reinforced plaster, can resist the additional compressive stress. Instead, the proposed strengthening elements counteract the jerk effects by providing additional tensile strength.

## 5 CONCLUSIONS

In existing masonry buildings, the design of strengthening interventions, both in case of repair or prevention, must ensure the proper connection of the floors to the load-bearing walls. However, this may not be sufficient to avoid local damages under jerk impulsive effects, with potential loss of robustness and trigger of progressive chaotic collapses, particularly fearsome in case of ruble stone masonry with poor quality mortar.

Therefore, the equilibrium and the resistance of floor-to-wall connections must also be assessed in relation to the continuous acceleration variation, which can generate local impulsive actions significantly higher than static and seismic inertial actions, with consequent stress concentrations and potential masonry disaggregation.

Confinement of masonry and insertion of tensile resistant elements aimed to absorb the impulsive stresses are necessary. Additional transversal tensile elements represent a natural extension of the reinforced plaster intervention, both in case of traditional and innovative techniques.

With the addition of bent tensile elements the continuity of the reinforced plaster in correspondence of structural nodes can be ensured, an aspect which is generally neglected, particularly in the connection between floor and load-bearing internal walls. The discontinuity of the reinforced plaster at the intrados and extrados of floors may in fact be the cause of local vulnerability.

## ACKNOWLEDGEMENTS

The authors appreciate the support of colleagues and collaborators that contributed to this research. They would like to thank Luca Ranocchia, Alessia Travanti and Nicola Pero Nullo for the composition and drawing of the construction details; Fulvio Massimo Mariani for the selection of records on ITACA database; Alessio Francioso for the elaborations of Fourier spectra and his support in the revision of this article. They also wish to thank Aedes Software for the software Seismic3D developed by Francesco Pugi as part of applied research activities.

## REFERENCES

[1] M. Mariani, F. Pugi, Jerk: effetti delle azioni sismiche impulsive e crisi locali nelle strutture in muratura, Ingenio, 2020

[2] M. Mariani, F. Pugi, Effects of Impulsive Actions Due to Seismic Jerk and Local Failures in Masonry Structures, Eurodyn 2020, Athens, Greece, 23–26 November 2020

[3] M. Tong, G.Q. Wang, G.C. Lee, Time derivative of earthquake acceleration, Earthquake Engineering and Engineering Vibration, Vol. 4, No. 1, 1-16, June, 2005.

[4] M. Mariani, F. Pugi, A. Francioso, Sisma verticale: modellazione e analisi in ambito professionale sugli edifici esistenti in muratura, Ingenio, 01.10.2018

[5] N. Chieffo, A. Formisano, P. Lourenco: Seismic vulnerability procedures for historical masonry structural aggregates: Analysis of the historical centre of Castelpoto (South Italy), Structures 48 (2023), 852-866.

[6] E.M. Rathje, N.A. Abrahamson, J.D. Bray, Simplified frequency content estimates of earthquake ground motions, J. Geotech. Geoenviron. Eng., 124(2), 150-159, 1998.

[7] V. Vukobratovic: The influence of jerk on the seismic responses of rigid linear elastic and nonlinear sdof systems, April 2022. Conference: 19th International Symposium of MASEAt: Ohrid, North Macedonia.

[8] V. Vukobratovic, S. Ruggieri: Jerk in Earthquake Engineering: State-of-the-Art, Buildings 2022, 12, 1123.

[9] C. Sansoni, Luís C.M. da Silva, R. Marques, S. Pampanin, Paulo B. Lourenço: SLaMA-URM method for the seismic vulnerability assessment of UnReinforced Masonry structures: Formulation and validation for a substructure, Journal of Building Engineering, Volume 63, Part A, 2023, 105487, ISSN 2352-7102,

[10] Haoxiang He, Ruifeng Li, Kui Chen: Characteristics of Jerk Response Spectra for Elastic and Inelastic Systems, Shock and Vibration, Vol. 2015, Article ID 782748.

COMPDYN 2023
9th ECCOMAS Thematic Conference on
Computational Methods in Structural Dynamics and Earthquake Engineering
M. Papadrakakis, M. Fragiadakis (eds.)
Athens, Greece, 12-14 June 2023

# RESILIENCE ASSESSMENT OF ROAD BRIDGES IN MULTI-HAZARD ENVIRONMENT

**Olga Markogiannaki[1], Anna Karatzetzou[1], Sotiria Stefanidou[1], Grigorios Tsinidis[2]**

[1] Postdoctoral Researcher, School of Civil Engineering, Aristotle University of Thessaloniki

Thessaloniki, Greece
e-mail: markogiannaki.olga@gmail.com, {akaratze,ssotiria}@civil.auth.gr

[2] Assistant Professor, Department of Civil Engineering, University of Thessaly, Volos, Greece
gtsinidis@uth.gr

## Abstract

*Highway transportation networks play a vital role in today's economic and societal life and affect growth and employment. Hence, their undisrupted functionality and their quick recovery even after extreme natural hazard events are critical. To this end, resilience assessment of transportation networks against natural hazards is needed for decision-making processes in planning maintenance and retrofit actions, as well as for post-event risk management. This study aims to propose a multi-hazard resilience assessment framework for bridges that are the key components of transportation networks. The first step of the framework is the identification of critical hazards (i.e., earthquakes, floods) and the derivation of hazard curves and scenarios based on their probability of occurrence. The second step consists of a fragility assessment process based on computational analysis for single or multi-hazard occurrences given a range of hazard intensities. The third step includes the evaluation of functionality losses based on fragility assessment. In the fourth step, the required restoration time is estimated, and resilience metrics are calculated as dimensionless indicators. The proposed framework is applied to a case study riverine bridge, and comparative results on the single hazard and the multi-hazard resilience metrics are discussed. It has been observed that the effect of the consideration of multi-hazard scenarios is significant on the resilience of bridges.*

**Keywords:** bridges, seismic hazard, flood hazard, resilience

# 1 INTRODUCTION

Multi-hazard resilience is a critical aspect of infrastructure design and management, especially in regions that are prone to natural disasters. Infrastructure assets are vulnerable to a variety of hazards, such as earthquakes, floods, hurricanes, landslides, and wildfires, which can cause severe damage, disrupt operations, and lead to economic losses [1]. Therefore, ensuring that infrastructure systems are resilient to multiple hazards is crucial for maintaining the safety, reliability, and functionality of these assets. The concept of multi-hazard resilience goes beyond the traditional approach of designing for a single hazard and considers the interdependencies and cascading effects that can occur when multiple hazards affect an infrastructure system. For example, a flood can cause damage to transportation networks, disrupt power supply, and contaminate water resources, which can in turn lead to further cascading effects. Hence, multi-hazard resilience, requires a holistic approach that considers the complex interactions among hazards, infrastructure assets, and the environment. Infrastructure systems that are resilient to multiple hazards have several benefits. They can withstand the impacts of disasters, minimize downtime, reduce damage and associated losses, and ensure the continuity of essential services. Additionally, multi-hazard resilience can help enhance social, economic, and environmental sustainability by improving the overall performance and efficiency of infrastructure assets.

In this context, it is critical to integrate resilience assessment into decision-making systems to support transportation network stakeholders in their strategic planning against natural hazards. For this reason, it is needed to provide appropriate metrics to quantify the capacity of civil engineering assets to “bounce back” from extreme events.

To facilitate the quantification of resilience considering various aspects, several methodological approaches have been developed. Cimellaro (2016) [2] provides a comprehensive overview of resilience indicators, e.g. indices, scorecards, tools and models, and their role in evaluating the resilience of different systems against natural and man-made hazards. Alipour and Shafei (2016) [3] presented the concept of resilience curves (time-functionality) and their use in quantifying the resilience of infrastructure systems against natural and man-made hazards. Numerous works focus on evaluating resilience against single hazard events. Deco et al (2013) [4] argue that traditional deterministic approaches for assessing seismic resilience are often limited by their reliance on simplified models and assumptions, which can lead to inaccurate predictions. The use of a probabilistic approach, such as the one presented in their paper, offers a more comprehensive and realistic way of modeling the complex uncertainties involved in seismic resilience. Capacci, Biondini, and Titi (2016) [5] also proposed a methodology to assess the seismic resilience of transportation networks. In recent years, the development of multi-hazard resilience strategies has become more popular since there has been a growing recognition that hazards can occur simultaneously or sequentially. Argyroudis et al (2020) [6] proposed a resilience assessment framework for critical infrastructure in a multi-hazard environment, with a specific focus on transport assets, including both quantitative and qualitative measures providing a detailed explanation of the framework, which includes four stages: (1) hazard analysis, (2) system analysis, (3) resilience assessment, and (4) resilience enhancement. The hazard analysis stage involves the identification and characterization of relevant hazards, while the system analysis stage involves the identification and modeling of the critical infrastructure system and its interdependencies. Most methodologies consider earthquake and flood hazards as the most critical ones for transportation assets and especially for bridges.

In line with the above, this study proposes a holistic methodology for the resilience assessment of assets of transport networks, which includes four distinct steps. The methodology

may be applied in case of single natural hazards (separated in time) or combined hazards in a multiple-hazard environment, regardless of the interaction scenario and the hazard sequence (flood followed by an earthquake and vice versa, successive flood or earthquake events) and it is presented for the assessment of bridges (as one of the most important assets of transportation networks) The novelty of the methodology lies in the consideration of the effect of cumulative damage of the examined transportation asset caused by subsequent and unrelated natural hazards, on the resilience assessment of the asset. This is done by employing fragility functions that were developed for multi-hazard scenarios. In this paper, the proposed methodology is applied to a reinforced concrete bridge and the results for various hazard scenarios are presented.

## 2 DESCRIPTION OF THE RESILIENCE ASSESSMENT METHODOLOGY

The methodology consists of four steps that are summarized in Figure 1 and presented below. It is acknowledged that due to the diversity of hazards and their combinations, it would be impractical to describe every possible hazard scenario. However, the proposed framework aims to be comprehensive and representative by including several critical hazard scenarios that cover a wide range of potential events in a multi-hazard environment.

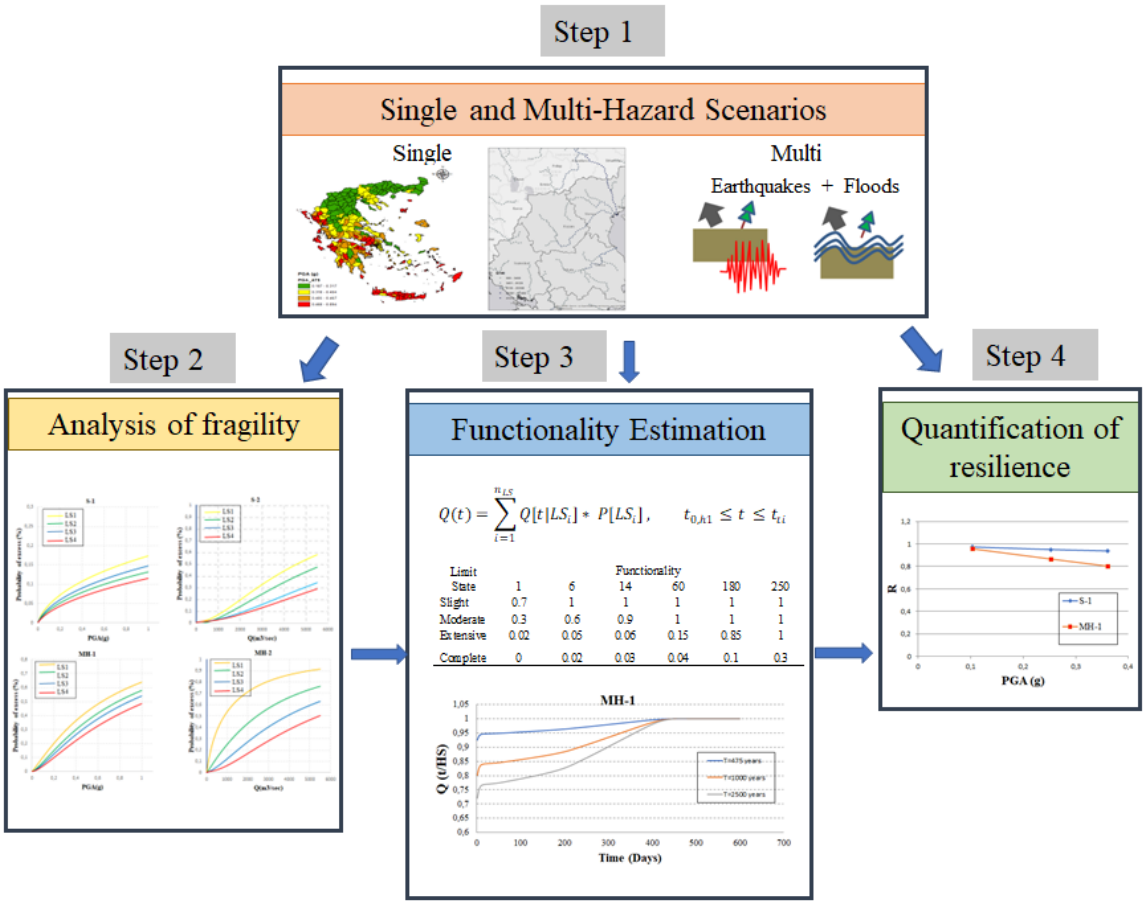


Figure 1: Multi-hazard Resilience Framework for road network components.

First step: Single and Multi-Hazard Scenarios

The purpose of this step is i) to identify the critical natural hazards that may occur at the location of the asset (location of interest) and ii) develop for these natural hazards appropriate single and multiple hazard models that will be taken into consideration in resilience assessment.

In this study, seismic and flood hazards are selected as the most critical natural hazards for the assessment of critical elements (i.e., bridges) of roadway networks in Greece [7].

For each critical hazard, appropriate intensity measures (IM) are defined accounting basically on their computability/availability and to some extent their effectiveness, efficiency, sufficiency and robustness. In seismic events, the Peak Ground Acceleration (PGA) or the Peak Ground Velocity (PGV) at ground surface may be used as adequate intensity measures to associate seismic hazard to structural damage. Accordingly, discharge (Q) can be used as the intensity measure for the assessment against flood hazard. After a literature review performed in the framework of INFRARES, Peak Ground Acceleration (PGA) is selected since this metric is used as intensity measure by the majority of studies proposing fragility functions for the assessment of bridges and tunnels.

In addition to the selection of an appropriate IM for each natural hazard, different scenarios with various return periods of the examined hazards should also be defined. These values could be derived from existing hazard maps, curves, or site-specific hazard analyses. Hazard analysis provides the probability of exceeding a specified level of demand in a given exposure period. Therefore, when hazard scenarios are considered in the analysis the occurrence probability is associated with specific return periods. Herein, each natural hazard is studied either separately or as a combination of the two hazards. In the framework of the multi-hazard assessment approach adopted herein, diverse natural hazards scenarios, as well as combined hazard scenarios are carefully selected and prioritized based on the potential to cause damage on the examined asset(s). It should be outlined that the present methodology accounts only for independent multi-hazard events that occur subsequently in time. The hazard assessment approach used in this study is presented in detail in [7].

Second step: Analysis of fragility

Fragility analysis is based on numerical analysis of a refined finite element model of the structure, conducted either for a single natural hazard or a multi-hazard occurrence for a given range of hazard(s) intensities. The approach employed herein is presented in detail in [8] whereas a short summary is presented in the following. The main core of the methodology is the same, regardless of the hazard considered. The critical components of the examined asset (e.g., bridge) are initially identified, and their capacity and limit state thresholds are estimated. An Engineering Demand Parameter (EDP) is selected for every component and damage is quantified based on the component's capacity curve, estimated on the basis of inelastic pushover analysis. The demand estimation at the component level is related to the hazard considered. Seismic analysis (i.e., dynamic analysis) is performed for selected earthquake ground motions and flood analysis (i.e., static analysis) is performed for selected discharge values, calculating the demand at control points of the selected components of the asset. To quantify

the uncertainties in capacity and demand, random variables for the material and modelling properties are considered (distribution, mean and dispersion values) and samples are generated, using the Latin Hypercube Sampling method. Multiple analyses are performed for the estimation of capacity and demand and the derivation of fragility curves according to Equation 1.

$$P[D \geq d|IM] = 1 - \Phi\left(\frac{ln(D)-ln(\theta_i)}{\beta_{tot|IM}}\right) \quad (1)$$

Where $P[.]$ is the conditional probability that the component will be damaged to damage state ith or a more severe damage state as a function of demand parameter, D, $\Phi$ denotes the standard normal (Gaussian) cumulative distribution function, $\theta_i$ denotes the median value of the probability distribution, and $\beta_{tot|IM}$ denotes the logarithmic standard deviation.

For the derivation of bridge system fragility curves ($P(F_{system})$), fragility of all critical components is considered ($P(F_i)$) and Equation 2 is applied (upper and lower bound) [9].

$$^{i=1}_{n}max[P(F_i)] \leq P(F_{system}) \leq 1 - \prod_{i=1}^{\pi}[1 - P(F_i)] \quad (2)$$

For the fragility assessment against multiple natural hazards, i.e., seismic and flood hazards, the same methodology is performed. Several scenarios of uncorrelated and different (separated in time) hazard events can be developed for the derivation of system fragility functions. It should be outlined that the events are applied subsequently and, therefore, cumulative damage is considered in all examined multi-hazard scenarios

Third step: Functionality Estimation

Functionality is estimated after an extreme event or at different time steps during the retrofit/restoration phase of the structure under study. The evaluation of functionality is based on the fragility assessment and is derived by Equation 3 [10].

$$Q(t|HS) = \sum_{i=1}^{n_{LS}} Q[t|LS_i] * P[LS_i|HS], \qquad t_{0,h1} \leq t \leq t_{ti} \quad (3)$$

Where $Q(t|HS)$ is the functionality level at time t for a selected hazard scenario (HS) (multi/single), $n_{LS}$ is the number of limit states used in fragility analysis, $Q[t|LS_i]$ is the functionality level at time t for the limit state $LS_i$, $P[LS_i]$ is the probability to be in this limit state as derived from the fragility curves $t_{ti}$ is the time in the restoration process that is investigated, $t_{0,h1}$ is the time that the hazard occurs (single or multi-hazard).

Unfortunately, restoration functions for critical assets of transportation networks (e.g., tunnels and bridges) are rarely available in the literature.

. Due to this lack of data, the FEMA restoration functions [11] are used in the proposed framework. To represent more accurately the local conditions in Greece based a multiplication factor was applied to FEMA values based on expert judgment. In Table 1 the restoration time for bridges is presented. When multi-hazard scenarios are considered, regarding the subsequent events, it is assumed that no restoration has started after the first hazard event (assum-

ing that the events have limited time difference). Therefore, the same restoration times are also applied for the multi-hazard scenarios.

| Limit State | Functionality | | | | | |
|---|---|---|---|---|---|---|
| | 1 | 6 | 14 | 60 | 180 | 250 |
| Slight | 0.7 | 1 | 1 | 1 | 1 | 1 |
| Moderate | 0.3 | 0.6 | 0.9 | 1 | 1 | 1 |
| Extensive | 0.02 | 0.05 | 0.06 | 0.15 | 0.85 | 1 |
| Complete | 0 | 0.02 | 0.03 | 0.04 | 0.1 | 0.3 |

Table 1: Restoration functions for Bridges in Greece

Fourth step: Quantification of resilience

In this final step, the results of the fragility assessment, the functionality losses, the estimated duration for repairs and the recovery process to restore functionality are combined to quantify the resilience of the bridge against single or multi-hazard scenarios.

More specifically, the resilience metric R is calculated based on Equation 4 [10].

$$R = \frac{\int_{t_{o,h1}}^{t_{ti}} Q(t)}{t_{ti} - t_{o,h1}} \tag{4}$$

Where R is the resilience index, $t_{ti}$ is the time in the restoration process that is investigated, $t_{0,h1}$ is the time that the hazard occurs (single or multi-hazard ) and $Q(t)$ is the functionality level at the time t.

## 3 CASE STUDY

### 3.1 Description of the case study bridge

The selected bridge is the Vardarovasi river bridge at the Thessaloniki-Giannitsa National Road Greece which was constructed in 1985. The case study is a typical river bridge with a deck of precast/prestressed beams, simply supported on three multicolumn piers with two cylindrical columns of diameter d =1.3 m each. The piers are founded on soil class C (according to Eurocode 8 [12]) by means of pile foundations, comprised of four reinforced concrete piles (length, l =33m, diameter d =1.0m) (Figure 2). The finite element model of the bridge was developed in Opensees [13]. Further details on the bridge simulation can be found in [8].

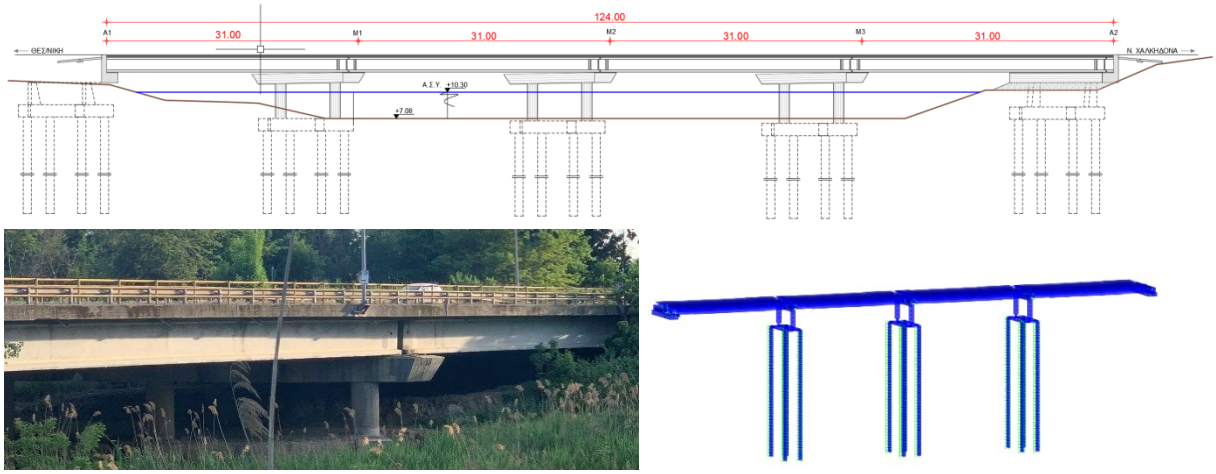


Figure 2: Drawings and 3D Model of the simply supported river bridge with prestressed/precast beam deck and multicolumn piers (Vardarovasi bridge).

### 3.2 Hazard Analysis

In the frame of the selected case study bridge, specific hazard scenarios are selected [7]. Table 2 depicts the potential hazard scenarios that are considered in a multi-hazard environment. More specifically, S-1 is a single earthquake event, S-2 is a single flood event, MH-1 are two subsequent events that are a flood followed by an earthquake event, MH-2 are two subsequent events that are an earthquake followed by a flood event, MH-3 are two subsequent flood events (i.e. flood event also considering for scour at bridge piers owning to previous flood event (3m scour)) and 4. a flood event also considering for scour at bridge piers owning to previous flood event (3m scour)) and an earthquake event have been considered.

| Hazard Scenarios | Event Combination |
|---|---|
| S-1 (Single) | Earthquake |
| S-2 (Single) | Flood |
| MH-1 (Multi) | Flood + Earthquake |
| MH-2 (Multi) | Earthquake + Flood |
| MH-3 (Multi) | Flood + Flood |

Table 2: Multi-hazard scenarios for earthquakes and floods

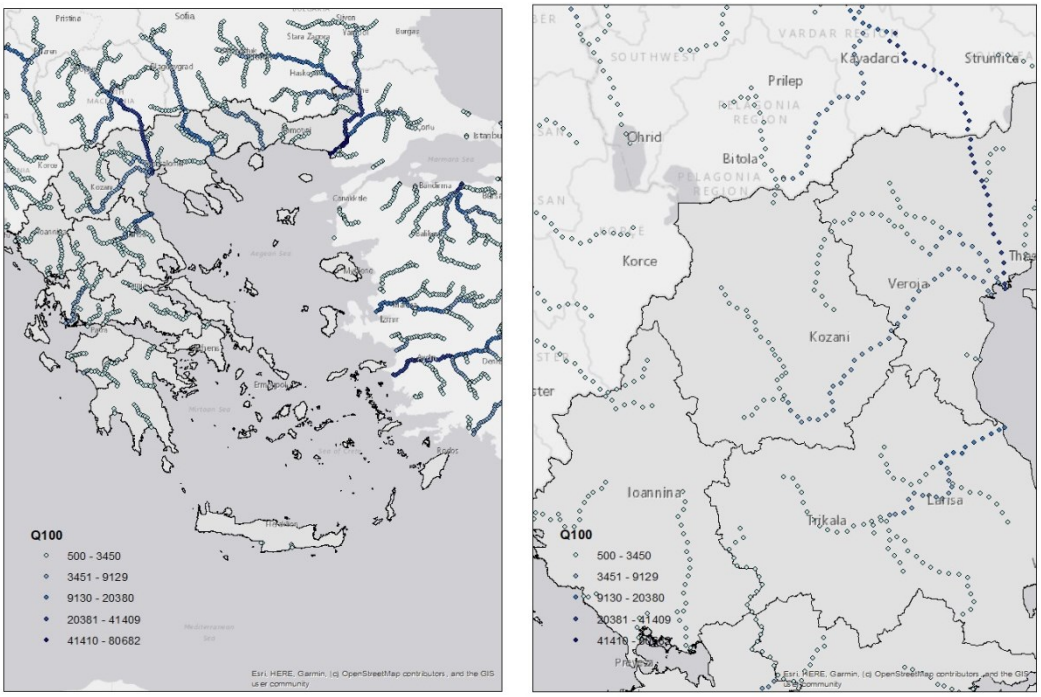


Figure 3: Flooding discharge Q values for T=100 years in a) Greece b) focus area

Regarding earthquake events, three return periods, T= 475 years, T=1000 years and T=2500 years were considered. For flooding events, the discharge values for a 100-year return period was investigated. In Figure 3, single hazard maps for the selected discharge in Greece and the investigated territory are shown.The corresponding values IM values for the selected return periods both for seismic and flooding events are presented in Table 3.

| IM | Return Period | Value |
|---|---|---|
| PGA | 475 | 0.103 g |
| PGA | 1000 | 0.252 g |
| PGA | 2500 | 0.36 g |
| Q | 100 | 4800 $m^3/s$ |

Table 3: IM values and their corresponding return periods

### 3.3 Fragility Analysis

The fragility curves of the bridge for the selected hazard scenarios were derived following the methodology presented in section 2. The development of the fragility curves is the basis for deriving the resilience metrics.

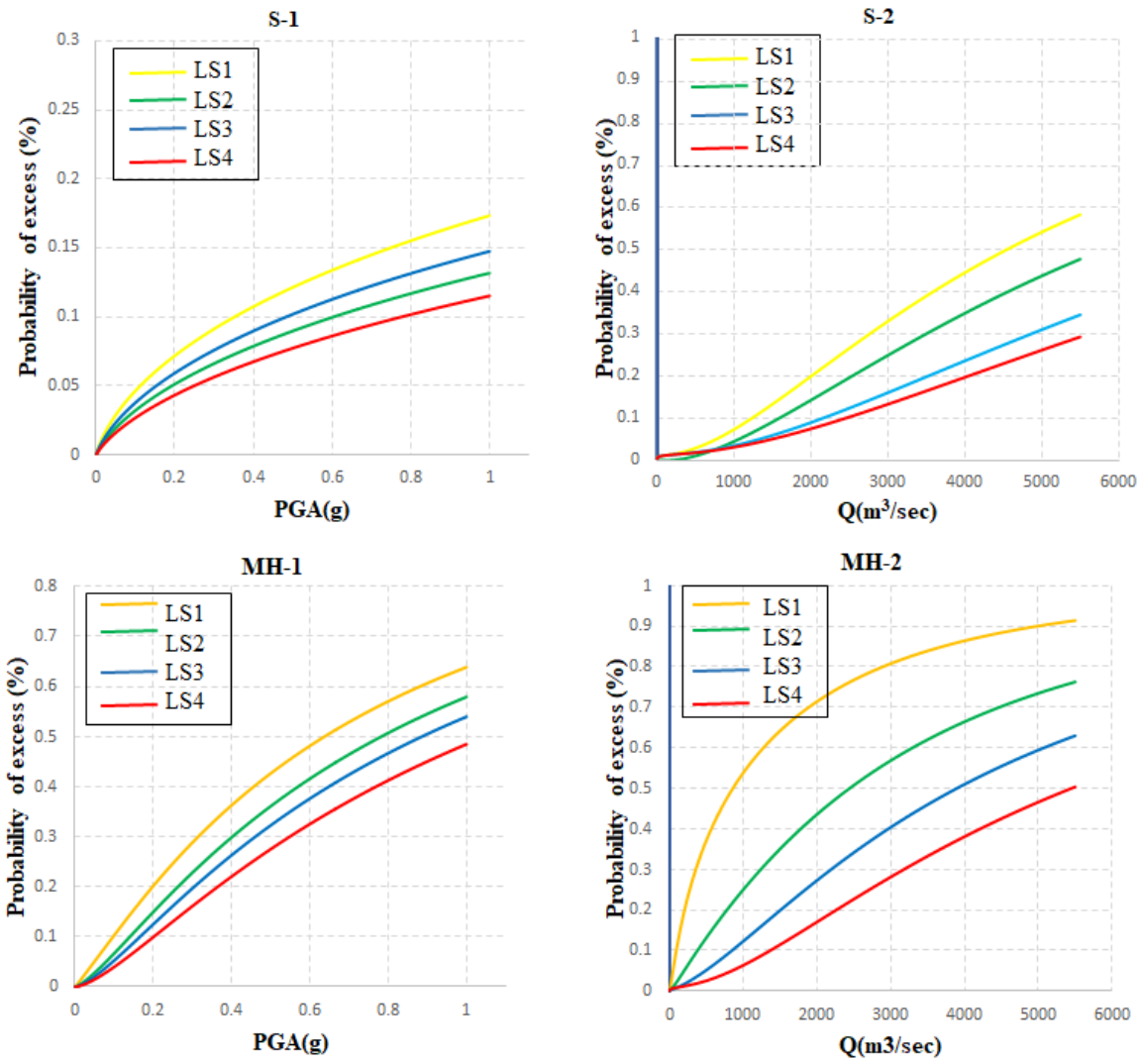


Figure 4: Fragility curves for Vardarovasi Bridge

To account for multi-hazard scenarios it is necessary to use the corresponding fragility curves that account for cumulative damage. Based on the elected multi-hazard scenarios as shown in Table 2, fragility analysis was performed. To assess seismic fragility, the y-direction was used to develop the fragility curves of the bridge system as it is more critical for the case study bridge. The occurrence of a flood prior to another hazard event is simulated as a 3m scour on the bridge foundation. In Figure 4, four of the derived fragility curves are presented, [8].

### 3.4 Restoration models

Based on the methodology described in section 2, the restoration models are developed as they are critical to perform resilience analysis. Immediately after the event occurrence, the functionality of the bridge is 70% for slight damage, 30% for moderate damage, and 2% for extensive damage and 0% for collapse. As recovery time increases the bridge functionality increases gradually. According to Table 1, the recovery of the bridge functionality is achieved

in about 6, 60, and 250 days for slight, moderate and extensive damage, respectively. In Figure 5, the restoration model for a single earthquake event and for a multi-hazard scenario, i.e. a flood event followed by an earthquake is depicted. It is evident that the functionality losses are larger during the recovery process after two subsequent events than after a single seismic event and that the post-event immediate residual functionality Q (t =0 day) of the bridge decreases significantly as the seismic intensity level increases for both single and multi-hazard scenarios.

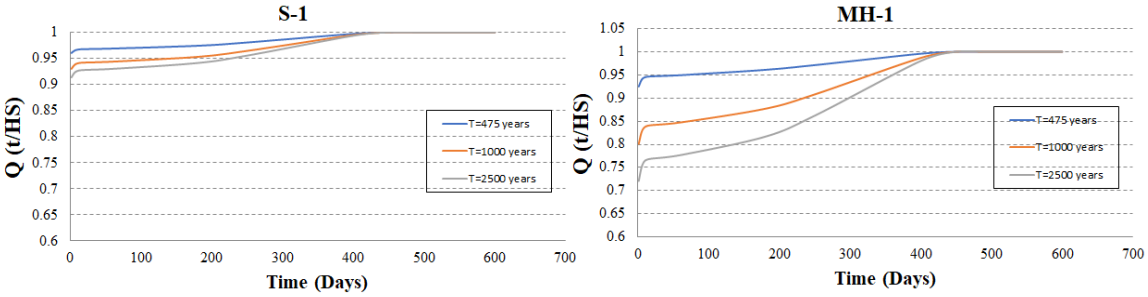


Figure 5: Restoration Models for Vardarovasi Bridge

### 3.5 Resilience Assessment

Resilience indices for the selected hazard scenarios are produced by utilizing the overarching framework depicted in Figure 1, along with the fragility and restoration models presented in sections 3.3 and 3.4. It is important to mention that the time frame $t_{ohi}$- $t_i$ in Equations (3)-(4) signifies the timeframe during which the assessment of resilience is conducted. This time frame enables the comparison of R values across different assets and/or various hazard scenarios. Typically, the maximum restoration time of the examined assets is considered to determine $t_i$. For the purposes of this paper, the resilience index is calculated with $t_i$ representing the recovery time for extensive damage which amounts to 250 days. More specifically, the fragility curves were used in the resilience analysis to determine the probability of occurrence of each damage state for the single and multi-hazard scenarios (see section 3.2). The functionality of the case study bridge was then computed for each damage state using the restoration model presented in Table 1. Figure 6 shows the R metric of the Vardarovasi Bridge for three shaking level intensities in the case of a single earthquake event compared to the corresponding intensities of the MH-1 scenario. It can be observed that the slope of the R trend line is higher for the MH-1 scenario which depicts the negative effect of the occurrence of subsequent events on the resilience of the bridge. In particular, the resilience metric R of the bridge is 20% lower in the MH-1 scenario compared to the S-1 for the PGA equal to 0.36g.

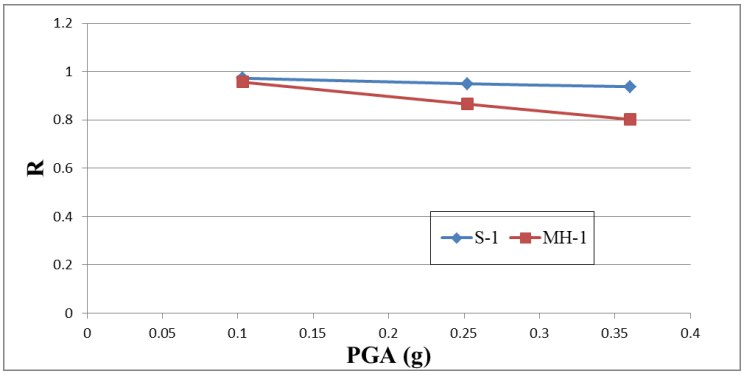


Figure 6: Resilience analysis for earthquake scenarios

In Figure 7, the resilience metrics R for S-2, MH-1 and MH-2 scenarios are presented. These scenarios correspond to T=100 years as the return period of the flood discharge Q for the single and the multi-hazard scenarios, respectively. The R values indicate that the differences on the computed resilience can become more than 50% lower in a multi-hazard environment.

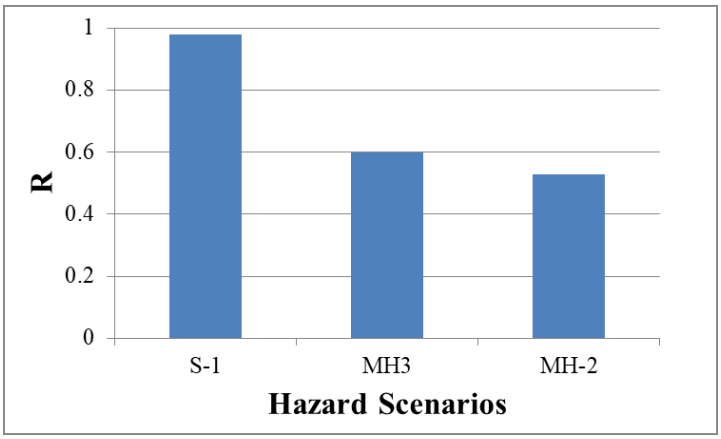


Figure 7: Resilience metric for discharge Q (T100)

## 4 CONCLUSIONS

The present study proposes a multi-hazard resilience assessment framework for key assets of transportation networks, focusing on bridges. The methodology includes the following steps: i. hazard analysis, ii. fragility assessment based on numerical analysis of the examined structures/assets against single or multi-hazard scenarios and for a range of hazard intensities, iii. evaluation of functionality level and iv. quantification of resilience metrics as dimensionless indicators of resilience. The proposed framework was applied to a riverine bridge. Regarding earthquake events, it has been observed that the post-event immediate residual functionality Q (t =0 day) of the bridge decreases significantly as the seismic intensity level increases. In particular, especially in the multi-hazard scenario the bridge functionality losses are more than 20% higher for the 2500 years return period than for the 475 years return period. Moreover, the bridge functionality losses are larger during the recovery process after two subsequent events than after a single seismic event. The difference between the functionality level values is more evident when the high seismicity level is considered. Regarding flooding

scenarios, the computed resilience metrics show that the bridge resilience is significantly lower when multi-hazard scenarios are taken into account than that considering only a single flood event occurrence. More specifically, the R metric becomes more than 50% lower in the case of a flood-flood scenario than that of a single flood event. Hence, the study highlights the significance of estimating resilience of bridges in a multi-hazard environment since the consideration of solely single events underestimates the effect

## ACKNOWLEDGEMENTS

The work reported in this paper was carried out in the framework of the research project INFRARES "*Towards resilient transportation infrastructure in a multi-hazard environment*" (https://www.infrares.gr/), funded by the Hellenic Foundation for Research and Innovation (HFRI) under the "2nd *Call for H.F.R.I. Research Projects to* support *Post-Doctoral Researchers*" (Project Number: 927).

## REFERENCES

[1] A. M. El-Maissi, S. A. Argyroudis and F. M. Nazri (2021). Vulnerability Assessment Methodologies for Roadway Assets and Networks: A State-of-the-Art Review. Sustainability, 13(1), 61; https://doi.org/10.3390/su13010061

[2] G. P. Cimellaro (2016). Resilience indicators. *Urban Resilience for Emergency Response and Recovery*, doi: 10.1007/978-3-319-30656-8_3

[3] A. Alipour, and B. Shafei (2016). Seismic Resilience of Transportation Networks with Deteriorating Components. Journal of Structural Engineering, 142(8):1–12. doi: 10.1061/(asce)st.1943-541x.0001399

[4] A. Decò, P. Bocchini, D.M. Frangopol (2013). A probabilistic approach for the prediction of seismic resilience of bridges. Earthquake Engineering and Structural Dynamics, 42(10), https://doi.org/10.1002/eqe.2282

[5] L. Capacci, F. Biondini and A. Titi. Seismic resilience of aging bridges and transportation networks. *Proceedings 8th International Conference on Bridge Maintenance, Safety and Management*, IABMAS 2016 (August 2019), 1129–1136, doi: 10.1201/9781315207681-172.

[6] S. A. Argyroudis, S. A. Mitoulis, L. Hofer, M. A. Zanini, E. Tubaldi, D. M. Frangopol (2020) Resilience assessment framework for critical infrastructure in a multi-hazard environment: Case study on transport assets. Science of The Total Environment, 714, https://doi.org/10.1016/j.scitotenv.2020.136854.

[7] A. Karatzetzou, S. Stefanidis, S. Stefanidou, G. Tsinidis, D. Pitilakis (2022). Unified hazard models for risk assessment of transportation networks in a multi-hazard environment. International Journal of Disaster Risk Reduction, 75, https://doi.org/10.1016/j.ijdrr.2022.102960.

[8] S. Stefanidou, A. Karatzetzou, G. Tsinidis, S. Mitoulis, S. Argyroudis, Multi-hazard fragility assessment of bridges: Methodology and case study application, *ICONHIC 2022,*

[9] Zhang, J., & Huo, Y. (2009). Evaluating effectiveness and optimum design of isolation devices for highway bridges using the fragility function method. Engineering Structures, 31(8), 1648–1660

[10] Z. Huang, D. Zhang, K. Pitilakis, G.Tsinidis, , Huang, H., Zhang, D. and et al. (2022) 'Resilience assessment of tunnels: Framework and application for tunnels in alluvial deposits exposed to seismic hazard'. Soil Dynamics and Earthquake Engineering, 162. pp. 1 - 13. ISSN: 0267-7261

[11] FEMA. Hazus 4.2 SP3: hazus earthquake model technical manual, *FEMA*, 2020

[12] CEN (2004). EN 1998-1 2004. Eurocode 8: Design of Structures for Earthquake Resistance.

[13] F. McKenna (1997). Object oriented finite element analysis: Frameworks for analysis algorithms and parallel computing. Ph.D. dissertation, University of California, Berkeley.

COMPDYN 2023
9th ECCOMAS Thematic Conference on
Computational Methods in Structural Dynamics and Earthquake Engineering
M. Papadrakakis, M. Fragiadakis (eds.)
Athens, Greece, 12-14 June 2023

# INFLUENCE OF CLADDING PANELS RETROFIT ON THE SEISMIC RISK OF AN EXISTING PRECAST BUILDING

**Marius Eteme Minkada, Marco Bosio, Andrea Belleri, Paolo Riva**

University of Bergamo
via Marconi 5, 24044, Dalmine, Bergamo, Italy
{marius.etememinkada, marco.bosio, andrea.belleri, paolo.riva}@unibg.it

## Abstract

*Recent research and past earthquakes have shown that precast industrial buildings built in Italy up to the 1980s are characterized by a considerable seismic risk, particularly considering inadequate connections between precast elements. It is therefore necessary to implement seismic retrofit interventions both at a local and global level to protect working activities and human lives.*
*In this work, the influence of local interventions, particularly of cladding panels, on the evolution of the seismic risk of a reference precast industrial building is assessed. The effects of the retrofitting interventions were verified by comparing the performance of the retrofitted structure with those of the structure in its current state, by means of multi stripe analyses, in terms of demand-capacity ratio associated with each element and each connection of the structural and non-structural system.*

**Keywords:** Precast Structures, Industrial Buildings, Seismic Risk

# 1 INTRODUCTION

Single-storey precast buildings represent the most common type of building in the industrial sector in Italy. Before the Ministerial Decree of 3 June 1981, the seismic classification of the Italian territory envisaged its subdivision into two categories: non-seismic zone and seismic zone. Nowadays, a large part of the heritage of precast industrial buildings in Italy is characterized by inadequate structural and non-structural details [1, 2, 3, 4, 5, 6, 7, 8, 9]. This leads to the inadequate seismic behavior observed during past seismic events [10, 11, 12, 13, 14, 15, 16, 17].

The seismic risk associated with one-storey existing precast buildings has been studied in various works [18, 19, 20, 21, 15]. The results obtained confirm the need to implement retrofit interventions to protect working activities and human lives. The Italian building code defines three classes of interventions on buildings: local interventions, improvement interventions, full-adequacy intervention. In the context of industrial buildings, it is important to note that local interventions are preferred over the global retrofit (improvement and full-adequacy interventions) which would require the temporary closure of the industrial activity. For local interventions the code allows the safety check to be performed by referring only to the parts and/or elements affected by the intervention. However, it is interesting to question the effect of local reinforcement interventions on the seismic risk of the entire building.

The aim of this paper is to evaluate the influence of local strengthening interventions on the evolution of the seismic risk of a precast industrial building. For this purpose, the effect of the adjustment of the connections between the external RC cladding panels and the main structural elements of a case study building is studied. Response spectrum analysis was carried out to determine the safety level of the building in its current state. The effects of the retrofitting interventions were verified by means of multi stripe analyses in Opensees [22] and the results are presented as demand-capacity ratio (*D/C*).

# 2 REFERENCE BUILDING

The reference building (Figure 1) was derived from a previous research work [21]. It is a single-storey building built in the 80s in the municipality of L'Aquila (Italy). The structural details reflect the design criteria established by the standards of the time in seismic area [23].

## 2.1 Description of the reference building

The vertical bearing structure is made up of 16 precast columns. A double tapered beam with a net span equal to 20m is placed onto the top of each pair of columns, housed inside RC forks; the portal-to-portal distance is 6m. The secondary roof system is made by double-tee roof elements. The cladding is made by horizontally and vertically spanning RC panels arranged along the longitudinal and transverse directions, respectively.

The columns have a square cross-section 50cm x 50cm with 4+4 Φ14 longitudinal rebars and Φ 8 stirrups placed every 200mm. The horizontal cladding panels are connected to the columns by two bearing connections at the bottom of the panel (a bearing bolt laying on a steel bracket) and two retaining hammer-head anchor bolts at the top [11, 12]. The vertical cladding panels are connected to the beam by a hammer-head stripe connection [12, 24].

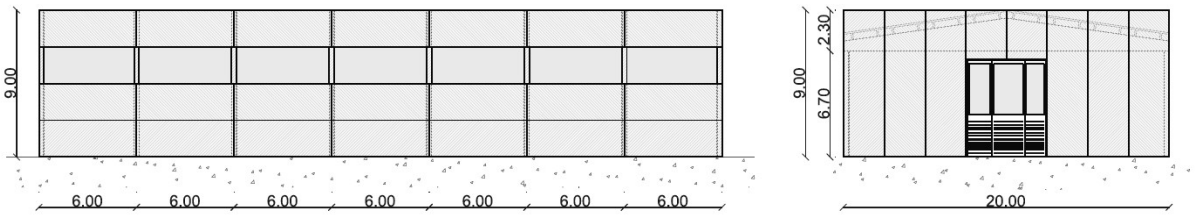


Figure 1: Longitudinal and transverse view of the reference building.

## 2.2 Level of safety in the as-is condition

The level of safety in the as-is condition was assessed in accordance with Italian technical standards [26] through the coefficient $\zeta_E$, defined as the ratio between the actual capacity and the demand required in the design of a new construction with the same characteristics. The value of $\zeta_E$ was evaluated for the columns, the roof element-to-beam connections and the cladding panels-to-structure connections. The demand was assessed through a modal response spectrum analysis. The main characteristics of the adopted finite element model are reported in Figure 2.

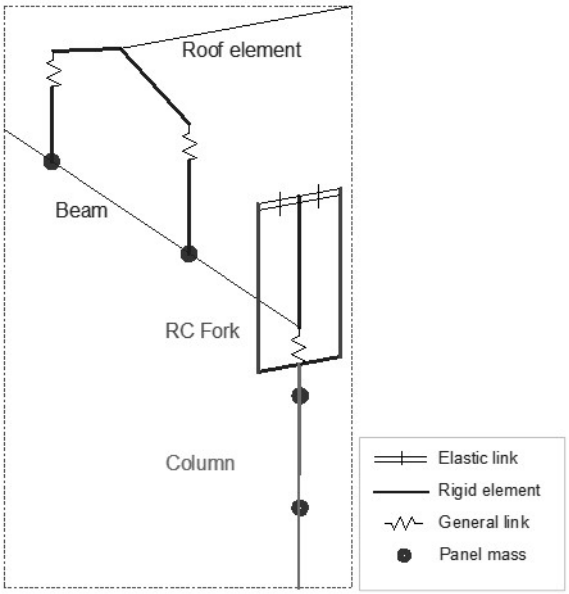


Figure 2: Modeling scheme for the finite element model used in the response spectrum analyses (MidasGen [26])

The main structural elements were modeled using beam type elements while the cladding panels were modeled only in terms of mass in correspondence with their connections with the main structural elements. To account for the cracking in the columns, a stiffness reduction factor equal to 0.27 was calculated as the ratio between the flexural stiffness at yield and the gross stiffness. As for constraints, the columns are fixed at the base while the roof element-to-beam and beam-to-column connections have been modeled using lumped springs ("general link") with a stiffness equal to 20'000 kN/m [27] and 64'000 kN/m [28], respectively. To capture the force on the RC fork, the "elastic link" type was inserted between the beam and the RC fork. The design spectrum in acceleration was defined with a behavior factor ($q$) equal to 1.5, assuming the topographic category $T_1$ and soil type C [25].

In determining the $\zeta_E$ coefficients, the demand at the roof element-to-beam connections was increased by 30% and for fragile mechanisms (e.g., shear failure), a safety factor of 1.25 was used [25]. The results (Table 1) highlight the deficiencies of the connections between the

panels and the main structure with a safety coefficient $\zeta_E$ equal to 16% and 41% for the vertical and horizontal panels respectively. For the roof element-to-beam connections and columns the coefficient $\zeta_E$ is respectively 92% and 53%.

| | $\zeta_E$ | | Demand | | |
|---|---|---|---|---|---|
| **Connection** | $F_{,X}$ | $F_{,Y}$ | $F_{,X}$ (kN) | | $F_{,Y}$ (kN) |
| Roof element - Beam | 0.92 | 5.31 | 45.22 | | 7.82 |
| | | | $F_{,X}$ (kN) | $F_a$ (kN) | d (m) |
| Panel – Column horizontal cladding | 2.52 | 0.41 | 6.52 | 2.38 | 0.064 |
| Panel-to-Beam Vertical Cladding | 0.67 | 0.16 | 7.30 | 2.93 | 0.160 |
| **Element** | Bending | Shear | Bending (kNm) | | Shear (kN) |
| Column | 0.53 | 1.10 | 344.20 | | 57.70 |

Table 1: Current levels of safety and demand in terms of force (from analysis: $F_{x/y}$; analytically: $F_a$) and displacement. Notes: x and y indicate the longitudinal and transverse direction, respectively.

## 3 RETROFIT MEASURES AND NON-LINEAR MODELING

In this section the retrofit measures selected for the local retrofit of cladding panels are presented. The selected retrofit consists of placing additional steel brackets (two at the bottom and two slotted brackets at the top) between each horizontal panel and the columns and one slotted bracket between each vertical panel and the beam.

The two-steel brackets at the bottom of the horizontal cladding panels are designed to carry the entire weight of the panel while the steel brackets arranged at the top of the panels (vertical and horizontal) are designed to counteract the overturning mechanism. Additionally, these top connections must accommodate the displacement demand in the panel plane. To this end, on the panel side, the steel angle is slotted for +/- 64 (mm) and +/- 160 (mm) respectively for the horizontal and vertical panels.

The out-of-plane design force ($F_a$) of the top connections can be determined by applying the formulation expected for non-structural elements [25]:

$$F_a = \frac{S_a W_a}{q_a} \tag{1}$$

where $S_a$ is the seismic coefficient applicable to non-structural element; $W_a$ and $q_a$ are the weight of the element and its behavior factor respectively. The seismic coefficient may be calculated using the formula proposed by EN 1998-1 [30].

$$S_a = \alpha S \left[ 3\left(1 + \frac{z}{H}\right) / \left(1 + \left(1 - \frac{T_a}{T_1}\right)^2\right) - 0.5 \right] \tag{2}$$

Where $\alpha$ is the ratio of the design ground acceleration ($a_g$) on soil type A to the acceleration of gravity ($g$); $S$ is the soil factor; $T_a$ and $T_1$ are respectively the fundamental period of vibration of the panel and of the building in the relevant direction; $z$ is the height of the non-structural element above the level of application of the seismic action and $H$ is the building height.
However, the strength values ($F_a$) determined analytically are much lower than the corresponding values obtained from the analysis; therefore, the values obtained from the analysis were directly used. S275 steel and 8.8 grade bolts were adopted.

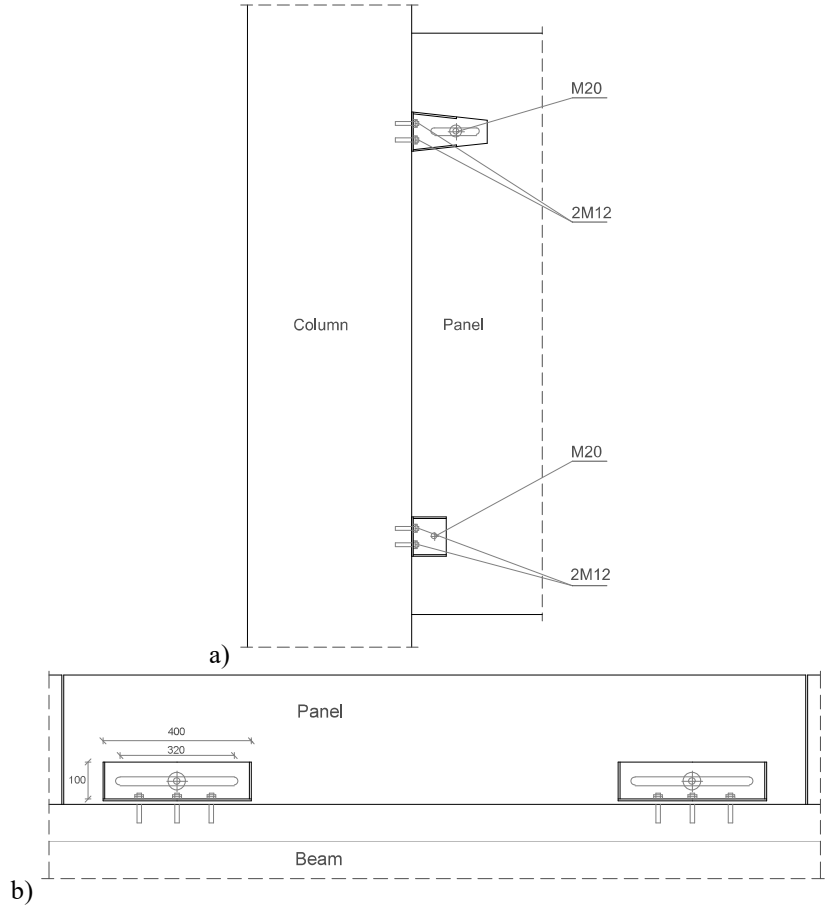


Figure 3: Details of the new connections for the (a) horizontal and (b) vertical panels.

### 3.1 Nonlinear modelling and analysis

The refined 3D model was created in OpenSees [22] according to the assumptions and approaches adopted in [21]. The new connections have been placed in the model by means of "Zero-Length" elements in parallel to other "Zero-Length" elements resembling the behaviour of the existing connections. The steel bracket at the bottom connections of the horizontal panels have been modeled with an "elasto-plastic" hysteresis material with stiffness ($k$) equal to 25'000 kN/m and yield strength ($F_y$) equal to 36.6 kN while those at the top have been modeled with "elasticPPgap" hysteresis material ($gap$=0.064 m, $k$=36'600 kN/m, $F_y$=36.60 kN), in the panel plane, and "elastoplastic" hysteresis material ($k$=22'000 kN/m, $F_y$=48.56 kN), in the out-of-plane of the panel. Similarly, the steel brackets connecting the vertical panels to the beams have been modeled with "elasticPPgap"' hysteresis material in the panel plane ($gap$=0.16 m, $k$=25'000 kN/m, $F_y$=42.74 kN) and "elastoplastic" hysteresis material in the out-of-plane of the panel ($k$=22'000kN/m, $F_y$=48.33 kN).

As regards the seismic input, two-hundred three-dimensions accelerograms were selected and grouped into ten increasing seismic intensity levels characterized by return periods equal to 10, 50, 100, 250, 500, 1000, 2500, 5000, 10000, 100000 years. Non-linear time-history analyses were performed by adopting mass and initial stiffness-proportional Rayleigh damping model. In addition, during the analyses, a check of the state of the plastic hinges inserted in the model was performed to assess failure of connections or elements.

## 4 RESULTS AND DISCUSSIONS

The results of the analyses are presented herein in terms of demand-on-capacity ratio (D/C) for two performance levels: Usability Preventing Damage (UPD) and Global Collapse (GC). The first refers to cladding panels while GC refers to roof elements and columns.

Figure 4 shows the beneficial effect of the retrofit intervention on the seismic response of the cladding panels. For the horizontal panels, the UPD is reached at intensities 2 and 5 for the as-is structure and the retrofitted structure, respectively; while referring to the vertical panels, UPD moves from intensity 3 to intensity 4. For the GC of the roof elements, the intervention does not alter the roof element falling from the support, while, considering the columns, we observe a slight reduction in the demand on the retrofitted structure compared to as-is conditions. This aspect might be related to the lower global acceleration demand due the higher fundamental period of vibration of the building with cladding panels (see for instance the mean acceleration spectrum of the ground motions of intensity 5 in Figure 5).

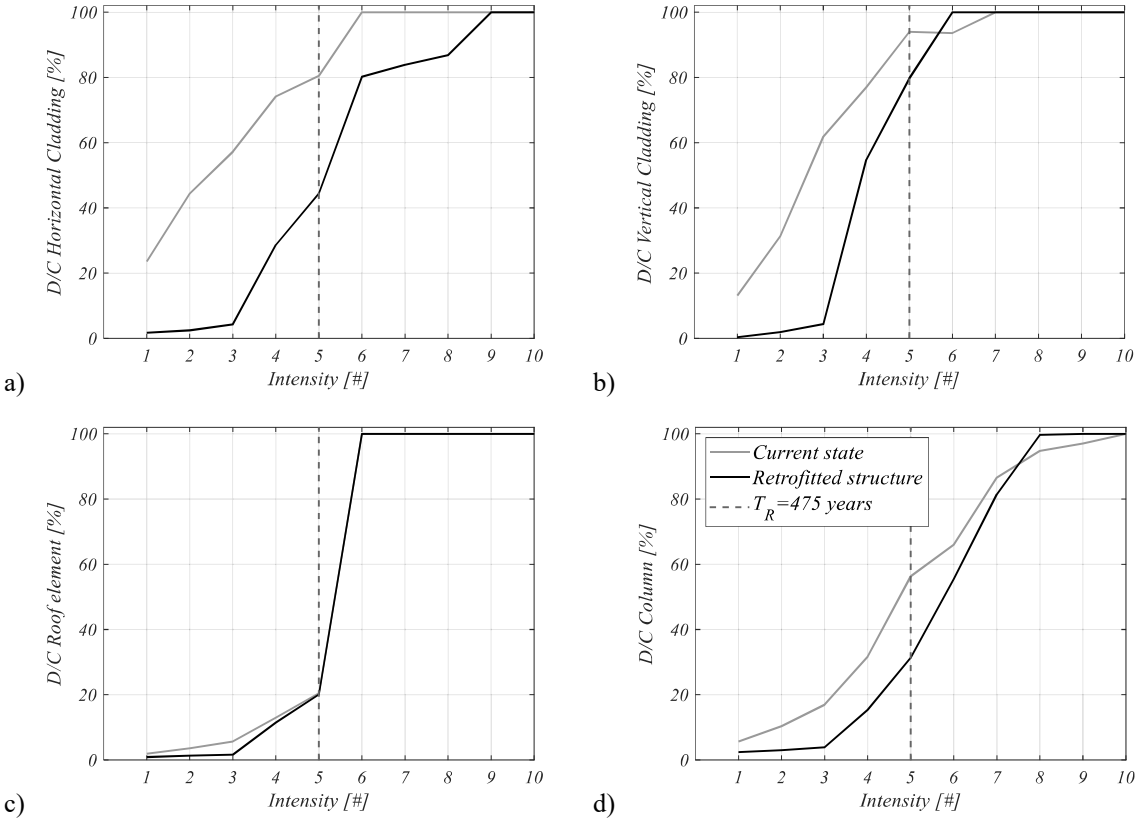


Figure 4: Demand-capacity (D/C) ratio for (a) horizontal and (b) vertical cladding panels, (c) roof elements and (d) columns. The dashed vertical line represents the seismic intensity for the life safety limit state.

Figure 6 shows the envelope for UPD of the cladding panels and GC for the columns and roof elements. The purpose of the retrofit intervention was related to the seismic risk reduction of the cladding system, and it successfully contributed to reducing it, although the effectiveness of the new connection of the vertically spanning panels was not optimal. This aspect needs to be further investigated. Regarding the GC, the envelope curve highlights a slight reduction of the D/C ratio.

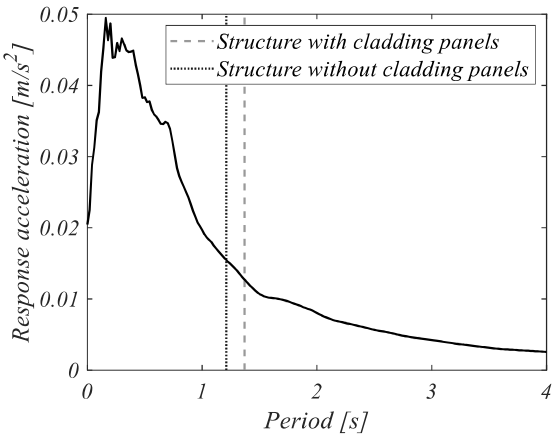


Figure 5: Mean elastic response spectrum (5% damping) for the ground motions of intensity 5. The vertical lines mark the fundamental period of the structure with and without cladding panels.

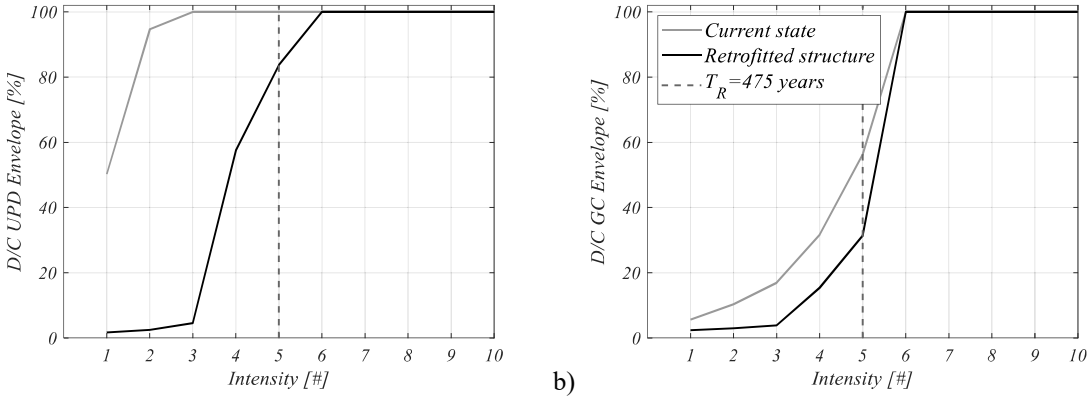


a) b)

Figure 6: Demand-capacity (D/C) ratio envelope for (a) UPD (vertical and horizontal cladding panels failure) and (b) GC (failure of roof elements and columns). The dashed vertical line represents the seismic intensity for the life safety limit state.

## 5 CONCLUSIONS

This paper investigated the change in seismic risk of a typical precast industrial building following a local retrofit intervention of the connections between the cladding panels and the main structure. The investigated interventions considered the placing of new steel backets, in parallel with the existing connections. The new connecting elements have been designed in accordance with the Italian building code thorough a response spectrum analysis considering as target the life safety limit state, indeed the failure of the panel may cause injuries.

Multi-stripe analyses were carried out to compare the performance of the retrofitted structure with the as-is conditions. The results have shown that the new cladding panel connections led as expected to a delay of the panel connection failure although not so effective for the vertically spanning cladding panels. On the other end, considering the global collapse related to the falling of roof elements no evident benefit was observed, while for the global collapse related to column's failure, a slight reduction of the demand was recorded probably due to the lower acceleration demand associated with the higher fundamental period of the building with cladding panels compared with the building with failed cladding panels.

## ACKNOWLEDGMENTS

This study was developed, in part, within the activities of the 2022-2024 ReLUIS-DPC research program funded by The Presidenza del Consiglio dei Ministri-Dipartimento della Protezione Civile. The views and opinions expressed in this document are those of the authors and do not necessarily reflect those of the research program as a whole.

## REFERENCES

[1] A. Belleri, E. Brunesi, R. Nascimbene, M. Pagani and P. Riva, "Seismic performance of precast industrial facilities following earthquakes in the italian territory," *Journal of performance of constructed facilities,* vol. 29, no. 5, 2015.

[2] A. Belleri, A. Torquati, P. Riva and R. Nascimbene, "Vulnerability assessment and retrofit solutions of precast industrial structures," *Earthquake and structures,* vol. 8, no. 3, pp. 801-820, 2015.

[3] A. Belleri, "Displacement based design for precast concrete frames with not-emulative connections," *Engineering structures,* vol. 141, pp. 228-240, 2017.

[4] M. Ercolino, G. Magliulo and G. Manfredi, "Failure of a precast RC building due to Emilia Romagna earthquakes," *Engineering structures,* vol. 118, pp. 262-273, 2016.

[5] D. A. Bournas, P. Negro and F. F. Taucer, "Performance of industrial buildings during the Emilia earthquakes in Northen Italy and raccomandation for strengthening," *Bulleting of earthquake engineering,* vol. 12, no. 5, pp. 2383-2404, 2014.

[6] G. Magliulo, M. Ercolino, C. Petrone, O. Coppola and G. Manfredi, "The Emilia earthquake: seismic performance of precast reinforced concrete buildings," *Earthquake spectra,* pp. 891-912, 2014.

[7] F. Minghini, E. Ongaretto, V. Ligabue, M. Savoia and N. Tullini, "Observational failure analyis of precast buildings after the 2012 Emilia earthquake," *Earthquake and structures,* vol. 11, no. 2, pp. 327-346, 2016.

[8] E. Nastri, M. Vergato and M. Latour, "Performance evaluation of seismic retrofitted RC precast industrial building," *Earthquakes and structures,* vol. 12, no. 1, 2017.

[9] M. Palanci, S. M. Senel and A. Kalkan, "Assessment of one story existing precast industrial buildings in Tukey based on fragility curves," *Bulleting of earthquake,* vol. 15, no. 1, pp. 271-289, 2017.

[10] E. Brunesi, R. Nascimbene, D. Bolognini and D. Belotti, "Experimental investigation of the cyclic response of reinforced precast framed structures," *PCI Journal,* vol. 60, no. 2, pp. 57-59, 2015.

[11] A. Belleri, M. Torquati, A. Marini and P. Riva, "Horizontal cladding panels: in-plane seismic performance in precast concrete buildings," *Bulletin of earthquake engineering,* vol. 14, pp. 1103-1129, 2016.

[12] A. Belleri, C. Cornali, C. Passoni, A. Marini and P. Riva, "Evaluation of out-of-plane seismic performance of column-to-column precast concrete cladding panels in one-storey industrial buildings," *Earthquake engineering aand Structural dynamics,* vol. 47, pp. 397-417, 2018.

[13] B. Dal Lago, P. Negro and A. Dal Lago, "Seismic design and performance of dry-assembled precast structures with adaptival joints," *Soil dynamics earthquake engineering,* vol. 106, pp. 182-195, 2018.

[14] M. Torquati, A. Belleri and P. Riva, "Displacement-based assessment for precast concrete frames with non-emulative connections," *Journal of earthquake engineering,* vol. 24, no. 10, pp. 1624-1651, 2018.

[15] I. Iervolino, A. Spillatura and P. Bazzurro, "RINTC-E project: towards the assessment of the seismic risk of existing building in Italy," in *7th ECCOMAS Thematic Conference on Computational Methods in Structural Dynamics and Earthquake Engineering*, Grete, 2019.

[16] M. Ercolino, D. Belotti, G. Magliulo and R. Nascimbene, "Vulnerability analysis of industrial RC precast buildings designed according to model seismic codes," *Engineering structures,* vol. 158, pp. 67-78, 2018.

[17] M. Bosio, A. Belleri and P. Riva, "Displacement-based simplified seismic loss assessment of italian precast building," *Journal of earthquake engineering,* vol. 24, no. 1, pp. 60-81, 2020.

[18] S. Labò, M. Eteme Minkada, A. Marini and A. Belleri, "Loss of support assessment for precast portal frames with friction connections and masonry infills," *Bullerin of earthquake engineering,* vol. 20, pp. 7983-8009, 2022.

[19] M. Angiolilli, M. Eteme Minkada, M. Di Domenico, S. Cattari, A. Belleri and G. M. Verderame, "Comparing the observed and numerically simulated seismic damage: a unified procedure for unreinforced masonry an reinforced concrete buildings," *Journal of earthquake engineering,* pp. 1363-2469, 2022.

[20] M. Bosio, C. Di Salvatore, D. Bellotti, L. Capacci, A. Belleri, V. Piccolo, F. Cavalieri, B. Dal Lago, P. Riva, G. Magliulo, R. Nascimbene and F. Biondini, "Modelling and seismic response analysis of non-residential single-storey existing precast buildings in Italy," *Journal of earthquake engineering,* vol. 27, no. 4, pp. 1047-1068, 2022.

[21] M. Bosio, S. Labò, P. Riva and A. Belleri, "Seismic risk and finite element modelling influence of an existing one-storey precast industrial building," *Journal of earthquake engineering,* vol. 24, no. 1, pp. 1363-2469, 2023.

[22] F. McKenna, G. L. Fenves and M. H. Scott, Open system for earthquake engineering simulation, Berkeley: University of California, 2000.

[23] "D.M. 24 gennaio 1986," in *Norme tecniche relative alle costruzioni antisismiche*, Rome Italy, Gazzetta Ufficiale della Repubblica Italiana, 1986.

[24] B. Zoubek, M. Fischinger and T. Isakovic, "Cyclic response of hammer-head strap cladding-to-structure connections in RC precast building," *Engineering structures,* vol. 119, pp. 135-148, 2016.

[25] "NTC18, Norme Tecniche per le costruzioni DM 17/1/2018," Gazzetta Ufficiale della Repubblica Italiana, Rome, Italy, 2018.

[26] MidasGEN, Analysis manual for Midas GEN, 2020.

[27] B. Dal Lago, G. Toniolo, R. Felicetti and M. Lamperti Tornaghi, "End support connection of precast roof elements by bolted steel angles," *Structural concrete,* vol. 18, pp. 755-767, 2017.

[28] A. Ferreira and M. El Debs, "Deformability of beam-tocolumn connection with elastomeric cushion and dowel bar to beam axial force," in *2nd international symposium on prefabrication Finland*, 2000.

[29] EC8 Design of structures for eathquake resistance Part 1: General rules, seismic actions and rules for buildings, EN 1998-1:2004.

COMPDYN 2023
9th ECCOMAS Thematic Conference on
Computational Methods in Structural Dynamics and Earthquake Engineering
M. Papadrakakis, M. Fragiadakis (eds.)
Athens, Greece, 12-14 June 2023

# NUMERICAL MODEL CALIBRATION OF A LOW IMPACT STRENGTHENING TECHNIQUE BASED ON BED-JOINTS SLIDING IN SEISMIC RETROFITTING OF MASONRY INFILLS

†**Marco Vailati**[1], **Amedeo Gregori**[1], **Federico Morelli**[1], **Giorgio Monti**[2], **Edoardo Ciuffetelli**[1], **Alfredo Peditto**[1]

[1] Department of Civil, Construction-Architectural and Environmental Engineering, University of L'Aquila, Italy

†*Corresponding author: marco.vailati@univaq.it

[2] Department of Structural Engineering and Geotechnics, Sapienza University of Rome, Rome, Italy

## Abstract

*The challenge against the waste of resources in the world of construction industry, starts from the seismic and thermal retrofitting of existing buildings with low environmental impact innovative technologies. When the buildings are especially vulnerable, for instance in the case of double-layer infills - often without thermal insulation - it's really hard to achieve satisfactory performance levels without resorting to radical interventions.*
*In these cases the interaction with the building internal activities is unavoidable and forms a further design constraints.*
*This work shows an innovative technology based on recycled plastic parts, optimized for the double-layer infills of existing buildings in which the maintaining of the internal activity is fundamental for the successful of the intervention. The system with recycled plastic joints is aiming at improving thermal and seismic performances, avoiding the residents relocation, consistently reducing the demolitions of existing infills and using plastic from recycled waste.*
*Such system was preliminarily tested on a real-scale double-layer infill equipped with two joint lines under horizontal force at the testing laboratory of materials and structures (LPMS) of the University of L'Aquila.*
*On the basis of this previous experimental tests, the present study proposes the calibration of a macroelement and a later numerical modelling of a multi-storey frame representative of r.c. buildings of the 80's.*
*The results of the retrofitted configuration with plastic joints were compared with bare frame and infilled frame with different macroelement available for traditional infills.*

**Keywords:** in-plane retrofitting of masonry buildings, bed-joints sliding, macroelements calibration, recycled plastic joints, double-layer infills, sustainable materials.

# 1 INTRODUCTION

In the past 12 years different effective and innovative techniques were developed to improve the seismic performances of single layer infills [1], [4].

However, for the double-layer configuration, no specific solution was developed and the predominant approach is still referred to reinforced coatings using either composite materials as Fiber Reinforced Polymers (FRP) in strips or sheets [5], [6], or fiber Reinforced Mortar (FRCM or FRLM) as external coating [7][8].

This type of infill can show high fragility in case of dynamic excitation; in fact, under out-of-plane force, the two layers generally have different motion since unlinked. This effect reduces the whole strength because the instability generally comes before ultimate strength.

Since 2012, one of the authors has started developing innovative devices for new building aiming at reducing in-plane fragility and preventing out-of-plane instability of the double-layer infills, through the combined effect of horizontal flexible joints and vertical bands made of recycled plastic [10], [11].

In further studies the previous joint waw upgraded to be use in the retrofitting of double-layer infills in which the mitigation of the pervasiveness is a priority requirement [12], also providing satisfactory results from a thermo-mechanical standpoint [13].

To date, the proposed technique stands out from the previous solutions by providing to the out-of-plane resistant mechanism two different mechanical contributions: a) the shear resisting mechanism due to plastic plate that links the two layers, b) the flexural resisting mechanism provided by the cantilevering elements placed behind the bricks where joint opens.

Figure 1 shows the mechanisms involved in the equilibrium of the infill undergoing out-of-plane inertia force induced by earthquake.

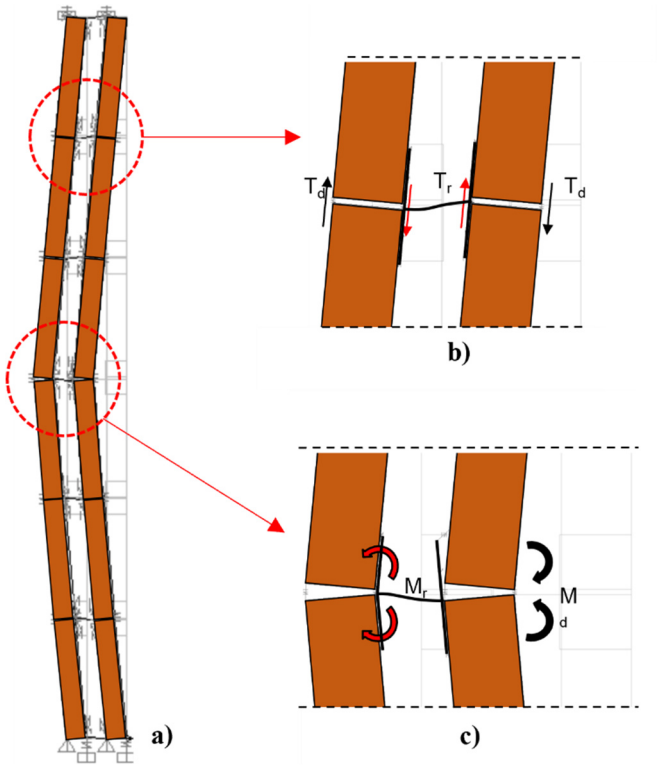


Figure 1. Resistant mechanisms involved in the equilibrium of the double-layer infill undergoing OoP loads: a) deformed configuration, b) shear resisting mechanism, c) flexural resisting mechanism.

## 2 NUMERICAL MODELLING OF BED-JOINT SLIDING

Bare concrete frames are structures with significantly more flexibility respect those infilled with common bricks and mortar, therefore when they work in parallel the stiffer element takes a large part of the inertia forces.

As a consequence, the elements are strengthened until to satisfy the performance demands provided by the current standard: this is what we can call “strength-based approach”.

Following this approach, the stiffness inevitably grows and therefore the demand on both structural and non-structural element, as a consequence of a stiffer structure.

The proposed technique based on the bed-joint sliding mechanism follows the opposite philosophy. All the deformations are channeled toward predefined lines in which special deformable joints are placed. In this way, blocks can slide without any cracks and the interaction between frame and infill can be neglected: this is what we have called “flexibility-based approach”. Following this second approach, we have low increasing in stiffness as well as having more dissipation – due to plastic deformation of the joints – and low interaction with the frame.

### 2.1 Calibration of a simplified macroelement

In this work the authors propose a modelling strategy via simplified macro-model developed for infill masonry panels undergoing in-plane forces [14] and implemented in Seismostruct [15], a FEM program of the software house SeismoSoft.

The calibration of the macroelement was carried out on a previous experimental campaign at the University of L'Aquila, in which a double-layer infilled frame of 12 and 8 cm thickness with 12 cm intermediate hollow space was tested [12].

The aim of the experimental test was to verify the triggering of the sliding mechanism due to special deformable joints made of recycled plastic, placed within an infill built in a wood frame with hinged ends. Figure 2 shows some assembly phases of the tested infill, while figure 3 shows the testing setup with the corresponding mechanical scheme with nonlinear central element developed by [14], respectively.

The non-linear behavior resulting from the arrangement of the plastic joints such as shown in figure 3, is concentrated in the central element, since its in-plane behavior is a function of the interstorey drift.

The advantage of the adopted macroelement is in the independence from the number of joint lines, so they can be always represented by an equivalent system in which the nonlinear properties are focused in the central element.



**a)** **b)** **c)**

Figure 2. Some assembly phases: a) first blocks rows placed into the frame, b) completed infill; c) removing of blocks to simulate the seismic retrofitting of masonry infills.

In figure 4 the experimental curve, the backbone curve - defined as a trilinear relationship - and the calibration curve are overlapped, while the bottom right graph represents the pinched asymmetric curve model, in which *da= pinchdisp·(dA'-dA'')+ dA''* and *fa= pinchforce·fkp.*

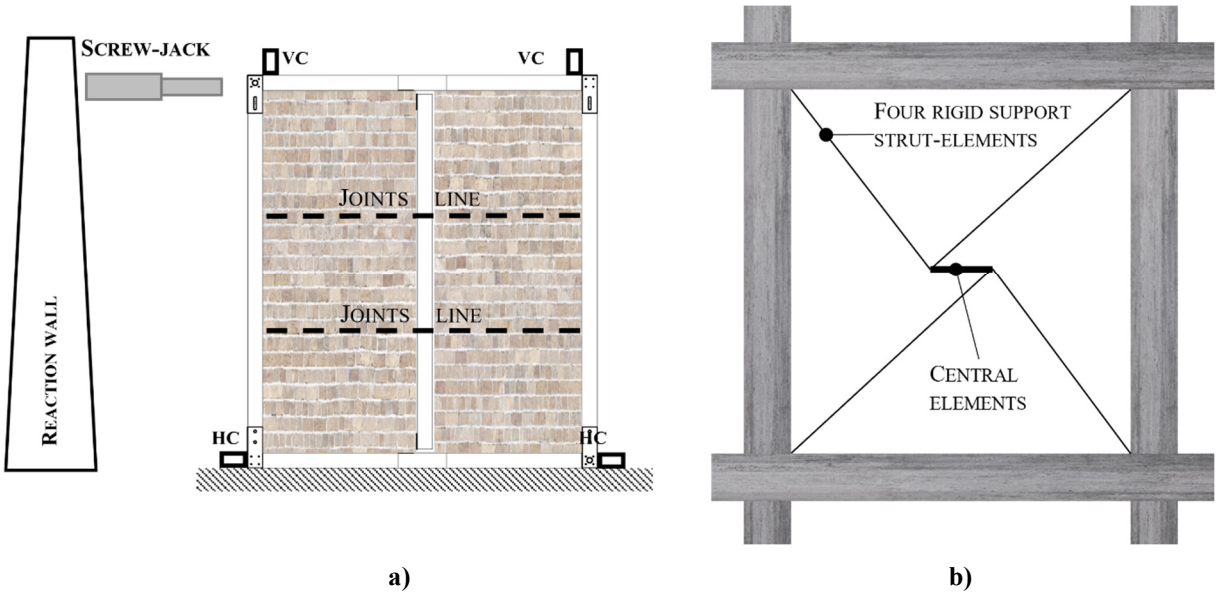


Figure 3. a) Test setup: in evidence the placement of the plastic joints. Vertical Constrains (VC) and Horizontal constrains (HC) fix the frame to the ground, allowing the horizontal deformation; b) the mechanical scheme of the adopted macroelement with non linear central element.

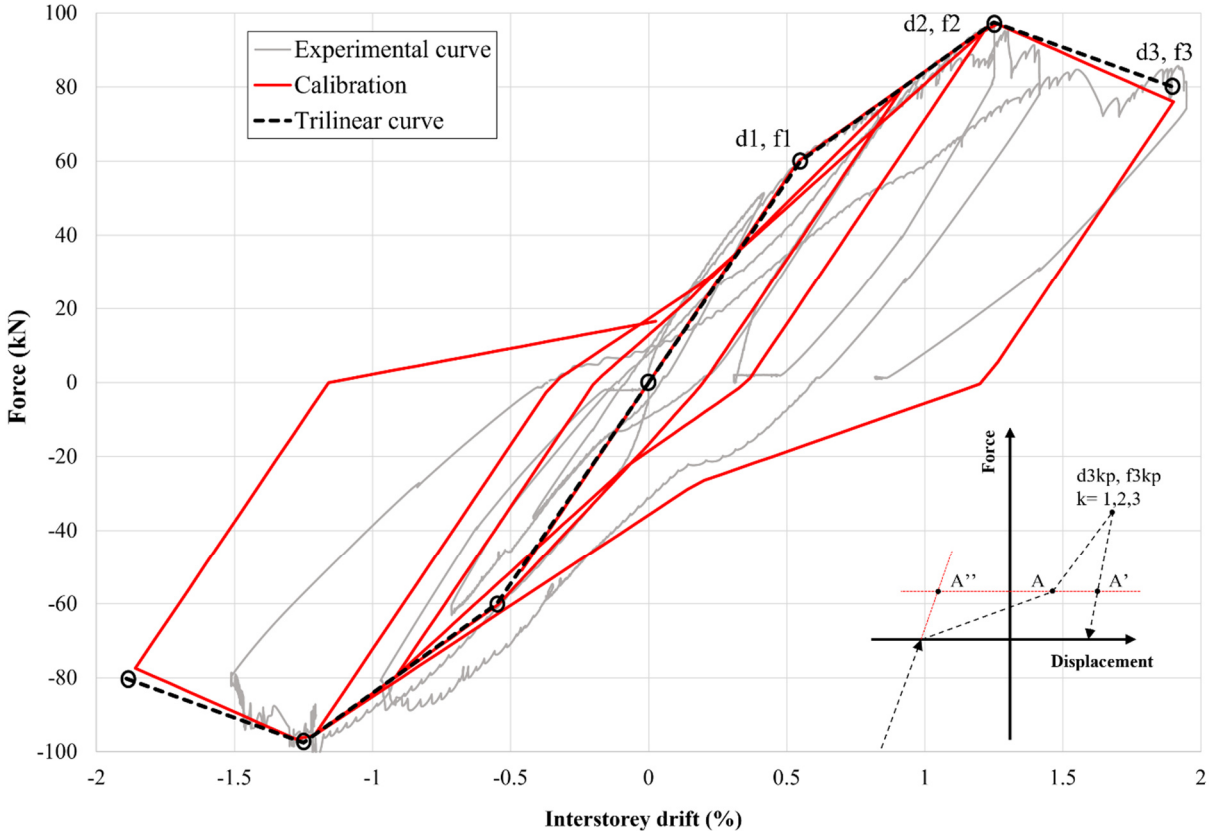


Figure 4. Calibration of the hysteretic response based on the in-plane experimental test conducted on a double-layer infill at the University of L'Aquila [12]. The bottom right graph shows the pinching rule.

The backbone curve of this macromodel is associated to both in-plane directions and it is fully described by five parameters that allow to describe the cycles of load/unload and the degradation as damage increases.

While the first three describe the points of the experimental curve where slope change, the last two allow to adjust the curve bottleneck and therefore are those subjected to calibration. The parameters *pichdisp* and *pinhforce* were therefore changed to minimize the gap between experimental data and the numerical simulation. Final set of the model parameters are listed in table 1.

| | Parameter | Value |
|---|---|---|
| **Backbone curve** | *d1* | 0.013 |
| | *f1* | 60 |
| | *d2* | 0.03 |
| | *f2* | 97.5 |
| | *d3* | 0.047 |
| | *f3* | 74.4 |
| **Pinching mechanism** | *pinchdisp* | 0.57 |
| | *pinchforce* | 0.28 |

Table 1. Setting parameters from calibration analysis.

## 3 MACROMODELLING IN SEISMIC ASSESSMENT OF INFILLED FRAME

### 3.1 Case study

In the present section the seismic assessment of a multi-storey frame representative of r.c. buildings of the 80's is shown.

More specifically, the study aims at both optimal modelling of the plastic joints system with a calibrated macroelement and comparing the performances with different frame configurations, as depicted in figure 5.

The considered structure is a frame consisting of three floors with height of 3.5 m each and two spans with width of 3.5 m each. Spacing among frames was assumed equal to 6 m.

The columns have 0.32 m width and 0.6 m height, while the beams have 0.4 m width and 0.5 m height.

The positioning of the vertical rebars is the following: 4ϕ20 at the corners and 2ϕ20 along each of four sides for the beams, 4ϕ20 at the corners and 5ϕ20 along each of the two longer sides. Columns and beams have stirrups with 2 arms ϕ6/80 mm and ϕ10/100, respectively.

The infilled frame with Crisafulli macroelement is realized with single layer wall of 20 cm thickness, while the one with plastic joint macroelement, calibrated in the previous section, is realized with double-layer wall with outer and inner side of 12 cm and 8 cm thickness, respectively, and 12 cm intermediate hollow space.

From the analysis of dead and live loads - equal to 4 kN/m$^2$ each - and live load combination coefficient $\varphi_{2j}$= 0.6, were defined two lumped masses: the first of 7 tons was applied at each nodes of the external columns, while the second of 14 tons was applied at each nodes of the central column, for a total number of 6 and 3, respectively.

The mean strength values of beams and columns are $f_{cm}$= 25.2 MPa and $f_{ym}$= 374 MPa for concrete and steel rebars, respectively, while the compressive strength, orthogonal and parallel to the brick holes, is $f_{bm\perp}$ = 2.2 MPa and $f_{bm//}$ = 11 MPa, respectively. In professional practice these values are defined by onsite test as the average of the compressive and tension test conducted on a meaningful number of specimens, but not less than three.

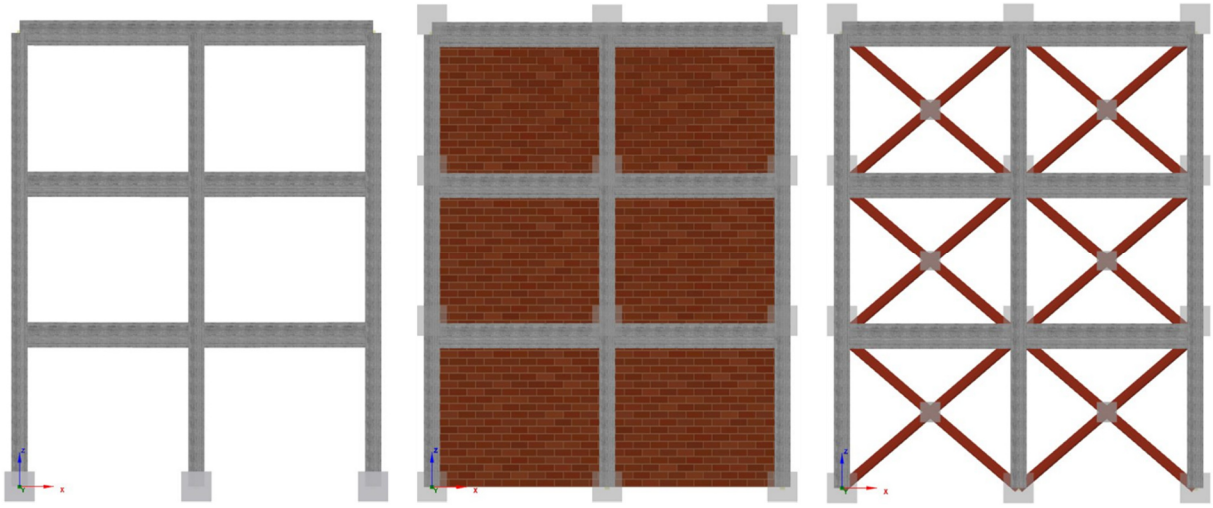

a) b) c)

Figure 5. Multi-storey frame representative of r.c. buildings of the 80': a) bare frame, b) full infilled frame with Crisafulli macroelement, c) full infilled frame with plastic joints macroelement.

The three pairs of points that define the backbone curve of the double layer infill with plastic joints used in the numerical model of figure 5c, were defined as described in table 2. It should be notice that the computed forces refer to the bed-joint sliding mechanism, made the weakest by introducing the plastic joints. Further details on the equations adopted in computing of the parameters of table 2 are reported in [12].

| | Parameter | Equation * | Reference code | Value |
|---|---|---|---|---|
| **Elastic threshold** | *f1* | $f_{1,120}+f_{1,80}$ | FEMA 306 | 68375 kN |
| | *d1* | $f_1/K_e$ | $K_e = \sum_{i=1}^{2} k_{e,i}$ (FEMA 273) | 17.20 mm |
| **Plastic threshold** | *f2* | $f_{2,120}+f_{2,80}$<br>$f_{2,120} = 0.8 f_{1,120}$<br>$f_{2,80}$ | $f_{2,80}$ (FEMA 306) | 107190 kN |
| | *d2* | 1.3% *h* | From experimental test | 35.75 mm |
| **Failure** | *f3* | $0.8 f_2$ | [15] | 85750 kN |
| | *d3* | 2.0% *h* | From experimental test | 55 mm |
| * the subscript 120 refers to the layer of 120 mm thickness, than 80 refers to the layer of 80 mm thickness, *fi, di* are the three pairs of backbone's points as depicted in figure 4, $k_{e,i}$ is the elastic stiffness of the layer i-th, *h* is the wall height | | | | |

Table 2. Backbone's points of the double layer infill used in numerical simulation.

Infill force capacity for Crisafulli's macroelement was defined as the weakest between the bed-joint sliding and diagonal cracking, while the infill deformation capacity was defined as 1.3% of the wall height, according to [12] and [16], respectively, and equal to 45.8 kN and 30 mm.

### 3.2 Numerical analysis

Numerical analysis were carried out with 2D model under the hypothesis of large displacement in case of geometric and material nonlinearity, using SeismoStruct FEM software [15]. The earthquake effect were simulated with two accelerograms obtained with the Rexel software [17], according to the design spectra of the Italian code NTC-18 [18] for the town of Norcia (42.792 lat. and 13.093 long.). Figure 6 shows the spectrocompatibility for the selected accelerograms, Amatrice of the 24$^{th}$ August 2016 and L'Aquila 6$^{th}$ April 2009, while the figure 7

shows the two accelerograms used in time-domain non linear analysis. Columns and beams are modelled with fibers cross-section and nonlinear force-based elements, while Kent-Park and Menegotto-Pinto models are assigned to concrete and steel rebars, respectively. Joints are considered exclusively elastic as a consequence of their intrinsic weakness due to the absence of stirrups (widespread condition for buildings built according to pre-seismic codes).

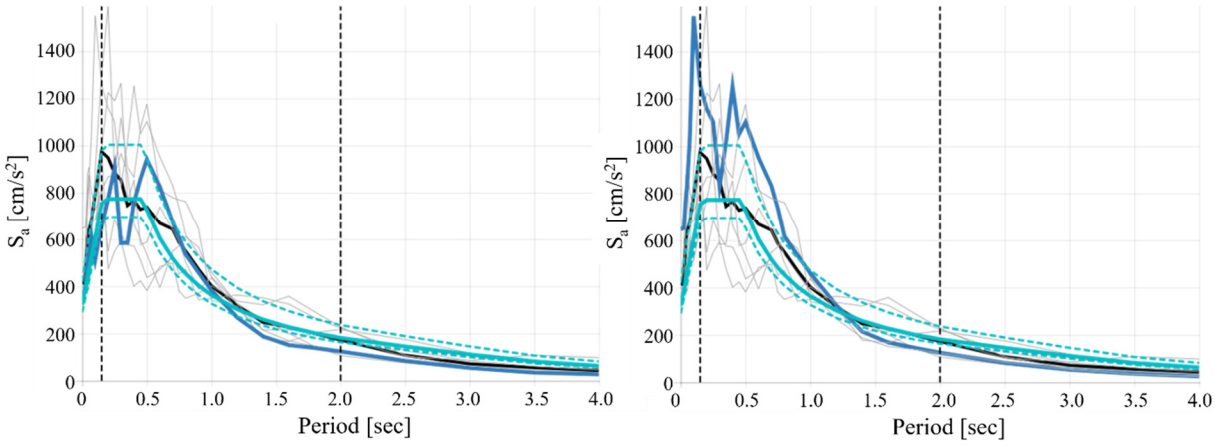


Figure 6. Highlighted in blue the response spectra of the selected accelerograms: a) Amatrice, b) L'Aquila.

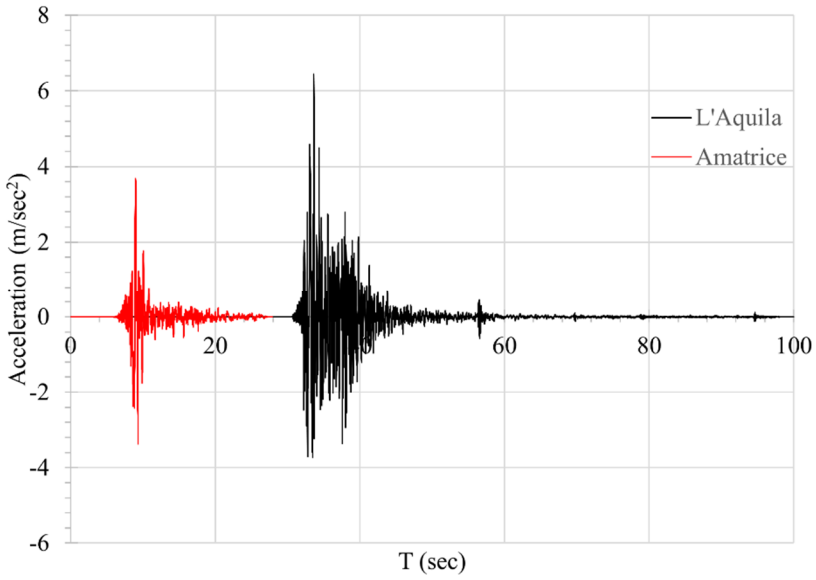


Figure 7. Accelerograms of Amatrice and L'Aquila for the time-domain non linear analysis.

The failure mechanisms are defined as performance criteria in three set, the first refers to the bare frame, while for infilled frames the set are coupled as follow: set 1 + set 2 for Crisafulli infilled frame, set 1 + set 3 for plastic joints infilled frame. The adopted values for the selected criteria are shown in table 3. Note that the first column on the right shows the assumption on the behavior of the elements after reaching the limit in force or deformation adopted in the corresponding criteria.

| | Criterion name | Control on | Value | Strength degradation |
|---|---|---|---|---|
| **SET 1 (Frame elements)** | Crush_conf. | Concrete strain | -8 ‰ | Keep strength |
| | Yield | Reinforcement strain | 2.5 ‰ | Keep strength |
| | Fracture | Reinforcement strain | 10‰ | Keep strength |
| | Chord_rot. | Frame element chord rotation capacity | (Variable) | Keep strength |
| | Shear | Frame element shear capacity | (Variable) | Keep strength |
| | | | | |
| **SET 2 (infilled Frame with Crisafulli macro-model)** | Infill_strut_force | Infill force | 45.9 kN | No residual strength |
| | Infill_shear_def. | Infill deformation | 30 mm | No residual strength |
| | | | | |
| **SET 3 (infilled Frame with plastic joints macro-model)** | Link_yield | Link deformation | 17.2 mm | Keep strength |
| | Link_max | | 35.75 mm | Keep strength |
| | Link_ult | | 55 mm | No residual strength |

Table 3. Performance criteria in defining of collapse mechanisms of the bare and infilled frames.

In resolving of non linear problem by means of time-domain non linear analysis, in addition to the hysteretic dissipation, the energy one was taken into account by using tangent stiffness proportional damping with damping ratio of 1% and first period of 0.48 s, 0.19 s and 0.35 s for bare frame, Crisafulli infilled frame and Plastic joints infilled frame, respectively.

# 4 RESULTS

## 4.1 Modal analysis

The analysis of natural frequencies of the three frames has confirmed the expectative. In fact, in case of infilled frame, the walls act increasing the global stiffness, and thus reducing the first period respect the bare frame. Comparing the two infilled frames, the one with Crisafulli macroelement shows higher stiffness respect the calibrated macroelement adopted for the plastic joints. By the fact that the mechanical properties of the materials are the same, the difference is likely due to different formulation of the macroelement. The following table 4 summarizes the results of the modal analysis for the three configuration of frames.

| | Bare frame | | Crisafulli infilled frame | | Plastic joint infilled frame | |
|---|---|---|---|---|---|---|
| | T (Sec) | f (Hz) | T (Sec) | f (Hz) | T (Sec) | f (Hz) |
| **1** | 0.48 | 2.08 | 0.19 | 5.26 | 0.35 | 2.86 |
| **2** | 0.16 | 6.25 | 0.07 | 14.60 | 0.12 | 8.33 |

Table 4. Modal analysis of the different frame configurations.

## 4.2 Non linear dynamic analysis

The results shown in the present section aiming at both proving the effectiveness of the strengthening technique with plastic joints through proper modelling with calibrated macroelement, and comparing results among different frame configurations, underlying pros and cons of the proposed modelling.

The analysis were carried out on the three frames using the accelerograms of Amatrice and L'Aquila, selected with disaggregation data analysis.

Figure 8 depicts two graphs in which the interstorey drift on the ground floor have been compared (the time axis were been truncated for a better yield of the curves).

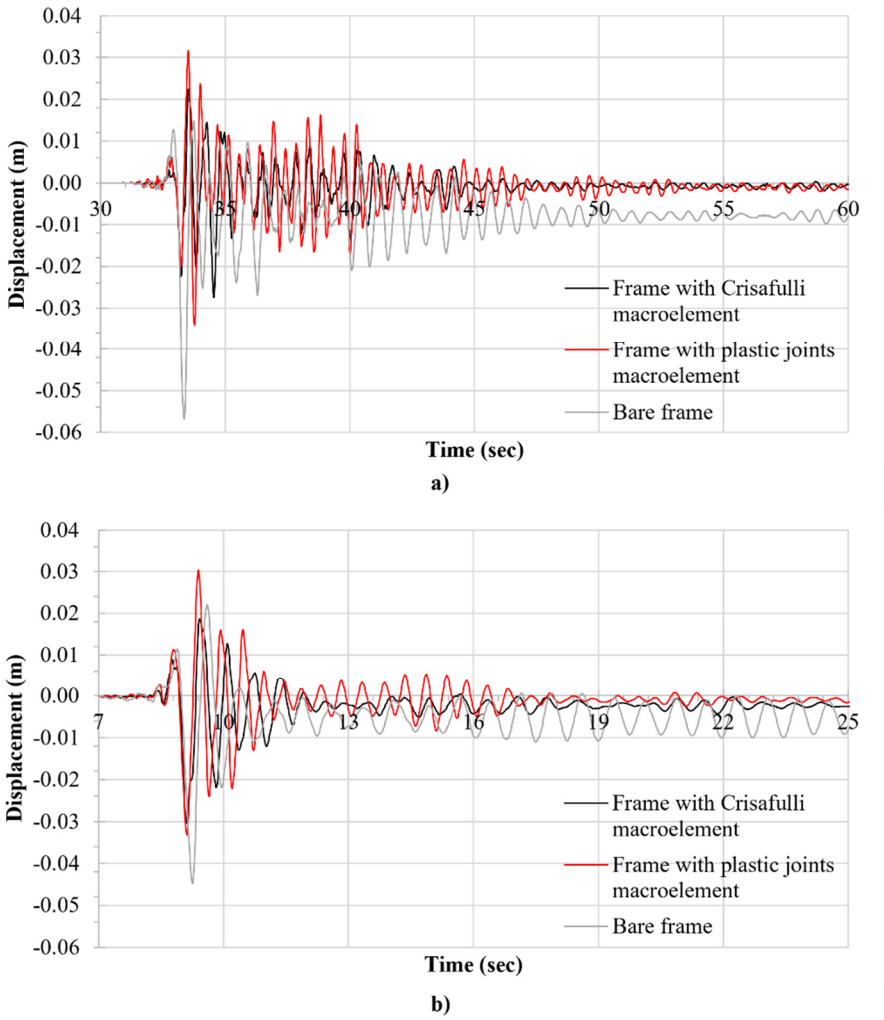


Figure 8. Interstorey drift on the ground floor for the three frame models undergoing to the effect of the selected natural accelerograms: a) L'Aquila, b) Amatrice.

Table 5 shows the maximum interstorey drift of all floor for both accelerograms, while the last row gives the average of the maximum. These displacement demands can be directly compared with the capacity of the infilled frame, according to the performance criteria listed in table 3.

| | **Bare frame** | | | **Crisafulli infilled frame** | | | **Plastic joint infilled frame** | | |
|---|---|---|---|---|---|---|---|---|---|
| | First | Second | Top | First | Second | Top | First | Second | Top |
| **L'Aquila** | 5.68 | 4.42 | 1.76 | 2.74 | 2.63 | 0.35 | 3.41 | 1.77 | 0.88 |
| **Amatrice** | 4.48 | 3.96 | 1.96 | 3.04 | 2.28 | 0.33 | 3.32 | 1.59 | 0.88 |
| Average | 5.08 | 4.19 | 1.86 | 2.89 | 2.46 | 0.34 | 3.36 | 1.68 | 0.88 |

Table 5. Maximum displacement at floors (given in cm).

The following figures 9 and 10 show the damaging of the three models of multistorey frame undergoing to the earthquakes of L'Aquila and Amatrice, respectively.

Analyzing the damage distributions, the bare frame reaches the same damaging level for both accelerograms, while the two infilled frames show opposite results: the one with Crisafulli macroelement suffers higher damage under the Amatrice earthquake, while the other with plastic joints reaches greater damage with L'Aquila earthquake. This is likely due to different energy content of the earthquakes: the armonics with higher energy are closer to Crisafulli infilled frame in case of Amatrice earthquake, respect to those of L'Aquila earthquake that are closer to the first period of the infilled frame with plastic joints. As general remark, the Crisafulli macroelement provide higher stiffness to the structures, shifting the first period toward the area of the response spectra where the acceleration are generally higher.

Beams and columns denote a widespread damaging due to rebars yielding in all three cases, while the infilled frame with Crisafulli macroelement shows brittle collapse of the infills on the ground floor in the case of Amatrice earthquake. The infilled frame with calibrated macroelements for plastic joints, shows only a few columns yielding - mostly placed on the ground floor - and the triggering of the bed-joint sliding of the infills on the ground and first floor, but without reaching the last displacement capacity, as shown in figure 11. The infills at the last level remain elastic. In case of bare frame we can observe the highest number of yielded beams and columns, as a consequence of a higher displacement demand due to lower stiffness.

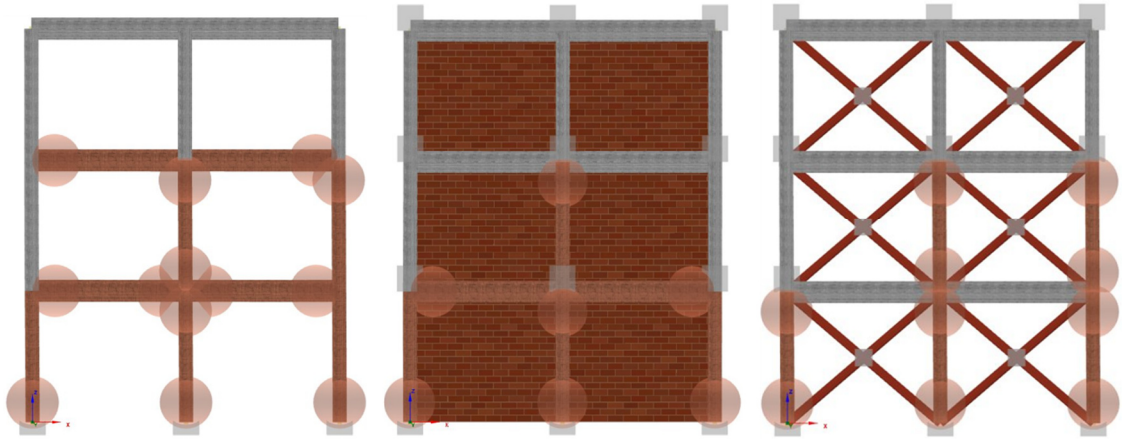

**a)** **b)** **c)**

Figure 9. Damaging of the three frame subjected to L'Aquila earthquake: a) bare frame, b) infilled frame with Crisafulli macroelement, c) infilled frame with calibrated macroelement for walls with plastic joints.

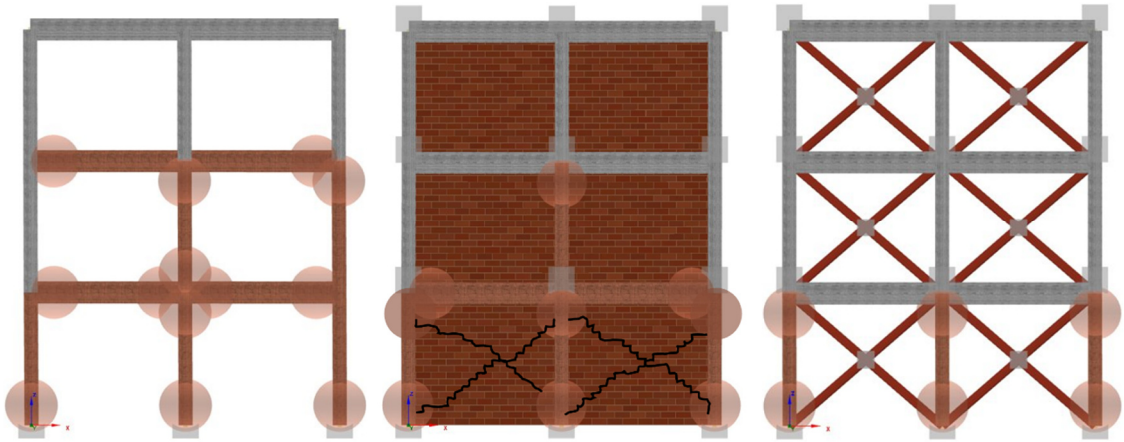

**a)** **b)** **c)**

Figure 10. Damaging of the three frame subjected to Amatrice earthquake: a) bare frame, b) infilled frame with Crisafulli macroelement, c) infilled frame with calibrated macroelement for walls with plastic joints.

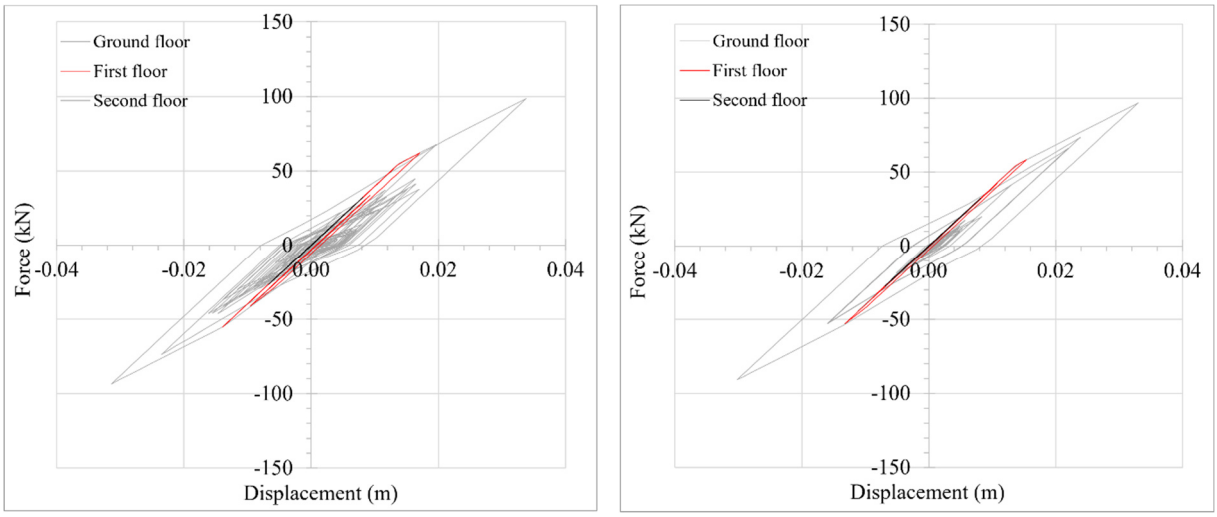


Figure 11. Hysteretic behavior of the walls strengthened with plastic joints at different floors for different accelerograms: a) L'Aquila, b) Amatrice.

## 5 CONCLUSIONS

In this study a macroelement available in literature has been calibrated on previous in-plane experimental test conducted at the University of L'Aquila on a double-layer masonry infill strengthened with an innovative technique based on recycled plastic joints.

The calibrated model was later used in seismic assessment of multistorey frames via numerical modelling by means of time-domain non linear analysis, using two natural accelerograms selected with Rexel software from disaggregation data of a location near Norcia. The research aims at both proving the effectiveness of the innovative strengthening technique with plastic joints through proper modelling, and comparing results among different configurations of multistorey frames representative of r.c. buildings of the 80's.

The considered structure is a frame consisting of three floors with total height of 10.5 m and two spans with total width of 7 m. Three configurations were studied: bare frame, infilled frame with Crisafulli macroelement and infilled frame with a calibrated macroelement based on the model proposed by Rodrigues et al. [14].

The calibration test have allowed to optimize the pinching mechanism parameters *pinchdisp*= 0.57 and *pinchforce*= 0.28 of the macroelement used in modelling of the bed-joints sliding mechanisms triggered by plastic joints.

The time-domain non linear analysis carried out on different multistorey frames, have shown a greater vulnerability of the infilled frame with Crisafulli macroelement, due to higher stiffness that shift the first modal shape toward the higher spectral accelerations. In particular, in the simulation with Amatrice earthquake, two beams and seven columns ends have reached the point of yielding, while two infills on the ground level have collapsed for the exceedance of shear deformation.

Regarding the infilled frame with plastic joints, the capacity of maintaining stable and large cyclic loading up to 2% of wall height, allows an high hysteretic dissipation that reduces the damaging on structural elements. Besides, the cantilever system behind bricks avoids the out-of-plane instability, thus preventing the early collapse of the infill.

Finally, the possibility to calibrate the triggering force of the bed-joints sliding mechanisms by means the increasing the number of joints per line, permits to reduce the main eigenfrequencies of the structure and thus decrease the inertia forces.

## REFERENCES


[1] M. Mohammadi, V. Akrami, R. Mohammadi-Ghazi, Method to improve infilled frame ductility. *Journal of Structural Engineering*, **137**, 646-653, 2011.

[2] M. Preti, N. Bettini, G. Plizzari, Infill walls with sliding joints to limit infill-frame seismic interaction: large-scale experimental test. *Journal of Earthquake Engineering*, **16** (1), 125-141, 2012.

[3] N. Mojsilović, Structural behavior of masonry walls with soft-layers: An overview of experimental work. *Current Perspectives and New Directions in Mechanics, Modelling and Design of Structural Systems*, 1928-1933, 2022.

[4] C. Zhang, T. Yu, Z. Chen, W. Huang, S. Zhang, Y. Zhou, D. Lu, Z. Lin, Seismic behavior of novel low-damage precast infill walls with sliding joints for reinforced concrete frame. *Earthquake Engineering & Structural Dynamics*, **51**(15), 3730-3754, 2022.

[5] J.G. Tumialan, F. Micelli, A. Nanni, Strengthening of masonry structures with FRP composites. In 551 Structures 2001: *A Structural Engineering Odyssey*, 1–8, 2001.

[6] S.A. Babatunde, Review of strengthening techniques for masonry using fiber reinforced polymers. *Composite Structures*, 161, 246-255, 2017. https://doi.org/10.1016/j.compstruct.2016.10.132.

[7] M. Angiolilli, A. Gregori, M. Vailati. Lime-Based Mortar Reinforced by Randomly Oriented Short Fibers for the Retrofitting of the Historical Masonry Structure. *Materials*, **13**(16):3462, 2020. https://doi.org/10.3390/ma13163462

[8] M. Vailati, M. Mercuri, M. Angiolilli, A. Gregori. Natural-Fibrous Lime-Based Mortar for the Rapid Retrofitting of Heritage Masonry Buildings. *Fibers*, **9**(11):68, 2021. https://doi.org/10.3390/fib9110068

[9] Mercuri, M., Vailati, M., Gregori, A. Lime-based mortar reinforced with randomly oriented polyvinyl-alcohol (PVA) fibers for strengthening historical masonry structures. *Development in the Built Environment*, **14**, 10152, 2023. https://doi.org/10.1016/j.dibe.2023.100152

[10] M. Vailati, G. Monti. Earthquake-Resistant and Thermo-Insulating Infill Panel with Recycled-Plastic Joints. In: D'Amico, S. (eds). *Earthquakes and Their Impact on Society. Springer Natural Hazards, Springer, Cham*., 417-432, 2016. https://doi.org/10.1007/978-3-319-21753-6_15

[11] M. Vailati, G. Monti. Earthquake-Safe and Energy-Efficient Infill Panels for Modern Buildings. In: Rupakhety, R., Ólafsson, S. (eds). *Earthquake Engineering and Structural Dynamics in Memory of Ragnar Sigbjörnsson. ICESD 2017. Geotechnical, Geological and Earthquake Engineering*, vol 44, 2018, Springer, Cham. https://doi.org/10.1007/978-3-319-62099-2_12

[12] M. Vailati, A. Gregori, M. Mercuri, G. Monti. A non-intrusive seismic retrofitting technique for masonry infills based on bed-joint sliding. *Journal of Building Engineering,* **69**, 106208, 2023. https://doi.org/10.1016/j.jobe.2023.106208

[13] M. Vailati, G. Di Gangi, G. Quaranta. Thermo-mechanical characterization and hysteretic behavior identification of innovative plastic joint for masonry infills in reinforced concrete buildings. *Journal of Building Engineering*, **65**, 105803, 2023. https://doi.org/10.1016/j.jobe.2022.105803

[14] H. Rodrigues, H. Varum, A. Costa. Simplified macro-model for infill masonry panels. *Journal of Earthquake Engineering*, **14**(3), 390-416, 2010. https://doi.org/10.1080/13632460903086044

[15] Seismosoft. SeismoStruct - A Computer Program for Static and Dynamic Nonlinear Analysis of Framed Structures. 2020. Available online: www.seismosoft.com.

[16] Alwashali, H., Torihata, Y., Jin, K., Maeda, M. Experimental observations on the in-plane behaviour of masonry wall infilled RC frames; focusing on deformation limits and backbone curve. Bulletin of Earthquake Engineering, 16, 1373-1397, 2018.

[17] Iervolino, I., Galasso, C., Cosenza, E. REXEL: computer aided record selection for code-based seismic structural analysis. Bulletin of Earthquake Engineering, 8, 339-362, 2010. DOI 10.1007/s10518-009-9146-1

[18] Norme Tecniche per le Costruzioni. Gazzetta Ufficiale n. 42 del 20/02/2018. Supplemento ordinario, (8), 2018. (in Italian).

COMPDYN 2023
9th ECCOMAS Thematic Conference on
Computational Methods in Structural Dynamics and Earthquake Engineering
M. Papadrakakis, M. Fragiadakis (eds.)
Athens, Greece, 12-14 June 2023

# PRELIMINARY RESULTS OF A SHAKING-TABLE DYNAMIC TEST ON A REPAIRED AND ENHANCED REINFORCED CONCRETE INFILLED STRUCTURE

**Riccardo R. Milanesi[1], Gabriele Guerrini[2], Davide Bolognini[1], Luca Grottoli[1], Filippo Dacarro[1], Paolo Morandi[1]**

[1] EUCENTRE Foundation
Via Ferrata, 1 - 27100, Pavia (PV) - Italy
{riccardo.milanesi, davide.bolognini, luca.grottoli, filippo.dacarro, paolo.morandi}@eucentre.it

[2] Department of Civil Engineering and Architecture
University of Pavia
Via Ferrata, 3 - 27100, Pavia (PV) - Italy
gabriele.guerrini@unipv.it

## Abstract

*Although several post-earthquake surveys and previous studies have addressed the seismic vulnerability of infilled reinforced concrete (RC) structures built without proper seismic design, investigations have focused on repair and enhancement techniques only in recent years thanks to the development of new materials and the increase of public awareness. Moreover, experimental investigations have more commonly addressed strengthening techniques of pristine specimens rather than repairing solutions for damaged elements, because of the difficulty in defining a proper level of pre-existing damage.*

*This paper describes an experimental campaign conducted at the EUCENTRE Foundation (Pavia, Italy) and discusses some preliminary results. The research work addresses the effectiveness of repair and strengthening techniques applied to a pair of identical structures through incremental dynamic shake-table tests. The specimens consisted of real scale three-story RC frames with clay masonry infills that were previously damaged up to two different levels to simulate two distinct post-earthquake conditions.*

*The structures were repaired and enhanced depending on the preexisting damage and then subjected to the same loading protocol to allow a direct comparison on the effectiveness of the adopted techniques. The interventions involved the most vulnerable structural and non-structural elements and can be summarized in: (i) strengthening of the first-story RC columns, (ii) repair and enhancing of first-story RC slab-column joints, and (iii) enhancement of the masonry infills for both in-plane and out-of-plane resistance.*

**Keywords:** existing reinforced concrete frames, masonry infills, seismic repair, seismic strengthening, dynamic shake-table test.

## 1 INTRODUCTION

Infilled reinforced concrete (RC) frames are among the most common structural typology in many countries worldwide: they have become popular during the XX century and are still frequently built. The knowledge acquired through post-earthquake field observations [1-2] or experimental and numerical scientific studies [3-12] has led to progressive improvements in the response of these structures, especially thanks to code prescriptions addressing new construction. However, a large number of existing buildings that were not designed for earthquake resistance are still in use, and are typically affected by severe damage in seismic events (Figure 1).

Despite the well-known deficiencies causing the seismic vulnerability of infilled RC structures, investigations have focused on repair and enhancement techniques only in recent years, thanks to the sharp evolution of the construction material industry and to the increased public awareness about seismic risk mitigation [11-12]. Strengthening techniques have usually been studied through separate experimental investigations to characterize, for example, the enhancement on RC column or beam elements [13-17], RC beam-column joints [18-19], or masonry infills [20-28]. Experimental studies more commonly address interventions applied to pristine specimens than repairing techniques for damaged elements, due to the difficulty in defining a proper level of pre-existing earthquake damage.

This work discusses the seismic behavior of a pair of real scale three-story infilled RC frames, considering the preliminary results of a unidirectional dynamic shake-table test and focusing on the effectiveness of repair and strengthening interventions applied to columns, slab-column joints, and infill walls. The two structures were identical except for the level of initial damage; in fact, they were previously tested on a different experimental campaign that induced severe damaged on one specimen, but only minor damage on the other one [29].



(a) (b)

Figure 1 Damage to infilled frames and RC elements after the 2016 Central Italy earthquake sequence: (a) infill panels; (b) RC beam-column joint.

# 2 DESCRIPTION OF THE SPECIMENS AND INTERVENTIONS

## 2.1 Original structures from the previous experimental campaign

The original structures were part of a previous experimental campaign [29]. The two test specimens (Figure 2) consisted of two three-dimensional infilled RC frames, with 4 columns each. Each building had a floor plan of 5.0 m x 2.1 m and clear story heights of 2.5 m. They were built side by side on the same RC foundation, fastened to the shaking table, leaving a gap of about 20 cm orthogonal to the shaking direction.

The RC columns had a 20 cm x 20 cm square cross-section. They were reinforced with 4 Φ16-mm longitudinal corner bars (with a reinforcement ratio of about 2%) and Φ8-mm closed square stirrups spaced at 100 mm (Figure 3). At the lower and upper ends of the first-story columns the stirrup spacing was reduced to 50 mm over a length of about 400 mm. The floors consisted of 400-mm-thick solid RC slabs. No stirrups or other shear reinforcement was provided at the slab-column joints within the slab thickness, to simulate non-seismic detailing.

9-cm-thick infills were provided within the 6 longitudinal bays (2 per floor) of each frame. They consisted of 8-cm-thick, hollow clay units with holes aligned horizontally and an about 65% perforation rate. An approximately 1-cm-thick plaster layer was applied on one side of the panels, using the same mortar of the infill bed joints. The internal infills at the first and second stories had respectively 3 and 2 openings of different sizes, to accommodate the elements of a safety steel frame; the external infills had identical perforations at the same stories to grant symmetry.

At the end of the previous testing campaign, the first-story RC joints and infills of the West building were heavily damaged (Figure 4), after reaching a peak interstory drift ratio of 0.88%.

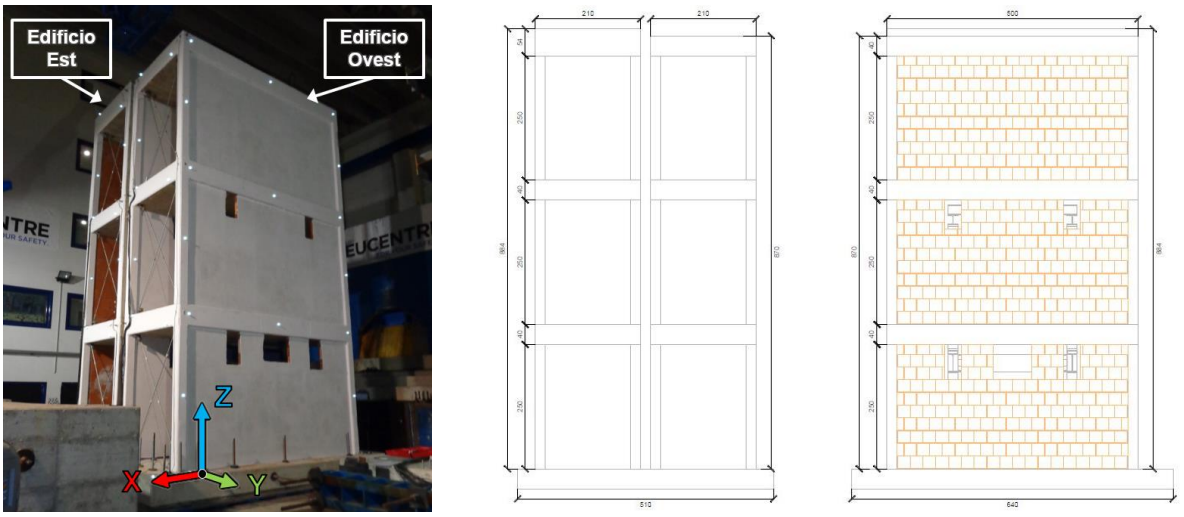


(a) (b) (c)

Figure 2 Specimens from the previous experimental campaign: (a) North-West corner photo; (b) North elevation; (c) West elevation [29].

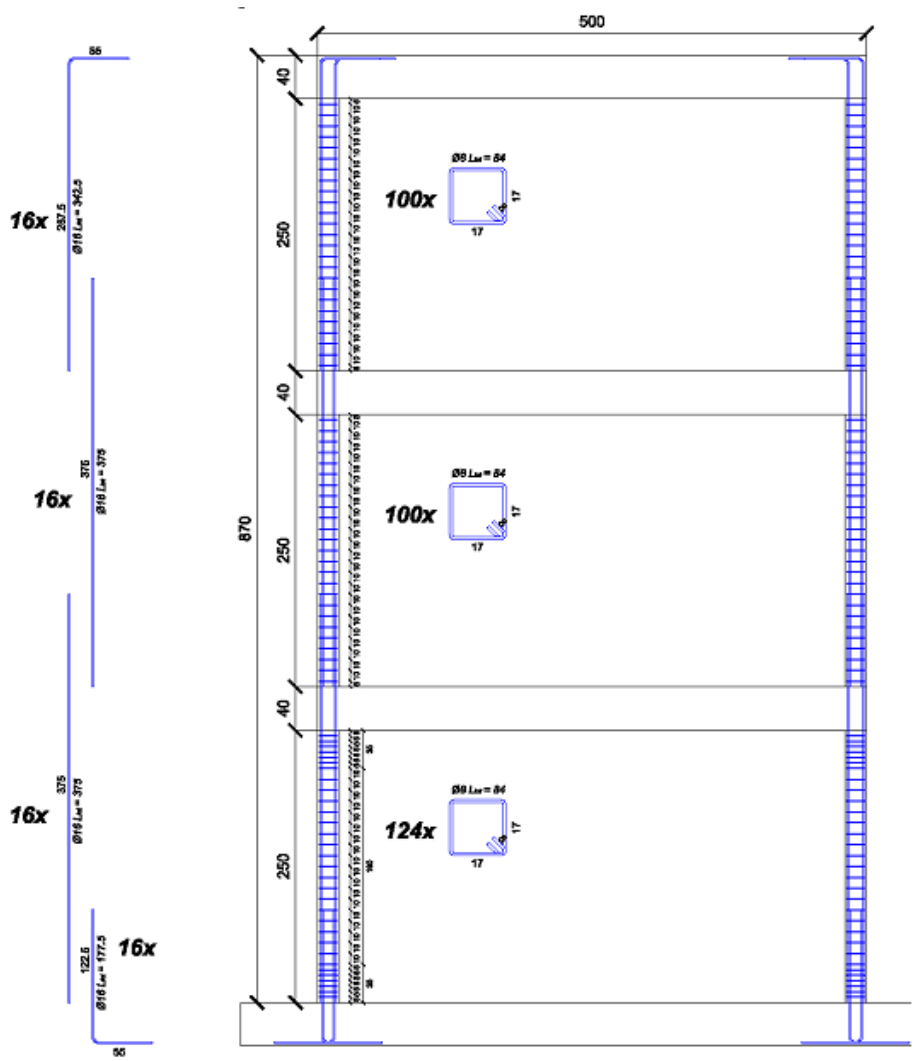


Figure 3 Column reinforcement details of the original RC structure.



(a) (b)

Figure 4 Damage at the end of the previous experimental campaign before interventions: (a) infill panels; (b) RC beam-column joint.

## 2.2 Interventions on RC members and masonry infills

The extent of damage found in both buildings at the end of the previous experimental campaign was comparable to situations that occur after a high-intensity seismic event. Such damage provided an ideal context for testing repair solutions and strengthening techniques on RC structural elements and masonry infills. Therefore, the following activities were carried out:

1. Demolition of the first-story masonry infills of both buildings;
2. Repair and strengthening of the first-story RC columns and slab-column joints of both structures with a high-performance, fiber-reinforced concrete jacket (Figure 5);
3. Reconstruction of the first-story masonry infills of both specimens, avoiding openings on the exterior panels, where not required by the steel safety frame (Figure 6a);
4. In-plane enhancement of all masonry infills, except for the two first-story panels of the East building (Figure 6b-c), by applying a basalt-fiber mesh within a specific mortar;
5. Construction of 4 double-leaf masonry infills (2 per building) at the second story and of 6 infills (3 per building) at the third story, perpendicular to the shaking direction, to be tested out of plane (Figure 7); these panels had a length of about 1.0 m, were restrained only at their top and bottom, and were left free along their vertical edges;
6. Enhancement of the out-of-plane masonry panels through several techniques, including (i) fastening to the top RC slab, (ii) adding rigid or flexible connections between the two masonry leaves, and (iii) providing different surface enhancements such as the application of a particular mortar on one or both sides, with or without a basalt-fiber mesh.



(a) (b) (c) (d)

Figure 5 Interventions on RC frame: (a) first-story beam-column joint of the East building at the end of the previous experimental campaign; (b) joint repairing; (c) column strengthening; (d) cross-section of the strengthened column during the demolition at the end of the tests.



(a) (b) (c)

Figure 6 Interventions on masonry infills: (a) first-story infill reconstruction; (b) in-plane infill enhancement with basalt-fiber mesh and mortar; (c) in-plane enhanced infill after completion.



(a) (b)

Figure 7 Masonry panels for out-of-plane testing: (a) construction of a double-leaf panel; (b) plastered panel before enhancement.

## 3 TEST SETUP, PROTOCOL, AND INSTRUMENTATION

In the chosen reference system, the northward X-axis coincides with the shaking direction, while the Y- and Z-axis point westward and upward, respectively (Figure 2). In its final configuration, the specimens consisted of two RC frames with masonry infills in the longitudinal (X) direction, both resting on the same foundation slab anchored to the shaking table. Therefore, the same unidirectional acceleration histories were applied along the X-axis to both buildings simultaneously during the tests.

One horizontal component of the November 23rd, 1980, Irpinia (Italy) earthquake was selected as the input signal and applied incrementally, with random noise run between each increment for dynamic identification and control calibration purposes. The original ground motion record is characterized by peak ground acceleration PGA = 0.32 g, effective duration $T_D$ = 6.32 s, Arias intensity $I_a$ = 1.41 m/s, and cumulative absolute velocity CAV = 10.88 m/s. Figure 8 shows the ground motion signal and its acceleration spectrum for 5% damping. Table 1 reports the nominal and actual PGA and maximum spectral accelerations.

Accelerometers and displacement transducers were installed to monitor the global response of the structures and the local behavior of the panels excited out of their planes. The two buildings were equipped with the same sensor layout, for a total of 27 accelerometers and 47 linear displacement transducers (Table 2).

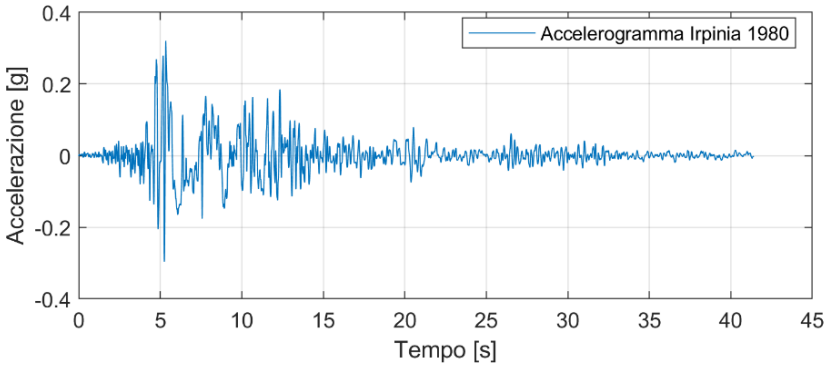


(a)

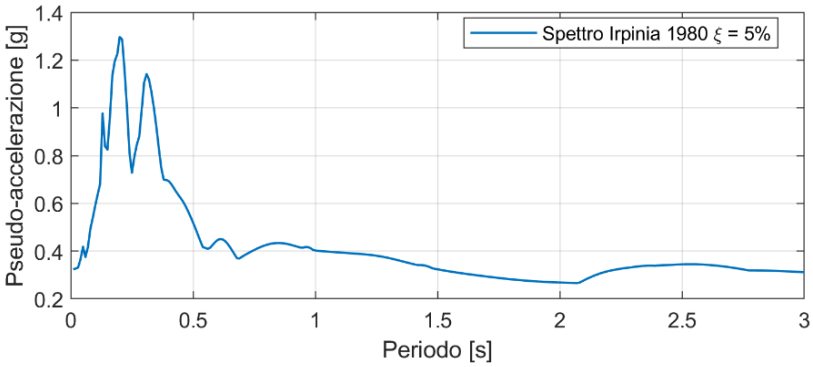


(b)

Figure 8 Irpinia 1980 earthquake: (a) reference time history ground motion; (b) spectrum at 5% damping.

| Test No. | PGA (nominal) [g] | PGA (actual) [g] | Max spectral acceleration (nominal) [g] | Max spectral acceleration (experimental) [g] |
|---|---|---|---|---|
| 2 | 0.08 | 0.06 | 0.33 | 0.15 |
| 3 | 0.08 | 0.08 | 0.33 | 0.27 |
| 4 | 0.08 | 0.09 | 0.33 | 0.29 |
| 6 | 0.32 | 0.22 | 1.31 | 0.66 |
| 8 | 0.32 | 0.36 | 1.31 | 1.06 |
| 10 | 0.32 | 0.42 | 1.31 | 1.42 |
| 12 | 0.40 | 0.58 | 1.64 | 1.84 |
| 14 | 0.48 | 0.79 | 1.97 | 2.36 |
| 17 | 0.56 | 0.41 | 2.30 | 1.24 |
| 18 | 0.56 | 0.35 | 2.30 | 1.27 |
| 20 | 0.40 | 0.49 | 1.64 | 1.60 |

Table 1 Main test sequence and input accelerations.

| **Accelerometers** | |
|---|---|
| 2 | Shaking table and RC foundation |
| 12 | 2 per floor on each structure |
| 5 | Setup elements where linear transducers were installed |
| 8 | Centre of each out-of-plane infill at the second story |
| **Linear displacement transducers** | |
| 4 | Relative displacement and uplift between the shaking table and the RC foundation |
| 1 | Displacement of the shaking table |
| 24 | Displacement and rotation of the floor slabs |
| 18 | Displacements of the out-of-plane infill panels (3 per panel) |

Table 2 Accelerometers and linear displacement transducers.

## 4 PRELIMINARY EXPERIMENTAL RESULTS

The great quantity of testing data provides both general and specific outcomes, dealing with the overall behavior of the structure and the seismic response of individual structural members and enhanced masonry infills. Furthermore, the comparison with the unstrengthened building tested in the previous experimental campaign allows for an interesting discussion. However, most of the results require a deeper interpretation that will be part of future work. In this section, the preliminary results are only briefly reported.

### 4.1 Damage evolution during the test

The damage evolution highlighted an overall satisfiying seismic response of the infilled structure, with evident effectiveness of the first-story RC column and joint repair/strengthening resulting in a soft-story mechanism at the unstrenghetend second storey in both structures. The main structural damage occurred at the second floor RC non-retrofitted slab-column joints (Figure 9).

The enhanced infills successfully reached a 1.20% peak interstory drift ratio with only localized and repairable damage (Figure 10). The improved panels also showed a superior out-of-plane behavior compared to the unstrengthened ones, although their detailed behavior will be addressed in future publications.

Table 3 summarizes the main aspects of the damage pattern.



(a) (b) (c)

Figure 9 Damage evolution of the unstrengthened second-floor slab-column joints: (a) after test 14; (b) after test 18; (c) after test 20.



(a) (b) (c)

Figure 10 Damage evolution of the infills excited in their plane: (a) after test 12; (b) after test 14; (c) after test 18.

| Test No. | PGA [g] | RC structures | Infills excited in plane |
|---|---|---|---|
| 4 | 0.09 | Flexural cracks on the 2nd-story columns. | Small cracks at the interface between all infills and RC elements. |
| 6 | 0.22 | Increased number/length of existing cracks. Shear cracks in the 2nd-floor slab-column joints of the West frame. | Cracks almost all along the 2nd- and 3rd-story infill interfaces. Unstrengthened 1st-story infills almost detached from the RC frame, yet stable. |
| 8 | 0.36 | Increased number/length of existing cracks. Flexural cracks along the 3rd-story columns. | Cracks all along the interfaces of all infills. Crushing of the top-north corner masonry unit of the 2nd-story West infill of the West frame. |
| 10 | 0.42 | Increased number/length of existing cracks. Cracks at the bottom of the 2nd-story slab near the columns of the West frame. | Increased width of interface cracks. Diagonal crack in the 1st-story unstrengthened infill between opening and top corner. Minor corner detachments of the strengthening plaster at the 2nd story. |
| 12 | 0.58 | Increased number/length of existing cracks. Flexural cracks along the 1st-story columns. Shear cracks in the 2nd- and 3rd-floor slab-column joints of the East frame. | Diagonal crack in the 1st-story enhanced infill between opening and top corner. Still limited corner detachments of the strengthening plaster (Figure 10a), now also at the 1st story. |
| 14 | 0.79 | Increased number/length of existing cracks. Considerable shear cracks in the 2nd-story joints (Figure 9a). Small flexural cracks on the 1st-floor slab side, close to the strengthened nodes. | Increased cracking on the 1st-story unstrengthened infill with openings (Figure 10b). Cracking of the 2nd-story strengthened infill with openings. Increased corner detachments of the strengthening plaster at the 2nd story. |
| 17<br>18 | 0.41<br>0.35 | Increased number/length of existing cracks. Spalling in the 2nd-story joints on the North sides of both frames (Figure 9b). | Increased cracking on the 1st-story unstrengthened infill with openings. Increased corner detachments of the strengthening plaster at the 2nd story, with masonry crushing of a few top corners in the West building (Figure 10c). |
| 20 | 0.49 | Increased number/length of existing cracks. Extensive spalling in the 2nd-story joints on the North sides of both frames (Figure 9c). | General worsening of existing damage patterns. Crushing of the top-north corner masonry unit of the 1st-story East infill of the East frame. |

Table 3 Summary of the damage evolution on RC elements and infills excited in plane.

## 4.2 Preliminary plots of the experimental results

The global results for the two infilled structures have been derived from the instrumentation installed on the slabs. The acceleration, force, and displacement values are taken along the X-axis, i.e. the shaking direction of the unidirectional test sequence.

Figure 11 shows the positive and negative floor acceleration envelopes for every test. In Table 4 and Table 5 also the peak floor accelerations are reported, together with the corresponding amplifications with respect to the applied table accelerations.

The positive and negative floor displacement envelopes are plotted in Figure 12 for every test. The interstory displacements concentrate at the second story, were peak interstory drift ratios of 1.0% and 1.2% were reached in the East and West building, respectively. The maximum first-story drift ratios were at 0.32% and 0.19% for the same buildings, whereas the second-story ratios peaked at 0.24% and 0.22%.

| Test No. | Maximum floor acceleration [g] | | | | Accel. amplification w.r.t table [-] | | |
|---|---|---|---|---|---|---|---|
| | Table | Floor 1 | Floor 2 | Floor 3 | Floor 1 | Floor 2 | Floor 3 |
| 2 | 0.059 | 0.070 | 0.087 | 0.095 | 1.192 | 1.479 | 1.607 |
| 3 | 0.085 | 0.113 | 0.158 | 0.160 | 1.341 | 1.863 | 1.885 |
| 4 | 0.094 | 0.157 | 0.199 | 0.198 | 1.673 | 2.121 | 2.101 |
| 6 | 0.215 | 0.366 | 0.501 | 0.633 | 1.701 | 2.331 | 2.940 |
| 8 | 0.356 | 0.624 | 0.887 | 1.014 | 1.752 | 2.487 | 2.846 |
| 10 | 0.424 | 0.741 | 1.188 | 1.233 | 1.745 | 2.799 | 2.906 |
| 12 | 0.583 | 0.761 | 1.311 | 1.327 | 1.305 | 2.248 | 2.276 |
| 14 | 0.894 | 0.951 | 1.309 | 1.430 | 1.197 | 1.649 | 1.801 |
| 17 | 0.408 | 0.630 | 1.063 | 1.162 | 1.546 | 2.607 | 2.851 |
| 18 | 0.349 | 0.666 | 0.975 | 1.174 | 1.907 | 2.790 | 3.362 |
| 20 | 0.491 | 0.933 | 1.127 | 1.373 | 1.901 | 2.296 | 2.797 |

Table 4 Maximum floor accelerations and amplifications of the East building.

| Test No. | Maximum floor acceleration [g] | | | | Accel. amplification w.r.t. table [-] | | |
|---|---|---|---|---|---|---|---|
| | Table | Floor 1 | Floor 2 | Floor 3 | Floor 1 | Floor 2 | Floor 3 |
| 2 | 0.059 | 0.066 | 0.103 | 0.120 | 1.125 | 1.741 | 2.042 |
| 3 | 0.085 | 0.131 | 0.182 | 0.214 | 1.543 | 2.153 | 2.531 |
| 4 | 0.094 | 0.150 | 0.219 | 0.272 | 1.591 | 2.328 | 2.890 |
| 6 | 0.215 | 0.417 | 0.496 | 0.675 | 1.936 | 2.306 | 3.138 |
| 8 | 0.356 | 0.590 | 0.799 | 1.067 | 1.654 | 2.241 | 2.993 |
| 10 | 0.424 | 0.707 | 1.113 | 1.363 | 1.666 | 2.623 | 3.210 |
| 12 | 0.583 | 0.941 | 1.415 | 1.504 | 1.614 | 2.428 | 2.508 |
| 14 | 0.894 | 1.089 | 1.265 | 1.430 | 1.372 | 1.593 | 1.801 |
| 17 | 0.408 | 0.664 | 1.183 | 1.322 | 1.630 | 2.903 | 3.242 |
| 18 | 0.349 | 0.698 | 1.145 | 1.235 | 1.999 | 3.278 | 3.534 |
| 20 | 0.491 | 0.915 | 1.225 | 1.299 | 1.865 | 2.495 | 2.645 |

Table 5 Maximum floor accelerations and amplifications of the West building.

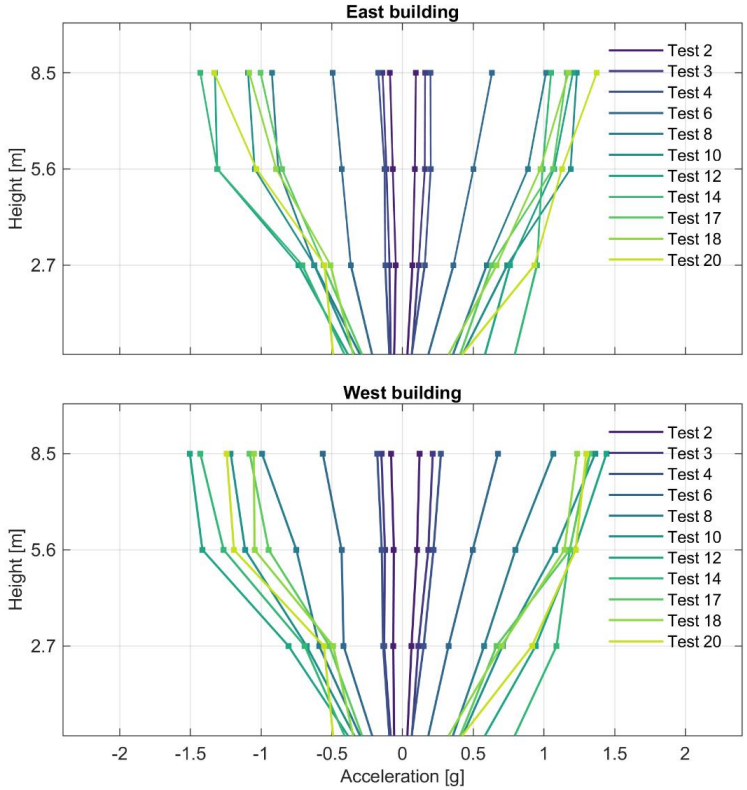


Figure 11 Positive and negative floor acceleration envelopes for both buildings and every test.

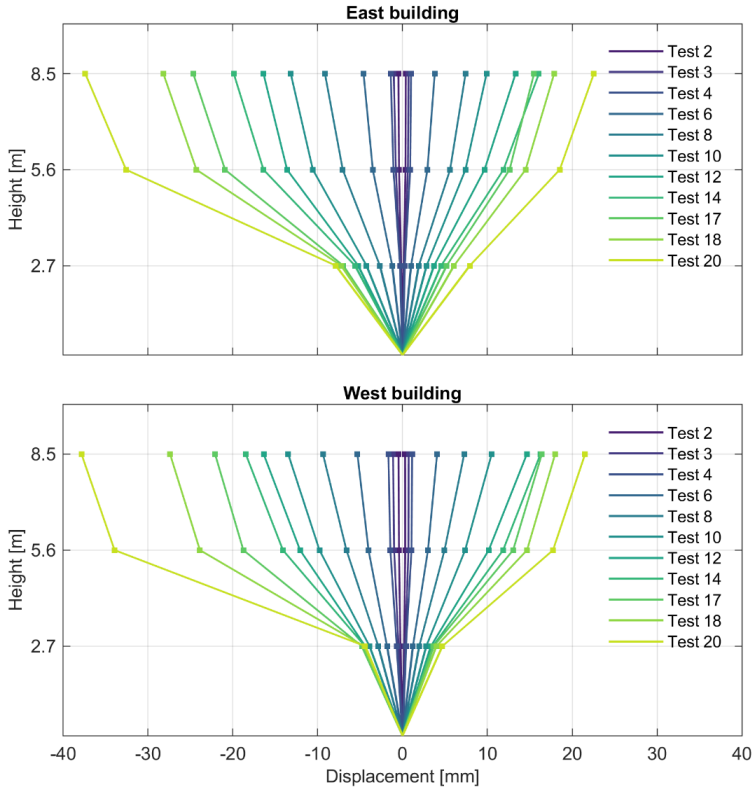


Figure 12 Positive and negative displacement envelopes for both buildings and every test.

Floor inertia forces were calculated by multiplying floor accelerations times tributary masses, according to Figure 13**Errore. L'origine riferimento non è stata trovata.**a. The shear-displacement backbone curves were plotted in terms of both global response (base shear vs top displacement, Figure 13**Errore. L'origine riferimento non è stata trovata.**b) and individual story response (story shear vs. interstory displacement, Figure 13**Errore. L'origine riferimento non è stata trovata.**c). These curves were obtained by taking the points of maximum positive and negative shear from each test run.

The specimens behaved similarly overall, with the East building showing slightly larger deformation of the first story (whose slab-column joints, even though repaired, were previously severely damaged) while the West building concentrating more at the second story.

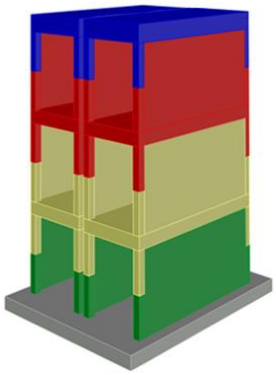

(a)

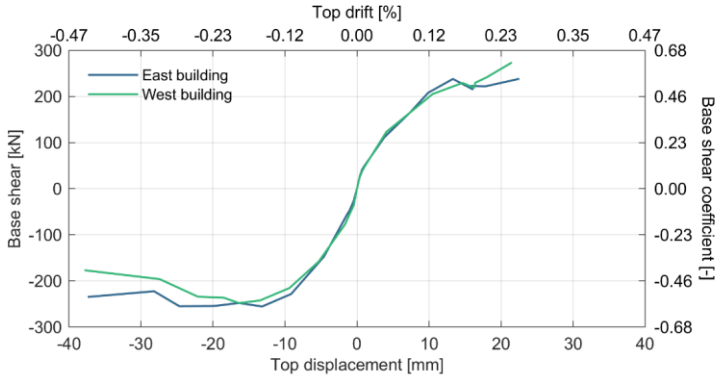


(b)

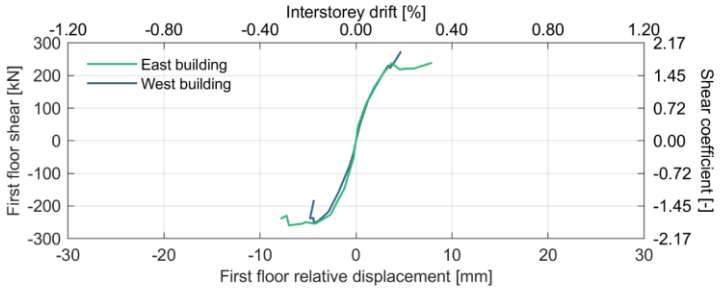


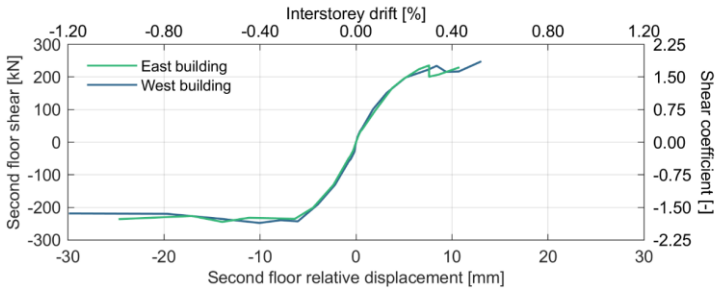


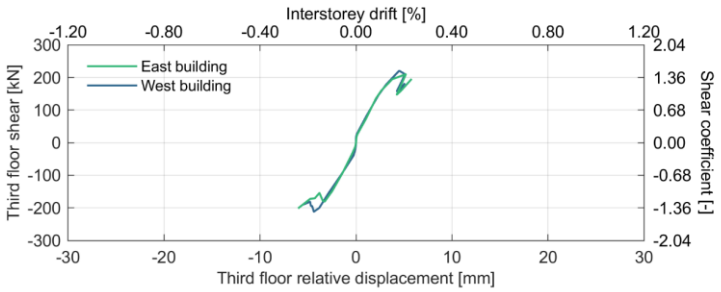


(c)

Figure 13 Lateral force-displacement responses: (a) mass distribution for the computation of inertia forces; (b) base shear vs. top displacement backbone curves; (c) individual story shear vs. interstory drift backbone curves.

## 5 CONCLUSIONS

The experimental study discussed in this paper is the continuation of a previous campaign [29] where two identical infilled RC structures were damaged to different extents through a unidirectional dynamic shake-table test, with a natural ground motion record applied in incremental steps. The two specimens, consisting of one-bay, three-story RC frames, were built at real scale, side by side on the same foundation. The masonry infills were made of hollow clay units with holes aligned horizontally.

For this work, the damaged structures were repaired (first-story RC slab-column joints) and strengthened (first-story RC joints and columns) with a high-performance, fiber-reinforced concrete jacket. The masonry infills parallel to the shaking direction were rebuilt at the first story and enhanced with a basalt-fiber mesh embedded in a plaster overlay, everywhere except for the first story of one building. Some infill panels were also built and strengthened perpendicular to the shaking direction, but their out-of-plane behavior is not the object of this paper.

The damage evolution, the floor acceleration and displacement envelopes, and the story shear-displacement backbone curves demonstrate an improved seismic performance of the structural and non-structural elements that had been repaired and/or enhanced. The failure mechanism transitioned from a soft first story (previous campaign) to a soft second story, controlled by shear on the unstrengthened second-floor slab-column joints. Indeed the interventions on the first-floor RC joints not only restored their original resistance, but also effectively increased it, making then stronger than the second-floor ones. Furthermore, the in-plane drift imposed on the enhanced infills at the second story demonstrated their increased deformation capacity, compared to the bare masonry ones.

This paper presents only the preliminary results of the experimental campaign, and future developments will cover several aspect such as a complete comparison with the unstrengthened infilled structure previously tested, a more detailed interpretation of the repair/strengthening effects on the global infilled frame response and on the in-plane infill behavior [28], and an analysis of the out-of-plane infill response with different enhancement interventions.

## ACKNOWLEDGEMENTS

The work presented is part of an ongoing study at the EUCENTRE Foundation in collaboration with Kerakoll S.p.A., that is acknowledged for its financial support.

## REFERENCES

[1] A. Masi, L. Chiauzzi, G. Santarsiero, V. Manfredi, S. Biondi, E. Spacone, C. Del Gaudio, P. Ricci, G. Manfredi, G.M. Verderame. Seismic response of RC buildings during the Mw 6.0 August 24, 2016 Central Italy earthquake: the Amatrice case study. *Bull Earthquake Eng*, 17, 5631–5654, https://doi.org/10.1007/s10518-017-0277-5, 2019.

[2] I.O. Demirel, A. Yakut, B. Binici, Seismic performance of mid-rise reinforced concrete buildings in Izmir Bayrakli after the 2020 Samos earthquake, *Engineering Failure Analysis*, 137, 106277, https://doi.org/10.1016/j.engfailanal.2022.106277, 2022.

[3] R.E. Klingner, N.R. Rubiano, T.R. Bashandy, S.C. Sweeney, Evaluation and analytical verification of shaking table data from infilled frames, *11th World Conference on Earthquake Engineering*, Acapulco, Mexico, June 23-28, 1996.

[4] A. Hashemi, K.M. Mosalam, Shake-table experiment on reinforced concrete structure containing masonry infill wall, *Earthquake Engineering and Structural Dynamics*, 35: 1827-1852, 2006.

[5] A. Stavridis, I. Koutromanos, P.B. Shing, Shake-table tests of a three-story reinforced concrete frame with masonry infill walls, *Earthquake Engineering and Structural Dynamics*, 41: 1089-1108, 2012.

[6] M. Tondelli, S. Petry, S. Peloso, K. Beyer, Shake-table test on four-storey structure with reinforced concrete and unreinforced masonry walls, *Proc. Recent Advances in Earthquake Engineering and Strucrural Dynamics 2013*, Vienna, Austria, August 28-30, 2013.

[7] M. Tondelli, S. Petry, I. Lanese, S. Peloso, K. Beyer. Shake Table Testing of a Half-Scaled RC-URM Wall Structure. *In: Taucer, F., Apostolska, R. (eds) Experimental Research in Earthquake Engineering. Geotechnical, Geological and Earthquake Engineering*, vol 35. Springer, Cham. https://doi.org/10.1007/978-3-319-10136-1_18, 2015.

[8] G.J. O'Reilly, T.J. Sullivan. Modeling Techniques for the Seismic Assessment of the Existing Italian RC Frame Structures, *Journal of Earthquake Engineering*, DOI: 10.1080/13632469.2017.1360224, 2017.

[9] G.M. Verderame, P. Ricci, M.T. De Risi, C. Del Gaudio, Experimental Assessment and Numerical Modelling of Conforming and Non-Conforming RC Frames with and without Infills, *Journal of Earthquake Engineering*, 26(2), 573-614, 2022.

[10] M.T. De Risi, M. Di Domenico, V. Manfredi, M. Terrenzi, G. Camata, F. Mollaioli, F. Noto, P. Ricci, P. Franchin, A. Masi, E. Spacone, G.M. Verderame. Modelling and Seismic Response Analysis of Italian Pre-Code and Low-Code Reinforced Concrete Buildings. Part I: Bare Frames, y*Journal of Earthquake Engineering*, 27:6, 1482-1513, DOI: 10.1080/13632469.2022.2074919, 2023.

[11] I. Koutromanos, M. Kyriakides, A. Stavridis, Shake-table tests of a 3-story masonry-infilled RC frame retrofitted with composite materials, *Journal of Structural Engineering*, 139(8), https://doi.org/10.1061/(ASCE)ST.1943-541X.0000689, 2013.

[12] M.T. De Risi, C. Del Gaudio, S.A. Scala, G.M. Verderame, Seismic retrofitting strategies for pre-70 RC buildings: the effectiveness of "local interventions", *Procedia Structural Integrity*, 44, 958-965, https://doi.org/10.1016/j.prostr.2023.01.124, 2023.

[13] M.K. Askar, A.F. Hassan, Y.S.S. Al-Kamaki, Flexural and shear strengthening of reinforced concrete beams using FRP composites: A state of the art, *Case Studies in Construction Materials*, 17, https://doi.org/10.1016/j.cscm.2022.e01189, 2022.

[14] S. Bahji, S. Omary, V. Steiner, F. Feugeas, Strengthening reinforced concrete beams by using different types and methods of fiber-reinforces polymers: a critical review, *Practice Periodical on Structural Design and Construction*, 27(4), 2022.

[15] H. Huang, M. Guo, W. Zhang, M. Huang, Seismic behavior of strengthened RC columns under combined loadings, *Journal of Bridge Engineering*, 27(6), 2022.

[16] K. Samy, M.A. Fouda, A. Fawzy, T. Elsayed, Enhancing the Effectiveness of Strengthening RC columns with CFRP sheets, *Case Studies in Construction Materials*, 17, https://doi.org/10.1016/j.cscm.2022.e01588, 2022.

[17] M. Elsayed, B.A. Tayeh, M.A. Elmaaty, Y. Aldahshoory, Behaviour of RC columns strengthened with Ultra-High Performance Fiber Reinforced concrete (UHPFRC) under eccentric loading, *Journal of Building Engineering*, 47, 103857, https://doi.org/10.1016/j.jobe.2021.103857, 2022.

[18] S. Pampanin, G.M. Calvi, M. Moratti, Seismic Behaviour of R.C. beam-column joints designed for gravity loads, *Proc. 12th European Conference on Earthquake Engineering*, London, United Kingdom, September 9-13, 2002

[19] M.T. De Risi, P. Ricci, G.M. Verderame, G. Manfredi, Experimental assessment of unreinforced exterior beam–column joints with deformed bars, *Engineering Structures*, 112: 215-232, https://doi.org/10.1016/j.engstruct.2016.01.016, 2016.

[20] G.M. Calvi, D. Bolognini. Seismic response of reinforced concrete frames inflled with weakly reinforced masonry panels. *Journal of Earthquake Engineering*, 5:153–185. https://doi.org/10.1080/13632460109350390, 2001.

[21] P. Ezzatfar, B. Binici, Ö. Kurç, E. Canbay, H. Sucuoğlu, G. Özcebe. Application of Mesh Reinforced Mortar for Performance Enhancement of Hollow Clay Tile Infill Walls. *In: Ilki, A., Fardis, M. (eds) Seismic Evaluation and Rehabilitation of Structures. Geotechnical, Geological and Earthquake Engineering*, vol. 26. Springer, Cham. https://doi.org/10.1007/978-3-319-00458-7_10, 2014.

[22] A. Furtado, H. Rodrigues, A. Arêde, H. Varum, Out-of-plane behavior of masonry infilled RC frames based on the experimental tests available: A systematic review, *Construction and Building Materials*, 168, 831-848, https://doi.org/10.1016/j.conbuildmat.2018.02.129, 2018.

[23] L.N. Koutas, Z. Tetta, D.A. Bournas, T.C. Triantafillou, Strengthening of Concrete Structures with Textile Reinforced Mortars: State-of-the-Art Review, *Journal of Composites for Construction*, 23(1), 2019.

[24] M. Minotto, N. Verlato, M. Donà, F. da Porto, Strengthening of In-Plane and Out-of-Plane Capacity of Thin Clay Masonry Infills Using Textile- and Fiber-Reinforced Mortar, *Journal of Composites for Construction*, 24(6), 2020.

[25] A. Furtado, H. Rodrigues, A. Arêde, H. Varum, Experimental tests on strengthening strategies for masonry infill walls: A literature review, *Construction and Building Materials*, 263, 120520, https://doi.org/10.1016/j.conbuildmat.2020.120520, 2020.

[26] M.T. De Risi, A. Furtado, H. Rodrigues, J. Melo, G.M. Verderame, A. Arêde, H. Varum, G. Manfredi, Influence of textile reinforced mortars strengthening on the in-plane/out-of-plane response of masonry infill walls in RC frames, *Engineering Structures*, 254, 113887, https://doi.org/10.1016/j.engstruct.2022.113887, 2022.

[27] R. R. Milanesi, P. Morandi, C. F. Manzini, L. Albanesi, G. Magenes. Out-of-plane Response of an Innovative Masonry Infill with Sliding Joints from Shaking Table Tests, *Journal of Earthquake Engineering*, 26:4, 1789-1823, DOI: 10.1080/13632469.2020.1739173, 2022.

[28] M. Kurukulasuriya, R.R. Milanesi, G. Magenes, D. Bolognini, L. Grottoli, F. Dacarro, P. Morandi. Investigation of seismic behaviour of existing masonry infills through com-

bined cyclic in-plane and dynamic out-of-plane tests, *Proc. COMPDYN 2023*, June 12-14, 2023.

[29] G. Rebecchi, P.M. Calvi, A. Bussini, F. Dacarro, D. Bolognini, L. Grottoli, M. Rosti, F. Ripamonti, S. Cii. Full-Scale Shake Table Tests of a Reinforced Concrete Building Equipped with a Novel Servo-Hydraulic Active Mass Damper. *Journal of Earthquake Engineering*, pp.1-24, 2022.

COMPDYN 2023
9th ECCOMAS Thematic Conference on
Computational Methods in Structural Dynamics and Earthquake Engineering
M. Papadrakakis, M. Fragiadakis (eds.)
Athens, Greece, 12-14 June 2023

# COLD FORMED STEEL PANELS FOR THE SEISMIC STRENGTHENING OF EXISTING RC BUILDINGS

**Simone Labò**[1], **Andrea Belleri**[1], **Michelle Gualdi**[1], **Atsushi Sato**[2]

[1] University of Bergamo
Department of Engineering and Applied Sciences
Dalmine (BG), Italia
e-mail: simone.labo@unibg.it, andrea.belleri@unibg.it, m.gualdi5@studenti.unibg.it

[2] Nagoya Institute of Technology
Department of Architecture and Design
Nagoya, Japan
e-mail: sato.atsushi@nitech.ac.jp

## Abstract

*In the last years, structural retrofit solutions for RC buildings have been studied and developed to meet the urgent need to renovate the existing building stock under multiple perspectives: seismic safety, architectural and comfort renovation, and thermal envelope enhancement. Cold-formed steel (CFS) panels could be used for this purpose among other strengthening solutions.*
*This paper investigates the behavior of CFS panels used as seismic strengthening for existing RC buildings. Reduced complexity finite element models are used to numerically simulate the structural behavior of CFS panels; simplified analyses are carried out to derive useful indications about the applicability of these panels in strengthening RC buildings such as, for example, the panel stiffness and strength for varying the panel components.*
*The applicability of CFS panels as a seismic retrofit solution for existing buildings not designed to withstand horizontal loads is herein preliminarily addressed through the application to a reference case study.*

**Keywords:** Renovation, Cold-Formed Steel, Seismic Retrofit System.

# 1 INTRODUCTION

Sustainability has become a huge priority in global development in all fields, including construction. Most European buildings have overcome their "design" end-of-life and manifest both structural and energy efficiency issues. The obsolescence of the existing reinforced concrete (RC) building stock concerns structural and non-structural components and can result in partial or total collapse, particularly under seismic loads. This condition can be found in Italy, where more than 50% of the existing RC buildings were built before 1974 [1], [2], i.e., before the enforcement of modern anti-seismic regulations. In recent years, many initiatives have been promoted to increase building energy performances. However, structural safety is rarely considered.

The concept of sustainability can't be related only to environmental aspects but must incorporate structural safety other than resilience. An integrated and holistic approach including all sustainability aspects in building retrofit was proposed by [3], [4], [5], which define a strategy targeting building renovation to reduce the impact along the building life cycle. Subsequently, the effective implementation of interventions with restorable, versatile, maintainable elements made with reusable materials is the key to reducing the impact of the building itself during its life.

In this regard, using prefabricated and standardized retrofit components allows to speed up the installation procedures and dismantle and reuse of the components at the end of life to reduce the refuse. In this context, the use of Cold-Formed Steel (CFS) panels as seismic-resistant elements is a valuable solution.

The first experimental investigations on the seismic behavior of CFS panels were conducted in the 90s [6], [7]. A series of tests were carried out on shear wall specimens consisting of CFS framing sheathed with sheet steel attached to a gypsum board on one side and with a plain gypsum board on the opposite side by [8] at the University of California. Full-scale shake table testing was run also in "CFS-NEES" North American projects [8].

In Italy, shake-table tests on a two-story full-scale building were conducted [10], showing that even though the box-building behavior and the presence of non-structural elements can increase the lateral resistance of the construction, sudden and undesirable brittle failures can appear. The dynamic behavior of reduced-scale three-story two-bay prototypes was analyzed by [11] where the main outcomes showed that the response to seismic action can be considered adequate thanks to the ductility of the system in the case of strap-braced walls.

Two interesting applications of cold-formed steel panels were tested at the Nagoya Institute of Technology (Nagoya, Japan) ([12], [13], [14], [15], [16]). Based on the results of the experimental campaigns on a) steel trapezoidal sheet shear walls [16], and b) steel sheet shear walls with burring holes [12], these systems are investigated herein with the purpose of evaluating their suitability as seismic retrofit systems for existing RC buildings. With this aim, first, the compatibility of this system with post-World War II RC buildings was assessed. Then a simplified finite element (FE) modeling strategy was developed to numerically investigate the effectiveness of the panel as a seismic force-resistant system (SFRS).

# 2 EXPERIMENTAL TESTS AND PRELIMINARY CONSIDERATIONS

## 2.1 Results of experimental campaigns and simplified backbone curves

For the sake of clarity, the trapezoidal sheet shear walls [16] and the steel sheet shear wall with burring holes [12], are called Panel 1 and Panel 2 in the following, respectively. The main geometries and layout are summarized in **Figure 1**; further details on the tested panels may be found in [16] and [12].

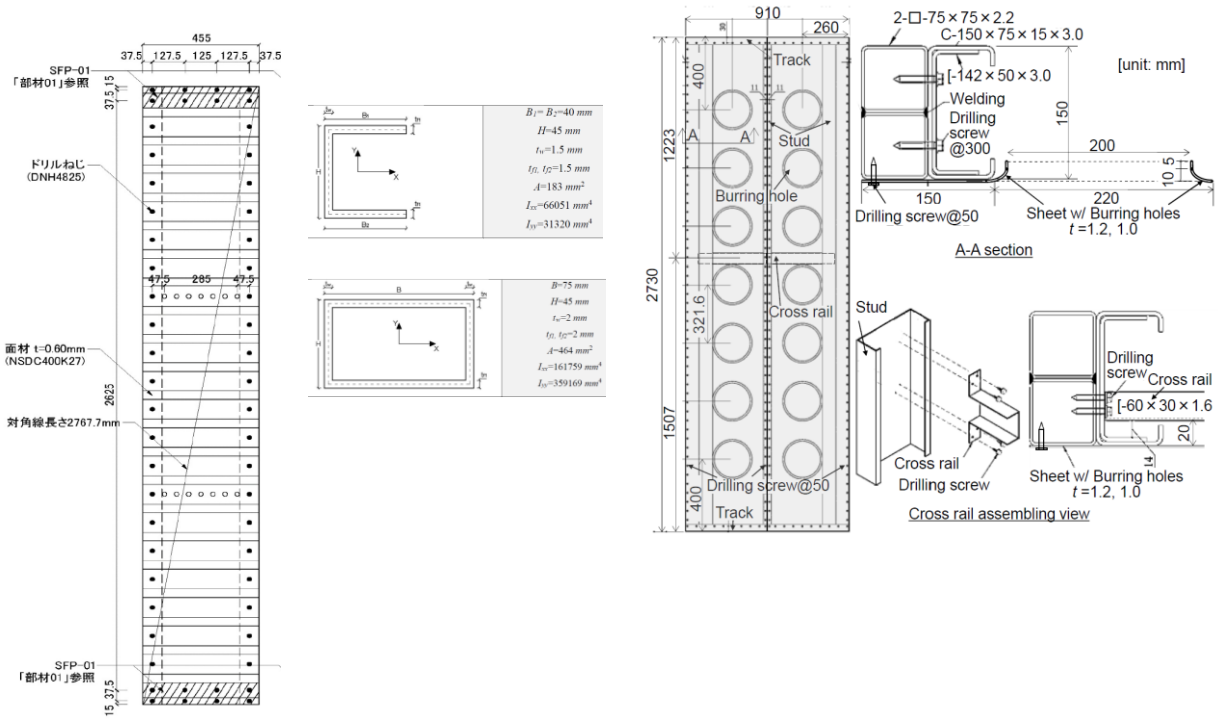


a) b)

Figure 1: Experimental campaigns analyzed: a) the corrugated shear walls. Figure from [16], and b) the steel sheet shear wall with burring holes. Figure from [12].

Both the panels were tested under cyclic loadings. Given the preliminary assessment purpose of this work, only the backbone curve was considered to preliminarily evaluate the panel applicability as seismic strengthening solutions for RC buildings. Experimental results and backbone curves are plotted in **Figure 2**. Since Panel 2 was two times larger than Panel 1, the backbone curve of Panel 1 was doubled (blue in **Figure 2a**).

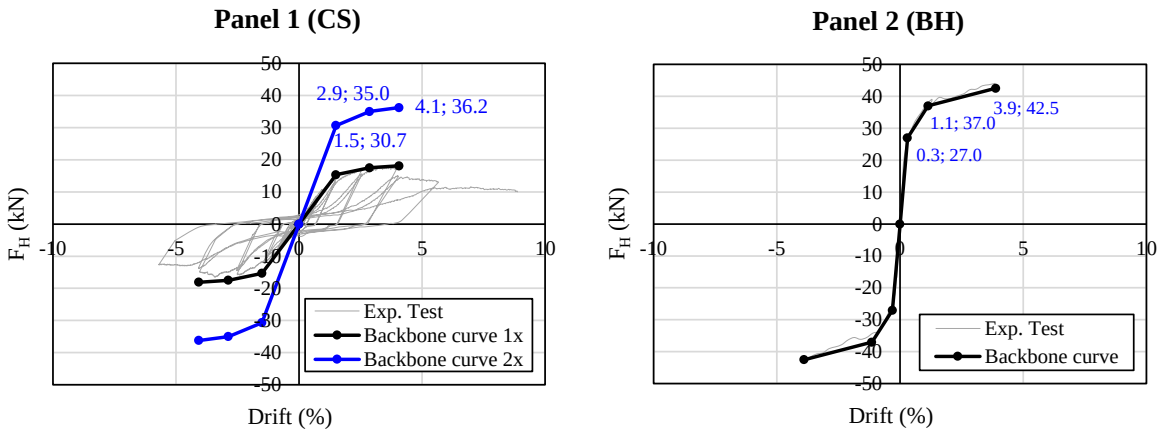


a) b)

Figure 2: Experimental results and backbone curves of the panels: a) Panel 1 – corrugated sheet (CS), and b) Panel 2 – burring holes (BS).

The main parameters of the backbone curves are summarized in **Table 1**.

| | Panel 1 (CS) | 2xPanel 1 (CS) | Panel 2 (BH) | Unit |
|---|---|---|---|---|
| $k_{El}$ | 0.4 | 0.8 | 3.2 | kN/mm |
| $F_y$ | 15 | 31 | 27 | kN |
| $\delta_y$ | 1.5 | 1.5 | 0.3 | (%) |
| $F_u$ | 18 | 36 | 42 | kN |
| $\delta_u$ | 4.1 | 4.1 | 3.9 | (%) |

Table 1: Main parameters of the backbone curves derived from the experimental results.

## 2.2 CFS panels as retrofit systems: preliminary considerations

To draw some preliminary considerations, CFS panels structural features were compared with those related to a post-World War II RC frame. The reference frame was 4.67 m width ($l$) and 3.15 m height ($h$); both the cases with (W) and without (W/O) infills were considered. As for the frame, (50x31.5) cm$^2$ horizontal beams, and (30x30) cm$^2$ RC columns reinforced with 2+2Φ12 mm at the corners and Φ6/120 mm stirrups were considered. For the sake of simplicity, a shear-type behavior was considered. According to the regulation code at the time, concrete C20/25 ($f_{ck}$=25 MPa) and steel Feb32k ($f_{ym}$=315 MPa, $f_{tk}$=490 MPa) were considered.

As for the infills, weak, medium, and strong masonry infills were considered according to [17]. Their contribution was accounted for by means of two compression-only diagonal struts converging in the beam-column joints as adopted by [18], among others. The infills behavior was described by means of a trilinear curve in which cracking and peak forces were evaluated according to Decanini et al. [18], while the cracking and the peak displacement capacities were set as 0.3 % for minor cracking and 0.5 % for the infill failure [19].

Infills trilinear curves are plotted in **Figure 3** in terms of horizontal force (kN) as a function of the inter-story drift ratio (%). The infill panel stiffness ($k_I$) depends on the infill typology considered (weak, medium, and strong) and can be derived by dividing the peak force by the peak displacement to obtain an equivalent stiffness that accounts for cracking.

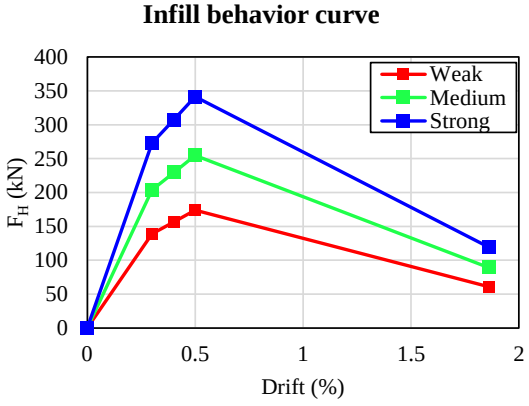


Figure 3: Trilinear curves of weak, medium, and strong infill panels.

The considered cases and the static schemes adopted to derive the stiffness and strength of the existing frame are depicted in **Figure 4**. Accordingly, the stiffness of the bare frame ($k_{BF}$) and of the infilled frame ($k_{IF}$) can be considered equal to $k_{BF} = 2 \cdot \left( \frac{12E^* I}{h^3} \right)$, and $k_{IF} = k_{BF} + k_I$, respectively where, $E^*$ and $I$ are the reduced elastic modulus (e.g., 0.5$E$, to account for cracking) and the inertia momentum of the RC columns, and $h$ is the frame height. The strength of

the bare frame was calculated according to the column dimensions, reinforcing bars, and material and accounting for a vertical load equal to 200 kN thus resembling the axial force of a residential three-floor building [15]. In the case of the infilled frame, the infill peak force was added.

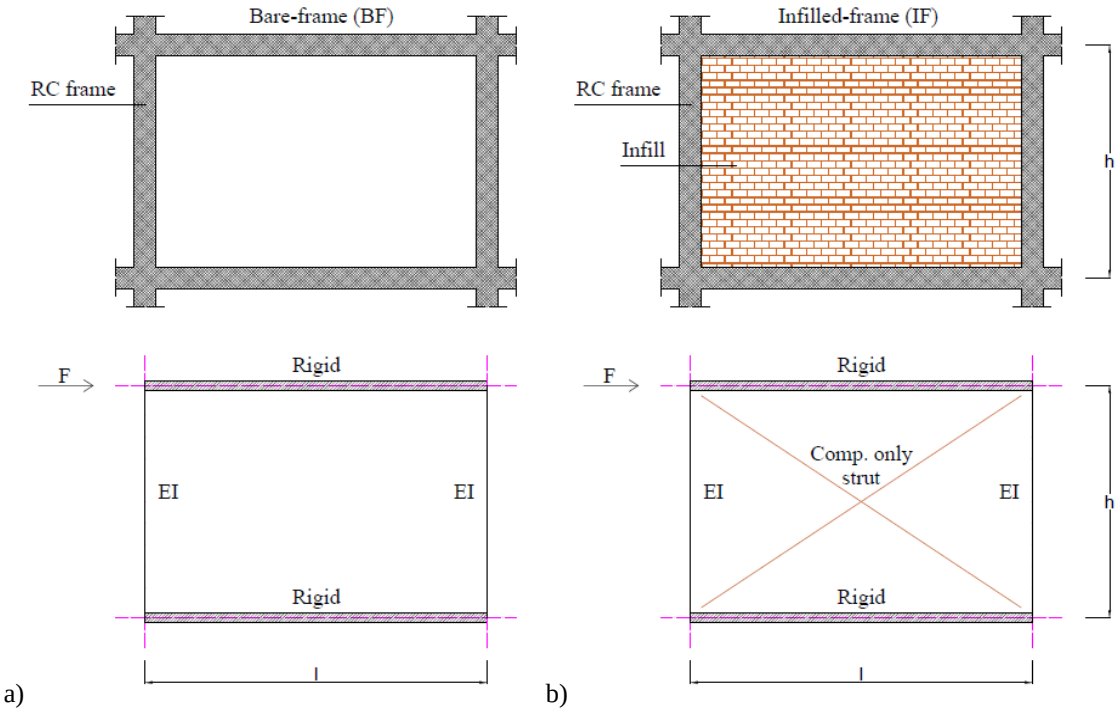


Figure 4: Sketches and static schemes of the reference frames considered: a) bare-frame, b) infilled-frame.

In this work, comparison is made on stiffness and strength considering that steel panels fully cover the frame surface (*l*x*h*); backbone curves were proportioned accordingly. Results are summarized in **Figure 5**. The stiffness and strength are plotted in **Figure 5a** and **Figure 5b**, respectively, for the bare frame (BF), the infilled frame with weak, medium, and strong infills (IF_w, IF_m, IF_s, respectively), Panel 1 (P1), Panel 2 (P2), and the cases in which Panel 1 and Panel 2 were considered as double (2xP1 and 2xP2) to resemble, for instance, sandwich-type panels.

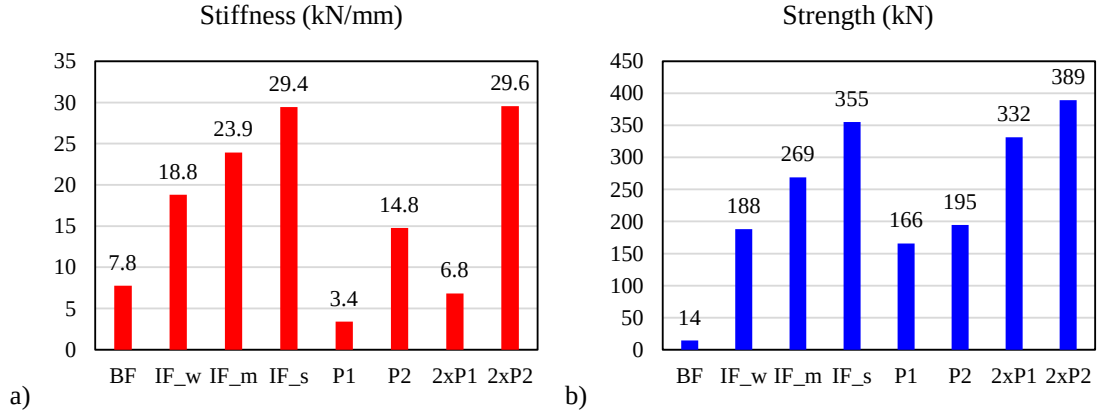


Figure 5: Stiffness and strength of the bare frame (BF), the infilled frame with weak, medium and strong infills (IF_w, IF_m, IF_s, respectively), the Panel 1 (P1), the Panel 2 (P2), and double P1, and P2 (2xP1 and 2xP2, respectively).

From **Figure 5** emerges that the major drawback in applying CFS panel as strengthening solution for RC existing buildings lays in the stiffness; to effectively preserve the existing structure (i.e., avoiding damages on both structural and nonstructural components) and transfer the seismic actions to the external CFS exoskeleton, the two systems stiffnesses must be comparable. Considering the CFS panel and existing frame as two springs in parallel, the seismic forces would be distributed according to their stiffnesses. Then, if the CFS panel stiffness is quite lower than that of the existing frame, even if the panel may provide equal or even greater strength than the existing wall, such a resource cannot be exploited unless extensive damage to the existing wall would allow for reducing its stiffness or selective weakening strategies are applied to the existing infills such as vertical cuts.

From **Figure 5a** emerges that Panel 1 stiffness is not even comparable to the BF case; only by considering a double panel (e.g., in a sandwich solution), its stiffness can be compared to the BF case. On the other hand, Panel 2 stiffness is comparable to a medium-capacity infilled frame (IF_m) and, if used as double (e.g., sandwich panel type), its stiffness may be compared to a strong-capacity infilled frame.

## 3 APPLICATION TO A REFERENCE FRAME

A reference 2D perimetral frame was designed to resemble a typical reinforced concrete (RC) post-World War II building (**Figure 6**). The bearing structure is made of RC beams and columns designed for vertical loads only; column dimensions and steel reinforcement are summarized in **Figure 6a**. To define the static loads, a residential building with a one-way RC beam-and-block flooring system featuring a 3 cm RC overlay for a total thickness of 19 cm was considered; the transversal span of the frame was 3.40 m. As for the non-structural elements, masonry infill panels are made of two layers of hollow bricks with two outer layers of plaster (corresponding to the medium infill in **Section 2**). According to the regulation code at the time of construction, concrete C20/25 ($f_{ck}$=25 MPa) and steel Feb32k ($f_{ym}$=315 MPa, $f_{tk}$=490 MPa) are considered.

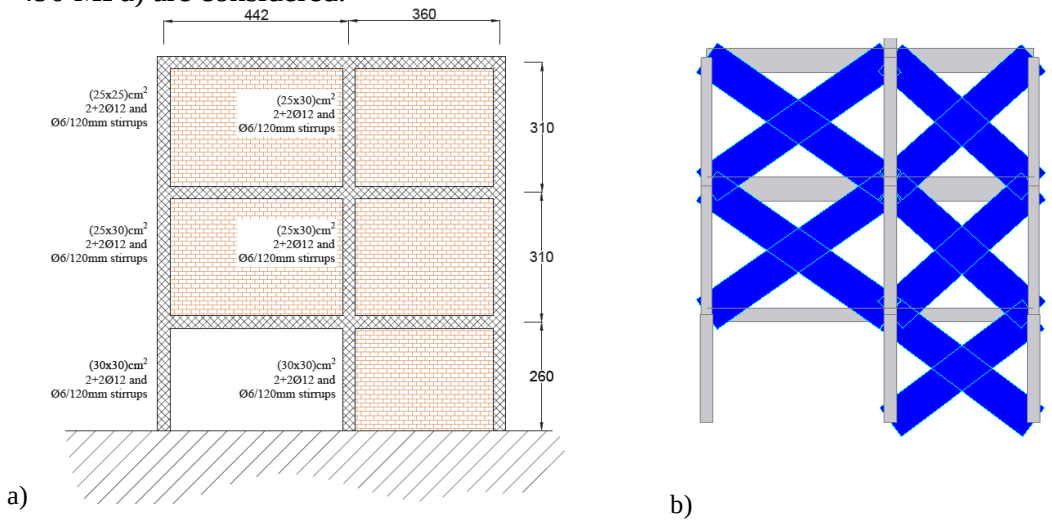


Figure 6: 2D reference frame. a) sketch of the reference 2D frame; b) sketch of the FEM.

The reference 2D frame was modeled with the software MidasGen [20]. *Beam*-type elements were implemented for the RC frame, while compression-only diagonal struts converging in the beam-column joints were adopted for the infills. The inelastic flexural and axial behaviors were accounted for by means of lumped plastic hinges. Strength, and deformation capacity of beams and columns were modelled according to the formulation suggested in the

European building code [21]; the non-linear behavior of the infills was modeled by means of the FEMA infill strut axial plastic hinge [22].

CFS panels were modeled by means of nonlinear *general links* acting in the frame plane. *General links* were calibrated according to the results discussed in **Section 2** and to the frame geometry. Given the infill irregularity, steel panels were supposed to be applied only to the fully infilled portion of the façade (right span in **Figure 6a**). Panels were rigidly connected to the frame.

Nonlinear static analyses were conducted, and the results are summarized in **Figure 7**; points 1, 2, and 3 represent the cracking, peak, and ultimate points of the infill panels, respectively.

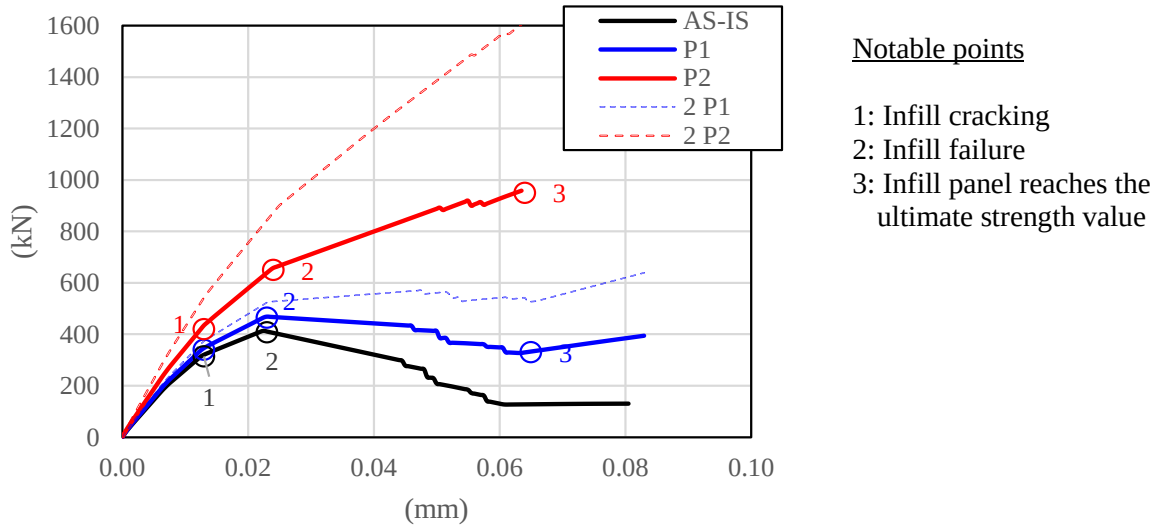


Figure 7: Capacity curves in the AS-IS condition (black) versus those obtained after introducing Panel 1 (blue) and Panel 2 (red) strengthening solutions. The double panels are plotted with dashed lines.

The capacity curve in the AS-IS condition is plotted in black line, Panel 1 solution in blue (P1), and Panel 2 solution in red (P2). As expected, by introducing Panel 1, stiffness and strength slightly increase (less than 30%). It is worth noting that when the infill panel at the base reaches its ultimate capacity (point 3) the capacity curve slightly increases due to the activation of the CFS panel. Although a further drop in the capacity curve was avoided thanks to the Panel 1 loading; however, this condition is associated with extensive damage in the infill panels. The results significantly change when Panel 2 is introduced (red line in **Figure 7)**. The stiffness almost doubled (1.7 times higher) and the global stiffness does not significantly vary at the infill panel failure. When double panels were introduced (dashed lines in **Figure 7**), the results do not significantly vary for the case of Panel 1, while stiffness and strength significantly increased (almost 3 times) in the case of Panel 2.

## 4 CONCLUSIVE REMARKS AND FUTURE DEVELOPMENTS

The paper aims to draw some preliminary consideration about the applicability of CFS panels as a seismic retrofit solution for existing post-World War II buildings. Moving from the results of two experimental campaigns, two solutions were investigated: in the first solution, corrugated steel panels were adopted, and in the second, steel sheet panels with burring holes were used. Preliminary considerations were drawn based on hand calculations and nonlinear analysis results. From the analyses emerged that:

- trapezoidal sheet panels are suitable in the case of bare-frame (without infill) or infilled frame with weak infill panels due to the limited stiffness of this strengthening system;

- sheet panels with burring holes may be an interesting retrofit solution since they allow for higher stiffness and strength with respect to the trapezoidal sheet panels;
- sheet panels with burring holes may develop stiffness and strength compared with those related to an ordinary infilled frame.

The effectiveness of such a retrofit solution deserves to be further evaluated. Moreover, the effectiveness of *sandwich*-type panels should be further investigated from a structural and technological point of view.

## REFERENCES

[1] ANCE, Audizione dell'Ance sulla situazione dell'edilizia scolastica in Italia, 2013.

[2] EU, Directive 2010/30/EU on the indication by labelling and standard product information of the consumption of energy and other resources by energy-related products (recasta), 2010.

[3] A. Marini, C. Passoni, A. Belleri, F. Feroldi, M. Preti, G. Metelli, P. Riva, E. Giuriani e G. Plizzari, Combining seismic retrofit with energy refurbishment for the sustainable renovation of RC buildings: a proof of concept. European Journal of Environmental and Civil Engineering, pp. 1-21, 2017.

[4] C. Passoni, A. Marini, A. Belleri e C. Menna, Redefining the concept of sustainable renovation of buildings: State of the art and LCT-based design framework. Sustainable Cities and Society, n. 64, 2021.

[5] C. Menna, C. Del Vecchio, M. Di Ludovico, G. M. Mauro, F. Ascione e A. Prota, Conceptual design of integrated seismic and energy retrofit interventions. Journal of Building Engineering, n. 38, 2021.

[6] S. Adham, V. Avanessian, G. Hart, R. Anderson, J. Elminger e J. Gregory, Shear wall resistance of lightgage steel stud wall systems. Earthquake Spectra, vol. 6, n. 1, pp. 1-14, 1990.

[7] E. Gad, C. Duffield, G. Hutchinson, D. Mansell e G. Stark, Lateral performance of cold-formed steel-framed domestic structures. Engineering Structures, vol. 21, pp. 83-95, 1999.

[8] M. S. Hoehler, C. M. Smith, T. C. Hutchinson, X. Wang, B. J. Meacham e P. Kamath, Behavior of steel-sheathed shear walls subjected to seismic and fire loads. Fire Safety Journal, vol. 91, pp. 524-531, 2017.

[9] B. Schafer, D. Ayhan, J. Leng, P. Liu, D. Padilla-Llano, K. Peterman, M. Stehman, S. Buonopane, M. Eatherton, R. Madsen, B. Manley, C. Moen, N. Nakata, C. Rogers e C. Yu, Seismic Response and Engineering of Cold-formed Steel Framed Buildings. Structures, vol. 8, pp. 197-212, 2016.

[10] L. Fiorino, V. Macillo e R. Landolfo, Shake table tests of a full-scale two-story sheathing-braced cold-formed steel building. Engineering Structures, vol. 151, pp. 633-647, 2017.

[11] L. Fiorino, B. Bucciero e R. Landolfo, Shake table tests of three storey cold-formed steel structures with strap-braced walls. Bulletin of Earthquake Engineering, vol. 17, pp. 4217-4245, 2019.

[12] Y. Kawai, S. Tohnai, S. Hashimoto, A. Sato e T. Ono, Steel Sheet Shear Walls with Burring Holes for Low-to Mid-rise Housings. 12th Pacific Structural Steel Conference, Tokyo, 2019.

[13] Y. Kawai, K. Fujihashi, S. Tohnai, A. Sato e T. Ono, Shear Resistance Mechanisms on Steel Sheet Shear Walls with Burring Holes and Cross-Rails. International Specialty Conference on Cold-Formed Steel Structures, 2018.

[14] Y. Kawai, T. Ono, A. Sato, S. Tohnai e M. Kondo, Allowable Design Formula for Steel Sheet Shear Walls with Burring Holes. 7th International Conference on Coupled Instabilities in Metal Structures, Baltimore, Maryland, 2016.

[15] S. Labò, A. Belleri, A. Marini e A. Sato, Numerical Study of a Cold Formed Steel Panel Assembly for Seismic Retrofit of RC buildings. XXVIII Congresso C.T.A., 2022.

[16] T. Serikawa, A. Sato and T. Ono, Strength and stiffness of corrugated steel sheet shear walls. Eighth International Conference on THIN-WALLED STRUCTURES, Lisbon, Portugal, 2018.

[17] S. Hak, P. Morandi and G. Magenes, Damage control of masonry infills in seismic desing. Research report., Pavia: Istituto Universitario di Studi Superiori (IUSS), 2013.

[18] L. Decanini, C. Gavarini and S. Bertoldi, Telai tamponati soggetti ad azioni sismiche, un modello semplificato: confronto sperimentale e numerico. In: VI Convegno Nazionale di Ingegneria Sismica in Italia, Perugia, 1993.

[19] K. Sassun, T. J. Sullivan, P. Morandi, and D. Cardone, Characterising the in-plane seismic performance of infill masonry. Bulletin of the New Zealand Society for Earthquake Engineering, 2016.

[20] MidasGEN, Analysis Manual for Midas GEN, 2022.

[21] EC8. (CEN), Design of structures for earthquake resistance. Brussels, Belgium: European Committee for Standardization, 2005.

[22] FEMA 273, F. E., Guidelines for the Seismic Rehabilitation of Buildings. Washington DC, 1997.

COMPDYN 2023
9th ECCOMAS Thematic Conference on
Computational Methods in Structural Dynamics and Earthquake Engineering
M. Papadrakakis, M. Fragiadakis (eds.)
Athens, Greece, 12-14 June 2023

# IMPROVEMENT OF SEISMIC SAFETY BY LOCAL STRENGHTNING IN ITALIAN PRE-70 RESIDENTIAL RC BUILDINGS DESIGNED FOR GRAVITY LOADS

**Santa A. Scala**[1], **Maria T. De Risi**[1], **Carlo Del Gaudio**[1], **and Gerardo M. Verderame**[1]

[1] University of Naples Federico II,
Department of Structures for Engineering and Architecture,
{santaanna.scala, mariateresa.derisi, carlo.delgaudio, verderam}@unina.it

## Abstract

*Pre-code reinforced concrete (RC) buildings in Italy are significantly vulnerable to seismic actions, especially those realized before '70s, since, up to '70, about 85% of the whole national territory was classified as not-seismic prone area. In such areas, buildings were designed to sustain gravity loads only, without capacity design principles, often resulting vulnerable to shear failures both in beams/columns and in beam-column joints under seismic loading. Thus, proper retrofit strategies should be analysed and implemented in order to solve such brittle failures, aiming at improving seismic performance at life safety limit state.*
*In this work, the seismic assessment of case-study Italian pre-70s RC buildings and the relevant retrofit design are carried out according to the current Italian technical code (D.M.2018). Two case-study residential buildings, designed for gravity loads only and different for number of stories, are analysed to assess their "as-built" capacity. The latter is compared with the seismic demand at the life safety limit state, considering all Italian municipalities classified as not-seismic area up to '70 as possible building locations. Thus, for each building/site, the capacity-to-demand ratio, is evaluated. Then, local strengthening interventions (wrapping with Fiber Reinforced Polymers strips for beams/columns and CAM® technology for joints) are designed aiming at the complete resolution of the detected shear failures. The post-strengthening seismic capacity is compared to seismic demand to finally quantify the effectiveness of such a local intervention depending on the building height and the current seismic hazard throughout the Italian country.*

**Keywords:** Existing buildings; seismic capacity; reinforced concrete; retrofit; shear failures; local strengthening.

## 1 INTRODUCTION

In areas prone to earthquakes, existing reinforced concrete (RC) buildings are often vulnerable to seismic loading and require retrofitting strategies and mitigation policies to ensure reliable seismic performance assessment and risk mitigation. Pre-code or low-code RC buildings present different failure typologies compared to newly designed buildings [1] and need to be considered for retrofitting. This is certainly true for RC buildings in Italy constructed before the 1970s [1], which often exhibited shear failures in beams/columns and beam-column joints after earthquakes. In the past 50 years, the Italian government has spent a significant amount (an annual cost of about four billion euros actualized to 2019) of money on direct and indirect costs due to earthquakes, half of which was related to assistance, recovery, and post-event reconstruction for residential buildings [2]. Therefore, a large-scale seismic strengthening intervention plan for those buildings is necessary to drastically reduce seismic losses and casualties in future events.

The primary aim of retrofitting is life safety prevention, which can be achieved through three main approaches according to the Italian code, D.M. 2018 [3]: achieving the new-design building safety level, improving the as-built safety level by a certain percentage, or with local strengthening interventions that do not change the lateral stiffness of the structure, producing an improvement of the seismic response of the involved primary elements.

This study presents the as-built assessment of Italian pre-70 RC buildings (characterized by different number of storeys) in about 6700 municipalities, characterized by different seismic hazard. The seismic capacity of each building/site has been evaluated at *Severe Damage* (SD) Limit State (LS) in a code-based approach according to Italian seismic prescriptions ([3], in tune with CEN, 2005, [4]). Retrofitting has been designed to solve the shear failures at SD LS in a local strengthening intervention approach, with post-strengthening seismic capacity compared to seismic demand to quantify the effectiveness of the intervention depending on building height and seismic hazard.

## 2 CASE STUDY BUILDINGS

This study focuses on a sample of Italian reinforced concrete (RC) buildings constructed before 1970, which are intended to represent most of the RC buildings built during this period. In fact, according to ISTAT 2011 [5], Italy has approximately 3.6 million RC buildings throughout the country, with about 1.1 million constructed before 1970. At this time, approximately 85% of the national territory (equivalent to about 6700 municipalities) was classified as a "non-seismic prone" area (see Figure 1). Despite this classification, several strong earthquakes have affected Italy in the last century, resulting in significant losses of life and damage to buildings. In response to these events, seismic hazard classification has been revised several times over the past century. Currently, the sites that were not considered to be seismic-prone until the 1970s are classified according to the hazard map shown in Figure 1, which divides Italy into four "seismic zones" based on the expected value of acceleration on stiff soil with a 10% probability of exceedance in 50 years. It should be noted that only 2% of the considered municipalities are in the first seismic zone (SZ1), while most of them (about 52%) are in the third seismic zone (SZ3). The remaining municipalities are almost equally distributed between the second (SZ2, 23%) and the fourth (SZ4, 17%) SZ.

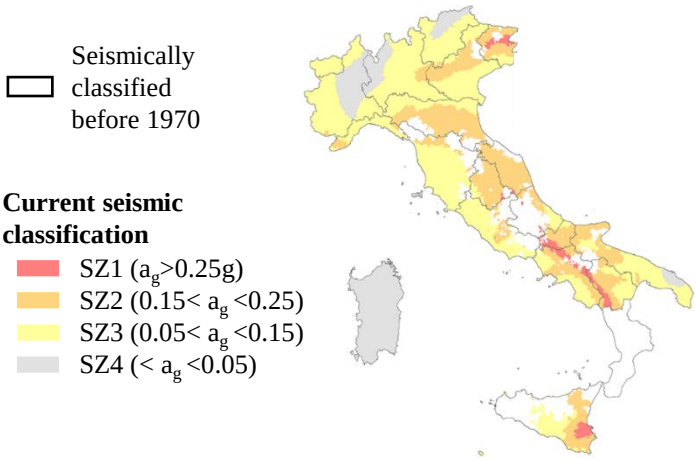


Figure 1. Current Italian seismic classification (based on acceleration on stiff soil $a_g$ with 10% probability of exceedance in 50 years) of municipalities not classified in 1970.

Accordingly, the large majority (88%) of reinforced concrete structures built before 1970 were designed to withstand only gravity loads, even though the current seismic classification acknowledges the need to consider seismic action. The case-study buildings selected for analysis in this study are two RC residential buildings with the same floor plan (approximately 200 $m^2$), but with different numbers of stories (3 and 6 stories), both designed according to the obsolete technical code in force in Italy until 1970 (Royal Decree, R.D. 1939, [6]).

Both the case-study buildings use the same moment resisting frames (MRFs) system, shown in Figure 2a. This system relies on parallel 2D resisting frames in the longitudinal (X) direction only, which was typical in pre-1970 reinforced concrete buildings in Italy.

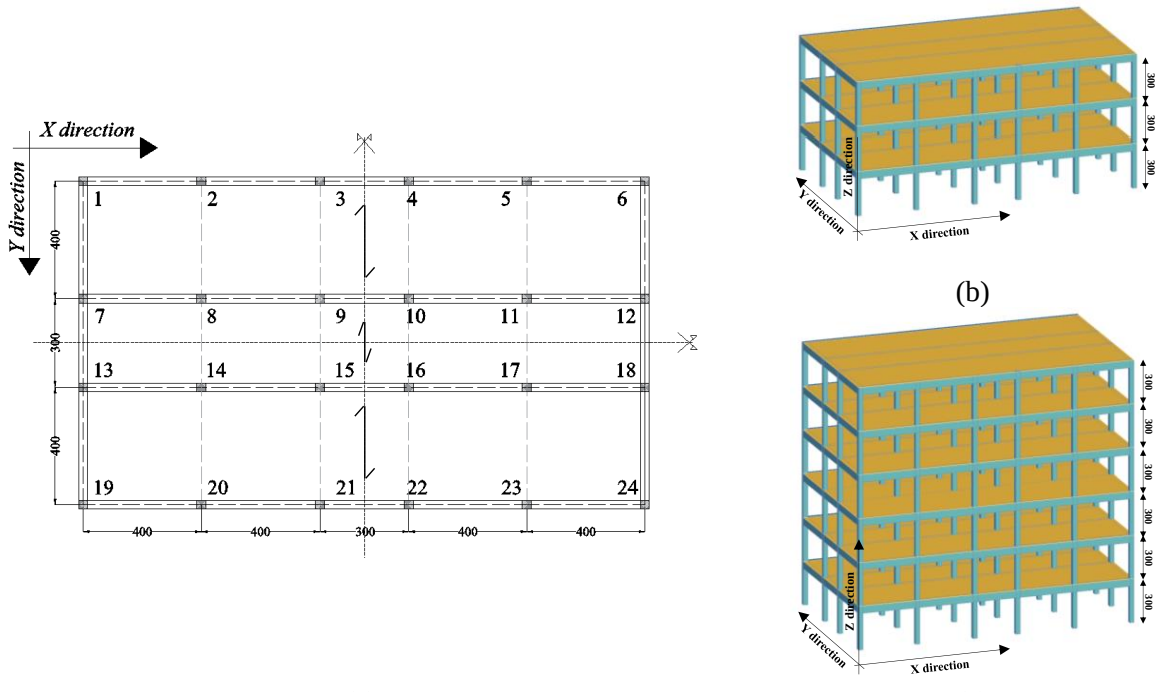


Figure 2 Plan (a) and 3D (b-c) views of analyzed case-study buildings. (Dimensions in centimeters)

Beams connecting columns in the transverse (Y) direction are absent, except for along the exterior perimeter. The floorplan, shown in Figure 2a, is symmetrical in both the main perpendicular directions (X and Y), with an interstory height of 3 meters (Figure 2b-c).

The *maximum allowable stress* method, adopted according to the Italian code in force until the construction time [6-7], assumes a maximum allowable stress of 5 or 6 MPa for concrete (in case of purely compressive loads or bending actions, respectively), and 140 MPa for reinforcing bars. Additionally, plain bars made of *AQ42* steel typology are assumed, which was typical during the reference period in Italy [8]. Design loads and infill weight are the same used in [9].

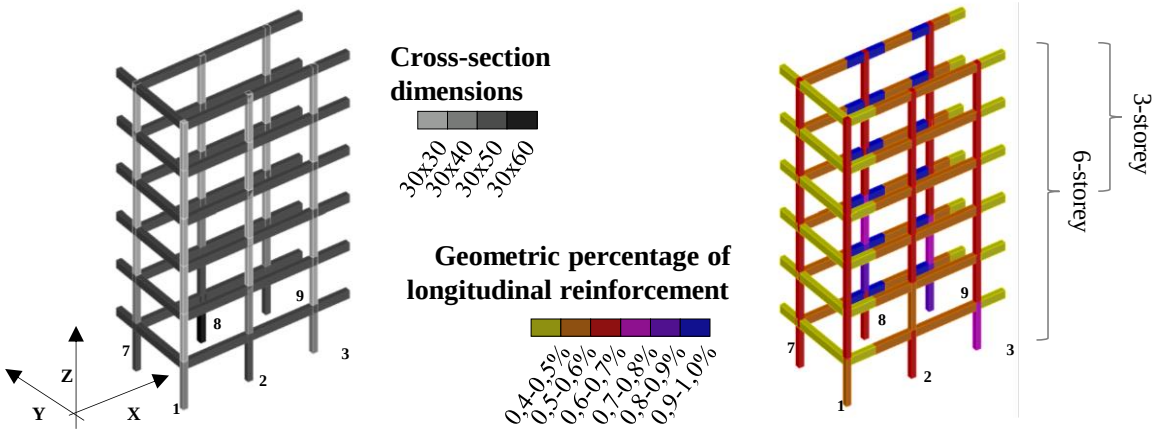


(a) (b)

Figure 3 Cross-section dimensions (a) and geometric percentage of longitudinal reinforcement (b) resulting from simulated design.

Figure 3 presents the main outputs of the simulated design, including resulted cross-sections (Figure 3a) and geometrical percentage of longitudinal reinforcement ρ (Figure 3b) for ¼ of the whole structures, relying on its double-plan symmetry. It should be noted that the simulated design of 6-storey buildings allows obtaining the cross-section dimensions and reinforcement details also for 3-storey case-study building. In fact, the 3-storey building matches the upper 3 storeys of the 6-storey building.

All beams have a 30×50 $cm^2$ cross-section, whereas column sections vary from a minimum of 30×30 $cm^2$ (for the upper storeys) to a maximum of 30×60 $cm^2$ (for central columns of the ground floor). Interior longitudinal beams have the highest ρ values (about 1%) since the floor weight is sustained by the longitudinal frames only. The minimum value of ρ (i.e., about 0.4%) characterizes the beams in the transverse direction. The reinforcement ratio in the columns decreases moving from the ground floor ( $\rho \approx 0.9\%$) to the upper stories ( $\rho \approx 0.6\%$). Stirrups with 140 mm spacing and 6 mm diameter are used in columns, complying with the minimum amount of transverse reinforcement required by the technical code in force in the considered time period [6, 1]. Stirrups with 250 mm spacing and 8 mm diameter characterize all beams, except for interior ones in the longitudinal direction, where 75 mm spacing is adopted at the beam ends.

## 3 ITALIAN CODE-BASED SEISMIC ASSESSMENT

This section shows the code-based assessment of "as-built" case-study buildings according to the current Italian code (D.M. 2018) via pushover (PO) analysis within the N2 framework [10]. Case-study buildings described above are located in the centroids of each Italian munic-

ipality classified as not-seismic prone area before ’70, also taking into account the current soil typology [11, 3, 4].

According to D.M. 2018 the code-based assessment at a given limit state ($LS_i$) can be expressed through the synthetic parameter $\zeta_e$ index, defined as the capacity-to-demand ratio generally calculated in terms of peak ground acceleration (PGA):

$$\zeta_e(LS_i) = \frac{PGA_C(LS_i)}{PGA_D(LS_i)} \quad (1)$$

where $PGA_C$ is the seismic capacity at a given limit state, obtained assuming a *Full Knowledge Level, KL* [3, 4], since the mean values of mechanical properties are used for capacity calculations without any further reduction. $PGA_D$ is the seismic demand at the same limit state, obtained considering both the site hazard on stiff soil and the site effects due to soil amplification (since a plan topography is always assumed).

Lastly, the seismic assessment is performed considering the *Severe Damage* (SD) limit state [3, 4], corresponding to seismic actions with a return period ($T_R$) of 475 years. The SD limit state is reached when for the first time a flexural or a shear failure occurs. In particular, as suggested by the Italian prescriptions, the ductile failure at SD LS is assumed to occur when the chord rotation demand reaches ¾ of the ultimate chord rotation capacity (calculated according to [12]. Joints shear failure occurs when its principal compressive stress overcomes 0.5fc (JF(C)), or if the principal tensile stress overcomes 0.3 √ fc (JF(T)). Lastly, columns/beams shear failure occurs when the shear demand overcomes the shear strength, the latter evaluated according to the model of [3, 13].

### 3.1 Modelling assumptions

The seismic response of the case-study buildings was numerically reproduced using the OpenSees platform [14]. To achieve this, each building was modelled as a 3D bare model, with infills modelled only in terms of masses and loads, as common in practice-oriented code-based assessment.

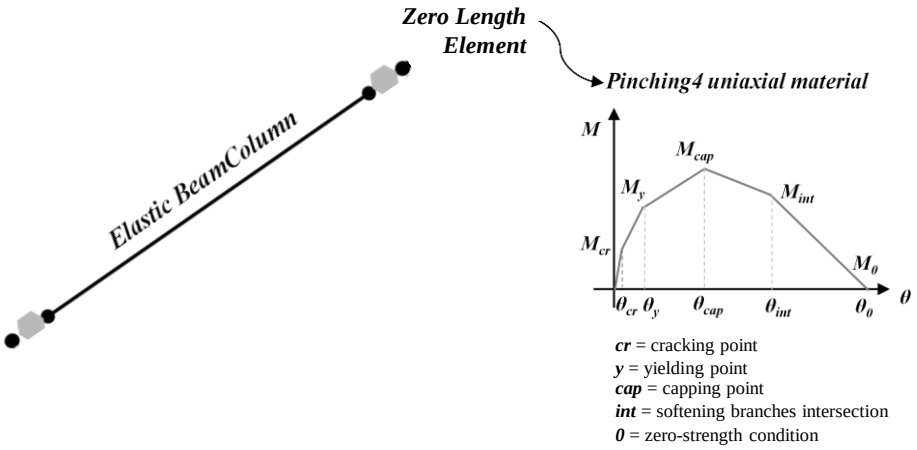


Figure 4. Adopted lumped plasticity approach implemented in OpenSees using elastic *BeamColumn Elements* in series with *Zero-Length Elements* located at each beam/column end and characterized by the *Pinching4* uniaxial material to reproduce the Verderame and Ricci (2018) flexural response.

The floors were assumed to be stiff in their own plane, while the joints' nonlinear response was not numerically reproduced, assuming them as rigid elements. The primary elements (beam/columns) were modelled as ductile elements, with only the nonlinear flexural response

being reproduced in the numerical model. Thus, any eventual shear failures in the columns, beams, or joints were detected by post-processing the static pushover results, which is also a common practice. To model the flexural response of the RC beams and columns, a lumped plasticity approach was used (as shown in Figure 4). This approach assumed a shear length equal to half the element length and adopted a moment-chord rotation (M-θ) relationship of [15], specific for RC elements with plain bars.

### 3.2 Static PO outcomes

Nonlinear static pushover analyses were conducted for each building in both longitudinal and transverse directions, using two different lateral load distributions as specified by [3]: *(i)* "modal" distribution, which was proportional to the first vibration modal shape in each direction, and *(ii)* "uniform" distribution, which was proportional to the storey horizontal accelerations. The resulting capacity curves are shown in Figure 5(a-b) in terms of spectral displacement ($S_d$) and spectral pseudo-acceleration ($S_a(T)$), along with the corresponding collapse mechanisms for each direction/load distribution.

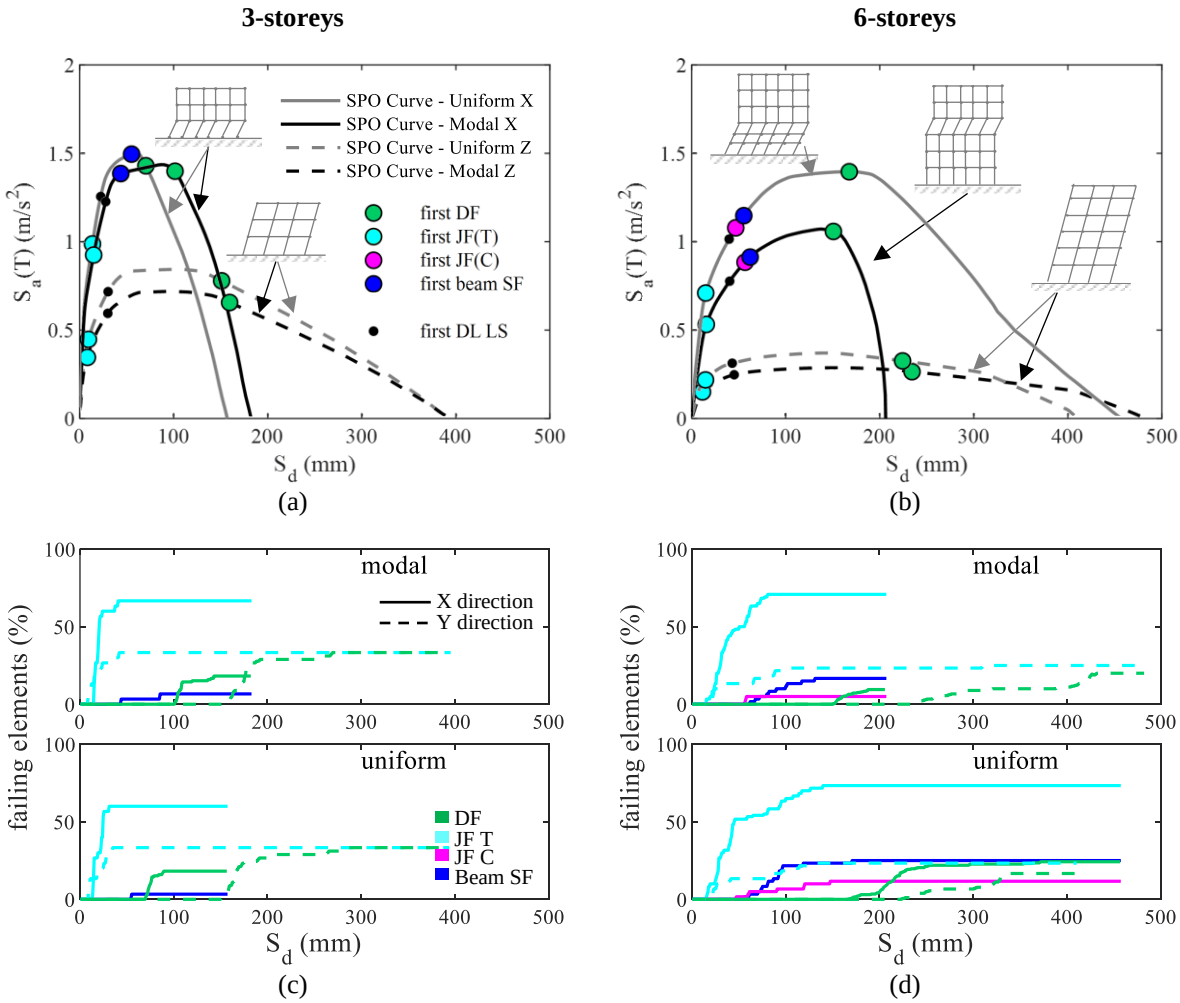


Figure 5 Capacity curves with relevant collapse mechanisms (a-b) and evolution of the considered failure typologies at SD LS (c-d) for both case-study buildings, both direction and load distributions.

A global collapse mechanism is observed in the transverse direction for both the case-study buildings and for both the lateral load patterns, whereas local mechanisms are observed in the longitudinal direction. In particular, for the 3-storey building local first-floor mechanisms is

observed applying both the load distributions; for 6-storey building a fourth floor and a pseudo-global mechanism are observed when modal and uniform distribution are applied, respectively. Moreover, each capacity curve shows the achievement of the first tensile (T) or compression (C) joint failure (JF), the first shear failure (SF) in beams or columns, the first ductile failure (DF), and also the capacity point at the Damage Limitation (DL) LS. The latter is assumed to be achieved when for the first time an inter-story drift ratio equal to 0.5% is achieved. It should be noted that JF(T) are exhibited (in both directions) by all case-study buildings, whereas only the tallest one (6- storey building) also shows JF(C) (only in the X direction). Beams SFs occur in X direction in each analyzed building, conversely columns SF is never observed.

Moreover, Figure 5(c-d) shows the percentage of failing elements in each pushover analysis step for both load distributions and directions. Going from the 3- to 6-storey building, the maximum percentage of JF(T) increase in the X direction, reaching about 75%. The percentage of JF(C) in the 6-storey building does not exceeds the 10% of the total number of beam-column joints, and the maximum percentage of beams SFs increases with the number of storeys, reaching about the 25%. DFs happen in less than 50% of the elements, mostly in the Y direction.

### 3.3 Safety index assessment

At each $LS_i$ the safety index $\zeta_e$ (as defined in Eq. 1) can be calculated. To obtain such result, starting from the capacity curves of Figure 5(a-b), first the equal-energy approach suggested by D.M. 2018 is applied, bi-linearizing each curve up to 85% of the peak load. In Figure 6(a), such procedure is shown for a single curve, for sake of example: an Elastic-Perfectly-Plastic (EPP) idealization is obtained, defining the elastic branch by the capacity curve point at 60% of the peak load.

As shown in Figure 6(a), the slope of this latter branches provides the effective period $T_{eff}$ (namely, 0.77-0.70 s in X direction and 1.11-1.00 s in Y direction for modal-uniform distribution respectively in 3-storey building; 1.23-1.07 s in X direction and 1.93-1.68 s in Y direction for modal-uniform distribution respectively in 6-storey building).

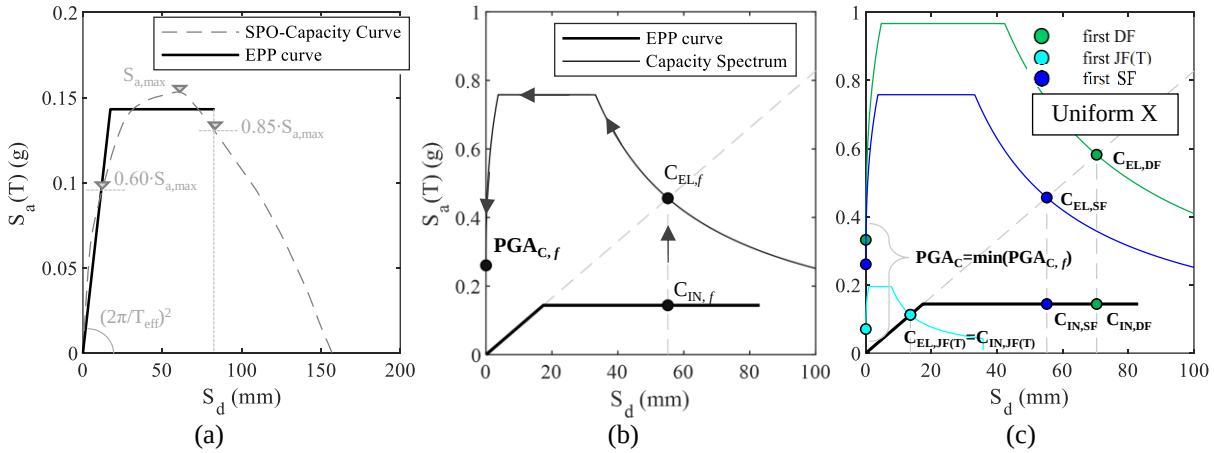


(a) (b) (c)

Figure 6 From capacity curve to EPP idealization (a); from EPP idealization to a capacity spectrum for a given f failure inelastic point (b); PGAC evaluation at the *SD* limit state (c), for a given site. (Case: 3-storey building in Uniform X distribution/direction).

In Figure 6(b), with reference to a given *f* failure, the corresponding capacity spectrum is obtained, first going from the inelastic capacity point, $C_{IN,f}$, to the elastic one, $C_{EL,f}$, by using

the R-μ-T relationship by [16, 3]. Then, the spectrum passing by $C_{EL,f}$ point is identified by a logarithmic interpolation among the nine spectra provided by code (with $T_R$ ranging from 30 to 2475 years).

Such procedure is shown in Figure 6(c) for each failure occurred in the 3-storey buildings in Uniform X distribution/direction, for a given site. In fact, the first achievement of each failure (i.e., the first tensile joint failure, the first shear and ductile failure in a primary element) are reported on obtained EPP curve, given the corresponding spectral displacement $S_d$ (i.e., $C_{IN,JF(T)}$, $C_{IN,SF}$, and $C_{IN,DF}$ respectively). Thus, the R-μ-T relationship allows going from inelastic to corresponding elastic points (i.e., $C_{EL,JF(T)}$, $C_{EL,SF}$, and $C_{EL,DF}$), then logarithmic interpolation allows moving from such elastic points to the relevant PGA values (i.e., $PGA_{C,JF(T)}$, $PGA_{C,SF}$, and $PGA_{C,DF}$ respectively). Thus, the $PGA_C$ for a given load distribution and direction is the minimum among all the obtained $PGA_{C,f}$ values (Figure 6(c)).

Moreover, the minimum of all values (derived for a given distribution/direction) is the building capacity in the as-built condition ($PGA_{C,\,ante}$) at the considered limit state, based on which the safety index is evaluated. Conversely, the seismic demand ($PGA_D$), at the same limit state, is obtained for each considered site by means of the pseudo-acceleration spectrum associated to the corresponding $T_R$.

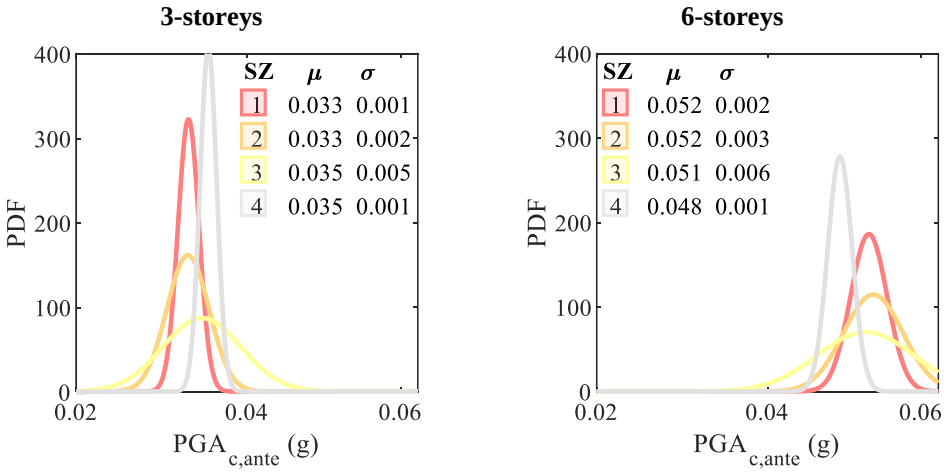


Figure 7. PDF of $PGA_{C,ante}$ at the Sever Damage (SD) limit state for 3- and 6-storey buildings.

Figure 7 shows the probability density function of as-built $PGA_{C,ante}$, at SD LS, thus obtained, fitted with a gaussian distribution, for all the considered sites, distinguishing for seismic zone (ZS), along with the associated mean (μ) and standard deviation (σ) values. It can be noted that, $PGA_{C,ante}$ is always very low, since it is always associated to the first JF(T) and to a capacity $T_R$ lower than 30 years. μ values of $PGA_{C,ante}$ range from 0.03g to 0.05g, slightly increasing from 3- to 6-storey buildings. For each building, σ values are always higher for ZS3 (i.e., the most populated ZS).

In Figure 8, $\zeta_{e,ante}$ indexes are shown as a function of $PGA_D$ for each analysed building, distinguishing in the current four SZs (see Figure 1(b)). The safety index is always lower than 1, except than for a very limited number of 6-storeys buildings located in ZS4. A decreasing trend is observed increasing the seismic demand (namely, going from the fourth to the first ZS), regardless of the number of storeys.

The fitting curve describing such decreasing trend is reported in Figure 8 following the functional law $aPGA_D^b$, where *a* and *b* are regression coefficients changing with the number of storeys. The obtained curves provide the expected $\zeta_{e,ante}$ value, given the seismic demand, for the Italian residential RC buildings designed between '50 and '70 for gravity loads only.

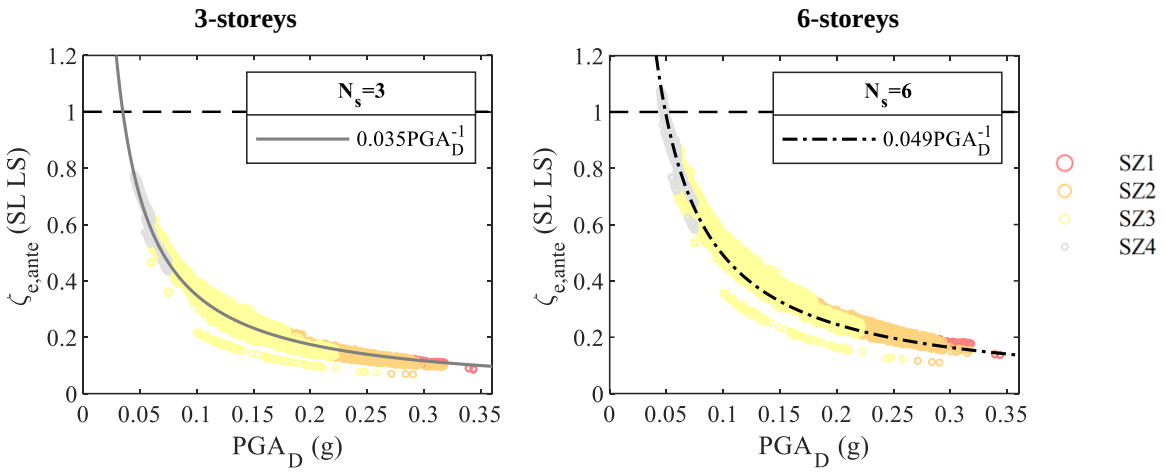


Figure 8. As-built safety index at the Sever Damage (SD) limit state for 3- and 6-storey buildings.

Thus, such mean curves could greatly shorten the time/effort for the seismic assessment of buildings like those analysed herein, directly providing the expected safety index (in KL3), starting from the seismic demand. Parameters *a* and *b* are reported in Figure 8 for each building. It is worth noting that, since the parameter *b* is equal to 1 for all buildings, *a* parameter actually represents the expected value of $PGA_{C,ante}$ at SD LS.

## 4 RETROFITTING STRATEGY

In the previous section, the building's seismic assessment has been performed, according to the normative prescriptions, thus leading to the definition of the safety index $\xi_{e,ante}$ at the *LS* limit state. In this section, the adopted retrofit strategy and the chosen techniques to increase $\xi_{e,ante}$ are explained. Thus, the retrofit design and the relevant $\xi_e$ increment are provided.

### 4.1 Local interventions and adopted retrofit strategies

In this work, an approach based on increasing building capacity (i.e., $PGA_C$) through local strengthening is adopted in order to improve the *ante-operam* safety index. In fact, shear failures can be solved using Fiber Reinforced Polymers (FRP) wrapping for shear-sensitive elements [17, 18, 19, 20] and CAM® technology [20, 21, 22, 23] for tensile failure of joints. The target is to solve shear failures at the plastic shear demand (modifying the shear-sensitive elements in ductile members), without modifying the pushover curve or seismic demand.

More in detail, to solve joints (tensile) failures, CAM® technology [22, 23] is adopted herein, relying on the use of pre-stressed steel strips confining the joint core [21]. The number of pre-stressed steel strips is designed by means of the "post-cracking" approach, according to [21] (in tune with [3, 4] for newly designed reinforced joints), thus considering steel strips as additional transverse reinforcement within the joint region. Joint shear demand is evaluated as the maximum tensile demand deriving from converging beams minus the shear load carried by the diagonal compressed concrete strut within the joint core [3, 4, 21].

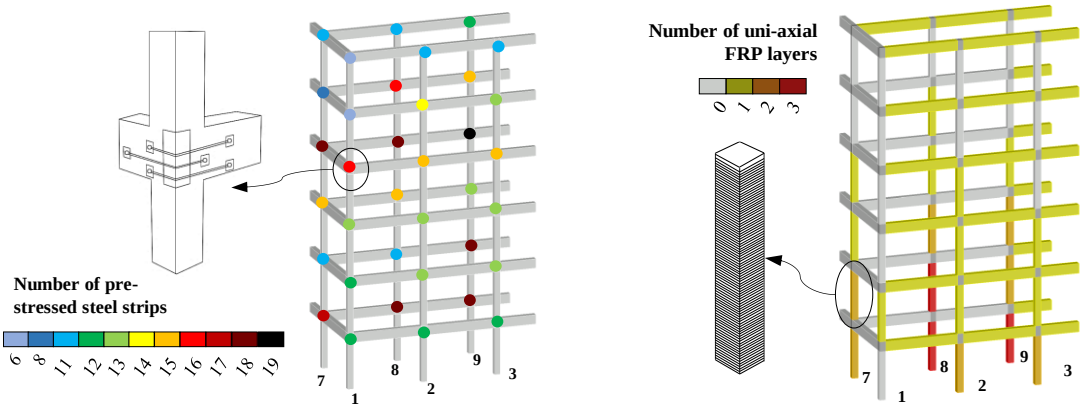


(a) (b)

Figure 9. Number of pre-stressed steel strips for beam-column joints (a); number of uniaxial FRP layers (b).

Figure 9 shows strengthening design outcomes for all shear-sensitive elements, detected by means of a-priori classification. In particular, Figure 9(a) provides the resulting number of pre-stressed steel stirrups for each (T-)shear sensitive joint, assuming a nominal yield strength equal to 400 MPa and a transverse section of 0.9×19 mm$^2$ [21]. Note that Figure 9 shows the design outputs for ¼ of the whole structure only, due to the plan symmetry in both directions, as already observed above. The maximum number of required steel strips is 19, thus making the designed intervention on joints feasible by distributing the obtained strips in 3 layers along beams height (as shown in Figure 9(a)). Moreover, the shear strengthening of beams and columns is designed, by using a uniaxial carbon fibre polymer whit high elastic modulus (230 GPa) and an equivalent thickness equal to 0.166 mm. The shear capacity of FRP-strengthened elements is evaluated according to CNR-DT 200/2004 [24]. For columns, wrapping on 4 sides is designed, along the whole column height; the resulting number of FRP layers is shown in Figure 9(b) for each shear-sensitive column. For all shear-sensitive beams, only one layer (in U-shape configuration) is sufficient, regardless of the number of stories, extended to the beams ends, ranging from the 14% to the 50% of the whole beam length, depending on the considered beam.

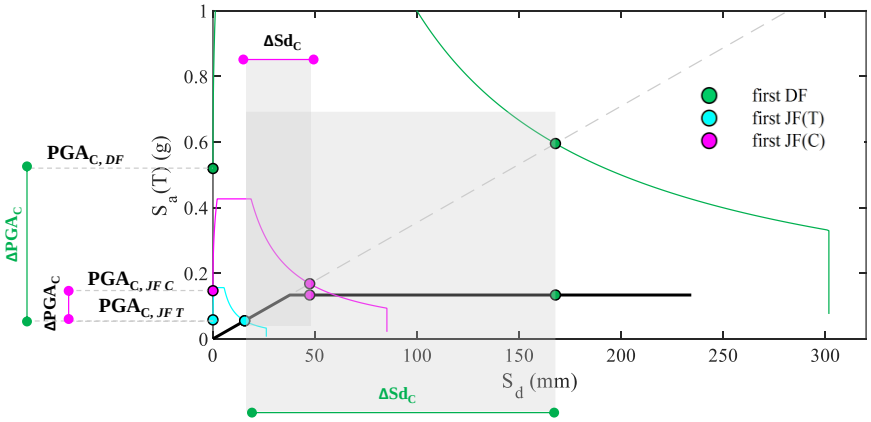


Figure 10. Seismic capacity increment at SD LS in terms of $S_d$ ($\Delta S_{d,c}$) and $PGA_C$ ($\Delta PGA_c$) moving from as-built to post-retrofit condition in presence (magenta marked) or absence (green marked) of JF(C) failures.

If any seismic analysis was performed, the local intervention should involve all shear sensitive elements, as in Figure 9. On the contrary, based on the SPO results shown in Figure 5(a-

b), the strengthening intervention can be optimised aiming at increase the seismic capacity from the first JF(T) (which always limits the as-built performance) ($PGA_{C,JF\,(T)}$) to the first DF ($PGA_{C,DF}$) (as shown in Figure 10 by means of green lines). To this aim, the retrofit can be limited to the shear-sensitive elements that actually exhibit a shear failure during the pushover analyses between the first JF(T) and the first DF, deriving the number of such failing elements from failure mapping of Figure 5(c-d). As a result, building $PGA_C$ can increase by $\Delta PGA_C$ (being the same the pushover curve in *ante-* and *post-operam* condition) and, in tune, the safety index increases. Nevertheless, it is worth noting that JF(C), if any, cannot be solved by means of local strengthening interventions, limiting the efficiency of the adopted strategy. If JF(C) occurs before the first DF, a limited $\Delta PGA_C$ can be obtained (Figure 10, magenta lines). Such circumstance occurs for the tallest building analysed here (6-storey building), reducing the maximum potential $\Delta PGA_C$ by 60%. Thus, in the post-retrofit phase, the seismic capacity is equal to that at the first DF for 3-storeys building, maximizing the effectiveness of the selected retrofit strategy. For 6-storey case-study building, the local strengthening leads to a displacement capacity equal to that at the first JF(C). In summary, the selected strengthening strategy allows increasing building displacement and, in tune, PGA capacity at SD LS from the first JF (T) to the minimum between the first DF and the first JF(C).

## 4.2 Safety index for retrofitted buildings

The safety index is re-assessed after the implementation of local strengthening, based on the same pushover curves of Figure 5a, for all the considered sites in Italy.

Figure 11 shows the PDF of $PGA_C$ at SD LS (fitted with a gaussian distribution) of post-retrofit buildings for all the considered sites, distinguishing for ZS. The increment of $PGA_C$ with respect to the as-built condition is very high for the lowest building, when JFs(C) do not occur at all: μ values of $PGA_{C,post}$ result about 9.7 times higher, for 3-storey buildings, than the as-built condition (averaging among all SZs). On the other hand, for the tallest building, such an increment is more limited: μ values of $PGA_{C,post}$ result 3.1 times the $PGA_{C,ante}$ for 6-storey buildings (averaging among all ZSs), due to the occurrence of JF(C) before DFs. For each building, σ values are always higher for ZS3 (i.e., the most populated ZS) also in post-retrofit condition, and, generally, given the ZS, they are higher for the post-retrofit condition with respect to as-built phase (except than for ZS1).

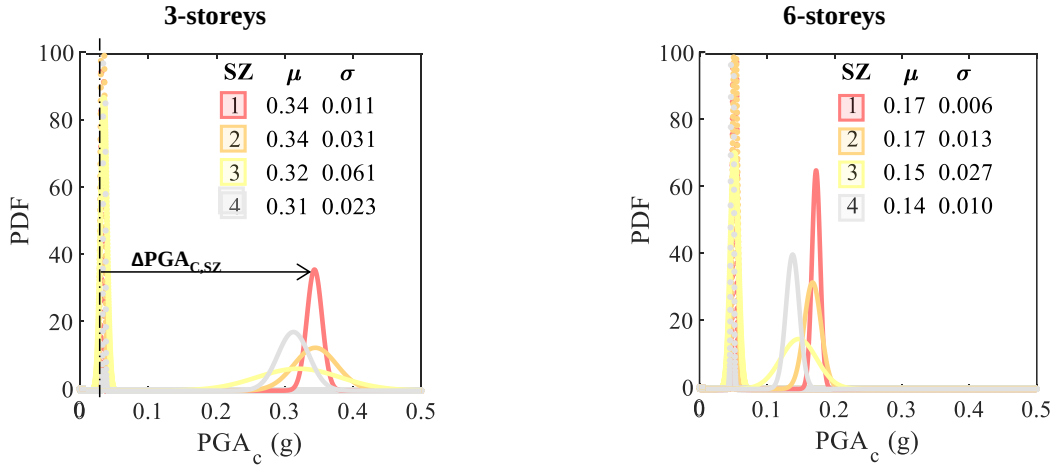


Figure 11. PDF of $PGA_{C,post}$ at the Sever Damage (SD) limit state for 3- and 6-storey buildings

In Figure 12(a-b), the safety index increment at SD LS, $\Delta\zeta_e$, (= $\zeta_{e,post}$- $\zeta_{e,ante}$) is provided, for each case-study buildings, showing its trend with the seismic demand expressed in terms of

$PGA_D$. Such $\Delta\zeta_e$ represents the maximum increment of $\zeta_{e,ante}$ that can be achieved with the selected retrofitting.

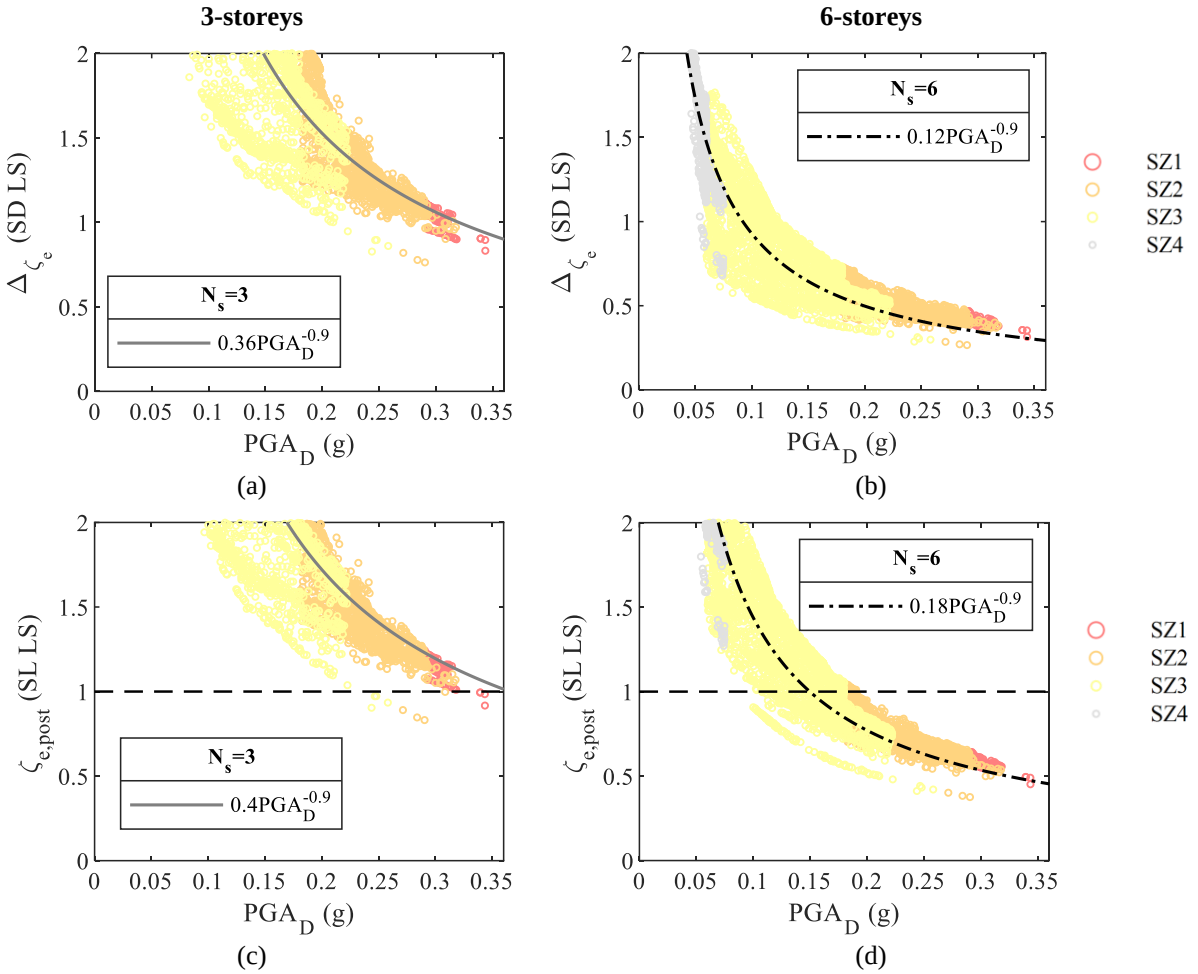


Figure 12. Safety index increment (a-b) and safety index in the post-operam condition (c-d) at SD LS.

Additionally, both the safety index increment at SD LS $\Delta\zeta_e$ (= $\zeta_{e,post}$ - $\zeta_{e,ante}$) and the relevant index in the post-operam condition ($\zeta_{e,post}$), show a decreasing trend, increasing the seismic demand. Fitting parameters for both $\zeta_{e,post}$ and $\Delta\zeta_e$ are reported in the relevant plot (see Figure 12).

Significant increments in $\zeta_e$ can be observed (Figure 12), especially in low-medium hazard sites (i.e., ZS3 and ZS4) and especially for 3-storey buildings, where there isn't any limitation due to JFs(C), as observed above.

In particular, the retrofitted 3-storeys building shows $\zeta_{e,post}<1$ only in the 0.2% of the sites (for high-medium hazard sites, ZS1 and ZS2), always reaching at least $\zeta_{e,post}=0.6$ (being the latter a threshold for seismic upgrading of strategic buildings). As expected, for the taller building (6-storeys ones), the occurrence of JFs(C) limits the $\Delta\zeta_e$ increment (Figure 12): the percentage of sites with $\zeta_{e,post}<1$ significantly increases (37%, mainly in ZS1,2,3) (Figure 12(c-d)). Moreover, $\zeta_{e,post}$ values can result even lower than 0.6 (5% of sites), especially for high-medium hazard sites.

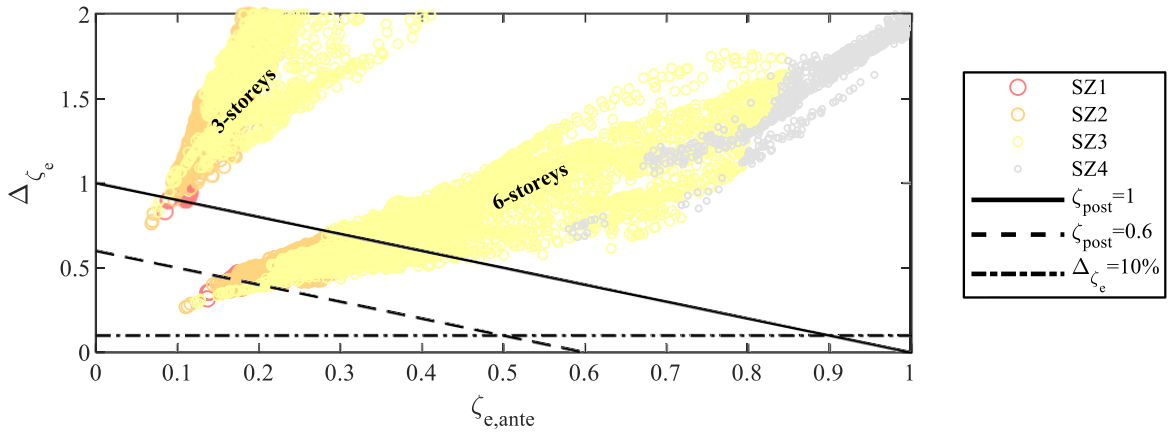


Figure 13. Safety index increment at SD LS versus the relevant as-built safety index for both case-study buildings.

However, the adopted intervention strategy always allows obtaining at least an increment $\Delta\zeta_e$ equal to 10% (being the latter the minimum requirement for a seismic improvement of residential buildings according to D.M. 2018), for all sites and number of storeys (Figure 13).

## CONCLUSIONS

Pre-1970 reinforced concrete buildings are commonly susceptible to seismic loads worldwide, and many buildings in Italy were designed to sustain only gravity loads despite being in high seismic hazard areas. To reduce their vulnerabilities, it is important to carefully assess their seismic performance by analyzing typical failures exhibited after past earthquakes and implementing efficient retrofitting strategies.

In this study, seismic assessment and retrofitting of pre-70 RC building case-studies in Italy were conducted through simulated designs and pushover analyses using 3D models in OpenSees.

The safety check highlighted a significant vulnerability to shear failures, particularly in beam-column joints, which were often characterized by tensile failure.

A retrofit intervention was designed using pre-stressed steel strips to solve tensile failures in joints and FRP wrapping for beams/columns against shear failure. The effectiveness of the retrofit technique was found to be more limited for taller buildings, as joint compression failure is often difficult to solve without changing lateral stiffness. However, on average, retrofitted buildings can achieve 100% of the seismic capacity of a new building at SD LS if the PGA demand is less than 0.15 g, and 60% of this "target" performance if the demand is less than 0.25 g.

Based on the seismic safety evaluation conducted both before and after the retrofit intervention on all Italian municipalities analyzed in the article, functional laws were derived. These are able to provide, for a building similar to those considered in the study (both in terms of geometry and construction period) and for a given number of floors (i.e., 3 or 6), the expected value of the *ante-operam* safety index, the expected index improvement by implementing local interventions, and therefore also the average *post-operam* safety index. These functional laws provide important indications both on the pre-intervention health status of the building and on the potential benefits of a local intervention, based solely on seismic demand (i.e., $PGA_D$).

## REFERENCES


[1] De Risi, M. T., Di Domenico, M., Manfredi, V., Terrenzi, M., Camata, G., Mollaioli, F., ... & Verderame, G. M. (2022a). Modelling and seismic response analysis of Italian pre-code and low-code reinforced concrete buildings. Part I: Bare frames. Journal of Earthquake Engineering, 1-32.

[2] Dolce, M., Speranza, E., De Martino, G., Conte, C., & Giordano, F. (2021). The implementation of the Italian National Seismic Prevention Plan: A focus on the seismic upgrading of critical buildings. International Journal of Disaster Risk Reduction, 62, 102391.

[3] D.M. 2018, Aggiornamento delle «Norme Tecniche per le Costruzioni» - D.M. 17/1/18. (in Italian)

[4] EN 1998-3-1-4. CEN (2005), Eurocode 8 - Design of Structures for Earthquake Resistance, Part 3, Assessment and Retrofitting of Buildings. European Committee for Standardization.

[5] ISTAT (2011) Istituto Nazionale di Statistica (National Institute of Statistics). 15° Censimento generale della popolazione e delle abitazioni. Dati sulle caratteristiche strutturale della popolazione, delle abitazioni e variabili (2011). (in Italian)

[6] R.D. Regio Decreto Legge n. 2229 del 16/11/1939. Norme per la esecuzione delle opere in conglomerate cementizio semplice od armato. G.U. n. 92 del 18/04/1940 (in Italian)

[7] Verderame, G.M., Polese, M., Mariniello, C., Manfredi, G., (2010). A simulated design procedure for the assessment of seismic capacity of existing reinforced concrete buildings. Advances in Engineering Software, 41(2), 323-335.

[8] Verderame, G.M., Ricci, P., Esposito, M., Manfredi, G., (2012). STIL v1.0 - Software per la caratterizzazione delle proprietà meccaniche degli acciai da c.a. tra il 1950 e il 2000. ReLUIS, http://www.reluis.it/

[9] De Risi M.T., Ricci P., Verderame G.M., (2022b). Experimental Analysis of the Effectiveness of Pre-Stressed Steel Strips for the Strengthening of Beam-Column Joints in Existing RC Buildings, XIX ANIDIS Conference, Seismic Engineering in Italy, September 2022, Torino, Italy.

[10] Fajfar, P. (2000). A nonlinear analysis method for performance-based seismic design. Earthquake spectra, 16(3), 573-592.

[11] Mori F, Mendicelli A, Moscatelli M, Romagnoli G, Peronace E, Naso G (2020). A new VS30 map for Italy based on the seismic microzonation dataset. Eng Geol 275:1–10.

[12] Biskinis, D., & Fardis, M. N. (2010). Flexure-controlled ultimate deformations of members with continuous or lap-spliced bars. Structural concrete, 11(2), 93-108.

[13] Circolare del Ministero dei Lavori Pubblici n. 65 del 10/4/1997 (1997) Istruzioni per l'applicazione delle "Norme tecniche per le costruzioni in zone sismiche" di cui al Decreto Ministeriale 16 gennaio 1996. G.U. n. 97 del 28/4/1997 (in Italian)

[14] McKenna, F. (2011). OpenSees: a framework for earthquake engineering simulation. Computing in Science & Engineering, 13(4), 58-66.

[15] Verderame, G. M., & Ricci, P. (2018). An empirical approach for nonlinear modelling and deformation capacity assessment of RC columns with plain bars. Engineering Structures, 176, 539-554.

[16] Vidic, T., Fajfar, P., & Fischinger, M. (1994). Consistent inelastic design spectra: strength and displacement. Earthquake Engineering & Structural Dynamics, 23(5), 507-521.

[17] Tsonos A.G., 2014. An innovative solution for strengthening of old R/C structures and for improving the FRP strengthening method. Structural Monitoring and Maintenance, 1(3), 323-338.

[18] Del Vecchio, C., Di Ludovico, M., Prota, A., & Manfredi, G. (2015). Analytical model and design approach for FRP strengthening of non-conforming RC corner beam–column joints. Engineering Structures, 87, 8-20.

[19] Pohoryles, D. A., Melo, J., Rossetto, T., D'Ayala, D., & Varum, H. (2018). Experimental comparison of novel CFRP retrofit schemes for realistic full-scale RC beam–column joints. Journal of Composites for Construction, 22(5), 04018027.

[20] De Risi, M. T., Del Vecchio, C., Ricci, P., Di Ludovico, M., Prota, A., & Verderame, G. M. (2020b). Light FRP Strengthening of Poorly Detailed Reinforced Concrete Exterior Beam–Column Joints. Journal of Composites for Construction, 24(3), 04020014.

[21] Verderame, G. M., Ricci, P., De Risi, M. T., & Del Gaudio, C. (2022). Experimental assessment and numerical modelling of conforming and non-conforming RC frames with and without infills. Journal of Earthquake Engineering, 26(2), 573-614.

[22] Dolce M., Gigliotti R., Laterza M., Nigro D., Marnetto R., 2001a. Il rafforzamento dei pilastri in c.a. mediante il sistema CAM. Atti del X Convegno ANIDIS "L'ingegneria sismica in Italia", September 9-13, Potenza-Matera, Italy. Paper F3-01. (in Italian)

[23] Dolce, M., Nigro, D., Ponzo, F.C., Marnetto, R., 2001b. Rafforzamento delle strutture murarie: il sistema CAM di Cuciture Attive per la Muratura. Atti del X Convegno ANIDIS "L'ingegneria sismica in Italia", September 9-13, Potenza-Matera, Italy. Paper E3-07. (in Italian)

[24] CNR-DT 200/2004. Istruzioni per la Progettazione, l'Esecuzione ed il Controllo di Interventi di Consolidamento Statico mediante l'utilizzo di Compositi Fibrorinforzati. (in Italian)

COMPDYN 2023
9th ECCOMAS Thematic Conference on
Computational Methods in Structural Dynamics and Earthquake Engineering
M. Papadrakakis, M. Fragiadakis (eds.)
Athens, Greece, 12-14 June 2023

# INFILL-FRAME INTERACTION: REFINED MODELLING FOR THE ANALYSIS AND THE ESTIMATION OF THE INTERNAL FORCES IN SEISMIC ASSESSMENT OF RC BUILDING STRUCTURES

**Fabio Di Trapani**[1], **Marilisa Di Benedetto**[1], **Massimo Petracca**[2], **Guido Camata**[3]

[1] Dipartimento di Ingegneria Strutturale, Edile e Geotecnica, Politecnico di Torino
Corso Duca degli Abruzzi 24, 10129, Turin, Italy
fabio.ditrapani, marilisa.dibenedetto@polito.it

[2] ASDEA Software Technology
Via Alide Breviglieri 8, Pescara, Italy
m.petracca@asdea.net

[3] Dipartimento di Ingegneria e Geologia, Università degli studi "G. D'Annunzio" di Chieti-Pescara
Viale Pindaro 42, Pescara, Italy
g.camata@unich.it

## Abstract

*The paper deals with the assessment of the internal force distribution in frame members due to masonry infills interaction under seismic loads. Special interest is addressed to shear demand, which cannot be evaluated by the common equivalent strut models, while refined finite element modelling is not computationally effective to be used in practice. With the aim to maintain the simplicity of the equivalent strut approach for the assessment of existing RC structures, the paper presents a detailed study of the infill-frame shear transfer mechanism. Refined 2D nonlinear models of real experimental tests on infilled frames have been defined using the OpenSees / STKO software platform. Shear demands at the columns ends of different case study tests have been extracted by integrating the nodal forces at specific section cuts of the RC members. An analytical relationship is finally proposed to correct the shear demand at the ends of the columns when using the equivalent strut approach. The new formula relates the additional shear demand to the current axial force on the equivalent struts and the geometrical and mechanical properties of the infilled frames. The formula is thought to be easily used to perform step-by-step shear safety checks in seismic safety assessments of existing RC structures.*

**Keywords:** Infilled frames, Shear, Masonry, Reinforced concrete, OpenSees, STKO.

## 1 INTRODUCTION

The interaction between infill and frame has been explored by researchers worldwide since the mid-20th century [1-5]. The complex contact interfacing between the infill and the surrounding frame members makes the behaviour under seismic loads highly nonlinear, posing a challenge for accurate prediction of the actual distribution of the internal forces in the frame members. Despite noteworthy advances of research on the topic [6-12], the assessment of the internal forces is still an object of investigation, as the accurate prediction of potential local shear failures [13-16] (Fig.1) is decisive to the assessment and the design of effective retrofitting interventions.



Figure 1: Local shear failure at column ends of infilled RC frames.

Numerical modelling techniques such as micro-modelling and macro-modelling approaches have been generally used for this purpose (Mehrabi et al. 1997 [7]; Di Trapani et al. [17]; Di Trapani et al. [18]). Micro-modelling methods allow simulating the behaviour of an infilled frame with a high level of accuracy, clearly highlighting the damage mechanisms as well as the localization of the stresses on the frame and on the infills. On the contrary, macro-models are simple and computationally effective, but since they are phenomenological models, they are useful to provide an estimation of the overall response, without predicting local interaction effects.

In this context, this study firstly provides a high-fidelity numerical micro-model of an infilled reinforced concrete (RC) frame using OpenSees [19] in combination with the Scientific ToolKit for OpenSees (STKO) [20] pre and post-processing suite. The micro-model provides continuum elements for masonry units, mortar, and RC members. Frictional interfaces are used to model the contact of the infill with the surrounding frame. The model is validated with the experimental results in terms of force-displacement response and failure mechanism. The distribution of the internal forces on the frame members is then obtained via numerical integration of the nodal forces at the different cross-sections. In the second step, the same tests were simulated using the equivalent strut approach. A simple analytical relationship is finally defined to predict the rate of the equivalent strut axial force, the is transferred as demand at the ends of the columns.

## 2 REFINED FE MICRO-MODELLING OF THE INFILLED FRAME

### 2.1 Modelling strategy

The micro-model employs a 2D continuum damage model, which allows for the simulation of the non-linear behaviour of masonry components (units and mortar) as well as concrete members. The model was arranged with the STKO software platform [20] which implements

OpenSees as a solver. Both the frame and the masonry were modelled using 2D *quadrilateral* elements. A scheme of the modelling approach is depicted in Fig. 2.

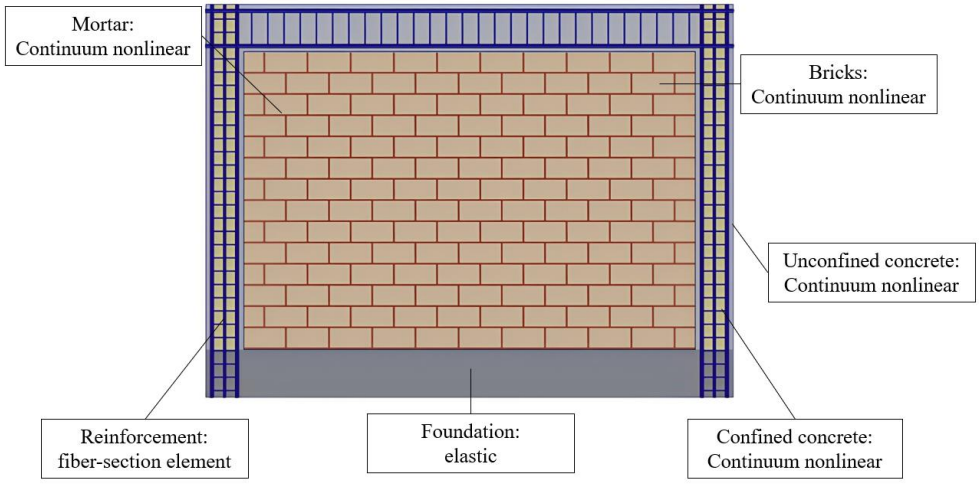


Figure 2: 2D Micro-model of the infilled-frame in OpenSees / STKO

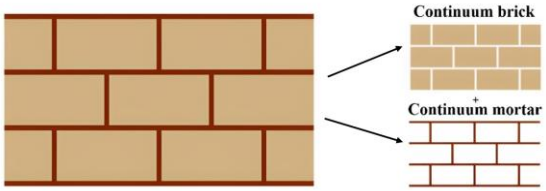


Figure 3: Masonry continuum micro-model

Masonry units and mortar were modelled as separate continuous elements (Fig. 3). The *DamageTC3D* constitutive model (Petracca et al. [21]) was used to model the nonlinear response and the damage evolution. This constitutive model is based on a continuum damage mechanism, which involves a tension-compression damage law, where the stress tensor $\sigma$ is defined as follows (Eq.1) [21]:

$$\sigma = (1-d^{+})\bar{\sigma}^{+} + (1-d^{-})\bar{\sigma}^{-} \tag{1}$$

in which $\sigma$ represents the nominal stress tensor, while $\sigma^{+}$ and $\sigma^{-}$ are the positive and negative parts of the effective stress tensors, respectively [21]. The damage indices $d^{+}$ and $d^{-}$ are based on the tensile and compressive laws of masonry units and mortar, which can be evaluated through the stress-strain curves of the material. According to this material constitutive law [21], fracture energy must be defined for the material. The latter accounts for the amount of energy required to propagate a crack per unit length. The fracture energy in tension ($G_t$) and compression ($G_c$) is here estimated according to Model Code 2010 [22] formulation, that is:

$$G_t = 0.073 \cdot f_c^{0.18} \tag{2}$$

$$G_c = \left(\frac{f_c}{f_t}\right)^2 \cdot G_t \tag{3}$$

where $f_c$ and $f_t$ are each time the tensile and compression strengths of the materials. The reinforced concrete elements are modelled as continuous 2D quadrilateral elements and the

*ASDConcrete3D* constitutive model was applied to the concrete frame members. The latter is an upgraded version of *DamageTC3D*, which is more capable in capturing the damage in concrete elements [19, 20].

Rebars are modelled as 1D *force beam-column* elements (Fig. 4b) embedded in the concrete elements. The uniaxial material model *Steel02* was used as constitutive model. The embedment condition of the rebars within the concrete elements is realized by defining the node-to-element links using the *ASDEmbedded Node Element* as depicted in Figure 4b. Finally, *zero-length* contact elements transferring normal contact forces and shear frictional forces are used to simulate the behaviour of the interface between the RC frame and the masonry infill panel (Fig. 4a).

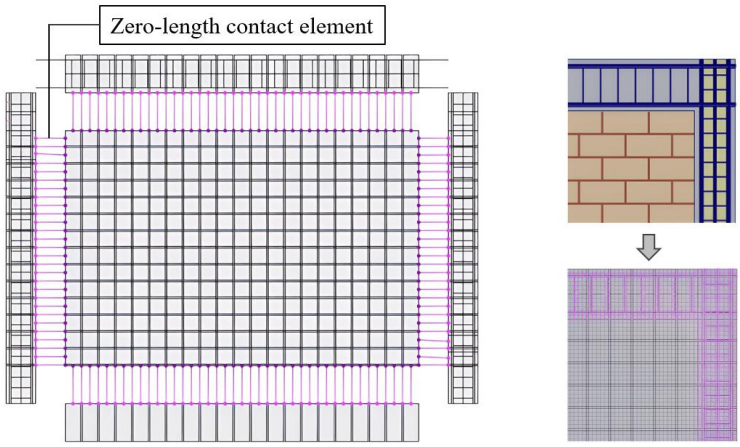


(a) (b)

Figure 4: (a) Frame-infill contact interface model (b) Reinforcement detail and node-to-element links (embedded rebars in concrete)

## 2.2 Details of the selected specimens

The proposed micro-modelling approach was applied to simulate four reference experimental tests on masonry-infilled frames. These tests were chosen from the experimental campaigns by Mehrabi and Shing [6] and Cavaleri and Di Trapani [2], with the goal of providing as much coverage as possible of various masonry infill typologies. Infill walls of specimens S8 and S9 from Mehrabi and Shing [6] were made by hollow clay brick masonry (8) and solid clay brick masonry (9). Infills of specimens S1A and S1B by Cavaleri and Di Trapani [2] were arranged with solid calcarenite and hollow clay masonry units, respectively.

The specimens by Mehrabi and Shing [6] experimental were tested to lateral monotonic loads with a constantly applied vertical load. Specimens S8 and S9 were subjected to a vertical load of 97.9 kN acting on the beam and 97.9 kN acting on each column. Specimens S1A and S1B by Cavaleri and Di Trapani [2] were subjected to a constant vertical load of 200 kN on each column, and then tested under cyclic load conditions. A summary of the main features of the reference experimental tests is provided in Table 1. mechanical properties of materials are also outlined in Tables 2 and 3.

| Reference | Specimen ID | Masonry type | Infill length (*l*) [mm] | Infill height (*h*) [mm] | Aspect ratio (*l*/*h*) [-] |
|---|---|---|---|---|---|
| Mehrabi & Shing [6] | S8 | Hollow clay bricks | 2134 | 1422 | 1.5 |
| | S9 | Solid clay bricks | 2134 | 1422 | 1.5 |
| Cavaleri & Di Trapani [2] | S1A | Solid calcarenite units | 1600 | 1600 | 1.0 |
| | S1B | Hollow clay units | 1600 | 1600 | 1.0 |

Table 1: General details of selected infilled frame specimens.

| Specimen | Concrete | | Units | | Mortar |
|---|---|---|---|---|---|
| | Elastic modulus [MPa] | Compressive strength [MPa] | Compressive strength ($f_{b,v}$) [MPa] | Compressive strength ($f_{b,h}$) [MPa] | Compressive strength [MPa] |
| S8 | 17225 | 26.8 | 16.48 | 8.51 | 8.01 |
| S9 | 17225 | 26.8 | 15.57 | - | 12.47 |
| S1A | 25500 | 25 | 7.06 | - | 3.06 |
| S1B | 25500 | 25 | 37.68 | 2.06 | 9.16 |

Table 2: Mechanical properties of concrete, masonry units and mortars of selected infilled frame specimens.

## 2.3 Model validation

Two steps were taken to carry out the analyses. First vertical loads were applied and kept constant. In the second phase, the horizontal monotonic load was applied. The lateral force versus lateral displacement responses from the micro-models were then compared to the positive and negative experimental monotonic envelopes (Fig.5). The latter show a satisfactory agreement both in terms of peak resistance, stiffness, and post-peak decay.

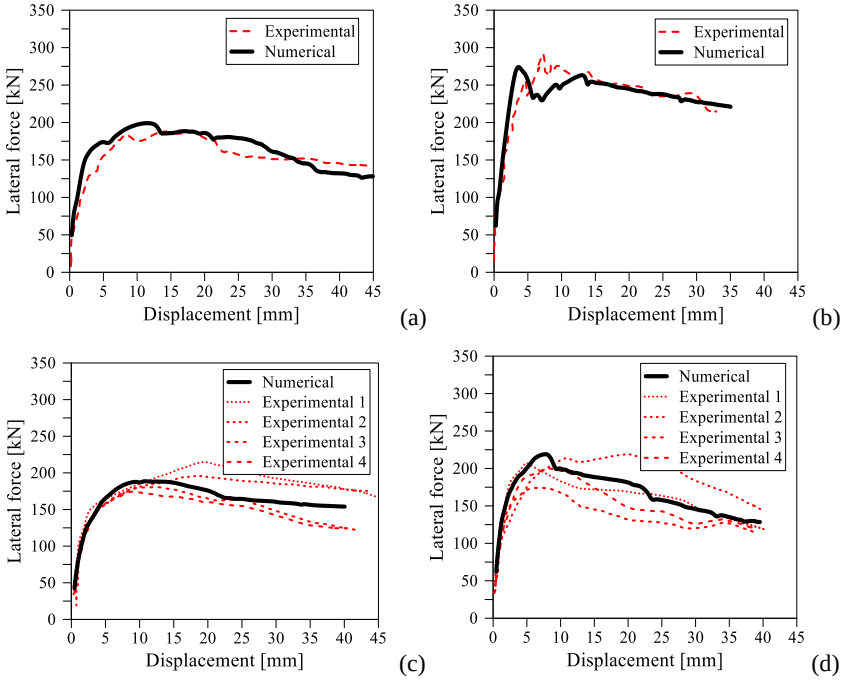


Figure 5: Comparison between experimental and numerical response:(a) S8 (b) S9 (c) S1A (d) S1B

In Fig.6 and Fig.7, experimental and numerical damage patterns are also compared. As it can be observed, the numerical models were also able to accurately predict the main cracking patterns in the masonry (bricks and mortar joints) as well as reinforced concrete elements (shear and flexural damage) in this case.

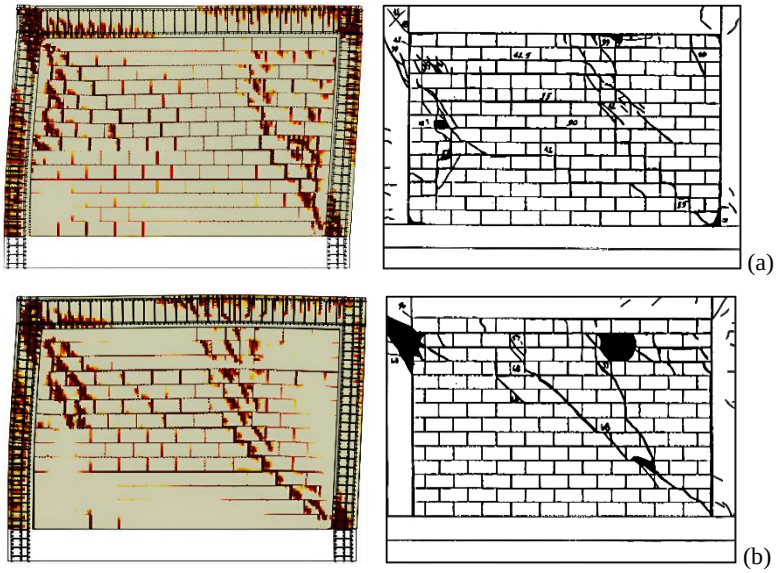


Figure 6: Numerical vs. Experimental damage pattern comparisons for Mehrabi and Shing [6]: (a) Specimen 8; (b) Specimen 9.

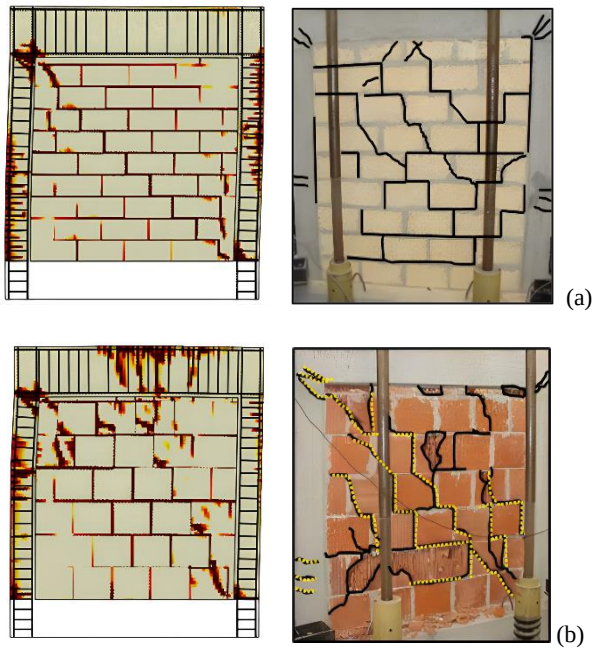


Figure 7: Numerical vs. Experimental damage pattern comparisons for Cavaleri and Di Trapani [2]: (a) Specimen S1A; (b) S1B.

## 3 EVALUATION OF THE INTERNAL FORCES DISTRIBUTION

The evaluation of the internal force has been carried out by implementing a TCL script in the STKO post-processing module. The latter allows the definition of a node set and collecting the nodal forces. The forces are then integrated across the defined section, called "section cut". As depicted in Figure 8, a total number of twenty section cuts was defined to reproduce the internal forces distribution over the concrete frame. A refinement of the section cuts was provided from the midspan to the ends of the columns, where it is expected the major force transfer, and so the major variability of the internal forces in the frame members.

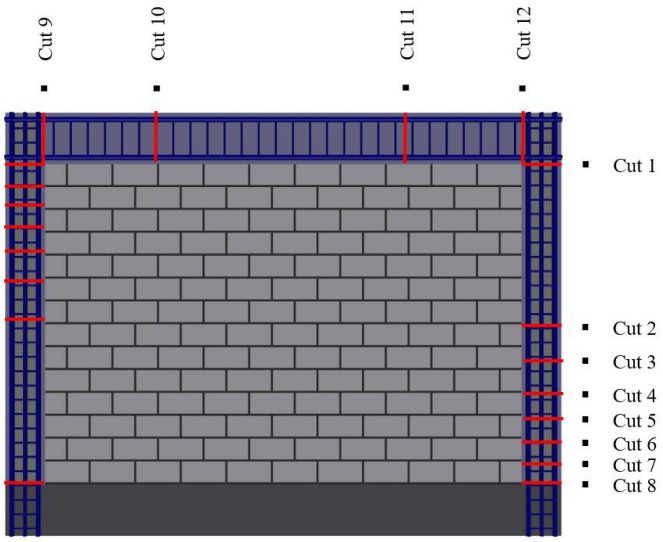


Figure 8: Section cuts' definition for RC frame

The internal forces were recorded at each step of the analysis. For the sake of brevity, only the shear demand distributions are here reported. In particular, three stages of the analysis are represented in Figures 9 and 10, namely those corresponding to the initial cracking, the peak resistance, and the final stage of analysis.

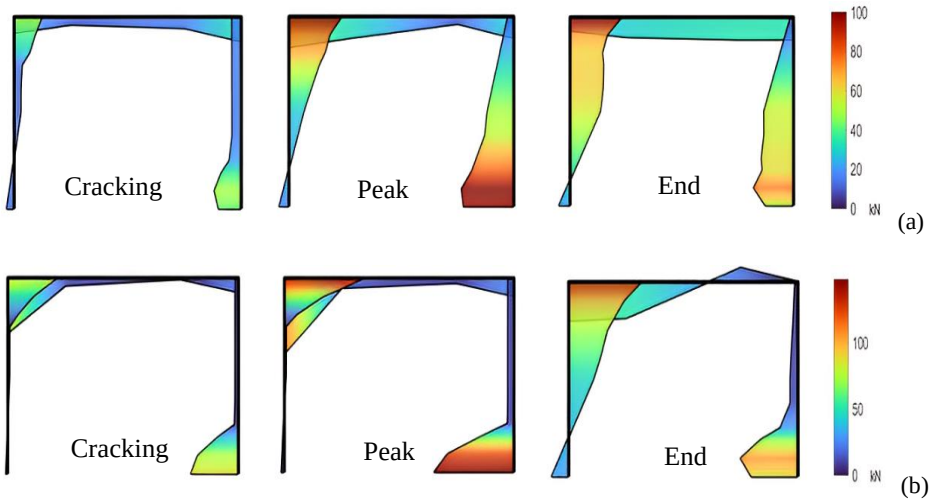


Figure 9: Shear demand distribution in frame members for Mehrabi and Shing [6] specimens: (a) S8; (b) S9.

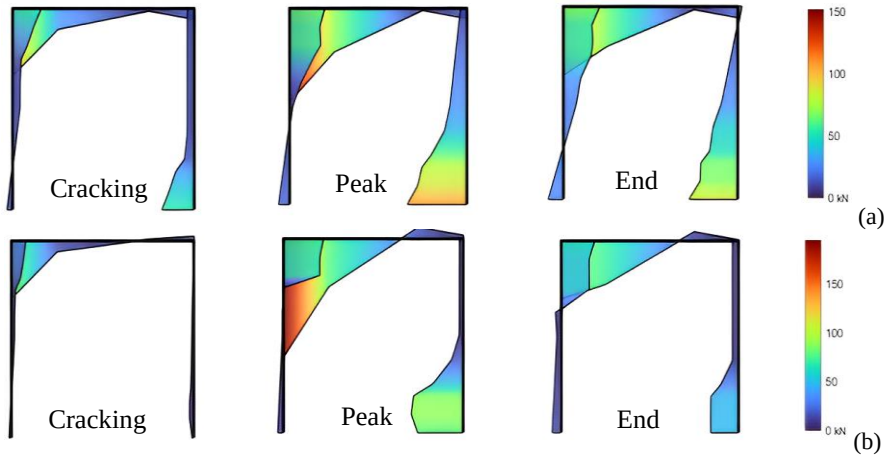


Figure 10: Shear demand distribution in frame members for Cavaleri and Di Trapani [2] specimens: (a) S1A; (b) S1B.

The evolution of shear force experienced by the selected infilled frame specimens was partially consistent with the findings of previous studies (e.g. D'Ayala et al. 2009 [23], Cavaleri and Di Trapani 2015 [24], Bolis et al. 2017 [25], Milanesi et al. 2018 [16]), generally highlighting a noticeable increase of shear demand of at the ends of beams and column. However, it has been found that such a shear demand increment at the ends is not always so pronounced. In fact, some cases (e.g. S8 or S1A) have shown a shear diagram that is linear throughout the entire column. This occurrence can be justified by the increase of the contact length which occurs because of a major sliding of the mortar joints, and that could be captured by the enhanced micro-model because of the physical modelling of the mortar joints. The section nodal forces integration was additionally used to assess the base shear demand of the individual components of the infilled frames. The sum of the shear demands at the base cross sections of the columns provided the lateral response of the RC frame coupled with the infill. By subtracting th so evaluated contribution of the frame from the overall response, the actual contribution of the infill is isolated. Results displaying the base shear-displacement curves by elements are illustrated in Fig. 11 for the analyzed specimens.

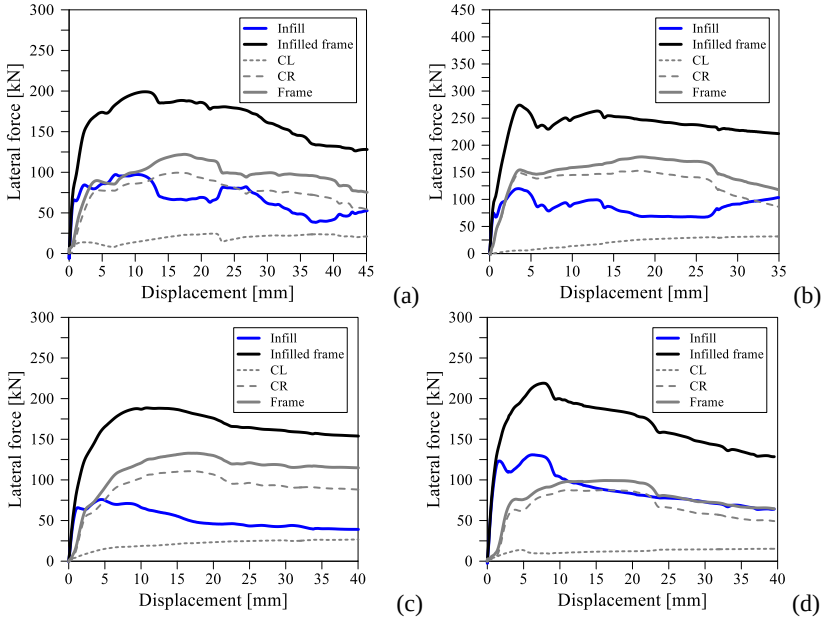


Figure 11: Shear demand in infilled-frame components: (a) S8 (b) S9 (c) S1A (d) S1B

## 4 EVALUATION OF THE ADDITIONAL SHEAR DEMAND USING MACRO-MODELLING

Equivalent strut macro-models do not allow assessing the local shear demand due to the interaction between the frame and the infill. In order to formulate a predictive analytical model it can be assumed (Fig.12a) that the total shear demand at the end of a column adjacent to the infill ($V_{d,tot}$) is the sum of the drift-induced shear on the frame ($V_{d,frame}$) and the extra shear demand arising from the frame-infill interaction ($V_{d,inf}$), as follows:

$$V_{d,tot} = V_{d,frame} + V_{d,\inf} \tag{4}$$

While $V_{d,frame}$ is already available as the shear internal force from the frame, the term $V_{d,inf}$ is unknown. However it can be reasonably assumed the shear force $V_{d,inf}$ is a rate of the axial force acting on the equivalent strut. In fact, considering the forces acting on a portion of infill at the end of a column, the translational equilibrium equation provides:

$$V_{d,\inf} = N\cos\theta - T \tag{5}$$

This implies that the extra amount of shear demand is the difference between the horizontal component of the axial force on the strut and the friction force at the interface, denoted as $T$. The latter is related to the vertical component ($\sigma_v$) of the normal stress acting on the strut ($\sigma_v$) through the friction coefficient ($\mu$) and acts on a contact length ($\alpha l$), which is a portion of the total length of the infill ($\alpha l$, with $\alpha \leq l$). The tangential force at the interface is therefore:

$$T = \mu \cdot \sigma_v \cdot t \cdot \alpha l \qquad \sigma_v = \sigma_n \sin\theta \;;\; \sigma_n = N / w \cdot t \tag{6}$$

By substituting Eq. (6) in Eq. (5) it follows:

$$V_{d,\inf} = N\cos\theta - \mu\sigma_n \sin\theta \cdot t \cdot \alpha l = N\cos\theta - \frac{\mu \cdot N \sin\theta \cdot t \cdot \alpha l}{w \cdot t} = N\left(\cos\theta - \frac{\mu \cdot \sin\theta \cdot \alpha l}{w}\right) \tag{7}$$

providing the additional shear demand as a function of the contact length ($\alpha l$) and the current axial force ($N$) on the corresponding strut.

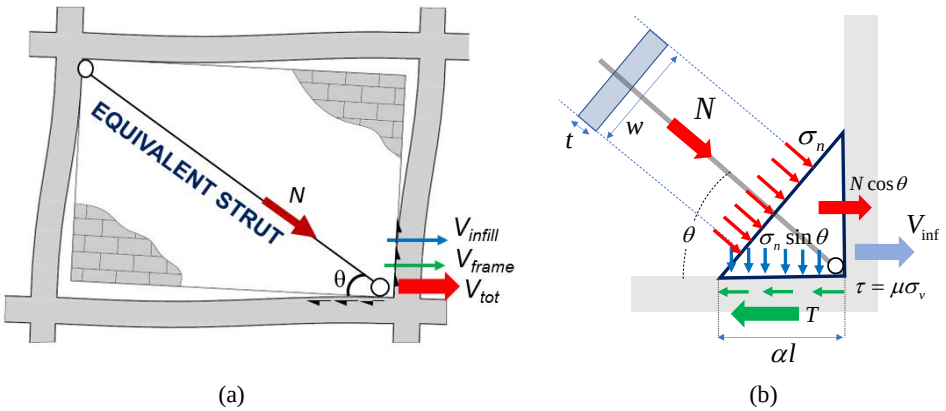


(a) (b)

Fig. 12: (a) Shear demand decomposition at the end of the columns of an infilled RC frame (b) Force transmission due to frame-infill interaction.

The validity Eq. (4) coupled with Eq. (7) has been tested by modelling the specimens mentioned according to using the macro-modelling approach suggested by Di Trapani et al. [18]. Figures 13 and 14 report the outcomes of the implementation of the proposed analytical model to adjust the shear demand, in comparison with the actual shear demand derived from the micro-model. A noticeable consistency with the results from the refined micro-model is ob-

served despite the simplicity of the analytical formulation. As regards the contact lengths, it was estimated that for the windward and leeward columns, $\alpha l$=0.30·$l$ and 0.4·$l$ for $l/h$=1, and $\alpha l$ =0.25· $l$ and 0.3· $l$ for $l/h$=1.5, respectively.

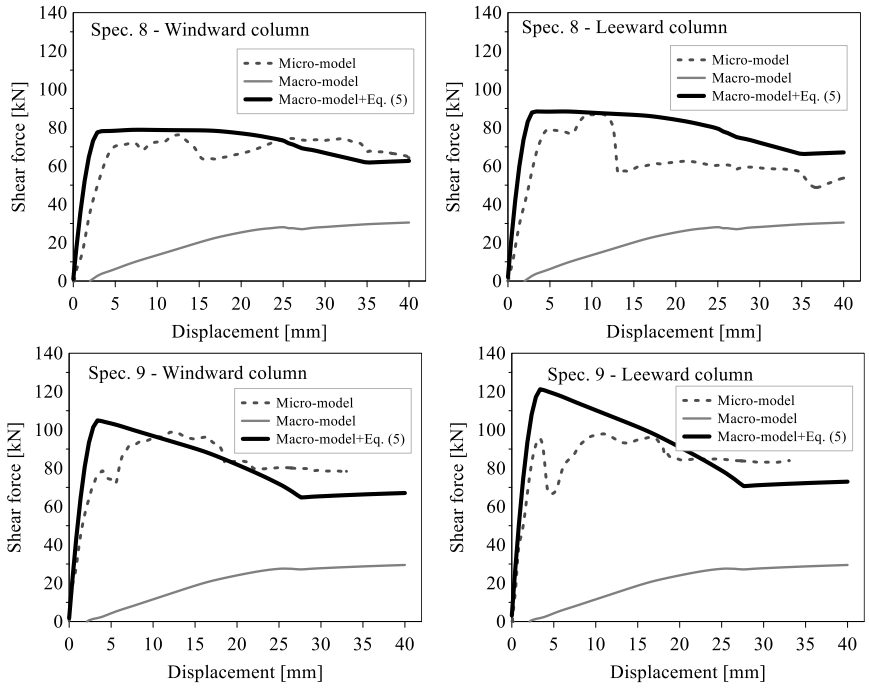


Fig. 13: Comparison between macro-model and micro-model predictions of shear demand at the windward and leeward column ends for Mehrabi & Shing [6] specimens: 8; 9.

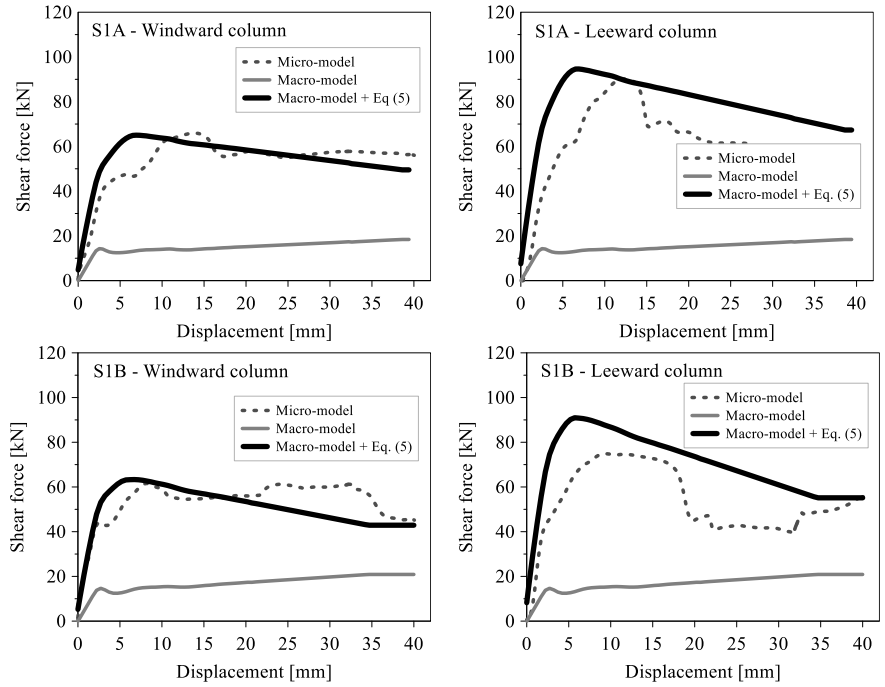


Fig. 14: Comparison between macro-model and micro-model predictions of shear demand at the windward and leeward column ends for Cavaleri & Di Trapani [2] specimens: S1A; S1B.

## 5 CONCLUSION

The additional shear demand resulting from the interaction between the frame and infill is crucial when assessing infill RC frames, as it may be responsible of local failures at the column ends and the joints. In this study, a refined micro-model for the infilled frame was formulated and realized with Open-Sees/STKO. The model validity was tested with four infilled frame specimens. The proposed micro-model enabled the evaluation of the internal forces distribution over the frame making use of a TCL script allowing the integration of the nodal forces across a specified cross-section. An analytical predictive model to estimate the additional shear demand when using the equivalent strut macro-modelling approach was also proposed. The latter relates the additional shear demand to the current axial force acting on the equivalent struts and also depends on the effective contact length of the infill with the frame ($\alpha l$). Preliminary comparisons of the shear demand extracted from the micromodel with that estimated by the macromodel, and adjusted by the proposed analytical formulation, had quite good agreement assuming contact length values in the range 0.25$l$ - 0.40$l$. This approach maintains the simplicity of the equivalent strut technique while ensuring accurate shear safety checks at the columns' ends. However, further research is necessary to determine more accurate contact length values and validate the proposed approach using a larger set of experimental tests.

## ACKNOWLEDGEMENTS

This paper was supported by DPC-ReLuis 2022–2024, WP10, Subtask 10.1.2 - Non-structural masonry.

## REFERENCES

[1] F. da Porto, M. Guidi, N. Dalla Benetta, F. Verlato, Combined in-plane/out-of-plane experimental behaviour of reinforced and strengthened infill masonry walls. *12th Canadian Masonry Symposium*, Vancouver, Canada, June 2–5, 2013.

[2] L. Cavaleri, F. Di Trapani, Cyclic response of masonry infilled RC frames: experimental results and simplified modeling. *Soil Dyn Earthq Eng*, **65**, 224–242, 2014.

[3] A. V. Bergami, C. Nuti, Experimental tests and global modeling of masonry infilled frames. *Earth Struct*, **9(2)**, 281–303, 2015.

[4] G. M. Verderame, P. Ricci, C. Del Gaudio, M.T. De Risi, Experimental tests on masonry infilled gravity- and seismic-load designed RC frames. *Proceedings of 16th international brick and block masonry conference (IBMAC)*, Padua, Italy, 2016.

[5] P. Morandi, S. Hak, G. Magenes, In-plane experimental response of strong masonry infills. *Eng Struct*, **156**, 503–521, 2018.

[6] A.B. Mehrabi, P.B. Shing, P.B., M.P. Schuller, L. Noland, Experimental evaluation of masonry-infilled RC frames. *J Struct Eng (ASCE)*, **122(3)**, 228–237, 1996.

[7] A.B. Merhabi, P.B. Shing, Finite Element Modeling of masonry-infilled RC frames, *Journal of Structural Engineering*, **123**, 604-613, 1997.

[8] M. Papia, L. Cavaleri, M. Fossetti, Infilled frame: developments in the evolution of the stiffening effect of infills, *Structural Engineering and Mechanics*,**16(6)**, 675-694, 2003.

[9] G. Uva, D. Rafaele, F. Porco, A. Fiore, On the role of equivalent strut models in the seismic assessment of infilled RC buildings. *Eng Struct*, **42**, 83–94, 2012.

[10] A. Fiore, F. Porco, D. Rafaele, G. Uva, About the influence of the infill panels over the collapse mechanisms active under pushover analyses: Two case studies. *Soil Dyn Earthq Eng*, **39**, 11–22, 2012.

[11] L. Cavaleri, F. Di Trapani, P.G. Asteris, V. Sarhosis, Influence of column shear failure on pushover-based assessment of masonry infilled reinforced concrete framed structures: A case study. *Soil Dyn Earthq Eng*, **100**, 98–112, 2017.

[12] F. Di Trapani, M. Malavisi, Seismic fragility assessment of infilled frames subject to mainshock/ aftershock sequences using a double incremental dynamic analysis approach. *Bull Earthq Eng*, **17(1)**, 211–235, 2019.

[13] I. Koutromanos, A. Stavridis, P.B. Shing, K. Willam, Numerical modelling of masonry-infilled RC frames subjected to seismic loads. *Comput Struct*, **89**, 1026–1037, 2011.

[14] L. Cavaleri, F. Di Trapani, Prediction of the additional shear action on frame members due to infills. *Bull Earthq Eng*, **13(5)**, 1425–1454, 2015.

[15] I. Caliò, B. Pantò, A macro-element modelling approach of Infilled Frame Structures. *Comput Struct*, **143**, 91–107, 2014.

[16] R.R. Milanesi, P. Morandi, G. Magenes, Local effects on RC frames induced by AAC masonry infills through FEM simulation of in-plane tests. *Bull of Earthq Eng* **16(1)**, 4053– 4080, 2018.

[17] F. Di Trapani, A. Vizzino, G. Tomaselli, A.P. Sberna, G. Bertagnoli, A new empirical formulation for the out-of-plane resistance of masonry infills in reinforced concrete frames. *Eng Struct* **266**, 114422, 2022.

[18] F. Di Trapani, G. Bertagnoli, D. Gino, M.F. Ferrotto, Empirical equations for the direct definition of stress-strain laws for fiber-section based macro-modeling of infilled frames. *J Eng Mech* **144(11)**, 04018101, 2018.

[19] F. McKenna, G.L. Fenves, M.H. Scott, *Open system for earthquake engineering simulation*. University of California, Berkeley, CA, 2000.

[20] M. Petracca, F. Candeloro, G. Camata, *ASDEA Software STKO user manual*, 2017.

[21] M. Petracca, L. Pelà, R. Rossi, S. Zaghi, G. Camata, E. Spacone, E, Microscale continuous and discrete numerical models for nonlinear analysis of masonry shear walls. *Construction and Building Materials* **149**, 296-314, 2017.

[22] John Wiley&Sons (Editor), "*fib Model Code for concrete structures 2010*", 2013.

[23] D. D'Ayala, J. Worth, O. Riddle, Realistic shear capacity assessment of infill frames: comparison of two numerical procedures. *Eng Struct*, **31**, 1745–1761, 2009.

[24] L. Cavaleri, F. Di Trapani. Prediction of the additional shear action on frame members due to infills. *Bull Earthq Eng* **13**(5), 1425–1454, 2015.

[25] V. Bolis, A. Stavridis, M. Preti, Numerical investigation of the in-plane performance of masonry-infilled RC frames with sliding subpanels. *J Struct Eng*, **143(2)**, 04016168, 2017.

COMPDYN 2023
9th ECCOMAS Thematic Conference on
Computational Methods in Structural Dynamics and Earthquake Engineering
M. Papadrakakis, M. Fragiadakis (eds.)
Athens, Greece, 12-14 June 2023

# SOIL-FOUNDATION-STRUCTURE PROBLEMS RELATED TO TRAIN-INDUCED VIBRATIONS – THE KINEMATIC INTERACTION OF TUNNEL EXCITED PILE FOUNDATIONS AND THE INERTIAL INTERACTION OF HIGH-RISE BUILDINGS

**L. Auersch**[1]

[1] Federal Institute of Material Research and Testing
Unter den Eichen 87, Berlin 12200
e-mail: lutz.auersch-saworski@bam.de

## Abstract

*The soil-foundation-structure interaction is always important when building vibrations due to train passages have to be considered. The frequency range for train vibrations is up to 100 Hz. Normally, soft surface soils are crucial so that the wavelength can be much smaller than the foundation dimensions. Three topics are of interest for the prediction and the understanding of building vibrations. 1. The „kinematic interaction" or the „added foundation effect", which is calculated either by the combined boundary-element finite-element method or by the wavenumber domain method, results in a reduction of the free-field vibration. The stiffness of the foundation resists the wave deformation, plates and walls for horizontally propagating waves or piles for vertically incident waves. 2. The „inertial interaction" or the „added building effect" yields an amplification around the vertical building resonance, which may be a rigid mode on the compliant soil or a flexible mode for high-rise buildings, and a reduction at higher frequencies. This has been analysed by detailed finite element models of apartment and office buildings. 3. Base isolation is a method to further reduce building vibrations. It is important to know the soil-foundation impedance for the possible reduction, as well as the correct building impedance. A high-rise building cannot be considered as a rigid mass model. It has a frequency-dependent behaviour with longitudinal waves travelling from the foundation to the top of the building which include the effect of floor vibrations. Experiences from building projects in Vienna, Frankfort and Berlin will give some additional results for the excitation from tunnel lines, the kinematic response of pile foundations, and the inertial response of the flexible multi-storey buildings.*

**Keywords:** Kinematic Interaction, Inertial Interaction, Surface Foundation, Pile Foundation, High-Rise Building.

## 1 INTRODUCTION

The problem is outlined in Figure 1. A building is founded on pile foundations and is excited by trains in a nearby tunnel. The problem is usually divided in the "kinematic interaction" and the "inertial interaction". The kinematic interaction, this is the reduction of the free field waves by a stiff foundation, is firstly analysed for surface foundations and secondly for pile foundations. The inertial interaction where the building-soil model is analysed for a uniform excitation, is then presented for three building examples.

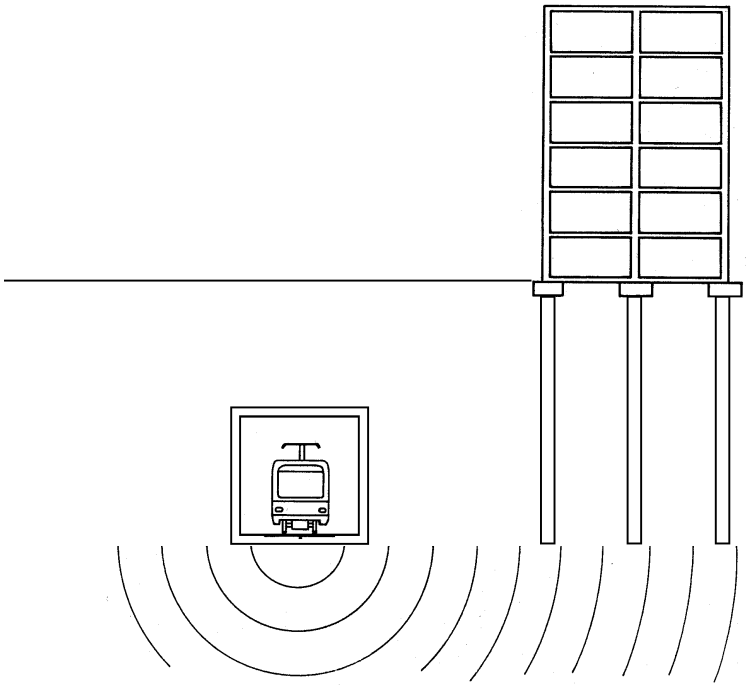

Figure 1: Train-induced building vibration, from the tunnel to the pile foundation into the multi-storey building.

## 2 THE COMBINATION OF THE FINITE-ELEMENT AND THE BOUNDARY-ELEMENT METHOD FOR THE SOIL-STRUCTURE INTERACTION

The behaviour (the dynamic stiffness and the kinematic interaction) of the foundation is calculated by the boundary-element method where the stiffness of a flexible foundation (beam, plate, wall) can be modelled by finite elements. In general, the whole building could also be modelled within the coupled FEBEM [1], but the large examples (tower buildings) presented here have been calculated with a commercial finite element software.

The boundary element method yields the frequency-dependent, complex dynamic stiffness matrix $\mathbf{K}_S(\omega)$ of the soil, where $\omega = 2\pi f$ is the circular frequency. The foundation (or building) structure is modelled by the finite element method. The global finite-element stiffness and mass matrices $\mathbf{K}_0$ and $\mathbf{M}$ yield also a frequency-dependent dynamic stiffness matrix $\mathbf{K}_F(\omega)$ of the foundation

$$\mathbf{K}_F(\omega) = \mathbf{K}_0 - \omega^2\mathbf{M} \tag{1}$$

The dynamic stiffness matrices of the soil and the structure are added to yield the global dynamic stiffness matrix $\mathbf{K}_{FS}(\omega)$

$$\mathbf{K}_{FS}(\omega) = \mathbf{K}_F(\omega) + \mathbf{K}_S(\omega) \tag{2}$$

of the combined foundation-soil system. The equation

$$\mathbf{K}_{FS}(\omega)\,\mathbf{u}(\omega) = \mathbf{p}(\omega) \tag{3}$$

of dynamic soil-structure interaction is solved to get the global displacements $\mathbf{u}(\omega)$ for any external global force excitation $\mathbf{p}(\omega)$.

In case of a free-field excitation $\mathbf{u}_0(\omega)$ of the soil, the equation

$$\mathbf{K}_{FS}(\omega)\,\mathbf{u}_F(\omega) = \mathbf{K}_S(\omega)\mathbf{u}_0(\omega) \tag{4}$$

has to be solved for the "kinematic interaction". A similar equation holds for the "inertial interaction" of the building-foundation system

$$\mathbf{K}_{BF}(\omega)\,\mathbf{u}(\omega) = \mathbf{K}_F^*(\omega)\mathbf{u}_F(\omega) \tag{5}$$

where the dynamic stiffness $\mathbf{K}_F(\omega)$ of the foundation is approximated by a number of spring and damper elements as $\mathbf{K}_F^*(\omega)$.

## 3 KINEMATIC INTERACTION OR ADDED FOUNDATION EFFECT

### 3.1 Beams, plates, and walls under horizontal wave excitation

The surface foundations are analysed for some standard parameters, the shear modulus $G$ = 8 $10^7$ N/m$^2$, the shear wave velocity $v_S$ = 200 m/s, and the compressional wave velocity $v_P$ = 400 m/s of the soil, the elasticity modulus of concrete $E$ = 3 $10^{10}$ N/m$^2$, and the length of the foundation $L$ = 20 m. The width ($a$ = 0.2, 0.5, 20 m) and the height (between 0.5 and 20 m) are varied with the different types of foundation. The free-field excitation $u_0$ is a horizontally propagating wave with the Rayleigh wave velocity of $v_R$ = 186 m/s.

At first, beams of different heights are presented in Figure 2a. The frequency-dependent transfer functions $u/u_0$ (for the centre of the foundation) start with the value 1 and decreases with increasing frequency. The reduction of the free-field depends strongly on the bending stiffness of the beams. For a beam height of 0.5 m, the reduction at 30 Hz is only 0.6 whereas for a beam with $h$ = 1.5 m (with a 30 times higher bending stiffness), the reduction reaches values smaller than 0.1 already at 25 Hz. The decrease (the slope) of this curve is also the strongest of all four curves.

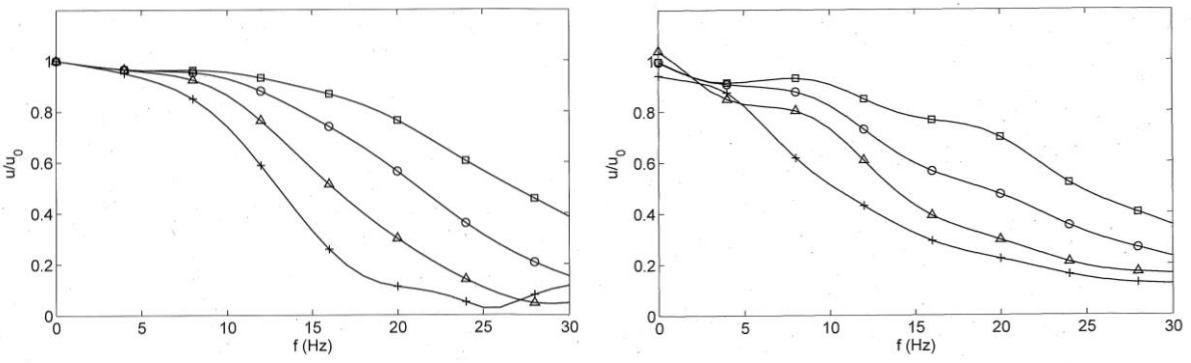


a) b)

Figure 2: Transfer function $u/u_0$ of a) concrete beams ($a$ = 0.5 m, $L$ = 20 m), b) concrete plates ($a$ = 20 m, $L$ = 20 m), with different heights $h$ = □ 0.5, ○ 0.7, △ 1.0, + 1.5 m, excited by a horizontally propagating wave.

Figure 2b shows comparable results for plate foundations with the same heights. The reduction is stronger than the reduction of the beams as far as the lower frequencies up to 15 Hz are observed. For higher frequencies, the beams have steeper curves and lower values. The higher soil-plate transfer values are due to the strong radiation damping for the wide soil area under the plate which is not present for the narrow beam foundation.

Next, low walls, which may exist in basement floors, are examined with Figure 3a for different masonry walls and a concrete wall. The reduction of the horizontally propagating waves is strongest for the stiffest material, the concrete. The reduction starts at low frequen-

cies and reaches values of 0.1 already at 10 Hz. The masonry walls reach their strongest reduction at about 20 Hz.

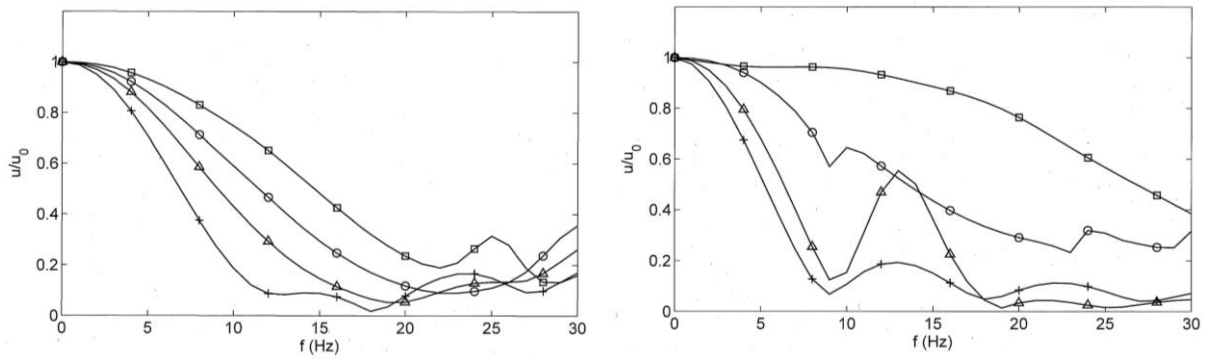


a) b)

Figure 3: Transfer function $u/u_0$ of a) low walls ($H$ = 5 m, $a$ = 0.2 m, $L$ = 20 m), with different $G$ = □ 1, ○ 2, △ 4, + 13 $10^9$ N/m$^2$, b) high walls with $G$ = ○ 1, △ 13 $10^9$ N/m$^2$, □ low beam ($h = a$ = 0.5 m, $L$ = 20 m), + rigid massless foundation ($L$ = 20 m), excited by a horizontally propagating wave.

Finally, high walls (20 m x 20 m large) are considered in Figure 3b. The behaviour of a soft masonry wall (circle markers) is completely different from the behaviour of a concrete wall (triangle markers). The reduction is quite similar to the low masonry wall with a continuously decreasing curve. The concrete wall, however, shows a strongly frequency-dependent behaviour. Zeros occur at 19 and 26 Hz and a strong maximum at 13 Hz. For comparison, the reduction of the smallest concrete beam and of a rigid (massless) foundation are also presented in Figure 3b. It can be understood that the high concrete wall responds like a rigid, but massive foundation which has the same zeros as the massless foundation and in addition an amplification at the wall-soil resonance frequency.

### 3.2 Rigid surface foundations and piles under horizontal and vertical wave excitation

A finite rigid foundation subjected to the wave-field excitation of a homogeneous soil can be calculated approximately by the simple formula of the kinematic interaction

$$\frac{u}{u_0} = \int_{-L^*/2}^{L^*/2} \exp ix^* \, dx^* / L^*/2 = \frac{\sin L^*/2}{L^*/2} \tag{6}$$

where $L^* = L\omega/v_R$. In Figure 3b, the curve with the plus markers shows the cancelation of the waves for a 20 m long foundation, which occurs at 9, 18 and 28 Hz if 1, 2 or 3 wavelengths fit into the foundation length. The length is the most relevant parameter for the wave reduction of a rigid foundation.

A similar formula holds for a rigid pile of length $H$ which is excited by a vertically incident P-wave. A second P-wave must be considered which is reflected at the stress-free surface of the soil. The superposition of these two waves yields a standing wave, and the average amplitude of this standing wave is

$$\frac{u}{u_0} = \int_0^{L^*} \cos z^* \, dz^* / H^* = \frac{\sin H^*}{H^*} \tag{7}$$

where $H^* = H\omega/v_P$. Formula (7) is similar to formula (6) but the full length $H$ of the pile is effective instead half the length $L$ of the beam, and the compressional wave velocity $v_P$ is used instead of the Rayleigh wave velocity $v_R$. Formula (7) holds for an earthquake excitation (see also Appendix A).

If the pile is excited by a metro train (a vertical point load at finite depth), the situation is more complex (Figure 4a presents the situation for a 10 m long rigid pile and the source at 30 m depth). The point load excites P- and S-waves travelling vertically upwards, which show strong interferences for the free field (square markers). Moreover, there is an attenuation (to

half the amplitude in the present case) from entering of the incident wave to the exit of the reflected wave. Figure 4 compares the amplitudes (admittances $v/F$) of the free field with the pile response at the soil surface (circle markers). There is a strong reduction for frequencies above 10 Hz. The maximum ratio would be 1/3, but the minimum values are nearly 0 at 14 and 28 Hz. These minima are at higher frequencies than for an earthquake excitation where minima at 10, 20 and 30 Hz are expected from equation (7).

Contrary, if the source is close to the pile end (at a depth of 11 m in Figure 4b), an amplification of the free field occurs instead of a reduction. This is due to the strong attenuation of the free field from 1 m (where the pile is excited) to 11 m distance of the soil surface to the source.

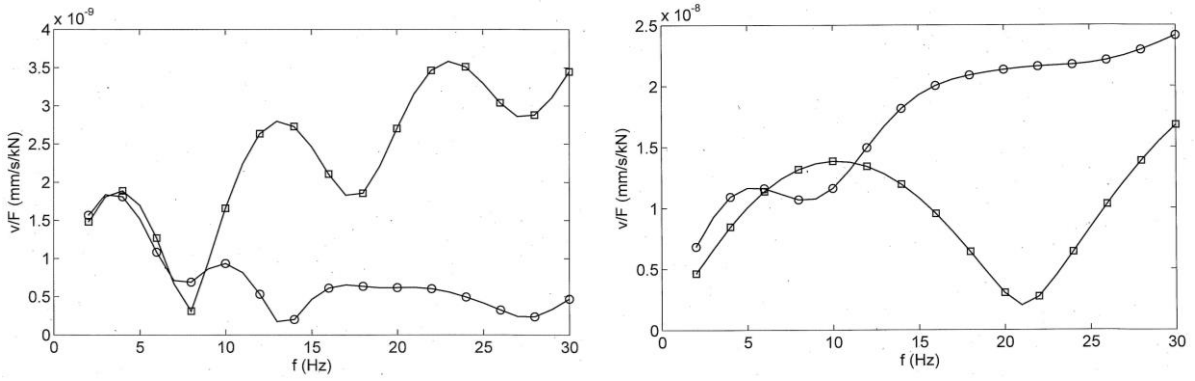


a) b)

Figure 4: Admittance functions $v/F$ of a rigid pile of length $H$ = 10 m excited by the vertically propagating wave field from a point load at depth $z_0$ = a) 30 m (far field), and b) 11 m (near field), □ free field, ○ response of the pile at the soil surface.

### 3.3 Pile groups under horizontal wave excitation

The following pile groups are considered [2]: A shallow foundation and a single pile for comparison, a line of 10 piles for theoretical studies, a circle of 16 piles (motivated by a wind

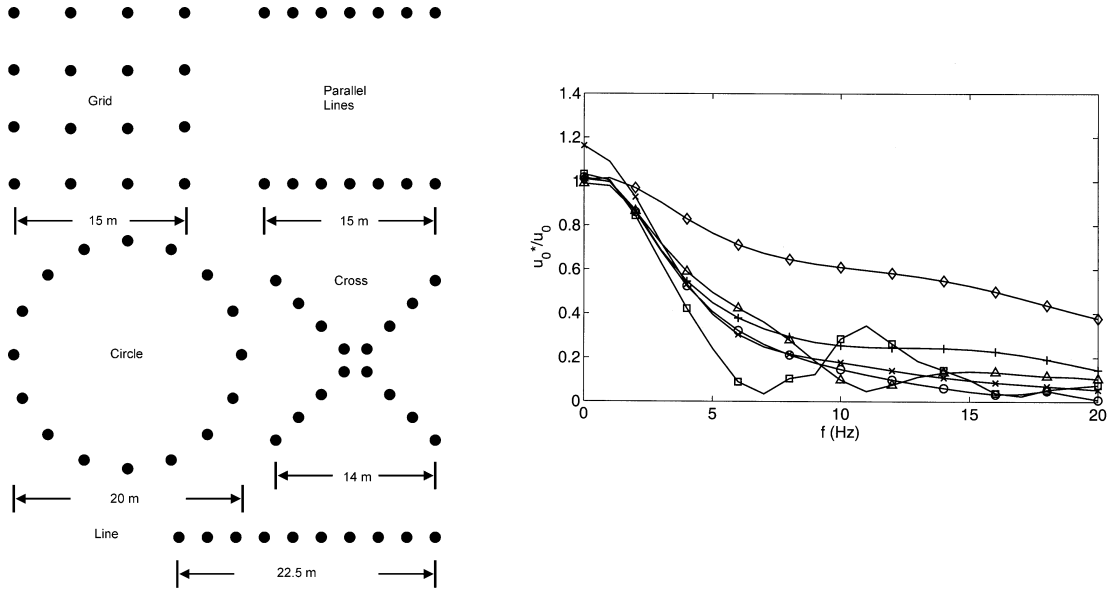


a) b)

Figure 5: Rigid pile groups (a) excited by a horizontally propagating wave, b) transfer functions $u/u_0$ for a □ circle, ○ grid, △ parallels, + cross, × line, ◇ single pile, ($H$ = 20 m, $2R$ = 1 m).

energy plant), two parallel lines of 2 x 7 piles (as a simple case of a building above a railway or motorway tunnel), a regular grid of 16 piles (typical for residential and office buildings), and a cross of 16 piles as a not so regular building foundation. The detailed dimension can be taken from Figure 5a. The diameter $2R$ of the circular piles is 1 m and the length $H$ is 20 m. The area which is covered by the pile groups is approximately 15 m x 15 m = 225 m$^2$. The excitation is a vertical point load at 20 m horizontal distance from the centre of the pile group. The kinematic interaction is described as the amplitude ratio between the response of the massless rigid foundation and the amplitude of the free field (Fig. 5b). The response at the free surface at the centre of the pile group (that is in 20 m distance of the loading point) is used as the reference $u_0$. In case of the single pile, the kinematic effect is due to the averaging of the different amplitudes at different depths which leads only to a moderate reduction of $u/u_0 \approx 0.4$ at 20 Hz. For all pile groups with rigidly connected piles, there are strong phase differences between the different foundation points. The averaging of amplitudes with different phases yields a strong reduction. Reductions down to $u/u_0 \approx 0.1$ are observed at 20 Hz, and the amplitudes clearly continue to decrease with increasing frequency.

## 4 INERTIAL INTERACTION OR ADDED BUILDING EFFECT

The effect of the building mass on the ground vibration has been called the "inertial interaction". As the simplest model, a rigid building can be added to the foundation model. Real buildings and namely high-rise buildings behave quite different from a rigid mass. An example for a six-storey apartment building with concrete walls is shown in Figure 6a. Longitudinal waves are propagating from the foundation to the roof and floor resonances (at 20 Hz) modify considerably the soil-building transfer functions. At 20 Hz, the floor resonance causes a minimum of the wall, and for frequencies higher than 32 Hz the different storeys behave different, minima can be found at different frequencies (higher frequencies for higher storeys), and the amplitudes vary around a constant value. In contrary, the rigid building models, which have been calculated for different soils (Fig. 6b) and different buildings (Fig. 6c), show a uniform strong decrease of amplitudes.

The same difference between the rigid and flexible modelling can be seen for buildings on different base isolations where the realistic high-frequency reduction (Fig. 6e) is considerably over-predicted by the rigid building model (Fig. 6d). A smooth prediction model for the average building amplitudes is suggested with Figure 6f, see Section 6.

Figure 7 shows the transfer functions of a 20-storey office tower calculated by the 1-dimensional soil-column-floor model

$$\frac{u_W}{u_0} = \frac{\cos\ a\xi}{\cos\ a}\ \frac{1}{1 + iq\ \tan\ a} \tag{8}$$

with $\xi$ indicating the storey, $a$ a normalised frequency parameter (which includes the stiffness of the columns and the effective mass of the floors), and $q$ a soil-structure interaction parameter (approximately the impedance ratio between columns and foundation), see [3]. The high-rise column-type building shows a clearer building-soil resonance at 3-4 Hz where amplitudes are increasing with the height in the building. At high frequencies, the amplitudes show a reduction which is stronger with increasing height in the building. This is due to the scattering damping of the floor slabs which has been added as a portion of the point impedance

$$\frac{F}{v} = 8\sqrt{Bm''} \tag{9}$$

of an infinite floor slab with bending stiffness $B$ and mass per area $m''$. Because of all these specialties of multi-storey buildings, detailed building models have been calculated under a uniform free-field excitation for several building projects, see the three examples in the following Section 5.

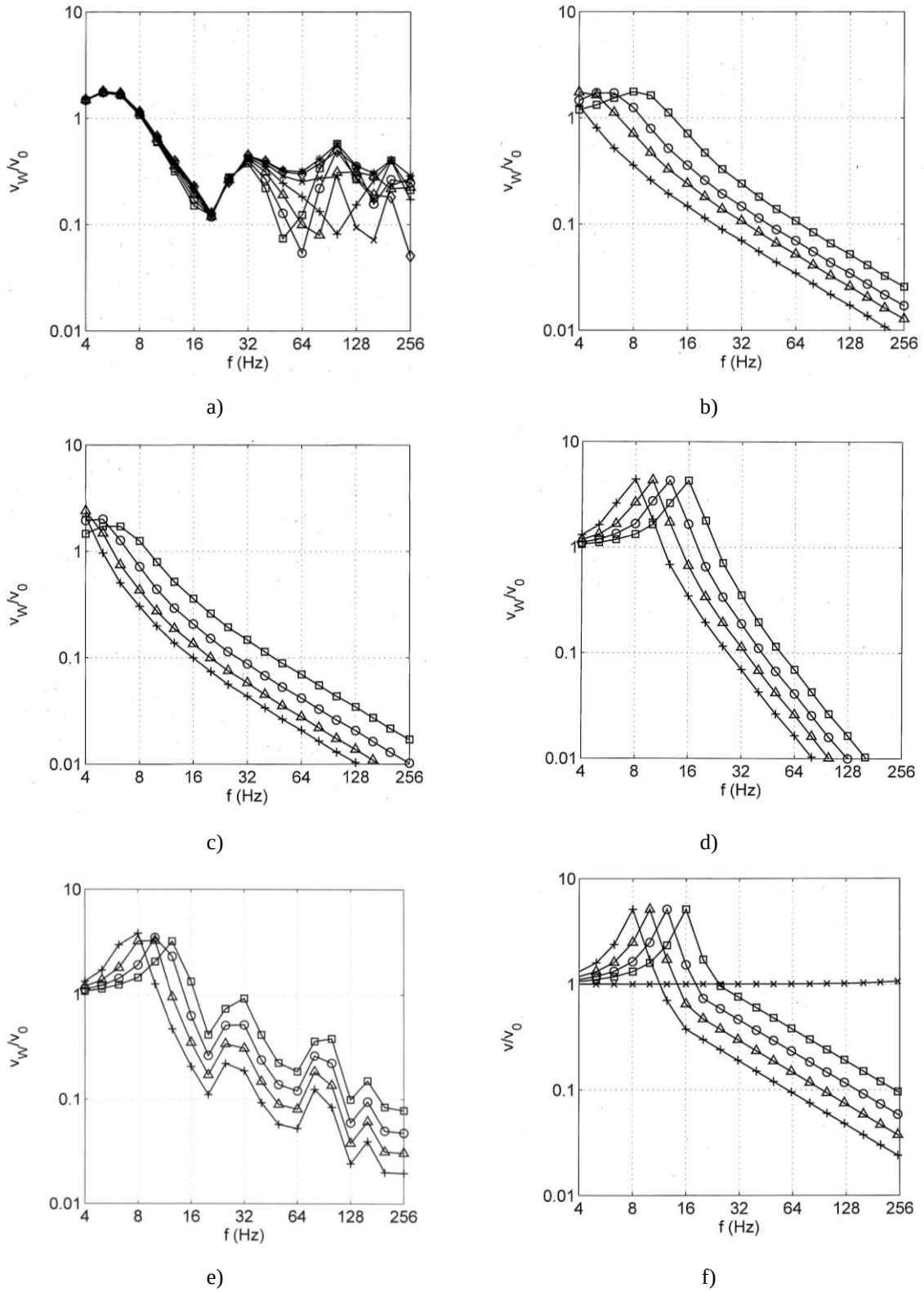


Figure 6: Transfer function $v/v_0$ of a six-storey apartment building a) at the □ 1st, ○ 2nd, △ 3rd, + 4th, × 5th, and ◇ 6th floor, b,c) rigid buildings for soils with $v_S$ = □ 300, ○ 200, △ 150, + 100 m/s (b), □ 6, ○ 10, △ 15, + 20 storeys (c), d-f) the same building on a base isolation with $f_0$ = □ 16, ○ 12.5, △ 10, + 8 Hz, d) rigid building, e) the building with flexible walls and floors, f) a simplified model consisting of a rigid mass at low frequencies and of an infinite building at high frequencies.

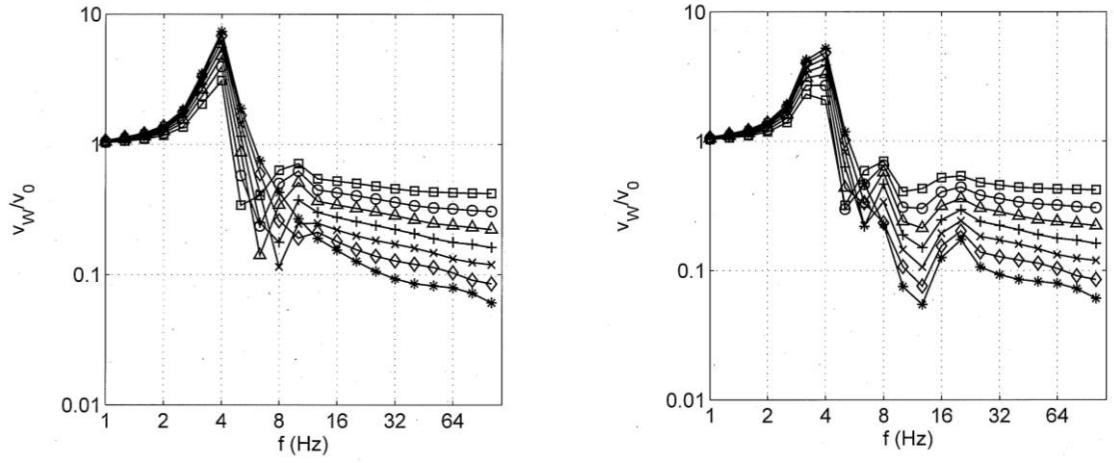


Figure 7: Transfer function $v/v_0$ of a 20-storey office tower at the □ 1st, ○ 4th, △ 7th, + 10th, × 13th, and ◇ 16th, ∗ 19th floor, e) model with rigid floors below $f_0$ = 10 Hz and floor dampers above, f) with floor resonance below 2 $f_0$ = 20 Hz and floor dampers above.

## 5 BUILDING EXAMPLES

### 5.1 Frankfort tower

A 40-storey tower in Frankfort has been analysed for the excitation by a metro tunnel in 10 m distance. The pile foundation consists of 50 piles of $H$ = 40 m and $R$ = 1 m which are connected by a 3 m thick concrete plate. The tower is founded on a stiff soil of $v_S$ = 400 m/s. The following foundation details can be taken from the analysis of Section 3.3. The values of the kinematic effect of the pile groups (Fig. 5) can be transferred to the present case by multiplying the frequencies by 2. In addition, the compliance (stiffness) of a single pile can be taken from Appendix A (Fig. 11b) as well as the group effect of 1/6 for the stiffness and 1 for the damping (Fig. 12).

The response of the whole soil-building system (the "inertial interaction effect") is calculated by a detailed finite-element model (Figure 8a). The building vibrations are quite different for the core, the near core areas, and the column areas. An average amplitude over several points has been built for every fifth storey and is presented for frequencies between 1 and 100 Hz as one-third octave spectra (Fig. 8b). A resonance amplification of up to $V$ = 6 is observed at 2 to 3 Hz where the amplitudes are clearly increasing with the height in the building. At high frequencies, a completely different behaviour can be found, the amplitudes decrease with increasing storey with 0.5 dB per storey. This attenuation is a result of the structural damping of the walls and columns, and of the scattering damping of the floors. The attenuation is stronger if the material damping of the building material is increased to 5 % (Fig. 8c). The attenuation is also stronger if the excitation is only applied at the first row of piles (Fig. 8d). The latter results in a general reduction by the stiff foundation slab, but also to a scatter of waves through the floors which is considerably stronger than for the uniform excitation of all piles (Fig. 8b,c). Therefore, the attenuation with increasing storey starts at a lower frequency of 12 Hz and reaches a stronger value of more than 1 dB per storey (Fig. 8d).

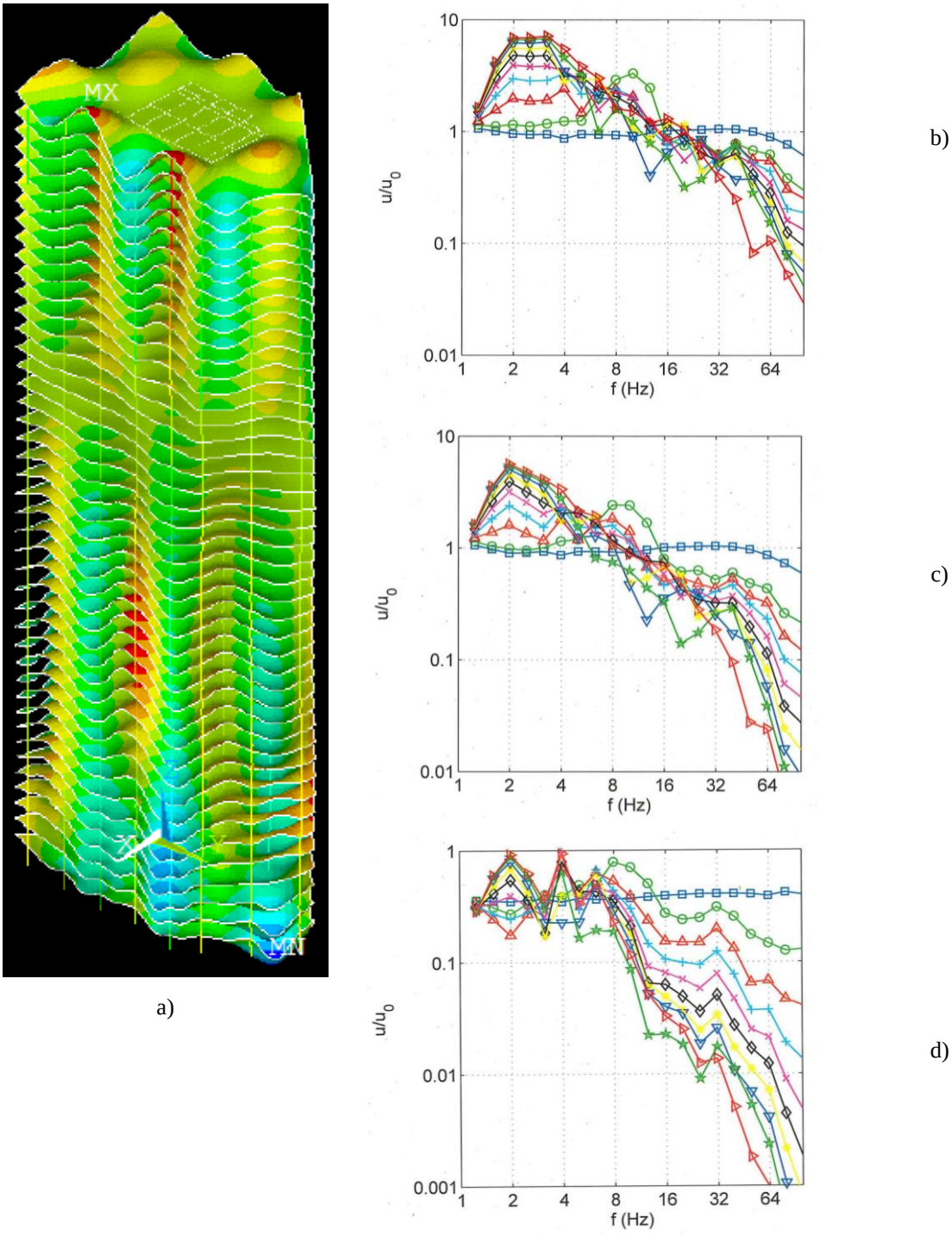


Figure 8: 40-storey Frankfort tower, a) vibration mode at 10 Hz, b) transfer functions $u/u_0$ of the building-soil system under uniform free-field excitation, □ base plate, ○ ground floor, △ 5th, + 10th, × 15th, ◇ 20th, ∗ 25th, ▽ 30th, ⋆ 35th, ▷ 40th storey, c) increased structural damping of 5%, d) increased scattering damping of the floors (only one row of piles excited).

The scattering damping of the floor slabs has also been included in the 1-dimensional soil-column-floor model, and the results for a 20-storey office tower clearly show the attenuation with increasing storey number (Fig. 7).

## 5.2 Hotel “Berlin Alexanderplatz”

The hotel consists of a 10-storey part and a 20-storey part (Fig. 9a). The metro is passing below the outer floors of the 10-storey part which is founded on piles. The vibration mode at 8 Hz (Fig. 9b) clearly shows that the central columns of both parts show a resonance amplification. The different parts of the building behave quite different although the model has been calculated for a uniform excitation. The wall has no amplification (Fig. 9c) whereas the column has a strong amplification at 10 Hz (Fig. 9d). At medium frequencies (40 – 60 Hz), the wall shows a characteristic spread of amplitudes, and the amplitudes are attenuated with increasing height at high frequencies. The different behaviour of different building parts seems to be a general characteristic of multi-storey buildings as has been found from a parameter study in [4].

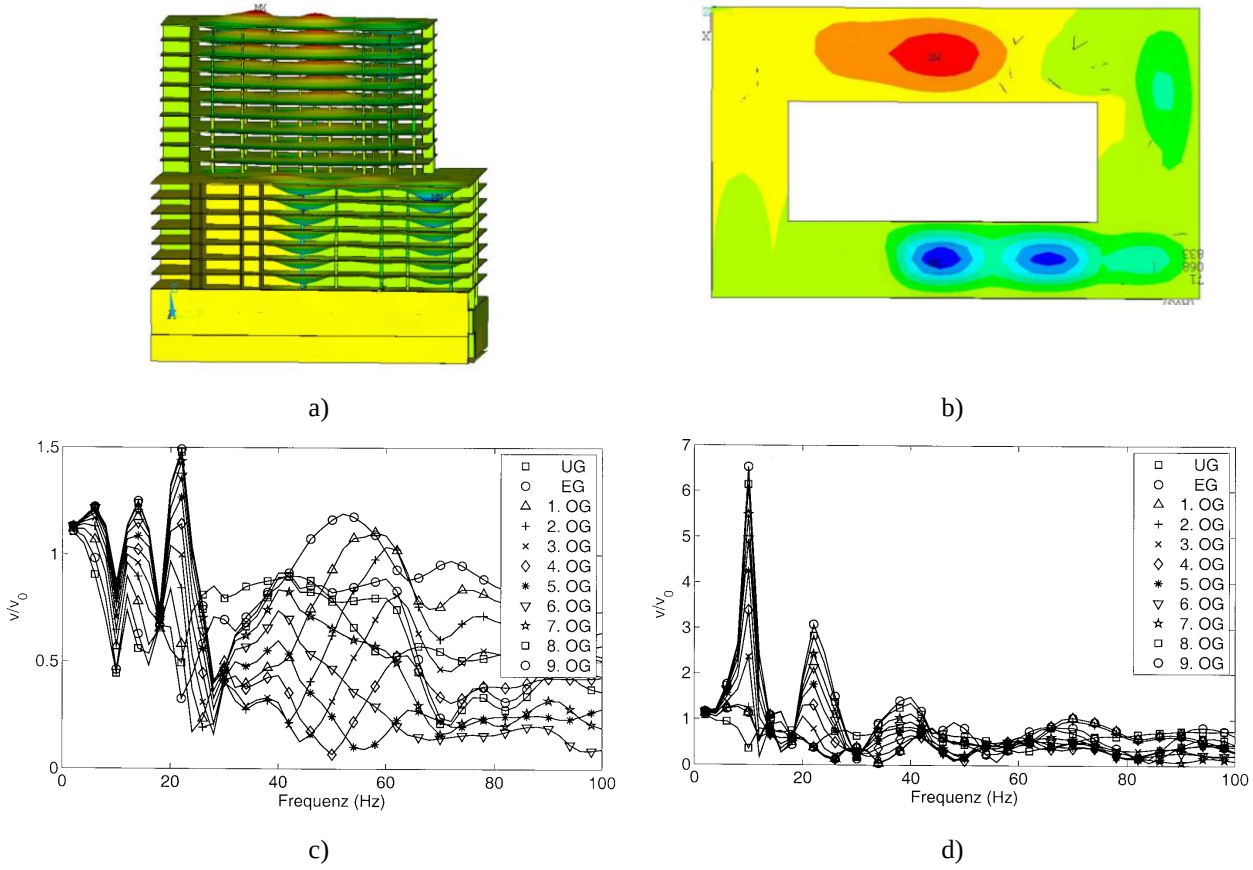


Figure 9: Hotel “Berlin Alexanderplatz” with 10- and 20-storey parts, calculated vibration mode at, a) 12 Hz, side view, b) 8 Hz, top view, c) transfer functions of a wall, d) transfer functions of a column.

## 5.3 City Tower Vienna

The vibrations of the 24-storey City Tower Vienna have been calculated and measured for trains running under the building (Fig. 10a,b). The transfer functions are shown in Figure 10c,d. The measurements and calculations show in good agreement the resonance amplification at about 6 Hz which is increasing with the height within the building. Moreover, the resonance amplifications of the floors between 10 and 20 Hz are also in good agreement.

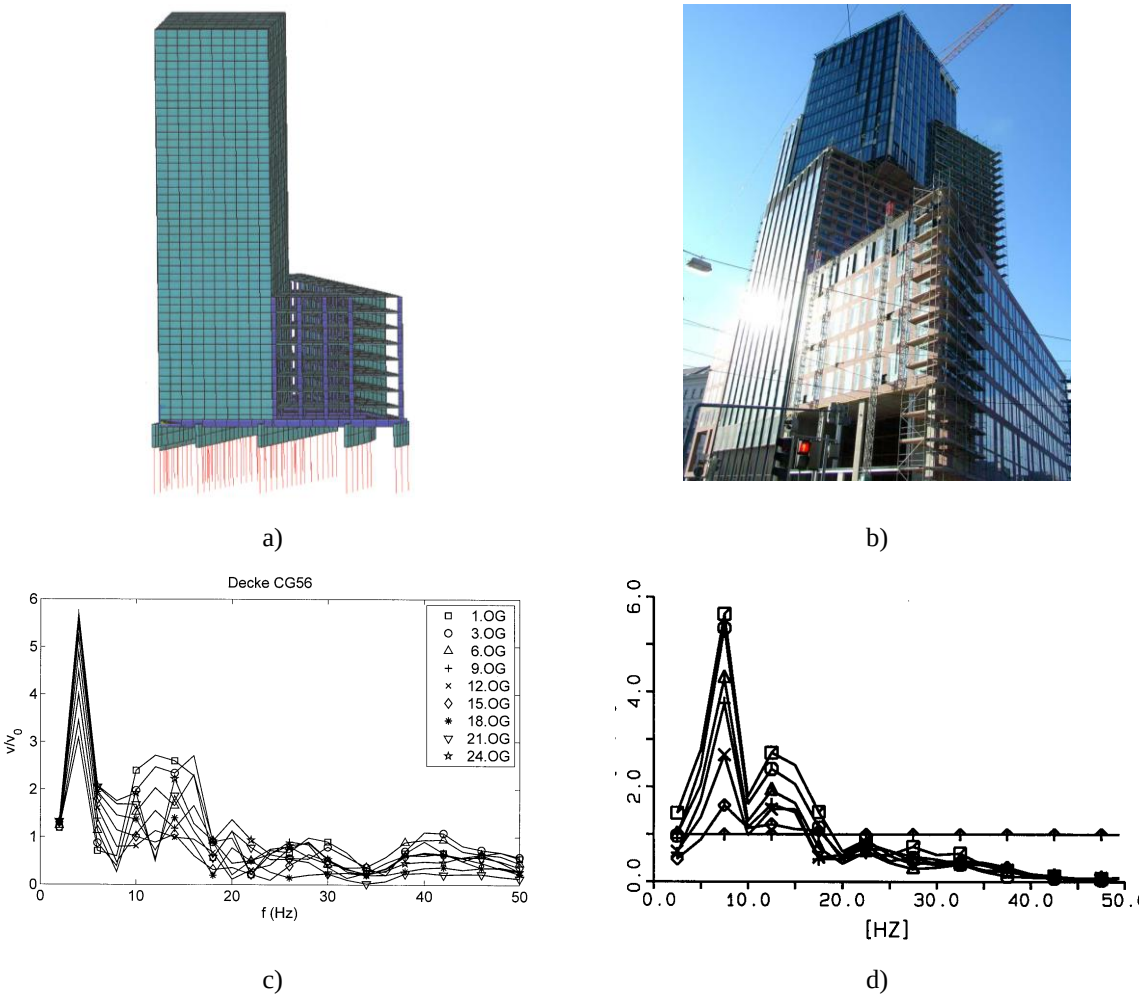


Figure 10: 24-storey City Tower Vienna (b), finite element model (a), calculated transfer functions (c), measured transfer functions (d, □ 24th, ○ 21st, △ 18th, + 15th, × 12th, ◇ 6th, ♦ ground storey)

## 6 BASE ISOLATION OF A BUILDING

Base isolations are often characterised by a frequency $f_0$, which is the resonance frequency of the rigid building on the isolation system. The reduction effect of a base isolation, however, should not be calculated by a rigid building model as neither the resonance frequency nor the reduction values are correct. This is demonstrated by Figures 6d and 6e where the frequency $f_0$ is varied between 8 and 16 Hz. These resonance frequencies can be clearly seen for the rigid building (Fig. 6d). Compared to the the strong reduction of the rigid building, the reduction of the flexible building is considerably weaker (Fig. 6e). The floor masses vibrate with the whole building at low frequencies. Then the floor resonance frequency at 20 Hz (with maximum of the floor response, not shown) is observed as a minimum of the wall response. Above the resonance frequency, the floor masses are decoupled from the building. Moreover, higher storeys are also decoupled from the lower building so that the reduction effect of the base isolation is weaker than for the full rigid mass. For a better prediction of the isolation effect, a different simple model can be used [5] which consists of a rigid building for the low frequencies and an infinitely high building for the high frequencies (Fig. 6f).

## 7 CONCLUSION

The kinematic reduction of the free field by stiff or rigid foundations has been presented for beams, plates low and high walls under horizontally propagating Rayleigh waves (see more results in [6]), and for piles under vertically incident compression waves. Reductions to 10 to 30 % of the free field are usually found at 30 Hz. Additional high-frequency reductions are due to the inertial interaction where a complete building-soil model has been calculated under a uniform free-field excitation. The amplitudes decrease with increasing height in the building due to the material damping and the scattering damping of the floors. At low frequencies, however, the amplitudes are amplified compared to the free field, increasing with the storey number. The prediction of the effect of a base isolation should regard these effects of a flexible building.

## 8 ACKNOWLEDGEMENT

M. Eidenmüller from ITA helped with the modelling and calculation of the Frankfort tower. My colleagues W. Wuttke and W. Schmid did the hard job of installing 120 sensors in the Vienna City Tower (without a lift!). Thanks to S. Said who helped with measuring, evaluating, modelling and calculating for several building projects in Berlin and Vienna.

## REFERENCES

[1] L. Auersch, G. Schmid, A simple boundary element formulation and its application to wavefield excited soil-structure interaction. *Earthquake Engineering and Structural Dynamics*, **19**, 931–947, 1990.

[2] L. Auersch, Wave propagation in the elastic half-space due to an interior load and its application to ground vibration problems and buildings on pile foundations. *Soil Dynamics and Earthquake Engineering*, **30**, 925–936, 2010.

[3] L. Auersch, Building response due to ground vibration – simple prediction model based on experience with detailed models and measurements. *International Journal of Acoustics and Vibrations*, **15**, 101-112, 2010.

[4] L. Auersch, S. Ziemens, The response of different buildings to free-field excitation – a study using detailed finite element models. M. Papadrakakis, eds. *EURODYN 2020*, Athens, Greece, November 23–26, 2020, 4560–4576.

[5] L. Auersch, Prediction of building noise and vibration – 3D finite element and 1D wave propagation models. *Proceedings of Euronoise 2021*, LNEC, Lisbon, 2021.

[6] L. Auersch, G. Sanitate, Effetto filtro esercitato dalle plate e pareti su onde incidente orizzontalmente. *Rivista Italiana di Geotecnica*, submitted 2023.

## 9 APPENDIX A: RIGID AND FLEXIBLE PILES AND PILE GROUPS UNDER VERTICAL WAVE AND FORCE EXCITATION

At first, a single pile is considered under a vertical earthquake excitation. A compressional wave is incident from infinity. The transfer function between the free field (incident and reflected wave) and the pile response is shown in Figure 11a for different pile materials. Strong variations with frequency can be found for the stiff piles, most clearly for the rigid pile (diamond marker). The flexible piles reach a different limit case, the infinitely long pile which is almost reached for the curve with square markers. This curve can be read as a function of the dimensionless frequency parameter $H^* = \omega H/v_P$, where 20 Hz relates to $H^* = 2\,\pi$. The stiffness ratio between pile and soil must be expressed as $h/H$ with the elastic length $h$

$$h = \sqrt{\frac{EA}{G}} \tag{10}$$

of the pile according to the correct dimensional analysis. The stiffness or length ratios of Figure 11 are 0.5, 0.7, 1.0, 1.5, 2.5, and infinity for the rigid pile. The infinitely long flexible limit can be read from the curve with the square markers where $f$ = 20 Hz corresponds to $h^* = \omega h/v_P = \pi$.

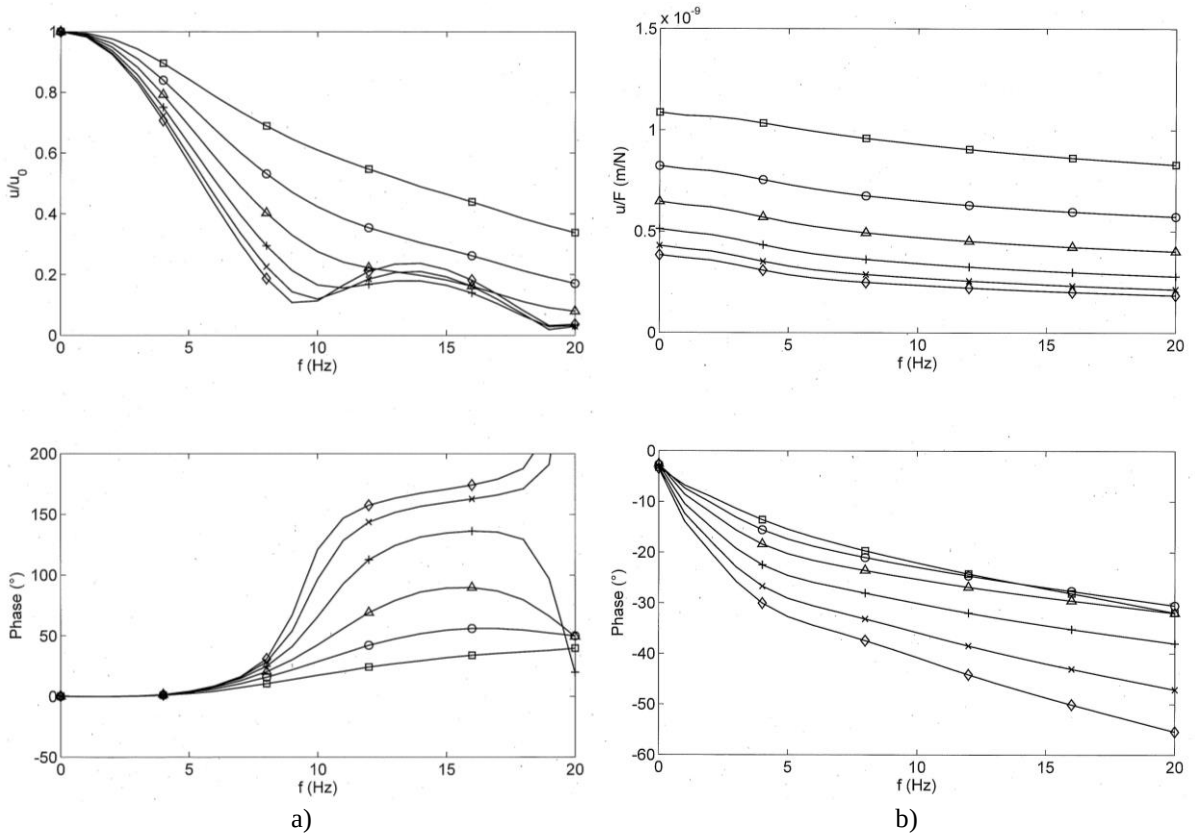


a) b)

Figure 11: Transfer functions $u/u_0$ resp. $u/F$ for single piles under a) earthquake and b) force excitation, pile material with $E$ = □ 0.7, ○ 1.5, △ 3.0 (concrete), + 7, × 21 $10^{10}$ N/m$^2$ (steel), ◇ ∞ (rigid), ($H$ = 20 m, 2$R$ = 1 m), amplitude (top), phase (bottom).

The same single piles are considered under a vertical force excitation in Figure 11b. The same limit cases can be observed. The non-dimensional compliances should be read from this figure as $C^* = uGH/F$ (≈ 0.6) for the rigid pile (diamond marker) and as $C^{**} = uGh/F$ (≈ 0.7) for the infinitely long flexible pile (square markers) where the static values are given in bra-

ckets. For higher values of $h/H$, the "rigid" limit is approached from above, for lower values the "infinitely long flexible" limit is approached also from above. The higher phase delays indicate the stronger damping of the stiff piles.

In Figure 12, groups of rigid and flexible piles are examined (see Figure 5a for the different configurations). The compliances are considerably frequency dependent, namely for the "grid" and "parallel" configurations. A general strong decrease of the amplitudes is found, and phases around 90° indicate that the damping is dominant. The results for the flexible (concrete) piles (Fig. 12b) are quite similar to the results for the rigid piles (Fig. 12a). The amplitudes are somewhat higher, and the phase (the damping) is reduced.

A group of $n$ piles has a higher compliance than $n$ single piles acting together. This group effect yields a factor of 5 to 7 for the different pile groups [2]. As the damping has (almost) no group effect, it becomes more dominant for the pile groups.

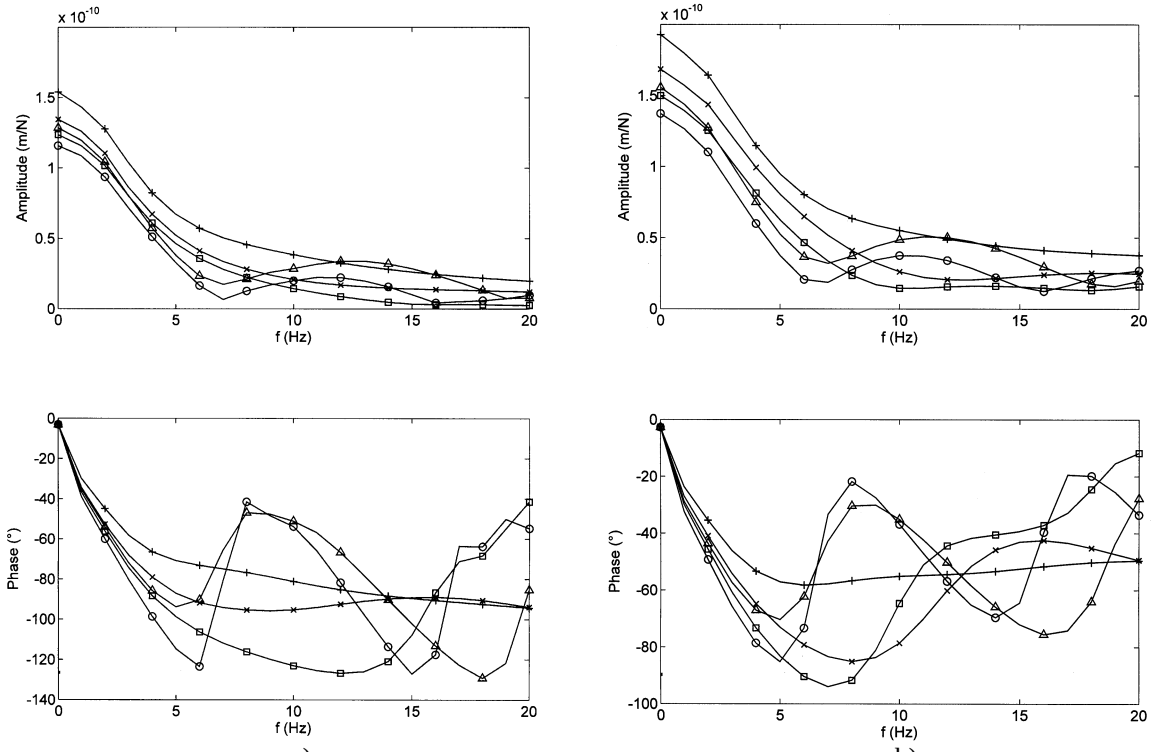


Figure 12: Groups of rigid (a) and flexible (b) pile groups excited by a vertical force, compliances $u/F$ for a □ circle, ○ grid, △ parallels, + cross, × line, ◇ single pile, ($H$ = 20 m, $2R$ = 1 m), amplitude (top), phase (bottom).

COMPDYN 2023
9th ECCOMAS Thematic Conference on
Computational Methods in Structural Dynamics and Earthquake Engineering
M. Papadrakakis, M. Fragiadakis (eds.)
Athens, Greece, 12-14 June 2023

# NUMERICAL BACK-ANALYSIS OF DYNAMIC CENTRIFUGE TESTS ON THE SEISMIC BEHAVIOUR OF CAISSON FOUNDATIONS SUPPORTING BRIDGE PIERS

**Domenico Gaudio**[1] **and Fabrizio Murillo**[2]

[1] University of Cambridge, UK (formerly Sapienza University of Rome, Italy)
High Cross, Madingley Road, Cambridge CB3 0EF, UK
e-mail: dg564@cam.ac.uk

[2] Politecnico di Milano
Piazza Leonardo da Vinci, 32, 20133 Milan, Italy
fabriziojose.murillo@mail.polimi.it

## Abstract

*Over the last few years, an ever-increasing interest on a sort of a "Reversed" Capacity Design of geotechnical systems has been emerging, particularly when looking at the seismic design of bridge foundations, such as shallow, piled and caisson foundations. In this approach, soil irreversible behaviour is triggered on purpose during strong seismic events, so as to protect the superstructure. Although the capacity of soil-caisson systems is quite high if compared to shallow and piled foundations, limit conditions of these systems may be actually attained during destructive seismic events.*

*The above-mentioned framework boosted the research on the dynamic response and interaction diagrams (i.e., failure envelopes) of rigid and massive caisson foundations [1][2]. Gaudio et al. [3] recently performed an experimental campaign via dynamic centrifuge tests, where a typical layout of a cylindrical caisson supporting a bridge pier was subjected to a series of ground motions. The caisson was embedded in a typical alluvial deposit, where the clay stratum was either soft and very soft.*

*In this paper, the results of preliminary 3D Finite Element back-analyses reproducing the centrifuge test are presented and discussed, for the specific soft-clay case. The analysis first aimed at reproducing and then extending the experimental investigation, so as to both validate and better understand the phenomena observed in the centrifuge. It is shown that, even with a simple but still comprehensive calibration of handy soil constitutive models, the main features ruling the seismic performance of the systems at hand can be fairly captured.*

**Keywords:** Caisson Foundations, Soft clay, Centrifuge testing, 3D Finite Element Analyses, Dynamic Soil-Structure Interaction, Earthquakes.

## 1. INTRODUCTION

It has been a long time since the engineering community realized that strong structure is not a synonym for safety when referring to earthquake-resistant systems. Nowadays, structural engineers rely on ductility for performing their designs. Nearly all the building codes worldwide allow plastic deformations to happen in focalized elements, reducing stresses in the critical ones, thus preventing collapse. Nonetheless, this concept is seldom applied to foundations.

Over the last decade, several studies have been performed to assess the effects of soil plasticity and soil-structure interaction on the performance of bridge piers under seismic actions. Studies like [4] and [5] showed that the inelastic behaviour of soils and the temporal attainment of bearing capacity could improve the performance of pier-deck systems. Following this framework, developments have been made concerning the "Reversed Capacity Design" (weak foundation-strong column) [6].

Most of these studies made use of numerical methods, taking advantage of the ongoing development of computational resources. However, commercial codes often rely on strong assumptions which may not correctly reproduce the system behaviour, whereas centrifuge experiments are more realistic but rarely available. This is why validation of the numerical models against centrifuge experiments is essential.

In this study, the centrifuge experiment performed by Gaudio *et al*. [3] is reproduced in the Finite Element (FE) code Plaxis 3D CE 2022 [7], where a caisson-pier-deck system embedded in a typical alluvial deposit with soft clay is subjected to a moderate-intensity earthquake. The comparison of the numerical results against the experimental ones shows that the main features ruling the seismic performance of the system may still be captured if a proper calibration of soil constitutive parameters is carried out.

## 2. PROBLEM LAYOUT

The study considers a typical configuration of a highway bridge pier, where the interaction with adjacent piers is neglected thanks to the assumption of a long span ($L$ = 50 m). The pier consists of a circular concrete column of diameter $d$ = 2.2 m and height $h_s$ = 15 m, subjected to the self-weight of the concrete deck.

Figure 1 shows the problem layout. The pier-deck system is supported by a massive cylindrical concrete caisson with a diameter $D$ = 8 m and height $H$ = 8 m (slenderness ratio $H/D$ = 1). The whole system is embedded in a typical alluvial deposit, consisting of a shallow 3-m-thick layer of loose sand overlying a 14-m-thick soft clay layer. The water table is located at the contact between the sand and clay, and the initial pore water pressure is hydrostatic.

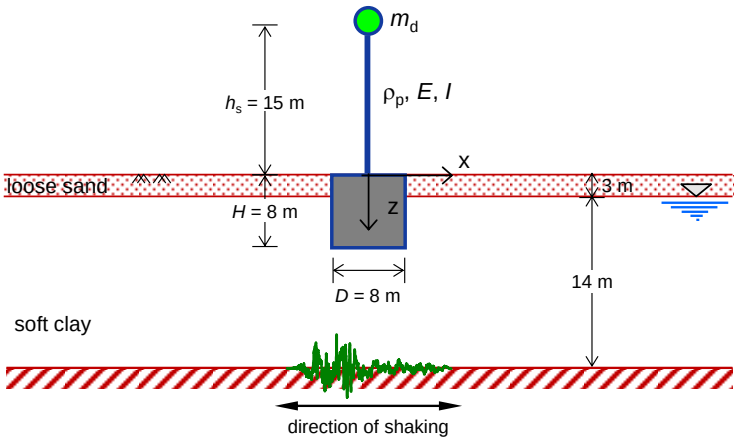


Figure 1: Schematic layout of the problem at prototype scale (modified from [8]).

For simplicity, the deck is assumed to be reproduced by a tip mass of $m_s$ = 194.40 Mg. The total mass of the caisson is $m_c$ = 1024.78 Mg, while the mass of the pier is $m_p$ = 143.64 Mg with a bending stiffness $EI$ = 30.7 GN·m$^2$, where $E$ and $I$ are Young modulus and cross-sectional moment of inertia, respectively. The system is subjected to ground motion at the bedrock depth ($z$ = 17 m), here represented as a horizontal acceleration time history.

Figure 2 shows a schematic view of the centrifuge model reproducing the prototype. The model was scaled down according to the laws reported in [9] for a centrifugal acceleration of 60$g$. To correctly reproduce the prototype model, aluminum was used (alloy 6028-T6) with unit weight $\gamma_{al}$ = 27 kN/m$^3$ both for the caisson (hollow cylinder) and the pier (rod). A brass cylinder (alloy CZ121) with $\gamma_{br}$ = 85.6 kN/m$^3$ was adopted to simulate the deck as a lumped mass. The sand layer was made of Hostun Sand with a relative density $D_R$ = 50%, while the clay layer was prepared from speswhite Kaolin powder. The physical and mechanical properties of the clay are listed in Table 1, where $w$ is the water content, which was measured right before spinning up the model in the centrifuge, $w_L$, $w_P$ are the liquid and plastic limits, $PI = w_L - w_P$ is the plasticity index, λ and κ are the slopes of the Normal Compression and of the Unloading–Reloading Lines in the semi-logarithmic $v$–$p'$ (log) plane, and Γ and M are the intercept and the slope of the Critical State Line in the $v$–$p'$ (log) and $q$–$p'$ plane, respectively, with Γ being computed at $p'$ = 1 kPa. The clay was consolidated at a stress level so that to obtain a soft clay ($\sigma'_{vc}$ = 512 kPa), together with suction applied at the bottom, $u$ = – 90 kPa. The model was placed into an Equivalent Shear Beam container (ESB) [10], whose dynamic boundary effects have been recently assessed [11]. In addition, the model was equipped with miniaturized instruments, such as those shown in Figure 2. The system was subjected to both recorded and sinusoidal time histories of the horizontal accelerations along the $x$-direction only, spanning a vast range of frequency contents and intensity levels, with peak accelerations ranging from 0.02$g$ (*weak*) to 0.21$g$ (*strong*). In this paper, reference to the Adana record is only made for the sake of brevity, which was characterised by a peak horizontal acceleration $a_{max, inp}$ = 0.133$g$ (*moderate* intensity).

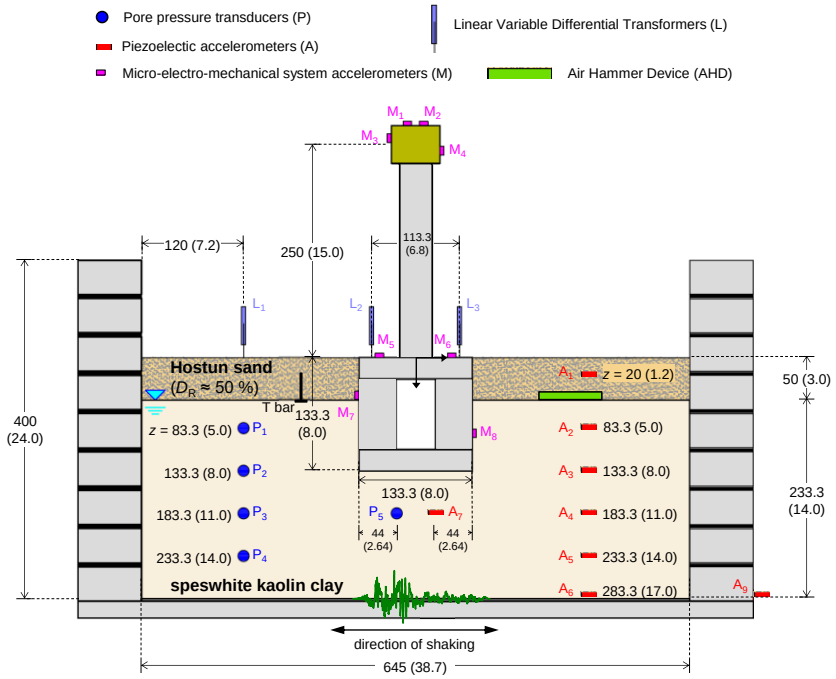


Figure 2: Elevation view of the centrifuge model at model scale (in mm) (bracketed prototype units: m) (modified from [8]).

| $w$ (%) | $w_L$ (%) | $w_P$ (%) | $PI$ (%) | $G_s$ (-) | Γ (-) | λ (-) | κ (-) | M (-) |
|---|---|---|---|---|---|---|---|---|
| 56 | 58 | 34 | 24 | 2.61 | 2.87 | 0.14 | 0.03 | 0.80 |

Table 1: Properties of the speswhite Kaolin clay adopted in the centrifuge tests (modified from [3]).

## 3. 3D NUMERICAL MODEL

A 3D FE model was implemented in the code Plaxis 3D [7] to simulate the centrifuge model shown in Figure 2 at the prototype scale. Thanks to the symmetry of the problem, just half of the ESB box domain was modelled, leading to the dimensions reported in Figure 3. The sand and clay layers were subdivided into multiple sub-layers with thickness ranging from 1 to 3 m, with the thinner layers located in the shallow 10 m. This was made with a twofold objective: first, to reproduce the variability with depth of the mechanical properties of the soil deposit, and second, to guide the automatic mesh refinement performed by the software, so as to limit the numerical distortion of shear waves propagating into the FE domain [12]. To this end, the seismic input motion was applied a low-pass filter with a maximum frequency $f_{max}$ = 8 Hz.

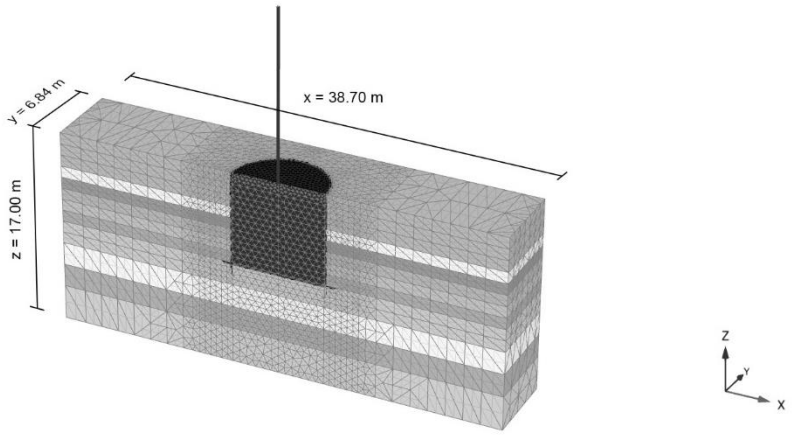


Figure 3: 3D FE model implemented in Plaxis 3D [7]

The soil and the caisson volumes were both modelled using 10-node tetrahedra, while the pier and the deck were modelled with *beam* elements. A very short beam element was adopted for the deck in order to reproduce a lumped mass. Finally, a rigid plate element was introduced atop the caisson to impose the continuity constraint between the beam element representing the pier and the tetrahedra simulating the caisson. The mesh was generated using the *coarse* option with a local coarseness factor equal to 0.2 for the volumes close to the caisson and to 1.5 for the farther ones, so that the desired mesh refinement was obtained (Fig. 3), which brought to 51225 elements and 75279 nodes.

In the static phases preceding the dynamic calculation, namely the $k_0$-procedure to initialise the lithostatic stress state and the *wished-in-place* activation of the caisson and the pier in drained conditions, the normal displacements were fixed along all the boundaries, and the horizontal displacement was also fixed at the bottom of the model ($u_x = u_y = 0$); the ground surface was assigned no restraint. Periodic boundaries (*i.e.*, tied-nodes) were adopted for the fully-undrained dynamic analysis, which means that the differential horizontal displacement between two nodes at the same depth along the vertical edges of the model was impeded ($\Delta u_x = 0$): this boundary condition allowed to mimic the dynamic boundary condition applied to the soil sample by the end walls of the ESB container, which are flexible and designed on the purpose of accommodating the deformation of an average dense/consistent soil deposit [10].

Both the structure and the caisson foundation were assigned non-porous linear-elastic materials, whereas the *HSsmall* constitutive model [13] was adopted for the soil layers.

The soil mechanical parameters were calibrated against those obtained in the centrifuge tests reported in Gaudio *et al*. [3]. First, the unit weight of the clay, $\gamma$, was obtained to reproduce the *in-flight* vertical effective stress profile, $\sigma'_{v0}$, which was measured before applying the ground motions: here it is worth mentioning that the stress state was affected by some residual excess pore water pressures in the clay, $\Delta u$, as the duration of consolidation preceding the dynamic phase did not last enough (1 hour only) to make $\Delta u$ dissipate completely. These $\Delta u$ were recorded at some specific depths with the Pore Pressure Transducers (PPT) (black crosses in Fig. 4a). Then, the OverConsolidation Ratio, *OCR*, was imposed to the different soil strata subdividing the clay layer (Fig. 4b). Moreover, the parameters ruling the small-strain shear modulus $G_0$, $G_0^{ref}$ and $m$, were calibrated to fit the values computed from the Air Hammer (AH) test, both for the sand and the clay layers (Fig. 4c), according to the equation

$$G_0 = G_0^{ref} \left( \frac{c' \cot \varphi' + \sigma'_3}{c' \cot \varphi' + p^{ref}} \right)^m \quad (1)$$

where $c'$ and $\varphi'$ are the effective cohesion and angle of shearing resistance, respectively, $\sigma'_3$ is the minimum effective stress and $p^{ref}$ = 100 kPa is a reference pressure. As for the clay, the effective cohesion $c'$ was calibrated in order to provide the undrained shear strength $s_u$ shown in Fig. 4d, providing a fair estimation of the experimental one, which in turn was measured with the T-bar penetrometer [14].

The remaining soil parameters are listed in Table 2, where the shear strain $\gamma_{0.7}$ was determined from the shear modulus decay curves, $G/G_0(\gamma)$, proposed in the literature ([15] for the sand and [16] for the clay layer), while moduli $E_{ur}^{ref}$ and $E_{oed}^{ref}$ were retrieved based on $\kappa$ and $\lambda$ reported in Table 1, respectively. A typical Poisson ratio $\nu_{ur}$ was assumed, and the elasto-plastic modulus $E_{50}^{ref}$ was computed based on typical ratios ($E_{50}^{ref}/E_{oed}^{ref}$ = 1.00 for the sand and 1.25 for the clay). Both the sand and the clay were assigned a null dilatancy angle ($\psi$ = 0), together with the default value $R_f$ = 0.9.

All materials adopted in the analyses were also assigned a damping ratio $\xi$ = 1 % to damp out the response of the system at very low strains, as the *HSsmall* model does not provide any hysteretic damping in the small-strain range ($\gamma = 10^{-4}$ %).

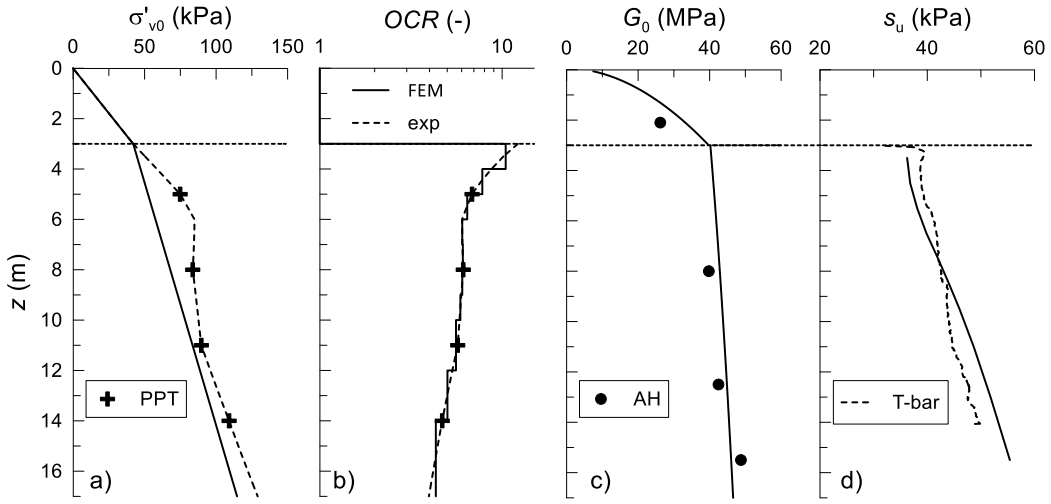


Figure 4**:** Calibration of the constitutive soil model: (a) effective vertical stress, (b) over consolidation ratio (c) initial shear modulus, and (d) undrained shear strength profiles.

| soil | $\gamma$ (kN/m$^3$) | $G_0^{ref}$ (MPa) | $m$ (-) | $\gamma_{0.7}$ (%) | $E_{ur}^{ref}$ (MPa) | $\nu_{ur}$ (-) | $E_{50}^{ref}$ (MPa) | $E_{oed}^{ref}$ (MPa) | $c'$ (kPa) | $\varphi'$ (°) |
|---|---|---|---|---|---|---|---|---|---|---|
| sand | 14.0 | 92.1 | 0.52 | 0.024 | 110.7 | 0.25 | 36.9 | 36.9 | 0.5 | 32.3 |
| clay | 15.0 | 45.5 | 0.23 | 0.044 | 11.4 | 0.25 | 2.2 | 1.7 | 15.0 | 20.7 |

Table 2: Mechanical parameters adopted in the *HSsmall* constitutive model.

## 4. NUMERICAL VS. EXPERIMENTAL RESULTS

In this section, the numerical results obtained from the fully-undrained dynamic calculation phase are compared to those from the centrifuge test. In particular, the time histories of the dimensionless deck drift ($u_{rel}/h_s$) are plotted in Fig. 5a, where the deck drift is defined as $u_{rel} = u_d - u_c$, with $u_d$ and $u_c$ being the deck and caisson horizontal displacement; in the same figure, the rigid rocking component ($tan\theta$) and the bending moment recorded at the base of the pier ($M_s$) are also plotted (Fig. 5b-c). The moment-rotation and relative settlement-rotation loops are also shown in Fig. 5d-e, where the moment was computed as follows:

$$M_s = m_{eff} \cdot a_d \cdot h_s \tag{2}$$

where $m_{eff}$ = 270.4 Mg is the effective mass related to the first mode of the pier [3], while the relative settlement $w_r$ was calculated as

$$w_r = w - w_{ff} \tag{3}$$

where $w$ is the average settlement of the caisson, and $w_{ff}$ is the settlement at the ground surface of the far-field alignment, which was measured with LVDT L1 in the centrifuge test (see Fig. 2).

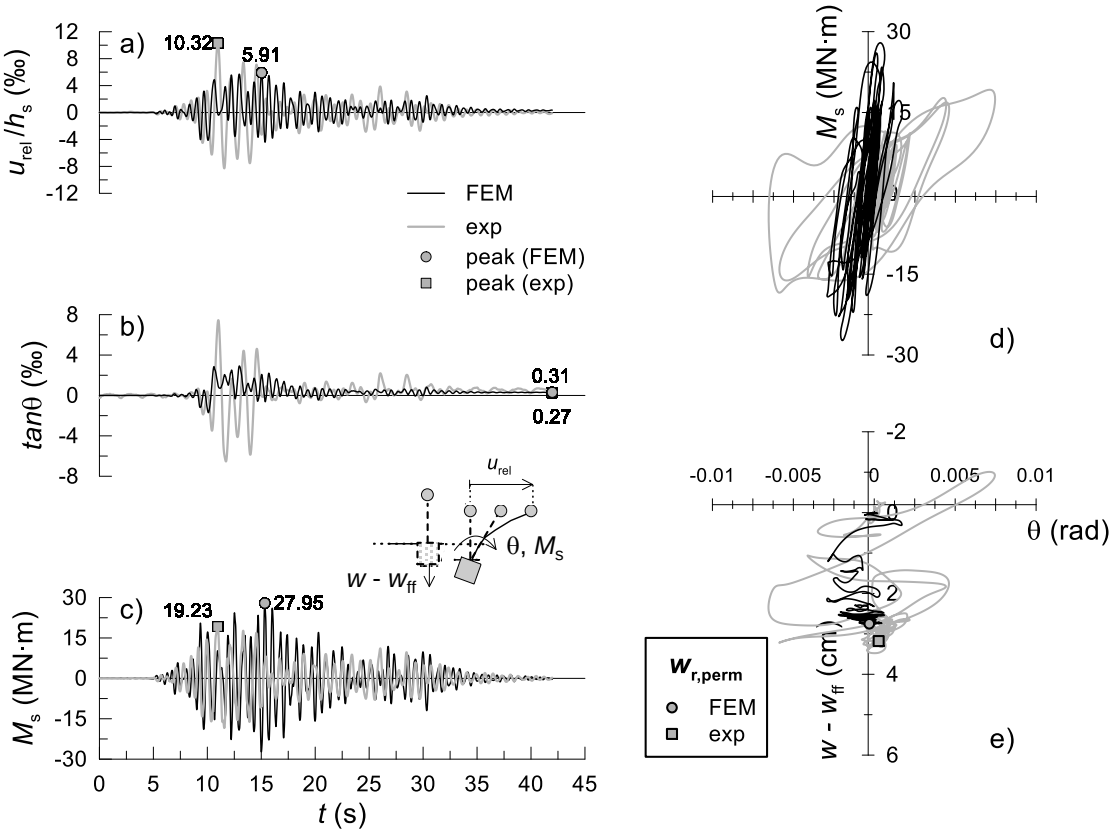


Figure 5: Time histories of the (a) total and (b) rigid component of deck drift, and of the (c) bending moment experienced by the system; (d) moment-rotation and (e) settlement-rotation loops.

The FE model provides a response which is stiffer than the experimental one, as it can be clearly seen in Figure 5a-d, where lower peak values of the deck drift and its rigid component are obtained, as a counterpart of the higher peak moment transmitted to the caisson. The frequency content of the time histories are quite similar though, which means that the period of the whole system is fairly captured by the numerical model. Moreover, permanent deformations, here expressed in terms of permanent tilting and settlement, are accurately reproduced in the FE analysis (Fig. 5e). As for these permanent values, it is worth noting that quite low values were computed, namely $tan\theta \sim 0.3$ % and $w_r \sim 3$ cm ($w_r/D \sim 0.4$ %), which clearly indicates that the system behaviour fell into the nonlinear elastic regime: the role of soil plasticity can be therefore deemed negligible, for the case at hand. This mostly holds true for the centrifuge test, where a broader area of the $M_s$-θ loop is observed, which entails more energy being dissipated in the soil deposit (Fig. 5d).

The comparison was also made in terms of the peak accelerations obtained at the far field, the caisson and the deck (Fig. 6). In the graphs, the results obtained in the centrifuge after applying the entire series of base excitations are reported, so as to provide the whole range of input accelerations $a_{max, inp}$ spanned during the test. The FE model provided a much higher acceleration at the far field (Fig. 6a): this is also true for the acceleration measured at the deck level (Fig. 6c), whereas a good agreement was obtained as for the caisson acceleration (Fig. 6b).

A much better agreement was achieved in terms of specific seismic performance indices [17], as reported in Figure 7. Here, the maximum and permanent drift of the deck, $u_{rel, max}/h_s$ and $u_{rel, perm}/h_s$, respectively, and the maximum bending moment at the base of the pier, $M_{s, max}$, were also plotted against $a_{max, inp}$. Figure 7a shows that the FE peak drift plotted close to the linear trend detected in [3] for the centrifuge results. As for the permanent drift, the agreement is even better (Fig. 7b). Lastly, higher bending moments were obtained for the numerical model than all the centrifuge experiments (Fig. 7c), which directly stems from the higher deck acceleration shown in Fig. 6c.

The differences between the FE model and the experimental layout may be mainly attributed to the difference in the initial effective stress profile (Fig. 4a), other than a stiffer sand in the numerical model due to a lack of experimental information. Nonetheless, permanent displacements, which are crucial for designing purposes, were reasonably reproduced in the FE analysis.

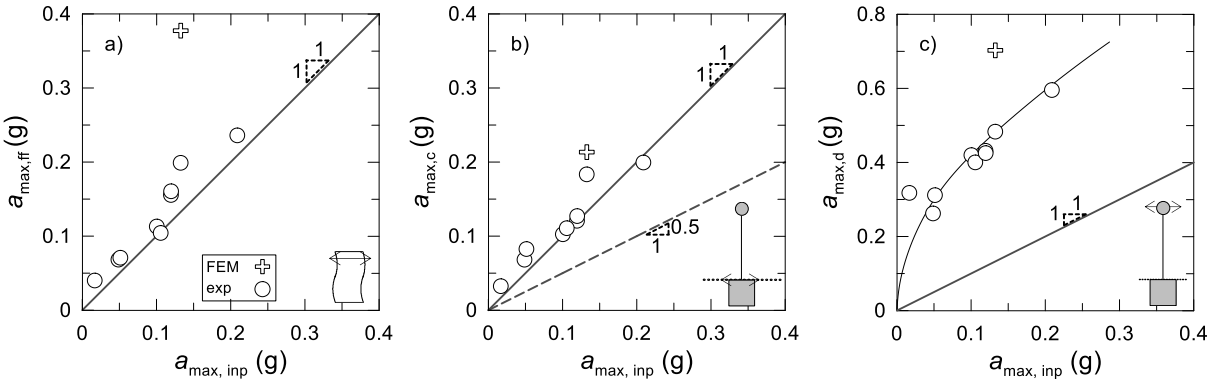


Figure 6: Peak horizontal accelerations recorded at the: (a) far-field ground surface; (b) top of the caisson; (c) deck level.

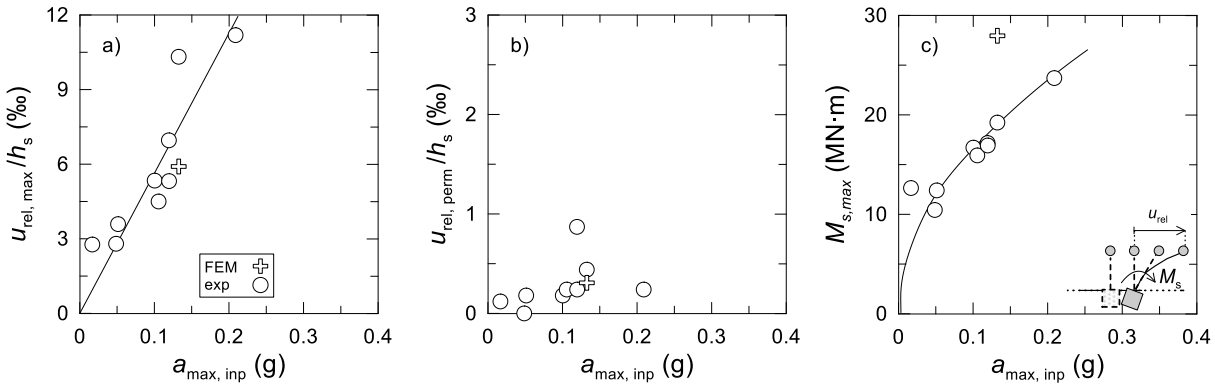


Figure 7: Indices of seismic performance against the peak input acceleration: (a) peak and (b) permanent deck drift; (c) peak bending moment.

## 5. CONCLUDING REMARKS AND FURTHER DEVELOPMENTS

This paper illustrated the preliminary results of a 3D Finite Element back-analysis reproducing a dynamic centrifuge test where a bridge pier on a caisson foundation, embedded in a soft clay layer, was subjected to a moderate-intensity ground motion. It is shown that it is still possible to fairly capture the seismic performance of the system even when adopting quite a customary constitutive model to describe the mechanical soil behaviour, provided that calibration of soil parameters is carried out in detail. A fair agreement between the numerical and experimental performance indices was obtained indeed, although some differences were actually observed, which may be deemed acceptable at an engineering level though. This result may enhance the reliability of advanced numerical analysis to be performed in the practice when critical infrastructures, such as long-span bridges, are to be designed.

Analyses with different intensity levels have been currently carried out to simulate the series of input motion which were applied in the centrifuge. Softer soil conditions will also be discussed in the next future to assess the predictability of the FE model when soil plasticity is triggered, and bearing capacity of the soil-caisson system is temporarily attained, which were not involved in the case discussed in this paper.

## ACKNOWLEDGEMENTS

The numerical analyses were performed thanks to the support by Bentley and Dr. Sandro Brasile. The authors also extend their appreciation to Prof. Gabriele Della Vecchia for his valuable supervision.

## REFERENCES

[1] N. Gerolymos, A. Zafeirakos, K. Karapiperis, Generalized failure envelope for caisson foundations in cohesive soil: static and dynamic loading. *Soil Dynamics and Earthquake Engineering*, **78**, 154-174, 2015.

[2] A. Rosati, D. Gaudio, C. di Prisco, S. Rampello, Use of interaction domains for a displacement based design of caisson foundations. *Acta Geotechnica*, **18** (1), 445-468, ISSN: 1861-1125, 2023, DOI: 10.1007/s11440-022-01547-z

[3] D. Gaudio, S.P.G. Madabhushi, S. Rampello, G.M.B. Viggiani, Experimental investigation of the seismic performance of caisson foundations supporting bridge piers. *Géotechnique*, Thomas Telford Ltd, 1-16, 2022, ISSN: 0016-8505, DOI: 10.1680/jgeot.22.00076

[4] I. Anastasopoulos, G. Gazetas, M. Loli, M. Apostolou, N. Gerolymos, Soil failure can be used for seismic protection of structures. *Bulletin of Earthquake Engineering*, **8** (2), 309-326, 2010, DOI: 10.1007/s10518-009-9145-2

[5] D. Gaudio, S. Rampello, The influence of soil plasticity on the seismic performance of bridge piers on caisson foundations. *Soil Dynamics and Earthquake Engineering*, **118**, 120-133, 2019, DOI: 10.1016/j.soildyn.2018.12.007

[6] A. Pecker, Development of the second generation of eurocode 8 – part 5: A move towards performance-based design. F. Silvestri & N. Moraci eds. *7th International Conference on Geotechnical Earthquake Engineering*, Rome, Italy, June 17-20, 273–281, 2019.

[7] Bentley, Plaxis 3D Connect Edition v22 – Reference Manual. Delft University of Technology. Delft, The Netherlands, 2022.

[8] D. Gaudio, S. Rampello, G.S.P. Madabhushi, G.M.B. Viggiani, The role of seismic intensity on the performance of caisson foundations supporting bridge piers: preliminary results from dynamic centrifuge testing. In *Proc. of the 3rd International Conference on Natural Hazard & Infrastructure (ICONHIC 2022)*, Athens, Greece, July 5-7, 2022.

[9] A.N. Schofield, Cambridge Geotechnical Centrifuge Operations. *Geotechnique*, **30** (3), 227-268, 1980, DOI: 10.1680/geot.1980.30.3.227

[10] A.J. Brennan, S.P.G. Madabhushi, Design and performance of a new deep model container for dynamic centrifuge testing. R. Philips, P. Guo, and R. Popescu eds. *International Conference on Physical Modelling in Geotechnics (ICPMG 2002)*, Rotterdam: Balkema, 183-188, 2002.

[11] D. Gaudio, J. Seong, S. Haigh, G.M.B. Viggiani, S.P.G. Madabhushi, R. Shrivatsava, R. Veluvolu, P. Padhy, Boundary effects on dynamic centrifuge modelling of onshore wind turbines on liquefiable soils. *International Journal of Physical Modelling in Geotechnics*, ICE Publishing, **23** (1), 16-34, 2023, ISSN: 1346-213X, DOI: 10.1680/jphmg.21.00085

[12] R.L. Kuhlemeyer, J. Lysmer, Finite Element Method Accuracy for Wave Propagation Problems. *Journal of the Soil Mechanics and Foundations Division*, ASCE, **99** (5), 421-427, 1973, DOI: 10.1061/jsfeaq.0001885

[13] T. Benz, P.A. Vermeer, R. Schwab, A small-strain overlay model. *International Journal for Numerical and Analytical Methods in Geomechanics*, **33** (1), 25-44, 2009.

[14] D.P. Stewart, M.F. Randolph, A new site investigation tool for the centrifuge. H.-Y. Ko and F. G. McLean eds. *Centrifuge '91: Proceedings of International Conference on Centrifuge Modelling*, Rotterdam, the Netherlands, Balkema, 531–538, 1991.

[15] H.B. Seed, I.M. Idriss, *Soil moduli and damping factors for dynamic response analyses*, Report No. EERC 70-10. Earthquake Engineering Research Centre, University of California, Berkeley, California, 1970.

[16] M. Vucetic, R. Dobry, Effect of soil plasticity on cyclic response. *Journal of Geotechnical Engineering*, **117** (1), 89-107, 1991.

[17] D. Gaudio, S. Rampello, The role of soil constitutive modelling on the assessment of seismic performance of caisson foundations. F. Silvestri & N. Moraci eds. *7th International Conference on Geotechnical Earthquake Engineering*, Rome, Italy, June 17-20, 2574-2582, 2019.

COMPDYN 2023
9th ECCOMAS Thematic Conference on
Computational Methods in Structural Dynamics and Earthquake Engineering
M. Papadrakakis, M. Fragiadakis (eds.)
Athens, Greece, 12-–14 June 2023

# A PHYSICS INFORMED NEURAL NETWORK (PINN) APPROACH FOR SOIL-PILE INTERACTION

**Michail Madianos[1], Panagiotis Lykourgias[1], Dimitris Loupas[1], Maria Papanikolaou[1], Stijn François[2], George Anoyatis[3] and Aggelos Tsikas[1]**

[1]Quantum Neural Technologies SA, Athens, Greece
address
{mcm, pml, dcl, mdp, ait}@quantumtech.ai

[2] KU Leuven, Department of Civil Engineering, Structural Mechanics Section, 3001 Leuven, Belgium
stijn.francois@kuleuven.be

[3] KU Leuven, Department of Civil Engineering, Hydraulics and Geotechnics Section, 8200 Bruges, Belgium
george.anoyatis@kuleuven.be

**Abstract.** *This work presents a reference solution for a typical soil-pile interaction problem, by means of a Physics Informed Neural Network (PINN). Advanced elastodynamic solutions for pile response can perform as scoping tools in early design stage and complement finite element simulations serving as "benchmark" solutions to allow the verification of more complex dynamic numerical models. Their intrinsic theoretical interest lies in tackling the Sturm-Liouville (SL) boundary value problem, which in presence of soil inhomogeneity is not straightforward, and can yield solutions only for specific types of soil inhomogeneity. Inspired by the recent advancements in scientific machine learning in a wide range of scientific disciplines, an application of a PINN to Soil-Structure Interaction (SSI) is presented herein. In this respect, eigenvalues and eigenfunctions of a SL operator, which arises in the classic elastic solution of a single axially loaded pile embedded in inhomogeneous soil deposit, are obtained. PINNs are physically motivated neural networks, in the sense that natural constraints such as physical laws, boundary conditions or other physical properties are embedded in either the cost function or the architecture of the network, to form a data-efficient universal function approximator. Moreover, their versatility (high adaptability to a wide range of problems), their straightforward extension to higher dimensions and, their meshfree nature (free from geometrical restrictions imposed by conventional numerical methods), can render them a valuable asset in the SSI toolkit of geotechnical engineers.*

**Keywords:** soil-pile interaction, PINNs, neural network, eigenfunctions, eigenvalues

## 1 INTRODUCTION

The analysis of pile foundations under axial load is an important topic in geotechnical engineering, and consequently there are several methods available for this purpose, each with its advantages and limitations. The selection of a suitable method depends on the complexity of the problem in question, the accuracy of the analysis, and the soil type. Current, commonly used, methods for determining pile settlements can be classified into four main groups: (A) experimental methods, which can provide direct measurement of the pile capacity and settlement, and can be used to validate the results of theoretical methods; such method can be expensive and time-consuming. (B) semi-empirical methods, which are relatively simple methods, to predict pile settlements in a wide range of soil conditions, yet its accuracy depends on calibration with field data. (C) numerical methods, such as the widely used finite element method, which can account for soil non-linearity, and can handle a variety of structure-soil configurations. Such methods require the use of specialized software and significant computational resources, especially for dynamic analyses. (D) elastic analytical models, which assume that the soil and the pile behave elastically, and could be used for preliminary design calculations, accounting implicitly for the effects of soil non-linearity by pertinent modifications of soil stiffness. An additional benefit of such methods is that they can act as complementary tools to finite element simulations, serving as benchmark solutions to allow the verification of more complex dynamic numerical models, and safeguard the design process from systemic risk caused by uncertainty in simulations.

With reference to models in group (D), a promising family of analytical models are those often referred to as Tajimi formulations, and are associated with the approximate continuum models of Matsuo and Ohara [1] and Tajimi [2]. Such models treat the pile as a rod or beam, following the classical strength-of-materials solution and assume perfect bonding at the soil-pile interface. The soil is modelled as an approximate continuum of the Tajimi type; yet retains the three-dimensional features of the problem. The number of dependent variables is reduced by eliminating certain stress and displacement components in the governing equations in the soil medium. The solution is then expressed in terms of ”soil modes” or eigenfunctions along the vertical spatial coordinate. A number of closed form solutions for homogeneous soils have been obtained by means of this approach for piles (e.g., [3, 4, 5, 6, 7, 8, 9, 10, 11]) and retaining walls (e.g., [12, 13, 14]). A detailed description of the advantages of this family of models against numerical solutions and simplified approaches is presented in Anoyatis *et al.* [11], for axially-loaded piles embedded in inhomogeneous soils.

An added, less explored, yet powerful advantage of models within group (D) is that they can serve as a valuable tool in the development and application of Physics-Informed Neural Networks (PINNs); whenever available, analytical models, can provide a useful tool to assess PINN’s performance. PINNs is a framework that combines physics-based models with neural networks to solve complex problems. They were introduced in the seminal work of Raissi, Perdikaris and Karniadakis [15], and, since then, they have attracted the increasing attention of the Scientific Machine Learning community. PINNs can be seen as a powerful alternative to provide numerical solutions by means of training a neural network, which respects the physical laws of the problem at hand, as described by the pertinent partial differential equations (PDEs). PINNs’ ability to provide solutions to PDEs and eigenvalue problems has been tested to a series of works (e.g., [15, 16, 17, 18, 19]).

Evidently, since PDEs are fundamental to the description of a wide range of physical processes, PINNs have the potential to become a valuable tool for scientists and engineers, in

particular where less data are available. This is achieved due to PINNs being physically motivated and requiring no external data, since training can be performed in terms of generated data samples. Another key advantage compared to traditional numerical differential equation solvers is that PINNs are inherently mesh-free, and can generate solutions that are readily differentiable, contrary to solutions at specified grid points. Being mesh-free adds to the flexibility of PINNs, rendering them applicable to a wide range of problems, including those with complex geometries or multi-physics problems. Further, in the same spirit, PINNs can be more robust to changes in geometry or boundary conditions of a problem, as they are not tied to a specific mesh. This also means that the computational time needed to solve a problem using PINNs can be significantly reduced, rendering them as a computationally efficient alternative to available and commonly used finite element method. As a final remark, PINNs can help reduce modeling errors, in particular where the underlying physics of a system are not well understood. This is because PINNs can be intrinsically trained on experimental or simulation data, which allows for the experimental or simulation error to be accounted for in the model.

This works aims to introduce the applications of PINNs to a classical soil-pile interaction problem, for which an analytical model has been recently developed by some of the Authors [11]. The analytical approach extends the model proposed by Mylonakis [3], following the seminal work of Nogami & Novak [4], to piles embedded in inhomogeneous soils (Fig. 1).

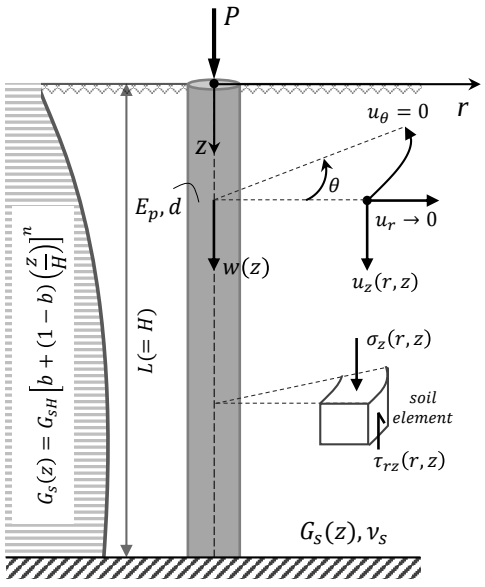


Figure 1: Stresses and displacements in a Tajimi type continuum.

Soil inhomogeneity is expressed via a depth-dependent soil shear modulus $G_s(z)$ which obeys a power law variation with depth; $n$ and $b = (G_{s0}/G_{sH})^{1/n}$ are dimensionless inhomogeneity factors, $G_{s0}$ and $G_{sH}$ are the soil shear moduli at the surface and the base of the soil deposit, respectively.

$$G_s(z) = G_{sH}\left[b + (1-b)\frac{z}{H}\right]^n \tag{1}$$

As shown in [11], handling an inhomogeneous soil medium of the Tajimi type is not straightforward; application of the orthogonality identity of the soil modes is used to satisfy the perfect bonding condition at the pile-soil interface. The solution is expressed in the form of series and

can handle different types of soil inhomogeneity using natural soil "modes" (eigenfunctions), and associated "eigenvalues", to describe the attenuation of soil displacement with depth and radial distance from the pile. The series' coefficients are coupled and are obtained as solutions to a set of simultaneous algebraic equations of rank equal to the number of modes considered in the analysis. The eigenvalues are obtained as the roots of of an algebraic non-linear equation, which especially in presence of dynamic loads, becomes an intricate task [20]. Herein a PINN is constructed to obtain the eigenfunctions and eigenvalues of the problem (Fig. 1).

## 2 THE ANALYTICAL MODEL

Key to the Tajimi approach in axial mode is the physically motivated assumption that the vertical normal and vertical shear stresses in the soil are controlled exclusively by the vertical soil displacement component. This reduces the two equations of classical axisymmetric elasticity to one [11] (Fig. 1). Thus, the equilibrium of vertical forces acting on a soil element in axisymmetric mode yields the following partial differential

$$\frac{\partial(\tau\, r)}{\partial r} \;+\; r\,\frac{\partial \sigma}{\partial z} \;=\; 0 \tag{2}$$

where $\tau = \tau_{rz}(r,z)$ is the vertical shear stress and $\sigma = \sigma_z(r,z)$ is the vertical normal stress. The stress-displacement relations in an axisymmetric Tajimi type continuum are obtained as

$$\sigma(r,z) \approx -\eta_s^2\, G_s(z)\,\frac{\partial u}{\partial z} \tag{3}$$

and

$$\tau(r,z) \approx -G_s(z)\,\frac{\partial u}{\partial r} \tag{4}$$

where $u = u(r,z)$ is the vertical soil displacement and $\eta_s = \sqrt{(2-\nu_s)/(1-2\nu_s)}$ is a dimensionless compressibility parameter, which accounts, indirectly, for the effect of vanishing the horizontal soil displacement on soil stresses, and depends solely on Poisson ratio $\nu_s$ [4]. Substituting Equations (3) and (4) into (2), the equilibrium equation is written in terms of displacements. The solution is then obtained using the method of separation of variables, which enables the decomposition of the governing partial differential equation into the pair of ordinary differential equations. The equation which involves the independent variable $z$ is a Sturm-Liouville (SL) equation with variable coefficients, and its solution depends on the functional form $G_s(z)$.

$$\frac{d}{dz}\left(\frac{G_s(z)}{G_{sH}}\,\frac{d\Phi}{dz}\right) \;+\; a^2\left(\frac{G_s(z)}{G_{sH}}\right)\Phi \;=\; 0, \quad z \in [0,H] \tag{5}$$

Finding the distinct values $a_m$ ($m = 1, 2, 3, \dots$), for which nontrivial solutions exist, is part of the SL theory. $a_m$'s are referred to as the eigenvalues of the boundary-value problem. Solutions to Equation (5) are the eigenfunctions $\Phi = \Phi_m(z)$ (i.e., soil modes), which satisfy the boundary conditions of the problem i.e., stress-free soil surface and zero displacements at the base. In the next section a PINN is constructed to obtain the eigenfunctions and eigenvalues of the SL problem, by considering the properties of SL operators. According to the *Universal Approximation Theorem*, any continuous function can be approximated using a neural network [21]. In this spirit, Hornik *et al.* demonstrated that neural networks can approximate any measurable function [22]. The special case of linear variation of shear modulus with depth and zero shear modulus at the surface is investigated in this work i.e., $b = 0$ and $n = 1$ in Equation (1).

## 3 THE NEURAL NETWORK

A fully-connected feed-forward Neural Network (NN) i.e., $\mathcal{N}^L : R \rightarrow R$ is employed to solve the SL problem. The NN transforms the input data to an output which approximates each eigenfunction $\Phi_m$. An input $x \in R$ is successively propagated through $L$ layers of neurons. Each neuron applies an affine transformation, followed by a nonlinear activation function. The training points are uniformly generated within the interval $[0, H]$, to effectively create an one-dimensional grid. The grid points created within each training iteration are slightly perturbed to capture extra points within the interval. This allows the network to train with additional points on top of the initial uniformly distributed points. A Neural Network with three hidden layers of 30 neurons each, and a trigonometric activation function $\sin x$ are selected. The input of each hidden layer is further fed directly to the next hidden layer. This way a Residual Network (ResNet) structure is created, where each layer is itself a block. The ResNet structure is quite ordinary in the context of deep learning. It usually aims to fix the problem of vanishing or exploding gradient, which is common in image recognition tasks [23]. Despite the radically different nature of the problem at hand, the ResNet structure turned out to be fruitful. The output of the NN can be written as:

$$N(z) = \mathcal{N}^L(z; \theta),\ \theta \in \Theta \tag{6}$$

The set of all weights span the parameter space $\Theta$, whilst the tunable parameters $\theta$ update iteratively during training. The training strategy lies in tuning the parameters $\theta$ and minimise a Residual Loss $L_\theta$ on the given data:

$$\text{Find } \theta^* \in \Theta :\ \theta^* = \underset{\theta}{\operatorname{argmin}}\, L_\theta \tag{7}$$

The ADAM optimizer, a learning rate equal to $10^{-2}$, and a loss function with four different terms are adopted to train the Neural Network. All four terms are essential for the successful training of the network. Each one accomplishes a specific task, which is explained in detail in the next subsections.

### 3.1 The parametric function

To enforce the boundary conditions, a parametric trick, commonly used in PINNs is adopted (e.g., [19, 24]): for Dirichlet and homogeneous boundary conditions, the output $N$ is multiplied with a suitable function $g(z)$. In the same fashion, to implement the mixed boundary conditions for the problem examined, $\Phi$'s are described as follows:

$$\Phi(z) \ = \ \tanh(z - H) \left[ (\tanh(z - H) - 2\, \tanh(-H))\, N \ + \ \tanh(-H)\, \tanh(z)\, \frac{\partial N}{\partial z} \right] \tag{8}$$

This way the boundary conditions are enforced directly to the output. This is commonly referred to as hard constraint, in contrast to soft constraints imposed via loss functions.

### 3.2 The loss function

The following loss function is adopted:

$$L \ = \ \lambda_{\mathrm{DE}}\, L_{\mathrm{DE}} \ + \ \lambda_{\mathrm{norm}}\, L_{\mathrm{norm}} \ + \ \lambda_{\mathrm{Bol}}\, L_{\mathrm{Bol}} \ + \ \lambda_{\mathrm{Slide}}\, L_{\mathrm{Slide}} \tag{9}$$

where $DE$ is the differential equation error, $norm$ is the normalization error, $Bol$ refers to the nodes error, and $Slide$ is the slide loss.

**Differential equation error** The following loss function is considered, which complies with the requirement for $\Phi$ to satisfy Equation (5)

$$L_{\mathrm{DE}} \;=\; \int_0^H \left[\frac{d}{dz}\left(\frac{G_s(z)}{G_{sH}}\,\frac{d\Phi}{dz}\right) \;+\; a^2\,\frac{G_s(z)}{G_{sH}}\,\Phi\right]^2 dz \tag{10}$$

where $a^2$ is given by the Rayleigh quotient:

$$a^2 \;=\; \frac{\displaystyle\int_0^H G_s(z)\,\left(\frac{d\Phi}{dz}\right)^2 dz}{\displaystyle\int_0^H G_s(z)\,\Phi^2\,dz}. \tag{11}$$

**Normalization error** The normalization loss enforces a non-zero solution and the eigenfunction's squared integral to be finite. This way it prevents the network from discovering trivial eigenfunctions and eigenvalues:

$$L_{\mathrm{norm}} \;=\; \left(1 - \int_0^H \frac{G_s(z)}{G_{sH}}\,\Phi^2\,dz\right)^2 \tag{12}$$

**Nodes error** In principle, the aforementioned steps should help discover the first eigenfunction. The challenge lies in guiding the NN to discover the higher eigenfunctions. In the work of Jin *et al.* this is achieved by considering the inherent orthogonality identity of the eigenfunctions of SL problems [19]. In this work a more efficient alternative is adopted. According to the SL theorem, the $m$-th eigenfunction $\Phi_m$ has exactly $m$ nodes in $(0, H)$ [25]. For a regular SL problem it can be proven that there is a sign alternation of $\Phi_{m+1}$ between two successive nodes of $\Phi_m, \forall m \in N$. This means that $\Phi_{m+1}$ has a node within that interval [25]. It can be shown that for Neumann boundary conditions, there is at least one node of $\Phi_{m+1}$ between the corresponding endpoint and the closest $\Phi_m$ root. In this work, an approach inspired by the root-finding Bisection method is employed to discover the nodes accounting for the alternating positive and negative behavior of the eigenfunction [26]. Thus, one can set:

$$L_{\mathrm{Bol}}^{m,m+1} \;=\; \sum_{i=0}^{m+1} \Phi_{m+1}(z_i)\,\Phi_{m+1}(z_{i+1}) \;+\; \left|\Phi_{m+1}(z_i)\,\Phi_{m+1}(z_{i+1})\right| \tag{13}$$

where $z_1, \ldots, z_m$ are the nodes of $\Phi_m$, and $\{z_0, z_{m+1}\} = \{0+\varepsilon, H-\varepsilon\}, \varepsilon \ll 1$. By minimising the loss term expressed by Equation (13) to zero, the network reproduces a function with a node within each desired interval.

**Slide loss** The last term is expressed by the following equation:

$$L_{\mathrm{slide}}^{m+1} \;=\; \frac{a_m^2}{a_{m+1}^2}. \tag{14}$$

In fact this is not a conventional loss term; it is not possible to minimize such term, since that would require the eigenvalue to become infinite. Instead, it is used herein to guide the neural network to search for eigenvalues greater than the previously obtained ones. This becomes

increasingly important for eigenvalues of higher modes. It is common knowledge that finding functions with high frequency components is not an easy task for neural networks [27]. For the problem at hand, such term creates some kind of inverse-squared slide in terms of the eigenvalue, which along with the other loss terms, enables the network to capture the more complicated, excited eigenfunctions.

Each loss term is multiplied by a suitable factor to ensure that they balance well with each other. Then the network parameters are updated to minimize all of them. The integrals in the loss functions are calculated using the Monte Carlo integration [28]. This way the Mean Squared Error (MSE) is reduced, following previous works on PINNs [15, 19, 29].

## 4 RESULTS

The neural network architecture consists of 3 blocks with 30 neurons each. Results are presented for the special case of $b = 0$ and $n = 1$, which correspond to piles in Gibson soil with zero stiffness at the soil surface. The terms in Equation (9) are selected as: $\lambda_{\mathrm{DE}} = 1$, $\lambda_{\mathrm{norm}} = 1$, $\lambda_{\mathrm{Bol}} = 10^5$ and $\lambda_s = 10^4$. Comparisons of the neural network predictions with results obtained from the semi-analytical model by Anoyatis *et al.* [11], demonstrate the predictive power of the proposed method.

Table 1 presents the results of the first fifteen eigenvalues $a_m$. The comparisons between the actual eigenvalues $a_{\mathrm{true}}$ obtained from the semi-analytical model by Anoyatis *et al.* [11], and the eigenvalues $a_{\mathrm{NN}}$ obtained from the proposed neural network are in excellent agreement.

| $m$-th eigenvalue | $a_{true}$ | $a_{\mathrm{NN}}$ | $\frac{a_{\mathrm{NN}} - a_{true}}{a_{true}} \times 10^{-5}$ |
|---|---|---|---|
| 1 | 2.405 | 2.405 | 0.0 |
| 2 | 5.520 | 5.521 | 18 |
| 3 | 8.654 | 8.655 | 11 |
| 4 | 11.792 | 11.793 | 0.8 |
| 5 | 14.931 | 14.932 | 0.6 |
| 6 | 18.071 | 18.073 | 11 |
| 7 | 21.212 | 21.213 | 0.4 |
| 8 | 24.352 | 24.355 | 12 |
| 9 | 27.493 | 27.495 | 0.7 |
| 10 | 30.635 | 30.637 | 0.6 |
| 11 | 33.776 | 33.778 | 0.5 |
| 12 | 36.917 | 36.920 | 0.8 |
| 13 | 40.058 | 40.062 | 0.9 |
| 14 | 43.200 | 43.204 | 0.9 |
| 15 | 46.341 | 46.345 | 0.8 |

Table 1: Results of the first fifteen eigenvalues $a_n$. Comparison between the actual eigenvalues $a_{\mathrm{true}}$ obtained from the semi-analytical model by Anoyatis *et al.* [11], and the eigenvalues $a_{\mathrm{NN}}$ obtained from the proposed neural network. $b = 0$, $n = 1$ in Eq. (1)

Figures 2 and 3 plot the eigenfunctions for the 1st-2nd-3rd and 11th-12th-13th soil modes, respectively. The predictions from the proposed PINN are compared against results from the

analytical model [11]. An excellent agreement is observed for all cases investigated, which demonstrate the accuracy of the proposed method.

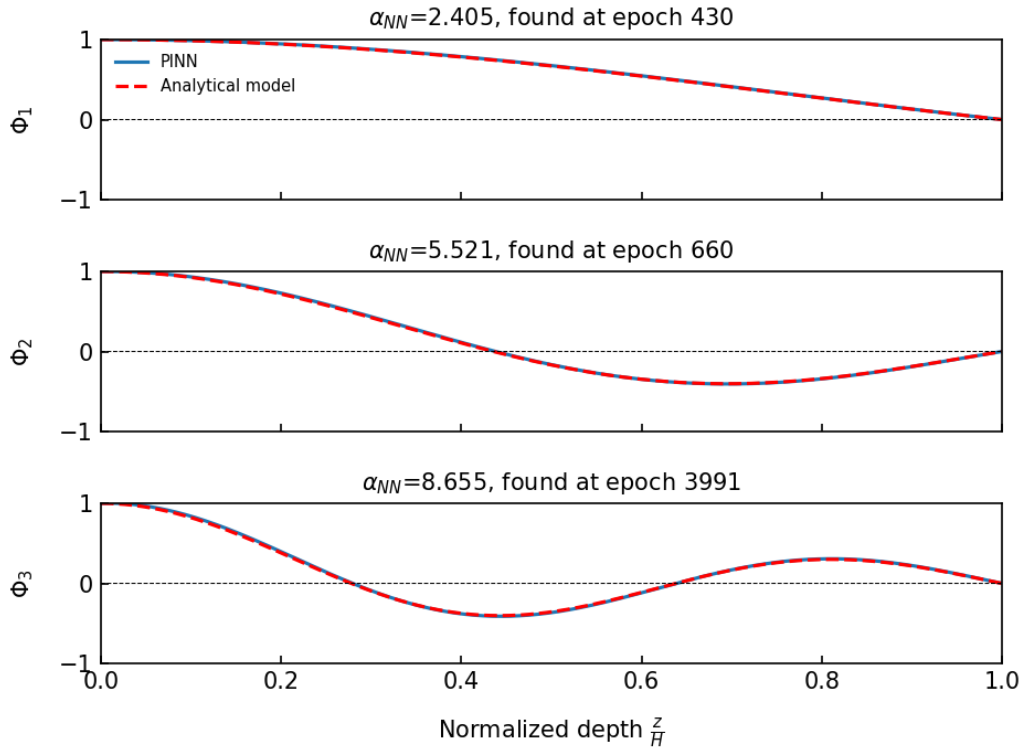


Figure 2: Profiles of the first three eigenfunctions $\Phi_1$, $\Phi_2$, $\Phi_3$. Comparisons between the proposed neural network approach and results from the analytical model by Anoyatis *et al.* [11].

Figures 4 presents the evolution of loss functions and eigenvalues with epochs, for the first three modes ($m = 1, 2, 3$, sub-figures (a) and (c)) and higher modes ($m = 11, 12, 13$, sub-figures (b) and (d)). In machine learning an epoch refers to the one entire passing of training data through the algorithm. It can be seen as a hyperparameter that determines the process of training the machine learning model. Each time a data set passes through an algorithm, completes an epoch. In both cases examined (low and high modes), the neural network detects the correct eigenvalue, and starts to build the corresponding suitable eigenfunction. It is evident that higher modes require training using a larger number of epochs.

## 5 SUMMARY AND CONCLUDING REMARKS

This study investigates the use of Physics-Informed Neural Networks (PINNs) as a method for solving classical problems in geotechnical engineering. For this reason, a soil-pile interaction problem for which an analytical model of the Tajimi type for the soil has been recently developed by some of the Authors, is selected [11]. The analytical approach extends the model proposed by Mylonakis [3], following the seminal work of Nogami & Novak [4] for end-bearing piles, to vertically inhomogeneous soils. Fundamental to the semi-analytical approach is the solution of the boundary value problem; the calculation of the eigenvalues and the corresponding eigenfunctions (soil modes). The eigenvalues are obtained as the roots of of an algebraic nonlinear equation, which especially in dynamic regime can be a challenging task [20].

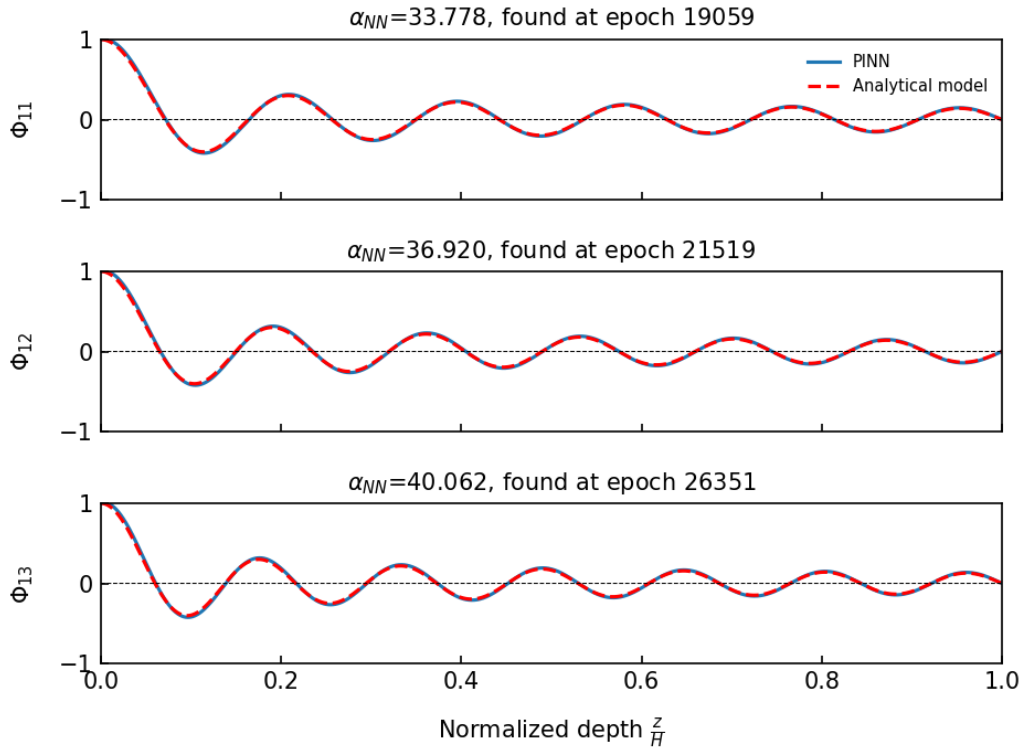


Figure 3: Profiles of higher eigenfunctions $\Phi_{11}$, $\Phi_{12}$, $\Phi_{13}$. Comparisons between the proposed neural network approach and results from the analytical model by Anoyatis *et al.* [11].

Herein a PINN is constructed to obtain the eigenfunctions and eigenvalues of the problem for an axially-loaded, end-bearing pile embedded in Gibson soil, by considering the properties of Sturm-Liouville operators. The ADAM optimizer, a learning rate equal to $10^{-2}$, and a loss function with four different terms are adopted to train the neural network. For the cases examined, it has been demonstrated that the PINN can be seen as a powerful alternative to provide numerical solutions by means of training a neural network, which respects the physical laws of the soil-pile interaction problem, as described by the governing partial differential equation. The predictive power of the proposed neural network based approach is demonstrated via the excellent agreement between proposed PINN results and results obtained from the existing analytical method in terms of both eigenvalues and eigenfunctions. It is also evident that higher modes require training using a larger number of epochs.

Overall, it is shown that analytical approach can be a valuable tool in the development and application of PINNs, allowing physical laws and relationships to be incorporated into machine learning models, which in turn lead to accurate and efficient predictions. Combining the power of neural networks with the precision of analytical models, render PINNs an attractive and promising alternative to predict the behavior of more complex foundation systems i.e., complex geometry, soil non-linearity, dynamic analyses without the need for expensive simulations or (limited) experimental data. It is though fair to mention that PINNs are a relatively new method and further systematic exploration is required. Nevertheless they are likely to play an increasingly important role in the development of advanced methodologies and scientific understanding in the coming years.

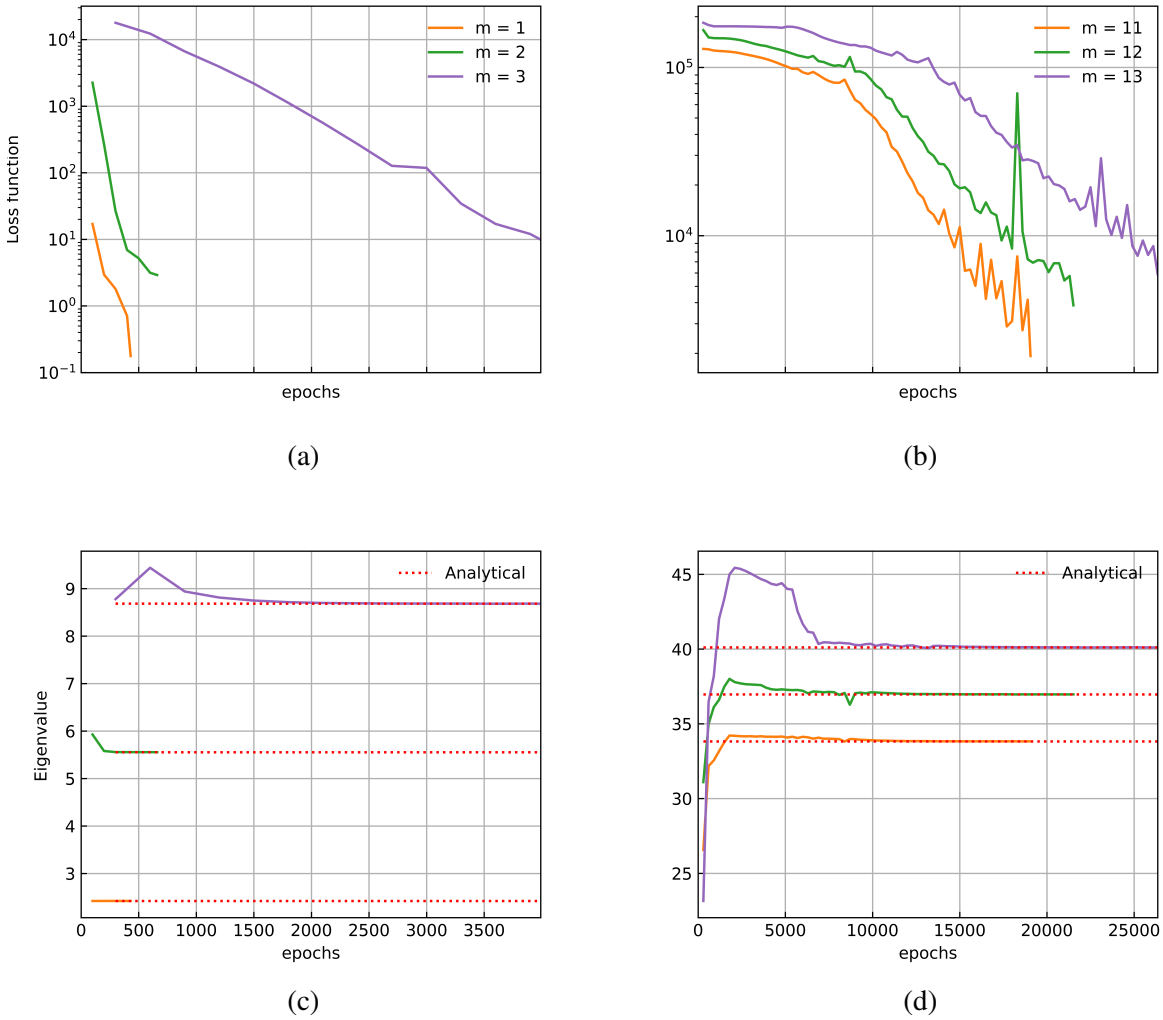


Figure 4: Evolution of loss functions and eigenvalues $a_m$'s during training, measured in epochs. (a)-(c) $m = 1, 2, 3$; (b)-(d) $m = 11, 12, 13$. Subfigures (c) and (d) show comparisons against the actual eigenvalues $a_{\text{true}}$, as obtained from the analytical solution by Anoyatis *et al.* [11].

## Acknowledgements

The research proposed in this paper was supported by KU Leuven through the project *ATHENA Analytical & programming efficiency in geoTecHnical ENgineering Applications* (C24E/22/009), KU Leuven Internal Funds. The authors are grateful for this support.

## REFERENCES

[1] H. Matsuo, S. Ohara, Lateral Earth Pressure and Stability of Quay Walls During Earthquake. *2nd World Conference on Earthquake Engineering*, Tokyo and Kyoto, Japan, July 11-18, 1960.

[2] H. Tajimi, Dynamic analysis of a structure embedded in an elastic stratum. *4th World Conference on Earthquake Engineering, Foundations and Soil-Structure Interaction (Session A6)*, Santiago de Chile, Chile, January 13-18, 1969.

[3] G. Mylonakis, Winkler modulus for axially loaded piles. *Géotechnique*, **51(5)**, 455–462, 2001.

[4] T. Nogami, M. Novak, Soil-pile interaction in vertical vibration. *Earthquake Engineering & Structural Dynamics*, **4(3)**, 277–193, 1976.

[5] T. Nogami, M. Novak, Resistance of soil to a horizontally vibrating pile. *Earthquake Engineering & Structural Dynamics*, **5(3)**, 249–261, 1977.

[6] M. Novak, T. Nogami. Soil-pile interaction in horizontal vibration. *Earthquake Engineering & Structural Dynamics*, **5(3)**, 263–281, 1977.

[7] G. Anoyatis, G. Mylonakis, Novel Tajimi models for static and dynamic soil-pile interaction. G. Lombaert, G. De Roeck eds. *8th International Conference on Structural Dynamics (EURODYN 2011)*, Leuven, Belgium, June 4-6, 2011.

[8] G. Anoyatis, G. Mylonakis, Dynamic Winkler modulus for axially loaded piles. *Géotechnique*, **62(6)**, 521–536, 2012.

[9] G. Anoyatis, G. Mylonakis, A. Lemnitzer, Soil reaction to lateral harmonic pile motion. *Soil Dynamics and Earthquake Engineering*, **87**, 164–179, 2016.

[10] G. Anoyatis, A. Lemnitzer, Dynamic pile impedances for laterally–loaded piles using improved Tajimi and Winkler formulations. *Soil Dynamics and Earthquake Engineering*, **92**, 279–297, 2017.

[11] G. Anoyatis, G. Mylonakis, A. Tsikas, An analytical continuum model for axially loaded end-bearing piles in inhomogeneous soil. *International Journal for Numerical and Analytical Methods in Geomechanics*, **43(6)**, 1162–1183, 2019.

[12] A. S. Veletsos, A. H. Younan, Dynamic soil pressures on rigid vertical walls. *Earthquake Engineering & Structural Dynamics*, **23(3)**, 275–301, 1994.

[13] A. S. Veletsos, A. H. Younan, Dynamic response of cantilever retaining walls. *Journal of Geotechnical and Geoenvironmental Engineering*, **123(2)**, 161–172, 1997.

[14] A. H. Younan, A. S. Veletsos, Dynamic response of flexible retaining walls. *Earthquake Engineering & Structural Dynamics*, **29(12)**, 1815–1844, 2000.

[15] M. Raissi, P. Perdikaris, G. E. Karniadakis, Physics Informed Deep Learning (Part I): Data-driven Solutions of Nonlinear Partial Differential Equations. *arXiv preprint arXiv:1711.10561*, 2017.

[16] B. Yu, The Deep Ritz Method: A deep learning-based numerical algorithm for solving variational problems. *Communications in Mathematics and Statistics*, **6(1)**, 1—12, 2018.

[17] A. D. Jagtap, E. Kharazmi, G. E. Karniadakis, Conservative physics-informed neural networks on discrete domains for conservation laws: Applications to forward and inverse problems. *Computer Methods in Applied Mechanics and Engineering*, **365**, 113028, 2020.

[18] M. Mattheakis, D. Sondak, A. S. Dogra, P. Protopapas, Hamiltonian neural networks for solving equations of motion. *Physical Review E*, **105(6)**, 065305, 2022.

[19] H. Jin, M. Mattheakis, P. Protopapas, Physics-Informed Neural Networks for Quantum Eigenvalue Problems. *2022 International Joint Conference on Neural Networks (IJCNN)*, Padua, Italy, July 18-23, 2022.

[20] G. Anoyatis, S. François, O. Orakci, A. Tsikas, Soil-pile interaction in vertical vibration in inhomogeneous soils. *Earthquake Engineering and Structural Dynamics*, Under Review.

[21] G. Cybenko, Approximation by superpositions of a sigmoidal function. *Mathematics of control, signals and systems*, **2(4)**, 303–314, 1989.

[22] K. Hornik, M. Stinchcombe, H. White, Multilayer feedforward networks are universal approximators. *Neural networks*, **2(5)**, 359–366, 1989.

[23] K. He, X. Zhang, S. Ren, J. Sun, Deep residual learning for image recognition. *IEEE conference on computer vision and pattern recognition (CVPR)*, 770–778, Las Vegas, NV, USA, June 27-30, 2016.

[24] L. V. Kantorovich, V. I. Krylov, *Approximate methods of higher analysis, 3rd Edition*. Noordhoff, Groningen, 1958.

[25] U. H. Gerlach, *Linear mathematics in infinite dimensions: Signals, boundary value problems and special functions, ISBN-10/ASIN: B00DJUA5DK, 2nd Beta Edition*. The Ohio State University, 2017.

[26] P. Henrici, *Elements of Numerical Analysis*. pp 328. New York. 1964.

[27] S. Wang, H. Wang, P. Perdikaris, On the eigenvector bias of Fourier feature networks: From regression to solving multi-scale PDEs with physics-informed neural networks. *Computer Methods in Applied Mechanics and Engineering*, **384**, 113938, 2021.

[28] R. E. Caflisch, Monte carlo and quasi-monte carlo methods. *Acta numerica*, **7**, 1–49, 1998.

[29] A. Kovacs, L. Exl, A. Kornell, J. Fischbacher, M. Hovorka, M. Gusenbauer, L. Breth, H. Oezelt, M. Yano, N. Sakuma, A. Kinoshita, Conditional physics informed neural networks. *Communications in Nonlinear Science and Numerical Simulation*, **104**, 106041, 2022.

COMPDYN 2023
9th ECCOMAS Thematic Conference on
Computational Methods in Structural Dynamics and Earthquake Engineering
M. Papadrakakis, M. Fragiadakis (eds.)
Athens, Greece, 12-14 June 2023

# FILTERING EFFECT FOR A PILE IN TWO-LAYER SOIL

**Raffaele Cesaro**[1] **and Raffaele Di Laora**[1]

[1] Università degli Studi della Campania "Luigi Vanvitelli"
Aversa (CE), Italy
e-mail: raffaele.cesaro@unicampania.it, raffaele.dilaora@unicampania.it

## Abstract

*The aim of this work is to investigate the kinematic response of fixed-head vertical floating piles embedded in two layer soils with shallow interfaces and subjected to upward-propagating seismic waves. The problem is explored numerically by means of a rigorous finite element analysis, to quantify the kinematically-induced reduction of the horizontal free-field spectral acceleration. Insight about the beneficial role of the stiffer layer is provided.*

**Keywords:** Kinematic pile interaction, earthquakes, finite element analysis, seismic design.

# 1 INTRODUCTION

It is widely recognized that the passage of seismic waves through the ground induces deformations in the soil mass. Piles embedded in the soil are not always able to follow the deformations of the surrounding soil, given their large flexural stiffness. Such inhability is more and more pronounced with increasing excitation frequency, i.e. with decreasing soil wavelength ($\lambda_s$) compared to the characteristic pile wavelength ($\lambda_p$) as highlighted by Di Laora & de Sanctis (2013). Therefore, piles can filter out the high-frequency components of the free-field motion, producing generally a beneficial effect on the Foundation Input Motion (FIM) which excites the structure (Fig. 1).

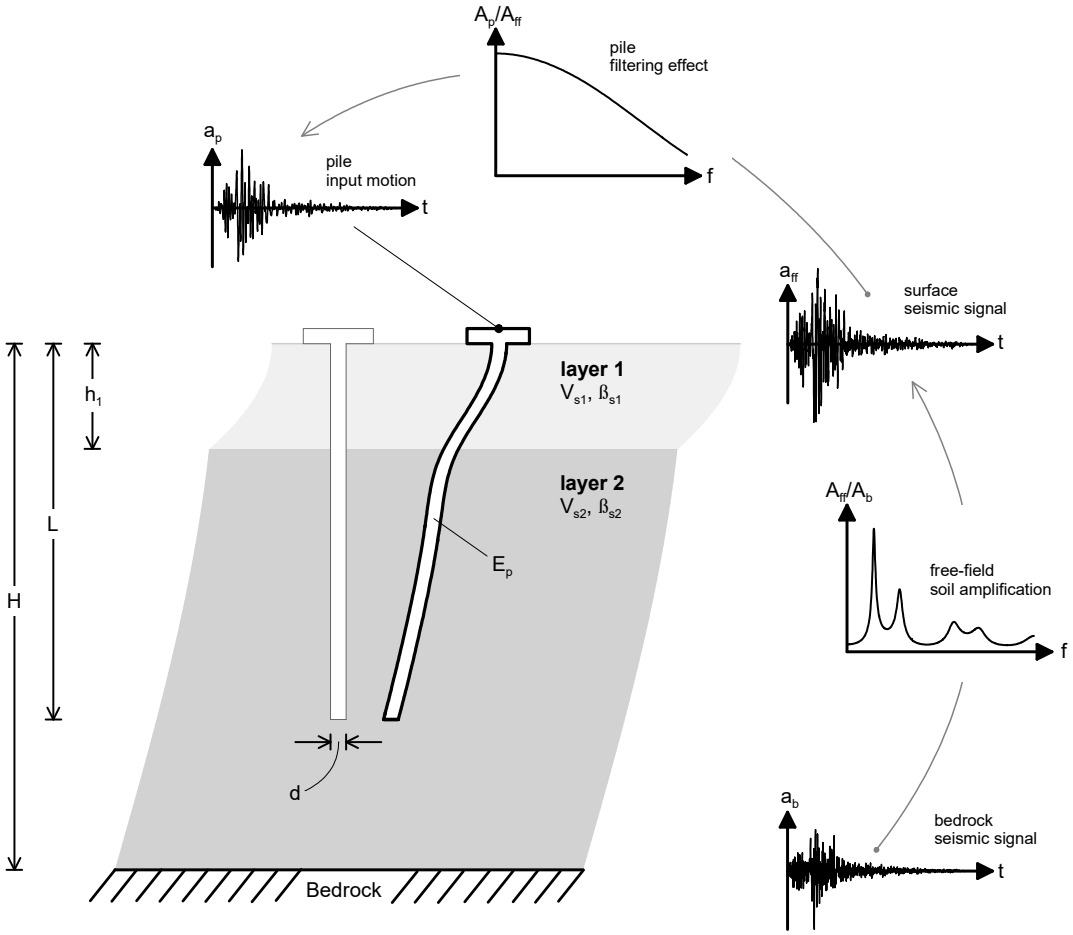


Figure 1: Problem under investigation.

Flores-Berrones and Whitman (1982) proposed the first closed-form analytical solution for the kinematic interaction factor for an infinitely long fixed-head pile, embedded in a homogeneous half space, based on the beam-on-dynamic-Winkler-foundation (BDWF) approach. With the same approach Nikolaou et al. (2001) provided the analytical solution for the case of a free-head pile; Anoyatis et al. (2013) proposed analytical solutions for the kinematic response of a single pile of finite length in homogeneous layer with different boundary conditions at its ends. Iovino et al. (2019) provided a simplified expression for the case of soil with stiffness varying continuously with depth according to a generalized power law function.
As regards the pile groups Fan et al. (1991) studied the kinematic behaviour of groups of vertical floating piles connected by a rigid massless cap, showing that the number of piles and the

group geometry have a negligible effect in terms of lateral displacements, while they affect significantly the rotation of the pile cap. Di Laora et al. (2017) proposed a simplified closed-form solution for the horizontal motion and rotation of a capped pile group generated by kinematic interaction.
Nevertheless, the case of a pile embedded in a two-layer soil with shallow interface, i.e. with interface depth lower than the active pile length, has been less investigated, despite it is a very common geotechnical scenario, for example in presence of made ground, when piles are required to transfer loads to a deeper, more competent soil layer.
In this work the kinematic response of a single fixed-head pile embedded in a two-layer soil is investigated through rigorous finite element analysis carried out in frequency domain, with the commercial FE code ANSYS. Adopting the kinematic interaction coefficient obtained through the finite element analysis, the transient response is studied evaluating the reduction of the design spectra for some cases employing 9 selected real accelerograms.

## 2 FE MODEL

Numerical analyses are performed using the commercial FE code ANSYS. The analyses were carried out in the frequency domain, pile is assumed to be a linear elastic medium, while soil possesses a complex shear modulus $G^* = G(1+2i\beta)$, with $\beta$ the constant hysteretic damping ratio. Although the problem is 3D, the geometry is axisymmetric whereas the load is antisymmetric. To simplify the analysis, stresses and displacements are expanded into a Fourier series in the circumferential direction, according to the technique introduced by Wilson (1965).
So the original three-dimensional problem is reduced to a 2D one. Four-noded axisymmetric elements were used to mesh soil and pile. After a thorough sensitivity analysis, the vertical size of the elements is set to 0.1 diameters for a width of 3 diameters close to layers interface and 0.5 diameters elsewhere. On the other hand, the horizontal size is 1/8 pile diameters at pile–soil interface, thereby increasing with radial distance up to 1.5 diameters at the free-field (Fig. 2). The nodes at the base of the model are restrained to both horizontal and vertical directions to represent a rigid bedrock. The lateral boundary, where vertical displacements are restrained, is placed at 400 m, a sufficiently large distance from the pile, thus allowing diffracted waves from pile-soil interface to attenuate because of the soil damping before being reflected at the boundary (Di Laora et al., 2012; Iovino et al. 2019; Iovino et al. 2022).

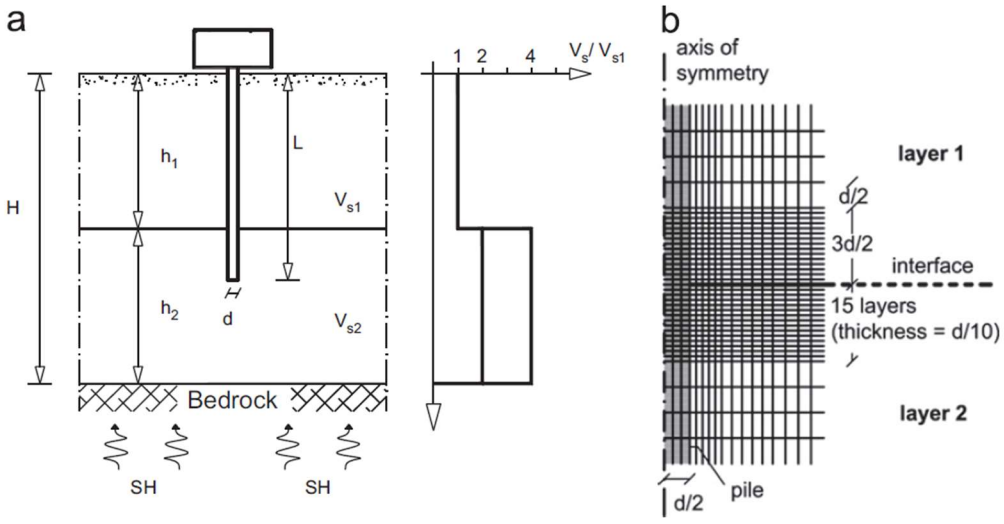


Figure 2: (a) problem considered; (b) finite element mesh employed in the analyses.

## 3 HARMONIC RESPONSE

Some FEM analysis results are depicted in Figure 3, in terms of pile-to-soil acceleration ratio $I_u$, against the dimensionless frequency as defined by Anoyatis et al. (2013), $\omega/\lambda_1 V_{s1}$, where $\lambda_1$ is the Winkler wavenumber of the soil-pile system, equal to:

$$\lambda_1 \approx \left( \frac{k_1}{4E_p I_p} \right)^{1/4} \tag{1}$$

The spring stiffness $k_1$ could be considered to be frequency-independent and expressed as a multiple of the soil Young's modulus $E_s$ (Gazetas & Dobry, 1984):

$$k_1 \approx \delta E_{s1} \tag{2}$$

where $\delta$ is a proportionality coefficient, which for the problem at hand varies in the range 1.5 to 2.5.
It can be observed that, when the interface depth becomes deep enough the kinematic interaction coefficient obtained converges with that related an infinitely long pile in homogeneous half space, that can be expressed as proposed by Flores-Berrones & Whitman (1982):

$$I_u = \Gamma_1 = \frac{4\lambda_1^4}{4\lambda_1^4 + q_1^4} \tag{3}$$

where $q_1 = \omega/V_{s1}^*$ is the complex wavenumber of the soil.

In particular, pile response is not affected by the presence of the second layer if the interface depth is greater than the active pile length which is typically equal to about 10 pile diameters (Poulos and Davis, 1980; Randolph, 1981).
For a fixed-head pile the pile-to-soil acceleration ratio is, even for the two layer case, always lower then unity and diminishes with increasing frequency (Fig. 3).
The presence of the second layer, stiffer than the first, may be beneficial since would act as a partial fixity for the embedded portion of the pile (Di Laora & de Sanctis, 2013). Indeed for a fixed interface depth the filtering effect increases (i.e. $I_u$ decreases) with the stiffness contrast between the two layers, as can be observed in Fig. 3a, 3c and 3e.
Nevertheless, this is not always the case. The effect of a stiffer second layer is beneficial only for an "intermediate" interface depth. This is because on one hand, as expected, if the interface depth is too deep the pile behaviour is unaffected by the presence of the second layer. On the other hand, if the interface is too shallow the pile response becomes close to that of a pile embedded in an homogeneous half space with the characteristics of the second layer, thus the overall pile-to-soil stiffness contrast decreases and so does the filtering effect for a given excitation frequency (Fig. 3).

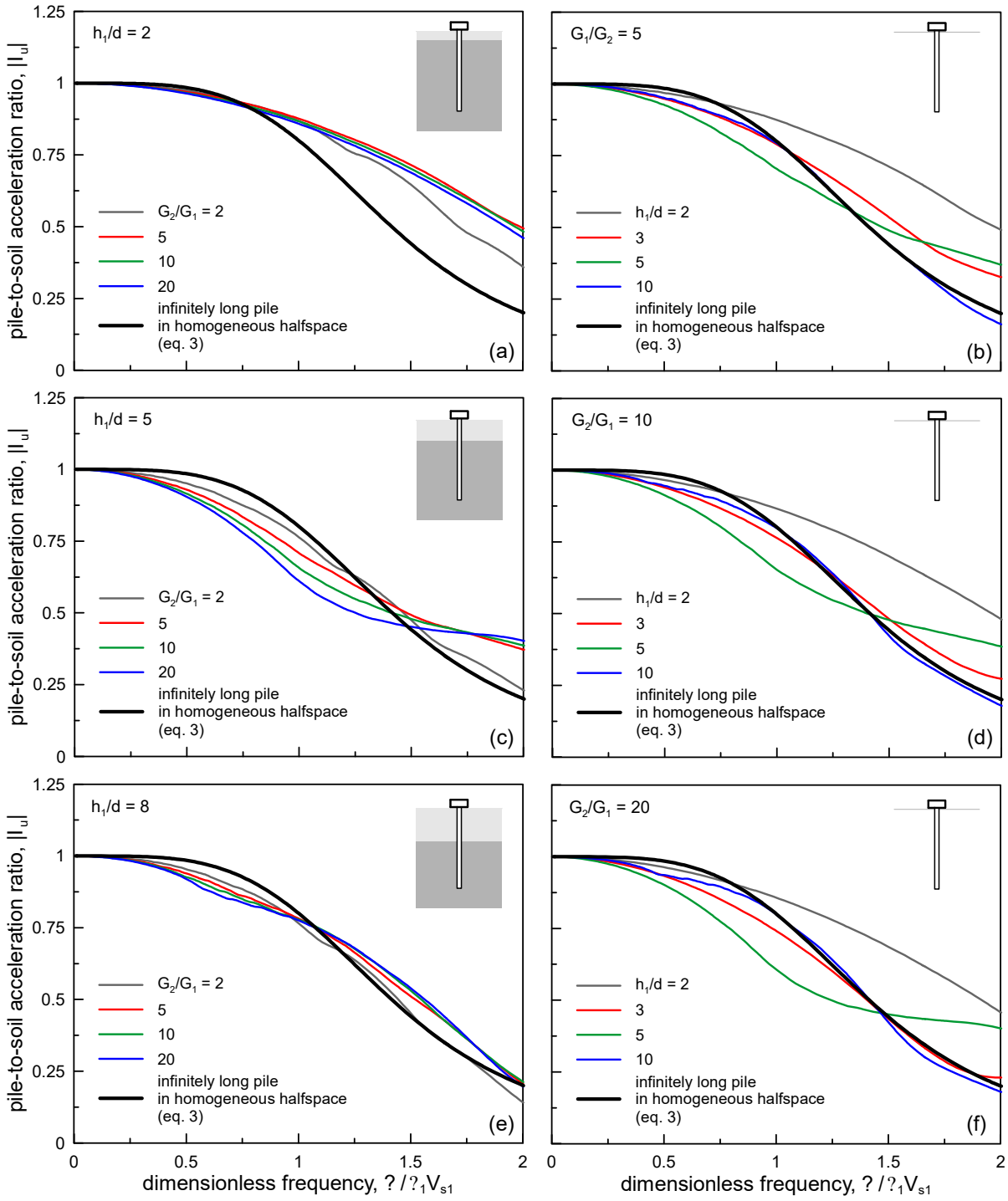


Figure 3: Numerical results for $E_p/E_l = 1000$, $\delta = 1.5$ and $\beta = 0.05$.

## 4 TRANSIENT RESPONSE

Transient response is investigated by using real acceleration time-histories selected from the Engineering Strong Motion Database (Luzi et al., 2020). In Fig. 4 and Fig. 5 time histories and Fourier spectra of the signals are depicted. Furthermore in Fig. 5 the mean frequency $f_m$ as defined by Rathje et al. (1998) is reported for each accelerogram.

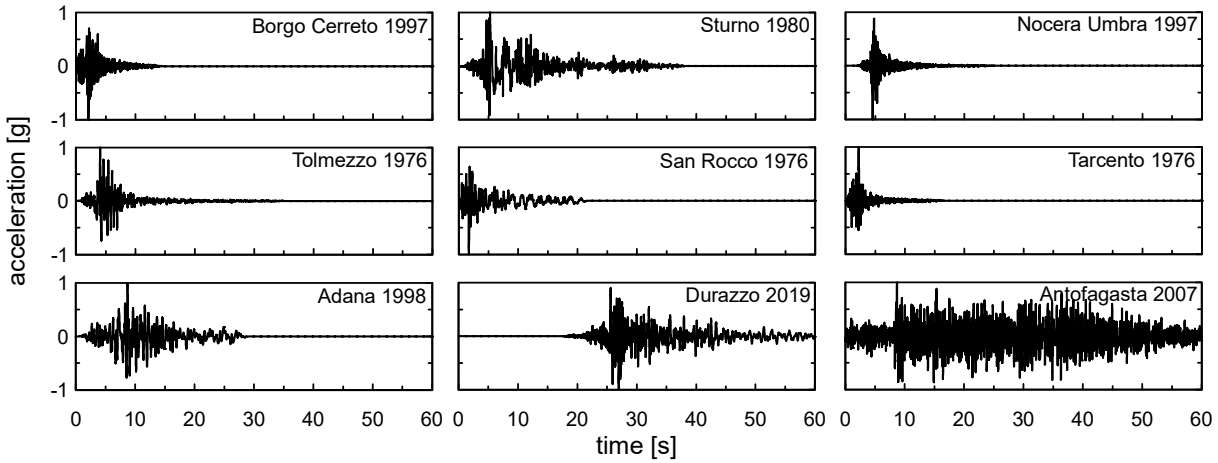


Figure 4: Acceleration time-histories.

Pile to soil acceleration spectral ratios were obtained deriving the transient response at the pile-head and free-field surface, then the corresponding acceleration response spectra were computed for each of the 9 accelerograms (Fig. 6).

The spectral acceleration rations $\xi$ were calculated as the mean response spectrum at the pile head over the mean response spectrum of the free-field motion.

Figure 6a shows the outcropping bedrock to soil surface amplification function for a dimensionless interface depth $h_1/d = 5$, layers stiffness contrast $G_2/G_1 = 10$ and total height of the soil medium $H = 30$ m. In the same figure the outcropping-bedrock to pile amplification function is also reported. Figure 6b shows the surface response spectra for each selected accelerogram, the pile response spectra, the outcropping-bedrock mean response spectrum, the surface mean response spectrum and the pile mean response spectrum. From inspection of the two graphs, it is evident that piles may provide a significant filtering effect within the frequency range of the selected signals, resulting in a reduction of seismic demand for structures having a fundamental period up to 0.5 s.

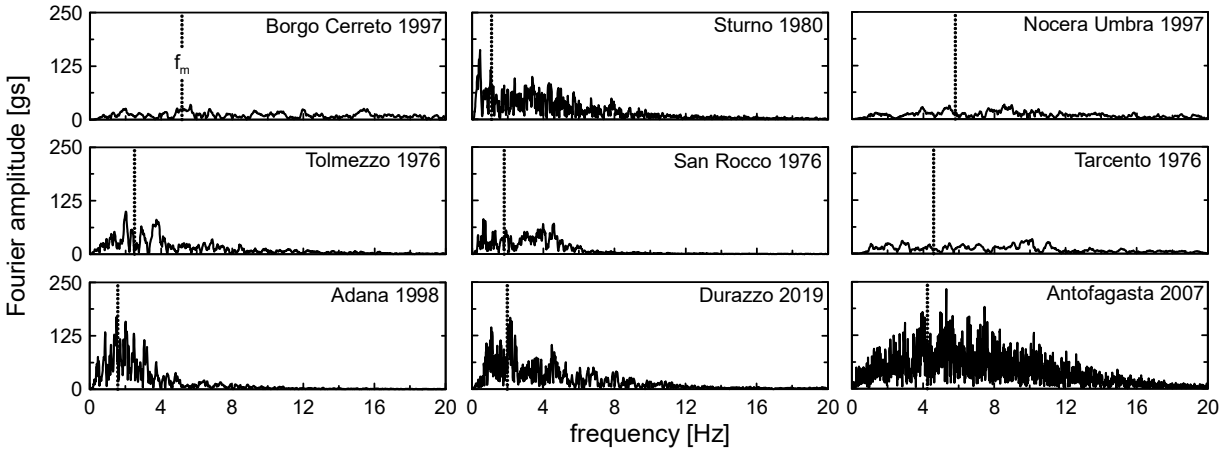


Figure 5: Fourier spectra of the acceleration time-histories.

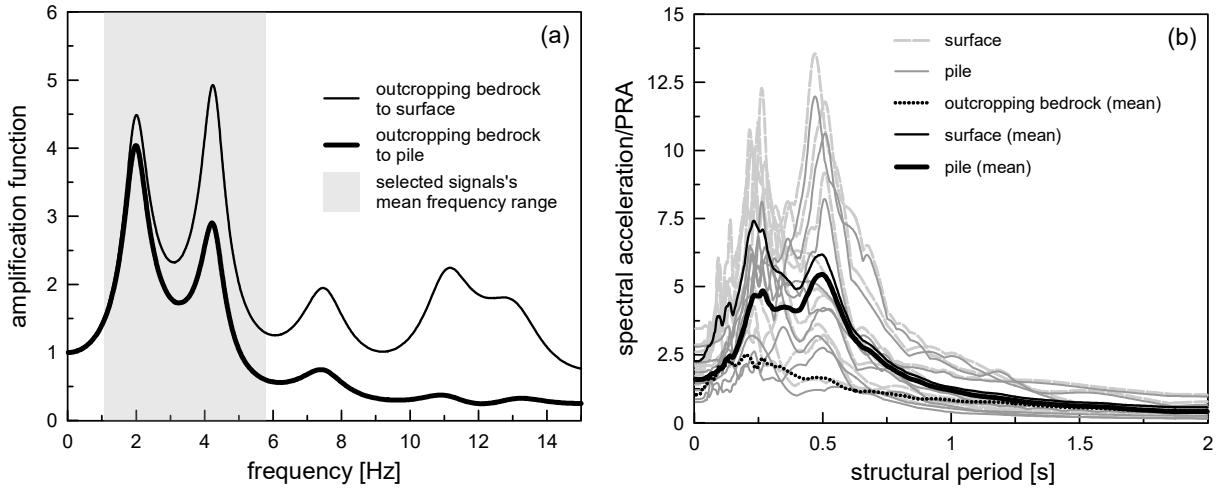


Figure 6: Amplification function (a) and spectral acceleration (b) for $d$ = 1 m, $E_p/E_{s1}$ = 1000, $h_1/d$ = 5, $G_2/G_1$ = 10 $\beta$ = 0.05, $H$ = 30 m.

The spectral acceleration ratio is shown in Fig. 7 for selected cases. A noteworthy point is that time-domain response seems more sensitive to the presence of a second layer as compared to the frequency domain, since even deep interfaces may affect spectral ratios in a significant manner. This is because the time-domain results reflect also the frequency content of the signal at soil surface, which is shifted to higher frequencies in presence of a stiffer second layer, rendering the filtering action more pronounced. For the same reason, a large layers' stiffness contrast has a double beneficial role. This is evident in Fig. 7(b,d): for an interface depth equal to 10 pile diameters, which in the frequency domain returns the same interaction factor as a homogeneous soil, the filtering effect is more pronounced than for a homogeneous halfspace with the proprieties of the first layer, and for some structural periods could be even more beneficial compared to an "intermediate" interface depth.

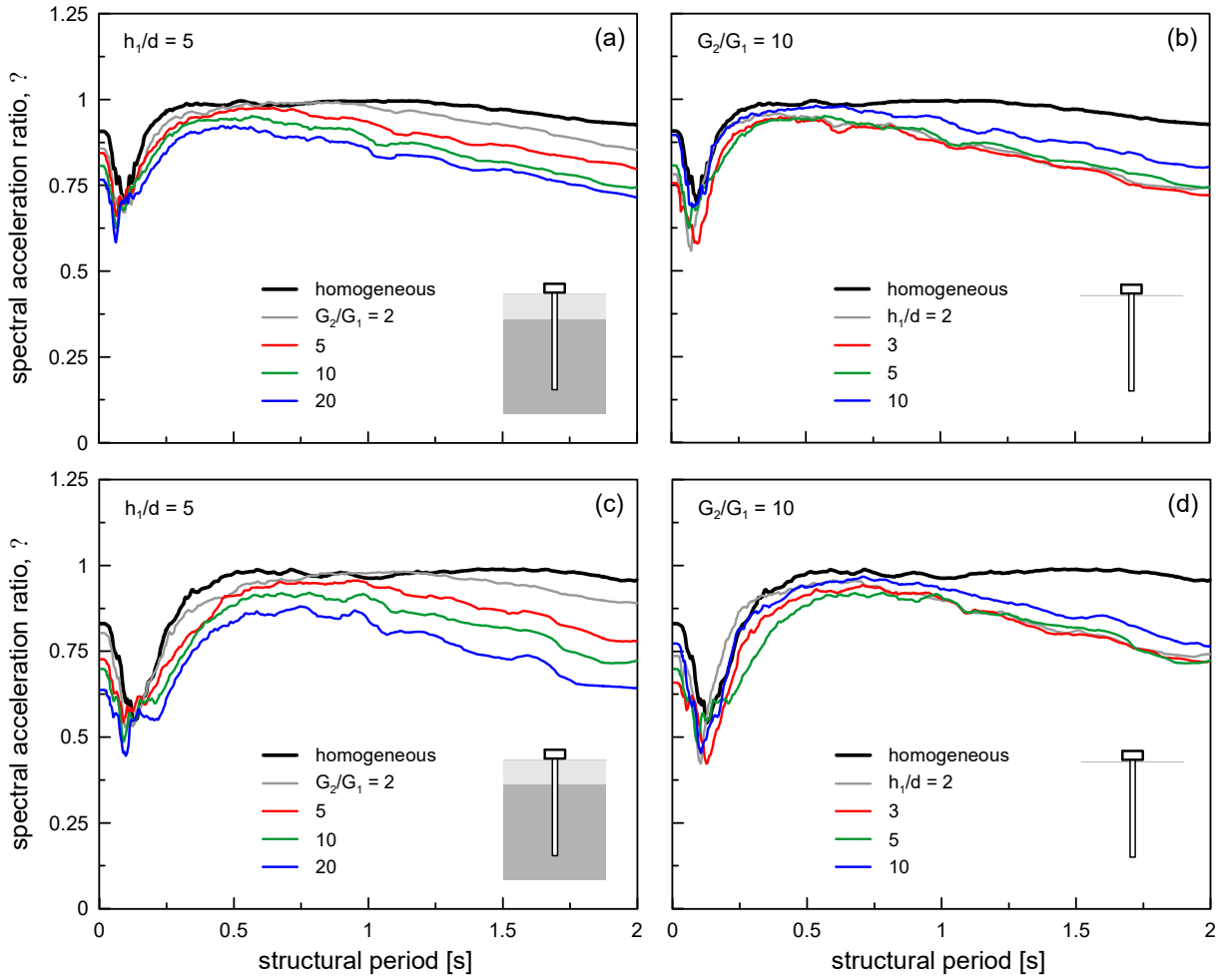


Figure 7: Spectral acceleration ratio for $d = 1$ m, $\beta = 0.05$, $H = 30$ m; $E_p/E_{s1} = 500$ for (a) and (b); $E_p/E_{s1} = 1000$ for (c) and d.

## 5 CONCLUSIONS

This work investigates the pile-induced filtering effect due to kinematic interaction in two-layer soil with shallow interfaces, i.e. when the first layer thickness is lower than the active pile length. A wide set of rigorous Finite Element (equivalent) linear analyses was carried out in the frequency domain using the commercial FE code ANSYS. Transient response has been analyzed with reference to 9 selected real acceleration time-histories. The beneficial role of the second layer, stiffer than the first, has been highlighted. It is shown that while the pile-to-soil acceleration ratio in the frequency domain is significant only for intermediate interface depths, the transient response shows that filtering effect may be very important also for deep interfaces. This is because the presence of a stiff layer shifts the frequency content of the signal at surface towards higher frequencies. From a general standpoint, a stiffer underlying layer is usually beneficial for pile filtering.

## ACKNOWLEDGMENTS

The authors wish to thank Università della Campania Luigi Vanvitelli for funding this work through Programma V:ALERE 2020, Project "Piles AS Seismic vulnerability Reduction Appliances".

## REFERENCES

[1] R. Di Laora & L. de Sanctis, Piles-induced filtering effect on the foundation input motion. *Soil Dynamics and Earthquake Engineering,* **46**, 52–63, 2013.

[2] R. Flores-Berrones & R.V. Whitman, Seismic response of end bearing piles. *Journal of the Geotechnical Engineering Division,* **108**(4), 554–69, 1982.

[3] A.S. Nikolaou, G. Mylonakis, G. Gazetas, T. Tazoh, Kinematic pile bending during earthquakes analysis and field measurements. *Géotechnique,* **51**(5), 425–40, 2001.

[4] G. Anoyatis, R. Di Laora, A. Mandolini, G. Mylonakis, Kinematic response of single piles for different boundary conditions: Analytical solutions and normalization scheme. *Soil Dynamics and Earthquake Engineering,* **44**, 183–195, 2013.

[5] M. Iovino, R. Di Laora, E. Rovithis, L. de Sanctis, The Beneficial Role of Piles on the Seismic Loading of Structures, *Earthquake Spectra,* **35**(3), 1141–1162, 2019.

[6] K. Fan, G. Gazetas, A. Kaynia, E. Kausel, S. Ahmad, Kinematic seismic response analysis of single piles and pile groups, *Journal of the Geotechnical Engineering Division,* **117**(2), 1860–1879, 1991.

[7] R. Di Laora, Y. Grossi, L. de Sanctis, M.G. Viggiani, An analytical solution for the rotational component of the foundation input motion induced by a pile group, *Soil Dynamics and Earthquake Engineering* **97**, 424–38, 2017.

[8] E. L. Wilson, Structural analysis of axisymmetric solids, *Am. Inst. Aeronaut. Astronaut,* **3**(12), 2269–2274, 1965.

[9] M. Iovino, L. de Sanctis, R. Di Laora, T.K. Garala, G.S.P. Madabhushi, The Filtering Effect of Pile Foundations in Clay, *Journal of Geotechnical and Geoenviromental Engineering* **148**(10), 04022077, 2022.

[10] G. Gazetas & R. Dobry, Horizontal response of piles in layered soils, *Journal of Geotechnical and Geoenviromental Engineering,* **110**(1), 20-40, 1984.

[11] H.G. Poulos & E.H. Davis, *Pile Foundation Analysis and Design*, Jonh Wiley and Sons, 1980.

[12] M. F. Randolph, The response of flexible piles to lateral loading, *Géotechnique* **31**(2), 247 – 259, 1981.

[13] L. Luzi, G. Lanzano, C. Felicetta, M.C. D'Amico, E. Russo, S. Sgobba, F. Pacor, ORFEUS Working Group 5. Engineering Strong Motion Database (ESM) (Version 2.0). *Istituto Nazionale di Geofisica e Vulcanologia* (INGV), 2020.

[14] M. Rathje, N.A. Abrahamson, J.D. Bray, Simplified frequency content estimates of earthquake ground motions, *Journal of Geotechnical and Geoenviromental Engineering* **124**(2), 150 – 159, 1998.

COMPDYN 2023
9th ECCOMAS Thematic Conference on
Computational Methods in Structural Dynamics and Earthquake Engineering
M. Papadrakakis, M. Fragiadakis (eds.)
Athens, Greece, 12-14 June 2023

# ON THE SSI PERIOD AND DAMPING FOR BRIDGE PIERS ON CAISSON FOUNDATIONS

**Riccardo Conti[1], Emmanouil Rovithis[2], and Raffaele Di Laora[3]**

[1] Università degli Studi di Roma "Tor Vergata"
Rome, Italy
e-mail: riccardo.conti@uniroma2.it

[2]Democritus University of Thrace
Xanthi, Greece
e-mail: erovithis@civil.duth.gr

[3]Università degli Studi della Campania "Luigi Vanvitelli"
Aversa (CE), Italy
e-mail: raffaele.dilaora@unicampania.it

## Abstract

*The vibrational period and damping of structure-foundation-soil systems are explored, with focus on the case of bridge piers on caisson foundations. To this end, a SDOF model resting on flexible supports is considered as reference model. A parametric study is then performed by considering different dimensions of the caisson, heights of the pier, mass of the deck and sub-soil. Rigorous results are compared with predictions of earlier solutions, obtained in the context of the "replacement oscillator" approach, to highlight the role of the double damping terms, foundation mass, reference system for the calculation of impedances and the cross swaying-rocking stiffness.*

**Keywords:** Soil-Structure Interaction, caisson foundation, dynamic impedance, replacement oscillator.

## 1 INTRODUCTION

Conventional modelling of structures considering the effects of Soil-Structure Interaction (SSI) involves a Single-Degree-Of-Freedom system resting on foundation impedances (i.e. springs and dashpots), as illustrated in Fig. 1. The above system is then converted into an equivalent SDOF system ([1], [2]), referred to as '*replacement oscillator*', having modified period and damping ratio, so that under a force *F*, equal to the mass *m* multiplied by the input acceleration *a*, it experiences the same response at resonance.

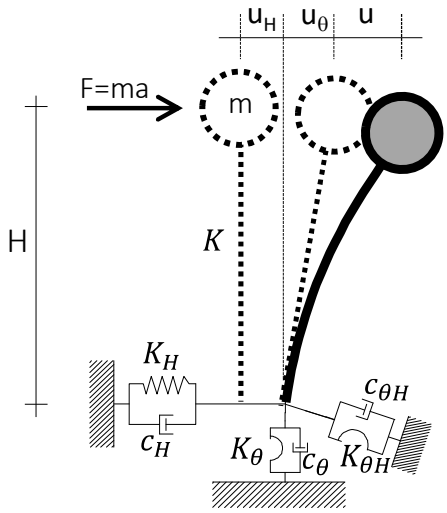


Figure 1: Single Degree-Of-Freedom system on foundation impedances to consider SSI.

Foundation impedances describe the compliance of the soil-foundation system along with its capability of dissipating energy by hysteresis and radiation of waves in the soil medium. Under harmonic force vibrations, these can be conveniently expressed as frequency-dependent complex functions in the following form:

$$K_H^* = K_H(1 + i2\xi_H)$$
$$K_\theta^* = K_\theta(1 + i2\xi_\theta) \quad (1)$$

where $K_H$, $K_\theta$ and $\xi_H$, $\xi_\theta$ are the stiffness and damping ratio of the foundation in swaying and rocking mode, respectively. It follows that the corresponding damping ratios can be back-calculated from the impedance functions as:

$$\xi_H(\omega) = \frac{\mathrm{Im}[K_H^*(\omega)]}{2\mathrm{Re}[K_H^*(\omega)]}$$
$$\xi_\theta(\omega) = \frac{\mathrm{Im}[K_\theta^*(\omega)]}{2\mathrm{Re}[K_\theta^*(\omega)]} \quad (2)$$

By imposing that the absolute displacement of the replacement oscillator, $\tilde{u}$, is equal to the displacement of the complete SSI system, $u + u_H + u_\theta$, it is possible to derive the ratio between the periods of the replacement oscillator, $\tilde{T}$, and the fixed-base SDOF system, $T_0$, as:

$$\frac{\tilde{T}}{T_0} = \frac{\omega_0}{\tilde{\omega}} = \sqrt{1 + \frac{K}{K_H} + \frac{KH^2}{K_\theta}} \quad (3)$$

where $K$ is the stiffness of the original fixed-base SDOF system, while the symbol $\omega$ stands for the cyclic natural frequency (= $2\pi/T$). Since foundation stiffnesses are frequency-dependent, the calculation of the elongated period $\tilde{T}$ requires some iteration, the final stiffness values being calculated at $\omega = \tilde{\omega}$. With reference to the solution reported by Wolf (1985), the equivalence of the peak response between the replacement oscillator and the coupled system at resonance provides the following expression for the equivalent damping ratio of the replacement oscillator:

$$\tilde{\xi} = \left(\frac{\tilde{\omega}}{\omega_0}\right)^2 \xi + \left[1 - \left(\frac{\tilde{\omega}}{\omega_0}\right)^2\right] \xi_s + \left(\frac{\tilde{\omega}}{\omega_H}\right)^2 \xi_H + \left(\frac{\tilde{\omega}}{\omega_\theta}\right)^2 \xi_\theta \tag{4}$$

where $\omega_H$ and $\omega_\theta$ are fictitious natural frequencies defined as:

$$\omega_H = \sqrt{\frac{K_H}{m}}$$
$$\omega_\theta = \sqrt{\frac{K_\theta}{mH^2}} \tag{5}$$

The hysteretic damping ratio of the soil ($\xi_s$) appears explicitly in Eq. (4). Therefore, proper treatment of the above solution requires that $\xi_H$ and $\xi_\theta$ refer only to the radiation part of the foundation damping mechanism. On the other hand, the solution provided by Veletsos and co-workers, formulated for $\xi_s = 0$, reads:

$$\tilde{\xi} = \left(\frac{\tilde{\omega}}{\omega_0}\right)^3 \xi + \left(\frac{\tilde{\omega}}{\omega_H}\right)^2 \xi_H + \left(\frac{\tilde{\omega}}{\omega_\theta}\right)^2 \xi_\theta \tag{6}$$

where in this case the ratio of $\tilde{\omega}/\omega_0$ in the right-hand side of the equation is raised in the power of 3 due to the assumption of a viscously-damped replacement oscillator.
Eqs. (4) and (6) were developed for structures resting on shallow foundations. Therefore, direct application of these solutions to the case of embedded caisson foundations may lead to inaccurate results for two main reasons: (1) mass and inertia of the foundation are not accounted for, which could be relevant with increasing height of the foundation; (2) the formulation lacks of the cross-swaying coupled stiffness, which, contrary to the case of shallow foundations, is of paramount importance for embedded and deep foundations. A procedure to account for these aspects is illustrated in the following. A parametric study is then carried out to quantify the inaccuracy introduced by the above approximations.

## 2 REFERENCE MODEL FOR INERTIAL INTERACTION ANALYSIS

Owing to the finite mass and height of the caisson, the calculation of impedances requires the following nontrivial choices: (1) considering the foundation as massless or massive and (2) referring the impedance to the top or the bottom of the foundation. Despite the choice of considering a massive foundation could appear somehow obvious, in reality it is not, as explained below.

The models for SSI only refer to the so called ‘inertial interaction’ analysis, that is the structure-foundation-soil system excited at the top. However, under the assumption of (equivalent) linear behavior for all materials, a rigorous analysis of the three-component system should be carried out using the substructure method, *i.e.* first computing the Foundation Input Motion (FIM), consisting of both a translational and a rotational component, by means of a ‘kinematic

interaction' analysis. Then, the results of the inertial and kinematic interaction analyses must be combined to obtain the overall response of the structure-foundation system.

The substructure method could be in principle applied in different, yet consistent, manners to ensure that the sum of kinematic and inertial effects makes the correct total response. However, in its most widespread application, the kinematic interaction is performed with reference to the bottom of a massless foundation. Accordingly, the consistent inertial interaction analysis requires modelling both the structure and the foundation, the latter with its mass and height; moreover, the springs and dashpots attached to its bottom are evaluated with reference to the bottom of a massless foundation. Modelling the foundation height and mass is rather complicated and makes the replacement oscillator model hard to be defined, at least in a rigorous manner.

To overcome this issue, Conti & Di Laora [3] proposed an alternative, yet exact, substructure method, where the kinematic interaction analysis is performed considering a massive foundation, while the inertial interaction analysis requires modelling only the superstructure, attaching directly to its base springs and dashpots evaluated with reference to the top of a massive foundation. This way, the replacement oscillator model can be (easily and) rigorously adopted. Many works in literature provide simplified formulae for the impedances at the bottom of a massless foundation. Among these, the recent expressions in Conti & Di Laora [3] furnish very accurate results for a rigid cylindrical caisson, allowing for a more accurate prediction of the SSI system response over earlier solutions, when the impedances at the bottom of a massless foundation are considered in the context of the classical substructure approach. However, a simple transformation ([4], [5]), allows to obtain the corresponding impedances at the top of a massive foundation.

With these premises, a replacement oscillator can be derived including the coupled impedance term. Although the mathematical passages are herein omitted in the interest of space, it is possible to express the natural frequency of the equivalent SDOF as:

$$\frac{\tilde{T}}{T_0} = \frac{\omega_0}{\tilde{\omega}} = \sqrt{1 + K\frac{K_\theta + K_H H^2 - 2K_{\theta H} H}{K_H K_\theta - K_{\theta H}^2}} \tag{7}$$

where $K_{\theta H}$ is the coupled stiffness of the caisson. This expression, already derived by Zania [6], degenerates to the one by Veletsos and co-workers [1] and Wolf [2] for $K_{\theta H} = 0$.

The effective damping ratio is:

$$\tilde{\xi} = \xi\left(\frac{\tilde{\omega}}{\omega_0}\right)^2 + 2\xi_{\theta H}\frac{1-\left(\frac{\tilde{\omega}}{\omega_0}\right)^2-\left(\frac{\tilde{\omega}}{\omega_{\theta H}}\right)^2}{1-\left(\frac{\omega_H\omega_\theta}{\omega_{\theta H}^2}\right)^2} + \xi_H\frac{1-\left(\frac{\tilde{\omega}}{\omega_0}\right)^2-\left(\frac{\tilde{\omega}}{\omega_\theta}\right)^2}{1-\left(\frac{\omega_{\theta H}^2}{\omega_H\omega_\theta}\right)^2} + \xi_\theta\frac{1-\left(\frac{\tilde{\omega}}{\omega_0}\right)^2-\left(\frac{\tilde{\omega}}{\omega_H}\right)^2}{1-\left(\frac{\omega_{\theta H}^2}{\omega_H\omega_\theta}\right)^2} \tag{8}$$

where $\xi_{\theta H}(\omega) = \frac{\mathrm{Im}[K_{H\theta}^*(\omega)]}{2\mathrm{Re}[K_{H\theta}^*(\omega)]}$ and $\omega_{H\theta} = \sqrt{\frac{K_{H\theta}}{mH}}$.

Eq. (8) coincides with the expression by Zania [6] if in the latter the coupled damping terms $\xi_i\xi_j$ are neglected. Based on the above discussion, Eqs. (7) and (8) furnishes correct values for period and damping ratio at resonance only if impedances at the top of the massive foundation are employed.

## 3 PARAMETRIC STUDY

An extended parametric study was carried out to explore the influence of the impedance formulation and of the coupled stiffness on the natural period and damping of the replacement oscillator. The ideal case of a bridge pier with a caisson foundation embedded on a homogeneous clayey soil deposit was analyzed. Two soil deposits were considered, whose relevant mechanical properties are summarized in Table 1: the Plasticity Index, *PI*; the undrained shear strength, $s_u$; the small strain shear wave velocity, $V_s$; the hysteretic damping ratio, $\xi_s$. To take into account the nonlinear soil behavior (i.e.: the variation of the shear modulus *G* and damping with the mobilized strain level, $\gamma$), three values of $V_s$ and $\xi_s$ were considered, corresponding to $G/G_0 = 1$, 2/3 and 1/3.

The cylindrical caisson foundation has diameter $D = 8$ and 12 m, with slenderness ratio $H_c/D = 0.5$, 1 and 2, where $H_c$ is the caisson depth. Three pier heights were considered ($H = 20$, 40 and 60 m). The hollow rectangular reinforced concrete cross section of the pier, as well as the mass of the deck, are representative of highway and railway bridges with span length of 20-150 m. Specifically, for each pier, the mass of the deck was designed taking into account three conditions: (i) to guarantee a minimum span length, $L/H \geq 0.5$; (ii) to avoid second order effects within the pier; and (iii) to provide a static global safety factor $SF = 1.5$ and 5 for the bearing capacity of the foundation against pure vertical loads.

The bridge pier was modelled as a single degree of freedom system with height *H*, structural damping $\xi$, stiffness *K* and lumped mass *m*, the latter including the mass of the deck and the mass of the upper half of the pier ($m = m_{deck} + 0.5 \cdot m_{pier}$). A total of 69 pier-foundation-soil systems were analyzed, comprising structural (fixed-base) periods $T_0$ in the range 0.3-2.8 s.

| *PI* [%] | 60 | | 200 | |
|---|---|---|---|---|
| $s_u$ [kPa] | 40 | | 140 | |
| | $\xi_s$ [%] | $V_s$ [m/s] | $\xi_s$ [%] | $V_s$ [m/s] |
| $G/G_0 = 1$ | 2 | 130 | 2 | 240 |
| $G/G_0 = 2/3$ | 7 | 110 | 5 | 200 |
| $G/G_0 = 1/3$ | 12 | 75 | 10 | 140 |

Table 1: Soil parameters considered in the parametric study.

## 4 SELECTED RESULTS

This section provides a comparison between different considerations in the evaluation of the SSI period, $\tilde{T}$ , and damping, $\tilde{\xi}$, by applying the replacement oscillator model [Eqs. (7) and (8)] to the pier-foundation-soil systems analyzed in the parametric study.

The reference (rigorous) solution, which is mentioned in the graphs as $\tilde{T}_{ref}$ and $\tilde{\xi}_{ref}$, is obtained by computing the SSI period and damping using the formulas derived by Zania (2014), thus including also double damping terms in the equations, and evaluating the dynamic impedances at the top of the massive foundation.

The effect of double damping terms is shown in Fig. 2. Considering that double damping terms have been omitted in Eq. (8), their effect can be directly explored by the comparison between $\tilde{\xi}$ and $\tilde{\xi}_{ref}$, as specified above. As expected, the effect is more pronounced on the effective damping rather than on the effective period, which in turn can be safely calculated by neglecting the products $\xi_i\xi_j$. The effective damping is generally not sensitive to this approximation, except few cases which, however, are difficult to detect a priori.

The role of the coupled stiffness is assessed in Fig. 3. Neglecting the cross swaying-rocking stiffness, $K_{HM}$, results in an underestimation of the effective period, leading to stiffer SSI systems with respect to the actual ones (Fig. 3b). Such an underestimation may be as high as 50%, depending on the properties of the SSI system. This is because, in the case of the actual SSI system with non-zero coupled stiffness, which also corresponds to a non-zero coupled compliance, the shear force produces an additional rotation and the moment produces an additional displacement. The effect of the coupled impedance term on the effective damping is more critical (Fig. 3a): neglecting this term may lead to a severe overestimation of damping ratio (by a factor of 2 or larger) and thereby a severe underestimation of structural response.

Figure 4 shows the effect of neglecting the mass of the foundation: except for few cases, the mass of the foundation has a minor influence with respect to a proper choice of the reference system for the evaluation of the dynamic impedances.

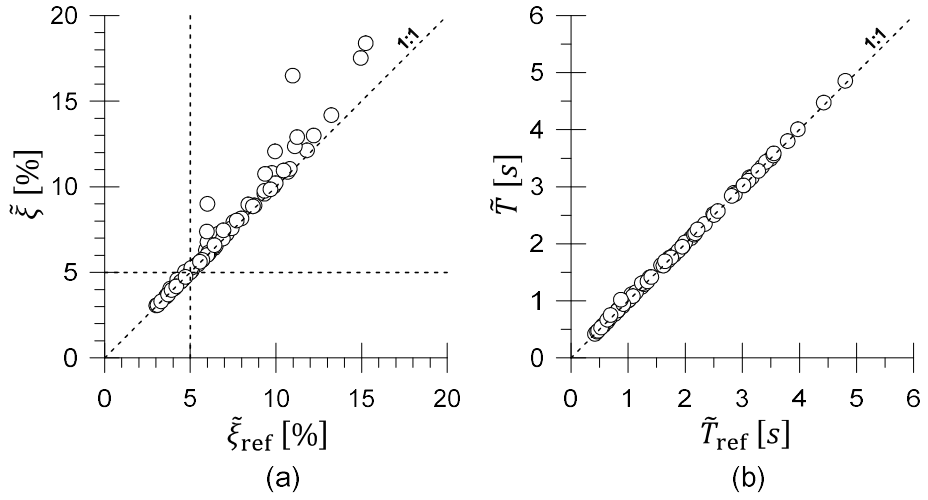


Figure 2: Effect of double damping terms on effective period and damping ratio.

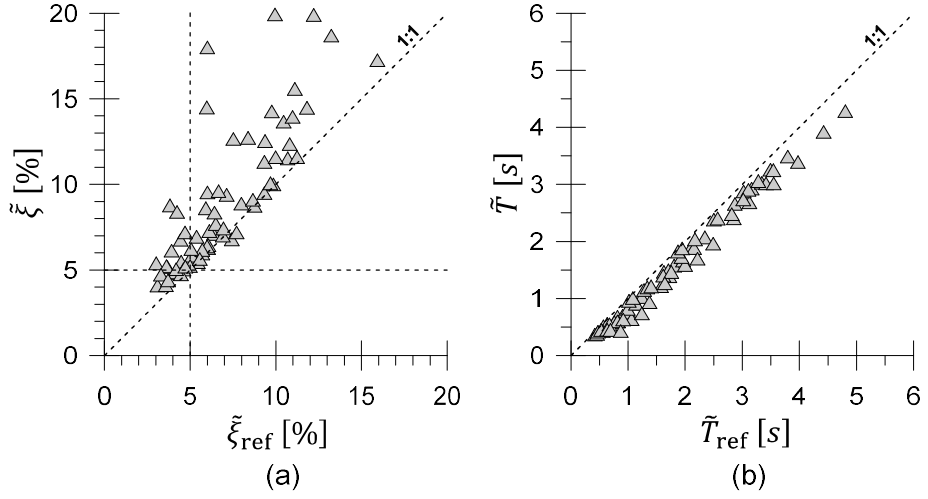


Figure 3: Effect of coupled impedance on effective period and damping ratio.

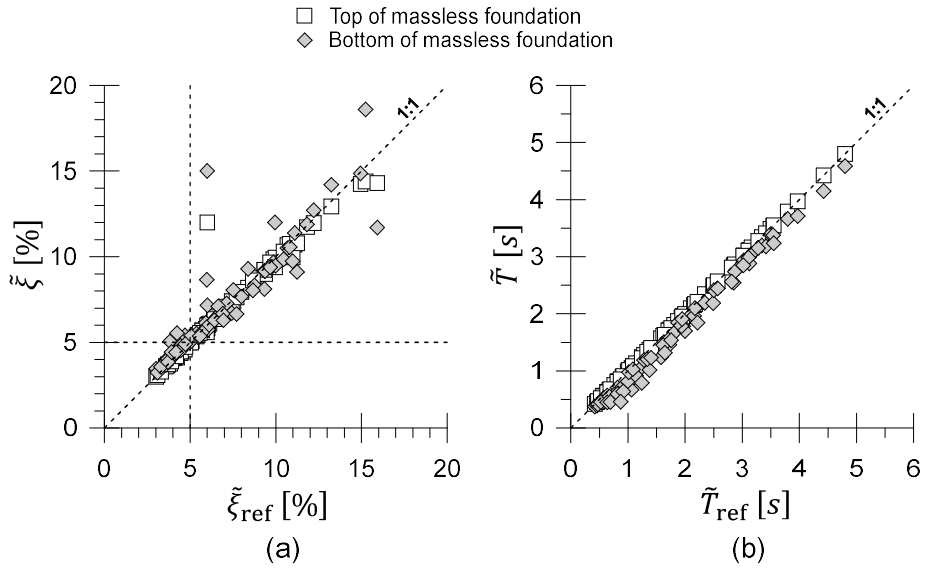


Figure 4: Effect of impedance reference system on effective period and damping ratio.

## 5 CONCLUSIONS

The natural period and damping of soil-foundation-structure systems, referring to bridge piers founded on caisson foundations, were explored by means of a SDOF model resting on flexible supports. The problem is treated numerically by implementing a hybrid substructure approach of the complete SSI system, where the foundation mass is introduced directly in the foundation input motion and caisson impedances. In light of the above considerations, closed-form expressions for the effective natural period and damping are reported in Equations 7 and 8, respectively, which allowed investigation of the importance of some critical components on the vibrational characteristics of the SSI system. The main findings of the study can be summarized as follows:

- The effect of double damping terms (i.e. products of $\xi_i\xi_j$) is more pronounced on the SSI damping of the system than on its natural period. The latter can thus be derived with sufficient accuracy if double damping terms are omitted.

- The role of the cross swaying – rocking stiffness of the caisson foundations on the vibrational characteristics of the replacement oscillator is critical. Neglecting the foundation impedance of this particular mode of vibration may lead to a strong underestimation of the effective natural period as high as 50% and a strong overestimation of the SSI damping by a factor of 2 or even larger, depending on the properties of the soil-caisson-structure system.

- Except for few cases, the foundation mass has a minor influence with respect to a proper choice of the reference system for the evaluation of the dynamic impedances.

## REFERENCES

[1] A. S. Veletsos and V.V.D. Nair, Seismic interaction of structures on hysteretic foundation. *Journal of Structural Divisions*, 101(1):109–29, 1975.

[2] J. P. Wolf, *Soil–structure interaction*. NewJersey, USA : Prentice Hall; 1985.

[3] R. Conti & R. Di Laora, Substructure Method Revisited for Analyzing the Dynamic Interaction of Structures with Em-bedded Massive Foundations. *Journal of Geotechnical and Geoenvironmental Engineering,* **148**(6), 040220292013.

[4] I. Takewaki, Takeda N. and Uetani K. Fast practical evaluation of soil–structure interaction of embedded structure. *Soil Dynamics and Earthquake Engineering*, 23 (3): 13–20, 2003.

[5] C. Tsigginos, N. Gerolymos, D. Assimaki, and G. Gazetas. Seismic response of bridge pier on rigid caisson foundation in soil stratum, *Earthquake Engineering and Engineering Vibrations*, 7 (1): 33–43, 2008.

[6] V. Zania. Natural vibration frequency and damping of slender structures founded on monopoles. *Soil Dynamics and Earthquake Engineering* 59: 8–20, 2014.

COMPDYN 2023
9th ECCOMAS Thematic Conference on
Computational Methods in Structural Dynamics and Earthquake Engineering
M. Papadrakakis, M. Fragiadakis (eds.)
Athens, Greece, 12-–14 June 2023

# ASSESSMENT OF MACRO-ELEMENTS IN THE PREDICTION OF THE RESPONSE OF OFFSHORE WIND TURBINES

**Olgu Orakci[1], Nunzia Letizia[1], Stijn François[2], Shiaohuey Chow[3], Yinghui Tian[3], George Anoyatis[1*]**

[1] KU Leuven, Department of Civil Engineering, Hydraulics and Geotechnics Section
Bruges, Belgium

[2] KU Leuven, Department of Civil Engineering, Structural Mechanics Section
Leuven, Belgium

[3] University of Melbourne, Department of Infrastructure Engineering, Offshore Geomechanics Group
Melbourne, Australia

[*]corresponding author, e-mail: @george.anoyatis@kuleuven.be

**Abstract.** *The dynamic excitation of Offshore Wind Turbines (OWTs) by wind, waves, and currents is an important issue to harness offshore wind energy, where the estimation of the OWT natural frequency is a key aspect. Advanced numerical models and simplified methodologies are used in engineering practice to optimize the design and performance of the turbines. This work provides an assessment of existing tools to determine the natural frequency and response of OWTs, by presenting an engineering study of an OWT in the general Dunkirk sand model from the PISA project. The selected foundation type is a hollow steel monopile, which is typically used in shallow-to-mid water depths and is a cost-effective solution to support the dead weight of the turbine and the environmental loads it experiences during the life span. In particular, this study involves: (i) the interpretation of geotechnical data from the PISA project Dunkirk site; (ii) the design of the monopile using spring models from PISA methodology for lateral springs, and the recently published unified method for vertical springs along the monopile shaft and at the base and following the API and DNV guidelines. This includes results from modeling the monopile as a Timoshenko beam; (iii) the selection of appropriate macro-elements from the literature to describe the relationship between load and displacement, and thus provide the pile head stiffness in swaying, rocking, cross swaying-rocking; (iv) the implementation of the selected macro-elements to predict the natural frequency of the system and its response using an available method by Arany et al. (2016) and the open source software OpenSees, respectively; (v) the assessment of the adopted simplified methodology for the study selected, using comparisons with results obtained from a finite element model.*

**Keywords:** Offshore wind turbines, Simplified method, Design of monopile, Dynamic analysis

## 1 INTRODUCTION

Offshore wind energy is becoming increasingly important as a source of renewable energy. It is a clean and renewable source of electricity that does not produce greenhouse gas emissions or other pollutants which are causing air pollution and climate change. This makes it an attractive alternative to fossil fuels and helps reduce dependence on non-renewable energy sources [2]. It can further increase energy security by diversifying the energy mix and reducing dependence on imported fuels. This can help to stabilize energy prices and reduce exposure to supply disruptions. In light of the above, many countries have set ambitious targets to increase the share of renewable energy in their electricity mix, in order to reduce greenhouse gas emissions and combat climate change. Offshore wind energy is seen as a key technology to help meet these targets, as it has the potential to provide large amounts of clean electricity. The year 2021 witnessed an exceptional increase in new offshore wind capacity installation globally, with a remarkable record of 21 GW, more than three times the capacity deployed in 2020 [11]. New ambitious aims worldwide give promises to new records to come. In particular, the European Union has set a target of installing at least 60 GW of offshore wind capacity by 2030, and 300 GW by 2050, which represents a significant increase from current levels [2]. Offshore wind farms are thus expected to play an increasingly important role in the overall energy system, as they are integrated with other sources of energy, such as onshore wind, solar, and storage, and are connected to the grid, to ensure the stability and reliability of the energy system.

The monopile foundation is a common type of fixed foundation used in offshore wind turbines (OWTs), which consists of a single steel pile driven into the seabed [25]. The foundation is designed to safely resist the loads imposed by wind, waves, and currents. The foundation design is a critical factor in ensuring the safe and reliable operation of OWT foundations, and the consideration of displacements and rotations is an important part of that process, as they affect the OWT performance [22]. Large displacements and rotations can result in fatigue damage to the foundation, tower, and turbine components and serviceability problems which can cause structural failure and operational problems [7].

The stability of an offshore wind turbine depends on limiting displacements and rotations of the foundation within specified thresholds. Specific limits for displacements and rotations are typically imposed by the manufacturer and can vary depending on the specific project conditions [5]. These limits ensure the turbine remains stable and operates efficiently without excessive deformations or structural damage. The response is dependent on the geometrical and mechanical foundation properties, soil conditions, and the loading that the OWT is exposed to in its lifetime [20]. Although an analysis is required by the design guidelines, there is not a unified methodology with a consensus on the serviceability analysis [5].

There are three main categories that can be used to calculate displacements and rotations of monopile foundations: spring methods such as p-y method, advanced methods such as finite element models, and simplified methods such as macro-elements [7]. This work focuses on assessing the performance of a simplified methodology to predict displacement and rotations of OWTs using macroelements available in the literature to represent the monopile-foundation system. The macroelements simplify the analysis significantly and enable a smooth connection to structural analysis by including the soil-foundation system's response at one single point at the base of the OWT (e.g., [17]). Herein a set of simple linear elastic macroelements are used, following the works of Gazetas (1984) [14], Poulos and Davis (1980) [24], Pender(1993) [23], Shadlou and Bhattacharya (2016) [26]. A monopile, which is embedded in a single layer of the "general Dunkirk sand model" (GDSM) of the PISA project [8], is first designed to support an

8 MW turbine. Geotechnical data are obtained from studies available in the literature [8, 28]. The monopile design is performed according to the design guidelines by API and DNV-GL [3, 13]. The recently proposed p-y curves from the PISA project [8, 9], and t-z and Q-z springs from the unified method [19] are implemented for the analysis of the monopile design. The calculations are executed in Python, by importing the OpenSeesPy library as a non-linear solver [21, 29]. The monopile is modelled as a Timoshenko beam, considering p-$\delta$ effect. Once the monopile design is complete, the macroelements are first used to estimate the first natural frequency of the OWT, which as shown later in the manuscript is an important aspect in the design of the OWT system. Then predictions of the displacement are compared with results obtained from a finite element monotonic analysis. Analyses under cyclic loading are not within the scope of this work.

## 2 DESIGN OF THE MONOPILE FOUNDATION

This section presents a design scenario for a monopile foundation for a 8 MW offshore wind turbine located in 30 m water. The loads and the geotechnical conditions are selected from the literature and are applicable to monopiles installed in offshore homogeneous sand sites, under drained loading conditions. The monopile foundation is designed using the recent PISA methodology [8, 10]. This offers a more realistic approach to current large diameter monopiles with short embedment depth, compared to API formulations which were developed based on field tests of small diameter, flexible piles [7]. The design follows the API and DNV-GL guidelines summarized in Table 1. Working Stress Design (WSD) for the structural steel and soil bearing capacity checks and Serviceability Limit State (SLS) for the pile ground level displacement check are considered for the monopile design according to [3] and [13] guidelines, respectively.

Table 1: Monopile design checks according to API [3] and DNV-GL [13] guidelines

| **Guideline** | **Checks** | **Condition** |
|---|---|---|
| API | Shear | $f_s = \frac{V}{0.5A} < F_s = 0.4F_y$ |
| API | Combined | $\frac{f_a}{0.6F_{xc}} + \frac{\sqrt{f_{bx}^2+f_{by}^2}}{F_b} \leq 1.0$ |
| API | Overload | $\frac{P/A}{F_{xc}} + \frac{2}{\pi}(\arcsin\frac{M/Z}{F_{xc}}) \leq 1.0$ |
| API | Soil Bearing | $\frac{F_v}{A} \leq \frac{Q_c}{2} = \frac{Q_p+Q_{fc}}{2}$ |
| DNV-GL | Service | $\delta < \frac{2L}{200}$ |

$f_a$ is the absolute value of acting axial stress, $f_{bx}$ is the absolute value of acting resultant bending stress in the x direction, $f_{by}$ is the absolute value of acting resultant bending stress in y direction $f_s$ is maximum beam shear stress, $A$ is the cross-sectional area, $F_b$ is allowable bending stress, $F_s$ is allowable beam shear stress, $F_{xc}$ is inelastic local buckling stress, $F_y$ is yield strength, $L$ is the total length of the monopile, $M$ is the bending moment, $P_v$ is axial loading, $Q_c$ is the ultimate axial capacity of piles in compression, $Q_{fc}$ is shaft friction capacity in compression, $Q_p$ is the end bearing capacity $V$ is transverse shear force, $Z$ is the plastic modulus, $\delta$ is lateral displacement.

### 2.1 Geotechnical data and design loads

The site considered in this study includes a deep homogeneous soil layer of the Dunkirk sand [8, 28]. This way the rule-based PISA design approach can be adopted using pre-defined functions of the soil reaction curves, following the General Dunkirk sand model (GDSM), as described in the work of Burd *et al.* [8]. The foundation soil is a normally consolidated marine sand that originates from a coastal site in Northern France. The site includes a 3 m hydraulically placed sand at the top to increase the ground level in the 1970s without compaction or surcharging. In line with previous studies [8], this fill is not considered in the analysis, and a hydrostatic pore pressure distribution is assumed for the underlying sand. The CPT data along with selected design tip resistance values $q_c$ (blue line) are given in Figure 1 ([28]). The relative density, $D_R$, is considered equal to 75%, and the critical state friction angle $\phi'_{\text{cs}}$ is 32°. All other geotechnical parameters necessary for the implementation of the PISA design approach, the macroelements and the rigorous three-dimensional finite element analysis are taken from relative publications of the PISA project [8, 28].

The OWT specifications and geometry, as well as pertinent design loads, are obtained from

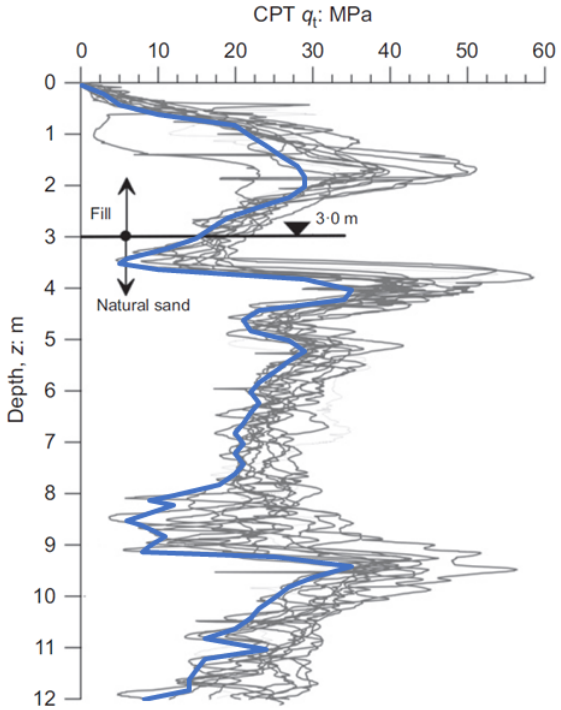


Figure 1: CPT data from sand soil profile in Dunkirk with selected design values (blue line) [28]

the work of Bhattacharya [7]. In particular, metocean data for the case of a 30 m water-deep site and 12 m of maximum wave height are used. The wind load depends on the wind speed, the rotor diameter, the controlling mechanism, and turbulence. The wave load depends on the water depth and the pile diameter. Typical lateral loads for the problem at hand are presented in Table 2. The vertical loads include the tower mass, $m_T$, together with rotor-nacelle assembly mass, $m_{\text{RNA}}$, and the dead weights of the monopile, $m_P$, and the transition piece, $m_{\text{TP}}$. Steel sections are made of $S355$ grade and unit weight of $78.6\ kN/m^3$. The following load cases are considered in the design [5, 7]: (1) normal operational conditions; (2) extreme wave load

Table 2: Typical wind and wave loads for an 8 MW offshore wind turbine according to Bhattacharya [7]

| **Input Parameter** | **Symbol** | **Unit** | **Case Study** |
|---|---|---|---|
| Rotor diameter | $D_{\text{rotor}}$ | m | 164 |
| Rated wind speed | $U_r$ | m/s | 13 |
| Hub height | $z_{\text{hub}}$ | m | 110 |
| Monopile diameter | $D$ | m | 7.5 |
| Horizontal wind force | $Fh_{\text{wind}}$ | MN | 2.3 |
| Horizontal wave force | $Fh_{\text{wave}}$ | MN | 6.1 |
| Moment from wind force | $M_{\text{wind}}$ | MN.m | 323 |
| Moment from waves | $M_{\text{wave}}$ | MN.m | 175 |
| Tower mass | $m_T$ | ton | 558 |
| Rotor-nacelle assembly mass (RNA) | $m_{\text{RNA}}$ | ton | 410 |

conditions; (3) extreme wind load conditions; (4) cut-out wind speed and extreme operating gust conditions; and (5) wind-wave misalignment condition (the same as in (2), only wind and wave act perpendicular).

## 2.2 p-y and t-z design analysis

The PISA method defines lateral load-displacement curves ($p - y$) and moment-rotation curves throughout the pile ($m - \theta$) and at the pile tip ($M_B - \theta$), as well as an additional base lateral load-displacement curve ($H_B - y$). The embedded pile is modelled as a Timoshenko beam, which allows for the realistic approximation of the shear strains in the pile [9]. An example of monopile discretization including lateral and axial springs is shown in Figure 2.

The PISA design method for sands is applicable to monopiles installed at offshore sand sites

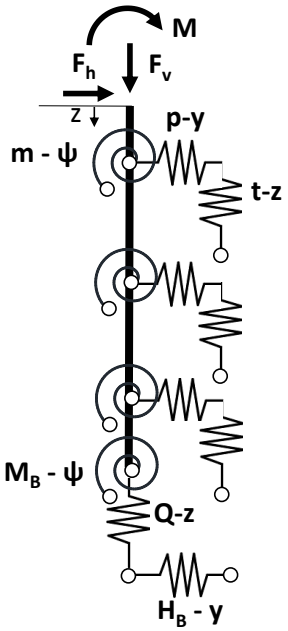


Figure 2: Pile discretization for the problem considered

with similar sand characteristics to the Flandrian sand found at Dunkirk, provided that the dimensions of the monopiles fall within the calibration space (i.e., $2 \leq L/D \leq 6, 5 \leq h/D \leq 15$, $45\% \leq D_R \leq 90\%$) [8]. In this work, only the load-displacement curves along the pile length i.e., $p-y$ curves, and an additional base lateral load-displacement curve $H_b - y$ are used.

The normalized soil reactions can be determined as a function of normalized displacements by the four-parameter conic function where the parameters are $k$ the initial slope, $\bar{y_u}$ the ultimate normalized soil reaction, $\bar{x_u}$ the normalized displacement or rotation at the ultimate soil reaction, and $k$ the shape parameter ($0 \leq n \leq 1$) of the soil reaction curve:

$$\bar{y} = \bar{y_u} \frac{2\,c}{-b + \sqrt{b^2 - 4ac}} \quad \text{for } \bar{x} \leq \bar{x_u} \quad \text{and} \quad \bar{y} = \bar{y_u} \quad \text{for } \bar{x} > \bar{x_u} \tag{1}$$

where

$$a = 1 - 2n, \qquad b = 2n\frac{\bar{x}}{\bar{x_u}} - (1-n)\left(1 + \frac{\bar{x}k}{\bar{y_u}}\right), \qquad c = \frac{\bar{x}k}{\bar{y_u}}(1-n) - n\frac{\bar{x}^2}{\bar{x_u}^2}$$

The actual values ($p$, $y$, $m$, $\theta$, $H_B$, $M_B$) are determined from the normalized values ($\bar{p}$, $\bar{y}$, $\bar{m}$, $\bar{\theta}$, $\bar{H_B}$, $\bar{M_B}$).

For $p-y$ and $H_B - y$ curves:

$$\bar{p} = \frac{p}{\sigma'_{\text{vi}}\,D}, \quad \bar{H_B} = \frac{H_B}{\sigma'_{\text{vi}}\,D^2}, \quad \text{and} \quad \bar{y} = \frac{y\,G_0}{\sigma'_{\text{vi}}\,D}$$

For $m - \psi$ and $M_B - \psi$ curves:

$$\bar{m} = \frac{m}{|p|D} \quad \bar{M_B} = \frac{M_B}{\sigma'_{\text{vi}}\,D^3}, \quad \text{and,} \quad \bar{\psi} = \frac{\psi\,G_0}{\sigma'_{\text{vi}}} \tag{2}$$

where $G_0$ is the small-strain shear modulus defined according to [16]:

$$G_0 = \frac{B\,p'_{\text{ref}}}{0.3 + 0.7\,e_0^2}\sqrt{\frac{p'}{p'_{\text{ref}}}} \tag{3}$$

where $p'_{\text{ref}}$ is 101.3 kPa, the atmospheric pressure.

The recently developed Unified Method is used for design under axial loads; comparisons against available methods demonstrated a very good performance in predicting the axial pile capacity [19]. This is a CPT-based method that is established using experimental data obtained from 71 static load tests of piles embedded in siliceous sand deposits. The plugging effect, effects of loading direction, sand-pile interface friction, friction fatigue, and radial stress changes during the loading of driven piles are considered. Axial deflection - axial force ($t-z$) curves and the tip deflection - axial force ($Q-z$) curve are presented in Figure 2.

Shaft capacity is calculated as follows:

$$Q_{\text{shaft}} = \pi D \int_0^L \tau_f\,dz \quad \text{where} \quad \tau_f = (f_t/f_c)(\sigma'_{\text{rc}} + \Delta\sigma'_{\text{rd}})\,\tan 29^\circ$$

$$\sigma'_{\text{rc}} = (q_c/44)\,A_{\text{re}}^{0.3}\,[\max(1,(L-z)/D)]^{-0.4} \quad \text{and} \quad \Delta\sigma'_{\text{rd}} = (q_c/10)\,(d_{\text{CPT}}/D)\left(\frac{q_c}{\sigma'_v}\right)^{-0.33}$$

$$A_{\mathrm{re}} = 1 - \mathrm{PLR}(D_i/D)^2 \quad \text{and} \quad \mathrm{PLR} \approx \tanh\left(0.3(D_i/d_{\mathrm{CPT}})^{0.5}\right)$$

where $f_t/f_c = 1$ in compression and $0.75$ in tension. $d_{\mathrm{CPT}} = 35.7\mathrm{mm}$

Base capacity is calculated as follows:

$$Q_{\mathrm{base}} = q_{\mathrm{b0.1}}(\pi\, D^2/4) \quad \text{where} \quad q_{\mathrm{b0.1}} = (0.12 + 0.38\, A_{\mathrm{re}})q_p$$

$$q_p \approx q_{\mathrm{c,av,1.5D}} = \frac{1}{3D}\int_{L-1.5D}^{L+1.5D} q_c(z)\, dz$$

For the curves, $z/z_{\mathrm{peak}}$ vs. $t/t_{\max}$ and $z/D$ vs. $Q/Q_p$ tables from the API guideline [4] are held to define $t-z$ and $Q-z$ curves, respectively; where $t_{\max} = (\pi D \tau_f)$ and $Q_p = Q_{\mathrm{base}}$. As was recommended for routine design purposes, $z_{\mathrm{peak}} = 0.01\, D$ is considered [4].

The open-source software tool OpenSees is used for load-controlled analyses [21, 29]. Nonlinear algebraic equations are handled by Krylov Newton method. The analyses are carried out in ten load steps, each with an increment of $0.1$, and the toleration level is set to $10^{-7}$ with a maximum iteration number of $1000$. The hollow steel cylindrical monopile has an embedded length $L_P$, a free length $L_S$, a diameter $D_P$, a thickness $t_P$, a cross-sectional area $A_P$, a moment of inertia $I_P$, Young's modulus $E_P$, a plastic modulus $Z_P$, and a radius of gyration $K_P$. The monopile is modelled as a Timoshenko beam and the horizontal load and the moment transmitted from the OWT are applied at the mud level as a point load in OpenSees.

**Final monopile design** is shown in Figure 3. The minimum wall thickness is $t_P = 6.35 + D_P/100$ where $D_P$ is in mm [3]. The embedded length is determined following a critical pile length methodology presented by Arany *et al.* [5]. According to this method, the pile length is obtained based on a critical length (beyond which an increment in the length has a negligible effect on the pile head displacement), which can be calculated based on pile diameter and relative pile-soil stiffness ratio.

## 3 SIMPLIFIED APPROACH USING MACRO ELEMENTS

The monopile-soil system can be represented by three impedances (macro elements) $K_{LL}$, $K_{RR}$ and $K_{LR}$ which correspond to swaying, rocking, and cross-swaying-rocking of the pile head, respectively. Figure 4 shows a simplified model of an OWT represented by a single degree of freedom system (SDOF) which rests on a "flexible base" represented by a set of macro elements. Prior to assessing the response of the OWT via the simplified approach, macroelements available in the literature are assessed on the basis of their ability to predict the natural frequency of the system.

### 3.1 Simple method to estimate the first natural frequency of an OWT

Calculating the first natural frequency of an offshore wind turbine-monopile system is crucial because it helps to ensure that the system can operate safely and efficiently. The natural frequency refers to the frequency at which a structure naturally vibrates when subjected to external forces or disturbances. In the case of an offshore wind turbine-monopile system, the natural frequency determines how the system will respond to wind and wave loads. If the natural frequency of the system is too low, it may experience resonance with the wind and wave

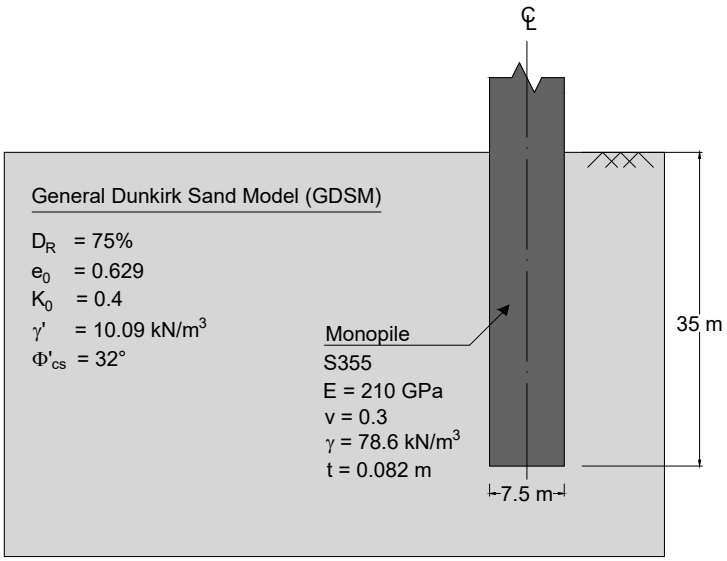


Figure 3: Final monopile design for an 8 MW OWT embedded in Dunkirk sand [8, 28].

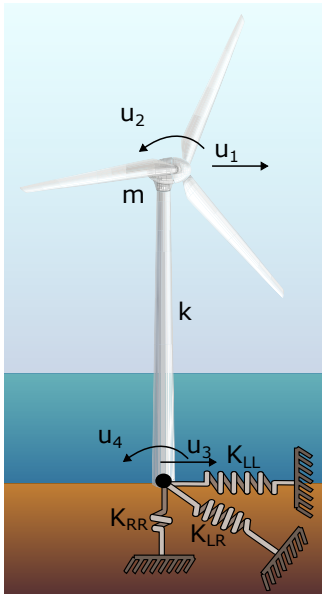


Figure 4: Schematic representation of an OWT which rests on a "flexible base".

loads, causing to excessive vibrations that can damage the structure and even cause it to fail. On the other hand, if the natural frequency is too high, the system may be too stiff and unable to absorb the dynamic loads from wind and waves, again leading to damage and failure. By calculating the first natural frequency of the offshore wind turbine-monopile system, engineers can determine whether the system's design and construction are adequate to withstand the environmental loads and operate safely and efficiently. Arany *et al.* [6] show typical wind and wave spectra, rotational speed (1P) and blade passing (3P) frequency bands for six commercial turbines as was given in Figure 5. The first natural frequency $f_1$ is intended to lie within the gap

between 1P and 3P. Otherwise, adjustments can be made to the system's design or operation to ensure that it can function as intended.

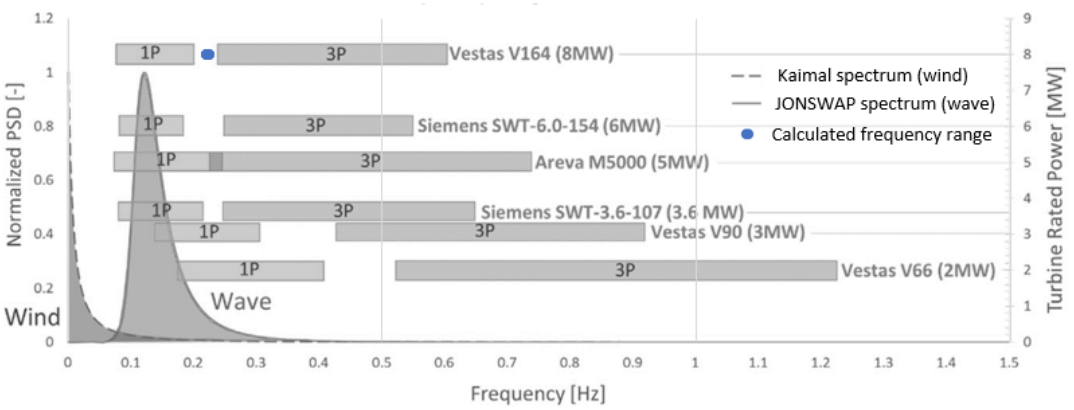


Figure 5: Typical wind and wave spetra together with 1P and 3P frequency bands for six commercial turbines (modified from [6])

In this work, the simplified methodology proposed by Arany *et al.* is used to obtain the first natural frequency of the OWT-monopile system using data from the Wind Turbine Generator, the tower and monopile geometry, and the foundation soil properties [5]. These data are included in Table 3. The tower refers to an 8MW offshore wind turbine as described in [12]. The

Table 3: Input parameters to estimate $f_1$

| **Input Parameter** | **Symbol** | **Unit** | **Case Study** |
|---|---|---|---|
| Tower height | $L_T$ | m | 106.3 |
| Tower bottom diameter | $D_t$ | m | 7.7 |
| Tower top diameter | $D_b$ | m | 5 |
| Average tower wall thickness | $t_T$ | m | 0.029 |
| Tower Young's modulus | $E_T$ | GPa | 210 |
| Platform height above mudline | $L_S$ | m | 45 |
| Monopile diameter | $D_P$ | m | 7.5 |
| Monopile embedment length | $L_P$ | m | 35 |
| Monopile wall thickness | $t_P$ | m | 0.082 |
| Monopile Young's modulus | $E_P$ | GPa | 210 |
| Monopile Poisson's ratio | $\nu$ | - | 0.3 |

expressions were derived by modelling the rotor– nacelle assembly (RNA) as a lumped top head mass, $m_{RNA}$, and the tower and the substructure as beams. The tower diameter is assumed to linearly decrease from $D_b$ at the bottom to $D_t$ at the top of the tower. The average diameter is used as the equivalent constant diameter for the idealised tower, $D_T$. The wall thickness $t_T$ is also assumed to be constant along the tower. The soil-foundation interaction is modelled by three springs characterised by lateral $\mathrm{K}_{LL}$, rotational $\mathrm{K}_{RR}$, and cross coupling $\mathrm{K}_{LR}$ stiffness, respectively.

The first natural frequency $f_1$ is obtained by multiplying the fixed base natural frequency $f_{FB}$ by two factors, namely $\mathrm{C}_R$ and $\mathrm{C}_L$, which take into account the flexibility of the foundation:

$$f_1 = C_R\, C_L\, f_{FB} \tag{4}$$

where

$$f_{FB} = \sqrt{\frac{1}{1+(1+\psi)^3\chi-\chi}}\, f_{FB,T} \qquad \chi = \frac{E_T\, I_T}{E_P\, I_P} \qquad \psi = \frac{L_S}{L_T}$$

$\chi$ is the bending stiffness ratio and $\psi$ is the platform-to-tower length ratio. $E_T\, I_T$ is the bending stiffness of the tower, $E_P\, E_p$ is the bending stiffness of the monopile, $L_S$ is the platform height above the seabed (represented by the distance from the mud line to the top of the transition piece), and $L_T$ is the height of the tower. $f_{FB,T}$ is the fixed base natural frequency of the tower:

$$f_{FB,T} = \frac{1}{2\pi}\sqrt{\frac{3\, E_T\, I_T}{L^3\left(m_{RNA}+\frac{33}{140}m'_T\right)}} \tag{5}$$

In the previous equation $m'_T$ is the mass of the tower and $m_{RNA}$ is the mass of the rotor–nacelle assembly. The second moment of area, $I_T$, and the mass, $m'_T$, are calculated considering an average diameter $D_T$ and an average wall thickness $t_T$:

$$I_T = \frac{1}{8}\,\pi\, D_T^3\, t_T \qquad m'_T = \rho_T\, D_T\, \pi\, t_T\, L_T \tag{6}$$

In Equation (4) $C_R$ and $C_L$ are empirical foundation flexibility factors:

$$C_R = 1\, -\, \frac{1}{1+a\left(\eta_R-\frac{\eta_{LR}^2}{\eta_L}\right)} \qquad C_L = 1\, -\, \frac{1}{1+b\left(\eta_L-\frac{\eta_{LR}^2}{\eta_R}\right)} \tag{7}$$

where $a = 0.6$ and $b = 0.5$ are empirical constants obtained as described in [5]. $\eta_L$, $\eta_{LR}$ and $\eta_R$ are the non-dimensional lateral, cross-coupling and rotational stiffness values, respectively:

$$\eta_L = \frac{K_{LL}\, L_T^3}{EI_\eta} \qquad \eta_{LR} = \frac{K_{LR}\, L_T^2}{EI_\eta} \qquad \eta_R = \frac{K_{RR}\, L_T}{EI_\eta} \tag{8}$$

$EI_\eta$ represents the equivalent bending stiffness of the tapered tower:

$$EI_\eta = E_T\, I_t\left(\frac{1}{3}\,\frac{2q^2\,(q-1)^3}{2q^2\,\ln q - 3q^2 + 4q - 1}\right) \tag{9}$$

where $I_t$ is the second moment of area at the top of the tower, and $q = D_b/D_t$. The applicability of Equation 7 is limited to:

$$\eta_R > 1.2\frac{\eta_{LR}^2}{\eta_L} \qquad \eta_L > 1.2\frac{\eta_{LR}^2}{\eta_R} \tag{10}$$

**Available macro elements** The pile head stiffness or macro elements can be estimated by analytical formulations available in literature, as suggested by [5]. The appropriate method for the pile head stiffness estimation depends on the pile behavior (i.e., rigid or slender). Piles can be considered rigid if the pile moves as a whole and does not deflect under operational loads [7]. This study considers both slender and rigid pile macroelement derivations to obtain $K_{LL}$, $K_{LR}$ and $K_{RR}$:

**i. Macro-elements derived for slender piles**

Parabolic inhomogeneous soils $n = 0.5$

Gazetas (1984) [14]:

$$K_{\mathrm{LL}} = 0.79 E_{S0} D_P \left(\frac{E_{eq}}{E_{S0}}\right)^{0.28} \quad K_{\mathrm{LR}} = -0.24 E_{S0} D_P^2 \left(\frac{E_{eq}}{E_{S0}}\right)^{0.53} \quad K_{\mathrm{RR}} = 0.15 E_{S0} D_P^3 \left(\frac{E_{eq}}{E_{S0}}\right)^{0.77}$$

Pender(1993) [23]:

$$K_{\mathrm{LL}} = 0.735 E_{S0} D_P \left(\frac{E_{eq}}{E_{S0}}\right)^{0.33} \quad K_{\mathrm{LR}} = -0.27 E_{S0} D_P^2 \left(\frac{E_{eq}}{E_{S0}}\right)^{0.55} \quad K_{\mathrm{RR}} = 0.1725 E_{S0} D_P^3 \left(\frac{E_{eq}}{E_{S0}}\right)^{0.776}$$

Shadlou and Bhattacharya (2016) [26]:

$$K_{\mathrm{LL}} = \frac{1.02 E_{S0} D_P}{f_{(V_s)}} \left(\frac{E_{eq}}{E_{S0}}\right)^{0.27} \quad K_{\mathrm{LR}} = \frac{-0.29 E_{S0} D_P^2}{f_{(V_s)}} \left(\frac{E_{eq}}{E_{S0}}\right)^{0.52} \quad K_{\mathrm{RR}} = \frac{0.17 E_{S0} D_P^3}{f_{(V_s)}} \left(\frac{E_{eq}}{E_{S0}}\right)^{0.76}$$

**ii. Macro-elements derived for rigid piles**

Homogeneous soils $n = 0$

Poulos and Davis (1980) [24]:

$$K_{\mathrm{LL}} = k_h D_p L_p \qquad K_{\mathrm{LR}} = \frac{-k_h D_p L_p^2}{2} \qquad K_{\mathrm{RR}} = \frac{k_h D_p L_p^3}{3}$$

Shadlou and Bhattacharya (2016) [26]:

$$K_{\mathrm{LL}} = \frac{3.2 E_{S0} D_P}{f_{(V_s)}} \left(\frac{L_P}{D_P}\right)^{0.62} \quad K_{\mathrm{LR}} = \frac{-1.7 E_{S0} D_P^2}{f_{(V_s)}} \left(\frac{L_P}{D_P}\right)^{1.56} \quad K_{\mathrm{RR}} = \frac{1.65 E_{S0} D_P^3}{f_{(V_s)}} \left(\frac{L_P}{D_P}\right)^{2.5}$$

Linear inhomogeneous soils $n = 1$

Poulos and Davis (1980) [24]:

$$K_{\mathrm{LL}} = \frac{1}{2} L_p^2 n_h \qquad K_{\mathrm{LR}} = -\frac{1}{3} L_p^3 n_h \qquad K_{\mathrm{RR}} = \frac{1}{4} L_p^4 n_h$$

Shadlou and Bhattacharya (2016) [26]:

$$K_{\mathrm{LL}} = \frac{2.35 E_{S0} D_P}{f_{(V_s)}} \left(\frac{L_P}{D_P}\right)^{1.53} \quad K_{\mathrm{LR}} = \frac{-1.775 E_{S0} D_P^2}{f_{(V_s)}} \left(\frac{L_P}{D_P}\right)^{2.5} \quad K_{\mathrm{RR}} = \frac{1.58 E_{S0} D_P^3}{f_{(V_s)}} \left(\frac{L_P}{D_P}\right)^{3.45}$$

Parabolic inhomogeneous soils $n = 0.5$

Shadlou and Bhattacharya (2016) [26]:

$$K_{\mathrm{LL}} = \frac{2.66 E_{S0} D_P}{f_{(V_s)}} \left(\frac{L_P}{D_P}\right)^{1.07} \quad K_{\mathrm{LR}} = \frac{-1.8 E_{S0} D_P^2}{f_{(V_s)}} \left(\frac{L_P}{D_P}\right)^{2.0} \quad K_{\mathrm{RR}} = \frac{1.63 E_{S0} D_P^3}{f_{(V_s)}} \left(\frac{L_P}{D_P}\right)^{3.0}$$

Table 4: Stiffness coefficients for the reference soil-foundation system according to existing rigid pile formulations and related natural frequency

| | Homogeneous $n = 0$ | | Linear inhomogeneous $n = 1$ | | Parabolic inhomogeneous $n = 0.5$ |
|---|---|---|---|---|---|
| | [24] | [26] | [24] | [26] | [26] |
| $K_{\mathrm{LL}}$ | 10.50 | 10.39 | 24.50 | 21.94 | 26.41 |
| $K_{\mathrm{LR}}$ | -183.75 | -176.12 | -571.67 | -553.79 | -561.59 |
| $K_{\mathrm{RR}}$ | 4287.50 | 5454.64 | 15006.25 | 15974.32 | 17799.31 |
| $f_1$ | 0.221 | 0.223 | 0.222 | 0.223 | 0.224 |

where

$$E_{eq} = \frac{E_p I_p}{D_p^4 \pi / 64}, \qquad f_{(v_s)} = 1 + |v_s - 0.25| \tag{11}$$

$k_h$ is the modulus of subgrade reaction, $n_h$ is the coefficient of subgrade reaction (the rate of increase of $k_h$ with depth) where $k_h = n_h(z/D_P)$ for sand [7].

$E_{S0}$ is the soil stiffness at $z = -D_P$. In Dunkirk site, the $G_0$ as was given in Equation 3 together with $E = G_0(2(1 + \mu))$ expression is held. A linear profile is fit considering the parabolic inhomogeneous soil stiffness (see Figure 6). Homogeneous soil stiffness is calculated following $[E_P/E_{S0}]_{linear} = 0.24\,[E_P/E_S]^{1.25}_{homogeneous}$ [27] to keep the lateral response in homogeneous and linear soil profiles equal. Calculated parabolic soil stiffness profile- and adopted homogeneous and linear soil stiffness profiles are shown in Figure 6.

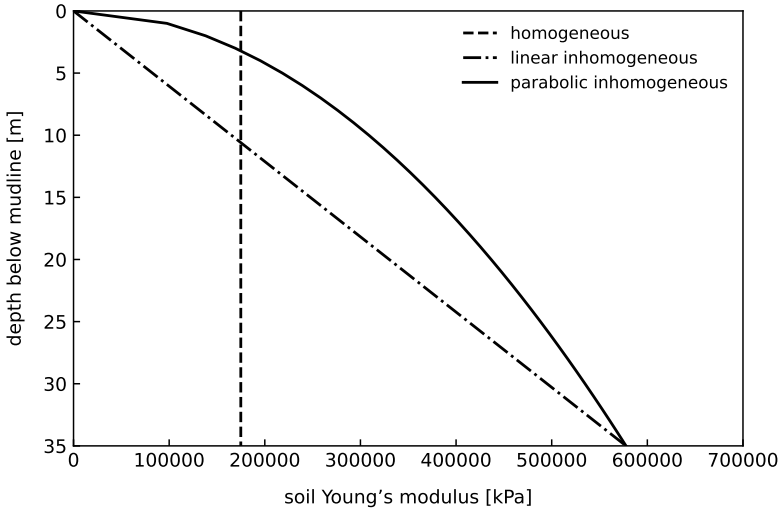


Figure 6: Homogeneous, linear, and parabolic soil stiffness profiles

The stiffness coefficients values adopted for the natural frequency estimation for rigid piles are reported in Table 4 for rigid pile estimation and Table 5 by slender pile estimation. $K_{\mathrm{LL}}$ in GN/m, $K_{\mathrm{LR}}$ in GN, and $K_{\mathrm{RR}}$ in GNm/rad. The natural frequency values for the presented structure-substructure-foundation system, estimated by the described methodology, are reported in the same table in Hz.

Table 5: Stiffness coefficients for the reference soil-foundation system according to existing slender pile formulations and related natural frequency

| | Parabolic inhomogeneous $n = 0.5$ | | |
|---|---|---|---|
| | [14] | [23] | [26] |
| $K_{\mathrm{LL}}$ | 5.13 | 5.89 | 6.05 |
| $K_{\mathrm{LR}}$ | -33.38 | -40.84 | -36.84 |
| $K_{\mathrm{RR}}$ | 428.42 | 505.25 | 443.42 |
| $f_1$ | 0.211 | 0.212 | 0.212 |

For the OWT at hand, the rotational frequency range (1P) is $0.105 - 0.175\,Hz$ and the turbine's blade passing frequency range (3P) is $0.315 - 0.525\,Hz$, as derived by the rotor speeds information provided by [6]. For the widely used soft–stiff design, the target first natural frequency must lie in the range between the maximum of 1P (0.175 Hz) and the minimum of 3P (0.315 Hz). The results reported in Table 4 and 5 show that the formulation for the stiffness coefficients does not affect the frequency estimation and that, according to the applied computation methodology, the design requirement is satisfied.

### 3.2 Displacement and rotation at sea bed level

Following Figure 4, the displacement and rotation of the monopile at the the level of the sea bed, $u_3$ and $u_4$, respectively, can be determined by the following matrix form equation:

$$\begin{bmatrix} F \\ M \end{bmatrix} = \begin{bmatrix} K_{LL} & K_{LR} \\ K_{LR} & K_{RR} \end{bmatrix} \cdot \begin{bmatrix} u_3 \\ u_4 \end{bmatrix} \tag{12}$$

The response of the offshore wind turbine is defined by the lateral displacement, $u_1$, and tilt or rotation, $u_2$. The response at the top is linked to the response at the seabed level by the turbine mass, $m$, and the tower stiffness, $k$.

The mud-line pile displacements for the presented structure-substructure-foundation system, estimated by different methods, are shown in Figure 7. Such displacements are calculated by the soil small-strain stiffness where the system is not expected to go into the nonlinear regime under free vibrations. However, the soil behavior is expected to be nonlinear under such high loads applied to the monopile.

Macroelements obtained for a homogeneous soil profile are deemed to be the most accurate representation of an elastic and homogeneous soil profile under lateral loading within the designated range of design loads. On the other hand, macroelements derived for a parabolic soil profile are considered to be the least precise representation of such a soil profile under lateral loading within the same range of design loads. This discrepancy can be attributed to the linear soil stiffness profile fit illustrated in Figure 6. Additional analyses are required to seek the more accurate macroelements for a parabolic inhomogeneous soil profile at hand.

## 4 3D FINITE ELEMENT MODEL

In order to predict the nonlinear load-deformation response, 3D FE analysis is held via OpenSees [21, 29]. Gmsh [15] is used for the mesh discretization, and gmsh2opensees module [1] is held to extract nodes and elements from gmsh to OpenSees. The axisymmetric finite element model has a computational domain size $L_x = 100\mathrm{m}, L_y = 50\mathrm{m}, L_z = 50\mathrm{m}$ as presented in Figure 8. The soil surrounding the pile, the plugged soil inside the pile, and the pile itself are modelled with standard four-node tetrahedron elements with one Gauss integration

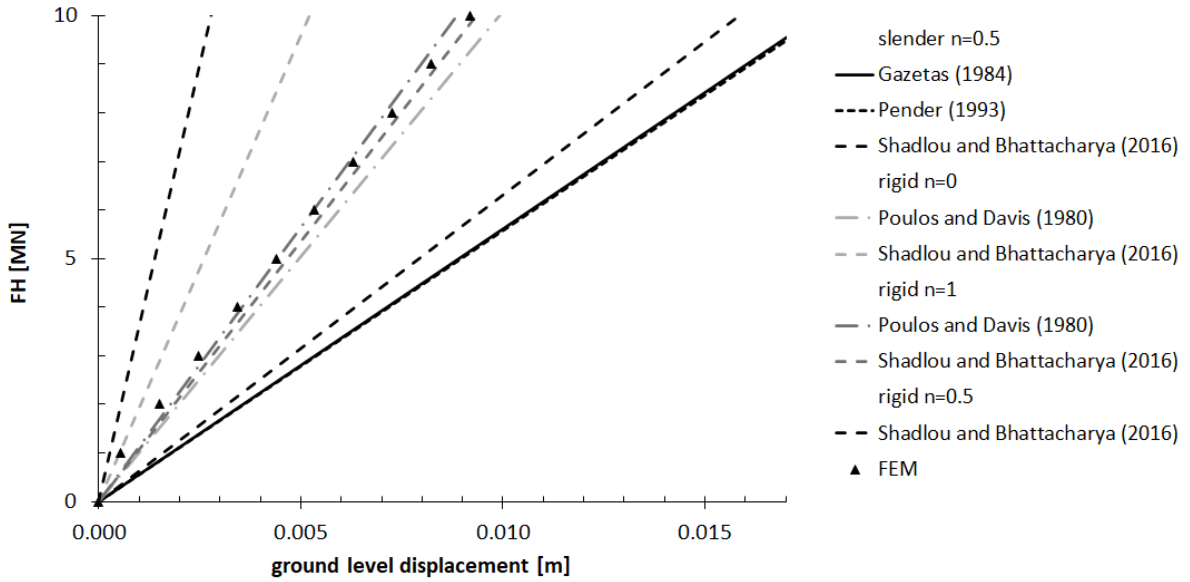


Figure 7: Pile lateral displacement at the mud-line

point (FourNodeTetrahedron elements in OpenSeesPy library). The boundary conditions for the model are a fixed bottom surface, a free upper surface, and no horizontal displacement perpendicular to the lateral surfaces. Axisymmetry surfaces are fixed in y direction 8.

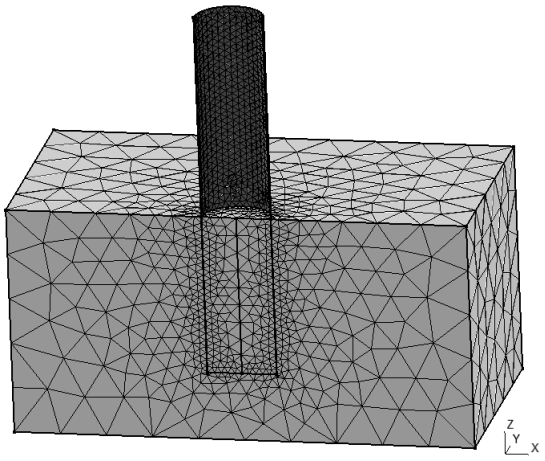


Figure 8: 3D FE model

The material of monopile is elastic (ElasticIsotropic in OpenSeesPy library) with material properties given in Table 3 for embedded and free lengths of $35$ and $45\mathrm{m}$ respectively. The lateral force is applied at the top of the model with an eccentricity, $h$, of $45\mathrm{m}$ in this case. This eccentricity value, $h = L_s$, is consistent with the relevant small-scale testing studies where $h \approx 1.2L_P$ [18, 20]. The material for soil is assumed elastic (ElasticIsotropic in OpenSeesPy library) with the homogeneous profile with Young's modulus given in Table 6. Initial $K_0$ analysis before pile installation is followed by wished-in-place pile condition analysis. Then, the load is applied

in 10 steps in a load-controlled way. The convergence is sought with a relative normal increment within a tolerance of 0.001 similar to [20]. Displacement results are shown in Figure 9 for a maximum load of 10 MN. Displacements are visually scaled 10 times for better representation.

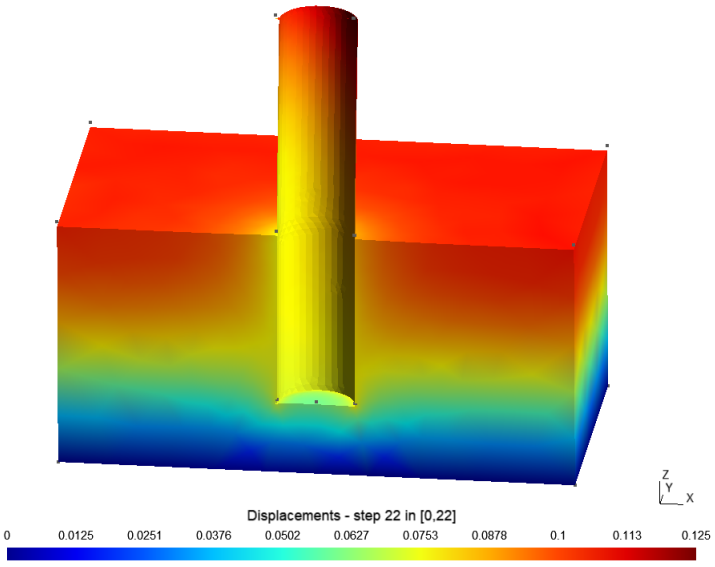


Figure 9: 3D FEA model displacement field [m]

## 5 CONCLUSIONS

This study aims to test a simplified method for predicting the displacement and rotation of OWTs by using readily available macroelements to represent the monopile-foundation system. The main findings of this study can be summarized as follows:

- Although the stiffness coefficients of macroelements diverge for different soil profile configurations (homogeneous, linear inhomogeneous, and parabolic inhomogeneous), they converge to a similar natural frequency (see Figure 5).
- The influence of the macroelement stiffness coefficients on frequency estimation is negligible and between the design limits for the 8 MW OWT designed.
- Macroelements derived for homogeneous soil profile are the most accurate representation of an elastic, homogeneous soil profile under lateral loading within the designated range of design loads.
- Macroelements derived for parabolic soil profile are the least accurate representation of an elastic, homogeneous soil profile under lateral loading within the designated range of design loads. This can be associated with the linear soil stiffness profile shown in Figure 6.

### Acknowledgements

The research proposed in this paper was supported by the *Cyclic soil-structure interaction framework for the foundations of offshore renewable energy structures* project, funded by the "KU Leuven Global PhD Partnerships with The University of Melbourne" scheme (GPUM/21/023).

## References


[1] J. A. Abell. *gmsh2opensees*, 2022. A simple Python module to use Gmsh and OpenSees together in Python.

[2] E. An. Strategy to harness the potential of offshore renewable energy for a climate neutral future. *European Commission: Brussels, Belgium*, 2020.

[3] API. *RP2A-WSD: Recommended Practice for Planning, Designing and Constructing Fixed Offshore Platforms – Working Stress Design*. American Petroleum Institute, 2014.

[4] API. *RP2GEO: Geotechnical and Foundation Design Considerations*. American Petroleum Institute, 2014.

[5] L. Arany, S. Bhattacharya, J. Macdonald, and S. Hogan. Design of monopiles for offshore wind turbines in 10 steps. *Soil Dynamics and Earthquake Engineering*, 92:126–152, 2017.

[6] L. Arany, S. Bhattacharya, J. H. Macdonald, and S. J. Hogan. Closed form solution of eigen frequency of monopile supported offshore wind turbines in deeper waters incorporating stiffness of substructure and ssi. *Soil Dynamics and Earthquake Engineering*, 83:18–32, 2016.

[7] S. Bhattacharya. *Design of foundations for offshore wind turbines*. John Wiley & Sons, 2019.

[8] H. J. Burd, D. M. Taborda, L. Zdravković, C. N. Abadie, B. W. Byrne, G. T. Houlsby, K. G. Gavin, D. J. Igoe, R. J. Jardine, C. M. Martin, et al. Pisa design model for monopiles for offshore wind turbines: application to a marine sand. *Géotechnique*, 70(11):1048–1066, 2020.

[9] B. W. Byrne, G. T. Houlsby, H. J. Burd, K. G. Gavin, D. J. Igoe, R. J. Jardine, C. M. Martin, R. A. McAdam, D. M. Potts, D. M. Taborda, et al. Pisa design model for monopiles for offshore wind turbines: application to a stiff glacial clay till. *Géotechnique*, 70(11):1030–1047, 2020.

[10] B. W. Byrne, R. A. McAdam, H. J. Burd, W. J. Beuckelaers, K. G. Gavin, G. T. Houlsby, D. J. Igoe, R. J. Jardine, C. M. Martin, A. Muir Wood, et al. Monotonic laterally loaded pile testing in a stiff glacial clay till at cowden. *Géotechnique*, 70(11):970–985, 2020.

[11] G. W. E. Council. Global offshore wind report 2022. *Global Wind Energy Council: Brussels, Belgium*, 2022.

[12] C. Desmond, J. Murphy, L. Blonk, and W. Haans. Description of an 8 mw reference wind turbine. *Journal of Physics: Conference Series*, 753:092013, 09 2016.

[13] DNV-GL. Support structures for wind turbines. *Offshore Standard DNVGL-ST-126*, 2016.

[14] G. Gazetas. Seismic response of end-bearing single piles. *International Journal of Soil Dynamics and Earthquake Engineering*, 3(2):82–93, 1984.

[15] C. Geuzaine and J.-F. Remacle. Gmsh: A 3-d finite element mesh generator with built-in pre-and post-processing facilities. *International journal for numerical methods in engineering*, 79(11):1309–1331, 2009.

[16] B. O. Hardin and W. L. Black. Vibration modulus of normally consolidated clay. *Journal of the Soil Mechanics and Foundations Division*, 94(2):353–369, 1968.

[17] G. Houlsby, C. Abadie, W. Beuckelaers, and B. Byrne. A model for nonlinear hysteretic and ratcheting behaviour. *International Journal of Solids and Structures*, 120:67–80, 2017.

[18] C. LeBlanc, G. Houlsby, and B. Byrne. Response of stiff piles in sand to long-term cyclic lateral loading. *Géotechnique*, 60(2):79–90, 2010.

[19] B. Lehane, Z. Liu, E. Bittar, F. Nadim, S. Lacasse, R. Jardine, P. Carotenuto, P. Jeanjean, M. Rattley, K. Gavin, et al. A new'unified'cpt-based axial pile capacity design method for driven piles in sand. In *4th International Symposium on Frontiers in Offshore Geotechnics*, pages 463–477. American Society of Civil Engineers, 2020.

[20] H. Liu, E. Kementzetzidis, J. A. Abell, and F. Pisanò. From cyclic sand ratcheting to tilt accumulation of offshore monopiles: 3d fe modelling using sanisand-ms. *Géotechnique*, 72(9):753–768, 2022.

[21] S. Mazzoni, F. McKenna, M. H. Scott, G. L. Fenves, et al. *OpenSees command language manual*, volume 264. Berkeley, California, United States, 2006.

[22] O. Orakci, N. Huvaj, S. François, and G. Anoyatis. Probability of unsatisfactory performance of monopile foundations for offshore wind turbines considering variations in seabed properties. *Ocean Engineering*, 277:114335, 2023.

[23] M. J. Pender. Aseismic pile foundation design analysis. *Bulletin of the New Zealand National Society for Earthquake Engineering*, 26:49–160, 1993.

[24] H. G. Poulos, E. H. Davis, et al. *Pile foundation analysis and design*, volume 397. Wiley New York, 1980.

[25] L. Ramirez, D. Fraile, and G. Brindley. Offshore wind in europe: Key trends and statistics 2020. 2021.

[26] M. Shadlou and S. Bhattacharya. Dynamic stiffness of monopiles supporting offshore wind turbine generators. *Soil Dynamics and Earthquake Engineering*, 88:15–32, 2016.

[27] K. C. Syngros. *Seismic response of piles and pile-supported bridge piers evaluated through case histories*. City University of New York, 2004.

[28] L. Zdravković, R. J. Jardine, D. M. Taborda, D. Abadias, H. J. Burd, B. W. Byrne, K. G. Gavin, G. T. Houlsby, D. J. Igoe, T. Liu, et al. Ground characterisation for pisa pile testing and analysis. *Géotechnique*, 70(11):945–960, 2020.

[29] M. Zhu. The openseespy library. `https://openseespydoc.readthedocs.io/en/latest/index.html#`, 2019. Accessed: 2021-11-20.

99COMPDYN 2023
9th ECCOMAS Thematic Conference on
Computational Methods in Structural Dynamics and Earthquake Engineering
M. Papadrakakis, M. Fragiadakis (eds.)
Athens, Greece, 12-14 June 2023

# DIMENSIONLESS FACTORS GOVERNING THE LATERAL DISCONNECTION EFFECTIVENESS

**Somma Fausto**[1], **Flora Alessandro**[1]

[1] University of Naples Federico II
Via Claudio 21, 80125 Naples, Italy
e-mail: fausto.somma@unina.it

## Abstract

*The lateral disconnection technique consists in removing the soil on the sides of the shallow foundations with considerable embedment. In this way, the foundation-soil contact will be through the foundation base only. The reduction of the translational and rotational soil-foundation stiffness, generated by the lateral disconnection, lengthens the fundamental period of the soil-structure system. Depending on the site-specific hazard, this may result in a significant reduction of the seismic actions on the structure itself. The paper shows the preliminary results of a parametric study aimed at identifying the main dimensionless groups governing the effectiveness of the lateral disconnection intervention in lengthening the fundamental period of the soil-structure system.*

**Keywords:** Geotechnical seismic isolation; Lateral Disconnection; Soil Structure Interaction.

## 1 INTRODUCTION

Geotechnical seismic isolation (named GSI) transposes the effects of traditional seismic isolation into the ground. Yegian & Catan (2004) demonstrated numerically and experimentally that the insertion of a sliding surface (*i.e*. a special geotextile), characterized by a low friction angle placed immediately below the foundations, would be able to dissipate the energy of earthquakes. Similarly, Kirtas et al. (2009) studied numerically the effect of creating vertical and horizontal, rigid or soft, barriers in the foundation soil. Brennan (2013) and Nappa (2016) validated the idea of seismically isolating a building by placing soft barriers in the ground through various centrifuge tests. Further aspects of seismic isolation of existing building through soft barriers such as advanced dynamic characterisation of soft mixtures, simplified modelling procedures and numerical analysis results can be found in Somma *et al.* 2023. On the contrary, sand-rubber mixtures (named rubber-soil), which can be placed with relatively easy as foundation soil for a new building, have also been particularly investigated in seismic loads mitigation (Pitilakis, 2015). All the procedures outlined have as a common strategy the increase of the natural period of vibration and/or the damping of the soil-structure system. However, there are still numerous uncertainties and difficulties linked to the technological installation procedures (especially for existing buildings), as well as a certain diffidence in operating only and exclusively through the modification of the foundation soil.

A technologically simple and intuitive way to lengthen the fundamental period of the soil-structure system is the lateral disconnection of the shallow foundations from the adjacent soil. In fact, the creation of a small gap, laterally the foundations side, modifies the horizontal and rotational stiffness of the soil-foundation, thus contributing to increase the fundamental period of the soil-structure system itself (Somma *et al.* 2021b). In some contexts of seismic hazard, and for foundations with a considerable embedment in the soil (*i.e.* masonry buildings), this technique determines a significant reduction of seismic actions and, therefore, an excellent low-cost seismic improvement technique (Somma *et al.* 2021a, Somma *et al.* 2022). However, in other cases, lateral disconnection has been shown to provide little benefit compared to classical structural retrofitting (Somma *et al.* 2023). Using dimensional analysis, this memory identifies, through FEM analysis, the parameters that most influence the period elongation produced by the lateral disconnection in order to determine the circumstances where this intervention could generate significant seismic benefits.

## 2 NUMERICAL ANALYSIS

The numerical analyses, aimed at identifying the natural period of vibration with soil-structure interaction, are conducted using the software Plaxis 2D (Brinkgreve, 2013). Fig. 1 generically shows the FEM model used.

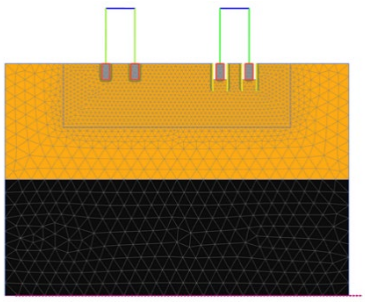

Fig. 1. Finite element model used for the numerical analysis

It is possible to see that the two structural models, with and without lateral disconnection, were studied simultaneously within each analysis. In particular the structure with lateral disconnection will be named *GSI* structure while the one without lateral disconnection *NO GSI* structure. The structural model used is a one-storey, one-bay building with discontinuous shallow foundations. The gap generated by the lateral disconnection technique is supported by the presence of four small rigid cantilever walls, modelled as plate elements, whose only task is to support the lateral load of soil. The relative distance between the two structures and between the structures and the boundaries of the model, ensures that there are no interferences (Jiang & Yan, 1998). The columns and the crossbeams of the structures are modelled as plate elements. In particular, the crossbeams are characterised by a very high normal stiffness, *EA,* and flexural stiffness*, EI,* values, equal to, respectively, $10^8$kN/m and $10^9$ kNm$^2$/m (where *E* is the Young modulus, *I* the inertia and A is the area of the plate in plane strain condition). The high flexural and normal stiffness of the crossbeams generates the so called "*Grinter frame*" effect. The flexural stiffness value of the columns is chosen, once the structural mass is selected, to generate the desired structural period in fixed base condition. The soil is modelled as homogeneous visco-elastic material model. Since the depth of the bedrock is one of the parameters influencing the dynamic soil-foundation stiffness coefficients (Gazetas 1991), it was explicitly modelled in the numerical model. The water table is not present.

The numerical procedure to calculate the period elongation, generated by the soil deformability on the two analysed structures, consists of several phases:

1. In a static phase, application of a horizontal force on the roof of the two structures.
2. In a dynamic phase, deactivation of the static force, and computation of the free oscillations decay generated.
3. From the free oscillations, using the Fourier transform, it is possible to know the predominant period of the structure with soil structure interaction and, therefore, to know the period elongation with respect to the fixed base case ($\frac{\tilde{T}}{T_s}$).
4. Finally, it is possible to evaluate the relative period elongation between the two systems, with and without intervention, as: $\Delta = \frac{\tilde{T}_{disc} - \tilde{T}_{conn}}{\tilde{T}_{conn}}$; this value can be understood as an efficiency measure of the lateral disconnection in the elongations of the soil-structure natural period.

As the free decay oscillations are produced by a static force applied within the mesh, it was preferred to use perfectly absorbent viscous contours on lateral boundaries (Lysmer and Kuhlemeyer, 1969).

## 2.1 Application of dimensional analysis on period elongation

In order to delineate the dimensionless parameters governing the period lengthening produced by lateral disconnection, it is necessary to identify all the independent variables involved, $q_i$, as well as their physical dimensions.

Table 1. Independent variables involved in the period elongation generated by the soil deformability

| Parameters | | Description of the variable |
|---|---|---|
| Variable | Dimension | |
| $T_s$ | T | Fixed base period of the structure |

| | | |
|---|---|---|
| $H_s$ | L | Height of mass centroid in the first modal form for the fixed base structure |
| $B$ | L | Width of single strip foundation |
| $W$ | L | Base width of the building |
| $D$ | L | Embedment of the foundation |
| $d$ | L | Effective soil-foundation contact |
| $m_s$ | $ML^{-1}$ | Participating mass of the first modal form in plane cond. |
| $v_f$ | - | Poisson coefficient of foundation material |
| $p_t$ | $ML^{-3}$ | Mass density of soil |
| $p_f$ | $ML^{-3}$ | Mass density of foundation |
| $v_t$ | - | Possion coefficient of soil material |
| $V_t$ | $LT^{-1}$ | Shear waves velocity in the soil material |
| $V_f$ | $LT^{-1}$ | Shear waves velocity of the foundation material |
| $H_b$ | L | Depth of the bedrock |

The fundamental period of the structure, considering the soil-structure interaction ($\widetilde{T}$), can therefore be expressed as a function of the identified variables:

$$\widetilde{T} = f(T_s, H_s, B, W, D, d, m_s, v_f, p_t, p_f, v_t, V_t, V_f, H_b) \quad (1)$$

The number of variables identified is 14, while the number of independent units is 3 (mass, time, length). Therefore, it would be possible to identify 14-3=11 dimensionless groups (Buckingham's Theorem). It is possible to identify the following dimensionless groups, using $V_t$, $W$, $p_t$ as the dimensionally independent variables (*dimensional base*). It should be remembered that this choice is arbitrary and other bases can be chosen to obtain other significant dimensionless groups. A characteristic value for the resonance period of the structure is obviously given by the fixed base period $T_s$, so $U = \frac{\widetilde{T}}{T_s}$ is a dimensionless number representing the period elongation compared to the fixed base case. The dimensionless period lengthening, can, therefore, be expressed as a function of the following dimensionless parameters:

$$\frac{\widetilde{T}}{T_s} = f\left(\frac{T_s V_t}{W}, \frac{H_s}{W}, \frac{B}{W}, \frac{D}{W}, \frac{d}{W}, \frac{m_s}{p_t W^2}, \frac{p_f}{p_t}, v_f, v_t, \frac{V_f}{V_t}, \frac{H_b}{W}\right) \quad (2)$$

$$U = F(\Pi_1, \Pi_2, \Pi_3, \Pi_4, \Pi_5, \Pi_6, \Pi_7, \Pi_8, \Pi_9, \Pi_{10}, \Pi_{11}) \quad (3)$$

It is possible to manipulate these dimensionless groups, obtaining other dimensionless groups produced from the originals (for example, $\Pi_1' = \frac{\Pi_2}{\Pi_1} = \frac{H_s}{V_s T_s}$). The following dimensionless groups can be found:

$$\frac{\widetilde{T}}{T_s} = f\left(\frac{H_s}{V_t T_s}, \frac{H_s}{W}, \frac{B}{W}, \frac{D}{B}, \frac{d}{D}, \frac{m_s}{p_t W H_s}, \frac{p_f}{p_t}, v_f, v_t, \frac{V_f}{V_t}, \frac{H_b}{B}\right) \quad (4)$$

The dimensionless period lengthening is therefore a function of 11 dimensionless parameters. It is obvious that an engineering problem governed by 11 dimensionless parameters is unmanageable and, for this reason, some of them will be neglected in the following sensitivity analysis. For example, it is possible to neglect small variations in the Poisson's modulus for the soil considered (~ 0.2-0.3) and for the concrete material of the foundation (~ 0.2). Assuming infinitely stiff foundations, it is possible to neglect the parameter $\Pi_{10}$ since it is much higher than unity in every possible scenario. It is possible to neglect the parameter $\Pi_{11}$ because, except for particular cases of outcropping bedrock, this ratio is always higher than 10, as well as it is possible to neglect the variations of the parameter $\Pi_7$ because it rarely assumes values that are significantly different from unity. It is also possible to note that some of these parameters (*i.e.* $\Pi_1$, $\Pi_6$) coincide with those found by Veletsos (1974) and Bielak (1975) (respectively, structure to soil relative stiffness and structure to soil relative mass ratio).

## 2.2. Illustrative example and demonstration of physical similarity

In order to demonstrate the effectiveness of the dimensionless groups found, it is possible to carry out parametrically similar numerical analyses. In particular, the following vector of dimensionless parameters has been fixed:

$$\pi = (0.15, 0.85, 0.15, 1, 1, 0.24, 1.10, 0.2, 0.25, 20, 20) \quad (5)$$

Eight different numerical models with the same dimensionless parameters were therefore produced (Table 2).

Table 2. Numerical models created with identical dimensionless parameters but different physical dimensions.

| Variables | | Numerical models produced | | | | | | | |
|---|---|---|---|---|---|---|---|---|---|
| Name | Unit | I | II | III | IV | V | VI | VII | VIII |
| $T_b$ | [s] | 0.3 | 0.5 | 0.8 | 0.8 | 0.3 | 0.5 | 0.3 | 0.8 |
| $H_s$ | [m] | 5.5 | 5.5 | 5.5 | 11 | 8.25 | 13.75 | 13.75 | 13.75 |
| $B$ | [m] | 1 | 1 | 1 | 2 | 1.5 | 2.5 | 2.5 | 2.5 |
| $W$ | [m] | 6.5 | 6.5 | 6.5 | 13 | 9.75 | 16.25 | 16.25 | 16.25 |
| $D$ | [m] | 1 | 1 | 1 | 2 | 1.5 | 2.5 | 2.5 | 2.5 |
| $d$ | [m] | 1 | 1 | 1 | 2 | 1.5 | 2.5 | 2.5 | 2.5 |
| $m_s$ | [Kg] | 16819 | 33639 | 61671 | 123343 | 25229 | 84097 | 42048 | 154179 |
| $v_f$ | - | 0.2 | 0.2 | 0.2 | 0.2 | 0.2 | 0.2 | 0.2 | 0.2 |
| $p_t$ | [Kg/m$^3$] | 1911 | 3822 | 7008 | 3504 | 1274 | 1529 | 764 | 2803 |
| $p_f$ | [Kg/m$^3$] | 2102 | 4204 | 7708 | 3854 | 1401 | 1681 | 840 | 3083 |
| $v_t$ | - | 0.25 | 0.25 | 0.25 | 0.25 | 0.25 | 0.25 | 0.25 | 0.25 |

| | | | | | | | | | |
|---|---|---|---|---|---|---|---|---|---|
| $V_t$ | [m/s] | 122 | 73 | 44 | 91 | 183 | 183 | 305 | 114 |
| $V_f$ | [m/s] | 2444 | 1466 | 916 | 1401 | 3666 | 3666 | 6111 | 2291 |
| $H_b$ | [m] | 20 | 20 | 20 | 40 | 30 | 50 | 50 | 50 |

By applying the procedure described in Section 2, Figure 2 shows the period lengthening related to the fixed base. Since the period elongation with respect to the fixed base case are practically constant in the 8 analyses conducted, it is possible to state that also the period variations between *GSI* and *NO GSI* structure (called Δ, see section 2) is constant too. It is possible to conclude that the selected dimensionless parameters control the physical process analysed. It is important to underline that small discrepancies may be due to numerical aspects such as the axial stiffness of the columns which has not been included in the dimensionless parameters space.

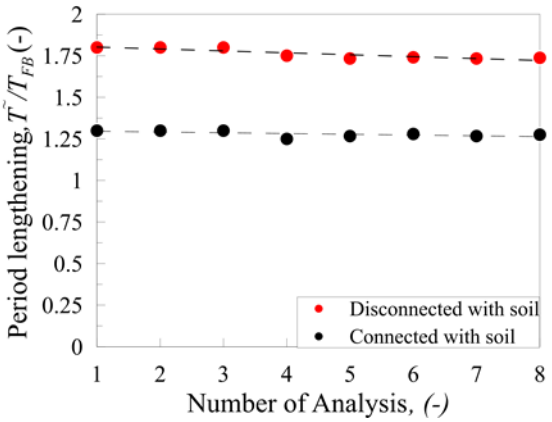


Fig. 2. Similar period lengthening, in different numerical analysis, using the same a-dimensional group

## 2.3. Sensitivity analysis

The previous paragraph has shown that the period variations between the two structures, with and without lateral disconnection, are the same as long as the dimensionless parameters are constant, confirming that the Buckingham's Theorem was correctly applied. In order to identify the most significant dimensionless parameters, it is possible to vary each dimensionless parameter individually, leaving the value of the others fixed (Fig. 3). In particular, each individual dimensionless parameter was varied up to a maximum of a 100%, increasing or decreasing, their initial value (see equation 5 for the initial values). The graphs show the period variations between *NO GSI* and *GSI* structure (called Δ) for two different types of lateral disconnection interventions. Indeed, in *"both sides"* case, the disconnection occurs on both sides of the foundations (*i.e.* inside and outside the structure itself, on the left and on the right of each strip foundation). In the *"externally only"* case, on the other hand, the disconnection was generated only on the external side of the structure leaving the ground between the two adjacent foundations untouched. This solution has been introduced because it obviously represents a considerable technological simplification.

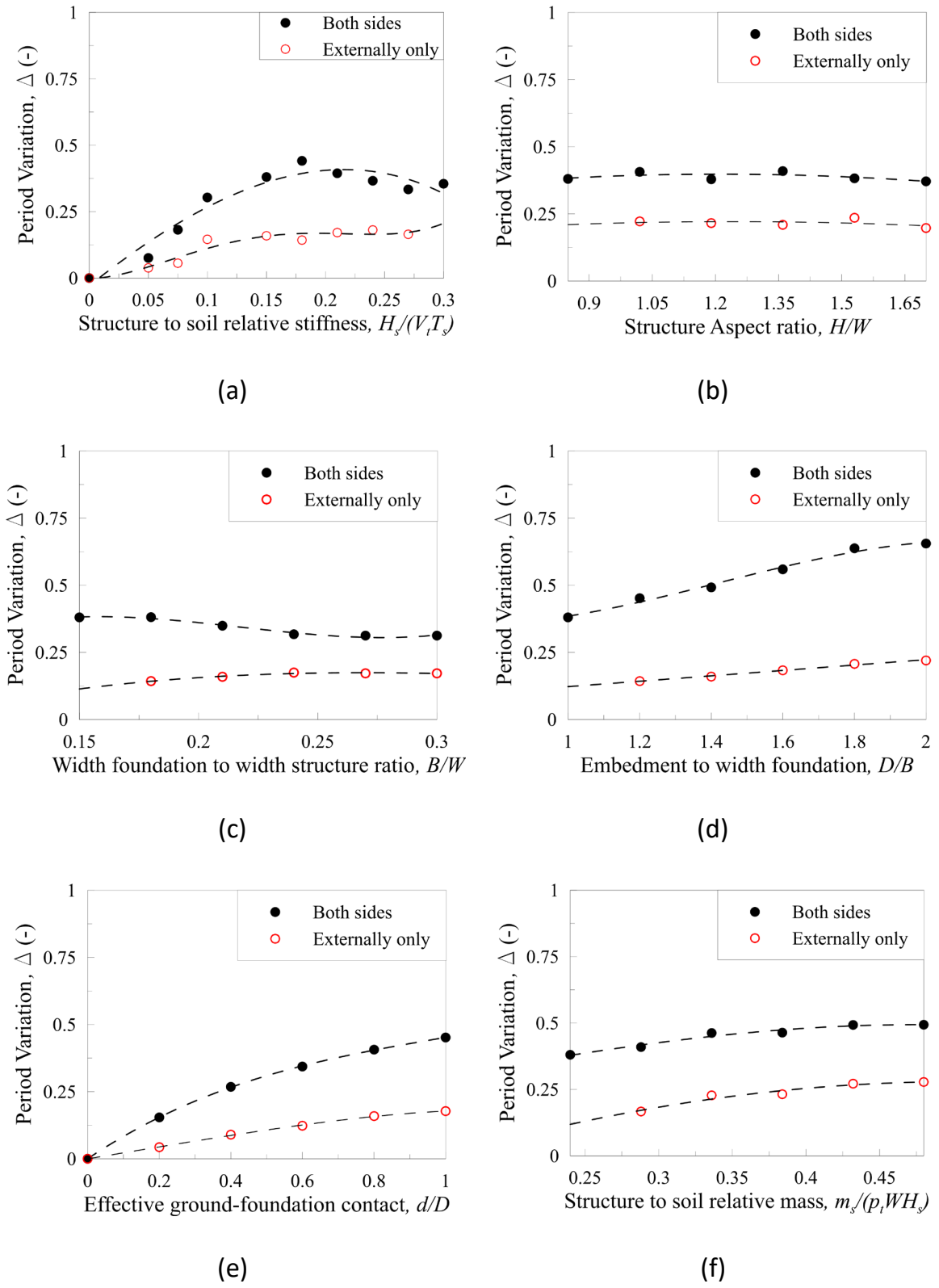


Fig. 3. Sensitivity analysis obtained by increasing or decreasing the dimensionless parameters up to a maximum of 100% of their initial value; (a) structure to soil stiffness ratio, (b) structure aspect ratio (c) width foundation to width structure ratio (d) Embedment to width foundation (e) Effective ground-foundation contact (f) Structure to soil relative mass

The graphs show that the *"externally only"* lateral disconnection solution, although easier to apply technologically, is less efficient than the *"both sides"* case. For all dimensionless parameters, it is possible to state that the efficiency, $\Delta$, is almost halved in the *"externally only"* solution.

Some dimensionless parameters seem to have a relatively small influence on the period variations between the connected and disconnected structure. In particular, for the parameters $\Pi_2$, $\Pi_3$ the period variation trend seems to be almost independent from the variation of the dimensionless parameter considered (*i.e.* horizontal tangent). As far as the parameter $\Pi_6$ is concerned, *i.e.* the ratio between the mass of the structure and the mass of participating soil involved, a slight increase in the period variation can be observed as this parameter increases. This could indicate a greater efficiency of the technique for particularly massive structures related to the participating mass of soil.

The modification of the relative structure to soil stiffness (Fig. 3a), in the engineering-significant range of 0.05-0.2 (NIST, 2012), seems to significantly influence the period elongation between the two structures. In particular, the more rigid the structure with respect to the soil, the more effective the disconnection. This is an interesting result since it is possible to understand that the applicability of this intervention, in contexts where the foundation soil is particularly rigid with respect to the structure, may be useless. This happens because the high stiffness of the soil below the foundations inhibits the global rotations of the structure more significantly than the lateral soil. For this reason, the two structures tend to have approximately the same period with and without intervention. Lateral disconnection, therefore, may give greater benefits, in terms of period extension, for rigid structures on deformable soils.

A further significant dimensionless parameter is the *D/B* ratio of the foundations. It is clear that this parameter affects a lot the effectiveness of lateral disconnection. Very high values of this ratio indicate foundations with considerable embedment for which the removal of adjacent soil can have a significant effect. For values less than unity the relative period elongations are reduced and the lateral disconnection technique loses its effectiveness.

The effective lateral contact of the soil with respect to the total embedment (*d/D*) of the foundation is also particularly important. In fact, if for the *NO GSI* structure the effective contact is particularly low, the relative period variations, $\Delta$, is reduced. In case of *d/D*=0, indeed, there is zero lateral effective contact between the foundation and the ground and no period variations, $\Delta$, will be generated by the lateral disconnection. In general, the effective contact is never equal to unity (perfect contact *d/D*=1) but tends to be reduced by soil non linearities such as gapping (Gazetas, 1991).

## 3 CONCLUSIONS

The memory summarised the results of a preliminar parametric study conducted using significant dimensionless groups. The purpose of the parametric study was to understand the importance of some dimensionless groups on the effectiveness of the lateral disconnection technique. The increase of the relative structure-to-soil stiffness as well as, to a lesser extent, the relative structure-to-soil mass ratio positively influence the effectiveness of the lateral disconnection technique. The *D/B* ratio plays a fundamental role in the effectiveness of this technique. Especially for existing masonry buildings, for which traditional construction technique included to thicken the load-bearing masonry walls and to sink it several metres into the ground,

this ratio can be considerably high and lateral disconnection can represent an economic and alternative seismic improvement technique.

## References


- Bielak J., (1975). Dynamic behaviour of structures with embedded foundations. Earthquake Engineering & Structural Dynamics, 3(3), 259–274.
- Brennan A.J., Klar A., Madabhushi S.P.G. (2013). "Mitigation of seismic accelerations by soft caissons". International Journal of Geotechnical Earthquake Engineering, 4, 1-17
- Brinkgreve, R. B. J., Engin, E., Swolfs, W. M. (2013). PLAXIS 3D. Reference Manual.
- Gazetas, G. (1991). Formulas and charts for impedances of surface and embedded foundations. J Geotech Eng, ASCE. 117(9):1363–81.
- Jiang, X., Yan, Z. (1998). Earthquake response analysis of building-foundation-building interaction system. Journal of vibration engineering, 11(1).
- Kirtas E., Rovithis E., Pitilakis K. (2009). Subsoil Interventions Effect on Structural Seismic Response. Part I: Validation of Numerical Simulations. Journal of Earthquake Engineering, 13(2):155-169.
- Kuhlemeyer, R.L., Lysmer, J. (1973). Finite Element Method Accuracy for Wave Propagation Problems. Journal of Soil Mechanics & Foundations. Div. ASCE. 99(5):421–427.
- Nappa V., Bilotta E., Flora A., Madabhushi S.P.G. (2016). Centrifuge modelling of the seismic performance of soft buried barriers. Bulletin of Earthquake Engineering, 14(10): 2881–2901.
- NIST. (2012). Soil-structure interaction for building structures. National Institute of Standards and Technology Report No. NIST GCR 12-917-21. Gaithersburg, MD.
- Pitilakis K., Karapetrou S., Tsagdi K. (2015). Numerical investigation of the seismic response of RC buildings on soil replaced with rubber–sand mixtures. Soil Dynam Earthq Eng., 79:237–52.
- Somma F., Bilotta E., Flora A., Viggiani G.M. (2021b). Centrifuge modelling of shallow foundations lateral disconnection to reduce seismic vulnerability. Journal of Geotechnical and Geoenvironmental Engineering. doi: 10.1061/(ASCE)GT.1943-5606.0002746
- Somma, F., Bilotta, E., Flora, A., Viggiani, G.M. (2022). "Lateral disconnection of foundations: a respectful seismic isolation of historic building". 3rd international symposium on geotechnical engineering for the preservation of monuments and historic sites. Naples, Italy, 22-24 June 2022.
- Somma, F., Flora, A. (2023). SAP-sand mixtures as a geotechnical seismic isolation technology: from the dynamic characterization to a simple analytical design approach. Bull Earthquake Eng. https://doi.org/10.1007/s10518-023-01660-8
- Somma, F., Flora, A., Bilotta, E., Viggiani, G.M. (2021a). "Numerical analysis on shallow foundations lateral disconnection". 8th ECCOMAS Thematic Conference on Computational Methods in Structural Dynamics and Earthquake Engineering. Athens, Greece, 27–30 June 2021.
- Somma, F., Lignola, G., Ramaglia, G., De Sanctis, L., Iovino, M., Oztoprak, S., Flora, A. (2023). An interdisciplinary investigation of the seismic performance of a historic tower in Istanbul during the 1999 Kocaeli earthquake. Bull Earthquake Eng (2023). https://doi.org/10.1007/s10518-023-01638-6
- Veletsos A., Meek J. (1974). Dynamic behaviour of building-foundation systems. Earthquake Engineering & Structural Dynamics, 3(2), 121–138.
- Yegian M.K, Catan M. (2004). Soil isolation for seismic protection using a smooth synthetic liner. J Geotech Geoenviron Eng, 130:1131–1139.

COMPDYN 2023
9th ECCOMAS Thematic Conference on
Computational Methods in Structural Dynamics and Earthquake Engineering
M. Papadrakakis, M. Fragiadakis (eds.)
Athens, Greece, 12-14 June 2023

# CONCRETING UNDER TRAFFIC: IN-DEPTH INVESTIGATION OF THE EFFECTS OF VIBRATIONS ON YOUNG CONCRETE

**Christian Gasser[1], Soufiane El Yassini[1], Alfred Lechner[1], Lukas Hausner[2], and Alois Vorwagner[1]**

[1] Austrian Institute of Technology (AIT)
Giefinggasse 4, 1210 Vienna, Austria
e-mail: Christian.Gasser@ait.ac.at, Soufiane.El-Yassini@ait.ac.at, Alfred.Lechner@ait.ac.at, Alois.Vorwagner@ait.ac.at

[2] Smart Minerals GmbH
Franz-Grill-Straße 9, 1030 Vienna, Austria
e-mail: Hausner@smartminerals.at

## Abstract

*In an ongoing research project, the effects of vibrations on young (reinforced) concrete are being investigated. Such a situation is often encountered at repair and widening works on bridges at the time when parts of newly cast concrete are connected to the existing bridge under running traffic. In the research project, a systematic approach is pursued to investigate the influence of different kinds of vibrations (harmonic, transient/"real"; intermittent, continuous), durations of vibration, concrete mixtures, and construction types (plain concrete, reinforced concrete, direct contact of concrete surfaces). The quality of the shaken test specimens (and respective reference specimens) is determined in terms of strength, density, elastic modulus, cracks, homogeneity, and permeability. Preliminary results indicate that plain concrete does not suffer deteriorations of strength or stiffness when excited by traffic vibrations, in general. However, the bond between concrete and rebar may not evolve properly.*

**Keywords:** Vibrations, Traffic-induced Vibrations, Structural Dynamics, Concrete Hardening, Young Concrete, Multiscale

## 1 INTRODUCTION

Regarding vibrations, extensive research has been conducted as far as the effects on both people and (historical) buildings are concerned. On the other side, investigations regarding harmful effects of vibrations on young concrete are very limited [3][4][5][6]. However, transport authorities, construction companies and engineering firms are aware that traffic induced vibrations might afflict permanent damage to concrete structures when the vibrations take place in a certain time range after concrete casting. Regarding this "critical time range", different values can be found in the literature ranging from 3 to 14 hours [8][7][1]. Obviously, this depends on the specific hardening process of the concrete used, which is a function of its composition, the temperature, and other parameters. Therefore, bridges and viaducts often need to be closed for traffic in case that they have direct contact to new components made of concrete, see Figure 1. Such a situation occurs frequently, e.g., when bridges and viaducts are reconstructed, extended, or partially restored.

The aim of the presented (ongoing) project is to investigate the influence of vibrations on young concrete in a very comprehensive and realistic manner. Experiments with plain concrete as well as with reinforced concrete are being performed. Different concrete mixtures are used. Moreover, realistic situations of contact between existing vibrating concrete plates and newly cast concrete parts are studied. A wide range of harmonic vibrations as well as traffic induced vibrations with different intensities and frequencies are being applied. Following the vibration procedure, a variety of material parameters are determined on the test specimens as well as on reference specimens: compression strength, tensile strength, elastic modulus, mass density. Laboratory tests are performed to identify flaws, cracks, and any changes in the concrete texture. The bond between concrete and reinforcement is investigated by means of pull-out tests. Experimental investigations are accompanied by analytical and numerical calculations. Results are verified by finite element analyses, in some cases also adopting multiscale approaches.

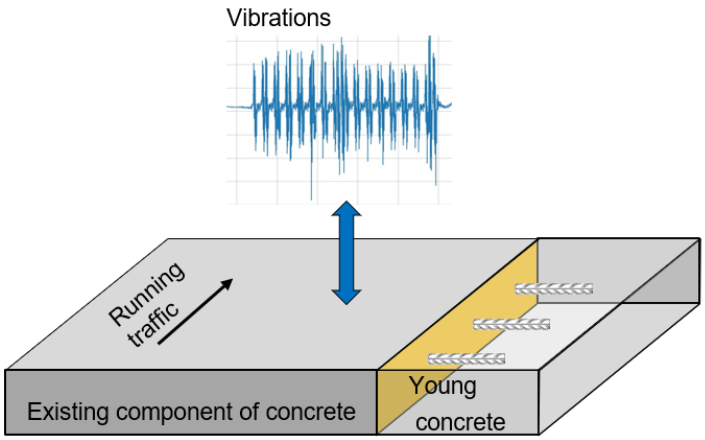


Figure 1: General illustration of the problem: young concrete adjacent to vibrating existent structure

## 2 TEST PROGRAM

To study the causes and mechanisms of damages, a test program consisting of three series was set up (see Figure 2):

- Series 1: Specimens of plain concrete (in general 150 mm cubes) are excited by a vibration generator, see Figure 3. In this series, the aim is to study the effects of vibrations on the concrete itself. Possible types of damage are especially cracks and segregation of the constituents.

- Series 2: In this series, the test specimens are moulds filled with concrete punched by a rebar through the middle. The test specimens are immobile, while the end of the rebar is excited by the shaker, see Figure 4. This test situation imitates a real situation where a newly cast part is at rest on a scaffold while it is connected to a vibrating existing bridge via rebars. In this series, the effects of vibrations are studied by means of pull-out tests conducted on the 28 days old concrete. Here, the relationship between applied tensile force and slip of the rebar is of interest. Thus, the bond behaviour can be inferred.
- Series 3: This test setup is the one most similar to most real-world problems. A plate of hardened concrete is placed on a platform which is excited by two small shakers. Another plate of young concrete is cast on a stationary pedestal. The two plates are in direct contact to one-another and are furthermore connected via rebars. Figure 5 shows the cross-section of the experimental setup. In this test series, it is expected that the vibrations will impair the bond between the two concrete plates as well as the bond between the rebars and the newly cast concrete. This will be studied by means of bending tests conducted on beams cut out from the shaken concrete slabs.

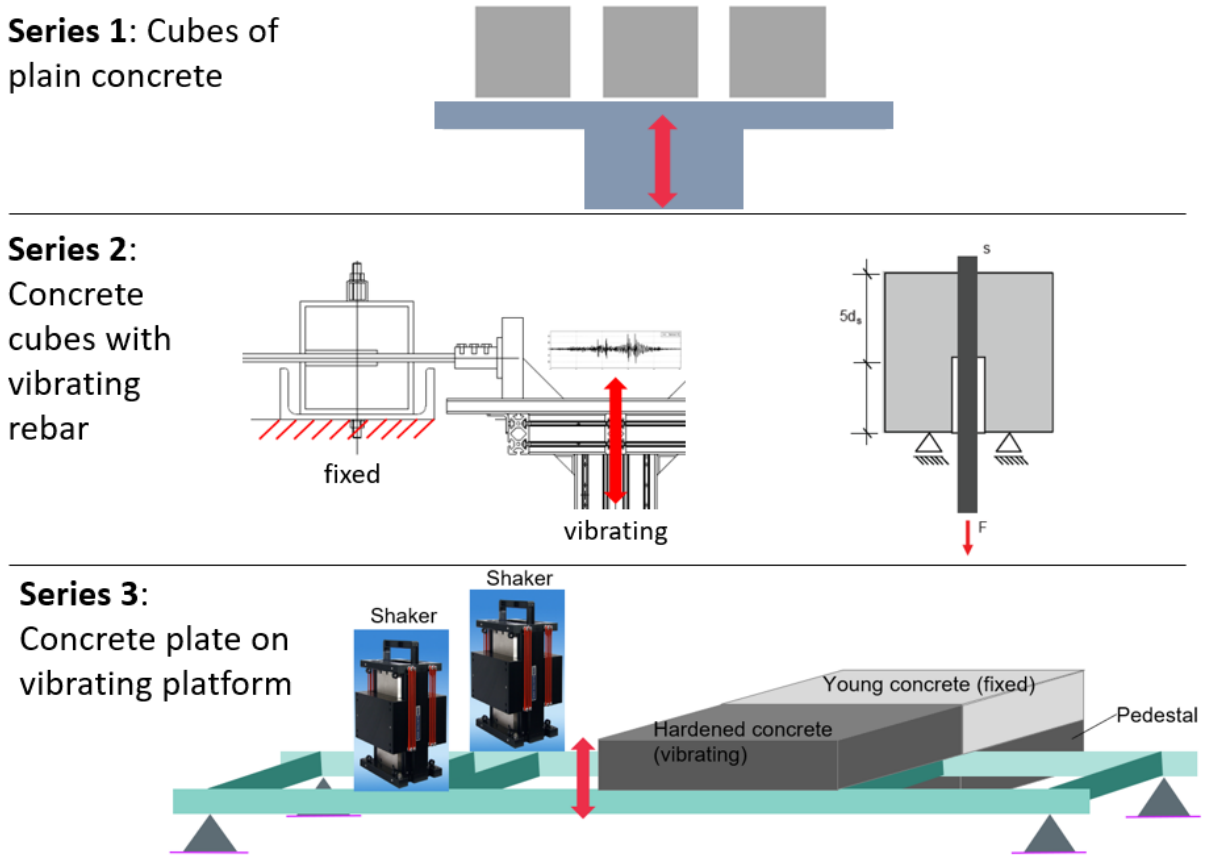


Figure 2: The three series of the test program

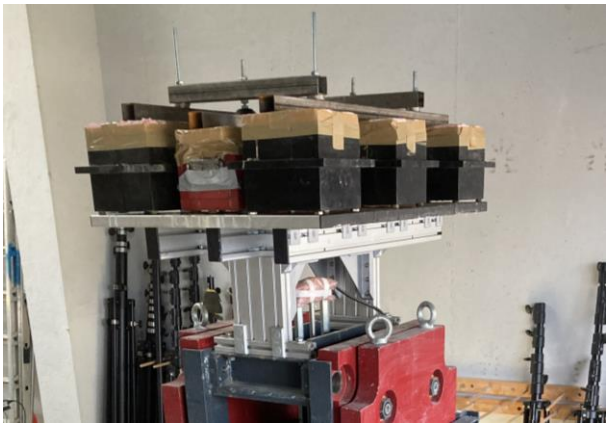

Figure 3: Specimens of plain concrete mounted on vibration generator (Series 1)

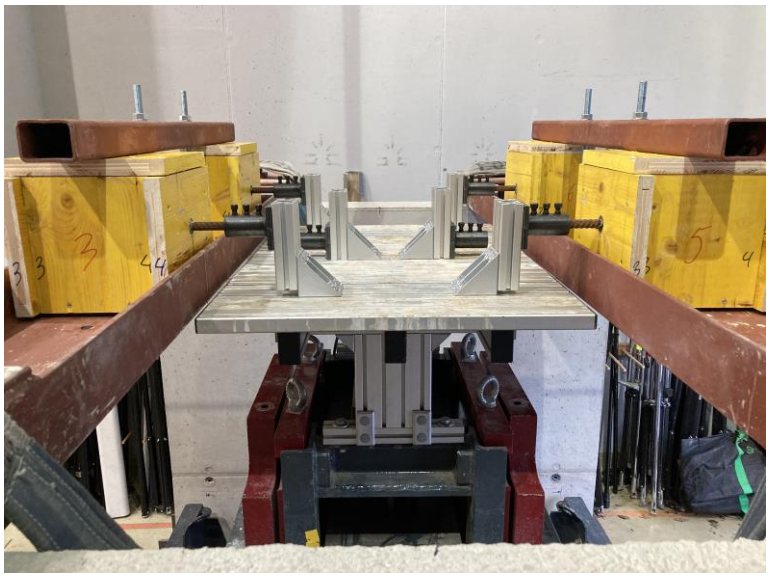

Figure 4: Fixed specimens of concrete with rebar which is subjected to vibrations (Series 2)

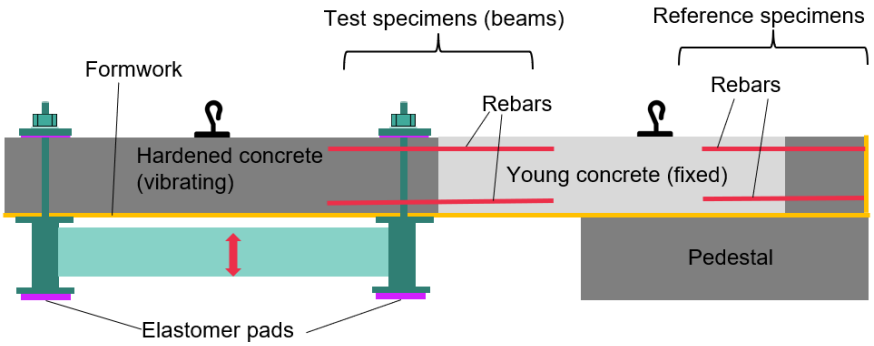


Figure 5: Cross-section of Series 3 setup

A summary of the parameters of the test setup is listed in Table 1. Note that not all the values are combined with all the other values of the parameters. The choice of combinations of parameter values is being done based on realistic situations, expected meaningfulness and outcomes of previous experiments.

<table>
<tr><td rowspan="6">Type of excitation</td><td rowspan="3">harmonic</td><td>5 Hz</td><td rowspan="3">Intermittent: excitation of 20 s each 10 min</td></tr>
<tr><td>20 Hz</td></tr>
<tr><td>35 Hz</td></tr>
<tr><td rowspan="3">transient</td><td>Train</td><td>Intermittent: 1 train each 20 min</td></tr>
<tr><td>Truck</td><td>Intermittent: 1 truck each 3 min</td></tr>
<tr><td>Motorcars</td><td>Continuous</td></tr>
<tr><td colspan="2" rowspan="7">Excitation peak velocity</td><td colspan="2">5 mm/s</td></tr>
<tr><td colspan="2">10 mm/s</td></tr>
<tr><td colspan="2">15 mm/s</td></tr>
<tr><td colspan="2">20 mm/s</td></tr>
<tr><td colspan="2">30 mm/s</td></tr>
<tr><td colspan="2">50 mm/s</td></tr>
<tr><td colspan="2">80 mm/s (adopted only exceptionally)</td></tr>
<tr><td colspan="2" rowspan="2">Duration of excitation</td><td colspan="2">In general: 15 h</td></tr>
<tr><td colspan="2">In some experiments less than 15 h</td></tr>
<tr><td rowspan="2">Type of concrete</td><td>B3</td><td>C30/37/F52/GK22<br>CEM II/B-M (S-L) 42.5 N<br>Cement: 340 kg/m³<br>Air: 2.5 – 6.5 %<br>Water/cement ratio: 0.55</td><td>Note: Typical type of concrete for supporting structure of bridges</td></tr>
<tr><td>B7</td><td>C25/30/F52/GK22<br>CEM II/A-M (S-L) 42.5 N<br>Cement: 380 kg/m³<br>Air: 4 – 8 %<br>Water/cement ratio: 0.45</td><td>Note: Typical type of concrete used for edge beams (increased frost resistance)</td></tr>
</table>

Table 1: Parameters of the test setup

## 3 EXCITATIONS

Next to harmonic signals, transient signals are being used for the excitations. The transient signals ought to reproduce vibrations of real bridges excited by traffic of trains, trucks, and passenger cars. However, after scrutinizing a great number of recorded signals of bridge vibrations, it became clear to us that the variations of signals, even measured on one and the same bridge, are very large. The reason is that the vibrations are also very much influenced by the traffic. In summary, the intensity, the frequency content, and the duration of the vibration due to passing of a vehicle are influenced by (cf. [7]):

- Natural frequencies of the bridge (primarily by the first one)
- Damping of the bridge
- (Periodic) “disturbances” on the track (e.g., expansion joints)
- Mass of vehicle
- Driving speed
- Distance between axles
- Other factors: Sleeper distance, interaction between wheel and rail/road surface, wheel suspension etc.

Nevertheless, the authors aspired to select sample signals which are somehow typical for the passage of the respective vehicle type over a bridge. Thus, e.g., the passage of the train lasts much longer (19 seconds) than the passage of a truck (2 seconds). Figure 6 shows the train

signal, Figure 7 shows the truck signal, and Figure 8 shows the bridge vibrations due to passenger car traffic. Peak velocity is scaled to 20 mm/s for all vehicle types.

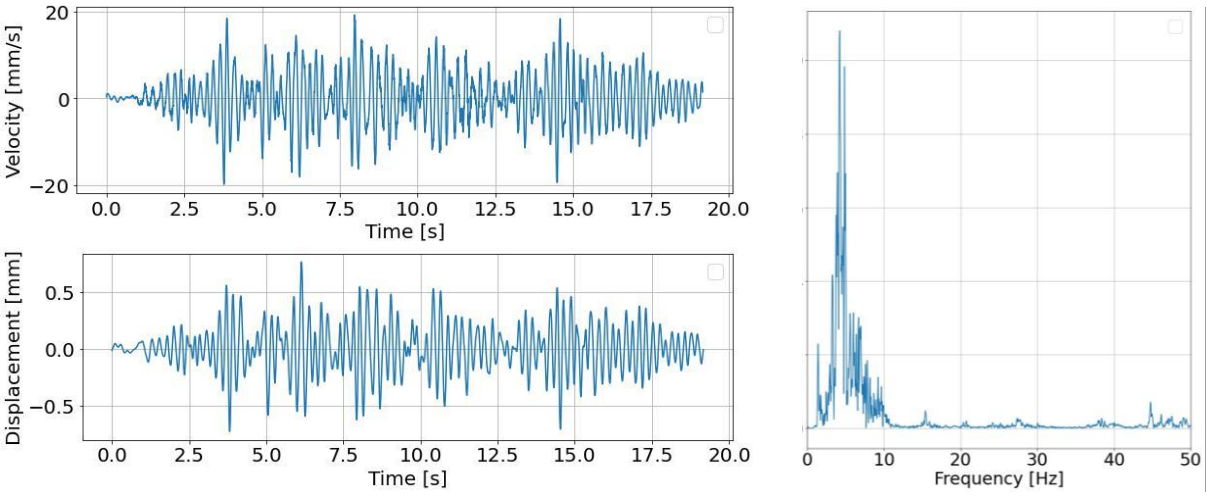


Figure 6: Velocity, displacement, and FFT of velocity caused by passage of (freight) train over a bridge

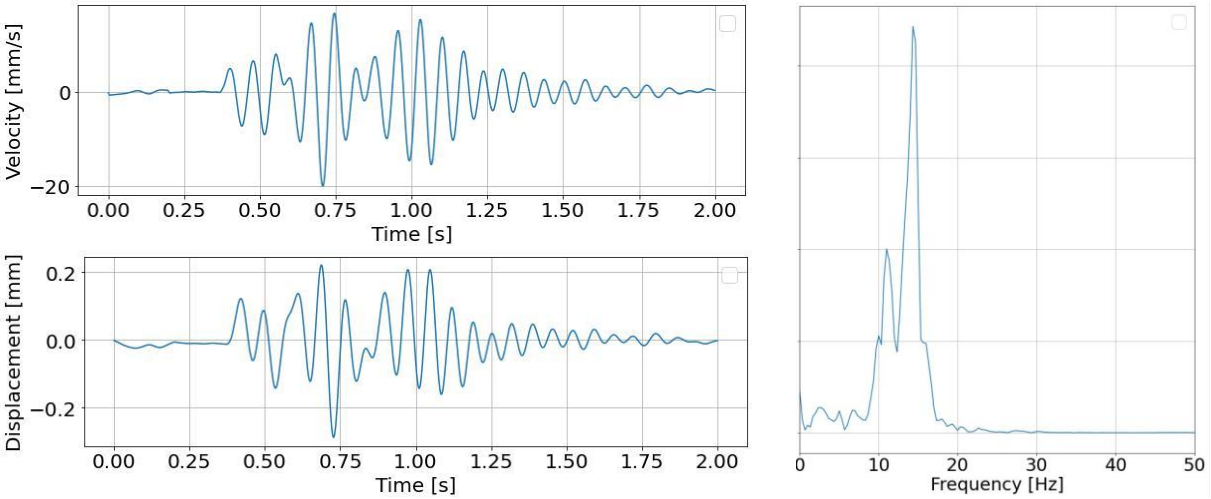


Figure 7: Velocity, displacement, and FFT of velocity caused by passage of truck over a bridge

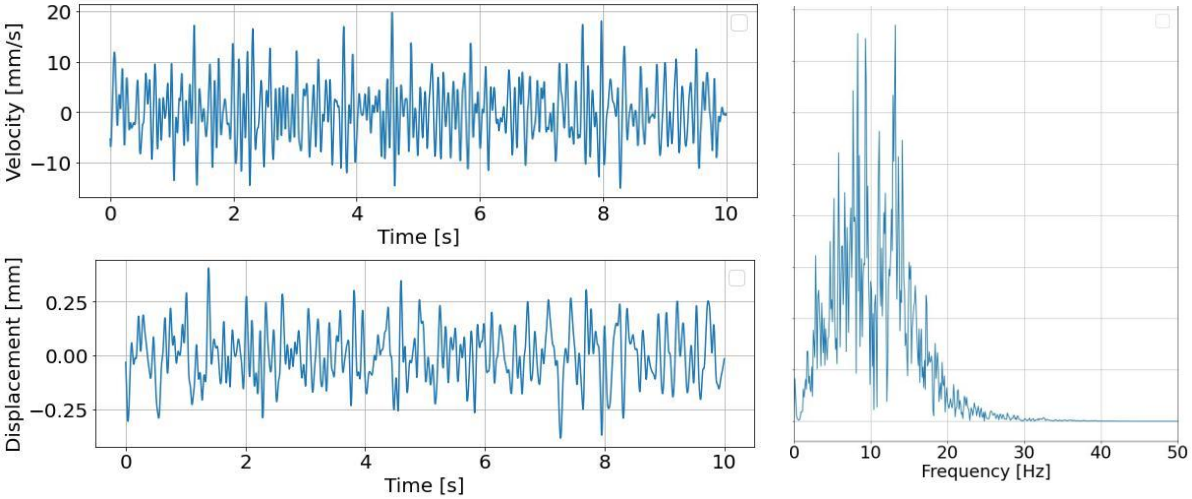


Figure 8: Velocity, displacement, and FFT of velocity caused by passage of passenger cars over a bridge

# 4 PRELIMINARY RESULTS

## 4.1 Series 1: Plain concrete

Preliminary lab results indicate that strength and stiffness of plain concrete, in general, are not reduced by vibrations caused by common traffic situations. There is no clear indication that a certain excitation type (a certain frequency) is especially critical. It is even more interesting that also the amplitude of the excitation does not seem to influence the properties of the concrete (the highest excitation amplitude adopted was 80 mm/s).
The following figures show the results in detail. Next to the test results of the specimens excited by harmonic signals (5, 20, and 35 Hz), also the results for traffic of passenger cars (p.c.), trucks, and trains are shown. The type of concrete is "B3", cf. Table 1. If available, also the mean values of respective reference results (of specimens at rest) are indicated (m.v.ref.).
The most noticeable result is that, for some test cases, the elastic modulus is considerable (ca. 35%) lower than the elastic modulus of most other specimens (which is usually around 42,000 MPa). However, the lowest values of the elastic modulus are observed for the middle frequency (10 Hz) and for the lower excitation amplitudes, and additionally for the passenger car excitation. From a rational point of view this behaviour is difficult to explain. Unfortunately, a reference elastic modulus is not available for each single experiment.
Hence, the elastic modulus of these "suspicious specimens" was additionally determined by dynamic testing (ultra-sonic). Interestingly, using this method, the elastic modulus of these specimens is equally high as the one of the other specimens. Further tests will provide more insight into these observations.

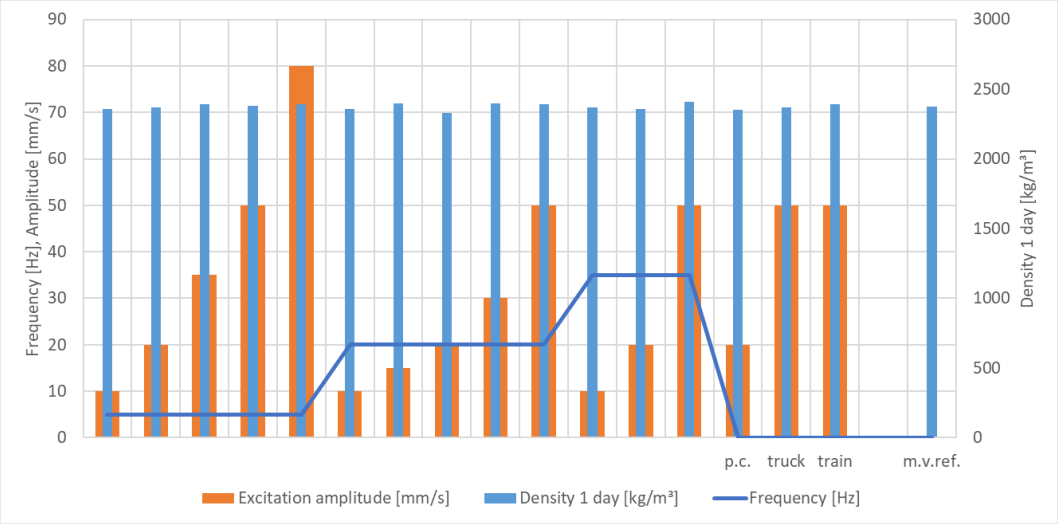


Figure 9: Density after 1 day

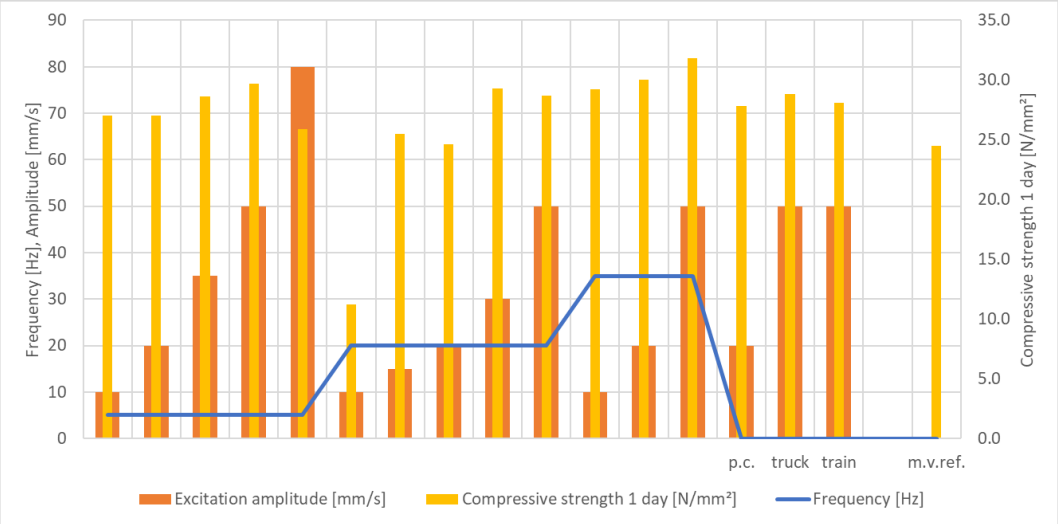


Figure 10: Compressive strength after 1 day

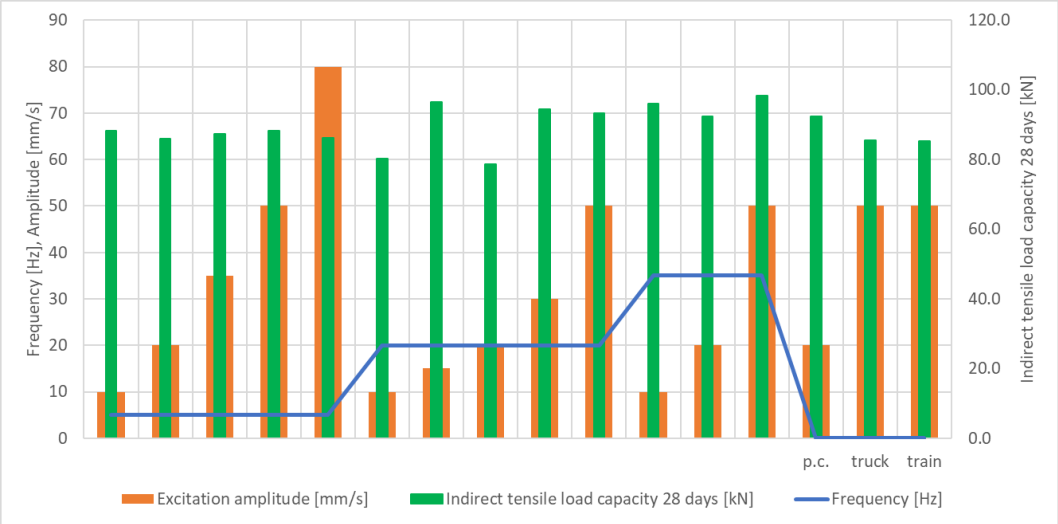


Figure 11: Indirect tensile load capacity after 28 days

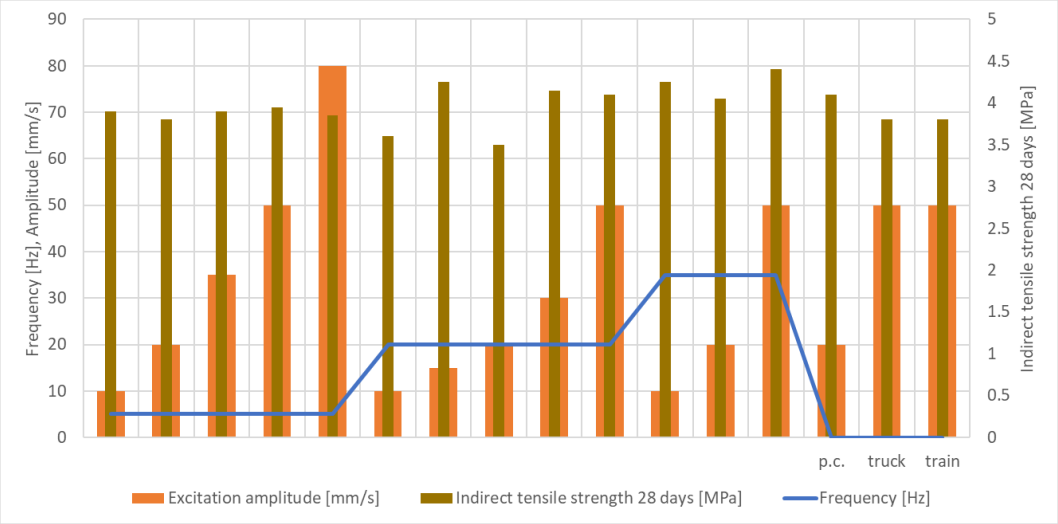


Figure 12: Indirect tensile strength after 28 days

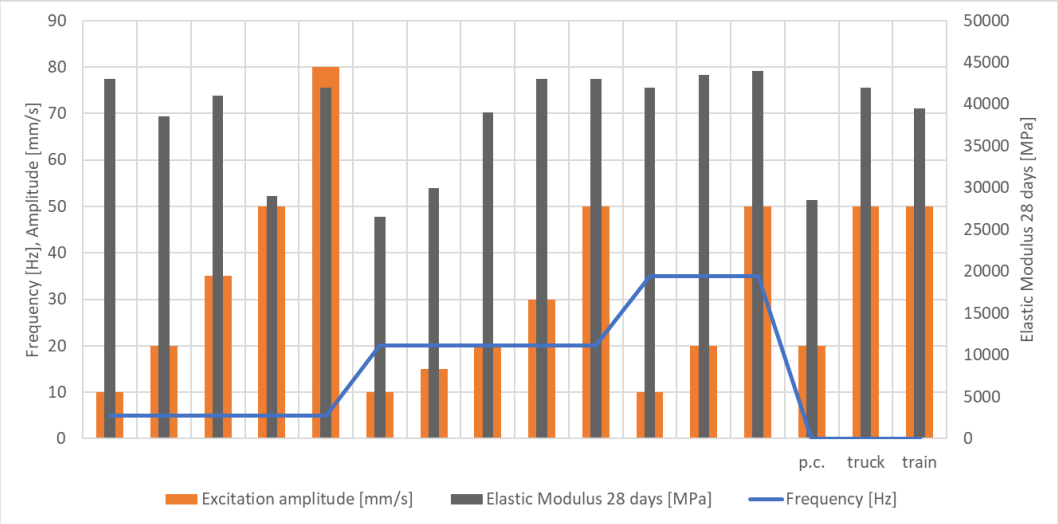


Figure 13: Elastic Modulus after 28 days

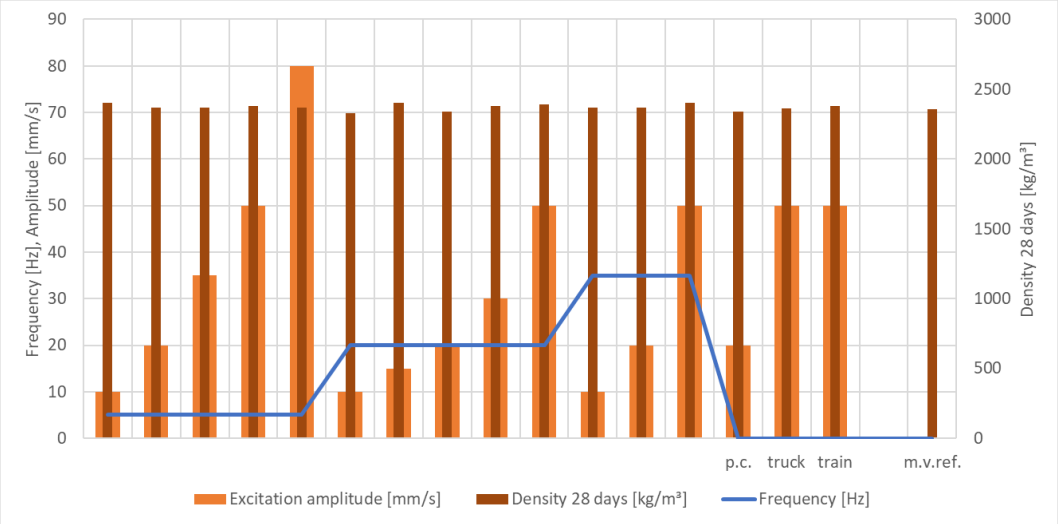


Figure 14: Density after 28 days

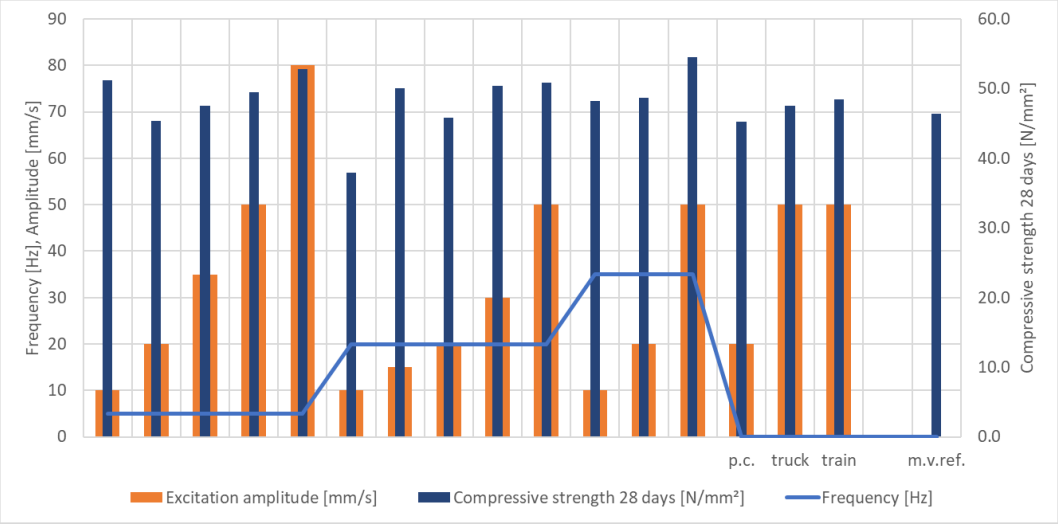


Figure 15: Compressive strength after 28 days

**Multiscale Modelling**

The specimens of plain concrete are being further tested for variations in porosity and microstructure. By means of a micro-X-ray fluorescence analysis, it was found that some shaken specimens exhibit a microstructure where the (larger) aggregates tend to accumulate rather in the lower area of the specimen while there is a higher concentration of cement in the upper part (compared to the reference specimens).
To see the expected macroscopic effects of such microscopic variations, a multiscale analysis was performed. The aim is to capture the behaviour of concrete at a macroscopic scale by accounting for the complex interactions between the different constituent phases at a microscopic level by averaging them. Hence, Representative Volume Elements (RVEs) are generated for both the reference sample and the vibrated sample, which differ slightly in terms of the distribution of aggregates, see Figure 16.

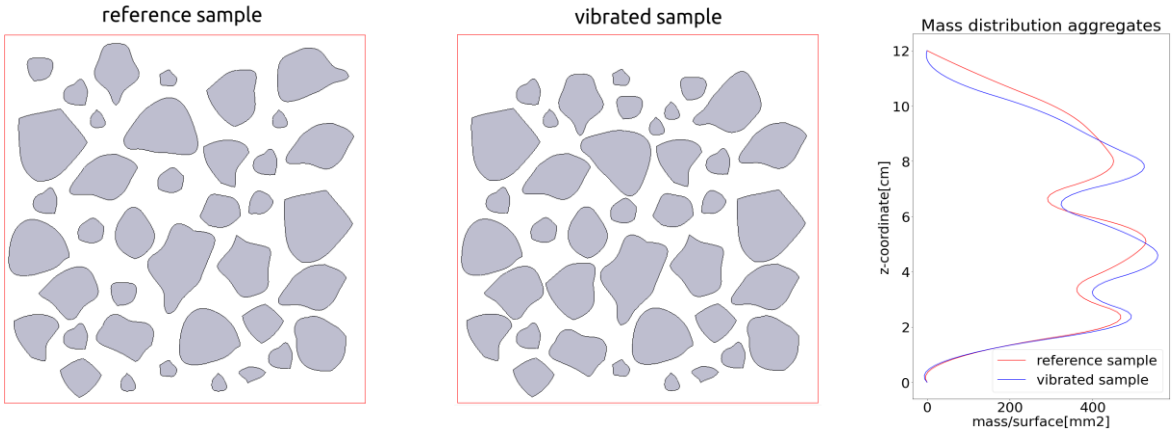


Figure 16: Representative volume element (RVE) used in the multiscale analysis: Left: reference sample (homogeneous distribution of aggregates), middle: vibrated sample (tendency of aggregates to accumulate in the lower part), right: distributions of aggregates over the hight of the sample.

In the analysis, cement is assigned an elastic modulus of 30,000 N/mm² and the aggregates are assigned an elastic modulus of 50,000 N/mm². For the homogenization method, periodic boundary conditions are used.
The resulting elastic moduli for the concrete are 34,460 N/mm² for the reference sample and 34,360 N/mm² for the sample exposed to vibrations, respectively. Thus, the difference is only 0.3%. This small demonstrative example shows that small rearrangements of the components that can occur due to vibrations do not alter the elastic properties of the concrete specimens significantly. This finding is in full congruence with the macroscopic test results presented previously.

## 4.2 Serie 2: Pull-out Tests

So far, only the results of the samples excited by train passage signals are available. The quality of the concrete-rebar bond was studied by means of pull-out tests [9]. The results are shown in Figure 17 in terms of the mean value of the maximum force reached in the pull-out test. The samples excited by a train passage signal with peak value equal to 10 mm/s reached a peak pull-out force of approximately 70 kN, which is in the range of fluctuation of the reference values (mean value 75 kN). However, the bond of the samples excited with a maximum of 20 mm/s is clearly damaged since the (mean) peak pull-out force is nearly 40% lower than for the reference samples. In the case of 50 mm/s, the peak pull-out force is again much reduced (minus 73% compared to reference).

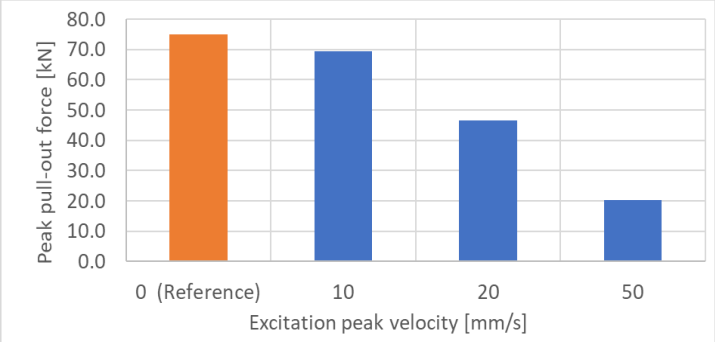


Figure 17: Peak pull-out forces performed with reinforced concrete samples excited by train passage signals

## 5 CONCLUSIONS

Preliminary lab results indicate that strength and stiffness of plain concrete, in general, are not reduced by vibrations caused by common traffic situations. However, latest results show very clearly that the bond between concrete and rebars may be damaged by strong vibrations.

## REFERENCES

[1] S. Krohn, M. Schrick, R. Maurer, Betonieren unter Verkehr: Einfluss von Erschütterungen auf die Betonerhärtung. *Beton- und Stahlbetonbau,* **116**, 89-100, 2021.

[2] B. Pichler, C. Hellmich, Upscaling quasi-brittle strength of cement paste and mortar: A multi-scale engineering mechanics model. *Cement and Concrete Research,* **41**, 467-476, 2011.

[3] SBB AG, Erschütterungen von jungem Beton bei Neubauten und Instandsetzungen – Empfehlungen für Beurteilungen, Vermeidung und Massnahmen

[4] D.G. Manning, Effects of traffic-induced vibrations on bridge-deck repairs. *National Cooperative Highway Research Program Synthesis of Highway Practice 86.* Washington DC (USA): Transportation Research Board, National Academy of Sciences, 1981

[5] A.K.H. Kwan, P.L. Ng, Effects of traffic vibration on curing concrete stitch: Part I – test method and control program. *Engineering Structures*, **29**, 2871-2880, 2007.

[6] P.L. Ng, A.K.H. Kwan, Effects of traffic vibration on curing concrete stitch: Part II – cracking, debonding and strength reduction. *Engineering Structures*, **29**, 2881-2892, 2007.

[7] M. Ralbovsky, A. Vorwagner, M. Kleiser, T. Kozakow, R. Geier, Verkehrsschwingungen bei Betonierarbeiten auf bestehenden Straßenbrücken. *Beton- und Stahlbetonbau,* **115**, 179-187, 2020.

[8] J. Bonzel, M. Schmidt, Einfluss von Erschütterungen auf frischen und auf jungen Beton. *Betontechnischer Bericht,* **80-81**. Verein Deutscher Zementwerke e.V., Düsseldorf, 1980.

[9] BS EN 10080:2005: Steel for the reinforcement of concrete – Weldable reinforcing steel – General.

COMPDYN 2023
9th ECCOMAS Thematic Conference on
Computational Methods in Structural Dynamics and Earthquake Engineering
M. Papadrakakis, M. Fragiadakis (eds.)
Athens, Greece, 12-–14 June 2023

# EFFECT OF THE LENGTH OF SEISMIC METASURFACES ON VIBRATION MITIGATION PERFORMANCE

**David Carneiro, Pieter Reumers, Geert Lombaert, and Geert Degrande**

KU Leuven, Department of Civil Engineering, Structural Mechanics Section
Kasteelpark Arenberg 40 box 2448, B-3001 Leuven, Belgium
e-mail: david.carneiro@kuleuven.be

**Abstract.** *This paper investigates the effect of the length of 2D seismic metasurfaces composed of an array of resonators on vibration mitigation performance. This is accomplished by means of computations using 3D and periodic finite element - boundary element (FE-BE) models. Whereas the 3D model considers a finite number of resonators on layered soils, the periodic approach assumes an infinite number of equally spaced resonators in the longitudinal direction. Behind longer metasurfaces, larger vibration reduction is found in a perpendicular direction from the source. The vibration mitigation performance of the metasurfaces reduces with distance from the source. The number of resonators also affects the frequency at which the metasurface has the best performance. The advantage of the periodic model is that only a line of resonators needs to be modeled resulting in a reduction in computational requirements. The computation time, however, depends on the number of terms in the Floquet transform, which is affected by the spacing between the resonators and the dynamic soil characteristics. Larger spacing increases the maximum distance between the periodic sources. Waves traveling on highly damped soils vanish at shorter distances. This enables a reduction of the number of terms in the Floquet transform and the use of coarser wavenumber samplings while still accurately predicting the response of metasurfaces.*

**Keywords:** Periodic seismic metasurfaces, dynamic soil-structure interaction, boundary element method.

## 1 Introduction

Seismic metamaterials have been widely investigated as a vibration mitigation measure over the past years. These are artificially engineered materials consisting of an arrangement of elementary cells exhibiting non-conventional dispersion properties that are usually not found in natural soils [1]. Non-resonant metamaterials induce Bragg scattering as a result of periodic arrangements of the same order of the surface wavelengths. Locally resonant metamaterials do not rely on structural periodicity, allowing their dimensions and spacings to be lower than the surface wavelengths [2].

Locally resonant seismic metasurfaces consisting of an array of resonators are employed in this paper. Their vibration mitigation performance depends on the soil properties, the number and arrangement of the resonators and their dynamic properties [3]. We focus on the effect of the number of resonators in the longitudinal direction for a fixed number of resonators in the perpendicular direction.

The band gap created by an array of resonators on a homogeneous halfspace under an incoming wave field from fixed sources can be predicted using numerical models [4]. Resonators with identical resonance frequency placed on top of a homogeneous soil induce narrow band gaps [5, 6]. This can be broadened over a wider frequency band using graded metamaterials [7]. 2D models considering uniform geometry in the longitudinal direction are frequently employed. In reality, metabarriers have finite dimensions in both directions. Therefore, their length in the longitudinal direction plays a crucial role, requiring further investigation.

The large computational cost to model a finite metabarrier interacting with soil is still a concern, in particular for very long and wide metabarriers in a broad frequency range. Numerical analyses are usually made with a finite element (FE) model coupled with absorbing boundary conditions such as perfectly matched layers (PML), as commonly available in commercial softwares [6, 8, 9]. This results in straightforward discretization and computation for both metasurfaces and embedded metabarriers. Extended 3D FE-PML meshes may become computationally very demanding, however.

Alternatively, coupled FE-BE formulations are developed to analyze the performance of seismic metabarriers [4]. As fundamental solutions of a layered halfspace can be employed, the boundary element (BE) mesh remains limited to the soil-structure interfaces. The drawback of this method is that fully populated matrices lead to high memory and CPU requirements, hindering the applicability of the BE method for a large number of resonators. In the case of metasurfaces with a periodic layout, an alternative is to model a slice of soil containing resonators using a periodic FE-BE model [10], resulting in a reduction of the computational requirements.

This paper investigates the effect of the number of resonators in the longitudinal direction on the vibration mitigation performance of metasurfaces. 3D and periodic FE-BE models are used to solve this problem. The periodic approach assumes a finite number of resonators in one direction and an infinite number of equally spaced resonators in the other direction. The corresponding formulations are developed for multiple resonators on top of layered soils. The excitation is a vertical harmonic point load applied on the surface of the soil. The computational performance of a periodic FE-BE model is compared with the 3D FE-BE model. We gradually increase the length of the metasurface in the longitudinal direction using a 3D FE-BE model, approaching the case of an infinitely long periodic metasurface. We assess the vibration mitigation performance of different configurations by computing the wave field on the surface of the soil and the corresponding insertion loss at selected receiver points behind the metasurfaces.

Memory requirements for computing boundary element matrices and CPU time are given.

The outline of the paper is as follows. Section 2 presents a 3D and periodic FE-BE formulation for a metasurface on layered soils. The vibration mitigation performance of seismic metasurfaces on a homogeneous soil and computational efficiency of the FE-BE models are described in section 3. Section 4 concludes the paper.

## 2 Seismic metasurface on a layered soil

### 2.1 Problem outline

Figure 1a depicts a finite metasurface comprising an array of $N$ resonators on top of a layered soil represented by the unbounded domain $\Omega_{\mathrm{s}}^{\mathrm{e}}$. The metasurface is placed at a perpendicular distance $D$ from the origin of the coordinate system. The layout is characterized by a rectangular grid of $N_x$ by $N_y$ resonators with lattice constants $a_x$ and $a_y$ in the $x$- and $y$-direction, respectively. The interface between a resonator $k$ and the soil is defined as $\Sigma_k$. The soil-structure interface for $N$ resonators is denoted as $\Sigma = \bigcup_{k=1}^{N} \Sigma_k$.

In cases where the array of resonators has a periodic arrangement, $N_x$ resonators in the $x$-direction and an infinite number of equally spaced resonators in the $y$-direction ($N_y = \infty$) are considered. The domain can then be restricted to a reference cell $\tilde{\Omega}_{\mathrm{s}}^{\mathrm{e}}$ with period $L = a_y$ in the longitudinal direction $\mathbf{e}_y$ (figure 1b).

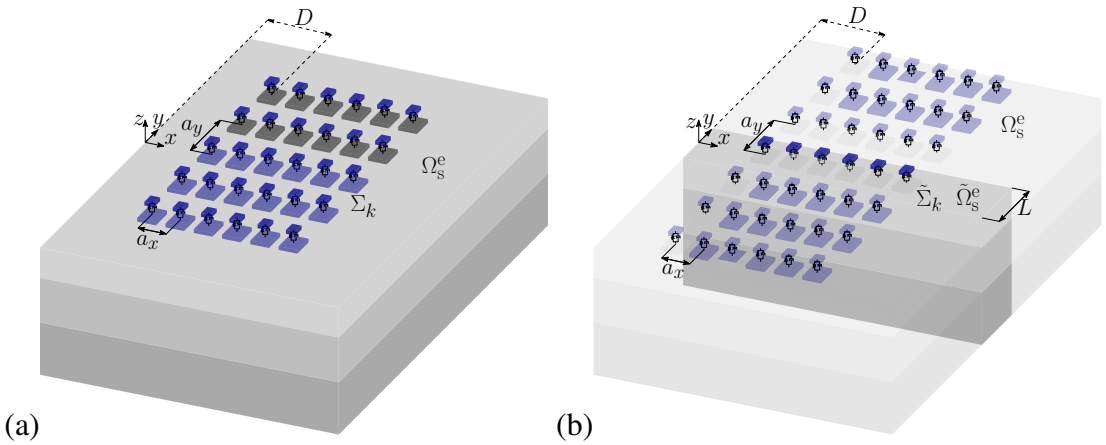


(a) (b)

Figure 1: (a) Finite and (b) periodic array of resonators.

### 2.2 3D FE-BE model

#### 2.2.1 Displacement and traction fields

The displacement of a resonator $k$ on top of the layered halfspace is denoted as $\hat{\mathbf{u}}_{\mathrm{r}k}(\mathbf{x}, \omega)$. A hat on a variable denotes its representation in the spatial-frequency domain. Continuity conditions and equilibrium of tractions are imposed on the soil-resonator interface $\Sigma_k$:

$$\hat{\mathbf{u}}_{\mathrm{r}k} - \hat{\mathbf{u}}_{\mathrm{s}} = \mathbf{0} \quad \text{on} \quad \Sigma_k \tag{1}$$

$$\hat{\mathbf{t}}_{\mathrm{r}}(\hat{\mathbf{u}}_{\mathrm{r}k}) + \hat{\mathbf{t}}_{\mathrm{s}}(\hat{\mathbf{u}}_{\mathrm{s}}) = \mathbf{0} \quad \text{on} \quad \Sigma_k, \tag{2}$$

where $\hat{\mathbf{u}}_{\mathrm{s}}(\mathbf{x}, \omega)$ is the soil displacement vector and $\hat{\mathbf{t}}_{\mathrm{r}}(\hat{\mathbf{u}}_{\mathrm{r}k})(\mathbf{x}, \omega)$ is the traction vector due to the displacement $\hat{\mathbf{u}}_{\mathrm{r}k}$.

Assuming that the resonators are subjected to an incident wave field, the soil displacement $\hat{\mathbf{u}}_{\mathrm{s}}(\mathbf{x},\omega)$ is decomposed into the incident wave field $\hat{\mathbf{u}}_{\mathrm{inc}}(\mathbf{x},\omega)$, the locally diffracted wave field $\hat{\mathbf{u}}_{\mathrm{d0}}(\mathbf{x},\omega)$ and the wave field $\hat{\mathbf{u}}_{\mathrm{sc}}(\mathbf{x},\omega)$ scattered by the displacements $\hat{\mathbf{u}}_{\mathrm{r}k}(\mathbf{x},\omega)$ of all resonators $k$ ($k=1,\ldots,N$) such that [11]:

$$\hat{\mathbf{u}}_{\mathrm{s}} = \hat{\mathbf{u}}_{\mathrm{inc}} + \hat{\mathbf{u}}_{\mathrm{d0}} + \sum_{k=1}^{N} \hat{\mathbf{u}}_{\mathrm{sc}}(\hat{\mathbf{u}}_{\mathrm{r}k}). \tag{3}$$

The incident wave field $\hat{\mathbf{u}}_{\mathrm{inc}}$ is computed with a source model. The locally diffracted wave field $\hat{\mathbf{u}}_{\mathrm{d0}}(\mathbf{x},\omega)$ is an elastodynamic field that obeys Sommerfeld's radiation condition. This is defined so that the combined wave field $\hat{\mathbf{u}}_{\mathrm{inc}}(\mathbf{x},\omega) + \hat{\mathbf{u}}_{\mathrm{d0}}(\mathbf{x},\omega)$ vanishes on the soil-structure interface $\Sigma$.

### 2.2.2 Soil-structure interaction problem

The dynamic equilibrium for a single structure $j$ ($j=1,\ldots,N$) can be expressed in a weak variational form. A virtual displacement field $\hat{\mathbf{v}}_{\mathrm{r}j}(\mathbf{x},\omega)$ is imposed on the structure $j$ in order to construct the virtual work expression, which is given by [12]:

$$\int_{\Omega_{\mathrm{r}j}} \hat{\boldsymbol{\epsilon}}_{\mathrm{r}}(\hat{\mathbf{v}}_{\mathrm{r}j}) : \hat{\boldsymbol{\sigma}}_{\mathrm{r}}(\hat{\mathbf{u}}_{\mathrm{r}j})\,\mathrm{d}\Omega - \omega^2 \int_{\Omega_{\mathrm{r}j}} \hat{\mathbf{v}}_{\mathrm{r}j}\cdot\rho_{\mathrm{r}j}\hat{\mathbf{u}}_{\mathrm{r}j}\,\mathrm{d}\Omega = \int_{\Sigma_j} \hat{\mathbf{v}}_{\mathrm{r}j}\cdot\hat{\mathbf{t}}_{\mathrm{r}}(\hat{\mathbf{u}}_{\mathrm{r}j})\,\mathrm{d}\Gamma, \tag{4}$$

where $\hat{\boldsymbol{\epsilon}}_{\mathrm{r}}(\hat{\mathbf{v}}_{\mathrm{r}j})(\mathbf{x},\omega)$ is the virtual strain tensor, $\hat{\boldsymbol{\sigma}}_{\mathrm{r}}(\hat{\mathbf{u}}_{\mathrm{r}j}))(\mathbf{x},\omega)$ is the Cauchy stress tensor due to displacements $\hat{\mathbf{u}}_{\mathrm{r}j}(\mathbf{x},\omega)$, and $\rho_{\mathrm{r}j}$ is the density of the structure. Introducing equations (2) and (3) into equation (4) yields:

$$\begin{aligned}\int_{\Omega_{\mathrm{r}j}} \hat{\boldsymbol{\epsilon}}_{\mathrm{r}}(\hat{\mathbf{v}}_{\mathrm{r}j}) : \hat{\boldsymbol{\sigma}}_{\mathrm{r}}(\hat{\mathbf{u}}_{\mathrm{r}j})\,\mathrm{d}\Omega - \omega^2 \int_{\Omega_{\mathrm{r}j}} \hat{\mathbf{v}}_{\mathrm{r}j}\cdot\rho_{\mathrm{r}j}\hat{\mathbf{u}}_{\mathrm{r}j}\,\mathrm{d}\Omega + \sum_{k=1}^{N}\int_{\Sigma_j} \hat{\mathbf{v}}_{\mathrm{r}j}\cdot\hat{\mathbf{t}}_{\mathrm{s}}(\hat{\mathbf{u}}_{\mathrm{sc}}(\hat{\mathbf{u}}_{\mathrm{r}k}))\,\mathrm{d}\Gamma \\ = -\int_{\Sigma_j} \hat{\mathbf{v}}_{\mathrm{r}j}\cdot\hat{\mathbf{t}}_{\mathrm{s}}(\hat{\mathbf{u}}_{\mathrm{inc}} + \hat{\mathbf{u}}_{\mathrm{d0}})\,\mathrm{d}\Gamma.\end{aligned} \tag{5}$$

This problem is solved by means of a coupled FE-BE model. The resonator is modeled with finite elements whereas boundary elements are used to discretize the unbounded soil on the interfaces $\Sigma_k$. The structural displacement vector for resonator $j$ is discretized as:

$$\hat{\mathbf{u}}_{\mathrm{r}j} \simeq \mathbf{N}_{\mathrm{r}j}\underline{\hat{\mathbf{u}}}_{\mathrm{r}j}, \tag{6}$$

where $\mathbf{N}_{\mathrm{r}j}$ is a matrix of global finite element shape functions for resonator $j$ and $\underline{\hat{\mathbf{u}}}_{\mathrm{r}j}(\omega)$ is the vector with nodal degrees of freedom. In a Galerkin approach, this approximation is also used for the virtual displacement field $\hat{\mathbf{v}}_{\mathrm{r}}(\mathbf{x},\omega)$. Equation (5) then yields:

$$\left[\mathbf{K}_j - \omega^2\mathbf{M}_j\right]\underline{\hat{\mathbf{u}}}_{\mathrm{r}j} + \sum_{k=1}^{N}\hat{\mathbf{K}}^{\mathrm{s}}_{jk}\underline{\hat{\mathbf{u}}}_{\mathrm{r}k} = \underline{\hat{\mathbf{f}}}^{\mathrm{s}}_{j}, \tag{7}$$

where $\mathbf{K}_j$ and $\mathbf{M}_j$ are the stiffness and mass matrices of the resonator $j$, respectively. The contribution of structural damping can be added to equation (7). In this work, proportional

damping is used where a damping ratio is defined for each mode of the structure. The summation in equation (7) accounts for through-soil coupling of resonator $j$ with all resonators. The soil stiffness matrix $\hat{\mathbf{K}}^{\mathrm{s}}_{jk}(\omega)$ is given by:

$$\hat{\mathbf{K}}^{\mathrm{s}}_{jk} = \int_{\Sigma_j} \mathbf{N}^{\mathrm{T}}_{\mathrm{r}j} \hat{\mathbf{t}}_{\mathrm{s}}(\hat{\mathbf{u}}_{\mathrm{sc}}(\mathbf{N}_{\mathrm{r}k}))\,\mathrm{d}\Gamma. \tag{8}$$

The force vector $\hat{\underline{\mathbf{f}}}^{\mathrm{s}}_{j}(\omega)$ due to an incident wave field is equal to:

$$\hat{\underline{\mathbf{f}}}^{\mathrm{s}}_{j} = -\int_{\Sigma_j} \mathbf{N}^{\mathrm{T}}_{\mathrm{r}j} \hat{\mathbf{t}}_{\mathrm{s}}(\hat{\mathbf{u}}_{\mathrm{inc}} + \hat{\mathbf{u}}_{\mathrm{d0}})\,\mathrm{d}\Gamma. \tag{9}$$

The scattered wave field and the locally diffracted wave field are computed by means of the BE method, as the problem is formulated in terms of displacements on the interfaces $\Sigma_k$. When the resonator $j$ is placed on the surface of the soil, $\hat{\mathbf{t}}_{\mathrm{s}}(\hat{\mathbf{u}}_{\mathrm{inc}})(\omega) = \mathbf{0}$. The tractions $\hat{\mathbf{t}}_{\mathrm{s}k}(\omega)$ on the soil-resonator interfaces are calculated as:

$$\sum_{k=1}^{N} \left[\mathbf{I}_{jk} + \hat{\mathbf{T}}_{jk}\right] \hat{\underline{\mathbf{u}}}_{\mathrm{s}k} = \sum_{k=1}^{N} \hat{\mathbf{U}}_{jk} \hat{\underline{\mathbf{t}}}_{\mathrm{s}k}, \tag{10}$$

where $\mathbf{I}_{jk}$ is an identity matrix, $\hat{\mathbf{U}}_{jk}(\omega)$ and $\hat{\mathbf{T}}_{jk}(\omega)$ are fully populated asymmetric boundary element matrices which require the integration of Green's functions for a layered halfspace, and $\hat{\underline{\mathbf{u}}}_{\mathrm{s}k}(\omega)$ and $\hat{\underline{\mathbf{t}}}_{\mathrm{s}k}(\omega)$ are the displacements and tractions on the soil-structure interface $\Sigma_k$. For a BE mesh on the surface of the soil, $\hat{\mathbf{T}}_{jk}(\omega) = \mathbf{0}$.

### 2.2.3 Craig-Bampton substructuring method

It is convenient to decompose the structural displacement vector $\hat{\underline{\mathbf{u}}}_{\mathrm{r}j}(\omega)$ of resonator $j$ into displacements of its foundation $\hat{\underline{\mathbf{u}}}_{\mathrm{r}_1 j}(\omega)$ and superstructure $\hat{\underline{\mathbf{u}}}_{\mathrm{r}_2 j}(\omega)$. Introducing this decomposition into equation (6) leads to:

$$\hat{\mathbf{u}}_{\mathrm{r}j} \simeq \begin{bmatrix} \mathbf{N}_{\mathrm{r}_1 j} & \mathbf{N}_{\mathrm{r}_2 j} \end{bmatrix} \begin{Bmatrix} \hat{\underline{\mathbf{u}}}_{\mathrm{r}_1 j} \\ \hat{\underline{\mathbf{u}}}_{\mathrm{r}_2 j} \end{Bmatrix}. \tag{11}$$

Using the decomposition (11), equation (7) becomes:

$$\begin{aligned} \left( \begin{bmatrix} \mathbf{K}_{\mathrm{r}_1\mathrm{r}_1 j} & \mathbf{K}_{\mathrm{r}_1\mathrm{r}_2 j} \\ \mathbf{K}_{\mathrm{r}_2\mathrm{r}_1 j} & \mathbf{K}_{\mathrm{r}_2\mathrm{r}_2 j} \end{bmatrix} - \omega^2 \begin{bmatrix} \mathbf{M}_{\mathrm{r}_1\mathrm{r}_1 j} & \mathbf{M}_{\mathrm{r}_1\mathrm{r}_2 j} \\ \mathbf{M}_{\mathrm{r}_2\mathrm{r}_1 j} & \mathbf{M}_{\mathrm{r}_2\mathrm{r}_2 j} \end{bmatrix} \right) \begin{Bmatrix} \hat{\underline{\mathbf{u}}}_{\mathrm{r}_1 j} \\ \hat{\underline{\mathbf{u}}}_{\mathrm{r}_2 j} \end{Bmatrix} \\ + \sum_{k=1}^{N} \begin{bmatrix} \hat{\mathbf{K}}^{\mathrm{s}}_{\mathrm{r}_1\mathrm{r}_1 jk} & \mathbf{0} \\ \mathbf{0} & \mathbf{0} \end{bmatrix} \begin{Bmatrix} \hat{\underline{\mathbf{u}}}_{\mathrm{r}_1 k} \\ \hat{\underline{\mathbf{u}}}_{\mathrm{r}_2 k} \end{Bmatrix} = \begin{Bmatrix} \hat{\underline{\mathbf{f}}}^{\mathrm{s}}_{\mathrm{r}_1 j} \\ \mathbf{0} \end{Bmatrix}. \end{aligned} \tag{12}$$

Since the resonator is composed of a superstructure coupled to a foundation interacting with the soil, it is advantageous to use a Craig-Bampton substructuring technique [13]. This reduces the problem size and avoids the recomputation of the BE matrices for the same dimensions and spacing of foundations whenever the superstructures change. Using the Craig-Bampton substructuring technique, the displacement vector $\hat{\mathbf{u}}_{\mathrm{r}j}$ of resonator $j$ is written as:

$$\hat{\mathbf{u}}_{\mathrm{r}j} = \begin{bmatrix} \mathbf{N}_{\mathrm{r}_1 j} & \mathbf{N}_{\mathrm{r}_2 j} \end{bmatrix} \begin{bmatrix} \boldsymbol{\Phi}_{\mathrm{r}_1 j} & \mathbf{0} \\ \boldsymbol{\Phi}^{\mathrm{s}}_{\mathrm{r}_2 j} & \boldsymbol{\Phi}_{\mathrm{r}_2 j} \end{bmatrix} \begin{Bmatrix} \hat{\underline{\boldsymbol{\alpha}}}_{\mathrm{r}_1 j} \\ \hat{\underline{\boldsymbol{\alpha}}}_{\mathrm{r}_2 j} \end{Bmatrix} = \mathbf{N}_{\mathrm{r}j} \boldsymbol{\Phi}_{\mathrm{r}j} \hat{\underline{\boldsymbol{\alpha}}}_{\mathrm{r}j}, \tag{13}$$

where the vector $\underline{\hat{\boldsymbol{\alpha}}}_{\mathrm{r}j}(\omega)$ collects the modal coordinates. The modes $\boldsymbol{\Phi}_{\mathrm{r}_2 j}$ are the eigenmodes of the superstructure with clamped base. The modes $\boldsymbol{\Phi}_{\mathrm{r}_1 j}$ are the eigenmodes of the foundation without the superstructure. The modes $\boldsymbol{\Phi}^{\mathrm{s}}_{\mathrm{r}_2 j}$ are the quasi-static transmission of the foundation modes $\boldsymbol{\Phi}_{\mathrm{r}_1 j}$ into the superstructure:

$$\boldsymbol{\Phi}^{\mathrm{s}}_{\mathrm{r}_2 j} = -\mathbf{K}^{-1}_{\mathrm{r}_2\mathrm{r}_2 j}\mathbf{K}_{\mathrm{r}_2\mathrm{r}_1 j}\boldsymbol{\Phi}_{\mathrm{r}_1 j}, \tag{14}$$

where $\mathbf{K}_{\mathrm{r}_2\mathrm{r}_2 j}$ and $\mathbf{K}_{\mathrm{r}_2\mathrm{r}_1 j}$ are submatrices of the stiffness matrix of resonator $j$ presented in equation (12). Introducing equation (13) in equation (5) and premultiplying with $\boldsymbol{\Phi}^{\mathrm{T}}_{\mathrm{r}j}$ gives:

$$\boldsymbol{\Phi}^{\mathrm{T}}_{\mathrm{r}j}\left[\mathbf{K}_j - \omega^2\mathbf{M}_j\right]\boldsymbol{\Phi}_{\mathrm{r}j}\underline{\hat{\boldsymbol{\alpha}}}_{\mathrm{r}j} + \sum_{k=1}^{N}\boldsymbol{\Phi}^{\mathrm{T}}_{\mathrm{r}j}\hat{\mathbf{K}}^{\mathrm{s}}_{jk}\boldsymbol{\Phi}_{\mathrm{r}k}\underline{\hat{\boldsymbol{\alpha}}}_{\mathrm{r}k} = \boldsymbol{\Phi}^{\mathrm{T}}_{\mathrm{r}j}\underline{\hat{\mathbf{f}}}^{\mathrm{s}}_{j}. \tag{15}$$

The modal soil stiffness matrix $\boldsymbol{\Phi}^{\mathrm{T}}_{\mathrm{r}_1 j}\hat{\mathbf{K}}^{\mathrm{s}}_{\mathrm{r}_1\mathrm{r}_1 jk}\boldsymbol{\Phi}_{\mathrm{r}_1 k}$ is given by:

$$\boldsymbol{\Phi}^{\mathrm{T}}_{\mathrm{r}_1 j}\hat{\mathbf{K}}^{\mathrm{s}}_{\mathrm{r}_1\mathrm{r}_1 jk}\boldsymbol{\Phi}_{\mathrm{r}_1 k} = \int_{\Sigma_j}\boldsymbol{\Phi}^{\mathrm{T}}_{\mathrm{r}_1 j}\mathbf{N}^{\mathrm{T}}_{\mathrm{r}_1 j}\hat{\mathbf{t}}_{\mathrm{s}}(\hat{\mathbf{u}}_{\mathrm{sc}}(\mathbf{N}_{\mathrm{r}_1 k}\boldsymbol{\Phi}_{\mathrm{r}_1 k}))\,\mathrm{d}\Gamma. \tag{16}$$

The modal soil tractions $\hat{\mathbf{t}}_{\mathrm{s}}(\hat{\mathbf{u}}_{\mathrm{sc}}(\mathbf{N}_{\mathrm{r}_1 k}\boldsymbol{\Phi}_{\mathrm{r}_1 k}))(\omega)$ are computed by means of equation (10) for each mode and integrated over the interface using equation (16).

Modifications of the superstructure do not affect the computation of the soil stiffness in equation (16) as it only depends on the foundation modes and the BE mesh.

### 2.3 Receiver points

Tractions $\underline{\hat{\mathbf{t}}}_{\mathrm{s}}(\omega)$ and displacements $\underline{\hat{\mathbf{u}}}_{\mathrm{s}}(\omega)$ on the interface $\Sigma$ are computed according to the procedure described in [4]. The radiated wave field $\underline{\hat{\mathbf{u}}}^{\mathrm{r}}_{\mathrm{s}}(\mathbf{x},\omega)$ in the soil domain $\Omega^{\mathrm{e}}_{\mathrm{s}}$ is evaluated as:

$$\underline{\hat{\mathbf{u}}}^{\mathrm{r}}_{\mathrm{s}} = \hat{\mathbf{U}}_{\mathrm{p}}\underline{\hat{\mathbf{t}}}_{\mathrm{s}} - \hat{\mathbf{T}}_{\mathrm{p}}\underline{\hat{\mathbf{u}}}_{\mathrm{s}}, \tag{17}$$

where $\hat{\mathbf{U}}_{\mathrm{p}}(\mathbf{x},\omega)$ and $\hat{\mathbf{T}}_{\mathrm{p}}(\mathbf{x},\omega)$ are boundary element transfer matrices computed with the Green's functions of a layered halfspace.

### 2.4 Periodic FE-BE model

Although a substantial reduction in computation time and memory requirements can be achieved using the Craig-Bamption method, the computation of the modal soil stiffness matrices can still be very demanding for a large number of resonators $N$. Alternatively, a periodic FE-BE formulation is proposed in combination with a Craig-Bampton substructuring method [14].

The problem in figure 1a can be limited to a reference cell $\tilde{\Omega}^{\mathrm{e}}_{\mathrm{s}}$ (figure 1b) by application of Floquet's theorem. The position vector $\mathbf{x}$ in the problem domain $\Omega^{\mathrm{e}}_{\mathrm{s}}$ can be decomposed into $\mathbf{x} = \tilde{\mathbf{x}} + n_y L\mathbf{e}_y$, where $\tilde{\mathbf{x}}$ is the position vector in the reference cell $\tilde{\Omega}^{\mathrm{e}}_{\mathrm{s}}$ and $n_y$ is the cell number. The Floquet transformation $\tilde{f}(\tilde{\mathbf{x}},\kappa_y)$ of a non-periodic function $f(\mathbf{x}) = f(\tilde{\mathbf{x}} + n_y L\mathbf{e}_y)$ defined on a 3D domain $\Omega^{\mathrm{e}}_{\mathrm{s}}$, that is periodic in the $y$-direction with period $L$, transforms the distance $n_y L$ between the $n_y$th cell and the reference cell $\tilde{\Omega}^{\mathrm{e}}_{\mathrm{s}}$ to the wavenumber $\kappa_y \in ]-\pi/L, +\pi/L[$ and is defined as [10]:

$$\tilde{f}(\tilde{\mathbf{x}},\kappa_y) = \sum_{n_y=-\infty}^{\infty} f(\tilde{\mathbf{x}} + n_y L\mathbf{e}_y)\exp\left(+\mathrm{i}n_y L\kappa_y\right). \tag{18}$$

The complex function $\tilde{f}(\tilde{\mathbf{x}}, \kappa_y)$ is a periodic function of $\kappa_y$ with a period $2\pi/L$ (or a periodic function of the first kind with respect to $\kappa_y$), as the following periodicity condition holds [10]:

$$\tilde{f}\left(\tilde{\mathbf{x}}, \kappa_y + \frac{2\pi}{L}\right) = \tilde{f}(\tilde{\mathbf{x}}, \kappa_y). \tag{19}$$

This complex function $\tilde{f}(\tilde{\mathbf{x}}, \kappa_y)$ is also periodic of the second kind with a period $L$ in the $y$-direction, since the following condition holds for all $\tilde{\mathbf{x}}$ [10]:

$$\tilde{f}(\tilde{\mathbf{x}} + L\mathbf{e}_y, \kappa_y) = \exp\left(+\mathrm{i}\kappa_y L\right)\tilde{f}(\tilde{\mathbf{x}}, \kappa_y). \tag{20}$$

The function $f(\tilde{\mathbf{x}} + n_y L\mathbf{e}_y)$ can be reconstructed for any $\mathbf{x} = \tilde{\mathbf{x}} + n_y L\mathbf{e}_y$ using the inverse Floquet transform [10]:

$$f(\tilde{\mathbf{x}} + n_y L\mathbf{e}_y) = \frac{L}{2\pi}\int_{-\pi/L}^{\pi/L} \tilde{f}(\tilde{\mathbf{x}}, \kappa_y)\exp\left(-\mathrm{i}n_y L\kappa_y\right)\mathrm{d}\kappa_y \tag{21}$$

Using the Floquet transformation defined in equation (18), all the displacement and traction fields $\hat{\mathbf{u}}(\mathbf{x}, \omega)$ and $\hat{\mathbf{t}}(\mathbf{x}, \omega)$ in the domain $\Omega_{\mathrm{s}}^{\mathrm{e}}$ are transformed to the fields $\tilde{\mathbf{u}}(\tilde{\mathbf{x}}, \kappa_y, \omega)$ and $\tilde{\mathbf{t}}_{\mathrm{s}}(\tilde{\mathbf{x}}, \kappa_y, \omega)$ in the reference cell $\tilde{\Omega}_{\mathrm{s}}^{\mathrm{e}}$ (figure 1b), where a tilde on a variable denotes its representation in the wavenumber-frequency domain. Only a line of $N_x$ resonators within the reference cell $\tilde{\Omega}_{\mathrm{s}}^{\mathrm{e}}$ is therefore modeled, reducing the summation term in equation (5) to $N_x$ resonators.

In case of structures connected between cells (e.g. periodic track in tunnels), kinematic bases that obey the periodicity condition of the second kind which depend on the wavenumber are employed [14]. The resonators used in the present paper, however, are not connected between cells, and hence, there is no need to adapt the eigenmodes computed from classical FE matrices. These are chosen as the basis in a Craig-Bampton substructuring technique. The periodicity is therefore incorporated in the soil stiffness matrix $\tilde{\mathbf{K}}_{jk}^{\mathrm{s}}(\kappa_y, \omega)$ and the force vector $\underline{\tilde{\mathbf{f}}}_j^{\mathrm{s}}(\kappa_y, \omega)$ using Green-Floquet fundamental solutions $\tilde{\mathbf{u}}^{\mathrm{GF}}(\tilde{\mathbf{x}}', \tilde{\mathbf{x}}, \kappa_y, \omega)$ computed as [10]:

$$\tilde{\mathbf{u}}^{\mathrm{GF}}(\tilde{\mathbf{x}}', \tilde{\mathbf{x}}, \kappa_y, \omega) = \sum_{n_y'=-N_c}^{N_c} \hat{\mathbf{u}}^{\mathrm{G}}(\tilde{\mathbf{x}}' + n_y' L\mathbf{e}_y, \tilde{\mathbf{x}}, \omega)\exp\left(+\mathrm{i}n_y' L\kappa_y\right), \tag{22}$$

where the Green's tensor $\hat{\mathbf{u}}^{\mathrm{G}}(\tilde{\mathbf{x}}' + n_y' L\mathbf{e}_y, \tilde{\mathbf{x}}, \omega)$ represents the displacement fields in the point $\tilde{\mathbf{x}}$ due to sources that are periodically located in space at $\tilde{\mathbf{x}}' + n_y' L\mathbf{e}_y$ and the infinite sum in equation (18) was truncated by a finite sum $n_y' = -N_c$ to $N_c$.

Using the Green-Floquet fundamental solutions, equation (15) becomes:

$$\boldsymbol{\Phi}_{\mathrm{r}j}^{\mathrm{T}}\left[\mathbf{K}_j - \omega^2\mathbf{M}_j\right]\boldsymbol{\Phi}_{\mathrm{r}j}\underline{\tilde{\boldsymbol{\alpha}}}_{\mathrm{r}j} + \sum_{k=1}^{N_x}\boldsymbol{\Phi}_{\mathrm{r}j}^{\mathrm{T}}\tilde{\mathbf{K}}_{jk}^{\mathrm{s}}\boldsymbol{\Phi}_{\mathrm{r}k}\underline{\tilde{\boldsymbol{\alpha}}}_{\mathrm{r}k} = \boldsymbol{\Phi}_{\mathrm{r}j}^{\mathrm{T}}\underline{\tilde{\mathbf{f}}}_j^{\mathrm{s}}. \tag{23}$$

The tractions $\underline{\tilde{\mathbf{t}}}_{\mathrm{s}k}(\kappa_y, \omega)$ on the interface $\Sigma_k$ are evaluated within the periodic domain $\tilde{\Omega}_{\mathrm{s}}^{\mathrm{e}}$ using the representation of equation (10) in the wavenumber-frequency domain:

$$\sum_{k=1}^{N_x}\left[\mathbf{I}_{jk} + \tilde{\mathbf{T}}_{jk}\right]\underline{\tilde{\mathbf{u}}}_{\mathrm{s}k} = \sum_{k=1}^{N_x}\tilde{\mathbf{U}}_{jk}\underline{\tilde{\mathbf{t}}}_{\mathrm{s}k}. \tag{24}$$

Equation (24) requires the computation of $\tilde{\mathbf{U}}_{jk}(\kappa_y, \omega)$ and $\tilde{\mathbf{T}}_{jk}(\kappa_y, \omega)$ which are obtained using the Green-Floquet fundamental solutions (22).

The radiated wave field $\underline{\tilde{\mathbf{u}}}_{\mathrm{s}}^{\mathrm{r}}(\tilde{\mathbf{x}}, \kappa_y, \omega)$ in the domain $\tilde{\Omega}_{\mathrm{s}}^{\mathrm{e}}$ is computed using equation (17) in the wavenumber-frequency domain and limiting the number of resonators to $N_x$. Its spatial-frequency domain representation $\underline{\hat{\mathbf{u}}}_{\mathrm{s}}^{\mathrm{r}}(\mathbf{x}, \omega)$ defined in $\Omega_{\mathrm{s}}^{\mathrm{e}}$ is obtained using the inverse Floquet transform (21).

## 3 Application: seismic metasurface as a mitigation measure

### 3.1 Problem outline

A uniform array of resonators interacting with a homogeneous halfspace is considered. The dynamic soil characteristics are summarized in table 1. We investigate the vibration mitigation performance of metasurfaces with six rows of resonators ($N_x = 6$) in the $x$-direction and $N_y = 7, 21,$ and $\infty$ resonators in the $y$-direction. These are denoted as $\mathrm{MS1}$, $\mathrm{MS2}$, and $\mathrm{MS3}$, respectively. Lattice constants $a_x = 1\,\mathrm{m}$ and $a_y = 1.5\,\mathrm{m}$ are considered. A resonator is composed of an oscillator on top of a surface foundation. The oscillator has mass of $50\,\mathrm{kg}$ and resonance frequency of $\mathrm{f_{res}} = 60\,\mathrm{Hz}$. A damping ratio $\xi = 0.01$ is incorporated. The foundation is a rigid concrete slab of dimension $0.5\,\mathrm{m} \times 0.5\,\mathrm{m} \times 0.1\,\mathrm{m}$ and mass $62.5\,\mathrm{kg}$. The metasurface is placed at a distance $D = 12\,\mathrm{m}$ so that mainly Rayleigh waves impinge on the resonators.

| Layer | $h$ [m] | $C_{\mathrm{s}}$ [m/s] | $C_{\mathrm{p}}$ [m/s] | $\beta_{\mathrm{s}}$ [-] | $\beta_{\mathrm{p}}$ [-] | $\rho$ [kg/m$^3$] |
|---|---|---|---|---|---|---|
| 1 | $\infty$ | 150 | 300 | 0.020 | 0.020 | 1800 |

Table 1: Dynamic soil characteristics for the homogeneous soil.

### 3.2 Algorithmic parameters

Calculations are made for frequencies between $40\,\mathrm{Hz}$ and $80\,\mathrm{Hz}$ with a frequency bin of $1\,\mathrm{Hz}$. A logarithmic sampling is adopted for the horizontal wavenumber $k_x$ in both 3D and periodic models, whereas a linear sampling is used for the wavenumber $\kappa_y$ with $\Delta\kappa_y = 2\pi/(N_c L)$. All computations were performed on 11th Gen Intel® Core™ i7-11850H ($2.50\,\mathrm{GHz}$) CPUs and $32\,\mathrm{Gb}$ RAM.

The homogeneous soil in table 1 has a Rayleigh wavelength $\lambda_{\mathrm{R}} = C_{\mathrm{R}}/f_{\max} = 1.75\,\mathrm{m}$ at $80\,\mathrm{Hz}$. A BE mesh consisting of $6 \times 6$ square 4-node linear elements is used, ensuring an accurate BE solution in the chosen frequency range.

The period $L$ influences the required number of terms $N_c$ in the Floquet summation (22) as it changes the distance $N_c L$ between the periodic sources [15]. In addition to this, $N_c$ also depends on the wavelength at a selected frequency, which is affected by the dynamic soil characteristics. Computations are obtained using $N_c = [90, 67]$ for a frequency band split into two ranges as $[(40-60), (61-80)]$ Hz. These correspond to a maximum distance $N_c L = [135, 100.5]\ \mathrm{m}$ from the source within the reference cell $\tilde{\Omega}_{\mathrm{s}}^{\mathrm{e}}$, ensuring that the periodic sources are far enough from the receiver points in the corresponding frequency bands. In cases where metasurfaces are on top of highly damped soils where elastic waves vanish at shorter distances, $N_c$ can be decreased yielding a significant reduction in computational cost.

### 3.3 Vibration mitigation performance

Figure 2 presents the real part of the vertical displacement $\hat{\mathrm{u}}_{zz}(\mathbf{x}, \mathbf{x}', \omega)$ on a large grid of receiver points on the surface of the homogeneous halfspace at $56\,\mathrm{Hz}$, $57\,\mathrm{Hz}$, and $58\,\mathrm{Hz}$ for $\mathrm{MS1}$, $\mathrm{MS2}$, and $\mathrm{MS3}$. Black lines connect the source location to the closest corners of the metasurface, delimiting the zone affected by the metasurface. A black square depicts a resonator. Black circles display receiver points behind the array of resonators at $x = 31\,\mathrm{m}$ and $y = 0$, $10\,\mathrm{m}$, and $20\,\mathrm{m}$, denoted as $\mathrm{R1}$, $\mathrm{R2}$, and $\mathrm{R3}$. $\mathrm{MS1}$ and $\mathrm{MS2}$ are computed using a 3D FE-BE model [4], while $\mathrm{MS3}$ is evaluated using the periodic FE-BE model.

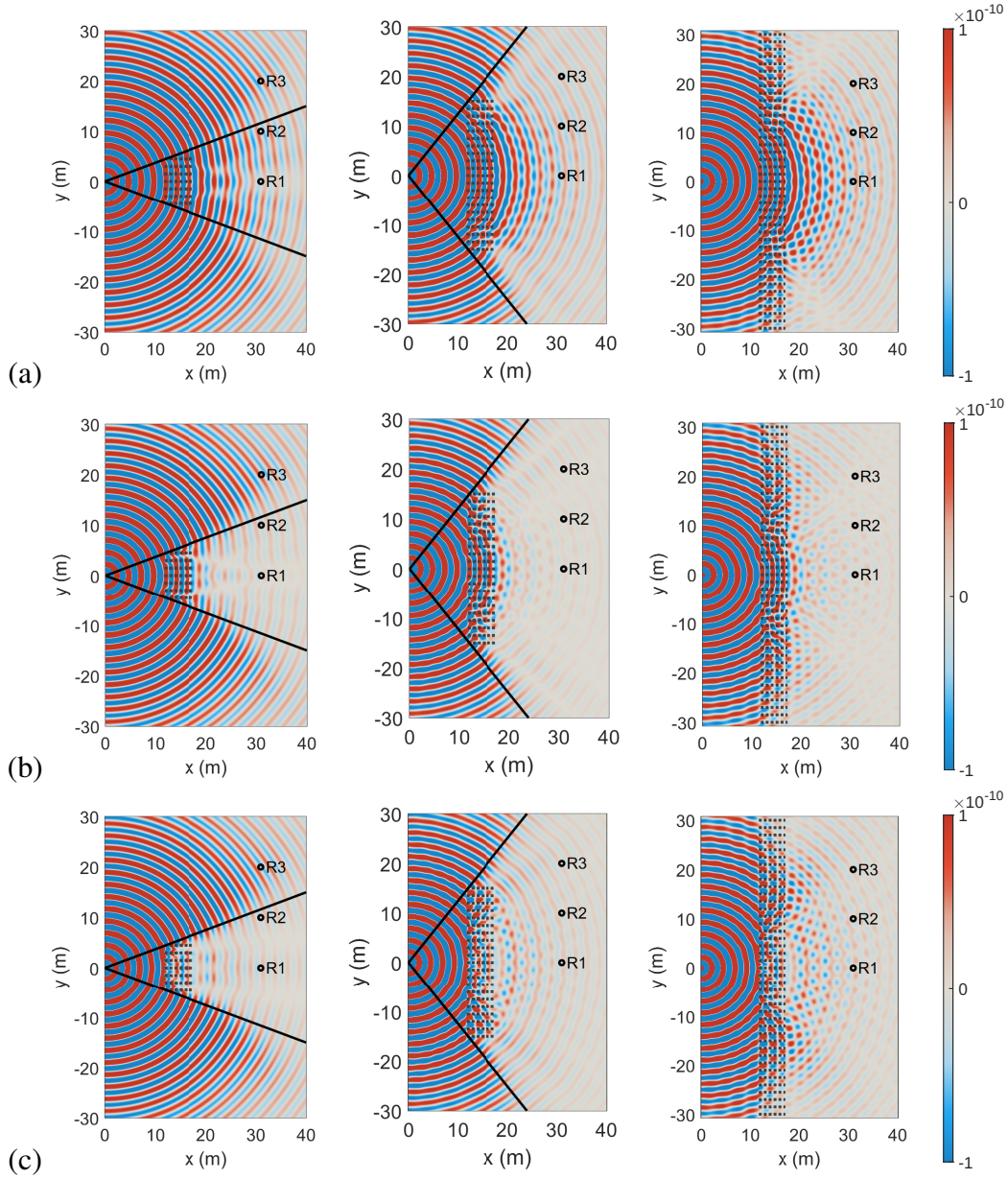


Figure 2: Real part of the vertical displacement $\hat{u}_{zz}(\mathbf{x}, \mathbf{x}', \omega)\,[\mathrm{m/Hz}]$ at (a) $56\,\mathrm{Hz}$, (b) $57\,\mathrm{Hz}$, and (c) $58\,\mathrm{Hz}$ on the surface ($z = 0$) of the homogeneous soil for $\mathrm{MS1}$ (left), $\mathrm{MS2}$ (middle), and $\mathrm{MS3}$ (right). Black lines connect the source to the corners of the metasurface.

Significant vibration reduction is found behind the metasurfaces within the shielded zone.

At $56\,\mathrm{Hz}$ (figure 2a), this is less pronounced as this frequency is relatively far from the resonance frequency of the resonators. The Rayleigh wave at $57\,\mathrm{Hz}$ and $58\,\mathrm{Hz}$ (figure 2b and 2c) interacting with the resonators splits into three portions, which propagate in the $x$-, $-y$-, and $+y$-direction. The waves traveling in the $y$-direction are not significantly affected by $\mathrm{MS1}$ as only three rows of resonators are not enough to attenuate the wave field. As a result, vibration is amplified outside the shielded zone, near its borders. This is no longer the case for $\mathrm{MS2}$ and $\mathrm{MS3}$ as the Rayleigh waves propagating in the $y$-direction are attenuated by the large number of resonators in this direction. A more important scattered wave field behind $\mathrm{MS2}$ and $\mathrm{MS3}$ in comparison to $\mathrm{MS1}$ is observed at these frequencies.

Figure 3 shows the insertion loss $\widehat{\mathrm{IL}}(\mathbf{x},\omega)$ of the vertical displacement at $\mathrm{R1}$, $\mathrm{R2}$, and $\mathrm{R3}$ on a logarithmic scale in dB for metasurfaces considered in figure 2. The insertion loss is defined as the ratio of the vertical displacement amplitude without and with the metasurface. Positive values of the insertion loss indicate a reduction of the vertical free field vibrations. A sharp peak in the insertion loss at the resonance frequency of the system is observed indicating significant vibration attenuation.

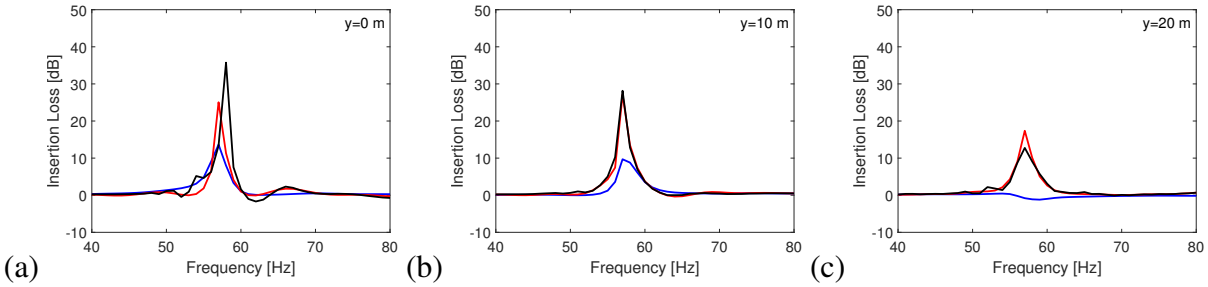


(a) (b) (c)

Figure 3: Insertion loss $\widehat{\mathrm{IL}}(x = 31\,\mathrm{m}, y, z = 0, \omega)$ on the surface of the soil at (a) $\mathrm{R1}$, (b) $\mathrm{R2}$, and (c) $\mathrm{R3}$, for $\mathrm{MS1}$ (blue), $\mathrm{MS2}$ (red), and $\mathrm{MS3}$ (black).

Although all configurations generate vibration reduction at $\mathrm{R1}$ at $56\,\mathrm{Hz}$, $57\,\mathrm{Hz}$, and $58\,\mathrm{Hz}$ (figure 2), figure 3a reveals a significant impact on the metasurface's efficiency of the number of resonators in the longitudinal direction. The frequency where the peak is observed and the vibration attenuation performance is influenced by $N_y$, where a change in this term results in an alteration in the mass density of the system, leading to a shift in frequency. For $\mathrm{MS1}$ and $\mathrm{MS2}$, a peak at $57\,\mathrm{Hz}$ is found. Infinitely extending the metasurface in the $y$-direction induces a shift of the peak to $58\,\mathrm{Hz}$, as well as boosts the vibration mitigation performance, as larger peak values are found for $\mathrm{MS3}$.

Peaks at the same frequency for the different metasurfaces are found when the insertion loss is evaluated at $\mathrm{R2}$ (figure 3b). A good agreement between the insertion loss of $\mathrm{MS2}$ and $\mathrm{MS3}$ is observed. The vibration mitigation performance of the metasurfaces is reduced at $\mathrm{R2}$ in comparison to the performance seen at $\mathrm{R1}$ (figure 3a).

Figure 3c shows the insertion loss at $\mathrm{R3}$. This receiver is outside the zone protected by $\mathrm{MS1}$ as depicted in figure 2, resulting in $\widehat{\mathrm{IL}} \approx 0$. Slightly negative values of insertion loss are obtained around the resonance frequency of the system due to the vibration amplification near the borders of the shielded zone. The peak values for $\mathrm{MS2}$ and $\mathrm{MS3}$ are distinguishable. More energy travels in the direction of $\mathrm{R3}$ behind $\mathrm{MS3}$ (figure 2b), resulting in a lower value of insertion loss at $57\,\mathrm{Hz}$ at this location in comparison to the response for $\mathrm{MS2}$.

The peak values of the insertion loss for all metasurfaces are reduced at farther points, indicating that the performance decreases with distance.

Similar results are obtained with the periodic model when the (finite) metasurface is effectively long in the $y$-direction. This indicates that the periodic method can be used as an alternative for a 3D model when the metasurface is long enough in the $y$-direction. Further investigation should be done to precisely quantify how long the metasurface has to be.

### 3.4 Computational performance

Table 2 summarizes the number of degrees of freedom $N_{\mathrm{DOF}}$, required memory to compute the boundary element matrices $\hat{\mathbf{U}}(\omega)$ and $\tilde{\mathbf{U}}(\kappa_y, \omega)$, the transfer matrices $\hat{\mathbf{U}}_{\mathrm{p}}(\mathbf{x}, \omega)$ and $\tilde{\mathbf{U}}_{\mathrm{p}}(\tilde{\mathbf{x}}, \kappa_y, \omega)$, and the CPU time to compute the response for all metasurfaces considered in figures 2 (case 1) and 3 at a single frequency (case 2). These matrices contain complex floating point entries in double precision.

| | $N_y$ [−] | $N_{\mathrm{DOF}}$ [−] | $\hat{\mathbf{U}}$ [Gb] | $\hat{\mathbf{U}}_{\mathrm{p}}$ [Gb] | Time (case 1) [s] | Time (case 2) [s] |
|---|---|---|---|---|---|---|
| MS1 | 7 | 6 174 | 0.57 | 16.70 | 1 368 | 118.8 |
| MS2 | 21 | 18 522 | 1.96 | 50.10 | 7 920 | 1 620 |
| | $N_c$ [−] | $N_{\mathrm{DOF}}$ [−] | $\tilde{\mathbf{U}}$ [Gb] | $\tilde{\mathbf{U}}_{\mathrm{p}}$ [Gb] | Time (case 1) [s] | Time (case 2) [s] |
| MS3 | 67 | 882 | 0.01 | 0.55 | 55 074 | 8710 |
| MS3 | 90 | 882 | 0.01 | 0.55 | 97 897 | 15 702 |

Table 2: Required memory to compute the boundary element matrices $\hat{\mathbf{U}}(\omega)$ and $\tilde{\mathbf{U}}(\kappa_y, \omega)$, the transfer matrices $\hat{\mathbf{U}}_{\mathrm{p}}(\mathbf{x}, \omega)$ and $\tilde{\mathbf{U}}_{\mathrm{p}}(\tilde{\mathbf{x}}, \kappa_y, \omega)$, and the CPU time to compute the response at a single frequency in figures 2 (case 1) and 3 (case 2).

In a 3D BE computation, a quadratic amount of memory ($\mathcal{O}(N_{\mathrm{DOF}}^2)$) in terms of the number of degrees of freedom $N_{\mathrm{DOF}}$ of the BE mesh is required to store $\hat{\mathbf{U}}(\omega)$. In order to solve equation (10) by means of direct solvers, for instance an LU-decomposition, a cubic amount of operations is demanded ($\mathcal{O}(N_{\mathrm{DOF}}^3)$). Therefore, using a 3D FE-BE model to assess the performance of a very long and wide metabarrier is limited by excessive memory requirements.

An amount of memory of $\mathcal{O}(N_{\mathrm{DOF_s}} N_{\mathrm{DOF}})$ is required to store the transfer matrix $\hat{\mathbf{U}}_{\mathrm{p}}(\mathbf{x}, \omega)$, where $N_{\mathrm{DOF_s}}$ is the number of degrees of freedom at all receiver points. MS2 requires $50.1\,\mathrm{Gb}$ to store this matrix, exceeding the RAM limits of the machine. Nevertheless, as the response at receiver points can be calculated separately, the wave field on a large grid can still be obtained. Storing this matrix for reuse to compute different superstructures requires a high amount of disk storage preventing parametric studies using this formulation.

A quadratic amount of memory is still required to store the boundary element matrix $\tilde{\mathbf{U}}(\kappa_y, \omega)$ in a periodic FE-BE model. However, the number of degrees of freedom $N_{\mathrm{DOF}}$ in the BE mesh is drastically reduced as modeling of only a line of resonators is needed. This model can therefore be used to compute the solution of metasurfaces with large number of resonators $N_x$.

The amount of memory necessary to store the transfer matrix $\tilde{\mathbf{U}}_{\mathrm{p}}(\tilde{\mathbf{x}}, \kappa_y, \omega)$ is also significantly lowered in comparison to a 3D BE computation. As the free field is restrained to the reference cell $\tilde{\Omega}_{\mathrm{s}}^{\mathrm{e}}$, $N_{\mathrm{DOF_s}}$ also reduces. This reduces the disk space required to store this matrix, enabling saving and reusing this matrix for further computations where only the superstructure is modified.

Besides using Green-Floquet fundamental solutions (22), the periodic FE-BE model requires a BE computation for all wavenumbers. As a result, the 3D FE-BE method turn out to be faster

than the periodic FE-BE model for moderate problem sizes. Periodic models can be an attractive alternative in cases where longer finite metasurfaces are needed (e.g. railway induced vibration). Moreover, since a significant decrease in CPU time is experienced when $N_c$ is reduced (table 2), larger $a_y$ or highly damped soils result in higher efficiency of the periodic FE-BE model as convergence can be achieved for smaller values of $N_c$.

## 4 Conclusions

The effect of the length of 2D seismic metasurfaces on vibration mitigation performance has been investigated. This is accomplished using 3D and periodic FE-BE models. Results for three metasurfaces with increasing $N_y$ approaching the have been presented. Behind longer metasurfaces, larger vibration reduction is found in a perpendicular direction from the source. Similar results are obtained in diagonal directions when the finite metasurface is effectively long in the $y$-direction. Finally, the vibration mitigation performance of the metasurfaces reduces with distance in the $y$-direction.

The computational efficiency of the periodic model has been compared with the 3D FE-BE approach. Although using a periodic FE-BE model results in a significant reduction in memory requirements, the CPU time to solve the problem increases in comparison to the 3D FE-BE model. This, however, strongly depends on the required number of terms $N_c$ in the Floquet transformation, which depends on the period $L$ and the soil properties. For a large period $L$ and highly damped soils, the periodic FE-BE model can be more efficient than the 3D model as $N_c$ is significantly reduced.

## Acknowledgement

Results presented in this paper were obtained within the frame of the project G0B8221N "Mitigation of railway induced vibration using seismic metamaterials" funded by the Research Foundation Flanders (FWO Flanders). The financial support is gratefully acknowledged.

## REFERENCES

[1] D. Colquitt, A. Colombi, R. Craster, P. Roux, and S. Guenneau, "Seismic metasurfaces: Sub-wavelength resonators and rayleigh wave interaction," *Journal of the Mechanics and Physics of Solids*, vol. 99, pp. 379–393, 2017.

[2] A. Palermo, S. Krödel, A. Marzani, and C. Daraio, "Engineered metabarrier as shield from seismic surface waves," *Scientific reports*, vol. 6, no. 1, pp. 1–10, 2016.

[3] C. He, S. Zhou, X. Li, H. Di, and X. Zhang, "Forest trees as a natural metamaterial for surface wave attenuation in stratified soils," *Construction and Building Materials*, vol. 363, p. 129769, 2023.

[4] D. Carneiro, H. Kato, P. Reumers, G. Lombaert, and G. Degrande, "Mitigation of environmental ground vibration using seismic metasurfaces," in *Proceedings of the 30th International Conference on Noise and Vibration Engineering, ISMA 2022* (W. Desmet, B. Pluymers, D. Moens, and S. Neeckx, eds.), (Leuven, Belgium), pp. 3247–3261, September 2022.

[5] S. Brûlé, E. Javelaud, S. Enoch, and S. Guenneau, "Experiments on seismic metamaterials: molding surface waves," *Physical review letters*, vol. 112, no. 13, p. 133901, 2014.

[6] A. Colombi, P. Roux, S. Guenneau, P. Gueguen, and R. V. Craster, "Forests as a natural seismic metamaterial: Rayleigh wave bandgaps induced by local resonances," *Scientific reports*, vol. 6, no. 1, pp. 1–7, 2016.

[7] A. Colombi, D. Colquitt, P. Roux, S. Guenneau, and R. Craster, "A seismic metamaterial: The resonant metawedge," *Scientific reports*, vol. 6, no. 1, pp. 1–6, 2016.

[8] A. Palermo, M. Vitali, and A. Marzani, "Metabarriers with multi-mass locally resonating units for broad band rayleigh waves attenuation," *Soil Dynamics and Earthquake Engineering*, vol. 113, pp. 265–277, 2018.

[9] C. Zeng, C. Zhao, and F. Zeighami, "Seismic surface wave attenuation by resonant metasurfaces on stratified soil," *Earthquake Engineering & Structural Dynamics*, vol. 51, no. 5, pp. 1201–1223, 2022.

[10] D. Clouteau, M. Elhabre, and D. Aubry, "Periodic BEM and FEM-BEM coupling: application to seismic behaviour of very long structures," *Computational Mechanics*, vol. 25, pp. 567–577, 2000.

[11] D. Aubry and D. Clouteau, "A subdomain approach to dynamic soil-structure interaction," in *Recent advances in Earthquake Engineering and Structural Dynamics* (V. Davidovici and R. Clough, eds.), pp. 251–272, Nantes: Ouest Editions/AFPS, 1992.

[12] S. François, *Nonlinear modelling of the response of structures due to ground vibrations*. PhD thesis, Department of Civil Engineering, KU Leuven, 2008.

[13] R. R. Craig Jr and M. C. Bampton, "Coupling of substructures for dynamic analyses.," *AIAA journal*, vol. 6, no. 7, 1968.

[14] G. Degrande, D. Clouteau, R. Othman, M. Arnst, H. Chebli, R. Klein, P. Chatterjee, and B. Janssens, "A numerical model for ground-borne vibrations from underground railway traffic based on a periodic finite element - boundary element formulation," *Journal of Sound and Vibration*, vol. 293, no. 3-5, pp. 645–666, 2006.

[15] S. Gupta, M. Hussein, G. Degrande, H. Hunt, and D. Clouteau, "A comparison of two numerical models for the prediction of vibrations from underground railway traffic," *Soil Dynamics and Earthquake Engineering*, vol. 27, no. 7, pp. 608–624, 2007.

COMPDYN 2023
9th ECCOMAS Thematic Conference on
Computational Methods in Structural Dynamics and Earthquake Engineering
M. Papadrakakis, M. Fragiadakis (eds.)
Athens, Greece, 12-14 June 2023

# LOW-COST HYBRID DESIGN STRATEGIES: LARGE-SCALE SHAKING TABLE TESTS AND CHALLENGES OF IMPLEMENTATION

**Anastasios Tsiavos**[1], **Anastasios Sextos**[2]

[1] Lecturer, ETH Zurich, Switzerland
tsiavos@ibk.baug.ethz.ch

[2] Professor, University of Bristol, United Kingdom
a.sextos@bristol.ac.uk

## Abstract

*The complexity of design, the high transportation cost and the use of materials of high carbon footprint inhibit the sustainable implementation of response modification strategies, such as seismic isolation systems and tuned mass dampers to a large number of countries worldwide. This study presents novel, low-cost response modification strategies that are constructed based on materials, which can be easily resourced. These strategies comprise low-cost engineering measures for the protection of the superstructure from seismic damage at the design hazard level and low-cost seismic isolation techniques for the seismic protection of structures for intensities that exceed the design one. These methods are based on the inclusion of a thin layer of sand or roller bearings between two rigid and smooth surfaces in a sandwich configuration, which facilitates the sliding of the upper surface against the bottom surface at an attractively low, yet reasonably configurable, friction coefficient. The efficiency of the aforementioned response modification strategies is demonstrated based on large-scale testing performed at University of Bristol that paved the way for the design and construction of a new building.*

**Keywords:** seismic isolation, low-cost response modification strategies, large-scale shaking table tests

## 1 INTRODUCTION

The design of strategies that modify the dynamic response of structures aims to utilize the attractive mechanical characteristics, the energy dissipation and the recentering ability of highly engineered devices to reduce the seismic demand during an earthquake excitation. These strategies, defined as response modification strategies, entail a wide range of seismic isolation devices and tuned mass dampers, which are extensively implemented worldwide in developed countries ([1], [2], [3], [4]).

However, the high transportation cost, the project-specific qualification testing, the use of materials of high embodied carbon footprint and the highly engineered construction of these devices inhibit their extensive application in regions of low- to moderate income, as well as in deprived areas in higher income countries. This is because owners and stakeholders have limited access to highly technology seismic protection systems or lack the resources to enforce compliance to modern codes, including those associated with seismic isolation [5]. Moreover, the lack of technical equipment and/or access to certified laboratories for project-specific testing of isolation devices and the potential absence of quality control in the field, increase the uncertainties related to the mechanical properties of the seismic isolation system that is constructed on site compared to a standard, highly engineered seismic isolation system. These uncertainties may impede the activation and the efficiency of the seismic isolation system and lead to severe damage to a superstucture that was not designed for the 'non-activated' seismic isolation configuration. This is of particular importance for the case of seismic motion intensities that exceed the design one as these structures would be lacking the adequate ductility.

In light of these challenges, the design of structures to develop different dynamic response mechanisms for different seismic intensity levels emerges as an engineering solution that is highly aligned with the context of countries or regions with limited financial resources, characterized by inadequate quality control and insufficient measures for ductile design. According to this design approach, defined as Low-Cost Hybrid Design (LC-HD) by Tsiavos et al. [6], the building is designed to respond in a 'fixed-based' mode for the design seismic intensity, and respond in a ductile manner according to the performance objectives outlined in the seismic code. For earthquake ground motions beyond the design level, the system is expected to slide on the low-cost foundation surface, thus introducing a "fuse" that is aimed to protect the structure in case of insufficient detailing, lack of code compliance or poor material properties. Essentially the Low-Cost Hybrid Design (LC-HD) refers to new buildings that are expected to be designed by the code, but given the lack of confidence on its implementation, it offers an additional safety factor against collapse.

Different alternatives have been proposed for the above foundation sliding interface. Tsiavos et al. [6,7,8] demonstrated experimentally, at large scale, the efficiency of a novel 'sand-wich' seismic isolation, based on the encapsulation of a thin sand layer (PVC sand-wich) or a layer of roller bearings (PVC-Rollers Sandwich) between two PVC surfaces below the foundation of a structure. The sliding of the superstructure at a configurable low friction coefficient that may vary in the range of 0.1 to 0.25 is enabled by the rolling motion of sand grains (PVC sand-wich [6]) or glass/steel roller bearings (PVC-Rollers Sandwich [8]). A similar system was explored by Banovic et al. [9], who investigated numerically and experimentally at large scale the sliding of structures founded on a layer of pebbles.

Several researchers have further investigated experimentally low-cost seismic isolation methods [10, 11] based on the use of fiber-reinforced, unbonded elastomeric isolators. Nevertheless, the vulcanization required for the production of rubber in these bearings inhibits their use in countries where this vulcanization cannot be performed, leading to high carbon footprint values and high transportation costs. Another group of low-cost seismic isolation

methods comprises a class of Geotechnical Seismic Isolation (GSI) methods [12], which are based on the use of flexible soil-based materials below the structure that modify its seismic response. Tsang [12] and Brunet et al. [13] investigated numerically and showed the efficiency of the use of a 2m thick, flexible sand-rubber foundation layer for the seismic isolation of structures in developing countries.
Tsiavos et al. [14] investigated experimentally the seismic response of structures founded on a sand-rubber layer. Gatto et al. [15] explored the injection of flexible polyurethane foam into the soil below the foundation of a building to create a low-cost seismic isolation system that reduces the seismic acceleration of the building during an earthquake excitation. However, this method requires a deep excavation below the structure and the deposition of a flexible GSI layer [16]. The main problem though of the implementation of rubber-based mixtures for the GSI of structures is the induced rocking motion that may be manifested during the excitation [7]. Within this context, the hybrid low-cost response modification strategies emerge as a promising combination of efficient seismic protection for a wide spectrum of intensity levels, that does not require significant resources of the use of materials that are not accessible in low-income regions. This paper presents a summary of the large-scale shaking table tests that demonstrate the efficiency of these low-cost response modification strategies and discusses the challenges related to the implementation of these strategies in real life structural design and construction.

## 2 LARGE-SCALE SHAKING TABLE TESTS

The conceptual design of a prototype, masonry building using the Low-Cost Hybrid Design method (LC-HD) is presented in Fig. 1. The design of the superstructure, which in this case is a masonry one, comprises the attachment of steel wire mesh and steel ties to the facade walls of the building. The latter is expected to increase substantially the in-plane and out-of-plane seismic strength and deformability of the building. The design of these engineering measures aims at the seismic protection of the building from seismic damage for the design seismic hazard level, as per the provisions of seismic codes for masonry construction. If this seismic hazard level is exceeded by a strong earthquake ground motion excitation, a secondary ‘fuse’ mechanism is designed to get activated at the foundation of the building. This mechanism comprises the novel, low-cost ‘sand-wich’ seismic isolation system, that was described previously. The RC foundation slab of the building is casted above the upper PVC surface. A 10-20 cm thick excavation further enables the construction of a hardcore layer, typically of concrete as well, allowing for the formation of a flat, rigid base below the sliding surface of the structure. The sand layer was initially designed with a 5cm thick sand layer but was gradually reduced to achieve the desirable friction coefficient.
The large-scale shaking table investigation of a three-times scaled down model of the above masonry building at the 3mx3m, 6-degree-of-freedom shaking table of University of Bristol [6] is shown in Fig. 2a. The magnified acceleration response of the superstructure subjected to the Chi-Chi 1999 earthquake ground motion is shown in Fig. 2b.
As shown in Fig. 2b, the building subjected to an earthquake ground motion excitation of PGA=0.4g that represents the design acceleration in several countries worldwide, manifested sliding, thus capping the maximum acceleration acting on the superstructure to an acceleration level of 0.2g. This corresponds to a kinetic friction coefficient of approximately 0.2. It is noted that the acceleration demand of 0.2g did not cause any damage to the superstructure, since that was designed following efficient and low-cost engineering practices (well anchored steel mesh around the masonry walls and steel ties connecting opposite wall surfaces).

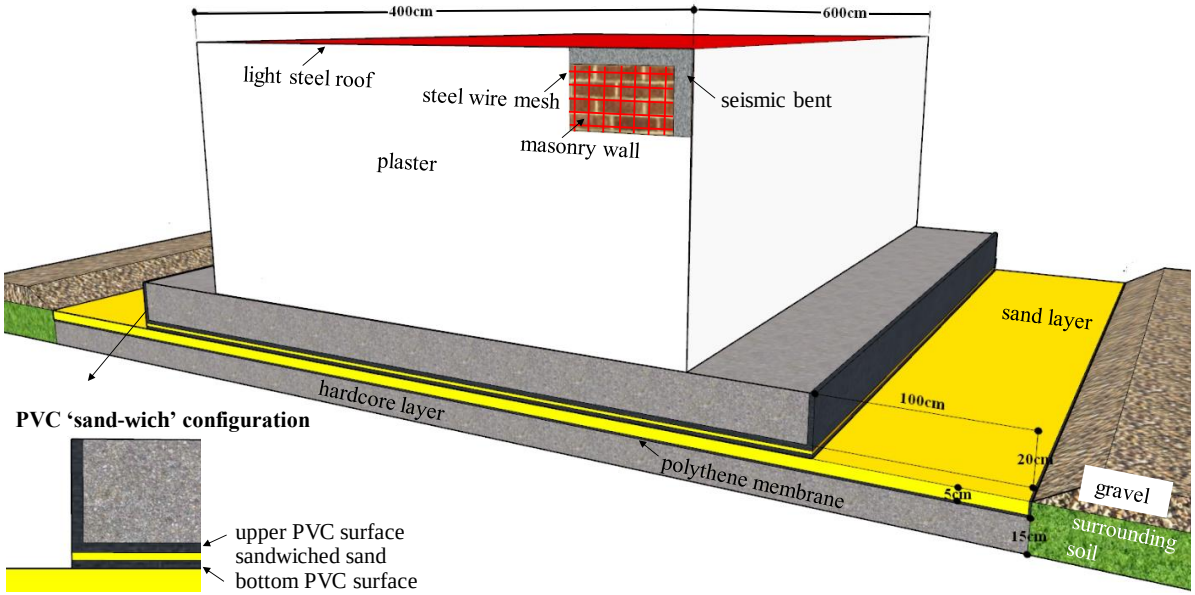


Fig. 1. Prototype building designed with the Low-Cost Hybrid Design (LC-HD) method.

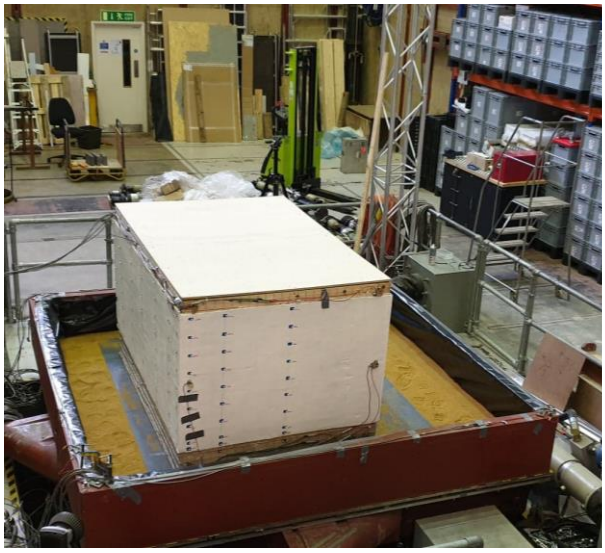

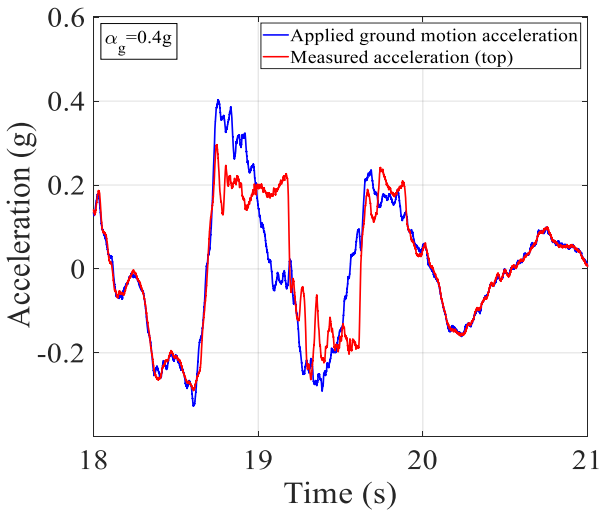


(a) (b)

Fig. 2. (a) Large-scale shaking table test of scaled masonry building designed using the LC-HD method at University of Bristol (b) Magnified acceleration response at sliding due to the activation of the PVC-sandwich seismic isolation for the Chi-Chi 1999 recorded earthquake ground motion excitation.

As a means to introduce a lower friction coefficient rolling elements were also encapsulated into the sliding surface. It was observed [8] that the replacement of sand with steel or glass bearings can decrease the friction coefficient of the interface, due to the smoother rolling motion of the spherical encapsulated elements, to 0.1 or below (Fig. 3).

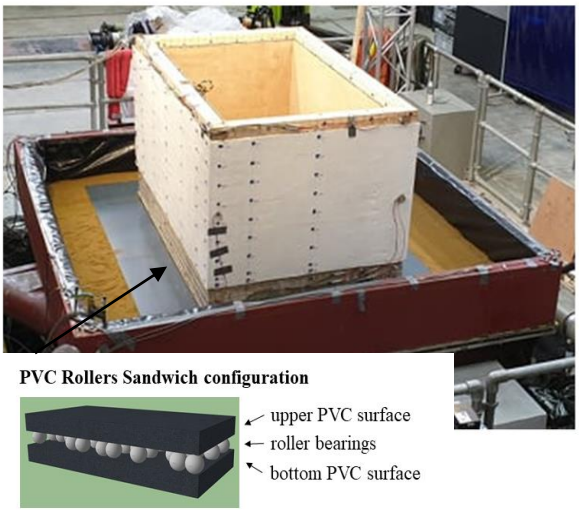


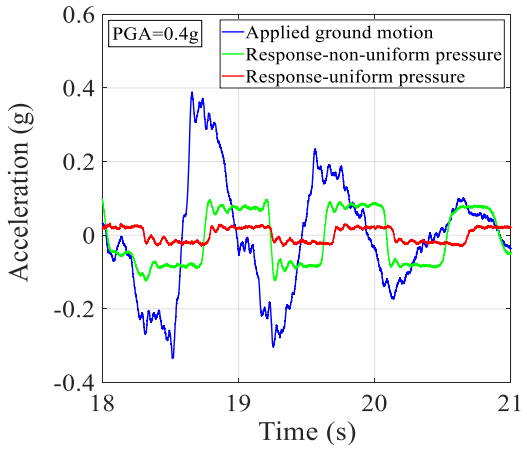


(a) (b)

Fig. 3. (a) Large-scale shaking table test of scaled masonry building designed using the LC-HD method at University of Bristol (b) Magnified acceleration response at sliding due to the activation of the PVC Rollers sandwich seismic isolation for the Chi-Chi 1999 recorded earthquake ground motion excitation.

This is shown in more detail in the magnified acceleration response of the superstructure subjected to the Chi-Chi 1999 earthquake ground motion of Fig. 3b: the building subjected to an excitation of PGA=0.4g manifested sliding at an attractively low acceleration level of 0.05g for a density of 800 rollers/m$^2$ facilitating uniform vertical pressure on the bearings. The use of 200 rollers/m$^2$ increased the sliding acceleration level to 0.1g due to the non-uniform pressure on the bearings, which inhibits the smoothness of their rolling motion. The masonry structure, which was designed following efficient and low-cost engineering practices (steel mesh, steel ties), was protected from seismic damage in this case as well, both in the state before sliding as well as during sliding.

## 3 CHALLENGES OF IMPLEMENTATION

The modern code provisions for the inelastic, seismic design of structures focus on the concentration of seismic damage at pretetermined locations, which are designed to behave in a ductile manner and dissipate seismic energy during an earthquake event. However, the ductile design of structures to satisfy displacement-based performance objectives related to their expected seismic damage is not always feasible in regions with limited financial resources, as observed in some areas during the recent 2023 Kahranmaras earthquake in Turkey. Within this frame, the fundamental performance objective for the design of structures located in these regions is the prevention of their collapse, not only for the design earthquake, but also for seismic intensites exceeding the design hazard level.

The efficiency of the LC-HD approach was demonstrated in the previous section. However, a major drawback of such a low-cost protective system is the inevitable lack of recentering capability. This was also observed during the large-scale shaking table tests performed by Tsiavos et al. [6,7,8] that indicated a residual sliding displacement of the isolated superstructure after the end of the ground motion excitation, of the order of 5cm-15cm. Detailed probabilistic assessment for the case of a 3-storey R/C building have also shown [5] a

mean value of residual displacement of the order of 10cm, with the maximum predicted transient displacement being approximately 30cm in the extreme case of motions twice as strong as the design acceleration (i.e., for Sa(T)=2g), see Fig. 4. Note that the PVC-s residual-to-maximum displacement ratio was found of the order of 2/3 [5].

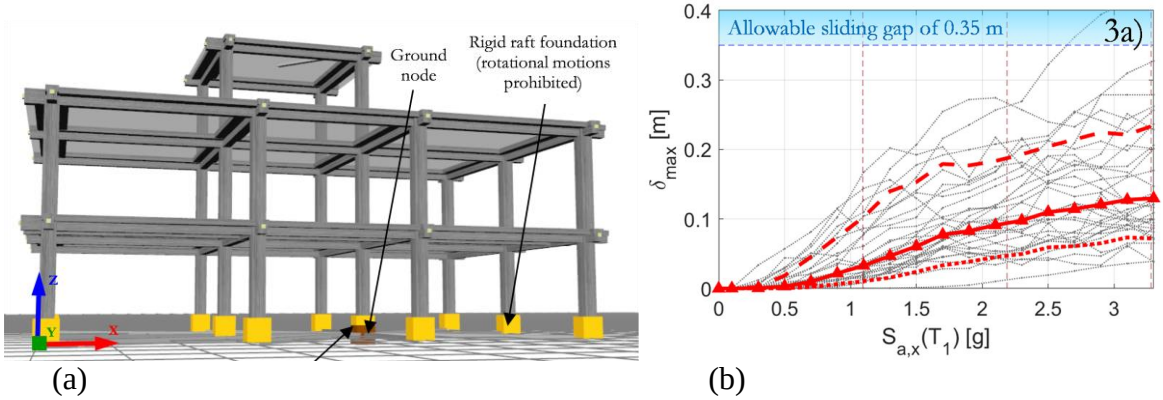


(a) (b)

Fig. 4. (a) Overview of the building numerically studied and (b) maximum PVC-s sliding displacement $\delta_{max}$ [m] [5].

From a practical viewpoint, for low-rise, low-weight structures, the recentering of the superstructure after the earthquake can be performed by means of trucks that are able to apply the necessary pulling force. Additionally, appropriate design measures should be considered for the accommodation of this sliding displacement in the design phase, by providing flexible connections for the pipes and sewage system and the implementation of a buffer zone in the form of a sacrificial parapet in the perimeter of the structure to inhibit pounding. Sextos et al. [5] report that given an allowable sliding gap of 0.35 m, the probability of pounding between the raft foundation of the PVC-s base-isolated building and the non-structural perimeter parapet wall is less than 2% at the extreme case of three times the design-level (see also Fig. 4b). In case the design requirements for the structure do not allow a residual sliding displacement or the weight of the structure does not allow the recentering by trucks, a recentering system that minimizes this residual sliding displacement has been proposed by ETH Zurich. Tsiavos et al. [17] demonstrated through large-scale shaking table tests at ETH Zurich the efficiency of a low-cost and sustainable recentering system based on low-cost steel springs and deformable timber plates [18]. This system, which is based on a 'sandwich' seismic isolation strategy, can be used either as low-cost seismic isolation with recentering or a low-cost tuned mass damper, leading to residual sliding displacement lower than 5mm. Alternative, low-cost recentering systems are also currently explored at the University of Bristol under the UKRI-funded project LASSIE (Low life cycle cost Sand-wich Isolation System for Seismic Risk Reduction, PI: N. Alexander, Co-Is: A. Sextos, A. Diambra).

The aforementioned novel engineering techniques for the combination of low-cost seismic isolation with recentering systems will increase substantially the potential of application of low-cost hybrid design and low-cost seismic isolation to a wide range of countries worldwide. It is the authors' position though that for case that the construction quality of the superstructure cannot be assured, the protective sliding 'fuse' mechanism is deemed critical to at least prevent collapse. This observation essentially paves the way for a wider discussion of rethinking what are the *desirable* and *feasible* performance objectives in the context of housing safety in the developing world.

## 4 CONCLUSIONS

This paper focuses on the presentation of the results of large-scale shaking table tests and the challenges of implementation of low-cost response modification strategies to developing countries. The uncertainties related to the implementation of ductile seismic design measures and highly engineered seismic isolation methods in low-income countries emerge from the lack of quality control, the improper inspection of the construction site and the inadequate application of the latest code provisions in these countries. These uncertainties require rethinking and contextualization of the conventional performance-based design approaches to align with the aforementioned construction limitations. Along these lines, this study aims to trigger a discussion on the feasibility of conventional performance-based design approaches in regions of low income raising the question of focusing on a single performance objective: Collapse Prevention. In this context, large-scale shaking table tests performed at University of Bristol [6,7,8] are demonstrated and the Low-Cost Hybrid Design (LC-HD) method is presented in detail. According to this method, the structure is designed as normal to modern seismic codes, however, in case these measures are not implemented or the design seismic intensity is exceeded, the low-cost seismic isolation located at the foundation level will act as an additional seismic protection mechanism.

## REFERENCES

[1] M.C. Constantinou, A. Kartoum, A.M. Reinhorn, P. Bradford, Sliding isolation system for bridges: Experimental study. *Earthquake Spectra*, **8**, 321–344, 1992.

[2] P. Castaldo, G. Amendola, Optimal DCFP bearing properties and seismic performance assessment in nondimensional form for isolated bridges. *Earthquake Engineering and Structural Dynamics*, **50**(9), 2442–2461, 2021.

[3] M. Furinghetti, A. Pavese, V. Quaglini, P. Dubini, Experimental investigation of the cyclic response of double curved surface sliders subjected to radial and bidirectional sliding motions. *Soil Dynamics and Earthquake Engineering*, **117**, 190–202, 2019.

[4] A. Tsiavos, D. Schlatter, T. Markic, B. Stojadinovic, Experimental and analytical investigation of the inelastic behavior of structures isolated using friction pendulum bearings. *Procedia engineering*, **199**, 465-70, 2017.

[5] A. Sextos, Z. Zhang, N. Alexander, Large-Scale Testing for Enhancing the Resilience of Schools in Seismic Regions: Challenges and Cost-Efficient Solutions, R. Vacareanu and C. Ionescu (Eds.): Progresses in European Earthquake Engineering and Seismology Third European Conference on Earthquake Engineering and Seismology – Bucharest, 433–448, 2022. https://doi.org/10.1007/978-3-031-15104-0_26.

[6] A. Tsiavos, A. Sextos, A. Stavridis, M. Dietz, L. Dihoru, F. Di Michele, A. Nicholas, Low-cost hybrid design of masonry structures for developing countries: shaking table tests. *Soil dynamics and Earthquake Engineering*, **146**, 106675, 2021.

[7] A. Tsiavos, A. Sextos, A. Stavridis, M. Dietz, L. Dihoru, N.A. Alexander, Large-scale experimental investigation of a low-cost PVC 'sand-wich' (PVC-s) seismic isolation for developing countries. *Earthquake Spectra*, **36(4)**, 1886–1911, 2020.

[8] A. Tsiavos, A, Sextos, A. Stavridis, M. Dietz, L. Dihoru, N.A. Alexander, Experimental investigation of a highly efficient, low-cost PVC-Rollers Sandwich (PVC-RS) seismic isolation. *Structures*, **33**, 1590-1602, 2021.

[9] I. Banović, J. Radnić, N. Grgić, Geotechnical seismic isolation system based on sliding mechanism using stone pebble layer: shake-table experiments, *Schock and Vibration*, **1-26**, 9346232, 2019.

[10] S. Galano, A. Calabrese, State of the Art of Seismic Protection Technologies for Non Engineered Buildings (N-EBs) in Developing Regions of the World, *Journal of Earthquake Engineering*, 2023.

[11] D. De Domenico, D. Losanno, N. Vaiana, Experimental tests and numerical modeling of full-scale unbonded fiber reinforced elastomeric isolators (UFREIs) under bidirectional excitation. *Engineering Structures*, **274**, 115118, 2023.

[12] H.H. Tsang, Seismic isolation by rubber–soil mixtures for developing countries. *Earthquake Engineering and Structural Dynamics*, **37**, 283–303, 2008.

[13] S. Brunet, J.C. de la Llera, E. Kausel. Non-linear modeling of seismic isolation systems made of recycled tire-rubber. *Soil Dynamics and Earthquake Engineering*, **85**, 134–145, 2016.

[14] A. Tsiavos, N.A. Alexander, A. Diambra, E. Ibraim, J.P. Vardanega, A. Gonzalez-Buelga, A. Sextos. A sand-rubber deformable granular layer as a low-cost seismic isolation strategy in developing countries: experimental investigation, *Soil Dynamics and Earthquake Engineering*, **125**, 105731, 2019.

[15] M.P.A Gatto, L. Montrasio, L. Zavatto. Experimental Analysis and Theoretical Modelling of Polyurethane Effects on 1D Wave Propagation through Sand-Polyurethane Specimens, Journal of Earthquake Engineering, 2021.

[16] A. Tsiavos, Methodologies and design parameters that influence the efficiency and sustainability of geotechnical seismic isolation systems, Proceedings of the Third European Conference on Earthquake Engineering and Seismology (3ECEES), Bucharest, 2022.

[17] A. Tsiavos, D. Kolyfetis, G. Panzarasa, I. Burgert, B. Stojadinovic, Shaking table investigation of a low-cost and sustainable timber-based energy dissipation system with recentering ability. Bulleting of Earthquake Engineering, 2022. https://doi.org/10.1007/s10518-022-01464-2

[18] J. Sun, H. Guo, J. Ribera, C. Wu, K. Tu, M. Binelli, G. Panzarasa, F. Schwarze, Z. Wang, I. Burgert, Sustainable and biodegradable timber sponge piezoelectric nanogenerator for sensing and energy harvesting applications. *ACS Nano*, **14**, 14665–16474, 2020.

COMPDYN 2023
9th ECCOMAS Thematic Conference on
Computational Methods in Structural Dynamics and Earthquake Engineering
M. Papadrakakis, M. Fragiadakis (eds.)
Athens, Greece, 12-14 June 2023

# DYNAMIC ANALYSIS OF RAILWAY BRIDGES CONSIDERING THE NONLINEAR AMPLITUDE-DEPENDENT SYSTEM BEHAVIOUR - SIMULATION AND IN-SITU TESTS

**M. Reiterer[1] and A. Firus[2]**

[1] REVOTEC gmbh
Hermanngasse 18, A-1070 Vienna
e-mail: michael.reiterer@revotec.at

[2] iSEA Tec GmbH
Am Flughafen 76, D-88046 Friedrichshafen
andrei.firus@iseatec.de

## Abstract

*The train-induced forced vibration responses of railway bridges are investigated and evaluated under consideration of nonlinear effects. The considered nonlinearities refer to the amplitude dependency of the natural frequencies, which was observed during in-situ measurements conducted by the authors for several existing railway bridges of different construction type. The nonlinearities detected during dynamic measurements on existing railway bridges are presented and discussed. The focus is on single-span steel and concrete slab bridges with ballasted superstructure. Numerical simulations of train crossings are carried out under assumption of nonlinear beam models for the considered railway bridges. The amplitude dependency of the natural frequencies is considered in these nonlinear simulations and the structural responses during train crossing are presented in the form of resonance curves. For comparison purposes, the calculations are also carried out on linear beam models with constant natural frequencies and the resulting deviations are discussed. The influence of the investigated nonlinearities on the vibration response behavior of railway bridges is highlighted and recommendations for the future consideration of these effects in dynamic calculations of train crossing are given.*

**Keywords:** Railway Bridges, Train Crossing, Train-Induced Vibrations, Nonlinear Effects, Beam Models.

## 1 INTRODUCTION

According to the currently valid standards [1] and regulations [2], [3], the effects of train-induced vibrations on the serviceability and structural safety of new railway bridges and the dynamic assessment of existing railway bridges must be investigated by means of a dynamic calculation of the train crossings. In [3], [4] and [5] the limit values of 3.5 m/s² and 6.0 m/s² respectively are defined for the permissible vertical bridge deck acceleration for new bridges and for existing bridges with ballast superstructure. In the dynamic calculation of train crossing, the considered HSLM trains and operating trains are usually assumed as moving individual loads in the sense of a "moving load model" and linear beam or plate models are created for the bridges of interest. The dynamic calculation of the structural responses resulting from train crossing simulations is usually carried out with finite element programs, whereby the equations of motion are solved by application of modal or direct time-step integration. Alternatively, the much more efficient combined numerical and analytical solution methods, such as the analytical time-step integration method presented by Pircher [6] or the DER- and LIR-method presented in ERRI D214/RP 6 [7] are also used.

All train crossing calculation methods applied in the past and currently in practice to determine the vertical structural bridge deck response are based on linear models for the considered railway bridge. The solution methods for linear differential equations of motion are implemented in the common software products and thus time-efficient calculations can be carried out (e. g. application of modal time-step integration). In the recent past, however, significant nonlinear effects have been detected during many dynamic measurements on existing railway bridges, especially regarding the amplitude dependence of the bridge natural frequencies [8]-[12]. In the dynamic measurements on existing railway bridges documented in [8] and [9], forced vibration testing was used to determine the dynamic characteristics and the natural frequencies could be determined by gradually increasing the excitation force amplitude at different levels of the vibration amplitude of the structure. It has been found that an increase of the bridge´s vibration amplitudes lead to a decrease of the measured natural frequencies, which may be related to a decrease in the stiffness of the structure during the loading phase. In [10], train acceptance tests were carried out during the commissioning of the new ICE 4 in Germany and a steel bridge susceptible to train induced vibrations was subjected to a detailed analysis of its resonance behaviour during train crossing. These investigations also showed that there was a significant deviation between the theoretically calculated resonance speed and the value determined out of the measurements. The actual resonance speed was significantly lower, and this was attributed, among other things, to occurring nonlinear stiffness effects in the ballast superstructure during train crossing. The theoretical principles of the oscillation behaviour of dynamic systems with an amplitude-dependent natural frequency were presented by Duffing in 1918 [13] and additional theoretical investigations of the Duffing-oscillator were carried out by Parkus [14] and Magnus [15].

In this paper actual findings regarding the nonlinear amplitude dependent behaviour of the natural frequencies of railway bridges during the loading phase are presented and train crossing simulations are carried out considering nonlinear beam models. The results of these simulations are compared to linear bridge model calculations. The amplitude dependence of the natural frequency is considered by a suitable choice of the nonlinear spring characteristic of a boundary restraint modelled at the supporting points of the considered beam. The nonlinear spring law is derived based on measurements already carried out from the authors on existing railway bridges. The effects of nonlinearity and amplitude dependence of the natural frequencies on the forced vibration response of railway bridges during train passage are further investigated.

## 2 ACTUAL FINDINGS ON NONLINEARITIES IN DYNAMIC MEASUREMENTS

### 2.1 Nonlinear effects in reinforced concrete slab bridges

In the paper by Vospernig & Reiterer [8], the results of measurement and numerical dynamic investigations carried out on two simple test bridges of identical execution as supported single span reinforced concrete slab bridges are presented. The span of the two identical bridge structures is $l$ = 8.0 m, the total length 9.0 m, the structure width 4.50 m, and the slab thickness 0.66 m. With $\rho$ = 2.5 t/m³ for the concrete density, this results in a total mass of 66.83 t without any additional masses. The two reinforced concrete slab structures were built side by side on a formwork floor and after curing for 28 days they were supported on prefabricated foundations with four elastomer mats each (250 × 300 × 52 mm). In the final state of the structure, the mass per unit length including all additional masses like track ballast, sleeper framework and concrete edge beams on both sides, resulted in a total mass per unit length of $\rho$A = 12595 kg/m. The value for the average Young´s Modulus of the structural concrete was determined from laboratory tests with $E_{cm}$ = 29.6 × 109 N/m². Together with the calculated bending stiffness $E_{cm}I_y$ = 3191 MNm² and the span $l$ = 8.0 m, the calculated first natural frequency of the vertical bending mode shape under assumption of an uncracked state of the concrete result to $f_{1,ZI}$ = 12.35 Hz [8].

The main objective of the investigations carried out in [8] was to determine the dynamic parameters (natural frequencies $f_i$ and the corresponding damping ratios $\zeta_i$) of single span reinforced concrete slab structures at different stages of construction and to investigate the influence of the cracking of the structural slab on the change in the dynamic parameters. For this purpose, dynamic measurements were carried out during the construction of the test bridges, starting from the raw structure up to the final state with the entire superstructure loads. One of the two test bridges was placed in the cracked state after construction by applying a correspondingly high static load. The second test bridge was left in the non-cracked state for the entire duration of the test, so that the results of the two identical executed test bridges could be directly compared and evaluated.

The longitudinal and cross-section of the two test bridges is shown in Figure 1 for the final executed state. The ballast superstructure with sleeper framework was not connected to an existing track and therefore the stiffness contribution of the transition area from the open track to the bridge is not realistically present in the test bridges under investigation.

The forced vibration testing was used to determine experimentally the natural frequencies $f_i$ and the corresponding damping rations $\zeta_i$ for the different assembly conditions of the concrete slab bridges. With two long-stroke vibration exciters in parallel operation, an amplitude-dependent determination of the dynamic characteristics could be carried out by gradually increasing the excitation force amplitude from one measurement to the next in the range of $F_E$ = 226 N ÷ 452 N. The gained amplitude-dependent frequency response functions are show in Figure 2 for the final state of the structure in the non-cracked state (a) and in the cracked state (b). It is seen that the maximum vertical bridge deck accelerations of 0.27 m/s² and 0.37 m/s² were achieved at the highest excitation force amplitude $F_E$ = 452 N in the steady state response of the structure. The frequency response functions shown in Figure 2b for the test bridge in the cracked condition (T2) show a significant nonlinearity and amplitude dependence, respectively, in the determined natural frequencies despite the very low vibration amplitudes. When the harmonic resonance excitation with the excitation force amplitude $F_E$ = 226 N is applied, the natural frequency of the cracked test bridge is 10.1 Hz. In contrast, applying the higher excitation force $F_E$ = 452 N results in a significantly lower first natural frequency of 9.97 Hz. The leftward bending of the frequency response curves is clearly visible here.

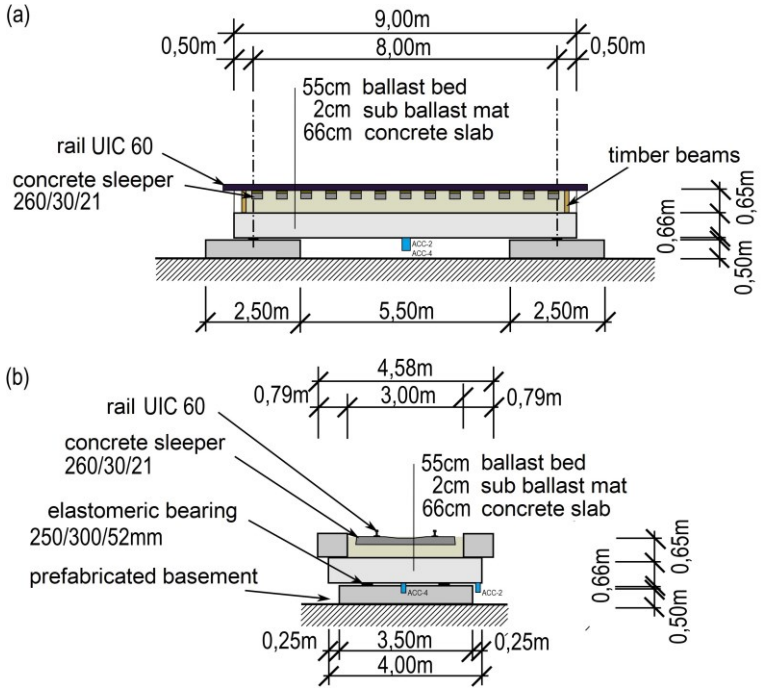


Figure 1: Longitudinal and cross section of the investigated test bridges (only one test bridge is shown; the second test bridge is identical in construction) [8]

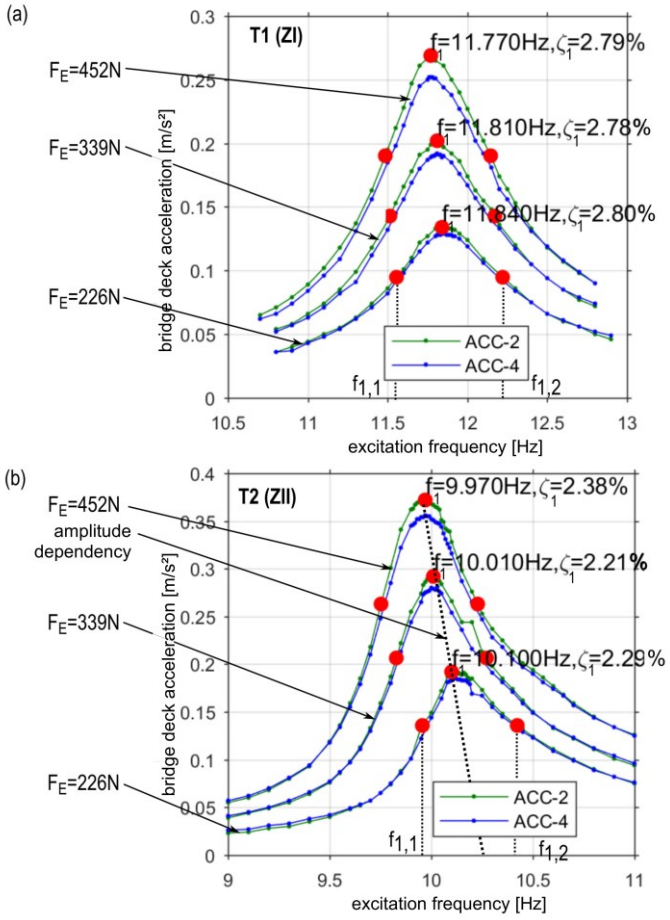


Figure 2: Amplitude dependent frequency response functions in the final state of the two test bridges [8]: a) structure T1 - uncracked state; b) structure T2 - cracked state

In Figure 2a the experimentally gained frequency responses of the test bridge in the non-cracked state also show a non-linearity and amplitude dependence, respectively, of the natural frequency, but this is somewhat lower than in the cracked structure. The test bridge´s damping ratios were determined with the half-power bandwidth method, and it does not show any non-linearities in the amplitude range considered in the measurements. It is assumed that the detected slight differences result from measurement inaccuracies.

It is noted that the amplitude dependence of the natural frequencies of the reinforced concrete slab structures determined from the dynamic measurements can be clearly assigned to a decreasing structural stiffness with increasing vibration amplitude in the case investigated. The kinetic equivalent moving mass of the two test bridges was kept constant in all measurements and the effect of the frequency shift due to the passing train [16], [17], which is often cited in the literature, does not occur here. In the case of the test bridge in cracked condition, the nonlinearity of the natural frequencies is attributed to the crack opening and closing mechanism occurring during the vibration process as well as changes in stiffness at the elastomeric supports. For the non-cracked structure, the nonlinearity is only attributed to stiffness changes in the supports. As the track and superstructure connection to the free track was not executed realistically in the investigated test bridges, no nonlinear effects can be attributed to the transition area here. In the existing structures, however, additional nonlinearities are expected to occur during the passage of the train in the bridge end area due to the changes in the adhesion forces of the ballast grains to each other during the vibration process [18]-[20].

## 2.2 Nonlinear effects in steel bridges

In [10], the experimental and numerical investigation of a single-span simple supported steel bridge with a span of 19.5 m carried out within the framework of the project "Bridge trafficability" [21] of DB Netz AG is presented. The structure consists of two adjacent identical hollow steel boxes, over each of which a track runs centrally (Figure 3). The two substructures are connected to each other via the ballast superstructure, resulting in coupled vibration modes. The main objectives of the investigation were the verification of the excitation mechanism of the ICE 4, the experimental determination of the resonance curve when excited by the ICE 4 at different crossing speeds, and the analysis of the influence of the longitudinal ballast joint and the ballast bed residual stress on the dynamic behavior of the bridge.

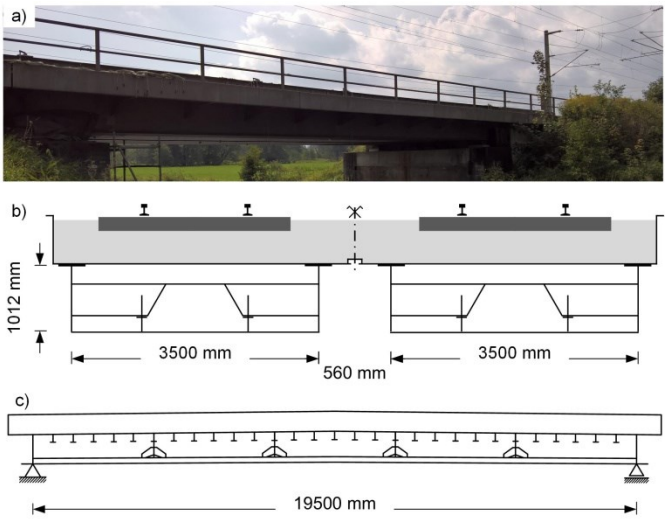


Figure 3: Investigated steel bridge [10]: a) photo caption; b) cross-section at mid-span; c) longitudinal section

Prior to the executed in-situ measurement, an operational modal analysis of the unloaded structure was carried out using the "Reference-Based Combined Deterministic-Stochastic Subspace Identification (CSI/ref)" method implemented in the MACEC software [22]. This resulted in an experimentally determined first natural frequency of the structure of $f_1$ = 5.75 Hz, which can be assigned to the first vertical bending mode. The expected resonance velocity of the considered ICE 4 vehicle can be determined as follows [1]:

$$v_{\text{res}} = f_1 \cdot \frac{L_{\text{üp}}}{i} \ , \tag{1}$$

where $L_{üp}$ is the length over the buffer of the coaches and $i$ is an integer between 1 and 4. For $i$ = 3 and $L_{üp}$ = 28.75 m, the resulting resonance velocity of ICE 4 is $v_{res}$ = 198 km/h. However, the resonance curve determined from in-situ measurements for excitations by the ICE 4 and shown in Figure 4 shows that the resonance overshoots of the structural response occur at a speed of approx. 171 km/h. This would correspond to a back-calculated natural frequency of the structure of approx. 4.95 Hz, and it differs significantly from the experimentally determined first natural frequency of 5.75 Hz. It can therefore be concluded that the first natural frequency of the structure during train passage is approx. 14 % lower than that of the unloaded structure. Detailed calculations with consideration of the vehicle-bridge interaction [10] have shown that the natural frequency drop caused by the mass effects of the vehicle only plays a minor role. Thus, the significant frequency drop was also attributed to a stiffness reduction, identical to the findings regarding the considered concrete slab bridge in section 2.1. It should be noted at this point that the maximum measured acceleration values, which significantly exceed the limit value of 3.5 m/s² [3], had no negative influence on the stability of the bridge´s ballast bed. This was observed from visual inspections of the track position after each train crossing.

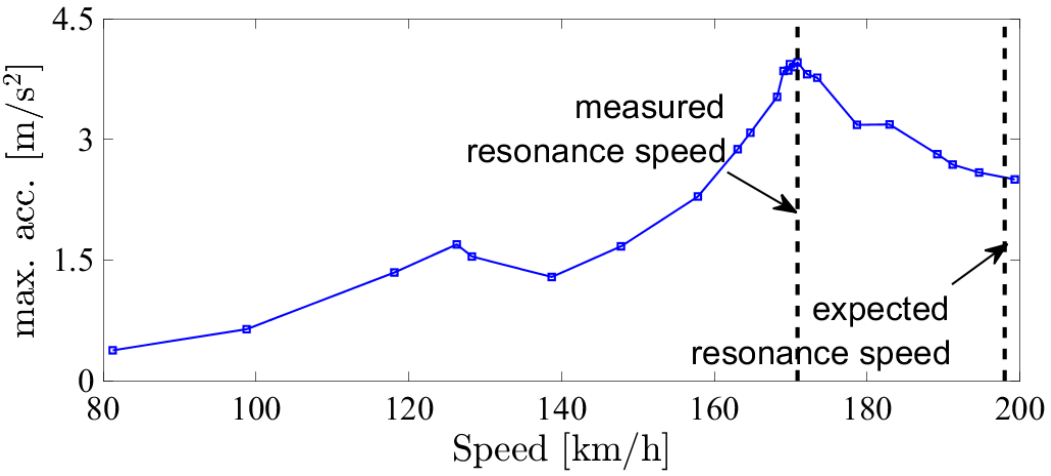


Figure 4: Experimental resonance curve of the considered steel bridge determined for the loaded substructure at midspan of the outer web using train passages of an ICE 4 vehicle [10]

Without going into a detailed discussion here, it should be mentioned that the experimentally determined results for the dynamic characteristic values of railway bridges comprehensively documented in [23] also show a significant reduction in natural frequency with increasing bridge deck vibration amplitudes.

# 3 LINEAR AND NONLINEAR BRIDGE MODELS FOR TRAIN CROSSING SIMULATIONS

## 3.1 Linear bridge model for train crossing simulations

In this section the numerical simulations of train crossings are carried out by application of a Finite Element Software and using the direct time step integration method considering a linear beam model for the bridge. All relevant bridge parameters necessary to conduct the numerical simulations are taken from the reinforced concrete slab bridge presented in section 2.1. At first, the numerical calculations are carried out under consideration of the test bridge in the cracked state without taking the non-linear effects into account. The linear numerical model was calibrated to the initial value of the measured first natural frequency $f_0$ = 10.10 Hz (Figure 2b) by properly adjusting the bending stiffness and the stiffness of the additional horizontal spring modelled at the end supports of the beam model. This natural frequency was measured using the forced testing method with the excitation force amplitude $F_E$ = 226 N (Figure 2b). The value of the properly adjusted bending stiffness was selected as $(E_{cm}I_y)_{red}$ = 0.5 · $E_{cm}I_y$ = 1595.5 MNm² to consider the reduction in stiffness due to cracking [24]. Additionally, to obtain the first natural frequency $f_0$ = 10.10 Hz in the linear numerical bridge model, the stiffness of the horizontal spring at the end supports was chosen to the value 3520 MN/m. Figure 5 shows the numerical model created in the finite element software. The model shown is used to simulate the train crossings in both the linear and nonlinear calculations. For the nonlinear calculations, the spring characteristic is defined as nonlinear (see section 3.2).

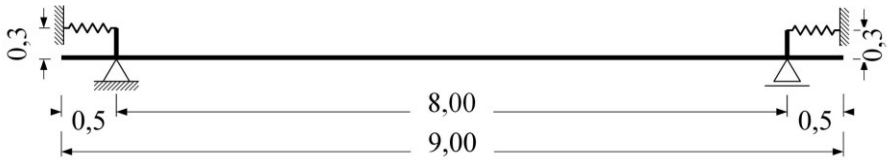


Figure 5: Applied Finite Element model for train crossing simulations of railway bridges (applied for linear and non-linear simulations of train crossing)

The train crossing simulations are carried out with the moving load model according to EN 1991-2 [1], whereby in addition to the standard HSLM-A trains, the operating trains ICE 4 and Railjet, relevant in Germany and Austria, are also considered. For simplification, only the critical model train HSLM-A01 of the ten different HSLM-A trains is considered. This results from the span of the examined reinforced concrete slab structure of $l$ = 8.0 m by applying the procedure described in Annex E of EN 1991-2 [1]. The axle loads and axle distances of the operating trains ICE 4 and are taken from RW 08.01.04 [2] and RIL 804 [3].

The train crossing calculations are carried out in the train speed range from 60 to 420 km/h. The speed step is chosen with 5 km/h. The equations of motion are solved by applying the direct time step integration, whereby the time step for the integration is set to $\Delta t$ = 0.01 seconds. This captures the contribution of the governing first vibration mode to the bridge´s train induced acceleration response with sufficient accuracy. The Rayleigh damping is defined for the first and second natural frequency of the bridge according to EN 1991-2 [1] with $\zeta_{total} = \zeta + \Delta\zeta$ = 2.56 %, where $\zeta$ = 2.34 % and $\Delta\zeta$ = 0.22 %. The evaluation of the maximum vertical bridge deck acceleration is carried out at each velocity step in the middle of the beam structure and the calculation results are used to create a resonance curve for each train type considered. The calculation results are presented and discussed in section 4.

### 3.2 Nonlinear bridge model for train crossing simulations

The train crossing simulations on nonlinear beam models of the considered reinforced concrete slab bridge are also caried out by applying direct time-step integration with the numerical model shown in Figure 5. Here again, the structure in cracked condition is considered, whereby the nonlinearities (amplitude dependencies) of the natural frequencies are here considered. This is done approximately by two additional nonlinear eccentrically arranged horizontal springs in the support area of the beam model (Figure 5). The definition of a realistic nonlinear spring characteristic for the simulation of train crossings is in itself a very complex task that can only be solved on a structure-specific basis and with a very high experimental effort. In the present case, a simplified approach is followed. Here, the frequency response curves determined from dynamic measurements and shown in Figure 2b are used for the structure in cracked condition. The reductions of the bridge´s natural frequencies due to the nonlinear amplitude-dependent behavior can be determined for the measured amplitude range ($a_{1,max}$ = 0.19 m/s² to $a_{3,max}$ = 0.37 m/s²) in the form of a negative gradient in the unit Hz / (m/s²) as follows:

$$k_{a3-a1} = \frac{f_{0,3} - f_{0,1}}{a_{3,\max} - a_{1,\max}} = \frac{9{,}97 - 10{,}1}{0{,}37 - 0{,}19} \approx -0{,}70 \ \frac{\text{Hz}}{\text{m/s}^2} \ . \tag{2}$$

The derived amplitude dependence of the natural frequency according to Equation 2 is used as a rough orientation value for finding the optimal nonlinear spring characteristic of the considered concrete slab bridge. This step was carried out in an iterative process. It provides for the iterative adjustment of the supporting points of the spring characteristic curve so that the behavior of the numerical model reaches the desired tendency of the frequency reduction. The spring characteristic curve obtained in this way is shown in Figure 6, while the resonance curves obtained with it at different excitation frequencies are shown in Figure 7. It is seen that the (initial) natural frequency drops from approx. 10.1 Hz at 0.5 kN excitation force amplitude to approx. 8.8 Hz at a correspondingly increased force amplitude of approx. 35 kN. A further increase of the force amplitude causes only a relatively small decrease of the natural frequency. Furthermore, it can be observed that the slope of the frequency reduction is on average approx. 0.3 Hz/(m/s²) and is therefore smaller than the experimentally determined negative slope from Equation 2. It should be mentioned that the expected behavior does not show a linear amplitude dependence. In the low amplitude range, as also examined in the measurement results in Figure 2, the frequency reduction can be approximated linearly. For larger amplitudes, the frequency dependence can no longer be represented by the linear relationship.

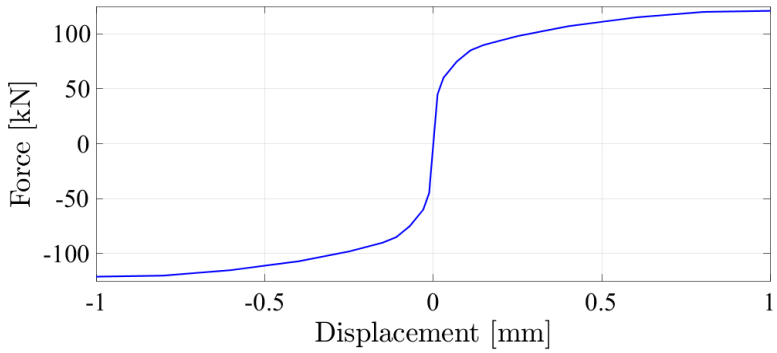


Figure 6: Nonlinear spring characteristic determined from an iterative process

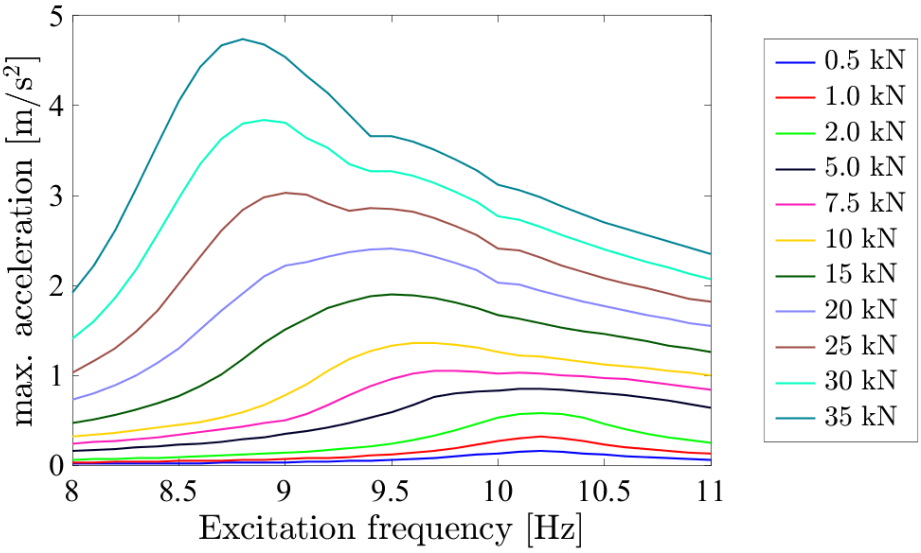


Figure 7: Resonance curves of the nonlinear beam model for harmonic excitation applied at midspan based on the nonlinear spring characteristic curve

## 4 COMPARISON OF THE RESULTS OF THE NON-LINEAR WITH THE LINEAR BRIDGE MODEL

The dynamic calculations of train crossings on the linear and nonlinear beam model of the investigated reinforced concrete slab bridge results the resonance curves shown in Figure 8 to 10 for the train types considered, HSLM-A01, ICE 4 and Railjet. In the linear beam model, the maximum value of the vertical bridge deck acceleration results 23.8 m/s² for the HSLM-A01 at the corresponding resonance speed of 320 km/h. In comparison, the resonance speed for the simulation of train crossings in the nonlinear beam model is significantly lower at 270 km/h. The reduction of the resonance speed and thus also of the resonance frequency is therefore approx. 16 % due to the considered nonlinear system behavior. At the same time, the maximum value of the vertical bridge deck acceleration of the nonlinear system is with 21.2 m/s² approx. 11 % lower.

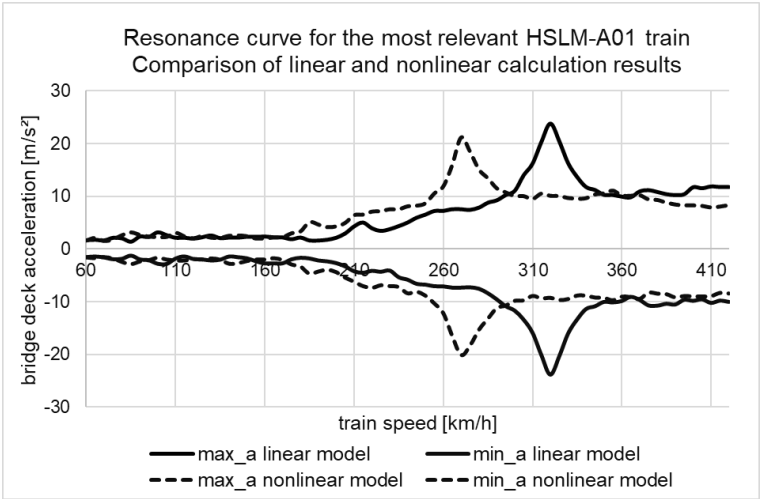


Figure 8: Calculated resonance curves due to crossing of the critical model train HSLM-A01 for the linear and nonlinear bridge model

For the operating train ICE 4, the maximum values of the vertical bridge deck acceleration in the linear and nonlinear beam model are 35.4 m/s² and 29.20 m/s respectively. In the nonlinear model, the maximum value is therefore approx. 18 % lower. It is seen from Figure 9 that the simulation of the ICE 4 in the nonlinear model results in a significant reduction of the resonance speed compared to the linear model (from 340 km/h to 285 km/h). The reduction amounts to approx. 16 %.

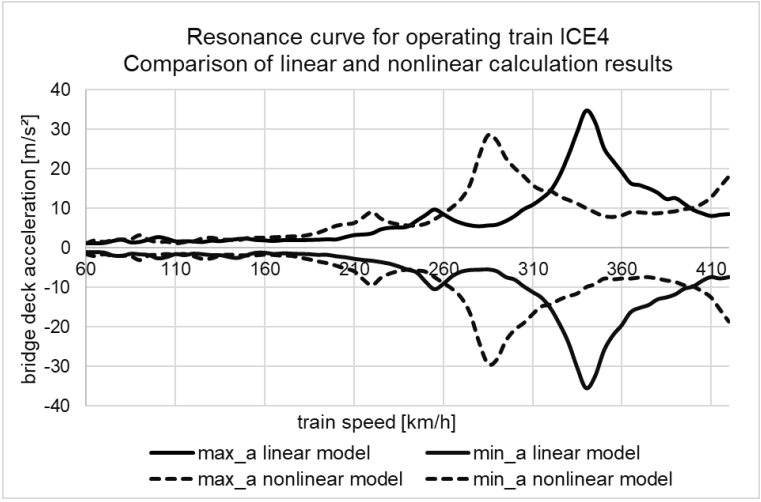


Figure 9: Calculated resonance curves due to crossing of the operating train ICE 4 according to [3] for the linear and nonlinear bridge model

The simulation of the Railjet crossings results in a maximum value of 24.1 m/s² for the vertical bridge deck acceleration in the linear beam model at the resonance speed of 315 km/h. In comparison, the nonlinear beam model yields a maximum value of 19.6 m/s² at the resonance speed of 265 km/h. The reduction of the resonance speed is therefore approx. 16 % and the reduction of the maximum vertical bridge deck acceleration is approx. 19 %.

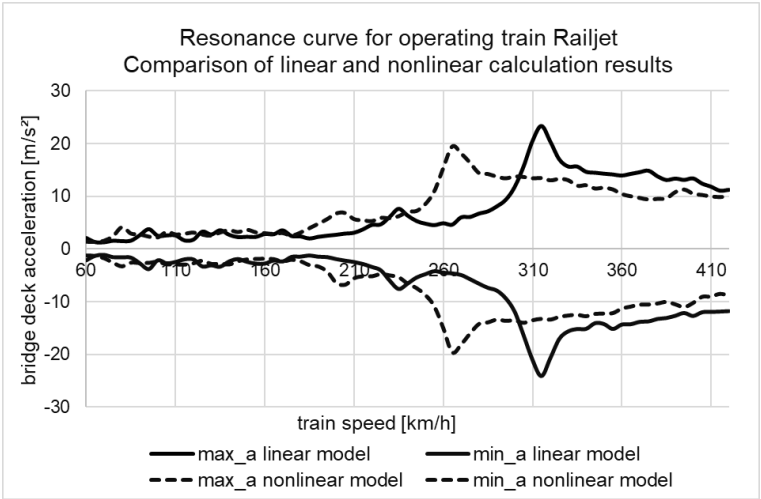


Figure 9: Calculated resonance curves due to crossing of the Railjet (configuration 1 according to [2]) for the linear and nonlinear bridge model

## 5 CONCLUSIONS

The influence of the observed nonlinear, amplitude-dependent behavior of the resonance frequencies of railway bridges was investigated in relation to the vibration response behavior occurring during train passage. Based on the authors' existing findings on the amplitude dependence of the resonance frequencies, which were determined during executed in-situ measurements on reinforced concrete slab bridges and steel bridges, a non-linear spring law approximating the real behavior was derived and numerical train crossing calculations were carried out. For the numerical calculations, a single-span simple supported reinforced concrete slab was considered, and the crossings were carried out with the HSLM-A01 train, which is critical for the structure, as well as with the operating trains ICE 4 and Railjet in the speed range from 60 km/h to 420 km/h. The linear and non-linear behavior of the train crossings was calculated. The calculation results obtained in the linear and nonlinear beam model for the maximum vertical bridge deck accelerations of the considered railway bridge during train passage show that due to the amplitude dependence of the natural frequencies, a significant reduction of the resonance velocity and lowering of the maximum vibration responses of the bridge results. The reduction of the resonance velocity resulting from the nonlinearity of the resonance frequency is approx. 16 % and this agrees very well with the observations made during in-situ measurements on existing railway bridges. This frequency reduction can play a major role if the calculated resonance velocity is outside the range to be calculated, but the actual resonance velocity falls within the relevant range due to the frequency reduction. The maximum vertical bridge deck acceleration of the structure was determined in the nonlinear beam model with a value up to approx. 19 % lower than in the linear model. The investigations carried out show that considering the nonlinearities of the resonance frequencies determined in in-situ measurements in dynamic calculations of the train passage, a more exact agreement between the measured and the computationally determined vibration response behavior is achieved. The findings presented in the article regarding the significant reduction of the resonance velocity due to the amplitude dependence of the natural frequencies should be taken into account in dynamic calculations of train crossings of railway bridges. However, it should be mentioned that further investigations are necessary in order to develop a generally valid approach for the representation of non-linearities in the dynamic calculation of railway bridges. Nevertheless, the findings of this paper can be used as a rough guide to highlight the extent of the effects of non-linear behavior.

## REFERENCES

[1] ÖNORM EN 1991-2 (2013) *Eurocode 1: Einwirkungen auf Tragwerke – Teil 2: Verkehrslasten auf Brücken (konsolidierte Fassung).* Austrian Standard Institute, Wien.

[2] RW 08.01.04 (2011) *Dynamische Berechnung von Eisenbahnbrücken.* ÖBB-Regelwerk. Wien.

[3] RIL 804: *Richtlinie 804 - Eisenbahnbrücken (und sonstige Ingenieurbauwerke) planen, bauen und instand halten.* DB Netz AG, Jänner 2013.

[4] ÖNORM EN 1990/A1 (2013) *Eurocode – Grundlagen der Tragwerksplanung – Änderung 1: Anwendung bei Brücken (konsolidierte Fassung).* Austrian Standard Institute, Wien.

[5] ÖNORM B 4008-2 (2019) *Bewertung der Tragfähigkeit bestehender Tragwerke - Teil 2: Brückenbau*. Austrian Standard Institute, Wien.

[6] H. Pircher, C. Stadler, J. Glatzl, P. Seitz (2009) *Dynamische Berechnung von Eisenbahnbrücken im Zuge von Hochgeschwindigkeitsstrecken Ein Alternatives Verfahren zur Simulation von Zugüberfahrten.* In: Bautechnik **86**, H. 01, S. 1–13.

[7] ERRI D 214/RP 6 (1999) *Berechnung einfach gelagerter Brücken bei der Durchfahrt eines Zugverbandes.* ERRI-Sachverständigenausschuss D 214.

[8] M. Vospernig, M. Reiterer (2020) *Evaluierung der dynamischen Systemeigenschaften von einfeldrigen Stahlbeton-Eisenbahnbrücken.* In: Beton- und Stahlbetonbau **115**, H. 06, S. 424-437.

[9] M. Reiterer, S. Lachinger, J. Fink, S.-Z. Bruschetini-Ambro (2018) *In-Situ Experimental Modal Testing of Railway Bridges.* In: Proceedings of 18th International Conference on Experimental Mechanics (OCEM 2018), 1-5 July 2018, Brussel, Belgium.

[10] A. Firus, H. Berthold, J. Schneider, G. Grunert (2018) *Untersuchungen zum dynamischen Verhalten einer Eisenbahnbrücke bei Anregung durch den neuen ICE 4.* In: VDI-Berichte 2321, 6. VDI-Fachtagung Baudynamik, Würzburg, Deutschland, S. 233-248.

[11] T. Mohamed, K. Abdellatif, B. Mohammed (2021) *Nonlinear analysis of the ballast effect on the dynamics of a simply supported high speed railway bridge.* In: Journal of Applied Sciences **11**, p. 1-20.

[12] L.R. Ticona Melo, J. Malveiro, D. Ribiero, R. Calcada, T. Bittencourt (2020) *Dynamic analysis of the train-bridge system considering the non-linear behaviour of the track-deck interface.* In: Engineering Structures **220**.

[13] G. Duffing (1918) *Erzwungene Schwingungen bei veränderlicher Eigenfrequenz und ihre Technische Bedeutung.* Vieweg, Braunschweig.

[14] H. Parkus (1988) *Mechanik der festen Körper.* Zweite Auflage, Springer Verlag Wien New York.

[15] K. Magnus (1961) *Schwingungen.* Band 3, B.G. Teubner Verlagsgesellschaft mbH, Stuttgart.

[16] J. Li, M. Su, L. Fan (2003) *Natural Frequency of Railway Girder Bridges under Vehicle Loads.* In: Journal of Bridge Engineering **8**, H. 4, p. 199-203.

[17] K. Liu, G. De Roeck, G. Lombaert (2009) *The effect of dynamic train-bridge interaction on the bridge response during a train passage.* In: Journal of Sound and Vibration **325**, p. 240-251.

[18] T. Rauert, H. Bigelow, B. Hoffmeister, M. Feldmann (2010) *On the prediction of the interaction effect caused by continuous ballast on filler beam railway bridges by experimentally supported numerical studies.* In: Engineering Structures **32**, p. 3981-3988.

[19] C. Rebelo, S. Da Silva, C. Rigueiro, M. Pircher (2008) *Dynamic behaviour of twin single-span ballasted railway viaducts – Field measurements and modal identification.* In: Engineering Structures **30**, H. 9, p. 2460-2469.

[20] C. Rigueiro, C. Rebelo, S. Da Silva (2010) *Influence of ballast models in the dynamic response of railway viaducts.* In: Journal of Sound and Vibration **329**, H. 15, p. 3030-3040.

[21] G. Grunert (2022) *Data and evaluation model for the description of the static–dynamic interface between trains and railway bridges.* In: Engineering Structures **262**, p. 1-19.

[22] E. Reynders, G. De Roeck (2008) *Reference-based combined deterministic stochastic subspace identification for experimental and operational modal analysis.* In: Mechanical Systems and Signal Processing **70-71**, p. 756-768.

[23] A. Anderson, R. Allahvirdizadeh, A. Kamali, A. Silva, D. Ribeiro, G. Ferreira, P. Montenegro, P. Museros (2021), *High-speed low cost bridges, background report.* Technical Report of the Shift2Rail project (KTH/FEUP/UPV).

[24] H. Bachmann (2002): *Erdbebensicherung von Bauwerken*. 2., überarbeitete Auflage, Springer Basel AG.

COMPDYN 2023
9th ECCOMAS Thematic Conference on
Computational Methods in Structural Dynamics and Earthquake Engineering
M. Papadrakakis, M. Fragiadakis (eds.)
Athens, Greece, 12-14 June 2023

# STATIC AND DYNAMIC EXPERIMENTAL VALIDATIONS OF THE LATERAL IMPACT RESILIENT DOUBLE CONCAVE FRICTION PENDULUM (LIR-DCFP) BEARING

**G. Auad[1], P. Castaldo[2], J. L. Almazán[1], and D. Quizanga[1]**

[2] Department of Structural Engineering, Pontificia Universidad Católica de Chile
Avenida Vicuña Mackenna, 4860, Santiago, Chile
{gaauad, jlalmaza, dmquizanga}@uc.cl

[2] Department of Structural, Geotechnical and Building Engineering (DISEG), Politecnico di Torino
Corso Duca degli Abruzzi, 24, Torino, Italy
paolo.castaldo@polito.it

## Abstract

*During high-magnitude earthquakes, large base displacements that exceed the lateral capacity of the isolation level can cause internal impacts jeopardizing the benefits of using seismic isolation. The Lateral Impact Resilient Double Concave Friction Pendulum (LIR-DCFP) bearing has been proposed to mitigate the adverse effects of internal lateral impacts between inner sliders and restraining rims of sliding surfaces. This device has an enhanced inner slider formed by two bodies. These bodies are in contact, generating a plane high-friction interface capable of dissipating additional energy and limiting the magnitude of the impact. A numerical model based on rigid body dynamics has been proposed to represent the dynamic response of structures equipped with LIR-DCFP bearings. The numerical formulation includes important modeling aspects such as lateral impact behavior and large displacements (P-Δ effects), among other essential phenomena. A prototype of this novel device was constructed to validate its lateral behavior through static experimental tests. As predicted, if the inner slider does not contact the restraining rims of the sliding surfaces, the response of the isolator will be identical to the response of the classical frictional isolators. On the contrary, for larger lateral displacements, the contact between the inner slider and the restraining rims triggers high friction sliding. Finally, experimental tests were conducted to validate the dynamic response of a stiff structure equipped with four LIR-DCFP devices. An accurate prediction of the dynamic response can be obtained by employing the suggested numerical model under the presence or absence of internal lateral impacts.*

**Keywords:** Seismic isolation, LIR-DCFP bearing, internal lateral impact, high-friction interface.

# 1 INTRODUCTION

Friction Pendulum System (FPS) bearings [1] are commonly used to achieve seismic isolation, protecting superstructures from high-magnitude earthquakes. Particularly, the FPS device consists of an articulated slider and one plate with a spherical sliding surface. A restraining rim is placed on the plate to limit the maximum base displacement. Several alternatives exist to construct isolation levels using frictional isolators with multiple sliding surfaces. Two of the most used devices with multiple sliding surfaces are the Double Concave Frictional Pendulum (DCFP) [2] and Triple Concave Friction Pendulum (TCFP) [3,4] bearings. The presence of more than one sliding surface allows a passive adaptive behavior to be generated. In this way, it is possible to change both damping and stiffness properties based on different base displacement demands. All the cited devices have shown excellent seismic performance [2,3,5–7].

Under extreme ground motions, large base displacement could cause internal lateral impacts between inner sliders and restraining rims. Internal impacts can produce an critical rise in the ductility demand of the superstructure [8–13] or the failure of the DCFP and TCFP isolators [14,15].

A new frictional isolator, called the Lateral Impact Resilient Double Concave Friction Pendulum (LIR-DCFP) bearing, has been suggested to mitigate the adverse effects of internal impacts [16–18]. This device has an improved inner slider with a high friction interface. The sliding in this interface starts when the inner slider impacts the restraining rims of the concave plates, dissipating an additional amount of energy and limiting the magnitude of the impact force. Numerical evaluations of the seismic performance of structures equipped with LIR-DCFP bearings have been conducted to determine the comparative advantages of using the novel friction bearing instead of classical isolation devices [16–18].

The first part of this paper presents a static experimental validation of the lateral behavior of the LIR-DCFP bearing is presented. This experimental test aims to determine if the hysteretic response obtained by imposing cyclic lateral displacements is consistent with the expected theoretical response.

The second part of this research aims to validate a numerical model based on rigid body dynamics developed by Auad & Almazán [16]. The numerical formulation includes important modeling aspects such as lateral impact behavior, large displacements ($P-\Delta$ effects), uplifting, bi-directional frictional coupling, and kinematics constraints, among other essential phenomena. Dynamic tests were conducted applying sinusoidal ground motions to generate experimental data valuable to validate the dynamic response of a numerical model of the tested base-isolated structure.

# 2 LATERAL BEHAVIOR OF THE LIR-DCFP BEARING

## 2.1 Geometric description

The Lateral Resilient Double Concave Friction Pendulum (LIR-DCFP) isolator has been suggested as an alternative to mitigate the adverse effects of impacts between inner sliders and restraining rims of frictional devices [16–18]. Typically, this isolator consists of two plates with spherical sliding surfaces characterized by a radius of curvature $R$. Between the concave plates, an enhanced inner slider is located. This slider is the key feature of the new device. The inner slider is composed of two bodies: the upper slider and the bottom slider. Both pieces are in contact, generating a planar high-friction interface. On the one hand, low friction contacts (between the spherical surfaces of the slider and the sliding surfaces) are typified by a low friction coefficient $\mu_d$ that depends on the sliding velocity $\dot{v}$ according to the following equation [5,6]:

$$\mu_d = f_{max} - (f_{max} - f_{min})\exp(-\alpha \dot{v}) \quad (1)$$

being, $f_{max}$ and $f_{min}$ the friction coefficient at a high and slow velocity, respectively, and $\alpha$ the rate parameter. On the other hand, the planar high friction contact between the upper and bottom sliders is assumed to be independent of the sliding velocity and denoted by the symbol $\mu_h$. In Figure 1, a schematic illustration of the LIR-DCFP bearing is presented, indicating the name of the components and the region where slow and high friction interactions are generated.

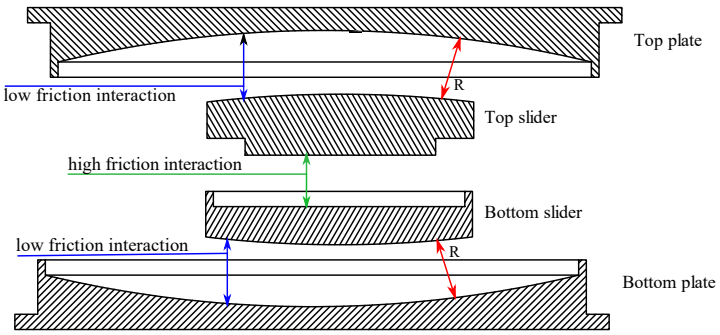


Figure 1: Illustration of the LIR-DCFP bearing.

The mechanism created to mitigate the adverse effects of internal lateral impacts consists of triggering the high friction sliding when the inner slider contacts the restraining rims of the concave plates. This condition is satisfied by ensuring in the design steps that $\mu_h > \mu_d$. If high friction sliding occurs, the magnitude of the impact force will be limited, and a critical amount of energy will be dissipated. In Figure 2, the expected lateral behavior in terms of normalized force-displacement relationship is shown, including different deformed configurations of the device.

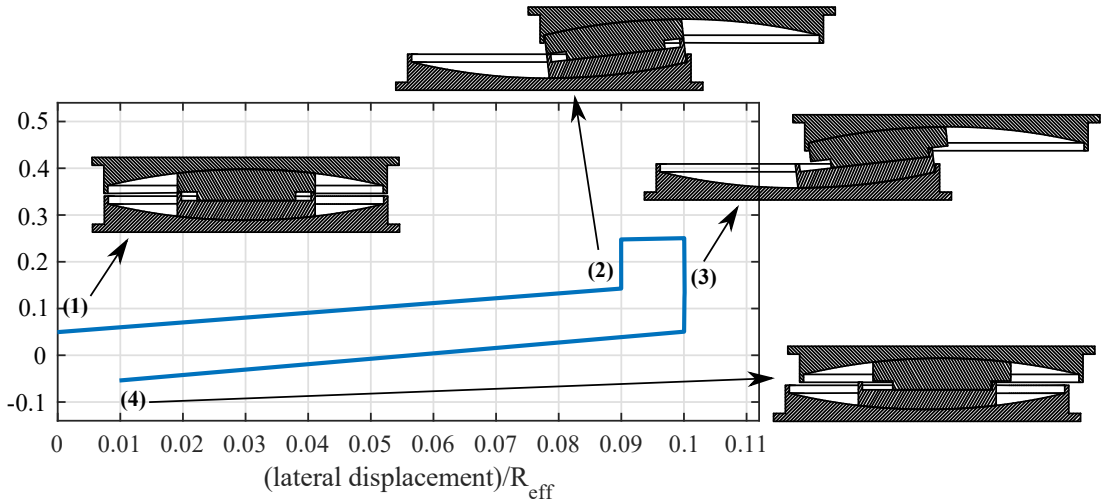


Figure 2: Expected lateral behavior of the LIR-DCFP bearing.

## 2.2 Experimental hysteretic validation of the LIR-DCFP bearing.

This subsection presents the main results of a cyclic static experimental test. This test was conducted to validate the expected lateral behavior of the novel device. The experimental setup is presented in Figure 3(a). While an axial load of 150 kN is applied using a horizontally

orientated actuator, the displacement of the bottom plate of the isolator is imposed employing a vertically orientated hydraulic actuator. Two constant velocity cycles with an amplitude of 18.5 cm were imposed on the prototype. The tested device has two identical sliding surfaces with a radius of curvature equal to $R = 0.75$ m. Since the inner slider has a height of 8.5 cm, the effective radius of curvature of the isolator is equal to $R_{eff} = 1.415$ m [2]. While the low friction interactions are defined by a friction coefficient of $\mu_d = 0.066$, the developed friction coefficient of the planar interface between the top and bottom slider was equal to $\mu_h = 0.126$.

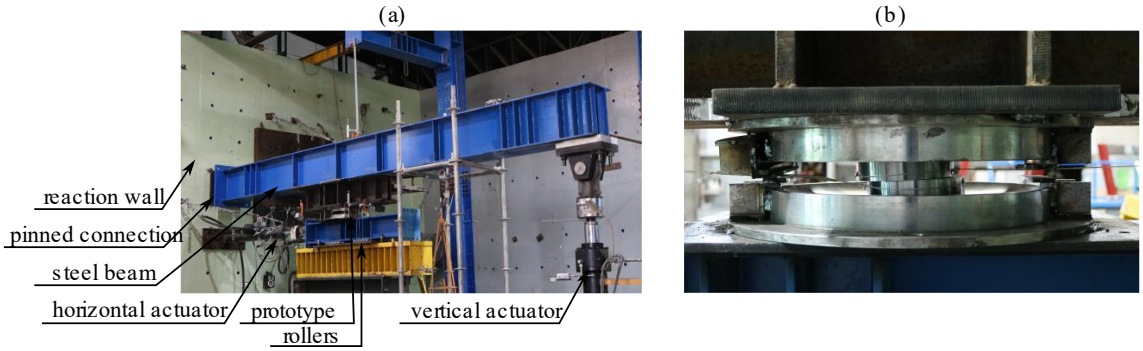


Figure 3: (a) Experimental setup; (b) Prototype of the LIR-DCFP bearing.

In Figure 4, the obtained normalized hysteretic loops that characterize the lateral behavior of the LIR-DCFP bearing are presented. As predicted, the displacement of the device starts with low friction sliding between spherical surfaces. The first high friction sliding is triggered by the impact between the inner slider and the restraining rims of the plates at a lateral displacement of 17.5 cm. Note that the magnitude of the impact force is limited to the force needed to overcome the sticking phase of the high-friction interface. Also, an additional amount of energy is dissipated during the planar sliding. This first high-friction sliding generates a relative displacement between the top and bottom sliders of 1 cm, explaining why the second high-friction sliding occurs for a displacement of 16.5 cm.

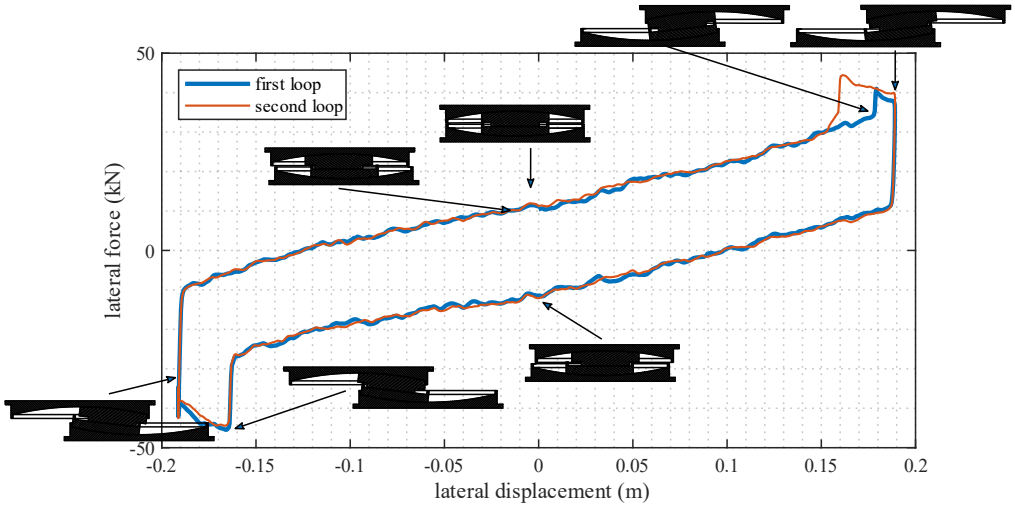


Figure 4: Experimental hysteretic loops.

## 3 NUMERICAL FORMULATION OF THE LIR-DCFP BEARING

In this Section, the numerical formulation of the LIR-DCFP bearing is briefly described. A complete report can be found in [16]. The three-dimensional modeling procedure is based on rigid body dynamics and was proposed by Bao and Becker [19]. The first step is to define a set of contact and projection points. As an example, in Figure 5, four pairs contact-projection points are defined for each interaction between bodies that form the isolator. The contact between the upper slider and the upper plate is considered using the pairs $A_i - A_i'$. The contact between the bottom slider and the bottom plate is included using the pairs $B_j - B_j'$. Finally, the high friction interaction between the slider is modeled using the points $C_k - C_k'$. Since contact points are located in a rigid body, it is possible to track their global location and velocity by knowing the displacements and velocities of the centroid of the rigid bodies and the angular velocity of the pieces that form the isolator. Suppose the position and velocity of all the contact and projection points are known. In that case, it is possible to determine the contact forces generation between the interaction of the rigid bodies. As an example, the interaction force of one generic couple $B_j - B_j'$ in local coordinates can be computed by determining the normal force $N_{B_j}$ and the two components of the friction force $\boldsymbol{f_{\mu,A_1}} = [\, f_{\mu,A_1}^{(x)} ;\, f_{\mu,A_1}^{(y)} \,]$ using the following equations:

$$N_{B_j} = \begin{Bmatrix} k\left(\boldsymbol{r_{B_j}}(3) - \boldsymbol{r'_{B_j}}(3)\right) + c\left(\dot{\boldsymbol{r}}_{\boldsymbol{B_j}}(3) - \dot{\boldsymbol{r}}'_{\boldsymbol{B_j}}(3)\right), if\left(\boldsymbol{r_{B_j}}(3) - \boldsymbol{r'_j}(3)\right) \geq 0 \\ 0, \text{ otherwise} \end{Bmatrix} \quad (2)$$

$$\boldsymbol{f_{\mu,B_j}} = -\mu_d N_{B_j} \boldsymbol{z_{B_j}} \quad (3)$$

in which $\boldsymbol{r_{B_j}}$ and $\boldsymbol{r'_{B_j}}$ are the position of the contact and projection point, respectively; and $\dot{\boldsymbol{r}}_{\boldsymbol{B_j}}$ and $\dot{\boldsymbol{r}}'_{\boldsymbol{B_j}}$ are the velocities of the contact and projection point, respectively. Note that the normal force is computed by employing a Kelvin-Voigth element [20], being $k$ and $c$, the stiffness and damping coefficient of the element. The friction phenomenon is modeled using the well-known biaxial Bouc-Wen's model, being $\boldsymbol{z_{B_j}}$ the vector that contains the two hysteretic parameters associated with the pair $B_j - B_j'$. Both forces can be arranged in a three-dimension vector as follows:

$$\boldsymbol{f_{n,B_j}} = [N_{B_j};\, \boldsymbol{f_{\mu,B_j}}] \quad (4)$$

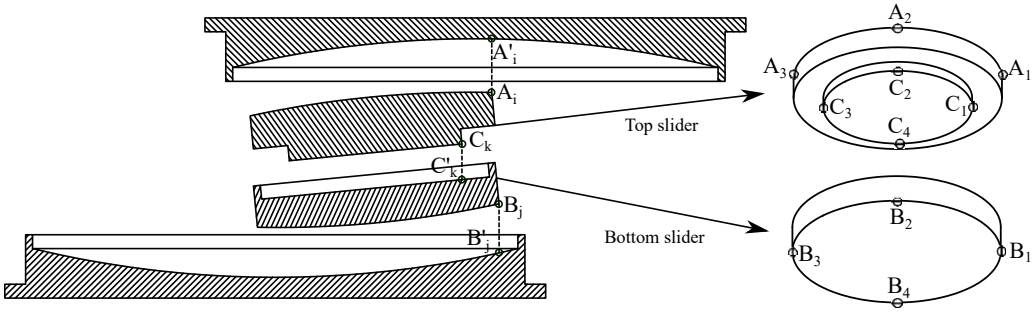


Figure 5: Location of a set of four contact-projection points for each interaction [16].

The vectorial force presented in Equation (4) is described in local coordinates. All the contact forces (external force according to the procedure) in local coordinates can be rotated to global coordinates. By considering the contribution of all the contact forces in global coordinates, it is possible to determine the generalized vector as follows:

$$\boldsymbol{F} = \sum_n \frac{\partial \boldsymbol{r_c}}{\partial \boldsymbol{q}} \cdot \boldsymbol{f_n} + \sum_n \left( (\boldsymbol{r_n} - \boldsymbol{r_c}) \times \boldsymbol{f_n} \right) \cdot \frac{\partial \bar{\boldsymbol{\omega}}}{\partial \boldsymbol{q}} \tag{5}$$

where, the symbol $\boldsymbol{f_n}$ denotes the $n$th contact force described in global coordinates; $\boldsymbol{r_c}$ is the vector from the origin of the global system to the centroid of the considered rigid body; and $\bar{\boldsymbol{\omega}}$ is the angular velocity vector of the considered rigid body. Assuming that the bottom plate is connected to the ground, there are three rigid bodies that can be displaced. Since a three-dimensional formulation is used, the motion of each rigid body can be described by 6 degrees of freedom (i.e., three displacements and three rotations), leading to a total of 18 degrees of freedom. The vector that contains the 18 degrees-of-freedom is denoted by the symbol $\boldsymbol{q}$.

### 3.1 Numerical model example

In this Subsection, the dynamic response of a LIR-DCFP bearing with sliding surfaces with a radius equal to $R = 1.185$ m and a slider with a height of $h = 0.12$ m (i.e., effective radius of $R_{eff} = 2.25$ m) is presented. The impact between the inner slider and the restraining rims of the sliding plate is produced if the base displacement exceeds 0.25 m. The low friction interactions are characterized by the following parameters: $f_{max} = 0.065$, $f_{min} = f_{max}/2$, and $\alpha = 15$ sec/m. The high-friction interface is defined by a constant friction coefficient of $\mu_h = 2f_{max}$. A lumped mass of $m_s = 204$ kN×sec$^2$/m was assigned to the top plate of the bearing. The numerical model was subjected to one horizontal component of the Newhall record (Northridge earthquake, 1994).

The motion of the bearing is presented in Figure 6. The displacements of the bodies that are not connected to the ground are shown in Figure 6(a). Note that the impact is observed at $t = 4.2$ sec, triggering the high friction sliding. This sliding is noticeable since a relative displacement between the bottom and top slider is generated. The numerical formulation is based on rigid dynamics. In this way, by adopting a large value of the stiffness in the contact-projection points interaction, the kinematic constraints of describing a spherical trajectory are satisfied. In Figure 6(b), the vertical displacement of the components of the LIR-DCFP isolator is shown, confirming that a vertical displacement accompanies a lateral displacement. The numerical formulation allows even to include the rotation. This response is presented in Figure 6(c).

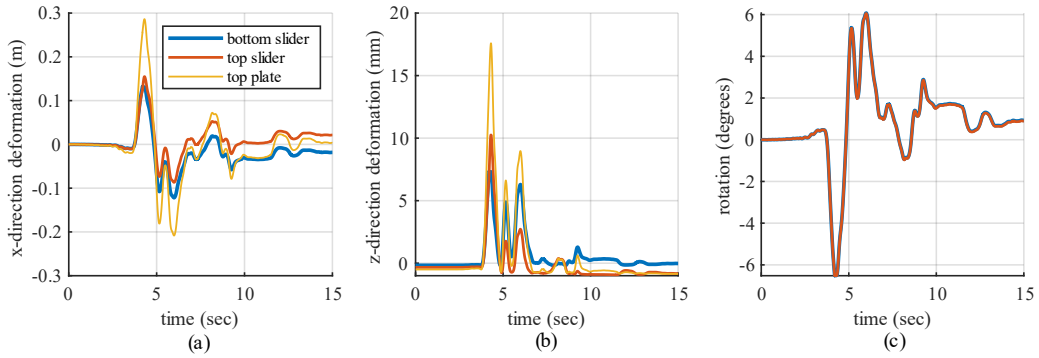


Figure 6: Dynamic Response of the numerical formulation of a LIR-DCFP bearing: (a) Lateral displacements; (b) Vertical displacements; (c) Rotations.

The configurations of the different bodies that form the isolator are depicted in Figure 7. In this figure, it is possible to check the position of the plates and sliders before, during, and after the impact.

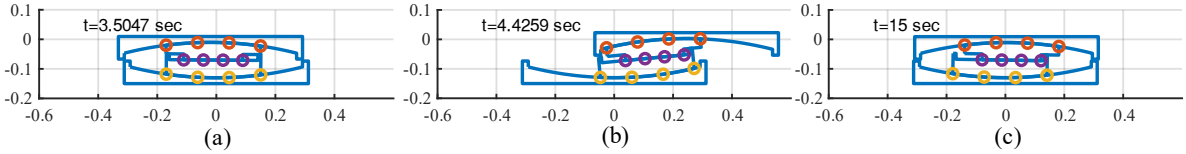


Figure 7: Deformed configurations of a LIR-DCFP bearing: (a) Before the impact; (b) During the impact; (c) After the impact.

The response of the isolator in terms of forces transmitted to the superstructure is presented in Figure 8. The lateral force generated in the device is presented in Figure 8(a). It is noticeable that even when the impact occurs ($t = 4.2$ sec), the magnitude of the lateral force does not present a dramatic increase but only increases until the high friction interface slides. The described numerical formulation allows including $P - \Delta$ effects, phenomenon that is critical when large displacements are expected. Figure 8(b) shows the evolution of the bending moment that the isolator transfers to the superstructure. The hysteric lateral response of the LIR-DCFP can be seen in Figure 8(c). The high friction sliding occurs when the lateral capacity of the bearing is exceeded. If the slider impacts the restraining rims of the plates, an additional amount of energy is dissipated.

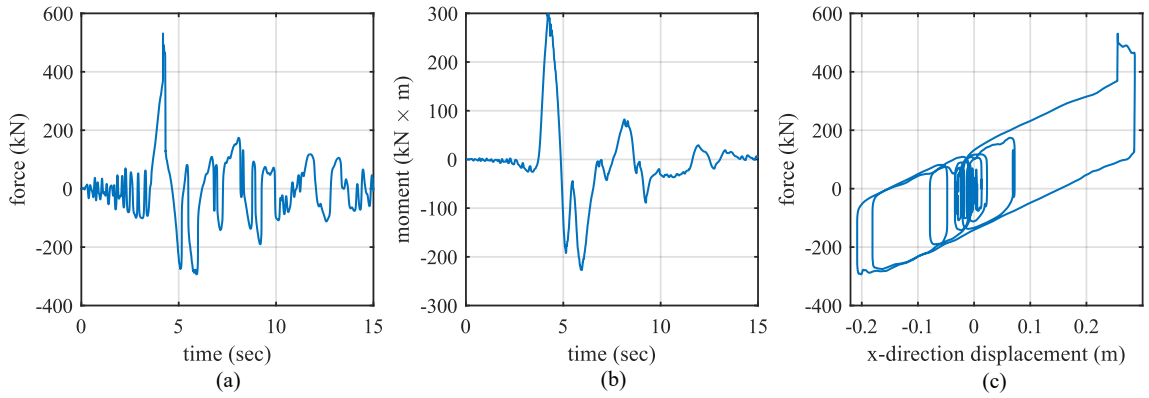


Figure 8: Dynamic Response of the numerical formulation of a LIR-DCFP bearing: (a) Lateral force; (b) Moment; (c) Hysteretic loops.

## 4 DYNAMIC VALIDATION OF THE LIR-DCFP LATERAL BEHAVIOR

A small-scaled stiff two stories structure equipped with four LIR-DCFP isolators was built to validate the dynamic response of the isolation system. In Figure 9, the base-isolated structure and one LIR-DCFP isolator are shown. The isolators that form the flexible level were characterized by the following parameters: radius of curvature $R = 0.75$ m, slider height $h = 0.05$ m, a lateral capacity of 0.11 m, maximum and minimum friction coefficient in the low friction interaction of $f_{max} = 0.14$ and $f_{min} = 0.11$, and a high friction coefficient in the high friction interface of $\mu_h = 0.27$. The total seismic weight acting on the isolation system was $W_{sis} = 26.6$ kN.

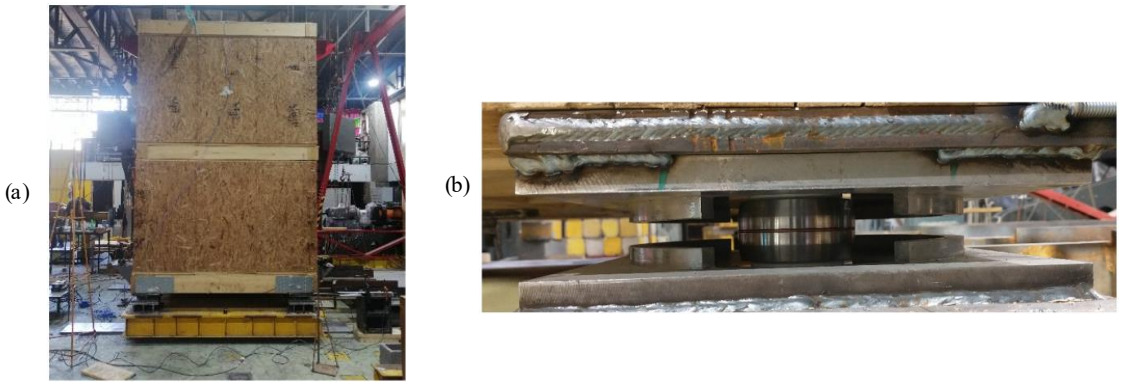

Figure 9: (a) Experimental setup of the dynamic tests; (b) LIR-DCFP bearing used in the dynamic tests.

Periodic waves were imposed on the dynamic system in one direction using a horizontal actuator. The objective of these tests was to validate the expected response of the isolation system under two conditions: (i) with internal lateral impacts and (ii) without internal lateral impacts. Periodic accelerations with different amplitudes were applied to observe both conditions. The input generated using the shaking table was measured to have the data to replicate the tests numerically. These signals are shown in Figure 10.

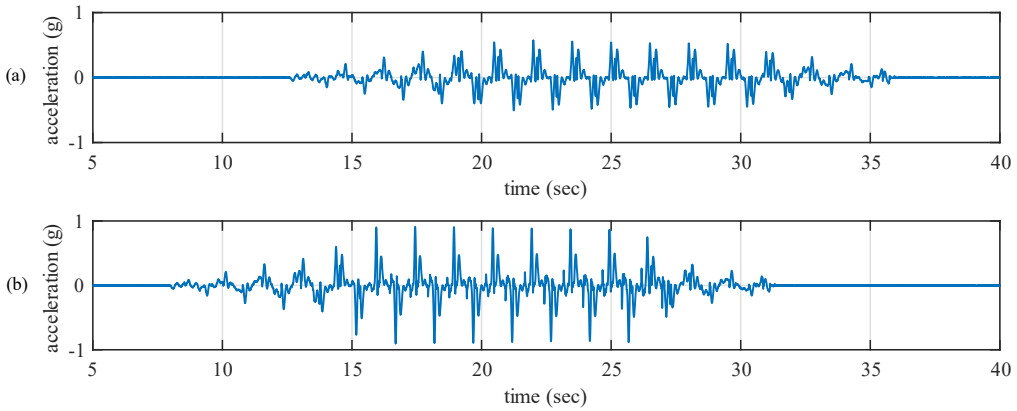


Figure 10: Experimental seismic inputs: (a) Test without impacts; (b) Test with impacts.

A numerical model of the base-isolated structure was developed in the MATLAB environment. The isolation devices were modeled employing the numerical formulation described in this work. A comparison between the experimental and numerical dynamic response of the isolation system is shown in Figure 11 in terms of base displacement and hysteretic loops generated in the isolation system. In Figure 11(a, b), the response without impacts is plotted. Note that since impacts between the inner slider and the restraining rims do not occur, high friction sliding is not generated. In this case, as expected, the dynamic behavior of the isolation system is equal to a classic isolation interface formed by DCFP bearings. In Figure 11(c, d), the dynamic response of the isolation system, including the lateral impact behavior, is presented. Similar responses are obtained, indicating that the developed numerical model can be an excellent tool to predict the response of an isolation system with LIR-DCFP bearing. A good match between the experimental and numerical response in terms of the maximum response of the base displacement and total base shear of the isolation system is obtained. It is essential to highlight that even in the presence of lateral internal impacts, the maximum base shear does not exceed the 60% of the seismic weight. Furthermore, the isolation devices can resist several high-

friction relative displacements between the top and bottom sliders. The use of LIR-DCFP bearing can be an effective way of mitigating the adverse effects of internal lateral impacts.

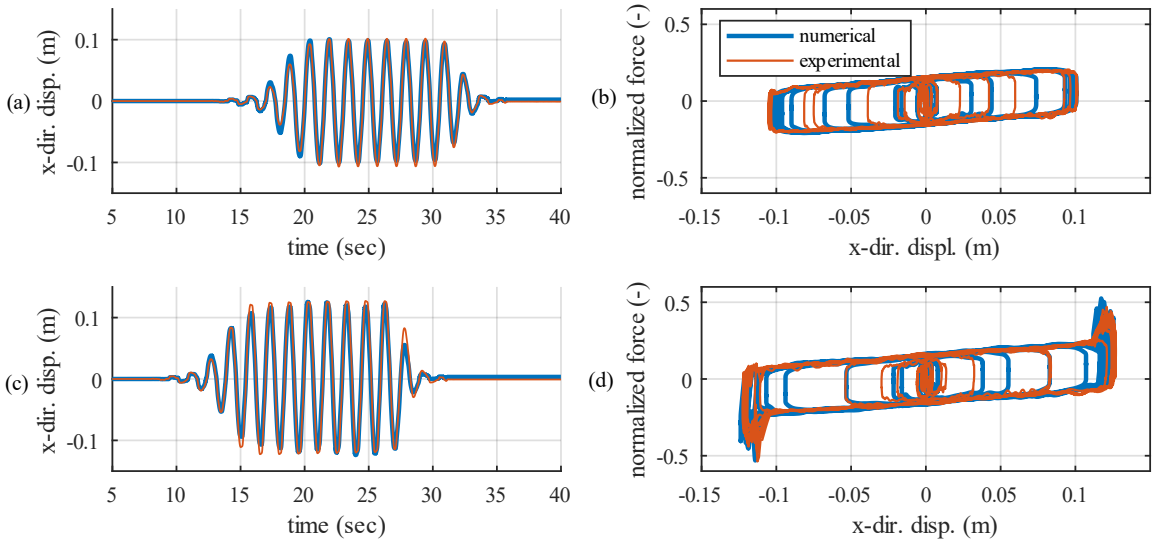


Figure 11: Comparison of the experimental and numerical response of the isolation system: (a) Base displacement without impacts; (b) Hysteretic loops without impacts; (c) Base displacement with impacts; (d) Hysteretic loops with impacts.

## 5 CONCLUSIONS

This paper presents an experimental validation of the constructability and lateral behavior of the Lateral Impact Resilient Double Concave Friction Pendulum (LIR-DCFP) bearing. This device has been suggested to mitigate the adverse effects of internal impacts between inner sliders and restraining rims of frictional isolators. The main advantage of the LIR-DCFP device over classical frictional bearings is its high friction interface. This interface allows to limit the impact force and dissipating an additional amount of energy during the internal lateral impact.

A static test of an LIR-DCPF prototype was conducted to validate the hysteretic behavior of the isolator. As expected, since the friction interaction in the high-friction interface is characterized by a friction coefficient larger than the friction coefficient generated between spherical surfaces, high-friction sliding occurs when the slider impacts the restraining rims of the concave plates. This static test indicates that the idea of creating a high-friction interface is feasible.

Dynamics tests were conducted to generate data on the response of an isolation system formed by four LIR-DCFP bearings. This data was used to validate a numerical model of the device. This numerical formulation is based on rigid body dynamics and includes essential modeling aspects such as lateral impact behavior, large displacements, $P-\Delta$ effects, among other phenomena. The numerical model of the novel device is able to accurately predict the dynamic response of the isolation system under the presence or absence of internal lateral impacts. Additionally, the responses obtained from the dynamic tests of the base-isolated structure indicate that this new technology can effectively mitigate the adverse effects of internal lateral impacts.

## REFERENCES

[1] V.A. Zayas, S.S. Low, S.A. Mahin, A Simple Pendulum Technique for Achieving

Seismic Isolation, Earthq. Spectra. 6 (1990) 317–333. https://doi.org/10.1193/1.1585573.

[2] D.M. Fenz, M.C. Constantinou, Behaviour of the double concave Friction Pendulum bearing, Earthq. Eng. Struct. Dyn. 35 (2006) 1403–1424. https://doi.org/10.1002/eqe.589.

[3] D.M. Fenz, M.C. Constantinou, Spherical sliding isolation bearings with adaptive behavior: Theory, Earthq. Eng. Struct. Dyn. 37 (2008) 163–183. https://doi.org/10.1002/eqe.751.

[4] D.M. Fenz, M.C. Constantinou, Modeling triple friction pendulum bearings for response-history analysis, Earthq. Spectra. 24 (2008) 1011–1028. https://doi.org/10.1193/1.2982531.

[5] A. Mokha, M. Constantinou, A. Reinhorn, Teflon Bearings in Base Isolation I: Testing, J. Struct. Eng. 116 (1990) 438–454. https://doi.org/10.1061/(ASCE)0733-9445(1990)116:2(438).

[6] M. Constantinou, A. Mokha, A. Reinhorn, Teflon Bearings in Base Isolation II: Modeling, J. Struct. Eng. 116 (1990) 455–474. https://doi.org/10.1061/(ASCE)0733-9445(1990)116:2(455).

[7] D.M. Fenz, M.C. Constantinou, Spherical sliding isolation bearings with adaptive behavior: Experimental verification, Earthq. Eng. Struct. Dyn. 37 (2008) 185–205. https://doi.org/10.1002/eqe.750.

[8] Y. Bao, T.C. Becker, Inelastic response of base-isolated structures subjected to impact, Eng. Struct. 171 (2018) 86–93. https://doi.org/10.1016/j.engstruct.2018.05.091.

[9] Y. Bao, T.C. Becker, T. Sone, H. Hamaguchi, To limit forces or displacements: Collapse study of steel frames isolated by sliding bearings with and without restraining rims, Soil Dyn. Earthq. Eng. 112 (2018) 203–214. https://doi.org/10.1016/j.soildyn.2018.05.006.

[10] Y. Bao, T.C. Becker, Effect of Design Methodology on Collapse of Friction Pendulum Isolated Moment-Resisting and Concentrically Braced Frames, J. Struct. Eng. 144 (2018) 04018203. https://doi.org/10.1061/(asce)st.1943-541x.0002183.

[11] E.A. Mavronicola, P.C. Polycarpou, P. Komodromos, Spatial seismic modeling of base-isolated buildings pounding against moat walls : effects of ground motion directionality and mass eccentricity, (2017) 1161–1179. https://doi.org/10.1002/eqe.

[12] P.C. Polycarpou, P. Komodromos, Earthquake-induced poundings of a seismically isolated building with adjacent structures, Eng. Struct. 32 (2010) 1937–1951. https://doi.org/10.1016/j.engstruct.2010.03.011.

[13] P. Komodromos, Simulation of the earthquake-induced pounding of seismically isolated buildings, Comput. Struct. 86 (2008) 618–626. https://doi.org/10.1016/j.compstruc.2007.08.001.

[14] Y. Bao, T.C. Becker, H. Hamaguchi, Failure of double friction pendulum bearings under pulse-type motions, Earthq. Eng. Struct. Dyn. 46 (2017) 715–732. https://doi.org/10.1002/eqe.2827.

[15] T.C. Becker, Y. Bao, S.A. Mahin, Extreme behavior in a triple friction pendulum isolated frame, Earthq. Eng. Struct. Dyn. 46 (2017) 2683–2698. https://doi.org/10.1002/eqe.2924.

[16] G. Auad, J.L. Almazán, Lateral Impact Resilient double concave Friction Pendulum

(LIR-DCFP) bearing: Formulation, parametric study of the slider and three-dimensional numerical example, Eng. Struct. 233 (2021). https://doi.org/10.1016/j.engstruct.2021.111892.

[17] G. Auad, P. Castaldo, J.L. Almazán, Seismic reliability of structures equipped with LIR-DCFP bearings in terms of superstructure ductility and isolator displacement, Earthq. Eng. Struct. Dyn. 51 (2022) 3171–3214. https://doi.org/10.1002/eqe.3719.

[18] G. Auad, Mitigating the adverse effects of internal lateral impacts in structures equipped with frictional isolators, Pontificia Universidad Católica de Chile, 2022.

[19] Y. Bao, T. Becker, Three-dimensional double friction pendulum bearing model including uplift and impact behavior: Formulation and numerical example, Eng. Struct. 199 (2019) 109579. https://doi.org/10.1016/j.engstruct.2019.109579.

[20] S.A. Anagnostopoulos, Equivalent viscous damping for modeling inelastic impacts in earthquake pounding problems, Earthq. Eng. Struct. Dyn. 33 (2004) 897–902. https://doi.org/10.1002/eqe.377.

COMPDYN 2023
9th ECCOMAS Thematic Conference on
Computational Methods in Structural Dynamics and Earthquake Engineering
M. Papadrakakis, M. Fragiadakis (eds.)
Athens, Greece, 12-14 June 2023

# SHAKE-TABLE TESTING OF LOW-COST, HIGH-PERFORMANCE SEISMIC ISOLATORS BASED ON ROLLING RUBBER SPHERES

**Antonios A. Katsamakas**[1] **and Michalis F. Vassiliou**[2]

[1] Institute of Structural Engineering, ETH Zurich, Stefano Francini Platz 5, CH-8097, Switzerland
e-mail: katsamakas@ibk.baug.ethz.ch

[2] Institute of Structural Engineering, ETH Zurich, Stefano Francini Platz 5, CH-8097, Switzerland
e-mail: vassiliou@ibk.baug.ethz.ch

## Abstract

*This study presents the results of a large-scale experimental investigation of low-cost, high-performance seismic isolators based on deformable rolling rubber spheres. The spheres roll on flat or concave concrete surfaces. Different types of spheres and design scenarios were examined. A potential application of the proposed isolator could be in low-rise structures in regions where conventional seismic isolators are unaffordable.*
*The spheres were initially subjected to monotonic uniaxial compression and sustained compression under vertical load to examine their compressive behavior. Subsequently, lateral cyclic tests under large displacements were performed. Finally, a total of 1170 shake-table tests were performed in 1:2 scale, with various different isolators subjected to a large number of ground motion excitations.*
*Results showed that the compressive strength of the spheres was substantially higher than the design load. The lateral cyclic response differs substantially from the one that a rigid body model would suggest due to the non-negligible deformability of the spheres. The rolling friction coefficient ranged between 3.7% and 7.1%. Hence, it is suitable for seismic isolation applications. The spherical concrete plates increase the restoring force of the system. When tested in a shake table under 1170 ground motions, the isolators substantially reduced the acceleration transmitted to the superstructure (to less than 0.2 g) while maintaining reasonable peak and zero residual displacements. Notably, the shake table tests were repeatable, and the isolators did not deteriorate even after subjected to 65 ground motion excitations.*

**Keywords:** Low-cost Seismic Isolation, Earthquake Engineering, Shake Table Testing, Rolling Isolators, Rubber Isolators.

## 1 INTRODUCTION

Earthquake-induced fatalities and economic loss are mainly concentrated in the developing world. This is due to the vulnerability of the building stock there, since modern structural codes are too expensive to be followed. Numerous recent examples prove that there is a pressing need to propose and implement earthquake-resistant solutions tailored to the needs and economic capabilities of the developing world.

Seismic isolation is a widely-acknowledged method of seismic protection. Its implementation includes the installation of devices (bearings) with low lateral resistance at the base of the structure. This allows for uncoupling the superstructure from the ground shaking. These bearings should have high bearing capacity under gravity loading to support the weight of the superstructure. Seismic isolation is mainly applied in important projects in the developed world, due to the associated high cost. The applications of the method in the developing world are much more limited. To this end, reduced-cost isolators have been proposed over the last decades. These isolators are distinguished into three main categories: flexible rubber bearings, sliding bearings, and rolling bearings.

Multiple studies [1-12] proposed the replacement of steel shims (used in conventional steel-laminated bearings) with flexible fiber reinforcement reduced the cost and weight of the isolators, leading to the "Fiber reinforced Elastomeric Isolator (FREI)". However, FREIs remain too stiff to isolate lightweight residential buildings.

Conventional sliding-based seismic isolators (such as the Friction Pendulum System, FPS) [13] require polished metals and Teflon surfaces from the sliding interfaces. This increases their cost and, therefore, limits their applications in the developing world. Recent studies proposed alternative sliding surfaces to reduce the cost of the isolators. Jampole et al. [14-15] studied high-density polyethylene sliders on galvanized steel. Brito et al. [16-17] used concrete-steel friction interfaces. In both previous systems restoring force is provided through the use of concave surfaces, similar to the FPS. Tsiavos et al. [18-19] used sand grains enclosed in PVC sheets as isolation layers below the foundation slab. This system lacks restoring force.

Rolling bearings, comprising steel spheres rolling on steel surfaces (Figure 1), have been used in [20-21]. The extensive use of steel may make the bearings unaffordable for low-income countries. The use of rubber was proposed in [22-26] to increase damping and avoid localized failure at the rolling interfaces.

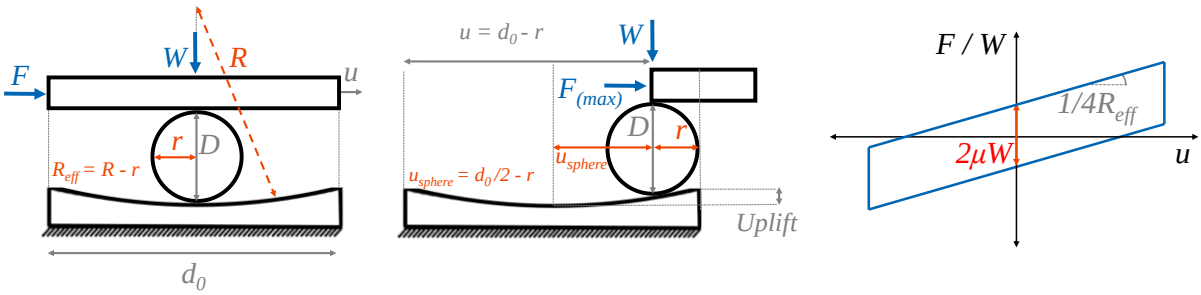


Figure 1: Rigid body model for rolling seismic isolators. Left, Isolator under compressive load and zero lateral displacement; Middle, Isolator under compressive load and maximum lateral displacement; Right, Bilinear force-displacement plot.

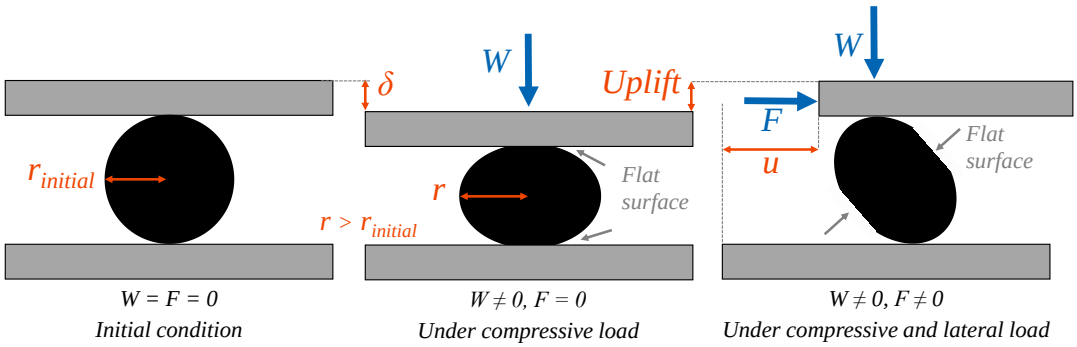


Figure 2: Left, Initial condition of the spherical isolator; Middle, Isolator under compressive load with evident compressive displacement; Right, Isolator under compressive and lateral load, with evident uplift.

## 2 DESCRIPTION AND POTENTIAL APPLICATION OF THE ISOLATOR

### 2.1 Description of the isolator and rigid-body equations

One of the most recent suggestions for seismic isolation of lightweight residential structures has been the Spherical Deformable Rolling Seismic Isolator (SDRSI) [27], initially proposed by Cilsalar and Constantinou [28-29]. Their work was based on the isolator proposed by Cui et al. [30]. The isolator comprises a deformable elastomeric sphere rolling on concrete surfaces (Figure 2). It is noted that the deformability of the sphere cannot be neglected and that the response is significantly different from an idealized rigid-body model [31]. This is due to residual "creep" deformation of the sphere under vertical compressive load that results in essentially rolling an oval-shaped sphere rather than a perfect sphere (Figure 2).

According to the rigid-body model, the force-displacement relation that describes the lateral response of the system is described by Equation (1) [28]:

$$F = \frac{W}{4R_{eff}}u + \mu_{roll} W sign(\dot{u}) \tag{1}$$

Where $F$ is the horizontal force applied to the isolator, $W$ is the vertical force (weight) applied to the isolator, $u$ is the lateral displacement of the isolator, $\delta$ is the compressive displacement under load $W$, $R_{eff} = R - r$, $R$ is the radius of curvature of the spherical concrete plate and $r = D/2$ is the radius of the rolling sphere (Figure 1). The quantity $\frac{W}{4R_{eff}}u$ is the restoring force of the system that originates from gravity and the use of concave concrete plates. The translational displacement of the sphere ($u_{sphere}$) is equal to half of the displacement of the isolator ($u$); hence, $u_{sphere} = u/2$. The isolation period of the system is equal to as $2\pi\sqrt{\frac{4R_{eff}}{g}}$. The $\mu_{roll}$ term is the rolling friction coefficient of the system and is equal to the lateral-to-vertical force ratio at zero lateral displacement. It is a macroscopic term that describes the initiation of rolling motion and the energy dissipation of the isolator.

It is recommended to use one concave concrete surface to guarantee restoring force to the system. Configurations with two flat plates are also tested in the present study to characterize the behavior of the rolling sphere without the curvature of the concrete surface influencing the response.

## 2.2 Potential application of the isolator

A potential application of the proposed isolator could be in one- or two-story masonry houses in countries where reinforced concrete is unavailable or unaffordable. In these regions, the construction of seismically isolated masonry houses could be a viable solution for earthquake-resistant structures. Communication with engineers from Cuba and Peru has unveiled that, in many low-income countries, seismic isolation cannot be financially viable for low-rise buildings because of the cost of the additional, heavily reinforced slab (diaphragm) that is typically constructed at the isolation level. Unless the cost of this slab is reduced, seismic isolation cannot be financially competitive. It is noted that the applications of the isolator are not limited to the aforementioned cases. The isolator could also be applicable in the developed world, in projects where conventional seismic isolation is too expensive to be applied.

We propose a combination of the systems of Cilsalar and Constantinou [28-29] and the one proposed by Tsiavos et al. [18-19], for the isolation of 1-2 story masonry houses (Figure 3). More specifically, the walls are supported on concrete beams that serve as the upper rolling surface of the isolators.

Two sheets of PVC (with sand in between) will continuously support the ground floor slab. This continuous support allows for reducing the thickness of the slab and for providing minimal (if any) reinforcement, making its cost similar to the cost of the cleaning concrete layer that is used in fixed base structures.

When the deformable rubber sphere rolls, the horizontal motion of the isolator also causes a vertical one. Therefore, a PVC joint could be used to connect the slab to the beams. This would allow the vertical motion of the beams while the slab only moves horizontally (Figure 3).

# 3 EXPERIMENTAL SETUP

## 3.1 Testing equipment and instrumentation

The uniaxial shake table of ETH Zurich was used in both the lateral cyclic and the shake-table tests. The experimental setup comprises four isolators placed symmetrically on the shake table platen in a two-by-two configuration (Figure 4). An isolator comprises a PU sphere rolling between two concrete plates. In all tested cases, the lower concrete plates were flat. The upper concrete plates were either flat (“flat configurations”) or spherical/concave (“spherical configurations”). The lower concrete plates were fixed to the shake table platen, whereas the upper ones were mounted on a steel slab.

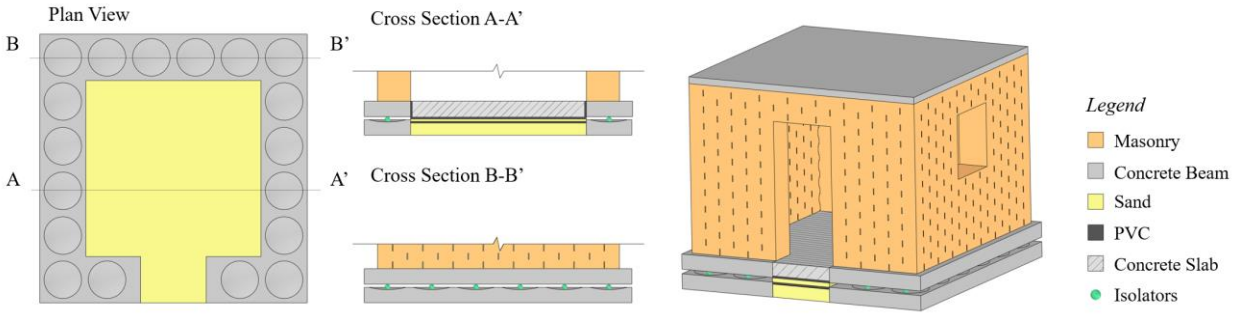


Figure 3: Representation of a potential application of deformable rolling isolators in low-rise masonry buildings.

During the lateral cyclic tests, the motion of the top slab parallel to the x-axis (and the out-of-plane y axis) was restrained by two rigid struts fixed to a rigid column (Figure 4). The shake table applied a sinusoidal motion by moving the bottom concrete plates, whereas the top plates were kept in place by the rods. Thus, shearing of the isolators was achieved. Large steel beams were placed on top of the steel slab to compress the isolators (emulating the weight of the isolated superstructure). For the shake table tests, the steel rods were removed, and the steel slab was free to move along the x-axis.

Three-dimensional accelerometers were placed on top of the steel slab and the shake table platen. The struts that hold the steel diaphragm in place were equipped with load cells, measuring the reaction force of the isolators to the applied motion during the lateral cyclic tests. Another load cell was placed at the actuator that drives the shake table. The movement of the shake table and the superstructure was measured using an NDI Optotrak Certus camera with an accuracy of 0.1 mm (Figure 4).

### 3.2 Materials and geometry

Three types of spheres were tested: Solid spheres with a diameter of 100 mm, spheres with a diameter of 100 mm and a 50 mm steel core inside (spheres 100/50 mm), and spheres with a diameter of 80 mm and a 50 mm steel core inside (spheres 80/50 mm). The spheres were made of polyurethane (PU) with a shore hardness of 95A. The steel core was made of Gcr15 steel. The cost of 100 mm, 100/50 mm, and 80/50 mm spheres was $23, $30, and $25 per piece, respectively. In a practical application, the price per piece is expected to be significantly lower due to the increase in the total number of spheres ordered.

A commercial M15 concrete mix was used for the construction of the concrete plates. Figure 5 shows the dimensions of the spherical (concave) concrete plates. The mean compressive strength of the concrete mix was 27.6 MPa. The plates were unreinforced. The material cost of each plate was $6. In plan view, the diameter of the spherical concrete plate was 350 mm (Figure 5). The radius of curvature of the spherical concrete plates (R) was $R$ = 750 mm.

### 3.3 Similitude laws and tested configurations

All tests were performed in 1:2 scale. To ensure similitude of stresses, the geometric, force, and time scaling factors were $S_L$=0.5, $S_F$ = 0.25, and $S_T$ = 0.707, respectively. A modern unconfined masonry house in Cuba was considered to calculate the expected vertical load, resulting in a gravity load of 11 kN (i.e., 2.75 kN in the model scale) per isolator. Four compressive loads (2.08 kN, 3.23 kN, 4.74 kN, or 8 kN per sphere in model scale) under two rolling surface curvatures (flat and concave) were planned for all three spheres. The actuator of the shake table had a stroke of 230 mm. To test the isolators under larger lateral displacements, two types of cyclic tests were performed: a) between -115 and +115 mm ("±115 mm") and b) between 0 and +230 mm and 0 and -230 mm ("±230 mm").

The shake table tests were performed under an ensemble of 61 different ground motions, selected from the three different categories of FEMA P695 [32] (i.e., far-field, near-field pulse-like, and near-field non-pulse-like). All ground motions were scaled in the frequency domain since the tested model corresponds to a half-scale ($S_L$=0.5) representation of a prototype structure. Subsequently, all ground motions were acceleration-scaled to comply with the capacity of the shake table, with the acceleration scaling factor ranging from 0.7 to 1. Figure 5 (B,C) plots the elastic response spectra of the pseudo-accelerations and displacements of the ground motions used in the shake table tests, together with the design spectrum for a site in Santiago, Cuba (model scale), assuming soil type C, 5% damping and a return period of 475 years. The example of Santiago, Cuba is used since it is considered representative of regions

of high seismicity and low availability of construction materials. Similar (or higher) seismicity and analogous lack of recourses can be found in many countries in Latin America, Asia, and Africa.

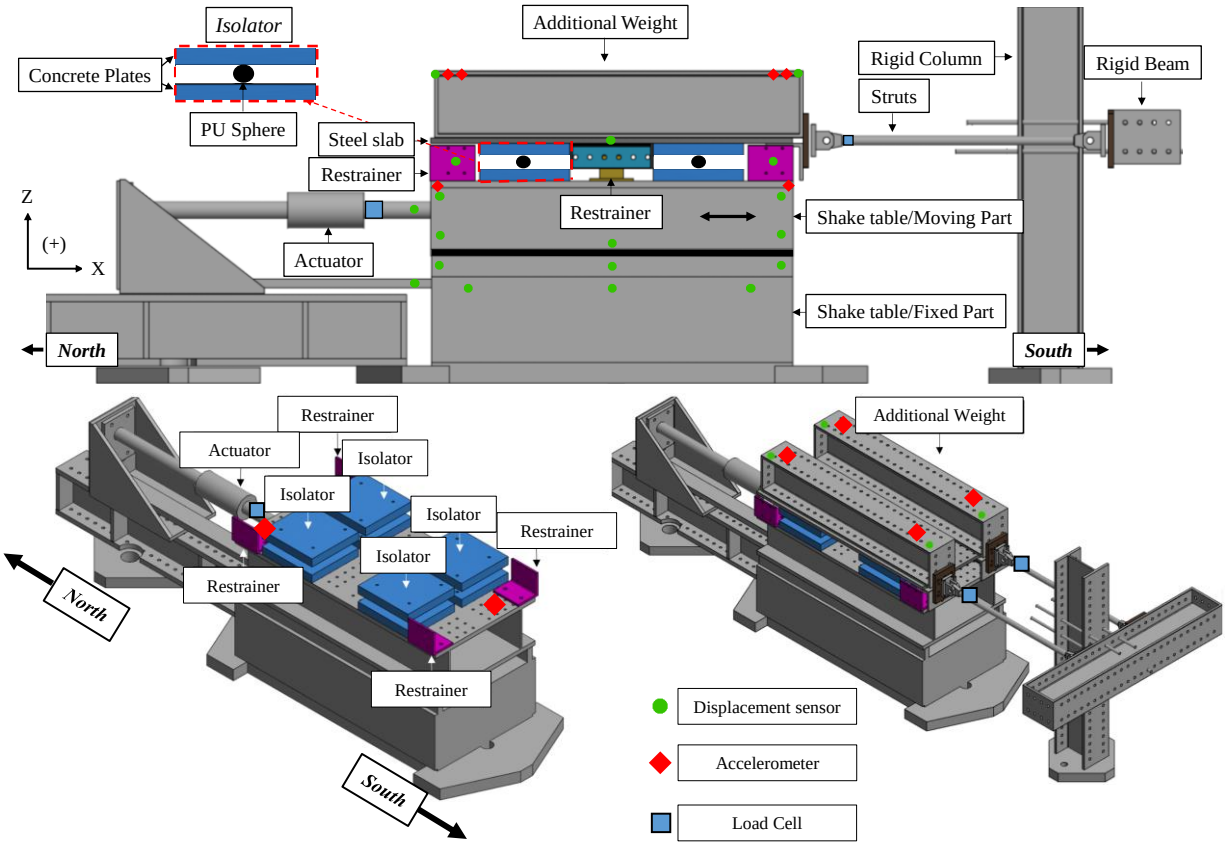


Figure 4: Representation of the experimental setup. Green circles, red diamonds, and blue squares show the location of the triaxial displacement sensors, the triaxial accelerometers, and the uniaxial load cells, respectively.

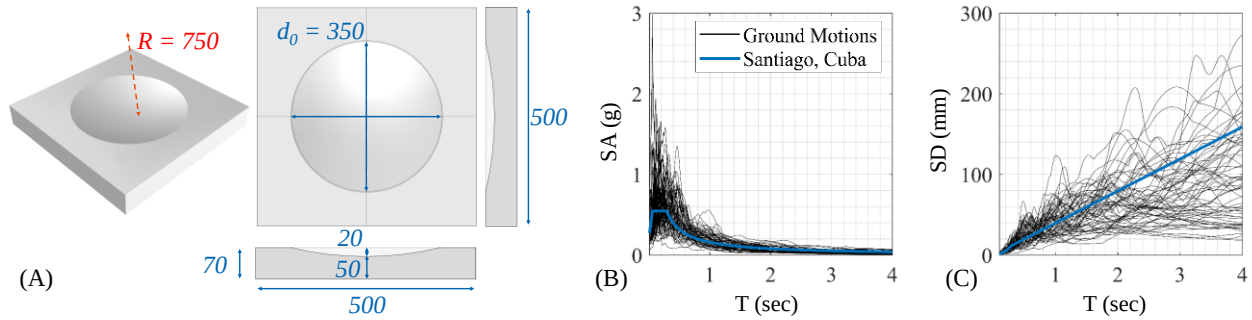


Figure 5: (A) Shape and dimensions of the utilized spherical concrete plates (in mm); Elastic response spectra of the applied ground motions and design spectrum of Santiago, Cuba (in model scale). (B), Pseudo-accelerations; (C) Displacements.

# 4 COMPRESSIVE AND LATERAL CYCLIC RESPONSE

## 4.1 Compressive response

The maximum load that the spheres sustained under monotonic uniaxial compression was 105.2 kN, 118.8 kN, and 102.5 kN for the 100 mm, 100/50 mm, and 80/50 mm spheres, respectively (Figure 6). These load levels are substantially higher than the ones that the spheres would have to sustain in a practical application (2.75 kN/sphere in model scale, Section 2). Therefore, the loss of vertical load-bearing capacity of the spheres is not the critical design parameter. Under design loads, the compressive displacement of the isolators is non-negligible, indicating the shape change of the spheres. A comparison of the 100 and 100/50 spheres shows that the presence of a steel core increases the stiffness of the sphere.

## 4.2 Lateral cyclic response

Before the lateral cyclic tests, the spheres were subjected to sustained compression for seven days, so their "creep" displacement and shape change is concluded. The excitation frequency of all cyclic tests was f = 0.2 Hz. Figure 7 collectively offers the force deformation loops for all lateral cyclic tests. The first and most important observation is that the behavior of the system is clearly not bilinear elastoplastic. In fact, since the sphere has deformed into an oval-shaped object, a vertical motion of the top plate was recorded both in the tests presented in this study and in [33-35]. This vertical motion influences the restoring force, which is positive for small displacements (up to 30 mm) but becomes negative for larger displacements due to the rolling of the sphere. The use of concave concrete plates adds positive stiffness to the system.

The rolling friction coefficient ($\mu_{roll}$), is defined as the lateral-to-vertical force ratio at zero lateral displacement and describes the energy dissipation capacity of the isolator. In all following sections, the rolling friction coefficient was obtained by the "±115 mm" cyclic tests and is noted in Figure 7. It is observed that as the vertical load ($W$) increases, the rolling friction coefficient also increases. This is more pronounced in spheres without a steel core since they are more flexible. A detailed explanation of this phenomenon appears in [27].

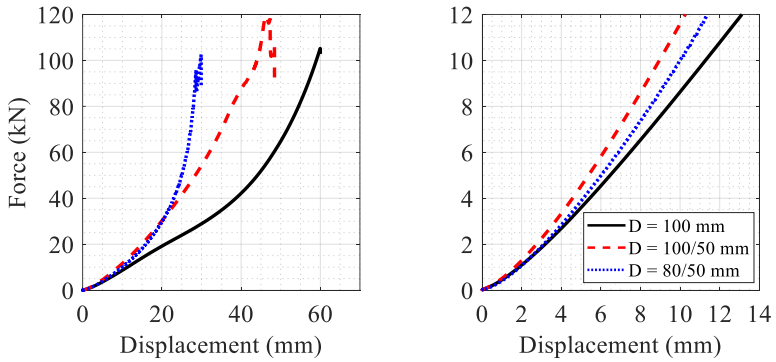


Figure 6: Compression testing results. Left: Force-displacement (overview); Right: Force-displacement (detail).

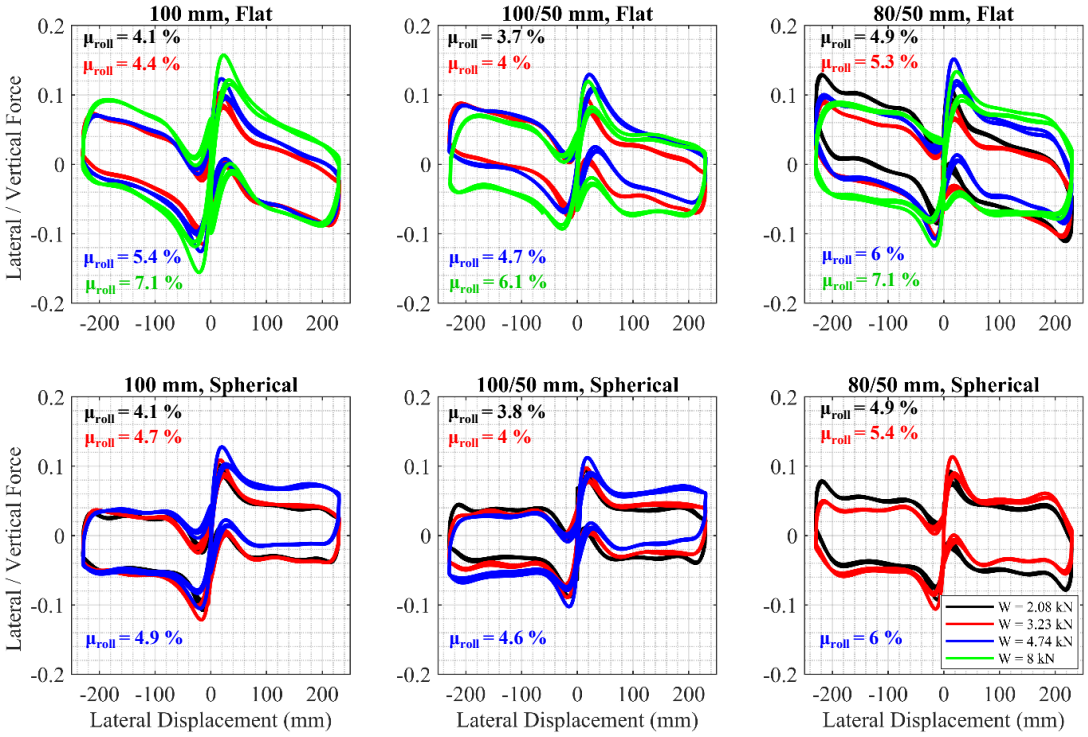


Figure 7: Influence of the vertical load (W) on the cyclic lateral response of the spherical isolator.

## 5 SHAKE-TABLE RESPONSE

Figures 8 and 9 show scatter plots between the Peak Ground Acceleration (PGA) and a) the acceleration of the top slab (Peak Superstructure Acceleration – PSA), b) the peak displacement of the isolators. Different categories of ground motions appear with different marks.

Excitations with relatively small PGAs (smaller than 0.10-0.15) are not strong enough to start rolling the system (activate the isolators). Hence, the superstructure acceleration is roughly equal to the PGA (Figure 8). However, for larger PGAs, the superstructure acceleration is capped at 0.15-0.2 g (Figure 8). These values are slightly higher than the peak of the force deformation loops of the cyclic loops (Figure 7).

The isolators maintained moderate peak displacements during ground motion shaking, which were below 120 mm and 100 mm for the flat and the spherical plates, respectively (model scale). No systematic trend that could correlate the category of the ground motion (e.g., near-field pulse-like) to the response (e.g., maximum displacement) is apparent (Figure 9).

Some shake table tests were performed three times (using the same ground motion input) to examine the repeatability of the results. The response of the isolators was practically identical, both in terms of accelerations and displacements, confirming the repeatability of the tests (Figure 10). Figure 10 also shows a detail of the isolation effect that appears collectively in Figures 8 and 9. More specifically, we observe that the isolators cap the acceleration transmitted to the superstructure (limit of less than 0.20 g), regardless of the intensity of the applied ground motion (Figure 10, top). This comes at the expense of large displacements at the isolation level (Figure 10, bottom).

After the shake table tests, another set of lateral cyclic tests was performed to evaluate the deterioration of the spheres. The lateral cyclic response of the isolators was practically the same as before the shake table tests (Figure 11). Hence, even after 65 ground motions, the spheres did not deteriorate.

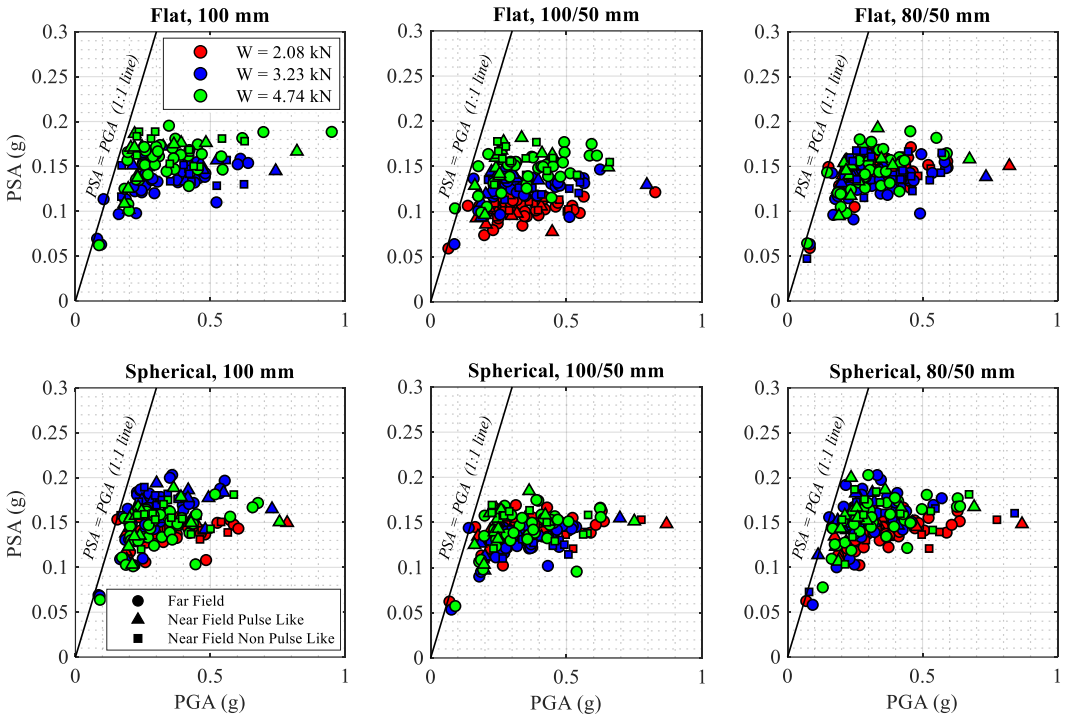


Figure 8: Correlation between the acceleration transmitted to the superstructure (PSA) and PGA for all tested configurations. Top, Flat concrete plates; Bottom, Spherical concrete plates.

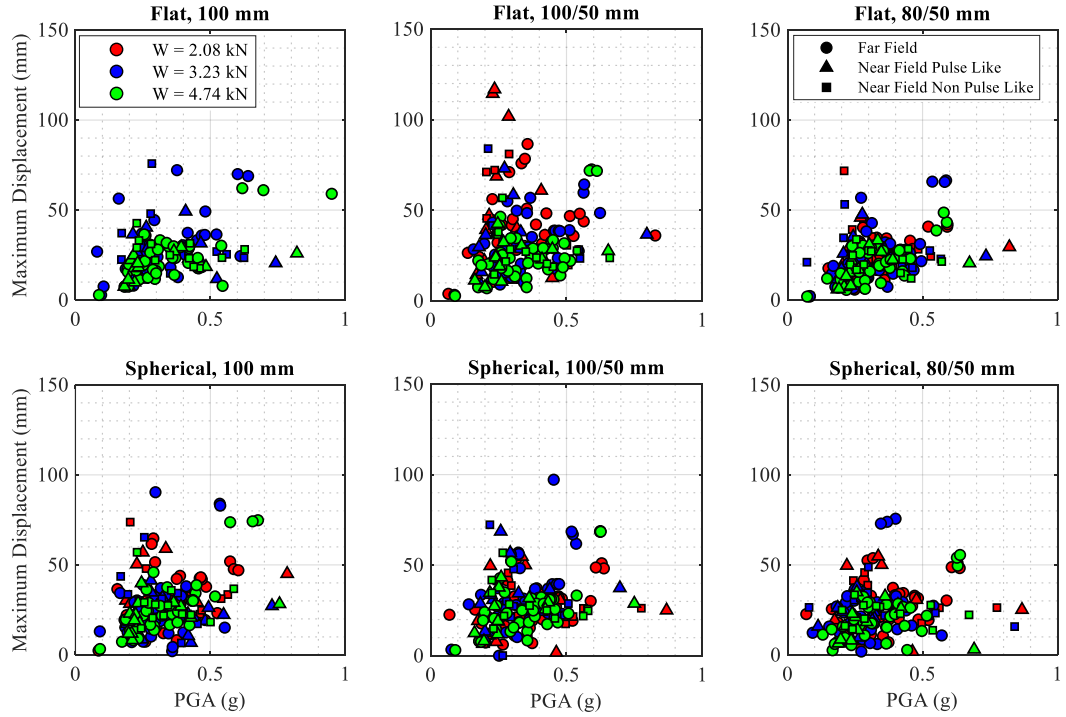


Figure 9: Correlation between the maximum displacement of the isolators and PGA for all tested configurations. Top, Flat concrete plates; Bottom, Spherical concrete plates.

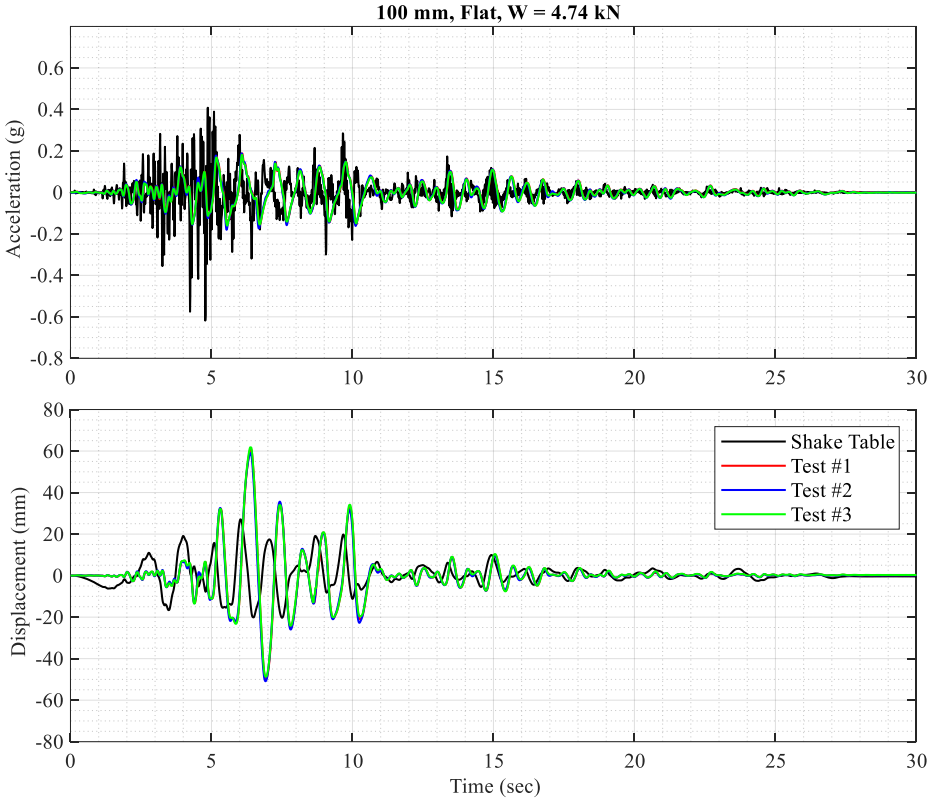


Figure 10: Repeatability of the shake table tests when using the same excitation in 3 sequential tests. Use of the 1989 Loma Prieta, USA, ground motion, component 0, as recorded at Capitola station.

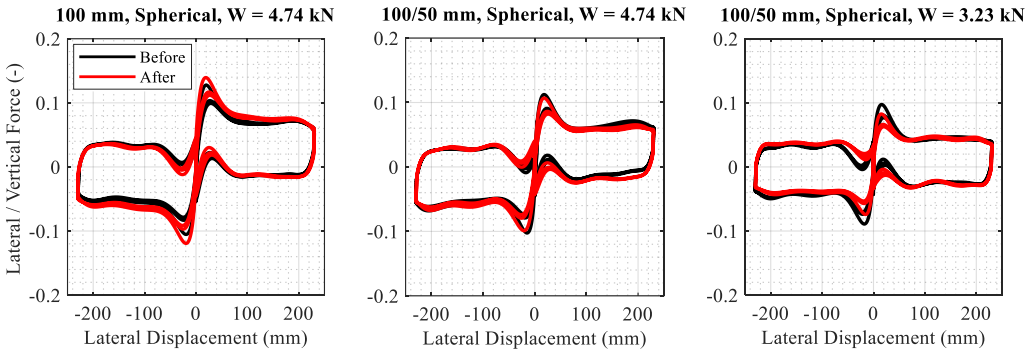


Figure 11: Lateral cyclic response of the isolators before and after being subjected to 65 ground motions. No deterioration was observed.

## 6 CONCLUSIONS

The present study investigated the compressive, lateral cyclic, and shake-table response of an isolator based on rolling PU spheres (with and without steel core) rolling on concrete plates. Different levels of supported weight and curvatures of concrete plates were considered. A total of 21 different combinations of vertical load, sphere dimensions, and concrete plate curvature were tested under lateral cyclic loading. In the shake-table tests, 18 combinations were tested with 65 ground motions each, leading to a total of 1170 shake-table tests. According to the experimental results, the following conclusions are drawn:

- The compressive strength of the spheres is substantially higher than the estimated design vertical load applied to the spheres, considering an application in a low-rise residential masonry structure in low-income countries.
- The lateral cyclic response differs substantially from the one that a rigid body model would suggest. This is due to the non-negligible deformability of the spheres that leads to both positive and negative stiffness branches.
- The curvature of the concrete surface affects the lateral cyclic response. When spherical (concave) plates are used, the stiffness of the system increases. The final stiffness of the isolators is affected by the deformed shape of the isolators (source of negative stiffness) and the curvature of the concrete plate (source of positive stiffness).
- During the shake-table tests with excitations at the order of the seismicity of Santiago, Cuba, the isolators significantly reduced the accelerations transmitted to the superstructure (in the range of 0.15g), while maintaining displacements below 120 mm in the model scale (240 mm in the prototype scale). This means that the proposed isolators cap the accelerations transmitted to the superstructure to less than 0.2 g, while they maintain reasonable displacements.
- When the same isolators were subjected to 3 identical sequential shake table excitations, the measured response, both in terms of accelerations and displacements, was practically the same. Therefore, the shake-table tests were repeatable.
- Even after subjected to 65 ground motion excitations, the isolators do not deteriorate, and their cyclic lateral response remains unaffected by the loading history.

## 7 ACKNOWLEDGEMENTS

Financial support to the authors was provided by the European Research Council (ERC) under Starting Grant 803908. The methods, results, opinions, findings, and conclusions presented in this report are those of the authors and do not necessarily reflect the views of the funding agency.

## REFERENCES

[1] A. Das, SK. Deb, A. Dutta, Shake table testing of un-reinforced brick masonry building test model isolated by U-FREI. *Earthquake Engng Struct Dyn*, 45(2), 253-272, 2016. https://doi.org/10.1002/eqe.2626

[2] D. De Domenico, D. Losanno, N. Vaiana, Experimental tests and numerical modeling of full-scale unbonded fiber reinforced elastomeric isolators (UFREIs) under bidirectional excitation. *Engineering Structures*. 274, 115118, 2023. https://doi.org/10.1016/j.engstruct.2022.115118

[3] D. Losanno, N. Ravichandran, F. Parisi, Seismic fragility models for base-isolated unreinforced masonry buildings with fibre-reinforced elastomeric isolators. *Earthquake Engng Struct Dyn*. 52:308–334, 2023. https://doi.org/10.1002/eqe.3761

[4] M. Spizzuoco, A. Calabrese, G. Serino, Innovative low-cost recycled rubber–fiber reinforced isolator: experimental tests and finite element analyses. *Engineering Structures.* 76: 99-111. 2014. https://doi.org/10.1016/j.engstruct.2014.07.001

[5] S. Galano, A. Calabrese, State of the Art of Seismic Protection Technologies for Non-Engineered Buildings (N-EBs) in Developing Regions of the World. *Journal of Earthquake Engineering*. 2023. https://doi.org/10.1080/13632469.2023.2165579

[6] P.M. Osgooei, M.J. Tait, D. Konstantinidis, Finite element analysis of unbonded square fiber-reinforced elastomeric isolators (FREIs) under lateral loading in different directions. *Composite Structures.* 113, 164-173, 2014. https://doi.org/10.1016/j.compstruct.2014.02.033

[7] H. Toopchi-Nezhad, M.J. Tait, R.G. Drysdale, Shake table study on an ordinary low-rise building seismically isolated with SU-FREIs (stable unbonded-fiber reinforced elastomeric isolators). *Earthquake Engineering & Structural Dynamics*. 38(11), 1335-1357, 2009. https://doi.org/10.1002/eqe.923 (2009).

[8] C. Tran, A. Calabrese, M.F. Vassiliou, S. Galano, A simple strategy to tune the lateral response of unbonded Fiber Reinforced Elastomeric Isolators (FREIs), 222, 111128, 2020. *Engineering Structures*

[9] N.C. Van Engelen, D. Konstantinidis, M.J. Tait, Structural and nonstructural performance of a seismically isolated building using stable unbonded fiber-reinforced elastomeric isolators. *Earthquake Engineering & Structural Dynamics,* 45(3), 421-439, 2016.

[10] N.C. Van Engelen, M.J. Tait, D. Konstantinidis, Model of the shear behavior of unbonded fiber-reinforced elastomeric isolators. Journal of Structural Engineering, 141(7), 04014169, 2014.

[11] G. Russo, M. Pauletta, A.A. Cortesia, A study on experimental shear behavior of fiber-reinforced elastomeric isolators with various fiber layouts, elastomers and aging conditions. *Engineering Structures*, 52, 422-433, 2013.

[12] D. Konstantinidis, J.M. Kelly, N. Makris, *Experimental investigations on the seismic response of bridge bearings*. Earthquake Engineering Research Center, Report No. EERC 2008-03, 2008.

[13] M.C. Constantinou, A.S. Mokha, A.M. Reinhorn, Teflon bearings in base isolation II: Modeling. *J. Struct. Eng.* 116(2), 455-474, 1990.

[14] E.A. Jampole, G. Deierlein, E. Miranda, B. Fell, S. Swensen, C. Acevedo, Full-scale dynamic testing of a sliding seismically isolated unibody house. *Earthquake Spectra.* 32(4), 2245-2270, 2016. https://doi.org/10.1193/010616EQS003

[15] E.A. Jampole, S.D Swensen, B. Fell, E. Miranda, G.G. Deierlein, Dynamic testing of a low-cost sliding isolation system for light-frame residential structures. 10NCEE. 2014.

[16] M.B. Brito, H. Ishibashi, M. Akiyama, Shaking table tests of a reinforced concrete bridge pier with a low-cost sliding pendulum system. *Earthquake Engng Struct Dyn*. 48: 366– 386, 2019.

[17] M.B. Brito, M. Akiyama, Y. Ichikawa, H. Yamaguchi, R. Honda, N. Ishigaki, Bidirectional shaking table tests of a low-cost friction sliding system with flat-inclined surfaces. *Earthquake Engng Struct Dyn.* 49: 817– 837, 2020 https://doi.org/10.1002/eqe.3266

[18] A. Tsiavos, A. Sextos, A. Stavridis, M. Dietz, L. Dihoru, N.A. Alexander, Large-scale experimental investigation of a low-cost PVC 'sand-wich'(PVC-s) seismic isolation for developing countries. *Earthquake Spectra*. 36(4), 1886-1911, 2020.

[19] A. Tsiavos, A. Sextos, A. Stavridis, M. Dietz, L. Dihoru, F. Di Michele, N.A. Alexander, Low-cost hybrid design of masonry structures for developing countries: Shaking table tests. *Soil Dynamics and Earthquake Engineering*. 146, 106675, 2021.

[20] P.S. Harvey, K.C. Kelly, A review of rolling-type seismic isolation: Historical development and future directions. *Engineering Structures*. 125, pp. 521-531, 2016. https://doi.org/10.1016/j.engstruct.2016.07.031.

[21] P.S. Harvey, G.P. Zéhil, H.P. Gavin, Experimental validation of a simplified model for rolling isolation systems. *Earthquake Engineering and Structural Dynamics*. 43:1067–1088, 2014.

[22] D. Foti, Rolling devices for seismic isolation of lightweight structures and equipment. Design and realization of a prototype. *Structural Control and Health Monitoring*. 26(3), e2311, 2019.

[23] A.A. Katsamakas, M. Chollet, S. Eyyi, M.F. Vassiliou, Feasibility Study on Re-Using Tennis Balls as Seismic Isolation Bearings. *Frontiers in Built Environment*. 2021; 7, 768303. 2021. https://doi.org/10.3389/fbuil.2021.768303

[24] A.A. Katsamakas, M. Chollet, S. Eyyi, M.F. Vassiliou, Re-using tennis balls as low-cost seismic isolation devices: Experimental Investigation. *3rd International Conference on Natural Hazards & Infrastructure (ICONHIC2022),* Athens, Greece, July 5-7, 2022.

[25] A.A. Katsamakas, M.F. Vassiliou, Low-cost and sustainable seismic isolation with re-used tennis balls: Lateral cyclic tests. *Third European Conference on Earthquake Engineering and Seismology (3ECEES)*, Bucharest, Romania, September 4-9, 2022.

[26] G.P. Zéhil, H.P. Gavin, Rolling resistance of a rigid sphere with viscoelastic coatings. *Int. J. Solids Struct.* 1;51(3-4):822-38, 2014.

[27] A.A. Katsamakas, M.F. Vassiliou, Experimental parametric study and phenomenological modeling of a deformable rolling seismic isolator. *Journal of Earthquake Engineering*, 2023. (under review)

[28] H. Cilsalar, M.C. Constantinou, Behavior of a spherical deformable rolling seismic isolator for lightweight residential construction. *Bull Earthquake Eng.* 17, 4321–4345, 2019. https://doi.org/10.1007/s10518-019-00626-z.

[29] H. Cilsalar, M.C. Constantinou, *Development and Validation of a Seismic Isolation System for Lightweight Residential Construction*. Technical Report MCEER, Report No.19-0001, University at Buffalo, USA, 2019.

[30] S. Cui, M. Bruneau, M.C. Constantinou, *Integrated Design Methodology for Isolated Floor Systems in Single-Degree-of-Freedom Structural Fuse Systems*. Technical Report MCEER, Report No. 12-0004, 2012.

[31] A.A. Katsamakas, G. Belser, M.F. Vassiliou, M. Blondet, Experimental investigation of a spherical rubber isolator for use in low income countries. *Engineering Structures*. 2022; 1; 250:113522, 2022. https://doi.org/10.1016/j.engstruct.2021.113522

[32] FEMA P695: *Quantification of Building Seismic Performance Factors*, Federal Emergency Management Agency, USA, 2009.

[33] A.A. Katsamakas, G. Belser, M.F. Vassiliou, M. Blondet, B. Stojadinovic, Experimental investigation of spherical rubber seismic isolation bearings. *8th ECCOMAS Thematic Conference on Computational Methods in Structural Dynamics and Earthquake Engineering (COMPDYN 2021),* Athens, Greece. June 27–30, 2021.

[34] A.A. Katsamakas, G. Belser, M.F. Vassiliou, B. Stojadinovic, M. Blondet, Shake-table testing of low-cost seismic isolation bearings based on rolling rubber spheres. *3rd International Conference on Natural Hazards & Infrastructure (ICONHIC2022)*, Athens, Greece, July 5-7, 2022.

[35] A.A. Katsamakas, M.F. Vassiliou, Lateral cyclic response of deformable rolling seismic isolators for low-income countries. *Third European Conference on Earthquake Engineering and Seismology (3ECEES)*, Bucharest, Romania, September 4-9, 2022.

COMPDYN 2023
9th ECCOMAS Thematic Conference on
Computational Methods in Structural Dynamics and Earthquake Engineering
M. Papadrakakis, M. Fragiadakis (eds.)
Athens, Greece, 12-14 June 2023

# BEHAVIOR OF COMPLEX CURVED SURFACE SLIDER IN DESIGN AND EXPERIMENTAL SITUATION

**Frederik Bomholt**[1], **Toshihisa Mano**[2]

[1] Technical Group Manager Vibration and Seismic Protection Devices MAURER SE
Frankfurter Ring 193, 80807 Munich
f.bomholt@mauer.eu

[2] Technical Group Manager Testing and Certification MAURER SE
Frankfurter Ring 193, 80807 Munich
t.mano@maurer.eu

## Abstract

*The performance of curved surface slider (CSS) is in general directly dependent on the dynamic coefficient of friction and the effective radius of curvature. For single CSS and double CSS with non-articulated slider the change of the leading results can be easily determined for the corresponding influence parameter. For more complex CSS, double CSS with articulated slider and adaptive CSS with differences in displacement capacity, coefficient of friction and effective radius of curvature for upper and lower sliding level, the resulting change in performance are much more complex. For the former, differences in coefficient of friction and effective radius can lead to one-sided moving of the slider due to non-geometrical restraint of the inner part. This behavior can lead to significant change in performance with changing restoring stiffness and significant deviations in effective stiffness and damping. Furthermore, the total displacement capacity can be reduced if one-sided sliding occurs with a significant high magnitude.*

*This change in behaviour is similar for the complex adaptive CSS but much more complex due to the designed sliding behaviour with change from one-sided sliding to simultaneously sliding to one-sided sliding of the other side with each different effective radius and coefficient of friction. The question is how the magnitude of the performance changes due to fluctuating input parameters, here for the coefficient of friction and the effective radius, is a typical task for monte-carlo simulations. In this work the findings of several monte-carlo simulations for a typically double and adaptive CSS will be presented in comparison with experimental results made on appropriate specimens for quality control and type testing.*

**Keywords:** Complex Curved Surface Slider, CSS, Adaptive Isolator, Stochastic Simulation, Experimental Testing,

## 1 INTRODUCTION

For the mitigation of earthquake loadings, the basic isolation is an established option which can be realized by means of isolator devices [1]. Especially for building of the critical infrastructure like hospitals or main bridges the basic isolation can ensure a high stability and probability of survival of the structure even during big shocks caused by maximum considered earthquakes (MCE). Besides the elastic isolators like high damping rubber bearings or lead rubber bearings the curved surface sliders are well-known products for the application in basic isolation systems. The friction pendulum bearing was developed from the overall movable spherical bearing which commonly will be designed with lubricated sliding material [2]. While a spherical bearing as a part of a bridge bearing system must operate with a minimum of resistance force, the curved surface slider mainly has an additional task of energy dissipation which will be achieved by means of a certain amount of friction. To achieve this friction coefficient the CSS will not be lubricated. The second and more important difference is the additional curvature in the main sliding surface. The evolution of an overall movable spherical bearing with a curvature in the main sliding surface leads to a Sliding Isolation Pendulum bearing with a single sliding surface (SIP-S). Due to the second curvature the CSS achieve a recentering capacity which is dependent on the actual friction of the sliding material as well as the passed horizontal displacement. Because inherently CSS are usable for a stable bearing of high vertical loads, the device does have all characteristics for the requirement of a basic isolation device:

- Vertical load transmission
- Horizontal movement capacity
- Recentering capacity
- Energy dissipation capacity

The last point is optional because a CSS with non-designed energy dissipation can be combined with an energy dissipation device like viscous damper as velocity dependent device or displacement dependent devices like hysteretic dampers.

To improve the second point horizontal movement capacity the SIP-S was further developed to the Sliding Isolation Pendulum bearing with double sliding surfaces (SIP-D). Instead of achieving the pendulum effect by means of a combination of main and secondary sliding surfaces, the SIP-D design has two identical main sliding surfaces which doubles the horizontal movement capacity compared to a SIP-S with almost identical isolator size. As a disadvantage of this improvement of horizontal movement capacity the SIP-D is significantly reduced in rotational capacity because a significant rotation can only occur if one-sided sliding occurs or if the sliding material allow small rotations due to small deformations on the edges. While the former reduces the horizontal movement capacity one-sided and needs in particular high forces to break the frictional resistance of the slider the latter leads to a partial reduction of the sliding gap which is an indicator for the wear of the CSS. This type of isolator is accordingly more related to applications in buildings than in bridges where high demands of rotations and service displacements are requested. But especially for buildings with higher stiffness of the superstructure the SIP-D is the best solution for cost-effective basic isolation systems [3].

A combination of both high horizontal movement capacity and high rotational capacity can be achieved by means of dividing the inner part of the SIP-D into two parts with an additional secondary sliding surface with a sufficient curvature to achieve a SIP-DR, see exemplary Figure 1. This additional hinge allows significant rotation not only in central position but also in a multitude of combinations of horizontal movement and rotational demand. Without any doubt this description fit perfectly to typical mid and width span bridges in seismic regions

which must work properly in service conditions with transmitting forces and translational and rotational movements between the substructure and the superstructure. In the event of earthquakes, the isolation system must provide sufficient decoupling of both parts of the structure by allowing high translational movements in horizontal direction. For this application the use of fully lubricated sliding surfaces is recommended in combination with energy dissipation devices like velocity dependent hydraulic devices. While the latter will have the highest reaction force at around zero displacement because of the highest velocity in this point, the CSS will have the highest reaction force at the maximum out centered position due to the recentering force. This combination leads to a very efficient system with high energy dissipation and low base shear forces acting on the structure. From design point of view the SIP-DR is a double CSS with decoupled sliding surfaces which not automatically slides both simultaneously like a SIP-D but rather only similar sliding occurs if the acting horizontal forces of both main sliding areas are in a certain equilibrium.

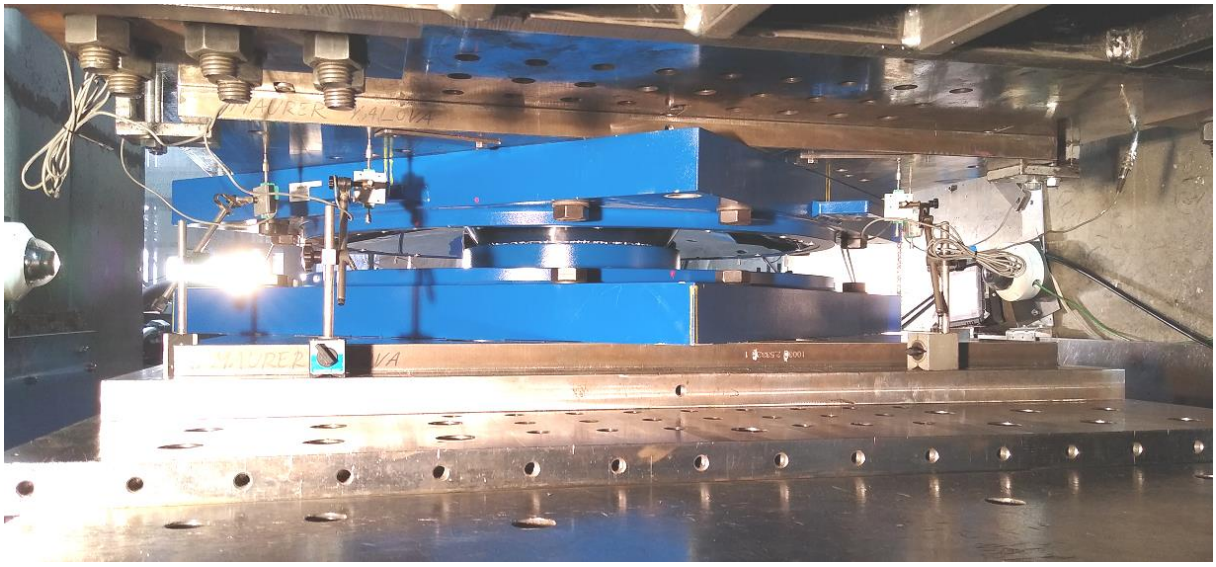

Figure 1: SIP-DR device in test machine of BTS Eucentre, Pavia.

This decoupling of sliding surfaces was the start point for the development of a second generation of CSS with not only decoupled sliding surfaces which shall slide simultaneously but rather which will be controlled for different sliding regimes to achieve different protection levels for different seismic situations. The development results in the adaptive CSS SIP-A [4, 5]. While high frequently earthquakes act with a low magnitude and with low energy impact the isolator must slide with little movements only but with very less friction to reduce the base shear. In case of a design base earthquake the isolator must switch into the second gear to achieve a significant energy dissipation and increase the period of the isolation system. The SIP-A can be designed with an overlapping of siding of both primary sliding surfaces with the different effective radii and design coefficient of friction to have a second working point for the DBE event. Switching into the third gear means for the SIP-A a contact between the bottom part of the slider and the restraint system of the lower sliding plate to allow sliding on the top surface only with the highest displacement capacity and with sufficient amount of design friction and restoring stiffness which are designed to meet the challenges of a maximum considered earthquake (MCE) [6]. The schematically development of the sliding isolation pendulum with and without recentering capacity can be seen in Figure 2.

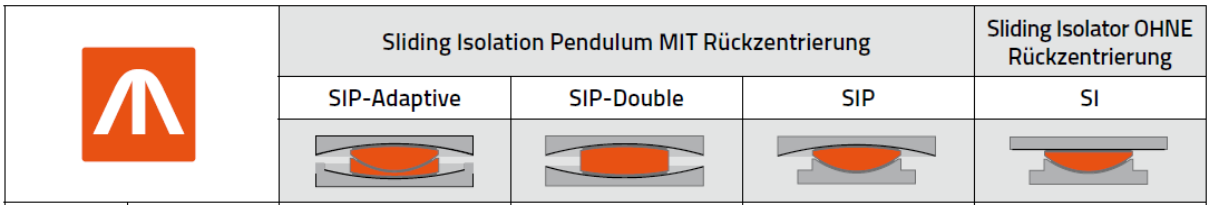


Figure 2: Summary of different SIP types

Like the SIP-DR the SIP-A must work with decoupled main sliding surfaces which only slides simultaneously if the equilibrium between restoring forces and friction forces is achieved. While the restoring stiffness $F_{Re}$ is dependent only on the actual geometry of the CSS (the actual condition of the several curvatures $R_{geo,act,i}$), the actual friction force $F_F$ is dependent not only on the actual pressure but rather on the actual condition of the surfaces, the sliding velocity v and the temperature T [7].

$$F_{Re} = f(N_S, d, R_{eff}) = N \cdot d/R_{eff} \text{ with } Reff = f\{R_{geo,act,i}\} \quad (1)$$

$$F_F = f(N_S, Area, T, v) \quad (2)$$

Obviously, this dependency of the actual forces leads to differences of both the SIP-DR as well as the SIP-A between the design performance and the actual performance. Especially the friction part is charged with a high uncertainty due to the stochastic nature of the dry friction between two materials. But also, $F_{Re}$ can deviate from the design performance significantly due to geometrical inexactness or softness of the connecting structural members. Both stochastic inevitabilities must be considered for the actual expectation of the device performance and the related assessment of the so-called complex curved surface sliders in experimental situations.

## 2 STOCHASTIC SIMULATIONS

### 2.1 Mechanical model

The behaviour of a curved surface slider can be described by means of a mechanical model based on the following assumptions and equations. First the acting horizontal forces are driven by the input parameters of the curved surface slider, which are presented in Table 1.

| Lower sliding element | Upper sliding element | Description |
|---|---|---|
| $d_{1,cap}$ | $d_{2,cap}$ | Displacement capacity |
| $R_{eff,1}$ | $R_{eff,2}$ | Effective radius |
| $\mu_1$ | $\mu_2$ | Coefficient of friction |

Table 1: Summary of main design parameters of complex CSS

On a sliding level a horizontal force act which comprise on two parts: friction force and restoring force.

$$F_{H,i} = \mu_i \cdot N_S + \frac{d_i}{R_{eff,1}} \cdot N_S \quad (3)$$

Where $N_S$ is the acting vertical load on the isolator and $d_i$ is the actual displacement on the corresponding sliding level. Each state of the CSS can be described by means of the six parameters plus the acting vertical load $N_s$ and the following equilibrium equation:

$$\mu_1 \cdot N_S + \frac{d_1}{R_{eff,1}} \cdot N_S = \mu_2 \cdot N_S + \frac{d_2}{R_{eff,2}} \cdot N_S \quad (4)$$

Due to different effective radii, actual displacement and different coefficient of friction, the sliding regime can become in three different states.

| | |
|---|---|
| $F_{H,1} < F_{H,2}$ | Sliding regime 1; only sliding on lower sliding level |
| $F_{H,1} > F_{H,2}$ | Sliding regime 2; only sliding on upper sliding level |
| $F_{H,1} = F_{H,2}$ | Sliding regime 3; sliding occurs simultaneously on both sliding levels |

Due to the different displacement capacity the following restrictions must be considered.

| | |
|---|---|
| $d_1 = d_{1,cap}$ | Sliding regime 2, only sliding on upper sliding level due to capacity restriction |
| $d_2 = d_{2,cap}$ | Sliding regime 1, only sliding on upper sliding level due to capacity restriction |
| $d_1 + d_2 = d_{1,cap} + d_{2,cap}$ | No further sliding can occur |

With the model equations and the restrictions, a program code was written in VisualBasic Application to determine hysteresis shape and resulting isolator performance indicator which are summarized in the following. Together with the maximum horizontal force, the effective stiffness is an interesting parameter for the seismic designer for modelling the horizontal stiffness of the base isolated building. The effective stiffness can be calculated by means of the maximum horizontal force at maximum displacement.

$$K_{eff} = \frac{(F_{H,max} - F_{H,min})}{(d_{max} - d_{min})} \quad (5)$$

In the bilinear model curve, the corresponding displacement of the maximum horizontal force is always the maximum displacement of the cycle while in experimental data the peak of horizontal force will be reached slightly before the maximum displacement. Next significant indicator of performance is the energy dissipation of a cycle EDC which can be calculated by means of the enclosed area of the hysteresis loop and is dependent of the friction component of the CSS.

$$EDC = 4 \cdot \mu \cdot N_S \cdot d \quad (6)$$

With the energy dissipation and the effective stiffness, the calculation of the effective damping of the isolator is possible.

$$\beta_{eff} = \frac{2}{\pi} \frac{EDC}{K_{eff} \cdot (d_{max} - d_{min})} \quad (7)$$

Due to the direct or indirect dependency of the indicators from the input parameter coefficient of friction and effective radius of the CSS it is obvious that a change in the input parameter will lead to different magnitude of the indicator.

## 2.2 Monte Carlo Simulations

According to EC8 and EN 15129 upper and lower bounds for the performance of isolators can be set for the assessment of the isolation system [8, 9]. Though the mechanical description of CSS is comprehensive, a significant deviation of the isolator performance indicator can be observed in isolator tests which is nevertheless a result of fluctuating input parameters of the mechanical model. With neglecting the fact that testing machines in particular have difficulties with maintain a constant vertical load into the isolator while high speed displacement occur, the parameter of the vertical load is assumed as non-fluctuating and the horizontal displacement is the controlling variable. It remains effective radius of curvature and the coefficient of friction. The scattering of the first input parameter is mainly dependent of the quality of production and can be assumed as significantly smaller than the latter influence by the coefficient of friction. In general PTFE or similar PE-materials are common for CSS in combination with austenitic steel which is threaten with fine polish for low roughness of the surface. The tribological behaviour of those materials is strongly dependent of pressure and sliding velocity [10]. Both parameters can be controlled in tests but even with constant pressure and sliding velocity a significant scatter can be still observed for the coefficient of friction. The instable pressure and the inherent changing sliding velocity during a cycle with a sinusoidal wave form intensify the scatter of this decisive influence parameter [11].
Additional to an inherent high scatter of the coefficient of friction at an assumed stable pressure the effect of frictional heating must be considered in the evaluation of understanding and assessment of CSS. Frictional heating occurs during the movement of the CSS due to the heating of the PE material which leads to a significant reduction of the dynamic coefficient of friction. The amount of frictional heating can be in general deterministic described by means of the acting pressure and sliding velocity but still a high stochastic amount must be considered [12].
The result of deviations from the design friction, design effective radius and the friction decrease due to frictional heating can be exemplary seen for a typical SIP-DR in Figure 3. The device with a friction of 5% under a load of 10000 kN has an effective radius of 5000 mm which means each sliding level will rotate with $R_{eff}$ = 2500 mm. Considering really bad and very unlikely deviations of each sliding level with a maximum deviation of 0.8 μ and 0.9 $R_{eff}$ for sliding level 1 and 1.2 μ and 1.1 $R_{eff}$ for sliding level 2, the performance of the device obviously change significant almost in the first cycle. The frictional heating was set to a random decrease in each cycle for the sliding surfaces up to 20% to demonstrate an exaggerated example for a maximum possible alteration of the hysteresis curve.

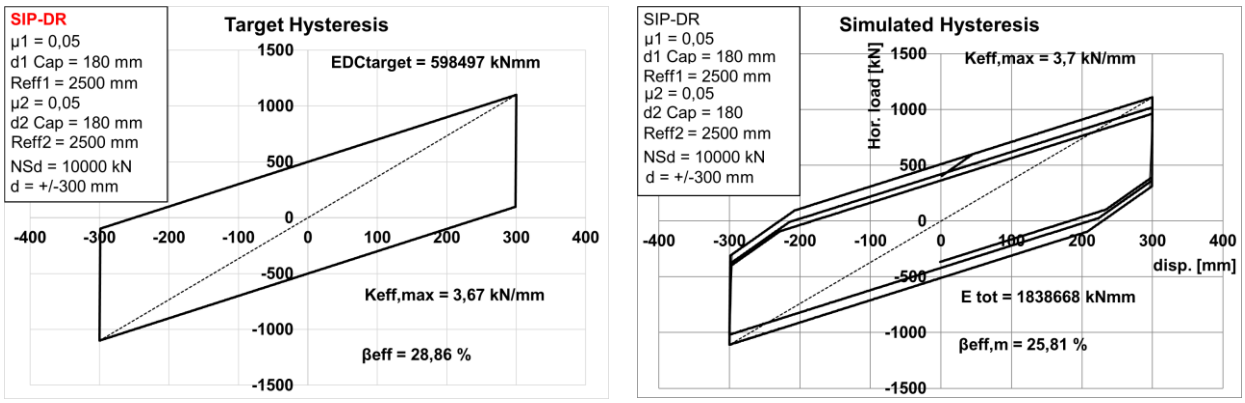


Figure 3: Comparison of target hysteresis and simulated hysteresis for an exemplary SIP-DR device.

For the Monte-Carlo-Simulation all three in detail unknown characteristics – effective radius of curvature, dynamic coefficient of friction and frictional heating – were generated by means of an expectation design value and an upper and lower bound level for each variable. The expression between the bound levels was selected randomly by means of the VBA random function which generates an equal distributed value between the boundaries. The bounds for μ were chosen to 0.8 and 1.2 to reflect the large scatter of friction. For the effective radius of each sliding surface the bounds were set to 0.9 and 1.0. The bounds for frictional heating were always from 0% to 15% for each new cycle i+1 with no frictional heating in the first cycle. For n = 100 simulations as well as for n = 1000 simulations the distribution of results can be seen exemplary for the effective stiffness and the effective damping in Figure 4. A review of stochastic simulations with n = 100 and n = 1000 with the same input parameters show no significant improvement for a number of simulations above n = 100.

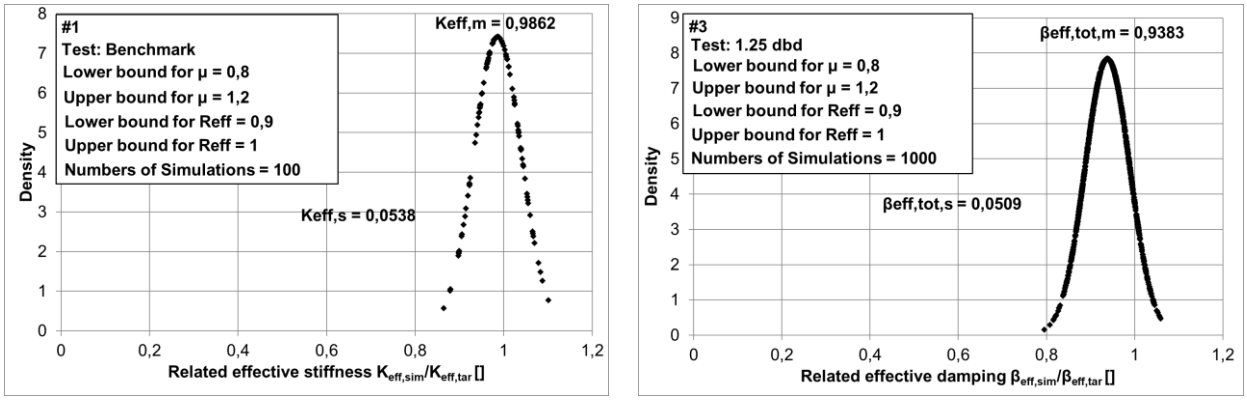


Figure 4: Distribution of related results from simulations with parameters of campaign #1 and #3.

## 3 EXPERIMENTAL STUDIES

### 3.1 General description

According to EN 15129 anti-seismic devices must be tested either as initial type tests (ITT) for a first qualification of the device or as part of a factory production control (FPC) with a reduced program compared to the initial type tests [8]. Latter is applicable if the manufacturer already tested similar devices with deviations in terms of friction, maximum load, and geometrical radii with certain tolerance levels. In both tests procedures the execution of a benchmark test is requested for CSS which is a dynamic test executed with the amplitude of +/- $d_{bd}$ and with the vertical design load of $N_{Sd}$. To allow the execution of the benchmark test in a multitude of test facilities the velocity demand is reduced to only 50 mm/s which is in most cases far below the design velocity of $v_{Ed}$.
For a statistical comparison the benchmark tests are most valuable because the results of a great number of tests are showing the distribution of performance. In the following the outcomes of two greater campaigns with 26 and 48 specimens tested for quality control will be used in comparison with the corresponding design performance from a statistical point of view. In both campaigns each one type of SIP-DR device was designed, manufactured, and tested. In Figure 5 the related results of $\beta_{eff}$ can be seen for both the experimental tests and the stochastic simulations.

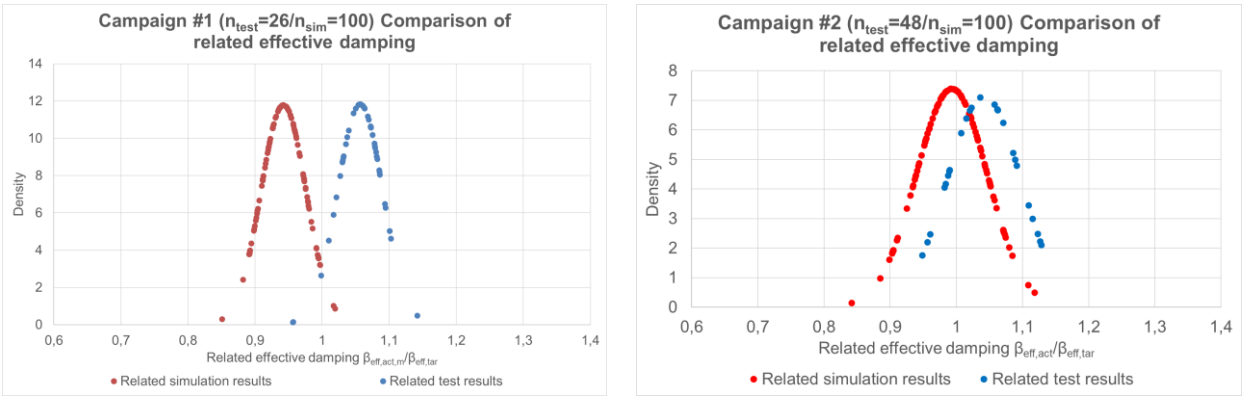


Figure 5: Comparison of distribution of test results and simulation results for the related $\beta_{eff}$.

A third test campaign will be finally used which contains the performance of a SIP-A device for which three specimens were tested according to the ITT procedure. Here only less statistical information can be collected but the comparison between theoretical and experimental outcomes will give a precious outlook to the applicability of a stochastically view to the performance of complex CSS.
For all performance results of experimental tests and stochastic simulations the mean of three cycles were used with exception of the maximum horizontal force for which the maximum value is mandatory.

## 3.2 Findings of the experimental studies

The findings of both experimental result and simulation results are presented in Figure 6 and Figure 7. Both experimental and simulated results are showing the highest scatter in the performance of the mean EDC. With exception of the effective damping all experimental performance indicators are significantly higher than the simulated results which is a result of the velocity effect of dry friction of sliding materials. As described above, the test velocity is significantly less than the design velocity for which the design friction can be controlled. For each of the here described outcomes $\beta_{eff}$ has the smallest dependency of the increase in friction.

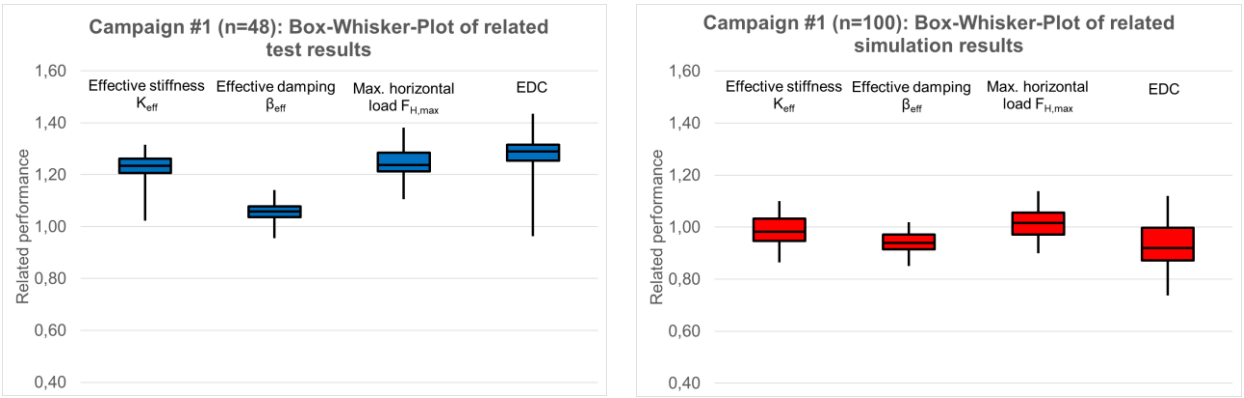


Figure 6: Comparison of SIP-DR performance from tests (left) and simulation (right) from campaign #1.

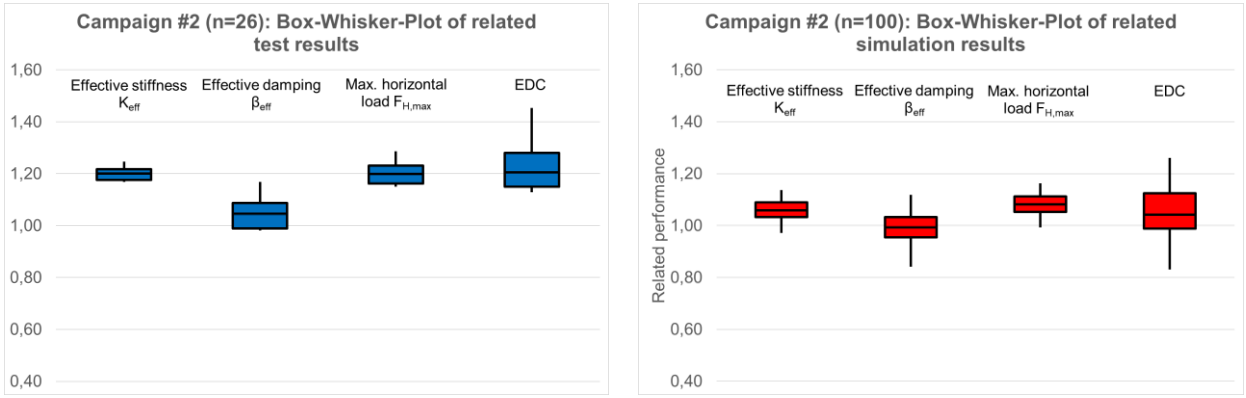


Figure 7: Comparison of SIP-DR performance from tests (left) and simulation (right) from campaign #2

In the next Figure 8 the stochastic simulations will be compared with the performance of the type tests on three SIP-A devices. The comparison was made for an extra dynamic test with 1.25 of $d_{bd}$ which was executed to proof the elevated performance of adaptive CSS beyond the DBE. From the distribution of the test results, a good repeatability of the performance was achieved for all three prototypes. In comparison with the simulation results it becomes obvious that in the simulation significantly too high values for effective stiffness and maximum load will be produced. Because of the simplified model several effects like the velocity effect of a sinusoidal wave form were not simulated. This effect for example reduces the reaction force in the last few percent of movement where the target hysteresis would have a steady increase. In contrast to that observation the effective damping in the tests were significantly higher than evaluated in the simulations. This directly affects the calculation of $K_{eff}$.

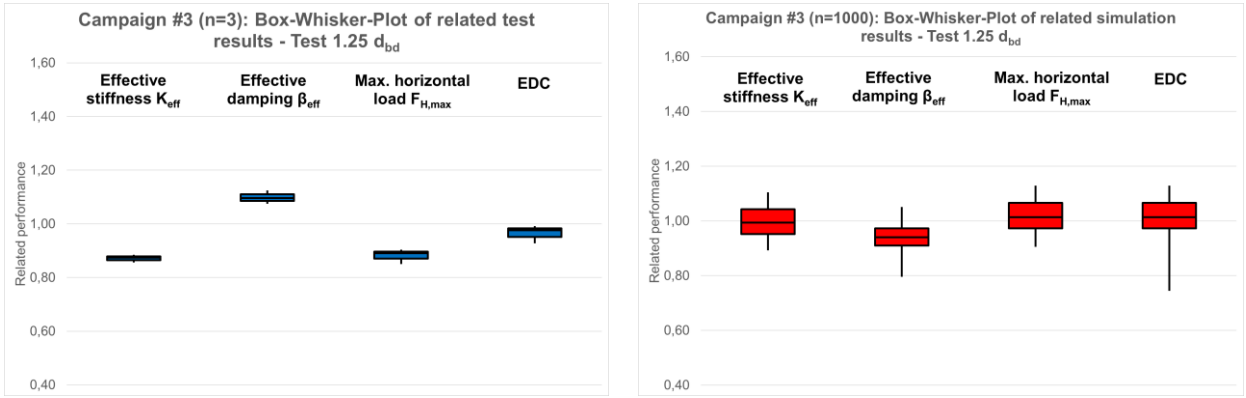


Figure 8: Comparison of SIP-A performance from tests (left) and simulation (right) from campaign #3 for test with 1.25 $d_{bd}$.

In the next step the development of the deviation from small amplitudes to maximum amplitudes will be checked from a stochastic point of view. By means of the results of the tests D1, D2 and D3 this development can be determined. While test D3 will be carried out with $d_{bd}$, $v_{Ed}$ and $N_{sd}$, the tests D1 and D2 will be carried out with only 0.25 $d_{bd}$ and 0.5 $d_{bd}$ but still with $v_{Ed}$ and $N_{Sd}$. In Figure 9 the development of the related performance is shown for 0.25 $d_{bd}$ to 1.25 $d_{bd}$. It can be seen that in the test campaign the related values for $K_{eff}$ and the $F_{h,max}$

will decrease with increasing displacement while the related values for $\beta_{eff}$ increase. In contrast to that the development of the simulation results are less flexible and have steady quantil values while in the tests the magnitude and distribution of the quantil compared to the median fluctuates more intensive, as can be seen in Figure 10. This can be explained by the smaller number of test results compared to the simulation results. Additionally, the mechanical model is not capable to calculate several effects of the test environment which influences the results significantly. Besides the velocity effect mentioned above, in tests with smaller amplitude but with same test velocity the control of the vertical load becomes more instable because of the frequent change of direction and consequently a frequent up and down of the isolator. This leads to high vertical load fluctuations which affects the whole isolator performance in a negative manner.

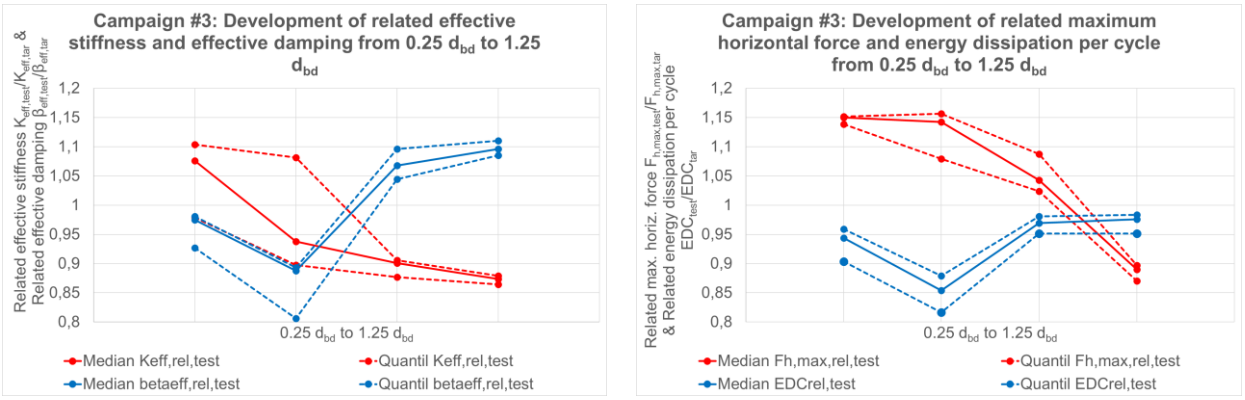


Figure 9: Development of SIP-A performance from 0.25 $d_{bd}$ to 1.25 $d_{bd}$ in experimental tests

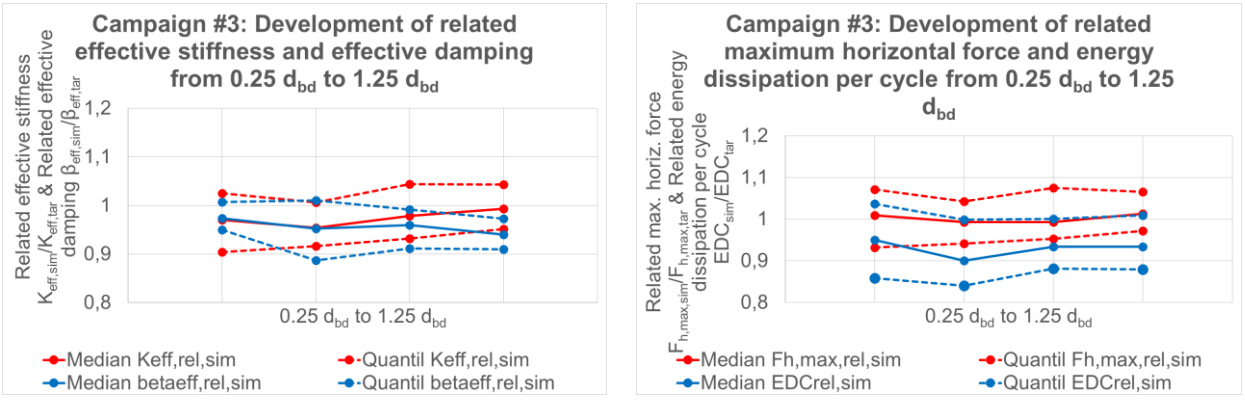


Figure 10: Development of SIP-A performance from 0.25 $d_{bd}$ to 1.25 $d_{bd}$ in stochastic simulation.

## 4 CONCLUSIONS

The mechanical background of complex CSS was investigated in this paper with the aim of connecting a mechanical model with a monte-carlo-simulation to achieve a stochastic tool for the assessment of complex CSS like SIP-DR or SIP-A. The model shows a good forecast of isolator performance with considering the stochastic nature of complex CSS which was evaluated by two test campaigns with a significant number of test specimens. For the prediction of single test results the model is fewer applicable because more dynamic effects must be con-

sidered like the velocity effect and the vertical load fluctuations with the corresponding influence on the actual friction.

## 5 REFERENCES


[1] C. Casarotti und A. Pavese, „Statistical results of a wide experimental campaign on full scale surface sliders," in 2nd European Conference on Earthquake Engineering and Seismology, Istanbul, Turkey, 2014.

[2] P. Huber und R. Medeot, „The Sliding Isolation Pendulum for the seismic protection of buildings," in *WIT Transaction on the Built Environment*, WIT Press, 2008, pp. 323-332.

[3] F. Weber, T. Mano, H. Distl und C. Braun, „Optimized Triple Friction Pendulum Versus Optimized Double Friction Pendulum," in *11th German-Japanese Bridge Symposium*, Osaka, 2016.

[4] F. Weber, R. Hamood, P. Huber, C. Braun und M. Halimi, „Adaptive Curved Surface Slider for Improved Seismic Structural Performance," in *8th International Conference on Seismology & Earthquake Engineering*, Tehran, Iran, 2019.

[5] F. Weber, F. Obholzer, M. Hartinger und J. Distl, „Adaptive Curved Surface Slider for Improved Seismic Structural Performance," *Practial Periodical on Structural Design and Construction*, August 2021.

[6] F. Weber, L. Meier, J. Distl, F. Obholzer, P. Huber und C. Braun, „SIP-Adaptive: improved structural isolation, reduced base shear,," in *12th Japanese-German Bridge Symposium*, Munich, Germany, 2018.

[7] C. Casarotti und A. Pavese, „Statistical results of a wide experimental campaign on full scale surface sliders," in *2nd European Conference on Earthquake Engineering and Seismology*, Istanbul, Turkey, 2014.

[8] Eurocode, *EN 15129: Anti Seismic Devices*, 2009.

[9] Eurocode, *EN 1998-1: Design of structures for - Part 1: General rules, seismic actions and*, 2004.

[11] C. Braun und C. Butz, „Static and Dynamic Friction in Curved Surface Sliders," in *IABSE Symposium: Large Structures and Infrastructures for Environmentally Constrained and Urbanised Areas*, Venedig, Italien, 2010.

[12] S. Barone, A. Pavese und G. Calvi, „Experimental dynamic response of spherical friction-based isolation devices," *Journal of Earthquake Engineering*, pp. 2-20, 2017.

[13] D. Domenico, D., G. Ricciardi, S. Infanti und G. Benzoni, „Frictional Heating in Double Curved Surface Sliders and Its Effect on the Hysteretic Behavior: An Experimental Study," *Frontiers in Built Environment*, Bd. 5, Nr. 74, 2019.

COMPDYN 2023
9th ECCOMAS Thematic Conference on
Computational Methods in Structural Dynamics and Earthquake Engineering
M. Papadrakakis, M. Fragiadakis (eds.)
Athens, Greece, 12-14 June 2023

# EXPERIMENTAL TESTS OF VARIOUS TYPES OF SEISMIC ISOLATION SYSTEMS

**Mohammed S. Mohammed[1], Scott C. Darling[1], Ahmed F. Ibrahim[1], and Ahmed O. Atiek[1]**

[1] Dynamic Isolation Systems Inc
885 Denmark Dr. Suite 101, McCarran, NV, 89437, USA
{mmohammed, sdarling, aibrahim, aatiek}@dis-inc.com

## Abstract

*Seismic isolation is one of the most effective means of earthquake hazard mitigation. This paper summarizes experimental studies on different types of seismic isolation systems that are used for structural applications such as buildings and bridges, and for non-structural systems such as computer servers, artwork, medical equipment and other sensitive equipment. The seismic isolation systems presented in the paper include: 1) Lead rubber bearings (LRB): Extreme testing of LRBs is presented. 1410 mm diameter bearings were subjected to large lateral displacements in addition to the axial load. The same bearings were subjected to combined shear and tension, with an extreme uplift of 20 mm. Limit state performance of full-scale bearings is also presented where the bearings are subjected to more than 500% shear strain. 2) Non-structural isolation system: A patented multi-directional spring isolation system that provides damping and self-centering capabilities. The system is used mainly to isolate sensitive equipment inside a building. Shake table test results are presented in the paper showing the effectiveness of the system. 3) Elastomeric slider bearings (ESB): Test results are presented of ESBs used in a unique application in the US. A vertical expansion of an existing building was required, and the isolation bearings were introduced between the existing structure below and the addition above. 4) Sliding systems: The paper presents test results of a polyamide nylon-based sliding material that has been used significantly in Japan and has been introduced to the US recently. The material has a lower coefficient of friction than the typical PTFE. The material has been used in a building project in the US where the SEOR used extensive test results to characterize and model the isolation system.*

**Keywords:** Earthquake, Seismic Isolation, Hazard Mitigation, Nonstructural Isolation, Shake table Testing, Lead Rubber Bearings.

# 1 INTRODUCTION

Seismic base isolation is widely recognized as one of the most effective and commonly employed methods for mitigating the hazards associated with earthquakes. The basic concept of seismic isolation is to substantially decouple a structure from damaging earthquake ground motions using seismic isolators (see Figures 1a & 1b). Consequently, when a seismic isolated structure is subjected to an earthquake, the inelastic deformations occur in the seismic isolators, reducing forces/accelerations in the structure compared to conventional, fixed-base structure. The modern concept of seismic isolation originated in New Zealand in the 1970's [1], and many studies have demonstrated the advantages of seismic isolation in mitigating structural damage during severe seismic events [2,3]. In contrast, conventionally designed structures depend on the inelastic response of selected structural elements to dissipate the earthquake energy, resulting in damage to these selected elements [4, 5, 6, 7, 8, 9]. In general, a seismic isolator that is used to protect a structure against earthquakes should have the following characteristics as a minimum:

- Flexibility from the low horizontal stiffness of the isolators, which lengthens the period of vibration of the structure and reduces the seismic forces (see Figure 1c).
- Energy dissipation from the introduction of significant level of hysteretic damping, which absorbs energy from the earthquake. This limits relative displacements and deformations to acceptable levels and further reduces the seismic forces (see Figure1c).



(a)



(b)

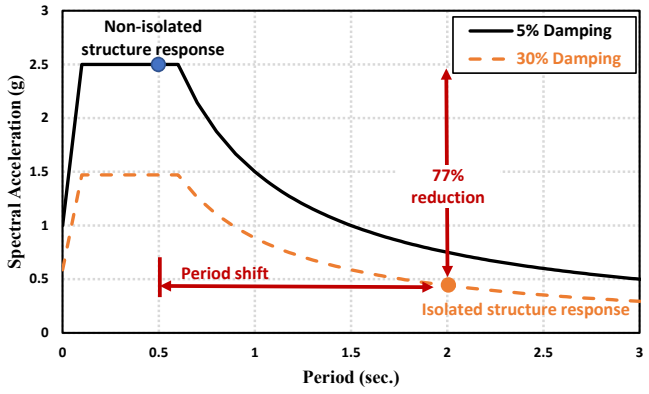


(c)

Figure 1: a) Installation of seismic isolators for a building in Taiwan. The superstructure will be connected to the isolators and decoupled from the ground, b) A completed building showing the seismic isolators fully installed, c) Effect of isolator flexibility and damping on a structure performance

Testing is considered an essential aspect of the design and review of seismic isolation systems. Extensive experimental campaigns conducted at advanced testing facilities have greatly enhanced the confidence level in seismic isolation technologies. The availability of high-capacity testing rigs, capable of conducting full-scale testing of devices under realistic loading conditions, has deepened and improved the knowledge and behavior of existing and new seismic isolation solutions [10]. The main objective of this paper is to present experimental studies on various types of seismic isolation systems that are used for conventional structural applications such as buildings and bridges, and for non-conventional non-structural applications. The seismic isolation solutions presented in the next sections are:

a) Lead-rubber bearings (LRB) and Rubber bearings (RB)
b) Non-structural/low mass seismic isolation system
c) Elastomeric sliding bearings (ESB)
d) Sliding system using polyamide (nylon-based) material

## 2 LEAD-RUBBER BEARINGS AND RUBBER BEARINGS

Lead-rubber bearings and rubber bearings are considered two of the most common seismic isolators in applications worldwide. LRBs and RBs have been extensively tested, and there are comprehensive guidelines on their design and modelling [11]. Figure 2a shows the main components of an LRB: layers of vulcanized low-damping rubber and steel shims. The rubber layers provide flexibility in the lateral direction, while the steel shims prevent bulging due to axial loads, creating high vertical stiffness. The bearing is fitted with a central lead core which is confined by the steel shims. The lead core provides resistance to service loads, then yields and dissipates energy under earthquake lateral movements. Steel mounting plates are placed on top and bottom of the bearing to connect to the substructure and superstructure. Finally, a resilient rubber compound is used as a cover rubber to protect the bearing's internal components from environmental effects. Figure 2b shows an idealized bilinear force-displacement relationship for an LRB. Figure 2c shows an actual force-displacement test loop for an LRB that was used in a bridge located in the United States. The RB is made of the same components as the LRB, except that there is no central lead core. This removes the majority of the resistance to service loads and energy dissipation, causing the RB to behave more like a simple lateral spring. RBs are commonly paired with LRBs to achieve a desired system performance and response.

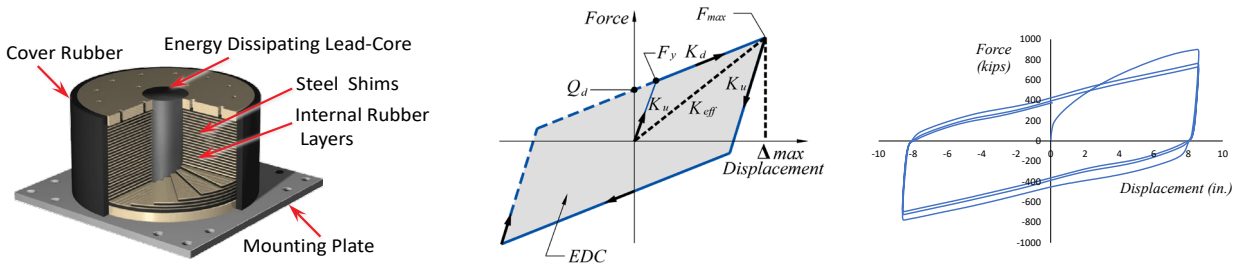


(a) (b) (c)

Figure 2: a) Main components of lead-rubber isolators, b) Bilinear force-displacement relationship for an LRB, c) Actual force-displacement test results for an LRB

## 2.1 LRB extreme uplift testing

Extreme prototype testing was conducted for a LRB used on a bridge project. The bearing has a diameter of 1410 mm and is composed of (50) 8 mm thick rubber layers (total rubber height = 400mm). A 390 mm lead core is used to resist bridge service loads and to provide the required damping. The LRB was extensively tested at both the Caltrans SRMD (Seismic Response Modification Device) testing facility at University of California San Diego and at Dynamic Isolation Systems (DIS) testing facility in NV. The prototype test protocol included compression and shear testing up to 1051 mm (263% shear strain) at both low and high velocities. The testing velocities ranged from 20 mm/sec up to 1571 mm/sec. In addition, an extreme uplift and shear test was conducted where an uplift of 20 mm was first applied to the bearing, and then sheared to a displacement of 450 mm. Selected test loops and results are shown in Figure 3. The bearings maintained performance and stability throughout the extreme testing protocol.

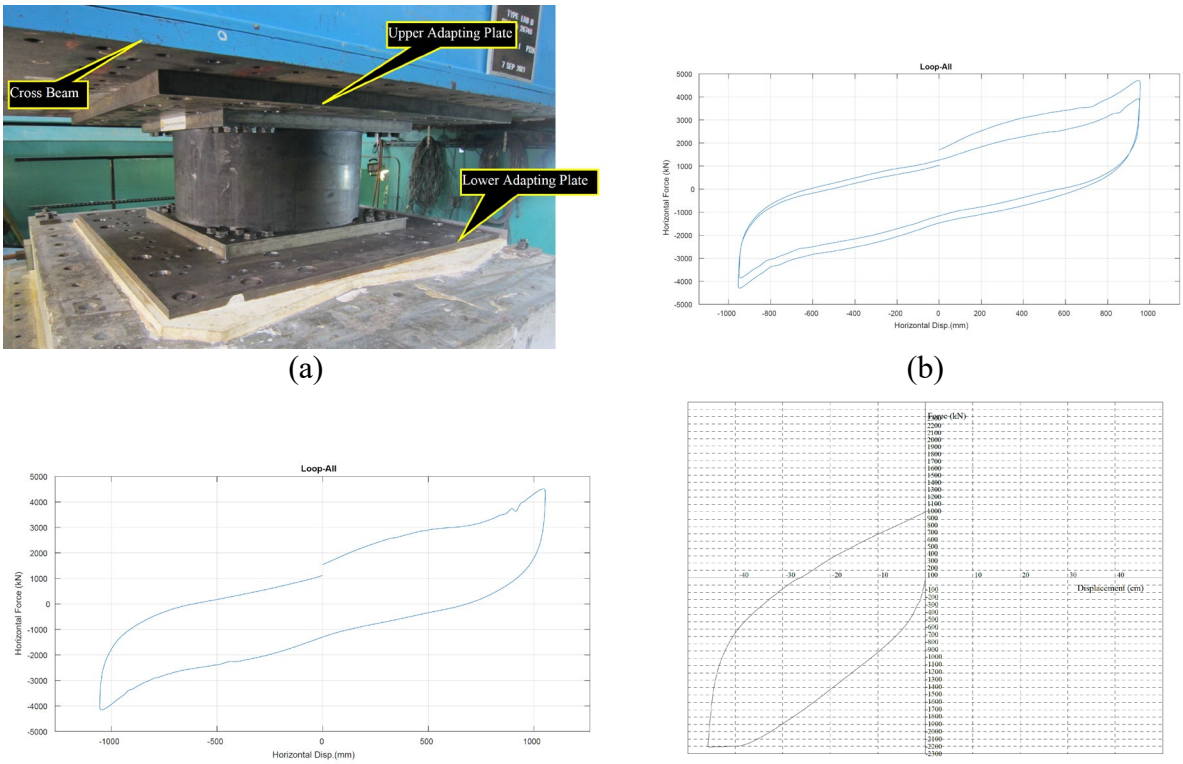


Figure 3: a) Installed bearing in the SRMD test machine, b) Force-displacement loop [axial load=3200 kN, displacement=955 mm, velocity=1571 mm/sec], c) Force-displacement loop [axial load=7000 kN, displacement=1051 mm, velocity=938 mm/sec], d) Force-displacement loop [uplift=20 mm, displacement=450 mm, velocity=20 mm/sec]

## 2.2 Limit state performance of rubber bearings

During strong ground motions, seismic isolation bearings are subjected to large lateral displacements that in some cases could be larger than expected in design. The designers are interested in evaluating the performance of elastomeric isolators beyond the standard design limits to ascertain the safety margin beyond the expected design displacements. This subsection evaluates the limit state performance of large rubber isolators through testing. 500 mm and 800 mm isolators were tested at DIS testing facility, and a 1300 mm isolator was tested at the SRMD facility.

a)

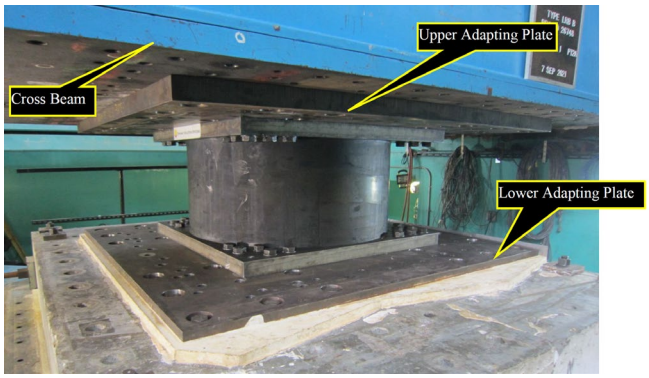


b)

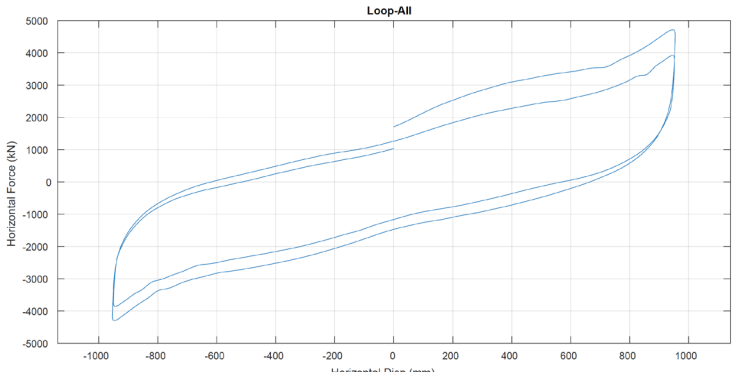


c)

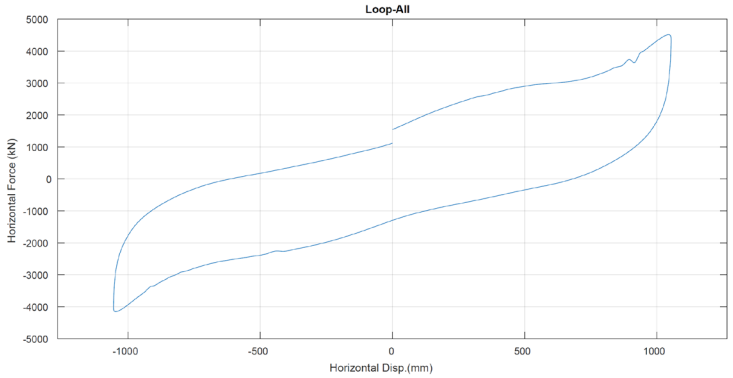


d)

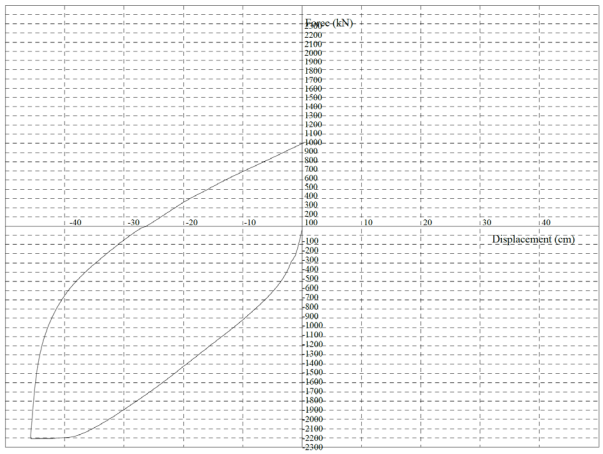


Figure 3: a) Installed bearing in the SRMD test machine, b) Force-displacement loop [axial load=3200 kN, displacement=955 mm, velocity=1571 mm/sec], c) Force-displacement loop [axial load=7000 kN, displacement=1051 mm, velocity=938 mm/sec], d) Force-displacement loop [uplift=20 mm, displacement=450 mm, velocity=20 mm/sec]

For the 500 mm isolators, linear force-displacement loops were observed until shear strains of 250% and then stiffening of the rubber was clearly observed. The isolators exhibited satisfactory behavior up to 550% shear strain and under a compression stress of 19.6 N/mm$^2$. During the final test with 9.8 N/mm2, the isolators failed at 574% shear strain.

For the 800 mm isolators, linear force-displacement loops were observed until shear strains of 250% and then stiffening of the rubber was clearly observed. The stiffness in the range of 300 to 400% was three to four times compared to stiffness under 200% strain. The isolators failed at 450% shear strain with a compression stress of 9.8 N/mm$^2$.

For the 1300 mm isolator, similar behavior was observed up to the 250% shear strain. The isolator successfully carried a compression stress of 29.4 N/mm$^2$ at 400% shear strain. The isolator failed at 446% shear strain with a compression stress of 14.7 N/mm$^2$.

Figure 4 presents selected force-displacement loops for the tree bearing sizes. Table 1 shows the isolator dimensions and ultimate strain test results.

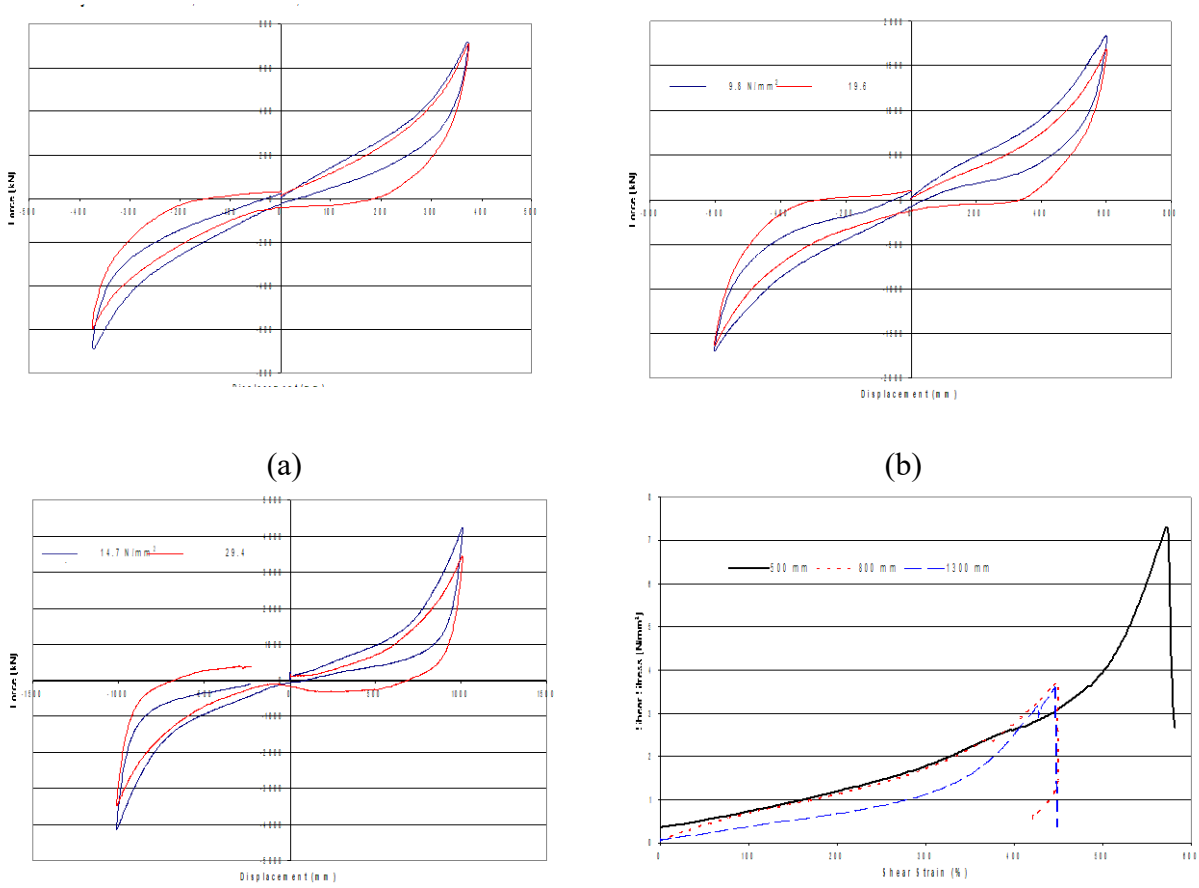


Figure 4: a) 500 mm isolator [strain:400%, stress 9.8 & 19.6 N/mm$^2$], b) 800 mm isolator [strain:400%, stress 9.8 & 19.6 N/mm$^2$], c) 1300 mm isolator [strain:400%, stress 14.7 & 29.4 N/mm$^2$], d) Shear stress vs shear strain behavior at failure

All bearings performed at displacements and strains well in excess of their design values and well beyond values used in design practice worldwide. This highlights that individual elastomeric bearings, produced by qualified, high quality manufacturers, have significant robustness and resiliency.

| Isolator | | 500 mm | 800 mm | 1300 mm |
|---|---|---|---|---|
| Bearing Diameter | mm | 500 | 800 | 1300 |
| Layer Thickness | mm | 3.7 | 6 | 9 |
| Number of Layers | | 25 | 25 | 28 |
| Shear Modulus of Rubber | $N/mm^2$ | 0.39 | 0.39 | 0.39 |
| Shape Factor (S) | | 33.6 | 33.9 | 36.1 |
| Stress at Failure | $N/mm^2$ | 9.8 | 9.8 | 14.7 |
| Strain at Failure | % | 574 | 450 | 446 |

Table 1: Rubber bearing dimensions and ultimate strain test results.

### 2.3 LRB instability in bridge shake table testing

A reduced-scale model (2/5th scale) of a three-span, curved girder bridge isolated with a 12 LRBs was tested on four shake tables. The bridge was subjected to ground motion excitations exceeding the design level earthquake to initiate instability of the seismic isolators (up to three times the design level). The displacements at selected locations exceeded the diameter of the isolators and triggered their instability. Shear strains exceeding 400% were observed which was more than 4 times the design level strain. The bridge did not collapse, the overall stability of the system was maintained, and full recovery of the unstable seismic isolators was observed [12]



Figure 5: Video snapshots showing the LRB during the extreme testing that caused the instability [12]

## 3 NON-STRUCTURAL/LOW-MASS SEISMIC ISOLATION SYSTEM

Lately, there has been an increasing interest in isolating particular floors within buildings or specific equipment and not isolating the whole structure. The unique challenges of isolating equipment arise from the relatively low mass supported by isolators, necessitating isolator stiffness that is significantly lower compared to conventional isolation. This section discusses seismic isolation of equipment using a patented Multi-Directional Spring Unit (MDSU) that provides damping, low stiffness, and self-centering capabilities. The MDSUs can be used for stand-alone equipment or to isolate a complete floor. More details about the inner workings of the MDSU, mechanical properties, and analytical modeling can be found in [13, 14].

Extensive bi-directional shake table testing was conducted at the University of Nevada Reno (UNR) to evaluate the effectiveness of the system in reducing the seismic forces/acceleration on server racks (see Figure 6a). Results showed that the isolation platform reduced accelerations on the server racks by a factor of 3 to 4. A sample acceleration history showing the input shake table motion and the isolation platform response is shown in Figure 6b.

Additional shake table testing was conducted on larger connected modules at University of California Berkeley. The system that was tested had a total isolated area of 140 square feet, which included two spring modules and many stringers. Three fully equipped computer racks

were part of the shake table testing (see Figure 7). The objective of the study was to evaluate the behavior of multiple spring modules in fully loaded, partially loaded, and unbalanced loaded conditions. Test results showed effectiveness of the system where reduction of accelerations over a wide range of frequencies was achieved (see Figure 8).

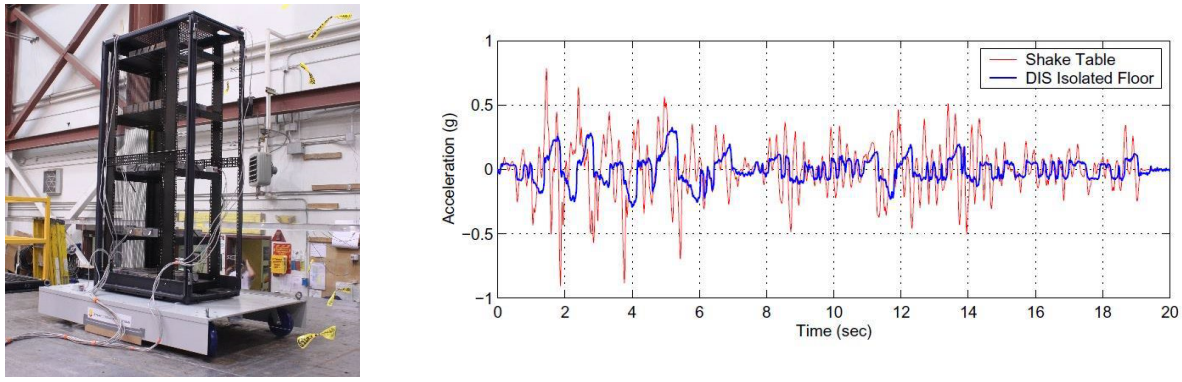


(a) (b)

Figure 6: a) Shake table testing of single server rack at UNR [14], b) Sample acceleration history showing reduction of input accelerations by a factor of 3 to 4 [14]



(a) (b)

Figure 7: Shake table testing of a floor isolation system at UC Berkeley [14] a) Floor isolation system with no tiles or server racks on top, b) Floor isolation system showing the tile -stringer-pedestal system installed on top along with server racks

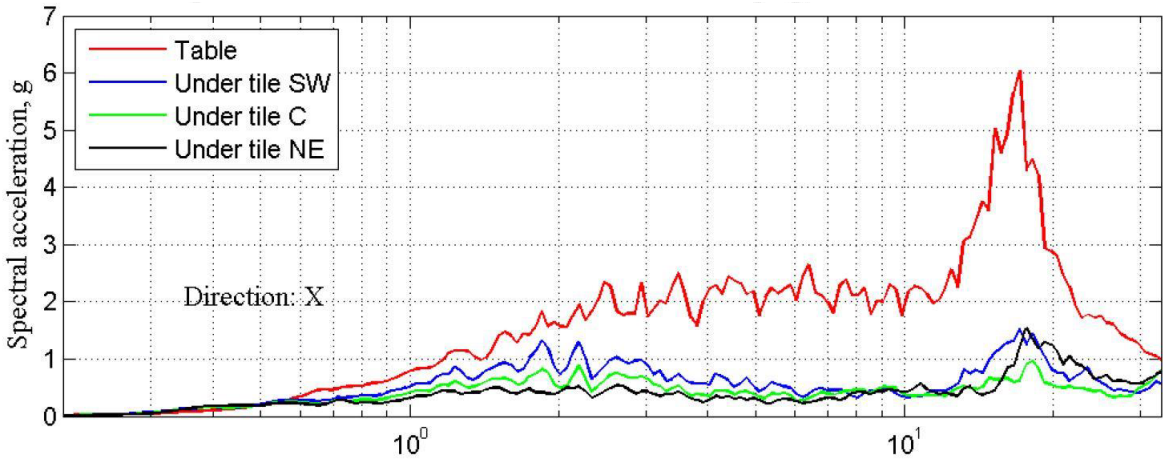


Figure 8: Response of the seismic isolation floor showing reduction of accelerations over a wide range of frequencies. The red line is the shake table input, and the other three plots are response spectra of accelerations on the isolated platform measured at three different locations [14]

## 4 ELASTOMERIC SLIDING BEARINGS

Elastomeric Sliding Bearings (ESB) were used as part of the seismic isolation system for a unique application in San Francisco. They were used in the first application of seismic isolation in the world that permits the vertical expansion of an existing structure by introducing isolation bearings between the existing structure and the addition (see Figure 9). More information about the building and the design can be found in [15].

Two different types of isolation bearing were used, a conventional LRB and an elastomeric sliding bearing (ESB) consisting of PTFE slider in series with an elastomeric bearing. A schematic showing the ESB's main components is presented in Figure 10a. The elastomeric bearing is intended to provide an initial lateral flexibility before sliding starts and provide additional flexibility if the EQ displacements exceed the dimensions of the sliding plate. Extensive testing have been conducted at the University of California San Diego to characterize the performance of the ESBs (see Figure 10b). Test results of one of the ESBs are presented in Figure 11.



Figure 9: The 185 Berry St. building showing the vertical expansion of the existing structure by introduce seismic isolation bearings between the existing structure and the addition

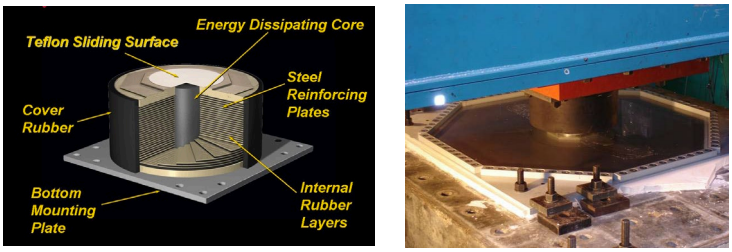


(a) (b)

Figure 10: a) Schematic of the ESB showing the main components, b) Testing of an ESB at UCSD [15]

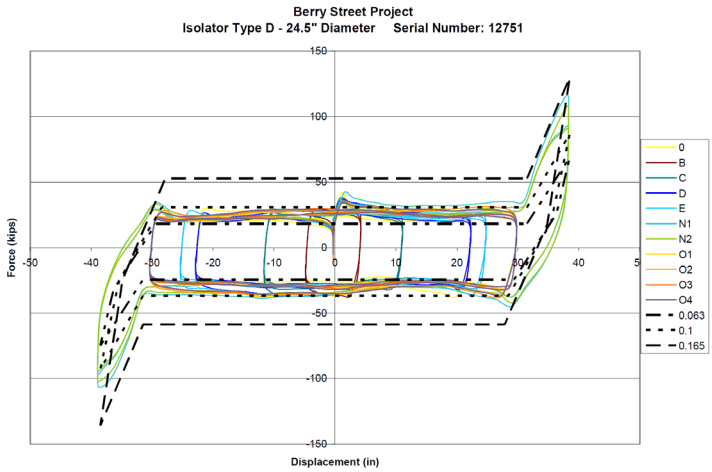


Figure 11: Force-displacement loops of one of the ESBs tested at UCSD [15]

## 5 SLIDING SYSTEM USING POLYAMIDE (NYLON-BASED) MATERIAL

This section presents test results of a polyamide (nylon-based) sliding material that has been extensively used in different applications in Japan. Thorough characterization tests under various axial stresses and testing velocities have been conducted, and the sliding material has been introduced and used in several seismic isolation applications in the US. The material test specimen and test setup are shown in Figure 12. Selected test results are shown in Figure 13, and a summary of all the characterization testing is shown in Figure 14. Like PTFE sliding materials, the measured COF is dependent on both velocity and axial pressure. The polyamide COF is consistently lower than the expected COF for PTFE for all combinations of velocity and pressure.

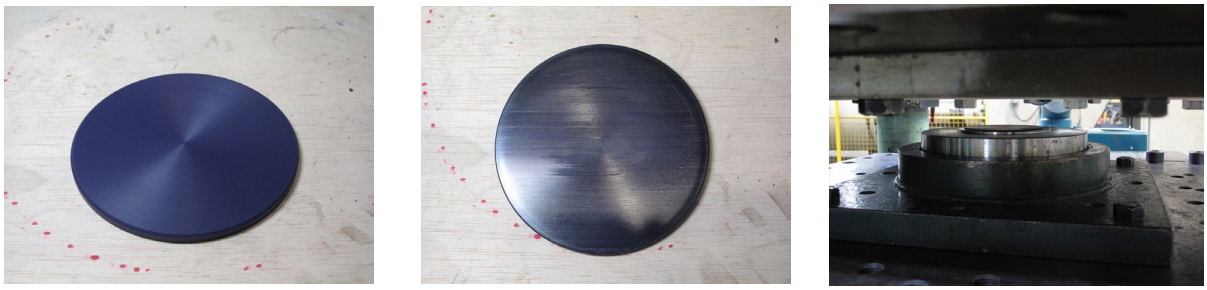

(a) (b) (c)

Figure 12: a) Polyamide test specimen before testing, b) polyamide test specimen after testing, c) test setup

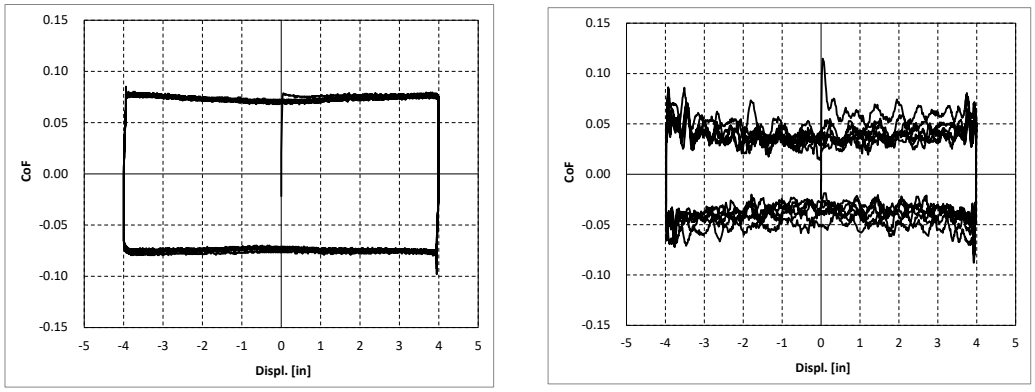


(a) (b)

Figure 13: Sample test loops for the polyamide material at stress = 4 ksi (27.6 MPa) a) test velocity = 1 in/sec (25.4 mm/sec), b) test velocity = 24.8 in/sec (630 mm/sec)

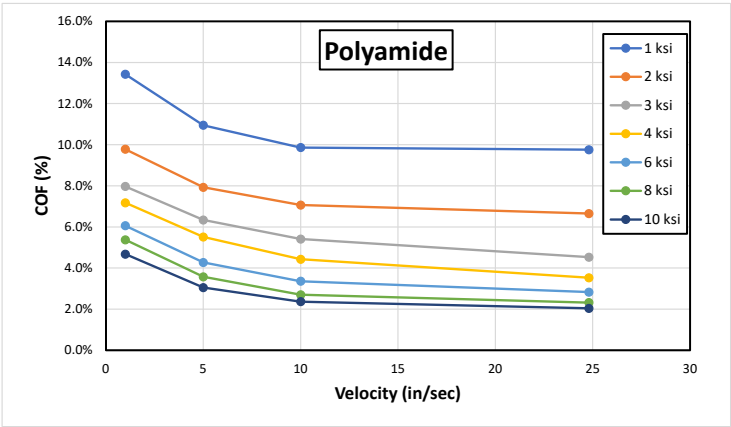


Figure 14: Summary of the characterization test results for the polyamide material conducted using various axial stresses and testing velocities

## 6 CONCLUSIONS

The paper summarized experimental testing of various types of seismic isolation systems. The test results demonstrate that the elastomeric isolators that are produced by qualified, high-quality manufacturers can undergo very large shear strains and axial demands and still exhibit stable hysteretic behavior. This demonstrates that individual Lead-Rubber Bearings (LRB) and Rubber Bearings (RB) are highly robust and resilient. The testing of a continuous curved bridge well in excess of the design displacement demonstrated that when placed in a system with other elastomeric bearings, an additional system robustness is achieved such that instability of individual isolators at one or two supports does not lead to bridge collapse. The system is able to fully recenter on its own and repeated instability of the LRBs does not cause permanent deformation in the isolation system or for the entire bridge. Effective seismic isolation of nonstructural equipment was achieved using the Multi-Directional Spring Units (MDSU). The MDSU has been utilized in seismically isolating individual equipment, server racks and full floors with excellent results in reducing the seismic forces and accelerations on the equipment. Different sliding products like the Elastomeric Sliding Bearings (ESB) or the Polyamide sliding material proved to be effective and has been recently used in many projects in the US.

## REFERENCES

[1] R.I. Skinner, W.H. Robinson, G.H. McVerry, An Introduction to Seismic Isolation. Wiley, England, 1993.

[2] I. Buckle, M. Constantinou, M. Dicleli, H. Ghasemi, Seismic Isolation of Highway Bridges. Report No. MCEER-06-SP07, Multidisciplinary Center for Earthquake Engineering Research, Buffalo, NY, 2006.

[3] K.B. Eriksen, M.S. Mohammed, C.B. Coria, Seismic Isolation in North and South America. *2018 NZSEE Conference*, New Zealand, 2018.

[4] M.S. Saiidi, A. Vosooghi, R.B. Nelson, Shake-Table Studies of a Four-Span Reinforced Concrete Bridge. *Journal of Structural Engineering,* 139(8), 1352-1361, 2013.

[5] M.S. Mohammed, D. Sanders, I. Buckle, Shake Table Tests of Reinforced Concrete Bridge Columns Under Long Duration Ground Motions. *6th International Conference on Advances in Experimental Structural Engineering*, 2015.

[6] M.S. Mohammed, Effect of Earthquake Duration on Reinforced Concrete Bridge Columns. Ph.D. Thesis, University of Nevada Reno, 2016

[7] M. Del Caprio R., G. Mosqueda, D.G. Lignos, Sidesway Collapse of a Steel Special Moment Frame Subjected to Earthquake Loading. *16th World Conference on Earthquake Engineering*, Santiago, Chile, January 9-13, 2017.

[8] M.S. Mohammed, D. Sanders, I. Buckle, Reinforced Concrete Bridge Columns Tested Under Long and Short Duration Ground Motions. *16th World Conference on Earthquake Engineering*, Santiago, Chile, January 9-13, 2017.

[9] G. Biasi, M.S. Mohammed, D. Sanders, Earthquake Damage Estimations: ShakeCast Case Study on Nevada Bridges. *Earthquake Spectra* 33(1), 45-62, 2017.

[10] G. Benzoni, G. Lomiento, N. Bonessio, Testing Protocols for Seismic Isolation Systems. *XIV Convegno ANIDIS, L'Ingegneria Sismica in Italia*, Bari, September 18-22, 2011.

[11] F. Naeim, J.M. Kelly, Design of Seismic Isolated Structures: From Theory to Practice. John Wiley & Sons, Inc, 1999.

[12] E.V. Monzon, I.G. Buckle, A.M. Itani, Effect of Isolator Instability on the Performance of Seismically Isolated Curved Bridges. Tenth U.S. national Conference on Earthquake Engineering, Anchorage, Alaska, July 21-25, 2014.

[13] S. Cui, M. Bruneau, A. Kasalanati, Behavior of Bidirectional Spring Unit in Isolated Floor Systems. *Journal of Structural Engineering,* 136(8), 2010.

[14] A. Kasalanati, T. Ng, K. Friskel, Seismic Isolation of Sensitive Equipment. *16th World Conference on Earthquake Engineering*, Santiago, Chile, January 9-13, 2017.

[15] A. Dutta et al., A Unique Application of base isolation Technology. *10th World Conference on Seismic isolation, Energy Dissipation and Active Vibrations Control of Structures*, Istanbul, Turkey, May 28-31, 2007.

COMPDYN 2023
9th ECCOMAS Thematic Conference on
Computational Methods in Structural Dynamics and Earthquake Engineering
M. Papadrakakis, M. Fragiadakis (eds.)
Athens, Greece, 12-14 June 2023

# ANALYSIS OF THE FORCE RESPONSE OF BEARING DEVICES FOR BRIDGE STRUCTURES

**Marco Furinghetti[1,2], Simone Reale[1], Matt J. Fox[1], Yuan Fan[1], Chiara Casarotti[2], and Alberto Pavese[1]**

[1] University of Pavia
via Ferrata 3, 27100 Pavia (Italy)
e-mail: marco.furinghetti@unipv.it, simone.reale01@universitadipavia.it, yuan.fan@unipv.it, matt.fox@unipv.it, a.pavese@unipv.it

[2] EUCENTRE Foundation
via Ferrata 1, 27100 Pavia (Italy)
marco.furinghetti@eucentre.it, chiara.casarotti@eucentre.it

## Abstract

*Bridge structural systems are often represented by high risk levels, from several standpoints. The strategic role they generally play in the infrastructure network leads to significant exposure characteristics, with a resulting high risk level. Even though the seismic action is not always a key issue for a considered bridge, excessive horizontal loading may lead to unexpected failures at specific local levels. Among all the possible structural elements, bearing devices can represent in some case the most vulnerable component of the overall system, which can cause sudden and brittle collapses, at ultimate conditions. In this work the behavior of bearing devices for bridge structural systems has been analyzed, by comparing the outcomes of experimental campaigns to numerical parameters, commonly adopted in analytical simulations. Then, some case study structures have been modeled, in order to carry out a parametric study, with varying mechanical properties, and consequently accounting for the effect of aging on the force response of the single devices. Special attention has been focused on the displacement at the bearing locations, rather than the internal forces of piers, and results have been normalized with respect to the mean values for the assumed mechanical properties.*

**Keywords:** Bridge, Reinforce Concrete, Bearing Devices, Experimental Campaign, Parametric Study.

## 1 INTRODUCTION

Bridge structural systems present several facets that need to be discussed to properly understand the structural response under different actions. Bridges generally play a strategic role in infrastructure networks, which leads to significant exposure characteristics and to a resulting high risk level.

The seismic action, which is not always a key issue for bridge structures, can lead to significant damage in the structural elements, with effects on the response of the whole bridge. The effects of multiple earthquakes on a bridge structure can reduce its seismic reliability [1]. The effects of aftershocks on the seismic response of bridges have been studied by Pang and Wu [2]. The study considered reinforced concrete continuous bridges, highlighting that aftershock events can increase the system fragility, the displacement of the bearings and the curvature of piers. Many existing bridges have been designed, when there were not specific requirements in terms of structural details. In such situation, it is reported that the fragility of the joints highly influences the seismic vulnerability of the whole structure [3].

Considering the case of the Italian road network, most of the bridges have been built around the middle of the last century and have reached or exceed their design life. The degradation in the properties of bridges has played a key role in some collapse events that occurred in recent years [4]. The rise in frequency of bridge collapses is a clear indicator of the effects of aging, with eventual lack of maintenance [5]. Proper maintenance is fundamental, since the most important element in the durability of bridges is the correct evolution of the structure within the design lifetime. Critical points of structures (especially for reinforced concrete bridges in particular) are not always easy to detect. Among all the possible structural elements, bearing devices can represent in some case the most vulnerable component of the overall system, causing sudden and brittle collapses, at ultimate conditions.

To properly assess the effects of aging on the materials, it is necessary to consider both experimental and numerical results. In particular, this work analyzes the behavior of bearing devices for bridge structural systems, comparing the outcomes of experimental campaigns to numerical parameters. A parametric study has been then carried out, in order to investigate the effect of aging on the response of bearing devices, focusing on displacements undergone by the device and on actions transmitted to the piers.

## 2 EXPERIMENTAL OUTCOMES ON FULL-SCALE DEVICES

In Figure 1 the specimens under investigation are shown.



a) b)

Figure 1: Full-scale *new generation* (a) and *naturally aged* (b) elastomeric bearings.

Full-scale bearing devices have been experimentally tested at the Laboratory of EUCENTRE Foundation in Italy, in order to assess the characteristics of the force response of elastomeric bearings, used for bridge structural systems in the last decades. Specifically, the plan sizes are 700mm and 350mm, with an average thickness of 35mm. The naturally aged bearings consist of dismissed devices, which were previously installed into an existing bridge structural system. Thus, the presented testing campaign can be considered as an evidence of the mechanical properties of commonly adopted elastomeric bearing devices, in agreement with the material properties used in the last 50 years.

## 2.1 Testing protocol

The testing protocol to be applied to the aforementioned devices has been defined, according to the European Standard Code for Bearing Devices, UNI:EN1337, and all tests are summarized in Table 1.

Table 1: Testing protocol for full-scale bearing devices.

| test # | test name | label | main dof | Ampl. | Max. vel. | Freq. | load shape | Vert. load [kN] | Cycles [#] |
|---|---|---|---|---|---|---|---|---|---|
| **1** | Shear Stiffness at ambient temperature | SS | long | ± 100% | 3 mm/s | 0.016 Hz | triangular | 1470 | 2 |
| **2** | Shear bond at ambient temperature | SB | long | ± 200% | 2 mm/s | 0.007 Hz | triangular | 2940 | 2 |
| **3** | Compression stiffness | CS | vert | - | 24.5 kN/s | - | loading ramp | 2940 | 3 |
| **4** | Static rotation eccentricity method | SR | vert | 0.470 deg | - | - | loading ramp | 1715 | 2 |
| **5** | Static rotation restoring moment | SR | vert | 0.172 deg | - | 0.030 Hz | triangular | 1715 | 10 |

In this work the analysis of the experimental outcomes of tests #1 and #2 are discussed, since the force response of the bearings is under investigation. Both tests are related to low-velocity longitudinal tests, performed by applying a triangular displacement waveform, with 100% and 200% of peak shear strain respectively for Shear Stiffness and Shear Bond tests. The vertical load is kept as constant during the whole duration of the tests, in order to simultaneously apply compression and shear states of stress.

## 2.2 Testing setup

All tests have been performed at the Laboratory of EUCENTRE Foundation in Italy, through the Bearing Tester System (BTS). Such a testing equipment is capable of performing static and dynamic tests on full-scale bearing and isolation devices, thanks to large displacement and force capacity levels for both longitudinal and vertical directions. In Figure 2 the testing equipment is shown.

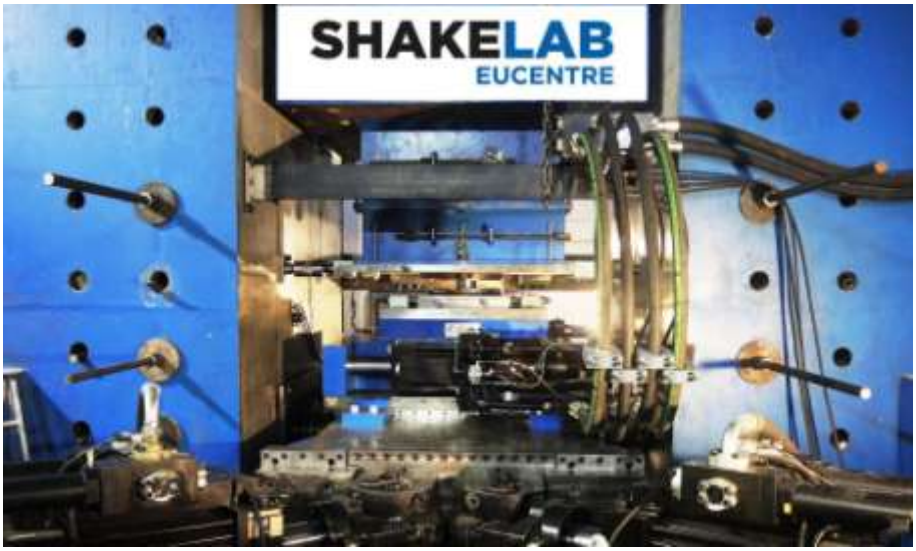


Figure 2: Bearing Tester System at EUCENTRE Foundation (Italy).

Since bearing devices are commonly tested just laid on the setup backing plates, by considering just a frictional coupling between the testing equipment and the bearings, special steel plates have been designed and installed, in order to ensure the correct application of the horizontal motion, without eventual sliding induced by high forces. To this aim, the roughness of the interfaces between bearings and testing equipment has been increased, through mechanical the realization of grooves, which allows to better apply horizontal displacements, with no sliding motions, which would result into small portion with constant horizontal force within the hysteretic loops.

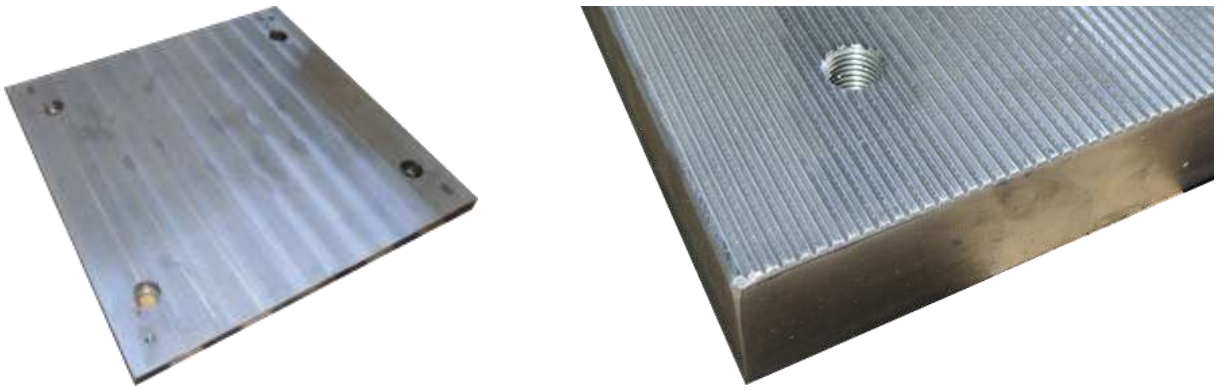

Figure 3: Backing plates for effective application of motion.

Consequently, the resulting mechanical properties of the devices can be correctly evaluated, since the effective hysteretic response of the devices is returned by the proper application of test horizontal motion.

## 2.3 Test results

In what follows testing results are analyzed. More specifically, hysteretic response is discussed, in addition to the shear modulus obtained as a function of the effective stiffness at maximum displacement, together with the equivalent viscous damping.

In Figure 4 the hysteretic loops are shown, for one new and one aged devices.

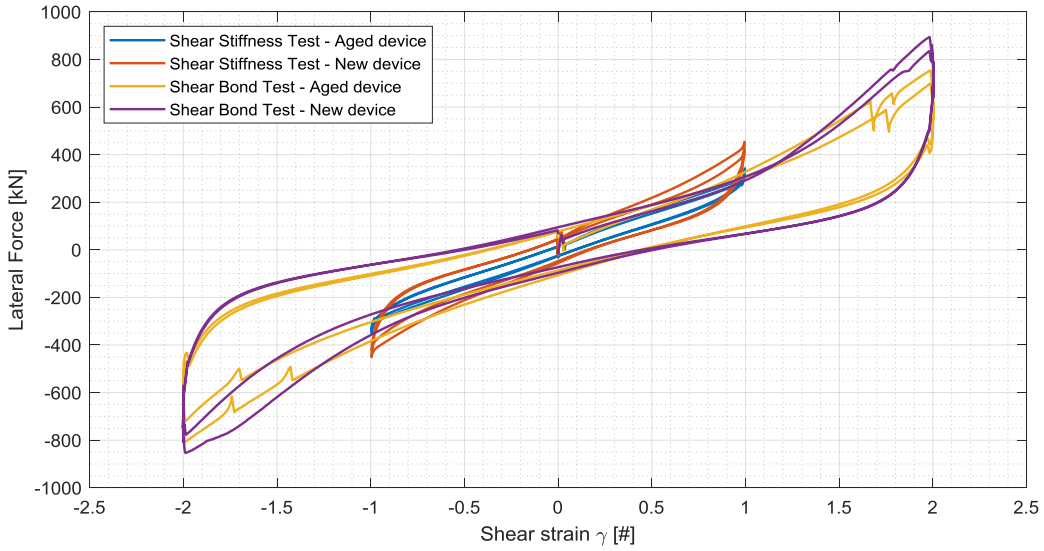


Figure 4: Example of hysteretic loops for both aged and new bearing devices.

As can be noted, the behavior of the bearings can be considered approximately linear elastic, with a certain value of equivalent viscous damping, as the lateral shear strain does not exceed 100%. For tests at 200% of shear strain, the hysteresis area significantly increases, together with a considerable hardening, which may result into increased values of both equivalent shear modulus and viscous damping.

In Figure 5 values of the equivalent shear modulus G are reported, obtained as a function of the effective stiffness at maximum displacement, by considering *Shear Stiffness* tests.

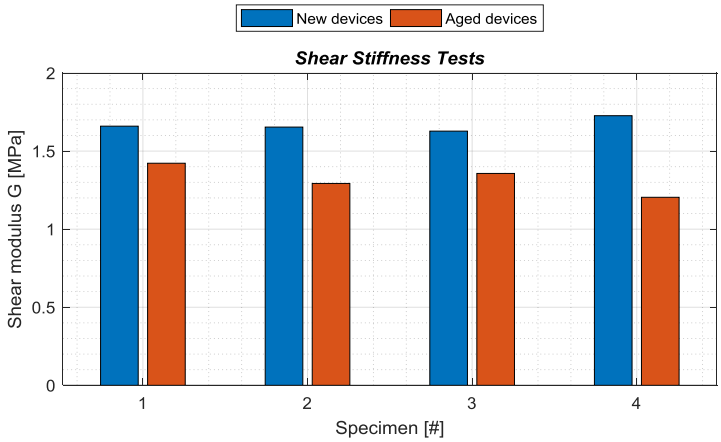


Figure 5: Equivalent shear modulus for *Shear Stiffness* tests.

Graphical results for the shear modulus at 100% shear strain show that the new compound has a higher shear modulus, in comparison to the naturally aged devices, for all specimens. However, since details of the original design value of the dismissed bearings are missing, it is not possible to directly address such differences to the aging effect, rather that possible discrepancies in the compound characteristics. On the other hand, it is possible to assess a range of variation of the shear modulus for elastomeric bearings, to be implemented in real practice applications of bridge structural systems.

Finally, in Figure 6 experimental results are reported, as equivalent viscous damping values.

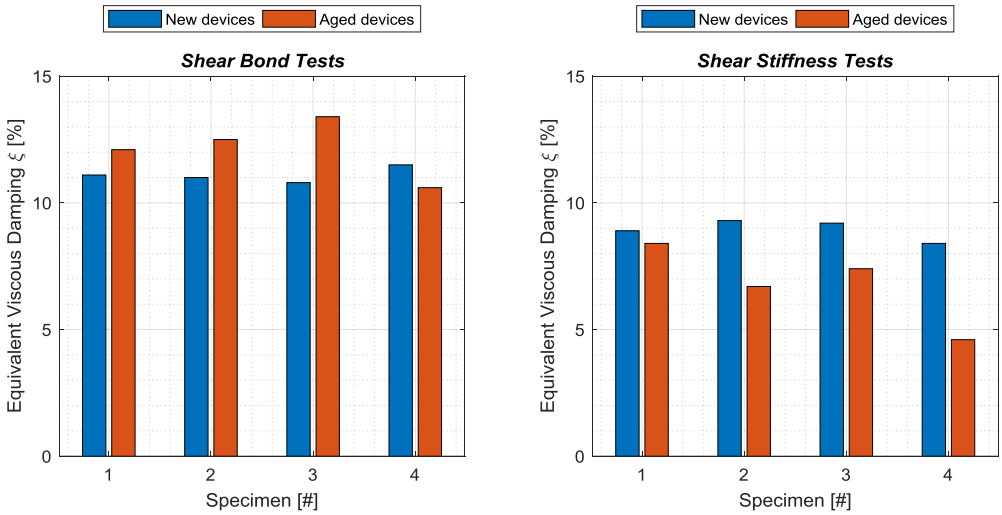


Figure 6: Equivalent Viscous Damping for *Shear Bond* and *Shear Stiffness* tests.

As previously discussed, tests with 200% of peak shear strain have larger values of damping ratios, due to the larger hysteresis area, in comparison to tests with 100% of shear strain. Concerning the comparison between naturally aged and new devices, it is not possible to detect a common trend, since damping results are higher for aged bearings at 200% of shear strain, and the opposite behavior can be noticed at 100% of shear strain. In addition, as the displacement demand does not exceed 100% of shear strain, the equivalent viscous damping, as expected, is quite low (between 5% and 10%), and consequently a lower bound of 5% damping is recommended, when no sufficient information about the compound mechanical properties are available.

## 3 ASSESSMENT OF CASE STUDY STRUCTURES

Two case study structures have been modeled, in order to perform a parametric study, by considering the effects of aging on the force and displacement responses of elastomeric bearing devices.

Bridge #1 is located in a region associated to low seismic hazard. The bridge is characterized by three simply supported spans. The total length of Bridge #1 is 44 m. The width of the deck is 16.5 m, with two carriageways, divided by a fixed traffic divider. The deck is composed of 14 prestressed concrete beams with I-shape section. The height of the beams is 1.3 m in the central span and 0.9 m in the lateral spans. Transversal reinforced concrete beams,

used as stiffeners, are present along the deck, which is completed by an upper slab 0.25m thick. A neoprene pad bearing is present below each beam. Six lines of devices have been identified. Each device is 3 cm high, with plan dimensions of 0.4 x 0.35 m. Each of the two piers of Bridge #1 is made up of four columns topped by an L-shaped pier cap. The columns present a square section with side 0.8 m. Shallow foundations are present below the piers. In particular, a continuous footing with section 2 x 1 m has been identified and modeled below each piers. No detailed information were available for the abutments, which have been modeled in a simplified way. The mechanical properties of the materials employed in the model have been defined, by considering the results of experimental tests.

On the other hand, the construction site of Bridge #2 is associated to a high seismic hazard. Four simply supported 12.5 m long spans characterize the case study. The total length of the bridge is 50 m. The width of the deck is 10.5 m. The carriageway is divided into two lanes (one for each direction of travel). The deck is composed of 5 reinforced concrete beams with section 0.4 x 0.95 m. Transversal reinforced concrete beams, used as stiffeners, are present along the deck. The deck is completed by a 0.3 m thick upper slab. A neoprene pad bearing is present below each beam. Eight lines of devices have been identified. Each device is 2.5 cm high, with plan dimensions of 0.4 x 0.6 m. Bridge #2 presents three piers with frame structure. In each pier, two columns with section 1.2 x 1 m are topped by a pier cap with section 1.3 x 1.25 m. The foundations of piers and abutments consist of piles with 1.2 m diameter. The data required to define the mechanical properties of the materials employed in the model have been obtained considering the results of experimental tests on the structure.

Figure 7 presents the FEM models developed to perform the parametric study on the two case studies. The models have been developed by using SAP2000 [6]. Longitudinal and transverse beams, columns, pier caps and continuous footing have been modeled using beam elements. The bearings have been modeled using two nodes link elements, assigning to each degree of freedom the corresponding stiffness to properly characterize the devices. The upper slab of the deck of each bridge has been modeled using Shell elements. This procedure was necessary to properly capture the response of the deck, as a result of the load configurations considered in this study. Given their inherently two-dimensional nature, abutments have also been model using Shell elements.

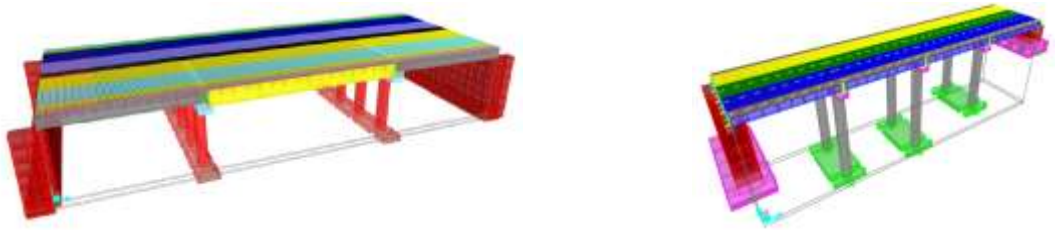

a) b)

Figure 7: Case study structures FEM models with low (Bridge #1 - a) and high (Bridge #2 - b) seismic hazard.

As briefly aforementioned, the two case studies have been considered in a parametric study with the aim of investigating the effects of aging in the variation of the mechanical properties of bearings, and the consequent modifications in the overall structural response, subjected to both ordinary and seismic loads.

As reported in the scientific literature, one of the possible modifications in the properties of the bearings due to aging effects is the increase or reduction of their stiffness [7][8]. Thus, a

wide range of variation of the mechanical properties of elastomeric bearings has been considered in the presented parametric study.

The parametric study has been carried out by performing linear dynamic analyses in SAP2000. For each case study, 11 models have been defined. Each model was characterized by a different value of horizontal stiffness of the bearings $K_h$, which is computed as follows:

$$K_h = GA/h \tag{1}$$

Where G is the shear modulus of the rubber compound, A is the plan area of the device and h is the total height of all the elastomeric layers.

Particularly, the bearing properties have been obtained, by varying the value of G between 0.5MPa and 1.5MPa. Once the linear dynamic analyses have been completed, the obtained results have been processed to define the variation of the considered response parameters with the value of G.

In order to summarize the procedure adopted for the parametric study, four main steps can be identified:

- Definition of the models of the case studies;
- Load analysis;
- Linear dynamic analyses for different values of G;
- Post-processing of the results.

### 3.1 Load configurations and combinations

To properly introduce the analysis of results returned by the parametric study, the description of the adopted configurations and combinations considered in the study is of fundamental importance. The following actions have been considered for both the case studies:

- Structural dead loads;
- Non-structural dead loads;
- Snow;
- Traffic loads (including the braking force);
- Seismic action.

The wind action has not been considered in the present study, since is not considered as a significant contribution. The Italian Building Code (NTC2018 [9]) represented the main reference in the definition of the acting loads. Structural dead loads have been automatically computed by the software, while a typical configuration of the roadway finishes has been considered, for the definition of the non-structural dead loads. The snow load has been defined considering the prescriptions of §3.4 of NTC2018. The seismic load has been defined as horizontal and vertical response spectra, corresponding to the Life-Safety and Damage Limit States, in agreement with NTC2018.

The definition of the traffic loads requires some specific considerations for both the case studies. Figure 8 represents the lane definition for Bridge #1 and Bridge #2. Both the case studies are road bridges, thus the traffic loads in the vertical direction are defined considering the Scheme 1, as ruled by NTC2018. The definition of the traffic loads is needed to identify the lanes. Given the configuration of Bridge #1, four 3 m wide lanes (two for each traffic direction) have been identified, whereas Bridge #2, has three 3 m wide lanes.

In the definition of the traffic loads, the braking force has been taken into account. The braking force is defined as a percentage of the vertical traffic load and is applied in horizontal direction, along the traffic direction.

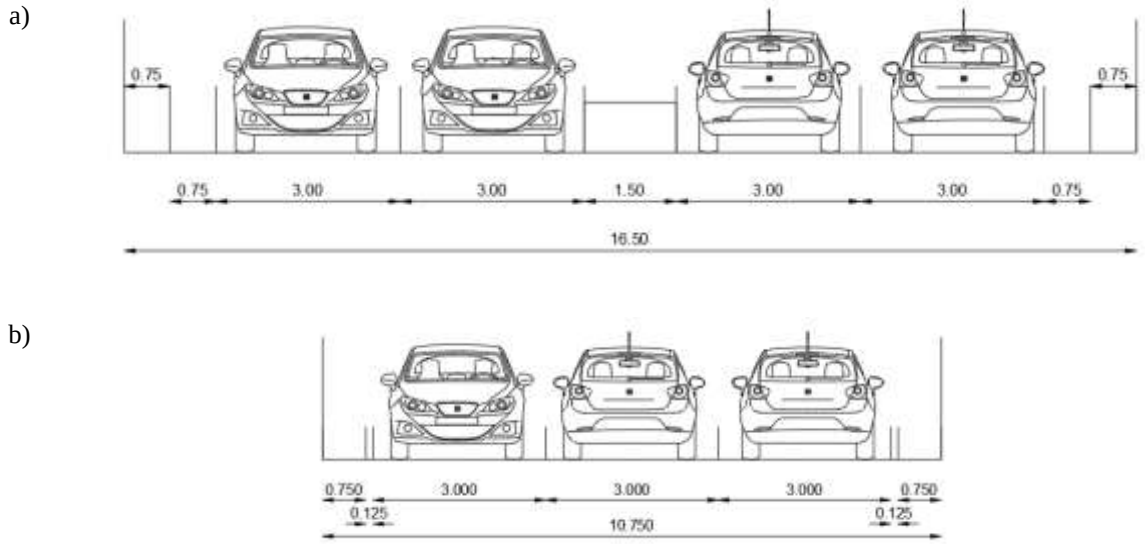


Figure 8: Lane definition for the traffic load computation: Bridge #1 (a) and Bridge #2 (b).

The parametric study required the definition of load combinations for static and seismic conditions. In both cases, the combinations have been defined following the prescriptions of NTC2018. Specific considerations are required in the definition of the static load combinations.

For static load combinations, the traffic loads must be defined with different configurations, in order to maximize the response of the structure. To this aim, six different configurations of the traffic lanes defined according to the NTC2018 have been considered for both the case study structures. The influence of the moving loads has been taken into account in the study, by employing the tandem loads defined in the NTC2018. For each span, three different positions (the two ends and the middle of the span) of the moving loads have been considered in order to maximize the structural response.

Figure 9 represents a scheme of the traffic load configurations for Bridge #1 and Bridge #2.

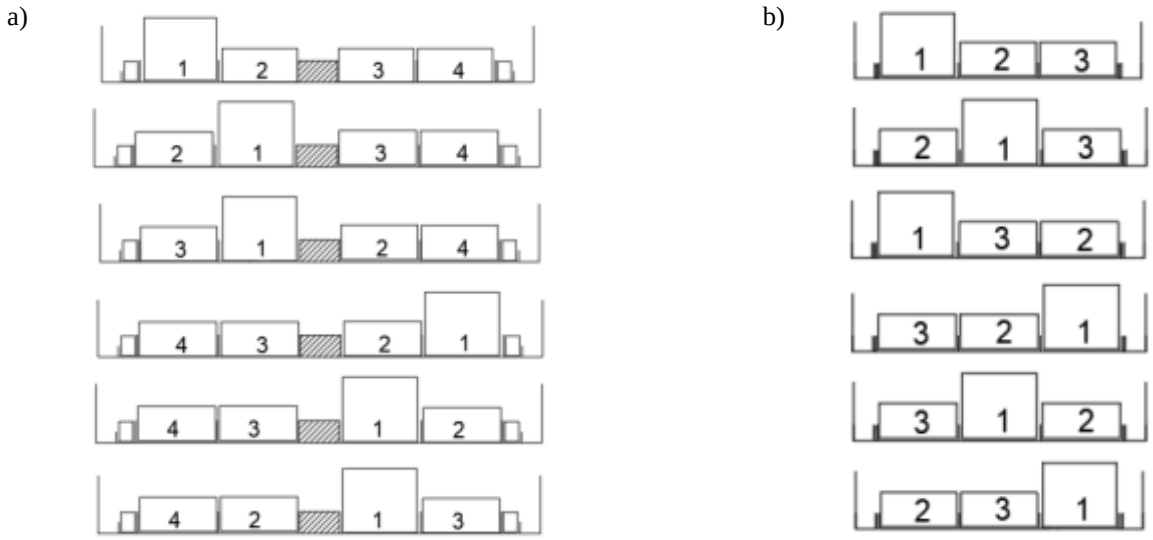


Figure 9: Traffic load configurations: Bridge #1 (a) and Bridge #2 (b).

## 3.2 Analysis of results

In this section the analysis of the results of the parametric study introduced earlier is presented. In the post-processing of results special attention has been focused on the horizontal displacements of the bearings, the shear force transmitted to the piers and the bending moment transmitted to the piers. Peak values of each response quantity have been normalized with respect to corresponding value returned by considering a shear modulus G equal to 1 MPa.

Figure 10 reports the displacement ratio for one line of bearings of Bridge #1 and Bridge #2. For each value of G and considering all the different load combinations, the maximum value of displacement in a given line of bearings in both longitudinal and transverse direction has been taken and successively normalized with respect to the value of displacement in the same direction, returned by considering the shear modulus G equal to 1 MPa. It has to be pointed out that $U_2$ is the displacement in the longitudinal direction of the bridge, while $U_3$ refers to the transverse direction.

Considering all the bearing lines, maximum peak displacements, for both the case studies, have been detected at the abutments locations. It can be noted that the displacement demands decrease with the increase of G, since the horizontal stiffness of the bearings increases. As expected, results provide evidence that the shear modulus G has a significant influence on the peak horizontal displacements of the bearings and that aging phenomena are relevant in this sense. Significant variations have been computed, bounded between -15% and 35%.

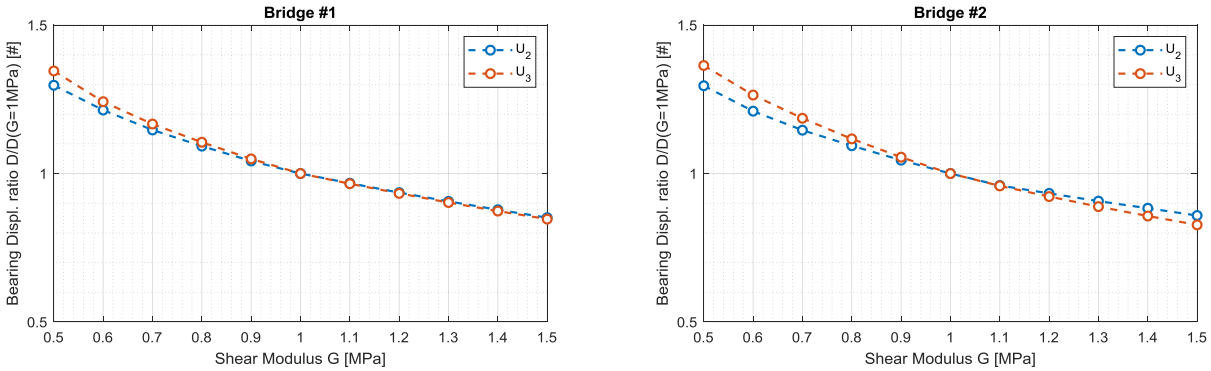


Figure 10: Numerical results: Displacement ratio for Bridge #1 (left) and Bridge #2 (right).

Figure 11 shows the results in terms of shear ratio for both the case studies. Data have been processed similarly to what has been done for the bearings' peak displacement demand. For each pier, the peak value of shear force transmitted to the columns has been identified, by considering all the load combinations, and results have been normalized with respect to the value corresponding to a shear modulus G equal to 1 MPa. $V_{22}$ indicates the shear in the plane parallel to the longitudinal direction of the bridge, while $V_{33}$ refers to the shear in the plane perpendicular to the longitudinal direction of the bridge.

Figure 12 is related to the bending moment ratio for Bridge #1 and Bridge #2. The post-processing of the data obtained with the analyses is almost equal to the procedure employed to derive the shear ratio. $M_{22}$ represents the moment acting in the plane perpendicular to the bridge longitudinal axis, while $M_{33}$ indicates the moment in the plane parallel to the bridge longitudinal axis.

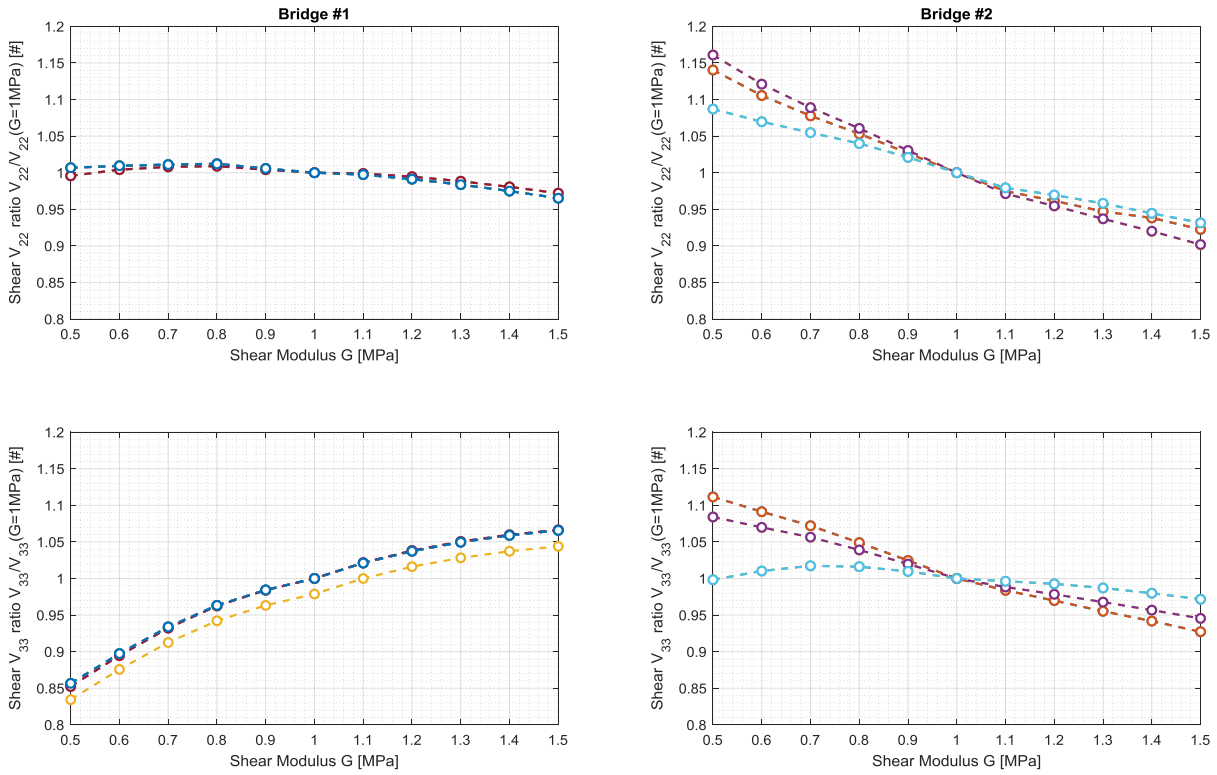


Figure 11: Numerical results: Shear ratio for Bridge #1 (left) and Bridge #2 (right).

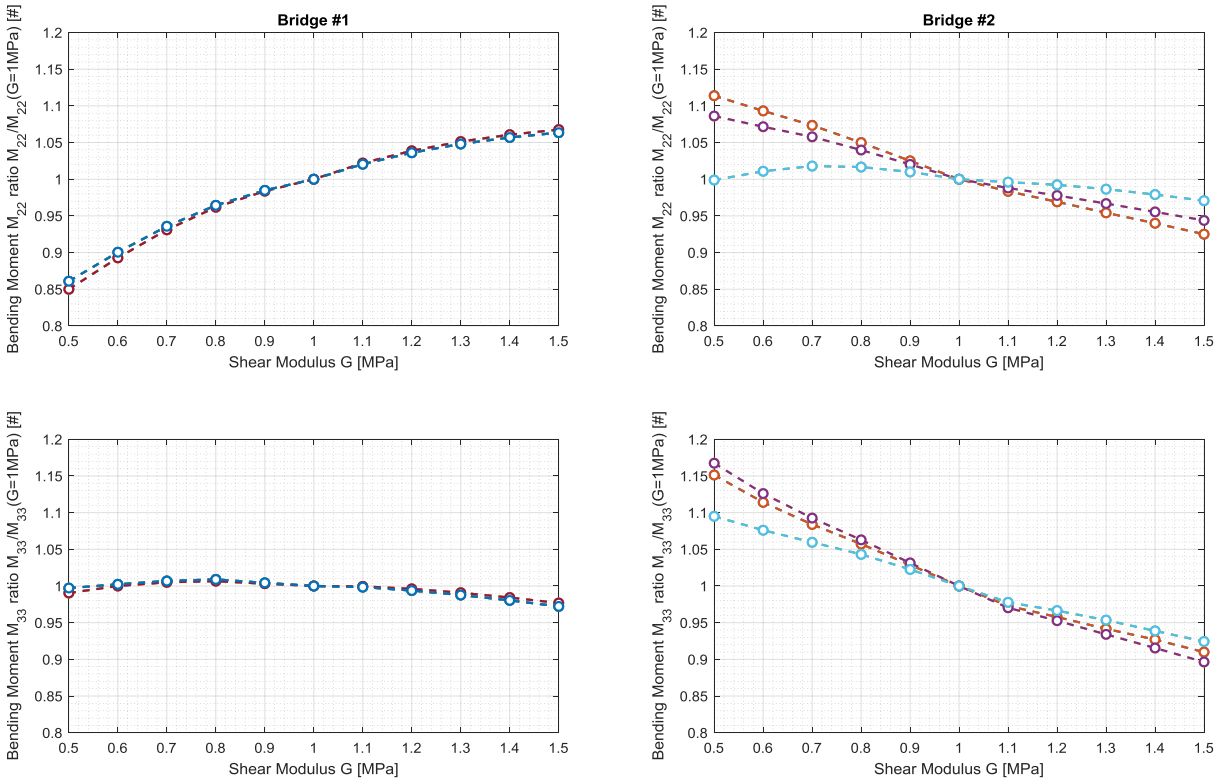


Figure 12: Numerical results: Bending Moment ratio for Bridge #1 (left) and Bridge #2 (right).

Considering Bridge #1, it can be noticed that the variation for $V_{22}$ is relatively small, while for $V_{33}$ values become more relevant (around 15% for values of G below 1 MPa, and approximately 6% for values of G greater than 1 MPa). Similar results can be observed in terms of bending moments, with $M_{22}$ exhibiting greater variations compared to $M_{33}$.

Considering the case of Bridge #2, for $V_{22}$ the variation is around 10% for values of G greater than 1 MPa and around 15% when G is less than 1 MPa. In the case of $V_{33}$, the variation is 10% for G less than 1 MPa and 8% when G is greater than 1 MPa. Similar results can be observed considering the moments $M_{22}$ and $M_{33}$.

The parametric study that has been carried out allows to understand how the aging effects on bearing devices can modify the actions transmitted to the piers. It has to be remarked, however, that the study considers only two case studies and that an extended sample of bridges could be useful to better generalize the drawn conclusions.

## 4 CONCLUSIONS AND FUTURE DEVELOPMENTS

The presented research show the outcomes of both experimental and numerical campaigns, with the aim of analyzing the characteristics of the force response of elastomeric bearings for bridge structural systems, and the influence of the mechanical properties of the adopted rubber compound on the overall response. The results have shown the following issues:

- Naturally aged devices seems to have a lower stiffness, in comparison to new generation bearings;
- On the other hand, it is not possible to detect a general trend for the equivalent viscous damping, since is seems to be significantly affected by the hardening and increase of hysteresis area for shear strains higher of 100%.
- The shear modulus variation leads to non-negligible variations in the displacement demand of the deck, as well as for shear and bending moment peak responses.

As a future development of this endeavor, the new generation devices will be artificially aged through a special procedure which implies a certain duration of high temperature application to the bearings, in order to better distinguish the effects of aging on the mechanical properties of the adopted rubber compound.

## ACKNOWLEDGEMENT

This work was funded by the agreement between the Italian Consiglio Superiore dei Lavori Pubblici and the ReLUIS Consortium on “Sperimentazione delle linee guida per la classificazione e gestione del rischio, la valutazione della sicurezza ed il monitoraggio dei ponti esistenti”, Decreto del Ministero delle Infrastrutture n. 578 del 17.12.2020.

## REFERENCES


[1] Kumar R, Gardoni P. Effect of seismic degradation on the fragility of reinforced concrete bridges. Eng Struct 2014;79:267–75. https://doi.org/10.1016/j.engstruct.2014.08.019.

[2] Pang Y, Wu L. Seismic Fragility Analysis of Multispan Reinforced Concrete Bridges Using Mainshock-Aftershock Sequences. Math Probl Eng 2018;2018:1–12. https://doi.org/10.1155/2018/1537301.

[3] Taghinia A, Vasseghi A, Khanmohammadi M, Soroushian A. Development of Seismic Fragility Functions for Typical Iranian Multi-Span RC Bridges with Deficient Cap Beam–Column Joints. International Journal of Civil Engineering 2022;20:305–21. https://doi.org/10.1007/s40999-021-00661-5.

[4] Fox MJ, Furinghetti M, Pavese A. Application of the new Italian assessment guidelines to a 1960s prestressed concrete road bridge. Structural Concrete. 2022. https://doi.org/10.1002/suco.202200884

[5] Cosenza E, Losanno D. Assessment of existing reinforcedconcrete bridges under road-traffic loads according to the new Italian guidelines. Structural Concrete 2021;22:2868–81. https://doi.org/10.1002/suco.202100147.

[6] CSI, "SAP2000 Integrated Software for Structural Analysis and Design," Computers and Structures Inc., Berkeley, California.

[7] Itoh, Y., and H. S. Gu. "Prediction of aging characteristics in natural rubber bearings used in bridges." *Journal of Bridge Engineering* 14.2, 2009.

[8] Oh, Ju, Jin Ho Kim, and Hwa Cho Yi. "Effects of thermal aging of laminated rubber bearing on seismic performance of bridges." *Journal of Vibroengineering* 18.6, 2016

[9] Norme Tecniche per le Costruzioni. Aggiornamento delle Norme tecniche per le costruzioni. Gazzetta Ufficiale Serie Generale 2018;42.

COMPDYN 2023
9th ECCOMAS Thematic Conference on
Computational Methods in Structural Dynamics and Earthquake Engineering
M. Papadrakakis, M. Fragiadakis (eds.)
Athens, Greece, 12-14 June 2023

# EXPERIMENTAL AND FINITE ELEMENT ANALYSIS OF THE CYCLIC BEHAVIOUR OF LINEAR DISSIPATIVE DEVICES

**Salvatore Pagnotta, Muhammad Ahmed and Piero Colajanni**

Department of Engineering, University of Palermo,
Viale delle Scienze, Ed. 8, 90128, Palermo, Italy.
email: {salvatore.pagnotta, muhammad.ahmed, piero.colajanni}@unipa.it

## Abstract

In the past years, low-damage design of structures is becoming an efficient approach by engineers and researchers in order to mitigate the structural damage to buildings during a seismic event. To this aim, one of the most popular strategies is to endow framed structures with either viscous, hysteretic metallic, or viscoelastic devices. As an alternative to these systems, friction devices have been also studied, proving to be an effective solution. Steel braces endowed with linear dissipative devices based on friction can be used effectively both in the case of new and existing structures. Studies conducted on these devices stressed that their behaviour is mainly influenced by type of friction materials, loss of bolt preload and effect of disc springs.
An experimental campaign has been performed at the Materials and Structures Laboratory of the University of Palermo on linear dissipative devices with different types of friction materials i.e., steel, thermal sprayed aluminium, and brass, to check their effectiveness. Finite element analysis using ABAQUS has been done to design, check the functionality, and get insight into the experimental results of the linear dissipative devices. An investigation has been done on the effectiveness of disc springs to limit the bolt preload variation in the device and the effect of thicknesses of plates on the functionality of linear friction dissipative device. The results showed that thermal sprayed aluminium, coupled with structural steel, is a good friction material as it provides stable hysteresis loops and high friction coefficient as compared to brass, and appropriately designed disc springs are able to limit bolt preload variation.
The experimental results showed that the thermal sprayed aluminium provides a friction coefficient between 0.57 and 0.6 without significant variation even for a large number of cycles, while for the brass the friction coefficient at the beginning of the test was 0.25 and then it increased to 0.45 at the end of test, exhibiting large variation due to stick and slip phenomenon. The FEM analysis proved that the disc springs are able to minimize the variation of the contact pressure due to the Poisson effect and proper thickness of friction plates are important for the performance of friction device.

**Keywords:** Friction, Energy dissipation, Pre-load, Cyclic loading.

## 1 INTRODUCTION

During the last decades, an increase in seismic events urges a need to ensure an effective dissipative global behaviour for structures in order to prevent them from collapsing and to mitigate the chances of loss of human lives. Design strategies for seismic-resistant buildings and seismic rehabilitation of existing buildings have become one of the most important topics among researchers. Depending on the type of structure different retrofitting techniques, either through a global modification of structural seismic behavior [1], or through simple local interventions [2], were proposed.

The use of dissipative connection in the designing of seismic resistant low damage steel frame was investigated by several authors [5]-[9], while more recently a friction device for beam to column connection was proposed for reinforced concrete frames with Hybrid Steel Truss Concrete Beams (HSTCB)s by [10]-[13].

Detailed and well-designed friction devices are an efficient solution to dissipate seismic energy and provide stable hysteresis behaviour using different friction materials [14]. Over the last few years friction devices have been also studied as an alternative to viscous, hysteretic metallic, viscoelastic etc. proving to be an effective solution.

Retrofitting of either steel or reinforced concrete frames by bracing equipped with dissipative devices has been recognized as one of the most performing and economic procedure. The use of friction-based dissipative devices started in the eighties of the last century [15] and recently has gained more popularity. Their use is still growing in the seismic active regions because of the economic and safety aspect [16].

In order to ensure a highly dissipative behaviour of linear friction dissipative device, two aspects are mainly investigated: variation of friction coefficient and contact pressure during the operational condition, that provide the sliding force of the device. In general, the main phenomena that can occur on the surfaces on which friction forces are generated are the increase in the roughness of surfaces with a smooth finish, which leads to an increase in the coefficient of friction and flattening of the roughness of surfaces with a rough finish, which leads to a decrease in the coefficient of friction. It is evident how such phenomena can make the behaviour of dissipative friction connections uncontrollable, that's why the choice of the friction material to be adopted must fall on those materials whose properties do not change significantly during the sliding of the surfaces.

As regards the second aspect, i.e., contact pressure, its value in operation is affected both by the application procedure of the bolt preload and by long-term phenomena. In fact, with the common techniques used to preload bolts (for example the use of a torque wrench), it is extremely complex to precisely control the level of force applied.

When friction devices are utilized as a dissipative source in beam-to-column friction joints, many aspects are investigated, such as stiffness and strength of the connection, amplitude, stability and symmetry of hysteresis cycles, recentering behaviour and influence on the global response of the structure.

Regarding the behaviour of linear dissipative devices, [17] investigated the cyclic response of linear dissipative devices using different friction materials by performing cyclic tests under the displacement control method, analyzing the variation of friction coefficient. They found that thermal sprayed aluminium on the steel interface has a consistent cyclic response and less variation of friction coefficient, remaining nearly constant with just 3-5% variation between the start and end of the test. It was also found that it has a high value of friction coefficient (0.5-0.6) as compared to the steel-steel, which ranges between 0.18 and 0.35 during the test, and brass on steel (ranging from 0.1 to 0.25).

To understand the preload behaviour, [18] investigated the actual preload levels applied on a series of bolts, applied by reading the tightening torque provided by a torque wrench. The force actually applied was measured by means of a load cell placed between the bolt head and the steel plate in which the bolt was inserted. They found that the dispersion of the data was significant, having a preload force with 95% fractile equal to 112.3% of the nominal value, while with 5% fractile equal to 96.4%. It is therefore evident that how such uncertainty of the preload force applied to the bolts directly influences the uncertainty of the sliding load of the friction device.

In addition to this uncertainty, the value of the prestressing load in operation is affected by the long-term preload loss that occurs in the bolts due to creep phenomena and by the crushing of the asperities on the surfaces in contact between the nut, pin and washer. In order to minimize these effects, several authors [19] proposed to keep the preload in the bolts between 30% and 60% of the maximum applicable according to Eurocode 3.

In addition to reducing the maximum preload applied to the bolts, the main solution adopted to limit the variations in preload is the use of cup springs or conical washers. These are truncated cone-shaped washers that are arranged below the nuts and bolt heads in different configurations based on the required force-lowering behaviour.

Another aspect to take into account in the design of structures equipped with friction devices is the dependence of the mechanical behaviour of these elements on the speed of application of the load. In fact, it has been seen that as the speed of displacement varies, these systems offer a mechanical response (in terms of force/sliding moment) which is greater than that obtained with quasi-static type tests [20][21]. This difference depends not only on the imposed movement speed, but also on the type of the used friction material.

In [22] experimental analysis was done on both friction-based linear dissipative devices and friction-based beam-to-column joints using thermal sprayed aluminium as a friction material. The material selection was done on the basis of its performance reported in the literature [8][17][19][23][24]. The results showed that in the friction-based beam-to-column joint hysteresis cycles were unexpectedly not symmetrical, so it urges a need to get more insight into the friction-based dissipative device behaviour, in order to detect the source of this unexpected behaviour.

In this paper, to develop the technical knowledge regarding the role of friction devices for the strengthening of frames and to check the functionality of a linear dissipative device, two approaches were adopted i.e., FEM and experimental analysis. To analyze the friction properties of different materials to be used in a linear dissipative device, a linear friction dissipative device was tested using the cyclic loading protocol as suggested in code [25].

In the experimental campaign, on the basis of the previously mentioned results in the literature, two materials were investigated, namely thermal-sprayed aluminium and brass, both coupled with structural steel. The variation of bolt preload during the test was evaluated using load cells, while the evaluation of the friction coefficient was done by a correlation between sliding force and the actual instant value of preload acting on the bolts.

FEM analysis has been done to further check the functionality and to deeply analyze the behaviour of aluminium plates with different thicknesses, and the role of disc springs. In the FEM analysis, the same testing protocols and properties were taken into consideration as of the experimental test but with different thicknesses of thermal sprayed aluminium plates.

## 2 DESIGN OF LINEAR DISSIPATIVE DEVICES

The reference test specimen was similar to that used in [17]. The device shown in Figure 1 is composed of two central steel plates, one with slotted holes and the other with standard clearance holes. Two friction shims of steel coated by thermal sprayed aluminium are sandwiched

on both sides between the central plates and steel cover plate. This whole assembly is fastened together using four preloaded bolts of M12 class 10.9 on the sliding side and six on the fixed side. The design of the linear friction device is carried out according to [26].

The design of the sliding force of the device is calibrated on the instrumentation available at the Laboratory of Materials and Structures of the University of Palermo. Zwick-Roell Z600 universal testing machine, with a maximum load of 600 kN is used. The design is carried out considering, initially, a sliding force equal to 150 kN. Based on the experimental results provided by [8], the friction coefficient for thermal sprayed aluminium is taken as equal to 0.5.

The maximum preload applicable on the bolts is taken as equal to 60% of the preload suggested by the standard (maximum work rate $t_{s,max}$ = 0.6). A friction connection is designed using 4 Bolts of M12 class 10.9 bolts having resistant area $A_{res}$ = 85 mm$^2$, yield strength $f_{yb}$ = 900 MPa and tensile strength $f_{ub}$ = 1000 MPa.

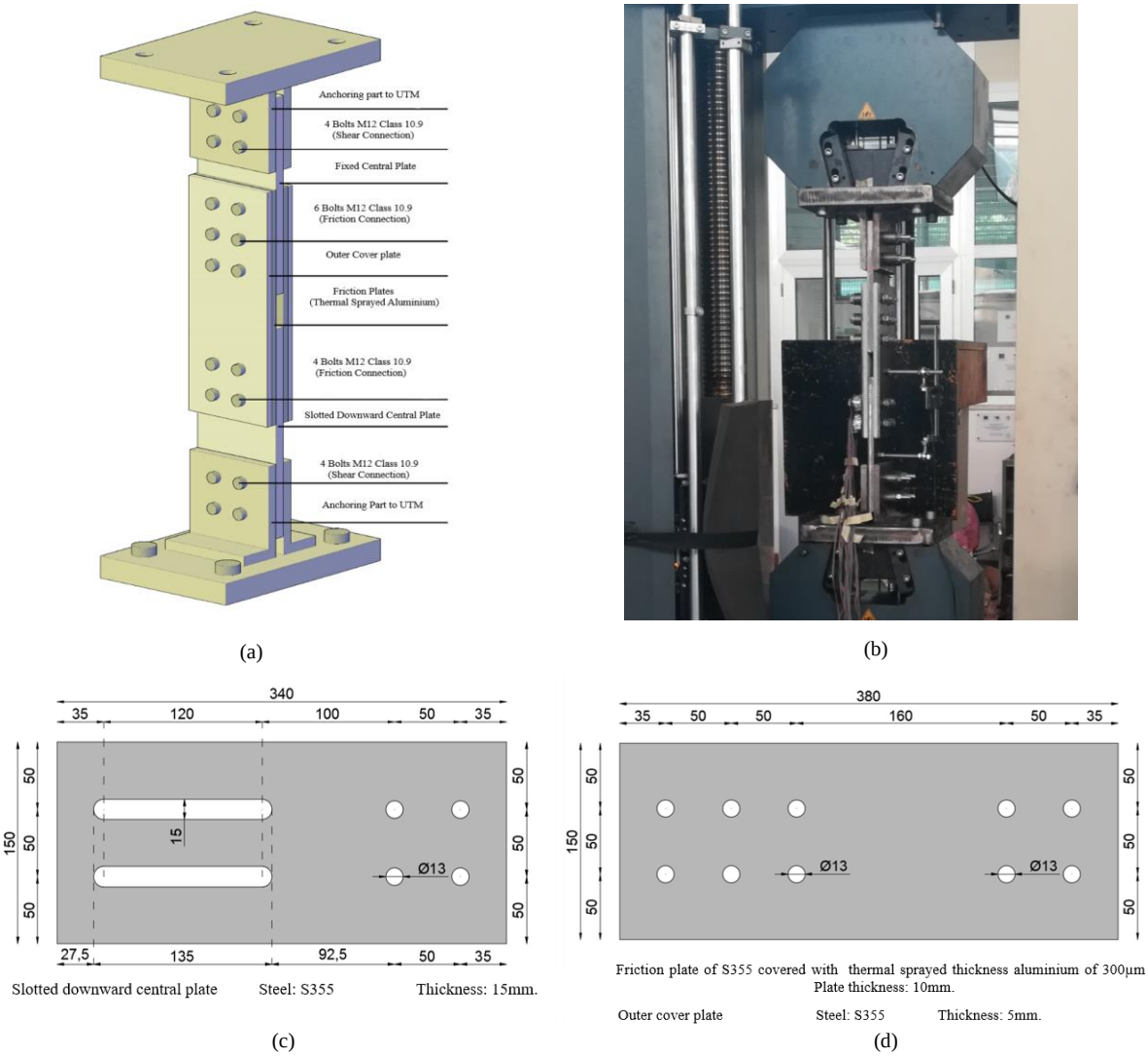


Figure 1: (a) Assembly details of friction dissipative device; (b) friction dissipative device during testing; (c); slotted downward central plate (d) friction plates and outer cover plates

The applicable preload on the bolt according to the regulations is:

$$F_{pc} = 0.7 f_{ub} A_{res} = 59.4 kN \quad (1)$$

Considering two surfaces on which the friction forces of the device are generated ($n_s$ = 2), the expected sliding force in the device to be tested is equal to:

$$F_{s,\max} = \mu t_{s,\max} n_s n_b F_{pc} = 0.5 \times 0.6 \times 2 \times 4 \times 59.4 = 142.6 kN \quad (2)$$

## 3 EXPERIMENTAL TESTS ON THE LINEAR FRICTION DISSIPATIVE DEVICE

In the experimental tests, the linear friction device was used to assess the friction properties of the two friction materials (thermal sprayed aluminium and brass). The device was tested using Universal Testing Machine (UTM). The thickness of outer cover plates and friction pads were taken as 10mm and 5mm respectively for all experimental tests. The central plates of the linear friction device were connected using bolted shear connections to four steel angles welded to 35 mm-thick steel plates bolted to the Universal Testing Machine (UTM). The disc springs were used to keep the bolt preload constant on the friction plates as possible. Three-disc springs arranged in series were added to each bolt. The bolt preload was set at 40% of the preload suggested by the standard (maximum work rate $t_{s,\,max}$ = 0.4). Thus, the expected experimental sliding force is:

$$F_{s,\max} = \mu t_{s,\max} n_s n_b F_{pc} = 0.5 \times 0.4 \times 2 \times 4 \times 59.4 = 95.04 kN \quad (3)$$

Displacement was monitored by a digital length gauge placed between the fixed downward central plate and the outer cover plate (see Figure 1(b)).

Two tests were carried out for each group of friction shims. Test 1 was performed using new thermal sprayed aluminium plates as friction pads having significant roughness. The force displacement curve of test 1 is shown in Figure 2(a). Two different trends can be seen in the graph, one is where the sliding force is constant and the other is where is a sudden variation of the sliding force. The sudden variation is due to the "stick and slip" phenomenon. It refers to the non-continuous sliding of friction pads and central plate. As it can be seen in Figure 2(a), the plate starts sliding after the attainment of sliding force, and then the force tends to decrease until it stops again and then the load start increasing until the attainment of sliding force. The device

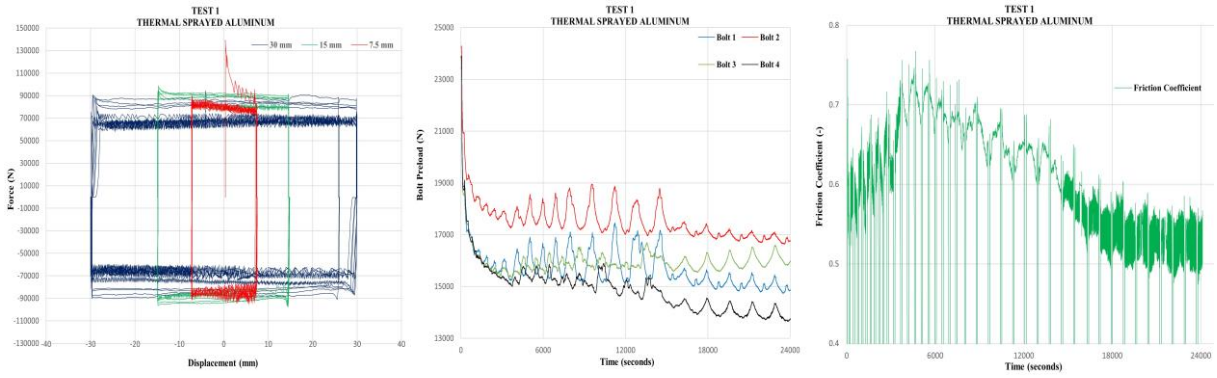


(a) (b) (c)

Figure 2: Results of test 1 for thermal sprayed aluminium (a) force displacement; (b) variation of bolt preload; (c) friction coefficient during test

starts sliding at 140kN and then during the first cycle, the load was significantly reduced up to 90kN. During the last cycles of ± 30mm displacement, the sliding force reduced up to 70kN which is almost half (50%) of the initial sliding force (140kN). Figure 2(b) shows the variation of bolt preload of all four bolts. A decrement in bolt preload can be observed during the test. At the beginning of the test, a large decrement due to the beginning of sliding of the central slotted

plate, namely from 24 kN up to (16 kN-19 kN) occurred, that was not successfully compensated by the disc spring. This phenomenon can be attributed to the sudden reduction of the unevenness of the thermal sprayed aluminium surface produced by a manual treatment. An average of 16 kN bolt load is observed at the end of the test which is almost 33.3% less than the initial bolt preload of 24kN. Figure 2(c) demonstrates the variation of friction coefficient during test 1, evaluated as the ratio of the sliding force and actual instantaneous bolt total load. It can be observed that the friction coefficient increased from 0.62 to 0.75 during the starting phase of the test while at the end of the test, it reduced up to 0.57. Due to this loosening and loss of bolt preload, there is a variation in sliding force and friction coefficient.

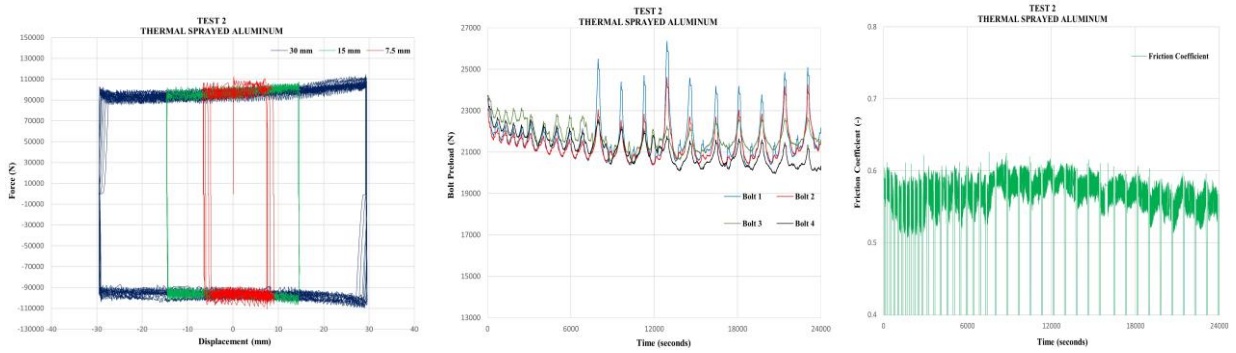


(a) (b) (c)

Figure 3: Results of test 2 for thermal sprayed aluminium (a) force displacement; (b) variation of bolt preload; (c) friction coefficient during test

To get more depth into the phenomenon, and to check the stability of the operational behaviour, test 2 was performed after applying again the bolt preload of 24kN without changing anything in the assembly configuration. The force-displacement curve of test 2 can be seen in Figure 3(a). Unlike the variations as in test 1, there is a very stable curve, and there is not much preload difference between the start and end of the test, proving that the disc spring are able to compensate bolt load fluctuation due to the residual roughness of the sliding surface. The initial sliding force is approximately 110kN while the final sliding force is 94.8kN so the difference is roughly 14% which is much less as compared to the 50% difference observed in test 1.

Similarly, Figure 3(b) shows the trend of bolt preload variation during test 2. It can also be observed that unlike test 1, there is less loss of bolt preload; only 5% loss of bolt preload observed at the start of the test during the initial sliding phase, while the average bolt preload value at the end of the test observed to be 21.5 kN which is 10% less than the initial value, significantly smaller than the loss of bolt preload observed at test 1 (33.3%). The variation of friction coefficient is depicted in Figure 3(c); it can be seen that there is very less variation of friction coefficient at the start phase of test 2 as compared to test 1. The initial friction coefficient is about 0.6 while the final is 0.57.

The results of test 2 are encouraging about the performance of thermal sprayed aluminium. Once the initial unevenness of the surface is reduced by a small number of cycles, the outermost roughness of the surface decreases and the wear rate of thermal sprayed aluminium stabilizes, which provides a stable friction coefficient. Thus, the loss of bolt load and the force-displacement variation is ultimately reduced; as a result, the load-displacement cycles are impressively stable, even for a larger number of cycles than that required by the code [25].

Test 3 was performed using the brass plates as the friction material. The brass seemed to be less rough as compared to thermal sprayed aluminium when touched. Figure 4(a) shows the force-displacement curve; there are large fluctuations in the slip force during the displacement

cycles, and the "stick and slip" phenomenon is more visible in this case. The sliding force increases with the increase of displacement and the number of cycles.
The sliding force was found to be 35kN at the start of the first five cycles of ± 7.5 mm, while it increased up to 62kN at the end of the cycle. At the end of ± 30mm, it was found near about 85kN, which is almost 141% more than the initial sliding value. Variation of bolt preload can be observed in Figure 4(b). Contrary to test 1, there is no loss of bolt preload at the initial phase of the test, and also the average bolt preload remained constant during the whole test. By contrast, in Figure 4(c), it can be seen that the friction coefficient increased as the number of cycles increased, from 0.25 at the start up to 0.42 at the end of the test.

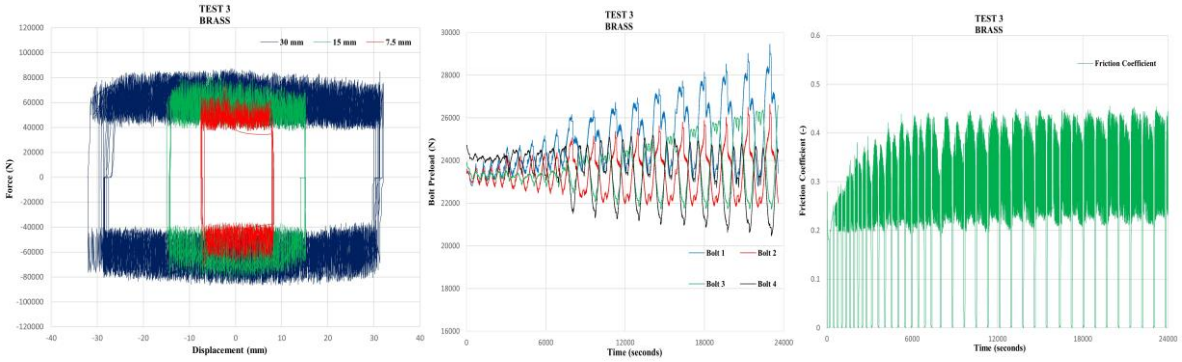


(a) (b) (c)

Figure 4: Results of test 3 for brass (a) force displacement; (b) variation of bolt preload; (c) friction coefficient during test

The increment is due to the wearing out of a brass plate surface, which increased the friction coefficient, and also influenced the force-displacement curve.
To deeply insight into the phenomenon, test 4 was performed after applying again the bolt preload of 24kN on each bolt and without changing the assembly configuration, as done in the previous test 2. Figure 5(a) reports the sliding force-displacement cycles. Unlike test 3, almost constant fluctuation of sliding force is observed for all displacement cycles, with a difference of about 8% from the initial mean to the final mean value, and a very large fluctuation of about 50% of the mean values. The trend of bolt preload as shown in Figure 5(b) demonstrates the high fluctuation during the test, but the average value of bolt preload remained constant at approximately 24kN. The friction coefficient also has large fluctuation, between 0.23 to 0.45, with an almost constant mean value (roughly 0.33) throughout the test as shown in Figure 5(c).

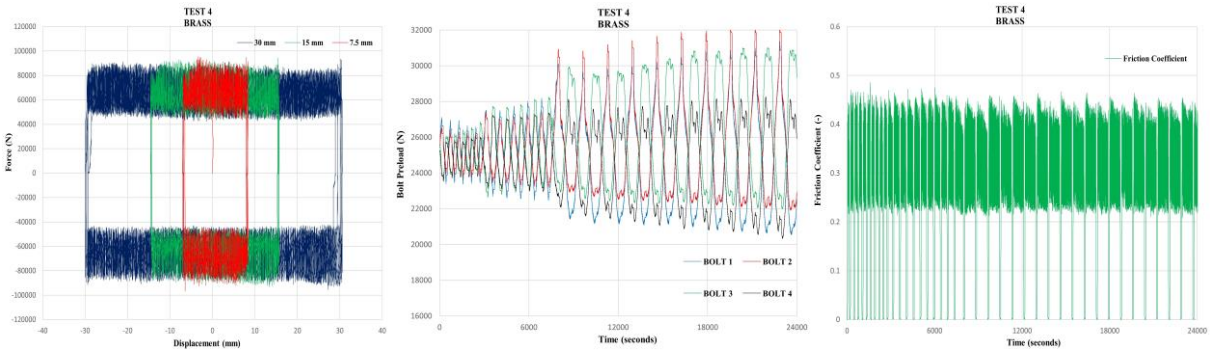


(a) (b) (c)

Figure 5: Results of test 4 for brass (a) force displacement; (b) variation of bolt preload ; (c) friction coefficient during test

By analyzing the results, it can be observed that, unlike thermal sprayed aluminium plates, for the brass plates during cyclic testing, a large fluctuation of the bolt load was obtained in the second test, and consequently a large fluctuation of the friction coefficient was found, both due to the relevant amplitude of the stick and slip phenomenon, that was not adequately compensated by the disc spring. The resulting large fluctuation of the sliding force, even characterized by a constant mean value, proves that the coupling of brass and steel is not as performing as coupling of steel and thermal sprayed aluminium for friction devices.

## 4 FINITE ELEMENT ANALYSIS OF LINEAR FRICTION DISSIPATIVE DEVICE

The Linear friction device was modelled in ABAQUS software as consistent with the experimental specimen shown in Figure 6. In the FEM analysis, to understand the effect of the thickness of friction pads and cover plates on the functioning of the friction device, three different configurations were adopted. In the first configuration, the thickness of thermal sprayed aluminium and outer cover plates were 10 mm and 5mm same as of the experimental specimen. In the second configuration friction shims and outer cove plates were taken thinner 5mm and 2.5mm while for third configuration, taken as thicker of thicknesses 20mm and 10mm respectively as shown in table 1.

| Thickness | Central Plate (mm) | Friction Plate (mm) | Outer Cover Plates (mm) |
|---|---|---|---|
| NT | 15 | 10 | 5 |
| HT | 15 | 5 | 2.5 |
| DT | 15 | 20 | 10 |

*NT=Normal Thickness, HT=Half Thickness, DT=Double Thickness

Table 1: Thickness of plates

To understand the effect of disc springs in maintaining the bolt preload and contact pressure, disc springs were also introduced in the first configuration. They were modelled by a segment of tube, with an internal radius of 13 mm, external radius of 19 mm, height of 12 mm, and elastic modulus able to reproduce the actual disc spring stiffness, that was 14300 N/mm. The bolt preload applied on each bolt was 24 kN, which is equal to 40% of the bolt preload corresponding to the code strength (60 kN), in total a preload of 96 kN was applied on four bolts. On the basis of the experimental results, in FEM modelling the friction coefficient was set equal to $\mu$=0.6. Thus, the expected sliding force is:

$$F_{s,\max} = \mu t_{s,\max} n_s n_b F_{pc} = 0.6 \times 0.4 \times 2 \times 4 \times 59.4 = 114.05 kN \quad (4)$$

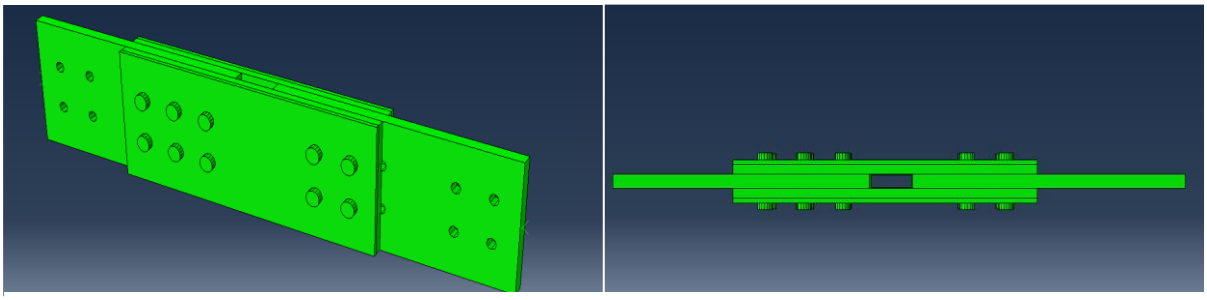

(a) (b)

Figure 6: (3D) views of FEM modelling of linear dissipative device (a) side view; (b) top View

The maximum displacement of the device was assumed as 30mm, consistent with the experimental approach and the loading protocol adopted according to the requirements of [25]. For each analysis, the device was tested by 5 cycles of ± 7.5 mm (25% of maximum displacement), 5 cycles of ± 15 mm (50% of maximum displacement) and 5 cycles of ± 30 mm (100% of maximum displacement).

In Figure 7 the contact pressure distribution of plates in tension (a), (c), (e) and in compression (b), (d), (f) are shown. Figures (a) and (b) represent the results of specimen with double thickness plates, (c) and (d) with normal thickness and (e) and (f) with half thickness.

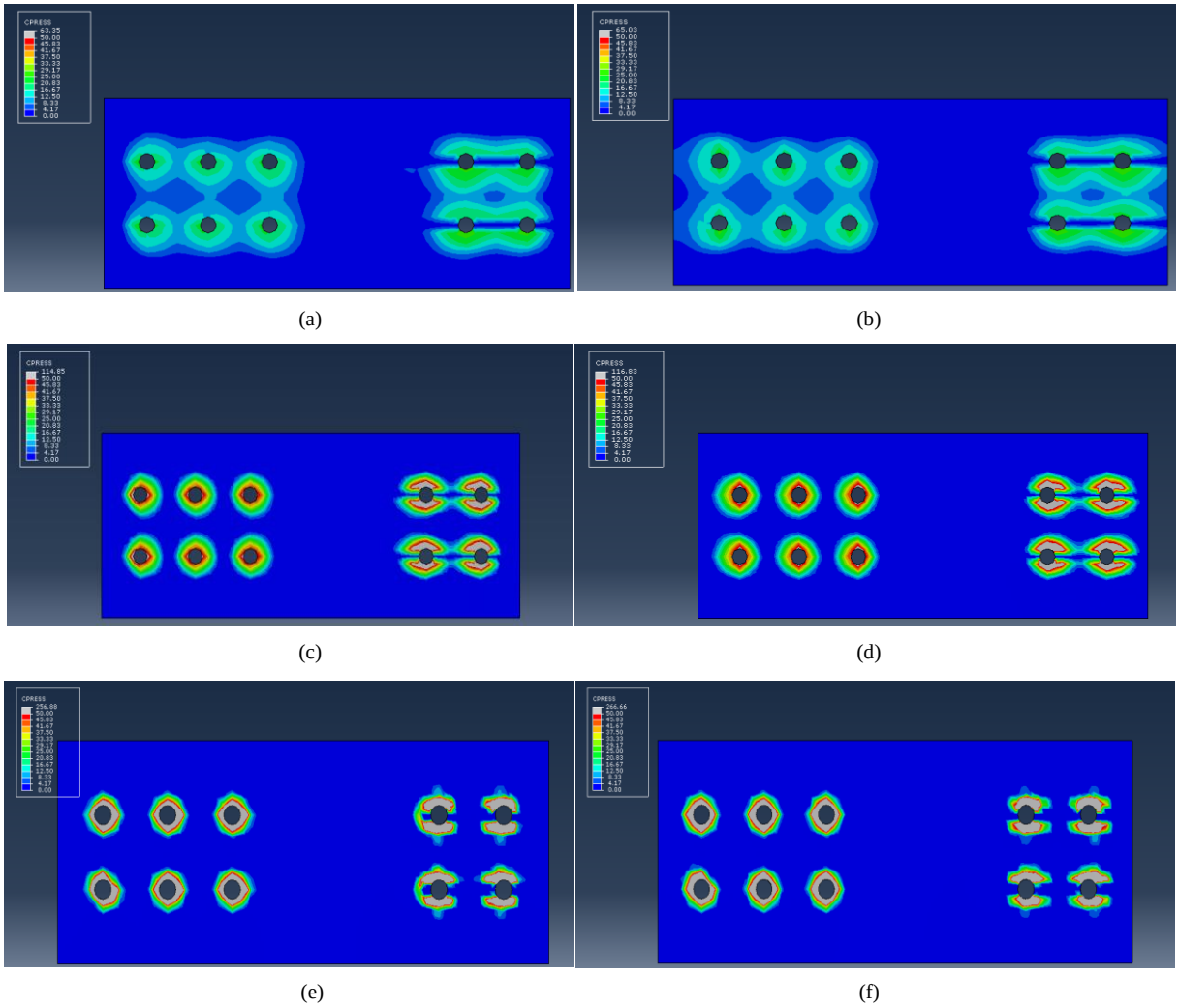

Figure 7: Contact pressure distribution of plates during sliding (a,c,e) in tension; (b,d,f) in compression; (a,b) double thickness; (c,d) normal thickness; and (e,f) half thickness

By comparing Figure 7(a) and Figure 7(b) it can be recognized that in double thick plates the contact pressure is uniformly distributed due to the small deformability of the plates, with a maximum value of 65 Mpa. By contrast, normal thick (Figure 7(c) and Figure(7d)), and half-thick (Figure 7(e) and Figure 7(f)) plates are characterized by stress concentration around the holes. Apparently, the color representation of the contact pressure is very similar, but a deeper inspection of the contact pressure scale focuses that for the latter case, the maximum contact pressure is around 260 Mpa, roughly double as compared to contact pressure for normal thickness plates (115 Mpa). The effect of the different stiffness of the plates of the three specimens on the deformed shape is stressed in Figure 8, where the displacement is magnified by 400%;

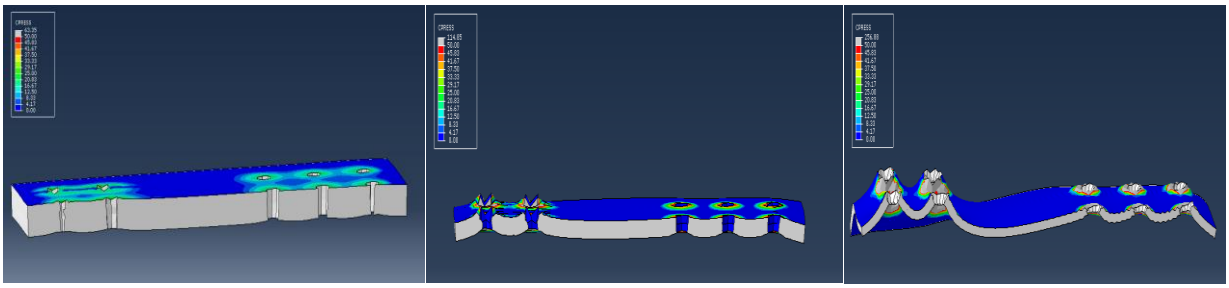

(a) (b) (c)

Figure 8: Deformed shape of plates (a) double thickness; (b) normal thickness; (c) half thickness

the ineffectiveness of the half-thick plate in avoiding transversal deformation can be easily recognized.

In Table 2 the maximum values of the resultant of contact pressure during the sliding phases in compression and tension are reported for the three specimens. A fourth couple of values, related to normal thickness specimen equipped with disc spring (NTWDS), that will be considered in the following, is also reported. The results show that, when sliding in compression is considered, an increment of the resultant of contact pressure, with respect to the initial value of 96 kN, of about 2% for all three specimens is detected; by contrast, when sliding in tension is considered, a reduction is detected, namely 1.6% for DT, 2.8% for NT and 6.45% for HT.

The variation should be attributed mainly to the variation of the plate thickness due to Poisson's effect, and to the uneven distribution of contact pressure especially for half thickness plates. However, it has to be stressed that the FEM model, as it was implemented, was not able to reproduce both the contact pressure variation due to the variation of the unevenness of the sliding surface, nor the variation of the friction coefficient that mainly affects the cycling behaviour of the device.

| Description | Compression (kN) | Tension (kN) |
|---|---|---|
| NT | 98.17 | 93.31 |
| NTWDS | 95.5 | 92.6 |
| HT | 98.22 | 89.8 |
| DT | 97.80 | 94.43 |

NT= Normal Thickness with No Disc Springs, NTWDS= Normal Thickness with Disc Springs
HT = Half Thickness with no Disc Spring, DT = Double Thickness with no Disc Spring

Table 2: Resultant of contact pressure maximum value at tension and compression. Initial value 96 kN.

The FEM model is able to capture the role of the disc spring in reducing the contact pressure variation due to the Poisson effect. To this aim, in Figure 9(a) and Figure 9(b), the distribution of the contact pressure during the sliding phase in tension and compression for the specimen with a normal thickness plate equipped with the disc spring is depicted.

Comparison with Figures 7(c) and 7(d) proves a reduction of the maximum contact pressure in tension of 15.51% and in compression of 22.72%. Regarding the resultant of contact pressure reported in Table 2, it can be recognized that disc springs are able to reduce the fluctuation of the contact pressure during the compression and tension slide phases to 3.4% of the initial value.

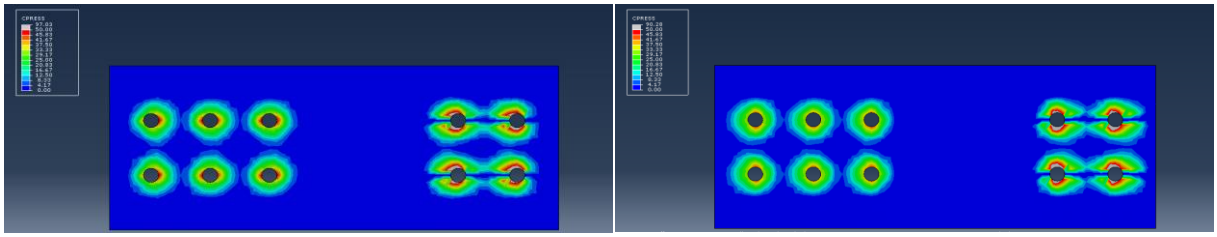

(a) (b)

Figure 9: Contact pressure distribution of plates of normal thickness with disc spring during sliding (a) in tension; (b) in compression.

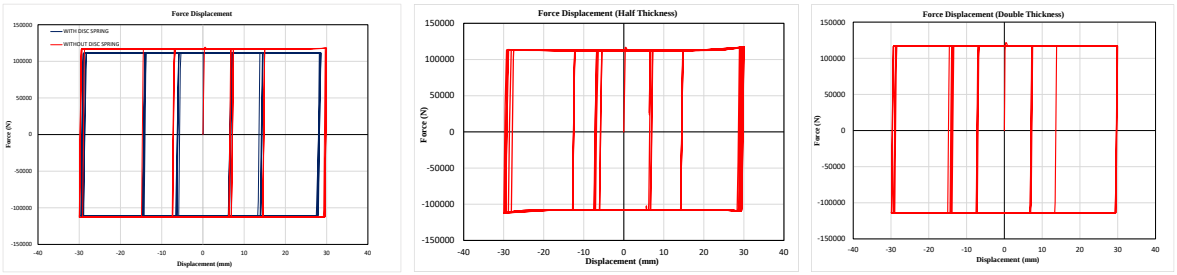


(a) (b) (c)

Figure 10: Force displacement graph for (a) plates of normal thickness with and without disc springs; (b) plates of half thickness; (c) plates of double thickness

The effect of these different configurations on the sliding force-displacement graphs obtained by FEM analysis is shown in Figure 10; the most stable force-displacement relationship behaviour can be observed in plates with normal and double thicknesses, while the force-displacement relationship of half-thickness plates (Figure 10(b)) have some discrepancy for the larger positive and negative displacement, showing that half thickness is not suitable to obtain a stable behaviour. Indeed, a small variation in the sliding force in compression can be observed for the specimen with normal thickness plates, but the presence of disc springs is able to almost eliminate this variation. Table 3 shows the maximum value of the sliding force at the end of

| Description | Compression[kN] | | Tension[kN] | |
|---|---|---|---|---|
| | -30mm | +30mm | -30mm | +30mm |
| NT | 117.13 | 117.83 | 113.13 | 112.23 |
| Difference [%] | 2.70 | 3.31 | -0.81 | -1.60 |
| NTWDS | 111.17 | 111.49 | 112.02 | 112.41 |
| Difference [%] | -2.53 | -2.24 | -1.78 | -1.44 |
| HT | 113.49 | 117.8 | 111.95 | 109.22 |
| Difference [%] | 0.49 | 3.29 | -1.84 | -4.23 |
| DT | 116.51 | 117.04 | 113.74 | 113.92 |
| Difference [%] | 2.16 | 2.62 | -0.27 | -0.11 |

*NT= Normal Thickness with No Disc Springs, NTWDS= Normal Thickness with Disc Springs, HT = Half Thickness with no Disc Spring, DT = Double Thickness with no Disc Spring

Table 3: Maximum value of force displacement graph

± 30 mm last cycle, and the value of the percentage errors with respect to the nominal sliding force (see Equation 4).The values for positive and negative displacement are different due to the different position of the bolts with respect to the slotted downward central plate.

For specimens without disc springs, the difference for positive displacement is mostly larger than the counterpart for negative displacement, and with the exception of HT, the value of the increment in compression is larger than the reduction in tension. The larger differences are found for the half-thick specimen and for positive displacement (-4.23% in tension and +3.29% in compression). The presence of disc springs produces a general reduction of the sliding force, minimizing the fluctuation to 1.09%.

## 5 CONCLUSIONS

Experimental tests on a linear friction dissipative device were performed, and the results were interpreted with the aid of a FEM modelling of the test. The results obtained with thermal sprayed aluminium-steel sliding surfaces were compared with those for brass-steel sliding surfaces. The results prove that the former is able to provide stable and predictable sliding force even for a larger number of cycles than that required by the code [25], once the initial irregularities of the aluminum surface due to manual spraying are reduced through a preventive application of a few load cycles. In this context, a paramount role is played by the role of disc springs when used in conjunction with the thermal sprayed aluminium surface. In friction shims with thermal sprayed aluminium coating, disc springs are able to control the variation of bolt preload that adjusts the sliding force. By contrast, for a brass sliding surface, the stick and slip phenomenon is more pronounced with increased amplitude in the initial cycles which rules the behaviour of the sliding force; this phenomenon is also characterized by undesired large fluctuation during all the subsequent load cycles.

The FEM analysis give more insight into the role of the thickness of the friction and cover plates, proving that the thickness chosen for the tested specimen is the smallest able to ensure a stable value of the sliding force, once is used in conjunction with the disc spring. The FEM analysis showed the disc spring's ability to minimize the variation of the contact pressure due to the Poison effect. Moreover, even if there were small variations of sliding force only, the FEM analysis was able to detect the influence of the relative position of the sliding plates of the device at the end of the cycles in determining the sliding force, and the different behaviour experienced when the sliding plates are loaded in compression and in tension.

## REFERENCES

[1] X.Y. Cao, D. Shen, D.C. Feng, C.L. Wang, Z. Qu, G. Wu, Seismic retrofitting of existing frame buildings through externally attached sub-structures: State of the art review and future perspectives, *Journal of Building Engineering*, **57**,104904, 2022.

[2] M. Ahmed, P. Colajanni, S. Pagnotta. Influence of Cross-Section Shape and FRP Reinforcement Layout on Shear Capacity of Strengthened RC Beams. *Materials*, **15**, 4545, 2022.

[3] S. Benfratello, S. Caddemi, L. Palizzolo, B. Pantò, D. Rapicavoli, S. Vazzano, Targeted steel frames by means of innovative moment resisting connections, *Journal of Constructional Steel Research*, **183**, 106695, 2021.

[4] S. Benfratello, L. Palizzolo, S. Vazzano. A New Design Problem in the Formulation of a Special Moment Resisting Connection Device for Preventing Local Buckling, *Applied Sciences*, **12**, 2022.

[5] T. S. Yang, E. P. Popov, *Experimental and analytical studies of steel connections and energy dissipators, UCB/EERC-95/13*, College of Engineering, University of California, Berkeley, USA, 1995.

[6] H. H. Khoo, G. C. Clifton, J. Butterworth, G. A. MacRae, G. Ferguson, Influence of steel shim hardness on the Sliding Hinge Joint performance, *Journal of Constructional Steel Research*, **72**, 119-29, 2012.

[7] M. Latour, V. Piluso, G. Rizzano, Free from damage beam-to-column joints testing and design of DST connections with friction pads, *Engineering Structures*, **85**, 219-233, 2015.

[8] M. Latour, V. Piluso, G. Rizzano, Experimental analysis of beam-to-column joints equipped with sprayed aluminium friction dampers, *Journal of Constructional Steel Research*, **146**, 33-48, 2018.

[9] S. Ramhormozian, G. C. Clifton, G. A. MacRae, H. H., Khoo, The sliding hinge joint: final steps towards an optimum low damage seismic-resistant steel system, *Key Engineering Materials*, **763**, 751-60, 2018.

[10] P. Colajanni, L. La Mendola, A. Monaco, S. Pagnotta, Dissipative connections of rc frames with prefabricated steel-trussed-concrete beams, *Ingegneria Sismica*, **37**, 51-63, 2020a.

[11] P. Colajanni, L. La Mendola, A. Monaco, S. Pagnotta, Design of RC joints equipped with hybrid trussed beams and friction dampers, *Engineering Structure*s, **227**, 111442, 2021a.

[12] P. Colajanni, S. Pagnotta, Friction-based beam-to-column connection for low-damage RC frames with hybrid trussed beams, *Structural Engineering and Mechanics*, **45(2)**, 231-248, 2022a.

[13] P. Colajanni, L. La Mendola, A. Monaco, S. Pagnotta, Seismic Performance of Earthquake-Resilient RC Frames Made with HSTC Beams and Friction Damper Devices, *Journal of Earthquake Engineering*, **26(15)**, 7787-7813, 2022b.

[14] Y. Cui, Z. Yan, X. Wang, T. Wang, Experimental studies on slip friction device using symmetric friction connections. *Structures*, **44**, 1886-1897, 2022.

[15] A.S. Pall, C. Marsh, Response of friction damped braced frames, *Journal of Structural division, ASCE*, **108**,1313-1322,1982.

[16] Y. Maida, H. Sakata, Finite Element Analysis of Reinforced Concrete Frames with Bracing-Friction Dampers for Seismic Resistance, *Journal of Earthquake Engineering*, 2022.

[17] M. Latour, V. Piluso, G. Rizzano, Experimental analysis on friction materials for supplemental damping devices, *Construction and Building Materials*, **65**, 159-176, 2014.

[18] G.F. Cavallaro, M. Latour, A. B. Francavilla, V. Piluso, G. Rizzano. Standardised friction damper bolt assemblies time-related relaxation and installed tension variability. *Journal of Constructional Steel Research*, **141**,145-55, 2018

[19] G.F. Cavallaro, A. Francavilla, M. Latour, V. Piluso, G. Rizzano, Experimental behaviour of innovative thermal spray coating materials for FREEDAM joints. *Composites Part B: Engineering*, **115**, 289-299, 2017

[20] J.C. Chanchi Golondrino, G.A. MacRae, J.G. Chase, G.W. Rodgers, and G.C. Clifton. Velocity effects on the behaviour of asymmetrical friction connections (AFC). *8th International conference on behavior of steel structures in seismic areas*. Shanghai, China, July 1-3, 2015.

[21] A.F. Santos, A. Santiago, M. Latour, G.Rizzano, L. Simòes da Silva. Response of friction joints under different velocity rates. *Journal of Constructional Steel Research,* **168**, 106004, 2020.

[22] S. Pagnotta, A. Monaco, P. Colajanni, L. La Mendola, Experimental characterization of friction properties of materials for innovative beam-to-column dissipative connection for low-damage RC structures. Giuseppe Ferro, Luciana Restuccia eds, *XIX ANIDIS conference, Seismic Engineering in Italy Procedia Structural Integrity,* Turin, Italy, September 11-15, 2022.

[23] G.A. MacRae, J.G. Chase, G.W. Rodgers, C.G. Clifton, Behaviour of Asymmetrical Friction Connections using different shim materials. *Proceedings of the New Zealand society for earthquake engineering conference.* New Zealand, 2012.

[24] S. Ramhormozian, G. Clifton, S. Maetzig, D. Cvitanich, G. MacRae. Influence of the Asymmetric Friction Connection (AFC) ply configuration, surface condition, and material on the AFC sliding behaviour. In *New Zealand Society for Earthquake Engineering (NZSEE) Annual Technical Conference, Reducing Risk Raising Resilience*. Christchurch, New Zealand, 2016.

[25] CEN EN 15129, anti-seismic devices. CEN, 2018.

[26] EN 1993-1-1, design of joints - Design of steel structures, 2005.

COMPDYN 2023
9th ECCOMAS Thematic Conference on
Computational Methods in Structural Dynamics and Earthquake Engineering
M. Papadrakakis, M. Fragiadakis (eds.)
Athens, Greece, 12-14 June 2023

# ROBUSTNESS OF RC FRAMES UNDER EARTHQUAKE AND BLAST CHAINED SCENARIOS

**Mattia Francioli[1], Juliano Ferreira Martins[1], Francesco Petrini[1], and Franco Bontempi[1]**

[1] Dept of Structural and Geotechnical Engineering, Sapienza University of Rome
{mattia.francioli, juliano.martins, francesco.petrini, franco.bontempi}@uniroma1.it

## Abstract

*In this paper the structural robustness assessment of concrete frame buildings under blast and under earthquake blast hazard chain scenarios is investigated. A deterministic methodology for connecting the robustness with the blast hazard intensity and for conducting the robustness analysis under earthquake-triggered blast is presented and applied to a 3D RC frame building by implementing nonlinear time history analyses considering both plastic behavior and large displacements. The robustness curves (residual structural capacity versus the level of damage occurring in the structure), evaluated both for the blast-only and for the earthquake-blast chained cases, are compared by considering different explosion locations inside the building (location of the blast-induced structural damage). Results show that neglecting the chained load scenarios would lead to the identification of an erroneous location as critical for the structural robustness performance..*

**Keywords:** Structural Robustness; Multi-Hazard; Blast; Earthquakes.

## 1 INTRODUCTION

Structural robustness is a global attribute required to structures when subjected to a local damage which, if not confined, can spreads inside the structural system until disproportionated damage or progressive collapse occur with the consequent mining of the global integrity ([1]). The structural robustness is commonly assessed by a well-established procedure called "damage-presumption approach", that is a "hazard-independent" analysis where a certain damage level is assumed for the structure (for a framed structure typically consisting in the removal of a column), and the residual capacity of the structure is then evaluated. Even if widely used in the literature, common damage-presumption approaches, indeed, do not directly and univocally link the presumed damage to a specific hazard and its intensity.

In addition, some natural disasters occurred in recent years shown that most dangerous scenarios for structural robustness performances are those called "hazard-chains" ([2]), where a certain initial hazard strikes on the structure, which can suffer a certain damage from it, and then a subsequent hazard impacts as well, affecting the structure already damaged by the previous one. The initial hazard of the chain has multiple consequences which can affect the structural robustness in the hazard-chain scenario ([3]):

- first, as already said, it can induce a damage who decreases (and in generally changes) the structural robustness of the structure to the subsequent hazard;
- second, the initial hazard can "trigger" the subsequent one. This is the case where a strong seismic shaking can damage electrical system or gas pipes inside the building, causing earthquake-induced fires or explosions.

When, in the literature, the behavior of structures in case of explosions is extensively discussed ([4]), the explosion is therefore not intended triggered by another main hazard.

In this paper, the structural robustness analysis of a RC frame building under blast and under earthquake-induced blast hazard chain scenario is conducted. All the analyses of this paper are conducted in deterministic terms, in case of hazard chains it is assumed that a high intensity earthquake striking the structure causes a subsequent explosion compromising the integrity of the structure.

Specific sensitivity analyses are carried out to highlight the issues arising when the robustness performances must be correctly linked to the considered hazards, by making specific reference to the blast-induced damage, and by introducing novel "blast scenario-dependent robustness curves". Then the design implications related to the consideration of earthquake induced explosion scenarios are highlighted by carrying out robustness analyses under hazard-chain scenarios and providing new insights regarding the multi-hazard structural design.

## 2 NUMERICAL PROCEDURE FOR STRUCTURAL ROBUSTNESS QUANTIFICATION OF RC FRAMES BY THE DAMAGE PRESUMPTION APPROACH

As already said, in the damage presumption approach ([26]), the dynamic response of the frame under the sudden removal of a number "n" of columns is evaluated by a nonlinear dynamic analysis (NDA) starting from the static equilibrium configuration reached by the non-damaged structure under vertical loads (generally due to the seismic "permanent+0.3*variable" mass combination). By the sudden column removal, the NDA can lead to ([5]): i) a new static equilibrium condition characterized by some residual plastic displacements after an initial damped transitory phase or, ii) the collapse of the structure.

The collapse can be defined to occur when: a) the time-response and/or the load-response diagrams are unconfined by certain boundary limits ([6]) (runaway behavior), or b) the vertical relative drift (DV) between the beam-column nodes located around the removed column

reaches the value of 20%, or c) the vertical displacement ratio (largest ratio of nodal vertical displacement to the story height) at the base floor, exceeds a specific threshold of 0.5 ([6]).

If the outcome of the NDA is not the collapse, an incremental static nonlinear analysis of the structure is carried out under lateral forces (pushover) in order to evaluate the residual capacity of the damaged structure. Also if common approaches use the pushdown analysis to assess the residual capacity of the structure under gravity incremental loads ([7]). For example by carrying out a pushover, the damage and the capacity under earthquakes can be coherently considered in the robustness analysis. This is particularly significant in earthquake-induced explosions, where the evaluation of the residual capacity of the blast-damaged structures under earthquake aftershocks is crucial. In this way, each damage level "DL" (i.e., number "n" of simultaneously removed columns) is associated to a residual lateral force capacity (λu) as evaluated by the pushover and expressed as percentage (λu/λ %) of the pushover capacity (λ) of the non-damaged structure.

As a result of the aforementioned numerical outcome, the deterministic robustness of the structure can be quantified and efficiently represented by the so-called "robustness curves" as introduced by Olmati et al. (2013) [8]. Robustness curves are represented on a cartesian plane in which on the x-axis there is the DL suffered by the structure ("n" in the text above), while on the y-axis the corresponding residual force capacity percentage (λu/λ % in the text above) is reported. See for example the robustness curves represented in Figure 1, where different colors and markers represent different locations along the structure for the presumed damage initiation.

The main indications about the global robustness performances which can be obtained by the robustness curves are: i) the maximum DL that the structure can suffer without collapsing, and ii) the residual capacity of the damaged structure at different DLs. Other considerations can be made by focusing on the steepness of the curve: the steepness of the robustness curve when the DL is incremented, is proportional to the decay of the residual capacity of the structure.

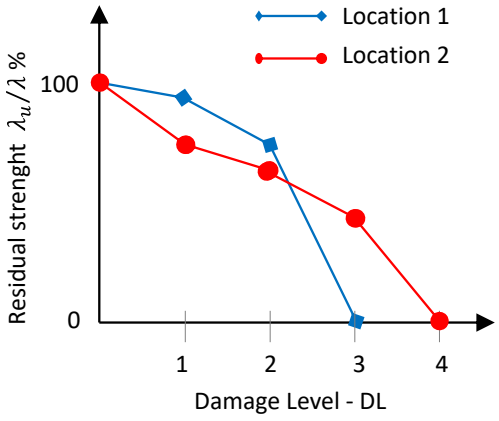


Figure 1: Example of robustness curves.

The response to the initial NDA (typically represented by the time history of the vertical displacement of the node at the top of the removed column), the successive pushover analysis and, consequently, the obtained robustness curves, are strongly influenced by several parameters regarding the nature of the damaging hazard, the analysis procedure, or the structural model. One of these parameters is the removal time interval ($\Delta t_d$) for the column: the less is the $\Delta t_d$, the more severe is the consequent structural response, and the less is the residual ca-

pacity obtained by the pushover [5]. In this view, the correct identification or setting of the $\Delta t_d$ for a certain "n" would be of value.

To understand the importance of the $\Delta t_d$ parameter related to the procedure described above, the RC 2D frame test structure shown in Figure 2a is considered. The structure is modeled using SAP2000® commercial code. The nonlinear behavior is implemented using the approximation of plastic hinges, which are obtained from the bending moment-rotation relationship (M-θ) evaluated from the equations provided by the Italian Standards NTC2018 (2018) [9] by considering the influence of the axial load. Moreover, geometric nonlinearity is considered by a large displacement analysis formulation.

The sensitivity analysis is carried out by the damage presumption approach, then it contemplates both a global NDA and the subsequent pushover analysis, the last one allowing the evaluation of the residual capacity of the structure after the considered DL (where DL=number of removed columns). The NDA is conducted by the following steps (see Fig. 3):

1. First, a static analysis under vertical loads is conducted to evaluate the reactions at the top of the columns that will be removed in the subsequent step (column-reaction forces). This will allow to develop a "surrogate" FE model of the structure in which the removed columns are substituted by the corresponding column-reaction forces, which reaches the same static equilibrium of the previous model under vertical loads.
2. In the second step of the analysis the surrogate FE model is used to conduct the NDA under sudden the columns removal. Here the two subsequent sub-steps are implemented: i) the vertical loads and the columns-reaction forces are applied by a slow ramp, and; ii) the columns-reaction forces are suddenly removed by a drop-to-zero ramp of duration Δtd (columns removal time-interval);

If the structure does not experiment the collapse at step 2 above, the pushover analysis is conducted by implementing triangular forces and by bi-linearizing the response curve as shown in Figure 4. Depending on the location of the damage (location of the first removed column), the results obtained by the lateral pushover analysis are different (Fig. 2b): since the internal columns (n°3, n°4 and n°5) are characterized by a large tributary area for vertical loads, the damage to one of them could cause a bigger reduction of the capacity with respect to the one caused to damages at external columns.

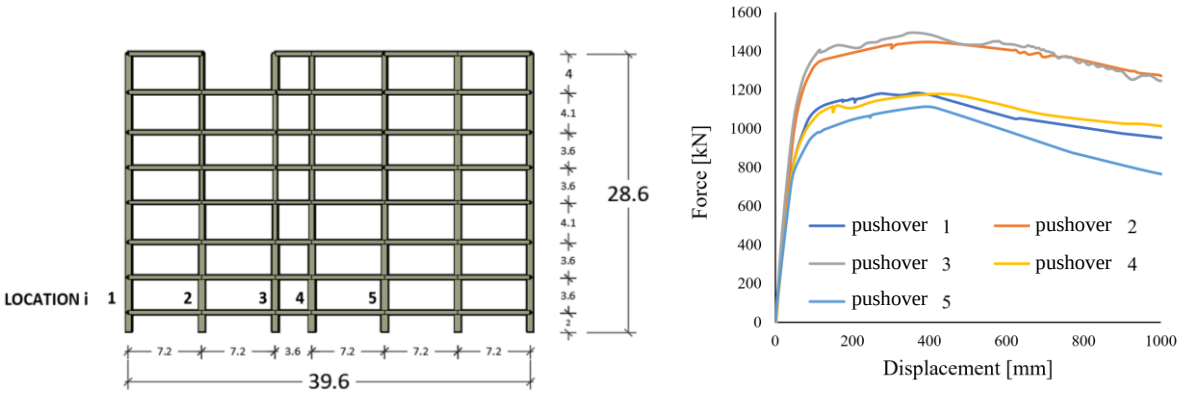


(a) (b)

Figure 2: (a) 2D RC frame structure (sizes in m) and (b) Pushover curves after different locations of damage (please note that the maximum displacements reached in pushover analyses are unrealistic and are obtained by forcing the numerical convergence).

Focusing on location 3 (see Fig. 2a), some sensitivity analyses have been carried out by varying the columns removal time interval $\Delta t_d$; the variation of this parameter influences the

behavior of the structure in terms of residual displacement after column removal as obtained by the NDA, the ultimate load and deformation as obtained by the pushover analysis, and then it changes the resulting robustness curve. Figure 4 shows the effect of the variation of $\Delta t_d$ for DL=1 at location 3.

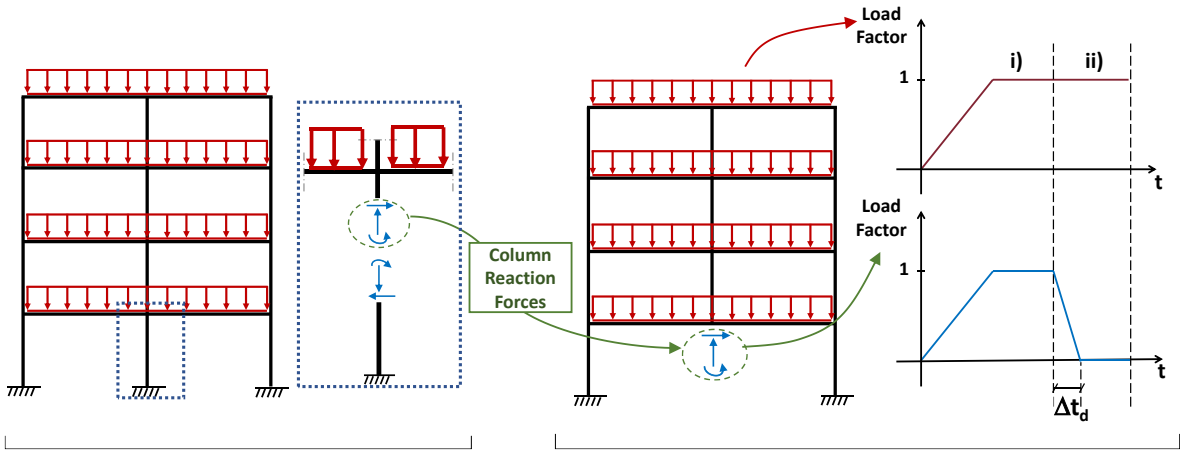


Figure 3: Two step procedure for the sudden column removal analysis: static analysis under vertical loads (a); NDA under sudden column removal with columns removal time-interval $\Delta t_d$.

The Figure 4 shows the bi-linearized results of pushover analyses for location 3 with DL= 1 and how the variation of $\Delta t_d$ affects the capacity of the damaged structure. Although there are just slight differences between the curves for the considered cases, it is shown that if the $\Delta t_d$ value decreases, the overall capacity decreases as well. It is important to understand the effect that different values of $\Delta t_d$ have in terms of decreasing the capacity of the structure because this parameter can be used to simulate the damage induced by different blast scenarios.

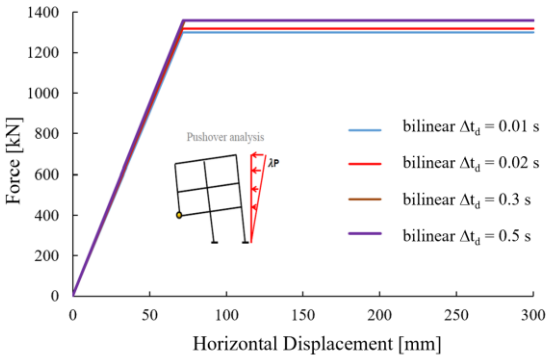


Figure 4. Bi-linearized pushover curve of 2D RC frame structure – DL=1: effect of variation of $\Delta$td (expressed in seconds).

In Figure 5, the effect of the variation of $\Delta t_d$ on the obtained robustness curves for damage at location 3 is shown: the decreasing of $\Delta t_d$ determines a decrease of the robustness. The DL= 2 (i.e., two columns simultaneously removed) always determines the progressive collapse of the structure due to the spontaneous collapse of the column adjacent to the initially removed one, while DL=1 causes a drop in initial capacity of about 20%. In the figure, DL=

0.5, corresponds to the loss of the 50% of the column cross-section; this means that the explosion results in a loss of element stiffness and capacity, but not in a collapse.

The decreasing of the pushover residual capacity at shorter $\Delta t_d$ it is due to the larger damage suffered by the elements adjacent to the removed column (e.g., beams) as a consequence of the large vertical displacement experimented by the nodes at the top of the removed columns.

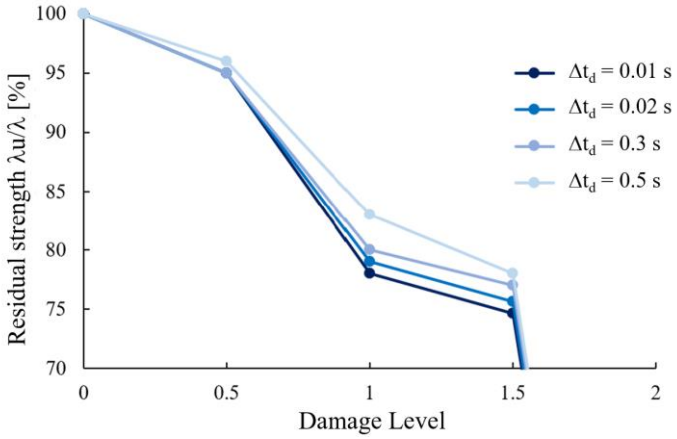


Figure 5. Robustness curves for 2D RC frame structure for location 1: effect of variation of Δtd (expressed in seconds).

In order to take into account for the above-mentioned sensitivity of the robustness to the column removal time interval ($\Delta t_d$) and to pertinently connect the robustness with the blast hazard, Francioli et al (2021) [5] proposed a procedure for determining the so-called "blast-scenario dependent robustness (BSR) curves" for RC frame structures, which take into consideration the parameters of the specific blast hazard, like the blast intensity and impulsive rate. The BSR curves are obtained by a two-stage analysis where, as a first step, the vulnerability of the frame's columns is assessed by capacity (pushover) and demand (nonlinear dynamic) analyses carried out by a "local" model (single column under lateral load). By the local NDA of the column, each damage level DL is associated to damage time interval $\Delta t_{local}$, the last one being defined by the time interval ranging from the explosion instant to the instant in which the considered damage occurs (column lateral deformation is larger than a fixed threshold value $d_U$). The damage time interval $\Delta t_{local}$ is then strictly related with the intensity parameters of the blast: for detonations, pertinent intensity parameters are the equivalent Kgs of TNT joint with the stand-off distance, while for deflagrations, peak pressures acting on the blast-invested elements should be considered as intensity parameter ([10]). In both cases, lower $\Delta t_{local}$ values can be reasonably associated with higher blast intensities. By assuming that $\Delta t_d = \Delta t_{local}$, if the previous mentioned local analysis is not carried out, the reasonable assumption where lower $\Delta t_d$ values are associated to larger DLs can be made in conducting the successive global analysis step (described below).

As a second step, the BSR curve is obtained by the damage presumption approach, where each DL is analyzed by a "global" NDA (whole building under sudden column removal) and using a removal time interval ($\Delta t_d$) for the columns, previously associated to each of the considered DL. Given a certain DL=n, the DL=n+1 is obtained by removing an additional column which is adjacent to the "n" columns removed at the previous DL. The "n" columns in a certain damage scenario are removed simultaneously by using the $\Delta t_d = \Delta t_{local}$ already associated to that DL=n at the first step. The procedure is carried out for different locations to obtain a set of BSR curves. The BSR curves, on the contrary of those obtained by the classical damage

presumption approach, are hazard-dependent, in the sense that each DL is joint to the intensity of the blast hazard, which is directly associable to (and identified by) the parameter $\Delta t_d$ (= $\Delta t_{local}$).

## 2.1 Robustness analysis hazard-chain scenarios

The scenarios when two chained hazards impact on the structure is one of the most demanding for robustness requirements. A typical chain of hazards is the one implying the sequence of earthquake as triggering action and explosion and/or fire as chained or triggered one. This is what can occur when a big earthquake strikes on the structure: it may cause structural damages and, at the same time, damages to electrical/gas pipes to generate an internal fire or explosion. It would be important to understand to what extent the blast robustness of a structure is changed from the damage suffered by an earthquake, and if the considerations of such a hazard chain scenario provides new design indications. As already said, it is not the goal of this paper to investigate probabilistic aspects of the hazard chain scenarios (e.g., probability for an earthquake to trigger an explosion), while the goal here is to investigate the structural consequences of the earthquake-induced damages on the blast structural robustness of an RC building. For this reason, the robustness analysis under hazard chain scenarios is conducted in deterministic terms. The robustness deterministic analysis under blast after earthquake is similar to the one under the blast hazard only, but it is conducted on the structure when it is already damaged by the earthquake: thus, a nonlinear time history seismic response analysis must be carried out before applying the procedure outlined in previous sections. The robustness analysis under earthquake-triggered hazards make sense only for high-intensity earthquakes, which can induce the damage in the structure before the blast occurs. A fruitful representation of the robustness under hazard chains is on the same graph of the "blast only" robustness curve of the same structure, meaning that the residual capacity percentage $\lambda u/\lambda$ % should be factorized by the residual capacity of the undamaged structure (see Fig. 6). This is something allowing the correct quantification of the robustness decrement due to the earthquake-induced damage.

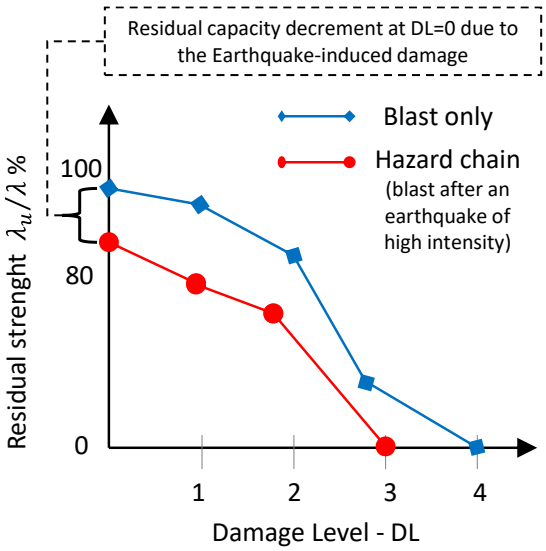


Figure 6. Robustness under hazard-chain.

## 3 CALCULATION: APPLICATION TO A 3D RC FRAME

The procedure for the BSR curves evaluation has been applied to an existing 3D RC structure serving as hospital building (Fig. 7). The building has a floor extension of about 42x35 meters and a global height of 28 meters (7 floors). It is a RC structure made of concrete C28/35 and steel B450C under the classification of Italian Standards ([9]), the increasing of the concrete elastic modulus (Ec) and of the concrete strength (fc) under impulsive load (strain rate effect) has been taken into account by assuming Ec= 42510 MPa and fc=41.73 MPa for a C28/35 concrete. The steel rebars elastic modulus Es is taken equal to 210000 MPa, while the yielding stress fy (increased under impulsive load) is 510 MPa (B450C steel grade).

The structure has been designed 40 years ago under the Italian Standards both for vertical and seismic loads. The seismicity of the site has been updated in Standards about 20 years after the construction, something that required a successive seismic vulnerability check in consideration of the increased seismic hazard.

As for the demonstrative 2D frame structure analyzed in previous sections, the finite element model has been realized by the commercial structural code SAP2000® using BEAM type element for beams and columns and the material nonlinearity has been taken into account with bending plastic hinges for beams and plastic hinges sensitive to the axial load for columns (modelled coherently with the Moment-Rotation (M-θ) bond required by Italian standards). Different removal time of the column ($\Delta t_d$) are considered, while the value of the damping ratio is fixed to 4%.

On the base of architectural drawings, two different locations (i.e., the position of the element removed at DL=1) have been considered, in correspondence to technical premises as shown in Figure 8. Key structural elements (the DL can be identified as the number of the damaged key elements) are the columns at the ground floor which, at the two selected locations have 60x60 and 65x90 (cmxcm) cross-sections.

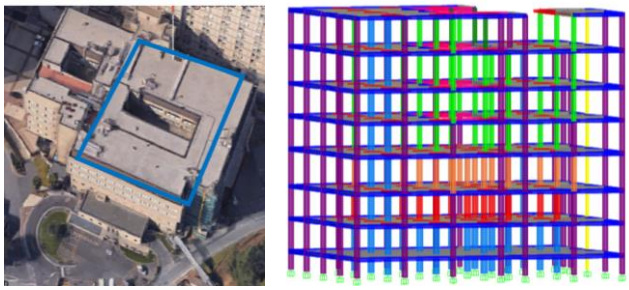

Figure 7. Case study structure: (left) Google Earth® view; (right) FE model of the structure.

The methodology used to assess the robustness performances of the structure is the one explained in Section 2: in a certain location, starting from a certain DL the structural response is evaluated by the NDA. If failure (as defined in section 2.1) doesn't occur spontaneously, first, the residual capacity of the structure is identified by a pushover analysis, then the damage level is increased (i.e., the previously removed plus an additional column are simultaneously removed) and the structural response is re-evaluated.

As already stated above, during the pushover analysis the criteria identifying the residual lateral force capacity ($\lambda u$) are: i) the occurring of the "run-away" behaviour observed in the vertical displacement time history of the nodes around the removed column; ii) the occurrence of a vertical drift ratio (DV) bigger than 20%; iii) a vertical displacement ratio bigger than 0.5.

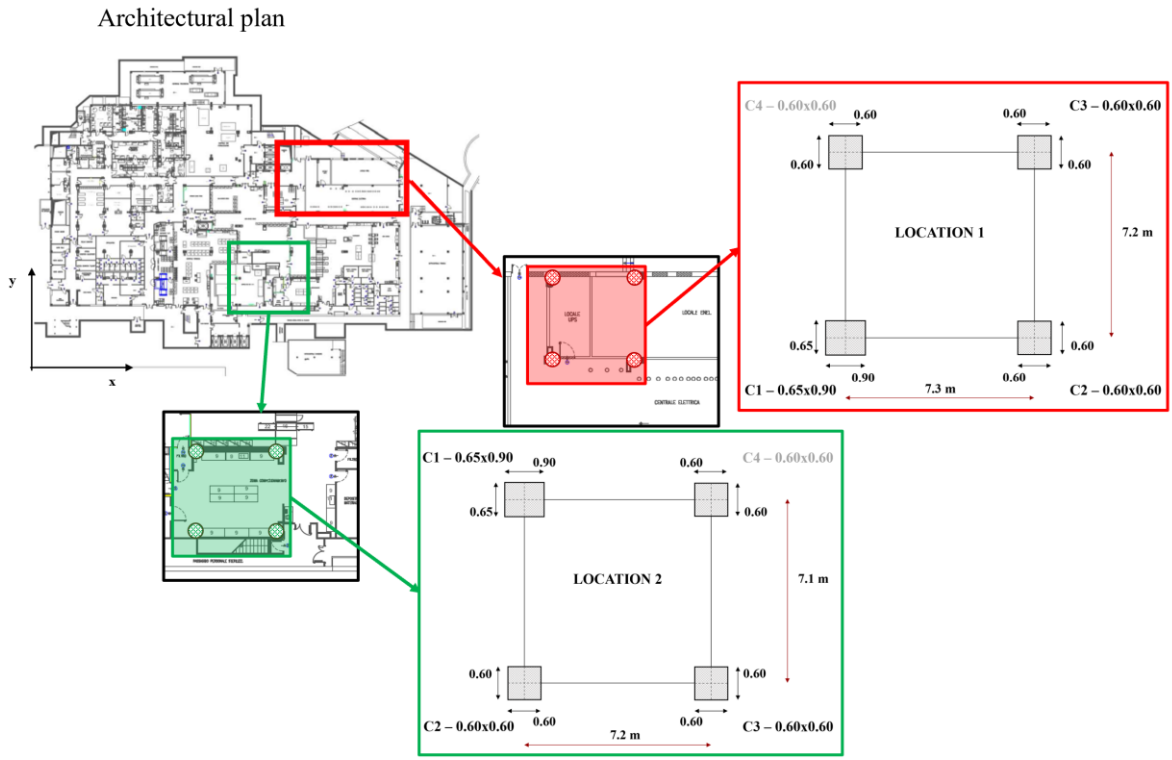


Figure 8. Architectural specifications: parts of the first floor with high concentration of components potentially subjected at risk of explosion; first (red) and second (green).

## 4 RESULTS AND DISCUSSION

### 4.1 BSR curves

As said, the explosion is assumed to occur in technical areas inside the building, then the structure is subjected to deflagrative explosions (of gaseous material). The deflagration overpressure peak $P_0$ can reach maximum values of 8 - 20 bar, while the duration of the positive pressure phase ($\Delta t_p$) may vary depending on the circumstances, with values ranging between a few milliseconds and hundreds of milliseconds ([11]). The typical pressure wave time history of deflagrative explosions it is usually obtained by ad hoc Computational Fluid Dynamic (CFD) analyses, which is not developed here, to explore the local effect (pressure time history on the columns) of the explosion.

In cases where such a local analysis is not conducted, it is a reasonable approximation to assume that larger DLs are associated to lower $\Delta t_d$ values. In other words, the lower considered $\Delta t_d$ is associated to the DL that involves the removal of the highest number of columns, while at the maximum $\Delta t_d$ is linked the one that causes the removal of the lowest number of columns. With this criterion, in order to obtain the BSR curves, pertinent points are selected from the set of damage presumption robustness curves shown above (obtained for all the considered $\Delta t_d$ and all pushing-over directions). Namely, since $\Delta t_{d_1} < \Delta t_{d_2} < \Delta t_{d_3} < \Delta t_{d_4}$, the $\Delta t_{d_1}$ is associated to DL=4, while $\Delta t_{d_2}$, $\Delta t_{d_3}$ and $\Delta t_{d_4}$ are associated to DL=3, DL=2 and DL=1 respectively.

In the present paper, a local model (single column under lateral load due to the explosion) has been developed in SAP2000® to associate different values of the $\Delta t_d$ to different blast intensities. T. In addition, since the structure is characterized by different residual capacities in both X direction ($\lambda_{u,\,X>0} \neq \lambda_{u,\,X<0}$) and Y direction ($\lambda_{u,\,Y>0} \neq \lambda_{u,\,Y<0}$), for each DL the lower capacity is chosen between the two alternative results in each direction. The resulting BSR

curves are shown in Figure 9 for the X direction (similar graphs, here neglected for sake of simplicity, are obtained for the Y direction).

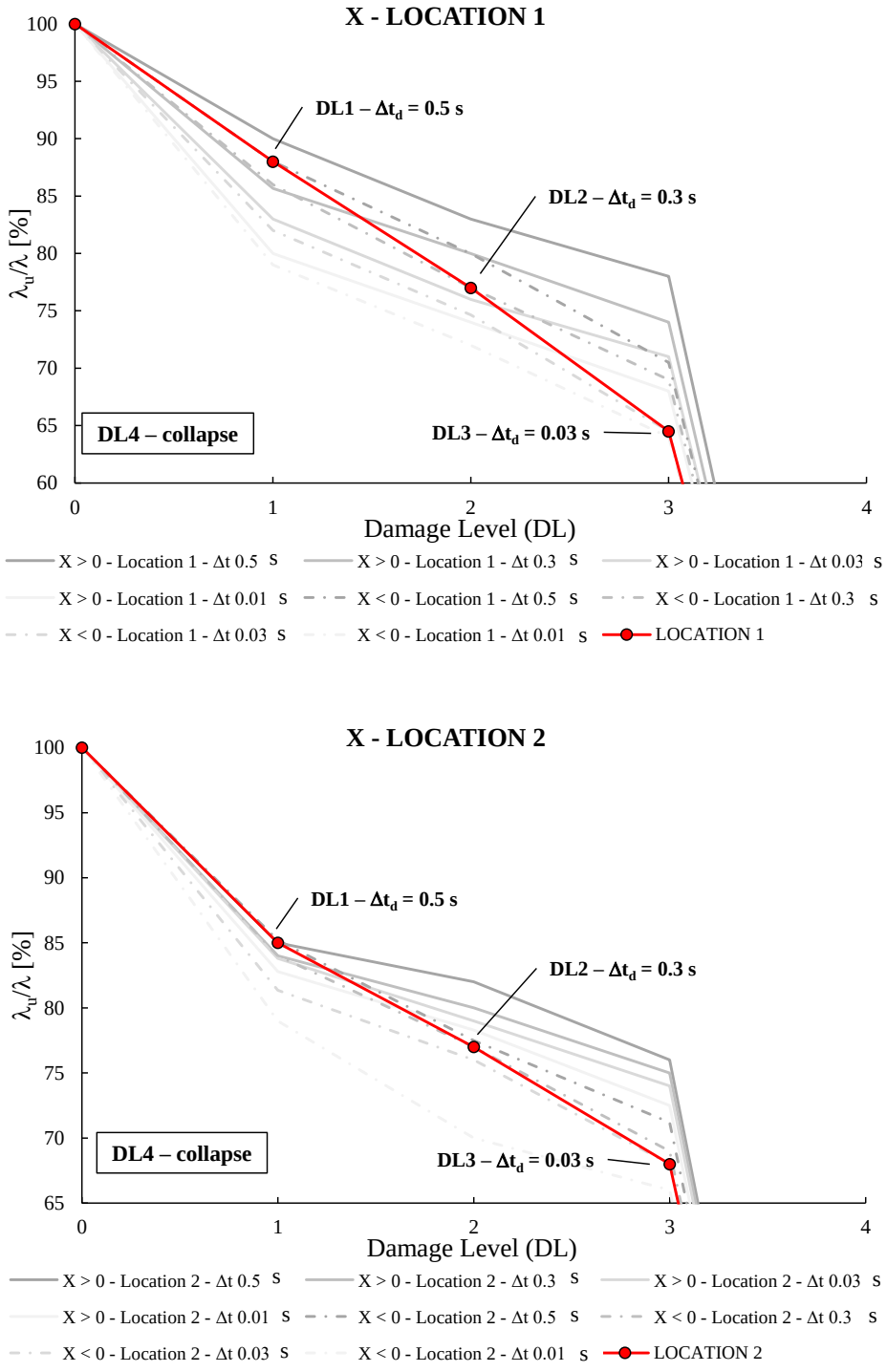


Figure 9. BSR curves associated to the X direction.

It is noted that, if four columns are simultaneously removed (DL=4), at least one of the threshold values of the adopted failure criteria are exceeded independently of the pushing direction, of the blast location, and of the value of the time interval $\Delta t_d$. The comparison of the BSR curves for the two considered locations in each direction is reported (Figure 10 (a) and

(b)). It appears a similar behaviour between the two locations, either in X or Y directions; in both cases the location 1 appears more robust than location 2 for low DLs, while for a DL equal to 3, location 1 is less performing than location 2. As said, the DL =4, here associated to the $\Delta t_d$ = 0.01 s, always determines the collapse of the structure. As general conclusion, it can be said that the critical location for the blast robustness of the considered structure is the location 1, with $\lambda_u/\lambda$ %=64% for DL=3.

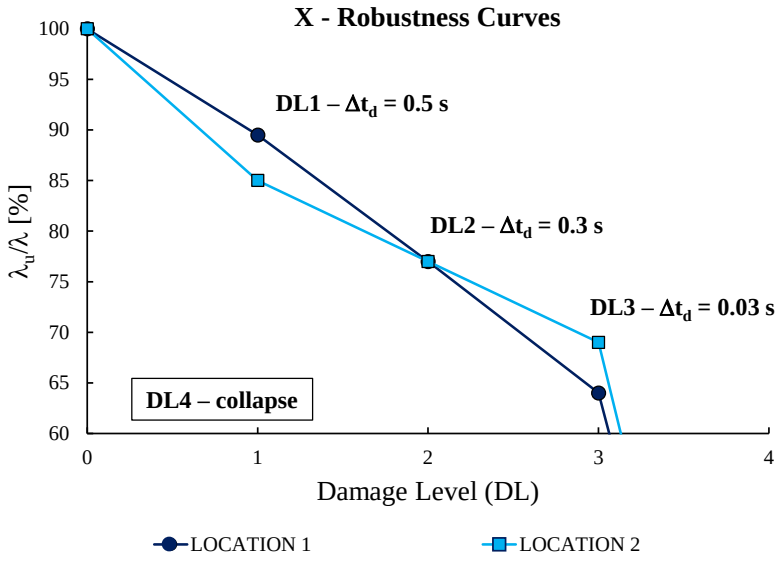


(a)

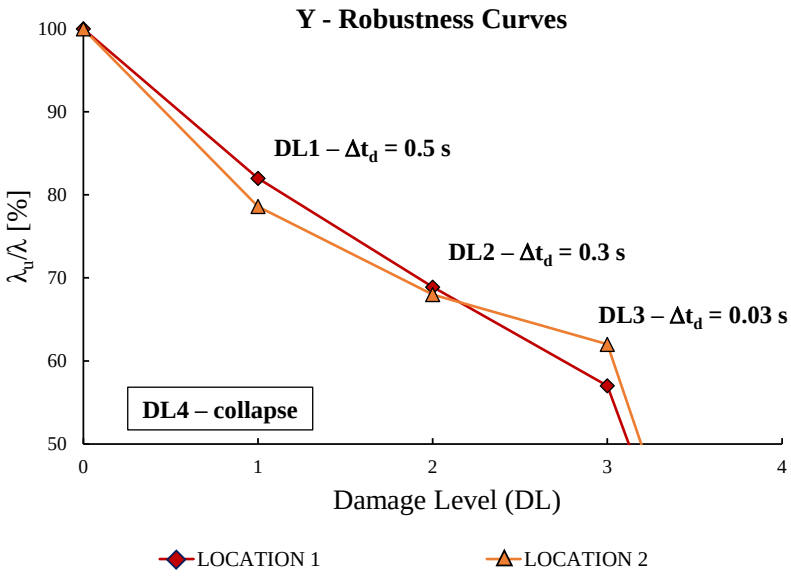


(b)

Figure 10. BSR curves associated to the X and Y directions.

### 4.2 Robustness under hazard chain scenarios

To highlights the consequences of an initial earthquake damage on the blast-robustness performances, a single earthquake is considered here, characterized in intensity for the considered structure by the spectral acceleration at the first natural period Sa($T_1$) of 0.37g, and a return period of 475 years.

The effect of the earthquake induced damage on the structural capacity is evident from the comparison of the bi-linear capacity curves obtained by the pushover analysis of the structure at different blast induced damages (DLs) obtained without considering the earthquake or after the earthquake-induced damage (Fig. 11 for the location 1). The capacity curves shown herein refer to one of the $\Delta t_d$ values considered in the analyses ($\Delta t_d$ = 0.3s).

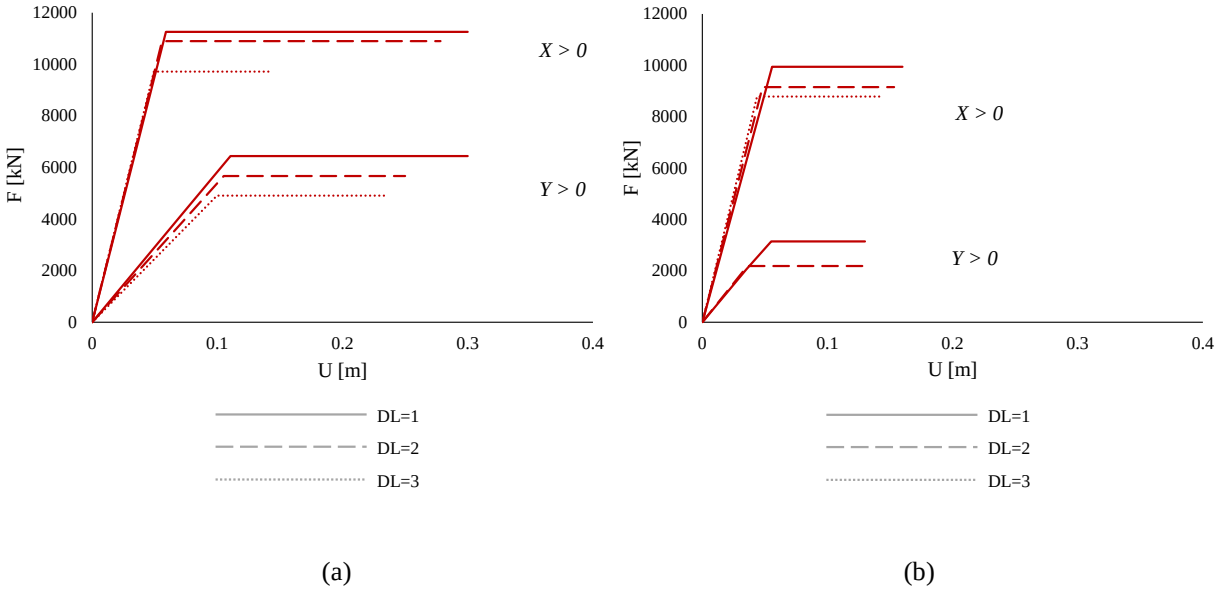


Figure 11. Pushover response curves of the 3D frame at different DLs (Dtd = 0.3 s); Location 1: (a) without considering earthquake damage, (b) with earthquake damage (DL=3 for Y>0 is null).

The effect of the earthquake induced damage on the structural robustness is also noticeable in Figure 12, where the BSR curves obtained for the directions X and Y for the structure when damaged or not by the earthquake are shown.

## 5 CONCLUSION

Looking at Figure 12, it can be highlighted that the earthquake-induced damage is quantified to be 18% and 45.5% in X direction and Y direction respectively (with residual capacities after earthquake at DL=0 being 82% and 54.5% respectively). In addition there is an important result to highlights, which can give new insights about the robustness design of RC frames against blast: when the hazard chain scenario is not considered, the critical location is the one identified as location 1, suggesting that eventual provisions for enhancing the structural robustness should focus on the blast-strength improvement at that location or, alternatively, they should focus on some management measures to decrease the blast hazard at that location, for example by keeping the technical premises away from location 1 and placing them at location 2.

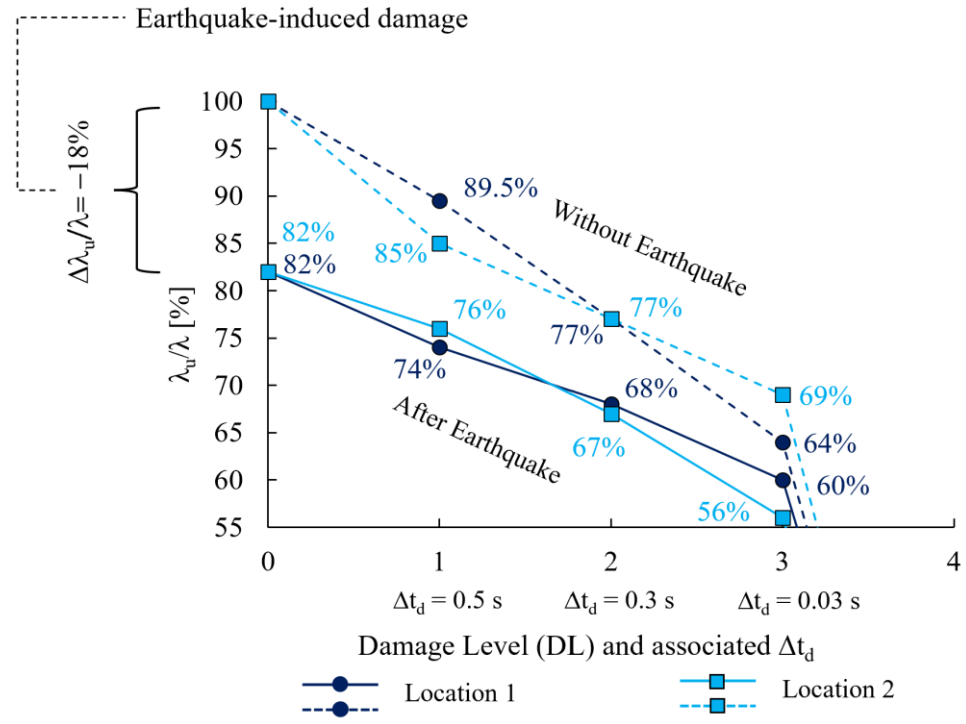


(a)

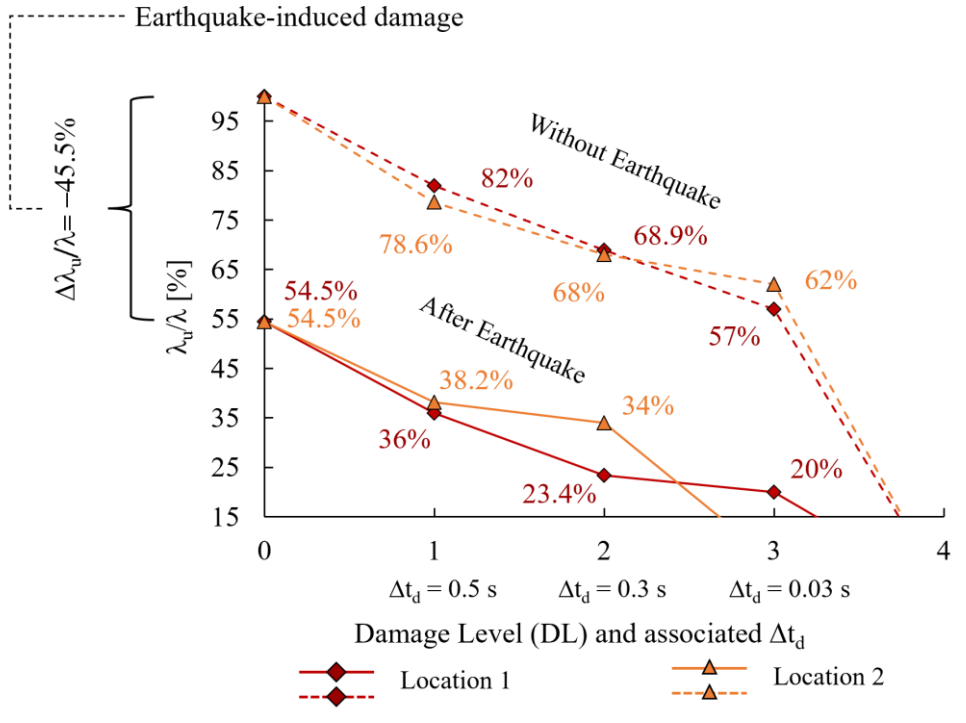


(b)

Figure 1. Effect of hazard chain on the BSR curves: (a) X direction, (b) Y direction.

On the contrary, if the hazard chain scenarios are considered in the robustness analysis, they lead to the identification of the location 2 as the critical one for robustness performances, meaning that moving technical premises at location 2 (one of the above-mentioned design

provisions) is not appropriate because this can increase the risk of progressive collapse. The change of critical location in terms of robustness when the hazard-chain scenarios are considered with respect to the blast-only scenario suggests that the effect of the initial earthquake-induced damage cannot be ignored in structural design, at least for important buildings located in seismic regions.

The result of this analysis show that the blast robustness of a previously earthquake-damaged structure dcreases as obvious, but most of that the analyses show that the critical location inside the structure for the blast-induced damage in terms of robustness performances is different if the hazard-chain scenario is taken into account or not, something indicating that, when buildings are located in seismic regions, these types of hazard chain scenarios cannot be neglected in the design of RC frames for robustness. All the analyses of the paper are deterministic. No references are made to the probabilistic occurrence of the hazard chain scenarios or to the probability for a fixed intensity of the earthquake to trigger explosions, a high intensity earthquake is rather deterministically assumed to cause an explosion.

## REFERENCES


[1] Starossek U., *Progressive Collapse of Structures*, 2nd edition. Institution of Civil Engineers (ICE) Publishing, 2018.

[2] F. Petrini, K. Gkoumas, C. Rossi, F. Bontempi, Multi-Hazard Assessment of Bridges in Case of Hazard Chain: State of Play and Application to Vehicle-Pier Collision Followed by Fire. *Frontiers in Built Environment - Bridge Engineering*, 2020.

[3] A.E. Zaghi, J.E. Padgett, M. Bruneau, M. Barbato, Y. Li, J. Mitrani-Reiser, A. McBride, Establishing Common Nomenclature, Characterizing the Problem, and Identifying Future Opportunities in Multihazard Design. *J. Struct. Eng*, **142**(12), H2516001, 2016.

[4] DoD UFC 3-340-01, *Structures to Resist the Effects of Accidental Explosions (UFC)*. Department of Defence (DoD), 2008

[5] M. Francioli, F. Petrini, P. Olmati, F. Bontempi, Robustness of reinforced concrete frames against blast induced progressive collapse. *Vibration*, **4**, 722–742, 2021.

[6] F. Parisi, M. Scalvenzi, Progressive collapse assessment of gravity-load designed European RC buildings under multi-column loss scenarios. *Eng Struct*, **209**, 110001, 2020.

[7] K. Lin, Z. Chen, Y. Li, X. Lu, Uncertainty analysis on progressive collapse of RC frame structures under dynamic column removal scenarios. *Journal of Building Engineering*, **46**, 103811, 2022.

[8] P. Olmati, F. Petrini, F. Bontempi. Numerical analyses for the assessment of structural response of buildings under explosions. *Structural Engineering and Mechanics*, **45**(6), 803-819, 2013.

[9] NTC 2018, *Italian Ministry for Transportations and Infrastructures*. Norme Tecniche per le Costruzioni (NTC2018) – Technical Standards for Structures, 2018.

[10] P. Olmati, F. Petrini, D. Vamvatsikos, C.J. Gantes, Simplified fragility-based risk analysis for impulse governed blast loading scenarios. *Eng Struct*, **117**, 457–469, 2016.

[11] F. Stochino. RC beams under blast load: Reliability and sensitivity analysis. *Engineering Failure Analysis*, **66**, 544–565, 2016.

COMPDYN 2023
9th ECCOMAS Thematic Conference on
Computational Methods in Structural Dynamics and Earthquake Engineering
M. Papadrakakis, M. Fragiadakis (eds.)
Athens, Greece, 12-14 June 2023

# EQUIVALENT DAMPING RATIO EVALUATION FOR HISTORICAL CHURCH REINFORCED BY CROSS LAM ROOF STRUCTURE FOR IMPROVING THE SEISMIC RESPONSE

**N. Longarini**[1] **, P. Crespi**[1], **M. Zucca**[2]

[1] Department of Architecture, Built Environment and Construction Engineering Politecnico di Milano
Piazza Leonardo da Vinci 32, Milano, Italy
{nicola.longarini,pietro.crespi }@polimi.it

[2]Department of Civil, Environmental Engineering and Architecture University of Cagliari, Italy
Via Marengo, 2, Cagliari, Italy
e-mail: marco.zucca2@unica.it

## Abstract

*The paper is focused on the evaluation of the Equivalent Damping Ratio (EDR) obtained by different cross lam roof structures for an historical church for improving the seismic response. The church has one nave configuration, masonry walls and original wooden roof-structures. The seismic response of this kind of construction is afflicted by the nave transversal response, therefore structural improvements inspired to the global box behavior must be pursued for avoiding the out-of-plane mechanisms of the perimetral walls. The dissipative roof-diaphragm able to contain the lateral displacements and to permit a controlled rocking is studied by choosing pithed panel cross lam timber (CLT) panels. The wooden based solutions permit to use materials compatible to the original ones as requested by Cultural Heritage Office. By this way the dissipative effect due to the CLT roof structure must be calibrated by a careful choice of the steel connections, in terms of stiffness and strength. The optimization of connections dissipative effects is here carried out by the estimation of EDR with three methods: FEMA 440, ATC-40 and time histories (TH). Each method is applied to equivalent finite elements models in which the nonlinear properties of the masonry walls and wooden roof with steel connections are considered by inelastic rotational springs (for the walls) and inelastic shear springs (for the roof). A comparison of the EDR values is shown and discussed.*

**Keywords:** Historical buildings, Cross Lam Timber Structure; Effective Equivalent Damping; Seismic Vulnerability, Nave Transversal Response

## 1 INTRODUCTION

The paper is focused on the seismic response optimization of historical one-nave configuration churches with masonry structures and wooden roof by the estimation of the Equivalent Damping Ratio (EDR) indicated by symbol $\beta_{eq}$ in FEMA 440 [1] or the definition Effective Viscous Damping and symbol $\beta_{eff}$ in ATC-40 [2].

In the post-earthquake survey, under transversal earthquake this kind of construction has shown several recurring collapse mechanisms as out-of-plane mechanisms of the perimeter walls or excessive in-plane stresses afflicting the seismic resistance elements [3],[4].

To avoid these mechanisms, a dissipative roof diaphragm represents a valid technique especially when it is not adequate to use steel chains for the poor quality of the masonry or for excessive geometrical slenderness of the perimeter walls.

The roof diaphragm can be represented by wooden elements and steel connections also considering the preservation of the original materials of the historical churches. The wooden pitched panels replacing or over-layering the original wooden planks must withstand to the in-plane shear stresses and the steel connections must be calibrated in terms of strength and stiffness to resist and to dissipate the inertia forces due to the seismic action. For these reasons Cross Lam Timber (CLT) panels can be used representing a valid precast solution with in-plane higher resistance with respect to the original wooden planks[5]. Moreover, the generic CLT panel is a smart technology thanks to its coupled hardwood layers, having 90° orientation themselves, able to reduce the resistance problems of the single planks related to the single orientation of the grains regardless of the total thickness.

With the CLT panels technology, the energy's dissipation must be occurred in the steel connections. In case nave transversal response in one nave configuration church, the panel-to-panel connections play a crucial role in the energy's dissipation either for reducing the in-plane shear actions stressing the wooden elements of the roof and for reducing the forces transmitted by the roof to the façade. The calibration of the stiffness due to the connections permits to control the lateral displacements of the church but it is mandatory to not create an over stiffness solution because the façade could be afflicted by in-plane shear stresses not compatible to the mechanical features of the masonry elements.

In the present paper the energy dissipation under transversal seismic action obtained by CLT panels with steel connections (in different geometrical configurations) is given in terms of EDR evaluated for the global construction[6], considering the contributes of the masonry walls and wooden roof diaphragm. The optimization of EDR is shown in relation to the transversal displacements obtained with different geometrical configuration of the steel connections. Therefore, a case study church is represented by equivalent finite element model (FEM) with nonlinear proprieties for the equivalent vertical elements – representing the head and perimeter walls) – and the equivalent horizontal elements – representing the wooden panels with the steel connections -. In the FEM, nonlinear properties can be introduced by inelastic hinges: (i) inelastic rotational hinges located at the base of the vertical elements represent the inelastic behavior of the masonry perimeter walls involved in the nave transversal response whereas (ii) shear inelastic hinges to attribute to the horizonal elements describe the dissipation occurring in the roof's in-plane connections[7,8]. The nonlinear behavior of the inelastic hinges represents an important issue in the performance based seismic design for several reasons. If the nonlinear behavior of the rotation hinges is evaluated by the geometrical and mechanical features of the existent masonry walls, the inelastic properties of the shear inelastic hinges of the roof can be opportunely changed to obtain the best result in terms of EDR. By adopting equivalent FEM, the EDR estimation can be performed without a strong computational effort by varying the properties of the shear inelastic hinges in relation to the geometrical features of

the CLT roof-diaphragm in terms of thickness of the panels and steel connections configuration (diameter of the connections, mutual distance and stiffness of the single connection evaluated by [9] as $K_{ser}$).

In this paper, the EDR is estimated by performing nonlinear static (pushover) and nonlinear dynamic analyses (time histories) where the inelastic features of the walls and the roof are introduced by the above-mentioned inelastic hinges, respectively by rotational springs and shear springs. When nonlinear static analyses are performed the strength capacity of the structure is detected when the elastic limit is passed, and the ultimate strength is achieved. In pushover analysis the equivalent linearization technique can be adopted for detecting the capacity curve of the structure. Finally, the EDR is estimated by adopting FEMA 440 and ATC-40 approaches when nonlinear static analyses are performed; the EDR values obtained in such analyses are compared to the one evaluated by nonlinear dynamic analyses (Time History, TH) in which the contribution of single inelastic hinge in terms of hysteretic cycle during the seismic event is considered. Moreover, the EDR values is compared to the transversal displacement optimization to find the best configuration of the roof diaphragm in terms of energy dissipation and EDR as well.

## 2 NUMERICAL APPROACH

### 2.1 Structural modelling

Nonlinear dynamic analyses are performed by equivalent finite element model in which mono-dimensional macro-elements represent the parts of the church involved in the nave transversal response [5]. In the one nave configuration church, it is possible to individuate macro-systems able to resist to the transversal earthquake. The macro-systems are the head wall, façade, coupled perimeter walls or triumphal arches (if present). Head wall and façade can be represented by a single vertical equivalent element whereas the coupled perimeter walls or the triumphal arch can be divided in sub-structures, for example in case of single perimeter walls, each sub structure is given by the part of the wall included between lateral openings or the part of wall belonged to a single abutment. The implementation of the equivalent model can be performed by observing the following three steps. In the first step, the sub structures are detected and implemented as single equivalent vertical element. Each sub-structure is divided in sections with fibers discretization; each fiber has nonlinear attributing by concrete trilinear model with zero tensile resistance [10] or the concrete damaged plasticity model ([11], [12]) in which tensile cracking and compressive crushing are the main failure modes [13]; pushover analyses performing on single sub-structure permit to obtain $(M\text{-}\chi)_I$ diagrams describing the behavior of single sub-structure. In the second step, the single sub-structures located on the left and right perimeter walls are implemented and connected themselves by a rigid link located at the top of the elements. The coupled sub-structures represent a transversal resistant system. At the base of the vertical elements, inelastic rotational hinges are located; these hinges are characterized by bi-linear behavior described by yielding and ultimate values already evaluated in $(M\text{-}\chi)_I$ . On the system characterized by the coupled sub-structures, pushover analyses are performed again detecting the shear-displacement curves of the transverse resistant system. Consequently, the $(M\text{-}\chi)_{II}$ diagrams of each system are obtained by multiplying and dividing the shear-displacements curves for the shear length (the distance between the section with zero bending moment and the section with maximum bending moment is considered as shear length). Finally, in the third step, the full construction is implemented. The head wall, the façade and the transverse resistant systems are modeled as vertical mono-dimensional equivalent elements by reproducing the in vertical mass distribution of the real elements of the church. Since the façade and the head wall have in-plane

strength and stiffness greater than the longitudinal walls, façade and head walls are fully restrained at the base [14]. At the same time, at the base of the transverse resistant systems, concentrated inelastic rotational hinges are present; these hinges are described by $(M\text{-}\chi)_{II}$ features previously obtained by the pushover analyses of second step. The roof-diaphragm is represented by horizontal mono-dimensional equivalent elements linked to the vertical ones by hinges located at the end of the vertical elements to allow the rocking's trigger and to release the bending moment transferred to the roof. The equivalent elements representing the end parts of the roof are pinned with respect to the head wall and façade. The roof's shear deformability and the nonlinear behavior of the connections are represented shear elastic-plastic hinges. The shear roof springs can be described by trilinear degrading model, Takeda Slip model opportunely modified [15] or by the Clough model in which the unloading stiffness gradually reduces when the deformation increases [16] and [17].

In the equivalent FEM, the earthquake is represented by a set of spectrums compatible accelerograms acting perpendicularly to the nave axis. Once the equivalent model is implemented and the seven-spectrum compatible accelerograms are applied it is possible to evaluate the seismic response for different configurations of the connections.

## 2.2 Nave transversal response simulation

The implementation of the finite element model described in the previous Section 2.1. permits to simulate the nave transversal response of the church in different configuration of the CLT diaphragm. In fact, CLT panels and connections represent a deformable diaphragm able to permit the rocking trigger of the perimeter walls but also able to limit the lateral displacements and the seismic loads on the rigid head walls when the stiffness of the inelastic shear hinges is opportunely calibrated, working as a roof's damper [18]. The nave transversal response of one nave historical church can be described by a flag-shaped diagram: the response of the seismic resistant elements (see Section 2.1) is represented by bi-linear free rocking curve [5,19] whereas presence of the dissipative hysteretic roof-diaphragm due to the nonlinear behavior of the connections is represented by elastic-plastic curve [20]. The bi-linear behavior of the free rocking can be described by the yielding and ultimate force (respectively $F_{frame,y}$ and $F_{frame,u}$) related to the yielding and the ultimate displacements of the generic resistant seismic frame (respectively $\delta_{frame,y}$ and $\delta_{frame,u}$). These values come out from the pushover analyses of the second step already described in Section 2.1. The stiffness of the frame $k_{frame}$ is consequently given by the ratio between $F_{frame,y}$ and $\delta_{frame,y}$.

The dissipative behavior of the roof can be described by the yielding and the ultimate force (respectively $F_{roof,y}$ and $F_{roof,u}$) related to the yielding and the ultimate displacements of the roof (respectively $\delta_{roof,y}$ and $\delta_{roof,u}$). These values can be determined from experimental tests on the connectors chosen for the connections [21]. The stiffness of the roof $k_{roof}$ is given by the ratio between $F_{roof,y}$ and $\delta_{roof,y}$.

Therefore, by varying the features of the roof diaphragm connections, the roof's stiffness changes and consequently the flag shaped diagram modifies as well. In order to describe the modification of the flag shaped diagram, the hysteretic variables β is introduced [19]; β represents an index of the energy dissipated by the roof (when β increases, the damping effect increases too), consequently it also represents the dissipative capacity of the roof with respect to the features of the masonry walls. The β optimal value could be included in the range $\beta = 0 \div 1.5$ because for higher values the self-centering rocking behavior is partially inhibited having a flag-shaped diagram with significant residual displacements; β is given by the following Equation 1:

$$\beta = 2\frac{F_{roof,y}}{F_{frame,y}} \tag{1}$$

Once β is defined, the yielding force and the stiffness of the roof can be expressed in terms of β, respectively Equation 2 and Equation 3:

$$F_{roof,y} = \frac{\left(F_{frame,y} \cdot \beta\right)}{2} \tag{2}$$

$$k_{roof,y} = k_{frame,y} \cdot \frac{\beta \cdot \delta_{frame,y}}{2 \cdot \delta_{roof,y}} \tag{3}$$

Initially the stiffness of the roof $k_{roof}$ depends on the geometrical and material properties of CLT panels with connections; it is evaluated based on preliminary seismic actions estimation as reported in [18]. The initial $k_{roof}$ is used in the dynamic nonlinear analyses but the optimum roof stiffness ($k_{roof\text{-}opt}$) is detected at the end of the analyses in in correspondence to optimal $\beta$ value ($\beta_{opt}$) able to limit the lateral displacement below the design value ($\delta_{design}$)m usually fixed as minor than 0.5% of the perimeter walls' height [18]. The $k_{roof\text{-}opt}$ value can be also expressed by Equation 4 where $\Delta$ is the ratio between the yielding displacements of the roof and the frame as it is indicated in Equation 5. It is worth nothing the preliminary approach focused on the limitation of the lateral displacement is crucial for avoiding possible out-of-plane collapse mechanisms [22], also because the stiffness of the roof-diaphragm (introduced in the model by means of the in-plane shear inelastic hinges) affects the maximum lateral displacement. The different configurations of the connections are simulated in the finite element model by varying $\beta$.

$$k_{roof-opt} = \frac{\beta_{opt} \cdot k_{frame}}{2 \cdot \Delta} \tag{4}$$

$$\Delta = \frac{\delta_{roof,y}}{\delta_{frame,y}} \tag{5}$$

## 3 EVALUATION OF THE EFFECTIVE DAMPING RATIO

### 3.1 Hysteretic models

The Effective Damping Ratio EDR is estimated by adopting FEMA 440 ([1]) and ATC-40 ([2]) approaches in case of nonlinear static analyses and by performing nonlinear dynamic analyses (Time History, TH). In FEMA 440, ATC-40 and TH approaches, the basic hysteretic models to adopt in the EDR estimation must be preliminary defined by assigning the suitable model to the inelastic hinges of the roof-diaphragm in the FEM. Generally, FEMA 440 and ATC-40 individuate four models of Figure 4: Elastic Perfectly Plastic (EPP), Stiffness Degrading (SD) corresponding to a modified Clough [16] in which the lateral stiffness decreases as the level of lateral displacements increases, Strength and Stiffness Degrading (SSD) in which the lateral strength and lateral stiffness decrease when subjected to cyclic reversals. By observing the cycles of connections in shear experimental tests (typically, nails or screws for wood) reproducing the pane-to-panel connections [6] (the more stressed ones in the nave transversal response), the cyclic behavior can be collocated in the halfway between SD and SSD.

Consequently, the inelastic shear hinges of the roof can be described by Clough for SD (characterized by stiffness degradation) and Takeda Slip[23] for SSD model (characterized by strength and stiffness degradation).

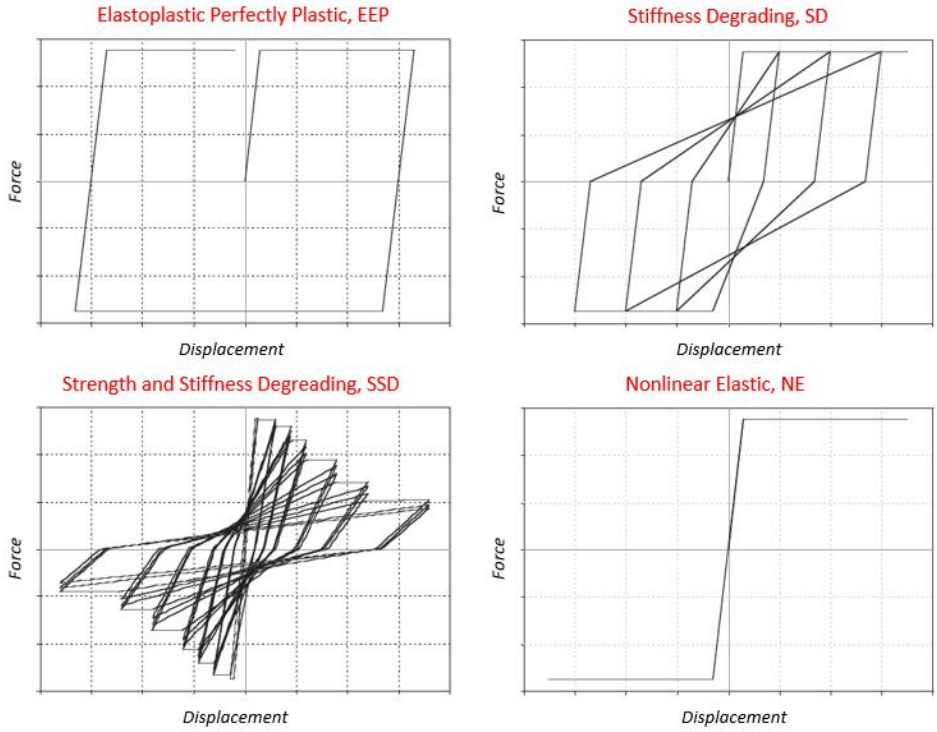


Figure 1 – Hysteretic models

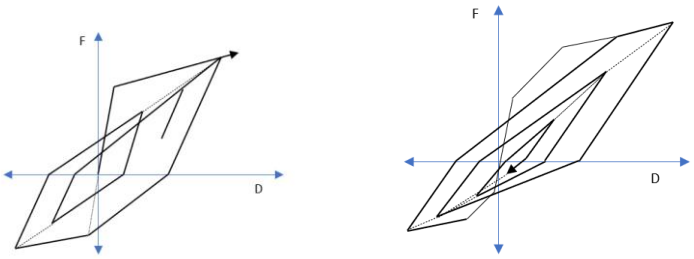


Figure 2 – Clough for SD model on the left and Takeda slip for SSD model on the right.

## 3.2 FEMA 440

In FEMA 440, EDR is estimated by equivalent linear method in which the period of the structure is evaluated from the initial vibrational period of the nonlinear system and the maximum ductility ratio μ. EDR depends on μ, the post-yield stiffness ratio α and a sort of adjustment factor k considering changes in hysteretic behavior, [1]. FEMA 440 indicates three kinds of behavior called Type A, Type B and Type C, respectively corresponding to the previous shown models EEP (without degrading), SD (stiffness degrading) and SSD (strength and stiffness degrading). In this paper, as suggested by ATC-40, the analyses consider that the initial elastic viscous damping ratio of the construction is 0.05 (5%). Consequently, EDR is estimated by Equation 6 in which the terms to the right of k are the equivalent hysteretic viscous damping for an idealized bilinear system (also called $\beta_0$ in ATC-40). When the Clough model

is adopted k = 0.67 considering the stiffness degradation, whereas Takeda slip is used k = 0.33 considering the stiffness and strength degradation. It is worth nothing that EDR corresponds to the Effective Viscous Damping called $\beta_{eq}$ in ATC-40.

$$EDR = 0.05 + k \cdot (2/\pi) \cdot \{[(\mu-1) \cdot (1-\alpha)] / [\mu \cdot (1+ \alpha \cdot \mu - \alpha)]\} \quad (6)$$

### 3.3 ATC-40

EDR estimation by ATC-40 is based on the Capacity Spectrum Method of Equivalent Linearization in which the maximum inelastic deformation of a nonlinear system is approximated from the maximum deformation of a linear elastic system having a period and damping ratio larger than the initial values of those of the nonlinear system. The Capacity Spectrum Method gives a force-deformation relationship for the structure. By the Capacity -Spectrum Method of equivalent linearization, EDR is graphically given by Figure 6 and Equation 7 in which: $E_d$ is the energy dissipated by damping (corresponding to the area enclosed by hysteresis loop), $E_{S0}$ is the maximum strain energy (graphically given by the area enclosed in the triangle defined by spectral displacement $d_{pi}$ and the spectral acceleration $a_{pi}$ of the performance point). The equivalent period, $T_{eq}$, is assumed to be the secant period at which the seismic ground motion demand, reduced for the equivalent damping, intersects the capacity curve.

$$EDR = (1/4\pi) \cdot (E_d / E_{S0}) \quad (7)$$

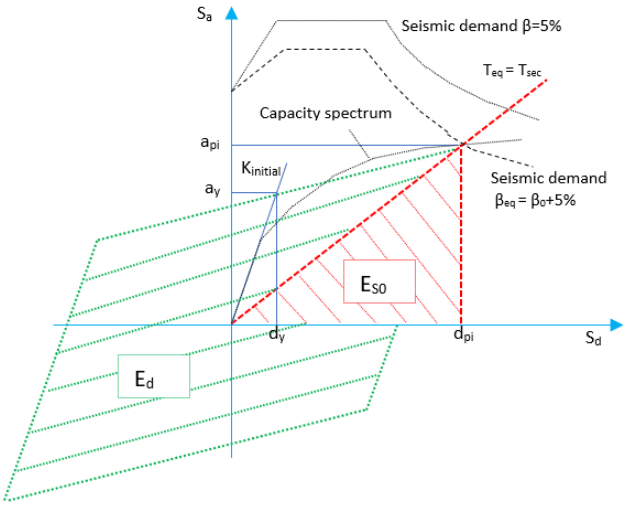


Figure 3 – EDR estimation by FEMA 440 and ATC-40

### 3.4 TH method

By TH method, EDR can be estimated by considering the cycles of the inelastic hinges of the walls and roof during the seismic events. Each inelastic hinge able to dissipate energy shows different closed cycles during the seismic event. Knowing the previous control nodes of FEMA 440 and ATC-40, when the generic control node is known, its lateral displacement's time history can be plotted, and the following instants (points 0÷4 of Figure 4) can be detected to determinate the enclosed cycle of the inelastic hinges. The first instant corresponds to the one in which the control node achieves for the first time during the seismic events the control displacement value already evaluated in FEMA or in ATC (point 1 in Fig-

ure 4). The second time instant is located before point 1 on the x-time axis; it represents the origin of the cycle, and it corresponds to the previous instant in which the displacement's time history meets the time axis (point 0 in Figure 4).

The following instants correspond to the maximum transversal displacements in both positive and opposite verse (points 2 and 3 in Figure 4). The last time instant corresponds to the end point of the cycle occurring when the displacement's time history meets again the time axis (point 4 in Figure 4). Consequently, the time instants of points 0÷4 are used to define the enclosed sub-cycle to extract from all the cycles representing the behaviors of each inelastic hinge (both for walls and roof). Each enclosed sub-cycle is included in the time instants already found in 1÷4 points (Figure 4).

For each inelastic hinge present on the roof, the inner area of the related enclosed sub-cycle represents the damping energy dissipated by the inelastic hinge ($E_D$). When the sub-cycle is drawn the maximum transversal displacements can be detected either along the seismic direction and in the opposite one. In correspondence of the maximum displacement value, the maximum strain energy ($E_{S0}$) of the enclosed sub-cycle can be calculated. The value of $E_{S0}$ is graphically calculated as the area enclosed in the triangle given by the origin point, the point corresponding to the maximum displacement and its vertical projection on the x-time axis. When the inelastic hinges do not give a contribute in terms of damping energy, enclosed sub-cycles do not exist; however, in these cases, the inelastic hinges are considered for their contribution in terms of strain energy (graphically evaluated as previously mentioned).

Therefore, by considering all the inelastic hinges of the walls and roof, the EDR of the entire structure can be estimated by Equation 6 where i represents the number of the inelastic hinges of the roof and the walls, $E_D$ and $E_{S0}$ respectively are the damping energy and the maximum strain energy of the i-th inelastic hinge evaluated in the time range extracted from the transverse displacement's time history of the control node defined by FEMA 440 or ATC-40. The graphically procedure illustrated in Figure 4 is performed for all the inelastic hinge under the seven-spectrum compatible accelerogram. The value to consider for the EDR estimation is the average one. Thus, in Equation 6 the average values of $E_D$ and $E_{S0}$ are considered.

$$\boldsymbol{EDR} = \frac{1}{4\pi}\frac{\sum_{i=1}^{n}(\boldsymbol{E_D})_i}{\sum_{i=1}^{n}(\boldsymbol{E_{S0}})_i} \tag{6}$$

The strategy here considered to evaluate the most suitable solution for the roof diaphragm by the TH approach is based on the hysteretic variable β introduced in Section 2.2. By changing β values in the range $0< \beta <1.5$ it is possible to simulate by FEM different roof diaphragm configuration to evaluate the seismic response under the seven spectrum compatible aerograms in terms of transversal displacements. By this way the optimal $\beta_{opt}$ value able to minimize the displacements without extremely increase the forces transmitted on the façade can be found. In parallel, by varying β, the response of the one nave church can be studied in terms of transversal displacement of the control node previously detected in FEMA 440 and ATC-40.

As it is above mentioned, once the transversal displacements' time histories of the control nodes are plotted for several β values, for each inelastic hinges in the FEM the cyclic behaviors are plotted as well and the sub-cycles to consider for EDR evaluation can be drawn. Finally, EDR can be analyzed in relation to the hysteretic variable β, and its trend can be compared to the one of the transversal displacements of the roof's central node (corresponding to the roof's part with the maximum deformation in the nave transversal response).

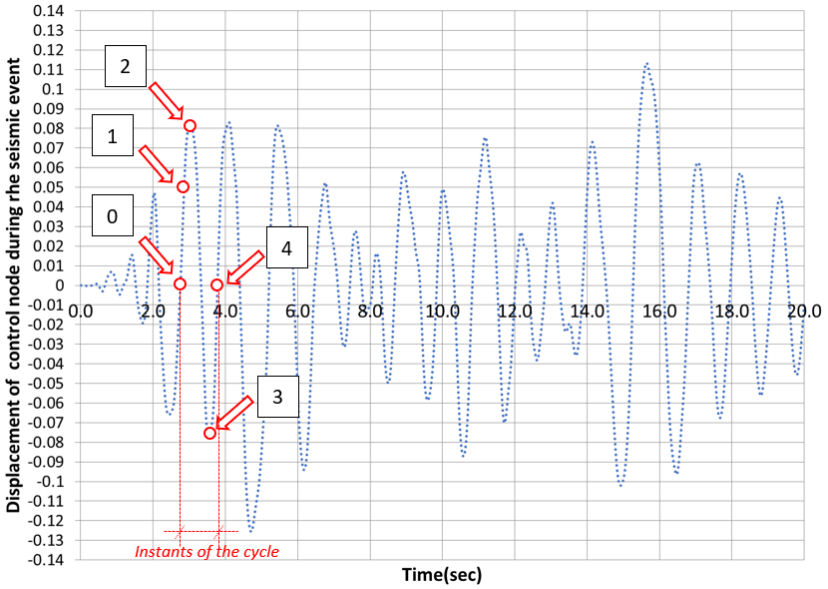


a)

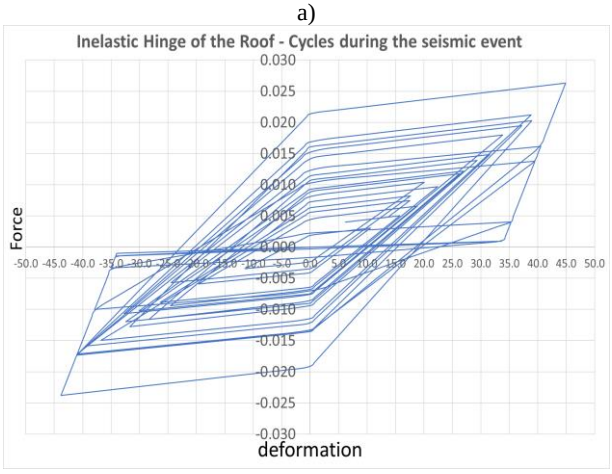


b)

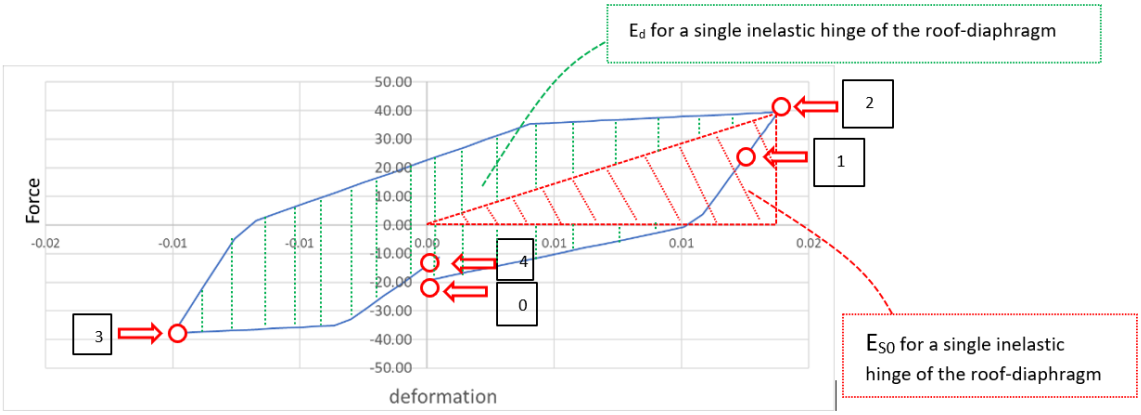


c)

Figure 4 – Definition of cycles for the inelastic hinges of the FEM: a) transversal displacement of the control node evaluated by FEMA or ATC during the seismic event – individuation of the points representing the cycle to consider; b) cycle of a generic inelastic hinge of the roof able to dissipate energy during the seismic event (in figure Clough model is adopted) – c) extrapolation of the single cycle to consider for evaluating the contribute of the roof's generic inelastic hinge in terms of energy dissipating by damping $E_d$ and maximum strain energy $E_0$.

## 4 CASE STUDY

The EDR evaluation is here performed for a single nave configuration church with masonry walls and wooden roof. The church has a 33m x 12m rectangular plan 0.90 m thickness head wall and façade, 0.60m thickness perimeter walls. The roof is characterized by hardwood trusses (a general branch is represented in Figure 8), and three openings are present in the perimeter walls (Figure 8). The masonry is characterized by Young modulus E = 1200 MPa and weight density $\rho$ = 18 kN/m$^3$. The equivalent FEM is represented by monodimensional equivalent elements representing the walls and the roof. The rotational inelastic hinges are located at the base of the vertical elements whereas the in-plane shear inelastic hinges are in the middle of the equivalent horizontal elements (Figure 8). Since the different distances among the vertical equivalent elements, there are two different values for the inelastic hinges located close the head wall and façade with respect to the others located in the central part of the roof. Starting from the design target behavior in which the energy dissipation in the steel connections of the roof occurs when the inelastic hinges of the walls achieve the yielding point, the yielding and ultimate values attributing to the inelastic hinges' properties are shown in Table 1. The properties vary by hysteretic variable $\beta$ while the properties of the inelastic hinges characterizing the masonry elements are evaluated as already described in Section 2.1. Table 1 resumes the inelastic hinges properties either for the walls (subscript frame) and the roof (symbol P1-D1 and P2-D2).

In Table 1, P1 and P2 respectively indicate the yielding and the ultimate force of the roof's inelastic hinges; D1 and D2 respectively are dimensionless values given by the ratio between the yielding or the ultimate deformations and the length of the church (symbol l in Table 1). P1-D1 and P2-D2 are used in Clough in case of SD model is adopted. When the Takeda slip is attributed to the inelastic hinges, three points P1-D1, P2-D2 and P3-D3 must be defined.

In [23], since the Takeda is normally adopted for reinforced concrete structure, it is possible to assume P2-D2 as the yielding points already found for the Clough, P3-D3 as the ultimate points already evaluated for the Clough, with P1-D1values (usually the cracking point) very close to the yielding ones. For the sake of brevity, the Takeda values are not present in Table 1.

In the case study the CLT panels have 6cm thickness with three 2 cm thickness layers. In the FEM the equivalent horizontal elements take in account the CLT panels' total thickness while the dead load due to the wooden beams is considered by the element beam loads uniformly applied. Also, the in-elevation part of the façade is applied as nodal load on the top of the equivalent vertical element representing the façade.

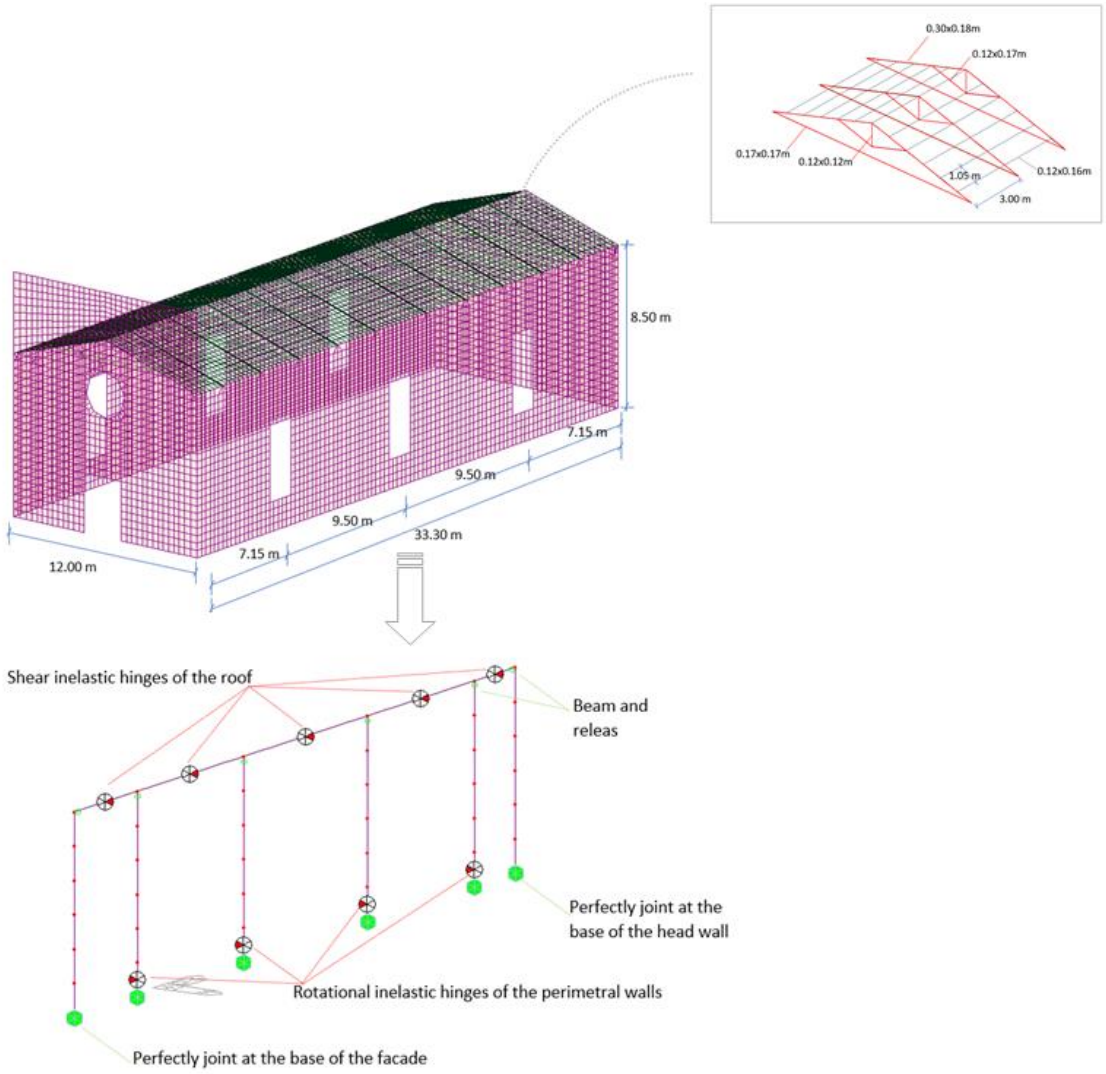


Figure 5: case study and FEM.

| Parts of the roof close to the head wall and facade | | | | | | | |
|---|---|---|---|---|---|---|---|
| β | $P_1$ [kN]=$F_{roof,y}$ | $P_2$ [kN]=$F_{roof,u}$ | $D_1=(P_1/K_{roof,y})/l$ | $D_2$ | $M_{frame,y}=M_{frame,u}$ [kNm] | $R_{frame,y}$ [rad] | $R_{frame,u}$ [rad] |
| 0.30 | 9.69 | 12.11 | 0.00062 | 0.01257 | 555.422 | 0.00086 | 0.00258 |
| 0.60 | 19.38 | 24.22 | 0.00062 | 0.01257 | 555.422 | 0.00086 | 0.00258 |
| 0.90 | 29.06 | 36.33 | 0.00062 | 0.01257 | 555.422 | 0.00086 | 0.00258 |
| 1.20 | 38.75 | 48.44 | 0.00062 | 0.01257 | 555.422 | 0.00086 | 0.00258 |
| 1.50 | 48.44 | 60.55 | 0.00062 | 0.01257 | 555.422 | 0.00086 | 0.00258 |
| 1.80 | 58.13 | 72.66 | 0.00062 | 0.01257 | 555.422 | 0.00086 | 0.00258 |
| 2.10 | 67.81 | 84.77 | 0.00062 | 0.01257 | 555.422 | 0.00086 | 0.00258 |
| Central parts of the roof | | | | | | | |
| β | $P_1$ [kN]=$F_{roof,y}$ | $P_2$ [kN]=$F_{roof,u}$ | $D_1=(P_1/K_{roof,y})/l$ | $D_2$ | $M_{frame,y}=M_{frame,u}$ [kNm] | $R_{frame,y}$ [rad] | $R_{frame,u}$ [rad] |
| 0.3 | 189.72 | 237.15 | 0.008619834 | 0.17239 | 10877.185 | 0.01182 | 0.03548 |
| 0.6 | 379.44 | 474.30 | 0.008619834 | 0.17239 | 10877.185 | 0.01182 | 0.03548 |
| 0.9 | 569.16 | 711.44 | 0.008619834 | 0.17239 | 10877.185 | 0.01182 | 0.03548 |
| 1.2 | 758.87 | 948.59 | 0.008619834 | 0.17239 | 10877.185 | 0.01182 | 0.03548 |
| 1.5 | 948.59 | 1185.74 | 0.008619834 | 0.17239 | 10877.185 | 0.01182 | 0.03548 |
| 1.8 | 1138.31 | 1422.89 | 0.008619834 | 0.17239 | 10877.185 | 0.01182 | 0.03548 |
| 2.10 | 1328.03 | 1660.04 | 0.008619834 | 0.17239 | 10877.185 | 0.01182 | 0.03548 |

Table 1: properties of the inelastic hinges

## 5 RESULTS

The transversal displacements are investigated in relation to the hysteretic variable β by fixing the target displacement referring to the 5% of the total height of the walls (in the case study the target displacement is 0.043m). It is considered β varies in the range 0÷2.1 to deep the seismic response also for values higher than the limit value 1.5 corresponding to an over-stiffness condition of the roof. Figure 6 shows the optimal value of the hysteretic variable is around $\beta_{opt}$ =1.35; beyond $\beta_{opt}$ the transversal displacement values not significantly decrease as it occurs in the previous branch of the diagram. Once the transversal displacements are investigated, FEMA 440 and ATC-40 approaches are used to evaluate EDR by pushover analyses (PO) for different β values and by considering SD and SSD models for the inelastic hinges' properties. PO analyses are performed therefore in FEMA 440 and ATC-40 the control nodes are detected and their displacements are evaluated as well (Table 2).

The node numbers indicated as 57 and 64 of Table 2 corresponds to the nodes determining the central beam element of the roof, present in the equivalent FEM, already shown in Figure 8. In the present case study, PO performed by FEMA 440 and ATC-40, EDR is estimated by adopting Procedures A. The EDR values detected by FEMA 440 and ATC-40 are plotted in Figure 7 and Figure 8 in relation to the hysteretic variable and in comparison to the values obtained by TH approach (which separately considers the control nodes and their displacements detected in FEMA440 and the ones of ATC-40).

From Figure 7 and Figure 8 the EDR evaluated by PO of FEMA 440 and ATC-40 are generally higher than the values evaluated by TH approach. The importance of the hysteretic model for the inelastic hinges of the roof are appreciable. In fact, the EDR values estimated

by SD model are higher than the ones of SSD model, as a consequence in SD model there is a higher percentage of the dissipated energy during the seismic event by the roof-diaphragm. EDR values of SD model are higher than the SSD ones. The difference between SD and SSD models is more evident for ATC-40 approach.

For all of the estimations, the range $0.3< \beta< 1.2$ shows a quasi-linear trend whereas the $1.2< \beta<1.5$ range shows a spike of EDR values. Once passed $\beta<1.5$ the energy dissipation due to the roof diaphragm is not significative, consequently the range $1.5<\beta<2.1$ is almost constant and even in ATC-40 and TH referring to ATC-40 the EDR decreases in this branch.

EDR's values evaluated by PO are overestimated especially in SD model for ATC-40.

Generally, the EDR trends detected by TH approaches (by considering either the FEMA 440 or ATC-40 control nodes) are similar to the one of the transversal displacements.

Finally, for the case study here presented, in the correspondence of the hysteretic variable's optimal value, the EDR values are shown in Table 3.

| β | Approach | Control node | Control node - displacement [m] |
|---|---|---|---|
| 0.3 | PO-FEMA / PO-ATC | 64/64 | 0.0382 / 0.0552 |
| 0.6 | PO-FEMA / PO-ATC | 64/64 | 0.0289 /0.0510 |
| 0.9 | PO-FEMA / PO-ATC | 64/64 | 0.0297 /0.0442 |
| 1.2 | PO-FEMA / PO-ATC | 64/64 | 0.0272 /0.0450 |
| 1.5 | PO-FEMA / PO-ATC | 57/57 | 0.0374 /0.0548 |
| 1.8 | PO-FEMA / PO-ATC | 57/57 | 0.0357 /0.0505 |
| 2.1 | PO-FEMA / PO-ATC | 64/64 | 0.0212 /0.039 |

Table 2: identification of the control nodes and their displacements by FEMA 440 (FEMA) and ATC-40 (ATC).

| Approach | Model | EDR [%] ($\equiv \beta_{eq}$ FEMA 440, $\beta_{eff}$ in ATC-40) |
|---|---|---|
| FEMA 440 | SD | ≃16.8 |
| ATC-40 | SD | ≃25.0 |
| TH refers to FEMA 440 | SD | ≃15.2 |
| TH refers to ATC-40 | SD | ≃14.8 |
| FEMA 440 | SSD | ≃ 16.0 |
| ATC-40 | SSD | ≃16.3 |
| TH refers to FEMA 440 | SSD | ≃12.5 |
| TH refers to ATC-40 | SSD | ≃12.1 |

Table 3: EDR' values for the case study (considering inelastic properties of the walls and roof) for the optimal value of the hysteretic variable $\beta_{opt} = 1.35$

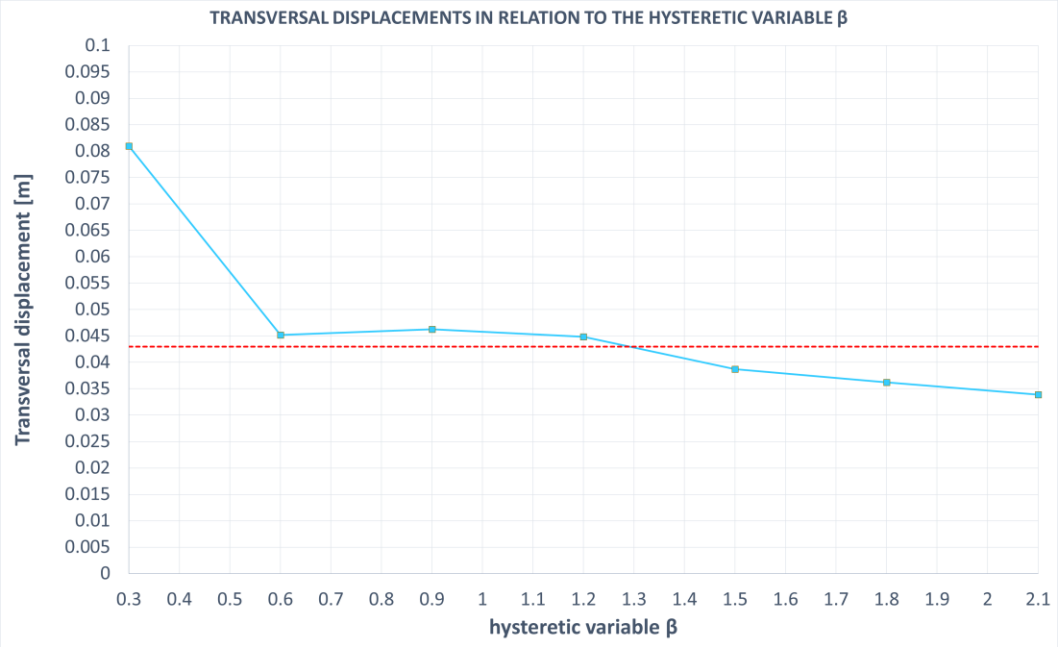


Figure 6: average values of the transversal displacements of the roof's central part under seven spectrum-compatible accelerograms.

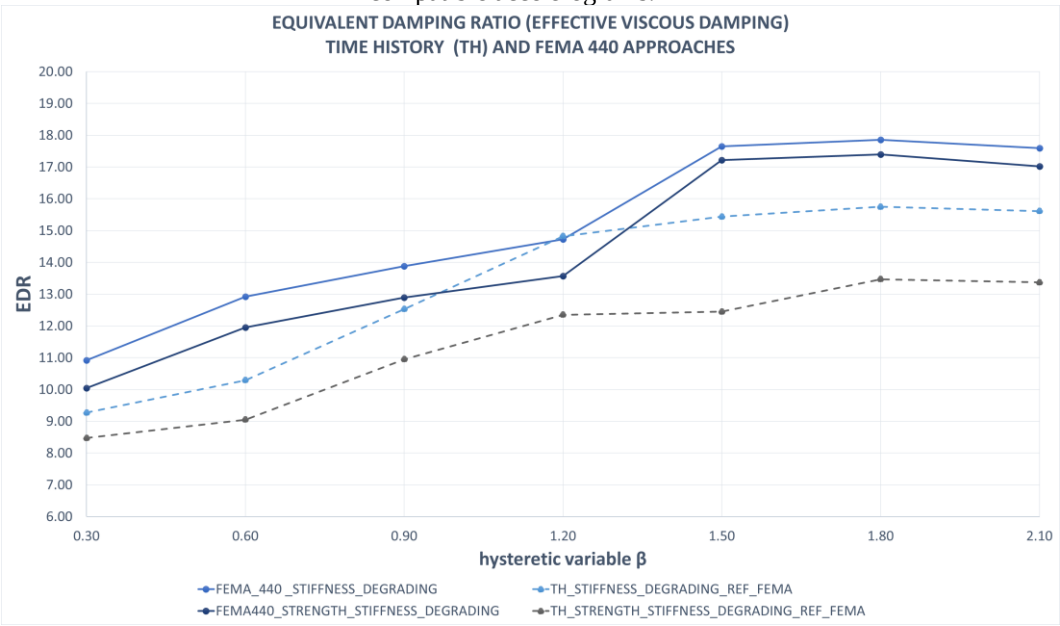


Figure 7: EDR evaluation by TH and FEMA 440 in relation to the hysteretic variable β in case of stiffness degrading SD and strength and stiffness degrading SSD hypotheses.

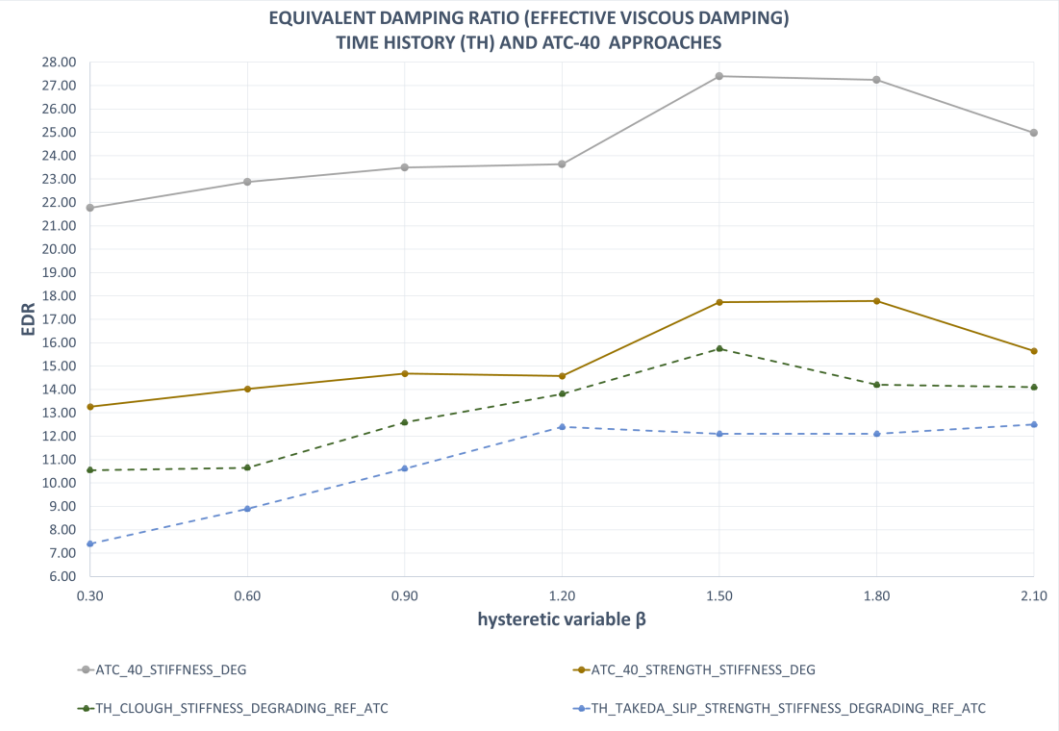


Figure 8: EDR evaluation by TH and ATC-40 in relation to the hysteretic variable β in case of stiffness degrading SD and strength and stiffness degrading SSD hypotheses.

## 6 CONCLUSIONS

In this paper the evaluation of the Equivalent Damping Ratio (EDR), also called equivalent damping in FEMA 440 or effective damping in ATC-40, is performed in the nave transversal response under a seismic event for a one nave configuration church (with masonry walls and CLT roof structure). The seismic response in studied adopting equivalent finite element model (Section 2.1) in terms of hysteretic variable β (Section 2.2) and by considering different models for the inelastic hinges of the roof (in particular Stiffness Degrading SD and Strength and Stiffness Degrading SSD, Section 3.1). EDR is evaluated by nonlinear static analyses (pushover analyses PO) by FEMA 440 and ATC-40, (Section 3.2 and Section 3.3) and nonlinear dynamic analyses by a Time Histories (TH) approach described in Section 3.4.

TH approach considers the control nodes and their displacements previously identified by FEMA 440 and ATC-40. Once the optimal values of the hysteretic variable $\beta_{opt}$ is detected, the target transversal displacement (5% of the perimeter walls' height), in correspondence of $\beta_{opt}$, the corresponding EDR is evaluated as well, by FEMA 440, ATC-40 and TH approaches. The results show:

- The EDR's variation in relation to the hysteretic variable β is very similar to the transversal displacements' one by performing nonlinear dynamic analysis.
- TH approach gives EDR values minor than the ones evaluated by FEMA 440 and ATC-40.
- The effects of SD and SSD models are significant in terms of dissipated energy during the seismic event.
- ATC-40 overestimates EDR values, especially if SD model is adopted.
- Generally, the TH approach gives EDR values minor the ones of FEMA 440 and ATC-40.
- The optimal $\beta_{opt}$ value detected in the transversal displacements diagram is also valid in the EDR estimation.

- Over $\beta = 1.5$ the dissipative effects of the roof-diaphragm decades testifying the important role of the dissipative roof-diaphragm in comparison to an over-stiffness configuration.

## REFERENCES

[1] FEMA. No Title. FEMA 440 Improv Nonlinear Static Seism Anal Proced 2005.

[2] ATC 40. SEISMIC EVALUATION AND RETROFIT OF CONCRETE BUILDINGS ATC -40. ATC 40 Rep SSC 96-01 n.d.;1.

[3] Milani G. Lesson learned after the Emilia-Romagna, Italy, 20-29 May 2012 earthquakes: A limit analysis insight on three masonry churches. Eng Fail Anal 2013. https://doi.org/10.1016/j.engfailanal.2013.01.001.

[4] Liberatore D, Doglioni C, AlShawa O, Atzori S, Sorrentino L. Effects of coseismic ground vertical motion on masonry constructions damage during the 2016 Amatrice-Norcia (Central Italy) earthquakes. Soil Dyn Earthq Eng 2019. https://doi.org/10.1016/j.soildyn.2019.02.015.

[5] Longarini, Nicola,CRESPI , PIETRO, ZUCCA M. The influence of the geometrical features on the seismic response of historical churches reinforced by different cross lam roof-solutions. Bull Earthq Eng 2022;20:6813–6852.

[6] Angelo Aloisio; Rocco Alaggio; and Massimo Fragiacomo. Equivalent Viscous Damping of Cross-Laminated Timber Structural Archetypes. J Struct Eng 2021;147(4): 04.

[7] Longarini N, Crespi P, Zucca M. Dissipative cross lam roof structure for seismic restoration of historical churches. REHABEND, 2018.

[8] Longarini N, Crespi P, Scamardo M. Numerical approaches for cross-laminated timber roof structure optimization in seismic retrofitting of a historical masonry church. Bull. Earthq. Eng., 2020. https://doi.org/10.1007/s10518-019-00661-w.

[9] EUROCODE 5 Design of timber structures UNI EN 1995-1-1. 1995.

[10] Midas. Midas GEN FX Program - General structure design system n.d.

[11] Lubliner J, Oliver J, Oller S, Oñate E. A plastic-damage model for concrete. Int J Solids Struct 1989. https://doi.org/10.1016/0020-7683(89)90050-4.

[12] Lee J, Fenves GL. Plastic-Damage Model for Cyclic Loading of Concrete Structures. J Eng Mech 2002. https://doi.org/10.1061/(asce)0733-9399(1998)124:8(892).

[13] Valente M, Milani G. Damage assessment and partial failure mechanisms activation of historical masonry churches under seismic actions: Three case studies in Mantua. Eng Fail Anal 2018. https://doi.org/10.1016/j.engfailanal.2018.06.017.

[14] Preti M, Bolis V, Marini A, Giuriani E. Example of the Benefits of a Dissipative Roof Diaphragm in the Seismic Response of Masonry. Proc 9th Int Conf Struct Anal Hist Constr 2014.

[15] Barbosa MJ, Pauwels P, Ferreira V, Mateus L. Towards increased BIM usage for

existing building interventions. Struct Surv 2016. https://doi.org/10.1108/SS-01-2015-0002.

[16] Genshu T, Yongfeng Z. Seismic force modification factors for modified-Clough hysteretic model. Eng Struct 2007;29:3053–70. https://doi.org/10.1016/j.engstruct.2006.12.007.

[17] Hossain A, Lakshman R, Tannert T. Shear Connections with Self-Tapping Screws for Cross-Laminated Timber Panels, 2015. https://doi.org/10.1061/9780784479117.195.

[18] Giuriani E, Marini A. Wooden roof box structure for the anti-seismic strengthening of historic buildings. Int J Archit Herit 2008. https://doi.org/10.1080/15583050802063733.

[19] Preti M, Loda S, Bolis V, Cominelli S, Marini A, Giuriani E. Dissipative Roof Diaphragm for the Seismic Retrofit of Listed Masonry Churches. J Earthq Eng 2017. https://doi.org/10.1080/13632469.2017.1360223.

[20] Johansen KW. Theory of Timber Connections. IABSE Int Assoc Bridg Struct Eng 1949.

[21] Sandhaas C, van de Kuilen JWG. Strength and stiffness of timber joints with very high strength steel dowels. Eng Struct 2017. https://doi.org/10.1016/j.engstruct.2016.10.046.

[22] Giuriani EP, Marini A, Preti M. Thin-folded Shell for the Renewal of Existing Wooden Roofs. Int J Archit Herit 2016. https://doi.org/10.1080/15583058.2015.1075626.

[23] Takeda T. Reinforced Concrete Response to Simulated Earthquakes 1971.

COMPDYN 2023
9th ECCOMAS Thematic Conference on
Computational Methods in Structural Dynamics and Earthquake Engineering
M. Papadrakakis, M. Fragiadakis (eds.)
Athens, Greece, 12-14 June 2023

# EVALUATION OF MAINTENANCES INTERVENTION PERIOD ON STOCK OF EXISTING RC BRIDGES SUBJECT TO DAMAGE PHENOMENA

**M. Zucca[1], P. Crespi[2], F. Stochino[1], M.L. Puppio[1], F. Mistretta[1], N. Longarini[2] and M. Sassu[1]**

[1]Department of Civil, Environmental Engineering and Architecture University of Cagliari, Italy
Via Marengo, 2, Cagliari, Italy
e-mail: {marco.zucca2,flavio.stochino,mariol.puppio,fausto.mistretta, msassu}@unica.it

[2] Department of Architecture, Built Environment and Construction Engineering Politecnico di Milano
Piazza Leonardo da Vinci 32, Milano, Italy
{pietro.crespi,nicola.longarini}@polimi.it

## Abstract

*During last decades, the attention of the scientific community on the evaluation of the load-bearing capacity of existing reinforce concrete (RC) bridges has significantly increased even as a result of the recent collapses which have occurred. Particular attention is focused on the seismic performance of the existing RC bridges especially if located in areas characterized by high seismicity level such as Italy. One of the most important problems that affects the seismic performance of this structures is the presence of corrosion effects due to carbonation phenomenon which may involve the steel reinforcements of the piers.*
*In this paper the evaluation of the seismic vulnerability of an existing RC bridge located in Italy and built around the 1960's is presented, considering three different corrosion scenarios (slightly, moderate, and high). Non-linear time history analysis has been performed considering a simplified Finite Element Model (FEM) where the structural elements have been implemented with beam elements and the non-linear behavior of the piers has been introduced using appropriate concentrated plastic hinges. The carbonation effects have been modelled considering the piers steel reinforcement area reduction as a function of the age of the bridge. Risk indices evaluated as the ratio of the peak ground acceleration leading to collapse of the first structural element and the design peak ground acceleration, are calculated to define the seismic vulnerability of the analyzed structure.*

**Keywords:** Existing RC Bridges, Seismic Vulnerability, Time-History Analysis, Corrosion Effects.

## 1 INTRODUCTION

Correct scheduling of maintenance interventions of existing reinforced concrete (RC) bridges represents one of the most important aspects useful to guarantee an adequate safety level of these strategic infrastructures. Focusing attention on seismic performance of existing RC bridges, corrosion effects due to carbonation acting on the RC piers can lead to a significant reduction of their load-bearing capacity when subjected to horizontal loads [1-4].

Several Italian RC motorway bridges were built between 1960's and 1970's and, consequently require a series of maintenance interventions in order to maintain an adequate safety level [5]. Furthermore, these structures have been realized without considering the presence of the seismic action, according to the design codes of the time.

To evaluate the seismic behavior of existing RC bridges, several approaches based on non-linear analysis method have been proposed during last decades. One of the most used methods is the pushover analysis but it is applicable only in presence of structures characterized by a dynamic behavior with a predominant translational vibration mode [6]. For this reason, the use of multi-modal pushover approach has been extended by [7,8] to the evaluation of the seismic vulnerability of existing RC bridges. Different probabilistic approaches, based on the use of fragility curves which define the seismic response of these structures have been proposed in literature [9-11].

Another approach developed in recent years and used for the evaluation of the seismic performance of existing RC bridges is the Incremental Dynamic Analysis (IDA) [12,13]. A simple alternative of the IDA method is represented by IMPAB approach proposed by [14] based on the use of Incremental Modal Pushover Analysis which allows a better representation of seismic input with respect to the standard selection of accelerograms to be scaled at different intensities, usually adopted in IDA. A good compromise between computational effort and accuracy of the results is represented by the Non-Linear Time-History Analysis (NTHA). In this case the correct choice of the seismic signals, the modelling of strength/stiffness degradation and the evaluation of the evolution of the damping play a role of primary importance. NTHA is one of the most used analysis methods thanks also to the technological evolution of computers and the software for numerical analyses.

Different approaches have been developed to consider the corrosion effects due to carbonation phenomena on the seismic performance of existing RC bridges. In this paper, a simplified analytical method which considers the corrosion effects only in terms of steel reinforcements area reduction has been taken into account. The approach has been applied to an RC existing motorway bridge located in Northern Italy, considering three different corrosion scenarios (slight, moderate and high) and evaluating the evolution of the seismic performance of the bridge until 75 years from the construction time, through the execution of a series of NTHA analyses. The seismic vulnerability of the bridge has been expressed in terms of appropriate risk indices based on the ratio between the peak ground acceleration which leads to the collapse of the first monitored structural element and the design peak ground acceleration obtained from the Italian Design Code [15] and the ratio of the related return periods. These indices have been useful to calculate the minimum time intervention period through the application of a simplified relation suggested by [16].

## 2 STRUCTURAL MODELLING

To evaluate the seismic behavior of existing RC bridges, the simplified procedure described in [17] have been used. The approach is based on the implementation of simplified 3D Finite Element models (FEM) where the main structural elements which characterize the

bridge as the piers, the pier caps and the deck have been modelled with beam elements while the elastomeric bearings have been introduced in the FEM using elastic links with translational and rotational stiffnesses have been calculated according to [18]. The connection between the elastomeric bearings and the other structural elements is realized through a series of rigid links as shown in Figure 1.

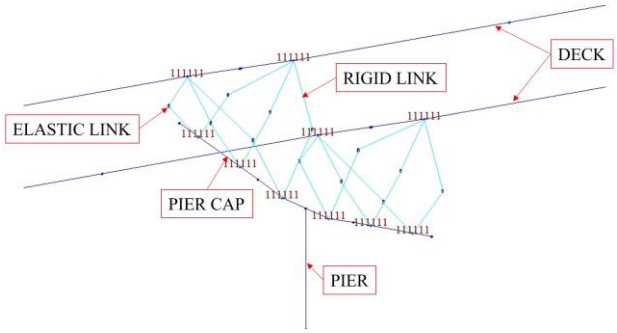


Figure 1: Elastomeric bearings connection.

The pier foundations have been considered as perfect constrain applied to the node at the base of each pier while the presence of the abutments have been represented by perfect constrains applied to the node located at the base of each elastic links representing the elastomeric bearings located at the abutment-deck interface. In order to reproduce the correct dynamic behavior of the bridge, the reduction of the bending stiffness of the gross-section of each pier due to the concrete cracking has been considered through the application of appropriate scale factors calculated starting from the moment-curvature diagram (M-χ) which characterize the gross-section of each pier, according to as reported in [19]. On the contrary, the deck stiffness is not reduced despite the formation of bridge decks cracks it is still in the elastic phase during seismic events [20]. In the FEM, the contribution of structural and non-structural masses is considered while the presence of traffic load is according to [15].

Two failure mechanisms of the piers have been monitored: (i) the ductile collapse mechanism related to the moment-curvature diagram of the gross-section and which is characterize by a linear elastic portion followed by a hardening branch and (ii) the brittle collapse mechanism regulated by the shear resistance of the pier. The ductile collapse mechanism is based on the plastic hinge rotational capacity while the fragile collapse mechanism is ruled by the ultimate shear strength of the considered pier.

To take into account the non-linear behavior of the materials, Kent and Park model [21] (Figure 2a) and Park Strain Hardening [22] (Figure 2b) constitutive law have been adopted respectively for the concrete and for the steel reinforcement.

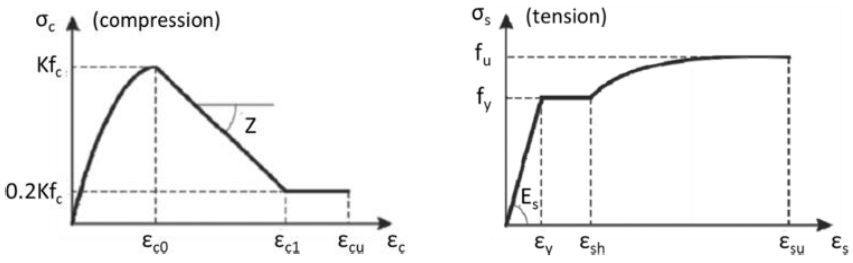


Figure 2: (a) Kent and Park and (b) Park Strain Hardening model.

Appropriate plastic hinges, calculated according to [23,24] have been applied to the base of each pier where the formation of the ductile mechanism is expected. The considered ultimate limit states are the following: (i) for the ductile failure mechanism, the achievement of ¾ of the ultimate rotation $\vartheta_u$ (Figure 3a) while (ii) for the brittle failure mechanism the overcome of the shear resistance $V_R$ of the considered structural element (Figure 3b) calculated considering the formulation proposed in [25] for the cyclic shear resistance based on the sum of three different terms depending on the axial load, the concrete strength, and the stirrups.

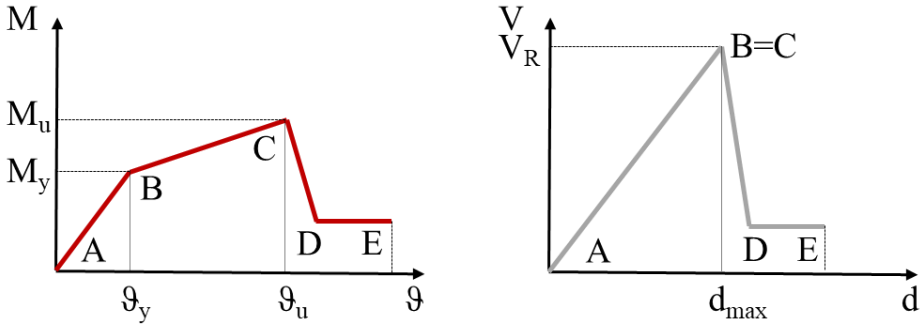


(a) (b)

Figure 3: (a) Ductile and (b) Brittle collapse mechanism.

The corrosion effects have been introduced in the FEM considering a simplified analytical approach based on the progressive reduction of steel reinforcement diameter [26] and where the penetration law in a generic concrete volume is characterized by a parabolic behavior (Equation 1):

$$s = k \cdot t^{1/n} \tag{1}$$

where $s$ is the thickness of the carbonated layer, $t$ the time and $k$ the penetration rate coefficient. The parameter $n$, which depends on the concrete characteristics, can be taken equal to 2 considering that the existing RC bridge analyze was built between the 1960's and 1970's with normal compacted concrete [27]. It possible to calculate the residual service life ($t_{res}$) of the bridge starting from the initiation time ($t_i$), the propagation time ($t_p$) and the maximum expected rebar radius reduction ($P_{lim}$) following the Equation 2 reported in [28]:

$$t_{res} = t_i + t_p - t = \left(\frac{c}{k}\right)^2 + \frac{P_{lim}}{i_{corr}} - t \tag{2}$$

where $t$ is the bridge age, $k$ the penetration rate coefficient (in mm/years$^{0.5}$), $i_{corr}$ is the mean corrosion current density (in μA/mm$^2$) and $c$ is the concrete cover thickness. The existing RC bridges considered in this work were designed without considering the presence of the seismic action and for this reason the evaluation of the residual service life ($t_{res}$) as proposed in Equation 2 is not useful. In this work the estimation of the correlation between the reduction of the steel reinforcement diameter and the seismic performance of the bridges has been considered, through the following Equations 3 and 4:

$$d(t) = d_0 - 2P(t) = d_0 - 2i_{corr}k(t - t_i) \tag{3}$$

$$A_s(t) = \pi[d_0 - 2i_{corr}k(t - t_i)]^2/4 \tag{4}$$

where $d$ is the reduction of the steel reinforcement diameter, $d_0$ is the initial steel reinforcement diameter and $P(t)$ is the corroded thickness.

Three different corrosion scenarios have been analysed: slight, moderate and high corrosion level characterized by a value of $i_{corr}$, respectively, equal to 0.1 μA/cm$^2$, 1 μA/cm$^2$ and 5 μA/cm$^2$. The reduction of steel reinforcement diameter is obtained ad the difference between the initial diameter ($d_0$) and the diameter referred to the time of interest ($d(t)$). It is possible to notice that the reduction of the steel reinforcement diameter strictly depends on the initiation time ($t_i$) considered as statistical variable and the corrosion current density ($i_{corr}$) calculated considering as reported in the design codes or obtained from experimental results. Considering an initial value of cover thickness equal to 25 mm, the iterative process has been developed for different concrete type. The following values of other parameters has been considering in this work: w/c = 0.6, $t_i$ = 13.5 years [28] while concrete compressive strength $f_{ck}$ = 28 MPa, penetration rate coefficient k = 0.0116 and steel rebar ultimate deformation $\varepsilon_{u,0}$ = 9 % have been considered as constants for each analyzed corrosion scenario.

To evaluate the seismic performance of the existing RC bridges subjected to corrosion phenomena due to carbonation, a series of non-linear time history analyses (NTHA) have been performed considering both ductile and brittle collapse mechanism in the same FEM in order to take into account the interaction between the two failure mechanisms.

## 3 CASE STUDY

The approach described in the previous Section has been applied to an existing RC bridge located in Northern Italy. Figure 4 shows the FE model of the considered bridge. The main seismic characteristics of the site where the bridge was built are the following: Soil type = C (evaluated according to Eurocode 8) and PGA = 0.156 g.

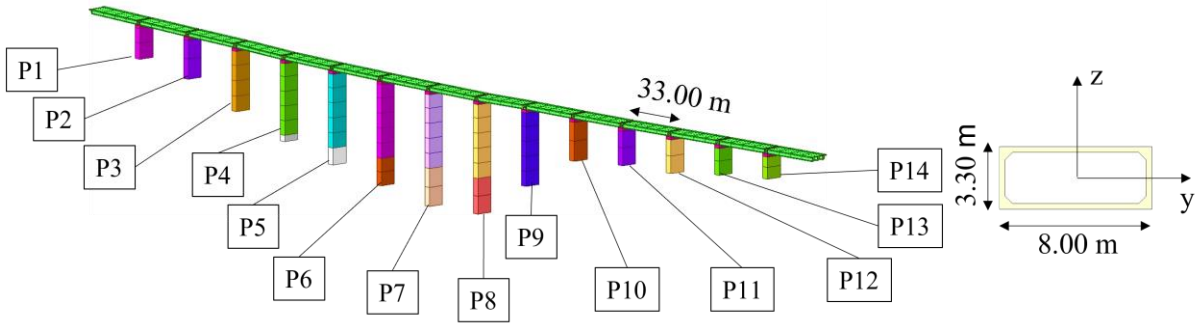


Figure 4: FEM.

In particular, the bridge is composed by two adjacent and independent carriageways having fifteen simply supported 34.50 m simply supported spans. The overall width of the roadway is equal to 9.84 m. Each span is realized in precast concrete of three prestressed I girders while the deck concrete slab is characterized by a thickness equal to 25 cm. The piers present a hollow rectangular cross-section with height ranging between 10.46 m and 53.00 m. All the viaducts analyzed, have been made with $f_{ck}$ = 28 MPa concrete and $f_{yk}$ = 440 MPa steel. The main characteristics of the bridge and of the piers are listed, respectively, in Table 1 and Table 2.

| Spans [n°] | Length [m] | Elastomeric bearings [n°] | Piers [n°] | Piers shape [-] | Piers thickness [m] |
|---|---|---|---|---|---|
| 15 | 515 | 2 x 3 | 14 | Rectangular hollow | 0.35 |

Table 1: Bridge structural characteristics.

| Pier [n°] | Cross section dimensions [m] | Height [m] | Longitudinal steel reinforcement [-] | Transverse steel reinforcement [-] |
|---|---|---|---|---|
| 1 | 8.0 x 3.3 | 14.50 | 164Ø14 | Ø10/20 |
| 2 | 8.0 x 3.3 | 18.50 | 164Ø14 | Ø10/20 |
| 3 | 8.0 x 3.3 | 28.53 | 164Ø14 | Ø10/20 |
| 4 | 8.0 x 3.3 | 37.00 | 164Ø14 | Ø10/20 |
| 5 | 8.0 x 3.3 | 43.00 | 164Ø14 | Ø10/20 |
| 6 | 8.0 x 3.3 | 48.00 | 164Ø14 | Ø10/20 |
| 7 | 8.0 x 3.3 | 53.00 | 164Ø14 | Ø10/20 |
| 8 | 8.0 x 3.3 | 51.97 | 164Ø14 | Ø10/20 |
| 9 | 8.0 x 3.3 | 34.76 | 164Ø14 | Ø10/20 |
| 10 | 8.0 x 3.3 | 18.46 | 164Ø14 | Ø10/20 |
| 11 | 8.0 x 3.3 | 16.31 | 164Ø14 | Ø10/20 |
| 12 | 8.0 x 3.3 | 15.98 | 164Ø14 | Ø10/20 |
| 13 | 8.0 x 3.3 | 12.75 | 164Ø14 | Ø10/20 |
| 14 | 8.0 x 3.3 | 10.46 | 164Ø14 | Ø10/20 |

Table 2: Piers main characteristics.

Considering the seismic parameters of the site where the bridge was built, seven spectrum-compatible accelerograms have been obtained using Rexel software [29]. Table 3 reports the fundamental characteristics of the seismic signals derived from the European Strong-Motion Database (ESD).

| Event [-] | Station ID [-] | Year [-] | PGA [$m/s^2$] | PGV [m/s] | Magnitude $M_w$ [-] |
|---|---|---|---|---|---|
| Umbria Marche | ST223 | 1997 | 0.567 | 0.048 | 5.3 |
| Lazio Abruzzo | ST152 | 1984 | 1.444 | 0.112 | 5.9 |
| Ionian | ST8 | 1973 | 2.498 | 0.255 | 5.8 |
| Umbria Marche | ST232 | 1997 | 0.501 | 0.012 | 5.3 |
| Basso Tirreno | ST47 | 1978 | 1.493 | 0.083 | 6.0 |
| Umbria Marche | ST223 | 1978 | 0.326 | 0.031 | 5.3 |
| Izmit | ST3273 | 1999 | 1.387 | 0.089 | 5.8 |

Table 3: Seismic signals considered in this work.

The first three fundamental natural periods which characterize the dynamic behavior of the bridge are: $T_1$ = 2.64 s, $T_2$ = 1.87 s and $T_3$ = 1.75 s.

Table 4 indicates the reduction of the steel reinforcement diameter and area due to corrosion effects evaluated for the three above-mentioned different corrosion levels taking into account different time intervals since the construction of the bridge.

| t | Slight Corrosion Scenario $i_{corr}$ = 0.1 [μA/cm$^2$] | | | | Moderate Corrosion Scenario $i_{corr}$ = 1 [μA/cm$^2$] | | | | High Corrosion Scenario $i_{corr}$ = 5 [μA/cm$^2$] | | | |
|---|---|---|---|---|---|---|---|---|---|---|---|---|
| | $d_0$ | d | $\Delta A_s$ | $\varepsilon_u$ | $d_0$ | d | $\Delta A_s$ | $\varepsilon_u$ | $d_0$ | d | $\Delta A_s$ | $\varepsilon_u$ |
| [year] | [mm] | [mm] | [%] | [%] | [mm] | [mm] | [%] | [%] | [mm] | [mm] | [%] | [%] |
| 0-13.5 | 10.00 | 10.00 | 0.00 | 9.00 | 10.00 | 10.00 | 0.00 | 9.00 | 10.00 | 10.00 | 0.00 | 9.00 |
| | 14.00 | 14.00 | 0.00 | 9.00 | 14.00 | 14.00 | 0.00 | 9.00 | 14.00 | 14.00 | 0.00 | 9.00 |
| 25 | 10.00 | 9.97 | 0.27 | 8.95 | 10.00 | 9.73 | 2.67 | 8.53 | 10.00 | 8.67 | 13.34 | 6.66 |
| | 14.00 | 13.97 | 0.19 | 8.97 | 14.00 | 13.73 | 1.91 | 8.67 | 14.00 | 12.67 | 9.53 | 7.33 |
| 50 | 10.00 | 9.93 | 0.73 | 8.90 | 10.00 | 9.27 | 7.31 | 7.97 | 10.00 | 6.35 | 36.54 | 2.59 |
| | 14.00 | 13.93 | 0.52 | 8.93 | 14.00 | 13.27 | 5.22 | 8.26 | 14.00 | 10.35 | 26.10 | 4.42 |
| 75 | 10.00 | 9.86 | 1.43 | 8.75 | 10.00 | 8.57 | 14.27 | 6.50 | 10.00 | 2.87 | 71.34 | 0.53 |
| | 14.00 | 13.86 | 1.02 | 8.82 | 14.00 | 12.57 | 10.19 | 7.21 | 14.00 | 6.87 | 50.96 | 0.72 |

Table 4: Area and diameter reduction of the steel reinforcement.

Taking into account the bridge service life and the considered three corrosion levels, it is possible to highlight that the corrosion effects are more evident for the transverse steel reinforcement having diameter equal to 10.00 mm. Considering as reported in the previous Section 2, the corrosion effects begin to develop after 13.5 years from the construction of the bridge. In fact, considering the age of structure ranging between 0 and 13.5 years, the corrosion effects are not yet present.

After 25 years since the construction of the bridge, the corrosion effects become significant only considering the high corrosion level with $i_{corr}$ = 5 μA/m$^2$ reaching values of steel reinforcement area reduction equal to 13.34 % for the steel rebars diameter $d_0$ = 10.00 mm.

Considering the case of 50 years after the construction time, the corrosion effects show significant values of steel reinforcement reduction area also in the case of moderate corrosion level ($i_{corr}$ = 1 μA/m$^2$) where, however, there are no reduction values that rich 10.00 %. Focusing attention on the high corrosion scenario ($i_{corr}$ = 5 μA/m$^2$) significant values of steel reinforcement area reduction has been obtained. In particular, considering the steel rebars characterized by $d_0$ = 10.00 mm the area reduction ($\Delta A_s$) is equal to 36.54 %.

After 75 years from the bridge construction also considering the moderate corrosion level $\Delta A_s$ is characterized by values greater than 10.00% for the steel reinforcement having diameter equal 10.00 mm ($\Delta A_s$ = 14.27 %) and 14.00 mm ($\Delta A_s$ = 10.19 %). In the case of high corrosion level very important steel reinforcement area reduction values are achieved: 71.34 % for $d_0$ = 10.00 mm and 50.96 % for $d_0$ = 14.00 mm.

Figure 5 reports the trend of the moment-curvature diagram of the gross-section of the pier 7 as a function of the age of the bridges. It is possible to highlight that after 25 years of service life, the slight and moderate corrosion scenarios do not affect the load-bearing capacity and the ductility of the pier gross-section.

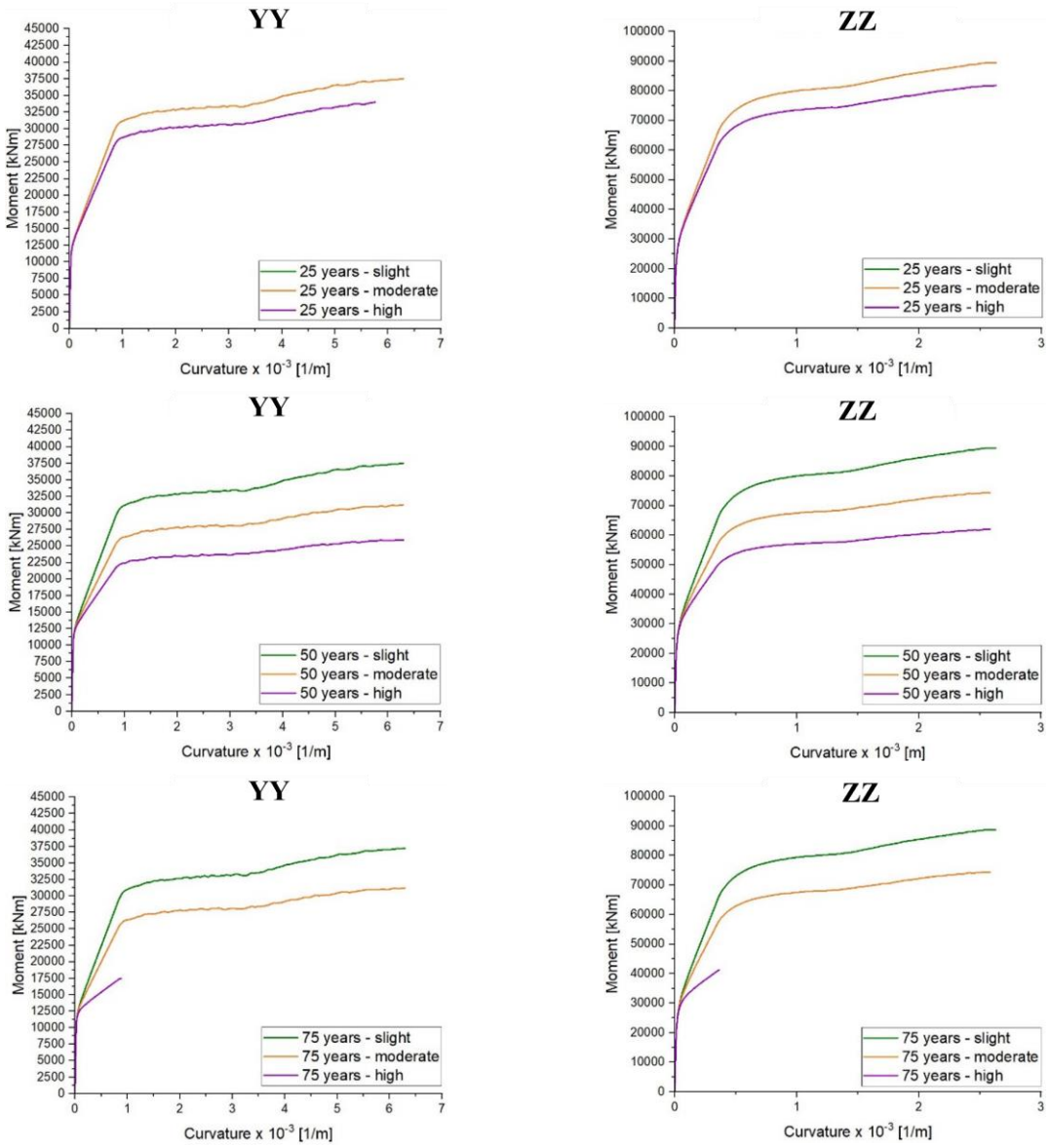


Figure 5: Moment-curvature diagrams of the pier 7.

The evolution of the corrosion effects with the service life of the viaducts, leads to a progressive reduction of the stiffness of the piers which slightly influence the dynamic behavior of the structures in terms of increment of the value of the first natural periods.

In order to define the seismic performance of the analyzed existing RC bridge at the construction time and after 13.5 years, 50 years and 75 years, non-linear time-history analyses have been performed using the seven seismic signals listed in Table 3 considering the seismic load action on 0°, 45° and 90° from the bridge longitudinal axis. Two different risk indices, reported in following Equations 5 and 6, have been considered for the evaluation of the seismic performance of the bridge:

$$RI_{PGA} = \frac{PGA_C}{PGA_D} \tag{5}$$

$$RI_{RP} = \left(\frac{T_{R,C}}{T_{R,D}}\right)^{0.41} \quad (6)$$

where $PGA_C$ is the value of the peak ground acceleration which leads to the collapse of the first monitored structural element, $PGA_D$ is the design value of the peak ground acceleration evaluated considering as reported in [15] and $T_{R,C}$ and $T_{R,D}$ are, respectively, the related return periods. Risk index characterized by a value less than one define a bridge with a significant risk to collapse under seismic load, while risk index equal or greater than one defines a seismically safe structure.

Table 5 summarizes the value of the risk indices obtained considering the different corrosion scenarios and the age of the bridge.

| | Corrosion level | 25 years | | | 50 years | | | 75 years | | |
|---|---|---|---|---|---|---|---|---|---|---|
| | | 0° | 45° | 90° | 0° | 45° | 90° | 0° | 45° | 90° |
| $RI_{PGA}$ | Slight | 2.300 | 1.986 | 1.300 | 2.300 | 1.986 | 1.300 | 2.300 | 1.986 | 1.300 |
| | Moderate | 2.300 (0.00%) | 1.986 (0.00%) | 1.300 (0.00%) | 2.000 (-13.04%) | 1.714 (-13.67%) | 1.129 (-13.19%) | 1.236 (-46.26%) | 1.344 (-32.33%) | 0.933 (-28.23%) |
| | High | 2.000 (-13.04%) | 1.714 (-13.67%) | 1.129 (-13.19%) | 1.214 (-43.35%) | 1.343 (-32.38%) | 0.971 (-25.31%) | 0.857 (-62.74%) | 0.900 (-54.68%) | 0.743 (-42.84%) |
| $RI_{RP}$ | Slight | 2.364 | 2.026 | 1.299 | 2.364 | 2.026 | 1.299 | 2.364 | 2.026 | 1.299 |
| | Moderate | 2.364 (0.00%) | 2.026 (0.00%) | 1.299 (0.00%) | 2.041 (-13.67%) | 1.735 (-14.33%) | 1.128 (-13.17%) | 1.295 (-45.21%) | 1.412 (-30.30%) | 0.921 (-29.10%) |
| | High | 2.041 (-13.67%) | 1.735 (-14.33%) | 1.128 (-13.17%) | 1.214 (-48.64%) | 1.342 (-33.76%) | 0.913 (-29.71%) | 0.875 (-62.99%) | 0.913 (-54.94%) | 0.750 (-42.26%) |

Table 5: Risk indices.

It is possible to notice an important reduction of the value of the risk indices as a function of the age of the bridge, mainly considering the moderate and the high corrosion scenarios. The slight corrosion scenario does not influence the seismic behavior of the bridge, according to the low levels of the steel reinforcement reduction area shown in previous Table 4. After 75 years from the construction of the bridge the risk indices, both in terms of peak ground acceleration (PGA) and in terms of related return period (RP), are characterized by reduction values greater than 30% considering the moderate and the high corrosion scenarios. It is possible to notice that taking into account the high corrosion scenario, all the risk indices obtained both for ductile and brittle collapse mechanism, are characterized by a value smaller than one, that define a structure with a significant risk to collapse if subject to a seismic event equal to the design one. On the contrary, for moderate corrosion scenario, the bridge maintains value of risk indices greater than one for each direction of the seismic action.

After 50 years from the construction, the bridge is characterized by values of risk indices always close or greater than one for all the corrosion scenarios analyzed.

Considering the case of 25 years from the construction, the bridge shows much more limited reduction values of the risk indices, equal to about 13 %.

Figure 6 summarizes the trend of the above-mentioned risk indices normalized to the initial value (evaluated when the bridge was built) as a function of the age of the bridge.

Starting from the values of the risk indices calculated for the different corrosion scenarios, it is possible to obtain the intervention time (IT), related to the considered limit state (life-safety limit state in this work), which characterized the bridge, considering the Equation 7 [16]:

$$IT = 0.105 \cdot \frac{\min(RP)}{C_u} \quad (7)$$

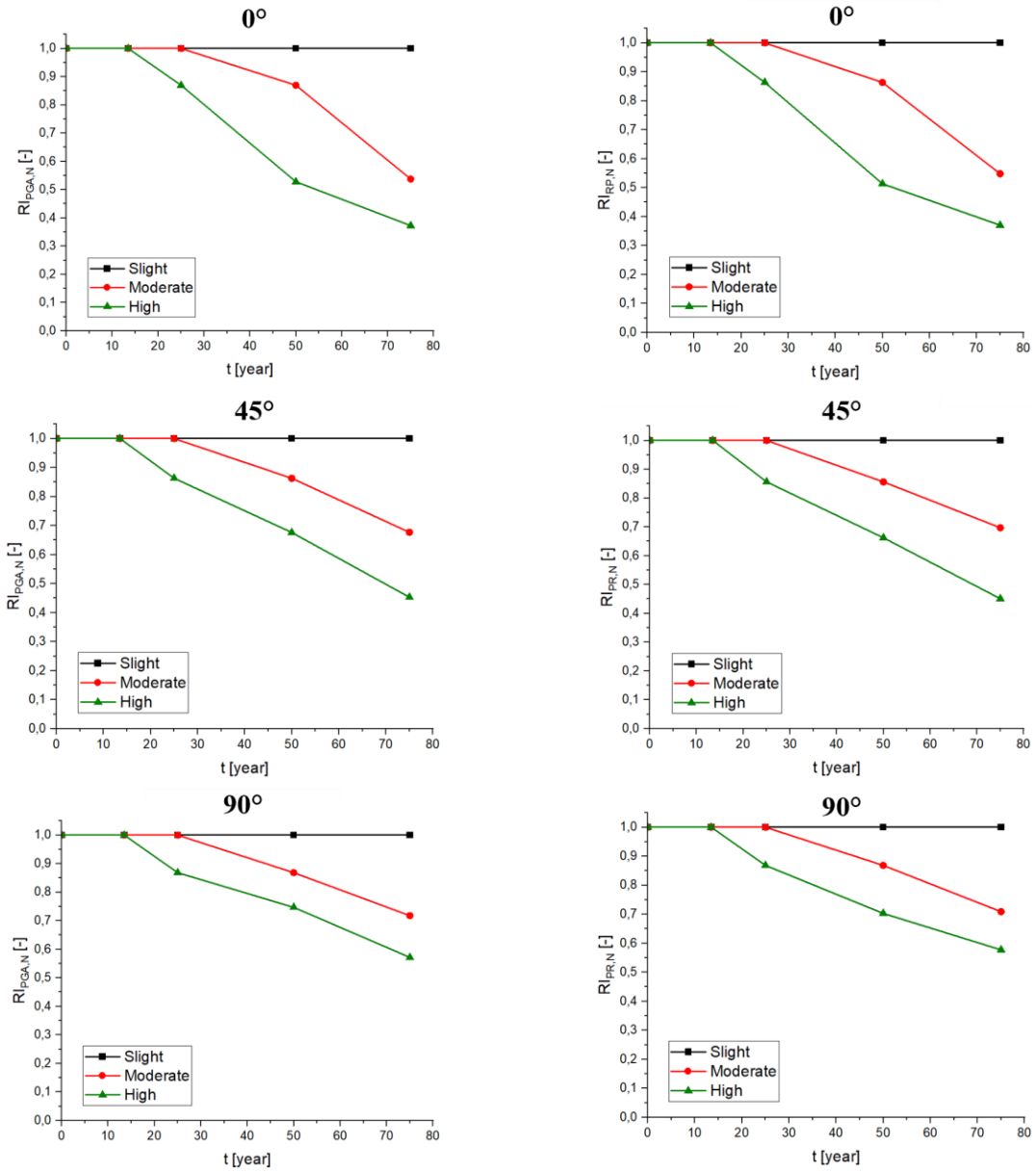


Figure 6: Evolution of the normalized risk indices value as a function of the bridge age.

where IT indicates the intervention time (in years), min(RP) represents the minimum return period obtained starting from the risk indices calculated and $C_u$ is the coefficient for use category taken, in this work, equal to 2 according to as reported in [15]. Table 6 summarizes the evolution of the intervention time as a function of the age of the analyzed bridge.

| | 25 | 50 | 75 |
|---|---|---|---|
| IT [years] | 66.84 | 39.90 | 24.70 |

Table 6: Evolution of the intervention time (IT).

It is possible to highlight that the intervention time decreases significantly with increasing aging of the viaducts, considering a high corrosion level for which the values of the lower risk

indices were obtained. In fact, the increase in the level of corrosion related to the age of the bridge leads to significant reduction values in terms of steel reinforcement areas, especially for the stirrups characterized by a smaller diameter than the longitudinal steel reinforcement. As a consequence, the shear strength of the piers decreases yielding to the activation of the brittle collapse mechanism.

## 4 CONCLUSIONS

In this work the influence of the corrosion effects due to carbonation on the seismic performance of existing RC bridges considering the age of the structure (0-75 years) is analyzed. In particular, the corrosion effects are considered only in terms of steel reinforcement area reduction by means of analytical formulation. Three different corrosion scenarios are evaluated: (i) slight, (ii) moderate and (iii) high characterized by a different value of corrosion current density ($i_{corr}$).

The seismic behavior of the bridge has been defined through the implementation of a simplified finite element model using Timoshenko beam elements and plastic hinges located at the base of the piers. Different non-linear time history analyses (NTHA) have been performed on an existing RC bridge built between 1960's and 1970's to obtain the values of the risk indices, expressed in terms of the ratio between the peak ground acceleration which leads to collapse of the first monitored structural elements considering both ductile and brittle failure mechanism and the design peak ground acceleration and the ratio between the related return periods, useful to calculate the intervention time which characterizes the analyzed structure.

The corrosion effects due to the carbonation start after 13.5 years from the construction of the structure and for this reason, three different time steps are considered in this work to evaluate the relation between the seismic performance of the brdige and the corrosion effects: 25, 50 and 75 years after the construction of the structure. From the results obtained, it is possible to notice that:

- the slight corrosion scenario, characterized by a value of $i_{corr} = 0.1$ $\mu A/mm^2$, does not influence the seismic performance of the bridge even after 75 years from the construction;
- considering the case of 25 years from the construction of the bridge, significant variations of the seismic performance have been obtained only considering the high corrosion scenario ($i_{corr} = 5$ $\mu A/mm_2$). The moderate corrosion scenario does not influence the bearing-capacity of bridge under seismic actions;
- after 50 years, considering the moderate corrosion level ($i_{corr} = 1$ $\mu A/mm^2$), the bridge shows values of risk indices always close or greater than one also considering the high corrosion scenario;
- analyzing the results obtained after 75 years from the construction time, a significant reduction of the seismic performance is observed also in the case of moderate corrosion level.

These results obtained are useful to schedule the correct maintenance interventions creating a priority queue within the same motorway network, also considering the decrease of the intervention time as a function of the age of the structures.

## REFERENCES


[1] P. Crespi, M. Zucca, M. Valente, N. Longarini. Influence of corrosion effects on the seismic capacity of existing RC bridges. *Engineering Failure Analysis*, **140**, 106546, 2022.

[2] S. Mahboubi, M. Kioumarsi. Damage assessment of RC bridges considering joint impact of corrosion and seismic loads: A systematic literature review. *Construction and Building Materials*, **295**, 123662, 2021.

[3] C. Do-Eun, P. Gardoni, D. Rosowsky, T. Haukaas. Seismic fragility estimates for reinforced concrete bridges subject to corrosion. *Structural Safety*, **31**, 275-283, 2009.

[4] M.A. Zanini, C. Pellegrino, R. Morbin, C. Modena. Seismic vulnerability of bridges in transport networks subjected to environmental deterioration. *Bulletin of Earthquake Engineering*, **11**, 561-579, 2013.

[5] M. Zucca, P. Crespi, F. Stochino, M.L. Puppio, M. Coni. Maintenance interventions period of existing RC motorway viaducts located in moderate/high seismicity zones. *Structures*, **47**, 976-990, 2023.

[6] H. Krawinkler, G.D.P.K. Seneviratna. Pros and cons of a pushover analysis of seismic performance evaluation. *Engineering Structures*, **20**, 452-464, 1998.

[7] T.S. Paraskeva, A.J. Kappos, A.G. Sextos. Extension of modal pushover analysis to seismic assessment of bridges. *Earthquake Engineering and Structural Dynamics*, **35**, 1269-1293, 2006.

[8] T.S. Paraskeva, A.J. Kappos. Further development of a multimodal pushover procedure for seismic assessment of bridges. *Earthquake Engineering and Structural Dynamics*, **39**, 211-222, 2009.

[9] S. Stefanidou, A.J. Kappos. Methodology for the development of bridge-specific fragility curves. *Earthquake Engineering and Structural Dynamics*, **46**, 73-93, 2017.

[10] C. Perdomo, R. Monteiro, H. Sucuoğlu. Development of fragility curves for single-column RC Italian bridges using nonlinear static analysis. *Journal of Earthquake Engineering*, **26**, 2328-2352, 2022

[11] Y. Zhang, I. Tien. Conjugate Bayesian updating of analytical fragility functions using dynamic analysis with application to corroded bridges. *Computers & Structures*, **270**, 106832, 2022.

[12] D. Vamvatsikos, A.C. Cornell. Incremental dynamic analysis. *Earthquake Engineering and Structural Dynamics*, **31**, 491-514, 2002.

[13] C. Bernuzzi, D. Rodigari, M. Simoncelli. Incremental dynamic analysis for assessing the seismic performance of moment resisting steel frames. *Ingegneria Sismica*, **4**, 23-44, 2020.

[14] C.P. Contiguglia, A. Pelle, B. Briseghella, C. Nuti. IMPA versus Cloud Analysis and IDA: different methods to evaluate structural seismic fragility. *Applied Sciences*, **12**, 3687, 2022.

[15] Decreto Ministeriale 17/01/2018, Ministero delle Infrastrutture e dei Trasporti, G.U. Serie Generale n.42 del 20/02/2018 – S.O.8.

[16] O.P.CM. 3 maggio 2005, n. 3431, Primi elementi in materia di criteri generali per la classificazione sismica del territorio nazionale e di normative tecniche per le costruzioni in zona sismica, Ministero delle Infrastrutture e dei Trasporti, G.U. Serie Generale n.107 del 10/05/2005 – S.O.85.

[17] P. Crespi, M. Zucca, M. Valente. On the collapse evaluation of existing RC bridges exposed to corrosion under horizontal loads. *Engineering Failure Analysis*, **116**, 104727, 2020.

[18] EN 1337-3:2005. Structural bearings – Part 3: Elastomeric bearings. CEN (European Committee for Standardization), Management Centre. Brussels.

[19] EN 1998-3:2005. Eurocode 8: Design of structures for earthquake resistance – Part 3: Assessment and retrofitting of buildings. CEN (European Committee for Standardization), Management Centre. Brussels.

[20] W.F. Chen, L. Duan. *Bridge Engineering – Seismic Design*. CRC Press, Boca Raton, FL, 2000.

[21] D.C. Kent, R. Park. Flexural members with confined concrete. *Journal of the Structural Division*, **97**, 1969-1990, 1971.

[22] R. Park, T. Paulay. *Reinforced Concrete Structures*. John Wiley and Sons, New York, 1975.

[23] FEMA 356. Prestandard and commentary for the seismic rehabilitation of buildings. Federal Emergency Management Agency: Washington, DC.

[24] FEMA 440. Improvement of nonlinear static seismic analysis procedure. Applied Technology (ATC-55 Project) Department of Homeland Security, Federal Emergency Management Agency: Washington, DC.

[25] EN 1998-2:2005. Eurocode 8: Design of structures for earthquake resistance – Part 2: Bridges. CEN (European Committee for Standardization), Management Centre. Brussels.

[26] A. Bossio, T. Monetta, F. Bellucci, G.P. Lignola, A. Prota. Modeling of concrete cracking due to corrosion process of reinforcement bars. *Cement and Concrete Research*, **71**, 78-92, 2015.

[27] A.V. Saetta, R. Vitaliani. Experimental investigation and numerical modeling of carbonation process in reinforced concrete structures: Part I: Theoretical formulation. *Cement and Concrete Research*, **34**, 571-579, 2004.

[28] L. Berto, R. Vitaliani, A.V. Saetta, P. Simioni. Seismic assessment of existing RC structures affected by degradation phenomena. *Structural Safety*, **31**, 284-297, 2009.

[29] I. Iervolino, C. Galasso, E. Cosenza. REXEL: computer aided record selection for code-based seismic structural analysis. *Bulletin of Earthquake Engineering*, **8**, 339-362, 2010.

COMPDYN 2023
9th ECCOMAS Thematic Conference on
Computational Methods in Structural Dynamics and Earthquake Engineering
M. Papadrakakis, M. Fragiadakis (eds.)
Athens, Greece, 12-14 June 2023

# STRUCTURAL BEHAVIOR OF STEEL STORAGE RACKS UNDER DIFFERENT FIRE SCENARIOS

**Marco Simoncelli[1], Marco Zucca[2], Flavio Stochino[2] and Livia Bardhi[1]**

[1] Politecnico di Milano, Department of Architecture, Built environment and Construction engineering
Piazza Leonardo da Vinci 32, Milano, Italy
e-mail: marco.simoncelli@polimi.it

[2] Università degli studi di Cagliari, Department of Civil, Environmental engineering and Architecture
Via Marengo 2, Cagliari, Italy
marco.zucca2@unica.it

## Abstract

*Steel solutions commonly used in logistic to store goods and products (i.e. racks) are assembled by thin-walled cold-formed components and their competitiveness on the market depends essentially on the total weight of the framed system. Despite great efforts have been done on seismic and static design, very limited attention was given to the problem of the fire design and to the robustness of such structures. Due to the limited thickness of the structural elements, it is well-known that their resistance to the fire load is quite limited. No specific design rules or design procedures have been developed till now. Nowadays, the only way to protect these frames against fire is the use of sprinkler or more complex solutions, like isolated chambers. However, fire hazard cannot be always eliminated and when these strategies were not effective, global structural collapse of the racks, during a fire, have been observed.*
*In this paper a parametric analysis is proposed to deeply understand the behavior of racks against fire. In particular, starting from an existing rack configuration, different fire scenarios were modeled by changing the fire position along the fame and the fire design curve. Moreover, the progressive collapse of the rack is discussed proposing also two reinforcing strategies.*
*Final results discuss about the best way to design these slender structures against fire, trying to prevent the global failure or, at least, to guarantee a safe collapse mode.*

**Keywords:** Fire design, thin-walled members, steel racks, global instability.

## 1 INTRODUCTION

An important area of the steel construction industry is represented by structural systems made by thin-walled cold-formed components [1], which are extensively employed in logistic to realize frames used for the long- and medium-term storage of goods and products. One of the most common types of storage solutions is the so-called adjustable selective storage pallet rack (in the following simply identified as *rack*), which is the core of the present paper. As shown in Fig. 1, the vertical elements (uprights) are jointed with diagonals and struts in the transversal (cross-aisle) direction forming a set of trussed columns connected in the longitudinal (down-aisle) direction to each other by pairs of pallet beams directly supporting the stored goods. At each beam end, a shop welded bracket with hooks is accommodated into special slots regularly pitched along uprights allowing for a rapid assemblage of the skeleton frame [2]. Generally, due to logistic reasons, bracing systems (spine bracings) are rarely used in the down-aisle direction.

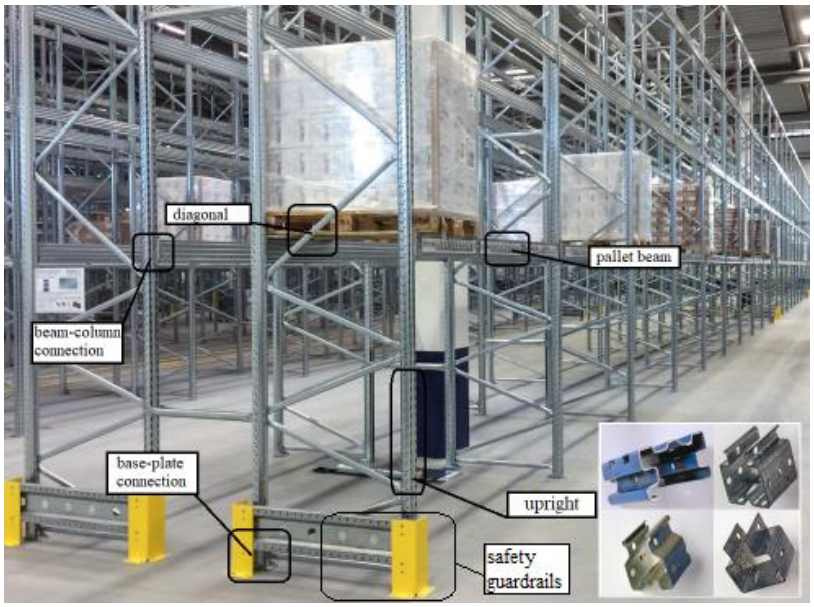


Figure 1: Example of unbraced rack(a) and its main components (b-d) [3].

Racks are widely adopted in warehouses, and they are loaded with tons of valuable goods. The loss of goods after a structural collapse may represent, for the owner, a very large economic loss, much larger than the cost of the whole rack on which the goods are stored, as highlighted by the quite recent collapses [4]. Racks are also frequently adopted in supermarkets and shopping centers, in areas open to the public. A global structural collapse, in this case, may endanger the lives of the customers, as well as that of the workmen and employees, involving not only Civil and Penal Right considerations about the liability of the owners, but also economic considerations related to insurance coverage.

A large number of research have been carried out on the behavior of racks, paying attention mainly to the seismic and static response. In fact, it is possible to assert that while the seismic behavior of these structures has been widely investigated [5], very limited attention has been focused on the problem of fire safety and structural robustness. Robustness is generally defined as the ability of a structure to withstand out-of-the-scheme events, such as impacts or fire without being damaged to an extent disproportionate to the original cause [6]. In case of fully loaded racks, a local damage generally propagates to the entire rack system and, in the worst case-scenario, to the neighboring ones causing the so-called *domino effect*.

Prediction of the structural performance of these structures is cumbersome because it is affected by many parameters like the non-standard geometries of their structural components which are thin-walled elements, the strong nonlinearity of the joint response and the great dead-to-live load ratio. For these reasons, the only way to design racks is to follow the *design assisted by testing* procedure: the numerical models used for the structural analyses must be based on *ad-hoc* components tests [7].

Fire effects on steel structures can be very dangerous: the variations of mechanical properties due to temperature variations can strongly reduce the bearing capacity and the induced thermal deformation can affect the global structural behavior [8]. For this reason, in case of fire, both mechanical and geometrical non linearities should be taken into account. The understanding of the fire effects on such structures is even more complex. The different protection strategies and methodologies proposed in the past for regular steel structures [9-12] cannot be directly extended to rack frames due to the limited thickness of the sections. The very thin thickness of zinc that is generally present on the structural members can guarantee only a poor protection [13] and the intumescent painting is not an efficient solution. In fact, the only effective strategy, which is in use nowadays, is the use of sprinklers.

In past research only local elements of rack under fire have been proposed: Ren et al [13] investigated the effect of localized fire on the uprights, proposing updated buckling curves for design purposes and Shah focused on the response of beam-to-column connections [14]. On the contrary, in the current paper, the whole structural system is investigated, by performing an extensive parametric analysis on an existing rack by varying the fire type, its position and intensity. In particular, attention is focused on the type of collapse induced by the fire position and different reinforcement strategies were investigated.

## 2 HYPOTESES FOR FIRE ANALYSIS

In this study, the fire load is represented by a temperature time history curve applied directly to a single span (Fig. 2a) or to a single beam element (like an upright), rather than to the entire structure. This simplification of the problem is considered acceptable for the purposes of the paper objectives. This procedure allows for the identification of most critical zone of the rack when subjected to a fire; on the contrary, if the same temperature were applied to the whole frame, only a global and simultaneous collapse would occur. Furthermore, numerous studies in the literature adopted a similar strategy for the application of the temperature curve [15].

In addition, it should be noted that the ISO temperature curves, used in the following, are representative of the time-temperature curve of a compartment and not of a single element. Indeed, it should be necessary to also consider convention and radiation of the heat to evaluate the element temperature. The increment of temperature can be represented by equation 1) reported in EN1993-1-2 [16]:

$$\Delta\theta_{a,t} = k_{sh} \cdot \frac{A_m}{V} \cdot \frac{1}{c_a \rho_a} \cdot \dot{h}_{net} \cdot \Delta t \tag{1}$$

where, $\Delta\theta_{a,t}$ is the increment of the temperature in the steel in a specific time $\Delta t$, $A_m/V$ is the section factor of the structural element under consideration, $c_a$ is the specific heat, $\rho_a$ steel density, $h_{net}$ heat flux and $k_{sh}$ factor for the shadow effect.

By applying eq. 1) to the elements of the considered rack, it should be noted that when thin-walled steel profiles are considered, the temperature of the compartment (blue line in Fig.

2b) can be considered the same of the one evaluated in the structural element (grey line in Fig. 2b).

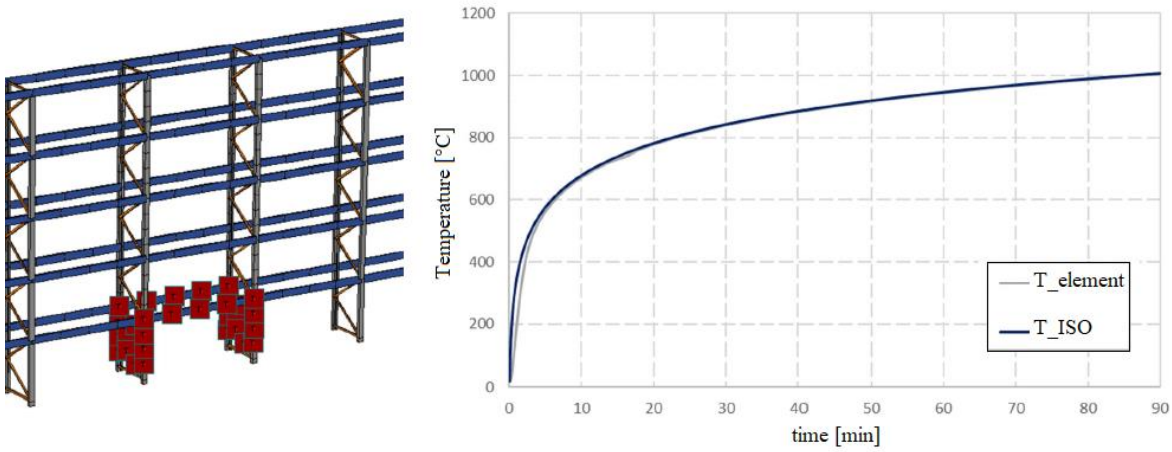


Figure 2: hypothesis on the application of the temperature curve.

## 3 THE CONSIDERED CASE STUDY

The case study consists of an existing rack having 9 bays with 2780mm of span and 5 storage floors, with 1330mm of interstorey, for a total height of 6650mm. In the transversal direction, the upright frame is composed by a k-bracing type with a step of 665mm and having 1000mm of width (Fig. 3). In the standard (S) configuration all the columns are made by a 75x115x50 lipped C-section with 2mm of thickness, all the beams are 40x160 rectangular hollow profile with a thickness of 1.3 mm and the diagonals are hollow square section of 35mm with a thickness of 2mm. The same geometric layout was considered with standard elements or with two different reinforcement hypotheses (R and RR). The material is the same for all the elements: steel S350GD with a Young modulus equal to 210 GPa and ν=0.3.

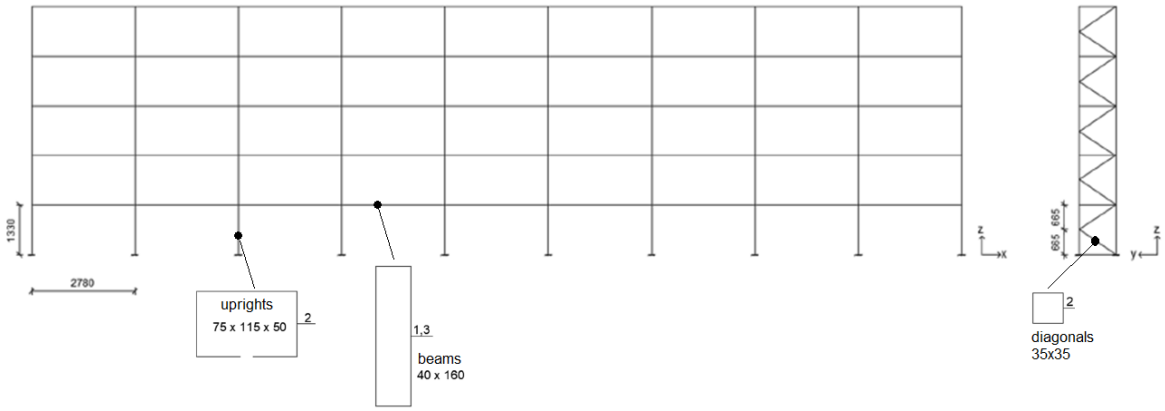


Figure 3: The considered rack geometry (dimensions in mm).

In the first reinforced model (R) the thickness of all the beams was increased up to 2mm; while in the second reinforced configuration (RR) together with the increase of the beams thickness, the first and the second storage level column thickness were increased too (4mm). The load was considered as uniform distributed on all the beams and equal to 4.0 N/mm to simulate the presence of 3 pallets of 800kg each. Beam-to-column and internal and external

base-plate connections have been assumed as non-linear, i.e. characterized by a moment-rotation rule, and their response have been calibrated based on previous cyclic and monotonic tests. The variability of the connection properties with the temperature were not considered in the paper. For all the configurations two different fire type were considered (ISO834, named ISO, and the fire hydrocarbon curve, named HYD [16]). Moreover, the fire position was varied considering the internal (C) or the external (L) position and from the first to the fifth storage levels. The fire was considered acting on a single column (SC) or on a complete bay (CB). The layout of all the considered analyses is depicted in Fig. 4.

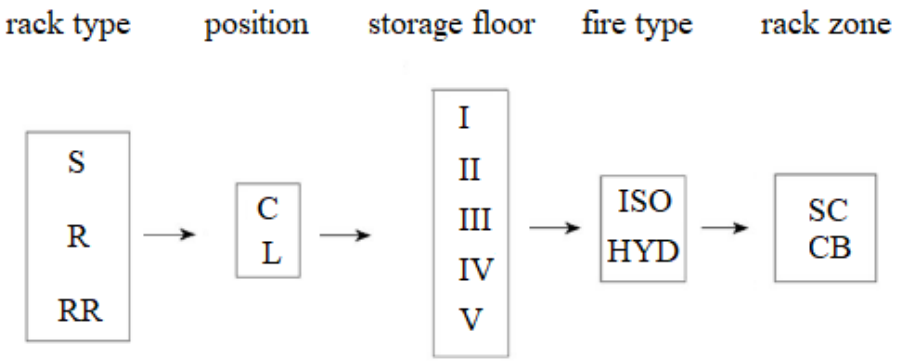


Figure 4: Layout of the considered cases.

As an example, the case S_C_III_ISO_CB case is depicted in Fig. 5. which represent the standard rack subjected to a fire (represented by the ISO curve) on a central bay at the third storage level.

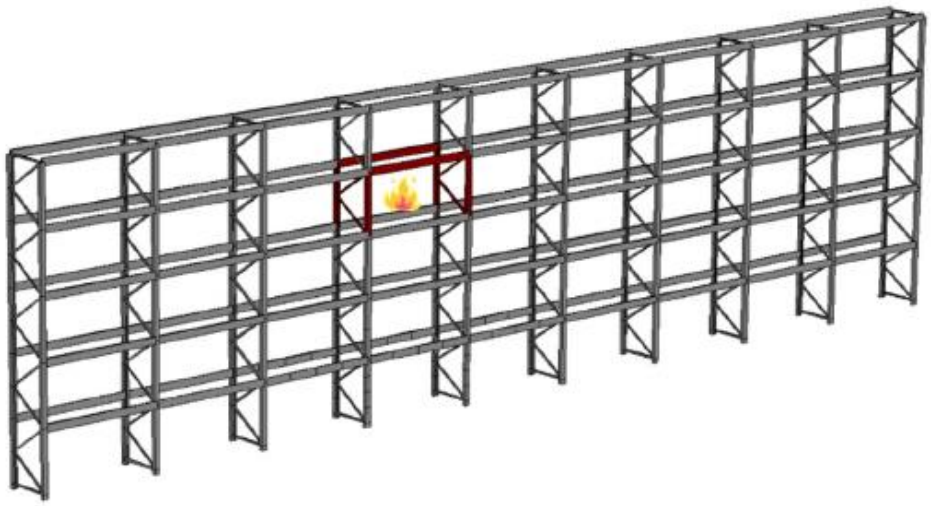

Figure 5: Example of the S_C_III_ISO_CB case (in red the elements in which the ISO curve was assigned).

Nonlinear thermomechanical analyses were performed by using the finite element software Straus7 [17], following two main steps: i) thermal analysis, which gives as output the temperature on each structural node for each time interval; ii) non-linear mechanical analysis by considering second order effects and mechanical nonlinearities. According to [16] the Young modulus, the yielding stress, the conductivity and the thermal expansion of the material were modeled as non-linear and dependent on the temperature value.

Once obtained the internal stresses for each step of the analyses the safety index, SI, were evaluated on all the elements in accordance with EN15512:2020 [7], considering the stability equation for the element in bending and compression:

$$\left(\omega_{x,y}\frac{N_{Ed}}{\chi_y N_{Rd}}\right)^{\alpha_y}+\left(\omega_{x,LT}\frac{M_{y,Ed}+\Delta M_{y,Ed}}{\chi_{LT}M_{y,Rd}}\right)^{\beta_y}+\left(\frac{M_{z,Ed}+\Delta M_{z,Ed}}{M_{z,Rd}}\right)^{\delta_y}\le 1{,}0$$

$$\left(\omega_{x,z}\frac{N_{Ed}}{\chi_z N_{Rd}}\right)^{\alpha_z}+\left(\omega_{x,LT}\frac{M_{y,Ed}+\Delta M_{y,Ed}}{\chi_{LT}M_{y,Rd}}\right)^{\beta_z}+\left(\frac{M_{z,Ed}+\Delta M_{z,Ed}}{M_{z,Rd}}\right)^{\delta_z}\le 1{,}0 \quad (2)$$

where $N_{Ed}$, $M_{y,Ed}$, $M_{z,Ed}$ are the acting axial force and bending moments along y- and z- directions; $N_{Rd}$, $M_{y,Rd}$, $M_{z,Rd}$ are the resistant axial force and bending moments along y- and z-directions; $\chi_y$, $\chi_z$, $\chi_{LT}$ are the reduction factors for the global buckling and $\omega_{x,y}$ $\omega_{x,z}$ $\omega_{x,LT}$ are the interaction factors.

From a numerical standpoint, it should be noted that also when in a specific step one or more elements reached the SI equal to one, the step forward happened anyway, until an eventual convergence problem. On the contrary, from a physical point of view the low redundancy of the structure, suggests that when one element lose is carrying capacity (upright or beam) also the whole frame collapse. The results are hence proposed continuously in time, but the global collapse has been assumed in correspondence of the first SI = 1.

## 4 RESULTS

The result obtained for the two considered temperature curves are really close to one another and, for the sake of brevity, only the ones associated with the ISO curve are discussed in the paper. for the S_C_I_ISO_CB case is proposed in Fig. 6a, in terms of SI versus time. In the figure the SI of all the columns and beams at the first storage level are proposed grouped together. This figure is representative of all the case, in particular it can be noted that before 5 minutes a great number of beams and columns reached the collapse, generating a global collapse of the whole frame. Due to the increase of the axial force in the beams and to their limited thickness, some of them reached the SI = 1 also within 1 minute, as showed in Fig. 6b for the same S_C_I_ISO_CB case. It can be concluded that for the specific case the collapse of the frame is reached in 1 minute.

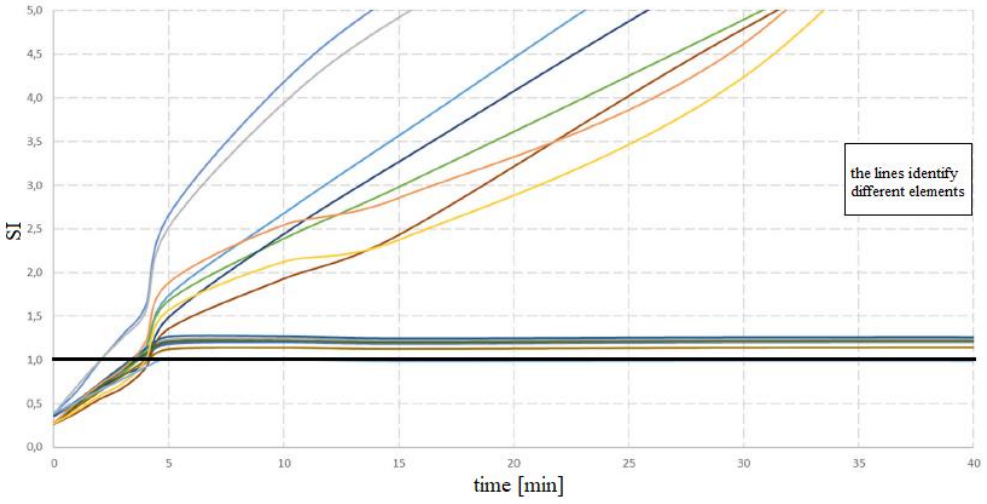


a)

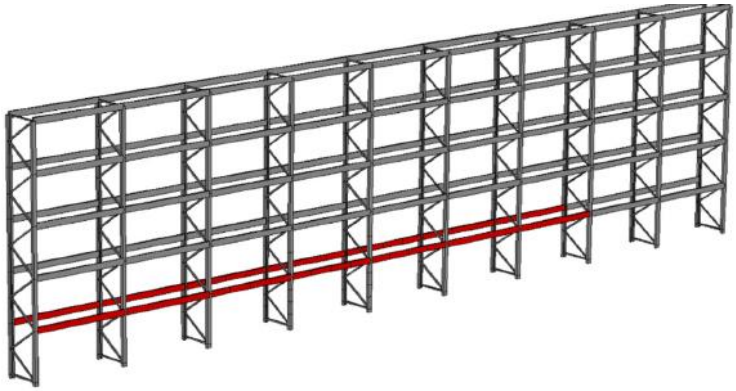

t=1min b)

Figure 6: S_C_I_ISO_CB case, (a) SI results versus time and (b) element collapsed after 1 minute (in red).

At the same way, when the fire is applied to a single column (SC) instead of to the whole bay, the collapse of the first storage level beams is reached in 1 minute. In this case the frame exhibits a lateral global displacement of the central upright frame (Fig. 7b). The failure of the frame in the first case happens with a local collapse of the first storage level beams followed by a longitudinal global displacement. In the second case the global collapse starts with the local failure of the burned upright cause a lateral global deformation of the structure. The second ode is the most dangerous because in a real warehouse where there are multiple racks next to each other, it would lead to a *domino effect*.

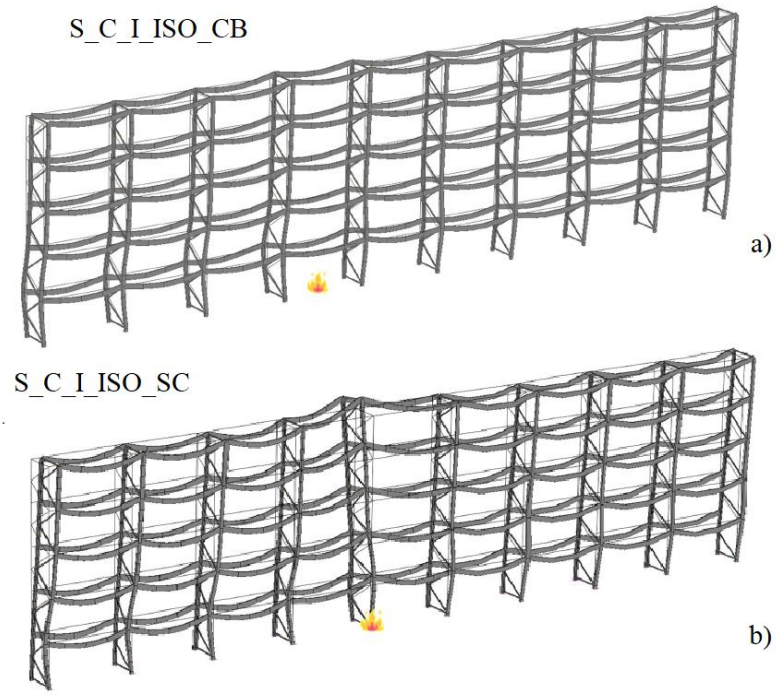


Figure 7: Global deformed shape after 1 minute of fire, (a) S_C_I_ISO_CB and (b) S_C_I_ISO_SC.

All the results obtained for the standard rack, are summarized in Fig. 8, in terms of number of collapsed elements versus the time of the analysis. The position of the fire has been varied by changing the storage floor and spatial zone (central or lateral). The ISO 834 curve is considered with a whole bay subjected to the fire action.

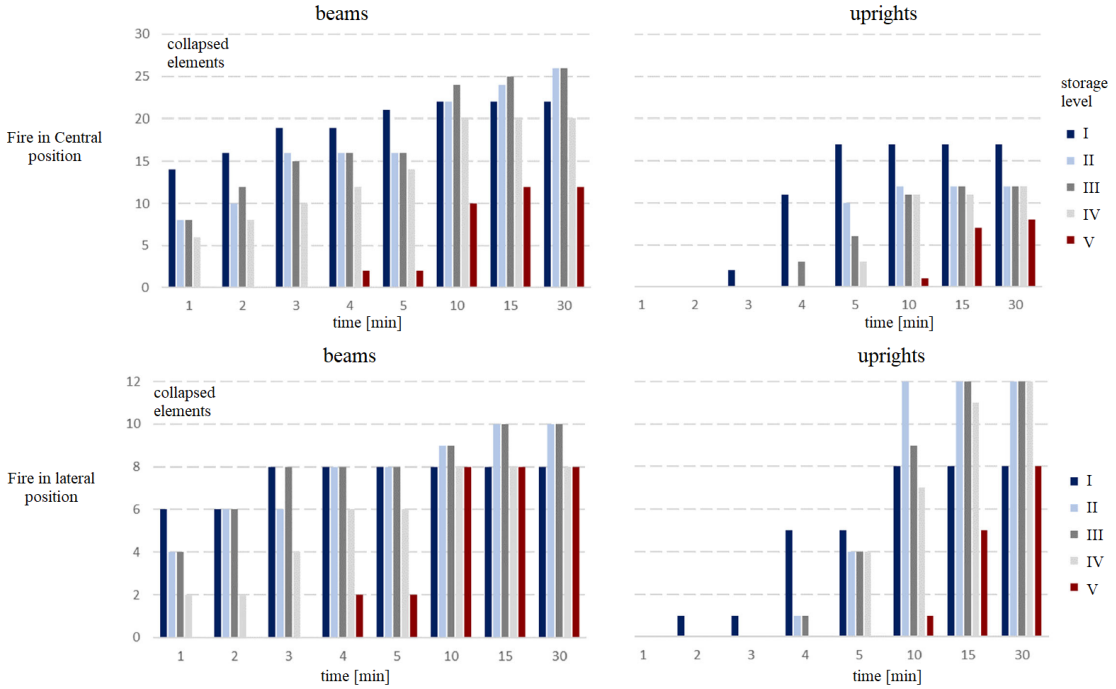


Figure 8: Number of collapsed element for S frame subjected to different frame scenarios.

For all the considered cases the time of collapse of the elements is always limited, in fact within the 5 minutes of exposition a non-negligible number of uprights and beams collapsed. For the other cases, independently on the location of the fire, the beams collapsed within the first minute of fire. The uprights are less sensitive to the fire and their collapse is more pronounced when the columns of the first storage level are directly exposed.

Finally, the comparison between the standard rack and reinforced ones is proposed in Tab. 1, for the case different scenarios.

Table 1: Collapse time of the first element for different scenario.

| scenario | S | R | RR |
|---|---|---|---|
| C_I_ISO_CB | 1 min | 1 min | 2 min |
| C_II_ISO_CB | 1 min | 1 min | 2 min |
| C_III_ISO_CB | 1 min | 2 min | 2 min |
| C_IV_ISO_CB | 1 min | 4 min | 4 min |
| C_V_ISO_CB | 4 min | 10 min | 10 min |
| L_I_ISO_CB | 1 min | 1 min | 2 min |
| L_II_ISO_CB | 1 min | 1 min | 2 min |
| L_III_ISO_CB | 1 min | 2 min | 2 min |
| L_IV_ISO_CB | 1 min | 4 min | 4 min |
| L_V_ISO_CB | 4 min | 10 min | 10 min |
| C_I_ISO_SC | 1 min | 1 min | 2 min |
| L_I_ISO_SC | 1 min | 1 min | 2 min |

As showed in the table, the proposed reinforcements are not effective because despite the thickness of the profiles have been increased more than 2 times, their value is still very low. As discussed in the introduction, also the application of painting or the zinc coating is not an effective solution to guarantee at least 15 minutes before the failure of 1 or more elements.

For this reason, the only effective solutions for such structures seem to be the use of *ad-hoc* well-designed sprinkler system or the use of special compartment with a controlled level of oxygen.

## 5 CONCLUDING REMARKS

In the paper, the response of a rack frame under different fire scenarios has been investigated, focusing attention on the safety of the structure during the time in which it is exposed. An extensive parametric analysis by varying the fire type, its position and intensity is discussed showing the very low level of reliability of such structures, mainly due to the very low thickness of the structural members. Nonlinear numerical thermo-mechanical analyses were performed by considering but geometrical and mechanical nonlinearities.

Two reinforcement strategies were discussed: i) the increasing of the thickness of the beams and ii) the thickness increment of both beams and columns. Both strategies were not really effective and are not able to satisfy a minimum level of performance. In fact, all the structures presented the failure of one or more structural element (beam or upright) in a time lower than 5 minutes, independently of the fire position and on the curve type.

For this reason, it can be concluded that the only effective solutions to design rack structures against fire seem to be the use of *ad-hoc* well-designed sprinkler system, which need of constant maintenance, or the use of special compartment with a controlled level of oxygen, which is quite expensive strategy and not always suitable. Both strategies will be investigated in the future.

## REFERENCES


[1] B. W. Shafer, Cold-formed steel structures around the world – a review of recent advances in applications, analysis and design, *Steel Construction*, **4**, 141-149, 2011.

[2] L. Dai, X. Zhao, K. J.R. Rasmussen, Flexural behaviour of steel storage rack beam-to-upright bolted connections, *Thin-walled structures*, **124**, 202-217, 2018

[3] M. Simoncelli. R. Montuori, B. Tagliafierro, Recent development on the seismic devices for steel storage structures, *Thin-walled structures*, **155**, 106827, 2020.

[4] F. Braga, R. Gigliotti, G. Monti, (..), I. Vanzi, Speedup of post-earthquake community recovery: the case of precast industrial buildings after the Emilia 2012 earthquake, *Bulletin of earthquake engineering*, **12**(5), 2405-2418, 2014.

[5] G. Gabbianelli, A. Kanyilmaz, C. Bernuzzi, C.A. Castiglioni, A combined experimental-numerical study on unbraced pallet rack under pushover loads, *Ingegneria Sismica*, **34**(1), 18-38, 2017.

[6] F. Stochino, C. Bedon, J. Sagaseta, D. Honfi, Robustness and resilience of structures under extreme loads. Advances in Civil Engineering, art. n. 4291703, 2019.

[7] CEN, EN15512:2020, Steel Static Storage Systems - Adjustable Pallet Racking Systems - Principles for Structural Design, CEN, 2020.

[8] P. Meloni, F. Mistretta, F. Stochino, G. Carcangiu, Thermal path reconstruction for reinforced concrete under fire. Fire Technology, **55**, 1451-1475, 2019.

[9] D. de Silva, N. Alam, (…), F. Ali, Finite element modelling for structural performance of slim floors in fire and influence of protection materials, *Applied Sciences*, **23**(11), 11291, 2021.

[10] D. de Silva, A. Bilotta, E. Nigro, Effect of the thermal input on the behavior of intumescent coatings, *Applications of Fire Engineering - Proceedings of the International Conference of Applcations of Structural Fire Engineering (ASFE 2017)*, Manchester, September 7-8, 2017.

[11] F. Pittau, F. Doveri, M. L. Puppio, F. Stochino, F. Mistretta, M. Sassu, Experimental tests on vapor and gas permeability of concrete boxes, *Procedia Structural Integrity*, **33**, 630-645, 2021.

[12] J. Jirku, F. Wald F, Influence of zinc coating to a temperature of steel members in fire, in *ASFE13 - Application of Structural Fire Engineering*, Prague, Czech Republic, 19-20 April 2013

[13] C. Ren, P. Zhang, S. Yan, L. Dai, Analysis and design of cold-formed steel storage rack uprights under localised fires, *Structures*, **27**, 2082-2095, 2020.

[14] S.N.R. Shah, N.H. Ramli Sulong, M. Shariati, R. Khan, M.Z. Jumaat, Behavior of steel pallet rack beam-to-column connections at elevated temperatures, *Thin-walled structures*, **106**, 471-483, 2016.

[15] F. Bontempi, (…), M. Ponticelli, P. Mastrogiuseppe, Modelli di incendio semplificati ed avanzati per la valutazione della sicurezza strutturale antincendio di edifici industriali in acciaio", Congresso *Collegio dei Tecnici dell'Acciaio*, Torino 2015.

[16] CEN, Eurocode 3 - Design of Steel Structures - Part 1-2: General rules, structural fire design. European Committee for Standardization CEN Brussels, 2005.

[17] Straus7, multidisciplinary finite element software, p://www.straus7.com, accessed 2023.

COMPDYN 2023
9th ECCOMAS Thematic Conference on
Computational Methods in Structural Dynamics and Earthquake Engineering
M. Papadrakakis, M. Fragiadakis (eds.)
Athens, Greece, 12-14 June 2023

# A NUMERICAL STUDY ON FIRE RESISTANCE OF BLAST DAMAGED REINFORCED CONCRETE COLUMNS

**Ravi Mudragada[1], Ankit Agrawal[1], and Pradeep Bhargava[1]**

[1] Dept. of Civil Engineering, Indian Institute of Technology Roorkee, Uttarakhand, 247667, India.
e-mail: mkumar13@ce.iitr.ac.in, ank.agr89@gmail.com, p.bhargava@ce.iitr.ac.in

## Abstract

*An explosion or blast can trigger a subsequent fire in the building structure. In the case of reinforced concrete (RC) structures, blast loading can result in relatively large residual deformations and locked in stresses in the affected members prior to fire exposure. Such residual deformations and locked in stresses can have a detrimental effect on the fire performance of RC members. Accordingly, this paper presents results from a numerical study on fire resistance of blast damaged RC columns. A three dimensional numerical model of an RC column was developed using general-purpose finite element software ABAQUS and validated against data from the experimental fire resistance tests. The developed continuum-based finite element model of RC column was subjected to blast loads of distinct scaled distances simulating the far-field and near-field scenario. Further, the blast-damaged RC columns were exposed to a standard fire, and calculated the fire resistance period corresponding to each blast case. Results indicate that the blast damaged RC column show a significant reduction in fire resistance period compared to the undamaged RC column.*

**Keywords:** RC Column, Blast, Post-blast Fire, Fire Resistance, Damage, ABAQUS.

## 1 INTRODUCTION

Fire is a plausible secondary hazard following accidental or intentional blasts (explosions). In the case of reinforced concrete (RC) structures, blast damage can result in residual (permanent) deformation and locked in stresses. Such residual deformation and locked in stresses can have a detrimental effect on the fire performance of RC members subject to a post-blast fire (PBF) scenario. Therefore, it is of interest to quantify the reduction in the fire resistance of RC members under the PBF conditions.

Recognizing the catastrophic consequences of a PBF scenario on structural systems, it has received noticeable attention in the past. Early works by researchers [1, 2] comprised an integrated environment for conducting fire and blast (explosion) analysis of steel frames. The framework was verified for a number of examples, including an isolated column subject to explosion followed by fire. Similarly, the combined effects of blast and fire and the PBF scenario of steel frames and isolated steel columns were investigated in various studies [3-9]. In some other studies [10], the progressive failure of steel framed structures was studied due to the combined effects of blast and fire.

The literature review suggests that the PBF scenario has received some attention in the past. However, very limited understanding exists on the topic, especially in the case of concrete members. This can be attributed to the complexities of modeling the interactions between blast and fire. Furthermore, no studies exist on critical load-bearing elements such as RC columns when subject to a PBF scenario.

Accordingly, this paper presents results from a numerical study on an isolated RC column subject to a PBF scenario using the general-purpose finite element software ABAQUS [11]. The blast loading is calculated using Kingery-Bulmash [12] relations and assumed to be uniformly distributed across one face of the RC column. The fire analysis is conducted in a sequentially coupled manner wherein the temperature field is independent of the stress field, i.e., the stresses do not alter the calculation of temperatures in the member. Results from the analysis are used to highlight the difference in fire resistance periods of the undamaged and post-blast fire damaged RC column obtained for four different blast loading conditions representing far-field and near-field conditions.

## 2 APPROACH FOR SIMULATING PBF SCENARIO

In order to simulate the PBF scenario on an isolated RC column under axial load, a step-by-step procedure of three steps was adopted. This approach could explicitly account for the interaction between blast loading and subsequent fire exposure. Details of this approach are presented in this section.

### 2.1 General Procedure

For simulating the PBF scenario, a three-step procedure was considered. The dead load and live load acting on the RC column were simulated as part of the first step of the approach. Subsequently, in the second step, blast loading was applied on a single face of the RC column. The peak pressure and impulse (duration) of each blast load were calculated based on an assumed charge weight and standoff distance using the Kingery-Bulmash [12] equations. Furthermore, the blast loading distribution was assumed to be uniform which is a reasonable assumption made in a number of previous studies [13-15]. The analysis was conducted using a dynamic implicit procedure available within the framework of ABAQUS [11] software. The analysis was continued for almost 100 times the duration of the blast pulse to ensure that a steady state of vibration following the pulse loading was attained within the member.

Once the blast loading was applied in the second step, a sequentially coupled thermo-mechanical analysis was conducted in the third step. A separate heat transfer model with identical geometry was developed as part of this step. The results from the heat transfer analysis were imported as a predefined field condition into the thermo-mechanical model in the third step to simulate fire exposure. Appropriate failure criteria were applied in the second and third steps to determine failure during blast loading or fire exposure. The three steps of analysis for simulating the PBF scenario are illustrated through a flowchart in Figure 1.

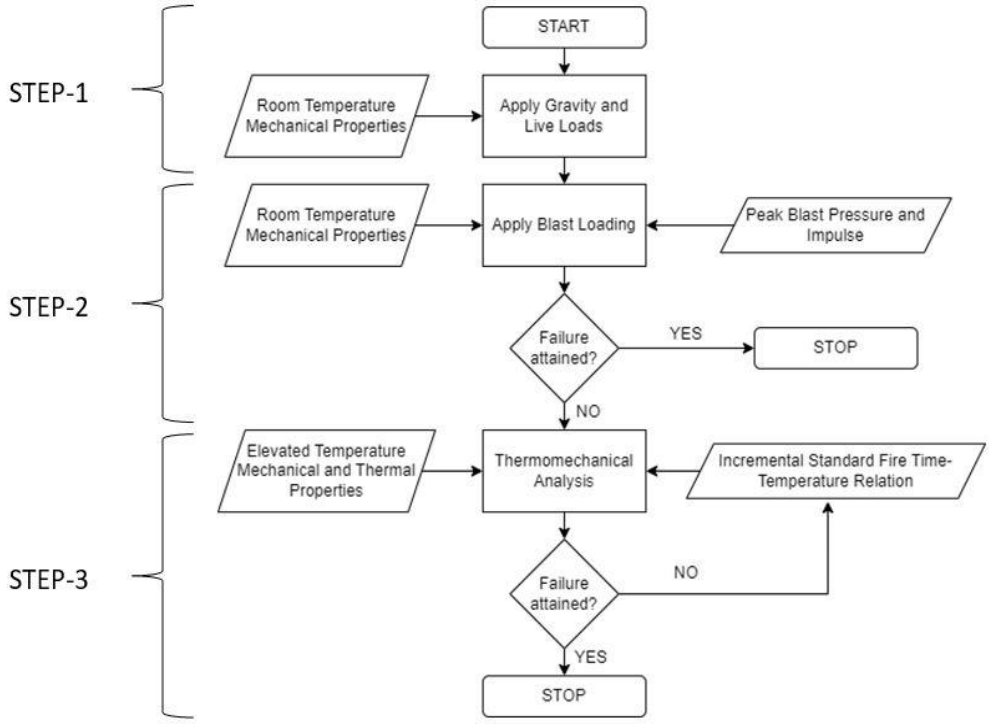


Figure 1: Flow chart describing the three steps in simulating the PBF scenario.

## 2.2 Properties of constituent materials

The properties of constituent materials, i.e., concrete and rebar, have a significant bearing on the PBF performance of the RC column. Since it is not possible to modify the material model, i.e., different suitable material models for blast (strain-rate dependent) and fire (temperature dependent), after initiating the analysis, the room temperature properties are utilized for the first two steps with the calculated average representative strain rate for each blast case, followed by temperature-dependent constituent models to be followed for the thermomechanical analysis during the fire.

The stress-strain relationship provided by Saenz (1964) [16] was modified to account for strain rate effects by employing the dynamic increase factors (DIFs) [17] to describe the dynamic behavior of concrete under uniaxial compression. Similarly, the tensile behavior of concrete under the strain rate effects was modeled by adopting the constitutive relation from the CEB-FIP Model code (2010) [18] with the inclusion of DIFs [19]. Furthermore, the elastic-plastic hardening models were used in modeling the reinforcement bars and updated the stress-strain relation with the DIFs to account for strain rate effects [20]. Numerical analysis was carried out for each blast case with a stress-strain model corresponding to static strain rate and observed the mechanical strain rate (ER) output obtained from the ABAQUS. Subsequently, for each trial, an average ER value was obtained, corresponding DIFs were calculat-

ed, and the stress-strain model was updated for both concrete and steel and used in Step-1 and Step-2 of the analysis (at room temperature conditions). During fire analysis in Step-3, the temperature ingress from the fire into concrete and the rebar is governed by their thermal properties, i.e., specific heat and thermal conductivity. Furthermore, the temperature-dependent mechanical properties, i.e., Young's modulus, yield strength, ultimate strength, and strain at ultimate strength, govern the structural response of the member. These properties were specified following the Eurocode EN 1992-1-2 [21] specifications.

### 2.3 Failure criteria

While simulating the PBF scenario, it is essential to consider failure limit states when evaluating response during blast loading as well as fire exposure. Step-1 of the analysis (at room temperature conditions) involves simulating gravity and live loading on the member; hence failure is unlikely as these loading conditions are well below the load-bearing capacity of the structure at ambient conditions. Subsequently, in Step-2 of the analysis (blast loading), deflection-based failure criteria in terms of support rotation are adopted as per UFC 3-340-02 [22] to check the failure of the RC column before the fire exposure. Finally, in Step-3 of the analysis, the rate of deflection and maximum deflection criteria as per ASTM E119 [23] is adopted to determine failure in the RC column during fire exposure.

## 3 NUMERICAL STUDY

In order to evaluate the performance of RC columns subject to the PBF scenario, finite element models were developed using the general-purpose finite element software ABAQUS [11]. The predicted response parameters from these models were used to evaluate the fire resistance period of the RC columns subject to the PBF scenario.

### 3.1 General

A normal strength RC column tested under combined effects of axial loading and temperature exposure as per ASTM E119 [23] standard time-temperature relation was selected from published literature [24]. The test parameters of the chosen column are summarized in Table 1.

| Column Designation | Fire Exposure | Initial Load (kN) | Fire Resistance (min) | Extent of Spalling |
|---|---|---|---|---|
| TNC1 | ASTM E119 | 930 | 278 | Minor |

Table 1: Summary of test parameters and results used for model validation.

Different input parameters such as the geometric details, gravity and live loading distribution, blast pressure application, fire scenario, and material properties are required to simulate the PBF scenario. The details of the column, the blast pulse and distribution, boundary conditions, and the time-temperature relation are shown in Figure 2.

The tested columns were fixed at the bottom and had only vertical translation as the degree of freedom at the top. The considered RC column had four longitudinal bars of 25mm size tied with 10 mm stirrups at a spacing of 75 mm on both ends and 145 mm in the middle. The M40 (40MPa) grade of concrete was considered with the reinforcement embedded inside with yield strength of 420 and 280 MPa for longitudinal and ties bars, respectively. Approximately 3000 mm of the entire column length was exposed to fire. The column was subject to a concentric load of 930 kN, corresponding to approximately 54% of its design capacity [25] prior to fire exposure. These loads were maintained constant throughout the fire exposure until the columns failed and could not sustain the applied loading. All four faces of the column were

subject to fire exposure. The same column selected for validation was subject to varying PBF scenarios with four different blast pulses. The analysis was continued for 500 milliseconds for each case to allow for a steady state of vibration (as no damping was considered in the model) to be attained prior to fire exposure. The blast pulse details for each of the four cases are summarized in Table 2.

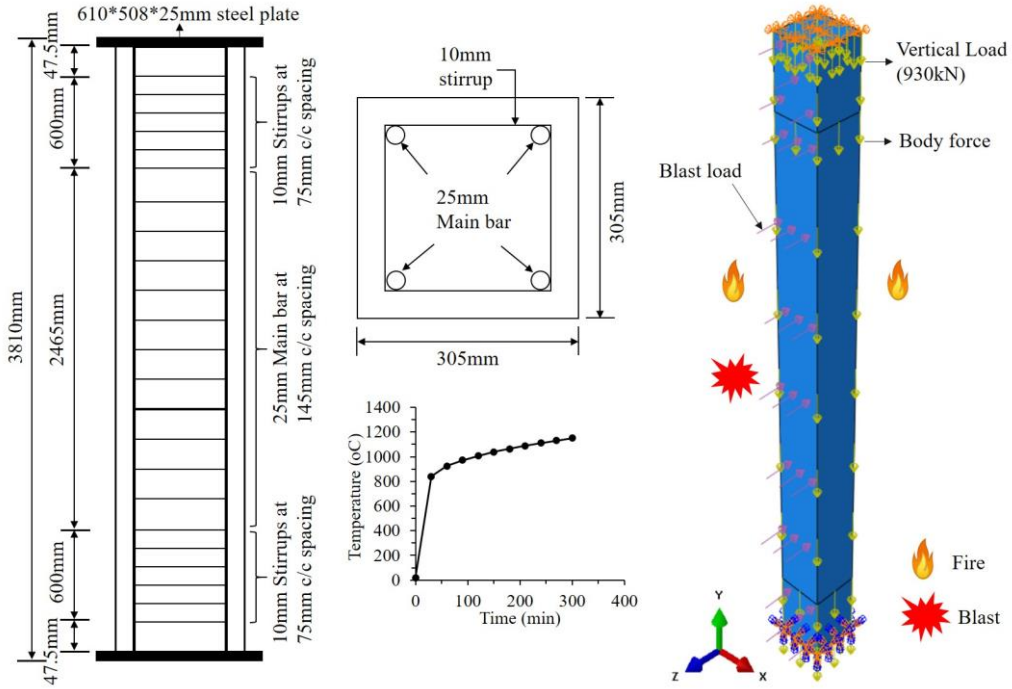


Figure 2: Dimensions, loading, and reinforcement details of the column selected for validation.

| Scenario Designation | Charge Weight (Kg) | Standoff Distance (m) | Scaled Distance ($m/kg^{1/3}$) | Peak Pressure (MPa) | Peak Impulse (MPa-ms) | Scenario Classification [26] |
|---|---|---|---|---|---|---|
| Case-1 | 1000 | 20 | 2 | 1.056 | 3.638 | Far-field |
| Case-2 | | 16 | 1.6 | 2.08 | 4.798 | Far-field |
| Case-3 | | 12 | 1.2 | 4.895 | 6.944 | Near-field |
| Case-4 | | 11 | 1.1 | 6.268 | 7.789 | Near-field |

Table 2: Summary of blast pulses for simulating the PBF scenario.

### 3.2 Finite element model

The analysis was carried out using the general-purpose finite element software ABAQUS. Two sub-models were developed to simulate the effects of the PBF scenario on the RC column. A structural model was required for conducting the room temperature loading analysis, blast loading analysis, and thermo-mechanical analysis. Also, a heat transfer model is needed to calculate the evolution of temperatures within the column cross-section. Accordingly, the structural model comprised of eight-noded continuum elements with full integration (C3D8) for modeling concrete and two-node link elements (T3D2) for modeling the steel reinforcement. The heat transfer model comprised of eight-noded linear brick elements (DC3D8) for discretizing concrete and two-noded link elements (DC1D2) for steel reinforcement, with only nodal temperature as the degree of freedom. A perfect bond between rebar and concrete was simulated through the tie constraint in the heat transfer model, whereas embedded region

constraint was used in the structural model. The constitutive models for concrete and steel were defined using plasticity models within the framework of the software. Concrete was modeled using a concrete-damaged plasticity model, and an elastic-plastic hardening model was used for steel reinforcement. A discretized view of the structural model of the RC column, along with the material models for both blast and fire analysis, are shown in Figure 3.

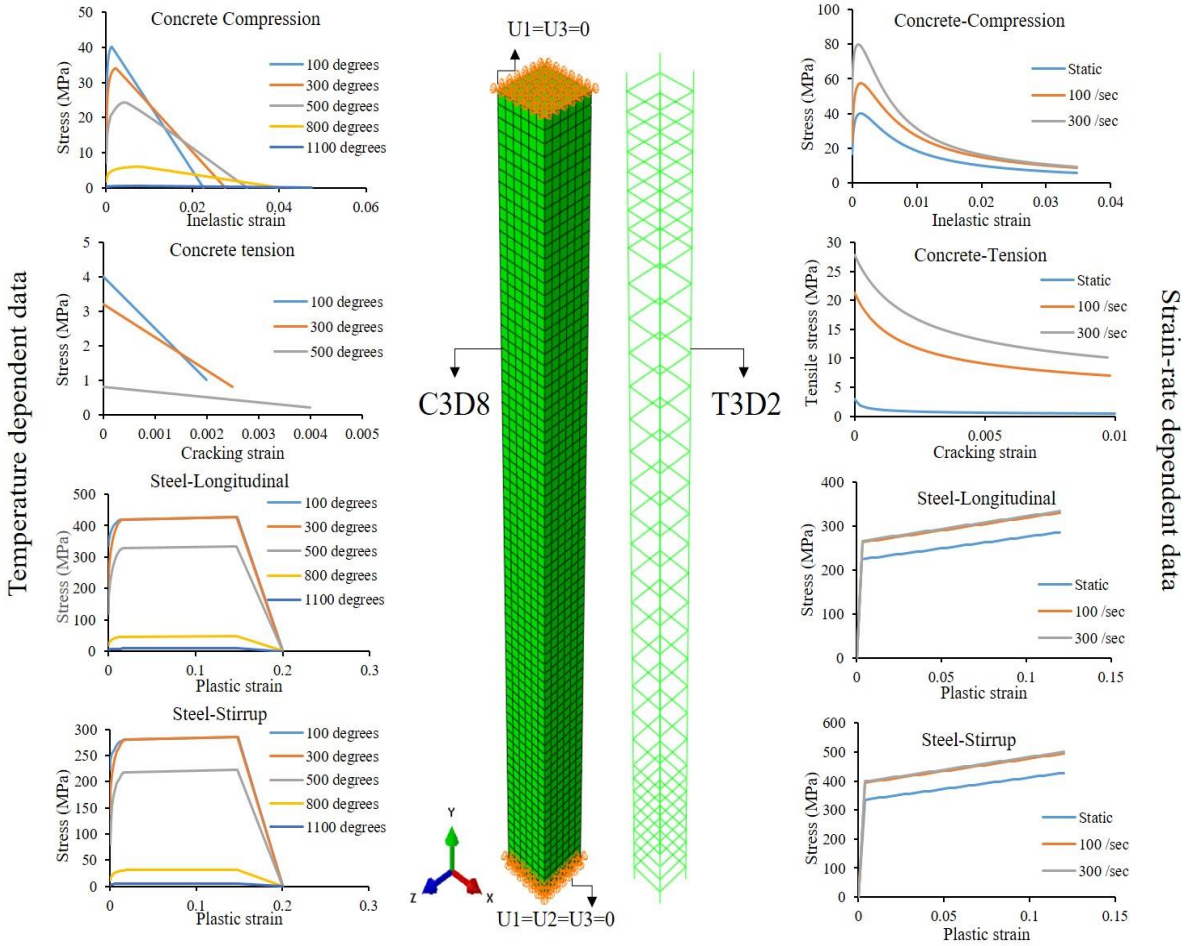


Figure 3: Discretized view of the RC column with adopted stress-strain relations for concrete and steel.

## 4 RESULTS AND DISCUSSION

Predictions of response parameters obtained through numerical simulation were compared against those measured during tests [24] for validation. Figure 4 shows temperature progression at various cross-sectional locations of the column as a function of time. The temperature within deeper layers of the column experiences a progressively lower rate of increase when compared with fire temperature due to low thermal conductivity and high specific heat of concrete. Overall, the measured and predicted temperatures at different cross-sectional locations are in agreement. This comparison establishes the validity of the heat transfer model.

Similarly, the axial deflections of the column measured during tests and predicted through the numerical model are compared in Figure 5. The deflection in the columns is governed by several factors, including load level, thermal expansion, and creep. The initial deflection (expansion) of the column is a consequence of thermal strains in the column due to monotonically increasing fire temperatures. Subsequently, as cross-sectional temperatures increase further, the mechanical strains begin to dominate due to temperature induced degradation in concrete and steel reinforcement as well as primary and secondary creep effects. As a result, the deflec-

tions in the column begin to decay after attaining a peak value despite fire temperatures increasing monotonically.

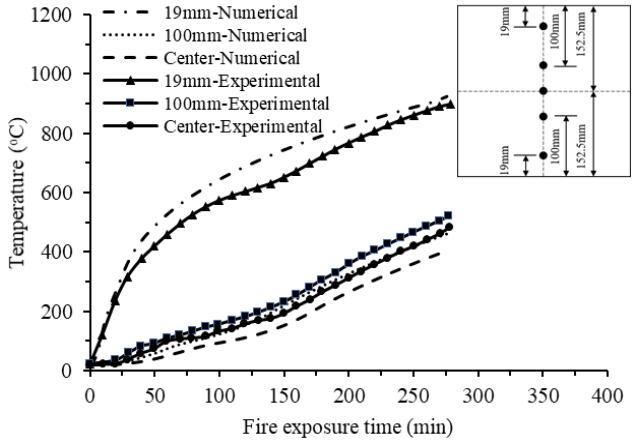


Figure 4: Comparison of measured versus predicted cross-sectional temperatures at various depths in column.

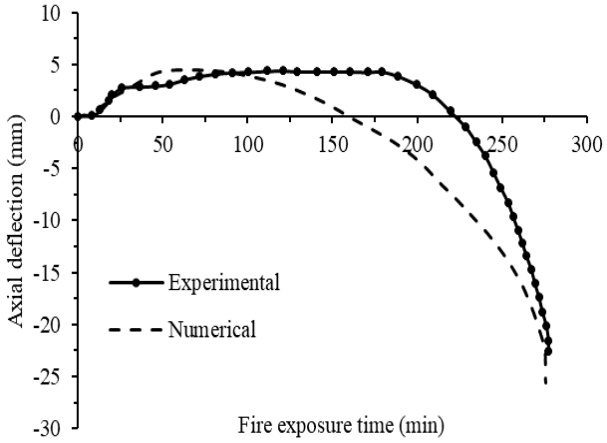


Figure 5: Comparison of measured versus predicted axial deflection during fire exposure alone.

Eventually, the increasing cross-sectional temperatures result in the yielding of reinforcement resulting in the contraction of the column followed by failure. It can be seen that the predicted and measured axial deformations agree well during the early phases of fire exposure, when the majority of the deflections occur due to thermal expansion. However, as fire exposure time progresses further, the numerical model over-predicts the contraction in the column. This can be attributed to the conservative nature of the temperature-dependent mechanical model prescribed by Eurocode 2 [21]. Nonetheless, the prediction of time to failure is in a close match with the experimental result.

The validated numerical model was modified to simulate the effects of the PBF scenario on the same RC column. In this numerical model, Step-1 comprised gravity loading as a distributed body force of 2.5 kN/m$^3$ and a vertical load of 930 kN on the column. Following the application of the ambient loads, blast loads were applied as pressure loading corresponding to peak pressure and pulse duration, as summarized in Table 2. Finally, after running the blast analysis for a sufficiently long time period (500 milliseconds) such that a steady state of vibration was attained, a sequentially coupled thermo-mechanical analysis was conducted to evaluate the fire resistance period for each case. During the blast analysis, it was observed that for all the considered blast cases, the central bending deflections of the RC column measured

in the lateral direction were within the permissible limits recommended by UFC 3-340-02 [22]. Therefore, the considered RC column can be subject to the PBF scenario.

Figure 6 shows axial deformations on the blast loaded edge of the top face from the blast loading step for all four cases of blast loading. As expected, the top edge on the blast loaded face begins to deflect downwards initially from its original equilibrium position under static loading. The downward deflection continues to increase during the initial phases of the triangular pulse loading. Eventually, as time progresses, the amplitude of the oscillations induced by the blast pulse diminishes and attains a steady state value which does not reduce as no damping is considered in the model. Also, a noticeable residual deformation can be observed in the column depending on the scaled distance.

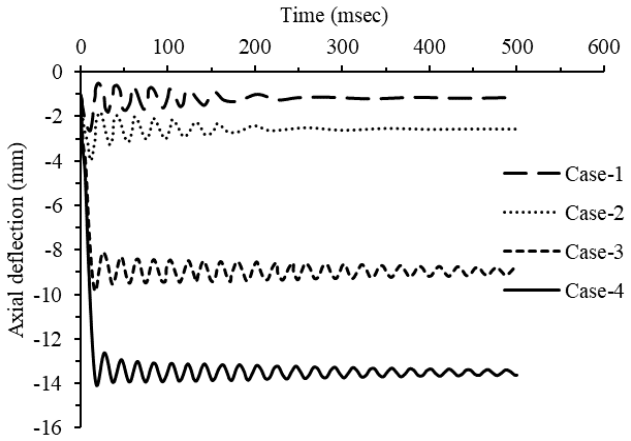


Figure 6: Predicted axial deflection at the top face of the column for different blast pulses.

Besides the blast response, a comparison of the response of the column subject to distinct PBF scenarios is contrasted with the fire response of the undamaged column in Figure 7. Clearly, the blast damaged columns subject to fire exposure exhibit a similar response to the undamaged column. Nonetheless, the initial imperfection in terms of the residual deflection and locked in stresses (as depicted for Case-2 and Case-4 in Figure 8) resulted in a significant reduction in the overall fire resistance period of the blast damaged columns. As a comparison, Table 3 shows the fire resistance period of undamaged and blast damaged RC columns (PBF). It can be observed that the fire resistance period of PBF columns reduces by almost 83% for the near-field blast (Case-4) and 22% for the far-field (Case-1).

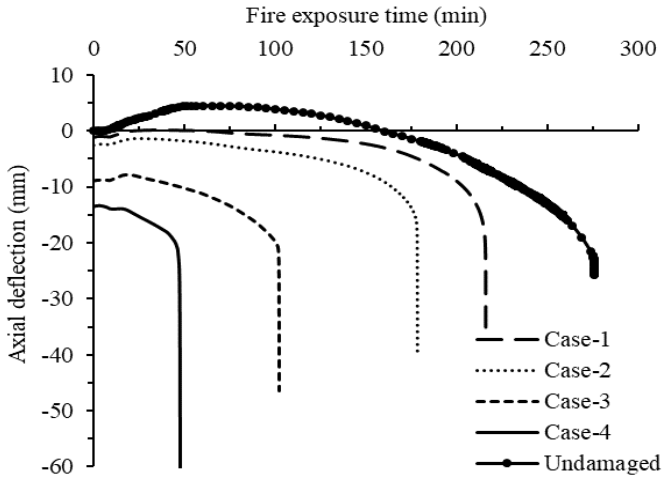


Figure 7: Comparison of axial deflection for undamaged column versus PBF scenario.

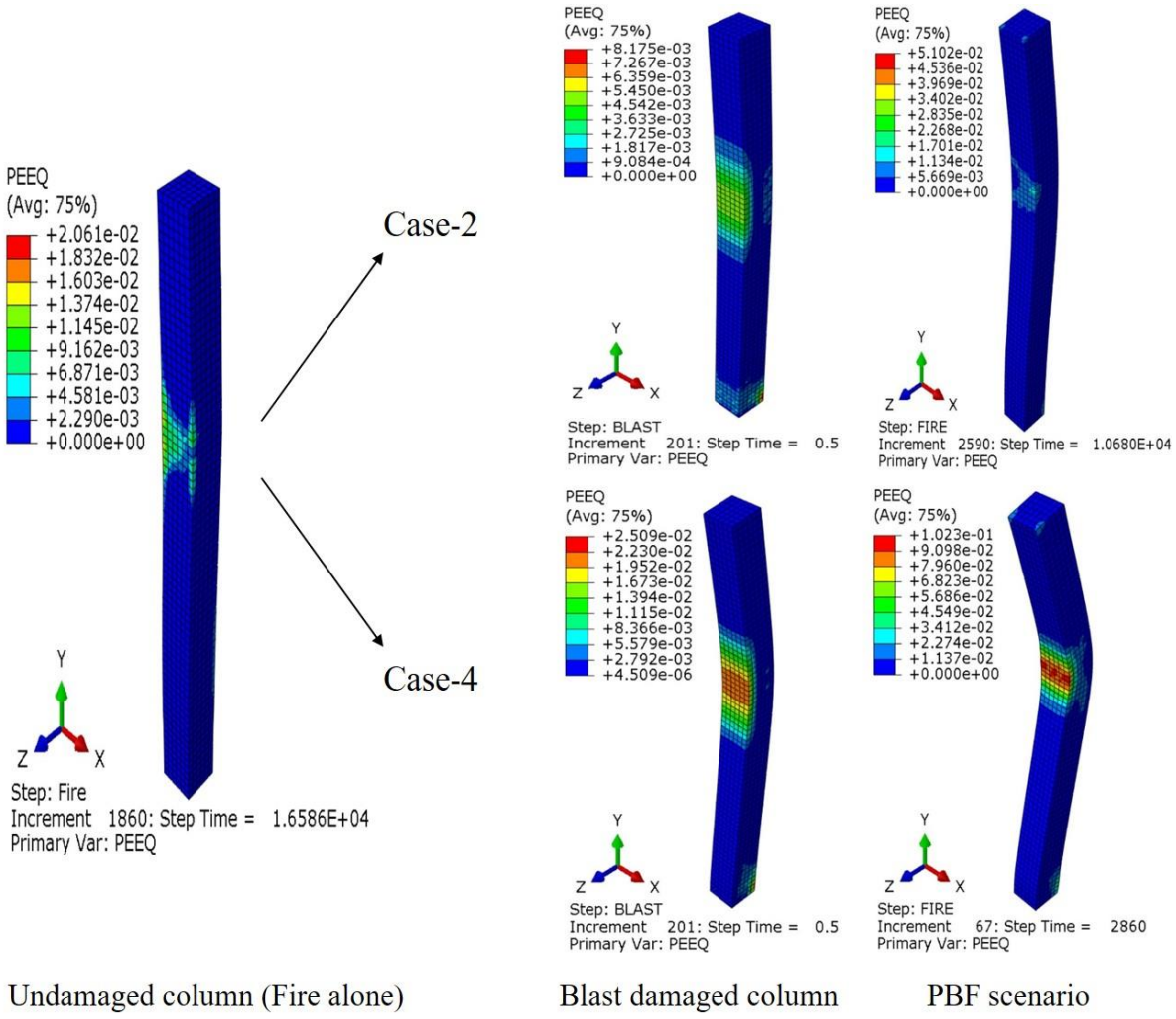


Figure 8: Equivalent plastic strain comparison of undamaged column versus PBF scenario for Case-2 and Case-4.

| Loading Scenario | Residual Axial Deflection (mm) | Fire Resistance Period (min) | % Reduction |
|---|---|---|---|
| Undamaged (Fire alone) | - | 276.4 | - |
| Damaged (Case-1) | 1.17 | 216 | 22.3 |
| Damaged (Case-2) | 2.56 | 178 | 35.9 |
| Damaged (Case-3) | 8.82 | 102.3 | 63.2 |
| Damaged (Case-4) | 13.6 | 47.7 | 82.8 |

Table 3: Comparison of fire resistance period between undamaged column versus PBF scenario.

## 5 CONCLUSIONS

In general, structural members or systems are designed for a required fire-resistance rating, which is defined as the duration in which a structural member or system exhibits resistance with respect to structural integrity, stability, and heat transmission. However, many of these criteria are developed for fire exposure under normal conditions without cumulative damage from the preceding blast scenario. The study presented here attempts to determine the fire resistance rating of RC axial members subject to post-blast fire. The following conclusions can be drawn based on the results of the numerical study.

- The developed continuum-based finite element model of the reinforced concrete column was validated with experimental studies on both blast and fire. The response measured during the tests agreed well with response predictions made by the numerical model, which shows the reliability of the developed numerical model in evaluating the post-blast fire scenarios of the reinforced concrete members.
- Post-blast fire scenarios can be simulated through a three-step procedure. The gravity loads acting on the reinforced concrete column were simulated as part of the first step, followed by the blast exposure in the second step at room temperature conditions. Finally, a sequentially coupled thermo-mechanical analysis was conducted in the third step.
- A comparison of the response of the column subject to distinct post-blast fire scenarios is contrasted with the fire response of the undamaged column. The initial imperfection in terms of the residual deflection and locked in stresses resulted in a significant reduction in the overall fire resistance period of the blast damaged columns.
- It can be observed that the fire resistance period of post-blast fire columns reduces by 22.3% to 82.8% at scaled distances varying from 2 to 1.1 m/kg$^{1/3}$ showing the severity of the post-blast fire scenario on the fire performance of reinforced concrete members.

## REFERENCES

[1] L. Song, B.A Izzuddin, A.S Elnashai, P.J Dowling, An integrated adaptive environment for fire and explosion analysis of steel frames. Part I: analytical models. *Journal of Constructional Steel Research*, 53, 63-85, 2000.

[2] B.A. Izzuddin, L. Song, A.S. Elnashai, P.J. Dowling, An integrated adaptive environment for fire and explosion analysis of steel frames — Part II: verification and application. *Journal of Constructional Steel Research*, 53, 63-85, 2000.

[3] Y. Ding, M. Wang, Z.X. Li, H. Hao, Damage evaluation of the steel tubular column subjected to explosion and post-explosion fire condition. *Engineering Structures*, 55, 44-55, 2013.

[4] L. Magenes, T.J. Mander, M.A. Morovat, Effects of Blast-Induced Permanent Deflections on the Performance of Load-Bearing Steel Elements in Fire. *Structures Congress*, Denver, Colorado, April 6–8, 2017.

[5] Q. Baoxin, S. Yan, J. Bi, Study on Collapse Mechanism of Steel Frame Structure under High Temperature and Blast Loading. *3rd International Conference on Energy Equipment Science and Engineering (ICEESE 2017)*, Beijing, China, December 28–31, 2017.

[6] T.B. Adeyanju, M.C. Christian, P.J. Stafford, A Numerical Study on the Structural Response of Steel Structures under Post-Blast Travelling Fires. *Structures Congress*, Orlando, Florida, April 24–27, 2019.

[7] W. Lu, Thermo-mechanical damage modelling for collapse assessment of steel buildings under blast and fire loads. *Unpublished Doctoral thesis*, University of London, UK, 2019.

[8] T.B. Adeyanju, Structural Performance of Steel Buildings under Travelling Fires and Blast. *Doctoral thesis*, Imperial College London, United Kingdom, 2020.

[9] H. Al-Thairy, Prediction of Behaviour and Failure of Steel Columns Subjected to Blast Followed by Fire Induced by Explosion. *International Journal of Steel Structures*, 21, 1431–1453, 2021.

[10] Y. Ding,Ye. Chen, Y. Shi, Progressive collapse analysis of a steel frame subjected to confined explosion and post-explosion fire. *Advances in Structural Engineering*, 19, 1780–1796, 2016.

[11] ABAQUS, *Theory Manual*. Dassault Systemes Simulia Corporation, Providence, RI, USA, 2017.

[12] C.N. Kingery, G. Bulmash, *Air blast parameters from TNT spherical air burst and hemispherical surface burst*. Aberdeen Proving Ground, MD: Ballistic Research Laboratories, 1984.

[13] E. Sammarco, E. Williamson, Dynamic Response Characteristics that Lead to Direct Shear Failure in Blast-Loaded Columns. *Journal of Structural Engineering*, 147, 1–17, 2021.

[14] S.J. Ju, H.G. Kwak, A FE model to evaluate the resisting capacity of RC beams and columns under blast loading based on P-I diagram. *International Journal of Impact Engineering*, 161, 104113, 2022.

[15] L.L. Ma, H. Wu, Q. Fang, A unified performance-based blast-resistant design approach for RC beams/columns. *International Journal of Impact Engineering*, 173, 104459, 2023.

[16] L.P. Sanez, Discussion of Equation for the Stress-Strain Curve of Concrete. *ACI Journal*, 61, 1227–39, 1964.

[17] Y. Al-Salloum, T. Almusallam, S.M. Ibrahim, H. Abbas, S. Alsayed, Rate-dependent behavior and modeling of concrete based on SHPB experiments. *Cement and Concrete Composites*, 55, 34–44, 2015.

[18] CEB-FIP, *Model code for concrete structures*. Switzerland: Committee Euro-International du Beton-Federation for Prestressing, 2010.

[19] X.Q. Zhou, H. Hao, Modelling of compressive behavior of concrete-like materials at high strain rate. *International Journal of Solids and Structures*, 45, 4648–4661, 2008.

[20] CEB Bulletin 187, *Concrete Structures under Impact and Impulsive Loading-Synthesis Report*. Lausanne, Switzerland: Committee Euro-International du Beton, 1988.

[21] EN 1992-1-2, *Eurocode 2: Design of concrete structures – Part 1-2: General rules – Structural fire design*. European Committee for Standardization, Brussels, Belgium, 2004.

[22] UFC 3-340-02, *Structures to Resist the Effects of the Accidental Explosions*. Washington, D.C: US Department of Army, Navy and the Air Force, 2008.

[23] American Society for Testing and Materials (ASTM-1990), *Standard methods of fire endurance tests of building construction and materials.* ASTM E119-88, Philadelphia, 1990.

[24] V.K.R. Kodur, C. Fu-Ping, W. Tien-Chih, M.A. Sultan, Effect of Strength and Fiber Reinforcement on Fire Resistance of High-Strength Concrete Columns. *Journal of Structural Engineering*, 129, 253-259, 2003.

[25] Canadian Standards Association (CSA), *Code for the design of concrete structures for buildings*. CAN3-A23.3-M94, Rexdale, Ontario, Canada, 1994.

[26] Americal Society of Civil Engineers (ASCE), Blast protection of buildings. ASCE SEI 59-11, Reston, VA, USA, 2011.

COMPDYN 2023
9th ECCOMAS Thematic Conference on
Computational Methods in Structural Dynamics and Earthquake Engineering
M. Papadrakakis, M. Fragiadakis (eds.)
Athens, Greece, 12-–14 June 2023

# THE INFLUENCE OF DAMPING ON PROGRESSIVE COLLAPSE ANALYSIS

**Alex S. Cao**[1] **and Andrea Frangi**[2]

[1]Institute of Structural Engineering, ETH Zurich
Stefano-Franscini-Platz 5, 8093 Zurich, Switzerland
e-mail: cao@ibk.baug.ethz.ch

[2] Institute of Structural Engineering, ETH Zurich
Stefano-Franscini-Platz 5, 8093 Zurich, Switzerland
e-mail: frangi@ibk.baug.ethz.ch

**Abstract.** *The most common method of modeling damping in structures is with equivalent viscous damping with the Rayleigh damping model. However, it is well-known that the Rayleigh damping model may cause spurious damping forces and nonphysical behavior for inelastic structures. Remedies have been proposed to overcome these problems, such as various incremental versions using the tangent stiffness or the use of modal damping instead. These may be appropriate for inelastic structures with negligible changes of the vibration modes, and without softening behavior for the Rayleigh damping models. In progressive collapse analyses, these damping models may be inappropriate because of the radical change in vibration modes, as well as the changes to the mass and stiffness matrix. In this paper, initial and incremental versions of the Rayleigh and modal damping models are presented and compared for a structure undergoing progressive collapse. The damping model is not critical if the objective is to assess the response until the first failure. However, the choice of the damping model may lead to large dissimilarities after the first failure in a progressive collapse analysis.*

**Keywords:** Equivalent Viscous Damping, Rayleigh Damping, Modal Damping, Structural Dynamics, Progressive Collapse, Nonlinear Response History Analysis.

## 1 INTRODUCTION

Nonlinear response history analysis is a versatile tool that can be used in performance-based design [1] and to simulate the response of structures subjected to various dynamic loading, such as earthquake loading [1], wind loading [2], blast and impact loading [3, 4], and progressive collapse [5]. The nonlinearities in nonlinear response history analysis may stem from large deformations, inelastic material behavior, and more. An important consideration for the dynamic response of a structure is the amount of damping and its model implementation.

For inelastic structures, the damping would ideally be modeled explicitly in the model as the hysteresis of the different materials [6]. This supposes that the hysteresis of the different materials used in the model is known, which may not be trivial. Besides, implementing hysteresis directly in the model as distributed or concentrated plasticity quickly leads to a bottleneck in terms of computational expenses for the analysis. A common alternative to the explicit modeling of hysteresis in the model is the use of equivalent viscous damping with the Rayleigh damping model or other damping models. A combination of equivalent viscous damping and the explicit modeling of hysteresis in the materials can also be used.

The advantage of using equivalent viscous damping is its computational efficiency in comparison with the direct modeling of hysteresis. For elastic structures or structures with moderate inelastic behavior, the use of equivalent viscous damping may result in acceptable results. However, the use of common damping models with equivalent viscous damping for strongly inelastic structures with large deformations may lead to large non-physical or spurious damping forces. This problem is particularly pronounced in Rayleigh damping [1, 6, 9]. Besides, equivalent viscous damping is often measured for structures in their elastic range [1] and it may not reflect the damping for inelastic structures [7].

To overcome the problems related to conventional Rayleigh damping, several researchers have suggested to use the tangent stiffness in Rayleigh damping [6, 8]. Another approach is to keep the calibration parameters in Rayleigh damping constant throughout the analysis [6]. Other alternative damping models are mass-proportionate damping [8], capped damping [10], modal damping [1, 11], and more.

In progressive collapse analysis, structures typically undergo large deformations and exhibit strong inelastic behavior. The failure and subsequent detachment and loss of structural members lead to changes in the remaining structure's stiffness and mass matrices. The loss of members also affects the damping properties of the structure. For damping models which rely on a combination of the initial stiffness and mass matrices to form the damping matrix, spurious damping forces are a certainty. Besides the spurious damping forces, the unchanged damping matrix may lead to convergence problems and a loss of computational efficiency associated with classical damping models.

This paper presents different variations of initial and incremental Rayleigh damping, as well as initial and incremental modal damping and their appropriateness for progressive collapse analysis. The performance of the different damping models is compared in a case study of a symmetric timber frame with four bays and four stories. Progressive collapse is introduced through the dynamic removal of an edge column, and the collapse is simulated using a recently developed collapse model [12]. The collapse model is parametric and includes element separation and detachment [13], element-removal [14], impact loading [15], and various damping models. The timber frame comprises glued laminated timber beams and columns, and laterally loaded timber connections with dowel-type fasteners and slotted-in steel plates. To find the equivalent viscous damping, a newly developed multi-scale hysteretic connection model is

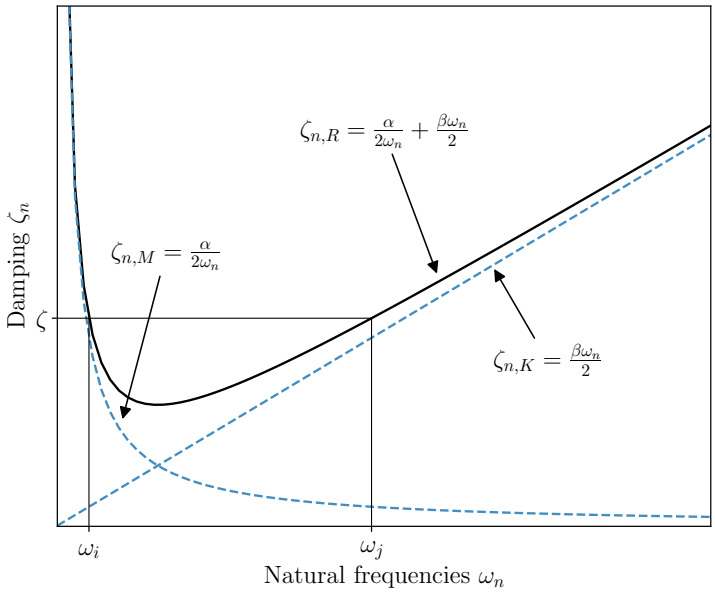


Figure 1: Damping $\zeta_n$ of frequency $\omega_n$ in Rayleigh damping.

used [16]. With the resulting hysteresis, a secant stiffness approach is used to model the frame connections.

## 2 DAMPING MODELS

In this paper, the Rayleigh damping and modal damping models were investigated. Rayleigh damping was assessed in its initial and incremental form, with initial and incremental calibration parameters. Similarly, modal damping was assessed in its initial and incremental form. The following subsections present the different damping models.

### 2.1 Rayleigh damping

In Rayleigh damping, the damping matrix **c** is a linear combination of the stiffness **k** and mass **m** matrices:

$$\mathbf{c} = \alpha\mathbf{m} + \beta\mathbf{k}, \tag{1}$$

where $\alpha$ and $\beta$ are calibration parameters. If the damping ratio $\zeta$ is constant throughout all the modes, the calibration parameters $\alpha$ and $\beta$ are:

$$\begin{aligned} \alpha &= 2\zeta\frac{\omega_i\omega_j}{\omega_i + \omega_j}, \\ \beta &= 2\zeta\frac{1}{\omega_i + \omega_j}, \end{aligned} \tag{2}$$

where $\omega_i$ and $\omega_j$ are the angular frequencies that the calibration parameters $\alpha$ and $\beta$ are computed for. The angular frequencies $\omega_i$ and $\omega_j$ often inherit the values of the first and a higher frequency mode of a structure, which are picked based on their importance for the dynamic response of the structure. With the calibration factors in Equation 2, it is assumed that the damping $\zeta$ is the same for frequency $\omega_i$ and $\omega_j$.

### 2.1.1 Initial Rayleigh

In the most common implementation of Rayleigh damping, an eigenvalue analysis is conducted before the dynamic analysis, and the damping matrix **c** is computed from the resulting eigenvalues at the initial state of the structure. In this paper, this approach is referred to as initial Rayleigh damping. Initial Rayleigh damping may lead to spurious or non-physical damping forces $\mathbf{f}_D = \mathbf{c}\dot{\mathbf{u}}$ for inelastic structures, where $\dot{\mathbf{u}}$ is the velocity [1, 6, 9, 10]. Besides, the results may not be conservative in a nonlinear response history analysis [11].

The root cause of the spurious damping forces $\mathbf{f}_D$ lies in the formulation of the Rayleigh damping model, which includes a contribution from the stiffness matrix **k**. For a certain displacement **u** of a structure, the resulting forces $\mathbf{f}_S = \mathbf{k}\mathbf{u}$ of a linear-elastic idealization would be larger than the real response of the structure in the inelastic range, where hardening or softening may be present and the actual stiffness **k** of the system may be lower. In initial Rayleigh damping, the stiffness contribution **k** does not change. This results in an increasing error from initial Rayleigh damping with the magnitude of inelasticity experienced by the structure.

Besides the spurious damping forces $\mathbf{f}_D$ that stem from the constant stiffness contribution $\mathbf{c}_k = \beta\mathbf{k}$, the inertia forces $\mathbf{f}_I = \mathbf{m}\ddot{\mathbf{u}}$ and the velocity $\dot{\mathbf{u}}$ may also encounter problems. If there is a change in the stiffness **k**, this implies that the natural frequency $\omega_n = \lambda_n\sqrt{k/m}$ would also change. If the structure experiences hardening or softening, the natural frequency $\omega_n$ would become smaller because of the reduced stiffness **k**. Consequently, the natural period $T_n$ would become longer and the velocity $\dot{\mathbf{u}}$ and acceleration $\ddot{\mathbf{u}}$ would be reduced. This would lead to a direct reduction in the inertia $\mathbf{f}_I$ and damping forces $\mathbf{f}_D$ as well. However, a linear-elastic idealization with initial Rayleigh damping cannot replicate this behavior for inelastic systems.

In the analysis of the progressive collapse of structures with elastic or inelastic material behavior, the use of initial Rayleigh may cause larger spurious damping forces. Suppose that a model can simulate a progressive collapse, including the separation and detachment of members upon failure. If the members of the structure have linear-elastic perfectly brittle materials, then the structure will only experience a change in the stiffness **k** and mass **m** matrices as the different members fail, separate, and detach from the remaining structure. Initial Rayleigh damping cannot reflect these changes, as the damping matrix **c** is computed from the initial stiffness **k** and mass **m** matrices. Therefore, initial Rayleigh damping results in an increasing amount of spurious damping forces $\mathbf{f}_D$ as more and more members fail during the progressive failure. Besides, the equation solving becomes inefficient and convergence problems may ensue as the damping matrix **c** retains non-zero entries for elements that are removed.

### 2.1.2 Incremental Rayleigh

To overcome the problem of spurious damping forces in initial Rayleigh damping, several remedies have been proposed. A common approach is to replace the initial stiffness in initial Rayleigh damping with the tangent stiffness, which is updated incrementally [6, 8, 10]. Here, this approach is slightly modified and is referred to as incremental Rayleigh damping, where both the stiffness **k** and mass **m** matrices are updated at each time-step. There are several variations of incremental Rayleigh damping, where the calibration factors in Equation 2 may be computed only once, or incrementally [1, 6, 8, 10]. This can also be combined with the tangent stiffness.

In progressive collapse analysis, the use of incremental Rayleigh damping solves some problems related to initial Rayleigh damping. To a certain extent, it also solves the problems related

to spurious damping forces for inelastic structures. However, the updating of the stiffness matrix $\mathbf{k}$ may lead to an unstable response if the structure experiences softening behavior. If softening behavior is present in the structure, the stiffness matrix $\mathbf{k}$ may become negative. This implies that the damping matrix $\mathbf{c}$ in Equation 1 may decrease and eventually become negative. Consequently, the damping force $\mathbf{f}_D$ may transition from being a resisting force to an exerting force. Therefore, the structure's vibrations may grow uncontrollably. Besides the aforementioned problems, it may also become impossible to find real-valued positive eigenvalues because of the negative stiffness matrix $\mathbf{k}$.

A physical interpretation of the growing vibrations is that the structure experiences an influx of energy from the work exerted on the structure from the negative damping force $\mathbf{f}_D$. This exerted work must materialize in kinetic or strain energy in the structure, which results in larger response amplitudes to accommodate the additional energy. Unless the structure is subjected to an external force, this mechanism is physically impossible. Therefore, incremental Rayleigh damping can only be used for structures which do not experience softening behavior.

Besides the aforementioned problems with incremental Rayleigh, there is another worrying property. Because incremental Rayleigh damping changes with the state of the stiffness matrix $\mathbf{k}$, the damping of a monotonically loaded structure may be accurate. If, however, the structure experiences an inelastic response with hysteresis, the stiffness matrix $\mathbf{k}$ will change throughout the hysteretic response. Consequently, the damping force $\mathbf{f}_D$ would inherit the hysteresis of the stiffness matrix $\mathbf{k}$. Because most vibration measurements are conducted for structures in their elastic range, it is largely unknown whether damping should have the property of hysteresis [1].

### 2.2 Modal damping

As an alternative to Rayleigh damping, modal damping can be used [1]. In modal damping, the damping matrix $\mathbf{c}$ is defined as a superposition of modal damping matrix contributions:

$$\mathbf{c} = \mathbf{m}\left(\sum_{n=1}^{N} \frac{2\zeta_n\omega_n}{M_n}\phi_n\phi_n^T\right)\mathbf{m}, \tag{3}$$

where $\zeta_n$ is the damping ratio, $\omega_n$ is the natural angular frequency, $M_n$ is the generalized mass, and $\phi_n$ is the eigenvector for mode $n$. The generalized mass matrix is defined as $\mathbf{M} = \Phi^T\mathbf{m}\Phi$, where $\Phi$ is the modal matrix. The generalized mass matrix $\mathbf{M}$ is a diagonal matrix comprising $M_n$ diagonal entries.

### 2.3 Initial modal damping

For the modal damping matrix in Equation 3, damping contributions of $N$ modes are included. If the modal damping matrix $\frac{2\zeta_n\omega_n}{M_n}\phi_n\phi_n^T$ from mode $n$ is not included, there is no damping $\mathbf{c}$ in this mode. To ensure that the response of the system is accurate, a sufficient number of modes $N$ must be included in the analysis.

Similarly to initial Rayleigh damping, modal damping computed for the initial elastic state may cause spurious damping forces $\mathbf{f}_D$ for inelastic structures. One of the main assumptions of modal analysis is that the structural response is linear and subjected to small deformations. Because the different parameters of modal damping in Equation 3 relies on solving the eigenvalue problem $\det\left[\mathbf{k} - \omega_n^2\mathbf{m}\right] = 0$ in modal analysis, their accuracy may be in question for the inelastic response of a structure with large deformations.

However, initial modal damping will not result in a negative damping matrix $\mathbf{c}$ and damping force $\mathbf{f}_D$ in most cases, as the eigenvalues of a structure $\omega_n^2$ are mostly non-negative in the elas-

tic state. Negative eigenvalues $\omega_n^2$ are physically plausible if a structure experiences dynamic buckling or snap-through. However, most cases of negative eigenvalues $\omega_n^2$ are associated with modeling errors and are not physically plausible. This is especially true for an eigenvalue analysis conducted for a structure in the elastic state.

Using initial modal analysis is less problematic than the different variations of Rayleigh damping. For the inelastic response of structures, initial modal damping offers superior performance compared with Rayleigh damping [1, 11]. For progressive collapse analysis, initial modal damping is fraught with similar challenges as incremental Rayleigh damping because of the changing mass **m** and stiffness **k** during a progressive collapse. The changing mass **m** and stiffness **k** leads to changes in the natural angular frequencies $\omega_n$ and the eigenvectors $\phi_n$, which affects the damping matrix **c** in Equation 3 directly.

### 2.4 Incremental modal damping

A remedy for overcoming the shortcomings of initial modal damping, is its incremental alternative. If a sufficiently small time-step $\Delta t$ is used in a dynamic analysis, the structural response between time $t_i$ and $t_{i+1}$ may be considered linear and the deformations may be small. Therefore, updating the modal damping incrementally throughout an analysis may better reflect the real response of a structure in its inelastic state.

A disadvantage of incremental modal damping is the need to conduct an eigenvalue analysis at each time $t_i$. For small models with a few degrees of freedom, this may be unproblematic. However, larger models will be substantially more computationally expensive in comparison with initial modal damping. To make the equation solving more efficient, the damping matrix **c** can be updated at every other time $t_i$, or the time-step $\Delta t$ can be increased. The trade-off between computational efficiency and numerical accuracy should be quantified for every analysis with a sensitivity study.

Besides the computational expense of conducting an eigenvalue analysis at each time $t_i$, convergence problems may ensue because of the eigenvalue analysis. For initial modal damping, the occurrence of negative eigenvalues $\omega_n^2$ is highly unlikely. However, a structure in its inelastic state may experience instabilities. These instabilities may occur because of changes in the stiffness matrix **k** from hardening or softening behavior. In progressive collapse analysis, or for structures subjected to extreme loading, the likelihood of instabilities is not negligible.

## 3 MATERIALS AND METHOD

### 3.1 Frame design

The frame was designed for gravity loads according to EN 1990:2002 [17] and EN 1991-1-1:2002 [18] with the following load combination:

$$p_{Ed} = \xi \gamma_G g_k + \gamma_Q q_k, \tag{4}$$

where $\xi$ is 0.85, $\gamma_G$ is 1.35, $\gamma_Q$ is 1.50, $g_k$ is 3.5 kN/m$^2$, and $q_k$ is 3.0 kN/m$^2$. Glued laminated timber with a strength class of GL24h was chosen for the beams and columns. Characteristic material parameters were assumed from EN 14080:2013 [19], and the beams and columns were designed with EN 1995-1-1:2004 [20]. The beams were assumed to have simply supported boundary conditions, and the columns were assumed to be continuous. The frame also satisfied the serviceability criterion for wind-induced vibrations from ISO 10137:2007 [21], where the peak accelerations were computed with EN 1991-1-4:2005 Annex B [22]. For the wind-induced vibrations, an equivalent viscous damping $\zeta_{eq}$ of 0.02 was chosen.

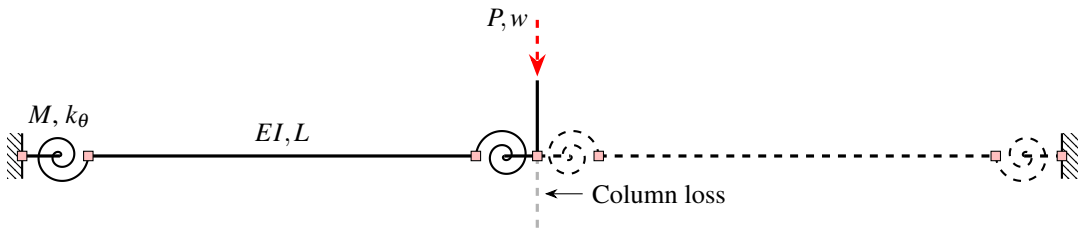


Figure 2: Structural system for the estimation of the equivalent viscous damping $\zeta_{eq}$.

To connect the beams and the columns, laterally loaded timber connections with dowel-type fasteners were designed with EN 1995-1-1:2004 [20]. The connections comprised a single slotted-in steel plate and six dowel-type fasteners arranged in a 3×2 rectangular pattern with minimum distances specified in EN 1995-1-1:2004 [20]. The slotted-in steel plate had a thickness of 10 mm, and the dowels had a diameter of 10 mm. Both the slotted-in steel plate and the dowels were S235 steel with a characteristic yield strength $f_{y,k}$ of 235 N/mm$^2$ and an ultimate strength $f_{u,k}$ of 360 N/mm$^2$.

### 3.2 Equivalent viscous damping

To estimate the equivalent viscous damping $\zeta_{eq}$, a multi-scale hysteretic model of laterally loaded timber connections with dowel-type fasteners [16] was used, with material parameters on the mean level [23, 24]. The multi-scale connection model was implemented for the simplified column-loss scenario in Figure 2, where it was assumed that the connections were subjected to a maximum rotation $\theta_u$ of $3\theta_y$, where $\theta_y$ is the yield rotation. For the connections in this paper, the yield rotation $\theta_y$ was 25.8 mrad, which corresponds to a maximum rotation $\theta_u$ of 77.5 mrad. If the beams are considered as rigid bodies, a maximum rotation $\theta_u$ of 77.5 mrad corresponds to approximately 279 mm in vertical deflections $u_z$ of the node above the removed column.

The maximum rotation $\theta_u$ was used to simulate the hysteresis of the connection for a fully reversed displacement-controlled loading cycle of the structure in Figure 2. In Figure 3, the resulting hysteresis of the connection is shown. The total dissipated energy $E_d$ was computed by integrating the area inside the envelope of the hysteresis, and the equivalent viscous damping $\zeta_{eq}$ was found from:

$$\zeta_{eq} = \frac{1}{4\pi}\frac{E_d}{E_s}, \tag{5}$$

where $E_s$ is the strain energy calculated from the secant stiffness $k_\theta$ of the point of maximum rotation. With Equation 5 and a maximum rotation of $3\theta_y$, the equivalent viscous damping $\zeta_{eq}$ of the connection was 17.94%.

### 3.3 Simulations

For the simulations, a symmetrical frame with four bays and four storeys was chosen. The frame was subjected to the removal of an edge column. This is shown in Figure 4, with the removed column in red. The connections in Section 3.1 were idealized with a linear-elastic perfectly brittle material behavior. For the rotational stiffness $k_\theta$ of the connections, the secant stiffness of the maximum rotation $\theta_u$ of the hysteresis in Figure 5 was used, and the maximum rotation $\theta_u$ was used to define the brittle failure. The simulations were conducted with a recently developed parametric nonlinear model for progressive collapse analysis [12]. The model

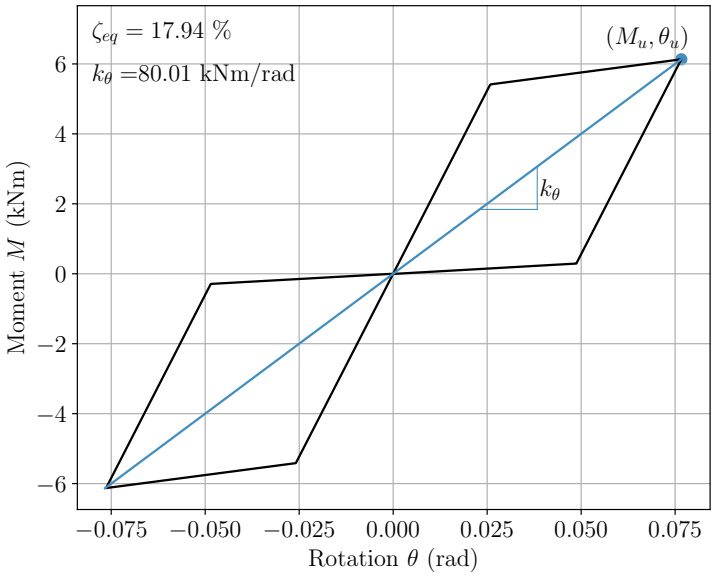


Figure 3: Hysteresis of the connection with a maximum rotation $\theta$ of $3\theta_y$, equivalent to 77.5 mrad. $k_{\theta,el}$ = 210 kNm/rad, $k_{\theta,pl}$ = 8.38 kNm/rad, $k_{\theta,sec}$ = 80.0 kNm/rad

| Damping | $\alpha$ and $\beta$ | **k** | **m** | Eigenvalues |
|---|---|---|---|---|
| Initial Rayleigh | Initial | Initial | Initial | Initial |
| Incremental Rayleigh | Constant | Incremental | Incremental | Incremental |
| Incremental Rayleigh | Incremental | Incremental | Incremental | Incremental |
| Initial modal | - | Initial | Initial | Initial |
| Incremental modal | - | Incremental | Incremental | Incremental |

Table 1: Overview of the different methods. In the incremental Rayleigh with incremental $\alpha_t$ and $\beta_t$ and initial Rayleigh with constant $\alpha_{t=0}$ and $\beta_{t=0}$ damping models, the first $\omega_1$ and fifth $\omega_5$ frequencies were used. For the incremental Rayleigh with constant $\alpha_{t=0}$ and $\beta_{t=0}$ damping model, the second calibration frequency $\omega_j$ in Equation 2 was $5\omega_1$.

includes features such as element removal, detachment of elements or structural assemblies, debris tracking, impact loading, and more.

In this paper, the different damping models described in Section 2 were investigated with an equivalent viscous damping $\zeta_{eq}$ of 17.94%. These are summarized in Table 1. For the initial Rayleigh damping and incremental Rayleigh damping with varying $\alpha_t$ and $\beta_t$ parameters, the first $\omega_1$ and fifth $\omega_5$ modes were used for the damping matrix **c** in Equation 1. In the simulation with incremental Rayleigh damping with constant $\alpha_{t=0}$ and $\beta_{t=0}$, the frequencies $\omega_1$ and $5\omega_1$ were used. For the modal damping models, analyses with 5, 10, and 20 modes $N$ were conducted. In addition, $N = 30$ modes were also simulated for the incremental modal damping model. Ten simulations of edge column removals were performed.

To quantify the deviations between the models, the root-mean-square deviation RMSD and normalized root-mean-square deviation NRMSD were used, which can be expressed as:

$$\mathrm{RMSD}\left(y_{mn}\right) = \sqrt{\frac{\sum_{t=1}^{T}\left(y_{m,t} - y_{n,t}\right)^2}{T}}, \tag{6}$$

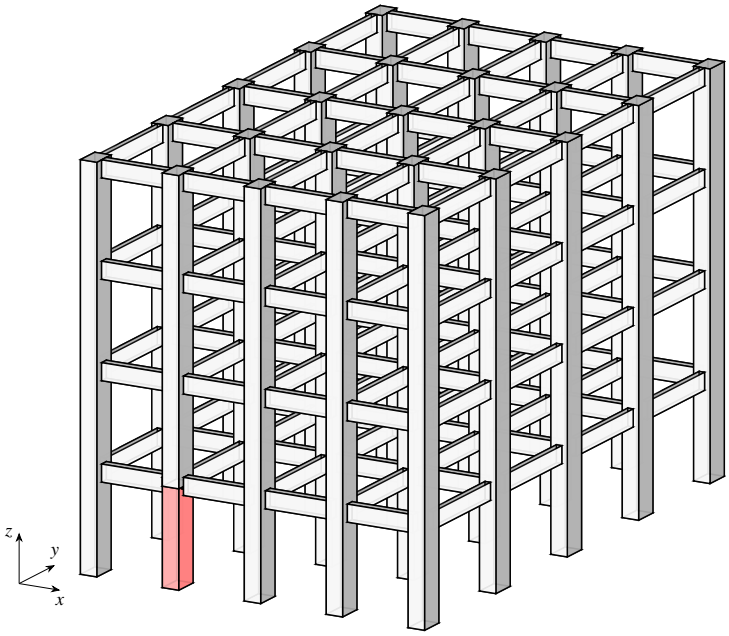


Figure 4: Structural system with the removed column in red.

$$\mathrm{NRMSD}\left(y_{mn}\right) = \frac{\mathrm{RMSD}}{\bar{y}_{mn}},$$

where $y$ is a time series, indices $m$ and $n$ are two different time series, $t$ is the time, $T$ is the length of the time series, and $\bar{y}$ is the mean value of the time series. The normalized root-mean-square deviation $\mathrm{NRMSD}$ can be interpreted as the coefficient of variation $cov$ of the compared time series, and the root-mean-square deviation $\mathrm{RMSD}$ as the standard deviation of the compared time series.

## 4 RESULTS AND DISCUSSION

### 4.1 Progressive collapse

Figure 5 shows the different damage states during the progressive collapse for the incremental modal damping model with $N = 20$ modes, with different nodes marked in Figure 5a. The course of the progressive collapse was similar for all the damping models. Following the removal of the column, node 4 deflected vertically to a deflection $u_z$ of 276 mm in Figure 5a. This is similar to the deflection level of the calibrated equivalent viscous damping $\zeta_{eq}$, presented in Section 3.2. Because of the large vertical deflections $u_z$ and the corresponding rotations $\theta$ of the adjacent connections in the $x$-direction of the structure above the removed column, most of these beam-column connections failed. This is shown in Figure 5b and is referred to as the secondary damage state. In the tertiary damage state, the beam-column connections in the $y$-direction adjacent to the columns above the removed column failed. In the final damage state, the two bays sharing the removed column had collapsed.

For this structure, the progressive collapse was contained within two bays, with a collapsed floor area above ground of 78 m$^2$. This is equivalent to 12.5% of the total floor area and is less than the indicative limit of 100 m$^2$ or 15% in EN 1991-1-7:2006 [25]. The limited damage propagation can be attributed to the connections, which acted as fuse elements or weak links. The connections did not have a sufficient rotational capacity $\theta_u$ to activate alternative load paths through catenary action or vertical suspension of the structure adjacent to and above the re-

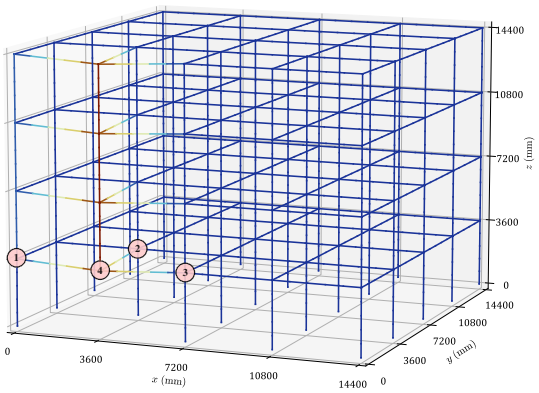


(a) Initial damage state with node numbering, $u_{z,\max} \simeq 276$ mm.

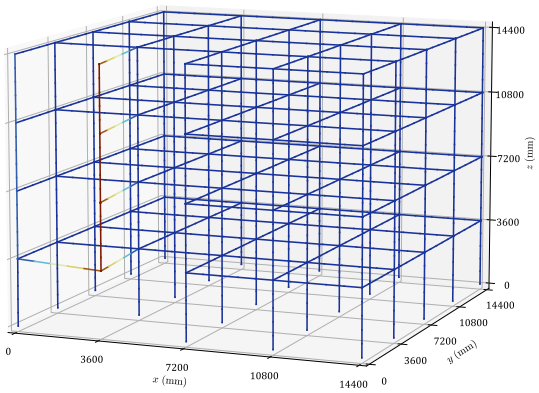


(b) Secondary damage state, $u_{z,\max} \simeq 277$ mm.

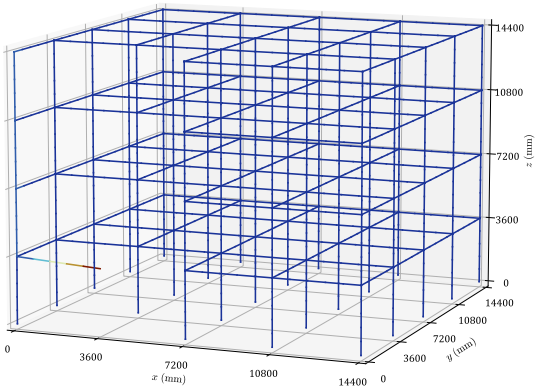


(c) Tertiary damage state, $u_{z,\max} \simeq 251$ mm.

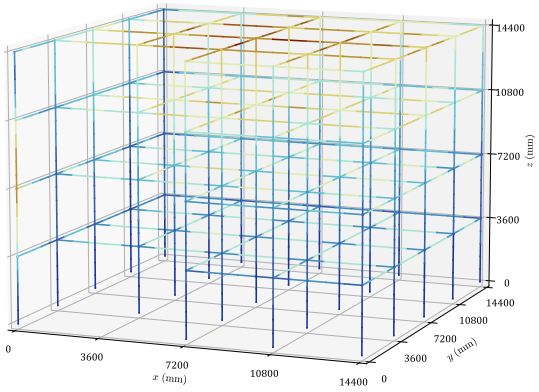


(d) Final damage state, $u_{z,\max} \simeq 10$ mm.

Figure 5: Damage states during the collapse.

moved column. Therefore, the collapse was limited to two bays. This is similar to the collapse of the Siemens arena [26]. With sufficient rotational capacity $\theta_u$ in the connections, alternative load paths could have developed, which might have led to the arrest of the collapse. Another scenario with an increased rotational capacity $\theta_u$ could be the propagation of collapse because of the absence of the fuse elements, similar to the collapse of the Bad Reichenhall ice-arena [26].

## 4.2 Convergence and computation time

The incremental Rayleigh model with incremental $\alpha_t$ and $\beta_t$ had a computation time of 50 453 s on a desktop computer with an Intel Xeon CPU E3-1225 V2 @3.20 GHz processor run-

ning on a single core, which was approximately 4.4 % longer than the initial Rayleigh damping model. There was no significant difference in the computation time between the initial Rayleigh damping model and the incremental Rayleigh model, with constant $\alpha_{t=0}$ and $\beta_{t=0}$. Because the structural responses of the different Rayleigh models were practically identical, it is sensible to use the incremental Rayleigh model with constant $\alpha_{t=0}$ and $\beta_{t=0}$ for similar analyses.

For the initial modal damping model, the response histories of the simulations with $N = 10$ and $N = 20$ modes were similar for node ①. The dissimilarities were slightly larger for nodes ② and ③, where the displacement magnitudes were slightly different. The computation time for the initial modal damping model with $N = 20$ modes was 105 720 s. This was approximately 5.4% longer than with $N = 10$ modes. Because of the gain in accuracy when using $N = 20$ modes compared to $N = 10$ modes and the relatively small difference in computation time, it is sensible to use $N = 20$ modes for similar analyses. In the following discussion in Section 4.3, the results from the analyses with $N = 20$ modes are used.

For the incremental modal damping model, convergence was reached for $N = 30$ modes. This can be seen in Figure 6, where the response histories of the $N = 20$ and $N = 30$ modes were fairly similar. The computation time for the incremental modal damping model with $N = 30$ modes was 75 554 seconds, or about 14.5% longer than with $N = 20$ modes. Although the response history for nodes ① and ③ were almost identical, there was a larger discrepancy for node ②. Therefore, $N = 30$ modes should be used for similar analyses with the incremental modal damping model. In the following discussion in Section 4.3, the results from the analyses with $N = 30$ modes are used.

### 4.3 Comparison of damping models

For the different nodes in Figure 5a, the response histories of the different damping models are shown in Figure 6. The response histories of the different variations of Rayleigh damping and initial modal damping models were quite similar for nodes ①, ②, and ③. Although all models resulted in the same oscillation trends, the magnitudes of the peaks for the incremental modal damping model were severely dissimilar from the other damping models. The maximum deformations for nodes ① to ③ with the incremental damping models were approximately five times higher than for the other damping models, and the peak deformations occurred later.

The Rayleigh variations and the initial modal damping models damped out higher-mode response, which can be seen from the relatively smooth curves in Figure 6. For initial modal damping with $N = 5$ modes, higher mode response was also present. However, the higher mode response became less pronounced as more modes $N$ were included in the damping matrix $\mathbf{c}$ in Equation 3. For the incremental modal damping model, higher mode response was much more pronounced. This can be seen from the ruggedness of the curves, especially for nodes ② and ③ after $t = 0.5$ s. Although higher mode response was captured better in the incremental modal damping model, its significance in progressive collapse simulations may be limited as long as the displacement magnitudes are correctly represented.

Figure 6d shows the response history of node ④ for the different damping models. The different Rayleigh and modal damping models result in almost identical response histories with similar failure points. If the objective of the analyses are to model the initial failure, the choice between the different damping models in this paper is not important, as the shape of the response history and the failure points are fairly similar. If the objective of the analyses is to assess the response of the structure past the first failure, the choice of the damping model is important. This can be seen in Figures 6a-c, with the large deviations between the incremental modal damping model and the other damping models.

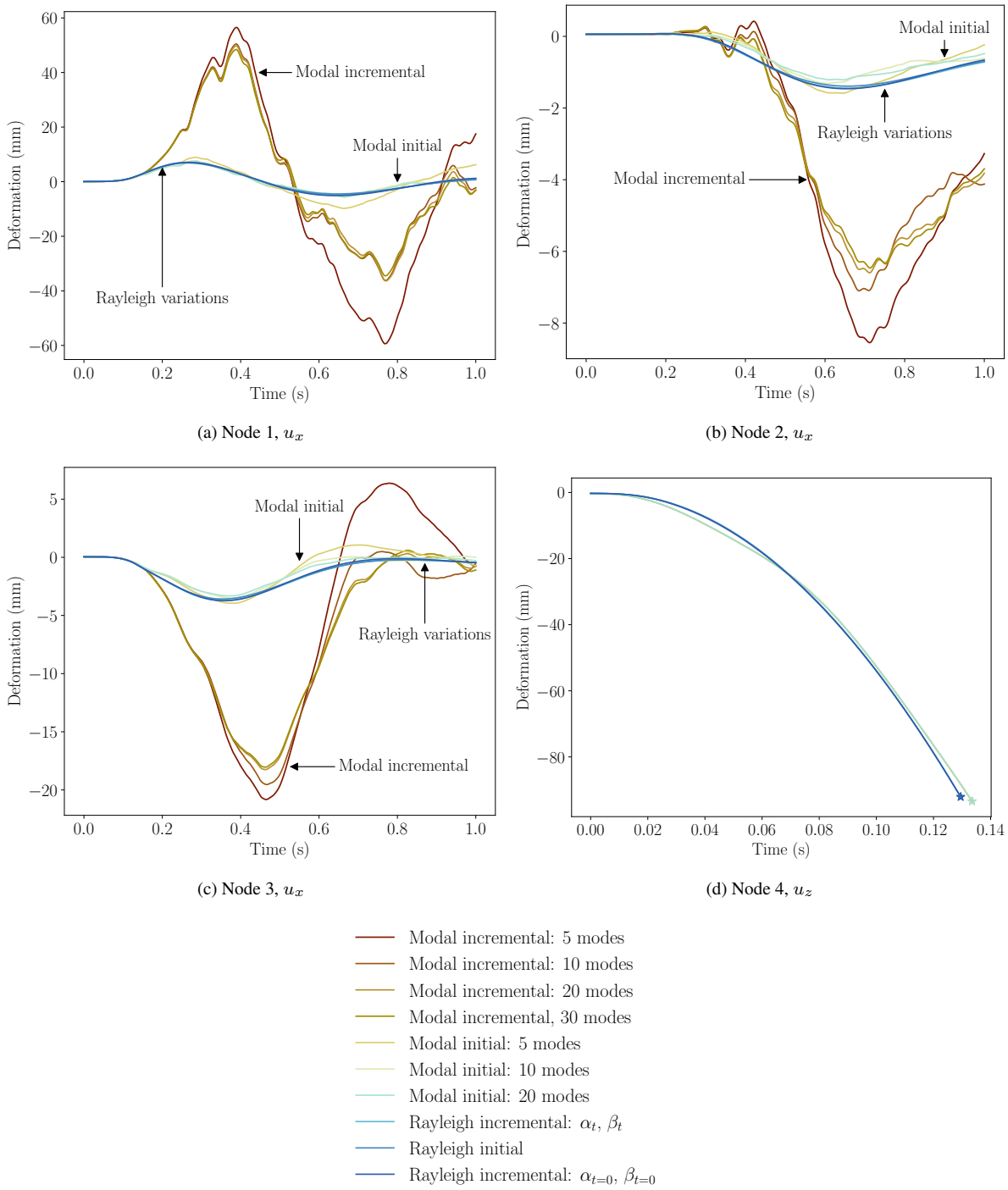


(a) Node 1, $u_x$

(b) Node 2, $u_x$

(c) Node 3, $u_x$

(d) Node 4, $u_z$

Figure 6: Nodal displacements for the different damping models.

Table 2 shows the root-mean-square deviation RMSD and normalized root-mean-square deviation NRMSD between the different damping models. As observed in Figure 6, the differences between the different Rayleigh damping models are quite small, with an RMSD less than 0.32. Similarly, the RMSD between the different Rayleigh damping models and the initial modal damping model is also of the same magnitude of around 0.55. The large dissimilarities between the incremental modal damping model and the other models result in an RMSD of

| NRMSD (RMSD) | | $R_{in}$ $\alpha_{t=0}$, $\beta_{t=0}$ | $R_{inc}$ $\alpha_{t=0}$, $\beta_{t=0}$ | $R_{inc}$ $\alpha_t$, $\beta_t$ | $M_{in}$ | $M_{inc}$ |
|---|---|---|---|---|---|---|
| $R_{in}$ | $\alpha_{t=0}$, $\beta_{t=0}$ | 0 | 1.14 (0.32) | 0.54 (0.15) | 1.87 (0.52) | 68.82 (19.03) |
| $R_{inc}$ | $\alpha_{t=0}$, $\beta_{t=0}$ | 1.14 (0.32) | 0 | 0.92 (0.19) | 2.73 (0.57) | 89.84 (18.90) |
| $R_{inc}$ | $\alpha_t$, $\beta_t$ | 0.54 (0.15) | 0.92 (0.19) | 0 | 2.11 (0.55) | 73.09 (18.92) |
| $M_{in}$ | | 1.87 (0.52) | 2.73 (0.57) | 2.11 (0.55) | 0 | 8.56 (19.17) |
| $M_{inc}$ | | 68.82 (19.03) | 89.84 (18.90) | 73.09 (18.92) | 8.56 (19.17) | 0 |

Table 2: Root-mean-square deviation RMSD and normalized root-mean-square deviation NRMSD in parenthesis.

around 19, which is over 30 times higher than the RMSD between the other models.

For conventional nonlinear response history analyses without the separation and detachment of elements, modal damping is superior to Rayleigh damping [1, 11]. On this basis, it is believed that its incremental version offers the highest precision of the different damping models presented in this paper. With incremental modal damping, the damping model can to represent the changes in the mass **m**, stiffness **k**, and mode shapes $\phi_n$ throughout a progressive collapse. If the time steps $\Delta t$ are small enough, the deformations from a time $t_i$ to $t_{i+1}$ are small, changes in stiffness can be reasonably idealized as linear, and the mode shapes do not change significantly. Therefore, the assumptions of modal analysis are not violated.

### 4.4 Issues with damping in progressive collapse

Although incremental modal damping may offer the highest precision of the different damping models in this paper, there is still an intrinsic problem with equivalent viscous damping $\zeta_{eq}$ for inelastic structures, and especially for structures undergoing a progressive collapse. Regardless of the damping models presented in this paper, the equivalent viscous damping $\zeta_{eq}$ was calibrated for a certain deformation level. Here, it was calibrated for an ultimate rotation $\theta_u$ of $3\theta_y$. The maximum vertical deflections $u_z$ in the analyses conformed well to an ultimate rotation $\theta_u$ of $3\theta_y$. However, the calibrated equivalent viscous damping $\zeta_{eq}$ was only appropriate for the most deformed connections in the immediate vicinity of the removed column. The other connections further away from the removed column did not undergo nearly as large deformations. Therefore, the calibrated equivalent viscous damping $\zeta_{eq}$ was not appropriate for much of the structure. Because of this, the accuracy of the response history would deteriorate with the time. It is also possible to choose a value of the equivalent viscous damping $\zeta_{eq}$ that averages the damping of the entire structure. However, this approach is fraught with similar issues, where the equivalent viscous damping is incorrectly modeled everywhere.

To increase the accuracy of the damping modeling, there are essentially two approaches. The first approach is to model the hysteresis of the different members explicitly in the model with lumped or distributed plasticity. By modeling the hysteresis directly, the damping of the modeled members would have the highest precision. However, this approach may lead to excessive computation times and convergence problems if the members with hysteresis experiences segments of zero stiffness. Moreover, most hysteretic models are phenomenological and rely on physical tests for their calibration. This means that it is difficult to generalize the hysteretic models to all structural components.

The second approach is to calibrate and implement equivalent viscous damping $\zeta_{eq}$ for each member, which contributes significantly to the damping of the structure. Because the modal damping models rely on the mode shape of the whole structure, these models cannot be used.

Alternative damping models such as Rayleigh damping or stiffness-proportionate damping could be used, especially in lumped plasticity approaches where the plasticity is concentrated in members with nearly zero mass. However, these alternative damping models would inherit the same weaknesses as Rayleigh damping, such as spurious damping forces and near-infinite damping for high frequencies. Additionally, the calibration of the equivalent viscous damping $\zeta_{eq}$ for each component would be a tedious iterative process with its own uncertainties. This would lead to the need to do multiple analyses to find the appropriate equivalent viscous damping $\zeta_{eq}$ for all the relevant components of the structure.

Regardless of the two approaches, an appropriate amount of equivalent viscous damping $\zeta_{eq}$ would also need to be implemented to account for other sources of damping in the structure. These may stem from friction, non-load-bearing members, furniture and appliances, and more. The ideal approach to model damping in a structure undergoing a progressive collapse would be the explicit modeling of hysteresis in the connections, as well as a service-level equivalent viscous damping $\zeta_{eq}$ in the form of incremental modal damping. The service-level equivalent viscous damping $\zeta_{eq}$ can be adopted from any forced or ambient vibration test of similar structures in their elastic range, which is typically a few percent.

## 5 CONCLUSIONS

This paper presented different equivalent viscous damping models and discussed their applicability for nonlinear response history and progressive collapse analyses. Initial and two versions of incremental Rayleigh damping were assessed, besides initial and incremental modal damping. These damping models were implemented in a recently developed nonlinear parametric model for progressive collapse analysis. To compare the damping models in a progressive collapse, a symmetrical timber frame subjected to the removal of an edge column was analyzed. The timber frame comprised four bays and storeys with laterally loaded timber connections with dowel-type fasteners, and the equivalent viscous damping was estimated from a newly developed multi-scale hysteretic model for such timber connections.

The results showed that the response histories followed the same trend, with one positive and negative peak. For the initial modal damping and the Rayleigh damping models, the response histories were similar and high-frequency responses were damped out. However, the incremental modal damping model resulted in peak amplitudes that were in the order of five times higher than the other damping models. It also showed high-frequency response and the peaks occurred later. If the objective is to assess the structure until the first failure, the damping model is not critical. For this purpose, one of the incremental Rayleigh damping models may be used because of their computational efficiency. If the objective is to assess a progressive collapse past the first failure, the damping model may heavily influence the structural response. For this, the incremental modal damping model is recommended.

The best representation of the damping in an inelastic response history analysis is to model the hysteresis explicitly in the materials of the structure in a lumped or distributed plasticity approach. This should be combined with service-level equivalent viscous damping to account for other sources of damping. Further research is necessary to quantify the accuracy gains between the explicit modeling of hysteresis and equivalent viscous damping models, as well as the appropriate amount of service-level equivalent viscous damping.

## REFERENCES


[1] A.K. Chopra, F. McKenna, Modeling viscous damping in nonlinear response history analysis of buildings for earthquake excitation. *Earthquake Engineering & Structural Dynamics*, **45**, 193–211, 2016.

[2] M.A. Bezabeh, G.T. Bitsuamlak, S. Tesfamariam, Nonlinear dynamic response of single-degree-of-freedom systems subjected to along-wind loads. I: Parametric study. *Journal of Structural Engineering*, **147**(11), 2021.

[3] G. Kaewkulchai, E.B. Williamson, Modeling the impact of failed members for progressive collapse analysis of frame structures. *Journal of Performance of Constructed Facilities*, **20**(4), 375–383, 2006.

[4] C. Viau, G. Doudak, Dynamic analysis methods for modelling timber assemblies subjected to blast loading. *Engineering Structures*, **233**, 2021.

[5] J.A.J. Huber, M. Ekevad, U.A. Girhammar, S. Berg, Structural robustness and timber buildings - a review. *Wood Material Science & Engineering*, **14**(2), 107–128, 2019.

[6] F.A. Charney, Unintended consequences of modeling damping in structures. *Journal of Structural Engineering*, **134**(4), 581–592, 2008.

[7] M.J.N Priestley, G.M. Calvi, M.J. Kowalsky, Direct displacement-based seismic design of structures. *2007 New Zealand Society for Earthquake Engineering Conference (2007 NZSEE)*, New Zealand, 2007.

[8] A.A. Correia, J.P. Almeida, R. Pinho, Seismic energy dissipation in inelastic frames: Understanding state-of-the-practice damping models. *Structural Engineering International*, **23**(2), 148–158, 2013.

[9] J.F. Hall, Problems encountered from the use (or misuse) of Rayleigh damping. *Earthquake Engineering & Structural Dynamics*, **35**, 525–545, 2006.

[10] J.F. Hall, Performance of viscous damping in inelastic seismic analysis of moment-frame buildings. *Earthquake Engineering & Structural Dynamics*, **47**, 2756–2776, 2018.

[11] X. Qian, A.K. Chopra, F. McKenna, Modeling viscous damping in nonlinear response history analysis of steel moment-frame buildings: Design-plus ground motions. *Earthquake Engineering & Structural Dynamics*, **50**, 903–915, 2021.

[12] A.S. Cao, L. Esser, B. Glarner, A. Frangi, A nonlinear dynamic model for collapse investigations in tall timber buildings - Preliminary results. *World Conference on Timber Engineering 2023 (WCTE2023)*, Oslo, Norway, June 19-22, 2023.

[13] A.S. Cao, A. Frangi, Mixed element method for progressive collapse analysis: Method description and verification. F. Di Trapani ed. *Proceedings of Eurasian OpenSees Days 2022 (OpenSeesDays2022)*, Torino, Italy, July 7-8, 2022.

[14] A.S. Cao, P. Palma, A. Frangi, Multi-scale hysteretic model of laterally loaded timber connections with dowel-type fasteners. *World Conference on Timber Engineering 2023 (WCTE2021)*, Santiago, August, July 9-12, 2021.

[15] A.S. Cao, M. Lolli A. Frangi, Pendulum impact hammer tests on spruce GLT - Preliminary results B.H.V. Topping, J. Kruis eds. *Proceedings of the Fourteenth International Conference on Computational Structures Technology (CST2022)*, Montpellier, France, August 23-25, 2022.

[16] A.S. Cao, P. Palma, A. Frangi, Multi-scale hysteretic model of laterally loaded timber connections with dowel-type fasteners. J.F. Silva Gomes ed. *20th International Conference on Experimental Mechanics (ICEM20)*, Porto, Portugal, July 2-7, 2023.

[17] European Committee for Standardization, *EN 1990:2002. Eurocode - Basis of structural design*. European Committee for Standardization (CEN), 2002.

[18] European Committee for Standardization, *EN 1991-1-1:2002. Eurocode 1: Actions on structures - Part 1-1: General actions - Densities, self-weight, imposed loads for buildings*. European Committee for Standardization (CEN), 2002.

[19] European Committee for Standardization, *EN 14080:2013. Timber structures - Glued laminated timber and glued solid timber - Requirements*. European Committee for Standardization (CEN), 2013.

[20] European Committee for Standardization, *EN 1995-1-1:2004. Design of timber structures - Part 1-1: General - Common rules and rules for buildings*. European Committee for Standardization (CEN), 2004.

[21] International Organization for Standardization, *ISO 10137:2007. Bases for design of structures - Serviceability of buildings and walkways against vibrations*. International Organization for Standardization (ISO), 2007.

[22] European Committee for Standardization, *EN 1991-1-4:2005. Actions on structures - Part 1-4: General actions - Wind actions*. European Committee for Standardization (CEN), 2005.

[23] S. Schilling, P. Palma, R. Steiger, A. Frangi, Probabilistic description of the mechanical properties of glued laminated timber made from softwood. R. Görlacher Ed. *Proceedings of the International Network on Timber Engineering Research, INTER, Meeting 54 (INTER 2021)*, Online, August 16-19, 2021.

[24] Joint Committee on Structural Safety, *JCSS - Probabilistic Model Code: Part III Resistance Models - Steel*. Joint Committee on Structural Safety (JCSS), 2000.

[25] European Committee for Standardization, *EN 1991-1-7:2006. Actions on structures - Part 1-7: General actions - Accidental actions*. European Committee for Standardization (CEN), 2006.

[26] J. Munch-Andersen, P. Dietsch, Robustness of large-span timber roof structures - Two examples. *Engineering Structures*, **33**(11), 3113–3117, 2011.

COMPDYN 2023
9th ECCOMAS Thematic Conference on
Computational Methods in Structural Dynamics and Earthquake Engineering
M. Papadrakakis, M. Fragiadakis (eds.)
Athens, Greece, 12-14 June 2023

# FRAGILITY CURVES FOR STEEL INDUSTRIAL SILOS ACCOUNTING FOR FILLING LEVEL OF GRANULAR-LIKE MATERIAL

**Mohammad Khalil** [1], **Sergio Ruggieri** [1], **Vito Tateo**[1], **Giuseppina Uva**[1]

[1] Politecnico di Bari, DICATECH Department, Via Orabona4, Bari, Italy

e-mail: {mohammad.khalil, sergio.ruggieri, vito.tateo, giuseppina.uva}@poliba.it

## Abstract

*This study presents an assessment on the seismic fragility of ground-supported steel silos storing solids. As key units in the different industrial sites, storage systems are crucial for the proper and continuous functionality of the relevant industrial operations that can be intended for vital activities such as the food supply. Nevertheless, it is undeniable that storage systems are more vulnerable to seismic events than other units as evidenced in the past. In this context, this work aims to estimate the seismic fragility of ground-supported steel silos, which represent a very common form of storage systems containing granular material. The effect of key factors, such as the silo geometry and the absence/existence of the filling material, which significantly affect the seismic behavior of silos was addressed. In addition, the governing damage patterns is determined. To achieve these goals, two different silos with different distinctive geometries (slender and squat) were investigated considering the empty case and the 90%-filled case. First, a detailed numerical model was built for the investigated cases by using finite element software ABAQUS. After a phase of model validation, the dynamic properties of the silos under investigation were assessed through eigenvalue analysis, while the seismic buckling capacity of the different silos were evaluated through nonlinear static and time-history analysis. Finally, fragility curves of silos were derived by identifying the most critical buckling capacity corresponding to the specific damage patterns, showing the influence of each parameter on the seismic vulnerability and behavior of these kinds of structures.*

**Keywords:** Steel Silos, Granular-like Materials, Nonlinear Time History Analysis, Seismic Fragility.

## 1 INTRODUCTION

Storage systems represent vital and critical units in the different industrial sectors. However, in order to ensure a safe and continuous operation of these systems, it is highly important to assess the behavior of the different components of the industrial sites under different sources of risk. Steel silos are storage units that almost no factory is devoid of. They are mainly used to store granular solids covering a wide range of material such as flour, iron ore pellets, cements, chemical materials. Most of these storage systems are steel silos, presenting a circular plan form, although different structural typologies can be adopted. A first classification can be made, distinguishing the ground-supported silos [1,2] and the elevated silos resting on a supporting structure [3,4]. Accounting for the first typology, steel silos are categorized as thin wall shell structures where they are extremely vulnerable to buckling under different load conditions. With this regard, seismic events can provoke disastrous impact on the storage facilities of the industrial systems as evidenced by past significant earthquakes (e.g., 2023 Turkey-Syria Earthquake; 2012 Emilia Earthquake). For instance, Figure 1 shows a recent satellite image of a factory in south of Turkey right after a powerful 7.8 magnitude earthquake struck the area (2023 Turkey-Syria Earthquake). As the image illustrates, the earthquake had the highest destructive impact on the storage systems as the majority of the silos were fully collapsed, although, the other units and ordinary framed industrial structures do not show any collapse. Therefore, it is undeniable that silos are more vulnerable to seismic events than other industrial component. In addition, the loss of containment, which could be encountered in the event of silo failure, can have a propagation effect causing irreparable damage to other units in the industrial sites. Therefore, evaluating the seismic risk of silos is of great importance to avoid the different industrial accident scenarios. The proper functionality of the relevant industrial activities can be guaranteed after an earthquake, as it can be directly connected to logistical activities of rescue operations, food supply, and later to the reconstruction process.



a b

Figure 1: A satellite image of an industrial site following the recent Turkey/Syria earthquake 2023:(a) before; (b)after the earthquake[5].

In the light of the state-of-art reported in Section 2, it is worth mentioning that among the most influencing factors governing the dynamic response of the grain-silo system are: (a) the geometry of the structure; (b) the existence of the ensiled material; (c) the ground motion characteristics. Moreover, as thin wall shell structure, the buckling of the silo wall is the main

concern that demands special attention. However, different damage patterns (DPs), or buckling failure modes, might develop in the silo wall under lateral pressure.

In this context, this study investigates the effect of the above-mentioned factors on the behavior and on the failure probability of the grain-silo system under seismic excitation, specifying the most dominant DP. To this aim, two different silos (squat and slender) are investigated under different conditions of functionality (full and empty), and the effect of the ground motion characteristics was implicitly accounted for since different ground motions records were used for performing seismic analysis. First, detailed numerical models were built and validated, after time history (TH) analyses were carried out for each case, finally seismic fragility curves were calculated for each case considering each possible DPs. The results showed in probabilistic term the possibility of each DP to develop, considering the variation of two main parameters: the silo geometry and the effect of the ensiled material existence.

## 2 BACKGROUND

### 2.1 Seismic behavior of ground-supported steel silos

Despite the continuous evolution of the knowledge on the performance-based seismic assessment of different components in the industrial sites such as tanks [6–8], piping systems [9], framed structure [10], elevated silos [3]. The seismic risk assessment of ground-supported steel silos is poorly investigated in the past research. Nevertheless, the principal dynamic behavior and the dynamic characteristics of silos were addressed in the scientific literature since the middle of the last century. In this respect, Lee [11] proposed an analytical model to estimate the portion of mass of the grain which pushes on the silos walls, known as the effective mass, when the system is subjected to dynamic excitation. In this work, a harmonic bass excitation was considered, and the proposed model allowed to observe the variation of the frequencies in the cases of empty and filled conditions. Trahair et al. [12] presented the concept of the additional normal pressure that represent the effect of the seismic response of the stored material on the shell. However, very simple and conservative expressions were introduced to quantify the radial and circumferential pressures applied on the silo wall under horizontal dynamic excitation. Yokota et al. [13] was among the early researchers who employed the finite element techniques to model the cylindrical shell and the ensiled material. This study assumed the coal as ensiled material. In this model, an increasing value in the coal Young's modulus, from the top to the bottom, was considered to account for the confining pressure. The results were compared with the corresponding experimental findings [13] and the natural frequencies calculated on the FE model were 30-40% larger than those obtained based on the experimental test. Shimamoto et al. [14] studied the dynamic response of silo containing coal based on the FE model, using conical shell elements. However, the numerical solution represented by the resonance curves were compared with those obtained based on the tested silo specimens. Rotter and Hull [15] studied the response of circular ground-supported silos (squat) based on elastic FE analysis. The seismic load was represented by quasi-static horizontal body force (uniform horizontal acceleration). In this work, expressions to calculate the stress induced, in the silo wall, by the seismic action were presented. However, this study stated that the membrane stress induced in the wall shell are proportional to R/t ratio and to H/R ratio (R is the radius of the silo, t is the wall thickness and H is the height). Sasaki and Yoshimura [16] presented a numerical model to reproduce a tested scaled silo. In their research, they evaluated the effective mass that pushes on the silo wall under an earthquake. Similarly, Hardin et al. [17] evaluated numerically the seismic response of a large scale steel silos storing wheat. In this study, the grail-silo system modelled by the means of composite shear-beam model accelerated by real

earthquake record. The linear elastic behavior was assumed for the silo wall. However, the study recorded the acceleration history, the amplification of the horizontal acceleration, and the stress-strain distribution. Later, Younan and Veletsos [18,19], examined analytically cylindrical silos storing linear viscoelastic solids subjected to earthquake-induced ground motions. The aim of the study was to provide an analytical formulation to describe the seismic response of the filled silo, accounting for the parameters of slenderness ratio and the wall flexibility. Holler and Meskouris [20] characterized the effect of the different component on the silo seismic behavior, mainly accounting for variation of some key parameters, such as the grain-wall interaction, the aspect ratio, the nonlinearity of the granular material, and soil-structure interaction (SSI). The study grounds on the basis of FE numerical modelling considering linear elastic wall behavior. The study concluded that for squat silos, a substantial portion of the ensiled weight does not participate to the horizontal pressures as it is transferred directly to the ground.

Further investigating on the effect of the aspect ratio on the seismic response of flat-bottomed ground-supported silos was presented by Nateghi and Yakhchalian [21]. The study emphasized, based on numerical observations, the influence of the aspect ratio and concluded that assuming a constant value of acceleration distribution along the height of squat silos (adopted by the current European standards EN 1998-4 [22]) leads to conservative design pressures for a squat silo, on the other hand, this assumption is fair for a slender silo. A study presented by Silvestri et al. [23] addressed the matter of the effective mass pushing on the silo wall under seismic action. Grounding on a new physically-based analytical approach, which was later refined by Pieraccini et al. [24], this study emphasized the conservatism of EN 1998-4 [22] provisions with regards to squat silos. In the same framework, a series of shaking table tests was performed by Silvestri et al. [25], on scaled silos made of polycarbonate sheets and containing wheat as ensiled material. This experimental campaign revealed the significant effect of the wall-friction coefficient on the base overturning moment and that is consistent with the analytical approach introduced in [23]. However, this effect is disregarded by the current European provisions of EN 1998-4 [22], which conservatively estimate the base overturning moment. Butenweg et al. [2] further investigated the static equivalent load (adopted by the current European standards EN 1998-4 [22]) by comparing it to more sophisticated approach based on the time history analysis considering nonlinear FE model. The study revealed that considering the equivalent static load, with a simplified linear acceleration along the height, is too conservative for a slender silo. Instead, an acceleration profile determined based on multimodal analysis on a simplified beam is more realistic. Moreover, the study suggested that using the nonlinear numerical modelling leads to more economical design as the equivalent static load approach yields in conservative stress values in case of squat silos and that is in agreement with the statement by [20,23]. Durmus and Livaoglu [26] investigated analytically the seismic behavior of the ground-supported silo based on a simplified model represented by a single degree of freedom flexural cantilever beam with a lumped mass. The study aimed at estimating the dynamic pressure, the base shear force, the fundamental frequency of vibration and the SSI effect. The results obtained by the analytical solution were compared with those obtained based on the numerical simulation. This study stated a good agreement between the results obtained by the two solutions, and it concluded that the effect of SSI can be ignored in practical applications, as it has negligible contribution especially in case of squat silos. Mehretehran and Maleki [27] investigated, by the means of incremental dynamic analysis (IDA), the dynamic buckling behavior of steel silos with a constant thickness. The silos were assumed filled up to 90% of the maximum capacity and the elephant foot buckling was the unique investigated DP. The study estimated the seismic buckling capacity of the relevant silos by the peak ground acceleration (PGA) that initiate the buckling. The main findings of this

study indicate that slender silos are more vulnerable to buckling failure while squat silos present a considerably higher resistance under same conditions. Later, the same authors extended their findings to include the stepped wall steel silos under seismic conditions[28]. This study stated that the vertical component of the seismic excitation is of a quite marginal effect. Recently, Silverstri et al. [29] reported a series of shaking table test on full scall flat-bottom steel silo. The considered silo was of corrugated walls and filled with wheat. Basically, this study reported the experimental observation on the static pressure, the dynamic properties, and the dynamic overpressure. On the level of the dynamic behavior, the study found that the fundamental frequency depends on the acceleration and on the compaction of the grains. In addition, the dynamic amplification increases along the height of the silo with maximum value at the top of the ensiled content and the additional normal pressure increases with the depth. Another recent experimental study was presented by Jing et al. [30] based on shaking table test and considering different real and artificial earthquake excitations. The study reported the favorable effect of the existence of the granular material on the energy dispassion of the grain-silo system. In addition, the effect of different filling states on the acceleration vertical profile and on the fundamental frequency of the system was quantified experimentally. For the sake of conciseness, the state-of-art reported above is limited to the ground-supported steel silos which is the most relevant to the subject of this work. Various examples about silos with different typologies, such as elevated silos [3] and reinforced concrete silos [31] can be found in the scientific literature. However, more elaborated state-of-art about the silo structure and their behavior under different conditions is presented in [32,33].

### 2.2 Possible failure modes of ground-supported steel silos

Early investigations on the behavior of storage systems under earthquakes allowed us to gain significant insight into the possible failure modes that can affect the functionality of silos as storage systems. Based on the post-earthquakes site inspections reported in [7,34], a wide variety of possible failure modes and mechanisms of similar structures were reported under earthquake. However, the DPs that can develop in the shell wall, under lateral pressure, are the only connected failure modes to this study. For the case at hand, the considered DPs are: (a) the elastic-plastic buckling known as elephant foot buckling (EFB) [35]; (b) the top-of-wall damage (TWD) which is a possible buckling occurs at the top of the wall [28,34], (c) the elastic buckling occurring near to the middle part of the silo (EB) [7,36].

## 3 CASE STUDY

### 3.1 Silos description

To reflect the variety in the geometry of the silos in the practice, two different silos with different dimensions were considered. A wider set of silos, with similar typology, were studied by Sadowski and Rotter [1] under the condition of discharge loads. The reader may consult the relevant study [1,37] for more details of the conceptual design of the relevant silos. However, the considered silos were chosen to cover slender and squat geometries with properties reported in Table 1. Both considered silos have the same storage capacity (510 m3).

| Typology | Acronym | Height (h) - m | Diameter (D) - m | Thickness (t) - mm | h/D | R/t |
|---|---|---|---|---|---|---|
| Slender | S | 18 | 6.00 | 6 | 3 | 500 |
| Squat | Q | 6.5 | 10.0 | 3 | 0.65 | 1667 |

Table 1: The geometric characteristics of the considered silos.

It is a matter of fact that the existence of the ensiled solids leads to a significant seismic demand. Nevertheless, the existence of the filling material has a favorable impact on the lateral stiffness and imperfection amplitude, and hence on the structure strength. With this regard, it is of high importance to evaluate the influence of the solids' existence on the seismic vulnerability of the silos under investigation and, in this view, the considered silos were studied for the case of empty and 90% filled silo.

### 3.2 Finite element modelling

The three-dimensional EE models of the case study silos were developed using the commercial package ABAQUS (Standard) [38]. Three parts form and assemble the numerical model, that is, the cylindrical steel silo (modelled using the S4R element type) the bulk material stored in the silo (modelled using the C3D8R element), and the concrete base (modelled using the S4R element). This latter was considered as a fully stiff element. Fixed boundary conditions were applied to the steel wall bottom. Giving that the behavior of the shell wall is the main focus of the investigation, the roof structure was ignored in the model. Nevertheless, the effect of the top roof was substituted by considering a rigid body constraint that ties the nodes at the upper edge of the silo wall to a reference point. A careful mesh convergence study was fulfilled for each silo under different analyses. Generally, the mesh considered in the models considers essential considerations. For instance, a greater number of elements should be considered where the stress change rate is high, and less number was used where it is low. For the ensiled material, a higher resolution of mesh was considered at the interface near the wall to ensure a proper developing of the friction interaction between the filling material and the wall. The critical shear stress between the ensiled material and the silo wall was defined according to Coulomb frictional model.

The steel material of the shell wall was assumed as elastic-hardening, with elastic modulus of 210 GPa, yield strength of 275 MPa, ultimate strength of 430 MPa, and strain hardening modulus of 3880 MPa. The considered silos are filled with 'Camacho' wheat [39] with density of 836 kg/m$^3$, angle of internal friction of 22.2°, Young's nodulus of 19.7 MPa, Poisson's ration of 0.37, cohesion of 0.0095 MPa, friction coefficient of 0.19 for steel walls and 0.42 for concrete base. Elastic properties for the filling material were considered to simulate its behavior in the numerical model.

### 3.3 Model validation

Two steps were performed in order to verify the FE model and its static/dynamic outcomes: (a) comparing the static pressure imposed by the filling material on the silo wall with the analytical solution provided by Janssen's theory [40] and modified Reimbert's theory [41]; (b) comparing the dynamic characteristics of the a scaled silo calculated by the numerical modelling with those reported in the literature based on experimental tests [25].

Regarding the first point, the static pressure exerted by the filling material on the silo wall and computed by the numerical analysis were compared with those calculated by the analytical solution provided by [40] for slender silo and [41] for squat silo. Figure 2 depicts the comparison for the considered silos filled up to 90% of the maximum storage capacity, showing a good agreement numerical and analytical solutions.

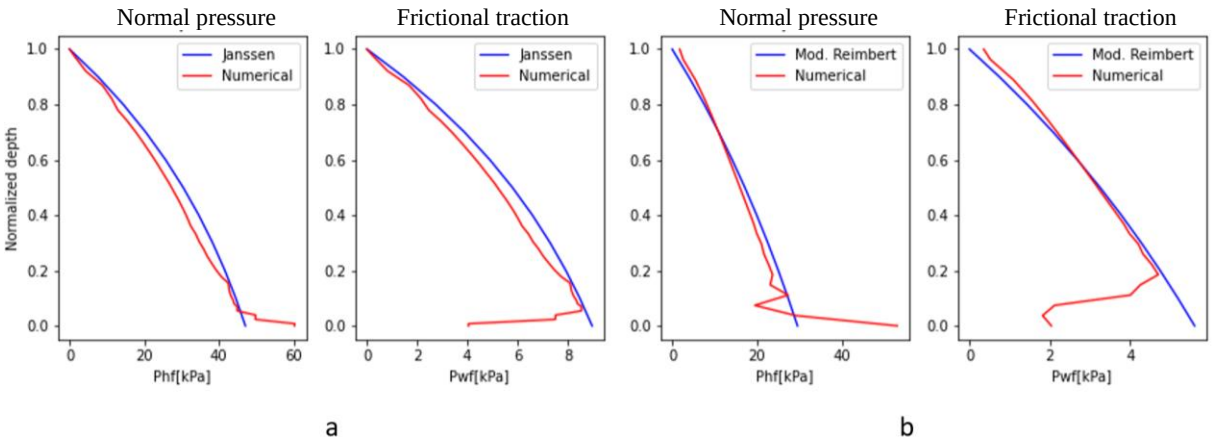


Figure 2: Filling static normal pressures and frictional tractions on the silo walls for the silos Q: (a) 90% filled S-silo; (b) 90% filled Q-silo.

For purpose of verifying the dynamic characteristics yielded from the numerical model, a scaled benchmark silo subjected to shaking table test presented in [25] was modelled. Consequently, eigenvalue analysis was performed and the dynamic characteristics represented by the natural frequency of the dominant vibration modes was calculated and compared with those reported based on the experimental study. The first and second natural frequencies calculated by the FE model were equal to 15.65 Hz and 43.79 Hz, while the ones provided by the experimental test were equal to 12.7-14.1 Hz for the first fundamental vibration mode and 43.9-44.9 Hz for the second one. Also in this case, the comparison between numerical and experimental solutions provided satisfying results.

## 4 SEISMIC ANALYSIS

### 4.1 Frequency analysis

The main dynamic characteristics of the silos under consideration were identified by performing frequency analysis. Fundamental modes of vibration for the silos were observed and the corresponding natural periods were collected. Table 2 reports the periods of vibration for slender and squat cases with empty and 90%-filled condition.

| | 90% | 0% |
|---|---|---|
| S | 0.27 | 0.06 |
| Q | 0.12 | 0.02 |

Table 2: The natural period (in second) of the investigated cases.

### 4.2 Pushover analysis and damage identification

For the purpose of predefining the most vulnerable buckling zones, nonlinear static pushover analysis was performed on the considered silos under investigation. The buckling zones are expected to exhibit severe deformations under lateral loads, and they should be observed when running the dynamic analysis. Nevertheless, the other key reason behind performing pushover analysis is to define the limit of deformation, $EDP_{DP}$, which represent the threshold that state the achievement of the DP, and it was quantified according to a specific engineering demand parameter (EDP) corresponding to each DP. As an instability phenomenon, the shell buckling can be quantified with the displacement magnitude, $\delta$, where this parameter is measured for a control node selected to represent the buckling area under investigation. The parameter $\delta$ was

adopted by other studies to quantify the dynamic buckling of silos and similar structures [8,27]. In practice, the buckling can develop in the silo shell body in different positions with different heights. Thus, in order to have a more practical height-unbiased parameter that can neutralize the position of the buckling zone and that account for the silo global behavior, an alternative parameter was used, which is represented by the ratio between the displacement at the monitored point over to the height of the relevant buckling zone, identified with $\theta$. Hence, this unitless parameter can be employed as EDP in the seismic analysis. Figure 3 shows the performance and the deformation shape for the S silo, under a monotonically increased lateral load.

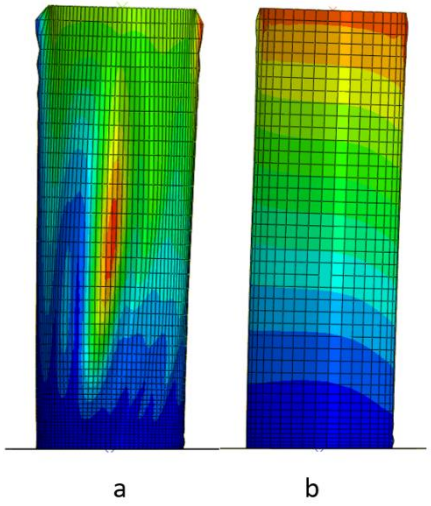


Figure 3: The deformed shape of S silo under lateral static load: (a) the empty case; (b) the 90%-filled case.

The performance of the silo can be interpreted by the behavior of zones prone to buckling corresponding to the distinct DPs. Practically, the behavior of these zones is interpreted by the F-$\theta$ curves, where F represents the global base shear. Consequently, the relevant threshold can be captured as illustrated Figure 4.

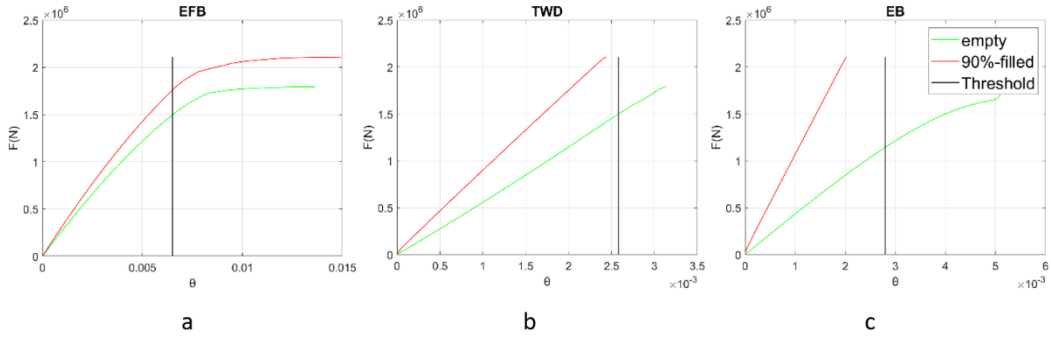


Figure 4: Buckling assessment of the DPs of S silo: (a) EFB; (b) TWD; (c) EB.

### 4.3 Time history analysis

For the purpose of evaluating the dynamic buckling capacity and the variation in the behavior based on the geometry and the absence/presence of the granular material, TH analyses were performed on the silos, accounting for the nonlinearities simulated in the numerical models. For this phase, only half of the system was analyzed since the structure is symmetrical. A damping ratio of 2% was considered for the system. To perform nonlinear TH analyses, the implicit time-integration technique provided by ABAQUS (standard) [38] was used. The model

was accelerated by unidirectional ground motions, using 11 natural ground motion records selected according to a high-intensity spectrum (i.e., PGA > 0.25g).

## 5 PROBABLISTIC SEISMIC RESPOSNE ANALYSIS

To estimate the vulnerability of the investigated silos under a seismic action, fragility curves are derived, in order to quantify the probability that a certain DP occurs in the structure for a given seismic intensity measure (IM). To this end, cloud analysis [42] was employed to calculate the fragility of the silo. The results of TH analysis were used to define the EDP-IM pairs that determine the demand-capacity relationship. As IM, the parameter chosen was the spectral acceleration of the first vibration mode, $Sa(T_1)$, in order to well describe the severity of the ground motion on the structure. Nevertheless, PGA could be used, as adopted in [6,27]. To derive the relation between IM and EDP, given the limited number of records, the power law by Cornell was used [43]. Eventually, fragility curves were computed for each case, considering the three possible DPs. Figure 5 presents the fragility curves as output of the analysis. In total, 4 different cases were investigated. As illustrated by the curves in Figure 5, the overall behavior indicates that both silos are most vulnerable to the EFB when the filling material exists, that is, the probability of occurrence of the other expected failure modes (i.e., TWD and EB) is much lesser than that one of EFB, which is the governing DP. However, for empty case the three DPs have roughly similar tendency to develop as graphically demonstrated by the corresponding fragility curves in Figure 5. Values of medians ($\mu$) and dispersions ($\sigma$) were depicted in Table 3, using as subscripts the related DPs.

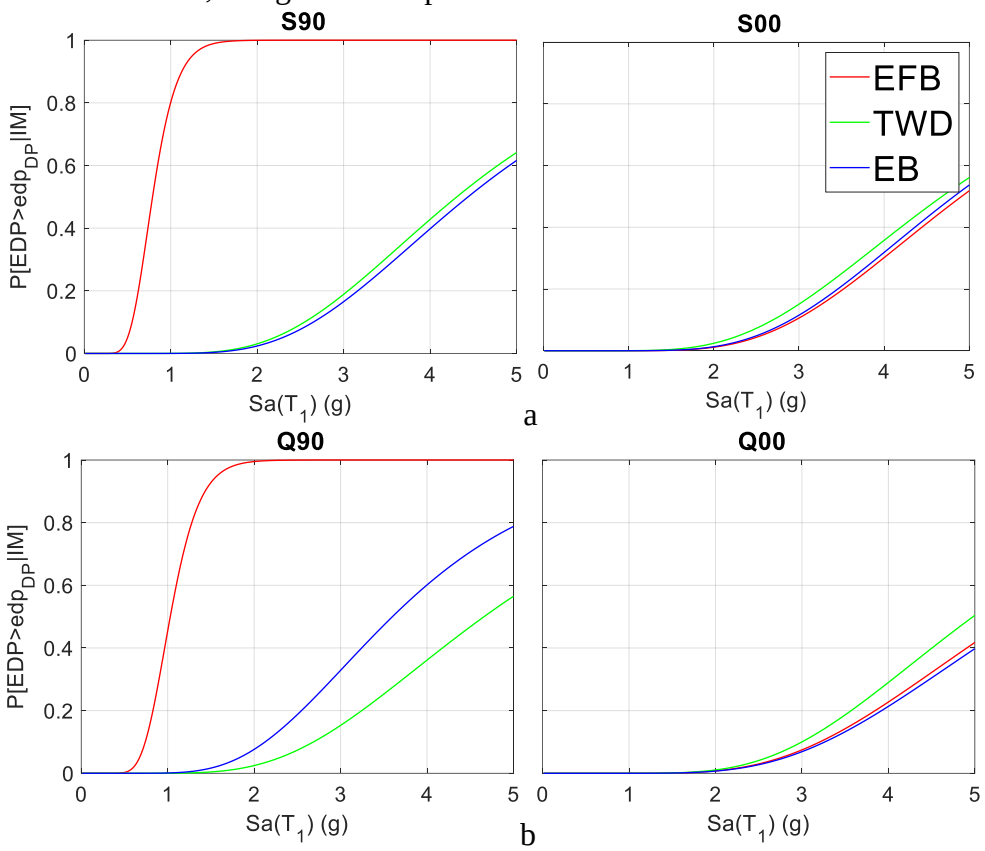


Figure 5. Fragility curves for the investigated silos considering different geometries and filling condition.

| Silo and filling level | | $\mu_{EFB}$ | $\sigma_{EFB}$ | $\mu_{TWD}$ | $\sigma_{TWD}$ | $\mu_{EB}$ | $\sigma_{EB}$ |
|---|---|---|---|---|---|---|---|
| S | 00% | 4.91 | 0.39 | 4.68 | 0.43 | 4.82 | 0.40 |
| | 90% | 0.79 | 0.28 | 4.31 | 0.41 | 4.44 | 0.40 |
| Q | 00% | 5.45 | 0.41 | 4.98 | 0.40 | 5.57 | 0.42 |
| | 90% | 1.03 | 0.26 | 4.66 | 0.43 | 3.60 | 0.41 |

Table 3. Results of fragility curves (μ and $\sigma$) derived for the 4 considered cases.

It is worth noting that the variation in terms of $\mu$ when accounting for 90%-filled or empty cases, reveals that for differences occur for different silo geometry. As a matter of fact, S silo results to be more vulnerable than Q case, looking at the EFB DP ($\mu_{EFB}$ for S equal to 0.79g vs. $\mu_{EFB}$ for Q equal to 1.03). In general, silos with lower aspect ratio performs stronger than those with high aspect ratio and medians corresponding to the governing DPs are higher for squat silos than slender ones, given the same conditions of functionality.

More influent is the role of the ensiled material in the fragility evaluation. Looking at the fragility parameters of the slender silo, the filled silo presents a $\mu_{EFB}$ equal to 0.79g, while the same parameter is equal to 4.91g in the empty case. Still, the relative-high increasing in the median for the empty case indicates very low seismic risk connected to the empty silo, that is, the silo rarely collapses under a natural seismic event for the empty condition. This achievement assume a physical sense, by considering that a very low total mass characterize the empty system, then leading to a low seismic demand.

## 6 CONCLUSIONS

This study presented a numerical evaluation of the seismic fragility for cylindrical ground-supported steel silos storing granular-like material. In detail, the influence of key factors such as the geometry (slender and squat silos) and functionality conditions (fully-filled and empty) were estimated. The governing damage patterns among the possible ones for this kind of structures, i.e. elephant foot buckling, top-wall diamond and elastic buckling in the middle-wall was determined, by computing the seismic fragility for each case.

On the effect of the silo geometry, the results revealed that silos storing solids are most vulnerable to the elephant foot buckling for both slender and squat silos, especially when structures are filled with 90% of the maximum capacity. In addition, both slender and squat silos do not present the tendency to exhibit top-wall damage or diamond elastic middle-wall buckling. In general, the results emphasized that the squat silo performs stronger than the slender one with about 25% higher capacity for the 90%-filled case. About the effect of the ensiled material existence, the results indicated that elephant foot buckling is the governing failure mode for 90%-filled silos while, in case of empty silos, the three investigated damage patterns present comparable probability of occurrence, under very high seismic intensity. On the other hand, empty silos exhibit very high seismic capacity regardless the failure mode and this indicates a very low possibility to fail under ordinary natural seismic events.

Further developments will aim to extend the work on silos to different typologies of silos, storing different class of materials, as well as to refine the numerical models to account other physical factors, e.g., compaction of solid materials during earthquakes action.

## REFERENCES

[1] A.J. Sadowski, J.M. Rotter, Steel silos with different aspect ratios: I — Behaviour under concentric discharge, J Constr Steel Res. 67 (2011) 1537–1544. https://doi.org/10.1016/J.JCSR.2011.03.028.

[2] C. Butenweg, J. Rosin, S. Holler, Analysis of Cylindrical Granular Material Silos under Seismic Excitation, Buildings. 7 (2017) 61. https://doi.org/10.3390/buildings7030061.

[3] A. Kanyilmaz, C.A. Castiglioni, Reducing the seismic vulnerability of existing elevated silos by means of base isolation devices, Eng Struct. 143 (2017) 477–497. https://doi.org/10.1016/j.engstruct.2017.04.032.

[4] R.J. Merino Vela, E. Brunesi, R. Nascimbene, Seismic assessment of an industrial frame-tank system: development of fragility functions, Bulletin of Earthquake Engineering. 17 (2019) 2569–2602. https://doi.org/10.1007/s10518-018-00548-2.

[5] satellite imagery via Google Earth, Maxar, Nurdagi, Turkey @WxNB, (n.d.). https://twitter.com/Maxar/status/1623874874769825793 (accessed March 14, 2023).

[6] M.J. O'Rourke, P. So, Seismic Fragility Curves for On-Grade Steel Tanks, Earthquake Spectra. 16 (2000) 801–815. https://doi.org/10.1193/1.1586140.

[7] E. Brunesi, R. Nascimbene, M. Pagani, D. Beilic, Seismic Performance of Storage Steel Tanks during the May 2012 Emilia, Italy, Earthquakes, Journal of Performance of Constructed Facilities. 29 (2015). https://doi.org/10.1061/(ASCE)CF.1943-5509.0000628.

[8] N. Buratti, M. Tavano, Dynamic buckling and seismic fragility of anchored steel tanks by the added mass method, Earthq Eng Struct Dyn. 43 (2014) 1–21. https://doi.org/10.1002/EQE.2326.

[9] M. Vathi, S.A. Karamanos, I.A. Kapogiannis, K. V. Spiliopoulos, Performance Criteria for Liquid Storage Tanks and Piping Systems Subjected to Seismic Loading, J Press Vessel Technol. 139 (2017). https://doi.org/10.1115/1.4036916.

[10] M. Khalil, Long Span Steel Structures: Structural Typology Optimization and Enhancement- The Conceptual Design of an Aircraft Hangar, in: 2022. https://doi.org/10.11159/iccste22.228.

[11] S.J. Lee, Experimental study of cylindrical silos subject to seismic excitation , Doctoral dissertation, The Ohio State University, 1981.

[12] N.S. Trahair, A. Abel, P. Ansourian, H.M. Irvine, J.M. Rotter, Structural Design of Steel Bins for Bulk Solids, AustralianInstitute of Steel Construction, Sydney, Australia, 1983.

[13] H. Yokota, M. Sugita, I. Mita, Vibration tests and analyses of coal-silo model, in: In Proc., 2nd Int. Conf. on the Design of Silos for Strength and Flow, , Powder Advisory Centre, Stratford-upon-Avon, 1983: pp. 107–116.

[14] A. Shimamoto, M. Kodama, M. Yamamura, Vibration tests for scale model of cylindrical coal storing silo, in: Proceedings of the 8th World Conference on Earthquake Engineering (Vol. 5, San Francisco., 1984: pp. 287–294.

[15] J.M. Rotter, T.S. Hull, Wall loads in squat steel silos during earthquakes, Eng Struct. 11 (1989) 139–147. https://doi.org/10.1016/0141-0296(89)90002-3.

[16] Y. Sasaki, J. Yoshimura, Dynamic discrete modeling and computer simulation of seismic response of concrete stave silos with structural discontinuity. In Earthquake Engineering, in: Proceedings of the Tenth World Conference, Balkema, Rotterdam , 1992: pp. 5065–6070.

[17] B. O. Hardin, R. A. Bucklin, I. J. Ross, Shear-beam Analysis for Seismic Response of Metal Wheat Bins, Transactions of the ASAE. 39 (1996) 677–687. https://doi.org/10.13031/2013.27552.

[18] A.S. Veletsos, A.H. Younan, Dynamics of Solid-Containing Tanks. II: Flexible Tanks, Journal of Structural Engineering. 124 (1998) 62–70. https://doi.org/10.1061/(ASCE)0733-9445(1998)124:1(62).

[19] A.H. Younan, A.S. Veletsos, Dynamics of Solid-Containing Tanks. I: Rigid Tanks, Journal of Structural Engineering. 124 (1998) 52–61. https://doi.org/10.1061/(ASCE)0733-9445(1998)124:1(52).

[20] S. Holler, K. Meskouris, Granular Material Silos under Dynamic Excitation: Numerical Simulation and Experimental Validation, Journal of Structural Engineering. 132 (2006) 1573–1579. https://doi.org/10.1061/(ASCE)0733-9445(2006)132:10(1573).

[21] F. Nateghi, M. Yakhchalian, Seismic behavior of silos with different height to diameter ratios considering granular material-structure interaction, International Journal of Engineering. 25 (2012) 25–35. https://doi.org/10.5829/idosi.ije.2012.25.01b.04.

[22] EN 1998-4, Eurocode 8: Design of Structures for Earthquake Resistance – Part 4: Silos, Tanks and Pipelines, CEN, Brussels, 2006, n.d.

[23] S. Silvestri, G. Gasparini, T. Trombetti, D. Foti, On the evaluation of the horizontal forces produced by grain-like material inside silos during earthquakes, Bulletin of Earthquake Engineering. 10 (2012) 1535–1560. https://doi.org/10.1007/s10518-012-9370-y.

[24] L. Pieraccini, S. Silvestri, T. Trombetti, Refinements to the Silvestri's theory for the evaluation of the seismic actions in flat-bottom silos containing grain-like material, Bulletin of Earthquake Engineering. 13 (2015) 3493–3525. https://doi.org/10.1007/s10518-015-9786-2.

[25] S. Silvestri, S. Ivorra, L. Di Chiacchio, T. Trombetti, D. Foti, G. Gasparini, L. Pieraccini, M. Dietz, C. Taylor, Shaking-table tests of flat-bottom circular silos containing grain-like material, Earthq Eng Struct Dyn. 45 (2016) 69–89. https://doi.org/10.1002/eqe.2617.

[26] A. Durmuş, R. Livaoglu, A simplified 3 D.O.F. model of A FEM model for seismic analysis of a silo containing elastic material accounting for soil–structure interaction, Soil Dynamics and Earthquake Engineering. 77 (2015) 1–14. https://doi.org/10.1016/j.soildyn.2015.04.015.

[27] A.M. Mehretehran, S. Maleki, 3D buckling assessment of cylindrical steel silos of uniform thickness under seismic action, Thin-Walled Structures. 131 (2018) 654–667. https://doi.org/10.1016/J.TWS.2018.07.040.

[28] A.M. Mehretehran, S. Maleki, Seismic response and failure modes of steel silos with isotropic stepped walls: The effect of vertical component of ground motion and comparison of buckling resistances under seismic actions with those under wind or discharge loads, Eng Fail Anal. 120 (2021) 105100. https://doi.org/10.1016/j.engfailanal.2020.105100.

[29] S. Silvestri, S. Mansour, M. Marra, J. Distl, M. Furinghetti, I. Lanese, E. Hernández-Montes, C. Neri, M. Palermo, A. Pavese, E. Rizzo Parisi, A.J. Sadowski, F. Selva, T. Taniguchi, L. Vadrucci, F. Weber, Shaking table tests of a full-scale flat-bottom manufactured steel silo filled with wheat: Main results on the fixed-base configuration, Earthq Eng Struct Dyn. 51 (2022) 169–190. https://doi.org/10.1002/eqe.3561.

[30] H. Jing, H. Chen, J. Yang, P. Li, Shaking table tests on a small-scale steel cylindrical silo model in different filling conditions, Structures. 37 (2022) 698–708. https://doi.org/10.1016/j.istruc.2022.01.026.

[31] F. Nateghi, M. Yakhchalian, Seismic Behavior of Reinforced Concrete Silos Considering Granular Material-Structure Interaction, Procedia Eng. 14 (2011) 3050–3058. https://doi.org/10.1016/j.proeng.2011.07.384.

[32] S. Mansour, S. Silvestri, A.J. Sadowski, The 'miniature silo' test: A simple experimental setup to estimate the effective friction coefficient between the granular solid and a horizontally-corrugated cylindrical metal silo wall, Powder Technol. 399 (2022) 117212. https://doi.org/10.1016/j.powtec.2022.117212.

[33] M. Khalil, S. Ruggieri, G. Uva, Assessment of Structural Behavior, Vulnerability, and Risk of Industrial Silos: State-of-the-Art and Recent Research Trends, Applied Sciences (Switzerland). 12 (2022). https://doi.org/10.3390/APP12063006.

[34] P.K. Malhotra, T. Wenk, M. Wieland, Simple Procedure for Seismic Analysis of Liquid-Storage Tanks, Https://Doi.Org/10.2749/101686600780481509. 10 (2018) 197–201. https://doi.org/10.2749/101686600780481509.

[35] J.M. Rotter, Elephant's foot buckling in pressurised cylindrical shells, Stahlbau. 75 (2006) 742–747. https://doi.org/10.1002/STAB.200610079.

[36] J.C. Virella, L.E. Suárez, L.A. Godoy, A Static Nonlinear Procedure for the Evaluation of the Elastic Buckling of Anchored Steel Tanks Due to Earthquakes, Journal of

Earthquake Engineering. 12 (2008) 999–1022. https://doi.org/10.1080/13632460701672714.

[37] A.J. Sadowski, J.M. Rotter, Steel silos with different aspect ratios: II — behaviour under eccentric discharge, J Constr Steel Res. 67 (2011) 1545–1553. https://doi.org/10.1016/J.JCSR.2011.03.027.

[38] Dassault Systèmes Simulia, Abaqus CAE User's Manual, (2012), (n.d.).

[39] M. Moya, P.J. Aguado, F. Ayuga, Mechanical properties of some granular agricultural materials used in silo design, Int Agrophys. 27 (2013) 181–193. https://doi.org/10.2478/v10247-012-0084-9.

[40] H.A. Janssen, Versuche uber getreidedruck in silozellen, Zeit. D. Ver. Dtsch. Ing. (1895) 1045–1049.

[41] M.L. Reimbert, A.M. Reimbert, Silos : theory and practice, (1976).

[42] P. Bazzurro, C.A. Cornell, N. Shome, J.E. Carballo, Three Proposals for Characterizing MDOF Nonlinear Seismic Response, Journal of Structural Engineering. 124 (1998) 1281–1289. https://doi.org/10.1061/(ASCE)0733-9445(1998)124:11(1281).

[43] C.A. Cornell, F. Jalayer, R.O. Hamburger, D.A. Foutch, Probabilistic Basis for 2000 SAC Federal Emergency Management Agency Steel Moment Frame Guidelines, Journal of Structural Engineering. 128 (2002) 526–533. https://doi.org/10.1061/(ASCE)0733-9445(2002)128:4(526).

COMPDYN 2023
9th ECCOMAS Thematic Conference on
Computational Methods in Structural Dynamics and Earthquake Engineering
M. Papadrakakis, M. Fragiadakis (eds.)
Athens, Greece, 12-14 June 2023

# EFFECT OF THE STRUCTURAL INTERACTIONS IN MULTI-STORY CLT SHEAR WALLS

**E. M. Ruggeri[1], G. D'Arenzo[2], M. Fossetti[3]**

[1] Faculty of Engineering and Architecture, Kore University of Enna, Italy
e-mail: e-mail: elisabettamaria.ruggeri@unikorestudent.it

[2] Timber Structures and Building Rehabilitation, University of Kassel, Germany
e-mail: giuseppe.darenzo@uni-kassel.de

[3] Faculty of Engineering and Architecture, Kore University of Enna, Italy
e-mail: e-mail: marinella.fossetti@unikore.it

## Abstract

*A CLT platform building is made up of horizontal and vertical panels, which are assembled on site to obtain a "box-type" structure, in which the lateral load resisting system consists of the assembly of different shear walls with their base connections, and other typologies of connections. The lateral behavior of a CLT platform building is governed by the wall base connections, but also influenced by different structural interactions including those between floor and wall segments and those between lintels and wall segments. The magnitude of the interactions between lintels and wall segments depends on the construction technique chosen for creating the openings, which can be realized through monolithic or assembled shear walls. Although multi-story CLT shear walls realized with these two different construction techniques exhibit a different lateral behavior, often, the same simplified modelling strategy is considered in the design practice, neglecting relevant aspects of the lateral behavior such as the structural interactions. This paper investigates in detail the differences of the lateral behavior of multi-story CLT shear walls realized with these two construction techniques by considering both simplified modelling strategies and more advanced modelling strategies, which consider the structural interactions between floor diaphragms and wall segments and between lintels and wall segments. Results of nonlinear static analyses showed significant differences between the two modelling strategies in terms of lateral performance and failure modes of the systems, emphasizing that simplified modelling strategies cannot always be reliable methodologies to describe the behavior of multi-story CLT shear walls.*

**Keywords:** CLT structures, multi-story shear walls, structural interactions, numerical modelling strategies, lateral capacity.

## 1 INTRODUCTION

Typically, in the design of a CLT building, it is assumed that the mechanical behavior of the shear walls is primarily governed by the mechanical properties of the panels and connections at the base of the wall. Based on this assumption, several analytical models that predict the lateral stiffness and lateral capacity of a CLT wall subjected to lateral loads were developed, see for instance [1]. CLT buildings, especially those built using the platform construction technique, have a significant structural redundancy because of the multiple connections between the exterior walls, interior partitions, and floor diaphragms. The lateral performance of a building constructed using the platform method is strongly influenced by the connection details. Moreover, the type of connection determines how lateral forces are transferred from the floors to the walls and thus to the foundation. In this context, in case of platform CLT buildings, in addition to the connections placed at the base of the walls (hold-downs and angle brackets), there are other connections that influence the mechanical behavior of CLT shear walls, such as those between perpendicular walls and between floors and walls.

The effects of interaction between horizontal floors and vertical walls have been found in several experimental tests of CLT buildings, see for instance the study by Popovski and Gavrić [2] and Yasumura et al. [3], as well as in analytical and numerical studies. D'Arenzo et al. [4] presented a study on the phenomenon of the floor-to-wall interaction and on its influence on the rocking behavior of segmented CLT shear walls. Results of this study showed that the floor-to-wall interaction increases the rocking stiffness of segmented shear walls and modifies the kinematic behavior of these systems. Tamagnone et al. [5] analyzed the influence of the out-of-plane stiffness of the floor diaphragm and floor-to-wall connections on the rocking behavior of segmented CLT walls. Results of this study showed that the stiffness of the floor-to-wall connections has a strong influence on the lateral behavior of the system, which modify the behavior of the panels. Gavrić et al. [6] and Ruggeri et al. [7] investigated the effects of the interactions between perpendicular walls in "box-type" CLT buildings. These studies showed that the properties of the hold downs of the perpendicular walls and the wall-to-wall connections between the shear walls and the perpendicular walls contribute to increase the lateral performances of CLT structures.

Since the lateral response of a CLT building depends on different structural interactions, the presence of the openings also plays an important role in the lateral behavior of multi-story CLT shear walls. In case of platform construction method, the openings may be realized following two different construction techniques: by cutting out of the CLT panel with an automated process during fabrication, or by assembling multiple CLT panel elements in situ [3,8]. In the first case, it is possible to schematize the system as a monolithic shear wall, whose lateral behavior is influenced by the structural continuity between the wall segments and the lintels, see Figure 1. In the second case, when lintels are assembled by means of mechanical connections to the wall segments (assembled shear wall), the system can be studied considering wall segments as cantilever elements due to the fact that lintels provide very limited interaction, see Figure 1.

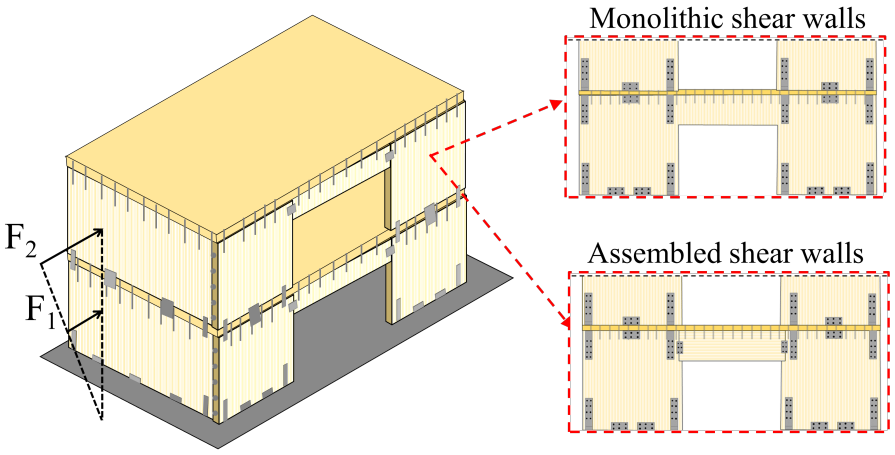


Figure 1: Typical platform CLT building with openings.

The mechanical behavior of CLT shear walls with door and window openings were studied by Casagrande et al. [9] through full-scale experimental tests and numerical analyses. Results of this study showed that, in case of shear wall with openings, the failure may occur in the lintel element either in bending or shear. Mestar et al. [10] studied the kinematic modes of CLT shear walls with openings and observed that the lintel geometry and the vertical stiffness of the wall base connections, govern the lateral behavior of these systems. D'Arenzo [11] investigated the lateral behavior of monolithic shear walls with openings with particular focus on the effects of the interactions between the CLT wall segments, the lintels and the parapets. Results of this study showed that there is an interaction between lintels, parapets and wall segments, which modifies the lateral deformation mechanism and the kinematic modes of the shear walls and lead to higher lateral performances. Similar results were found by Khajehpour et al. [12], who studied the effects of the interactions between lintel, parapets and wall segments in multi-story shear wall systems.

Although the results documented above reveal that the presence of the floor and its connections to the underlying walls and the two different shear wall construction techniques (monolithic and assembled), lead to different lateral behavior of CLT systems, it is common practice in structural design to model multi-story CLT shear walls by considering the same simplified modelling strategy. This modelling strategy considers wall segments and their connections at the base, but neglects the contribution given by the interactions between lintel and wall segments and between floor elements and wall segments [13,14].

To overcome this limitation and realistically simulate the behavior of a CLT structures under lateral loads, it is necessary to implement numerical models that take into account these structural interactions, since they can profoundly influence the lateral response of CLT structures. In this study, two advanced modelling strategies, which consider the structural interactions between floor diaphragms and wall segments and between lintels and wall segments are proposed. The different modeling strategies were applied to the two construction techniques in the presence of openings, see Figure 1. In order to compare the results obtained from the simplified modelling strategy with those obtained from the advanced modelling strategies that take into account the structural interactions, nonlinear static analyses were conducted. Results of the current study will show how the different modelling strategies lead to significantly different lateral performance of the structures in terms of lateral stiffness, capacity and failure modes.

## 2 MODELLING STRATEGIES

Typically, multi-story CLT shear walls are modelled by means of simplified modelling strategy in the numerical analyses. In this context, the wall segments provide the stability for horizontal loads and are schematized as cantilever elements, while lintels and parapets are modelled as pinned elements and are considered as non-structural components. Hold-downs are placed at both extremities of each wall segment to prevent it from overturning, while angle brackets, that transfer the shear loads to the foundation, are placed along the length of the wall panels. Using this modelling strategy for multi-story CLT shear walls, the bending contribution of floor diaphragms and lintels is neglected, see Figure 2. In this simplified modelling strategy, called SM, the lintels (and parapets) have the function of transferring vertical and horizontal loads to the wall segments [8,15]; as result no bending moment is transmitted between the wall segments and the lintels, and the system failure occurs in the mechanical anchors placed at the base of the wall segments.

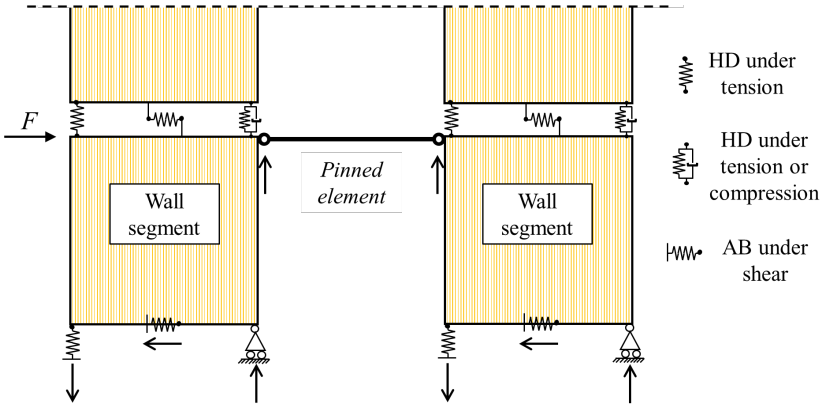


Figure 2: Simplified modelling strategy of multi-story CLT shear walls (SM).

In order to realistically simulate the lateral behavior of a multi-story CLT shear walls, it is necessary to adopt a more advanced modelling strategy, which takes into account the interactions between lintels and wall segments and the interactions between floors and wall segments. In this context, an advanced modelling strategy that consider these structural interactions (IM) is proposed. In particular, this advanced modelling strategy is applied for both monolithic walls (IM-MSW) and assembled walls (IM-ASW).

In case of monolithic shear walls (IM-MSW), see Figure 3, the structural continuity between lintels and wall segments is ensured and the failure of the system can occur either in the connections at the base of the wall segments or in the corner of the openings between the lintel and the wall segments, depending on the level of stresses in this critical zone [2,16,17]. Using this modelling strategy, higher lateral performance can be achieved than the SM strategy due to the fact that the lintels have the ability to transfer bending actions, but also due to the bending contribution of the floor diaphragms. According to D'Arenzo [11] the bending stiffness of monolithic shear walls with openings is governed by the stiffness of the lintels, parapets, hold-downs and it also depends on the geometry of the system. Furthermore, a strong correlation was found between the kinematic behavior and the rocking stiffness of the system, in fact, the kinematic behaviors with a one center of rotation are associated with values of rocking stiffness generally higher than those achieved by the kinematic behaviors with two centers of rotation. Based on the results of this study, in case of monolithic shear walls (IM-MSW), a different lateral deformation mechanism may occur with a different distribution

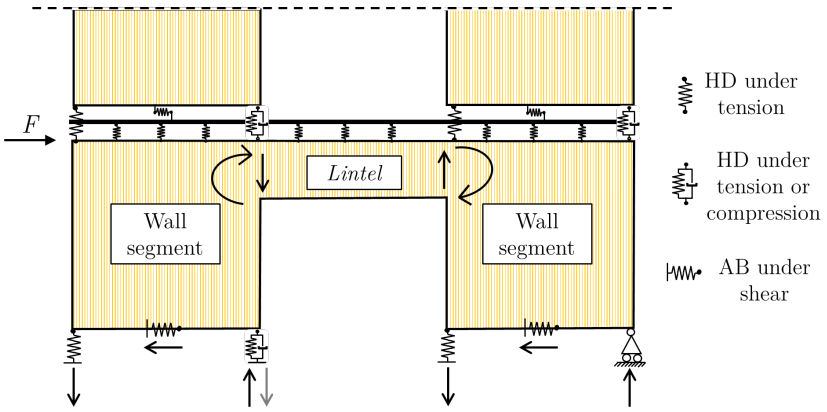


Figure 3: Advanced modelling strategy with interactions of multi-story CLT shear walls (IM-MSW).

of the centers of rotation of the system [18], depending on the bending stiffness and the capacity of lintels and floor diaphragms.

Also in case of assembled shear walls (IM-ASW), see Figure 4, modelled considering the structural interactions, higher lateral performances are expected compared to the SM strategy, due to the bending contribution of the floor diaphragms. Unlike the case of monolithic walls (IM-MSW), in this construction technique it is not possible to obtain full structural continuity between lintels and wall segments with the typical mechanical connections used in practice, and consequently, the failure of the system may occur in the floor panel or in the connections placed at the base of the wall segments.

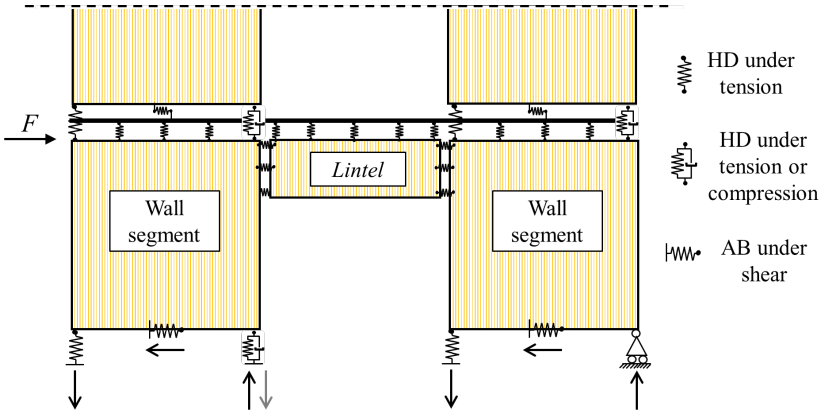


Figure 4: Advanced modelling strategy with interactions of multi-story CLT shear walls (IM-ASW).

In the next sections, the numerical study aimed at investigating the effects of the interactions provided by floor diaphragms, lintels, and wall segments in multi-story CLT shear walls is presented.

## 3 NUMERICAL STUDY

In the following, the configurations, the mechanical parameters, the numerical modelling, including the failure mode criteria, of different multi-story CLT shear wall systems used for the numerical study are presented.

### 3.1 Configuration and mechanical parameters

In order to investigate the effects of the two different construction techniques (see Figure 1) and the structural interactions due to floors, lintels, and wall segments the lateral behavior of different CLT multi-story shear wall geometries, with different panel and connection properties were studied. Figure 5 shows the nine different multi-story CLT shear wall configurations and the distribution of the mechanical anchors used in this study. These structures consist of one-, three-, and five-story systems and three different geometries, with a lintel height of 400 mm. For all stories and for all geometries, the same CLT wall segment height and the same CLT floor thickness were assumed. The geometrical dimensions of the three different geometries are shown in Figure 6.

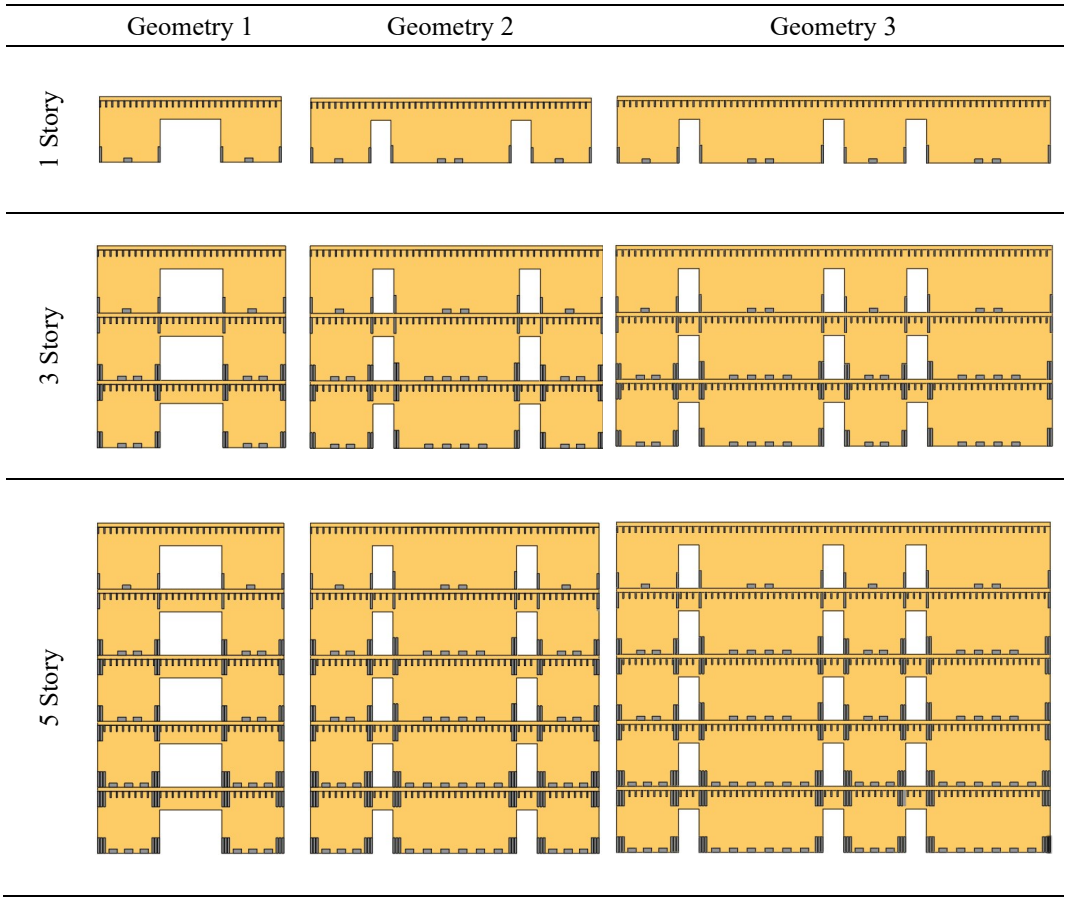


Figure 5: Multi-story CLT shear walls configurations and connections distribution.

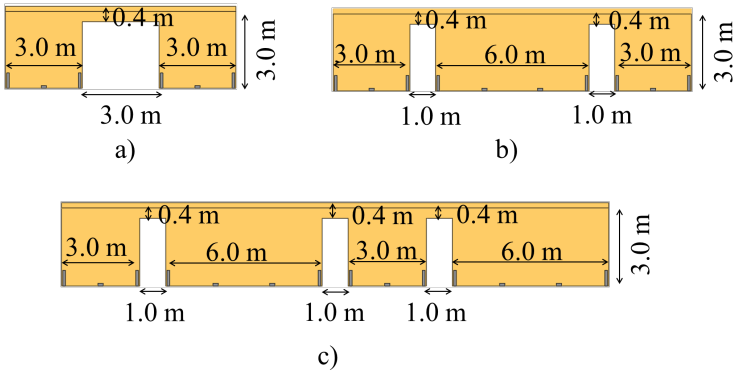


Figure 6: CLT shear walls geometries and dimensions: a) Geometry 1, b) Geometry 2 and c) Geometry 3.

The numerical study was conducted by considering three different thicknesses of CLT wall panels along the height of the structures, as is usually done in the practical construction of multi-story CLT buildings. Figure 7 shows the different layer's thicknesses for the Floor panel (FP), the same for all stories, and for the Wall panel 1 (WP1), Wall panel 2 (WP2) and Wall panel 3 (WP3), used along the height of the structures. Depending on the construction technique, a different direction of the external wooden laminates was assumed for the wall segments and lintels. In case of monolithic shear walls, the orientation of the external wooden laminates of CLT panels was assumed to be in the vertical direction for both wall segments and lintels, while in case of assembled shear wall, a vertical orientation was assumed for wall segments and a horizontal orientation was assumed for lintels. The distribution of the different CLT panels considered along the height of the structures are shown in Table 1.

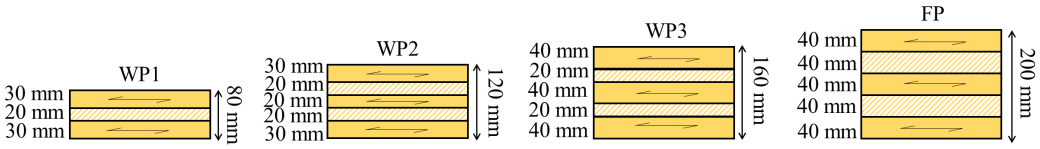


Figure 7: Layers thicknesses.

| CLT panels thickness [mm] | | | |
|---|---|---|---|
| | 1 story | 3 story | 5 story |
| Fifth story | | | WP1 |
| Fourth story | | | WP2 |
| Third story | | WP1 | WP2 |
| Second story | | WP2 | WP3 |
| First story | WP1 | WP2 | WP3 |

Table 1: Distribution of the CLT panel sections along the height of the structures.

The modulus of elasticity parallel to the grain, $E_0$, perpendicular to the grain, $E_{90}$, and the in-plane shear modulus $G_0$ of the wooden laminates of all CLT panels were assumed to be 11700 MPa, 390 MPa and 730 MPa, respectively. The mechanical properties of the connections at the base of the shear walls, hold-downs and angle brackets, were chosen on the basis of the experimental results of Casagrande et al [19]. In this study, the WHT440 type hold-

downs with thirty 4×60 mm annular ring nails and the TTF200 type angle brackets with thirty 4×60 mm annular ring nails were tested for tension and shear loads, respectively. On the basis of these results, the values of vertical elastic stiffness and maximum strength of a hold-down were set respectively equal to 6.61 kN/mm and 78.14 kN, while the values of horizontal elastic stiffness and maximum strength of an angle bracket were set equal to 8.94 kN/mm and 70.04 kN, respectively. The number of the mechanical anchors of the CLT multi-story shear walls was set considering the increase of the shear force from the upper stories to the foundation. In fact, a different number of hold-downs along the height of the structures, placed at the ends of each wall segment, and a different number of angle brackets, distributed along the base of the wall segments, were considered (see Figure 5). The mechanical properties of one hold-down and one angle bracket used for the numerical analyses are summarized in Table 2.

| | $K_{el}$ [kN/mm] | $F_y$ [kN] | $F_{max}$ [kN] | $F_{ult}$ [kN] | $v_y$ [mm] | $v_{max}$ [mm] | $v_{ult}$ [mm] | D [-] |
|---|---|---|---|---|---|---|---|---|
| Hold-down | 6.61 | 61.33 | 78.41 | 62.51 | 9.28 | 18.87 | 28.47 | 3.07 |
| Angle bracket | 8.94 | 57.69 | 70.04 | 56.03 | 6.45 | 16.26 | 26.07 | 4.04 |

Table 2: Parameters of the base connections used for the numerical analyses.

Mechanical properties of the floor-to-wall connections were assigned based on the experimental results of Gavric et al.[20]. Based on this study, the withdrawal stiffness (vertical direction) and the shear stiffness (horizontal direction) of one screw was set equal to 4.00 and 1.45 kN/mm, respectively. The spacing between each wall-to-wall connection is chosen equal to 300 mm in all analyses. A vertical load $q$ equal to 10 kN/m was applied on each story of the system, while a triangular distribution of horizontal loads $F$ was adopted. The value of the base shear force used in each configuration are reported in Table 3.

| Base shear [kN] | | | |
|---|---|---|---|
| | Geometry 1 | Geometry 2 | Geometry 3 |
| 1 story | 21.4 | 33.3 | 50.0 |
| 3 story | 128.6 | 200.0 | 300.0 |
| 5 story | 321.4 | 500.0 | 750.0 |

Table 3: Base shear used for each configuration.

### 3.2 Description of the numerical modelling

Numerical models were developed using the software package SAP2000 [21]. Orthotropic homogeneous shell elements [22] were adopted to reproduce the wall segments and the lintels considering the different thicknesses of the CLT panels. Effective modulus of elasticity in the vertical, $E_{eff,v}$, and horizontal, $E_{eff,h}$, direction of the panel were assigned considering the layered distribution of the different CLT panel sections, according to the composite theory of Blaß and Fellmoser [23]. Whereas, the effective in-plane shear modulus of the wooden laminates, $G_{eff}$, was defined according to Bogensperger et al. [24]. The mechanical properties of the CLT panels used in the numerical models (WP1, WP2, WP3) are summarized in Table 4.

Quadrilateral shell elements with a mesh size equal to 100×100 mm were adopted in all numerical analyses. In case of SM strategy, the pinned elements connecting the wall segments were modeled as frame elements, see Figure 8.

| | $E_{eff,v}$ [MPa] | $E_{eff,h}$ [MPa] | $G_{eff}$ [MPa] |
|---|---|---|---|
| WP1 | 8872 | 3217 | 573 |
| WP2 | 7930 | 4160 | 598 |
| WP3 | 8872 | 3217 | 570 |

Table 4: Mechanical properties of CLT panels.

In case of structures analyzed with the modelling strategies with interactions (IM strategy), the floor diaphragms were modelled as beam elements with effective bending stiffness $E_0 I_{eff}$. The effective moment of inertia $I_{eff}$ was calculated considering the layered structure of the panel and in particular the thickness of each layer, the distance of each layer from the centroid of the section, and the floor width. The calculation of the floor width relied on the method presented by Masoudnia et al [25] for determining the effective collaborative section in situations of internal bending actions. Based on this, the effective bending stiffness of the floor was set equal to 5793 kNm$^2$.

In case of monolithic shear wall analyzed with the advanced modelling strategy taking into account the structural interactions (IM-MSW), wall segments and lintels were modelled as unique shell element with the same orientation of the external wooden laminates (z), see Figure 9 (a). Whereas, in case of assembled shear walls analyzed considering the effect of the interactions (IM-ASW), wall segments and lintels were modelled as separate shell elements with different orientation of the external wooden laminates (z and x, respectively) and connected by means of wall-to-lintel connections (w-l), see Figure 9 (b).

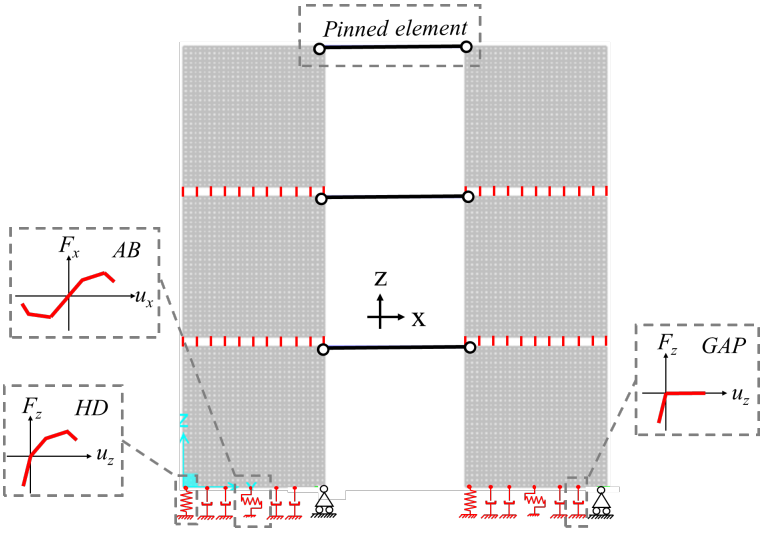


Figure 8: Simplified modelling strategy of multi-story CLT shear walls (SM).

In case of simplified modelling strategy, the analyses were conducted applying the horizontal forces $F$ on the top of wall segments at each story, while a vertical load $q$ was applied on the first row of shell elements of the walls and on the pinned elements as equivalent load per unit area and as uniformly distributed load, respectively. While, in case of advanced modelling strategies with interactions, the horizontal forces $F$ were applied on the top of the wall segments at each story and a vertical load $q$ was applied to the first row of shell elements of the walls as equivalent load per unit area.

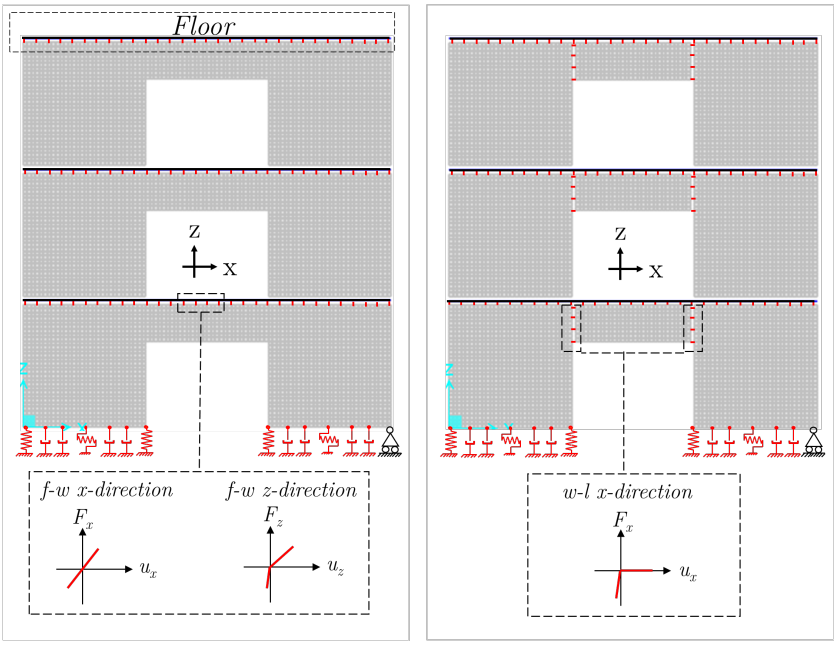


Figure 9: Advanced modelling strategy with interactions: a) of monolithic(IM-MSW). and b) assembled multi-story CLT shear walls (IM-ASW).

Hold-downs and angle brackets (HD and AB, respectively) were modelled by means of one- and two-joint multilinear elastic links, for both modelling strategies, SM and IM. The hold-downs were characterized by different multilinear behavior for tensile and compressive forces: for tensile forces the tensile stiffness of the hold-downs was considered, while for compressive forces the link simulated the contact between panel and foundation through high stiffness values, see Figure 8. The vertical tensile behavior (z) of the hold downs was modelled with a trilinear curve according to the values reported in Table 2. Angle brackets were modelled with symmetrical tri-linear curve in the horizontal shear direction (x), in order to reproduce the nonlinear behavior of the angle brackets for shear loads, see Figure 8.

To simulate the contact between the wall segments and the foundation, gap elements with rigid compression-only behavior were defined for both modelling strategies, SM and IM, see Figure 8. These gap elements were also used between the wall segments of the different stories in the SM strategy.

In the IM strategy, the floor-to-wall connections (f-w) were modelled as a series of two-joint multilinear elastic links from the SAP2000 library, see Figure 9. These connections were characterized by a symmetric elastic behavior in the horizontal shear direction (x), while they were modelled with elastic behavior, for tensile loads, in order to simulate the withdrawal behavior of the connection, and with a stiff behavior, for compressive loads, to simulate the contact between floor and wall. Finally, in case of assembled shear wall (IM-ASW) the wall-to-lintel connections (w-l) were modelled as a series of multilinear elastic two-joint links with stiff compression-only properties in the horizontal (x) direction in order to reproduce the contact between the wall segments and the lintels, see Figure 9.

Results obtained from the modelling strategies that consider the structural interactions (IM-MSW and IM-ASW) were compared with those obtained from the SM strategy and with another additional numerical model that represents a comparison system. This comparison model, called CS, considers the same multi-story CLT shear wall configurations without openings modelled according to the IM strategy, see Figure 10. SM and CS strategies represent respec-

tively the case of maximum and minimum lateral flexibility, while the modelling strategies with interactions in case of monolithic and assembled shear wall (IM-MSW and IM-ASW) should have lateral flexibility between these two cases.

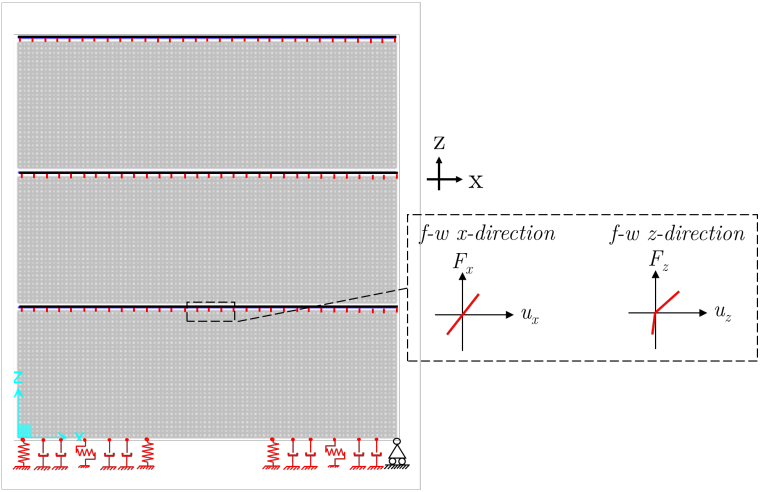


Figure 10: Advanced modelling strategy with interactions in case of multi-story CLT shear walls without openings (CS).

### 3.3 Failure modes of the systems

CLT shear wall systems are composed of massive timber walls that are fastened together to form "box-type" structures. Due to the high in-plane stiffness of the CLT panels, the lateral response of such systems strongly depends on the connection properties. In fact, in case of shear walls without openings, the failure of the CLT panel is unlikely because it is typically preceded by the failure of the connections. Whereas, in case of monolithic shear wall systems with openings, the high concentrations of forces in the corners of the openings may cause brittle failures of the wooden panel in this critical zone before the failure of the connections take place. This failure type occurs when the strength of the wooden panels in this region is exceeded, involving the formation of cracks around the corner of the openings.

In case of systems with monolithic shear walls (IM-MSW), the failure condition was determined by checking step-by-step in the nonlinear analysis the level of the internal stresses of the panel in the corner around the openings. This verification was performed by verifying the shear ($\tau$) and the horizontal and vertical normal ($\sigma_h$ and $\sigma_v$) stresses of each mesh along the critical region above the corner of the openings, between lintels and wall segments. In particular, in case of monolithic shear walls, the verification was done using the RVSE model, according to Bogensperger et al. [24].

In case of assembled shear walls (IM-ASW), bending failure of the CLT floor panel above the corner of the openings is likely to be observed, according to Yasumura et al. [16]. On the other hand, no failure takes place in the CLT shear walls due to the discontinuity between lintels and wall segments. In these systems, the floor failure was monitored by verifying step-by-step in the nonlinear analysis that the floor bending stresses did not exceed the bending strength of the CLT floor panels. The bending strength of the floor panel was calculated considering the bending strength of the CLT and the effective inertia of the CLT floor panel.

In all numerical modelling strategies considered in this study, the failure of the wall base connections, hold-downs and angle brackets, was monitored considering their ultimate displacement, which is given in Table 2.

## 4 RESULTS AND DISCUSISON

The influence of the interactions provided by the bending contribution of the floor diaphragms and the structural continuity between lintels and wall segments on the lateral behavior of one- and multi-story CLT shear walls is shown in this section. Nonlinear static analyses were performed, considering the geometry and the connection properties of the systems shown in Figure 5. The results of the nonlinear static analyses in terms of lateral performances and failure modes are presented below. In all analyses conducted in this study, the results obtained from the advanced modelling strategy (IM-MSW and IM-ASW), which takes into account the structural interactions, were compared with those obtained from the structures modelled with the simplified modelling strategy (SM), and the additional numerical model representing a comparison system (CS), which considers the same configurations of multi-story CLT shear walls without openings.

Figure 11 shows the pushover curves and the failure modes of the multi-story CLT shear walls, plotting graphs organized in matrix form. Each graph shows four curves, each one representing the results of multi-story CLT shear walls modelled with one of the four modelling strategies discussed above. The results of the nonlinear analyses show that the pushover curves of the multi-story CLT shear walls obtained from the modelling strategies with interactions (IM-MSW and IM-ASW) are between those obtained from the SM and CS strategies. From Figure 11, it can be observed that when the structural interactions are taken into account, the lateral behavior of the systems is close to that of a structure composed of the same shear walls without openings, which in this study is represented by the comparison system (CS). The exception to this is the Geometry 1, in three- and five-story, in which a behavior between SM and CS strategy is detected. Generally, these results emphasize the significant effect of the structural interactions on the lateral behavior of the multi-story CLT shear walls, meaning that the contribution provided by floors and lintels strongly influences the lateral response of these systems.

For each analyzed case, the failure modes of the systems were investigated, which can occur in the connections placed at the base of the wall segments (hold-down, HD, and angle brackets, AB), in the ends of the lintel elements (critical region), or in the floor section, as described in section 3.3. In the case of systems with monolithic shear walls, failure occurred in the lintel ends. However, it should be noted that the failure of the lintel ends does not represent the failure of the whole structural system, see for instance [26]. In fact, in this circumstance, it is expected that the failure of the lintels leads to a discontinuity between lintel and wall segments and to an overall behavior of the system as that of a multi-story assembled shear walls. On the other hand, in the case of the systems with assembled shear walls, the failure was reached in the wall base connections, while floor section failures never occurred.

Figure 11 shows that, in the case of one-story systems, the pushover curves obtained from each modelling strategy achieve approximately the same lateral stiffness and lateral capacity. This is due to the fact that the systems deform with a predominant sliding mechanism and low rocking, generating negligible structural interactions. As a consequence, shear failure of angle brackets was the failure mode of the one-story systems in all modelling strategies considered.

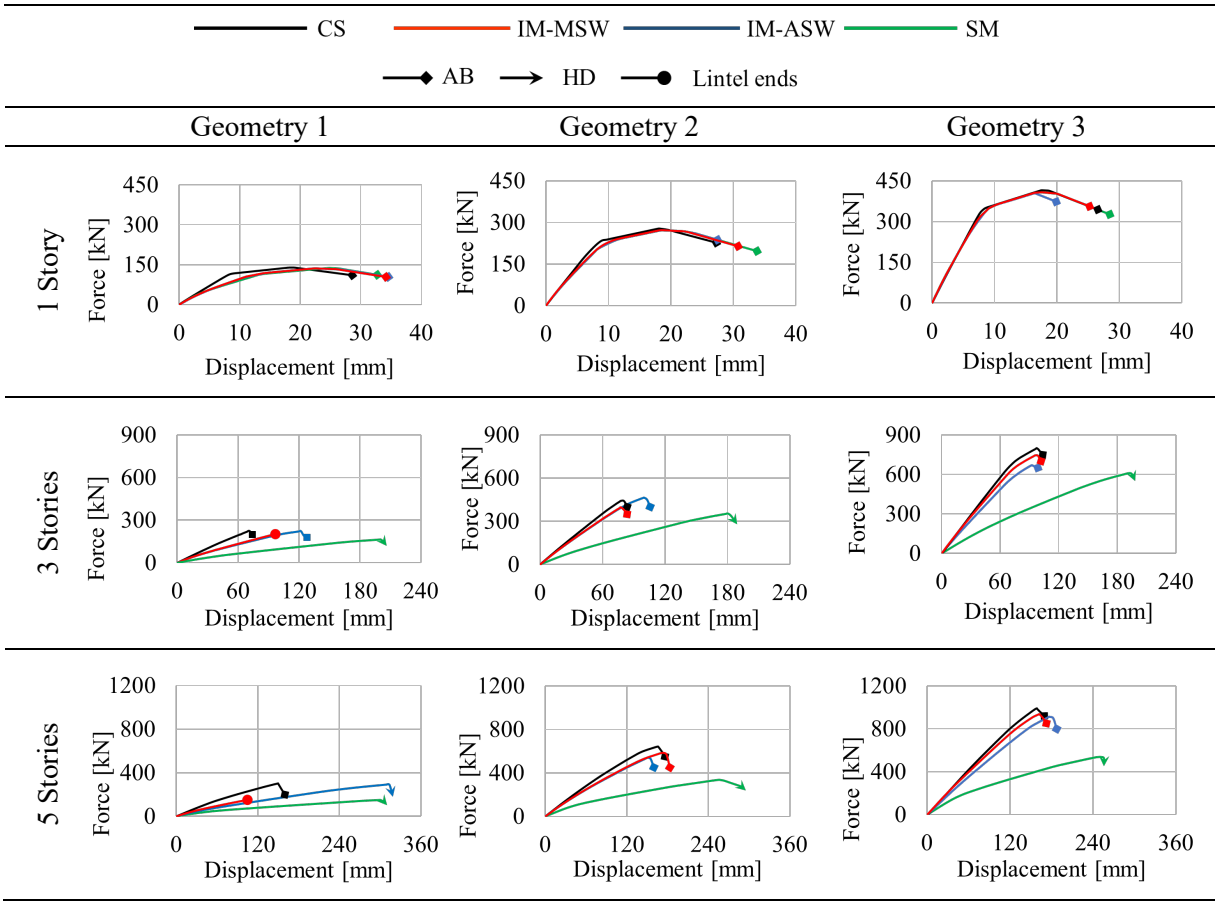


Figure 11: Pushover curves obtained from the nonlinear analyses.

In case of three-story systems, the results of the structures without openings (CS), show that sliding was the predominant deformation mechanism, resulting in shear failure of the angle brackets. On the other hand, for three-story CLT shear walls with openings modelled using the SM strategy, deformation was the consequence of a predominant rocking mechanism, resulting in tensile failure of the hold-downs. Whereas, in case of monolithic and assembled shear walls modelled with interactions (IM-MSW and IM-ASW, respectively), a combination of sliding and rocking deformation mechanisms occurred. In particular, these systems exhibit a predominant sliding mechanism; in fact, their lateral behavior is close to that of a system without openings (CS). Regarding the lateral performances, the maximum increments of the lateral capacity of the IM-MSW and IM-ASW strategies respect to the SM strategy are 22% and 35%, respectively, and occur for the cases with Geometry 1. On the other hand, the maximum decrements of the lateral capacity of the IM-MSW and IM-ASW strategies respect to the CS strategy are 10%, for Geometry 1, and 16%, for Geometry 3. This highlights that the lateral behavior of systems modeled with interactions is closer to that of systems without openings (CS) rather than that of systems modeled with the SM strategy.

Similar results were obtained in case of five-story systems, see Figure 11. Also in this case, multi-story shear walls modelled with interactions (IM-MSW and IM-ASW, respectively) deformed with a combination of sliding and rocking mechanism. Yet, in case of assembled shear walls (IM-ASW) with Geometry 1, a predominant rocking mechanism took place, which led to tensile failure of the hold-downs. Regarding the lateral performances of the five-story systems, the maximum increments of the lateral capacity of the IM-MSW and IM-ASW strategies respect to the SM strategy are equal to 75%, for the Geometry 3, and 93%, for the

Geometry 1. On the other hand, the maximum decrements of the lateral capacity of the IM-MSW and IM-ASW strategies respect to the CS strategy are equal to 51%, for the Geometry 1, and 16%, for the Geometry 2.

## 5 CONCLUSIONS

This study utilized numerical methods to examine the lateral behavior of multi-story Cross-Laminated Timber (CLT) shear walls. The study compared simplified modeling strategies (SM) to more advanced modeling strategies (IM) that account for structural interactions between lintels and wall segments, as well as between floors and wall segments. The study analyzed nine different structural configurations, including one-, three-, and five-story shear wall systems with three different geometries and varying mechanical properties at the base of the wall segments. The lateral performance of the advanced modeling strategies (IM-MSW and IM-ASW) for monolithic and assembled shear walls was compared to that of the simplified modeling strategy (SM) and a comparison system (CS) that modeled the same configurations of multi-story CLT shear walls without openings.

The results of the study showed that numerical models of monolithic and assembled shear walls, which take into account the structural interactions, resulted in significantly higher lateral stiffness and capacity values compared to the simplified modeling strategy (SM). In particular, these systems exhibit lateral performance close to the CS systems, which indicates that the structural interactions provided a significant contribution to the lateral performance of the multi-story CLT shear walls, due to the bending contribution of lintels and floors.

The study also suggested that the simplified modeling strategies often used for the design of CLT structures may not always properly describe the behavior of a multi-story CLT building subjected to horizontal loads. Therefore, the use of advanced modeling strategies that account for structural interactions should be considered when designing multi-story CLT shear walls to accurately predict their lateral behavior.

This study highlights the importance of considering the lateral behavior of multi-story CLT shear walls in the design of CLT structures. By using advanced modeling strategies that account for structural interactions, it is possible to accurately predict the lateral behavior of multi-story CLT shear walls and ensure the safety and stability of the building lateral loads.

## REFERENCES

[1] Lukacs I, Björnfot A, Tomasi R. Strength and stiffness of cross-laminated timber ( CLT ) shear walls : State-of- the-art of analytical approaches. Eng Struct 2019;178:136–47. https://doi.org/10.1016/j.engstruct.2018.05.126.

[2] Popovski M, Gavric I. Performance of a 2-Story CLT House Subjected to Lateral Loads. J Struct Eng 2015;142:1–12. https://doi.org/10.1061/(asce)st.1943-541x.0001315.

[3] Yasumura M, Kobayashi K, Okabe M, Miyake T, Matsumoto K. Full-Scale Tests and Numerical Analysis of Low-Rise CLT Structures under Lateral Loading. J Struct Eng 2016;142:1–12. https://doi.org/10.1061/(asce)st.1943-541x.0001348.

[4] D'Arenzo G, Schwendner S, Seim W. The effect of the floor-to-wall interaction on the rocking stiffness of segmented CLT shear-walls. Eng Struct 2021;249:113219. https://doi.org/10.1016/j.engstruct.2021.113219.

[5] Tamagnone G, Rinaldin G, Fragiacomo M. Influence of the Floor Diaphragm on the Rocking Behavior of CLT Walls. J Struct Eng 2020;146:1–11. https://doi.org/10.1061/(ASCE)ST.1943-541X.0002546.

[6] Gavric I, Popovski M. Design models for CLT shearwalls and assemblies based on connection properties. Proc Meet 47, INTER- Int Netw Timber Eng Res 2015. https://doi.org/10.13140/RG.2.1.3845.0728.

[7] Ruggeri EM, D'Arenzo G, Fossetti M, Seim W. Investigating the effect of perpendicular walls on the lateral behaviour of Cross-Laminated Timber shear walls. Structures 2022;46:1679–95. https://doi.org/10.1016/j.istruc.2022.10.141.

[8] Fanti R, Polastri A, Doudak G, Casagrande D. Analisi del comportamento meccanico di pareti in X-Lam con aperture. Ingenio n.d.

[9] Casagrande D, Fanti R, Doudak G, Polastri A. Experimental and numerical study on the mechanical behaviour of CLT shearwalls with openings. Constr Build Mater 2021;298:123858. https://doi.org/10.1016/j.conbuildmat.2021.123858.

[10] Mestar M, Doudak G, Polastri A, Casagrande D. Investigating the kinematic modes of CLT shear-walls with openings. Eng Struct 2020:111475. https://doi.org/10.1016/j.engstruct.2020.111475.

[11] D'Arenzo G. An elastic model for the prediction of the lateral response of Cross-Laminated Timber shear walls with openings. Eng Struct 2023;274:115055. https://doi.org/10.1016/j.engstruct.2022.115055.

[12] Khajehpour M, Casagrande D, Doudak G. The role of lintels and parapets on the mechanical performance of multi-storey cross laminated timber shearwalls with openings. Eng Struct 2022;255:113912. https://doi.org/10.1016/j.engstruct.2022.113912.

[13] Rinaldi V, Casagrande D, Cimini C, Follesa M, Fragiacomo M. An upgrade of existing practice-oriented FE design models for the seismic analysis of CLT buildings. Soil Dyn Earthq Eng 2021;149:106802. https://doi.org/10.1016/j.soildyn.2021.106802.

[14] Hummel J, Seim W. Displacement-based design approach to evaluate the behaviour factor for multi-storey CLT buildings. Eng Struct 2019;201. https://doi.org/10.1016/j.engstruct.2019.109711.

[15] Calderoni B, Giubileo C, Sandoli A. Criteri di progettazione strutturale di edifici in legno a pannelli X-lam. XV CONVEGNO ANIDIS, Padova 2013 2013. https://doi.org/10.13140/RG.2.1.4686.9202.

[16] Yasumura M, Kobayashi K, Okabe M, Miyake T, Matsumoto K. Full-Scale Tests and Numerical Analysis of Low-Rise CLT Structures under Lateral Loading. J Struct Eng (United States) 2016;142:1–12. https://doi.org/10.1061/(ASCE)ST.1943-541X.0001348.

[17] Yue K, Liang B, Shao Y, Xie C, Hu W, Zhao M, et al. Lateral behavior of wood frame shear walls sheathed with densified plywood under monotonic loading. Thin-Walled Struct 2021;166:108082. https://doi.org/10.1016/j.tws.2021.108082.

[18] Mestar M, Doudak G, Casagrande D. Kinematic modes of CLT single-storey shearwalls with openings in the inelastic range. World Conf Timber Eng 2021, WCTE 2021 2021.

[19] Casagrande D, Polastri A, Sartori T, Loss C, Chiodega M. Experimental campaign for the mechanical characterization of connection systems in the seismic design of timber buildings. WCTE 2016 - World Conf Timber Eng 2016.

[20] Gavric I, Fragiacomo M, Ceccotti A. Cyclic behavior of typical screwed connections for cross-laminated ( CLT ) structures. Eur J Wood Wood Prod Vol 2015;73:179–91. https://doi.org/10.1007/s00107-014-0877-6.

[21] CSI. Integrated software for structural analysis and design. CSI-SAP2000. Berkeley, CA: CSI. I Berkeley (CA, USA) Comput Struct INC 2013.

[22] Izzi M, Casagrande D, Bezzi S, Pasca D, Follesa M, Tomasi R. Seismic behaviour of Cross-Laminated Timber structures : A state-of-the-art review. Eng Struct 2018;170:42–52. https://doi.org/10.1016/j.engstruct.2018.05.060.

[23] Blaß HJ, Fellmoser P. Design of solid wood panels with cross layers. Proc, World Conf Timber Eng Helsinki, Finl Finnish Assoc Civ Eng © 2004:604.

[24] Bogensperger T, Moosbrugger T, Silly G. Verification of CLT-plates under loads in plane. 11th World Conf Timber Eng 2010, WCTE 2010 2010;1:231–40.

[25] Masoudnia R, Hashemi A, Quenneville P. Predicting the Effective Flange Width of a CLT Slab in Timber Composite Beams. J Struct Eng 2018;144:04018084. https://doi.org/10.1061/(asce)st.1943-541x.0001979.

[26] Sato M, Isoda H, Araki Y, Nakagawa T, Kawai N, Miyake T. A seismic behavior and numerical model of narrow paneled cross-laminated timber building. Eng Struct 2019;179:9–22. https://doi.org/10.1016/j.engstruct.2018.09.054.

COMPDYN 2023
9th ECCOMAS Thematic Conference on
Computational Methods in Structural Dynamics and Earthquake Engineering
M. Papadrakakis, M. Fragiadakis (eds.)
Athens, Greece, 12-14 June 2023

# TIMBER CARPENTRY WITHOUT STEEL CONNECTORS

**Luigi Massaro**[1], **Roberto Serpieri**[1], **Giorgio Frunzio**[1] **and Luciana Di Gennaro**[1]

[1] Department of Architecture and Industrial Design, University of Campania Luigi Vanvitelli
81033, Aversa, Italy
{luigi.massaro, roberto.serpieri, giorgio.frunzio, luciana.digennaro}@unicampania.it

## Abstract

*Use in modern timber constructions of wood-wood connections inspired by traditional timber carpentry can take advantage today of the many available digital technologies aiding stress analysis and automated control of machining tools. Such methodologies of more recent introduction, if properly employed, allow for a reduction in time and of human error in the design and manufacturing phases of timber structures. Wood-wood connections without metal elements are encountered in many historical buildings. However, not infrequently in intervention on existing timber elements as well as in new timber constructions, the original connection typologies are renounced in favor of other connection typologies due to higher costs and the difficulty of thoroughly analyzing the structural behaviour of wood-only joints under the full set of loading conditions and design seismic actions prescribed by the building regulations currently in force. The connection typologies between timber elements may differ according to the loading types (stress-resultant) for which they are designed to. The most common are carpentry joints and mechanical joints. The former is the traditional union of timber carpentry using woodworking of contacting surfaces. Mechanical joints provide, instead, for the use of metal connections and/or glue layers. Fostering the use of wood-wood connections brings several advantages: (i) exploring the value of timber-timber connections as an ancient cultural heritage amenable to provide methodologies suitably implementable in the design processes of the modern construction industry, with a specific view towards the rehabilitation of historical and monumental buildings; (ii) understanding by parametric computer-aided analyses, in desirable retracing of the past rules of the art, the influence of wood fiber orientation also in the use of engineered composite timber assemblies like CLT; (iii) foster the use of local wood; (iv) measure the fire-resistance of timber joints. This contribution has the twofold purpose of summarizing the state-of-the-art in the structural design of a wood carpentry joint in absence of strengthening metal connectors and exploring the possibilities offered by an ad-hoc stress analysis software for the parametric finite-element analysis of timber joints.*

**Keywords:** connections, timber, CLT, existing structures, design processes.

## 1 INTRODUCTION

Several economic and technological factors recently brought into prominence in Italy, also caused by geopolitical processes of larger geographical and temporal scales, ultimately traceable to ecological and environmental problems [1,2], suggest today a more conscious reconsideration of timber as building construction material in civil engineering. Wood has always been used as a building material and, thanks to its characteristics, it responds well to current environmental needs [1–3]. This applies both to solid wood and engineered woods such as glued laminated timber (GLT) and cross-laminated timber (CLT). The latter has been widely used in recent decades both for interventions on existing structures [4] and for the construction of new buildings. The connections between the wooden elements play a key role in the intervention's stability. Selective use of wood-wood connections without metal elements can be found in many historical buildings and bridges [5–7]. This suggests analyzing the connection of wood elements without the use of steel connectors.

In the Campania area in southern Italy, an example of wooden structures of monumental historical value is the roof in solid chestnut wood covering the local warehouse and storage building of the Cemetery of Santa Maria del Popolo (known as the cemetery of the 366 pits), designed by Ferdinando Fuga in the second half of the '700 [8] and located in Naples in the Poggioreale district (Fig.1).



Figure 1: Chestnut truss of the roof of the Cimitero delle 366 fosse, Naples.

Still in the Campania area, an example of renovation in GLT, of the roof of a historic structure, is the relatively recent replacement of the trusses of the graduation hall at the Faculty of Architecture of the University of Campania "Luigi Vanvitelli", within the monastery complex of San Lorenzo "ad Septimum" in Aversa (Fig.2).



Figure 2: GLT roof truss in Monastery complex of Lorenzo ad Septimum, Aversa.

The monastery, founded around the year one thousand by the Benedictines and located on the Roman consular road near Capua, became with the Normans one of the most important abbeys in southern Italy and was subsequently used as a military school, a military orphanage, and later as institute of art and mechanics, as well as for other educational activities [9,10].

In this contribution, a computational study is presented addressing structural analyses accounting for dynamic loads for a future replacement in solid wood of the trusses of San Lorenzo's roof, without using glues or metal connectors. Such a research problem is identified as a relevant one, proceeding from the consideration that it can be of general interest for interventions of sustainable renovation of the wooden roofing structures of many buildings of historical and monumental importance both of sacred and civil architecture [11]. Special attention is devoted herein to the analysis of the central connection between the kingpost and left and right struts by questioning the capability of this joint to sustain seismic loads avoiding exit of the struts' lower ends from the notched saddle supports in absence of metallic restraints or glues. Details of these notched saddles are shown in Fig.3a, which is an enlargement of the bottom connections of Fig.2, and in Fig.3b showing similar notched supports in the wooden trusses of the roof of the Church of the Nativity in Bethlehem [12,13].



a)



b)

Figure 3: Detail of notched saddle supports in kingpost-struts connections. a), enlargement from Fig.2; b), detail from the Church of the Nativity in Bethlehem.

Computational analyses were carried out employing the finite-element code for static and environmental sustainability of structures: MORES (Multipurpose Object-oriented Research Environment for Structures).

Section 2 introduces a few selected aspects concerning the approach to structural and computational analysis of wood-wood connections. In Sect. 3, the truss structure is described, and a design problem is presented relevant to the response to dynamic loads of the connection between kingpost and struts, together with some numerical results.

## 2 WOOD-WOOD JOINTS IN DYNAMIC STRUCTURAL ANALYSIS

Wood has long been used for building structurally connected assemblies subjected to dynamic loading, an example of which can be the *capra*, an ancient Roman machinery which, according to some authors, may have been at the very origin of the Italian name *capriata* for timber roof truss. The capability of timber to reliably sustain dynamic loads is also testified by its ordinary employment, at the beginning of the past century, as a construction material for manufacturing specific structural components in aircraft engineering [14]. In the field of building constructions, where wood is frequently employed for roofing systems, the treatise of Architecture by Sebastiano Serlio [6] remarked on the importance of duly considering the dynamic action of wind loads for selecting

the proper structural typology and dimension of roof truss structures. Book VII of this treatise illustrates, in particular, several wood joint typologies, many of which, at selected connection sites of specific truss typologies, are constructed without any use of nails and steel reinforcements [6]. This category of joints, where connection can be guaranteed solely by friction and interlocking between the contacting wooden surfaces, are denominated carpentry joints. On the opposite side are mechanical joints where stress transmission is ensured by other non-ligneous materials or devices such as glue, metallic connectors and/or restraints including ropes. Some typologies of carpentry joints are exemplified in Fig.4.

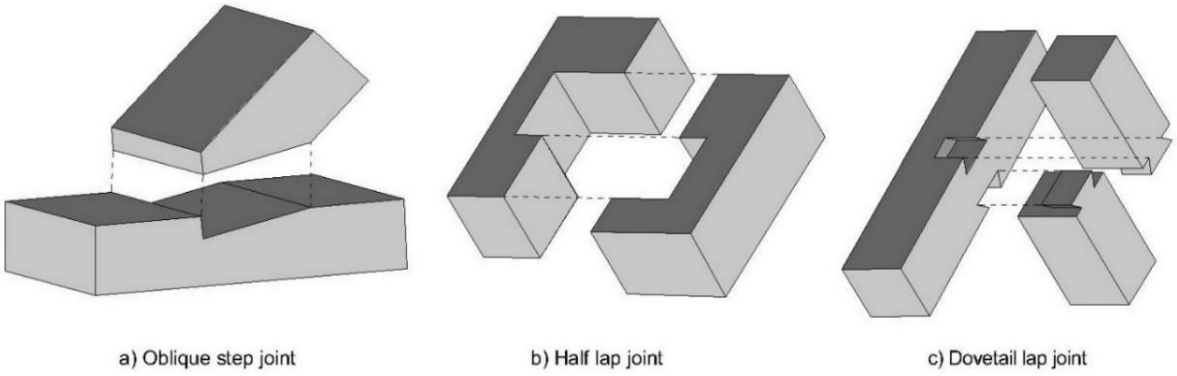


Figure 4: Some traditional typologies of carpentry joints.

Computational stress analysis of wood connections cannot rule out the orthotropic features of timber, given the considerable difference – usually even higher than a tenfold factor – of strength and stiffness between values attained in grain direction and orthogonal to grain direction [15,16].

The mechanical characteristics of wood strongly vary between conifers and deciduous trees and often even between individual trees of the same species. In general, in a tree, most of the wood-cells are elongated, like a hollow cylinder oriented along the axis of the trunk. The residual ones are arranged in radial direction. By virtue of these considerations, wood can be seen as a material having at any point three perpendicular planes of elastic symmetry, identified by three axes. Herein, as shown in Fig.5, L is the grain direction, R the radial direction, while T is orthogonal to L and R.

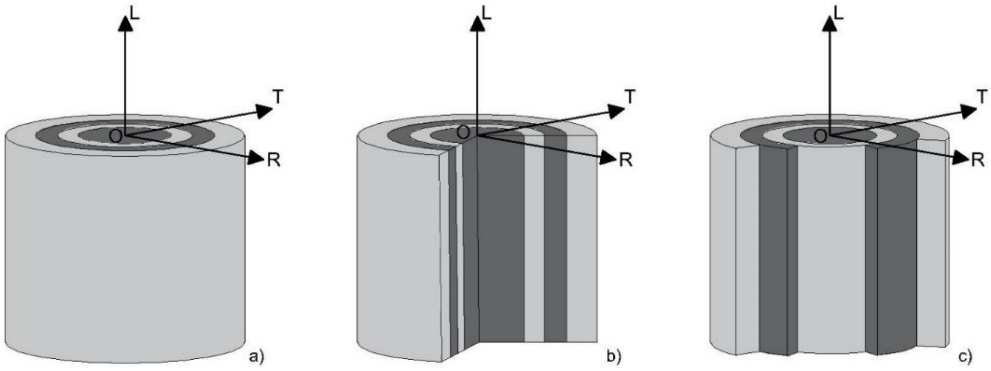


Figure 5: Reference system based on wood nature.

The computational analyses in this study employ frame-element models and 2D plane-stress membrane models. In the latter, transverse isotropy is assumed as an approximation acceptable to the benefit of simplicity in setting input parameters, thus treating directions T and R as identical from the mechanic point of view. Working in a reference frame $x_1x_2$ of axes of transverse-isotropy coinciding with plane-stress membrane axes (with axis $x_1$ being aligned to OL), plane-stress elastic relations admit in Voigt notation the following representation:

$$\{\sigma\} = [K]\{\varepsilon\}: \qquad \begin{Bmatrix} \sigma_{x_1} \\ \sigma_{x_2} \\ \tau_{x_1x_2} \end{Bmatrix} = \begin{bmatrix} \frac{E_1}{1-\nu_{12}\nu_{21}} & \frac{E_1\nu_{21}}{1-\nu_{12}\nu_{21}} & 0 \\ \frac{E_2\nu_{12}}{1-\nu_{12}\nu_{21}} & \frac{E_2}{1-\nu_{12}\nu_{21}} & 0 \\ 0 & 0 & 2G_{12} \end{bmatrix} \begin{Bmatrix} \varepsilon_{x_1} \\ \varepsilon_{x_2} \\ \gamma_{x_1x_2}/2 \end{Bmatrix} \tag{1}$$

where the usual notation for orthotropy is employed to denote Young moduli $E_1, E_2$, the shear modulus $G_{12}$ and Poisson ratios $\nu_{12}, \nu_{21}$, and where, in compliance with transverse isotropy, the constraint $\nu_{21}E_1 = \nu_{12}E_2$ must hold.
In modeling connections among wood frames of different direction by 2D plane-stress membrane models, coordinates changes become necessary. The usual formula giving components-change of a fourth-order tensor $c_{ijhk}$ as a consequence of a rotational change of reference axes directions $x_1x_2x_3 \longrightarrow x_1,x_2,x_3$, (defined by the orthonormal $3 \times 3$ one-covariant and one-contravariant tensor $Q_{ij}$), reading $c'_{ijhk} = Q_{li}\, Q_{mj} Q_{ph} Q_{qk} c_{lmpq}$, achieves, by virtue of the hypotheses and notational conventions above and of minor and major symmetries of the elastic tensor, the following simpler representation in Voigt matrix format

$$[K]' = \left[M_Q\right][K]\left[M_Q\right]^{-1}, \tag{2}$$

where $\left[M_Q\right]$ is a matrix, associated with an in-plane rotation by an angle $\vartheta$, defined as:

$$\left[M_Q\right] = \begin{bmatrix} \cos^2\vartheta & \sin^2\vartheta & 2\cdot\sin\theta\cos\theta \\ \sin^2\vartheta & \cos^2\vartheta & -2\cdot\sin\theta\cos\theta \\ -\sin\theta\cos\theta & \sin\theta\cos\theta & \cos^2\vartheta - \sin^2\vartheta \end{bmatrix}. \tag{3}$$

The properties of the wood material considered in the analyses of the following section are calibrated upon chestnut (Castanea sativa). This choice stems from the copious presence of chestnut elements in many structures and historic buildings, especially in southern Italy. References for these values are taken from [14,17–20] and summarized in Table 1.

| Wood Species | density [Kg/mc] | moisture [%] | E [GPa] |
|---|---|---|---|
| Chestnut | 508 | 12 | 13,8 |

Table 1: Properties of chestnut and walnut.

## 3 NUMERICAL ANALYSIS OF A WOOD-WOOD TIMBER ROOF TRUSS JOINT

The structural analyses reported in this section examine a replacement in solid chestnut of the wood truss sustaining the roof of the graduation hall within the monastery complex of San Lorenzo ad Septimum in Aversa. The truss typology is an *Italian capriata* with kingpost-struts joint – in Italian technical nomenclature termed *giunto monaco-saette* and hereafter referred to in brief as KS joint – statically unconnected from the horizontal *catena*, conforming to the classical static scheme and carpentry details already documented by Luciano da San Gallo and retraceable to the ancient Roman empire, since already present in the original paleo Christian Basilica of San Paolo fuori le Mura [5]. In such scheme the lower catena element is conveniently exempt from flexural loads, except for those originated by self-weight, thus acting as a pure tie.
The span as well as the characteristic dimensions and carpentry joint details considered in the analyses are dimensioned upon those of the currently existing GLT structure. Span and height are approximately 12.0 m and 3.2 meters. Fig.6 shows the single-line frame-assembly 2D scheme with constraints employed in frame analyses. In the structural analyses herein presented, left and right struts are modelled as elements bearing only axial force, by addition of terminal hinges, assuming rotational capacity granted by the notched saddles visible in Fig.3 left and sketched in Fig.7 with geometrical details. Roof struts AC and CB are continuous. Bearing B was modeled both as a simple

support, to gain insight into the stress on the tie A-B, and as a as complete external hinge, to obtain a symmetric model.

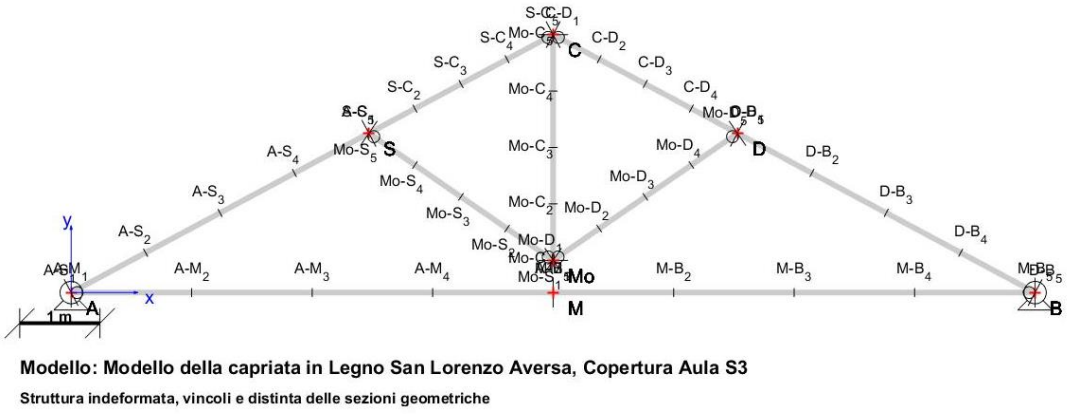


Figure 6: **S**ingle-line frame-assembly diagram with constraints of San Lorenzo's roof truss structure.

Kingpost and struts have section 24x24 cm, roof struts are 24x30 cm, while the tie is 24x40 cm.
A front-planar sketch of the KS joint with relevant dimensions and carving angles is shown in Fig.7.

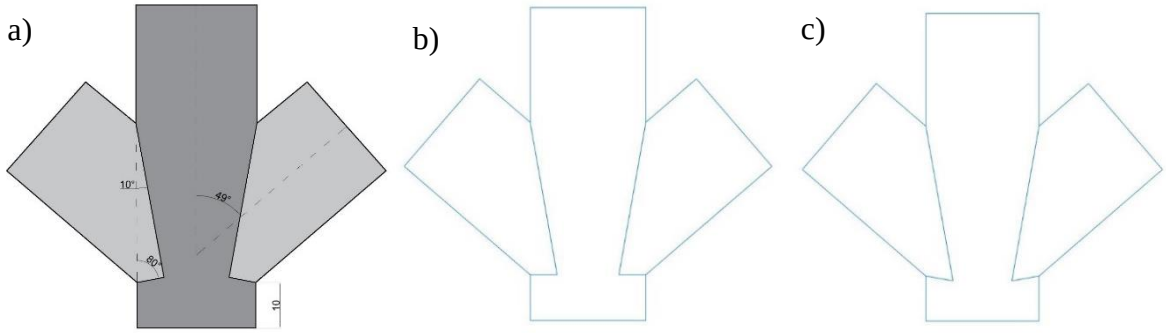


Figure 7: Detail sketch of the analyzed geometries for the KS joint with dimensions of carving angles. In all sketches upper carving angles are 10° while lower carving angles are: a) 80°; b) 90°; c) 100°.

Response of this structure to dynamic loads is investigated by examining the capability of the KS joint to resist seismic loads while preventing, even in complete absence of metallic restraints or glues, the struts falling off the notched saddle supports at the lower end of the kingpost element.

Computer-aided stress analyses were carried out employing frame and plane-stress membrane finite-element models within the multi-criteria object-oriented code MORES for static and environmental sustainability of structures. A first beta version of this code has been developed and benchmarked in Matlab® at the Department of Architecture of the University of Campania as an open-source multiplatform project.

From pre-dimensioning, dynamic loads which are found significant for the potential activation of such a collapse mechanism are identified only in seismic loads, since dimensioning of wind loads based upon NTC 2018 section 3.3 [21] – leads to much lower and negligible actions. The gravity load (1,700 kN), the horizontal seismic load (210 kN) and the vertical seismic load (105 kN), were essentially determined based on NTC 2018 [22], and are modeled as distributed forces over the roof struts. Fig.8 shows the four elementary load cases considered in the analyses: a) gravity load, b) horizontal seismic load, c) vertical seismic load, d) seismic asynchronous oscillation of roof pitches. The fourth load case is contemplated proceeding from considerations about structural and loading symmetries. In the symmetric scheme with hinges in both A and B, the KS joint remains unloaded

when subjected to load case b) alone, since this load case constitutes an antisymmetric loading distribution over a structure which is both geometrically symmetric and symmetrically constrained. Such symmetries, and the property of the kingpost tie of being only amenable to symmetric centered axial loads and located above the symmetry axis and located over the symmetry axis, bring the consequence that the KS joint remains unloaded under full-span horizontal seismic loading which is antisymmetric. Load case d) was consequently included among the elementary cases to be combined, referred to a hypothetical asynchronous horizontal movement of one pitch possibly originated by backlash between the left and right frames of the truss.

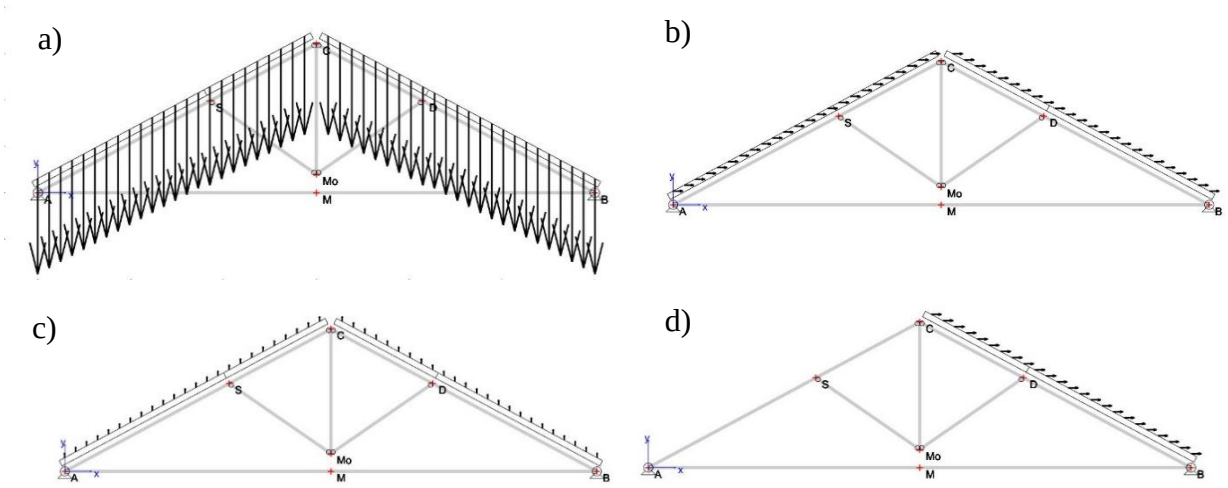


Figure 8: Elementary load cases considered: a) gravity load, b) horizontal seismic load, c) vertical seismic load d) seismic asynchronous oscillation. Representation of distributed loads are in scale.

The response of the KS joint to dynamic loading has been also investigated by 2D plane-stress finite-element membrane hierarchical sub-models, providing detailed analyses of the joint connections of the primary frame-element model. The 2D mesh consists of the structured hierarchical mesh of Constant Stress Triangles (CST) [23] shown in Fig.9a. Prior to its use, the element implementation was benchmarked based on analytical solutions of isotropic and transversely isotropic beams by also exploiting the closed-form analytical solution with full account of shear deformability and shear principal axes originally proposed in [24] . The structure is supported at the upper kingpost cross section and forces acting on struts' cross sections are hierarchically determined. The joint is modeled assuming, as first-step condition, perfect bilaterally contacting surfaces.

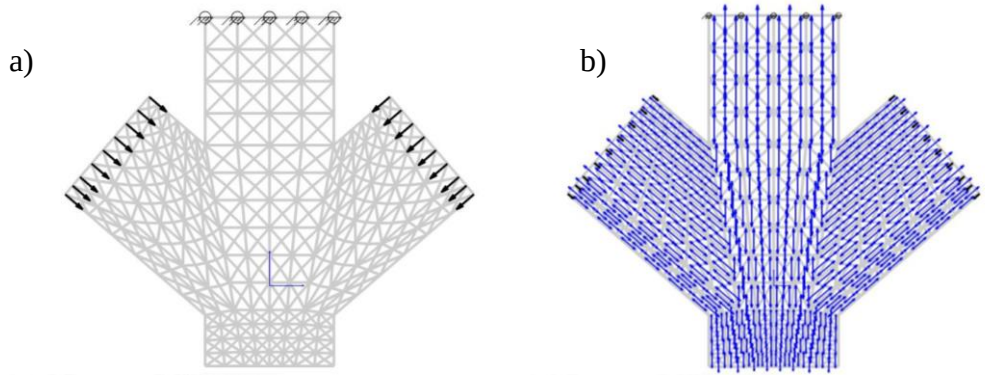


Figure 9: KS finite-element model: a) employed mesh; b) grain directions.

Different grain orientations in the three membrane subparts are shown in Fig.9b and are computationally addressed as described in the previous section.

## 4 RESULTS AND CONCLUSION

Fig.10 illustrates a selection of moment diagrams and axial force diagrams associated with some of the elementary load cases of Fig.8 for the symmetric and unsymmetric constraint schemes. In particular, Fig.10a shows, for the symmetric scheme with two external hinges, the function of struts in creating an intermediate support reducing span, maximum moment and deflection in struts AC ed CB. For the same constraint scheme, Fig.10b shows that the KS joint remains unloaded under full-span horizontal loads since this load case constitutes an antisymmetric loading distribution over a structure which is both geometrically symmetric and symmetrically constrained. Fig.10c illustrates the response in the unsymmetric simply supported scheme, with linear variation of axial force in AC and BC due to the longitudinal component of distributed horizontal load, and with the function exerted by the horizontal tie in preventing external transfer of horizontal loads to the bearing structure. Fig.10d shows the elementary demand of axial tensile type over the struts for the seismic half-span loading.

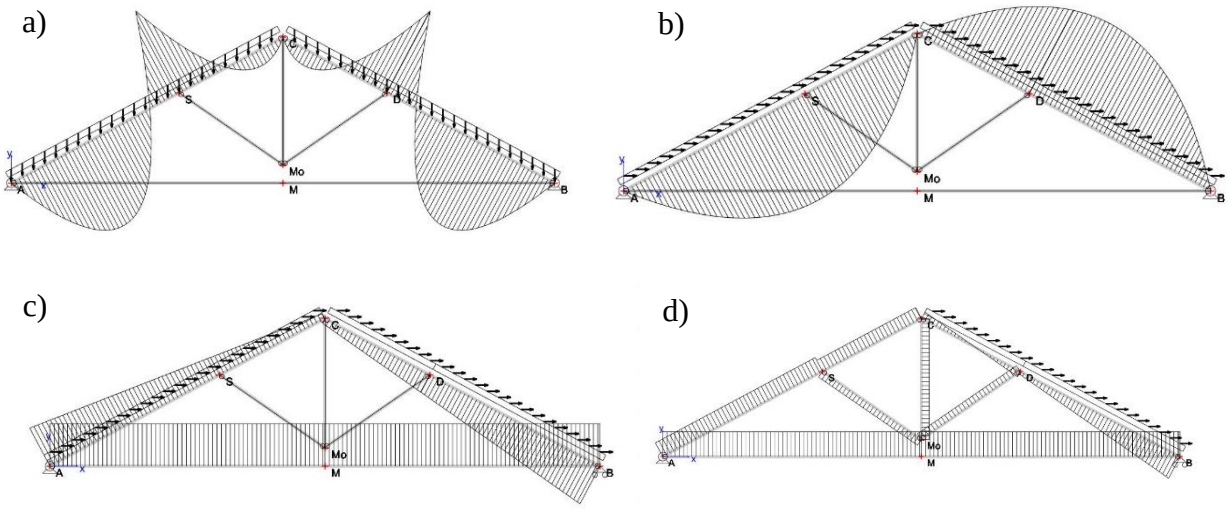


**Figure 10:** a) Moment diagrams with complete external hinges at both bearings (gravitational load case); b) Moment diagrams with complete external hinges at both bearings (seismic full-span load case); c) Axial load diagrams in the unsymmetric scheme with hinge on the left and simple support on the right (seismic full-span load case; d) Axial load diagrams in the unsymmetric scheme with hinge on the left and simple support on the right (seismic half-span). Scale factors of diagrams are not the same in figures.

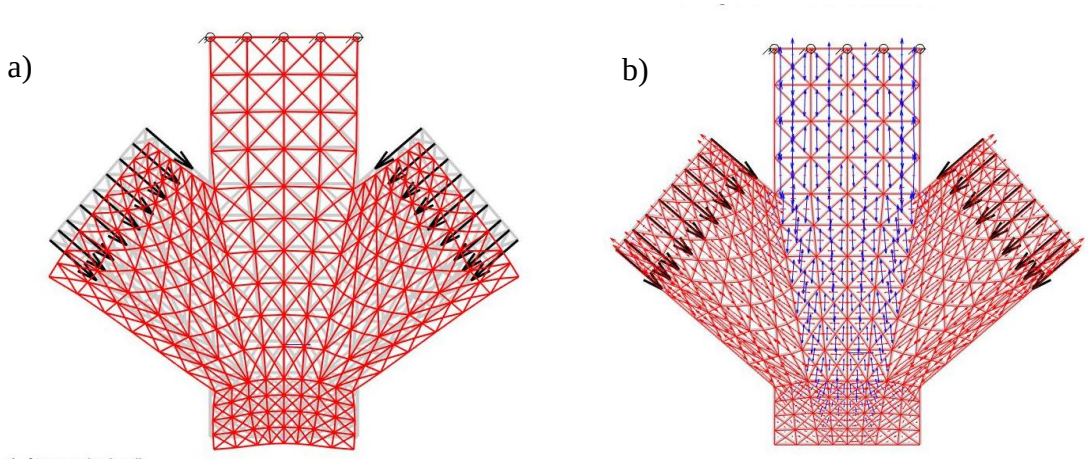


**Figure 11:** KS finite-element model: a) deformed mesh (displacements magnified by a factor **10** ×; b) principal stresses (tensile stresses in blue, compressive stresses in red).

Stress-resultant actions across node 'Mo' contributed by elementary load cases have been used, upon suitable linear combination, as input loading demands for determining the static performance of this node by higher-detail 2D membrane models of the typology exemplified in Fig.9. A deformed mesh and principal stresses for a 2D analysis for the purely gravitational load case are shown in Fig.11.

Altogether, the computer-aided finite-element analyses have shown the capability of the KS joint to sustain seismic loads avoiding exit of the struts' lower ends from the notched saddle supports with no appearance of tensile stresses over contacting surfaces and in absence of any supplemental non-wood bilateral restraints. Such result would show that – at least as far as the modelling hypotheses herein assumed for interaction of elementary frames, loading, mechanical contact, and geometry are concerned – it is possible to construct the KS joint according to the 'rules of the art' and sustain dynamic loads without metal connectors or glues.

Future lines of research departing from this study will address nonlinear contact, friction and explore minimum-maximum problems for optimal selection of materials, joint details and structural schemes, in a perspective of sustainability.

## REFERENCES


[1] *Kyoto Protocol to the United Nations Framework Convention on Climate Change*, 2303 U.N.T.S., 1997.

[2] United Nations General Assembly, United Nations, The 2030 Agenda and the Sustainable Development Goals, 2015.

[3] *Legge 28 dicembre 2015, n. 221 - Disposizioni in materia ambientale per promuovere misure di green economy e per il contenimento dell'uso eccessivo di risorse naturali.*

[4] G. Frunzio, S. Rinaldi, M. Guadagnuolo, L. Massaro, and L. di Gennaro, "Use of engineered wood for the retrofitting of existing structures," in *9th International conference on harmonisation between architecture and nature - Eco-Architecture 2022*, 2022.

[5] S. Valeriani, "Monaci, dardi e colonnelli: genesi e caratteristiche delle capriate italiane," 2005.

[6] S. Serlio, *Il settimo libro d'Architettura*, Francesco de' Franceschi, 1600.

[7] G. da Sangallo and C. Hülsen, *Il libro di Giuliano da Sangallo: Codice vaticano barberiniano latino 4424*, Biblioteca apostolica vaticana, 1984.

[8] P. Giordano, "Il restauro e la riconfigurazione architettonica del Cimitero delle 366 Fosse e del Sepolcreto dei Colerici a Napoli," *Festival dell'Architettura Magazine*, 42–49, Festival Architettura Edizioni, 2021.

[9] L. Santagata, "Storia di Aversa", Eve Editrice, 1991.

[10] L. Santagata, "Storia di Aversa", Eve Editrice, 1991.

[11] G. Frunzio and L. di Gennaro, "Seismic structural upgrade of historical buildings through wooden deckings strengthening: The case of study of Palazzo Ducale in Parete, Italy," *Procedia Structural Integrity* **11**, 153–160, Elsevier B.V., 2018.

[12] C. Alessandri, V. Mallardo, B. Pizzo, and E. Ruocco, "The roof of the Church of the Nativity in Bethlehem: Structural problems and intervention techniques," *Journal of Cultural Heritage* **13**, e70–e81, Elsevier Masson SAS, 2012.

[13] G. Faella, G. Frunzio, M. Guadagnuolo, A. Donadio, and L. Ferri, "The Church of the Nativity in Bethlehem: Non-destructive tests for the structural knowledge," *Journal of Cultural Heritage* **13**, e27–e41, Elsevier Masson SAS, 2012.

[14] C. F. Jenkin, “Report on materials of construction used in aircraft and aircraft engines,” 1920.

[15] J. Bodig and B. A. Jayne, “Mechanics of wood and wood composites,” 712, Van Nostrand Reinhold, 1982.

[16] A. T. Price, “A mathematical discussion on the structure of wood in relation to its elastic properties,” *Philosophical Transactions of the Royal Society of London. Series A, Containing Papers of a Mathematical or Physical Character* **228**, 1–62, 1929.

[17] M. Nocetti, M. Brunetti, and M. Bacher, “Efficiency of the machine grading of chestnut structural timber: prediction of strength classes by dry and wet measurements,” *Materials and Structures/Materiaux et Constructions* **49**, 4439–4450, Kluwer Academic Publishers, 2016.

[18] M. Brunetti, M. Nocetti, and P. Burato, “Strength Properties of Chestnut Structural Timber with Wane,” *Adv Mat Res* **778**, 377–384, Trans Tech Publications Ltd, 2013.

[19] M. Nocetti, M. Bacher, S. Berti, M. Brunetti, and P. Burato, “Machine Grading of Chestnut Structural Timber with Wane,” 2013.

[20] M. Nocetti, M. Bacher, M. Brunetti, A. Crivellaro, and J.-W. G. van de Kuilen, “Machine grading of Italian structural timber: preliminary results on different wood species,” 2010.

[21] D. Min. Infrastrutture e Trasporti 17gennaio 2018, *Norme tecniche per le costruzioni (NTC 2018), paragrafo 3.3 Azioni del vento - (Technical standards for construction - section 3.3. wind actions)*, 2018.

[22] D. Min. Infrastrutture e Trasporti 17gennaio 2018, *NTC 2018 - Norme tecniche per le costruzioni. (Technical standards for construction)*, 2018.

[23] N. Carpenter, H. Stolarski, and T. Belytschko, “Improvements in 3-node triangular shell elements,” *Int J Numer Methods Eng* **23**, 1643–1667, 1986.

[24] R. Serpieri, “On the Equivalence of Energetic and Geometric Shear Factors Based on Saint Venant Flexure,” *J Elast* **116**, 115–160, 2014.

COMPDYN 2023
9th ECCOMAS Thematic Conference on
Computational Methods in Structural Dynamics and Earthquake Engineering
M. Papadrakakis, M. Fragiadakis (eds.)
Athens, Greece, 12-14 June 2023

# EXPERIMENTAL AND NUMERICAL ASSESSMENT OF AN IMPROVED PLYWOOD-BASED IN-PLANE RETROFITTING METHOD FOR TIMBER FLOORS IN HIGHLY SEISMIC AREAS

**Michele Mirra**[1] **and Andrea Gerardini**[2]

[1] Delft University of Technology, Section of Bio-Based Structures and Materials
Stevinweg 1, 2628 CN Delft, The Netherlands
e-mail: m.mirra@tudelft.nl

[2] Gerardini Ingegneria Sismica
Via Castiglione 131, 25060 Collio (BS), Italy
e-mail: gerardini.a@gmail.com

## Abstract

*Wood-based retrofitting techniques for seismic upgrading and architectural conservation of existing buildings have found increasing application in the last decades. With reference to the in-plane seismic strengthening of existing timber floors, a particularly efficient solution consists of an overlay of plywood panels fastened to the sheathing. This technique allows a great improvement in strength, stiffness, and energy dissipation of the floors. Yet, when adopting this strengthening solution for existing floors in highly seismic regions, the target design loads could require large values of in-plane strength and stiffness for the retrofitted diaphragms, and this could cause their beneficial, dissipative potential to be reduced. Thus, in this work, a strengthening solution is presented, able to retrieve high strength and at the same time activate large energy dissipation in the floors. The proposed technique consists of the creation of two independent shear planes by means of two different superimposed overlays of plywood panels. Previously developed analytical and numerical models describing the in-plane response of floors retrofitted with a single plywood overlay were adapted for the present case with two overlays, validating the results against an experimental test conducted on a sample representing a floor portion. Very good agreement was obtained between experimental and analytical as well as numerical results, thus the proposed approaches enable an efficient design process and an accurate simulation of the proposed retrofitting technique.*

**Keywords:** Timber floors, Plywood Panels, Seismic Retrofitting, Existing Buildings, Numerical modelling.

## 1 INTRODUCTION

In several architectural contexts all over the world, unreinforced masonry (URM) structures featuring timber floors as horizontal elements, constitute a large part of the building stock. Numerous seismic events have highlighted the vulnerability of URM buildings to earthquakes, mainly due to poor-quality masonry, excessive in-plane flexibility of timber floors, and absence of effective connections among structural elements.

In this framework, several retrofitting methods for timber diaphragms [1]-[14] and timber-masonry connections [15]-[20] have been developed in the recent years, progressively focusing on more reversible techniques [21],[22]. With regard to the floors, the main proposed and tested retrofitting methods consisted of the traditional cast of a concrete slab on the existing sheathing, a widely adopted retrofitting in the last decades [1],[6]; the superposition of a second layer of planks arranged at 45° [1]-[4] or 90° [6],[7] with respect to the existing sheathing; the bracing of the floors with steel plates [1],[3],[4] or fibre reinforced polymer (FRP) laminae [1],[6]; the overlay of cross-laminated timber (CLT) [7],[8], oriented strand board (OSB) [8], or plywood panels [9]-[14]. Among these techniques, reversible ones are usually preferred because of their lower impact on existing buildings, especially when they are monumental or protected. In particular, the overlay of plywood panels on the existing sheathing has proved to be a valid and versatile strengthening method, as demonstrated by several investigations and applications in different contexts, e.g. in the United States [10],[12], New Zealand [9],[12],[13], the Netherlands [14],[23]-[27], and Italy [28],[29].

When considering highly seismic areas with more demanding requirements for the in-plane strength and stiffness of the plywood-retrofitted diaphragms, their beneficial dissipative effect, highlighted by several studies [12], [23]-[27], could be reduced. The in-plane strength and stiffness of the floors can be increased by means of e.g. lateral steel chords, thicker and more interlocked or blocked plywood panels, or fasteners in a larger number or with wider diameter. These design choices can strongly reduce the displacement capacity of the floor, and an excessive number of fasteners could also cause splitting of the existing wooden boards.

In this work, a simple method is proposed, allowing to achieve a large improvement in strength of the retrofitted diaphragms, while also keeping sufficient displacement capacity and, consequently, the possibility of activating large hysteretic energy dissipation. The proposed technique consists of the creation of two independent shear planes by means of two different superimposed overlays of plywood panels (Figure 1). The first layer, featuring smaller panels, is fastened directly to the existing sheathing; the second, with larger panels, is fixed to the sheathing through plywood boards surrounding each smaller panel. A small gap is left between the plywood boards and the smaller panel, enabling its free rotation and sliding.

With this strengthening method, the two overlays are not directly connected to each other, combining the strength of two plywood layers with an improved ductility linked to their independent movement. This solution of creating two separate shear planes proved to be very effective in the case of light timber shear walls [30], thus its application for the retrofitting of existing wooden floors was also investigated.

Previously developed analytical and numerical models describing the in-plane response of floors retrofitted with a single overlay of plywood panels proved to be accurate in predicting strength, stiffness and energy dissipation of such diaphragms [23],[25]. These models were adapted and used to simulate the present case with two overlays, validating the results against an experimental test conducted on a prototype sample representing a floor portion. Very good agreement was obtained between experimental and analytical/numerical results, and additional sensitivity analyses were also conducted, assessing the influence of fasteners diameter and plywood thickness.

## 2 MATERIALS AND METHODS

### 2.1 Materials

The principle for the execution of the proposed retrofitting method is shown in Figure 1. The plywood panels of the first overlay are fastened along their perimeter to the existing sheathing between two subsequent joists, with in-plane dimensions smaller than the joists' spacing. Most of the material resulting from the cut of these panels can then be used to create the interlayer between the existing sheathing and the second overlay (see Figure 1), leaving a small gap around the panels themselves, to enable their rotation during in-plane loading. The second overlay consists once more of plywood panels, fastened along their perimeter to the existing sheathing and the joists, through the previously placed interlayer made of plywood boards. Because of the modular structure of this retrofitting method, and accounting for its shear-related in-plane deflection, only a small, representative portion of the floor was selected for testing (Figure 1), resulting in the sample shown in Figure 2 along with its construction sequence.

As can be noticed, the prototype consisted of 100×18×500 mm planks, fastened to two 50×120×500 mm joists with two 3×65 mm nails at each end. The first, smaller plywood panel measured 380×380×18 mm, whereas the second had dimensions of 450×450×18 mm. For fastening the panels along their perimeter, 5×70 mm screws were used, in such a way that five screws for each side were present. With regard to material properties, the structural elements of the sample featured the following densities, referred to 12% moisture content:

- 530±58 kg/m$^3$ for the planks;
- 457±1 kg/m$^3$ for the joists;
- 511±10 kg/m$^3$ for the plywood panels.

Finally, the screws featured a characteristic yield moment $M_{y,k}$ = 8800 Nmm and a characteristic withdrawal-resistance parameter $f_{ax,k}$ = 15.5 MPa.

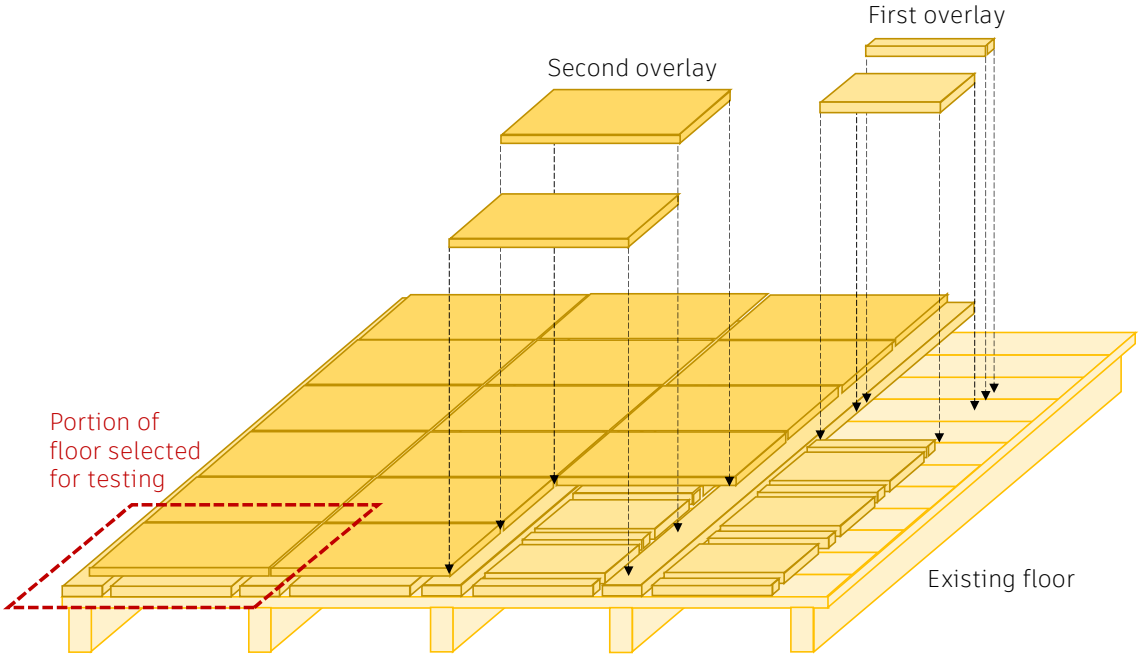


Figure 1: Principle for the execution of the double plywood panels overlay.

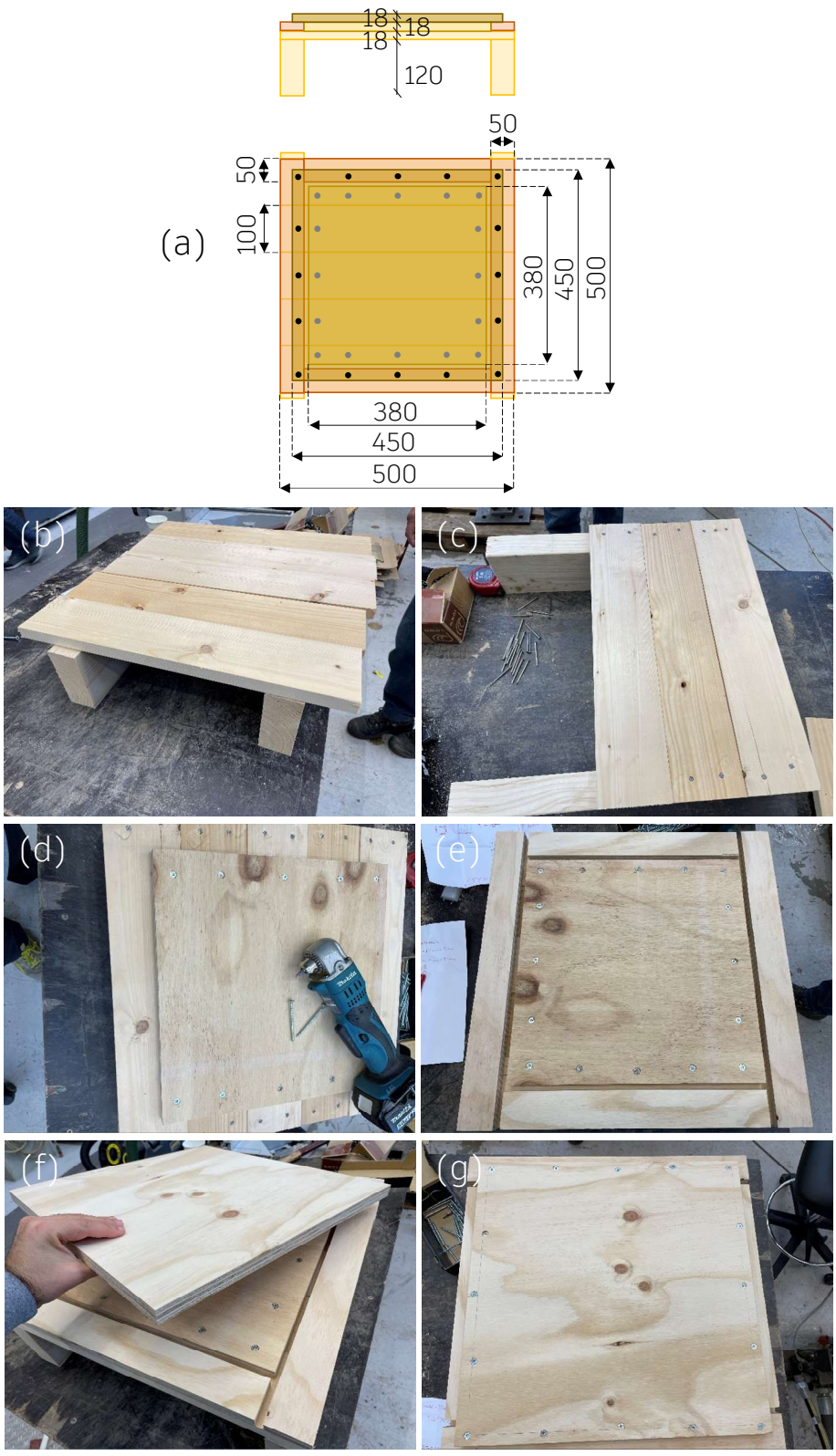


Figure 2: (a) Geometry and dimensions (in mm) of the tested prototype and construction sequence: (b) preparing joists and boards; (c) nailing the planks; (d) fastening the first plywood panel; (e) preparing the interlayer with plywood boards; (f) placing the second plywood panel; (g) fastening the second plywood panel.

## 2.2 Testing methods

The test setup adopted for the sample, shown in Figure 3, consisted of a compact steel frame to which the prototype and a hydraulic actuator (100 kN capacity, ±120 mm stroke) were fixed. To detect the in-plane displacements of the sample, two lasers and an additional sensor integrated in the actuator were placed. Additionally, digital image correlation (DIC) technique was adopted, thus the sample was provided with markers and a central reference pattern (Figure 3b). The DIC system consisted of two cameras, placed at 750 mm from the prototype, having a resolution of 4096×3000 pixels each. This allowed to detect the in-plane response of the sample in detail.

The specimen was subjected to displacement-based quasi-static cyclic tests following the loading protocol of ISO 16670 [31]. To this end, an ultimate displacement of 30 mm was assumed to derive the amplitude of each cycle, based on the analytical model presented in the following. The test was conducted at a constant displacement rate of 0.3 mm/s.

## 2.3 Analytical modelling

The adopted analytical model, also used for numerical implementation, was an extension of the formulation presented in [23],[25] to predict the in-plane response of the retrofitted diaphragms starting from the load-slip response of the single screws. This load-slip curve was modelled by means of a combination of a linear and a parabolic branch, representing the initial stiffness and the global behaviour, respectively [23]:

$$F_s = (F_0 + a\, d_s + b\, d_s^2)[1 - \exp(-K_0\, d_s/F_0)] \geq 0; \text{ with } a > 0,\ b < 0 \tag{1}$$

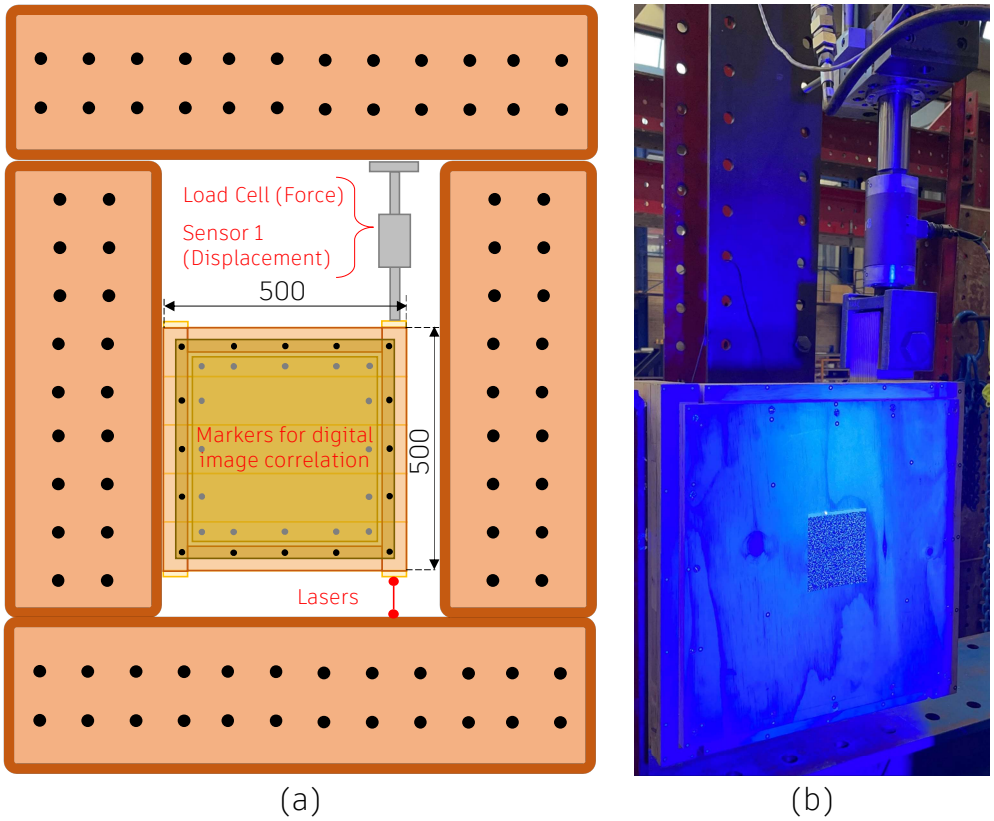


Figure 3: (a) Test setup used for the in-plane testing of the sample; (b) prototype in the setup while testing.

In Equation 1, $F_s$ and $d_s$ are the force and displacement of the screw, respectively; $F_0$, $a$ and $b$ are the coefficients of the parabola representing the global behaviour, while $K_0$ is the slope of the line representing the initial stiffness [23],[25]. As a failure criterion, in agreement with the provisions of ISO 16670 [31], the ultimate displacement was considered as the one for which the transferred load dropped below 80% of the peak strength during the softening phase.

All parameters of Equation 1 can be derived from tests on single screwed joints (see [23]), but can also be analytically determined. For the initial stiffness, the expression proposed in [32], i.e. $K_0 = 50\ d^{1.7}$, with $d$ nominal diameter of the screw, can be adopted. $F_0$ can be predicted starting from the knowledge of the maximum force $F_{max}$ determined according to EN 1995 [33] and Johansen's theory for timber-to-timber joints, and with a screw sufficiently slender to develop two plastic hinges. Then, $F_0$ can be estimated as $F_{max}/8$ [23],[25]. The remaining two parameters $a$ and $b$, identifying the parabolic branch, have the following expressions: $a = 2(F_{max} - F_0)/d_{max}$ and $b = -(F_{max} - F_0)/(d_{max})^2$. In the former equations, $d_{max}$ is the slip of the screw at $F_{max}$, estimated as $d_{max} = (b_1 + b_2)\tan(\alpha)$, with $(b_1 + b_2)$ distance between the two plastic hinges according to Johansen's theory [34], and $\alpha$ angle at which the yield moment of the screw is evaluated [35]. Based on the load-slip response of the single screw, the in-plane response of a whole retrofitted floor can be derived simply considering equilibrium relations [23],[25],[26].

This analytical model has shown very good agreement with previously reported experimental results on timber floors strengthened with a single overlay of plywood panels [14],[23],[25],[26]. The use of the presented formulation appeared thus to be promising for the prediction of the in-plane response of diaphragms retrofitted with the methodology proposed in this work. In fact, only one adjustment is needed, and namely in the expression for $F_{max}$. When the plywood panels are directly fastened to the sheathing (this is the case for the first overlay), the usual formulation from [33],[34] is adopted:

$$F_{max} = \sqrt{\frac{2\,\beta}{1+\beta}}\sqrt{2\,M_y\,f_{h,1}\,d} + \frac{F_{ax}}{4} \tag{2}$$

In Equation 2, $M_y$ is the yield moment of the fastener, $d$ its diameter, and $F_{ax}$ its withdrawal strength; $f_{h,1}$ is the embedment strength of the sheathing, and $\beta = f_{h,2}/f_{h,1}$ is the ratio between the embedment strength of the plywood overlay and that of the sheathing.

When, instead, the second overlay is considered, the screws connecting the panels to the sheathing now also cross the interlayer made of plywood boards. This interlayer does not contribute to the shear strength, and constitutes in fact an interposed gap between the second overlay of plywood panels and the sheathing. This effect corresponds to a reduction of the distance $b_1$ of the plastic hinge in the sheathing from its interface with the interlayer. Thus, because of the presence of this interlayer (having thickness $t$), $b_1$ can now be expressed as [36]:

$$b_1 = \sqrt{\frac{2\,\beta}{1+\beta}}\sqrt{\frac{2\,M_y}{f_{h,1}\,d} + \frac{\beta}{1+\beta}\frac{t^2}{2}} - \frac{\beta}{1+\beta}t \tag{3}$$

Finally, the shear strength of a fastener in such configuration is $F_{max} = f_{h,1}\ b_1\ d + F_{ax}/4$, whereas $d_{max} = (b_1 + t + b_2)\tan(\alpha)$. With this adjustment it was possible to separately calculate the in-plane response of the first overlay (using $F_{max}$ from Equation 2) and of the second one (using $F_{max}$ from Equation 3), starting from the load-slip response of the single screws and considering the two different dimensions of the panels (Figure 4).

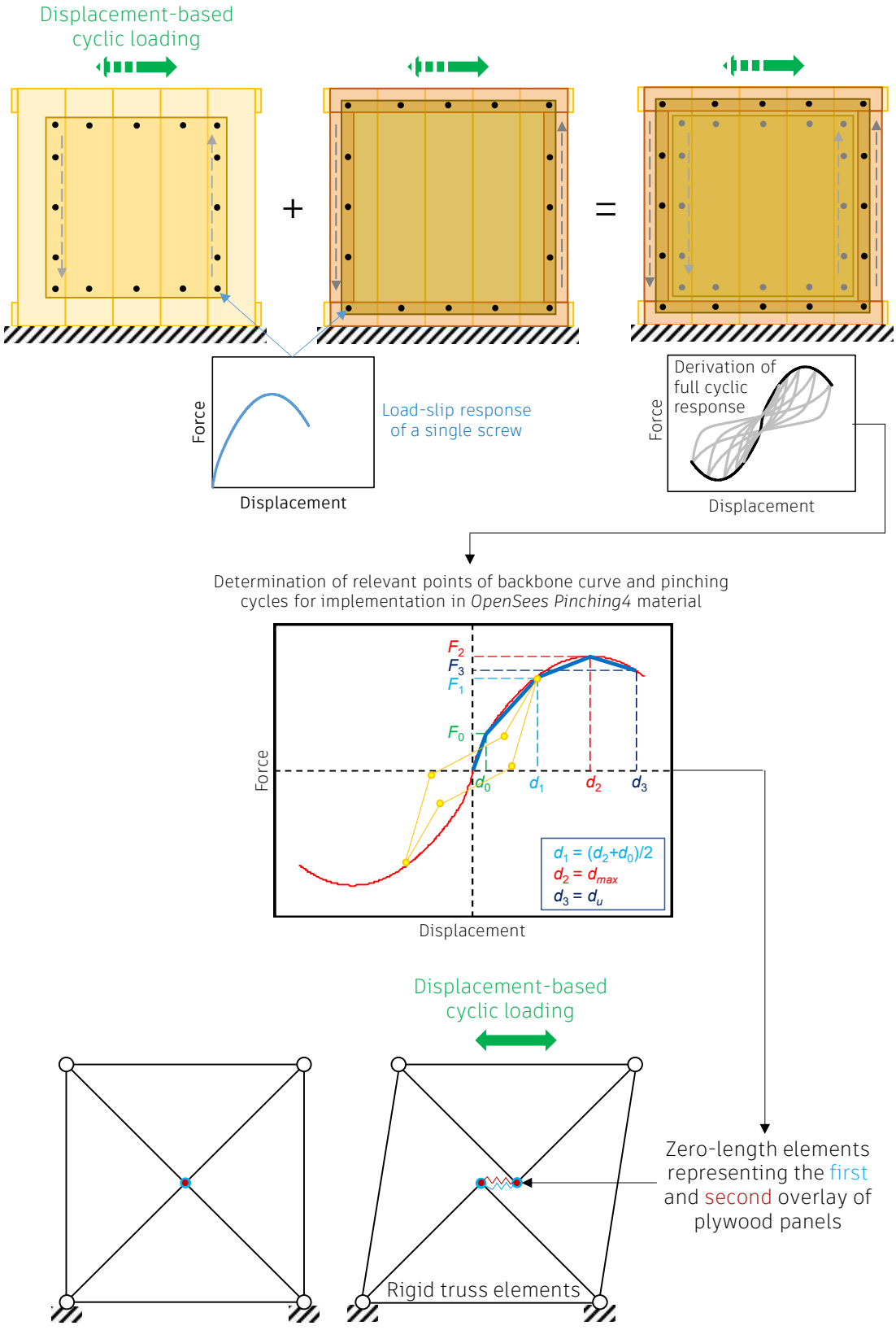


Figure 4: Adopted analytical formulation and its implementation in a macro-element modelling strategy for simulating the in-plane response of the tested sample.

### 2.4 Numerical modelling

Besides reproducing the conducted experimental test, sensitivity analyses were performed, in order to assess the influence of parameters such as the diameter of the screws and the plywood thickness. Thus, the aforementioned analytical formulation was implemented in the open-source software *OpenSees* [37], adopting a macro-element modelling strategy (Figure 4). The macro-element representing the prototype was composed of rigid truss elements forming an upper and a lower triangle connected to each other; in the middle of the macro-element, two *zero-length elements* [37] were present, representing the nonlinear, in-plane response of the first and second overlay of plywood panels. The two zero-length elements featured the *Pinching4* uniaxial material model [37], whose input parameters are the load-displacement points of the backbone curve and the internal pinching cycles. These quantities were derived directly from the analytically calculated backbone curve, following the approach presented in [23] and recalled in Figure 4.

## 3 RESULTS AND DISCUSSION

### 3.1 Experimental results

The tested sample exhibited large in-plane strength and stiffness, and considerable hysteretic energy dissipation (Figure 5). The presence of the double plywood panels overlay proved to be beneficial from this point of view, ensuring a stable softening phase after the peak load, and large strength with sufficient displacement capacity even for the limited dimensions of the prototype.

Diffused yielding of the fasteners was observed, responsible for the large dissipation: depending on the considered cycle, an equivalent hysteretic damping ratio of 13 to 17% was determined. The tested prototype reached a peak load of 13.7 kN, with a corresponding in-plane deflection of 38 mm. As will be shown in the next section, these values were in line with those expected from the analytical prediction.

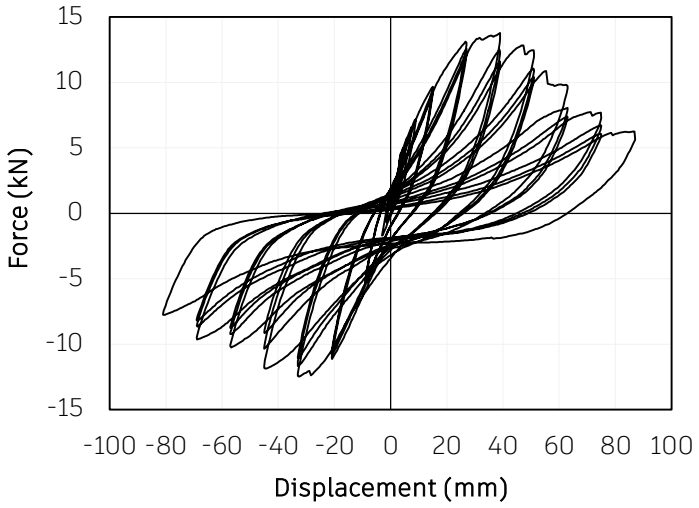


Figure 5: Experimental in-plane cyclic response of the tested specimen.

### 3.2 Comparison of the analytical and numerical models with the experiment

The analytical formulation presented in Section 2.3 allowed to construct two separate backbones for the two plywood overlays. Since the two panels ultimately contribute to the same in-plane deflection, the analytically determined backbone curves of the overlay were summed together, obtaining the graph shown in Figure 6b. The internal pinching cycles were derived from the resulting backbone curve (see once more Figure 4), following the geometrical procedure already presented in previous works [23],[25]. As can be noticed, a very good agreement between the analytical model and the experimental response of Figure 6a was obtained. In particular, from the performed calculations, based on the material properties reported in Section 2.1, values of $F_{max}$ = 12.5 kN and $d_{max}$ = 37 mm were determined. These values appear to be very close to those recorded from the experiment (see Section 3.1): $F_{max}$ was underestimated by only 9% and $d_{max}$ by only 3%. It should be noticed that, with respect to a single-panel overlay, the strength could be almost doubled, while still keeping the same displacement capacity.

Since the constitutive laws adopted for the zero-length elements of the numerical model were based on the previously reported analytical formulation (Figure 4), also the results of the simulations in *OpenSees* can accurately capture the in-plane response of the prototype (Figure 6c). The good agreement with the experiment is not only visible from the very similar shape of the numerical hysteretic response, but also when considering the energy dissipation per cycle: as can be noticed from Figure 7, the energy accumulation derived from the experiment is well described by the numerical model, with only minor discrepancies. In other words, the adopted modelling strategy and constitutive laws can reliably simulate not only the in-plane strength and stiffness of the proposed retrofitting method, but also its cyclic energy dissipation, confirming also for this strengthening configuration the results obtained for a single plywood overlay [23],[25].

### 3.3 Influence of diameter of screws and plywood thickness

Since the proposed analytical formulation and the performed numerical analyses showed good agreement with the experiment, these approaches were also used to assess the influence of different diameters of screws (4, 5, 7 mm) and plywood thicknesses (9, 12, 15, 18 mm) (Figure 8). Because the main failure mode of the prototype involves the development of two plastic hinges in the fasteners, the impact of screw diameter is, as expected, very relevant, with a great in-plane strength and stiffness increase for larger diameters. For the same reason, the influence of plywood thickness is lower, but can lead to a variation in strength of 2%/mm of panel thickness for the investigated range, similarly to past findings on floors retrofitted with a single plywood overlay [13].

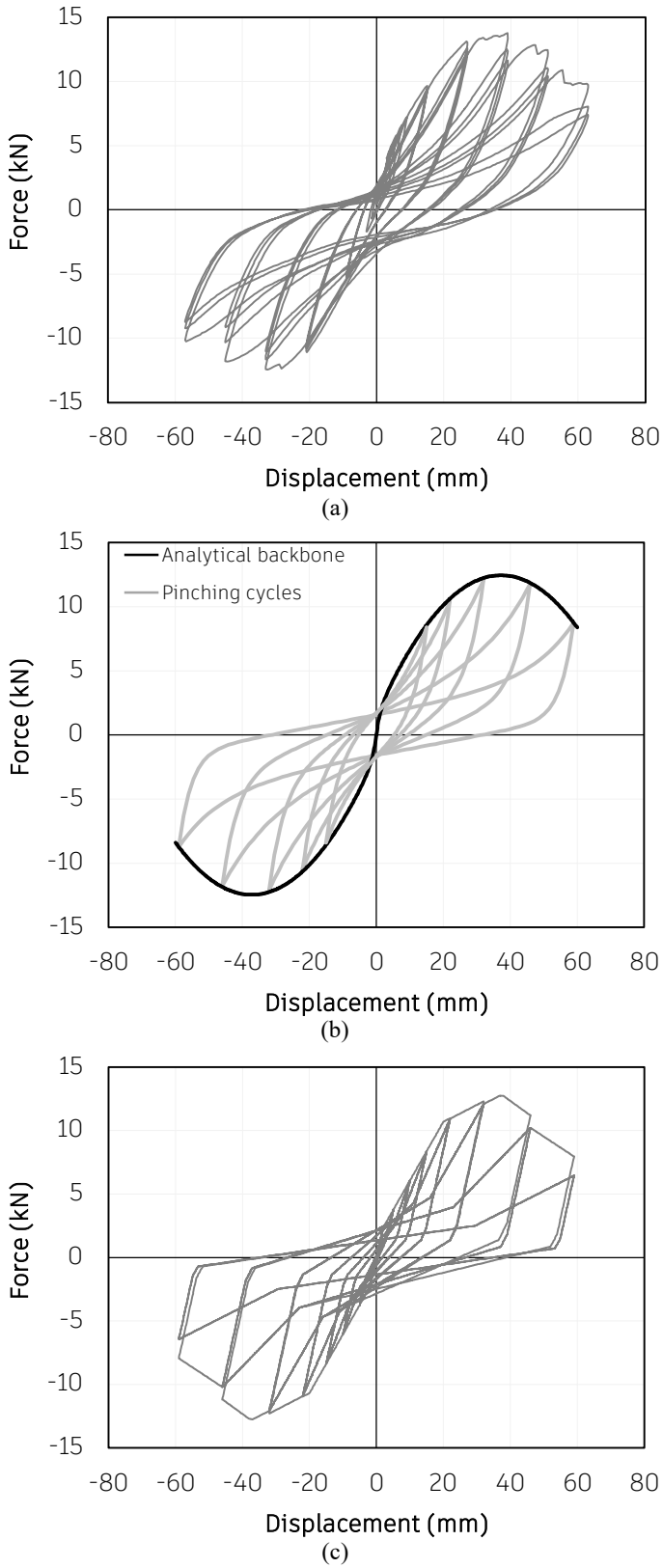


Figure 6: (a) Experimental response of the prototype including softening phase up to 80% of peak load; (b) prediction based on the presented analytical formulation; (c) cyclic response of the specimen simulated in *OpenSees*.

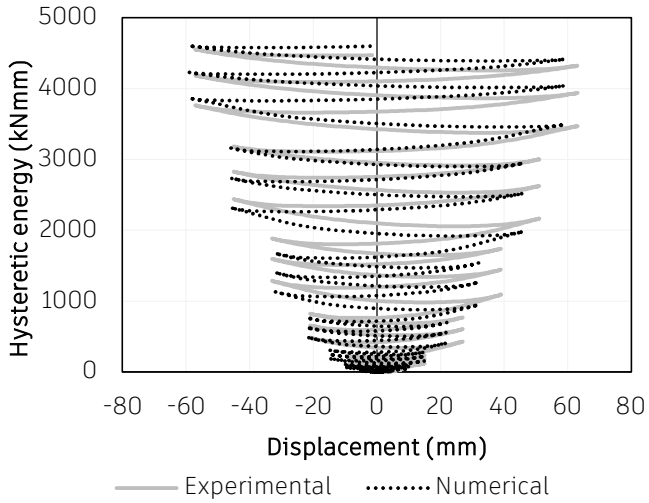


Figure 7: Comparison between the experimental and numerical hysteretic energy accumulation.

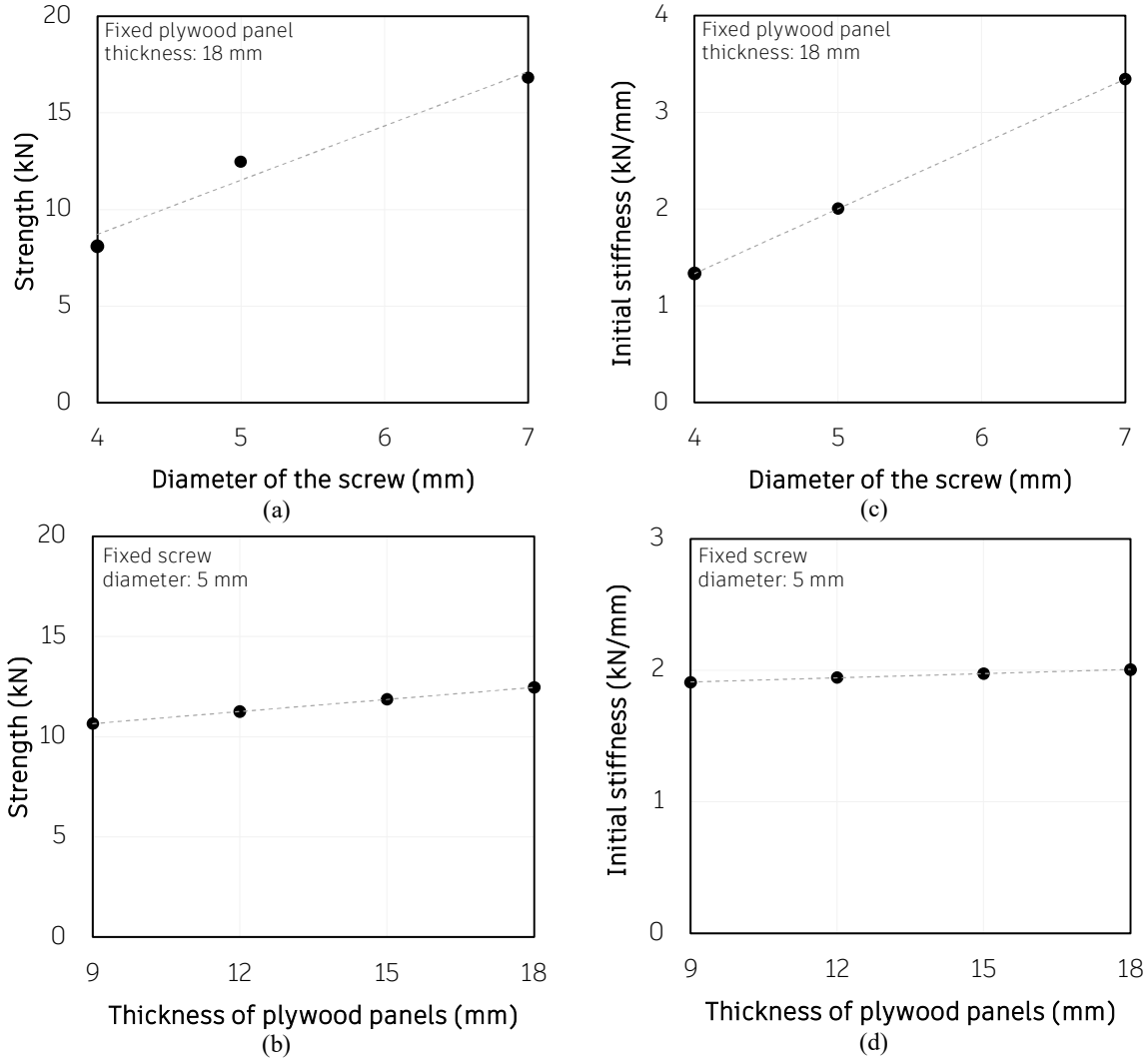


Figure 8: Influence of screw diameter and plywood thickness on strength (a, b) and initial stiffness (c, d) of the tested sample.

## 4 CONCLUSIONS

In this work, a plywood-based in-plane retrofitting for existing timber floors has been presented. The proposed strengthening method consists of the creation of two independent shear planes by means of two different superimposed overlays of plywood panels. The first layer is fastened directly to the existing sheathing, while the second is fixed to the sheathing through plywood boards surrounding each panel of the first overlay. A small gap is left between the boards and the panels, enabling free rotation and sliding. With this solution, the two overlays are not directly connected to each other, combining the strength of two plywood layers with an improved ductility linked to their independent movement.

Firstly, an experimental test was conducted on a prototype representing a 500×500 mm portion of a floor retrofitted with the aforementioned method. The results from this test were used to validate the analytical formulations and numerical modelling strategies previously developed for a single plywood overlay, and adapted in the present study for the case of the double overlay. Although the tested sample had relatively small dimensions, it exhibited an in-plane strength of 13.7 kN reached at 38 mm displacement, with large energy dissipation, corresponding to an equivalent hysteretic damping ratio of 13 to 17%, depending on the considered cycle.

The outcomes from the test were then compared with the analytical and numerical modelling approaches adapted for the case of two plywood panels overlay, showing an overall good agreement with the experiment. The influence of the variation of parameters such as screw diameter and plywood thickness was also evaluated. The developed modelling strategies can be adopted to design retrofitting interventions on existing timber floors with the proposed method, and to accurately simulate their in-plane response. Furthermore, these approaches can also be used for optimizing the layout of the two plywood overlays and their fasteners, in order to combine the target strength and stiffness of the floor with large energy dissipation, making the technique very adaptable and versatile.

The outcomes of this work can contribute to the research framework supporting the use of wood-based techniques for the seismic upgrading and architectural conservation of existing and historical structures.

## REFERENCES

[1] M. Piazza, C. Baldessari, R. Tomasi, The Role of In-Plane Floor Stiffness in the Seismic Behaviour of Traditional Buildings. *14th World Conference on Earthquake Engineering*, Beijing, 2008.

[2] C. Modena, M.R. Valluzzi, E. Garbin, F. da Porto, A strengthening technique for timber floors using traditional materials. *Proceedings of the Fourth International Conference on Structural Analysis of Historical Constructions SAHC 04*, Padua, Italy, 10–13 November 2004, 911–921, 2004.

[3] M.R. Valluzzi, E. Garbin, M. Dalla Benetta, C. Modena, In-Plane Strengthening of Timber Floors For The Seismic Improvement Of Masonry Buildings. *11th World Conference on Timber Engineering*, Riva del Garda, 2010.

[4] M.R. Valluzzi, E. Garbin, M. Dalla Benetta, C. Modena, Experimental Assessment and Modelling of In-Plane Behaviour of Timber Floors. D. D'Ayala and E. Fodde (Eds.), *Proceedings of the VI International Conference on Structural Analysis of Historic Construction, SAHC 08*, 2–4 July 2008, Bath, UK, 2008, 755-762.

[5] N. Gattesco, L. Macorini, High reversibility technique for in-plane stiffening of wooden floors. D. D'Ayala and E. Fodde (Eds.), *Proceedings of the VI International Conference on Structural Analysis of Historic Construction, SAHC 08*, 2–4 July 2008, Bath, UK, 2008, 1035–1042.

[6] M. Corradi, E. Speranzini, A. Borri, A. Vignoli, In-Plane Shear Reinforcement of Wood Beam Floors With FRP. *Composites: Part B* **37**, 310-319, 2006.

[7] J.M. Branco, M. Kekeliak, P.B. Lourenço, In-Plane Stiffness of Timber Floors Strengthened with CLT. *European Journal of Wood Products* **73**, 313-323, 2015.

[8] A. Gubana, M. Melotto, Experimental tests on wood-based in-plane strengthening solutions for the seismic retrofit of traditional timber floors, *Construction and Building Materials* **191**, 290–299, 2018.

[9] E. Rizzi, M. Capovilla, M. Piazza, I. Giongo, In-plane behaviour of timber diaphragms retrofitted with CLT panels. Chapter in book: R. Aguilar et al. (Eds.): *Structural Analysis of Historical Constructions*, RILEM Bookseries 18, 1613-1622, 2019.

[10] D.F. Peralta, M.J. Bracci, M.B.D. Hueste, Seismic Behavior of Wood Diaphragms in Pre-1950s Unreinforced Masonry Buildings. *Journal of Structural Engineering* **130**, 2040-2050, 2004.

[11] A. Brignola, S. Pampanin, S. Podestà, Experimental Evaluation of the In-Plane Stiffness of Timber Diaphragms. *Earthquake Spectra*, Volume 28, No. **4**, 1–23, 2012.

[12] A. Wilson, P.J.H. Quenneville, J.M. Ingham, In-Plane Orthotropic Behavior of Timber Floor Diaphragms in Unreinforced Masonry Buildings. *Journal of Structural Engineering* **140**, 2014.

[13] E. Rizzi, I. Giongo, J. Ingham, D. Dizhur, Testing and Modeling In-Plane Behavior of Retrofitted Timber Diaphragms. *Journal of Structural Engineering*, vol. 146, **2**, 2020.

[14] M. Mirra, G. Ravenshorst, J.W. van de Kuilen, Experimental and analytical evaluation of the in-plane behaviour of as-built and strengthened traditional wooden floors. *Engineering Structures* **211**, 110432, 2020.

[15] T.-J. Lin, J.M. LaFave, Experimental Structural Behavior of Wall-Diaphragm Connections for Older Masonry Buildings. *Construction and Building Materials* **26**, 180–189, 2012.

[16] S. Moreira, D.V. Oliveira, L.F. Ramos, P.B. Lourenço, R.P. Fernandes, J. Guerreiro, Experimental study on the seismic behavior of masonry wall-to-floor connections. *Proceedings of the 15th World Conference on Earthquake Engineering*, Lisbon, Portugal, 2012.

[17] S. Moreira, L.F. Ramos, D.V. Oliveira, P.B. Lourenço, L. Mateus, Developing a seismic retrofitting solution for wall-to-floor connections of URM with wood diaphragms. *Proceedings of the 9th International Masonry Conference*, Guimarães, Portugal, 2014.

[18] D. Dizhur, M. Giaretton, J.M. Ingham, URM wall-to-diaphragm and timber joist connection testing. *Proceedings of the 10th International Masonry Conference*, Milan, Italy, 2018.

[19] M. Mirra, G. Ravenshorst, J.-W. van de Kuilen, Monotonic, cyclic and dynamic behaviour of timber-masonry connections. *World Conference on Timber Engineering*, Santiago, Chile, August 9-12, 2021.

[20] M. Mirra, G. Ravenshorst, P. de Vries, F. Messali, Experimental characterisation of as-built and retrofitted timber-masonry connections under monotonic, cyclic and dynamic loading. *Construction and Building Materials* **358**, 129446, 2022.

[21] A. Gubana, State-of-the-Art Report on high reversible timber to timber strengthening interventions on wooden floors. *Construction and Building Materials* **97**, 25-33, 2015.

[22] M. Mirra, G. Ravenshorst, J.W. van de Kuilen, Comparing in-plane equivalent shear stiffness of timber diaphragms retrofitted with light and reversible wood-based techniques. *Practice Periodical on Structural Design and Construction* **26**(4), 2021.

[23] M. Mirra, G. Ravenshorst, P. de Vries, J.W. van de Kuilen, An analytical model describing the in-plane behaviour of timber diaphragms strengthened with plywood panels. *Engineering Structures* **235**, 112128, 2021.

[24] M. Mirra, G. Ravenshorst, J.W. van de Kuilen, Dissipative properties of timber diaphragms strengthened with plywood panels. *World Conference on Timber Engineering*, Santiago, Chile, August 9-12, 2021.

[25] M. Mirra, M. Sousamli, M. Longo, G. Ravenshorst, Analytical and numerical modelling of the in-plane response of timber diaphragms retrofitted with plywood panels. *8th International Conference on Computational Methods in Structural Dynamics and Earthquake Engineering*, COMPDYN 2021, Athens, Greece, June 28-30, 2021.

[26] M. Mirra, G. Ravenshorst, A seismic retrofitting design approach for activating dissipative behaviour of timber diaphragms in existing unreinforced masonry buildings. *Current Perspectives and New Directions in Mechanics, Modelling and Design of Structural Systems - Proceedings of the 8th International Conference on Structural Engineering, Mechanics and Computation*, Cape Town, South Africa, September 5-7, 2022.

[27] M. Mirra, G. Ravenshorst, Optimizing Seismic Capacity of Existing Masonry Buildings by Retrofitting Timber Floors: Wood-based Solutions as Dissipative Alternative to Rigid Concrete Diaphragms. *Buildings* **11**(12), 604, 2021.

[28] M. Mirra, A. Gerardini, G. Ravenshorst, Application of timber-based techniques for seismic retrofit and architectural restoration of a wooden roof in a stone masonry church. *XIX ANIDIS Conference, Seismic Engineering in Italy*, Turin, Italy, September 12-15, 2022.

[29] M. Mirra, A. Gerardini, S. Ghirardelli, G. Ravenshorst, J.W. van de Kuilen, Combining architectural conservation and seismic strengthening in the wood-based retrofitting of a monumental timber roof: the case study of St. Andrew's Church in Ceto, Brescia, Italy. *International Journal of Architectural Heritage*, 2023.

[30] V. Wilden, G. Balaskas, B. Hoffmeister, L. Rauber, B. Walter, High performance light timber shear walls and dissipative anchors for damage limitation of wooden buildings in seismic areas. *Current Perspectives and New Directions in Mechanics, Modelling and Design of Structural Systems - Proceedings of the 8th International Conference on Structural Engineering, Mechanics and Computation*, Cape Town, South Africa, September 5-7, 2022.

[31] ISO 16670:2003. Timber structures — Joints made with mechanical fasteners — Quasi-static reversed-cyclic test method.

[32] P. Dubas, E. Gehri, T. Steurer, Einführung in die Norm SIA 164 (1981) – Holzbau. Publication No. 81-1, Baustatik und Stahlbau, ETH Zürich, Switzerland, 1981.

[33] EN 1995-1-1:2004+A2:2014. Eurocode 5: Design of timber structures - Part 1-1: General - Common rules and rules for buildings. CEN (European Committee for Standardization).

[34] K.W. Johansen, Theory of timber connections. Publ. 9 Bern. International Association of Bridge and Structural Engineering, 1949.

[35] EN 409:2009. Timber structures - Test methods - Determination of the yield moment of dowel type fasteners. CEN (European Committee for Standardization).

[36] P. Gelfi, E. Giuriani, A. Marini, Stud Shear Connection Design for Composite Concrete Slab and Wood Beams. Journal of Structural Engineering **128**(12), 1544-1550, 2002.

[37] S. Mazzoni, F. McKenna, M.H. Scott, G.L. Fenves, OpenSees Command Language Manual. University of California, Berkeley, 2006.

COMPDYN 2023
9th ECCOMAS Thematic Conference on
Computational Methods in Structural Dynamics and Earthquake Engineering
M. Papadrakakis, M. Fragiadakis (eds.)
Athens, Greece, 12-14 June 2023

# LIGHT TIMBER FRAME WALLS WITH CLADDING – NUMERICAL INVESTIGATION OF THE SEISMIC PERFORMANCE OF A MULTI-STORY BUILDING BASED ON TEST RESULTS

**L. Rauber[1], C. Vulcu[1], V. Wilden[1], G. Balaskas[1] and B. Hoffmeister[1]**

[1] Center for Wind and Earthquake Engineering, RWTH Aachen University
Mies-van-der-Rohe-Str. 1, Aachen, Germany
e-mail: {l.rauber, c.vulcu, v.wilden, g.balaskas, hoff}@stb.rwth-aachen.de

## Abstract

Light Timber Frame Walls (LTFWs) are increasingly used to provide lateral stiffness and resistance to multi-story timber buildings. They consist of several components (frame, sheathing, fasteners and anchorage) and act as shear diaphragms for the global stability of the structure. Additional cladding, e.g. gypsum fiberboard (GFB), is common practice for fire protection in multi-story buildings. Yet, according to Eurocode 5, this cladding is not considered in the structural analyses. Three different LTFW configurations were tested under monotonic and cyclic loading: (i) typical LTFWs sheathed with OSB sheathing on each side; (ii) enhanced LTFWs with three OSB sheathings (two external and one internal); (iii) typical LTFWs with OSB sheathing covered by GFB cladding. Aim of the tests was to determine the – stiffness, resistance and ductility – of typical LTFWs, to examine the improved seismic behavior of the enhanced LTFWs and identify the influence of the fire protection cladding. The response of the investigated walls (i.e. initial stiffness, hysteretic behavior) was implemented in a structural model (SAP2000) using multi-linear plastic link elements. Nonlinear static and dynamic analyses were performed on a set of multi-story buildings containing the three LTFW typologies. The paper presents the following aspects: (i) overall experimental results of the tested LTFWs; (ii) numerical model of the 3D structure and modelling parameters of the link elements; (iii) outcomes of the nonlinear static/dynamic analyses; (iv) comparison of results and main conclusions. The seismic performance of the multi-story building is outlined for each LTFW typology, the strengths and weaknesses of each wall configuration are discussed.

**Keywords:** Light Timber Frame Walls; Nonlinear Static/Dynamic Analyses; Performance Based Design.

## 1 INTRODUCTION

Light timber frame walls (LTFW) are commonly used to provide lateral stiffness in low and mid-rise buildings. Given the increasing interest for timber multi-story buildings, the demands for timber elements capable to provide lateral stiffness grows as well.

LTFWs are built-up members consisting of the frame, the sheathing(s) and the fasteners. Each component with its corresponding material properties contributes to the total load-bearing capacity of the walls. The frame usually consists of structural timber, while for sheathing oriented strand boards (OSB) are usually employed. Fasteners are typically nails, staples or – less common – screws. Due to the ductile behavior of the mechanical fasteners, LTFWs can be utilized in buildings for energy dissipation in seismic events. Design provisions provided by *Eurocode 5* [1] and *Eurocode 8* [2] are applied to ensure this desired fastener failure mode and exclude brittle ones. Within a dissipative design concept, the nonlinear behavior of the walls must be considered in the structural design process.

*Eurocode 8* allows design against seismic actions either using force-based methods (equivalent static method, response spectrum analysis), in which the nonlinear response of the structural members can be considered only indirect through the behavior factor, or implementing more sophisticated methods, in which the nonlinear response of particular structural elements is directly simulated. Non-linear static analysis (pushover) and nonlinear dynamic analysis (response history analysis) can assess this possible nonlinear response of a structure under seismic actions. For a safe nonlinear design, the lateral load-bearing parameters (i.e. stiffness, load-bearing capacity and ductility) of all structural elements must be adequately estimated. These parameters can be derived from tests.

Experimental investigations at RWTH Aachen and other research projects demonstrated that the calculation of the load-bearing capacity and stiffness of LTFWs by the provisions given in *Eurocode 5* [1] are underestimated for OSB sheathing [3][4].

In Europe, it is common practice for timber multi-story buildings to clad the walls with fire protective boards, e.g. gypsum fiber boards (GFB). According to *Eurocode 5* [1], the stiffness and resistance of the cladding is not taken into consideration for the structural design. As a result, the initial stiffness and load-bearing capacity of the cladded LTFWs are even more undervalued by the analytical design model of *Eurocode 5* [1]. This was proven by recent experimental tests conducted at RWTH Aachen, whose results are present below.

The outcomes of the tests are of great importance, mainly regarding the seismic design of LTFWs. Their initial stiffness influences the modal properties of the structure and consequently the spectral acceleration. Moreover, in case timber walls are considered as dissipative elements, their resistance governs the design of non-dissipative elements (i.e. in case of the capacity-based design). A possible underestimation of resistance could lead to premature, undesired, brittle failure of non-dissipative elements (i.e. anchoring).

In the current paper, the seismic performance of conventional LTFWs, enhanced LTFWs and cladded LTFWs is outlined. First of all, the results of the experimental tests on real-scale LTFWs are briefly summarized. Furthermore, a mid-rise case study building – stabilized in both directions by the tested LTFWs – is numerically investigated (i.e. through non-linear static and dynamic analyses) – with the aim to quantify the response to lateral forces and to evaluate the seismic performance. Initially, the influence of the cladding was neglected, as it is done in practice. Afterwards, the contribution of the GFB-cladding was simulated. The outcomes of numerical investigations – on both case studies (without and with GFB-cladding) – are compared and discussed. The main conclusions regarding the performance of the investigated LTFWs, the seismic performance of the case study buildings, and the influence of GFB-cladding are finally presented.

## 2 EXPERIMENTAL INVESTIGATIONS OF LTFWs

Within a recent research project (*HOLZBEBEN*), quasi-static monotonic and cyclic experimental investigations on real-scale LTFW's with different configurations were carried out at the *Centre of Wind and Earthquake Engineering / RWTH Aachen University*. The experimental campaign included tests on typical LTFWs (labeled as "TW"), enhanced walls (labeled as "EW") [3][5] and anchorage elements [6]. Tests on walls with additional fire-protection cladding (labeled as "CW") were conducted in the aftermath of the project and their results were the inspiration for the research project *HELEPOLIS* [7]. The test results are outlined briefly below.

The structure of the LTFW test specimens is shown in Figure 1. All specimens used structural timber C24 for the frame, resin coated staples (applied considering a spacing of 75 mm) as fasteners and two HTT31 (Simpson Strong-Tie) anchorage elements at the supports of each wall. The TW test specimen (see Figure 1a) had OSB sheathing (t=15 mm) on both sides. The EW test specimen (see Figure 1b) used OSB sheathing on both sides. Furthermore, one additional sheathing layer was placed in the interspace of the wall by recessing the studs on one side.

The CW test specimen (see Figure 1c) represented a common exterior wall. It was sheathed with OSB (t=15 mm) on one side. The sheathing was cladded by gypsum fiber boards (t=12.5 mm) with an offset of half the sheathing length – typical for fire protection. The staples were driven into the frame trough the sheathing – "doubling" shear joints. The results of both TW and CW are comparable, as the resistance is proportional to wall length and number of sheathings. The influence of the wood fiber board (FB) positioned on the back side can be neglected based on the outcomes within [7].

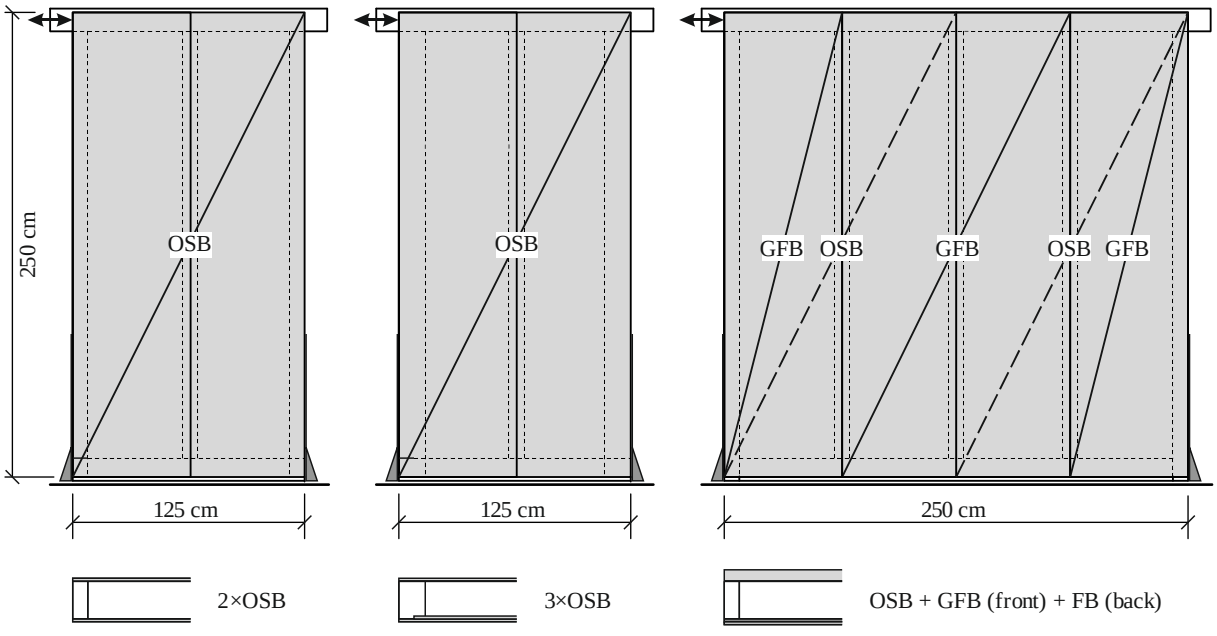


Figure 1: Structure of test specimens

The experimental program and the main properties of the specimens are summarized in Table 1. All mentioned specimens were tested without vertical loading. High performance anchorages were used to prevent a possible failure there and to allow the realization of a "shear mechanism" according to *Dujic* [8]. Horizontal cyclic loading was introduced according to *ISO*

*21581* [9]. The results of the tests in terms of force-displacement curves are presented in Figure 2. As it can be observed, the additional sheathing layer of the EW leads to about 38% higher resistance. Moreover, the influence of cladding can be distinguished from the comparison of the envelope curves corresponding to TW and CW (see Figure 2d).

| Name | | L × h [m] | Sheathing t [mm] | Fasteners ⌀-length-spacing [mm] | Loading |
|---|---|---|---|---|---|
| h-c-01 | (TW) | 1.25 × 2.50 | 2 × OSB 15 | Staples 1.80 - 65 - 75 | Cyclic |
| h-c-11 | (EW) | 1.25 × 2.50 | 3 × OSB 15 | Staples 1.80 - 65 - 75 | Cyclic |
| | | | 1 × OSB 15 (front) | Staples 1.80 - 65 - 75 | |
| h-c-21 | (CW) | 2.50 × 2.50 | 1 × GFB 12.5 (on OSB) | Staples 1.80 - 75 - 75 | Cyclic |
| | | | 1 × FB 60 (back) | Staples 2.00 - 80 - 95 | |

Table 1: Test program of LTFWs with cyclic lateral loading according to *ISO 21581* [9]

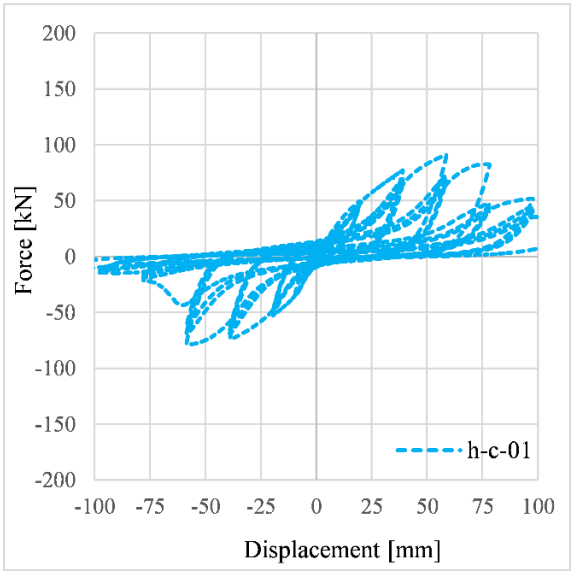


(a) Cyclic load-displacement curve of typical wall (TW)

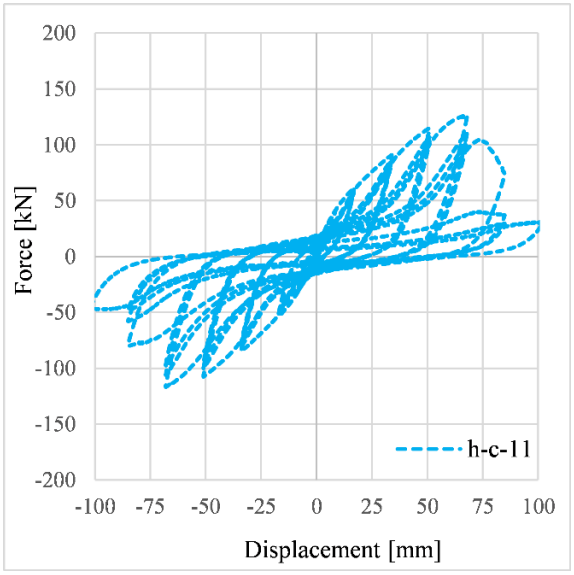


(b) Cyclic load-displacement curve of enhanced wall (EW)

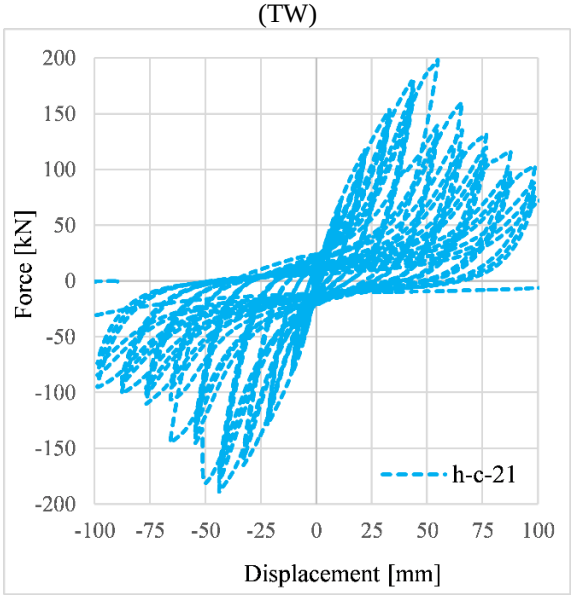


(c) Cyclic load-displacement curve of cladded wall (CW)

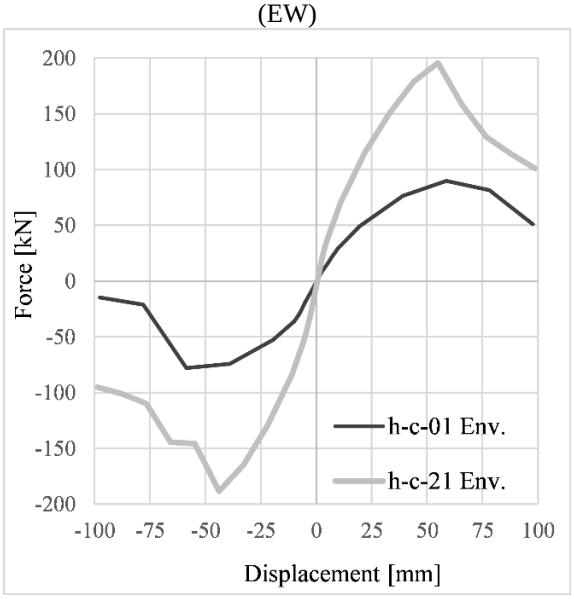


(d) Comparison of TW and CW "force-displacement" envelope curves

Figure 2: Experimental results of the different LTFW specimens

## 3 SEISMIC PERFORMANCE OF A MULTI-STORY BUILDING WITH LTFWs

The aim of the current study was to investigate the seismic performance of a multi-story building with light timber frame walls (LTFW) in the following two configurations: (i) typical / enhanced LTFWs (see Figure 3); (ii) typical / enhanced LTFWs covered by one gypsum fireboard (GFB) (see Section 3.5). Furthermore, one of the main objectives was to compare the response of the two multi-story building structures and to show the influence of the gypsum fireboard with regard to the response and the seismic performance.

The current chapter is divided into the following main topics: (i) definition of the case study buildings (including a brief description of the structural configuration, geometry, loading, modeling procedure and simplifications); (ii) outcomes of the nonlinear static analysis performed on the multi-story building with typical / enhanced LTFWs; (iii) outcomes of the nonlinear dynamic analysis performed on the multi-story building with typical / enhanced LTFWs; (iv) comparison of nonlinear static and dynamic results; (v) influence of the gypsum fireboard (GFB) on the "nonlinear static and dynamic response" of the multi-story building with LTFWs.

### 3.1 General data (definition of the case study buildings)

#### 3.1.1. Structural configuration / geometry / loading / seismic action

In order to illustrate the potential of LTFWs for the use as part of a lateral load resisting structure, as well as for the seismic performance evaluation – a 5-story building was developed and analyzed. The overall dimensions of the 3D building are shown in Figure 3a, while the types of LTFWs that were considered within the current study are presented in Figure 3b.

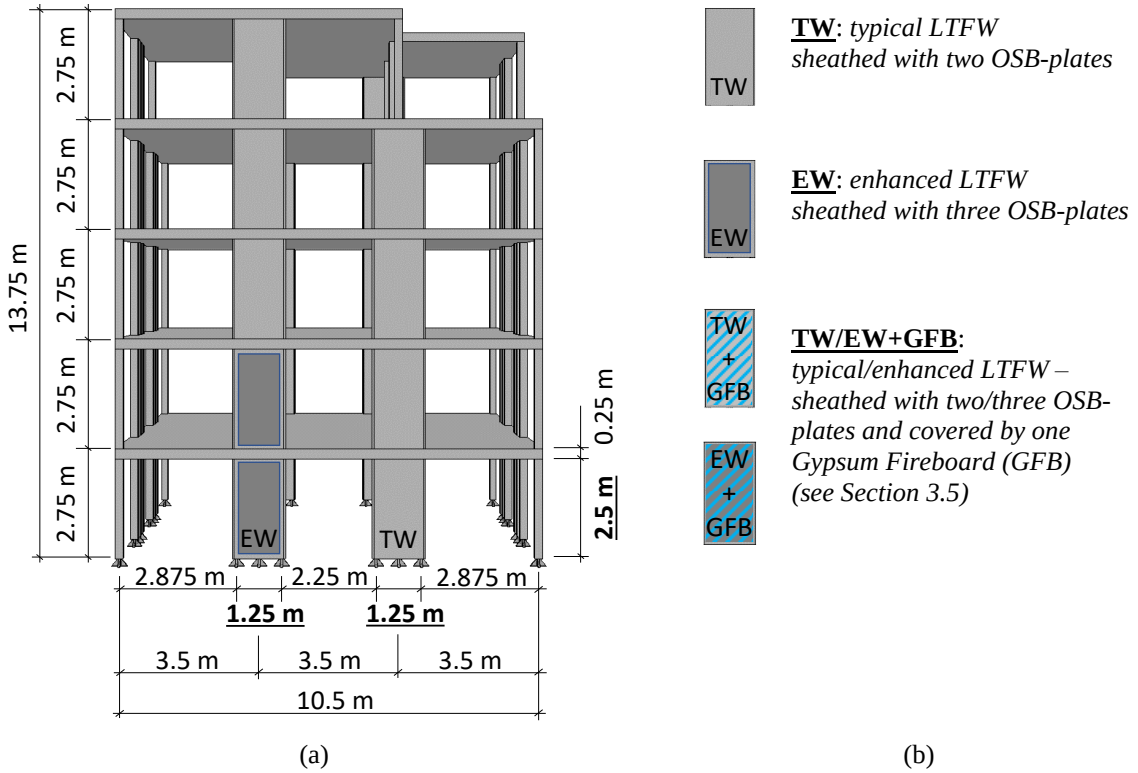


(a) (b)

Figure 3: 5-floor case study building with perimeter lateral load resisting timber structure: (a) overall dimensions and position of the walls; (b) types of light timber frame walls

As it can be observed in Figure 3a, the total height of the building is 13.75 m and the width is 10.5 m on both horizontal directions. Each of the five floors has 2.75 m height, out of which

0.25 m represents the thickness of the timber deck and 2.5 m is the available floor-to-ceiling height. With regard to the floor layout, it can be observed that the first four floors are identical, while the fifth floor has terrace space (i.e. 20% of the floor area) corresponding to two opposite corners. From the structural point of view, the loads are transferred from the various floors to the foundation as follows:

- The gravity loads (i.e. permanent and variable loads) are transferred from the "*timber floor systems*" to the timber beams (i.e. internal and on the perimeter), then to the timber columns (i.e. internal and on the perimeter), and further to the foundations;
- The lateral loads (i.e. seismic and wind loads) are transferred from the "*timber floor systems*" to the perimeter lateral load resisting structures and further to the foundations.

The perimeter lateral load resisting structures consist of: (i) timber beams which were considered to be continuous over a 5.25 m length (i.e. the connection between two beams is performed in the mid span); (ii) timber columns which were considered to be continuous just over a 2.5 m length (i.e. equal to the floor to ceiling height); (iii) LTFWs, which consist of timber studs and rails which form a "frame" and two or three layers of OSB-plates (leading to TW or EW – see Figure 1 and Figure 3b). Considering the floor layout and the perimeter lateral load resisting structure, it needs to be highlighted that the structural configuration is symmetric on the two orthogonal directions. Furthermore, as it can be observed in Figure 3a, the perimeter lateral load resisting structure consists of two rows of LTFWs. Aiming for an identical arrangement of the windows (i.e. within the two external spans 2.5 m × 2.875 m, as well as in the middle span 2.5 m × 2.25 m) over the height of the building, and for an optimal transfer of the lateral loads (e.g. avoiding a soft story mechanism) – the type and number of LTFWs was customized for each floor. The main components corresponding to each perimeter lateral load resisting system are summarized in Table 2. In addition, Table 3 and Table 4 show the adopted - permanent, variable and seismic - loads.

| Floor | LTFW - Row I | LTFW - Row II | Timber columns (h×b) | Timber beams (h×b) |
|---|---|---|---|---|
| 5th | TW | - | 200×200 mm | 250×400 mm |
| 4th | TW | ½ × TW | 200×200 mm | 250×400 mm |
| 3rd | TW | TW | 200×200 mm | 250×400 mm |
| 2nd | EW | TW | 200×200 mm | 250×400 mm |
| 1st | EW | TW | 200×200 mm | 250×400 mm |

Table 2: Main components of the perimeter lateral load resisting system

| Design loads | | Description | Load value |
|---|---|---|---|
| Roof | Permanent | Self-weight of: timber deck, isolation, etc. | 2 kN/m$^2$ |
| | Variable | Snow; personnel working on the roof, etc. | 1 kN/m$^2$ |
| Floors 1÷5 | Permanent | Self-weight of: timber deck, finishing etc. | 3 kN/m$^2$ |
| | | Perimeter walls | 2.5 kN/m |
| | Variable | Offices (Class B) | 3 kN/m$^2$ |

Table 3: Permanent and variable loads

| Seismic design action | Value / Description |
|---|---|
| Peak ground acceleration | $a_{gR} = 0.24 \times g$ |
| Importance factor | $\gamma_1 = 1.0$ (Class II) |
| Ground type | C-R (S = 1.15, $T_B$ = 0.1 s, $T_C$ = 0.3 s, $T_D$ = 2.0 s) |

Table 4: Seismic design action according to DIN EN 1998/NA [10]

### 3.1.2. Modeling procedure and simplifications

The numerical modeling and analysis of the two case study buildings was performed using the SAP2000 [12] software. Consequently, an illustration of the 3D structural model (with extruded elements) – is shown in Figure 4.

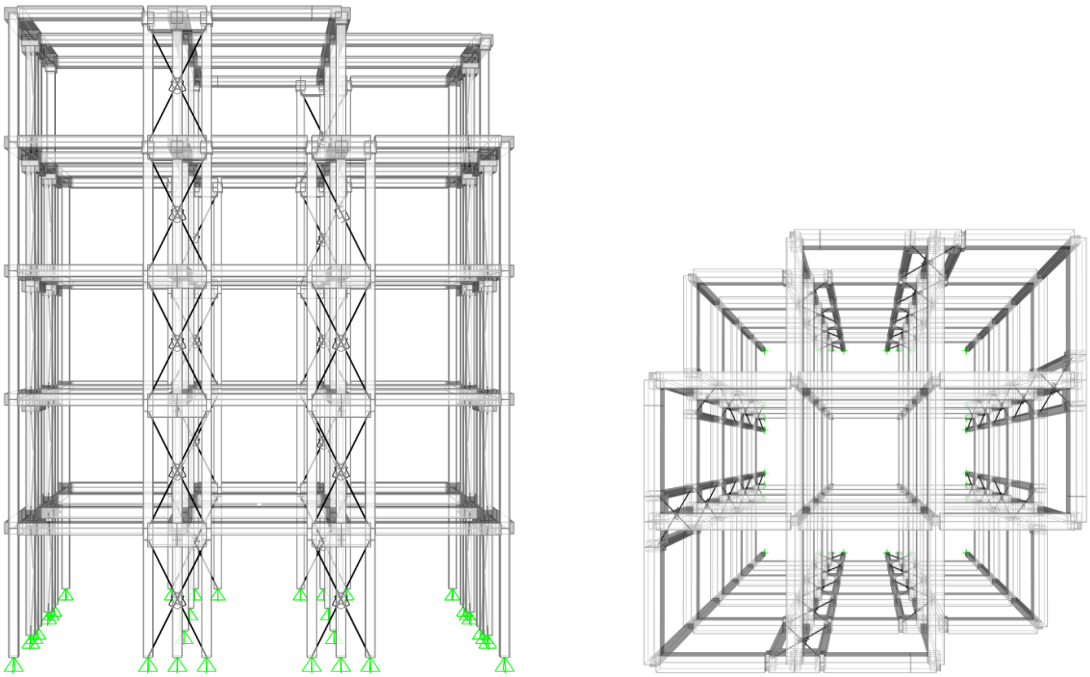

(a) (b)

Figure 4: 3D structural model of the case study building: (a) side view; (b) top view

As can be observed in Figure 4, the timber beams and columns were modeled as beam elements considering the cross-sections described in Table 2. Even though the timber deck was not explicitly modeled, its weight was included as part of the permanent load (see Table 3), while its stiffening effect was accounted for through a diaphragm constraint, which was defined at each floor. All column bases were modeled considering pinned connections to the foundation. Furthermore, the connection between the columns (i.e. from one story to the other) was considered to be pinned as well based on the technical solutions that are current used in the practice. The main simplifications that were adopted in the numerical model are as follows:

- The anchorage devices (e.g. those used for the connection between columns from different floors, respectively between columns and foundation) have sufficient capacity;
- The timber decks have sufficient stiffness for working as rigid diaphragms, and consequently for transmitting the seismic forces to the perimeter lateral load resisting system;
- Torsional effects are not considered;
- While the case study buildings are modeled as 3D structures, the nonlinear static and dynamic analyses are performed only on the X-orthogonal direction (plane frame analysis);
- The investigated structures are characterized by a 5% damping coefficient, as within EN 1998-1 [2];
- The LTFWs transfer the lateral forces (i.e. from one floor to another) - through their capacity to resist in-plane shear forces.

Even though the connection between two timber columns cannot be realized as full-rigid, and the actual stiffness of the connection should be included within the numerical model – the

first simplification was considered to be conservative. Indeed, by introducing in the structural model – the actual stiffness of the connection between timber columns, the fundamental period of the structure would increase and the seismic demand would decrease.

With regard to the LTFWs that are part of the perimeter lateral load resisting systems, as it can be observed in Figure 4 – these were modeled through multi-linear plastic link elements – as within [11]. The input (in terms of force-deformation curve) for the different LTFWs was defined based on the cyclic experimental investigations described in Section 2. In particular, an envelope curve was constructed corresponding to the first, second and third force-deformation cycle (see Figure 5a for TW and Figure 5c for EW). Additionally, an average envelope curve was computed corresponding to each loading direction (i.e. positive and negative – see Figure 5b for TW and Figure 5d for EW). From the average positive / negative envelope curve, the least favorable (i.e. with lower capacity / ductility) was used to define the input for the multi-linear plastic link elements.

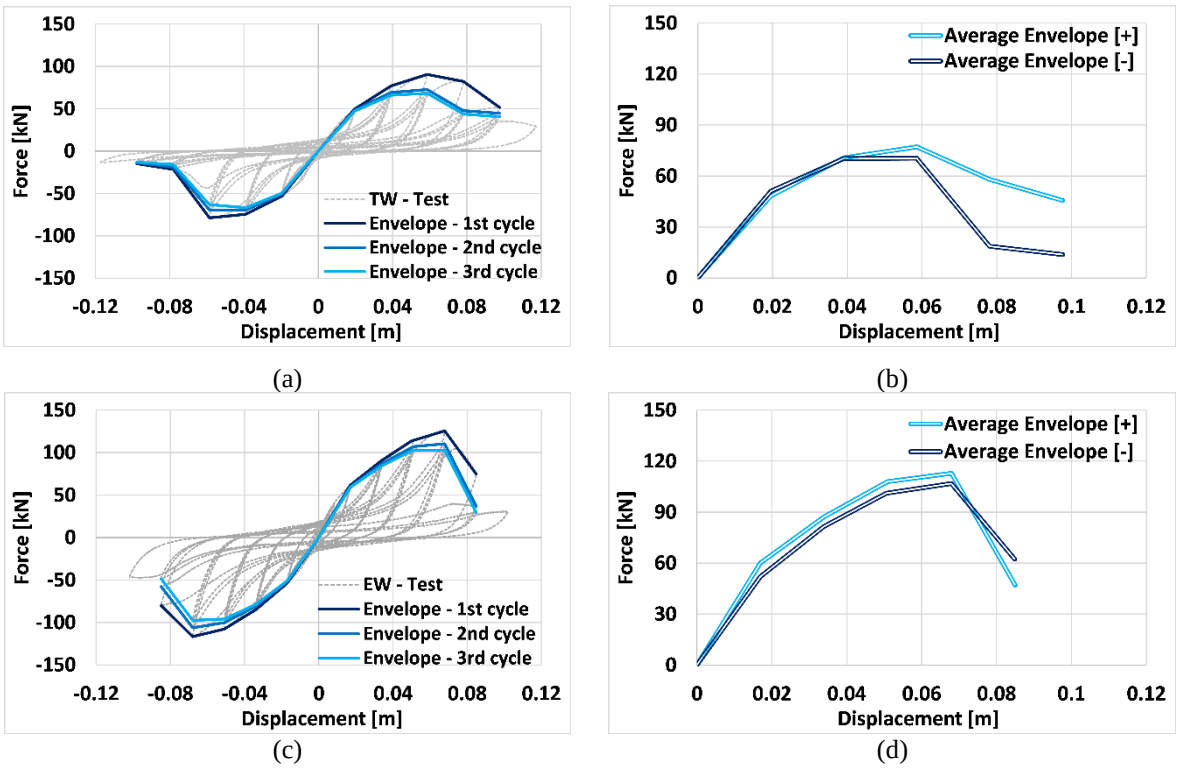


Figure 5: Envelope curves for the 1st, 2nd and 3rd "force-deformation" cycle and average envelope curves corresponding to: (a)-(b) typical wall (TW); (c)-(d) enhanced wall (EW)

A summary of the input for the multi-linear plastic link elements corresponding to the TW and EW is presented in Table 5. In particular the hysteretic behavior of the link elements was defined by a force-displacement curve and by a set of parameters for the "pivot" hysteresis. It is to be noted that the force-displacement curves within Table 5 characterize one link element, which means that the deformation and force correspond to the direction of the link (i.e. the diagonal of the LTFW panel).

In order to validate the input for the multi-linear plastic link elements summarized in Table 5, a simplified numerical model was developed in SAP2000 [12] for both typical and enhanced LTFWs (see Figure 6a). Two link elements were used for each LTFW with the input in Table 5. Pinned connections were used at the base of the panel as well as between timber studs and rails. Furthermore, a "pushover" analysis was performed considering the deformation

pattern illustrated in Figure 6a, i.e.: (i) displacement to the right (approx. +0.06 m); (ii) displacement to the left (approx. -0.16 m); (iii) displacement to the right (approx. +0.18 m). The outcomes (in terms of force-displacement curves) of these numerical investigations were compared to the experimental response of the LTFWs under cyclic loading (see the comparison in Figure 6b corresponding to the TW, and in Figure 6c corresponding to the EW). As it can be observed, the input for the multi-linear plastic link elements (i.e. force-deformation curve and parameters for the pivot hysteresis) from Table 5 – lead to a similar hysteretic response of the LTFWs as the one obtained experimentally. Some minor differences can be observed in terms of capacity; nevertheless, these originate from the use of an average envelope curve and from the selection of the most detrimental of the "+/-" average envelope curves.

| TW - LTFW | | | EW - LTFW | | |
|---|---|---|---|---|---|
| Displacement [m] | Force [kN] | Pivot hysteresis parameters | Displacement [m] | Force [kN] | Pivot hysteresis parameters |
| -0.042 | -15.4 | $\alpha_1$=100 | -0.037 | -69.6 | $\alpha_1$=100 |
| -0.034 | -20.9 | $\alpha_2$=100 | -0.030 | -119.4 | $\alpha_2$=100 |
| -0.026 | -78.8 | $\beta_1$=0.15 | -0.022 | -113.1 | $\beta_1$=0.2 |
| -0.017 | -78.5 | $\beta_2$=0.15 | -0.015 | -91.2 | $\beta_2$=0.2 |
| -0.009 | -57.2 | $\eta$=0.2 | -0.007 | -58.3 | $\eta$=0.2 |
| 0 | 0 | | 0 | 0 | |
| 0.009 | 57.2 | | 0.007 | 58.3 | |
| 0.017 | 78.5 | | 0.015 | 91.2 | |
| 0.026 | 78.8 | | 0.022 | 113.1 | |
| 0.034 | 20.9 | | 0.030 | 119.4 | |
| 0.042 | 15.4 | | 0.037 | 69.6 | |

Table 5: Input for multi-linear plastic link elements – force-displacement curve & "pivot" hysteresis parameters

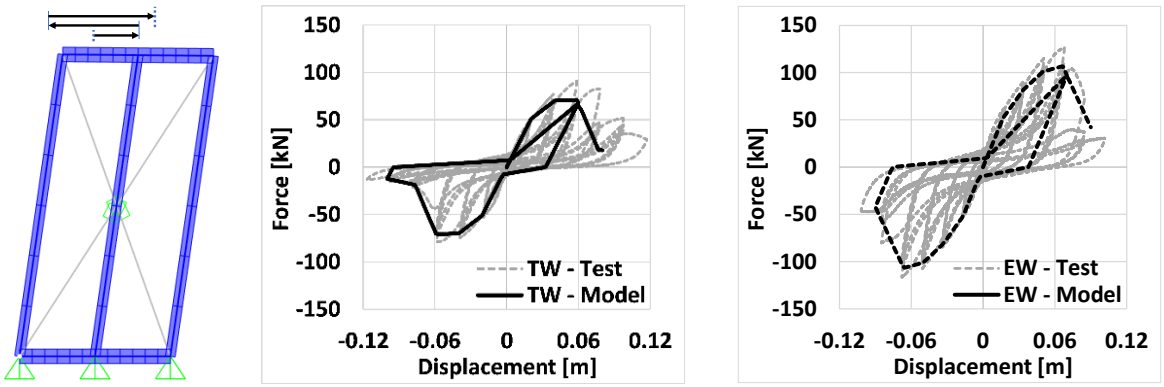


(a) (b) (c)

Figure 6: (a) Numerical model of a LTFW with "loading pattern"; (b) response of FEA model for TW; (c) response of FEA model for EW.

### 3.2 Nonlinear static analysis (Pushover + N2)

The first step for the seismic performance evaluation of the [TW+EW] case study building – was represented by the nonlinear static analysis (pushover - PO) and evaluation of the target displacements with the N2 method [13]. The 3D structural model (see Figure 4 and Section 3.1.2), together with the input for link elements (see Table 5) was used for this purpose. Under a constant gravity load (i.e. from the seismic combination), the structure was laterally loaded (i.e. displacement control at the top floor up to 0.211 m) – considering a modal distribution of the lateral forces. Consequently, the main outcome of the nonlinear static analysis was represented by the capacity curve illustrated in Figure 7a. It is to be noted that the analysis was

performed on the 3D structural model but considering only the X-direction. As the structural configuration is symmetric, the response on the Y-direction would be identical. Furthermore, the capacity curve in Figure 7a characterizes the response of two perimeter lateral load resisting structures. The capacity curve and the N2 method [13] allowed to determine the target displacements corresponding to the following limit states (LS): (i) damage limitation (DL); significant damage (SD); near collapse (NC). The obtained target displacements are reported in Table 6 and marked on the capacity curve from Figure 7a. The response of the perimeter lateral load resisting structure corresponding to each of the three limit states is also shown in terms of: (i) inter-story drift (see Figure 7b); (ii) deformed shape (see Figure 7c-e).

| Limit States (LS) | Return period | Performance factors | Target displacements |
|---|---|---|---|
| Damage Limitation (DL) | 60 years | 0.5 | $D_{t,DL}$ = 0.060 m |
| Significant Damage (SD) | 475 years | 1.0 | $D_{t,SD}$ = 0.119 m |
| Near Collapse (NC) | 1600 years | 1.5 | $D_{t,NC}$ = 0.179 m |

Table 6: Limit states, corresponding scaling factors for the seismic input and target displacements for computed for the [TW/EW] case study building

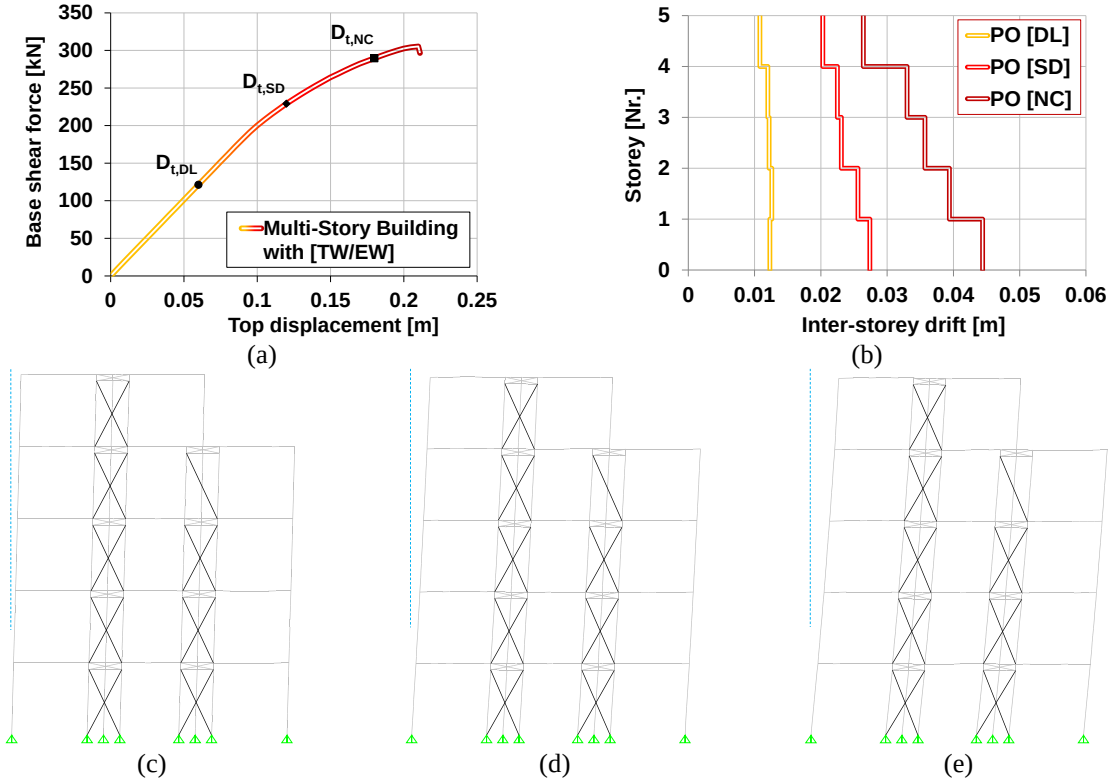


Figure 7: Outcomes of the nonlinear static analysis on the case study building with [TW/EW]: (a) capacity curve with marked target displacements; (b) inter-story drifts at DL / SD / NC limit states; (c) / (d) / (e) deformed shape of the perimeter lateral load resisting structure with [TW/EW] at DL / SD / NC limit states

Based on the outcomes of the nonlinear static analysis with N2 method (i.e. capacity curve, target displacements and inter-story drifts at the three limit states), and the comparison with the experimental outcomes (see Figure 5), the following were observed:

- at DL limit state: the response of the structure was in the elastic range – as confirmed by the computed target displacement (see $D_{t,DL}$ on the capacity curve in Figure 7a), and the maximum inter-story drift value (i.e. 0.012 m);

- at SD limit state: the response of the structure was in the nonlinear range – with relatively low but nevertheless plastic deformations occurring at each story except at the 5th floor; the maximum inter-story drift (i.e. 0.027 m) occurred at the ground floor, while at the upper stories the drifts slightly decreased in intensity;
- at NC limit state: the response of the structure was completely in the nonlinear range – with significant plastic deformation and energy dissipation at each floor; the inter-story drifts ranged between 0.026 m at the 5th floor and 0.044 m at the 1st floor; despite the over-all significant plastic deformations and a slightly higher inter-story drift at the 1st floor – the partial or total collapse of the structure was not evidenced.

Based on the pushover analysis and the above observations (DL / SD / NC limit states) – the seismic performance of the investigated case study building was found to be adequate.

### 3.3 Nonlinear dynamic analysis (RHA – response history analysis)

For the nonlinear dynamic analyses, a set of seven artificial accelerograms (see Table 7) were chosen from the ESM ground motion database [14] [15]. A tolerance of 30% was imposed to the ratio between the pseudo-acceleration spectrum of the accelerograms and the target spectrum. Based on the modal analysis, the investigated structure was characterized by a fundamental period of vibration in amount of $T_1 = 1.475\ sec$.

| #A | ESM ID | Date | Earthquake Name | Event ID | Magnitude | Sc. Fact. |
|---|---|---|---|---|---|---|
| 1 | EU.ULA-HNN.D | 1979-04-15 | Montenegro | ME-1979-0003 | 6.9 | 1.03 |
| 2 | HI.KAL1-HN2.D | 1986-09-13 | Southern Greece | GR-1986-0006 | 5.9 | 0.80 |
| 3 | IT.NRC-HGE.D | 2016-10-26 | Central Italy | EMSC-20161026_77 | 5.4 | 1.10 |
| 4 | IT.CSC-HGN.D | 2016-10-30 | Central Italy | EMSC-20161030_29 | 6.5 | 1.85 |
| 5 | IT.PCB-HGE.D | 2017-01-18 | Central Italy | EMSC-20170118_37 | 5.4 | 1.95 |
| 6 | IT.TLN-HGE.D | 2016-10-30 | Central Italy | EMSC-20161030_29 | 6.5 | 2.60 |
| 7 | TK.1607-HNN.D | 2006-10-24 | Turkey | TK-2006-0107 | 4.8 | 2.60 |

Table 7: Recorded acceleration time histories used for dynamic analyses [14] [15]

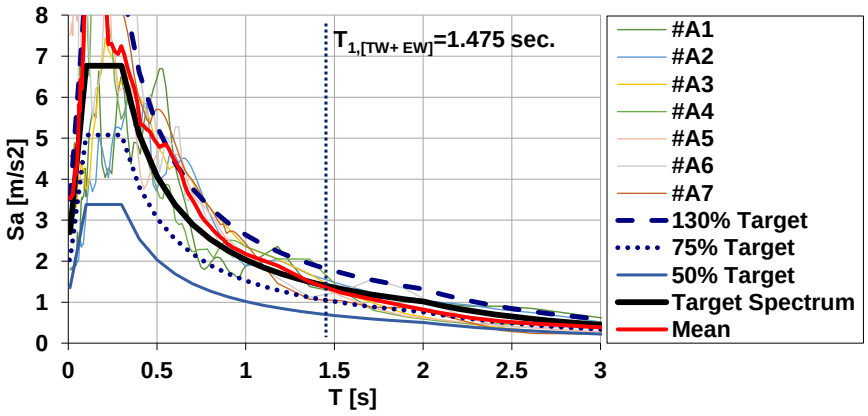


Figure 8: Elastic response spectra of mean and individual accelerograms compared to the target spectrum

The nonlinear dynamic analysis (or response history analysis - RHA) was performed on the X-direction only. In order to evaluate the dynamic response and the seismic performance of the case study building with [TW/EW], the following parameters were monitored corresponding to the three limit states (DL / SD / NC) and the seven accelerograms: (i) displacement at the top floor vs. time; (ii) force-deformation within each LTFW; (iii) inter-story drifts. An overview of the structural response, corresponding to the most demanding accelerogram (i.e. Acc.#2) and to the three limit states, is illustrated in Figure 9.

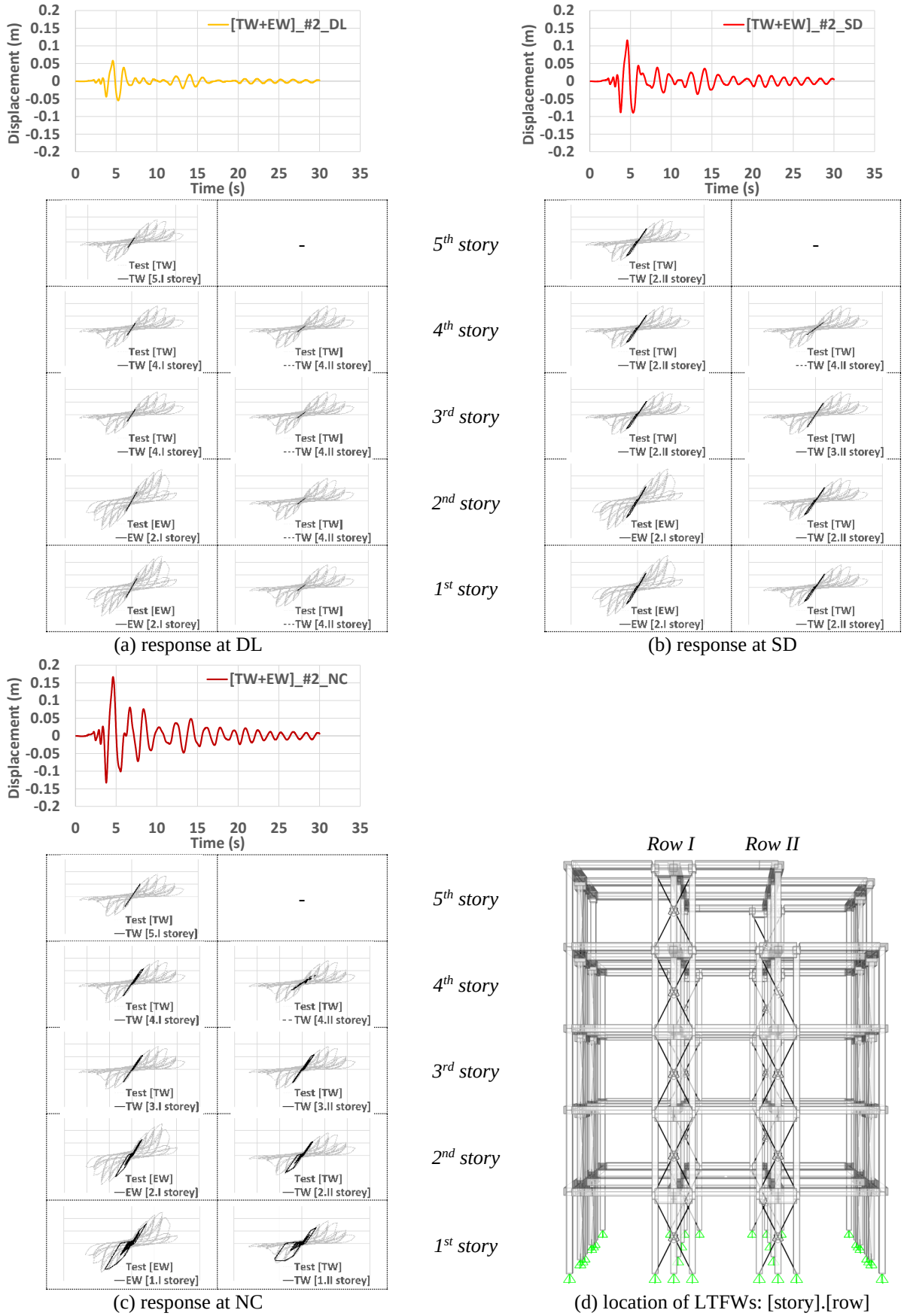


(a) response at DL

(b) response at SD

(c) response at NC

(d) location of LTFWs: [story].[row]

Figure 9: RHA outcomes (i.e. top displacement vs. time, force-deformation of LTFWs) corresponding to Acc.#2

Additional to the outcomes in Figure 9, the response of the case study building with [TW/EW] is also illustrated in terms of inter-story drifts computed as: (i) min. / max. drifts from Acc.#2 (see Figure 10a); (ii) average of the min. / max. from the 7-selected accelerograms (see Figure 10a). As can be observed, for each of the three limit states – the average inter-story drifts are lower compared to the min. / max drifts resulted from accelerogram #2.

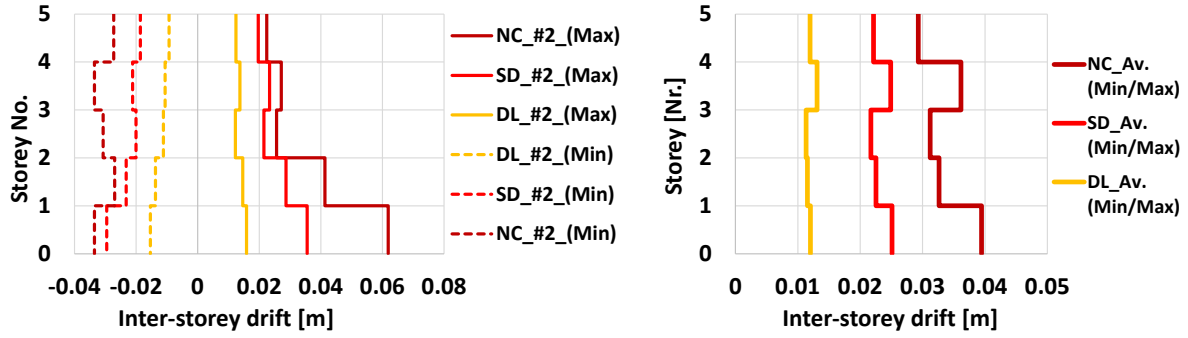


(a) (b)

Figure 10: Inter-story drifts for the case study building with [TW/EW] computed as: (a) min. / max. from Acc.#2; (b) average of the min. / max. from the 7-selected accelerograms.

Based on the outcomes of the nonlinear dynamic analysis (i.e. displacements at the top floor, force-deformation response of the LTFWs, and inter-story drifts – see Figure 9 and Figure 10), and the comparison with the experimental outcomes (see Figure 5), the following were observed:

- at DL limit state: the response of the structure was in the elastic range – as confirmed by the force-deformation curves within TW and EW panels (see Figure 9a), and the maximum of the average inter-story drifts (i.e. 0.013 m – see Figure 10b);
- at SD limit state: the response of the structure was in the nonlinear range – with relatively low but nevertheless plastic deformations occurring at each story including the 5$^{th}$ floor (see Figure 9b); the maximum of the average inter-story drifts (i.e. 0.025 m) occurred at the 1$^{st}$ and 3$^{rd}$ floor, while at the other three stories the drifts were slightly lower – and therefore a relative uniform distribution of deformations was evidenced – as for DL;
- at NC limit state: the response of the structure was completely in the nonlinear range – with significant plastic deformation and energy dissipation at each floor (see Figure 9c and Figure 10b); the average inter-story drifts ranged between 0.029 m at the 5$^{th}$ floor and 0.039 m at the 1$^{st}$ floor (see Figure 10b); despite the overall significant plastic deformations and a slightly higher inter-story drift at the 1$^{st}$ floor (see Figure 9c and Figure 10a corresponding to Acc.#2) – the partial or total collapse of the structure was not evidenced.

Based on the RHA and the above observations (i.e. response at the DL / SD / NC limit states) – the seismic performance of the investigated case study building with LTFWs was found to be adequate.

### 3.4 Comparison of nonlinear static and dynamic results

For the investigated case study building with LTFWs, a brief comparison was performed – for each of the three limit states – between the nonlinear static and nonlinear dynamic analyses in terms of the following:

- Displacement at the top floor (see Table 8);
- Inter-story drifts (see Figure 11).

As can be observed in Table 8, the outcomes of the nonlinear static analysis are conservative – with values of the displacement at the top floor that are closer to the values from the most

demanding accelerogram (Acc. #2). The average values of the displacement at the top floor (i.e. from the RHA), were approximately 13% lower compared to the target displacements obtained with the capacity curve and the N2 method [13].

Regarding inter-story drifts, differences between the nonlinear static and dynamic analyses – were observed in terms of both values and pattern. As can be observed in Figure 11, while for the pushover analysis the highest drifts occur at the lower floors, in case of the RHA a relative uniform distribution of drifts was evidenced – with maximum values corresponding to the 1st and 4th floor.

| Limit States (LS) | Pushover | Response History Analysis (RHA) | |
|---|---|---|---|
| | Target displacements (at the top floor) | Maximum top displacements (i.e. from Acc. #2) | Average of maximum top displacements |
| Damage Limitation (DL) | $D_{t,DL}$ = 0.060 m | $D_{RHA\#2,DL}$ = 0.058 m | $D_{RHA\text{-}avg,DL}$ = 0.052 m |
| Significant Damage (SD) | $D_{t,SD}$ = 0.119 m | $D_{RHA\#2,SD}$ = 0.116 m | $D_{RHA\text{-}avg,SD}$ = 0.103 m |
| Near Collapse (NC) | $D_{t,NC}$ = 0.179 m | $D_{RHA\#2,NC}$ = 0.167 m | $D_{RHA\text{-}avg,NC}$ = 0.145 m |

Table 8: Comparison of the nonlinear static (pushover) and the nonlinear dynamic (RHA) analyses – in terms of displacement at the top floor

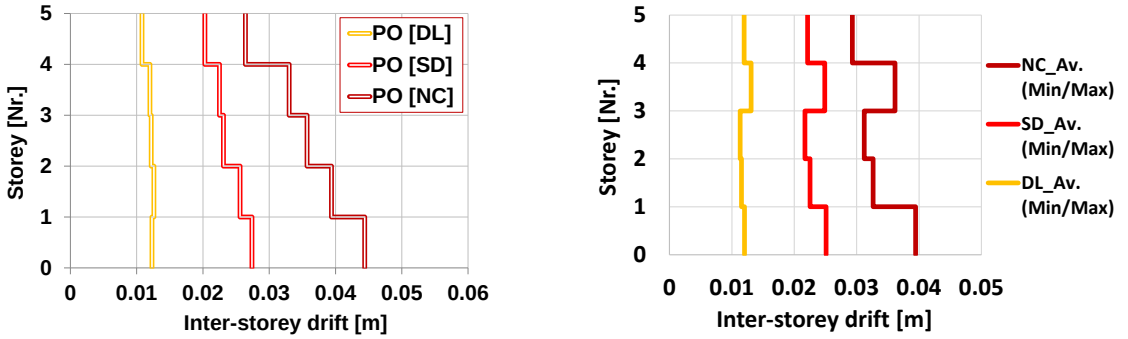


(a) (b)

Figure 11: Comparison of the (a) nonlinear static analysis and (b) nonlinear dynamic analysis in terms of inter-story drifts at DL / SD / NC limit states

### 3.5 Influence of GFB on the "nonlinear response" of the multi-story building

One of the main objectives of the current study was to investigate the influence of the gypsum fireboard (GFB) on the nonlinear static and nonlinear dynamic response of the case study building with LTFWs. Based on the experimental outcomes of the LTFWs with GFB (see Section 2), the effect of the gypsum fireboard panels was filtered and inserted within the structural model (i.e. corresponding to each TW and EW – see Figure 12a) as a multi-linear plastic link element. The influence of the GFBs on the structural response, was evaluated in terms of the following:

- Fundamental period of vibration;
- Capacity curve (see Figure 12b);
- Reaction force (i.e. tension force in the connection between LTFWs and foundation – see Table 9);
- Displacement at the top floor corresponding to the DL / SD / NC seismic intensity – as resulted from the nonlinear dynamic analysis using the most demanding accelerogram (i.e. Acc. #2 – see Figure 13).

Based on the outcomes of the modal analysis, the following periods of vibration were obtained: $T_{1,[TW/EW]}$=1.475 seconds; $T_{1,[TW/EW+GFB]=}$1.189 seconds. The use of GFBs lead to a stiffening effect and therefore to a reduction of the fundamental period of vibration.

The influence of the GFBs was observed to be significant also corresponding to the other monitored indicators. In terms of capacity curve and target displacements, as can be observed in Figure 12b, the use of GFBs lead to an increase of the stiffness and capacity, as well as to a reduction of the target displacements.

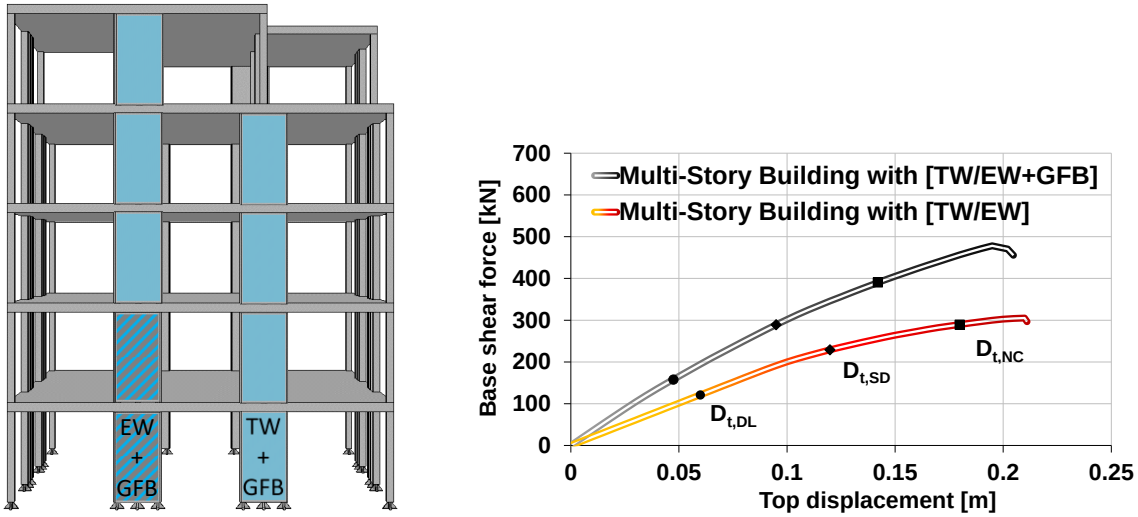


(a) (b)

Figure 12: (a) Case study building with fire protected LTFWs [TW/EW+GFB]; (b) Influence of the gypsum fireboard (GFB) on the nonlinear static response (i.e. capacity curve).

With regard to the reaction forces corresponding to the LTFWs with GFBs, as summarized in Table 9 – corresponding to the nonlinear static analysis and to the SD limit state – it was observed that reaction forces (e.g. the tension forces within the connections between LTFWs and foundations) increased. For the current case study, the reaction forces increased with more than 26%, which can be explained by the fact that the demand increased with approximately 32% (i.e. the spectral acceleration corresponding to $T_{1,[TW/EW]}$=1.475 sec. was 1.55 m/s$^2$, while the spectral acceleration corresponding to $T_{1,[TW/EW+GFB]=}$1.189 sec. was 2.046 m/s$^2$).

| LTFWs without cladding | | LTFWs with GFB cladding | | Increase factor |
|---|---|---|---|---|
| RF from PO at $D_{t,SD}$=0.119 m | | RF from PO at $D_{t,SD}$=0.095 m | | $RF_{w/o}/RF_{GFB}$ |
| [TW] | 106 kN | [TW+GFB] | 154 kN | 45% |
| [EW] | 218 kN | [EW+GFB] | 275 kN | 26% |

Table 9: Influence of the gypsum fireboard (GFB) on the reaction forces (RF)

Regarding the influence on the dynamic response, as can be observed in Figure 13, the use of GFBs lead to a decrease of the period of vibration, as well as to a reduction of the displacements at the top floor – corresponding to each of the three limit states. These two observations were also confirmed by the modal analysis (i.e. lower fundamental period of vibration) and the nonlinear static analysis combined with the N2 method (i.e. lower values for the computed target displacements).

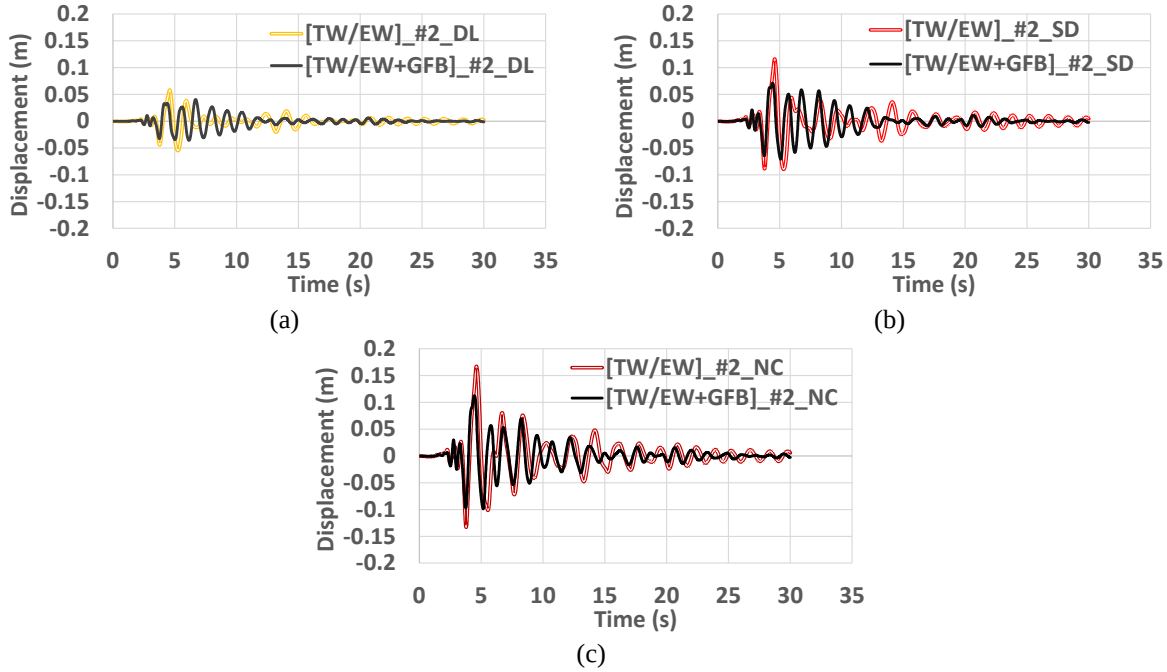


Figure 13: Influence of the gypsum fireboard (GFB) on the nonlinear dynamic response (top displacement vs. time) corresponding to – (a) DL, (b) SD, (c) NC – seismic intensity.

## 4 CONCLUSIONS

The objective of this contribution was to evaluate the safety of neglecting fire protection cladding in seismic design. For this purpose, the following aspects were presented: (i) overall experimental results of tested light timber frame walls (LTFWs) without and with additional GFB cladding; (ii) numerical model of a 3D reference structure in SAP2000 and modelling parameters of the used link elements representing the LTFWs; (iii) outcomes of the nonlinear static/dynamic analyses for both structure configurations (i.e. without and with cladding).

From the presented experimental investigations on typical walls (TW), enhanced walls (EW) and cladded walls (CW) the following could be concluded: (i) the EW were characterized by an increase of the load-bearing capacity in comparison with the TW (i.e. by 38%); (ii) the CW were characterized by an increase of the load-bearing capacity in comparison with the TW (i.e. by 109%). The initial stiffness was doubled (i.e. increase of 102%). The increase in stiffness and load-bearing capacity is mainly related to the doubling of the shear planes (i.e. number of fasteners) between sheathing and frame, but also, to the additional diaphragm action of the GFB cladding.

Basic “multi-linear plastic” link elements were presented for modeling the hysteretic behavior of LTFWs. These link elements were calibrated and validated with the presented test results for each wall configuration (i.e. TW / EW / CW) on wall level. The calibrated wall models were used as part of the lateral load resisting structure on a 5-storey case study building – modeled and analyzed with SAP2000 [12]. Numerical investigations (i.e. nonlinear static and dynamic analyses) were performed with the aim to evaluate the seismic performance of the case study buildings.

Based on the outcomes of the nonlinear static (pushover) analysis in combination with the N2 method - the seismic performance of the case study building was found to be adequate (i.e. satisfied DL / SD / NC limit states). Furthermore, the seismic performance was confirmed also by the outcomes of the nonlinear dynamic analysis (RHA). In particular, the average values of

the displacements at the top floor and the inter-story drifts were slightly lower compared to the outcomes of the nonlinear static analysis. The response at DL limit state was in the elastic range, while corresponding to SD and NC limit states – the structure responded in the nonlinear domain: (i) at SD seismic intensity – only with minor plastic deformations corresponding to the LTFWs; (ii) at NC seismic intensity – with significant plastic deformations mainly corresponding to the 1st and 2nd floors, but without any partial or total collapse of the structure.

For investigating the influence of GFBs, the case study building was adapted by additional multi-linear plastic link elements representing the GFB cladding. The following was observed within the comparison of the structures without and with additional GFB elements – based on the nonlinear static and dynamic analyses:

- The cladding decreased the fundamental period of the case study building to 1.189 seconds compared to the 1.475 seconds corresponding to the building without cladding;
- The response of the structure (i.e. in terms of base shear force) was increased by the GFB cladding;
- The top displacement was decreased by the presence of the GFB cladding;
- The total capacity reserves of the LTFWs was increased by the cladding;
- The decisive reaction forces increased by a minimum of 26%.

The results of the presented investigations are of interest in two respects: (i) economic efficiency and (ii) safe-sided seismic design.

The unused enhancement of the load-bearing behavior by claddings in the structural design is not resource efficient, as the full capacity is not utilized. By adding the effects in the design process, timber frame buildings could become more economic and architectonically sophisticated – as fewer stiffening walls are required.

Capacity design of brittle components (e.g. anchorages) with use of sufficient overstrength factors is key to safe seismic design. This contribution shows, that a neglection of fire protective cladding would lead to a non “safe sided” capacity design of the anchorage for the presented case study building. Considering the fire protection cladding in seismic design is therefore not only recommended, but also classified as relevant for safety.

Further, more elaborate studies should be carried out with regard to the influence of cladding on the seismic performance of multi-story timber buildings. Overstrength factors for cladded LTFWs should be elaborated for practice. An adaption of the design provisions of *Eurocode 5* and *Eurocode 8* with regard to cladding is proposed.

## ACKNOWLEDGEMENTS

The authors gratefully acknowledge the financial support of the ZIM research project *HOLZBEBEN* by the BMWI and the FNR research project *HELEPOLIS* funded by BMEL. We are also grateful for the cooperation with the project partners Walter • Reif Ingenieurgesellschaft mbH and Adams Holzbau-Fertigbau GmbH.

## REFERENCES

[1] EN 1995-1-1. *Eurocode 5: Design of timber structures - Part 1-1: General – Common rules and rules for buildings*, 2004.

[2] EN 1998-1. *Eurocode 8: Design of structures for earthquake resistance - Part 1: General rules, seismic actions and rules for buildings*, 2009.

[3] V. Wilden, B. Hoffmeister: Experimental analyses of innovative wood-shear walls under seismic loads. *IABSE Congress - Resilient Technologies for sustainable infra-structure*, Christchurch, New Zealand, pages 1222-1229, 3-5 February, 2021.

[4] M. Schick, T. Vogt, W. Seim. Connections and anchoring for wall and slab elements in seismic design. *CIB-W18/46-15-4*, 2013.

[5] V. Wilden, G. Balaskas, B. Hoffmeister, L. Rauber, B. Walter, High performance light timber shear walls and dissipative anchors for damage limitation of wooden buildings in seismic areas. *Current Perspectives and New Directions in Mechanics, Modelling and Design of Structural Systems*, pages 1713-1719, 2022.

[6] G. Balaskas, V. Wilden, B. Hoffmeister, Experimental numerical investigation of innovative ductile and replaceable anchoring systems for wood shear walls under seismic loads. *COMPDYN 2021 - Computational Methods in Structural Dynamics and Earthquake Engineering*, Athens, Greece, 27-30 June, 2021.

[7] L. Rauber, V. Wilden, B. Hoffmeister. Untersuchung zum Einfluss von Brandschutzbekleidungen auf das Tragverhalten von Holztafelwänden. *Doktorandenkolloquium Holzbau Forschung + Praxis*, Stuttgart, 10-11 March, 2022.

[8] B. Dujic, S. Aicher, R. Zarnič. Investigations on in-plane loaded wooden elements – influence of loading and boundary conditions. *Otto-Graf-Journal Vol. 16*, 2005.

[9] ISO 21581. *Timber structures - Static and cyclic lateral load test methods for shear walls*, 2010.

[10] DIN EN 1998-1/NA. *National Annex – Nationally determined parameters – Eurocode 8: Design of structures for earthquake resistance – Part 1: General rules, seismic actions and rules for buildings*, 2021.

[11] G. Rinaldin, Hervé Poh'sié, C. Amadio, M. Fragiacomo. Modelling of seismic behaviour of light-frame timber structures. *Ingegneria Sismica 30(4):82-98*, 2013.

[12] CSI Berkley, SAP2000 v21, Copyright Computers and Structures, 2019.

[13] P. Fajfar. A nonlinear analysis method for performance-based seismic design, *Earthquake Spectra*, 16(3):573-92, 2000.

[14] Luzi L, Puglia R, Russo E & ORFEUS WG5. Engineering Strong Motion Database. Istituto Nazionale di Geofisica e Vulcanologia, Observatories & Research Facilities for European Seismology. doi: 10.13127/ESM, 2016.

[15] Working Group ESM. *European strong motion database*, http://esm.mi.ingv.it, 2015.

COMPDYN 2023
9th ECCOMAS Thematic Conference on
Computational Methods in Structural Dynamics and Earthquake Engineering
M. Papadrakakis, M. Fragiadakis (eds.)
Athens, Greece, 12-14 June 2023

# AN INSIGHT ON THE ROLE OF THE DESIGN PROCEDURES ON DAMAGE TOLERANCE AND COST OF CLT BUILDINGS IN SEISMIC AREAS

**Antonio Sandoli**[1], **Bruno Calderoni**[2], **Carla Ceraldi**[2], **and Giovanni Fabbrocino**[1,3]

[1] University of Molise, Dept. of Biosciences and Territory
via Francesco De Sanctis 1, 86100, Campobasso, Italy
{antonio.sandoli, giovanni.fabbrocino}@unimol.it

[2] University of Naples Federico II, Dept. of Structures for Engineering and Architecture
via Claudio 21, 80125, Naples, Italy
{calderon, ceraldi}@unina.it

[3] Institute for Construction Technologies, National research Council of Italy
Secondary branch of L'Aquila, 67100, L'Aquila, Italy, 80125, Naples, Italy
fabbrocino@itc.cnr.it

## Abstract

*Physical characteristics of timber as a construction material offer a high-performance option for the design and erection of buildings in seismic-prone area. Massive Cross-Laminated Timber (CLT) buildings represent a vehicle to increase the building sustainability and a robust workaround to heavyweight constructions.*
*This paper is intended as a contribution in the reviewing the most common design procedures for the seismic design of CLT buildings and their implications on structural features and technological solutions, focusing the attention particularly on overall seismic performance, damage tolerance, construction costs and environmental impact. As a starting point of a more comprehensive study, the assessment is made with reference to a real building, which is representative of a wide class of buildings recently designed and erected in many Italian regions exposed to low and moderate seismic hazard. As a common reference, the analysis has been carried out according to a two-dimensional model of the panels, assumed to be elastic, varying the type of connections at the base, the presence of pre-stressing steel bars for rocking control and of dissipative devices. The main outcomes of the study can be summarized as follows: (i) the structural seismic behavior of CLT buildings is significantly influenced by the structural schemes adopted for walls and connections; (ii) construction costs and environmental impact decrease when enhanced design procedures are used.*

**Keywords:** CLT, Damage tolerance, Timber Buildings, Connections, Construction Costs, Sustainability in construction.

## 1 INTRODUCTION

Low and mid-rise Cross-Laminated Timber (CLT) buildings represent a valid alternative to traditional masonry or reinforced concrete buildings, both for residential and non-residential use [1, 2, 3]. In principle, the beneficial properties of the base material related to reduced weight, thermal insulation and its natural origin place timber buildings at very high levels of structural and seismic, energetic, and sustainability performances [4].

The rapid progression of these constructions on the market has been mainly boosted by the technology and production advances of the timber components and subassemblies; nevertheless, at International (European) level this process has not been complemented by a rational development and updating of the design, mainly seismic, codes. This circumstance is confirmed by the current form of the Eurocode 5 [5] and Eurocode 8 [6], which currently partially cover seismic design and are currently in a revision and enhancement phase [7, 8]. At a National (Italy), the Technical Document CNR DT-206/R1 2018 [9] can be addressed as one of the early technical documents defining a more comprehensive framework of seismic design rules for timber buildings coherent with the capacity design method [10]. Experimental and numerical studies proved that, for *traditional* CLT buildings, a rational design of the connections at panel-to-panel and panel-to-foundation interface is crucial to achieve satisfactory seismic response [11]. Herein, 'traditional' CLT buildings are those having connections made with hold-downs (HDs), bearing tensile forces due to moment demand, and angle-brackets (ABs) aimed at covering the shear demand. Those connections are designed according to Johansen's failure mechanisms under seismic-like actions, i.e. localized timber embedding combined with yielding of metal fasteners [12]. This circumstance points out the activation of permanent damage mechanisms allocated in the timber panels due to embedding of wood, as documented in Fig. 1, where typical failure mechanisms of HDs and ABs observed during experimental testing are shown. Due to timber damage, vertical timber panels result heavily damaged making their reparation impractical after an earthquake, so that the demolition of the building (or some its portions) results the most rational option entailing additional costs due to both demolition and reconstruction, recycle of materials and an environmental impact.

To overcome the problem of damaging of CLT walls, alternative connection systems have been proposed in literature for CLT buildings, the so-called *low damage* CLT buildings. A novel class of mechanical connections recalled the attention of the technical community [11, 13, 14]. They are conceived to concentrate the seismic damage in steel plates (or bars) only, protecting the vertical timber panel against permanent damage. Indeed, the concept of 'low-damaging' or better 'damage tolerance' for timber systems was firstly claimed in New Zealand referring to post-tensioned rocking timber walls [15]; they consist of self-centering rocking walls provided or not with additional plug and play dissipating systems at the base of the wall made with mild-steel buckling-restrained bars [16].




Figure 1: Typical damage in connections made with hold-downs and angle-brackets.

To obtain high-performant CLT buildings, a rational design approach devoted to optimizing and integrating the global performance of CLT buildings - in terms of seismic, economic and Life Cycle Assessment (LCA) - is needed (Fig 2). In this framework, structural solutions oriented towards damage control in structural components, and then costs reduction related to demolition of structural and non-structural components and improvement of the aspects influencing the LCA should be selected in engineering practice [1].

This paper presents an insight on the relationship between design criteria of the connecting systems and global performances of CLT buildings in seismic area by means of a comparative analysis of traditional and damage tolerant CLT buildings. This task is accomplished by means of the analysis of a real two-storey CLT school building, located in Northern of Italy, and its seismic design made varying the geometry of the walls and typology of connections. A comparative analysis of the different structural layouts has been then performed depending on the results of nonlinear static analyses (e.g., pushover).

So doing, some reflections on the relevance of optimized and integrated design procedures for CLT buildings are proposed, highlighting the major role of the connecting system design on the overall structural response of the buildings in terms of seismic capacity, ductility, damage control and tolerance, interaction with architectural and non-structural features, overall construction costs, and impact on the Lifecycle performance of the buildings.

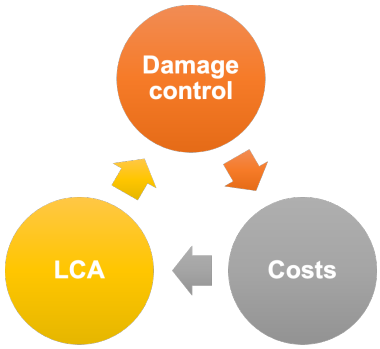


Figure 2: Optimized design approach for timber buildings.

## 2 ON THE DESIGN THE CONNECTIONS

In the context of the capacity design methodology, the design of the connections is severely ruled by the Strength Hierarchy (SH) criterion established among the components present in panel-to-panel and panel-to-foundation contact zone [8].

To date, National and International codes [5, 6] and guidelines [9] refer to a single type of dissipative mechanisms – those required for the traditional CLT buildings - based on the Johansen's theory. For such an approach (identified as Approach A1 in the following) the non-dissipative elements are the HDs and ABs, while the dissipative ones are the timber-to-steel interactions characterized by a combination of timber embedding and cyclic yielding of steel metal fasteners (Table 1). Due to the cyclic nature and intensity of earthquakes, a high and permanent damage of timber panels in the connecting zones is accepted in the absence of detailed evaluations of the damage level of the timber panels. This may be the case of buildings located in high seismicity regions, where high levels of ground shaking may appear even at the Damage Limit States and high demand at the connection level may occur to activate the overall ductility required to survive at the Life Safety and Collapse limit states [17]. As a consequence, a relevant impact on the costs related to demolition and/or reconstruction of structural and non-structural component, recycle of materials, and sustainability of the construction seems to be intrinsically accepted.

As above discussed, alternative damage tolerant connections can represent an effective solution to reduce costs related to damage of structural components after an earthquake, although HS rules are not still included in the current standards. The seismic dissipation is concentrated into sacrificial 'plug and play' metallic elements which yields in tension or shear (bars, steel plates, etc.), while timber elements are non-dissipative and behaves elastically. As advantage, timber components are preserved to plastic damage after the seismic event and no costs related to demolition and/or reconstruction, recycle arise. This approach has been named as Approach A2 in Table 1.

Furthermore, problems related to damage tolerance of non-structural elements, forced to accommodate the inter-story drift of the seismic resistant-structure, can impact significantly on repair/reconstruction costs and on safety of peoples in the case of low-and high-intensity earthquakes [18]. In the following, some considerations on this issue are addressed.

| Type | Non dissipative element | Dissipative element | SH formulation |
|---|---|---|---|
| Approach A1 | Steel plates (HD/AB) | Timber-to-steel interaction | $N_{pl} \geq R_d \gamma_{Rd}$ |
| Approach A2 | Timber-to-steel interaction | Steel elements (bars, plates, etc.) | $R_d \geq N_{pl} \gamma_{Rd}$ |

$N_{pl}$ = plastic axial strength of the non-dissipative element - $R_d$ = maximum strength of the dissipative element - $\gamma_{Rd}$= over-strength factor of the connection

Table 1: Description of the Strength Hierarchy criteria.

## 3 METHODOLOGY

### 3.1 Description of the mockup building

The mockup building is a two-story CLT school building located in Northern of Italy (Fig. 3), whose structural project was available to the authors. The building belongs to the class of use III (as defined by IBC 2018 [19]). The real building is designed to be built in a low-intensity seismic zone, where a peak-ground acceleration on bed-rock is equal to $a_g$=0.081*g* at Life Safety (LS) limit state.

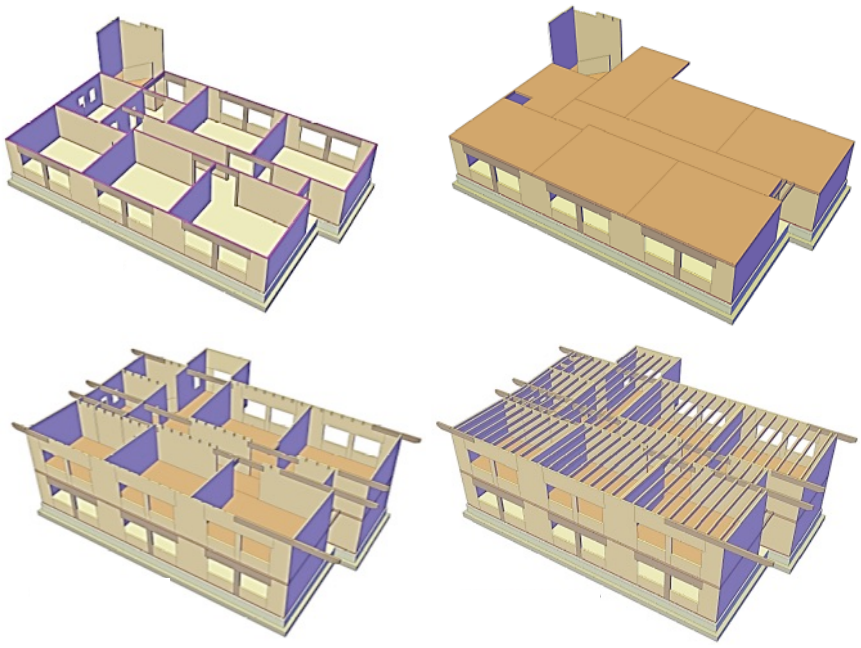

Figure 3: Views of the mockup CLT building.

The structure is made of 140 mm thick five-ply seismic-resistant CLT walls, where the thick of the two vertical external layers is equal to 40 mm and those internal (both in vertical and horizontal directions) are 20 mm thick. The strength class of CLT corresponds to solid wood class C24 derived according to ETA-14/0349 [20].

The construction technology follows the platform-type system, where vertical walls are interrupted at inter-story by horizontal CLT floors interposed between two consecutive vertical panels. The floors are composed by seven-layered CLT panels with strength class C24.

It is worth noting that the comparative analysis has no relation with the real design and erection of the building; indeed, available technical material has been used to refer to realistic building geometry, material properties, and live and dead loads. The arrangement of the walls herein addressed is the same provided by the real project and shown in Fig. 3, while different solutions have been adopted for the connections.

### 3.2 Test cases

To investigate the role of the design procedures on the seismic performances, damage and costs of CLT buildings, different structural schemes have been considered to model the CLT walls. Fig. 4 shows the four structural schemes adopted, divided in two main Groups: *a*) Group 1 (G1) includes Monolithic (M), Coupled (C), and Uncoupled (U) CLT walls, designed considering both Approach A1 and A2 listed in Table 1; *b*) Group 2 (G2) instead includes post-tensioned CLT walls only, characterized by a pure rocking behaviour only (i.e., without additional dissipaters at the base).

Coupling between the walls is assumed to be made of horizontal metal fasteners uniformly distributed along the vertical joints designed to behave elastically. Whereas the geometries of the walls, number of layers of CLT panels and number of the angle-brackets are the same in each scheme. Note that the vertical timber panels are not in direct contact with the reinforced concrete foundation, but it is interposed a horizontal timber beam between the vertical panel and the foundation involving orthogonal-to-grain timber to timber contact at the interface.

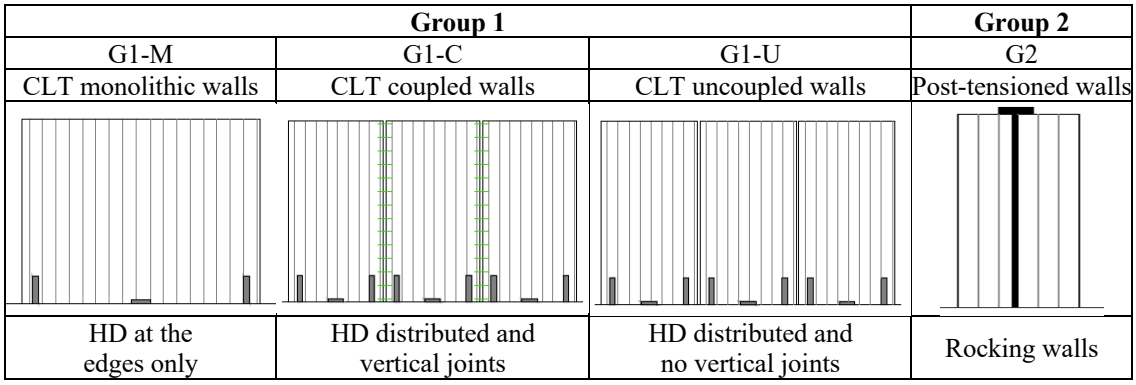


Figure 4: Schematic representation of geometry and connection arrangements of the investigated cases.

### 3.3 Design of the connections

For the cases belonging to the Group 1 (Fig. 4), panel-to-panel and panel-to-foundation mechanical connections have been designed considering both the approaches A1 and A2. In the case A2 the connections are supposed made with sacrificial dissipative steel elements, whose cross-section areas have been determined as the minimum area required by the flexural demand and which stratify the inequality $R_d > N_{pl}\,\gamma_{Rd}$.

Commercial HDs have been designed in the case of the approach A1 to bear the tensile forces induced by the moment demand and, consequently, the number of nails is determined

to satisfy the inequality $N_{pl} > R_d \gamma_{Rd}$.

The design of the connection for both approaches (A1 and A2) require the calculation of the moment and shear demand on each panel according to an iterative procedure [11]. In a first phase, an attempt value of the first vibration period - belonging to the constant branch of the design response spectrum - has been used to compute the equivalent horizontal seismic actions acting on the building. Those forces have been applied to the numerical model of the building (for the dir. X and Y, separately), which does not include the mechanical connections; this is the way the dimensions of the tensile and shear-resistant elements can be set depending of the moment and shear demand, respectively. In a second step, the same building has been modelled including panel-to-panel and panel-to-foundation connections to re-calculate the first vibration period: if the new period ranges in the constant branch of the response spectrum the design procedure of the first phase is accurate, otherwise a new attempt must be done by varying the period. Note that equivalent seismic actions have been determined by assuming a behavior factor q=2.0 in compliance with relevant design standards [6, 9].

Focusing on post-tensioned CLT walls (Group 2), no additional mild-steel components for energy dissipation are provided at the base of the panel, so that the response of the wall is dominated by the rocking motion. The design of post-tensioned walls (cross-section of the cable and its pre-stressing axial force) has been carried out the displacement-based approach after the New Zealand design guidelines [21].

### 3.4 Modelling of the wall-system

Modelling of CLT structures involves three different levels: *a*) CLT 'material', *b*) connecting zones, *c*) global structural scheme (floors, spandrels, etc.) [11, 22, 23]. Being out of the scope of this paper a detailed description of the modelling strategies and their effectiveness, the modelling criteria herein adopted in are summarized the following. The structural models have been developed with the software SAP 2000 v.18 [24].

With regards to CLT 'material', simplified methodologies suitable for macro-scale modelling of the CLT material are available in literature proving comparable results [1]. In this paper, the in-plane behaviour of the CLT panel has been modelled through homogenized orthotropic 2D-shell elements: the panel thick is equal to the actual one, while the elastic moduli of the base material are reduced as a function of the effective number of layers present in vertical and horizontal direction.

More sophisticated is the schematization of wall-to-wall and wall-to-foundation connection zones. Generally, they are modelled on analogy with the reinforced concrete cross-sections, assuming the HDs as the tensile-resistant elements, the ABs as shear-resistant elements and timber-to-timber and timber-to-concrete contact as the part devoted to resist to compression forces [1, 25]. In this study, the tensile-resistant elements have been schematized as provided with tensile resistance only and unable to resist to compression, moment and shear (i.e., pendulums); instead, the timber-to-timber (or timber-to-foundation) contact has been schematized with pendulums provided with compression resistance only. Whereas the angle brackets have been schematized with flexural and shear-resistant frame elements. Tensile-resistant and contact elements have been schematized with an elastic-perfectly plastic (axial) behaviour, whose maximum strength is defined according to the selected SH criterion ($R_d$ or $N_{pl}$ in the case of approach A1 and A2, respectively). Instead, the maximum axial displacement capacity of the tensile-resistant elements has been assumed variable and equal to the values $\varepsilon = 1\%$ and $\varepsilon = 2\%$. This strain range has been used to account for the uncertainties associated with the calibration of the threshold; this especially in case of HDs nailed to CLT panels where the length on which evaluate the axial strain is still of difficult evaluation [11]. The limit value of the axial

strain in orthogonal-to-grain direction of the compressed elements has been set equal to 5% [11, 22].

Vertical joints fasteners of the coupled walls have been modelled with elastic springs, linked to the nodes of the adjacent panels, and provided with shearing stiffness ($k_{ser}$) calculated according to Eurocode 5 [5].

The modeling of the post-tensioned walls is made by means shells characterized by the same constitutive relationships used to describe traditional CLT walls complemented with a prestressed element to simulate the vertical cable, whose primary role is to ensure the system recentering. Timber-to-foundation contact has been modelled with zero-length contact elements.

To reduce the computational efforts related to the dense mesh adopted to model the CLT panels, two separate models have been developed to analyze the structural behavior in the two orthogonal directions X and Y. For seismic analysis purposes, the CLT floors have been modelled as in-plane infinitely rigid diaphragms connected to the vertical walls. The flexural and shear contribution of the spandrels has been neglected, being simply supported to the adjacent walls [11]. Figs. 5 and 6 show the 2D-shell models of the buildings relative to the Group 1 and 2, respectively.

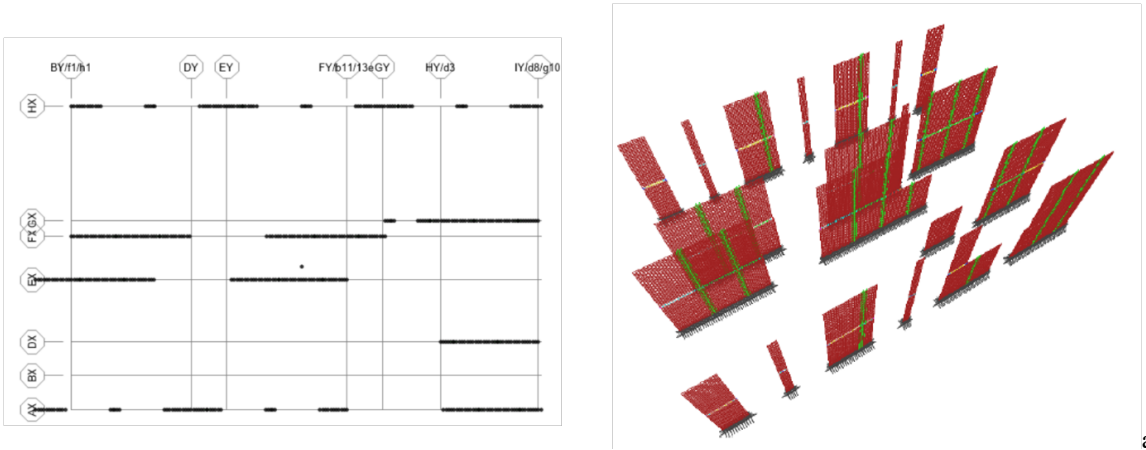


a)

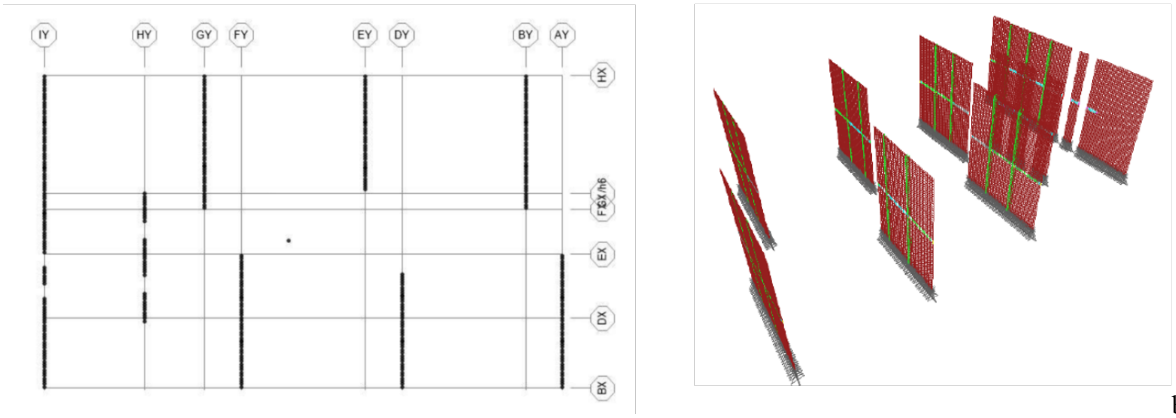


b)

Figure 5: Wall geometry and the structural model of the cases of the Group 1: a) direction X, b) direction Y.

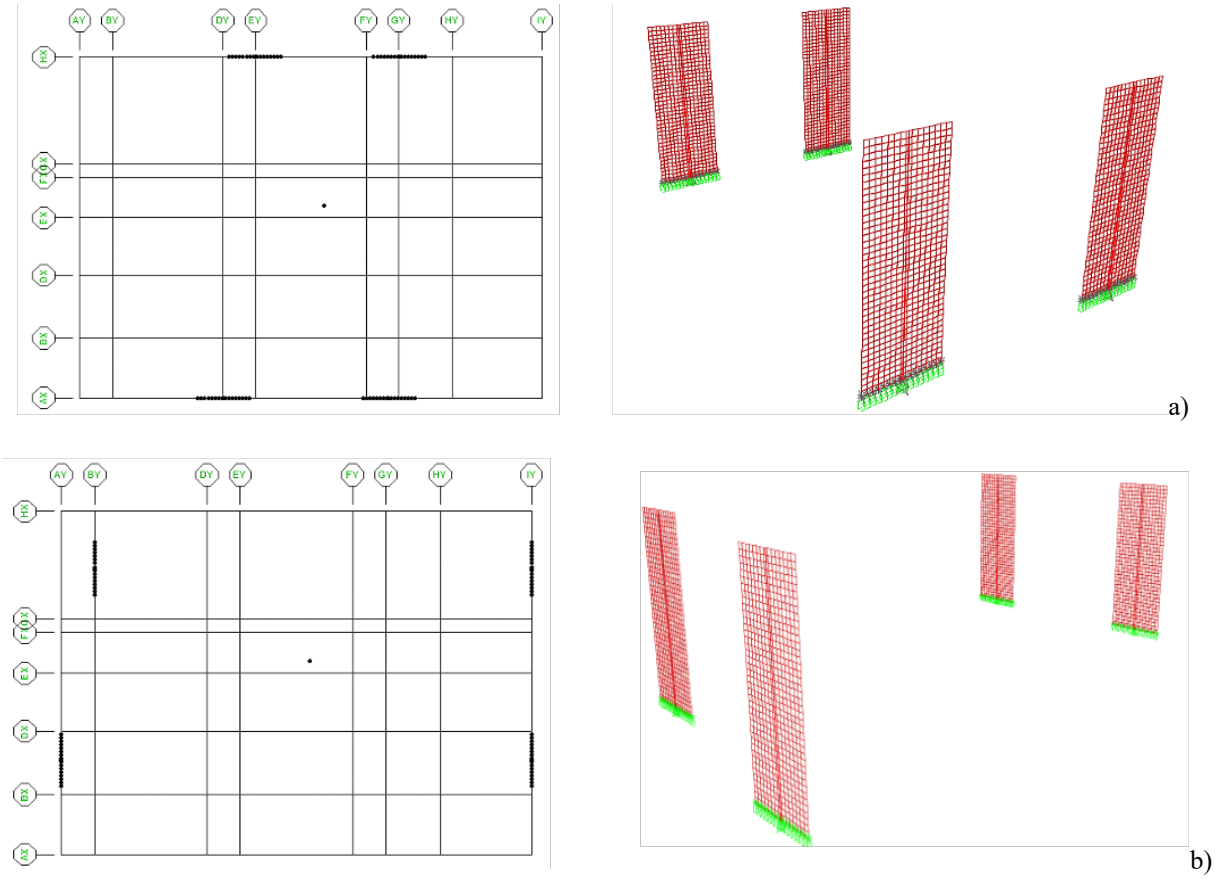


Figure 6: Position of the walls and view of the numerical model - Group 2: a) direction X, b) direction Y.

## 4 DISCUSSION OF RESULTS

### 4.1 Structural response

Figs. 7a and 7b report the pushover curves of the four analyzed numerical models described in Table 1 for the directions X and Y, separately. Moreover, the curves obtained with the two different values of axial strain of the tensile-resistant elements (ε= 1% and ε=2%) are reported for the sake of comparison.

The pushover curves point out some differences in terms of structural response of the system depending on the layout and performance of the connections. As a comparison between the two SH criteria, it is resulted that (*i*) the approach A2 involves higher post-elastic displacements than approach A1 (either for ε= 1% and ε=2%) and that (*ii*) the maximum base shear obtained in the case of the approach A1 is higher than those of the approach A2.

Both statement (*i*) and (*ii*) are due to the higher overstrength of the tensile-resistant element designed with approach A1 than approach A2. The higher overstrength of the approach A1 is due to the adoption of commercial cross-section for the HDs, while in the case of approach A2 the cross-section area of the tensile-resistant elements is calibrated to be equal to that strictly required by the moment demand. In particular, in the case (*i*) the overstrength of the tensile-resistant elements designed according to approach A1 address the failure mechanisms towards the crisis of compressed timber before that of the tensile-resistant element.

The overstrength resulted from the approach A1 with respect to A2 is accentuated in the cases of coupled walls, probably because of additional strength given by vertical joints in combination with overstrength of the base connections. Whereas this additional strength is not completely exploited in the case of approach A2, being the ultimate displacement of the walls

achieved with a plasticization in both tensile and compressed zone. With regards the influence of the ultimate axial strain (ε) of the cases belonging to Group 1 it is evident that, despite double values of ε, the displacement capacity of the walls does not increase proportionally. This is occurs as the failure mechanisms of the walls are ruled by the achievement of maximum axial strain of timber in compression zones which limit the overall displacement capacity of the walls.

As fa as the Group 2 is concerned, the pushover curves are the same in comparison with direction X and Y. This because the same number of walls (four) - and with the same cross-section area and pre-stressed forces - have been used in the two orthogonal directions X and Y (Fig. 6). Comparisons between the pushover curves of the Group 1 and 2 show that in the second case additional overstrength is avoided, because the walls are designed to achieve exactly the base shear demand at ULS. Contrariwise, the displacement capacity of post-tensioned system is significantly higher than that of the Group 1 because dissipating seismic energy through the rooking behavior of the walls, without plastic dissipation concentrated in few tensile-resistant elements. The overstrength generated from the design approaches A1 and A2 of the Group 1 are more evident by looking at Fig. 8, where the maximum seismic capacity bearable by the structure at LS limit state expressed in terms of PGA/g is evaluated according to N2 method [26]. From the structural point of view, post-tensioned systems are optimal because designed to satisfy the seismic demand without additional overstrength and with optimal displacement capacity.

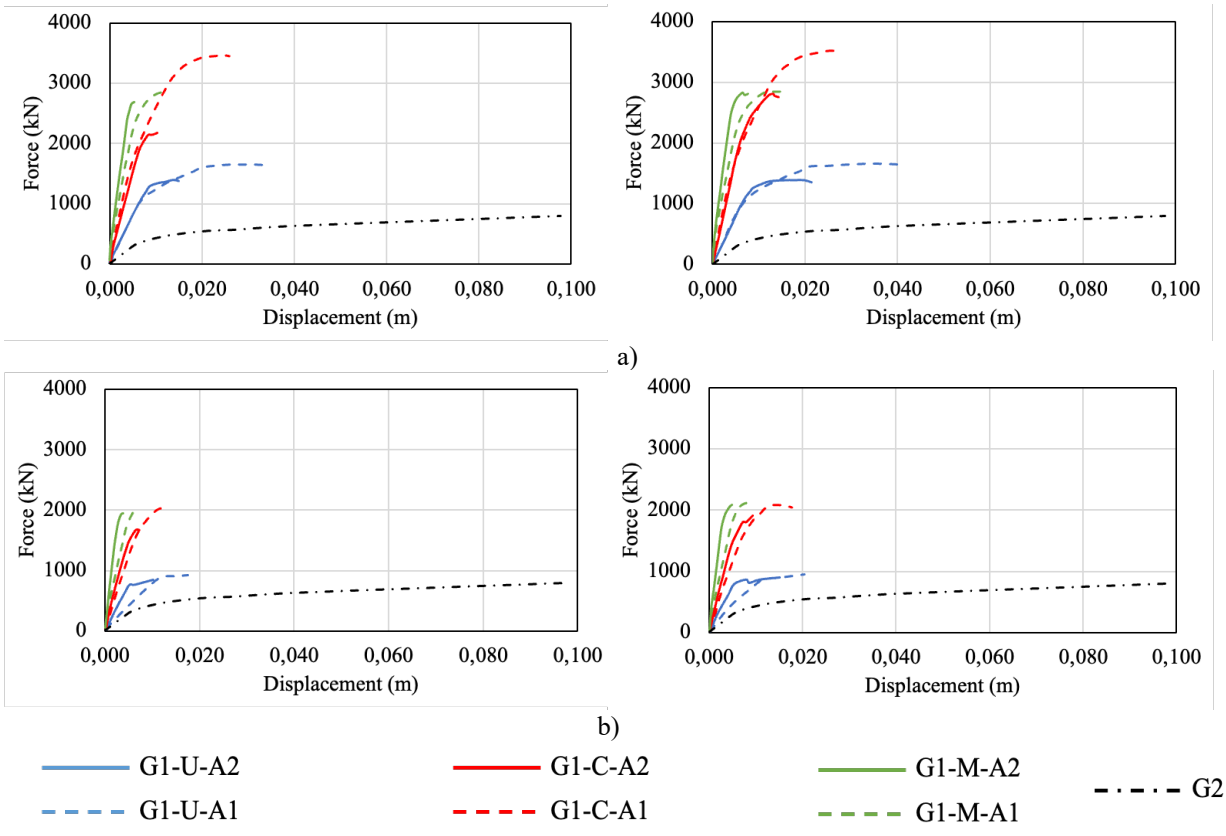


Figure 7: Comparison between the pushover curves: a) walls in direction X, b) walls in direction Y.

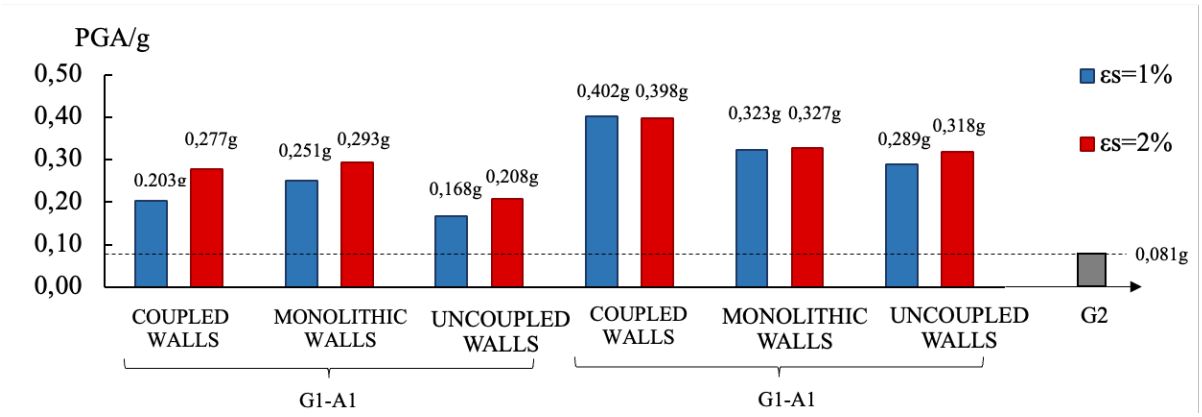


Figure 8: Comparison between the maximum PGAs at ULS bearable by the different structural solutions.

## 4.2 Some remarks on the damage tolerance

The obtained results - concerning the structural behavior of the various structural systems listed in Table 1 with respect to Life Safety Limit State condition - shown that low damage structural solutions (either those of the Group 1-A2 and Group 2) are more performant than Group 1-A1 (traditional CLT buildings), in terms of seismic behavior and particularly because the damage is gradually decreasing in the connecting zone passing from Group1-A1, to Group 1-A2, to Group 2.

Nonetheless, in these analyses, the influence of damage tolerance of the non-structural components on the overall seismic performance of CLT buildings has not been considered. In the general framework of Performance-Based Design (PBD) of buildings, the influence of non-structural components - such as infill walls and partitions, ceilings, claddings, contents etc. - cannot be neglected any more worldwide. In fact, many codes treat the problem of safety related to non-structural components, also including criteria for determining the seismic demand at different Limit States [6, 19, 27].

Even in presence of low-damage principal structural systems, damage to non-structural elements has severe impact in the building recovery, increasing the socioeconomic losses even for low intensity events (i.e., Damage Limit State) [18]. This aspect is not secondary, especially when (*i*) the displacement capacity and/or the inter-story drift of the structural system are significant, being the non-structural elements forced to accommodate such displacements with high probability to achieve high-level of damaging and needs to be removed and replaced with new components; (*ii*) the number of non-structural elements is elevated.

The latter two statements are typically recognized in post-tensioned systems because the reduced number of seismic-resistant walls due to the high seismic performance of the systems involves (necessary) the introduction of a significant number of non-structural components to realize infill and partitions. From this perspective, the system of the Group 1-A2 appears optimal because limits the damage of structural components and contemporarily requires a lower number of non-structural elements to realize the construction.

On the other hand, studies on the behavior of non-structural timber-based drywall equipped with low damage connections are available in literature [28, 29, 30]. Obviously, such systems reduce the nonstructural damage and serviceability of the construction is preserved especially for low-intensity earthquakes. Moreover, economic and environmental cost of a timber wall structure should take into account the probability of a reduced or nullified efficiency of non-structural elements, especially in presence of severe earthquake.

As final remark, it should be also considered that another issue affects the damage level of CLT buildings belonging to the Group 1. It regards the damage of CLT floors due to rocking

motion of the vertical panels: due to the platform-type constructional technology (i.e., floor inserted between two vertical walls) the rocking movements of the vertical panels cause the crushing of the floors in orthogonal-to-grain direction, whose values of strength are very low about 2-3 MPa. Thus, it is worth revising the idea behind the traditional CLT building and introducing the '2.0 CLT building' composed with full-height CLT walls (i.e., balloon-type technology) equipped with damage tolerant connections at the base of the walls.

### 4.3 Construction Costs and Life Cycle Assessment

This Section reports preliminary observations on the influence on costs related to the different structural schemes investigated in this paper, also including Life Cycle Assessment (LCA) aspects. The latter measures the environmental impact associated with all stages of a building's life cycle as provided by the International Organization for Standardization ISO 14040 [31] and the European Standard EN 15978 [32].

In Group 1, advantages of approach A2 with respect to approach A1 can be mainly referred to the repairing phase after the seismic event. In fact, low damage-based approach A2, avoiding removing and disposal of damaged CLT walls, reduces demolition and reconstruction costs, material and energy use, pollution due to transport and fabrication. In fact, solutions which provide permanent damage of the connecting zones (e.g., Group 1-A1) require the demolition of the structure involving additional costs.

Conversely, a comparison from an economical and environmental point of view of the different structural systems of Group 1 and that of Group 2 requires analyzing many factors, concerning designing, and building aspects. All the solutions of the Group 1 (be it designed according to approach A1 or A2) are particularly massive; they require higher number of walls, and then quantities of material, because the CLT seismic-resistant walls are distributed all over the perimeter and in the inner of the building, while few internal partitions are present. Whereas, in the case of the Group 2, few seismic-resistant walls were required, and in addition non-structural lightweight timber infill panels (or glass façades) are used to close the perimeter of the buildings, as well as internal partitions.

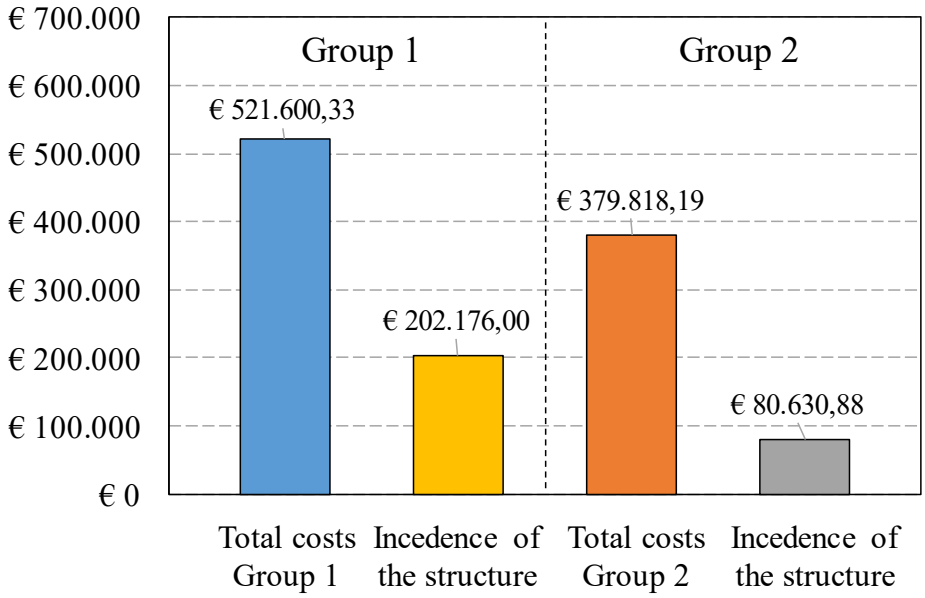


Figure 9: Comparison between construction costs.

As the structural components only are concerned, the weight of timber in cases of the Group 1 is greater than 30% with respect to the Group 2. Obviously, this aspect has an impact also on the construction costs involving transports and installing costs, material and energy use in producing as well as building phases. For the case study herein analyzed, the incidence of the costs of the structural system on total building costs of the Group 1 is about 38%, while in the case of post-tensioned solution (Group 2) is about 22%. In Fig. 9, the total costs of the solutions relative to the Groups 1 and 2, with indication of the incidence of the structural elements, are summarized.

Being out of the scope of the paper a detailed LCA, some remarks can be proposed based on the comparative analysis of the design procedures described herein:

- Structural solution of the Group 1 involved higher quantities of structural material than that of the Group 2, and consequently high environmental impact on the phases of extraction, production, packaging, and transport is expected in the first case.
- Traditional CLT buildings (Group 1-A1) characterized by severe seismic damage in the connecting zones imply higher environmental impact related to the phases of 'use' and 'end of life' due to demolition and disposal: whereas for those based on low damage (Group 1-A2 and Group 2) reduced or null damage is expected, also under high-intensity earthquakes.
- Costs related to non-structural components of the Group 2 are greater than those of the Group 1, because a higher number of nonstructural elements are required for such structural solution.

As matter of the fact, low-damage based solutions represented by the Group 1-A2 and Group 2 are both evidently more effective in terms of damage control and sustainability than that of the Group 1-A1. Those of the Group 1-A2 have the further advantage of reducing the number of non-structural components and then costs related to their eventual damaging. Note that in both cases of the Group 1-A2 and Group 2 low damaged non-structural components can be also enclosed in the structure, but with the disadvantages of additional costs related to the high level of prefabrication and specialized technology required by such systems.

Furthermore, it is worth noting that in the case of Group 2 few seismic-resistant walls are distributed over the perimeter of the building and in the inner. This characteristic is positive because lead to a larger architectural freedom in organizing inner spaces and outer openings, but it is negative because enlarges the need of introducing infill panels and partitions if compared to the systems of the Group 1-A2.

## 5 CONCLUSIONS

Among the various timber building typologies, massive CLT buildings have grown rapidly in the last decades both for residential and non-residential buildings. This rapid development has not been supported by up-to-date and codified design rules, leading to design approaches which limit the overall performances of the CLT buildings because based on structural considerations only.

In this context, an insight on the influence of design approaches of the connections on the overall performance of CLT buildings has been presented in this paper, highlighting the needs of a comprehensive and integrated design methodologies including the aspects related to damage control, costs and environmental impact also. The results of the conducted research con be summarized as follows:

i. The adoption of low damage structural systems is a fundamental requisite to achieve high performances of CLT buildings in terms of structural behavior, damage control, costs and environmental impact.
ii. Traditional CLT buildings (Group 1-A1) are low performant because damage is

expected in the connecting zones depending on the level of the seismic demand. After an earthquake the structural components must be demolished/repaired and then reconstructed involving additional costs and environmental impact.

iii. Low damage solutions (Group 2) are efficient from structural, architectural and environmental point of view, but the high damage to non-structural components - related to high displacement capacity of the structure - can compromise their serviceability. In fact, if damage control systems for nonstructural components are not installed, costs related to their damage can become very significant. On the other hand, low damage solutions are expansive for non-structural elements and increase the construction costs.

iv. CLT buildings equipped with low damage connecting systems at the base of the panels (Group 1-A2) represent a balance between traditional constructions (Group 1-A1) and those post-tensioned (Group 2), as no damage in structural components is expected and the use of non-structural element is limited.

The comparative analyses described herein are not certainly comprehensive and need further investigations and validations. Attention must be primarily focused on the technology and on the expected dissipative capabilities of the connections, whose optimization requires a rigorous scientific approach and an efficient code implementation.

## REFERENCES

[1] A. Sandoli, C. D'Ambra, C. Ceraldi, B. Calderoni, A. Prota. Sustainable Cross-Laminated Timber Structures in a Seismic Area: Overview and Future Trends. *Applied Science*, **11**, 2078, 2021. doi.org/10.3390/app11052078.

[2] S. Lehmann. Sustainable construction for urban infill development using engineered massive wood panel systems. *Sustainability*, **4**, 2707–42, 2012. https://doi.org/10.3390/SU4102707.

[3] A. Iqbal. Development in tall wood buildings and hybrid buildings and environmental impacts. *Sustainability*, **13**, 11881, 2021.

[4] CLT Handbook: Cross Laminated Timber; FP Innovation Special Publication SP-529E; U.S. Edition: St. Jean Pointe-Claire, QC, Canada, 2013.

[5] EN 1995-1-1:2004 Eurocode 5: Design of Timber Structures, Part 1-1: General rules and rules for buildings. Brussels.

[6] EN 1998-1:2005 Eurocode 8: Design of structures for earthquake resistance-part 1: general rules, seismic actions and rules for buildings. Brussels.

[7] P. Dietsch, S. Winter. Eurocode 5 - Future Developments towards a more comprehensive code on timber structures. *Struct Eng Int* 2012, **22**(2), 223-31.

[8] A. Sandoli, C. D'Ambra, M. Lippiello, C. Ceraldi, B. Calderoni, A. Prota. Moment-curvature diagrams for CLT panels accounting for orthogonal to grain compression timber properties. Proc of the 8th COMPDYN Conf. Eccomas Procedia. Athens Greece, 28-30 June 2021.

[9] CNR DT 206-R1/2018. Instructions for Design, Execution and Control of Timber Structures. Italian National Council of Research, 2018. Rome.

[10] B. Faggiano, A. Sandoli, G. Iovane, M. Fragiacomo et al. The Italian instructions for the

design, execution and control of timber constructions (CNR-DT 206 R1/2018). *Eng Struct*, **253**, 113753, 2022.

[11] A. Sandoli, C. D'Ambra, C. Ceraldi, B. Calderoni, A. Prota. Role of perpendicular to grain compression properties on the seismic behavior of CLT walls. *Journal of Building Engineering,* **34**, 101889, 2021.

[12] K.W. Johansen. Theory of timber connections. Int. Ass Bridges Struct. Eng. 9, 1949, 249-262.

[13] R. Scotta, L. Marchi, D. Trutalli, L. Pozza. A dissipative connector for CLT buildings: Concept, design and testing. *Materials* **9**, 139, 2016.

[14] M. Latour, G. Rizzano. Seismic behavior of cross-laminated timber equipped with traditional and innovative connectors. *Arch Civ Mech Eng* **17**, 382–399, 2017.

[15] A. Palermo, S. Pampanin, A. Buchanan, M. Newcombe. Seismic design of multi-storey buildings using laminated veneer lumber (LVL). *Proc of the NZSEE Conference*, New Zealand, Wairakei, 2005.

[16] Sarti, F.; Palermo, A.; Pampanin, S. Quasi static cyclic testing of two-thirds scale unbonded posttensioned rocking dissipative timber walls. *J. Struct. Eng*. **142**, 2016, E40115005.

[17] Cito, P., Iervolino, I. Peak-over-threshold: Quantifying ground motion beyond design. *Earth Eng and Struct Dyn* **49**, 458-478, 2020.

[18] S. Bianchi, J. Ciurlanti, D. Perrone, A. Filiatrault, A. Campo Costa, P.X. Candeias, A.A. Correirea, S. Pampanin. Shake-table test of innovative drift sensitive nonstructural elements in a low-damage structural system. *Earth. Eng. And Struct. Dyn* , 1-23, 2021.

[19] IBC 18- Italian Building Code for Construction. Ministry of infrastructures and Transportation, 24/01/2018. Rome. Italy.

[20] ETA-14/0349. (2019). European Technical Assessment, issued in accordance with Regulation EU n° 305/2011.

[21] STIC (2013). Design guide Australia and New Zealand – Post-tensioned timber buildings. *Structural Timber Innovation Company*, Christchurch, New Zealand.

[22] A. Sandoli, D. Moroder, S. Pampanin, B. Calderoni. Simplified analytical models for coupled CLT walls. *16th World Conference on Timber Engineering* (WCTE 2016), Wien, Austria, August 11-25, 2016.

[23] J.H. Blass, P. Fellmoser, P. Design of solid wood panels with cross layers. In Proceedings of the WCTE 2004, Lahti, Finland, 14-17 June 2004, 543-548.

[24] SAP2000 (v.18). Structural Analysis Program. CSI.

[25] G. Tamagnone, G. Rinaldin, M. Fragiacomo. A novel method for non-linear design of CLT wall systems. *Eng. Struct.* **167**, 760-771, 2018.

[26] P. Fajifar, P. Gaspersic, "The N2 method for the seismic damage for RC buildings", *Earth Eng and Struct Dyn*, 23-67, 2000.

[27] AWCI – Code of practice for seismic design and installation of non-structural internal walls and partitions. Association of Wall and Ceiling Industries of New Zealand Inc.New Zealand, 2018.

[28] A.S. Tasligedik, S. Pampanin, A. Palermo (2014) Low damage seismic solutions for non-structural drywall partitions. *Bull of Earth Eng* **13**, 1029–1050, 2014.

[29] C. Petrone, G. Magliulo, G. Manfredi. Shake-table tests on standard and innovative temporary partition walls. *Earth Eng and Struct Dyn* **46**, 1599-1624, 2017.

[30] C. Zhang, T. Yu, Z. Chen, W. Huang, S. Zhang, Y. Zhou, D. Lu, Z. Lin. Seismic behavior of novel low-damage precast infill walls with sliding joints for reinforced concrete frame. *Earth Eng and Struct Dyn*, 1-25, 2022.

[31] ISO14040: 2006. Environmental management — Life cycle assessment — Principles and framework

[32] EN 15978: 2011. Sustainability of construction works - Assessment of environmental performance of buildings - Calculation method.

COMPDYN 2023
9th ECCOMAS Thematic Conference on
Computational Methods in Structural Dynamics and Earthquake Engineering
M. Papadrakakis, M. Fragiadakis (eds.)
Athens, Greece, 12-14 June 2023

# SEISMIC FRAGILITY ANALYSIS TO ASSESS THE IMPACT OF TIMBER VERTICAL ADDITIONS ON EXISTING RC BUILDINGS: A CASE STUDY

**A. Bartolotti[1], M. Sartori[1] and I. Giongo[1]**

[1]Department of Civil, Environmental and Mechanical Engineering, University of Trento
via Mesiano 77, 38123 Trento (Italy)
e-mail: {andrea.bartolotti, ivan.giongo}@unitn.it

## Abstract

*Construction of vertical expansions on top of existing structures can be considered as an economical and practical solution to contain urban sprawl. The use of timber, due to its lightness, suitability for modularity and prefabrication, and due to environmental benefits, emerges as an interesting option for the realisation of vertical additions in existing buildings. Unfortunately, in seismic-prone areas, the construction of vertical expansions clashes with seismic safety. Current standards require that the safety level of the existing structure after the expansion be that prescribed for new buildings. This requirement represents a major obstacle to vertical expansion because vintage buildings rarely comply with the provisions of the seismic standards even without any addition, making costly retrofit intervention necessary. In this paper, a case study is selected and analysed to try and understand how the vertical timber addition of existing buildings can impact their seismic behaviour. The selected case study is a 1980s four-story RC frame building with masonry infill walls. Following current design practices, a one-storey timber vertical expansion was designed by adopting a cross-laminated timber shear-wall system. The seismic response of the building with and without the timber expansion was then simulated via finite element modelling. The outcomes of the numerical simulations were then used to perform a seismic fragility analysis and assess the effect of vertical expansion on the seismic performance of the case study building. The results of the analysis showed how, in some cases, the vertical timber addition not only does not worsen the safety level of the building but can actually improve it. This outcome opens new paths for future research to further investigate the effect of vertical expansions and maximize their beneficial effect on the seismic response of existing buildings.*

**Keywords:** Vertical Addition, Cross-laminated Timber, Fragility Analysis, Existing RC Buildings, Infilled RC Frames.

# 1 INTRODUCTION

Urban sprawl, that is the rapid expansion of the geographic extent of cities and towns, is a hoary problem that threatens natural and rural environments and accelerates climate change due to an increase in greenhouse emissions. The gravity of the impact of unchecked urban sprawl has prompted the European Commission to take action and propose in the EU Environment Action Programme a specific plan that aims to achieve 'no net land take" by 2050 [1]. The consequence of this policy is that in the near future new housing volume can only be obtained by intervening on the existing building stock.

Within this scenario, there are many reasons why vertical building expansion, with one or more storeys built ex-novo on top of an existing structure, could be a valuable strategy to increase the housing volume with no land take. First, vertical expansion is efficient and economical: there is no need to allocate budget to purchase new land and new housing volume can be created where no land is available but where the extra-value of the expansion would be maximum (i.e., most prestigious neighbourhood in the city centres). In addition, the cost for services and supplies (e.g., power, water, gas) is lower because direct access is already available onsite. In case of buildings that have ageing roof structures in need of repair, adding one or more storeys can solve the roof problem while increasing the living space, and hence the building value with limited extra cost. Another strong point of vertical expansion is the speed of construction thanks to extensive adoption of prefabrication and modularity [2].

In earthquake-prone countries, seismic vulnerability of existing building stock is a critical issue that often discourages from intervening on existing structures and, as a consequence, it contributes to soil consumption. Historic, centuries old masonry buildings, as well as masonry infilled reinforced concrete (RC) frames built in the central decades of the 20th Century, constitute the largest part of the building stock of many cities and towns in Europe [3]. Such structures were not designed to resist lateral loading and therefore have been shown to be highly vulnerable to earthquakes [4][4]-[7]. Current standards such as NTC and ASCE 7 [8], [9], require for existing buildings, when significant modifications are made to their structure, as the case of vertical expansion, the same safety level prescribed for new buildings. This requirement represents a formidable obstacle to vertical expansion because existing structures may be far from complying with the provisions from seismic standards even without the inertial extra-load from the vertical addiction. This means that expensive retrofit interventions need to be designed in order for the building to be able to accommodate additional storeys. Adopting light building solutions such as those relying on timber walls or steel frames, that limit the extra weight due to the vertical expansion, is certainly positive, but it might not be sufficient to guarantee the viability of the intervention.

Sustainability is another key aspect to be considered [10] when selecting the optimal construction technology for the building expansion. In this regard, timber-based systems appear as the most promising option. "Environmental benefits" from using timber in construction have been proven by many studies that have provided numerous examples of life cycle assessment (LCA) evidencing advantages in terms of carbon sequestration, greenhouse emission and energy saving [11]-[14]. In addition, the large availability of wood on the entire EU territory (43% of EU land is covered by forests [15]) can be exploited to develop short and smart supply chains and foster local circular economies [16], [17].

The scope of the present paper is to investigate the influence of vertical expansion on the seismic performance of existing buildings. Previous research has mainly focused on RC frames with vertical steel expansions. The findings indicated the ability of the addition to prolong the natural period of the structure usually resulting in lower seismic forces at the ground floor. However, the so-called whip effect, due to the lower stiffness of the steel superstructure, may

cause an increase in interstorey drift at higher floors, such as to exceed deformation acceptance criteria and thus making the expansion unfeasible [18]. Recently, some authors [18]-[20] focused on timber vertical expansion using timber light frame as well as cross-laminated (CLT) shear wall systems. Also in this case, via modal analysis, a reduction in seismic force was found due to a shift in the natural period of the expanded building. In addition, this type of superstructure can be easily adjusted to fit a desired stiffness by changing the composition of the elements and using different fasteners with different arrangements [18], thus having a greater control over the period shift.

To analyse the effect of vertical timber expansion on the seismic safety of existing building, a case study was selected representing a typical example from the Italian mid-20$^{th}$ century residential building stock.

## 2 CASE STUDY BUILDING

The case study building selected for the present research is the one analysed by Manfredi et al. in [21]. It is a four-storey RC frame with masonry infill walls that was built in 1984 in the Molise region (South of Italy). It represents a typical multi-storey residential building for the period, with rectangular plan (circa 2:1 aspect ratio) and central staircase (Figure 1a). The openings are mainly distributed along the lengthwise direction. There is also a wide unobstructed space at the ground floor, due to the presence of the garages and the front porch (Figure 1b and Figure 1c).

The structure consists of parallel two-dimensional RC frames running in the longitudinal direction and having beams and columns with rectangular and square cross-sections, respectively. The columns are 35 cm wide on the ground floor and 30 cm on the upper storeys. The internal beams, and the external ones located in correspondence with the balconies, are wide-shallow beams with 80x20 cm cross-section geometry. The remaining external beams are characterized by a 30x50 cm cross-section. Transversal 50x20 cm beams are also present, connecting the longitudinal framing. A one-way hollow clay block slab (20 cm thick) constitutes the flooring system. The external infills are made of cavity walls with a hollow clay block wythe (8 cm thick) facing inwards and a solid clay brick wythe (12 cm thick) facing outward.

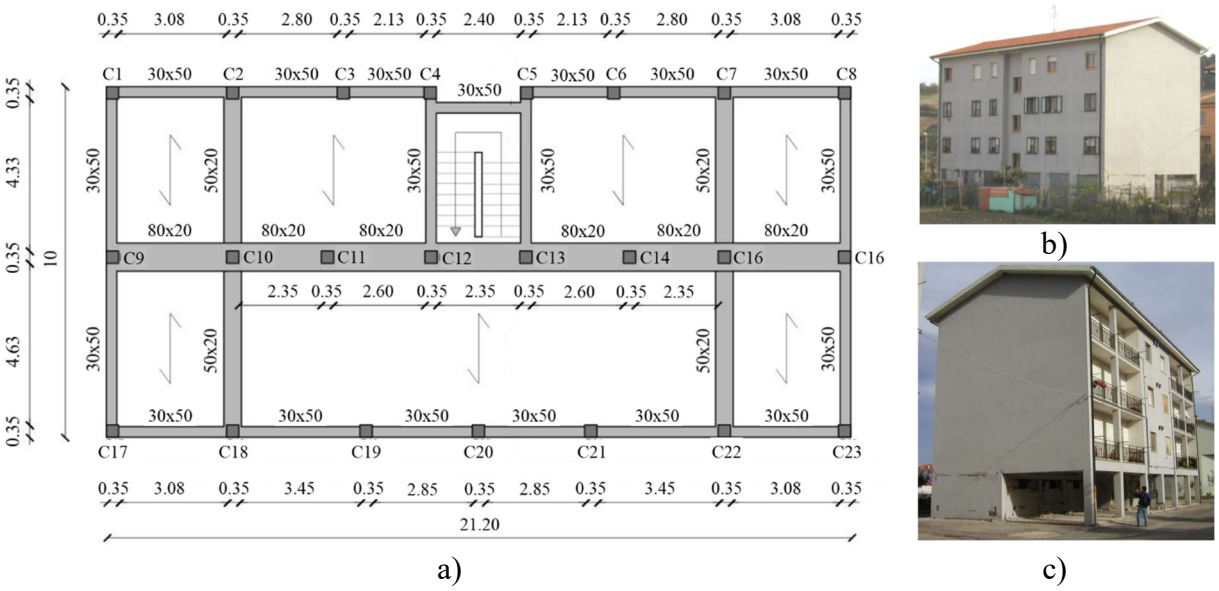


Figure 1: a) Plan of the ground floor of the case study building. b) Back view and c) front view

## 2.1 Timber vertical addition

From an architectural point of view, the objective of the vertical expansion is to substitute the unused roof space of the case study building with a completely new floor (Figure 2b) thus increasing the habitable space by more than 25%. The vertical structure of the timber addition is constituted by a CLT shear-wall system. The timber panels are connected to the concrete beams using angle brackets (TCF200) and hold down connectors (WHT620) whose geometrical properties are summarised in Figure 4. In the case of CLT walls not directly supported by concrete beams, a supporting steel joist was inserted to transfer the panel forces to the RC frame (dashed lines in Figure 2b). The plan distribution of the CLT panels is shown in Figure 2c together with the arrangement of the steel connectors designed according to [22], taking into account the seismic action. To evaluate the seismic loads H and T (see Figure 3) acting on the angle brackets and hold down connectors, respectively, the horizontal seismic forces were calculated through an equivalent static analysis where the response spectrum for the region, corresponding to 475 years return period, was used [9]. The total shear force acting on the fourth floor of the expanded building was distributed among the CLT walls proportionally to their length thus obtaining the shear force H. Then, according to the scheme reported in Figure 3, the tension force T was also evaluated through simple equilibrium considerations.

To complete the vertical expansion, a new wooden roof and extension of the stairs were also designed.

Thanks to the lightness of the construction system based on timber panels, the total weight of the building after the expansion resulted to be approximately the same as the original case study building (Figure 2a).

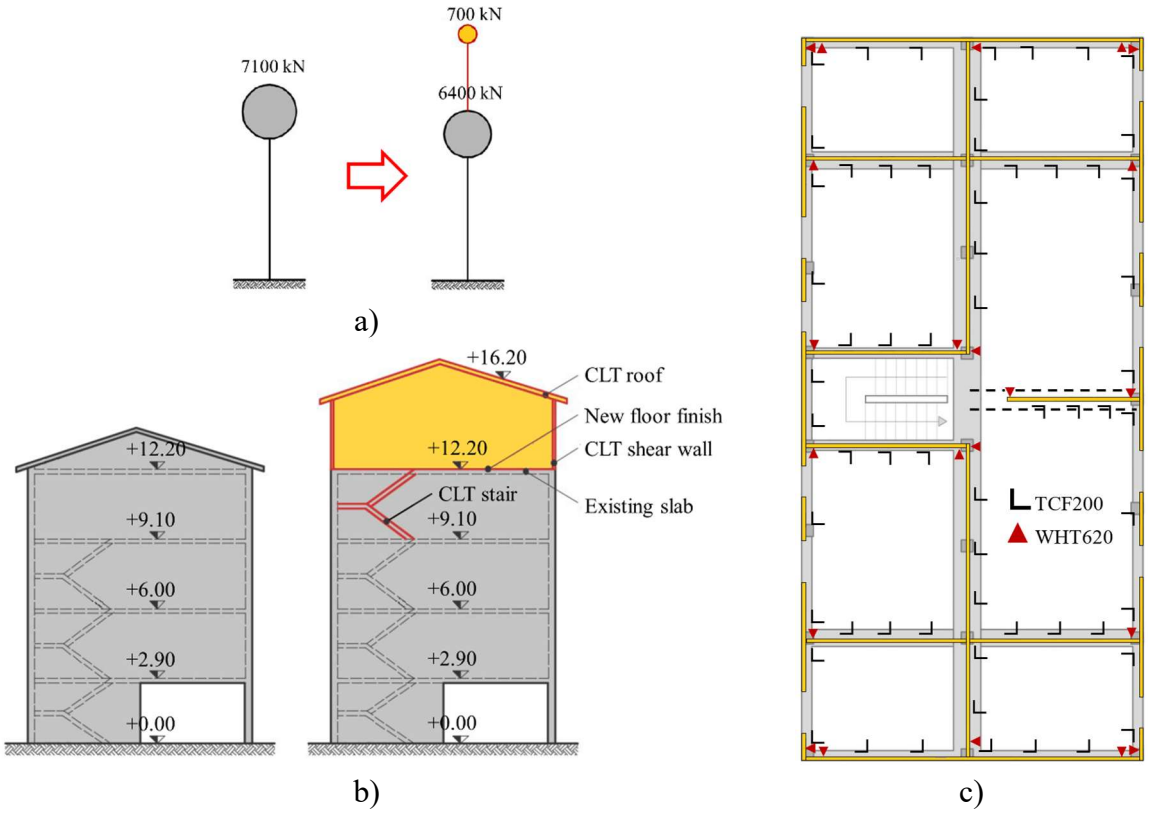


Figure 2: a) Total weight of the case study building before and after the timber vertical addition. b) Vertical expansion of the case study building. c) Plan of the CLT shear wall and of the steel connectors of the timber vertical expansion.

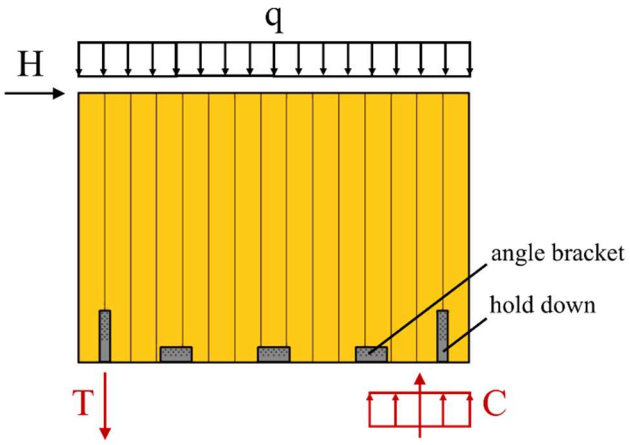


Figure 3: Scheme for the calculation of the seismic load of the shear wall connection system: q is the distributed load acting on the wall; H is the horizontal force acting on the panel equal to the shear load absorbed by the angle brackets; T is the tension force absorbed by the hold-down connector, which, together with the compression force C, generates the stabilising moment that opposes the one caused by the horizontal force H.

## 2.2 Finite element modelling

The structure of the building was modelled using the SAP2000 finite element software [23]. RC members are represented by frame elements and reinforcement detailing was defined in accordance with [21]. To account for the nonlinearities of the RC members a concentrated plasticity approach was used, and plastic hinges automatically defined by the software according to [24] were assigned to the frame elements.

The slab floor was not explicitly modelled by means of bi-dimensional elements, but a rigid diaphragm constraint was assigned to the nodes of each floor to enforce the same lateral displacements to any point laying on the floor area. A different approach was used for the sloped slabs of the existing pitched roof that were modelled through linear shell elements considering the out-of-plane stiffness.

The masonry infill walls were added to the model through nonlinear link elements by adopting the equivalent concentric strut macromodel proposed by Liberatore et al. [25]; hysteresis was described by using a pivot model [26] as suggested by [27].

The main material properties used in the model are reported in Table 1 and were assumed based on the information collected by Manfredi et al. [21] relying on test certificates from the construction period (compression tests on concrete cores and tension tests on steel rods) and the results of an in-situ testing campaign.

Table 1: Material properties assigned to the structural elements within the numerical model.

| **Concrete** | | **Steel** | | **Masonry infill wall** | |
|---|---|---|---|---|---|
| Compressive strength (MPa): | 16.7 | Yield strength (MPa): | 440 | Compressive strength (MPa): | 6.5 |
| Modulus of elasticity (GPa): | 25.7 | Modulus of elasticity (GPa): | 210 | Shear strength (MPa): | 0.13 |
| | | | | Diagonal cracking strength (MPa): | 0.28 |
| | | | | Modulus of elasticity (GPa): | 4.5 |

Concerning the timber expansion, the CLT shear wall system was modelled considering an elastic behaviour for the timber panels. Mechanical nonlinearities were only accounted for in the steel connectors, which were modelled through multilinear plastic link elements. The

accuracy of this approach relies on the hypothesis that plastic deformation only occurs at the level of the connection system. The CLT walls were thus modelled through orthotropic linear shell elements whose elastic properties were derived from [28][29]. The multilinear backbone curves reported in Figure 4 (solid red line), representing the mechanical behaviour of the steel connectors (steel bracket TCF200 and WHT620 hold-down connector), were derived from the results of the experimental campaign conducted by Piazza and Sartori [30]. A pivot model suitably calibrated on the results of the aforementioned experimental campaign was adopted to describe the hysteretic behaviour of the steel connectors.

| TCF200 | |
|---|---|
| H = | 200 mm |
| B = | 103 mm |
| P = | 71 mm |
| t = | 3 mm |

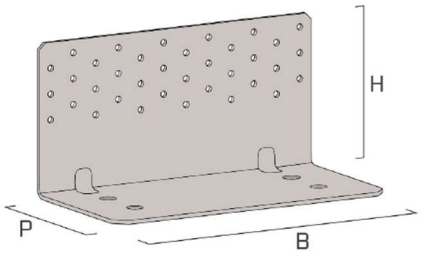


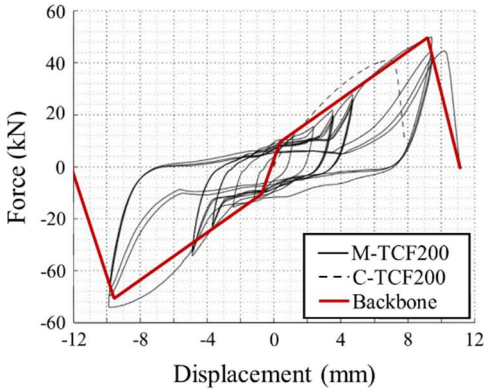


| WHT620 | |
|---|---|
| H = | 620 mm |
| B = | 80 mm |
| P = | 83 mm |
| t = | 3 mm |

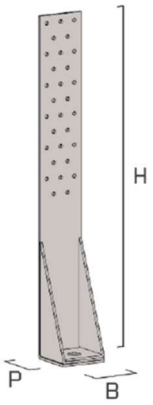


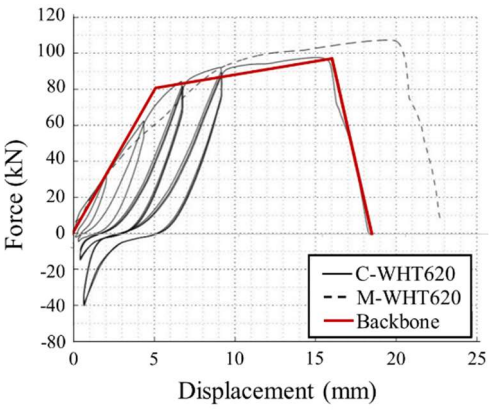


Figure 4: Geometrical and mechanical properties of the steel connectors.

## 3 COMPARATIVE FRAGILITY ANALYSIS

Fragility analysis is a valuable tool to assess the seismic vulnerability of structures. It has a long tradition in the nuclear industry and, since the late 1990s, it has been used also for ordinary buildings, fostering the development of new seismic standards [31]. Over the years, thanks to the improving computation power, fragility analysis has become, among researchers, the go-to tool for studying the seismic behaviour of a multitude of different structures [32].

The primary outcome of a fragility analysis is a set of curves that describe the probability of exceeding a specified limit state (e.g., collapse or life safety) given the intensity measure (IM) of earthquake ground motions [33]. Limit states are usually defined by damage thresholds expressed by suitable values of a selected damage measure (DM).

Among the various methods described in the literature [31], the one that relies on linear regression in log-space and incremental dynamic analysis (IDA) [34] was chosen to derive the fragility curves of the case study building, in both "as built" (AB) and vertically expanded (VE) configuration. Firstly, a set of seven ground-motion records (see Table 2) was selected from the

PEER Ground Motion Database [35], considering the spectral shape of the region and different earthquake mechanisms. For simplicity only the median capacity of the log-normal distribution was estimated by regression. The estimation of dispersion (β), which would have required a greater sample [31] was achieved by using tabulated values [36]. Peak ground acceleration (PGA) was adopted as IM and maximum interstory drift ratio was selected as DM. To define appropriate thresholds of the DM, reference was made to FEMA's Hazus program [36], and four damage levels were defined according to Table 3.

Table 2: Set of records selected from PEER to perform fragility analysis.

| Earthquake name | Record number | Year | Mechanism | Magnitude |
|---|---|---|---|---|
| Christchurch | 8119 | 2011 | Reverse oblique | 6.2 |
| Coyote Lake | 148 | 1979 | Strike slip | 5.74 |
| Bam | 4040 | 2003 | Strike slip | 6.6 |
| Gazli | 126 | 1976 | Reverse | 6.8 |
| Managua | 96 | 1972 | Strike slip | 5.2 |
| San Fernando | 77 | 1971 | Reverse | 6.61 |
| Norcia | 156 | 1979 | Normal | 5.9 |

Table 3: Damage thresholds defined within the FEMA's Hazus program and adopted to define limit state conditions in the present fragility analysis.

| Damage level | Drift ratio threshold | β |
|---|---|---|
| Slight | 0.0016 | 0.9 |
| Moderate | 0.0032 | 0.86 |
| Extensive | 0.008 | 0.9 |
| Complete | 0.0187 | 0.96 |

The results of the fragility analysis are summarised in

Figure 5. The regression curves (

Figure 5a) show that the VE building (black line) tends to exhibit lower drifts as the seismic intensity increase with respect to the AB configuration (red line). This behaviour becomes more and more evident as the PGA values exceed 0.2g corresponding to a damage threshold comparable to that defining the "extensive" damage level. This fact is reflected by the resulting fragility curves (

Figure 5b) of the VE configuration (dashed line) that show an appreciable reduction in the risk of exceedance respect to the AB configuration only when considering "extensive" and "complete" damage level. Specifically, the maximum reduction in the risk of exceedance between the AB and VE configurations moved from 1.9% and 4.3%, respectively for the "slight" and "moderate" damage level, to 8.7% and 13.5% for the "extensive" and "complete".

In the first place, the results indicate that the vertical timber addition did not worsen the seismic performance of the case study building, in addition, although it did not drastically improve it either, the seismic safety level of the RC frame building can still be enhanced through the vertical expansion.

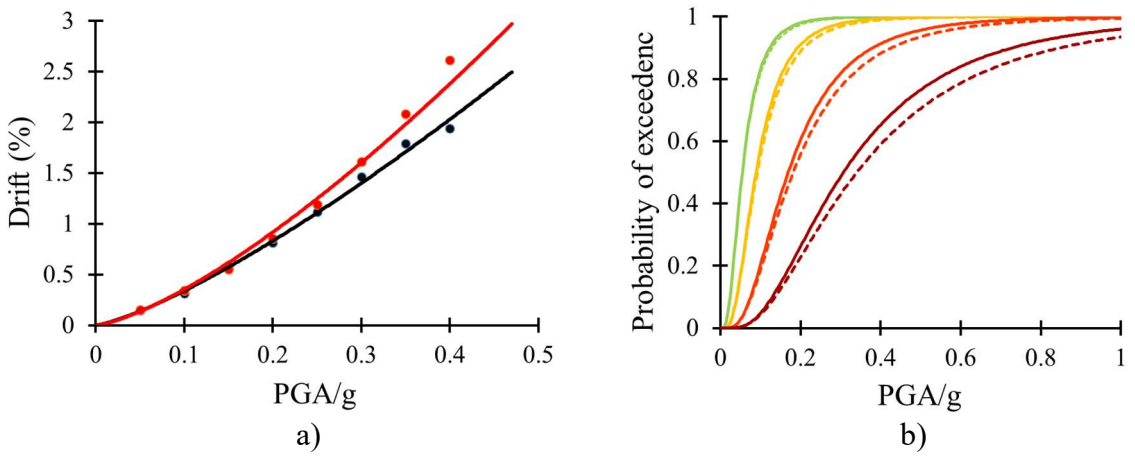


Figure 5: a) Regression curves (solid lines) that express the median DM as a function of IM for the AB (—) and VE (—) configurations; circle marks represent the median values used for the regression and obtained by the multi-IDA analysis. b) Fragility curves obtained for the AB (solid) and VE (dashed) configurations, and for the considered damage level: slight (—) , moderate (—), extensive (—), complete (—).

## 4 CONCLUSIONS

In this paper a RC frame case study building from the literature was subjected to a vertical timber addition with cross-laminated shear-wall structure. A comparative seismic fragility analysis was performed on the case study building before and after the expansion. The results provided a proof of concept of the following:

- the addition of vertical expansions on an existing RC frame building, when made of timber, does not necessarily produce a worsening of the seismic performance of the building;
- vertical timber additions can actually enhance the seismic safety of RC buildings;
- in this study, such a beneficial effect was more noticeable for higher seismic intensity and damage thresholds.

## REFERENCES

[1] EEA, Urban Sprawl in Europe: The Ignored Challenge. Report No 10/2006. Office for Official Publications of the European Communities; Luxembourg, 2006.

[2] A. Jellen and A. Memari, Residential Vertical Expansion of Existing Commercial Buildings Using Modular Construction Methods. *2nd Residential Building Design & Construction Conference*, Penn State University Park, Pennsylvania, February 19-20, 2014.

[3] G. Tsionis, European building inventory framework. Report EUR 27603 EN, Publications Office of the European Union, Luxembourg, 2015.

[4] A. Penna, P. Morandi, M. Rota, C.F. Manzini, F. da Porto and G. Magenes, Performance of masonry buildings during the Emilia 2012 earthquake. *Bulletin of Earthquake Engineering*, **12(3)**, 2255-2273, 2013.

[5] J.M. Ingham, and C. Griffith, Performance of unreinforced masonry buildings during the 2010 Darfield (Christchurch, NZ) earthquake. *Australian Journal of Structural Engineering*, **11**, 207-224, 2016.

[6] K.M. Mosalam and S. Günay, Progressive Collapse Analysis of Reinforced Concrete Frames with Unreinforced Masonry Infill Walls Considering In-Plane/Out-of-Plane Interaction, *Earthquake Spectra*, **31(2)**, 921–943, 2015.

[7] F. Di Trapani and M. Malavisi, Seismic fragility assessment of infilled frames subject to mainshock/aftershock sequences using a double incremental dynamic analysis approach, *Bulletin of Earthquake Engineering*, **17(1)**, 211–235, 2019.

[8] ASCE (American Society of Civil Engineers), ASCE/SEI 7-16: Minimum Design Loads for Buildings and Other Structures. Reston, Virginia, 2016.

[9] Ministero delle Infrastrutture, Norme Tecniche per le Costruzioni (NTC). Aggiornamento delle «Norme tecniche per le costruzioni» Decreto Ministero delle Infrastrutture, 17 gennaio 2018, G.U. n. 42 del 20 febbraio 2018 - Suppl. Ordinario (in Italian).

[10] European Standards, CSN EN 15978: Sustainability of construction works - Assessment of environmental performance of buildings - Calculation method. Czech Republic, 2011.

[11] H.J. Darby, A. A. Elmualim and F. Kelly, A case study to investigate the life cycle carbon emissions and carbon storage capacity of a cross laminated timber, multi-storey residential building. *Sustainable Building Conference*, Munich, Germany, April 23-25, 2013.

[12] B. Grann, A comparative life cycle assessment of two multistory residential buildings: Cross-laminated timber vs. concrete slab and column with light gauge steel walls. *FPInnovations Report,* Vancouver, Canada. pp. 1-121, 2013.

[13] A. B. Robertson, F.C.F. Lam F. and R.J. Cole, A Comparative Cradle-to-Gate Life Cycle Assessment of Mid-Rise Office Building Construction Alternatives: Laminated Timber or Reinforced Concrete. *Buildings*, **2(3)**, 245-270, 2012.

[14] C.X. Chen, F. Pierobon, S. Jones, I. Maples, Y. Gong, Comparative life cycle assessment of mass timber and concrete residential buildings: a case study in China. *Sustainability*, **14(1)**, 144, 2022. https://doi.org/10.3390/su14010144

[15] Eurostat database. https://ec.europa.eu/eurostat/data/database

[16] M. Romagnoli, M. Fragiacomo, A. Brunori, M. Follesa, G. Scarascia Mugnozza, Solid Wood and Wood Based Composites: The Challenge of Sustainability Looking for a Short and Smart Supply Chain. *Digital Wood Design: Innovative Techniques of Representation in Architectural Design*; F. Bianconi, M. Filippucci, Eds., Springer International Publishing: Cham, Switzerland, 783-807, 2019.

[17] M. H. Ramage, et al., The wood from the trees: the use of timber in construction. *Renew Sustain Energy Rev*, **68**, 333-359, 2017.

[18] J. Jančar, T. Zafirov, M. Premrov and B. Dujič, Seismic resistance of existing buildings with added light timber structure storeys. *Gradevinar*, **74**, 403-4017, 2022.

[19] I. Šušteršič, B. Dujič, and S. Gostič, Timber upgrade of structures on seismically active areas. *World conference of timber engineering (WCTE)*, Riva del Garda, Italy, June 20-24, 2010.

[20] S. Calderón, S. Carcamo, C. Sandoval and F. Chateau Gannon, Structural feasibility of timber-structured vertical expansions for social housing buildings in Chile. *World conference of timber engineering (WCTE)*, Seoul, South Korea, August 20-23, 2018.

[21] G. Manfredi, A. Masi, R. Pinho, G. Verderame, M. Vona, Valutazione degli edifice esistenti in Cemento Armato. IUSS Press, Pavia, Italy; 2007 (in Italian).

[22] Swedish Wood, The CLT Handbook. Stockholm, Sweden; 2019.

[23] CSI, SAP2000 Integrated Software for Structural Analysis and Design, Computers and Structures Inc., Berkeley, California.

[24] FEMA-356: Prestandard and Commentary for the Seismic Rehabilitation of Buildings American Society of Civil Engineers, 2000.

[25] L. Liberatore, F. Noto, F. Mollaioli, P. Franchin. In-plane response of masonry infill walls: Comprehensive experimentally-based equivalent strut model for deterministic and probabilistic analysis. *Engineering Structures*, **167(7),** 533-548, 2018.

[26] O. Dowell, F. Seible, E.L. Wilson. Pivot hysteresis model for reinforced concrete members. *ACI structural journal*, **95**, 607-617, 1998.

[27] L. Cavaleri, F. Di Trapani. Cyclic response of masonry infilled RC frames: Experimental results and simplified modeling. *Soil Dynamics and Earthquake Engineering,* **65**, 224-242, 2014.

[28] T. Bogensperger, G. Silly. Two-axial load transfer of Cross-Laminated-Timber plates. *Bautechnik*, **91 (10),** 742-752, 2014.

[29] R. Brandner, P. Dietsch, J. Droscher, M. Schulte-Wrede, H. Kreuzinger, M. Sieder. Cross laminated timber (CLT) diaphragms under shear: Test configuration, properties and design. *Construction and Building Materials*, **147**, 312-27, 2017.

[30] M. Piazza, T. Sartori. Caratterizzazione meccanica attraverso prove monotone e cicliche dei principali dispositivi di connessione utilizzati negli edifci multipiano in legno. Test Report, Trento 2015.

[31] I. Zentner, M. Gündel, N. Bonfils. Fragility analysis methods: Review of existing approaches and application. *Nuclear Engineering and Design*, **323**, 245-258, 2017.

[32] S. Rajkumari, K. Thakkar, H. Goyal. Fragility analysis of structures subjected to seismic excitation: A state-of-the-art review. *Structures*, **40**, 303-016, 2022.

[33] K. Kiani, C. Camp, S. Pezeshk. On the application of machine learning techniques to derive seismic fragility curves. *Computers & Structures*, **218**, 108-122, 2019.

[34] D. Vamvatsikos, C.A. Cornell. Incremental dynamic analysis. *Earthquake Engineering & Structural Dynamics*, **31 (3)**, 491-514, 2002.

[35] Database. Pacific Earthquake Engineering Research Center, University of California, Berkeley. California (2006)

[36] Department of Homeland Security, FEMA. HAZUS-MH, Multi-hazard loss estimation methodology: earthquake model. Washington (DC), 2003.

COMPDYN 2023
9th ECCOMAS Thematic Conference on
Computational Methods in Structural Dynamics and Earthquake Engineering
M. Papadrakakis, M. Fragiadakis (eds.)
Athens, Greece, 12-14 June 2023

# A PARAMETRIC STUDY ON THE CYCLIC RESPONSE OF POST-TENSIONED LOW DAMAGE TIMBER WALLS WITH DISSIPATIVE DEVICES.

**V. Tomei[1], M. Zucconi[2], H. Monsef[2], B. Ferracuti[2]**

[1] Department of Civil and Mechanical Engineering, University of Cassino and Southern Lazio, via Di Biasio 43, Cassino, 03043, Italy
e-mail: v.tomei@unicas.it

[2] Department of Engineering, Niccolò Cusano University, via Don Carlo Gnocchi 3, 00166 Rome, Italy
e-mail: {maria.zucconi, hadi.monsefahmadi, barbara.ferracuti}@unicusano.it

## Abstract

*Low-damage Post-tensioned timber walls arose from the requirement to develop structural solutions capable of ensuring fast re-use of the structure without permanent damage after a seismic event while also protecting human life. These kinds of solutions require rocking timber walls equipped with hysteretic dampers. The rocking behavior guarantees the recentering of the walls, and it is mainly entrusted to post-tensioned bars placed in ad hoc cavities in the wall. Likewise, the energy dissipation mechanisms are provided by axial or shear hysteretic dampers which easily replaceable after a seismic event. In this context, the investigation presents a non-linear numerical model strategy able to reproduce the cyclic behavior of post-tensioned timber walls at global and local levels by non-linear static analyses. The proposed model considers both material and geometrical non-linearities: the former due to entering the plastic field of hysteretic dampers and the latter due to the rocking behavior which causes base uplifts. Along the same lines, in this paper, a parametric analysis is developed to investigate the various parameters that affect the local and global behavior of the systems and influence the recentering capacity and dissipative behaviors of the building. The main parameters investigated are: the initial level of post-tension in the bars, the number of axial dampers, the geometrical dimensions of the walls, the mechanical characteristics of the wall.*

**Keywords**: post-tensioned timber walls, dissipative dampers, rocking timber walls, numerical modeling, parametric analysis.

## 1 INTRODUCTION

In the last decades, the ever-increasing need for structural solutions that are sustainable, seismically safe, and ensure rapid reuse of the buildings has drawn attention to Post-tensioned (PT) rocking dissipative timber wall systems, which are mainly comprised of timber walls equipped with Post-tesioned bar (PT-bar) which are able to guarantee system recentering, and provided by steel damper for energy dissipation. The idea is that, during a seismic event, the timber wall works in the elastic field, while the dampers, which provide energy dissipation, are vulnerable to damage owing to their entry into plastic field, which also guarantees the energy dissipation; then, the damaged dampers can be easily replaced. The global Force/Displacement (F/Δ) response of the PT wall system is a typical flag-shape behavior as shown in Figure 1: the bilinear backbone curve is mainly controlled by the system's rocking behavior due to the presence of PT- bars, but the amplitude of the flag is governed by the dissipative contribution of steel dampers. Several experimental campaigns on post-tensioned wall systems can be found in the scientific literature [1–6], but also on whole buildings or on multi-story/ multi-panel solutions [7–10]. The growing diffusion of this structural system suggests the significance of developing numerical models capable of capturing their experimental responses, indeed, several contributions can be found in this field [11–15].

In this framework, the non-linear numerical model implemented in the open-source software OpenSEES [16] and presented in [15], is here adopted to perform a parametric study, to investigate the effect of several different parameters, such as: timber wall dimensions, initial post-tensioned force in the bars, mechanical properties of the timber wall and the number of axial dampers, on the global response of PT-wall systems in terms of Force/Displacement curves and PT-Force responses.

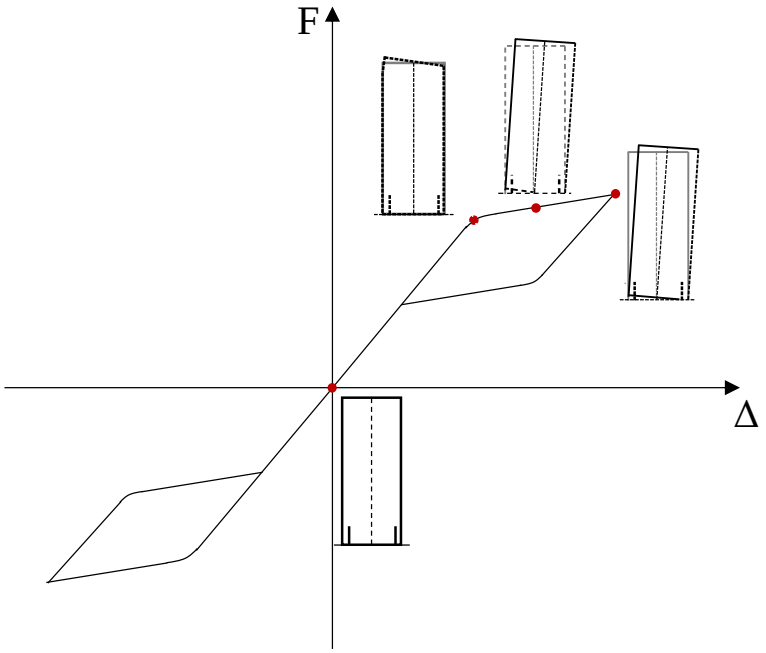


Figure 1: Typical flag-shape force/ displacement (F/Δ) curve of a PT- system subjected to cycling loading.

# 2 NUMERICAL MODEL

## 2.1 Description of the numerical model

The PT-wall configuration employed to carry out parametric analysis is a single wall configuration which has been equipped with one PT-bar and two couples of axial dampers disposed along the base of the wall [15]. The proposed numerical model, which is developed as a 2D model in OpenSEES [16], takes into account both geometrical and material non-linearities to get the rocking behavior of the timber wall and the entry into the plastic field of hysteretic dampers, respectively. As shown in Figure 2, the timber panel is schematized with 2D quad elements to which an orthotropic material is assigned in terms of stress/strain curve (σ/ε). The PT-bar is modeled with a two-node link element, fixed at the base and connected at the top of the wall, to which a steel material is assigned with an elastoplastic force-displacement curve, characterized by an elastic stiffness K and a yielding force $F_y$; further, an initial level of deformation $\varepsilon_{in}$ is introduced to simulate the initial PT-Force. The axial dampers are modeled with zero-length elements and a hysteretic force-displacement curve is calibrated according to experimental results (section2.2). Furthermore, the wall is connected at the base with unilateral constraints able to provide displacements once upward (gap elements), in order to simulate the rocking behavior of the timber wall. The numerical model is subjected to cyclic static nonlinear analysis, and the control point is disposed at the top of the wall; the loading protocol is chosen in analogy to that employed in the experimental analyses used to validate the proposed numerical model.

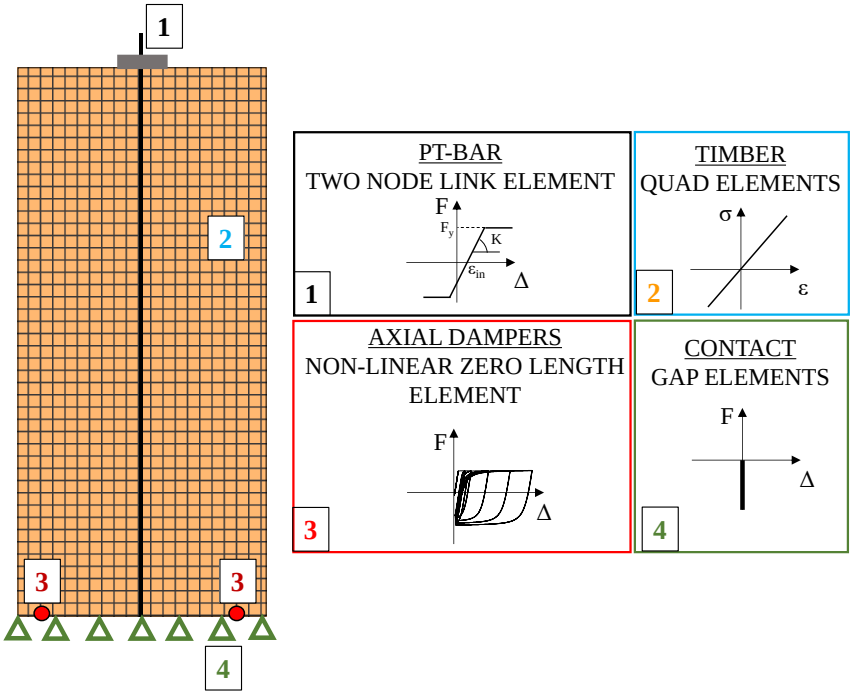


Figure 2: Numerical meshes of PT-wall setup.

In order to validate the numerical model, the experimental tests performed by Chen et al. 2020 [4] were employed as a reference. In particular, the setup has been characterized by a single CLT panel equipped with one PT-bar positioned in the middle of the wall, and with two couples of axial dampers located along the base. Further detailed information on the selected experimental campaigns are reported in Table; in particular, there are information on geometrical characteristic and material properties, where: $E_L$ and $E_T$ are the elastic moduli of the timber,

$G_{LT}$ and $G_{LR}$ are the shear moduli of the timber, with subscripts L, T, R that indicate longitudinal, transverse and radial directions, respectively; $E_b$ is the elastic modulus of the steel of the PT-bar, PT-$F_{in}$ is the initial PT-Force imposed on the PT-bar; $f_{y,A}$ and $E_A$ are the yielding stress and the relevant elastic modulus of the axial damper.

| Element | Material | Property | Value |
|---|---|---|---|
| Wall | CLT | $E_L=E_T$ | 6000 MPa |
| | | $G_{LT}=G_{LR}$ | 348 MPa |
| PT-bar | Steel | Fb | 205 GPa |
| | | PT-$F_{in}$ | 89 kN |
| | | Diameter | 20 mm |
| Axial Damper | Mild Steel | $F_{y,A}$ | 300 MPa |
| | | $E_A$ | 200 GPa |

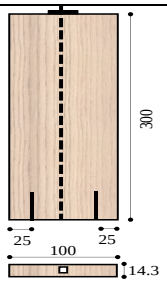


Table 1: Geometrical and mechanical parameters of the selected experimental campaign [4]

The nonlinear law adopted for the dampers is calibrated based on preliminary axial experimental tests performed on the axial dampers, by minimizing differences in terms of strength, stiffness and cyclic behavior between the numerical response and the experimental one. The adopted numerical law is the Giuffré-Menegotto-Pinto Model with Isotropic Strain Hardening [17], which is implemented in OpenSEES as "Steel 02". Table 2 shows the values assigned to the parameters of the "Steel 02" law: $F_y$, the yield strength; E, initial elastic tangent stiffness; b, hardening ratio; R0, $c_{R1}$ and $c_{R2}$, i.e. the parameters that control the transition from elastic to plastic branches [17].

| Constitutive law | Parameters | Values |
|---|---|---|
| STEEL 02 | $F_y$ (kN) | 42.5 |
| | E (MPa) | 43000 |
| | b | 0.02 |
| | R0 | 50 |
| | $c_{R1}$ | 0.955 |
| | $c_{R2}$ | 0.2 |

Table 2: Parameters assigned to Steel 02" law for axial dampers.

## 2.2 Outcomes of the numerical evaluation

The comparison between the experimental cyclic behavior of the axial dampers and the calibrated numerical one, is reported in Figure 3 in terms of force-displacement curve. The Force/ Drift responses and Post-tension force/ Drift curves are reported in Figure 4a and b, respectively. The strong contribution of the hysteretic dampers is evident in the Force/ Drift response; in particular, a drift value other than zero at zero force is provided, due to the contribution of the dampers that is more pronounced than that of the PT-bars, leading to a poor recentering system and no evident flag behaviour, as illustrated in Figure 1. The high contribution of dampers is also evident in terms of strenght, since the Force/Drift envelope slightly differs from the bilinear trend, as shown in Figure 1. The rocking behaviour is emerged by the Post-tension force/ Drift curves, in which the PT-Force substantially increases while moving from the position of zero drift to the position of drift larger than zero in absolute value. Both the Force/ Drift responses

and Post-tension force/ Drift ones are well captured by the numerical models, with the exception of a small difference in terms of PT-force variation which reaches 20% for the Drift of 2.5%.

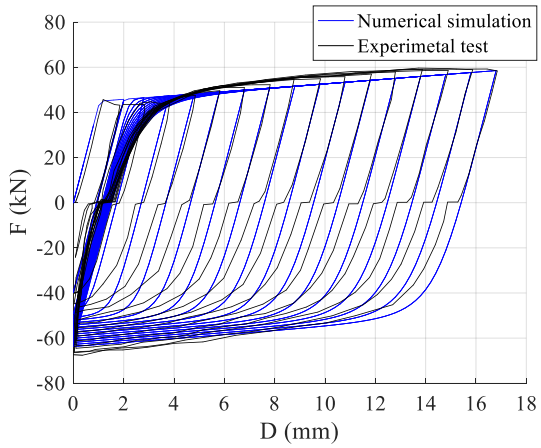


Figure 3: Calibration of axial dampers – Force/Displacement (F/D) response.

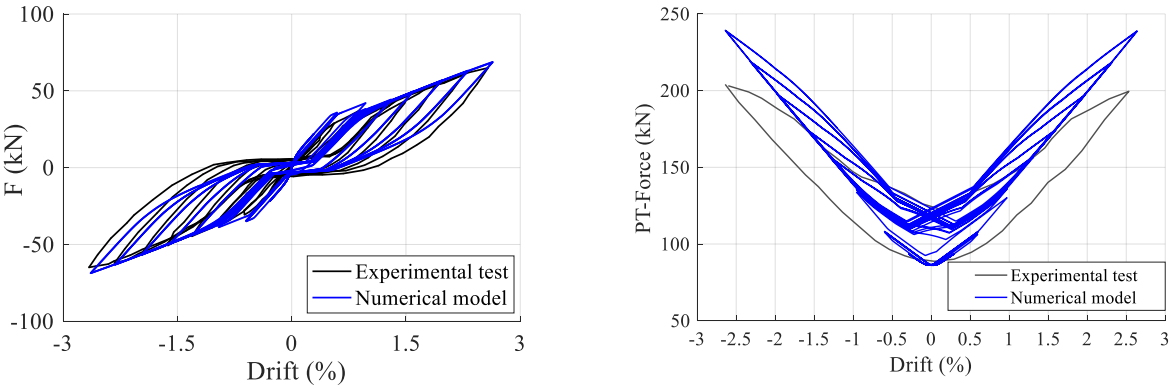


(a) (b)

Figure 4: Comparison of numerical and experimental Force/Drift responses.

## 3 PARAMETRIC INVESTIGATION

Starting with the setup analysed in section 2.2, a set of parametric analysis is carried out to assess the effect of different paremeters on the response of PT-wall systems. The investigated parameters are the main geometrical and mechanical parameters, as well as the applied post-tensioned force, which are as follows: B = the wall base; H = the wall height; the initial PT-force of the bars, E= the timber characteristics in terms of elastic modulus (that indicates, for simplicity, the value of $E_L$=$E_T$ defined in section 2.2) and G= shear modulus (that indicates the value of $G_{LT}$ =$G_{LR}$ defined in section 2.2) and the number of axial dampers. All the analysis are carried out imposing an initial level of PT-Force of 135 kN, unless otherwise indicated.
Figures 5 to 7 illustrate the results in terms of Force/Drift curves. Figure 5 shows the effect of wall dimensions on increasing strength and stiffness. These increases become more evident as B increases (Figure 5a), due to the presence of axial dampers, which are subjected to higher displacement if the distance from the corners remains constant, and therefore they provide an ever more evident contribution in terms of strength, stiffness and dissipative capacity. Figure 6 shows the variety of mechanical properties in terms of E and G (Figure 6a) as well as PT-force

(Figure 6b). As seen in Figure 6a, strength and stiffness may be slightly influenced by changing E and G, while, as expected, no effective difference in terms of dissipative capacity is provided, since no difference in the amplitude of the Force/Drift curves is noticed The effect of the initial value of PT-Force is shown in Figure 6b: increasing this value, the system's strength , stiffness and re-centering capability enhance, as shown by the well defined flag shape of the Force/ Drift curve obtained for an initial PT-Force of 270 kN. Figure shows the influence of the number of axial dampers: a greater number of axial dampers assures higher strength, stiffness and dissipative capacity of the system, at the detriment of the re-centering capability, which instead reduces.

In syntesis, the effect of the analysed parameters on the global behaviour of the system can be summarized as follows:

- increasing the base of the wall B, also initial stiffness, strength, and dissipative capacity significantly increase;
- increasing height of the wall H, the initial stiffness and strength show a slight variation;
- there is a slight effect of changing mechanical properties in terms of E and G on strength, stiffness and energy dissipation;
- increasing initial PT-Force of the bar, strength and stiffness of the system increase, but the most important effect is in significantly improve the re-centering capacity of the system;
- increasing number of axial damper, strength and dissipative capacity of the system increase, while the the re-centering capacity decreases.

Downstream of this brief description, in order to design a PT-wall system with good re-centering capacity and a good dissipative capacity, it is important to pay attention to the number of dampers to provide in the function of the initial PT-Force of the bars. Moreover, with the same number of dampers and initial PT-Force, it is possible to improve strength and stiffness of the system by increasing the dimensions of the walls.

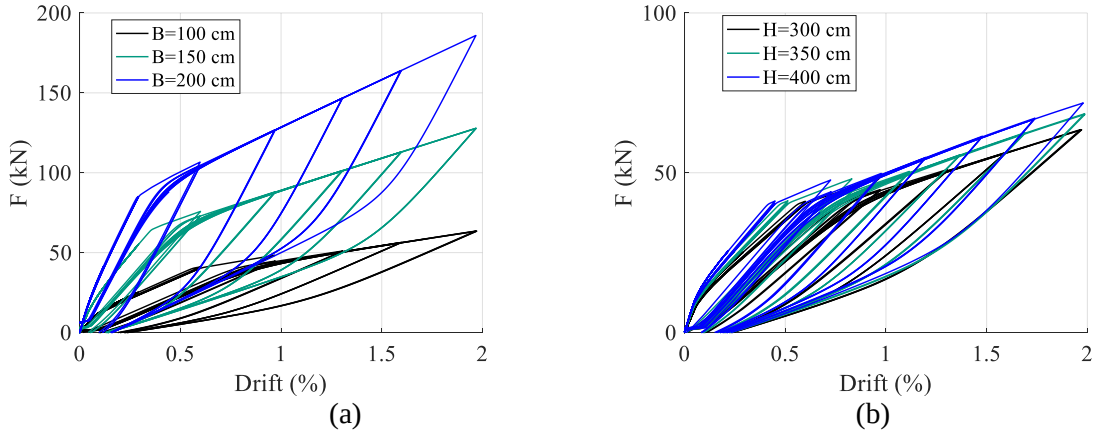


Figure 5: Effect of the timber wall geometrical parameters on Force/ Drift response: wall base B (a) and wall height H (b).

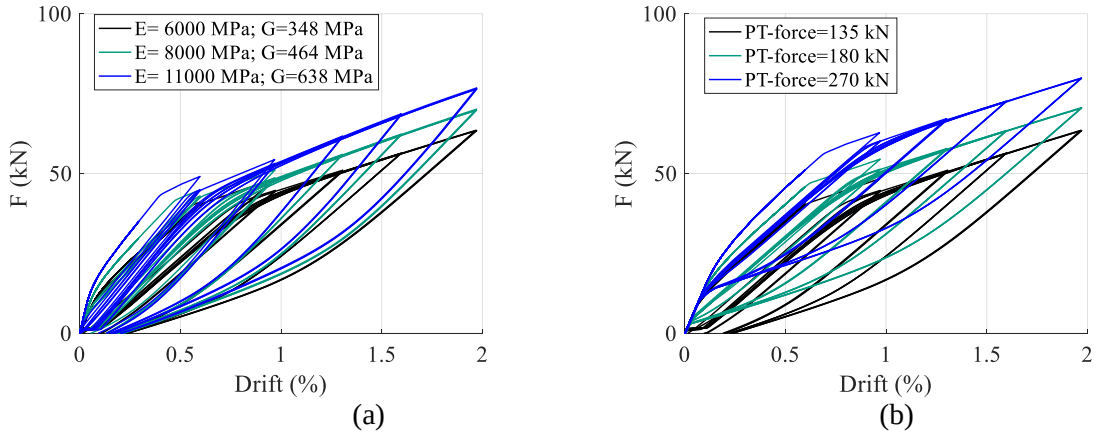


Figure 6 Effect of the mechanical characteristics E and G (a) and of the initial PT-Force on Force/ Drift response (b).

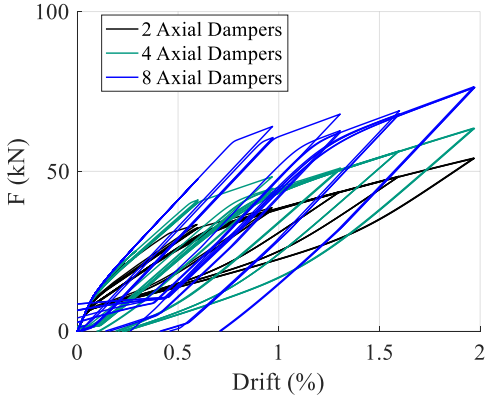


Figure 7:Effect of the number of axial dampers on the Force/ Drift response.

## 4 CONCLUSIONS

A Finite Element nonlinear numerical model was developed in the OpenSEES environment for the evaluation of the cyclic response of Post-Tensioned dissipative timber walls systems. The numerical model, which takes into account of both material and geometrical non-linearities, was validated firstly with the results of an experimetal campaign carried out on a single wall system equipped with one PT-bar and two couples of axial dampers disposed near the corners, along the base. The validation was performed by comparing the global results in terms of Force/Drift curves and PT-bar/Drift responses, showing a good agreement in terms of stiffness, strength, cyclic behaviour, and energy dissipation. After validation, a parametric analysis was carried out in order to analyse the role of different parameters on the global behavior of post-tensioned timber walls: the wall base; the wall heigh; the initial post-tensioned force of the bars; the timber mechanical properties; the number of axial dampers. The results highlight that an important effect on initial stiffness, strength, and PT-Force variation is due to the variation of the base wall, while the initial post-tension in the bar has an important role on the re-centering capacity of the system; the number of dampers strongly affects both the dissipative capacity and the recentering contribution of the system.

## 5 ACKNOWLEDGEMENT

The financial support of ENHANCE 2021-2023 - Research Groups 2020, financed by the POR FESR Lazio 2014 - 2020 (Action 1.2.1), are gratefully acknowledged.

## 6 REFERENCES

[1] A. Iqbal, S. Pampanin, A. Palermo, A.H. Buchanan, Performance and design of LVL walls coupled with UFP dissipaters, *J. Earthq. Eng*. **19** (2015) 383–409. https://doi.org/10.1080/13632469.2014.987406.

[2] F. Sarti, A. Palermo, S. Pampanin, Development and Testing of an Alternative Dissipative Posttensioned Rocking Timber Wall with Boundary Columns, *J. Struct. Eng. (United States)*. **142** (2016). https://doi.org/10.1061/(ASCE)ST.1943-541X.0001390.

[3] M. Massari, M. Savoia, A.R. Barbosa, Experimental and Numerical Study of Two-Story Post-Tensioned Seismic Resisting CLT Wall with External Hysteretic Energy Dissipaters, *in: Atti Del XVII Convegno ANIDIS L'ingegneria Sismica Ital*., 2017.

[4] Z. Chen, M. Popovski, A. Iqbal, Structural Performance of Post-Tensioned CLT Shear Walls with Energy Dissipators. *Journal of Structural Engineering, J. Struct. Eng*. **146** (2020). https://doi.org/doi:10.1061/(asce)st.1943-541x.0002569.

[5] L. Pozza, L. Benedetti, V. Tomei, B. Ferracuti, M. Zucconi, C. Mazzotti, Cyclic response of CLT Post-Tensioned Walls: Experimental and numerical investigation, Constr. *Build. Mater*. 308 (2021) 125019. https://doi.org/10.1016/J.CONBUILDMAT.2021.125019.

[6] L. Pozza, L. Benedetti, V. Tomei, B. Ferracuti, M. Zucconi, C. Mazzotti, Post-Tensioned low damage CLT walls with replaceable hysteretic devices – concept, experimental and numerical characterization, in: *M. Papadrakakis, M. Fragiadakis (Eds.), 8th Int. Conf. Comput. Methods Struct. Dyn. Earthq. Eng. Streamed from Athens*, Greece 28-30 June 2021, Institute of Structural Analysis and Antiseismic Research School of Civil Engineering National Technical University of Athens (NTUA) Greece, Streamed from Athens, Greece, 2021: pp. 2352–2358.

[7] S. Pei, J.W. Van De Lindt, A.R. Barbosa, J.W. Berman, E. McDonnell, J. Daniel Dolan, H.E. Blomgren, R.B. Zimmerman, D. Huang, S. Wichman, Experimental Seismic Response of a Resilient 2-Story Mass-Timber Building with Post-Tensioned Rocking Walls, *J. Struct. Eng*. (United States). 145 (2019). https://doi.org/10.1061/(ASCE)ST.1943-541X.0002382.

[8] J.R. Brown, M. li, A. Palermo, S. Pampanin, F. Sarti, Nokes. Roger, Experimental testing and analytical modelling of single and double post-tensioned CLT shear walls, *Eng. Struct*. **256** (2022).https://doi.org/https://doi.org/10.1016/j.engstruct.2022.114065.

[9] A. Polastri, D. Casagrande, Mechanical behaviour of multi-panel cross laminated timber shear-walls with stiff connectors, Constr. *Build. Mater*. **332** (2022) 127275. https://doi.org/10.1016/j.conbuildmat.2022.127275.

[10] R. Thiers-Moggia, C. Málaga-Chuquitaype, Performance-based seismic design and assessment of rocking timber buildings equipped with inerters, *Eng. Struct*. **248** (2021) 113164. https://doi.org/10.1016/j.engstruct.2021.113164.

[11] A.W. Wilson, C.J. Motter, A.R. Phillips, J.D. Dolan, Modeling techniques for post-tensioned cross-laminated timber rocking walls, *Eng. Struct*. **195** (2019) 299–308. https://doi.org/10.1016/j.engstruct.2019.06.011.

[12] V. Tomei, M. Zucconi, B. Ferracuti, Cyclic model of post-tensioned low damage timber walls with dissipative devices, *Procedia Struct. Integr*. **44** (2023) 598–604. https://doi.org/10.1016/J.PROSTR.2023.01.078.

[13] T.X. Ho, T.N. Dao, S. Aaleti, J.W. van de Lindt, D.R. Rammer, Hybrid System of

Unbonded Post-Tensioned CLT Panels and Light-Frame Wood Shear Walls, *J. Struct. Eng*. **143** (2017) 04016171. https://doi.org/10.1061/(asce)st.1943-541x.0001665.

[14] V. Tomei, M. Zucconi, B. Ferracuti, Post-tensioned rocking dissipative timber wall systems: Numerical prediction, *J. Build. Eng*. **66** (2023). https://doi.org/10.1016/J.JOBE.2023.105897.

[15] Z. Chen, M. Popovski, Material-based models for post-tensioned shear wall system with energy dissipators, *Eng. Struct*. **213** (2020). https://doi.org/10.1016/j.engstruct.2020.110543.

[16] F. McKenna, M.H. Scott, G.L. Fenves, Nonlinear finite-element analysis software architecture using object composition, *J. Comput. Civ. Eng*. **24** (2010). https://doi.org/10.1061/(ASCE)CP.1943-5487.0000002.

[17] F.E. Fllippou, E.P. Popov, V. V Bertero, Effects of bond deterioration on hysteretic behavior of reinforced concrete joints, Report EERC 83-19, *Earthquake Engineering Research Center*, University of California, Berkeley, 1983.

COMPDYN 2023
9th ECCOMAS Thematic Conference on
Computational Methods in Structural Dynamics and Earthquake Engineering
M. Papadrakakis, M. Fragiadakis (eds.)
Athens, Greece, 12-14 June 2023

# THE USE OF STRUCTURAL TIMBER IN EUROPE: AN OVERVIEW ON RECENT DEVELOPMENTS

**Valentina Tomei[1], Martina Sciomenta[2], and Antonio Sandoli[2]**

[1] University of Cassino and Southern Lazio
Department of mechanical and Civil Engineering
e-mail: v.tomei@unicas.it

[2] University of L'Aquila
Department of Civil, Building and Architecture and environmental Engineering
martina.sciomenta@univaq.it

[2] University of Molise
Department of Biosciences and Territory
antonio.sandoli@unimol.it

## Abstract

*The prerogatives of sustainability, excellent strength-to-weight ratio and high prefabrication level, make the structural timber as a highly performant construction material widely used in Europe for new constructions or for retrofitting the existing ones. The recent development of structural timber was due to the introduction of engineered wood products that gave the possibility to realize buildings for residential and commercial destinations, also in seismic- prone areas. Moreover, in the light of the Next Generation EU Plan - released be the European Parliament as aid to the economy recovery following the covid-19 pandemic - which introduced the concept of green transition to reduce emissions of carbon dioxide into the atmosphere, timber surely occupies a prominent place among the building materials.*
*This paper deals with an insight on the use of timber in Europe as sustainable, green, and highly seismic and energetic performant construction material. The aim is that of providing a comprehensive overview on the state-of-art and highlighting recent advancements and future trends both in research field and engineering practice in Europe. Particular emphasis is paid to (i) new timber-based products and/or subassemblies used for low, medium and high-rise seismic-resistant constructions; (ii) timber-based solution for combined seismic and energetic retrofit of existing masonry and reinforced concrete buildings; (iii) new prospective of short chains to improve life cycle of material and its impact on environment, (iv) codes and guidelines. The peculiarities of each topic treated are discussed in detail.*

**Keywords:** Structural Timber, Timber Products, Timber Buildings, Retrofit, Codes.

# 1 INTRODUCTION

Timber based constructions are spreading in Europe in the last two decades in order to pursue the growing need to have high-performance buildings, both from structural and energetic points of view [1,2]. In this context, the (relative) recent introduction of engineered timber products - such as Glue-Lam, Cross-Laminated Timber, Laminated Veneer Lumber, OSB, etc., realized with automated-control industrial processes - offered new possibilities in realizing timber-based structures with respect to traditional solid wood elements [3,4]. In addition to classic timber roofs, single or multiple span bridges, engineered products have led to the possibility of realizing new structural solutions for timber buildings in seismic-prone area, concerning fully timber low- or mid-rise constructions and hybrid structural solutions (i.e., that couples timber elements with concrete or steel) [5, 6, 7]. The growing interest towards the use of timber elements and the introduction of engineered timber buildings (both for residential and industrial sector) has motivated the scientific community to update the existing timber codes; the aim is that of align and transfer the scientific background concerning the seismic design rules developed for other construction type (i.e., reinforced concrete or steel) to timber structures [8, 9].

Due to the potentials offered by raw material - related to structural and environmental aspects - timber constructions strongly attracted the attention of the researchers in the last years, especially in Europe. Moreover, the Next Generation EU plan, released by the European Parliament following the Covid-19 pandemic, accentuated the use of timber products because particularly suitable in the framework of integrating structural performances and energetic aspects both for new buildings and for retrofitting the existing ones [10,11].

Looking at existing buildings, studies on the use of timber elements for retrofitting existing masonry and reinforced concrete buildings occupy a prominent position in the last two/three years in Europe [12]. Several solutions, mostly oriented to integrate seismic and energetic aspects, have been recently introduced in the scientific literature and other are under development.

The aim of the paper is to provide an overview on recent developments and trends concerning the use of structural timber in Europe, with particular emphasis on structural, energetic and short chain/life cycle aspects. The work is subdivided in three main Sections, organized as follows: Section 2 focuses on timber-based products available in Europe and the structural solutions mainly used for low-, mid- and high-rise timber buildings; Section 3 focuses on the potentialities offered by timber-based solutions for seismic and energetic retrofit of existing buildings and reports a state of the art on scientific studies conducted on this topic; Section 4 discusses about the new prospective of short chains to improve life cycle; Section 5 reports a brief recognition on codes and guidelines devoted to structural design of timber elements, subassemblies and buildings.

# 2 TIMBER-BASED PRODUCTS FOR LOW, MEDIUM AND HIGH-RISE BUILDINGS IN SEISMIC-PRONE AREA

## 2.1 Products

Thanks to technological innovations and research advancements, the performance of timber-based products become more and more excellent over the years. Basically, timber products were made by solid hard- or soft-wood elements in the past, whose dimensions were regulated by natural limits of base material. All the products illustrated in this section are summarized in the Tables 1, 2 and 3. Thereafter, the introduction of industrial production gave the opportunity to introduce on the market the so-called *engineered timber products*, where Glue-Laminated Timber (GLT) surely represents the emblematic example [13]. On the other hand, also glued solid wood elements are performant products, such as the KVH whose main advantage is that

of using solid wood element joined with finger joints along its longitudinal axis; thus, they represent a right compromise between solid and GLT to realize one-dimensional timber elements used for beams and columns (https://lnx.dartalegno.com/wp/product/kvh/).

New opportunities offered by the industrial production processes, allowed to realize bi-dimensional elements also. For instance, Oriented Strand Board (OSB) is a structural panel product realized by bonding together thin wood strands with adhesive, mainly used as infill panel into light-timber frame structures or to realize web-element in composite I-beams. Plywood fibreboards panels, instead, are made of stacked veneers organized in an odd number of layers bonded together to produce a flat sheet. (https://timberproducts.com/softwood-plywood/).

| **Products for one-dimensional elements** | | | | |
|---|---|---|---|---|
| Product | Description | Advantages | Disadvantages | |
| Solid wood | Solid wood | High strength | Dimensional limits |  |
| https://royomartin.com/product/solid-wood-timbers/ (accessed on 20 March 2023) | | | | |
| KVH | Solid structural sawn construction finger-jointed timber, made from softwood | High strength | Standardization of solid wood |  |
| https://lnx.dartalegno.com/wp/product/kvh/ (accessed on 20 March 2023) | | | | |
| GluLAm | Pieces of wood glued together under pressure and heat | Curved shapes<br>Availability | Production cost |  |
| https://www.naturallywood.com/products/glulam/ (accessed on 20 March 2023) | | | | |
| I-beams | The top and bottom flanges are made with LVL, the web is made with plywood or OSB | Lightness<br>High strength and Stiffness | |  |
| https://www.woodsolutions.com.au/wood-species/wood-products/i-beams (accessed on 20 March 2023) | | | | |

Table 1: Timber products for one-dimensional elements.

| **Products for both one-dimensional and two-dimensional elements** | | | | |
|---|---|---|---|---|
| Product | Description | Advantages | Disadvantages | |
| CLT | Wood panel product made from gluing together at least three layers of solid-sawn lumber | More uniform mechanical properties than wood<br>High load bearing capacity | Production cost<br>Renovations and changes are difficult |  |
| https://www.naturallywood.com/products/cross-laminated-timber/ (accessed on 20 March 2023) | | | | |
| LVL | Composite product manufactured from multiple thin layers of veneer that are aligned with the length of the finished lumber | High strength properties<br>Low cost<br>Stronger than wood | Susceptible to warm if not properly stored |  |
| https://www.steico.com/en/solutions/product-advantages/lvl-laminated-veneer-lumber (accessed on 20 March 2023) | | | | |

Table 2: Timber products for both one-dimensional and two-dimensional elements.

As extremely versatile product, plywood is used for a wide range of structural interior and exterior applications; instead, particleboard panel is an interior-use engineered wood panel product, manufactured from wood particles. Among the engineered products, CLT surely represents the structural element most used to realize panels or beams in mid- and high-rise timber buildings in the last years [14]. CLT was introduced in Austria about thirty years ago, and its success is mainly due to (*i*) strength and stiffness both in-plane and out-of-plane, (*ii*) high dimensional stability, (*iii*) elevated in-plane isotropic strength and stiffness with respect to sawn timber, (*iv*) high speed of installation; and (*v*) the environmental benefits compared to other construction materials like steel, concrete and masonry [15,16]. CLT, and in general mass timber products, can be made from both softwoods or hardwoods timber species if engineered properly, but construction-grade softwoods such as spruce, pine, and fir are commonly employed [17].

| **Products for two-dimensional elements** | | | | |
|---|---|---|---|---|
| Product | Description | Advantages | Disadvantages | |
| OSB | Thin wood strands disposed in crosshatch orientation bonded together with adhesive | Cheap with respect plywood<br>Uniform mechanical properties | Prone to retaining moisture that can result in the swelling of the board's edges<br>It doesn't look very nice |  |
| https://noyekplywood.co.uk/products/osb-board/ (accessed on 20 March 2023) | | | | |
| Plywood | Strong panel made by thin veneers pressed together in perpendicular layers | Cheap with respect solid wood<br>No susceptible to water damage<br>Uniform strength | Difficult to cut |  |
| https://timberproducts.com/softwood-plywood/ (accessed on 20 March 2023) | | | | |
| Fibreboard | Wallboard made of wood chips, plant fibres, softwood flakes | Thermal insulation<br>Light weight and easy to handle | Weaker than wood |  |
| https://www.floorsave.co.uk/blog/fibreboard/ (accessed on 20 March 2023) | | | | |
| LSL | Panels made of dried and graded wood veneers, strands or flakes that are layered upon one another and bonded together with a moisture-resistant adhesive | Low cost<br>Stronger than wood | It doesn't look very nice |  |
| https://www.naturallywood.com/products/laminated-strand-lumber/ (accessed on 20 March 2023) | | | | |
| NLT | Structural elements realized by dimension lumber stacked together on its edge and fastened together with nails | Easily to fabricate | Once nailed, there is no possibility for rearrangement of timber panels |  |
| https://wbdg.org/ (accessed on 20 March 2023) | | | | |
| DLT | It is an evolution of NLT, with the inclusion of wooden dowels, used to replace the nails or adhesives | Flexible in terms of attachment and construction | Hardwood fasteners or dowels lose their stiffness over time |  |
| https://www.naturallywood.com/products/dowel-laminated-timber/ (accessed on 20 March 2023) | | | | |

Table 3: Timber products for two-dimensional elements.

With regards to LVL, which is used both for two- or one-dimensional elements, it is made of dried and graded wood veneers, strands or flakes that are layered upon one another and bonded together with a moisture resistant adhesive [18]. Similarly, Solid Wood Panels (SWP) are made with timber boards glued on the edges and, if multi-layered, glued also on the upper and bottom surfaces. Laminated Strand Lumber (LSL) instead is another product similar to LVL; the difference is that it is made of flakes in lieu of layers of veneers, which are bonded together employing heat and adhesives (https://www.naturallywood.com/products/laminated-strand-lumber/). Literature studies highlighted (experimentally) the benefit in employing LSL with respect CLT in terms of bending properties [19].

Among the mass timber products, Nail-Laminated Timber (NLT) and Dowel-Laminated Timber (DLT) should be mentioned too. NLT and DLT, whose concept is dated back to the renaissance, consist of single lamellae superimposed one each other and mechanically fastened together with nails (or screws) or by hardwood timber dowels, respectively. The lamellae are disposed with its base in vertical direction and are used to realize floors mainly, also in union with a concrete slab on the top [4].

Among engineered wood products, it is interesting to mention composite elements, such as wood I-beams, light beams realized by gluing LVL flanges and plywood or OSB webs (helpful to provides high strength and stiffness thanks to the I-configuration) (https://www.woodsolutions.com.au/wood-species/wood-products/i-beams).

### 2.2 Buildings

In the last two decades, different factors lead to a global increase in the construction of mid- and high-rise multi-storey timber buildings: new developments in both engineering and timber manufacturing, and, overall, the ever growing need to reduce the environmental impact [20].

Until few years ago, low-rise timber buildings made with one-, two- or three-storey light-timber frame or log-haus buildings were mainly realized, while only in the last decades CLT buildings were introduced [21, 22]. Nevertheless, the recent introduction of hybrid systems, which couple timber elements with concrete or steel ones, leads the construction of mid- and high-rise timber-based buildings in seismic prone area too [23]. Indeed, the term high-rise building is not yet standardised for timber buildings but in literature it is suggest considering high-rise constructions when surpassing 10 floors or 25 meters high [22]. In Europe, the first example of high-rise timber building is the 14-storey Treet building in Bergen built in 2014 in Norway [22], completely realized with timber elements Figure 1 (a). In particular, the main structural system is composed by a glu-lam truss, which takes inspiration from contemporary bridge design, while the cellular units are realized by assembling prefabricated CLT modules and framework in laminated timber. It should be emphasised that this building is located in a low seismic area, this has make possible to realize the structure entirely with timber.

The first mid-rise European timber building is the E3 building built in Berlin in 2007 (Figure 1 (b)), designed by architects Kaden and Klingbeil. It is a seven-storey timber structure realized with glu-lam frame and CLT timber panels for walls, and equipped with two concrete cores; instead, the horizontal structures are realized with timber-concrete composite floors [24]. In 2013, the largest CLT residential complex was realized in low-seismic prone area in Milan (Italy), the Social Housing in via Cenni (Figure 1 (c)). The complex is divided into four timber towers of 27 meters high, connected between them by several two-storey linear buildings.

In Switzerland, timber high-rise buildings that reaches a height of 30 m have been realized. The first two buildings are the Suurstoffi S22 (Figure 1 (d)) completed in 2018 and the Arbo (Figure 1 (e)) completed in 2019, having 10 and 15 floors respectively. In particular, the Suurstoffi S22 is an hybrid building characterized by a concrete core, first floor in concrete,

and the higher floors are provided by structural elements in laminated timber. The Arbo is a 60-storeys timber-hybrid building provided with reinforced concrete cores, frame is realized with elements in LVL and GluLam and the floors are in composite timber-concrete elements [25].

The high structural performances provided by hybrid timber buildings, lead to several design proposal aiming to overcome the height limits. Just some European example will be highlighted. Arup Group Limited proposed a 21-storey, 73 m high, tall timber building in Amstelkwartier, Netherland, i.e. the tallest timber building in the country, and further one of the tallest in the world upon completion; it is composed by internal CLT load bearing walls and CLT panels in the facades, while the ground and first floor are made of concrete. To date, two hybrid solutions have been explored during the design phase: a concrete-timber hybrid lateral stability system and a steel-timber hybrid one; after the preliminary analysis, the first solution has been chosen. [26]. Anders Berensson Architects proposed the Tratoppen building (Figure 1 (f)), a 40-story timber building to be built in Stockholm, made in laminated timber from the sixth-floor ad made of concrete for the firts floors. Finally, the Department of Architecture at Cambridge University, conceptually designed a 300 m high high-rise timber building in London, England [27], provided by timber mega-diagonals (Figure 1 (g)).

Coming out of Europe, a pioneering hybrid timber building is the 53 m tall Brock Commons Tallwood House in Vancouver (Figure 1 (h)), Canada [26], an 18-story hybrid mass timber residence at the University of British Columbia. Also in this case, 17 storeys are realized in mass timber elements, upon a concrete podium and two concrete stirs cores; the floor structure is made of CLT panels supported by Glulam columns, while the roof is made of steel beams and metal decking (https://www.thinkwood.com/construction-projects/brock-commons-tallwood-house). Ever in Canada, Michael Green and Eric Karsh proposed a 30-story hybrid tall mass-timber building known as “Finding the Forest through the Trees” [27], designed with 3 CLT panels connected by hinged steel beams (Figure 1 (i)). In the USA, the SOM (Skidmore, Owings and Merrill) proposed a design of a 42-story hybrid tall timber building, presented at the 2016 Mass Timber Conference in Portland, in which discuss the great benefits in terms of combining wood, concrete and steel in order to achieve highly efficient buildings with a reduced carbon footprint with respect the same building realized in concrete (https://www.ingenio-web.it/articoli/som-realizza-il-timber-tower-research-project/).

The most diffuse structural system for low-rise timber buildings in Europe is made of Cross Laminated Timber (CLT) walls connected to each other and to the foundation with thin-steel plates nailed to timber panels and anchored in foundation by means of steel anchors [7, 9, 30]. Since the timber panels cannot provide a ductile behaviour, they should work in the elastic field also during a seismic event, meaning that the energy dissipation is mainly entrusted to steel connectors, which, therefore, can be severely damaged after a seismic event. In this context, low-damage rocking systems, firstly introduced in New Zealand [31], are today studied also in Europe as an alternative to traditional CLT buildings above-described.

As advantage, post-tensioned walls entrust the energy dissipation to steel dampers, easily replaceable after a seismic event, while the re-centering contribution is provided by post-tensioned bars inserted in ad hoc cavities in the CLT walls [32, 33, 34].

In order to increase the sustainability of post-tensioned rocking dissipative solutions, these are also recently investigated by Lu et al. [32] employing Cross-Laminated Bamboo (CLB) panels instead of timber ones. In the proposed system, an innovative dissipation damper is also proposed, composed by friction dampers disposed at the lower corners of the walls, equipped with steel bars orthogonal to the friction plates, which provide dissipation energy through bending deformation.



(a) (b) (c)



(d) (e) (f)



(g) (h) (i)

Figure 1: Timber-based buildings: (a) Treet building [28]; (b) E3 building - available online: https://www.world-constructionnetwork.com/projects/e3-leaf/ (accessed on 03 March 2023); (c) Social Housing - available online: http://www.rossiprodi.it/?project=social-housing-via-cenni-2 (accessed on 09 March 2023); (d) Suurstoffi S22 - available online https://burkardmeyer.ch/projekte/suurstoffi-22-risch-rotkreuz/ (accessed on 03 March 2023); (e) Arbo - available online http://www.skyscrapercentre.com/building/arbo-cabral/37225 (accessed on 07 March 2023); (f) Tratoppen building - available online https://www.skyscrapercenter.com/building/tratoppen/24866; (accessed on 07 March 2023); (g) 300 m tall buildings - available online https://plparchitecture.com/oakwood-timber-tower-london-uk/ (accessed on 07 March 2023); (h) Brock Commons Tallwood House in Vancouver available online https://www.thinkwood.com/construction-projects/brock-commons-tallwood-house (accessed on 07 March 2023); (i) Finding the Forest through the Trees [29]).

# 3 TIMBER-BASED SOLUTIONS FOR SEISMIC AND ENERGETIC RETROFIT OF EXISTING BUILDINGS

## 3.1 Brief state of the art

Timber-based solutions for retrofitting existing buildings can be considered a novel topic, either in research field and engineering practice. Literature overview remarks that most of the scientific works have been developed in the last few years substantially, while applications to real buildings are not still available (at least in the authors knowledge).

Table 4 reports a summary of some of the literature papers available on this topic, focusing on those investigating the effectiveness of specific techniques of interventions only. In addition to timber products, the Table reports the investigated aspects (e.g., seismic, energetic, or both), modes of applications (as endo- or exoskeletons) and a brief description of the interventions from structural point of view.

By looking at Table 4, some considerations arise: *a*) the great part of the research are developed in southern Europe (and in particular in Italy), this probably because the problem of updating existing buildings is particularly felt in seismic-prone areas; *b*) a large use of CLT panels as structural timber products can be observed, this is the reason of its high structural and energetic performant behavior.

Due to the great variety of the seismic-resistant interventions suitable with timber products, a classification in *exoskeletons* or *endoskeletons* appears necessary and useful for practical purposes: in the first case the retrofitting system is applied from outside of the building, while in the second one from inside. Such nomenclature, already used in Di Lorenzo et al. [38] for additional systems made with steel, has been declined to the case of timber-based systems [12]. Basically, the latter identifies two- or three-dimensional parallel or orthogonal additional skeletons applied to masonry or RC buildings. With respect to endoskeletons, exoskeletons are systems particularly beneficial in terms of monetary losses, damage reduction (to structural and nonstructural component) due to the operative working phases, and low invasiveness of interventions. Thus, they are particularly suitable in case of strategics structures- such as hospitals, police stations, first aided associations etc. – because no interruption of activities cause.

## 3.2 General features

Europe, and in particular the Mediterranean basin area, is constituted by significant percentage of old and vulnerable buildings stock made with no-code compliant - both from *seismic* and *energetic* points of view - masonry and reinforced concrete (RC) constructions.

Figure 2 reports the building stock distribution by age of construction in Europe provided by Ref [35]. About of 50% of the building stock is older than 50 years and many buildings in use today are hundreds of years old (i.e, historical masonry buildings). As matter of the fact, the great part of existing buildings has been constructed before the 1960s when seismic and energy regulations were very limited in Europe. About of 75% of the European buildings are inadequate to the current building standards in terms of energy efficiency [36]; whereas, about of 40% of them have been designed without particular seismic prescriptions or detailing (i.e., pre-1960).

| Scholars | Timber products | Investigated aspects | Application | Brief description of the intervention |
|---|---|---|---|---|
| | | Reinforced Concrete buildings | | |
| Sustersic and Dujic 2012 [39] | CLT panels | S+E | EnS | CLT infill panels for RC buildings |
| Sandoli et al. 2021 [37] | Post-tensioned CLT walls | S | ExS | CLT walls placed parallel to RC frames |
| Smiroldo et al. 2021 [40] | CLT panels | S+E | EnS+ExS | CLT infill panels for RC buildings |
| Barbagallo et al. 2021 [43] | CLT panels | S | EnS | CLT infill panels for RC buildings equipped with friction damper connections |
| Aloisio et al. 2022 [41] | CLT panels | S | EnS | CLT infill panels equipped with friction connections for RC buildings |
| Badini et al. 2022 [42] | CLT panels | S+E | ExS | Additional orthogonal CLT walls |
| Li Cavoli et al. 2023 [44] | CLT panels | S | EnS | CLT infill panels for RC buildings |
| | | Masonry buildings | | |
| Pozza et al. 2017 [45] | CLT panels | S | EnS+ExS | Exo- or Endoskeletons parallel to masonry walls |
| Valluzzi et al. 2021 [46] | CLT panels | S+E | ExS | CLT panels which envelope the buildings |
| Cassol et al. 2021 [50] | Vertical elements | S | EnD | Interior strong-backs made with vertical timber elements connected to masonry walls |
| Miglietta et al. 2021 [48] | Light-timber frame | S | EnS | Light-timber frame to reinforce masonry walls |
| Iuorio et al. 2021 [49] | OSB panels | S | ExS | OSB panels to prevent out-of-plane of masonry walls |

Legend: S= seismic, E=energetic, EnS=endoskeleton, ExS= esoskeleton

Table 4. Summary of some of the literature papers on timber-based solutions for retrofitting existing buildings.

With regard to energy efficiency, consumptions associated to spaces heating is the most significant contribution (about 60-80% of the total employed energy - https://ec.europa.eu/energy/eu-buildings-factsheets_en ), meaning that the skins of the buildings are inadequate to limit heat dispersions. Concerning the seismic aspects, buildings erected before 1960s rarely are designed according to seismic prescriptions or detailing, while those erected in the period 1960-1990 often observed limited seismic rules.

Fortunately, the awareness of the seismic risk and of the climate change - to which the Covid-19 pandemic has gravely added - has motivated massive financial measures to be applied around the strategic axes of digitalization and innovation, ecological transition and social inclusion. The Next Generation EU programme, released by the European Union in the aftermath of Covid-19 pandemic, has allocated funds devoted to seismic and energetic retrofitting of existing buildings.

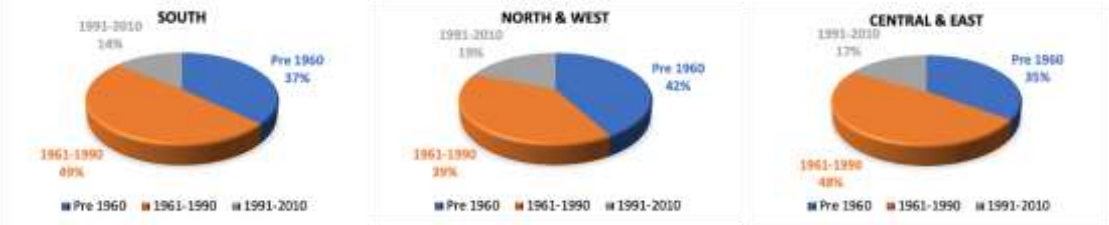


Figure 2. Age of construction of the building stock in Europe

In this framework, timber engineering has taken serious advancements in the research field introducing innovative integrated seismic and energetic retrofitting solutions for existing buildings. This has been strongly endorsed since the introduction of the engineered timber products (Glue-Lam, CLT, LVL, KVH, etc.) which represent an optimal alternative to traditional techniques of interventions. The main benefits related to the use of such products are (*i*) enhancement of the structural safety of the constructions against earthquakes (or other natural or man-made hazards) because increasing global shear capacity, stiffness and ductility of the retrofitted building; (*ii*) reduction of energetic consumption through the introduction of insulating systems of the perimetral skin of the buildings, (*iii*) the eco-sustainability of the interventions, due to natural intrinsic properties of wood material [37].

### 3.3 Intervention for RC buildings

Additional exo- or endoskeletons are adopted to improve the overall performances of existing RC buildings. Among the various timber engineered products, CLT panels are those frequently adopted in the scientific papers: due to their multi-layered configuration and intrinsic material properties, CLT can integrate seismic and energetic performance [14]. Some of the solutions, selected among the paper listed in Table 4, are discussed in the following. Following to 2012, where one of the pioneering studies was introduced by Sustersic and Dujic [39], a period of inactivity has characterized this research on this topic. A renewed interest on the potentiality offered by timber-based systems for retrofitting existing systems arise in the last few two/three years only. In 2021, Smiroldo et al. [40] proposed the use of CLT as infilled panels applied both from inside (endoskeleton) or from outside (exoskeleton) to existing RC framed buildings. Existing infill masonry are not demolished and CLT walls are connected to masonry by means of dry steel connectors. Inside the system, insulating layers made with wood fibers and polyurethane are also incorporated. Figure 3 reports the image of the system applied from outside of the building and the comparison among the pushover curves referred to as built and retrofitted RC frame. In the same image, the computation of the reduction energy consumption in the case of intervention made from outside or inside are indicated, in comparison with the un-retrofitted configuration.

In Figure 4, instead, is represented the reinforcing system proposed by Aloisio et al. [41], which consists of infill CLT panels connected to existing frames by means of asymmetric friction dampers (named with e-CLT). The Figure also compares the cyclic behavior of bare frame, infilled masonry RC frame and the e-CLT system: the introduction of CLT panel implies a strength reduction with respect the infill masonry frame but a significant increase in energy dissipation.

Sandoli et al. [37] proposed and investigated the potential offered by additional external post-tensioned CLT rocking walls applied to RC buildings by means of numerical analyses. CLT walls are connected to the existing frame through high-diameters steel connectors placed in the beam-to-column intersections at each story and in foundation through the post-tensioned cable (and shear key). Contrary to the case of infill CLT panels, an own foundation system (or an enlargement of that existing) devoted to withstanding the rocking behavior of timber walls is required in case of post-tensioned walls. The effectiveness of the system has been studied with reference to a real existing substandard six-storey RC building (designed for gravity loads only in Italy in 1960s) and analyzed through nonlinear static analyses.

Bandini et al. 2022 [42], instead proposed an integrated system able to join the enhancement of seismic and energetic performance with the need/opportunity of introducing additional spaces to existing RC buildings. The additional system consists of CLT-resisting walls inserted

in the plane perpendicular to the external facades, connected to CLT slabs. Connection to foundation and existing structure is made with traditional hold-downs and angle brackets; horizontal slabs are connected by means post-tensioned system. The structural performances of the system have been assessed by means of linear dynamic and nonlinear static analyses.

Result outcomes obtained either in Refs. [37] and [42] are the same, and summarized as follows: additive CLT external walls provide significant increases of strength and stiffness with respect to the existing structure; CLT walls are able to distribute the deformation demand along the elevation of the RC frames, changing the collapse mechanisms from local (brittle) mechanisms at ground story to mix collapse mechanisms which involve higher seismic energy dissipation; minimum or null damage into CLT walls is expected.

Nevertheless, other interesting studies have been conducted by Barbagallo et al. [43] which proposed infill CLT wall connected to existing structure by means of friction damper and by Li Cavoli et al. [44] which proposed infill CLT panels connected to existing RC frame through classic angle-brackets nailed to the panels a dowelled to the frame or with steel plated connected to CLT panels with high ductile dowels and dowelled to the frame.

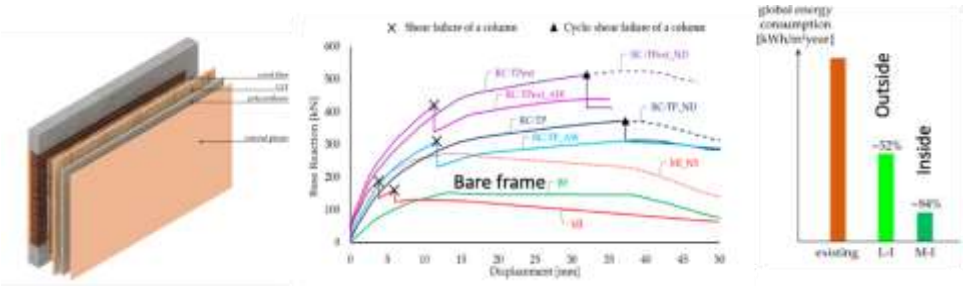


Figure 3: Retrofit solution proposed by Smiroldo et al. 2021 [40].

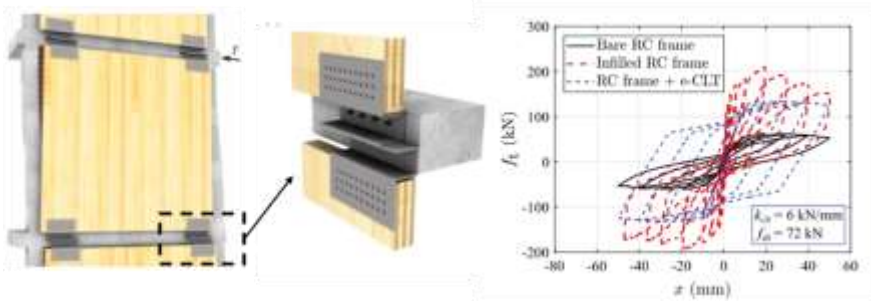


Figure 4: Retrofit solution proposed by Aloisio et al. 2022 [41].

### 3.4 Interventions for masonry buildings

Masonry buildings represent the structural typology most recurrent in the inner areas of Europe and in the historical centers of the most populated cities. Being, in most cases, buildings designed with lack of seismic or energetic prescriptions, integrated retrofitting interventions are crucial to reduce economic losses due to seismic damage or to reduce carbon emissions. In the perspective of seismic strengthening, retrofit solutions devoted to withstanding out-of-plane or in-plane mechanisms - often integrated with energetic solutions – are available in literature.

One of the first solution was proposed in Pozza et al. 2017 [45]. They studied, through experimental tests and numerical analyses, the effectiveness of CLT panels used as exo-or endo-skeleton to improve the seismic structural behavior (in- and out-of-plane) of masonry walls (Figure 5a). Whereas the thermal aspects have not been studied again. In Figure 5b is reported a comparison between the cyclic tests conducted on a single masonry panel unreinforced and

reinforced with a single CLT panel. Comparing results of the unreinforced and reinforced walls it is possible to state that the retrofit technique induces: no increase in terms of elastic stiffness, increase of post-elastic stiffness; negligible variation of the yielding point, significant increase of the peak force, significant increase of the displacement capacity and therefore of the ductility, since the yielding condition does not vary.

Valluzzi et al. [46] presented a valuable integrated structural and energy solution based on the concept of 'nested building' (Figure 6): it enables to retrofit and reuse existing buildings by (i) preserving the external envelope, (ii) removing the internal elements, and (iii) inserting a new inner coat layer with high structural and energetic performances. The efficacy of such solution has been analyzed from seismic and energetic points of view. Stone and hollow clay brick masonry has been considered as base material, reinforced with CLT panels provided with additional insulating material layers: the reinforcing system is connected to existing walls by means of steel bars injected in the masonry walls. It has been studied the seismic behavior, both in-plane and out-of-plane, of the reinforced systems. The higher stiffness of the panels reduced about 30% the in-plane displacement of the walls, while the coupling in the OOP direction was not fully reached even with the minimum spacing of the connectors. Thus, the CLT-stone masonry connection may not be sufficient to exclude OOP mechanisms and a careful evaluation of construction details able to ensure the connection of masonry walls at floor levels is needed.

The hygrothermal performance resulted different in the case of stone masonry and hollows clay-brick masonry. In the first case a significant reduction in both the steady and the periodic thermal transmittance reached values of 0.278 $W/m^2K$ and 0.007 $W/m^2K$, while in the second values of 0.235 $W/m^2K$ and 0.006 $W/m^2K$, respectively; in both cases, the achieved values are lower than that provided by the Italian code [47].

Iuorio and Dauda [48] investigated the possibility to use oriented strand boards (OSB) panels to improve the out-of-plane performance of brick masonry walls. They performed both experimental tests and numerical analyses (with reference to a four-point bending test) aimed at characterizing the structural behavior of the proposed systems.

Miglietta et al [49] tested on shake-table a two-storey masonry building (the first unreinforced and the second reinforced) to assess the effectiveness of a retrofit solution made with light timber frame systems. It is an innovative sustainable, lightweight, reversible, and cost-effective technique, which could be extensively applied to actual buildings. Timber frames were connected to the interior surface of the masonry walls and completed by oriented strands boards nailed to them. Moreover, the second-floor timber diaphragm was stiffened and strengthened by a layer of oriented-strand boards, nailed to the existing joists and to additional blocking elements through the existing planks. Test result highlighted that the retrofit was effective at enhancing the walls in-plane and out-of-plane capacities, also improving the connections between structural elements, and thus inducing a global box-type behavior on the retrofitted building, with full exploitation of the in-plane capacities of all masonry piers. Despite changing the failure mechanism and the overall lateral resistance of the building, the retrofit application did not affect the initial fundamental period of 0.17 s, thanks to its small mass and stiffness compared to those of the masonry structure.

Cassol et al. [50], instead, proposed to prevent put-of plane of masonry walls through vertical timber elements (strong-backs) placed as endoskeleton, connected to masonry using mechanical screws or bolts. The out-of-plane behavior of as-built and retrofitted masonry walls was investigated by conducting full scale static airbag tests. The walls were subjected to semi-cyclic out-of-plane loading through the application of uniformly distributed loads, using inflated airbags in order to simulate the self-weight inertia force induced by an earthquake. A simplified numerical model to predict the response of the masonry wall retrofitted using timber strong-backs was

developed using the finite element software SAP2000. As main result, the capacity of the retrofitted walls was found to be > 3.5 times that of the URM walls when the strong-back is on the compression side and > 5.6 times when the strong-back is on the tension side.

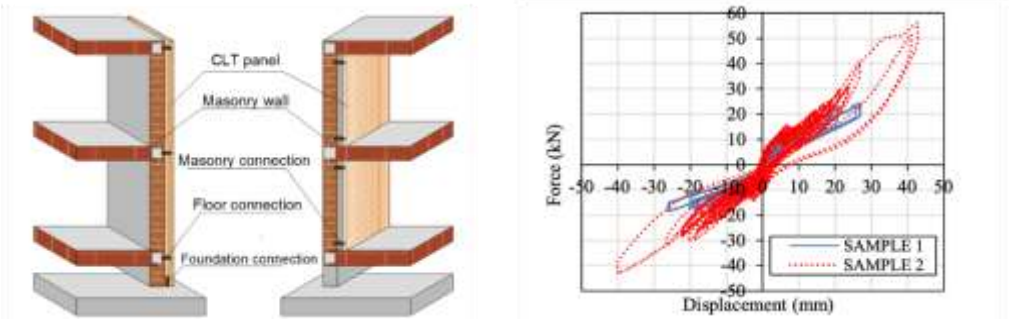


a) b)

Figure 5: Retrofit solution proposed by Pozza et al. 2017 [45].

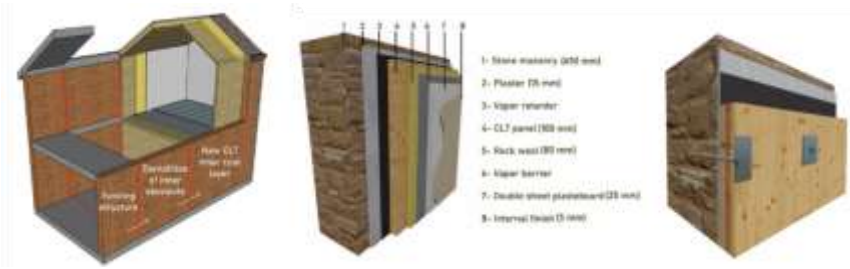

Figure 6: Retrofit solution proposed by Valluzzi et al. 2021 [46].

## 4 PROSPECTIVE OF SHORT CHAINS TO IMPROVE LIFE CYCLE OF MATERIAL AND ITS IMPACT ON ENVIRONMENT

Sustainable constructions embraces several aspects, such as design and management of buildings and constructed assets, choice of materials, building performance as well as interaction with urban and economic development and management. Timber as a material and as a structural system could be an ideal for a new era of construction.

One of the most favorable aspects of timber short supply chain development is the reduction of carbon emission and the carbon sequester. The built environment generates 40% of annual global $CO_2$ emissions. Of those total emissions, building operations are responsible for 27% annually, while building and infrastructure materials and construction (typically referred to as embodied carbon) are responsible for an additional 13% annually. So it has become crucial determining the full lifecycle impact of mass timber on carbon emissions starting from the transport of the row cut log to the amount of carbon embedded in the timber itself, where it is sequestered in buildings that could last anywhere from 50 to hundreds of years [51].

Over the past decade, there has been growing interest in mid- and high-rise buildings constructed from mass timber materials as a means to achieve greater urban density with more sustainable construction [20, 52].

A rise in the demand for wooden construction, especially for residential and commercial construction sectors along with the large amount of material required to supply the construction of tall timber buildings put the timber global supply chain under pressure and require overhauling the timber market rules.

In the last years many efforts have been addressed to exploit wooden species of short supply chain to obtain timber products also suitable for structural building [53, 54], according to the

principles of the European and Italian Bioeconomy strategy (https://ec.europa.eu/research/bioeconomy/index.cfm?pg=policy) launched at 2012 aiming to accelerate the deployment of a sustainable European bioecomomy by developing a circular economy and by reducing the dependence on non-renewable resources.

Samples of this good practice are repoted in Sikora et al. [55] which analized the influence of the thickness on mechanical performance in bending and shear of Irish Sitka spruce CLT panels, Fortune and Quenneville [56] who analized the behavior of CLT panels realized by using locally grown Radiata Pine and Concu et al. (2018) [57] and Fragiacomo et al. (2015) [58] respectively examinated the behavior of Italian Marine Pine in Sardinia for the CLT short procurement chain in the Mediterranean area. Short supply Italian beech in homogeneous and hybrid configuration with Calabrian Corsican pinewas investigated by Sciomenta et al. (2021) [59] for the manufactoring of CLT panel as well for the production of glulam beams [60] (Figure 7). These tests aimed to prove the goodness for structural applications of one of the most widespread hardwood species in Italy.

Recently, also national codes have stepped forward to enhance short supply chain products. The New Zeeland Standard NZS AS 1720.1:2022 (ICS Codes, 2022) [61] has included information specifically for New Zealand-grown timber such as stress grade, density, tension, bending, compression, modulus of elasticity, and load-bearing capacity. Consideration for New Zealand-grown timber is especially important since timber properties rely on not only the species grown, but where it is grown, hence the need for modification of the AS and measures to accommodate.



Figure 7. Short supply beech CLT panel under out plane load [59]

## 5 CODES AND GUIDELINES

The growing interest in wooden structures is also evidenced by the updates of the codes deriving from various part of the world. At European level, the two main documents for the design of timber constructions are Eurocode 5 [62] and Eurocode 8 [63] - the first dedicated to basic of design of structural members and connections, and the second to the design of seismic-resistant structures – both updating. In line with the Eurocodes, the Technical Document CNR-DT 206-R1/ 2018 (Instructions for the Design, Execution and Control of Timber Structures - has been recently update in Italy and represent (probably) one of the most advanced documents oriented to seismic design of timber buildings available in Europe. In its first version the Document included both rules for check and design single timber member or subassemblies (such as arches, diaphragms, braces etc.) only, while in 2018 a revised version was released containing seismic design rules for timber buildings based on capacity deign [8].

The Eurocode 8 provides harmonized technical rules to achieve uniform levels of safety in the field of seismic design of structures. In the current version, only six pages of specific rules for new timber buildings are provided in Chapter 8 of EN 1998-1: General rules, seismic actions and rules for buildings while, no specific chapters on existing timber buildings are defined in EN 1998-3: Assessment and retrofitting of buildings.
In the next generation of Eurocode 8 relevant updates will be provided. It was proposed to subdivide Part 1 in Part 1-1: General rules and seismic action and Part 1-2- Rules for new buildings (Chapter 13: Timber) respectively. This latter Chapter will be extended from 6 to 40 pages with novelties concerning different aspects. At first, some new wood-based panels with related rules will be introduced as the Oriented Strain Boards (OSB), the Gypsum Fibre board (FF) and in particular, the Cross Laminated Timber (CLT). Will be revised the definition of structural types according to their behavior under horizontal seismic actions in ten different typologies.

New safety format for seismic verifications will be specified, in particular the previous dissipative classes named with Low Ductility Class (DCL), Medium Ductility Class (DCM) and High Ductility Class (DCH) will be respectively replaced with DC1 (non-dissipative), DC2 (medium dissipative) and DC3 (highly dissipative) classes. For the verification of DC2 and DC3 in SD Limit State, the design strength of dissipative zones will be calculated by introducing: *i)* the $k_{deg}$ strength reduction factor due to cyclic degradation, assumed to be equal to 0.8 when no experimental results are available or estimated experimentally as ratio between $F_{1,cycle}$ (EN12512) / $F_{monotonic}$ (EN26891); *ii)* the values of $\gamma_m$=1 as those given in EN 1995-1-1:2004 and A1:2008 for accidental situations.

Another novelty will regard the new definition of behavior factors q according to EN1998-1-1. It will be given as product of three components: $q_S$ the over-strength component introduced in the design phase (1.5 material independent), $q_R$ the over-strength component due to the redistribution of seismic action in redundant structures; $q_D$ the deformation capacity and energy dissipation component. For each of the ten structural types will be specified: for design in DC1, the q factor and maximum value of the seismic action index $S_\delta$; for the design in DC2 and DC3 the values of q, and/or $q_R$ and $q_D$ when applicable.

Moreover, new ductility rules for dissipative zones will be specified. The dissipative zones for each structural type designed in DC2 and DC3 should be located in joints and connections where the energy dissipation should take place by flexural yielding of metal fasteners, whereas the timber members themselves should be designed to behave elastically.

The values of ductility are specified for DC2 and DC3 and for each dissipative zone of each structural type (i.e., CLT structures: shear walls, hold-downs, screwed wall panel-to-panel joints).

Another update will concern the capacity design and the specification of novel over-strength factors. These latter will be specified for capacity design at connection and 2D/3D nailing plate level or at wall and building level considering the different possible brittle/non-dissipative failure modes occurring.

The last novelty concerns the introduction of detailing rules for the correct design of all the structural types.

## 6 CONCLUSIONS

This paper reports a state of the art on recent developments concerning the use of structural timber in Europe, focusing on new single products, structural systems for buildings, new solution for seismic and energetic retrofit of existing masonry and RC buildings, aspects related to short chain and life cycle assessment, and last advancements for codes and guidelines.

Due to the potentials offered by raw material - related to structural and environmental aspects - timber constructions have become more and more attractive over the years. The ever-increasing demand in terms of quantity and performance of timber-based products led to great technological innovations and research advancements.

One of the most evident results is the global increase of mid- and high-rise multi-storey timber building, which design, combined with the diffusion of some products for structural purposes such as CLT, required an update of the regulations (i.e., EC8).

The potential of timber is not limited only to new constructions but also extends to existing buildings. The Europe, and in particular the Mediterranean basin area, is constituted by significant percentage of old and vulnerable buildings both under the energetic and seismic point of view. In this framework, timber engineering has taken serious advancements in the research field introducing innovative integrated seismic and energetic retrofitting solutions for existing buildings.

To conclude, the environmental benefits of wood are immense and up to now not maximized. This is the reason why several scientific studies have been carried to investigate the structural performances of short supply timber to produce novel engineered wood products.

## REFERENCES


[1] Swedish Wood. *The CLT Handbook-CLT Structures*, Fact and Planning; Swedish Wood: Stockholm, Sweden, 2019.

[2] M. Dzian, H. Palus, J. Parobek . Global Trends Affecting the EU Timber Trade. *Proc of Digitalisation and circular economy: forestry and forestry based industry implications*, Bulgaria, 297-301, 2019.

[3] H. Svatoš-Ražnjevi´c, L. Orozco, Menges, A. Advanced Timber Construction Industry: A Review of 350 Multi-Storey Timber Projects from 2000–2021. *Buildings*, **12**, 12, 404, 2022. https://doi.org/ 10.3390/buildings12040404.

[4] M. Gong, Meng. "Lumber-Based Mass Timber Products in Construction." *Timber Buildings and Sustainability*, 2019. IntechOpen. doi:10.5772/intechopen.85808.

[5] V. Salvadori. Multi-Storey Timber-Based Buildings: An International Survey of Case-Studies with Five or More Storeys Over the Last Twenty Years; *Technische Universität Wien: Vienna*, Austria, 2021.

[6] U. Kuhlmann, J. Schänzlin. A Timber-Concrete Composite Slab System for Use in Tall Buildings, *Structural Engineering International*, **18** (2), 2008. DOI: 10.2749/101686608784218707

[7] A. Sandoli, C. D'Ambra, C. Ceraldi, B. Calderoni, A. Prota. Sustainable Cross-Laminated Timber Structures in a Seismic Area: Overview and Future Trends. *Applied Sciences*, **11**(5), 2078, 2021.

[8] B. Faggiano, A. Sandoli, G. Iovane, M. Fragiacomo et al. The Italian instructions for the design, execution and control of timber constructions (CNR-DT 206 R1/2018). *Eng Struct*, **253**, 113753, 2022,.

[9] M. Follesa, M. Fragiacomo, D. Casagrande, R. Tomasi, M. Piazza, D. Vassallo, D. Canetti, S. Rossi. The new provisioned for the seismic design of timber buildings in Europe, *Eng. Struct*, **168**, 736–747, 2018.

[10] M. Busselli, D. Cassol, A. Prada, I. Giongo. Timber Based Integrated Techniques to Improve Energy Efficiency and Seismic Behaviour of Existing Masonry Buildings. *Sustainability*, **13**, 10379, 2021.

[11] G. Iovane, A. Sandoli, D. Marranzini, R. Landolfo, A. Prota, B. Faggiano. Timber based systems for the seismic and energetic retrofit of existing structures. *Proc Struct Integrity* **44**,1870-1876, 2023.

[12] F. Smiroldo, I. Giongo, M. Piazza. Use of timber panels to reduce the seismic vulnerability of concrete frame structures. *Eng Struct*, **244**(2),112797, 2021.

[13] R. Brandner, G. Flatscher, A. Ringhofer, G. Schickhofer, A. Thiel. Cross laminated timber (CLT): overview and development. *European Journal of Wood and Wood Products*, **74**(3), 2016 https://doi.org/10.1007/s00107-015-0999-5

[14] M. Jeleč, D. Varevac, V. Rajčić: Cross-laminated timber (CLT) – a state of the art report, *GRAĐEVINAR,* **70**(2), 75-95, 2018. doi: https://doi.org/10.14256/JCE.2071.2017

[15] J.W.G. Van De Kuilen, A. Ceccotti, Z. Xia, M. He,Very Tall Wooden Buildings with Cross Laminated Timber, *Procedia Engineering*, **14**, 1621-1628, 2011, ISSN 1877-7058, https://doi.org/10.1016/j.proeng.2011.07.204

[16] J. Comnick, L. Rogers, K. Wheiler. Increasing Mass Timber Consumption in the U.S. and Sustainable Timber Supply. *Sustainability*, **14**, 381, 2022. https://doi.org/10.3390/su14010381

[17] CLT Handbook: *Cross Laminated Timber; FP Innovation Special Publication* SP-529E; U.S. Edition: St. Jean Pointe-Claire, QC, Canada, 2013.

[18] Z. Wang, M. Gong, Y.H. Chui. Mechanical properties of laminated strand lumber and hybrid cross-laminated timber. *Constr Build Mater* **101**, 622-7, 2015. https://doi.org/10.1016/J.CONBUILDMAT.2015.10.035.

[19] S. Breneman, L. Podesto. Timber Skyline: A Review of Structural Systems for High-Rise Wood Structures. *2013 SEAOC Convention Proceedings*. San Diego, September 2013, 2013.

[20] M. Jeleč, D. Varevac, V. Rajčić: Cross-laminated timber (CLT) – a state of the art report, *GRAĐEVINAR,* **70** (2), 75-95, 2018. doi: https://doi.org/10.14256/JCE.2071.2017

[21] V.Ž. Leskovar, M. Premrov. *A Review of Architectural and Structural Design Typologies of Multi-Storey Timber Buildings in Europe*, **12**, 2021, https://doi.org/10.3390/F12060757.

[22] A. Iqbal. Development in tall wood buildings and hybrid buildings and environmental impacts. *Sustainability*, **13**, 11881, 2021.

[23] S. Lehmann. Sustainable construction for urban infill development using engineered massive wood panel systems. *Sustainability*, **4**, 2707–42, 2012. https://doi.org/10.3390/SU4102707.

[24] R. Jockwer, P. Grönquist, A. Frangi. Long-term deformation behaviour of timber columns: Monitoring of a tall timber building in Switzerland. *Eng Struct*, **234**, 1118552021; 2016:. https://doi.org/10.1016/J.ENGSTRUCT.2021.111855.

[25] R. Verhaegh, M. Vola, J. de Jong, Haut - A 21-storey Tall Timber Residential Building. International Journal of High-Rise, *Building*, **9**(3), 213-220, 2020.

[26] M.A. Bezabeh, G.T. Bitsuamlak, M. Popovski, S. Tesfamariam. Probabilistic serviceability-performance assessment of tall mass-timber buildings subjected to stochastic wind loads: Part I - structural design and wind tunnel testing. *J Wind Eng Ind Aerodyn*, **181**, 85–103, 2018;. https://doi.org/10.1016/J.JWEIA.2018.08.012.

[27] A. Sandoli, D. Moroder, S. Pampanin, B. Calderoni. Simplified analytical models for coupled CLT walls. *Proc. Of the World Conf on Timb Eng*, Wien, 2016.

[28] S. Tulebekova, K.A. Malo, A. Rønnquist, P. Nåvik. Modeling stiffness of connections and non-structural elements for dynamic response of taller glulam timber frame buildings. *Eng Struct*, **261**, 114209, 2022. https://doi.org/10.1016/J.ENGSTRUCT.2022.114209.

[29] M. Fairhust, Z. Xiaoyue, T. Tannert. Nonlinear dynamic analyses of novel timber-steel hybrid system. *World Conference on Timber Engineering*, Canada, Quebec City, 10-14 August, 2014.

[30] A. Palermo, S. Pampanin, A. Buchanan, M. Newcombe. Seismic design of multi-storey buildings using laminated veneer lumber (LVL). *Proc of the NZSEE Conference*, New Zealand, Wairakei, 2005.

[31] A. Iqbal, S. Pampanin, A. Palermo, A.H. Buchanan. Performance and design of LVL walls coupled with UFP dissipaters. *J Earthq Eng* 2015. https://doi.org/10.1080/13632469.2014.987406.

[32] Y. Lu, Q. Lv, Y. Liu. Experimental and numerical study on seismic performance of CLB rocking wall with bending-friction coupled dampers. *J Build Eng*, **45**, 103622, 2022. https://doi.org/10.1016/j.jobe.2021.103622.

[33] L. Pozza, L. Benedetti, V. Tomei, B. Ferracuti, M. Zucconi, C. Mazzotti. Cyclic response of CLT Post-Tensioned Walls: Experimental and numerical investigation, *Construction and Building Materials*, **308**, 125019 ,2021.

[34] V. Tomei, M. Zucconi, B. Ferracuti. Post-tensioned rocking dissipative timber wall systems: Numerical prediction, *Journal of Building Engineering*, **66**, 105897, 2023.

[35] EU building database. An official website of the European Union. Available at: https://ec.europa.eu/energy/eu-buildings-database_en .

[36] F. Filippidou, J. Jimenez Navarro. Achieving the cost-effective energy transformation of Europe's buildings, EUR 29906 EN. *Publication office of the European Unioni, Luxemburg*, 2019.

[37] A. Sandoli, B. Calderoni, A. Prota. A displacement-based design methodology devoted to post-tensioned timber walls for seismic retrofit of an existing RC building. *Ingegneria Sismica*, **38**(2), 70-94, 2021.

[38] G. Di Lorenzo, F. Colacurcio, A. Formisano, A. Massimilla, R. Landolfo. State-of-the-art on steel exoscheletons for seismic retrofit of existing RC buildings. *Ingegneria Sismica*, **37**(1), 33-50, 2022

[39] I. Sustersic, B. Dujic. Seismic strengthening of existing buildings with cross laminated timber panels. *Proc. of World Conf on Timb Eng*, Auckland, New Zealand, 2012.

[40] F. Smiroldo, I. Paviani, I. Giono, P. Zanon, R. Albatici, M. Piazza. An integrated approach to improve seismic and energetci behaviour of RC framed buildings using timber panels. *Sustainability*, **13**, 11304, 2021.

[41] A. Aloisio, M. Pellicciari, S. Sirotti, F. Boggian, R. Tomasi. Optimization of the structural coupling between RC frames, CLT shear walls and asymmectric friction connections. *Bull of Earth Eng*, **20**, 3775-3800, 2022.

[42] L. Bandini, P. Aondio, S.J. Ott, S. Winter. Seismic Strengthening of Existing RC Buildings With External Cross-Laminated Timber (CLT) Walls Hosting an Integrated Energetic and Architectural Renovation. *Bull of Earth Eng*, **20**, 5963–6006, 2022.

[43] F. Barbagallo, G. Margani, E.M. Marino, A. Moretti, C. Tardo. Impact of retrofit of rc frames by clt panels and friction dampers. *Proc of 8th Int Conf on Comp Meth in Struct Dyn and Earth Eng (COMPDYN)*, Greece, Athens, 2021, DOI: 10.7712/120121.8636.18851

[44] D. Li Cavoli, G. D'Arenzo, M.E. Ruggeri, M. Fossetti. On the use of CLT infills to improve the lateral performance of RC frames. *Lecture Notes in Civil Eng*, 2023, DOI: 10.1007/978-3-031-21187-4_75

[45] L. Pozza, F. Evangelista, R. Scotta. CLT used as seismic strengthener for existing masonry walls. *Proc of the XVII Italian Conf on Earth Eng (ANIDIS)*, 210–220, 2017.

[46] M.R.Valluzzi, E. Saler, A. Vignato et al. Nested buildings: An innovative strategy for the integrated seismic and energy retrofit of existing masonry buildings with CLT panels. *Sustainability*, **13**(3), 118, 2021

[47] DM 26/06/2015—Italian Interministerial Decree: Application of Calculation Methods for Energy Performance and Definition of Minimum Building Requirements; *Official Gazette of the Italian Republic: Rome*, Italy, 2015. (In Italian).

[48] O. Iuorio, J.A. Dauda. Retrofitting Masonry Walls against Out-Of-Plane Loading with Timber Based Panels. *Applied Sciences*, **11**(12), 5443, 2021.

[49] M. Miglietta, N. Damiani, G. Guerrini, F. Graziotti. Full-scale shake-table tests on two unreinforced masonry cavity-wall buildings: effect of an innovative timber retrofit, *Bulletin of Earthquake Engineering*, **19**(6): 2561-2596, 2021.

[50] D. Cassol, I. Giongo, J. Ingham, D. Dizhur. Seismic out-of-plane retrofit of URM walls using timber strong-backs. *Constr. Build. Mater*, **269**, 121237, 2021.

[51] D. Roberts, The hottest new thing in sustainable building is, uh, wood, Vox Media, LLC, 15 Jan 2020, Online: https://www.vox.com/energy-and-environment/2020/1/15/21058051/climate-change-building-materials-mass-timber-cross-laminated-clt (accessed on 21 March 2020).

[52] Timmers M, Rogowksi B, Jacobs AT, Jones B. Mass Timber High-Rise Design Research: Museum Tower in Los Angeles Reimagined in Mass Timber. *2015 SEAOC Convention Proceedings*, Bellevue, WA. September, 2015.

[53] M. Romagnoli, M. Fragiacomo, A. Brunori, M. Follesa, and G. Scarascia Mugnozza, "Solid wood and wood based composites: The challenge of sustainability looking for a short and smart supply chain," *Lect. Notes Civ. Eng.*, **24**, 783–807, 2019, doi: 10.1007/978-3-030-03676-8_31.

[54] G. Scarascia Mugnozza, M. Romagnoli, M. Fragiacomo, M. Piazza , B. Lasserre, M. Brunetti, R. Zanuttini, M. Fioravanti, M. Marchetti, L. Todaro, M. Togni, T. Ferrante, M. Maesano, M. Nocetti, G.B. De Dato, M. Sciomenta, T. Villani. La filiera corta del legno:

un'opportunità per la bio-economia forestale in Italia. *Forest@* **18**, 64-71, 2021. doi: 10.3832/efor0052-018

[55] K.S. Sikora, D.O. McPolin, A.M. Harte. Effects of thickness of cross-laminated timber (CLT) panels made from Sitka spruce on mechanical performance in bending and shear. *Constr. Build. Mater*, **116**, 141–150, 2016

[56] A.L. Fortune, P. Quenneville. A feasibility study of New Zealand Radiata Pine crosslam, *S. Setunge*, **116**, 141-150, 2011.

[57] G. Concu, B. De Nicolo, M. Fragiacomo, N. Trulli, M. Valdes, Grading of maritime pine from Sardinia (Italy) for use in cross-laminated timber, *Proc. Inst. Civ. Eng. Constr. Mater*. **171**(1), 11–21, 2018. https://doi.org/10.1680/jcoma.16.00043.

[58] M. Fragiacomo, R. Riu, R. Scotti, Can structural timber foster short procurement chains within Mediterranean Forests? A research case in Sardinia, South-east Eur. *For.* **6**(1), 107–117, 2015. https://doi.org/10.15177/seefor.15-09.

[59] M. Sciomenta, L. Spera, C. Bedon, V. Rinaldi, M. Nocetti, M. Brunetti, M. Fragiacomo, M. Romagnoli. Mechanical characterization of novel Homogeneous Beech and hybrid Beech-Corsican Pine thin Cross-Laminated timber panels. *Constr. Build. Mater.*, **271**, 2021. doi: 10.1016/j.conbuildmat.2020.121589

[60] M. Sciomenta, Spera L., Peditto A., Ciuffetelli E., Savini F., Bedon C., Romagnoli M., M. Nocetti, M. Brunetti, M. Fragiacomo, Mechanical characterization of homogeneous and hybrid beech-Corsican pine glue-laminated timber beams, *Engineering Structures*, **264**, 114450, ISSN 0141-0296, 2022,.

[61] ICS Codes, NZS AS 1720.1:2022 Timber structures. Part 1: Design methods.

[62] EN 1995-1-1:2004 Eurocode 5: Design of Timber Structures, Part 1-1: General rules and rules for buildings.

[63] EN 1998-1:2005 Eurocode 8: Design of structures for earthquake resistance-part 1: general rules, seismic actions and rules for buildings.

COMPDYN 2023
9th ECCOMAS Thematic Conference on
Computational Methods in Structural Dynamics and Earthquake Engineering
M. Papadrakakis, M. Fragiadakis (eds.)
Athens, Greece, 12-14 June 2023

# CYCLIC BEHAVIOR OF AN INNOVATIVE JOINT PROTOTYPE FOR CLT PANELS

**A. Tancredi[1], I. Marchionni[1], M.G. Masciotta[1], G. Brando[1]**

[1] University "G. d'Annunzio" of Chieti-Pescara, Department of Engineering and Geology
Viale Pindaro 42, Pescara 65127, Italy
e-mail: antonio.tancredi@unich.it; italo.marchionni@gmail.com; g.masciotta@unich.it; giuseppe.brando@unich.it;

## Abstract

*CLT (Cross-Laminated Timber) panels represent one of the most used technologies for wooden structures. The design and the details of panel-to-panel connections represent an aspect of utmost importance to understand the overall behavior of timber structures subject to lateral loads, such as seismic loads. For these reasons, new solutions for connections have been -and continue to be- proposed in the last years.*

*In this framing of research, this paper proposes a new type of dissipative steel connection for timber structures. As an alternative to traditional solutions, such as hold-down and angle brackets, this connection is conceived to be easy to fabricate and to be installed, allowing, moreover, the use of a small number of connectors. Different joint-panel model combinations are presented, and numerical analyses are carried out to study the behavior of CLT panels equipped with the proposed connection under lateral load. The performed FEM analyses lead to the identification of two innovative optimized solutions of connections, recently patented by the authors, which will be prototyped in the next future.*

**Keywords:** Cross-laminated timber, Wooden structures, Seismic behavior, Cyclic Analysis, Dissipative connection, Steel connection.

## 1. INTRODUCTION

In recent years, X-LAM solid wooden panel technologies have been gaining increasing attention as a sustainable and low-impact solution for building construction. X-LAM is a construction system based on bi-dimensional panels made of solid cross laminated timber, which offers numerous advantages over traditional construction methods. Although relatively young, this technology has been already employed in many parts of the world to build multi-story residential and commercial buildings.

An X-LAM building is configured as a box structure made of vertical and horizontal panels with biaxial load-bearing performance. In the design process of X-LAM structures, connections between panels are crucial for the transmission of horizontal loads, as they have to ensure adequate load transfer between adjacent panels. Although many solutions are available to this purpose, however, the type of connection to use largely depends on the type of assemblies to be connected (i.e., panel-to-panel, floor-to-wall, etc.). Generally, they can be classified into traditional and innovative connections. The former group includes:

- hold-downs (HD): metal connections commonly placed at the corners of the panel to provide uplift resistance against the overturning moment of the wall under in-plane lateral loading (Figure 1).
- angle brackets (AB): metal connections typically located at the base of the panel to absorb in-plane shear loads and prevent sliding mechanisms (Figure 2).
- in-plane screwed joints: metal connectors used to connect each other adjacent panels and to take combined axial and lateral loads, preventing relative displacements.



Figure 1 Hold-downs (from[1])



Figure 2 Angle brackets (from[1])

Many studies about the behavior of traditional connections in CLT assemblies subjected to lateral loads are available in literature. Among these, it must be mentioned the study performed by Gavric et al. [3], who carried out both cyclic tensile tests on hold-downs and cyclic shear tests on angular brackets, stressing that all connections feature a cyclic behavior characterized by significant pinching phenomena. The experimental tests also revealed that both HDs and ABs own a significant deformation capacity, therefore a reasonable ductility, despite the low overall energy dissipation capacity.

Calderoni et al. [4] conducted a numerical study to investigate the role played by specific performance parameters of traditional connections, such as deformation and resistance capacity, in the seismic behavior of CLT structures They observed an increase in strength and ductility by considering larger strains for the metal components that work in tension (HD), as it allows the plastic hinge to develop in these elements. This facilitates easier replacement in case of damage. In the framing of the SOFIE project, Dujic et al [5], compared the results obtained from the shake table tests of a full-scale seven-story building made of X-LAM panels and

traditional connections (HDs and ABs) with those obtained from numerical analyses in order to better investigate the seismic behavior and the influence of panels thickness and connectors arrangement.

On the other hand, innovative connections can be distinguished as follows:

- Point-to-point connections: dissipative connections designed to withstand simultaneously both shear and tensile stresses and typically installed in the peripheral areas of the panels. They require careful evaluations to determine the connection location. Examples include: (i) XL-stub, (ii) X-rad and (iii) X-bracket.
- Wall/core systems: systems made of several monolithic panels spanning the entire height of the building and designed to withstand all types of loads. Examples of these connections are: (i) PRES-LAM WALL/CORE and (ii) IPC – Integrated Panel Core.

The XL-stub connection is designed to take advantage of the dissipative characteristics of steel throughout its entire length. This is possible owing to the hourglass shape of the flange plate, which creates a weaker area that allows for plasticization and prevents failures in the flange-web link section and in the bolt area. A study by Latour et al. [6], who tested the XL-STUB connection through monotonic and cyclic load tests to verify its efficiency, showed that collapse occurred in the expected area and the hysteresis cycles revealed a hardening plastic trend without pinching effect.

The X-rad connection is designed for being installed at the corners of X-LAM panels and consists of three fundamental elements: an external enclosure combined with an internal steel plate, a seasoned wood core, and six fully threaded self-tapping screws. Polastri et al. [7] tested the shear-tension and shear-compression behavior of this type of connection through cyclic analyses. The hysteresis curves showed pinching, but, however, the connection featured good energy dissipation and ductility.

The X-bracket connection (Figure 3) is also designed for installation at the corners of X-LAM panels and features an X-shaped metallic profile screwed to timber panels that assures a spread plasticization of the material, thus preventing localized failures. Careful design is required for the anchorage to minimize the bearing effect in the wood-connector contact area. A study by Scotta et al. [2] evaluated the behavior of the X-bracket through laboratory tests of pure traction and pure shear cyclic load tests. The hysteresis curves showed an elastic-plastic behavior without pinching.

The Pres-Lam system [8] consists of coupled timber walls post-tensioned with steel tendons passing either externally or through internal ducts. To improve the dissipative behavior of such a system, Iqbal et al. [9] proposed a “hybrid” solution combining unbonded post-tensioned vertical tendons with U-shaped flexural plates (UFPs) inserted between panels. Energy dissipation occurs through metal yielding of the UFPs during rocking of the walls. The experimental investigation confirmed that the Pres-Lam system exhibits efficient energy dissipation.

The IPC (Integrated Panel Core) system is designed to resist forces through a central core constructed of integrated X-LAM panels running the full height of the building [10]. This system showcases several advantages, including: 1) integration of various X-LAM panels to create larger and stiffer components as compared to individual panels; 2) transfer of gravity loads parallel to the grain through proper positioning of vertical panels; 3) transfer of loads between panels through direct contact without the need of steel connectors.

This paper arises within the research framework outline above and intends to move a step forward towards the prototyping of enhanced dissipative steel connections for timber structures. The main purpose is to present an innovative connection technology that is easy to be installed

and to be assembled, allowing to optimize time on site, as well as easy of fabrication, allowing for the use of local skilled labor, thereby providing a valid alternative to the most widely used connections such as hold-downs and angular brackets.

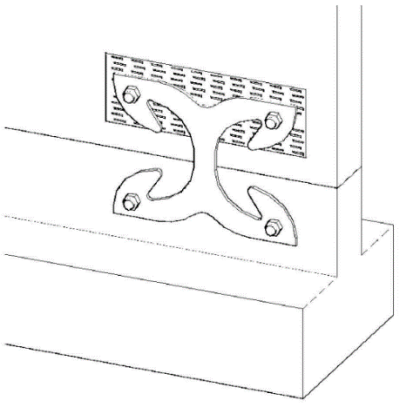

Figure 3 X-bracket (from [2])

In order to optimize the design of the proposed connection, many numerical analyses are conducted adopting different types of geometry, dimensions, and material for the connectors. In the present work, due to space constraints, only the two solutions meeting the criteria of capacity design (strong panel-weak connection) are described.

## 2. DESCRIPTION OF NEW JOINT PROTOTYPE

The proposed prototypes are composed of two different resisting systems, one designed to resist tensile forces and the other to resist shear forces (Figure 4). The system for tensile forces is the same for the two joint prototypes, whereas different solutions are adopted for the shear stress resisting system:

- Solution 1: system made of plates with simple curvature (Figure 5);
- Solution 2: system made of plates with double curvature (Figure 6).

The tensile connection is provided at the left and right sides of the panel and has been designed to resist only by contact with the panel, with no connector connecting it to the Cross Laminated Timber (CLT) panel. The connection is composed of a semi-circular shaped steel plate, housed in a space created inside the panel, and two steel bars inclined at 45° and placed outside to the panel, which connect the semi-circular plate to the intrados of the floor. The housing space created to insert the two semi-circular steel plates into the panel has a curvilinear shape at the bottom and a straight shape at the top, which allows for easy lifting of the panel an facilitates the positioning of the wall during installation.

Similarly, the connection designed to resist shear stresses is provided at the left and right edges of the panel, which is properly shaped in order to accommodate it. Like the tensile connection, this connection is conceived to resist only by direct contact without the need for additional connectors to the CLT panel. The connection consists of a plate with a straight base and a semi-circular section that has an interruption at about 2/3 of its development, thus providing greater flexibility to the connection and reducing stresses when it reaches plastic

deformation. The straight section of the plate allows the connection to the floor through a steel bar.

## 3. NUMERICAL MODELLING AND ANALYSES

In order to study the behavior of the connection and its interaction with a X-LAM shear panel under horizontal forces, a FEM model was created, also to understand the different reaction of the components (plates, bars, nuts, panel), with the goal of proving if the assumed design criteria, concerning most of all the first component that have to yield, work well.

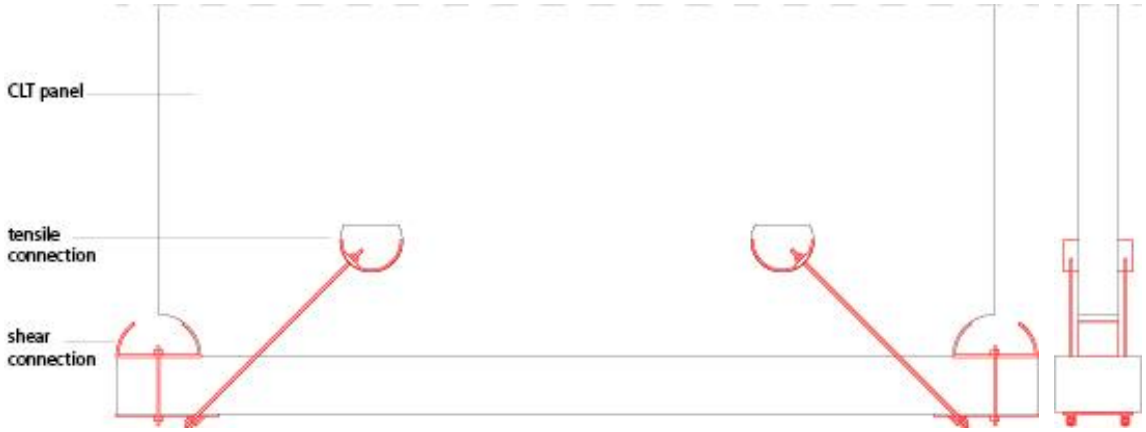


Figure 4 Example of CLT panel with tensile and shear connections

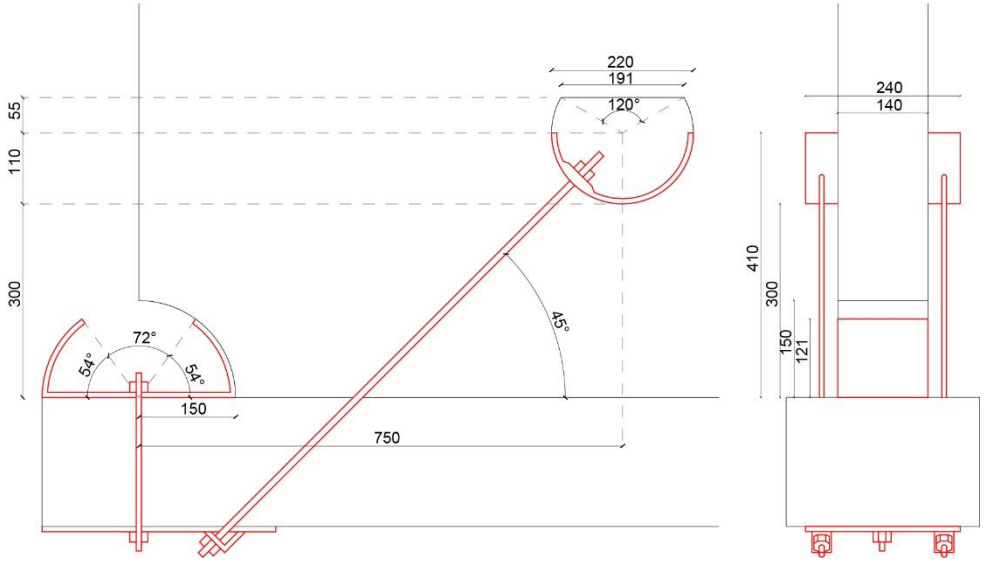


Figure 5 Prototype with simple curvature

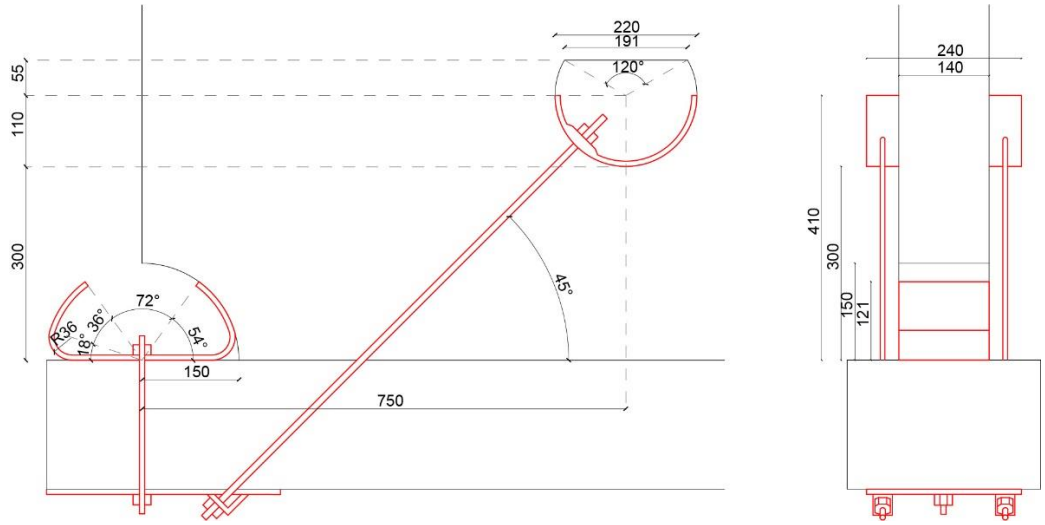


Figure 6 Prototype with double curvature

The proposed joint prototypes were modelled through the ABAQUS [11]software and analyzed. To this end, a floor-to-wall system was created assuming the following hypotheses:

- Infinitely rigid floor slab, fixed at the base.
- Infinitely rigid ceiling slab subjected to horizontal and vertical translations and rotation about the center of mass.
- Connection between CLT panel and floor slab: a constrain is adopted that allows the transfer of force and displacement between two parts in contact.

The CLT panel was created by replicating the geometric dimensions (B, H) of the wall tested in the SOFIE project (Ceccotti el at. [1]), which was 2950 mm wide and 2950 mm high with a thickness of 140 mm. The panel is composed of three layers, the outer ones with fibers arranged longitudinally and the intermediate layer with fibers in the transverse direction.

The model was created and meshed with different type of elements corresponding to different type of material described (Figure 7).

The wall modeling in the calculation software was carried out using continuum SC8R shell elements (8-node quadrilateral in-plane general-purpose continuum shell, reduced integration with hourglass control, finite membrane strains). The type of wood adopted is a homogeneous glued laminated timber with strength class GL24h (Table 1), described as elastic using the Tsai-Wu failure criterion (Figure 8) for orthotropic materials which have different strengths in tension and compression.

The steel connection elements were modelled through solid 3D elements of the C3D8R type (8-node linear brick, reduced integration, hourglass control). The material was described using a bi-linear hardening curve (Figure 9). Different types of steel were used for the various components of the connection: class 3.6 elements for the nuts, B450C steel for the cylindrical bars and S235 steel for the plates.

The CLT system was subjected to both vertical and lateral loads. To limit instability phenomena of the bars, a preload $F_{p,Cd}$ was applied.

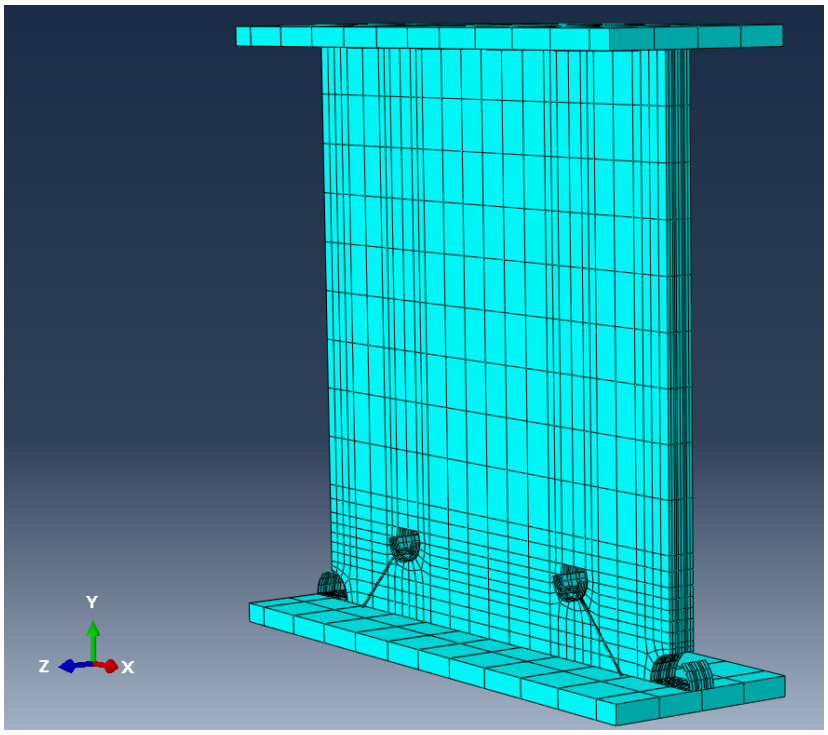


Figure 7 Model meshed

| GL24h | | | | |
|---|---|---|---|---|
| $\sigma_{t0}$ (MPa) | $\sigma_{c0}$ (MPa) | $\sigma_{t90}$ (MPa) | $\sigma_{c90}$ (MPa) | $\tau_{90}$ (MPa) |
| 14 | -21 | 0.4 | -2.5 | 4 |

Table 1 Material properties

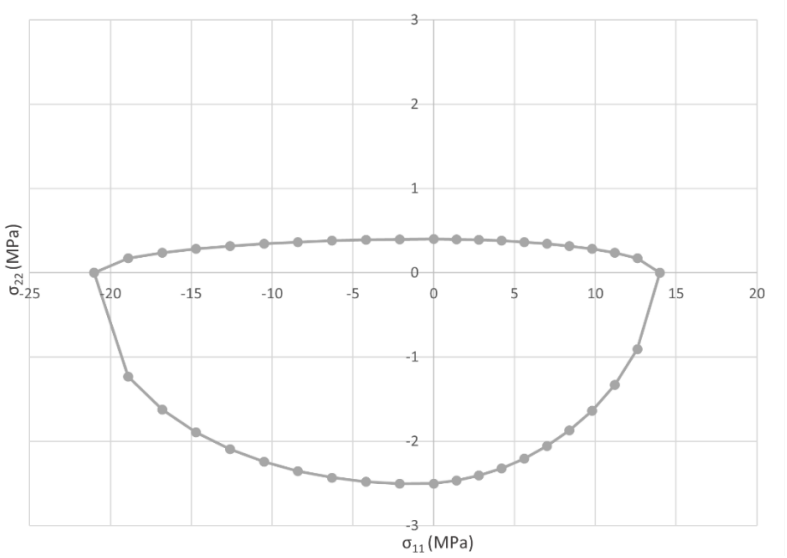


Figure 8 Tsai-Wu failure criterion

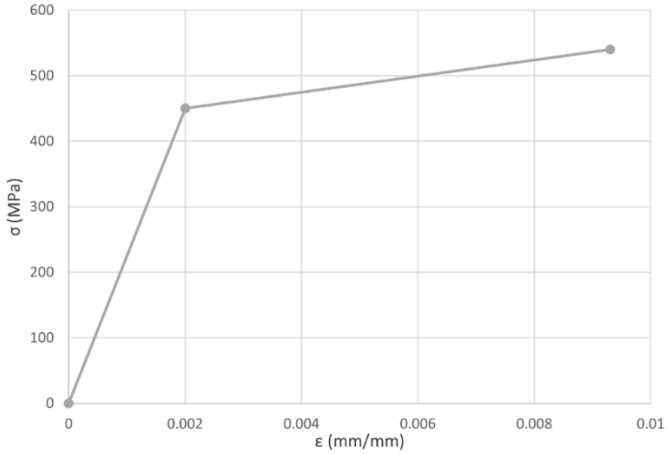


Figure 9 Steel inelastic behavior (B450C)

This value was calculated using the expressions of the Italian building code, based on the connector diameter and the ultimate strength of the material. As such, the preload was computed as reported in eq. (1)

$$F_{p,Cd} = \frac{0.7 f_{tbk} A_{res}}{\gamma_{M7}} \tag{1}$$

To properly evaluate the behavior of CLT panels under cyclic loading, the ECCS 85 loading protocol [12] was used as a reference. The protocol recommends to impose the following cyclic history depending on an esteem of the lateral displacement at the yielding attainment $u_y$:

- A symmetric displacement cycle for each displacement equal to $0.25u_y$, $0.50u_y$, $0.75u_y$ and 1.00 $u_y$.
- Three displacement cycles equal to $2.00u_y$, $4.00u_y$, 6.00 $u_y$.

In this study, in order to reduce the computational effort, the applied loading protocol differs from the reference protocol and includes:

- One cycle of symmetric displacement equal to 1.00 $u_y$ .
- ¼ cycle of displacement at $u_y$ .

As for the single curvature model shown (detail in Figure 5), a stiff behavior with a re-centering mechanism and low ductility was observed (Figure 10). The connection allowed the panel to automatically reposition itself to the initial configuration after the seismic event, thanks to the imposed gravitational loads. During the input application, energy dissipation occurred through rocking. The behavior of the connection system throughout the cyclic loading, expressed in terms of base shear versus top displacement, is shown in Figure 10. It is observed that the system maintains its full capacity during the cycle and a low energy dissipation.

Conversely, the analysis of the double curvature connection (detail of Figure 6) showed the occurrence of both rocking and sliding phenomena. The latter can be explained by the presence of a gap between the wall and the shear-resisting connection. This gap causes a delay in the plasticization of the panel near the shear connection, also leading to sliding, which resulted in a loss of self-centering capacity, but in supplemental damping (Figure 11). It is observed that the system maintains a shear capacity similar to the configuration with single curvature but had a better capacity to dissipate energy.

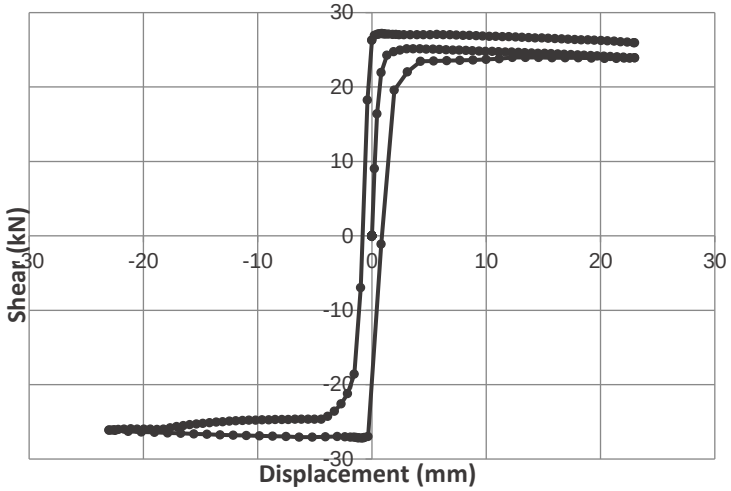


Figure 10 Cycle behavior of single curvature model, base shear and displacement at the top

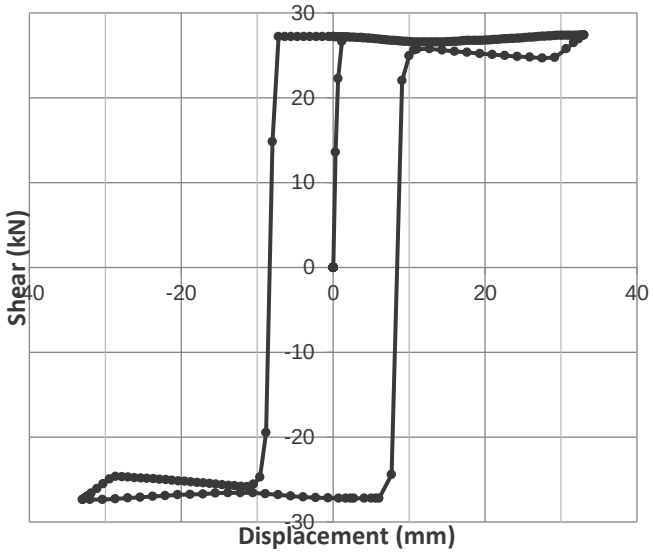


Figure 11 Cyclic behavior of double curvature model, base shear and displacement at the top

## 4. CONCLUSION

The study carried out in this paper led to the definition of two innovative types of steel connections for X-Lam wooden panels. The connections work for tension and shear, taking advantages from the following characteristics:

- Loads are transmitted exclusively by contact, thus avoiding the problem of material bearing.
- Connections are attached to the floor using only threaded bars and steel fixing bolts, simplifying the installation process and reducing the construction time.

The two modeled connection types, in the "single curvature" and the "double curvature" configurations, showed different behaviors both in terms of ductility and developed kinematics but a similar shear capacity.

The natural empirical continuation of the modeling activity involves a significant campaign of experimental investigations aimed at validating the results obtained from numerical analyses.

## 5. ACKNOWLEDGEMENTS

This research was developed during the Italian Research Project “Collegamenti innovativi per edifici in legno in zona sismica” framed in the PON action “Dottorati e contratti di ricerca su tematiche dell’innovazione” funded by the Italian Ministry of University and Research.

## REFERENCES

[1] A. Ceccotti, C. Sandhaas, M. Okabe, M. Yasumura, C. Minowa, and N. Kawai, “SOFIE project - 3D shaking table test on a seven-storey full-scale cross-laminated timber building,” *Earthq Eng Struct Dyn*, vol. 42, no. 13, pp. 2003–2021, Oct. 2013, doi: 10.1002/eqe.2309.

[2] R. Scotta, L. Marchi, D. Trutalli, and L. Pozza, “A dissipative connector for CLT buildings: concept, design and testing,” *Materials*, vol. 9, no. 3, Feb. 2016, doi: 10.3390/ma9030139.

[3] I. Gavric *et al.*, “Experimental-numerical analyses of the seismic behaviour of cross-laminated wall systems,” *WCEE*. 2012. [Online]. Available: https://www.researchgate.net/publication/332528990

[4] B. Calderoni, C. Giubileo, A. Sandoli, and V. Onotri, “L’influenza dei sistemi di connessione sul comportamento strutturale di pannelli in legno X-lam per edifici in zona sismica,” *ANIDIS*. 2015. [Online]. Available: https://www.researchgate.net/publication/282667294

[5] B. Dujic, K. Pirmanšek, R. Zarnić, A. Ceccotti, K. Strus, and R. Zarnic, “Predition of dynamic response of a 7-storey massive XLam wooden building tested on a shakinjg table,” *WCTE*, 2010, [Online]. Available: https://www.researchgate.net/publication/265204580

[6] Latour M., Rizzano G., Terrano G., and Torello G., “Comportamento sismico di edifici a pannelli in legno a strati incrociati realizzati con connessioni di tipo innovativo,” *ANIDIS*. 2013.

[7] A. Polastri, I. Giongo, and M. Piazza, “An innovative connection system for cross-laminated timber structures,” *Structural Engineering International*, vol. 27, no. 4, pp. 502–511, Nov. 2017, doi: 10.2749/222137917X14881937844649.

[8] A. Palermo, S. Pampanin, A. Buchanan, and M. Newcombe, “Seismic Design of multi-storey buildings using laminated veneer lumber (LVL),” 2005. [Online]. Available: https://www.researchgate.net/publication/29486939

[9] A. Iqbal, S. Pampanin, A. Palermo, and A. H. Buchanan, “Performance and design of LVL walls coupled with UFP dissipaters,” *Journal of Earthquake Engineering*, vol. 19, no. 3, pp. 383–409, Apr. 2015, doi: 10.1080/13632469.2014.987406.

[10] J. Chapman, “Integrating cross-laminated timber panels to construct buildings to twenty levels.”

[11] “ABAQUS/Standard User’s Manual, Version 6.6.”

[12] ECCS “European Convention fot Constructional Steelwork,” “Recommended testing procedure for assessing the behaviour of steel elements under cyclic loads,” 1986. [Online]. Available: www.eccspublications.eu

COMPDYN 2023
9th ECCOMAS Thematic Conference on
Computational Methods in Structural Dynamics and Earthquake Engineering
M. Papadrakakis, M. Fragiadakis (eds.)
Athens, Greece, 12-14 June 2023

# DEVELOPMENT OF A HOLISTIC PARAMETRIC FRAMEWORK FOR MULTI-PERFORMANCE LIFE-CYCLE EVALUATION OF POST-TENSIONED TIMBER BUILDINGS

**Giada Formichetti**[1], **Michele Matteoni**[1], **and Stefano Pampanin**[1]

[1] Department of Structural and Geotechnical Engineering, Sapienza University of Rome
Via Eudossiana 18, 00184 Rome, Italy
{giada.formichetti, michele.matteoni, stefano.pampanin}@uniroma1.it

## Abstract

*Catastrophic events and climate change represent major challenges for modern society, which calls for new solutions able to provide acceptable performances with low carbon footprint. The environmental impact of buildings, already accounting for 39% of Carbon Dioxide (CO2) emissions in the European Union (EU), becomes much more important in seismic prone areas, where buildings are vulnerable to extensive damage, significantly influencing the sustainability as well as the resilience of the entire community. The low-damage post-tensioned engineered timber structural system, also known as Pres-Lam (Prestressed Laminated timber), meets the need for a shift towards a damage-control approach while using sustainable materials. Beside the material choice, the design phase has a strong influence over the environmental impact along the life cycle of buildings. Hence, decision-making process has to take into account multiple aspects related to the proposed solution, that have to be combined into a comprehensive framework. This paper proposes a holistic parametric approach able to evaluate simultaneously the seismic performance and the environmental impact of three different Pres-Lam case studies, developing an integrated model within Rhino-Grasshopper platform using independently developed packages. The seismic response is assessed through a probabilistic approach, whereas the carbon footprint is estimated through the Life-Cycle Assessment (LCA) procedure using the extensive database of the Grasshopper plugin One Click LCA. Given the parametric nature of the framework, a wide range of solutions can be analysed to make the optimal choice, with the possibility to include also energy simulations and combine all the results within a Multi-Criteria Decision Analysis to guide the decisional process.*

**Keywords:** Post-tensioned timber, Pres-Lam, Low-damage, Seismic performance, Sustainability, Integrated parametric design.

# 1 INTRODUCTION

In line with the 2030 Agenda for Sustainable Development [1], the construction sector is moving towards the promotion of sustainability in all its activities. A sustainable construction is a multi-performance product, dealing with the different requirements related to Planet preservation, People satisfaction and Profit achievement, according to the three Ps (or Pillars) of Sustainability. Hereby, it is necessary to include all the possible hazards, such as earthquakes, that may occur during the building life cycle compromising its sustainable features, showing the mutual dependency between the structural performance and the environmental footprint [2, 3].

The material and socio-economic consequences of the recent earthquakes on the built stock have highlighted the crucial need to build up a resilient community, able not only to ensure life-safety and safeguard to the cultural heritage, but also to look at the future providing a smart and sustainable building environment. The modern buildings designed following the current seismic code approach targeting Life-Safety, although performing as expected as per Hierarchy of Strength principles, might incur in severe damage to their structural and non-structural components which can be deemed as not cost-effective to repair [4, 5]. To overcome the equivalence between damage and ductility in code-compliant earthquake-resisting buildings, earthquake engineering community has been recently focusing on innovative high-performance technologies aiming at raising the bar in seismic design, shifting the no-more adequate targeted performance to a more appropriate damage-control objective (Figure 1a). Among these technologies, the so-called PRESSS system (PREcast Seismic Structural System) has been largely investigated and tested in the past two decades starting from the US-PRESSS programme, in the 1990's, at the University of California San Diego (UCSD) with substantial developments and actual implementations on site at the University of Canterbury in New Zealand. [6, 7, 8]. Based on the use of precast concrete elements joined together through "dry" ductile connections, this technology replaces the traditional plastic hinge (expected in monolithic solutions) with a peculiar rocking and dissipating mechanism at the interface between structural members by the use of two types of reinforcement: (i) unbonded post-tensioned cable/bars ensuring the self-centering capacity of the structure, and (ii) internal mild steel or external fuse-type replaceable Plug&Play dissipaters [9], which ensure the energy dissipation (Figure 1b). During the earthquake, a rocking mechanism is expected at the interface between structural members, while at the end of the shacking, the post-tensioned reinforcement ensures the pre-existing gap closure between members, leading to negligible residual displacements/deformations. The combination of the self-centring and energy dissipation capabilities of the system defines the so called "flag-shape" hysteresis rule of the connection system.

More recently, such technology has been extended to the use of laminated timber with the Pres-Lam (Prestressed Laminated Timber) systems [10] (Figure 1c). Today, it is well recognized how the use of timber can be a way to achieve the concept of sustainability in construction. The state-of-the-art technologies have made possible to have engineered products (the so-called mass timber) with structural performances comparable to the more common steel and concrete, with the lightness and renewability that characterize the wood. Hence, mass timber creates an opportunity to use renewable methods of constructions while still ensuring the expected building performances [11]. This development represents a step towards a circular model in constructions, which, in its highest expression, aims to keep products in use maintaining their embedded value as long as possible, avoiding waste and energy-consumer processes and leaving recycling as the "last-resort" in favour of the more resilient-based concept of re-use [12]. The high seismic structural performance of Pres-Lam technology could make it

a competitive choice when dealing with the need of a durable construction, capable of withstand hazardous events during the building life cycle, modular to be easily replaced and made by materials easily separated for recycling if re-use it is not possible.

To date, many assessment tools have been employed and developed to effectively drive decision-making processes in the direction of achieving sustainability goals in the construction sector. Some methodological frameworks analyse single or multiple aspects of environmental scenarios that are related to construction activities (protocollo ITACA [13], LEED [14], DGNB [15], BREEAM [16], CASBE [17]). Besides these tools, the Life-Cycle Assessment (LCA), regulated by ISO 14040 and ISO 14044, has the potential to analyse overall environmental factors related to the entire life cycle of a building [18]. For this reason, its use is spreading among the engineering community. The LCA allows to quantify the environmental impact of a building during its life cycle, from raw materials extractions to the End-of-Life (with different bounding conditions depending on the scope of the analysis), not only in terms of CO2 emissions but also in the form of different impacts on the ecosystem, the use of resources and the human health (Life-Cycle Impact Assessment). Given that, the LCA can be usefully adopted in the construction industry to evaluate different design options for a new building in the early design stage, in order to guide decision-makers towards the adoption of a more sustainable solution.

Nevertheless, the current approach to the LCA of buildings that involves gathering the relevant environmental data of the different materials manually in an Excel file tends to discourage designers from applying LCA. Implementing an automated LCA in a dedicated parametric design software tool, such as Rhino+Grasshopper (McNeel, 2007) [19] can help to achieve a time-effective process while creating an integrated environment that enables to stay on top of all the different aspects of a complex building system, considering them simultaneously. Furthermore, the parametric nature of the software enables to assess different solutions in pursuing the optimal choice, making this design approach ideal for (multi-)decision-making processes.

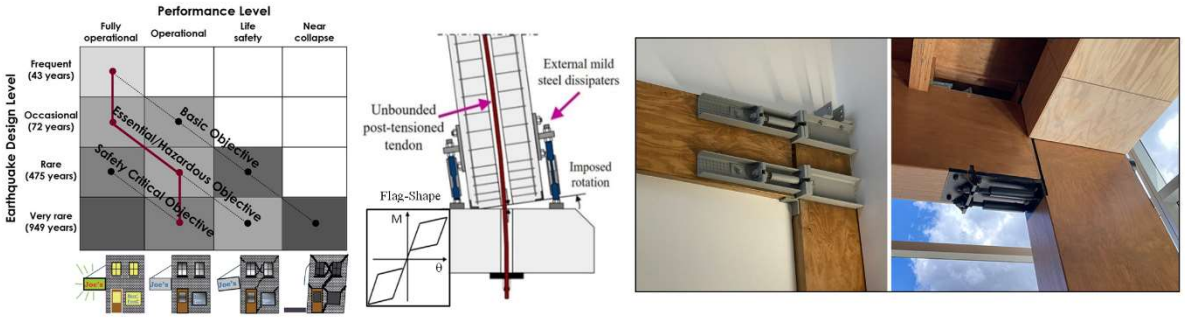


a) b) c)

Figure 1. a) Proposed modification of the seismic performance design objective matrix [20], with the identification of the damage state at each performance level; b) Example of low-damage column-to-foundation connection using external Plug&Play dissipaters and a sketch of the "flag-shape" hysteresis rule [21]; c) Pres-Lam beam-to-column connections with two different configurations of Plug&Play dissipaters: on the face of the beams and columns, Trimble building (left), on top and bottom of beams, Young Hunter House, Merritt Building (right).

## 1.1 Pres-Lam State-of-the-Art

The Pres-Lam technology is a low-damage solution for earthquake-resisting structural systems making use of mass timber products.

Despite being relatively new, the technology was proved to be effective by extensive testing [22, 23, 24, 25] that showed how the engineered connections are able to withstand several loading cycles while maintaining a stable response. By combining frames and walls is possible to achieve a complete and robust structural system able to withstand higher levels of drift without showing significant damage [26, 27].

The technology, making extensive use of timber, is characterized by easier prefabrication, shipping, and assembly processes, making it a prime solution even for low-seismic areas. Several buildings have already been built using this technology as it was deemed cost-effective for different applications [28, 29, 30, 31, 32, 33] (Figure 2).

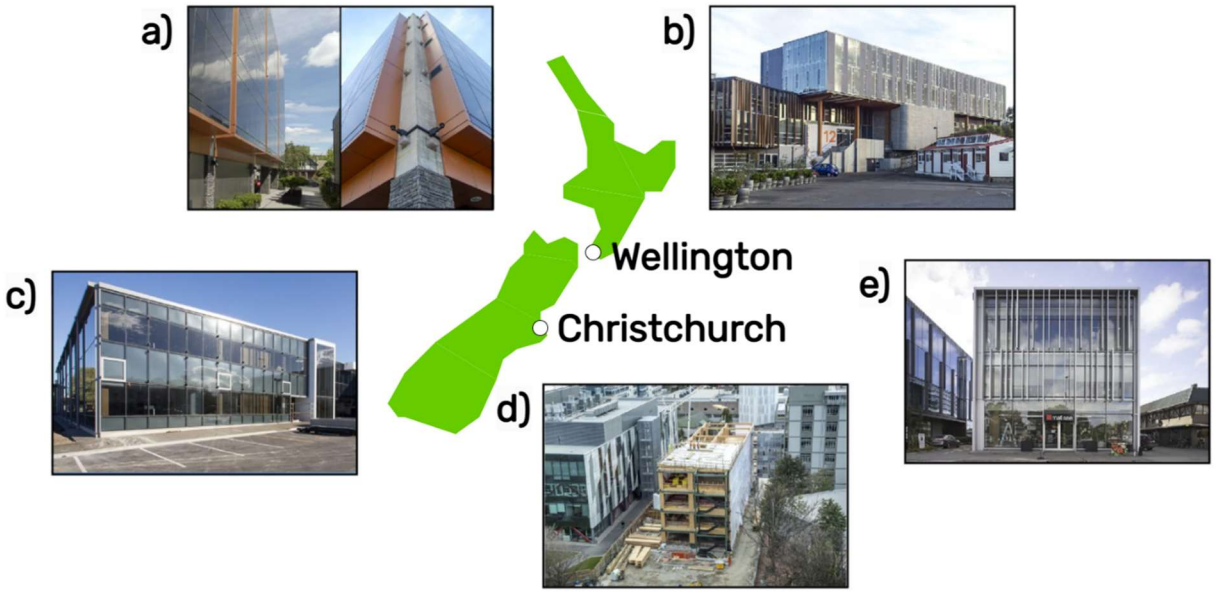


Figure 2. Examples of buildings that make use of Pres-Lam frames in New Zealand: (a) St. Elmo Courts building, Christchurch, (b) College of Creative Arts building, Wellington (courtesy of Andy Buchanan/PTL structural consultants), (c) Trimble building, Christchurch, (d) Beatrice Tinsley building, Christchurch (courtesy of University of Canterbury), and Young Hunter House, Christchurch (modified after [34]).

One major shortcoming of the technology is the strong anisotropy (actually orthotropy) of the timber which exhibits a lower stiffness when loaded perpendicular-to-the-grain, when compared to parallel-to-the-grain, leading to a reduced connection stiffness in the beam-to-column joint connection. To address this issue, several protecting solutions have been proposed and implemented regarding the joint interface detailing using nails, screws, and steel plates [34]. Some authors even proposed and tested solutions which make use of different materials for columns such as reinforced concrete or steel [35, 36]. Moreover, the combination of this technology with non-structural components able to withstand high levels of drift, made it possible to develop an integrated solution capable of facing high-intensity level seismic events without reporting any significant damage [37].

A detailed state-of-the-art on the structural systems regarding testing against seismic and fire hazards can be found in [38].

## 2 AIMS AND METHODOLOGY

This paper proposes an integrated methodology for the seismic and environmental performance of low-damage laminated timber buildings. The two performances are evaluated individually but, combining them within the same parametric framework in the Rhino+Grasshopper environment, it allows for a comprehensive understanding of the proposed

solutions and for a time-saving automated evaluation process. Among the scopes of the work, the authors want to investigate and confirm that the achievement of high seismic performance in building design, through the use of pre-cast low-damage structural technologies, does not hinder low carbon footprint.

## 2.1 Life-Cycle Assessment

A Life-Cycle Assessment (LCA) procedure is an effective tool that helps to monitor the direction through less environmental impact. Regulated by ISO 14040 and ISO 14044 [39, 40], the aim of the method follows the one of the study. The main steps in which the analysis is divided are (Figure 3a): (i) Goal and Scope Definition; (ii) Inventory Analysis; (iii) Life-Cycle Impact Assessment; (iv) Interpretation.

The first phase establishes the functional unit, i.e., the reference parameter for the results of LCA (in our case the Gross Floor Area (GFA) of the building), the reference time, set as 50 years for residential/commercial buildings, and the boundaries of the system, according to which four LCA alternatives are possible [41, 42] (Figure 3b): (i) Cradle-To-Grave, where the complete life-cycle of the product is assessed, from the manufacturing processes to the End-of-Life (EoL) scenario; (ii) Cradle-To-Gate, which involves the phases between the manufacture and the factory; (iii) Cradle-To-Cradle, that consider the product back on the market after the recycling process at the EoL; (iv) Gate-To-Gate, considering only the processes in the factory. In this paper, a Cradle-To-Grave LCA is performed, with the possibility to select the recycling of steel and glass components as their EoL scenario, as well as the reuse of timber elements enabled by the low-damage structural system; the operational phase is neglected because it would not be meaningful in the comparison, having the case-study buildings roughly the same GFA and the same envelope. It is worth saying that this work considers the recycling and reuse EoL scenarios just as a reduction of CO2 emissions in the EN 15978/EN 15804 C1-C4 stages, without taking into account the consequential cutting of the required raw-materials (stages A1-A3) in the following product cycle.

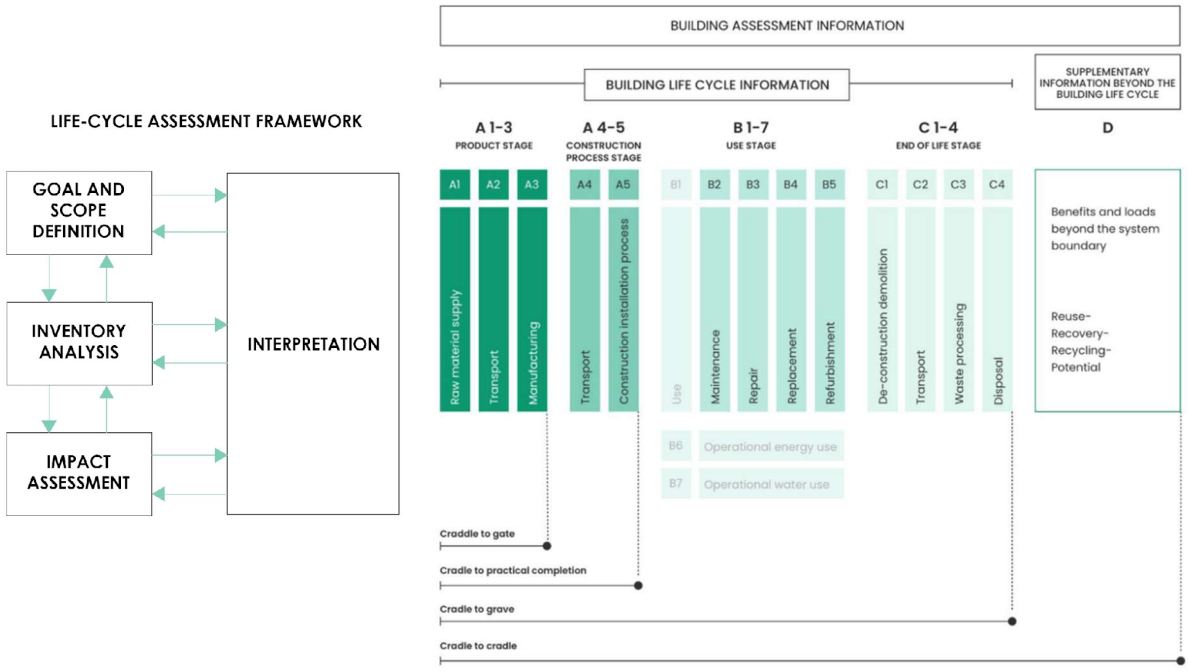


a) b)

Figure 3. a) LCA framework according to ISO 14040; b) Life-Cycle stages according to EN standards and the related four different LCA alternatives (modified from One Click LCA website).

As far as the Inventory Analysis phase is concerned, the energy flows of each material and processes involved in the study are analysed. This is the part where the software tool comes handy, since the Environmental Product Declaration (EPD) of the project's components and data on energy and consumption must be collected. The framework proposed in this paper uses the extended database of the One Click LCA software for building design, consisting of both manufacturer-specific data, useful if a particular product has already been chosen, and country-specific average data, convenient in the early-design of the project.

Once the environmental data of the project materials and components are gathered, the results of LCA can be presented in the form of Green-House Gases Emissions, computed as kgCO2 equivalent, and Embodied Energy (GJ). If one wants to assess the impact on different aspects of the eco-system and the human health, the Life-Cycle Impact Assessment should be carried out. This phase assigned each energy flow to impact categories represented, for example, by Climate Change (Global Warming Potential), Acidification, Eutrophication, Ozone Depletion Potential. However, this phase is often avoided, since it relies on the assessment models chosen and, hence, it's not standardized.

The interpretation and the evaluation of the results of LCA can eventually bring the process back to its initial phase and lead to changes in the proposed design; therefore, the automation of the entire design and assessment procedure makes this iterative process less daunting.

## 2.2 Seismic Performance

To assess the seismic performance of the frame structural systems, a probabilistic approach was chosen making use of fragility curves to obtain the Mean Annual Frequency of Exceedance (MAFE) related to various limit states.

To develop the fragility curves for the case-study buildings a Non-Linear Time History Analysis (NLTHA) approach is used implementing the Incremental Dynamic Analysis (IDA, [43]) methodology. The procedure employs a suite of ground motions that are progressively increased until the onset of the desired limit state is achieved. The suite of 44 ground motions (22 recordings times 2 directions) provided by FEMA P-695 [44] is used to perform the procedure.

The considered limit states for the Pres-Lam frames are:

- DS1: failure of the external mild steel dissipaters, considered as the gap opening that induces a 6% axial deformation in the fuse-shaped devices.
- DS2: yielding in compression of the timber beam's interface parallel to the grain.
- DS3: yielding of the post-tensioning tendons inside the beam elements.

The global onset of each limit state is achieved once at least one section reaches the defined limit state.

Because every section might reach the above-defined limit states for a different amount of gap opening, the Demand Capacity Ratio (DCR) instead of the gap opening has been defined as the Engineering Demand Parameter (EDP). The DCR is computed as the ratio between the maximum gap opening that occurred during the NLTHA and the gap opening corresponding to the onset of the considered limit state in the specific connection. Finally, the global DCR is defined as the maximum between all the connections (Eq. 1).

$$DCR_{LS} = max_j^n DCR_{LS,j} = max_j^n \frac{D_{gap,j}}{C_{gap,j}(LS)} \quad (1)$$

where:

- $D_{gap,j}$ is the maximum gap opening occurred during NLTHA.

- $C_{gap,j}(LS)$ is the gap opening corresponding to the onset of the limit state for the considered connection.
- $n$ is the number of connections in the frame.

The chosen Intensity Measure (IM) is the spectral acceleration of the first mode period ($Sa(T_1)$).

Because all the different solutions have a different value of the first mode period, the MAFE is used to compare the results. The MAFE is computed by integrating the fragility curves with the hazard curve [45]. However, the values of the hazard curve according to the Italian seismic hazard model [46] do not cover a wide enough range to perform the integration. For this reason, an approach like the one proposed by the SAC-FEMA [47, 48] methodology is used to fit the hazard curve on an analytical model. The analytical model chosen as representative of the hazard curve is the second-order hazard approximation proposed by [49] (Eq. 2):

$$Hazard(im) = k_0 exp[-k_2 ln^2(im) - k_1 ln(im)] \quad (2)$$

Finally, following the same approach as [45], the integration is truncated to a $T_R$ (return period) of 100,000 years after which a probability of 1 is considered for the occurrence of the damage state (Eq 3):

$$\lambda_{LS} = \int_0^{IM_{T_R^*}} P[DCR_{LS} \geq 1 \mid IM = x] \cdot |d\lambda_{IM}(x)| + 10^{-5} \quad (3)$$

## 2.3 Parametric Integrated Model

As shown in Figure 4, a comprehensive parametric framework is developed in order to investigate the best solution in terms of both seismic and environmental performance. The workflow consists of independently developed packages and Python-based modules all inside the same Grasshopper parametric model, which enables to analyze a wide range of solutions just varying the input parameters in an even user-friendly manner.

Geometry and material properties of the building are set as input as well as the seismic hazard level related to the construction area and the importance class of the building. Through a set of algorithms represented by a series of boxes dragged into the canvas of the visual programming software and linked to each other by wires, the whole building 3D parametric model is defined, considering both the structural and the non-structural components (facades).

Then, the main workflow activities within the model are the following:

- *Structural design*. The Python programming language directly integrated in Grasshopper allows to develop the seismic design procedure within the model; specifically, the Direct Displacement-Based Design methodology [50, 51] is carried out for the lateral force-resisting systems, returning the Base-Shear as output which is in turn the input for the following Python-based box that returns the force demand along the structure. The structural members are then dimensioned to carry the force-demand at the serviceability limit state (SLS), being the size of timber structural elements and the amount of post-tensioning in Pres-Lam structures usually governed by this limit state [34], and then designed in detail and verified at the ultimate limit state (ULS) [52].
- *Structural modelling and seismic analyses.* Once the design phase is completed, the building's parameters, together with connection reinforcement details, are stored and broadcasted to a Python script that defines a numerical model using the OpenSEES software [53, 54]. The script is able to perform non-linear static and dynamic analyses to assess the building's performance against seismic action.

- *Life-Cycle Assessment*. Using the One Click LCA Grasshopper module, LCA is carried out getting data directly from the 3D model and the materials properties set as input. All the building components are parametrically mapped to LCA profiles, defined by the type of material and the EPD database chosen to assess the environmental impact. At this stage, by easily pressing a "button" in Grasshopper, the LCA can be run in the cloud importing the construction to the web platform, where is possible to adjust the feature of the elements concurring to the evaluation of the carbon footprint, e.g., the EoL scenario, the distance from the manufacturing plant and the energy grid used during the production. The results are visualized through a set of diagrams and images.

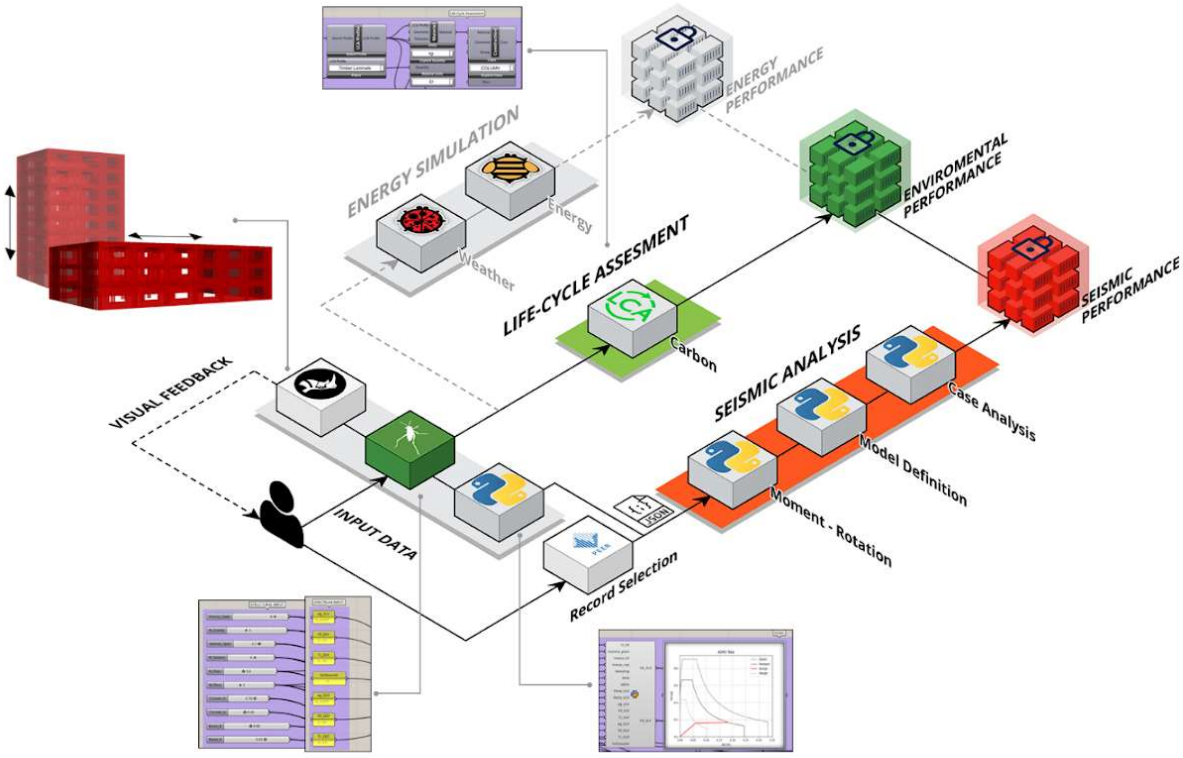


Figure 4. Grasshopper-Phyton parametric workflow for the multi-performance evaluation of buildings, from the selection of input to the 3D geometric model, to DDBD design, to seismic numerical analyses and LCA analysis.

It is worth saying that the Grasshopper-Python-based workflow herein presented allows to account also for the implementation of energy simulation for the building, evaluating the energy efficiency of the building (or set of buildings, given the parametric nature of the model), and use it for the operational phase in the LCA.

## 3 PARAMETRIC DESIGN

### 3.1 Case-study buildings

The parametric integrated framework is applied to three different Pres-Lam case-study office buildings, sharing solely the same inter-story height of 3.6 m and the same GFA of around 2800 square meters. All the three buildings feature two lateral force resisting systems: post-tensioned timber frame in the longitudinal direction and post-tensioned timber walls in the transversal one. In this paper, for simplicity, seismic analyses are carried out only for the longitudinal direction, i.e., for the post-tensioned timber frames. The different number of

stories, span number and lengths, the number of lateral resisting frames and the beams and columns dimensions are shown in Figure 5a.

The hybrid Pres-Lam frame connections details, i.e., the number and diameters of external Plug&Play dissipaters and the number of post-tensioned tendons, are determined following the DDBD procedure implemented within the Grasshopper-Phyton model, whose key parameters are summarized in Table 1. The buildings are designed considering the high seismicity of L'Aquila (Abruzzo, Italy, C soil type), and an importance class of level 3 [55].

The considered beam-column joint configuration was the one shown in Figure 5b, taking as a reference the Young Hunter House (Merritt) building in Christchurch, New Zealand (2014). The external mild steel fuse-shaped short-bar are placed at the top and the bottom of the beam, while the post-tensioned cables run through the hollow beams at mid-height; structural steel rods passing right through the column reinforce against crushing perpendicular to the grain. The plates, nails and bolts for the Plug&Play dissipater anchorage are dimensioned following the EN 1995-1-1:2004 for timber and EN 1993-1-8:2005 for steel [56, 57].

For timber beams and columns, Laminated Veneer Lumber (LVL) has been chosen, with a flexural strength of 44 MPa and a parallel-to-grain modulus of elasticity of 14700 MPa, while the external dissipaters are made of S355 steel. The internal post-tension occurs through unbonded 7-wire strands characterized by a yielding tensile strength of 1670 MPa.

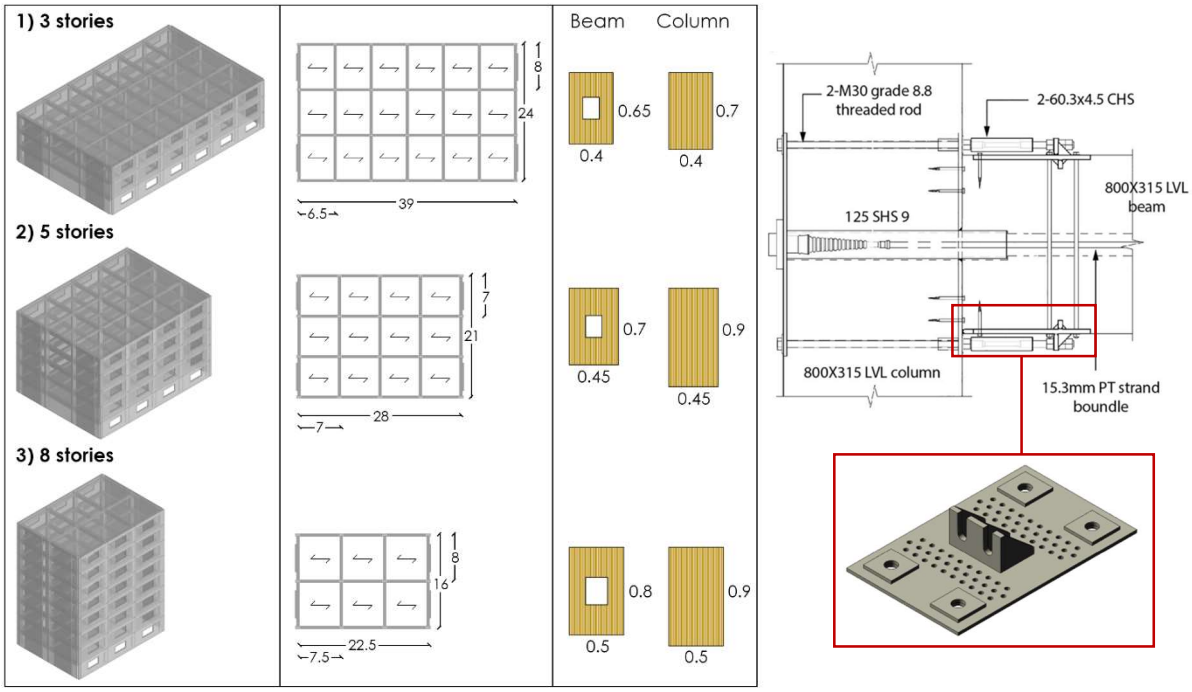


Figure 5. a) Geometry and structural data of the 3 case-study buildings; b) Beam-column connection detail from the Young Hunter House [34], and the top and bottom anchor plate for the Plug&Play dissipaters (courtesy of Federica Felici).

| | Case-study 1 | | Case-study 2 | | Case-study 3 | |
|---|---|---|---|---|---|---|
| Parameter | SLS | ULS | SLS | ULS | SLS | ULS |
| $\theta_{design}$ (%) | 0.5 | 1.7 | 0.5 | 1.8 | 0.5 | 1.55 |
| $\Delta_{design}$ (m) | 0.04 | 0.11 | 0.06 | 0.18 | 0.1 | 0.24 |
| $m_{effective}$ (ton) | 1272 | 1332 | 1485 | 1555 | 1674 | 1754 |
| $H_{effective}$ (m) | 7.2 | 7.1 | 11.9 | 11.6 | 19.12 | 18.64 |
| $\xi_{equivalent}$ (%) | 5 | 11 | 5 | 11.1 | 5 | 10.7 |
| $T_{effective}$ (s) | 0.73 | 1.1 | 1.2 | 2.07 | 1.93 | 2.77 |
| $K_{effective}$ (kN/m) | 93821 | 34977 | 40486 | 14348 | 17670 | 9057 |
| $V_{base}$ (kN) | 3392 | 3729 | 2408 | 2578 | 1689 | 2205 |

Table 1. Parameters from the DDBD procedure for the three case-study buildings, at Serviceability Limit State (SLS, SLD in Italian Building Code) and Ultimate Limit State (ULS, SLV in Italian Building Code).

The building skeleton is coated with two types of facades: a timber-based cladding system (Figure 6a) with multiple insulation layers in the frames direction, connected by low-damage bearing connections and UFP connections (Figure 6b) [37, 58], and spider-glazing façades made of 12 + 1.52pvb + 12 mm glass panels in the walls direction. The study of this type of connections and non-structural components is not covered in this paper [59].

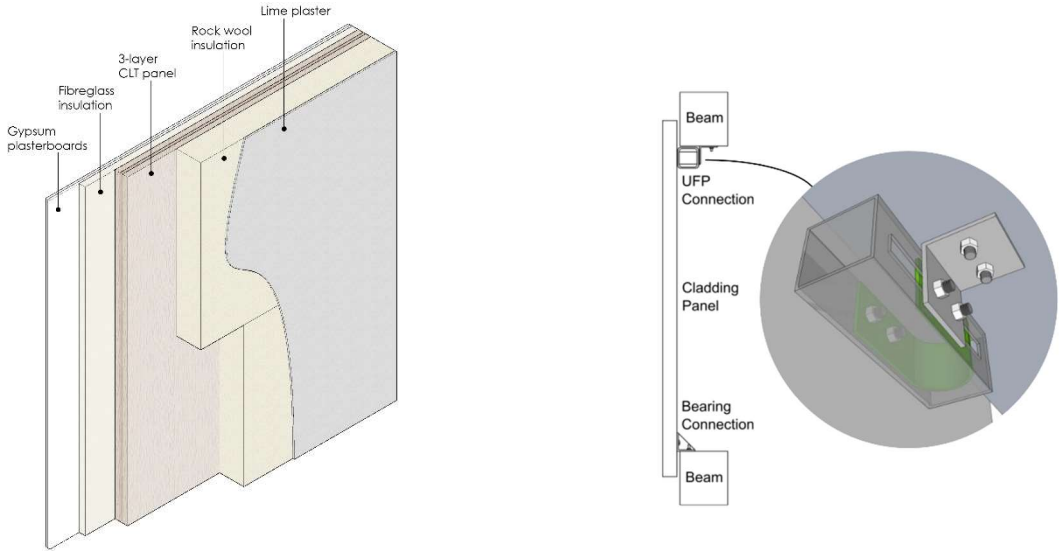


a) b)

Figure 6. a) Detail of the facade in the longitudinal direction; b) Cladding system with low-damage UFP connection [58].

## 3.2 Modelling approach

To model the response of the Pres-Lam frames, a lumped plasticity approach is used as it was shown that it can adequately predict the behavior of the hybrid connections [60].

The beam-column connection was modelled accounting for three different contributions (Figure 7):

- The post-tensioning unbonded tendons are modelled using a multi-linear elastic link.
- The mild steel external damping devices are modelled using a Giuffrè-Menegotto-Pinto (GMP) hysteretic behaviour.
- The joint shear deformation is modelled using a linear elastic link.

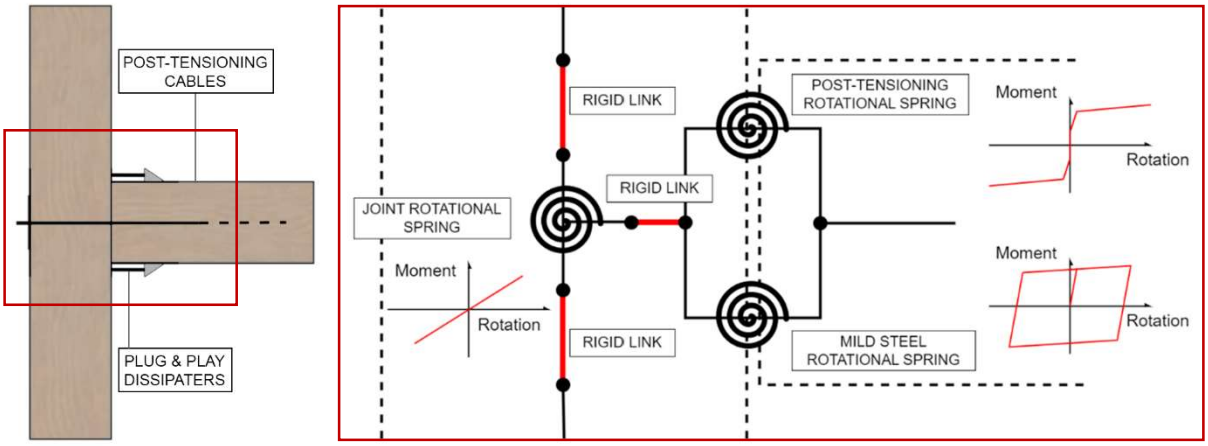


Figure 7. Modelling of a hybrid connection for a beam-column joint.

To define the parameters of the mild steel and post-tensioning, an iterative analytical procedure was used. Originally developed by [61] using the concept of *member compatibility* known as the "monolithic beam analogy" for rocking concrete connections, the procedure was further developed by [62], then adapted to Pres-Lam by [25] and finally revised by [63].

The model was validated on the results of the experimental testing by [64].

The GMP link is set to fail once a gap opening corresponding to a 6% axial deformation in the damping devices is reached. Similarly, the multi-linear elastic link modelling of the tendons is set to fail once a gap opening corresponding to the yielding deformation of the post-tensioning element is achieved. This choice was made because once the tendons are yielded, the residual deformation cannot ensure a correct rocking mechanism leading to the unpredictability of the dynamic behaviour of the connection. Finally, when the yielding deformation of the timber is reached, the moment rotation is computed considering the partially plasticized connection, thus leading to a reduction in stiffness.

The stiffness of the elastic link modelling the panel is derived by the formulation proposed by [52] for internal (Eq. 4) and external (Eq. 5) joint panels:

$$K_{joint,int} = \frac{4}{3}\frac{\alpha_{s,ave} A_{col} h_b G_t}{\left(1-\frac{h_c}{L}\right)(2-\beta)} \tag{4}$$

$$K_{joint,ext} = \frac{2}{3}\frac{\alpha_{s,ave} A_{col} h_b G_t}{\left(1-\frac{h_c}{L}\right)} \tag{5}$$

where:

- $\alpha_{s,ave}$ is the effective shear area assumed 0.85 for rectangular beam.
- $A_{col}$ is the area of the column.
- $h_b$ is the height of the beam.
- $G_t$ is the shear modulus of the timber.
- $\beta$ is the ratio of the effective height of the beam assumed 2/3.

# 4 RESULTS AND DISCUSSION

In this section, the results of the Life Cycle Analysis as well as seismic performance assessment are presented first separately then together to evaluate the optimal solution among the 3 case studies presented.

## 4.1 Life-Cycle Assessment

As shown in the performance matrix of Figure 8, all the three case-study buildings share a low environmental impact when compared to similar buildings, i.e., office buildings, in Italy [65]. Amongst the three case-studies, the 8-storey building set is the one with the highest CO2 emissions both in terms of total value (expected due to the larger size) and per square meter values. The latter is probably due to the highest amount of vertical structures and facades due to the greater height; these are in fact one of the main actors in determining carbon emissions, especially when considering the spider-glazing curtain wall characterized by the two most contributing materials to the Global Warming, glass and steel, even if recycled at the EoL.

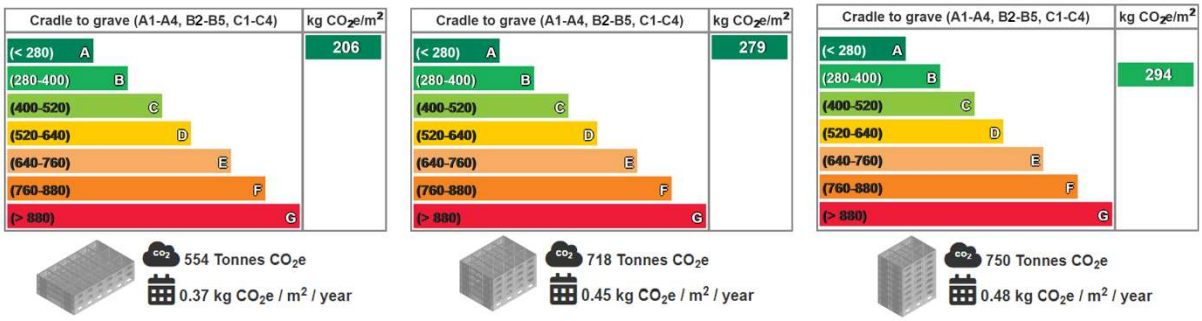


Figure 8. Embodied carbon associated to the three case-study buildings compared to benchmark buildings with the same service class (offices) in the same country (Italy). The performance metric is built on the results of standardized LCA on 1000 anonymized, verified sample buildings with data breakdown for over 100 different materials, developed by building type and countries [65].

When looking at life-cycle stages (Figure 9), having neglected the operational phase, it appears that most of the emissions are related to the A1-A3 production phase, also because all the materials have been considered as virgin resources at the beginning of their life cycle. On the contrary, the C1-C4 End-of-Life phase shows a nearly zero global warming potential, since the majority of the building components, among which an important role is played by the high-performance low-damage Pres-Lam structural system, are designed to be durable and reusable at the end of their life, while those not suitable for that scenario are recycled. As far as the construction stage is concerned, the results are based on the data available for standard prefabricated timber-frame structures; thus, the value of kgCO2eq related to this phase would be cut if considering the easy of assembly of Pres-Lam technology [66].

The results of LCA are expressed also in the form of Embodied Energy, that is the total use of primary energy during the life-cycle stages (Figure 10).

It is worth saying that in this paper the maintenance and replacement stages consider only the impacts from restoring the building products after they reach the end of their service life within the 50-year LCA reference time of the building, without taking into account the rehabilitation required if any type of hazard, such as earthquakes [2, 3, 67], should happen during the life time of the structure, for which further studies are undergoing.

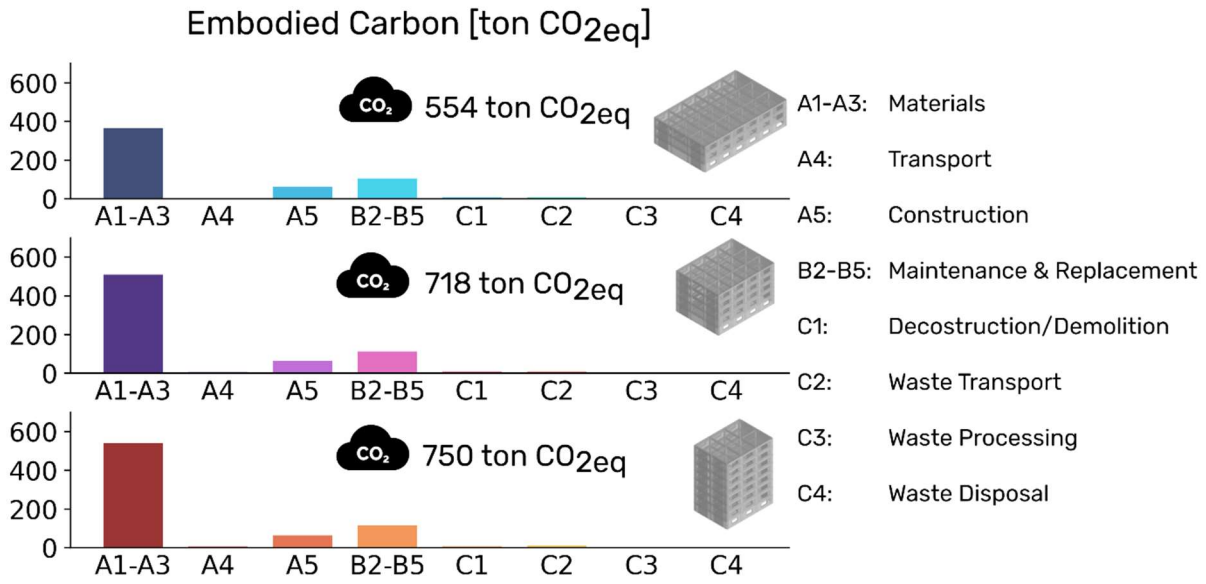


Figure 9. Global Warming Potential (kg CO2 equivalent) associated with the EN 15978 LCA stages and cumulative total values for the three case-study buildings.

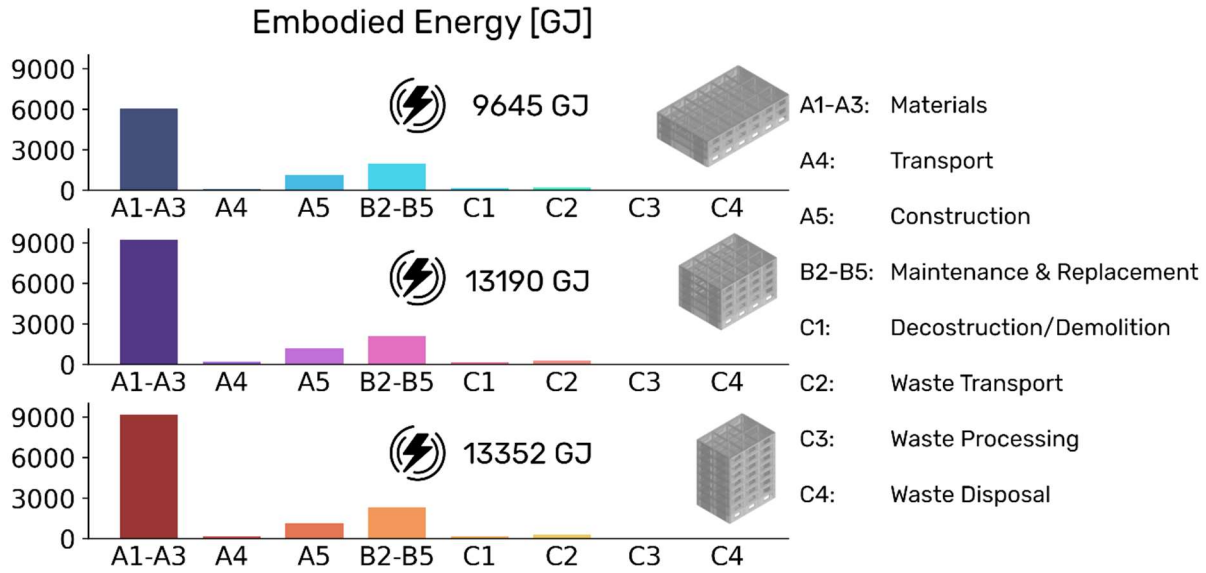


Figure 10. Embodied Energy (GigaJoule) associated with the EN 15978 LCA stages and cumulative total values for the three case-study buildings.

## 4.2 Seismic Performance

The analyses performed were used to assess the performance of the building under seismic action using time history non-linear analyses with a probabilistic approach. The Mean Annual Frequencies of Exceedance (MAFE) of the various damage states were computed using the fragility curves obtained through the IDA methodology and integrated using the fitted hazard curves.

Since the chosen intensity measure used to compute the fragility curve is the first mode spectral acceleration, the hazard curves had to be fitted for each building using the data obtained by the Italian Hazard model relative to the given first mode period and then adjusted for the soil

category C. A modal analysis was performed to determine the periods of the first mode and are reported in Figure 11 along the relative hazard curves.

The fragility curves were finally combined with the hazard curves to compute the MAFE for each limit states. The MAF integrand functions from Eq. 3 are show in in Figure 11.

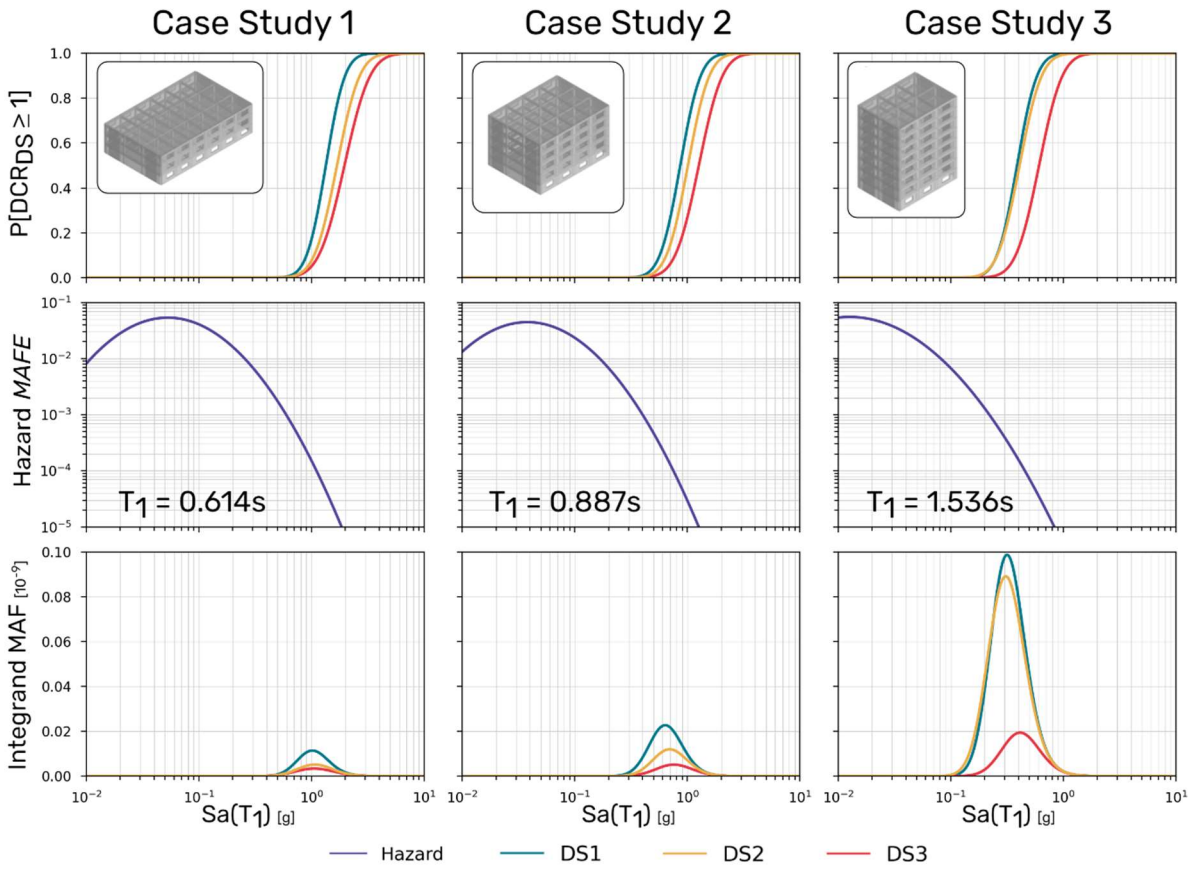


Figure 11. Damage state fragility in logarithmic scale (top); site hazard curve fitted using Eq. (2) for the specific T1 (centre); and MAF integrand scaled by a factor of $10^9$ (bottom).

Results show that in every case study the DS2 is achieved after the DS1, as it is desirable, even if the fragilities of the higher building experience a slight crossing which is more evident in the MAF integrand function. The crossing is related to the proximity between the two median values and to the fact that the DS2 experience a higher dispersion, which leads to a higher beta than the DS1. However, despite being undesirable, is possible in certain circumstances to experience the DS2 damage state before the DS1 in sections where the axial load is higher, or even after DS3, especially for sections at the last floor where the axial stress (induced by tendons) is lower. In fact, in the case of the higher building, as the case study 3, the DS2 insurgence is dominated by the base column sections which bear a higher level of axial load.

The values of the MAFE related to the various damage states show how case studies 1 and 2 are less prone to damage and failure respect to the higher building (Figure 12). Moreover, the lower case-study, even if does not exhibit a lower MAFE for the DS3, is less prone to damage both for DS1 and DS2.

It must be noted that the damage associated with DS1 is minimal because of how the connections are designed, as long as external dissipaters are employed. Instead, the DS2 is related to a more severe level of damage which falls into a gap on knowledge due to the lack of experience with this technology. For this reason, would be desirable to keep the DS2 as close

as possible to the DS3 that is related to a life-threatening or even a collapse-threshold level of damage beyond which the control over the response might be lost.

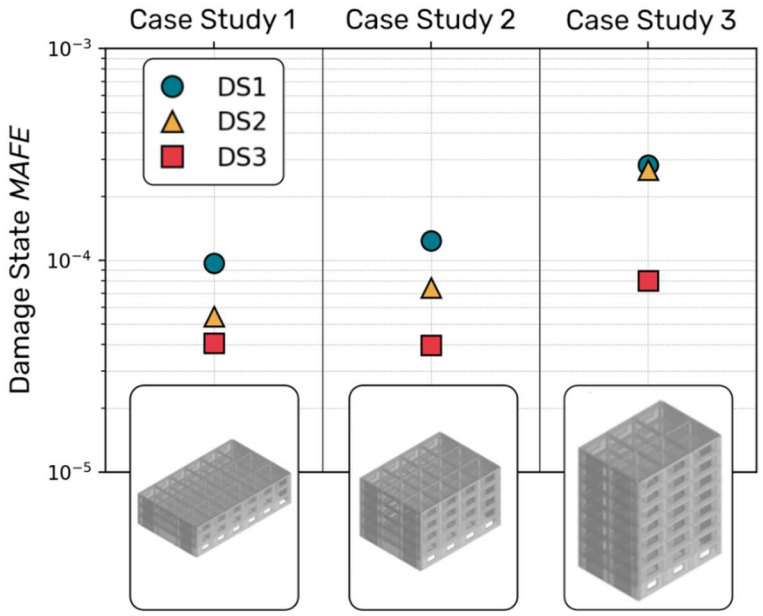


Figure 12. Mean Annual Frequency of Exceedance (MAFE) for the case studies and relative damage states.

### 4.3 Holistic Performance Assessment

Once the single building performances are evaluated for the three case-study building sets, their combination allows for a comprehensive understanding of which can represent the ideal solution. Thanks to the holistic parametric framework developed within the Grasshopper environment, is possible to control all the aspects involved in the multi-performance evaluation of the buildings in an automated and user-friendly manner and, changing the input parameters, to find out which building features influence the most its performance and adjust them towards the optimal solution.

Figure 13 shows how the 8-stories case-study building set, the highest as well as most slender one, represents the worst solution in terms of both seismic and environmental performance. All the damage states are expected for lower MAFE and its GWP is slightly higher than those of the 5-storey case study building despite being more compact in its floor area (as previously said, the greater amount of vertical facades due to the greater number of floors could be responsible for this difference).

The multi-performance approach becomes much more important when comparing the 5-storey case study to the 3-storey one: in fact, the 5-storey building, despite showing a slightly better performance than the 3-storey over the DS3, related to life-threatening behaviour, it comes with a greater carbon footprint, which can make it a less desirable choice. Furthermore, if the lower damage states are taken into account, the 5-storey shows a worse performance, highlighting how the sensibility and objectives of the stakeholder making the decision influence the outcome of the project. However, a multitude of factors are not included in this evaluation such as the fact that the 3-story requires a larger plot of land leading to a higher land use and higher costs. For this reason, a parametric, yet user-friendly, approach into an integrated environment can become very powerful as it allows the decision-maker to develop ad-hoc procedures that plugs into the model to aid the design process.

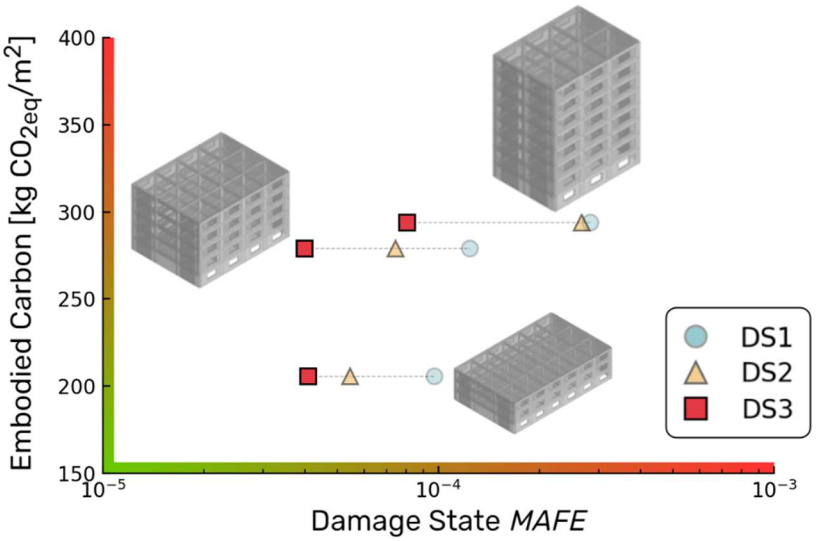


Figure 13. Combined seismic (MAFE for each DS) and environmental (Embodied Carbon, GWP) performance for the three case-study buildings.

The 3-storey case study building set, on the other hand, exhibit a significant better performance in terms of environmental impacts, while it does not really differ from the 5-storey building set in terms of seismic performance. The slightly lower carbon emissions are realistically due to the smaller dimensions of the structural elements, i.e., beams and columns, resulting from the seismic design.

Looking at the overall values for both seismic and environmental performance, it seems clear that the Pres-Lam technology allows for a low carbon footprint while, at the same time, delivering a high capability of withstanding severe earthquakes with a reduced level of damage, which is a fundamental aspect also for the reusability of the building elements in a circular economy perspective, leading, in turn, to a more sustainable performance.

## 5 CONCLUSIONS

This paper proposes a step towards a holistic multi-performance parametric approach for the seismic and environmental evaluation of Pres-Lam buildings. The framework herein presented is developed within Grasshopper-Python environment and has the potential to enhance the early stages of the design phase allowing for a rapid and user-friendly simultaneous check of multiple building performance towards the optimal solution.

Three Pres-Lam case-study buildings has been analysed using the parametric framework, geometrically defined and directly designed, using the DDBD procedure, within the Rhino+Grasshopper tool through a Python-based algorithm. Using a lumped plasticity model for the Pres-Lam frames, the seismic performance has been evaluated through fragility curves for different damage states obtained by the IDA methodology implemented in a Python script automatically linked to the Grasshopper model, while the environmental assessment has been carried out running the LCA procedure through the extensive EPD database of the OneClickLCA plug-in in the Rhino+Grasshopper environment.

The MAFE related to the various damage states, resulting from the seismic analyses, identified the higher case-study building as the more prone to damage, while the other two buildings are slightly similar in terms of seismic performance. On the other hand, the environmental assessment strongly declared the lower case-study as the best one in terms of

both GWP and Embodied Energy, while the other two buildings show approximately the same impact, with the higher one being the worst solution as it falls in a lower environmental class.

When putting together the two performances, a comprehensive understanding of the buildings' behaviour is possible, confirming which of those analysed is the best overall solution. Among the outcomes, particular emphasis shall be placed on how the use of laminated timber low-damage high-performance earthquake-resistant technologies allows also to cut the environmental footprint of buildings and to introduce circular economy principles within the building design.

The workflow introduced in this paper is therefore an easy and useful tool to evaluate if several proposed solutions are suitable for the designer's aims. The way it was conceived enables the stakeholders to monitor various building aspects simultaneously, analysing an unlimited number of options thanks to its parametric nature and identifying which parameter influences mostly the whole building's performance.

As a further development, the framework might also include energy simulations and insert the resulting energy consumptions within the LCA procedure as regards the operational phase of the building life cycle, in order to taking into account all the LCA stages. Similarly, the seismic performance should enter the environmental analysis through a revised Performance-Based Environmental Assessment by a Grasshopper algorithm, further confirming the benefits of using Pres-Lam structures. Finally, the results from all the different analyses could be combined using a Multi-Criteria Decision Making method to select the best solution amongst the alternatives.

## 6 REFERENCES

[1] United Nations, *Transforming our world: the 2030 Agenda for Sustainable Development–A/RES/70/1*, 2015.

[2] C. Menna, D. Asprone, F. Jalayer, A. Prota, G. Manfredi, Assessment of ecological sustainability of a building subjected to potential seismic events during its lifetime. *The international journal of life cycle assessment*, **18**, 504-515, 2013.

[3] A. Belleri, A. Marini, Does seismic risk affect the environmental impact of existing buildings?. *Energy and Buildings*, **110**, 149-158, 2016.

[4] S. Pampanin, Reality-check and renewed challenges in earthquake engineering: Implementing low-damage systems–from theory to practice. *Bulletin of the New Zealand Society for Earthquake Engineering*, **45(4)**, 137-160, 2012.

[5] S. Pampanin, Towards the "ultimate earthquake-proof" building: Development of an integrated low-damage system. *Perspectives on European Earthquake Engineering and Seismology*, **2**, 321-358, 2015.

[6] J. Stanton, W. C. Stone, G. S. Cheok, A hybrid reinforced precast frame for seismic regions. PCI journal, **42(2)**, 20-32, 1997.

[7] M. N. Priestley, S. Sritharan, J. R. Conley, S. Pampanin, Preliminary results and conclusions from the PRESSS five-story precast concrete test building. *PCI journal*, **44(6)**, 42-67, 1999.

[8] M. N. Priestley, Overview of PRESSS research program. *PCI journal*, **36(4)**, 50-57, 1991.

[9] F. Sarti, A. Palermo, S. Pampanin, Fuse-type external replaceable dissipaters: Experimental program and numerical modelling. *Journal of Structural Engineering*, **142(12)**, 04016134, 2016.

[10] A. Palermo, S. Pampanin, A. Buchanan, M. Newcombe, Seismic design of multi-storey buildings using laminated veneer lumber (LVL). *New Zealand Society for Earthquake Engineering Conference*, Wairakei, Taupo, New Zealand, March 11-13, 2005.

[11] A. Campbell, Mass timber in the circular economy: paradigm in practice? *Proceedings of the Institution of Civil Engineers - Engineering Sustainability*, **172(3)**, 141-152, 2018.

[12] R. Jockwer, Y. Goto, E. Scharn, K. Crona, Design for adaption–making timber buildings ready for circular use and extended service life. *IOP Conference Series: Earth and Environmental Science*, **588 (5)**, 052025, 2020.

[13] ITACA Italia Protocol, Roma, Italy, http://www.itaca.org/valutazione_sostenibilita.asp.

[14] U.S. Green Building Council, Washington, DC, http://www.usgbc.org/leed.

[15] DGNB, German Sustainable Building Council, http://www.dgnb.de/en.

[16] BREEAM, http://www.breeam.org.

[17] CASBEE, Comprehensive Assessment System for Built Environment Efficiency, Japan, http://www.ibec.or.jp/CASBEE/english.

[18] M. C. Caruso, C. Menna, D. Asprone, A. Prota, A., G. Manfredi, Methodology for life-cycle sustainability assessment of building structures. *ACI Structural Journal*, **114(2)**, 323, 2017.

[19] D. Apellániz, P. Pasanen, C. Gengnagel, A holistic and parametric approach for life cycle assessment in the early design stages. *Symposium on Simulation for Architecture and Urban Design (SimAUD)*, April 15-17, 2021.

[20] Structural Engineers Associate of California, *Performance-based seismic engineering*. SEAOC Vision 2000, Sacramento, California, USA, 2000.

[21] D. Marriott, S. Pampanin, D. Bull, A. Palermo, Dynamic Testing of Precast, Post-Tensioned Rocking Wall Systems with Alternative Dissipating Solutions. *New Zealand Society for Earthquake Engineering Conference*, Wairakei, Taupo, New Zealand, April 11-13, 2008.

[22] D. Moroder, T. Smith, A. Dunbar, S. Pampanin, A. Buchanan, Seismic testing of post-tensioned Pres-Lam core walls using cross laminated timber. *Engineering Structures,* **167**, 639–54, 2018.

[23] F. Sarti, A. Palermo, S. Pampanin, Quasi-Static Cyclic Testing of Two-Thirds Scale Unbonded Posttensioned Rocking Dissipative Timber Walls. *Journal of Structural Engineering,* **142**, 2016.

[24] F. Wanninger, A. Frangi, Experimental and analytical analysis of a post-tensioned timber connection under gravity loads. *Engineering Structures,* **70**, 117–29, 2014.

[25] M.P. Newcombe, S. Pampanin, A. Buchanan, A. Palermo, Section Analysis and Cyclic Behavior of Post-Tensioned Jointed Ductile Connections for Multi-Story Timber Buildings. *Journal of Earthquake Engineering,* **12**, 83–110, 2008.

[26] M.P. Newcombe, S. Pampanin, A. H. Buchanan, Global response of a two-storey Pres-Lam building. *New Zealand Society for Earthquake Engineering Conference*, Wellington, New Zealand, March 26-28, 2010.

[27] New Zealand Society for Earthquake Engineering. Kaikoura earthquake special issue. Bulletin of the New Zealand Society for Earthquake Engineering, **50(2)**, 73–362, 2016.

[28] F. Sarti, A. Palermo, S. Pampanin, J. Berman, Determination of the seismic performance factors for post-tensioned rocking timber wall systems. *Earthquake Engineering & Structural Dynamics,* **46**,181–200, 2016.

[29] T. Holden, C. Devereux, S. Haydon, A. Buchanan, S. Pampanin, NMIT Arts & Media Building - Innovative structural design of a three storey post-tensioned timber building. *Case Studies in Structural Engineering,* **6**, 76–83, 2016.

[30] C. Leyder, F. Wanninger, A. Frangi, E. Chatzi, Dynamic response of an innovative hybrid structure in hardwood. *Proceedings of the Institution of Civil Engineers - Construction Materials,* **168**, 132–43, 2015.

[31] B. Curtain, D. Dekker, S. Chung, et al., Design of Carterton Event Centre: An example of innovative collaboration between architecture and timber engineering. *12th world conference on timber engineering (WCTE),* Auckland, New Zealand, July 15–19, 2012.

[32] A. Brown, J. Lester, S. Pampanin, D. Pietra. Pres-Lam in practice - A damage-limiting rebuild project. *Structural Engineering Society (SESOC) New Zealand Conference*, Auckland, New Zealand, November 2-3, 2012.

[33] A. Kirstein, J. Siracusa, T. Smith, The new timber von Haast replacement building in Christchurch. *New Zealand Society for Earthquake Engineering Conference,* Auckland, New Zealand, April 13-15, 2018.

[34] A. Miliziano, G. Granello, A. Palermo, S. Pampanin, Overview of connection detailing for post-tensioned dissipative timber frames. *Structural Engineering International*, **30(2)**, 209-216, 2020.

[35] S. Pampanin, J. Ciurlanti, S. Bianchi, M. Palmieri, D. Grant, G. Granello, A. Palermo, A. Correia, Overview of SERA project: 3Dshaking table tests on an integrated low-damage building system. *4th International Workshop on the Seismic Performance of Non-Structural Elements (SPONSE),* Pavia, Italy, May 22-23, 2019.

[36] M. J. Mancini, S. Pampanin, Numerical and experimental investigation on low damage steel-timber post-tensioned beam-column connection. *16th European Conference on Earthquake Engineering*. Thessaloniki, Greece, 18-21 June, 2018.

[37] S. Bianchi, J. Ciurlanti, S. Pampanin, Comparison of traditional vs low-damage structural and non-structural building systems through a cost/performance-based evaluation. *Earthquake Spectra*, **37(1)**, 366-385, 2021.

[38] G. Granello, A. Palermo, S. Pampanin, S. Pei, J. van de Lindt, Pres-Lam Buildings: State-of-the-Art. *Journal of Structural Engineering,* **146**, 2020.

[39] International Standards Organization, ISO 14040. *Environmental Management—Life Cycle Assessment - Principles and Framework*, Geneva, Switzerland, 2006.

[40] International Standards Organization, ISO 14044. *Environmental Management—Life Cycle Assessment, Requirements, and Guidelines*, Geneva, Switzerland, 2006.

[41] British Standard Institution, EN 15978. *Sustainability of Construction Works - Assessment of Environmental Performance of Buildings - Calculation Method*, 2011.

[42] British Standard Institution, EN 15804. *Sustainability of construction works. Environmental product declarations. Core rules for the product category of construction products*, 2012.

[43] D. Vamvatsikos, C.A. Cornell, Incremental dynamic analysis. *Earthquake Engineering & Structural Dynamics*, **31**, 491–514, 2002.

[44] Federal Emergency Management Agency, FEMA P-695. *Quantification of building seismic performance factors,* Washington, DC, USA, 2009.

[45] I. Iervolino, A. Spillatura, P. Bazzurro, Seismic Reliability of Code-Conforming Italian Buildings. *Journal of Earthquake Engineering* **22**, 5–27, 2018.

[46] M. Stucchi, C. Meletti, V. Montaldo, H. Crowley, G.M. Calvi, E. Boschi, Seismic Hazard Assessment (2003-2009) for the Italian Building Code. *Bulletin of the Seismological Society of America* **101**, 1885–911, 2011.

[47] SAC Joint Venture, Federal Emergency Management Agency, SAC/FEMA. *Recommended seismic design criteria for new steel moment-frame buildings. Report No. FEMA-350*, Washington, DC, USA, 2000.

[48] SAC Joint Venture, Federal Emergency Management Agency, SAC/FEMA. *Recommended seismic evaluation and upgrade criteria for existing welded steel moment-frame buildings*. *Report No. FEMA-351*, Washington, DC, USA, 2000.

[49] D. Vamvatsikos, Derivation of new SAC/FEMA performance evaluation solutions with second-order hazard approximation. *Earthquake Engineering & Structural Dynamics,* **42**, 1171–88, 2012.

[50] M. N. Priestley, Direct displacement-based design of precast/prestressed concrete buildings. *PCI journal*, **47(6)**, 66-79, 2002.

[51] M. N. Priestley, G. M. Calvi, M. J. Kowalsky, Displacement-Based Seismic Design of Structures. *Earthquake Spectra*, **24(2)**, 555–557, 2007.

[52] S. Pampanin, A. Palermo, A. H. Buchanan, *Design Guide Australia and New Zealand-Post-Tensioned Timber Buildings*, 2013.

[53] F. McKenna, OpenSees: A Framework for Earthquake Engineering Simulation. *Computing in Science & Engineering,* **13**, 58–66, 2011.

[54] M. Zhu, F. McKenna, M.H. Scott, OpenSeesPy: Python library for the OpenSees finite element framework. *SoftwareX,* **7**, 6–11, 2018.

[55] Ministero delle Infrastrutture e dei Trasporti (MIT), NTC 2018. *D.M. del Ministero delle Infrastrutture e dei trasporti del 17/01/2018. Aggiornamento delle Norme Tecniche per le Costruzioni,* 2018 (in Italian)

[56] European Committee for Standardization (CEN), *Eurocode 5 - Design of timber structures - Part 1-1: General - Common rules and rules for buildings*, Brussels, Belgium, 2004.

[57] European Committee for Standardization (CEN), *Eurocode 3 - Design of steel structures - Part 1-8: Design of joints*, Brussels, Belgium, 2005.

[58] A. Baird, A. Palermo, S. Pampanin, Controlling seismic response using passive energy dissipating cladding connections. *New Zealand Society for Earthquake Engineering Conference,* Wellington, April 26-28, 2013.

[59] S, D'Amore, S. Bianchi, J. Ciurlanti, S. Pampanin, Seismic assessment and finite element modeling of traditional vs innovative point fixed glass facade systems (PFGFS). Bulletin of Earthquake Engineering, 2023.

[60] A. Di Cesare, F.C. Ponzo, D. Nigro, S. Pampanin, T. Smith, Shaking table testing of post-tensioned timber frame building with passive energy dissipation systems. *Bulletin of Earthquake Engineering,* **15**, 4475–98, 2017.

[61] S. Pampanin, M.J.N. Priestley, S. Sritharan, Analytical modelling of the seismic behaviour of precast concrete frames designed with ductile connections. *Journal of Earthquake Engineering,* **5**, 329–67, 2001.

[62] A. Palermo, The use of controlled rocking in the seismic design of bridges. *PhD Thesis*, Technical Institute of Milan, Milan, Italy, 2004.

[63] T. Smith, Post-tensioned timber frames with supplemental damping devices. *PhD Thesis*, University of Canterbury, Christchurch, New Zealand, 2014.

[64] A. Iqbal, S. Pampanin, A. Palermo, Seismic performance of prestressed timber beam column sub-assemblies. *New Zealand Society for Earthquake Engineering Conference*, Wellington, New Zealand, March 26-28, 2010.

[65] P. Pasanen, R. Castro, Carbon Heroes Benchmark Program–whole building embodied carbon profiling. *IOP Conference Series: Earth and Environmental Science,* **323(1)**, 012028, 2019.

[66] T. Smith, R. Wong, M. P. Newcombe, D. Carradine, S. Pampanin, A. Buchanan, R. Seville, E. McGregor, The Demountability, Relocation and Re-use of a High-Performance Timber Building. *9th Pacific Conference on Earthquake Engineering (PCEE): Building an Earthquake-Resilient Society*, Auckland, New Zealand, April 14-16, 2011.

[67] Federal Emergency Management Agency, *Seismic Performance Assement of Buildings, Volume 1. Technical report FEMA-P-58-1*, Department of Homeland Security, Washington, DC, USA, 2012.

COMPDYN 2023
9th ECCOMAS Thematic Conference on
Computational Methods in Structural Dynamics and Earthquake Engineering
M. Papadrakakis, M. Fragiadakis (eds.)
Athens, Greece, 12-14 June 2023

# SYSTEM IDENTIFICATION OF LONG-SPAN BRIDGES VIA SYNCHRO-SQUEEZED ADAPTIVE WAVELET TRANSFORM BASED OPTIMIZED MULTIPLE ANALYTICAL MODE DECOMPOSITION

**Hongya Qu[1], Mwenda Lomthundzi[1], Yan Xu[1] and An Chang[1]**

[1] Department of Bridge Engineering, Tongji University
1239 Siping Rd. Shanghai 200092, China
e-mail: hqu@tongji.edu.cn, lomymwenda@outlook.com, 05203@tongji.edu.cn, ox@tongji.edu.cn

## Abstract

*In this study, a new system identification method, synchro-squeezed adaptive wavelet transform based optimized multiple analytical mode decomposition (SSAWT-oMAMD), is proposed and introduced. The SSAWT adaptively adjusts the wavelet parameters, which provides the optimal representation over the entire time-frequency plane and minimizes the energy dispersion. In this way, SSAWT yields the time-frequency representation that is close to actual signal characteristics. Then, SSAWT is utilized as the preprocessing for oMAMD method, which is to determine bisecting frequencies with high accuracy. The oMAMD is then applied to the structural health monitoring signals, for denoising, decomposition, and identification. The proposed SSAWT-oMAMD is first verified with various analytical and numerical examples, and the identification accuracy of the complex time-varying systems are generally within 5%, demonstrating the effectiveness of the method. Based on SSAWT-oMAMD, shake table test of a scaled cable-stayed bridge model is then carried out. The parameters of the implemented viscous damper are identified with the SSAWT-oMAMD algorithm, and damage progression of the bridge structure is also identified with the algorithm through damping and stiffness coefficient. It is proved that the proposed SSAWT-oMAMD is effective in identifying key features of the bridge system under earthquake loading based on basic structural health monitoring data, which further facilitates the resilience evaluation of bridge damage subjected to earthquake loading.*

**Keywords:** Signal Processing, System Identification, Structural Dynamics, Seismic Response, Shake Table Test.

## 1 INTRODUCTION

Signal processing typically includes two categories: representation and decomposition. For signal representation, it transforms the viewing angle of a signal, which includes but not limited to Wigner-Ville distribution [1], short-time Fourier transform [2], and wavelet transform [3]. To further improve time-frequency resolution of conventional wavelet transform, synchro-squeezed wavelet transform is proposed [4]. Adaptation algorithm [5] is then proposed to formulate synchro-squeezed adaptive wavelet transform (SSAWT) [6], which provides the optimal time-frequency representation of the signal. For signal decomposition, some typical decomposition methods include: filters [7], empirical mode decomposition [8], Hilbert vibration decomposition [9], and analytical mode de-composition (AMD) [10]. Empirical mode decomposition is one of the most popular method for decomposition of signal with time-varying characteristics. AMD retains the capability of time-varying signal decomposition with high accuracy.

A number of cable-stayed bridge has been constructed in recent years, and some of these bridges are located in earthquake-prone zones. Shake table tests are carried out by limited research works, which includes structural response analysis under non-uniform excitation [11]; comparison of various isolation devices in cable-stayed bridge [12]; the effect of viscous damper on seismic performance [13]. In addition, there is only a few studies that focus on the system identification of cable-stayed bridge under earthquake load [14-18]. Therefore, it is necessary to perform parameter identification of cable-stayed bridge components during an earthquake with shake table test, in order to understand the seismic behavior or even damage progression.

In this study, synchro-squeezed adaptive wavelet transform based multiple analytical mode decomposition (SSAWT-MAMD) is proposed, to perform the system identification of a 1/20-scale cable-stayed bridge model. Based on the numerical and experimental study of cable-stayed bridge, it is demonstrated that the SSAWT-MAMD algorithm is capable for identification of nonlinear behaviors of bridge structural components.

## 2 SSAWT-MAMD ALGORITHM

At given time instant $\tau_k$ over the time history of a signal, short-time wavelet transform is performed for the $k^{th}$ short-time segment. The short-time segment ($n = (T - T_{\tau_n})/\Delta t$ in total) retains the time duration of $[\tau_k, \tau_k + T_{\tau_k}]$. The optimal center frequency ($\omega_c$) and window length ($T_{\tau_k}$) are determined by the adaptation algorithm. To eliminate the discontinuity of segment, adjacent edges of the transformed segments are overlapped, summed, and averaged. The adaptive wavelet transform with Morlet mother wavelet can therefore be formulated. Synchro-squeezing is finally applied, and SSAWT is defined as:

$$SSAWT\{x(t)\}(\omega, b) = \int_{A(b)} \sum_{k=0}^{n} \frac{q_k}{p_k} \frac{1}{\sqrt{2\pi\omega_c(\tau_k)/\omega}} \int_{\tau_k}^{\tau_k + T_{\tau_k}} x(t) e^{-\frac{(t-b)^2\omega^2}{2\omega_c^2(\tau_k)}} e^{-i\omega(t-b)}\, dt\, a^{-3/2} \delta(\omega_x(a,b) - \omega) da \quad (1)$$

where $\omega_c(\tau_k)$ and $a(\tau_k)$ is center frequency and scaling factor at time $\tau_k$, $T_{\tau_k}$ is the window length, $p_k$ is the parameter for averaging that counts the number of windowed segments spanning over $\tau_k$, $q_k$ is the normalization factor of each short-time segment, and $\omega_x(a,b) = -i\frac{1}{W_x(a,b)}\frac{\partial[W_x(a,b)]}{\partial b}$.

$AMD_{\omega_b(t)}[\cdot]$, decomposed low frequency component of a signal $s(t)$ with respect to the time-varying bisecting frequency of $\omega_b(t)$, is the tool for mode decomposition:

$$s(\theta)=\begin{cases}\frac{1}{2}AMD_{\omega_b(t)}[s(\theta)]+\frac{1}{2}AMD_{\omega_b(t)}\left[AMD_{\omega_b(t)}[s(\theta)]\right] & 0<\omega_b(t)<\frac{1}{4}\omega_s(t)\\ s(t)+\frac{1}{2}AMD_{\omega_b(t)}[s(\theta)]-\frac{1}{2}AMD\left[AMD_{\omega_b(t)}[s(\theta)]\right] & \frac{1}{4}\omega_s(t)<\omega_b(t)<\frac{1}{2}\omega_s(t)\end{cases} \tag{2}$$

The MAMD integrates the AMD for multiple applications for identification of nonlinear system with fast-varying components. It starts from the equation of motion of a time-varying nonlinear system:

$$\ddot{x}(t)+2h(t)\dot{x}(t)+\omega^2(t)x(t)=p(t) \tag{3}$$

where $2h(t)=2h_s(t)+2h_f(t)$ and $\omega^2(t)=\omega_s^2(t)+\omega_f^2(t)$, and the subscripts $s$ and $f$ indicates the slow- and fast-varying components of the coefficients.

AMD is used for the first time to denoise original signal. It is then applied for the second time to decompose the coefficients to obtain slow-varying components:

$$\omega_{s'}^2=AMD_{\min[\omega_{x1}(t),\omega_{x2}(t)]}\{\omega_{0x}^2(t)\} \tag{4}$$

$$2h_{s'}=AMD_{\min[\omega_{\dot{x}1}(t),\omega_{\dot{x}2}(t)]}\{2h_{0x}(t)\} \tag{5}$$

where $\omega_{x1}(t)$, $\omega_{x2}(t)$, $\omega_{\dot{x}1}(t)$ and $\omega_{\dot{x}2}(t)$ are the bisecting frequencies, and $\omega_{0x}^2(t)$ and $2h_{0x}(t)$ are the raw stiffness and damping coefficients mixed with both fast- and slow-varying components. The actual slow-varying components are then obtained as $\omega_s^2=\omega_{s'}^2+\omega_{0p}^2$ and $2h_s=2h_{s'}+2h_{0p}$.

By utilizing AMD for the third time, the fast-varying components with lower frequency is decomposed first, and the other is obtained afterwards:

$$2h_f=AMD_{\omega_b'(t)}\{2\tilde{h}_f\} \tag{6}$$

$$\omega_f^2=AMD_{\omega_b'(t)}\{\tilde{\omega}_f^2\} \tag{7}$$

where $2\tilde{h}_f$ and $\tilde{\omega}_f^2$ are the fast-varying coefficients with mixing terms, and the bisecting frequency $\omega_b'(t)$ is determined by SSAWT.

Actual coefficients are thus derived from:

$$2h=2h_s+2h_f \tag{8}$$

$$\omega^2=\omega_s^2+\omega_f^2 \tag{9}$$

The SSAWT-MAMD algorithm is summarized in Figure 1.

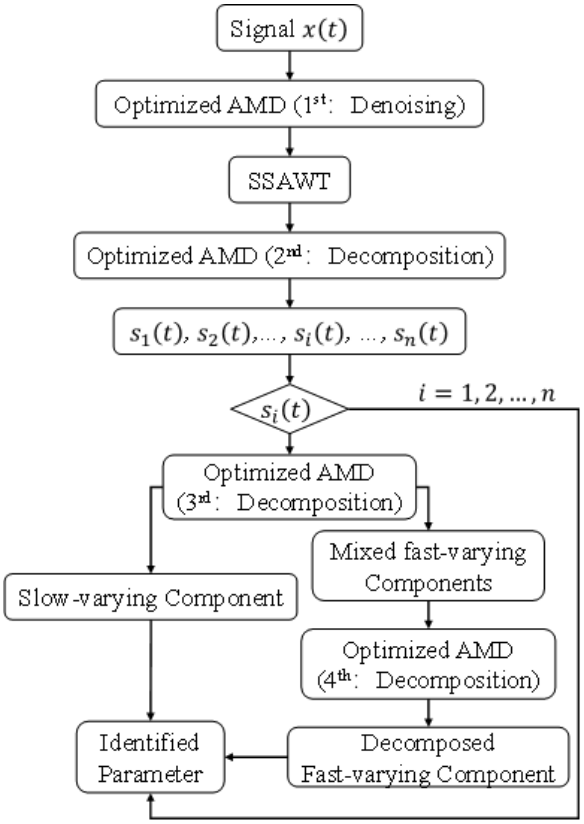


Figure 1: SSAWT-MAMD algorithm.

## 3 ALOGRITHM VERIFICATION WITH ANALITCAL MODEL

The effectiveness of the proposed SSAWT-MAMD algorithm is first demonstrated by two closely-spaced Duffing systems. Both systems are with the initial displacement of 100 and can be mathematically expressed as: $\ddot{x} + 0.05\dot{x} + x + 0.01x^3 = 0$ (system 1) and $\ddot{x} + 0.05\dot{x} + 3x + 0.02x^3 = 0$ (system 2).

SSAWT is performed for the time history function with Morlet mother wavelet, as shown in Figure 2. The adaptation algorithm is able to provide optimal time-frequency representation of time history function. The SSAWT result is also compared with conventional wavelet transform, and it is clearly shown in the figure that conventional wavelet transform is of thicker curves, and the two curves are interconnected with distorted representation. On the other hand, SSAWT provides clear and concentrated time-frequency representation of the two systems.

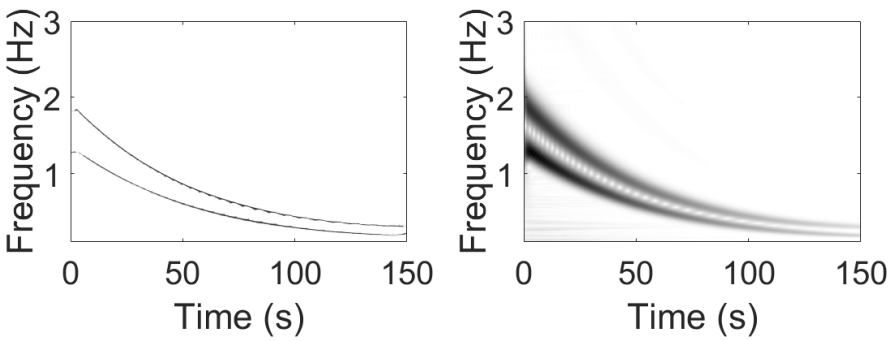


(a) (b)

Figure 2: Comparison of wavelet transforms: (a) SSAWT; (b) Wavelet transform.

Based on SSAWT results, time-varying bisecting frequency can be determined, and AMD is performed to decompose the two systems. For Duffing system, damping coefficient does not contain fast-varying component but stiffness coefficient. By applying MAMD, the final identification of the stiffness coefficient from Duffing system is given in Figure 3. It shows that SSAWT-MAMD can be effective for parameter identification of analytical models with fast-varying system.

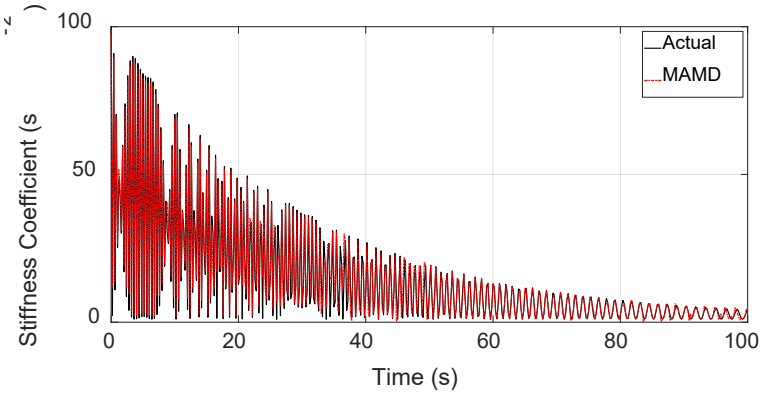


Figure 3: Identified stiffness coefficient by SSAWT-MAMD.

## 4 ALOGRITHM APPLICATION IN SHAKE TABLE TEST MODEL

The prototype bridge is a typical cable-stayed bridge (110 m + 260 m + 110 m). Concrete tower is 108 m tall, concrete box girder is used for the entire span, and piers of side span are thin-walled hollow-section reinforced concrete. The bridge model is scaled to 1/20 of the prototype (Figure 4), which is to investigate the nonlinear behavior of the bridge structure under seismic load. Earthquake input is a near-fault earth-quake occurred in June 28th, 1992 at Landers, California (LCN266). The PGA of the earthquake record is scaled from 0.1g to 0.4g by the step size of 0.1g.



Figure 4: Experiment bridge model.

For parameter identification of the bridge tower, the time history of acceleration at the top of the bridge tower and its SSAWT under the 0.4g (PGA) earthquake input are selected. Based on the time-frequency representation of SSAWT, the first four vibration modes can excited by the seismic load. SSAWT-MAMD it then performed, and the identified stiffness and damping of the test model under 0.4g earthquake input are shown in Figure 5. As shown in the figure, damping and stiffness of the dominant mode stays relatively constant within the time of interest (3 s to 6 s where strong earthquake motion occurs), which is in accordance with the observation from the experiment. This confirms that the bridge specimen has experienced little damage throughout the entire process of experiment.

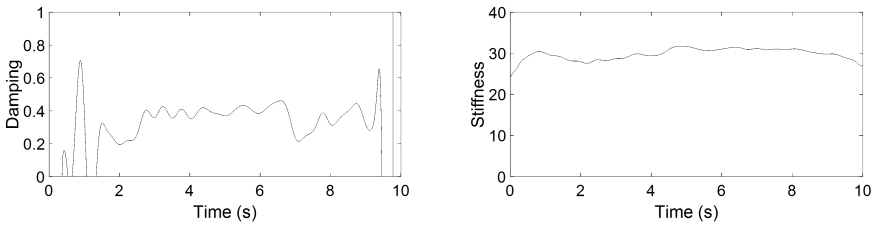


(a) (b)

Figure 5: Identified parameter: (a) damping; (b) stiffness

## 5 CONCLUSIONS

In this study, SSAWT-MAMD is proposed and applied to system identification of analytical and experimental models, and the following conclusions can be drawn:

- The synchro-squeezing algorithm lowers energy dispersion and sharpens the ridgelines of the time-frequency representation.
- MAMD integrates de-noising, decomposition and identification, which effectively identifies system parameters with better accuracy.
- Clear separation of signals is presented and accurate identification of complex time-varying coefficient is achieved.
- Based on experimental results of a cable-stayed bridge model, the proposed method is effective in identifying the structural conditions.

## REFERENCES

[1] Wigner EP. On the quantum correction for thermodynamic equilibrium. InPart I: Physical Chemistry. Part II: Solid State Physics 1997 (pp. 110-120). Springer, Berlin, Heidelberg.

[2] Jacobsen E, Lyons R. The sliding DFT. IEEE Signal Processing Magazine. 2003 Mar 10;20(2):74-80.

[3] Daubechies I. Ten lectures on wavelets. Society for industrial and applied mathematics; 1992 Jan 1.

[4] Daubechies I, Lu J, Wu HT. Synchrosqueezed wavelet transforms: An empirical mode decomposition-like tool. Applied and computational harmonic analysis. 2011 Mar 1;30(2):243-61.

[5] Qu H, Li T, Chen G. Adaptive wavelet transform: Definition, parameter optimization algorithms, and application for concrete delamination detection from impact echo responses. Structural Health Monitoring. 2019 Jul;18(4):1022-39.

[6] Qu H, Li T, Chen G. Synchro-squeezed adaptive wavelet transform with optimum parameters for arbitrary time series. Mechanical Systems and Signal Processing. 2019 Jan 1;114:366-77.

[7] Jackson LB. Digital Filters and Signal Processing: With MATLAB® Exercises. Springer Science & Business Media; 2013 Jun 29.

[8] Huang, Norden E., Zheng Shen, Steven R. Long, Manli C. Wu, Hsing H. Shih, Quanan Zheng, Nai-Chyuan Yen, Chi Chao Tung, and Henry H. Liu. "The empirical mode decomposition and the Hilbert spectrum for nonlinear and non-stationary time series analysis." Proceedings of the Royal Society of London. Series A: mathematical, physical and engineering sciences 454, no. 1971 (1998): 903-995.

[9] Feldman M. Time-varying vibration decomposition and analysis based on the Hilbert transform. Journal of Sound and Vibration. 2006 Aug 22;295(3-5):518-30.

[10] Wang ZC, Chen GD. Analytical mode decomposition of time series with decaying amplitudes and overlapping instantaneous frequencies. Smart materials and structures. 2013 Jul 25;22(9):095003.

[11] Zong ZH, Zhou R, Huang XY, Xia ZH. Seismic response study on a multi-span cable-stayed bridge scale model under multi-support excitations. Part I: shaking table tests. Journal of Zhejiang University SCIENCE A. 2014 May;15(5):351-63.

[12] Xu Y, Wang R, Li J. Experimental verification of a cable-stayed bridge model using passive energy dissipation devices. Journal of Bridge Engineering. 2016 Dec 1;21(12):04016092.

[13] Guo W, Li J, Guan Z. Shake table test on a long-span cable-stayed bridge with viscous dampers considering wave passage effects. Journal of Bridge Engineering. 2021 Feb 1;26(2):04020118.

[14] Kim JT, Ho DD, Nguyen KD, Hong DS, Shin SW, Yun CB, Shinozuka M. System identification of a cable-stayed bridge using vibration responses measured by a wireless sensor network. Smart Struct. Syst. 2013 May 1;11(5):533-53.

[15] Lozano-Galant JA, Nogal M, Paya-Zaforteza I, Turmo J. Structural system identification of cable-stayed bridges with observability techniques. Structure and Infrastructure Engineering. 2014 Nov 2;10(11):1331-44.

[16] Asadollahi P, Li J. Statistical analysis of modal properties of a cable-stayed bridge through long-term wireless structural health monitoring. Journal of Bridge Engineering. 2017 Sep 1;22(9):04017051.

[17] Sun M, Makki Alamdari M, Kalhori H. Automated operational modal analysis of a cable-stayed bridge. Journal of Bridge Engineering. 2017 Dec 1.

[18] Siringoringo DM, Fujino Y, Namikawa K. Seismic Responses Analyses of the Yokohama-Bay Cable-Stayed Bridge in the 2011 Great East Japan (Tohoku) Earthquake. J. Bridge Eng. ASCE,(In press) DOI. 2013;10.

COMPDYN 2023
9th ECCOMAS Thematic Conference on
Computational Methods in Structural Dynamics and Earthquake Engineering
M. Papadrakakis, M. Fragiadakis (eds.)
Athens, Greece, 12-14 June 2023

# RESTORATION OF A LANDMARK BALANCED CANTILEVER BRIDGE CONSIDERING DIFFERENT RESILIENCE AND SUSTAINABILITY STRATEGIES

**Marco Domaneschi[1], Stergios A. Mitoulis[2], Raffaele Cucuzza[1], Valentina Villa[1] and Roberta Di Bari[3], Gopika Siva[2]**

[1]Politecnico di Torino, Department of Structural, Geotechnical and Building Engineering (DISEG), Corso Duca degli Abruzzi, Turin, Italy; e-mail: {marco.domaneschi, valentina.villa, raffaele cucuzza, giuseppe.marano} @polito.it

[2] Department of Civil Engineering, School of Engineering, University of Birmingham and www.infrastructuResilience.com; email: {S.A.Mitoulis, gxs268 } @Bham.ac.uk

[3] Department Life Cycle Engineering (GaBi), School of Engineering, Instute for Acoustics and Building Physics, Germany; email: roberta.di.bari@ibp.fraunhofer.de

## Abstract

*This paper examines a landmark bridge upon which the road network functionality and life of people living in the region are heavily dependent. The Servia High Bridge, also known as the Lake Polyfytos Bridge, and it is the second longest bridge in Greece, spanning 1,372 meters. It was constructed by XEKTE SA and designed by Prof Riccardo Morandi. The bridge was designed around about the same time with the artificial Polyfytos lake, its construction started in 1972 and was completed in 1975. Strong connections exist between the nation's 48-year-old iconic bridge and the most significant power plants in South East Europe. The risk and resilience of the bridge and surrounding network have been assessed using a combination of visual inspections and digital data collection based on: (a) a digital twin, which provides a snapshot of the asset's current geometry and a dynamically evolving model that can inform advanced simulations; (b) satellite imagery, which offers ongoing updates and information about the asset's deformations and geometry; and (c) advanced numerical modeling, where based on back analysis an interpretation of the current deflections is attempted. The bridge exhibits degradation typically met in reinforced concrete (RC) and PRC (prestressed RC) bridges. In particular, the present case study is faced with challenges relating to the corroded tendons and concrete bonding. In this paper, different retrofitting measures are examined either the speed of recovery and the CO2 of the materials for retrofit, which reflect the resilience and sustainability of the examined strategies, based on FEM and monitoring data that lead to decisions.*

**Keywords:** bridge, sustainability, resilience, cost-effectiveness.

## 1 INTRODUCTION

Over the last 50 years, the balanced cantilever construction method has become prominent in bridge construction as it has proved itself to be both structurally effective and economically sound as a solution for medium spans, approximately 100 to 200 meters [1]. However, it is now evident that long-term effects of materials, such as creep and shrinkage of concrete and corrosion and relaxation of steel tendons, can cause damage to the deck, in the form of excessive vertical deflections of the cantilever ends an effect that was reported since the 90's by prominent researchers [2-4]. Numerous cases of bridge deterioration leading to excessive deflections have been documented before [5] with the damage in some instances extending to more than serviceability issues, e.g. resulting to partial collapse of the structure and fatalities. Although the main causes are almost positively confirmed to be the long-term effects, the ever-increasing traffic loads [6] and potential constructability issues [7], the detailed mechanism of the faults, as well as a streamlined method to calculate and predict them in a satisfactory level, are not yet established despite multiple researchers' endeavors [8-10].

The lack of a standard approach to this problem gave motivation to the authors to put forward an alternative solution, quite different approaches to the traditional ones that consist of multiple on-site inspections and measurements. This paper can be used in cases where the fragile nature of the asset and the uncertainty revolving its structural integrity poses as a barrier to destructive testing (e.g. loading with heavy vehicle) and extensive sample collection (e.g. cores of the deck concrete). In addition to that, as the construction sector is slowly but steadily moving towards digitalization and extensive monitoring, the proposed solution relies heavily on computer analysis and cutting-edge measuring tools such as drone-based photogrammetry [11], providing an inexpensive and time-efficient solution, while also being in accordance with environmental concerns. Laser scanning technology is rising in popularity [12] and has been found to achieve highly detailed results, even in restricted periods of time [13].

In this paper, a proposal using state-of-the-art surveying tools (laser-photogrammetry) paired with an advanced analysis is implemented to the Polyfytos bridge, a balanced cantilever segmentally constructed box girder bridge that developed excessive deformations and is now under investigation by the local Government and owner in Western Macedonia in Greece. The process begins with collecting data that were quite fragmented and scattered through the initial design report (written in 1974) and using it to create a 3D non-linear model of a typical cantilever (advanced modelling). After a thorough literature review, the most commonly mentioned possible causes of the problem were decided and a scenario based on each one was created (scenario-based modelling). The detailed measurements were compared to the results of the analyses and the scenarios were rated based on their resemblance to the actual state of the bridge.

The combination of the laser-scanning output and the detailed modelling deflection curves may be considered as evidence that can drive the project engineers to make a more precise assumption about the structural defects of the balanced cantilever part of the deck. Numerous examples across literature show that a misconception of the fault source may lead to erroneous repair methods, resulting in more extensive damage and sometimes even partial collapse [14]. At the same time, our proposal is time and cost efficient, carries little to no carbon footprint and helps engineers make decisions while having no physical interaction with the bridge.

## Background of the challenge

According to SGS [15], a leading inspection and verification multinational company, the usual process in damage assessment at an infrastructure asset includes a preliminary report, design supervision, on-site inspections, materials and construction units testing, monitoring and a final report of the repair process. However, there may be cases where one or more steps of

this process are not feasible, and an alternative route should be followed in order to assess the condition of the asset. A technically sound solution to this problem should be in line with the two main contemporary principles around which all engineering innovation revolves nowadays; digitalization and sustainability.

The Polyfytos bridge is an asset built in 1975 in the Municipality of Western Macedonia, Kozani, Greece and bridges the artificial homonymous lake of Polyfytos, with the local and the national road network relying entirely on its integrity. The balanced cantilever method was used to build a part of the bridge, specifically six cantilevers spanning from piers 22, 23 and 24 (Fig.1) accounting for a total of 260 meters (total length of the bridge is 1372 m).

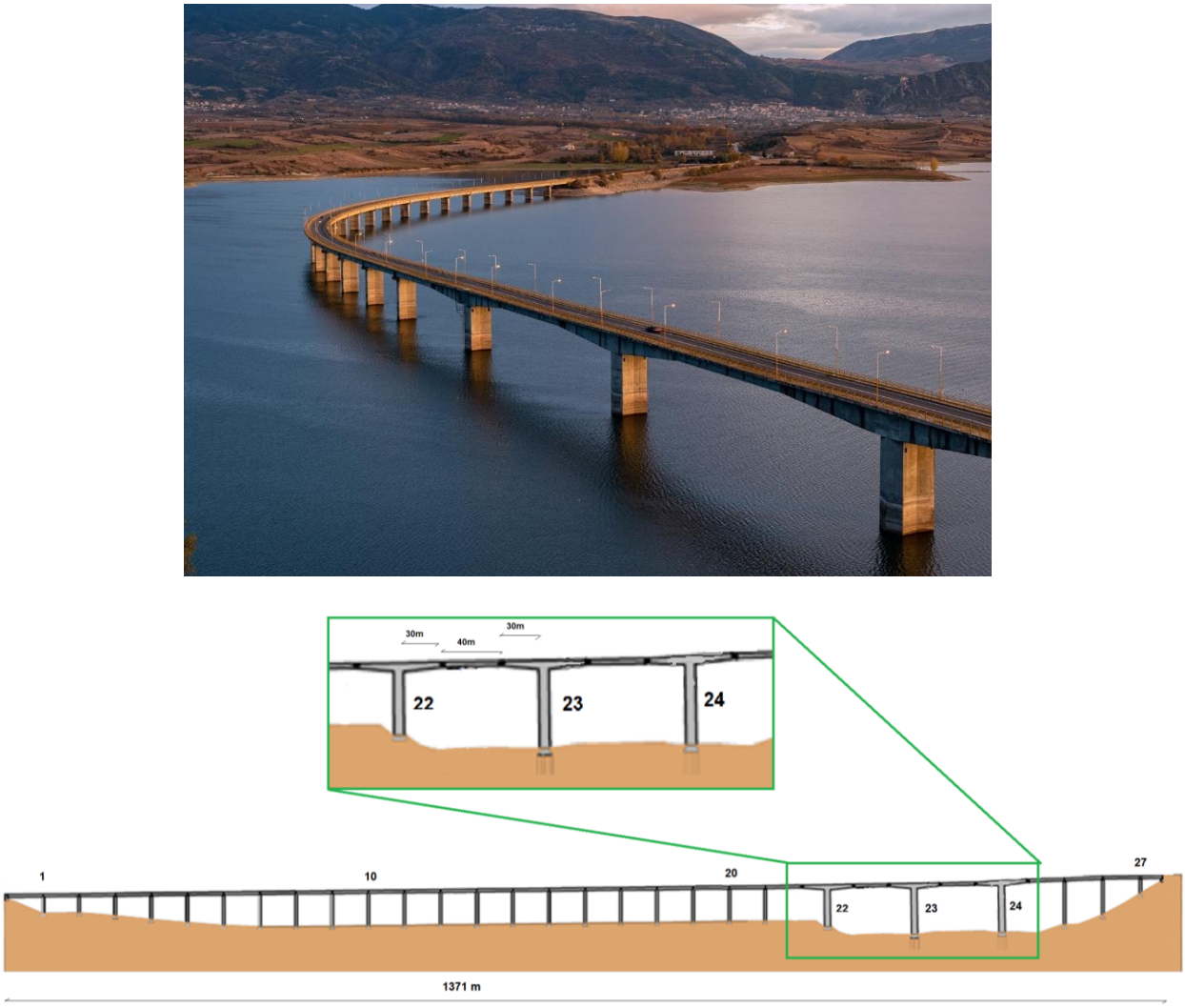


Figure 1: Bridge layout.

Very recently, excessive deflections at the free ends of the cantilevers were reported [16] during multiple inspections from inspectors and from one of the authors of this paper, a very common problem typically observed on old balanced cantilever bridges. Preliminary reports found evidence of corrosion and local concrete crashing, leading engineers to question the capacity and structural integrity of the bridge and as a result traffic restrictions were imposed, i.e. weight restrictions for heavy vehicles and reduction of the speed limit to minimize dynamic amplification impacts. The traditional way to extract meaningful conclusions about the condition of the materials would be extensive sampling, destructive testing methods and extensive

vibration/loading checks, methods that was not authorized by the owners, as there are serious concerns about the bearing capacity of the deck at critical positions. At the same time, the road served by the bridge is part of a busy national road network traffic (part of the E65 Central Greece Highway) and detouring through the local road network is extremely difficult, and long, posing an extra challenge to engineers that would normally stop vehicles from crossing in order to conduct tests.

As a way to bypass many of the above-mentioned considerations our team proposes a digitalized approach to damage assessment, which can be applied on a wide range of structural assets (both residential and infrastructure) and relies heavily on state-of-the-art computational tools. Numerous approaches with different levels of interaction with the structure have been proposed through recent years, for example deflection-based monitoring system using sensor and signal processing technology [17] or connected pipe systems [18]. However, no approach is currently streamlined and considered as most optimum due to the fluctuating accuracy levels between the techniques in various occasions. The approach herein proposed as innovative contribution in the field requires minimum invasion and interaction with the structure, is extremely time efficient and includes minimal cost and carbon footprint.

The procedure starts with the fault report, where a decision has to be made around the degree on which on-site inspection and testing is allowed. In cases where the fragile nature of the structure poses as an obstruction, then high-tech surveying tools may be deployed. These tools should provide the engineers with viable information considering possible deflections, rotations, out-of-plane motions and even places where cracking is highly visible, all without ever setting foot on the actual structure. Two major options in order to obtain these measurements are drone-based photogrammetry (digital twin) and satellite imaging, with the former being chosen in the application of our proposal. Then the results should be interpreted and deflection curves should be created in order to provide a more mathematical view on the measurements, making them easier to compare with other data sets. At this point, any available information from official design reports should be also collected, however there might be cases where due to the passing of time they may have been misplaced or destroyed.

Based on design reports, information found in literature and scientifically backed assumptions, an advanced model of the structure is created. Contrary to the technological and academic advancements, numerous commonly found problems are not fully understood, leading to knowledge gaps that can only be approached in indirect ways. For example, the fault mechanism behind excessive deflections usually reported in balanced cantilever structures is not 100% documented yet, although creep and shrinkage have been observed by multiple research papers to play a significant part [19-22]. In order to save time, simplifications of some effects may be used when proven by literature to not significantly compromise result accuracy. The proposed way to cover multiple probable causes is a scenario-based analysis where each one will examine an individual parameter and its effect on the structure. In cases where the girder's behavior doesn't extend beyond its elastic limits, a simple superimposition is enough to examine the combined action of two or more parameters, although this is not possible in a non-linear analysis. Deflection curves from each scenario will be created in order to compare them with the measured results and conclude whether there is a data set that significantly resembles the initial ones in magnitude and/or shape.

If such a scenario is found, then engineers may use this approach as evidence to drive any possible investigation processes towards the probable cause that was used to create it. It should be clear that this method is not sufficient to produce absolute conclusions, it is a reliable source of information that may benefit both the engineers and the asset. Our proposal presents a highly digitalized, cost and time efficient solution, while also being environmentally friendly and requiring minimum interaction with the structure.

## A few words about corrosion

Corrosion in the tendons of prestressed concrete bridges is deemed to be among those principal factors that could undermine their structural integrity. Tendon corrosion failures/incidents have been reported in the past, e.g. the 1985 catastrophic failure of the prestressed Ynys-y-Gwas bridge in the United Kingdom that was constructed in 1953 without any prior warning [23], even at the early years in a bridge's lifespan. For instance, several post-tensioned tendons were replaced in the Mid-Bay bridge in Florida due to corrosion related concerns only after eight years of its operation [24].

Herein, corrosion was assumed to be the main source of deterioration for the investigated bridge essentially disregarding additional failure mechanisms that might contribute (e.g. scouring, spalling of the reinforced concrete). In fact, when a strand is exposed to moisture its exposed interface becomes particularly prone to corrosion induced damages. Of particular concern is the so-called "localized corrosion" that could lead to substantial local reductions in the cross section of the stand and consequently to severe reductions of its tension capacity. Each strut could have (a) corroded and uncorroded wires within the same section and (b) corroded and uncorroded parts across its length.

## 2 BRIDGE DESCRIPTION

Located in the North-West part of the country, the Polyfytos bridge held the record for the largest overall length in Greece at the time of its construction, only surpassed by the Rio-Antirrio bridge almost 35 years later. The part of the bridge under interrogation consists of 3 segmentally constructed balanced cantilever sets, extending 30 meters either side of the abutments. Neighbouring cantilevers are connected by 40m long precast members forming an overall span of 100m (Fig. 1). The geometry and individual sizes of the segments were measured in the original drawings and verified on a point cloud model (Fig. 2).

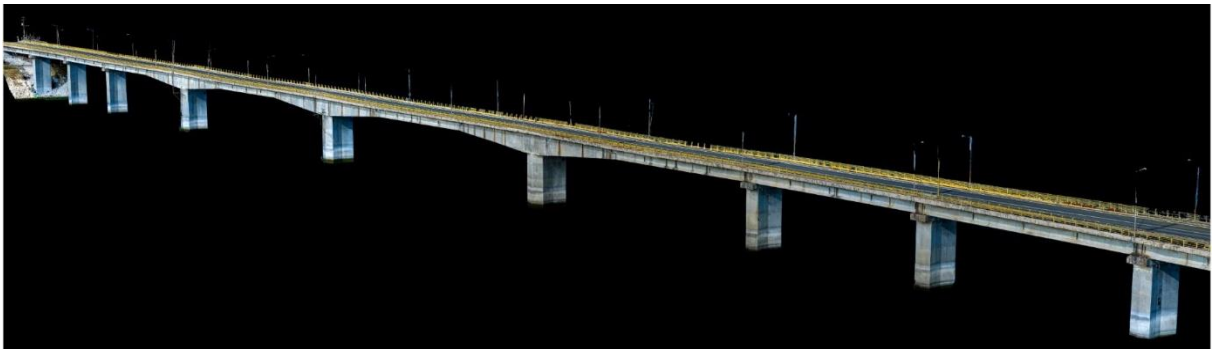

Figure 1: Point cloud model.

Prestressing concrete technique has been used in both the cantilever and precast beams (Fig. 3). The current view of the bridge deck with the original configuration of the prestressing cables in the cantilever beams and the precast beams between the half-joints is also depicted in Figure 3. Besides, Figure 4 reports the scheme of the current configuration of the bridge after about 50 years of in-service conditions. It can be seen that the failures of the brackets due to long-term material effects and the progression of prestressing cables in particular induced differential failures of the central beam between the half-joints. However, due to the property of the simply supported central beam, no additional coercive stresses developed.

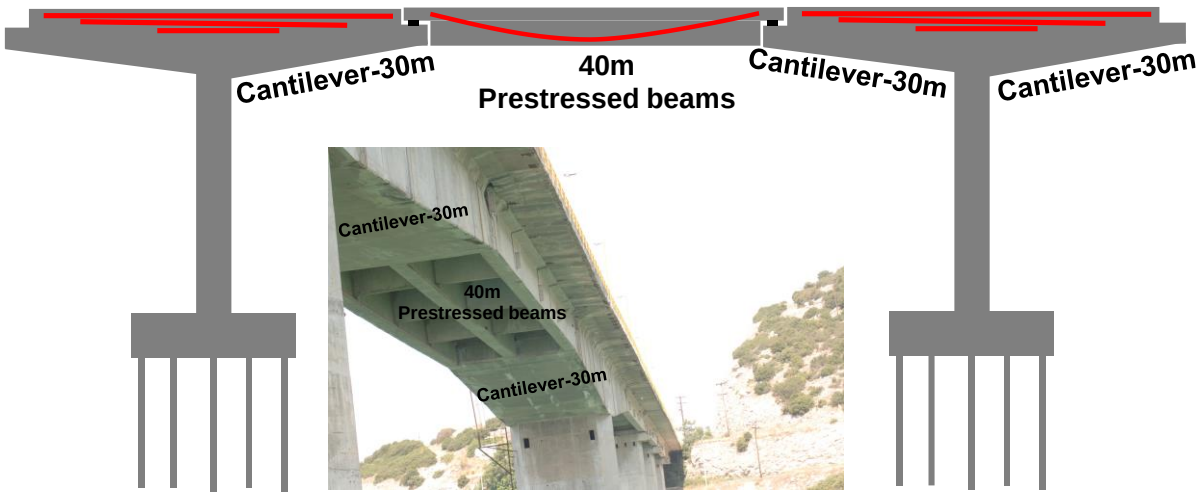


Figure 3: Schematic (not true) configuration with prestressing cables (red lines) and the actual view of the deck between Piers 23-24.

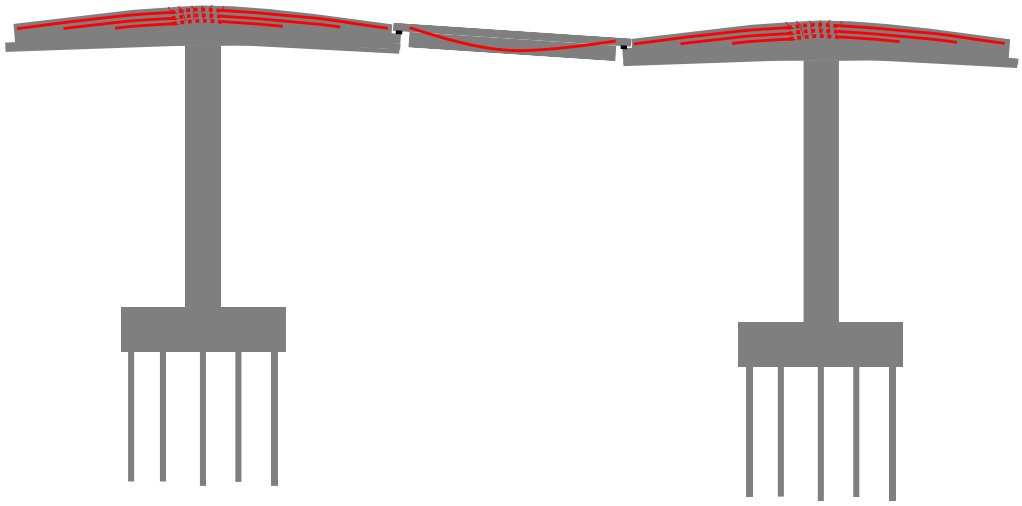

Figure 4: Current deteriorated condition of the cantilevers of the bridge after 48 years of service. The sketch shows the corrosion of the tendons above the piers (hypothesis based on extensive cracking observed on the locations) and the deflection of the deck (measured on a point cloud).

## 2.1 Geometry and materials

The part of the bridge under interrogation consists of 3 segmentally constructed balanced cantilever sets, extending 30 meters either side of the abutments. Neighboring cantilevers are connected by 40m long precast members forming an overall span of 100m. The geometry and individual sizes of the segments were measured in the original drawings and verified on a point cloud model. The position and trajectory of the prestressing tendons was not mentioned in the drawings so they were modelled according to standard practice of balance cantilever construction (all tendons on top flange of segment). Figure 5 depicts some critical cross sections of the cantilevers and details.

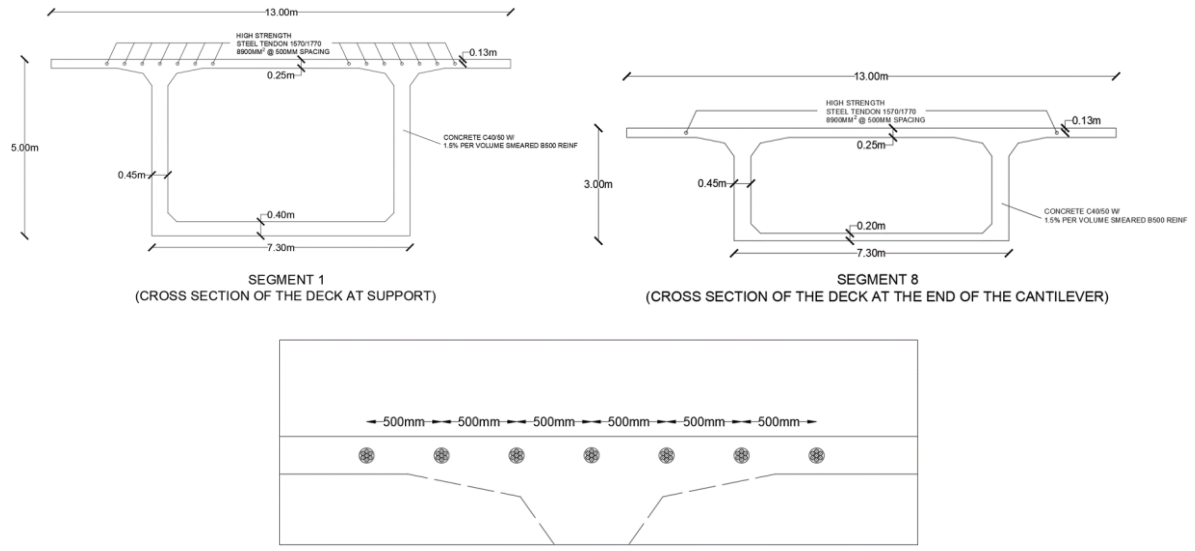


Figure 5: critical cross sections of the cantilevers and details.

Table 1: materials' properties.

| Material | Assumed properties |
|---|---|
| Reinforced concrete B450 | Young's modulus E= Varies |
| | Compressive strength $f_{ck}$= 40 MPa |
| | Tensile strength $f_{ctm}$ = 3.5 MPa |
| | Ultimate strain $\varepsilon_{cu1}$= 3.5 ‰ |
| Prestressing steel 160/180 | Young's modulus E = 195 GPa |
| | Tensile strength $f_{pk}$ = 1770 MPa |
| | 0.1% proof stress $f_{p0.1k}$ = 1570 |
| Passive reinforcement | Yield strength $f_{yk}$ = 500 MPa |
| | Strain at maximum force $\varepsilon_{uk}$ = 2.5% |

The materials characteristics were found in the original design report, however their characteristic properties do not exactly match contemporary materials so a theoretical match was made between older and recent (Table 1). However, the fact that construction practice has come a long way since 1974 in terms of quality control, monitoring and protection against environmental parameters adds a degree of uncertainty. There is a number of mechanical properties that may have been affected by poor quality control:

- Young's modulus (E) and compressive strength of the in-situ cast concrete ($f_{ck}$)

- Strength of passive ($f_{yk}$) and active ($f_{pk}$) reinforcement
- Permeability of concrete, water/cement ratio (affecting the microscopic properties)
- Imperfections during casting leading to permanent displacements

## 2.2 Analysis and degradation assessment

The bridge was constructed as a hybrid of two methods, the majority of spans were simple cast in-situ concrete decks and the rest of them, which will be the focus of our investigation, were constructed as balanced cantilevers. To the best of the author's knowledge the damage mechanism hasn't been described accurately to this day, however expert judgment and literature suggest some probable reasons behind the faults. Although it is highly probable that a multitude of mechanisms are at work, a previous study [25] bypassed the underlying cause and focuses more on the damage manifestation, which has been assumed to be extensive corrosion within the prestressed tendons of the bridge deck. A thorough review of the existing drawings and expert judgement to cover for the missing information resulted in the preparation of a numerical model which was used to carry-out a predetermined amount of analyses based on an optimal input for the k-NN algorithm. The non-linear analyses included vertical loads and prestressing. All the results were then collected and used as an input to the prediction algorithm after undergoing some statistical processing. The quantitative of corrosion is estimated almost 50% based on back analyses of the balanced cantilevers [25].

The model used in the analysis was created in such a way that the analysis process would resemble the actual construction process (staged construction approach). Balanced cantilever segmental construction is an iterative process including a casting concrete stage followed directly by a prestressing stage after the concrete has reached the desired strength. So, in an endeavour to make the model follow the same principles the following reasoning was used; finite element analysis primarily revolves around stiffness, external forces and displacements in order to calculate the rest of the values like stress, strain etc. By significantly reducing the bending stiffness and by removing the self-weight of a segment it is made practically "undetectable" during the analysis. This property was used for the concrete elements, as it is not possible to create them with different timing through the analysis, contrary to the steel elements which can be inserted during a specific construction stage. To explain it in more detail, the modelling process is laid out below:

- Concrete elements have been defined with 35 GPa modulus of elasticity and 25 kN/m$^3$ self-weight.
- All concrete elements have been presented at the start of the analysis, however this contradicts the segmental construction process.
- The desired state is for the two central segments to be the only ones present at the beginning and all the others to be neglected in the calculations.
- By reducing the bending stiffness of segments 2-8 to almost zero and by not applying self-weight, their contribution to the overall stiffness and loading of the analysis is diminished.
- With each next construction stage, the properties of the next segment in line to be constructed will change and it will be able to bear loading and deflect together with the rest of the already casted concrete segments.

This change in properties can be induced by changing the material of the segments. In the beginning, a "soft" material is created and assigned to all segments except the first two (Construction stage 1). During the next part of the analysis, the first two segments are post-tensioned by tendons which are created with specific timing and the application of a tensile strain (construction stage 2). After post-tensioning the first two segments, the next set is casted; meaning that the Young's modulus and the self-weight of the concrete get their correct value (construction stage 3). An iterative process, alternating concrete casting and post-tensioning, is then followed until all 16 segments are completed (Table 2). At this point the only load on the girder is the self-weight of the prestressed segments, so the rest of the external loads are applied. A pre-cast girder, represented by a load of 7200 kN on each side, is applied on the deck followed by an area load considering the asphalt layers, sidewalks etc. evaluated at a uniform value of 2 kN/m$^2$ (Figure 20)

Table 2. Construction stages and their corresponding load cases (CC-concrete casting, PT-post tensioning).

| Construction stage # | Load case | Construction stage # | Load case |
|---|---|---|---|
| 1 | Segment 1 CC | 10 | Segment 5 PT |
| 2 | Segment 1 PT | 11 | Segment 6 CC |
| 3 | Segment 2 CC | 12 | Segment 6 PT |
| 4 | Segment 2 PT | 13 | Segment 7 CC |
| 5 | Segment 3 CC | 14 | Segment 7 PT |
| 6 | Segment 3 PT | 15 | Segment 8 CC |
| 7 | Segment 4 CC | 16 | Precast girder load |
| 8 | Segment 4 PT | 17 | Surface load |
| 9 | Segment 5 CC | | |

## 3 EXISTING DATA ON THE CURRENT CONDITION OF THE BRIDGE

The point cloud of the bridge with some details of the cantilever and the half-joint is depicted in Figure 6. The deflection of the most critical cantilever of the bridge is reported in Figure 7, where the dashed line is the expected elevation, while the solid line is the measured position, i.e. 133mm and 207mm lower than the expected. Such deflections are the cantilever displacements downward at the tip (end) of the most critical cantilever.



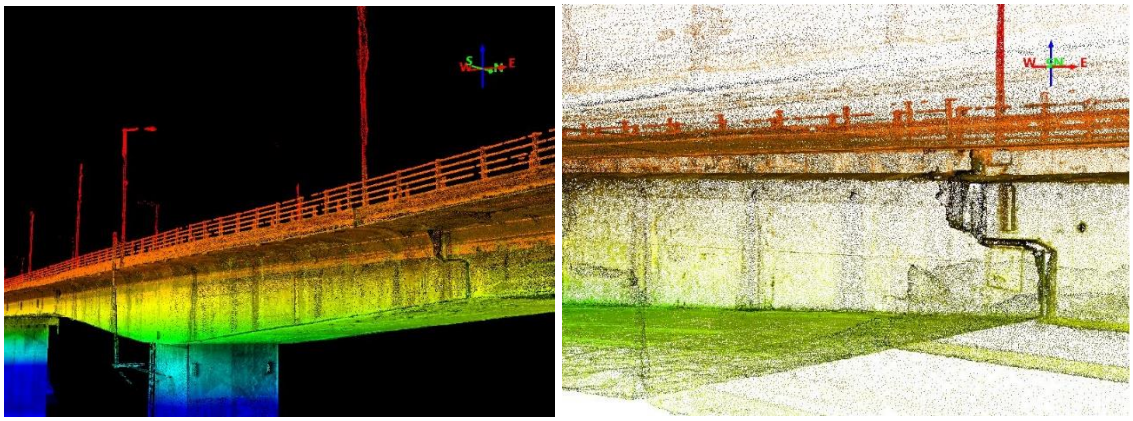

Figure 6: point cloud.

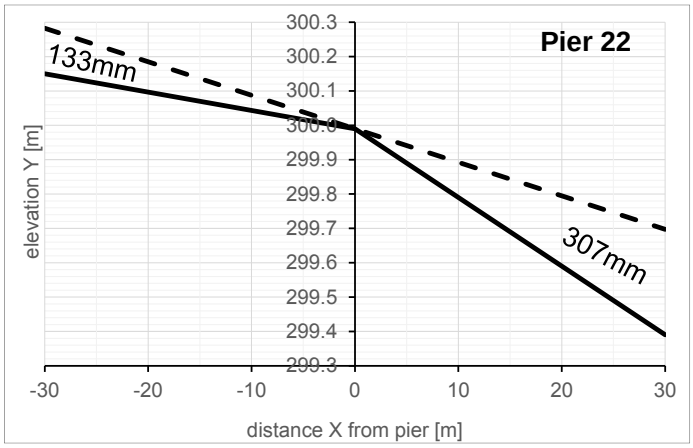


Figure 7: Measured deflection of the critical cantilever. Dashed line shows the hypothetical original elevation. Solid lines show the measured deflected cantilevers.

## 4 ADOPTED RETROFIT TECHNIQUES AND COST ASSESSMENT

In this section, the retrofitting techniques were preliminarily designed aiming to improve the structural performance of the bridge and enhance the safety levels by respecting standard regulation. As previously described, critical damages of the bridge can be manly attributed to insufficient maintenance strategies, possible poor workmanship at the construction phase, critical increase in the traffic levels and/or maximum traffic loads during the service-life and the aggressive environment. Critical losses of prestressing stress at the level of cantilever supports is the main cause of the functionality reduction as shown by Figure 4 and 7. For these reasons, two scenarios have been considered as feasible retrofitting solutions to restore the original serviceability of the bridge:

1. **Demolition and reconstruction:** this approach consists of demolishing the continuous deck composed by n.6 tapered box girder cantilevers and n.3 girder bridges, while existing piers have been maintained. It has been assumed that the reconstruction phase considers to maintain the same static scheme, materials and structural behaviors. This assumption can be considered reasonable since the bridge topology adopted by the designer is still widely used nowadays.
2. **Local interventions and replacement of the girder** bridge (Gerber bridge sections): in this scenario, external prestressing cables have been installed to restore the correct level of compression stresses into the n.6 cantilevers and the functionality of

the entire bridge. Moreover, the substitution of the n.3 girder bridge has been considered with a steel box girder section to avoid the corrosion effects into the prestressing cables. Therefore, as demonstrated by evaluations provided by the authors, this proposed solution results in an improvement of slenderness and an overall reduction of weight carried by cantilevers.

Once the retrofitting techniques have been identified, the authors proceed in order to define a detailed list of interventions for each scenario.
For scenario #1, the following activities have been considered:

a) Demolition of both defected balanced cantilever part of the deck and reinforced concrete girder bridge by adopting non-explosive agents with chemical action instead of explosive charges;
b) Reconstruction of decks by restoring the original static scheme of the bridge. In this phase, the authors have computed the cost for the construction for both concrete deck and steel reinforcement. The latter includes the steel reinforcement into the deck and the anchorages to fix the new cantilever to the existing piers' head;
c) Installation of elastomeric bearings at the end of the cantilever;
d) Installation of expansion joints at the level of the girder bridge deck in order to avoid thermal constraints or damage along the traffic pavement;
e) Road pavement realized by surfacing course top layer, asphalt bond coat, protective course, epoxy bonding layer, waterproofing and reinforced concrete deck;
f) Realization of all functional facilities like road signs, safety barriers, etc.

On the other hand, for scenario #2 the following activities have been taken into account:

a) Demolition of the Gerber bridge sections only adopting the same techniques of scenario 1;
b) Installation of a steel box deck which has been designed by adopting thumb rules aiming to reduce the total weight and assuring a minimum height for easier maintenance. Operations related to the realization of the reinforced concrete slab by adopting predalles system;
c) Application of hot-dip galvanizing (passivating treatment of the steel surface) to all steel surfaces of deck;
d) Substitution of girder deck bearings with FPS system aiming to avoid slip phenomena between deck and supports;
e) Installation of expansion joints at the level of the girder bridge deck in order to avoid thermal effect or damage along the traffic pavement;
f) Road pavement realized by surfacing course top layer, asphalt bond coat, protective course, epoxy bonding layer, waterproofing and reinforced concrete deck;
g) Realization of all functional facilities like road signs, safety barriers, etc;
h) External prestressing system realized by the addition of 4 cables along each cantilever in order to restore the original deflection. At this design stage, additional cables are supposed to be of the same section of that one recognized in the technical drawings. Moreover, the level of compression stress introduced into the system should be designed aiming to avoid cracking as depicted in Figure 8.

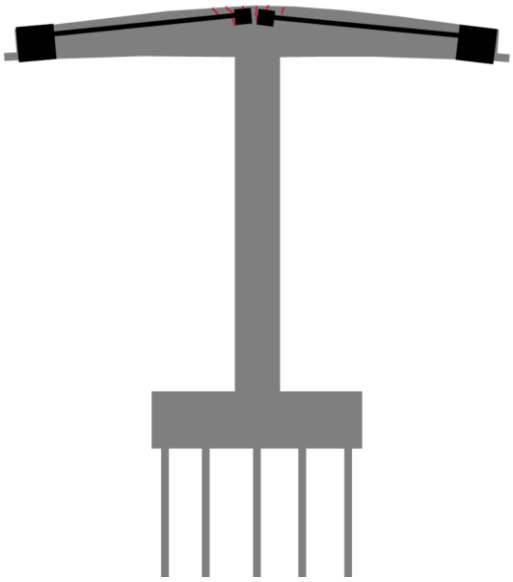

Figure 8: Scheme of prestressing system

The costs associated to each scenario have been evaluated by using the Italian price lists provided by ANAS S.p.A [26], with the exception of the prestressing system assessment for which the authors adopted the parametric cost pointed out by [27]. Thought price list may change from one country to another, although not drastically within the European community, authors focused mainly on the comparisons between different retrofitting scenarios.
Aiming to realize a comparison between the 2 scenarios, the authors selected a module of the bridge for which all the operations have been evaluated from an economical point of view (see Figure 9). The final amount of the estimations for each scenario is referred to the adopted module, hence, the cost of the overall intervention can be easily derived.

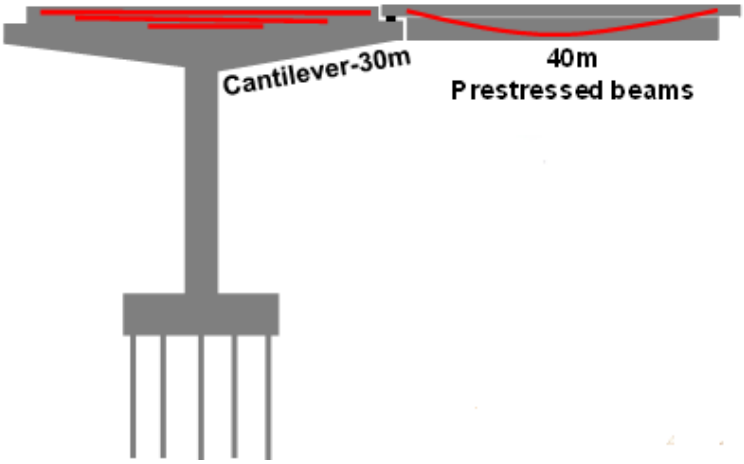


Figure 9: Module of the bridge considered for the cost evaluation

In Figures 10 and 11 report the spreadsheets with the calculations provided for each scenario. In the first column corresponds to the ID code of the adopted standard cost list. More details concerning with the description of the specific voice can be detected by ANAS S.p.A. [26]. The second column is a fast description of the activity. Columns 3 and 4 represent the unit for each operational phase and the geometrical properties of the considered element, respectively.

Finally, columns 5, 6 and 7 represent the total amount expressed in the unit indicated by the price list, the unit price and the total cost of the intervention, respectively.

| ID NUMBER | DESCRIPTION | U.M. | DIMENSIONS | | | | Amount | UNIT PRICE | TOTAL AMOUNT |
|---|---|---|---|---|---|---|---|---|---|
| | | | Numb. | L | P | H | | Euro | Euro |
| **SCENARIO 1** | | | | | | | | | **€ 2.242.046,60** |
| A.03.008 | Bridge demolition phase | mc | - | - | - | - | 750,84 | € 107,43 | € 80.662,74 |
| B.08.025.b | Bridge constructon with precast segmental elements | mq | - | 100 | 13 | - | 1300 | € 1.423,39 | € 1.850.407,00 |
| B.07.070.a | Expantion joints | ml | 2 | - | 13 | - | 26 | € 522,05 | € 13.573,30 |
| **Brdge supports** | | | | | | | | | |
| B.07.007.a | uni-direction elastomeric bearings | kN | 6 | - | - | - | 3000 | € 3,74 | € 11.220,00 |
| **Cast-in-place elements and reinforcement** | | | | | | | | | |
| B.03.040.a | Slab concrete (Rck 40/50) | m^3 | - | 100 | 13 | 0,2 | 260 | € 203,64 | € 52.946,40 |
| B.05.050.a | Slab reinforcement | kg | - | - | - | - | 12940,2 | € 2,37 | € 30.668,27 |
| B.05.030 | Steel reinforcement (anchorages included) - B450C class | kg | - | - | - | - | 51695,28 | € 1,86 | € 96.153,22 |
| **Pavement** | | | | | | | | | |
| D.01.005.a | Primer layout (10 cm) | m^3 | - | 100 | 13 | 0,1 | 163,8 | € 162,68 | € 26.646,98 |
| B.06.085 | waterproofing layout (4 mm) | m^2 | - | 100 | 13 | 0,004 | 1300 | € 25,69 | € 33.397,00 |
| D.01.017.a | binder layout (10 cm) | m^3 | - | 100 | 13 | 0,1 | 163,8 | € 183,02 | € 29.978,68 |
| D.01.036.a | draining wear layer (4 mm) | m^2 | - | 100 | 13 | 0,004 | 1300 | € 12,61 | € 16.393,00 |
| **FUNCTIONAL FACILITIES** | | | | | | | | | **€ 1.820,00** |
| | Road signs | €/mq | - | 100 | 13 | - | 1300 | € 1,40 | € 1.820,00 |
| **Electrical system** | | | | | | | | | **€ 52.000,00** |
| | Electrical system | €/mq | - | 100 | 13 | - | 1300 | € 40,00 | € 52.000,00 |
| **Drainage stormwater system** | | | | | | | | | **€ 39.000,00** |
| | Drainage stormwater system | €/mq | - | 100 | 13 | - | 1300 | € 30,00 | € 39.000,00 |
| **Safety barriers** | | | | | | | | | **€ 40.789,00** |
| G.02.005.b | Safety barriers (class H4) | ml | - | 100 | - | - | 100 | € 407,89 | € 40.789,00 |
| | | | | | | | | Total | **€ 2.375.655,60** |

Figure 10. Detailed calculations provided for Scenario #1

| ID NUMBER | DESCRIPTION | U.M. | DIMENSIONS | | | | Amount | UNIT PRICE | TOTAL AMOUNT |
|---|---|---|---|---|---|---|---|---|---|
| | | | Numb. | L | P | H | | Euro | Euro |
| **SCENARIO 2** | | | | | | | | | **€ 1.328.088,76** |
| A.03.008 | Bridge demolition phase | mc | - | - | - | - | 237,84 | € 107,43 | € 25.551,15 |
| B.05.008.b | Steel box bridge (incremental launching for lifting) | kg | - | 40 | 13 | | 194600 | € 5,61 | € 1.091.706,00 |
| B.09.160.a | Hot-dip galvanizing | m^2 | - | - | - | - | 520 | € 18,41 | € 9.573,20 |
| B.07.070.a | Expantion joints | ml | 2 | - | 13 | - | 26 | € 522,05 | € 13.573,30 |
| **Brdge supports** | | | | | | | | | |
| B.07.007.a | FPS isolation system bearings | kN | 6 | - | - | - | 3000 | € 3,74 | € 11.220,00 |
| **Cast-in-place elements and reinforcement** | | | | | | | | | |
| B.03.040.a | Slab concrete (Rck 40/50) | m^3 | - | 40 | 13 | 0,2 | 104 | € 203,64 | € 21.178,56 |
| B.05.050.a | Slab reinforcement | kg | - | - | - | - | 12940,2 | € 2,37 | € 30.668,27 |
| B.05.030 | Steel reinforcement (anchorages included) - B450C class | kg | - | - | - | - | 25847,64 | € 1,86 | € 48.076,61 |
| **Pavement** | | | | | | | | | |
| D.01.005.a | Primer layout (10 cm) | m^3 | - | 40 | 13 | 0,1 | 163,8 | € 162,68 | € 26.646,98 |
| B.06.085 | waterproofing layout (4 mm) | m^2 | - | 40 | 13 | 0,004 | 520 | € 25,69 | € 13.358,80 |
| D.01.017.a | binder layout (10 cm) | m^3 | - | 40 | 13 | 0,1 | 163,8 | € 183,02 | € 29.978,68 |
| D.01.036.a | draining wear layer (4 mm) | m^2 | - | 40 | 13 | 0,004 | 520 | € 12,61 | € 6.557,20 |
| **FUNCTIONAL FACILITIES** | | | | | | | | | **€ 728,00** |
| | Road signs | €/mq | - | 40 | 13 | - | 520 | € 1,40 | € 728,00 |
| **Electrical system** | | | | | | | | | **€ 20.800,00** |
| | Electrical system | €/mq | - | 40 | 13 | - | 520 | € 40,00 | € 20.800,00 |
| **Drainage stormwater system** | | | | | | | | | **€ 15.600,00** |
| | Drainage stormwater system | €/mq | - | 40 | 13 | - | 520 | € 30,00 | € 15.600,00 |
| **Prestressing system** | | | | | | | | | **€ 35.120,00** |
| AICAP | Prestressing system | ml | - | 40 | - | - | 40 | € 878,00 | € 35.120,00 |
| **Safety barriers** | | | | | | | | | **€ 16.315,60** |
| G.02.005.b | Safety barriers (class H4) | ml | - | 40 | - | - | 40 | € 407,89 | € 16.315,60 |
| | | | | | | | | Total | **€ 1.416.652,36** |

figure 11. Detailed calculations provided for Scenario #2

In table 3 and 4, each intervention has been collected in order to evaluate the total cost of each. The final value for each scenario has been expressed in terms of economical cost per km of bridge.

Table 3. Total interventions cost related to Scenario #1

| Activity | Cost (€) |
|---|---|
| (a) | 80.662,74 |
| (b) | 2.030.174,89 |
| (c) | 11.220,00 |
| (d) | 13.573,30 |
| (e) | 106.415,66 |

| | |
|---|---|
| (f) | 133.609,00 |
| **Total cost/km** | 1.827.427,38 |

Table 4. Total interventions cost related to Scenario #2

| Activity | Cost (€) |
|---|---|
| (a) | 25.551,15 |
| (b) | 1.191.629,44 |
| (c) | 9.573,00 |
| (d) | 11.200,00 |
| (e) | 13.573,30 |
| (f) | 76.541,66 |
| (g) | 53.443,60 |
| (h) | 35.120,00 |
| **Total cost/km** | 1.089.732,58 |

## 5 ENVIRONMENTAL IMPACT OF THE RETROFIT INTERVENTIONS

For the environmental sustainability assessment of the presented restoration scenarios, a Life Cycle Assessment (LCA) has been carried out according to ISO 14040 and ISO 14044 [28]. For LCA specifications regarding building products and construction works, European standards EN 15804, EN 15978 and EN15678 [29-3] have been furthermore considered.

As for the cost analysis, main goal of LCA is allowing a comparison between the different two scenarios and understanding their environmental impact on the whole infrastructure level, i.e. the bridge. Consequently, the established functional unit is the bridge surface (km² bridge). The analysis here presented is limited to the Global Warming Potential impact category (GWP 100ys, CML 2001), where the environmental data are provided from GENERIS® software [32] and selected from available product-specific (Environmental Product Declarations, EPD) and average generic construction materials' datasets [33]. Average datasets served also as a basis for a preliminary environmental assessment of products for which environmental information is not available, such as expansion joints, and bridge support systems. In particular, both bearing systems have been modelled as a double steel plate and an elastomeric intermediate element. Differently from cost analysis, in LCA functional facilities, electrical systems, drainage stormwater system and safety barriers are neglected. These are in fact deemed out of scope of the analysis, which is focused rather on the restoration scenarios solely.

Figures 12 and 13 outline the data collected for the Lifecycle Inventory (LCI) and the subsequent Lifecycle Impact Assessment (LCIA) stage. Each material is matched with a suitable environmental dataset. For a correct dataset match, products' composition, densities and applications are checked. Afterwards, lifecycle information regarding GWP is extracted. The environmental impact is calculated for the total products' amount and, lastly, the environmental impact of the scenario is derived per km² bridge.

| ID NUMBER | DESCRIPTION | Selected dataset | Dataset type | Lifecycle phases [EN15978] | Density [kg/m³] | Reference Unit | GWP [kg CO2 eq./unit] | Amount | Total |
|---|---|---|---|---|---|---|---|---|---|
| **SCENARIO 1** | | | | | | | | | |
| A.03.008 | Bridge demolition phase | Spannbeton-Fertigteildecken | EPD | C3-C4; D | | m³ | *228.92* | 751 | 171885.7 |
| B.08.025.b | Bridge construction with precast segmental elements | Spannbeton-Fertigteildecken | EPD | A1-A3; C3-C4; D | | m² | *58.19* | 1300 | 75644.4 |
| B.07.070.a | Expantion joints | Bitumen-based adhesive(60% Bitumen, 23%LM, 17% Water) | avarage | A1-A3; C3-C4; D | *930* | kg | *0.61* | 628680 | 385569.4 |
| **Bridge supports** | | | | | | | | | |
| B.07.007.a | uni-direction elastomeric bearings | Steel sections + Elastomer | avarage | A1-A3; C3-C4; D | | item | *10.18* | 3000 | 30546.8 |
| **Cast-in-place elements and reinforcement** | | | | | | | | | |
| B.03.040.a | Slab concrete (Rck 40/50) | Beton der Druckfestigkeitsklasse C 45/55 | EPD | A1-A3; C3-C4; D | *2400* | | *270.61* | 260 | 70358.6 |
| B.05.050.a | Slab reinforcement | Reinforcement steel | avarage | A1-A3; C3-C4; D | *7850* | kg | *0.29* | 12940 | 3766.7 |
| B.05.030 | Steel reinforcement (anchorages included) - B450C class | Reinforcement steel | avarage | A1-A3; C3-C4; D | *7850* | kg | *0.29* | 51695 | 15047.6 |
| **Pavement** | | | | | | | | | |
| D.01.005.a | Primer layout (10 cm) | Bitumen-based adhesive(60% Bitumen, 23%LM, 17% Water) | avarage | A1-A3; C3-C4; D | *1300* | kg | *0.6133* | 212940 | 130596.1 |
| B.06.085 | waterproofing layout (4 mm) | Joint sealing strips, polyisobutylene | avarage | A1-A3; C3-C4; D | *1300* | kg | *5.821* | 6760 | 39350.0 |
| D.01.017.a | binder layout (10 cm) | Binder Products based on epoxy-resin | EPD | A1-A3; C3-C4; D | *1750* | kg | *11.1756* | 286650 | 3203485.7 |
| D.01.036.a | draining wear layer (4 mm) | Bitumen emulsion (40% bitumen, 60% water) | avarage | A1-A3; C3-C4; D | *1000* | kg | *0.41524* | 5200 | 2159.2 |
| **FUNCTIONAL FACILITIES** | | | | | | | | | |
| **Electrical system** | | | | | | | | | |
| **Drainage stormwater system** | | | | | | | | | |
| **Safety barriers** | | | | | | | | | |
| | | | | | | | **Total GWP [kg CO2eq.]** | | **4128410.26** |
| | | | | | | | **GWP [kg CO2eq./km²]** | | **3175700.20** |

Figure 12: LCA, Scenario 1. Lifecycle impact assessment.

| ID NUMBER | DESCRIPTION | Selected dataset | Dataset type | Lifecycle phases [EN15978] | Density [kg/m³] | Reference Unit | GWP [kg CO2 eq./unit] | Amount | Total |
|---|---|---|---|---|---|---|---|---|---|
| **SCENARIO 2** | | | | | | | | | |
| A.03.008 | Bridge demolition phase | Spannbeton-Fertigteildecken | EPD | C3-C4; D | | m³ | *228.925* | 238 | 54447.41 |
| B.05.008.b | Steel box bridge (incremental launching for lifting) | Steel sections | avarage | A1-A3; C3-C4; D | *7850* | kg | *0.7714* | 194600 | 150114.44 |
| B.09.160.a | Hot-dip galvanizing | Hot dip galvanized steel; area weight | avarage | A1-A3; C3-C4; D | *7850* | m² | *7.394* | 520 | 3844.88 |
| B.07.070.a | Expantion joints | Bitumem based adhesive | avarage | A1-A3; C3-C4; D | *930* | kg | *0.6133* | 628680 | 385569.44 |
| **Bridge supports** | | | | | | | | | |
| B.07.007.a | FPS isolation system bearings | Steel sections + Elastomer | avarage | A1-A3; C3-C4; D | | item | *10.1822821* | 3000 | 30546.85 |
| **Cast-in-place elements and reinforcement** | | | | | | | | | |
| B.03.040.a | Slab concrete (Rck 40/50) | Beton der Druckfestigkeitsklasse C 45/55 | EPD | A1-A3; C3-C4; D | *2400* | m³ | *270.61* | 104 | 28143.44 |
| B.05.050.a | Slab reinforcement | Reinforcement steel | avarage | A1-A3; C3-C4; D | *7850* | kg | *0.2910821* | 12940 | 3766.66 |
| B.05.030 | Steel reinforcement (anchorages included) - B450C class | Reinforcement steel | avarage | A1-A3; C3-C4; D | *7850* | kg | *0.2910821* | 25848 | 7523.79 |
| **Pavement** | | | | | | | | | |
| D.01.005.a | Primer layout (10 cm) | Bitumen-based adhesive (60% Bitumen, 23%LM, 17% Wasser) | avarage | A1-A3; C3-C4; D | *1300* | kg | *0.6133* | 212940 | 130596.10 |
| B.06.085 | waterproofing layout (4 mm) | Joint sealing strips, polyisobutylene | EPD | A1-A3; C3-C4; D | *1300* | kg | *5.821* | 2704 | 15739.98 |
| D.01.017.a | binder layout (10 cm) | Binder Products based on epoxy-resin | EPD | A1-A3; C3-C4; D | *1750* | kg | *11.1756* | 286650 | 3203485.74 |
| D.01.036.a | draining wear layer (4 mm) | Bitumen emulsion (40% bitumen, 60% water); | avarage | A1-A3; C3-C4; D | *1000* | kg | *0.41524* | 2080 | 863.70 |
| **FUNCTIONAL FACILITIES** | | out of scope; neglected | | | | | | | |
| **Electrical system** | | | | | | | | | |
| **Drainage stormwater system** | | | | | | | | | |
| **Prestressing system** | | | | | | | | | |
| **Safety barriers** | | | | | | | | | |
| | | | | | | | **Total GWP [kg CO2eq.]** | | **4014642.43** |
| | | | | | | | **GWP [kg CO2eq./km²]** | | **3088186.49** |

Figure 13: LCA, Scenario 1. Lifecycle impact assessment.

Analogously with cost analysis, in table 5 and 6, GWP is calculated and aggregated in interventions.

Table 5. Total interventions GWP related to Scenario #1

| Activity | GWP [kg CO2eq] |
|---|---|
| (a) | 171 885.69 |
| (b) | 164 817.23 |
| (c) | 30 546.85 |
| (d) | 385 569.44 |

| | |
|---|---|
| (e) | 3 373 431.80 |
| (f) | out of scope |
| **Total GWP** | **4 126 251.02** |
| **Total GWP /km²** | **3 174 039.24** |

Table 6. Total interventions GWP related to Scenario #2

| Activity | GWP [kg CO2eq] |
|---|---|
| (a) | 54 447.41 |
| (b) | 189 548.33 |
| (c) | 38 44.88 |
| (d) | 30 546.85 |
| (e) | 385 569.44 |
| (f) | 3 350 685.53 |
| (g) | out of scope |
| (h) | out of scope |
| (i) | out of scope |
| **Total GWP** | **4 014 642.43** |
| **Total GWP /km²** | **3 088 186.49** |

## 6 CONCLUSIONS

- This preliminary study arises from the need to evaluate possible retrofit interventions for the degradation of the Polyfytos bridge.
- Different interventions have been evaluated with respect to costs and their environments sustenaibility.
- The study is based on state-of-the-art surveying tools (laser-photogrammetry) paired with an advanced analysis to the Polyfytos bridge.
- The preliminary results show a reasonable equivalence in terms of environmental sustainability with an essential difference in terms of costs of intervention.
- Although the study is preliminary with a limited number of scenarios, it is observed that there is a difference between the two types of intervention in terms of cost that was expected. Forthcoming developments intend to consider additional scenarios and parameters for evaluating the possible interventions, such as the validity of each solution over time.

## ACKNOWLEDGMENT

The research leading to these results has received funding from the European Research 501 Council under the Grant agreement ID: 101007595 of the project ADDOPTML, MSCA RISE 502 2020 Marie Skodowska Curie Research and Innovation Staff Exchange (RISE). Paola Cavallaro is gratefully acknowledgement for supporting LCA preliminary analysis.

## REFERENCES


[1] Concrete Bridge Development Group, *Development of prestressed concrete bridges*, 2017. https://www.cbdg.org.uk/

[2] Z.P. Bažant, J.C. Chern Bayesian statistical prediction of concrete creep and shrinkage, *ACI Journal*, **81** (4), 319-330, 1984.

[3] Z.P. Bažant, J.K. Kim Improved prediction model for time-dependent deformations of concrete: Part 2 - basic creep, *Mater. Struct.*, **24** (6), 1991.

[4] Z.P. Bažant, L. Panula Creep Shrinkage Characterization for Prestressed Concrete Structures, *J. of the Prestressed Concrete Institute*, **25**, 86-122, 1980.

[5] N. Lu, M. Beer, M. Noori, Y. Liu Lifetime Deflections of Long-Span Bridges under Dynamic and Growing Traffic Loads, *J. Bridge Eng.*, 04017086, 1-12, 2017

[6] M. Morgese, F. Ansari, M. Domaneschi, G. P. Cimellaro, Post-collapse analysis of Morandi's Polcevera viaduct in Genoa Italy, *Journal of Civil Structural Health Monitoring*, **10**, 69–85, 2020.

[7] G. Lucko, Jesu´s M. de la Garza, Constructability Considerations for Balanced Cantilever Construction, *Pract. Period. Struct. Des. Constr.*, **8**(1): 47-56, 2003.

[8] T. Guo, R. Sause, D. Frangopol, A. Li, Time-Dependent Reliability of PSC Box-Girder Bridge Considering Creep, Shrinkage, and Corrosion, *J. Bridge Eng.*, **16**(1): 29-43, 2011.

[9] S. Wang, C.C. Fu, Simplification of Creep and Shrinkage Analysis of Segmental Bridges, *J. Bridge Eng.*, **20**(8): B6014001, 2015.

[10] M. Domaneschi, C. Pellecchia, E. De Iuliis, G. P. Cimellaro, M. Morgese, A.A. Khalil, F. Ansari, Collapse analysis of the Polcevera Viaduct by the Applied Element Method", *Engineering Structures*, **214**, 110659, 2020.

[11] S. Varbla, E.Artu, P. Raido, Centimetre-range deformations of built environment revealed by drone-based photogrammetry, *Automation in Construction*, **128**, 103787, 2021.

[12] Lõhmus, H., et al. "Terrestrial laser scanning for the monitoring of bridge load tests–two case studies." Survey review 50.360 (2018): 270-284.

[13] T.R. Witcher, From disaster to prevention: The silver bridge, *Civil Engineering Magazine Archive*, **87**(11), 44-47, 2017.

[14] Z.P. Bažant, Q. Yu, G.H. Li, Excessive long-time deflections of prestressed box girders. I: Record-span bridge in Palau and other paradigms, *Journal of structural engineering* **138**(6), 676-686, 2012.

[15] SGS https://www.sgs.com/en

[16] O. Markogiannaki, X. Hang, F. Chen, S. Mitoulis, I. Parcharidis Monitoring of a landmark bridge using SAR interferometry coupled with engineering data and forensics, *International Journal of Remote Sensing*, **43**, 95-119, 2022.

[17] S. Li, W. Wang, B. Lu, X. Du, M. Dong, T. Zhang, Z. Bai Long-term structural health monitoring for bridge based on back propagation neural network and long and short-term memory, *Structural Health Monitoring*, 14759217221122337, 2022.

[18] J. Zhou, Z. Sun, B. Wei, L. Zhang, P. Zeng, P., Deflection-based multilevel structural condition assessment of long-span prestressed concrete girder bridges using a connected pipe system, *Measurement*, 169, 108352, 2021.

[19] Bažant 2015

[20] Bažant 2018

[21] Strauss 2017

[22] Lee 2019

[23] W. Podolny Corrosion of prestressing steels and its mitigation, *PCI journal* **37**(5), 34-55, 1992.

[24] W.H. Hartt, S. Venugopalan *Corrosion evaluation of post-tensioned tendons on the Mid Bay Bridge in Destin*, Florida, Florida Department of Transportation Research Center report 33890, 2002.

[25] Ref for the k-NN analyses and estimation of 50% corrosion in prestressing strands

[26] ANAS S.p.A. (2022), Price list for New Construction and scheduled maintenance (in Italian). https://www.stradeanas.it/it/elenco-prezzi

[27] A. Devitofranceschi Repair of prestressed road viaducts: intervention techniques and cost-benefit analysis (in Italian) *Italian Concrete Days-AICAP*, 2018.

[28] International Organization for Standardization 2006 Principles and Framework (Geneva, Switzerland) Environmental management- Life cycle assessment ISO EN 14040:2006

[29] International Organization for Standardization 2006 Environmental management- Life cycle assessment - Requirements and guidelines (Geneva, Switzerland) ISO EN 14044:2006

[30] European Committee for Standardization 2020 Sustainability of construction works - Environmental product declarations - Core rules for the product category of construction products (Brussels, Belgium) EN 15804:2020 https://www.cencenelec.eu

[31] European Committee for Standardization 2011 Calculation method (Brussels, Belgium) Sustainability of construction works. Assessment of environmental performance of buildings EN 15978:2011 https://www.cencenelec.eu

[32] Fraunhofer IBP GENERIS®: www.generis-solution.eu

[33] Im BBSR Ö D ÖKOBAUDAT https://oekobaudat.de/

COMPDYN 2023
9th ECCOMAS Thematic Conference on
Computational Methods in Structural Dynamics and Earthquake Engineering
M. Papadrakakis, M. Fragiadakis (eds.)
Athens, Greece, 12-14 June 2023

# DEEP LEARNING-BASED CRACK, LOCATION AND AREA IDENTIFICATION FOR A PIPELINE BY THE CONVOLUTIONAL NEURAL NETWORK BASED ON CRACK CONTOUR NETWORK METHOD

**Wael A. Altabey** [1,2], **Mohammad Noori** [3,4,*], **and Zhishen Wu**[1,*]

[1] International Institute for Urban Systems Engineering (IIUSE), Southeast University, Nanjing 210096, Jiangsu, China.
e-mail: wael.altabey@gmail.com; zsw@seu.edu.cn

[2] Department of Mechanical Engineering, Faculty of Engineering, Alexandria University, Alexandria (21544), Egypt.

e-mail: wael.altabey@gmail.com

[3] Department of Mechanical Engineering, California Polytechnic State University, San Luis Obispo, CA 93405, USA.

[4] Visiting Professor, School of Civil Engineering, University of Leeds, Leeds, LS2 9JT, UK.

e-mail: mnoori@outlook.com

[*]Corresponding author: Mohammad Noori; Zhishen Wu

## Abstract

*In this work, the Convolutional Neural Network (CNN) algorithm is introduced in pipeline surface cracks monitoring-based image processing method for improving the efficiency and accuracy of crack type, location, and area identification. The method is used to extract the cracks area called the CNN based on crack contour network (CCN-CNNs) method from locate and extract the crack shape. CCN-CNNs is provides the accuracy rate (P%), recall rate (R%), and F-score (F%) index to assess the algorithm in the problem while identifying the cracks, and then according to the maximum F-score, we computes the crack corresponding contour area. In this work the pipeline crake images datasets are provided using an inspection drone with high definition camera. To the best of the authors' knowledge, the methodology presented in this paper for pipeline crack identification is an original contribution to the literature. This work introduces an efficient approach that also significantly reduces the time for crack type, location, and area identification of pipelines, the accuracy rate (P%), recall rate (R%), and F-score (F%) are recorded 91.8% ,86.1%, and 84.6% respectively.*

**Keywords:** Image processing; Convolutional Neural Network (CNN); Pipeline crack identification; Crack contour Network method.

## 1 INTRODUCTION

In recent decades, the rapid development of pipeline construction in various countries, play an important role in gas, water and liquids transportation over long distances. [1-5].

With the rapid development of pipelines construction, pipeline maintenance and management tasks also follow. In particular, a number of high-grade pipelines in the early stage have entered the period of intermediate or major repair, and the relevant pipelines maintenance and management departments have paid more and more attention to the monitoring of pipelines surface diseases and the collection of disease data. However, at present, there are few researches on pipelines disease detection, and the related detection equipment is seriously backward or even insufficient. Therefore, many pipelines maintenance management departments are still in the stage of traditional manual inspection. However, there are many problems in traditional manual detection, such as low detection efficiency, high labor intensity, long time consumption, and inability to guarantee detection accuracy. With the continuous increase of the scale of pipeline mileage, traditional pipelines detection methods can no longer meet the needs of pipelines disease detection. Therefore, research and development of advanced pipelines disease detection technology have become an urgent problem to be solved in pipelines development.

However, due to the harsh environment of the construction locations, pipelines always suffer from structural damage problems caused by corrosion, cracks, etc. Pipeline corrosion has been defined for decades as a major source of pipeline deterioration in transmission lines.

With the continuous development of the social economy, harsh environment of the construction locations, during the long-term operation of pipelines, various types of damages will occur. Damages such as cracks, and corrosion on the pipeline surface during pipeline operation will adversely affect environment and pipeline safety. Rapid and accurate detection of pipeline surface damages is an effective guarantee for maintaining the health and safety of pipeline surfaces [6-21].

At present, the management department generally collects the apparent image information of the pipe through the pipeline inspection drones and uses the traditional manual method to identify the damages, which is time-consuming and labor-intensive. Vision-based pipeline damages detection methods use adaptive threshold segmentation method, edge detection method, morphological method, wavelet analysis, and other algorithms for identification, but still face the following problems:

1) It is difficult to deal with the rich and diverse pipeline damage scenes;
2) Image noise interference leads to recognition the accuracy and efficiency are low;
3) The algorithm has many parameters, which require manual intervention, and the accuracy is low.

In addition, a single image of pipeline damages has high resolution and a large amount of image processing data. The current method is difficult to achieve rapid, quantitative, and refined identification of pipeline apparent defects.

With the development of deep learning technology [22-24] Convolutional Neural Network CNN has been widely used in the field of computer vision.

In recent years, some scholars have also tried to apply CNN to the apparent disease extraction of civil engineering structures. For example, Cha et al. [25] applied CNN combined with sliding window technology to crack recognition. The training data of CNN is 40,000 pictures

(256 pixels × 256 pixels), and the final verification accuracy is about 98%. The test picture size is 5888 × 3584. The test duration is 4.5s. Dorafshan et al. [26] constructed an SDNET 2018 crack image database that is convenient for engineers and technicians to use and applied CNN to crack recognition, which is different from the traditional edge detection method.

Compared with other methods, a hybrid identification method based on CNN and edge detection were proposed, and the effect was better [27]. Ni et al. [28] developed a CDN based on the CNN framework to automatically deal with structural apparent cracks through convolutional feature fusion and pixel-level classification.

Therefore, it takes a long time, and the use of CNN for target detection is generally easy to cause misidentification caused by over-fitting, and other methods still need to be used for subsequent processing. In order to solve the above problems, Girshick et al. [29] used CNN as the kernel and combined it with the Selective Search algorithm. Uijlings et al. [30] proposed a regional convolutional neural network (R-CNN) method. This method uses selective search to generate 2000 candidate regions, Then, CNN feature extraction is performed on each candidate region, and target classification is performed on each (Support Vector Machine, SVM) method. This method does not share the features of each candidate region extracted by CNN, resulting in information redundancy and long training and testing time. He et al. [31] proposed Spatial Pyramid Pooling (SPP-Net) which uses the full-image convolution shared feature map method to reduce the training and testing time of R-CNN. The target detection accuracy has also improved.

This paper introduces the local pipeline surface cracks localization and shape extraction based on CCN-CNNs methods. The location and area for the extracted disease area with borders are computed. For evaluation of the method is proposed, the accuracy rate (P), recall rate (R), and F-score index are introduced, which shows the effectiveness of the proposed approach.

## 2 METHODOLOGY

The process of pipeline cracks identification is shown in Figure 1. At present, the collection methods of pipeline surface images is inspection drones and other cameras that can achieve fast and non-contact high-quality image collection. The collected sample pictures are preprocessed, including cropping and segmentation of disease pictures, size unification, contrast adjustment, and image data enhancement to increase the number of samples; and then according to the classification of typical cracks in pipeline pictures, special software is used to mark the images and establish corresponding samples database; then input the training samples into the constructed CNN network, adjust the parameters, and perform deep learning on the entire network; finally, test the trained network.

For damages such as cracks, the algorithm directly outputs the bounding box and gives the cracks contour area and classification confidence. For horizontal and vertical cracks, after the bounding box is determined, the crack shape will be extracted and obtained the crack area, which makes the crack information richer and more accurate.

## 3 SYSTEM CONFIGURATION

### 3.1 CNN Architecture

As shown in Figure 2, typically a CNN model consists of both alternating convolution operation and sub-sampling operation, and the last layer is de-noted as a general multi-layer network. Interspersed with sub-sampling layers, convolutional layers are established to increase computation efficiency and further improve configural and spatial invariance. [32-34].

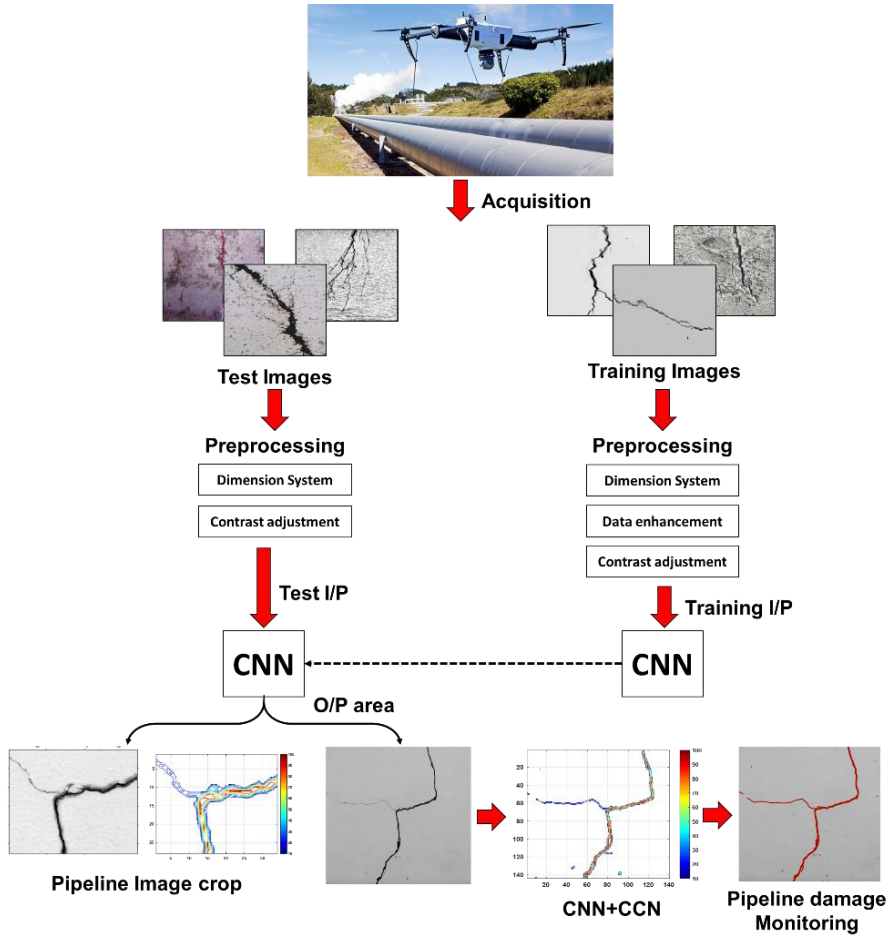


Figure 1: Illustration of the proposed method for pipeline disease identification.

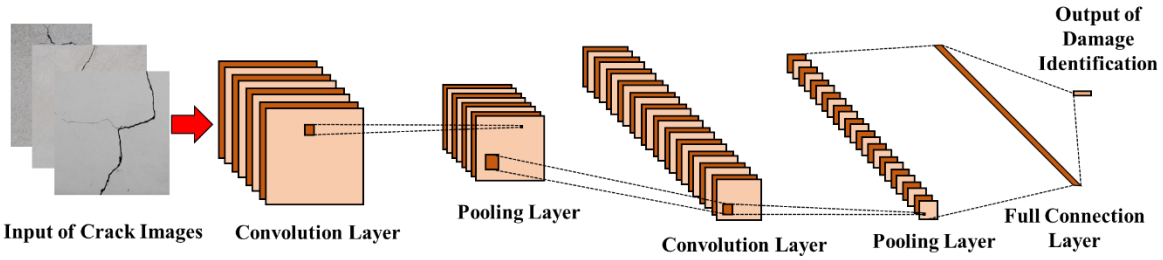


Figure 2: The architecture of a CNN model.

### 3.1.1 Convolution Layers

At a convolution layer, feature maps extracted from previous layers are convoluted with specific kernels and then activated to generate new feature maps. Multiple input feature maps are combined through the convolution operation until output is expressed as the following:

$$\boldsymbol{x}_j^l = f\left(\sum_{i \in M_j} \boldsymbol{x}_i^{l-1} * \boldsymbol{k}_{ij}^l + b_j^l\right). \tag{1}$$

where $M_j$ denotes a set of input feature maps, and each output feature map is added with an additive bias $b$. The input feature maps are convolved with distinct kernels for a particular output feature map.

### 3.1.2 Pooling layer

The pooling layer is usually arranged between sequential convolution layers. It is used to reduce the feature maps locative size. This is also called undersampling, by which network overfitting can be controlled. The operations can be used for undersampling are such as maximum pooling and average pooling. It can be expressed the average pooling feature of pooling layer in Eq. (2) for assuming the pooling size is $c$, $j^{th}$ is the region, and $l^{th}$ is number of pooling layer.

$$\boldsymbol{x}_j^l = f\left(B_j^l mean\left(\boldsymbol{x}_j^{l-1}\right) + b_j^l\right) \tag{2}$$

where $B_j^l$ is multiplicative; $mean(.)$ is average operation; The convolution and pooling layer are work together to detect the local connections and merges similar features and removes unnecessary irrelevant details.

## 3.2 Training, Validation, and Test Sets

In the CNN crack sample library, the cracks come from the actual collected pipeline crack pictures. The size of the source picture is 2048 × 2000 pixels. After slicing, the size of the small sample pictures is 32 × 32 pixels, and then data enhancement (rotation, mirroring, etc.) to obtain a training sample set, in which the number of samples with cracks is 15235 and the number of samples without cracks is 21642. After that, the pre-training network is used for migration learning, and all data are rotated 50 Epochs, and the final recognition accuracy can reach 95% above. Figure 3 presents the training performance using supervised mode. The key parameters for CNN training are shown in Table 1.

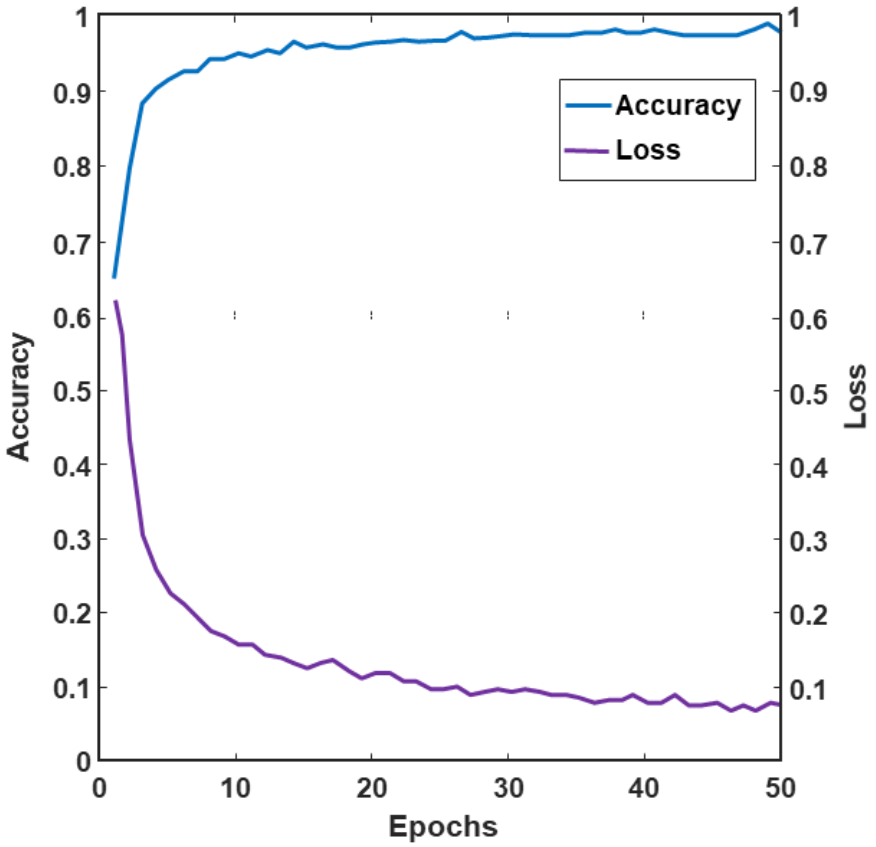


Figure 3: CNN Training Performance.

Table 1: CNN key parameters.

| Training Time | Gauge | Training Rate | Attenuation Factor |
|---|---|---|---|
| 50 sec | 32 | $10^{-4}$ | $10^{-6}$ |

## 4 RESULTS AND DISCUSSION

In the previous section, CNN feature maps training, validation and test were studied for the intact and damaged pipeline system, the processing method of pipeline should be processed by the two-value image processing methods. It can be seen that the background noise is difficult to remove, and the effect is not ignored. As a result, some traditional image processing algorithms are difficult to get crack. A series of image processing operations based on shape is to extract the image component that is meaningful to express and depict the shape of the regional shape, the most essential shape characteristics of the target objects are identified, such as the contour and object areas. The typical CCN method is used for processing pipeline images, which are widely used in digital image processing. The crack shape is restored according to the minimum gray value in the bounding box area. The process is shown in Figure 4. The detection of pipeline crack can be described through the following steps in Figure 5.

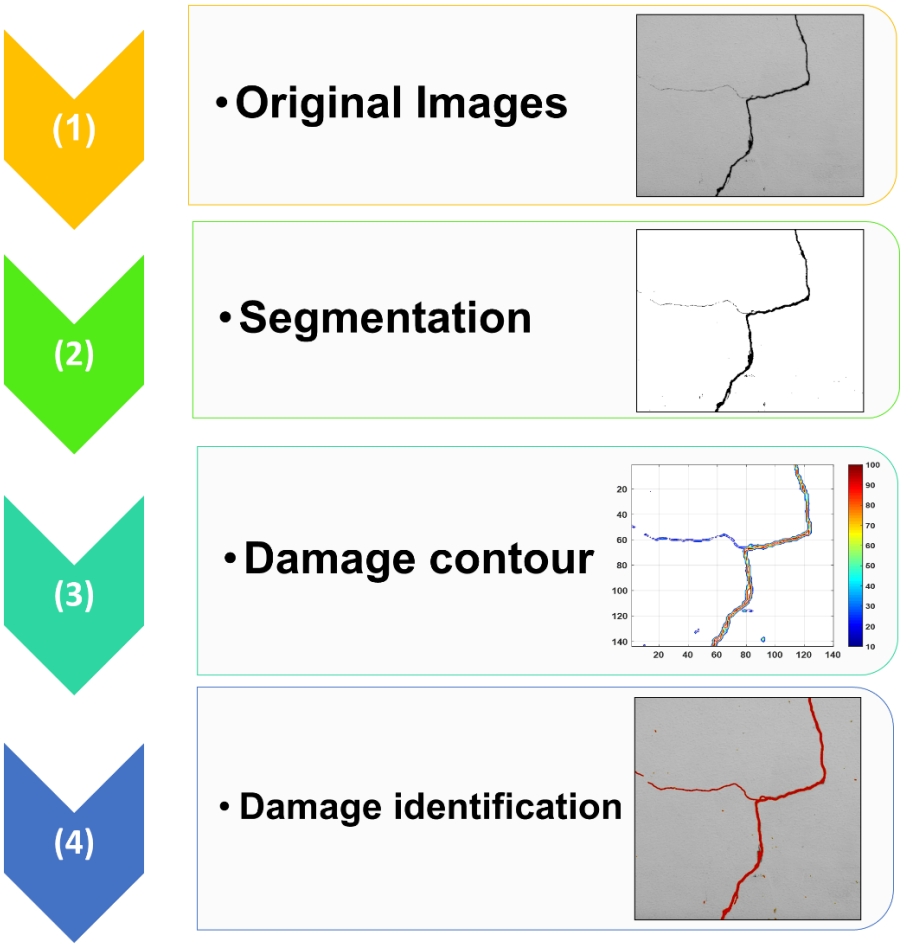


Figure 4: pipeline crack extraction flowchart.

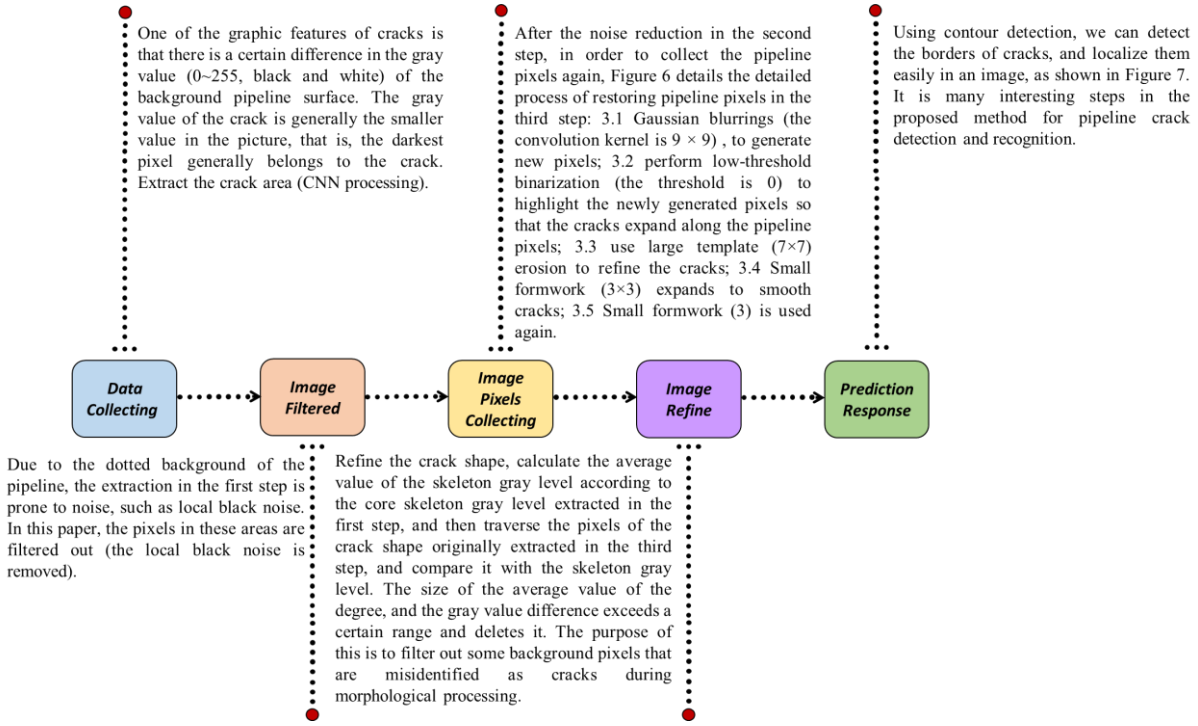


Figure 5: The steps of CCN-CNNs develop.

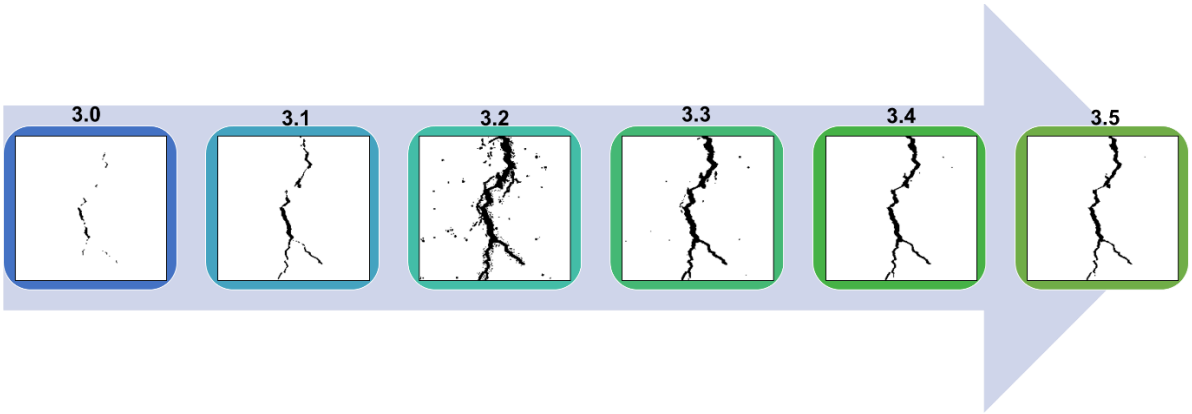


Figure 6: Collect the pipeline pixels again steps.

Four indexes that include the true-positive rate (TPR), true-negative rate (TNR), false-positive rate (FPR), and false-negative rate (FNR) are computed to estimate the proposed method performance measures for training and testing sets by calculating three indicators of the accuracy rate ($P$%), regression rate ($R$%), and F-score ($F$%), these three indexes can be determined:

$$P\%, = \frac{N_{TPR}}{N_{TPR} + N_{FPR}} \tag{3}$$

$$R\% = \frac{N_{TPR}}{N_{TPR} + N_{FNR}} \tag{4}$$

$$F\% = \frac{2N_{TPR}}{2N_{TPR} + N_{FNR} + N_{FPR}} \tag{5}$$

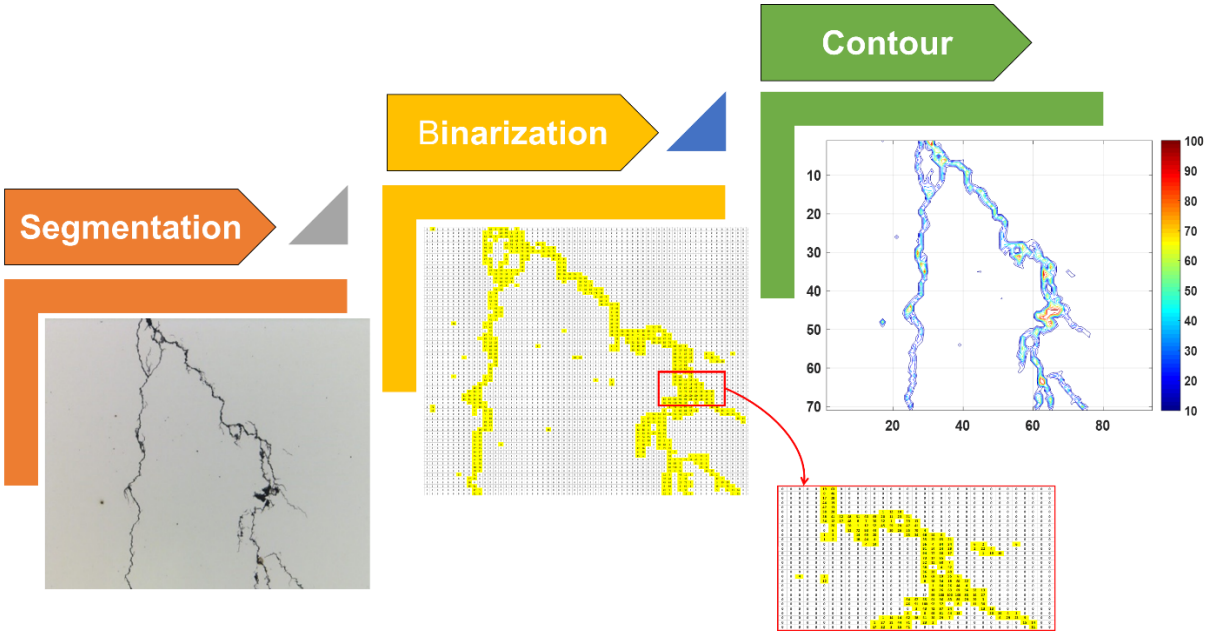


Figure 7: The crack contour extraction from pipeline Image.

Figure 8 plots the resulting accuracy (%), regression rate (%), and F-score (%) values in terms of the 50 Epochs number. In general P%, R%, and F% versus the overall performance are 91.8%, 86.1%, and 84.6%, respectively.

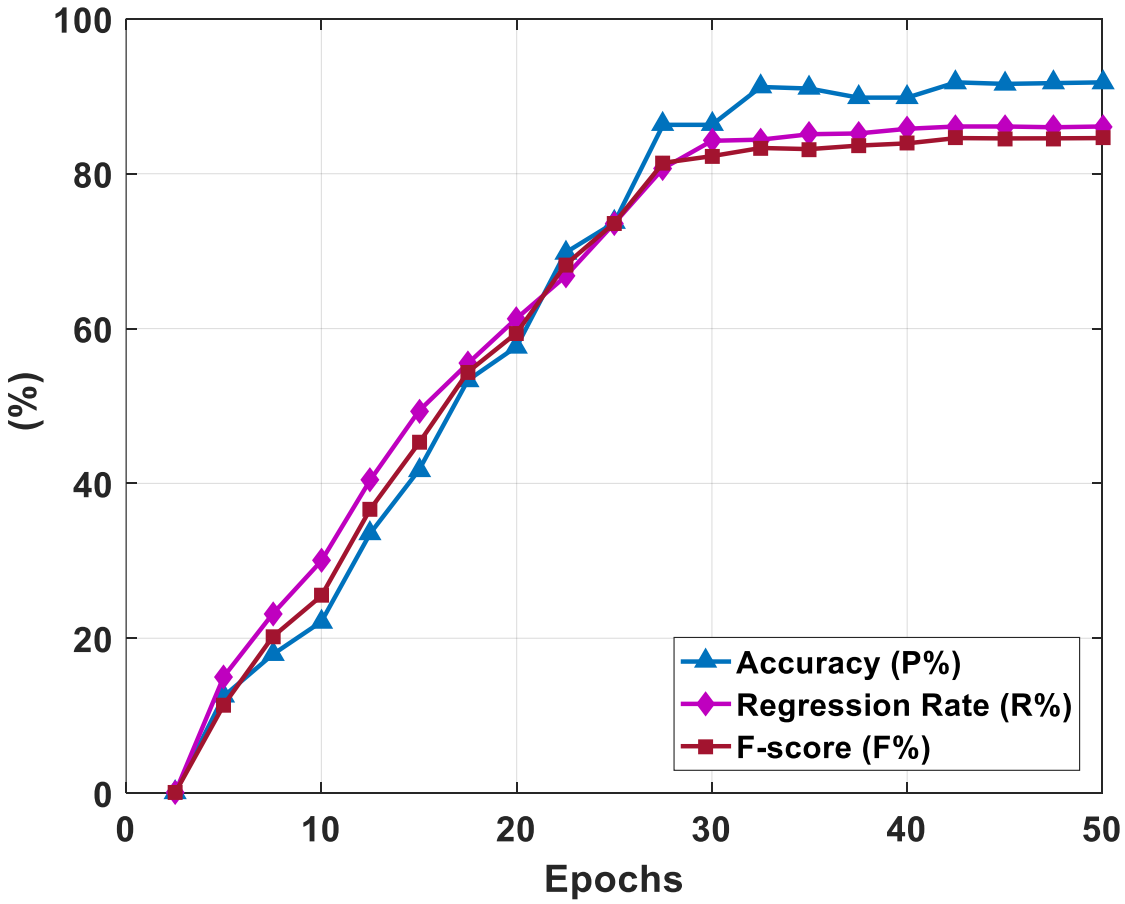


Figure 8. The training proceed comparison based on the crack identification test data.

## 5 CONCLUSIONS

This paper proposed the framework for pipeline crack detection method based on a learning-based model. The CNN algorithm in target detection is introduced to quickly identify the type, location, and area for the extracted disease area with borders, the CCN-CNNs method used to locate and extract the crack shape. The following conclusions can be drawn from the results:

1) The integrated method of CCN-CNNs can effectively search and locate the disease on the pictures collected by the pipeline inspection drones, and accurately extract the crack shape.
2) The test results show that its work efficiency is high, although the missed detection rate of the algorithm is low, the false detection rate is high, and it is difficult to be directly applied to the automatic detection of pipeline cracks.
3) Indexes such as the accuracy rate (*P%*), recall rate (*R%*), and F-score precision rate (*F%*) are introduced to evaluate the algorithm and determine the corresponding contour area of the disease frame according to the maximum F-score. A pipeline image was carried out by using an inspection drone with high definition camera.
4) The dataset used in this work, modeled with high *P%*, *R%*, and *F%*, and the overall performance are 91.8%,86.1%, and 84.6% respectively, highlighting the potential of using deep learning for the detection of pipeline crack.

## REFERENCES

[1] R. Ghiasi, M. Noori, W.A. Altabey, T. Wang, Z. Wu, Structural Damage Detection under Uncertain Parameters using Non-Probabilistic Meta-Model and interval mathematics, Lifeline 2022: Advancing Lifeline Engineering for Community Resilience, ASCE Library, 2022, 670-679. https://doi.org/10.1061/9780784484449.061.

[2] R. Ghiasi, M. Noori, W.A. Altabey, T. Wang, Z. Wu, Uncertainty Handling in Structural Damage Detection using Non-Probabilistic Meta-Model and interval mathematics, International Conference on Structural Health Monitoring of Intelligent Infrastructure: Transferring Research into Practice, SHMII 2021, Volume 2021-June, 819–824, 2021.

[3] R. Ghiasi, M.R. Ghasemi, M. Noori, W.A. Altabey, non-parametric approach toward structural health monitoring for processing big data collected from the sensor network. Structural Health Monitoring 2019: Enabling Intelligent Life-Cycle Health Management for Industry Internet of Things (IIOT). In Proceedings of the 12th International Workshop on Structural Health Monitoring (IWSHM 2019), Stanford, CA, USA, 10–12 September 2019; doi:10.12783/shm2019/32395.

[4] A. Silik, M. Noori, W.A. Altabey, D. Ji, R. Ghiasi, A New Denoising Technique via Wavelet Analysis of Structural Vibration Response for Structural Health Monitoring Applications, Lifeline 2022: Advancing Lifeline Engineering for Community Resilience, ASCE Library, 2022, 691–706. https://doi.org/10.1061/9780784484449.063.

[5] A. Silik; M. Noori, R. Ghiasi; T. Wang; S. Kuok; N. S. D. Farhan; J. Dang; Z. Wu, W. A. Altabey, Dynamic wavelet neural network model for damage features extraction and patterns recognition, Civil Structural Health Monitoring, 2023, https://doi.org/10.1007/s13349-023-00683-8.

[6] W.A. Altabey, M. Noori, Z. Wu, M. A. Al-Moghazy, S. A. Kouritem, Studying Acoustic Behavior of BFRP Laminated Composite in Dual-Chamber Muffler Application Using Deep Learning Algorithm, Materials, 15(22), 807, 2022, https://doi.org/10.3390/ma15228071.

[7] W.A. Altabey, S. A. Kouritem, M. I. Abouheaf, N. Nahas, Research in Image Processing for Pipeline Crack Detection Applications, IEEE conference, 2nd International Conference on Electrical, Computer, Communications and Mechatronics Engineering (ICECCME-2022), Maldives, 16-18 November 2022. https://doi.org/10.1109/ICECCME55909.2022.9988417.

[8] W.A. Altabey, The Damage Identification in Laminated Composite Plate under Fatigue Load through Wavelet Packet Energy Curvature Difference Method. Composites Part C: Open Access, 9, 100304, 2022, https://doi.org/10.1016/j.jcomc.2022.100304.

[9] A. Silik, M. Noori, W. A. Altabey, R. Ghiasi, Z. Wu, J. Dang, Evaluation of analytic wavelet parameters effet for data analyses in civil structural heath monitoring, International Conference on Structural Health Monitoring of Intelligent Infrastructure: Transferring Research into Practice, SHMII 2021, Volume 2021-June, 813–818, 2021.

[10] W.A. Altabey, S. A. Kouritem, M. I. Abouheaf, N. Nahas, A Deep Learning-Based Approach for Pipeline Cracks Monitoring, IEEE conference, 2nd International Conference on Electrical, Computer, Communications and Mechatronics Engineering (ICECCME-2022), Maldives, 16-18 November 2022, https://doi.org/10.1109/ICECCME55909.2022.9987998.

[11] H. Weixing, W. Ju, G. Dangui, W. Xiaodong, S. Gongzuo, X. Yan-liang, Z. Chuanyue, M. Noori, W.A. Altabey, Artificial intelligence Technique for Pavement Diseases Identification, ACM Digital Library, Proceedings of the 4th International Conference on Intelligent Science and Technology (ICIST '22), August 2022, 66–72, https://doi.org/10.1145/3568923.3570515.

[12] A. Silik, W. Hong, J. Li, M. Mao, M. Noori, W. A. Altabey, Develop a Health Monitoring Technique for Analysis a Big Data of Bridges, Lecture Notes in Civil Engineering, 292, 59–78, 2023, https://doi.org/10.1007/978-981-19-5783-3_5.

[13] W. Hong, M. Noori, H. Jiang, Y. Liu, W. A. Altabey, Machine Vision-Based Structural Diagnosis Application, Lecture Notes in Civil Engineering, 292, 79–88, 2023, https://doi.org/10.1007/978-981-19-5783-3_6.

[14] X. Yanliang, Z. Chuanyue, S. Gongzuo, J. Ye, Q. Yujin, M. Xueshun, X. Jingtao, M. Noori, W. A. Altabey, Research of pavement crack detection system based on image processing, Proc. SPIE 12590, Third International Conference on Computer Vision and Information Technology (CVIT 2022), 1259007, 2023; https://doi.org/10.1117/12.2669715.

[15] Z. Li, D. Feng, M. Noori, D. Basu, W. A. Altabey, Dynamic response analysis of Euler–Bernoulli beam on spatially random transversely isotropic viscoelastic soil. Proceedings of the Institution of Mechanical Engineers, Part L: Journal of Materials: Design and Applications, 236(5), 1037-1052, 2022, https://doi.org/10.1177/14644207211067442.

[16] Z. Li, M. Noori, D. Basu, E. Taciroglu, Z. Wu, W.A. Altabey, Dynamic analysis of soil structure interaction shear model for beams on transversely isotropic viscoelastic soil,

Proceedings of the Institution of Mechanical Engineers, Part L: Journal of Materials: Design and Applications, 236(5), 999-1019, 2022, https://doi.org/10.1177/14644207211067437.

[17] P. Mohebian, B. B. A. Seyed, M. Noori, N. Lu, W. A. Altabey, Visible Particle Series Search Algorithm and Its Application in Structural Damage Identification, Sensors, 22(3), 1275, 2022, https://doi.org/10.3390/s22031275.

[18] W. A. Altabey, M. Noori, Z. Li, Y. Zhao, Seyed Bahram Beheshti Ava, Farsangi, E. N., Ghiasi, R. Silik, A. A Novel MRE Adaptive Seismic Isolator Using Curvelet Transform Identification, Applied Sciences, 11(23), 11409, 2021, https://doi.org/10.3390/app112311409.

[19] W. A. Altabey, Z. Wu, M. Noori, H. Fathnejat, Structural Health Monitoring of Composite Pipelines Utilizing Fiber Optic Sensors and an AI-Based Algorithm—A Comprehensive Numerical Study. Sensors, 23, 3887, 2023, https://doi.org/10.3390/s23083887.

[20] B. B. A. Seyed, M. Ghabdian, M. Noori, W. A. Altabey, Simultaneous Effect of Temperature, Shrinkage, and Self-Weight Creep on RC Beams: A Case Study, Proceedings of the Institution of Mechanical Engineers, Part L: Journal of Materials: Design and Applications, 236(5), 1020-1036, 2022, https://doi.org/10.1177/14644207211067440.

[21] R. Arash, S. B. B. Aval, M. Noori, V. Sarhosis, W. Zhishen, A. Nikkhoo, W. A. Altabey, A simplified beam model for the numerical analysis of masonry arch bridges –A case study of the Veresk railway bridge, Structures, 45, 1253-1266, 2022, https://doi.org/10.1016/j.istruc.2022.09.087.

[22] W. A. Altabey, M. Noori, Z. Wu, M. A. Al-Moghazy, S. A. Kouritem, A deep-learning approach for predicting water absorption in composite pipes by extracting the material's dielectric features, Engineering Applications of Artificial Intelligence,121, 105963, 2023, https://doi.org/10.1016/j.engappai.2023.105963.

[23] T. Wang, H. Li, M. Noori, R. Ghiasi, S. Kuok, W. A. Altabey, Seismic response prediction of structures based on Runge-Kutta recurrent neural network with prior knowledge, Engineering Structures, 279, 115576, 2023, https://doi.org/10.1016/j.engstruct.2022.115576.

[24] H. Fathnejat, B. Ahmadi-Nedushan, S. Hosseininejad, M. Noori, W.A. Altabey, A data-driven structural damage identification approach using deep convolutional-attention-recurrent neural architecture under temperature variations, Engineering Structures, 276, 115311, 2023, https://doi.org/10.1016/j.engstruct.2022.115311.

[25] Y. J. Cha, W. O. Choi, Deep Learning - based Crack Damage Detection Using Convolutional Neural Networks. Computer-aided Civil and Infrastructure Engineering, 32(5), 361-378, 2017.

[26] S. Dorafshan, R. J. Thomas, M. Maguire, Comparison of Deep Convolutional Neural Networks and Edge Detectors for Image - based Crack Detection in Concrete. Construction and Building Materials, 186, 10 3 -1045, 2018.

[27] S. Dorafshan, R. J. Thomas, M. Maguire, An Annotated Image Dataset for Non-contact Concrete Crack Detection Using Deep Convolutional Neural Networks. Data in Brief, 21, 1664-1668, 2018.

[28] F. T. Ni, J. Zhang, Z. Q. Chen, Pixel - level Crack Delineation in Images with Convolutional Feature Fusion. Structural Control and Health Monitoring, 26(1), e2286, 2019.

[29] R. Girshick, J. Donahue, T. Darrell, Rich Feature Hicrarchies for Accurate Object Detection and Semantic Segmentation, IEEE. Proceedings of the IEEE Conference on Computer Vision and Pattern Recognition. New York: IEEE, 2014.

[30] J. R. Uijlings, K. E. A. Van De Sande, T. Gevers, Selective Search for Object Recognition, International Journal of Computer Vision, 104 (2), 154-171, 2013.

[31] K. He, X. Zhang, S. Ren, Spatial Pyramid Pooling in Deep Convolutional Networks for Visual Recognition. IEEE Transactions on Pattern Analysis and Machine Intelligence, 37(9), 1904 – 1916, 2015.

[32] W.A. Altabey, M. Noori, Artificial-Intelligence-Based Methods for Structural Health Monitoring, Appl. Sci. 2022, 12(24), 12726. https://doi.org/10.3390/app122412726.

[33] M. Noori, W.A. Altabey, Hysteresis in Engineering Systems. Appl. Sci. 2022, 12, 9428. https://doi.org/10.3390/app12199428

[34] Z. Li, M. Noori, C. Wan, B. Yu, B. Wang, W.A. Altabey, A Deep Learning-Based Approach for the Identification of a Multi-Parameter BWBN Model. Appl. Sci. 2022, 12, 9440. https://doi.org/10.3390/app12199440.

COMPDYN 2023
9th ECCOMAS Thematic Conference on
Computational Methods in Structural Dynamics and Earthquake Engineering
M. Papadrakakis, M. Fragiadakis (eds.)
Athens, Greece, 12-14 June 2023

# EFFECTIVE TECHNIQUE FOR STRUCTURES DAMAGE DETECTION BASED ON THE STRUCTURAL FREQUENCY MAPS

**Wael A. Altabey [1,2], Mohammad Noori [3,4,*], Zhishen Wu[1,*], Ahmad Silik[1], and Nabeel S. D. Farhan [5]**

[1] International Institute for Urban Systems Engineering (IIUSE), Southeast University, Nanjing 210096, Jiangsu, China.
e-mail: wael.altabey@gmail.com; zsw@seu.edu.cn; silikth@gmail.com

[2] Department of Mechanical Engineering, Faculty of Engineering, Alexandria University, Alexandria (21544), Egypt.

e-mail: wael.altabey@gmail.com

[3] Department of Mechanical Engineering, California Polytechnic State University, San Luis Obispo, CA 93405, USA.

[4] Visiting Professor, School of Civil Engineering, University of Leeds, Leeds, LS2 9JT, UK.

e-mail: mnoori@outlook.com

[5] School of Civil Engineering, Southeast University, Nanjing 210096, China.

e-mail: eng.nabeel.saeed@gmail.com

[*]Corresponding author: Mohammad Noori; Zhishen Wu

## Abstract

*This research studies a novel damage detection framework for beam structure systems using displacement sensors. First, a finite element model is established under the impact load. Based on this model, an accumulative damage model is introduced to model the beam damage, and the damage case is considered. Both static and transient displacement are collected from the beam sensors installing a long beam structure. A system transfer function (TF) is proposed and applied to the "open loop" beam system. Results show these approaches perform great promises when damage evolves in beam structure.*

**Keywords:** Beam structure systems, Damage detection, Displacement, Open Loop System, Transfer Function, Frequency analysis.

# 1 INTRODUCTION

In recent years, the construction of beam structures has developed rapidly, and the health monitoring of beam structures has become a research hotspot at home and abroad. Reasonable configuration of sensors is the premise to ensure the quality of beam structure health monitoring, and it is very important to obtain accurate and real-time information on the health status of beam structures and realize the monitoring and evaluation of beam structures [1-12].

Nowadays, more and more use intelligent and digital means to automatically capture various structural safety-related data such as environmental temperature and humidity, expansion joint displacement, etc. through the beam and plate structural health monitoring system, identify and record the development of existing diseases in real time, Discover new diseases and report it, assist in decision-making and judgment, reduce maintenance costs, and improve monitoring efficiency and quality [13-26].

System's frequency response function using conventional valve closure signals was proposed to study the influence of various faults, friction and pipe wall viscoelasticity on this response function and were compared with the corresponding impacts in the time domain [27]. The applicability of the transient-based frequency-response function (FRF) method was investigated for detecting leaks in complex series pipelines [28]. Frequency response method requiring the measurement of pressure and discharge fluctuations at only one location was used as the potential to detect leaks in real-life pipe systems conveying different types of fluids [29]. An analytical simplification of the original system frequency response-based method was used to identify the key blockage parameters governing the frequency shifts and showed that the magnitude of the frequency shift increases with the severity of blockages and is related to the changes in characteristic impedance and wave propagation coefficient of pipeline (pipe diameter, thickness, and / or wave speed) imposed by the blockage [30].

This paper discuss a new damage detection strategy of beams structure in both static and transient sensing approaches using displacement sensors, the displacement as system inputs and outputs of transfer function system is proposed and applied to the "open loop" beam system. To the best of the author's knowledge, no work related to a new damage indicator based on "system control theory" has been conducted on beams structure. By applying static and dynamic load to the displacement sensor distributed on beam, damage area of the beam can be identified by detecting signal changes with an order of magnitude.

# 2 BEAM MODELING

## 2.1 Beam Description

Consider a beam subjected to an impact force, as shown in Fig.1 as an example, the beam length is $20m$, $E = 210\ GPa$, $\rho = 7850\ kg/m^3$, $A = 1m^2$, $I = 0.083m^4$. An impact exciting force of $1000\ N$ is applied at the midpoint of the beam. Fig. 2 introduced the force-time relation. Various sensors were installed on the longitudinal direction of the beam at total of 20 orders element, 21 nodes, as shown in Fig.1 the sensors positions ate each node. Use ANSYS performs a transient analysis, simulating damage with stiffness drop at each element. The suitable finite elements were selected, i.e. for simulating structural characteristics is used BEAM3 element with material model EX 210000, PRXY: 0.3, and DENS: 7.85e-6. The displacement of the 21 nodes before and after the damage under the action of the exciting force is shown in Fig. 3.

Fig. 4 shows the acceleration responses of Impact excitation measured from the various sensors installed on the longitudinal direction of the beam. The acceleration responses change due to the structural damage. So, the time history acceleration responses are sensitive to structural damage and can be used as a damage indicator. Fig.5 shows the energy variations strength or

shows at which frequencies variations are strong and at which frequencies variations are weak. Any changes in the PSD can be used as indicator of damage. Also it can be used to reduce the effect of noise in the signal and also can be used to trace the damage through the curvature of the power spectrum energy. Fig. 6 shows 1st, 2nd and 3rd frequency of the intact pipeline. Table 1 lists all the values of frequency orders for different damage case (D0 & D1).

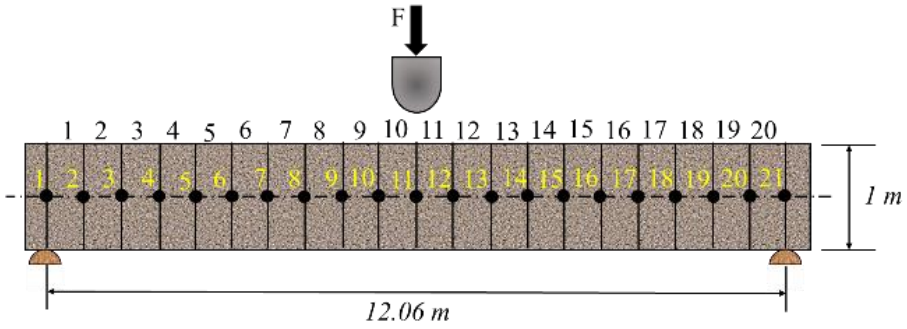


Figure 1: General View of beam.

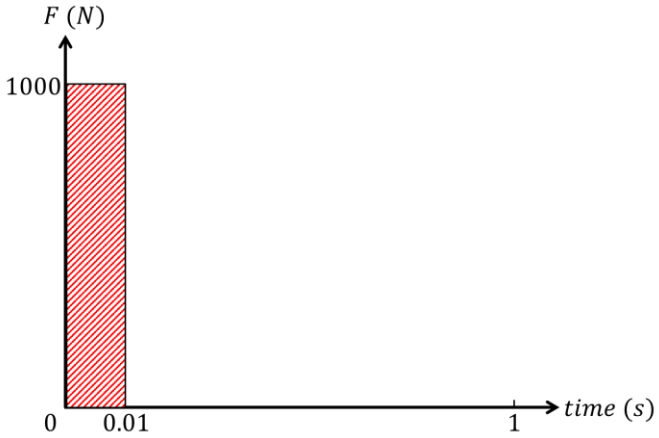


Figure 2: Impact Excitation.

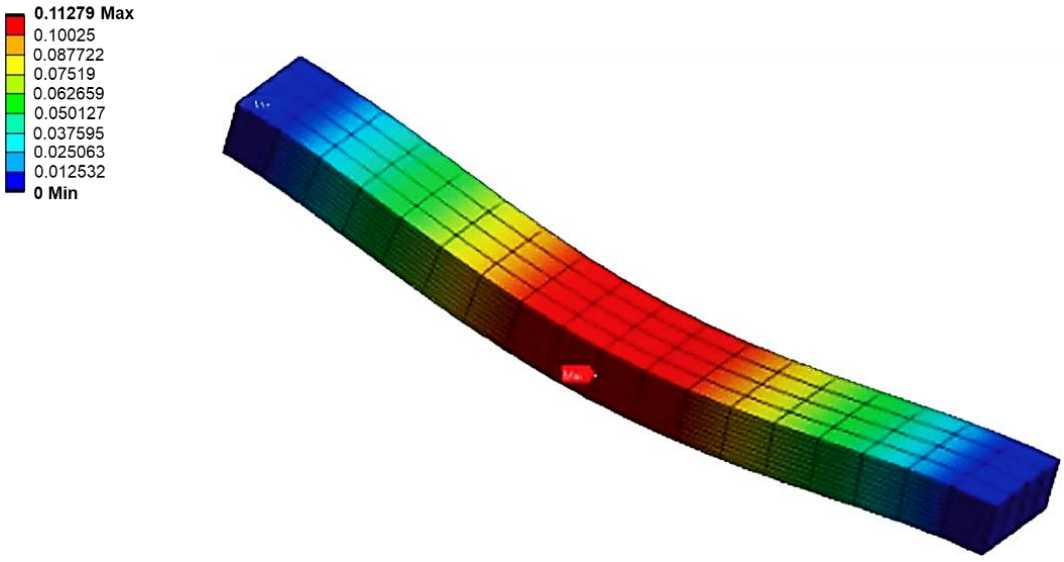


Figure 3: Displacement of a beam.

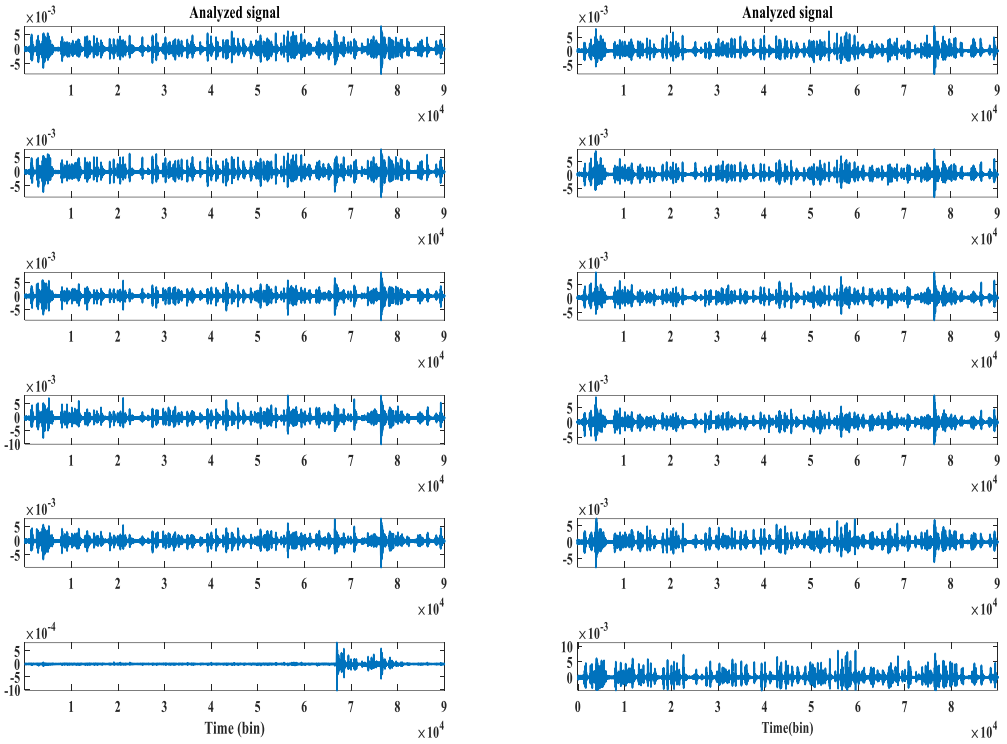


Figure 4: The acceleration of impact excitation.

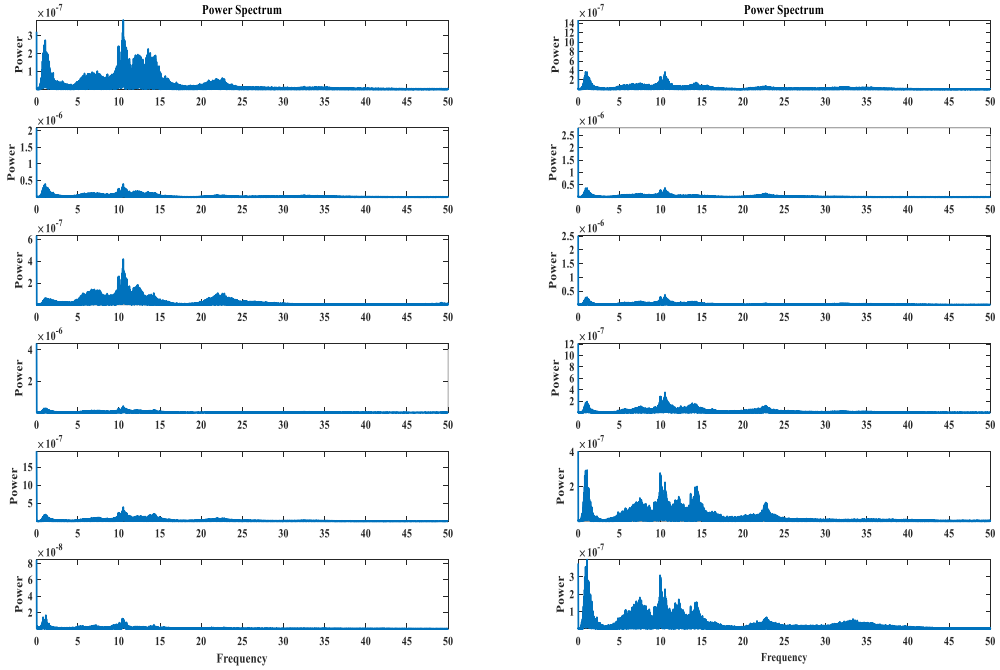


Figure 5: The Power spectral density.

Table 1: Structural frequency.

| Frequency Order | D0 (Hz) | D1 (Hz) |
|---|---|---|
| 1st order (Lateral Bending) | 233.55 | 232.85 |
| 2nd order (Vertical Bending) | 315.62 | 312.67 |
| 3rd order (shear) | 824.38 | 822.90 |

## 3 RESULTS AND DISSECTIONS

### 3.1 Acceleration Responses Analysis in the Frequency Domain

Considering the uncertainties of modeling, the typical fitting curves (average values) of acceleration variation response are selected (Equation 2) to describe the output of the structure field system excited by impact input, where the Cubic, Quadratic, Linear, and Constant terms of the fitting equation are 0.0287, -0.0016, 0.0063, 0.0005, respectively.

$$X(t) = 0.0287t^3 - 0.0016t^2 + 0.0063\mathrm{t} + 0.0005 \tag{1}$$

The differential equation can represent herein:

$$a_0 x_o^{(n)}(t) + a_1 x_o^{(n-1)}(t) + \cdots + a_{n-1} x_o^{(1)}(t) + a_n x_o(t) = b_0 x_i^{(m)}(t) + b_1 x_i^{(m-1)}(t) + \cdots + b_{m-1} x_i^{(1)}(t) + b_m x_i(t), n \geq m \tag{2}$$

Where $x_o$ is the system output, $x_i$ is the system input.

$$\mathrm{G(s)} = \frac{\mathrm{X_o(s)}}{\mathrm{X_i(s)}} = \frac{\mathrm{b_0 s^m + b_1 s^{m-1} + \cdots + b_{m-1} s + b_m}}{\mathrm{a_0 s^n + a_1 s^{n-1} + \cdots + a_{n-1} s + a_n}} \tag{3}$$

System input can be expressed as:

$$\mathrm{X_i(s)} = \frac{2232\pi}{\mathrm{s^2 + 35642\pi^2}} \tag{4}$$

System output can be expressed as:

$$\mathrm{X_o(s)} = \frac{213}{854\mathrm{s}^4} - \frac{1}{2232\mathrm{s}^3} \tag{5}$$

System TF can be expressed as follows according to the presented damage case (D1).

$$\mathrm{G_1(s)} = \frac{(\mathrm{s^2 + 35642\pi^2})(854\mathrm{s} - 11160)}{2.5\mathrm{E9}\pi\mathrm{s}^4} \tag{6}$$

### 3.2 Frequency Domain Analysis Methods

The beam system subjected to different conditions of damage features when excited by a impact signal input. Let us regard it as a "control system" with an input excitation and an output measurement sensors. When considering the system as an open loop control system, this means that no feedback from output to the system, the main control on the system is from input only. The frequency domain analysis methods (Zero-Pole, Nyquist, Bode, Nichols) are applied to measure the dynamic response characteristics of the system regarding damage using Simulink software.

The Zero-Pole Point Map analysis for the presented damage case is plotted in Fig. 5(a). For the presented damage we can see that the Zero point of system TF (0.4) moves towards zero when the damage range increases. The Nyquist map analysis for the presented damage case is plotted in Fig. 5(b). As shown in the Figure, for the presented damage we can see the variation of the endpoint trajectory of the vector $G(j\omega) = A(\omega)e^{j\varphi(\omega)}$ (Where shows $A(\omega_i)$ appears the vector magnitude $G(j\omega_i)$ when the frequency equals $\omega_i$, and The case of polar coordinates is $\varphi(\omega)$) when frequency $\omega$ changes from $0 \to \infty$. The Nyquist diagram shows in the non-overlapped part the system frequency of $G$ is -13.3. The system frequency decreases as the damage range increases. The Bode map analysis for the presented damage case is plotted in Fig. 5(c). As shown in the Figure, for the presented damage we can see the frequency of the excitation signal is 100π. In detail, when damage occurs the absolute value of magnitude increases over 40dB, and the corresponding phase changes more than $165^{\circ}$. The Nichols map for the presented damage case is plotted in Fig. 5(d). As shown in the Figure, for the presented damage phase

reaches about 180, accordingly G change at the inflection point with Gain 20 at the frequency is 100π.

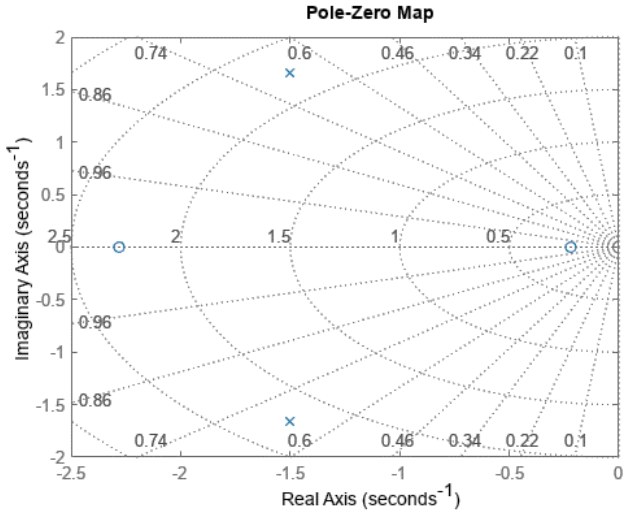


(a) Pole-Zero Map

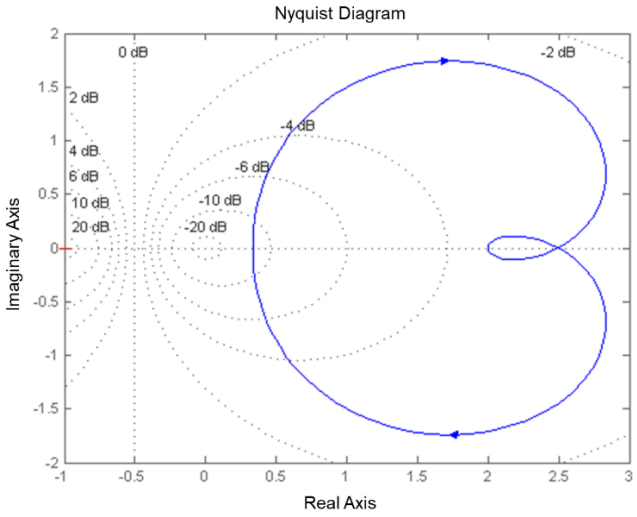


(b) Nyquist Map

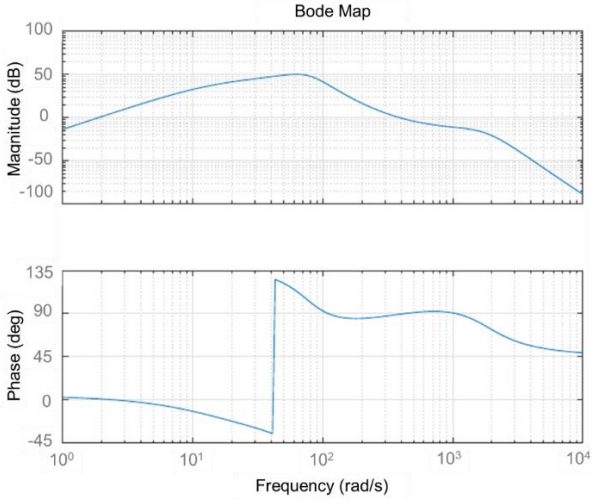


(c) Bode Map

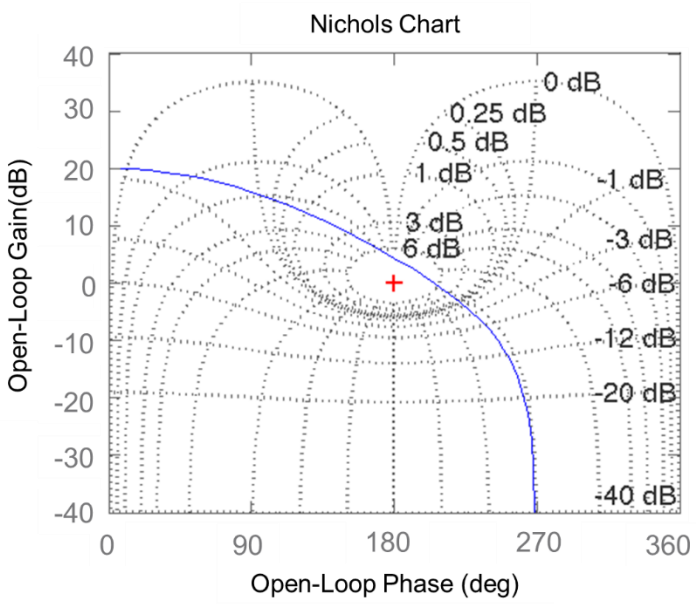


(d) Nichols Map

Figure 6: The frequency domain analysis methods for steel beam.

## 4 CONCLUSIONS

This paper established a FEM of steel beam damage system from the impact load, by extracting the measurements of sensors and loaded with impact signal. Results show that the signal magnitude will suddenly and sensitively change when the damage starts. The beam system TF and the frequency domain are established and applied to reflect damage evolution through plotting the zero-pole points map, Nyquist Map, Bode Map, and Nichols Map. The most motivating conclusion in this work is that, instead of using the vibration signals of the responses of the structural system, the variation of the frequency is used to observe the time and displacement characteristics variation of the system due to structural damage.

## REFERENCES

[1] R. Ghiasi, M. Noori, W.A. Altabey, T. Wang, Z. Wu, Structural Damage Detection under Uncertain Parameters using Non-Probabilistic Meta-Model and interval mathematics, Lifeline 2022: Advancing Lifeline Engineering for Community Resilience, ASCE Library, 2022, 670-679. https://doi.org/10.1061/9780784484449.061.

[2] R. Ghiasi, M. Noori, W.A. Altabey, T. Wang, Z. Wu, Uncertainty Handling in Structural Damage Detection using Non-Probabilistic Meta-Model and interval mathematics, International Conference on Structural Health Monitoring of Intelligent Infrastructure: Transferring Research into Practice, SHMII 2021, Volume 2021-June, 819–824, 2021.

[3] Z. Li, D. Feng, M. Noori, D. Basu, W. A. Altabey, Dynamic response analysis of Euler–Bernoulli beam on spatially random transversely isotropic viscoelastic soil. Proceedings of the Institution of Mechanical Engineers, Part L: Journal of Materials: Design and Applications, 236(5), 1037-1052, 2022, https://doi.org/10.1177/14644207211067442.

[4] Z. Li, M. Noori, D. Basu, E. Taciroglu, Z. Wu, W.A. Altabey, Dynamic analysis of soil structure interaction shear model for beams on transversely isotropic viscoelastic soil,

Proceedings of the Institution of Mechanical Engineers, Part L: Journal of Materials: Design and Applications, 236(5), 999-1019, 2022, https://doi.org/10.1177/14644207211067437.

[5] M. Ghabdian, B. B. A. Seyed, M. Noori, W. A. Altabey, Reliability of reinforced concrete beams in serviceability limit state via microprestress-solidification theory, a structural health monitoring strategy, Proceedings of the Institution of Mechanical Engineers, Part L: Journal of Materials: Design and Applications, 236(5), 1077-1093, 2022, https://doi.org/10.1177/14644207211069035.

[6] B. B. A. Seyed, M. Ghabdian, M. Noori, W. A. Altabey, Simultaneous Effect of Temperature, Shrinkage, and Self-Weight Creep on RC Beams: A Case Study, Proceedings of the Institution of Mechanical Engineers, Part L: Journal of Materials: Design and Applications, 236(5), 1020-1036, 2022, https://doi.org/10.1177/14644207211067440.

[7] R. Arash, S. B. B. Aval, M. Noori, V. Sarhosis, W. Zhishen, A. Nikkhoo, W. A. Altabey, A simplified beam model for the numerical analysis of masonry arch bridges –A case study of the Veresk railway bridge, Structures, 45, 1253-1266, 2022, https://doi.org/10.1016/j.istruc.2022.09.087.

[8] M. Noori, W.A. Altabey, Hysteresis in Engineering Systems. Appl. Sci. 2022, 12, 9428. https://doi.org/10.3390/app12199428

[9] A. Silik, W. Hong, J. Li, M. Mao, M. Noori, W. A. Altabey, Develop a Health Monitoring Technique for Analysis a Big Data of Bridges, Lecture Notes in Civil Engineering, 292, 59–78, 2023, https://doi.org/10.1007/978-981-19-5783-3_5.

[10] A. Silik, M. Noori, W.A. Altabey, D. Ji, R. Ghiasi, A New Denoising Technique via Wavelet Analysis of Structural Vibration Response for Structural Health Monitoring Applications, Lifeline 2022: Advancing Lifeline Engineering for Community Resilience, ASCE Library, 2022, 691–706. https://doi.org/10.1061/9780784484449.063.

[11] W. A. Altabey, Z. Wu, M. Noori, H. Fathnejat, Structural Health Monitoring of Composite Pipelines Utilizing Fiber Optic Sensors and an AI-Based Algorithm—A Comprehensive Numerical Study. Sensors, 23, 3887, 2023, https://doi.org/10.3390/s23083887.

[12] P. Mohebian, B. B. A. Seyed, M. Noori, N. Lu, W. A. Altabey, Visible Particle Series Search Algorithm and Its Application in Structural Damage Identification, Sensors, 22(3), 1275, 2022, https://doi.org/10.3390/s22031275.

[13] X. Yanliang, Z. Chuanyue, S. Gongzuo, J. Ye, Q. Yujin, M. Xueshun, X. Jingtao, M. Noori, W. A. Altabey, Research of pavement crack detection system based on image processing, Proc. SPIE 12590, Third International Conference on Computer Vision and Information Technology (CVIT 2022), 1259007, 2023; https://doi.org/10.1117/12.2669715.

[14] W.A. Altabey, M. Noori, Z. Wu, M. A. Al-Moghazy, S. A. Kouritem, Studying Acoustic Behavior of BFRP Laminated Composite in Dual-Chamber Muffler Application Using Deep Learning Algorithm, Materials, 15(22), 807, 2022, https://doi.org/10.3390/ma15228071.

[15] W.A. Altabey, S. A. Kouritem, M. I. Abouheaf, N. Nahas, Research in Image Processing for Pipeline Crack Detection Applications, IEEE conference, 2nd International Conference on Electrical, Computer, Communications and Mechatronics Engineering (ICECCME-2022), Maldives, 16-18 November 2022. https://doi.org/10.1109/ICECCME55909.2022.9988417.

[16] W.A. Altabey, The Damage Identification in Laminated Composite Plate under Fatigue Load through Wavelet Packet Energy Curvature Difference Method. Composites Part C: Open Access, 9, 100304, 2022, https://doi.org/10.1016/j.jcomc.2022.100304.

[17] W. A. Altabey, M. Noori, Z. Wu, M. A. Al-Moghazy, S. A. Kouritem, A deep-learning approach for predicting water absorption in composite pipes by extracting the material's dielectric features, Engineering Applications of Artificial Intelligence,121, 105963, 2023, https://doi.org/10.1016/j.engappai.2023.105963.

[18] A. Silik, M. Noori, W. A. Altabey, R. Ghiasi, Z. Wu, J. Dang, Evaluation of analytic wavelet parameters effet for data analyses in civil structural heath monitoring, International Conference on Structural Health Monitoring of Intelligent Infrastructure: Transferring Research into Practice, SHMII 2021, Volume 2021-June, 813–818, 2021.

[19] W.A. Altabey, S. A. Kouritem, M. I. Abouheaf, N. Nahas, A Deep Learning-Based Approach for Pipeline Cracks Monitoring, IEEE conference, 2nd International Conference on Electrical, Computer, Communications and Mechatronics Engineering (ICECCME-2022), Maldives, 16-18 November 2022, https://doi.org/10.1109/ICECCME55909.2022.9987998.

[20] H. Weixing, W. Ju, G. Dangui, W. Xiaodong, S. Gongzuo, X. Yan-liang, Z. Chuanyue, M. Noori, W.A. Altabey, Artificial intelligence Technique for Pavement Diseases Identification, ACM Digital Library, Proceedings of the 4th International Conference on Intelligent Science and Technology (ICIST '22), August 2022, 66–72, https://doi.org/10.1145/3568923.3570515.

[21] W. Hong, M. Noori, H. Jiang, Y. Liu, W. A. Altabey, Machine Vision-Based Structural Diagnosis Application, Lecture Notes in Civil Engineering, 292, 79–88, 2023, https://doi.org/10.1007/978-981-19-5783-3_6.

[22] A. Silik; M. Noori, R. Ghiasi; T. Wang; S. Kuok; N. S. D. Farhan; J. Dang; Z. Wu, W. A. Altabey, Dynamic wavelet neural network model for damage features extraction and patterns recognition, Civil Structural Health Monitoring, 2023, https://doi.org/10.1007/s13349-023-00683-8.

[23] T. Wang, H. Li, M. Noori, R. Ghiasi, S. Kuok, W. A. Altabey, Seismic response prediction of structures based on Runge-Kutta recurrent neural network with prior knowledge, Engineering Structures, 279, 115576, 2023, https://doi.org/10.1016/j.engstruct.2022.115576.

[24] H. Fathnejat, B. Ahmadi-Nedushan, S. Hosseininejad, M.Noori, W.A. Altabey, A data-driven structural damage identification approach using deep convolutional-attention-recurrent neural architecture under temperature variations, Engineering Structures, 276, 115311, 2023, https://doi.org/10.1016/j.engstruct.2022.115311.

[25] W.A. Altabey, M. Noori, Artificial-Intelligence-Based Methods for Structural Health Monitoring, Appl. Sci. 2022, 12(24), 12726. https://doi.org/10.3390/app122412726.

[26] Z. Li, M. Noori, C. Wan, B. Yu, B. Wang, W.A. Altabey, A Deep Learning-Based Approach for the Identification of a Multi-Parameter BWBN Model. Appl. Sci. 2022, 12, 9440. https://doi.org/10.3390/app12199440.

[27] P. J. Lee, H. Duan, M. S. Ghidaoui, B. Karney, Frequency domain analysis of pipe fluid transient behavior, Journal of Hydraulic Research, 51(6), 609-622, 2013.

[28] H. Duan , P. J. Lee , M. Ghidaoui, Y. Tung, Leak detection in complex series pipelines by using the system frequenc M. S. Ghidaoui y response method, Hydraulic Research, 49 (2), 213-221, 2011.

[29] W. Mpesha; S. L. Gassman; M. H. Chaudhry, Leak Detection in pipes by frequency response method, Hydraulic Engineering, 127 (2), 127-134, 2001.

[30] H. Duan; P. J. Lee; A. Kashima; J. Lu; M. S. Ghidaoui; Y. Tung, Extended Blockage Detection in Pipes Using the System Frequency Response, Analytical Analysis and Experimental Verification, Hydraulic Engineering, 139 (7), 2013.

COMPDYN 2023
9th ECCOMAS Thematic Conference on
Computational Methods in Structural Dynamics and Earthquake Engineering
M. J. A. Fritzsche, M. M. Rupp, S. R. Lorenzen, L. Hofmann, L. Birmele, J. Schneider
Athens, Greece, 12-14 June 2023

# INVERSE IDENTIFICATION OF CABLE FORCES USING ITS MODAL BEHAVIOR BY DIRECT AND NON-CONTACT VIBRATION MEASUREMENTS

**Max J. A. Fritzsche**[1], **Maximilian Michael Rupp**[1], **Steven R. Lorenzen**[1], **Lucia Hofmann**[1], **Lia Birmele**[1] **and Jens Schneider**[1]

[1] Technical University of Darmstadt, Institute of Structural Mechanics and Design (ISM+D)
Franziska-Braun-Straße 3, DE-64287 Darmstadt, Germany
{fritzsche,rupp,lorenzen,schneider}@ismd.tu-darmstadt.de
{lucia.hofmann,lia.birmele}@stud.tu-darmstadt.de

## Abstract

*Cables are essential in civil engineering for constructing slender, lightweight structures with large spans. To ensure serviceability and load-bearing capacity, a monitoring of the cable forces is necessary. Conventional, static methods are not suitable for systems with highly prestressed cables or large cable diameters, so dynamic measurements using the cable's vibration behavior offer an alternative. This study presents laboratory test results on inverse identification of cable forces using eigenmodes and the corresponding frequencies, comparing contact and non-contact dynamic measurement methods. Two methods for determining the cable force will be investigated within this study: (1) the linear theory of vibrating strings neglects internal sag and bending stiffness, and (2) an inverse identification of the cable force for a cable tensioned on both sides, accounting for bending stiffness. Contact based measurement with accelerometers can identify many eigenmodes and frequencies unambiguously and is suitable for simple systems like single span systems. In the conducted investigations, the non-contact measurement with microwave interferometers could only identify up to 4 natural frequencies.*
*The study also examines the influence of the free vibration length, which, in addition to the bending stiffness of the cable, the fork fitting and utilization, has a significant influence on the determined cable forces. The implications for using different fork fittings and cable cross-sections are discussed. This study offers valuable insights into the challenges and limitations of cable force identification and highlights the importance of choosing the appropriate measurement method based on the design of the cable structure.*

**Keywords:** dynamic measurements, inverse identification, free vibration length, linear theory of vibrating strings, experimental determination of natural frequencies

# 1 INTRODUCTION

Cables have numerous applications in the construction industry, including as bracing, stiffening elements, and suspension and tensioning cables for suspension bridges and facades. Prestressed cables are often used to avoid failure or too large deformation under compressive stress from external loads. Long-term environmental influences and fatigue can lead to a reduction in prestressing forces, which in turn results in greater deformation that compromises the integrity of the structures or limits their serviceability. Therefore, preventive inspections and periodic checks of cable structures are necessary to detect and address maintenance issues. While permanent monitoring of prestressing forces using installed measuring equipment is an option for some structures, it may not be economically feasible for complete equipment on a cable net facade. Instead, this paper focuses on measurement methods for structure inspections that do not require cables with pre-installed measurement technology, such as static and dynamic measuring methods. Integrated sensors like LoadScan® [1] from Pfeifer Systems GmbH, which measure cable forces with a force measuring unit embedded in clevis joints, will not be considered further.

## 1.1 Static measurement methods

A conventional method for determining cable forces is through static measurements using a tensioning device. This method involves displacing the tensioning cable at two points relative to a centrally located third point, and the cable force can be determined via the angle or transverse load required to produce a defined sag [2]. Based on Figure 1 and equation (1), the unknown cable force $N$ can be calculated using the angle $\alpha$ and sag $s$. The cable is then tensioned at two points.

$$N = \frac{s}{2} \cdot \frac{1}{\sin \alpha} \tag{1}$$

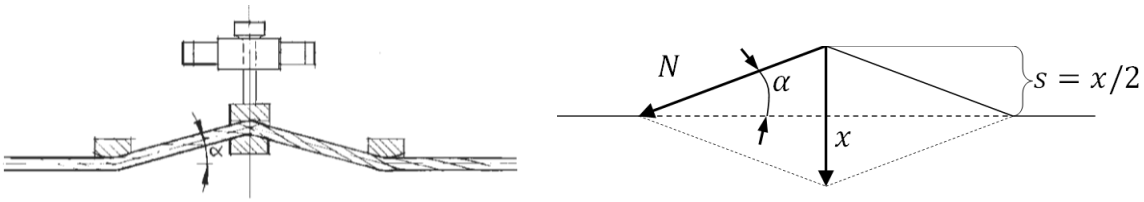


Figure 1: Principle application of a static cable force gauge [2] with illustration of the attachment of the device (left) and evaluation of the cable force according to the cable-tensioning method (right).

A commonly used cable tension measuring device is the PIAB RTM 20 D, manufactured by PIAB Kraftmesstechnik [2]. This device is suitable for cable cross-sections ranging from 6-38 mm diameter, calibrated for four cable ranges using a minicomputer, and provides an accuracy in cable force determination of 2-6% depending on the cable construction. Another widespread device is the CableBull® cable tension sensor from Honigmann [3]. It can be used for material diameters ranging from 1-46 mm but requires one of up to five series with different measuring distances depending on the measuring task. While the manufacturer does not specify a defined accuracy, they claim to have "high accuracy".

## 1.2 Dynamic measurement methods

An alternative method for measuring dynamic cable force is by determining the cable's natural frequencies. This can be achieved through direct and non-contact vibration measurements, where the linear theory of the vibrating string is utilized to estimate the cable force [4]. However, neglecting the bending stiffness of the cable can lead to inaccurate results, especially for larger

diameters or small span-to-diameter ratios. To account for the bending stiffness, methods such as Morse's approximate solution [5] and Geier and Petz's method [6] have been developed.

To determine the natural frequencies, displacement, velocity or acceleration signals of the cables can be used. Accelerometers are often used due to their versatility, reliability, and low costs, although other sensors such as strain gauges, gyroscopes, or force sensors may be more suitable depending on the application. Direct dynamic measurements on the cable are challenging due to the high effort required to carry out the measurement and ensure accessibility and power supply for wired sensors.

Non-contact measurement methods such as photogrammetry [7], laser scanning [8], and microwave technology [9] are becoming increasingly popular for structural monitoring. However, there are also disadvantages associated with these systems, such as higher signal-to-noise ratio, lower sensitivity, and limited sampling rates for photogrammetry and laser scanning. Consequently, determining higher-order natural frequencies, including harmonics, is challenging during system identification. Our experimental results align with observations from [10] that indicate the first natural frequency can be determined relatively unambiguously, but usually no more than 2-3 harmonics can be identified from the measured signals. Additionally, the evaluation range in this measurement method is carried out in evaluation cells, providing relative displacements in the entire radial resolution cell. The MetaSensing FastGBSAR microwave interferometer used in our study has an evaluation range of approximately 0.75m, which also corresponds to the maximum bandwidth of the waves with an accuracy of ±0.01 mm [11].

## 2 METHODS

In this section, we will explain the established methods for determining the cable forces based on frequency, with a focus on those applicable to single cables. We will first present the linear theory of the vibrating string, followed by Morse's approximate solution, which considers the bending stiffness of the cable and forms the basis of Geier and Petz's third method. Geier and Petz's method requires at least two natural frequencies to solve the system of linear equations with the two variables, namely the idealized first natural frequency $f_{1s}$ and the related stiffness $\xi$. Since additional natural frequencies can often be identified, the excess ones can be utilized for optimization using a gradient method [12]. We will not delve into the equations that account for discontinuities in the form of local single masses, as the scope of our research is restricted to single and multi-span cable systems with a constant mass occupancy. Lastly, we investigate the methods that consider the incorporation of individual masses. [13] provides an approach without, and [14] an approach including the consideration of bending stiffness.

### 2.1 Methods for frequency-based identification of cable forces

#### 2.1.1. Linear theory of the vibrating string

The linear theory of the vibrating string provides the most straightforward approach for determining cable forces. This theory assumes an ideal cable with no bending stiffness that is tightly tensioned. A detailed theory, which accounts for vibrations inside and outside the cable's sheaves, can be found in [4]. According to this theory, Equation (2) can be used to determine the unknown natural frequency $f_n$ as a function of the cable force, where $n$ is the order of the natural frequency $f_n$, $l$ is the span of the cable, and $\mu$ is the mass occupancy.

$$f_n = \frac{\omega}{2 \cdot \pi} = \frac{n}{2} \cdot \sqrt{\frac{N}{\mu \cdot l^2}} \quad with\ n = 1,2,\ldots \tag{2}$$

### 2.1.2. Method according to Geier and Petz

In [6], several studies on cable-stayed bridges using dynamic measurements of natural frequencies to investigate cable forces concluded that the previously assumed linear relationship between the natural frequencies and their order is only a sufficient approximation for the first 4-5 natural frequencies. These investigations also considered the influence of bending stiffness and bearing conditions of the cable, which can significantly affect the identification of cable forces based on measured natural frequencies. Therefore, Geier modified the linear relationship between the idealized fundamental frequency $f_{1s}$ and the $n$-th harmonic $f_{ns}$ as a function of cable normal force $N$ and mass occupancy $\mu$, described by equation (3), by developing an approximate solution based on the approximate solution according to Morse [6] for a beam clamped on both sides.

$$f_{ns} = \frac{n}{2 \cdot l} \cdot \sqrt{\frac{N}{\mu}} \tag{3}$$

By additionally introducing the associated stiffness $\xi$ according to equation (4) and inserting it into the Morse nutrient solution, equation (3) simplifies to equation (5):

$$\xi = L \cdot \sqrt{\frac{N}{EI}} \tag{4}$$

$$f_n = n \cdot f_{1s} \cdot \left[1 + \frac{2}{\xi} + \left(4 + \frac{n^2 \cdot \pi^2}{2}\right) \cdot \frac{1}{\xi^2}\right] \tag{5}$$

With the two unknowns $f_{1s}$ and $\xi$ there is a pair of values that can be solved from a number of at least two measured natural frequencies $f_n$ and their corresponding order $n$. The solution can be done with a gradient method like the Gauss-Newton method [12]. In [17], the method was applied to numerous inclined cables and concluded that the method can reliably determine the cable force with an accuracy of ± 1% when solved with usually 10 to 15 identified natural frequencies. In [6], the method was applied with 10 natural frequencies at a fundamental frequency of the cables of about 3 Hz. It was confirmed that in addition to the natural frequency, the bending stiffness, the bearing conditions and the cable sag must also be taken into account in order to be able to achieve an accuracy of ± 1%.

Since own investigations for smaller spans especially for measurements with the microwave interferometer used in this study often could not identify more than 5 natural frequencies unambiguously, the Levenberg-Marquardt method as explained in [18] was applied as an alternative to the Gauss-Newton method, which due to its robustness requires less natural frequencies to solve in order to achieve the same accuracy in the inverse force identification(cf. Section 3.3).

### 2.1.3. Approaches with additional consideration of single masses

The approach for additional consideration of single masses of a wire according to [13] is given in equation (6) and the approach with consideration of bending stiffness given in [14] is shown in equation (7), where $m_i$ defines the mass and $x_i$ the Position of all single masses $i$ across the cable.

$$N = \frac{2 \cdot l}{n^2 \cdot \pi^2} \cdot \left[4 \cdot \pi^2 \cdot f_n^2 \cdot \left(\frac{\mu \cdot l}{2} + \sum m_i \cdot \sin^2\left(\frac{n \cdot \pi \cdot x_i}{l}\right)\right) - \frac{n^4 \cdot \pi^4}{2 \cdot l^3} \cdot EI\right] \tag{6}$$

$$N = 2 \cdot \pi^2 \cdot f_1^2 \cdot \left(2 \cdot \mu \cdot \frac{l^2}{\pi^2} + m \cdot \sum \sqrt{x_i \cdot (l - x_i)}\right) \tag{7}$$

## 2.2 Measurements

### 2.2.1. Experimental setup

Two dynamic measurement methods were conducted to test the applicability of cable force identification on the test setup shown in Figure 3. The response of an open spiral cable was measured by a microwave interferometer and seismic acceleration sensors that were compared to a load cell as a reference value. The cable was horizontally tensioned with solid steel brackets bolted to an underlying steel beam. The cable is of PG20 type from Pfeifer with a nominal diameter of 14.1 mm and a tensile force of 109 kN [19].

The cable is secured on both ends using fork fitting type 980 and bolt connections with bending-resistant vane plates that are welded onto head plates. The fork cable ends are arranged to allow for free oscillation from top to bottom, which is where most of the excitation and measurements occur. A load cell is attached to the right support between the steel angle as bearing and the head plate to provide a reference value for the cable forces identified via the natural frequencies (cf. Figure 3). To prevent the increase in free vibration length caused by not fixing the head plate to the steel angle, steel profiles were bolted to the substrate and a clamp was used to press against the substructure from above. The background is covered with paperboard to prevent the interference of moving objects with the evaluation of the relative displacement of the microwave interferometer.

The system response is measured using 8 3D acceleration sensors of type TLD356A17 from PCB Piezotronics, with a measuring range of ±10 g and a sensitivity of 500 mV/g [20]. Figure 4 shows the positions of the accelerometers (labeled 1 to 8) and also indicates the locations of the trihedral (square) radar reflectors labeled A to D that were mounted during some measurements. These radar reflectors have orthogonal surfaces and improve the measurement signals of the microwave interferometer compared to measuring the displacement of the cable's pure cross-section [21]. The self-made radar reflectors were 3D printed and covered with stainless steel blanks. Two sizes of radar reflectors were used to investigate the influence of their individual masses (227 g for the small and 290 g for the large) and the reflector edge lengths (6.5 cm and 9.5 cm) on the cable vibration and measurement signals of the microwave interferometer. Figure 5 shows the smaller reflectors arranged eccentrically in relation to the cable axis in the vertical direction on the left, and the larger reflectors arranged concentrically on the right. The orientation of the microwave interferometer in relation to the point of origin (fork joint, left support) is shown in the images in Figure 6 and with the specified coordinates in Table 1. Figure 7 shows an example of the position of the microwave interferometer in plain view with representation of the resolution cells.

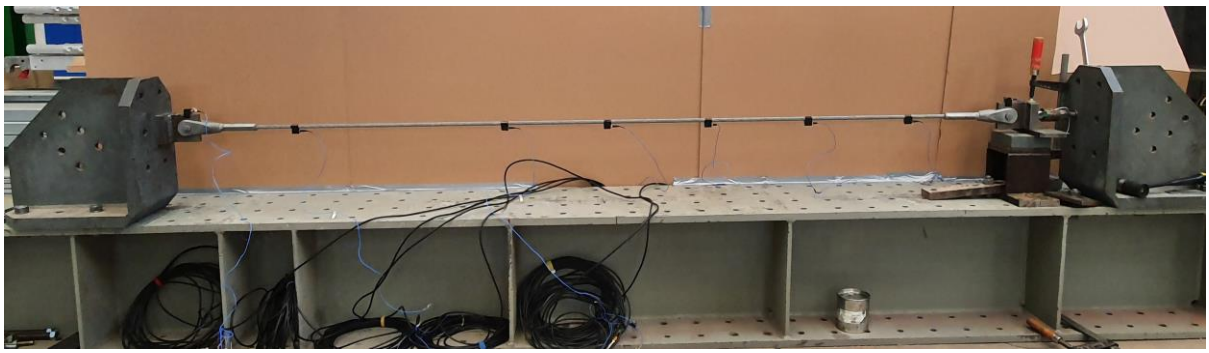

Figure 2: Side view of the test setup.

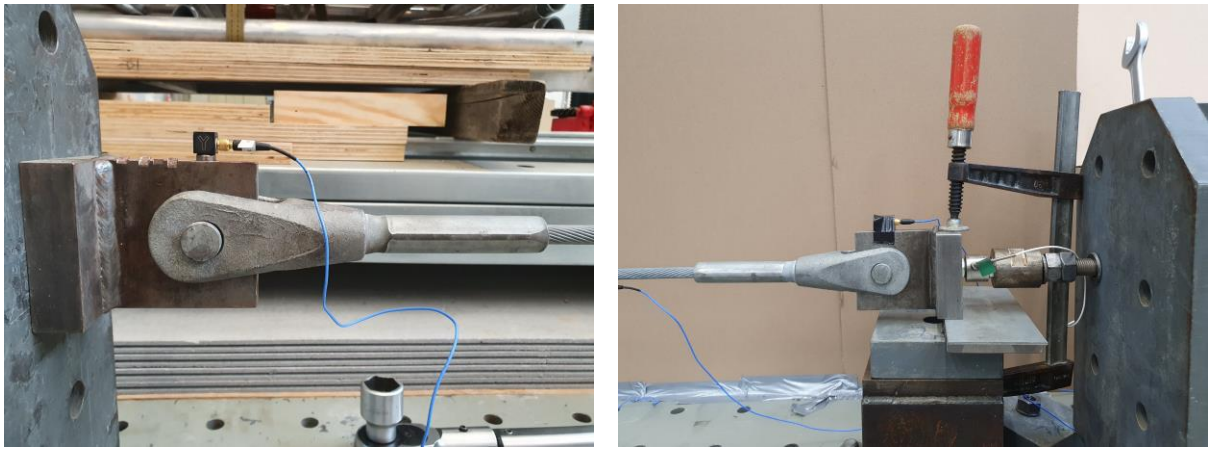

Figure 3: Details of the left and right support.

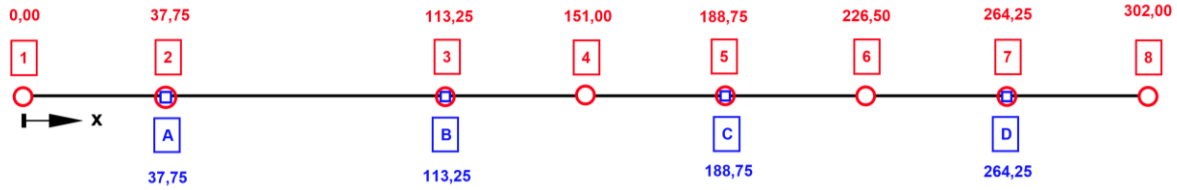


Figure 4: Position of accelerometers {1:8} and optional reflectors {A:D} in cm in relation to the joint in the fork fitting on the left support.



Figure 5: Illustration of the experimental setup with the microwave interferometer positioned at position 3 according to Table 1 with centrally arranged reflectors (left: small reflectors, eccentric; center: large reflectors, centric; right: illustration of experimental setup with 4 reflectors).

| Position | X [m] | Y [m] | Z [m] | Inclination [°] |
|---|---|---|---|---|
| 1 | -1.32 | -0.95 | 0.00 | ≈ 0 |
| 2 | -1.26 | -0.92 | 0.60 | ≈ 15 |
| 3 | -1.13 | 0.00 | 0.59 | ≈ 13 |

Table 1: Coordinates and inclination of the microwave interferometer with respect to the cable axis measured from the left support (clevis pin).



Figure 6: Illustration of the experimental setup with the microwave interferometer positioned according to the orientation given in Table 1 (left: Pos. 1; center: Pos. 2; right: Pos. 3).

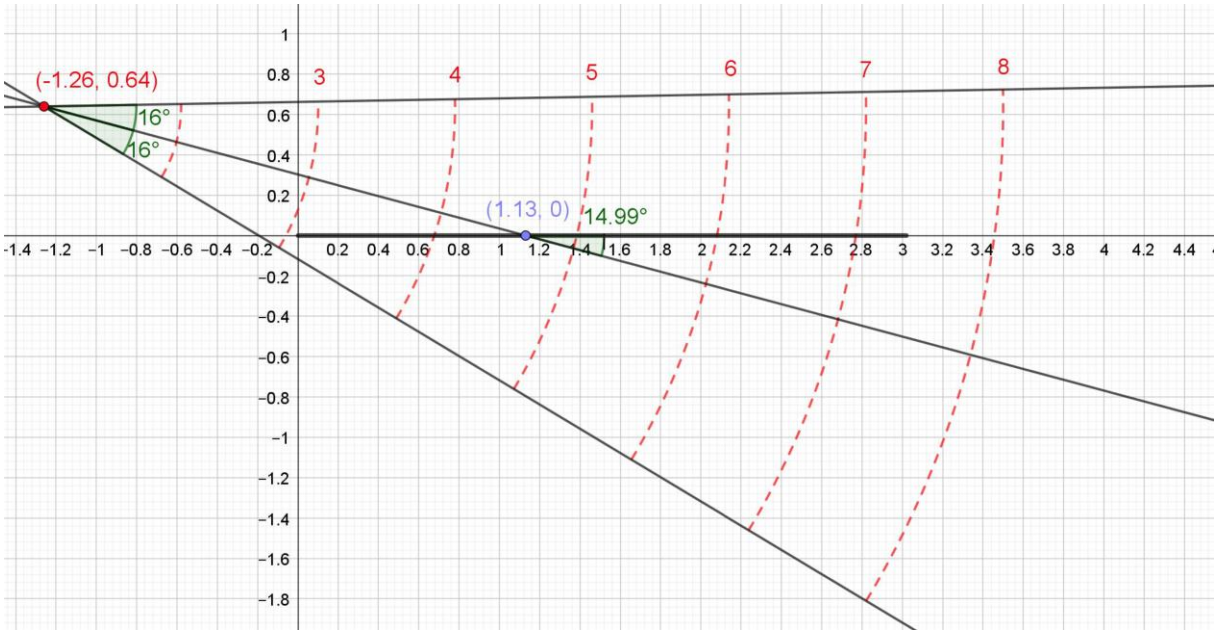


Figure 7: View of position 2 of the microwave interferometer showing the resolution cells $\boldsymbol{i}$ = {1:8}.

### 2.2.2. Experimental procedure

The experiments were conducted under varying conditions with different test setups involving the use of small and large radar reflectors. Table 2 displays the varied parameters that were employed in the measurement protocol, resulting in a total of 108 recordings with different permutations. For each of the three positions of the microwave interferometer measurements, the target tension forces of 10, 20, 30, and 40 kN were applied, which correspond to utilization rates ranging from 9.2 to 36.7 % concerning the limiting tension force of 109 kN. Higher utilization rates were not possible due to the operating limit of the load cell, which allows a maximum load of 45 kN.

The measurement signal for each of the utilization rates was obtained once without and with small and large radar reflectors, and differentiated between vertical, horizontal, and mixed excitation using an impulse hammer on the cable.

| Position | Force in kN | Reflector | Excitation |
|---|---|---|---|
| ➢ 1 | ➢ 10 ($\eta = 0.092$) | ➢ none | ➢ vertical |
| ➢ 2 | ➢ 20 ($\eta = 0.183$) | ➢ small one | ➢ horizontal |
| ➢ 3 | ➢ 30 ($\eta = 0.275$) | ➢ big one | ➢ mixed |
| | ➢ 40 ($\eta = 0.367$) | | |

Table 2: Variable parameters in microwave interferometer measurements.

The acceleration sensors, impulse hammer for forced excitation, and the preload force of the force sensor were measured time-synchronously using a QuantumX MX840B measuring amplifier from Hottinger Brüel & Kjaer GmbH at a sampling rate of 4,800 Hz. The microwave interferometer FastGBSAR from MetaSensing has a resolution cell size of 0.75 m for the bandwidth of approximately 200 MHz, and a sampling rate of 3,787.8788 Hz specified in the program, which results from the wave properties and device configurations. Since the two measuring systems are not synchronized with each other in terms of time, each measurement is first initiated at the measuring amplifier via the Catman® software with a duration of 210 s. Then, the measurement is conducted on a second computer using the Catman® software.

Subsequently, a 180 s measurement is initiated on a second computer using the FastGBSAR controller software, and excitation is applied to record the excitation in both measuring systems over a period of 3 minutes. To achieve a defined pre-tensioning force without effort at the beginning of each measurement, the bar, which is locked with a lock nut on the back of the steel angle, is tightened before each measurement. Subsequently, it was waited until the cable force adjusted to an almost constant value. Then, if necessary, the cable, which is increasingly tensioned flatter with increasing pre-tension, is supported by filler plates and tensioned with the screw clamp. The small normal force from the cable's dead weight at the beginning of the measurement is disregarded due to its short cable length.

# 3 RESULTS

## 3.1 Raw measurement data

Experimental results are presented in Figure 8, which shows an example of the measured preload force of the force sensor (left) and the measured acceleration for each sensor (right). In this example, acceleration data of sensor no. 6 with vertical orientation is shown for a measurement with 10 kN preload force and vertical excitation without reflectors. The preload force curve remains nearly constant over time. The time point of the non-periodic force excitation with an impulse hammer is easily recognizable from the large deflection and subsequent free vibration of the cable in the sensor signals. The signals are unambiguous and can be analyzed to study the dynamic system response by filtering the relevant frequency ranges.

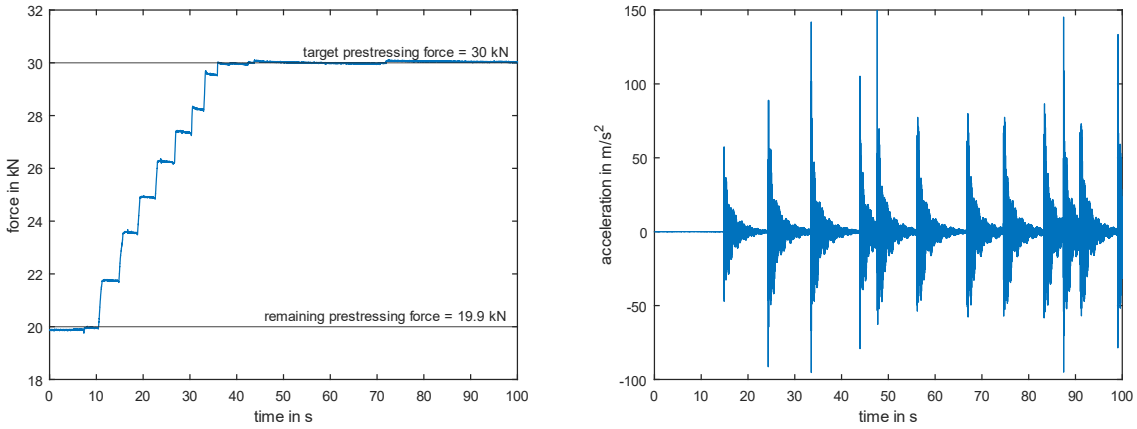


Figure 8: Measurement res ult of the load cell when prestressing force from 30 to 40 kN (left) and representation of the acceleration sensor data from sensor 6 in the local Z direction (right).

The microwave interferometer results were inconclusive. Resolution cells 3-5 did not yield useful measurement results due to low signal noise ratios (SNR). Therefore, Figure 9 only shows the relative displacements for cells 6 - 8 recorded by the measuring instrument. Since resolution cells 6 and 8 displayed jumps with subsequent plateaus and could not be corrected through post-processing, they were not suitable for further evaluation. Hence, Figure 10 shows only the measured displacement values for resolution cell 7, which appears plausible despite the very high noise level.

In the following, we will focus solely on the evaluation of the results obtained from evaluation cell 7, based on the same observations and measurements of other system configurations and prestressing forces. Despite the displacement amplitude being less than 1 mm and the uncertainty regarding whether it was accurate or caused by a defect in the measuring device, we

will proceed with our analysis, since the subsequent analysis of the measurement results will focus on the frequency analysis of the signals, rather than the amplitude of the displacement.

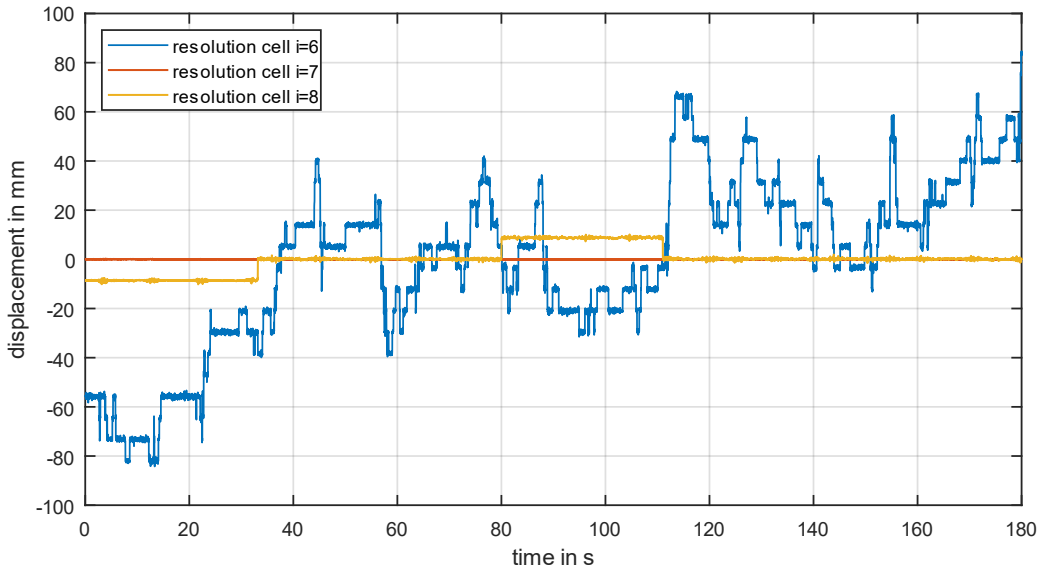


Figure 9: Time-displacement curves for resolution cells 6 to 8 for a measurement without reflector.

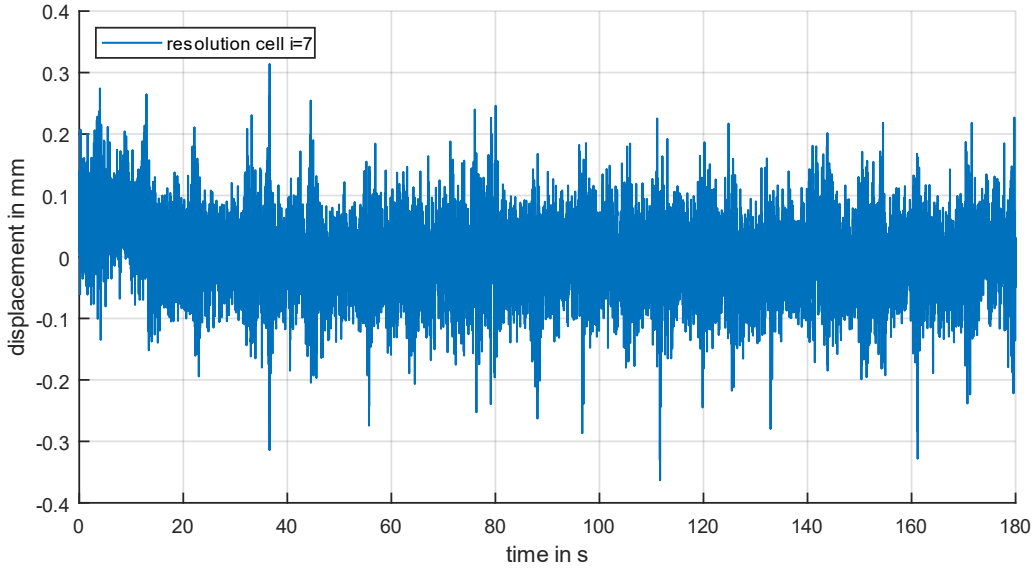


Figure 10: Time-displacement plot for resolution cells 7 without reflector.

## 3.2 Frequency analysis of the data of both measuring systems

In order to analyze the system response of the measured acceleration sensors and microwave interferometer displacements, a Fast Fourier Transformation (FFT) is applied to the raw data. The resulting frequency spectrum is used to identify the natural frequencies of the system response, by locating the peaks in the spectrum using the fft() function in Matlab®. While the measurement signals of the acceleration sensors exhibit numerous natural frequencies, the microwave interferometer signal is often characterized by a high level of noise, making it challenging to identify any frequencies beyond the fundamental one. To improve peak clarity in the FFT, the signal from the microwave interferometer is divided into eight subintervals. A FFT is

then performed for each subinterval to reduce noise, and the first natural frequency is identified by detecting the local extreme value. The phase angle of the (complex) value of the FFT belonging to the first natural frequency is then calculated to enable synchronization of the partial FFTs over the first natural frequencies identified in all partial FFTs. The resulting averaged FFTs, depicted in Figure 11 and Figure 12, reveal up to four natural frequencies. Since a narrow main lobe of the signal is desired, no explicit windowing (rectangular window) is utilized. The leakage effect due to the relatively short observation period of the subintervals is compensated for by averaging the individual FFTs.

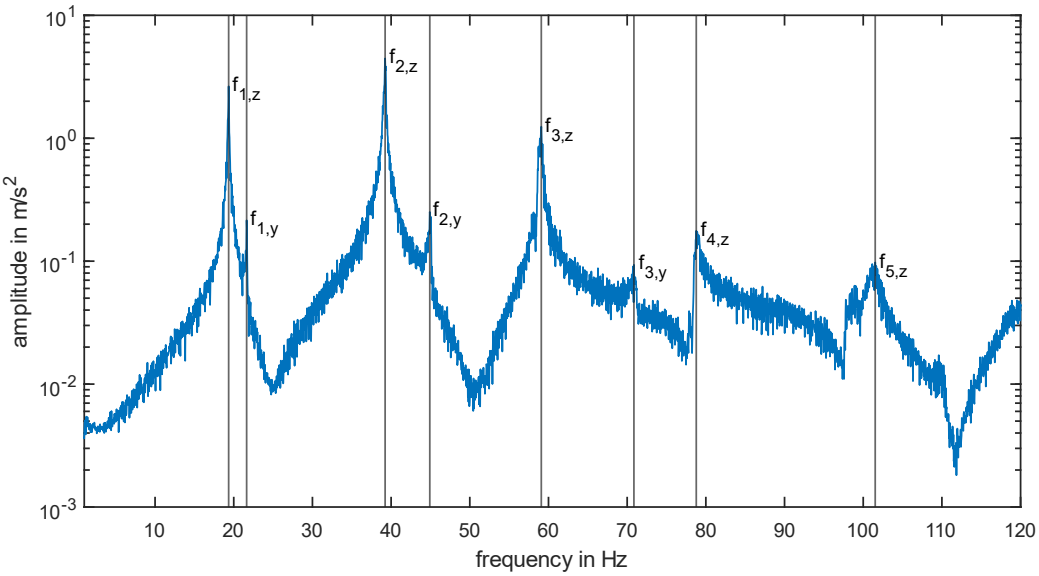


Figure 11: FFT of 8 time intervals for the acceleration data of sensor 6.

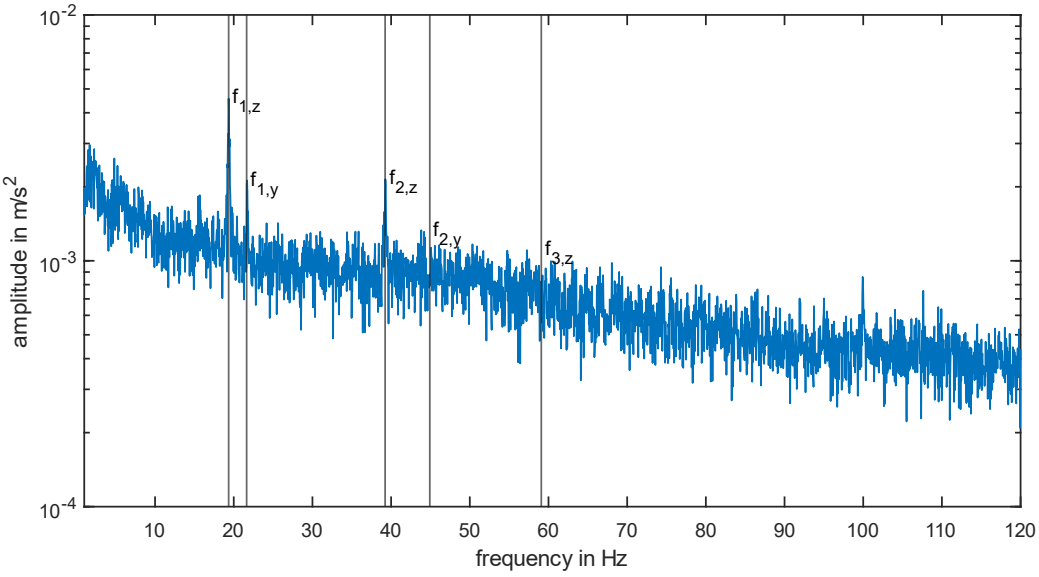


Figure 12: FFT of 8 time intervals for the displacement data from resolution cell 7 for a measurement without radar reflectors.

In brief, the analysis of the frequency of both measurement signals indicates that identification of the fundamental frequency is feasible using FFT for both systems. The acceleration signals exhibit numerous harmonics that can be readily identified without further post-

processing, enabling optimization of the cable force identification through gradient methods. However, the frequency spectra of the microwave interferometer displacements exhibit a significantly higher noise level, making it challenging to identify harmonics without subdividing and analyzing individual partial intervals and subsequently superimposing the partial FFTs. Even with this extensive post-processing of the measured data, typically no more than 2 to 4 natural frequencies can be identified, limiting the optimization of force identification using gradient methods.

### 3.3 Inverse cable force determination

In this section, the results for cable force identification via natural frequencies are compared with the reference values of the load cell. Not the absolute values, but the relative deviation $\Delta N$ of the identified cable force $N_{\mathrm{cal}}$ to the reference value of the load cell $N_{\mathrm{ref}}$ are determined.

$$\Delta N = \frac{(N_{\mathrm{ref}} - N_{\mathrm{cal}})}{N_{\mathrm{ref}}} \cdot 100\ \% \tag{8}$$

The frequency analysis of the microwave interferometer data identified only the first four natural frequencies. The aim of this study is to investigate the suitability of both methods - direct measurement with acceleration sensors and non-contact measurement using a microwave interferometer - for determining the inverse cable force. Therefore, we will only use the first four natural frequencies in the solution approaches below.

In addition to the identification according to the linear theory of the vibrating string using the fundamental frequency, the influence of the optimization based on including the first four harmonics is also considered using the Levenberg-Marquardt method. For the measurements with radar reflectors, the approaches considering additional concentrated loads according to section 2.1.3 with additional consideration of the bending stiffness are correctly used.

The results in in Figure 13 show that all approaches yield deviations of less than 20 % compared to the reference value of the load cell, with deviations becoming smaller with increasing utilization. The method according to Geier and Petz (cf. 2.1.2) shows the lowest error with a maximum deviation of 10 %, with deviations decreasing rapidly with increasing utilization or pre-stress force, amounting to only about 5 % at the highest utilization of 36.7 %. The results from the back calculation considering concentrated loads due to the radar reflectors show good agreement with the approximation from [14]. For the linear theory of the vibrating string, no improvement can be derived from the consideration of several natural frequencies compared to the calculation using only the fundamental frequency. Therefore, a calculation based on one frequency is sufficient if this approach is followed. Finally, it is investigated to what extent a modified system length defined as effective cable length $l_{\mathrm{eff}}$ can be used to achieve smaller deviations in identified forces, excluding the measurements with radar reflectors. A compensation line function is determined as a function of the prestressing force $N$ (cf. equation (9)) to determine the effective cable length $l_{\mathrm{eff}}$.

Figure 14 shows the measurement results without reflectors compared to the system length $l$ for comparison of the results adjusted with $l$. It can be seen that the deviations from the reference value can be significantly reduced and are below 5 % regardless of the process.

$$l_{eff} = \frac{N}{3kN/cm} + 0.92 \cdot l \tag{9}$$

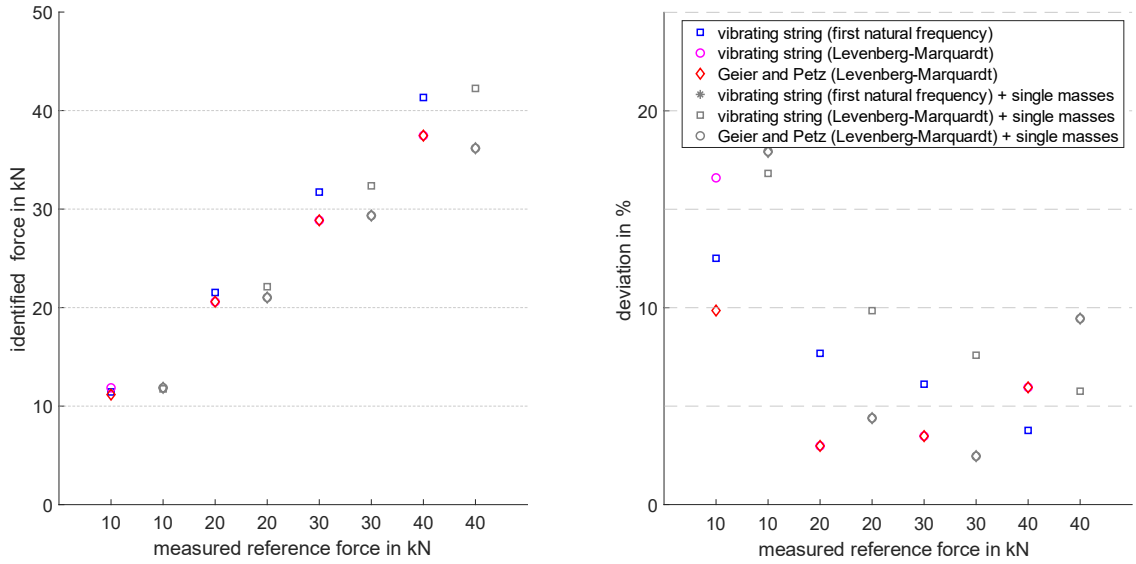


Figure 13: Identified forces and deviations for measurements considering the individual masses from the reflectors for the measurements from position 3.

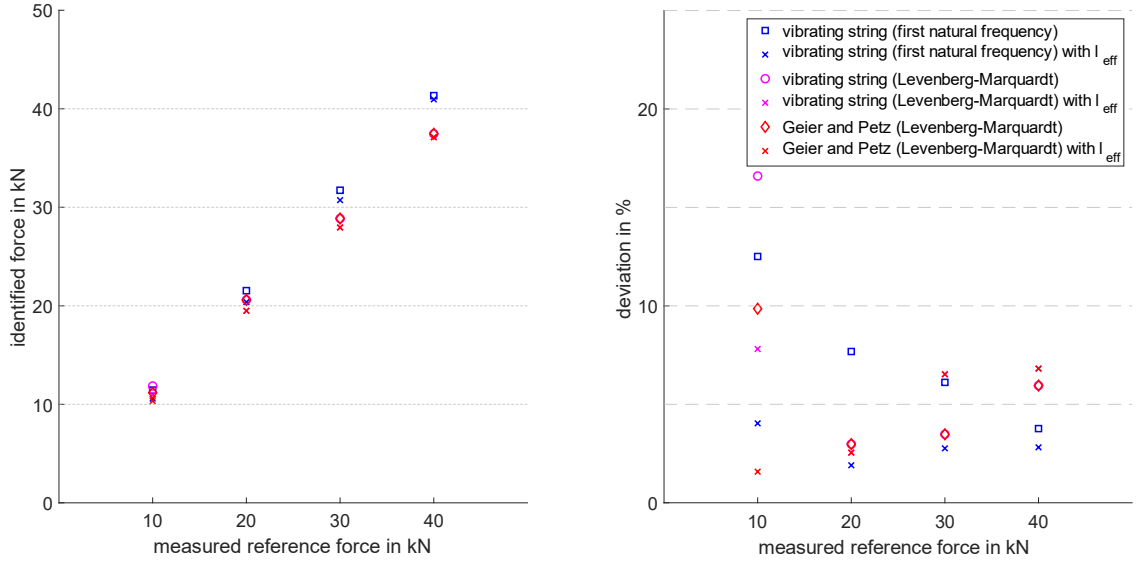


Figure 14: Identified forces and deviations with experimentally determined effective oscillation length $\boldsymbol{l_{eff}}$ for position 3 for measurements without reflectors.

Finally, we utilized the effective cable length as the system length and applied the linear theory of the oscillating string to identify the cable forces based on the first natural frequency. This frequency was determined using both measurement methods. Figure 15 shows the results obtained for the four utilization rates and all measurements without the radar reflector. The outcomes reveal an average deviation of less than 5%, which was further reduced to less than 3% with higher and more realistic utilization rates exceeding 20%. However, the largest standard deviation, observed in the case of the highest utilization with a pre-stressing force of 40kN, was 0.92%.

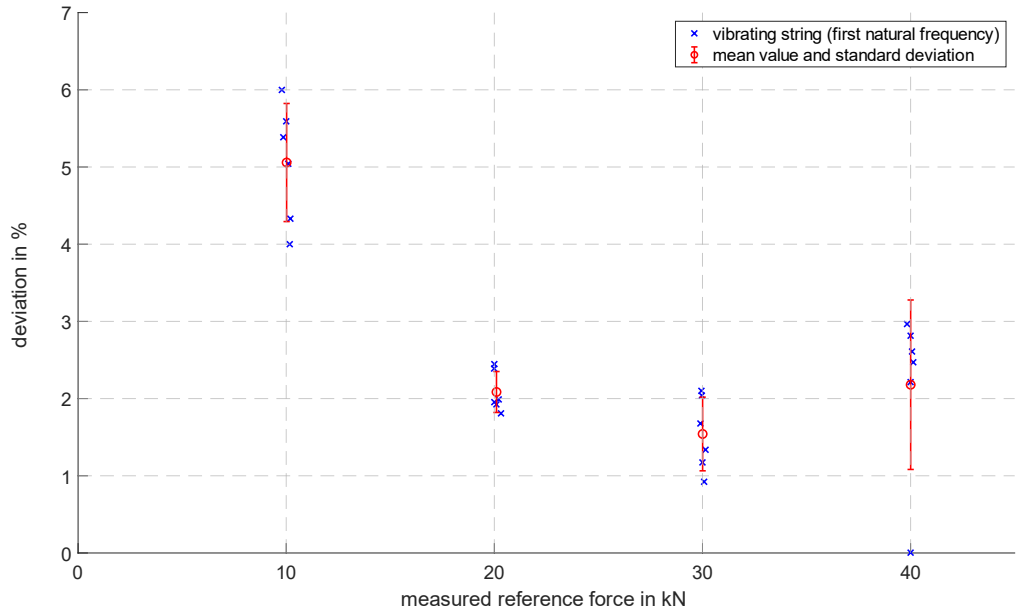


Figure 15: Deviations of the identified cable forces from the first natural frequency according to string theory considering a reduced oscillation length for measurements without reflectors.

## 4 CONCLUSION

In this investigation, two measurement concepts were evaluated for identifying the natural frequencies of a horizontally tensioned single-span cable. The first approach used acceleration sensors, while the second utilized ground-based microwave interferometers for deformation monitoring. The identified natural frequencies were then used to investigate the validity of equations available in the literature for frequency-based identification of the cable forces.

The use of acceleration sensors was found to be effective for system identification and could identify a large number of harmonics. However, difficulties with accessibility and interaction of secondary supporting or facade elements could arise in real structures. On the other hand, using the microwave interferometer for measurement was much simpler in terms of device placement. However, documenting the position of the resolution cells after the measurement required significant effort to ensure accurate orientation with respect to the measurement object. Strongly oscillating substructures could also have an influence on the measuring results, making them useless. In terms of accuracy, no significant difference was found between the two measuring systems, and both were suitable to identify the fundamental frequency of a cable. Despite the ease of using the microwave interferometer for measurement, documenting and analysing the friction data required a significantly more complex effort. Therefore, the relatively lower additional cost of installing acceleration sensors, even in positions that may require elevating platforms for access, seems justifiable compared to the documentation and evaluation efforts associated with the microwave interferometer.

The results of the cable force identification showed deviations from the reference value of the load cell between 10-20%, which became smaller with increasing utilization of the respective prestressing. Modifying the system length to the effective cable length of the system reduced the deviation to less than 5% using the linear theory of the vibrating string with fundamental frequency approach. However, investigations on other cable cross sections, spans and utilization rates showed that this approach is not generally valid and varies for each system configuration.

To summarize the findings regarding cable force identification, while modifying the effective cable length can improve accuracy, this approach is not universally applicable and varies depending on the specific cable configuration. Therefore, further investigations are necessary to account for influences such as bending stiffness, span length, prestressing force, and cable end formation. Additionally, the use of a microwave interferometer is not suitable for measuring small cable cross-sections and systems with adjoining substructures, unlike for cable-stayed bridges.

## REFERENCES

[1] "Permanent monitoring Temporäre Lastkontrolle Permanente Überwachung Accuracy Genauigkeit Universeller Einsatz." PFEIFER Seil- und Hebetechnik GmbH, Memmingen, p. 2, 2023. [Online]. Available: https://fabritecstructures.com/wp-content/uploads/2020/06/2020-Loadscan-brochure.pdf

[2] "PIAB RTM 20 D mit Beschreibung," vol. 1, no. 12. Matthias Nier PIAB, Haldensleben, pp. 0–12. [Online]. Available: http://www.piab-deutschland.de/wp-content/uploads/brosch/RTM_Bedienungsanleitung.pdf

[3] "Honigmann Industrielle Elektronik GmbH - Seilspannungssensor CableBull®.pdf." Honigmann GmbH, Gevelsberg, p. 4, 2023. [Online]. Available: https://honigmann.com/i437/Seilkraftmesser-Seilspannungsmesser-Seilspannungsmessgerät-CableBull.html?lang=1

[4] H. M. Irvine and T. K. Caughey, "The linear theory of free vibrations of a suspended cable," *Proc. R. Soc. London. A. Math. Phys. Sci.*, vol. 341, no. 1626, pp. 299–315, 1974, doi: 10.1098/rspa.1974.0189.

[5] P. M. Morse and K. U. Ingard, *Theoretical acoustics*. Princeton university press, 1986.

[6] R. Geier and J. Petz, "Kraftbestimmung in Schrägseilen durch dynamische Messungen," *Beton- und Stahlbetonbau*, vol. 99, no. 12, pp. 985–991, 2004, doi: 10.1002/best.200490285.

[7] D. Erdenebat and D. Waldmann, "Application of the DAD method for damage localisation on an existing bridge structure using close-range UAV photogrammetry," *Eng. Struct.*, vol. 218, no. March, p. 110727, 2020, doi: 10.1016/j.engstruct.2020.110727.

[8] F. Schill and A. Eichhorn, "Deformation Monitoring of Railway Bridges with a Profile Laser Scanner," *ZfV-Zeitschrift für Geodäsie, Geoinf. und Landmanagement*, vol. 2, pp. 109–118, 2019, doi: 10.12902/zfv-0248-2018.

[9] A. Firus, J. Schneider, M. Becker, J. J. Pullamthara, and G. Grunert, "Microwave interferometry measurements for railway-specific applications," *COMPDYN 2017 - Proc. 6th Int. Conf. Comput. Methods Struct. Dyn. Earthq. Eng.*, vol. 2, no. January, pp. 2705–2718, 2017, doi: 10.7712/120117.5600.17334.

[10] W. Zhao, G. Zhang, and J. Zhang, "Cable force estimation of a long-span cable-stayed bridge with microwave interferometric radar," *Comput. Civ. Infrastruct. Eng.*, vol. 35, no. 12, pp. 1419–1433, 2020, doi: 10.1111/mice.12557.

[11] "FASTGBSAR FAST Ground-Based Synthetic Aperture Radar FastGBSAR is a family of Ku-band ground based radars for deformation monitoring designed to work

FastGBSAR-S." MetaSensing BV, Noordwijk (Netherlands), p. 2, 2017. [Online]. Available: https://metasensing.com/wp-content/uploads/2022/09/MetaSensing-FastGBSAR-general.pdf

[12] M. Stadler, E. Penka, and K. Zilch, "Ermittlung der freien Schwingungslänge zur Bestimmung der Vorspannkraft externer Bandspannglieder durch dynamische Messungen," *Bauingenieur*, vol. 1, no. 82, 2007, [Online]. Available: https://structurae.net/en/literature/journal-article/ermittlung-der-freien-schwingungslange-zur-bestimmung-der-vorspannkraft-externer-bandspannglieder-durch-dynamische-messungen

[13] U. Kuhlmann, "Bauen mit Seilen," *Stahlbau Kal.*, pp. 689–755, 2000.

[14] R. Kempter, *Längskraftmessung von Zugstäben durch Messung der Eigenfrequenz*. München: Hochschule München, 2009.

[15] F. Lottersberger, *Untersuchung einer schienengebundenen Seilbahnfahrt*. Graz (Österreich): Technische Universität Graz, 2010.

[16] M. Schlaich, A. Bögle, and A. Bleicher, *Brückenbau II - Seile*. Berlin: Technische Universität Berlin, 2011.

[17] R. Geier, *Brückendynamik - Schwingungsuntersuchungen von Schrägseilen*. Norderstedt: BoD – Books on Demand, 2004.

[18] W. Dahmen, *Numerik für Ingenieure und Naturwissenschaftler*. 2006. doi: 10.1007/3-540-29883-5.

[19] P. S. Hebetechnik, "PFEIFER-Zugglieder." PFEIFER Seil- und Hebetechnik GmbH, Memmingen, 2015. [Online]. Available: https://www.pfeifer.info/out/assets/PFEIFER_TENSION-MEMBERS_BROCHURE_EN.PDF

[20] P. C. B. Piezotronics, "Model 352C04 General purpose , ceramic shear ICP ® accel ., 10 mV / g , 0 . 5 to 10k Hz , 10-32 Installation and Operating Manual," 2007.

[21] S. Rödelsperger, *Real-time Processing of Ground Based Synthetic Aperture Radar (GB-SAR) Measurements*. 2011. [Online]. Available: http://tuprints.ulb.tu-darmstadt.de/id/eprint/2755

COMPDYN 2023
9th ECCOMAS Thematic Conference on
Computational Methods in Structural Dynamics and Earthquake Engineering
M. Papadrakakis, M. Fragiadakis (eds.)
Athens, Greece, 12-–14 June 2023

# STRUCTURAL DEFORMATION RECONSTRUCTION USING THE HYBRID SHELL-BEAM INVERSE FINITE ELEMENT METHOD: THEORY & NUMERICAL RESULTS

**Rinto Roy[1], Marco Esposito[2], Marco Gherlone[2], and Cecilia Surace[1]**

[1] Department of Structural, Geotechnical and Building Engineering, Politecnico di Torino,
Corso Duca degli Abruzzi, 24, 10129 Torino, Italy
e-mail: {rinto.roy,cecilia.surace}@polito.it

[2] Department of Mechanical & Aerospace Engineering, Politecnico di Torino,
Corso Duca degli Abruzzi, 24, 10129 Torino, Italy
e-mail: {marco.esposito,marco.gherlone}@polito.it

**Abstract.** *This work introduces a robust and computationally efficient method for reconstructing the full-field elastic deformations of thin-walled and stiffened panel structures using discrete strain-sensor measurements. The approach presented is based on the inverse Finite Element Method (iFEM), a variationally-based shape sensing technique that attempts to reconstruct the structural displacements by matching a set of experimental and analytically defined strains in a least-squares sense. The novelty of the present work is the introduction of a hybrid discretisation paradigm for the iFEM whereby both beam and shell inverse finite elements are conjointly used to model the structure and capture its deformations. The theoretical framework for this new method and the kinematic coupling between shell and beam inverse elements, proposed based on the first-order shear deformation theory, is presented. Adoption of such a hybrid discretization scheme reduces the number of inverse elements required for structural modelling, thereby reducing computational time and effort. Additionally, beam elements reduce the number of in-situ strain sensors required compared to a solely shell-based inverse model. The hybrid iFEM approach is demonstrated numerically for the shape sensing of a stiffened panel under different load conditions. The preliminary results are accurate and efficient, demonstrating the capabilities of the hybrid iFEM as a potential monitoring approach, especially for aerospace applications where high strength and low mass requirements have led to the widespread adoption of thin-walled and stiffened structural geometry designs.*

**Keywords:** Inverse Methods, Shape Sensing, Beam-Shell Models, Stiffened Panel

## 1 INTRODUCTION

Inverse problems in structural engineering are key to estimating important characteristics of a structure when only indirect measurements are available. Reconstructing structural displacements in real-time from discrete strains, termed shape sensing, is such an inverse problem with the potential for real-time damage diagnosis and prognosis in the domain of Structural Health Monitoring (SHM) [1]. However, inverse problems are ill-posed, requiring efficient methods to ensure accurate, unique, and stable solutions. Although solution approaches to shape sensing based on strain integration, basis functions, and neural networks have been proposed in literature [2], those using a variational principle, such as the inverse Finite Element Method (iFEM) [3], have perhaps found the widest acceptance.

Displacement reconstruction using the iFEM is based on solving a functional defined as the least-squares error between analytical and experimental strains. The two main ingredients of the iFEM are the adoption of the finite element discretisation framework and the use of interpolation functions and the strain-displacement relations to approximate the analytical strains. The former allows complex geometries to be modelled, while the latter ensures that the iFEM is inherently independent of the material properties or loading conditions of the structure. iFEM developments have primarily focused on novel inverse element formulations to model one-dimensional (1D) beam and frame structures (called 1D iFEM) or two-dimensional (2D) plate or shell structures (called 2D iFEM). In the context of the 2D iFEM, the three- and four-node Mindlin shell [4, 5], eight-node curved shell [6], and multi-layered composite [7] elements have been developed and applied for monitoring aerospace, civil, or marine structures involving metallic and composite constructions [8, 9, 10]. When analysing complex structures, a precise 2D iFEM model involving a high-fidelity inverse shell element discretisation can be used to obtain accurate results. However, in this case, the analysis is computationally intensive, requiring strain measurements from a relatively large number of sensors instrumented on the structure. In contrast, the 1D iFEM offers a low-cost (computational and sensor) alternative for monitoring beam or frame structures, with inverse elements for thick [11] and thin beams [12], complex cross-sectional beams [13], and composite structures [14] comprising the major developments. They have also been applied for various aerospace [15] and marine structures [16]. As the 1D iFEM uses a low-fidelity finite beam element discretisation, the validity of the results is highly dependent on the kinematic relations used. As geometric complexity increases, the assumptions can break down, leading to inaccurate results. Hence, neither 1D nor 2D iFEM offers an optimal solution between accuracy, computational cost, and sensor requirement for monitoring structures such as a stiffened panel or a wing box.

This work proposes a solution to this problem by developing a hybrid iFEM scheme where the structure is discretised using both beam and shell elements. Such a coupling ensures greater accuracy than the 1D iFEM, while requiring fewer strain measurements and computational effort than the 2D iFEM. The hybrid iFEM is applied in this work for the numerical shape sensing of a cantilevered stiffened panel instrumented with fibre optic sensors. As per the hybrid scheme, the flat panel is discretised using shell elements, and the stringers use beams. The iFEM accuracy in reconstructing the bending and twisting deformation of the panel is evaluated by comparing results with a high-fidelity finite element (FE) model of the structure. The paper is organised as follows: the theoretical formulation of the hybrid iFEM is given in Section 2. The hybrid iFEM is demonstrated numerically in Section 3 for the shape sensing of a stiffened panel under different loading conditions. Finally, Section 4 concludes with the main conclusions and opportunities for future work.

## 2 HYBRID INVERSE FINITE ELEMENT METHOD

The 1D and 2D iFEM formulations, proposed by Gherlone et al. [11] and Tessler et al. [3], respectively, are briefly recollected in this section. Subsequently, the theoretical formulation of the hybrid iFEM is presented.

### 2.1 1D Inverse Finite Element Method

The 1D iFEM for beams or frames is based on the kinematic assumptions of Timoshenko beam theory [11], where the kinematic variables $\mathbf{u}_b \equiv \{u, v, w, \theta_x, \theta_y, \theta_z\}^T$ are used to describe the Cartesian components of the displacement vector as

$$u_x(\mathbf{x}) = u(x) + z\theta_y(x) - y\theta_z(x) \;\;,\;\; u_y(\mathbf{x}) = v(x) - z\theta_x(x) \;\;,\;\; u_z(\mathbf{x}) = w(x) + y\theta_x(x) \quad (1)$$

where the kinematic variables, $u$, $v$, and $w$, are the beam displacements at the shear centre along the $x$, $y$ and $z$-axis, respectively (see Fig. 1), and $\theta_x$, $\theta_y$, and $\theta_z$ are the torsional and bending rotations about the $x$, $y$, and $z$-axis, respectively.

Using the linear strain-displacement relations, the corresponding strain field is computed

$$\begin{Bmatrix} \varepsilon_x(\mathbf{x}) \\ \gamma_{xz}(\mathbf{x}) \\ \gamma_{xy}(\mathbf{x}) \end{Bmatrix} = \begin{Bmatrix} u_{x,x} \\ u_{x,z} + u_{z,x} \\ u_{x,y} + u_{y,x} \end{Bmatrix} = \begin{Bmatrix} e_1(x) + ze_2(x) + ye_3(x) \\ e_4(x) + ye_6(x) \\ e_5(x) - ze_6(x) \end{Bmatrix} \quad (2)$$

where $e_i$ $(i = 1, ..., 6)$ are the sectional strains defined along the beam axis. Using element shape functions to interpolate the nodal degrees-of-freedom (DOF) and approximate the displacements and strains within an element, the sectional strains can be written as

$$\begin{aligned} \mathbf{e}(\mathbf{u}_b) &= \{e_1, e_2, e_3, e_4, e_5, e_6\}^T \\ &= \{u_{,x}, \theta_{y,x}, -\theta_{z,x}, w_{,x} + \theta_y, v_{,x} - \theta_z, \theta_{x,x}\}^T = \mathbf{B}^s \mathbf{u}_b^e \end{aligned} \quad (3)$$

where $\mathbf{B}^s$ is a matrix of shape function derivatives and $\mathbf{u}_b^e$ is the nodal DOF vector of the element.

Although Eq. 3 provides the analytical form of the sectional strains, they can also be computed experimentally from strain measurements. For a strain sensor instrumented at an axial location $x_i$ and orientation $\beta$ on the beam surface, the surface strain measurement can be written in terms of the experimental sectional strains, $\mathbf{e}^\epsilon = \{e_1^\epsilon, e_2^\epsilon, e_3^\epsilon, e_4^\epsilon, e_5^\epsilon, e_6^\epsilon\}^T$ as [13]

$$\begin{aligned} \varepsilon^*(x_i, c, \beta) = (e_1^\epsilon(x_i) + e_2^\epsilon(x_i) z_i + e_3^\epsilon(x_i) y_i) (\cos^2\beta - \nu \sin^2\beta) + \\ \left( \frac{1}{k_{\epsilon z}} e_4^\epsilon(x_i) f_1(y_i, z_i) + \frac{1}{k_{\epsilon y}} e_5^\epsilon(x_i) f_2(y_i, z_i) + e_6^\epsilon(x_i) f_3(y_i, z_i) \right) \cos\beta \sin\beta \end{aligned} \quad (4)$$

where $f_1$, $f_2$, $f_3$, $k_{\epsilon y}$ and $k_{\epsilon z}$ are functions and coefficients used to model the shear strains variation due transverse or torsional loads and are only a function of the beam profile. Given a discrete set of strain measurements, Eq. 4 can be solved to compute $\mathbf{e}^\epsilon$.

The 1D iFEM is based on the finite element framework where the structural domain is discretised using 1D finite elements. For each element $e$, a weighted-least-squares error functional can be formulated as

$$\Phi_b^e(\mathbf{u}_b^e) \equiv \mathbf{w}_s \mathbf{\Phi}_s(\mathbf{u}_b^e) \equiv \mathbf{w}_s \sum_{i=1}^{N} \frac{l_e}{N} \left[ \mathbf{e}(x_i) - (\mathbf{e}^\epsilon)_i \right]^2 \quad (5)$$

where $\mathbf{w}_s = \{w_k\}$ $(k = 1, ..., 6)$ is a vector of weighing coefficients used to control the enforcement of the least-squares compatibility of each sectional strain component and ensures the dimensional consistency of Eq. 5, $l_e$ is the element length, and $N$ is the total number of axial sections with strain measurements.

Eq. 5 is minimized with respect to the nodal DOF of the element to obtain the following element set of linear algebraic equations

$$\frac{\partial \Phi_b^e(\mathbf{u}_b^e)}{\partial \mathbf{u}_b^e} = \mathbf{k}_b^e \mathbf{u}_b^e - \mathbf{f}_b^e = 0 \rightarrow \mathbf{k}_b^e \mathbf{u}_b^e = \mathbf{f}_b^e \tag{6}$$

where matrix $\mathbf{k}_b^e$ is only a function of the sensor positions while vector $\mathbf{f}_b^e$ is a function of the sensor positions and measured strains. These element matrices can also be written as the weighted sum of contributions from each sectional strain as

$$\mathbf{k}_b^e(\mathbf{u}_b^e) = \sum_{k=1}^{6} w_k \left( \frac{l_e}{N} \sum_{i=1}^{N} \left(\mathbf{B}_k^s(x_i)\right)^T \mathbf{B}_k^s(x_i) \right), \; \mathbf{f}_b^e(\mathbf{u}_b^e) = \sum_{k=1}^{6} w_k \left( \frac{l_e}{N} \sum_{i=1}^{N} \left(\mathbf{B}_k^s(x_i)\right)^T (e_k^\epsilon)_i \right) \tag{7}$$

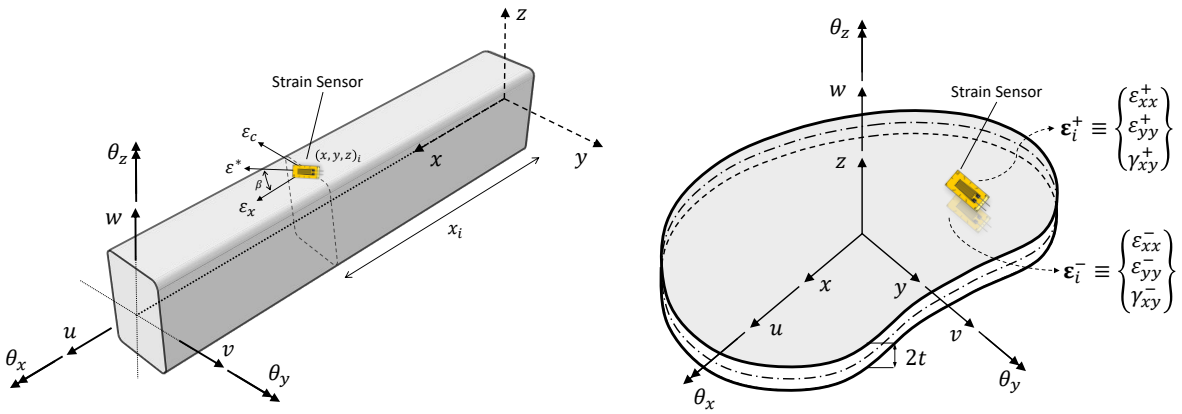


(**a**) (**b**)

Figure 1: Definition of the variables used to define the (a) beam and (b) plate kinematics

## 2.2 2D Inverse Finite Element Method

The 2D iFEM for plates or shells is formulated based on the kinematic assumptions of Mindlin theory [4], where the kinematic variables $\mathbf{u}_p \equiv \{u, v, w, \theta_x, \theta_y\}^T$ are used to describe the Cartesian components of the displacement vector as

$$u_x = u(\mathbf{x}) + z\theta_y(\mathbf{x}) \quad , \quad u_y = v(\mathbf{x}) - z\theta_x(\mathbf{x}) \quad , \quad u_z = w(\mathbf{x}) \tag{8}$$

where the variables $u$ and $v$, are the mid-plane displacements in the $x$ and $y-$directions; $w$ is section-averaged transverse deflection; and $\theta_x$ and $\theta_y$ are the section rotations about the $x$ and $y$-axes, respectively (see Fig. 1).

The in-plane and transverse shear strains of the plate are computed from Eq. 8 using the linear strain-displacement relations

$$\begin{Bmatrix} \varepsilon_{xx} \\ \varepsilon_{yy} \\ \gamma_{xy} \end{Bmatrix} = \begin{Bmatrix} u_{x,x} \\ u_{y,y} \\ u_{x,y} + u_{y,x} \end{Bmatrix} = \begin{Bmatrix} u_{,x} \\ v_{,y} \\ u_{,y} + v_{,x} \end{Bmatrix} + z \begin{Bmatrix} \theta_{y,x} \\ -\theta_{x,y} \\ -\theta_{x,x} + \theta_{y,y} \end{Bmatrix} = \mathbf{m}(\mathbf{u}_p) + z\mathbf{k}(\mathbf{u}_p)$$
$$\begin{Bmatrix} \gamma_{xz} \\ \gamma_{yz} \end{Bmatrix} = \begin{Bmatrix} u_{z,x} + u_{x,z} \\ u_{z,y} + u_{y,z} \end{Bmatrix} = \begin{Bmatrix} w_{,x} + \theta_y \\ w_{,y} - \theta_x \end{Bmatrix} = \mathbf{g}(\mathbf{u}_p) \tag{9}$$

where **m**, **k**, and **g** are the strain measures defined in the mid-plane surface and representing the membrane, curvature, and transverse shear strain of the mid-plane.

Using element shape functions to interpolate the nodal DOF and approximate the displacements and strains within an element, Eq. 9 can be written as

$$\begin{Bmatrix} \varepsilon_{xx} \\ \varepsilon_{yy} \\ \gamma_{xy} \end{Bmatrix} = \mathbf{m}(\mathbf{u}_p^e) + z\mathbf{k}(\mathbf{u}_p^e) = \mathbf{B}^m\mathbf{u}_p^e + z\mathbf{B}^k\mathbf{u}_p^e \quad , \quad \begin{Bmatrix} \gamma_{xz} \\ \gamma_{yz} \end{Bmatrix} = \mathbf{g}(\mathbf{u}_p^e) = \mathbf{B}^g\mathbf{u}_p^e \tag{10}$$

where $\mathbf{B}^m$, $\mathbf{B}^k$, and $\mathbf{B}^g$ are matrices of shape function derivatives and $\mathbf{u}_p^e$ is the nodal DOF vector. An additional drilling DOF, $\theta_z$, can be introduced in $\mathbf{u}_p^e$ by means of interdependent shape functions (discussed by Kefal et al. [5] for the iQS4 element). Hence, even though $\theta_z$ is not one of the kinematic variables of Mindlin theory, it appears among the nodal DOF.

The strain measures of Eq. 10 can also be computed from experimental strain measurements. Using plate top, $\boldsymbol{\varepsilon}_i^+ = \{\varepsilon_{xx}^+, \varepsilon_{yy}^+, \gamma_{xy}^+\}_i^T$, and bottom, $\boldsymbol{\varepsilon}_i^- = \{\varepsilon_{xx}^-, \varepsilon_{yy}^-, \gamma_{xy}^-\}_i^T$, surface strains measured by sensors placed at discrete in-plane locations, $\mathbf{x}_i = (x, y)_i$, the membrane and curvature strain measures can be computed using the relations

$$\mathbf{m}_i^\epsilon = \frac{1}{2}\left( \begin{Bmatrix} \epsilon_{xx}^+ \\ \epsilon_{yy}^+ \\ \gamma_{xy}^+ \end{Bmatrix} + \begin{Bmatrix} \epsilon_{xx}^- \\ \epsilon_{yy}^- \\ \gamma_{xy}^- \end{Bmatrix} \right)_i \quad , \quad \mathbf{k}_i^\epsilon = \frac{1}{2t}\left( \begin{Bmatrix} \epsilon_{xx}^+ \\ \epsilon_{yy}^+ \\ \gamma_{xy}^+ \end{Bmatrix} - \begin{Bmatrix} \epsilon_{xx}^- \\ \epsilon_{yy}^- \\ \gamma_{xy}^- \end{Bmatrix} \right)_i \tag{11}$$

The 2D iFEM uses the finite element framework to discretise the structure using 2D inverse finite elements. For each element, $e$, a weighted least-squares error functional is formulated as

$$\Phi_p^e(\mathbf{u}_p^e) \equiv \mathbf{w}_m\boldsymbol{\Phi}_m(\mathbf{u}_p^e) + \mathbf{w}_k\boldsymbol{\Phi}_k(\mathbf{u}_p^e) + \mathbf{w}_g\boldsymbol{\Phi}_g(\mathbf{u}_p^e) \tag{12}$$

where $\mathbf{w}_m$, $\mathbf{w}_b$, and $\mathbf{w}_s$, are row vectors of weighting coefficients, while the corresponding error functionals are given as

$$\boldsymbol{\Phi}_m \equiv \frac{1}{A_p^e}\int_{A_p^e}[\mathbf{m}(\mathbf{u}_p^e) - \mathbf{m}^\epsilon]^2 dA \ , \ \boldsymbol{\Phi}_k \equiv \frac{(2t)^2}{A_p^e}\int_{A_p^e}[\mathbf{k}(\mathbf{u}_p^e) - \mathbf{k}^\epsilon]^2 dA$$
$$\boldsymbol{\Phi}_g \equiv \frac{1}{A_p^e}\int_{A_p^e}[\mathbf{g}(\mathbf{u}_p^e)]^2 dA \tag{13}$$

The weighting coefficients are used to specify the correlation between the analytical and experimental strain measurements. They are set to unity ($\mathbf{w}_m = \mathbf{w}_b = \{1, 1, 1\}$) when experimental strains are available for an element and to a small value ($10^{-3}$–$10^{-5}$) otherwise to reduce the element contribution from the global functional. As $\mathbf{g}^\epsilon$ cannot be computed directly from experimental measurements, the square norm follows the form of Eq.13 with $\mathbf{w}_g = \{10^{-5}, 10^{-5}\}$.

Minimising Eq. 12 with respect to the nodal DOF gives to rise to the following element set of equations

$$\frac{\partial \Phi_p^e(\mathbf{u}_p^e)}{\partial \mathbf{u}_p^e} = \mathbf{k}_p^e \mathbf{u}_p^e - \mathbf{f}_p^e = 0 \rightarrow \mathbf{k}_p^e \mathbf{u}_p^e = \mathbf{f}_p^e \tag{14}$$

where matrix $\mathbf{k}_p^e$ and vector $\mathbf{f}_p^e$ are given in terms of the shape function derivatives as

$$\begin{aligned} \mathbf{k}_p^e(\mathbf{u}_p^e) &= \frac{1}{A_p^e} \int_{A_p^e} \left[ \mathbf{w}_m (\mathbf{B}^m)^T \mathbf{B}^m + \mathbf{w}_k (2t)^2 (\mathbf{B}^k)^T \mathbf{B}^k + \mathbf{w}_g (\mathbf{B}^g)^T \mathbf{B}^g \right] dA, \\ \mathbf{f}_p^e(\mathbf{u}_p^e) &= \frac{1}{A_p^e} \int_{A_p^e} \left[ \mathbf{w}_m (\mathbf{B}^m)^T \mathbf{m}^\epsilon + \mathbf{w}_k (2t)^2 (\mathbf{B}^k)^T \mathbf{k}^\epsilon + \mathbf{w}_g (\mathbf{B}^g)^T \mathbf{g}^\epsilon \right] dA. \end{aligned} \tag{15}$$

### 2.3 Hybrid Formulation

The hybrid iFEM formulation discretises the structure using both beam and shell inverse finite elements. Combining beam, $\Phi_b$, and shell, $\Phi_p$, element contributions, the global error functional of the structure is written as

$$\Phi(\mathbf{u}) \equiv \Phi_b(\mathbf{u}) + \Phi_p(\mathbf{u}) \tag{16}$$

where $\mathbf{u} \equiv \{u, v, w, \theta_x, \theta_y, \theta_z\}^T$ is the vector of kinematic variables.

Minimising Eq. 16 with respect to $\mathbf{u}$ produces the global equations of the structure,

$$\mathbf{KU} = \mathbf{F} \tag{17}$$

where matrix $\mathbf{K}$ and vector $\mathbf{F}$ can be written as the superposition of $n_b$ beam and $n_p$ shell element contributions with the appropriate local-to-global transformations, $\mathbf{T}^e$, as

$$\begin{aligned} \mathbf{K}(\mathbf{u}) &= \mathbf{K}_b(\mathbf{u}) + \mathbf{K}_p(\mathbf{u}) = \sum_{e=1}^{n_b} (\mathbf{T}^e)^T \mathbf{k}_b^e \mathbf{T}^e + \sum_{e=1}^{n_p} (\mathbf{T}^e)^T \mathbf{k}_p^e \mathbf{T}^e \\ \mathbf{U}(\mathbf{u}) &= \mathbf{U}_b(\mathbf{u}) + \mathbf{U}_p(\mathbf{u}) = \sum_{e=1}^{n_b} (\mathbf{T}^e)^T \mathbf{u}_b^e + \sum_{e=1}^{n_p} (\mathbf{T}^e)^T \mathbf{u}_p^e \\ \mathbf{F}(\mathbf{u}) &= \mathbf{F}_p(\mathbf{u}) + \mathbf{F}_b(\mathbf{u}) = \sum_{e=1}^{n_p} (\mathbf{T}^e)^T \mathbf{f}_p^e \mathbf{T}^e + \sum_{e=1}^{n_b} (\mathbf{T}^e)^T \mathbf{f}_b^e \mathbf{T}^e \end{aligned} \tag{18}$$

As in the direct FEM, nodal boundary conditions are used to constrain the structure against rigid-body motion and ensure a non-singular system matrix. Finally, Eq. 17 is solved to obtain the iFEM reconstructed nodal displacements, $\mathbf{U}$, of the structure.

## 3 NUMERICAL STUDY

The hybrid iFEM formulation is applied for the numerical shape sensing of a cantilevered stiffened panel in this section. The panel is 300 mm long, 180 mm wide, and 2 mm thick and is composed of six longitudinal stringers of rectangular cross-section $2\times10$ mm$^2$ (shown in Fig. 2). It is made of an aluminium alloy of Young's Modulus $E = 73$ GPa and Poisson's ratio $\nu = 0.3$. The panel is tested as a cantilever by clamping along one of its short ends. In contrast, the other end is subjected to two different load conditions: a uniformly distributed transverse load that causes the panel to bend and a concentrated transverse load at the corner, causing panel

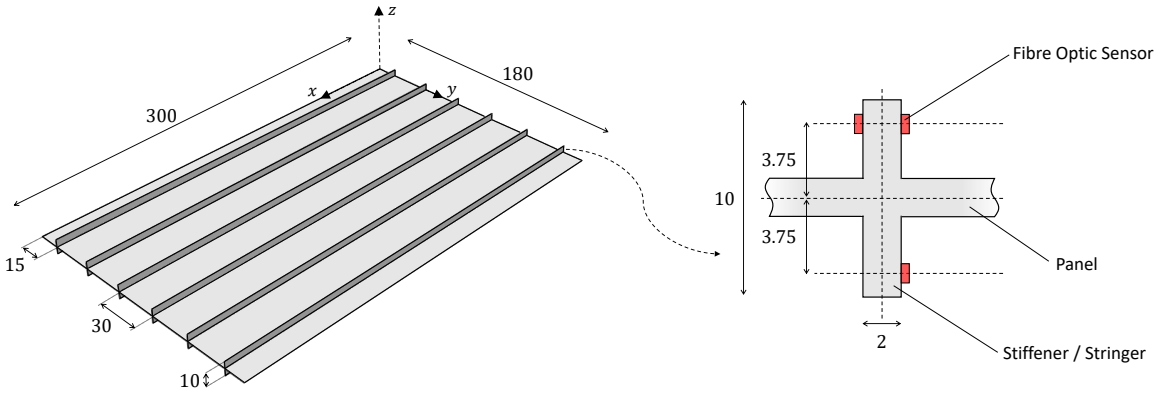


Figure 2: Images of the stiffened panel showing the panel and stringer dimensions, and the location of the fibre optic sensors on each stringer (all dimensions are in mm)

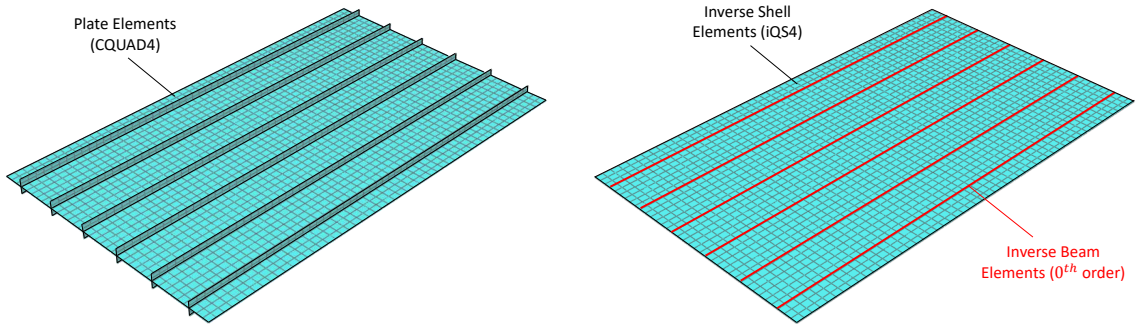


(**a**) (**b**)

Figure 3: The element discretisation for the (a) direct FEM model composed of 3180 CQUAD4 elements, and (b) iFEM model composed of 1908 iQS4 and 318 $0^{\text{th}}$-order beam elements

twisting. The panel is instrumented with a 5.4 m long fibre optic strain sensor to measure the strains during deformation. The fibre is instrumented on the stringers, with each stringer having three sensing lines along which the longitudinal ($x$-direction) strains are measured.

Given the absence of an experimental model, a high-fidelity finite element (FE) model developed in NASTRAN is used for the present study. The FE strains are inputs for the iFEM analysis, while the FE displacements are the reference for iFEM comparisons. In the direct model, the stiffened panel (including the stringers) is modelled using 3180 CQUAD4 elements, a four-node isoparametric plate element in NASTRAN. The stringers are discretised with 4 subdivisions along their vertical dimension and 53 along their length. The hybrid scheme is adopted for the inverse iFEM model. The flat panel is modelled using 1908 iQS4 elements [5], a four-node inverse shell element with bi-quadratic displacement interpolations and bi-linear rotations, whereas, the stingers are modelled with 318 $0^{\text{th}}$-order inverse beam elements (proposed by Gherlone et al. [11]) with a linear interpolation of axial displacement and torsional rotation, parabolic bending rotations, and cubic transverse deflections. As the fibre optic sensors are instrumented along the stringers, only the beam elements are sensorised in the inverse model.

Hence, the error norms for the shell elements are penalised with a low value of weights ($10^{-5}$). Additionally, as only longitudinal strains are measured, the transverse shears ($e_4$ and $e_5$) and torsional ($e_6$) sectional strain of the beam cannot be computed directly, and their corresponding weights are set to a small value ($10^{-4}$).

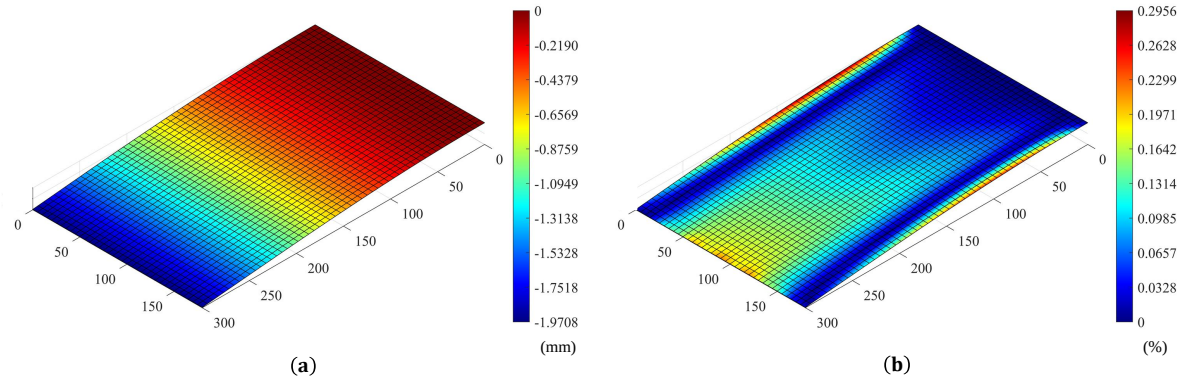


Figure 4: Contour plots of iFEM results for load case 1: (a) $w_{\text{iFEM}}$ and (b) $w^{err}$

The results of the iFEM analysis for load case 1 are given in Fig. 4, where the contour plots of transverse deflection, $w_{\text{iFEM}}$, and its corresponding error, $w^{err} = 100 \times (w_{\text{FE}} - w_{\text{iFEM}})/\{w_{\text{FE}}\}_{max}$, are shown. The iFEM results are seen to be very accurate ($w^{err} < 0.3\%$), with the strains measured on the stringers accurately describing the bending displacements on the panel. The highest errors are at the panel extremities, where local deflection changes might not be captured due to the absence of sensorised elements in its vicinity. Load case 2 presents a more interesting case with the concentrated load causing the panel to twist. Although the beam elements used no information regarding the torsional strain, the differential bending of the stringers accurately captured the global twisting behaviour of the panel ($w^{err} < 0.9\%$ as shown in Fig. 5). In contrast to a complete shell model of the same structures, these results obtained at a low computational cost and relatively lower number of strain measurements indicate the benefits of the hybrid iFEM approach.

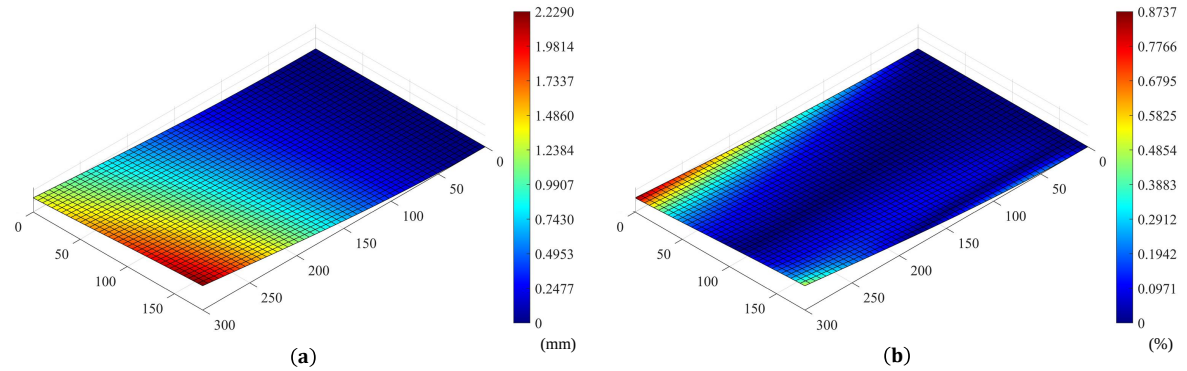


Figure 5: Contour plots of iFEM results for load case 2: (a) $w_{\text{iFEM}}$ and (b) $w^{err}$

## 4 CONCLUSIONS

This work introduced a hybrid beam-shell inverse Finite Element Method for the accurate, robust, and computationally efficient displacement reconstruction monitoring of thin-walled and stiffened panel structures using discrete strains. The crux of the proposed approach is a novel discretisation paradigm whereby the monitored structure is discretised using both beam and shell inverse finite elements. Such a discretisation scheme reduces the number of inverse elements required for structural modelling, thereby reducing computational time and the number of strain measurements needed. This novel approach was demonstrated for the numerical shape sensing of a cantilevered stiffened panel undergoing bending and twisting deformations. Accurate results were obtained in an efficient manner, highlighting the capabilities of the hybrid iFEM as a structural monitoring tool. Future work aims to combine higher-order inverse elements within this hybrid paradigm and experimentally demonstrate its capabilities for complex structures such as a composite wing box.

## REFERENCES

[1] C. R. Farrar and K. Worden. An Introduction to Structural Health Monitoring. *Philosophical Transactions of the Royal Society A: Mathematical, Physical and Engineering Sciences*, 365(1851):303–315, 2007. ISSN 1364503X. doi: 10.1098/rsta.2006.1928.

[2] M. Gherlone, P. Cerracchio, and M. Mattone. Shape sensing methods: Review and experimental comparison on a wing-shaped plate. *Progress in Aerospace Sciences*, 99: 14–26, April, 2018. ISSN 03760421. doi: 10.1016/j.paerosci.2018.04.001. URL https://doi.org/10.1016/j.paerosci.2018.04.001.

[3] A. Tessler and J. L. Spangler. A least-squares variational method for full-field reconstruction of elastic deformations in shear-deformable plates and shells. *Computer Methods in Applied Mechanics and Engineering*, 194(2-5 SPEC. ISS.):327–339, 2005. ISSN 00457825. doi: 10.1016/j.cma.2004.03.015.

[4] A. Tessler and J. Spangler. Inverse FEM for Full-Field Reconstruction of Elastic Deformations in Shear Deformable Plates and Shells. *Proceedings of Second European Workshop on Structural Health Monitoring*, pages 83–90, 2004.

[5] A. Kefal, E. Oterkus, A. Tessler, and J. L. Spangler. A quadrilateral inverse-shell element with drilling degrees of freedom for shape sensing and structural health monitoring. *Engineering Science and Technology, an International Journal*, 19(3):1299–1313, 2016. ISSN 22150986. doi: 10.1016/j.jestch.2016.03.006. URL http://dx.doi.org/10.1016/j.jestch.2016.03.006.

[6] A. Kefal. An efficient curved inverse-shell element for shape sensing and structural health monitoring of cylindrical marine structures. *Ocean Engineering*, 188:106262, 2019. ISSN 00298018. doi: 10.1016/j.oceaneng.2019.106262. URL https://doi.org/10.1016/j.oceaneng.2019.106262.

[7] A. Kefal, A. Tessler, and E. Oterkus. An enhanced inverse finite element method for displacement and stress monitoring of multilayered composite and sandwich structures. *Composite Structures*, 179:514–540, 2017. ISSN 02638223. doi: 10.1016/j.compstruct.2017.07.078. URL http://dx.doi.org/10.1016/j.compstruct.2017.07.078.

[8] E. J. Miller, R. Manalo, and A. Tessler. Full-Field Reconstruction of Structural Deformations and Loads from Measured Strain Data on a Wing Test Article using the Inverse Finite Element Method. *NASA/TM—2016–219407*, 2016.

[9] P. Cerracchio, M. Gherlone, and A. Tessler. Real-time displacement monitoring of a composite stiffened panel subjected to mechanical and thermal loads. *Meccanica*, 50(10): 2487–2496, 2015. ISSN 15729648. doi: 10.1007/s11012-015-0146-8.

[10] M. Esposito and M. Gherlone. Composite wing box deformed-shape reconstruction based on measured strains: Optimization and comparison of existing approaches. *Aerospace Science and Technology*, 99:105758, 2020. ISSN 12709638. doi: 10.1016/j.ast.2020.105758. URL https://doi.org/10.1016/j.ast.2020.105758.

[11] M. Gherlone, P. Cerracchio, M. Mattone, M. Di Sciuva, and A. Tessler. Shape sensing of 3D frame structures using an inverse Finite Element Method. *International Journal of Solids and Structures*, 49(22):3100–3112, 2012. ISSN 00207683. doi: 10.1016/j.ijsolstr.2012.06.009. URL http://dx.doi.org/10.1016/j.ijsolstr.2012.06.009.

[12] P. Savino, M. Gherlone, and F. Tondolo. Shape sensing with inverse finite element method for slender structures. *Structural Engineering and Mechanics*, 72(2):77–87, 2019. doi: https://dx.doi.org/10.12989/sem.2019.72.2.217.

[13] R. Roy, M. Gherlone, and C. Surace. A shape sensing methodology for beams with generic cross-sections: Application to airfoil beams. *Aer. Sci. and Tech.*, 110:106484, 2021. ISSN 1270-9638. URL https://www.sciencedirect.com/science/article/pii/S1270963820311664.

[14] F. Zhao, H. Bao, J. Liu, and K. Li. Shape sensing of multilayered composite and sandwich beams based on Refined Zigzag Theory and inverse finite element method. *Composite Structures*, 261:113321, 2021. ISSN 02638223. doi: 10.1016/j.compstruct.2020.113321. URL https://doi.org/10.1016/j.compstruct.2020.113321.

[15] Y. Zhao, J. Du, Q. Xu, and H. Bao. Real-time monitoring of the position and orientation of a radio telescope sub-reflector with fiber bragg grating sensors. *Sensors (Switzerland)*, 19(3), 2019. ISSN 14248220. doi: 10.3390/s19030619.

[16] Haiming Zhu, Zunfeng Du, and Yougang Tang. Numerical study on the displacement reconstruction of subsea pipelines using the improved inverse finite element method. *Ocean Engineering*, 248:110763, 2022. ISSN 0029-8018. doi: https://doi.org/10.1016/j.oceaneng.2022.110763.

COMPDYN 2023
9th ECCOMAS Thematic Conference on
Computational Methods in Structural Dynamics and Earthquake Engineering
M. Papadrakakis, M. Fragiadakis (eds.)
Athens, Greece, 12-–14 June 2023

# STRUCTURAL DEFORMATION RECONSTRUCTION USING THE HYBRID SHELL-BEAM INVERSE FINITE ELEMENT METHOD: EXPERIMENTAL APPLICATION ON A THIN-WALLED STIFFENED PANEL

**Marco Esposito[1], Rinto Roy[2], Marco Gherlone[1] and Cecilia Surace[2]**

[1]Department of Mechanical and Aerospace Engineering, Politecnico di Torino
Corso Duca degli Abruzzi, 24, Torino, Italy
e-mail: {marco.esposito, marco.gherlone}@polito.it

[2] Department of Structural, Geotechnical and Building Engineering, Politecnico di Torino
Corso Duca degli Abruzzi, 24, Torino, Italy
e-mail: {rinto.roy, cecilia.surace}@polito.it

**Keywords:** Inverse Methods, Shape Sensing, iFEM, Beam-Shell Models, Stiffened Panel, Experimental validation.

**Abstract.** *The continuous developments in the field of Structural Health Monitoring (SHM) and the simultaneous push toward the realization of the digital twin paradigm has generated a strong request for the on-line monitoring of structural responses that are usually difficult to measure through direct sensing. Among these responses, the displacements, and the stresses that can be derived from them, play a crucial role. The indirect computation of the displacement field from easily measurable surface strains, known as shape sensing, has inspired the definition of an inverse formulation of the Finite Element Method, the iFEM. As for the standard FEM, this approach is based on the discretization of the structural domain with finite elements. Therefore, 2D inverse shell elements and 1D inverse beam elements have been separately proposed and tested for the shape sensing of plate and beam-like structures, respectively. However, especially in aerospace applications, thin-walled stiffened panels are often adopted. These structures can be discretized using hybrid shell-beam models. In this work, the iFEM hybrid shell-beam formulation is applied for the first time to the experimental shape sensing of an aluminum stiffened panel instrumented with strain sensing optic fibres. The displacements' reconstruction is compared to the one obtained with a high-fidelity shell-only inverse model of the same structure. The comparison shows that the hybrid iFEM is capable of the same level of accuracy of the shell-only one, using a more computationally efficient model with less degrees of freedoms. These results prove that the proposed hybrid formulation is a valuable displacements' monitoring tool for applications where computational efficiency is paramount and the level of detail achieved by low-fidelity hybrid models is sufficient, as it occurs in aeroelastic models.*

## 1 INTRODUCTION

Structural Health Monitoring (SHM) is rapidly imposing itself as a crucial tool for the future of structural design in every technological area where damages and failures can occur. Within the SHM framework, different tools and technologies have been developed, depending on the specific characteristics of the structure that they are designed to monitor. In particular, several techniques for the monitoring of the displacements during the service life of a structure are rapidly developing [1]. The reconstruction of the displacement field from discrete strain sensors is defined as shape sensing. The shape sensing methods represent an important tool to improve the efficiency of the structural maintenance operations [2] and can also be implemented for damage detection activities[3, 4]. Among the existing approaches, the inverse Finite Element Method (iFEM) has emerged has one of the most accurate and efficient [5].

The iFEM is based on an inverse formulation of the Finite Element Method that allows, from a sparse set of strain measures, to compute the displacement field that induced those strains [6]. As for the standard FEM, it is based on the discretization of the structural domain with finite elements. Therefore, several inverse finite elements have been developed, with characteristics that adapt to different structural components. One-dimensional inverse elements for the analysis of beam structures have been developed in [7], whereas two-dimensional elements for the analysis of thin plates have been introduced in [8].

Several applications of the iFEM have involved the separate use of either 1D or 2D models for the displacement reconstruction of beam-like or thin-walled structures. Beam inverse elements have been successfully used for the shape sensing of sub-sea [9] and buried [10] pipelines. In [11] an inverse 1D element based on the Timoshenko beam theory has been applied to the displacement reconstruction of an airfoil beam. On the other hand, 2D shell inverse elements have been successfully involved in the shape sensing of aerospace and marine structures. In [12] 2D quad inverse elements have been used to model and analyse an aeronautical stiffened panel. In [13] the iFEM has been applied on the displacement and stress monitoring of a a capsize bulk carrier, using inverse quad elements.

Although a consistent research effort has concerned the development of different formulations and applications of 2D and 1D inverse elements, the application of beam and shell elements within the same model has never been explored. In the case of thin-walled stiffened structures, the standard FE structural analysis often involves the use hybrid shell-beam models, where the shell elements are used to simulate the thin-walled part and the beam elements are associated to the stiffeners. In this work, for the first time, the same approach is adopted for the experimental shape sensing of an aluminium stiffened panel. In fact, the displacement reconstruction is performed by discretizing the panel with quadrilateral inverse elements and the stiffeners with beam inverse elements. The results obtained with the hybrid shell-beam model are compared with the one computed trough the use of a more detailed standard shell-only inverse model. The study proves that the hybrid model is able to reach the same accuracy of the detailed model with a less computationally demanding model and with a slightly reduced number strain sensors.

The paper is structured as follows. In Section 2, the hybrid iFEM formulation is briefly described. In Section 3 the experimental setup and the structure object of the analysis are presented. The inverse models and the strain sensors' configurations for the shape sensing are introduced in Section 4. The results of the experimental campaign are reported in Section 5. Finally, the concluding remarks and the recommendations for the future development of the hybrid models are included in Section 6.

## 2 Hybrid inverse shell-beam formulation

The inverse Finite Element Method is based on the discretization of the structural domain with finite elements. This discretization leads to the formulation of the displacement field in terms of the shape functions and of the nodal degrees of freedom.

Once the discretized displacement field is defined, the dicretized strain field can be easily obtained by deriving the shape functions, thus obtaining the expression of the strain field in terms of the nodal values of the nodal degrees of freedom:

$$\mathbf{e}(\mathbf{u}^e) = \mathbf{B}\mathbf{u}^e \tag{1}$$

where $\mathbf{B}^s$ is a matrix of shape function derivatives and $\mathbf{u}^e$ is the vector of nodal DOF of element $e$ of the inverse model. $\mathbf{B}$, $\mathbf{u}_e$ and the strain components that define the vector $\mathbf{e}(\mathbf{u}^e)$ depend on the kind and formulation of the selected inverse element.

This analytical expression of the strain field can be compared with the one experimentally measured at discrete locations, in order to compute the nodal degrees of freedom value that best fit the measured strain field. The procedure is obtained by defining an error functional. For the beam element $e$, the error functional $\mathbf{\Phi}_b^e$ is defined as:

$$\Phi_b^e(\mathbf{u}_b^e) = \sum_{k=1}^{6} \lambda_k^b w_k^b \sum_{i=1}^{N} \frac{l_e}{N} \left[e_k(x_i) - (e_k^\varepsilon)_i\right]^2 \tag{2}$$

where $e_k(x_i)$ is the k-th analytical sectional strain computed at the section identified by the $x_i$ axial coordinate, $(e_k^\varepsilon)_i$ is the k-th measured sectional strain coming from a sensor at the same axial location, N is the number of sections within the beam element where the strains are measured and $l_e$ is the length of the beam element. The index $k$ identifies the six sectional strains that define the strain field for a Timoshenko beam, namely: axial stretching ($k = 1$), bending curvatures ($k = 2, 3$), transverse shear ($k = 4, 5$) and torsional strain ($k = 6$). $\lambda_k^b$ are coefficients that guarantee the dimensional consistency between the different sectional strains. $w_k^b$ is a weight used to take into account for sparse strain sensors configurations. It is set to 1 if the corresponding sectional strain is measured or to a small vale ($10^{-5}$) if it is not. For the application concerning this work, only sensors that measure axial stretching and bending curvatures are considered. Therefore, for sensorized beam elements, the value of $w_k^b$ for ($k = 4, 5, 6$) is set to $10^{-5}$ and for ($k = 1, 2, 3$) is set to 1. On the the other hand, for unsensorized elements all the weights are set to $10^{-5}$. A more detailed description of the iFEM formulation for the beam elements can be found in [11].

Using the same approach, the error functional can also be defined for shell elements. In this case the functional $\mathbf{\Phi}_p^e$ is defined as:

$$\Phi_p^e(\mathbf{u}_p^e) = \sum_{k=1}^{8} \lambda_k^p w_k^p \iint_{A^e} [e_k(\mathbf{u}^e) - e_k^\varepsilon]^2 dxdy \tag{3}$$

where $e_k(\mathbf{u}^e)$ is the k-th analytical strain measure, $e_k^\varepsilon$ is the k-th strain measure derived from sensors' measurements and $A^e$ is the area of the shell element. In this case, the $k$ index identifies the eight strain measures that define the strain field for a Mindlin plate, namely: the membrane strain ($k = 1, 2, 3$), the bending curvatures ($k = 4, 5, 6$) and the transverse shear strains ($k = 7, 8$) of the plate. In this case, the $\lambda_k^p$ and $w_k^p$ coefficient assume the same role as $\lambda_k^b$ and $w_k^b$. Since the transverse shear strains are not measurable through strain sensors, the values of $w_k^p$

for ($k = 7, 8$) is always set to $10^{-5}$. The detailed formulation of the inverse shell elements can be found in [14].

The minimization of the functional with respect to the nodal DOFs for each element generates a system of linear equations. In the case of a hybrid model, the simultaneous minimization of the error functional for the beam and shell elements needs to be performed:

$$\frac{\partial \Phi_b^e(\mathbf{u}_b^e)}{\partial \mathbf{u}_b^e} = \mathbf{k}_b^e \mathbf{u}_b^e - \mathbf{f}_b^e = 0 \tag{4}$$

$$\frac{\partial \Phi_p^e(\mathbf{u}_p^e)}{\partial \mathbf{u}_p^e} = \mathbf{k}_p^e \mathbf{u}_p^e - \mathbf{f}_p^e = 0 \tag{5}$$

The standard FE assembly procedure for all the $N^e$ elements, taking into account for the necessary transformations from the local DOFs of the elements to the global ones, generates the global matrices:

$$\begin{aligned} Assembly(\mathbf{k}_b^e; \mathbf{k}_p^e)_{e=1:N^e} &\rightarrow \mathbf{K} \\ Assembly(\mathbf{f}_b^e; \mathbf{f}_p^e)_{e=1:N^e} &\rightarrow \mathbf{F} \end{aligned} \tag{6}$$

where $\mathbf{K}$ is a matrix depending on the shape functions and strain sensor locations, whereas $\mathbf{F}$ is a vector incorporating the measured strains. The matrix $\mathbf{K}$ is a well-conditioned square matrix that, upon enforcement of the displacement boundary conditions, can be inverted to compute the vector of the global DOFs, $\mathbf{U}$, that best fit in a least-square sense the measured strains:

$$\mathbf{U} = \mathbf{K}^{-1}\mathbf{F} \tag{7}$$

It is important to highlight that the iFEM is only based on the strain-displacement relationship and, therefore, does not require any knowledge of the material characteristics or the loading condition of the monitored structure.

## 3 Experimental setup

The test case for the experimental validation of the hybrid shell-beam inverse model is an aluminium stiffened panel. The panel is made of a Aluminium-Lithium alloy, whose mechanical characteristics are reported in Table 1. The geometry of the panel is presented in Fig. 1 and 2. It

| | Al-Li alloy |
|---|---|
| $E\ [MPa]$ | 75,958 |
| $\nu$ | 0.3 |
| $\rho\ [g/cm^3]$ | 2.78 |

Table 1: Mechanical properties of the Aluminium-Lithium alloy.

has three L-section stringers and it is 3.92 mm thick, except for four areas between the stringers where the thickness is reduced to 1.91 mm.

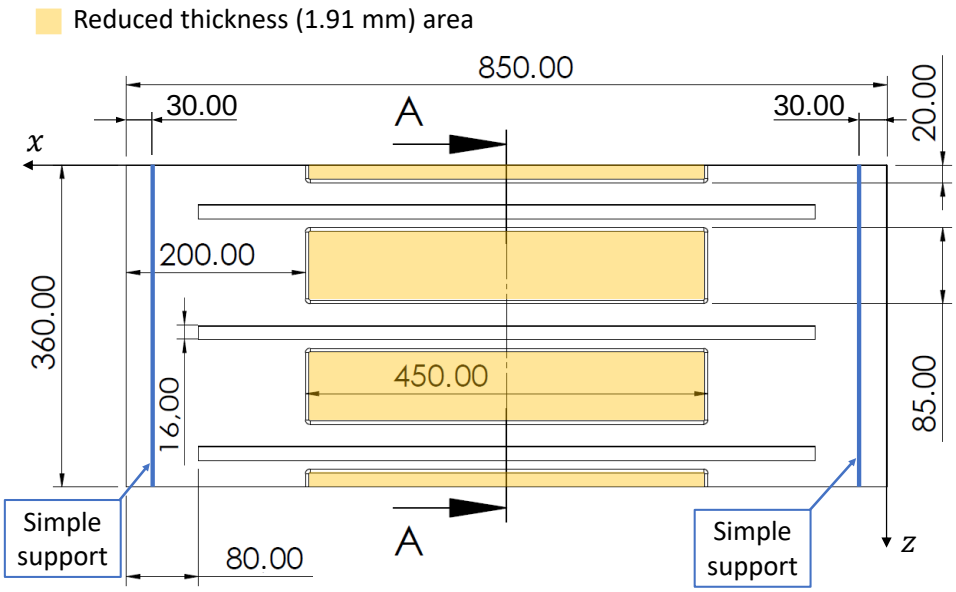


Figure 1: Geometry of the panel - Bottom view of the panel. All dimensions are expressed in mm.

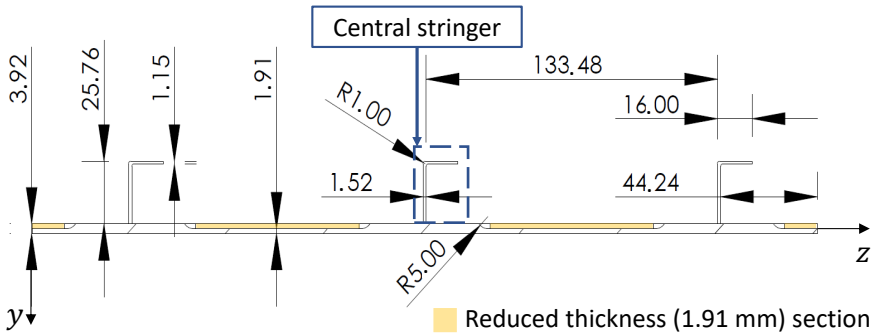


Figure 2: Section A - Section view of the panel. The section A is defined in Figure 1. All dimensions are expressed in mm.

The panel is tested in a simply supported condition. The simple support is obtained by placing the panel between two half-cylinder iron bars that constrain the transverse displacement but allow the rotations (Figure 3). The two supports are parallel to the shortest edges and located at a distance of 30 mm from them. The panel is loaded on the flat surface with a concentrated transverse force. The load is transmitted to the midpoint of the panel through an iron sphere that is pushed downwards by a iron bar installed on two threaded bars. By tightening two bolts on the threaded bars, the iron bar is pushed down and the load is transmitted to the panel by the sphere. The threaded bars are instrumented with two load cells in order to measure the applied load. The experimental setup is shown in Figure 4.

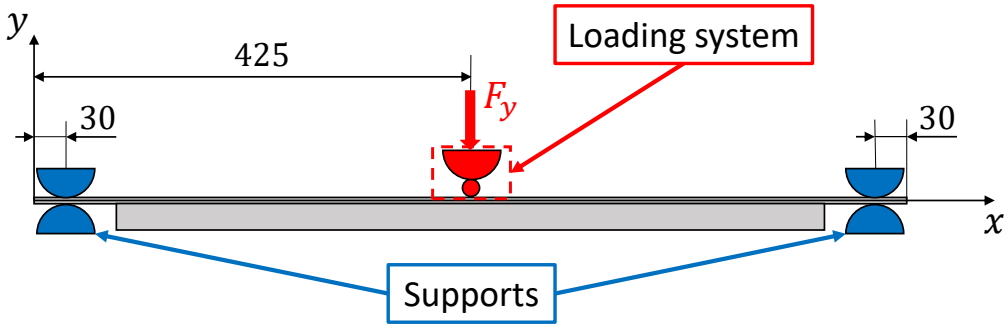


Figure 3: Loading system and boundary conditions. All dimensions are expressed in mm.

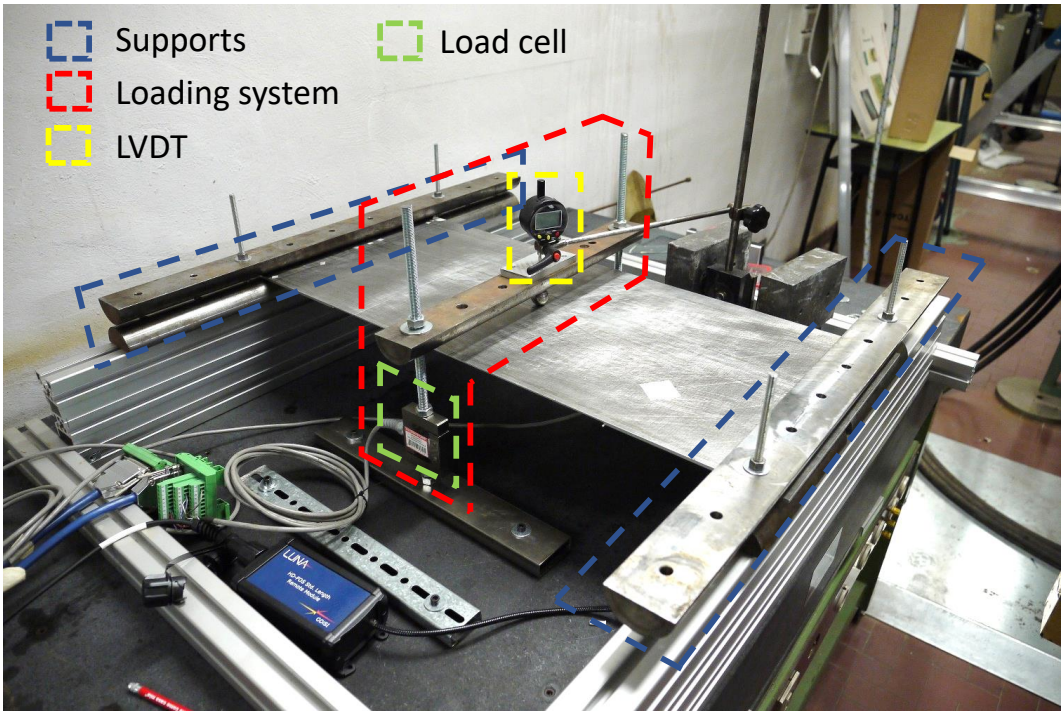


Figure 4: Experimental setup - The test is performed using four LVDTs. In the picture only one of the four LVDTs is shown. The detailed configuration of the LVDTs is presented in Fig. 7

## 4 Inverse models and strain sensors

Two inverse models of the structure have been realized. The first one is a standard shell-only model, made of 914 inverse quad elements and 978 nodes, accounting for a total of 5868 DOFs (Figure 5a). In this case, all the components of the panel are simulated using quad shell elements. This model is used as benchmark to evaluate the accuracy and the efficiency of the hybrid model. The focus of this work, the hybrid model, on the other hand, is constituted of 608 inverse quad elements to simulate the panel and of 102 inverse beam elements to model the three stiffeners (Figure 5b). The model has 663 nodes and 3978 DOFs. The reduced number of DOFs indicates that this model is less computationally demanding than the shell-only one.

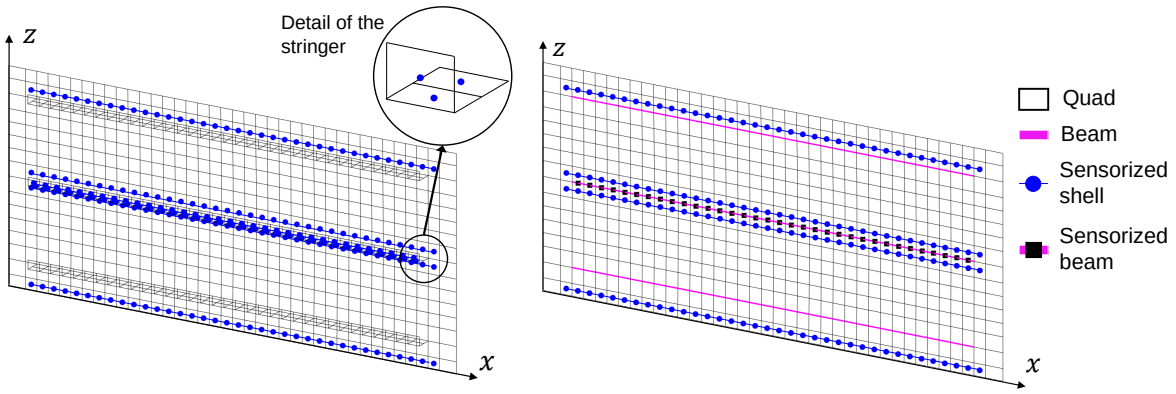


(a) Shell-only model (b) Hybrid model

Figure 5: Inverse models and strain sensors' configurations - The two inverse models are shown. The sensorized elements illustrated in the figures consider uni-axial strain sensors along the x direction.

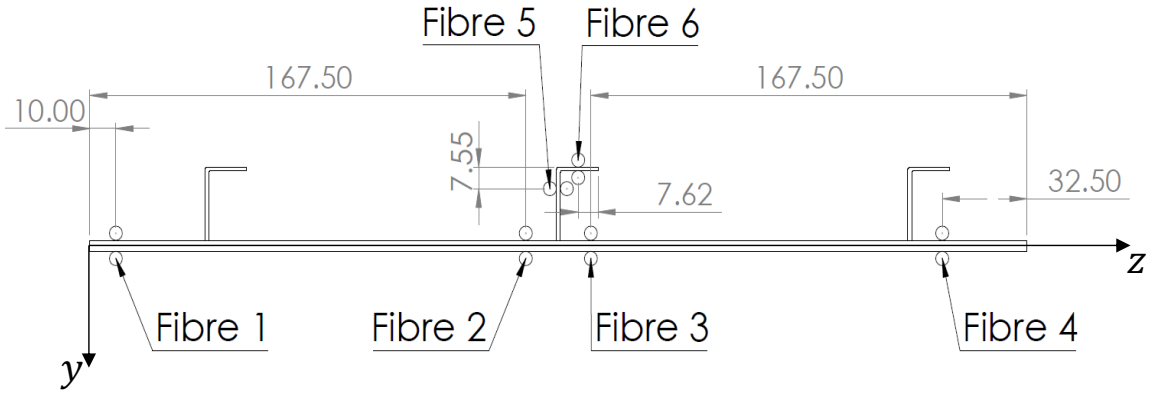


Figure 6: Distribution of the fibres on the panel. The fibres are numbered considering only one side of the back-to-back configuration. All dimensions are expressed in mm.

The strain sensors' configuration for the two models is illustrated in Figure 5. The configuration only considers mono-axial strain measurements in the direction of the longest edge of the panel. The configurations are experimentally obtained by instrumenting the panel with fibre optic strain sensors based on the Rayleigh scattering. These sensors allow the measurement of the strain along the fibre direction with an impressive density of a strain measurement every 1.3 mm. The strain sensors' configuration adopted for this test includes six sensing lines along the panel's length in a back-to-back configuration, i.e. every line on one side of the panel has a corresponding line on the other side as well. The six sensing lines of fibre are distributed on the panel as illustrated in Figure 6. The first four lines (Fibre 1-4), that are installed on the panel, are common to both the models' configurations. They guarantee, thanks to the sensors' density of the fibre, the sensing of the mono-axial strain in the x direction at the centroid of every sensorized shell element on both the bottom and top surface, as prescribed by the inverse

shell's formulation. For the shell-only model, Fibre 5 and 6, in the back-to back configuration, allow the sensorization of the shell elements simulating the central stringer, in the same way described for the panel. On the other hand, for the hybrid model, the sensorization of the beam elements, relative to the central stinger, only need three sensing lines, Fibre 5 in the back-to-back configuration, and Fibre 6, without the internal sensing line. In fact, the full sensorization of each beam element is obtained by measuring the three axial strains, coming from the fibres, at two sections($l_e/4$; $3l_e/4$) along the element's length ($l_e$).

To summarize, the hybrid model has less DOFs with respect to the shell-only one and, therefore, is less computationally demanding. Morover, because of the beam elements' formulation, to obtain a strain sensors' configuration that monitors the same components of the structure, slightly fewer sensors than the shell-only model are needed.

## 5 Experimental Results

The experimental test is performed by loading the structure with a concentrated load of 879 N. To assess the accuracy of the shape sensing for the two models, during the test, the transverse deflections of the panel in four points are experimentally measured with LVDTs. One LVDT is placed on the loading system and measures the maximum transverse deflection of the panel. The other three LVDTs are randomly distributed over the flat surface of the panel, as shown in Figure 7.

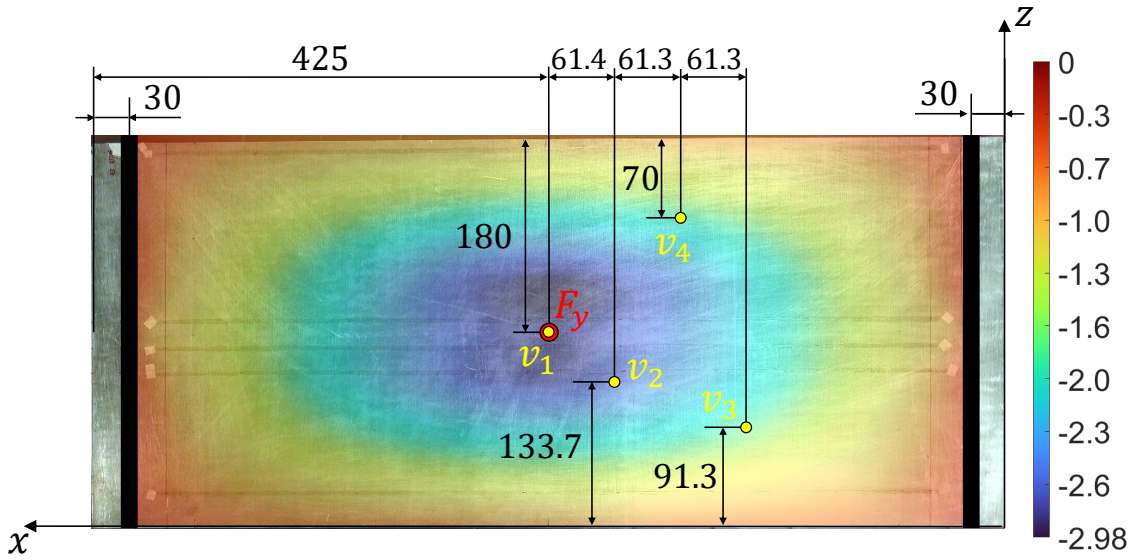


Figure 7: Results and LVDTs' configuration - The contour plot of the reconstructed transverse deflection with the hybrid model is shown on the panel. Moreover the location of the four LVDTs is presented. All dimensions are expressed in mm.

Once the test is performed, the data from the optic fibre are collected to perform the iFEM analysis with the two models. The reconstruction of the transverse deflection for the whole panel, using the hybrid model, is presented in Figure 7. More in details, the experimental values of the measured deflections and the reconstructed values for the two inverse models are reported in Table 2. In the table, the percentage errors and the mean absolute percentage errors are also reported. From the analysis of these values, it can be noted that the average accuracy

of the two model is strongly correlated. Both models show an extremely low value of the mean error, that is lower than $2\%$. Moreover, also the evaluation of the errors relative to the single displacements shows that the level of accuracy of the hybrid model is totally comparable with the one obtained by the shell-only model. In fact, although small differences exist for the single values, all the errors, for both the considered cases, are comprised between $0.6\%$ and $2.0\%$.

| | Experimental | Hybrid iFEM | Shell-only iFEM |
|---|---|---|---|
| $F_y\ [N]$ | 879 | | |
| $v_1\ [mm]$ | 3.030 | 2.983 | 2.988 |
| $(\%Err_{v_1})$ | | (-1.5%) | (-1.4%) |
| $v_2\ [mm]$ | 2.698 | 2.715 | 2.661 |
| $(\%Err_{v_2})$ | | (+0.6%) | (-1.4%) |
| $v_3\ [mm]$ | 1.670 | 1.652 | 1.636 |
| $(\%Err_{v_3})$ | | (-1.1%) | (-2.0%) |
| $v_4\ [mm]$ | 1.691 | 1.657 | 1.660 |
| $(\%Err_{v_4})$ | | (-2.0%) | (-1.8%) |
| $\mu(\lvert\%Err\rvert)$ | | 1.3% | 1.6% |

Table 2: Shape sensing results - In parenthesis, the percentage errors with respect to the experimental values are reported. The errors are computed considering the absolute value of the displacements. Moreover the mean absolute value of the percentage error is reported ($\mu(\lvert\%Err\rvert)$).

## 6 Conclusions

In this work, an hybrid shell-beam iFEM model is experimentally tested on the shape sensing of an aluminium stiffened panel. The model is constituted of shell inverse quad elements for the modelization of the panel and of beam inverse elements for the simulation of the L-section stringers. The accuracy of the hybrid model is compared with the one obtained using a standard shell-only model, where also the stiffeners are modeled using inverse quad elements. The configuration of the strain sensors adopted to perform the shape sensing for the two models is equivalent in terms of sensorized components. In fact, four strain sensing lines are installed on the panel and the central stringer is instrumented with strain sensing optic fibres. However, because of the different modelization of the stringer, the sensorization of this component needs one less sensing line for the beam elements belonging to the hybrid model. Therefore, the hybrid model has a little advantage in terms of required sensors. Another advantage of the hybrid model is related to the computational efficiency. This model has a reduced number of nodes and, as a consequence a smaller amount of Degrees of Freedom to be computed.

The experimental campaign proves that the accuracy in the reconstruction of the displacements obtained by the hybrid model is comparable with the one achieved by the shell-only model. In fact, both the models show the same excellent level of the error in the reconstruction of the displacements, never exceeding the value of $2\%$. This results demonstrate that the hybrid modelization for thin-walled stiffened structures can be beneficial for the shape sensing with the iFEM. In fact, this formulation allows to reach a significant accuracy with a more computationally efficient model and a slightly reduced number of strain sensors.

The use of hybrid shell-beam iFEM models should be further investigated in future works. In particular, the effect of different strain sensors' configurations and the possibility to further decrease the number of required sensors should be explored.

## REFERENCES


[1] M. Gherlone, P. Cerracchio, and M. Mattone. Shape sensing methods: Review and experimental comparison on a wing-shaped plate. *Progress in Aerospace Sciences*, 99:14 – 26, 2018. doi:10.1016/j.paerosci.2018.04.001.

[2] T. Nakamura, H. Igawa, and A. Kanda. Inverse identification of continuously distributed loads using strain data. *Aerospace Science and Technology*, 23(1):75 – 84, 2012. doi:10.1016/j.ast.2011.06.012.

[3] R. Roy, M. Gherlone, C. Surace, and A. Tessler. Full-field strain reconstruction using uniaxial strain measurements: application to damage detection. *Applied Sciences*, 11(4), 2021. doi:10.3390/app11041681.

[4] L. Colombo, D. Oboe, C. Sbarufatti, F. Cadini, S. Russo, and M. Giglio. Shape sensing and damage identification with ifem on a composite structure subjected to impact damage and non-trivial boundary conditions. *Mechanical Systems and Signal Processing*, 148:107163, 2021. doi:10.1016/j.ymssp.2020.107163.

[5] M. Esposito and M. Gherlone. Material and strain sensing uncertainties quantification for the shape sensing of a composite wing box. *Mechanical Systems and Signal Processing*, 160:107875, 2021. doi:10.1016/j.ymssp.2021.107875.

[6] A. Tessler and J. L. Spangler. A variational principle for reconstruction of elastic deformations in shear deformable plates and shells. Report NASA/TM-2003-212445, NASA Langley Research Center, Hampton, VA, United States, 2003.

[7] M. Gherlone, P. Cerracchio, M. Mattone, M. Di Sciuva, and A. Tessler. Shape sensing of 3d frame structures using an inverse finite element method. *International Journal of Solids and Structures*, 49(22):3100–3112, 2012. doi:https://doi.org/10.1016/j.ijsolstr.2012.06.009.

[8] A. Tessler and J. L. Spangler. Inverse fem for full-field reconstruction of elastic deformations in shear deformable plates and shells. In *Proceedings of the 2nd European Workshop on Structural Health Monitoring*. Munich, 2004.

[9] H. Zhu, Z. Du, and Y. Tang. Numerical study on the displacement reconstruction of subsea pipelines using the improved inverse finite element method. *Ocean Engineering*, 248:110763, 2022. doi:10.1016/j.oceaneng.2022.110763.

[10] J. Wang, L. Ren, R. You, T. Jiang, Z. Jia, and G. xin Wang. Experimental study of pipeline deformation monitoring using the inverse finite element method based on the ibeam3 element. *Measurement*, 184:109881, 2021. doi:10.1016/j.measurement.2021.109881.

[11] R. Roy, M. Gherlone, and C. Surace. A shape sensing methodology for beams with generic cross-sections: Application to airfoil beams. *Aerospace Science and Technology*, 110:106484, 2021. doi:10.1016/j.ast.2020.106484.

[12] D. Oboe, L. Colombo, C. Sbarufatti, and M. Giglio. Shape sensing of a complex aeronautical structure with inverse finite element method. *Sensors*, 21(4), 2021. doi:10.3390/s21041388.

[13] A. Kefal, J. B. Mayang, E. Oterkus, and M. Yildiz. Three dimensional shape and stress monitoring of bulk carriers based on ifem methodology. *Ocean Engineering*, 147:256 – 267, 2018. doi:10.1016/j.oceaneng.2017.10.040.

[14] M. Esposito, M. Mattone, and M. Gherlone. Experimental shape sensing and load identification on a stiffened panel: A comparative study. *Sensors*, 22(3), 2022. doi:10.3390/s22031064.

COMPDYN 2023
9th ECCOMAS Thematic Conference on
Computational Methods in Structural Dynamics and Earthquake Engineering
M. Papadrakakis, M. Fragiadakis (eds.)
Athens, Greece, 12-–14 June 2023

# EXPERIMENTAL AND NUMERICAL DYNAMIC EVALUATION OF PROFILED STEEL DECKING SLAB IN A CONTAINER HOUSE USING MEMS

**Henrique Tavares Lima[1], Luis Ernesto de Medeiros Alas[1], Mateus Narcizo de Almeida Nunes[1], Iálysson da Silva Medeiros[1], and Douglas Mateus de Lima[1]**

[1]Graduate Program of Civil and Environmental Engineering Academic Center of Agreste
Federal University of Pernambuco
Avenida Marielle Franco, Bairro Nova Caruaru, Caruaru - PE, Brazil, ZIP Code: 55014-900
e-mail: {henrique.tlima, luis.alas, mateus.narcizo, ialysson.medeiros, douglas.mlima}@ufpe.br

**Abstract.**
*The reuse of shipping containers is common in civil construction, not only for ecological reasons but also for speeding up the construction time, thus favoring the decrease in the payback time of the applied financial investment. Consequently, technological developments guarantee this trend with lighter structural elements, thus occurring natural frequencies closer to the frequency ranges of dynamic excitations associated with human activities. Therefore, a direct consequence of this new design trend is a considerable increase in problems related to unwanted vibrations in steel and concrete composite slabs, which arise from rhythmic actions, and external vibrations arising from earthquakes, which must be analysed to meet the comfort and safety of residents. Thus, this study aims to present a vibration analysis in a composite floor slab, built in steel deck 59S, of a residence built with reuse maritime containers in the municipality of Gravatá in Pernambuco, Brazil. The structure consists of three floors, with the cantilever slab analysed with dimensions of 8.24 m wide and 4.00 m long. In the experimental phase, vibration analysis was carried out through the heel impact test to obtain the natural frequencies, which had average values of 7.0 Hz, and average values of 7.14% for the damping ratio of the slab, a MicroElectroMechanical System (MEMS) was used, which are accelerometers of signals present in smartphone devices. Subsequently, using the software SCIA Engineer, the numerical analysis of the model was carried out, where usual discretization techniques were used through the Finite Element Method (FEM) to evaluate the structural behavior against dynamic actions, thus obtaining the results of natural frequencies, average values of 6.46 Hz, and modal shapes. With this, it was possible to verify the results regarding the natural frequencies of vibration, analysing the usability, comfort, and health of the structure according to the current normative codes. Finally, this study presents a comparison of modal parameters in numerical and experimental simulations against the dynamic actions that must be considered in the design of steel deck slabs when in a cantilever situation for the type of structure studied to validate comfort and building safety caused by dynamic effects developed by human behavior.*

**Keywords:** reuse of maritime containers, vibratory system, modal analysis, natural frequency, damping.

## 1 INTRODUCTION

It is notorious that construction processes are becoming increasingly modern, with the objectives of reducing costs, efficiency in construction, reducing execution time and being an ecologically friendly approach. With these topics in focus, some characteristics of new constructions became more evident, such as the overall weight reduction of the structure, due to the implementation of more modern and lighter materials in constructions, modularity, which allowed the industrialization of construction, the possibility increase in the height of buildings and the possibility of long free spans in bridges and given the proportions, in buildings [1].

With these mass reduction factors and increased supported structural lengths, it is common for structures to present lower natural frequencies, being more susceptible to excitations by dynamic loads and perceptible to human use, since human beings have high sensitivity to dynamic movements [2, 3, 4].

Structural dynamics involve the study of vibrational forces and the properties of any type of structure, with dynamic amplification as the phenomenon caused when the frequencies of this vibration have values close to the natural frequency of the structure, which should be avoided. Therefore, the participation of the mass of the building must be analyzed in relation to the degrees of freedom of the structure [5].

The processes of evaluating the dynamics of the structures, using sensors, allowed the development and optimization of the structures against the use of computational processes, which even allowed structural health monitoring (SHM)[6].

With the advancement of miniaturization of microchips, the emergence of Electro-Mechanical Systems allowed accelerometers to be miniaturized and inserted into cell phones for various purposes. Thus, it is possible to use telephone devices equipped with these systems for dynamic monitoring of structures. With this, it is possible to carry out dynamic monitoring with a smaller financial investment, when compared to traditional commercial accelerometer systems [6, 7].

Therefore, this work has the objective of verifying the dynamic behavior of the cantilevered slab of the structure using an experimental and numerical approach to obtain dynamic behavior data of the building, verifying the applicability of the reuse of maritime containers in civil construction works.

## 2 METHODOLOGY

This work sought to analyse the vibration characteristics of the cantilevered slab, with dimensions of $8.24\ m$ in longitudinal length and $4.00\ m$ in cantilever, composing a portion of the structure of the building, which has $313.02\ m^2$ in total area built, distributed in three floors, one semiunderground, ground floor and an upper floor, as illustrated in accordance with Figure 1a. Figure 1b illustrates the rear of the building during the construction process, likewise Figure 1c shows the east façade and Figure 1d shows us the façade west, illustrating the completion of the structural elements.

The cantilevered slab structures of a single-family residence built with the reuse of shipping containers, Figura 1, in the city of Gravatá, in the Agreste region of the state of Pernambuco, Brazil, are described as the object of study. The structure of the cantilevered slabs presents their composition according to Figure 1e, responsible as a linking element between the two upper containers, as shown in Figure 1f.

Thus, it is possible to perceive that the structure of this slab is composed partly by the floor structure of the maritime container and the other part by a composite structure, with steel deck plates supported on cold-formed profiles, connected to each other through welded connections,



(a) North facade.

(c) East facade.

(d) West facade.

(e) Structural cantilever of composite slabs.

(f) Containers locations.

Figure 1: Container house.

considered the title of this work to be rigid links.

Table 1 presents the materials used to compose the slab floors present in the building's cantilever, a portion that also connects the structure between the two upper containers.

| Element | Specification | Material | Norm |
|---|---|---|---|
| Slab Beam | U-150x50x3 | Cold-Formed Steel - CFS | ABNT NBR6355 [8] |
| Steel deck | Polydeck 59S | Profiled Steel | ABNT NBR16421 [9] |
| Concrete topping | $25MPa$ | Reinforced concrete | ABNT NBR6118 [10] |

Table 1: Slab structural specifications.

Therefore, based on the characteristics of the materials that make up the structure of the cantilevered slab, it was possible to define the mechanical properties of these elements in the elaboration of the numerical model of the analysed structure.

The methodology was constituted by two main phases of analysis of the dynamic behavior of the slabs of the structure, being an experimental phase, with local analysis to obtain the vibrations with the aid of a smartphone device using the software *MyFrequency* [11], and another numerical phase, using the commercial software *SCIA Engineer V21.1* [12], to carry out the modelling. The study was carried out on the floor structure present in the cantilevered region of the building, located on the upper floor, built with steel deck slabs supported on cold-formed profiles and another portion of the slab, made with the reuse of the floor structure of the container.

Figure 2 presents the flowchart proposed for the development of the research and obtaining the vibrational parameters of the analysed structure to obtain the results and compare them with the methodologies employed. Therefore, the structure analysis process was defined to obtain the vibrational modes of the studied slabs to identify the points of the structure that meets or

does not meet the frequency characteristics available in Annex L of NBR8800:2008 [13].

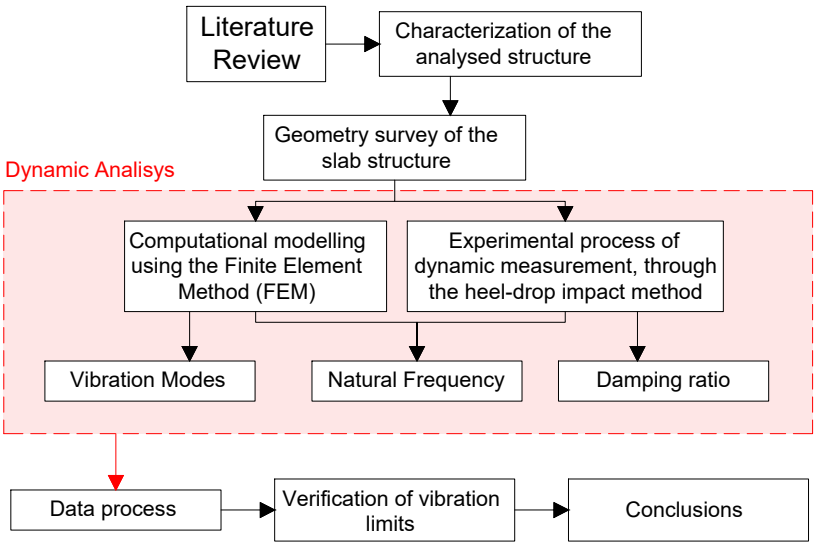


Figure 2: Metodology fluxogram.

Although there are vibration considerations in the Brazilian current, the subject is treated with simplicity and undergoes a review process; therefore it is also necessary to consider other standards and procedures of international relevance that become important for verifying the vibration parameters, such as AISC Design Guide 11 - Vibrations of steel-framed structural systems due to human activity:2016 [14] and PCI Design Handbook - precast and prestressed concrete:2004 [15].

## 2.1 Experimental Phase

To carry out the procedure, the flowchart defined by Figure 3 illustrates the execution process of this step. The experimental part of the work consisted of carrying out the heel impact test on the cantilevered region of the structure, at the points numbered from P1 to P5, defined in the cantilevered region, according to Figure 4, and at the points P6, P7, P8, P9, P10, P11, P12 and P13, located in other regions of building, with dimensions in $mm$, to excite the structure and obtain the vibrational parameters of the slab[16, 17].

Data were captured using a smartphone, model S21 Ultra from Samsung, equipped with a microelectromechanical system (MEMS) model LSM6DSO, manufactured by STMicroelectronics, with a maximum sample resolution rate of $500\ Hz$.

Therefore, with the points for carrying out the procedures defined, the region where the smartphone device would be fixed to the floor was cleaned. To perform the fixation, a double-sided acrylic tape with a resistive capacity of 180 g per meter, according to the manufacturer, was applied directly to the posterior region of the device, without the use of protective covers to reduce interference by elements in the collection of the data. Points P1 and P2 are covered with ceramic tiles, point P3 is laminated with wood and points P4 and P5 are finished with carpet.

To observe the dynamic behavior of other regions of the building, with different structural characteristics, the study regions described in points P6, P7, P8, P9, P10, P11, P12 and P13, according to Figure 5 presented other provisions of structural design. The characteristics of

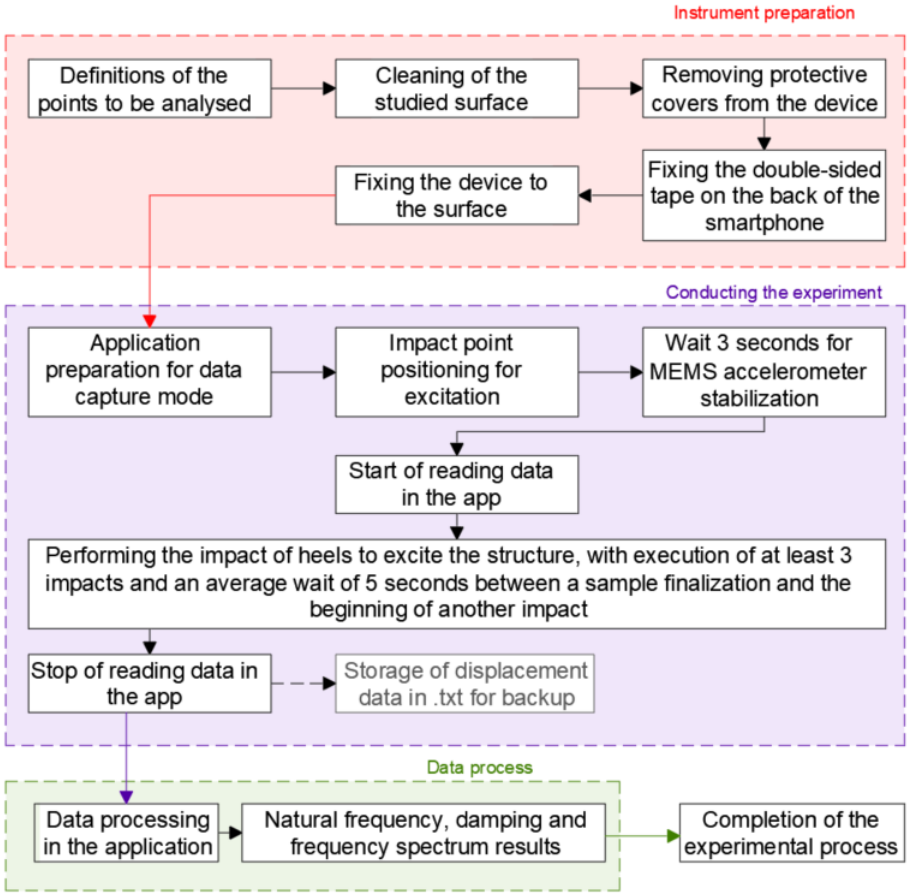


Figure 3: Experimental phase flowchart.

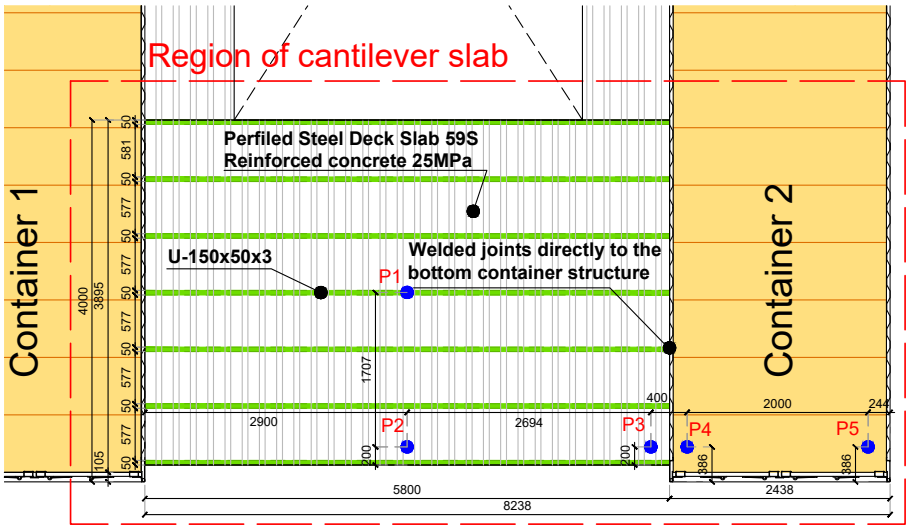


Figure 4: Analysed region of the cantilever slab.

the structural conditions of the slabs at these points are defined by different means of design, regarding the type of slab element, the type of horizontal elements and supporting conditions with support, according to Table 2.

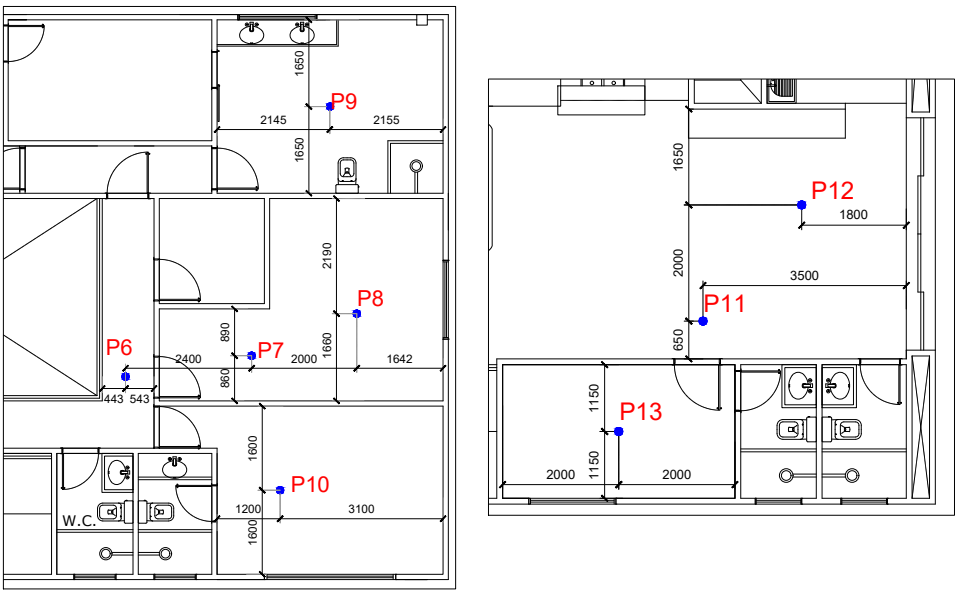


(a) $2^{nd}$ floor. (b) $1^{st}$ floor.

Figure 5: Container house regions.

| Point of analysis | Slab type | Support horizontal element | Region |
|---|---|---|---|
| P6 | Steel deck | Truss - CFS | Hall |
| P7 | Steel deck | Truss - CFS | Office |
| P8 | Steel deck | Truss - CFS | Office |
| P9 | Steel deck | Truss - CFS | Bathroom |
| P10 | Steel deck | Truss - CFS | Suite 1 |
| P11 | Steel deck | I profile - laminated steel | Playroom |
| P12 | Steel deck | I profile - laminated steel | Playroom |
| P13 | Concrete on container floor | Container floor structure | Suite 2 |

Table 2: Description of the structural typology in other parts of the building.

The processing of the experimental data was performed using software developed for the Android operating system, which allowed us to calculate the damping and obtain the frequency spectrum through the fast Fourier transform (FFT).

The software used was MyFrequency, which has the ability to obtain displacement values according to the axis possibilities present in the MEMS sensor available on the device. In this case, the sensor used has the ability to evaluate three axes; however, the analysed data were restricted to the vertical displacement of the structure.

The accelerometer sensitivity was $200\ Hz$ to reduce the capture of external signals due to bad weather, local traffic and other activity dynamics present at the site that could generate

excessive noise in the collected samples.

After attaching the smartphone to the point under analysis, a few seconds were waited for the calibration of the MEMS accelerometer signal, and the heel impact was performed at average intervals of 3 seconds, after returning to the resting state of the previous impact. The impact was made by a person measuring $1.65\ m$ tall and weighing 79 $kg$.

Through the application, during the experiment, it was possible to obtain the natural frequency in $Hz$, and the percentage damping values, displayed according to the variable $D$ in the application.

The frequency spectrum was obtained through the use of the FFT, using the application, and it is possible to observe in the spectrum the variation of the frequency data obtained in the test, with values in $Hz$ and in acceleration values, in $m/s^2$. With the frequency spectrum, the variation of the dynamic values in the evaluated range can be evaluated.

The measurements of the practical heel impact test underwent statistical control according to the precision intervals described by [18], in which test precision values are presented according to the coefficient of variation (D.V.C.) present in Table 3.

| D.V.C. | D.V.C. Evaluation | Precision |
|---|---|---|
| $< 10\%$ | Low | Very High |
| 10% to 20% | Medium | High |
| 20% to 30% | High | Low |
| $> 30\%$ | Very High | Very Low |

Table 3: Data variation coefficients.

## 2.2 Numerical Model

Numerical analysis was performed using the Scia Engineer V21.1 software, which uses the usual discretization techniques through the Finite Element Method (FEM). With this software, it is possible to model, analyse, dimension and optimize a three-dimensional model, regardless of the structural system and material adopted, due to the different analysis options, using Brazilian, American or European regulations. Plus, it plugs into a BIM workflow with a logical and intuitive CAD-like interface.

Based on the measurements carried out in loco, it was possible to perform preprocessing, processing and postprocessing of the structure of the container house, as shown in Figure 6.

In the pre-processing stage, the finite elements were defined for each structural component to simulate the real behavior of the structure; definition of the type (steel and concrete) and characteristics of the materials (modulus of elasticity, Poisson coefficient, characteristic compressive strength of concrete, yield strength and ultimate strength of steel, etc.); cross sections, in the case of bar elements, (e.g., C profile, W profile, angle and others); and thickness of two-dimensional components. To facilitate the visualization and distinction of each structural element in the modelling phase, layers were used, a functionality that allows the variation of colors between the modelled elements, as seen in Figure 7.

Still in the preprocessing stage, the linkages of the structural components (columns, beams and trusses) were defined; restrictions on the base supports, with clamping at the bases of the columns and other elements in contact with the ground; connections of elements and nodes, that is, interconnection between one-dimensional and two-dimensional elements that are in contact;

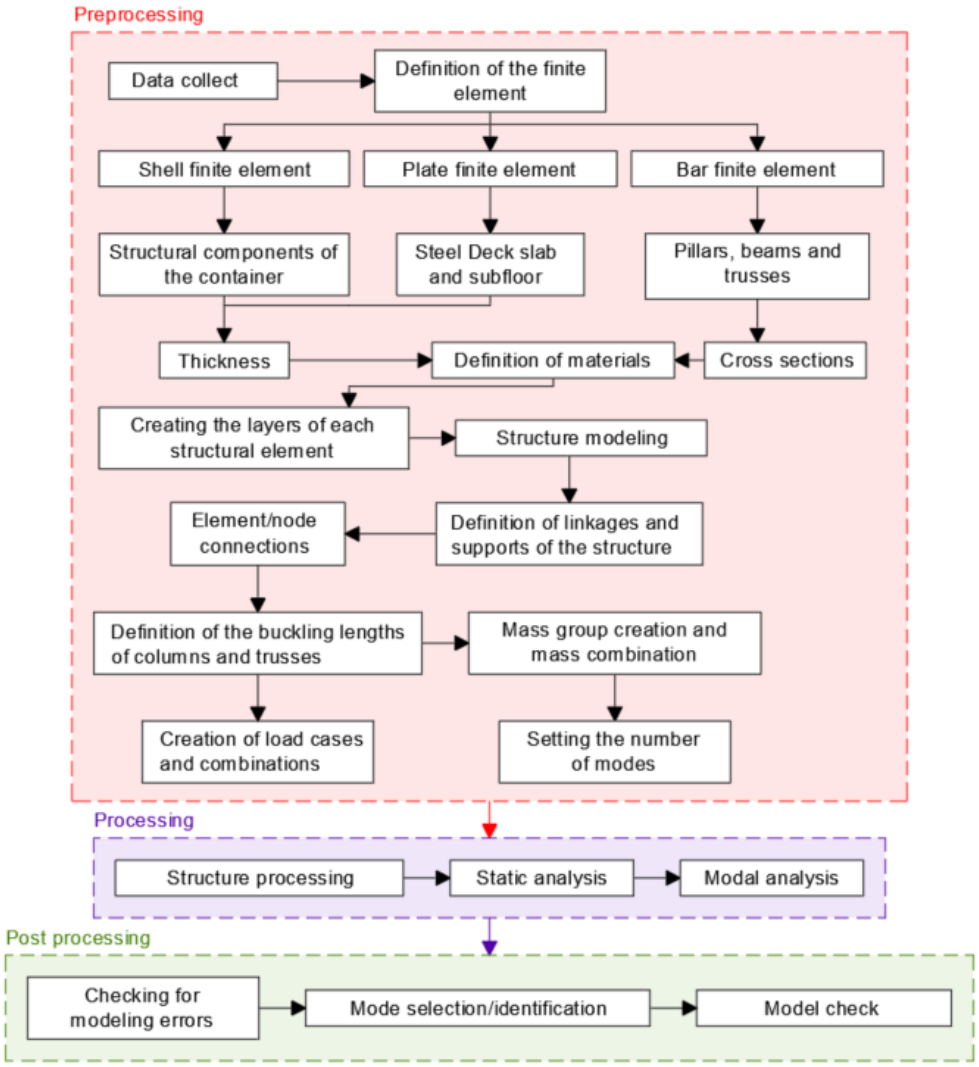


Figure 6: Numerical model flowchart.

configuration of the buckling coefficients of columns and trusses. Cases of loads and combinations were also created for the static analysis phase, and groups of mass and mass combinations were created for the modal analysis phase. The last definition was the number of natural modes, which at first were processed in six ways to understand the movement of the system, and soon after, the structure was processed with thirty modes.

In the processing and postprocessing stage, the model was processed, and then a static and modal analysis was carried out. The first analysis was carried out with the objective of verifying the modelling errors and guaranteeing the functioning of the structure in accordance with the real one. In the modal analysis, the identification and selection of the important vibration modes for the analysis were performed. To obtain the results of the analysis, 80423 two-dimensional elements, 2810 one-dimensional elements and 65257 nodes were used.

It is worth mentioning that in view of the analyses carried out, it can be seen that the Steel Deck slabs, modelled on the ground and upper floors outside the perimeter of the containers, were not following the movement of the support elements, which was found that the assigned plate element behaved like a rigid diaphragm, so a modification was made to the FEM model.

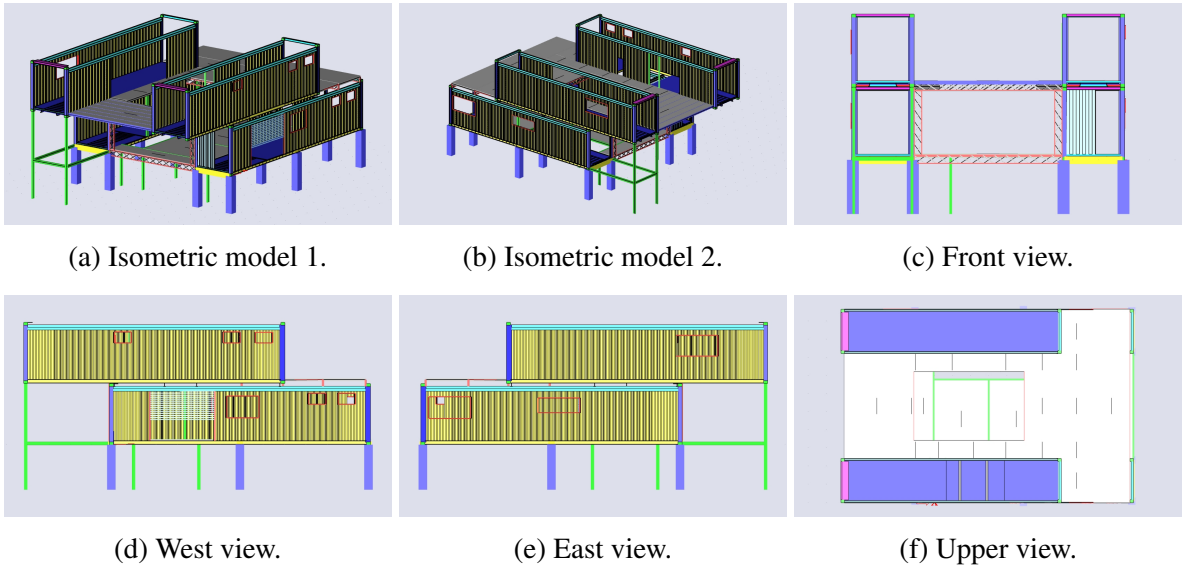

(a) Isometric model 1. (b) Isometric model 2. (c) Front view.

(d) West view. (e) East view. (f) Upper view.

Figure 7: Container house FEM model.

## 3 RESULTS AND DISCUSSION

After carrying out the processes proposed by this work, this section will present the results and their respective discussions of the numerical and experimental models to compare the results obtained between the two methodologies and verify the usability conditions of the studied structure.

### 3.1 Experimental Dynamic Results

The experimental phase obtained displacement data after the heel impact test, which were recorded and processed at points distributed throughout the building. Figure 8 shows the values obtained for the analysis of points P1, P2, P3, P4 e P5, showing the accelerations in $m/s^2$ caused by each impact as a function of time.

Table 4 presents the data obtained for each of the analysed points on the cantilevered floor slab, presenting the frequency values and the damping rate of the floor. Additionally, the average values were calculated, as well as the standard deviation of the collected samples.

The acceleration results presented in the graphs shown in Figure 9, correspond to the analysed points on the upper floor of the building, outside the cantilever region, located in previously described rooms.

The processing of data from points P2, P3, P6, P7, P8, P9 and P10 showed average frequency and damping values according to Table 5. Some of these points, P6 in particular, showed high damping values, obtained through the average of the samples. Some factors internal to the structure can influence the data obtained, such as movements between structural elements, internal material dissipation, and supports. Other external, nonstructural factors may also have had an influence, such as furniture and the drywalls[19]. The energy dissipation is caused by material damping which basically depends on three factors: amplitude of stress, number of cycles and geometry. In the case of nonhomogeneous stress distribution the geometry of the structure influences the vibration damping [21, 20].

Figure 10 shows the displacement points recorded on the ground floor of the building. The processing of data from points P11, P12 and P13 showed average frequency and damping values

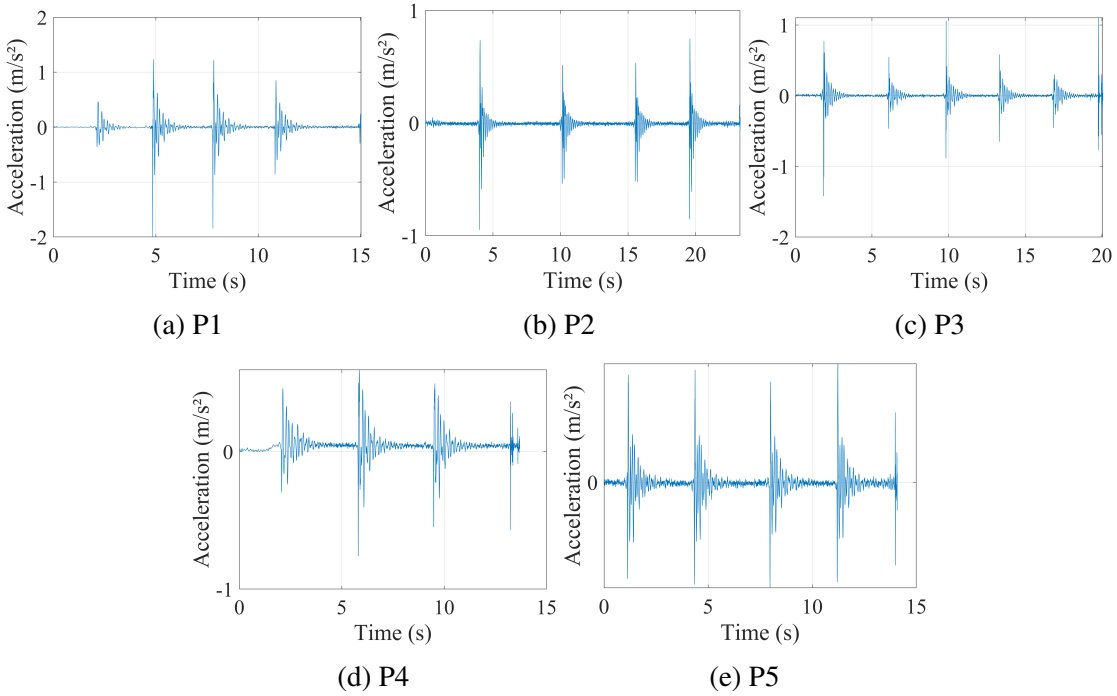


(a) P1 (b) P2 (c) P3

(d) P4 (e) P5

Figure 8: Accelerations recorded on the cantilevered slab in the heel impact test.

| Analysed Point | Sample | Frequency ($Hz$) | Damping Ratio (%) | Average Frequency ($Hz$) | Average Damping Ratio (%) |
|---|---|---|---|---|---|
| P1 | 1 | 10.8 | 3.53 | 10.77 | 3.48 |
| | 2 | 10.8 | 3.52 | | |
| | 3 | 10.7 | 3.4 | | |
| P2 | 1 | 7.1 | 9.25 | 7.10 | 8.29 |
| | 2 | 7.2 | 7.32 | | |
| | 3 | 7.1 | 7.99 | | |
| | 4 | 7.0 | 8.61 | | |
| P3 | 1 | 7.1 | 9.25 | 7.10 | 8.29 |
| | 2 | 7.2 | 7.32 | | |
| | 3 | 7.1 | 7.99 | | |
| | 4 | 7.0 | 8.61 | | |
| | 5 | 7.0 | 8.61 | | |
| P4 | 1 | 7.2 | 4.21 | 7.10 | 3.99 |
| | 2 | 7.2 | 4.38 | | |
| | 3 | 6.9 | 3.39 | | |
| P5 | 1 | 11.1 | 3.18 | 10.95 | 2.88 |
| | 2 | 11.1 | 2.73 | | |
| | 3 | 11.0 | 2.49 | | |
| | 4 | 10.6 | 3.12 | | |

Table 4: Frequency and damping values of the analysed points of the cantilevered slab.

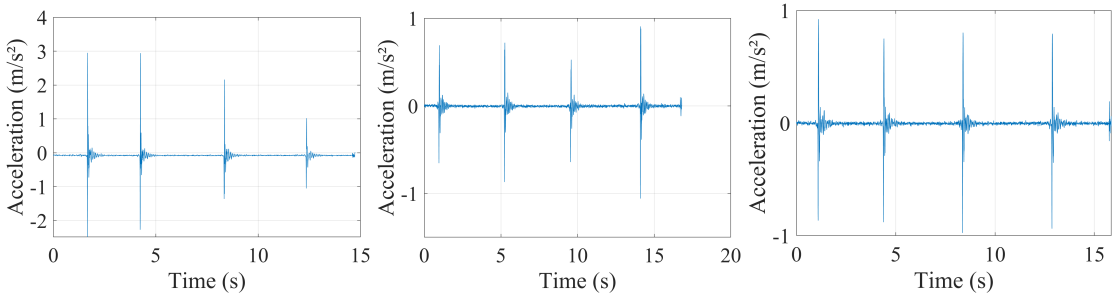


(a) P6 (b) P7 (c) P8

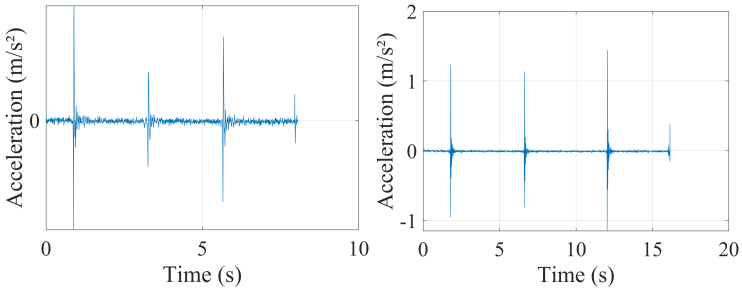


(d) P9 (e) P10

Figure 9: Accelerations on the posterior part of the $2^{nd}$ floor in the heel impact test.

| Analysed Point | Sample | Frequency ($Hz$) | Damping Ratio (%) | Average Frequency ($Hz$) | Average Damping Ratio (%) |
|---|---|---|---|---|---|
| P6 | 1 | 11.0 | 25.5 | 10.80 | 23.94 |
| | 2 | 10.6 | 27.56 | | |
| | 3 | 10.3 | 17.91 | | |
| | 4 | 11.3 | 24.79 | | |
| P7 | 1 | 11.4 | 8.06 | 10.98 | 9.22 |
| | 2 | 11.5 | 8.76 | | |
| | 3 | 10.4 | 9.84 | | |
| | 4 | 10.6 | 10.23 | | |
| P8 | 1 | 14.4 | 8.08 | 14.25 | 7.82 |
| | 2 | 14.2 | 7.18 | | |
| | 3 | 14.3 | 8.34 | | |
| | 4 | 14.1 | 7.67 | | |
| P9 | 1 | 17.1 | 7.44 | 17.30 | 7.36 |
| | 2 | 17.3 | 8.09 | | |
| | 3 | 17.5 | 6.55 | | |
| P10 | 1 | 23.7 | 10.58 | 22.83 | 11.53 |
| | 2 | 23.4 | 13.19 | | |
| | 3 | 21.4 | 10.81 | | |

Table 5: Frequency and damping values of the points in the posterior region of the $2^{nd}$ floor.

according to Table 6.

To verify the precision of the sample results, Table 7 presents the evaluation of data precision

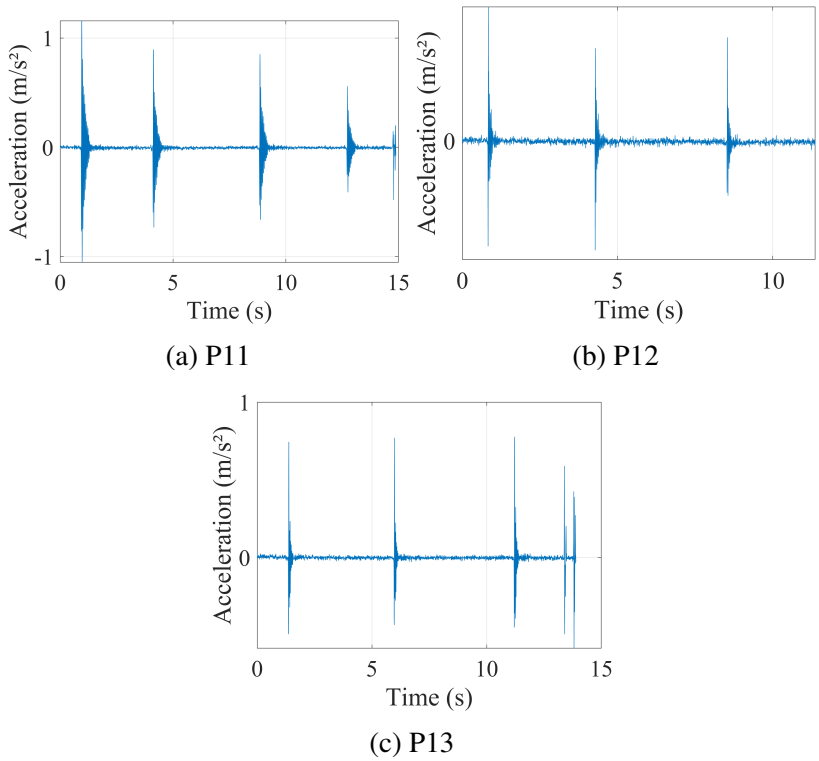


(a) P11 (b) P12

(c) P13

Figure 10: Accelerations on the $1^{st}$ floor in the heel impact test.

| Analysed Point | Sample | Frequency ($Hz$) | Damping Ratio (%) | Average Frequency ($Hz$) | Average Damping Ratio (%) |
|---|---|---|---|---|---|
| P11 | 1 | 28.6 | 4.61 | 29.15 | 4.58 |
| | 2 | 29.4 | 4.69 | | |
| | 3 | 28.8 | 4.35 | | |
| | 4 | 29.8 | 4.68 | | |
| P12 | 1 | 35,0 | 4.64 | 35.37 | 4.53 |
| | 2 | 35.8 | 4.74 | | |
| | 3 | 35.3 | 4.22 | | |
| P13 | 1 | 37.8 | 5.51 | 38.40 | 6.29 |
| | 2 | 38.1 | 6.77 | | |
| | 3 | 39.3 | 6.59 | | |

Table 6: Frequency and damping values of the points in the posterior region of the $1^{st}$ floor.

according to the coefficients of variation of the data.

The results obtained in the experimental model showed similar values in all observed regions of the floor made of steel deck and cold-formed profiles, consisting of points P1, P2 and P3, and in point P4, which already presents an analysis inside the container in balance. Point P5 presented a sampling frequency above $10\ Hz$, indicating greater rigidity in this studied point of the structure.

Therefore, after summarizing the experimental results, it is possible to identify some important points in the analysed regions:

| Analysed Point | Average Frequency ($Hz$) | Average Damping (%) | D.V.C Frequency | D.V.C Ratio Damping |
|---|---|---|---|---|
| P1 | 10.77 | 3.48 | 0,54% | 1,70% |
| P2 | 7.10 | 8.29 | 1.15% | 8.64% |
| P3 | 7.16 | 6.88 | 4.14% | 9.29% |
| P4 | 7.10 | 3.99 | 2.44% | 10.82% |
| P5 | 10.95 | 2.88 | 2.17% | 9.85% |
| P6 | 10.80 | 23.94 | 4.07% | 15.15% |
| P7 | 10.98 | 9.22 | 5.07% | 9.33% |
| P8 | 14.25 | 7.82 | 0.91% | 5.61% |
| P9 | 17.30 | 7.36 | 1.16% | 8.58% |
| P10 | 22.83 | 11.53 | 5.48% | 10.24% |
| P11 | 29.15 | 4.58 | 1.89% | 3.01% |
| P12 | 35.37 | 4.53 | 1.14% | 4.97% |
| P13 | 38.40 | 6.29 | 2.07% | 8.85% |

Table 7: Results and accuracy rate.

- The points described by the cantilever region showed low frequency in the edge regions, with an increase in the natural frequency when approaching the support of the slab, described by point P1;
- The cantilevered region of the container structure has a lower frequency in the connection region with the cold-formed profile slab composition, point P4, showing an increase in the frequency obtained in the corner region, described by point P5. This phenomenon may indicate a possible influence of the cantilevered slab made with a cold-formed profile on the shell element with container;
- The rear region of the property on the second floor, described by points P6, P7, P8, P9 and P10, presented frequencies above $10\ Hz$, which may indicate increased rigidity in the region. However, high values were also noticed in the damping data, which may indicate that the structure has a complex design, due to the wide variety of materials used in the structure, in floor coverings and their interactions with each other. Loads of use, such as furniture, can also be a factor that influenced these results, as well as the disposition of the nonstructural closing elements, the drywall panels, made with aluminum profiles, drywall boards and internal filling with foam of expanded polypropylene;
- The rear region of the property on the first floor, described by points P11, P12 and P13, also showed frequencies above $10\ Hz$, indicating high rigidity. The structural configuration of this region was elaborated with laminated steel profiles between the union of the containers, indicated according to points P11 and P12, with a significant increase in the central region of the floor, point P12. Point P13 determines the floor region where the container structure was used, without changing the original shape, presenting a high degree of rigidity, due to the high frequencies.

### 3.2 Numerical Model Results

After defining, modelling and dimensioning the numerical model of the structure, it was observed that within the possibilities of floor bending, in the range of thirty modes obtained,

two modal conditions presented deformation behavior according to the deformations induced by the experiment, displayed in Figure 11.

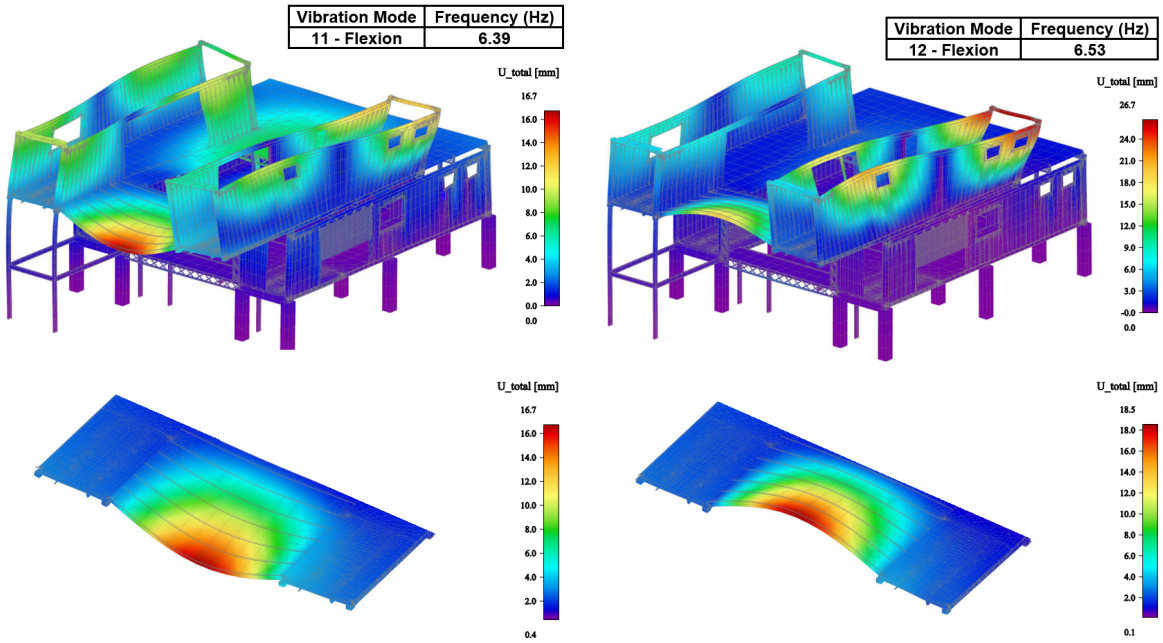


(a) Mode 11 - Flexion (b) Mode 12 - Flexion

Figure 11: Slab deformation modes through the numerical model.

The deformation of the floor occurs in the vertical axis of the structure, as evaluated in the experimental phase of the study. It is also possible to identify that the model presented a greater deformation of the steel deck slab element with cold formed profiles.

The observed vibration modes also exhibited a response regarding the deformation of the structure panels; however, experimental verifications of this behavior were not carried out.

The biggest challenge found in numerical solutions in dynamic behavior is the difficulty of obtaining and inserting real data from the analysed structure. Several factors can influence the dynamic results of a structure, such as the actual mass installed in the structure, contemplating precise loads of coatings, walls and furniture. It is also worth noting that special factors may vary in real situations, such as the wear and tear of the building due to redox over the years since its conception.

### 3.3 Comparison

The results obtained through the two approaches used in this article for points P1, P2, P3, P4 and P5 can be found in Table 8.

Due to the amount of modal analyses carried out in the numerical model, it was not possible to identify the behavior of vertical bending in floor slabs for the regions delimited by points P6, P7, P8, P9 and P10, on the $2^{nd}$ floor, and the same goes for points P11, P12 and P13, present on the $1^{st}$ floor of the building, which have experimental data of very high frequencies, characterizing themselves as rigid elements. However, it is perceived that the numerical and experimental models coincide in the observed points with a lower frequency, that is, in the points where the greater deformation of the structure was presented.

| Analysed Point | Experimental Frequency | Numerical Frequency | | Percentage Similarity | |
|---|---|---|---|---|---|
| | | Mode 11 | Mode 12 | Mode 11 | Mode 12 |
| P1 | 10,77 | | | 59% | 61% |
| P2 | 7,10 | | | 90% | 92% |
| P3 | 7,16 | 6,39 | 6,53 | 89% | 91% |
| P4 | 7,10 | | | 90% | 92% |
| P5 | 10,95 | | | 58% | 60% |

Table 8: Comparison of frequencies between numerical and experimental models.

## 4 CONCLUSIONS

The adoption of structures in maritime containers can be a satisfactory alternative for use in civil construction; however, it is important to observe some dynamic requirements on the floor to comply with current regulatory standards.

The dynamic characteristics on the floor have already been studied by several authors who contributed their research to the study of the area [22, 23, 24]. Among the possible conclusions in this study, it is possible to highlight the following:

- The experimental model presented results similar to those dimensioned in the numerical model through the finite element method (FEM). By observing vibration modes 11 and 12, it was possible to excite the structure to collect data in the experimental phase, including following the frequency variation curve studied between points P1 and P5;
- The cutouts made in the panels that make up the container enclosures can affect their performance in terms of use as a structural element in buildings. Therefore, static and dynamic behavioral studies are pertinent to verify the resistive alterations of these elements;
- Annex L of ABNT NBR8800:2008 considers limits for the natural frequencies on floors depending on the use of the floor region, which may affect activity restrictions on the slab in a free bludger, as the standard does not recommend intense rhythmic activity for slabs with a natural frequency below $8\ Hz$, for maximum vertical displacements of $5mm$ in the support structures, in accordance with the conditions provided in topic 4.7.7.3.3 of this same standard. Therefore, considering that some human activities, such as walking, rhythmic and aerobic activities may not be recommended due to the natural frequency of some slabs;
- According to Steel Design Guide Series n°11 and its approach parameters regarding the flexion of the floors, it is possible to assume that the cantilevered floor presents itself as flexible, since it has sample values below $9\ Hz$ in some regions;
- The structure of the container floor itself showed satisfactory rigidity for use with residential purposes; however, the floor structures and connection between the modules of the containers can influence the structural behavior of the containers, presenting considerable flexibility;
- It is recommended for future work to consider the roof structure to analyse the influence of this element on the conditions of vibration modes of the structure, with details of the model currently built;

- It is proposed for future studies to increase the analysis of structure vibration modes to investigate the structure flexion modes for higher frequencies that may coexist with the frequencies of other regions of the building analysed in the experimental phase;
- The damping factors obtained with the experimental phase showed great variety along the points analysed through the global structure, and the factors that can influence the damping rates are numerous and varied, being linked or not to the components of structural design. Therefore, it is suggested for future work a more in-depth analysis of the structural elements used to make the structure of the property, the methodology of connections between laminated, cold-formed elements and the structure of the container, as well as loads due to furniture and coatings present in these regions.

## REFERENCES

[1] THAI, H.-T.; NGO, T.; UY, B. A. A review on modular construction for high-rise buildings. *Structures,* Elsevier BV. v. 28, p. 1265–1290, dec. 2020. https://doi.org/10.1016/j.istruc.2020.09.070.

[2] RIJAL, R.; SAMALI, B.; SHRESTHA, R.; CREWS, K. Experimental and analytical study on dynamic performance of timber-concrete composite beams. *Construction and Building Materials,* Elsevier BV, v. 75, p. 46–53, jan. 2015. https://doi.org/10.1016/j.conbuildmat.2014.10.020.

[3] BERNARDO, L. F. A.; OLIVEIRA, L. A. P.; NEPOMUCENO, M. C. S.; ANDRADE, J. M. A. USE OF REFURBISHED SHIPPING CONTAINERS FOR THE CONSTRUCTION OF HOUSING BUILDINGS: DETAILS FOR THE STRUCTURAL PROJECT. *Journal of Civil Engineering and Management,* Vilnius Gediminas Technical University, v. 19, n. 5, p. 628–646, oct. 2013 https://doi.org/10.3846/13923730.2013.795185

[4] RAMOS, A. C. S.; PEREIRA, N. N. Reducing the response time to the homeless with the use of humanitarian logistics bases (blhs) composed of shipping containers adapted as temporary shelters. *Gest. Ambient. e Sust. - GeAS,* 2022 https://doi.org/10.5585/geas.v10i1.19494

[5] REZAIEFAR, A.; GALAL, K. Free vibration of thin rectangular steel plates with geometrically-nonlinear load-displacement behavior. *Thin-Walled Structures,* Elsevier BV, v. 129, p. 381–390, aug 2018. https://doi.org/10.1016/j.tws.2018.02.032

[6] HURLEBAUS, S.; GAUL, L. Smart structure dynamics. *Mechanical Systems and Signal Processing,* Elsevier BV, v. 20, n. 2, p. 255–281, feb. 2006. https://doi.org/10.1016/j.ymssp.2005.08.025

[7] LAGO, F. S.; KRIPKA, M.; SALEM, O. S.; PRAVIA, Z. M. C. Experimental and analytical study of vibration parameters in waffle concrete slabs. *Engineering Structures,* Elsevier BV, v. 199, p. 109593, nov. 2019. https://doi.org/10.1016/j.engstruct.2019.109593

[8] NBR 6355. Perfis estruturais de aço formados a frio — Padronização. *ASSOCIAÇÃO BRASILEIRA DE NORMAS TÉCNICAS - ABNT,* 2012.

[9] NBR 16421. Telha-forma de aço colaborante para laje mista de aço e concreto - Requisitos e ensaios. *ASSOCIAÇÃO BRASILEIRA DE NORMAS TÉCNICAS - ABNT,* 2015.

[10] NBR 6118. Projeto de estruturas de concreto — Procedimento. *ASSOCIAÇÃO BRASILEIRA DE NORMAS TÉCNICAS - ABNT,* 2014.

[11] APPtodate. MyFrequency app. *Mobile app* 24 jan. 2023. https://myfrequency.jimdofree.com/english

[12] BIM Works. SCIA Engineer V21.1. *Desktop app* 20 jan. 2023. https://bimworks.com.br/scia-engineer/

[13] NBR 8800. Projeto de estruturas de aço e de estruturas mistas de aço e concreto de edifícios. *ASSOCIAÇÃO BRASILEIRA DE NORMAS TÉCNICAS - ABNT,* 2008.

[14] MURAY T. M. et al. Steel Design Guide Series n°11: Vibrations of steel-framed structural systems due to human activity. *American Institute of Steel Contruction (AISC),* 2 ed., USA, 2016.

[15] PCI Design Handbook. Precast and Prestressed Concrete. *Precast and Prestressed Institute,* 6 ed., Chicago, IL, 2004.

[16] BEHNIA, A.; HONG, A. K. B.; SHABAZI M. M.; RANJBAR N.; BEHNIA N.; VAFAEI M. R. Finite element analysis of high modal dynamic responses of a composite floor subjected to human motion under passive live load. *Latin American Journal of Solids and Structures,* FapUNIFESP (SciELO), v. 10, n. 3, p. 601–630, may 2013. https://doi.org/10.1590/s1679-78252013000300009

[17] DAVIS, B.; LIU, D.; MURRAY, T. M. S. Simmplified experimental evaluation of floors subject to walking-induced vibration. *Journal of Performance of Constructed Facilities, American Society of Civil Engineers (ASCE),* v. 28, n. 5, oct. 2014. https://doi.org/10.1061/(asce)cf.1943-5509.0000471

[18] GOMES, F. P. Curso de estatística Experimenta. *FEALQ,* 15 edition, 2009.

[19] Soriano, H. L. Introdução à dinâmica das estruturas. *Elsevier,* 1ed, Rio de Janeiro, 2014.

[20] Wang, Y. -H.; Yan, W. M.; Lo, K. F. Damping-ratio measurements by the spectral-ratio method. *Can. Geotech - NRC Canada,* J. 43, 1180-1194. 2016. https://doi.org/10.1139/t06-067

[21] CAI, C;Sun, Q. Measurement and evaluation of damping proprieties of damping material. *Metrology in Modern Context,* IMEKO 2010 TC3, TC5 and TC22 Conferences, nov 2010. https://www.imeko.org/publications/tc22-2010/IMEKO-TC22-2010-002.pdf

[22] HEDAOO N.; GUPTA L.; RONGHE G. Design of composite slabs with profiled steel decking: a comparison between experimental and analytical studies. *Springer Science and Business Media,* v. 4, n. 1, sep. 2014. https://doi.org/10.1186/2008-6695-3-1

[23] HE, J.-H.; ANJUM, N.; SKRZYPACZ, P. S. A variational principle for a nonlinear oscillator arising in the microelectromechanical system. *Journal of Applied and Computational Mechanics,* nov. 2020. https://doi.org/10.22055/jacm.2020.34847.2481

[24] ERPINSKA, M.; IRBE, M. Specifics of natural frequency measurements for floor vibration. *Engineering for Rural Development,* 2017. https://doi.org/10.22616/erdev2017.16.n031

## ACKNOWLEDGEMENTS

The authors would like to thank the Fundação de Amparo à Ciência e Tecnologia de Pernambuco (FACEPE), the Pro-Rectory of Graduate Studies (PROPG) and the Coordenação de Aperfeiçoamento de Pessoal de Nível Superior - Brasil (CAPES) - Finance Code 001, for funding the research developed in the Graduate Program in Civil and Environmental Engineering (PPGECAM) at the Federal University of Pernambuco (UFPE) at the Caruaru Campus.

COMPDYN 2023
9th ECCOMAS Thematic Conference on
Computational Methods in Structural Dynamics and Earthquake Engineering
M. Papadrakakis, M. Fragiadakis (eds.)
Athens, Greece, 12-14 June 2023

# Machine Learning Approach for Predicting Flexural Behavior Variations of I-Shaped Steel Beams due to Manufacturing Tolerances

**Cyrus Eshaghi [1*], Arefeh Mazarei[2], Rui Carneiro de Barros [1], Xavier Romão [1] and José Miguel Castro [1]**

[1] *Construct, Faculty of Engineering University of Porto, 4200-465 Porto, Portugal*
*up202010595@up.pt*

[2] *INESCTEC, Campus of faculty of Engineering of University of Porto, 4200-465 Porto Portugal*

## Abstract

*The main subject of this paper is the impact that manufacturing tolerances have on the cyclic performance of steel beams constructed with European I-shaped profiles, particularly in moment-resisting frames (MRF). The paper also examines the effectiveness of AL models in anticipating this behavior. Past research has shown that the behaviour of a structural steel member in bending is greatly affected by the variability of geometrical and material parameters. Most previous research that focused on the cyclic behaviour of MFR members used the nominal sections in their research, however regarding the geometry, in Europe, hot-rolled profiles, are produced with dimension tolerances that are specified and limited in the European standard EN 10034. In this research, a numerical study was performed to evaluate the influence of geometrical variability on the strength and deformation capacity of steel beams subjected to cyclic flexural loading conditions. For this purpose, an advanced finite element model was developed in Abaqus and validated against experimental test data. A parametric study was conducted in which the geometrical dimensions of the beam were considered as random input. Probabilistic distributions derived from experimental data were defined for each of the 6 random input variables associated with the cross-section dimensions. Then a total set of 1600 samples were generated using Latin Hypercube sampling for a range of profiles (IPE300 to IPE600) with different lengths to evaluate the effect of dimension tolerances on the behaviour of beams. The results showed that the variability in beam behaviour is significant and can cause over strength or reduced ability of steel members to deform under load, resulting in less ductile behaviour. Then using AI techniques, some models developed to predict maximum moment and rotation capacity of beams. Various models were evaluated, including nonlinear and linear regression analysis, neural network, decision tree, and random forest.*

**Keywords:** Manufacturing Tolerance, Machine learning, Cyclic Loading, Rotation Capacity, Seismic Moment Resisting Frames, Steel

## 1 Introduction

The latest international codes encourage the use of advanced numerical modeling and design checks for a thorough seismic assessment of structures. In particular, nonlinear structural analysis that employs concentrated plasticity phenomenological models is effective in simulating the flexural behavior of steel beams subjected to large deformation. However, the accuracy and acceptance criteria of these models heavily rely on the rotation and bending strength parameters utilized, which need to be calibrated based on experimental results or advanced finite element models that accurately replicate the physical behavior of the structural component.

Several studies have suggested various parameters for nonlinear modeling that could be utilized for the calibration of concentrated plasticity models. For example, Lignos and Krawinkler [1] established empirical equations for estimating plastic rotations prior to and after capping, as well as the rate of cyclic deterioration in special moment connection tests. Additionally, they provided quantitative information for determining moment capacity at capping and residual moment after cyclic deterioration. Araujo et al. [2] proposed empirical equations for estimating plastic rotations in steel beam-columns with European profiles subjected to monotonic and cyclic loading. Mohabeddine et al. [3] derived an empirical equation for estimating rotation capacity in steel beams with European profiles, which can be utilized as acceptance criteria for performance-based assessment of structures or for calibration purposes in push-over analysis. Lignos et al. [4] suggested modeling criteria for the first-cycle envelope and monotonic backbone curves of steel wide-flange columns, which can be employed in nonlinear static and dynamic frame analyses. Previous studies that have examined the cyclic behavior of steel moment resisting frame components have primarily been based on nominal geometric dimensions provided by manufacturers. However, actual cross sections often deviate considerably from the nominal dimensions, as outlined by the tolerance limit deviations specified in the EN 10034:1993 standard [5]. Furthermore, while the standard provides acceptable intervals for section width, height, and thickness, the local slenderness of the plates within those intervals can vary significantly for a given profile. Since local slenderness is a critical factor in the flexural behavior of steel beams subjected to large deformation, understanding the extent of this effect is crucial.

Several researchers have explored the impact of these types of geometrical imperfections on the design and load-carrying capacity of steel members subjected to monotonic loading, including Byfield and Nethercott [6], Melcher et al. [7], and Kala et al. [8]. However, to the authors' knowledge, no studies have examined the impact of cross section dimension variability on the cyclic behavior of steel beams. While existing experimental tests may include these effects, large numbers of tests would be required to identify the effect of these imperfections, making such an approach infeasible.

Therefore, this study conducted 1600 finite element simulations in ABAQUS of cantilever beams (IPE300-IPE600) subjected to cyclic loading to investigate the effect of manufacturing tolerances on the rotation capacity of beams.

## 2 Methodology

This study aims to examine the impact of manufacturing tolerances on the cyclic behavior of steel flexural members with I-shaped cross-sections. To achieve this, a high-fidelity finite element model is created using ABAQUS software and the standardized SAC loading protocol is adopted. The model is a cantilever beam, assumed to represent the beam's behavior from one

end to the mid-point of inflection. This approach is commonly used in experimental and numerical studies. The study focuses on IPE300 to IPE600 profiles, which are widely used in practice, and considers a member with a length of 2, 2.5, 3, 3.5m. Figure 1 shows a 3D schematic view of the model with one edge fully restrained in all 6 degrees of freedom to ensure fixed boundary conditions. The cyclic loading is applied on the other edge, which is restrained in the X-X direction to prevent out-of-plane displacements at the top of the specimen.

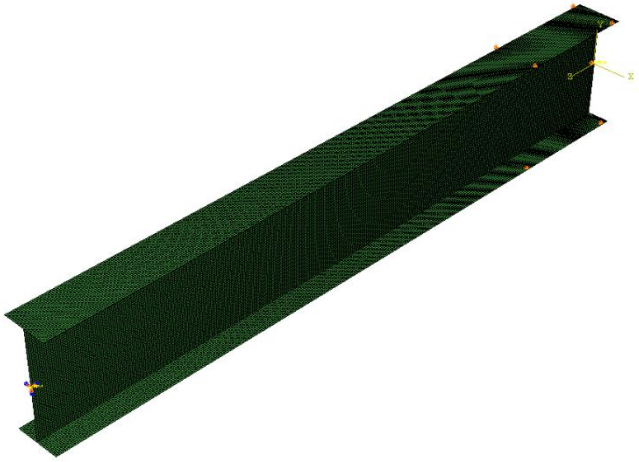

Figure 1: Beam model in Abaqus.

To avoid too much LTB, lateral restrictions were added in the flanges. According to ANSI/AISC 341-16 [23], the unbraced length ($L_b$), which is the distance between the lateral restraints, was calculated using Eq. 1

$$L_b = 0.095 i_z \frac{E}{F_y} \tag{1}$$

where $i_z$ is the radius of gyration of the cross-section, E is the young modulus, $F_y$ is the yield stress obtained from coupon tests.

$$\sigma^0 = \sigma|_0 + Q_\infty(1 - e^{-be^{pl}}) \tag{2}$$

In equation (2), the term $\sigma^0$ represents the alteration in the yield surface size as a function of equivalent plastic strain $e^{pl}$. The yield stress at zero equivalent plastic strain is represented by $\sigma|_0$, while $Q_\infty$ indicates the maximum change in the yield surface size. parameter b describes the rate at which the yield surface size changes as plastic strain increases. The nonlinear kinematic hardening component involves the movement of the yield surface in the stress space through the vector backstress α, which is used to capture complex phenomena like the Bauschinger effect. Equation (3) represents the backstress evolution law, which is a mathematical expression of the vector function that shifts the center of the Mises yield surface.

$$\dot{\alpha_k} = C_k \frac{1}{s^0}(\sigma - \alpha)\dot{\bar{e}}^{pl} - \gamma_k \alpha_k \dot{\bar{e}}^{pl} \tag{3}$$

Where $C_k$ and $\gamma_k$ are material parameters calibrated from stabilized cycle, σ is the stress matrix, $\dot{\alpha_k}$ is the evolution of the back stress, and $\dot{\bar{e}}^{pl}$ is the equivalent plastic strain rate. The subscript

$''_k''$ defines the backstress number. The constitutive parameters for this model were obtained through an optimization process using data from Chen et al.'s coupon test [14]. A comparison between the coupon test and the Voce-Chaboche model is illustrated in Figure 2, and Table 1 lists the parameters used to describe the constitutive model. The finite element model was then validated against various experimental tests on different members, and the outcomes are depicted in Figure 2.

Table 1 Nonlinear Isotropic and Kinematic hardening parameters.

| Material | σ\|0 (N/mm2) | Q∞ (N/mm2) | b | C (N/mm2) | γ |
|---|---|---|---|---|---|
| Q355b/S355 | 285 | 69 | 2.86 | 14238 | 96.15 |

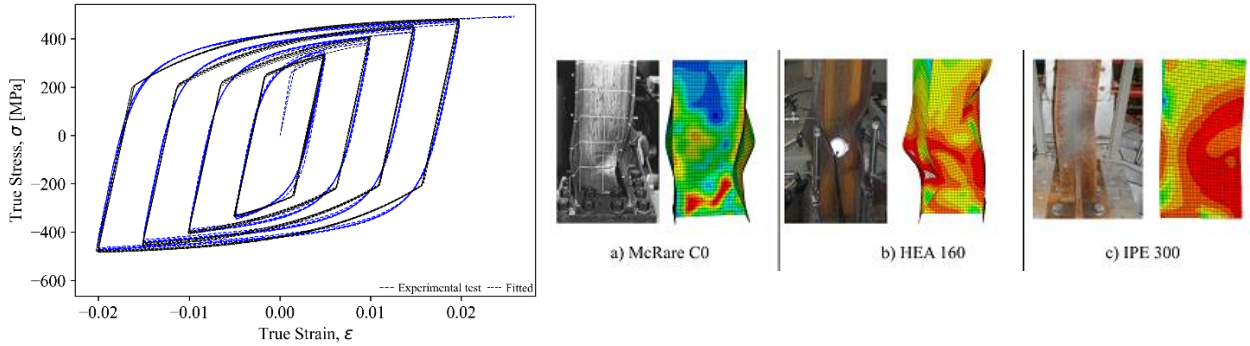


Figure 2: comparison between the buckling behavior simulated in the numerical model and from the numerical model: (a) anti-symmetric local buckling Specimens C0 (McRae[16]); (b) non-symmetric local buckling of HEA160 (D'Aniello et al [12]); (c) lateral buckling of IPE 300 (D'Aniello et al [12]).

## 3 Considering the dimension characteristics variability

Table 2 presents the tolerances on the shape dimensions of I and H sections of structural steel, as specified by the European standard [5]. The descriptions of the profile dimensions are illustrated in Figure 3 and their meanings are explained in Table 2.

**Table 2**-Dimensional tolerance for structural steel I and H sections (EN 10034:1993) (units in mm)

| Section Height (h) | | Flange Width (b) | | Web Thickness ($t_w$) | | Flange Thickness ($t_f$) | |
|---|---|---|---|---|---|---|---|
| h<=180 | +3<br>-2 | b<=110 | +4<br>-1 | $t_w$<7 | ±0.7 | $t_f$<6.5 | +1.5<br>-0.5 |
| 180<h<=400 | +4<br>-2 | 110<b<=210 | +4<br>-2 | 7=< $t_w$ <10 | ±1 | 6.5=<$t_f$<10 | +2<br>-1 |
| 400<h<=700 | +5<br>-3 | 210<b<=325 | +4<br>-4 | 10=< $t_w$ <20 | ±1.5 | 10=<$t_f$<20 | +2.5<br>-1.5 |
| h>700 | +5<br>-5 | b>325 | +6<br>-5 | 20=< $t_w$ <40 | ±2 | 20=<$t_f$<30 | +2.5<br>-2 |
| | | | | 40=< $t_w$ <60 | ±2.5 | 30=< $t_f$ <40 | +2.5<br>-2.5 |
| | | | | 60< $t_w$ | ±3 | 40=< $t_f$ <60 | +3<br>-3 |
| | | | | | | 60< $t_f$ | +4<br>-4 |

**Table 3** Relative statistical geometric characteristics and Correlation matrix of geometric characteristics [7]

| Quantity | Mean | Standard deviation | Skewness | Kurtosis | Min Value | Max value |
|---|---|---|---|---|---|---|
| h | 1.001 | 0.00443 | -0.4063 | 3.0150 | 0.989 | 1.013 |
| $b_1$ | 1.012 | 0.01026 | -0.3939 | 4.239 | 0.975 | 1.049 |
| $b_2$ | 1.015 | 0.00961 | -0.5448 | 3.887 | 0.975 | 1.037 |
| $t_1$ | 1.055 | 0.04182 | 1.0545 | 7.4730 | 0.949 | 1.3 |
| $t_{21}$ | 0.988 | 0.04357 | -0.2991 | 2.663 | 0.880 | 1.094 |
| $t_{22}$ | 0.998 | 0.04803 | 0.3303 | 2.766 | 0.858 | 1.129 |

| Quantity | h | $b_1$ | $b_2$ | $t_1$ | $t_{21}$ | $t_{22}$ |
|---|---|---|---|---|---|---|
| h | 1 | -0.0068 | 0.0534 | 0.0399 | -0.0686 | -0.0989 |
| $b_1$ | -0.0068 | 1 | 0.6227 | - 0.214 | -0.2681 | -0.1456 |
| $b_2$ | 0.0534 | 0.6227 | 1 | -0.2132 | -0.1596 | -0.0423 |
| $t_1$ | 0.0399 | -0.214 | -0.2132 | 1 | 0.2368 | 0.2451 |
| $t_{21}$ | 0.0686 | -0.2681 | -0.1596 | 0.2368 | 1 | 0.7634 |
| $t_{22}$ | -0.0989 | -0.1456 | 0.0423 | 0.2451 | 0.7634 | 1 |

Table 2 shows that the code allows for significant variation in width and height, and reductions in thicknesses, which can greatly affect the slenderness ratios and overall performance of the profile. The coefficient of variation for geometric imperfections is based on research from the 1970s, but some studies have questioned whether these estimates are still valid due to advancements in manufacturing methods [6]. Melcher et al. [7] conducted experimental research on Czech steel hot rolled IPE profiles, and statistically evaluated the geometrical characteristics of the cross-section dimensions, as presented in Table 3. This study used the results from those tables to define the next steps in the paper.

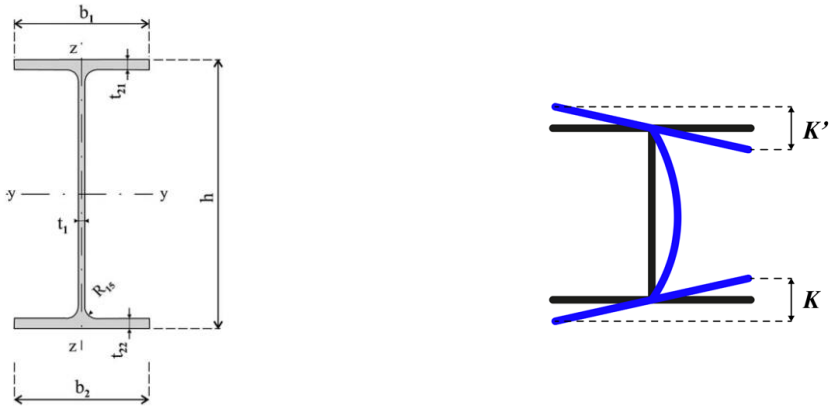


Figure 3: IPE profiles according to EN1993-1-1 and imperfection according to EN 10034:1993

As seen in Fig. 3, h is the height of the beam, $b_1$, $b_2$ are the top and bottom flange widths, $t_1$ is the web thickness, and $t_{21}$, $t_{22}$ are the top and bottom flange thicknesses.

## 4 Stochastic Model

Latin hypercube sampling (LHS) is a statistical technique used to generate a nearly random set of parameter values from a multidimensional distribution. This study employs the LHS method to define the random geometries for finite element analysis. The LHS method is computationally efficient compared to standard Monte Carlo sampling since it reduces the number of samples significantly. However, the results of LHS sections are dependent on whether the components of X (variables) are independent or dependent. In this paper, a procedure for producing Latin hypercube samples is used based on a correlation matrix of geometric characteristics, as presented in Table 4, since section variables are dependent. An experimental distribution is defined to capture the true distribution of the variables.

For each profile considered in this study, 50 samples with varying dimensions are generated using the LHS method and this process repeated for 4 different lengths of each profile. The different variations of an IPE300 are illustrated in Figure 4

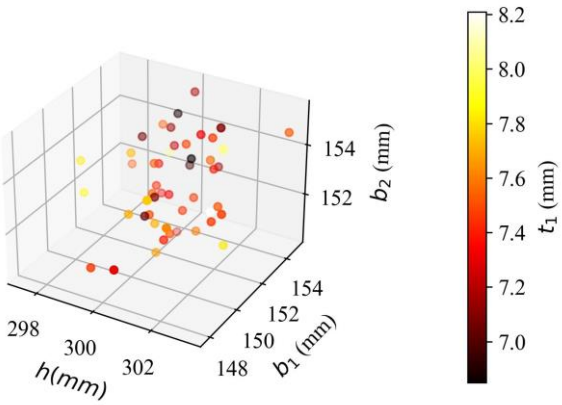


Figure 4 Latin hypercube sampling for IPE300

## 5 Results and Discussion

Figure 5 displays two graphs illustrating the behavior of IPE300 profiles, specifically the cyclic moment-rotation curve and the first cycle envelope, which is determined by moment and rotation values at yielding, maximum moment, and an 20% reduction in strength (M_80%). Figure 6 shows the first cycle curves for IPE300 to IPE600, based on 50 samples for the profile. The results indicate that changes in the dimensions of the beams significantly affect their strength and rotation capacity. The average first cycle curve is similar to the nominal cross section curve, but the average strength shows a higher maximum moment when the strength begins to drop. However, higher strength can increase the over-strength factor, which is not desirable for seismic design which can decrease the seismic performance of the structure. These results could be useful for reliability analysis and risk assessment, considering the variability of input modeling parameters.

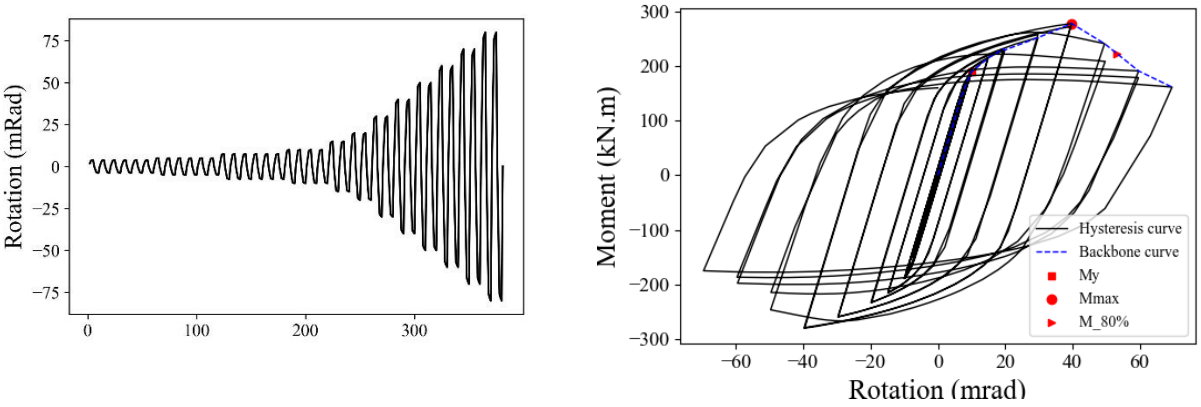


Figure 5: SAC protocol and cyclic hysteresis moment-rotation curves with first cycle curve of IPE300.

The rotation at of strength drop ($\theta_{80\%}$) is widely accepted as the parameter that defines the rotation capacity of the beam when subjected to large deformation.

Figure 6 illustrates the diversity of the $\theta_{80\%}$ values for various profiles with a length of 2 meters. The manufacturing tolerances in the dimensions of the cross-section have a significant impact on the variability of the data. In addition, Figure 6 demonstrates that there is greater variation in profiles with lower heights compared to those with higher heights. This is because the impact of tolerance on a slenderer profile is greater.

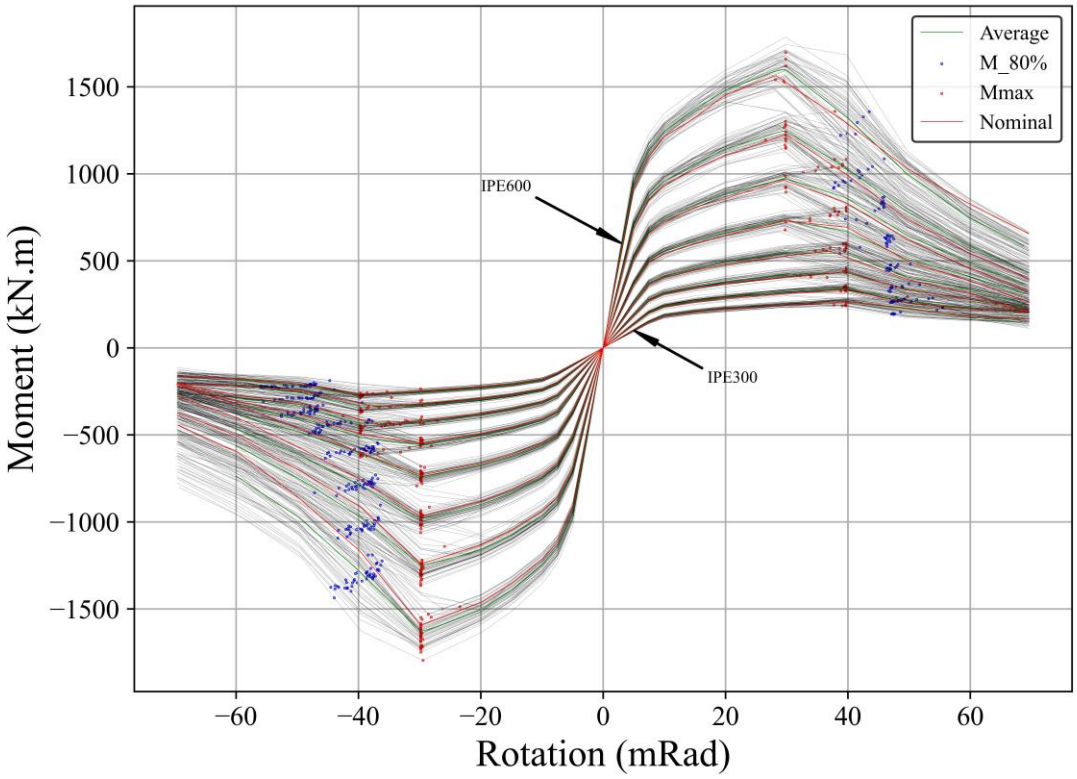


Figure 6: backbone curves of IPE300 to IPE600 and the impact of dimension tolerances on parameters

### 5.1. Strong beam, Weak column

The problem of "strong beam, weak column" in seismic design refers to a situation where the beams of a structure are much stronger than the columns. In this scenario, during a seismic event, the beams can cause the columns to fail due to the high forces that are transmitted through them.

The strong beam, weak column problem is a critical issue in seismic design because it can result in catastrophic failure of the structure, leading to loss of life and property damage. To avoid this problem, seismic design standards typically require that the strength and stiffness of the beams and columns be balanced to ensure that they work together to resist seismic loads.

According to the findings of this study, there is a high likelihood of overstrength for various profiles of different lengths, as demonstrated by the graph in figure 6.

The following section involved creating several models using machine learning methods to predict the maximum moment and rotation capacity and evaluating the accuracy of these models. Moreover, an empirical equation was developed to predict the rotation capacity at maximum moment and when the maximum moment has decreased by 20%. Several models

were evaluated, including nonlinear regression, linear regression analysis, neural network, decision tree, and random forest, with the aim of achieving the desired outcome. To evaluate the models, 80% of the data was used for training, while the remaining 20% was used for testing. Additionally, the training data was divided into two sets: a training set and a validation set, which were used to optimize the hyperparameters of the models under consideration.

### 5.2. nonlinear regression analysis

Nonlinear regression analysis requires careful consideration of the model assumptions, such as the distribution of errors, and the choice of model and parameters can have a significant impact on the results. It is important to evaluate the fit of the model to the data, often using diagnostic plots or statistical tests, to ensure that the model is appropriate, and the results are reliable. Current construction steels can develop large deformation without loss of strength. The rotation capacity of a steel member depends strongly on geometrical instabilities. Flange and web slenderness present the major influencing parameters of a given plated beam. Therefore, an empirical equation based on nonlinear regression analysis to estimate rotations corresponding to maximum moment and 20% drop in maximum moment of all the profiles is presented in Eq. 4.

$$\theta_{80\%} = a\left(\frac{L}{h}\right)^{b}\left(\frac{hw}{t_w}\right)^{c}\left(\frac{b_f}{2t_f}\right)^{d} \quad (4)$$

Where $\frac{h}{t_w}$ represent the web slenderness and $\frac{b}{2t_f}$ represent flange slenderness. The following are the regression coefficients:

| Dataset | a | b | c | d |
|---|---|---|---|---|
| All data | 889.56 | 0.39 | -0.75 | -0.56 |

L length of cantilever beam
$t_f$ flange thickness
$t_w$ web thickness
h beam depth
$b_f$ flange width
$L_b$ unbraced length.
$i_z$ radius of gyration

There is a strong correlation between measured and anticipated results.

The study examined three methods to assess the precision of the models, which were absolute error, mean square error, and r square. The equation 5 and 6 in the study describes these methods.

$$\text{MAE} = \frac{1}{n} * \sum\left|y_{pred} - y_{true}\right| \quad (5)$$

$$\text{MSE} = \frac{1}{n} * \sum(y_{pred} - y_{true})^2 \quad (6)$$

n is the number of samples in the dataset
$y_{true}$ is the predicted value of the model.
$y_{true}$ is the true value of the target variable.

The proposed equation underwent extensive research before being suggested, as indicated by the mean absolute error of 1.05 and the mean squared error of 1.8 in the nonlinear regression. However, when attempting to estimate the maximum moment of beams, there was unacceptable inaccuracy, as evidenced by the R^2 correlation of 0.78 and the following error values, mean absolute error of 146.29 and mean squared error of 41669.38. The benefit of this approach is that we arrive at a final equation that researchers and engineers may utilize with ease.

### 5.3. Linear regression

The linear regression method is widely used in civil engineering to model the relationship between various factors affecting the performance of structures, such as load-bearing capacity, deflection, and durability. In this part a liners regression model developed to predict $\theta_{80\%}$ and $\theta_{max}$ and $M_{max}$. The mean squared error of the linear regression for predicting $\theta_{80\%}$ is 2.04. R-Square for the test set is 0.94 and 1.12 means absolute error from this model.

### 5.4. Neural networks

Neural networks are a type of machine learning model that is inspired by the structure and function of the human brain. They consist of layers of interconnected nodes, also known as neurons, which process and transmit information using mathematical functions.

In this part a liners regression model developed to predict $\theta_{80\%}$ and $\theta_{max}$ and $M_{max}$. The neural network's mean squared error for $\theta_{80\%}$ is 0.77. The neural network's mean absolute error is 0.64 and R-Square for the test set is 0.98

### 5.5. Decision tree

Decision trees are a versatile tool that can be used for both classification and regression problems. When applied to regression analysis, decision trees aim to predict continuous target variables by dividing the feature space into smaller subsets based on input feature values [22].

The authors of the paper utilized decision tree analysis to predict the variables of interest, and the resulting metrics indicated a mean squared error of 3.09 and a mean absolute error of 1.21. The testing set R-squared value was found to be 0.91.

### 5.6. Random forest

Random forest is a powerful machine learning algorithm that can be used for both classification and regression tasks. In regression, the goal is to predict a continuous target variable, and random forest is particularly well-suited for this task because it can capture complex nonlinear relationships between input features and the target variable.

Random forest has several advantages for regression, such as its ability to handle high-dimensional data and outliers, and its ability to capture complex nonlinear relationships between the input features and the target variable. Additionally, the importance of input features can be easily interpreted based on their contribution to the variance reduction in the individual decision trees.

The study utilized random forest regression analysis to predict the variables of interest. The results revealed that the mean squared error was 1.98 and the mean absolute error was 0.94. The R-squared value for the testing set was determined to be 0.94.

By repeating the previous analysis for predicting maximum moment, we can obtain more encouraging outcomes. Even though the R-squared value is almost 1, non-linear regression still

produces substantial mean absolute and mean squared errors. The results of this section show that the neural net's mean squared error is 15.20 and the mean absolute error is 2.19, while the linear regression's mean squared error is 1503.04 and the mean absolute error is 32.30. The testing set R-squared values for the neural net and linear regression are 0.9999 and 0.9908, respectively. Moreover, the decision tree has a mean squared error of 156.43 and a mean absolute error of 8.53, with a testing set R-squared value of 0.9991. Finally, Random Forest has a mean squared error of 122.08 and a mean absolute error of 7.11, with a testing set R-squared value of 0.9993.

## Conclusion

The primary focus of this study was to examine how manufacturing dimensional tolerances impact the flexural behavior of steel beams when subjected to cyclic loading. To accomplish this objective, the study conducted 1600 analyses on eight distinct steel profiles, ranging from IPE300 to IPE600. After evaluating the results, the study found that this tolerance has a significant effect and can potentially cause either overstrength or a reduction in the rotation capacity of steel beams in MRF. Therefore, future design and analysis of steel structures should give greater consideration to this geometrical imperfection.

In this study, various techniques such as linear regression, nonlinear regression analysis, neural network, decision tree and random forest, were employed to predict the maximum moment and rotation at maximum moment and 20% of maximum moment. The findings suggest that neural network models are more accurate in predicting both variables, making it a reliable approach for predicting moment and rotation. It is interesting to note that utilizing a neural network can be highly beneficial in this context since running a model with Abaqus can be both time-consuming and expensive.

## Acknowledgements

This paper has been prepared within the scope of the Project “SD Poles - Steel and Dampers for Poles” with reference POCI-01-0247-FEDER-039865, co-financed by European Regional Development Fund (ERDF) through the Operational Program for Competitiveness and Internationalization (COMPETE 2020) under the PORTUGAL 2020, of which the first author is a grantee. This work is also integrated in the R&D activities of the CONSTRUCT Institute on Structures and Constructions (Instituto de I&D em Estruturas e Construções), financially supported by Base Funding UIDB/04708/2020 through national funds of FCT/MCTES (PIDDAC).

## REFRENCES

[1] Lignos, D.G.; Krawinkler, H.; (2011) *Deterioration Modeling of Steel Components in Support of Collapse Prediction of Steel Moment Frames under Earthquake Loading.* Journal of Structural Engineering. **137**(11): p. 1291-1302.

[2] Araújo, M.; Macedo, L.; Castro, J.M.; (2017) *Evaluation of the rotation capacity limits of steel members defined in EC8-3.* Journal of Constructional Steel Research. **135**: p. 11-29.

[3] Mohabeddine, A.; Koudri, Y.W.; Correia, J.A.F.O.; Castro, J.M.; (2021) *Rotation capacity of steel members for the seismic assessment of steel buildings.* Engineering Structures. **244**: p. 112760.

[4] Lignos, D.G.H.; Elkady, A.; Deierlein, G.G.; (2019) *Proposed Updates to the ASCE 41 Nonlinear Modeling Parameters for Wide-Flange Steel Columns in Support of Performance-Based Seismic Engineering.* Journal of Structural Engineering. **145**(9): p. 04019083.

[5] Standards, B., *BS EN 10034:1993 Structural steel I and H sections Tolerances on shape and dimensions*. (1993).

[6] Byfield, M. P.; Nethercot, D A.; (1997) *Material and geometric properties of structural steel for use in design.* The Structural Engineer. **75**(25).

[7] Melcher, J.K., Z. Holicky´, M. Fajkus, M. Rozlı ´vka, L. . (2004) *Design characteristics of structural steels based on statistical analysis of metallurgical products.* Journal of Constructional Steel Research. **60**(3-5): p. 795-808.

[8] KALA, Z.; Kala, J.; (2005) *Sensitivity analysis of lateral buckling stability problems of hot-rolled steel beams.* Slovac Journal of Civil Engineering. **2**: p. 9-14.

[9] Mohabeddine, A.I.; Eshaghi, C.; Correia, José A.F.O.; Castro J. M. (2022) *Analytical investigation of the cyclic behaviour of I-shaped steel beam with reinforced web using bonded CFRP.* Steel and Composit Structures. **43**(4): p. 447-456.

[10] Kato, B.; (1989) *Rotation capacity of H-section members as determined by local buckling.* Journal of Constructional Steel Research. **13**(2-3): p. 95-109.

[11] Kato, B.; Nakao, M.; (1994) *Strength and deformation capacity of h-shaped steel members governed by local buckling.* Journal of Structural and Construction Engineering (Transactions of AIJ). **59**(458): p. 127-136.

[12] D'Aniello, M. .;Landolfo, R. .;Piluso, V.Rizzano, G.; (2012) *Ultimate behavior of steel beams under non-uniform bending.* Journal of Constructional Steel Research. **78**: p. 144-158.

[13] Cheng, X.; Chen, Y.; (2018) *Ultimate strength of H-sections under combined compression and uniaxial bending considering plate interaction.* Journal of Constructional Steel Research. **143**: p. 196-207.

[14] Chen, Y.; Wei, S.;Tak-Ming, C. (2014) *Cyclic stress-strain behavior of structural steel with yieldstrength up to 460 N/mm2.* Frontiers of Structural and Civil Engineering. **8**(2): p. 178-186.

[15] Mohabeddine, A. I.; Kuidri, Y.W.; Castro, J. M.; Correia, J. A. F. O.; *Numerical Simulation and Calibration of the Cyclic Behavior of Structural Steel Under Different Loading Protocols*, in *XIX International Colloquium on Mechanical Fatigue of Metals*. (2018): Porto, Portugal. p. 97–98.

[16] MacRae, G.A.; *The seismic response of steel frames," University of Canterbury Christchurch*, in *Civil Engineering*. (1989), University of Canterbury: New Zealand.

[17] CEN, *Eurocode 3: Design of steel structures-part 1.1: General rules and rules for buildings*, in *CEN, European Committee for Standardization*. (1992).

[18] McKay, M.D.; R. J. Beckman, W. J. Conover. (1979) *A Comparison of Three Methods for Selecting Values of Input Variables in the Analysis of Output from a Computer Code.* Technometrics 21. **2**: p. 239-45.

[19] Tang, B.; (1988) *Orthogonal Array-Based Latin Hypercubes.* Journal of the American Statistical Association. **88**: p. 1392–1397.

[20] Anders M. J. Olsson, G.E.S.; (2002) *Latin Hypercube Sampling for Stochastic Finite Element Analysis.* Journal of Engineering Mechanics. **128**(1).

[21] Stein, M.; (1987) *Large Sample Properties of Simulations Using Latin Hypercube Sampling.* Technometrics. **29**(2): p. 143-151.

[22] Witten, I. H.; Frank, E.; Hall, M. A. (2011) Data Mining: Practical Machine Learning Tools and Techniques (3rd edition).

[23] Breiman, L. (2001). Random forests. Machine learning. 45(1): p. 5-32.

COMPDYN 2023
9th ECCOMAS Thematic Conference on
Computational Methods in Structural Dynamics and Earthquake Engineering
M. Papadrakakis, M. Fragiadakis (eds.)
Athens, Greece, 12-14 June 2023

# RESPONSE OF A SMALL WIND TURBINE TOWER UNDER EARTHQUAKE LOADS

**Dick Anelise[1], Barros C. Rui[1], and Braz-César T. Manuel[2]**

[1] CONSTRUCT/FEUP, Faculty of Engineering of the University of Porto
Porto, Portugal
{anelise.dick, rcb}@up.pt

[2] CONSTRUCT/IPB, Polytechnic Institute of Bragança
Bragança, Portugal
brazcesar@ipb.pt

## Abstract

*As the concern with the environment and the economical aspect of the use of fossil energies grows, the studies and application of renewable energy systems also increase. Wind energy is an important renewable energy system that can be used on a large or small scale. Indeed, the small-scale systems, known as small wind turbines (SMT) are used as an attractive solution to solve energy problems in rural or difficult access areas, that can be affected by seismic forces. The present paper analyses the seismic response of metallic tower used as a support for a SWT submitted to modal response spectrum method (MRSA) and response history analysis (RHA). The analyses were performed with the elastic response spectrum function given by Portuguese Annex to Eurocode 8, while the time history used the accelerations records of El Centro Earthquake scaled to match the elastic response spectrum*

*The results suggest that the beam model is appropriate for studying the seismic response of the tower, although it has some limitations. The horizontal accelerations at the ground surface were amplified by a factor of 6 at the top of the tower, but the displacements were not significant. However, the base reactions for a strong ground motion could be compared to those obtained by the wind forces that the tower and wind turbine experience.*

*The MRSA base responses were 30 to 40% lower than those obtained by RHA. For the northern region of Portugal, far-fault type led to higher responses than the near-fault. Overall, this study provides valuable insights into the seismic behavior of small wind turbines and highlights the importance of accounting for seismic loads in their design and construction to ensure their structural safety and stability.*

**Keywords:** small wind turbine, metallic tower, dynamic responses, finite element analysis, seismic analysis, Eurocode 8.

## 1 INTRODUCTION

The events that occurred at the outset of 2022 highlight the significance of Europe's energy independence, with the potential for advancements in the renewable energy sector to grow even further in the upcoming years. Notwithstanding, research in the wind energy domain has typically focused on large, on-grid wind turbines, with little attention given to the potential of small wind turbines (SWT) for off-grid utilization in rural or remote areas.

While wind-driven forces are widely considered as the primary hazard for wind turbines, earthquakes are not typically regarded as a significant concern for large wind turbines due to their vibration period ranging from 1.5 to 12 seconds, which corresponds to the low-intensity portion of seismic events [1-5]. When compared to shorter-period structures, the long vibration period of large wind turbine support structures allows them to absorb some of the energy from earthquakes, lowering the force and impact on the structure. this statement might not apply to small wind turbines (SWT) since they have a shorter natural vibration period than their larger counterparts due to their smaller rotor diameters and lower tower heights. Furthermore, the cantilever design of SWT structures exacerbates their susceptibility to earthquake excitation.

Current guidelines, such as Risø [6], GL [7], and IEC [8], recommend that seismic design must comply with seismic loading requirements outlined in design building code of the installation site. Unlike building projects, in which structures must develop inelastic deformation in response to seismic activity, for wind turbines, the objective is to minimize operation interruption, thus verifying service limit state parameters, i.e damage limitation [6].

Seismic evaluation of structures can be conducted using three methods: simplified, modal response spectrum analysis (MRSA), or response history analysis (RHA). In the Eurocode 8 [9], the simplified method, also known as the static load method, employs static loads to estimate the structural response to earthquake forces, but should only be employed for structures that meet the standard requirements. The MRSA method employs structural natural frequencies and corresponding mode shapes to calculate the response of a structure to earthquake forces based on the spectral acceleration, which is useful and widely used. However, this method has some limitations, such as assumptions of linear behavior, limited accuracy for irregular structures and high-frequency content, lack of consideration of soil-structure interaction, and limited applicability to non-building structures. On the other hand, RHA is a complex method that analyzes the dynamic behavior of a structure under earthquake forces based on the actual recorded or synthesized ground motion time history. It considers the nonlinear behavior of the structure and provides detailed information on the structural response. However, due to its complexity, it is computationally intensive [10].

The present study aims to analyze a metallic tapered tower utilized as a support for an SWT subjected to strong ground motion in accordance with seismic specifications for the North region of Portugal, where the real structure is installed, characterized by the El Centro earthquake. The MRSA method was employed using the response spectrum in accordance with Eurocode 8, while the same spectrum was used to scale the El Centro earthquake time history used in the RHA method.

## 2 DESCRIPTION OF THE TOWER

The School of Technology and Management of the Polytechnic Institute of Bragança in Portugal houses a 17.8 m tall metal tower constructed from steel S275. The tower has a hexadecagonal section, with an outside diameter of 0.5890 m at the base and 0.1954 m at the top, and a constant wall thickness of 4 mm. The tower is securely fastened to a gravity-based foundation by 16 anchor bolts attached to a flange at the base. Further details regarding the key properties of the tower can be found in Table 1.

| | | |
|---|---|---|
| **Density** | 7850.000 | [kg/m³] |
| **Young's modulus** | 210.000 | [GPa] |
| **Poisson's ratio** | 0.300 | -- |
| **Yield strength** | 275.000 | [MPa] |
| **Height** | 17.800 | [m] |
| **Top diameter** | 0.195 | [m] |
| **Bottom diameter** | 0.589 | [m] |
| **Nacelle mass** | 75.000 | [kg] |
| **Tower mass** | 664.277 | [kg] |

Table 1: Tower properties.

In this study, the wind turbine tower is represented as a multi-degree of freedom system, with the rotor and nacelle masses being modeled as a lumped mass located at the hub height. Two distinct models were evaluated using the SAP2000 software: a beam model and a more sophisticated shell model. To ensure the accuracy of the models, they were validated against experimental results obtained from Experimental and Operational Modal Analysis [11].

## 2.1 Modal Response Spectrum analysis (MRSA)

To perform Modal Response Spectrum Analysis, an elastic response spectrum function was constructed according to the EN 1998-1-1:2004 Section 3.2.2.5 [9], taking into account the Portugal national Annex specifications and the site location. The north region of Portugal is categorized as a low seismic region with a seismic zone of 1.6 for far-fault actions and 2.5 for near-fault actions, both having the lowest ground acceleration reference, $a_{gR}$, as shown in Table 2. Soil type is another crucial factor that needs consideration in seismic evaluations, even when not accounting for specific soil-structure interaction in fixed base. For this analysis, soil type D was chosen, which comprises soils with low shear strength, such as loose sands and silts, and soils with high plasticity, such as clayey soils [9].

| **Seismic Zone** | **1.6** | **2.5** |
|---|---|---|
| $a_{gR}[\,m/s^2]$ | 0.35 | 0.8 |
| class IV- $\gamma_I$ | 1.95 | 1.5 |
| Soil type D – Smax | 2.0 | 2.0 |

Table 2: Seismic parameters.

Wind turbines have traditionally been considered structures of low importance and have been assigned to the lowest importance class (Importance Class II) in Eurocode 8. However, given the growing global reliance on wind energy and the increasing role of wind turbines as critical infrastructure, there is a need to reconsider the importance class assigned to these structures [1]. In this study, the importance class of a wind turbine structure was reassigned to Class IV, taking into account its vital role in maintaining operational civil protection services, as prescribed by Eurocode 8-6 [12].

The uniaxial analysis of the models was carried out to enable a comparison between the MRSA and RSA methods. The modal analysis involved the use of load-dependent Ritz vectors with a modal participation factor of up to 90%, consistent with the recommendations set out in Eurocode 8. In order to achieve this level of modal participation factor in both x and y directions, 16 modes were considered for the shell-type model and 12 modes for the beam model.

The expected maximum seismic load was determined by combining the respective modal responses using the Complete Quadratic Combination (CQC) method as detailed in [13, 14]. The design response spectrum was then evaluated for accuracy and reliability through comparison with time series analysis.

## 2.2 Response History Analysis (RHA)

The time history analysis was performed using the time series accelerations presented in Figure 2 from the El Centro Earthquake, which occurred in Southern California on May 18, 1940. This earthquake had a magnitude of 6.9 on the Richter scale and a peak ground acceleration (PGA) of 0.289g. The El Centro Earthquake is frequently used as an acceleration signal for seismic analysis due to its well-documented characteristics and its status as a benchmark earthquake.

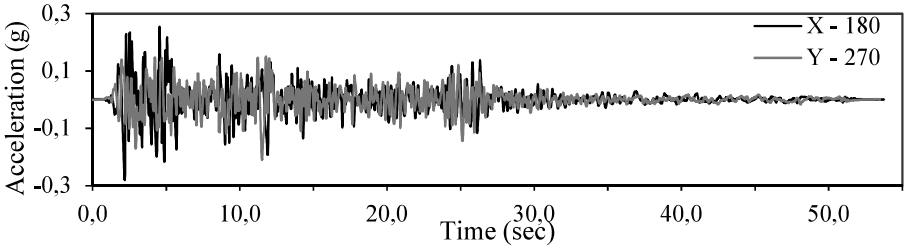


Figure 1 : Imperial Valley-06 1979, El Centro Array #4 time-history accelerations

In this study, the aim was to compare the results of time history response with those of response spectra analysis. In order to accomplish this, it was necessary to scale the time series accelerations to conform to the response spectrum. The response spectra were matched using the Frequency Domain Method, which preserves the Fourier phase of the reference time history while adjusting the Fourier amplitude spectrum to match the target response spectrum. The matched response spectra for both types of seismic action and directions are show in Figure 3.

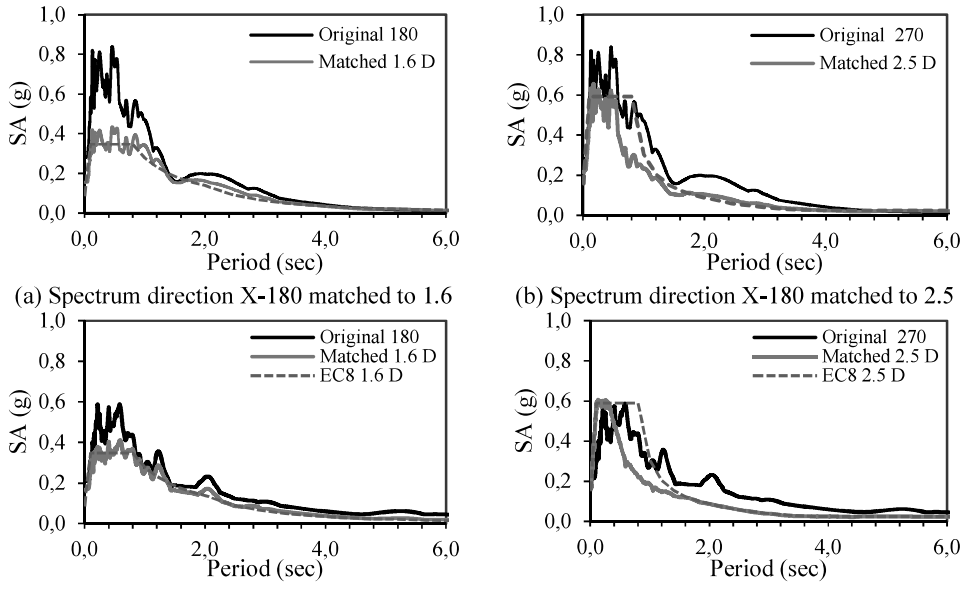


(a) Spectrum direction X-180 matched to 1.6

(b) Spectrum direction X-180 matched to 2.5

(c) Spectrum direction Y-270 matched to 1.6

(d) Spectrum direction Y-270 matched to 2.5

Figure 2 : Response spectrum functions

## 3 RESULTS

The analysis of the structure using the Finite Element Method (FEM) is performed using the SAP2000 Software, modal analysis was conducted to validate the models used in the study. The results of the analysis are presented in Table 2, which indicates that both models show good agreement with the experimental results [11].

In modern structural analysis, the lowest modes of vibration are often considered sufficient to meet the requirement of a 90% participation factor. However, relying solely on the lowest modes may not provide a complete understanding of the dynamic behavior of a structure. Higher modes can significantly contribute to the overall response of the structure, and their inclusion in the analysis can lead to a more accurate representation of the structural response under seismic loads. In the current analysis higher modes are needed to achieve at least 90% participation factor in each direction.

| | **Shell** | | **Beam** | | **Experimental** |
|---|---|---|---|---|---|
| Mode | Period (sec) | Frequency (Hz) | Period (sec) | Frequency (Hz) | **[11]** |
| 1 | 0.625 | 1.600 | 0.621 | 1.611 | 1.55±0.05 |
| 2 | 0.625 | 1.601 | 0.621 | 1.611 | 1.55±0.05 |
| 3 | 0.142 | 7.043 | 0.142 | 7.066 | 5.8 ±0.05 |
| 4 | 0.142 | 7.045 | 0.142 | 7.066 | 5.8 ±0.05 |
| 5 | 0.054 | 18.414 | 0.054 | 18.466 | 18.16 ±0.05 |
| 6 | 0.054 | 18.421 | 0.054 | 18.466 | 18.16 ±0.05 |
| 7 | 0.028 | 35.885 | 0.028 | 35.988 | |
| 8 | 0.028 | 35.898 | 0.028 | 35.988 | |
| 9 | 0.017 | 59.208 | 0.017 | 60.512 | 61.65 ± 0.05 |
| 10 | 0.017 | 59.229 | 0.017 | 60.512 | 61.65 ± 0.05 |
| 11 | 0.011 | 88.225 | | | 87.6 ± 0.05 |
| 12 | 0.011 | 88.255 | | | 87.6 ± 0.05 |
| 13 | 0.008 | 131.055 | 0.008 | 123.046 | |
| 14 | 0.008 | 131.089 | 0.008 | 123.046 | |
| 15 | 0.004 | 269.802 | | | |
| 16 | 0.004 | 270.105 | | | |

Table 3: Modal frequencies.

The seismic analysis results for the tower using both shell and beam models are tabulated in Table 3. The comparison of the results indicates that both models demonstrate comparable behavior. However, the beam model exhibits slightly higher peak ground acceleration (PGA) values while the displacements are marginally lower for the TH ElCentro and TH 1.6 D in the X direction. These observations suggest that the beam model is suitable for seismic analysis of the tower up to a certain extent. It is important to note that buckling analysis was not evaluated in this study, and therefore, the suitability of the beam model may vary in the presence of buckling effects.

Furthermore, the maximum displacement observed for the Y-270 component of the El Centro earthquake was found to be 91.393 mm. This result highlights the importance of accounting for seismic loads in the design and construction of tall structures, as these displacements can cause significant damage and compromise the integrity of the tower. Overall, the results demonstrate the effectiveness of the seismic analysis approach adopted in this study, and the suitability of the beam model for analyzing the seismic behavior of the tower.

| | Dir. | Ground PGA [m/s²] | Top PGA [m/s²] | | Amplification | Displacement [mm] | |
|---|---|---|---|---|---|---|---|
| | | | Beam | Shell | | Beam | Shell |
| TH ElCentro | X | 2.80 | 13.211 | 13.127 | 4.7 | 82.230 | 84.578 |
| TH 1.6 D | X | 1.50 | 7.163 | 7.145 | 4.8 | 53.873 | 55.530 |
| TH 2.5 D | X | 2.20 | 10.220 | 10.114 | 4.6 | 57.080 | 56.992 |
| EC8 1.6 D | X | | 5.584 | 5.585 | | 49.037 | 49.654 |
| EC8 2.5 D | X | | 5.904 | 5.894 | | 41.022 | 41.344 |
| TH ElCentro | Y | 2.10 | 11.075 | 10.228 | 5.3 | 91.393 | 84.183 |
| TH 1.6 D | Y | 1.64 | 7.724 | 7.166 | 4.7 | 65.319 | 60.896 |
| TH 2.5 D | Y | 1.99 | 9.873 | 9.303 | 5.0 | 61.571 | 56.360 |

Table 4: Comparisons accelerations and displacements responses.

The seismic analysis of the tower presented in this study provides valuable insights into the dynamic behavior of the structure under seismic loads. The maximum displacement of 91.393 mm observed for the Y-270 component of the El Centro earthquake indicates that the tower has the ability to withstand seismic events of similar intensity. Moreover, the displacement values obtained from MRSA and RSA analyses, which were matched to Eurocode spectrum for both far-fault and near-fault, were found to be within the allowable limit of 89 mm, as required by Eurocode 8-6 for damage limitation. These findings suggest that the tower is adequately designed to resist seismic loads.

Additionally, the analysis using EC8 showed that seismic displacements are not a SLS concern, as wind action leads to larger displacements around 200 mm [15]. The top of the tower was found to exhibit the maximum amplification of accelerations, with both the beam and shell models exhibiting an amplification factor of approximately 5 for both horizontal components. This was observed through the analysis of various time histories, with Figure 1 showcasing the amplification in the X-180 component. Similar behavior was observed in other time histories.

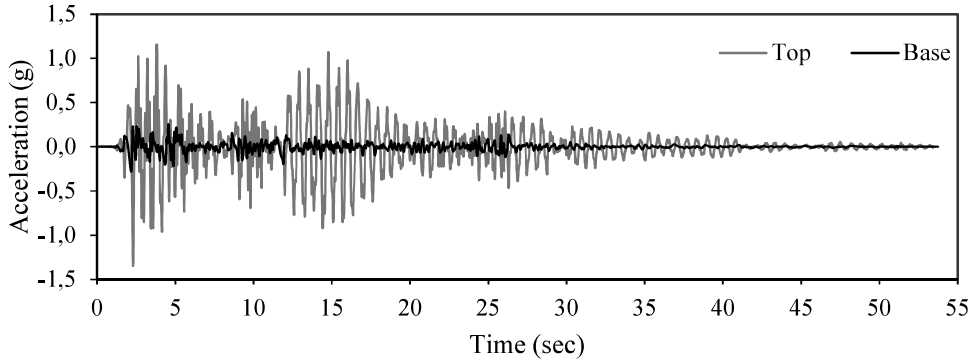


Figure 4: Base and top accelerations X-180 direction component of El Centro earthquake

Although the displacements are not a concern for this structure, it is still necessary to check the shear base forces and moments. Table 5 summarizes the base reaction forces obtained from the seismic analysis. A detailed examination of the table reveals that the seismic actions can produce shear forces and overturning moments that are comparable to those induced by wind forces [15]. Therefore, the design should consider both the seismic and wind loads to ensure the structural safety and stability.

| Analysis | Direction | F [kN] | M [kN.m] |
|---|---|---|---|
| TH ElCentro | X | 3.017 | 32.368 |
| TH 1.6 D | X | 1.801 | 19.736 |
| TH 2.5 D | X | 1.995 | 21.340 |
| EC8 1.6 D | X | 1.345 | 17.432 |
| EC8 2.5 D | X | 1.423 | 15.288 |
| TH ElCentro | Y | 2.794 | 33.480 |
| TH 1.6 D | Y | 2.099 | 24.506 |
| TH 2.5 D | Y | 1.985 | 22.859 |

Table 5: Base reaction forces beam type.

Research has shown that the base shear force and overturning bending moment calculated via time-history analysis were larger than those obtained from the elastic response spectrum analysis. Specifically, the time histories TH 1.6D and TH 2.5D in the Y-270 direction resulted in moments that were 41% and 50% higher than those from MRSA EC8 1.6D and 2.5D.

It is interesting to note that the unscaled El Centro time-history response generated overturning moments that were 64% higher than the matched time history for seismic zone 2.5D in the X-direction and only 36% higher for seismic zone 1.6D in the Y-direction.

Overall, the research revealed that the far-fault excitation (1.6) resulted in higher responses than the near-fault (2.5). Figure 5 shows that the far type's frequency content is closest to the lower modes than the near types. It is noteworthy since if the frequency content of the time history is close to the structure's natural frequency, the structure's response can indeed be substantially amplified.

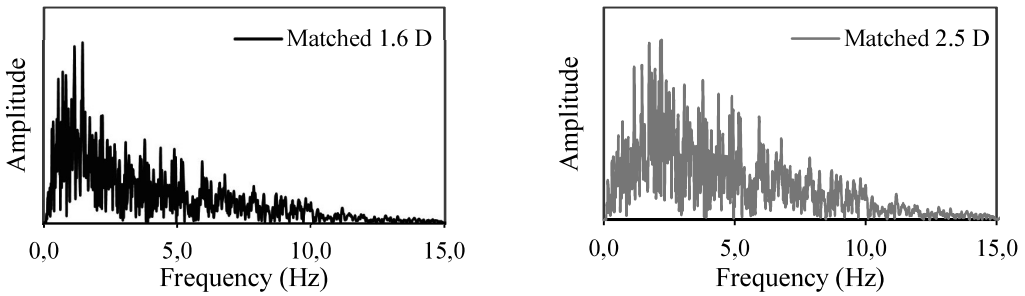


Figure 5: Frequency content of X-180 direction component of El Centro earthquake matched to seismic zone 1.6 and 2.5

## 4 CONCLUSIONS

The seismic response of a small wind turbine tower was analyzed by finite element models (beam and shell), for modal response spectrum analysis using the elastic response spectrum function in accordance with Eurocode 8, and respective Portuguese annex and a time history analysis corresponding to the El Centro earthquake with the time histories matched to elastic response function used in MRSA.

The results of the seismic analysis for the tower using both shell and beam models demonstrated comparable behavior. However, the beam model exhibited slightly higher PGA values, while the displacements were marginally lower for certain earthquake components in the X direction. These observations suggest that the beam model is suitable for seismic analysis of the tower up to a certain extent, but the suitability may vary in the presence of buckling effects.

The analysis using showed that the displacement values obtained by MSRA and correspondent matched time histories were within the allowable limit of 89 mm, as required by Eurocode 8-6 for damage limitation. This suggests that the tower is adequately designed to resist seismic loads. However, it is still necessary to check the shear base forces and moments as seismic actions can produce shear forces and overturning moments that are comparable to those induced by wind forces.

The research also showed that the base shear force and overturning bending moment calculated via time-history analysis were larger than those obtained from the elastic response spectrum analysis. Moreover, the far-fault excitation (1.6) resulted in higher responses than the near-fault (2.5), with the frequency content of the far type closest to the lower modes than the near types. This indicates that if the frequency content of the time history is close to the structure's natural frequency, the structure's response could be substantially amplified.

In conclusion, the seismic analysis approach adopted in this study was effective in providing valuable insights into the dynamic behavior of the structure under seismic loads. The results demonstrate the suitability of the beam model for analyzing the seismic behavior of the tower and highlight the importance of accounting for seismic loads in the design and construction of small wind turbines towers to ensure structural safety and stability, even in areas with low to moderate seismic activity.

## ACKNOWLEDGEMENTS

This paper is within the scope of the first author's Ph.D. degree in progress, financially supported by the Portuguese Foundation for Science and Technology (FCT) through the PhD grant reference SFRH/BD/147789/2019 under the programme POCH (N2020 – P2020) and subsidized by the European Social Fund (FSE) and national funds from MCTES. The authors also acknowledge the use of the experimental equipment [11] under the Project "SD Poles - Steel and Dampers for Poles" with reference POCI-01-0247-FEDER-039865, co-financed by European Regional Development Fund (ERDF) through the Operational Programme for Competitiveness and Internationalization (COMPETE 2020) under the PORTUGAL 2020, of which the second co-author is the FEUP's coordinator. This work is also integrated in the R&D activities of the CONSTRUCT Institute on Structures and Constructions (Instituto de I&D em Estruturas e Construções), financially supported by Base Funding UIDB/04708/2020 through national funds of FCT/MCTES (PIDDAC).

## REFERENCES

[1] E. I. Katsanos, S. Thöns, and C.T. Georgakis, C. T. Wind turbines and seismic hazard: a state-of-the-art review. *Wind Energ.*, 19: 2113– 2133, 2016.. doi: 10.1002/we.1968

[2] N. Bazeos, G. D. Hatzigeorgiou, I. D. Hondros, H. Karamaneas, D. L. Karabalis, and D. E. Beskos, Static, seismic and stability analyses of a prototype wind turbine steel tower, *Eng. Struct.*, vol. 24, no. 8, 1015–1025, 2002. Doi: 10.1016/S0141-0296(02)00021-4

[3] J. Fan, Q. Li, and Y. Zhang, Collapse analysis of wind turbine tower under the coupled effects of wind and near-field earthquake. *Wind Energy*, vol. 22, no. 3, pp. 407–419,2019. Doi: 10.1002/we.2294

[4] A. Patil, S. Jung, and O. S. Kwon, Structural performance of a parked wind turbine tower subjected to strong ground motions. *Eng. Struct.*, vol. 120, 92–102, 2016. doi: 10.1016/j.engstruct.2016.04.020

[5] Z. Zhao, K. Dai, A. Camara, G. Bitsuamlak, and C. Sheng, Wind Turbine Tower Failure Modes under Seismic and Wind Loads. *J. Perform. Constr. Facil.*, vol. 33, no. 2, 2019. Doi: 10.1061/(asce)cf.1943-5509.0001279

[6] Risø. *Guidelines for Design of Wind Turbines.* Det Norske Veritas & Wind Energy Department of Risø National Laboratory, 2002.

[7] GL. *Guideline for the Certification of Wind Turbines.* Germanischer Lloyd, Hamburg, Germany, 2010.

[8] IEC. *IEC 61400-1: Wind Turbines – Part 1: Design Requirements.* International Electronical Commission, 3rd edition, 2005.

[9] EN 1998-1. *Eurocode 8: Design of Structures for Earthquake Resistance – Part 1: General Rules Seismic Actions and Rules for Buildings.* European Committee for Standarization, 2004.

[10] CSI. *CSI Knowledge Base*. Computers & Structures Inc. 2022. URL: https://wiki.csiamerica.com/display/doc/Home

[11] A. Dick, R.C. Barros, and M.T.B. César. Experimental and operational modal analysis of a small wind turbine tower, J.F. Silva Gomes and S.A. Meguid eds. *9th International Conference on Mechanics and Materials in Design (M2D2022),* Funchal, Portugal 26-30 June 2022, 829-836. URL:https://paginas.fe.up.pt/~m2d/proceedings_m2d2022/

[12] EN 1998 -6. *Eurocode 8: Design of structures for earthquake resistance – Part 6: Towers, masts and chimneys*. European Committee for Standarization, 2005.

[13] ISO. *ISO 3010 Bases for design of structures – Seismic actions on structures*. International Organization for Standardization, 2017.

[14] E.L. Wilson, A. Der Kiureghian and E.P. Bayo. A replacement for the SRSS method in seismic analysis. *Dynamic analysis of soil / structure seminar*, Japan, 1981.

[15] A. Dick, R.C. Barros, and M.T.B. César. Finite element model calibration effecst on the static and dynamic response of a metallic hollow tower. M. Papadrakakis & M. Fragiadakis Eds. *8th International Conference on Computational Methods in Structural Dynamics and Earthquake Engineering,* vol. 1, 2121-2131 , Athens, Greece, 28-30 June 2021. ISBN (set): 978-618-85072-5-8

COMPDYN 2023
9th ECCOMAS Thematic Conference on
Computational Methods in Structural Dynamics and Earthquake Engineering
M. Papadrakakis, M. Fragiadakis (eds.)
Athens, Greece, 12-14 June 2023

# COMPARATIVE STUDY OF OPTIMUM FORMULATIONS FOR TUNED MASS DAMPERS IN SMALL WIND TURBINE TOWERS

**Dick Anelise[1], Barros C. Rui[1], and Braz-César T. Manuel[2]**

[1] CONSTRUCT/FEUP, Faculty of Engineering of the University of Porto
Porto, Portugal
{anelise.dick, rcb}@up.pt

[2] CONSTRUCT/IPB, Polytechnic Institute of Bragança
Bragança, Portugal
brazcesar@ipb.pt

## Abstract

*In the field of wind turbines, supplemental dampers have been utilized to control vibration and improve the response of slender structures. Although studies on vibration control in large wind turbines are common, studies on small structures are scarce. This article aims to analyze the dynamic behavior of a metallic hollow tower used as a horizontal small wind turbine support and design a vibration control device, namely a tuned mass damper (TMD), which is one of the most commonly used systems in large wind turbines due to its simplicity and effectiveness. The study investigates the influence of different formulations and parameters on the performance of TMDs in wind turbine towers. The results reveal that the selection of optimum parameters significantly influences the performance of the TMD system, and different formulations can lead to significant differences in the structure's response. The Single Degree of Freedom (SDOF) method accurately represents the main structure's behavior under harmonic excitation if the correct modal parameters are used. The study also finds that the maximum amplification factor for the main structure can be significantly reduced by the use of TMD systems, by up to 43% even for a mass ratio of 0.01 of the modal mass. However, using inadequate parameters can lead to a reduction of only 2.5%. Therefore, it is crucial to carefully evaluate and select the optimal parameters for the TMD system, which depends on the specific characteristics and requirements of the system.*

**Keywords:** Wind turbines, Tuned mass damper, Vibration control, Small wind turbines, Dynamic behavior, Structural response.

## 1 INTRODUCTION

Wind turbine towers are subjected to significant dynamic loads due to the fluctuating wind loads that they experience during their lifetime. These dynamic loads can cause undesirable vibrations in the tower, which can lead to fatigue and ultimately failure of the structure. To mitigate these vibrations, various vibration control techniques have been developed, and among them, tuned mass dampers (TMDs) have emerged as a promising solution.

TMDs stands out as a reliable and effective structural vibration control device that can be attached to a primary system to suppress undesirable vibrations induced by wind and earthquake loads. Typically, the TMD consists of a mass, damping component, and spring. The natural frequency of the TMD is tuned to resonate with the fundamental mode of the primary structure, allowing it to absorb a significant amount of the structural vibrating energy and dissipate it through the damping component when the primary structure is subjected to external disturbances [1].

Over the past century, several researchers have analyzed the optimal parameters of TMD systems for different types of structures. Many of these studies have been carried out using numerical analysis, and more recently, with the advent of advanced computational techniques, finite element analysis (FEA) has become a popular tool for studying TMD systems. However, despite the extensive research, there is no consensus on the optimal TMD parameters for a given structure.

In wind turbine engineering, TMDs are recognized as the standard for vibration absorption. Installing a TMD in a wind turbine tower can improve the dynamic response and reliability of the structure by increasing its damping. The effectiveness of the TMD depends on its mass and point of installation. Tuning its mass and damping to match the frequency of the tower's fundamental vibration mode allows the TMD to absorb and dissipate a significant portion of the structural vibrating energy. Proper placement of the TMD is also crucial for optimal energy transfer.

The first vibration absorbers were introduced by Frahm in 1909 [2], and over the following years, several authors proposed optimal design theories for TMDs according to different types of excitation. The first optimal frequency tuning formulation was given by Ormondroyd and Den Hartog in 1928 [3]. They minimized the steady-state response of the undamped main system subjected to a harmonic external force. According to Den Hartog, the optimum TMD parameters are found when the dynamic amplification curves cross two fixed points independent of the damping ratio. The main objective is to obtain a flat curve near the resonant frequency and suppress the dynamic response of the structure. Meanwhile, Brock derived the optimal damping for the same system [4]. He also derived solutions for the case in which the amplitude of the disturbing force varies with the square of its frequency [5], which is the same result obtained by [6] when the optimized parameter is the acceleration of the main mass. Following the same procedure, Neubert [7] proposed a formulation where the optimum parameters are obtained to minimize the velocity response.

The work of Warburton [6] presented several optimum absorber parameters for various excitations and response quantities, including force (main mass) and acceleration excitation (base), for harmonic and random white noise. The parameters are optimized by displacement, velocity, and acceleration of the main mass, as well as for the relative displacement between the main mass and ground. However, all the proposed formulations were made under the assumption of an undamped main mass. In the absence of structural damping, the optimal frequency tuning of the TMD can be determined based solely on the mass ratio between the TMD and the structure. But for real structures, some structural damping is always present, and the

above formulations may not be adequate. Ioi and Ikeda proposed some optimization parameters for damped structures using numerical calculation in 1978 [8].

The work of Fujino and Abé in 1993 derived analytical expressions for the frequency response function of the structure with the TMD and used a perturbation technique to obtain the design formulas [9]. In the same edition, Tsai and Lin derived analytical expressions for the frequency response function of the structure with the TMD and used the energy method to obtain the optimal mass, damping, and stiffness of the TMD using series representations [10]. Asami and Nishihara obtained a closed-form exact solution for the H∞ optimization, which can be applied to a range of transfer functions and damped systems [11].

In 2005, Krenk proposed a simplified analytical model to estimate the optimal parameters of a tuned mass damper (TMD) system, following a theoretical study focused on frequency analysis [12]. Another closed-form optimization criterion, proposed by Ghosh and Basu in 2007 [13], is based on the minimization of a cost function derived from the energy of the system under consideration. The optimization is subject to constraints on the maximum displacement and acceleration of the primary structure, using the equal peak theory employed by Den Hartog.

Krenk and Høgsberg (2008) demonstrated that the classical frequency tuning for harmonic loads of a system with both structural and applied damping, under the effects of random white noise, can be simplified by making an approximation that involves a small term in the structural damping coefficient. This approximation reduces the complexity of the formula, making it easier to apply in practice. The authors also found that the magnitude of the optimal applied damping depends only on the mass ratio, but is independent of the structural damping [14].

Anh and Nguyen (2013) utilized the Equivalent Linearization Method and a Dual Criterion of Equivalent Linearization Method to optimize a TMD, and also found that the expression of the optimal tuning ratio is independent of the TMD's damping [15].

Puzyrov and Awrejcewicz (2017) revised the classical formulations and proposed an alternative method for determining the optimum absorber parameters that takes into account the frequency response of the absorber and the frequency response of the primary system. The proposed formula does not rely on the existence of invariant points [16].

While the general formulations are proposed under the assumption that the system can be represented by a single degree of freedom (SDOF) system, when this assumption is not true, the optimum parameters may be found by numerical analysis. In this scope, Kordi and Alamatian (2019), based on the complex stiffness theory, proposed closed-form solutions that are applicable to both single and multiple-degree-of-freedom systems [17].

Numerous researchers have employed numerical analysis to investigate the optimal parameters of tuned mass damper (TMD) systems [18]–[20]. In the context of wind turbine towers, studies have primarily focused on numerical and finite element analyses [21]–[26].

The objective of the present study is to compare the outcomes of various TMD parameter formulations described in the literature when applied to a metallic tapered tower functioning as a support for a wind turbine. Specifically, the maximum dynamic amplification factor for both the main structure and TMD will be compared across several formulations. Furthermore, the maximum displacement of both the structure and TMD will be evaluated by numerically integrating the 2-degree-of-freedom (2DOF) system under harmonic excitation. The findings of this study will help determine the optimal TMD parameters for metallic tapered towers supporting wind turbines.

## 2 ANALYTICAL PROCEDURE

### 2.1 Formulation of the problem

Considering the structure represented as a SDOF system the damper system Kelvin-Voigt model [27] can be represented according to Figure 1. In the context of structural engineering, when the primary structure is represented as a single degree of freedom system (SDOF), only the dominant mode of energy dissipation is considered and involves the integration of a mass element ($m_s$) with a spring element ($k_s$) and a viscous damper element ($c_s$). The SDOF system offers a straightforward yet effective approach to analyzing the dynamic behavior of structures under external loads. The effects of TMD are accounted for within the SDOF model, by incorporating the mass of the TMD ($m_d$), its spring stiffness constant ($k_d$) and damping coefficient ($c_d$).

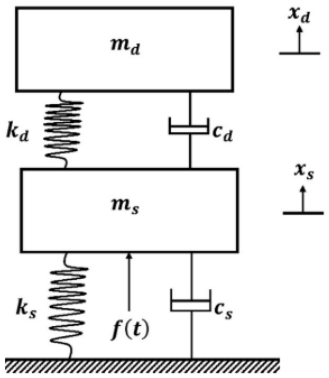


Figure 1 : Theoretical model of a damped main structure and TMD under force excitation f(t) [15].

Equation (1) presents the dynamic equilibrium equation for the 2DOF system illustrated in Figure 1.

$$\begin{aligned} m_s\,\ddot{x_s} + (c_s + c_d)\dot{x_s} - c_d\dot{x_d} + (k_s + k_d)x_s - k_d x_d &= f(t) \\ m_d\,\ddot{x_t} - c_d\dot{x_s} + c_d\dot{x_d} - k_d x_s + k_d x_d &= 0 \end{aligned} \tag{1}$$

The amplitude magnification of the steady-state response of a system, also referred to as the frequency transfer function, is determined as Equation (2) and (3) for the main structure and TMD, respectively. Appropriate substitutions are made in accordance with Equations (4-5) to obtain these equations. Utilizing Equations (2) and (3), it is feasible to evaluate the response of the system in relation to the dimensionless parameters outlined in Equation (5).

$$\left|\frac{x_s}{f_0/k_s}\right| = \sqrt{\frac{(\gamma^2-\beta^2)^2 + (2\gamma\beta\xi_d)^2}{[\gamma^2 - (1 + 4\gamma\xi_s\xi_d + \gamma^2 + \mu\gamma^2)\beta^2 + \beta^4]^2 + [2\beta\xi_s(\gamma^2-\beta^2)^2 + 2\gamma\beta\xi_d(1-\beta^2-\mu\beta^2)]^2}} \tag{2}$$

$$\left|\frac{x_d}{f_0/k_s}\right| = \sqrt{\frac{\gamma^4 + (2\gamma\beta\xi_d)^2}{[\gamma^2 - (1 + 4\gamma\xi_s\xi_d + \gamma^2 + \mu\gamma^2)\beta^2 + \beta^4]^2 + [2\beta\xi_s(\gamma^2-\beta^2)^2 + 2\gamma\beta\xi_d(1-\beta^2-\mu\beta^2)]^2}} \tag{3}$$

$$\omega_s = \sqrt{\frac{k_s}{m_s}}, \qquad \xi_s = \frac{c_s}{2m_s\omega_s}, \qquad \omega_d = \sqrt{\frac{k_d}{m_d}}, \qquad \xi_d = \frac{c_d}{2m_d\omega_d}, \tag{4}$$

$$\mu = \frac{m_d}{m_s}, \qquad \gamma = \frac{\omega_d}{\omega_s}, \qquad \beta = \frac{\omega}{\omega_s} \tag{5}$$

## 2.2 Optimum parameters

Based on the previous research outlined in Section 1, Table 2 presents the optimal values for the frequency ratio ($\gamma$) and damping of the damper system ($\xi_d$). To assess the efficacy of the proposed formulations, Equations (2) and (3) were solved using each of the 22 different configurations. The value of $\mu$ was held constant at 0.01 throughout the analysis.

| Code | Author | Frequency ratio $\gamma_{opt}$ | Damping TMD $\xi_{dopt}$ |
|---|---|---|---|
| DHUH | Den Hartog (1928) [3] | $\frac{1}{1+\mu}$ | $\sqrt{\frac{3\,\mu}{8(1+\mu)}}$ |
| NUUHVEL | Neubert (1964) [7] | $\frac{\sqrt{1+0.5\mu}}{1+\mu}$ | $\sqrt{\frac{3\,\mu\left(1+\mu+\frac{5\mu^2}{24}\right)}{8(1+\mu)(1-0.5\mu)^2}}$ |
| WBUH | Warburton (1982)[6] | $\frac{1}{\sqrt{1+\mu}}$ | $\sqrt{\frac{3\,\mu}{4(2+\mu)}}$ |
| WBUHB | Warburton (1982)[6] | $\frac{\sqrt{1+0.5\mu}}{1+\mu}$ | $\sqrt{\frac{3\mu}{8(1+\mu)(1-0.5\mu)}}$ |
| WBUR | Warburton (1982)[6] | $\frac{\sqrt{1+0.5\mu}}{1+\mu}$ | $\sqrt{\frac{\mu(4+3\mu)}{8(1+\mu)(2+\mu)}}$ |
| WBURVEL | Warburton (1982)[6] | $\frac{1}{\sqrt{1+\mu}}$ | $\frac{\mu}{4}$ |
| WBURB | Warburton (1982)[6] | $\frac{\sqrt{1+0.5\mu}}{1+\mu}$ | $\sqrt{\frac{\mu(4-\mu)}{8(1+\mu)(2-\mu)}}$ |
| IKDH | Ioi and Ikeda (1978) [8] | $\frac{1}{1+\mu} - (0.241 + 1.7\mu - 2.6\mu^2)\xi_s - (1 + 1.9\mu + \mu^2)\xi_s^2$ | $\sqrt{\frac{3\,\mu}{8(1+\mu)}} + (0.13 + 0.12\mu + 0.4\mu^2)\xi_s - (0.01 + 0.9\mu + 3\mu^2)\xi_s^2$ $with\ 0.1 \le \mu \le 0.3\ and\ 0 \le \xi_s \le 0.125$ |
| IKDHB | Ioi and Ikeda (1978) [8] | $\frac{\sqrt{1+0.5\mu}}{1+\mu} - (0.33 + 0.28\mu - 0.5\mu^2)\xi_s + (0.8 - \mu)\xi_s^2$ | $\sqrt{\frac{3\,\mu}{8(1+\mu)}} + (0.135 - 0.28\mu - 0.2\mu^2)\xi_s + (0.05 + 1.8\mu - \mu^2)\xi_s^2$ |
| FAUL | Fujino & Abé (1993) [9] | $\frac{1}{1-\mu}$ | $\sqrt{\frac{\mu}{(1+\mu)}} = \xi_{bif}$ |
| FADL | Fujino & Abé (1993) [9] | $\frac{1}{1+\mu} - \frac{\sqrt{\mu}\xi_s}{(1+\mu)\sqrt{1+\mu-\xi_s^2}}$ | $\frac{\xi_s}{1+\mu} + \frac{\sqrt{\mu}\sqrt{1+\mu-\xi_s^2}}{1+\mu}\ with\ \xi_s^2 \le \mu$ |
| TGDH | Tsai & Lin (1993) [10] | $\left(\frac{\sqrt{1+0.5\mu}}{1+\mu} + \frac{1}{\sqrt{1-2\xi_s^2}} - 1\right) - (0.288 - 0.611\sqrt{\mu} + 1.12\mu)\sqrt{\mu}\xi_s - (2.298 - 6.739\sqrt{\mu} + 8.316\mu)\sqrt{\mu}\xi_s^2$ | $\sqrt{\frac{3\,\mu}{8(1+\mu)}} + 0.151\xi_s - 0.187\xi_s^2 + 0.238\xi_s\mu$ |

| | | | |
|---|---|---|---|
| TGDHB | Tsai & Lin (1993) [10] | $\left(\frac{\sqrt{1+0.5\mu}}{1+\mu}+\sqrt{1-2\xi_s^2}-1\right)-(2.375-1.034\sqrt{\mu}-0.426\mu)\sqrt{\mu}\xi_s-(3.73-16.903\sqrt{\mu}+20.496\mu)\sqrt{\mu}\xi_s^2$ | $\sqrt{\frac{3\mu}{8(1+\mu)(1-0.5\mu)}}+(0.151\xi_s-0.170\xi_s^2)+(0.163\xi_s+4.98\xi_s^2)\mu$ |
| ANUH | Asami & Nishihara (2003) [11] | $\frac{2}{1+\mu}\sqrt{\frac{2(16+23\mu+9\mu^2+2(2+\mu)\sqrt{4+3\mu})}{3(64+80\mu+27\mu^2)}}$ | $\frac{1}{4}\sqrt{\frac{(8+9\mu-4\sqrt{4+3\mu})}{1+\mu}}$ |
| KRUL | Krenk (2005)[12] | $\frac{1}{1-\mu}$ | $\sqrt{\frac{\mu}{2(1-\mu)}}$ |
| GB | Ghosh & Basu (2007) [13] | $\sqrt{\frac{1-4\xi_s^2-\mu(2\xi_s^2-1)}{(1+\mu)^3}}$ | |
| KHDR | Krenk & Høgsberg (2008) [14] | $\frac{1}{1-\mu}$ | $\frac{\sqrt{\mu}}{2}$ |
| KHDRB | Krenk & Høgsberg (2008) [14] | $\frac{1}{1-\mu}$ | $\frac{1}{2}\sqrt{\frac{\mu}{(1-\mu)}}$ |
| AND1 | Anh & Nguyen (2013) [15] | $\frac{\sqrt{1+\frac{\pi^2}{(\pi^2-2)^2}\xi_s^2}-\frac{\pi}{\pi^2-2}\xi_s}{1+\mu}$ | |
| AND2 | Anh & Nguyen (2013) [15] | $\frac{1}{(1+\mu)\left(\sqrt{1+\frac{4}{\pi^2}\xi_s^2}+\frac{2}{\pi}\xi_s\right)}$ | |
| PAUH | Puzyrov & Awrejcewicz (2017) [16] | $\sqrt{\frac{8(16+23\mu+9\mu^2+2(2+\mu)\sqrt{4+3\mu})}{3((1+\mu)^2(64+80\mu+27\mu^2))}}$ | $\sqrt{\frac{8+9\mu-4\sqrt{(4+3\mu)}}{16(1+\mu)}}$ |
| KAUL | Kordi & Alamatian (2019)[17] | $\frac{\sqrt{1+\mu}}{1+\mu}$ | $\frac{\sqrt{\mu}}{1-\mu}$ |

Table 2: Optimum frequency ratio and damping of TMD according to Authors.

## 2.3 Time history analysis

The present study involved the analysis of the response of a system subjected to a harmonic force, where $f(t) = f_0.\sin(\omega t)$. This was accomplished through numerical integration of the equations of motion of the system, as presented in equation (1). In accordance with the optimal formulations detailed in Table 2, the parameters were varied while keeping $\mu$ constant at 0.01. The harmonic force was standardized at 1kN and applied over 10 seconds after that the structure are in free vibration, while the frequency excitation was set at $\omega = \omega_s$.

## 2.4 Finite element analysis

To obtain the modal parameters for the first mode of the wind turbine tower structure, an eigenvalue analysis was performed using Finite Element Method (FEM). The tower was represented as a multi-degree of freedom system, wherein the rotor and nacelle masses were modeled as a lumped mass situated at the hub height. To ensure the accuracy of the FEM model, it was evaluated using the SAP2000 software as a beam model. The accuracy of the model was then validated against experimental results obtained from Operational Modal Analysis [28].

Furthermore, a time history analysis was conducted on the beam model according to section 2.3. The resulting response was then utilized to validate the response of the SDOF model, which was obtained through time history integration.

## 3 DESCRIPTION OF THE TOWER

The focus of this investigation is a metal tower with a height of 17.8 meters, which has been constructed utilizing S275 steel. The tower features a hexadecagonal cross-section, exhibiting an outer diameter of 0.5890 meters at the base and tapering down to 0.1954 meters at the top, with a uniform wall thickness of 4 millimeters. Further significant details related to the key characteristics of the tower are provided in Table 3.

The dynamic characteristics of the tower, comprising of the initial frequency and damping ratio of the primary structure, were determined via in-situ vibration testing using operational modal analysis techniques [28]. The outcomes have been tabulated in Table 3 for easy reference. Additionally, Table 3 also includes the modal mass of the first mode obtained through modal analysis, where the mode shape was normalized to unity at maximum displacement.

| | | |
|---|---|---|
| **Density** | 7850.000 | [kg/m³] |
| **Young's modulus** | 210.000 | [GPa] |
| **Poisson's ratio** | 0.300 | -- |
| **Yield strength** | 275.000 | [MPa] |
| **Height** | 17.800 | [m] |
| **Top diameter** | 0.195 | [m] |
| **Bottom diameter** | 0.589 | [m] |
| **Nacelle mass** | 75.000 | [kg] |
| **Tower mass** | 631.355 | [kg] |
| **1st frequency** | 1.601 | [Hz] |
| $\xi_{s1^{st}}$ | 0.034 | -- |
| **1st modal mass** | 165.113 | [kg] |

Table 3: Tower properties.

## 4 RESULTS

In this section, we present the results of our analysis of the optimum TMD parameters for a metallic tapered tower supporting a SWT. The analysis involved comparing the results obtained using several formulations for estimating the TMD parameters, as described in the previous section. Specifically, we compared the maximum dynamic amplification factor and maximum displacement of the main structure and TMD, as determined through numerical integration under a harmonic excitation.

Figure 2 shows the comparison between the time history analysis of the main structure, comparing the MDOF system solved by FEM and the SDOF solved by numerical integration under harmonic excitation force where $\omega = 2\pi$. The correct modal parameters were used to accurately represent the behavior of the main structure. The graph plots the top displacement of the tower over time, highlighting the agreement between the FEM and SDOF methods. These results provide evidence that the behavior of the structure can be effectively captured through a SDOF system.

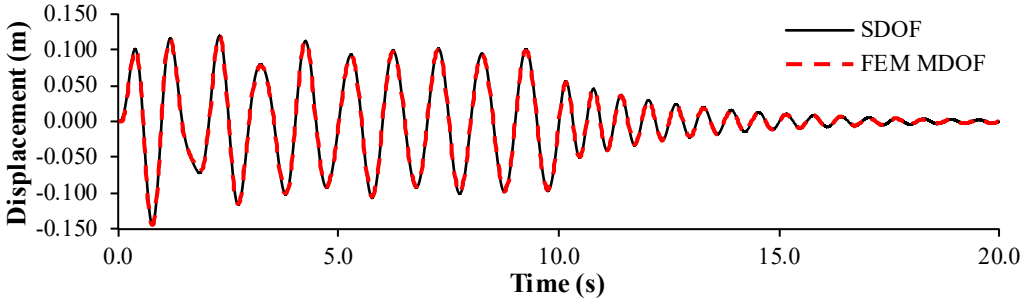


Figure 2 : Comparison of top displacement of main structure under harmonic excitation force

The results of the amplification response of the structure and the TMD system are illustrated in Figure 3, for all formulations listed in Table 2. The figure clearly shows that different formulations provide vastly different responses, with some of them proving to be unsuitable for the analyzed structure. Specifically, some formulations exhibit lower amplification factors around the resonance frequency, but at the same time, exhibit high amplification in the vicinity of this frequency, thereby leading to non-flat AM curves.

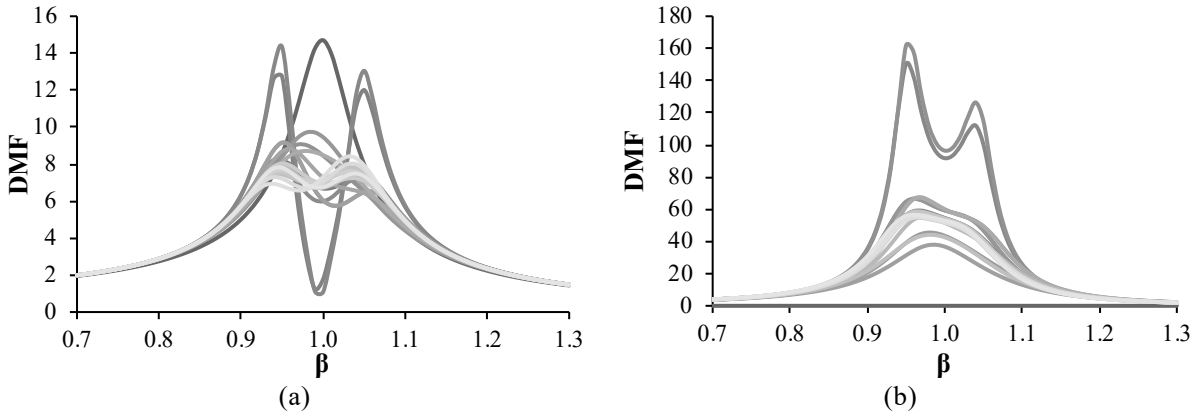


Figure 3 : Amplification magnification curves μ= 0.01 (a) main structure, (b) TMD

Figure 4 shows that, in general, all maximum amplification factors for the main structure do not exhibit high variation. The original structure amplification factor of 14.7 can be reduced by approximately 40% in almost all formulations, except for the codes WBUHB and WBUR VEL, which represent the two AM curves with two peaks around the resonant frequency. When these two values are excluded, the reduction of the DMF maximum factor when the TDM is used is 43 ± 3% for a μ=0.01.

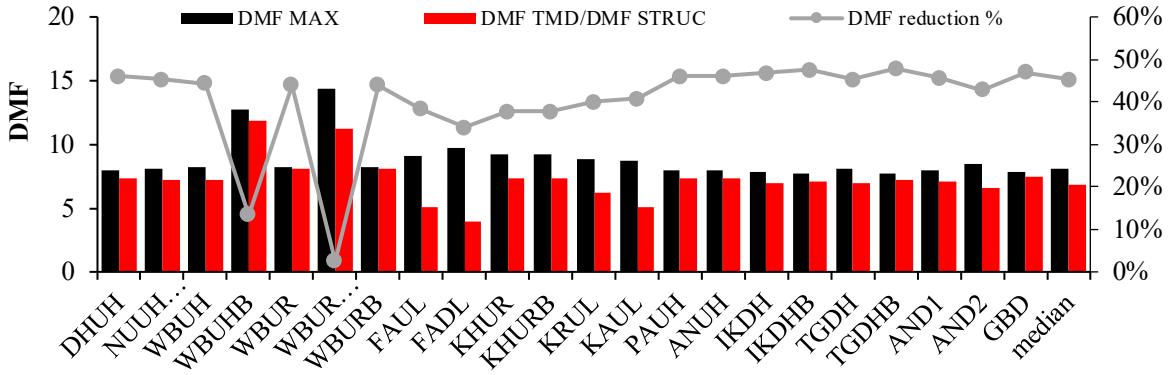


Figure 4 : Comparison DMF for the authors with μ= 0.01

In Figure 5, it is noteworthy that for some cases, the DMF MAX and the attenuation of the Xs exhibit an inverse relation, as in the case of FAUL and FADL, where the DMF MAX exhibits the highest values obtained by the steady-state response, while the Xs reduction is at lower values in the time history. This implies that the DMF curve has peaks near the resonant frequency.

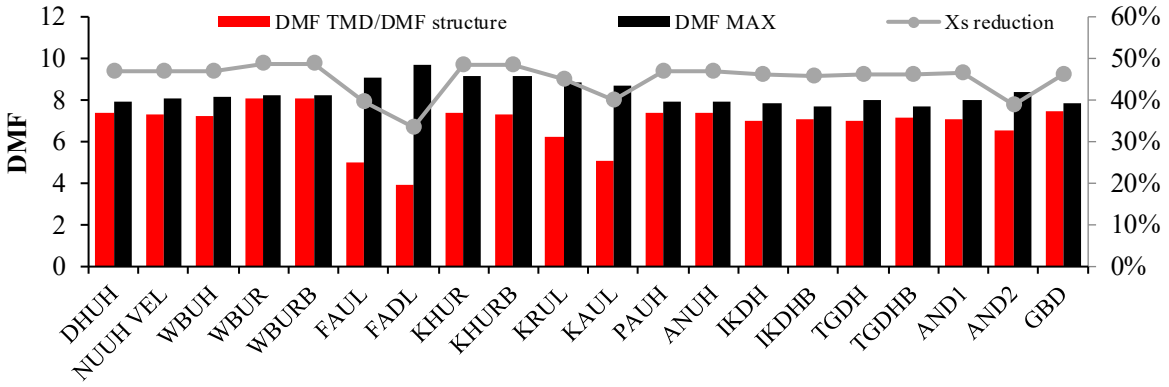


Figure 5 : Comparison DMF and the % reduction of Xs in the time history analysis for $\omega = 2\pi 1.601$

Regarding the time history response presented in Figure 6, it is evident that for the main structure, the classical DHUH formulation exhibits better performance than the FADL formulation. However, for the TMD system, the opposite is true, and FADL performs better. This result highlights the fact that optimal parameters depend on the system's specific requirements. In the case of wind towers, where space for TMD movement is limited, it is essential to find a solution that balances the main structure and TMD displacements.

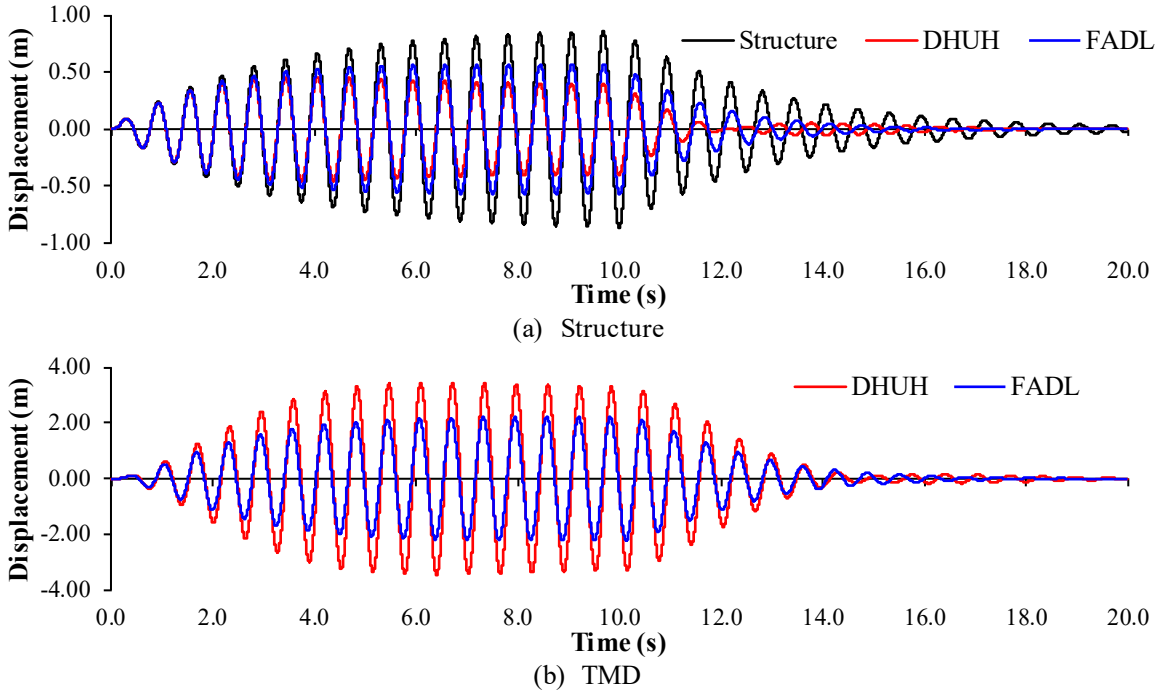


Figure 6: time history response of the system subjected to harmonic force with $\omega = 2\pi 1.601$

## 5 CONCLUSIONS

Based on the findings of this investigation, it can be inferred that the efficiency of the Tuned Mass Damper (TMD) system in wind turbine towers is significantly impacted by the choice of optimal parameters, and distinct formulations can result in significant variations in the structure's response. In general, for the metallic tapered tower considered in this study, all optimal formulations yielded comparable outcomes. Among these, the classical DHUH formulation demonstrated superior performance for the main structure, whereas the FADL formulation exhibited better performance for the TMD system. Nonetheless, the selection of optimal parameters must be tailored to the specific characteristics and demands of the system, and should therefore be evaluated for each case.

It is also demonstrated that the SDOF method is capable of accurately depicting the dynamic response of the main structure subject to harmonic excitation, assuming that the appropriate modal parameters are employed. Moreover, the results revealed that the utilization of TMD systems can result in a considerable reduction in the maximum amplification factor for the main structure, even at a relatively low mass ratio of 0.01 of the modal mass. Specifically, in the presented case, the use of a mass of 1.65 kg proved to be effective in significantly diminishing the primary vibration of the system, resulting in a reduction of up to 43%.

## ACKNOWLEDGEMENTS

This paper is within the scope of the first author's Ph.D. degree in progress, financially supported by the Portuguese Foundation for Science and Technology (FCT) through the PhD grant reference SFRH/BD/147789/2019 under the programme POCH (N2020 – P2020) and subsidized by the European Social Fund (FSE) and national funds from MCTES. The authors also acknowledge the use of the experimental equipment [11] under the Project "SD Poles - Steel and Dampers for Poles" with reference POCI-01-0247-FEDER-039865, co-financed by European Regional Development Fund (ERDF) through the Operational Programme for Competitiveness and Internationalization (COMPETE 2020) under the PORTUGAL 2020, of which the second co-author is the FEUP's coordinator. This work is also integrated in the R&D activities of the CONSTRUCT Institute on Structures and Constructions (Instituto de I&D em Estruturas e Construções), financially supported by Base Funding UIDB/04708/2020 through national funds of FCT/MCTES (PIDDAC).

## REFERENCES

[1] J. M. Henriques and R. C. Barros, "Design of a lattice wind tower and a comparison of the structural response with and without a TMD," *Civil-Comp Proc.*, vol. 102, no. January, 2013, doi: 10.4203/ccp.102.45.

[2] H. Frahm, "Device for Damped Vibrations of Bodies," 989958, 1909

[3] J. P. Den Hartog, *Mechanical Vibrations*, 4th ed. New York, 1956.

[4] J. E. Brock, "A Note on the Damped Vibration Absorber," *J. Appl. Mech. Trans. ASME*, vol. 13, no. 4, p. A284, 1946, doi: 10.1115/1.4009588.

[5] J. E. Brock, "Theory of the Damped Dynamic Vibration Absorber for Inertial Disturbances," *J. Appl. Mech. Trans. ASME,* vol. 16, no. 1, pp. 86–92, 1949, doi: 10.1115/1.4009897.

[6] G. B. Warburton, "Optimum absorber parameters for various combinations of response

and excitation parameters," *Earthq. Eng. Struct. Dyn.*, vol. 10, no. 3, pp. 381–401, 1982, doi: 10.1002/eqe.4290100304.

[7] V. H. Neubert, "Dynamic Absorbers Applied to a Bar That Has Solid Damping," *J. Acoust. Soc. Am.*, vol. 36, no. 4, pp. 673–680, 1964, doi: 10.1121/1.1919039.

[8] T. Ioi and K. Ikeda, "On the dynamic vibration damped absorber of the vibration system," *Bull. JSME*, vol. 21, no. 151, pp. 64–71, 1978, doi: 10.1299/jsme1958.21.64.

[9] Y. Fujino and M. Abé, "Design formulas for tuned mass dampers based on A perturbation technique," *Earthq. Eng. Struct. Dyn.*, vol. 22, no. 10, pp. 833–854, 1993, doi: 10.1002/eqe.4290221002.

[10] H. -C Tsai and G. -C Lin, "Optimum tuned-mass dampers for minimizing steady-state response of support-excited and damped systems," *Earthq. Eng. Struct. Dyn.*, vol. 22, no. 11, pp. 957–973, 1993, doi: 10.1002/eqe.4290221104.

[11] T. Asami and O. Nishihara, "Closed-form exact solution to H∞ optimization of dynamic vibration absorbers (application to different transfer functions and damping systems)," *J. Vib. Acoust. Trans. ASME*, vol. 125, no. 3, pp. 398–411, 2003, doi: 10.1115/1.1569514.

[12] S. Krenk, "Frequency analysis of the tuned mass damper," *J. Appl. Mech. Trans. ASME*, vol. 72, no. 6, pp. 936–942, 2005, doi: 10.1115/1.2062867.

[13] A. Ghosh and B. Basu, "A closed-form optimal tuning criterion for TMD in damped structures," *Struct. Control Heal. Monit.*, vol. 14, no. 4, pp. 681–692, 2007, doi: 10.1002/stc.176.

[14] S. Krenk and J. Høgsberg, "Tuned mass absorbers on damped structures under random load," *Probabilistic Eng. Mech.*, vol. 23, no. 4, pp. 408–415, 2008, doi: 10.1016/j.probengmech.2007.04.004.

[15] N. D. Anh and N. X. Nguyen, "Design of TMD for damped linear structures using the dual criterion of equivalent linearization method," *Int. J. Mech. Sci.*, vol. 77, pp. 164–170, 2013, doi: 10.1016/j.ijmecsci.2013.09.014.

[16] V. Puzyrov and J. Awrejcewicz, "On the optimum absorber parameters: Revising the classical results," *J. Theor. Appl. Mech.*, vol. 55, no. 3, pp. 1081–1089, 2017, doi: 10.15632/jtam-pl.55.3.1081.

[17] F. Kordi and J. Alamatian, "Analytical Method for Designing the Tuned Mass Damper Based on the Complex Stiffness Theory," *Iran. J. Sci. Technol. - Trans. Civ. Eng.*, vol. 43, no. 4, pp. 673–684, 2019, doi: 10.1007/s40996-018-0222-0.

[18] R. Rana and T. T. Soong, "Parametric study and simplified design of tuned mass dampers," *Eng. Struct.*, vol. 20, no. 3, pp. 193–204, 1998, doi: 10.1016/S0141-0296(97)00078-3.

[19] C. L. Lee, Y. T. Chen, L. L. Chung, and Y. P. Wang, "Optimal design theories and applications of tuned mass dampers," *Eng. Struct.*, vol. 28, no. 1, pp. 43–53, 2006, doi: 10.1016/j.engstruct.2005.06.023.

[20] M. Morga and G. C. Marano, "Optimization criteria of TMD to reduce vibrations generated by the wind in a slender structure,"*JVC/Journal Vib. Control*, vol. 20, no. 16, pp. 2404–2416, 2014, doi: 10.1177/1077546313478296.

[21] I. Enevoldsen and K. J. Mørk, *Effects of a vibration mass damper in a wind turbine tower*, vol. 24, no. 2. 1996. doi: 10.1080/08905459608905260.

[22] G. M. Stewart and M. A. Lackner, "The impact of passive tuned mass dampers and wind-wave misalignment on offshore wind turbine loads," *Eng. Struct.*, vol. 73, pp. 54–61, 2014, doi: 10.1016/j.engstruct.2014.04.045.

[23] M. Ghassempour, G. Failla, and F. Arena, "Vibration mitigation in offshore wind turbines via tuned mass damper," *Eng. Struct.*, vol. 183, no. December 2018, pp. 610–636, 2019, doi: 10.1016/j.engstruct.2018.12.092.

[24] O. Altay, F. Taddei, C. Butenweg, and S. Klinkel, *Vibration mitigation of wind turbine towers with tuned mass dampers*, no. 9783319084121. 2014. doi: 10.1007/978-3-319-08413-8_12.

[25] H. L. Guntur, W. Hendrowati, A. Daman, and A. D. Wilujeng, "The effect of tuned mass damper to the vibration of wind turbine structure model," *AIP Conf. Proc.*, vol. 2187, no. December, 2019, doi: 10.1063/1.5138357.

[26] X. Tong, X. Zhao, and S. Zhao, "Load reduction of a monopile wind turbine tower using optimal tuned mass dampers," *Int. J. Control*, vol. 90, no. 7, pp. 1283–1298, 2017, doi: 10.1080/00207179.2015.1124143.

[27] A. M. Baz, *Active and Passive Vibration Damping*. 2019. doi: 10.1002/9781118537619.

[28] A. Dick, R. C. De Barros, and M. T. B. César, "Experimental and operational modal analysis of a small wind turbine tower," in *M2D2022 - 9th International Conference on Mechanics and Materials in Design*, 2022, no. June, pp. 829–836. [Online]. Available: https://paginas.fe.up.pt/~m2d/proceedings_m2d2022/index.htm

COMPDYN 2023
9th ECCOMAS Thematic Conference on
Computational Methods in Structural Dynamics and Earthquake Engineering
M. Papadrakakis, M. Fragiadakis (eds.)
Athens, Greece, 12-14 June 2023

# MODELLING STRATEGIES OF INFILL MASONRY WALLS FOR SEISMIC ANALYSIS OF BUILDING STRUCTURES

**Pedro P. Folhento**[1], **Rui C. Barros**[1], **and Manuel T. Braz-César**[2]

[1] CONSTRUCT, Faculdade de Engenharia da Universidade do Porto
Porto, Portugal
{up201811645@edu.fe.up.pt, rcb@fe.up.pt}

[2] CONSTRUCT, Instituto Politécnico de Bragança
Bragança, Portugal
brazcesar@ipb.pt

## Abstract

*Infill walls in frame structures greatly influence the dynamic behaviour of buildings and consequently their performance when under seismic loads. In building construction, unreinforced masonry walls constitute one of the oldest and worldwide used materials. Despite of great simplicity of their application due to their assemblage process, their behaviour under earthquake events is rather complex, and it is usually neglected in the design phase of building structures. Numerous studies have been conducted over the years to model and assess the influence of non-structural infill walls in buildings. Micro-, meso- and macro-models are available in the literature, although the choice of one of these types of models depends on the problem under consideration. For the current investigation, macro-models are more adequate, in particular equivalent strut models. This kind of modelling has been evolving over the years accounting for a large number of phenomena intrinsic to these elements: the failure modes expected by the infill walls; the relative infill-frame lateral stiffness; the consideration of openings in infills and partially infill walls; bounding frame columns' shear failure; vertical loading effect; out-of-plane behaviour of the infill and its interaction with in-plane behaviour; applicability to multiple degrees-of-freedom systems with multiple stories and bays, etc. This study considers two well-known macro-modelling strategies of unreinforced infill masonry walls in reinforced concrete frame structures modified to improve the in-plane and out-of-plane behaviour simulation under seismic actions. Results showed that these modifications allowed for better reproduction of infill walls' behaviour compared with experimental tests.*

**Keywords:** Infill masonry walls, Non-structural elements, Seismic analysis, Model Validation, Building structures.

## 1 INTRODUCTION

Infill masonry walls in frame structures are known for their relevant influence on the dynamic behaviour of building structures and consequently the influence on their performance when subjected to seismic loads. In building construction, unreinforced masonry walls constitute one of the oldest and worldwide used materials. Despite of great simplicity in the application of these non-structural elements due to their assemblage process, their behaviour under earthquake events is rather complex, and thus it is usually neglected in the design phase of building structures. The interaction between the surrounding frame structure and the infill panel is not straightforward, it depends on numerous factors such as brick materials, mortar mechanical characteristics, brick geometry, workmanship quality, relative stiffness between the frame and the infill panel, etc. [1], which contribute for uncertainties in the accurate modelling of such non-structural elements.

Numerous studies have been conducted over the years to model and assess the influence of non-structural infill walls in buildings. Micro-, meso- and macro-models are available in the literature, although the choice of one of these types of models depends on the problem under consideration [1, 2].

The current investigation deals with macro-models, particularly equivalent strut models, which are more adequate for building structures with multiple stories and bays. This kind of modelling has been evolving over the years and can now account for a large number of physical phenomena intrinsic to these elements [3 – 12].

Two well-known macro-modelling strategies of unreinforced infill masonry walls in reinforced concrete (RC) frame structures are considered and modified to improve in-plane and out-of-plane behaviour simulation under seismic actions. The procedures are explained by presenting the modelling choices and assumptions used. The accuracy of such models is verified against different experimental results found in the literature [13 – 15], by calibrating the constitutive parameters of the infill wall elements with the subsequent use of a simplex and genetic algorithm [16].

Results indicate that these modifications allowed for better reproduction of the in-plane and out-of-plane behaviour of infill masonry walls when compared with different experimental tests, being appropriate for the use in numerical models of RC building structures, provided that the models' parameters are adequately chosen and calibrated.

## 2 MODELLING STRATEGIES

Generally, the bare frame withstands the gravity loads, whilst the frame and infill walls jointly carry the horizontal loads, e.g., winds or earthquakes, with a prevalent truss action mechanism in the infills [1]. Under these conditions, the infills tend to react with the bounding structure between the upper corner of the windward column and the lower corner of the leeward column, resulting in a compression-only diagonal. Large deformations cause the frame and the infill panel to interact at these corner regions (the contact lengths) and to separate in the opposite corners due to the differences in deformation of these elements, producing cracks at these interfaces.

Infill masonry wall macro-models generally consider equivalent diagonal strut elements. The standard strut model usually considers two struts in each direction as represented in Figure 1, functioning in a compression-only fashion. However, this modelling approach has been through an evolutionary process, in which different phenomenological features were added, whether by changing the number and arrangement of the struts and/or attributing different material laws to simulate different kinds of behaviour. Such features may include: the in-plane (IP) failure modes of the infill walls [3, 4]; the relative infill-frame lateral stiffness [5]; open-

ings in the infill panel and partially infill walls [6]; brittle failure of columns of the bounding frame [7]; vertical loading influence [8]; out-of-plane (OOP) stiffness, strength and failure, and its interaction with IP behaviour [9 – 11]; applicability to structural systems as buildings with multiple stories and bay [12], etc.

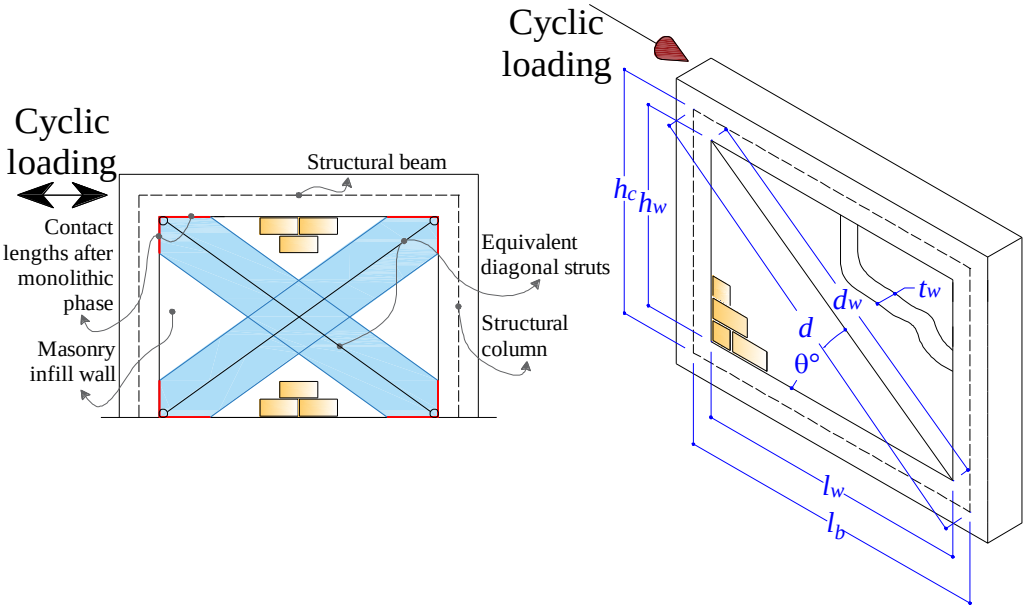


Figure 1: Standard equivalent diagonal strut model.

Among a large number of choices of macro-modelling techniques using equivalent diagonal struts, two approaches were selected for their relevance in the literature: Kadysiewski and Mosalam [9] model and Furtado et al. [10] model represented in Figure 2. Both models account for IP and OOP effects in the infill walls and can consider the collapse of individual infills upon exceedance of certain threshold values of drift. However, and despite the common disadvantage of not considering the possible shear failure of columns in the bounding frame (a disadvantage not addressed at this time), Furtado's model considers OOP linear behaviour and Kadysiewski and Mosalam's model does not properly captures the initial elastic and post-yield softening behaviour of infill walls.

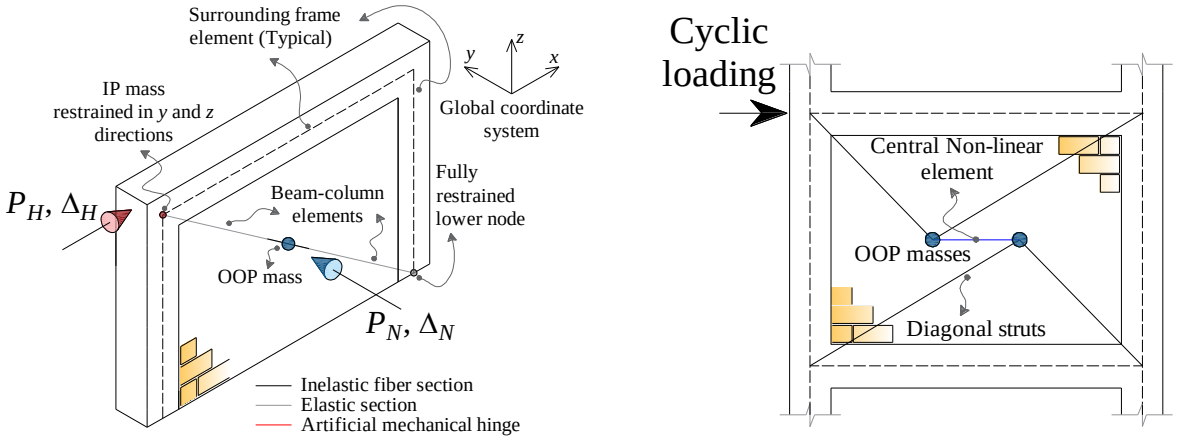


(a) Kadysiewski and Mosalam model; (b) Furtado et al. model.

Figure 2: Adopted modelling strategies for modification.

This study will address these points based on modifications carried out in these modelling techniques [17, 18]. Numerical models are developed using the OpenSees software [19, 20], and the calibration/optimization procedure and postprocessing of results are carried out using MATLAB [21]. Scripts were developed in Python language comprising functions for each of these models. The aim is to develop a model that could represent both the IP and OOP cyclic behaviour of infill masonry walls in RC frame structures using real provided mechanical parameters (when available), and in the absence of these, derivations of such parameters based on empirical assumptions. In addition, a Python function was developed to convert automatically the OpenSeesPy commands written directly to a Tcl file. This Tcl file containing specific information about the model will work as a batch file to be interpreted by MATLAB and used in parallel computing for model optimization and calibration purposes.

To model the RC beams and columns, force-based beam-column finite elements are used [22] with finite-length lumped plasticity using the modified Gauss-Radau plastic hinge integration method [23] and the Paulay and Priestly [4] expression to calculate the plastic hinge length in beams and columns. Linear geometric effects are considered by introducing the P-Δ term in the equilibrium upon geometric transformation [24]. The uniaxial materials are assigned to the different fibres in the critical sections following the Kent-Scott-Park model [25] for confined and unconfined concrete (respectively, *Concrete02* and *Concrete01* uniaxial materials in OpenSees) and a hysteretic law for the steel reinforcement (using the *Hysteretic* uniaxial material in OpenSees) that considers strength hardening and stiffness degradation. A cyclic shear law is also aggregated as a uniaxial material to the critical sections of columns, accounting for shear deformations and the possible shear failure in columns. All models are developed in a three-dimensional environment, so that elastic torsion is also included by aggregation to the element sections.

For both models a backbone curve of IP force-displacement as represented in Figure 3a is defined considering cracking, yielding, maximum, and ultimate points. However, this backbone is applied and used differently for each model as will be explained in the further two subsections.

Cracking and maximum IP forces are, respectively, calculated as follows [3, 4]

$$V_{\max} = \min\left( \underbrace{\frac{2}{3} z\, t_w\, f_m \sec(\theta)}_{R_{DC}\ \text{(Diagonal compression)}},\ \underbrace{\frac{\tau_0}{1-\mu\left(h_c/l_b\right)} t_w\, d_w}_{R_{SS}\ \text{(Shear sliding)}} \right) \cos(\theta) \tag{1}$$

$$V_{\text{crack}} = 0.5\pi t_w\, d_w\, f_{tm} \cos(\theta) \tag{2}$$

in which μ is the coefficient of friction [26], $z$ is the columns to infill contact lengths, and λ [5] is the frame-infill relative stiffness parameter, respectively,

$$z = \frac{\pi}{2}\frac{h_c}{\lambda} \quad \text{and} \quad \lambda = \sqrt[4]{\frac{E_{m0} t_w \sin(2\theta)}{4 E_c I_c h_w}} \tag{3}$$

where $f_{tm}$ is the masonry tensile strength, assumed as 5% of masonry compressive strength along the mortar bed-joints [27], $f_{m0}$, and $f_{m0}$ depending on the direction of voids in the masonry units is herein assumed to suffer an increase or reduction of 20% compared with the compressive strength of masonry perpendicular to the mortar bed-joints, $f_{m90}$. The Young's modulus of the masonry material along, $E_{m0}$, and orthogonal to the bed joints, $E_{m90}$, were computed in function of masonry compressive strength and the shear modulus, $G_{m0\text{-}90}$ (=0.4$E_{m90}$), implicitly assuming the Poisson's ratio, $\nu_{m0\text{-}90}$, as 0.25 [28]. A homogenous ortho-

tropic behaviour is assumed for the masonry with directions coinciding with the horizontal and vertical directions, the elastic properties can be derived along any direction (θ direction in Figure 1) [29]

$$E_{m\theta} = \left\{ \frac{\cos^4(\theta)}{E_{m0}} + \left[ \frac{1}{G_{m0\text{-}90}} - \frac{2\nu_{m0\text{-}90}}{E_{m0}} \right] \cos^2(\theta)\sin^2(\theta) + \frac{\sin^4(\theta)}{E_{m90}} \right\}^{-1} \tag{4}$$

The diagonal masonry compressive strength can now be found by assuming a linear proportion between Young's modulus and compressive strengths' ratio [30]. Considering the stress-strain relationship of unreinforced masonry in Figure 3b, the maximum IP displacement, $x_{max}$, can be calculated [31]

$$E_{t,m\theta} = 2E_{sec,m\theta} \rightarrow E_{sec,m\theta} = f_{m\theta} / \varepsilon_{m\theta,max} \rightarrow x_{max} = \varepsilon_{m\theta,max} d_w / \cos(\theta) \tag{5}$$

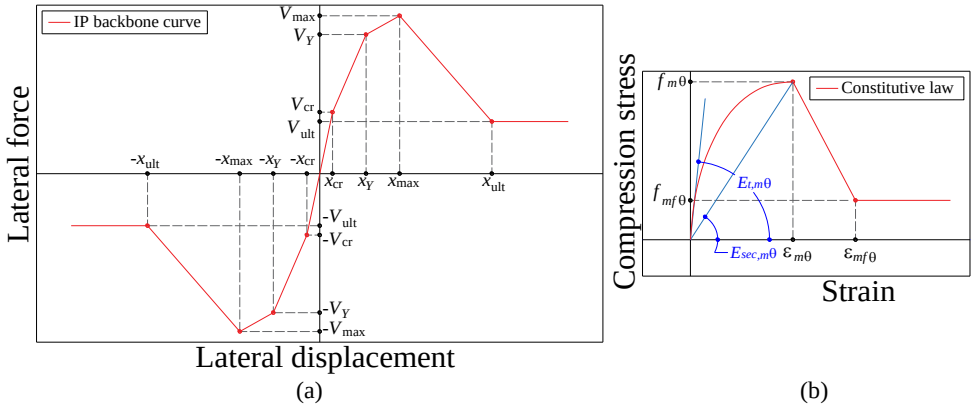


Figure 3: Constitutive relations adopted for IP behaviour of infill masonry walls.

It should be noted that this latter procedure of calculation of the masonry material elastic properties is only used when it is considered that enough real parameters are provided to adequately characterize such properties along the compression-only strut direction.

The infill wall's initial lateral stiffness, $k_{0w}$, can be estimated by considering double the ratio between the $V_{max}$ and $x_{max}$. The IP displacement at the cracking point is computed with the values of $V_{crack}$ and $k_{0w}$. The yield IP displacement, $x_Y$, is computed as an intermediate point between the cracking and maximum displacement [10]. The yield IP force, $V_Y$, is determined by assuming that the initial stiffness is modified by a factor of $a$ (assumed 0.05),

$$V_Y = \left(V_{max} - a k_{0w} x_{max}\right) / \left(1 - a\right) \tag{6}$$

The ultimate lateral IP force, $V_{ult}$, and ultimate IP displacement, $x_{ult}$, are assumed based on the observation of the experimental results. However, values of the force are assumed to range between 20% to 50% of the $V_{max}$, and displacements are considered to vary between 3 and 10 times the $x_{max}$.

The modifications to the above-mentioned modelling strategies are briefly expounded in the next two subsections.

## 2.1 Modification of Furtado et al. model

Besides the different approach to the IP behaviour previously explained, a further modification to this modelling strategy is considered, being focused on the attribution of a non-linear OOP bending moment–curvature law (instead of an elastic one) to the infill wall elements'

sections at the middle of the infill panel as illustrated in Figure 4a. This backbone curve shown in Figure 4b is defined by four points (uniaxial material *pinching4* [32] in OpenSees): cracking, maximum, softening, and residual points similar to the one adopted by [11].

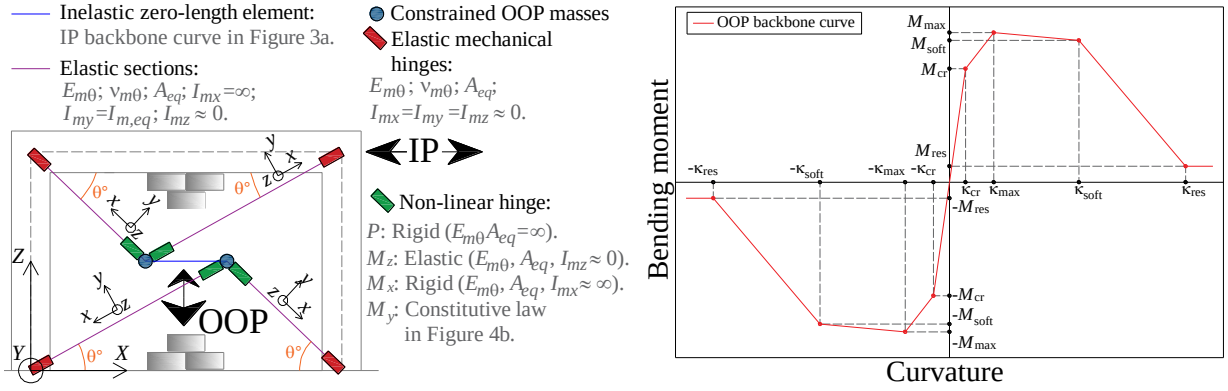


(a) Schematic representation of the model; (b) OOP moment-curvature backbone curve.

Figure 4: Modified Furtado et al. model.

The maximum point, corresponding to the maximum bending moment, is computed by adopting a similar procedure presented in [9]. This procedure follows the idea of an equivalent beam-column element spanning diagonally (derived from an original base system, i.e., a simply-supported element spanning vertically), which possesses an equivalent moment of inertia, $I_{m,eq}$,

$$I_{m,eq} = 1.644\left(\frac{d_w}{h_w}\right)^3 I \tag{7}$$

implying the first-mode effective mass (the OOP masses in Figure 4a) of 81% of the total mass of the infill. Parameter $I$ is the moment of inertia of the original infill panel cross-section, assuming half of this value to account for cracked infill. Hence, from the equivalence between the original and equivalent systems, the maximum bending moment can be calculated by the following expression

$$M_{\max,eq} = 1.570\left(\frac{d_w}{h_w}\right) M_{\max} \tag{8}$$

in which $M_{\max}$ is the maximum moment at mid-span of a simply-supported beam (original system) with a transverse uniform distributed applied load, that can be determined as follows

$$M_{\max} = \frac{q_{OOP} d_w h_w^2}{8} \tag{9}$$

The OOP strength or capacity of the infill wall, $q_{OOP}$, is computed as follows

$$q_{OOP} = \begin{cases} 0.85 f_{m90}\left(\dfrac{t_w}{h_w}\right)^2 & \text{if } SL \text{ and } 2E, \\ 0.85 f_{m90}\left(\dfrac{t_w}{h_w}\right)^2 + 0.85 f_{m0}\left(\dfrac{t_w}{l_w}\right)^2 & \text{if } (WL \text{ or } ML) \text{ and } 4E. \end{cases} \tag{10}$$

The terms *WL*, *ML* and *SL* are referred to as weak layout, moderate layout and strong layout infill wall leaves, respectively, and 2*E* and 4*E* mean the infill supported on two edges and four (all) edges, respectively. These terms and corresponding equations in Equation 10 were herein chosen based on the definitions provided by Di Domenico [15]. The first expression in the system of equations (top equation) is based on the one provided by Eurocode 6 [28] (although the author in [15], modified it according to McDowell et al.'s model [33] to include the term 0.85), being more appropriate to strong infills (*SL*) that may develop one-arching mechanism being thus supported on two edges.

Di Domenico [15] considered the Eurocode 6 [28] formulation to estimate the OOP strength of infills supported on four edges (4*E*) by summing the contributions of the two arching mechanisms expected to occur in *WL* and *ML* infills. Then by performing non-linear regression analysis, the established regression coefficient values on this formulation were determined for different deformed shapes, load shapes and boundary conditions, revealing good results in predicting the OOP strength of such infills. In this study, the second expression (bottom expression) simply assumes the sum of the two arching mechanisms' contributions, by considering the same value for the stress block ($0.85f_m$ of stress distribution at the ends of the arching mechanism parts [33]) for both contributions and adjusting the definition of slenderness ratio (inverse in Equation 10) depending on the arch direction. The choice of one or another expression is herein simplified to the value of the slenderness ratio of the infill, i.e., if the slenderness value is less than 15 the first expression is used, otherwise the second expression holds.

The cracking OOP moment on the OOP backbone curve is calculated by assuming $0.70q_{OOP}$ in the calculation of the respective bending moment. The softening moment is considered as a 5% reduction of the $M_{max,eq}$ and the residual moment is taken as 15% of the $M_{max,eq}$ for simulation convergence purposes (a smaller value can be considered).

The cracking and maximum curvatures are computed using the respective moments and bending stiffnesses. The softening and residual curvatures are assumed three and fifteen times the maximum curvature, respectively (although these values can be adjusted depending on the experimental result and numerical application).

The calculation of these parameters (excluding the maximum point parameters) was carried out based on a limited study with few experimental results. Further research should establish proper relations that can characterize the OOP behaviour of a wider range of infill masonry walls.

## 2.2 Modification of Kadysiewski and Mosalam model

This modelling strategy considers at the centre of the infill panel, sections with fibres along the orthogonal direction to the infill wall plane. The area and position of each fibre govern the IP and OOP behaviours of the infill wall. These parameters' values are obtained by satisfying the forces interaction limit curve shown in Figure 5 and certain geometric conditions of the corresponding sections derived from the actual infill wall geometric characteristics. Further details can be found in [9].

The main modification to this modelling strategy is in the constitutive relation assumed for the fibres. The original model considers a bilinear or elastoplastic behaviour assigned to each fibre of the infill wall. In the current study, a pentalinear constitutive relation is assumed for each fibre by using the uniaxial material *pinching4* [32] in OpenSees. In contrast with the original modelling formulation, expressions to calculate the IP and OOP capacity, respectively, represented by Equations 1 and 10 are used instead in the current modified model.

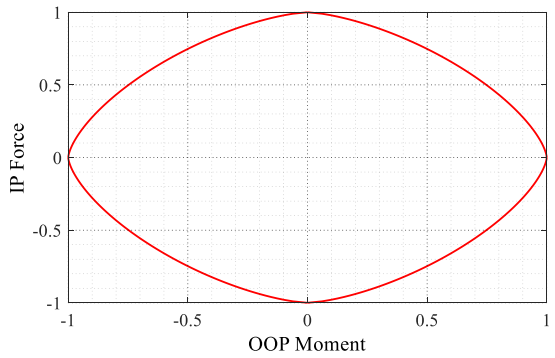


Figure 5: Interaction curve in terms of forces.

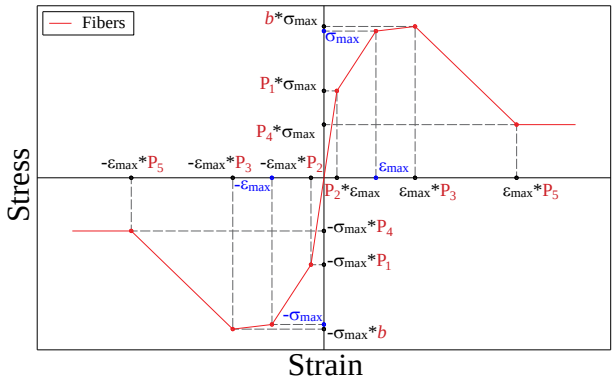


Figure 6: Pentalinear backbone curve and identification of scalar parameters.

From the sixteen parameters defining the pentalinear backbone curve (four stresses and four strains, positive and negative), twelve will be multiplied by a scalar to adjust both the IP and OOP behaviour of the infill wall. In reality, only six scalars will be needed since the response will be considered symmetric. This adjustment allows for the consideration of the initial elastic stiffness and post-yield softening behaviour verified in the infill masonry walls response while satisfying the interaction curve in Figure 5. Figure 6 shows the backbone curve and the identification of the scalar parameters for the stress-strain fibre response adjustment. It is seen that every parameter is derived from the maximum stress, $\sigma_{max}$, and strain, $\varepsilon_{max}$, calculated for each fibre using the procedure in [9]. The strain values are always calculated concerning the stress and the masonry Young's modulus ($\varepsilon_{max} = E_m \, \sigma_{max}$).

Parameter *b* will account for the strength hardening response, which in this case is assumed a very small value (nearly zero) to respect the referred interaction curve. Parameters $P_1$ to $P_5$ account for the stress-strain adjustments shown in Figure 6. However, parameters $P_1$ and $P_2$ are always set to 0.55 and 0.50, respectively.

As an example, Figure 7 shows an application of this model by using the elastoplastic material behaviour for the fibres as in the original Kadysiewski and Mosalam model. As can be verified, the use of such an approach may not be appropriate for replicating the cyclic response of frame structures with infill walls. However, in this example, the collapse-removal algorithm was not used, which could have added a steep softening branch to the response.

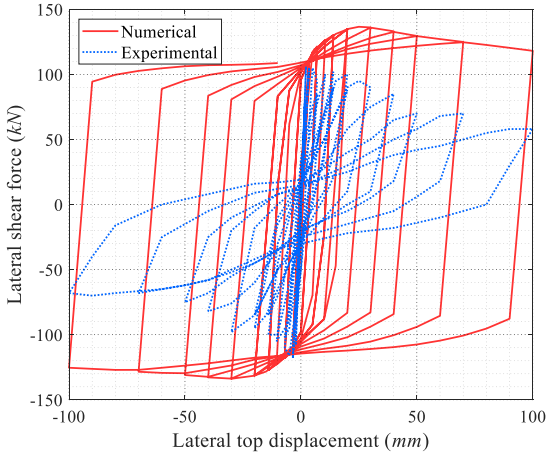


Figure 7: Kadysiewski and Mosalam model using an elastoplastic material for each fibre to replicate the cyclic response of specimen M2 in Pires and Carvalho's [13] experimental campaign.

The modified approach also allows for the further calibration of the intervenient parameters in the fibres' material constitutive relation, which can thus account for stiffness and strength degradation, and pinching effects.

Values for the remaining scalar parameters ($P_3$ to $P_5$) will be calculated (among the targets for optimization/calibration) in the next section for the different experimental results considered.

## 3 MODELS VALIDATION AND RESULTS

As evident in the previous brief description of the modified models, whether the original or modified Furtado et al. model [10] does not account directly for IP and OOP interaction of forces, i.e., it does not enforce this condition in the same way as the original Kadysiewski and Mosalam model [9], where the force response point would travel along the force interaction curve in Figure 5 when intersected. Instead, it includes based on the original Kadysiewski and Mosalam model, an interaction curve in terms of drifts that when reached signifies collapse, activating the element removal algorithm, which removes the collapsed infill wall elements from the model for further time-steps of the analysis.

This element removal algorithm is also included in the present modified versions of the models, although it is not activated in the process of optimization to be carried out for analysis purposes.

An optimization procedure is used similar to the one used in [16] and presented in Figure 8. This procedure makes use of a simplex algorithm where boundaries are applied [34]. Then, subsequently, a genetic algorithm (built-in function in MATLAB [21]) is implemented, which uses as an initial guess the previous solution obtained with the simplex algorithm.

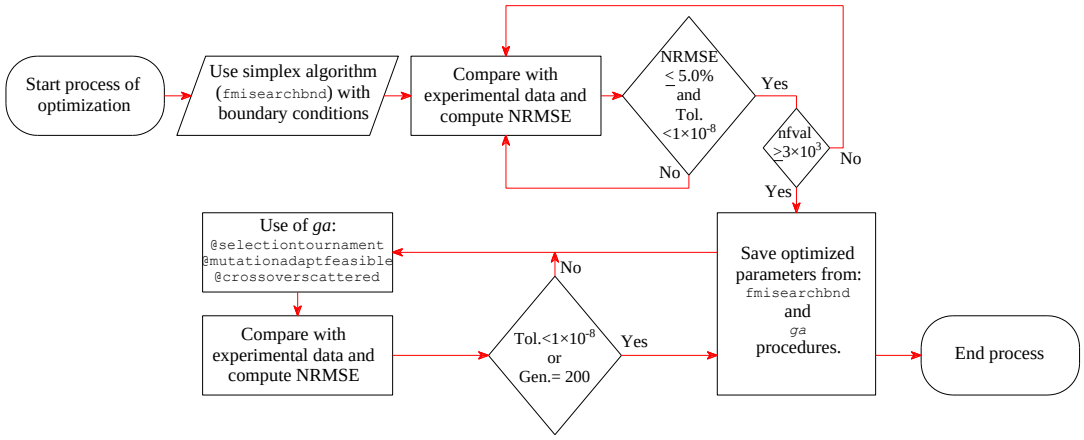


Figure 8: Flowchart of the optimization procedure used in this study.

Certain parameters are allowed to vary depending on the response to be replicated. In this sense, different experimental results are considered in this study for model validation: Pires and Carvalho [13] which considers the quasi-static cyclic analysis of RC portal frame structures with and without infill masonry walls exclusively loaded in the IP direction (Specimens used: M2 and M6); Di Domenico [15], that tested numerous portal frame specimens loaded in the IP and OOP direction in a quasi-statically manner (Specimens used: 120_OOP_4E, 120_IP+OOP_L, 120_IP+OOP_M, 120_IP+OOP_H, 120_OOP_4E_cyclic); and Negro et al. [14] which performed pseudo-dynamic tests on a full-scale RC building without infill walls and with infill walls in different configurations (Specimens used: Full-infilled wall RC building).

From here on the modified model of Furtado et al. will be named “modified model 1” and the modified model of Kadysiewski and Mosalam as “modified model 2”. The results of the optimization procedure are presented in Figures 9 to 15. For the modified model 1, 9 parameters are considered for optimization, whose results are presented in Table 1. Modified model 2 has 10 parameters for optimization. Its results are presented in Table 2. These parameters are related to the definition of the uniaxial material *pinching4* [32] in OpenSees [19, 20].

Figures 9a and 10a show the optimized response for specimens M2 and M6. These parameters shown in Table 1, correspond directly to the *pinching4* parameters defining the backbone curve in Figure 3a (always assuming from now on that the limit degradation parameters are equal to unity – *gKLim*, *gDLim*), except for the last two parameters (*dP*, *fP*), that scale the values of the last point in the backbone curve (displacement and force, respectively).

Figures 11a and 12a represent the results of the optimization of the backbone curve parameters in Figure 4b, i.e., related to the OOP behaviour of the infill using the modified model 1.

Figures 9b, 10b, 11b, 12b, 13, 14, and 15 are related to the optimization procedure using the modified model 2, thus considering the *pinching4* material parameters associated with the backbone curve in Figure 6. Table 2 shows the outcomes of the optimization, in which the last three parameters are scalars defined in the previous section ($P_3$, $P_4$, and $P_5$). Having the advantage of possessing only one constitutive law shared by both IP and OOP behaviours.

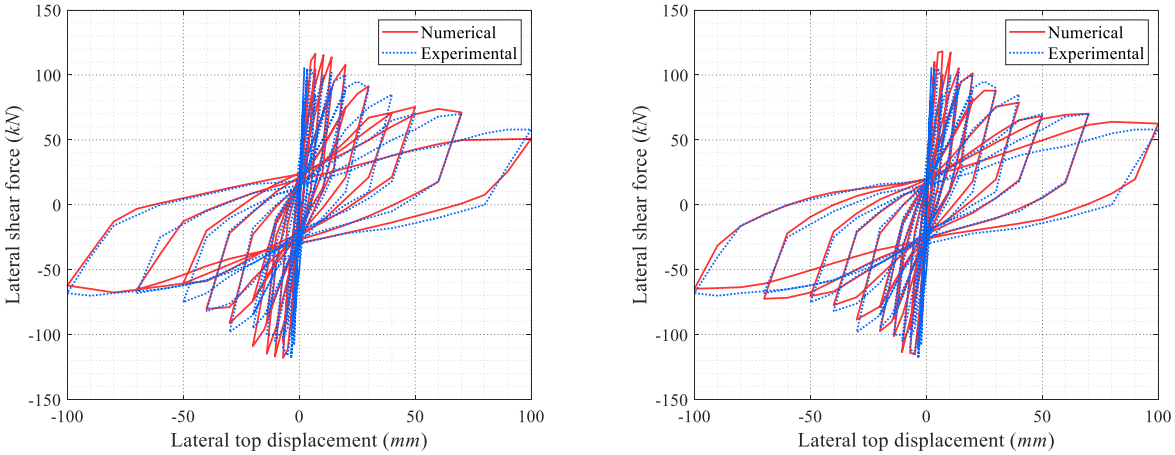


(a) Modified model 1; (b) Modified model 2.

Figure 9: Results of optimization related to specimen M2.

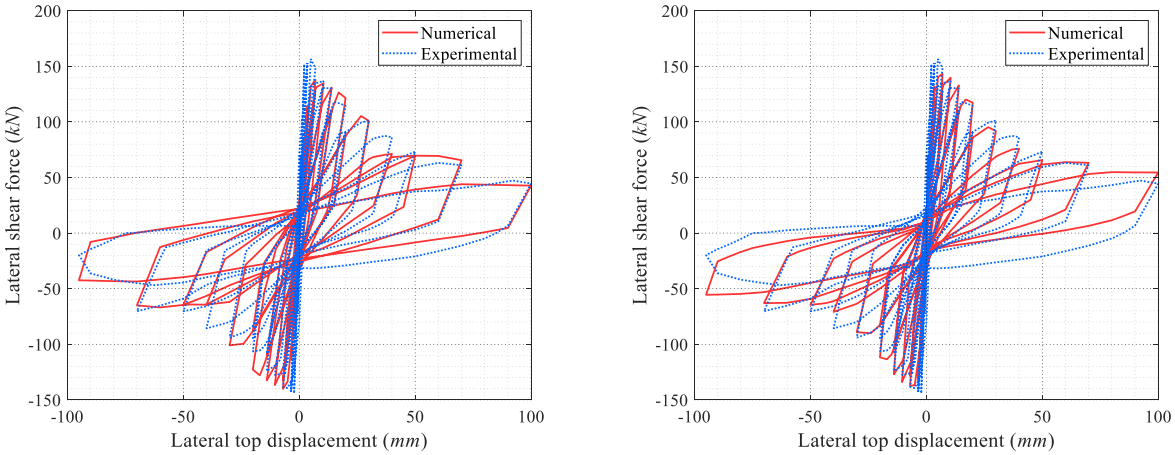


(a) Modified model 1; (b) Modified model 2.

Figure 10: Results of optimization related to specimen M6.

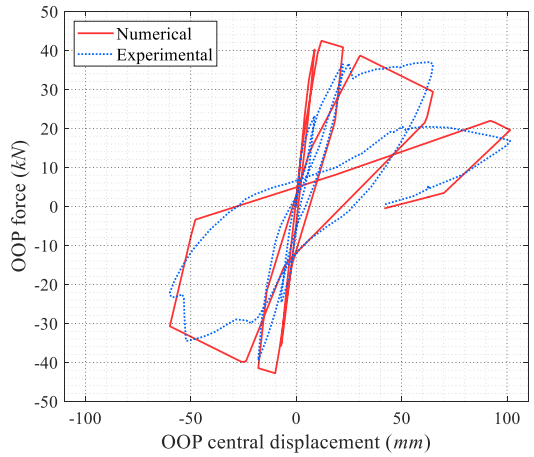


(a) Modified model 1;

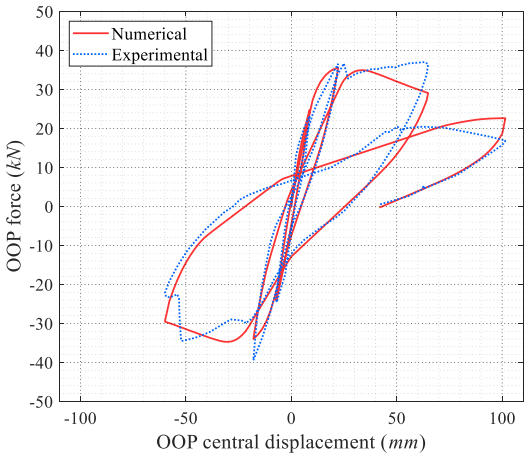


(b) Modified model 2.

Figure 11: Results of optimization related to specimen 120_OOP_4E_cyclic.

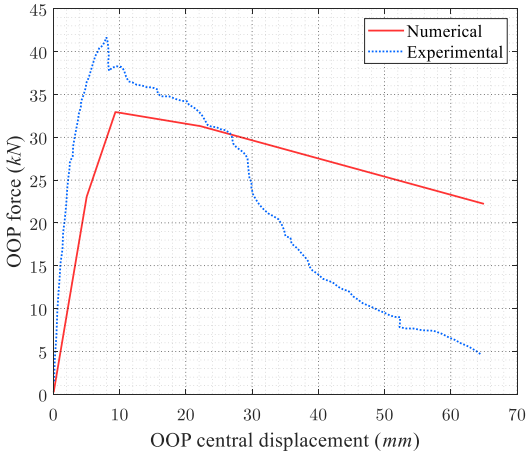


(a) Modified model 1;

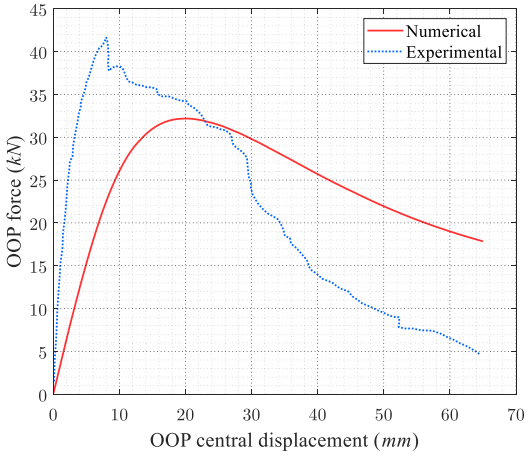


(b) Modified model 2.

Figure 12: Results of optimization related to specimen 120_OOP_4E.

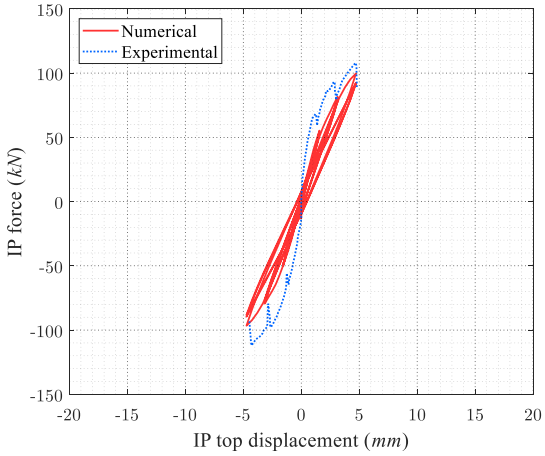


(a) Previous IP cyclic loading;

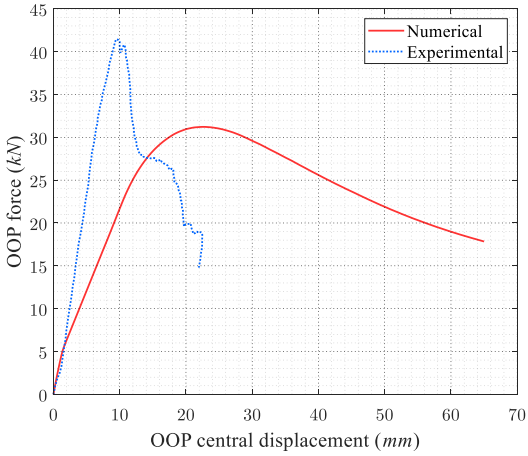


(b) Post OOP monotonic behaviour.

Figure 13: Results regarding OOP response with previous low IP damage of specimen 120_IP+OOP_L.

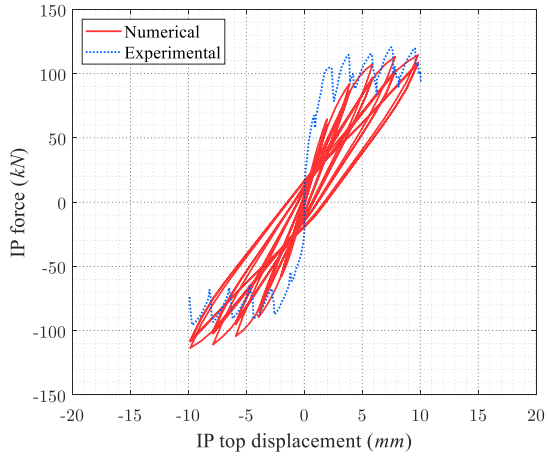


(a) Previous IP cyclic loading;

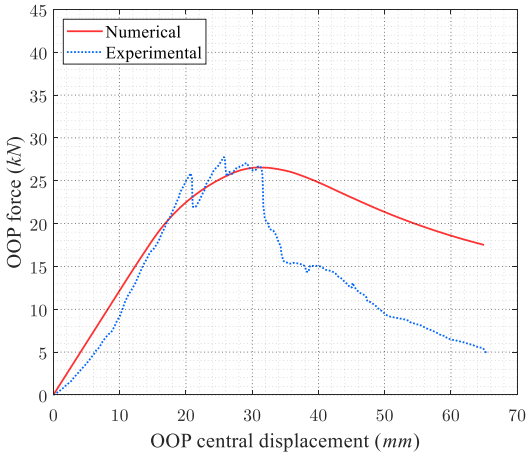


(b) Post OOP monotonic behaviour.

Figure 14: Results regarding OOP response with previous intermediate IP damage of specimen 120_IP+OOP_M.

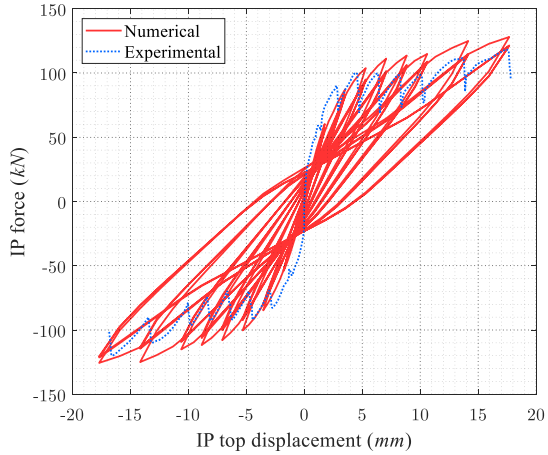


(a) Previous IP cyclic loading;

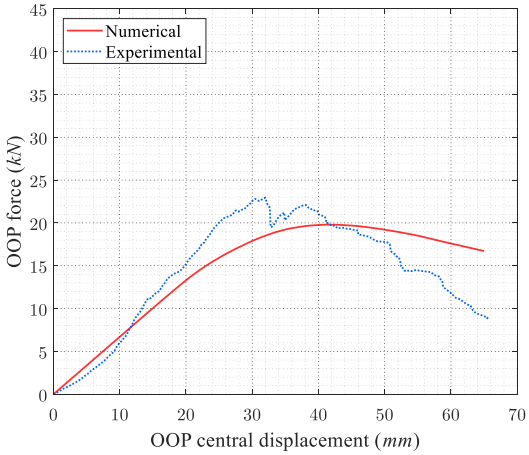


(b) Post OOP monotonic behaviour.

Figure 15: Results regarding OOP response with previous high IP damage of specimen 120_IP+OOP_H.

Figures 16 and 17 show an application of the modified models to full-scale buildings with infill walls that are only subjected to IP loads. Model parameters were manually calibrated.

In general, by graphical observation, tabled results in Table 3, and verification of the Correlation Coefficient [18] and Normalized Root Mean Square Error (NRMSE) in Figure 18, both modified models performed very well in replicating cyclic and monotonic behaviour of infill masonry walls in RC frame structures.

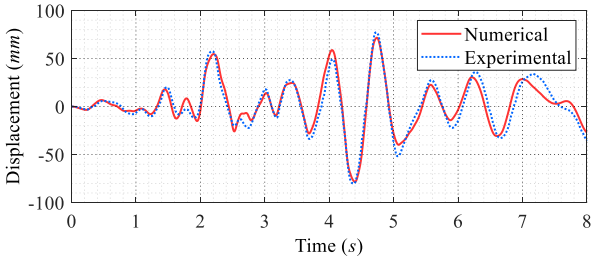


(a) Top story displacement;

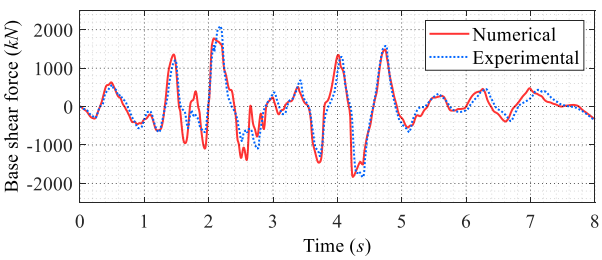


(b) Base shear force.

Figure 16: Response of the full-scale full-infilled wall building structure using the modified model 1.

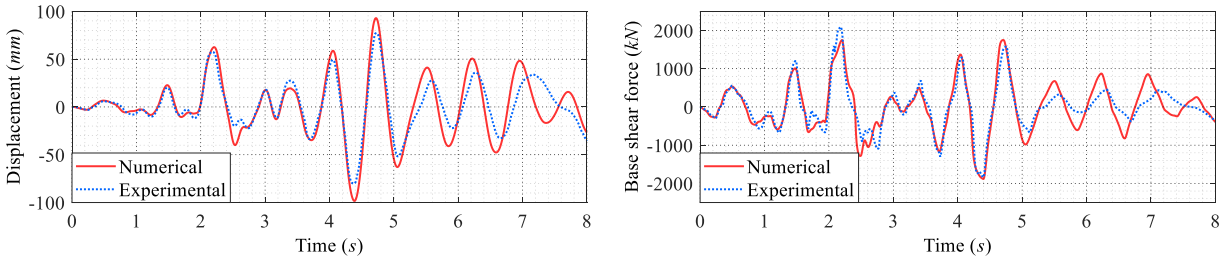


(a) Top story displacement; (b) Base shear force.

Figure 17: Response of the full-scale full-infilled wall building structure using the modified model 2.

| Specimen | *rDisp* | *rForce* | *uForce* | *gK1* | *gK3* | *gD1* | *gD3* | *dP* | *FP* |
|---|---|---|---|---|---|---|---|---|---|
| *M2* | 0.44 | 0.54 | -0.12 | 0.71 | 0.37 | 0.82 | 1.10 | 5.30 | 0.50 |
| *M6* | 0.43 | 0.53 | -0.10 | 0.70 | 0.03 | 0.98 | 1.59 | 5.83 | 0.42 |
| *120OOP4E* | 0.20 | 0.37 | -0.54 | 1.94 | 0.06 | 0.47 | 0.05 | 22.50 | 0.15 |

Table 1: Results of the calibrated parameters for the modified model 1.

| Specimen | *rDisp* | *rForce* | *uForce* | *gK1* | *gK3* | *gD1* | *gD3* | $P_3$ | $P_4$ | $P_5$ |
|---|---|---|---|---|---|---|---|---|---|---|
| *M2* | 0.25 | 0.39 | -0.01 | 0.88 | 0.07 | 1.95 | 1.24 | 25.20 | 0.48 | 35.00 |
| *M6* | 0.35 | 0.45 | -0.23 | 0.60 | 0.24 | 1.13 | 1.94 | 24.80 | 0.37 | 42.00 |
| *120OOP4E* | -0.06 | 0.42 | -0.33 | 0.05 | 0.05 | 2.00 | 1.46 | 3.10 | 0.25 | 7.60 |

Table 2: Results of the calibrated parameters for the modified model 2.

| Model | *M2* | *M6* | *120OOP4E_Cyclic* |
|---|---|---|---|
| *Modified 1* | 4.47 % | 4.67 % | 6.92 % |
| *Modified 2* | 3.81 % | 4.94 % | 3.69 % |

Table 3: Normalized Root Mean Square Errors of the different calibrations performed.

Modified model 1 is straightforward and it can represent well the IP and OOP behaviour. However, it does not enforce directly any interaction of forces between these behaviours, and hence it cannot properly consider prior damage in one direction influencing the other. Furthermore, it needs five elements in its definition, while modified model 2 only needs one. The modified model 2 can account for this interaction directly by the sequential yielding of each fibre. Figures 12 to 15 demonstrate this phenomenon very well, where previous IP loading affects the OOP behaviour by reducing it since some fibres have already yielded.

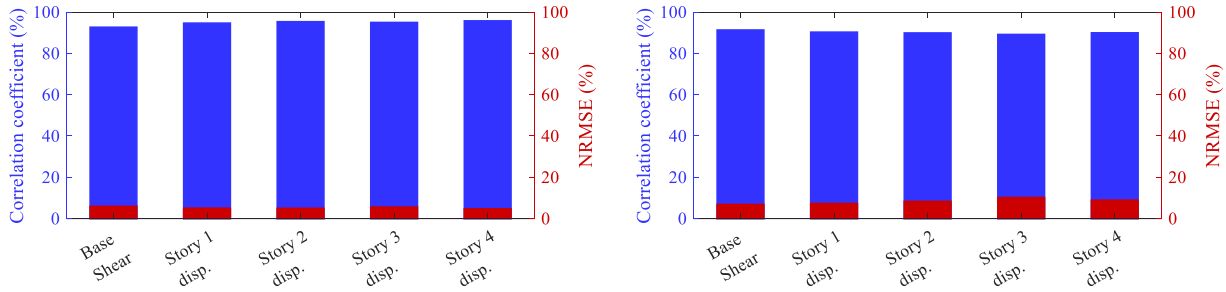


(a) Modified model 1; (b) Modified model 2.

Figure 18: Correlation between the numerical and experimental results of story displacements and base shear force time history responses.

Nevertheless, calibration of the modified model 2 may be difficult, as two-in-one behaviour is considered, which may lead to a solution fitting one behaviour and disfavoring the other. The possibility of increasing the number of fibres at the expense of computational effort can be a possible solution, even when converging problems arise. In addition, it was verified that due to the sequential yielding of fibres in this model by adopting the constitutive relation in Figure 6, may cause the infill wall to begin the softening phase without ever reaching the maximum response, i.e., without touching the interaction curve.

## 4 CONCLUSIONS

Two different modelling strategies were developed based on existing models, to replicate the in-plane and out-of-plane behaviour of infill masonry walls in reinforced concrete structures when subjected to horizontal loading. Generally, all responses were well predicted with either model. Nonetheless, the modified model based on Kadysiewski and Mosalam allowed for the interaction between in-plane and out-of-plane behaviour. This made it possible to satisfactorily predict the out-of-plane behaviour with prior in-plane damage, due to the sequential yielding feature of the fibres constituting the sections of the equivalent strut defining the infill panel. However, calibration can be difficult and an ideal solution may not be found due to the two-on-one behaviour defined by only one constitutive relation.

In conclusion, results showed that these modifications allowed a better reproduction of the in-plane and out-of-plane behaviour of infill masonry walls when compared with different experimental tests, being appropriate for the use in numerical models of reinforced concrete building structures, provided that the models' parameters are adequately chosen and calibrated.

Further studies should include more experimental results to aid the search for model parameters' values that better characterize the response of RC frame structures with infill masonry walls. The drawbacks of each modified model must be addressed to improve performance, stability and less computational effort for application in large structural systems subjected to different kinds of dynamic actions.

## ACKNOWLEDGEMENTS

This paper is within the scope of the first author's Ph.D. degree in progress. The present research was financially supported by the Portuguese Foundation for Science and Technology (FCT) through the PhD grant reference SFRH/BD/139570/2018 under the programme POCH (N2020 – P2020) and subsidized by the European Social Fund (FSE) and national funds from MCTES. This work was also financially supported by Base Funding UIDB/04708/2020 of the *CONSTRUCT* R&D Institute on Structures and Constructions (Instituto de I&D em Estruturas e Construções), through national funds of FCT/MCTES (PIDDAC).

## REFERENCES

[1] F. Nicola, C. Leandro, C. Guido, S. Enrico, Masonry infilled frame structures: state-of-the-art review of numerical modelling. *Earthquakes and Structures*, **8**(1), 225-251, 2015.

[2] P. B. Lourenço, *Computational strategies for masonry structures*. Ph.D. Thesis. Delft University, Delft, The Netherlands, 1996.

[3] M. Priestley, G. Calvi, Towards a Capacity-Design Assessment Procedure for Reinforced Concrete Frames. *Earthquake Spectra*, **7**(3), 414-436, 1991.

[4] T. Paulay, M. Priestley, *Seismic Design of Reinforced Concrete and Masonry Buildings*. John Wiley & Sons Inc., New York, USA, 1992.

[5] B. Stafford Smith, Methods for Predicting the Lateral Stiffness and Strength of Multistorey Infilled Frames. *Building Science*, **2**(3), 247-257, 1967.

[6] G. Al-Chaar, *Evaluating strength and stiffness of unreinforced masonry infill structures*. ERDC/CERL-TR-02-1, Engineer Research, and Development Center, Construction Engineering Research Lab, Champaign, IL, USA, 2002.

[7] F. Crisafulli, A. Carr, R. Park, Analytical modelling of infilled frame structures - a general review. *Bulletin of the New Zealand Society for Earthquake Engineering*, **33**(1), 30-47, 2000.

[8] G. Amato, L. Cavaleri, M. Fossetti, M. Papia, Infilled frames: influence of vertical loads on the equivalent diagonal strut model. In: *The 14th World Conference on Earthquake Engineering*, Beijing, China, October 12-17, 2008.

[9] S. Kadysiewski, K. Mosalam, *Modeling of Unreinforced Masonry Infill Walls Considering In-Plane and Out-of-Plane Interaction*. PEER Report 2008/102, Pacific Earthquake Engineering Research Center, College of Engineering, University of California, Berkeley, Berkeley, CA, USA, 2009.

[10] A. Furtado, H. Rodrigues, A. Arêde, and H. Varum, "Simplified macro-model for infill masonry walls considering the out-of-plane behaviour," Earthquake Engineering and Structural Dynamics, vol. 45, no. 4, pp. 507-524, 2016.

[11] M. Di Domenico, P. Ricci, G. Verderame, Effect of in-plane/out-of-plane interaction in infill walls on the floor spectra of reinforced concrete buildings. In: *COMPDYN2021 8th ECCOMAS Thematic Conference on Computational Methods in Structural Dynamics and Earthquake Engineering*, pp. 84-101, M. Papadrakakis, M. Fragiadakis (eds.) Streamed from Athens, Greece, 28-30 June, 2021.

[12] A. Furtado, N. Vila-Pouca, H. Varum, A. Arêde, Study of the Seismic Response on the Infill Masonry Walls of a 15-Storey Reinforced Concrete Structure in Nepal. *Buildings*, **39**(9), 2019.

[13] F. Pires, E.C. Carvalho, Cyclic Behaviour of Reinforced Concrete Frames Infilled with Brick Masonry Walls. In: *The 10th International Brick and Block Masonry Conference*, Calgary, Canada, 5-7 July, 1994.

[14] P. Negro, A. Anthoine, D. Combescure, G. Magonette, J. Molina, P. Pegon, G. Verzeletti, Tests on the Four-Storey Full-Scale Reinforced Concrete Frame with Masonry Infills: Preliminary Report. *Special Publication No.I.95.54*. European Commission. ELSA Laboratory, 1995.

[15] M. Di Domenico, Out-of-plane seismic response and modelling of unreinforced masonry infill walls. PhD Thesis. Università degli Studi di Napoli Federico II, 2018.

[16] P. Folhento, R. Barros, M. Braz-César, Optimization of the cyclic in-plane response of reinforced concrete frames with infill masonry walls using a genetic algorithm. *Controlo2022, 15th APCA ICACSC*, Caparica, Lisbon-Region, Portugal, 2022.

[17] F. Longo, G. Granello, G. Tecchio, F. da Porto, C. Modena, A Masonry infill wall model with in-plane–out-of-plane interaction applied to pushover analysis of RC frames. In: *Proceedings of 16th Brick and Block Masonry Conference (IBMAC 2016)*, Padova, Italy, June 26-30, 2016.

[18] M. H. Al Hanoun, L. Abrahamczyk, J. Schwarz, Macromodeling of in- and out-of-plane behaviour of unreinforced masonry infill walls. *Bulletin of Earthquake Engineering*, **17**, 519-535, 2019.

[19] F. Mckenna, M. Scott, G. Fenves, L. Gregory, Nonlinear Finite Element Analysis Software Architecture Using Object Composition. *Journal of Computing in Civil Engineering*, **24**(1), 95-107, 2010.

[20] M. Zhu, F. McKenna, M. H. Scott, OpenSeesPy: Python library for the OpenSees finite element framework. *SoftwareX*, **7**, 6-11, 2018.

[21] MATLAB 9.6.0.1072779 R2019a, Natick, Massachusetts, USA: MathWorks Inc., 2019.

[22] A. Neuenhofer, F. Filippou, Evaluation of Nonlinear Frame Finite-Element Models. *Journal of Structural Engineering*, **123**(7), 958-966, 1997.

[23] M. H. Scott, G. L. Fenves, Plastic Hinge Integration Methods for Force-Based Beam–Column Elements. *Journal of Structural Engineering*, **132**(2), 244-252, 2006.

[24] F. C. Filippou and G. L. Fenves, Methods of analysis for earthquake-resistant structures. In: *Earthquake Engineering: From Engineering Seismology to Performance-Based Engineering. Boca Raton: Y. Bozorgnia, and V. V. Bertero, eds.*, CRC Press, 2004, 316-393

[25] B. Scott, R. Park, M. Priestley, Stress–strain behaviour of concrete confined by overlapping hoops at low and high strain rates. *ACI Journal*, **79**(2), 13–27, 1982.

[26] Y.-H. Chen, *Seismic Evaluation of RC Buildings Infilled with Brick Walls*. PhD thesis. National Cheng-Kung University, Tainan, Taiwan, (in Chinese), 2003.

[27] FEMA 306, ATC: Evaluation of earthquake damaged concrete and masonry wall buildings, basic procedures manual, prepared by the applied technology council (ATC-33 project) for the partnership for response and recovery, published by the federal emergency management agency, Washington, D.C., USA: Report no. FEMA306, 1998.

[28] European Committee for Standardization (ECS): Eurocode 6 (EC6), EN 1996-1-1: Design of masonry structures - Part 1-1: General rules for reinforced and unreinforced masonry structures. Brussels, Belgium, 2005.

[29] R. Jones, Mechanics of composite materials. 2nd edn. Taylor & Francis, London (1998).

[30] W. El-Dakhakhni, A. Hamid, M. Elgaaly, Strength and Stiffness Prediction of Masonry Infill Panels. In: *13th World conference on earthquake engineering*. Vancouver, B.C., Canada, Paper No. 3089, 1–6 August, 2004.

[31] A. Reinhorn, H. Roh, M. Sivaselvan, S. Kunnath, R. Valles, A. Madan, C. Li, R. Lobo, Y. Park, *IDARC2D V7.0: A Program for the Inelastic Damage Analysis of Structures*. Technical Report MCEER-09-0006, State University of New York, Buffalo, USA, 2009.

[32] L. N. Lowes, M. Mitra, A. Altoontash, A Beam-Column Joint Model for Simulating the Earthquake Response of Reinforced Concrete Frames. PEER Report 2003/10, Pacific

Earthquake Engineering Research Center. College of Engineering, University of California, Berkeley USA, February, 2004.

[33] E. L. McDowell, K. E. McKee, E. Sevin, Arching action theory of masonry walls. *Journal of the Structural Division*, **82**(2), 1-8, 1956.

[34] J. D'Errico, fminsearchbnd, fminsearchcon. Available from: https://www.mathworks.com/matlabcentral/fileexchange/8277-fminsearchbnd-fminsearchcon), MATLAB Central File Exchange. Retrieved August 3, 2021.

COMPDYN 2023
9th ECCOMAS Thematic Conference on
Computational Methods in Structural Dynamics and Earthquake Engineering
M. Papadrakakis, M. Fragiadakis (eds.)
Athens, Greece, 12-14 June 2023

# SEISMIC COLLAPSE RISK OF A ISOLATED TRANSMISSION TOWER AND A TRANSMISSION LINE SYSTEM IN NORTHERN PORTUGAL

**Paiva Fabio M.**[1], **Rui C. Barros**[2]

[1] PhD student at Instituto Superior Técnico, Universidade de Lisboa, Lisboa, Portugal
Collaborator of CONSTRUCT R&D Center at FEUP, Porto, Portugal
e-mail: fabiopaiva@tecnico.ulisboa.pt

[2] Jubilled Prof of Structural Engineering
CONSTRUCT, FEUP (Faculdade de Engenharia da Universidade do Porto - Portugal)
email: rcb@fe.up.pt

## Abstract

*The collapse of the Transmission Line System (TLS) caused by a natural disaster can have serious consequences on the power grid, leading to challenges in the construction or reconstruction of critical infrastructure, reduced quality of community living, compromised disaster response, and potential secondary disasters resulting from interconnected infrastructure. This paper presents a methodology for assessing the seismic collapse risk of a transmission tower (TT) and transmission line system in Northern Portugal. A high-fidelity Finite Element Model of both the isolated tower and the remaining line components (i.e. TLS) was created using the OpenSees framework, and the seismic collapse fragility functions were derived through implementing Incremental Dynamic Analysis. The record-to-record variability of earthquake input is investigated with a set of 40 ground motions records (GMR), using the conditional spectrum for a specific site in Portugal as the target spectrum. The results showed that both the isolated TT and the TLS have acceptable seismic risk of collapse, but the latter system exhibiting a higher seismic collapse risk.*

**Keywords:** Fragility analysis, Three-dimensional modelling, Incremental Dynamic Analysis, Ground motion record selection

# 1 INTRODUCTION

Transmission lines system (TLS), or overhead power-lines, is a critical lifeline in modern societies. The electrical grid enables developed countries to sustain high standards of living; however, the risk of local line faults resulting in large-area power outages exists and is growing [1]. Transmission line collapse during a natural disaster may induce cascade failure, which could affect tremendously the local/global economy, and society lifestyle [2]. Seismic waves can transfer an excessive amount of energy in the TLS, which can lead to critical limit states being exceeded, potentially causing local member failures or even the collapse of the transmission tower in the worst-case scenario. However, other earthquake-induced hazards such as ground failure or soil liquefaction are often the primary cause of such collapses, as noted in studies by [3,4].

Assessing the ultimate seismic capacity of the TLS, which is a complex and large-scale electrical and mechanical system, is considered to be one of the most challenging tasks for analysts. To assist in the effort, a high fidelity numerical model of the isolated TT and TLS (three towers and four spans) case study were developed in OpenSees [5]. The isolated TT acts as a baseline for the subsequent TLS (a segment). The main TT has received considerable attention, as the numerical model can capture different member failures modes (yielding, buckling and post-buckling), gusset-plate flexural resistance, in addition to specific lattice tower characteristics joint effects as bolt slippage, joint eccentricities and semi-rigid behaviour at leg-diagonal connection. The IDA is a well-known approach for evaluating the overall collapse condition of a structure and is part of the methodology for generating the collapse fragility function (FF) [6]. To achieve the prior goal, a set of forty multi-component (with two horizontal components) properly selected ground motion records (GMR), based on the conditional spectrum (CS) is employed. The mean annual frequency of collapse (more details in [7]) may be calculated by performing the convolution of the collapse FF and the derivative of the hazard curve (a product of a probabilistic seismic hazard analysis). This allows the analysist to compare with acceptable risk (i.e. empirical approach or code based reliability index) in the TT industry [4].

# 2 TRANSMISSION LINE DESCRIPTION AND MODELLING ASPECTS

Seismic risk analysis requires a realistic and practical modelling approach that can incorporate various aspects such as tower member/joint ultimate behaviour, tower-line structural coupling and account demand and capacity uncertainties at several stages in the evaluation of the TLS collapse process. This section includes a summary of the TLS case study as well as a concise discussion of the modelling approach that was employed.

## 2.1 Transmission Line System description

The main TT under investigation is a component of an Overhead High Voltage Line, specifically the Sub-transmission 60 kV Line from EDP, Distribuição (Energias de Portugal). The power line's general layout is illustrated in Fig. 1a), and it “begins” (i.e. main segment represented in figure) in tower 1 and finishes in tower 10, with two significant angle line deviations (i.e. at tower 4 and 6). The TLS case study spans (i.e. segment) are also depicted in the same figure (dashed polygon). As shown in Fig. 1.b), tower 4 (a type F165CD in the operator terminology) was chosen as the critical component for the site-specific risk analysis. Furthermore, because of the substantial horizontal line angle deviation, this TT can be classified as a strain tower type (also known as tension towers in some works) [8].

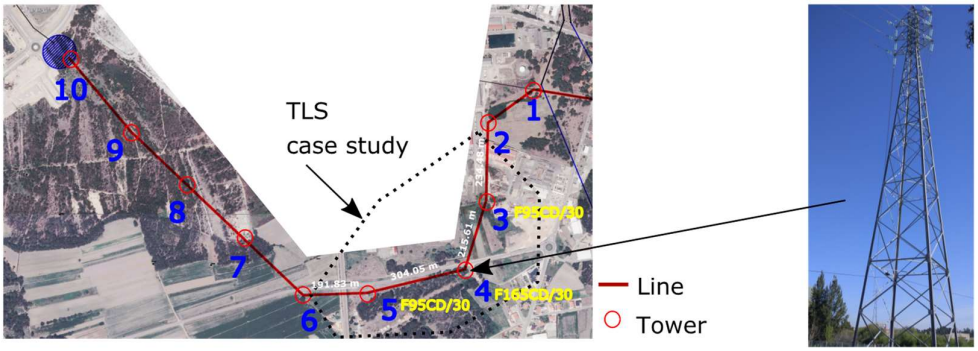


Figure. 1: a) 60 KV Overhead Power-line; b) Tower 4 –F165/CD Strain Tower

The TLS case study consists of four spans of transmission lines (line segment between tower 2 to 6), which are 234.48 m, 215.61 m, 304.05 and 191.83 m, respectively. Additionally, it consists of three towers (38.8-m height) designated as Towers 3 (F95CD/30), Tower 4 (165CD/30) and Tower 5 (F95CD/30) shown in Fig. 2. Despite the fact that tower 4 is less flexible than the adjacent towers, it has a substantial line angle deviation, a line condition that has received less attention.

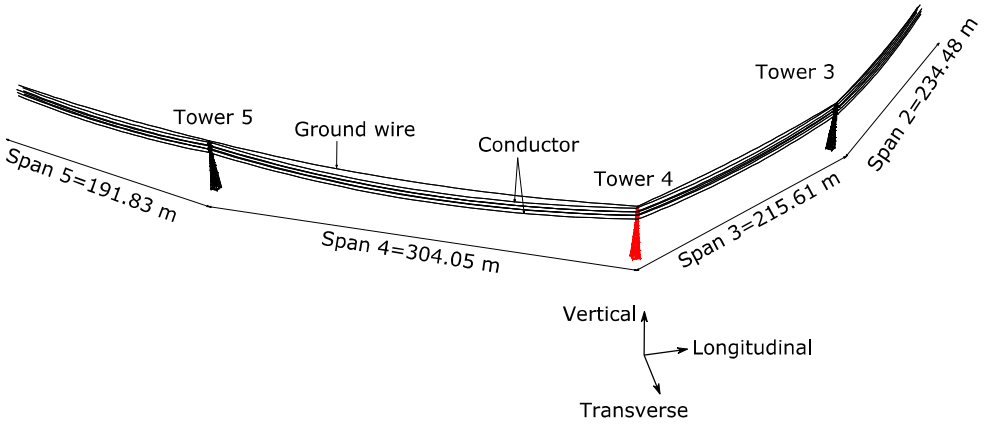


Figure. 2: 3D sketch of the TLS case study

The model's X, Y, and Z axes correspond to the transverse, longitudinal, and vertical directions of the transmission tower-line system, respectively. The line spans are variable, as indicated in the figure. Several significant deviations occur along the power line's path in this segment. The maximum line angle deviation, corresponds to $\Delta = 59.19°$. The overhead power line is supported on three cross-arms, each carrying two conductors (i.e. a double vertical three-phase electric circuit), while the top of the tower is reserved for the ground/shield wire (also known as earth wire).

A recent article by the authors [9] offers an in - depth description of the main TT 4 (cross-sections, main geometry, joint details, material characteristics), which is excluded in this work for brevity. In summary, the lattice tower is made up of steel angles from the S275 class.

For the transmission lines, the conductor (type: ASCR 325 (Bear)) is supported by the top, middle and bottom cross arms, while the ground wire (type: OPGW-AA/ACS/ST 157/60) hang from the top of the lattice tower. Strain insulators (U100 BLP) in toughened

glass L=1.2 m attach the conductor to the TT. Further information about the conductor lines and ground wires is presented in Table 1.

| Description | Conductor | Ground wire | Insulator |
|---|---|---|---|
| Designation | ASCR 325 | OPGW-AA/ACS/ST 157/60 | U100 BLP |
| Outside Diameter (mm) | 23,45 | 19,60 | - |
| Modulus of Elasticity (GPa) | 79,5 | 84,5 | 76,5 |
| Cross-sectional area ($mm^2$) | 325 | 219,66 | - |
| Mass per unit length (kg/km) | 1260 | 868 | 30 (total mass) |
| Nominal breaking load (kN) | 109,38 | 112,6 | 100 |

Table 1. Mechanical properties of conductor, ground wire and insulator

### 2.2 A high fidelity Transmission tower numerical model

It is widely acknowledged that the inclusion the full TLS (for example, from tower 1 to tower 10) in the computer model is impracticable and computationally costly. Furthermore, because the coupling action between a tower and a line is confined to a certain extension (usually two-three spans is ideal) from a specific TT, only a sub-system consisting of four transmission line spans and three supporting TT was considered in this study. This TLS dimension is expected to provide sufficient accuracy at an acceptable computation cost.

Typical modelling strategies (e.g., linear analysis of 3D truss models) have major limitations in replicating TT's complex nonlinear behaviour [10]. Damage assessment close to the system ultimate capacity frequently involves the application of algorithms to track the deterioration process throughout the TT brace components (i.e. yielding, buckling, and post-buckling) as well as other nonlinear effects at the joint. Regardless of the fact that the TT should have sufficient strength, stiffness, and ductility to endure large earthquakes events, earlier research has shown a brittle collapse mechanism [11]. When analysing such a complex system, a number of assumptions are made, each of which may have a different influence on seismic capacity assessment and subsequent risk analysis. Examples include component input of the seismic action, numerical models capabilities and neglecting aspect as: ground motion spatial variability effects, material spatial variability in the TT (member and bolts), fabrication errors and improper detailing [12].

In OpenSees, a Fiber-FEM modeling approach was used to mimic the behaviour of steel TT 4 to the collapse state ([13]; [14]; [15]). Member buckling, gusset plate yielding, and joint effects (e.g. slippage, eccentricities and semi-rigid behaviour) may all be simulated with developed numerical model. Paiva and Barros [9] provide detailed information about the development of the TT 4 numerical model in OpenSees.

### 2.3. Other TLS components

Despite the focus on the high-fidelity TT 4, the remaining transmission line components were modelled to evaluate their impact on the overall risk. This featured two adjacent towers (as simplified elastic models) to the main TT 4, conductors and wire shields, resulting in a system with three towers and four spans. To represent the curved geometry of cables (considered parabolic for small curvatures), a sequence of straight elastic beam-column elements with

a sag equal to 5% of the span is utilized (assumed at serviceability conditions) [16]. Each transmission line was modelled with 30 elastic beam-column. An overview of OpenSees TLS numerical model is given in Fig. 3.

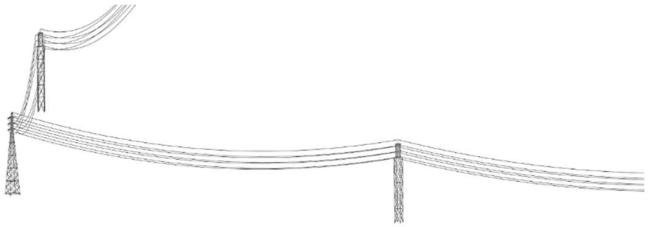

Figure. 3 –Overview of OpenSees TLS numerical model

The remote ends spans of the TLS, were controlled at the relevant heights with zero-length elements in the longitudinal direction and restrained from translational motion in the other directions. These elements were utilized to simulate the tensile restraints imposed by the remaining TT placed beyond the virtual system's two ends. The zero-length element longitudinal stiffness was first computed using equation (35) in [17], and then calibrated to meet the experimental data (identification of TLS fundamental vibration modes in the horizontal directions) [18]. The final remote longitudinal spring stiffness of span 5 (extreme left span) and span 2 (extreme right span), were determined as 50.4 kN/m and 39.78 kN/m, respectively.

### 2.4. Other modelling considerations

The mass of the TTs has been approximated as lumped at the main joints (leg-braces). This only occurred on TT lowest sections, with the remaining tower having a more realistic distribution. The mass densities of the transmission line materials and the line cross-section were utilized to define the line mass (e.g. kg/km), which was then assigned to the line nodes. In addition, the mass of the strain insulator was added as lumped mass to cross-arm tips.

The damping model in the Rayleigh form, proportional to the mass and to the initial stiffness matrix ($C=\alpha M+\beta K0$) is adopted [19]. The parameters α and β are grounded on the fundamental frequency $f_1$ and a second frequency equal to $5*f_1$. The $f_1$ frequency corresponds to the fundamental frequency of each subsystem (i.e. towers or transmission lines). Damping ratios of 5% and 1% were applied in the supporting steel towers and transmission lines, respectively. The dynamic properties of the transmission tower-line system of the OpenSees model are evaluated in terms of natural frequencies and compared to experimental data [18]. The first flexural vibration mode in the transversal direction was 2.47 Hz, while in the longitudinal direction the value was 2.23 Hz. As can be noted, the frequencies of the TLS were observed to be lower than those of the isolated TT (3.3 Hz).

## 3 SITE HAZARD AND SELECTION OF GROUND MOTION RECORDS UNDER SELEQ APPLICATION

An optimal IM is crucial in the seismic risk evaluation process [20]. TT seismic fragility studies have recognized the significance of using the spectral acceleration $S_a(T_1,5\%)$ at the fundamental period of the structure as having significant properties of an optimal IM [21]. Typically, the Sa reveals adequate properties for first dominated structures, which exhibit a brittle

or poor ductility behaviour [22]. With this in account, $S_{agm}$, as defined by earth scientists (geometric mean of spectral acceleration of two orthogonal horizontal components), is used as the IM in the current study [23].

### 3.1. Site hazard characterization

PSHA was carried out at the site of interest with the use of the open source program OpenQuake [24]. This was made possible with SelEQ software [25], and the seismic hazard models delivered in the SHARE project. In addition to the model supplied by the SHARE project, other hazards sources for the Portuguese territory were incorporated into PSHA [26].

At the TLS location (i.e. TT4), the site-specific median hazard curve is shown in terms of the IM= $S_{agm}(T_{eq},5\%)$ in Figure 4. The ground type C was assumed at the site location. All computations assume a 5% damping and are thus omitted. The IM=$S_{agm}$= $\sqrt{S_{ax}(T_{eq}) \cdot S_{ay}(T_{eq})}$ is denoted as $S_a(T_{eq},5\%)$ in this work, where $S_{ax}$ is the spectral acceleration of x horizontal component and $S_{ay}$ is the spectral acceleration of y horizontal component. The IM adopted is computed at the equivalent period $T_{eq}$ for the TLS and $T_{eq}$=$T_1$ for the isolated TT. This equivalent period is defined as the geometric mean of the two periods of vibration, $T_{1x}$ and $T_{1y}$, where $T_{1x}$ is fundamental period in the x direction (transversal direction in this work), and $T_{1y}$ fundamental period in the y direction (longitudinal direction), resulting in $T_{eq} = \sqrt{T_{1x} \cdot T_{1y}}$ as the option selected in this work [23]. For TLS this value is equal to $T_{eq}$=0.42 s and for isolated tower corresponds to $T_1$=0.30s

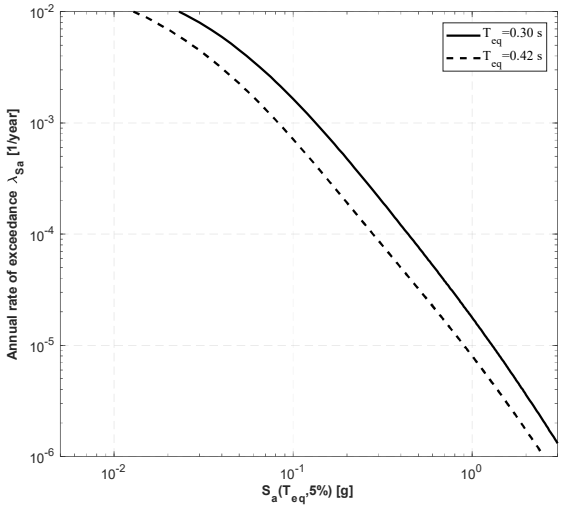


Figure. 4 - Seismic Hazard curve (median) for Teq= 0.42 and 0.30 s for a soil type C

### 3.2. Selection of Ground motion records

The importance of the spectral shape has been noted by several researchers, as a critical element improve the quality of ground motion set [7], [27]. Conditional Spectrum (CS) is one of the most important methods for selecting GMR developed in the last decades [25]. Unlike traditional code-based spectrum or Uniform Hazard Spectrum (UHS), a CS-based target spectrum selection explicitly considers for spectral shape.

The CS-based record selection comprises the use of SelEQ framework to compute the target CS for the case study site of interest (in the north of Portugal). The CS at the site was computed using a hazard level associated with a 475-year mean return period. The preliminary seismological criteria (e.g. magnitudes, epicentre distance and ground type) were established using PSHA disaggregation data. The record selection method consisted of minimizing the determined record set's mean and variance mismatches with regard to the CS target mean and standard deviation [25]. The set of forty GMR selected and scaled according to the aforementioned criteria is shown in Fig. 5-6. The set of records' mean and variance response spectrum closely follows the target spectrum. The response spectra of the GMR studied in this paper demonstrate the inherent uncertainty that they entail.

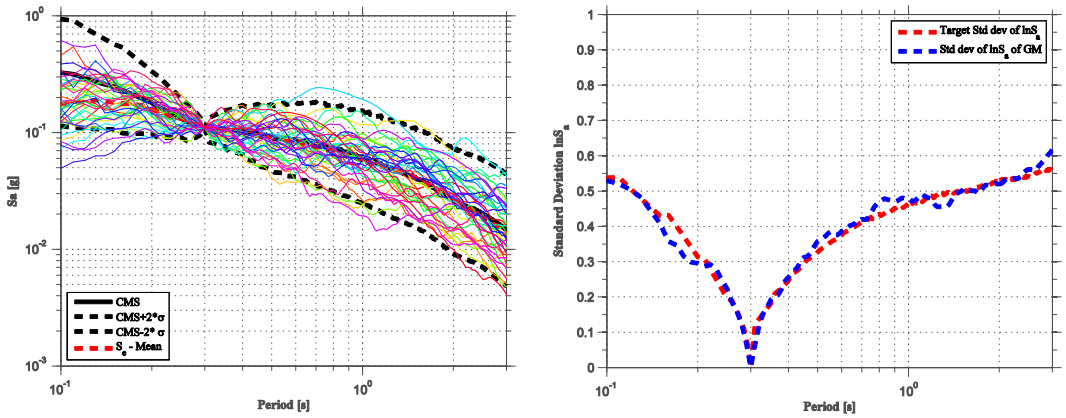


a) b)

Figure. 5 - Application of SelEQ to a CS-based record selection case, Isolated TT ($T_1$=0.30s), 10% in 50y a) mean; b) variance

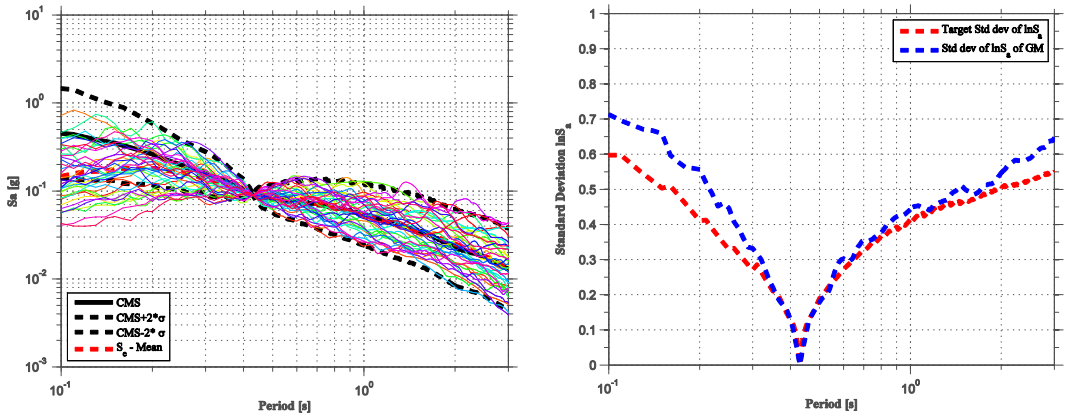


a) b)

Figure. 6 - Application of SelEQ to a CS-based record selection case, TLS ($T_{eq}$=0.42s), 10% in 50y a) mean; b) variance

The two horizontal components of each GMR are applied to the numerical model in both the transversal and longitudinal directions.

## 4 TT/TLS SEISMIC COLLAPSE RISK

The results here presented constitute an updated more detailed and justified version, of those presented earlier [28]-[29].

IDA will serve as the foundation of the applied seismic collapse risk framework in this study. Using the IDA approach, the GMR are scaled up (IM=$S_a(T_{eq},5\%)$) until collapse is achieved. Structural collapse is defined as a non-numerical convergence.

### 4.1. Seismic Collapse Fragility analysis of isolated TT and TLS

The plot of IM versus maximum Inter Section Drift Ratio (ISDR) ([11] provides further information) is calculated for each GMR, hence describing the evolution of the IDA curves. Figure 7 shows the IDA curves of the isolated TT for the ISDR. It is possible to verify that some degree of nonlinearity exists in multiple IDA curves, despite the fact that it does not appear to be particularly significant. This clearly suggest a fragile failure mode developed by the TT.

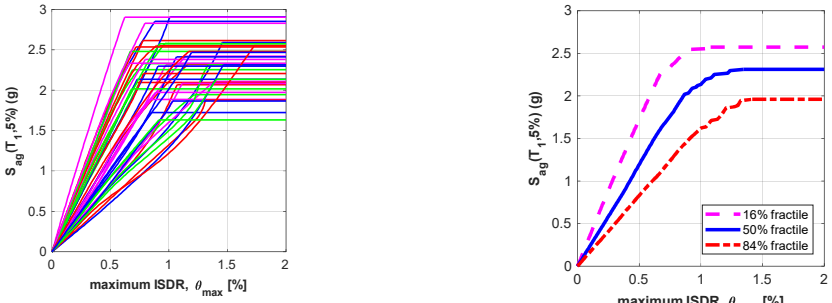


a) b)

Figure. 7 - IDA curves of isolated TT in terms of $S_{ag}(T_1)$ and the maximum ISDR a) all IDA curves b) IDA curves summarized in fractiles

As can be observed in Fig. 8, the IDA curve's initial behaviour for TLS is somewhat unexpected; however, the explanation is connected to the influence of gravity action on the transmission lines (i.e. unbalance tension imposed to the TT). Following that, the curve exhibits a linear trend in nearly every GMR until it reaches the ultimate state. This suggests that the TT4 has developed a brittle failure mode.

The $S_a$ capacities range within the 0.56g to 1.94g. It is possible to observe ISDR capacities associated with the collapse state in the 0.25-0.95% range.

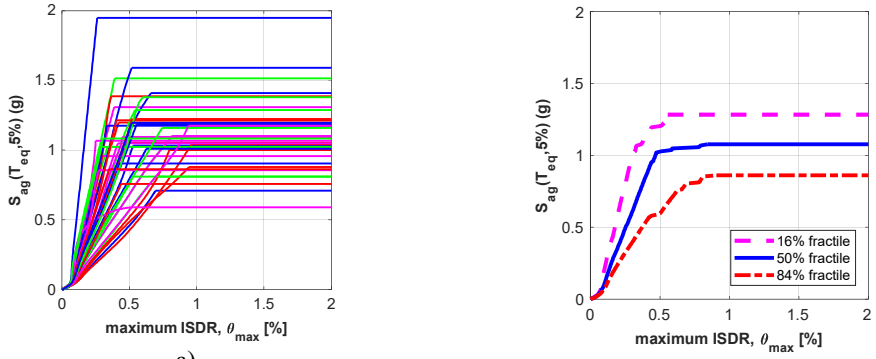


a) b)

Figure. 8 - IDA curves of TLS in terms of $S_a(T_{eq})$ and the maximum ISDR a) all IDA curves b) IDA curves summarized in fractiles

The collapse FF of the isolated TT and TLS is plotted in Fig. 9. The resulting function (i.e. lognormal distribution [30]) of the isolated TT has a median capacity of $\widehat{\boldsymbol{\theta}_r}$=2.28g and dispersion of $\widehat{\boldsymbol{\beta}_r}$=0.139. In the case of the TLS the generated FF has a median capacity of $\widehat{\boldsymbol{\theta}_r}$=1.08g and a dispersion of $\widehat{\boldsymbol{\beta}_r}$=0.226 .

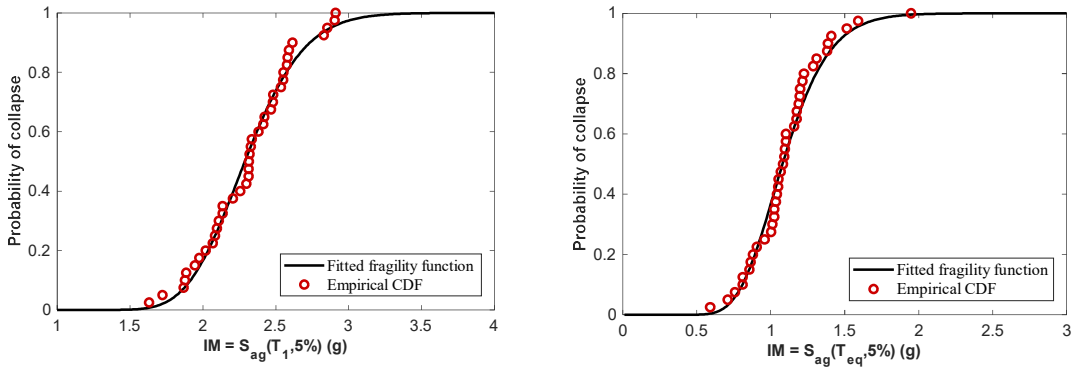


a) Isolated TT b) TLS

Fig. 6 - Collapse fragility function of the TT and TLS under multi-component ground motion records

The TLS collapse probability under a very rare earthquake scenario ($S_a(T_{eq})$=0.64g, mean return period of 2475 years) is close to 1%. This satisfies the 10 % collapse probability limit proposed in FEMA – P695 [31] under the Maximum Credible Earthquake (MCE). The isolated TT's collapse probability under a Maximum Credible Earthquake scenario ($S_a(T_1)$ =0.90g) is near zero, satisfying the guideline collapse probability limit by a large margin.

When an extremely rare earthquake scenario (exceedance probability of 1%/ in 50y) is considered, the probability of collapse approaches 0.002% for the isolated TT and 24 % for the TLS. The last scenario in the TLS, because of its magnitude, depicts a situation that may necessitate some attention for important structures. The collapse margin ratio (CMR) is another metric used to assess structural collapse resistance capacity [31]. In the case of the isolated TT the CMR translates to a value of around 2.5, indicating a moderate/high CMR, implying that the current TT is not susceptible to collapse. For the TLS, a CMR of about 1.69 suggests a low to moderate vulnerability to collapse.

### 4.2. Seismic Risk Analysis

The annual frequency of collapse $\boldsymbol{\lambda_c}$ is main metric for assessing risk of collapse of the TT in this study. The $\boldsymbol{\lambda_c}$ IM-based approach (more details in [7] and [30]), and involves integrating the structure specific seismic FF with the ground motion hazard curve. Because these two ingredients have previously been identified, the computation is accomplished by numerical integration [7]. The predicted annual frequency of collapse and other equivalent risk metrics (i.e. probability of collapse in 50y and reliability index in 1y or 50 y) for the two system under analysis are shown in Table 2.

| Model | $\hat{\lambda}_c$ (1/year) | $\hat{P}$c,50y(%) | $\hat{\beta}$1y | $\hat{\beta}$50y |
|---|---|---|---|---|
| Isolated TT | 2.41*10$^{-6}$ | 0.012% | 4.57 | 3.67 |
| TLS | 6.91*10-6 | 0.034% | 4.34 | 3.39 |

Table 2. Summary of the seismic collapse risk analysis in equivalent metrics

Additional efforts have been made to characterize the $\lambda_c$ estimation uncertainty, owing to the response variability from record to record ground motion [32]. Since a point estimate of the annual frequency, defined as the mean, has already been obtained, the aim now is to evaluate the expected value and variance of the risk estimator. To better characterize this risk metric, the bootstrap method (random sampling with replacement) is used [33]. This calculation employs 1000 parametric simulation extractions, under the assumption that FF has a parametric representation (i.e. lognormal model), and the main statistics generated are included in table 3.

| Model | $E[\hat{\lambda}_c]$ (1/year) | $Var[\hat{\lambda}_c]$ | $C.o.v[\hat{\lambda}_c]$ |
|---|---|---|---|
| Isolated TT- Parametric Bootstrap | $2.39*10^{-6}$ | $2.14*10^{-14}$ | 6% |
| TLS-Parametric Bootstrap | 6.95*10-6 | 3.86*10-14 | 9% |

Table 3. Quantification of collapse seismic risk uncertainty due to record to record variability

With this information, the annual frequency of collapse associated with 2 standard deviations, for example, yields $\lambda_c$= $2.09*10^{-6}$- $2.68*10^{-6}$ for the isolated TT and $\lambda_c$= $5.71*10^{-6}$ - $8.19*10^{-6}$ for the TLS. This translates to a roughly threefold increase in the likelihood of collapse of the TLS compared to the isolated TT. The determined probability of failure for TT is significantly lower (almost a magnitude lower) than the suggested acceptable values in the literature, such as Kempner [4], which "proposed" an acceptable target of 0.15 % in 50 y (risk category III according to the American code practice). This demonstrates that the both examples examined have a more than satisfactory seismic risk of collapse.

## CONCLUSIONS

In the OpenSees framework a complex TLS numerical model was built. In addition to taking into account critical system components (e.g. TTs and transmission lines), the emphasis was on a particular high-fidelity TT model. For an accurate collapse evaluation, many nonlinear phenomena were accounted for in the study. The isolated TT model was also compared throughout all the study to the TLS, as a mean to address the effect of tower-line coupling in the seismic response. The IDA approach forms the backbone of the collapse seismic fragility study. In order to undertake a robust analysis of the system's ultimate dynamic behaviour, forty GMR were chosen based on the CS target spectrum at the site of interest. This, together with PSHA and one of its outputs, the hazard curve, enabled the determination of the annual frequency of collapse ($\lambda_c$) of the TT (with and without the line effects).

Aside from the collapse seismic fragility function, the $\lambda_c$ was another notable contribution of this risk study. Its relevance may assist transmission line operators to manage the seismic risk revealed by their infrastructures more effectively. According to the conclusions of this study, the TLS has a minimal risk of collapse (a mean of 0.034% in 50 years). This was found to be three times larger than the seismic collapse risk displayed by isolated TT. In both situations, the seismic collapse risk achieved was considered acceptable.

## ACKNOWLEDGEMENTS

The first author acknowledges the financial support from Fundação para a Ciência e a Tecnologia (FCT, Ministério da Educação e Ciência, Portugal) through the scholarship PD/BD/127799/2016 - FCT Doctoral Program: Analysis and Mitigation of Risks in Infrastructures (INFRARISK).

This work is also supervised by the second author within the scope of the Project "SD Poles - Steel and Dampers for Poles" with reference POCI-01-0247-FEDER-039865, co‐financed by European Regional Development Fund (ERDF) through the Operational Programme for Competitiveness and Internationalization (COMPETE 2020) under the PORTUGAL 2020. Besides, this work is also integrated in the general R&D activities of the CONSTRUCT Institute on Structures and Constructions (Instituto de I&D em Estruturas e Construções), financially supported by Base Funding UIDB/04708/2020 through national funds of FCT/MCTES (PIDDAC).

## REFERENCES

[1] Organization for Security and Co-operation in Europe (OSCE). *Protecting Electricity Networks from Natural Hazards*, Vienna, Austria, 2016.

[2] E. Ghannoum. A Rational Approach to Structural Design of Transmission Line. *IEEE Transactions on Power Apparatus and Systems*, **PAS-100** (7): 3506–3512, 1981. https://doi.org/10.1109/TPAS.1981.316694

[3] G. Karagiannis, C. Stamatios, E. Krausmann, Z.I. Turksever. *Power Grid Recovery after Natural Hazard Impact. JRC Science for policy Report*, Luxembourg, 2017. https://doi.org/10.2760/87402

[4] L. Kempner. Question: What Is an Acceptable Target Reliability for High-Voltage Transmission Lines? *In Electrical Transmission and Substation Structures 2018*: Dedicated to Strengthening Our Critical Infrastructure - Proceedings of the 2018 Electrical Transmission and Substation Structures Conference, 281–289. https://doi.org/10.1061/9780784481837.026

[5] S. Mazzoni, F. Mckenna, M.H. Scott, G.L. Fenves. *Open System for Earthquake Engineering Simulation, User Command-Language Manual (Report NEES Grid-TR 2004–21*). Pacific Earthquake Engineering Research (PEER) Center, 2006.

[6] D. Vamvatsikos, C.A. Cornell. Incremental Dynamic Analysis. *Earthquake Engineering and Structural Dynamics*, 31 (3): 491–514, 2002. https://doi.org/10.1193/1.1737737.

[7] L. Eads. *Seismic Collapse Risk Assessment of Buildings: Effects of Intensity Measure Selection and Computational Approach*. Ph.D. Thesis, Stanford University, USA, 2013.

[8] F. Kiessling, P. Nefzger, J.F. Nolasco, U. Kaintzyk. *Overhead Power Lines - Planning, Design and Construction*. Heidelberg: Springer-Verlag, Berlin, Germany, 2003.

[9] F. Paiva, R.C. Barros. Capacity Assessment of a High-Voltage Lattice Tower Under Different Loading Patterns. *7th International Conference on Integrity-Reliability-Failure (IRF2020)*, Funchal, Portugal, 2020.

[10] E. Tapia-Hernández, S. Ibarra-González , D. De-León-Escobedo. Collapse Mechanisms of Power Towers under Wind Loading. *Structure and Infrastructure Engineering,* **13** (6): 766–82, 2017 https://doi.org/10.1080/15732479.2016.1190765.

[11] L. Tian, R. Ma, Q. Bing. Influence of Different Criteria for Selecting Ground Motions Compatible with IEEE 693 Required Response Spectrum on Seismic Performance Assessment of Electricity Transmission Towers. *Engineering Structures*, **144**: 337–350, 2018. https://doi.org/10.1061/(ASCE)ST.1943-541X.0002000.

[12] R.N. Prasad, G.M. Samuel Knight, S.J. Mohan, N. Lakshmanan. Studies on Failure of Transmission Line Towers in Testing. *Engineering Structures*, **35**: 55–70, 2012. https://doi.org/10.1016/j.engstruct.2011.10.017.

[13] P. Uriz P, S.A. Mahin. *Toward Earthquake-Resistant Design of Concentrically Braced Steel-Frame Structures* - PEER 2008/08 Report. Pacific Earthquake Engineering Research Center, Berkeley, California, USA, 2008.

[14] E. Karamanci, D.G. Lignos. Computational Approach for Collapse Assessment of Concentrically Braced Frames in Seismic Regions. *Journal of Structural Engineering* 140 (8): A4014019, 2014. https://doi.org/10.1061/(ASCE)ST.1943-541X.0001011.

[15] A. Aguero, C. Izvernari, R. Tremblay. Modeling of the Seismic Response of Concentrically Braced Steel Frames Using the OpenSees Analyis Environment. *Int. J. Adv. Steel Constr.* 2: 33, 2006.

[16] R. C. Battista, R.S. Rodrigues, M.S. Pfeil. Dynamic behavior and stability of transmission line towers under wind forces. *Journal of Wind Engineering and Industrial Aerodynamics* ,91 (8),1051-1067, 2003.

[17] Y.M. Desai, P. Yu, M. Popplewell, A.H. Shah A.H. Finite Element Modelling of Transmission Line Galloping. *Computers & Structures* **57** (3): 407–420, 1995. https://doi.org/10.1016/0045-7949(94)00630-L.

[18] F. Paiva F, R.C. Barros, L. Guerreiro. Dynamic Structural Health Monitoring of a Transmission Tower using Interferometric radar. *6th International Conference on Integrity-Reliability-Failure (IRF2018)*, Lisbon, Portugal, 2018.

[19] A. Hardyniec, F. Charney. An Investigation into the Effects of Damping and Nonlinear Geometry Models in Earthquake Engineering Analysis. *Earthquake Engineering & Structural Dynamics* **44** (July): 2695–2715, 2015. https://doi.org/10.1002/eqe

[20] S. Ghosh, S. Ghosh, S. Chakraborty. Seismic Fragility Analysis in the Probabilistic Performance-Based Earthquake Engineering Framework: An Overview." *International Journal of Advances in Engineering Sciences and Applied Mathematics*, no. December: **14**, 2017. https://doi.org/10.1007/s12572-017-0200-y.

[21] H. Pan, T. Li, F. Xing, L. Hongnan. Sensitivities of the Seismic Response and Fragility Estimate of a Transmission Tower to Structural and Ground Motion Uncertainties. *Journal of Constructional Steel Research* **167**: 105941, 2020. https://doi.org/10.1016/j.jcsr.2020.105941.

[22] D. Vamvatsikos. Analytic Fragility and Limit States [P(EDP|IM)]: Nonlinear Dynamic Procedures. In *Encyclopedia of Earthquake Engineering*, 15, 2015. https://doi.org/https://doi.org/10.1007/978-3-642-35344-4_247.

[23] J.W. Baker, C.A. Cornell. Which Spectral Acceleration Are You Using? *Earthquake Spectra*, **22** (2): 293–312, 2006. https://doi.org/10.1193/1.2191540.

[24] M. Pagani, F.Monelli, G. Weatherill, L. Danciu, H. Crowley, V. Silva, P. Henshaw, et al.. OpenQuake Engine: An Open Hazard (and Risk) Software for the Global Earthquake Model. *Seismological Research Letters* **85** (3): 692–702, 2014. https://doi.org/10.1785/0220130087.

[25] L. Macedo, J.M. Castro. SelEQ: An Advanced Ground Motion Record Selection and Scaling Framework. *Advances in Engineering Software*, **0**: 1–16, 2017. https://doi.org/10.1016/j.advengsoft.2017.05.005.

[26] S.P. Vilanova, J.F.B.D. Fonseca. Probabilistic Seismic-Hazard Assessment for Portugal. *Bulletin of the Seismological Society of America* **97** (5): 1702–1717, 2007. https://doi.org/10.1785/0120050198.

[27] J.W. Baker, C.A. Cornell. A Vector-Valued Ground Motion Intensity Measure Consisting of Spectral Acceleration and Epsilon. *Earthquake Engineering and Structural Dynamics*, **34** (10): 1193–1217, 2005. https://doi.org/10.1002/eqe.474.

[28] F. Paiva, R.C. Barros. Seismic Collapse Risk of a Transmission Tower. Contribution 8926 at the 3rd European Conference on Earthquake Engineering & Seismology, Bucharest, Romania, 2022.

[29] F. Paiva, R.C. Barros. Seismic Collapse Risk of a Transmission Line System. Contribution 0754 at the 3rd European Conference on Earthquake Engineering & Seismology, Bucharest, Romania, 2022.

[30] J.W. Baker. Efficient Analytical Fragility Function Fitting Using Dynamic Structural Analysis. *Earthquake Spectra*, **31** (1): 579–599, 2015. https://doi.org/10.1193/021113EQS025M

[31] Federal Emergency Management Agency (FEMA). *Quantification of Building Seismic Performance Factors - FEMA P695*, Washington, DC, USA, 2009.

[32] I. Iervolino. Assessing Uncertainty in Estimation of Seismic Response for PBEE. *Earthquake Engineering & Structural Dynamics*, **13**, 2017. https://doi.org/10.1002/eqe.2883.

[33] R. Baraschino, G. Baltzopoulos, I. Iervolino I. R2R-EU: Software for Fragility Fitting and Evaluation of Estimation Uncertainty in Seismic Risk Analysis. *Soil Dynamics and Earthquake Engineering,* **132** (February): 106093, 2020. https://doi.org/10.1016/j.soildyn.2020.106093

COMPDYN 2023
9th ECCOMAS Thematic Conference on
Computational Methods in Structural Dynamics and Earthquake Engineering
M. Papadrakakis, M. Fragiadakis (eds.)
Athens, Greece, 12-14 June 2023

# STUDY OF THE SEISMIC VULNERABILITY OF A REMODELLED REINFORCED CONCRETE BUILDING IN LISBON

**Raquel C. Pedreiras**[1], **Rui C. Barros**[2]

[1] Structural Engineer, M.Sc.
e-mail: up201709932@fe.up.pt

[2] Jubilled Prof of Structural Engineering
CONSTRUCT, FEUP (Faculdade de Engenharia da Universidade do Porto - Portugal)
email: rcb@fe.up.pt

## Abstract

*The main objective of this work is to assess the seismic vulnerability of a remodelled building in reinforced concrete, situated in Lisbon area. This evaluation is performed through the elaboration of a seismic vulnerability report through the analysis of the building seismic behaviour and the verification of the need to elaborate a seismic reinforcement project, if such report concludes that the building does not comply with structural safety requirements. In order to fulfil the objective, this work is divided into two parts: the first part concerns the application of the expedite methodologies I and II proposed by LNEC (2019); the second part, the seismic safety is verified for the reference method described in NP EN 1998-3 (2017), which also coincides with methodology III proposed by LNEC (2019), through a Pushover analysis.*

**Keywords:** Seismic Vulnerability, Expedite Methods, Eurocode 8 part 3 Portuguese version NP EN 1998-3, Pushover Analysis, SeismoStruct.

# 1 INTRODUCTION

The building that will be analysed under this seismic vulnerability assessment is a hotel located in Lisbon; but for data protection reasons, its location and ownership will not be identified. This building was designed in 1999 as an industrial building, consisting of 3 floors with high ceilings. However, in 2019 the building was subject to a remodelling, and two new floors were added between the existing floors, as well as new pillars, and some of the pre-existing ones were also reinforced (Figure 1). Another relevant aspect was the implementation of a lift shaft at each floor.

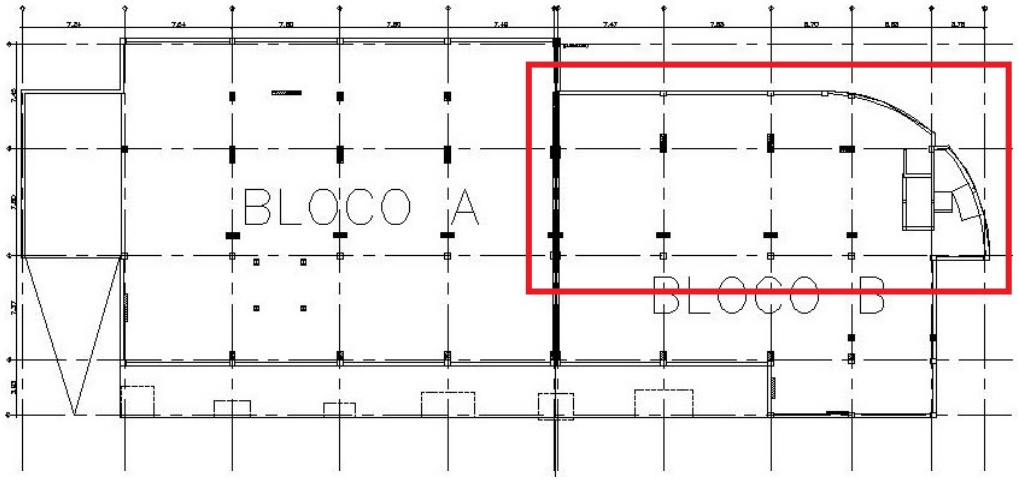


Fig. 1 – Part of the building to be studied - Floor plan.

# 2 EVALUATION OF THE APPLICABILITY OF THE EXPEDITE METHODOLOGIES I AND II IN THE BUILDING UNDER STUDY

Through the expedite methodologies I and II proposed by Report 81/2019 of LNEC [1], it is possible to evaluate the resistant capacity of the building subjected to seismic actions. However, it is necessary to verify certain criteria for their application, given in Tables 1-2-3.

## 2.1 Plant regularity and Structural regularity

| Plant regularity | Direction x | | | | Direction y | | | |
|---|---|---|---|---|---|---|---|---|
| Verification | **Floor** | **$0{,}3r_x$** | **$e_{o,x}$** | Verification | **Floor** | **$0{,}3r_y$** | **$e_{o,y}$** | Verification |
| **$e_{0,x} \leq 0{,}30r_x$** | Floor 1 | 7,86 | 7,00 | **OK** | Floor 1 | 3,25 | 2,49 | **OK** |
| | Floor 1 | 8,17 | 6,00 | **OK** | Floor 1 | 16,07 | 15,65 | **OK** |
| | Floor 1 | 8,17 | 6,00 | **OK** | Floor 1 | 16,07 | 15,65 | **OK** |
| | Roof | 8,33 | 6,00 | **OK** | Roof | 17,29 | 16,49 | **OK** |
| Verification | Floor | **$r_x$** | **$l_{sx}$** | Verification | **Floor** | **$r_y$** | **$l_{sy}$** | Verification |
| **$r_x \geq l_s$** | Floor 1 | 26,20 | 5,00 | **OK** | Floor 1 | 10,82 | 8,87 | **OK** |
| | Floor 2 | 27,22 | 5,00 | **OK** | Floor 1 | 53,58 | 9,40 | **OK** |
| | Floor 3 | 27,22 | 5,00 | **OK** | Floor 1 | 53,58 | 9,40 | **OK** |
| | Roof | 27,76 | 4,00 | **OK** | Roof | 57,63 | 7,85 | **OK** |

Table 1- Verification of $e_o$, $r_x$ and $l_s$, along x and y directions on each floor.

The boundary conditions considered for the columns correspond to built-in conditions. In this sense, Table 1 presents the verification of plant regularity; while Table 2 presents the verification of the non-existence of short columns.

| **Floor** | Unfavourable section **($b_i$ x $h_i$)** | **$h_i$** of the unfavourable column (m) | Column heights - **H** (m) | **$H/h_i$** | **Verification** If $H/h_i \geq 2.5 \rightarrow$ Slender column |
|---|---|---|---|---|---|
| Floor 1 | 0,60x1,00 | 1,00 | 5,00 | 5,00 | **OK** |
| Floor 2 | 0,75x0,25 | 0,75 | 4,00 | 5,33 | **OK** |
| Floor 3 | 0,40x0,70 | 0,70 | 3,50 | 5,00 | **OK** |
| Roof | 0,40x0,80 | 0,80 | 3,50 | 4,38 | **OK** |

Table 2 - Verification of the inexistence of short columns.

## 2.2 General criteria for application of expedite methods

| **Criteria required for applying method I and II** | | **Criteria observed in the building** |
|---|---|---|
| Class of importance | I or II (NP EN 1998-1 [2]) | II |
| Nº. of floors | Up to 4<br>Note: *In LNEC Report 81/2019 [1], buried basements are not considered as floors.* | 4 |
| Implantation area | Below 400 $m^2$ | ≈300 $m^2$ |
| Structural regularity | No short pillars | *(Subchapter 2.1)* |
| Plant regularity | $e_{ox} \leq 0,3r_x$ (1)<br>$r_x \geq l_s$ (2)<br>- $e_{ox}$ - distance between the centre of rigidity and the centre of gravity, measured in the x direction;<br>- rx- radius of torsion;<br>- ls- radius of gyration of the floor mass in plan. | *(Subchapter 2.2)* |
| | - The floor setback does not affect its rigidity;<br>- The setback area is less than 5% of the floor area. | - No floor setbacks. |
| | - Floor stiffness sufficiently large in relation to the lateral stiffness of the vertical elements. | - Satisfies the rigid diaphragm condition. |
| | $\lambda = L_{máx}/L_{min} < 4$ (3)<br>- $L_{máx}$ – largest dimension in the plan of the building;<br>- Lmin - smallest dimension in the plan of the building | $\lambda = 31/12 < 2,6$ |
| Regularity in height | - Continuous structural systems in height;<br>- Gradual reduction of lateral stiffness on each storey (kl);<br>- Gradual reduction of the mass on each floor (mi). | - No discontinuity between floors;<br>- Difference of kl of approximately 18% between floors;<br>- Difference of mi of approximately 12% between floors. |
| No interaction between adjacent buildings | - Alignment between adjacent slabs lower than the thickness of the respective slab (LNEC Report 81/2019 [1]);<br>- Height between adjacent buildings equal or less than 50% of the assessed one (LNEC Report 81/2019 [1]). | - No disparity between adjacent slabs;<br>- Equal height between adjacent buildings. |
| Local geotechnical conditions | - Soil type A, B or C (NP EN 1998-1 [2]). | - Type C |

Table 3 – Criteria of the expedite methods applicability for the building under study.

# 3 SEISMIC SAFETY EVALUATION ACCORDING TO METHOD II

## 3.1 Shear and flexural resistances

To determine the flexural and shear strengths of the vertical elements of the building, the expressions suggested in Report 81/2019 of LNEC [1] were applied, which are simplifications to those exposed in NP EN 1998-3 (2017) [3]. The first phase in the application of this method consisted in collecting data of the cross sections of all the vertical elements of the floors, only given in Table 4 for the most critical results obtained for floor 2.

| Vertical elements | New | | | | Existing | | | | $b_{wx}$ (m) | $b_{wy}$ (m) | $f_{wd}$ (Kpa) |
|---|---|---|---|---|---|---|---|---|---|---|---|
| | φw (mm) | branch-esSx | branch-esSy | $S_h$ (m) | φw (mm) | branch-esSx | branch-esSy | $S_h$ (m) | | | |
| PB' 6 | 8 | 2 | 4 | 0,15 | - | - | - | - | 0,25 | 0,75 | 434782 |
| PB'7 | 8 | 2 | 4 | 0,15 | - | - | - | - | 0,25 | 0,75 | |
| PB'5 | 8 | 2 | 4 | 0,15 | - | - | - | - | 0,25 | 0,50 | |
| PB'8 | 8 | 2 | 4 | 0,15 | - | - | - | - | 0,25 | 0,75 | |
| P31 | 8 | 2 | 2 | 0,15 | 0,28 | 4 | 4 | 0,15 | 0,60 | 0,60 | 289855 |
| P37 | 8 | 2 | 2 | 0,15 | 0,28 | 2 | 2 | 0,15 | 0,60 | 0,60 | |
| P47 | 8 | 2 | 2 | 0,15 | 0,28 | 2 | 2 | 0,15 | 0,60 | 0,60 | |
| P33 | 8 | 2 | 2 | 0,15 | 0,28 | 4 | 4 | 0,20 | 0,60 | 0,60 | |
| P29 | 8 | 4 | 2 | 0,15 | 0,50 | 3 | 2 | 0,25 | 0,80 | 0,40 | |
| P38 | - | - | - | - | 0,28 | 2 | 2 | 0,15 | 0,40 | 0,40 | |
| P39 | 8 | 2 | 2 | 0,15 | 0,28 | 2 | 2 | 0,15 | 0,60 | 0,60 | |
| P40 | - | - | - | - | 0,50 | 2 | 2 | 0,25 | 0,40 | 0,40 | |
| P41 | - | - | - | - | 0,50 | 2 | 2 | 0,25 | 0,40 | 0,40 | |
| P42 | 8 | 2 | 2 | 0,15 | 0,50 | 2 | 2 | 0,25 | 0,60 | 0,60 | |
| P46 | 8 | 2 | 2 | 0,15 | 0,50 | 3 | 2 | 0,25 | 0,60 | 0,40 | |
| P68 | - | - | - | - | 0,28 | 2 | 2 | 0,20 | 0,30 | 0,30 | |
| P53 | - | - | - | - | 0,28 | 2 | 2 | 0,20 | 0,30 | 0,40 | |
| Lift Wall 1 | 10 | 6 | 2 | 0,15 | - | - | - | - | 0,20 | 1,95 | 434782 |
| Lift Wall 2 | 10 | 2 | 4 | 0,15 | - | - | - | - | 1,75 | 0,20 | |
| Lift Wall 3 | 10 | 18 | 2 | 0,15 | - | - | - | - | 0,20 | 5,25 | |
| Lift Wall 4 | 10 | 2 | 6 | 0,15 | - | - | - | - | 2,15 | 0,20 | |

Table 4 - Cross section data for each vertical element on storey 2.

Equation (4) was applied to obtain the shear strength values for each vertical element, as shown in Table 5. Equally, Table 6 synthesizes calculation of flexural resistance also for each vertical element on floor 2, taken from the thesis of Pedreiras [4].

$$\rho_{sx} = \frac{A_{sx}}{b_w s_h} \tag{4}$$

Where: $\rho_{sx}$ - percentage of transverse reinforcement parallel to the x direction of loading; $A_{sx}$ - area of existing transverse reinforcement, parallel to the x direction; $b_w$ - base of the cross section, perpendicular to x-direction of loading; $s_h$ - stirrups spacing, in x-direction of loading. Thus, after analysing the shear and flexural strengths of all the vertical elements existing on each floor, it was possible to verify that the most unfavourable resistance corresponds to the flexural strength for each vertical element, as shown in Table 7.

| Vertical elements | New | Existing | $\rho_{swx}$ (%) | $\rho_{swy}$ (%) | $V_{C,x}$ (kN) | $V_{C,y}$ (kN) | $V_{C,i}$ (kN) |
|---|---|---|---|---|---|---|---|
| | $A_{sw}$ ($cm^2$) | $A_{sw}$ ($cm^2$) | | | | | |
| PB' 6 | 0,50 | - | 0,27 | 0,18 | 209 | 135 | 209 |
| PB'7 | 0,50 | - | 0,27 | 0,18 | 209 | 135 | 209 |
| PB'5 | 0,50 | - | 0,27 | 0,27 | 132 | 132 | 132 |
| PB'8 | 0,50 | - | 0,27 | 0,18 | 209 | 135 | 209 |
| P31 | 0,50 | 0,28 | 0,23 | 0,23 | 338 | 338 | 338 |
| P37 | 0,50 | 0,28 | 0,17 | 0,17 | 256 | 256 | 256 |
| P47 | 0,50 | 0,28 | 0,17 | 0,17 | 256 | 256 | 256 |
| P33 | 0,50 | 0,28 | 0,20 | 0,20 | 297 | 297 | 297 |
| P29 | 0,50 | 0,50 | 0,25 | 0,27 | 315 | 360 | 315 |

| | | | | | | | |
|---|---|---|---|---|---|---|---|
| P38 | - | 0,28 | 0,09 | 0,090 | 61 | 61 | 61 |
| P39 | 0,50 | 0,28 | 0,17 | 0,17 | 256 | 256 | 256 |
| P40 | - | 0,50 | 0,10 | 0,10 | 67 | 67 | 67 |
| P41 | - | 0,50 | 0,10 | 0,10 | 67 | 67 | 67 |
| P42 | 0,50 | 0,50 | 0,18 | 0,18 | 270 | 270 | 270 |
| P46 | 0,50 | 0,50 | 0,21 | 0,27 | 200 | 261 | 200 |
| P68 | - | 0,28 | 0,09 | 0,090 | 34 | 34 | 34 |
| P53 | - | 0,28 | 0,09 | 0,070 | 45 | 36 | 45 |
| Lift wall 1 | 0,79 | - | 0,16 | 0,53 | 252 | 847 | 252 |
| Lift wall 2 | 0,79 | - | 0,53 | 0,12 | 758 | 174 | 758 |
| Lift wall 3 | 0,79 | - | 0,18 | 0,53 | 759 | 2308 | 759 |
| Lift wall 4 | 0,79 | - | 0,53 | 0,15 | 935 | 262 | 935 |

Table 5 -$V_{C,i}$ - Calculation of the shear strength of each vertical element i existing on floor 2.

| Vertical elements | Area of reinforcements | | | $L_x$ | $L_y$ | ρ | $f_{yl}$ | $V_{F,x}$ | $V_{F,y}$ | $V_{F,i}$ |
|---|---|---|---|---|---|---|---|---|---|---|
| | Reinforced | Existing | Total | (m) | (m) | (%) | (kPa) | (kN) | (kN) | (kN) |
| PB'6 | 39,27 | - | 39,27 | 0,75 | 0,25 | 2,09 | 434782 | 117 | 52 | 117 |
| PB'7 | 39,27 | - | 39,27 | 0,75 | 0,25 | 2,09 | | 117 | 52 | 117 |
| PB'5 | 31,69 | - | 31,69 | 0,50 | 0,25 | 2,54 | | 74 | 45 | 74 |
| PB'8 | 49,56 | - | 49,56 | 0,75 | 0,25 | 2,64 | | 139 | 62 | 139 |
| P31 | 16,08 | 38,18 | 54,29 | 0,60 | 0,60 | 1,51 | 289855 | 94 | 94 | 94 |
| P37 | 16,08 | 29,64 | 45,73 | 0,60 | 0,60 | 1,27 | | 83 | 83 | 83 |
| P47 | 16,08 | 25,12 | 45,73 | 0,60 | 0,60 | 1,27 | | 83 | 83 | 83 |
| P33 | 16,08 | 25,12 | 33,17 | 0,60 | 0,60 | 0,92 | | 65 | 65 | 65 |
| P29 | 57,14 | 24,62 | 78,75 | 0,40 | 0,80 | 2,46 | | 92 | 152 | 92 |
| P38 | - | 20,60 | 20,60 | 0,40 | 0,40 | 1,29 | | 34 | 34 | 34 |
| P39 | - | 14,32 | 14,32 | 0,60 | 0,60 | 0,40 | | 35 | 35 | 35 |
| P40 | - | 42,02 | 42,02 | 0,40 | 0,40 | 2,63 | | 58 | 58 | 58 |
| P41 | - | 14,32 | 14,32 | 0,40 | 0,40 | 0,90 | | 26 | 26 | 26 |
| P42 | - | 27,68 | 27,67 | 0,60 | 0,60 | 0,77 | | 57 | 57 | 57 |
| P46 | - | 10,30 | 10,30 | 0,40 | 0,60 | 0,43 | | 20 | 28 | 20 |
| P68 | - | 12,56 | 12,56 | 0,30 | 0,30 | 1,40 | | 19 | 19 | 19 |
| P53 | - | 12,56 | 12,56 | 0,40 | 0,30 | 1,05 | | 24 | 19 | 24 |
| Lift wall 1 | 41,70 | - | 41,70 | 0,20 | 1,95 | 1,07 | 434782 | 47 | 247 | 47 |
| Lift wall 2 | 34,93 | - | 34,93 | 1,75 | 0,20 | 1,00 | | 201 | 41 | 201 |
| Lift wall 3 | 184,86 | - | 184,86 | 0,20 | 5,25 | 1,76 | | 139 | 1511 | 139 |
| Lift wall 4 | 69,98 | - | 69,98 | 2,15 | 0,20 | 1,63 | | 388 | 68 | 388 |
| $\sum V_{F,\,total}$ | | | | | | | | 1921 | 2841 | 1921 |

Table 6 - $V_{F,i}$- Calculation of the flexural resistance of each vertical element i existing on floor 2.

| Vertical elements | Floor 1 | | | Floor 2 | | | Floor 3 | | | Roof | | |
|---|---|---|---|---|---|---|---|---|---|---|---|---|
| | $V_{F,i}$ (kN) | $V_{c,i}$ (kN) | $V_{H,i}$ (kN) | $V_{F,i}$ (kN) | $V_{c,i}$ (kN) | $V_{H,i}$ (kN) | $V_{F,i}$ (kN) | $V_{c,i}$ (kN) | $V_{H,i}$ (kN) | $V_{F,i}$ (kN) | $V_{c,i}$ (kN) | $V_{H,i}$ (kN) |
| PB' 6 | 74 | 135 | 74 | 117 | 209 | 117 | 67 | 132 | 67 | 67 | 132 | 67 |
| PB'7 | 74 | 135 | 74 | 117 | 209 | 117 | 67 | 132 | 67 | 67 | 132 | 67 |
| PB'5 | 44 | 132 | 44 | 74 | 132 | 74 | 74 | 132 | 74 | 51 | 68 | 51 |
| PB'8 | 62 | 135 | 62 | 139 | 209 | 139 | 78 | 132 | 78 | 78 | 132 | 78 |
| P31 | 267 | 846 | 267 | 94 | 338 | 94 | 94 | 359 | 94 | 40 | 347 | 40 |
| P37 | 98 | 256 | 98 | 83 | 256 | 83 | 98 | 256 | 98 | 75 | 256 | 75 |
| P47 | 38 | 256 | 38 | 83 | 256 | 83 | 77 | 256 | 77 | 32 | 256 | 32 |
| P33 | 246 | 778 | 246 | 65 | 297 | 65 | 65 | 200 | 65 | 40 | 347 | 40 |
| P29 | 139 | 360 | 139 | 92 | 316 | 92 | 94 | 297 | 94 | 87 | 279 | 87 |
| P38 | 38 | 61 | 38 | 34 | 61 | 34 | 34 | 61 | 34 | 32 | 147 | 32 |
| P39 | 46 | 256 | 46 | 35 | 256 | 35 | 35 | 256 | 35 | 32 | 256 | 32 |
| P40 | 58 | 67 | 58 | 58 | 67 | 58 | 58 | 61 | 58 | 24 | 61 | 24 |
| P41 | 47 | 67 | 47 | 26 | 67 | 26 | 26 | 61 | 26 | 24 | 61 | 24 |
| P42 | 64 | 270 | 64 | 57 | 270 | 57 | 57 | 256 | 57 | 32 | 256 | 32 |
| P46 | 61 | 360 | 61 | 20 | 200 | 20 | 20 | 264 | 20 | 15 | 252 | 15 |
| P68 | 28 | 34 | 28 | 19 | 34 | 19 | 19 | 44 | 19 | 12 | 44 | 12 |
| P53 | 28 | 36 | 28 | 24 | 45 | 24 | 24 | 59 | 24 | 18 | 45 | 18 |
| Existing wall | 262 | 1883 | 262 | - | - | - | - | - | - | - | - | - |
| Lift wall 1 | 2097 | 3591 | 2097 | 775 | 2704 | 775 | 775 | 2704 | 775 | 569 | 2350 | 413 |
| Lift wall 2 | 67 | 174 | 67 | 201 | 758 | 201 | 201 | 758 | 201 | 156 | 121 | 121 |
| Lifet wall 3 | 1 534 | 2308 | 1 534 | 139 | 759 | 139 | 139 | 759 | 139 | 79 | 1 513 | 79 |
| Lift wall 4 | 100 | 262 | 100 | 388 | 935 | 388 | 388 | 935 | 388 | 285 | 164 | 164 |
| $\sum V_{H\,total}$ | | | 3783 | | | 1921 | | | 1771 | | | 1147 |

Table 7 - $V_{H,\,i}$ - Calculation of the most unfavourable resistance for each vertical element i existing on each floor.

### 3.2 Obtaining the total weight of the studied building

The total weight of the building was determined considering the masses related to the gravitational forces on each floor, obtaining the values presented in Table 8.

| Floor | $G_{K,i}$ (kN/m$^2$) | $\Psi_{E,i}$ | $Q_{k,i}$ (kN/m$^2$) | Area of the floor, j - $A_{p,i}$ (m$^2$) | $w_{E,i}$ (kN/m$^2$) | $W_E$ (kN) |
|---|---|---|---|---|---|---|
| Floor 1 | 9,45 | 0,24 | 2 | 291,483 | 9,93 | 2894,43 |
| Floor 2 | 8,70 | 0,24 | 2 | 291,483 | 9,18 | 2675,81 |
| Floor 3 | 9,45 | 0,24 | 2 | 291,483 | 9,93 | 2894,43 |
| Roof | 9,25 | 0,30 | 2 | 300,483 | 9,85 | 2959,76 |

Table 8-$W_E$ - Total weight per Floor.

### 3.3 Evaluation of the seismic vulnerability

In this phase, it was possible to obtain the seismic capacity coefficients that describe the resistance of each floor of the building, which are presented in Table 9.

| Floor | $V_{H,j}$ (kN) | $W_E$ (kN) | $CS_{c,j}$ |
|---|---|---|---|
| Floor 1 | 3782,58 | 2894,43 | 1,31 |
| Floor 2 | 1920,63 | 2675,81 | 0,72 |
| Floor 3 | 1771,24 | 2894,43 | 0,61 |
| Roof | 1146,66 | 2959,76 | 0,39 |

Table 9 - $CS_{c,j}$- Seismic capacity coefficient for each floor of the building

It is now necessary to know the seismic coefficient required at each floor. In a first phase, the global seismic coefficient is obtained for the building composed of 4 floors founded on type C ground, for the seismic actions of types 1 and 2, from the data obtained by the LNEC Report 81/2019 [1] (and resulting from reliability analyses), that assumes the values of 0.19 and 0.07, respectively.

In this sense, the seismic action type 1 is the most demanding, which is why the comparison of the seismic coefficients (capacity and required) will be analyzed only for the seismic action type 1. Thus, it is necessary to proceed to the definition of the demand for each floor, based on the coefficient ηj, as shown in Table 10.

| Floor | $CS_E$ Type 1 | $CS_E$ Type 2 | $\eta_j$ | $CS_{E,i}$ Type 1 | $CS_{c,j}$ | ≥ | $CS_{E,j}$ | Verification |
|---|---|---|---|---|---|---|---|---|
| Floor 1 | 0,19 | 0,07 | 1 | 0,19 | 1,31 | ≥ | 0,19 | **OK** |
| Floor 2 | | | 0,9 | 0,17 | 0,72 | ≥ | 0,17 | **OK** |
| Floor 3 | | | 0,7 | 0,13 | 0,61 | ≥ | 0,13 | **OK** |
| Roof | | | 0,4 | 0,08 | 0,39 | ≥ | 0,08 | **OK** |

Table 10-$CS_{E,j}$ – Seismic coefficient required on each floor, and verification of methodology II.

Thus, comparing the two coefficients obtained, it is possible to verify that the requirement or demand in each floor of the building does not override its capacity.

However, it is necessary to verify the same for methodology I, since it is characterized by being more conservative than the previous one, and for taking into account the values that a certain building should present in terms of shear capacity.

## 4 SEISMIC SAFETY ASSESSMENT ACCORDING TO METHOD I

In this method, the percentage of column area required in relation to the area of floor j ($A_{PE,j}$), will be compared with the percentage of column area existing on same floor ($A_{PC,j}$).

In this way, the building under study does not present seismic vulnerability, according to method I, if each floor obeys the following expression:

$$\boldsymbol{A_{PC,j} \geq A_{PE,j}} \quad (5)$$

To determine the percentage of $A_{PC,j}$, it was necessary to calculate the ratio of the area of the vertical elements of each floor, $\sum A_{pi}$, by the area of the respective floor, $A_{p,j}$, which are represented in Table 11.

| Floor | $\sum A_{pi}$ ($m^2$) | $A_{pj}$ ($m^2$) | $A_{PC,j}$ (%) |
|---|---|---|---|
| Floor 1 | 14,81 | 291,483 | 5,082 |
| Floor 2 | 6,32 | 291,483 | 2,167 |
| Floor 3 | 6,57 | 291,483 | 2,254 |
| Roof | 6,75 | 300,483 | 2,245 |

Table 11 -$A_{PC,j}$- Percentage of the area of all the columns on floor j in relation to the area of the respective floor.

Subsequently, from Report 81/2019 of LNEC (2019) [1] it was possible to determine the required column area, expressed as a percentage of the floor area. However, this area refers to floor 1 of the building to be analysed. To obtain the required column areas in relation to the area of the respective floor it was necessary to apply the coefficient, $\eta_j$, also used in method II, obtaining the values presented in Table 12 below.

| Floor | $A_{PE,1}$ | $\eta_j$ | 100% x $A_{PE,i}$ (%) | Verification | | | |
|---|---|---|---|---|---|---|---|
| | | | | $A_{PC,j}$ | ≥ | $A_{PE,j}$ | |
| Floor 1 | 2,5 | 1 | 2,50 | 5,082 | ≥ | 2,50 | **OK** |
| Floor 2 | | 0,9 | 2,25 | 2,167 | ≤ | 2,25 | **KO** |
| Floor 3 | | 0,7 | 1,75 | 2,254 | ≥ | 1,75 | **OK** |
| Roof | | 0,4 | 1,00 | 2,245 | ≥ | 1,00 | **OK** |

Table 12 - $A_{PE,j}$- Percentage of column area required on the floor in relation to the area of the respective floor, and verification of expression (5).

Through the results obtained, it is possible to verify safety, analyzing on each floor, if the percentage of the area of the existing elements, satisfies the percentage of area of elements required. This comparison is demonstrated in the last column of Table 12, where it is possible to conclude that in method I, the requirements for 100% of the seismic action on floor 2 are not verified.

However it is mentioned in Ordinance nº 302/2019 [5], in its paragraph 3 of article 1, that in case the seismic vulnerability report does not satisfy the safety requirements related to 90% of the seismic action, defined by the masses associated with the gravitational force of the building, it is mandatory to elaborate the seismic reinforcement project. Therefore, in this sense, it will be necessary to apply methodology I for 90% of the seismic action. Thus, from expression (6) it was possible to determine the required column area for 90% of the seismic action:

$$\boldsymbol{A_{PE} = \frac{C_{SE}\, n\, w_E}{\tau_{Ml}}} \quad (6)$$

Where: $n$ – number of floors existing in the building; $\tau_{Ml}$ - equivalent transverse stress (MPa); $w_E$ - weight per unit area resulting from the seismic combination of actions ($kN/m^2$).

In turn, the equivalent transverse stress was calculated by equation (7), based on the values of resistance to horizontal forces of the vertical elements, obtained by method II and the parameter $A_{pi}$, corresponding to the area of each column i existing on floor 2:

$$\tau_{MI} = \frac{min(V_{F,i}; V_{C,i})}{A_{pi}} \quad (7)$$

Thus applying equation (7) it was possible to obtain the equivalent stress (334.79 kPa) represented in the last column of Table 13, as the arithmetic mean of the stress obtained for each column i (of this floor 2).

| Vertical elements | $V_{F,i}$ (kPa) | $V_{C,i}$ (kPa) | $min(V_{F,i}V_{C,i})$ (kPa) | $L_x$ (m) | $L_y$ (m) | $A_{p,i}$ ($m^2$) | $\tau_{MI,i}$ (kPa) |
|---|---|---|---|---|---|---|---|
| PB'6 | 117 | 209 | 117 | 0,75 | 0,25 | 0,19 | 628 |
| PB'7 | 117 | 209 | 117 | 0,75 | 0,25 | 0,19 | 628 |
| PB'5 | 74 | 132 | 74 | 0,5 | 0,25 | 0,13 | 599 |
| PB'8 | 139 | 209 | 139 | 0,75 | 0,25 | 0,19 | 744 |
| P31 | 94 | 338 | 94 | 0,6 | 0,60 | 0,36 | 262 |
| P37 | 83 | 256 | 83 | 0,6 | 0,60 | 0,36 | 231 |
| P47 | 83 | 256 | 83 | 0,6 | 0,60 | 0,36 | 231 |
| P33 | 65 | 297 | 65 | 0,6 | 0,60 | 0,36 | 182 |
| P29 | 92 | 316 | 92 | 0,4 | 0,80 | 0,32 | 287 |
| P38 | 34 | 61 | 34 | 0,4 | 0,40 | 0,16 | 216 |
| P39 | 35 | 256 | 35 | 0,6 | 0,60 | 0,36 | 99 |
| P40 | 58 | 67 | 58 | 0,4 | 0,40 | 0,16 | 363 |
| P41 | 26 | 67 | 26 | 0,4 | 0,40 | 0,16 | 165 |
| P42 | 57 | 270 | 57 | 0,6 | 0,60 | 0,36 | 160 |
| P46 | 20 | 200 | 20 | 0,4 | 0,60 | 0,24 | 86 |
| P68 | 19 | 34 | 19 | 0,3 | 0,30 | 0,09 | 217 |
| P53 | 24 | 45 | 24 | 0,4 | 0,30 | 0,12 | 200 |
| Lift wall 1 | 46 | 252 | 46 | 0,2 | 1,95 | 0,39 | 120 |
| Lift wall 2 | 200 | 758 | 200 | 1,75 | 0,20 | 0,35 | 573 |
| Lift wall 3 | 117 | 209 | 117 | 0,75 | 0,25 | 0,19 | 132 |
| Lift wall 4 | 117 | 209 | 117 | 0,75 | 0,25 | 0,19 | 901 |
| | | | | | | $\sum A_{p,i}$=6,32 | $\tau_{MI}$= 334,79 |

Table 13 - $\tau_{MI}$ - Determination of equivalent transverse stress - Floor 2.

In this sense, considering 90% of the masses related to the gravitational forces existing on each floor, it was possible to obtain the values presented in Table 14.

| Floor | 90% $xA_{PE,j}$ | $A_{PC,j}$ | Verification $A_{PC,j} \geq 90\% xA_{PE,j}$ |
|---|---|---|---|
| Floor 1 | 2,380 | 5,082 | **OK** |
| Floor 2 | 1,687 | 2,167 | **OK** |
| Floor 3 | 1,502 | 2,254 | **OK** |
| Roof | 1,157 | 2,245 | **OK** |

Table 14 - Verification of seismic safety by method I on each floor.

It can be observed, that seismic safety is verified on each floor by this method I.

## 5 NONLINEAR PUSHOVER ANALYSIS

### 5.1 The N2 method in SeismoStruct software

The N2 method proposed by Fajfar [6] and universally divulgued by Fajfar *et al* [7-9], used at FEUP by Barros *et al* [10-15], was implemented in successive versions of the SeismoStruct software [16] which allows using uniform static Pushover analysis and adaptive static Pushover analysis. For each analysis seismic actions of types 1 and 2 were considered, as well as in the X and Y directions, applying the accidental eccentricity at the centre of mass of the floor, for the positive and negative direction of each seismic action. However, only

the results obtained for seismic action type 1, according to direction X, will be demonstrated, because it is the most unfavorable case.

In this sense, after the calculation of the program, the following deformation was obtained (Fig. 2), as well as the capacity curve and idealized curve necessary for the application of the N2 (Fig.3).

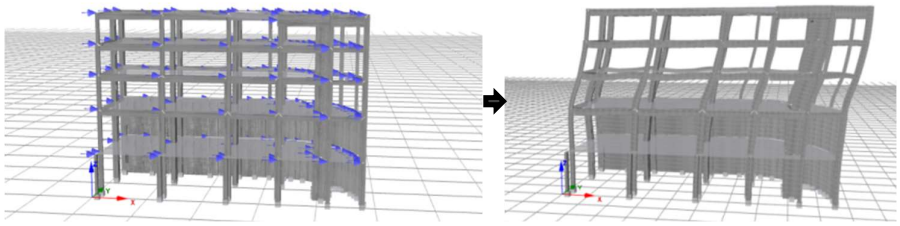

Fig. 2 - Deflection referring to seismic action type 1, according to X direction.

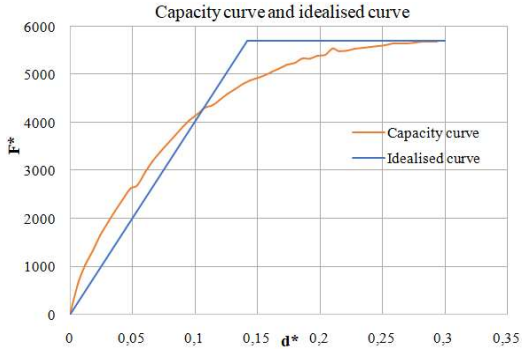


Fig. 3- Capacity curve and idealised curve, according to the X direction.

### 5.3 Evaluation of the resistant capacity of the building

In order to evaluate the resistant capacity of the structure, the seismic action was applied in the X direction with a target displacement of 49.19 mm; and it was verified that in none of the analysed elements the required requirement exceeded its capacity. However, the shear capacity was exceeded in columns P41, P40 and P53, after the structure assumed a displacement about 50% higher than the target displacement. In P41, the formation of two plastic hinges was observed in the two ends between the 2nd and 3rd floors of the building; Regarding P40, as well as P53, a plastic hinge occurred in one of its ends at floor 2, (assuming the same definition of floor used in the expedite methods). It should be noted that the columns referred, represented in brown in Fig. 4, are pillars existing before the remodelling and were not subjected to structural strengthening.

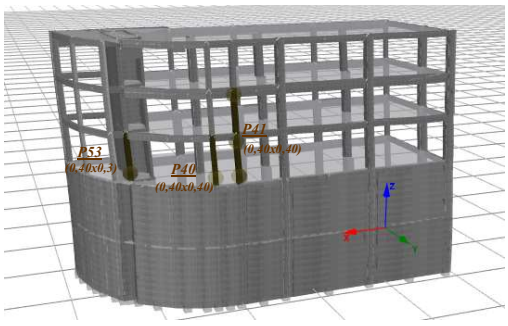


Fig. 4 - Formation of plastic hinges at the ends of columns P41-P40-P53 for a displacement of 78 mm.

## CONCLUSIONS

From the exposed analyses, it is concluded that the seismic safety of the building considered by the methods I and II, as well as by the reference method, is verified, not being necessary its seismic reinforcement according to current legislations and ordinances translating the current level of technical knowledge.

Besides, the building has a good performance to the seismic action. In this sense, the results obtained from the adaptive Pushover analysis allowed for the conclusion that the building had a good flexural deformation capacity, since the capacities associated to the shear of the elements were reached first than the ultimate rotation of the chord (associated to flexural capacities); since the post-elastic resistance of the vertical elements existing in the building was considered. Moreover, the cyclic shear strength decreases according to the ductility requirements of the plastic part, according to NP EN 1998-3 (2017) [3], so it is natural, its increase in the expedite method II. However, it is important to mention that through the results obtained in the adaptive nonlinear Pushover analysis, it was possible to verify an adequate cyclic shear capacity in the vertical elements of the building, since only the formation of the first hinge in the structure occurred, after exceeding the target displacement of the real structure of n degrees of freedom.

## ACKNOWLEDGEMENTS

The first co-author is grateful to Jubilled Professor Rui Carneiro Barros, for his dedication and help during the supervision of the master's thesis that was the genesis of this article.

A special recognition is given to the company Seismosoft, and indirectly to researchers of the Rose School of the University of Pavia, for the generous and collaborative supply of the software SeismoStruct-2021 with conditional use license, which proved to be indispensable for the realization of part of this article.

This work was financially supported by: Base Funding - UIDB/04708/2020 of the CONSTRUCT - Instituto de I&D em Estruturas e Construções - funded by national funds through the FCT/MCTES (PIDDAC).

## REFERENCES

[1] "Metodologia para a avaliação da segurança sísmica de edifícios existentes baseada em análises de fiabilidade estrutural - Edifícios de betão armado", *LNEC – Laboratório Nacional de Engenharia Civil, Relatório 81/2019 - DE/NESDE, Versão revista outubro 2019,* 134 p.

[2] NP EN 1998-1 – "Eurocódigo 8: Projecto de estruturas para resistência aos sismos. Parte 1: Regras gerais, ações sísmicas e regras para edifícios". Instituto Português da Qualidade (IPQ), Caparica – Portugal, 2010, 230 p.

[3] NP EN 1998-3 – "Eurocódigo 8: Projecto de estruturas para resistência aos sismos. Parte 3: Avaliação e reabilitação de edifícios". Instituto Português da Qualidade (IPQ), Caparica – Portugal, 2017, 87 p.

[4] R.C. Pedreiras – "Estudo da Vulnerabilidade Sísmica de um Edifício Remodelado em Betão Armado". *Tese de Mestrado, Faculdade de Engenharia da Universidade do Porto (FEUP)*, Porto, Portugal, 2022.

[5] "Portaria nº 302/2019, de 12 de Setembro, Infraestruturas e Habitação", *Diário da República n.º 175/2019*, *Série I*, 2019, 1 p.

[6] P. Fajfar – *The story of the N2 Method*. International Association for Earthquake Engineering (IAEE), Tokyo, Japan, 2021, 148 p.
[7] Fajfar, P., Fischinger, M. – "N2 : A method for non-linear seismic analysis of regular buildings". Proceedings of the 9th World Conference in Earthquake Engineering, Vol.5, 111-116, Tokyo, Japan, 1988.
[8] P. Fajfar, H. Krawinkler(eds.) - *Nonlinear Seismic Analysis and Design of Reinforced Concrete Buildings*. Elsevier Science Publishers Ltd, London and New York, 1992.
[9] P. Fajfar – "A nonlinear analysis method for performance based seismic design". *Earthquake Spectra*, 16(3), 2000, pp. 573-592.
[10] R. Carneiro Barros, Ricardo F. Almeida – "Pushover Analysis of Asymmetric Three-Dimensional Building Frames". *Journal of Civil Engineering and Management*, Vol. XI, Nº 1, pp. 3-12, Vilnius, Lithuania, 2005.
[11] M.T. César, Rui M.M.C. Barros – "Seismic performance of metallic braced frames by pushover analysis". *Computational Methods in Structural Dynamics and Earthquake Engineering*, ISBN: 978-960-254-682-6, M. Papadrakakis, N.D. Lagaros, M. Fragiadakis (eds.); p.264, CD 573, Institute of Structural Analysis & Seismic Research, NTUA, Athens, Greece, 2009.
[12] V.G. Pereira, R.C. Barros, M.T. César – "A Parametric Study of a R/C Frame based on Pushover Analysis". *Integrity Reliability and Failure (Challenges and Opportunities)*, ISBN: 978-972-8826-22-2, JF Silva Gomes and SA Meguid (eds.), INEGI editions; *Symposium on Dynamics and Stability* coordinated by Rui C Barros and M. Braz Cesar, Chapter 23, pp. 657-670; ref: S2604_A0581 – 30 pages, Porto, Portugal, 2009.
[13] V.G. Pereira, R.C. Barros, M.T.B. César – "Pushover Analyses of a R/C Frame by Distinct Software". *Proceedings of the Second International Symposium on Computational Mechanics and the Twelfth International Conference on the Enhancement and Promotion of Computational Methods in Engineering and Science* (Hong-Kong and Macao, 30th Nov-3rd Dec 2009), ISBN: 978-0-7354-0778-7, ISSN: 0094-243X, Editors: Jane WZ Lu, Andrew YT Leung, Vai Pan Iu, Kai Meng Mok; Part Two, pp. 1618-1623; AIP Conference Proceedings 1233, Melville, New York, 2010.
[14] R.C. Barros, M.T. Braz-César, et al. – "Comparative Review of the Performance Based Design of Building Structures Using Static Non-Linear Analysis - Part A: Steel Braced Frames". *Journal of Rehabilitation in Civil Engineering*, Volume 1, Issue 2, August 2013, pp. 24-39.
[15] R.C. Barros, M.T. Braz-César, et al. – "Comparative Review of the Performance Based Design of Building Structures Using Static Non-Linear Analysis, Part B: R/C Frames". *Journal of Rehabilitation in Civil Engineering*, Volume 2, Issue 1, February 2014, pp. 75-92.
[16] Seismosoft – "SeismoStruct 2021: A computer program for static and dynamic nonlinear analysis of framed structures", available from https://seismosoft.com/

COMPDYN 2023
9th ECCOMAS Thematic Conference on
Computational Methods in Structural Dynamics and Earthquake Engineering
M. Papadrakakis, M. Fragiadakis (eds.)
Athens, Greece, 12-14 June 2023

# SEISMIC ASSESSMENT OF TYPOLOGICAL MASONRY BUILDINGS USING SIMULATED GROUND MOTION RECORDS: A CASE STUDY FOR AZORES, PORTUGAL

**Shaghayegh Karimzadeh[1], Vasco Bernardo[1], Sayed Mohammad Sajad Hussaini[1], Daniel Caicedo[1], Alexandra Carvalho[2], and Paulo B. Lourenço[1]**

[1] University of Minho
Department of Civil Engineering, ISISE, Campus de Azurém 4800-058
Guimarães, Portugal
{ shaghkn, vbernardo, hussaini, dcaicedod, pbl }@civil.uminho.pt

[2] LNEC
Structural Department 17000-111
Lisbon, Portugal
xanacarvalho@lnec.pt

## Abstract

*Earthquakes are the major causes of damage and loss to the built environment, including cultural heritages, monumental buildings, and historical centres. Many regions with predominant active tectonic plates and high seismicity lack recorded ground motion datasets regarding large-magnitude events or near-field records. Among them, the Azores islands in Portugal are the regions with high seismicity. The traditional buildings from the Azores are mainly constituted of rubble stone masonry, which represents one of the weakest materials once subjected to seismic loads. The seismic performance of buildings has recently increased, given the public awareness related to damage prediction and risk mitigation during earthquakes. This study uses the stochastic finite-fault ground motion simulation approach to simulate region-specific scenario earthquakes in the Azores Plateau at bedrock. Simulations are accomplished by considering the stochastic behaviour of input-model parameters in terms of source and path attenuation effects. As a result, the dataset includes a wide range of moment magnitude and source-to-site distance due to the rupture of active faults in the Azores Plateau. Structural models are simulated using an equivalent frame model. Subsequently, analytical fragility curves are derived for these structures using the generated ground motion datasets. Results reveal that the studied structures are vulnerable to seismic actions.*

**Keywords:** Azores region, Stochastic Finite-Fault Ground Motion Simulation, Bedrock, Nonlinear analyses, Masonry structures, Seismic assessment.

# 1 INTRODUCTION

In earthquake-prone zones, earthquakes are the primary cause of fatalities and economic losses. Faial Island in the Azores Plateau experienced an earthquake of Mw=6.2 in 1998 [1]. This earthquake significantly damaged traditional masonry buildings characterised by load-bearing walls made of stone masonry and flexible timber floors. These structures are highly vulnerable to seismic damage and are prevalent on Faial Island [2]. As a result, this earthquake piqued the interest of researchers in investigating the seismic vulnerability of buildings in the area, as well as estimating potential damage and human losses that may occur in future seismic events [3]. The limited availability of recorded accelerograms for large-magnitude events in regions like the Azores Plateau presents a significant challenge for assessing the seismic performance of structures. This scarcity, particularly for severe events at short distances, has encouraged the application of synthetic records.

Several studies have investigated the seismic vulnerability of traditional masonry buildings in the Azores region. Guerreiro et al. [4] studied 30 masonry churches to identify the damage modes and possible collapse mechanisms based on in-situ observations. The observed damage was correlated with the structural typology, seismic action level, masonry quality, and previous retrofit or structural interventions. Similarly, Neves et al. [5] carried out a three-stage study that included a thorough description of the building stock, damage grade classification based on observed damage mechanisms, and seismic vulnerability assessment. The considered buildings ranged from old traditional rubble stone masonry to reinforced concrete frame structures. Their findings showed a high probability of collapse, around 30%, for intensities ranging from moderate to high (I=VII and I=VIII) according to the EMS 98 scale [6]. Ferreira et al. [7] investigated the seismic vulnerability of the historic centre of Horta in the Azores by analysing 192 buildings with a simplified vulnerability assessment method. They estimated the number of buildings likely to collapse or become unusable under various seismic intensities, linking their findings to the structures' low resistance and high vulnerability. In another study, Maio et al. [8] performed the Capacity Spectrum Method (CSM) and N2 Method on two stone masonry buildings in Faial Island to evaluate the seismic vulnerability. They utilised a set of ground motion records representative of the 1998 Faial earthquake. The results of their study indicated that retrofitting could greatly enhance the seismic resilience of at-risk structures. Zonno et al. [9] addressed the lack of recorded accelerograms by employing the stochastic finite-fault method [10] to generate representative synthetic time series of the islands affected by the 1998 Faial Earthquake. The records were used to estimate structural damage by comparing the mean damage index [11] (in Italian) and a macro-seismic method [12].

Ground motion simulations can provide alternative full time series of motions for potential scenario events in regions lacking recorded motions. Ground motion simulation techniques consist of various methodologies such as deterministic, stochastic, and hybrid models, each having specific limitations due to the modelling challenges [13]. In engineering applications, stochastic methods are more common due to their relative simplicity, as they don't require full wave propagation that relies on precise source and velocity models [10,14,15]. However, they require accurate input-model parameters to produce a ground-shaking pattern that matches the specific characteristics of real regional records. Once these methods are calibrated with input-model parameters specific to a region of interest, they can serve as powerful tools for assessing the potential impact of future earthquake hazards and disasters [16].

Within the field of earthquake engineering, ground motion simulation techniques are widely utilised to assess the impact of earthquakes on various structures such as buildings and bridges [17,18]. A rigorous analysis and validation process must be conducted to ensure the reliability of ground motion simulations in engineering applications. Previous studies in the literature have

evaluated stochastic ground motion simulations for estimating seismic demand in reinforced concrete and steel structures, including works by Karimzadeh et al. [19,20] and Cao et al. [21]. A recent study by Hoveidae et al. [22] utilised stochastically simulated ground motion records to evaluate seismic damage to a historic masonry building, namely Arge-Tabriz, in Iran. Ozsarac et al. [23] employed a stochastic finite-fault method to investigate the potential of simulated records in the probabilistic seismic assessment of reinforced concrete bridges. As proposed by Motazedian and Atkinson [10], Finite-fault stochastic simulations have been tested and verified for various regions of the world from both seismological and engineering perspectives [24,25]. Additionally, the synthetic records can be used in lieu of or in conjunction with recorded accelerograms to perform ground motion selection. The impact of ground motion selection criteria specified in ASCE/SEI 7-16 [26] and Eurocode 8 (EC8) [27] on estimating seismic demand for masonry structures using both real and simulated datasets was explored by Karimzadeh et al. [28].

The main objective of this study is to analyse the seismic performance of conventional masonry constructions situated on Faial Island, a part of the Azores Plateau in Portugal. To accomplish this, synthetic acceleration time series will be utilised. The stochastic finite-fault method based on a dynamic corner frequency approach is employed to obtain region-specific records. Then, sets of records are selected covering the distribution of Peak Ground Acceleration (PGA) for various scenario earthquakes. Non-linear numerical models are utilised to calculate the capacity of building structures using a probabilistic performance-based seismic approach. Capacity curves are obtained for various seismic scenarios to evaluate the seismic performance of the structures. The numerical findings indicate that the structures are highly susceptible to moderate to extensive damage when subjected to large-magnitude events.

## 2 SIMULATED GROUND MOTION DATASET IN THE STUDY AREA

The present study focuses on the Azores Plateau in Portugal as the study area for constructing a ground motion dataset. This region is dominated tectonically by the Azores triple junction between the North American plate, the Eurasian plate, and the African plate. The central and eastern parts of the plateau are characterised by a diffuse and complex deformation zone, which underwent shearing under a dextral trans-tensile regime. The study area comprises five islands, namely Faial, Pico, Sao Jorge, Terceira, and Graciosa [29]. The following sections describe the ground motion simulation methodology, input-model parameters, and the results obtained from the simulations.

### 2.1 Ground motion simulation methodology

The research employs the stochastic finite-fault ground motion simulation methodology of Atkinson and Assatourians [30], implemented using the EXSIM12 platform [31], to model the acceleration time series of the scenario events. The simulation algorithm, proposed by Motazedian and Atkinson [32] and based on the original FINSIM code by Beresnev and Atkinson [33], is enhanced by incorporating improvements suggested by Boore [34]. This approach considers various factors such as earthquake magnitude, fault geometry, slip distribution, density, rupture velocity, and strike to identify the fault rupture. The method combines the source contribution with attenuation parameters and site effects to obtain the seismic signal in the time domain at any observation site.

In the stochastic finite-fault method, the ruptured fault plane is divided into smaller sub-sources represented as a grid, with each sub-source assumed to be a point-source with a $\omega^{-2}$ source spectrum, as proposed by Boore [35,36]. The sub-sources rupture with a time delay that depends on their distance from the hypocentre, and the time domain summation of the

contributions from the delayed sub-sources is carried out to obtain the final ground motion simulation as follows:

$$A(t) = \sum_{i=1}^{N} H_i Y_i \left(t + \Delta t_i + T_i\right) \quad (1)$$

where $A(t)$ represents the total seismic signal at a specific time $t$, $N$ refers to the total number of sub-sources, $Y_i$ indicates the seismic signal of ith sub-source, which is calculated by performing the inverse Fourier transform of the $i^{th}$ sub-source spectrum [34,36]. The value $\Delta t_i$ is calculated by adding the time delay due to the distance of the $i^{th}$ sub-source from the hypocentre to the time of fracture initiation. The term $T_i$ denotes a fraction of rise time considered for additional randomisation. In contrast, the term $H_i$ represents the normalisation factor of the $i^{th}$ sub-source, which is introduced for energy conservation. The equation for $H_i$ is given as follows:

$$H_i = \frac{M_0}{M_{0i}} \sqrt{\sum\nolimits_j \left( \frac{f_0^2 f_j^2}{f_0^2 + f_j^2} \right)^2 \Bigg/ N \sum\nolimits_j \left( \frac{f_{0i}^2 f_j^2}{f_{0i}^2 + f_j^2} \right)^2} \quad (2)$$

where, the symbol $f_0$ represents the corner frequency of the primary fault plane, $f_j$ corresponds to the $j^{th}$ frequency ordinate. $M_0$ denotes the total seismic moment, and the terms $M_{0i}$ and $f_{0i}$ signify the seismic moment and corner frequency, respectively, of the $i^{th}$ sub-source. The expressions for $M_0$ and $f_{0i}$ are given below:

$$M_{0i} = \frac{M_0 \times S_i}{\sum_{i=1}^{N} S_i} \quad (3)$$

$$f_{0i} = 4.9 \times 10^6 \beta_s \left( \frac{\Delta\sigma}{p \times M_0} \right)^{\frac{1}{3}} \text{ where } p = \begin{cases} \frac{N_R}{N} & \text{if } N_R \prec N \times PP \\ PP & \text{if } N_R \geq N \times PP \end{cases} \quad (4)$$

where $s_i$ denotes the slip of the $i^{th}$ sub-source in Equation 3. In Equation 4, the term $N_R$ represents the total number of sub-sources that become active when the $i^{th}$ sub-source is triggered, and $\Delta\sigma$ denotes the stress drop in bars. The term PP is the pulsing percentage. The algorithm employs a dynamic corner frequency approach where the corner frequencies of the activated sub-sources decrease as the rupture progresses until it reaches a predefined level of PP. In contrast, the corner frequency of the remaining sub-sources remains constant.

### 2.2 Information on the simulations

In this study, a set of 23 scenario events featuring varying magnitudes ranging from 5.0 to 6.8 with a bin size of 0.1 are simulated on ruptured fault planes. All simulations are performed in the bedrock. To calibrate the simulation parameters for these events, region-specific input-model parameters provided by Karimzadeh and Lourenco [37], based on simulation validations against observed motions from the 1998 Faial (Mw=6.2) event, are employed. However, to account for the uncertainty associated with the parameters representing source and attenuation

effects, key parameters such as hypocentre location, stress drop, pulsing percent, quality factor, and kappa are treated as random variables. Regional models with probability distribution functions and their ranges are implemented using the study by Carvalho et al. [38]. For every event, 30 Monte Carlo simulations are performed, each with distinct combinations of input parameters. The study area, depicting the tectonic plates and stations utilised for the simulations, is presented in Figure 1. The simulations are conducted at 359 nodes on bedrock, as indicated by the triangular symbols in Figure 1.

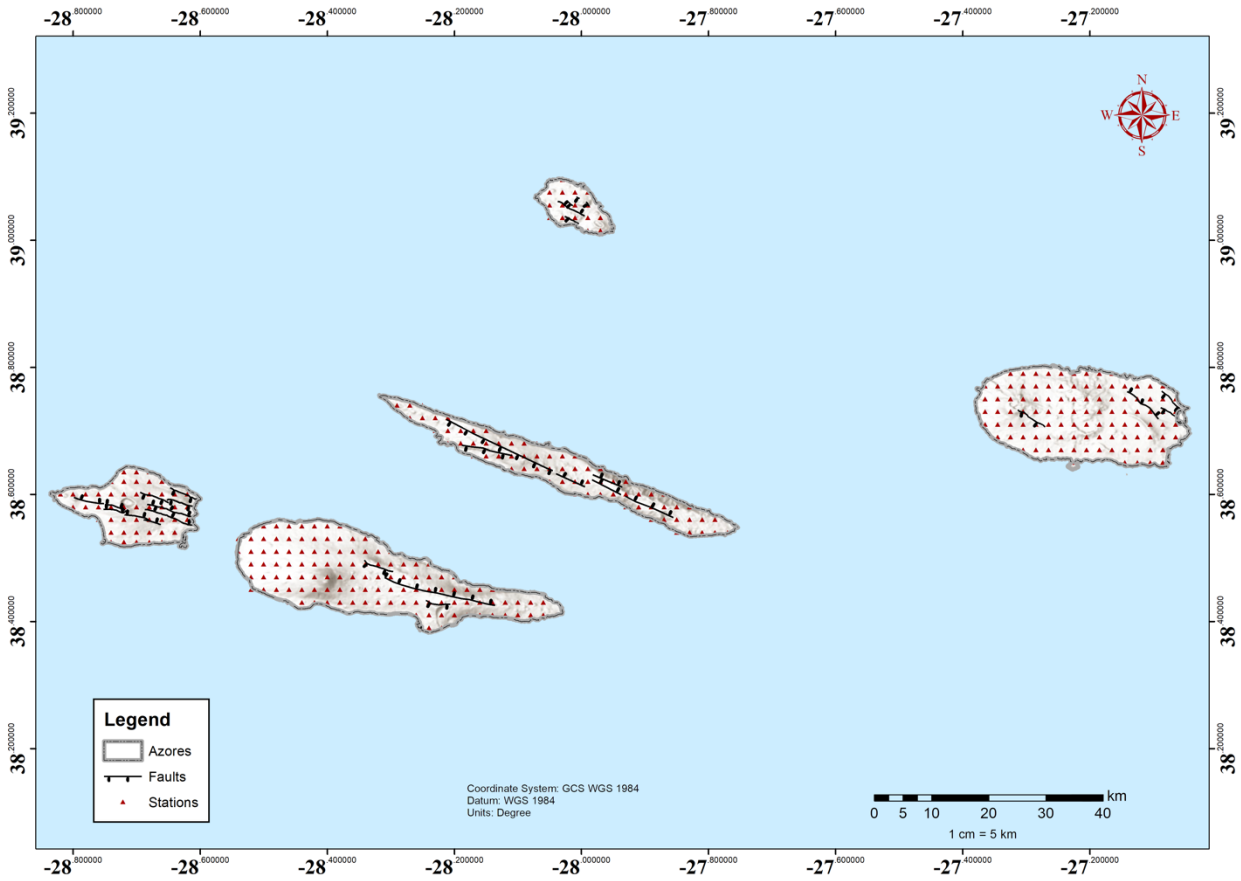


Figure 1 Study area illustrating the tectonic plates, with triangular symbols denoting the stations utilised for ground motion simulations.

## 2.3 Results of simulations

The 5% damped Pseudo Spectral acceleration (PSa) values of the simulated dataset are computed for randomly selected stations located in the centre of each island. These computations are performed for the scenario event with the largest magnitude (Mw=6.8) and the resulting PSa values are plotted in Figure 2. The figure provides a comprehensive representation of the PSa values at each station, including the individual, mean, median, standard deviation (std), minimum (min), and maximum (max) values for all simulations. This information is useful in providing a clear understanding of the variability in the dataset and the potential range of PSa values that could be observed at each station. The range of probable spectral values demonstrated by the plotted PSa values serves as evidence of the stochastic behaviour of the dataset.

(a) (b)

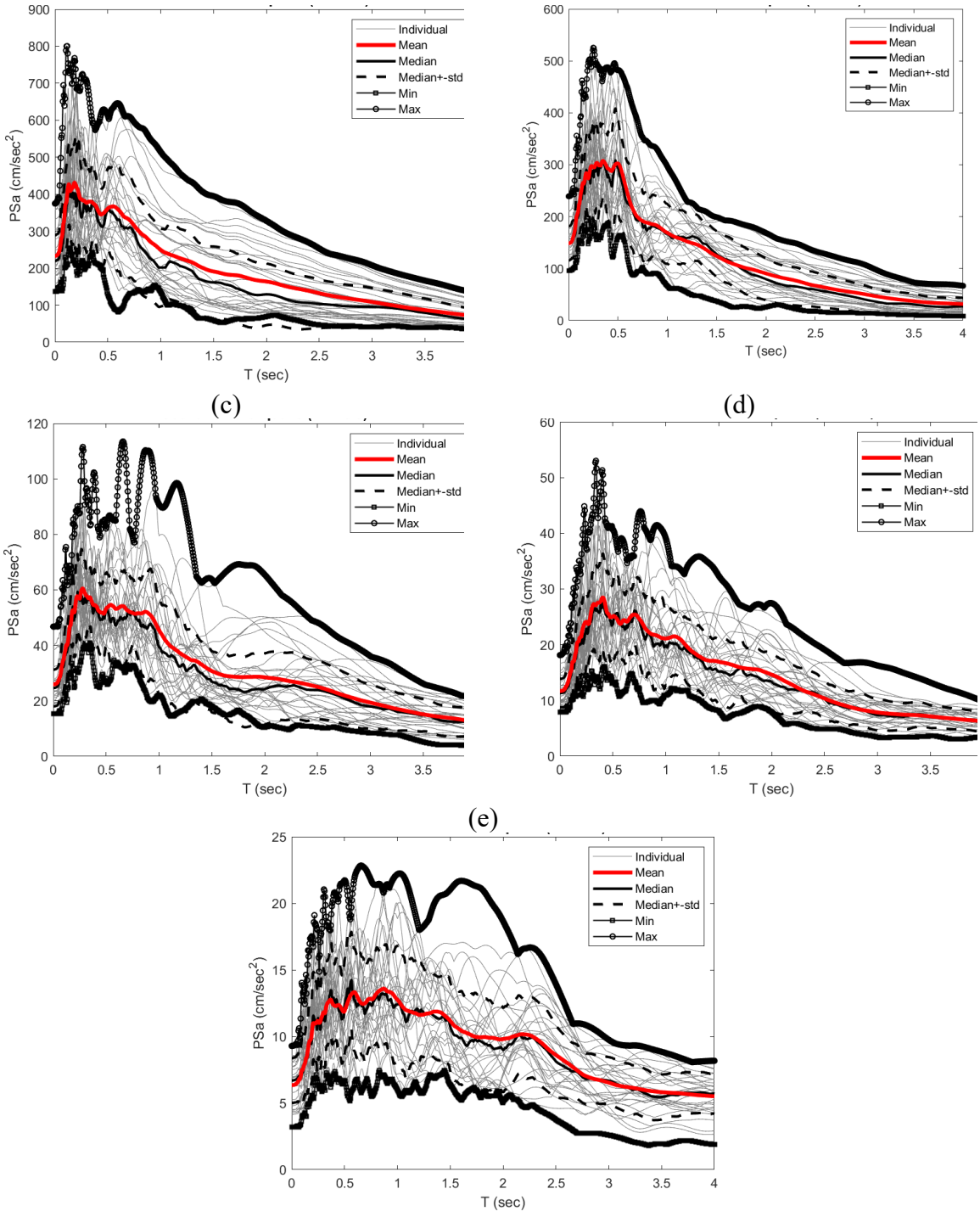


Figure 2. 5% damped PSa for stations in the centre of Azores islands, including (a) Faial, (b) Pico, (c) Sao Jorge, (d) Graciosa, and (e) Terceira.

## 3 GROUND MOTION SELECTION APPROACH

Various sets of simulated records are selected considering Mw values of 5.0, 5.1, 5.2, 5.5, 5.6, 5.8, 6.0, 6.2, 6.4, and 6.6. In this regard, each suite of records corresponds to a specific value of Mw, and 10 records within the set are selected to cover the PGA dispersion for each

scenario earthquake. Figure 3 shows the acceleration response spectra (Sa) of the 10 sets of the selected records, covering the distribution of PGA for each scenario earthquake.

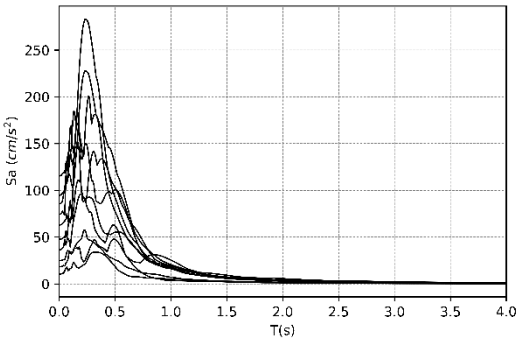


(a) Set 1, Mw = 5.0

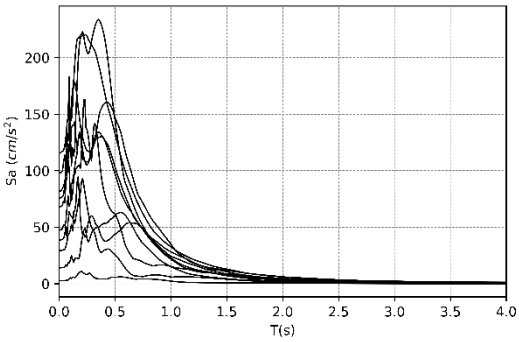


(b) Set 2, Mw = 5.1

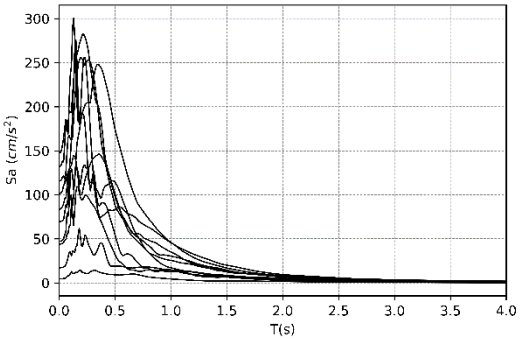


(c) Set 3, Mw = 5.2

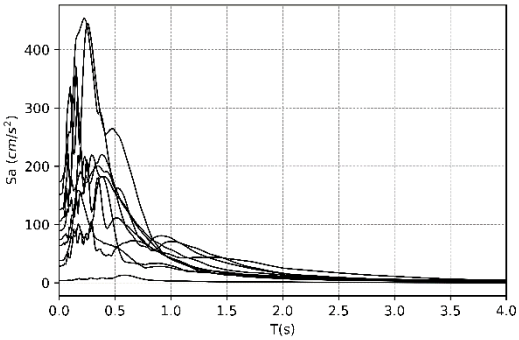


(d) Set 4, Mw = 5.5

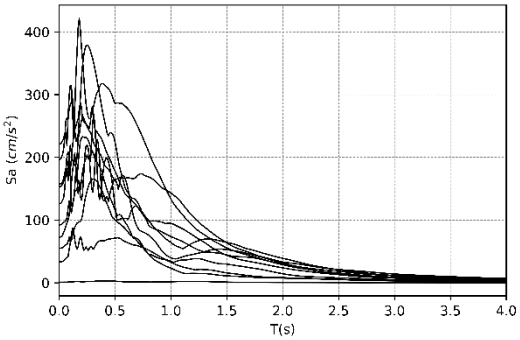


(e) Set 5, Mw = 5.6

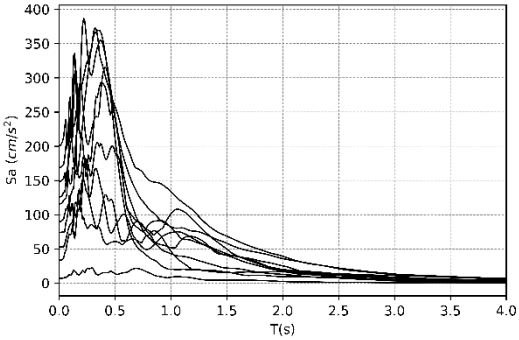


(f) Set 6, Mw = 5.8

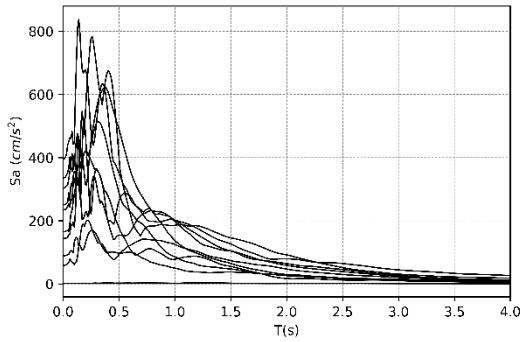


(h) Set 7, Mw = 6.0

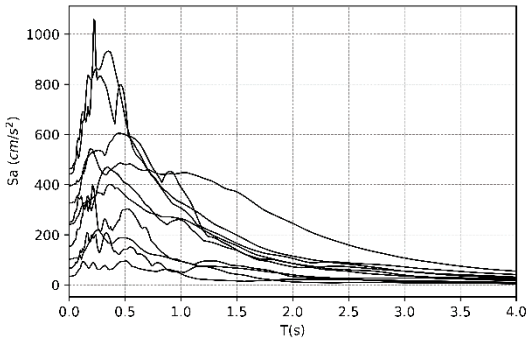


(i) Set 8, Mw = 6.2

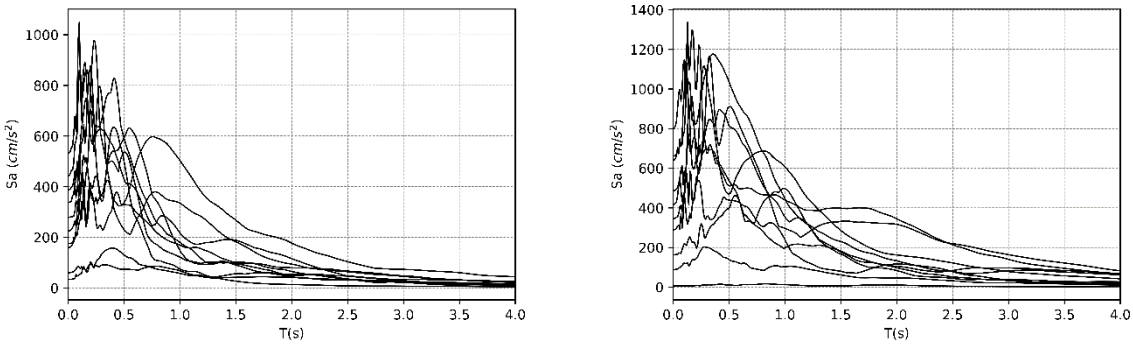


(j) Set 9, Mw = 6.4 (k) Set 10, Mw = 6.6

Figure 3. Sets of record for each scenario earthquake.

## 4 STRUCTURAL CAPACITY AND SEISMIC RESPONSE

### 4.1 Building typology and numerical modelling

One of the most traditional building typologies in Fail is characterised by rubble stone masonry walls and flexible timber floors, representing more than 50% of the building stock in that region.

In the scope of the present study, a representative URM building typology of Azores with three stories high and rectangular plan (7.5 m x 12.0 m) is used for the subsequent analysis. Details regarding the geometry parameters and material properties can be found in Bernardo et al. [39] and Costa [40].

The tridimensional numerical model of the buildings was developed using an equivalent frame modelling strategy where the in-plane behaviour only governs the capacity. Some of the model's features include the accurate representation of the principal in-plane failure mechanism, including the stiffness and strength degradation, such as bending rocking, diagonal shear and sliding. Further details regarding the modelling formulation can be consulted by Penna et al. [41].

Figure 4 depicts the numerical model considered for the subsequent analysis.

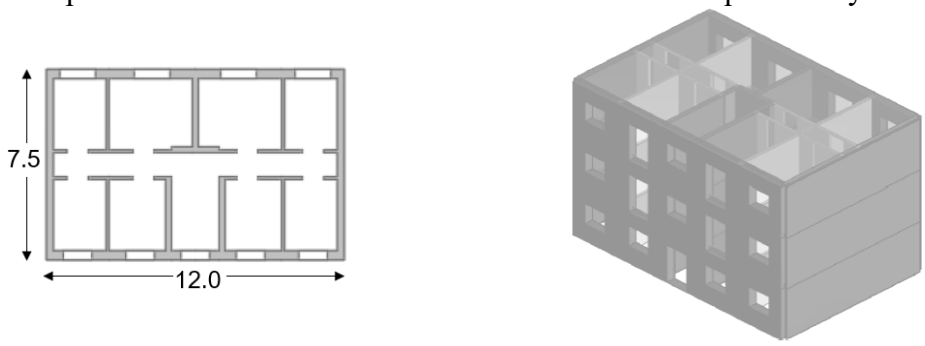


Figure 4. Typology layout and 3D-model considered.

### 4.2 Limit states and seismic assessment

The capacity curve is computed using nonlinear static analyses with a load pattern proportional to the damage (adaptive pushover). Then, the seismic performance is obtained for different spectra using the improved Capacity Spectrum Method [42] and considering the median of 10 PSa in each scenario.

The Damage States (DSs) considered in the present study for the seismic assessment are defined at a global scale in the capacity curves as a function of the yielding (Sdy) and ultimate displacement (Sdu). The ultimate displacement is considered a 20% decay of the maximum shear strength, while the yielding displacement corresponds to the immediate occupancy. The limit states adopted are summarised in Table 1 [42].

Table 1 – Damage states adopted.

| Limit state | Description | Global scale |
|---|---|---|
| DS1 (slight) | Appearance of diagonal hairline cracks in the walls' surface and parapets, being larger around openings. | 0.7*Sdy |
| DS2 (moderate) | Diagonal cracks and large cracks around the parapets. Element's separation. | Sdy |
| DS3 (severe) | Extensive cracking and relative movements to their supports. Some masonry may have fallen. | Sd (Sa,max) |
| DS4 (extensive) | Near to collapse due to in-plane of the walls. | Sdu = Sd (0.80*Sa,max) |

Figure 5 shows the capacity curve with the limit states considered and the seismic performance for different scenarios. As can be seen, the Mw=5.0 and Mw=5.2 produce performance values lower than the DS1, while the Mw =5.5 almost reaches DS1. For Mw =5.8, the performance is above DS2. Finally, for Mw =6.0 and 6.2, the expected performance reaches DS3, where the latter is slightly getting closer to DS4. Note that the results discussed assume a deterministic capacity for the buildings, and the uncertainty in the seismic scenario is not addressed. Thus, further studies are needed in a probabilistic seismic assessment framework.

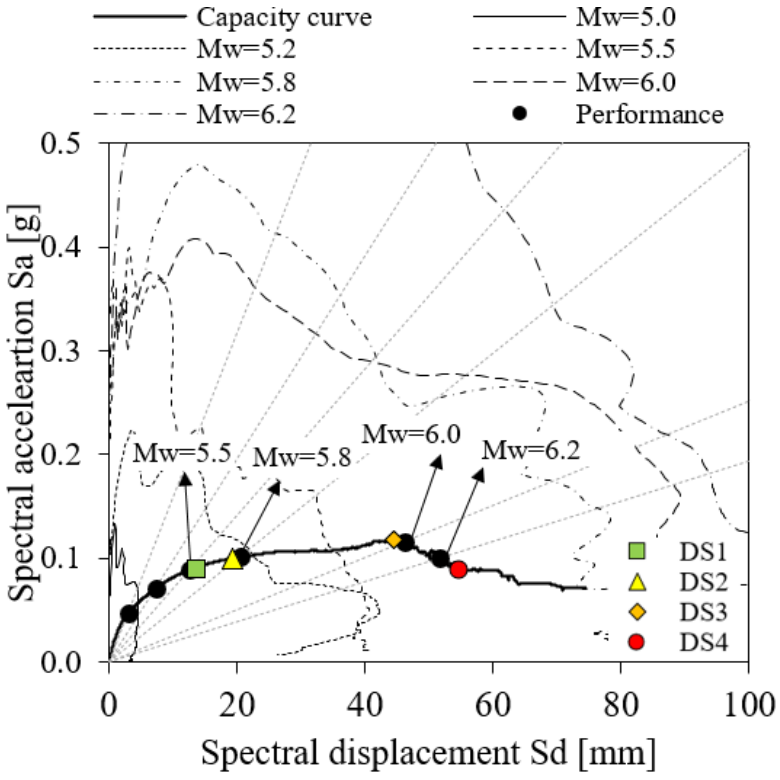


Figure 5. Seismic performance of the structure.

## 5 CONCLUSIONS

The evaluation of the seismic performance of topological masonry buildings using ground motions simulations after the 1998 Faial (Mw=6.2) earthquake is addressed in this study. The simulations are generated using the stochastic finite-fault method for region-specific scenario earthquakes in the Azores Plateau at bedrock. The stochastic behaviour of input-model parameters is considered regarding source and path attenuation effects. The dataset comprised a wide range of moment magnitude and source-to-site distance due to the rupture of active faults in the Azores Plateau. Additionally, the numerical structural model consists of a representative URM building typology of the Azores region, which is developed using an equivalent frame modelling strategy where the in-plane behaviour only governs the capacity.

Ground motion simulations offer a substantial benefit by capturing the random characteristics of earthquakes, as they provide a more precise depiction of potential seismic hazards. This enables informed decision-making in terms of seismic risk management and mitigation strategies. Regarding the numerical results on the seismic response and structural capacity, the structural system exhibited performance levels up to moderate damage for scenarios with Mw $\leq$5.8, while for scenarios with larger magnitudes (Mw=6.0 and 6.2), the expected performance reaches from severe up to extensive damage. These results demonstrate the vulnerability of typological URM buildings in the Azores region to seismic actions.

**ACKNOWLEDGMENTS**

This work was partly financed by FCT / MCTES through national funds (PIDDAC) under the R&D Unit Institute for Sustainability and Innovation in Structural Engineering (ISISE), under reference UIDB/04029/2020, and under the Associate Laboratory Advanced Production and Intelligent Systems ARISE under reference LA/P/0112/2020. This study has been partly funded by the STAND4HERITAGE project that has received funding from the European Research Council (ERC) under the European Union's Horizon 2020 research and innovation program (Grant agreement No. 833123), as an Advanced Grant. This work is financed by national funds through FCT - Foundation for Science and Technology, under grant agreement UI/BD/153379/2022 attributed to the third author.

## REFERENCES

[1] Morais EC, Ferreira TM, Estêvão JMC, Oliveira CS. Implementation and validation of an approach for the estimation of the magnitude of historical earthquakes in Azores Islands. International Journal of Disaster Risk Reduction 2021;53:102000. https://doi.org/10.1016/J.IJDRR.2020.102000.

[2] Costa A, Arêde A. Strengthening of structures damaged by the Azores earthquake of 1998. Constr Build Mater 2006;20:252–68. https://doi.org/10.1016/J.CONBUILDMAT.2005.08.029.

[3] Fontiela J, Rosset P, Wyss M, Bezzeghoud M, Borges J, Cota Rodrigues F. Human Losses and Damage Expected in Future Earthquakes on Faial Island–Azores. Pure Appl Geophys 2020;177:1831–44. https://doi.org/10.1007/S00024-019-02329-7/FIGURES/5.

[4] Guerreiro L, Azevedo J, Proença J, Bento R, Lopes M. Damage in ancient churches during the 9th of July 1998 Azores earthquake. Proceedings of the 12th World Conference on Earthquake Engineering, vol. 12, 2000.

[5] Neves F, Costa A, Vicente R, Oliveira CS, Varum H. Seismic vulnerability assessment and characterisation of the buildings on Faial Island, Azores. Bulletin of Earthquake Engineering 2012;10:27–44. https://doi.org/10.1007/S10518-011-9276-0/METRICS.
[6] Grünthal G. European macroseismic scale 1998. 1998.
[7] Ferreira TM, Maio R, Vicente R. Seismic vulnerability assessment of the old city centre of Horta, Azores: calibration and application of a seismic vulnerability index method. Bulletin of Earthquake Engineering 2017;15:2879–99. https://doi.org/10.1007/S10518-016-0071-9/TABLES/7.
[8] Maio R, Estêvão JMC, Ferreira TM, Vicente R. The seismic performance of stone masonry buildings in Faial island and the relevance of implementing effective seismic strengthening policies. Eng Struct 2017;141:41–58. https://doi.org/10.1016/J.ENGSTRUCT.2017.03.009.
[9] Zonno G, Oliveira CS, Ferreira MA, Musacchio G, Meroni F, Mota-de-Sá F, et al. Assessing seismic damage through stochastic simulation of ground shaking: The case of the 1998 Faial earthquake (Azores Islands). Surv Geophys 2010;31:361–81. https://doi.org/10.1007/S10712-009-9091-1/FIGURES/15.
[10] Motazedian D, Atkinson GM. Stochastic finite-fault modeling based on a dynamic corner frequency. Bulletin of the Seismological Society of America 2005;95:995–1010. https://doi.org/10.1785/0120030207.
[11] Dolce M, Goretti A, Masi A. Analisi dei danni causati dal sisma del settembre 1998 nel Pollino. Ingegneria Sismica 1999;16:5–15.
[12] Lagomarsino S, Giovinazzi S. Macroseismic and mechanical models for the vulnerability and damage assessment of current buildings. Bulletin of Earthquake Engineering 2006;4:415–43. https://doi.org/10.1007/S10518-006-9024-Z/METRICS.
[13] Rezaeian S, Sun X. Stochastic Ground Motion Simulation. Encyclopedia of Earthquake Engineering, Berlin, Heidelberg: Springer Berlin Heidelberg; 2014, p. 1–15. https://doi.org/10.1007/978-3-642-36197-5_239-1.
[14] Beresnev IA, Atkinson GM. FINSIM--a FORTRAN Program for Simulating Stochastic Acceleration Time Histories from Finite Faults. Seismological Research Letters 1998;69:27–32. https://doi.org/10.1785/gssrl.69.1.27.
[15] Dabaghi M, Der Kiureghian A. Stochastic model for simulation of near-fault ground motions. Earthq Eng Struct Dyn 2017;46:963–84. https://doi.org/10.1002/eqe.2839.
[16] Wang T, Shen Y, Xie X, Weng W. Ground motion simulation for the 21 May 2021 Ms 6.4 Yangbi, China, earthquake using stochastic finite-fault method. Earthquake Spectra 2022. https://doi.org/10.1177/87552930221129636/ASSET/IMAGES/LARGE/10.1177_87552930221129636-FIG11.JPEG.
[17] Halldórsson B, Mavroeidis GP, Papageorgiou AS. Near-Fault and Far-Field Strong Ground-Motion Simulation for Earthquake Engineering Applications Using the Specific Barrier Model. Journal of Structural Engineering 2011;137:433–44. https://doi.org/10.1061/(asce)st.1943-541x.0000097.
[18] Mavroeidis GP. Modeling and simulation of near-fault strong ground motions for earthquake engineering applications. State University of New York at Buffalo; 2004.
[19] Karimzadeh S, Askan A, Yakut A, Ameri G. Assessment of alternative simulation techniques in nonlinear time history analyses of multi-story frame buildings: A case study. Soil Dynamics and Earthquake Engineering 2017;98:38–53. https://doi.org/10.1016/J.SOILDYN.2017.04.004.

[20] Karimzadeh S, Askan A, Erberik MA, Yakut A. Seismic damage assessment based on regional synthetic ground motion dataset: a case study for Erzincan, Turkey. Natural Hazards 2018;92:1371–97. https://doi.org/10.1007/S11069-018-3255-6/FIGURES/15.

[21] Cao X-Y, Feng D-C, Li Y. Assessment of various seismic fragility analysis approaches for structures excited by non-stationary stochastic ground motions. Mech Syst Signal Process 2023;186:109838. https://doi.org/10.1016/J.YMSSP.2022.109838.

[22] Hoveidae N, Fathi A, Karimzadeh S. Seismic damage assessment of a historic masonry building under simulated scenario earthquakes: A case study for Arge-Tabriz. Soil Dynamics and Earthquake Engineering 2021;147:106732. https://doi.org/10.1016/J.SOILDYN.2021.106732.

[23] Ozsarac V, Monteiro R, Calvi GM. Probabilistic seismic assessment of reinforced concrete bridges using simulated records. Https://DoiOrg/101080/1573247920211956551 2021;19:554–74. https://doi.org/10.1080/15732479.2021.1956551.

[24] Karimzadeh S. Seismological and Engineering Demand Misfits for Evaluating Simulated Ground Motion Records. Applied Sciences 2019, Vol 9, Page 4497 2019;9:4497. https://doi.org/10.3390/APP9214497.

[25] Karimzadeh S, Ozsarac V, Askan A, Erberik MA. Use of simulated ground motions for the evaluation of energy response of simple structural systems. Soil Dynamics and Earthquake Engineering 2019;123:525–42. https://doi.org/10.1016/J.SOILDYN.2019.05.024.

[26] ASCE 7. Minimum Design Loads and Associated Criteria for Buildings and Other Structures. Reston, VA: American Society of Civil Engineers; 2016. https://doi.org/10.1061/9780784414248.

[27] EN 1998-1. Eurocode 8: Design of structures for earthquake resistance - Part 1: General rules, seismic actions and rules for buildings. vol. 50. Brussels: 2004.

[28] Karimzadeh S, Hussaini SMS, Funari marco F, Lourenço PB. On the Effect of Different Code-Based Ground Motion Selection Approaches for the Estimation of the Seismic Demand of Masonry Structures by Using Real Ground Motion Data Set. Earth and Space Science Open Archive 2021:14. https://doi.org/10.1002/essoar.10509375.1.

[29] J. Madeira, A. Brum da Silveira. Active tectonics and first paleoseismological results in Faial, Picoand S. Jorge islands (Azores, Portugal). Annals of Geophysics 2009;46. https://doi.org/10.4401/ag-3453.

[30] Atkinson GM, Assatourians K. Implementation and validation of EXSIM (a stochastic finite-fault ground-motion simulation algorithm) on the SCEC broadband platform. Seismological Research Letters 2015;86. https://doi.org/10.1785/0220140097.

[31] Atkinson GM, Goda K, Assatourians K. Comparison of nonlinear structural responses for accelerograms simulated from the stochastic finite-fault approach versus hybrid broadband approach. Bulletin of the Seismological Society of America 2011;101. https://doi.org/10.1785/0120100308.

[32] Motazedian D, Atkinson GM. Stochastic finite-fault modeling based on a dynamic corner frequency. Bulletin of the Seismological Society of America 2005;95. https://doi.org/10.1785/0120030207.

[33] Beresnev IA, Atkinson GM. FINSIM - A FORTRAN program for simulating stochastic acceleration time histories from finite faults. Seismological Research Letters 1998;69. https://doi.org/10.1785/gssrl.69.1.27.

[34] Boore DM. Comparing stochastic point-source and finite-source ground-motion simulations: SMSIM and EXSIM. Bulletin of the Seismological Society of America 2009;99. https://doi.org/10.1785/0120090056.

[35] Boore DM. Strong-motion seismology. Reviews of Geophysics 1983;21. https://doi.org/10.1029/RG021i006p01308.
[36] Boore DM. Simulation of ground motion using the stochastic method. Pure Appl Geophys 2003;160:635–76.
[37] Karimzadeh S, Lourenço PB. Stochastic Ground Motion Simulation of the 9th of July 1998 Faial Earthquake (Azores, North Atlantic). Authorea Preprints 2022.
[38] Carvalho A, Reis C, Vales D. Source and high-frequency decay parameters for the Azores region for stochastic finite-fault ground motion simulations. Bulletin of Earthquake Engineering 2016;14. https://doi.org/10.1007/s10518-015-9842-y.
[39] Bernardo V, Campos Costa A, Candeias P, Costa A. Seismic Vulnerability Assessment and Fragility Analysis of Pre-code Masonry Buildings in Portugal (under review - BEEE-D-21-00264R2). Bulletin of Earthquake Engineering 2021.
[40] Costa A. Determination of mechanical properties of traditional masonry walls in dwellings of Faial Island, Azores. Earthq Eng Struct Dyn 2002. https://doi.org/10.1002/eqe.167.
[41] Penna A, Lagomarsino S, Galasco A. A nonlinear macroelement model for the seismic analysis of masonry buildings. Earthq Eng Struct Dyn 2014;43:159–79. https://doi.org/10.1002/eqe.
[42] Bernardo V, Campos Costa A, Candeias P, Costa A, Marques A, Carvalho A. Ambient vibration testing and seismic fragility analysis of masonry building aggregates. Bulletin of Earthquake Engineering 2022. https://doi.org/https://doi.org/10.1007/s10518-022-01387-y.

COMPDYN 2023
9th ECCOMAS Thematic Conference on
Computational Methods in Structural Dynamics and Earthquake Engineering
M. Papadrakakis, M. Fragiadakis (eds.)
Athens, Greece, 12-–14 June 2023

# EVALUATION OF SIMULATED GROUND MOTIONS FOR SEISMIC ASSESSMENT OF A STEEL FRAME STRUCTURE USING MULTI-CRITERIA SELECTION AND SCALING APPROACH BASED ON EVOLUTIONARY ALGORITHMS

**Manolis Georgioudakis[1], Shaghayegh Karimzadeh[2], Michalis Fragiadakis[1] and Paulo B. Lourenço[2]**

[1]School of Civil Engineering
National Technical University of Athens, Zografou Campus, Greece
e-mail: {geoem, mfrag}@mail.ntua.gr

[2] Civil Engineering Department, ISISE, ARISE
University of Minho, Campus of Azurem, Guimaraes, Portugal
e-mail: {shaghkn, pbl}@civil.uminho.pt

**Abstract.** *Recently, simulated ground motion records have supplanted real records as a key alternative. Unlike real motions, simulations encompass various intensities, source-to-site distances, and site characteristics. However, determining whether they are appropriate for engineering applications takes time and effort. Another challenging topic is the proper selection and scaling of ground motion records to assess the seismic performance of structures. This study aims to investigate the difference between the real and simulated motions selected according to the code design spectra. Simulations are accomplished through the stochastic finite-fault method, considering the uncertainty of the rupture of the North Tabriz Fault Plane in northwestern Iran, one of the hazardous regions with a seismic gap. A real ground motion dataset with consistent seismological characteristics is compiled. The records are selected and scaled through a multicriteria approach using the evolutionary algorithm. In this approach, the mean spectrum and the (period-depended) dispersion fit best with the target spectrum and its dispersion. Variations in real and simulated record sets are assessed using several ground motion intensity metrics. This study also investigates the effectiveness of the simulated motions for seismic demand evaluation of a three-story steel moment frame.*

**Keywords:** Simulated ground motions, Selection, Scaling, Evolutionary algorithms, Steel Moment Frame.

## 1 Introduction

In recent times, simulated ground motion records have emerged as a significant alternative to real records. These records offer a wide range of intensities, source-to-site distances, and site characteristics that are not easily accessible through real records. However, the suitability of simulated records for engineering applications requires a considerable amount of time and effort for thorough evaluation. Furthermore, selecting and scaling ground motion records in a proper manner for the evaluation of seismic performance of structures poses significant challenges. Recent research endeavours have centred on the examination of simulation effectiveness utilising diverse methodologies across the world, covering a broad spectrum of engineering implementations. These include seismic assessment evaluations of distinct structures or investigations into seismic loss and risk assessments [1, 2, 3, 4, 5].

This study aims to investigate the difference between the real and simulated motions selected according to the code design spectra. Simulations are accomplished through the stochastic finite-fault method, considering the uncertainty of the rupture of the North Tabriz Fault Plane (NTFP) in northwestern Iran, one of the hazardous regions with a seismic gap. A real ground motion dataset with consistent seismological characteristics is compiled. The records are selected and scaled through a multi-criteria approach using the evolutionary algorithm. In this approach, the mean spectrum and the (period-depended) dispersion fit best with the target spectrum and its dispersion. Variations in real and simulated record sets are assessed using several ground motion intensity metrics. This work also investigates the effectiveness of the simulated motions for seismic demand evaluation of a three-story steel moment frame.

## 2 Simulated Ground Motion Records

Simulated records are generated through the stochastic finite-fault method, considering the uncertainty of the rupture of the NTFP in Northwestern Iran, one of the hazardous regions with a seismic gap (Fig. 1). NTFP is an active fault with a length of greater than 120 km, having a dextral strike-slip mechanism and an approximate right-lateral slip rate of 8 mm per year [6]. In spite of high seismicity of the region (it has the potential of rupturing with an approximated magnitude of 7.7), there is lack of recorded ground motions for moderate-large magnitude events in the instrumental area.

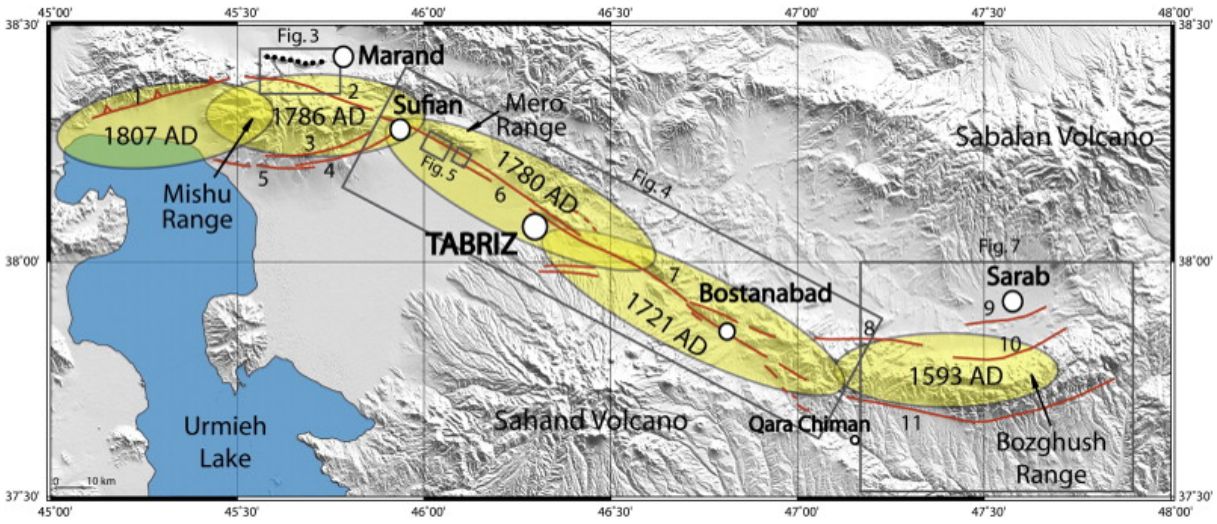


Figure 1: The North Tabriz Fault Plane located in Northwestern Iran [6].

In this study, potential scenario earthquakes with different moment magnitudes ($M_w$) are simulated to evaluate the seismic damage of a benchmark structure. For ground motion simulation of the scenario earthquakes, the stochastic finite-fault method is used. The simulation methodology is introduced by Motazedian et al. [12] and employs a finite-fault model comprised of point-source models as introduced by Boore. The method simulates the frequencies of engineering interest practically compared to the other approaches. Simulations of the scenario events are performed within the EXSIM platform. The simulation technique subdivides the rectangular fault plane into sub-faults with smaller dimensions, each of them having a $\omega^{-2}$ shape. The rupture initiates from the hypocenter, which is located in the center of one of the sub-faults. Then, rupture propagation achieves from the hypocenter to the other sub-faults in a radial direction with a constant rupture velocity. The technique uses a dynamic corner frequency approach in order to conserve the total radiated energy at high frequencies irrespective of the sub-fault size. The amplitude of the shear wave acceleration spectrum for the $ij$-th sub-fault in the frequency domain is obtained as follow:

$$A_{ij}(f) = CM_{0ij}H_{ij}\left[(2\pi f)^2 / \left[1+\left(\frac{f}{f_{cij}}\right)^2\right]\right] e^{\frac{-\pi f R_{ij}}{Q(f)\beta}} G(R_{ij})A(f)e^{-\pi\kappa f} \tag{1}$$

where:

$$\begin{aligned} C &= \tfrac{R^{\theta\phi}\sqrt{2}}{4\pi\rho\beta^3} \\ M_{0ij} &= \tfrac{M_0 S_{ij}}{\sum_{k=1}^{nl}\sum_{l=1}^{nw} S_{kl}} \end{aligned} \tag{2}$$

in which $C$ is the scaling factor, $R^{\theta\phi}$, $\rho$, $\beta$, $M_{0ij}$ and $S_{ij}$ correspond to radiation pattern, density, shear-wave velocity, seismic moment and relative slip weight of the $ij$-th sub-fault, respectively. The term $H_{ij}$ is a scaling factor given as follows:

$$H_{ij} = \sqrt{\left[N \cdot \sum\left(\frac{f^2}{1+(f/f_0)^2}\right) / \sum\left(\frac{f^2}{1+(f/f_{0ij})^2}\right)\right]} \tag{3}$$

where N corresponds to total number of sub-faults and $f_{0ij}$ expresses the dynamic corner frequency of the $ij$-th sub-fault. This scaling factor is employed for conserving the spectral shape at high-frequency portion. The dynamic corner frequency is given as:

$$f_{cij}(t) = (N_R(t))^{-\frac{1}{3}} \cdot 4.9 \cdot 10^6 \beta \left(\frac{\Delta\sigma}{M_{0_{ave}}}\right)^{\frac{1}{3}} \tag{4}$$

which is a function of stress drop ($\Delta\sigma$), number of ruptured sub-faults ($N_R(t)$) at the time $t$, and average seismic moment of sub-faults ($M_{0_{ave}} = M_0/N$). The term $R_{ij}$ corresponds to the distance of the $ij$-th sub-fault from the observation point. The quality factor is expressed by the term $Q(f)$. The term $G(R_{ij})$ is the geometric spreading factor as a function of $R_{ij}$. The site amplification factor is shown by $A(f)$. Finally, the term $e^{-\pi\kappa f}$ stands for the high-cut filter, which controls the spectral shape at high frequencies. In this formula, the kappa factor of soils is expressed by $\kappa$.

Finally, the acceleration time history at each site is calculated by summing the contribution of all sub-faults in time domain where the time delay of each sub-fault is taken into account as follows:

$$a(t) = \sum_{i=1}^{nl} \sum_{j=1}^{nw} a_{ij}(t + \Delta t_{ij}) \tag{5}$$

where, $a(t)$ corresponds to the acceleration time series at time $t$, $a_{ij}(t)$ stands for the acceleration time series of the $ij$-th sub-fault and $\Delta t_{ij}$ expresses the appropriate delay time which is defined as the difference of the time when the seismic wave radiates from the $ij$-th sub-fault to the time of reaching the observation point.

## 3 Selection and Scaling of Ground Motion Records

The current state-of-practice is followed by various design codes and guidelines, where the records are *selected* using engineering judgement and some simple filters based on qualitative criteria. Such criteria require that the records have to match the magnitude, fault mechanism, soil conditions of the site of interest [9]. The selected ground motions are subsequently *scaled*, usually so that their their mean spectrum, matches on average and over a wide range of periods the target spectrum. Amplitude scaling to a target acceleration value $S_T(T_i, \zeta)$ is obtained multiplying the ground motion with a scalar $s = S_T(T_i, \zeta)/S_a(T_i, \zeta)$, where $S_a(T_i, \zeta)$ is the spectral acceleration of the unscaled ground motion at $T_i$. The whole process is well-known as *spectrum matching*.

In this study, spectrum matching is performed considering a two-objective mixed-integer optimization problem which is formulated in order to consistently consider both the mean $F_\mu$ and the variability $F_\beta$ [11] functions where:

$$\begin{aligned} F_\mu(\mathbf{X}) &= \sqrt{\int_{T_l}^{T_u} \Big[\mu_{log}\Big(\mathbf{s}^T \mathbf{S}_a(T,\zeta)\Big) - log\Big(S_T(T,\zeta)\Big)\Big]^2 dT} \\ F_\beta(\mathbf{X}) &= \sqrt{\int_{T_l}^{T_u} \Big[\sigma_{log}\Big(\mathbf{s}^T \mathbf{S_a}(T,\zeta)\Big) - \beta_T(T,\zeta)\Big]^2 dT} \end{aligned} \tag{6}$$

In addition, $\zeta$ is the damping ratio of the structure and $\mathbf{s} = [s_1, s_2, \dots s_N]^T$ and $\mathbf{S}_a(T, \zeta)$ are the vectors contain the scaling factors and the spectral accelerations of each record, while $T_l$ and $T_u$ define the period range of interest. If $T_1$ is the fundamental vibration period, EC8 recommends that $T_l = 0.2T_1$ and $T_u = 2.0T_1$ and $\beta(T, \zeta)$ is the logarithmic dispersion (function of the period T), assumed, or provided by a ground motion model (GMM). Subsequently, the problem formulation is written as follows:

$$\begin{aligned} &\text{minimize} \quad [F_\mu(\mathbf{X}), F_\beta(\mathbf{X})] \\ &\text{subject to:} \quad g_k(\mathbf{X}) \leq 0 \end{aligned} \tag{7}$$

where $g_k(\mathbf{X})$ are the constraints of the problem. Eq. (7) describes a Pareto problem, whose solution is a set of optimum solutions. This is further explained in Fig. 2 where a set of optimum solutions is plotted in a graph; the two axes represent the two objective functions: $F_\mu$ and $F_\beta$. This curve is known as the "Pareto front" (red solid line). Pareto problems have meaning only if the objectives functions are "competing". In the problem at hand, due to the nature of the two objectives functions, i.e. mean and its variability, $F_\mu$ and $F_\beta$ are always competing and thus the shape of the Pareto front will always be convex. This allows to select the three optimum design solutions shown in Fig. 2 as 'A', 'B' and 'C'. Designs 'A' and 'C' are the optimum designs corresponding to the best optimum design with respect to $F_\mu$ and $F_\beta$, respectively. Design 'B' can be defined as the member of the Pareto front that has the minimum distance $min(D)$ from the origin and will always provide a good compromise solution, suitable for engineering practice.

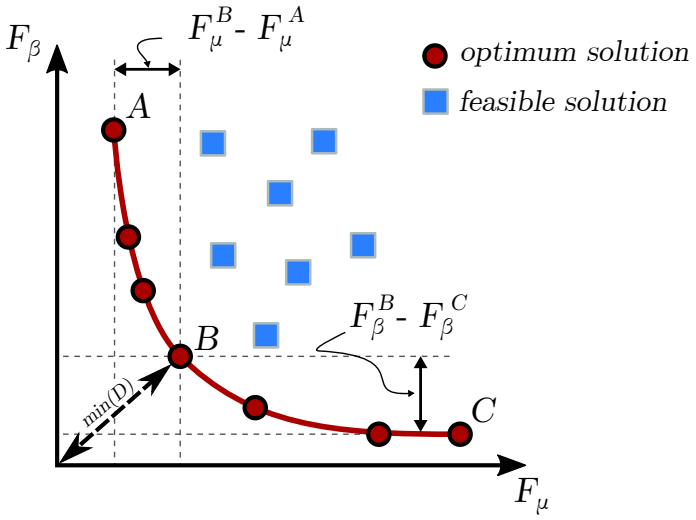


Figure 2: Pareto front solutions and selection of Point B as good compromise solution.

For solving the multi-objective optimization problem we adopt the differential evolution for multi-objective optiomization (DEMO) algorithm [15]. DEMO takes advantage of the differential evolution alorithm [14] in combination with the mechanisms of Pareto-based ranking and crowding distance sorting, used by evolutionary algorithms in multi-objective optimization problems. To preserve a uniformly spread Pareto-front of non-dominated solutions, it uses the following principle: the offspring replaces the parent if it dominates it. If the parent dominates the offspring, the offspring is discarded. Otherwise, when the offspring and parent are non-dominated with regard to each other, the offspring is added to the population. This step is repeated until the number of offsprings created reach the population size. If the population has enlarged, a truncation scheme is applied for the next step of the algorithm. The truncation scheme is based on the non-dominated sorting process which individuals of the same front are evaluated with the crowding distance metric [16]. The truncation ensures that only the best individuals, considering all objective functions, will be in the population.

## 4 Spectrum Matching of Simulated and Real Ground Motion Records

Two sets of ground motions datasets, i.e. *simulated* and *real*, are compiled. Simulations are accomplished through the stochastic finite-fault method, considering the uncertainty of the rupture of the NTFP in north-western Iran. Subsequently, a real ground motion dataset is compiled with consistent seismological characteristics.

### 4.1 Generation of the Ground Motions Datasets

**The Simulated Ground Motion Dataset**: The stochastic finite-fault methodology based on a corner frequency approach as described in Sec. 2 was utilized to conduct ground motion simulations for scenario earthquakes of magnitude ($M_w$) equal to 6.8, 7.1, 7.4 and 7.7 at random nodes in the city centre. The ruptured fault length and width are estimated according to Wells and Coppersmith [17] for scenario events of the same magnitude levels. To account for the aleatory uncertainty of earthquakes, in the entire length of the NTFP, alternative ruptured fault planes and hypocenters are considered. Each magnitude is investigated separately, and

multiple ruptured fault lines are generated for each magnitude value. The input model parameters for simulation, which include source, path, and site effects, are adopted from Hoveidae et al. [18] and calibrated accordingly. Finally, the simulated dataset includes 6207 ground motion records in total and were validated using different ground motion models (GMMs), including BA08 [19], AC10 [20], ASB14 [21] and KAAH15 [22]. Fig. 3 illustrates a validation example in terms of peak ground acceleration (PGA) for a scenario event with $M_w$ = 7.1.

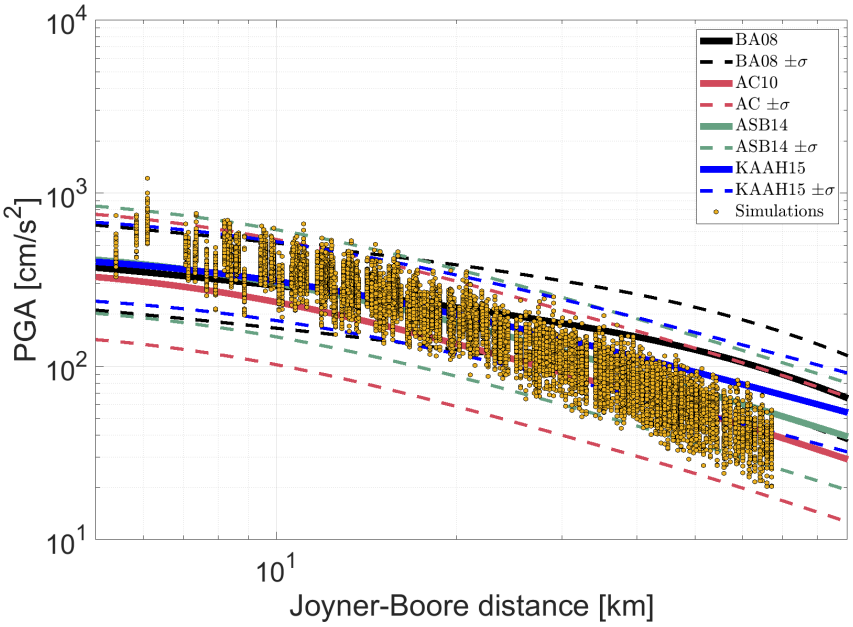


Figure 3: Comparison of PGA against GMMs for $M_w$ = 7.1.

**The Real Ground Motion Dataset**: For the compilation of the real ground motion dataset, the PEER NGA-West2 [24] ground motion records database was used. The database includes 21,336 (mostly) three-component records from 599 events. The parameter space covered by the database is $M_w$ 3.0 to 7.9, closest distance of 0.05 to 1,533 km, and site time-averaged shear-wave velocity in the top 30 m of $V_{S30}$ = 94 m/s to 2,100 m/s. Using consistent seismological characteristics related to NTFP region, the Criteria Set #1 from Table 1 were applied for each parameter to extract a compatible subset of ground motion records. This first search returned a subset of only 30 ground records from 6 events. Hence, to enlarge the real ground motion dataset, an extended range of parameters set were applied (Criteria Set #2) which finally returned 52 ground motion records from 8 events.

| | Parameter | | | | | |
|---|---|---|---|---|---|---|
| Criteria Set | Magnitude | $V_{S30}$ [m/s] | $R_{JB}$ [km] | Depth [km] | Fault Mechanism | Pulse-like |
| #1 | 6.8 - 7.7 | 175 - 375 | 0.5 - 80 | 6 - 18 | Strike-Slip (SS) | No |
| #2 | 6.8 - 7.7 | 30 - 500 | 0.5 - 150 | 6 - 18 | Strike-Slip (SS) | No |

Table 1: Criteria range applied to PEER database.

Fig. 4 shows a comprehensive histogram that portrays various seismological parameters, namely $M_w$, and Joyner-Boore distance ($R_{JB}$), along with ground motion intensity measures, namely PGA and Sa($T_1$) for both the simulated and real datasets compiled. In Fig. 5 the spectra of the two datasets along with their mean spectrum are also depicted.

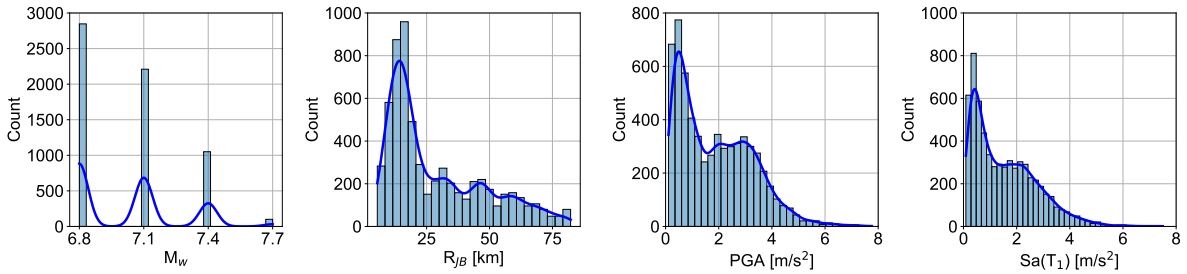


(a) Simulated records

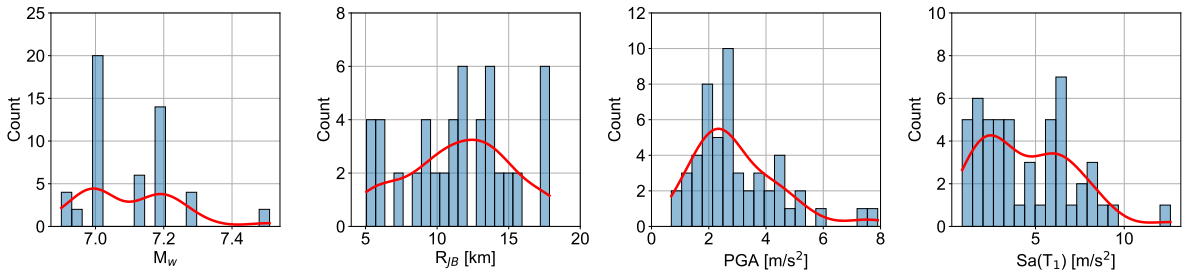


(b) Real records

Figure 4: Histograms of various parameters of the (a) simulated and (b) real ground motion datasets.

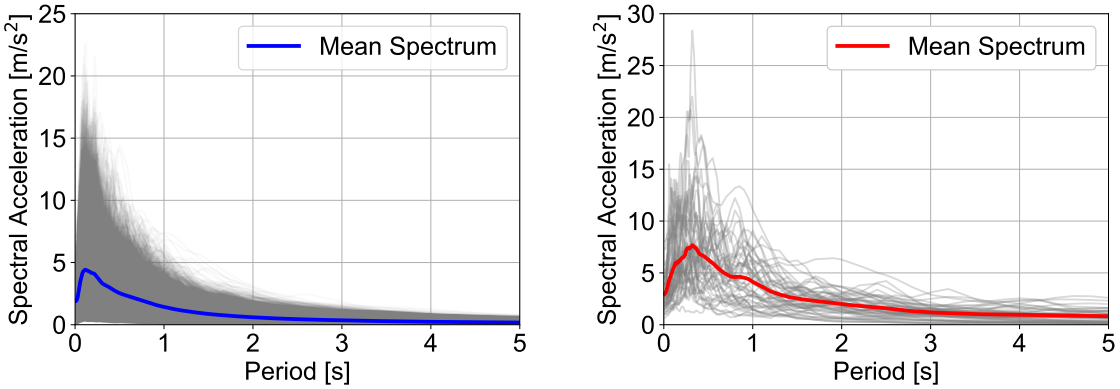


(a) Simulated records

(b) Real records

Figure 5: Spectra of the (a) simulated and (b) real ground motion dataset, along with their mean spectrum.

## 4.2 Spectrum Matching Results

Seven ground motion records were selected from the two ground motion datasets (i.e. simulated and real ones) and two-objective optimisation problems was subsequently solved where the mean and the dispersion of ground motion subset are matched to the elastic spectrum of EC8 [7]. The DEMO algorithm was adopted assuming values equal to 200, 0.6 and 0.9 for the population size, the mutation factor and the crossover probability, respectively. For both cases the parameters assumed for the target spectrum, are: peak ground acceleration $\alpha_g = 0.4g$, soil type "A", damping $\zeta = 2\%$ and importance factor $\gamma_I = 1$. Following EC8 guidelines, we have chosen a period matching range of $0.2 \sim 1.9$ s, assuming that the building's fundamental period is $T_1$ = 0.93 s. The scaling factors are allowed to vary in the range: $0.1 \sim 2$.

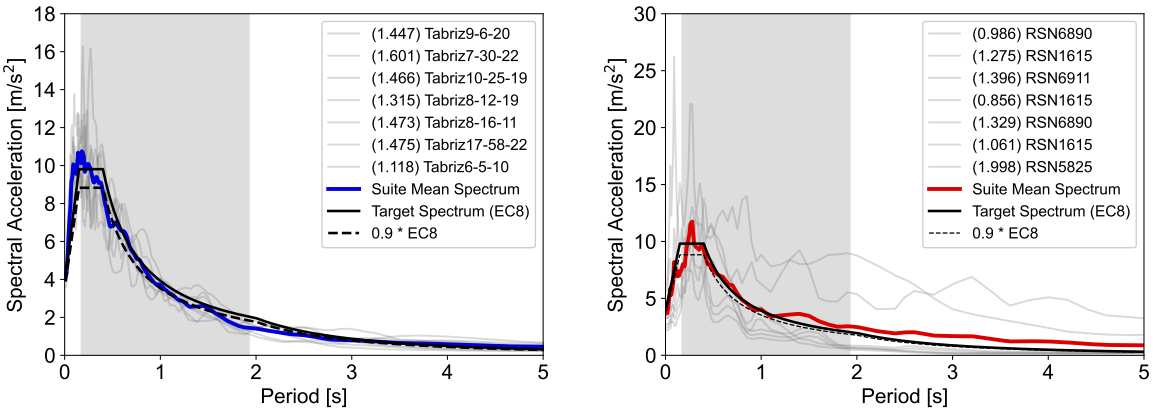


(a) Simulated records (b) Real records

Figure 6: Spectrum matching results for (a) simulated and (b) real ground motion records. In parenthesis the scale factor of each selected record.

Fig. 6 shows the Pareto front obtained after 300 DE generations for the trade-off solution of both datasets. A comparative analysis of the plots of the two datasets reveals that simulations are capable of generating consistent and evenly-distributed seismological parameters and ground motion intensity levels, in contrast to the real dataset. This underscores the effectiveness of simulated records in providing homogeneous scatteredness of seismological parameters and ground motion intensity levels.

## 5 Impact Investigation on Dynamic Response of a Steel Building

The effectiveness of the simulated motions for seismic demand evaluation of a benchmark structure is also investigated. The benchmark structure is a three-storey steel moment-resisting frame designed for a Los Angeles site and known as the "LA3 building" following the 1997 NEHRP (National Earthquake Hazard Reduction Program) provisions in the framework of the SAC/FEMA program [8]. The dynamic response of the building is dominated by the fundamental mode and has a fundamental period equal to $T_1 = 0.93$ s. All response history analyses were performed in OpenSees [23] using a force-based, beam-column fiber element with five integration sections and a material bilinear with pure kinematic hardening. Rayleigh damping is used to obtain a damping ratio of 2% for the first and the fourth mode.

Fig. 7 shows the distribution of interstorey drift demand when both $F_\mu$ and $F_\beta$ are considered (trade-off solution). The distribution clearly shows a rather small error on the mean value and excellent estimates of the dispersion of the demand when simulated ground motions are considered, compared to the real ones. The reason for this observation is the use of region-specific simulated records compared to real motions that originate from various regions worldwide, resulting in differing spectral shapes and higher dispersion compared to the target spectra. This finding further is supported also from the comparison of various intensity metrics (see Tables 2 and 3), emphasizing the usefulness of simulations in regions with a scarcity of real motions.

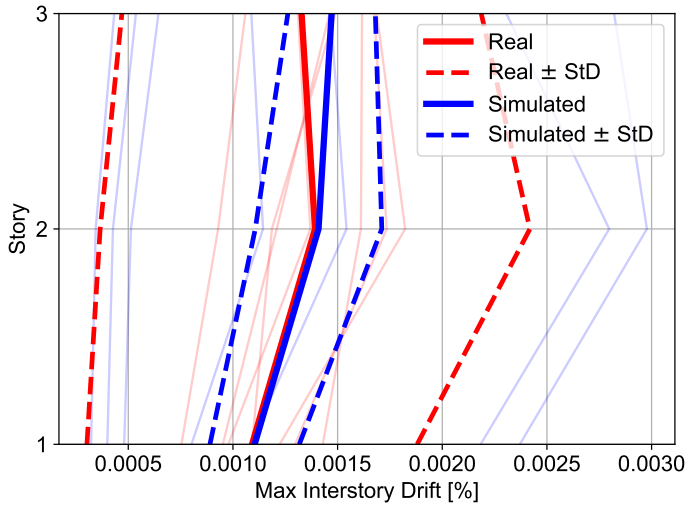


Figure 7: Interstory drifts comparison for LA3 building.

| | Record | Scaling Factor | | PGA [m/s$^2$] | PGV/PGA [s] | Sa(T1) [m/s$^2$] | Arias Intensity [m/s] |
|---|---|---|---|---|---|---|---|
| 1 | Tabriz9-6-20 | 1.447 | Unscaled | 2.867 | 0.082 | 0.874 | 2.753 |
| | | | Scaled | 4.150 | 0.082 | 1.830 | 3.985 |
| 2 | Tabriz7-30-22 | 1.601 | Unscaled | 2.789 | 0.086 | 1.037 | 2.382 |
| | | | Scaled | 4.465 | 0.086 | 2.659 | 3.814 |
| 3 | Tabriz10-25-19 | 1.466 | Unscaled | 2.422 | 0.093 | 0.606 | 3.439 |
| | | | Scaled | 3.550 | 0.093 | 1.303 | 5.040 |
| 4 | Tabriz8-12-19 | 1.315 | Unscaled | 3.336 | 0.076 | 1.631 | 2.683 |
| | | | Scaled | 4.388 | 0.076 | 2.820 | 3.529 |
| 5 | Tabriz8-16-11 | 1.473 | Unscaled | 2.771 | 0.103 | 0.923 | 2.022 |
| | | | Scaled | 4.081 | 0.103 | 2.002 | 2.979 |
| 6 | Tabriz17-58-22 | 1.475 | Unscaled | 2.770 | 0.111 | 1.985 | 2.845 |
| | | | Scaled | 4.087 | 0.111 | 4.320 | 4.197 |
| 7 | Tabriz6-5-10 | 1.118 | Unscaled | 3.619 | 0.087 | 0.802 | 3.128 |
| | | | Scaled | 4.047 | 0.087 | 1.003 | 3.499 |
| | | Mean Values | Unscaled | 2.939 | 0.091 | 1.123 | 2.750 |
| | | | Scaled | 4.110 | 0.091 | 2.277 | 3.863 |

Table 2: Intensity metrics for simulated dataset.

| | Record | Scaling Factor | | PGA [m/s$^2$] | PGV/PGA [s] | Sa(T1) [m/s$^2$] | Arias Intensity [m/s] |
|---|---|---|---|---|---|---|---|
| 1 | RSN6890_DARFIELD_CMHSS80E | 0.986 | Unscaled | 2.462 | 0.086 | 1.031 | 2.793 |
| | | | Scaled | 2.427 | 0.086 | 1.002 | 2.753 |
| 2 | RSN1615_DUZCE_1062-N | 1.275 | Unscaled | 1.166 | 0.088 | 0.202 | 0.867 |
| | | | Scaled | 1.486 | 0.088 | 0.328 | 1.106 |
| 3 | RSN6911_DARFIELD_HORCN18E | 1.396 | Unscaled | 4.414 | 0.240 | 3.195 | 6.125 |
| | | | Scaled | 6.160 | 0.240 | 6.222 | 8.548 |
| 4 | RSN1615_DUZCE_1062-N | 0.856 | Unscaled | 1.166 | 0.088 | 0.202 | 0.867 |
| | | | Scaled | 0.997 | 0.088 | 0.148 | 0.742 |
| 5 | RSN6890_DARFIELD_CMHSS80E | 1.329 | Unscaled | 2.462 | 0.086 | 1.031 | 2.793 |
| | | | Scaled | 3.273 | 0.086 | 1.823 | 3.713 |
| 6 | RSN1615_DUZCE_1062-N | 1.061 | Unscaled | 1.166 | 0.088 | 0.202 | 0.867 |
| | | | Scaled | 1.237 | 0.088 | 0.228 | 0.920 |
| 7 | RSN5825_SIERRA.MEX_GEO000 | 1.998 | Unscaled | 2.806 | 0.150 | 3.156 | 3.732 |
| | | | Scaled | 5.606 | 0.150 | 12.597 | 7.456 |
| | | Mean Values | Unscaled | 2.234 | 0.118 | 1.288 | 2.578 |
| | | | Scaled | 3.026 | 0.118 | 3.193 | 3.605 |

Table 3: Intensity metrics for real dataset.

## 6 Conclusions

- This study investigated the difference between the real and simulated motions selected according to the code design spectra.
- Two ground motion datasets (simulated and real) with consistent seismological characteristics are compiled.
- The records are selected and scaled through a multicriteria approach using the evolutionary algorithm. In this approach, the mean spectrum and the (period-depended) dispersion fit best with the target spectrum and its dispersion.
- In the context of real records, because the data is scarce, the same event records are used multiple times. However, this issue does not arise for the simulated ones.
- Variations in simulated and real record sets are assessed using several ground motion intensity metrics.
- Investigation of the effectiveness of the simulated motions for seismic demand evaluation of a three-story steel moment frame, emphasizing the usefulness of simulations in regions with a scarcity of real motions.

## ACKNOWLEDGEMENTS

This work was partly financed by FCT/MCTES through national funds (PIDDAC) under the R&D Unit Institute for Sustainability and Innovation in Structural Engineering (ISISE), under reference UIDB/04029/2020, and under the Associate Laboratory Advanced Production and Intelligent Systems ARISE under reference LA/P/0112/2020. Also, it was partly funded by the STAND4HERITAGE project that has received funding from the European Research Council (ERC) under the European Union's Horizon 2020 Research and Innovation Program (Grant Agreement No. 833123) as an Advanced Grant.

## REFERENCES


[1] S. Koboevic, K. Guilini-Charrette, P.X. Castonguay and R. Tremblay (2011). *Selection and scaling of NBCC 2005 compatible simulated ground motions for nonlinear seismic analysis of low-rise steel building structures*. Canadian Journal of Civil Engineering, **38**12.

[2] J. Fayaz, M. Dabaghi and F. Zareian. *Utilization of Site-Based Simulated Ground Motions for Hazard-Targeted Seismic Demand Estimation: Application for Ordinary Bridges in Southern California*. Journal of Bridge Engineering, **25**11, BE.1943-5592.0001634.

[3] S. Karimzadeh, K.Kadas, A. Askan and A. Yakut. *Comparison of real and simulated records using ground motion intensity measures*. Soil Dynamics and Earthquake Engineering, **147**, 106796.

[4] M. Causse, A. Laurendeau, M. Perrault, J. Douglas, L.F. Bonilla and P. Guéguen (2014). *Eurocode 8-compatible synthetic time-series as input to dynamic analysis*, Bulletin of Earthquake Engineering, **12**, pages 755—768.

[5] G. Pousse, L.F. Bonilla, F. Cotton and L. Margerin (2006). *Nonstationary stochastic simulation of strong ground motion time histories including natural variability: Application to the K-net Japanese database*. Bulletin of the Seismological Society of America, **96**(6): 2103.

[6] S. Azad, H. Philip, S. Dominguez, K. Hessami, M. Shahpasandzadeh, M. Foroutan, H. Tabassi and M. Lamothe (2015). *Paleoseismological and morphological evidence of slip rate variations along the North Tabriz fault (NW Iran)*. Tectonophysics, **640–641**, 20-–38.

[7] EN 1998-1 (2004). *Eurocode 8: Design of structures for earthquake resistance – Part 1: General rules, seismic actions and rules for buildings*. European Committee for Standardization.

[8] FEMA-355C (2000). *State of the Art Report on Systems Performance of Steel Moment Frames Subject to Earthquake Ground Shaking*. SAC Joint Venture, EMW-95-C-4770.

[9] J.J. Bommer, A.B. Acevedo (2004). *The use of real earthquake accelerograms as input to dynamic analysis*, Journal of Earthquake Engineering, 8, 43–91.

[10] D. M. Boore (1983). *Strong-motion seismology*. Reviews of Geophysics, **21**(6), 1308–1318.

[11] M. Georgioudakis and M. Fragiadakis (2020). *Selection and scaling of ground motions using multicriteria optimization*, Journal of Structural Engineering (ASCE), **146**(11), 04020241.

[12] D. Motazedian and GM. Atkinson (2005). *Stochastic finite-fault modeling based on a dynamic corner frequency*. Bulletin of the Seismological Society of America, **95**(3), 995-–1010.

[13] NIST Report GCR 11-917-15 (2011). Selecting and Scaling Earthquake Ground Motions for Performing Response-History Analyses, NEHRP Consultants Joint Venture.

[14] K. Price, R. Storn, M. Rainer and J.A. Lampinen (2005). *Differential Evolution: A Practical Approach to Global Optimization*, Springer.

[15] T. Robič and B. Filipič (2005). DEMO: Differential Evolution for Multiobjective Optimization, in *Evolutionary Multi-Criterion Optimization: Third International Conference, EMO 2005*, eds.C.A. Coello Coello, A. H. Aguirre, E. Zitzler, 520–533.

[16] K. Deb, A. Pratap, S. Agarwal, T. Meyarivan (2002). *A fast and elitist multiobjective genetic algorithm: NSGA-II*, IEEE Transactions on Evolutionary Computation, 6(2), 182–197.

[17] D. Wells and K. Coppersmith (1994). *New Empirical Relationships among Magnitude, Rupture Length, Rupture Width, Rupture Area, and Surface Displacement*. Bulletin of the Seismological Society of America, **84**, 974-1002.

[18] N. Hoveidae, A. Fathi and S. Karimzadeh (2021). *Seismic damage assessment of a historic masonry building under simulated scenario earthquakes: A case study for Arge-Tabriz.* Soil Dynamics and Earthquake Engineering, **147**:106732.

[19] D. M. Boore and G. M. Atkinson (2008). *Ground-Motion Prediction Equations for the Average Horizontal Component of PGA, PGV, and 5%-Damped PSA at Spectral Periods between 0.01 s and 10.0 s*. Earthquake Spectra, **24**(1), 99–138.

[20] S. Akkar and Z. Cagnan (2010). *A Local Ground-Motion Predictive Model for Turkey, and Its Comparison with Other Regional and Global Ground-Motion Models*. Bulletin of the Seismological Society of America, **100**(6), 2978—2995.

[21] S. Akkar, M. A. Sandıkkaya and J. J. Bommer (2013). *Empirical ground-motion models for point- and extended-source crustal earthquake scenarios in Europe and the Middle East*. Bulletin of Earthquake Engineering, **12**(1), 359-–387.

[22] Ö. Kale, S. Akkar, A. Ansari and H. Hamzehloo (2015). *A Ground-Motion Predictive Model for Iran and Turkey for Horizontal PGA, PGV, and 5% Damped Response Spectrum: Investigation of Possible Regional Effects*. Bulletin of the Seismological Society of America, **105**(2A), 963—980.

[23] S. Mazzoni, F. McKenna, M.H. Scott and G.L. Fenves (2006). *OpenSEES command language manual*, Pacific Earthquake Engineering Research (PEER) Center.

[24] Ancheta, Timothy D. and Darragh, Robert B. and Stewart, Jonathan P. and Seyhan, Emel and Silva, Walter J. and Chiou, Brian S.-J. and Wooddell, Katie E. and Graves, Robert W. and Kottke, Albert R. and Boore, David M. and Kishida, Tadahiro and Donahue, Jennifer L. *NGA-West2 Database*. Earthquake Spectra, **30**(3), 989–1005.

COMPDYN 2023
9th ECCOMAS Thematic Conference on
Computational Methods in Structural Dynamics and Earthquake Engineering
M. Papadrakakis, M. Fragiadakis (eds.)
Athens, Greece, 12-14 June 2023

# QUAKEMANAGER: A COMPREHENSIVE SOFTWARE TOOL FOR GROUND MOTION SELECTION, MODIFICATION AND ANALYSIS

**Mahmoud M. Hachem[1], Bashar M. Abdo[2], Hamza A. Al-Jundi[2], Sohaib A. Al-Jundi[2], Bahaa T. Tayba[2], Bahaa S. Ghieh[2], Yousra A. Hachem, and Khaled A. Chandab[2]**

[1] Earthquake Solutions
Tripoli, Lebanon
e-mail: mahmoud@eqsols.com

[2] Earthquake Solutions
Tripoli, Lebanon
{bashar,hamza,sohaib,bahaa,bghieh,yousra,kchandab}@eqsols.com

## Abstract

*Given the increasing usage of Response-History Analysis in the analysis and design of existing and new structures and infrastructure, ground motion records must be selected properly and adjusted to attain the best possible fit to the site-specific response spectrum. QuakeManager addresses many of the limitations of existing tools by integrating various functionalities into a single, powerful, yet simple-to-use program, allowing the selection, analysis and adjustment of ground motions to be conducted more accurately and effectively. It includes state-of-the-art methods in the ground motion science and earthquake engineering fields, as well as the two primary methods used in engineering application: Amplitude Scaling and Spectral Matching. In addition, it can perform nonlinear site response analysis and generate simulated artificial bidirectional near-fault ground motion records that can be used in earthquake simulations. QuakeManager features a customizable searchable database that allows the storage, search and analysis of records of various file formats from global databases. Additional tools allow record rotation of records to fault-normal/parallel or other orientations, computation of intensity measures, and generation of engineering reports of the ground motion selection and scaling or spectral matching of suites.*

**Keywords:** Baseline correction, Ground Motion Selection and Scaling, Spectral Matching, Site Response Analysis, Artificial Ground Motion Simulation

## 1 INTRODUCTION

The usage of ground motion data is increasing due to the continuous rise in the use of Response-History Analysis in the design and analysis of new and existing structures and infrastructure. The ground motions are required to be properly selected and modified to acquire an appropriate suite of records that provide the best possible fit to the site-specific response spectrum.

Engineers routinely expend substantial efforts in building and refining finite element models in order to ensure the highest possible accuracy, but usually pay significantly less attention to the selection, scaling and modification of the ground motion records, which can have an equal if not larger effect on the accuracy of the analysis. The selection of an appropriate suite of ground motions with the proper characteristics, that possesses the correct seismological characteristics, and mean and dispersion statistics can have a substantial impact on the accuracy and validity of the analysis results.

The QuakeManager software addresses many of the shortcomings of current software tools by integrating several functionalities in one easy-to-use program and allowing the process of ground motion selection, analysis and modification to be performed more effectively and accurately.

QuakeManager is an integrated software for the management, analysis, selection and modification of earthquake ground motions and related waveforms. The software incorporates the latest state-of-the-art techniques in the earthquake engineering field and ground motion science. QuakeManager incorporates the two primary methods used in engineering practice: Amplitude Scaling and Spectral Matching. The software consists of multiple modules that are tightly integrated within a common user-interface which allows data to flow seamlessly between modules: *QuakeSelect*, *QuakeMatch*, *QuakeSim*, *QuakeLibrary*, *QuakeSignal* (under development), and *QuakeSpec*, with other modules that are under development**.**

## 2 USER-INTERFACE

The software has a highly interactive and configurable user interface that is intuitive and easy to learn. These interactive features combined with the advanced capabilities of QuakeManager will make it easier for earthquake engineering professionals, students and researchers to search and utilize ground motion data.

Significant effort was invested in designing a graphical user interface that is modern, powerful, efficient, intuitive and easy to use. This enhanced the software capability and maximized the user productivity [1]. The user interface (Figure 1) draws on the latest developments in user-interface design, such as using moveable and resizable panes, providing the ability to browse record database information and display record histories, as well as the ability to instantly compute record properties including spectral values and intensity measures.

The workspace is fully configurable, and the various panes can be arranged and sized in a multitude of ways. Panes can be docked, floated or hidden, which maximizes space use and allows the use of multiple screens if desired (Figure 2). An emphasis was placed on visual output and immediate feedback from the user interface.

QuakeManager's ribbon guides users to browse, find and use commands efficiently. QuakeManager's ribbon allows users to discover the software features and functions faster and quickly enables learning of the software as a whole. The project pane (project tree) includes the list of commands that can be performed in QuakeManager (defining Target Spectra, Selection & Scaling, Spectral Matching…). The Ground Motion Database Library includes all the stored records in the libraries. History charts panes display the time-history charts (AVD, Acceleration, Velocity and Displacement) of one or multiple records, in addition to the Arias,

Polar chart and the geographical Mapping of the selected records. The spectra chart pane shows the various spectral quantities in various formats, or other types of spectra such as Fourier spectra and Power Spectral Density. The records view pane is at the center of the QuakeManager user interface. It displays a list of records, which can be all the records belonging to a given database collection, a filtered set of records, or the result of a selection or spectral matching. The view can be customized to remove or add columns (fields). Up to 147 different fields can be shown. This allows the user to show the fields of interest and hide all other fields in order to preserve screen space. The record properties (metadata) pane includes the properties and stored parameters of the ground motions. More than 160 fields are currently supported including a large number of automatically computed intensity measures. The "GM Search & Select" pane (Auto-Hidden by default) enables manually selecting as-recorded ground motions from the database for scaling, matching, modification and/or rotation. QuakeManager provides users a wide range of filtering criteria in which users may define, and GM Search Panel will generate all records that satisfy these criteria.

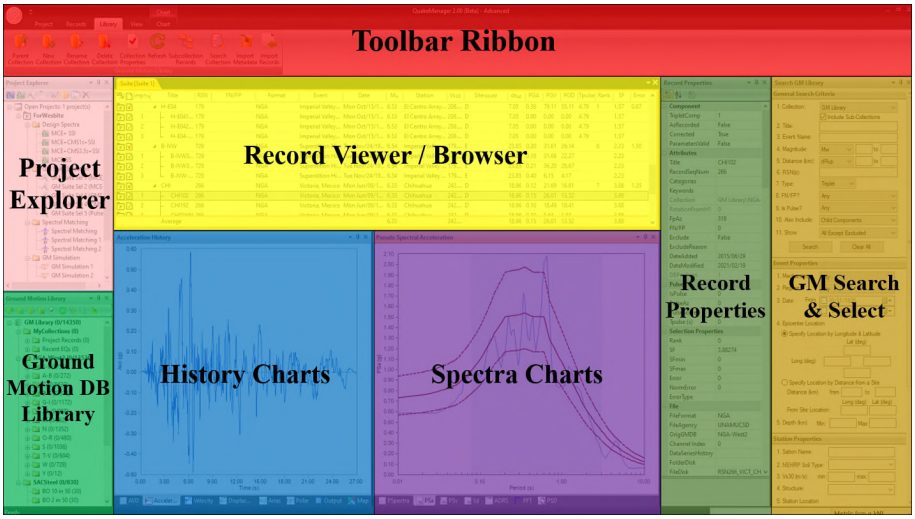


Figure 1: QuakeManager user interface

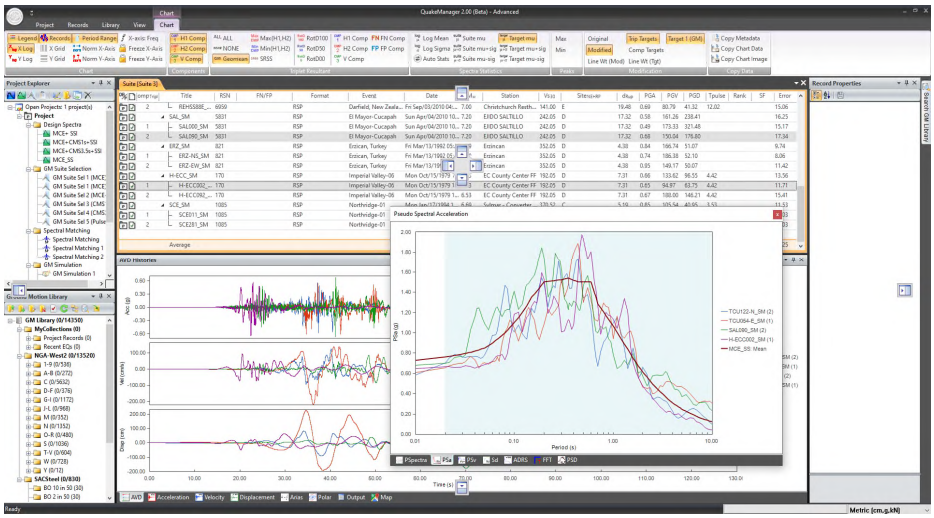

Figure 2 : Dockable user interface

QuakeManager can plot a wide range of time histories charts. The supported history charts are: AVD (Figure 3), Acceleration (Figure 4), Velocity (Figure 5), Displacement, Polar chart (Figure 6) and Arias (Figure 7). The Arias (Figure 7) chart plot the Husid plot of the recorded ground motion which reflects the variation of the cumulative ground motion input energy as a function of time. QuakeManager is also able of showing the locations of the selected records on a Google Map (Figure 8); the records can be viewed as clusters or individual markers representing the event and station of the record.

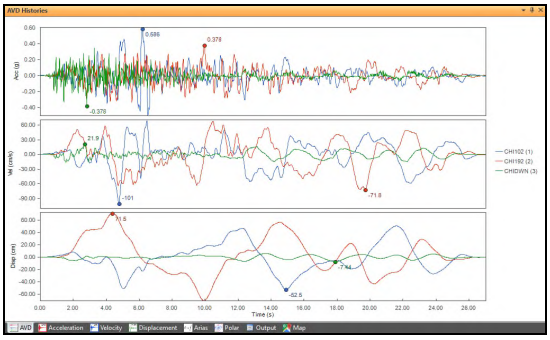

Figure 3: Acceleration-velocity-displacement time histories

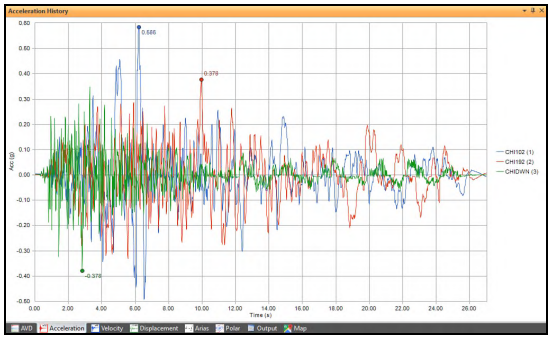

Figure 4 : Acceleration time history

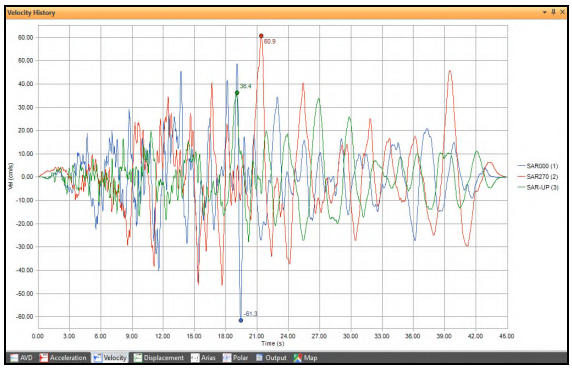

Figure 5 : Velocity time history

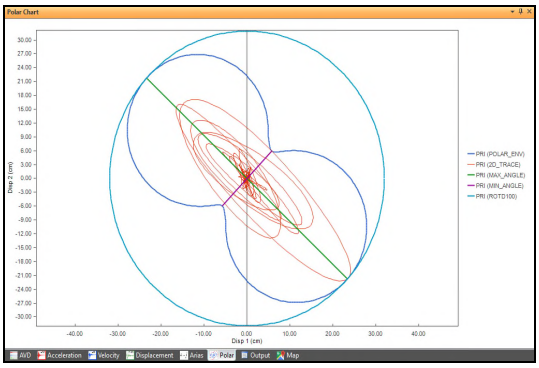

Figure 6 : Polar interaction 2D trace and Envelope

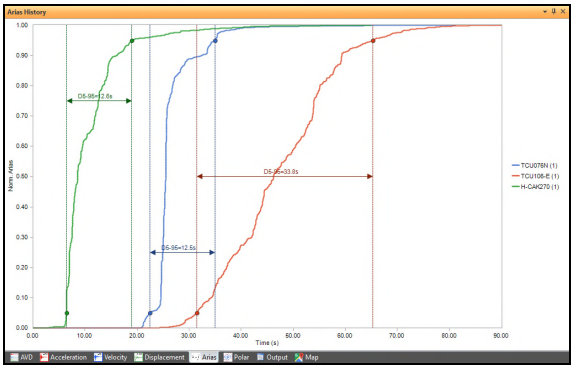

Figure 7: Husid plot (Arias Intensity) with D5-95 duration

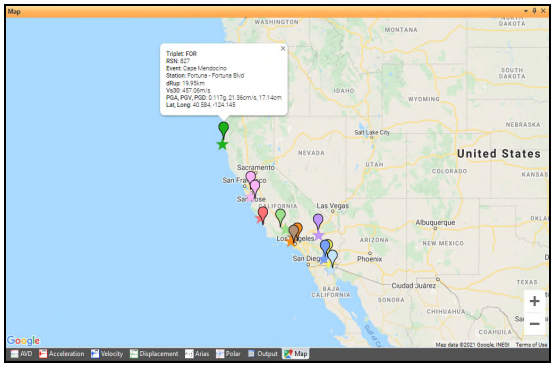

Figure 8 : Map of selected records

## 3 CODE AND USER-DEFINED DESIGN SPECTRA

The Design response spectra can be defined by the user and are typically used as Target Response Spectra for several operations within QuakeManager including selection and scaling and spectral matching of ground motions. Design spectra are used while performing ground motion search and ranking by spectral shape and when performing ground motion selection and scaling or spectral matching for suites of records or individual records.

Prior to defining the target spectrum, the user can use the Site dialog to define the site location (Street Address or Latitude/Longitude) and soil condition by site class (A, B, C…) or shear wave velocity (Vs30). QuakeManager supports two methods to define the target spectrum: Code Design Spectrum or User-Defined Spectrum.

Using the Code Design Spectrum dialog (Figure 9), the design spectrum parameters can be automatically retrieved from the USGS webs services [2] based on the defined site conditions and QuakeManager will calculate and plot the spectrum. The tool supports all codes supported by USGS including: ASCE 7-16, ASCE 7-10, ASCE 41-17, ASCE 41-13, NEHRP 2020, NEHRP 2015, NEHRP 2009 IBC 2015, IBC 2012, CBC 2019, CBC 2015, CBC 2010 and AASHTO 2009, with support for ASCE 7-22 becoming available once officially released. In addition to that, QuakeManager can develop the two-period and multi-period (NEHRP 2020 and ASCE 7-22) of MCE and DBE horizontal and vertical spectra. Spectra parameters that are downloaded include $S_S$, $S_1$, $T_L$, Fa, Fv, $S_{MS}$, $S_{M1}$, $S_{DS}$ and $S_{D1}$. QuakeManager also reads additional hazard parameters such as: risk category, PGA, seismic design category, $S_{suh}$ and others.

When the design spectrum is obtained from a site-specific probabilistic seismic hazard analysis, the User-Defined Spectrum dialog may be used in which the user can enter data directly in the table (T vs Sa), or by pasting the data which is copied from another software such as Excel. The user-defined spectrum allows the design spectral values and dispersion logSigma (optional) to be defined for each period independently. The data table and spectrum curve will update automatically when input parameters are defined or modified. Users may also select to plot to the **Standard Deviation** and **Target Mean +/- Standard Deviation** in a **Linear** or **Logarithmic** scale on the same plot (Figure 10).

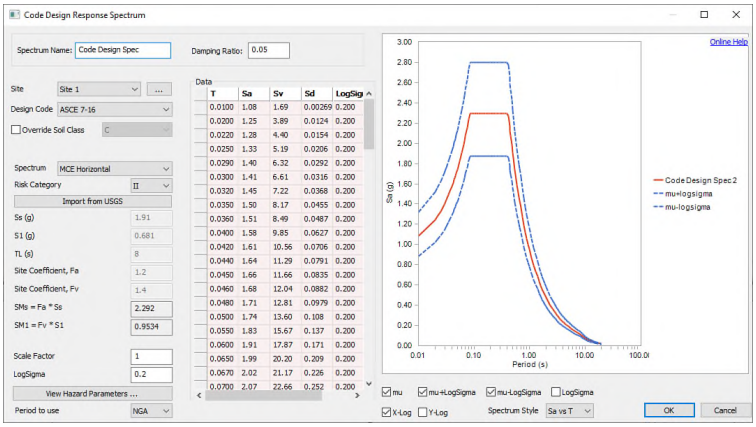


Figure 9 : Code design spectrum dialog

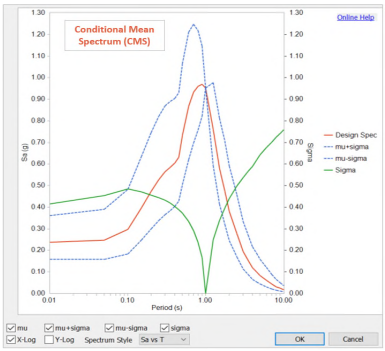


Figure 10: User-defined spectrum

## 4 QUAKEMANAGER MODULES

QuakeManager was designed as a framework that supports common functions and operations needed for the management and analysis of ground motion records. The software was fully developed in C++ under Microsoft Visual C++ [1]. The software incorporates the latest state-of-the-art techniques in the earthquake engineering field and ground motion science. The

design of the framework was conceptually and functionally separated into several modules. This has several benefits in conceptual design as well as actual software development. The software consists of multiple modules that are tightly integrated within a common user-interface which allows data to flow seamlessly between modules: QuakeSelect, QuakeMatch, QuakeSim, QuakeLibrary, QuakeSignal (under development), and QuakeSpec, with additional modules that are planned or under development.

### 4.1 QuakeSelect

The QuakeSelect module (Figure 11) provides enhanced record selection and scaling by selecting suites with optimal spectral shapes and statistics matching those of the target spectrum, while satisfying a variety of seismological, statistical, and code constraints. QuakeManager has the full capability (advanced and basic options) for ground motion selection and scaling to match the target spectrum.

The software allows scaling the records to the target-spectrum over a user-specified period range. It enables the user to define and control how the error between the records and the target spectrum is defined over the specified period range.

QuakeManager supports multiple types of selection targets including: Components (H1 component, H2 component and vertical), Bidirectional (SRSS, Geomean, RotD100, RotD50, RotD00, H1 component, H2 component, vertical component, FN component, FN component and the maximum of H1 component and H2 component) and a Custom Match. With Custom Match, QuakeManager enable defining up to three different target spectra with different matching types (RotD100, FN/FP Comp…) and fitting criteria.

The GM fitting criteria (Figure 12) allow the user to define parameters for selecting and optimizing the record selection and scale factors. In the dialog, minimum and maximum allowed scale factors may be defined. QuakeManager supports three different period range options including: Uniform Weight, Weighted Period and Weighted Frequency. The advanced options enable controlling the error types by specifying the evaluation method as Linear or Logarithmic and setting the desired error measure techniques of different spectral parameters as follows: Absolute Difference Sum, Absolute Difference Integral, Square Sum (SSE) or Square Integral. QuakeManager is capable of matching suite mean (Figure 13), suite dispersion (Standard Deviation (Figure 14) or Logarithmic Sigma) or individual records. The suite mean can be calculated arithmetically or using the geometric mean. Using the individual records feature, top records (records with smallest error) will be matched individually to the target spectrum, which is usually desired when the records will be subsequently spectrally matched. The suite scaling constraint is an additional adjustment in which the selected suite does not fall below the specified factor compared to the target spectrum. For example, if the average of the records generated in a suite may be specified to not fall below 90% of the target spectrum, which is used to satisfy the scaling requirements of some codes (e.g., ASCE 7-16 [3]).

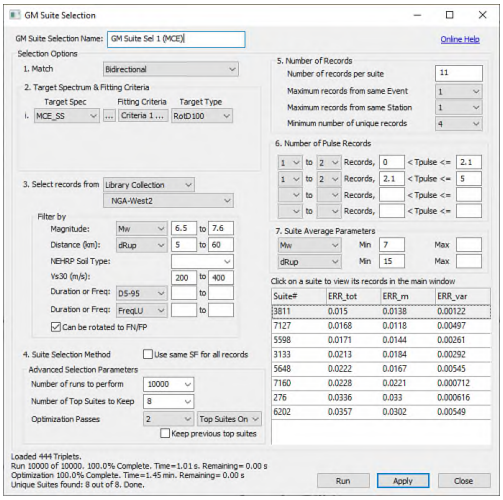


Figure 11: Ground motion selection

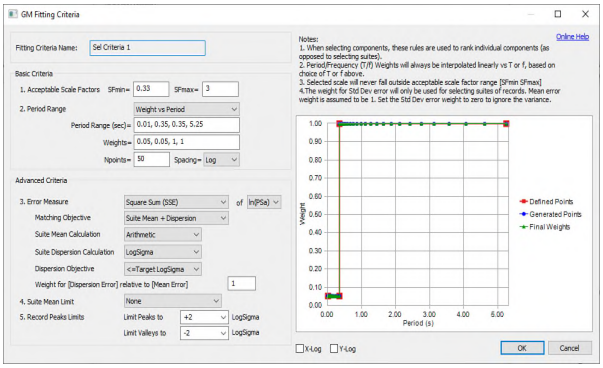


Figure 12 : Fitting criteria dialog

QuakeManager supports several record filtering options while performing ground motion selection. Filtering helps to select records that are a subset of the ground motion database that match the desirable tectonic and hazard properties of the site. Filter options include magnitude ($M_w$, $M_L$, or $M_S$, etc.), distance ($d_{epicenteral}$, $d_{hypocentral}$, $d_{rupture}$, $d_{Joyner\text{-}Boore}$…), frequency & duration ($D_{5\text{-}95}$, $D_{5\text{-}75}$, High-Pass Frequency, Low-Pass Frequency and Lowest-Usable Frequency), NEHRP Soil Class, Shear Wave Velocity (Vs30) and whether records can be rotated to FN/FP. The FN/FP rotation option will only select records that can be rotated to the fault axes. Finally, two suite target ranges can be set: Average Magnitude and Average Distance. When used, the magnitude and distance averages of the selected suite records will fall within the defined ranges.

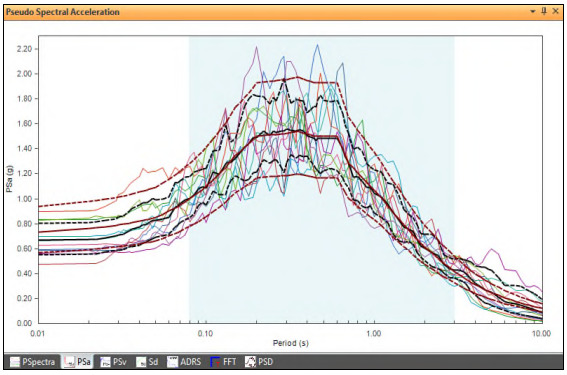


Figure 13: Ground motion selection and scaling

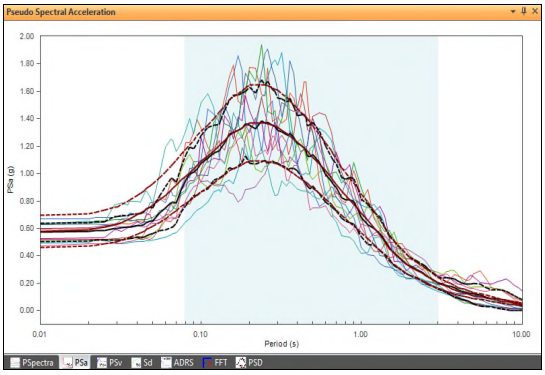


Figure 14: Ground motion selection and scaling

## 4.2 QuakeMatch

The Spectral Matching module provides the ability to modify a suite of records in order to achieve an ideal fit to the target spectrum, beyond what can be achieved by scaling alone.

QuakeMatch can perform both tight and mean spectral matching to further adjust ground motion suites for an improved fit to the target. Furthermore, the implemented mean spectral matching technique helps in maintaining record characteristics and controlling variability while meeting code requirements.

1. **Tight Matching:** This is the conventional spectral matching typically performed, where each ground motion is modified such that its spectrum perfectly matches the

target. This minimizes the potential amplification of higher modes and significantly reduces the variability in spectral ordinates (Figure 15)

2. **Mean Matching**: Is a hybrid spectral matching method, where records in the suite are each slightly modified such that the average (and optionally the dispersion) of the suite perfectly matches the target. Mean Matching preserves the peaks and valleys, characteristic period and energy content of the records (Figure 16). This method reduces the peak values of the individual spectra and hence, minimizes the amplification effects on higher modes, and is also better at preserving the natural characteristics of the records [4].

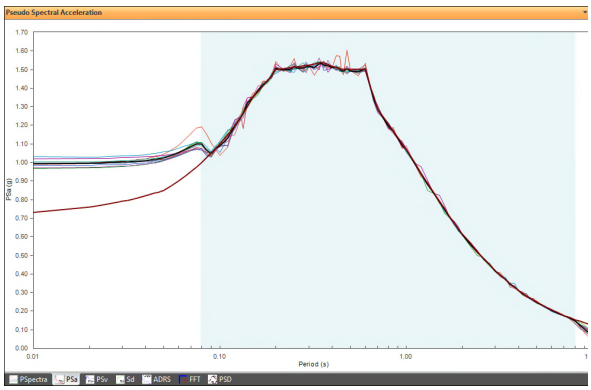


Figure 15: Tight spectral matching

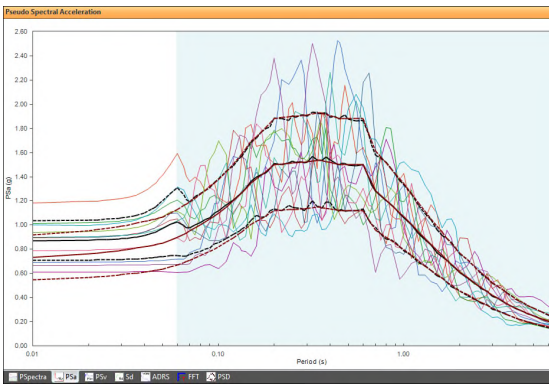


Figure 16: Mean spectral matching

The spectral matching dialog (Figure 17) is the main tool for performing spectral matching. Despite its simplicity, it offers a large number of possibilities for spectrally matching records. For example, it can match individual components as well as pairs and triplets of records. And it can be used to directly match record resultants such as SRSS, Geomean, RotD100 [5], RotD100 (approximate and exact), RotD50 (approximate and exact), and RotD100/RotD00 simultaneously, and can match all 3 components of a record including the vertical component.

The Matching Criteria (Figure 18) allows the user to control the parameters of the spectral matching including the definition of wavelet model to produce better solutions. QuakeManager enables defining period or frequency ranges that could be split into multiple matching steps, pre-scaling records at specific periods, applying additional factors and baseline correction. QuakeManager also supports different wavelet models including: Reverse Acceleration Impulse Response Function, Tapered Cosine Function and Improved Tapered Cosine Function [6].

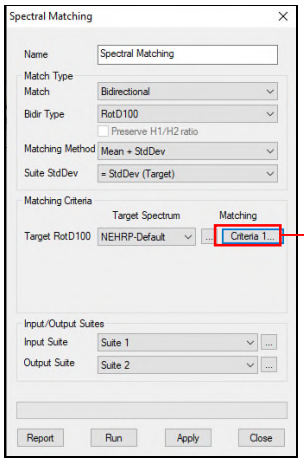


Figure 17: Spectral matching dialog

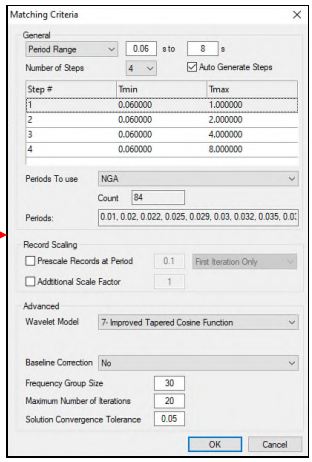


Figure 18: Matching criteria

## 4.3 QuakeSim

The QuakeSim module (Figure 19) can be used to generate simulated artificial bidirectional near-fault ground motion records that can be used in earthquake simulations (Figure 20), using a published algorithm for artificial ground motion simulation [7].

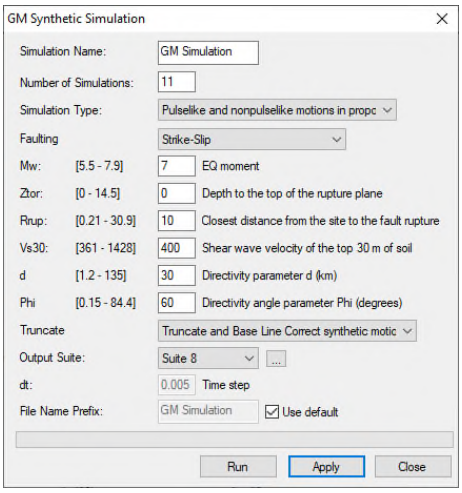


Figure 19: GM simulation Dialog

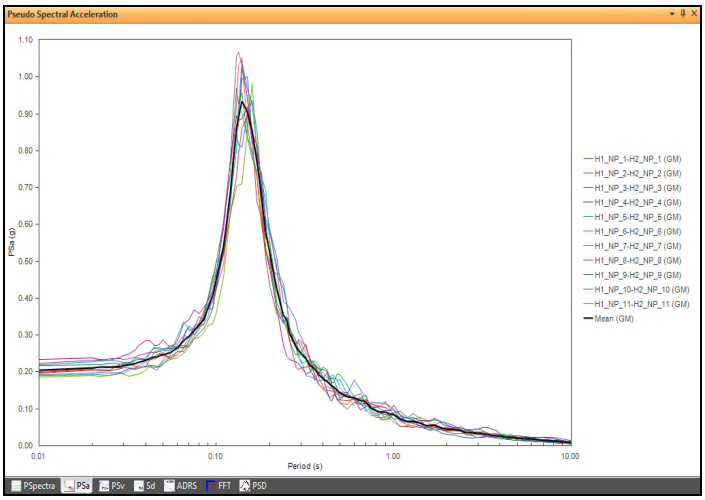


Figure 20 : GM record simulation

## 4.4 QuakeSpec

The QuakeSpec can calculate and plot a wide range of spectra including: PSa, PSv and Sd (Figure 21), Maximum and Minimum components, SRSS, Geomean, RotD100, RotD50, RotD00 (Figure 22) and FN/FP components. The spectra chart pane shows the various spectral quantities in various formats, or other analytical quantities such as Power Spectral Density and Fourier spectra (Figure 23). In addition to that, the software calculates and plots the Acceleration-Displacement Response Spectum (ADRS) as shown in Figure 24. The charts are organized in a tabbed interface to provide quick and easy switching between different chart types. They also allow comparison of multiple records. It is possible to export chart data as an image or to text format (to be pasted in spreadsheets or other software).

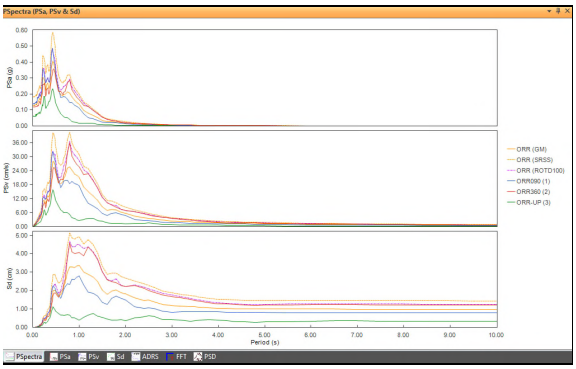

Figure 21: Pseudo spectra

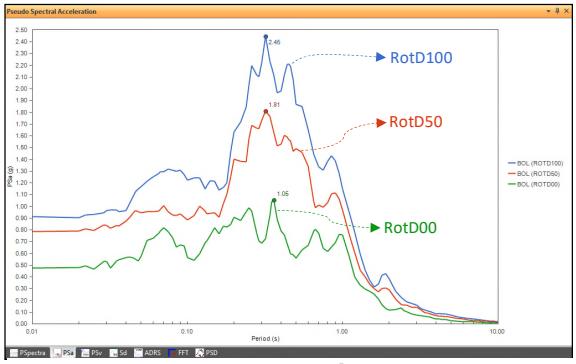


Figure 22: Rotated spectra

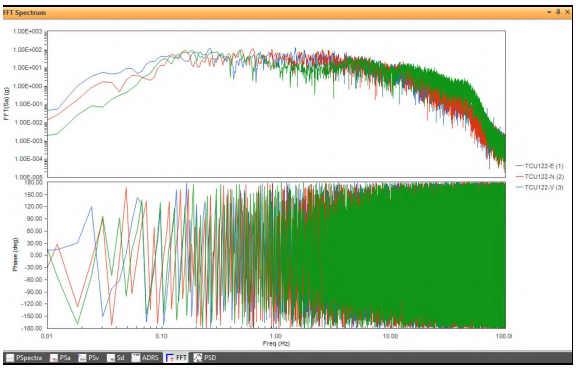

Figure 23: Fast fourier transform

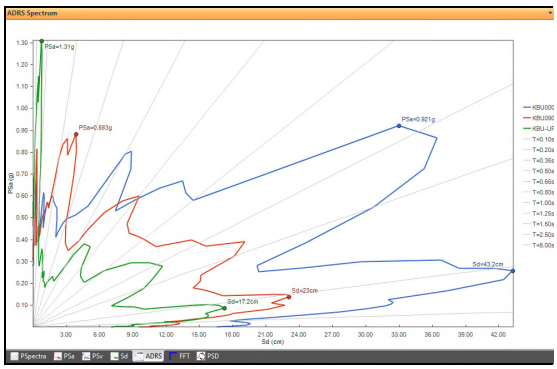

Figure 24: Acceleration-displacement response spectrum (ADRS)

## 4.5 QuakeLibrary

The QuakeLibrary module includes a massive searchable database enabling storing, searching and analyzing records with different file formats from worldwide libraries.

The Ground Motion Library is a ground motion database record manager within the user interface that provides the capability to organize, browse, and search a large number of ground motion records, both individual Components and Triplets. QuakeManager comes with pre-loaded and fully searchable ground motion databases including the metadata of NGA-West2 [8] database metadata and the SAC Steel ground motion set. The software allows users to add additional data, which can be obtained from multiple sources:

- Online ground motion databases
- Published sets of ground motions
- Simulated, user-generated, or proprietary ground motion records

The QuakeManager ground motion database includes multifaceted data as follows:

- Record metadata: which includes all the information about the event, station, time, place, etc. There could hundreds of metadata field values for each record that need to be saved, browsed, searched and imported from and to files and databases.
- The record file: this is usually a file on disk, but it could be located on a network.
- The data series (or time history): recorded data, which includes acceleration, velocity, and/or displacement. This represents the bulk of the recorded data and is extremely valuable for engineering and seismological analysis.

- Response spectra (Sa, Sv, Sd, PSa, PSv, etc): needed to perform useful engineering search, scaling, matching and other operations using the records.
- Intensity Measures: includes numerous types of intensity measures and indices intended to provide simple representations of the records damaging or shaking potential.

The software supports worldwide file formats including: USGS (SMC), PEER NGA, NRC, SAC Steel, K-Net and Kik-net, CSMIP/CGS, Chile, New Zealand, RSP Match, Generic File Format, COSMOS, NBCC, Multi-Column Format, Costa Rica and a User-Defined File Format

## 4.6 QuakeSite

The QuakeSite Module (Figure 25) is a one-dimensional site response analysis tool that can perform: nonlinear time domain analyses with and without pore water pressure generation, equivalent linear frequency domain analyses including convolution and deconvolution, linear time and frequency domain analyses convolution and deconvolution, and linear time and frequency domain analyses.

The module allows users to define the properties of the soil layers (Figure 26), including their density, stiffness, and damping characteristics. It can model nonlinear soil behavior, including hysteretic damping and strain softening, and can simulate the effects of soil liquefaction.

Below are some of the capabilities of QuakeSite Module:

1. One-dimensional (1D) site response analysis using linear and nonlinear soil models.
2. Time-domain and frequency-domain analyses to simulate seismic response.
3. Supports multiple Soil Models including GQ/H, MKZ, Yee, Linear and Points.
4. Incorporation of pore water pressure effects in the soil.
5. Visualization of results through various plots and graphs (Figure 27).

QuakeSite relies on DEEPSOIL [11] to perform analysis.

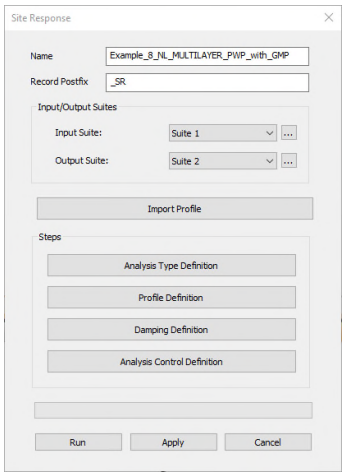


Figure 25: QuakeSite user interface

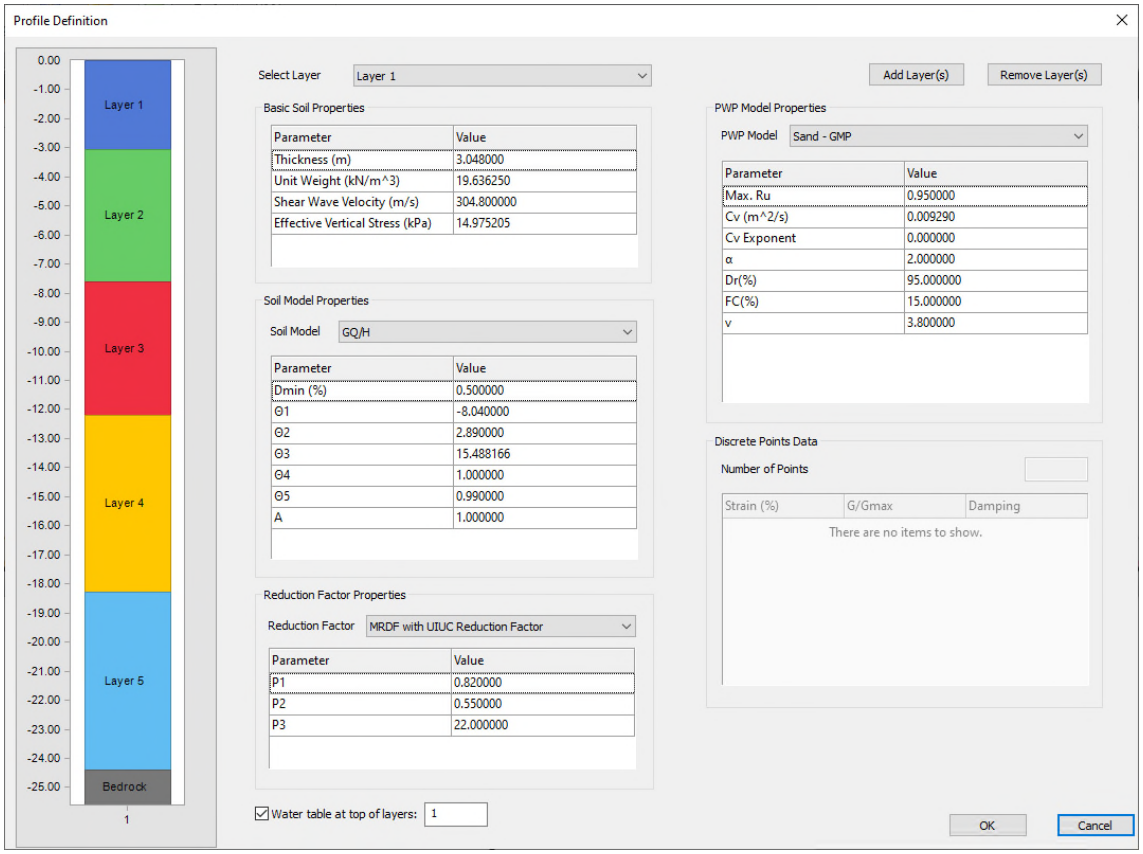


Figure 26: QuaeSite profile definition

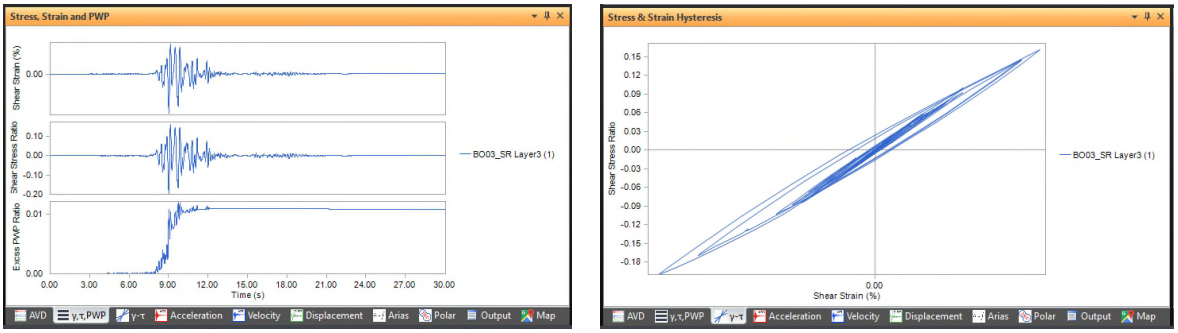


Figure 27: QuakeSite results charts

# 5 QUAKEMANAGER TOOLS

## 5.1 Ground Motion Rotation Tool

In general, it is assumed that the angle corresponding to the FN/FP directions will lead to the most critical structural response. Hence, some codes require that records be rotated to their FP/FN orientations (Figure 28) before being applied to a building, if the building is within the near-fault zone of a significant seismic fault.

Near-fault records are also likely to exhibit a pulse effect. Near-source effects cause most of the seismic energy from the rupture to arrive in a short coherent long-period pulse of motion in the FN (and/or FP) direction(s).

The Ground Motion Rotation Tool allows records to be rotated from their original as-recorded orientation to any desired orientation. Some records may also be rotated to their fault-normal (FN) and fault-parallel (FP) components, often without further input from the user. QuakeManager provides Basic and Advanced options and parameters for defining very specifically how the rotation should be performed and allows for scale the records. This feature guides users to search and compute the near-fault and pulse records. The software enables rotating a record or multiple records in a suite. The basic options allow scaling and rotating the records by a specific angle, rotate to FN, rotate to FP, rotate to FN plus an additional angle to account for building orientation or rotate to the record Azimuth.




Figure 28: Ground motion rotation example to FN/FP

## 5.2 Intensity Measures

There are numerous intensity measures that can be used to represent the shaking intensity and damage potential of a ground motion record. The variation of these values depends mainly on the distance of the fault rupture area, due to the distribution across the geographical area from the epicenter. Other parameters that contribute to the variation of the Intensity Measure is the rupture direction and surface geology. QuakeManager has the capability of computing various ground motion parameters (intensity measures). These measures are usually computed from the acceleration, velocity or displacement history, but some are related to the ground motion spectrum (acceleration, velocity, displacement), or other related quantities such as the PSD (Power Spectral Density), etc. QuakeManager can compute a large number (30+) of intensity measures like PGA (peak ground acceleration), PGV, PGD, RMSa (Root-Mean-Square Acceleration), EPA (effective peak acceleration - average spectral acceleration over the period range 0.1 to 0.5 sec divided by 2.5), SPA (sustained peak acceleration - third highest absolute value of the acceleration in the time history) [9], IV (Incremental Velocity), CAV (cumulative absolute velocity), Arias intensity, duration measures, cross-correlations of acceleration components, etc. Duration measures include $D_{5\text{-}75}$ and $D_{5\text{-}95}$ representing the Arias duration and $D_{b5PcG}$ corresponding to the bracketed duration of accelerations over 5%g [9].

## 5.3 Report Generator

The Report Generator tool generates engineering reports of the ground motion selection and scaling or spectral matching of suites. The Report Generator extracts all the output data and automatically generates a complete MS-Word report for the selected records. Users can

easily navigate through the report, make adjustments and save the report. Users may also select and define the data tables and figures to retrieve and have the ability to choose various display options. This is a tremendous time saver when generating long reports (Figure 29).

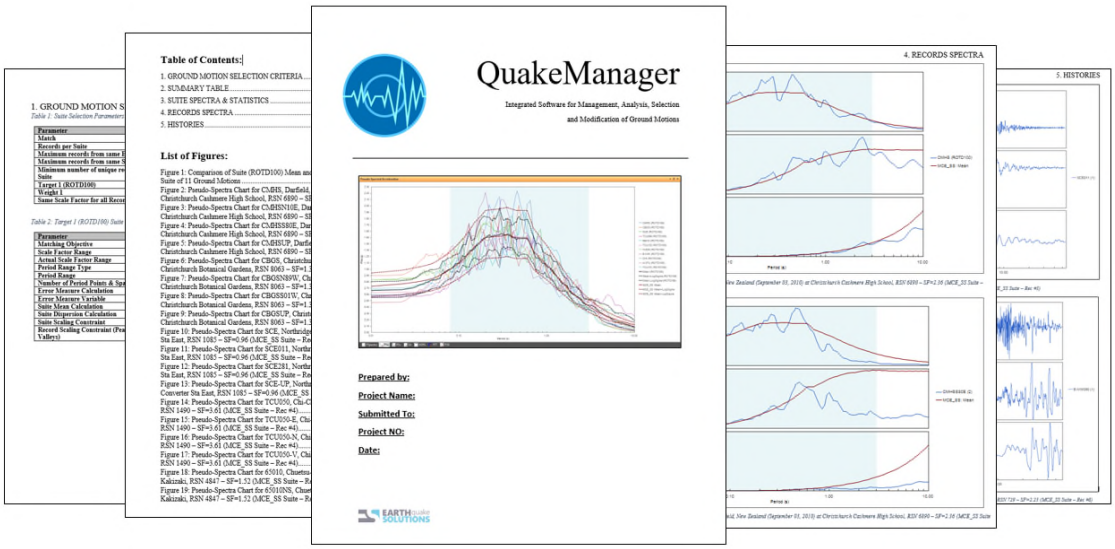


Figure 29: Sample generated report

## 5.4 Import Tool

The QuakeManager supports multiple methods to import records to the GM Library or the suite including:

- Drag and Drop
- Import from CSV
- QuakeManager Import Tool

The QuakeManager Import Tool enables importing records from a local source on the disk. The tool imports unlimited number of records and QuakeManager automatically detects the correct record file format if not specified. In case the record file format was not identified, QuakeManager, provides helpful debugging information for files that do not match the any of the file formats.

In the "Drag & Drop" method, the files are dragged from a folder on the computer disk into a collection in the Ground Motion Library. QuakeManager then checks all the files for a valid ground motion format and imports the valid ones to the database. If the record has header information, metadata is extracted and stored in the database.

In the "Import from csv" method, the user prepares a csv file that defines the metadata of each record and specifies the file disk location for each record (which contains the acceleration history data). This method can require more work but allows a large number of metadata to be imported for each record (e.g., from a flat file). Note that the acceleration history is not included in the csv, but only record properties.

## 5.5 Pulse Calculation Tool

Ground motions with significant velocity pulses are of particular importance to structural engineers because they can place greater demands on structures than non-pulse-like ground motions. The pulse calculation tool calculates up to 5 different pulses for a triplet and allows the user to select the most appropriate pulse. Once the desired pulse is selected, the user can

plot the time histories and the spectra of 1) The pulse, 2) The record rotated to the pulse direction, and 3) The residual. The pulse calculation is based on the algorithm presented in Shahi and Baker [10].

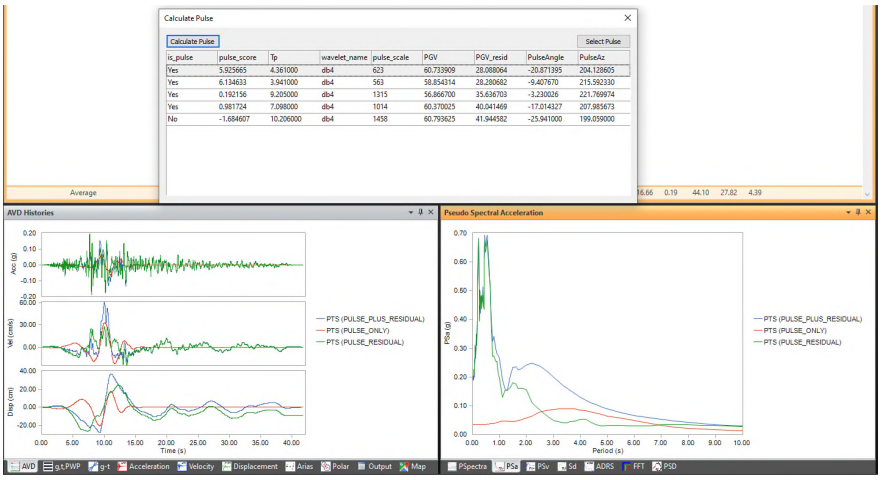


Figure 30: Time histories and spectra of the pulse, pulse direction and residual

## 5.6 Baseline Correction Tool

The baseline correction tool is required for some time series to correct the resulting drift in the velocity and displacement time series. This is done by doing a least square fitting of a polynomial of the specified order (from 0 to 15) on the acceleration time history and subtracting it from the original acceleration.

# 6 CONCLUSION

The QuakeManager is an integrated software for the management, selection, modification and analysis of ground motion records. The software incorporates the latest state-of-the-art techniques in the earthquake engineering field and ground motion science. QuakeManager incorporates the two primary methods used in engineering practice: Amplitude Scaling and Spectral Matching. The software consists of multiple modules that are tightly integrated within a common user-interface which allows data to flow seamlessly between modules: QuakeSelect, QuakeMatch, QuakeSim, QuakeLibrary, QuakeSignal (under development), and QuakeSpec, with other modules that are under development.

This software introduces an integrated and dynamic approach for using ground motion records that increases productivity and provides new capabilities that are not available in other ground motion analysis software. The major infrastructure and user interface components have been developed, and development is continuing on additional record modification and analysis features.

The usage of ground motion data is increasing due to the continuous rise in the use of Response-History Analysis in the design and analysis of new and existing structures and infrastructure. Engineers may expend efforts in the selection, scaling and modification of the ground motion records as they can largely affect the accuracy of the analyses and models. The selection of an appropriate suite of ground motions with the proper characteristics, that possesses the correct seismological characteristics, mean and dispersion statistics can have a substantial impact on the accuracy and validity of the analysis results.

## REFERENCES

[1] M. Hachem: QuakeManager: A Software Framework for Ground Motion Record Management, Selection, Analysis and Modification, *14WCEE Beijing, 2008*..

[2] Seismic Design Web Service Documentation (Beta), United States Geological Survey, [Online]. Available: https://earthquake.usgs.gov/ws/designmaps/.

[3] ASCE, ASCE 7-16 Minimum Design Loads for Buildings and Other Sturtures, 2016.

[4] S. Mazzoni, M. Hachem, M. Sinclair: An Improved Approach for Ground Motion Suite Selection and Modification for Use in Response History Analysis, *15WCEE Lisbon, 2012*.

[5] D. Grant: Response Spectral Matching of Two Horizontal Ground-Motion Components, *Journal of Structural Engineering © ASCE*, vol. 137, nº 3, p. 9, 2011.

[6] L. Attik, N. Abrahamson: An Improved Method for Nonstationary Spectral Matching, *Earthquake Spectra*, vol. 26, nº 3, p. 17, 2010.

[7] M. Dabaghi, A. Der Kiureghian: Simulation of orthogonal horizontal components of near- fault ground motion for specified earthquake source and site characteristics, *International Association for Earthquake Engineering*, vol. 47, nº 6, p. 25, 2018.

[8] PEER Ground Motion Database. [Online]. Available: https://ngawest2.berkeley.edu/.

[9] S. Kramer: *Geotechnical Earthquake Engineering*, Prentice Hall

[10] Shahi, Shrey & Baker, Jack.. An Efficient Algorithm to Identify Strong-Velocity Pulses in Multicomponent Ground Motions. Bulletin of the Seismological Society of America. 104. 2456-2466. 10.1785/0120130191, 2014.

[11] Hashash, Y.M.A., Musgrove, M.I., Harmon, J.A., Ilhan, O., Xing, G., Numanoglu, O., Groholski, D.R., Phillips, C.A., and Park, D. 2020 “DEEPSOIL 7.0, User Manual”. Urbana, IL, Board of Trustees of University of Illinois at Urbana-Champaign, 2020

COMPDYN 2023
9th ECCOMAS Thematic Conference on
Computational Methods in Structural Dynamics and Earthquake Engineering
M. Papadrakakis, M. Fragiadakis (eds.)
Athens, Greece, 12-14 June 2023

# SCALING GROUND MOTION RECORDS BY CONSIDERING THE INELASTIC RESPONSE OF SOILS

Yeudy F. Vargas-Alzate [(1)], Ana M. Zapata-Franco [(2)], Rodolfo J. Tirado[(3)], Ramón González-Drigo[(4)], and Jean Vaunat[(5)]

[(1)] *Adjunct professor, Universitat Politècnica de Catalunya, yeudy.felipe.vargas@upc.edu*
[(2)] *PhD Student, Universitat Politècnica de Catalunya, ana.maria.zapata@upc.edu*
[(3)] *PhD Student, Universitat Politècnica de Catalunya, rodolfo.javier.tirado@upc.edu*
[(4)] *Full professor, Universitat Politècnica de Catalunya, jose.ramon.gonzalez@upc.edu*
[(5)] *Full professor, Universitat Politècnica de Catalunya, jean.vaunat@upc.edu*

## Abstract

*One of the main shortcomings of several seismic databases is the lack of ground motion records exhibiting high-intensity values. Consequently, when characterizing seismic risk, or in the design process of a civil infrastructure, it is generally necessary to scale up a significant amount of low-intensity records so that the nonlinear response of the analyzed system can be fully explored. However, this type of records does not reflect neither the stiffness degradation nor the increasing of damping in soils affected by high-intensity ground motions. This paper presents an innovative approach for scaling seismic records by taking into account both effects. To do so, the equivalent linear method has been employed in an iterative manner to scale up and get records meeting these important conditions. A database from Colombia containing almost two-thousand ground motion records has been used to characterize the seismic hazard. Results show that low-amplitude records scaled following the presented approach exhibit an increase of intensities at certain periods, which is consistent with the one observed in actual high-intensity ground motion records. In addition, the inelastic response of the soil tends to modify the expected risk, showing that scaling using constant values can produce biased results. It has been observed after comparing fragility functions derived for records scaled using a single scalar vs those considering the inelastic response of the soil.*

**Keywords:** Scaling ground motion records, Stiffness degradation, Damping Increase, Equivalent linear method

## 1 INTRODUCTION

In places of high seismic risk, and depending on the complexity (or importance) of a civil infrastructure, it is recommended to analyze its dynamic interaction with the ground through the use of advanced nonlinear models. There are several ways to model this interaction depending on the type of foundation [1]. Yet, in most cases, it is necessary to develop a set of signals that act at the base of a soil model, below which elastic rebound theory is expected to apply [2]. These signals should be recorded on a hard rock site for the last assumption to hold. Therefore, a key aspect of the study of seismic risk is the characterization of the dynamic response of the soil profile [3]. In this respect, it is common practice to use simplified 1D soil models to extensive 3D finite-element-method-based representations [4]. However, the higher the complexity of the model the higher the computational time involved in solving dynamic problems. In order to tackle this computational effort, more simplified soil models are widely used. One of the most employed is the 1D model, in which the soil layers are modeled as Kelvin–Voigt solids [5]. This model is represented by a purely viscous damper and purely elastic spring connected in parallel. In several cases, it allows a good approximation of the dynamic response of a soil mass. Moreover, this model has been extended to consider no-linearities associated to the loss of stiffness of the soil and the consequent increase in damping due to shear strains [6].

In line with the above, the frequency content of the ground motions at the surface produced by earthquakes depends on several complex phenomena like the type of rupture, the proximity to the epicenter and depth, and the mechanical properties of the media traversed by seismic waves. Regarding this latter, depending on the depth, seismic waves may degrade the stiffness of the media at very low shear strains [7]; the deeper, the less stiffness degradation. Therefore, in each location, there is a depth limit in which one could consider the stiffness degradation, and the consequent increase of damping, do not occur. Hence, close to the surface, and depending on the seismic intensity [8] and soil type, it is expected a significant degradation of the soil properties. This effect should be included when scaling the same ground motion record to several intensity values.

There are several methodologies to scale ground motions from a database. Typically, the goal is to find a significant set of records leading the structure to multiple performance levels. However, as indicated by the well-known Richter's law, the number of high-intensity ground motion records is much smaller than the number of low-intensity ones. Consequently, it is sometimes necessary to scale low intensity records by significantly high factors. In doing so, it has to be considered that some types of soil modify their dynamic properties at very low shear strains. Therefore, scaling a single record to increased intensity values may not take into account the likely inelastic response of soils. Accordingly, in this article is compared results stemming from two type of scaling methods: i) scale the entire ground motion record using a single scalar; ii) scale the record by considering the inelastic response of the ground, which implies an elongation of the fundamental period of the soil mass. To do so, a 5-storey reinforced concrete building has been used as a case of study. It has been assumed that this structure rests on a specific soil profile, which propagates seismic waves from the bedrock to the surface by considering the equivalent linear method. The resulting seismic waves at the surface are used to perform several nonlinear dynamic analyses of the structure. A database that collects almost two-thousand ground motion records acquired in Colombia has been used to characterize the seismic hazard. Finally, fragility functions based on both scaling approaches are derived and compared. This comparison indicates a non-negligible difference in the expected probabilities of damage.

## 2 MODELLING CONSIDERATIONS

### 2.1 Soil model

There are several ways to model the dynamic response of the soil beneath a structure [9]. The most appropriate way to do it depends to a large extent on the type of soil to be analyzed. In this article, the soil mass has been considered as a cohesionless soil, whose physical properties at very low shear strains are summarized in Table 1. This soil profile is thirty meters deep and it has been divided into eight different layers. Figure 1 shows the evolution with depth of the soil properties at very low shear strains.

Numerically, site response analysis based on 1D models can be performed using linear, equivalent linear and nonlinear methodologies. Amongst these three methodologies, equivalent linear is widely followed because of its simplicity and reasonable accuracy with respect to nonlinear-based results. This methodology has been used herein to assess the stiffness degradation and the consequent increasing of damping of the soil profile.

At present, there are numerous softwares and codes which can perform site response analysis following 1D models. In this article, the waveprop program has been used as solver to develop the iterative procedure related to the equivalent linear method [10].

| Width (m) | Vs (m/s) | ρ (kg/m$^3$) | ξ |
|---|---|---|---|
| 2.5 | 430 | 1947 | 0.037 |
| 3.5 | 515 | 1947 | 0.036 |
| 4.5 | 600 | 1947 | 0.035 |
| 3.0 | 655 | 2446.5 | 0.035 |
| 5.5 | 805 | 2446.5 | 0.034 |
| 4.5 | 1005 | 2446.5 | 0.033 |
| 3.0 | 1260 | 2446.5 | 0.033 |
| 3.5 | 1550 | 2446.5 | 0.032 |

Table 1 Soil properties at very low shear strains

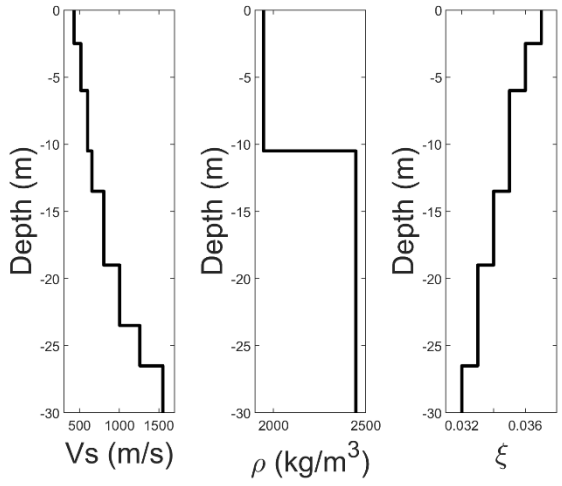


Figure 1 Scheme of the soil profile properties

## 2.2 Building model

As a case study, the five-story reinforced concrete building shown in Figure 2 has been analyzed. Table 2 summarizes the details of the main properties of its structural elements. This building rests on a soil profile whose dynamic properties at very low shear strains are the ones shown in Table 1. Thus, it has been assumed that seismic waves act at the top of the bedrock level (see Figure 2), from which elastic and inelastic propagations have been made towards the surface. Then, the resulting seismic waves have been used as input to perform structural calculations with the building model.

The modified Takeda hysteresis law, [11] has been used to represent the in-cycle behavior of the structural elements (beams and columns). This law allows considering strength degradation due to large deformations and excessive number of inelastic cycles. To do so, a strength degradation function, which depends on the ductility reached by the structural elements, as well as a degrading coefficient associated to the number of inelastic cycles has been considered in the hysteretic model [12]. For stiffness degradation, the degrading factor has been fixed to 0.4. The yielding surfaces are defined by the bending moment-axial load interaction diagram for columns and bending moment–curvature for beams. P-Delta effects has been considered in the numerical model, as the structure analyzed may experience deformations beyond the elastic range, sometimes exceeding their capacity to withstand gravity loads. The Ruaumoko software has been employed to perform the structural calculations [12].

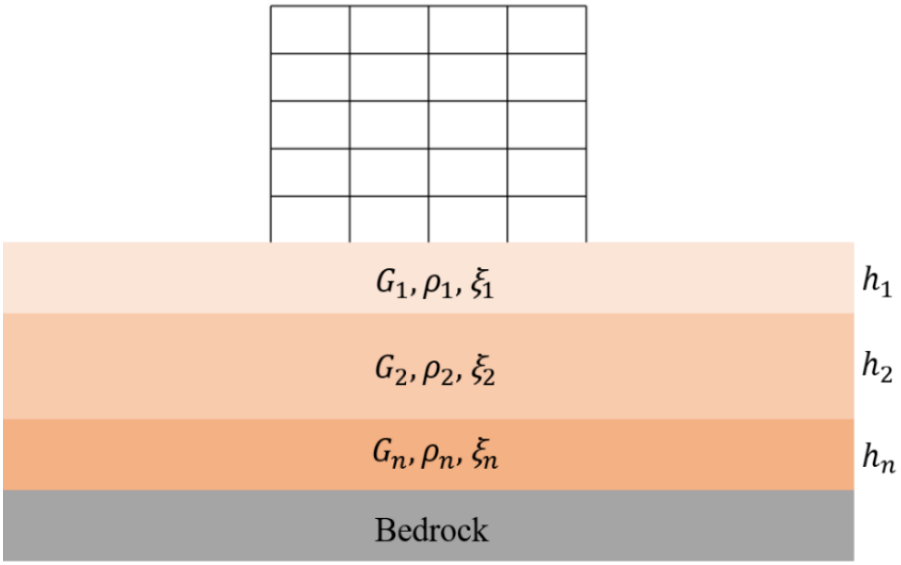


Figure 2 Soil and structural model

| Story | $W_c$ (m) | $B_c$ (m) | $W_b$ (m) | $D_b$ (m) | $\rho_c$ (%) | $\rho_b$ (%) |
|---|---|---|---|---|---|---|
| 1 | 0.55 | 0.55 | 0.30 | 0.40 | 1.5 | 0.66 |
| 2 | 0.55 | 0.55 | 0.30 | 0.40 | 1.5 | 0.66 |
| 3 | 0.50 | 0.50 | 0.30 | 0.40 | 1.5 | 0.66 |
| 4 | 0.50 | 0.50 | 0.30 | 0.40 | 1.5 | 0.66 |
| 5 | 0.45 | 0.45 | 0.30 | 0.40 | 1.5 | 0.66 |

Table 2 Characteristic of the structural elements. $W_c$ and $B_c$ represent the size of the columns; $W_b$ and $B_b$ represent the size of the beams; $\rho_c$ and $\rho_b$ represent the steel percentages of columns and beams, respectively

## 3 SEISMIC HAZARD

A compilation has been made of the ground motions recorded in Colombia between 1993 and 2017, with a magnitude greater than 4.0 Mw. These records have been extracted from the SGC [13]. They have been divided into two groups according to the ground conditions in which they were acquired. The first one corresponds to signals recorded on bedrock, from which a total of 1236 records were identified. The second group are signals recorded on less rigid ground, with a total of 756 records. Figure 3 shows the geometric mean of the horizontal spectra of these ground motion records. With the exception of a couple of ground motion records, this figure shows that the ground motions recorded in soils tend to provide increased spectral ordinates when compared to the ones acquired in rock. This can be easily seen by comparing some percentiles of both sets. Thus, Figure 4 compares percentiles 50th and 95th for records acquired in rock and soil. Two main conclusions can be drawn from this figure: i) Records acquired in soil provide higher spectral ordinates than the ones in rock; ii) the higher the intensity, the higher the response at higher period values. The latter can be seen in the 95th percentile figure, where two peaks appear in the soil spectrum. The one on the right side is likely to appear due to expected stiffness degradation for higher intensity values. It demonstrates the importance of accounting for this effect in the scaling process.

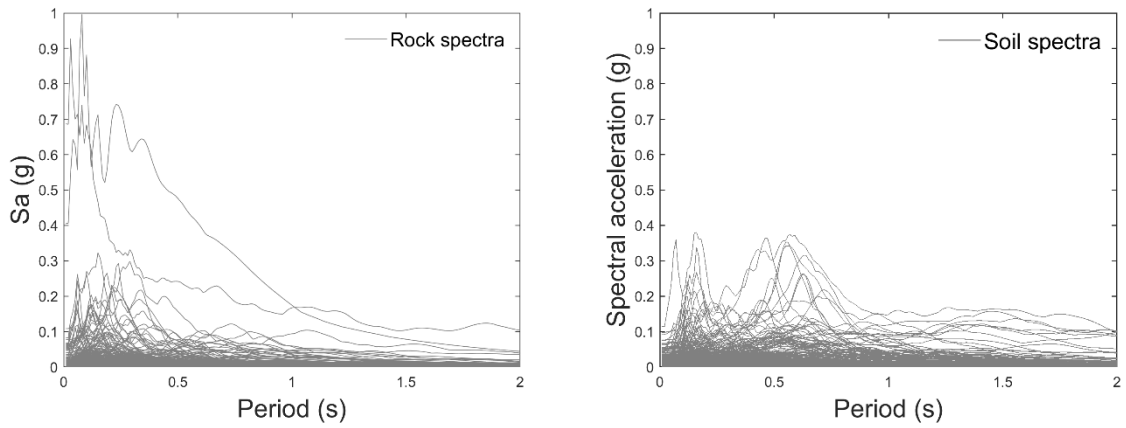


Figure 3 Geometric Mean Spectra of the horizontal components (Left: Rock Right: Soil)

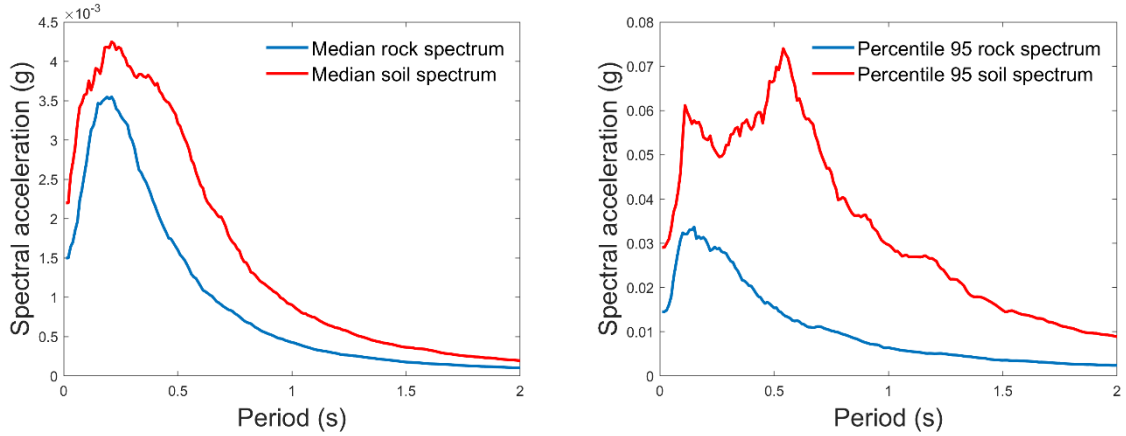


Figure 4 Median (Left) and percentile 95 (Right) of the entire set of spectra

From this database, one of the horizontal components of 20 ground motion records acquired in rock have been selected. These records have been used to analyze the influence of scaling, considering or not the effect of stiffness degradation.

## 4 EQUIVALENT LINEAR METHOD

The propagation of the seismic waves produces the degradation of the soil stiffness and, consequently, the increase of the material damping in each layer. These changes depend on the maximum shear strain reached during a seismic event. There are several methods to consider this modification of the physical properties of the soil in the seismic analysis. One of the most used is the linear equivalent method. This method consists in estimating, from iterative linear approximations, the physical properties of a modified soil profile, whose elastic dynamic response is similar to that obtained via nonlinear dynamic analysis. These calculations are performed in the frequency domain, which substantially reduces the computational effort.

In the equivalent linear method, the degradation of the stiffness, and the consequent increase in the damping of the material in each layer, are considered using the normalized shear modulus (G/Gmax) and hysteretic damping curves; both as a function of the maximum shear strain reached during the dynamic process. For the case of study, these reference curves have been selected from the EPRI report for a cohesionless soil [14]. Figure 5 shows the stiffness degradation and damping curves used in this study.

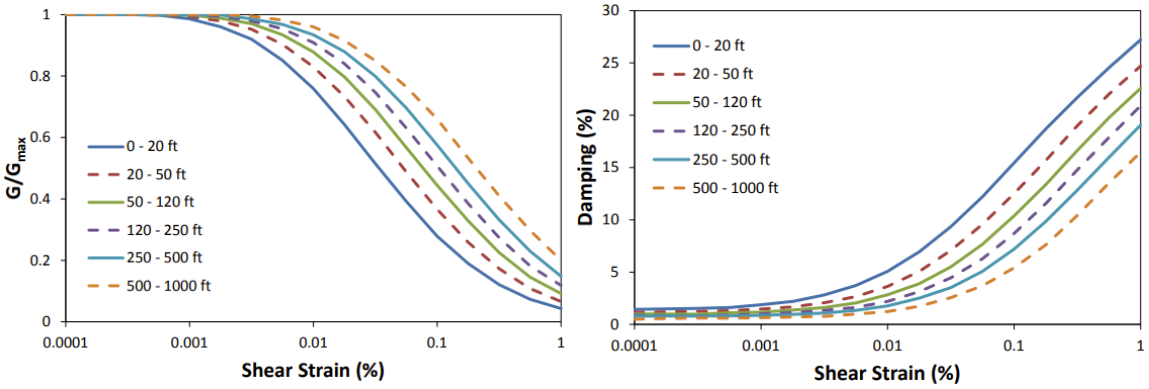


Figure 5 G/Gmax and hysteretic damping as a function of the shear strain for a cohesionless soil, [14]

In the following, the iterative process associated with the equivalent linear approximation is described step by step:

1. Initially, each soil layer is modeled considering values of stiffness ($G_0$) and damping ($\zeta_0$) corresponding to very low shear strains (<10-3) (see Table 1)
2. From the properties described in the previous step, the history of shear strains in each soil layer is calculated, $\gamma(t)$
3. From the maximum strain reached during the propagation, $\gamma_{max} = \max(|\gamma(t)|)$, the effective strain in each layer is estimated as $\gamma_{eff} = \alpha * \gamma_{max}$; in this research $\alpha$ =0.65
4. For each layer, a new pair of $G_i$ and $\zeta_i$ values is obtained from the degrading curves for stiffness and damping (see Figure 5)
5. Steps 2 to 4 are repeated until the difference between two consecutive values of $G_i$ and $\zeta_i$ are less than 1%
6. From the final values of $G$ and $\zeta$, for each soil layer, a linear site response analysis can be performed

This procedure has been used to estimate the nonlinear response of the soil profile shown in Figure 1 in front of a set of linear scaled versions of the 20 ground motion records selected from the Colombian database. That is, each ground motion record has been scaled so that an intensity measured identified as AvSv [15] ranges from 0.02 m/s, at intervals of 0.02 m/s, until reaching a value equal to 1 m/s. Figure 6 shows the resulting spectra of the ground motion at the surface

after applying the equivalent linear method. The spectra of records whose AvSv value is equal to 0.2 m/s have been included in order to show the elongation of the fundamental period of the soil profile for higher intensity values. It can be seen that depending on the ground motion record, the stiffness degradation is variable. Anyhow, the increased response at elongated periods observed in Figure 6 is consistent with that of the real records (see Figure 4, left).

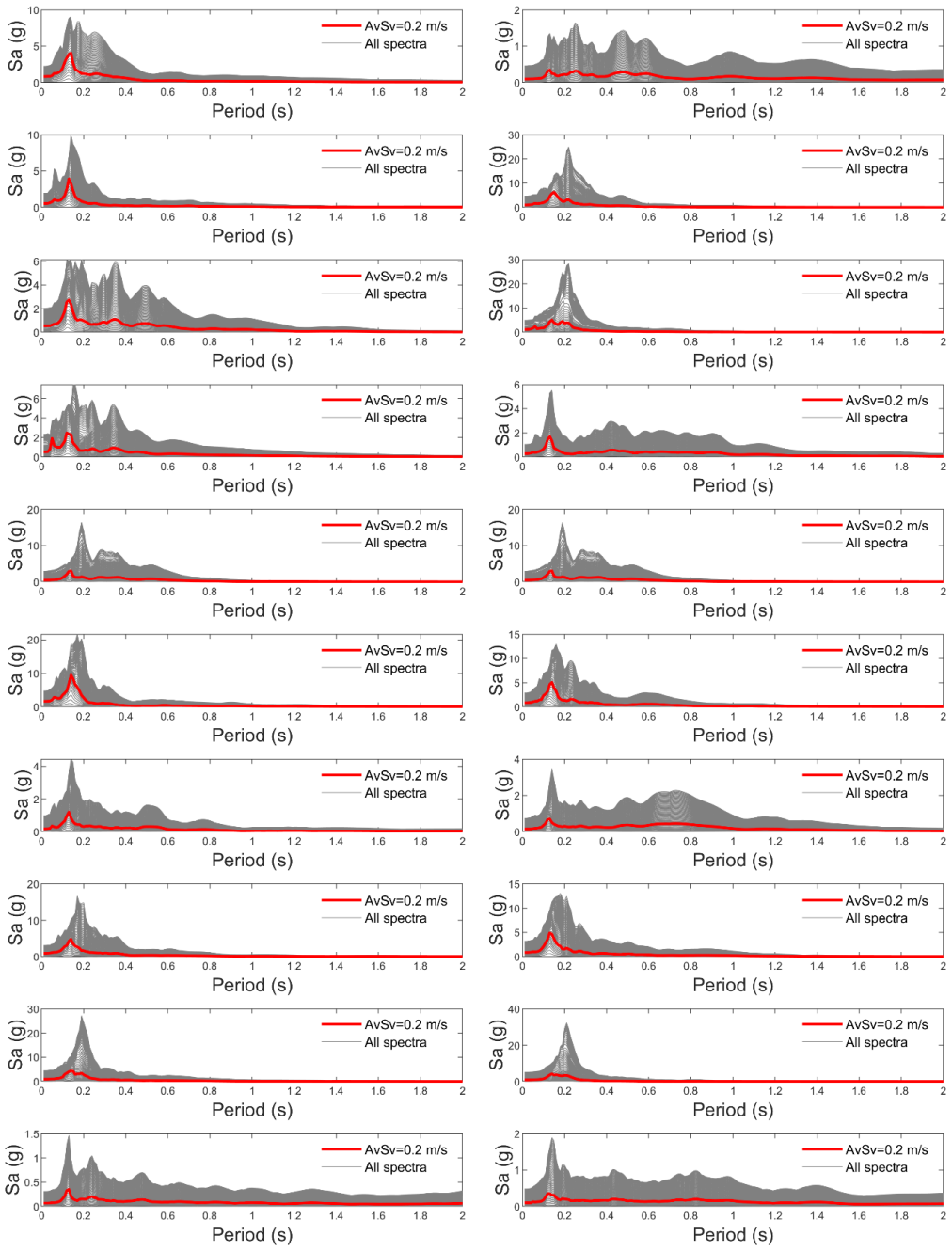


Figure 6 Spectra of the scaled records by considering the equivalent linear method

As discussed above, two approaches are considered when seismic waves traverse the soil profile (elastic and inelastic). Therefore, the set of seed signals has also been scaled using a linear propagation method. Figure 7 shows the resulting spectra at the surface after this

operation. Again, the spectra of the records scaled so that AvSv equals 0.2 m/s have been highlighted in red as reference.

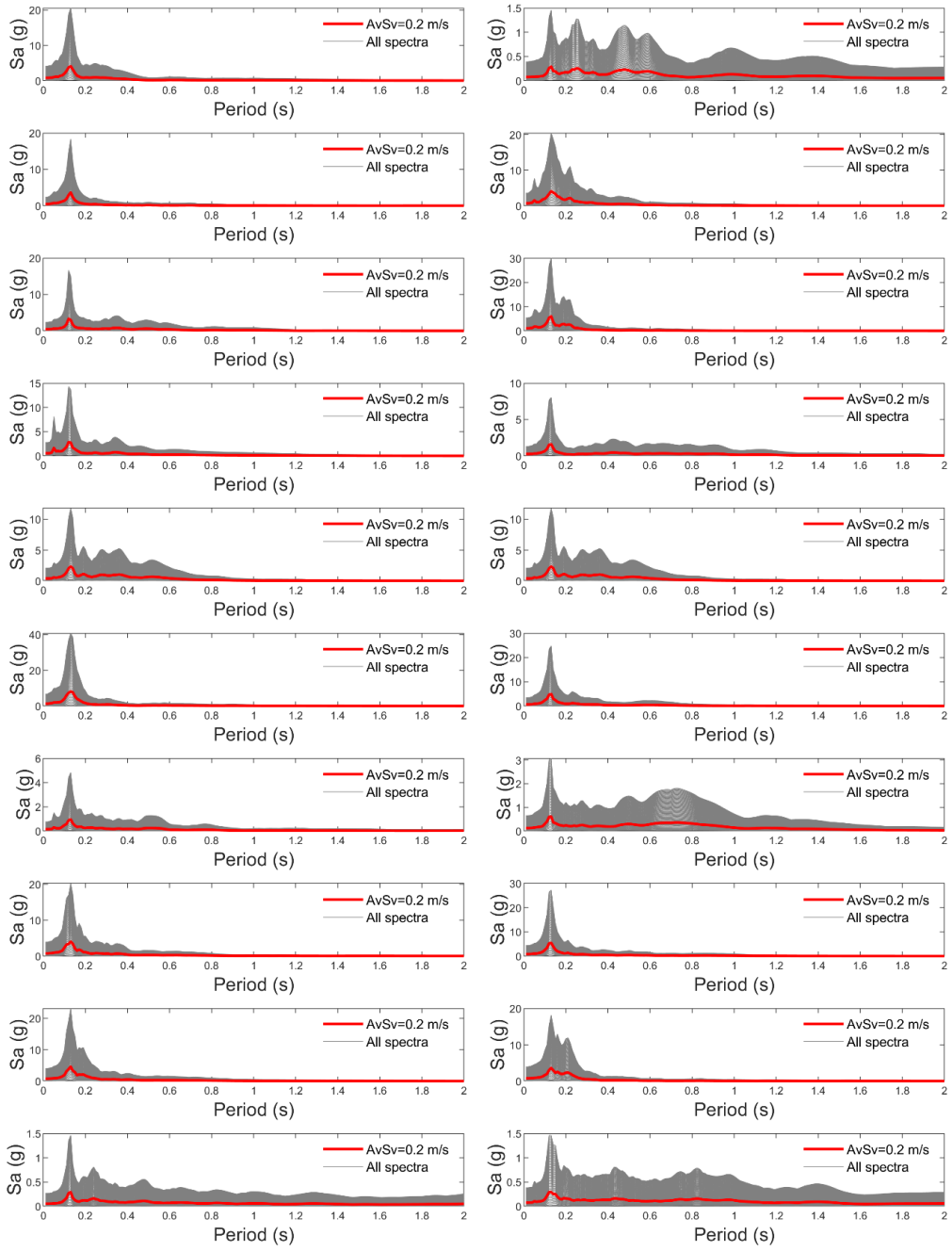


Figure 7 Spectra of the scaled records by considering a linear method

The resulting ground motions at the surface derived from both scaling approaches are then used as input to the building model. The nonlinear dynamic analysis has been used to perform these calculations. From each analysis, the maximum inter-storey drift ratio (MIDR) has been calculated and considered as engineering demand parameter (EDP).

## 5 FRAGILITY ANALYSIS

From the AvSv-MIDR relationship, one could derive fragility functions according to the so-called 'cloud analysis' approach [16]. This methodology requires to calculate the best fit curve between a set of IM and EDP realizations in the log-log space. In general, the aforementioned fitting is performed using linear regression analysis. However, some IM-EDP clouds are better represented by considering a nonlinear regression analysis [15]. This type of regression has been employed in this research. Then, the resultant curve is used to estimate the median of a parametric statistical distribution, given an IM value. The variability of this parametric distribution is estimated as the standard deviation of the IM-EDP residuals with respect to the fitted curve. In this way, the probability of exceeding a certain damage threshold can be calculated. These thresholds are particular realizations of the EDP under consideration, $EDP_C$.

Figure **8** shows the AvSv-MIDR pairs obtained based on both scaling approaches. It can be seen that at lower intensity values, MIDRs coming from the linear propagation method tend to be higher than those based on the equivalent linear method. At higher intensity values, this tendency is not that clear.

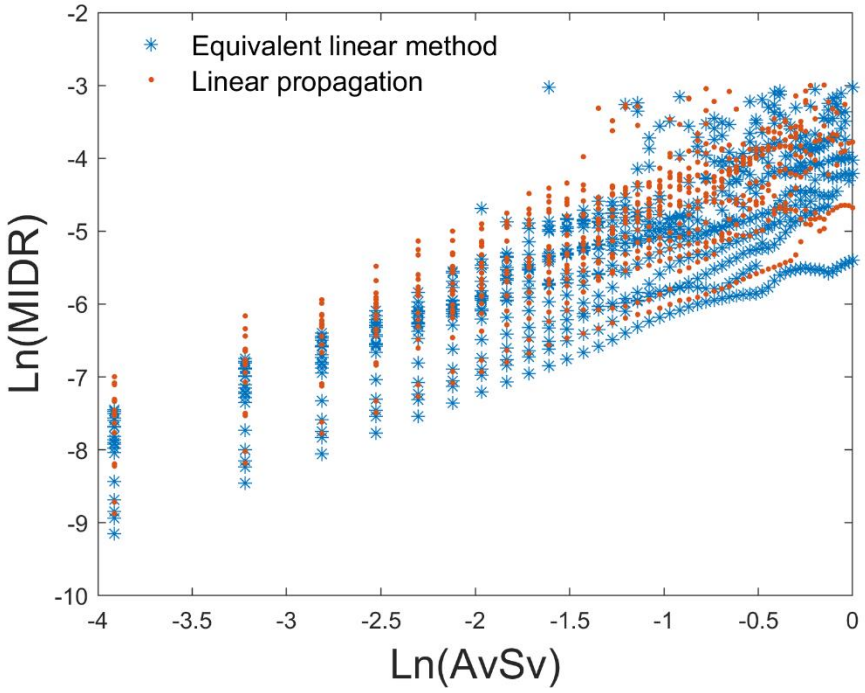


Figure 8 Clouds of IM-EDP points for both scaling approaches

Then, fragility curves for two performance levels have been derived: *slight* and *extensive*. They can be related to MIDR values equal to 0.005 and 0.02, respectively. Hence, Figure 9 shows the fragility functions for both damage thresholds and by considering both scaling approaches. In this figure it is also shown the absolute value of the difference in probability between both scaling methods. These functions show that the difference in probability can reach values of the order of 0.2 for the slight damage state whilst for the extensive 0.1. In both cases, a significant shift between fragility curves related to the same damage state can be observed.

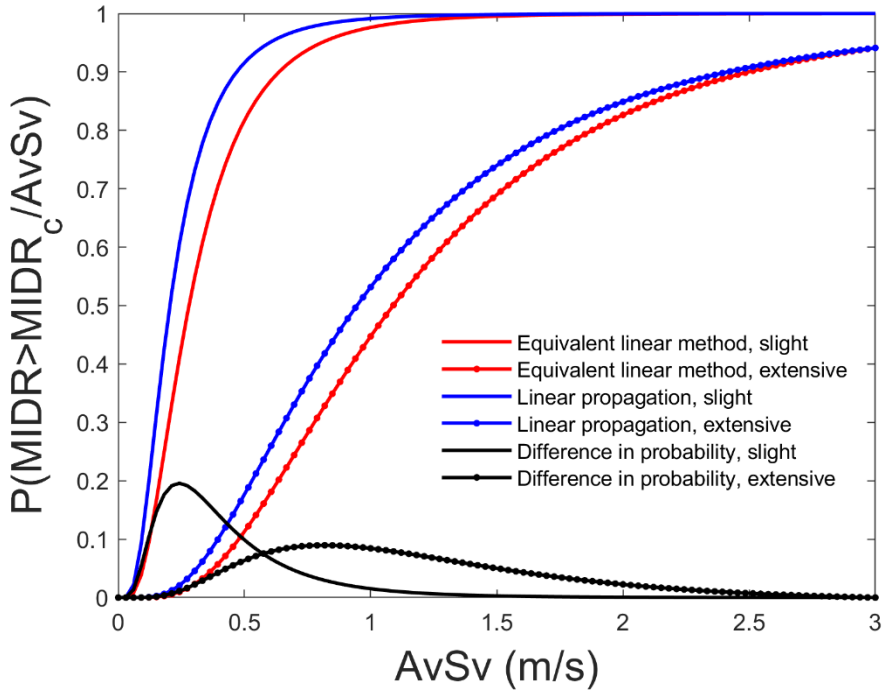


Figure 9 Fragility curves considering both scaling approaches

## 6 CONCLUSIONS

In this article, it has been analyzed the influence on the derivation of fragility functions when scaling ground motion records by taking into account the modification of the dynamic properties of the soil mass below a structure. As a case of study, a soil profile of cohesionless material and a 5-storey reinforced concrete building have been analyzed. Seismic hazard has been characterized by using a set of ground motion records acquired in Colombia [13]. These seed records have been scaled considering or not the influence of the stiffness degradation in the soils due to seismic waves. Using these records, several nonlinear dynamic analyses have been performed. Finally, fragility functions have been derived and compared.

The main conclusion of this study is that the consideration or not of the stiffness degradation of soils, when scaling, affects the derivation of fragility curves. However, the results are far from conclusive that the fragility functions derived by considering soil stiffness degradation always provide lower exceedance probabilities than those associated with linear propagation. This is because only one soil profile and one building model have been analyzed.

Advanced probabilistic calculations that consider the highly probabilistic nature of both the dynamic properties of soil and buildings can shed light on this regard. This would allow the development of advanced mathematical arrangements that take into account the influence of the main properties of the ground motion record applied at the bedrock level and the dynamic properties of soil and buildings.

## ACKNOWLEDGMENT AND FUNDING

This research has been funded by the Spanish Research Agency (AEI) of the Spanish Ministry of Science and Innovation (MICIN) through the projects with references: PID2020-117374RB-I00/AEI/10.13039/501100011033 and TED2021-132559B-I00 – J-02970.

## REFERENCES


[1] Lou, M., Wang, H., Chen, X., & Zhai, Y. (2011). Structure–soil–structure interaction: Literature review. Soil dynamics and earthquake engineering, 31(12), 1724-1731.

[2] Ohnaka, M. (1976). A physical basis for earthquakes based on the elastic rebound model. Bulletin of the Seismological Society of America, 66(2), 433-451.

[3] Pagliaroli, A., Lanzo, G., Tommasi, P., & Di Fiore, V. (2014). Dynamic characterization of soils and soft rocks of the Central Archeological Area of Rome. Bulletin of earthquake engineering, 12(3), 1365-1381.

[4] Kaklamanos, J., Baise, L. G., Thompson, E. M., & Dorfmann, L. (2015). Comparison of 1D linear, equivalent-linear, and nonlinear site response models at six KiK-net validation sites. Soil Dynamics and Earthquake Engineering, 69, 207-219.

[5] Hardin, B. O., & Scott, G. D. (1966). Generalized Kelvin-Voigt used in soil dynamics study. Journal of the Engineering Mechanics Division, 92(1), 143-156.

[6] Yoshida, N., Kobayashi, S., Suetomi, I., & Miura, K. (2002). Equivalent linear method considering frequency dependent characteristics of stiffness and damping. Soil Dynamics and Earthquake Engineering, 22(3), 205-222.

[7] Okur, D. V., & Ansal, A. (2007). Stiffness degradation of natural fine grained soils during cyclic loading. Soil Dynamics and Earthquake Engineering, 27(9), 843-854.

[8] Kostinakis, K., Fontara, I. K., & Athanatopoulou, A. M. (2018). Scalar structure-specific ground motion intensity measures for assessing the seismic performance of structures: a review. Journal of Earthquake Engineering, 22(4), 630-665.

[9] Wong, H. L. (1975). Dynamic soil-structure interaction.

[10] Dimitris Pitilakis (2023). waveprop, MATLAB Central File Exchange.

[11] Otani S (1974) Inelastic analysis of RC frame structures. J Struct Div ASCE 100:1433–1449

[12] Carr AJ (2000) Ruaumoko-inelastic dynamic analysis program. University of Canterbury, Department of Civil Engineering, Christchurch

[13] Colombian geological survey (SGC), Sistema de Consulta de la Amenaza Sísmica de Colombia. https://amenazasismica.sgc.gov.co/ (accessed January, 2023).

[14] ELECTRIC POWER RESEARCH INSTITUTE, «Seismic Evaluation Guidance - Screening, Prioritization and Implementation Details (SPID) for the Resolution of Fukushima Near-Term Task Force Recommendation 2.1: Seismic» Report 1025287, Palo Alto, CA, February 2013.

[15] Vargas-Alzate, Y. F., Hurtado, J. E., & Pujades, L. G. (2022). New insights into the relationship between seismic intensity measures and nonlinear structural response. Bulletin of Earthquake Engineering, 1-37.

[16] Jalayer F, De Risi R, Manfredi G (2015) Bayesian cloud analysis: efcient structural fragility assessment using linear regression. Bull Earthq Eng 13:1183–1203

COMPDYN 2023
9th ECCOMAS Thematic Conference on
Computational Methods in Structural Dynamics and Earthquake Engineering
M. Papadrakakis, M. Fragiadakis (eds.)
Athens, Greece, 12-14 June 2023

# SELECTION AND SCALING VALIDATION OF GROUND MOTIONS ACCORDING TO TBEC-2018 FOR THE SEISMIC ASSESSMENT OF MASONRY STRUCTURES

**Marco F. Funari[1], Shaghayegh Karimzadeh[2], Daniel Caicedo[2], Sayed M. S. Hussaini[2], Aysegul Askan[3], and Paulo B. Lourenço[2]**

[1] University of Surrey
School of Sustainability, Civil and Environmental Engineering
Guildford GU2 7XH, UK
m.funari@surrey.ac.uk

[2] University of Minho
Department of Civil Engineering, ISISE, Campus de Azurém 4800-058
Guimarães, Portugal
{ shaghkn, dcaicedod, hussaini, pbl }@civil.uminho.pt

[3] Middle East Technical University
Civil and Earthquake Engineering Departments
Ankara, Turkey
aaskan@metu.edu.tr

## Abstract

*This paper addresses the selection and scaling of earthquake time histories for analysing masonry structures' Out-Of-Plane (OOP) response according to the 2018 Turkish Building Earthquake Code (TBEC-2018) guidelines. Ground motion simulations are proposed for regions with limited seismic networks or lacking information regarding recorded accelerograms for large-magnitude events. Selection and scaling procedures are automatised according to the TBEC-2018 recommendations. The pre-selection is conducted according to specific seismological characteristics, and the optimal scaling factors of individual records are computed using a metaheuristic optimisation based on the Differential Evolution Method (DEM). Two sets of records (11 real and 11 simulated) are generated and used as input to conduct non-linear dynamic analyses. A U-shaped masonry prototype is adopted as a structural benchmark. The structural response is monitored with an emphasis on the OOP response.*

**Keywords:** Selection and Scaling, Ground motion simulation, Masonry Structures, OOP Response, Metaheuristic optimisation.

# 1 INTRODUCTION

Earthquakes have the potential to severely damage historic masonry structures. In order to preserve their structural integrity, advanced numerical models can be utilised to simulate potential ground shaking scenarios and implement appropriate conservation measures. In the last decade, numerical models, either based on the discrete element method or Finite Element Method (FEM), have been extensively used for non-linear dynamic analysis of Historical Masonry Structures (HMS) [1–6]. Discrete element method is particularly suitable for modelling large displacement static or dynamics problems. However, FEM is still the most common approach because of the large spread among practitioners and researchers, despite the limitations of modelling masonry as a homogeneous material [4,7–10]. FEM or DEM are adopted in conjunction with non-linear time history analysis to integrate the equations of motion and determine the structural behaviour. Besides developing a reliable numerical model, the selection of an earthquake input representative of local hazard is a major challenge that might cause uncertainty in assessing the seismic performance of a given structure [11]. In this regard, most relevant seismic codes provide simplified guidelines for scaling and selecting motion records, which have been adopted in past research to evaluate moment-resistant frame structures or bridges [12,13]. However, practitioners tend to use real accelerograms for code-based design validations, which on occasion might be a cumbersome task because of the lack of recorded accelerograms, specifically for the case of large-magnitude events in European regions. To overcome this limitation, simulation techniques have been implemented to reproduce synthetic motions. Ugurhan and Askan [14] performed stochastic simulation based on the dynamic corner frequency approach [15], considering the Duzce (Turkey) Earthquake that took place on November 12$^{th}$ of 1999 (Mw 7.1). Similarly, stochastic simulation has been employed for other historical records, such as the 9$^{th}$ of July 1998 Faial Earthquake (Azores, Portugal) [16].

On the other hand, some authors performed validations on synthetic records. Galasso et al. [17] addressed the validation of hybrid broadband simulation against historical events by considering the response of multiple degrees of freedom systems. Bijelić et al. [18] focused on validation through comparative assessments of building performance using sets of recorded and simulated motions. Similarly, Tsioulou et al. [19] compared the seismic demand of inelastic single-degree-of-freedom systems of hazard-compatible recorded ground motions to the demand of stochastic ground motion modified to match the same target hazard. Furthermore, other investigations adopted simulated records to address engineering and design-related problems. Among them, Karimzadeh et al. [20] performed non-linear time history analyses of multi-story reinforced concrete frames under synthetic records reproduced after the April 6$^{th}$ of 2009 L′Aquila, Italy, earthquake. Recently, the research by Zhong et al. [21] implemented site-specific simulated accelerograms to conduct ASCE 7-16 code-based design checks and performance-based assessment of a 20-story RC moment frame and a 42-story shear wall building.

In this regard, this paper aims to address the seismic assessment of masonry structures by using suites of real and simulated records generated according to TBEC-2018 provisions. The paper is divided as follows. Section 2 presents the derivation of sets of real and simulated motions based on the TBEC-2018 criteria. Section 3 provides a description of the numerical model and FE modelling implementation. The discussion of the results of the non-linear dynamic analyses with a focus on the out-of-plane (OOP) direction is presented in Section 4. Finally, section 5 delivers some relevant conclusions of the study.

# 2 GROUND MOTION SCALING AND SELECTION

The specific recommendations for selection from TBEC-2018 can be summarised as (i) A minimum of 11 acceleration records should be considered for the analysis; (ii) The spectral

matching should be carried out in the range $0.2T_1$-$1.5T_1$, where $T_1$ is the fundamental period of the structure; (iii) In the range of matching, the mean spectrum computed from each individual record should be above 1.0 times the code elastic response spectrum for 1- and 2-D analyses or 1.3 for 3-D analyses; (iv) Individual scaling factors lower than 1.3 should be considered. The following subsections describe the process of formulating these guidelines as a constrained optimisation problem and the subsequent selection of both, real and simulated records, to match the target design spectrum.

## 2.1 Algorithm for selection and scaling

The code-based selection and scaling of groups of acceleration records are handled as a constrained optimisation problem. For this purpose, the Sum of Square Error (SSE) between the mean and target spectral acceleration (*Sa*) spectra is defined as follows:

$$F(x) = \sum_{i=1}^{n} (Sa_{mean}(T_i) - Sa_{ref}(T_i))^2 \tag{1}$$

where *n* is the number of vibration periods considered in the matching domain.

This function is the main objective for minimising to achieve convergence with the target design spectrum. Nonetheless, additional constraints should be taken into consideration to create a global optimisation problem with penalty functions. The first one is referred to as a lower bound for the mean spectrum normally established as 90% with respect to the target spectrum as in [22,23]. An upper bound for the mean spectrum can be defined to construct the generalised first constraint in the form:

$$C_1(x) = \begin{cases} lower\ bound_{mean} - \min\left[{Sa_{mean}(T_i)}/{Sa_{target}(T_i)}\right];\ if\ \min\left[{Sa_{mean}(T_i)}/{Sa_{target}(T_i)}\right] < lower\ bound_{mean} \\ \max\left[{Sa_{mean}(T_i)}/{Sa_{target}(T_i)}\right] - upper\ bound_{mean};\ if\ \max\left[{Sa_{mean}(T_i)}/{Sa_{target}(T_i)}\right] > upper\ bound_{mean} \\ 0;\ otherwise \end{cases} \tag{2}$$

Analogously, a second constraint is defined, this time for lower and upper limits regarding each individual record:

$$C_2(x) = \begin{cases} lower\ bound_{ind} - \min\left[{Sa_{ind}(T_i)}/{Sa_{target}(T_i)}\right];\ if\ \min\left[{Sa_{ind}(T_i)}/{Sa_{target}(T_i)}\right] < lower\ bound_{ind} \\ \max\left[{Sa_{ind}(T_i)}/{Sa_{target}(T_i)}\right] - upper\ bound_{ind};\ if\ \max\left[{Sa_{ind}(T_i)}/{Sa_{target}(T_i)}\right] > upper\ bound_{ind} \\ 0;\ otherwise \end{cases} \tag{3}$$

This constraint was originally proposed in the work of Macedo and Castro [24] to reduce the individual mismatch, so called record-to-record variability. Therefore, the global optimisation problem yields the final form:

$$F(x) = \sum_{i=1}^{n} (Sa_{mean}(T_i) - Sa_{ref}(T_i))^2 + C_1(x) + C_2(x) \tag{4}$$

An additional penalty should be imposed when the same ground motion, or event, is considered more than one in the set. However, a different approach is adopted to decrease the complexity of the objective function. First, a series of seismological conditions (i.e., source mechanism, magnitude, source-to-site distance, and soil conditions) are considered to apply a scenario-based filter to the dataset. Then, the SEE between the acceleration spectrum and the target spectrum is computed, considering the two horizontal components of each record. The filtered set is reorganised by ranking the SEE of each record from lowest to largest in the two directions of analysis, and just the component with the lowest SEE is considered for the next stage. Finally, records from the same event are dropped from the dataset saving only the record of the event with the highest (unscaled) compatibility to the target code spectrum.

Next, a vector **x** is introduced as follows:

$$\boldsymbol{x} = \{x_1, x_2 \cdots x_N\}^T \tag{5}$$

where the value of $x_i$ denotes the $i^{th}$ scaling factor affecting the $i^{th}$ record in a set of $N$ accelerograms, in such a way that the $Sa_{mean}(T)$ vector can be calculated as:

$$Sa_{mean}(T) = \frac{\sum_{i=1}^{N} x_i \, Sa_{ind_i}(T)}{N} \quad (6)$$

where $Sa_{ind}$ is the individual spectra acceleration and N is the number of records, and $x_i$ is the scaling Factor (SF) of the $i^{th}$ record.

The optimisation problem is now aimed at determining the SFs that will reduce the total cost defined earlier in Equation 4. To solve this optimisation problem, the DEM metaheuristic technique is adopted [25].

## 2.2 Target elastic response spectrum

The city of Istanbul has been selected as location to derive site-specific target spectra considering a standard design earthquake ground motion (10% probability of exceedance in 50 years and return period Tr = 475 years), denoted as earthquake level DD-2 in the TBEC-2018. For the sake of simplicity, the dimensionless spectral acceleration values $S_S$=0.977 and $S_1$=0.270 were taken directly from the parameters reported by Işık et al. [26]. These values are utilised for estimating local ground effect coefficients Fs and $F_1$, the design spectral acceleration coefficients $S_{DS}$ and $S_{D1}$, and corner periods $T_A$ and $T_B$. The site-specific design spectrum is computed for a soil class ZC with shear-wave velocity to a depth of 30 meters ($V_{s30}$) values oscillating in the ranges 360-760 m/s and 180-360 m/s, following the procedure specified in the TBEC-2018.

## 2.3 Selection of real records

A dataset composed of 1520 three-component recorded accelerograms from various regions in Turkey is considered. For this purpose, two well-known datasets are adopted, including the reference database for seismic ground motion in Europe (RESORCE), [27] and the Turkish Accelerometric Database and Analysis System [28]. The fully integrated dataset consists of 37 earthquake scenarios, with the dominant fault mechanism being strike-slip. Although $M_w$ ranges from 2.8 to 7.6, the most frequent magnitudes are in the range of 4.8-5.2 and 6.4-6.8. The stations are distributed within Joyner and Boore distances ($R_{JB}$) of up to 744 km and $V_{s30}$ between 131-1862 m/s.

Regarding the selection process, a first scenario-based filter is applied to the complete dataset by fixing some significant seismological parameters (fault mechanism = strike-slip; $M_w \geq 5.5$; fault depth $\leq 40$ km; $R_{JB} \geq 15$ km; and $V_{s30}$ in the range 360–760 m/s). The reduced dataset is reorganised according to the SSEs, and the component with less SSE with respect to the target design spectrum is selected. Subsequently, records from the same event with the largest values of SSE are removed from the dataset, and only the first 11 records (best candidates) are taken for the fitting process.

The TBEC-2018 restricts the scaling factors for the modification of real accelerograms to an upper value of 1.3. Nevertheless, and as expected based on the experiences of previous research [29], using SFs lower than 2 led to a poor representation of target spectra. Thus, the searching domain of SFs is fixed in the range of 0.5-5.0. Moreover, the lower and upper bounds for the mean spectrum are set as 1.0 and 1.20 times the target design spectrum, respectively. The spectral mismatch of individual records is limited to ± 50% relative to the target spectrum following Macedo and Castro [24] suggestions. Figure 1 shows the results after scaling 11 real records according to TBEC-2018. Although a good level of matching of the mean spectrum with the target is observed in the relevant domain $0.2T_1$-$1.5T_1$, some values of the mean are below the target spectrum, specifically in the short period range. This behaviour is attributed to

the lack of real accelerograms meeting all the imposed conditions in the scenario-based filtering as well as the limitations of SFs up to 5.0. Similar results were reported in [24] where the implementation of metaheuristic techniques led to suites of records that minimises as better as possible the cost function although not all constraints are fully met in the process.

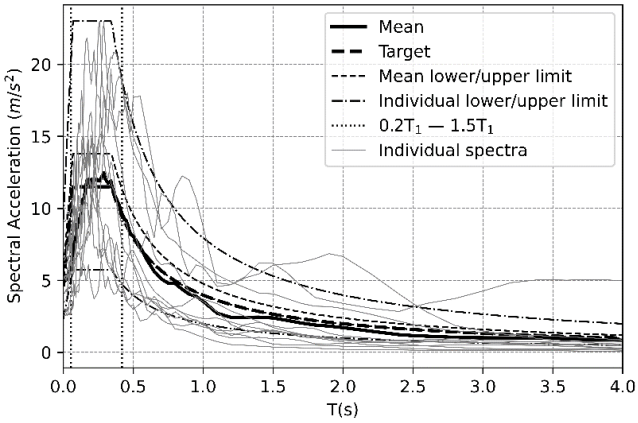


Figure 1. Selection of 11 real records using DE metaheuristic according to TBEC-2018 regulations.

## 2.4 Selection of simulated records

The dataset of simulated ground motions used in this study consists of 7358 time-series from simulations performed in different regions in Turkey, including Istanbul, Duzce, Van, Afyon, and Erzincan. Among these regions, Duzce, Van, Afyon and Erzincan simulation parameters are validated against previous events [14,30–32] while for Istanbul, the parameters for the hypothetical scenarios are validated against ground motion models [33]. For all regions, three distinct soil types characterised by mean $V_{s30}$ values of 255, 310, and 520 m/s were considered in the simulations. The dataset contains scenarios with $M_w$ ranging from 5.0 to 7.5 and $R_{JB}$ values up to 270 km. For Duzce simulations, the $M_w$ values of the scenario events are 5.0, 5.5, 6.0, 6.5, 7.0, 7.1, and 7.5. For Erzincan simulations, $M_w$ values include 5.0, 5.5, 6.0, 6.5, 7.0, 7.1, and 7.5. For Istanbul, $M_w$ values are 5.0, 5.5, 6.0, 6.5, 7.0, and 7.4, while for Afyon, the $M_w$ range includes 5.0, 5.5, 6.0, 6.5, 6.6, and 7.0. Finally, for the scenario events in Van, the $M_w$ values are 5.0, 5.5, 6.0, 6.5, 7.0, and 7.1.

All of the simulated datasets are constructed using the stochastic finite-fault method as developed by Motazedian and Atkinson [15]. In this approach, the rectangular fault plane is divided into multiple sub-faults, each of which is treated as a stochastic point source. Then, the contribution of each sub-fault is summed up in the time domain with kinematic time delays. This method has been efficiently employed for many regions in the world to simulate the ground motions of large earthquakes.

As with the real records, the preliminary selection is applied to the full simulated ground motion dataset considering the same seismological conditions. The SSEs are also computed, and the records are organised accordingly. However, the selection stage of the earthquake component with a smaller deviation from the target spectrum can be omitted since the simulations are carried out to obtain only a 1-component time-series. Figure 2 depicts the results of the metaheuristic optimisation of the 11 best candidate records to match the target spectrum, considering the same boundaries for the mean spectrum and individual spectra.

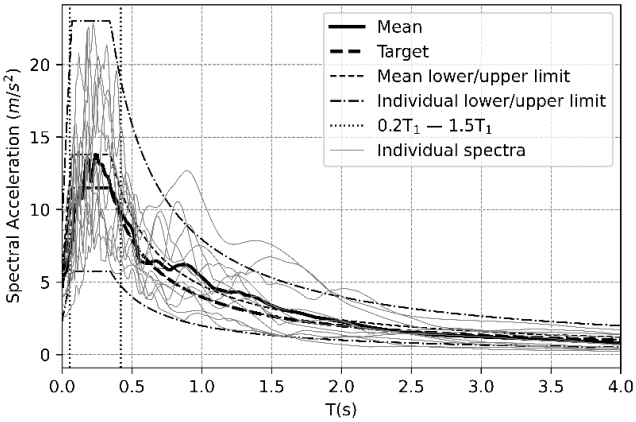


Figure 2. Selection of 11 simulated records using DE metaheuristic according to TBEC-2018 regulations.

For the selection process of simulated records, it was possible to limit the value of SFs up to 2.0, equally achieving an acceptable level of fitting with the target spectrum. These results agree with the discussion presented by Zhong et al. [21] arguing that simulated records reproduce with better accuracy spectral shapes, and therefore, large scaling is not required. Table 1 summarises the selected records alongside their seismological features and SFs. From Table 1 it might be observed that the distribution of SFs is coherent with the distribution of PGA. Real accelerograms exhibit lower values of PGA with higher SFs. An opposite observation is valid for the simulated time-series with higher PGA values; therefore, a better match with the target spectrum is obtained.

Table 1. Seismological characteristics and scaling factors of selected records.

| Record Nº | Depth [km] | Comp | Mw | $V_{s30}$ [m/s] | $R_{JB}$ [km] | PGA [m/s$^2$] | SF |
|---|---|---|---|---|---|---|---|
| *Real records* | | | | | | | |
| 1 | 8.06 | N-S | 6.8 | 450 | 17.86 | 2.36 | 2.61 |
| 2 | 15.90 | N-S | 7.6 | 701 | 38.00 | 2.65 | 3.48 |
| 3 | 6.09 | E-W | 5.6 | 363 | 15.00 | 2.46 | 2.64 |
| 4 | 10.00 | S49E | 7.0 | 652 | 41.00 | 1.01 | 4.97 |
| 5 | 14.30 | E-W | 5.6 | 481 | 54.00 | 1.00 | 4.97 |
| 6 | 20.00 | E-W | 6.3 | 366 | 52.00 | 1.32 | 4.89 |
| 7 | 15.00 | E-W | 6.0 | 369 | 31.00 | 0.70 | 5.00 |
| 8 | 10.00 | E-W | 6.7 | 433 | 62.00 | 0.86 | 5.00 |
| 9 | 15.00 | N-S | 6.1 | 520 | 43.00 | 0.53 | 4.99 |
| 10 | 11.20 | N-S | 7.1 | 616 | 17.00 | 0.52 | 4.99 |
| 11 | 5.00 | N-S | 6.1 | 529 | 30.00 | 0.55 | 4.98 |
| *Simulated records* | | | | | | | |
| 1 | 8.50 | — | 7.0 | 520 | 18.28 | 3.70 | 1.74 |
| 2 | 9.50 | — | 7.0 | 520 | 15.90 | 4.67 | 1.82 |
| 3 | 7.00 | — | 6.5 | 520 | 18.19 | 4.92 | 2.00 |
| 4 | 11.23 | — | 7.5 | 520 | 16.37 | 3.41 | 1.87 |
| 5 | 9.50 | — | 6.6 | 520 | 18.19 | 3.16 | 1.67 |
| 6 | 8.00 | — | 6.5 | 520 | 15.93 | 2.08 | 1.91 |
| 7 | 11.23 | — | 7.1 | 520 | 17.88 | 2.84 | 2.00 |

| | | | | | | | |
|---|---|---|---|---|---|---|---|
| 8 | 7.00 | — | 6.0 | 520 | 16.21 | 2.02 | 1.95 |
| 9 | 6.74 | — | 7.0 | 520 | 17.89 | 1.69 | 2.00 |
| 10 | 8.00 | — | 6.0 | 520 | 15.83 | 2.06 | 2.00 |
| 11 | 9.55 | — | 7.0 | 520 | 215.98 | 1.32 | 1.99 |

## 3 PROTOTYPE DESCRIPTION AND FE MODELLING IMPLEMENTATION

A U-shaped masonry prototype is adopted as a structural benchmark in this study. Figure 3 depicts the geometry and overall characteristics of the masonry prototype, which is an abstraction of a single-nave church commonly encountered in earthquake-prone areas of Europe and the Middle East. It is worth noting that these masonry structures have been reported to be among the most damaged typologies in post-earthquake surveys [34].

To account for masonry non-linearities, the Concrete Damage Plasticity (CDP) method, which couples plasticity with a scalar-based damage model [35], is adopted. A linear softening descending branch is used to represent the quasi-brittle nature of masonry in tension. In compression, a plateau is observed after the compressive strength, followed by a linear type of softening. When softening is active, damage variables are introduced to reduce the initial (undamaged) elastic modulus, as expressed by the following equations:

$$\boldsymbol{\sigma_c = (1 - d_c) E_0 (\varepsilon_c - \varepsilon_c^{pl})} \qquad \sigma_t = (1 - d_t) E_0 (\varepsilon_t - \varepsilon_t^{pl}) \tag{7}$$

where $E_0$ is the elastic modulus of the undamaged masonry, $\sigma_i$ is the effective stress value; d is the damage parameter relating the effective stress with the corresponding inelastic strain, $\varepsilon_i$ is the total strain value, and $\varepsilon_i^{pl}$ is the inelastic (plastic) strain value. The subscript $i$ reads as $c$ or $t$, if associated with the compressive or tensile regime, respectively. A scalar-based damage model describes the damage in tension $d_t$ (cracking) and compression $d_c$ (crushing), which can assume a value between zero (no damage) and one (fully damaged). Under cyclic loading, the masonry structure may experience some loss of stiffness during the unloading phase due to cracking and crushing. To account for non-linear masonry behaviour, the CDP method has been adopted. This method assumes a non-associative flow rule that is represented by a Drucker-Prager hyperbolic function and relies on physically based parameters for accurate modelling. Material properties adopted in the numerical analysis are reported in Table 2.

Table 2. Material properties and model parameters.

| $E_0$ [MPa] | $\nu$ | $\rho$ [kg m$^{-3}$] | Dilatation angle | Eccentricity | $f_{b0}/f_{c0}$ | $K_c$ | Viscosity parameter |
|---|---|---|---|---|---|---|---|
| 1000 | 0.2 | 1450 | 10° | 0.1 | 1.16 | 2/3 | 0.002 |

| *Compressive behaviour* | | | *Tensile behaviour* | | |
|---|---|---|---|---|---|
| Stress [MPa] | Inelastic strain | $d_c$ | Stress [MPa] | Inelastic strain | $d_t$ |
| 2.20 | 0 | 0 | 0.150 | 0 | 0 |
| 2.60 | 0.005 | 0 | 0.001 | 0.003 | 0.9 |
| 0.20 | 0.012 | 0.9 | 0.001 | 0.010 | 0.9 |
| 0.20 | 0.020 | 0.9 | - | - | - |

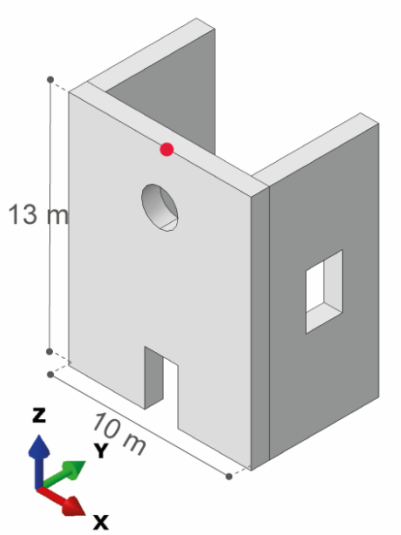


Figure 3. Overall geometry of the U-shaped prototype.

To model damping effects, in this work, the Rayleigh damping model has been adopted. The Rayleigh model approximates the damping coefficient as a linear combination of mass and stiffness, and a damping ratio equal to 3%. The fundamental period of the structure is equal to 0.28 s.

## 4 RESULTS

This section examines the results of the non-linear dynamic analyses, which have been conducted by using both real and simulated records in the OOP direction of the façade at both polarities. A total of 44 non-linear dynamic analyses are being performed to compare response measures. The results are categorised as “Real” and “Simulated” in Figure 4, which shows their distributions. It is noteworthy that the simulated records provide a more conservative prediction for both base shear and maximum displacement.

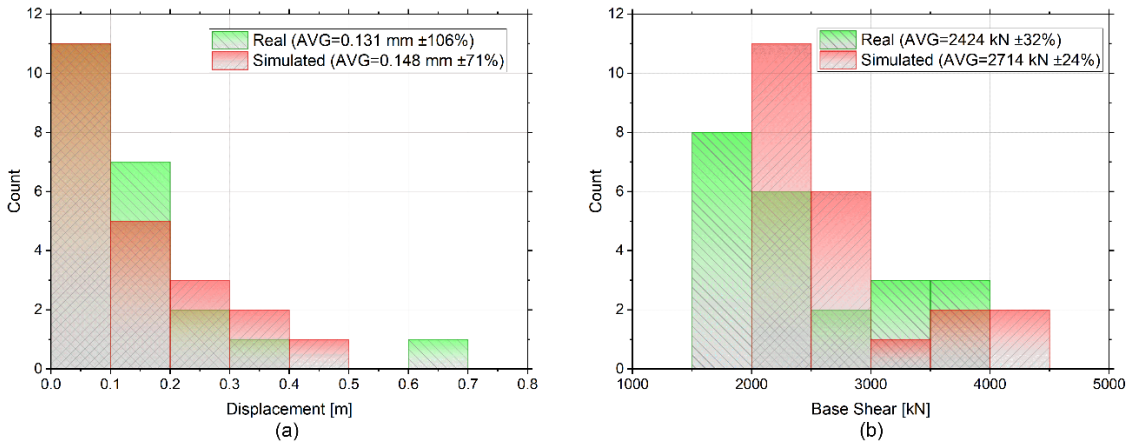


Figure 4. Overall geometry of the U-shape prototype.

## 5 CONCLUSIONS

This paper addresses the selection and scaling of real and simulated ground motions for the analysis of the OOP response of masonry structures according to the TBEC-2018 provisions. The selection process is formulated as a constrained optimisation problem where the DEM metaheuristic technique is applied to derive the optimal scaling factors of individual records. Two

sets of records (11 real and 11 simulated) matching the DD-2 ZC spectrum in Istanbul city were selected as input to conduct non-linear dynamic analyses for a U-shaped masonry prototype. Simulations are accomplished through the stochastic finite-fault simulation approach based on a dynamic corner frequency concept. The masonry non-linearities were considered by means of the CDP method.

Regarding the selection process, the mean of both sets exhibited close fitting with the target spectrum in the relevant domain $0.2T_1$-$1.5T_1$, although not all constraints were fully met in the optimisation process. In addition, lower SFs were reported for the case of simulated time-series denoting a better match with the target spectrum. The numerical results of the 22 non-linear dynamic analyses conducted for the benchmark structure reveal a clear trend for simulated records to provide a more conservative prediction when analysing shear base and maximum displacement metrics. The findings of this investigation assert that the implementation of a simulated suite of ground motion records exhibits great potential in earthquake engineering applications, particularly with respect to the seismic evaluation of masonry structures.

**ACKNOWLEDGMENTS**

This work was partly financed by FCT / MCTES through national funds (PIDDAC) under the R&D Unit Institute for Sustainability and Innovation in Structural Engineering (ISISE), under reference UIDB/04029/2020, and under the Associate Laboratory Advanced Production and Intelligent Systems ARISE under reference LA/P/0112/2020. This study has been partly funded by the STAND4HERITAGE project that has received funding from the European Research Council (ERC) under the European Union's Horizon 2020 research and innovation program (Grant agreement No. 833123), as an Advanced Grant. This work is financed by national funds through FCT - Foundation for Science and Technology, under grant agreement UI/BD/153379/2022 attributed to the second author.

## REFERENCES

[1] Pulatsu B, Gonen S, Parisi F, Erdogmus E, Tuncay K, Funari MF, et al. Probabilistic approach to assess URM walls with openings using discrete rigid block analysis (D-RBA). Journal of Building Engineering 2022;61:105269. https://doi.org/https://doi.org/10.1016/j.jobe.2022.105269.

[2] Funari MF, Pulatsu B, Szabó S, Lourenço PB. A Solution for the Frictional Resistance in Macro-Block Limit Analysis of Non-periodic Masonry. STRUCTURES 2022.

[3] D'altri AM, Sarhosis V, Milani G, Rots J, Cattari S, Lagomarsino S, et al. Modeling Strategies for the Computational Analysis of Unreinforced Masonry Structures: Review and Classification 2020;27:1153–85. https://doi.org/10.1007/s11831-019-09351-x.

[4] Sarhosis V, Lemos J V, Bagi K. Chapter 13 - Discrete element modeling. In: Ghiassi B, Milani GBT-NM of M and HS, editors. Woodhead Publishing Series in Civil and Structural Engineering, Woodhead Publishing; 2019, p. 469–501. https://doi.org/https://doi.org/10.1016/B978-0-08-102439-3.00013-0.

[5] Funari MF, Spadea S, Lonetti P, Fabbrocino F, Luciano R. Visual programming for structural assessment of out-of-plane mechanisms in historic masonry structures. Journal of Building Engineering 2020;31. https://doi.org/10.1016/j.jobe.2020.101425.

[6] Guo Y, Nagy AP, Gürdal Z. A layerwise theory for laminated composites in the framework of isogeometric analysis. Compos Struct 2014;107:447–57. https://doi.org/10.1016/j.compstruct.2013.08.016.

[7] Bertolesi E, Silva LC, Milani G. Validation of a two-step simplified compatible homogenisation approach extended to out-plane loaded masonries. International Journal of Masonry Research and Innovation 2019;4:265. https://doi.org/10.1504/IJMRI.2019.10019407.

[8] Funari MF, Silva LC, Mousavian E, Lourenço PB. Real-time Structural Stability of Domes through Limit Analysis: Application to St. Peter's Dome. Https://DoiOrg/101080/1558305820211992539 2021:1–23. https://doi.org/10.1080/15583058.2021.1992539.

[9] Fortunato G, Funari MF, Lonetti P. Survey and seismic vulnerability assessment of the Baptistery of San Giovanni in Tumba (Italy). J Cult Herit 2017;26:64–78. https://doi.org/10.1016/j.culher.2017.01.010.

[10] Funari MF, Hajjat AE, Masciotta MG, Oliveira D v., Lourenço PB. A Parametric Scan-to-FEM Framework for the Digital Twin Generation of Historic Masonry Structures. Sustainability 2021, Vol 13, Page 11088 2021;13:11088. https://doi.org/10.3390/SU131911088.

[11] Katsanos EI, Sextos AG, Manolis GD. Selection of earthquake ground motion records: A state-of-the-art review from a structural engineering perspective. Soil Dynamics and Earthquake Engineering 2010;30. https://doi.org/10.1016/j.soildyn.2009.10.005.

[12] Araújo M, Macedo L, Marques M, Castro JM. Code-based record selection methods for seismic performance assessment of buildings. Earthq Eng Struct Dyn 2016;45. https://doi.org/10.1002/eqe.2620.

[13] Iervolino I, Maddaloni G, Cosenza E. A note on selection of time-histories for seismic analysis of bridges in Eurocode 8. Journal of Earthquake Engineering 2009;13. https://doi.org/10.1080/13632460902792428.

[14] Ugurhan B, Askan A. Stochastic strong ground motion simulation of the 12 november 1999 Düzce (Turkey) earthquake using a dynamic Corner frequency approach. Bulletin of the Seismological Society of America 2010;100. https://doi.org/10.1785/0120090358.

[15] Motazedian D, Atkinson GM. Stochastic finite-fault modeling based on a dynamic corner frequency. Bulletin of the Seismological Society of America 2005;95. https://doi.org/10.1785/0120030207.

[16] Karimzadeh S, Lourenço PB. Stochastic Ground Motion Simulation of the 9th of July 1998 Faial Earthquake (Azores, North Atlantic). Authorea Preprints 2022.

[17] Galasso C, Zhong P, Zareian F, Iervolino I, Graves RW. Validation of ground-motion simulations for historical events using MDoF systems. Earthq Eng Struct Dyn 2013;42. https://doi.org/10.1002/eqe.2278.

[18] Bijelić N, Lin T, Deierlein GG. Validation of the SCEC Broadband Platform simulations for tall building risk assessments considering spectral shape and duration of the ground motion. Earthq Eng Struct Dyn 2018;47. https://doi.org/10.1002/eqe.3066.

[19] Tsioulou A, Taflanidis AA, Galasso C. Validation of stochastic ground motion model modification by comparison to seismic demand of recorded ground motions. Bulletin of Earthquake Engineering 2019;17:2871–98.

[20] Karimzadeh S, Askan A, Yakut A, Ameri G. Assessment of alternative simulation techniques in nonlinear time history analyses of multi-story frame buildings: A case study. Soil Dynamics and Earthquake Engineering 2017;98. https://doi.org/10.1016/j.soildyn.2017.04.004.

[21] Zhong K, Lin T, Deierlein GG, Graves RW, Silva F, Luco N. Tall building performance-based seismic design using SCEC broadband platform site-specific ground motion simulations. Earthq Eng Struct Dyn 2021;50. https://doi.org/10.1002/eqe.3364.
[22] Code P. Eurocode 8: Design of structures for earthquake resistance-part 1: general rules, seismic actions and rules for buildings. Brussels: European Committee for Standardization 2005.
[23] Engineers AS of C. Minimum design loads for buildings and other structures, American Society of Civil Engineers; 2013.
[24] Macedo L, Castro JM. SelEQ: An advanced ground motion record selection and scaling framework. Advances in Engineering Software 2017;114. https://doi.org/10.1016/j.advengsoft.2017.05.005.
[25] Storn R, Price K. Differential Evolution - A Simple and Efficient Heuristic for Global Optimization over Continuous Spaces. Journal of Global Optimization 1997. https://doi.org/10.1023/A:1008202821328.
[26] Işık E, Büyüksaraç A, Ekinci YL, Aydın MC, Harirchian E. The effect of site-specific design spectrum on earthquake-building parameters: A case study from the Marmara region (NW Turkey). Applied Sciences (Switzerland) 2020;10. https://doi.org/10.3390/app10207247.
[27] Akkar S, Sandıkkaya MA, Şenyurt M, Sisi AA, Ay B, Traversa P, et al. Reference database for seismic ground-motion in Europe (RESORCE). Bulletin of Earthquake Engineering 2014;12. https://doi.org/10.1007/s10518-013-9506-8.
[28] Disaster, Authority EM. Turkish National Strong Motion Network 1973. https://doi.org/10.7914/SN/TK.
[29] Du W, Ning CL, Wang G. The effect of amplitude scaling limits on conditional spectrum-based ground motion selection. Earthq Eng Struct Dyn 2019;48. https://doi.org/10.1002/eqe.3173.
[30] Zengin E, Cakti E. Ground motion simulations for the 23 October 2011 Van, Eastern Turkey earthquake using stochastic finite fault approach. Bulletin of Earthquake Engineering 2014;12. https://doi.org/10.1007/s10518-013-9527-3.
[31] Karimzadeh S. Seismological and engineering demand misfits for evaluating simulated ground motion records. Applied Sciences (Switzerland) 2019;9. https://doi.org/10.3390/app9214497.
[32] Can G, Askan A, Karimzadeh S. An assessment of the 3 February 2002 Cay (Turkey) earthquake (Mw=6.6): Modeling of ground motions and felt intensity distribution. Soil Dynamics and Earthquake Engineering 2021;150. https://doi.org/10.1016/j.soildyn.2021.106832.
[33] Uckan E, Umut Ö, Sisman FN, c S, Askan A. Seismic response of base isolated liquid storage tanks to real and simulated near fault pulse type ground motions. Soil Dynamics and Earthquake Engineering 2018;112. https://doi.org/10.1016/j.soildyn.2018.04.030.
[34] Lulić L, Ožić K, Kišiček T, Hafner I, Stepinac M. Post-Earthquake Damage Assessment—Case Study of the Educational Building after the Zagreb Earthquake. Sustainability 2021, Vol 13, Page 6353 2021;13:6353. https://doi.org/10.3390/SU13116353.
[35] Lubliner J, Oliver J, Oller S, Oñate E. A plastic-damage model for concrete. Int J Solids Struct 1989;25:299–326. https://doi.org/10.1016/0020-7683(89)90050-4.

COMPDYN 2023
9th ECCOMAS Thematic Conference on
Computational Methods in Structural Dynamics and Earthquake Engineering
M. Papadrakakis, M. Fragiadakis (eds.)
Athens, Greece, 12-14 June 2023

# PERMANENT DISPLACEMENT DATABASE OF STRONG EARTHQUAKES IN TURKEY, AND AN ADJUSTED PREDICTIVE MODEL

**Emrecan Adanır**[1] **and Gülüm Tanırcan**[1]

[1] Boğaziçi University Kandilli Observatory and Earthquake Research Institute Department of Earthquake Engineering
emrecan.adanir@boun.edu.tr, birgore@boun.edu.tr

## Abstract

*For seismic design and performance assessment of structures in near-fault regions, international codes recommend selecting sufficient number of strong ground motion recordings containing pulse characteristics. Permanent displacements (PD), also known as fling steps, on the other hand cannot be easily recovered from strong ground recordings because the standard filtering techniques eliminate the low- frequency portions of the motion. Recently, data processing schemes, which are based on de-trending in separate time windows, are proposed to unveil the PDs on the recordings. In this work, the data processing scheme eBASCO (Schiappapietra et al., 2021) is improved and the PDs of strong motion records calculated with new scheme is compared with GPS data of 21 worldwide earthquakes. Then, PDs in horizontal, fault normal, fault parallel and maximum direction components of Mw≥ 6 shallow crust earthquakes in Turkey are calculated to create a fling inventory for the first time. A database comprising 288 recordings ($R_{JB} \leq 50$ km) of 20 earthquakes occurred between 1983-2022 is utilized. Results are also utilized to improve the fling step prediction model of Burks and Baker (2016). Three major outcomes of this study are (1) a new comprehensive automatic data processing scheme; (2) a contribution of 22% and 33% to the fling values of normal and strike-slip earthquakes in the NESS-v2 database, respectively. Moreover, the modified processing scheme on worldwide data possibly will result in a much larger database based on our findings; (3) A Turkey-adjusted fling step predictive model.*

**Keywords:** Permanent displacement, fling step, near fault effects, strong motion database, scaling relation, baseline correction, earthquake waveform processing.

# 1 INTRODUCTION

Directivity and fling step are distinct characteristics of near-fault strong ground motions detected as full and half cycle pulses, respectively, on the velocity waveforms. In seismic design of structures, near-fault effects are taken into consideration through site specific evaluation since they are capable of causing damages on long period structures. Seismic design codes such as International Building Code (IBC, ICBO 2006) [24] and California Building Code (CBC, ICBO 2007) [25], which are based on ASCE7-22 (ASCE 2005) [26], recommend to select strong motion records including pulse characteristics of the motions for use in nonlinear response history analysis of structures. However, due to the fact that the widely utilized data processing schemes such as filtering mask the PDs, these records cannot be identified. To overcome disadvantages of filtering, 2 methods are adopted (1) constructing an artificial fling step and superimposing it on to processed time histories (Abrahamson, 2002 [4]); (2) processing the raw records by special data processing schemes to reveal fling step (Iwan et al., 1985 [1]; Boore, 2001 [2];Wu and Wu, 2007 [6]; D'Amico et al., 2018 [11]; Schiappapietra et al., 2021 [13]).

All available proposed special data processing procedures are based on baseline correction of the waveforms. Iwan et al. (1985) [1] presented a correction algorithm which consists of the evaluation of the baseline offsets in the strongest portion of the motion and the following end part. Later, Boore (2001) [2] redefined the correction points of the former study. Wu and Wu (2007) [6] altered the former methodology so that the ground motions are separated into 3 windows; and selection of the corrected trace is connected to flatness of the last portion. D'Amico et al. (2018) [11] presented eBASCO semi-automatic processing scheme. Schiappapietra et al. (2021) [13] upgraded the eBASCO procedure in that they introduced the comparison of the acceleration amplitudes at the correction points before and after processing of the records. In this paper, eBASCO by D'Amico et al. (2018) [11] is improved to increase the number of possible combinations of correction points. Validation of the improved processing scheme is done by comparing the PDs of processed strong motion records both from Turkey and worldwide earthquakes with those derived from the co-located GPS stations. Then, by exposing the near fault ground motion records to the proposed scheme, the PD database of Turkey is created.

Next, performance of the PD predictive models of Burks and Baker (2016) [8] is evaluated through a residual analysis. It is found that Burks and Baker (2016) [8] predictive model underestimates values for small earthquakes whereas overestimates them for slightly larger earthquakes. The best estimates of this model are found for the events with magnitudes ranging between Mw 6.6 to 6.9. Burks and Baker (2016) [8] fling predictive model is then adjusted by using earthquakes in Turkey. The adjusted model is found much more effective to capture the PDs in Turkey.

# 2 METHODOLOGY

In this study, eBASCO data processing scheme is improved. Differences of the improved procedure from eBASCO are presented as follows:

- The first amplitude of the acceleration time history is assigned as zero to make sure that the velocity oscillates around zero at the beginning of the motion, instead of subtracting it from the whole trace.

- Energy distribution for the selecting of the time correction points is defined by normalized Arias intensity.
- The time correction points are assigned as seconds to increase the possible combinations and thus the accuracy of the obtained corrected waveform.
- Constant detrending in post-event window together with the linear detrending in other time windows shows a reliable trend that was defined as a ramp function and thus used. Conformity is provided through an additional constant baseline correction between the sample point when the strongest pulse finishes and the end.
- Instead of relying on only the acceleration amplitude comparisons, the possible erroneous spurious spikes on the obtained acceleration time history is corrected by assigning the means of the nearest acceleration amplitudes to the amplitude corresponding to time correction points [19].
- It is assumed that the ground displacement fades by oscillating around the permanent displacement level after the most of the excitation energy is dissipated. Therefore, the fade level, also known as PD, is defined as the mean of the 95% of the dissipated cumulative energy to the end of the record [20].
- In contrast to eBASCO, cut of the record in the beginning of the processing is not recommended unless it is inevitable. Moreover, the Butterworth filter at the end of the processing scheme is also not recommended to preserve the low frequency portion of the motion.

To test the capability of the proposed scheme, revealed PDs from GPS data of worldwide earthquakes are compared with the those obtained with processed records at stations in similar locations. As an example, Figure 1 illustrates the comparison of PDs of the 1999 Chi Chi earthquake station TCU 074 obtained by Yu et al (2001) [3] with those found after processing the records. Similarly, the proposed scheme is managed to capture PDs from 1 cm to 260 cm in the validation process. Comparisons of the PDs obtained from the processed records and those derived from co-located GPS data are presented with magnitudes of the events in Figure 2.

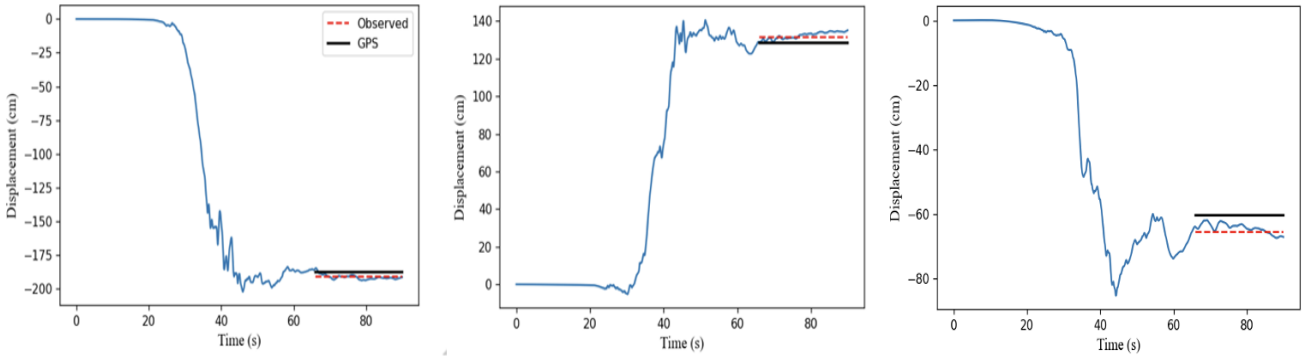


Figure 1: Displacement time history of 1999 Chi Chi earthquake EW, NS and UD components of the station TCU 074 with the findings from GPS data.

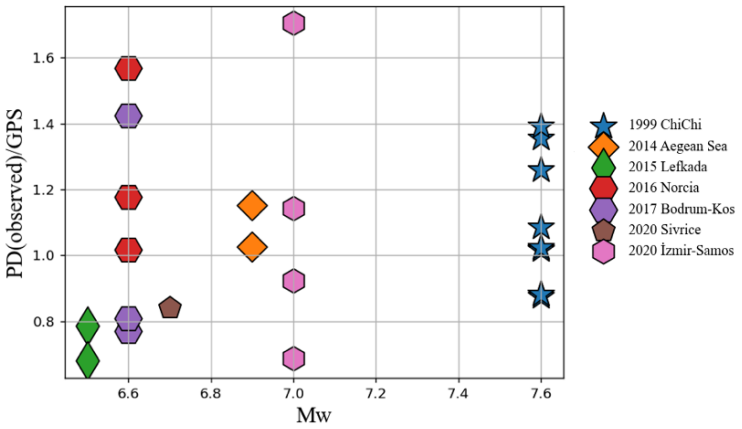


Figure 2: The comparison of PDs obtained on records with those derived from GPS

## 3 PERMANENT DISPLACEMENT (PD) DATABASE OF STRONG EARTHQUAKES IN TURKEY

To compile the ground motion records containing fling-steps, the new Turkish strong ground motion dataset of Turkey N-TSMD presented by Akbaş et al. (2023) [23] is utilized. Raw ground motion records are obtained from Earthquake Research Department of Disaster and Emergency Management Authority (AFAD, https://tadas.afad.gov.tr/list-waveform, last accessed December 2022) and Engineering Strong Motion Database (ESM, https://esm-db.eu/#/waveform/search, last accessed December 2022). Shallow crustal earthquakes Mw>6 and with depth <30 km have been selected. Distance limitation is set as 50 km from the surface projection of the rupture plane ($R_{JB}$ ≤50 km). A total of 288 near-fault records, 14 strike slip, 5 normal and 1 reverse faulting earthquakes are found within the defined criteria (Figure 3). The database includes 74 records from strike slip and 81 records from normal earthquakes. Considering the fact that normal faulting earthquakes were not common in the previous studies, knowledge of the fling step occurrence in normal faulting earthquakes is increased.

Table 1: Summary of Earthquakes and Number of Data Incorporated to the study. SoF: Style of Faulting; SS: Strike Slip; N: Normal; R: Reverse; $M_0$: Seismic Moment

| Date | SoF | Magnitude (Mw) | Number of Stations/Records | Date | SoF | Magnitude (Mw) | Number of Stations/Records |
|---|---|---|---|---|---|---|---|
| 30.Oct.83 | SS | 6,60 | 1/3 | 1.May.03 | SS | 6,30 | 1/3 |
| 13.Mar.92 | SS | 6,60 | 1/1 | 8.Mar.10 | SS | 6,10 | 1/3 |
| 6.Nov.92 | SS | 6,00 | 2/6 | 23.Oct.11 | R | 7,10 | 1/3 |
| 1.Oct.95 | N | 6,10 | 3/7 | 10.Jun.12 | SS | 6,10 | 2/6 |
| 27.Jun.98 | SS | 6,20 | 1/3 | 24.May.14 | SS | 6,90 | 6/18 |
| 31.Jul.98 | SS | 6,20 | 6/18 | 12.Jun.17 | N | 6,30 | 3/9 |
| 17.Aug.99 | SS | 7,60 | 13/37 | 20.Jul.17 | N | 6,60 | 9/27 |
| 12.Nov.99 | SS | 7,10 | 14/42 | 24.Jan.20 | SS | 6,70 | 10/30 |
| 6.Jun.00 | SS | 6,00 | 1/3 | 30.Oct.20 | N | 7,00 | 11/33 |

| | | | | | | | |
|---|---|---|---|---|---|---|---|
| 3.Feb.02 | N | 6,50 | 1/3 | 23.Nov.22 | SS | 6,00 | 11/33 |

PDs are calculated and results in 3 orthogonal components are presented in Figure 3. The largest PD is observed in the horizontal components of TK 8101 recording during the 1999 Düzce earthquake as 263 cm and 212 cm. They are followed by 186 cm during the 1999 Kocaeli earthquake.

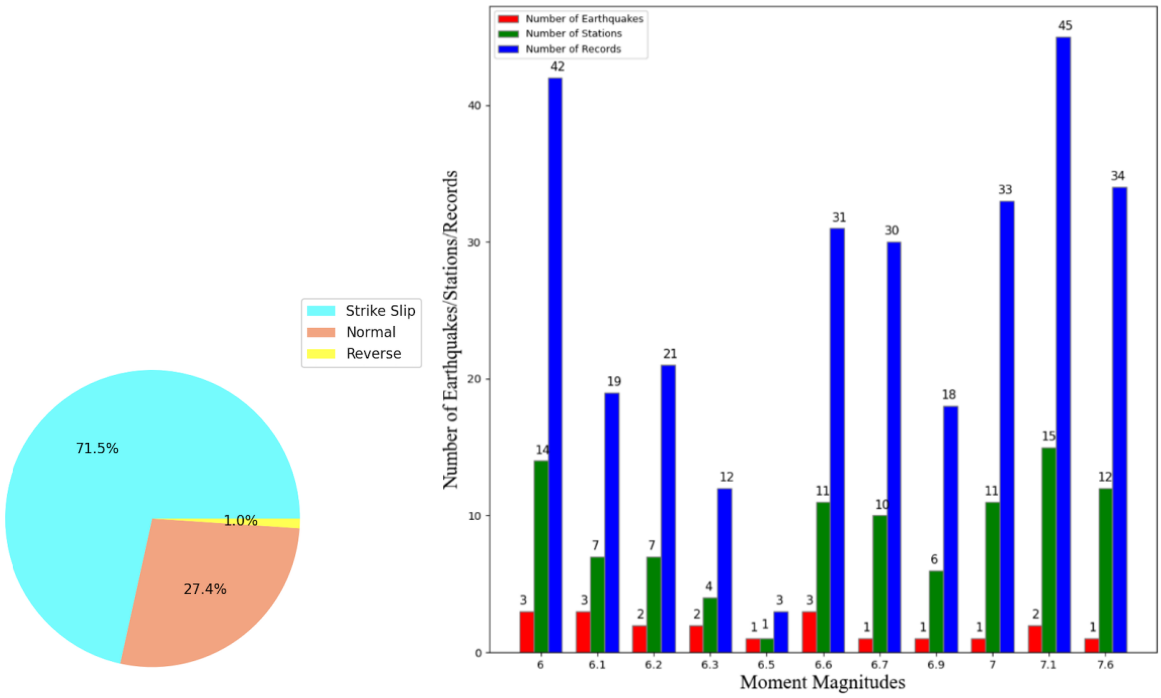


Figure 3: (Left) Distribution of the earthquakes in the dataset in terms of style of faulting (right) Distribution of the records with respect to Moment Magnitudes

As an example, resulting waveforms of the 1999 Kocaeli earthquake North-South component of YPT station and 1999 Düzce earthquake East-West component of station TK 8101 are demonstrated in Figure 4. The distribution of the PDs is illustrated in Figure 5.

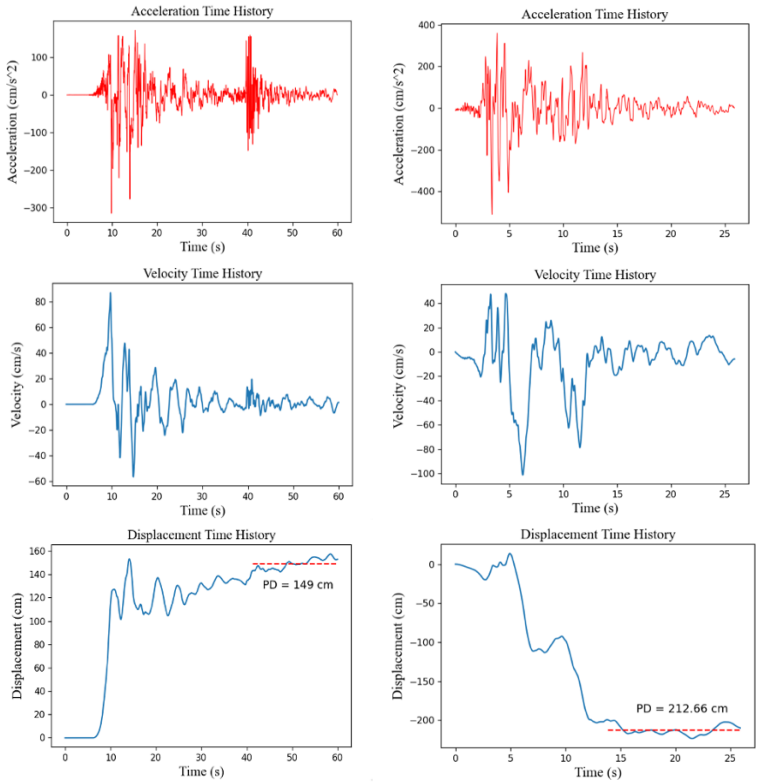


Figure 4: Processed waveforms of (left) the 1999 Kocaeli earthquake North-South component of YPT station and (right) the1999 Düzce earthquake East-West component of TK 8101 station

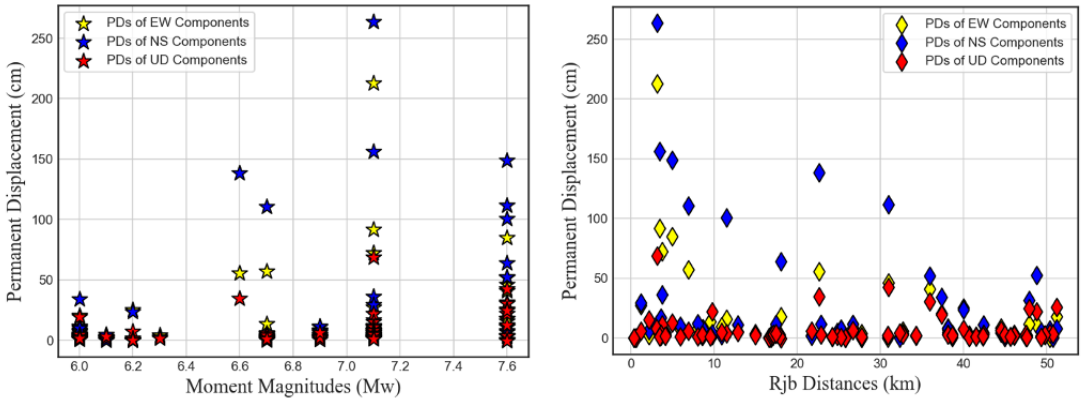


Figure 5: Distribution of the obtained PDs in EW, NS, and UD components with Mw (left) and Rrup (right)

## 4 EVALUATION OF PERMANENT DISPLACEMENT (PD) PREDICTION MODELS

Among several PD prediction models, Burks and Baker (2016) [8] model has been considered in this study. This model was created by inspecting the FP and FN components that obtained on kinematic and hybrid broadband earthquake simulations. Although the utilized scenario earthquakes are either strike slip or reverse faulting, Burks and Baker (2016) [8] does not depend on style of faulting as follows:

$$ln(D_p) = ln(cot^{-1}(0.3R)) + 1.3M - 5.1 \quad (1)$$

where $D_p$ is predicted fling, R is the closest distance, Rrup, and M is moment magnitude.

Residual analyses are conducted according to Gülerce et al. (2016) [21] by considering each record (i) from each event (j) as follows:

$$R_{ij} = ln(a_{ij}) - ln(p_{ij}) = c_k + \Delta_{Bj} + \Delta_{Wij} \quad (2)$$

where $R_{ij}$ is the total residual, $a_{ij}$ is the PD observed on the processed record and $p_{ij}$ is the predicted value. The total residual is divided into three parts: $c_k$, the average bias of the real PDs relative to predicted ones, $\Delta_{Bj}$, inter-event residuals, and $\Delta_{Wj}$, intra-event residuals.

With the view of engineering perspective, the calculated directions with PD≥ 3 cm are included in the residual analyses. Since the Burks and Baker (2016) [8] predictive model is based on the PDs in the slip direction of earthquake simulations, the computed values are compared with those obtained on FP components of strike slip earthquakes and FN component of normal faulting earthquakes. Figure 6 exhibits the obtained total, inter- and intra-event residuals with the Burks and Baker (2016) [8].

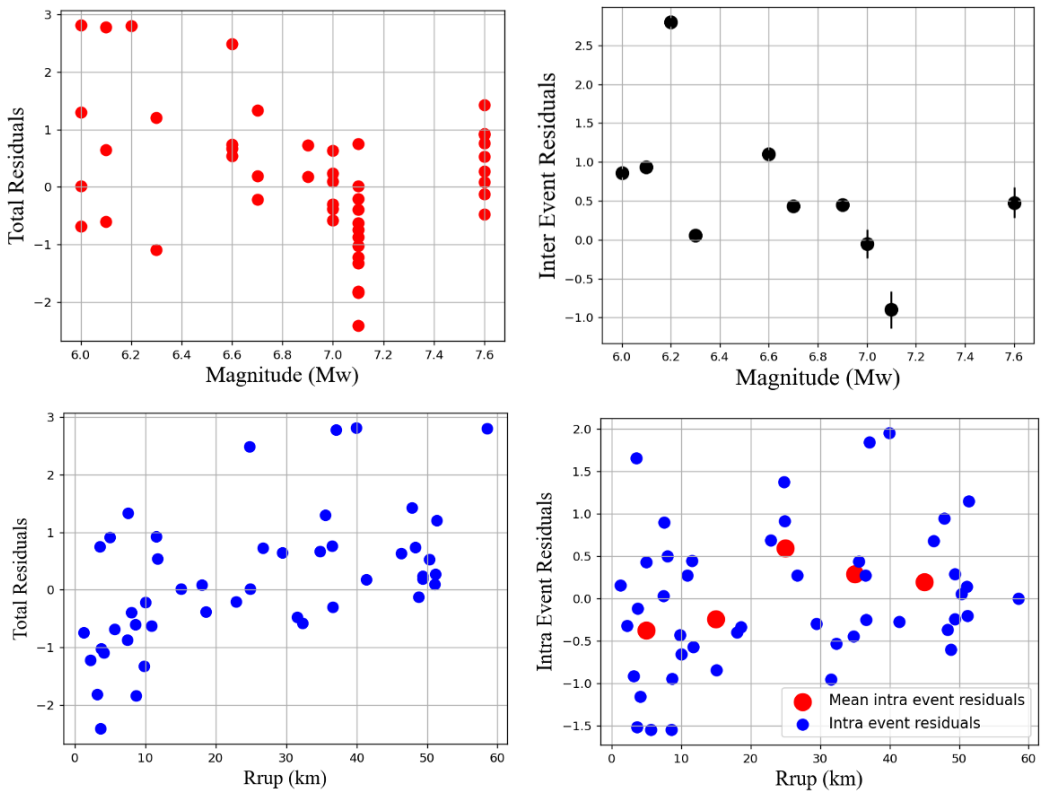


Figure 6: Distribution of (left) the total residuals of PDs with Mw and the Rrup (right) inter-event and intra-event residual distribution of PDs with Mw and the Rrup

Burks and Baker (2016) [8] is found useful to estimates the PDs to some extent. For instance, PDs of the 1999 Kocaeli (Mw 7.6) earthquakes and those of the earthquakes with magnitude ranging between Mw 6.6 to Mw 6.9 are well captured by Burks and Baker (2016) [8] predictive model. Nevertheless, in a broader sense, it is found that the model needs to be adjusted to Turkey earthquakes.

## 5 TURKEY ADJUSTED VERSION OF BURKS AND BAKER (2016) PD PREDICTIVE MODEL

Burks and Baker (2016) [8] model is revised with PD values of Turkish strong motion records. A random-effects regression is executed and plots of the residuals are utilized to evaluate the differences in magnitudes and distances. Modification of the predictive model is conducted by removing the observed trends on the residual graphics. First, a linear trend is found in the distribution of the inter-event residuals of the earthquakes and it is removed by incorporating in the prediction equation. Then, the intra-event residuals of the partly modified model are evaluated. It is found that in the first 10 km, the scatter of data with Rrup is quite different. Therefore, the distribution of intra event residuals are evaluated separately for the first 10 km and 10-50 km. Consecutive inter- and intra-event adjustments are defined as cycles. After 4 cycles, Turkey adjusted version of Burks and Baker (2016) [8] predictive model is obtained as:

Rrup > 10km:

$$Ln(cot^{-1}(0.3Rrup)) + 0.672Mw + 0.0113Rrup - 0.63994$$

Rrup ≤ 10km: (3)

$$Ln(cot^{-1}(0.3Rrup)) + 0.672Mw + 0.0327Rrup - 0.9847$$

Comparisons of the inter-event residuals of Burks and Baker (2016) [8] and its Turkey-adjusted version are illustrated in Figure 7. The conformity of the adjusted equation is found well.

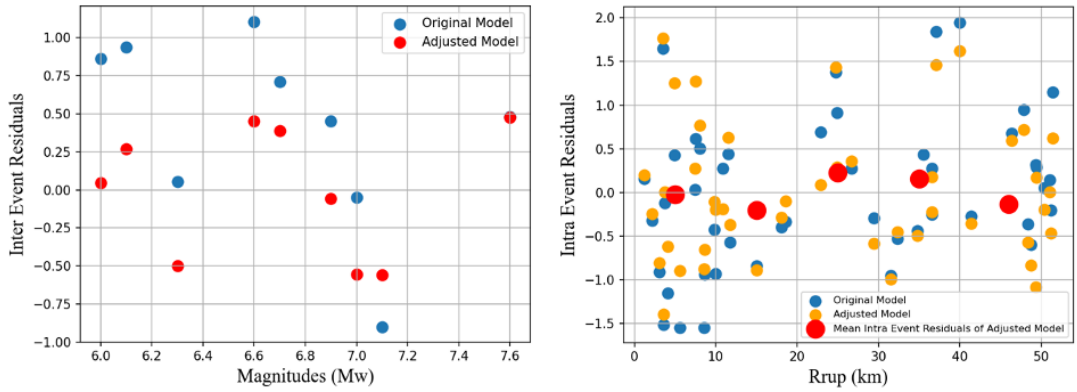


Figure 7: The comparison of the inter- and intra-event residuals of Burks and Baker (2016) and its Turkey-adjusted version

## 6 CONCLUSION

Near fault effects can be incorporated in seismic design of structures by selecting and scaling the actual ground motions. However, since the PD is hidden on account of the standard processing methods such as filtering the low frequency portion of the motion, there has been a need for identification of the fling containing ground motion records. In this study, an improved data processing scheme is presented. Then, by exposing the near fault records to the proposed scheme, for the first time, PD database of Turkey is compiled, which enables structural engineers to select the appropriate motions. Through the processed earthquakes in Turkey, NESS-v2 database containing the worldwide data is remarkably augmented.

In addition, obtained PDs are utilized to evaluate the performance of the Burks and Baker (2016) [8] predictive models. Due to scarcity of empirical data, prediction models are mainly based

on earthquake simulations, which is possibly the reason behind the discrepancies. Aligned with this interpretation, Burks and Baker (2016) [8] is adjusted to Turkey earthquakes by utilizing the residual plots of the created database.

## ACKNOWLEDGEMENTS

This study was supported by Boğaziçi University Research Fund Grant Number 19201.

## REFERENCES

[1] Iwan, W.D.; Moser, M.A.; Peng, C. Some observations on strong-motion earthquake measurement using a digital accelerograph. Bull. Seismol. Soc. Am. 1985, 75, 1225–1246.

[2] Boore DM. Effect of baseline corrections on displacements and response spectra for several recordings of the 1999 Chi-Chi, Taiwan, earthquake. Bulletin of the Seismological Society of America 2001;91(5):1199–211

[3] Yu, S.-B., L.-C. Kuo, Y.-J. Hsu, H.-H. Su, C.C. Liu, C.-S. Hou, J.-F. Lee, T.-C. Lai, C.C. Liu, C.-L. Liu, T.-F. Tseng, C.-S. Tsai, and T.-C. Shin, Preseismic deformation and coseismic displacements associated with the 1999 Chi-Chi, Taiwan, earthquake., Bulletin of the Seismological Society of America., 91 (5), 995-1012, 2001.

[4] Abrahamson NA. Velocity pulses in near-fault ground motions. In: Proceedings of the UC Berkeley - CUREE Symposium in Honor of Ray Clough and Joseph Penzien. Berkeley, California; 2002, p. 40–1.

[5] Kalkan E, Kunnath SK. Effects of fling step and forward directivity on seismic response of buildings. Earthquake Spectra 2006;22(2):367–90

[6] Wu YM, Wu CF. Approximate recovery of coseismic deformation from Taiwan strong-motion records. Journal of Seismology 2007;11:159–70.

[7] Chao, W. A., Y. M. Wu, and L. Zhao (2010). An automatic scheme for baseline correction of strong- motion records in coseismic deformation determination, J. Seismol. 14, no. 3, 495–504

[8] Burks, L. S., and J. W. Baker (2016). A predictive model for fling-step in near-fault ground motions based on recordings and simulations, Soil Dynam. Earthq. Eng. 80, 119–126, doi: 10.1016/j.soil- dyn.2015.10.010.

[9] Istituto Nazionale di Geofisica e Vulcanologia (INGV) Working Group "GPS Geodesy (GPS Data and Data Analysis Center)" (2016). Preliminary Co-seismic Displacements for the October 26 (Mw 5.9) and October 30 (Mw 6.5) Central Italy Earthquakes from the Analysis of GPS Stations, doi: 10.5281/zenodo.167959.

[10] Konca, A. O., Guvercin, S. E., Ozarpaci, S., Ozdemir, A., Funning, G. J., Dogan, U., Ergintav, S., Floyd, M., Karabulut, H., Reilinger, R., Slip distribution of the 2017 Mw6.6 Bodrum–Kos earthquake: resolving the ambiguity of fault geometry, Geophysical Journal International, Volume 219, Issue 2, November 2019, Pages 911–923, https://doi.org/10.1093/gji/ggz332

[11] D'Amico, M.; Felicetta, C.; Schiappapietra, E.; Pacor, F.; Gallovicˇ, F.; Paolucci, R.; Puglia, R.; Lanzano, G.; Sgobba, S.; Luzi, L. Fling, Effects from Near-Source Strong-Motion Records: Insights from the 2016 Mw 6.5 Norcia, Central Italy, Earthquake. Seism. Res. Lett. 2018, 90, 659–671.

[12] Konca, A. O., Cetin S., Karabulut, H., Reilinger, R., Dogan, U., Ergintav, S., Cakir, Z., Tari, E.,The 2014, MW6.9 North Aegean earthquake: seismic and geodetic evidence for coseismic slip on persistent asperities, Geophysical Journal International, Volume 213, Issue 2, May 2018, Pages 1113–1120, https://doi.org/10.1093/gji/ggy049

[13] Schiappapietra,E.; Felicetta, C.; D'Amico, M. Fling-Step Recovering from Near-Source Waveforms Database. *Geosciences* **2021**, *11*, 67. https://doi.org/ 10.3390/geosciences11020067

[14] Dogru, A., Bulut, F., Yaltirak, C., Aktug, B.,Slip distribution of the 2020 Elazığ Earthquake (Mw 6.75) and its influence on earthquake hazard in the Eastern Anatolia, Geophysical Journal International, Volume 224, Issue 1, January 2021, Pages 389–400, https://doi.org/10.1093/gji/ggaa471

[15] Aktuğ, B., Tiryakioğlu, İ., Sözbilir, H., Özener, H., Özkaymak, Ç., Yiğit, C. Ö., Softa, M. (2021). GPS derived finite source mechanism of the 30 October 2020 Samos earthquake, Mw = 6.9, in the Aegean extensional region. Turkish Journal of Earth Sciences, 30(S1), 718–737

[16] Disaster And Emergency Management Authority (1973). Turkish National Strong Motion Network [Data set]. Department of Earthquake, Disaster and Emergency Management Authority, https://doi.org/10.7914/SN/TK

[17] Engineering Strong Motion Database (ESM) (Version 2.0). Istituto Nazionale di Geofisica e Vulcanologia (INGV). https://doi.org/10.13127/ESM.2

[18] Burks, Lynne S., and Jack W. Baker. Fling in near-fault ground motions and its effect on structural collapse capacity. *Proceedings of the 10th National Conference in Earthquake Engineering*, Earthquake Engineering Research Institute, Anchorage, AK, 2014.

[19] Boore DM, Bommer JJ. Processing of strong-motion accelerograms: needs, options and consequences. *Soil Dynamics and Earthquake Engineering* 2005; **25**: 93–115.

[20] Trifunac, M. D. and Brady, A. G. (1975) A study on the duration of strong earthquake ground motion. Bulletin of the Seismological Society of America, 65 (3). pp. 581-626. ISSN 0037-1106.

[21] Gülerce Z, Kargıoğlu B., Abrahamson N.A., Turkey-Adjusted NGA-W1 Horizontal Ground Motion Prediction Models. Earthquake Spectra. 2016;32(1):75-100. doi: 10.1193/022714EQS034M

[22] Hisada, Y., and J. Bielak (2003). A theoretical method for computing near-fault ground motions in layered half-space considering static offset due to surface faulting, with a physical interpretation of fling step and rupture directivity, Bull. Seismol. Soc. Am. 93, no. 3, 1154–1168.

[23] Akbaş B., Tetik T., Önder F.M., Sopacı E., Tanırcan G., Ozacar A.A., and Gulerce Z. (2023). The New Turkish Strong Motion Dataset (N-TSMD) for earthquake engineering applications. Submitted to Bulletin of Earthquake Engineering

[24] International Conference of Building Officials (2006). International Building Code, Whittier, CA.

[25] International Conference of Building Officials (2007). California Building Code, Whittier, CA.

[26] American Society of Civil Engineers (2005), ASCE-7 Minimum Design Loads for Buildings, Reston, VA.

COMPDYN 2023
9th ECCOMAS Thematic Conference on
Computational Methods in Structural Dynamics and Earthquake Engineering
M. Papadrakakis, M. Fragiadakis (eds.)
Athens, Greece, 12-14 June 2023

# NUMERICAL PRE-DICTION OF THE SEISMIC BEHAVIOUR OF A MASONRY VAULT MOCK-UP USING THE NOSA-ITACA CODE

**Daniele Pellegrini**[1]

[1] Institute of Information Science and Technologies "A. Faedo" (ISTI-CNR), Pisa, Italy

e-mail: daniele.pellegrini@isti.cnr.it

## Abstract

*Masonry vaults are widely employed in ancient constructions and play a crucial role in their static and dynamic response. Even if they are designed to withstand gravity and dead loads, these structural elements must also resist dynamic excitations caused by traffic and earthquakes; hence, the knowledge of their behaviour still requires in-depth analyses from experimental and numerical points of view. Within the framework of the SERA.TA project (Seismology and Earthquake Engineering Research Infrastructure Alliance for Europe), a blind pre-diction contest has been organized to assess the numerical analyses capability to predict the seismic response of a 1:1 scale model of masonry cross vault, realized and tested at LNEC laboratory (Portugal). This paper describes the analyses conducted on a numerical model of the vault created by NOSA-ITACA, a code developed in-house by ISTI-CNR for the analysis and calibration of masonry structures. The experimental accelerations, displacements, and crack patterns have been compared with the predicted numerical ones achieved in the blind pre-diction phase, by performing a nonlinear dynamic analysis of the unstrengthened finite element model of the vault.*

**Keywords:** no tension material, masonry vault, groin vault, nonlinear elasticity, nonlinear dynamic analysis, seismic behavior, masonry material.

## 1 INTRODUCTION

Masonry vaults are widely employed in ancient constructions and play a crucial role in their static and dynamic behaviour. Even if they are specifically designed to endure heavy vertical loads, they must usually also withstand dynamic excitations caused by traffic and earthquakes; hence, the knowledge of their behaviour still requires in-depth analyses from experimental and numerical points of view.

Focusing on groin vaults, often employed to cover churches' naves and palaces' rooms, the most frequent cause of their failure is represented by the support movements resulting in a shearing action in the horizontal plane of the structure.

From an experimental point of view, few researchers conducted full experimental campaigns on vault shear behaviour as reported and described in detail in [1], while from a numerical perspective, plenty of approaches were developed to examine the structural behaviour of these structures ranging from limit analysis to Finite Element Method (FEM) and Discrete Element Method (DEM) [2, 3].

Nowadays, FEM is one of the most adopted procedures for structural analysis, with many constitutive equations capable of analysing the masonry response, modelled as an equivalent continuum [4-7], or as an assemblage of macro elements with few degrees of freedom and a pre-established behaviour [3, 8, 9].

Within the framework of the SERA.TA project (Seismology and Earthquake Engineering Research Infrastructure Alliance for Europe), a blind pre-diction contest has been organised to assess the numerical analyses approaches' capability to predict the seismic response of a full-scale masonry cross vault tested at LNEC laboratory (Portugal), considering its un-strengthened and strengthened configuration [10].

This paper describes the analyses conducted on a numerical model of the vault created by NOSA-ITACA (www.nosaitaca.it/software/), a finite element code developed in-house by ISTI-CNR, for the analysis and calibration of masonry structures.

The numerical simulations were performed before the experimental tests, modelling the masonry vault by the constitutive equation of no-tension (or *masonry-like*) materials implemented in NOSA-ITACA [4].

The numerical results obtained for the vault un-strengthened configuration have been compared to the experimental one in terms of frequencies, mode shapes, accelerations, displacements, and crack patterns [11].

## 2 MASONRY VAULT FINITE ELEMENT MODEL

The groin vault investigated in this paper has been built and tested at the National Laboratory for Civil Engineering (LNEC) in Portugal.

The geometry of the mock-up is about 3.5x3.5 m in plan and includes: two semi-circular barrel vaults with a net span of 2.9 m, a rise of 0.80 m and a constant thickness of 0.12 m; two masonry piers clamped at the base representing the fixed vault’s support; two 0.84x0.84m steel blocks representing the movable supports; three couples of steel rods linking the four abutments [10].

The specimen numerical model has been created by importing the vault CAD model in the NOSA-ITACA code.

NOSA-ITACA is free software developed in-house by ISTI-CNR to disseminate the use of mathematical models and numerical tools in the field of Cultural Heritage. The code has been developed to study the static and dynamic behaviour of masonry structures. In recent years, it has been updated by adding several features that enable modal analysis, linear perturbation analysis [12], and model updating [13].

A refined finite-element model of the vault has been built, assuming a macro-modelling approach. The mesh, shown in Figure 1, consists of 83664 4-node isoparametric tetrahedrons, 7612 8-node isoparametric hexahedrons and six 2-node isoparametric truss elements (element n.25, n.8 and n.35 of the NOSA-ITACA library) with 29353 nodes, for a total of 88056 degrees of freedom. Truss elements are used to model the tie-rods, assuming a cross-section of $8.04 \cdot 10^{-4}$ m$^2$ (corresponding to steel bars of 32 mm diameter). The material forming the vaults has been modelled by the constitutive equation of *masonry-like* (or no-tension) materials that models masonry as an isotropic homogeneous nonlinear elastic material with zero or low tensile strength $\sigma_t$ and infinite or bounded compressive strength $\sigma_c$ [4]. This equation can consider some of the masonry's peculiarities, particularly its inability to withstand significant tensile stresses.

The other parts of the mesh (steel blocks, beams, tie-rods, pillars and infill material) are modelled assuming a linear elastic behaviour. The materials' mechanical properties used in the blind pre-diction analysis are summarized in Table 1; the masonry's elastic modulus $E$ and Poisson ratio $\nu$ properties used are based on preliminary experimental tests provided to the participants beforehand [10]. Tensile and compressive strengths $\sigma_t$ and $\sigma_c$ are taken equal to 0.0 and 4.55 MPa (the latter obtained as a ratio between the experimental compressive strength [10] and a partial factor for material equal to 2 as suggested by Italian regulations NTC2018 [14]). Regarding the boundary conditions, the piers are assumed to be clamped at the base (red dots in Figure 1). At the same time, the steel masses and IPE beams have the vertical direction fixed, allowing movement in the longitudinal and transverse directions (blue dots in Figure 1).

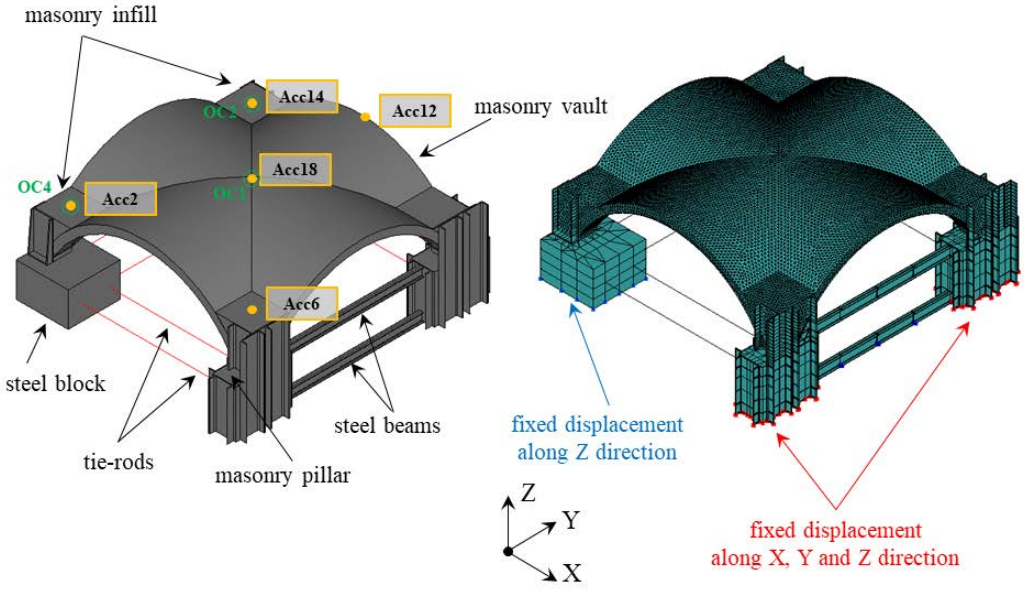


Figure 1: Vault geometry and finite element model

| | Masonry vault | Infill and pillars | Steel blocks and beams |
|---|---|---|---|
| $E$ [GPa] | 2.223 | 2.223 | 210.0 |
| $\rho$ [kg/m$^3$] | 2255.2 | 2255.2 | 7880.0 |
| $\nu$ | 0.2 | 0.2 | 0.3 |

| | | | |
|---|---|---|---|
| $\sigma_t$ [MPa] | 0.00 | -- | -- |
| $\sigma_c$ [MPa] | 4.55 | -- | -- |

Table 1: Mechanical materials properties. $E$, Young's modulus; $\rho$, mass density; $\nu$, Poisson ratio; $\sigma t$, tensile strength; $\sigma c$, compressive strength

## 3 DYNAMIC BEHAVIOUR OF THE UN-STRENGTHENED VAULT

In the blind pre-diction phase, a preliminary modal analysis has been performed to estimate the numerical model's dynamic behaviour and check the correspondence between experimental and numerical mode shapes.

Table 2 reports the experimental $f_{exp}$ [11] and numerical frequencies $f_{num}$, the absolute relative error and modal participation factors calculated by NOSA-ITACA. The table shows that the frequencies of the un-strengthened model are higher than the measured one, probably due to an unsuitable masonry's elastic modulus provided by the blind pre-diction organizers. At the same time, there is a good matching between the first, second and fourth numerical mode shapes and the first three experimental ones reported in [11] that are, respectively, a shear mechanism along the Y direction, a bending mode in the X direction and a vertical mode shape along Z, as sketched in Figure 2 [11].

| | $f_{exp}$ [Hz] | $f_{num}$ [Hz] | Relative error [%] | Mx [%] | My [%] | Mz [%] |
|---|---|---|---|---|---|---|
| Mode 1 | 6.15 | 9.33 | 51.50 | 0.00 | 73.30 | 0.00 |
| Mode 2 | 11.62 | 24.85 | 113.86 | 63.53 | 0.00 | 0.04 |
| Mode 3 | -- | 29.59 | -- | 0.00 | 0.00 | 0.00 |
| Mode 4 | 19.39 | 30.88 | 59.26 | 0.06 | 0.00 | 0.08 |

Table 2: Experimental vs numerical frequencies and modal participation factors

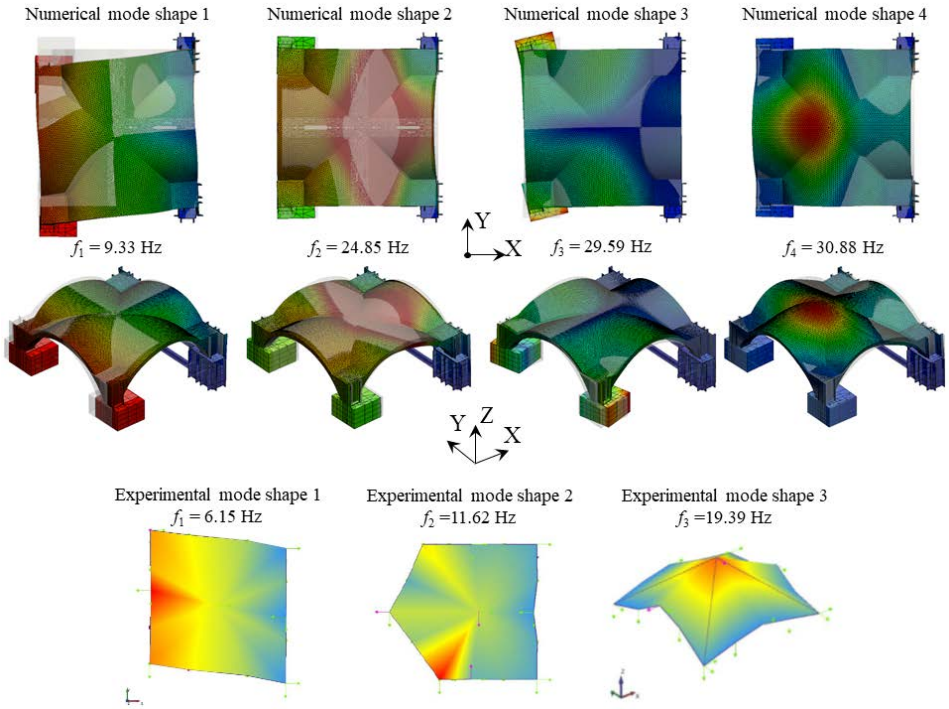


Figure 2: First four numerical mode shapes and the three experimental mode shapes

Subsequently, a nonlinear dynamic analysis has been performed considering the self-weight of the vault and applying at the base, in the Y direction, the accelerogram recorded during the L'Aquila earthquake (Figure 3). The analysis has been carried out assuming a time step of 0.0025 sec and scaling the accelerogram magnitude by 25%, as indicated by the organizers of the contest. The damping matrix has been calculated according to the Rayleigh hypothesis with a damping ratio equal to 2.5%.

In particular, the two Rayleigh coefficients are estimated, assuming the first and the twenty-second frequency as the reference, which involves 86% of the mass in the horizontal directions.

The failure mechanism obtained from the nonlinear dynamic analysis is shown in Figure 3. As seen in the picture, it is predominantly an in-plane shear mechanism accompanied, albeit to a lesser extent, by an in-plane bending of the south and north faces arches; the deformation follows the second mode shape of the vault that looks like a typical asymmetrical mode shape of an arch with lateral displacement according to one direction. The deformed shape, sketched in Figure 3 with a deformation scaling factor equal to 20, occurs at the time t = 4.25 seconds; the contour band refers to the value of the norm of the displacements expressed in meters.

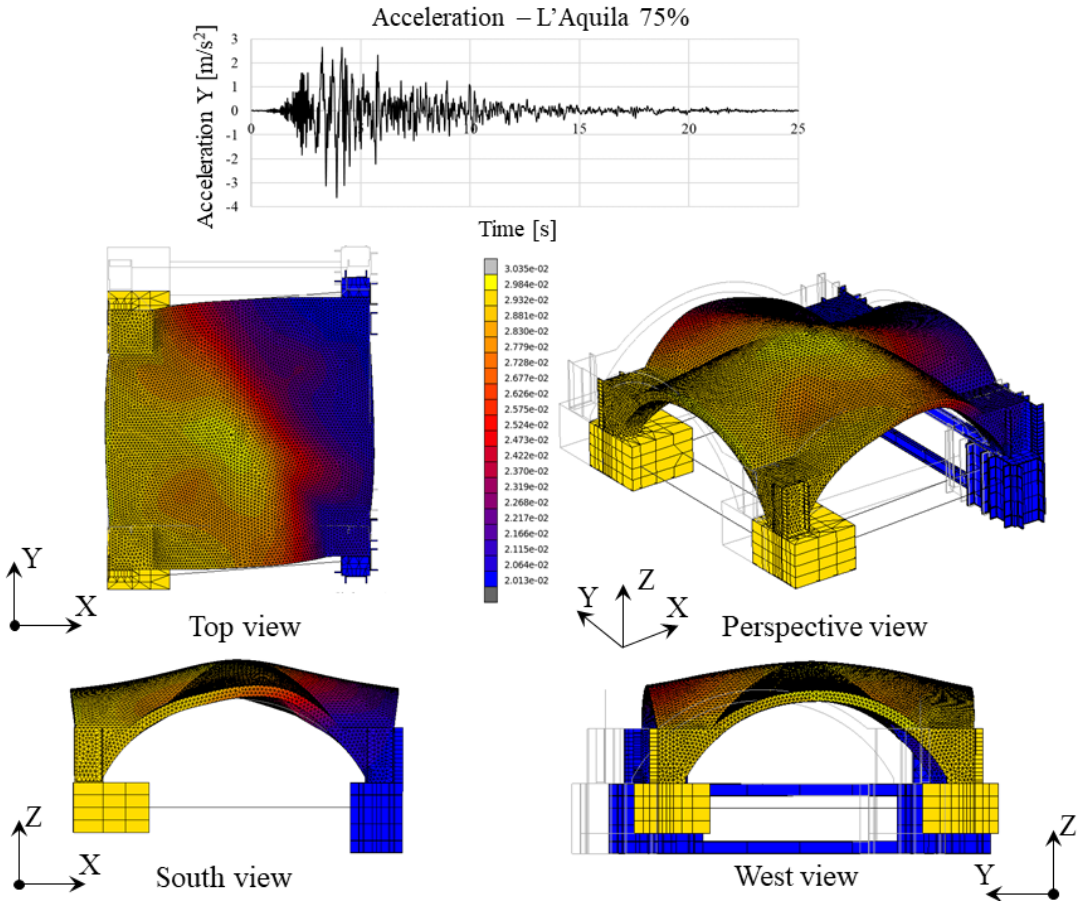


Figure 3: Acceleration time history and vault's deformation shape at failure

Figure 4 shows the crack pattern in terms of EFEQV (the norm of the fracture strain tensor); it is characterized by diagonal cracks, with a high concentration of fracture strain at the top of the vault extrados and near the infill. The numerical fracture distribution matches the experimental damage (shown in the middle of Figure 4), except for the cracks on the webs

that are not visible in the numerical solution. Furthermore, the numerical results show a limited concentration of crushing cracks in small areas near the filling material.

Tables 3 and 4 compare the maximum experimental and numerical total displacements and accelerations of the selected points shown in Figure 1. In terms of displacement, the discrepancy between the results is greater than 90% in the X direction, while in the Y direction it is about 13% except for $OC_{2\text{-}y}$. As concerns the acceleration, the numerical model overestimates, in general, its value in the X and Y directions.

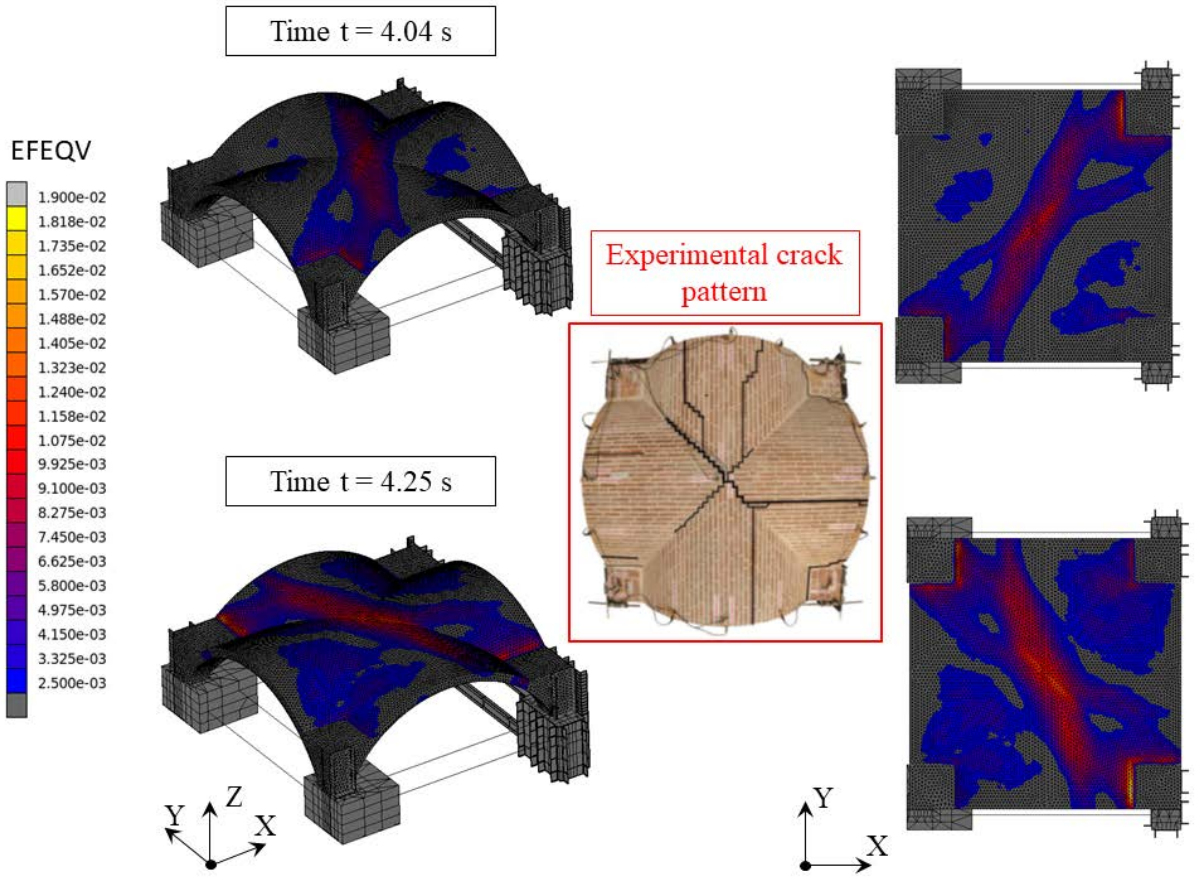


Figure 4: Crack pattern

| | Experimental [mm] | Numerical [mm] | Relative error [%] |
|---|---|---|---|
| $OC_{2\text{-}x}$ | 4.01 | 0.29 | 92.77 |
| $OC_{4\text{-}x}$ | 7.78 | 0.24 | 96.92 |
| $OC_{1\text{-}y}$ | 27.90 | 31.39 | -12.51 |
| $OC_{2\text{-}y}$ | 70.66 | 31.40 | 55.56 |
| $OC_{4\text{-}y}$ | 35.83 | 31.37 | 12.45 |

Table 3: Maximum total displacements (absolute value in mm)

| | Experimental | Numerical | Relative |
|---|---|---|---|

| | [m/s$^2$] | [m/s$^2$] | error [%] |
|---|---|---|---|
| $Acc_{2\text{-}x}$ | 4.39 | 8.56 | -94.99 |
| $Acc_{6\text{-}x}$ | 3.98 | 4.63 | -16.33 |
| $Acc_{12\text{-}x}$ | 3.44 | 4.88 | -41.86 |
| $Acc_{14\text{-}x}$ | 5.23 | 9.55 | -82.60 |
| $Acc_{18\text{-}x}$ | 3.77 | 5.03 | -33.42 |
| $Acc_{2\text{-}y}$ | 4.53 | 5.66 | -24.94 |
| $Acc_{6\text{-}y}$ | 4.51 | 4.90 | -8.65 |
| $Acc_{12\text{-}y}$ | 4.92 | 8.89 | -80.69 |
| $Acc_{14\text{-}y}$ | 4.44 | 6.43 | -44.82 |
| $Acc_{18\text{-}y}$ | 3.44 | 6.11 | -77.62 |

Table 4: Maximum total accelerations (absolute value in m/s$^2$)

## 4 CONCLUSION

The paper describes the results of numerical analyses conducted under the blind pre-diction contest organized within the framework of the SERA.TA project (Seismology and Earthquake Engineering Research Infrastructure Alliance for Europe). The seismic response of a 1:1 unstrengthened masonry cross vault specimen, realized and tested at the LNEC laboratory, has been simulated by the NOSA-ITACA code, a non-commercial software developed by ISTI-CNR.

A refined finite-element model of the vault has been created, modelling masonry as a no-tension material with zero tensile strength and limited compressive strength. A preliminary modal analysis has shown the ability of the model to fit the specimen experimental mode shapes despite an overestimation of the associated frequencies.

Then, a nonlinear dynamic analysis was carried out, assigning a scaled real accelerogram at the mesh base. The numerical results have been compared to the experimental ones in terms of crack pattern, failure mechanism, maximum total displacements and accelerations at selected points. The crack pattern fits the experimental damage even if the fractures along the specimen diagonals do not form simultaneously. A damage concentration is also close to the infill, while cracks on the webs are missing.

Regarding the displacements and accelerations, the numerical model generally overestimates their values. The model will be calibrated and improved in the post-diction phase using the experimental modal properties and model updating techniques.

## ACKNOWLEDGEMENT

This research has been supported by Italian National Research Council within the call Progetti di Ricerca @CNR, 2022–2024 (Revolution Project- open-source platform oriented toward digital twins: 3d digitization techniques, vibration monitoring and finite element models for evaluating the conservation status of historical buildings and civil infrastructures). This support is gratefully acknowledged.

## REFERENCES

[1] Bianchini, N., Mendes, N., Calderini, C. et al. “Seismic response of a small-scale masonry groin vault: experimental investigation by performing quasi-static and shake table tests”. *Bulletin of Earthquake Engineering* 20, 1739–1765, 2022. https://doi.org/10.1007/s10518-021-01280-0.

[2] Gaetani, A. Seismic performance of masonry cross vaults: Learning from historical developments and experimental testing (Vol. 91), 2020. Sapienza Università Editrice. ISBN 978-88-9377-144-3. https://doi.org/10.13133/9788893771443

[3] Cattari, S., Calderoni, B., Caliò, I. et al. “Nonlinear modeling of the seismic response of masonry structures: critical review and open issues towards engineering practice”. *Bulletin of Earthquake Engineering* 20, 1939–1997, 2022. https://doi.org/10.1007/s10518-021-01263-1.

[4] Lucchesi, M., Padovani, C., Pasquinelli, G., & Zani, N. (2008). Masonry constructions: mechanical models and numerical applications. Springer Science & Business Media. https://doi.org/10.1007/978-3-540-79111-9

[5] Nodargi, N. A., & Bisegna, P. (2019). “A mixed finite element for the nonlinear analysis of in‐plane loaded masonry walls”. International Journal for Numerical Methods in Engineering, 120(11), 1227-1248. https://doi.org/10.1002/nme.6179

[6] Bilko P, Małyszko L. (2020) “An Orthotropic Elastic-Plastic Constitutive Model for Masonry Walls”. Materials. 13(18):4064. https://doi.org/10.3390/ma13184064

[7] Lourenço, P. B., & Gaetani, A. (2022). Finite Element Analysis for Building Assessment: Advanced Use and Practical Recommendations. Taylor & Francis. eBook ISBN 9780429341564 https://doi.org/10.1201/9780429341564

[8] Malomo, D., & DeJong, M. J. (2022). “A Macro‐Distinct Element Model (M‐DEM) for simulating in‐plane/out‐of‐plane interaction and combined failure mechanisms of unreinforced masonry structures”. Earthquake Engineering & Structural Dynamics, 51(4), 793-811. https://doi.org/10.1002/eqe.3591

[9] Vadalà, F., Cusmano, V., Funari, M. F., Caliò, I., & Lourenço, P. B. (2022). “On the use of a mesoscale masonry pattern representation in discrete macro-element approach”. Journal of Building Engineering, 50, 104182. https://doi.org/10.1016/j.jobe.2022.104182

[10] Blind Pre-diction Competition - Sera.ta - Seismic Response of Masonry Cross Vaults: Shaking table tests and numerical validations. Blind pre-diction data: DOI 10.5281/zenodo.7624666

[11] Postdiction Competition - Sera.ta - Seismic Response of Masonry Cross Vaults: Shaking table tests and numerical validations. Post diction data: DOI 10.5281/zenodo.7624791

[12] D. Pellegrini, M. Girardi, P.B. Lourenco, M.G. Masciotta, N. Mendes, C. Padovani, L.F. Ramos “Modal analysis of historical masonry structures: linear perturbation and software benchmarking” Construction and Building Materials, Volume 189, 20 November 2018, pp 1232-1250, doi: https://doi.org/10.1016/j.conbuildmat.2018.09.034.

[13] M. Girardi, C. Padovani, D. Pellegrini, L. Robol “Model updating procedure to enhance structural analysis in the FE code NOSA-ITACA” Journal of Performance of

Constructed Facilities, Vol. 33, Issue 4 (August 2019), DOI: 10.1061/(ASCE)CF.1943-5509.0001303.

[14] Ministero delle Infrastrutture e dei Trasporti “Aggiornamento delle Norme tecniche per le costruzioni”. Decreto 17 gennaio 2018.

COMPDYN 2023
9th ECCOMAS Thematic Conference on
Computational Methods in Structural Dynamics and Earthquake Engineering
M. Papadrakakis, M. Fragiadakis (eds.)
Athens, Greece, 12-14 June 2023

# BLIND PREDICTION OF SHAKE TABLE TESTS ON A FULL-SCALE UNSTRENGTHENED MASONRY CROSS VAULT: COMBINED FINITE-DISCRETE ELEMENT MODEL

**O. AlShawa[1], D. Liberatore[2] and L. Sorrentino[1].**

[1] Sapienza University of Rome, Department of Structural and Geotechnical Engineering
Via Antonio Gramsci 53, 00197 Rome, Italy
e-mail: {*omar.alshawa; luigi.sorrentino}@uniroma1.it

[2] Sapienza University of Rome, Department of History,Representation and Restoration of Architecture
Piazza Borghese 9, 00186 Rome, Italy
e-mail: domenico.liberatore@uniroma1.it

## Abstract

*This work presents the blind results of the non-linear dynamic response of a three-dimensional finite-discrete element model of a full-scale unstrengthened masonry cross vault tested on a shake table. The cross vault is generated by the intersection of two semi-circular barrel brick vaults. The boundary conditions are asymmetric, with two piers fixed to the shake table and a steel frame between them to simulate the presence of a continuous lateral wall, while the other two piers are free to move along all directions on wheels to simulate the colonnade-between-naves condition. The seismic action was applied along the longitudinal direction of the specimen (parallel to the simulated lateral wall), and several sequential seismic tests, with increasing amplitude, were scheduled. The model used to blindly predict the test response allows for the elastic finite element modelling of masonry units, or blocks, and the discrete element modelling of the interfaces between them. A tension cut-off governs the interaction at a standard block interface: once this strength is exceeded, no tensile stress can be transmitted,. Shear response is defined by cohesion and friction, and once the cohesive contribution is exceeded, the interface interacts in shear according to Coulomb's behavior. The model was analysed under the scheduled experimental sequence of four amplitude intensity steps. The analysis at a 75% intensity of the selected natural ground motion accelerogram showed the activation of a shear mechanism, with hinges at about one-third of the span of the lateral circular arch, with negligible permanent displacement at the end of the analysis. The model capacity was reached at an amplitude intensity to 200% of the natural accelerogram.*

**Keywords:** Numerical analysis, Church; Seismic behaviour, Unreinforced Masonry, Sequence

## 1 INTRODUCTION

Recent earthquakes have emphasised the high vulnerability of vaulted structures. The behaviour of the vaults plays a relevant role in the seismic response of heritage masonry buildings, as observed in Italy for the 2009 L'Aquila earthquake [1], the 2012 Emilia earthquakes [2] and the 2016–2017 Central Italy earthquake sequence [3], but also for ancient events [4]. The verification of the safety of vaults is crucial [5] as collapse may either entail local damage or affect the whole building the vaults belong to, because of their heavy mass and the significant horizontal thrust on supporting elements. Despite the importance of this topic, evaluating the complex three-dimensional behaviour of vaults is still a significant challenge for both practitioners and researchers.

With the aim of investigating the dynamic response of vaulted structures, a full-scale unstrengthened masonry cross vault was tested on a shake table (Figure 1a) at the Civil Engineering National Laboratory (LNEC) in Lisbon, Portugal, within the Seismology and Earthquake Engineering Research Infrastructure Alliance for Europe (SERA) program and a blind prediction competition was organised [6]. The cross vault was generated by the intersection of two semi-circular barrel brick vaults with constant thickness 0.12 m; the size in plan is about 3.50 × 3.50 $m^2$. The boundary conditions are asymmetric, as costumary in churches, with two piers fixed to the shake table and a steel frame between them to simulate the presence of a continuous lateral wall, whereas the other two piers are free to move on wheels along all directions to simulate the colonnade-between-naves condition. In addition, each pier is connected to the adjacent ones by a couple of steel tie rods to restrain support rotation. Steel plates were added along the height of the supports to increase their stiffness and avoid local failure. An infill, made of brickwork with horizontal courses, is placed on top of each pier, stabilising the vault thrust. Finally, steel masses were added to the supports to simulate the roof weight.

The seismic action was applied along the longitudinal direction of the specimen (parallel to the simulated lateral wall), and an accelerogram, recorded at AQA station during the 2009 L'Aquila earthquake, with peak ground acceleration (PGA) of 4.85 m/$s^2$, was used. Incremental shake-table tests were planned by applying to the natural ground motion the following scale factors: 25, 50, 75 and 100% [6].

In this contribution, a finite-discrete element modelling is used, similar to what done in previous studies on other unreinforced masonry structures [7–12], but never before of a cross vaults.

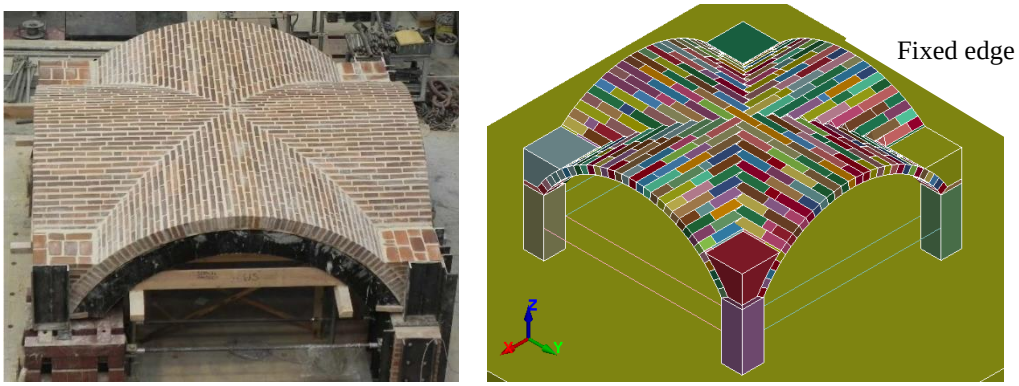


Figure 1Fig. 1 3D view: a) Physical model [6] and b) Numerical model. Blocks are coloured only for presentation purposes, their material properties being homogeneous.

## 2 OVERVIEW OF THE MODELING STRATEGY

The model foundation, as the shake table, was restrained along the *X* and *Z* directions. The overall geometry of the vault model is the same as the prototype, but all piers have a cross-section equal to that at the interface with the vault, neglecting steel additions (Figure 1b). The four piers are monolithic and cannot fracture along their height to account for the steel elements used in the physical prototype. Two piers are fixed at the base whereas the other two, corresponding to those resting on wheels in the prototype, have a very low strength interface at their base. The steel frame between piers A and C (Figure 2b) was not modelled, but the top of these piers experiences the same displacement of the shake table along the *Y* direction.

The model was implemented within LS-DYNA [13–15], allowing for the elastic finite element modelling of masonry units and the discrete modelling of the interfaces between them. Units are modelled as linear elastic 8-node solid elements with a single integration point. The major disadvantage of one-point integration is the need to control the zero-energy modes that arise, called hourglassing modes, which might entail divergence of the solution. Hourglass is controlled by utilising a Flanagan-Belytschko stiffness-type stabilisation [13]. The model does not explicitly consider mortar; instead, contact interfaces are used. Masonry blocks have the following boxing size: 250 × 120 × 118 mm$^3$, basically having the same length and width and double the average thickness of actual units. The blocks are wedge-shaped because interfaces have zero thickness and cannot account for the variable thickness of prototype mortar joints. The total number of blocks is 313, the total number of finite elements is 1147, and the total number of nodes is 4952. Two cutting planes are present along the groins, as in the actual construction (Figure 3).

The properties of the materials are reported in Table 1. Given the differences between the physical prototype and the numerical model, and in order to get the same mass, the non-fixed-base piers have a density equal to 26 438 kg/m$^3$, whereas in the fixed ones the density is equal to 3645 kg/m$^3$.

The tie rods are modelled as discrete elastic springs and, in order to account for the different lengths, the four rods along the *X* direction have an elastic stiffness equal to 7.23 $10^4$ kN/m, whereas in the case of the two rods along the *Y* direction, the stiffness is equal to 6.16 $10^4$ kN/m (Figure 1). No prestress force was applied.

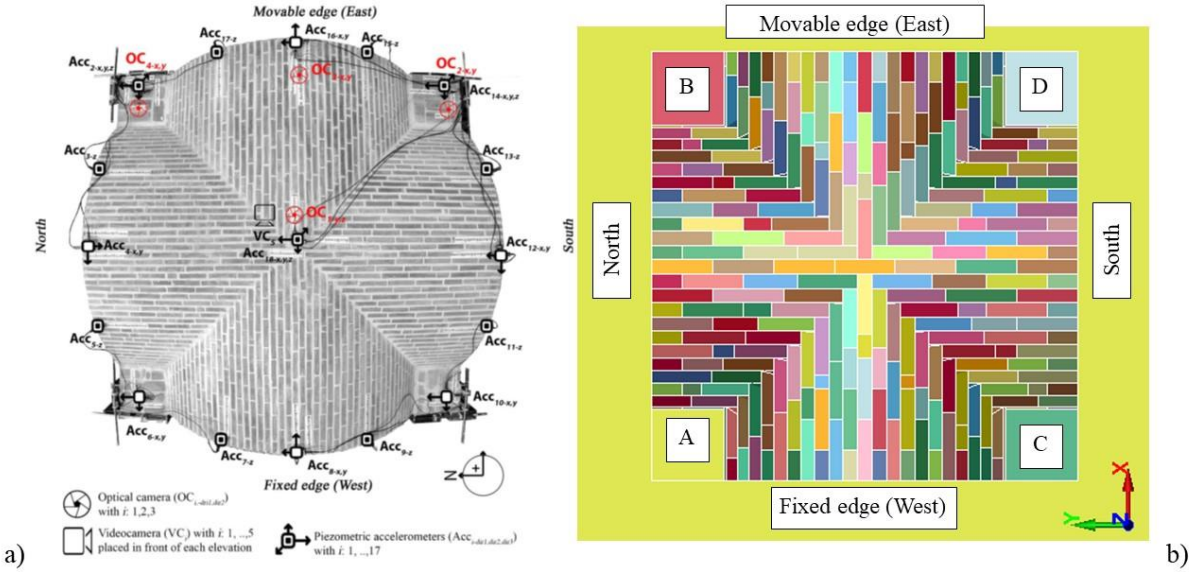


Figure 2 top view: a) Setup of the configuration [6] and b) Numerical model.

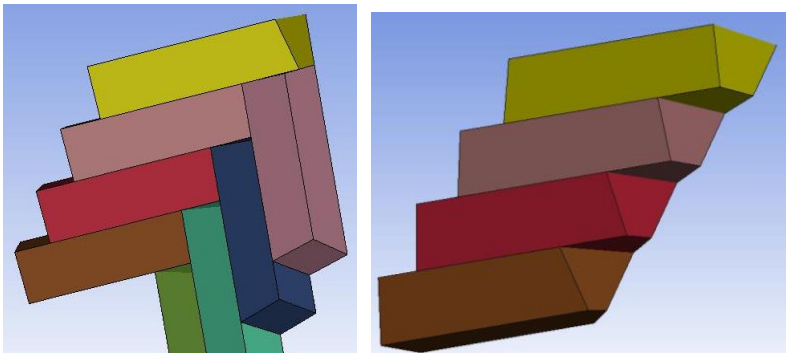

Figure 3 Blocks interlocked along the intersection between the webs of the vault.

| parameter | block[(1)] | non-fixed-base piers [(2)] | fixed-base piers [(2)] |
|---|---|---|---|
| Density, $\rho$ (kg/m$^3$) | 2225 | 26 438 | 3645 |
| Young's modulus, $E$ (GPa) | 2.223 | 2.223 | 2.223 |
| Poisson's ratio, $\nu$ (-) | 0.25 | 0.25 | 0.25 |

[(1)] informative leaflet [6]; [(2)] estimated

Table 1 Material properties

The adopted failure criterion at a standard block interface is based on tensile normal stress, i.e. failure occurs when the following inequality is satisfied:

$$\sigma_n \geq NFLS \tag{1}$$

where:
$\sigma_n$ is the normal stress on the contact surface;
*NFLS* is the normal (tensile) failure limit stress.

Once this strength is exceeded, complete separation occurs at the interface, and the latter can interact only in compression once the crack is closed. The shear response is defined by cohesion, *SFLS*. Once cohesion is exceeded, the interface interacts in shear according to Coulomb's friction behaviour, depending on static and dynamic friction coefficients (*FS*, *FD*). All interfaces present the same properties, with the only exception of the interface at the base of the non-fixed piers which has negligible cohesion. The most relevant parameters are reported in Table 2. Finally, a 5% stiffness-proportional damping coefficient was assumed for all materials.

| parameter | interface between blocks | interface at the base of the two non-fixed piers |
|---|---|---|
| *NFLS* (kPa) | 31.000[(1)] | 0.100[(2)] |
| *SFLS* (kPa) | 31.000[(2)] | 0.100[(2)] |
| *FS*, *FD* (-) | 0.785[(2)] | 0.785 [(2)] |

[(1)] informative leaflet [6]; [(2)] estimated

Table 2 Interface parameters

## 3 PREDICTIONS

The model was analysed under a sequence of four amplitude intensity steps (10, 25, 50 and 75%) of the ground accelerogram, according to the scheduled testing sequence. In Figure 4 the maximum response during the analysis at 75% shaking intensity is shown. The analysis at the last step shows the activation of an in-plane shear failure mechanism with hinges at about one-third of the length of the free span of the lateral circular arch, as recognisable from the East and West views in Figure 4. No cracks along the diagonals or close to the groins are present. At the end of the analysis, permanent displacements are negligible.

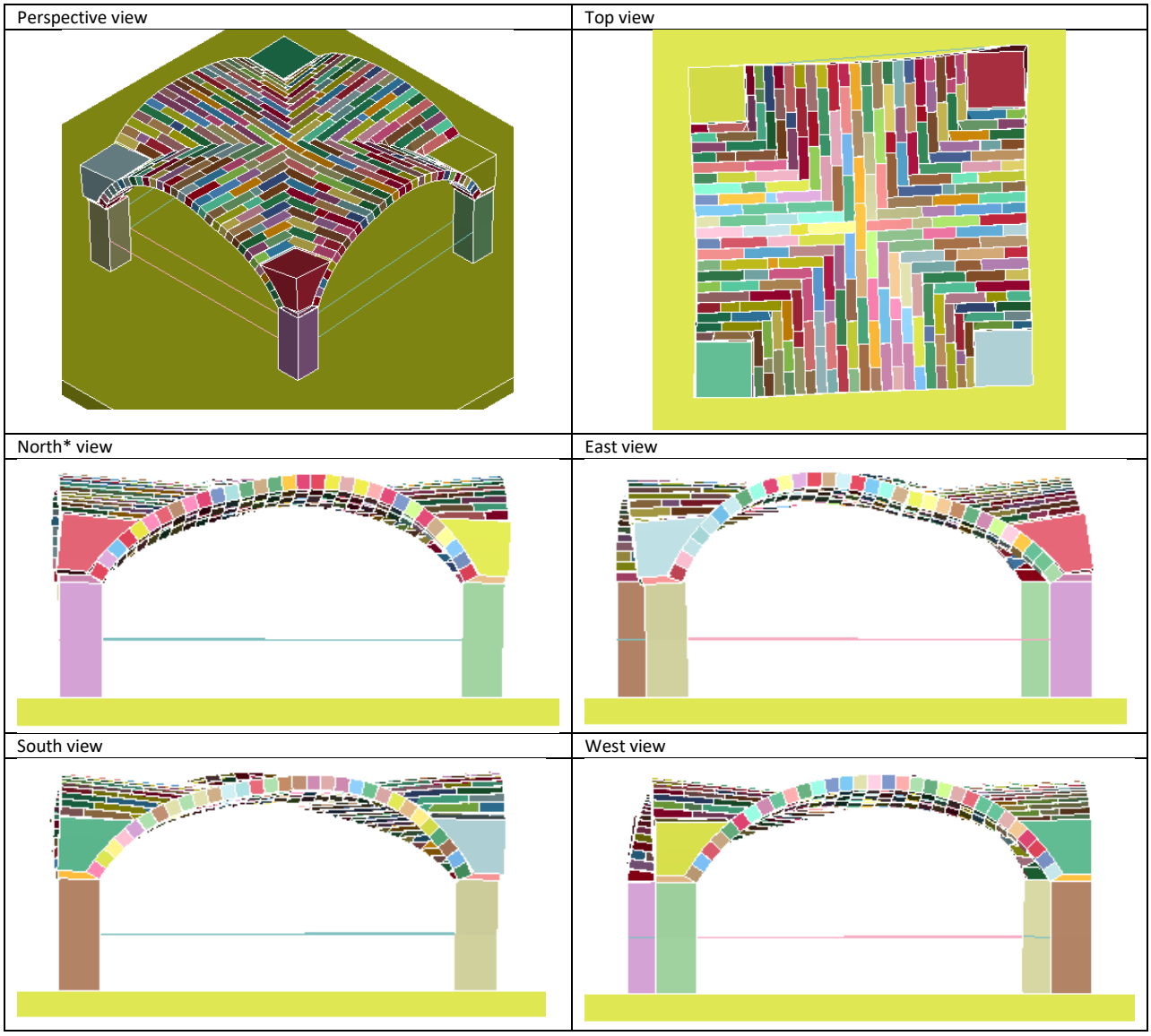


Figure 4 Numerical prediction of damage (75% intensity of shaking). Scale factor 5 applied to the deformations.

Further sequential analyses were performed according to the following intensity steps: 100, 125, 150, 175, and 200%. The collapse occurred at the very beginning of the last step, with PGA about 9.70 m/s$^2$ (Figure 5).

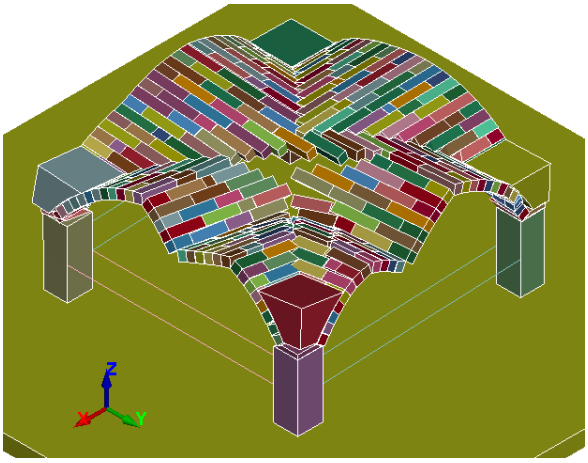

Figure 5 Numerical prediction of damage (200% shaking intensity). Scale factor 5 applied to the deformations.

## 4 CONCLUSIONS

The blind test prediction competition of a full-scale unstrengthened masonry cross vault tested in Lisbon represented the opportunity to implement a finite-discrete element model, which accounts for crack formation, complete separation and new contact formation. The modelling strategy was used to evaluate the ultimate displacement, the load-bearing capacity and the progressive deformation of the vault up to collapse under seismic action. While material properties were set equal to the experimental ones, the main limitation of the model resides in the size of the typical block, which is larger than its physical counterpart. In addition, the interface parameters were estimated to simulate the presence of wheels at the base of the two non-fixed piers. These features may lead to an overestimation of the capacity of the vault.

## ACKNOWLEDGEMENT

The authors thank architect Elena Pagliuso for her assistance in the creation of the 3D geometrical model of the vault. This work was partially funded by the 'Dipartimento di Protezione Civile – Consorzio RELUIS' program. The opinions expressed in this publication are those of the authors and are not necessarily endorsed by the funding bodies. OA acknowledges the financial support provided by Regione Lazio (Progetto Fare Ricerca anno 2022).

## REFERENCES

[1.] Podestà S, Brignola A, Curti E, Parodi S, Lemme A. Damage assessment and seismic vulnerability of churches: the Abruzzo earthquake. In: *Ingegneria Sismica, XXVII*; 2010:21–35.

[2.] Milani G. Lesson learned after the Emilia-Romagna, Italy, 20–29 May 2012 earthquakes: A limit analysis insight on three masonry churches. *Engineering Failure Analysis* 2013; **34**:761–778. doi:https://doi.org/10.1016/j.engfailanal.2013.01.001.

[3.] Borri A, Corradi M, Castori G, Sisti R, De Maria A. Analysis of the collapse mechanisms of medieval churches struck by the 2016 Umbrian earthquake. *International Journal of Architectural Heritage* 2019; **13**(2):215–228. doi:10.1080/15583058.2018.1431731.

[4.] Sorrentino L, Bruccoleri D, Antonini M. Structural interpretation of post-earthquake (19th century) retrofitting on the Santa Maria degli Angeli Basilica, Assisi, Italy. In: *Structural Analysis of Historic Construction: Preserving Safety and Significance - Proceedings of the 6th International Conference on Structural Analysis of Historic*

*Construction, SAHC08*, vol 1; 2008:217–225.
[5.] Rossi M, Calderini C, Roselli I, Mongelli M, Canio, G. D, Lagomarsino S. Seismic analysis of a masonry cross vault through shaking table tests: the case study of the Dey Mosque in Algiers. *Earthquakes and Structures* 2020; **18**(1):57–72.
[6.] Bianchini N, Calderini C, Mendes N, Candeias P, Lourenço PB. Blind Prediction Competition - Sera.ta - Seismic Response of Masonry Cross Vaults: Shaking table tests and numerical validations. 2023.
[7.] Abrams DP, AlShawa O, Lourenço PB, Sorrentino L. Out-of-Plane Seismic Response of Unreinforced Masonry Walls: Conceptual Discussion, Research Needs, and Modeling Issues. *International Journal of Architectural Heritage* 2017; **11**(1):22–30. doi:10.1080/15583058.2016.1238977.
[8.] AlShawa O, Sorrentino L, Liberatore D. Simulation Of Shake Table Tests on Out-of-Plane Masonry Buildings. Part (II): Combined Finite-Discrete Elements. *International Journal of Architectural Heritage* 2017; **11**(1):79–93. doi:10.1080/15583058.2016.1237588.
[9.] de Felice G, Liberatore D, De Santis S, et al. Seismic behaviour of rubble masonry: shake table test and numerical modelling. *Earthquake Engineering and Structural Dynamics* 2022; **51**(5):1245–1266. doi:10.1002/eqe.3613.
[10.] AlShawa O, Liberatore D, Sorrentino L. Effect of the vertical component of ground motion on a rubble masonry wall model. *Procedia Structural Integrity* 2023; **44**:1396–1402. doi:https://doi.org/10.1016/j.prostr.2023.01.179.
[11.] Liberatore D, Doglioni C, AlShawa O, Atzori S, Sorrentino L. Effects of coseismic ground vertical motion on masonry constructions damage during the 2016 Amatrice-Norcia (Central Italy) earthquakes. *Soil Dynamics and Earthquake Engineering* 2019; **120**:423–435. doi:10.1016/j.soildyn.2019.02.015.
[12.] AlShawa O, Liberatore D, Sorrentino L. Pre- and post-simulations of shake-table tests on a stone masonry building aggregate using finite-discrete elements. *Bulletin of Earthquake Engineering* 2022. doi:10.1007/s10518-022-01550-5.
[13.] Hallquist J. *LS-DYNA theory manual*. Livermore: Livermore Software Technology Corporation. 2006.; 2006.
[14.] Smoljanović H, Živaljić N, Nikolić Ž. A combined finite-discrete element analysis of dry stone masonry structures. *Engineering Structures* 2013; **52**:89–100. doi:10.1016/j.engstruct.2013.02.010.
[15.] Munjiza A. *The combined finite-discrete element method*. Chichester, UK: John Wiley and Sons; 2004.

COMPDYN 2023
9th ECCOMAS Thematic Conference on
Computational Methods in Structural Dynamics and Earthquake Engineering
M. Papadrakakis, M. Fragiadakis (eds.)
Athens, Greece, 12-14 June 2023

# NUMERICAL INVESTIGATION ON THE SEISMIC RESPONSE OF A MASONRY CROSS VAULT BASED ON THE DISCRETE MACRO-ELEMENT METHOD

**César Chácara[1], Bartolomeo Pantò[2], Francesco Cannizzaro[3], Davide Rapicavoli[3], and Ivo Caliò[3]**

[1] Pontificia Universidad Católica del Perú
Avenida Universitaria 1801, San Miguel 15088, Lima, Perú
e-mail: c.chacara@pucp.pe

[2] Durham University
South Road Durham, DH1 3LH, UK
bartolomeo.panto@durham.ac.uk

[3] University of Catania
Viale Andrea Doria 6, 95125 Catania, Italy
{francesco.cannizzaro, davide.rapicavoli, ivo.calio}@unict.it

## Abstract

*This paper focuses on the application of an innovative numerical approach to assessing the nonlinear dynamic response of an unstrengthened masonry cross vault subjected to shaking table testing performed within a blind prediction context. The numerical approach corresponds to the Discrete Macro-Element Method (DMEM), which consists of the assemblage of 2D panels and allows the assessment of the main in-plane and out-of-plane mechanisms of masonry structures according to a simplified mechanical scheme. A sensitivity analysis was carried out to determine the influence of the linear and nonlinear properties on the seismic response of the unstrengthened masonry cross vault. The calibration of the numerical model allowed reasonable agreement between experimental and numerical dynamic properties (natural frequencies and mode shapes). In addition, the numerical model provided acceptable results in terms of history of displacement and collapse mechanisms due to the application of nonlinear dynamic analyses. The results presented in this paper demonstrate the applicability of a simplified numerical method for assessing the seismic response of complex structures.*

**Keywords:** HiStrA Software, Fiber Calibration, Sensitivity Analysis, Model Updating, Nonlinear Dynamic Analysis.

## 1 INTRODUCTION

Masonry vaults constitute structural elements that play a relevant role in the seismic performance of existing historical buildings. These elements influence the global performance by increasing the lateral stiffness and affecting the load distribution during a seismic event. Nonetheless, these elements are characterized by a brittle response due to the constituent material's nature, which reduces the building capacity. Due to their complex geometrical characteristics, the heterogeneous material composition, or the presence of backfill, the structural and seismic assessment of these elements constitutes a complicated task. The failure of these structural typologies is mainly associated with the in-plane shear distortions or the lack of lateral instability due to relative displacements [1, 2]

To better understand the behavior of these elements, experimental and numerical research has been carried out considering different loading and boundary conditions. For instance, laboratory testing focused on assessing the response of these elements due to vertical loadings such as imposed differential displacements or concentrated loads [3-7] and shaking table tests [8-10] have been performed in the last decades. On the other hand, the numerical investigations associated with masonry cross vaults involved applying nonlinear analyses based on different approaches, such as the Finite Element Method [11-15] or the Discrete Element Method [16-18]. Nonetheless, it is worth noting that experimental and numerical approaches present relevant limitations due to the affordability of laboratory testing or the significantly high computational demand of nonlinear simulations.

This paper presents the seismic response assessment of an unstrengthened masonry cross vault using an innovative and simplified modeling approach known as the Discrete Macro-Element Method (DMEM). In addition, this investigation focused on determining the accuracy of this modeling approach to simulate the complex response of a masonry cross vault subjected to shaking table tests. This method was initially conceived for assessing the in-plane response of masonry structures [19]. Furthermore, the method was enhanced to simulate unreinforced masonry structures' combined in-plane and out-out-plane behavior [17], which was implemented in the HiStrA software [20]. The presented study is part of a competition involving several research teams on the blind prediction of the shaking table response of a masonry cross vault [21, 22]. Precisely, the presented analyses refer to the post-diction phase. The numerical model was calibrated to reproduce the modal properties from dynamic identification tests, obtaining acceptable results in natural frequencies and mode shapes. The seismic assessment of the unstrengthened cross vault was numerically investigated by nonlinear dynamic analyses. A reasonable agreement was obtained when comparing histories of displacements and collapse mechanisms. These results demonstrated that the proposed modeling approach represents a suitable tool for assessing the seismic response of masonry cross vaults.

## 2 DISCRETE MACRO-ELEMENT METHOD

The Discrete Macro-Element Method (DMEM) was initially developed to assess the in-plane response of masonry structures [19]. The mechanical scheme of the DMEM consists of 2D panels composed of a hinged quadrilateral composed of rigid edges. Adjacent panels are connected by zero-thickness interface elements whose calibration procedure follows a straightforward fiber approach. Based on its initial formulation, the DMEM can simulate in-plane failure mechanisms of masonry panels such as flexural, shear-sliding, and shear-diagonal. Additional mechanisms were subsequently implemented for assessing the out-of-plane response of unreinforced masonry walls [23] and curved structural components such as arches [24]. To this aim, the panels are composed of four rigid plates and plane interface elements (see Figure 1a). The kinematics of these panels is described by seven degrees of free-

dom (DOF): six rule the rigid body motion, and one governs the in-plane shear deformability. Simplified constitutive laws rule the simulation of the different collapse mechanisms. The bi-flexural response is described by a Takeda constitutive law in which the post-peak response in tension and compression can be ruled by exponential, linear, or parabolic softening curves with different unloading conditions. On the other hand, the shear mechanisms can be ruled by a Mohr-Coulomb yielding criterion in which the initial stiffness can define the unloading cycles. Examples of the constitutive laws available in the DMEM are depicted in Figure 1b.

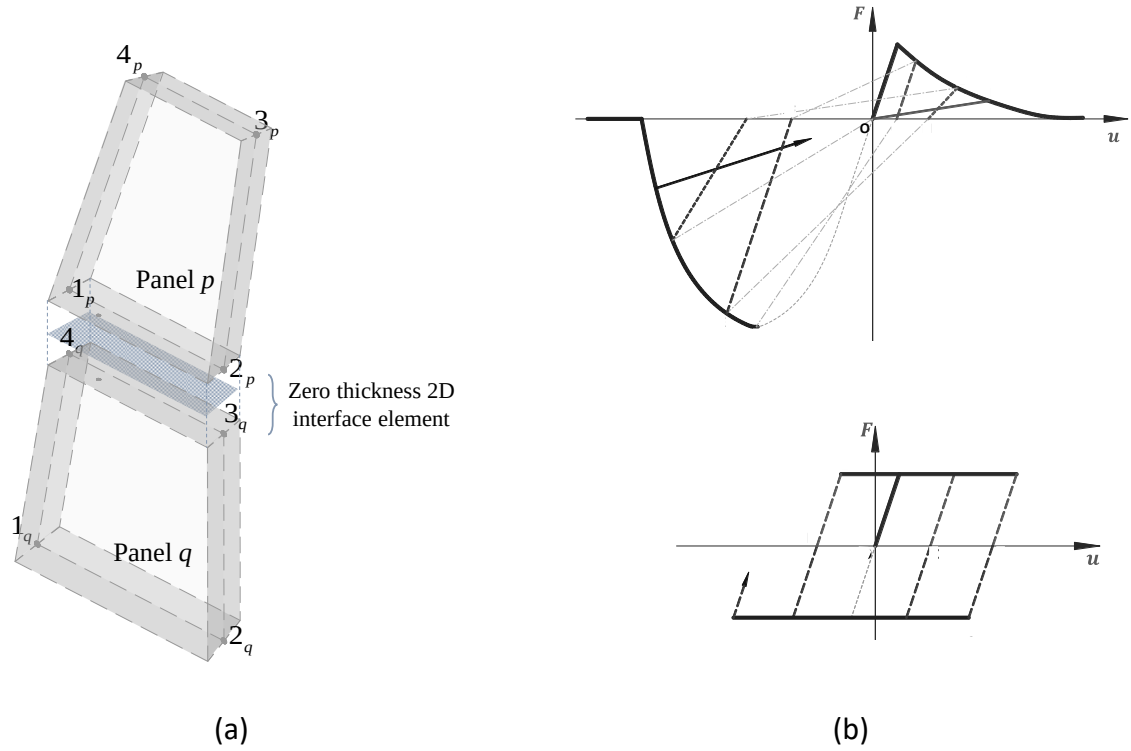


Figure 1. Discrete Macro-Element Method: (a) mechanical scheme, (b) cyclic constitutive laws.

## 3 UNSTRENGTHENED MASONRY CROSS VAULT

An unstrengthened masonry cross vault was built at the National Laboratory of Civil Engineering (LNEC) in Lisbon in December 2020 within the scope of the **SERA Project – Seismic Response of Masonry Cross Vaults: Shaking table tests and numerical validations** [21, 22]. The brick units used to construct the cross vault presented average dimensions of 4.5 cm x 12.0 cm x 23 cm, whereas a thickness of approximately 1 cm characterized the mortar joints. The units were arranged so that the bed joints were orthogonal to the four edges of the cross vault (see Figure 2a). The cross vault was characterized by a rectangular shape in which the lateral edges presented a length of approximately 3.0 m. On each corner of the vault, an infill compound made of brick masonry was placed to introduce additional weight. However, it is worth noting that the infill did not present any structural contribution to the cross vault. In addition, the corners of the vaults are supported by two steel masses and two masonry piers that simulate the presence of walls and columns. Finally, steel plates and rods were introduced to the specimen to restrain the rotations of the elements and to enhance and simulate the actual conditions of cross vaults. The 3D geometrical model of the full-scale masonry cross vault is depicted in Figure 2b.

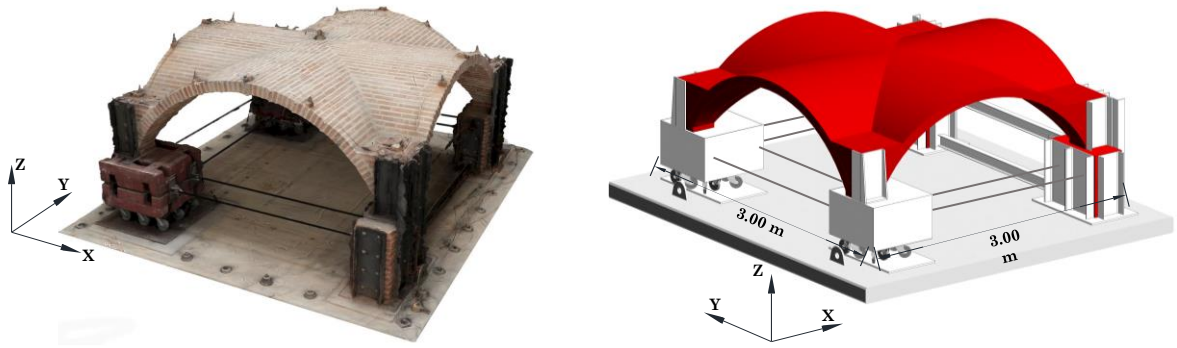


(a) (b)

Figure 2. Unstrengthened masonry cross vault: (a) plan and (b) isometric views [21].

The boundary conditions were defined to guarantee the occurrence of an in-plane shear mechanism when assessing the seismic response of the unstrengthened masonry cross vault [21]. As illustrated in Figure 3, two sets of boundary conditions along two edges of the structure were considered. The first focused on the masonry piers, which restrained their displacements and rotations (fixed edge). The second was characterized by the introduction of wheels below the steel masses, which enabled the displacements along X, and Y directions (moveable edge) and the rotation around the vertical axis [21].

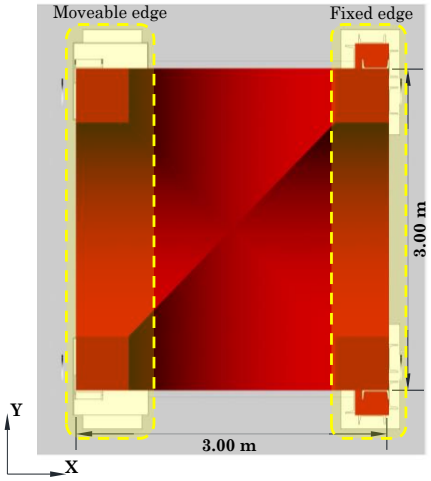


Figure 3. Boundary conditions of the unstrengthened masonry cross vault [21].

The instrumentation setup implemented for the unstrengthened masonry cross vault consisted of piezoelectric accelerometers (Acc), optical cameras (OC), and video cameras (VC), as illustrated in Figure 4. The piezoelectric accelerometers were placed in seventeen points of the masonry cross vault, measuring 29 directions. It is worth noting that additional accelerometers were placed close to one fixed pier and on the shaking table. Displacements were measured at four points of the structure using optical cameras. Measured point OC1 was at the center of the masonry cross vault, whereas OC2 and OC4 were on top of the masonry infill. The remaining measured point (OC3) was placed on the middle span of the moveable edge. In addition, four video cameras were located at each edge and one on top of the masonry vault. It is worth noting that the axial forces of the steel rods were measured during the experimental campaign using six load cells [21].

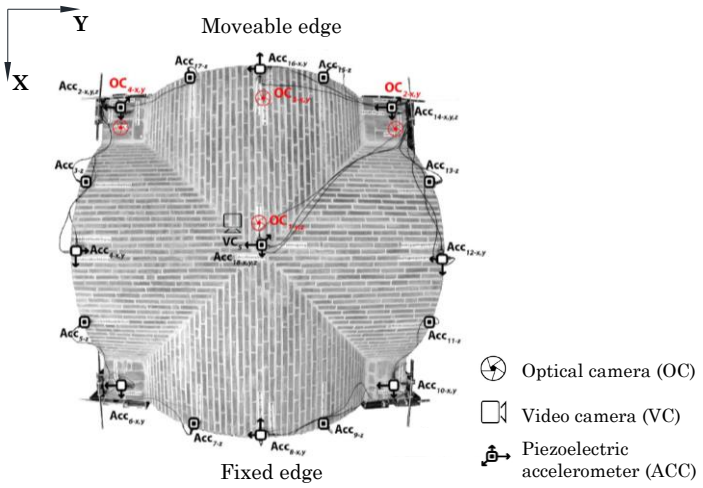


Figure 4. Instrumentation setup for the dynamic identification and shaking table tests [21].

## 4 LABORATORY TESTING

An experimental campaign involving the application of laboratory tests was carried out at the LNEC. These tests aimed at characterizing the mechanical properties of the constituent materials, identifying the dynamic properties, and assessing the seismic response of the unstrengthened masonry cross vault. The dynamic properties of the structure were identified under different damage conditions due to the application of shaking table tests with a certain seismic intensity. The application sequence of dynamic identification and shaking table tests is summarized in Table 1. It is worth noting that further details regarding the mechanical characterization can be found in [21].

| Shaking table tests | Dynamic identification tests |
|---|---|
| | 1. Under no damage condition |
| 2. Considering 25% of seismic input | 3. After 25% of seismic input |
| 4. Considering 50% of seismic input | 5. After 50% of seismic input |
| 6. Considering 75% of seismic input | 7. After 75% of seismic input |

Table 1. Testing sequences for the dynamic identification and shaking table tests.

### 4.1 Mechanical characterization

The experimental campaign consisted of three-point bending and uniaxial compression tests for mortar [25] and masonry units [26]. Based on these tests, the Young's modulus of mortar presented a mean value of 370 MPa and compressive and flexural strengths with average values of 1.68 MPa and 0.66 MPa. The units were characterized by average Young's modulus and compressive strength of 6200 MPa and 25.0 MPa, respectively. The mechanical characterization of the composite material involved the application of triplet [27], uniaxial compression [28], and diagonal compression tests [29]. The triplet tests (see Figure 5a) were carried out on twelve samples of three fired brick units with total approximate dimensions of 17.3 cm x 22.3 cm x 11.8 cm. Four specimens with dimensions of 61.9 cm x 46.8 cm x 11.8 cm (see Figure 5b) were subjected to uniaxial compression tests. Finally, the diagonal compression tests were applied to two masonry specimens (see Figure 5c).

Based on the application of these tests, it was possible to determine the main mechanical properties of the fired brick masonry material. From the triplet tests, it was possible to obtain mean cohesion and friction coefficient values of 0.031 MPa and 0.785, respectively. In the case of the uniaxial compression tests, the mean value of Young0s modulus was 2223 MPa,

whereas the mean compressive strength was 9.1 MPa. Finally, the diagonal compression tests allowed the estimation of a mean tensile strength of 0.31 MPa and a shear modulus of 762 MPa. A summary of the mean values, together with their corresponding coefficient of variation (COV), is reported in Table 2.

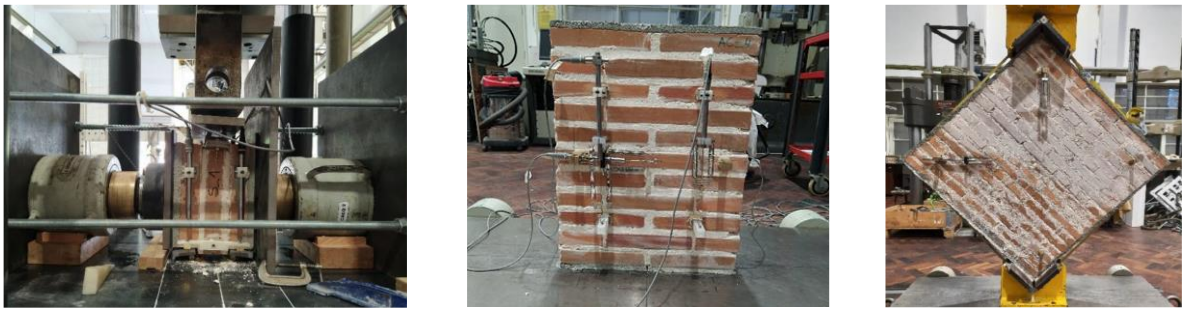

(a) (b) (c)

Figure 5. Mechanical characterization of the masonry material: (a) triplet, (b) uniaxial compression, and (c) diagonal compression tests [21].

| | Triplet tests | | Uniaxial compression tests | | Diagonal compression tests | |
|---|---|---|---|---|---|---|
| | Cohesion | Friction coefficient | Young's modulus | Compressive strength | Shear modulus | Tensile strength |
| Mean value | 0.031 MPa | 0.785 | 2223 MPa | 9.1 MPa | 762 MPa | 0.31 MPa |
| COV | - | - | 14.0% | 2.0% | 68.0% | 14.3% |

Table 2. Results of the mechanical characterization of fired brick masonry material [21].

## 4.2 Dynamic identification

Dynamic identification tests were conducted to estimate the structure's modal properties, namely mode shapes and vibration modes. The dynamic identification tests were carried out by applying an artificial accelerogram and measuring the corresponding response using piezoelectric acceleration transducers with a sensitivity of 100 mV/g and a measurement range of ±50 g pk. The duration of the dynamic identification tests was approximately 160 seconds with a sampling frequency of 200 Hz. The acceleration data's signal processing was carried out using the ARTeMIS software [30] following a Frequency Domain Decomposition (FDD) method. A detailed description of the results of the dynamic identification tests is reported in [22].

The identification of the dynamic properties of the structures was first carried out considering an undamaged condition. As illustrated in Figure 6a, the first vibration mode is associated with a pure shear vibration mode with a natural frequency of 6.15 Hz. The second mode, with a natural frequency of 11.62 Hz, was characterized by a horizontal displacement of the movable edge (see Figure 6b). Finally, the third one is associated with a vertical mode in which the maximum displacement is focused on the center of the vault (see Figure 6c), presenting a natural frequency of 19.39 Hz.

The natural frequencies of the unstrengthened masonry cross vault were compared to those identified after applying each shaking table test. It was possible to observe no relevant variation between the results from the undamaged condition and after the shaking table test with 25% of seismic input. This may indicate that the structure did not experience significant or permanent damage. On the other hand, the natural frequencies identified after the shaking table tests with 50% and 75% of seismic input were characterized by lower frequencies which may be related to the stiffness degradation of the material and the propagation of cracks, especially for the first and second vibration modes. For the dynamic identification after 50% of

seismic input, the reduction in natural frequencies of these modes presented absolute values of 4.23% and 7.14%, respectively. This reduction increased after the shaking test with 75% of seismic input with absolute values of 9.43 for the first mode and 13.08 for the second mode. It is worth noting that it was not possible to identify the third vibration mode after applying the shaking table test with 75% of seismic input. A summary of the natural frequencies throughout the different damage conditions is presented in Table 3.

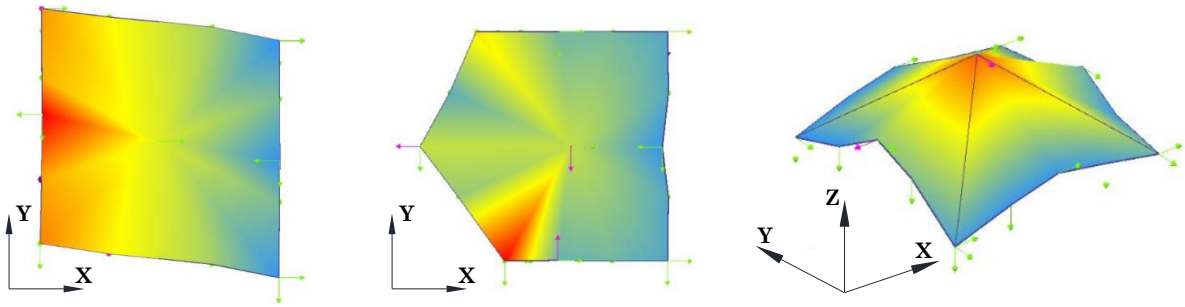


$f_1$ = 6.152 Hz $f_2$ = 11.621 Hz $f_3$ = 19.385 Hz

Figure 6. Identified vibration modes of the unstrengthened masonry cross vault (undamaged condition) [22].

| | Mode 1 | Mode 2 | Mode 3 |
|---|---|---|---|
| Undamaged | 6.15 Hz | 11.62 Hz | 19.39 Hz |
| After shaking table tests with 25% of seismic input | 6.15 Hz | 11.38 Hz | 19.38 Hz |
| After shaking table tests with 50% of seismic input | 5.89 Hz | 10.79 Hz | 19.30 Hz |
| After shaking table tests with 75% of seismic input | 5.57 Hz | 10.10 Hz | - |

Table 3. Natural frequencies identified at different damage conditions [22].

### 4.3 Shaking table tests

The application of shaking table tests allowed assessing the response of the unstrengthened masonry cross vault under dynamic loading with different intensities. The seismic input considered for these tests corresponded to the record of the 2009 L'Aquila earthquake. The record was subjected to a baseline correction, a bandpass filter ranging between 0.05 Hz and 20 Hz, and a Butterworth filter with a sixth pole order. The one-component input (see Figure 7) was applied along the Y–Y direction to assess the structure's in-plane shear seismic response. In addition, three sequential shaking table tests were carried out with increasing steps of 25% amplitude increment.

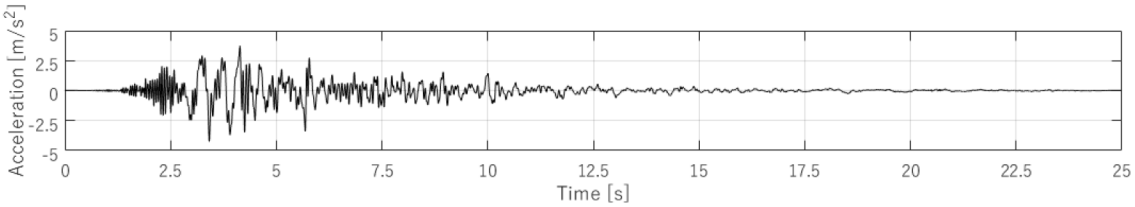


Figure 7. Filtered history of acceleration considered for the shaking table tests [21].

As reported in [22], the collapse mechanism of the unstrengthened masonry cross vault after applying the shaking table test with 75% of the seismic input was described as a crack propagation along the main diagonals of the structure due to a shear mechanism. Moreover, it was possible to observe that the structure also suffered damage in terms of plastic hinges at the masonry webs. Additional cracks were identified in the connection between the masonry

web and the infill. This detachment was mainly focused on the fixed edge. A top view of the collapse mechanism of the unstrengthened masonry cross vault is illustrated in Figure 8.

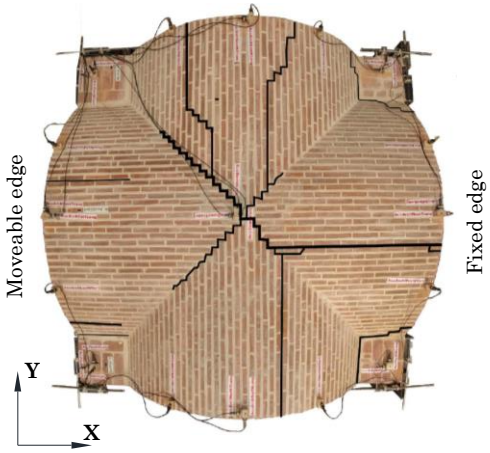


Figure 8. Collapse mechanism of unstrengthened masonry cross vault [22].

## 5 NUMERICAL SIMULATIONS

The numerical assessment of the unstrengthened masonry cross vault's seismic response was performed using the DMEM implemented in the HiStrA software [20]. The numerical model was composed of 2D quadrilateral and triangular elements for the idealization of the masonry vault, infill, binder, and steel components. In addition, trusses were used to model the steel rods and steel profiles that connect the masonry piers and the steel masses (see Figure 9). Two sets of boundary conditions were defined to simulate the actual laboratory characteristics. The first consisted of a fixed restraint of the piers, and the second one allowed the displacements in the X–X and Y–Y directions and the rotation around the Z axis. Based on the number of computational elements and the boundary conditions, the DME model of the masonry cross vault was described by 4822 DOFs.

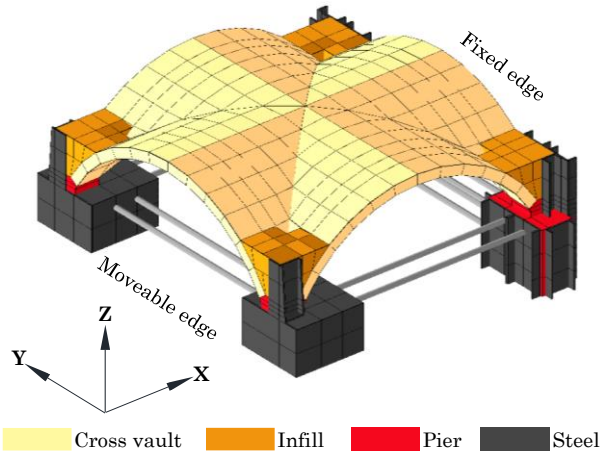


Figure 9. DME model of the masonry cross vault

The initial linear elastic mechanical properties defined for the numerical models were taken primarily from the mechanical characterization. Regarding the fired brick masonry material, the Young's and shear moduli presented values of 2,223 MPa and 762 MPa, respectively, and a specific weight of 22.55 kN/m$^3$. In the case of the structural steel material, typical val-

ues of Young's modulus and Poisson ratio were considered in this investigation. A summary of the mechanical properties is reported in Table 4.

| | Young's modulus $E$ [MPa] | Poisson ratio $\nu$ [-] | Shear modulus $G$ [MPa] | Specific weight $\gamma$ [kN/m$^3$] |
|---|---|---|---|---|
| Fired brick masonry | 2,223 | - | 762 | 22.55 |
| Structural steel | 210,000 | 0.25 | - | 78.50 |

Table 4. Linear elastic mechanical properties of fired brick masonry and structural steel materials.

## 5.1 Model updating

The numerical simulations initially consisted of updating the DME model following a sensitivity analysis and comparing experimental and numerical modal parameters. The sensitivity analysis focused on assessing the influence of the Young's modulus of the fired brick masonry material in the natural frequencies and mode shapes of the unreinforced cross vault. The accuracy of the mode shapes was evaluated using the Modal Assurance Criterion (MAC), which is determined as a function of experimental and numerical mode shapes. The MAC value ranges between when there is no resemblance and 1 when there is a perfect resemblance between experimental and numerical results [31].

The comparison of the dynamic properties focused on the first and third experimental modes since it was not possible to identify the second one with the DME model. In contrast, the estimation of the MAC value considered the mode shapes associated with the numerical model's first and fourth vibration modes. A first comparison between experimental and numerical results was carried out considering the initial value of the fired brick masonry material (2223 MPa). It was observed that there was s significant difference in natural frequencies, presenting absolute differences of 19.6% and 22.0% for the first and third experimental modes, respectively. In the case of mode shapes, there was a reasonable agreement regarding the first mode presenting a MAC equal to 0.878. Unfortunately, the MAC associated with the third experimental mode presented a value of 0.404. It was noted that these differences were associated with the rigidity of the numerical model. In this sense, the initial value of the Young's modulus of the masonry material was subjected to five reduction factors (RF = 0.9, 0.8, 0.7, 0.6, and 0.5) aiming at assessing its influence on the dynamic properties of the unstrengthened cross vault. It was observed that the difference in terms of natural frequency reduced, and the MAC ratio of the third experimental mode increased with a lower RF. In addition, it was evidenced that when using RFs of 0.6 and 0.5, the absolute differences in natural frequencies and the MAC presented acceptable results. The sensitivity analysis results are reported in Table 5.

| | | Initial | RF = 0.9 | RF = 0.8 | RF = 0.7 | RF = 0.6 | RF = 0.5 |
|---|---|---|---|---|---|---|---|
| 1$^{st}$ num mode / 1$^{st}$ exp mode | $f_{num}$ [Hz] | 7.35 | 7.05 | 6.74 | 6.38 | 5.99 | 5.55 |
| | error [%] | 19.6 | 14.6 | 9.7 | 3.8 | 2.6 | 9.7 |
| | MAC [-] | 0.878 | 0.879 | 0.881 | 0.883 | 0.885 | 0.887 |
| 4$^{th}$ num mode / 3$^{rd}$ exp mode | $f_{num}$ [Hz] | 23.65 | 22.88 | 22.04 | 21.09 | 20.02 | 18.79 |
| | error [%] | 22.0 | 18.0 | 13.7 | 8.8 | 3.3 | 3.1 |
| | MAC [-] | 0.404 | 0.458 | 0.533 | 0.609 | 0.685 | 0.751 |

Table 5. Frequency and mode shape comparison between experimental and numerical results.

Based on this sensitivity analysis, it was decided to use an average RF equal to 0.55 as the optimum value for the Young's modulus of the fired brick masonry. The mode shapes of the numerical model considering a RF of 0.55 are illustrated in Figure 10. The first mode presented a natural frequency of 5.78 Hz (with an absolute difference of 6% and a MAC ratio of

0.89), and it involved a pure shear behavior of the cross vault (see Figure 10a). The remaining dynamic properties were associated with the fourth vibration mode, whose response was mainly governed by the vertical component of the displacements, presenting a natural frequency of 19.34 Hz (difference of 0.2%) and a MAC ratio of 0.72.

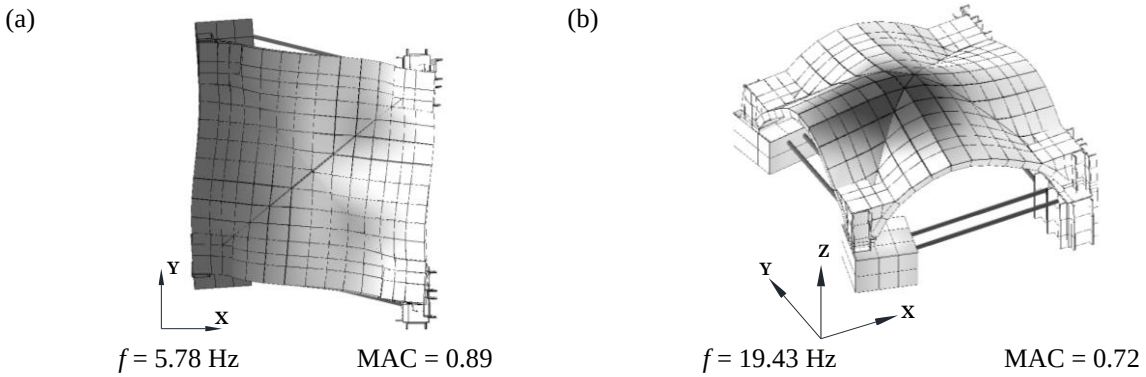


Figure 10. DME dynamic properties: (a) first and (b) fourth vibration modes

## 5.2 Nonlinear dynamic analysis

The unstrengthened cross vault's seismic response was numerically investigated through nonlinear dynamic analyses. The physical nonlinearity was focused on the mechanical properties of the masonry material, whereas structural steel was considered elastic. Exponential and parabolic curves described the tensile and compressive behaviors, whereas an elasto-plastic approach characterized the shear-sliding mechanism. The values of tensile and compressive strengths were taken from the mechanical characterization. In this sense, the tensile and compressive strengths presented values of 0.31 MPa and 9.10 MPa. The compressive fracture energy presented a value of 14.56 N/mm, and the tensile fracture energy was assumed to be equal to 0.012 N/mm. For the shear-sliding behavior, the friction coefficient was also taken from the mechanical characterization; however, cohesion was initially assumed equal to the tensile strength. A summary of the nonlinear mechanical properties of the masonry material is reported in Table 6.

| Compressive strength $f_c$ [MPa] | Compressive fracture energy $G_c$ [N/mm] | Tensile strength $f_t$ [MPa] | Tensile fracture energy $G_c$ [N/mm] | Cohesion $c$ [MPa] | Friction coefficient $\mu$ [-] |
|---|---|---|---|---|---|
| 9.10 | 14.56 | 0.31 | 0.012 | 0.31 | 0.785 |

Table 6. Nonlinear mechanical properties for fired brick masonry material

For the dynamic nonlinear analyses, the numerical solution used in this investigation correspondeded to the Newmark Method with average acceleration, whereas damping was defined following a Rayleigh approach. Two vibration modes with cumulative effective masses of approximately 71% and 84% and a damping ratio of 2.5% were considered for the definition of the Rayleigh damping matrix. Following the experimental campaign, three subsequent nonlinear dynamic analyses were conducted to account for damage accumulation. Such numerical simulations were associated with the shaking table tests with 25%, 50%, and 75% of seismic input. The signals used for the numerical simulations corresponded to the acceleration registered by the transducers placed at the shaking table, which were subjected to a baseline correction and a filtering process. The results presented correspond to the numerical simulations of the 75% of seismic input whose history of acceleration is depicted in Figure 11.

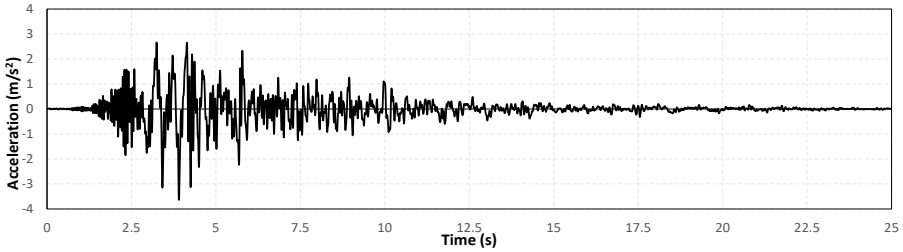


Figure 11. History of acceleration registered at the base of the shaking table for the 75% seismic input.

The comparison between experimental and numerical results was focused on the displacement histories at the points with optical cameras. Considering the initial value of tensile strength reported in the mechanical characterization, it was possible to observe a significant variation in maximum relative displacements. In the experimental campaign, the maximum relative displacement at the top of the moveable edge (measured point OC3) presented an approximate value of approximately 18 mm, whereas the numerical one was around 8.7 mm (see Figure 12a). The tensile strength and cohesion values were reduced to improve the correspondence between experimental and numerical displacements. For this purpose, tensile strength and cohesion with values equal to 0.248 MPa, 0.186 MPa, 0.124 MPa, 0.062 MPa, and 0.031 MPa were considered for further analyses. The numerical results experienced a significant improvement when considering low values of such mechanical properties. As illustrated in Figure 12b, there is a reasonable agreement regarding maximum displacement, assuming a value equal to 0.031 MPa. Nonetheless, the residual displacements observed in the experimental shaking table tests were not reproduced with the numerical model, which may be a limitation of the proposed modeling approach.

(a)

(b)

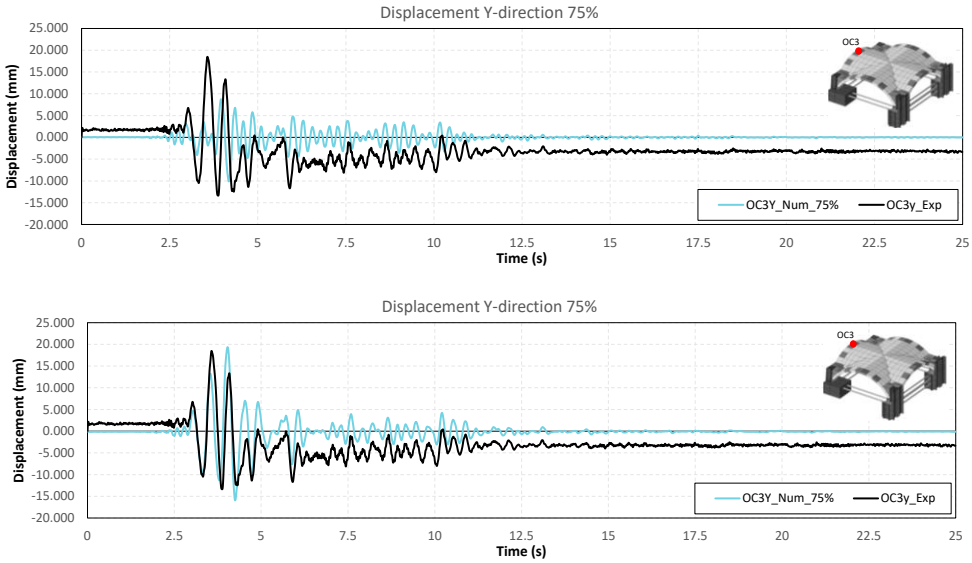


Figure 12. Comparison between experimental and numerical results for the 75% of seismic input considering tensile and cohesion equal to: (a) 0.310 MPa and (b) 0.031 MPa.

As illustrated in Figure 13, the collapse mechanism of the DME model of the unstrengthened cross vault consisted of plastic hinges along the masonry web and diagonal cracking. Additional damage was identified in the connection between the masonry cross vault and the infill. It was observed that the experimental and numerical collapse mechanisms presented an acceptable agreement. The crack pattern obtained after the shaking table tests coincides with

the appearance of plastic strains in the numerical model. These results demonstrate the capability of the DMEM to simulate the complex response of masonry cross vaults with an acceptable degree of accuracy.

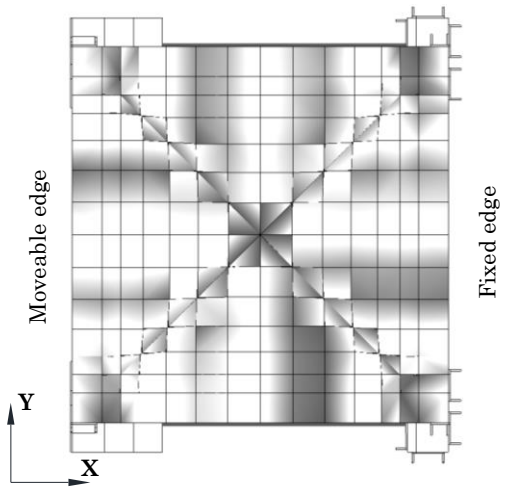


Figure 13. Numerical collapse mechanism of the numerical model of the unstrengthened masonry cross vault.

## 6 CONCLUSIONS

- This paper presents the simulation of the seismic response of an unstrengthened masonry cross vault using an innovative numerical tool known as the Discrete Macro-Element Method (DMEM).
- The proposed method is described by a simplified mechanical scheme that allows the simulation of the collapse mechanism of masonry structures with a reduced number of DOFs and computational demand.
- The numerical model could simulate the dynamic properties of the unstrengthened masonry cross vault with an acceptable degree of accuracy. This process involved applying a sensitivity analysis which evidenced that the vault's mechanical response does not accurately agree with the material's mechanical properties.
- The unstrengthened masonry cross vault's seismic response was investigated through nonlinear dynamic analysis using the DMEM. A reasonable agreement between the experimental and numerical models was obtained in terms of history of displacement and collapse mechanism. It is worth noting that the proposed model still presents some limitations, especially in simulating the residual displacement.

## REFERENCES

[1] D. Theodossopoulos and B. Sinha, "Structural safety and failure modes in Gothic vaulting systems," in *8th International Seminar on Structural Masonry*, Instanbul (2008).

[2] A. Plavsic, B. Pantò, C. Chisari, L. Macorini, B. A. Izzuddin, I. Boem, and N. Gattesco, "Nonlinear Simulation of Masonry Vaults Under Earthquake Loading," in *Conference on Computational Methods in Structural Dynamics and Earthquake Engineering*, Athens, Greece, pp. 595-606 (2021).

[3] P. Foraboschi, "Strengthening of masonry arches with fiber-reinforced polymer strips strengthening of masonry arches with fiber-reinforced polymer strips", *Journal of Composites for Construction,* vol. 8, p. 191:202, (2004).

[4] P. Krajewski and Ł. Hojdys, "Experimental Studies on Buried Barrel Vaults", *International Journal of Architectural Heritage,* vol. 9, pp. 834–843, (2014). doi: https://doi.org/10.1080/15583058.2013.860499

[5] M. Fagone, T. Rotunno, and S. B. Bati, "The groin vaults of St. John Hospital in Jerusalem: an experimental analysis on a scale model", *International Journal of Architectural Heritage,* vol. 10, pp. 903-918, (2016). doi: https://doi.org/10.1080/15583058.2016.1158331

[6] B. Torres, E. Bertolesi, J. J. Moragues, P. A. Calderón, and J. M. Adam, "Experimental investigation of a full-scale timbrel masonry cross vault subjected to vertical settlement", *Construction and Building Materials,* vol. 221, pp. 421-432, (2019).

[7] M. Rossi, C. C. Barentin, T. Van Mele, and P. Block, "Experimental study on the behaviour of masonry pavilion vaults on spreading supports", *Structures,* vol. 11, pp. 110-20, (2017). doi: https://doi.org/10.1016/j.istruc.2017.04.008

[8] G. De Matteis and F. M. Mazzolani, "The Fossanova Church: seismic vulnerability assessment by numeric and physical testing", *International Journal of Architectural Heritage,* vol. 4, pp. 222-45, (2010).

[9] M. Rossi, C. Calderini, I. Roselli, M. Mongelli, G. De Canio, and S. Lagomarsino, "Seismic analysis of a masonry cross vault through shaking table tests: the case study of the Dey Mosque in Algiers.", *Earthquakes and Structures,* vol. 18, pp. 57-72, (2020). doi: https://doi.org/10.12989/eas.2020.18.1.057

[10] E. Vintzileou, C. Mouzakis, L. Karapitta, and A. Miltiadou-Fezans, "Shake-Table Testing of a Cross Vault.", *Buildings,* vol. 12, p. 1984, (2022). doi: https://doi.org/10.3390/buildings12111984

[11] D. Theodossopoulos, B. P. Sinha, and A. S. Usmani, "Case study of the failure of a cross vault: Church of Holyrood Abbey", *Journal of architectural engineering,* vol. 9, pp. 109-17, (2003).

[12] G. Milani, M. Simoni, and A. Tralli, "Advanced numerical models for the analysis of masonry cross vaults: a case-study in italy", *Engineering Structures,* vol. 76, pp. 339–58, (2014). doi: https://doi.org/10.1016/j.engstruct.2014.07.018

[13] G. Milani, M. Rossi, C. Calderini, and S. Lagomarsino, "Tilting plane tests on a small-scale masonry cross vault: Experimental results and numerical simulations through a heterogeneous approach", *Engineering Structures,* vol. 123, pp. 300-312, (2016). doi: https://doi.org/10.1016/j.engstruct.2016.05.017

[14] A. Gaetani, N. Bianchini, and P. B. Lourenço, "Simplified micro-modelling of masonry cross vaults: stereotomy and interface issues", *International Journal of Masonry Research and Innovation,* vol. 6, pp. 97-125, (2021). doi: 10.1504/IJMRI.2021.112076

[15] G. Lengyel and K. Bagi, "Numerical analysis of the mechanical role of the ribs in groin vaults", *Computers & Structures,* vol. 158, pp. 42–60, (2015). doi: https://doi.org/10.1016/j.compstruc.2015.05.032

[16] J. McInerney and M. J. DeJong, "Discrete Element Modeling of Groin Vault Displacement Capacity", *International Journal of Architectural Heritage*, vol. 9, pp. 1037–49, (2014).

[17] G. Lengyel, "Discrete element analysis of gothic masonry vaults for self-weight and horizontal support displacement", *Engineering Structures*, vol. 148, pp. 195–209, (2017).

[18] D. Foti, V. Vacca, and I. Facchini, "DEM modeling and experimental analysis of the static behavior of a dry-joints masonry cross vaults", *Construction and Building Materials*, vol. 170, pp. 111–20, (2018).

[19] I. Caliò, M. Marletta, and B. Pantò, "A new discrete element model for the evaluation of the seismic behaviour of unreinforced masonry buildings", *Engineering Structures*, vol. 40, pp. 237-338, (2012).

[20] Gruppo Sismica s.r.l., "HiStrA (Historical Structure Analysis)," (2015), Catania, Italy, Release 17.2.3, http://www.histra.it.

[21] N. Bianchini, C. Calderini, N. Mendes, P. Candeias, and P. B. Lourenço, Blind Prediction Competition - Sera.ta - Seismic Response of Masonry Cross Vaults: Shaking table tests and numerical validations (Version 1), [Data set]. Zenodo, (2023). doi: https://doi.org/10.5281/zenodo.7624666

[22] N. Bianchini, C. Calderini, N. Mendes, P. Candeias, and P. B. Lourenço, Postdiction Competition - Sera.ta - Seismic Response of Masonry Cross Vaults: Shaking table tests and numerical validations (Version 1). [Data set]. Zenodo, (2023). doi: https://doi.org/10.5281/zenodo.7624791

[23] B. Pantò, F. Cannizzaro, I. Caliò, and P. B. Lourenço, "Numerical and experimental validation of a 3D macro-model for the in-plane and out-of-plane behaviour of unreinforced masonry walls", *International Journal of Architectural Heritage*, (2017). doi: 10.1080/15583058.2017.1325539

[24] S. Caddemi, I. Caliò, F. Cannizzaro, G. Occhipinti, and B. Pantò, "A Parsimonious Discrete Model for the Seismic Assessment of Monumental Structures," in *Fifteenth International Conference on Civil, Structural and Environmental Engineering Computing*, Prague, Czech (2015).

[25] EN 1015-11. (2006). *Methods of Test for Mortar for Masonry - Part 11: Determination of flexural and compressive strength of hardened mortar*

[26] BS EN 772-1. (2011). *Methods of test for masonry units*

[27] EN 1052-3. (2002). *Methods of test for masonry - Part 3: determination of initial shear strength*

[28] EN 1052-1. (1998). *Methods of test for masonry - Part 1: determination of compressive strength*

[29] ASTM E519/E519M – 10. (2010). *Standard Test method for Diagonal Tension (Shear) in Masonry Assemblages*

[30] Structural Vibration Solution (SVS), "ARTeMIS SVS User's Manual (8.4)", (2015).

[31] R. J. Allemang, "A correlation coefficient for modal vector analysis," in *1st International Modal Analysis Conference*, pp. 110-116 (1982).

COMPDYN 2023
9th ECCOMAS Thematic Conference on
Computational Methods in Structural Dynamics and Earthquake Engineering
M. Papadrakakis, M. Fragiadakis (eds.)
Athens, Greece, 12-14 June 2023

# SIMPLIFIED EVALUATION FOR THE SERA-TA BLIND PREDICTION: SEISMIC BEHAVIOR OF MASONRY CROSS VAULTS

**G. Ramaglia[1], G.P. Lignola[1], and A. Prota[1]**

[1] Department of Structures for Engineering and Architecture, University of Naples "Federico II"

Via Claudio, 21 - 80125 - Naples, Italy.

{giancarlo.ramaglia,glignola,aprota}@unina.it

## Abstract

*Experimental tests performed on prototypes provide important information to improve the knowledge under dynamic actions. Masonry vaults play a much relevant role in the seismic response of heritage masonry buildings and their behavior is very hard to predict due to the strong variability and heterogeneity of the physical and mechanical and input parameters. Since it is not possible to perform initial blind calibrations, the development of simplified models able to capture the main aspects is certainly a useful tool to plan experimental tests. In this specific case, the development of a model able to provide the following outputs has been the main goal: the threshold at which evident damage is expected; identify the areas where the damage is concentrated; identify the type of damage.*
*The masonry cross vault has been modelled by means of non-linear shell elements both for unreinforced and strengthened configuration. Managing simple models allowed also performing some consecutive time histories including the effects of previous signals, as tested prototype was subjected to replicas. The results obtained by the FE model have been compared with the experimental results. The simplified approach discussed in this paper represents a useful support tool to design dynamic tests on full-scale or scaled masonry structures.*

**Keywords:** Dynamics of concrete and masonry structures, Numerical simulation methods for dynamic problems, Reliability of dynamic systems.

## 1 INTRODUCTION

The planning of experimental programs both for single elements [1] and for scaled structures [2, 3] is a very critical phase. It increases when the goal focuses on masonry scaled buildings subjected to dynamic actions. Since it is not possible to make numerical calibrations before the test [4], the development of simplified models able to fix the main aspects represents a useful tool to set up experimental tests. In this case, simplified numerical modelling able to estimate the threshold at which evident damage is expected, the areas where the damage is concentrated, the type of damage and the expected maximum displacement values was developed. The data initially provided in terms of elastic and mechanical properties of the materials were adopted as main input for the development of the numerical model. The physical and mechanical properties have been assigned starting from tests performed on similar masonries [5]. In fact, in an initial blind phase, the level of knowledge is very low and the numerical model must be compatible with it [6, 7]. Excessively refined models are often more sensitive to input parameters and the cannot be used at initial phases [8, 9]. The main goal of the experimental program was to investigate the behavior of brick masonry cross vaults under different seismic inputs, in terms of damage, displacement capacity and peak acceleration [10].

## 2 STRUCTURAL ANALYSIS

Authors preferred a simplified approach, with some further very simple assumptions mainly due to original time constraints and initial knowledge level; the time extension did not allow to use a more refined approach (eventually a different more refined FEM code, also in use in our research group), but allowed to perform some consecutive time histories including the effects of previous signals.

In particular, since it is not possible to perform initial calibrations, the development of simplified models able to capture the main aspects is certainly a useful tool to plan experimental tests [11]. In this specific case, the development of a model able to provide the following output has been the main goal:

- The threshold at which evident damage is expected;
- Identify the areas where the damage is concentrated;
- Identify the type of damage.

Such simplified model has been successfully used before for similar problems of masonry structures and components modeling [12-18]. The masonry structure has been modelled by means of non-linear shell elements in SAP2000 (developed by “Computers and Structures”). A perspective view of numerical model is shown in the figure 1.

The real scale masonry specimen is made of a main cross vault modelled by means of non-linear shell elements. The boundary conditions reproduce the experimental setup made of steel elements, some are fixed, while others are able to slide only in horizontal direction, while steel bars reproduce their mutual connections.

The masonry stress-strain constitutive relationship must be compatible with a simplified approach. The masonry has been modelled as elastic perfectly plastic in compression. The maximum value of the compressive stress is always lower than the compressive strength for all time histories [19].

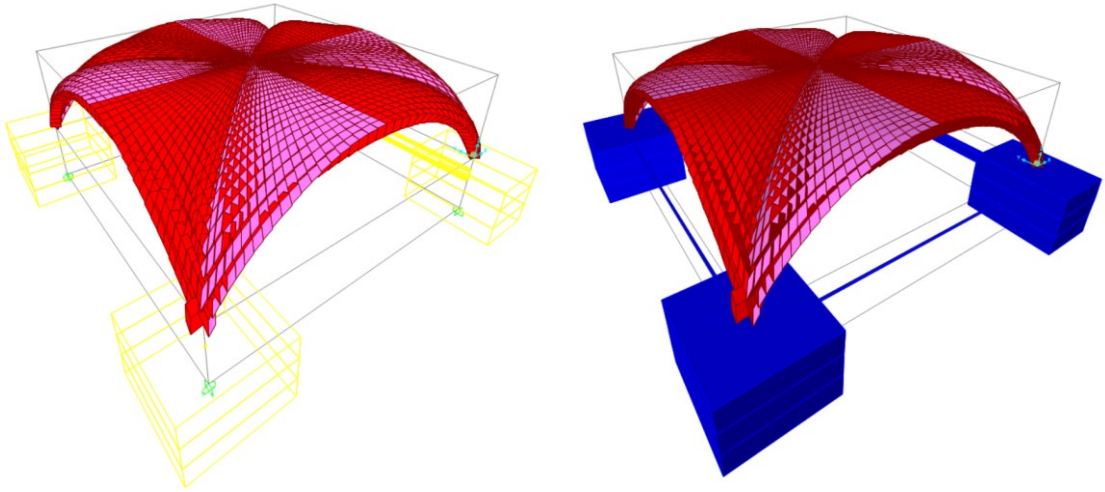

Figure 1: Numerical model: three dimensional views.

For this reason, no further improvement of the compressive behaviour was performed. The masonry behaviour in tension has been modelled limiting the maximum tensile strain of masonry at $3\times\varepsilon_T$, where $\varepsilon_T$ represents the cracking (peak) strain of the masonry in tension. The tensile behaviour is certainly the most critical, and it was assumed a reduced fracture energy based on preliminary information and this was confirmed after the dynamic tests [20, 21].

Figure 2 shows the nonlinear stress-strain constitutive relationship used for masonry, modelled with quadrilateral shell finite elements.

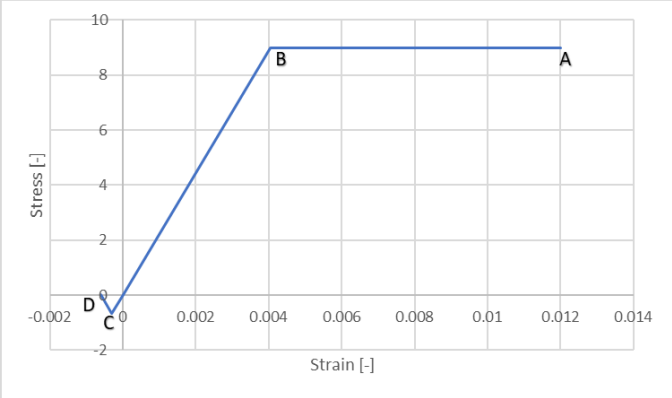


| Point | Strain [-] | Stress [MPa] |
|---|---|---|
| ***A*** | 0.012 | 9.0 |
| ***B*** | 0.00405 | 9.0 |
| ***0*** | 0 | 0 |
| ***C*** | 0.0003 | -0.66 |
| ***D*** | 0.00059 | 0 |

Figure 2: Stress-strain constitutive relationship for masonry.

Parameter for viscous model has been fixed equal to 5% for all time history analyses as shown in many tests performed on similar masonry [22, 23].

The numerical model was subjected to a sequence of dynamic signals at the base. The accelerograms refer to the desired signal. However, the experimental practice has shown that the desired signals are always affected by an alteration due to many disturbing factors. It has been seen that the experimental variations from the desired signal do not negligibly affect the numerical results. However, this statement is subordinate to the goals of this study which are aimed at a simplified analysis of the structure. Therefore, the theoretical signals were considered to assess the capacity of the masonry cross vault.

## 2.1 Dynamical behavior

A modal analysis was performed to assess the dynamical behavior of masonry vault. The vault shows a prevalently torsional behavior as shown in the following figures. This aspect is probably due to the non-symmetric restraint conditions of specimen [24, 25].

The boundary conditions reproduce the setup; some steel blocks are fixed, while others can slide only in some directions, and finally there are steel bars constraining their relative displacements, modelled as trusses.

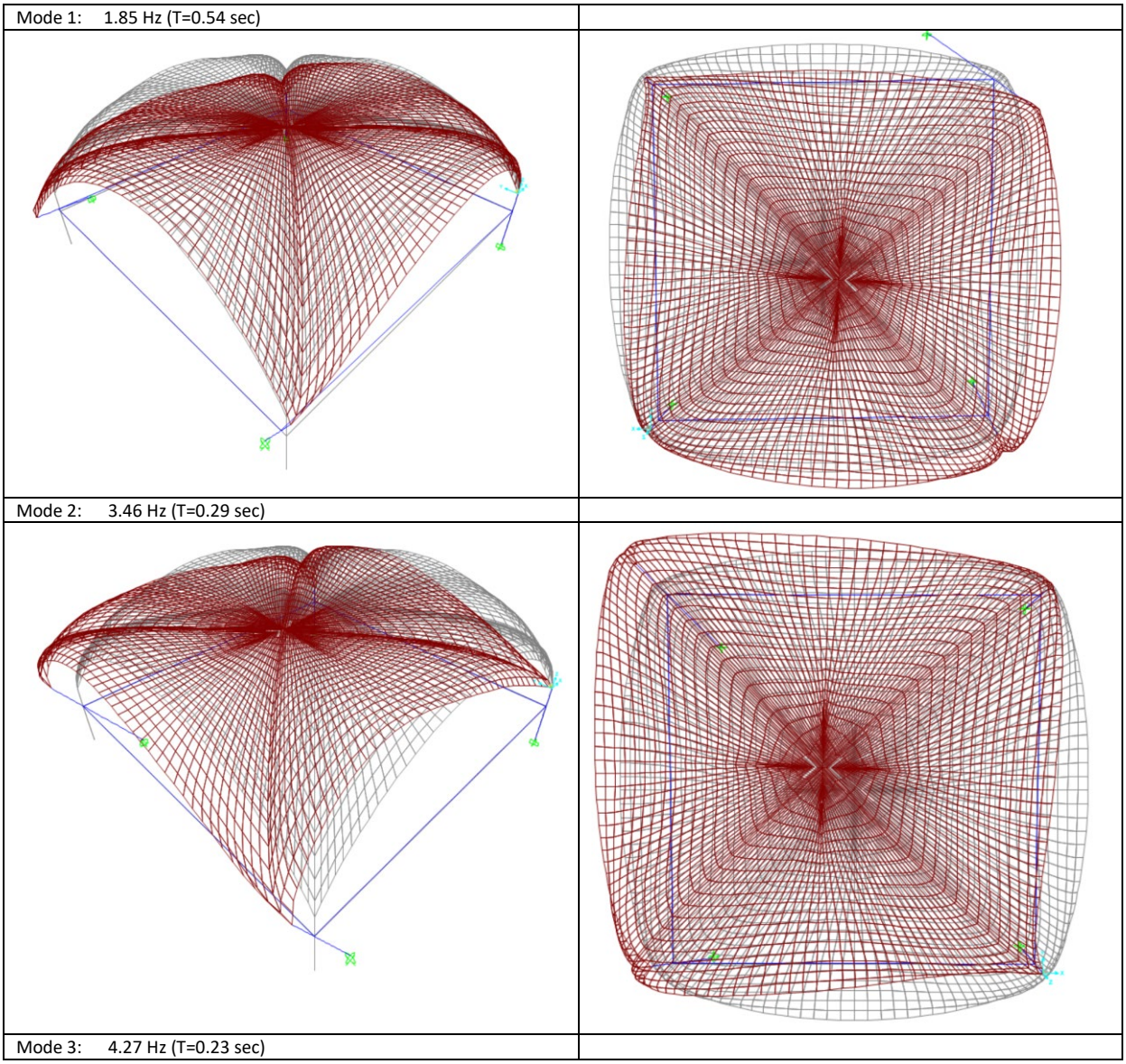


Figure 3: Main modal shapes, prospective view and top view, in the left and right column respectively.

A time history analysis was performed to assess the structural behavior of the real scale masonry vault. The time histories were assigned like as sequential analyses. In particular, in the output of sequential shaking analyses, the residual displacements of the previous shakings have been subtracted, for representation only, but from a mechanical point of view, residual displacements were found at the end of previous shakings and affect the numerical modelling.

## 2.2 Numerical results and experimental comparison

The adopted numerical approaches do not allow to plot a failure mechanism. However, a probable failure mechanism and the linked crack pattern can be identified starting from the internal stresses configuration, by means of Engineering judgment. In particular, for several steps of the time history, the principal stresses are shown in the following figures.

The torsional behavior/in-plane shear is the most significant mechanism. In main load direction the aligned longitudinal arches have the typical failure mode with longitudinal arch behavior (cracks at keystone and springers) according to the plotted stress contour maps. This is more evident in the opposite arches at the two sides (yellow rectangles, of figure 4). Torsional effects yield to cracks along the diagonal ribs of the vault, starting from Nord side (red dashed lines in figure 4).

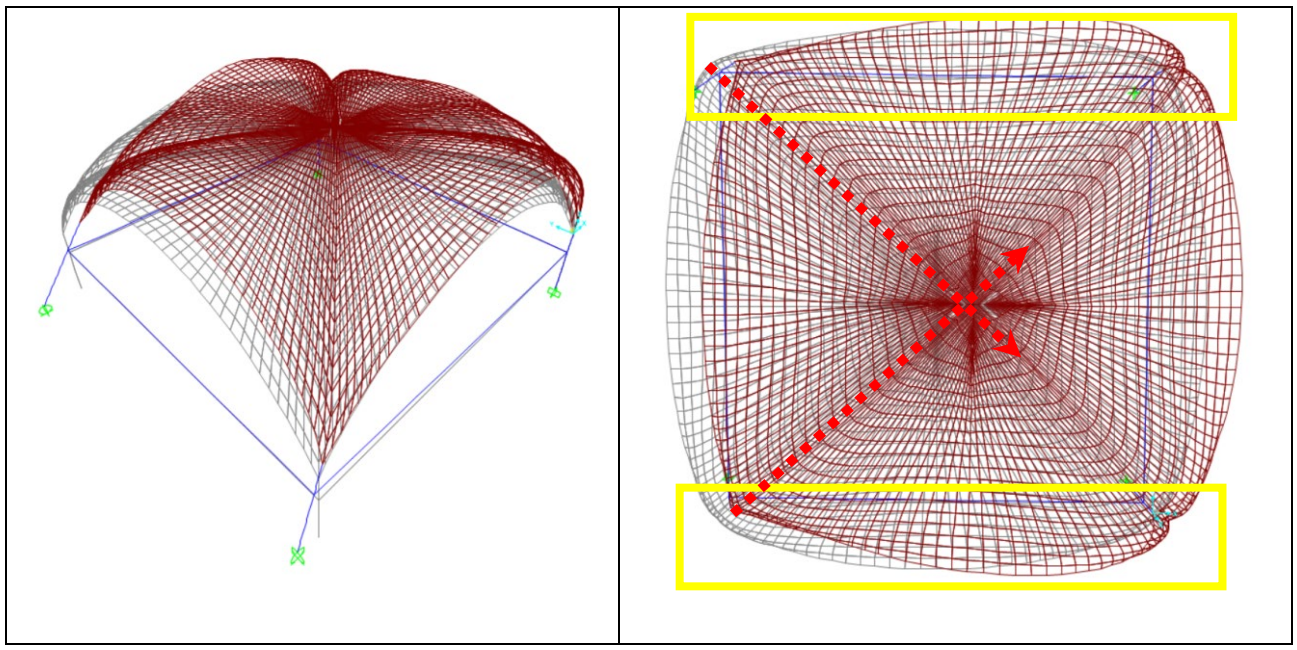

Figure 4: Torsional effects yield to cracks along the diagonal ribs of the vault.

The results in terms of internal principal stresses were shown in figures 5. In particular, the localization of the principal tensile stresses both at the intrados (blue areas of figure 5 a, c and e) and at the extrados (figure 5 b, d and f) was shown with reference to several steps of the last dynamic signal.

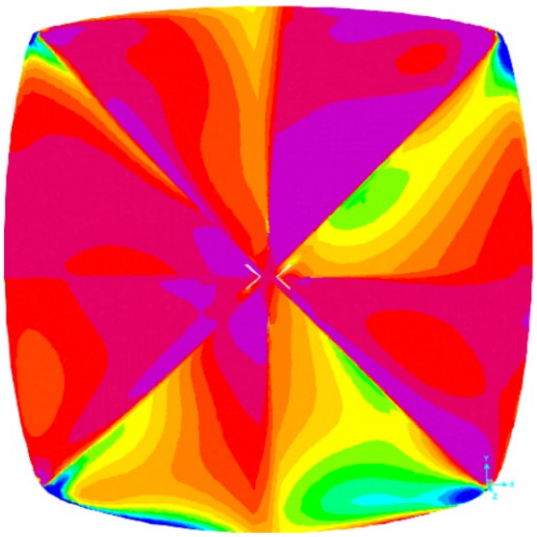

a)
Localization of the principal tensile stresses (blue areas intrados), timestep 3.905 sec

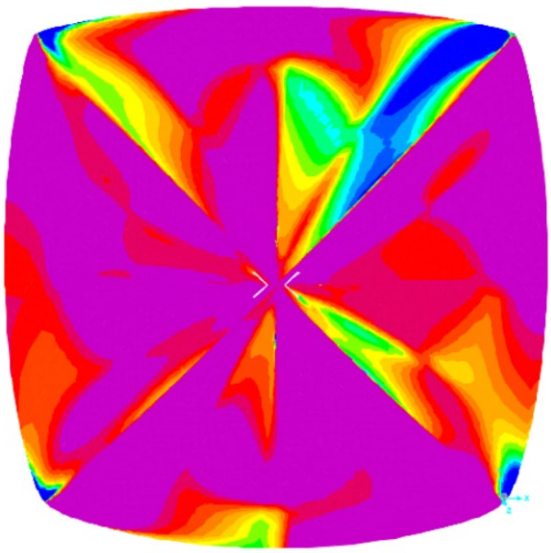

b)
Localization of the principal tensile stresses (blue areas extrados), timestep 3.905 sec

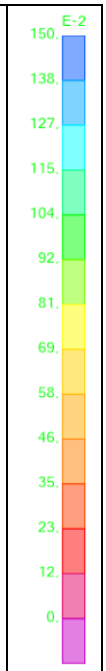


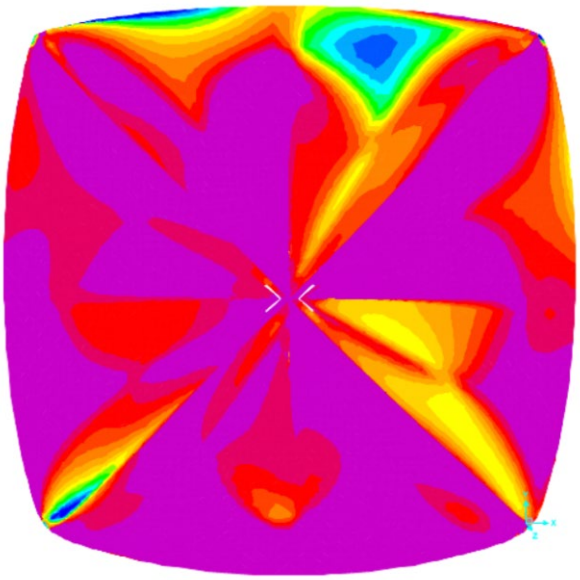

c)
Localization of the principal tensile stresses (blue areas intrados), timestep 4.415 sec

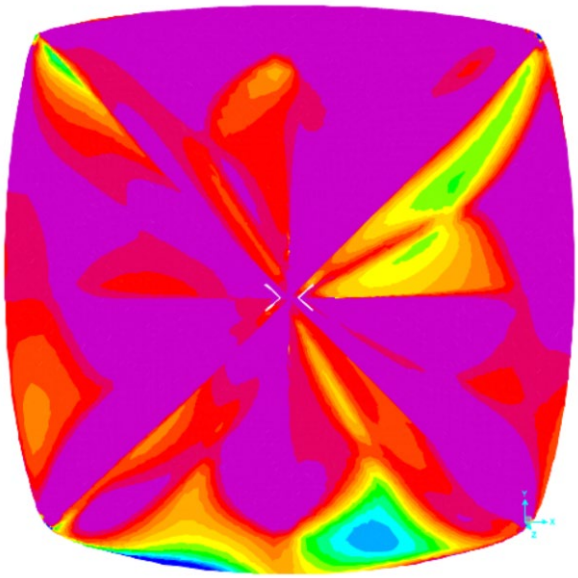

d)
Localization of the principal tensile stresses (blue areas extrados), timestep 4.415 sec

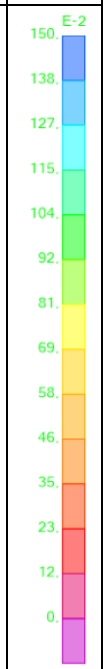

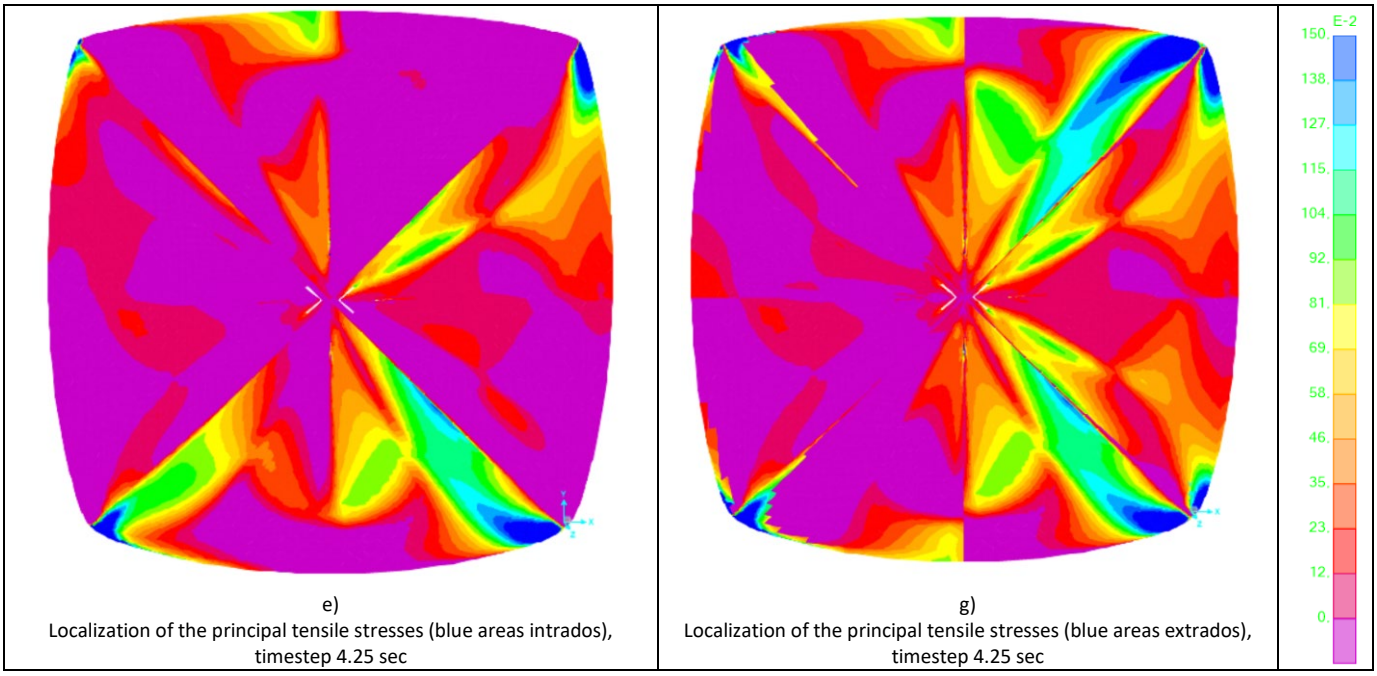


e)
Localization of the principal tensile stresses (blue areas intrados), timestep 4.25 sec

g)
Localization of the principal tensile stresses (blue areas extrados), timestep 4.25 sec

Figure 5: Simulated internal principal stresses (contour map in MPa).

The internal stresses provide important information about the identification of an expected crack pattern as shown in figure 6.

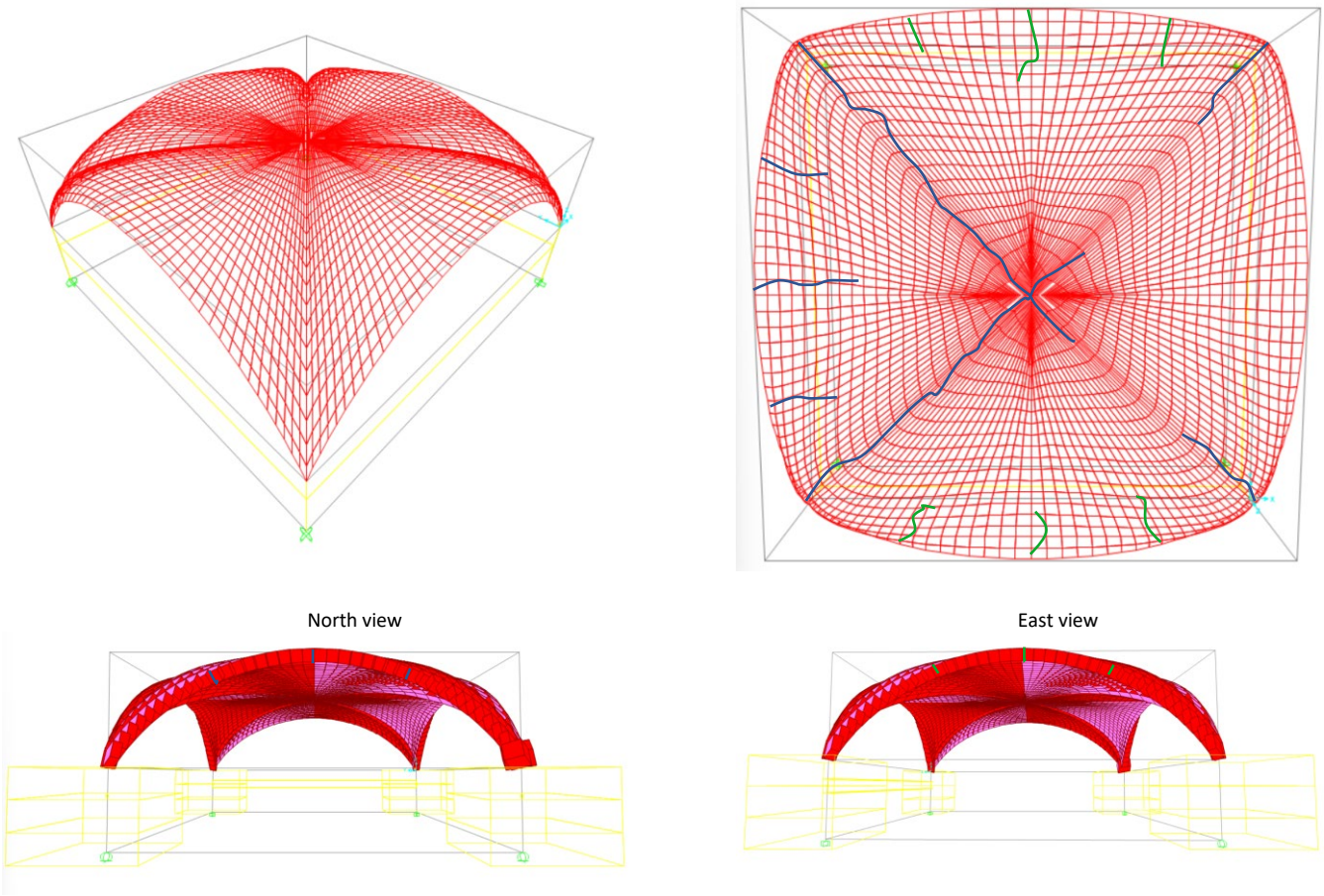

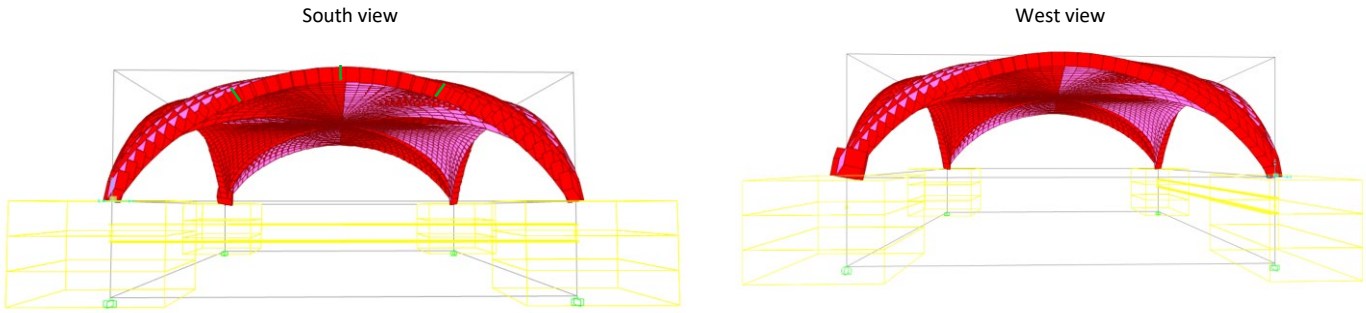


Figure 6: Simulated crack patterns.

## 3 CONCLUSIONS

The main goal of this work was to develop a simplified model compatible with preliminary analysis. Many experimental programs are planned on the basis of assumptions and choices which are subsequently amended. This is a very key issue, especially for masonry structures subjected to dynamic actions. A model able of simulating the main information on structural behavior is a useful tool, especially in the planning phase of experimental programs. The numerical model was in fact developed on the basis of initially available mechanical properties. Therefore, the numerical model was developed to test the reliability of a simplified approach (pre diction [9]) and not to accurately model the behavior of the tested masonry vault (post diction [26]). A reliable model is necessarily calibrated on the basis of deeper data from experimental tests. However, such refined calibration would make the simulations highly sensitive to the peculiarities of the case study, while this simplified modelling and approach would provide a more general outcome.

The approach is unable to accurately predict internal redistribution once evident damage has been achieved. It is obviously necessary to develop more refined models. They can be developed after specific numerical calibrations should be used.

From the point of view of damage, the developed numerical model was satisfactory. Main damage pattern was satisfactorily identified in accordance with the location, load threshold and typology experimentally found.

## REFERENCES

[1] H. R. Tabatabaiefar, B. Mansoury. Detail design, building and commissioning of tall building structural models for experimental shaking table tests. *Structural Design of Tall and Special Buildings*, **25**(8), 2006. https://doi.org/10.1002/tal.1262

[2] K. Fujii, Y. Sakai. Shaking table test of adjacent building models considering pounding. *International Journal of Computational Methods and Experimental Measurements,* **6**(5), 2018. https://doi.org/10.2495/CMEM-V6-N5-857-867

[3] A. Meoni, A. D'Alessandro, N. Cavalagli, N. Gioffré, F. Ubertini. Shaking table tests on a masonry building monitored using smart bricks: Damage detection and localization. *Earthquake Engineering and Structural Dynamics*, **48**(8), 2019. https://doi.org/10.1002/eqe.3166

[4] S. I. Kajii, C. Yasuda, T. Yamashita, H. Abe, H. Kanki. Development of synchronized control method for shaking table with booster device (verification of the capabilities based on both real facility and numerical simulator). *Nippon Kikai Gakkai Ronbunshu, C Hen/Transactions of the Japan Society of Mechanical Engineers, Part C*, **70**(7), 2020. https://doi.org/10.1299/kikaic.70.1889

[5] S. Noor-E-Khuda, F. Albermani. Mechanical properties of clay masonry units: Destructive and ultrasonic testing. *Construction and Building Materials*, **219**, 2019. https://doi.org/10.1016/j.conbuildmat.2019.05.166

[6] A.M. D'Altri, V. Sarhosis, G. Milani, J. Rots, S. Cattari, S. Lagomarsino, S., E. Sacco, A. Tralli, G. Castellazzi, S. de Miranda, S. Modeling Strategies for the Computational Analysis of Unreinforced Masonry Structures: Review and Classification. *Archives of Computational Methods in Engineering*, **27**(4), 2020. https://doi.org/10.1007/s11831-019-09351-x

[7] G. Rizzano. A Simplified Approach for the Seismic Analysis of Masonry Structures. *The Open Construction and Building Technology Journal*, **5**(1), 2011. https://doi.org/10.2174/1874836801105010097

[8] F. Aras, T. Akbaş, H. Ekşi, S. Çeribaşı. Progressive Damage Analyses of Masonry Buildings by Dynamic Analyses. *International Journal of Civil Engineering*, **18**(8), 2011. https://doi.org/10.1007/s40999-020-00508-5

[9] F. Saviano, F. Parisi, G.P. Lignola "Material aging effects on the in-plane lateral capacity of tuff stone masonry walls: a numerical investigation.". SPRINGER Materials and Structures, 2022. **55**, 198. Pages 1-24. https://doi.org/10.1617/s11527-022-02032-5

[10] N. Bianchini, C. Calderini, N. Mendes, P. Candeias, P.B. Lourenço. (2023). Blind Prediction Competition - Sera.ta - Seismic Response of Masonry Cross Vaults: Shaking table tests and numerical validations (Version 1) [Data set]. Zenodo. https://doi.org/10.5281/zenodo.7624666

[11] M.G. Masciotta, D. Pellegrini, M. Girardi, C. Padovani, A. Barontini, P.B. Lourenço, D. Brigante, G. Fabbrocino. Dynamic characterization of progressively damaged segmental masonry arches with one settled support: Experimental and numerical analyses. *Frattura Ed Integrita Strutturale*, **14**(51), 2020. https://doi.org/10.3221/IGF-ESIS.51.31

[12] G. Ramaglia, G.P. Lignola, A. Prota "Preliminary nonlinear analysis of a scaled masonry building under shaking test for the blind prediction of the SERA AIMS project". Special Issue "Adjacent Interacting Masonry Structures", on the SPRINGER Bulletin of Earthquake Engineering, 2023. https://doi.org/10.1007/s10518-023-01639-5

[13] F. Somma; G.P. Lignola; G. Ramaglia; L. de Sanctis; M. Iovino; S. Oztoprak; A. Flora "An interdisciplinary investigation of the seismic performance of a historic tower in Istanbul during the 1999 Kocaeli earthquake". Bull of Earth Engineering. 2023. https://doi.org/10.1007/s10518-023-01638-6

[14] G.P. Lignola, A. Prota "Deformability of base connections in shotcreted concrete sandwich load bearing perforated walls". ELSEVIER Engineering Structures, **268**, 114720, Pages 1-10. https://doi.org/10.1016/j.engstruct.2022.114720

[15] G. Ramaglia, G.P. Lignola, F. Fabbrocino, A. Prota "Structural analysis of historical masonry churches: the case study of S. Giuseppe delle Scalze (Naples, Italy)". Special Issue "Simple Mechanical Models for Unreinforced Historic Masonry Constructions",

on the International Journal of Masonry Research and Innovation. **6**(4):472 – 501. 2021. https://doi.org/10.1504/IJMRI.2021.10037509

[16] C. D'Ambra, G.P. Lignola, A. Prota "Multi-scale analysis of in-plane behaviour of tuff masonry". Advances in Masonry Materials and Structures Experimental & Numerical Modelling Aspects. The Open Construction and Building Technology Journal, **10**(Suppl 2: M10):312-328. 2016. https://doi.org/10.2174/1874836801610010312

[17] G.P. Lignola, G. Manfredi "Damage assessment and design of structural interventions for Monte di Pietà in Naples, Italy". International Journal of Architectural Heritage **5**:6, 2011:647-676. https://doi.org/10.1080/15583058.2010.483565

[18] V. Russo, G.P. Lignola, E. Vassallo, A. Zinno "Second World War damages of the architectural heritage: St. Maria del Popolo agli Incurabili church in Naples". Advanced Materials Research. Vols. **133-134**, 2010:1137-1142, https://doi.org/10.4028/www.scientific.net/AMR.133-134.1137

[19] B. Shrestha, H. Hao. Building Pounding Damages Observed during the 2015 Gorkha Earthquake. *Journal of Performance of Constructed Facilities*, **32**(2), 2018. https://doi.org/10.1061/(asce)cf.1943-5509.0001134

[20] M. TufailKhalil, J. Hafeez, M. Hasnain, A. AdeedKhan, M. Munir. Exploring the capabilities of building information modelling for a real life structure. *Journal of mechanics of continua and mathematical sciences*, **14**(2), 2019. https://doi.org/10.26782/jmcms.2019.04.00013

[21] N. Ravichandran, D. Losanno, F. Parisi. Comparative assessment of finite element macro-modelling approaches for seismic analysis of non-engineered masonry constructions. *Bulletin of Earthquake Engineering*, **19**(13), 2021. https://doi.org/10.1007/s10518-021-01180-3

[22] J. Segura, L. Pelà, P. Roca. Monotonic and cyclic testing of clay brick and lime mortar masonry in compression. *Construction and Building Materials*, **193**, 2018. https://doi.org/10.1016/j.conbuildmat.2018.10.198

[23] V. Giamundo, G.P. Lignola, G. Maddaloni, F. da Porto, A. Prota, G. Manfredi. Shaking table tests on a full-scale unreinforced and IMG retrofitted clay brick masonry barrel vault. *Bulletin of Earthquake Engineering*, **14**(6), 2016. https://doi.org/10.1007/s10518-016-9886-7

[24] R. Gagliardo, F. Portioli, L. Cascini, R. Landolfo, P.B. Lourenço. A rigid block model with no-tension elastic contacts for displacement-based assessment of historic masonry structures subjected to settlements. *Engineering Structures*, **229**, 2021. https://doi.org/10.1016/j.engstruct.2020.111609

[25] F. Solarino, D. Oliveira, L. Giresini. Wall-to-horizontal diaphragm connections in historical buildings: A state-of-the-art review. *In Engineering Structures*, **199**, 2019. https://doi.org/10.1016/j.engstruct.2019.109559

[26] N. Bianchini, C. Calderini, N. Mendes, P. Candeias, P.B. Lourenço. (2023). Postdiction Competition - Sera.ta - Seismic Response of Masonry Cross Vaults: Shaking table tests and numerical validations (Version 1) [Data set]. Zenodo. https://doi.org/10.5281/zenodo.7624791

COMPDYN 2023
9th ECCOMAS Thematic Conference on
Computational Methods in Structural Dynamics and Earthquake Engineering
M. Papadrakakis, M. Fragiadakis (eds.)
Athens, Greece, 12-14 June 2023

# COMPRESSION AND RECONSTRUCTION OF AUTOCOVARIANCE FUNCTIONS FOR DAMAGE DETECTION AND LOCALIZATION UNDER VARIABLE ENVIRONMENTAL CONDITIONS

**Jyrki Kullaa**

Department of Automotive and Mechanical Engineering
Metropolia University of Applied Sciences
Leiritie 1, 01600 Vantaa, Finland
P.O. Box 4071, 00079 Metropolia, Finland
e-mail: jyrki.kullaa@metropolia.fi

## Abstract

*Vibration-based structural health monitoring using autocovariance functions (ACFs) as damage-sensitive features is studied. ACFs are spatiotemporally correlated, which can be utilized in damage detection in the time domain. For accurate ACF estimates, a long measurement period with a high sampling frequency is needed. Storing data from repeated measurements will soon become exhaustive. A huge amount of space can be saved by storing much shorter ACFs instead. Further data compression can be achieved by storing only an optimally selected set of ACFs together with a coefficient matrix, from which the discarded ACFs can be reconstructed. The selection of the stored ACFs is done individually for each measurement based on the reconstruction accuracy. This ensures that the variability between measurements due to environmental or operational conditions or damage remains in the data. The stored and reconstructed ACFs are used for damage detection and localization by applying novelty detection techniques. The proposed method was studied with a numerical model of a bridge deck having 28 accelerometers. Only about four ACFs were stored together with the coefficient matrix for reconstruction. The space saving was more than 80%. The stored and reconstructed ACFs and the full set of original ACFs performed equally well in damage detection and localization. ACFs also outperformed direct measurement data in damage detection.*

**Keywords:** Autocovariance Function, Data Compression and Reconstruction, Damage Detection, Optimal Sensor Placement, Environmental Effects, Spatiotemporal Correlation.

## 1 INTRODUCTION

Structural health monitoring (SHM) is based on measurement data. Vibration-based SHM is a global technique, in which damage can be detected remotely from a sensor. Nevertheless, it is often necessary to equip structures with a sensor network consisting of several vibration sensors. Information about the structure's condition is extracted from the response time histories. This process typically requires training data from the undamaged structure under different environmental or operational conditions. The excitation is often unknown, but can be assumed colored white noise. In order to obtain accurate vibration characteristics from the data, a long measurement period must be used. Moreover, the sampling frequency must be sufficiently high resulting in a large amount of data. These data must be stored to train a data model of the undamaged structure and then to monitor possible damage evolution by applying unsupervised learning techniques.

Due to a large amount of data, data management soon becomes an issue. The amount of data can be considerably reduced by extracting damage-sensitive features from the time records. The most common features are probably natural frequencies, mode shapes, and modal damping of the structure. They can be obtained using output-only system identification algorithms [1]. The algorithms must run automatically, which may be an issue. Also, a high-dimensional feature vector may result in the curse of dimensionality in statistical data analysis, especially if mode shapes are used in damage detection. On the other hand, if natural frequencies are only used, they may not be sensitive enough to detect damage, and damage localization would be difficult.

In this paper, autocovariance functions (ACFs) are proposed for damage detection and localization. Each sensor results in an ACF consisting of covariances at different time lags. This is advantageous for statistical analysis, because the feature vector is low-dimensional and has several data points per measurement. Also, damage can be associated to a sensor, which can be utilized in damage localization. ACFs have the same form as a free decay of the system [1]. This form is very advantageous, because there is a strong spatial and temporal correlation between ACFs of different DOFs [2]. The estimation of ACFs can be easily automated, but the measurement period should be long for sufficient accuracy. ACFs have been found to outperform raw measurement data in time-domain damage detection [2].

Correlation functions have been proposed for damage detection also in other studies. Li and Law [3] used cross-covariance functions with one sensor acting as a reference. In many cases, only a single data point is selected from the correlation functions, either the value at lag $\tau = 0$ [4–8], or the maximum of the cross-correlation function [9, 10].

The space requirement of autocovariance functions may also be an issue. Fortunately, ACFs are much shorter signals than the measured time histories, from which they are estimated. Storing AFCs instead of the actual measurements results already in an enormous space saving. Further data compression is possible by storing only a limited set of ACFs so that the discarded ACFs can be reconstructed using the stored ACFs. This is the main objective of this study.

It may first appear that because of redundancy, the stored ACFs alone would be sufficient for damage detection and no further information would be gained using also the reconstructed ACFs. This is, however, not true as will be shown in the numerical experiment. The redundancy in a single measurement is utilized in data compression, where the environmental and operational conditions remain unchanged. However, pooling many measurements under different environmental conditions in damage detection requires a higher-dimensional feature vector. In addition, damage localization is possible also to sensors whose data are reconstructed [11], fully exploiting all sensor data.

Neither excitation nor environmental variables need be measured. Quite a few methods to eliminate environmental or operational effects from data have been proposed, in which

measurement of the underlying variables is not necessary [12]. In this study, different environmental conditions between measurements are considered using whitening transformation of the training data acquired from the undamaged structure [13].

Sensor selection for storage is performed using optimal sensor placement (OSP) algorithms. The backward sequential sensor placement (BSSP) algorithm has proven efficient and practical [14–16] and is also used in this study. Initially, a full set of ACFs is available and one ACF is removed in each round until the stopping criterion is met. The selection is based on the most accurate reconstruction of the discarded data. The cost function is thus related to the reconstruction error, which must be minimized.

Damage detection is based on changes in the dynamic characteristics of the structure. In this paper, damage detection and localization are performed in the time domain. The data are the stored and reconstructed ACFs. Statistically significant differences between the training and test data are assumed to reveal damage. The discrepancy can be projected to each sensor, and the largest value is assumed to locate damage in the vicinity of the corresponding sensor.

The paper is organized as follows. Autocovariance functions are introduced in Section 2. An algorithm to optimally select ACFs for storage and reconstruct the discarded ACFs is proposed in Section 3. Damage detection and localization using the stored and reconstructed ACFs is also outlined. In Section 4, a numerical experiment is conducted with a bridge structure under variable environmental conditions. Damage is a propagating crack in the steel girder. Concluding remarks are given in Section 5.

## 2 AUTOCOVARIANCE FUNCTIONS

The autocorrelation function (ACF) of a zero-mean random process $\{x(t)\}$ is [17]:

$$R_{xx}(\tau) = \mathrm{E}[x(t)x(t+\tau)] \tag{1}$$

where E[·] is the expectation operator. The ACF at lag $\tau = k\Delta t$ can be estimated from the sampled measurement record having $N$ samples with sampling period $\Delta t$:

$$R_{xx}(k) = \frac{1}{N-k}\sum_{j=1}^{N-k} x(j)x(j+k) \tag{2}$$

where $x(k) = x(k\Delta t)$ and $R_{xx}(k) = R_{xx}(k\Delta t)$. ACFs can alternatively be estimated using FFT computations [17]. This is much faster, if the measurement period is very long.

Autocovariance functions are time-domain features. For a viscously damped SDOF system under white noise excitation with a constant power spectral density $S_0$, the displacement autocorrelation function at a non-negative lag $\tau$ can be expressed as [18]:

$$R_{xx}(\tau) = \frac{\pi\omega_\mathrm{n}S_0}{2k^2\zeta}\left(\cos\omega_\mathrm{d}\tau + \frac{\zeta}{\sqrt{1-\zeta^2}}\sin\omega_\mathrm{d}\tau\right)\exp(-\omega_\mathrm{n}\zeta\tau) \tag{3}$$

where $\omega_\mathrm{n}$ is the natural angular frequency, $k$ is the spring constant, $\zeta$ is the damping ratio, and $\omega_\mathrm{d} = \omega_\mathrm{n}\sqrt{1-\zeta^2}$ is the damped natural angular frequency. Note that Equation (3) has the following form.

$$R_{xx}(\tau) = (A\cos\omega_\mathrm{d}\tau + B\sin\omega_\mathrm{d}\tau)\exp(-a\tau) \tag{4}$$

where $A$, $B$, $a$, and $\omega_\mathrm{d}$ are constants. Equation (4) has the same form as the free vibration of a viscously damped SDOF system. This particular form was studied in [2] showing that temporal correlation applies, so that values at different lags are redundant. The same form (4) applies also to velocity and acceleration ACFs [8].

For a MDOF system, ACFs include contributions from all modes, resulting in the following formula for DOF $j$ (see also [1, 7, 19]).

$$R_{jj}(\tau) = \sum_{s=1}^{n} e^{-\zeta_s \omega_s \tau} \left[ A_{jjs} \cos(\omega_{\mathrm{d}s}\, \tau) + B_{jjs} \sin(\omega_{\mathrm{d}s}\, \tau) \right] \tag{5}$$

where $n$ is the number of modes, and

$$A_{jjs} = \sum_{r=1}^{n} \frac{F_{rs}}{2 m_r \omega_{\mathrm{d}r} m_s \omega_{\mathrm{d}s}} \boldsymbol{\phi}_{jr} \boldsymbol{\phi}_{js}\, \boldsymbol{\phi}_r^T \mathbf{B} \mathbf{Q} \mathbf{B}^T \boldsymbol{\phi}_s \tag{6}$$

$$B_{jjs} = \sum_{r=1}^{n} \frac{G_{rs}}{2 m_r \omega_{\mathrm{d}r} m_s \omega_{\mathrm{d}s}} \boldsymbol{\phi}_{jr} \boldsymbol{\phi}_{js}\, \boldsymbol{\phi}_r^T \mathbf{B} \mathbf{Q} \mathbf{B}^T \boldsymbol{\phi}_s \tag{7}$$

$$F_{rs} = \frac{-\zeta_r \omega_r - \zeta_s \omega_s}{(\zeta_r \omega_r + \zeta_s \omega_s)^2 + (\omega_{\mathrm{d}r} + \omega_{\mathrm{d}s})^2} + \frac{\zeta_r \omega_r + \zeta_s \omega_s}{(\zeta_r \omega_r + \zeta_s \omega_s)^2 + (\omega_{\mathrm{d}r} - \omega_{\mathrm{d}s})^2} \tag{8}$$

$$G_{rs} = \frac{\omega_{\mathrm{d}r} + \omega_{\mathrm{d}s}}{(\zeta_r \omega_r + \zeta_s \omega_s)^2 + (\omega_{\mathrm{d}r} + \omega_{\mathrm{d}s})^2} + \frac{\omega_{\mathrm{d}r} - \omega_{\mathrm{d}s}}{(\zeta_r \omega_r + \zeta_s \omega_s)^2 + (\omega_{\mathrm{d}r} - \omega_{\mathrm{d}s})^2} \tag{9}$$

in which $m_r$, $\omega_r$, $\omega_{\mathrm{d}r}$, $\zeta_r$, $\boldsymbol{\phi}_r$, are, respectively, the modal mass, the undamped natural circular frequency, the damped natural circular frequency, the damping ratio, and the mode shape vector of the mode $r$. Matrix **B** is the load distribution matrix, and **Q** is a diagonal matrix with spectral densities of the loads. From Equation (5), it can be seen that it has the same form as a free decay of the system. The redundancy applies also in a MDOF system within a single measurement under constant environmental and operational conditions.

However, between measurements, the situation is more complicated. First, under different environmental conditions, the dynamic characteristics may differ, resulting in different ACFs. Second, even if the environmental conditions remain the same, the excitation may vary, or more specifically, matrices **B** and **Q** may be different between measurements affecting the constants $A_{jjs}$ and $B_{jjs}$.

Due to reasons stated above, it is important to process each measurement individually for data compression and reconstruction. On the other hand, in damage detection, in which the training data are comprised of several measurements, the data covariance matrix includes normal variability due to different environmental or operational conditions. Therefore, damage detection is supposed to require a higher-dimensional feature vector to take these variabilities into account. This can be realized by using all ACFs, stored and reconstructed, and applying spatiotemporal correlation.

## 3 DAMAGE DETECTION USING COMPRESSED DATA

Data analysis for damage detection is done using a full set of ACFs. However, it is often not necessary to store all ACFs. The objective is to store only a limited set of the ACF data so that the discarded ACFs can be reconstructed with sufficient accuracy using the stored signals. It is important to process each measurement individually to ensure that the variability between measurements due to different environmental or operational conditions or damage remains in the data.

Each measurement may result in a different set of stored data, depending on the reconstruction accuracy. Because all AFCs of a measurement are initially available, data compression and reconstruction can be actually tested before making the decision. The data analysis process is illustrated in Figure 1.

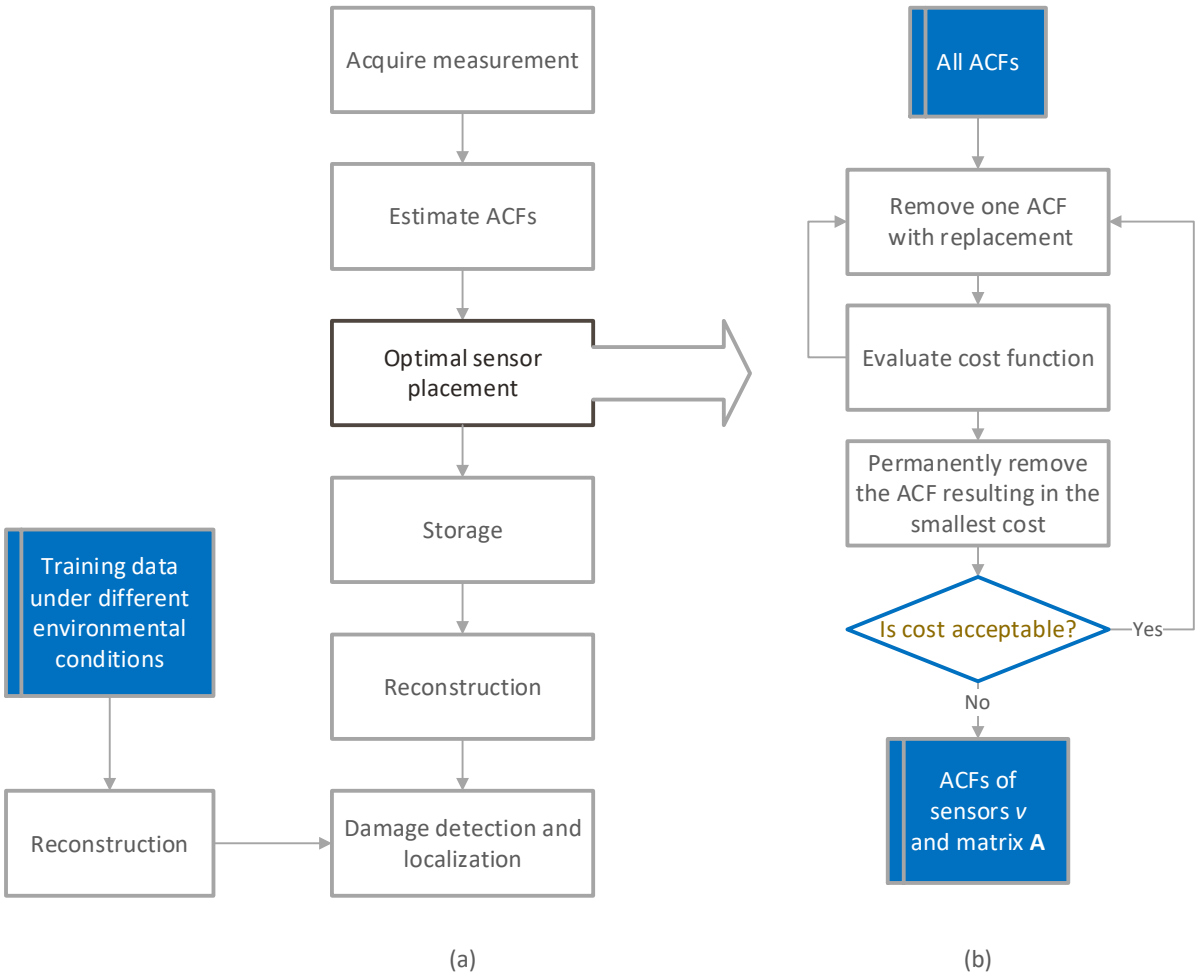


Figure 1: a) Flowchart for data compression and reconstruction for damage detection and localization. b) Flowchart for optimal sensor placement (OSP) to select the ACFs for storage.

### 3.1 Data compression and reconstruction

The flowchart to optimally select sensors for storage is depicted in Figure 1b. Consider a sensor network with $p$ sensors resulting in $p$ ACF estimates $\hat{R}_{ii}(\tau),\ i = 1,2,\ldots,p$. For simplicity, denote the ACF estimates with

$$\mathbf{r}(k) = \begin{Bmatrix} \hat{R}_{11}(k\Delta t) \\ \hat{R}_{22}(k\Delta t) \\ \vdots \\ \hat{R}_{pp}(k\Delta t) \end{Bmatrix} \tag{10}$$

After a single measurement, the ACFs from all sensors are available. If only a subset of the ACFs is stored, a lot of space can be saved. Assume that the ACFs of channels $v$ are only stored, while the discarded ACFs of the remaining channels $u$ must be reconstructed.

Divide $\mathbf{r}$ into stored data $\mathbf{r}_v$ and discarded data $\mathbf{r}_u$. The discarded data can be reconstructed using spatiotemporal correlation, as follows. Assuming model order $m$, the following data vectors are defined.

$$\mathbf{y}_u(k) = \boldsymbol{r}_u(k), \qquad \mathbf{y}_v(k) = \begin{Bmatrix} \mathbf{r}_v(k) \\ \mathbf{r}_v(k+1) \\ \mathbf{r}_v(k+2) \\ \vdots \\ \mathbf{r}_v(k+m) \end{Bmatrix} \tag{11}$$

$$\mathbf{y}(k) = \begin{Bmatrix} \mathbf{y}_u(k) \\ \mathbf{y}_v(k) \end{Bmatrix} \tag{12}$$

The data covariance matrix is

$$\boldsymbol{\Sigma} = \mathrm{E}[\mathbf{y}\mathbf{y}^T] = \begin{bmatrix} \mathrm{E}(\mathbf{y}_u\mathbf{y}_u^T) & \mathrm{E}(\mathbf{y}_u\mathbf{y}_v^T) \\ \mathrm{E}(\mathbf{y}_v\mathbf{y}_u^T) & \mathrm{E}(\mathbf{y}_v\mathbf{y}_v^T) \end{bmatrix} = \begin{bmatrix} \boldsymbol{\Sigma}_{\mathbf{y}_u\mathbf{y}_u} & \boldsymbol{\Sigma}_{\mathbf{y}_u\mathbf{y}_v} \\ \boldsymbol{\Sigma}_{\mathbf{y}_v\mathbf{y}_u} & \boldsymbol{\Sigma}_{\mathbf{y}_v\mathbf{y}_v} \end{bmatrix} \tag{13}$$

Note that for model order equal to $m = 0$, $\mathbf{y}_v(k)$ is simply equal to $\mathbf{r}_v(k)$, representing spatial correlation only.

The discarded data can be reconstructed by applying linear minimum mean-square error (MMSE) estimation. The mean square-error is minimized by the conditional mean [20]:

$$\mathrm{E}(\mathbf{y}_u|\mathbf{y}_v) = \boldsymbol{\Sigma}_{\mathbf{y}_u\mathbf{y}_v}\boldsymbol{\Sigma}_{\mathbf{y}_v\mathbf{y}_v}^{-1}\mathbf{y}_v = \mathbf{A}\mathbf{y}_v \tag{14}$$

where $\mathbf{A} = \boldsymbol{\Sigma}_{\mathbf{y}_u\mathbf{y}_v}\boldsymbol{\Sigma}_{\mathbf{y}_v\mathbf{y}_v}^{-1}$ is the coefficient matrix that has to be stored together with the stored signals $\mathbf{r}_v$. The covariance matrix of the conditional distribution $p(\mathbf{y}_u|\mathbf{y}_v)$ is [20]:

$$\mathrm{cov}(\mathbf{y}_u|\mathbf{y}_v) = \boldsymbol{\Sigma}_{\mathbf{y}_u\mathbf{y}_u} - \boldsymbol{\Sigma}_{\mathbf{y}_u\mathbf{y}_v}\boldsymbol{\Sigma}_{\mathbf{y}_v\mathbf{y}_v}^{-1}\boldsymbol{\Sigma}_{\mathbf{y}_v\mathbf{y}_u} \tag{15}$$

which can be used to estimate the reconstruction error for optimal sensor selection.

### 3.2 Optimal sensor placement

The selection of ACFs for storage utilizes optimal sensor placement (OSP) methods. Starting with a full set of ACFs, one ACF is removed in each round until the stopping criterion is met. This is referred as backward sequential sensor placement (BSSP) algorithm [16].

Note that unlike in damage detection, each measurement under constant environmental and operational conditions is analyzed separately. Therefore, each measurement may result in different ACFs selected with a unique coefficient matrix.

Once the model order $m$ is determined, the covariance matrix is estimated using Equation (13). One sensor in turn is removed with replacement, and all the removed ACFs are estimated using the retained ACFs. Once all ACFs have been gone through and the cost function evaluated, one ACF is permanently removed corresponding to the minimum value of the cost function. The process is repeated until the stopping criterion is met. Then the retained ACFs together with the coefficient matrix $\mathbf{A}$ in Equation (14) are stored.

The cost function and the stopping criterion are related to the error of reconstruction, Equation (15), which is minimized in each round.

### 3.3 Damage detection and localization

Damage detection starts by defining the training data, which are the selected ACFs (either directly estimated or stored and reconstructed) from the undamaged structure. Once the model order $m$ is determined, another covariance matrix is estimated for all training data including influences of different environmental or operational conditions, but not damage.

The time-shifted covariance matrix estimate, with a time shift $k$, is computed by

$$\mathbf{R}_k = \mathrm{E}[\mathbf{x}(j)\mathbf{x}^T(j+k)] \approx \frac{1}{N-k}\sum_{j=1}^{N-k}\mathbf{x}(j)\mathbf{x}^T(j+k) \tag{16}$$

where $\mathbf{x}(k) = \mathbf{x}(k\Delta t)$ are the ACFs of the training data at a time instant $k\Delta t$, $\Delta t$ is the sampling period, and $N$ is the total number of samples. Equation (16) is similar to Equation (2), but in Equation (16) cross-covariances are also included. In Equation (2), $N$ denotes the length of a single measurement, while in Equation (16) $N$ denotes the total length of the training data. If $m$ is the model order, the covariance matrix is:

$$\mathbf{R} = \begin{bmatrix} \mathbf{R}_0 & \mathbf{R}_1 & \cdots & \mathbf{R}_m \\ \mathbf{R}_1^T & \mathbf{R}_0 & \cdots & \mathbf{R}_{m-1} \\ \vdots & \vdots & \ddots & \vdots \\ \mathbf{R}_m^T & \mathbf{R}_{m-1}^T & \cdots & \mathbf{R}_0 \end{bmatrix} \tag{17}$$

For a model order equal to $m = 0$, $\mathbf{R} = \mathbf{R}_0$ corresponding to spatial correlation only.

Whitening transformation is applied to the training data using the covariance matrix in Equation (17). Whitening acts as data normalization considering also the effects of environmental or operational variability [13]. After whitening transformation, the training data points are located inside a unit hypersphere. The test data are then subjected to the same transformation. If damage (or any other novelty) is present, the corresponding transformed data points are presumably located outside the unit hypersphere. This can be detected e.g. by principal component analysis. Retaining only the first principal component reveals the direction of the largest variance. This direction projected on each sensor DOF and searching for the maximum is assumed to identify the sensor closest to damage.

A generalized extreme value statistics (EVS) probability distribution [21] is identified for the first principal component scores of the training data. An EVS control chart is then designed for the scores with appropriate control limits and subgroup size [22]. In this paper, the subgroup size equal to 100 and the probability of a false alarm equal to 0.001 have been used.

## 4 NUMERICAL EXPERIMENT

### 4.1 Structure and monitoring data

Sensor data were generated numerically using a finite element model of a bridge deck with a concrete slab and steel stiffeners (Figure 2). The structure was 30 m long and 11 m wide. More details can be found in [23]. The structure was equipped with 28 accelerometers. Vertical random excitation was applied at two points shown in green in Figure 2. The unmeasured excitations were mutually independent and different in each measurement in the frequency range between 0 and 20 Hz with random amplitudes and phases. The first 30 modes were used in the simulation. Modal damping was assumed with damping ratios of $\zeta_{1\text{–}2} = 0.01$, $\zeta_{3\text{–}4} = 0.02$, and $\zeta_{5\text{–}30} = 0.03$.

Steady state analysis was performed in the frequency domain using modal superposition. The sampling frequency was 100 Hz and the measurement period was more than 43 min. Each sensor produced $2^{18}$ samples per measurement. Gaussian random noise with equal standard deviations was added to each sensor. The average signal-to-noise ratio was 30 dB.

The bridge ends were at random temperatures between –20°C and +40°C. The relationship between the Young's modulus $E$ of the concrete slab and temperature $T$ (°C) was piecewise linear (see Figure 3a):

$$E = \begin{cases} E_0 + k_1 T, & T < 0 \\ E_0 + k_2 T, & T \geq 0 \end{cases} \tag{18}$$

where $E_0 = 40$ GPa, $k_1 = -1.0$ GPa/°C, and $k_2 = -0.25$ GPa/°C. The temperature distribution between the bridge ends was linear, except for Gaussian noise $N(0, 0.2°C)$, which was added to

the temperature values in each element row. Note that the temperature or the Young's modulus were not measured, but they were considered latent variables.

Damage was an open crack in a steel girder with an increasing severity (Figure 2). Due to damage and the temperature effect, the natural frequencies varied between measurements. Figure 3b shows the seven lowest natural frequencies of the structure in all measurements. The data points on the right-hand side of the vertical line are from the damaged structure. It is difficult to detect damage visually from the frequency changes due to the strong environmental effect. Natural frequencies were not used in damage detection in this paper.

The first 100 measurements were acquired from the undamaged structure and each damage level was monitored with six measurements under different and unknown environmental conditions. Training data were the first 70 measurements. Extreme value statistics (EVS) control charts were designed using the same training data.

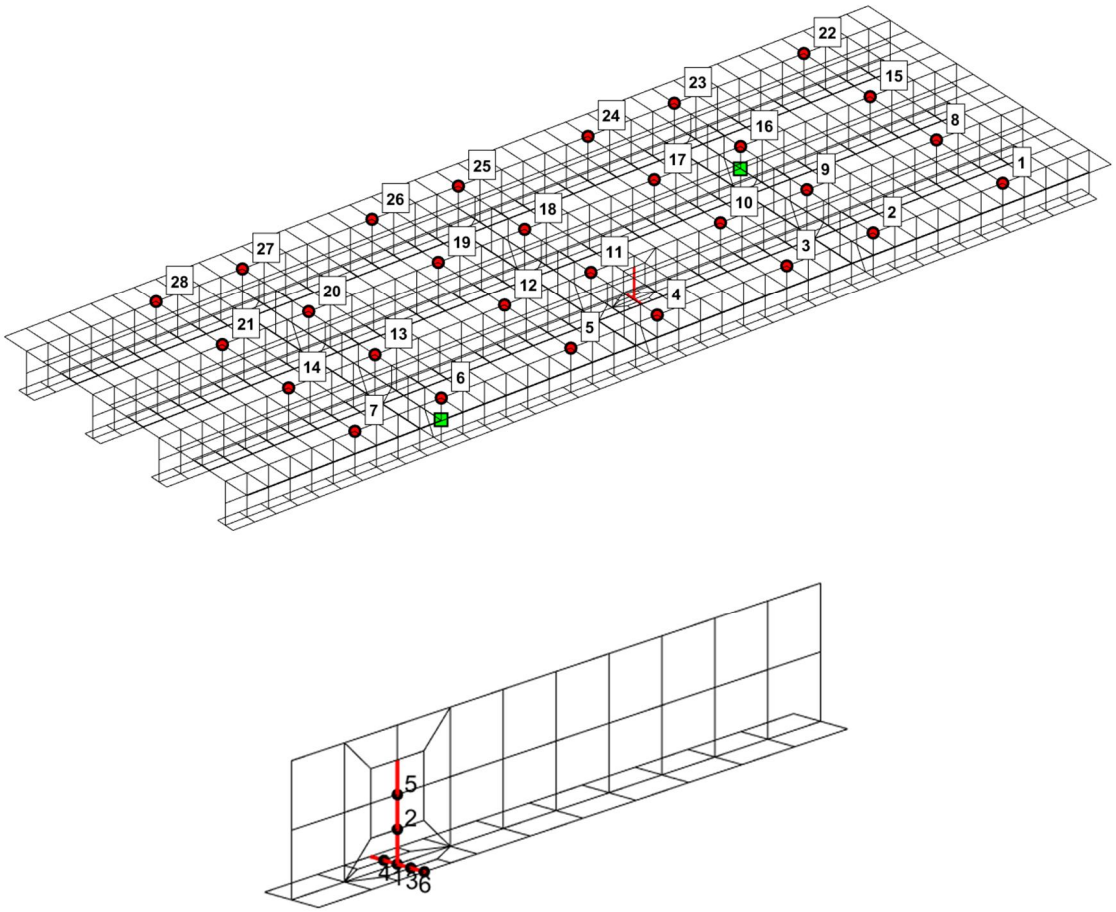


Figure 2: Top: Bridge deck with 28 accelerometers, two excitation points (green), and damage in a steel girder. Bottom: Detail of the crack damage with numbers indicating the order of damage evolution.

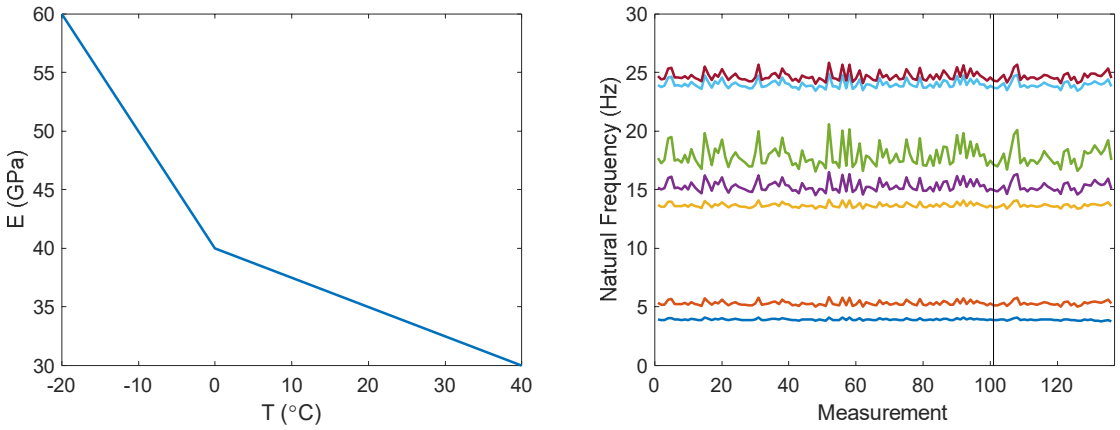


(a) (b)

Figure 3: (a) Young's modulus of concrete versus temperature. (b) Variation of the seven lowest natural frequencies due to temperature and damage. Frequencies on the right of the vertical line are from the damaged structure.

### 4.2 Data compression and reconstruction

Autocovariance functions were estimated from each sensor signal at time lags 0–3 s, resulting in 300 samples in each ACF ($n = 300$). As an example, the ACF of sensor 1 in measurement 4 is plotted in Figure 4. Compared with the actual sensor data, ACFs resulted in a huge space saving.

Having all 28 ACFs of a single measurement ($p = 28$), the next step was to select a limited number of ACFs for storage so that the discarded ACFs could be reconstructed with sufficient accuracy. The algorithm described in Section 3 was applied. The stopping criterion was that the estimation error, or more precisely, the square root of the conditional variances in Equation (15) had to be less than the estimated random errors of the ACF estimates at lag $\tau = 0$. The normalized rms error is [17]:

$$\varepsilon\left[\hat{R}_{xx}(0)\right] \approx (BT)^{-1/2} \tag{19}$$

where $B$ is the bandwidth and $T$ is the record length. With $B = 20$ Hz and $T = 2621$ s resulted in the normalized rms error $\varepsilon = 0.0044$. Multiplying this with $\hat{R}_{xx}(0)$ gave the absolute error. This value was computed for all data records and used in sensor selection.

Starting with all 28 ACFs, the backward sequential sensor placement (BSSP) algorithm was applied by removing a single sensor (ACF) in turn so that the maximum difference between the current and allowed reconstruction errors in any sensor in the network was minimized. Sensor removal continued until the accuracy requirement was violated. Model order $m = 4$ was used in data compression and reconstruction. Figure 4 shows the direct ACF estimate of sensor 1 in measurement 4 together with the reconstruction estimated using only three stored ACFs and the coefficient matrix of size 25×15. The difference is hardly visible. Only at higher lags is the discrepancy more pronounced.

The required number of stored ACFs varied between 3 and 6. Even with the relatively large stored coefficient matrices for each measurement, the total space saving was more than 81%.

With a higher model order, the accuracy of reconstruction would have been higher and the number of stored sensors would have been smaller. However, the size of the coefficient matrix would have increased. The size of the data matrix is $(n - m) \times (m + 1)p$. With a large model order $m$, the covariance matrix becomes singular. In the present case, the maximum allowed

model order would have been $m_{\max} = 9$. Therefore, a relatively small model order had to be used. In damage detection, the model order can be selected independently as can be seen in the following.

Once a single ACF was permanently removed, the mean error of the reconstructed ACFs was evaluated. The mean error as a function of the number of stored ACFs is plotted in Figure 5 for measurement 4. It can be seen that storing 11 ACFs instead of all 28 ACFs did not significantly increase the average noise level. When the number of stored ACFs was further decreased below 11, the reconstruction error considerably increased. In this case, only 3 ACFs had to be stored before the accuracy criterion was violated.

The reconstruction errors in each measurement, or more specifically, the square roots of the diagonal terms of $\mathrm{cov}(\mathbf{y}_u|\mathbf{y}_v)$ in Equation (15), are plotted in Figure 6 for all 28 sensors. The heavy line on top is the error limit. The criterion was not applied to the stored ACFs, and for those sensors the plotted value was zero.

A histogram of the selected sensors for storage in all measurements is shown in Figure 7a. The most often selected sensors can be clearly seen. However, both the number and location of the stored sensors varied between measurements. The placement of the stored three sensors in measurement 4 is plotted in Figure 7b.

The data compression ratio was computed as follows. If all ACF data were stored, the number of floating-point numbers in each measurement was 28·300 = 8400 numbers. Storing three ACFs (3·300 = 900 numbers) and the coefficient matrix **A** (Equation 14) of size 25×15 resulted in 1275 numbers. Consequently, only 15.2% of the total data had to be stored. Note also that the space saving was huge compared to the case if all raw acceleration data had been stored.

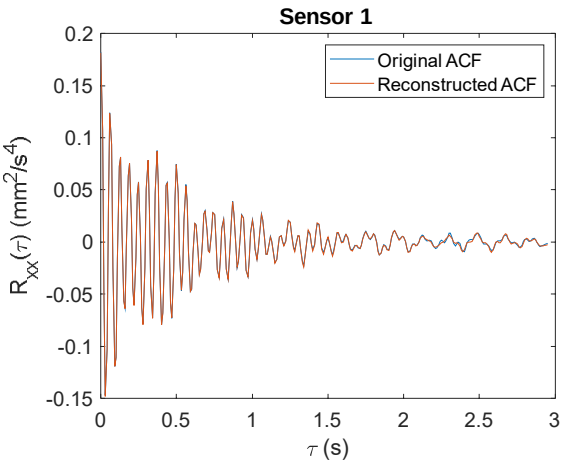


Figure 4: Directly estimated and reconstructed ACF of accelerometer 1 in measurement 4.

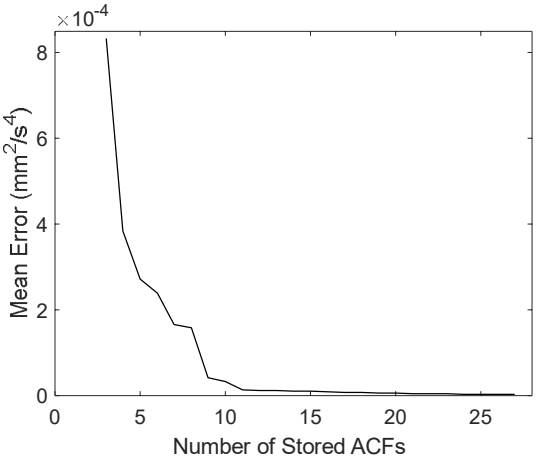


Figure 5: Mean reconstruction error as a function of the number of stored ACFs in measurement 4.

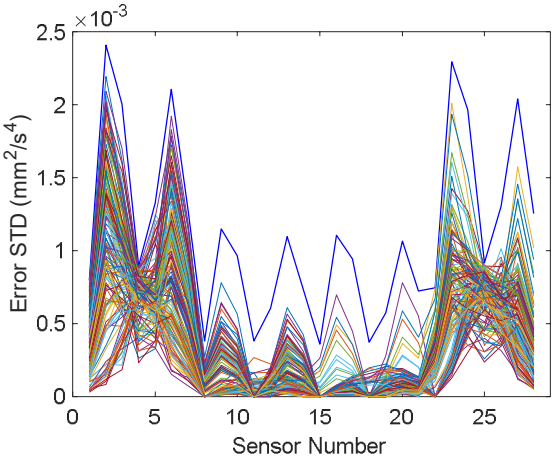


Figure 6: Accuracy criterion (blue heavy line on top) and the reconstruction errors of each sensor in all measurements.

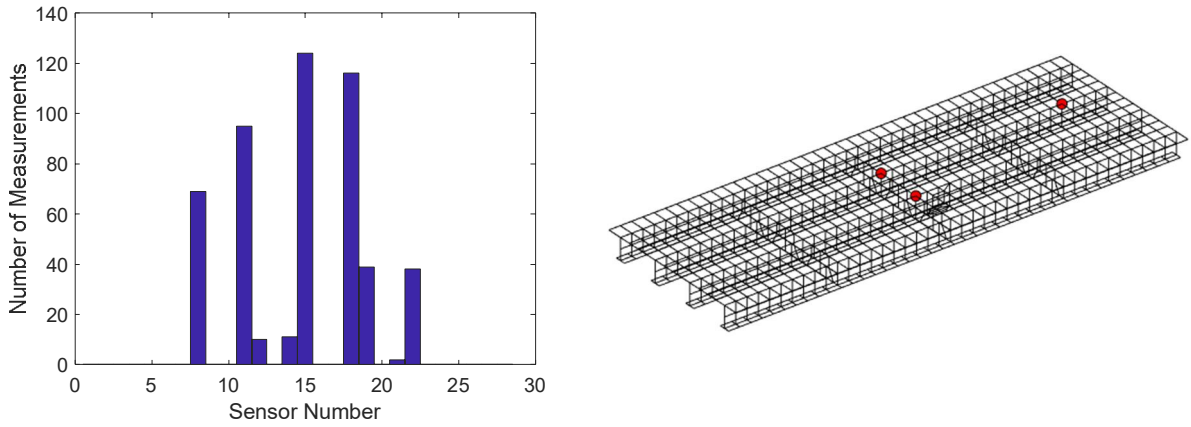


(a) (b)

Figure 7: a) Histogram of selected sensors for storage in all measurements. b) Selected sensors for storage in measurement 4: sensors 11, 15, and 18.

### 4.3 Damage detection and localization

Damage detection was studied using four different data: (1) ACFs estimated from the measurement data, (2) stored and reconstructed ACFs, (3) raw acceleration measurements, and (4) the stored ACFs only. Model order equal to 10 was used in all cases.

EVS control charts designed with a subgroup size of 100 are plotted in Figure 8. The data points to the left of the blue vertical line correspond to the training data, while the black vertical lines indicate the onset of each six damage levels. Logarithmic scaling was applied to the vertical axis for clarity.

When using all directly estimated ACFs, all damage levels could be detected with only three false positives (Figure 8a). Detection of damage level 1 was however not clear. As a comparison, using the stored and reconstructed ACFs resulted in a slightly better detection performance with two false alarms (Figure 8b). This was surprising, because the accuracy probably decreased in data compression. Notice also that in one measurement, the maxima exceeded the lower control limit, which could be ignored.

If the measurement data were directly used [23], only the largest damage level could be detected (Figure 8c). Also, if the four most stored ACFs of sensors 8, 11, 15, and 18 were only used, damage levels 5 and 6 were only detected (Figure 8d). Due to different environmental conditions between measurements, a higher-dimensional feature vector would have been needed to remove the environmental influences. This could be achieved by using all 28 ACFs instead of the four stored ACFs alone.

Damage localization was done by plotting the squared projection of the first principal component on each sensor (Figure 9). Using the direct ACF estimates, damage was localized to sensor 11, and using the stored and reconstructed ACFs, damage was localized to sensor 10. The correct position was between sensors 10 and 11, slightly closer to sensor 11.

Applying spatial correlation only with the model order equal to $m = 0$, the control charts in Figure 10 resulted. Compared to the spatiotemporal correlation, damage detection was less reliable. Direct ACF estimates outperformed the reconstructed ones. The number of false positives remained at the same level as with spatiotemporal correlation.

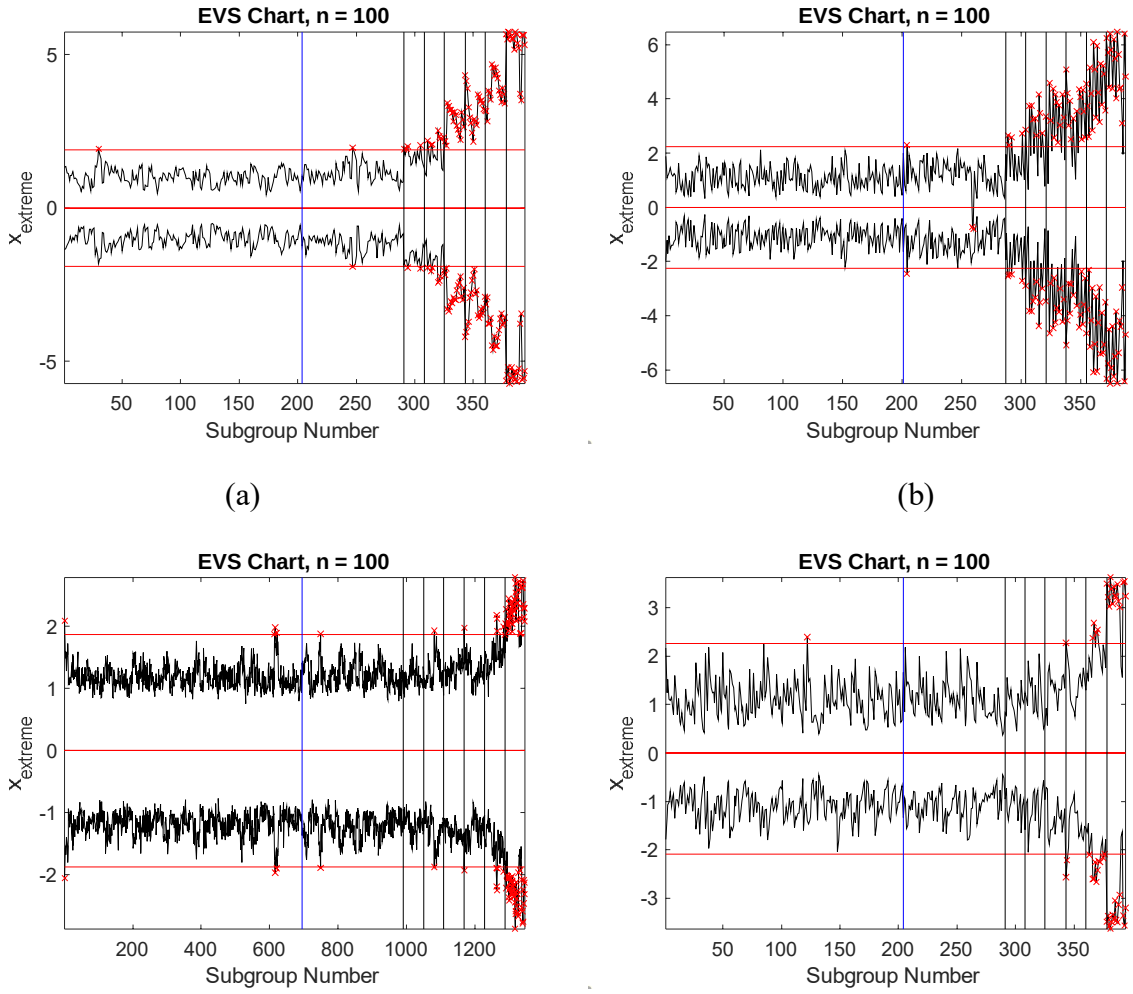


Figure 8: Damage detection using model order $m$ = 10. (a) All ACFs, (b) stored and reconstructed ACFs, (c) raw measurement, and (d) ACFs of sensors 8, 11, 15, and 18. The vertical lines correspond to the end of training data (blue) and the six damage levels (black).

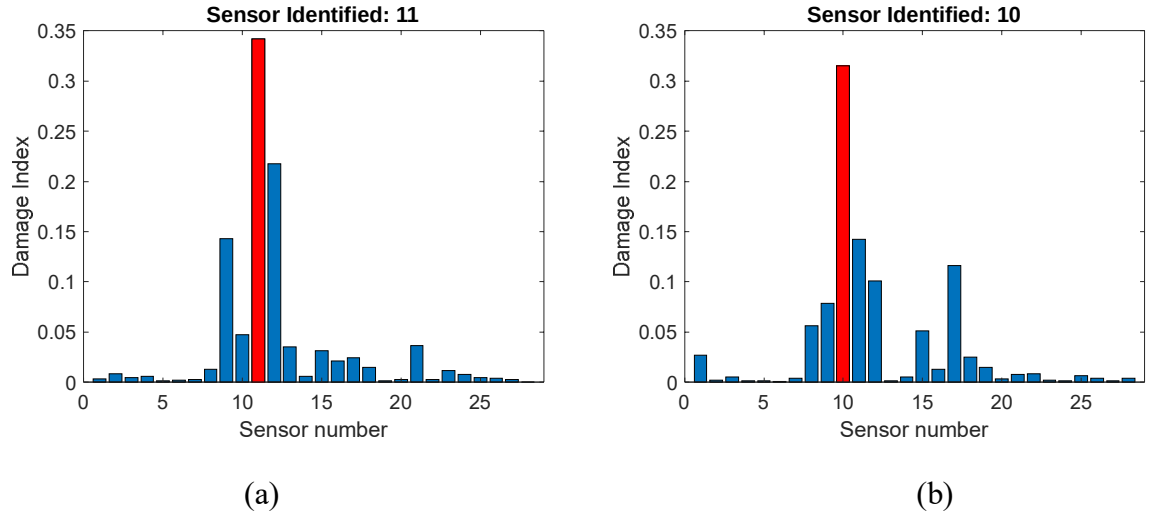


Figure 9: Damage localization. (a) All ACFs, (b) stored and reconstructed ACFs. The correct damage position was between sensors 10 and 11.

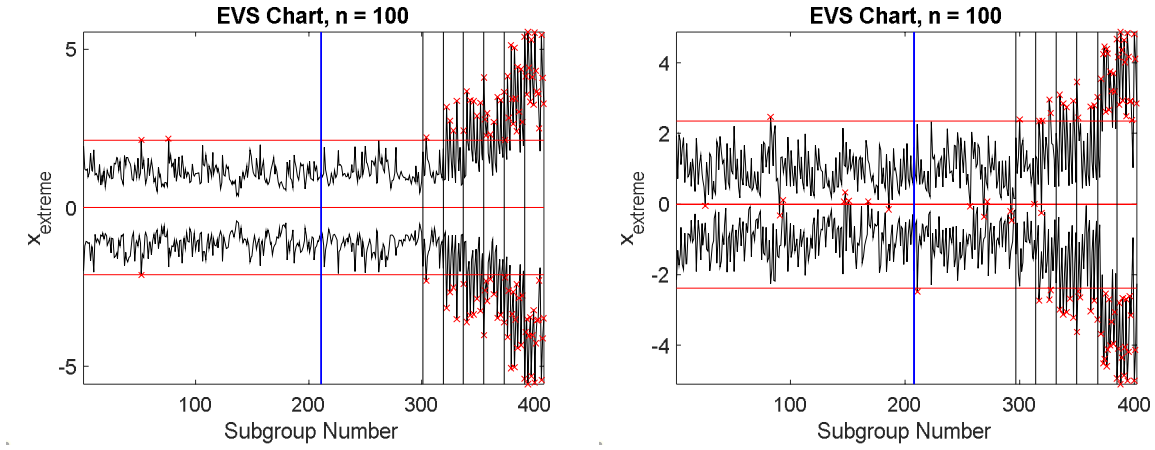


(a) (b)

Figure 10: Damage detection using model order = 0. (a) All ACFs, (b) stored and reconstructed ACFs. The vertical lines correspond to the end of training data (blue) and the six damage levels (black).

## 5 CONCLUSION

Data management in structural health monitoring applications is important, because the system is operating for a long time and each measurement produces lots of data. In order to save disk space without compromising damage detection performance, the following conclusions were drawn.

- Instead of using raw data, autocovariance functions were suggested as damage-sensitive features. They are much shorter signals to store, they are easy to estimate, and spatiotemporal correlation applies. Their accuracy can also be controlled with the measurement period.
- Storing only a limited set of ACFs, a further space saving can be obtained. In the given example, the additional space saving was more than 80%.
- The stored and reconstructed data were used to detect and localize damage.
- Spatiotemporal correlation was utilized both in data compression and reconstruction as well as in damage detection. The model orders need not be equal. Increasing the model order also increases the size of the covariance matrix. In data compression, the model order should be kept small making sure that the data covariance matrix is not singular and at the same time taking care that the number of stored ACFs is minimal.
- In damage detection, a full set of ACFs was used. The variability between measurements required a higher-dimensional feature vector than only the stored signals in order to consider also the environmental or operational variability.
- The original and reconstructed ACFs performed equally well in damage detection. In the given numerical experiment, it was seen that spatiotemporal correlation outperformed spatial-only correlation in damage detection.
- ACFs outperformed raw data in damage detection.
- Several functions were used in damage detection and localization: Whitening was applied to the training data to take different environmental or operational conditions into account. Principal component analysis was used to find the direction of the largest change, which

was also used in damage localization. Finally, extreme value statistics control chart was plotted to detect damage.

- Damage localization to a reconstructed DOF was possible.
- Experimental results are needed to validate the proposed technique.

## ACKNOWLEDGEMENTS

This research was supported by Metropolia University of Applied Sciences.

## REFERENCES

[1] R. Brincker, C. Ventura, *Introduction to operational modal analysis.* Wiley, 2015.

[2] J. Kullaa, Damage detection and localization using autocorrelation functions with spatiotemporal correlation. Z. Wu, T. Nagayama, J. Dang, R. Astroza, eds. *Experimental Vibration Analysis for Civil Engineering Structures. Lecture Notes in Civil Engineering, vol 224*. Springer, Cham. 83–95, 2023.

[3] X.Y. Li, S.S. Law, Matrix of the covariance of covariance of acceleration responses for damage detection from ambient vibration measurements. *Mechanical Systems and Signal Processing*, **24**, 945–956, 2010.

[4] M. Zhang, R. Schmidt, Sensitivity analysis of an auto-correlation-function-based damage index and its application in structural damage detection. *Journal of Sound and Vibration*, **333**, 7352–7363, 2014.

[5] M. Zhang, R. Schmidt, Study on an auto-correlation-function-based damage index: Sensitivity analysis and structural damage detection. *Journal of Sound and Vibration*, **359**, 195–214, 2015.

[6] W. Li, Y. Huang, A method for damage detection of a jacket platform under random wave excitations using cross correlation analysis and PCA-based method, *Ocean Engineering*, **214**, 107734, 2020.

[7] Z. Yang, L. Wang, H. Wang, Y. Ding, X. Dang, Damage detection in composite structures using vibration response under stochastic excitation. *Journal of Sound and Vibration*, **325**, 755–768, 2009.

[8] L. Wang, Z. Yang, T.P. Waters, Structural damage detection using cross correlation functions of vibration response. *Journal of Sound and Vibration*, **329**, 5070–5086, 2010.

[9] I. Trendafilova, A method for vibration-based structural interrogation and health monitoring based on signal cross-correlation. *Journal of Physics Conference Series*, **305**, 012005, 2011.

[10] L.-S. Huo, X. Li, Y.-B. Yang, H.-N. Li, Damage Detection of Structures for Ambient Loading Based on Cross Correlation Function Amplitude and SVM. *Shock and Vibration* **2016**, 3989743, 2016.

[11] J. Kullaa, Damage detection and localization under variable environmental conditions using compressed and reconstructed Bayesian virtual sensor data. *Sensors*, **22**, 306, 2022.

[12] H. Sohn, Effects of environmental and operational variability on structural health monitoring, *Philosophical Transactions of the Royal Society A: Mathematical, Physical and Engineering Sciences*, **365**, 539–560, 2007.

[13] J. Kullaa, Whitening transformation in damage detection. A.E. Del Grosso, P. Basso eds. *Smart structures: Proceedings of the 5th European Conference on Structural Control — EACS 2012*, Genoa, Italy, June 18–20, 2012.

[14] D.C. Kammer, Sensor placement for on-orbit modal identification and correlation of large space structures, *Journal of Guidance, Control, and Dynamics*, **14**, 251–259, 1991.

[15] D.C. Kammer, Effects of noise on sensor placement for on-orbit modal identification of large space structures, *Journal of dynamic systems, measurements and control—Transactions of the ASCE*, **114**, 436–443, 1992.

[16] C. Papadimitriou, G. Lombaert, The effect of prediction error correlation on optimal sensor placement in structural dynamics, *Mechanical Systems and Signal Processing*, **28**, 105–127, 2012.

[17] J.S. Bendat, A.G. Piersol, *Random data: Analysis and measurement procedures. 4th Edition.* Wiley, 2010.

[18] R.W. Clough, J. Penzien, *Dynamics of structures. 2nd Edition*. McGraw-Hill, 1993.

[19] G.H. James III, T.G. Carne, J.P. Lauffer, The natural excitation technique (NExT) for modal parameter extraction from operating structures. *Modal Analysis: The International Journal of Analytical and Experimental Modal Analysis* **10**, 260–277, 1995.

[20] H.W. Sorenson, *Parameter Estimation: Principles and Problems*. Marcel Dekker, 1980.

[21] S. Coles, *An introduction to statistical modeling of extreme values*. Springer, 2001.

[22] D.C. Montgomery, *Introduction to statistical quality control, 3rd edition*, Wiley, 1997.

[23] J. Kullaa, Robust damage detection in the time domain using Bayesian virtual sensing with noise reduction and environmental effect elimination capabilities, *Journal of Sound and Vibration*, **473**, 115232, 2020.

COMPDYN 2023
9th ECCOMAS Thematic Conference on
Computational Methods in Structural Dynamics and Earthquake Engineering
M. Papadrakakis, M. Fragiadakis (eds.)
Athens, Greece, 12-14 June 2023

# KURTOSIS AND SKEWNESS BASED COMPARISON OF HERMITE POLYNOMIAL AND JOHNSON TRANSFORMATIONS

**Ayse S. Giz and Ata Mugan**

Istanbul Technical University, Department of Mechanical Engineering
34437 Beyoglu, Istanbul, Turkey

{giza, mugan}@itu.edu.tr

## Abstract

*In fatigue analyses and structural health monitoring applications, frequency domain theoretical fatigue life estimation models work best on Gaussian data, while many natural occurrences that influence the stress history have non-Gaussian properties. In order to handle realistic stress data, various transformations from non-Gaussian to Gaussian distributions are used. In this study, two transformation methods namely moment based Hermite polynomial model and Johnson transformation model were examined that have both a non-Gaussian to Gaussian transformation and a Gaussian to non-Gaussian transformation. These established transformation methods were compared for their distortion with reference to increasingly leptokurtic behavior and skewness.*
*Normally distributed Gaussian data were distorted to a non-Gaussian form and then re-stored back to Gaussian form using parameters estimated from the non-Gaussian data were compared according to their kurtosis and skewness values. It was found that the restored da-ta contains significant deviation from Gaussian form the deviation depending on the distortion in the initial transformation and the deviations are more prominent in the Hermite Polynomial Transformation. These deviations in turn affect fatigue life estimations.*

**Keywords:** Non-Gaussian, Gaussian Transformation, Hermite, Johnson Transformation Method, Fatigue Analysis.

## 1 INTRODUCTION

The analysis of service life with respect to fatigue failure gains more importance as structures are designed, primarily for economic reasons, to have a finite life. Obtaining a realistic estimation of fatigue lifetime of mechanical systems is of crucial importance. Various estimation methods have been developed based on stress history. These methods work in time domain or frequency domain. Frequency domain methods based on fast Fourier transform are less computationally intensive and are preferred for long data streams. They have been developed [1] and found to give results consistent with more precise methods such as cycle counting for stress distributions in Gaussian form. Normally distributed, also known as Gaussian random data is symmetric, with a skewness of zero and has kurtosis of three. These methods have limitations on them in regards to the sampling rate [2] and Gaussianity of the data. On the other hand, many natural phenomena like wind pressure or wave pressure, which are important for wind turbines and off-shore structures have non-Gaussian properties.

To treat non-Gaussian data in the frequency domain it is commonly converted to Gaussian form by a transformation technique which preserves time domain properties such as peak count and upcrossing rate. The fatigue lifetime is calculated for the Gaussian data for which analytical formulae are available [3–5]. The estimated lifetime is corrected using a conversion factor which depends on the kurtosis and skewness of the non-Gaussian data.

Various methods have been developed to transform non-Gaussian load histories to Gaussian data. Most prominent of these are based on Hermite Polynomials [5], power law [6], series expansions, logarithms and hyperbolic functions [7], and empirical methods as well [8,9]. Most of these are one-way transformations [10], turning the non-Gaussian to Gaussian or vice versa, and few are transformations to both transform the data into Gaussian or into non-Gaussian. The two most prominent of which, the Hermite polynomial based Winterstein's transformation [1,11] and Johnson transformation will be studied here.[12]

In life estimation studies using simulations, and initial Gaussian random is transformed into a non-Gaussian data for analysis. The usual procedure is to start with Gaussian data, convert it to non-Gaussian data form using the inverse of the transform then attempt to go back to Gaussian data by estimating the transform parameters.[10] Obviously if the inverse transform is performed using the exact same parameters the original data would be recovered exactly. However, since the underlying Gaussian would not be available in real cases, the parameters for the restoring transformation are estimated based on kurtosis and skewness of this created non-Gaussian data or its percentile rankings.

Liu and group have developed a modified version of the Hermite polynomial method [13] and compared it with original Hermite method and the Johnson Transformation method [14–16] (with parameters estimated by the moments) in life estimation using simulated and wind data. They found that both the Johnson transformation and the modified Hermite polynomial methods gave better results than the original Hermite polynomial method.

Since the correction factor is based on the assumption that the transformed function is completely Gaussian, the level of distortion between transformations can significantly affect the accuracy measure in fatigue calculations. When the transformation affects the subsequent calculations and assumptions dramatically, it becomes difficult to make accurate fatigue life evaluations.

Here, we compare the Hermite polynomial method and Johnson transformation on how they perform with different distorted skewness and kurtosis values. Random Gaussian data is distorted to a non-Gaussian form of various kurtosis and skewness values using both the Hermite and the Johnson methods. The distorted data are then brought back to the Gaussian form. Parameters for the back transform are estimated using the formulae given in [10] for the Hermite

method and by Slifker and Shapiro for the Johnson method in [12]. The kurtosis and skewness of the final form of the data is discussed and accuracy of fatigue calculations of transformed data is compared with that of the initial load, using Dirlik's method [1,17]. This is done to obtain a more realistic assessment of both transformation methods' performance in transforming non-Gaussian data to Gaussian form.

## 2 METHOD

In order to compare transformation methods, the random data was simulated with a sampling rate of 500 samples per second and a frequency range between 0 to 60Hz. Three samples were prepared and results were averaged for statistical significance. All three had a zero mean, and a kurtosis of three and skewness of zero as per Gaussian standards. For both methods the skewness between -2.5 and 2.5 with 50 intervals. Softening cases were analyzed, kurtosis was scanned between 4 and 18, in 140 intervals.

Non-Gaussian distorted data were obtained by following the Johnson and Hermite polynomial transformations described above. Lifetime estimation was performed by the Dirlik method. The average of the three datasets results is quoted and plotted in the figures.

### 2.1 Johnson transformation method

N.L. Johnson in 1949 suggested three families of transformations to transform non-Gaussian data, which can be unbounded, bounded on one side or bounded on both sides, to Gaussian form. All three families involve a shift and scale operation before and after the transform by a monotonically increasing function. [7]

To obtain a Gaussian $X_2$, a non-Gaussian $Z$ is first shifted and scaled to form an intermediate variable:

$$u = (Z - \xi)/\lambda \tag{1}$$

Then the transformation function $f(u)$ and finally another scaling and shifting is applied.

$$X_2 = \gamma + \delta f(u) \tag{2}$$

The stress distribution is expected to be unbounded. So, for our purposes the unbounded distribution, with the transformation function $f_U(u) = \sinh^{-1}(u)$ is the more relevant.

Thus, the Johnson transform for unbounded Z is:

$$X_2 = \gamma + \delta \sinh^{-1}((\mathrm{Z} - \xi)/\lambda) \tag{3}$$

To estimate Johnson's parameters one can follow three strategies, namely; percentage and moment fitting and fitting by non-linear least squares (NLLS).

Slifker and Shapiro [12] developed an estimation method based on percentage fitting. Their method takes a real $x_p$ and take four percentages of a normal distribution corresponding to; $\zeta = [3x_p, x_p, -x_p, -3x_p]$. Letting these percentages to be $[Z_{3xp}, Z_{xp}, Z_{-xp}, Z_{-3xp}]$ they defined the quantities:

$$p = Z_{xp} - Z_{-xp},\ m = Z_{3xp} - Z_{xp},\ n = Z_{-xp} - Z_{-3xp} \text{ and } d = mn/p^2. \tag{4}$$

The parameter estimates for Johnson's $U$ distribution are:

$$\begin{aligned} \delta_e &= \frac{2x_p}{\operatorname{arccosh}\left(\frac{1}{2}\left(\frac{m}{p}+\frac{n}{p}\right)\right)} \\ \gamma_e &= \delta_e \operatorname{arcsinh}\left(\frac{\frac{n}{p}-\frac{m}{p}}{2\sqrt{d-1}}\right) \\ \lambda_e &= \frac{2p\sqrt{d-1}}{\left(\frac{m}{p}+\frac{n}{p}-2\right)\left(\frac{m}{p}+\frac{n}{p}+2\right)^{1/2}} \end{aligned} \tag{5}$$

$$\xi_e = \frac{(x_{zp}+x_{-zp})}{2} + \frac{p\left(\frac{n}{p}-\frac{m}{p}\right)}{2\left(\frac{m}{p}+\frac{n}{p}-2\right)}$$

Simulated non-Gaussian data can be generated from a random Gaussian data X by applying the inverse of the transformation. For the unbounded case the inverse transform is:

$$\mathrm{Z} = \xi + \lambda \sinh((\mathrm{X}-\gamma)/\delta) \tag{6}$$

This non-Gaussian data is then transformed to Gaussian form via the Johnson transformation using the estimated parameters.

$$\mathrm{X}_2 = \gamma_e + \delta_e \sinh^{-1}((\mathrm{Z}-\xi_e)/\lambda_e) \tag{7}$$

## 2.2 Hermite Polynomial Method

For Hermite Polynomial method, the formulations developed by Winterstein for softening processes [5] were used. To get the distorted non-Gaussian version (Z) from the initial random generated Gaussian $(X)$ the below formulae were used, as it is stated in [10], with $\gamma_3$ and $\gamma_4$ are the skewness and kurtosis, μ is the mean and $\sigma^2$ is the variance.

$$\begin{gathered} Z = \mu_z + \sigma_z K\left[X + \widetilde{h_3}(X^2-1) + \widetilde{h_4}(X^3-3X)\right] \\ \widetilde{h_4} = \widetilde{h_{40}}\left[1 - \frac{1.43\gamma_3^2}{\gamma_4-3}\right]^{1-0.1\gamma_4^{0.8}} \\ \widetilde{h_3} = \frac{\gamma_3}{6}\left[\frac{1-0.15|\gamma_3|+0.3\gamma_3^2}{1+0.2(\gamma_4-3)}\right] \\ K = \frac{1}{\sqrt{1+2\widetilde{h_3}^2+6\widetilde{h_4}^2}} \\ \widetilde{h_{40}} = \frac{[1+1.25(\gamma_4-3)]^{\frac{1}{3}}-1}{10} \end{gathered} \tag{8}$$

And to achieve the underlying Gaussian $(X_2)$ of the non-Gaussian (Z) the inverse of the previous expression is used, with the following formula for the transformation;

$$\begin{gathered} X_2 = \left[\sqrt{\xi^2(Z)+c}+\xi(Z)\right]^{\frac{1}{3}} - \left[\sqrt{\xi^2(Z)+c}-\xi(Z)\right]^{\frac{1}{3}} - a \\ \xi(Z) = 1.5b\left(a + \frac{Z-\mu_z}{K\sigma_z}\right) - a^3 \\ a = \frac{\widetilde{h_3}}{3\widetilde{h_4}} \\ b = \frac{1}{3\widetilde{h_4}} \\ c = (b-1-a^2)^3 \end{gathered} \tag{9}$$

## 2.3 Fatigue Life Calculation

Properties of s355j10 steel were used in fatigue life analyses. The Gaussian data before and after the transformation procedures were analyzed with Dirlik's fatigue damage estimation method, which was proposed in 1985 and is considered as one of the most popular method among frequency domain estimation methods for wide band Gaussian data [1]. The fatigue life is computed from the damage, with T=1/D and the damage formula as;

$$D = K^{-1}\upsilon_p m_0^{\frac{k}{2}}\left[G_1 Q_k \Gamma(1+k) + \left(\sqrt{2}\right)^k \Gamma\left(1+\frac{k}{2}\right)(G_2|R|^k + G_3)\right] \tag{10}$$

The percent difference in estimated life was calculated with $100*(T_2-T_0)/T_0$. All three results for each 7000 points in plot, was averaged.

# 3 NUMERICAL RESULTS

## 3.1 Numerical results using the Johnson transformation method

The figure 1 shows the kurtosis (in color code) of data distorted to a wide range of skewness values from -2.5 to + 2.5 and kurtosis values from 3 to 18. As can be seen from the color code the kurtosis values of the restored data were between 2.8 and 2.9.

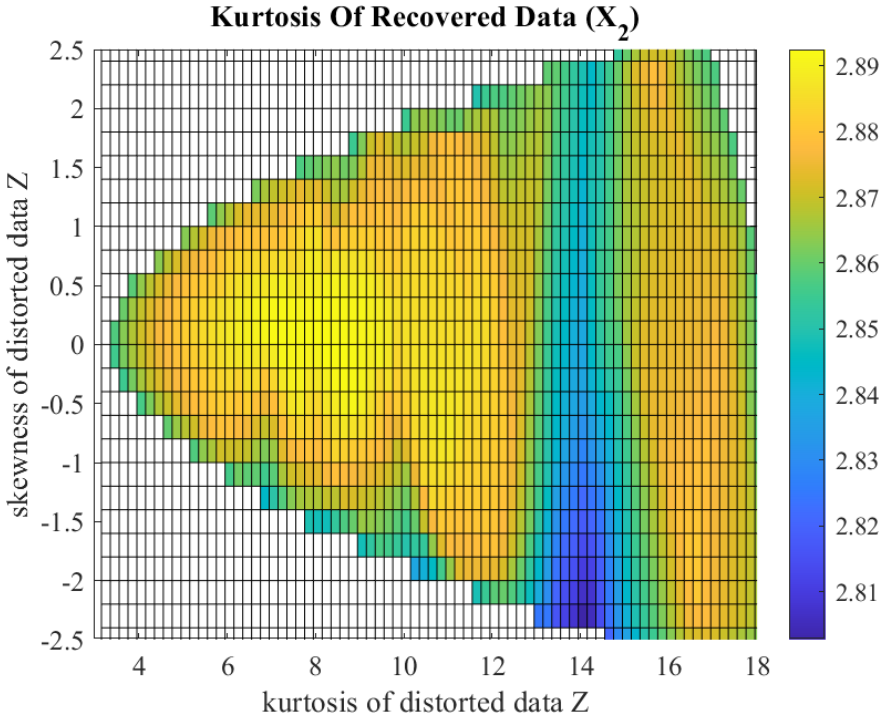


Figure 1 Kurtosis of the "Gaussian" data after distortion and transformation via Johnson transformation method, plotted against the skewness and kurtosis values the data were distorted to

The skewness results shown in Figure 2 were very close to the Gaussian value of zero; that is, they were between 0.007 and 0.028 for the average, and within the dataset never got values above 0.036 or below -0.007

Distorting the data to negative skewness was slightly less robust, resulting in relatively higher skewness values for the final Gaussian distribution. Whereas for positive skewness distortions in the non-Gaussian transformation resulted in very close to zero values, all below 0.02 across all kurtosis values. The resulting skewness was only higher in cases with distortions to extreme kurtosis values and negative skewness.

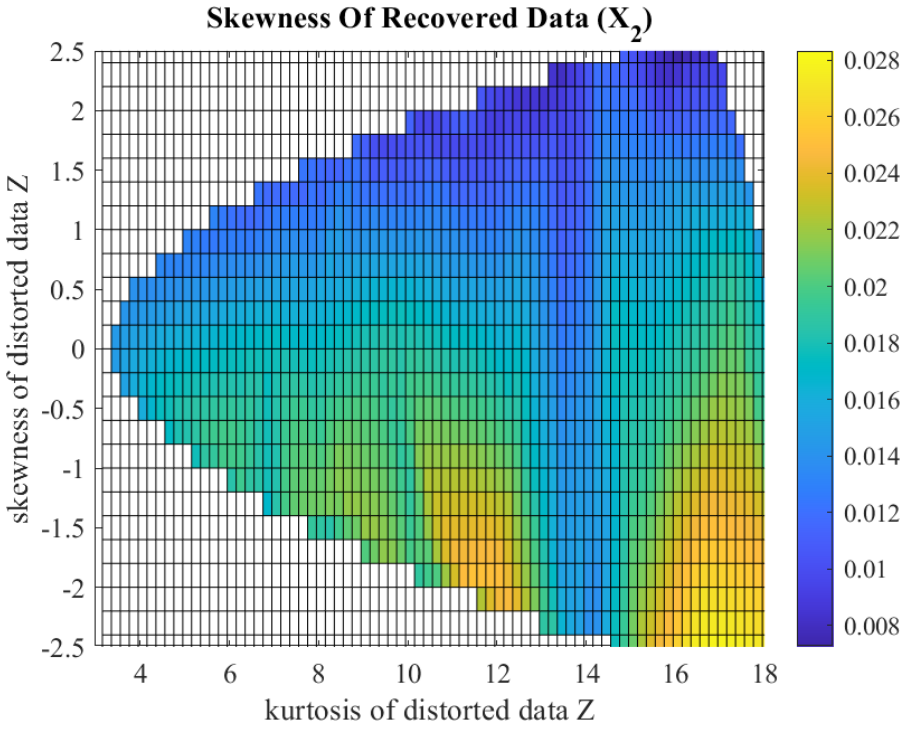


Figure 2 Skewness of the Gaussian data after distortion and transformation via Johnson transformation method, plotted against the skewness and kurtosis values the data were distorted to

The fatigue life estimation values after the process were around 28% lower compared with that of the before transformation, this can be considered because of the decrease in kurtosis, as a result of around 0.2 decrease in the kurtosis values, since it made the final loading slightly smoother with less extremities.

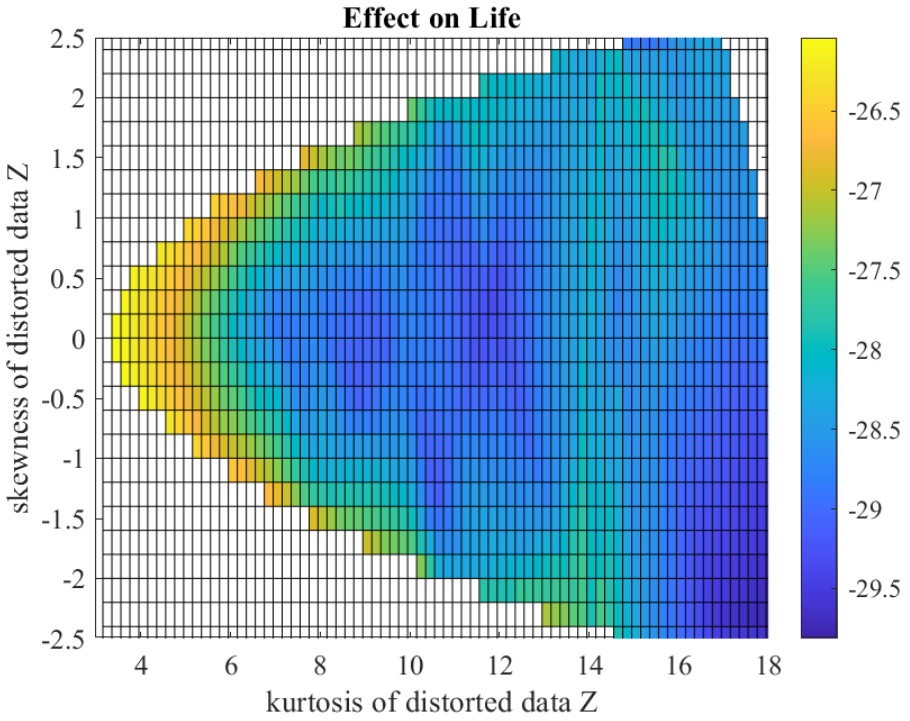


Figure 3 Percent change in estimated life, between the original data and the restored data, plotted against the skewness and kurtosis values of the distorted data

The difference in fatigue estimation results here depend mostly on the kurtosis change, as the graph follows a similar pattern and does not seem to be affected by the same trends visible in the skewness graph. This is also because the change in skewness before and after the process was minimal, especially compared the kurtosis.

### 3.2 Numerical results using Hermite transformation method

Figure 4 shows the kurtosis of the data restored by the Hermite polynomial method. It is seen that the kurtosis values range from less than 3 to 3.5 for most of the parameter space but varied on the edges of the applicable zone with negative skewness values, reaching up to 6.973 for the average and 12.251 in one of the datasets.

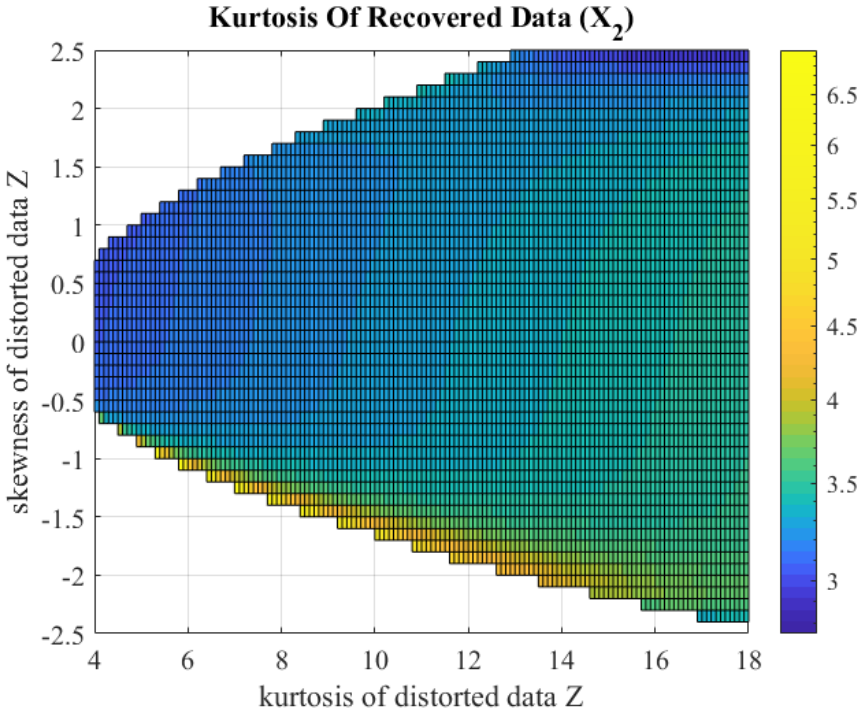


Figure 4 Kurtosis of the Gaussian data after distortion and transformation via Hermite transformation method, plotted against the skewness and kurtosis values the data were distorted to

Though the edges showed great change in kurtosis, and not enough recovery from the distortion procedure, the rest of the data was less varied. There was an increase in final kurtosis values with increasing distorted kurtosis values. Smaller kurtosis values were found as the distortion in skewness increases.

The data was mostly higher than 3, only going below down 2.756 in the cases of extreme kurtosis and highest skewness values. In individual datasets, these points went down to 1.958.

For almost zero skewness distortion, the resulting kurtosis slowly increased from 3.081 to 3.504 as the distorted kurtosis increased.

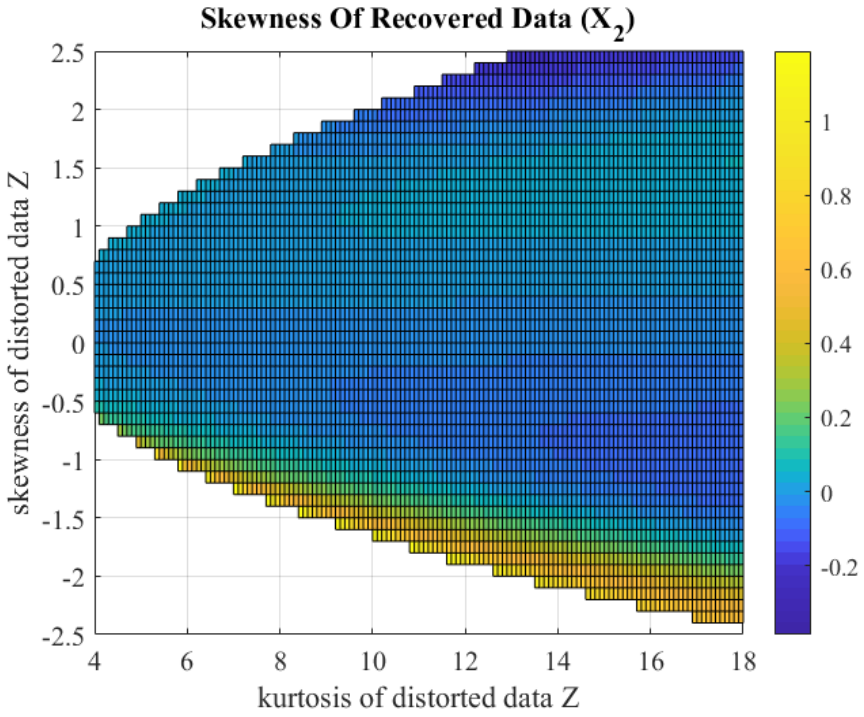


Figure 5 Skewness of the Gaussian data after distortion and transformation via Hermite transformation method, plotted against the skewness and kurtosis values the data were distorted to

Less monotonic behavior was seen from the skewness values, though the edges were once again heavily affected by the transformation sequence. Skewness values as low as -0.382 were observed in with higher skewness and extreme kurtosis values. Considering the individual datasets, the resulting skewness went as low as -1.042 and as high as 2.214. The highest average value is 1.189, still significantly higher than the values produced by using the Johnson transformation method. For no skewness distortion, the recovered skewness decreased monotonically from -0.008 to -0.03. Positive skewness distortion resulted in mostly positive skewness until the edges, where the behavior was the opposite with negative results. And negative skewness distortion resulted in mostly negative resulting skewness, however at the edges once again the sign quickly changed to higher positive values.

The change in fatigue life estimation values with the transformation sequence were between 70% less and 20% more, a large variance depending on both the kurtosis and skewness values as can be seen from the graph patterns. The edges with both higher and lower skewness show a heavily decreased fatigue result. And a higher than before estimation at low absolute skewness distortion with the gradual soft increase with kurtosis, similar to the resulting kurtosis graph.

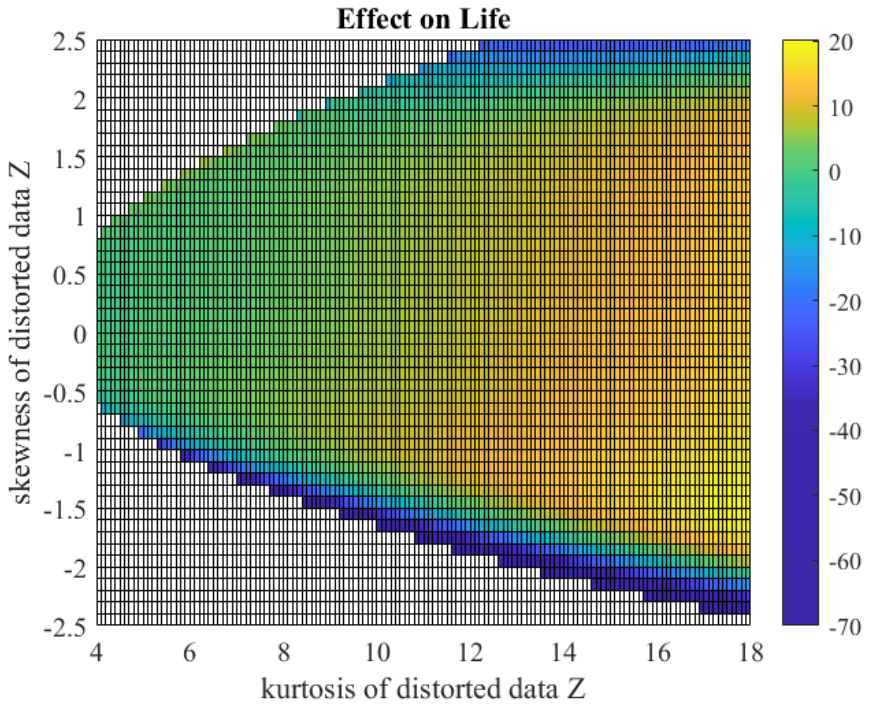


Figure 6 Change in estimated life of load, before and after distortion and Gaussian transformation via Hermite transformation, plotted against the skewness and kurtosis values the data were distorted to

## 4 DISCUSSION

The variation of both kurtosis and skewness with Johnson transformation were much smaller in range than that of Hermite transformation.

The kurtosis values after Johnson transformation all skewed towards 2.8, regardless of the values, it was distorted to original values. The average values were between 2.802 and 2.892 and considering the load samples individually, the secondary Gaussian kurtosis values had a range between 2.77 and 2.92

The edges of the viable range had a lower kurtosis values and the closest to 3 was towards the center, where no skewness change was applied to the data to begin with. However, kurtosis consistently undershooting to below 3, which also affected the fatigue calculations.

The resulting kurtosis and skewness values from distorting the loads to non-Gaussian and then using the inverse function to retransform them to Gaussian by the Hermite method were much more varied. For both the kurtosis and skewness of the final load, the edges of the data behaved wildly differently than the majority, while the rest of the data behaved more monotonously than those of the Johnson transformation method

The effect of this series of Hermite polynomial transformations on life estimation was very varied and followed a similar trend as the kurtosis and skewness results, showing extremities on the edges and a monotonically increasing pattern with increasing kurtosis in the center of the graph where skewness was changed less. The changes in fatigue mildly followed a merge of the patterns seen in kurtosis and skewness graphs. As the kurtosis and skewness changes were more varied for this transformation, the fatigue calculation was also more varied than its Johnson transformation counterpart. The part of the graph with smaller kurtosis values were more accurate, with less than 5% difference up to kurtosis of 8, and 10% up to a kurtosis of 11 for the majority of skewness spectrum.

## 5 CONCLUSIONS

When a Gaussian time series is distorted by transforming into a highly leptokurtic form and back using the Slifker formulation for the Johnson transformation and Winterstein's formula for the Hermite polynomial transformation, the final result is not exactly Gaussian in that the kurtosis as differs from 3.0.

Distortion and recovery by the Johnson Method resulted in skewness very close to zero and kurtosis consistently between 2.8 and 2.9. As a consequence, lifetimes estimated by the Dirlik method were consistently 28 – 30 % less than the lifetime of the original data.

Hermite polynomial method gave good results for most of the parameter space but at the edge of maximal skewness the results of this method showed large variations. Skewness, kurtoses and lifetimes of the restored data for this part of parameters were far from the original data. Kurtoses as large as 10 and skewness with absolute values as large as 0.8. These deviations from normal distribution resulted in expected fatigue life to vary by up to 60 % for data distorted to kurtosis of 18 and skewness of $\pm 2$.

## 6 ACKNOWLEDGEMENT

This study is supported by the Scientific and Technological Research Council of Türkiye (TUBITAK) under the grant number 120M214

## REFERENCES

[1] T. Dirlik, D. Benasciutti, Dirlik and Tovo-Benasciutti Spectral methods in vibration fatigue: a review with a historical perspective. *Metals 2021,* **11**, 1333, 2021.

[2] A. Trapp, Q. Hoesch, P. Wolfsteiner, Effects of insufficient sampling on counting algorithms in vibration fatigue. *Procedia Structural Integrity*, **38**, 260–270, 2021.

[3] M. Grigoriu, Crossings of non-Gaussian translation processes. *Journal of Engineering Mechanics*, **110**, 610–620, 1984.

[4] S.R. Winterstein, Non-normal responses and fatigue damage. *Journal of Engineering Mechanics*, **111**, 1291–1295, 1985.

[5] S.R. Winerstein, Nonlinear vibration models for extremes and fatigue. *Journal of Engineering Mechanics*, **114,** 1772–1790, 1988.

[6] G.E.P. Box, D.R Cox, An analysis of transformations. *Journal of the Royal Statistical Society: Series B (Methodological)*, **26**, 211–243, 1964.

[7] N.L. Johnson, Systems of frequency curves generated by methods of translation. *Biometrika*, **36,** 149, 1949.

[8] C. Braccesi, F. Cianetti, G. Lori, D. Pioli, The frequency domain approach in virtual fatigue estimation of non-linear systems: The problem of non-Gaussian states of stress. *International Journal of Fatigue*, **31**, 766–775, 2009.

[9] F. Cianetti, M. Palmieri, C. Braccesi, G. Morettini, Correction formula approach to evaluate fatigue damage induced by non-Gaussian stress state. *Procedia Structural Integrity*, **8**, 390–398, 2018.

[10] D. Benasciutti, Fatigue analysis of random loadings. 2004.

[11] D. Benasciutti, R. Tovo, Frequency-based analysis of random fatigue loads:Models, hypotheses, reality. *Materialwissenschaft und Werkstofftechnik,* **49**, 345–367, 2018.

[12] J.F. Slifker, S.S. Shapiro, The Johnson system: selection and parameter estimation. *Technometrics*, **22**, 239–246, 1980.

[13] M. Liu, X. Chen, Q. Yang, Estimation of peak factor of non-Gaussian wind pressures by improved moment-based Hermite model. *Journal of Engineering Mechanics,* **143,** 2017.

[14] F. Wu, G. Huang, M. Liu, Simulation and peak value estimation of non-Gaussian wind pressures based on Johnson transformation model. *Journal of Engineering Mechanics,* **146**, 2020.

[15] Q. Yang, X. Chen, M. Liu, Bias and sampling errors in estimation of extremes of non-Gaussian wind pressures by moment-based translation process models. *Journal of Wind Engineering and Industrial Aerodynamics,* **186,** 214–233, 2019.

[16] L. Peng, M. Liu, Q. Yang, G. Huang, B. Chen, An analytical formula for Gaussian to non-Gaussian correlation relationship by moment-based piecewise Hermite polynomial model with application in wind engineering. *Journal of Wind Engineering and Industrial Aerodynamics*, **198**, 2020.

[17] T. Dirlik, Application of computers in fatigue analysis. 1985.

COMPDYN 2023
9th ECCOMAS Thematic Conference on
Computational Methods in Structural Dynamics and Earthquake Engineering
M. Papadrakakis, M. Fragiadakis (eds.)
Athens, Greece, 12-14 June 2023

# FEASIBILITY STUDY OF MICROTREMOR SIGNALS FOR STRUCTURAL HEALTH MONITORING ON REAL STEEL BUILDING STRUCTURES

**Chih-chun Ou**[1], **and Jun Iyama**[2]

[1] Graduate Student Researcher, Graduate School of Engineering, The University of Tokyo
7 Chome-3-1 Hongo, Bunkyo City, Tokyo, Japan 113-8654
moods0707@g.ecc.u-tokyo.ac.jp

[2] Associate Professor, Graduate School of Engineering, The University of Tokyo
7 Chome-3-1 Hongo, Bunkyo City, Tokyo, Japan 113-8654
iyama@arch1.t.u-tokyo.ac.jp

## Abstract

*Square hollow section (SHS) columns are widely used in many Asian countries such as Japan and China for the construction of low- and middle-rise steel buildings. Post-earthquake damage surveys and structural condition assessments of this common type of structure have attracted increasing attention in order to ensure business continuity. Many measuring instruments for structural health monitoring (SHM) of buildings such as accelerometers have been commercially available; however, measuring acceleration response alone does not allow for direct estimation of damage to individual structural members. Another potential structural health monitoring instrument is the strain gauge; however, it has very limited application in structures. This research aims to establish a method to evaluate the severity of structural damage by strain measurement under microtremor and ambient vibration. A 1-story steel frame was designed to examine the applicability of this method in real buildings. Steel base plates for columns are fixed to the concrete foundations by anchor bolts, whose loosening will be used to simulate different levels of structural damage. The strains measured directly from the anchor bolts showed to be very sensitive to the loosening of the bolts. In addition, the local stiffness observed from the lower part of the column, which has a smaller cross-sectional area, tends to be more significant compared to that measured from the upper part. The reduction of stiffness at the column base can be observed from the bending moment distribution under microtremor. In this research, the classification models were trained with different machine learning tools for structural damage assessment. In general, trained models can successfully classify the different damage states and the severity of the damage.*

**Keywords:** Structural health monitoring, Damage detection, Steel frame structure, Strain measurement, Microtremor, Machine learning.

## 1 INTRODUCTION

Steel frames have been used all over the world due to the relatively well ductility compared to the concrete structures. However, during the 1995 Hyogo-ken Nambu earthquake in Japan, substantial damages were still observed [1][2]. Meanwhile, enterprises and factories suffered damage to their buildings and equipment, disrupting the supply chain and hitting the local economies of steel, automobiles, liquor brewing, and the chemical and footwear industries [3]. In the 1999 Chi-Chi earthquake in Taiwan, damage to the electronic component industry even temporarily caused a global crisis in computer production [4].

To ensure the business continuity and safety, structure health monitoring (SHM) has acquired increasing attentions and many measuring instruments have become commercially available. For example, many attempts have been made to apply accelerometers for SHM and the overall behavior of the structure can be monitored [5][6]. However, because changes in structural response behavior due to structural damage are usually very minor, measuring the acceleration solely tends to be difficult for evaluating the damage state of individual structural members [7][8]. Instead of evaluating the damage condition only by accelerometer, some studies have focused on the strain response under small vibration. Iyama et al. proposed a method using an index "local stiffness" including the strain response measured by the strain gauges attached to the beam flanges and the displacement measured by the displacement transducer; the results confirmed that this method is effective for fracture localization especially for buckling damage [9][10].

Steel column base plays an important role in transmitting the earthquake load from concrete base to the superstructure in the steel frame system. Therefore, the connection mechanism between the concrete part and the steel member has gained a lot of interest. Some studies have been made to clarify the mechanism of this connection [11]. Square hollow section (SHS) columns are widely used in many Asian countries such as Japan and China for the construction of low- and middle-rise steel buildings. In this research, a 1-story steel frame with SHS columns was designed to examine the applicability of this method in real buildings. Steel column base is fixed to the concrete foundations by anchor bolts, whose loosening will be used to simulate different levels of structural damage. Whenever a bolt is loosened, the test structure is manually shaken to apply small vibrations.

The strains measured directly from the anchor bolts are shown in this study. Comparisons were made between the local axial stiffness and local bending stiffness as measured from the upper and lower column sections. It is addressed how the distribution of bending moments changes as a result of the loosening of anchor bolts. These results suggest the possibility of a quantitative assessment of damage by strain measurements.

In recent years, machine learning has been applied to many areas of research, such as biotechnology and medical science, and many believe it has great potential for the SHM method [12]. In this research, the strain data measured under microtremor and small vibration was used as the training materials to build a model for damage condition classification of steel frame structures. For creating the training data set, the short-time Fourier transform can be used to convert the measured vibration data into a spectrogram. In addition to exploring the potential for structural damage assessment, the classification models were trained utilizing a variety of tools to make it simpler for more people to use and promote this approach.

## 2 EXPERIMENT OVERVIEW

### 2.1 Test setup

A 1-story steel frame was designed to examine the applicability of the proposed SHM method in real buildings. Figure 1 and 2 show the photograph and schematic, respectively, of the test structure. Each column can be separated into two parts: the 1500 mm lower part (□-150x150x12; b/t = 12.5) and the 2600 mm upper part (□-200x200x9; b/t = 22.2). Both two parts were manufactured using the material STKR400, which has the Young's modulus = 205000 N/mm$^2$; yielding strength = 245 N/mm$^2$; maximum strength = 400 N/mm$^2$. Each column was held in place by four anchor bolts illustrated in Figure 3. The loosening of these bolts is used to simulate the damage of column base.



Figure 1: Photograph of the test structure.

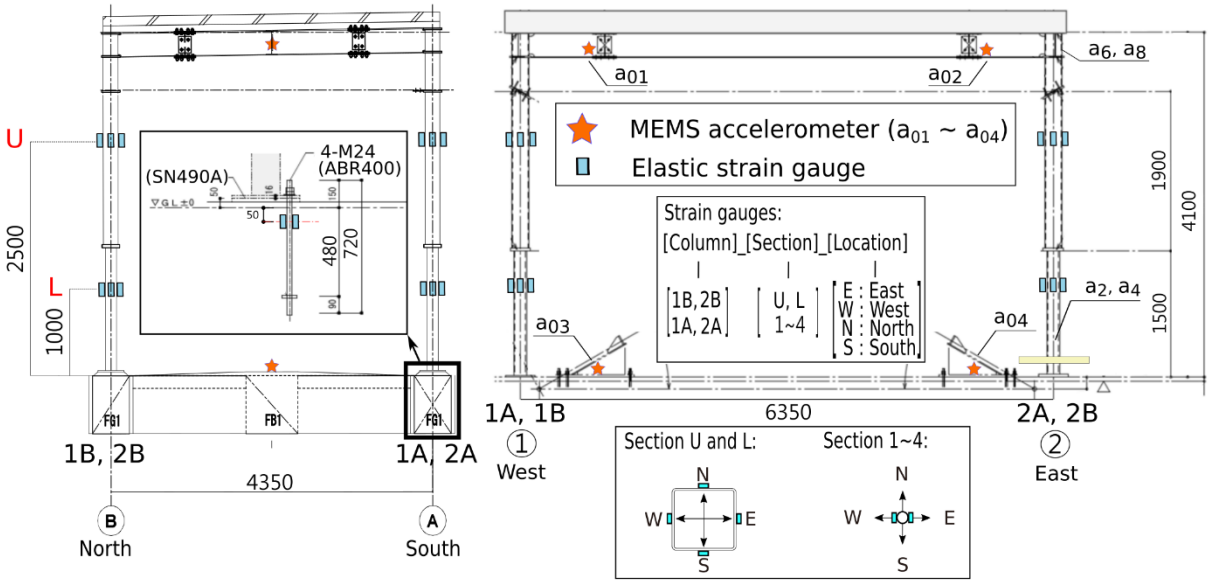


Figure 2: Test setup and measurement.

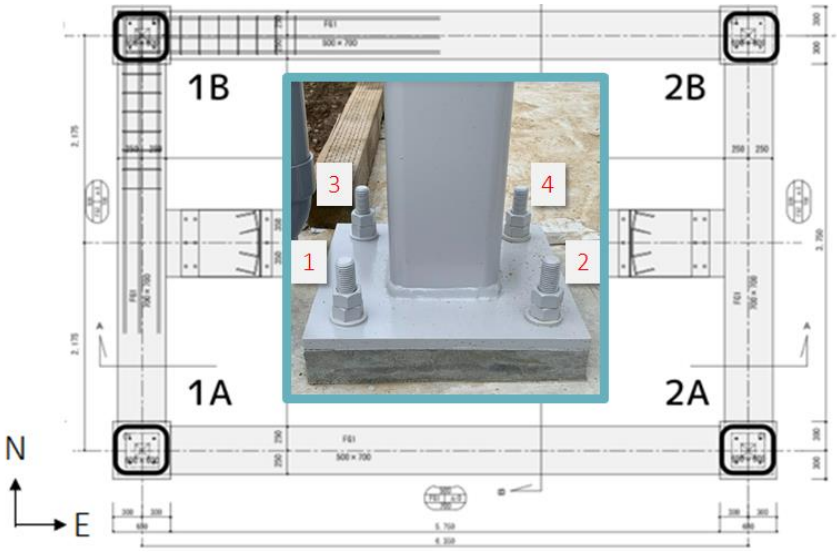


Figure 3: Structure plan view and the name of anchor bolts.

### 2.2 Data acquisition devices

The data acquisition was implemented using Raspberry Pi units as shown in Figure 4, which was used to collect the acceleration data and strain data during small vibration with a sampling rate up to 86 Hz for strain and 125 Hz for acceleration, respectively.




(a) Strain gauge units (b) Accelerometer unit

Figure 4: Raspberry Pi units.

## 3 DAMAGE DETECTION METHOD

### 3.1 Detection principle

In this paper, we aim to capture small response under microtremor before and after the damage occurred to capture changes in vibration characteristics.

Suppose a column suffers the horizontal displacement, $d$, at the top and accordingly the strain, $\varepsilon_W$ and $\varepsilon_E$ are occurred at the east and west sides of a certain section as shown in Figure 2. If the column is in an elastic state, $d$ and $\varepsilon$ are proportional. The ratio, $\frac{\varepsilon}{d}$, is hereinafter referred to as "local stiffness" and denoted by $K_\varepsilon$. This includes the "local axial stiffness", $K_{\varepsilon,a}$, and the "local bending stiffness", $K_{\varepsilon,b}$, that are illustrated in the equations bellow:

$$K_{\varepsilon,a} = \frac{\hat{\varepsilon}_{i,W} + \hat{\varepsilon}_{i,E}}{2\hat{d}} \quad ; \quad K_{\varepsilon,b} = \frac{\hat{\varepsilon}_{i,W} - \hat{\varepsilon}_{i,E}}{2\hat{d}} \tag{1}$$

Here, ^ represents the Fourier transform to a certain parameter. For the location of the displacement measurement, it is desirable to select a location the displacement at which is considered strongly correlated to the measured strain. Therefore, the displacement, *d*, was measured using the accelerometers placed at the top ($a_{01}$, $a_{02}$) and bottom ($a_{03}$, $a_{04}$) of the test specimen, as shown in Figure 2. Because $K_{\varepsilon,a}$ and $K_{\varepsilon,b}$ have similar physical meaning with axial force and bending moment, respectively, when the distribution of bending moment changed due to the damage of column base, it is expected that similar change can be captured by strain measurement even under microtremor as shown in Figure 5.

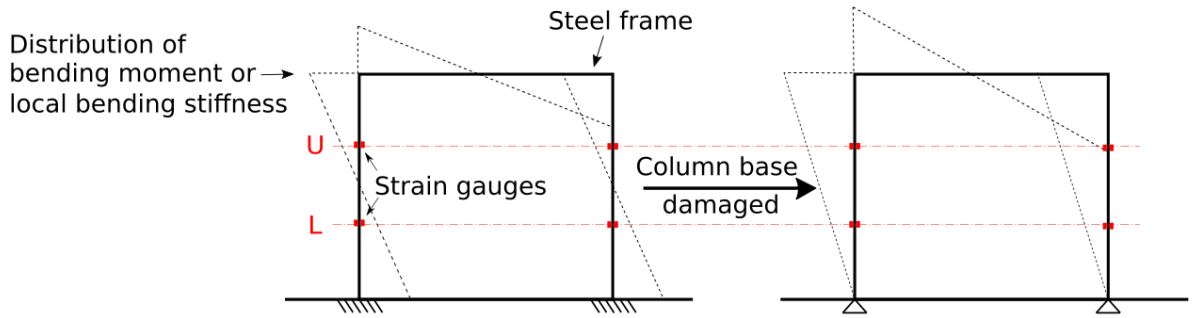


Figure 5: Concept of the damage detection method based on strain measurement.

### 3.2 Test procedure

Table 1 shows the test procedure. The capital, M, represent microtremor which is applied manually by man power before and after each step. The name of the steps is written as the column name followed by the bolt number and the process. For example, 1A -1 loosened means the bolt number 1 of column 1A was loosened. After the M16 step, all bolts in four column bases were loosened. From the M17 step, the bolts started to be fastened one by one until the final step.

| Step. | Status | Step. | Status | Step. | Status |
|---|---|---|---|---|---|
| M00 | Intact | M12 | 1B -3 loosened | M24 | 2A -3 fastened |
| M01 | 1A -1 loosened | M13 | 2B -1 loosened | M25 | 1B -1 fastened |
| M02 | 1A -4 loosened | M14 | 2B -4 loosened | M26 | 1B -4 fastened |
| M03 | 1A -2 loosened | M15 | 2B -2 loosened | M27 | 1B -2 fastened |
| M04 | 1A -3 loosened | M16 | 2B -3 loosened | M28 | 1B -3 fastened |
| M05 | 2A -1 loosened | M17 | 1A -1 fastened | M29 | 2B -1 fastened |
| M06 | 2A -4 loosened | M18 | 1A -4 fastened | M30 | 2B -4 fastened |
| M07 | 2A -2 loosened | M19 | 1A -2 fastened | M31 | 2B -2 fastened |
| M08 | 2A -3 loosened | M20 | 1A -3 fastened | M32 | 2B -3 fastened (Intact) |
| M09 | 1B -1 loosened | M21 | 2A -1 fastened | | |
| M10 | 1B -4 loosened | M22 | 2A -4 fastened | | |
| M11 | 1B -2 loosened | M23 | 2A -2 fastened | | |

Table 1: Test procedure.

### 3.3 Measurement

Figure 6 shows an example of the time history of acceleration and strain measured by the instrument that the attachment position is shown in Figure 2 while the lower graphs show an enlarged view of the upper graphs. The measured time history and spectrum of the MEMS accelerometers and strain gauges show almost identical shapes, indicating successful measurement.

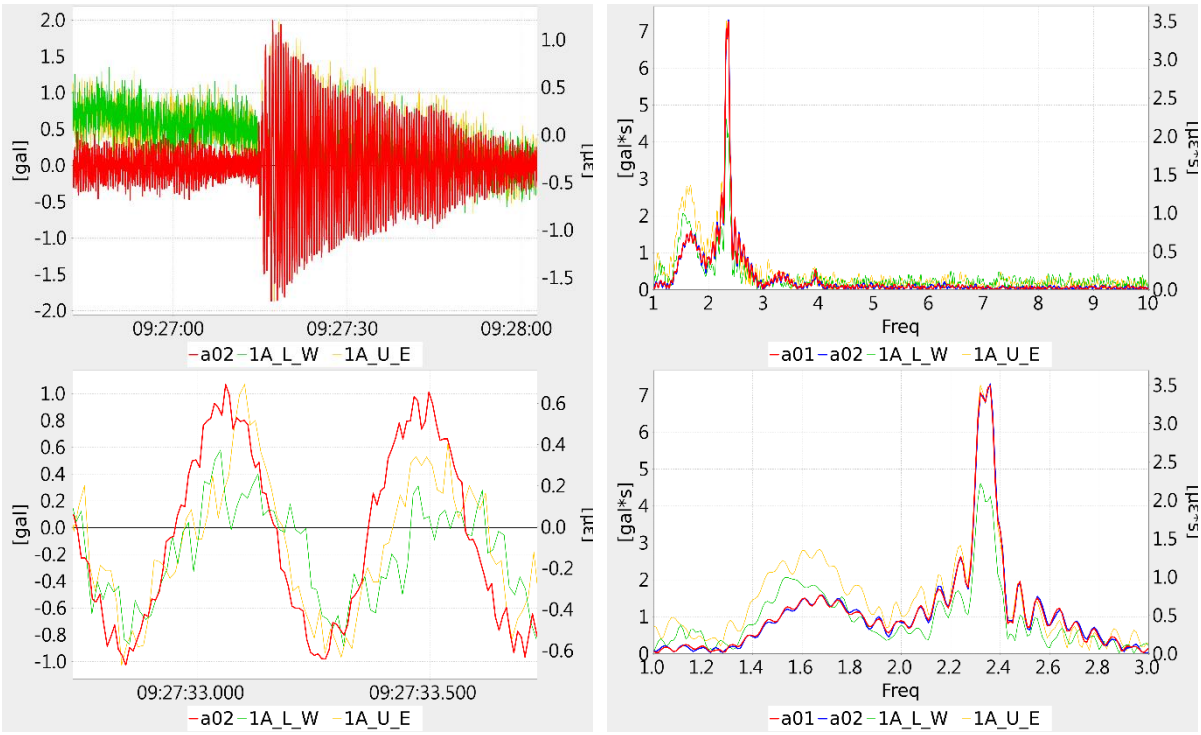


Figure 6: Recorded time history and spectrum

### 3.4 Training materials for machine learning

The strain data measured from all 64 strain gauges are used to create the training dataset for machine learning. Figure 7 shows an example of generating the training data of the column 1A.

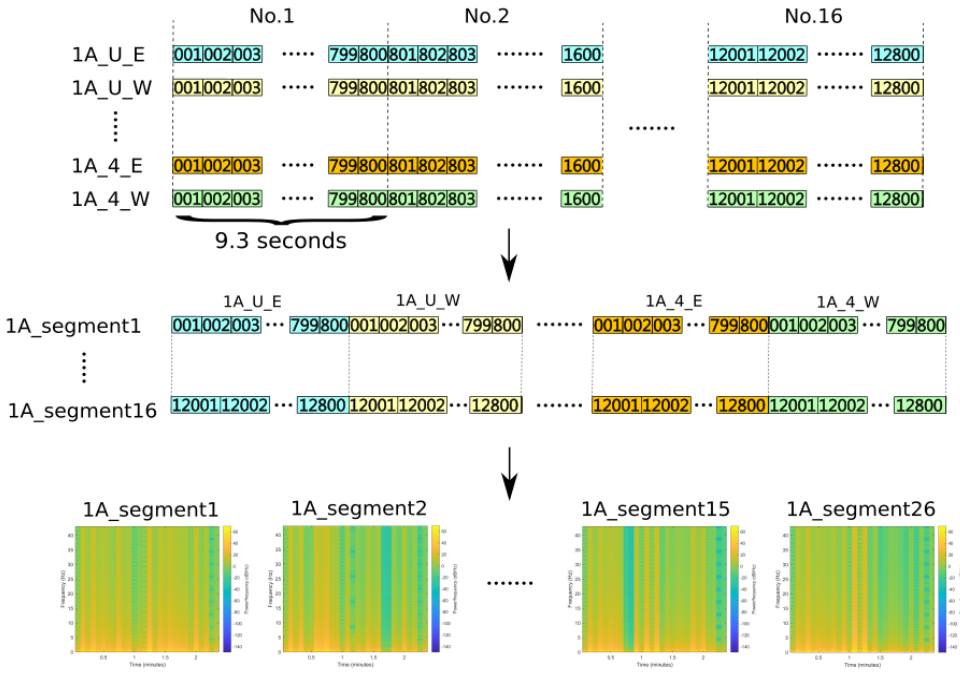


Figure 7: Concept of generating training dataset

As shown in Figure 7. The strain was measured starting from the time when the vibration was applied and last for a duration of 150 seconds. Each data set is composed of strain data

measured from 16 strain gauges on 1 column. The strain data measured in 150 seconds is split into 16 segments and numbered. All segments with the same number will then be connected to form a training data. Finally, the training data will be converted into spectrograms by means of a short-time Fourier transform form to train the model.

# 4 TEST RESULT

## 4.1 Strain measurement on anchor bolts

Figure 8 shows an example of the time history of the axial strain on the anchor bolts. The horizontal axis shows the time, while the vertical axis shows the average of strain measured on the two sides of the anchor bolt, respectively.

According to Figure 8(a) and (b), the strain gauges attached to the anchor bolts are sensitive to changes in the loosening and fastening of the bolts. Due to systematic errors, the strain data needs to be zeroed manually. In this diagram, the strain measured right before the tightening of the nut is set to zero. Therefore, in order to monitor damage to anchor bolts through strain time histories, continuous measurements are necessary to capture the changes.

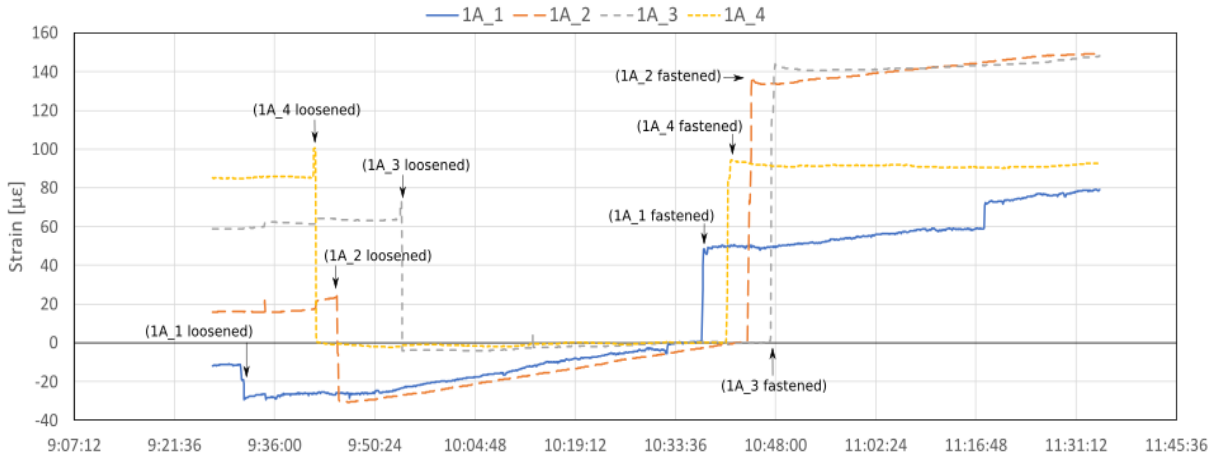


(a) Column 1A

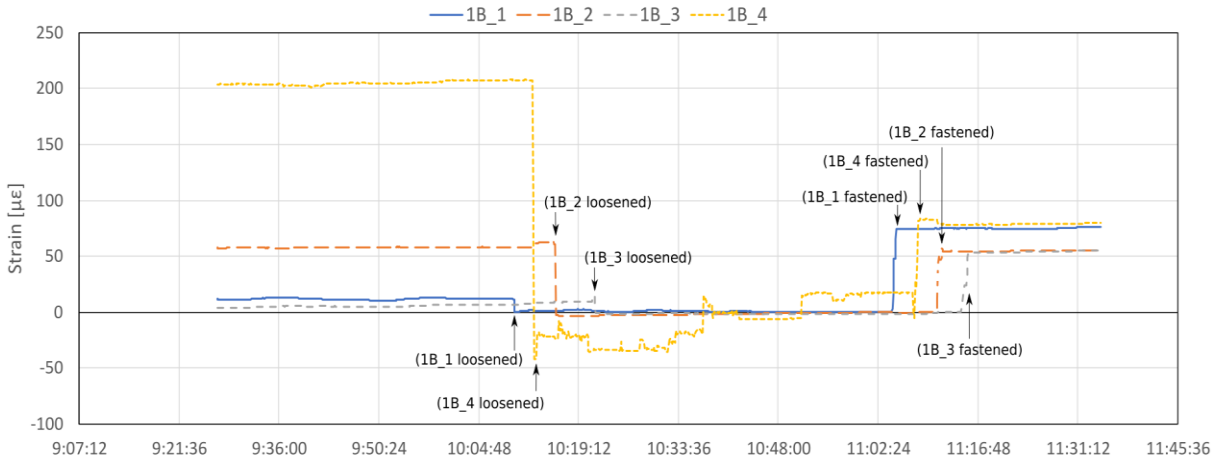


(b) Column 1B

Figure 8: Change in strain measured from individual anchor bolt

### 4.2 Local stiffness of column sections

Local stiffness of the upper and lower section of the column 1A calculated using Eq. (1) are illustrated in Figure 9. Unlike the time history of the axial strain on the anchor bolt, the local axial stiffness ($K_{\varepsilon,a}$) remains almost constant. On the other hand, the local bending stiffness ($K_{\varepsilon,b}$) is relatively sensitive to changes in the loosening and tightening of the bolt especially in the lower section, which can be used as a potential indicator for damage detection.

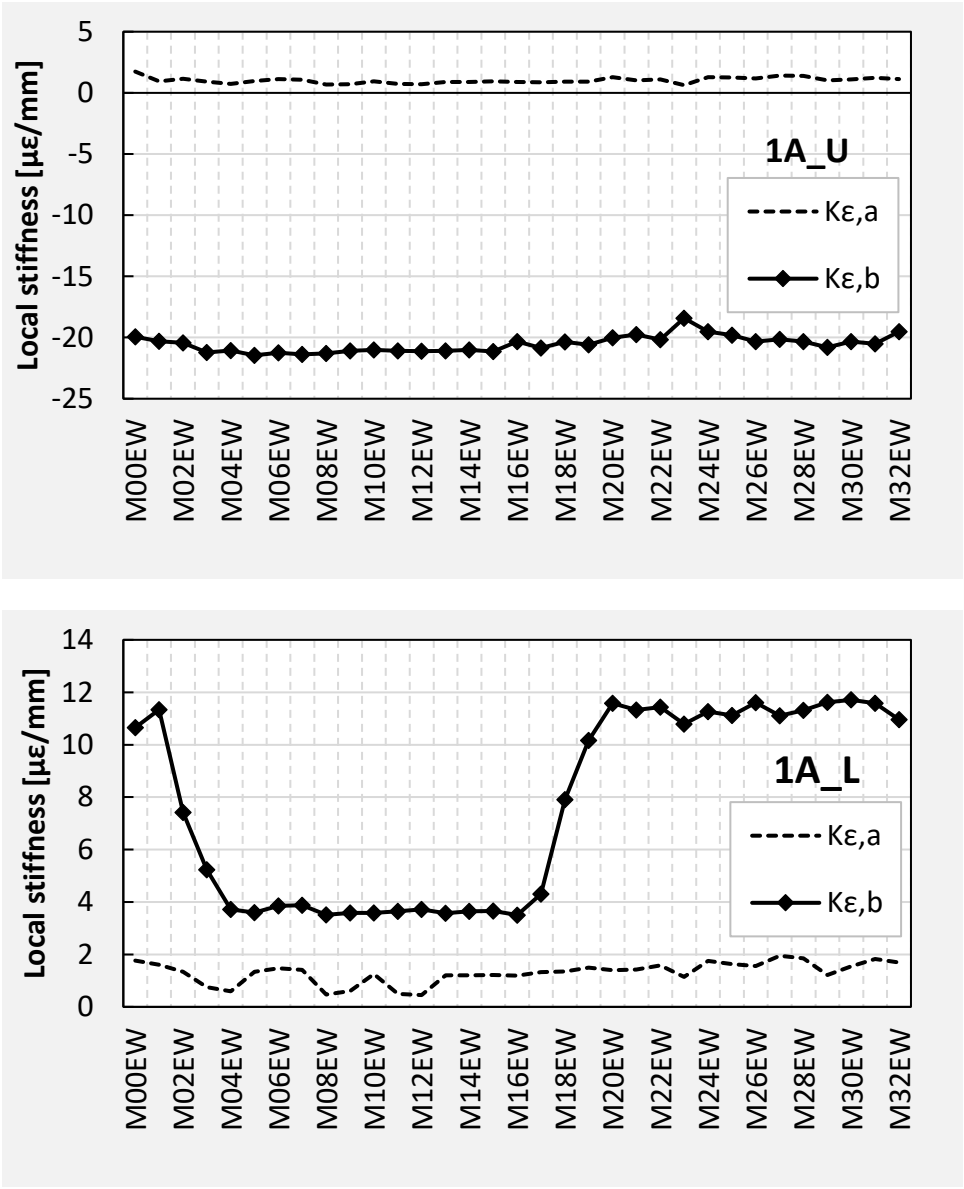


Figure 9: Local stiffness measured on sections 1A_U and 1A_L

### 4.3 Bending moment distribution

Because the local stiffness does not consider the different sectional properties between the upper part and lower part of the column, it may also be preferable to use the bending moment distribution. In general, the bending moment can be written as Eq. (2):

$$M = EI\varphi = EI \times \frac{\varepsilon_{i,W} - \varepsilon_{i,E}}{H} = \frac{EI}{H}\left(\varepsilon_{i,W} - \varepsilon_{i,E}\right) \tag{2}$$

Using the concept of local stiffness, the bending moment normalized by displacement can be calculated as Eq. (3):

$$\widehat{M} = \frac{EI}{H} \times \frac{\hat{\varepsilon}_{i,W} - \hat{\varepsilon}_{i,E}}{2\hat{d}} = \frac{EI}{H} \times K_{\varepsilon,b} \tag{3}$$

Figure 10 shows the bending moment distribution of the column 1A calculated using Eq. (3). The values at the top and bottom sections are calculated by extrapolation. A reduction in the bending moment at the bottom of the column can be observed, indicating a reduction in the stiffness at the column base.

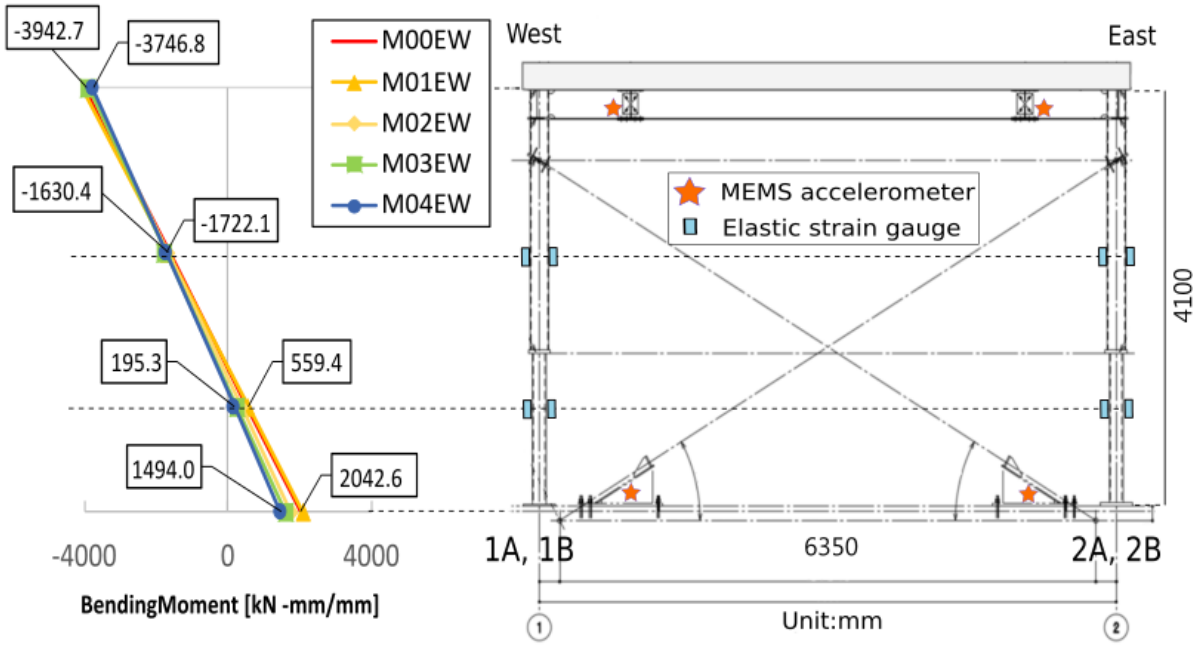


Figure 10: Bending moment distribution of the column 1A

### 4.4 Damage classification using machine learning

In this research, the amount of total data sets is relatively small. Therefore, spectrograms created from all four columns are combined and classified into five damage classes: 1. No bolts have been loosened; 2. One bolt has been loosened; 3. Two bolts have been loosened; 4. Three bolts have been loosened; and 5. All bolts have been loosened. For each damage class, 128 spectrograms were used as the image samples and the batch size was set as 16.

Figure 11 and Figure 12 illustrate the training result using Teachable Machine where the learning rate was set as 0.0005. The default validation rate is 0.15, which cannot be changed. The trained model performed well, and the training time was less than 30 seconds. The training values are close to the test values, meaning that there is less overfitting. Furthermore, the model can successfully identify extreme situations (Class 1 and Class 5), but it performs poorly when classifying images from Class 3. In conclusion, thanks to the powerful cloud server, the teachable machine can easily classify different damage cases with minimal training time.




Figure 11: Accuracy and loss per epoch trained by Teachable Machine

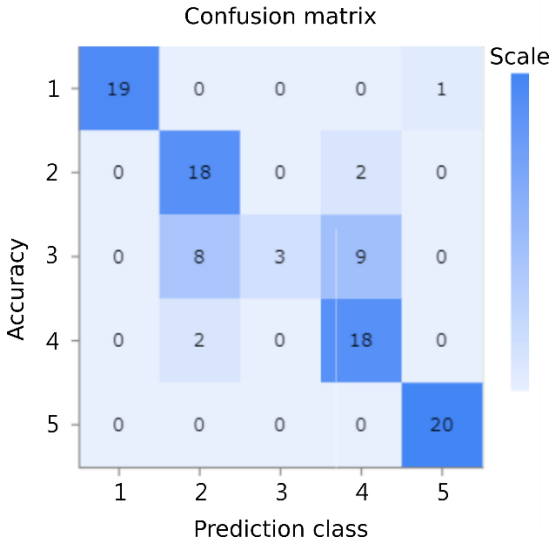


Figure 12: Confusion matrix created by Teachable Machine

Figure 13 and Figure 14 illustrate the training result using the Deep Network Designer in MATLAB. While the Teachable Machine is based on MobileNet, a pretrained image recognition network, in this research, we also use a pretrained image network called NasNet-Mobile which has 913 layers and 1071 connections. Due to the small amount of data, the validation frequency was set to 5 iterations. The initial learning rate was set as 0.01 while the drop ratio was set as 0.1.

According to the result, the trained model performed well; however, it takes about 3 hours to train using the 11th Generation Intel Core i7. Because the training values are close to the test values, there is less overfitting. In addition, similar to the result made by Teachable Machine, while the model is capable of identifying extreme situations (Class 1 and Class 5), it performs relatively poorly when classifying images from Class 2 to Class 3. However, compared to Teachable Machine, because the network created in MATLAB can be manually tuned, it has the potential to train a better model if the parameters are properly adjusted.

In conclusion, it has been demonstrated that training damage classification models using raw strain data is efficient and only requires a limited amount of data processing. Once the

technology matures, the level of technological expertise required for structural health monitoring will significantly decrease.

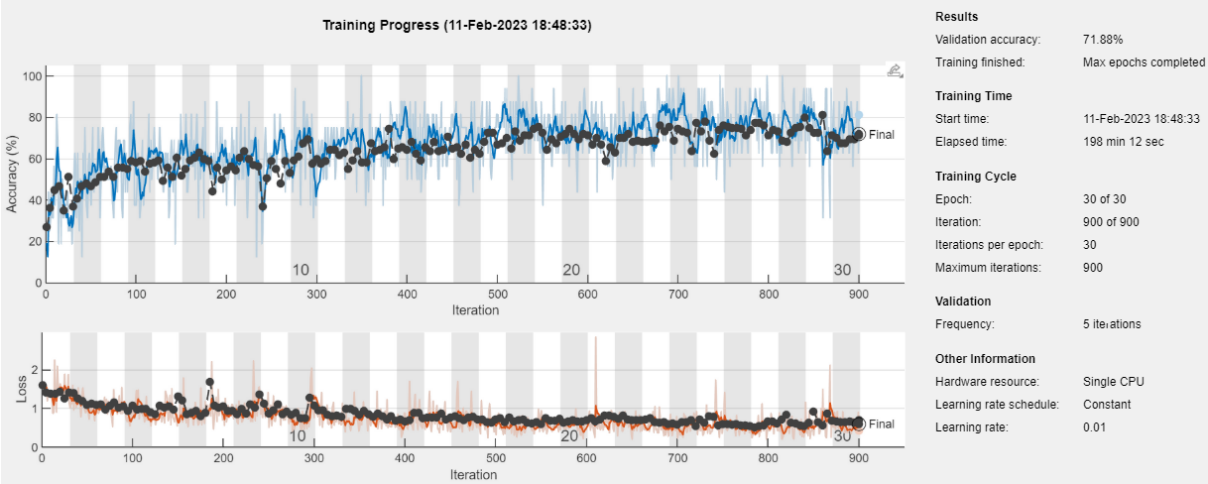


Figure 13: Accuracy and loss per epoch trained by NasNet-Mobile

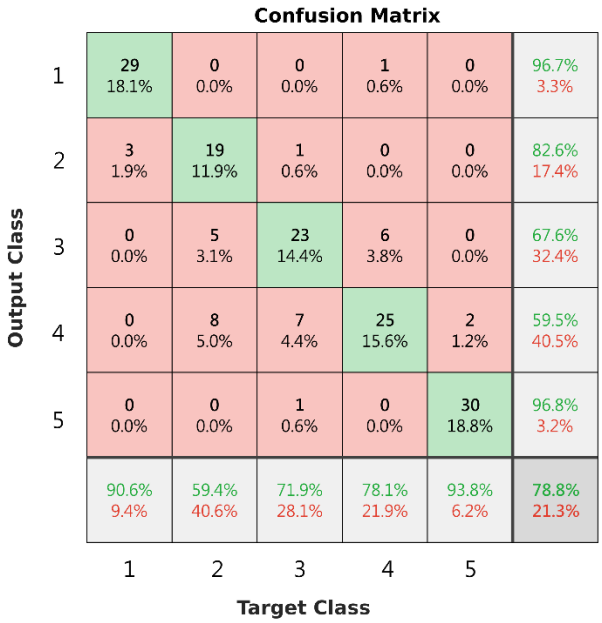


Figure 14: Confusion matrix created by the model trained by NasNet-Mobile

## 5 CONCLUSIONS

- The strain gauges attached to the anchor bolts are sensitive to changes in the loosening and fastening of the bolts.
- In order to monitor damage to anchor bolts through strain time histories, continuous measurements are necessary to capture the changes.
- Compared to the local axial stiffness ($K_{\varepsilon,a}$), the local bending stiffness ($K_{\varepsilon,b}$) measured on the column surface is relatively sensitive to changes in the loosening and tightening of the bolt especially in the lower section

- Using the concept of local stiffness, the bending moment distribution normalized by displacement shows a trend of reduction at the bottom of the column, indicating a reduction in the stiffness at the column base.
- For both Teachable Machine and NasNet-Mobile, the trained model performed well with an accuracy of 70-80%; However, the Teachable Machine is more time saving while NasNet-Mobile implemented using MATLAB is more customizable.
- Once the proposed methods mature, the level of technological expertise required for structural health monitoring will significantly decrease.

## REFERENCES

[1] Scawthorn, C., & Yanev, P. I. (1995). 17 January 1995, Hyogo-ken Nambu, Japanese earthquake. Engineering Structures, 17(3), 146-157.

[2] Watanabe, E., Sugiura, K., Nagata, K., & Kitane, Y. (1998). Performances and damages to steel structures during the 1995 Hyogoken-Nanbu earthquake. Engineering Structures, 20(4-6), 282-290.

[3] Maruya H (2008) Significance and Economic Effect of Business Continuity Plan, Gyosei Co., p.2, (in Japanese).

[4] Lee Y, Watanabe K, Li WS (2019) Enhancing Regional Disaster Resilient Trade and Investment – Business Continuity Management. In: Murayama Y, Velev D, Zlateva P. (eds) Information Technology in Disaster Risk Reduction. ITDRR 2017. IFIP Advances in Information and Communication Technology, vol. 516. Springer, Cham. https://doi.org/10.1007/978-3-030-18293-9_10

[5] Brownjohn JMW (2003) Ambient vibration studies for system identification of tall buildings. Earthquake Eng Struct Dyn 32(1): 71–95.

[6] Yousefianmoghadam S, Behmanesh I, Stavridis A, Moaveni B, Nozari A, Sacco A (2018) System identification and modeling of a dynamically tested and gradually damaged 10‐story reinforced concrete building. Earthq Eng Struct Dyn 47: 25‐47.

[7] Kubota J, Suzuki Y, Suita K Sawamoto Y, Kiyokawa T, Koshika N, Takahashi M (2017) Experimental study on the collapse process of an 18-story high-rise steel building based on the large-scale shaking table test. In: 16th World Conference on Earthquake Engineering, Santiago, Chile, 9–13 January 2017.

[8] Kubota J, Takahashi M, Sawamoto Y, Suzuki Y, Koetaka Y, Iyama J, Nagae T (2018) Collapse behavior of 18-story steel moment frame on shaking table test. J. Struct. Constr. Eng. AIJ 83(746): 625–635 (in Japanese).

[9] Iyama J (2017) Detection of damage and fracture of steel members based on micro strain measurement. In: 9th International Symposium on Steel Structures, Jeju, Korea, 1–4 November 2017.

[10] Iyama J, Hasegawa T, Nakagawa H, Kaneshiro Y (2019) Beam end fracture detection of two-story steel frame based on micro strain measurement under microtremor. In: 12th Pacific Structural Steel Conference, Tokyo, Japan, 15–17 December 2019.

[11] Sato, K., & Ikarashi, K.: Local buckling behavior and evaluation method for structural performance of square hollow section members under bending shear force. Journal of Structural and Construction Engineering 82(731), 123-133 (2017) (in Japanese)

[12] Wang, S., Shi, J., Ye, Z., Dong, D., Yu, D., Zhou, M., ... & Tian, J. (2019). Predicting EGFR mutation status in lung adenocarcinoma on computed tomography image using deep learning. European Respiratory Journal, 53(3).

COMPDYN 2023
9th ECCOMAS Thematic Conference on
Computational Methods in Structural Dynamics and Earthquake Engineering
M. Papadrakakis, M. Fragiadakis (eds.)
Athens, Greece, 12-14 June 2023

# SEVEN YEARS OF CONTINUOUS DYNAMIC MONITORING OF BAIXO SABOR DAM

**Sérgio Pereira[1], Filipe Magalhães[1], Jorge Gomes[2], Álvaro Cunha[1] and José V. Lemos[2]**

[1] Construct-ViBest, Faculty of Engineering of the University of Porto (FEUP)
Rua Dr. Roberto Frias, 4200-465 Porto, Portugal
{sbp, filipema, acunha}@fe.up.pt

[2] National Laboratory for Civil Engineering (LNEC)
Av. do Brasil 101, 1700-066 Lisboa, Portugal
{jgomes, vlemos}@lnec.pt

## Abstract

*The Baixo Sabor dam is a 123 meters high concrete arch dam located in the north of Portugal. After the performance of a forced vibration test, a quite unique experimental programme was initiated in the dam during the first filling of the reservoir, with the installation of a continuous dynamic monitoring system in December 2015. The implementation of such a system aimed to study the evolution of the dam's dynamic behaviour during the first filling, as well as to monitor its condition in the long-term through the development of vibration-based damage detection supported by robust operational modal analysis.*
*After a description of the dam and the monitoring system, this paper presents an overview of the tools developed to perform the automated tracking of the dam's modal parameters. Finally, using the database collected during the last seven years, the long-term evolution of the dam dynamic parameters is analysed, and their seasonal fluctuations interpreted. The eventual occurrence of structural anomalies is evaluated after the minimization of the most influential operational and environmental effects on the dam, such as temperature and the reservoir water level.*

**Keywords:** operational modal analysis; continuous dynamic monitoring; dam monitoring; minimization of operational conditions; structural health monitoring.

## 1 INTRODUCTION

From the point of view of renewable energies exploitation, hydroelectricity has an essential position in Europe. In Portugal, for instance, it covers about one third of the country's installed capacity to produce electricity and it plays an important role in energy storage, through complementarity with other energy sources. Moreover, having in mind the high number of dams with 30-70 years of age existing in the vicinity of populations and the important deterioration processes induced by the ageing of structural materials, dam safety control is of fundamental importance.

In this context, the development and implementation of efficient Structural Health Monitoring (SHM) systems is of utter priority in the long-term management of large civil infrastructures [1], both to prevent catastrophes and to guarantee an efficient and long due operation of these structures, through timely structural interventions

Though the monitoring of concrete dams is historically associated with the study of quasi-static quantities, such as horizontal displacements, the installation of robust vibration based SHM systems have become more common in the past decade [2-4]. The continuous dynamic monitoring of Baixo Sabor arch dam, in Portugal, which is being carried out by the Laboratory of Vibrations and Structural Monitoring (ViBest-FEUP) and by the National Laboratory for Civil Engineering (LNEC) is a good example of the integration of such systems in the daily monitoring activities of large dams. Despite the complexity introduced by the disadvantageous signal-to-noise ratio, the influence of significant reservoir fluctuations and the disturbances induced by the operation of nearby power plants [5], it has been possible to successfully characterize the dynamic behaviour of this structure over a period of 7 years.

In this context, a brief description of Baixo Sabor dam and its dynamic monitoring system are presented in this work, followed by a summary of the tools that have been developed and implemented to assure of the monitoring of structures, as well as the results obtained since the first filling in late 2015. Operational modal analysis is used to identify the structure's dynamic properties over time and data normalization techniques are used to minimize the effects of operational and environmental conditions on modal properties. Finally, control charts are applied to the residuals obtained from the comparison between observed and predicted results, and used to detect shifts that may indicate the occurrence of novel structural behavior.

## 2 BAIXO SABOR DAM AND MONITORING SYSTEM

The Baixo Sabor hydroelectric development is located across the Sabor river, in the basin of the Douro river, in the northeast of Portugal. The dam is double curvature, 123 m high and 505 meters long and crest height. Its arch is composed by 32 concrete blocks, separated by vertical contraction joints, including six horizontal visit galleries. The reservoir originated by the dam (see left part of Figure 1) has a capacity of 1095 $hm^3$ at exploration level, which is defined for 234 m above sea level.

In order to continuously identify the dam's dynamic characteristics and their evolution over time, while considering the variation of operational and environmental conditions, a vibration-based monitoring system has been designed for the dam in 2015 considering both a numerical model and a forced vibration test developed and performed by LNEC [6]. The system was installed and testes in late 2015, being in continuous operation since December 2015. It consists of 20 uniaxial accelerometers that have been radially disposed in the dam's three upper visit galleries, three digitizers, a central computer for data storage and GPS antennas that assure the need synchronization between different measuring channels. The right part of Figure 1 shows the position of the accelerometers installed in the dam, marked with red dots over a picture of the structure. The dynamic monitoring system is configured to continuously

record acceleration time series with a sampling rate of 50 Hz and a duration of 30 minutes at all instrumented points, therefore, producing 48 groups of time series every day.

A monitoring software developed at ViBest/FEUP called DynaMo [7] is being used to process the data collected by the monitoring system. This software is responsible for backing up the original data samples, performing pre-processing procedures on the acceleration time series (such as trend elimination, filtering and re-sampling), as well as for the characterization of vibration levels and the identification of the dam modal properties through automatic operational modal analysis.



Figure 1 – Baixo Sabor arch dam: a) aerial view (on the left); b) position of accelerometers marked with red dots (on the right).

## 3 MODAL TRACKING

Given that only the vibration of the structure is being recorded by the monitoring system and that no excitation is purposedly imposed on it, operational modal analysis is being used to identify the modal properties of the dam. An automated procedure is considered, which takes advantage of the combination between the SSI-Cov method, as presented in [8, 9], and the algorithm for hierarchical clustering proposed in [10], to group poles with similar modal properties.

To separate physical modes from numerical ones, the modal estimates identified in each setup are compared with reference mode shapes, which were obtained from selected datasets with very clear stabilization diagrams. Each new set of modal properties is only accepted as a physical mode if the MAC (Modal Assurance Criterion) [11] between the estimated mode shape and the reference mode shape is higher than 0.55, and if the variation between their frequency values is lower than 5%.

The modal properties of the structure are strongly affected by the operational and environmental conditions of the dam surroundings. The level of water in the reservoir, for instance, has a major impact on the dam's natural frequencies. This can be observed on the left part of Figure 2, where the estimates obtained for first mode's natural frequency over one year of monitoring is represented (in blue) together with the variation of the level of water in the reservoir (represented in orange) for the same period. It is clear that an inverse relation exists between these two variables, that is, when the water level rises, the natural frequency decreases, and vice-versa. Moreover, temperature variations impact the dynamic behavior of the structure as well, has can be observed in the right part of Figure 2, where the evolution of the natural frequency of the seventh mode follows an oscillatory pattern characteristic of a daily thermal wave. Though to a lesser extent, the same is verified for the sixth mode.

Therefore, the procedure for modal tracking has been improved through the consideration of these effects and multiple linear regressions are used to predict the expected frequency val-

ues at each moment, continuously updating modal references and increasing the identification rates [12].

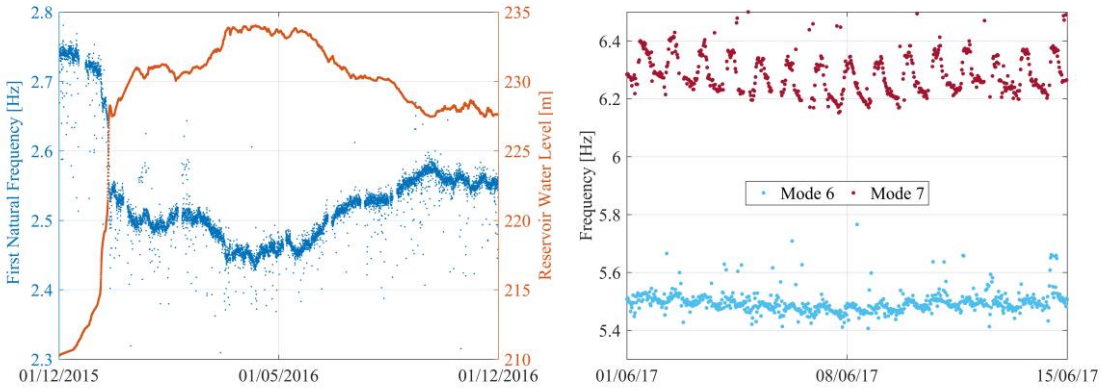


Figure 2 – Relation between the first natural frequency and reservoir water level (on the left); Effect of daily temperature variations on natural frequency of modes 6 and 7 (on the right).

The operation of the power plant is another external factor affecting the modal identification process and introducing bias in the analysis. While using operational modal analysis in general, and the SSI-Cov method, it is assumed that the excitation on the structure is a white noise. Good results can still be achieved even if the excitation noise is not completely white, but problems arise when well-defined frequencies are significantly present in the excitation. This is the case with the power production turbines operating in the power plant nearby the dam, which rotate at 214 rpm (~3.57 Hz).

The turbine rotation frequency is close to the frequency of the dam's third vibration mode, leading to several misidentifications by the automated procedure when the power plant is operating. This can be observed in the left part of Figure 3, where an unusual number of identifications around 3.57 Hz is found in the histogram of the third mode's identified frequencies. To solve this problem, a procedure using the uncertainties associated with the modal properties estimated by the SSI-Cov was proposed, considering that the turbine rotation frequency is very well-defined and, therefore, presents low uncertainty [13]. In this sense, the frequency estimates identified for the third mode that present frequency standard deviations lower than 0.005 Hz were represented in yellow in the right part of Figure 3. The vast majority of yellow points correspond to frequencies very close to 3.57 Hz, therefore associated with the turbine rotation frequency.

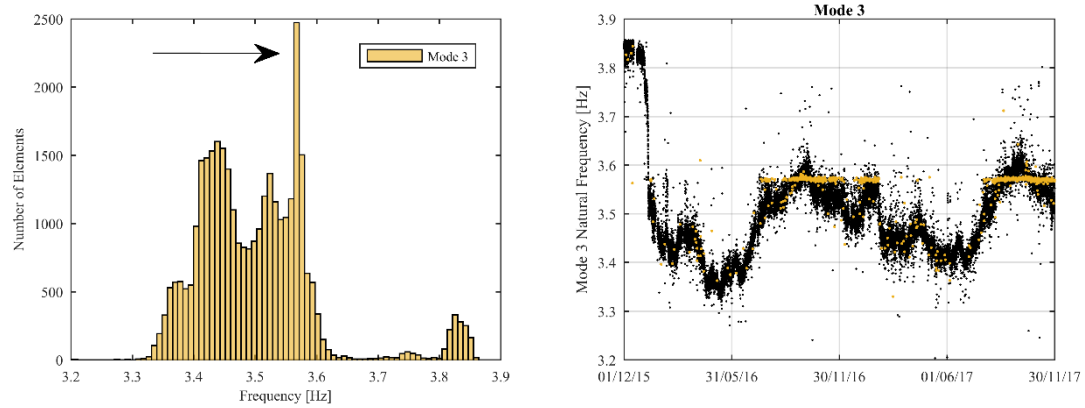


Figure 3 – Histogram of frequencies identified for the third mode (on the left); Evolution of the third mode natural frequency with estimates associated with the turbine operation highlighted in yellow (on the right).

The set of tools presented was used to identify the first 10 vibration modes of the structure for more than 7 seven years, between 01/12/2015 and 31/12/2022. In this sense, the evolution of the natural frequencies of the dam is presented in Figure 4, where each point represents 1 hour of data and each mode is represented by a different color. Visually inspecting Figure 4 it is verified that natural frequencies are significantly affected by external factors, and that higher scatter occurs for higher order modes. This is corroborated by Table 1, where mean values and standard deviations are presented for each mode's frequency. The standard deviation varies from 0.048 Hz for the first mode, to 0.228 Hz in the case of the tenth mode.

It should be noted that blank spaces correspond to periods when the monitoring system was either malfunctioning or under maintenance procedures. Excluding a period in 2020 when Portugal was under general lockdown due to the COVID-19 pandemic and access to the system was severely restricted, the system has been behaving as expected for the past seven years.

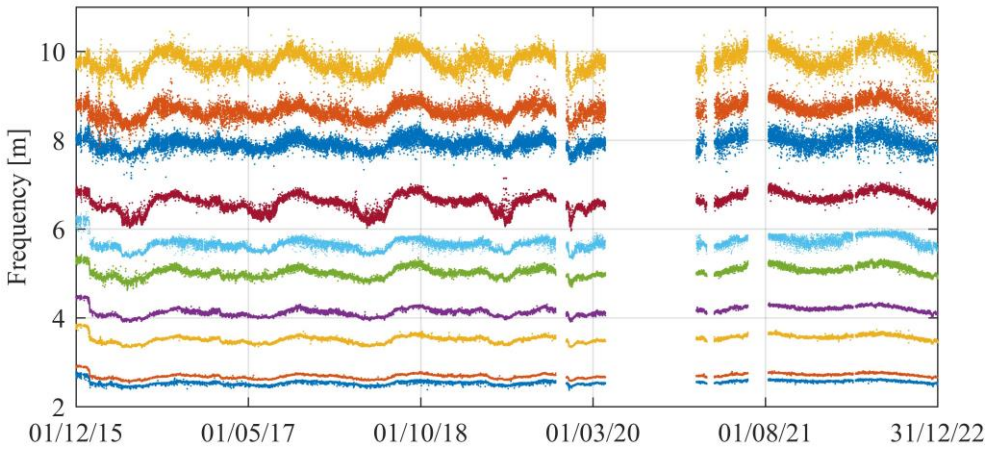


Figure 4 – Natural frequencies of the first 10 vibration modes between 01/12/2015 and 31/12/2022.

| Mode | 1 | 2 | 3 | 4 | 5 | 6 | 7 | 8 | 9 | 10 |
|---|---|---|---|---|---|---|---|---|---|---|
| $f_{mean}$ [Hz] | 2.54 | 2.69 | 3.52 | 4.15 | 5.03 | 5.67 | 6.62 | 7.92 | 8.67 | 9.80 |
| $f_{std}$ [Hz] | 0.048 | 0.054 | 0.083 | 0.095 | 0.113 | 0.140 | 0.189 | 0.148 | 0.174 | 0.228 |

Table 1: Statistical characterization of the natural frequencies estimates from 01/12/2015 to 31/12/2022

## 4 DATA NORMALIZATION AND NOVEL BEHAVIOUR

The occurrence of novel structural behavior in a structure, which may be due to damage, can be detected through variations in their natural frequencies. However, the effects of small damages on frequencies can be significantly lower than those resulting from the variation of environmental and operational conditions. Therefore, it is necessary to minimize data variability due to external factors, such as reservoir water level and temperature.

For this, the Minimum Mean Square Error (MMSE) estimator [14] has been used to predict the evolution of each mode's natural frequency, based on the observed frequencies of the remaining modes. The model was trained using data obtained between 01/12/2015 and 30/11/2017. Finally, the residuals that result from the difference between the observed and the

predicted data, are characterized by significantly lower standard deviations and distributions close to the normal distribution.

The distributions of the natural frequencies of the first two vibration modes (in blue and orange) and those of the corresponding residuals (in black) are represented in Figure 5, as examples, showing the success of this approach in minimizing the effects of external conditions. It should be noted that the mean frequency of each mode was added to the corresponding set of residuals, for representation purposes.

The reduction in data variability achieved is ascertained in Table 2, where the standard deviations of the identified natural frequencies are compared to those of the residuals obtained after the data normalization procedure. In most cases, reductions of over 50% are achieved. For the first five modes the reductions achieved are between 65% and 82%.

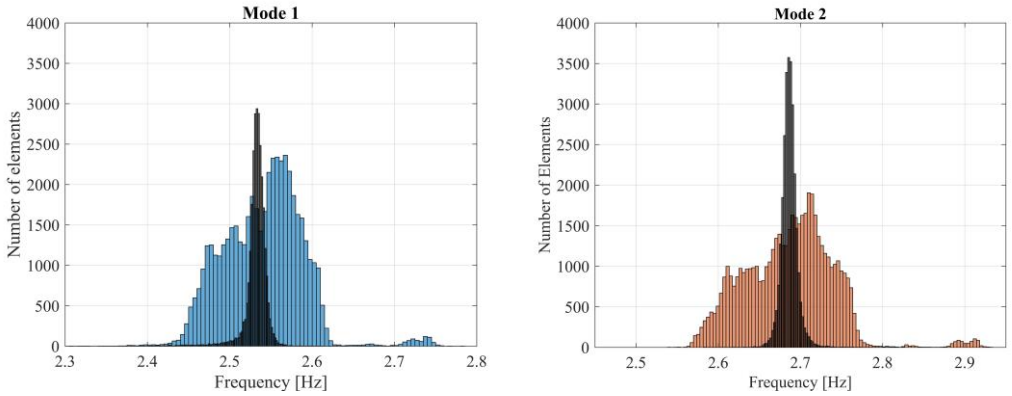


Figure 5 – Histograms of natural frequencies (in blue and orange) and residuals (in black), for the first two vibration modes.

| Mode | 1 | 2 | 3 | 4 | 5 | 6 | 7 | 8 | 9 | 10 |
|---|---|---|---|---|---|---|---|---|---|---|
| $f_{std}$ [Hz] | 0.048 | 0.054 | 0.083 | 0.095 | 0.113 | 0.140 | 0.189 | 0.148 | 0.174 | 0.228 |
| $r_{std}$ [Hz] | 0.016 | 0.010 | 0.016 | 0.018 | 0.040 | 0.074 | 0.086 | 0.126 | 0.129 | 0.151 |

Table 2: Comparison between the standard deviation of the identified natural frequencies ($f_{std}$) and those of the residuals ($r_{std}$) achieved after data normalization.

Control charts are especially adequate to detect changes in processes characterized by several variables, such as the natural frequencies of the different tracked vibration modes, being commonly used in the detection of novel structural behavior.

In this context, the residuals obtained after the application of the MMSE procedure, were used to build a control chart resorting to the statistical test $T^2$, which is presented in Figure 6. Data from 01/12/2015 to 30/11/2017 was used as reference period, whereas observations from 01/12/2017 to 31/12/2022 were considered for the validation period, each point corresponding to 2 days of data. The training period was also used to determine the upper control limit (UCL), which was set as the $[0; 3\sigma]$ interval, where $\sigma$ represents the standard deviation of the process.

It was verified that 3.2 % points were above the UCL during the training period, while only 2.8 % of the points were above the UCL during the validation period, indicating that the process is in control and, therefore, that the structure is not showing novel structural behavior.

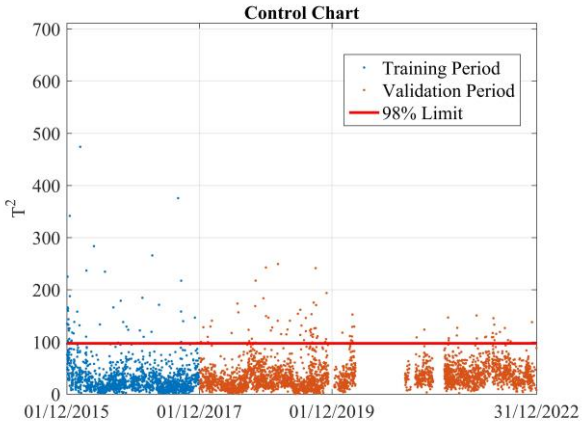


Figure 6 – Natural frequencies of the first 10 vibration modes between 01/12/2015 and 31/12/2022.

## 5 CONCLUSIONS

The dynamic monitoring system of Baixo Sabor arch dam has been installed in 2015 and it has been operating continuously ever since, showing efficiency and robustness. Additionally, the characterization of the dynamic behavior of the structure for a period of over 7 years, constitutes quite an unusual database that now allows the study of the long-term health of the structure based on modal properties.

To achieve an efficient automated procedure for the performance of operational modal analysis in the dam, state of the art methods were used and complemented with processing tools developed specifically for this application, that can now be generalized for similar structures. It was verified that natural frequencies present high variability, mostly due to the effects of operational and environmental conditions. The analysis of such effects revealed an inverse relation between frequencies and the level of water in the reservoir, and that the effect of daily temperature variations should not be despised.

It was possible to significantly minimize the effects of external factors on natural frequencies through data normalization techniques, considering only two years of monitoring data for the training period, which resulted in (close to) normally distributed residuals. Finally, the residuals obtained in the previous step allowed to build a control chart, using the same training period. It was verified that the process is in control, suggesting that the structure is not presenting novel behavior.

## ACKNOWLEDGEMENTS

This work was financially supported by national funds through the FCT/MCTES (PIDDAC), under the project PTDC/ ECI-EST/29558/2017, and by Base Funding - UIDB/04708/2020 and Programmatic Funding - UIDP/04708/2020 of the CONSTRUCT - Instituto de I&D em Estruturas e Construções - also funded by national funds through the FCT/MCTES (PIDDAC). The authors would also like to thank the collaboration and support provided by Engie/Movhera.

## REFERENCES


1. Gomes, J.P., et al. *Seismic monitoring system of baixo sabor scheme for structural dynamic behaviour monitoring and risk management*. in *26th International Congress on Large Dams, 2018*. 2018.
2. Darbre, G.R. and J. Proulx, *Continuos ambient-vibration monitoring of the arch dam of Mauvoisin.* Earthquake Engineering and Structural Dynamics, 2002. **31**(2): p. 475-480.
3. Oliveira, S. and A. Alegre, *Seismic and structural health monitoring of Cabril dam. Software development for informed management.* Journal of Civil Structural Health Monitoring, 2020. **10**.
4. Pereira, S., et al., *Modal tracking under large environmental influence.* Journal of Civil Structural Health Monitoring, 2022. **12**(1): p. 179-190.
5. Pereira, S., et al., *Modal identification of concrete dams under natural excitation.* Journal of Civil Structural Health Monitoring, 2021. **11**(2): p. 465-484.
6. Gomes, J.P. and J.V. Lemos, *Characterization of the dynamic behavior of a concrete arch dam by means of forced vibration tests and numerical models.* Earthquake Engineering & Structural Dynamics, 2020. **49**(7): p. 679-694.
7. Magalhães, F., et al. *DynaMo - Software for vibration based structural health monitoring*. in *Bridge Maintenance, Safety, Management, Resilience and Sustainability - Proceedings of the Sixth International Conference on Bridge Maintenance, Safety and Management*. 2012.
8. Reynders, E., R. Pintelon, and G. De Roeck, *Uncertainty bounds on modal parameters obtained from stochastic subspace identification.* Mechanical Systems and Signal Processing, 2008. **22**(4): p. 948-969.
9. Döhler, M. and L. Mevel, *Efficient multi-order uncertainty computation for stochastic subspace identification.* Mechanical Systems and Signal Processing, 2013. **38**(2): p. 346-366.
10. Magalhães, F., Á. Cunha, and E. Caetano, *Online automatic identification of the modal parameters of a long span arch bridge.* Mechanical Systems and Signal Processing, 2009. **23**(2): p. 316-329.
11. Allemang, R.J., *The modal assurance criterion–twenty years of use and abuse.* Sound and vibration, 2003. **37**(8): p. 14-23.
12. Pereira, S., et al., *Vibration-based damage detection of a concrete arch dam.* Engineering Structures, 2021. **235**: p. 112032.
13. Pereira, S., et al., *The role of modal parameters uncertainty estimation in automated modal identification, modal tracking and data normalization.* Engineering Structures, 2020. **224**: p. 111208.
14. Kullaa, J., *Sensor validation using minimum mean square error estimation.* Mechanical Systems and Signal Processing, 2010. **24**(5): p. 1444-1457.

COMPDYN 2023
9th ECCOMAS Thematic Conference on
Computational Methods in Structural Dynamics and Earthquake Engineering
M. Papadrakakis, M. Fragiadakis (eds.)
Athens, Greece, 12—14 June 2023

# EVOLUTION OF THE MODAL PARAMETERS DUE PROGRESSIVE DEGRADATION OF AN RC BEAM-COLUMN JOINT

**Angelo Aloisio[1], Amedeo Gregori[1,*], Lorenzo Bizzarri[1], Caterina D'Agostino[1], Riccardo Cirella[1], Rocco Alaggio[1]**

[1] Università degli Studi dell'Aquila, Civil Environmental and Architectural Engineering Department,
via Giovanni Gronchi n.18, L'Aquila 67100, Italy
e-mail: {angelo.aloisio1,amedeo.gregori,riccardo.cirella,rocco.alaggio}@univaq.it

**Abstract.** *This paper presents an experimental characterization of the progressive damage in reinforced concrete beam-columns joints from ambient vibration tests. During the quasi-static cyclic tests on an RC joint, the authors estimated the modal parameters corresponding to different stages of joint degradation. The variation of the modal parameters has been correlated to damage indicators of concrete, thus providing an answer to a well-debated topic concerning this case study: Are ambient vibration measurements informative for damage assessment? Which is the sensitivity of the modal parameters to the increasing damage levels? This preliminary study aims to understand the feasibility of vibration-based damage assessment at a component level for concrete structures to understand the modal parameters' sensitivity to damage at a system level.*

**Keywords:** Instructions, Structural Dynamics, Earthquake Engineering, Proceedings.

## 1 INTRODUCTION

Operational and cost constraints make often unfeasible forced-vibration tests (e.g., shaker and impact/pull-back tests) in civil structures. Consequently, ambient vibration (AV) is often the sole alternative method for damage detection purposes. In this approach, operational modal analysis (OMA) or output-only system identification techniques are used with AV data recorded before and after the structure has potentially suffered damage. According to Astroza et al. [3], there are three main limitations and challenges related to the use of OMA for damage detection.

- The need for automatic operational modal analysis. The automatic procedure allows to distinguish between spurious and physical modes, This is the most research aspect which received more attention, since many methods have been proposed in the last twenty years [17, 19, 12, 21, 16, 22, 7, 1, 14, 6].

- The statistical variability of the identified modal properties needs to be adequately investigated and understood because sources different to damage can also induce variations in the dynamic characteristics of civil structures, for example, temperature, measurement noise level, change in the boundary conditions, wind speed, etc. (e.g., [16, 13, 15, 4, 24]), as well as the uncertainty of the parameter estimation method itself.

- Third, the availability of data recorded on real structures undergoing real damage and degradation processes has been extremely limited. Most of the full-scale tests have been conducted on in-situ bridge structures condemned for demolition, in which artificial damage (e.g., partial saw cuts in steel girders, partial cuts of post-tensioning tendons) was induced during the demolition process [11, 9, 23, 5]. However, the induced type of artificial damage is not representative of real damage caused by natural loads or ageing.

There are a few studies attempting to assess the modal parameters of reinforced concrete (RC) buildings at different states of damage (e.g., [14, 10, 8]). However, except for the study by [3], none of the existing test, programs recorded AV data continuously and therefore implemented an automatic system identification approach, based on the data data recorded on a real structure subjected to damage induced by a realistic source of dynamic excitation. In this paper, the authors estimate the modal parameters of an RC joint subjected to progressive damage from quasi-static tests. The analyses reveal the variation of the modal parameters at a component level approach, never done before for RC joints.

## 2 EXPERIMENTAL TEST

The tested specimen consists of a T-shaped RC joint [2]. It represents the cellular unit of an RC frame. Fig.1(a) shows the tested specimen, while Fig.1(b) displays the layout of the ambient vibration test using Force Balance Accelerometers.

The experimental investigation derives from the superposition of two tests typology. (i) Quasi-static tests of the RC frame, as displayed in Fig.2(a), that shows the loading point and the constraints of the RC frame. (ii) Ambient vibration tests corresponding to different damage levels, identified by the maximum displacement value attained during the quasi-static test. The authors considered seven damage levels corresponding to the displacement values in mm: 23.70, -28.27, -31.27, 40.75, -52.55, -150, 300. Six accelerometers have been positioned on the RC frame, as shown in Fig.2(a). The acquisition duration is approximately 10 minutes at a 200Hz sampling frequency.



(a) (b)

Figure 1: (a) Tested specimen and (b) Experimental layout

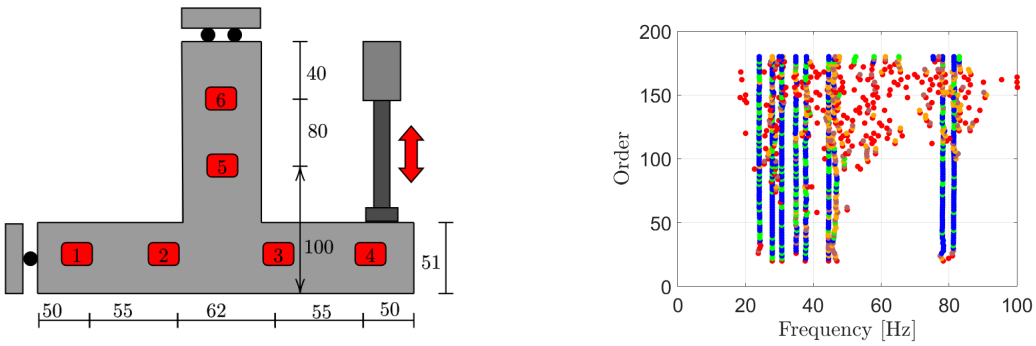


(a) (b)

Figure 2: (a) Experimental setup; (b) Stabilization diagram at the stage 0, no damage.

The data were processed using the SSI-cov algorithm [20], using the open-source software PyOMA [18]. Fig.2(b) shows the stabilization diagram obtained from the SSI-cov on the data corresponding to no damage. The dynamic identification provided a high-quality estimate of approximately seven modes in the range 0-100Hz.

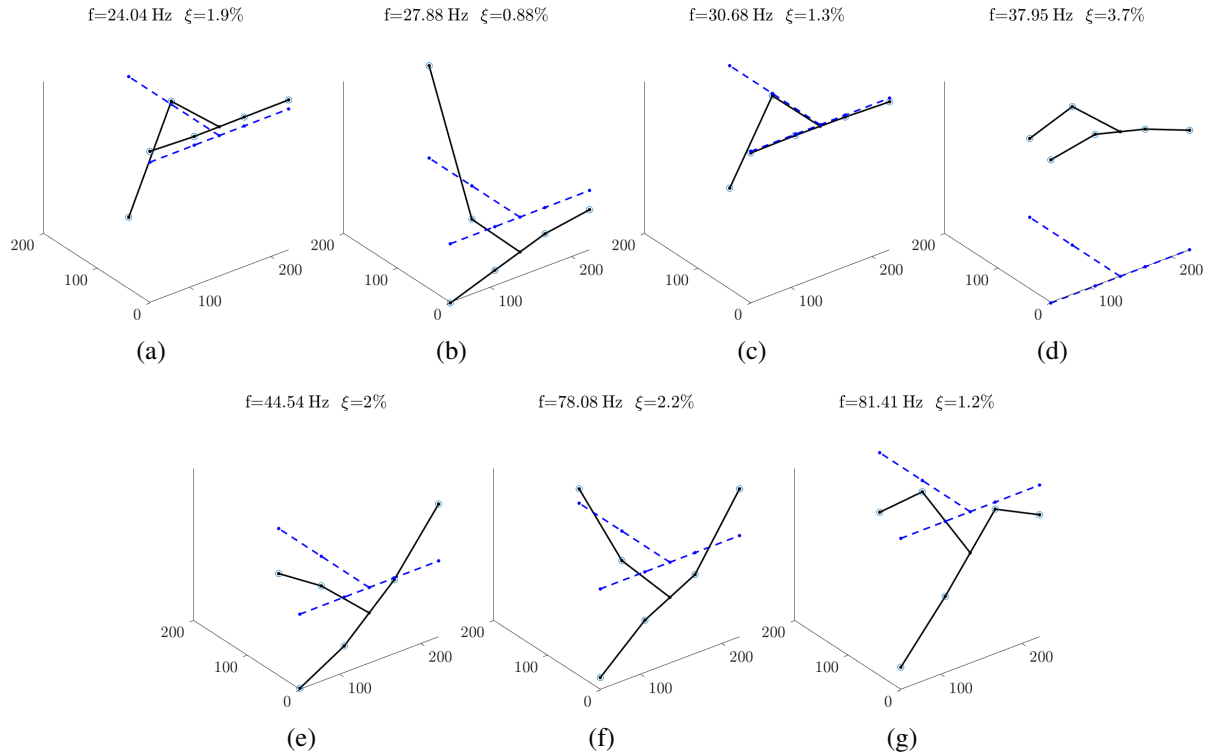


Figure 3: 3d representation of the experimental mode shapes corresponding to the undamaged phase.

Fig.3 shows a 3d representation of the experimental mode shapes corresponding to the undamaged phase. Additionally, Fig.4 shows a 2d representation of the experimental mode shapes corresponding to the undamaged phase. This representation helps us understand the in-plane distortion of the T-shaped element. The first mode at 24.04 Hz is characterized by more evident distortion at the joint. Therefore, its tracking might be the most informative approach to assess the effects of damages.

## 3 RESULTS AND DISCUSSION

Tab.1 resumes all the results of the dynamic identification for the eight considered stages. It collects the natural frequencies and damping values estimated in the undamaged phase (0) and the seven considered damage levels, labelled progressively from 1 to 7.

Tab.2 shows with a colour formating the Modal Assurance Distribution Matrices (MAC), obtained by comparing the modes estimated in two consecutive phases, namely states 0-1, 1-2, 2-3, 3-4, 4-5, 5-6, and 6-7.

The main aspects arising from the observation of the experimental data resumed in Tabs.1 and Tab.2 are:

- The progression of damage within the RC joint does not allow carrying out a modal tracking. The presence of damage significantly modifies the mode shape, as highlighted

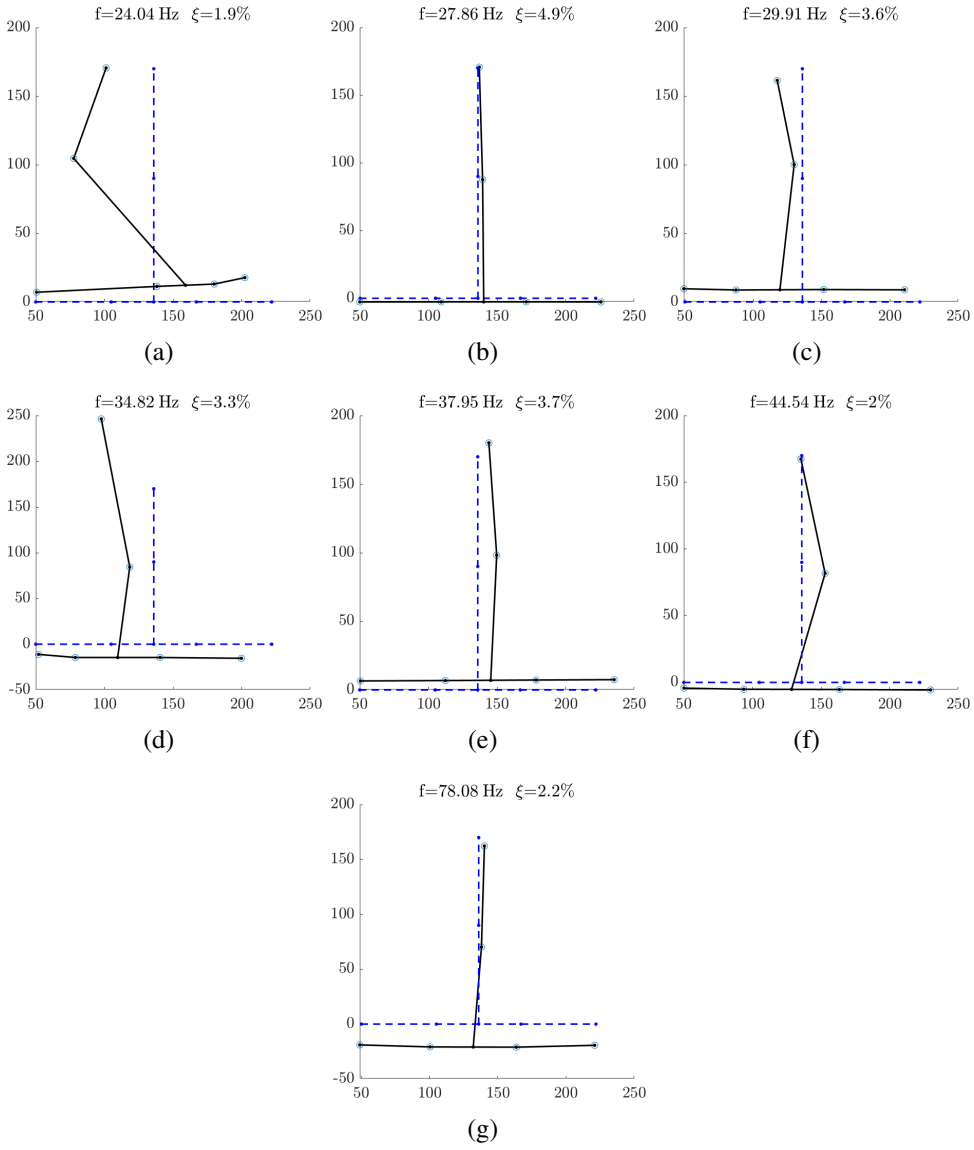


Figure 4: 2d representation of the experimental mode shapes corresponding to the undamaged phase.

Table 1: Natural frequencies and damping values estimated in the undamaged phase (0) and the seven considered damage levels.

| | Damage level | | | | | | | |
|---|---|---|---|---|---|---|---|---|
| | 0 | 1 | 2 | 3 | 4 | 5 | 6 | 7 |
| $f_1$ | 24.04 | 24.52 | 24.03 | 24.21 | 23.74 | 20.71 | 18.51 | 12.67 |
| $f_2$ | 27.86 | 33.04 | 32.59 | 33.40 | 33.43 | 31.29 | 19.61 | 26.07 |
| $f_3$ | 29.91 | 37.30 | 37.38 | 38.60 | 39.25 | 39.86 | 32.74 | 32.35 |
| $f_4$ | 34.82 | 48.44 | 49.21 | 42.26 | 42.20 | 49.34 | 40.00 | 33.32 |
| $f_5$ | 37.95 | 52.15 | 50.25 | 50.12 | 50.10 | 50.60 | 42.59 | 39.18 |
| $f_6$ | 44.54 | 53.29 | 52.68 | 51.99 | 52.26 | 55.35 | 52.27 | 46.00 |
| $f_7$ | | | | 54.96 | 55.28 | 63.57 | 55.20 | 49.06 |
| $f_8$ | 78.08 | 65.99 | 65.58 | 65.21 | 65.39 | 79.81 | 64.89 | 75.01 |
| $f_9$ | 81.41 | 86.98 | 83.53 | 82.17 | 80.19 | 85.07 | 81.15 | 84.24 |
| $\xi_1$ | 1.85 | 0.60 | 1.54 | 0.88 | 1.17 | 1.29 | 2.38 | 0.50 |
| $\xi_2$ | 4.92 | 1.70 | 4.55 | 0.99 | 1.31 | 3.09 | 2.18 | 0.89 |
| $\xi_3$ | 3.60 | 3.46 | 2.96 | 3.86 | 0.61 | 1.61 | 1.29 | 0.62 |
| $\xi_4$ | 3.26 | 3.63 | 1.39 | 4.79 | 4.39 | 2.16 | 2.63 | 2.69 |
| $\xi_5$ | 3.72 | 1.48 | 3.92 | 1.36 | 1.32 | 2.22 | 2.44 | 2.45 |
| $\xi_6$ | 2.02 | 1.10 | 1.55 | 1.33 | 2.26 | 1.89 | 0.40 | 1.21 |
| $\xi_7$ | | | | 0.82 | 1.16 | 1.28 | 1.10 | 2.08 |
| $\xi_8$ | 2.17 | 2.23 | 1.77 | 1.74 | 1.99 | 0.93 | 1.49 | 2.02 |
| $\xi_9$ | 1.21 | 1.41 | 1.77 | 2.73 | 1.08 | 4.12 | 2.09 | 1.64 |

Table 2: Representation of the MAC matrices. Each table shows the MAC computed between the modes of two consecutive states.



by the MAC values, which are generally very low, also when comparing mode shapes between two consecutive states of damage.

- The first modes are the ones characterized by the most evident decrement of the natural frequency. This is because the first mode is a distortion mode of the T-element, the one more affected by a stiffness reduction of the RC joint due to the presence of damage. The natural frequency reduces from almost 24.04 to approximately 12.67 Hz.

- Conversely, the higher modes are not characterized by a manifest in-plane deformation of the T- This is confirmed by the natural frequencies of the higher modes, which are almost independent of the damage phase. Paradoxically, the natural frequency of the last mode rises from 81 to 84 due to possible variations of the boundary conditions associated with the last damage phase.

## 4 CONCLUSIONS

This paper presents the results of an experimental campaign aiming at characterizing the effects of damage on an RC joint, tested quasi-statically in terms of modal parameters. The authors identified seven stages of the quasi-static test of the joint for carrying out seven ambient vibration tests. The supposed goal was to make a sort of modal tracking, i.e. following the evolution of the mode shape of the specimen as the damage progresses inside the node. However, the experimental tests highlighted two aspects. Only the modes associated with a significant distortion component manifest a frequency reduction associated with a stiffness loss in the RC joint. The second aspect relates to the difficulty in modal tracking. The mode shapes exhibit a significant variation between the different phases of damage. Accordingly, it is nearly impossible to state which mode became what since the modes modified substantially, yielding MAC values lower than 0.4, approximately. The frequency of the first distortion mode reduced from nearly 24 to 12 Hz. Future research efforts will assess the relationship between the frequency and stiffness loss of the joint through FE numerical modelling.

## REFERENCES

[1] Rocco Alaggio, Angelo Aloisio, Elena Antonacci, and Riccardo Cirella. Two-years static and dynamic monitoring of the santa maria di collemaggio basilica. *Construction and Building Materials*, 268:121069, 2021.

[2] Michele Angiolilli, Amedeo Gregori, Roberto Tonelli, Claudio Tonelli, Edoardo Ciuffetelli, and Alfredo Peditto. Structural performance of unreinforced full-scale façade concrete beam-column joint under cyclic load. *Procedia Structural Integrity*, 44:870–877, 2023.

[3] Rodrigo Astroza, Hamed Ebrahimian, Joel P Conte, José I Restrepo, and Tara C Hutchinson. Statistical analysis of the modal properties of a seismically-damaged five-story rc building identified using ambient vibration data. *Journal of Building Engineering*, 52:104411, 2022.

[4] R. Ceravolo, G. Coletta, G. Miraglia, and F. Palma. Statistical correlation between environmental time series and data from long-term monitoring of buildings. *Mechanical Systems and Signal Processing*, 152, 2021. cited By 17.

[5] M. Dilena and A. Morassi. Dynamic testing of a damaged bridge. *Mechanical Systems and Signal Processing*, 25(5):1485–1507, 2011. cited By 84.

[6] M. Fraser, A. Elgamal, X. He, and J.P. Conte. Sensor network for structural health monitoring of a highway bridge. *Journal of Computing in Civil Engineering*, 24(1):11–24, 2010. cited By 95.

[7] C. Gentile, A. Ruccolo, and F. Canali. Continuous monitoring of the milan cathedral: dynamic characteristics and vibration-based shm. *Journal of Civil Structural Health Monitoring*, 9(5):671–688, 2019. cited By 20.

[8] H. Hien and A. Mita. Damage identification of full scale four-story steel building using multi-input multi-output models. volume 7981, 2011. cited By 4.

[9] O. Huth, G. Feltrin, J. Maeck, N. Kilic, and M. Motavalli. Damage identification using modal data: Experiences on a prestressed concrete bridge. *Journal of Structural Engineering*, 131(12):1898–1910, 2005. cited By 160.

[10] X. Ji, G.L. Fenves, K. Kajiwara, and M. Nakashima. Seismic damage detection of a full-scale shaking table test structure. *Journal of Structural Engineering*, 137(1):14–21, 2011. cited By 79.

[11] R.G. Lauzon and J.T. DeWolf. Ambient vibration monitoring of a highway bridge undergoing a destructive test. *Journal of Bridge Engineering*, 11(5):602–610, 2006. cited By 25.

[12] F. Magalhães, A. Cunha, and E. Caetano. Online automatic identification of the modal parameters of a long span arch bridge. *Mechanical Systems and Signal Processing*, 23(2):316–329, 2009. cited By 365.

[13] B. Moaveni, X. He, J.P. Conte, M. Fraser, and A. Elgamal. Uncertainty analysis of voigt bridge modal parameters due to changing environmental condition. *International Conference on Modal Analysis*, 2009. cited By 1.

[14] B. Moaveni, X. He, J.P. Conte, J.I. Restrepo, and M. Panagiotou. System identification study of a 7-story full-scale building slice tested on the ucsd-nees shake table. *Journal of Structural Engineering*, 137(6):705–717, 2011. cited By 115.

[15] R.D. Nayeri, S.F. Masri, R.G. Ghanem, and R.L. Nigbor. A novel approach for the structural identification and monitoring of a full-scale 17-story building based on ambient vibration measurements. *Smart Materials and Structures*, 17(2), 2008. cited By 145.

[16] C. Pan, X. Ye, and L. Mei. Improved automatic operational modal analysis method and application to large-scale bridges. *Journal of Bridge Engineering*, 26(8), 2021. cited By 6.

[17] R.S. Pappa, G.H. James III, and D.C. Zimmerman. Autonomous modal identification of the space shuttle tail rudder. *Journal of Spacecraft and Rockets*, 35(2):163–169, 1998. cited By 66.

[18] Dag Pasquale Pasca, Angelo Aloisio, Marco Martino Rosso, and Stefanos Sotiropoulos. Pyoma and pyoma_gui: A python module and software for operational modal analysis. *SoftwareX*, 20:101216, 2022.

[19] B. Peeters and G. De Roeck. One-year monitoring of the z24-bridge: Environmental effectsversus damage events. *Earthquake Engineering and Structural Dynamics*, 30(2):149–171, 2001. cited By 821.

[20] Bart Peeters and Guido De Roeck. Reference-based stochastic subspace identification for output-only modal analysis. *Mechanical systems and signal processing*, 13(6):855–878, 1999.

[21] C. Rainieri and G. Fabbrocino. Automated output-only dynamic identification of civil engineering structures. *Mechanical Systems and Signal Processing*, 24(3):678–695, 2010. cited By 161.

[22] E. Reynders, J. Houbrechts, and G. De Roeck. Fully automated (operational) modal analysis. *Mechanical Systems and Signal Processing*, 29:228–250, 2012. cited By 311.

[23] D.M. Siringoringo, Y. Fujino, and T. Nagayama. Dynamic characteristics of an overpass bridge in a full-scale destructive test. *Journal of Engineering Mechanics*, 139(6):691–701, 2013. cited By 27.

[24] F. Ubertini, G. Comanducci, N. Cavalagli, A. Laura Pisello, A. Luigi Materazzi, and F. Cotana. Environmental effects on natural frequencies of the san pietro bell tower in perugia, italy, and their removal for structural performance assessment. *Mechanical Systems and Signal Processing*, 82:307–322, 2017. cited By 135.

COMPDYN 2023
9th ECCOMAS Thematic Conference on
Computational Methods in Structural Dynamics and Earthquake Engineering
M. Papadrakakis, M. Fragiadakis (eds.)
Athens, Greece, 12-–14 June 2023

# PROPAGATION OF EPISTEMIC UNCERTAINTY IN MODAL PARAMETERS AND ITS INFLUENCE ON DAMAGE

**Saranika Das**[1], **and Koushik Roy**[1]

[1]Department of Civil and Environmental Engineering
Indian Institute of Technology Patna, India
e-mail: koushik@iitp.ac.in

**Abstract.** *The physical properties of a real structure are stochastic in nature. Mass density, cross-sectional area, Poisson's ratio, modulous of elasticity, etc., develop non-homogeneity in real systems due to spatial distribution. These parameter uncertainties propagate into modal responses involved in structural health monitoring techniques. A detailed literature survey has been performed to identify the suitable probability distribution recommended for defining material uncertainty. Although Gaussian distribution cannot replicate realistic material behaviour, its explicit implementation makes it prevalent. However, based on the principle of maximum entropy, gamma distribution is the appropriate recommendation among all non-Gaussian continuous distributions ranging [0, $\infty$). In this study, elastic modulous has been considered the primary source of uncertainty. Karhunen–Loève (KL) expansion has been adapted to discretize the stochastic field to determine spectral stiffness of a multi-damaged cantilever bar. Closed-form orthogonal pairs of eigensolutions considering exponential covariance function have been derived. The uncertainty propagation in modal properties have been estimated in both damaged and undamaged system. Extensive simulation studies have been performed to evaluate the effectiveness of the present study.*

**Keywords:** Uncertainty propagation, Spectral element method, Karhunen–Loève (KL) expansion, Damage quantification.

## 1 INTRODUCTION

The term uncertainty or stochasticity is described as the multiple outcomes of repeated measurements that do not follow any pattern [1]. The sources of uncertainty cannot be limited. Mathematical models, model parameters, numerical algorithms, measurement data are the key sources of uncertainty. In case of uncertainty propagation, tools are developed to obtain the probabilistic descriptions of dynamic responses of any structure depending on the given probabilistic description of system parameters. However, uncertainty quantification is the inverse process in which results obtained from large dataset of identical structures are used to estimate the probability density function (PDF) of the unknown structural parameters. The objectives of stochastic study include understanding the uncertainties inherited by a system, prediction of responses due to various uncertainties, quantification of the confidence interval and minimizing unexpected failures. In this study, modulous of elasticity has been considered as the main source of uncertainty. Now material property being a continuous system parameter, continuous PDFs have been preferred over discrete PDFs for uncertainty modelling.
A detailed literature review of more than hundred science citation indexed (Sci) articles and other documents published in the last two decades (2000-2022) has been performed to identify the best possible PDF recommended for defining material uncertainty in any stochastic study. From Fig. 1(a) it can be observed that priority has been provided to Gaussian, log normal, Weibull and gamma distributions in stochastic modelling of material properties. As there is

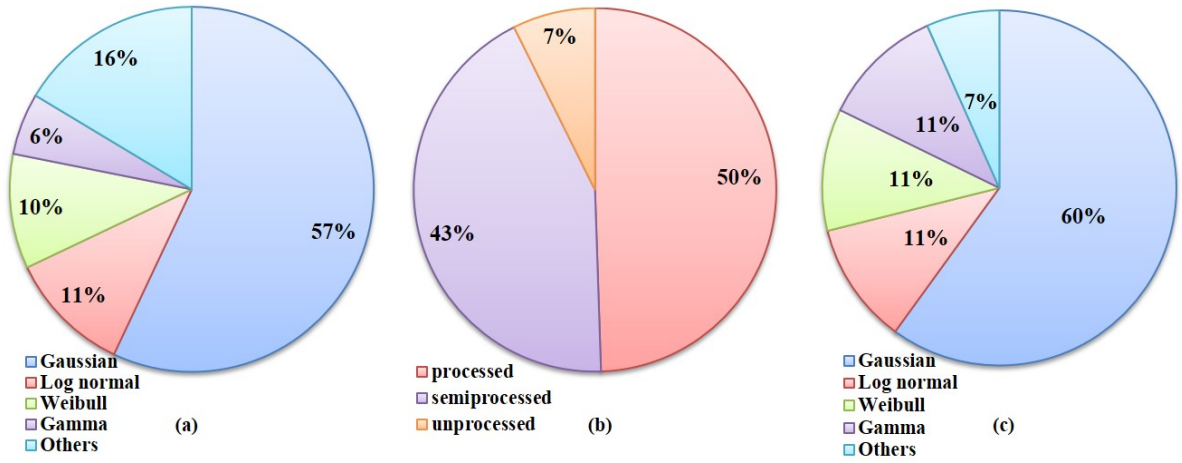


Figure 1: Literature survey (2000-2022): (a) PDFs considered for modelling material uncertainty, (b) types of engineering material and (c) PDFs considered for modelling processed material uncertainty.

no straightforward recommendation of a particular PDF for material uncertainty modelling, to perceive clarity, the dataset of articles has been differentiated into processed or manufactured materials (e.g. steel, aluminium, metals, etc.), semi-processed items (like composites) and unprocessed materials (i.e. concrete, bamboo, etc.). It can be observed from Fig. 1(b) that most of the stochastic study considering material uncertainty has been performed on processed and semi-processed materials. Again, similar trend of adopting various PDFs has been followed as observed in Fig. 1(c) for processed materials. However, there still persists scepticism about the most appropriate PDF for material modelling. The Gaussian distribution function has been prevalently used irrespective of material-type due to its explicit implementation in simulation studies. However, it cannot replicate the realistic behaviour as material property cannot take

negative values and its second moment tends to infinity based on the maximum entropy principle [2]. Various studies considering non-Gaussian distribution functions those are valid between $0$ to $\infty$ have been also performed. The application of both normal and log normal distribution function have been discarded [3] stating that the PDF defining material uncertainty must be bounded along with higher moments available. The auto-correlation function must be non-negative and monotonically decreasing function. An approach has been suggested considering beta distribution due to its large variety of shapes. Again gamma distribution has been recommended [4] as it includes other popular distributions like exponential, chi-squared, and Erlang distribution, etc. However, it has been concluded that similar approach may be followed for normal as well as log normal distributions such that it diminishes the importance of considering gamma distribution for the study. Another widely used PDF is the Weibull distribution. Although it has been considered in the studies of ductile materials (e.g. steel) [5] in the initial years of literature considered. However in recent studies, it has been mainly implemented in modelling natural fibers [6] like jute, coconut and for brittle materials [12] especially. Therefore, the Weibull distribution has been discarded from the list of priority of the stochastic study of ductile material. Now in the recent research articles, it has been observed that gamma distribution has been preferred for material uncertainty modelling. The principle of maximum entropy [2] stated that the probability distribution for a positive-valued random variable with a reparameterization leads to gamma distribution. Thus among all the various types of PDFs involved in defining material uncertainty, gamma distribution is the most suitable recommendation to the researchers for the future stochastic studies.

If values of a real variable associated with the outcome of a random experiment such that its values depend on chance, it is called a random variable or a stochastic variable or a variate. If a random variable takes a finite set of values, it is called a discrete variate and if it assumes infinite number of uncountable values, it is called a continuous variate [7]. A random variable is defined by its distribution function and is characterized by its mean and variance. When the quantities vary temporally or spatially, then random process or random field comes into play. Now, any random field can be described as a combination of infinite-dimensional random variables. The vast dimensional problem is difficult to handle by simulation. Thus the dimension need to be truncated to a finite dimension such that the truncated random process turn out to be similar as the original random process with maximum accuracy and minimum computational cost. KL expansion is one of the method for approximation of a random process. It decomposes a random field into finite number of random variables depending on the covariance function considered [8]. In brief, KL expansion discretizes a random process into a series of finite number of orthogonal pairs of eigenvalues and corresponding eigenvectors of the concerned covariance function. This is a sophisticated method. The eigenvalues obtained are gradually decaying such that considering only the higher eigenvalues will estimate the approximated sample space.

In this study, the spectral mass and stiffness of a multi-damaged cantilever bar have been derived. Followed by a detailed mathematical background of KL expansion and estimation of eigensolutions for recreating random field. The spectral stiffness for stochastic condition have been also derived. Further, the application of KL expansion has been described through simulation studies for undamaged cantilever bar considering Gaussian and gamma distribution to evaluate the effectiveness of the present study.

## 2 MATHEMATICAL ILLUSTRATION ON A CANTILEVER BAR

### 2.1 Deterministic

An axially vibrating cantilever prismatic bar of length $L$ has been considered as an assembly of $N$ discrete spectral elements of length $\epsilon$ each as shown in Fig. 2. The notches between each element indicate the non-propagating cracks. Based on Castigliano's theorem and laws of fracture mechanics, the damages between any $p^{\text{th}}$ and $(p+1)^{\text{th}}$ element can be defined by crack flexibility ($\Theta_p$). If there is no damage in between any two segments then the corresponding crack flexibility ($\Theta_p$) is considered to be 0. Therefore, when $\Theta_p$= 0 $\forall$ $p$ =1,2,$\cdots$ $(N-1)$, then the formulation represented undamaged system and for non-zero $\Theta_p$ the formulation modifies to damaged system. The spectral deformation ($\widehat{u}_p(x,\omega)$) at any location of the $p^{\text{th}}$ spectral element of the system can be given as,

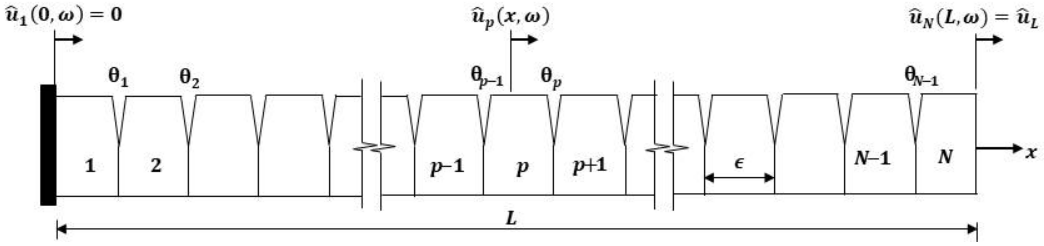


Figure 2: One end restrained axially vibrating prismatic bar having multiple damages $(\Theta_1, \Theta_2, \ldots, \Theta_p, \ldots, \Theta_{N-1})$ uniformly discretized into $N$ spectral elements

$$\widehat{u}_p(x,\omega) = \begin{Bmatrix} e^{ikx} & e^{-ik(p\epsilon - x)} \end{Bmatrix} \begin{Bmatrix} a_{2p-1} \\ a_{2p} \end{Bmatrix} = s_p(x,\omega)\widehat{a}_p \quad , \text{for } (p-1)\epsilon \leq x \leq p\epsilon$$

where, $x$ is distance of any location on the bar from the fixed-end and $k = \frac{\omega}{c}$ is wavenumber corresponding to longitudinal wave propagation. $s_p(x,\omega)$ and $\widehat{a}_p$ are spectral shape function matrix and coefficient matrix respectively corresponding to the $p^{\text{th}}$ element. Here, $i$ represents unit imaginary number $\sqrt{-1}$. The spectral deformation $\widehat{u}(x,\omega)$ of the total system can be represented in a matrix form as,

$$\widehat{u}(x,\omega) = \begin{Bmatrix} \widehat{u}_1(x,\omega) \\ \vdots \\ \widehat{u}_p(x,\omega) \\ \vdots \\ \widehat{u}_N(x,\omega) \end{Bmatrix} = \begin{bmatrix} s_1(x,\omega) & \cdots & 0 \\ \vdots & \ddots & \vdots \\ \vdots & s_p(x,\omega) & \vdots \\ \vdots & \ddots & \vdots \\ 0 & \cdots & s_N(x,\omega) \end{bmatrix} \begin{Bmatrix} \widehat{a}_1 \\ \vdots \\ \widehat{a}_p \\ \vdots \\ \widehat{a}_N \end{Bmatrix} = S(x,\omega)\widehat{a} \tag{1}$$

To obtain the coefficient matrix $\widehat{a}$, the boundary and compatibility conditions need to be applied. For a fixed-free system, the boundary conditions include

$$\widehat{u}_1(0,\omega) = 0 \tag{2a}$$
$$\widehat{u}_N(N\epsilon,\omega) = \widehat{u}_L \tag{2b}$$

Again, for any intermediate damage between elements $p$ and $(p+1)$, the compatibility equations are given as,

$$\widehat{u}_{p+1}(p\epsilon,\omega) - \widehat{u}_p(p\epsilon,\omega) = \Theta_p \frac{\partial \widehat{u}_p(p\epsilon)}{\partial x} \tag{3a}$$

$$\frac{\partial \widehat{u}_p(p\epsilon)}{\partial x} = \frac{\partial \widehat{u}_{p+1}(p\epsilon)}{\partial x} \tag{3b}$$

where, $\Theta_p$ indicates crack flexibility corresponding to damage between $p^{\text{th}}$ and $(p+1)^{\text{th}}$ element. Combining Eqs. (1-3), the nodal spectral displacements $\widehat{u}_{\text{node}}$ can be expressed as

$$\widehat{G}\,\widehat{a} = \widehat{u}_{\text{node}} \tag{4}$$

where, $\widehat{a} = \{\widehat{a}_1, \widehat{a}_2, \cdots, \widehat{a}_{2N-1}, \widehat{a}_{2N}\}^T_{2N\times 1}$ , $\widehat{u}_{\text{node}} = \{0, 0, \cdots, 0, \widehat{u}_L\}^T_{2N\times 1}$ and $\widehat{G}$ can be expressed as,

$$\begin{bmatrix}
1 & e^{-ik\epsilon} & 0 & 0 & 0 & \cdots & \cdots & \cdots & \cdots & \cdots & \cdots & \cdots & 0 \\
(ik\Theta_1-1)e^{-ik\epsilon} & -(ik\Theta_1+1) & e^{-ik\epsilon} & e^{-ik\epsilon} & 0 & \cdots & \cdots & \cdots & \cdots & \cdots & \cdots & \cdots & 0 \\
-ike^{-ik\epsilon} & ik & ike^{-ik\epsilon} & -ike^{-ik\epsilon} & 0 & \cdots & \cdots & \cdots & \cdots & \cdots & \cdots & \cdots & \vdots \\
\ddots & \ddots & \ddots & \ddots & \ddots & \ddots & \ddots & \ddots & \ddots & \ddots & \ddots & \ddots & \vdots \\
0 & \cdots & \cdots & \cdots & 0 & (ik\Theta_p-1)e^{-ikp\epsilon} & -(ik\Theta_p+1)e^{-ikp\epsilon} & e^{-ik\epsilon} & 0 & \cdots & \cdots & \cdots & 0 \\
\vdots & \cdots & \cdots & \cdots & 0 & -ike^{-ikp\epsilon} & ik & ike^{ikp\epsilon} & ike^{ik\epsilon} & 0 & \cdots & \cdots & \vdots \\
\vdots & \cdots & \cdots & \cdots & \cdots & \ddots & \ddots & \ddots & \ddots & \ddots & \ddots & \ddots & 0 \\
\vdots & \cdots & \cdots & \cdots & \cdots & 0 & \cdots & \cdots & 0 & (ik\Theta_{N-1}-1)e^{-ik(N-1)\epsilon} & -(ik\Theta_{N-1}+1)e^{-ik(N-1)\epsilon} & e^{-ik\epsilon} & \\
\vdots & \cdots & \cdots & \cdots & \cdots & \cdots & \cdots & \cdots & 0 & -ike^{-ik(N-1)\epsilon} & ik & ike^{ik(N-1)\epsilon} & ike^{ik\epsilon} \\
0 & \cdots & \cdots & \cdots & \cdots & \cdots & \cdots & \cdots & \cdots & \cdots & 0 & e^{-ikN\epsilon} & 1
\end{bmatrix}$$

$\widehat{G}$ has been introduced to establish a relationship between the spectral nodal displacements under boundary conditions $\widehat{u}_{\text{node}}$ and the constant coefficient matrix $\widehat{a}$. The expression of $\widehat{a}$ can be obtained from Eq. (4) as,

$$\widehat{a} = \widehat{G}^{-1}\,\widehat{u}_{\text{node}} = \widehat{\mathcal{F}}\,\widehat{u}_{\text{node}} \tag{5}$$

Applying boundary conditions on $\widehat{\mathcal{F}}$, the spectral stiffness matrix $\widehat{K}(\omega)$ of a multi-damage cantilever bar can be obtained as,

$$\widehat{K}(\omega) = EA_0\widehat{\mathcal{F}}(:,2N)^T \begin{bmatrix}
\int_0^{\epsilon} {s_1'}^T(x,\omega)s_1'(x,\omega)dx & \cdots & 0 \\
\vdots & \ddots & \vdots \\
\vdots & \int_{(p-1)\epsilon}^{p\epsilon} {s_p'}^T(x,\omega)s_p'(x,\omega)dx & \vdots \\
\vdots & \ddots & \vdots \\
0 & \cdots & \int_{(N-1)\epsilon}^{L} {s_N'}^T(x,\omega)s_N'(x,\omega)dx
\end{bmatrix} \widehat{\mathcal{F}}(:,2N) \tag{6}$$

## 2.2 Stochastic

### 2.2.1 Mathematical background of KL expansion

Any random process $S(x,\theta)$ with non-zero mean can be expressed as a sum of a deterministic part that contains the mean value $\mu_S(x) = \mathbb{E}\{S(x,\theta)\}$ of the concerned random process and a zero mean random process $Y(x,\theta)$ [9], and is given as

$$S(x,\theta) = \mu_S(x) + Y(x,\theta) \tag{7}$$

Here, $x$ is a function of position vector with the domain $D$ and $\theta$ is element of sample space of random events $\Omega$ [10]. The covariance function and the correlation function of $Y(x,\theta)$ is same as the covariance function of $S(x,\theta)$ and is denoted as $C_S(x_1,x_2)$. The simplest form of expressing a stochastic process is by using random polynomials and can be expressed as

$$f(x,\theta) = \sum_{k=0}^{q} \xi_k(\theta) x^k \tag{8}$$

where $q$ is a finite value, $\xi_k$ are uncorrelated random coefficients and $x^k$ represents each element of parameter space. These random polynomials are difficult to analyze. To simplify the study, stationary processes are considered and mathematical background for random polynomials have been modified to cosine field. The representation of a complex random process as a summation of simple ones is complicated. Thus, the idea of orthogonal expansions have been introduced. Let $\{\varphi_n(x)\}$ be a set of functions on parameter space $D$ and $\{\xi_n(\theta)\}$ be a set of uncorrelated random variables. The zero-mean random process can be written as

$$Y(x,\theta) = \sum_{n=1}^{\infty} \xi_n(\theta)\varphi_n(x) \tag{9}$$

The covariance function of the concerned zero-mean random process can be obtained as

$$\begin{aligned} C_s(x_1,x_2) &= \mathbb{E}\{Y(x_1,\theta)Y(x_2,\theta)\} \\ &= \sum_{m=1}^{\infty}\sum_{n=1}^{\infty} \varphi_m(x_1)\varphi_n(x_2)\mathbb{E}\{\xi_m(\theta)\xi_n(\theta)\} = \sum_{n=1}^{\infty} \varphi_n(x_1)\varphi_n(x_2) \end{aligned} \tag{10}$$

The above equation is obtained by considering the orthonormality property of $\{\xi_n(\theta)\}_n$, such that they can be considered as Hilbert space basis satisfying $\int \xi_n(\theta)\xi_m(\theta)d\theta = \delta_{mn}$, where $\delta_{mn}$ is the Kronecker delta.
Let the parameter set $D$ be a compact domain such that $\lambda_1 \geq \lambda_2 \geq ...$ and $\psi_1, \psi_2, ...$ are the ordered negative eigenvalues and corresponding normalized eigenfunctions of the covariance function $C_s(x_1,x_2)$, respectively. The space of square integrable functions on $D$ to itself can be given in the integral form of Fredholm integral equation of second kind. This can be solved by eigenvalue and corresponding normalized eigenfunction pairs. The integral equation is given as

$$\int_D C_s(x_1,x_2)\psi_n(x_1)dx_1 = \lambda_n\psi_n(x_2) \tag{11}$$

The KL expansion form can be achieved by applying Mercer's theorem. If the covariance function is symmetric, bounded and positive semi-definite then it can be expressed in uniformly convergent series expansion as

$$C_S(x_1,x_2) = \sum_{n=1}^{\infty} \lambda_n\psi_n(x_1)\psi_n(x_2) \tag{12}$$

An expression for $\xi_n$ can be obtained by eliminating $C_S(x_1,x_2)$ from Eqs. (10) and (12), and is given as

$$\varphi_n = \sqrt{\lambda_n}\psi_n \tag{13}$$

Substituting Eq. (13) in (9), the KL expansion of $Y(x,\theta)$ can be obtained as

$$Y(x,\theta) = \sum_{n=1}^{\infty} \xi_n(\theta)\sqrt{\lambda_n}\psi_n(x) \tag{14}$$

provided $\xi_n(\theta)$ are independent and identically distributed and follows Gaussian distribution i.e. $\mathcal{N}(0,1)$. The final expression of a stochastic process in infinite terms of KL expansion is given as

$$S(x,\theta) = \mu_S(x) + \sum_{n=1}^{\infty} \xi_n(\theta)\sqrt{\lambda_n}\psi_n(x) \tag{15}$$

If the parameter space is replaced by a finite number of points then the infinite series expansion can be reduced to a truncated series of eigensolutions of the concerned covariance function. The analytical solution for all covariance functions are not available. However, the eigenvalue problems can be solved numerically. The beauty of KL expansion is that it can represent a random process by a finite number of terms known as the order ($\overline{N}$) of the KL expansion. The major advantage of the truncation is that it optimizes the truncation error for a given order. The final expression of a stochastic process is given by

$$\widehat{S}(x,\theta) = \mu_S(x) + \sum_{n=1}^{\overline{N}} \xi_n(\theta)\sqrt{\lambda_n}\psi_n(x) \tag{16}$$

### 2.2.2 Estimation of eigensolutions

Consider a one dimensional exponential decaying Gaussian covariance function. The covariance function is given by

$$C(x_1,x_2) = e^{\frac{-|x_1-x_2|}{b}} \tag{17}$$

where $b$ is the correlation length. It is assumed that the analytical solution will be in the range $[-a < x < a]$ such that the mean is zero and produces the random field following Eq. (15). Based on Eq. (11), the Fredholm integral equation can be written as

$$\int_{-a}^{a} e^{-c|x_1-x_2|}\psi(x_2)dx_2 = \lambda\psi(x_1) \tag{18}$$

Considering $c = \frac{1}{b}$. Eq. (18) can be rewritten as

$$\int_{-a}^{x_1} e^{-c(x_1-x_2)}\psi(x_2)dx_2 + \int_{x_1}^{a} e^{-c(x_2-x_1)}\psi(x_2)dx_2 = \lambda\psi(x_1) \tag{19}$$

The first and second order derivative of the eigenfunctions with respect to $x_1$ can be obtained by applying Leibniz integral rule. Differentiating Eq. (19) twice with respect to $x_1$ and rearranging, the expression can be obtained as,

$$\psi''(x_1) = \frac{-2c+\lambda c^2}{\lambda}\psi(x_1) = \omega_k^2\psi(x_1) \ , \left(\text{let } \omega_k^2 = \frac{-2c+\lambda c^2}{\lambda}\right) \tag{20}$$

Now, substituting $x_1 = -a$ and $x_1 = a$ and solving, the eigenvalues can be expressed as

$$\left[\omega_k^2 \geq 0; \tan(\omega_k a) = \frac{c}{\omega_k}\right] \cup \left[\omega_k^2 \geq 0; \tan(\omega_k a) = -\frac{\omega_k}{c}\right] \tag{21}$$

The graphical solution of Eq. (21) shows that $\tan(\omega_k a)$ takes decreasing sequence of positive and negative numbers for odd and even sequence of $\omega_k a$ respectively. The odd sequence corresponds to $\tan(\omega_k a) = \frac{c}{\omega_k}$ and the even sequence corresponds to $\tan(\omega_k a) = -\frac{\omega_k}{c}$. The eigenvalues can be obtained after determining $\omega_k$ by using

$$\lambda_j = \frac{2c}{c^2 - {\omega_k}_j^2}, j = 1, 2, 3 \ldots \tag{22}$$

The odd sequence of eigenvalues are obtained from,

$$\psi_j(x) = C_o \cos(\omega_{kj} x) \tag{23}$$

where $C_o$ is a constant such that it satisfies

$$\int_{-a}^{a} C_o^2 \cos^2(\omega_{kj} x) dx = 1 \tag{24}$$

Thus normalizing the eigenfunction gives

$$C_o = \frac{1}{\sqrt{a + \frac{\sin(2\omega_{kj} a)}{2\omega_{kj}}}} \tag{25}$$

The corresponding eigenfunction is obtained as,

$$\psi_{jo}(x) = \frac{\cos(\omega_{kj} x)}{\sqrt{a + \frac{\sin(2\omega_{kj} a)}{2\omega_{kj}}}}, j = 1, 3, 5 \ldots \tag{26}$$

Similarly the even eigenvalues can be obtained from,

$$\psi_j(x) = C_e \sin(\omega_{kj} x) \tag{27}$$

where $C_e$ is a constant such that it satisfies

$$\int_{-a}^{a} C_e^2 \sin^2(\omega_{kj} x) dx = 1 \tag{28}$$

Thus normalizing the eigenfunction gives

$$C_e = \frac{1}{\sqrt{a - \frac{\sin(2\omega_{kj} a)}{2\omega_{kj}}}} \tag{29}$$

The corresponding eigenfunction is obtained as,

$$\psi_{je}(x) = \frac{\sin(\omega_{kj} x)}{\sqrt{a - \frac{\sin(2\omega_{kj} a)}{2\omega_{kj}}}}, j = 2, 4, 6 \ldots \tag{30}$$

However for non-Gaussian stochastic field, the KL expansion can be applicable by modifying through memoryless transformation [11] involving cumulative distribution function of both the underlying Gaussian and target non-Gaussian distributions.

### 2.2.3 Stochastic expressions

Stochastic formulation of a vibrating rod is similar to the deterministic formulation but parameter like cross-section area ($A_0$), mass density ($\rho$), and Young's modulous of elasticity ($E$) may be assumed as spatially distributed random variables. The spectral stiffness for a cantilever bar-type structure considering material uncertainty can be expressed as

$$\widehat{K}_s(\omega,\theta) = \widehat{K}(\omega) + \varepsilon_1 \sum_{j=1}^{\overline{N}} \xi_{Kj}(\theta)\sqrt{\lambda_{Kj}}\widehat{K}_j(\omega) \tag{31}$$

where $\varepsilon_1$ indicates deterministic constant ranging between 0 and 1. $\widehat{K}(\omega)$ is the deterministic part as derived in Eq. (6). $\overline{N}$ is the number of terms of the truncated series in the KL expansion while $\xi_{Kj}(\theta)$ denotes uncorrelated Gaussian random variables with zero mean and unit standard deviation. Now based on the eigenvalues ($\lambda_{Kj}$) along with even and odd eigenfunctions i.e. Eqs. (26) and (30), the expressions of $\widehat{K}_j(\omega)$ can be obtained as,

$$\widehat{K}_j(\omega) = EA_0\widehat{\mathcal{F}}(:,2N)^T \begin{bmatrix} \int_0^{\epsilon} \psi_j {s_1'}^T(x,\omega)s_1'(x,\omega)dx & \cdots & 0 \\ \vdots & \ddots & \vdots \\ \vdots & \int_{(p-1)\epsilon}^{p\epsilon} \psi_j {s_p'}^T(x,\omega)s_p'(x,\omega)dx & \vdots \\ \vdots & \ddots & \vdots \\ 0 & \cdots & \int_{(N-1)\epsilon}^{L} \psi_j {s_N'}^T(x,\omega)s_N'(x,\omega)dx \end{bmatrix} \widehat{\mathcal{F}}(:,2N) \tag{32}$$

## 3 NUMERICAL SIMULATION

### 3.1 System specifications

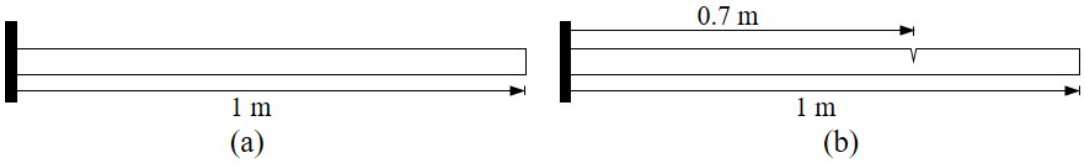


Figure 3: Cantilever bar: (a) undamaged and (b) damaged at 0.7m

Table 1: Details of system specifications

| | |
|---|---|
| length ($L$) | 1 m |
| cross-sectional area ($A_0$) | 0.0003 m$^2$ |
| Young's modulous ($E$) | 200e9 Pa |
| mass density ($\rho_0$) | 7850 kg/m$^3$ |

A cantilever bar has been modelled as shown in Fig 3. The structural specifications have been shown in table 1. Now for the damaged system, damage severity of 20% has been considered at 0.7 m from the fixed-end. Both deterministic as well stochastic analysis have been performed for undamaged and damaged system. In case of stochastic study both Gaussian and gamma distribution have been considered to generate the stochasticity in spectral stiffness of the undamaged system. However, only Gaussian distribution has been analysed in damaged

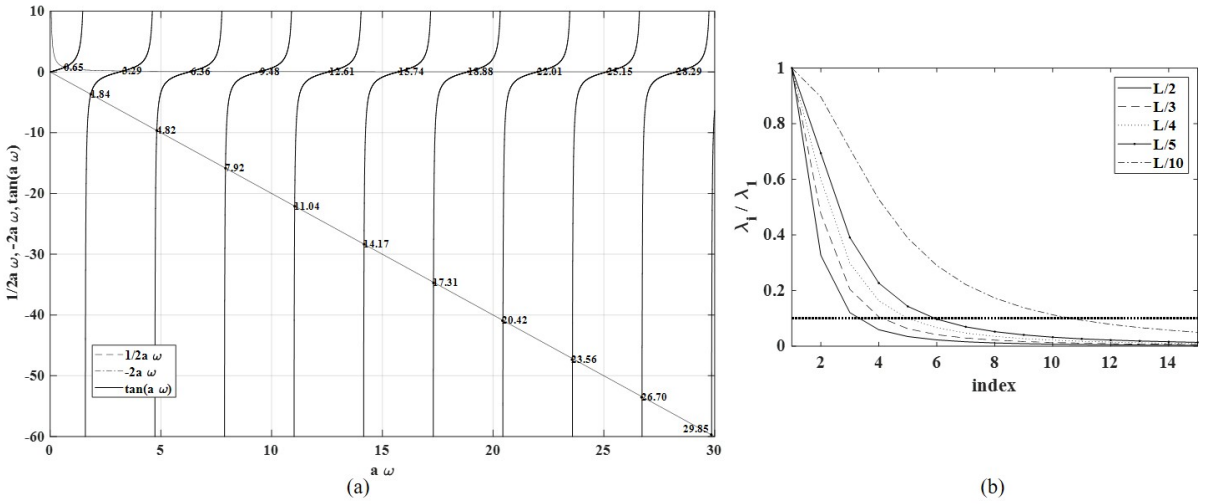


Figure 4: (a) Graphical solution of $\omega_k$ for even and odd terms and (b) Number of eigenvalues required to capture 90% of the stochastic field for different correlation lengths considering unit domain exponential covariance function

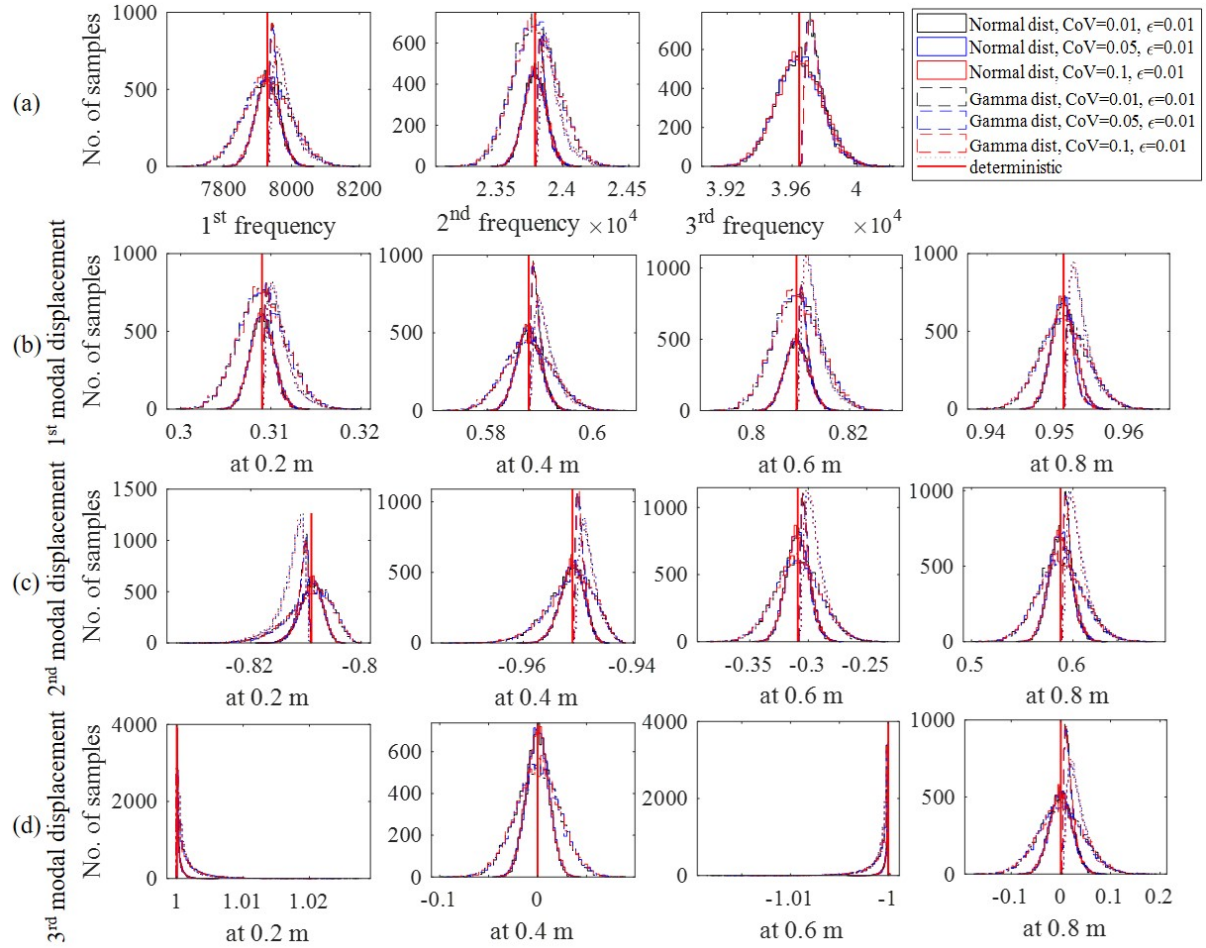


Figure 5: Distribution of responses due to different stochastic conditions in undamaged bar: (a) first three natural frequencies, (b) 1st, (c) 2nd and (d) 3rd modal displacements at 0.2, 0.4, 0.6 and 0.8 m from fixed-end, respectively.

bar. The coefficient of variation (CoV) of 0.01, 0.05 and 0.1 have been considered in the input randomness along with a deterministic constant ($\epsilon_1$) of 0.01 for both undamaged and damaged system. A set of 20 random variables with zero mean and unit standard deviation has been considered for the Gaussian distribution. However for gamma distribution, memoryless transformation has been applied. Considering the correlation length $b = \frac{L}{2}$, the eigensolutions have been obtained as shown in Fig. 4(a). It has been observed from Fig. 4(b) that in case of this system, first 5 eigensolutions can capture 90% of the stochastic field [13]. The simulation study has been performed for 10000 samples for each case of damaged and undamaged system.

| Normal, CoV=0.01, ε=0.01 | mode 1 | | | | | mode 2 | | | | | mode 3 | | | | |
|---|---|---|---|---|---|---|---|---|---|---|---|---|---|---|---|
| | deter. | mean | CoV | skew. | kurt. | deter. | mean | CoV | skew. | kurt. | deter. | mean | CoV | skew. | kurt. |
| frequency | 7928.7 | 7928.9 | 0.0043 | 0.0316 | 2.89 | 23786 | 23787 | 0.0036 | 0.0448 | 2.92 | 39643 | 39644 | 0.0035 | 0.0461 | 2.92 |
| at 0.2 m | 0.30902 | 0.30903 | 0.0042 | 0.0617 | 2.90 | -0.80902 | -0.80914 | -0.0025 | -0.3635 | 3.09 | 1 | 1.0004 | 0.0005 | 2.8027 | 15.06 |
| at 0.4 m | 0.58779 | 0.58781 | 0.0037 | 0.0611 | 2.90 | -0.95106 | -0.95116 | -0.0022 | -0.2681 | 3.02 | 2.32E-16 | -8.61E-05 | -129.54 | -0.0464 | 2.93 |
| at 0.6 m | 0.80902 | 0.80904 | 0.0030 | 0.0600 | 2.90 | -0.30902 | -0.30898 | -0.0312 | 0.0280 | 2.92 | -1 | -1.0002 | -0.00035 | -2.8021 | 15.06 |
| at 0.8 m | 0.95106 | 0.95108 | 0.0018 | 0.0584 | 2.90 | 0.58779 | 0.58789 | 0.0186 | 0.0607 | 2.92 | -4.65E-16 | 0.000172 | 129.59 | 0.046356 | 2.93 |
| Normal, CoV=0.05, ε=0.01 | mode 1 | | | | | mode 2 | | | | | mode 3 | | | | |
| | deter. | mean | CoV | skew. | kurt. | deter. | mean | CoV | skew. | kurt. | deter. | mean | CoV | skew. | kurt. |
| frequency | 7928.7 | 7928.3 | 0.0044 | 0.0249 | 2.98 | 23786 | 23785 | 0.0036 | 0.0421 | 2.99 | 39643 | 39642 | 0.0036 | 0.0422 | 3.00 |
| at 0.2 m | 0.30902 | 0.30901 | 0.0043 | 0.0569 | 2.98 | -0.80902 | -0.80912 | -0.0025 | -0.3798 | 3.18 | 1 | 1.0004 | 0.0005 | 2.7511 | 13.82 |
| at 0.4 m | 0.58779 | 0.58778 | 0.0038 | 0.0562 | 2.98 | -0.95106 | -0.95119 | -0.0022 | -0.2883 | 3.10 | 2.32E-16 | 7.96E-05 | 142.78 | -0.04235 | 3.00 |
| at 0.6 m | 0.80902 | 0.80901 | 0.0030 | 0.0550 | 2.98 | -0.30902 | -0.30912 | -0.0317 | 0.0244 | 2.99 | -1 | -1.0003 | -0.00037 | -2.7506 | 13.81 |
| at 0.8 m | 0.95106 | 0.95105 | 0.0018 | 0.0533 | 2.98 | 0.58779 | 0.58774 | 0.0189 | 0.0590 | 2.99 | -4.65E-16 | -0.00016 | -142.72 | 0.042319 | 3.00 |
| Normal, CoV=0.1, ε=0.01 | mode 1 | | | | | mode 2 | | | | | mode 3 | | | | |
| | deter. | mean | CoV | skew. | kurt. | deter. | mean | CoV | skew. | kurt. | deter. | mean | CoV | skew. | kurt. |
| frequency | 7928.7 | 7928.6 | 0.0044 | 0.0048 | 2.94 | 23786 | 23786 | 0.0037 | 0.0136 | 2.95 | 39643 | 39643 | 0.0036 | 0.0163 | 2.96 |
| at 0.2 m | 0.30902 | 0.30902 | 0.0043 | 0.0363 | 2.94 | -0.80902 | -0.80913 | -0.0025 | -0.3454 | 3.09 | 1 | 1.0004 | 0.0005 | 2.6775 | 13.08 |
| at 0.4 m | 0.58779 | 0.58779 | 0.0038 | 0.0356 | 2.94 | -0.95106 | -0.95118 | -0.0022 | -0.3122 | 3.08 | 2.32E-16 | 3.12E-06 | 3661.9 | -0.01633 | 2.96 |
| at 0.6 m | 0.80902 | 0.80902 | 0.0030 | 0.0345 | 2.94 | -0.30902 | -0.30905 | -0.0319 | -0.0039 | 2.95 | -1 | -1.0003 | -0.00036 | -2.6771 | 13.07 |
| at 0.8 m | 0.95106 | 0.95106 | 0.0018 | 0.0328 | 2.94 | 0.58779 | 0.58781 | 0.0190 | 0.0302 | 2.95 | -4.65E-16 | -6.26E-06 | -3647.8 | 0.016327 | 2.96 |
| gamma, CoV=0.01, ε=0.01 | mode 1 | | | | | mode 2 | | | | | mode 3 | | | | |
| | deter. | mean | CoV | skew. | kurt. | deter. | mean | CoV | skew. | kurt. | deter. | mean | CoV | skew. | kurt. |
| frequency | 7928.7 | 7956 | 0.002233 | 1.3186 | 5.0032 | 23786 | 23858 | 0.001855 | 1.3559 | 5.1817 | 39643 | 39761 | 0.00184 | 1.3585 | 5.1855 |
| at 0.2 m | 0.30902 | 0.31005 | 0.002185 | 1.3374 | 5.086 | -0.80902 | -0.81079 | -0.00144 | -1.5438 | 6.0802 | 1 | 1.0004 | 0.000487 | 3.1876 | 17.984 |
| at 0.4 m | 0.58779 | 0.58955 | 0.001955 | 1.337 | 5.0842 | -0.95106 | -0.94941 | -0.00099 | 1.1392 | 4.2762 | 2.32E-16 | -0.00931 | -0.62409 | -1.3642 | 5.2147 |
| at 0.6 m | 0.80902 | 0.81094 | 0.001548 | 1.3363 | 5.0811 | -0.30902 | -0.30095 | -0.01652 | 1.3471 | 5.1433 | -1 | -1.0002 | -0.00032 | -3.187 | 17.977 |
| at 0.8 m | 0.95106 | 0.9524 | 0.000923 | 1.3353 | 5.0766 | 0.58779 | 0.597 | 0.009572 | 1.3676 | 5.2359 | -4.65E-16 | 0.018616 | 0.62395 | 1.3633 | 5.2098 |
| gamma, CoV=0.05, ε=0.01 | mode 1 | | | | | mode 2 | | | | | mode 3 | | | | |
| | deter. | mean | CoV | skew. | kurt. | deter. | mean | CoV | skew. | kurt. | deter. | mean | CoV | skew. | kurt. |
| frequency | 7928.7 | 7955.9 | 0.002264 | 1.3799 | 5.2696 | 23786 | 23857 | 0.001879 | 1.419 | 5.4576 | 39643 | 39760 | 0.001865 | 1.4223 | 5.4633 |
| at 0.2 m | 0.30902 | 0.31005 | 0.002216 | 1.3998 | 5.3584 | -0.80902 | -0.81079 | -0.00146 | -1.617 | 6.4105 | 1 | 1.0004 | 0.000502 | 3.2861 | 18.107 |
| at 0.4 m | 0.58779 | 0.58954 | 0.001982 | 1.3993 | 5.3565 | -0.95106 | -0.94942 | -0.00101 | 1.1894 | 4.4835 | 2.32E-16 | -0.00928 | -0.63471 | -1.4284 | 5.4945 |
| at 0.6 m | 0.80902 | 0.81093 | 0.00157 | 1.3986 | 5.3531 | -0.30902 | -0.30097 | -0.01673 | 1.4098 | 5.4166 | -1 | -1.0002 | -0.00033 | -3.2856 | 18.101 |
| at 0.8 m | 0.95106 | 0.9524 | 0.000936 | 1.3975 | 5.3483 | 0.58779 | 0.59697 | 0.0097 | 1.4315 | 5.5155 | -4.65E-16 | 0.018549 | 0.63456 | 1.4274 | 5.4892 |
| gamma, CoV=0.1, ε=0.01 | mode 1 | | | | | mode 2 | | | | | mode 3 | | | | |
| | deter. | mean | CoV | skew. | kurt. | deter. | mean | CoV | skew. | kurt. | deter. | mean | CoV | skew. | kurt. |
| frequency | 7928.7 | 7956 | 0.002269 | 1.3365 | 5.0325 | 23786 | 23858 | 0.001888 | 1.3685 | 5.1859 | 39643 | 39761 | 0.001872 | 1.3736 | 5.199 |
| at 0.2 m | 0.30902 | 0.31005 | 0.002221 | 1.3555 | 5.1139 | -0.80902 | -0.81079 | -0.00147 | -1.5566 | 6.0523 | 1 | 1.0004 | 0.000499 | 3.1469 | 16.775 |
| at 0.4 m | 0.58779 | 0.58955 | 0.001987 | 1.3551 | 5.1121 | -0.95106 | -0.94941 | -0.00101 | 1.1498 | 4.2976 | 2.32E-16 | -0.00931 | -0.63484 | -1.3794 | 5.2271 |
| at 0.6 m | 0.80902 | 0.81094 | 0.001573 | 1.3544 | 5.1091 | -0.30902 | -0.30094 | -0.01681 | 1.3596 | 5.1485 | -1 | -1.0002 | -0.00033 | -3.1465 | 16.77 |
| at 0.8 m | 0.95106 | 0.9524 | 0.000938 | 1.3534 | 5.1047 | 0.58779 | 0.597 | 0.009743 | 1.3803 | 5.2385 | -4.65E-16 | 0.018616 | 0.6347 | 1.3784 | 5.2223 |

Figure 6: Statistical indicators obtained from modal parameters due to different stochastic conditions in undamaged system

### 3.2 Results and discussion

The material uncertainty propagates into the modal parameters of any system. In this study, the first three natural frequencies and the modal displacements at 0.2, 0.4, 0.6 and 0.8 m from the fixed end of both the damaged and undamaged bar have been determined. The probability distribution corresponding to the undamaged system considering material randomness as Gaussian and gamma distribution has been shown in Fig. 5. The statistical indicators namely, mean, standard deviation, CoV, skewness and kurtosis for all samples have been considered as the key parameters for describing the randomness in response parameters. The statistical results corresponding to the undamaged bar has been presented in Fig. 6. Similarly, for the damaged bar element, the study has been performed considering only the Gaussian randomness as the material uncertainty. The probability distributions and the statistical indicators of the damaged system have been shown in Figs. 7 and 8, respectively. It has been observed that as the modal displacement gets closer to zero crossing of any mode shape, the skewness increases. Again in most of the cases of Gaussian randomness in material, the kurtosis is around 3 as should be in Gaussian distribution. Whereas, in case of material uncertainty as gamma distribution, the obtained kurtosis is mostly around 5. Some discrepancies have been observed in determination of fundamental frequency of the damaged system which requires modifications. Again, the uncertainty propagation in the damage quantification need to be studied along with the variation in mode shape difference and damage severity due to various input uncertainty.

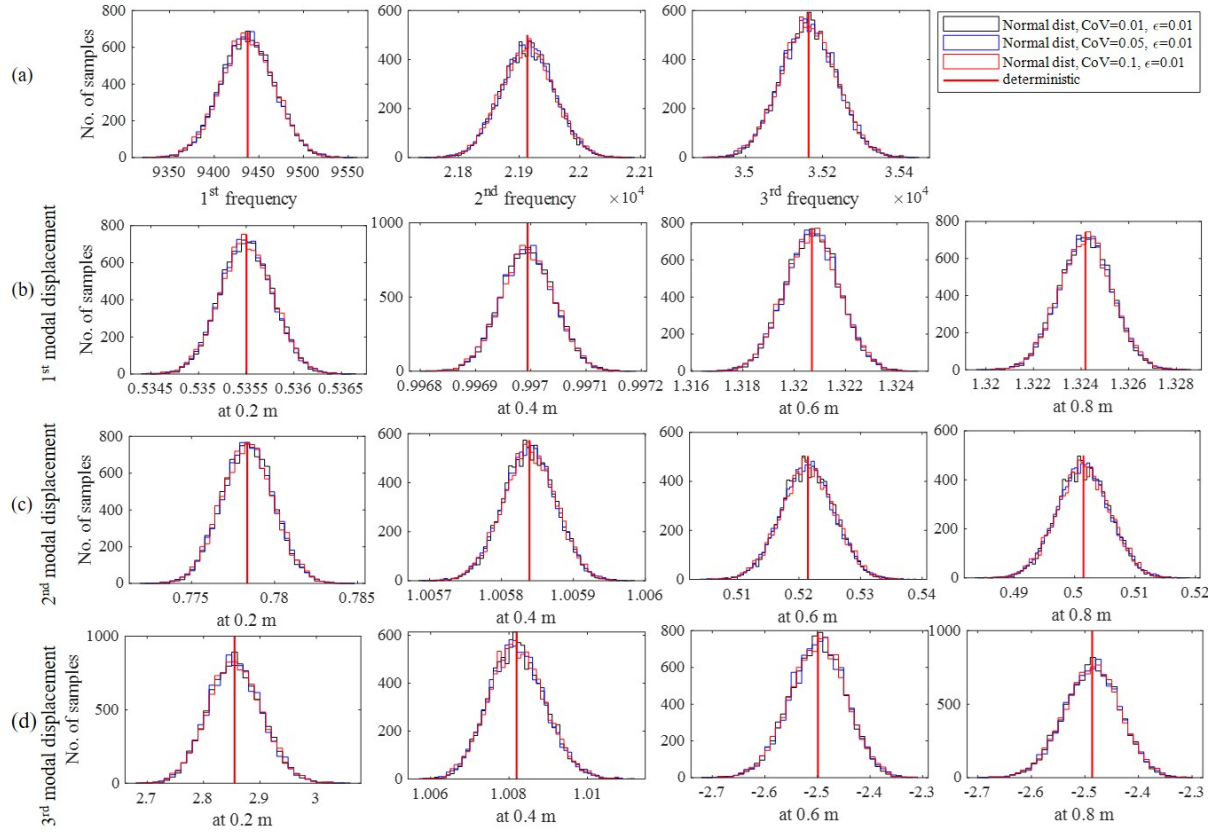


Figure 7: Distribution of responses due to different stochastic conditions in damaged bar: (a) first three natural frequencies, (b) 1st, (c) 2nd and (d) 3rd modal displacements at 0.2, 0.4, 0.6 and 0.8 m from fixed-end, respectively.

| Normal, CoV=0.01 , ε=0.01 | mode 1 | | | | | mode 2 | | | | | mode 3 | | | | |
|---|---|---|---|---|---|---|---|---|---|---|---|---|---|---|---|
| | deter. | mean | CoV | skew. | kurt. | deter. | mean | CoV | skew. | kurt. | deter. | mean | CoV | skew. | kurt. |
| frequency | 9437.4 | 9437.4 | 0.003151 | 0.018758 | 2.9327 | 21914 | 21914 | 0.001969 | -0.00678 | 2.9272 | 35164 | 35164 | 0.002044 | 0.034104 | 2.9297 |
| at 0.2 m | 0.5355 | 0.5355 | 0.00051 | 0.029416 | 2.9332 | 0.77835 | 0.77836 | 0.001984 | 0.008457 | 2.928 | 2.8551 | 2.8562 | 0.016595 | 0.13317 | 2.9604 |
| at 0.4 m | 0.99699 | 0.99699 | 4.77E-05 | 0.019705 | 2.9326 | 1.0058 | 1.0058 | 3.60E-05 | -0.0322 | 2.9299 | 1.0082 | 1.0082 | 0.000699 | 0.16452 | 2.9754 |
| at 0.6 m | 1.3207 | 1.3207 | 0.00079 | -0.02886 | 2.9332 | 0.52146 | 0.52143 | 0.008086 | -0.00171 | 2.9275 | -2.4991 | -2.5002 | -0.02112 | -0.12299 | 2.956 |
| at 0.8 m | 1.4159 | 1.3242 | 0.000827 | -0.02868 | 2.9331 | 0.10443 | 0.50146 | 0.008517 | -0.0013 | 2.9275 | -2.8616 | -2.4875 | -0.02083 | -0.12288 | 2.956 |
| Normal, CoV=0.05 , ε=0.01 | mode 1 | | | | | mode 2 | | | | | mode 3 | | | | |
| | deter. | mean | CoV | skew. | kurt. | deter. | mean | CoV | skew. | kurt. | deter. | mean | CoV | skew. | kurt. |
| frequency | 9437.4 | 9437.1 | 0.003207 | 0.014415 | 2.9961 | 21914 | 21914 | 0.002005 | -0.00433 | 2.9909 | 35164 | 35163 | 0.002074 | 0.01709 | 2.9862 |
| at 0.2 m | 0.5355 | 0.5355 | 0.000519 | 0.025619 | 2.9964 | 0.77835 | 0.77838 | 0.002019 | 0.011686 | 2.9921 | 2.8551 | 2.8554 | 0.016828 | 0.12053 | 3.014 |
| at 0.4 m | 0.99699 | 0.99699 | 4.86E-05 | 0.015415 | 2.996 | 1.0058 | 1.0058 | 3.67E-05 | -0.03658 | 2.9947 | 1.0082 | 1.0082 | 0.000708 | 0.1533 | 3.0283 |
| at 0.6 m | 1.3207 | 1.3207 | 0.000804 | -0.02503 | 2.9964 | 0.52146 | 0.52139 | 0.008232 | -0.00459 | 2.9914 | -2.4991 | -2.4993 | -0.02142 | -0.1099 | 3.0099 |
| at 0.8 m | 1.4159 | 1.3242 | 0.000841 | -0.02484 | 2.9964 | 0.10443 | 0.50141 | 0.00867 | -0.00416 | 2.9914 | -2.8616 | -2.4866 | -0.02113 | -0.10979 | 3.0099 |
| Normal, CoV=0.1, ε=0.01 | mode 1 | | | | | mode 2 | | | | | mode 3 | | | | |
| | deter. | mean | CoV | skew. | kurt. | deter | mean | CoV | skew. | kurt. | deter. | mean | CoV | skew. | kurt. |
| frequency | 9437.4 | 9437.3 | 0.003226 | -0.01633 | 2.957 | 21914 | 21914 | 0.002019 | 0.03048 | 2.9539 | 35164 | 35164 | 0.002079 | 0.00266 | 2.9571 |
| at 0.2 m | 0.5355 | 0.5355 | 0.000522 | -0.00528 | 2.956 | 0.77835 | 0.77837 | 0.002034 | 0.046311 | 2.9568 | 2.8551 | 2.8557 | 0.016874 | 0.10468 | 2.9737 |
| at 0.4 m | 0.99699 | 0.99699 | 4.89E-05 | -0.01534 | 2.9568 | 1.0058 | 1.0058 | 3.69E-05 | -0.07095 | 2.9621 | 1.0082 | 1.0082 | 0.00071 | 0.13697 | 2.9843 |
| at 0.6 m | 1.3207 | 1.3207 | 0.000808 | 0.005858 | 2.9561 | 0.52146 | 0.52142 | 0.008291 | -0.0393 | 2.9554 | -2.4991 | -2.4997 | -0.02148 | -0.09421 | 2.9708 |
| at 0.8 m | 1.4159 | 1.3242 | 0.000846 | 0.006048 | 2.9561 | 0.10443 | 0.50144 | 0.008732 | -0.03888 | 2.9553 | -2.8616 | -2.487 | -0.02119 | -0.0941 | 2.9707 |

Figure 8: Statistical indicators obtained from modal parameters due to different stochastic conditions in damaged system

## 4 CONCLUSION

In this study, a detailed literature survey regarding the appropriate probability distribution to model material uncertainty has been conducted. A detailed derivation of KL expansion has been described for modelling stochasticity in material properties of any system. It has been then applied to obtain the closed-form expression of spectral stiffness for a multi-damaged cantilever bar-type structure. Extensive simulation study has been performed on both undamaged and damaged bar-type system to understand the propagation of material uncertainty in the modal parameters. Both Gaussian and gamma distribution-based randomness have been introduced as input in the undamaged system. However in case of damaged system, only Gaussian distribution has been followed as material uncertainty. Statistical indicators have been determined to understand the uncertainty propagation in the structural responses. However, the study may be further extended in quantifying multi-damage in bar-type systems as well as in real civil structures.

## REFERENCES

[1] S. Mahadevan, A. Haldar, *Probability, reliability and statistical method in engineering design* . John Wiley & Sons, 2000.

[2] C. Soize, *An Accelerated Course with Advanced Applications in Computational Engineering, Vol. 47 of Interdisciplinary Applied Mathematics* . John Wiley & Sons, 2000.

[3] Y. Liu, S.T. Quek, F. H. Lee, Translation random field with marginal beta distribution in modeling material properties. *Structural Safety* , **61**, 57–66, 2016.

[4] Y. Liu, M.D. Shields, A direct simulation method and lower-bound estimation for a class of gamma random fields with applications in modelling material properties. *Probabilistic Engineering Mechanics*, **47**, 16–25, 2017.

[5] P. E. Hess, D. Bruchman, I. A. Assakkaf, B. M. Ayyub, Uncertainties in material and geometric strength and load variables. *Naval engineers journal* , **114**, 139–166, 2002.

[6] S. Shahinur, *Quantification of uncertainty of material properties and its application* , 2018.

[7] B. S. Grewal, *Higher engineering mathematics* . Khanna Publishers, New Delhi, 2002.

[8] S. Rahman, H. Xu, A meshless method for computational stochastic mechanics. *International Journal for Computational Methods in Engineering Science and Mechanics* , **6**, 41–58, 2005.

[9] M. Schevenels, G. Lombaert, G. Degrande, Application of the stochastic finite element method for Gaussian and non-Gaussian systems. *ISMA2004 International Conference on Noise and Vibration Engineering* , 3299–3314, 2004.

[10] R. G. Ghanem, P. D. Spanos, *Stochastic finite elements: a spectral approach* . Courier Corporation, 2003.

[11] M.R. Machado, S. Adhikari, J.M.C. Dos Santos, A spectral approach for damage quantification in stochastic dynamic systems. *Mechanical Systems and Signal Processing* , **88**, 253–273, 2017.

[12] B. Basu, D. Tiwari, D. Kundu, R. Prasad, Is Weibull distribution the most appropriate statistical strength distribution for brittle materials? *Ceramics International* , **35**, 237–246, 2009.

[13] S. Adhikari, M. I. Friswell, Distributed parameter model updating using the Karhunen–Loève expansion. *Mechanical systems and signal processing*, **24**, 326–339, 2010.

COMPDYN 2023
9th ECCOMAS Thematic Conference on
Computational Methods in Structural Dynamics and Earthquake Engineering
M. Papadrakakis, M. Fragiadakis (eds.)
Athens, Greece, 12-14 June 2023

# LASER SCANNING OF JUMA MACHIT'S COURTYARD AND DETAILED NUMERICAL STUDY ACCOUNTING FOR ROOF MEMBERS COMPROMISED BY TERMITE INFESTATION

**Shakhzod M. Takhirov[1], Bakhodir S. Rakhmonov[2], Ravshanbek Nafasov[2], Abbos Samandarov[2] , Sevara Sultanova[2], Sultan Kudratov[3], Mirzokhid M. Akhmedov[4], and Ravshan A. Shamansurov[5]**

[1] University of California, Berkeley: 337 Davis Hall, Berkeley, California, 94720, USA
takhirov@berkeley.edu

[2] Urgench State University: 14, Khamid Olimjon Str., Urgench, Uzbekistan
rah-bahodir@yandex.com

[3] Tashkent University of Information Technologies: 108 Amir Temur Ave., Tashkent, Uzbekistan
s.kudratov@gmail.com

[4] Miyamoto International – Silk Road: Tashkent, Uzbekistan
m.akhmedov@miyamotointernational.com

[5] Sigma Innovative Tech: Tashkent, Uzbekistan
shamansurov@rambler.ru

## Abstract

*This paper is focused on a study of Juma Machit's courtyard in Ichan Kala (Khiva, Uzbekistan). The courtyard represents an enclosed space surrounded by four walls that resulted in a trapezoidal overall plan view. It is fully covered by a roof supported by numerous lumber columns. The roof is constructed of lumber with a modern addition of a concrete layer on top of it. The relatively recent addition of the concrete layer creates additional structural demand on the room diaphragm. A detailed study of this demand is especially important now as there are obvious signs of a termite infestation in the lumber pieces. To address this issue, the courtyard was laser scanned from the inside and the outside, which allowed for the creation of a point cloud with high accuracy. A simplified numerical model of the roof was generated in order to study the effect of both static and dynamic loads. Based on the outcomes of this study, a more sophisticated model of the monument will be created that will include the brick walls, the columns, and the composite roof. Numerical simulations of the performance of this system under a combination of seismic loading and a snow load will be studied.*

**Keywords:** Structural health monitoring, Non-destructive measurements, Termite infestation, Seismic loading, Snow loading, Laser scanning, Finite element modeling.

## 1 INTRODUCTION

The objective of the paper is to study an effect of the ongoing termite infestation on the structural performance of the roof covering the courtyard of Juma Machit in Itchan Kala (Khiva, Uzbekistan). The roof is supported by the columns. Some of the columns are more than a thousand years old and were taken from the old Juma Machit which had been destroyed in a fire. During one of the recent reconstruction efforts a concrete layer was poured on top of the roof. As a result the roof was converted into a much heavier composite structural diaphragm consisting of lumber covered with a layer of concrete. To achieve the objective of the project Juma Machit was laser scanned to capture its geometry with high accuracy. The resulting point cloud was used for finite element modeling of the monument. The ongoing termite infestation was introduced by reducing the cross sections of the supporting roof members at the infestation locations.

## 2 LASER SCANNING

The courtyard of the mosque was previously laser scanned by a research team from Poland [1]. The study was limited to capturing the geometry of the monument's interior. The current research team expanded the research project. In the first phase of the project (2020), the exterior surface of the monument was scanned from eleven positions, the so-called stations [2]. A terrestrial laser scanner, C10 from Leica Geosystems [3], was utilized. In the summer of 2022, the second phase was conducted and the interior surface of the courtyard of the monument was scanned from six stations. These point clouds of the interior surface of the courtyard were stitched together with the point cloud of the exterior of the monument that had been collected earlier. The stitching was conducted in Cyclone [4]. The latter point cloud included the minaret and the interior walls of the courtyard. Laser scans conducted from the roof were added to the overall registration. As a result, the thickness of the wall, openings in the wall, column locations, and roof thickness can be obtained from the fully registered point cloud.

### 2.1 Overall point cloud

The complete registration that includes the point clouds collected in 2020 and 2022 is presented in Figure 1. It contains points of the exterior, interior, and roof surfaces.

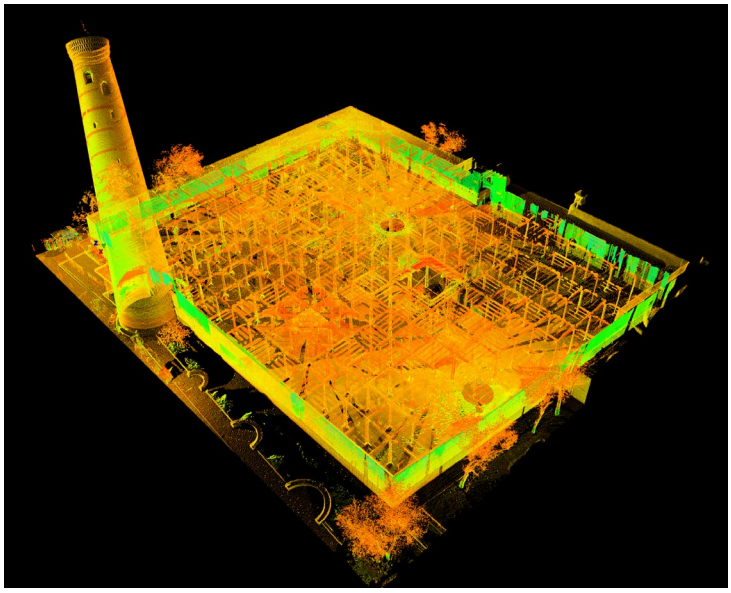

Figure 1: The complete registration containing exterior, interior, and roof surfaces.

It is worth noting that the 2020 phase of the project was conducted in December, so the roof surface was captured with a limited amount of snow.

The view of the courtyard is presented in Figure 2. The roof is supported by 213 columns which are located at the grid intersections as presented in Figure 3.

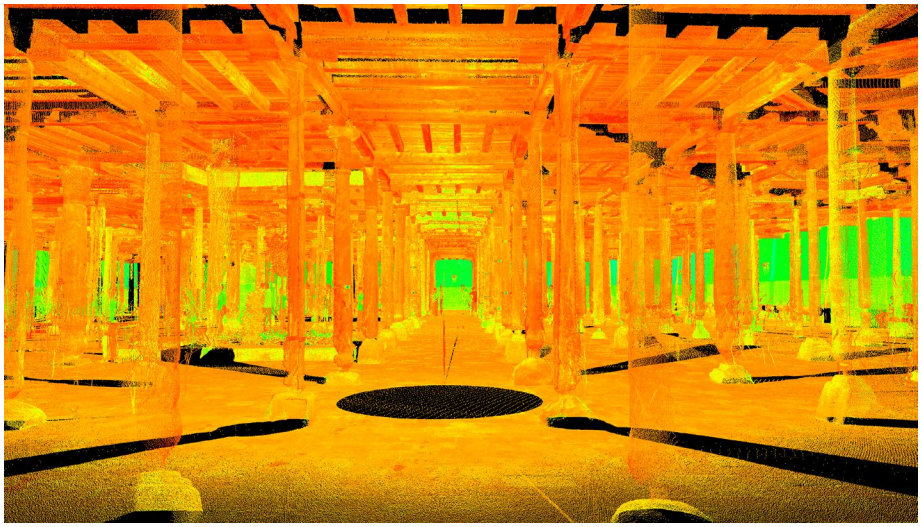

Figure 2: The courtyard's point cloud.

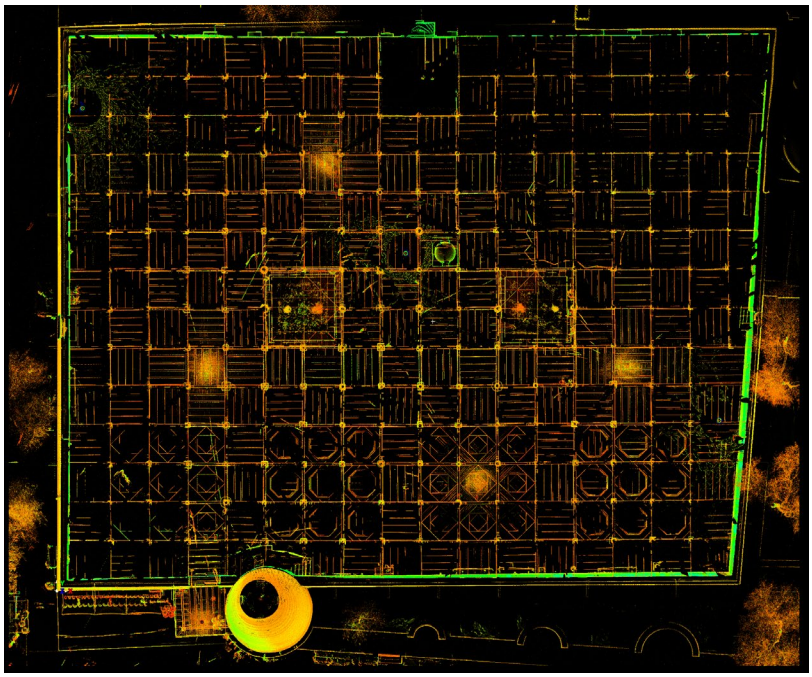

Figure 3: The supporting grid of the roof.

The processing of the fully registered point cloud was conducted in the Matlab environment. [5].

## 3 FINITE ELEMENT MODELING

The finite element modeling was conducted in the SAP2000 environment [6]. Some preliminary models were developed earlier [7]. Since the point cloud of the roof was incomplete

the earlier models were limited to modeling the masonry structures, i.e., the walls and the minaret.

### 3.1 Selecting a column row to study

To assess the effect of the termite infestation the following approach was taken. It was assumed that the roof load is evenly distributed over the area of the roof. As a representative case for studying a load-carrying capacity, a row of columns along the width of the courtyard was selected as presented in Figure 4. This image shows the columns along the fourth row counted from the left of the image in Figure 3. It also contains half of the roof on each side of the column row in order to account for the roof's weight supported by these columns.

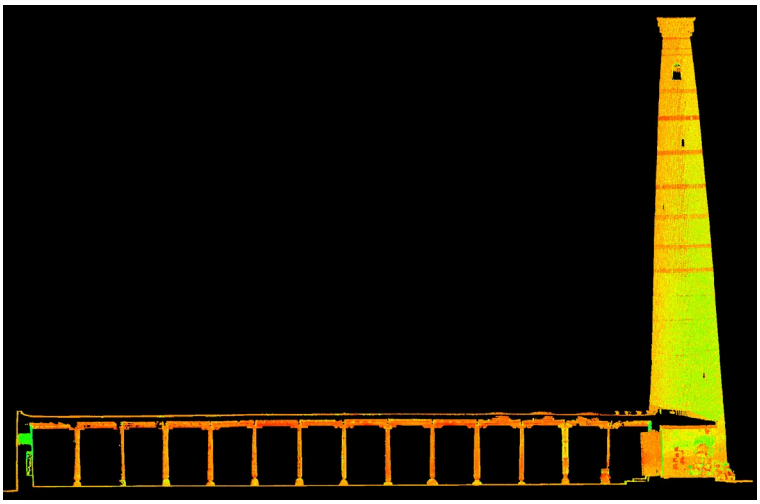

Figure 4: Typical row of columns.

### 3.2 Modeling of column row

The thickness of the roof was estimated from the point cloud as presented in Figure 5. As shown in the image, the roof thickness is close to 0.4 m. The bottom portion is constructed of round lumber pieces and it was assumed that their diameter does not exceed 0.1 m. Based on this assumption, the thickness of the concrete layer is close to 0.3 m.

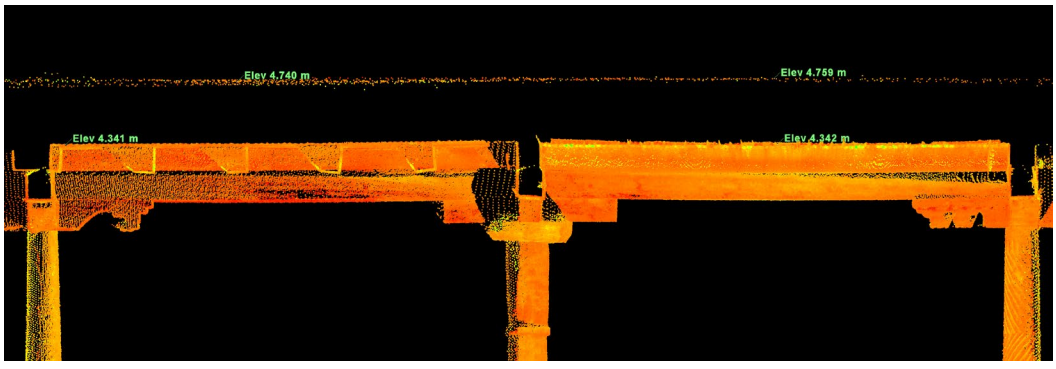


Figure 4: Typical row of columns.

The modeling of this part of the roof was conducted in SAP2000 and it is presented in Figure 5.

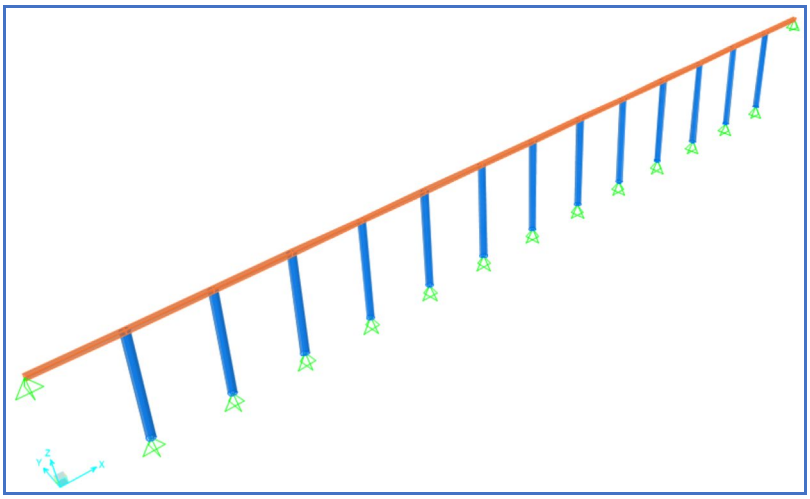

Figure 5: Model of column row.

### 3.3 Static analysis

A few finite element models were generated. The original roof cover of Juma Machit was likely done by laying a thick layer of wet clay on top of the wooden ceiling. This construction approach was commonly. Hence, Model A was generated for the case of the clay cover. Model B was generated for the case of the concrete cover. Model C represents the case with snow on top of the concrete layer. Model D corresponds to the case without any layer above the wooden ceiling. A summary of the results obtained for the static dead load analysis is presented in Table 1.

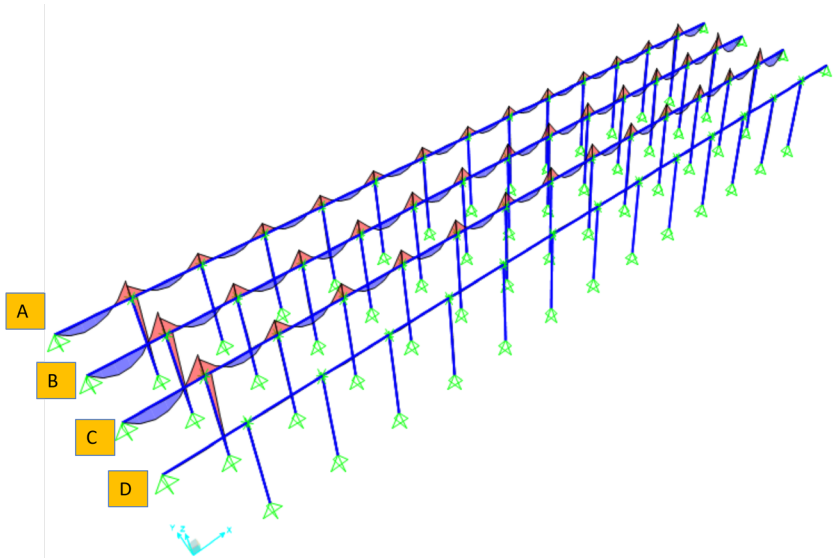


Figure 6: Four models with different load combinations on top of wooden ceiling.

| Model | Description | Percentage to Model A |
|---|---|---|
| A | Clay | 100% |
| B | Concrete | 128% |
| C | Concrete+snow | 131% |

Table 1: Maximum static moments in the beams normalized to that for Model A.

As presented in Table 1, the modern replacement of the clay layer with the concrete layer most likely increased the bending moments in the beams by about 28%. When accounted for the snow load the moments increased to about 31%. For the snow load, it was assumed that the roof has a uniform layer of snow that is 0.3 m thick, which is a common amount of snow for this region of Uzbekistan.

### 3.4 Dynamic analysis

A historic record obtained during the 1976 Gazli earthquake in Uzbekistan was utilized for the dynamic analysis. All models described above were excited with this earthquake record. Only two components of this record were used as presented in Figure 7. Note that the "NS-axis" stands for the north-south axis. Figure 7a shows the acceleration time histories. Figure 7b shows spectral accelerations which indicate that the spectral demand in the vertical direction was about two times greater than the demand in the horizontal direction.

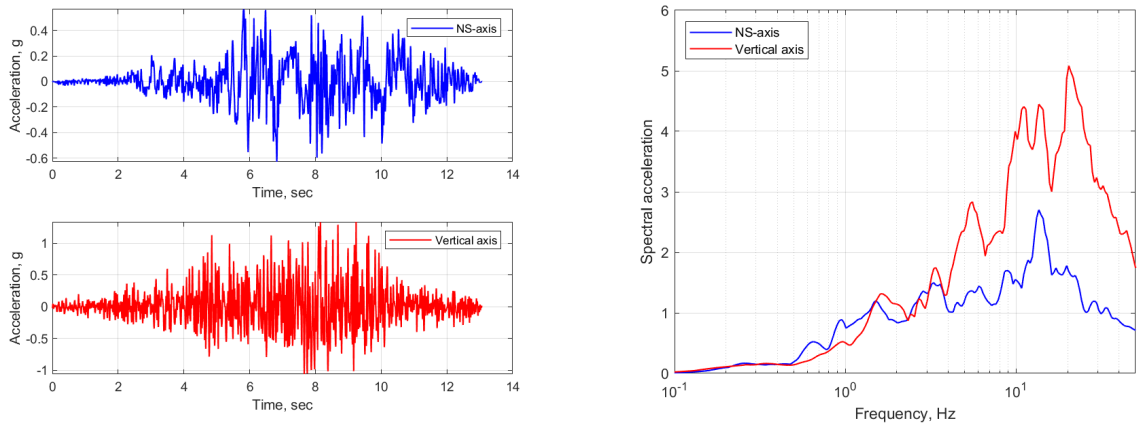


a) Acceleration time histories b) Spectral accelerations

Figure 7: Four models with different load combinations on top of wooden ceiling: dynamic analysis.

The results of the dynamic analysis are presented in Figure 8 which are summarized in Table 2.

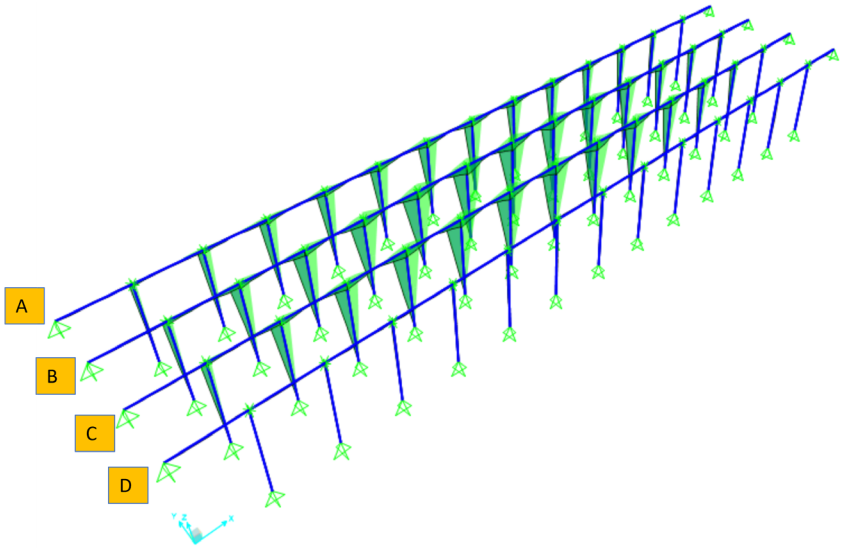


Figure 8: Four models with different load combinations on top of wooden ceiling: dynamic analysis.

| Model | Description | Percentage to Model A |
|---|---|---|
| A | Clay | 100% |
| B | Concrete | 139% |
| C | Concrete+snow | 145% |

Table 2: Maximum dynamic moments in the beams normalized to that for Model A.

As presented in Table 2, the modern replacement of the clay layer with a concrete layer-most likely increased the bending moments in beams by about 39%. When accounting for the snow load the moments increased to about 45%.

### 3.5 Sagging analysis and accounting for termite infestation

Analysis of the point cloud indicates that a few beams had noticeable sagging. A typical case of beam sagging along with other roof elements is shown in Figure 9.

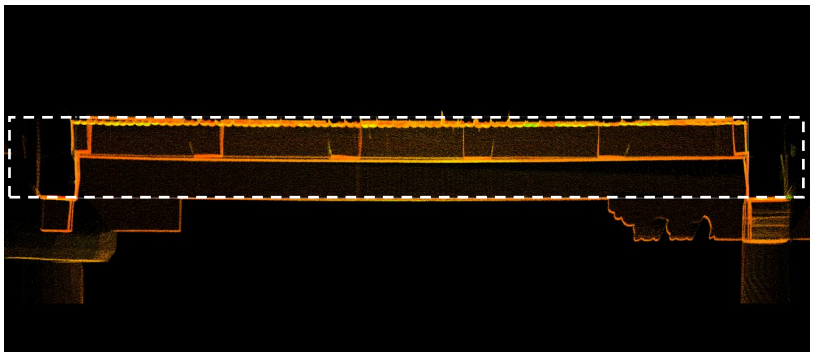

Figure 9: Sagging of the beam and roof elements (a reference straight block shown in white).

When a beam is affected by a termite infestation a load-carrying capacity of the beam in bending can be reduced due to the reduction of a cross-sectional area that will resist bending. A simple case is presented in Figure 10a which shows a cross-section of the beam before (right) and after infestation (left). The area compromised by the termite infestation is shown in red. The change in capacity of carrying the bending load is presented in Figure 10b.

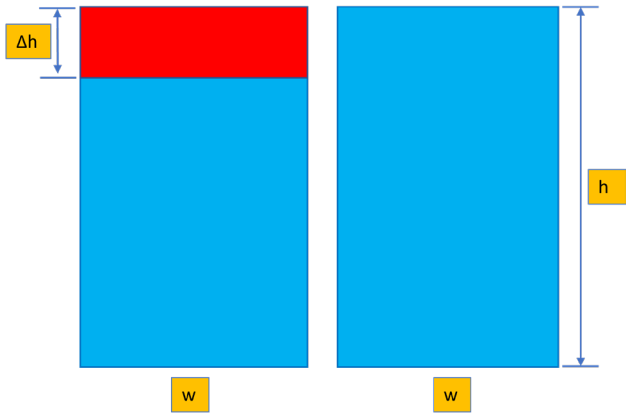


a) Beam's cross section before (right) and after (left) infestation: red indicates affected area

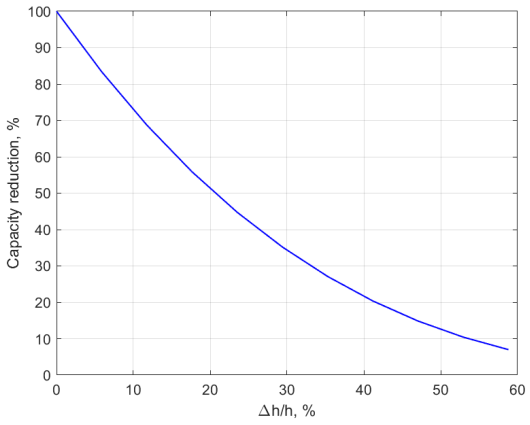


b) Capacity reduction: ratio of stresses after to that before the infestation

Figure 10: Simplified case of termite infestation and reduction in the beam's load-carrying capacity.

The results provided in Figure 10b are based on the well-known calculation of the bending stresses, σ (see, [8] as an example):

$$\sigma = M/(EI) \tag{1}$$

Where $M$ is the bending moment, $E$ is the Young modulus of the lumber and $I$ is the moment of inertia of the beam's cross section.

The moment of inertia for the rectangular cross section is estimated by a commonly known expression ($w$ is the width and $h$ is the depth of the cross section as shown in Figure 10a):

$$I = wh\text{^}3/12 \tag{2}$$

For the case in which a portion of the cross section with a depth of $\Delta h$ is affected by termite infestation the reduction of the stress capacity in bending can be computed by the following expression:

$$Reduction\ in\ stress\ capacity = (1 - (\Delta h/h)\text{^}3) \tag{3}$$

The expression (3) is presented in a graphical form in Figure 10b. The plot shows that the bending capacity of the beams drops dramatically when the depth of the compromised area increases. For example, when the compromised area is half of the original depth of the beam the load-carrying capacity drops to less than 15% of the capacity before infestation.

## 4 CONCLUSIONS

The paper is the first attempt in studying the stability of the roof in the Juma Machit monument (Khiva, Uzbekistan). The courtyard of the minaret was scanned from the outside, inside, and top of the roof. As a result an accurate point cloud of the monument including its roof and all supporting elements was captured. As a starting point of this investigation a simple numerical model was generated from the collected point cloud. The numerical model was investigated under static loading. The recent addition of a thick concrete layer to the top of the roof was studied through FE modeling. It was assumed that the top layer of the roof was constructed of clay. This model was compared to an FE model with the top layer built of concrete. It was shown that the concrete layer increased the demand for the beams by about 31% for static dead load analysis. The same models were subjected to dynamic loading that replicate the ground motions recorded during the 1976 Gazli earthquake. It was shown that the concrete layer increased the demand on the beams by about 45% in a time history analysis. The large demand can result in significantly larger stresses in the areas where the supporting beams are affected by the termite infestation. In the next phase of the project a detailed finite element model will be developed that will investigate the impact of both static and dynamic loadings. A reduced cross section will be introduced at the locations with a severe termite infestation. The results of the numerical simulations will be used for developing restoration strategies.

## ACKHOWLEDGMENTS

The project would not be possible without funding provided by the Central Asia University Partnerships Program (UniCEN) for the 2020 phase of the project. UniCEN is sponsored by the U.S. Embassy in Tashkent, Uzbekistan and administered by the American Councils for International Education. The second phase of the project in 2022 was sponsored by Urgench State University (Urgench, Uzbekistan), which is greatly appreciated. The authors would like to acknowledge Ms. Holly Halligan of UC Berkeley for editing the paper.

## REFERENCES

[1] Miłosz, M., Kęsik, J., and Badurowicz, M. 3D scanning of the interior of Juma Mosque in Khiva, International Conference "3D Digital Silk Road Project" (3DSR'2022). September 7-9, 2022 (https://silkroad3d.com/wp-content/uploads/2022/08/14_3D-scanning-of-the-interior-of-Juma-Mosque-in-Khiva.pdf).

[2] Takhirov, S., Rakhmonov, B., Nafasov, R., Samandarov, A., Sultanova, S., Musurmanov, J., Takhirov, B. Structural health monitoring of Juma Mosque in Itchan Kala, Uzbekistan by laser scanning. International Conference on Structural Health Monitoring of Intelligent Infrastructure: Transferring Research into Practice, SHMII, 2021-June, pp. 1331-1337.

[3] Leica Geosystems AG (2011). Leica ScanStation C10. https://w3.leicageosystems.com/downloads123/hds/hds/ScanStation%20C10/brochures datasheet/Leica_ScanStation_C10_DS_en.pdf (accessed on 19 October 2021).

[4] Leica Geosystems (2018). Cyclone Version 9.2.1.

[5] MathWorks. Matlab Version R2020a. 2020.

[6] Computers and Structures, Inc. (CSI). SAP2000 Ultimate Version 16.1.1. Structural Analysis Program. 2014.

[7] Takhirov, S.M., Rakhmonov, B.S. Finite element analysis of Juma Mosque in Uzbekistan based on laser scanning and Ambient studies. COMPDYN Proceedings, 2021-June. DOI:10.7712/120121.8506.19400.

[8] Popov, E.P. Engineering Mechanics of Solids. Prentice Hall, 1990.

COMPDYN 2023
9th ECCOMAS Thematic Conference on
Computational Methods in Structural Dynamics and Earthquake Engineering
M. Papadrakakis, M. Fragiadakis (eds.)
Athens, Greece, 12-14 June 2023

# DYNAMIC IDENTIFICATION OF A HISTORICAL MASONRY BUILDING: THE CASE STUDY OF PALAZZO ROSCIANO

**Raffaele Tarantini[1], Alessandro Cardoni[1], Gian Paolo Cimellaro[1], Marco Domaneschi[1], Enrico Pribaz[2], Gianluca Rupolo[2]**

[1] Department of Structural, Geotechnical and Building Engineering, Politecnico di Torino, Corso Duca degli Abruzzi 24, 10129, Turin (TO), Italy
e-mail: {raffaele.tarantini, alessandro.cardoni, gianpaolo.cimellaro, marco.domaneschi}@polito.it

[2]Autorità di Sistema Portuale del Mar Tirreno Settentrionale, Calata Carrara 1, 57123 Livorno (LI), Italy

## Abstract

*This paper focuses on the dynamic characterization of a historical building located in the port city of Livorno (Italy), Palazzo Rosciano. It is a masonry structure built in the second half of the 1600 and fully renovated in the nineties to accommodate the offices of the North Tyrrhenian Sea Port Authority. The research was carried out starting from a preliminary inspection and a historical-critical analysis. Then, a detailed geometric survey was carried out using a 3D laser scanner. To define the mechanical properties of materials a series of minor destructive tests, i.e., flat jacks, shove test, and penetrometer, were performed. A structural health monitoring campaign was also carried out under ambient vibrations using a wireless sensor network. The acquired data was processed to characterize the dynamics of the structure by means of two different output-only techniques, the frequency domain decomposition, and the stochastic subspace identification.*

**Keywords:** Historical masonry building, Materials testing, Structural Health Monitoring, Ambient Vibration Test, Operational Modal Analysis, Structural Dynamic Identification.

## 1 INTRODUCTION

Traditional masonry buildings have an extensive and prominent heritage in Europe, especially in Italy. It is crucial to preserve this built heritage in historic cities, above all those that are located in seismically active regions. In fact, the recent earthquakes in Italy have highlighted the necessity of comprehensive monitoring and safety evaluation of the built environment.

*Structural Health Monitoring (SHM)*, a tool of particular relevance that allows for the analysis and estimation of the state of health of civil works with the goal of determining their safety, represents a reliable support that professionals and researchers may rely on [1, 6].

The inspection and testing campaign carried out on the historic building "Palazzo Rosciano" will be examined in the following paragraphs, starting with the historical-critical analysis, and ending with the dynamic identification, by way of the in-situ testing and investigation.

## 2 GENERAL OVERVIEW

Located in the Venezia Nuova district (Livorno, Italy), the building under study is a branch of the Port System Authority of the Northern Tyrrhenian Sea. It is a historic building built in the early decades of the 1600s, part of a larger masonry aggregates (Figure 1).

The building has four floors above ground and a basement, with a pseudo-rectangular shape. The load-bearing structure consists of masonry walls of various thicknesses, that widen below the ground level to shape the foundations system. The above ground floors are one-way timber-concrete composite slabs, while the ground floor consists of masonry vaults.

In Figure 2 the architectural plan of the ground floor is shown.




Figure 1 – Google Earth view

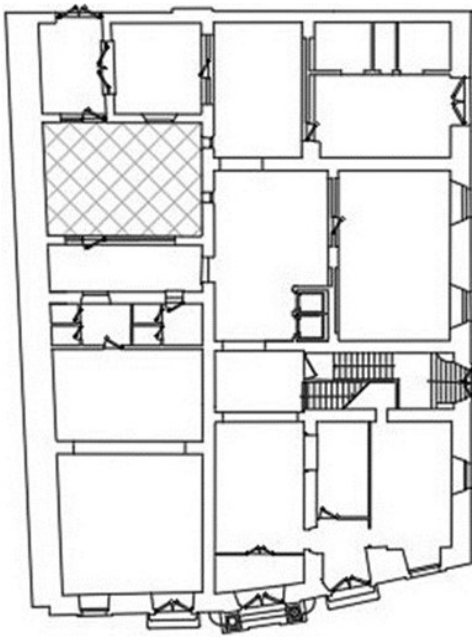

Figure 2 – Architectural plan of the ground floor

## 3 HISTORICAL-CRITICAL ANALYSIS

Despite being a city with an important historical past, Livorno has seen its cultural heritage greatly reduced following the devastation caused by war events and an invasive reconstruction plan. However, there were several urban redevelopment projects that have affected the Venezia Nuova district and, consequently, Palazzo Rosciano after the first half of the 1900s. The building was built between 1580 and 1620. Originally, only the construction of a warehouse for remittances of port equipment had been planned and, only later, the above floors were built. After its construction, the building underwent many transformations mainly due to the bombings that devastated the city during World War II. Ignored for several years, it regained its splendor thanks to the 1989 restoration.

The retrofitting history of the building has been extracted from technical reports and geological surveys and used to develop the FEM model of the building.

A program of investigations and testing has been planned, as described in the following paragraphs, to confirm the accuracy of the information acquired from the historical-critical analysis and collect the extra information.

## 4 IN-SITU TESTING AND INVESTIGATION CAMPAIGN

First, visual investigations were conducted, allowing for the analysis of the cracking pattern, the texture of the walls and their degree of interlocking. Based on these findings, a set of *minor-destructive tests (MDT)* were planned to evaluate the mechanical properties of the constituent materials, such as single and double flat jacks, shove test, and penetrometer [1, 2, 3, 4].

Regarding the geometric survey of the building, the BLK360 3D laser scanner produced by Leica was used. The point cloud (Figure 3) acquired in such a way can be used to create a future BIM model.



Figure 3 – Point cloud

## 5 DYNAMIC IDENTIFICATION

### 5.1 SHM acquisition system

The TRITON model of the LUNITEK data gathering and processing system was employed. An integrated Force Balance triaxial accelerometric sensor is part of the system. The 24-bit resolution A/D conversion device was configured with synchronous sampling at a sampling rate of 250 samples/second per channel. The device has a microSD memory that you may use to manage a ring-buffer for prolonged continuous recordings and a GPS receiver for absolute time synchronization. A local network connection (cable or WiFi) or a UMTS/HSPA modem can be used to connect to the instrument and enable remote control of its operation. The system has an internal battery (LiPo) that ensures continuous operation for more than 30 hours and is powered by an external network [1, 2, 3, 4].

### 5.2 Sensors setup

The accelerometers were placed on the extrados of the slabs to carry out the recordings. The different configurations of accelerometers have all been oriented in accordance to a single global reference system (N,E,Z). Figure 4 represents a setup example used during the building's dynamic characterization tests.

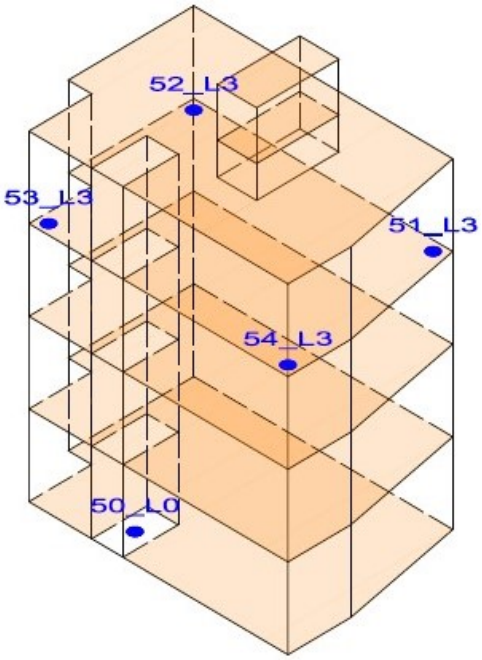


Figure 4 – Example of sensors setup

### 5.3 Ambient Vibration Test (AVT)

*Ambient Vibration Tests (AVT)* were performed on the structure in compliance with operational modal analysis to identify its modal properties (natural frequencies and mode shapes).

The sensors' data consists of acceleration time histories. A "clean" sub-window, which is one that is free of anomalous peaks caused by bumps, for example, and can therefore be recognized as white noise, was then obtained within the actual recording window [1, 5, 7].

### 5.4 Frequency Domain Decomposition (FDD)

*Frequency Domain Decomposition (FDD)*, a dynamic identification approach, was used. It works in the frequency domain and is based on the *Power Spectral Density (PSD)* matrix's singular value decomposition algorithm.

It is possible to determine the spectral density eigenfunctions corresponding to each mode of the system and, consequently, to estimate the modal shape at each peak, from the assessment of the *Singular Values - SV* (Figure 5) that are returned in the output [7, 8].

### 5.5 Stochastic Subspace Identification (SSI)

The dynamic identification method known as *Stochastic Subspace Identification (SSI)*, that operates in the time domain, was then used. These kinds of methods are considered as a robust output-only identification approach, compared to other methods currently available.

A stochastic state-space model of the structure is found through *SSI* algorithms. The final model can then be converted into a more practical structural model form for the results' engineering interpretation. Both the modal model and the *Finite Element (FE)* model formulations can be related to the state-space model.

In practice, once the analysis has been performed, the output will be determined by stabilization diagrams (Figure 6) which align the distribution of the values obtained in the frequency peaks, identifying the modes of vibration of the system [9, 10]

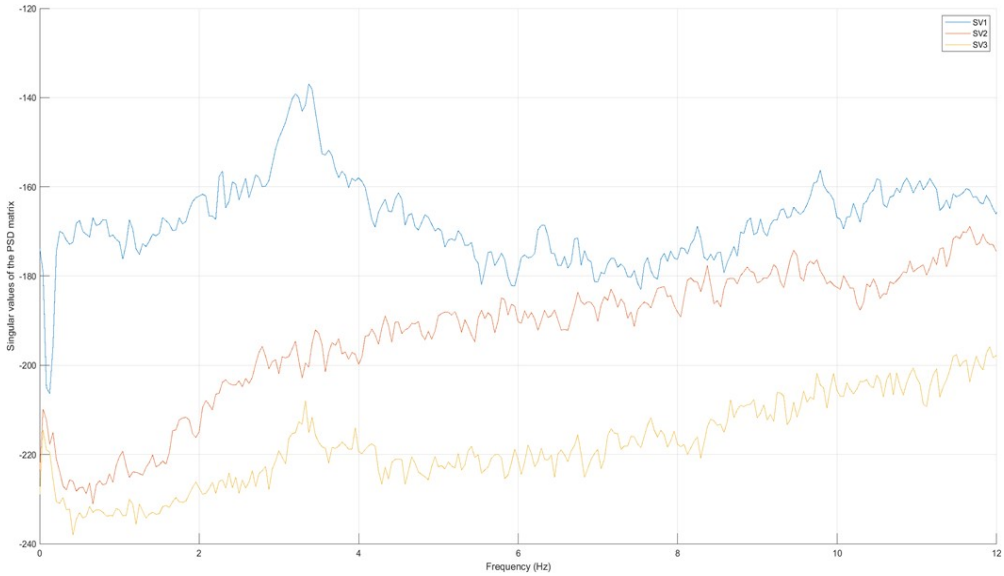


Figure 5 – Example of SV-frequency diagram

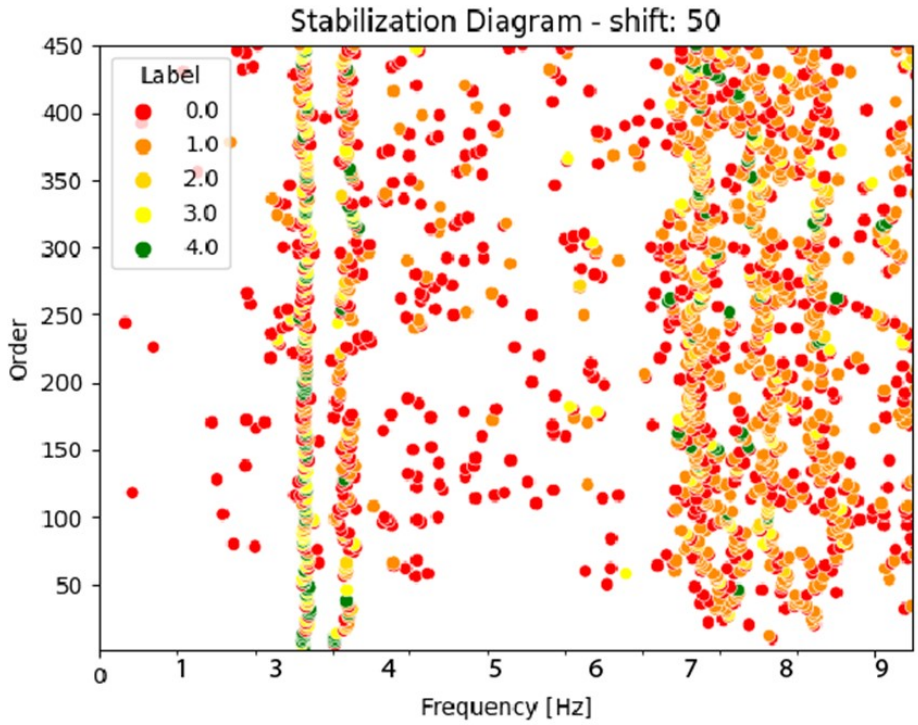


Figure 6 – Example of stabilization diagram

## 5.6 Results

The *FDD* algorithm has led to the identification of a single mode shape of the structure. In fact, considering the results for all the different sensors setups, it was possible to identify a natural frequency corresponding to the identified mode equal to 3.24Hz. While, the stabilization diagram obtained with the *SSI* technique has returned a distribution of remarkable values

around 3.21 Hz. By performing a final comparison between the outputs of the two analyzes performed, with the necessary approximations, the procedure and the obtained results have been validated.

Figure 7 shows the comparison between the normalized modal shapes obtained with *FDD* (dash-dotted line) and *SSI* (solid line). The first mode of vibration of the structure is a flexural type mode shape in the global east direction, the only free angle of the structure.

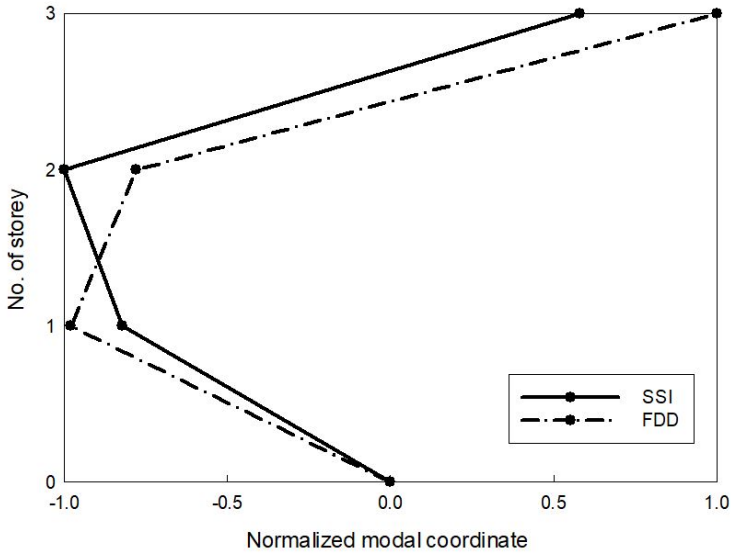


Figure 7 – Comparison of mode shapes

## 6 CONCLUSIONS

The aim of the present paper is to assess the dynamic behavior of the Palazzo Rosciano, a historical masonry building located in the port city of Livorno (Italy).

First, a preliminary inspection and a historical-critical analysis were carried out to obtain as much information as possible. Secondly, a detailed geometric survey was conducted using a 3D laser scanner at the same time. Then, a test campaign, which included a series of *minor destructive tests (MDT)*, was carried out to evaluate the mechanical properties of materials.

Finally, an ambient vibration modal identification campaign was carried out to detect the dynamic characteristics of the structure. Two different output-only techniques, frequency domain decomposition and stochastic subspace identification, provide reliable and comparable results. The latter could be the starting point for the development and calibration of future numerical models.

## REFERENCES

[1] Tarantini, R., Cardoni, A., Marasco, S., Merlin, J., Pribaz, E., Rupolo, G., Domaneschi, M., Cimellaro, G. P.: *Dynamic Characterisation and Seismic Vulnerability Assessment of Existing Masonry Port Structures*. In: Cimellaro, G.P. (eds) Seismic Isolation, Energy Dissipation and Active Vibration Control of Structures. WCSI 2022. Lecture Notes in Civil Engineering, vol 309. Springer, Cham. (2023). https://doi.org/10.1007/978-3-031-21187-4_90

[2] Cimellaro, G.P., Piantà, S., De Stefano, A.: *Output-only modal identification of ancient L'Aquila city hall and civic tower*, Journal of structural engineering 138(4), (2012).

[3] Marasco, S., Zamani Noori, A., Domaneschi, M., Cimellaro, G.P.: *Seismic vulnerability assessment indices for buildings: proposals, comparisons and methodologies at collapse limit states*, International Journal of Disaster Risk Reduction 63, 102466 (2021).

[4] Domaneschi, M., Zamani Noori, A., Pietropinto, MM.V., Cimellaro, G.P.: *Seismic vulnerability assessment of existing school buildings*, Computers & Structures 248, 106522 (2021).

[5] Beck JL, Vanik MW, Katafygiotis LS (1994). *Determination of model parameters from ambient vibration data for structural health monitoring*. Proceedings of the 1st World Conference on Structural Control, Pasadena, California.

[6] M. G. Masciotta, L. F. Ramos, and P. B. Lourenço, "The importance of structural monitoring as a diagnosis and control tool in the restoration process of heritage structures: A case study in Portugal," Journal of Cultural Heritage, vol. 27, pp. 36–47, Oct. 2017, doi: 10.1016/j.culher.2017.04.003.

[7] R. Brincker, "*Introduction to Operational Modal Analysis*", John Wiley & Sons, 2015. doi: 10.1002/9781118535141.

[8] R. Brincker, L. Zhang, and P. Andersen, "*Modal identification of output-only systems using frequency domain decomposition*", Smart Mater. Struct., vol. 10, no. 3, pp. 441–445, Jun. 2001, doi: 10.1088/0964-1726/10/3/303.

[9] Brincker R, Andersen P (2006). *Understanding Stochastic Subspace Identification.* Proceedings of the International Modal Analysis Conference (IMAC-XXIV), A Conference & Exposition on Structural Dynamics. Society for Experimental Mechanics.

[10] K. Zhou, Q.-S. Li, and X.-L. Han, "*Modal Identification of Civil Structures via Stochastic Subspace Algorithm with Monte Carlo–Based Stabilization Diagram*", J. Struct. Eng., vol. 148, no. 6, p. 04022066, Jun. 2022, doi: 10.1061/(ASCE)ST.1943-541X.0003353.

COMPDYN 2023
9th ECCOMAS Thematic Conference on
Computational Methods in Structural Dynamics and Earthquake Engineering
M. Papadrakakis, M. Fragiadakis (eds.)
Athens, Greece, 12-–14 June 2023

# APPLICATION OF THE WAVELET TRANSFORM INVERSE ANALYSIS FOR MODAL IDENTIFICATION AND DAMAGE DETECTION

**Pierre Argoul**[1,2] **and Michalis Fragiadakis**[2,3]

[1]LVMT, Ecole des Ponts, Université Gustave Eiffel
77454 Marne la Vallée, France
e-mail: pierre.argoul@enpc.fr

[2]Université Gustave Eiffel, MAST-EMGCU
F-77454 Marne-la-Vallée, France
e-mail: pierre.argoul@univ-eiffel.fr

[3]National Technical University of Athens
Iroon Polytechneiou 15780, Zografou Campus, Athens, Greece
e-mail: mfrag@mail.ntua.gr

**Keywords:** wavelet transform, modal identification, damage detection, building vibrations

**Abstract.** *The use of the Continuous Wavelet Transform method for modal identification and structural damage analysis is discussed in this paper. The wavelet transform method can be used to understand the responses of different structures under different loading conditions, i.e. after noise-embedded shock signals. The method allows the processed signal to be displayed in the time-frequency plane, making it possible to estimate modal characteristics, or study the effect of structural defects on the vibration behaviour of the structure. The paper summarises the important aspects of the method and proposes a novel formulation for structural assessment. Two example applications are presented, a four-degree-of-freedom linear system vibrating freely and a damaged masonry wall subjected to shear compression and ambient vibration tests. The examples show that the CWT method can be used to obtain valuable information for structural characterization.*

## 1 INTRODUCTION

The Wavelet Transform (WT) method appeared in mathematics more than a century ago, starting with Haar who discovered in 1909 an orthonormal basis consisting of step functions. The Haar basis construction is a precursor of what is known today as the multiresolution analysis [1] which refers to the expansion of a signal into components that can reproduce the original signal when added together. The principle of multiresolution spaces is to decompose a signal of finite energy $\mathcal{L}^2(\mathbf{R})$ to two complementary spaces: $(i)$ a space of approximation; and $(ii)$ a detail space that contains the approximation error. Multi-resolution analysis can be seen as a way to zoom into, or out of, the signal without losing information. From the beginning of 1980s, under the impetus of several French researchers, especially Grossmann and Morlet [2], wavelet research in mathematics has grown steadily with significant contributions from many authors. Figure 1 provides a quick overview of the history of the WT method. Since then, the WT has been used in many areas of science and engineering. For example, is a recent reference published by A. Guillet and his co-workers,the method has been applied to physiological signals. In reference [14], the authors introduced time-log-frequency ratio distributions based on WT with analytic mother wavelets (the Grossmann wavelet belonging to the Morse wavelets family cf. [19]) that they applied to voice recordings. Two main trends exist in how the WT is computed and used: the Continuous Wavelet Transform (CWT) and the Discrete Wavelet Transform (DWT) method [3]. Our work will focus on the former.




Figure 1: Short History of Wavelet Transform (WT).

The wavelet transform method, allows the time-frequency (TF) analysis of a signal. An interesting analogy between TF analysis and modern music notation is shown in Figure 2. Modern music notation gives an illustration of the time-frequency representation where the vertical position of the note-head within the staff indicates its pitch which can be modified by accidentals, associated with a frequency. For example, the frequency of A3 is set at 440 Hz. The time duration (note length, or note value) is indicated by the form of the note-head or with the addition of a note-stem plus beams or flags (cf. 2).

Among the large number of books on the wavelet transform method [4, 6, 3], few are dedicated to applications on civil engineering structures. The book by Chatterjee [7] describes several applications of wavelets to civil engineering problems and shows their importance, for example, in the analysis of non-stationarities in seismic ground motions, in the study of bridge vibrations caused by vehicle passage, or in the identification of structural damage. Furthermore, damaging events often result in short-time, non-stationary vibration characteristics that are difficult to analyse using classical modal approaches. Methods based on time-frequency representations, such as wavelet transform methods, are better suited to analysing signals generated by time-varying systems than those using the Fourier transform that are better suited to signals generated by time-invariant systems. This makes these time-frequency based methods a very interesting tool for structural damage detection.

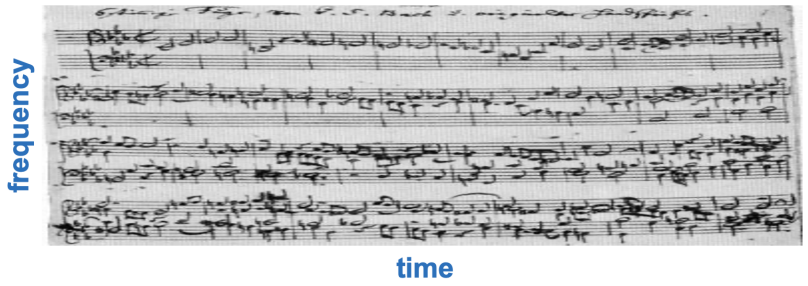


Figure 2: Writing of a musical piece: a famous illustration of time-frequency representation.

## 2 THE CONTINUOUS WAVELET TRANSFORM METHOD

The basic idea of the Continuous Wavelet Transform (CWT) method is to use a function $\psi(t) \in L^1(\mathbb{R}) \cap L^2(\mathbb{R})$ called the "mother wavelet"[1], which can generate an infinite continuous basis of functions, by varying the parameters $a$ and $b$:

$$\psi_{a,b}(t) = (1/a)\psi[(t-b)/a], \tag{1}$$

where $a$ is a scale parameter and $b$ a temporal localization parameter.

There is a clear relationship between the scale parameter $a$ and the frequency $f$. More specifically, a low value of $a$ results in a compressed wavelet, allowing to capture details that change rapidly in the processed signal, thus resulting in a high frequency content. On the other hand, a large value of $a$ results in a stretched wavelet, which captures slowly changing coarse features in the processed signal, resulting in a high frequency content. Thus, the ratio $1 \,/\, a$ can be assimilated to a frequency parameter $f$. There are several possible approaches that relate the scale $a$ to the inverse of the frequency, typically denoted: $a = f_\psi^* / f$. In the references [8, 10], $f_\psi^*$ is chosen to be equal to the peak frequency $f_\psi^0$, where $f_\psi^0 = \arg\max(|\widehat{\psi}|)$ and $\widehat{\psi}$ is the Fourier transform of the mother wavelet. Two other meaningful frequencies, classically found in literature, are the energy frequency: $\tilde{f_\psi}$[2] and the time-varying instantaneous frequency of the

[1] A function $\psi(t) \in L^1(\mathbb{R}) \cap L^2(\mathbb{R})$ can be admissible to a mother wavelet if it satisfies the admissibility condition : $C_\psi = \int_{-\infty}^{+\infty} \frac{|\widehat{\psi}(f)|^2}{|f|} df < \infty$ where $\widehat{\psi}(f) = \int_{-\infty}^{+\infty} \psi(t) e^{-2i\pi ft} dt$ is the Fourier transform of $\psi(t)$, which implies that $\int_{-\infty}^{+\infty} \psi(t) dt = 0$ . cf. [4].

[2] $\tilde{f}_\psi = \frac{\int_{-\infty}^{+\infty} f \left|\widehat{\psi}(f)\right|^2 df}{\int_{-\infty}^{+\infty} |\widehat{\psi}(f)|^2 df}$.

wavelet at its time center $\breve{f}_\psi(0)$ [3] (cf. [17]). These three definitions of $f_\psi^*$ result to three different mappings between scale and frequency. The first will correctly give the frequency of a pure harmonic signal from the scale $a$ at which its transform obtains a maximum. The second will correctly give the frequency of a pure cosine from the energy mean scale of the CWT $\widetilde{a_\psi}(b)$ [4]. The third fixes the frequency to be the same as the phase progression of the transform at the location of an infinitesimally narrow impulse.

To better highlight the importance of the choice of $f_\psi^0$, consider the example of the CWT of a cosine $u(t) = A_1 \cos(2\pi f_1 t + \theta_1)$. The CWT can be written as: $T_\psi[u](a,b) = \frac{1}{2} A_1 \widehat{\psi}(af_1) e^{i\theta_1}$ and its modulus $|T_\psi[u](a,b)| = \frac{1}{2} A_1 |\widehat{\psi}(af_1)|$ is maximal when $|\widehat{\psi}(af_1)|$ is maximal, so that $af_1 = f_\psi^0$ and $|T_\psi[u](a,b)| = A_1$. In addition, the energy mean scale of the CWT $\widetilde{a_\psi}(b)$ in the case of a pure cosine is equal to: $\widetilde{a_\psi}(b) = \tilde{f}_\psi \,/\, f_1$ [5].

Using a mother wavelet $\psi$, the CWT method is then used to decompose a function $u(t)$ into the time-frequency domain as follows:

$$T_\psi[u](a,b) = \frac{1}{a} \int_{-\infty}^{+\infty} u(t) \overline{\psi}\left(\frac{t-b}{a}\right) dt, \tag{2}$$

where $\overline{\psi}$ is the conjugate of $\psi$.

Regarding the regularizing term $1/a$ in the definition of Eq. 2. This term is appropriate when the magnitude of the modulus wavelet transform is wished to reflect the amplitude of the analysed signal $u(t)$. It is generally more useful to describe time-localized signals by their amplitude; hence, Eq. 2 uses the $1/a$ normalization which is known as the $L_1$ norm, it is used in Carmona *et al.* [4], preferred by Argoul [12, 13], or Lilly[15]. Instead, the factor $1/\sqrt{a}$ can guarantee that the wavelet maintains constant energy. This is known as the $L_2$ norm of $T_\psi$ and is more appropriate when one wishes that the modulus-squared wavelet transform reflects the energy of the analyzed signal.

The definition of CWT of Eq. 2 can be rewritten in the frequency domain:

$$T_\psi[u](a,b) = \int_{-\infty}^{+\infty} \widehat{u}(f) \widehat{\psi}(af) e^{2i\pi fb} df, \tag{3}$$

where $\widehat{u}(f) = \int_{-\infty}^{+\infty} u(t) e^{-2i\pi ft} dt$ is the Fourier transform of $u(t)$ and $\widehat{\psi}$ is the mother wavelet in the frequency domain. Eq. 3 allows for an easy numerical computation by means of the fast Fourier transform (FFT) algorithm.

### 2.1 Selection of mother wavelet

Apart from the widely-used Morlet wavelet, which is only approximately analytic, various analytic wavelets have been proposed, including the Cauchy-Paul, the derivative of the Gaussian wavelet, the lognormal or log Gabor, the Shannon and the Bessel, among others. Olhede and Walden [16] and Lilly and Olhede [17] have showed that all known analytic wavelets can be grouped together in a much larger family, first introduced by Daubechies and Paul [18], whose properties were studied in detail [19]. This broad "superfamily" of wavelets is known as the

[3] $\breve{f}_\psi(t) = \frac{1}{2\pi} \frac{d}{dt} \Im\{\ln \psi(t)\} = \frac{1}{2\pi} \frac{d}{dt} (arg\{\psi(t)\})$.

[4] $\widetilde{a_\psi}(b) = \frac{\int_{-\infty}^{+\infty} a |T_\psi[u](a,b)|^2 da}{\int_{-\infty}^{+\infty} |T_\psi[u](a,b)|^2 da}$.

[5] $\widetilde{a_\psi}(b) = \frac{\int_{-\infty}^{+\infty} a |T_\psi[u](a,b)|^2 da}{\int_{-\infty}^{+\infty} |T_\psi[u](a,b)|^2 da} = \frac{\frac{1}{4} A_1^2 \int_0^{+\infty} a \left|\widehat{\psi}(af_1)\right|^2 da}{\frac{1}{4} A_1^2 \int_0^{+\infty} \left|\widehat{\psi}(af_1)\right|^2 da} = \frac{1}{f_1} \frac{\int_0^{+\infty} f \left|\widehat{\psi}(f)\right|^2 df}{\int_0^{+\infty} \left|\widehat{\psi}(f)\right|^2 df} = \frac{\tilde{f}_\psi}{f_1}$.

generalized Morse wavelets. Within that family, one can objectively say which wavelet choice is the "best" for the problem at hand. The generalized Morse wavelets $\psi_{\beta,\gamma}$ depend on two parameters $\beta$ and $\gamma$ which control the shape of the wavelet. The general expression is as follows:

$$\widehat{\psi}_{\beta,\gamma}(f) = c_{\beta,\gamma} f^{\beta} e^{-(2\pi f)^{\gamma}} H(f) \tag{4}$$

where $c_{\beta,\gamma}$ is a normalization constant and $H(f)$ is the unit step function.

Among the broad family of generalised Morse wavelets, the Cauchy-Paul mother wavelet $\psi_n(t)$ has been preferred in our work. This is a complex single parameter mother wavelet where $n$ is an integer that controls the shape of the wavelet. With respect to Eq. 4, the Cauchy-Paul wavelet belongs to the Morse family when $\beta = n$ and $\gamma = 1$. The definition with respect to parameter $n$, becomes:

$$\widehat{\psi}_n(f) = c_n f^n e^{-2\pi f} H(f) \tag{5}$$

where $c_n$ is a normalization constant. An asymmetry in the frequency domain of the Cauchy-Paul wavelet leads to distinct values for the frequencies previously introduced in order to define the scale parameter $a = f_{\psi}^{*}/f$, i.e.:

$$f_{\psi_n}^{0} = \frac{n}{2\pi}, \quad \tilde{f}_{\psi} = \frac{n+\frac{1}{2}}{2\pi}, \quad \breve{f}_{\psi_n} = \frac{n+1}{2\pi}, \tag{6}$$

There are several ways to define the $c_n$ parameter. In older papers [11, 12, 13] we preferred the $L^{\infty}$ norm in the time domain: $\|\psi_n\|_{\infty} = 1$. In this paper we have chosen the norm: $\|\widehat{\psi}_n\|_{\infty} = \max|\widehat{\psi}_n(f)| = 2$, which leads to $c_n = 2(2\pi e/n)^n$. Therefore, the peak frequency is: $f_{\psi}^{0} = n/2\pi$, for which the maximum value is: $\widehat{\psi}_n(f_{\psi}^{0}) = 2$. This is the same choice as in Lilly [15], since it provides a direct equality between $|T_{\psi}[u](t, a(t))|$ and the amplitude of $u$.

There are several reasons for choosing an analytic mother wavelet, and in particular the Cauchy-Paul wavelet. The first is that an analytic mother wavelet which is a complex function whose spectrum contains only positive frequencies, leading to: $\widehat{\psi}_n(f) = 0 \ \forall \ f < 0$. As an analytic mother wavelet, it only responds to non-negative frequencies in the signal being analysed and it produces a transform whose modulus is less oscillatory than in the case of a real mother wavelet. This property is a real advantage for detecting and tracking the instantaneous frequencies contained in the signal. Eq. 3 is simplified as follows:

$$T_{\psi}[u](a,b) = \int_0^{+\infty} \widehat{u}(f)\widehat{\psi}(af)\, e^{2i\pi fb} df. \tag{7}$$

The second reason concerns the phase retrieval problem which is related to the reconstruction of a function from its scalogram, that is, from the modulus of its wavelet transform. Mallat and Waldspurger [20] mathematically proved that the reconstruction of the analyzed function from the modulus of its Cauchy-Paul wavelet transform is unique up to a global phase. They have also showed that the reconstruction operator is continuous but non uniformly continuous. The authors specify that the proofs are special to Cauchy-Paul wavelets and cannot be extended to generic wavelets because they make intensive use of the link between Cauchy wavelets and holomorphic functions.

### 2.2 Resolution in the time-frequency domain

For the successful CWT decomposition, it is essential to control the *time-frequency resolution* of the signal wavelet transform. This is necessary in order to correctly interpret the CWT plot and also to take into account *edge effects* [13].

Referring to the conventional frequency analysis of constant-$Q$ filters, Le and Argoul [13] introduced a parameter $Q_m$ called "quality factor". This parameter can be used in order to control the time-frequency resolution of the CWT. Introducing the duration $\Delta t$ and the frequency bandwidth $\Delta f$ of the wavelet transform and its relationship with the the duration $\Delta t_\psi$ and the frequency bandwidth $\Delta f_\psi$ of the mother wavelet are as follows:

$$\Delta t \;=\; a\,\Delta t_\psi \qquad\qquad \Delta f \;=\; \frac{\Delta f_\psi}{a}, \tag{8}$$

where $\Delta t_\psi$ and $\Delta f_\psi$ are stated in terms of root mean squares for $L_2$ norm which are equivalent to the standard deviation in statistics:

$$\begin{aligned} \Delta t_\psi &= \frac{1}{\|\psi\|_2^2}\int_{-\infty}^{+\infty}\left(t-t_\psi\right)^2\,|\psi(t)|\,dt \\ \Delta f_\psi &= \frac{1}{\|\widehat{\psi}\|_2^2}\int_{-\infty}^{+\infty}\left(f-f_\psi\right)^2\,|\widehat{\psi}(f)|^2\,df, \end{aligned} \tag{9}$$

where $t_\psi$ and $f_\psi$ are the centre of $\psi$ and $\widehat{\psi}$, respectively:

$$t_\psi \;=\; \frac{1}{\|\psi\|_2^2}\int_{-\infty}^{+\infty} t\,|\psi(t)|^2\,dt \qquad\qquad f_\psi \;=\; \frac{1}{\|\widehat{\psi}\|_2^2}\int_{-\infty}^{+\infty} f\,|\widehat{\psi}(f)|^2\,df. \tag{10}$$

It is noteworthy to introduce the CWT uncertainty $\mu$, equal to the mother wavelet uncertainty $\mu_\psi$:

$$\mu \;=\; \Delta t\,\Delta f \;=\; \Delta t_\psi\,\Delta f_\psi \;=\; \mu_\psi \tag{11}$$

Using the relationship between scale and frequency previously discussed ($a \;=\; f_\psi^*/f$), Eq. 8 becomes:

$$\Delta t \;=\; \frac{f_\psi^*\,\Delta t_\psi}{f} \propto \frac{1}{f} \qquad\qquad \Delta f \;=\; \frac{\Delta f_\psi}{f_\psi^*}\,f \propto f, \tag{12}$$

This $Q_m$ factor introduced in [13] is defined as the ratio of the mean value $\tilde{f}$ (for $L_2$ norm) previously defined over two times its standard deviation $\Delta f$ of the wavelet transform, i.e.:

$$Q_m = \frac{\tilde{f}}{2\Delta f} = \frac{\frac{\tilde{f}_\psi}{a}}{2\frac{\Delta f_\psi}{a}} = \frac{\tilde{f}_\psi}{2\Delta f_\psi}. \tag{13}$$

Notice from Eq. 13 that the resolution parameter $Q_m$ is independent of the frequency parameter $a$. From the formulae above, it is easy to see that:

$$\Delta t \;=\; 2\,Q_m\,\mu_\psi\,\frac{f_\psi^*}{\tilde{f}_\psi}\,\frac{1}{f} \qquad\qquad \Delta f \;=\; \frac{1}{2\,Q_m}\,\frac{\tilde{f}_\psi}{f_\psi^*}\,f. \tag{14}$$

where the ratio $\frac{\tilde{f}_\psi}{f_\psi^*}$ is close to 1 and equal to 1 if $f_\psi^* \;=\; \tilde{f}_\psi$; for example for Cauchy wavelet it depends on the value of $n$ (Eq. 6).

Thus, a small $Q_m$ value increases the resolution in the time axis ($\Delta t$ small), while a large value increases the frequency resolution ($\Delta f$ small).

Properly adjusting the $Q_m$ parameter is particularly important in the case of two close Eigenmodes which allows to separate them. In reference [13], it was shown that the value of $Q_m$ can be chosen within the limits below:

$$Q_m^{(min)} = c_f \frac{f_j}{2\,D f_j} \leq Q_m \leq Q_m^{(max)} = \frac{\pi L f_j}{c_t}, \tag{15}$$

where $L$ is the length of the signal, $c_t$, $c_f$ are constants that are used to identify edge effects in the time and the frequency domain, respectively, $f_j$ is the Eigenfrequency of interest and $Df_j$ is its distance from the closest Eigenfrequency. Note that typically $c_t$ and $c_f$ receive values between 3 and 5.

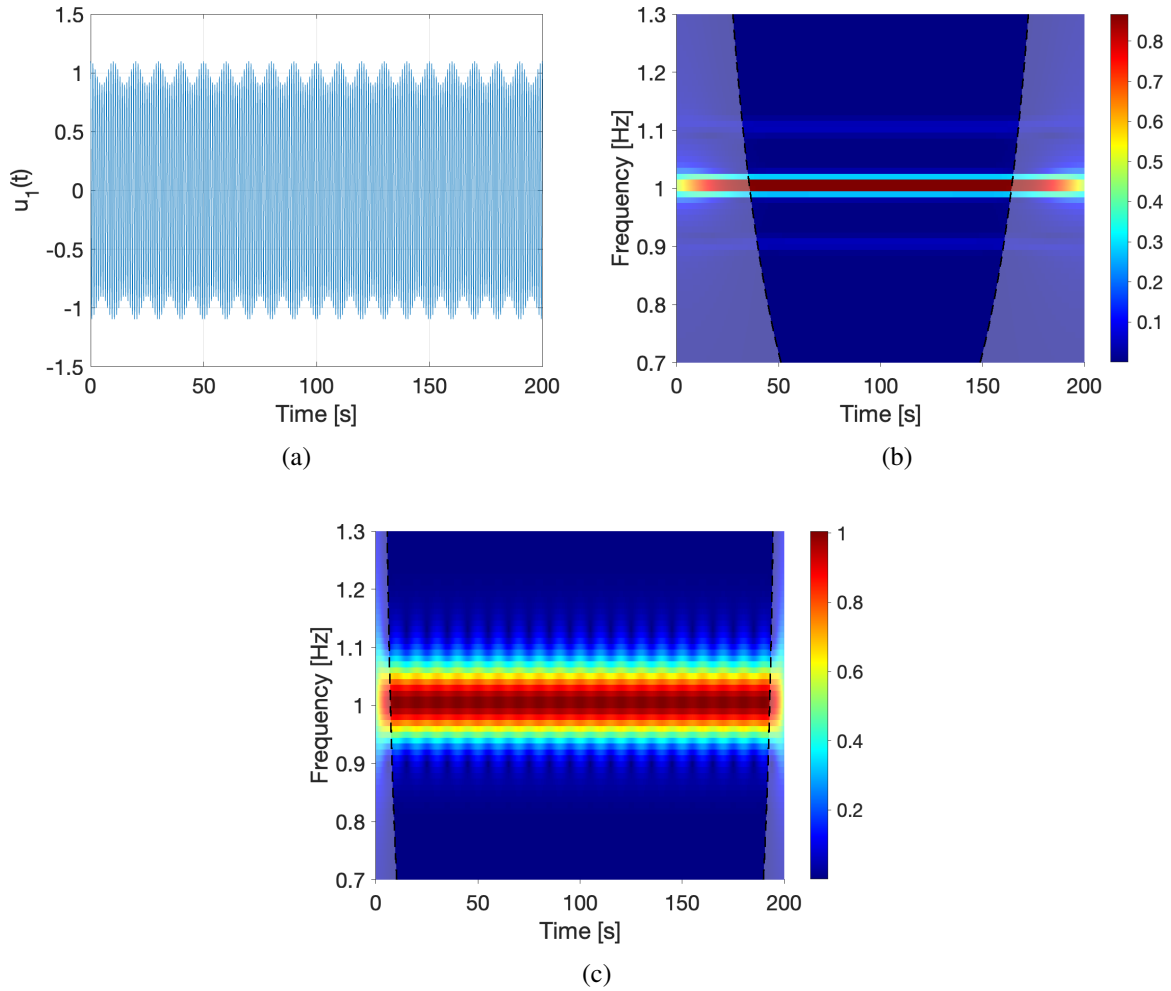


Figure 3: Wavelet analysis on a amplitude-modulated signal $u_1(t) = A(t)\cos(2\pi t)$ with $A(t) = 1 + 0.2\cos(2\pi t/10)$: (a) the signal $u_1(t)$ in the time domain, (b) scalogram computed with $Q_m = 75$ and (c) scalogram computed with $Q_m = 15$.

The importance of the resolution parameter can be understood from the two examples of Figures 3 and 4. The figures present two examples of signals, with their time-frequency scalogram plots.

The first example concerns the amplitude modulated signal $u_1(t) = A(t)\cos(2\pi t)$, where $A(t) = 1 + 0.2\cos(2\pi t/10)$ (Figure 3a). The expression for $u_1(t)$ can be misleading. By developing the equation using trigonometric formulae, it can be shown that $u_1(t)$ is the sum of three cosines: $u_1(t) = \cos(2\pi t) + 0.1\cos(\frac{11}{10}2\pi t) + 0.1\cos(\frac{9}{10}2\pi t)$ which can be identified in the scalogram plot of Figure 3b) as three horizontal ridges. Due to the amplitude dominance of the first term at 1Hz, the other two frequencies at $9/10$ and $11/10$Hz cannot be seen unless the quality factor $Q_m$ is chosen "correctly". According to Eq. 15, the bounds are: $Q_m^{(min)} = 25$ and $Q_m^{(max)} = 125.6$ respectively, with $c_t = c_f = 5$, $f_j = 1Hz$, $\Delta f = 1$ / 10 Hz and $L = 200s$. If we had chosen a quality factor lower than $Q_m^{(min)} = 25$, giving precedence to time resolution over frequency resolution, the scalogram plot would have shown oscillations at the edges, as shown in Figure 3c.

The second example (Figure 4) is that of an acoustic signal $u_2(t)$ measured when the passage of a semi-trailer on a joint of pavement in very good condition on a motorway bridge and plotted in Fig. 4a). The frequency content of this signal is mainly between $0$ Hz and $2500$ Hz (see. Fig. 4b)). Zooming in on the amplitude spectral density of $u_2(t)$, which is the square root of its classical Pseudo Spectral Density (PSD) over this frequency range, we see three main peaks around the frequencies $250, 600$ and $900$Hz. Table 1, shows the limits of the $Q_m$ factor: $Q_m^{(min)}$ and $Q_m^{(max)}$, for the three frequency values obtained using Eq. (15). Two scalograms of this signal are then plotted for two different values of the quality factor in Figures 4c) and 4d): $Q_m = Q_m^{(min)} = 2$ and $Q_m = Q_m^{(max)} = 125$, respectively, corresponding to the limits: $Q_m^{(min)} = 2$ and $Q_m^{(max)} = 125$ for the relevant frequency: $f_j = 250Hz$ given in Table 1.

A comparison of these two scalograms provides an obvious interpretation. The lower the value of $Q_m$, the more visible the time effect is, with the vertical lines corresponding to the times that the 5 axles of the semi-trailer passed over the pavement joint.

Table 1: Values of the limits of the quality factor $Q_m^{(min)}$ and $Q_m^{(max)}$ from Eq. (15) corresponding to the three frequency peaks in the FT of the signal generated by the passage of a semi-trailer over the joint.

| Relevant frequency | | |
|---|---|---|
| $f_j\ (Hz)$ | $Q_m^{(min)}$ | $Q_m^{(max)}$ |
| 250 | 2 | 125 |
| 600 | 5 | 301 |
| 900 | 7.5 | 452 |

Another point of interest, also related to $Q_m$ is the *edge-effect* problem. The problem is attributed to the finite length of the signal, the discretization of the measured data record and to the nature of the CWT. Edge effects cannot be removed and there will always be a domain in the time-frequency plane that should be neglected due to this problem. Edge effects are seen with dashed lines in Figs. 3 and 4; the effect of the quality parameter $Q_m$ on edge effects is evident. As the $Q_m$ value increases, the edge effects become more significant, thus the useful time interval for modal identification is reduced but the decoupling of the modes is more effective.

In reference [14], based on a study on simulated digital signals, the authors concluded that the choice of $Q_m$ is a compromise between two objectives, (i) to discriminate close frequencies (in which case larger values of $Q_m$ are preferred), (ii) to adopt a correct temporal resolution

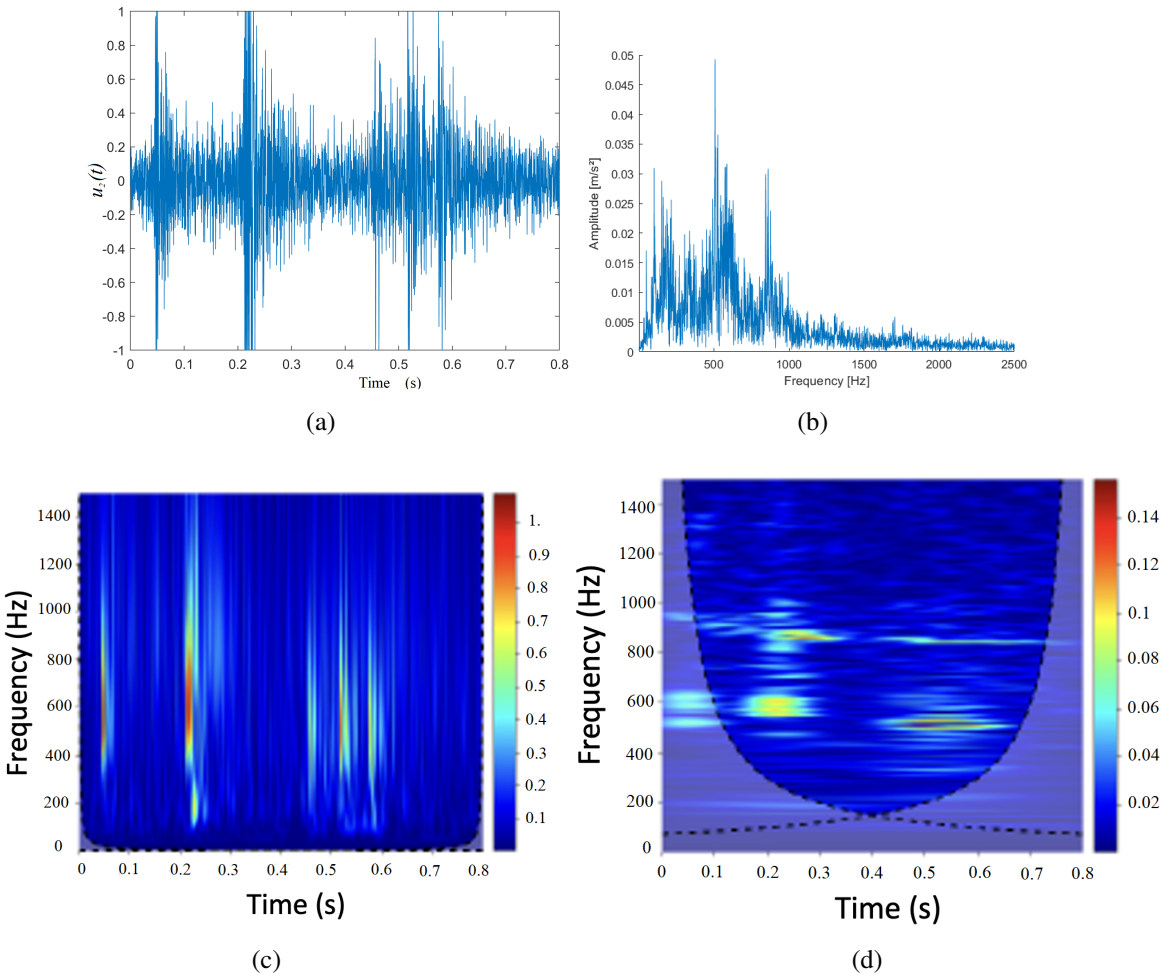


Figure 4: Acoustic response $u_2(t)$ of a joint of pavement on a motorway bridge measured when a semi-trailer passes by: (a) time response, the amplitude is normalised between $[-1, 1]$, note that on this recording, the passage of a lorry saturates the microphone, (b) amplitude spectral density of $u_2(t)$ over the range [0, 2500]Hz, (c) Scalogram of $u_2(t)$ computed with $Q_m = Q_m^{(min)} = 2$ for $f_j = 250Hz$ and (d) Scalogram of $u_2(t)$ computed with $Q_m = Q_m^{(max)} = 125$ for $f_j = 250Hz$.

for the detection of abrupt frequency changes (in which case smaller values of $Q_m$ are more effective).

In conclusion, the computation of CWT of Eq. 7 can be performed for $f = f_\psi^0 \,/\, a = n \,/\, (2\pi a)$ within a chosen frequency band and with an adapted time-frequency resolution $Q_m$. This remark led Rouby *et al.* [21] to introduce an adapted CWT: $T_\psi[u](f_\psi^0 \,/\, f, b)$ with a time-frequency resolution varying for each frequency, leading to a uniform resolution in the whole time-frequency plane.

## 3 ASYMPTOTIC SIGNALS - RIDGE DEFINITION AND EXTRACTION

### 3.1 One component signal

Several authors [4, 5, 22, 23] have worked on the use of CWT for so-called asymptotic signals. The typical example is the chirp model [4, 5] which is a pseudo-periodic signal modulated in frequency around a carrier frequency and also modulated in amplitude by an envelope whose

variations are slow compared with the oscillations of the phase [23]. The CWT results that are obtained in the context of asymptotic signals are very useful in particular for modal analysis [13]. The first step is to uniquely associate to any real signal $u(t)$ a canonical amplitude $A^{(u)}(t)$, assumed to be positive, and a phase $\theta^{(u)}(t)$ assumed to be increasing, and satisfying: $u(t) = A^{(u)}(t)\,\cos(\theta^{(u)}(t))$. $A^{(u)}(t)$ and $\theta^{(u)}(t)$ can be determined with the aid of the Hilbert transform $\mathcal{H}[u]$ which is defined in the Fourier domain as: $\widehat{\mathcal{H}[u]}(f) = -isgn(f)\,\widehat{u}(f)$ and allows the definition of the analytical signal $Z_u(t)$ associated to $u(t)$ such as:

$$Z_u(t) = u(t) + i\mathcal{H}[u](t) = A^{(u)}(t)\,e^{i\,\theta^{(u)}(t)} \tag{16}$$

Several authors have showed that the CWT of an asymptotic signal will tend to "concentrate" in the neighborhood of a curve $a_1(t)$ called "ridge" that consists of an aggregation of points called ridge points. The ridge points are commonly obtained either from the CWT modulus of the signal, or from its phase, and are called *amplitude ridge points* and *phase ridge points*, respectively [24].

In the time-scale map, a ridge can be defined (see reference [23]) from its canonical phase $\theta^{(u)}$ by:

$$a_1(t) = \frac{2\pi\, f_\psi^*}{\dot{\theta}^{(u)}(t)}, \tag{17}$$

where $f_\psi^*$ appears in the chosen mapping between scale and frequency previously detailed. The restriction of the CWT to the ridge $a_1(b)$, is called the "skeleton" of the wavelet transform. From the skeleton, it is possible to reproduce the signal, or more precisely, what is associated with the analytical signal $Z_u(b)$), while it behaves like the product of $Z_u(b)$ by a multiplicative factor entirely characterised by the mother wavelet and the ridge $a_1(b)$ :

$$T_\psi[u](a_1(b), b) \;=\; \frac{1}{2}\,\overline{\widehat{\psi}}\left(a_1(b)\dot{\theta}^{(u)}(b)\right) Z_u(b) = \frac{1}{2}\,\overline{\widehat{\psi}}\left(2\pi\, f_\psi^*\right) Z_u(b). \tag{18}$$

The process of estimating the ridge from the absolute value and/or from the phase information of the CWT of the signal is called "ridge extraction". Different techniques for extracting ridges exist [4] and can be classified into two categories: the "differential" and the "global" methods [13].

Differential methods rely on local properties of the CWT of the signal $u(t)$, they are verified theoretically on the ridge curve and they are based on the partial differential equations of the CWT. The differential method used here is based on the modulus of $T_\psi[u](a, b)$, which is maximum at $b$ in the vicinity of the ridge, and therefore verifies a cancellation of its partial derivative at $a$. This definition is given in [24] and its implementation has the advantage that it is particularly simple and stable since it is a simple search for maxima.

The global methods, introduced in reference [25], are based on the search for curves that maximize the energy of the CWT while maintaining a certain regularity of the solution. When the considered frequency and amplitude modulated signal is embedded in noise and near the ridges, the contribution of the signal is much larger than that of the noise, while the wavelet transform of the noise spreads in the whole time-frequency plane. Several algorithms for global ridge extraction are detailed in the book by Carmona *et al.* [4] and are discussed with reference to their robustness to noise.

Once the ridge extraction method has been chosen and the ridge has been determined, the analytical signal $Z_u(b)$ can be obtained. Its real and imaginary parts give the signal and its Hilbert transform, respectively. The final goal of ridge extraction is to get an estimate of $\dot{\theta}_u(t)$ from Eq. 17 and then of $Z_u(b)$ feeding it back into Eq. 18.

### 3.2 Multicomponent signals

The analytical expression of the structural responses of linear systems is well-known, even in the case of non-proportionally damped systems [26]. The aim of this section is to characterise the behaviour of structures from multi-channel dynamic signals obtained from measurements made by a set of $N$ sensors, typically accelerometers. The set of displacement measurements at these sensor points is grouped into the vector: $\mathbf{u} = [u_1, u_2, \cdots, u_N]^T$. Note that this notation is generic and can also be used when the signal is an acceleration. The modal decomposition expresses the state equation as a linear combination of the various modes of the system. Thanks to the modal decomposition approach for linear systems, every signal can be expanded as a linear combination of the different modes of the system, e.g. $M$ components, each corresponding to a different Eigenmode of the structure [26]. The CWT of each component of $\mathbf{u}$ is also grouped in the vector $\boldsymbol{T_\psi}[\mathbf{u}]$, as follows:

$$\boldsymbol{T_\psi}[\mathbf{u}](a,t) = \left[T_\psi[u_1](a,t), T_\psi[u_2](a,t), \ldots, T_\psi[u_N](a,t)\right]^T \tag{19}$$

Therefore, the displacement $u_k(t)$, taking into account the $M$ modes, can be obtained as:

$$u_k(t) = \Re \sum_{l=1}^{M} \left\{ A_l^{(u_k)}(t)\, e^{i\,\theta_l^{(u_k)}(t)}\, \Phi_k^{(l)} \right\}, \tag{20}$$

where $A_l^{(u_k)}(t)\, e^{i\,\theta_l^{(u_k)}(t)}$ is the analytical modal participation factor of the $l$-th complex mode $\boldsymbol{\Phi^{(l)}}$ ($\Phi_k^{(l)}$ being its $k$-th component) to the structural response $\boldsymbol{u_k}(t)$, while its real part are assumed to be asymptotic [6].

The vector $\boldsymbol{\phi^{(l)}}$ is the complex $l$-th mode, which we have chosen to normalise as $(\boldsymbol{\phi^{(l)}})^T\, \boldsymbol{\phi^{(l)}} = 1$, based on the generalisation of a criterion usually used for real modal deformations: $||\boldsymbol{\phi^{(l)}}||^2 = 1$ (cf. Carpine [10]). In the case of free responses, the dynamic signals contain the vibrations of each mode of the structure, associated with an exponentially damped sinusoidal component. Thus, Eq. (20) becomes:

$$u_k(t) = \Re \sum_{l=1}^{M} \left\{ A_l^{(u_k)}(t)\, e^{i\,\theta_l^{(u_k)}(t)}\, \Phi_k^{(l)} \right\} = \Re \sum_{l=1}^{M} \left\{ Z_l^{(u_k)} e^{i\,\lambda_l t} \Phi_k^{(l)} \right\}, \tag{21}$$

where $Z_l^{(u_k)}$ is a complex constant, $\lambda_l = 2\pi\, i\, f_l \sqrt{1-\xi_l^2} - \xi_l\, 2\pi\, f_l$ is the $l$-th pole and $f_l$, $\xi_l$ are the Eigenfrequency and the modal damping ratio associated with mode $l$, respectively.

With the aid of the above form, which is a sum of asymptotic amplitude and frequency modulated components, in the case of a single asymptotic amplitude and frequency modulated signal, the absolute value of its CWT tends to concentrate near the "ridges" of the transform [4]. In the time-frequency plane, the ridge is a well-defined region, but most importantly, the wavelet transform acts as a "regularizing" filter that concentrates the information that is carried within the signal and hence allows to characterize the instantaneous frequencies.

Based on the discussion above, the linearity of the CWT and a good choice of the mother wavelet $\psi$ can allow to separate these different components and extract the ridge for each of them. There are several approaches for detecting multiple ridges, the final choice depends on their interaction, or their independence. When these ridges do not interact and are located at

[6] the real part of $u_k$ is equal to $A_l^{(u_k)}(t)\, \cos\left(\theta_l^{(u_k)}(t)\right)$

distinct regions of the time-frequency plane, a frequently encountered case in the analysis of dynamic signals for which each instantaneous frequency remains in the vicinity of a horizontal straight line, the methods previously mentioned can be implemented as in [13, 27].

As previously discussed, the ridges can then be deduced using Eq. 17. A common problem is when there are two close Eigenfrequencies, $f_j$ and $f_k$. The possibility of extracting the ridges is guaranteed if the following condition is satisfied:

$$\xi_j \leq \frac{\sqrt{2}}{c_f} \frac{|f_j - f_k|}{f_j}, \tag{22}$$

where $c_f$ is a constant related to edge effects [28], $\xi_j$ is the modal damping ratio of the $j$-th mode and the $j$ and $k$ indexes correspond to two neighboring modes $j$ and $k$, respectively. If the condition of Eq. 22 is not met, the extraction of accurate ridges is not guaranteed and may even not be possible since the modes are too close and they cannot be separated in the case that they are heavily damped. This tells us that two close modes cannot be well separated from each other if they are damped too much. Figure 5 plots the $\xi_j$ values as function of $f_j$ and $\Delta f = |f_j - f_k|$ for $c_f = 3$. If the condition of Eq. 22 is met, the extraction of accurate ridges is guaranteed, provided that the quality factor $Q_m$ is appropriately chosen, as already discussed in Eq. 13 and Section 2.1.

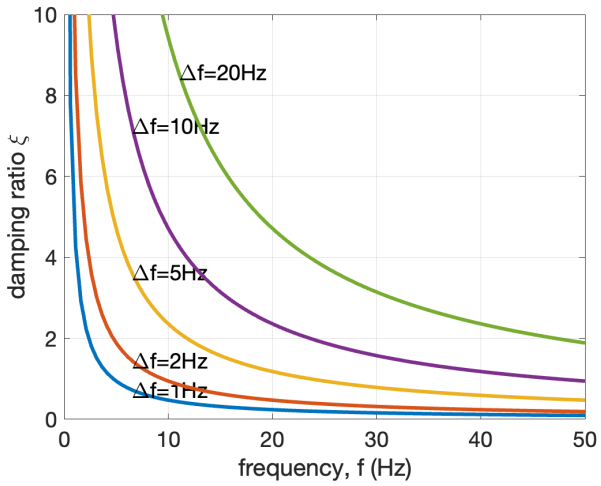


Figure 5: Relationship between damping ration and frequency for ridge identification according to Eq. 22 ($c_f = 3$).

As already discussed, at each measurement point $u_k$, $k \in [1, N]$, a set of ridges $a_k^{(l)}(t)$ can be extracted from the time-frequency plot, for the $l$-th mode excited by the shock, where $l = 1, \ldots, M$. For the extraction of ridges, differential methods based on a local analysis of the extrema of the CWT modulus are here preferred. Thus the ridges, or the instantaneous frequencies $a_l^{(k)}(t)$, are extracted by the computation of local maxima of $\left|T_\psi[u_k](a,t)\right|$ as function of time $t$ and for the $l$-th mode excited by the shock:

$$a_l^{(k)}(t) = arg_a max \left|T_\psi[u_k](a,t)\right|. \tag{23}$$

So, for a mode $l$, a set of $k = 1, \ldots, M$ ridges $a_l^{(k)}(t)$ is obtained, and a procedure to retain only one ridge for the instantaneous frequency must be then made, in [13], for example assuming the

average of the $k$ signals:

$$a_l^{\text{mean}}(t) = \frac{1}{N}\sum_{k=1}^{N} a_l^k(t) \tag{24}$$

An alternative way of obtaining a single ridge $a_\Sigma^{(l)}(t)$ for mode $l$ instead of several ridges $a_l^{(k)}(t)$ (one for each measurement point) was recently been proposed by the authors in [8]. This new procedure is based on the computation of the Averaged Continuous Wavelet Transform (ACWT) $\widetilde{T_\psi}[\boldsymbol{u}](a,t)$, which combines the CWTs of each measurement point $u_k$ ($k \in [1, N]$), as follows:

$$\widetilde{T_\psi}[\boldsymbol{u}](a,b) = \sum_{k=1}^{N} [T_\psi[u_k](a,b)]^2. \tag{25}$$

Eq. (25) is suitable for ridge extraction in the case of free responses of systems whose Eigenvectors are real or with a negligible imaginary part, which is the case of weakly damped systems [26] and practically refers to all civil engineering structures. In fact, the use of the squares of the transforms makes it possible to orient the contributions of the useful signal in each measurement channel according to the same orientation in the complex plane, while those of noise remain a priori randomly distributed. Therefore, Eq. (25) allows to obtain a single ridge $a_\Sigma^{(l)}(t)$ for mode $l$ as follows:

$$a_\Sigma^{(l)}(t) = arg_a \max \left| \left[\widetilde{T_\psi}[\boldsymbol{u}](a,t)\right] \right|^{\frac{1}{2}} = arg_a \max \left| \sum_{k=1}^{N} \left[T_\psi[u_k](a,t)\right]^2 \right|^{\frac{1}{2}}. \tag{26}$$

Finally, for both definitions of the ridges, i.e. $a_l^{\text{mean}}(t)$ (Eq. 23), or $a_\Sigma^{(l)}(t)$ (Eq. 26), a procedure has been proposed in [8] to smooth the result of the maxima obtained for each time $t$; for two neighbouring points in frequency of a maximum to the right and to the left make it possible to perform a parabolic interpolation from which we obtain the coordinates of a new ridge in the time scale plane for the mode $l$ under consideration $(t, \breve{a}_k^{(l)}(t))$, or $(t, \breve{a}_\Sigma^{(l)}(t))$. A procedure for chaining the discrete points of the time-frequency plane to transform them into ridges is finally performed (cf. [4]). The set of maxima of the absolute value of the CWT along the ridges present in the signal forms the skeleton of the CWT of the signal. According to the definition chosen for a ridge $l$ in eq. (23) or in eq. (26), the absolute value of the CWT along each ridge $T_\psi[u]\left(\breve{a}_k^{(l)}(t), t\right)$ or the ACWT along the single ridge $\widetilde{T_\psi}[\boldsymbol{u}]\left(\breve{a}_\Sigma^{(l)}(t), t\right)$ is preferred.

## 4 SYSTEM DYNAMIC CHARACTERIZATION

The modal parameters of a system under transient vibrations can be identified by extracting the ridges and the skeleton of the CWT time-frequency representation. Once the ridges of the CWT have been extracted, the instantaneous frequencies, the modal damping ratio and the modal shapes can be estimated. If the system is purely linear, the shape of the ridges associated with the Eigenfrequencies will be a straight horizontal line. Furthermore, the damping ratio of the modes of interest can be estimated from the exponential decrease in amplitude associated with these ridges, and finally the modal shapes can be obtained from the relative amplitudes and phase shifts between the channels corresponding to the different sensors.

Therefore, the extraction of the "ridges" is a critical aspect for the successful application of the CWT for modal identification in the case of transient structural responses. Among the authors who have used the CWT for modal identification from transient structural responses, we

can cite two references published in 1997: Staszewski [29] and Ruzzene *et al.* [30]. Staszewski [29] proposed several CWT-based methods for estimating damping ratios and applied them to simulated multi Degree-of-freedom (DoF) systems. Ruzzene *et al.* [30] showed that the CWT analysis of the free response of a system allows the estimation of its natural frequencies and viscous damping ratios. A more complete procedure, which also gives access to frequencies and modal shapes, can be found in Lardies & Gouttebroze [31]. In Le & Argoul [13], the authors propose a more precise and complete method where the choice of the mother wavelet, its quality factor and the management of the edge effects of the TOC are studied in depth. The subsequent article by Erlicher & Argoul [27] discusses the use of this procedure in the case of systems with non-proportional damping, and therefore in the presence of complex deformations.

For amplitude and phase modulated signals of the form: $u(t) = A(t)\cos(\phi(t))$, the restriction of the wavelet transform to its ridge behaves mainly as the associated complex signal of $u(t)$: $A(t)\exp[i\phi(t)]$. This representation also allows the reconstruction of such original signals in non-significant noise situations [4]. If the system behaviour is close to be linear, from the CWT (or the ACWT) of its transient responses, the extracted ridges are similar to horizontal lines and the associated skeleton has an exponential decrease [13]. The logarithm $\log\left|\widetilde{T_\psi}[\boldsymbol{u}](\breve{a}_k^{(l)}(t),t)\right|$ for the CWT, or $\log\left|\widetilde{T_\psi}[\boldsymbol{u}](\breve{a}_\Sigma^{(l)}(t),t)\right|$ for the ACWT can be then deduced and the calculation of the slope of the "straight lines" for each mode $l$ can be performed in order to estimate the corresponding modal damping ratio of the $l$-th mode. The slope allows to get an estimate to the near sign of the product $2\pi\, f_l\, \xi_l$ that is the reciprocal of the time constant characterizing the exponential decay of the $l$-th mode.

The calculation of the Eigenshapes requires a set of measurements grouped in the vector: $\mathbf{u} = [u_1, u_2, \cdots, u_N]^T$. The CWT of each component of $\mathbf{u}$ along the smoothed ridge $\breve{a}_\Sigma^{(l)}$ of mode $l$ are also grouped in the vector $\boldsymbol{T_\psi}[\mathbf{u}]$, as follows:

$$\boldsymbol{T_\psi}[\mathbf{u}](\breve{a}_\Sigma^{(l)}(t),t) = \left[T_\psi[u_1](\breve{a}_\Sigma^{(l)}(t),t), T_\psi[u_2](\breve{a}_\Sigma^{(l)}(t),t), \cdots, T_\psi[u_N](\breve{a}_\Sigma^{(l)}(t),t)\right]^T \quad (27)$$

Depending on the choice made for the definition of the ridge, i.e. either Eq. 23, or Eq. 26, the instantaneous complex modal shapes $\phi^{(l)}(t)$ can be derived from the relative amplitude and phase of the CWT calculated along each ridge. There are several ways to normalise the modal vector. One way is to choose the unit amplitude for the measurement point $u_{\max}$, where the $\max$ index corresponds to the measurement point where the modal amplitude is greatest [13]. The $k$-th component $\phi_k^{(l)}(t)$ of the "instantaneous" complex mode can be expressed as follows:

$$\phi_k^{(l)}(t) = \frac{T_\psi[u_k](\breve{a}_k^{(l)}(t),t)}{T_\psi[u_{max}](\breve{a}_l^{(l)}(t),t)}. \quad (28)$$

As already discussed above, in this work we prefer the following scaling condition: $\left(\phi^{(l)}(t)\right)^{\mathrm{T}}\phi^{(l)}(t) = 1$ for instantaneous mode shape $\phi^{(l)}(t)$ [8, 10]. This definition results to:

$$\phi_k^{(l)}(t) = \pm\frac{\mathbf{T}_\psi[u_k](\breve{a}_\Sigma^{(l)}(t),t)}{\left[\mathbf{T}_\psi[\mathbf{u}](\breve{a}_\Sigma^{(l)}(t),t))^{\mathrm{T}}\,\mathbf{T}_\psi[\mathbf{u}](\breve{a}_\Sigma^{(l)}(t),t))\right]^{1/2}}, \quad (29)$$

where the sign follows the continuity of $\phi_k^{(l)}$ over time. The amplitude of mode $l$ is then equal to:

$$A_l(t) = \left|\mathbf{T}_\psi[\mathbf{u}](\breve{a}_\Sigma^{(l)}(t),t)^{\mathrm{T}}\,\mathbf{T}_\psi[\mathbf{u}](\breve{a}_\Sigma^{(l)}(t),t)\right|^{1/2} \quad (30)$$

To obtain a "constant" mode, especially in the case of linear behaviour, the mean value over time, denoted $\overline{\phi}$, can be calculated for each component $k$ of the $l$-th mode:

$$\overline{\phi_k}^{(l)} = \frac{1}{t_f - t_i} \int_{t_i}^{t_f} \phi_k^{(l)}(t)\, dt. \tag{31}$$

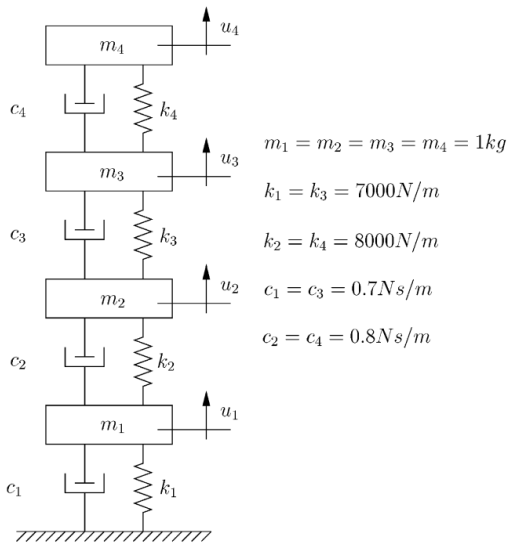


Figure 6: Characteristics of the four DoF system [13].

## 5 Applications

### 5.1 Numerical example: Transient response of a four DoF structure

The first example is the four DoF mass spring-damper model originally studied by Le and Argoul [13] and revisited here. The characteristics of the system are shown in Figure 6. The structure is displaced from original position by imposing initial displacements: $u_1 = 1.00$m, $u_2 = 0.75$m, $u_3 = 0.50$m and $u_4 = 0.25$m and zero velocities ($\ddot{u}_1 = \ddot{u}_2 = \ddot{u}_3 = \ddot{u}_4 = 0$). The system is left to freely oscillate after the initial displacements. The sample of duration $L = 5$ sec is taken over $M = 1024$ points (sampling period $T = 0.0049$ sec). The wavelet analysis is performed using the Cauchy wavelet, while for the edge effect $c_t = c_f = 3$ is assumed.

Figure 7 shows the displacement response histories of the four DoF system. Furthermore, Figure 8 shows the modulus of the squared ACWT for three $Q_m$ values, i.e $Q_m = 5, 15$ and $30$. The large $Q_m$ value ($Q_m = 30$) allows to clearly see the Eigenfrequencies, but the edge effects become more prominent, since the value $Q_m = 30$ exceeds the maximum value $Q_m^{(max)}$ according to Eq. 15 (see also Table 2).

Figure 9a shows the squared ACWT for $Q_m = 20$ and the four ridges identified, i.e. $a_\Sigma^{(i)}(t)$, $i = 1, 2, 3, 4$. Due to the linear response, the ridges are straight, while due to the large $Q_m$ value, the ridge identification of the first mode is restricted to a narrow region by the edge effects. Moreover, Figure 9b shows the plots of $\widetilde{T_\psi}[\boldsymbol{u}](a, b)$, i.e. of the squared ACWT ridges versus time and the corresponding ridges $\alpha_\Sigma^{(l)}(t)$. The slope of each curve provides the modal damping ratio. Notice that, since the ACWT is squared (see Eq. 25), the slope should be divided by 2. Finally, Figure 10 shows the four averaged Eigenmodes $\overline{\phi}$ obtained after applying Eq. 29

and Eq. 31. The integration limits $[t_f, t_i]$ of Eq. 31 are determined by the edge effects for the frequency of interest.

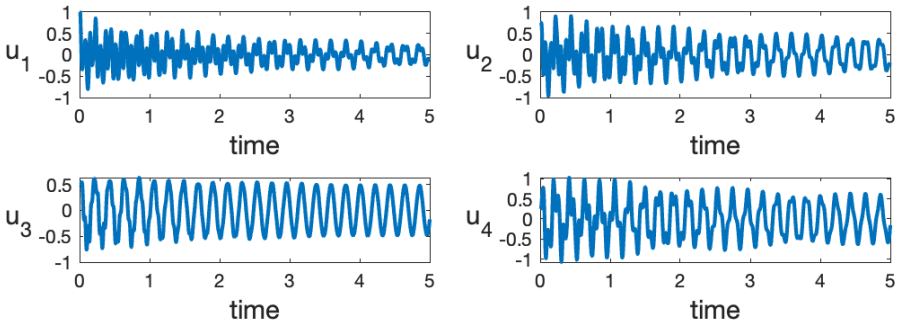


Figure 7: Response histories for the four-DoF system.

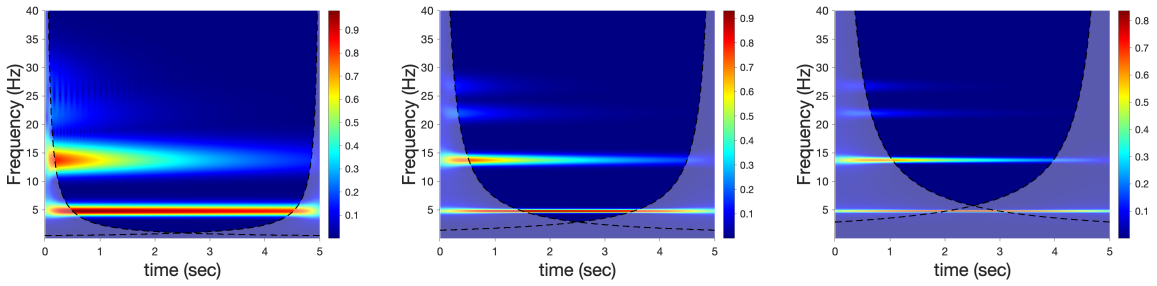


(a) (b) (c)

Figure 8: Scalogram $\left|\widetilde{T_\psi}[\boldsymbol{u}](a,b)\right|$ computed for: (a) $Q_m = 5$, (b) $Q_m = 15$, (c) $Q_m = 30$.

Table 2 summarizes the results of this first example. The first three columns provide the minimum and maximum values of the $Q_m$ parameter obtained with Eq. 15. Since the problem is simulated, the exact Eigenfrequencies and the modal damping ratio values have been exactly calculated. Table 2 compares the exact values with those obtained with the aid of the proposed ACWT approach, proving its accuracy and efficiency.

Table 2: Identified modal characteristics using the ACWT method and compared with analytical characteristics.

| | | | | Eigenfrequency $f_i$ (Hz) | | Damping ratio $\xi_i$ (%) | |
|---|---|---|---|---|---|---|---|
| Mode | $\Delta f$ (Hz) | $Q_m^{min}$ | $Q_m^{max}$ | exact | identified | exact | identified |
| 1 | 4.7397 | 1.50 | 24.9 | 4.7397 | 4.7430 | 0.15 | 0.17 |
| 2 | 8.8503 | 2.3 | 71.4 | 13.5900 | 13.6915 | 0.43 | 0.42 |
| 3 | 7.9135 | 4.08 | 112.9 | 21.5035 | 21.9165 | 0.68 | 0.66 |
| 4 | 4.4379 | 8.8 | 136.3 | 25.9414 | 26.6851 | 0.81 | 0.79 |

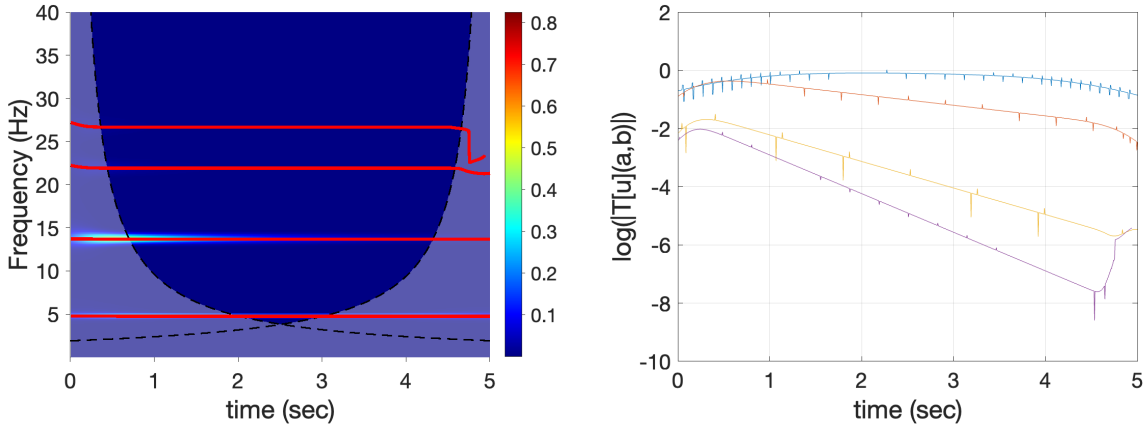


(a) (b)

Figure 9: (a) Scalogram $\left|\widetilde{T_\psi}[\boldsymbol{u}](a,b)\right|$ (computed with: $Q_m = 20$) and ridges identified, (b) damping calculation from the slope of log of the ridge. Note that since the ACWT transform is the sum of transforms that are in the power of two (Eq. 25), the slope of $\log\left(\left|\widetilde{T_\psi}[\boldsymbol{u}](a,b)\right|\right)$ has to be divided by 2. From top to bottom: $f_i = 4.7, 13.7, 21.9, 26.6$ Hz.

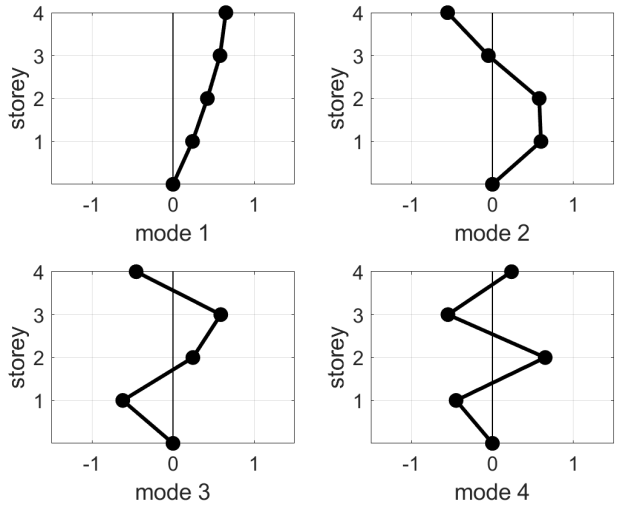


Figure 10: The four identified Eigenmodes obtained using Eq. 29.

### 5.2 "Damaged" masonry wall under dynamic excitation

The second example focuses on vibration data that were acquired during an experimental campaign carried out on masonry wall specimens. The tests were performed in LabSCo laboratory of IUAV University, Venice [32]. These data were used to apply the CWT method for the dynamic identification through transient responses embedded into noise responses.

The experimental campaign was carried out on UnReinforced Masonry (URM) panels subjected to Shear-Compression (SC) and ambient-vibrations tests using a system of nine accelerometers (Fig. 11). The test specimens are ordinary URM walls with Flemish bond pattern as masonry arrangement. The unit dimensions of a brick are: $250 \times 120 \times 55$mm and each wall is 150cm tall, 130cm width and 25cm thick, with 1cm for the thickness of mortar joints.

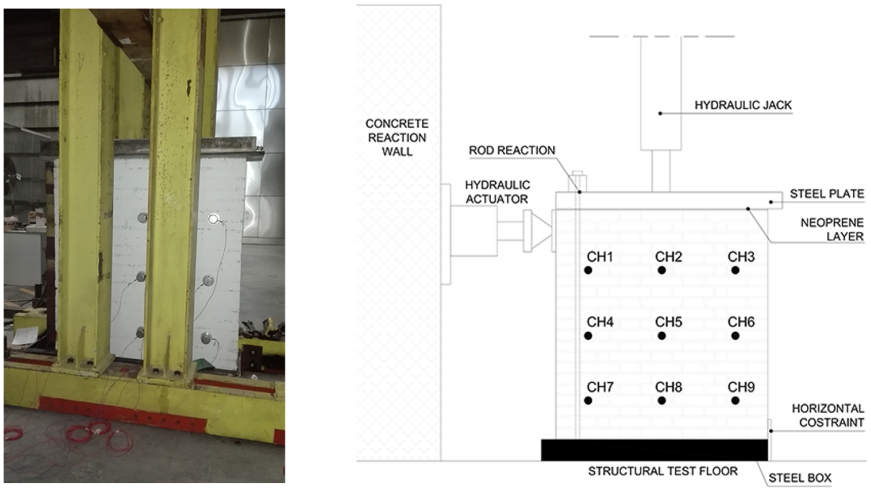


Figure 11: Masonry wall test. Location of the nine accelerometric sensors.

Among the types of URM panels tested by the Italian team, including the undamaged walls already analysed by the wavelet transform method in [8, 33], only those with the fired brick masonry walls have been processed here and are compared with the undamaged masonry wall at the loading step, immediately after the appearance of the diagonal crack, shown in Figs. 12a and 12b for the undamaged and damaged wall, respectively. A core of bricks that were exposed to high temperature were put in the wall arrangement, aiming to reproduce discontinuities and irregularities of the wall cross-section as they can be found in existing walls and buildings. In particular, $12$ brick units were subjected to a cycle of exposition to high temperature ($600°$C) for $40$ minutes and they were cooled at ambient temperature as shown in Figure 12b. The final modified panel can be seen as a "damaged" panel where the so-called "damage" is controlled by the number of fired bricks, their location and their firing temperature.

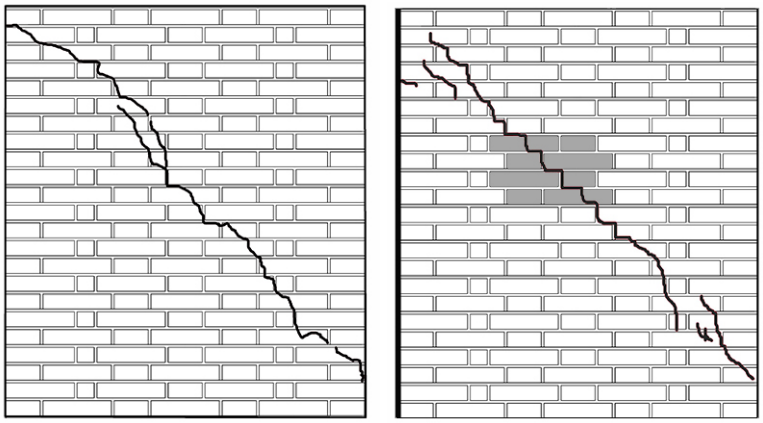

(a) (b)

Figure 12: Photo of the wall at the loading step, immediately after the appearance of the diagonal crack, ($a$) "Undamaged" masonry wall, and ($b$) "Damaged" wall with the group of 12 fired bricks (6 for each side) drawn in hatched lines.

The signals acquired, contain some discontinuities in the waveform that can be assumed as transient responses, i.e. change in the steady-state of the system. These responses are probably

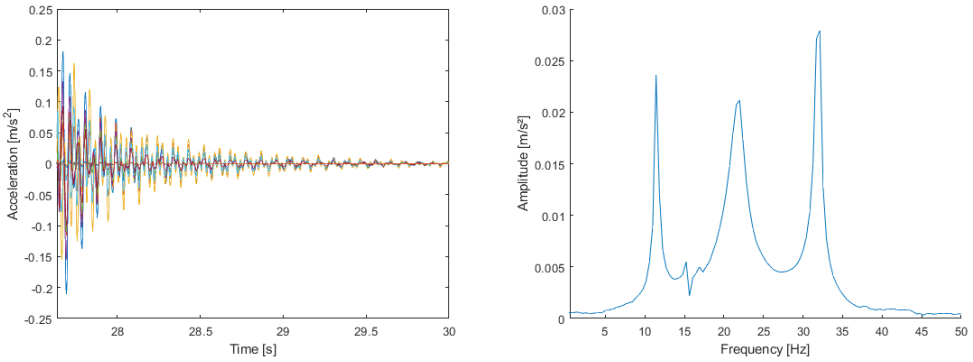


(a) (b)

Figure 13: "Damaged" masonry wall - After impact responses : $(a)$ The nine "transient" acceleration signals data set used for the processing, and $(b)$ Averaged Fourier Transform (Eq.32).

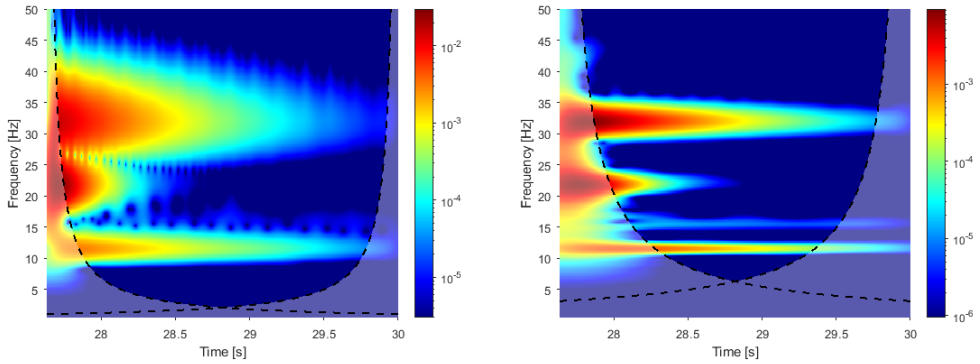


(a) (b)

Figure 14: "Damaged" masonry wall testing. Scalograms of the ACWT for the nine acceleration signals. Effect of the quality factor: $(a)$ $Q_m = 5.42$, and $(b)$ $Q_m = 18.06$.

due to the testing environment triggered by other testing machines. The set of a "transient" acceleration signals $\ddot{u}_k(t)$ data set $k \in [1, 9]$ plotted in Figure 13a, has been processed using the CWT method. An Averaged Fourier Transform (AFT) $\tilde{\tilde{\ddot{u}}}(f)$ combining the Fourier transform of each of the $N = 9$ channel acceleration signals is introduced, defined by the square root of the sum of the squared FT of each individual acceleration signal by:

$$\tilde{\tilde{\ddot{u}}}(f) = \left( \sum_{k=1}^{N} \tilde{\ddot{u}}_k^2(f) \right)^{\frac{1}{2}}, \tag{32}$$

and its absolute value is plotted in Figure 13(b). The effect of the quality factor is illustrated in Figure 14, where the absolute value of the square $\left(\widetilde{T_\psi}[\ddot{u}](a,b)\right)^2$ of the ACWT given in Eq. (25) is plotted in the time-frequency domain for two different quality factor values $Q_m^{(1)} = 5.42$ and $Q_m^{(2)} = 18.06$. For the first three modes, Eigenfrequencies $f_i$ and modal amplitudes $A_i$ are then estimated by the classical peak picking method applied to the AFT, the corresponding modal damping ratios are obtained with the classical half power technique (cf. [34, 35]) and listed in Table 3.

Table 3: "Damaged" masonry wall testing - After impact signals. - Identified modal characteristics (Eigenfrequency $f_i(Hz)$, modal amplitude $A_i$ (m/s$^2$) and modal damping ratio $\xi_i$ (%)) for the first three modes) by classical identification techniques (peak picking and half power) from the AFT versus the ACWT identification technique (indication of the quality factor $Q_m$).

| | estimated with classical techniques from AFT | | | estimated with ACWT techniques | | | |
|---|---|---|---|---|---|---|---|
| Mode | $f_i(Hz)$ | $A_i$ (m/s$^2$) | $\xi_i$ (%) | $f_i(Hz)$ | $A_i$ (m/s$^2$) | $\xi_i$ (%) | $Q_m$ |
| 1st | 11.41 | 0.024 | 1.98 | 11.54 | - | 0.96 | 18.06 |
| 2nd | 21.97 | 0.0212 | 4.25 | 22.12 | - | 3.07 | 18.18 |
| 3rd | 32.11 | 0.0279 | 1.31 | 31.79 | - | 0.73 | 40.17 |

The ridges corresponding to the first three modes are plotted in Figure 15(a), and are similar to horizontal straight lines showing that the mechanical behaviour of the wall remains "linearized" during its response to the impact. Finally, the average value along each ridge allows to estimate the three first Eigenfrequencies whose values are given in Table 3. The two first modal characteristics have then been compared to those obtained with the undamaged wall during a similar step of loading after diagonal cracking. The calculation of the slope of the three "straight lines" is then performed and the modal damping ratios $\xi_i$ for $i \in [1, 3]$, of the three first modes are deduced and given in Table 3. The values obtained are of the same order of magnitude but slightly lower than those obtained by the half-power method applied to the AFT given in Eq. (32). The three complex "constant" modal shapes are then computed from Eq. (31). The imaginary part of the three first complex modal shapes being quite small, thus only their real part is plotted in Figures 16(a), (b) and (c) for the undamaged wall and in Figures 17(a), (b) and (c) for the damaged wall, respectively. In both cases "undamaged" and "damaged", the shape of these three identified modes is similar and appears to correspond to the first bending mode for the first mode identified, the first torsion mode for the second mode and a combination of the two for the third. The identified modal Eigenfrequency $f_i$ and modal damping ratio $\xi_i$ for the first three modes ($1 \leq i \leq 3$), between the "undamaged" and "damaged" wall, estimated by ACWT techniques are given and compared in Table 4. It can be seen that the modal characteristics identified for the second mode (torsional type) for the "undamaged" wall are very different from those for the "damaged" wall (lower eigenfrequency and higher modal damping ratio).

Table 4: Comparison of identified modal characteristics (Eigenfrequency $f_i(Hz)$, and modal damping ratio $\xi_i$ (%)) for the first three modes, between the "undamaged" and "damaged" wall, estimated by ACWT techniques with indication of the corresponding quality factor $Q_m$.

| | "undamaged" wall at horizontal load of $224.2kN$ | | | "damaged" wall at horizontal load of $186.79kN$ | | |
|---|---|---|---|---|---|---|
| Mode | $f_i(Hz)$ | $\xi_i$ (%) | $Q_m$ | $f_i(Hz)$ | $\xi_i$ (%) | $Q_m$ |
| 1st | 11.01 | 0.90 | 18.94 | 11.54 | 0.96 | 18.06 |
| 2nd | 28.18 | 0.83 | 18.33 | 22.12 | 3.07 | 18.18 |
| 3rd | 34.11 | 0.74 | 63.45 | 31.79 | 0.73 | 40.17 |

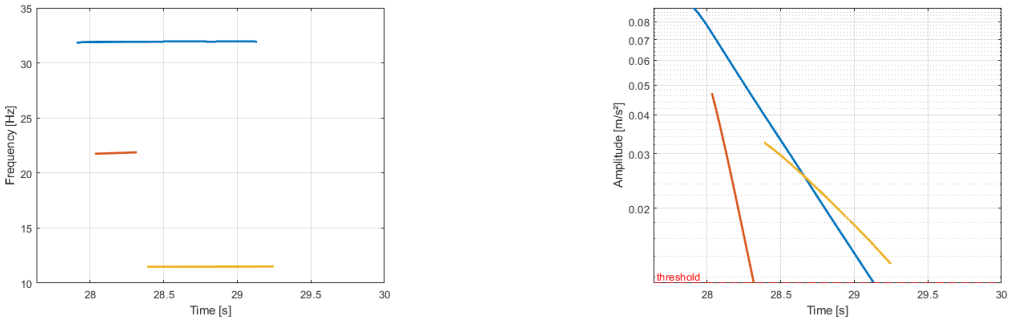


(a) (b)

Figure 15: "Damaged" masonry wall testing - After impact signals. Extraction of ridges and skeletons from the ACWT: ($a$) instantaneous eigen frequencies (ridges), and ($b$) Logarithm of the absolute value of the ACWT along each ridge. For both figures, yellow curves correspond to the first mode, red curves to the second mode and blue curves to the third mode.

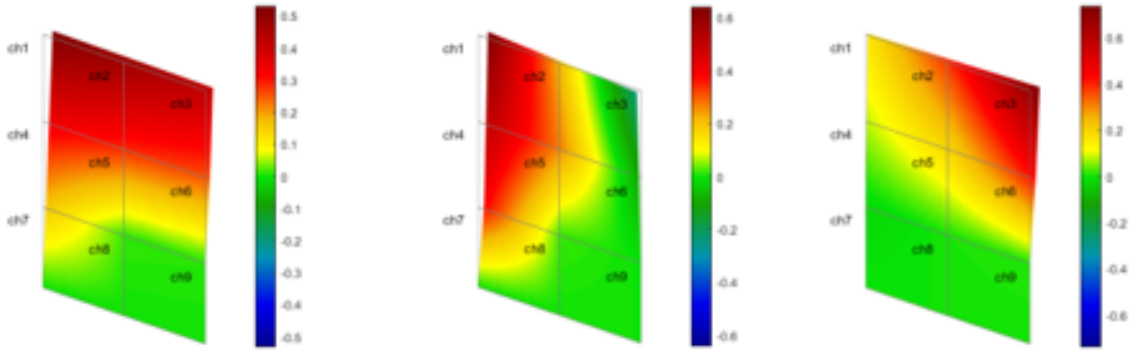


(a) (b) (c)

Figure 16: "Undamaged" masonry wall testing. Modes shapes: ($a$) First mode ($f_1 = 11.01\,Hz$), ($b$) Second mode ($f_2 = 28.18\,Hz$), and ($c$) Third mode ($f_3 = 34.11\,Hz$).

## 6 CONCLUSIONS

The wavelet analysis method allows the processed signal to be represented in the time-frequency domain, thus facilitating access to the estimation of modal characteristics. Applied to transient signals, it allows the detection of spurious modes generated by noise or redundant DoF of the model, and the identification of the presence of close modes and their associated modal parameters. Two application examples are presented, showing that inverse CWT analysis can provide valuable information for structural modal identification and for evaluating the effect of damage on the modal characteristics of the structure under study. The next step is to apply it to damage assessment, as demonstrated by first studies to be published soon.

## ACKNOWLEDGMENTS

The authors would like to thank the Laboratory of Resistance Materials of the IUAV University of Venice, its director (Antonella Cecchi) and the technical team (Giosuè Boscato) for their help in assembling and carrying out the tests on the masonry walls. They are also grateful for

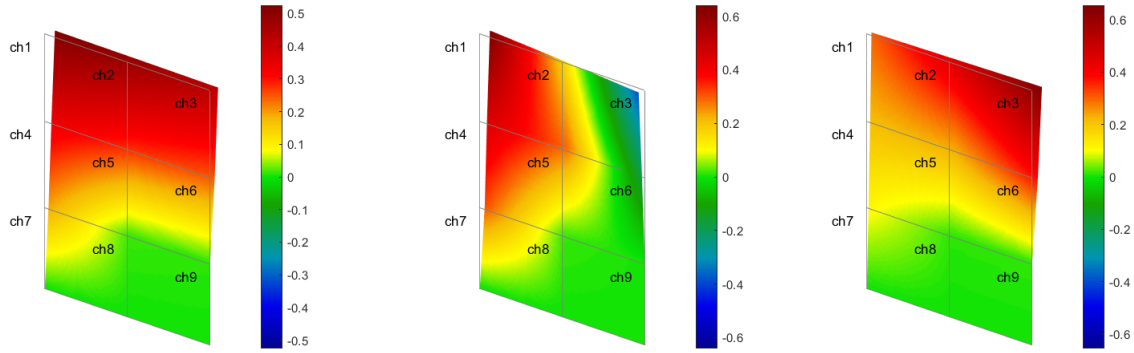


(a) (b) (c)

Figure 17: Damaged masonry wall testing. Modes shapes: $(a)$ First mode ($f_1 = 11.54\,Hz$), $(b)$ Second mode ($f_2 = 22.12\,Hz$), and $(c)$ Third mode ($f_3 = 31.79\,Hz$).

the contributions of Dr Silvia Ientile of the EMGCU/MAST laboratory of the Gustave Eiffel University, for the data processing of the dynamic tests on masonry walls, and for the detailed review of this paper. They are also very grateful to Charles Cynober of Freyssinet for authorising the use of the set of measurements relating to the passage of a semi-trailer over a joint in the pavement of a road bridge. They express their deep appreciation to Françoise Argoul for proofreading this article and for her wise advice and expertise on the use of the CWT. The first author would then like to thank his two former PhD students Nicolas Vacca and Raphaël Carpine for their thesis work [9, 10] respectively, and a student trainee at the Ecole des Ponts ParisTech Mohammed-Ta Hamzaoui for his help in drawing some figures in this article. The second author would also like to thank the Université Gustave Eiffel for its financial support through the 'iSite-FUTURE' project.

## REFERENCES

[1] Mallat, S. (1989). "A theory of multiresolution signal decomposition: The wavelet representation." *IEEE Transactions on Pattern Analysis and Machine Intelligence*, 11:674-693.

[2] Grossmann, A. and Morlet, J. (1984). "Decomposition of Hardy functions into square integrable wavelets of constant shape." *SIAM Journal on Mathematical Analysis*, 15(4):723-736.

[3] Mallat S.G. (1989). "Multiresolution approximations and wavelet orthonormal bases of L2(R)" *Trans. Amer. Math. Soc*, 315, 69-87.

[4] Carmona, R., Hwang, W-L. and Torrésani, B. "Practical Time-Frequency Analysis: Gabor and wavelet transforms, with an implementation in S", *Wavelet Analysis and its Applications, Vol. 9*, Academic Press, San Diego, 1998.

[5] Chassande-Mottin E., Flandrin P. (1998) "On the stationary phase approximation of chirp spectra." *Proc. IEEE Int. Symp. on Time-Frequency and Time-Scale Analysis*, Pittsburgh, 117–120.

[6] Flandrin, P. (1999). “Time-Frequency/Time-Scale Analysis” *Wavelet Analysis and its Applications*, Vol. 10) Academic Press, San Diego.

[7] Chatterjee P. (2018). “Wavelet Analysis in Civil Engineering” *CRC Press*, isbn = 978-1-4822-1056-9.

[8] Carpine R., Ientile S., Vacca N., Boscato G., Rospars C., Cecchi A., Argoul P. (2021). “Modal identification in the case of complex modes – Use of the wavelet analysis applied to the after-shock responses of a masonry wall during shear compression tests.”, *Mechanical Systems and Signal Processing*, 160, 107753.

[9] Vacca, N. (2022). “Fonctions analytiques et signaux asymptotiques pour la transformée en ondelettes” (’Analytic functions and asymptotic signals for the wavelet transform’), *PhD thesis of Paris-Est University*, 29-04-2022, in French.

[10] Carpine R. (2022). “Détection de défauts dans les structures de génie civil par analyse en ondelettes de réponse vibratoire.”, *PhD thesis of Paris-Est University*, in French.

[11] Argoul, P., Le, T.P. (2004). “Wavelet Analysis of Transient Signals in Civil Engineering”. In: Frémond, M., Maceri, F. (eds) Novel Approaches in Civil Engineering. *Lecture Notes in Applied and Computational Mechanics*, Vol 14. Springer, Berlin, Heidelberg.

[12] Argoul, P., Le, T.-P. (2003). “Instantaneous indicators of indicators of structural behaviour based on the continuous Cauchy wavelet analysis”, *Mechanical Systems and Signal Processing*, 17(1), 243-250.

[13] Le T.-P., Argoul, P. (2004). “Continuous wavelet transform for modal identification using free decay response”, *Journal of Sound and Vibration*, 277(1-2), 73–100.

[14] Guillet, A., Arneodo, A., Argoul, P. and Argoul, F. (2023). “Quantifying the rationality of rhythmic signals”, In Theoretical Physics, Wavelets, Analysis, Genomics, Springer International Publishing, Series Title: Applied and Numerical Harmonic Analysis, Flandrin, P., Jaffard, S. , Paul, T. and Torresani, B. Editors, 565–593.

[15] Lilly, J.M. (2017). “Element analysis: A wavelet-based method for analysing time-localized events in noisy time series”, *Proceedings of the Royal Society A: Mathematical, Physical and Engineering Sciences*, 473(2200).

[16] Olhede S. C. & Walden A. T. (2002). “Generalized Morse wavelets.” *IEEE Transactions on Signal Processing*, 50(11), 2661-2670.

[17] Lilly J. M. & Olhede S. C., (2009). “Higher-Order Properties of Analytic Wavelets.” *IEEE Transactions on Signal Processing*, 57(1), 146-160.

[18] Daubechies I. & Paul T. (1988). “Time-frequency localization operators—A geometric phase space approach: II. The use of dilations,” *Inverse Problems*, Vol. 4, pp. 661–680.

[19] Lilly J. M. & Olhede, S. C. (2012). “Generalized Morse Wavelets as a Superfamily of Analytic Wavelets” in *IEEE Transactions on Signal Processing*, Vol. 60(11): 6036-6041.

[20] Mallat, S., Waldspurger, I. (2015). “Phase Retrieval for the Cauchy Wavelet Transform.” *J Fourier Anal. Appl.*, 21:1251–1309.

[21] Rouby C., Rémond, D. and Argoul P. (2010). "Orthogonal polynomials or wavelet analysis for mechanical system direct identification". *Ann. Solid Struct. Mech.*, 1:41–58.

[22] Delprat, N., Escudie, B., Guillemain, P., Kronland-Martinet, R., Tchamitchian, P., & Torresani, B. (1992). "Asymptotic wavelet and Gabor analysis: extraction of instantaneous frequencies." *IEEE Transactions on Information Theory*, 38(2): 644–664.

[23] Torrésani, B. (2012). "Analyse continue par ondelettes.", EDP Sciences, 256 pages.

[24] Lilly, J. M., & Olhede, S. C. (2010). "On the Analytic Wavelet Transform." *IEEE Transactions on Information Theory*, 56(8): 4135–4156.

[25] Carmona, R., Hwang, W. L., & Torrésani, B. (1995). "Identification of chirps with continuous wavelet transform." In P. Bickel, P. Diggle, S. Fienberg, K. Krickeberg, I. Olkin, N. Wermuth, S. Zeger, A. Antoniadis, & G. Oppenheim (Eds.), *Wavelets and Statistics*, 103:95–108. New York.

[26] Geradin M. & Rixen D.-J. (2015). "Mechanical Vibrations: Theory and Application to Structural Dynamics", John Wiley & Sons, 616 pages.

[27] Erlicher, S., Argoul, P. (2007). "Modal identification of linear non-proportionally damped systems by wavelet transform." *Mechanical Systems and Signal Processing*, 21(3): 1386–1421.

[28] Argoul P. and Erlicher S. (2005). "Mechanical modelling and computational issues in civil engineering", Volume 23 of Lecture Notes in Applied and Computational Mechanics, In "On the use of continuous wavelet analysis for modal identification",359-–368. Springer.

[29] Staszewski W.J. (1997). "Identification of damping in MDOF systems using time-scale decomposition", *Journal of Sound and Vibration,* 203(2): 283-305.

[30] Ruzzene M., Fasana A., Garibaldi L., & Piombo B., (1997). "Natural frequencies and dampings identification using wavelet transform: application to real data", *Mechanical Systems and Signal Processing*, 11(2): 207-218,

[31] Lardies, J., Gouttebroze, S. (2002). "Identification of modal parameters using the wavelet transform." *International Journal of Mechanical Sciences*. 44(11): 2263—2283.

[32] Ientile, S., Cecchi, A., Boscato, G., Argoul, P., Schmidt, F., Nedjar, B., Siegert, D. (2018). "Methodology for the dynamic identification of damaged unreinforced masonry walls through vibrations tests", *40th IABSE Symposium 2018: Tomorrow's Megastructures*, Int. Assoc. for Bridge and Structural Engineering, 26-29.

[33] Ientile S. (2017). Sensitivity and dynamic identification of damaged unreinforced masonry walls, PhD Thesis, IUAV University of Venice, Venice, Italy.

[34] Maia, N.M.M., Silva, J.M.M. (1997). Theoretical and Experimental Modal Analysis, Engineering dynamics series, *Research studies*, Pre Edts, 468 p.

[35] Ewins, D.J. (2000). Modal testing, 2nd edn. Research Studies Press, Baldock.

COMPDYN 2023
9th ECCOMAS Thematic Conference on
Computational Methods in Structural Dynamics and Earthquake Engineering
M. Papadrakakis, M. Fragiadakis (eds.)
Athens, Greece, 12-14 June 2023

# ASSESSMENT OF THE SEISMIC VULNERABILITY AND MODELLING OF EXISTING BRIDGE WITH DIFFERENT LEVELS OF ACCURACY: STRENGTHS AND WEAKNESSES

**C. Pettorruso**[1], **V. Quaglini**[2]

1 Politecnico di Milano, Department of Architecture, Built Environment and Construction Engineering,
Piazza Leonardo da Vinci 32, 20133 Milan, Italy
e-mail: { carlo.pettorruso, virginio.quaglini }@polimi.it

## Abstract

*The assessment of the seismic vulnerability of existing bridges is a topic of primary relevance for the infrastructure field, as the knowledge of the vulnerability allows to design the management of the aftermath of the earthquake. To appreciate the vulnerability of the structure, different modelling approaches with different levels of accuracy are available and modern seismic design code provide recommendation about their use.*
*The study aims at assessing the reliability of less complex methods, but with low computational cost and calibrate them against the results of nonlinear dynamic analyses in order to obtain an acceptable level of accuracy.*
*The study will be developed considering a bridge prototype, representative of features such as the structural scheme (simply supported), the material of the piers (reinforced concrete), and the geometry of the piers (framed piers). The bridge will be analyzed first through nonlinear dynamic analyses, to define the benchmark solution. Then, the same bridges will be analyzed through linear dynamics analysis (Linear Time history and Response Spectrum) and nonlinear static analyses, such as MPA (Modal Pushover Analysis) and, in the end, through simplified Equivalent Static Analysis, and a comparison among the different modeling approaches will be proposed. Strengths and weaknesses of each model will be highlighted and discussed.*

**Keywords:** Existing bridge, Seismic Vulnerability, Earthquake Engineering, Linear Static Analysis, Linear Dynamic Analysis, Modal Pushover Analysis, Nonlinear Dynamic Analysis.

## 1 INTRODUCTION

To appreciate the vulnerability of the structure, different modelling approaches with different levels of accuracy are available and modern seismic design code provide recommendation about their use, in this work it's considered the Italian Building Code (IBC) [1] and the Eurocode 8 [2].

The work presents a two different comparison of analyses, taking nonlinear time history analysis (NTHA) [3] as a benchmark. The first compare the result of linear dynamic analysis, which can be Linear Time History Analysis (LTH) and Response Spectrum (RS) [2] with the NTHA; the second compare the benchmark with the Modal Pushover Analysis (MPA) [4,5] and the Equivalent Static Analysis (ESA).

## 2 CASE STUDY

The work considers a simply supported bridge with geometries reflect typical configurations available in the Italian stock, namely the frame pier composed of three circular columns and the deck with four T-shaped beams. In the work three seismic scenarios corresponding to three different seismic zones according to the Italian Building Code are analyzed, relevant to the municipalities of Reggio Calabria for zone 1(Z1), Sirmione (BS) for zone 2 (Z2) and Pavia for zone 3 (Z3). The selected typology turns out to be among the most widespread ones in the Italian stock, where they represent more than 90% of existing bridges [6,7].

### 2.1 Bridge characteristics

The considered case study is a simply supported bridge with a 20m span and 5m pier's high. The static scheme was assumed, in the longitudinal direction, a fixed support axis and a moving support axis, while in the transverse direction both axes have fixed supports (the same would be if the presence of transverse restraints were considered) (Figure 1). In terms of seismic mass distribution this means that in the longitudinal direction the seismic mass acting on the pier under consideration will be the mass of the rigidly connected deck, in the transverse direction the seismic mass will be given by half of the seismic masses of both decks' laying on the analyzed pier.

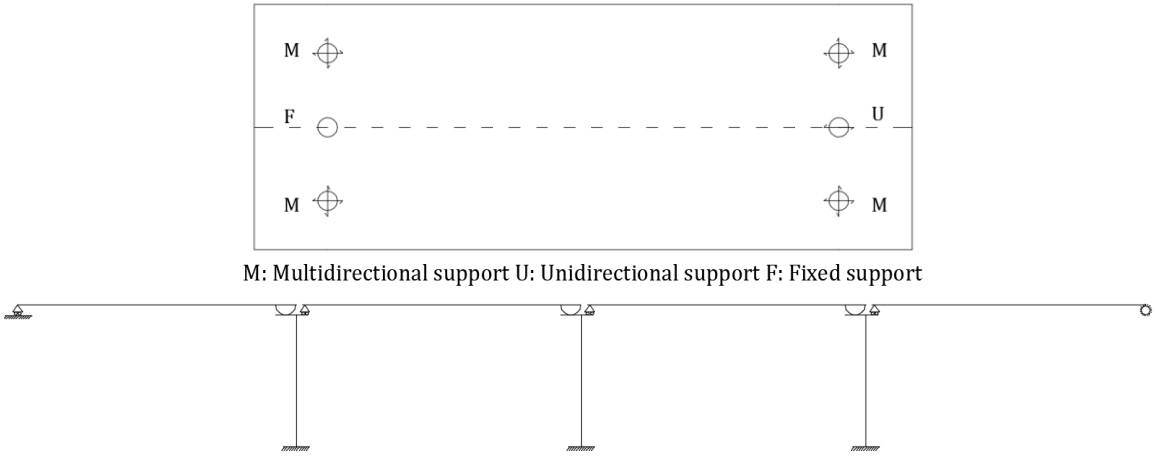


Figure 1: Static scheme for simply supported bridges

For the piers, C25/30 concrete is assumed, with a Young's modulus $E_c$ = 31475,8 MPa and a characteristic cylindrical resistance $f_{ck}$ = 25MPa; steel for the rebar is FeB44k, with Young's

modulus $E_s$ = 200GPa, characteristic yield strength $f_{yk}$ = 430 MPa and characteristic tensile strength at break $f_{tk}$ = 540MPa.

Three columns with diameter 1m connected at the top by a pier cap make the frame piers. Volumetric ratios of $\rho_s$=0,4% and $\rho_w$ =0,09% (defined as the volume of longitudinal bars divided by the volume of concrete, and the volume of stirrups divided by the volume of confined concrete) are assumed for the longitudinal and the transverse reinforcement [8,9].

Each column is reinforced with longitudinal bars arranged circumferentially and consisting of 12φ18 bars, in the case of a 5m high pier (Figure 2). The transverse reinforcement for each column, in both heights, consists of circular φ10 stirrups with 20cm pitch.

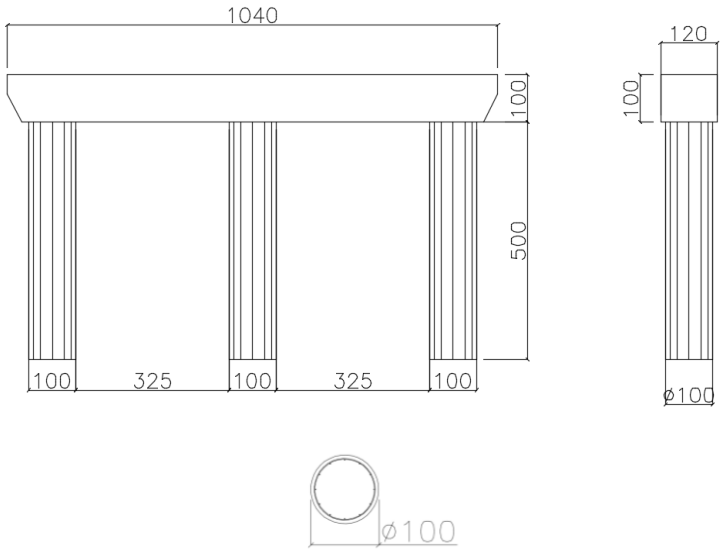


Rebar 12Ø18; stirrups Ø12/20

Figure 2 Pier and reinforcement

The type of deck considered have been associated to static layout and span length typical of the Italian scenario. In the case study it was considered the T-shaped beams of 20m span (Figure 3), the considered section is shown below with their characteristics summarized in the Table 1, in terms of geometry and loads.

| | | |
|---|---|---|
| A | 5,434 | m2 |
| $\gamma_{cls}$ | 25 | kN/m3 |
| $G_1$ | 135,85 | kN/m |
| $G_2$ | 47 | kN/m |
| L | 20 | m |
| $G_{deck}$ | 3657 | kN |
| $Q_{0,2}$ | 276 | kN |

**Table 1 T-shape deck characteristics**

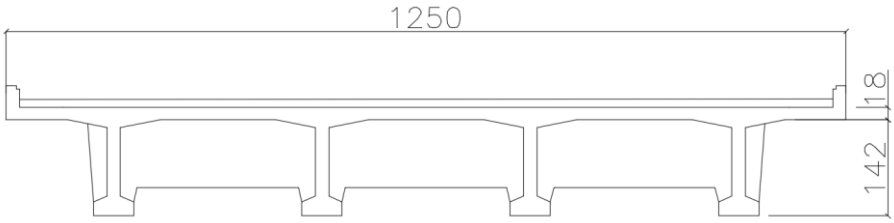


Figure 3 T-shape deck section

## 2.2 Seismic scenarios

Three scenarios were defined according to IBC [1], assuming a design life $V_N$ = 50 years and use class IV (cu = 2.0) (IBC, § 2.4.3), to which the following structure reference periods (IBC, § 3.2.1) $V_R = V_N c_u$ = 100 years. Only ULS is examined, with a period of 949 years.

The three seismic scenarios correspond to seismic zones 1, 2 and 3 according to the Italian Building Code. The code classifies the entire Italian territory into 4 zones according to the horizontal acceleration with a probability of exceedance equal to 10% in 50 years.

For the first three zones a municipality was chosen to define the seismic scenario: for zone 1, Reggio Calabria, located in Calabria region; for zone 2, Sirmione, located in Lombardy region in the province of Brescia; for zone 3 Pavia, located in Lombardy region. For all zones, topographic class T1 and soil type B were assumed.

In Figure 4, the design spectra considered for the parametric analysis are represented.

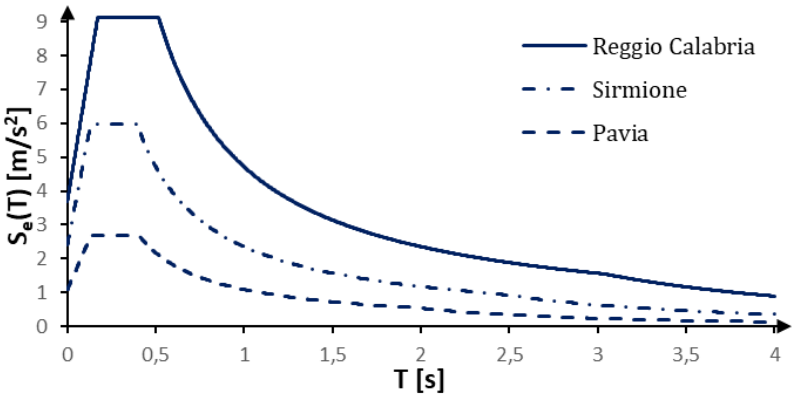


Figure 4 Design spectrum

Starting from the design spectra defined according to IBC, seismic inputs were defined for the different analyses.

The spectra themselves are the seismic input for the response spectrum analysis (RSA) and the equivalent static analysis (ESA).

The input for the nonlinear static (MPA) was derived from the acceleration spectrum and the displacement spectrum, thus obtaining the demand curve in the ADRS plane and are shown in Figure 5.

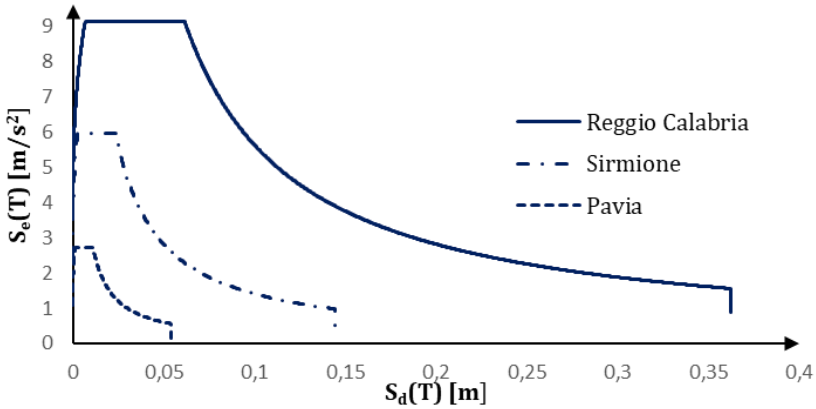


Figure 5 Demand curves for MPA

Three sets of seven bidirectional ground motions consistent with the target spectra were selected one set for each seismic scenario for the dynamics analysis (nonlinear and linear); these are selected with REXEL v3.4 beta [10] software from the European Strong-motion Database [11].

Relevant information on the ground motion data set is reported in Table 2, and the scaled horizontal spectra at 5% damping are shown in Figure 6.

| **Reggio Calabria** | | | | | | | |
|---|---|---|---|---|---|---|---|
| **Earthquake Name** | **Waveform ID** | **Earthquake ID** | **Mw** | **PGA_X [m/s^2]** | **PGA_Y [m/s^2]** | **SFx** | **SFy** |
| Umbria Marche | 600 | 286 | 6 | 1,6852 | 1,0406 | 2,186 | 3,5401 |
| Adana | 1726 | 561 | 6 | 2,1575 | 2,6442 | 1,7074 | 1,3932 |
| Izmit | 1231 | 472 | 8 | 1,5764 | 2,1922 | 2,3368 | 1,6804 |
| Duzce 1 | 1703 | 497 | 7 | 3,6988 | 5,0358 | 0,9959 | 0,7315 |
| Campano Lucano | 290 | 146 | 7 | 2,1206 | 3,1662 | 1,7371 | 1,1635 |
| South Iceland | 4674 | 1635 | 7 | 3,1176 | 3,3109 | 1,1816 | 1,1126 |
| Gazli | 74 | 43 | 7 | 6,0382 | 7,065 | 0,6101 | 0,5214 |
| **Sirmione** | | | | | | | |
| **Earthquake Name** | **Waveform ID** | **Earthquake ID** | **Mw** | **PGA_X [m/s^2]** | **PGA_Y [m/s^2]** | **SFx** | **SFy** |
| Campano Lucano | 292 | 146 | 7 | 0,5878 | 0,5876 | 4,0921 | 4,0934 |
| Friuli (aftershock) | 147 | 65 | 6 | 1,3841 | 2,3189 | 1,7377 | 1,0372 |
| Spitak | 439 | 213 | 7 | 1,7932 | 1,7958 | 1,3413 | 1,3394 |
| Tabas | 182 | 87 | 7 | 3,316 | 3,7789 | 0,7253 | 0,6365 |
| Montenegro | 198 | 93 | 7 | 1,7743 | 2,1985 | 1,3556 | 1,0940 |
| Umbria Marche | 594 | 286 | 6 | 5,1383 | 4,5383 | 0,4681 | 0,5300 |
| Campano Lucano | 290 | 146 | 7 | 2,1206 | 3,1662 | 1,1342 | 0,7597 |
| **Pavia** | | | | | | | |
| **Earthquake Name** | **Waveform ID** | **Earthquake ID** | **Mw** | **PGA_X [m/s^2]** | **PGA_Y [m/s^2]** | **SFx** | **SFy** |
| Campano Lucano | 292 | 146 | 7 | 0,5878 | 0,5876 | 1,8426 | 1,8432 |
| Montenegro (aftershock) | 232 | 108 | 6 | 0,56 | 0,5426 | 1,9341 | 1,9961 |
| Friuli (aftershock) | 147 | 65 | 6 | 1,3841 | 2,3189 | 0,7825 | 0,4670 |
| South Iceland (aftershock) | 6335 | 2142 | 6 | 1,2481 | 1,1322 | 0,8677 | 0,9566 |
| South Iceland | 6263 | 1635 | 7 | 6,1359 | 5,018 | 0,1765 | 0,2158 |
| Umbria Marche | 594 | 286 | 6 | 5,1383 | 4,5383 | 0,2108 | 0,2386 |
| Campano Lucano | 291 | 146 | 7 | 1,5256 | 1,7247 | 0,7099 | 0,628 |

Table 2 Selected accelerogram for each scenario

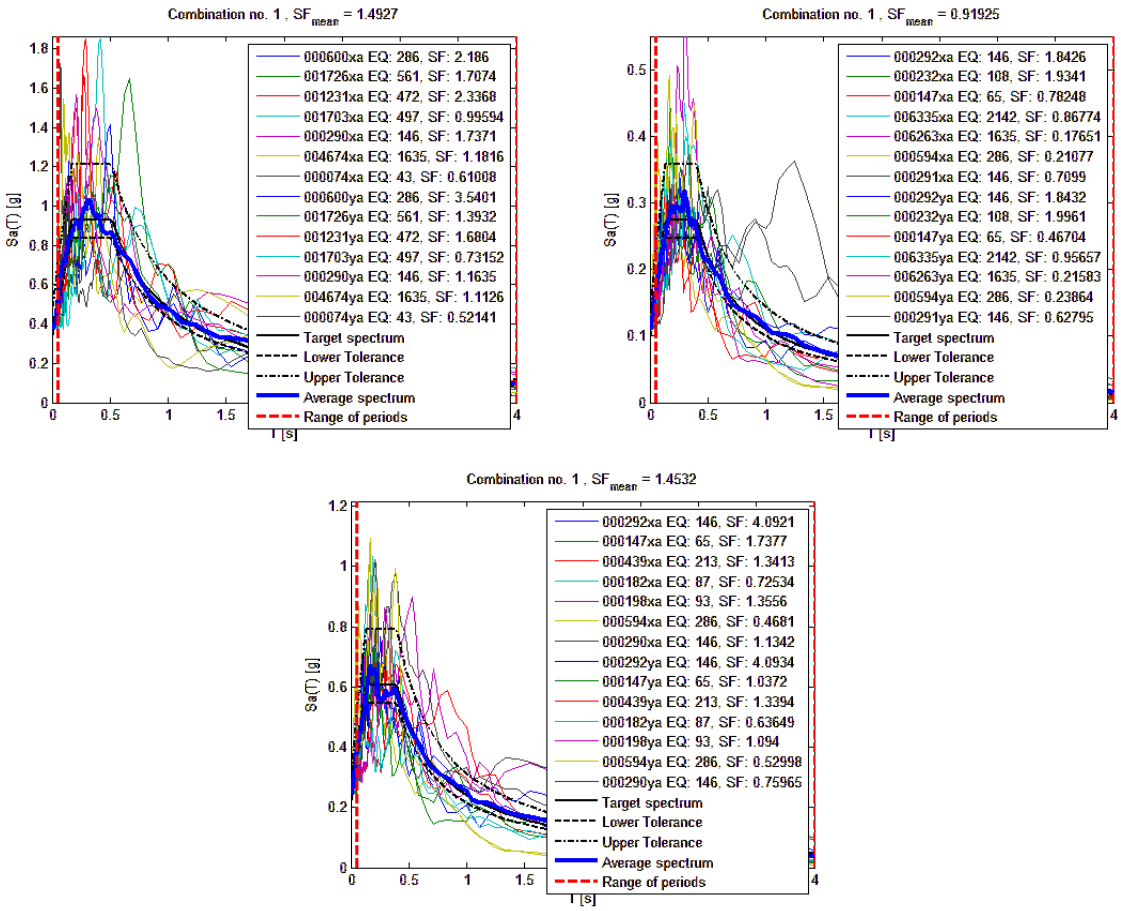


Figure 6 Scaled ground motion acceleration spectra and target spectra

## 2.3 Numerical model

The structural model was implemented in SAP2000 v23.1.0 software [12]. The geometry represents that expressed in the previous section (Figure 7).

The framed piers were rigidly fixed to the ground and the abutments are one hinged and one longitudinally free to move.

The deck is modelled as linear elastic elements and on this are applied the permanent non-structural load and the variable loads.

The connection between the deck and the pier was modelled through a rigid links [34], the locked degrees of freedom change as the fixed or moving axis of the simply supported bridge changes.



Figure 7 Numerical model

The work presents different types of analysis, for linear analysis the material is purely elastic, while for nonlinear analysis the design values for C25/30 and Fe44k are used.

The material nonlinearity is modeled with concentrated plasticity, the framed piers were rigidly fixed to the ground and modelled as linear elastic elements, with a bidirectional plastic hinge (parametric P-M2-M3) at the basis formulated according to Table 10-8 (concrete columns) of ASCE 41-13 [13] in order to account for inelastic concrete deformation. The plastic hinges backbone is computed in function of the vertical load.

The internal structural damping is modeled as Rayleigh damping [3], with parameters assigned to achieve 5% damping ratio at the first two frequencies.

## 3 RESULTS

The results shown in this section refer to the NTHA benchmark for each seismic scenario. The percentage change in base reactions and pier head displacement between the linear dynamic analyses (LTH and RS) and the NTHAs, and later between the nonlinear and linear static analyses (MPA and ESA) and the NTHAs, are shown below.

Figure 8 shows the variation in response between NTHAs and linear dynamic analyses (LTH and RS) in terms of base reaction, and there are two interesting aspects to note: first, it can be seen that as seismic intensity varies, the variation in response decreases, this is easily inferred to be due to the capped response induced by modeling nonlinearities in NTHAs; second, it is possible to see that the difference between of result of the two linear methods is minimal, especially as the seismic intensity decreases.

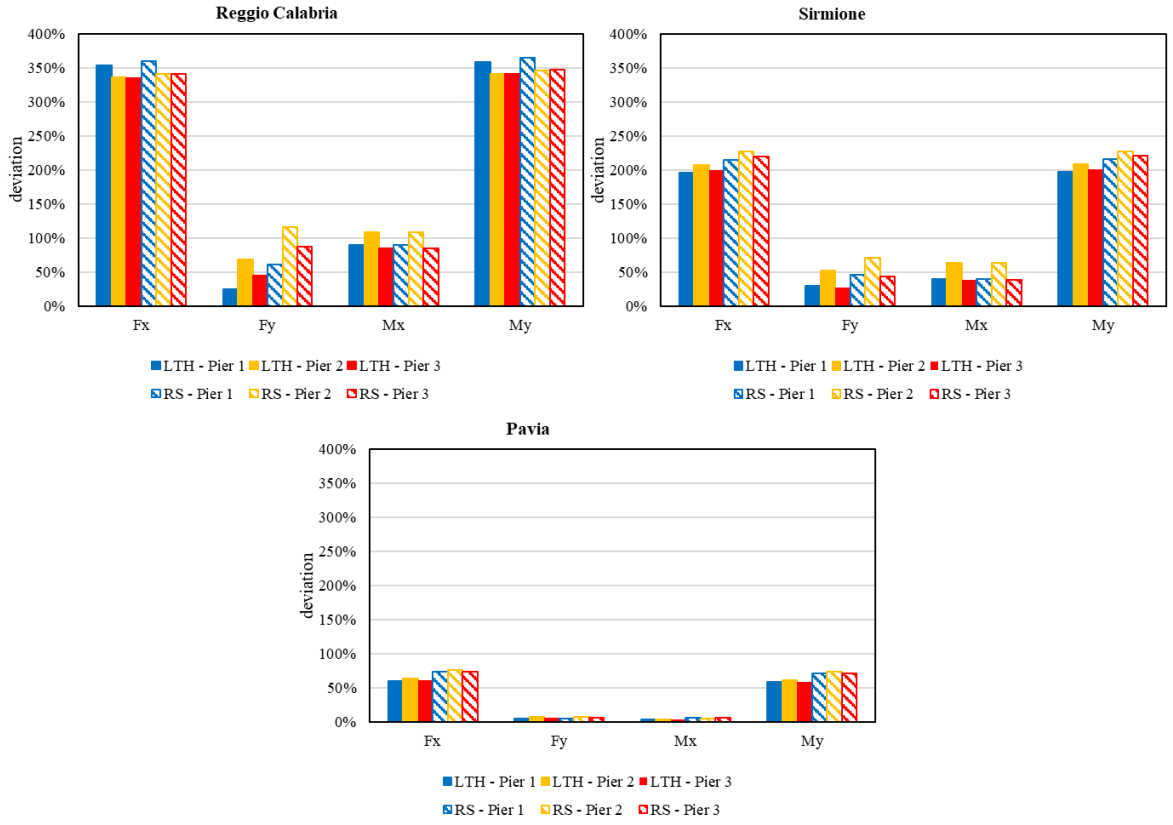


Figure 8 Reactions variation NTHAs vs LTH and RS

Figure 9 shows the variation in terms of displacement, and it can be seen that the percentage variations are generally smaller than those of the reactions. For the medium- and low-intensity seismic scenarios, a larger variation is seen in the x-direction than for the heaviest

seismic scenario; this result should be attributed to the large plastic displacement in that scenario with the NTHAs.

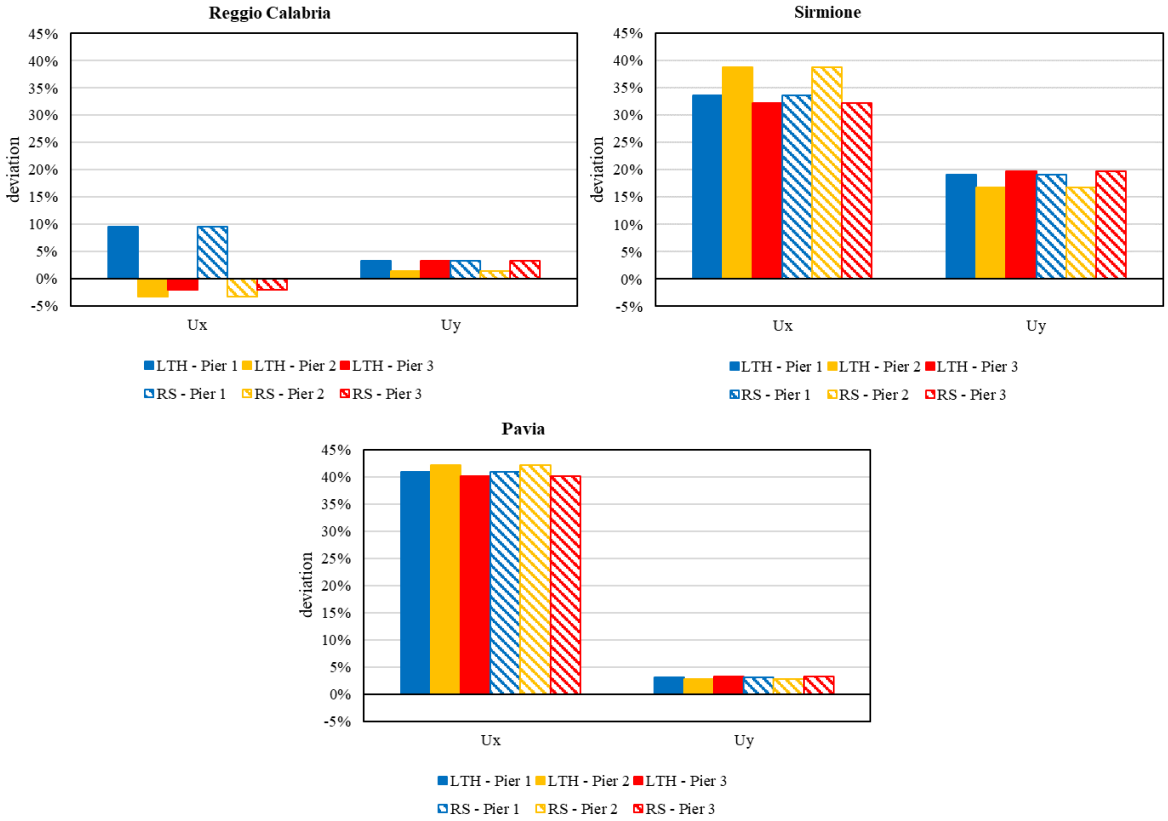


Figure 9 Displacements variation NTHAs vs LTH and RS

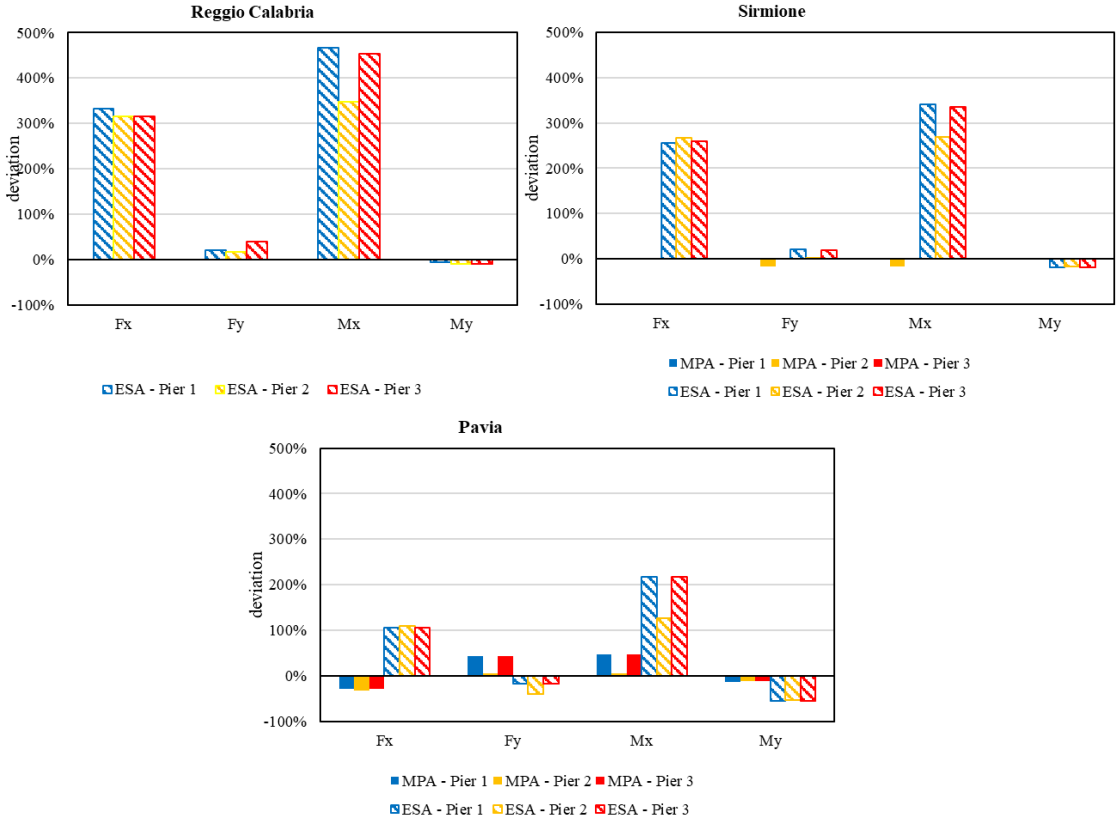


Figure 10 Reactions variation NTHAs vs MPA and ESA

In figure 10 there isn't all the result because in most severe scenario and in x-direction of the medium scenario the performance point doesn't exist. In this comparison, when a performance point exists, the MPA gives a good approximation. Instead, ESAs show a response similar to what we have seen in linear dynamic analyses, with the error decreasing with li decreasing earthquake intensity.

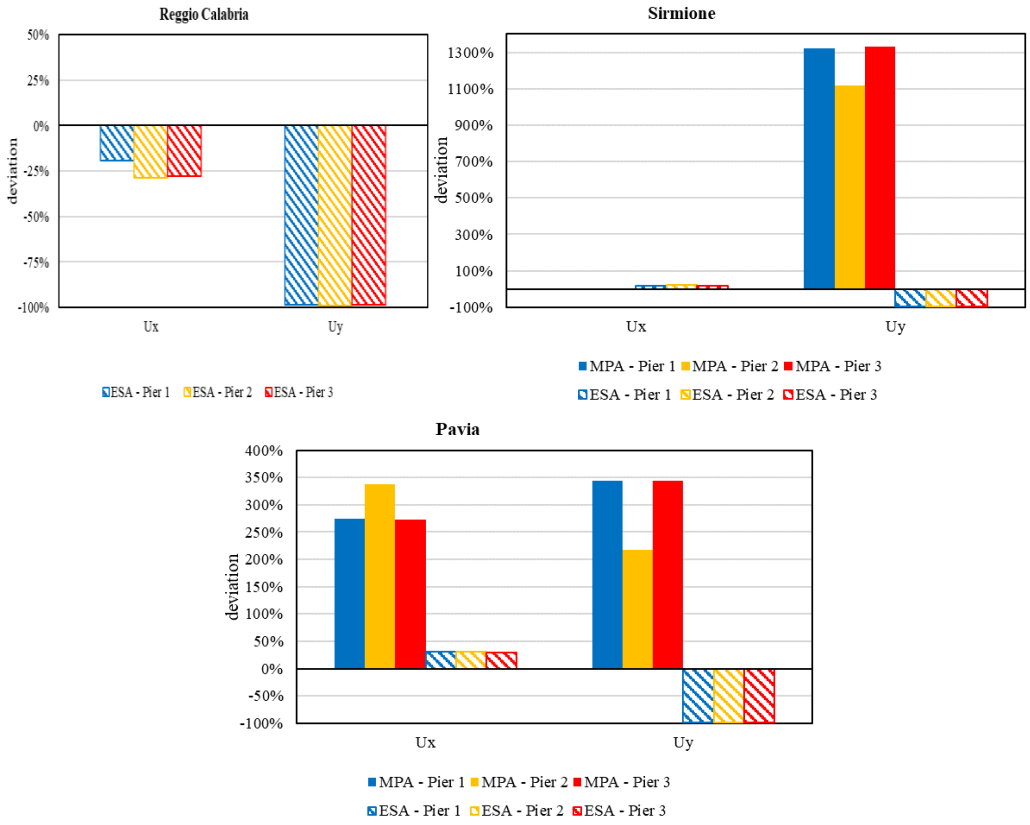


Figure 11 Displacements variation NTHAs vs MPA and ESA

In the last figure there is the results in terms of displacement, the ESAs confirm the previous consideration, a result that has to be commented is the displacement in y-direction for the medium seismic scenario with MPA that is one order on magnitude higher than the benchmark, this is due to the fact that performance point is for higher plastic deformation.

## 4 CONCLUSIONS

The work presents the results obtained with the different analysis methodologies counted in the current seismic codes. By analyzing the accuracy, it was possible to see that the linear methods for heavier seismic scenarios deviate greatly from the benchmark response, as the modeling for NTHAs has a cap in the strength that cannot be captured of the linear modeling. The accuracy of MPAs comes very close in terms of base reactions, as they capture the resources of the structure.

In terms of computational cost, two cost items can be identified: first, modeling, which in the case of nonlinear analyses (NTHAs and MPAs) involves more effort than in linear dynamic (LTH and RS) and ESAs; second, reading the result, in the case of LTHs is very expensive, as for NTHAs, for MPAs it is less expensive than the former, while for the other analyses (RS and ESAs) it is immediate.

## REFERENCES


[1] Italian Building Code. Technical Recommendations for Buildings—D.M. 17/02/2018. Italian Building Code: Rome, Italy, 2018. (In Italian)

[2] EN 1998-1 Eurocode 8: Design of Structures for Earthquake Resistance—Part 1: General Rules, Seismic Actions and Rules for Buildings; CEN European Committee for Standardization: Brussels, Belgium, 2004.

[3] Chopra, A.K. Dynamics of Structures, 5th ed.; Pearson: London, UK, 2017.

[4] Paraskeva, T.S.; Kappos, A.J.; Sextos, A.G. Extension of modal pushover analysis to seismic assessment of bridges. Earthq. Eng. Struct. Dyn. 2006, 35, 1269–1293.

[5] 17. Paraskeva, T.S.; Kappos, A.J. Further development of a multimodal pushover analysis procedure for seismic assessment of bridges. Earthq. Eng. Struct. Dyn. 2009, 39, 211–222.

[6] Pinto and Franchin, 2010. Issues in the upgrade of Italian highway structures. Journal of Earthquake EngineeringVolume 14, Issue 8, Pages 1221 – 1252, 10.1080/13632461003649970

[7] Borzi et al, 2015. Seismic vulnerability of the Italian roadway bridge stock. Earthquake Spectra, Volume 31, Issue 4, Pages 2137 – 2161, 10.1193/070413EQS190M

[8] Pinto et al, 2003. Cyclic tests on large-scale models of existing bridge piers with rectangular hollow cross-section. Earthquake Engineering and Structural DynamicsVolume 32, Issue 13, Pages 1995 – 2012, 10.1002/eqe.311

[9] Delgado et al, 2009. Shear effects on hollow section piers under seismic actions: Experimental and numerical analysis. Bulletin of Earthquake EngineeringVolume 7, Issue 2, Pages 377 – 389, 10.1007/s10518-008-9098-x

[10] Iervolino, I.; Galasso, C.; Cosenza, E. REXEL: Computer aided record selection for code-based seismic structural analysis. Bull. Earthq. Eng. 2010, 8, 339–362, http://dx.doi.org/10.1007/s10518-009-9146-1.

[11] Ambraseys, N.; Smit, P.; Sigbjornsson, R.; Suhadolc, P.; Margaris, B. Internet-Site for European Strong-Motion Data, European Commission, Research-Directorate General, Environment and Climate Programme. Available online: http://www.isesd.cv.ic.ac.uk/ESD/ (accessed on 20 December 2022).

[12] SAP2000 Analysis Reference, Volume 1; Computer and Structures Inc.: Berkeley, CA, USA, 1997.

[13] ASCE/SEI 41-13 Seismic Evaluation and Retrofit of Existing Buildings; American Society of Civil Engineers: Reston, VA, USA, 2014.

COMPDYN 2023
9th ECCOMAS Thematic Conference on
Computational Methods in Structural Dynamics and Earthquake Engineering
M. Papadrakakis, M. Fragiadakis (eds.)
Athens, Greece, 12-14 June 2023

# STOCHASTIC MODEL UPDATING OF RC TIED-ARCH BRIDGE

**A. Gennaro[1], A. Caprino[2], V. Pernechele[2], F. Lorenzoni[2] and F. da Porto[2]**

[1] University of Brescia, Dept. of Civil and Environmental Engineering, International cooperation and Mathematics (DICACIM)
Via Branze 43, 25123 Brescia, Italy
e-mail: a.gennaro@unibs.it

[2] University of Padova, Dept. of Geosciences,
Via Gradenigo 6, 35131 Padova, Italy
e-mail: {amedeo.caprino,valentina.pernechele,filippo.lorenzoni,francesca.daporto}@unipd.it

## Abstract

*The finite element (FE) method is a powerful tool in the civil engineering field for the design, analysis, and assessment of structures. Although FE models attempt to replicate structures' behaviour, discrepancies always exist between experimental and numerical model responses. These are related to aleatoric uncertainties, such as measurement noise and epistemic uncertainties, like modelling assumptions. Epistemic uncertainties may negatively affect the FE model to the point that it may not correctly represent the structure behaviour, becoming unreliable for structural assessment. The FE model updating method has been successfully used to reduce the error between experimental tests and numerical output by updating uncertain FE model parameters, usually adopting data from dynamic tests. In this framework, experimentally derived dynamic responses in terms of natural frequency and mode shape can be used to reduce uncertainties. Although the general methodology for updating the FE model is well known, specific implementation techniques should be investigated and adapted to the analysed structure to fulfil more accurate results. In this paper, a model updating procedure through experimental data is applied to an existing Reinforced Concrete (RC) tied-arch bridge. The structural characteristics were assessed by an onsite test campaign, including and ambient vibration test (AVT). The updating procedure involves applying a stochastic method for quantifying the variability of parameters.*

**Keywords:** Model updating; RC tied-arch bridge; Dynamic identification; Experimental test.

# 1 INTRODUCTION

The finite element (FE) method is widely used in the engineering field to simulate real structures, making model-based activities easier, including but not limited to damage identification, structural health monitoring (SHM), structural safety, and risk assessment. Therefore, a "high-fidelity" FEM that accurately characterises structural behaviour is of fundamental importance. However, it is known that the results obtained from an FE model built only on the original designs, may differ from the actual measurements made on the real structure. Therefore, experimental measurements should be used to validate the numerical results. The structural response can be thoroughly described in terms of natural frequencies and mode shapes through dynamic identification test, particularly by ambient vibration test (AVT).

To reduce the discrepancies between experimental and numerical dynamic characteristics, specific methodologies have been implemented [1–6]. These methods use uncertain parameters including material quality, geometric characteristics, boundary conditions, etc., to calibrate the numerical model.

In general, the model updating problem can be divided into two groups: deterministic and stochastic [7, 8].

In the deterministic model updating method, a single FE model is optimised by minimising the error between the numerical results and the test data of the physical structure. However, predictions based on a single calibration of model parameters cannot give a measure of confidence in the numerical models' capability in representing the physical structure [1, 2, 9]. Instead, stochastic model updating refers to the numerical model with measurement variability, and the updating parameters are estimated from the interval or probability density function (PDF).

This paper presents a case study of probabilistic model updating of a historic RC tied-arch bridge (1931) located in Padua, northern Italy. The paper is organized as follows: in chapter 2, the description of the case study is presented, including the modal parameters for the model updating, and the preliminary FE model. In chapter 3, the results of AVT and the deterministic and stochastic model updating are discussed.

# 2 MATERIAL AND METHODS

## 2.1 Description of the case study

The case-study selected is a bridge situated in Padua, northeast Italy, built in the 1930s. The bridge is a reinforced concrete tied-arch bridge with 13 vertical hangers per side and 3 horizontal braces between the arches. The deck consists of longitudinal and transverse girders and a flat reinforced concrete slab. One abutment of the bridge has sliding supports, called pendulums, while the other end has fixed supports. During the restoration works carried out in 1994, the flat slab was repaired, and two cantilevered cycle-pedestrian walkways were added to either side of the bridge. The general configuration of the bridge is reported in Figure 1, with the dimensions of its components being consistent with those reported in the original project documents.

## 2.2 Dynamic identification

An Ambient Vibration Test (AVT) was performed to extract the modal characteristics of the bridge. The test was conducted by means of 14 uniaxial accelerometers, performing the recordings in two separate setups, namely North and South (as illustrated in Figure 2). Seven recordings were made with the North setup and four with the South setup.

The experimental parameters were extracted using MACEC 3.3 toolbox [10] applying the poly-reference Least Square Complex Frequency domain (p-LSCF) technique [11–13]. Modal parameters were estimated for each recording and the resulting data from the two setups were combined, obtaining 28 configurations. The correlation between the modal shapes of these configurations was calculated using the MAC index [14].

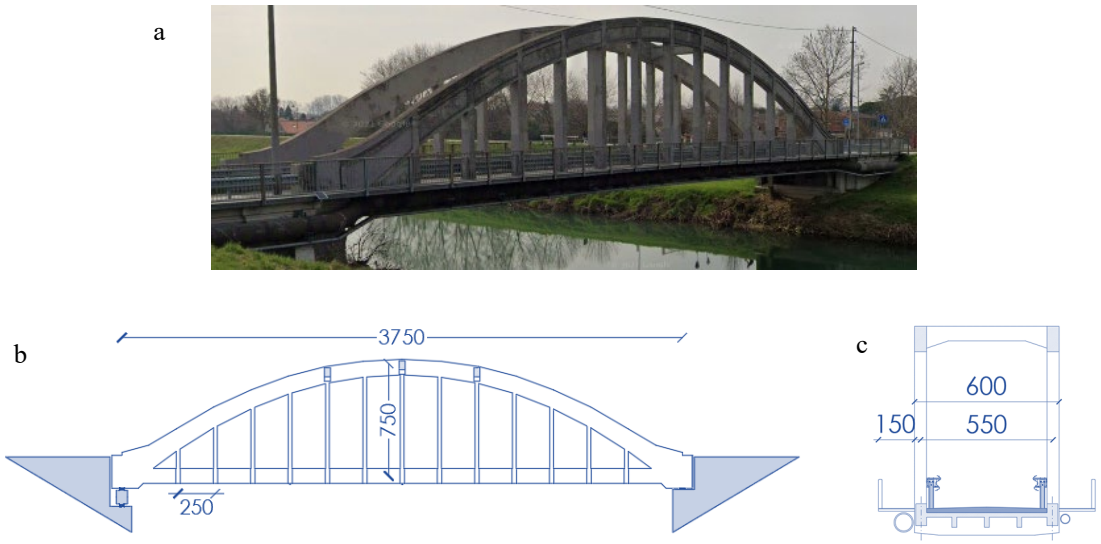


Figure 1: a) Case study view b) longitudinal view; c) transverse view of the bridge.

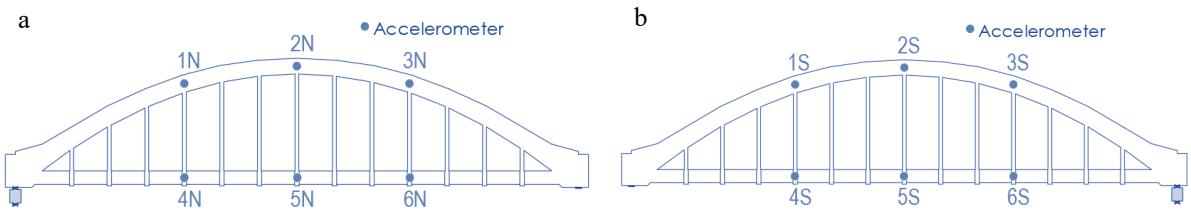


Figure 2: Ambient vibration test: a) North setup; b) South setup.

### 2.3 Numerical model and model updating

A 3D FE model was realised through the utilization of Midas Civil [15]. In this FE model, all bridge members were modelled via beam elements, except for the slab which was modelled as a plate. The loads of the road pavement, barriers, and cycle-pedestrian walkways were applied as non-structural masses. The arch-hanger, tie-hanger and arch-brace connections are simulated by inserting rotational springs, while the boundary conditions were simulated by translational springs, except for the vertical direction, assumed fixed. An eigenvalue analysis was conducted, and the first four mode shapes are presented in Figure 3: Frist four modal shapes of the case study bridge.

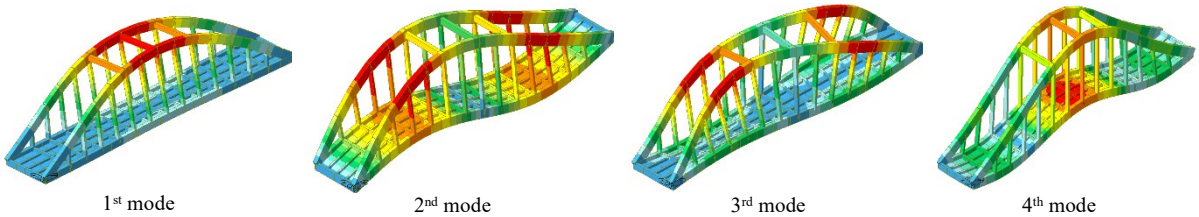


Figure 3: Frist four modal shapes of the case study bridge.

Finally, the FE model updating was performed using the software FEMtools 3.6 [16]. The updating process consists into two parts: deterministic updating and stochastic updating. First, deterministic model updating was performed. The procedure is based on a sensitivity formulation that can be written as [17]:

$$\{R_e\} = \{R_a\} + [S]\left(\{P_u\} - \{P_0\}\right) \quad \text{or} \quad \{\Delta R\} = [S]\{\Delta P\} \tag{1}$$

where $\{R_e\}$ is the vector containing the reference system responses (experimental data); $\{R_u\}$ is the vector containing the predicted system responses for a given state $\{P_0\}$ of the parameters values; $\{P_u\}$ is the vector containing the updated parameter values, and $[S]$ is the sensitivity matrix. Eq. (1) is usually underdetermined, so the Bayes Parameter Estimation (BPE) [18] technique was performed to solve it.

Parameter values updated with the deterministic process are assumed as the mean value for the probabilistic model updating. The other stochastic characteristics of the parameters are estimated with the Mean Value First Order Reliability Method (MVFOSM) [19]. The MVFOSM method assumes a normal distribution for the model parameters, while the standard deviation of the parameter distributions is estimated using the following relationship [20]:

$$\sigma_{R_i}^2 \approx \sum_{j=1}^{n} s_{ij}^2 \sigma_{P_j}^2 \tag{2}$$

where $s_{ij}$ is the sensitivity coefficient of response $R_i$ with respect to the parameter $P_j$, $\sigma_{R_i}$ is the standard deviation of response $R_i$, and $\sigma_{P_j}$ is the standard deviation of the parameter $P_j$. The sensitivity coefficient $s_{ij}$ is computed using the FE model, while the standard deviation $\sigma_{R_i}$ is estimated from the available test data. In this way, Eq. (2) allows the estimation of $\sigma_{P_j}$.

The statistical properties of the parameters are used to perform a Monte Carlo Simulation [21] and re-analyse the FE model with the obtained sample values to investigate the scatter of the numerical frequencies in relation to the experimental ones.

## 3 Results

### 3.1 Summary of AVT results

Table 1presents statistical information of the 28 experimental configurations concerning the first four identified frequencies and the error in relation to numerical model. Correlations between experimental modal shapes are calculated with the MAC index, and the results are reported in Figure 4. Figure 5 shows the correlation between the average of experimental and the numerical modal shapes. The maximum error in both frequency and MAC index occurs in the third modal shape.

| n° mode | Mode type | Mean [Hz] | Std dev | Std rsd | Initial FEM [Hz] | Error |
|---|---|---|---|---|---|---|
| 1 | I° Trans | 3.015 | 0.009 | 0.30% | 2.768 | 8.19% |
| 2 | I° Vert | 4.057 | 0.079 | 1.94% | 3.094 | 23.74% |
| 3 | I° Tors | 4.796 | 0.009 | 0.18% | 3.633 | 24.25% |
| 4 | II° Vert | 7.216 | 0.063 | 0.88% | 5.986 | 17.16% |

Table 1: Statistics of the first four identified frequencies.

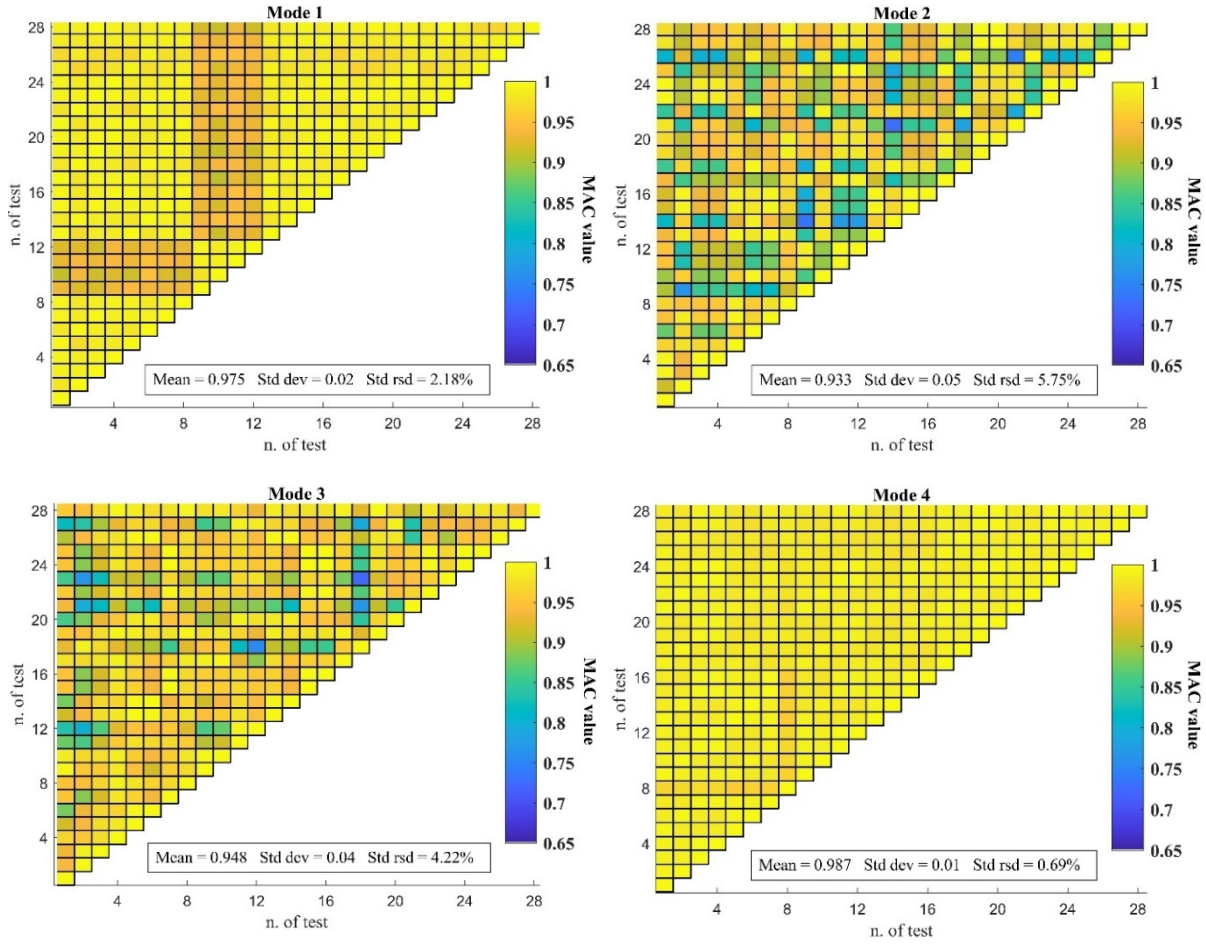


Figure 4: Statistics of the first four identified modal shape.

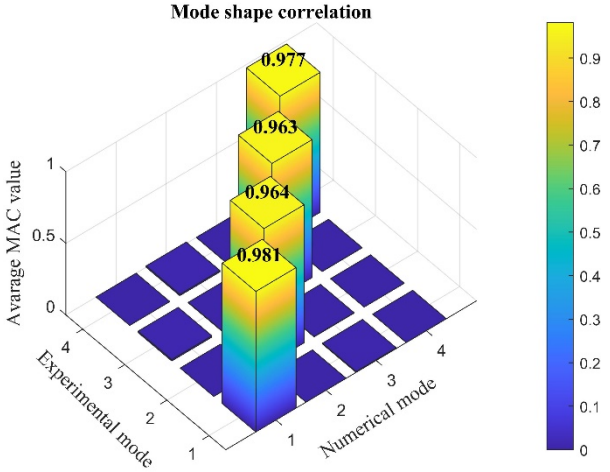


| n° mode | Mean | Std dev | Std rsd |
|---|---|---|---|
| 1 | 0.981 | 0.022 | 2.26% |
| 2 | 0.964 | 0.022 | 2.33% |
| 3 | 0.963 | 0.025 | 2.58% |
| 4 | 0.977 | 0.009 | 0.94% |

Figure 5: Mode shape correlation between test and numerical model.

### 3.2 Deterministic model updating

First, a sensitivity analysis was employed to investigate the impact of various parameters on the first four frequencies of the numerical model. Initially, 9 variables were selected for the updating procedure, including the elastic modulus ($E$), material density ($\rho$), non-structural mass ($NSM$), rotational stiffness of the arch-hanger and tie-hanger connections ($k_1$), rotational stiffness of arch-braces connections ($k_2$), and horizontal boundary conditions ($k_3$). The 9 variables were presented in Table 2 with the respective reference values. The results of the sensitivity analysis reported in Figure 6 indicated that the elastic modulus and mass density exhibited the highest influence on the frequencies response. As a result, only these two parameters were taken into consideration for the model updating procedure.

| n° | Description | Symbol | Ref. value | Units |
|---|---|---|---|---|
| 1 | Elastic modulus | $E$ | 34.3 | GPa |
| 2 | Mass density | $\rho$ | 2.40 | t/m$^3$ |
| 3 | Non-structural mass | $NSM$ | 0.31 | t/m$^2$ |
| 4 | Rotational spring stiffness hangers (x-axis) | $k_{1x}$ | $10^5$ | kNm/rad |
| 5 | Rotational spring stiffness hangers (y-axis) | $k_{1y}$ | $10^4$ | kNm/rad |
| 6 | Rotational spring stiffness braces (x-axis) | $k_{2x}$ | $10^5$ | kNm/rad |
| 7 | Rotational spring stiffness braces (z-axis) | $k_{2y}$ | $10^5$ | kNm/rad |
| 8 | Translational spring stiffness (x-axis) | $k_{3x}$ | $10^{10}$ | kN/m |
| 9 | Translational spring stiffness (y-axis) | $k_{3y}$ | $10^{10}$ | kN/m |

Table 2: Initial Input parameters of the FEM base model.

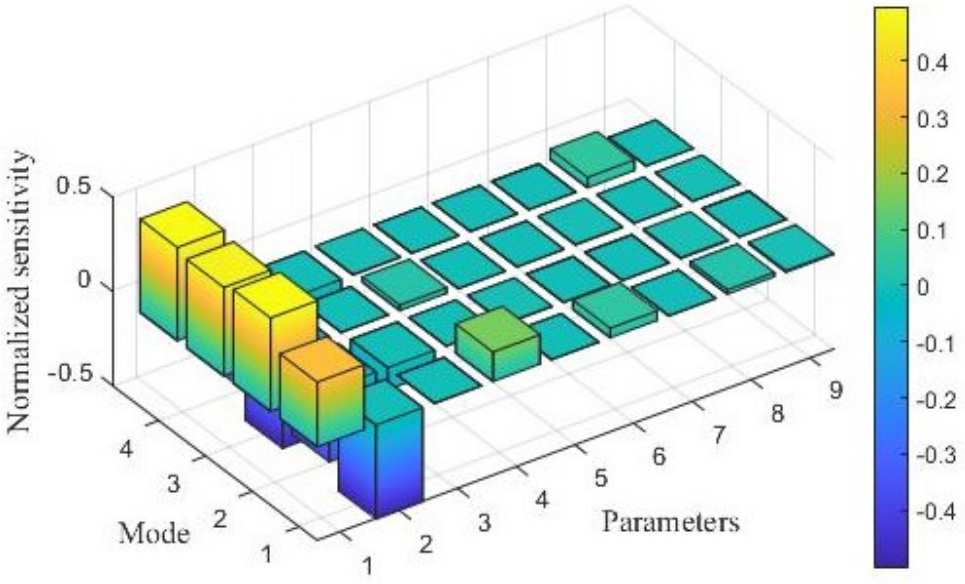


Figure 6: Sensitivity of numerical model frequencies to initial input parameters.

Initially, a first-step calibration strategy was performed on a FE model, whose elements have the same values of elastic modulus and mass density that have been varied in a range between -30% and +30% of the reference values. The average values of the experimental frequencies were assumed as targets.

The final results of the deterministic calibration process are presented in Table 3 while the updated parameter values are summarized in Table 4. This calibration strategy reduced the maximum error between the experimental and model frequencies from 24.25% to 15.20%. The updated model presents an increment of +30% of the elastic modulus and +10.5% of the mass density. Despite only the experimental frequencies were used as target, the average MAC index value indicates a solid correlation between the experimental and numerical modal shapes.

After the first calibration process, a second-step calibration was performed varying the elastic modulus and mass density parameters for specific elements, such as ties, arches, hangers, braces, and deck. The decision to model separately ties and deck is based on the assumption that ties were constructed with a higher performance concrete mix-design [22]. The initial values and range of variation of the parameters are the same as those used in the first-step updating process, and the sensitivity analysis is reported in Figure 7. Through the second-step deterministic model updating, the maximum error between experimental and numerical frequencies was reduced from 24.25% to 8.23%, as reported in Table 5. As reported in Table 6, the updating process caused an increase of +30% of the elastic modulus of ties and arches and a reduction of about -30% in all other elements. Mass density decreased in all elements except in the arches, where it remained almost unchanged, and in the braces (+30% increment). Also, in this case no significant changes in the MAC index are reported.

| n° mode | Mode type | Exp freq. [Hz] | FEM freq, [Hz] | $\Delta f_{resp}$ [%] | Mean MAC |
|---|---|---|---|---|---|
| 1 | I° Trans | 3.015 | 3.057 | -1.39 | 0.951 |
| 2 | I° Vert | 4.057 | 3.486 | 14.07 | 0.972 |
| 3 | I° Tors | 4.796 | 4.067 | 15.20 | 0.923 |
| 4 | II° Vert | 7.226 | 6.777 | 6.21 | 0.878 |

Table 3: Comparison between experimental and numerical modal characteristics of the updated FE model with first-step strategy.

| n° | Description | Symbol | Ref. value | Update value | $\Delta_{par}$ [%] | Units |
|---|---|---|---|---|---|---|
| 1 | Elastic modulus | $E$ | 34.3 | 44.5 | +30 | GPa |
| 2 | Mass density | $\rho$ | 2.40 | 2.65 | +10.5 | t/m$^3$ |

Table 4: Comparison between the structural properties of the FEM model before updating (Ref. value) and after updating (Updated value) with first-step strategy.

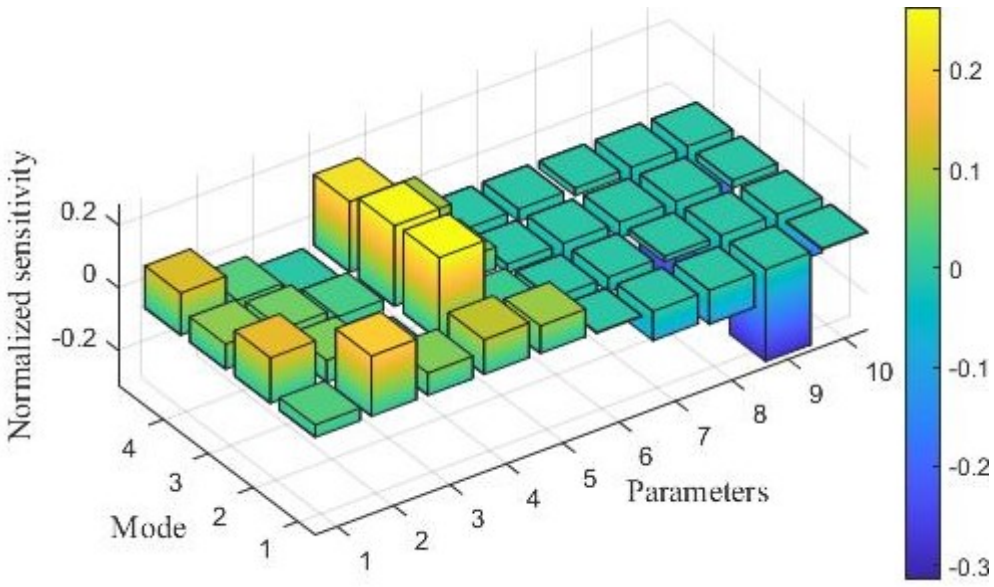


Figure 7: Sensitivity of numerical model frequencies to second-step calibration input parameters.

| n° mode | Mode type | Exp freq. [Hz] | FEM freq, [Hz] | $\Delta f_{resp}$ [%] | Mean MAC |
|---|---|---|---|---|---|
| 1 | I° Trans | 3.015 | 2.973 | 1.39 | 0.939 |
| 2 | I° Vert | 4.057 | 3.723 | 8.23 | 0.991 |
| 3 | I° Tors | 4.796 | 4.465 | 6.90 | 0.938 |
| 4 | II° Vert | 7.226 | 6.977 | 3.44 | 0.930 |

Table 5: Comparison between experimental and numerical modal characteristics of the updated FE with second-step strategy.

| n° | Description | Symbol | Ref. value | Update value | $\Delta_{par}$ [%] | Units |
|---|---|---|---|---|---|---|
| 1 | Tie elastic modulus | $E_t$ | 34.3 | 44.5 | +30 | GPa |
| 2 | Hanger elastic modulus | $E_h$ | 34.3 | 24.8 | -27.5 | GPa |
| 3 | Brace elastic modulus | $E_b$ | 34.3 | 24.0 | -30 | GPa |
| 4 | Arch elastic modulus | $E_a$ | 34.3 | 44.5 | +30 | GPa |
| 5 | Deck elastic modulus | $E_d$ | 34.3 | 24.0 | -30 | GPa |
| 6 | Tie mass density | $\rho_t$ | 2.40 | 1.68 | -30 | t/m$^3$ |
| 7 | Hanger mass density | $\rho_h$ | 2.40 | 1.68 | -30 | t/m$^3$ |
| 8 | Brace mass density | $\rho_b$ | 2.40 | 3.12 | +30 | t/m$^3$ |
| 9 | Arch mass density | $\rho_a$ | 2.40 | 1.68 | -30 | t/m$^3$ |
| 10 | Deck mass density | $\rho_d$ | 2.40 | 2.38 | -1.0 | t/m$^3$ |

Table 6: Comparison between the structural properties of the FEM model before updating (Ref. value) and after updating (Updated value) with second-step strategy.

### 3.3 Stochastic model updating

For all parameters, a normal distribution was assumed, with the mean value assumed from the deterministic model updating results [20]. The standard deviation was estimated using Eq. (2), which uses the dispersion of the experimental tests and the sensitivity values calculated on the calibrated FE models. The resulting probabilistic parameters proprieties of the first-step and second-step calibration strategies are shown respectively in Table 7 and Table 8.

| n° | Description | Symbol | Mean value | Std dev | Std rsd | Units |
|---|---|---|---|---|---|---|

| | | | | | | |
|---|---|---|---|---|---|---|
| 1 | Elastic modulus | $E$ | 44.5 | 0.046 | 0.10% | GPa |
| 2 | Mass density | $\rho$ | 2.65 | 0.045 | 0.02% | t/m$^3$ |

Table 7: Probabilistic parameters proprieties of the first-step strategy.

| n° | Description | Symbol | Mean value | Std dev | Std rsd | Units |
|---|---|---|---|---|---|---|
| 1 | Tie elastic modulus | $E_t$ | 44.5 | 0.069 | 0.16% | GPa |
| 2 | Hanger elastic modulus | $E_h$ | 24.8 | 0.114 | 0.46% | GPa |
| 3 | Brace elastic modulus | $E_b$ | 24.0 | 0.030 | 0.13% | GPa |
| 4 | Arch elastic modulus | $E_a$ | 44.5 | 0.094 | 0.21% | GPa |
| 5 | Deck elastic modulus | $E_d$ | 24.0 | 0.103 | 0.43% | GPa |
| 6 | Tie mass density | $\rho_t$ | 1.68 | 0.039 | 2.32% | t/m$^3$ |
| 7 | Hanger mass density | $\rho_h$ | 1.68 | 0.015 | 0.89% | t/m$^3$ |
| 8 | Brace mass density | $\rho_b$ | 3.12 | 0.043 | 1.38% | t/m$^3$ |
| 9 | Arch mass density | $\rho_a$ | 1.68 | 0.079 | 4.70% | t/m$^3$ |
| 10 | Deck mass density | $\rho_d$ | 2.38 | 0.100 | 4.20% | t/m$^3$ |

Table 8: Probabilistic parameters proprieties of the second-step strategy.

The probabilistic properties of parameters were used to generate 200 random Monte Carlo samples and re-analyse the FE model with the sample values. Natural frequencies for all the samples are reported in Table 9 considering only those values that fall within the 95th percentile ellipse. The results indicate that the second-step strategy shows better convergence with the experimental data cloud, with the centre of the 95th percentile ellipses positioned closer. Specifically, the Euclidean distance calculated between the experimental and numerical data obtained with the first-step strategy is 0.589 [Hz] for the scatter plot between frequency 1 and frequency 2 (Figure 8a), and 0.887 [Hz] for that between frequency 3 and frequency 4 (Figure 8b). Whereas, for the second-step strategy, these values drop to 0.186 [Hz] (Figure 9a) and 0.290 [Hz] (Figure 9b), respectively, providing further evidence of its better convergence with the experimental data.

| n° mode | Mode type | Mean freq. [Hz] | | | Std dev | | | Std rsd | | |
|---|---|---|---|---|---|---|---|---|---|---|
| | | Exp | Prim. | Sec. | Exp | Prim. | Sec. | Exp | Prim. | Sec. |
| 1 | I° Trans | 3.015 | 3.038 | 2.968 | 0.009 | 0.091 | 0.074 | 0.30% | 3.00% | 2.49% |
| 2 | I° Vert | 4.057 | 3.466 | 3.877 | 0.079 | 0.097 | 0.101 | 1.95% | 2.80% | 2.61% |
| 3 | I° Tors | 4.796 | 4.041 | 4.581 | 0.009 | 0.121 | 0.123 | 0.19% | 2.99% | 2.69% |
| 4 | II° Vert | 7.226 | 6.739 | 7.025 | 0.011 | 0.186 | 0.171 | 0.15% | 2.76% | 2.43% |

Table 9: Comparison between experimental and numerical frequencies after Monte Carlo Simulation.

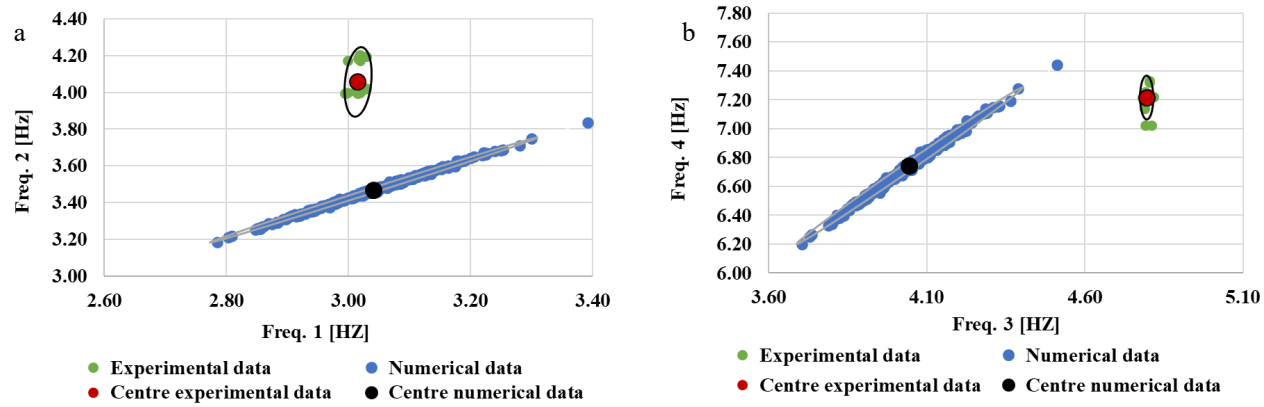


Figure8: Overlaid scatter plots of experimental and numerical frequencies for first-step strategy: a) freq.1-freq.2, b) freq.3-freq.4.

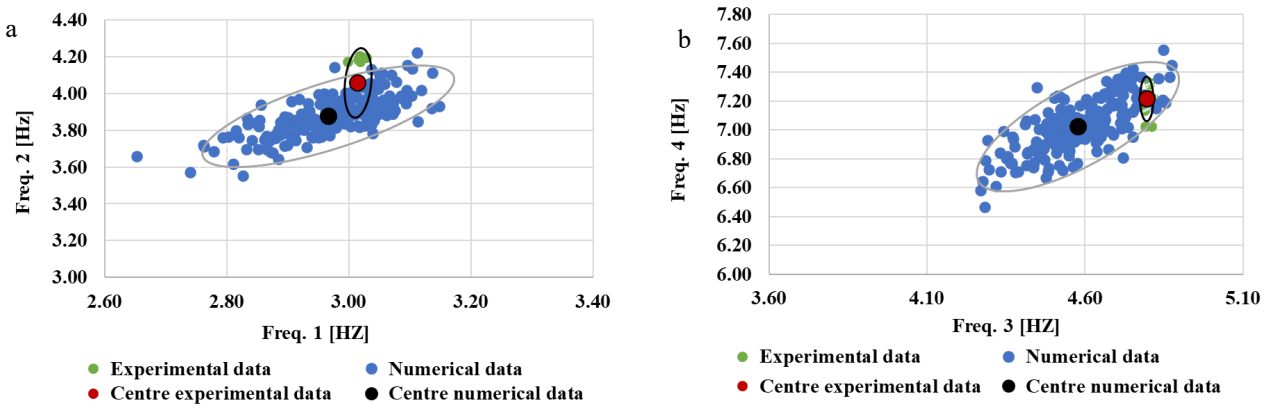


Figure 9: Overlaid scatter plots of experimental and numerical frequencies for second-step strategy: a) freq.1-freq.2, b) freq.3-freq.4.

## 4 CONCLUSION

This paper presents a stochastic model updating of an RC tied-arch bridge. The initial model was calibrated using dynamic identification test results. The recordings were made on two set-ups, and the extracted modal parameters were appropriately combined create 28 combination tests. The model updating procedure assumed the frequencies of the first four modes as targets, and a sensitivity analysis was conducted to determine the most sensitive parameters. The analysis revealed that the elastic modulus and mass density were the most sensitive parameters. Next, deterministic model updating was performed using an iterative procedure based on the Bayes Parameter Estimation (BPE) technique. Two strategies were adopted, first-step and second-step, where the first considered a FE model with identical material characteristics for all elements, while the second considered different material characteristics for specific elements. The results showed that the second-step strategy provided better results, reducing the frequencies error from 24.25 % to 8.23 %, while the first-step strategy stopped at 15.20 %. The FE model that best represented the real behaviour of the bridge present an increase in elastic modulus for the arch and tie elements and a reduction for all other elements. As for mass density, a reduction was observed for all elements except for the arch, which remained constant, and for the braces, where it increased. Next, stochastic model updating was performed, where the statistical properties of the parameters were estimated using the Mean Value First Order Reliability

Method (MVFOSM) assuming as mean values the results value of the deterministic model updating.

Finally, a Monte Carlo simulation was performed using the statistical properties of the model parameters to generate 200 random samples and re-analyse the FE model with these values. The frequencies of these models were statistically processed to obtain a scatter plots. It has been demonstrated that in probabilistic model updating, more reliable results can be obtained by using a larger number of calibration parameters. In particular, it was shown how the scatter of the numerical data generated by the Monte Carlo Simulation of the second-step strategy is closer to the distribution of the experimental data, reducing the Euclidean distance from 0.589 [Hz] to 0.186 [Hz], for the scatter plot between frequency 1 and frequency 2, and from 0.887 [Hz] to 0.290 [Hz] for frequency 3 and frequency 4, compared with the first-step strategy.

## REFERENCES

[1] J. . Mottershead and M. . Friswell, Model Updating In Structural Dynamics: A Survey, *J. Sound Vib.*, *Vol 167, no. 2,* pp. 347–375, 1993.

[2] M. I. Friswell and J. E. Mottershead, *Finite Element Model Updating in Structural Dynamics*, *Vol 38*. in Solid Mechanics and its Applications, Dordrecht: Springer Netherlands, 1995.

[3] M. Link, Updating of analytical models—review of numerical procedures and application aspects, *Proc., Struct. Dyn. Forum SD2000*, 193–223, 1999.

[4] J. M. W. Brownjohn, P. Q. Xia, H. Hao, and Y. Xia, Civil structure condition assessment by FE model updating: Methodology and case studies, *Finite Elem. Anal. Des.*, *Vol 37, no. 10*, 761–775, 2001.

[5] S. V. Modak, T. K. Kundra, and B. C. Nakra, Comparative study of model updating methods using simulated experimental data, *Comput. Struct.*, *Vol 80, no. 5–6*, 437–447, 2002.

[6] A. Brandt, *Noise and vibration analysis: signal analysis and experimental procedures*, *1st Edition*, 2010.

[7] C. Mares, J. E. Mottershead, and M. I. Friswell, Stochastic model updating: Part 1-theory and simulated example, *Mech. Syst. Signal Process.*, *Vol 20*, *no. 7*, 1674–1695, 2006.

[8] J. E. Mottershead, C. Mares, S. James, and M. I. Friswell, Stochastic model updating: Part 2-application to a set of physical structures. *Mech. Syst. Signal Process.*, *Vol 20*, *no. 8*, 2171–2185, 2006.

[9] F. M. Hemez, S. W. Doebling, and M. C. Anderson, A brief tutorial on verification and validation. *22nd SEM International Modal Analysis Conference*, 26–29, 2004.

[10] E. Reynders, M. Schevenels, and G. De Roeck, MACEC 3.3 A Matlab Toolbox for Experimental and Operational Modal Analysis, 2014.

[11] P. Verboven, P. Guillaume, S. Vanlanduit, H. Van Der Auweraer, and B. Peeters, A Poly-Reference Implementation of the Least-Squares Complex Frequency-Domain Estimator, 2003.

[12] B. Peeters, G. Lowet, H. Van Der Auweraer, and J. Leuridan, A New Procedure for Modal Parameter Estimation. *J. Sound Vib.*, 24–28, 2004.

[13] B. Peeters and H. Van Der Auweraer, PolyMax: a revolution in operational modal analysis. *Proceedings of the 1st International Operational Modal Analysis Conference, Copenhagen, Denmark*, 2005.

[14] R. Allemang and L. Brown, A Correlation Coefficient for Modal Vector Analysis. *Proc. 1st Int. Modal Anal. Conf.*, 110–116, 1982.

[15] midas Civil, "Manuals and Tutorials," Jun. 13, 2022.

[16] FEMtools, *FEMtools 3.6 Release Notes*. Leuven, Belgium, 2012.

[17] FEMtools, *FEMtools 3.6 Model Updating Theoretical Manual*. Leuven, Belgium, 2012.

[18] W. L. Hays, Scientific Reasoning: The Bayesian Approach. *Contemp. Psychol. A J. Rev.*, *Vol 36, no. 8*, 726–726, 1991.

[19] A. Haldar and M. Sankaran, *Probability, Reliability, and Statistical Methods in Engineering Design*. John Wiley & Sons Incorporated, 2000.

[20] FEMtools, *FEMtools 3.6 Model Updating User's Guide.* Leuven, Belgium, 2012.

[21] R. Y. Rubinstein and D. P. Kroese, *Simulation and the Monte Carlo Method*. John Wiley & Sons, 2016.

[22] G. Albenga, *I ponti: la pratica, Vol. 1*, 1953.

COMPDYN 2023
9th ECCOMAS Thematic Conference on
Computational Methods in Structural Dynamics and Earthquake Engineering
M. Papadrakakis, M. Fragiadakis (eds.)
Athens, Greece, 12-14 June 2023

# THE EFFECT OF GROUND MOTION INCIDENCE ANGLE FOR SCOURED HIGHWAY BRIDGES

**S. Ateş[1] and Ö. Avşar[2]**

[1] Department of Civil Engineering, Eskisehir Technical University
Iki Eylul Kampusu, 26555 Eskisehir, Turkey
e-mail: serenayates@ogr.eskisehir.edu.tr

[2] Department of Civil Engineering, Eskisehir Technical University
Iki Eylul Kampusu, 26555 Eskisehir, Turkey
e-mail: ozguravsar@eskisehir.edu.tr

## Abstract

*Bridges are usually built to connect two pieces of land where water flows between them. Over time, for the water crossing bridges it is inevitable to occur scour around bridge substructure and this may affect both the seismic demands and capacity of bridge members. Besides, the ground motion incidence angle is another critical issue that can amplify the seismic demands imposed on the bridges. In this study, it is aimed to investigate the seismic performance of a highway bridge which has a uniform scour around its piles. A soil structure interacted reinforced concrete bridge consisting of prestressed I-sectioned beams and deck is modeled in OpenSees program. Scour depth is varied from 0 m (no scour) to 5 m depth with a uniform increment of 1 m. During nonlinear time history analysis, 7 different strong ground motion records with their 3 components are used. To obtain critical incidence angle, horizontal components of ground motions are rotated from 0° to 180° with an increment of 15° by using linear transformation equations. Superstructure displacement, pier curvature and shear force demands are investigated for each scour depth and earthquake incidence angle in the scope of the study. Both scour depth and earthquake incidence angle affect the seismic response of the investigated highway bridge under the selected ground motion records.*

**Keywords:** Scour, Incidence angle, Reinforced concrete bridge, Nonlinear time history analysis.

# 1 INTRODUCTION

Bridges are particularly expensive and vital type of construction since they are the backbone of community life and one of the most crucial parts of the road network. In the event of an earthquake, the existing bridges should be serviceable to provide connection for the emergency and rescue teams to the affected area and to maintain the sustainability of social life. Even if bridge-like structures are constructed in compliance with the regulations, they are still susceptible to damage from many external factors including aging, natural disasters etc. In such circumstances, it is crucial for designers to calculate the actual demands that will be imposed on the structural members in order to predict potential structural damage. As a result, in recent years, researchers have examined the demands that occur in bridges under various effects [1, 2, 3]. Scour, which is an important phenomenon, is caused by water erosion as it flows and it becomes a stunning occurrence for bridges built in flood region areas. According to U.S. Department of Transportation [4], 3 types of scour can exist in a flood region area; long term aggradation and degradation of the river bed, contraction scour at the bridge and local scour at the piers or abutments. The most important one is the local scour for bridge type structures because it occurs around the substructure of bridge and it may affect the seismic demand of members during earthquake or any other natural hazards. Moreover, unexpected damage to bridges may occur when the combined effects of scour and earthquake occur [5, 6, 7]. Nonlinear time history analysis is frequently used to calculate the seismic demands of bridge elements during an earthquake. Real or artificial ground motion suits are employed for the simulations. Although the horizontal ground motion components are frequently applied on the global axes of the structure, the incidence angle at which the horizontal ground motion components affecting the structure is generally different from the global axis. Numerous investigations have found that when the earthquake incidence angle is taken into account, the seismic demands of elements are affected considerably [8, 9, 10, 11, 12].

In this study, it is aimed to determine the effect of ground motion incidence angle in nonlinear analysis for scoured highway bridges. A soil structure interacted concrete bridge model with prestressed I beams, and a single column bent was modelled in the OpenSees platform. It has 4 spans with 35 m span length and 12 m width and total length of the bridge is 140 m. Scour depth was changed starting from 0 m (no Scour) to 5 m with a uniform increment of 1m for each piles. According to the Principles for the Design of Highway and Railroad Bridges and Viaducts Under the Impact of Earthquakes [13], nonlinear time history analyses should be conducted under 7 strong ground motion records. The incidence angle of the ground motion pairs was rotated starting from 0° to 180° with an increment of 15° by using linear transformation equations. Deck displacement in longitudinal and transverse direction, shear and curvature demand for bridge piers are the seismic demand parameters for investigating the effectiveness of the method. It is thought that this study will contribute to the evaluation of the seismic demands more realistically that arise under multiple effects, such as earthquake and scour, in the elements of a typical bridges.

# 2 CHARACTERISTICS AND ANALYTICAL MODELING OF BRIDGES

## 2.1 Bridge properties

The bridge used in the study is a reinforced concrete highway bridge consisting of prestressed I-section beams and continuous deck and it is found mostly in Turkey. The bridge superstructure has 4 spans as seen in Figure 1, each span has 35 m length and 12 m width and the total length of the bridge is 140 m. The superstructure consists of 8 prestressed beams and a continuous reinforced concrete deck. Deck thickness is 22 cm. Concrete grade is C40 for the

prestressed beams, C25 for other elements, and reinforcing steel grade is S420. The bridge substructure consists of a cap beam, single column piers and abutments. Each of the column piers is H=8.7 m high and consists of an oval section of $B_c$=1.2 m and D=4 m. Both the piers and abutments are supported on the pile cap. The cap beam has a rectangular section with a width of 1.2 m and a depth of 1.75 m. There are 450x250x40 mm elastomeric bearings under each prestressed beam. Moreover, pile cap has a rectangular section with dimensions $B_{cap}$=2.5m, $L_{cap}$=5m and a height of $H_{cap}$=1.5m. Under this pile cap, there are 6 circular piles with a diameter of $D_{pile}$=1m and a height of $H_{pile}$=20m. Concrete grade is also taken as C25 and steel grade is S420 for pile elements.

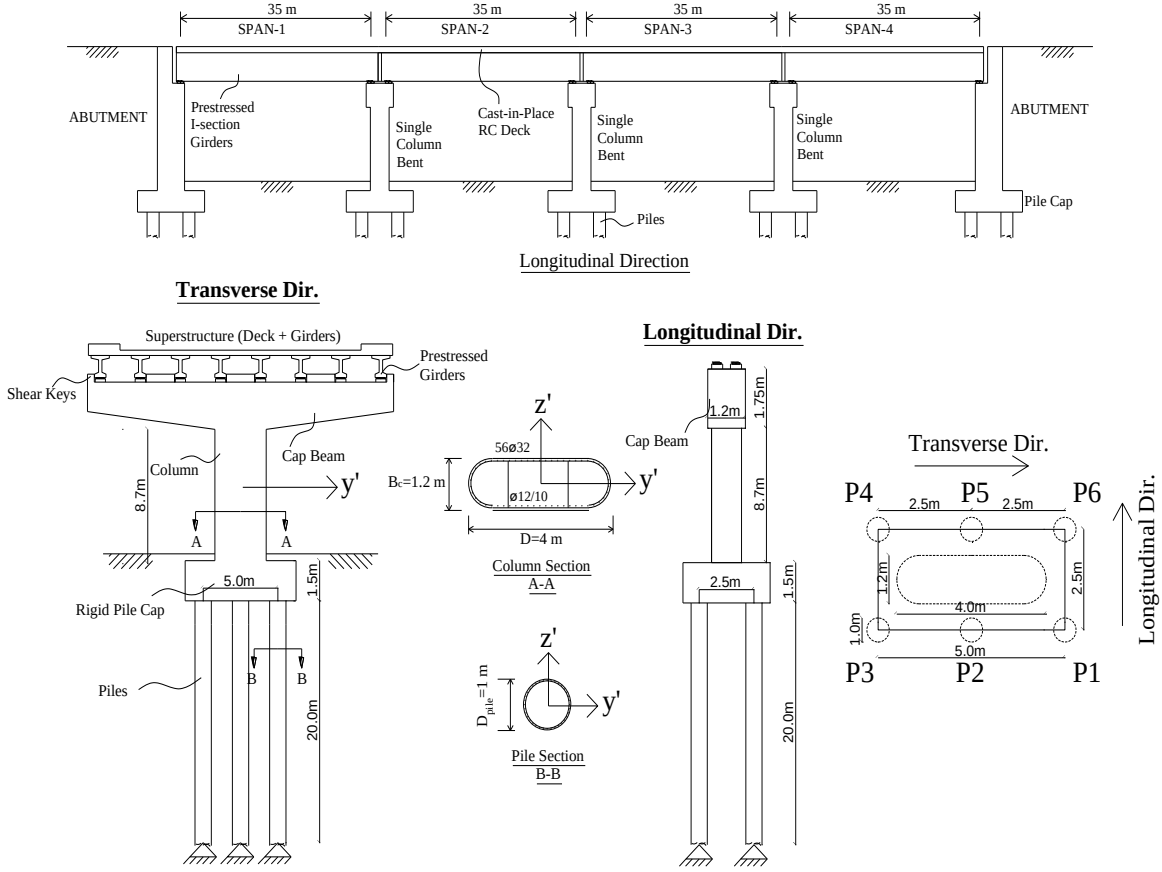


Figure 1: Properties of bridge members.

## 2.2 Analytical modeling

The 3 dimensional analytical model of the reinforced concrete highway bridge used in the study was created using the frame elements in the OpenSees program as seen in Figure 2. Because of the elastomeric bearings between superstructure and substructure, superstructure members such as deck and girders were modelled by using elastic beam column elements and masses are distributed at equally spaced nodes. Fiber section elements were used to create bent columns in order to simulate the nonlinear behavior. Abutment-deck pounding and deck-shear key pounding were defined using nonlinear pounding elements in both the longitudinal and transverse directions, respectively. They have 5 cm gap in longitudinal and 2.5 cm gap in transverse direction. In addition, springs were used at the abutments to simulate the soil - structure interaction with regard to Caltrans [14]. While defining the pile cap, rigid elastic beam column elements were used in OpenSees. Column pier and piles were connected to the

pile cap with also rigid elements. Piles were assumed to be in the elastic limits during earthquake therefore, they were defined by using elastic beam column elements in the model.

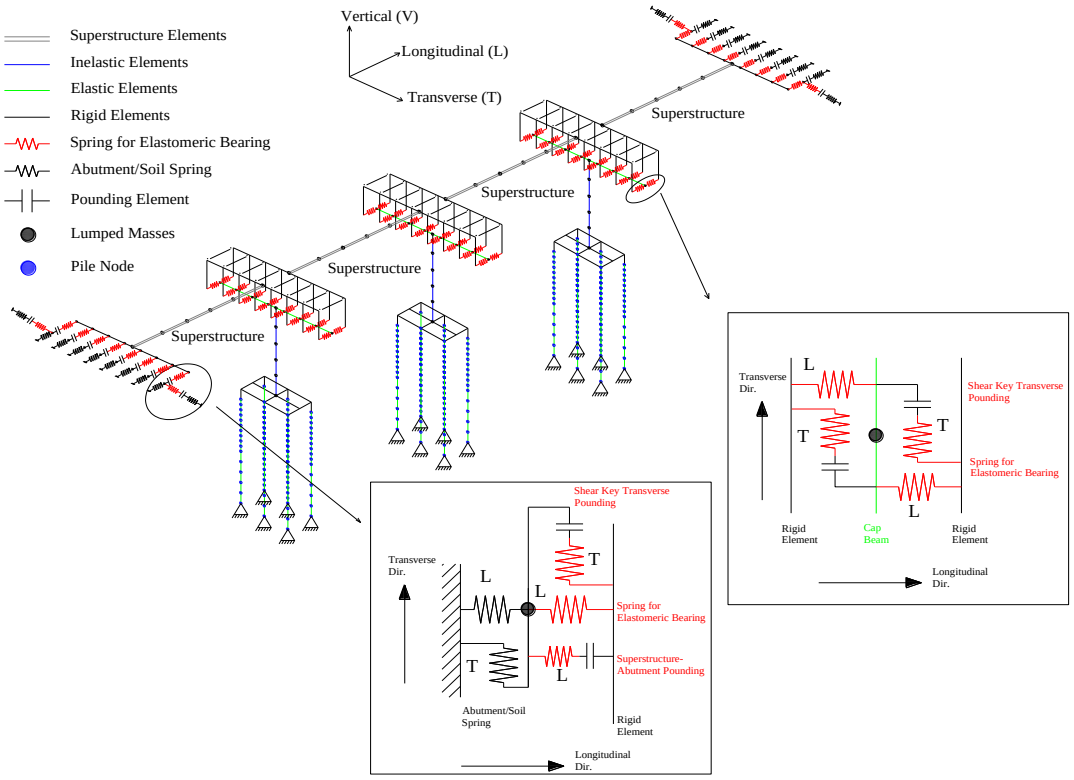


Figure 2: Analytical bridge model constructed in OpenSees.

## 2.3 Soil-structure interaction

The foundation of the piles is affected by axial and lateral loads caused by the surrounding soil, particularly during earthquakes. In order to achieve realistic results, it is essential to take soil structure interaction into account while modeling the structural system for bridges. In the literature, many of the researchers used soil springs to reflect this interaction [2, 5, 15, 16] During the modeling process in the OpenSees program, “Py Simple1” material model was used for lateral soil resistance and “Tz Simple1” material model was used for axial resistance. The pile elements were divided into 0.5 m long members for the first 10 m length below the pile cap and 1 m long members for the last 10 m. The springs were assigned to the nodes of these small elements. P-y springs were defined in the horizontal direction (both longitudinal and transverse directions) of the bridge and t-z springs were assigned in the vertical direction as seen in Figure 3.

The soil around the piles was chosen as sand with a unit weight $\gamma_{sand}$=18 kN/m$^3$ and angle of internal friction Ø=25°. Uniaxial material properties of p-y springs were calculated according to the American Petroleum Institute (API) [17]. The relationship between lateral soil resistance (P) and deflection (y) can be calculated by using Equation (1);

$$P = A \cdot P_u \cdot tanh\left[\frac{k \cdot H}{A \cdot P_u} \cdot y\right] \quad (1)$$

where, A=factor to account for cyclic or static loading condition and evaluated by A=0.9 for cyclic loading. $P_u$ (kN/m) is the ultimate bearing capacity at depth H (m), k is the initial modulus of subgrade reaction, given in API [17] as function of internal friction Ø. H (m) is the depth from ground level and y (m) is the lateral deflection. The ultimate lateral capacity for sand can be calculated by using Equation (2) and (3) for shallow and deep depths, respectively. At a given depth the smallest value of the given equation should be used as $P_u$.

$$P_{us} = (C_1 \cdot H + C_2 \cdot D) \cdot \gamma \cdot H \tag{2}$$

$$P_{ud} = C_3 \cdot D \cdot \gamma \cdot H \tag{3}$$

In these equations, $P_u$ is the ultimate resistance (kN/m) for s=shallow and d=deep. γ is the effective soil weight (kN/m3), H is depth (m), $C_1$, $C_2$ and $C_3$ are the coefficients determined from API [17] as function of Ø and D is the average pile diameter from surface to depth (m).

The uniaxial material properties of t-z spring was calculated for sand type soil [18]. Ultimate axial soil resistance was calculated by using Equation (4);

$$T_{ult1} = K_0 \cdot \gamma \cdot H \cdot P_{Perimeter} \cdot tan\delta \tag{4}$$

$$T_{ult} = T_{ult1} \cdot L \tag{5}$$

$$Z_{50} = \frac{t_{ult}}{K_f} \tag{6}$$

where, $T_{ult1}$ is the ultimate axial bearing capacity of pile with a unit of kN/m. $K_0$ is the coefficient of the lateral earth pressure at rest, taken as $K_0$=0.4, H is the depth (m), P is the perimeter of pile surface and δ is interface friction between soil and pile, take as δ=0.8xØ to be representative of a smooth precast concrete pile [18]. After calculating $T_{ult1}$, it should be converted to the force unit ($T_{ult}$) by multiplying length of the pile section as given in Equation (5). $Z_{50}$ represents displacement at 50% of $T_{ult}$. It can be calculated by using Equation (6) and $K_f$ is initial modulus of side resistance [19].

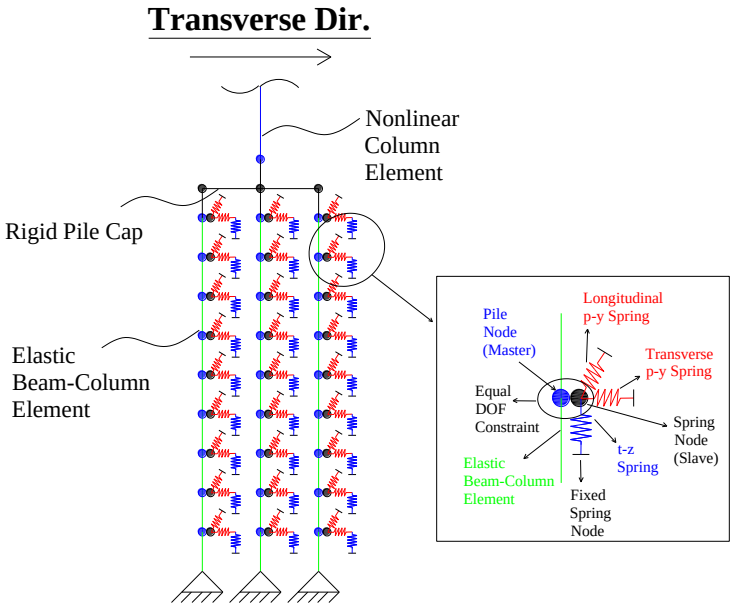


Figure 3: Description of nonlinear p-y and t-z springs on the bridge piles.

### 2.4 Scour Effect

Scour is a significant phenomenon that, as previously mentioned, may have an impact on the seismic demands for bridge members. In this study, it is aimed to determine seismic demands of scoured bridge members under the effect of strong ground motions. Therefore 6 different scour cases were created in the OpenSees program. The depth of scour around bridge piles was changed starting from 0 m (no scour) to 5 m with an increment of 1 m as seen in Figure 4. For each scour depth, nonlinear springs were removed from the pile nodes and soil properties were recalculated for each depth.

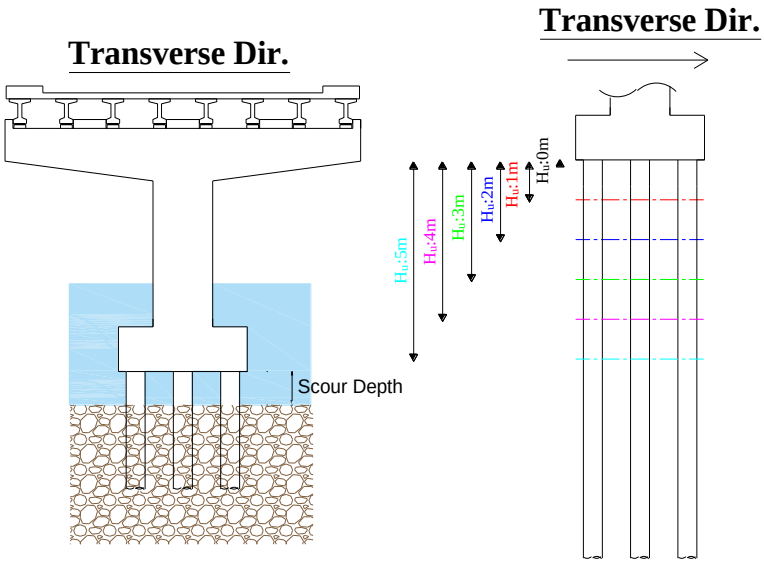


Figure 4: The change of uniform scour depth (Hu).

## 3 GROUND MOTION PROPERTIES

### 3.1 Selection and scaling of ground motion records

Nonlinear time history analysis of the bridge analytical model created within the scope of the study were performed using the OpenSees program. By using Pacific Earthquake Engineering Research Center [20] database, 7 strong ground motion suits selected and scaled according to Principles for the Design of Highway and Railroad Bridges and Viaducts Under the Impact of Earthquakes [13]. The properties of the horizontal components of selected ground motions are given in Table 1. Assuming that the bridge used in the study is located in Eskisehir, a location was chosen by using the Turkey Earthquake Hazard Map [21] web interface. Spectral acceleration-period graph was obtained for the ZD soil class and DD-2 (earthquake ground motion level with 10% probability of exceedance in 50 years) level of this location. The amplitudes of the selected earthquake ground motion components are scaled according to the rule given in section 2.5.2.2. in the regulations that the ratio of the average amplitudes of the resultant spectra of all selected records between the 0.2 $T_p$ and 1.5 $T_p$ period range to the amplitudes of the design acceleration spectrum in the same period range is not less than 1.3 as given in Figure 5, where $T_p$ is the fundamental period of the bridge. The specified scale factor should be considered for both perpendicular horizontal components and vertical component of the ground motion records.

| No | Event | Station | Mw | Fault Type | Component | PGA (g) | PGV (cm/s) | PGD (cm) | Scale Factor |
|---|---|---|---|---|---|---|---|---|---|
| 1 | Coyote Lake, 1979 | Gilroy Array #6 | 5.74 | Strike slip | 230°<br>320° | 0.42<br>0.31 | 44.34<br>25.39 | 12.44<br>4.38 | 1.0 |
| 2 | Morgan Hill, 1984 | Anderson Dam | 6.19 | Strike slip | 250°<br>340° | 0.42<br>0.28 | 25.40<br>27.80 | 4.43<br>6.43 | 1.0 |
| 3 | Imperial Valley, 1979 | El Centro Array #4 | 6.53 | Strike slip | 140°<br>230° | 0.48<br>0.37 | 39.64<br>80.41 | 25.13<br>74.26 | 1.0 |
| 4 | Landers, 1992 | Lucerna | 7.28 | Strike slip | 260°<br>345° | 0.72<br>0.78 | 133.40<br>28.10 | 113.92<br>25.53 | 1.0 |
| 5 | Düzce, 1999 | Duzce | 7.14 | Strike slip | 180°<br>270° | 0.40<br>0.51 | 71.15<br>84.23 | 49.69<br>48.03 | 1.0 |
| 6 | Superstition Hills, 1987 | El Centro Imp. Co. Cent | 6.54 | Strike slip | 0°<br>90° | 0.35<br>0.25 | 48.07<br>41.79 | 19.27<br>21.85 | 1.0 |
| 7 | Kocaeli, 1999 | İzmit | 7.51 | Strike slip | 90°<br>180° | 0.23<br>0.16 | 38.29<br>22.33 | 24.29<br>11.84 | 1.0 |

Table 1: Properties of the selected ground motion records

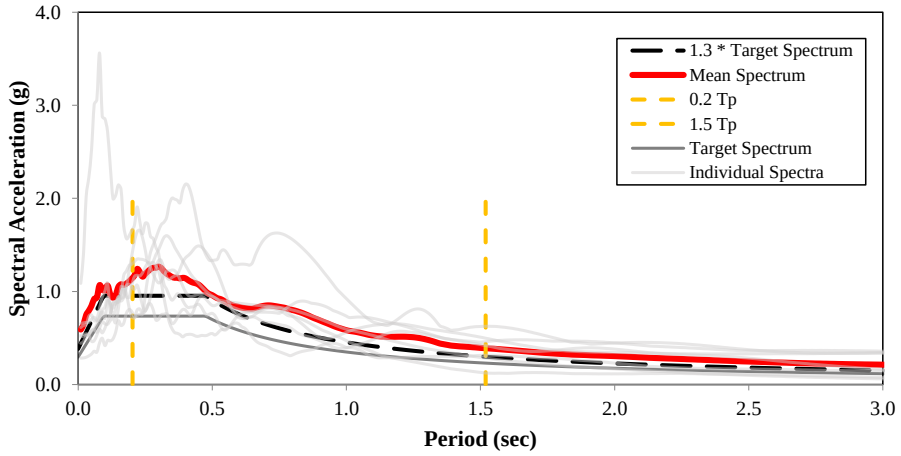


Figure 5: Elastic response spectra for selected ground motions with 5% damping ratio.

## 3.2 Rotation of ground motion records

It is a general assumption that the ground motion components affect the global axis of the structure in time history analysis. However, in reality, it is not known at which angle the earthquake ground motion components affect a structure. Furthermore, as per Caltrans [14], the ground motion must be applied at a sufficient number of angles to capture the maximum deformation of all critical components. For this reason, in recent years, researchers have carried out several studies on the effect of critical incidence angle on bridge performance [9, 10, 12, 20]. In this study, horizontal ground motion components were rotated by using linear transformation equations. Ground motion components were recalculated using Equation (7) and the new earthquake record components obtained were applied to the bridge global axis as shown in Figure 6. The $a_1(t)$ and $a_2(t)$ specified in Equation (1) are the original horizontal earthquake records that should be applied to the local axes (1) and (2) determined by the angle $\theta$. However, to be used in the analysis, $a_X(t)$ and $a_Y(t)$ which are their equivalents on the glob-

al axes are converted by linear transformation. With this method, analyses were performed by rotating the original components of ground motion from 0° to 180° at 15° intervals. Also, the horizontal component of ground motion which has the highest PGV was affected to the bridge transverse direction. Vertical component of the ground motions was included in each analysis.

$$\begin{Bmatrix} a_X(t) \\ a_Y(t) \end{Bmatrix} = \begin{bmatrix} cos\theta & -sin\theta \\ sin\theta & cos\theta \end{bmatrix} \cdot \begin{Bmatrix} a_1(t) \\ a_2(t) \end{Bmatrix} \tag{7}$$

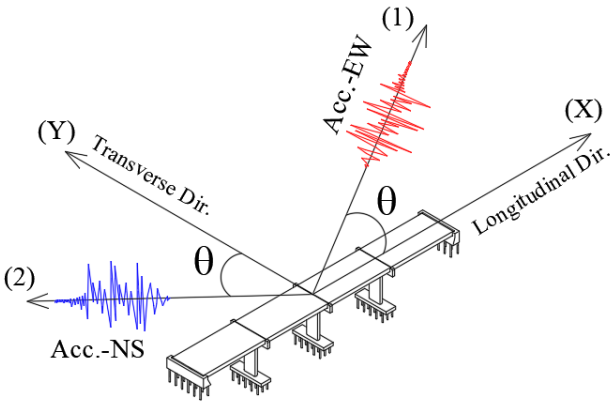


Figure 6: The rotation of the horizontal ground motion pair and its application to the bridge [10]

## 4 ANALYSIS RESULTS

Nonlinear time history analyses were carried out for given bridge model to investigate the combined effect of scour and earthquake. Scour depth was changed starting from 0 m to 5 m with an increment of 1 m and horizontal ground motion components was rotated from 0° to 180° in counterclockwise direction with an increment of 15°. 6 different scoured bridges exposed to 7 ground motion acceleration time series with 13 particular incidence angles independently. As seen in Figure 7, the 1st and 2nd vibration periods of the bridge increase when scour depth increases. This is because, the clear height of the bent piles increases when the soil around piles is removed. This situation increases the flexibility of the bridge and so do the periods.

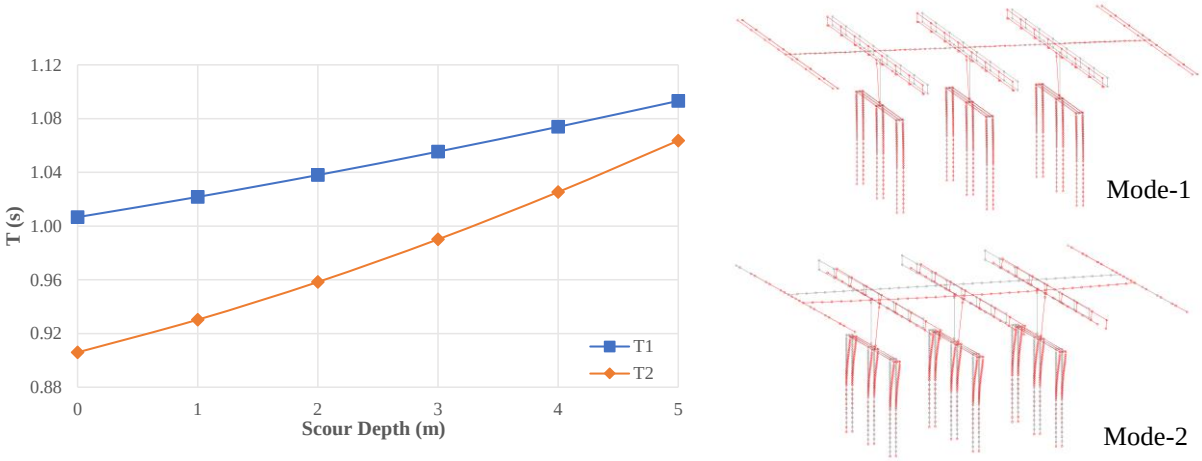


Figure 7: The variation of 1st and 2nd vibration period of bridge depending on uniform scour depth.

Deck displacement in both longitudinal and transverse direction, curvature and shear force demands for bent column piers are inspected as engineering demand parameters and results are given in the sections below.

### 4.1 Superstructure displacement

Consideration of uniform scour depth change is a practical way while modeling soil structure interaction for the scoured bridges. For each scour depth, nonlinear springs were removed from the pile nodes therefore, the scoured bridge models were obtained easily.

Superstructure displacement demands obtained from nonlinear analysis results belong to the midpoint displacement of the bridge deck. In Figure 8, average maximum displacement demands in longitudinal and transverse direction of the bridge are given. Also, average maximum resultant displacement is calculated by taking the maximum of square root of the sum of squares of these directions. When we examine the results in terms of the change of the earthquake incidence angle, the average maximum displacement in longitudinal direction of bridge has an increasing trend between 0° and 75° although in transverse direction it is decreasing between 0° and 90°. Therefore, the resultant displacement is not much affected from the change of scour depth. According to the radar and bar charts, the average maximum superstructure displacement increases in both directions of bridge when scour depth ($H_u$) increase uniformly around piles. Because as the depth of scour increases, the effective height of the bridge pier increases, which causes more displacement of the superstructure elements. The maximum difference of average displacement demands in longitudinal direction between no scoured ($H_u$=0m) and 5 m scoured ($H_u$=5m) bridge is occurred at 75° incidence angle is 12.4%. In transverse direction, it is at 165° as 18.1%. If it is checked for resultant displacement, the maximum difference becomes 13% at 0° incidence angle.

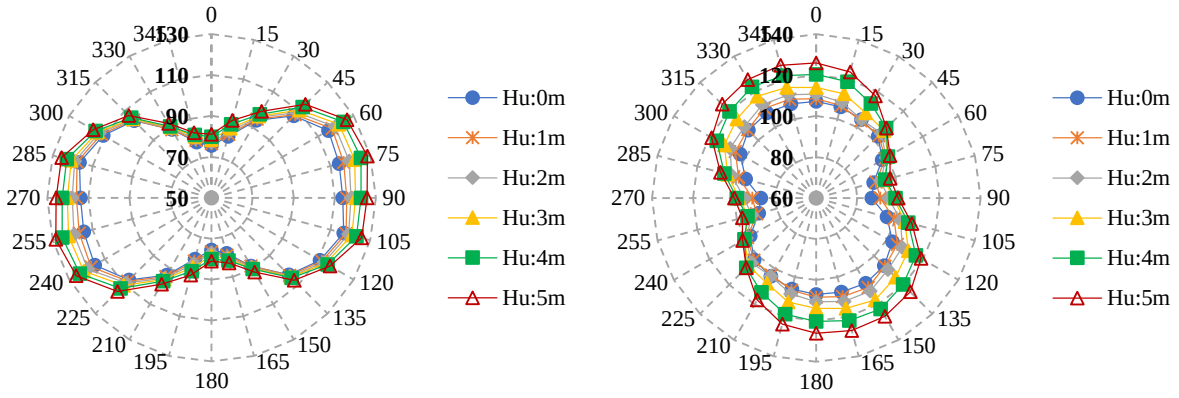


(a) Longitudinal (b) Transverse

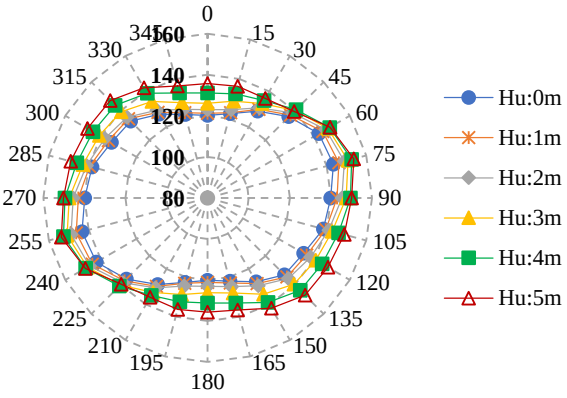
0
15
30
45
60
75
90
105
120
135
150
165
180
195
210
225
240
255
270
285
300
315
330
345
160
140
120
100
80
Hu:0m
Hu:1m
Hu:2m
Hu:3m
Hu:4m
Hu:5m

(c) Resultant

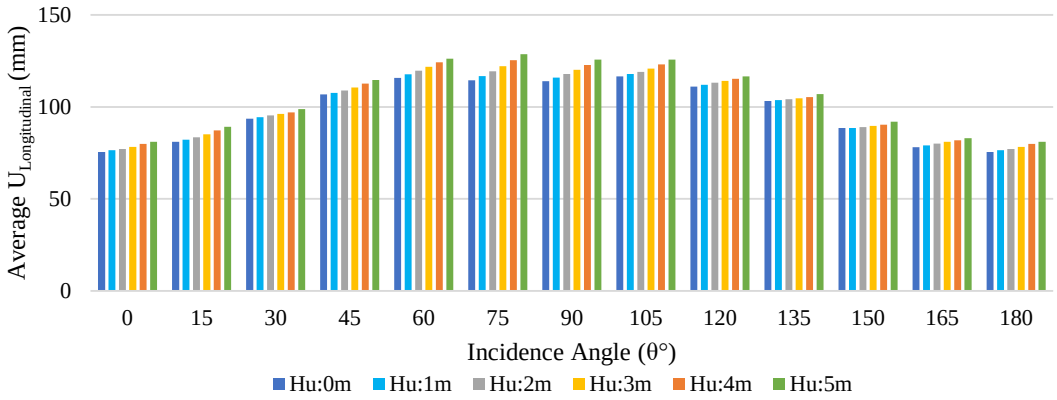
Average U Longitudinal (mm)
150
100
50
0
0
15
30
45
60
75
90
105
120
135
150
165
180
Incidence Angle (θ°)
Hu:0m
Hu:1m
Hu:2m
Hu:3m
Hu:4m
Hu:5m

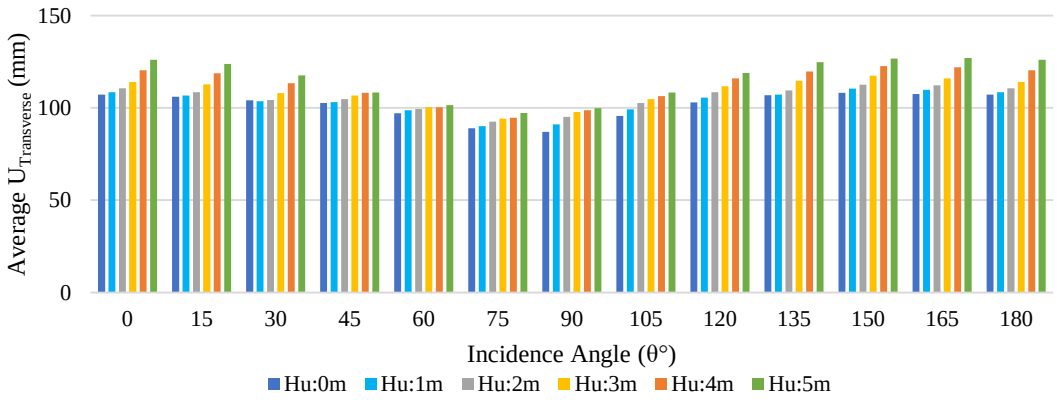
Average U Transverse (mm)
150
100
50
0
0
15
30
45
60
75
90
105
120
135
150
165
180
Incidence Angle (θ°)
Hu:0m
Hu:1m
Hu:2m
Hu:3m
Hu:4m
Hu:5m

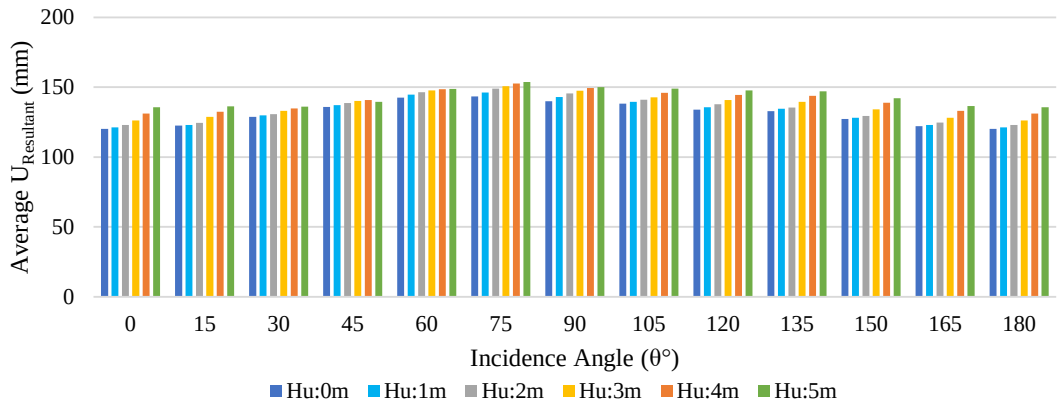


Figure 8: Maximum displacement demands of the bridge for different uniform scour depths and earthquake incidence angles.

## 4.2 Curvature demand of bridge pier

The superstructure of the bridge maintains in the elastic region due to elastomeric bearings, and these members only transfer axial loads to the bridge columns. Therefore, in terms of nonlinear response during earthquakes, bent columns are the most impacted elements that can expose to seismic damage. Section analyses using the XTRACT program have been carried out for both weak and strong axes to determine the capacity of bridge columns. The yield curvature of the column section is determined by the moment-curvature curves as 0.0033 1/m for the weak axis and 0.0011 1/m for the strong axis.

In Figure 9, the average maximum curvature demands of the middle column of bridge in weak (y') and strong (z') axis is given. Average curvature demand is increasing when ground motion incidence angle is changed from 0° to 75° in weak axis (y'). Also, it is increasing between 0° and 105° in strong axis (z'). Also, average maximum column curvature demand has a decreasing trend when scour depth ($H_u$) increases in both axes and for all ground motion incidence angles. The reason of this, bridge column becomes more flexible as scour depth increases and this causes to decrease in curvature. Especially in strong axis (z'), the average maximum curvature demand of column is under the yield curvature ($\Phi_{z_yield}$) for all incidence angles when scour depth becomes 4 and 5 m. The maximum difference of curvature demands in the weak axis (y') of column between no scoured ($H_u$=0m) and 5 m scoured ($H_u$=5m) bridge is occurred at 0° incidence angle is 45.5%. Also, in strong axis (z'), it becomes 68.7% at 60° incidence angle. These results show that the scour around the piles has a positive contribution to the curvature demands of the bridge column piers.

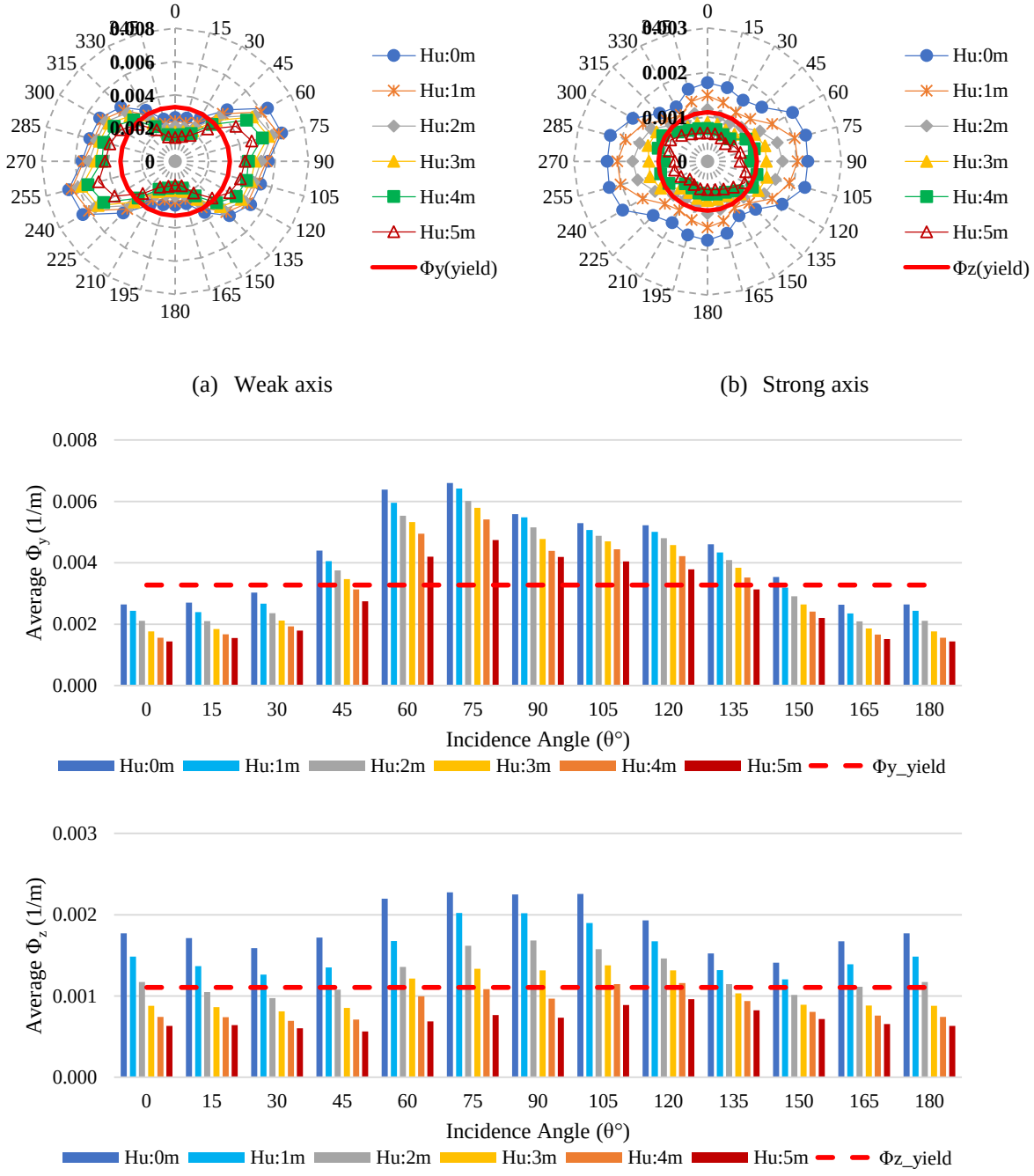


Figure 9: Maximum curvature demands of column weak axis (y') and strong axis (z') for different uniform scour depths and earthquake incidence angles.

## 4.3 Shear force demand of bridge pier

Member shear force demand, which is a forced-based engineering demand parameter, indicates whether it exceeds its shear capacity. For the purpose of preventing brittle shear failure during earthquakes, all codes recommend ductile section design.

In Figure 10, average maximum shear force demands of the middle column of bridge in local y' and z' axis is given. Average shear demand is decreasing when ground motion incidence angle is changed from 0° to 90° in local y' axis. Besides, it has an increasing trend between that angle range in local z' axis. Moreover, shear force demands decrease as the

depth of scour increases for all incidence angles. The maximum difference of average demands in local y' axis of no scoured ($H_u$=0m) and 5m scoured ($H_u$=5m) models occurs at 60° incidence angle and nearly 27.7%. Also, it is about 14.2% at 150° incidence angle in local z' axis. The shear capacity demands of column was calculated in previous sections as 5198.2 kN in local y' axis and 6519.9 kN in local z' axis. When the average maximum shear force demands are compared to these capacities, it is seen that shear force demands are below the limits for all scour depths and incidence angles. Therefore, it can be said that no shear damage occurred in the bridge column during the nonlinear analysis.

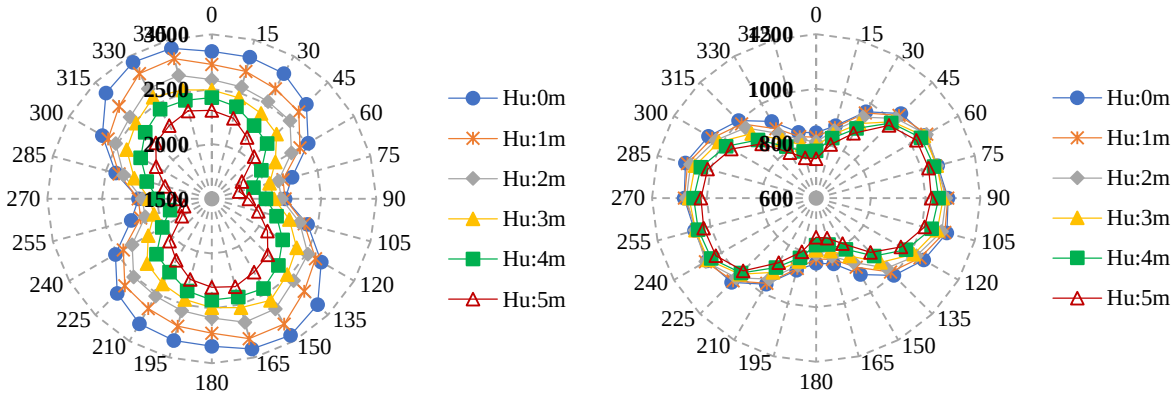


(a) Local y' axis (b) Local z' axis

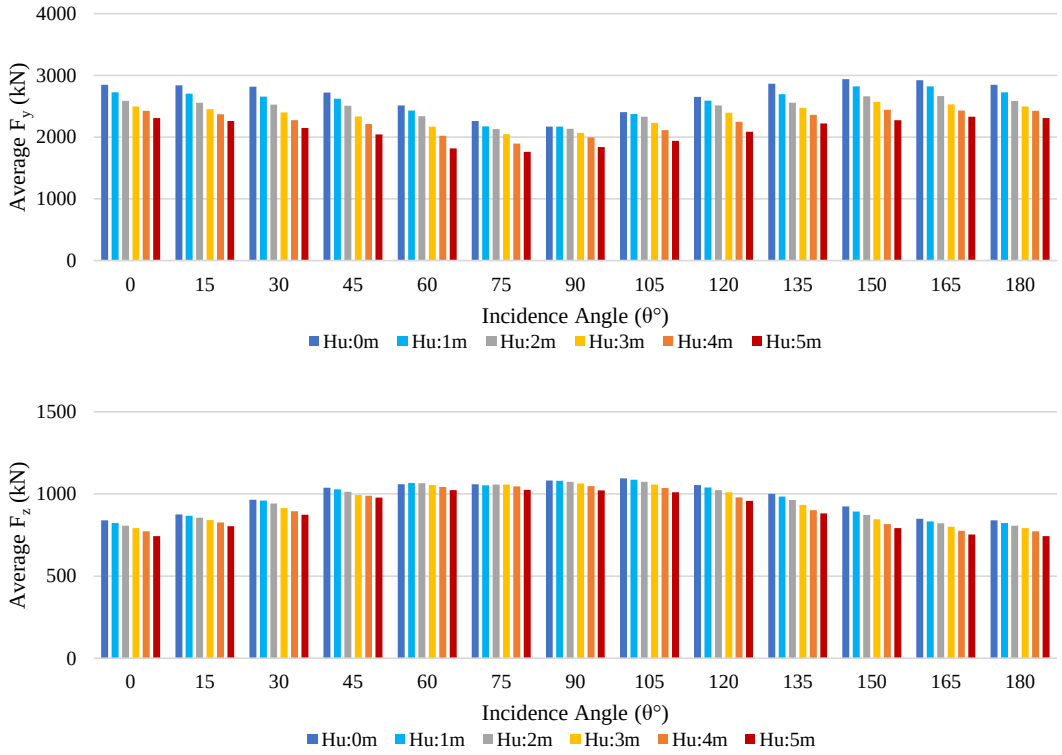


Figure 10: Maximum shear force demands of column local y' and local z' axis for different uniform scour depths and earthquake incidence angles.

## 5 CONCLUSIONS

Bridges are one of the critical components of lifeline systems that should be in service during and after a natural disaster. Especially the bridges built on the stream bed, scour may occur over time around substructure members and this situation affects the demand parameters of the bridge elements in the event of an earthquake. Furthermore, ground motion may act on bridges with a different angle and it may cause change in seismic demands. Therefore, a series of nonlinear response history analysis was done for 6 different scoured bridge models by using 7 strong ground motion records with 3 components. Also, horizontal components of ground motions were rotated starting from 0° to 180° with an increment of 15° by using linear transformation equations and demands belong to these bridge models were compared with each other. Below outcomes were achieved from all the investigated parameters;

- Scour is a significant event that has a major impact on the seismic demands of bridge members. Bridge member demands are substantially higher in circumstances of extensive scour than in cases of no scour. Therefore, it is crucial to take it into account when designing bridge-type structures built in flood-prone areas.
- The natural vibration period of the bridge increases with the increase in scour depth. The main cause is an increase in the effective column clear height followed by an increase in scour depth. Therefore, scour increases the vibration periods of the bridge and makes it more flexible.
- Superstructure displacement has an increasing trend with an increase in scour depth for both longitudinal and transverse direction of bridges for all scour cases. Because the effective height of the bridge pier increases along with the depth of scour, as a result superstructure elements displaced more.
- Curvature and shear force demands of bridge column has a decreasing trend with the increase in scour depth. This situation can be explained as the increase in the bridge period results in less earthquake force on the structure. Additionally, in the fixed supported situation, the deformations are primarily concentrated in the bridge columns. However, in scour conditions, the deformations in the piles lessen the deformations in the columns.
- For each demand parameter, there is no particular ground motion incidence angle that results in the most critical seismic demands. It depends on a variety of factors, including the ground motion data used, the chosen soil type, the characteristics of the bridge, the scour depth, etc. However, analytical results demonstrate that it significantly affects demand parameters. Especially superstructure displacement and curvature demand have an increasing trend between 0° and 75° earthquake incidence angles. Therefore, ground motion directionality should be considered in nonlinear time history analysis. According to Caltrans [14], each set of ground motions shall be rotated in 45° increments for at least a total of three angular directions (i.e., 0°, 45°, and 90°) to maximize the structural response. As a result, the analysis of the earthquake incidence angle within the scope of the study highlights the significance of this regulation's article.

## REFERENCES

[1] T. Yilmaz and O. C. Aygin, Çoklu Bozulma Etkileri Alt ı nda Ya ş lanan Karayolu Köprülerinin Sismik Kırılganlık ve Riskinin Değerlendirilmesi, no. October, 2019.

[2] Ö. Avsar, B. Atak, and A. Caner, In-Depth Investigation of Seismic Vulnerability of an

Aging River Bridge Exposed to Scour, *J. Perform. Constr. Facil.*, vol. 31, no. 5, pp. 1–13, 2017.

[3] L. G. He, H. H. Hung, C. Y. Chuang, and C. W. Huang, Seismic assessments for scoured bridges with pile foundations, *Eng. Struct.*, vol. 211, no. October 2019, p. 110454, 2020.

[4] F. H. Administration, *Evaluating scour at bridges (HEC-18), fifth edition*, no. 18. 2012.

[5] A. Alipour and B. Shafei, Performance Assessment of Highway Bridges Under Earthquake and Scour Effects, *15th World Conf. Earthq. Eng.*, vol. 18, no. 18, 2012.

[6] X. Guo and Z. Chen, Lifecycle multihazard framework for assessing flood scour and earthquake effects on bridge failure, *ASCE-ASME J. Risk Uncertain. Eng. Syst. Part A Civ. Eng.*, vol. 2, no. 2, pp. 1–10, 2016.

[7] X. Guo, Y. Wu, and Y. Guo, Time-dependent seismic fragility analysis of bridge systems under scour hazard and earthquake loads, *Eng. Struct.*, vol. 121, pp. 52–60, 2016.

[8] I. F. Moschonas and A. J. Kappos, Assessment of concrete bridges subjected to ground motion with an arbitrary angle of incidence: Static and dynamic approach, *Bull. Earthq. Eng.*, vol. 11, no. 2, pp. 581–605, 2013.

[9] A. Roy, G. Bhattacharya, and R. Roy, Maximum credible damage of RC bridge pier under bi-directional seismic excitation for all incidence angles, *Eng. Struct.*, vol. 152, pp. 251–273, 2017.

[10] B. Atak, Ö. Avşar, and A. Yakut, Directional effect of the strong ground motion on the seismic behavior of skewed bridges, *Proc. Int. Conf. Struct. Dyn. , EURODYN*, vol. 2014-Janua, no. June, pp. 1253–1258, 2014.

[11] U. R. Bhatnagar and S. Banerjee, Fragility of skewed bridges under orthogonal seismic ground motions, *Struct. Infrastruct. Eng.*, vol. 11, no. 9, pp. 1113–1130, 2014.

[12] H. R. Noori, M. M. Memarpour, M. Yakhchalian, and S. Soltanieh, Effects of ground motion directionality on seismic behavior of skewed bridges considering SSI, *Soil Dyn. Earthq. Eng.*, vol. 127, no. July, p. 105820, 2019.

[13] Ministry of Transport and Infrastructure of The Republic of Turkey, Principles for the Design of Highway and Railroad Bridges and Viaducts Under the Impact of Earthquakes, 2020.

[14] Caltrans, Seismic Design Criteria, State of California Department of Transportation, no. April, 2019.

[15] S. Banerjee Basu and M. Shinozuka, Effect of ground motion directionality on fragility characteristics of a highway bridge, *Adv. Civ. Eng.*, vol. 2011, 2011.

[16] T. Yilmaz, S. Banerjee, and P. A. Johnson, Performance of Two Real-Life California Bridges under Regional Natural Hazards, *J. Bridg. Eng.*, vol. 21, no. 3, p. 04015063, 2016.

[17] API, Recommended Practice for Planning , Designing and Constructing Fixed Offshore Platforms — Working Stress Design, *Api Recomm. Pract.*, vol. 24-WSD, no. December 2000, p. 242, 2000.

[18] F. H. Kulhawy, Drilled Shaft Foundations, *Found. Eng. Handb.*, vol. 1991, no. c, pp. 537–552, 1991.

[19] R. L. Mosher, Load-Transfer Criteria for Numerical Analysis of Axially Loaded Piles in Sand, 1984.

[20] PEER, PEER Ground Motion Database - PEER Center, https://ngawest2.berkeley.edu/ (accessed Jun. 24, 2021).

[21] TEHM, Turkish Earthquake Hazard Map, https://tdth.afad.gov.tr (accessed Dec. 06, 2021).

[22] Y. Wang, L. Ibarra, and C. Pantelides, Effects of Ground Motion Incidence Angles in a Reinforced Concrete Skewed Bridge Retrofitted with Bucking Restrained Braces, *Struct. Congr. 2017 Bridg. Transp. Struct. - Sel. Pap. from Struct. Congr. 2017*, no. Chopra 2012, pp. 481–493, 2017.

COMPDYN 2023
9th ECCOMAS Thematic Conference on
Computational Methods in Structural Dynamics and Earthquake Engineering
M. Papadrakakis, M. Fragiadakis (eds.)
Athens, Greece, 12-14 June 2023

# OPTIMIZED DYNAMIC DESIGN RULES FOR HIGH-SPEED BRIDGES BY USING DIGITAL TWIN

**Vincent Mathouraparsad[1*], Muriel Ragueneau[1], T. T. Huyen Nguyen[1]**

[1] SNCF Réseau Direction Générale Industrielle et Ingénierie
15/17 rue Jean-Philippe Rameau – 93212 La Plaine Saint Denis, France
vincent.mathouraparsad@reseau.sncf.fr, muriel.ragueneau@reseau.sncf.fr,
huyen.nguyen@reseau.sncf.fr

## Abstract

*Dynamic behaviors of bridges on high-speed railway are often the main criteria in bridges design. It has a huge impact on the technical choices and thus on the building cost. In the European Union, civil engineers rely on the Eurocode standards which defines the dynamic constitutive law for bridge designing. Those laws were based on the results of the European research program ERRI with few experimental test results. Therefore, to guarantee the structural safety, the design rules are disadvantageous that implies the design of oversized bridges and thus extra building costs.*

*In the interest of improving the safety of the infrastructure and optimizing the cost, SNCF Réseau realized a research program in a two-step approach. Firstly, it has carried out a great monitoring campaign of its bridges on the high-speed railway network. This experimental campaign consists of measuring the acceleration and the dynamic displacement of the deck under train traffic. Secondly, we create a digital twin of measured bridges by modeling them with an in-house software for dynamic solution. An important number of measurement data were used to correct the simulation of the digital twin. In the end, through the digital twin of bridges, we were able to refine the dynamic constitutive law of bridges by extracting the adjusted values like the damping coefficient or the structural stiffness from the numeric model.*

**Keywords:** Digital Twin, Dynamic Bridge Behavior.

## 1 MOTIVATION OF THE PROJECT

The consideration of dynamic effects is often critical for the design of rail bridges, particularly for high-speed. As the speed of a train increases on a bridge, the effects of the loading on the bridge intensifies compared to the corresponding static values. Thus, the deflection, bending stresses and similar effects due to torsion and shear stresses are higher than the static values. Annex A2 of Eurocode 0 [4] presents the deformation and vibration checks for railway bridges. The points to be checked in the dynamic calculations are the deck twist, the vertical deflection, the transverse and longitudinal displacements of the deck and the uplift of the bearings. In addition to these criteria, the limitation of the vertical accelerations of the bridge must be considered. This criterion is one of the most important safety parameters for ballasted bridges. Excessive acceleration can lead to reduce the interlocking of the ballast and consequently to reduce the friction at the interfaces between sleepers/ballast and ballast/deck. Under these conditions, the bearing of the track by the ballast is no longer guaranteed, increasing the risk of track buckling in warm weather.

These excessive accelerations are due to resonance effects between the bridge and the regularly spaced loads of the rolling stock. This phenomenon was detected at the opening of the first high-speed line in France. The passage of TGVs at 250 km/h caused excessive vibrations destabilizing the ballast on several structures. One of bridges caused a track buckling. After this incident, studies and laboratory tests were undertaken by the European Railway Research Institute (ERRI) to determine a permissible vertical acceleration limit for bridges on high-speed railway. The results of the tests [4] indicated that unfavorable dynamic behavior of the ballast occurred at deck accelerations exceeding 7 $m \cdot s^{-2}$. The current regulatory limit for the design of new structures has been limited to 3.5 $m \cdot s^{-2}$ by EN 1990 [5].

To determine the accelerations of bridges under rail traffic, it is necessary to identify the parameters that dominate the dynamic response. The boundary conditions of the deck, the skew, the span, the mass, the stiffness, and the damping must all be carefully considered to be relevant in the dynamic simulations. Damping is particularly important because it characterize how the energy dissipated and thus how the amplitudes of the oscillations are reduced. But damping is difficult to quantify and depends on many parameters (materials, support conditions, type of structure, etc.).

The critical damping coefficient expressed in percentage can be deduced from the acceleration measurements made at mid-span of the structure. In free oscillation, when the load is no longer present on the bridge, the oscillations decrease, and this decreasing rate can be used to determine the damping. However, this parameter has a large dispersion because it depends on the stresses, and it is therefore necessary to carry out numerous measurements to deduce a reliable value. In the absence of sufficiently numerous data, the statistical values indicated in the Eurocode 1991-2 must be used. These values come from tests carried out in the framework of the work of committee D 214 [4], the number of exploitable results was very limited, and no results could be obtained in the vicinity of resonance speeds given the danger of the phenomenon for traffic. The laws used for damping are therefore very conservative and have a very important impact on the design cost of rail bridges.

Therefore, SNCF has initiated a major test campaign in order to obtain more relevant data, particularly in the vicinity of the resonance speed. To do this, new measurement methods have been developed to adapt to the strong constraints on railway, particularly on high-speed railway. Numerous tests have been carried out on the entire network, and more than a hundred structures have been instrumented by SNCF since the first high-speed railway was put in use.

Finally, the tests were compared with the results of numerical simulations and helped to create digital twins of the bridges, facilitating in the future the verification of the dynamic compatibility of new rolling stock.

## 2 MONITORING CAMPAIGN OF BRIDGES

The railway infrastructure of SNCF has around 30 000 railway bridges with a span greater than 2 m. The monitoring campaign could be limited to a subset of bridges. They are selected in order to have a panel of bridges covering the different kind of bearing, numbers of spans, numbers of tracks and the rolling stock.

| Bridge type | Number |
|---|---|
| Masonry bridge | 12 000 |
| Filler beam bridge | 7 000 |
| Reinforced or prestressed concrete slab bridge | 5 000 |
| Modern metal or composite steel/concrete bridge | 4 000 |
| Old metal bridge | 2 000 |

Table 1: Distribution of bridge types in the French railway network.

Instrumentation of bridges was to measure the vertical acceleration and dynamic displacement of the deck at its mid-span while a train was traveling. Measure should be sampled at 108 Hz at least which is the Nyquist frequency of 2 axles at the highest speed. The maximum speed on the French railway network is 350 km/h (97.2 m/s) and the minimal distance between 2 axles in bogie is 1.8 m, which gives a frequency of 54 Hz.

There are many constraints in the high-speed infrastructure. Access to the tracks is highly controlled, and installation the measuring equipment can require halting the train running which strongly increases the cost of the monitoring campaign. The sensors should be installable from underneath the bridge without having an impact on the gauge below.

### 2.1 Acceleration measurement

For measuring the acceleration, we used the wireless MEMS accelerometer G-Link-200 from Lord Microstrain. They were mounting on magnetic base to be installed directly upon metallic surface. In the case of reinforced concrete deck, a steel plate was preinstalled on the lower side if the deck.

Accelerometers were configured with a sampling rate of 4 096 Hz, a measurement range of 8g, a low-pass filtering at 800 Hz, and no high-pass filter. Acceleration recording were manually triggered.

### 2.2 Displacement measurement

The digital book [1] presents several instruments used in civil engineering to measure the displacement of the deck. For the dynamic displacement, there is 4 ways to measure it:

- A rod made in a material with a low thermal expansion coefficient (often rod in Invar) is fixed under the bridge on one side and connected on the other side to an instrument which records the displacement. The instrument can be a rotating drum with an arm to graph the displacement (“Jules Richard” mechanical fleximeter) or a displacement sensor like a LVDT.

It's an affordable solution but its installation and use are quite constraining because the area under the measurement point must be free of traffic during the record. It cannot be used if the measurement point is over a river.

- A motorized theodolite tracks a retroflector on the bridge and records its rotations. The displacement is computed by triangulation.

  Unlike the first solution, there are very few constraints on the installation et use. But equipment able to measure the position of a reference at 108 Hz are expensive. Moreover, the accuracy depends strongly on the distance from the bridge because the displacement is computed by triangulation.

- A laser emitter installed outside the bridge (fixed reference) points to an instrument able to track the laser beam (Flexigraph LASER) fixed on the deck. Inside the instrument, there is a light-sensitive sensor able to move. The instrument centers the sensor on the laser beam and records the movement which corresponds to the displacement of the deck.

  Like the motorized theodolite, the use has few constraints, and the displacement is directly recorded. However, the installation can be cumbersome because the equipment is heavy and must be strongly fixed to the deck. Because of the equipment size, it cannot be installed where the gauge below the deck is limited.

- Railway bridges have sometime a concrete beam next to the deck called heavy shoulder. They are installed for protecting the deck against vehicle collisions and are independent of the deck. The vertical displacement of the deck can be measure by measuring the distance between the deck and the heavy shoulder with a distance sensor as shown in figure 1.

  It a low cost, easy to install and easy to use solution. But not all bridges have heavy shoulders, and because we monitor bridges on highspeed line there are constraints for accessing to heavy shoulders from tracks. Another problem is the heavy shoulders have the same bridge support as the deck. They vibrate during the passage of trains bringing measurement errors. We use a laser distance sensor from ACUITY.

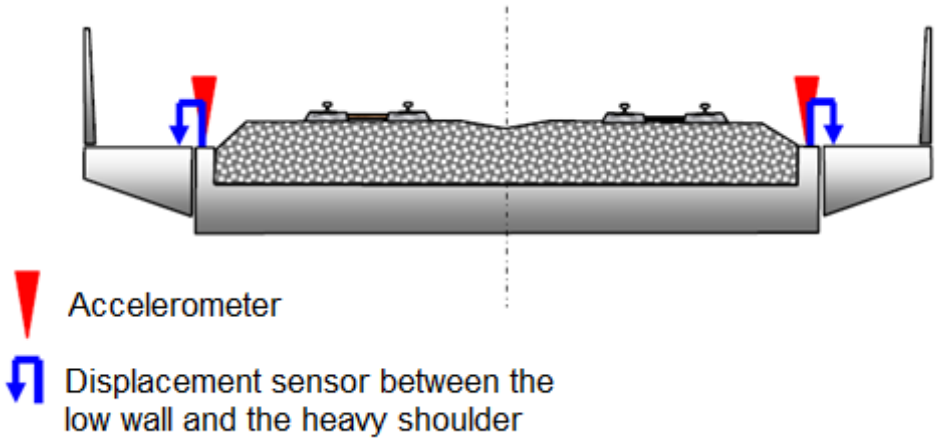


Figure 1: Layout of the sensors when measurement is taken from heavy shoulders

The first 3 measurement system cannot be used because there are expensive and/or not practical. The last one can be used for just a subset of bridges which contains mainly metal bridges. For those reasons, we had to develop an instrument which is easy to install, to use and ideally cheap [2]. The solution created works on the principle to track a laser beam on a normalized

target with a camera. The target and the camera are installed on the deck. The laser emitter is outside the bridge for creating a fixed reference.

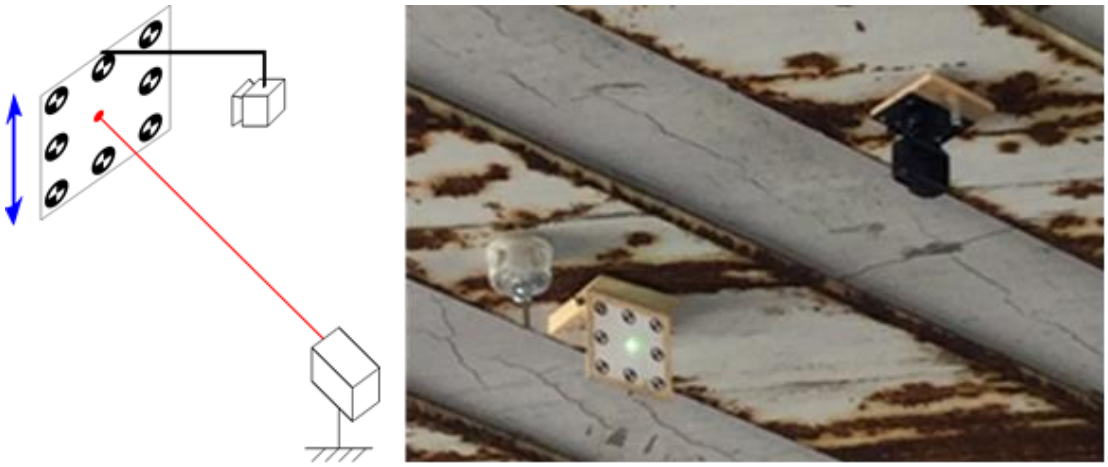

(a) (b)

Figure 2: Schema of the system tracking (a) and photo of the system installed under a bridge deck (b)

On the target, 8 beacons are printed, including one that represents the origin. When the deck moves, the beacons move relative to the laser dot of the emitter. The camera records the displacement of the dot relative to the beacons.




Figure 3: Processed image from the video with the laser dot position

Then the video is processed to extract the position of the dot relative to the beacons thanks to an in-house software (figure 5). Its algorithm is presented figure 4.

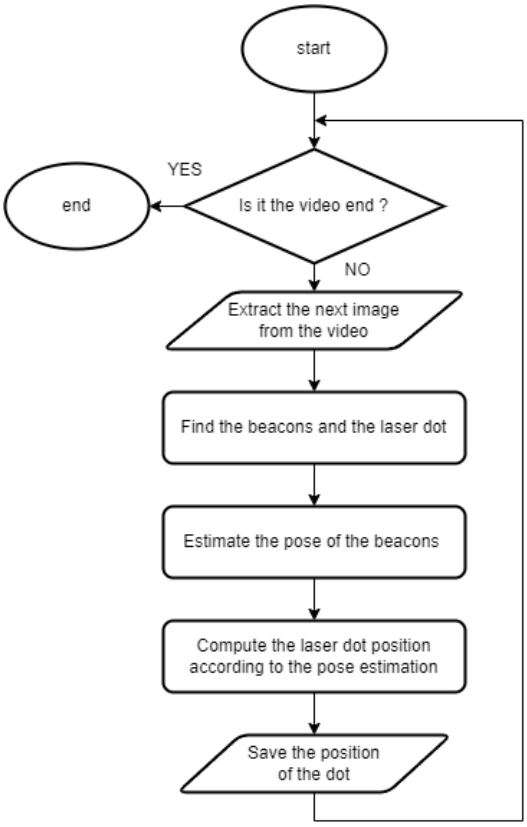


Figure 4: Algorithm for extracting the displacement from the video

For detecting the beacons, the contrast of the image is improved, and threshold is applied to keep the darkest pixels. Then a blob detection is applied on the black pixels. The beacon representing the origin is recognized by finding the beacon which has more black pixels. For detecting the laser dot, we apply a threshold to keep the brightest pixels then we apply a blob detection on the white pixels. The beacons on the target form a square of 80 mm by 80 mm. We compute the homography matrix (pose estimation) between their real positions and their position on the image. The matrix is used for computing the real position of the laser dot on the target.

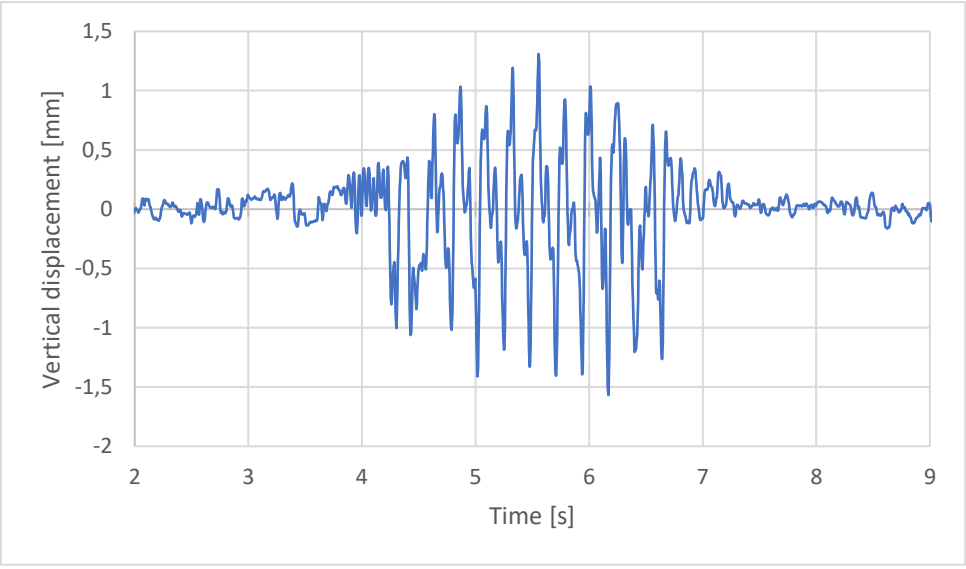


Figure 5: Resulting graph of the vertical displacement of a deck

The system is very inexpensive. We use a simple laser pointer. For the camera, we use an action camera because there are cheap, small, wireless, and able to record a video at a framerate higher than 110 Hz. We used a GoPro Hero 5 recording at 240 frame per second with a resolution 720×1280 pixels. The target and the camera were mounted on magnetic bases to be installed like the accelerometers. The camera was manually triggered.

## 3 EXTRACTING OF THE DYNAMIC CHARACTERISTICS

For each deck and train travels, we have an acceleration and a displacement signal. the following dynamic characteristics to be compared to the numerical simulation:

- The absolute maximal displacement
- The 1st natural frequency of the unloaded deck
- The damping of the unloaded deck
- The absolute maximal acceleration

On the acceleration signal, we firstly apply high-pass frequency with a cut-off frequency of 0.5 Hz to remove the constant component in the signal. In the free vibration period, we extract the 1st natural frequency by applying a Fourier transform.

For computing the damping coefficient, we use the Logarithmic Decrement method by selecting local maximal values in the free vibration period, or the Peak-Picking method by selecting the 1st natural frequency and computing the Q-factor (bandwidth of the peak at -3 dB). We keep the lowest value of both. the Peak-Picking method is more robust than the Logarithmic Decrement method when the structure is a little excited, but the 1st frequency must be well separated from the 2nd one. The Logarithmic Decrement method is less sensitive in this case, but the free vibration period must be clearly visible (for vibrations less than 0.3 $m/s^2$, damping is strongly underestimated. Figure 6 shows the signal processing.

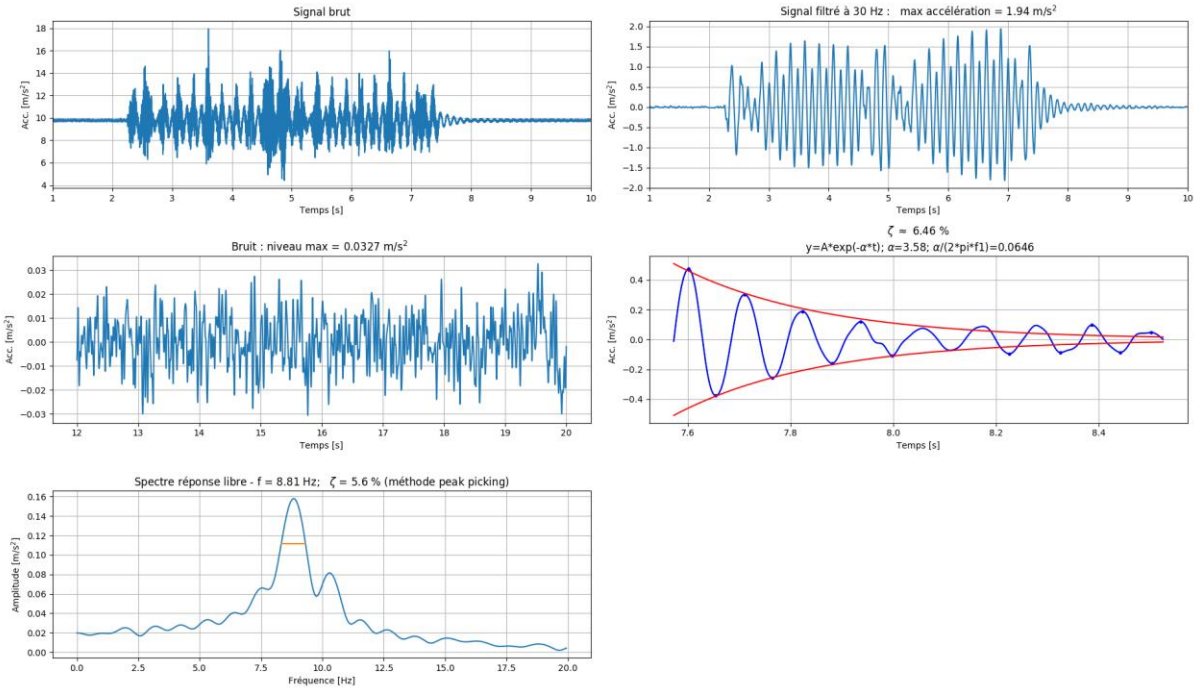


Figure 6: Result from the signal processing for a reinforced concrete slab bridge with a 12 m span under a TGV MU at 282 km/h

For extracting the absolute maximal acceleration, we apply a low-pass filter with a cut-off frequency at 30 Hz. We extract the absolute maximal acceleration in the signal, excluding isolated peaks because they don't contribute to destabilize the ballast (figure 13 shows a peak which is excluded).

On the displacement signal, we remove the constant component by applying a high-pass frequency with a cut-off frequency of 0.5 Hz and a low-pass filter with a cut-off frequency at 30 Hz. Then we extract the absolute maximal displacement.

After the processing, we have a table with the dynamic characteristics for each deck like the table 2. There are compared the numerical simulation and used for fitting our digital twins of bridges.

| Train | Speed [km/h] | Displacement [mm] | Acceleration [m/s²] | Natural frequency [Hz] | Damping [%] |
|---|---|---|---|---|---|
| TGV SU | 281 | 2.0 | 1.8 | 8.9 | 4.1% |
| TGV SU | 293 | 2.0 | 2.2 | 8.9 | 5.3% |
| TGV MU | 282 | 2.1 | 1.9 | 8.9 | 5.6% |
| TGV SU | 283 | - | 1.8 | 8.8 | 5.2% |
| TGV MU | 285 | - | 2.1 | 8.9 | 3.9% |
| TGV MU | 291 | - | 2.1 | 8.9 | 3.9% |
| TGV US | 293 | 2.1 | 2.1 | 8.8 | 3.9% |
| TGV | 240 | - | 0.9 | 9.8 | 2.5% |
| TGV | 262 | - | 1.2 | - | - |
| TGV | 272 | - | 1.1 | - | - |

Table 2: Results for a reinforced concrete deck on the high-speed railway.

For each measure, we note the kind of train. The speed of the train is estimated from the acceleration signal or displacement signal knowing the kind of train. A peak in the forced vibration period corresponds to the passage of a bogie. Dividing the distance between 2 bogies by the duration between 2 peaks gives the speed of the train.

## 4 MEASURES AND COMPARAISON WITH SIMULATIONS

The measurement campaign concerned all types of rail bridge (metal, composite, concrete, filler-beam) in proportion to their number on the network. Figures 7 to 9 show critical damping and maximal acceleration for different kind of bridges.

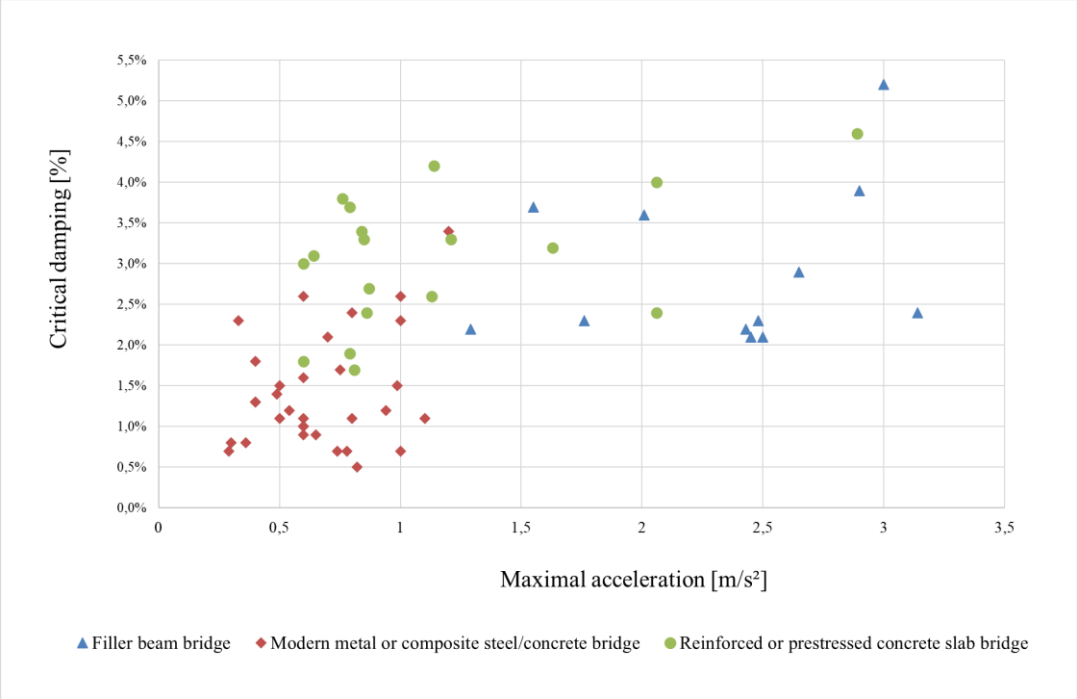


Figure 7: Critical damping according to the maximum acceleration for different kind of bridges

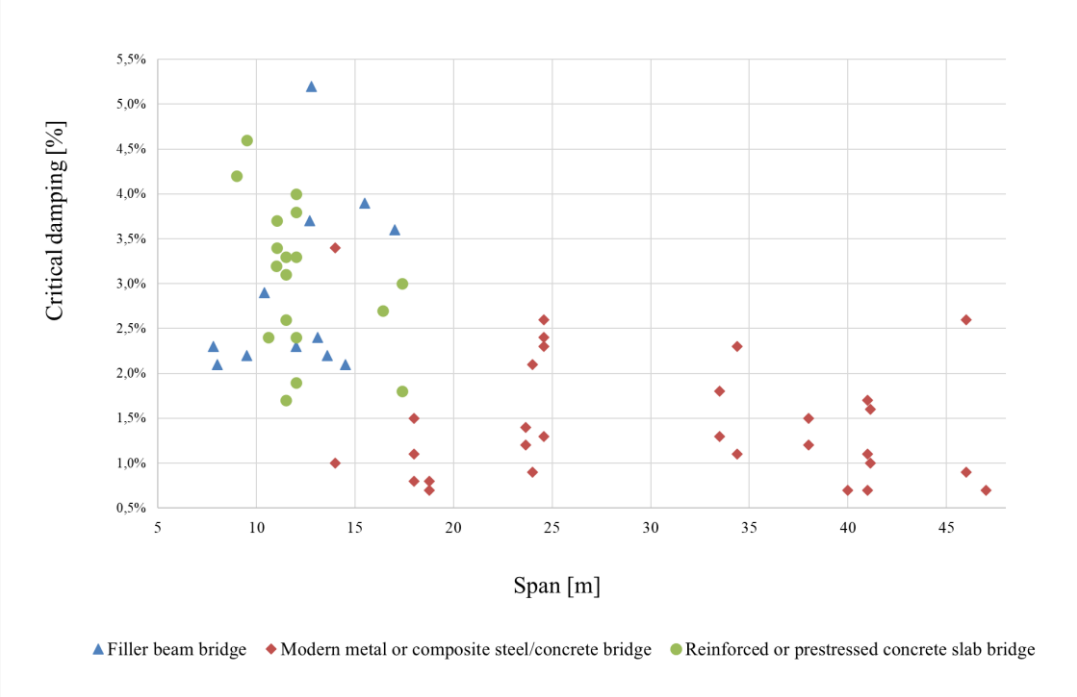


Figure 8: Critical damping percentage according to span for different kind of bridges

Metal and composite bridges have a critical damping around 0.75% which is higher by 50% than the value of 0.5% recommended by the Eurocodes for those kinds of bridges. For the concrete slab bridges or filler beam bridges, minimal values of damping correspond to ones from the Eurocodes.

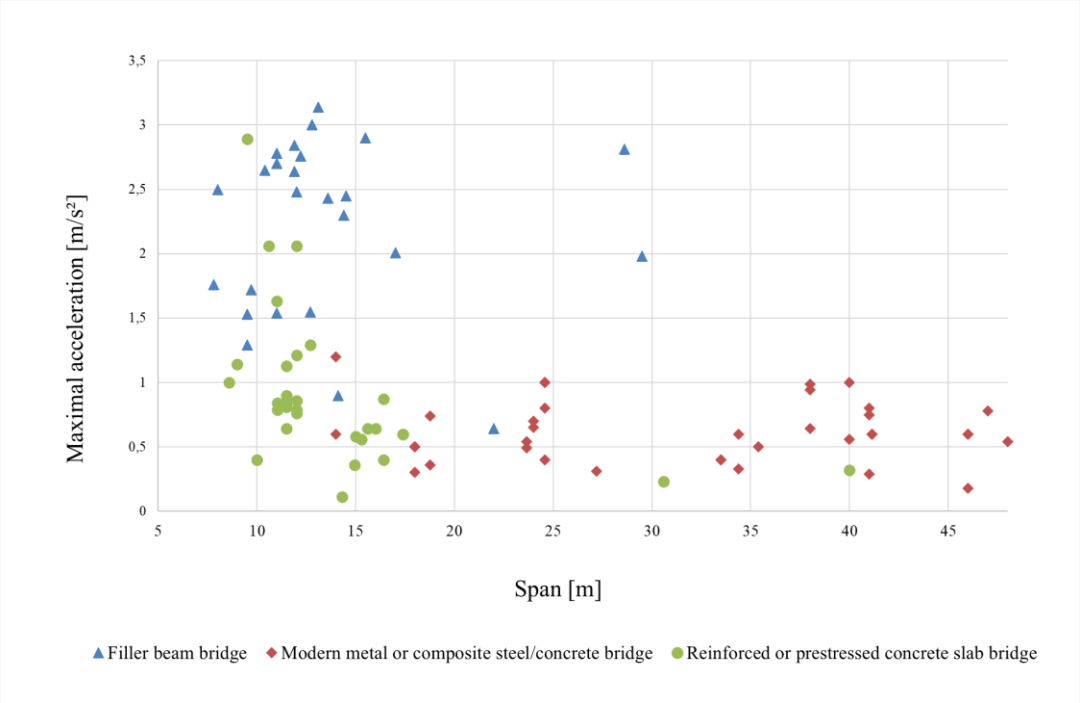


Figure 9: Maximal acceleration according to the span for different kind of bridges

The results confirmed that the most sensitive structures in terms of dynamics are the short, very slender structures with a high-speed traffic. Decks with coated girders and isostatic concrete slabs carrying a single track are the most sensitive. These kinds of structures became scarcer on new high-speed lines. Thus, instrumentation was mostly carried out on the oldest high-speed line designed before the advent of dynamic rules. On this line, the encased girder bridges were mainly reinforced to meet the regulatory criteria, however some reinforced concrete structures were kept as is and present a significant slenderness which is very interesting for studying the dynamic behavior of bridges.

As an example, figures 10 to 14 below illustrate the comparison between the different measurements carried out on an isostatic reinforced concrete slab bridge with a span of 12 m and a natural frequency of 8.8 Hz equal to twice the exciting frequency of the high-speed train which is 4.4 Hz. The exciting frequency is equal to the train speed (296 km/h) by the distance between the train bogies (18.7 m).

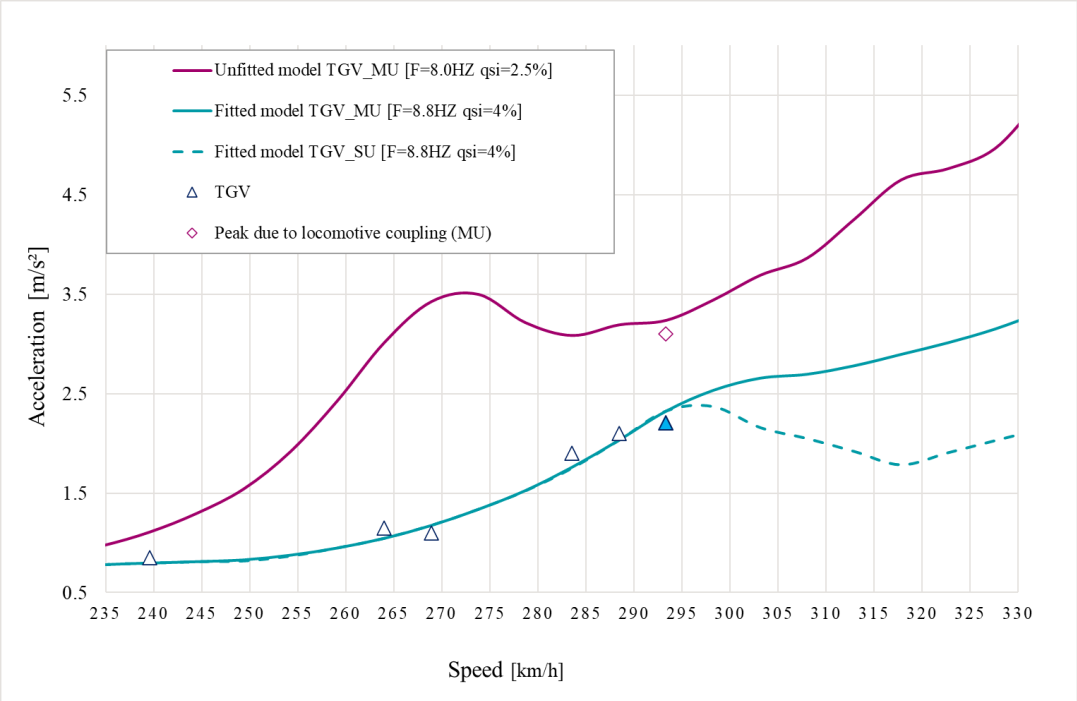


Figure 10: Comparison of the acceleration between measurement results and the digital twin

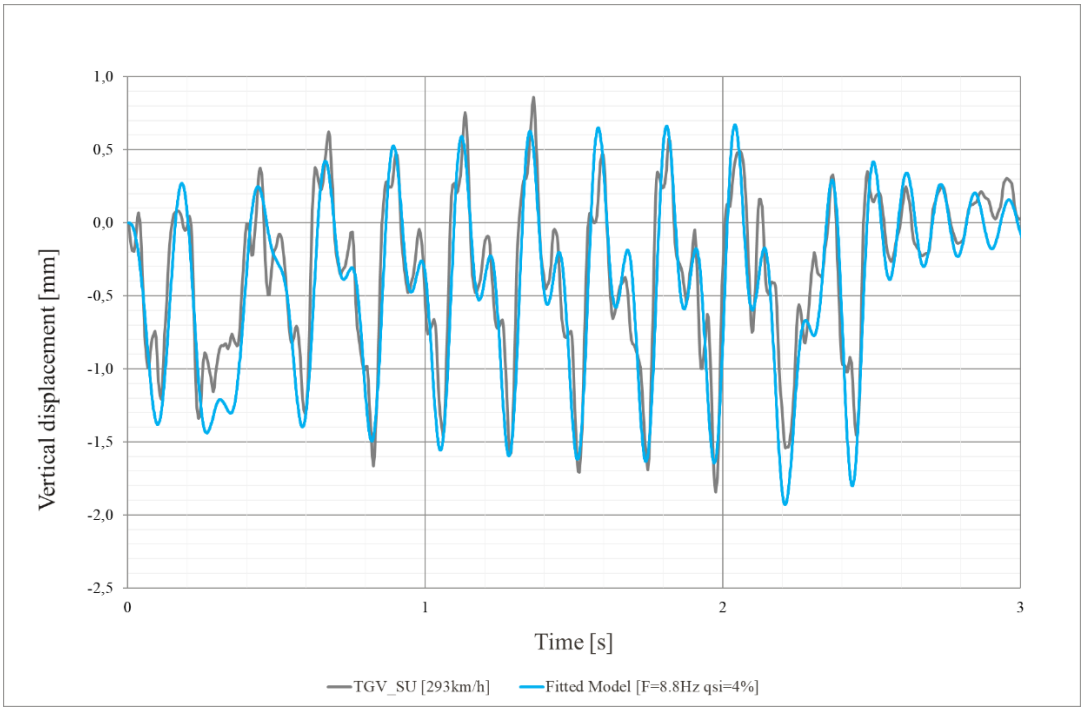


Figure 11: Comparison of the vertical displacement between measurement results and the digital twin TGV SU at 293 km/h

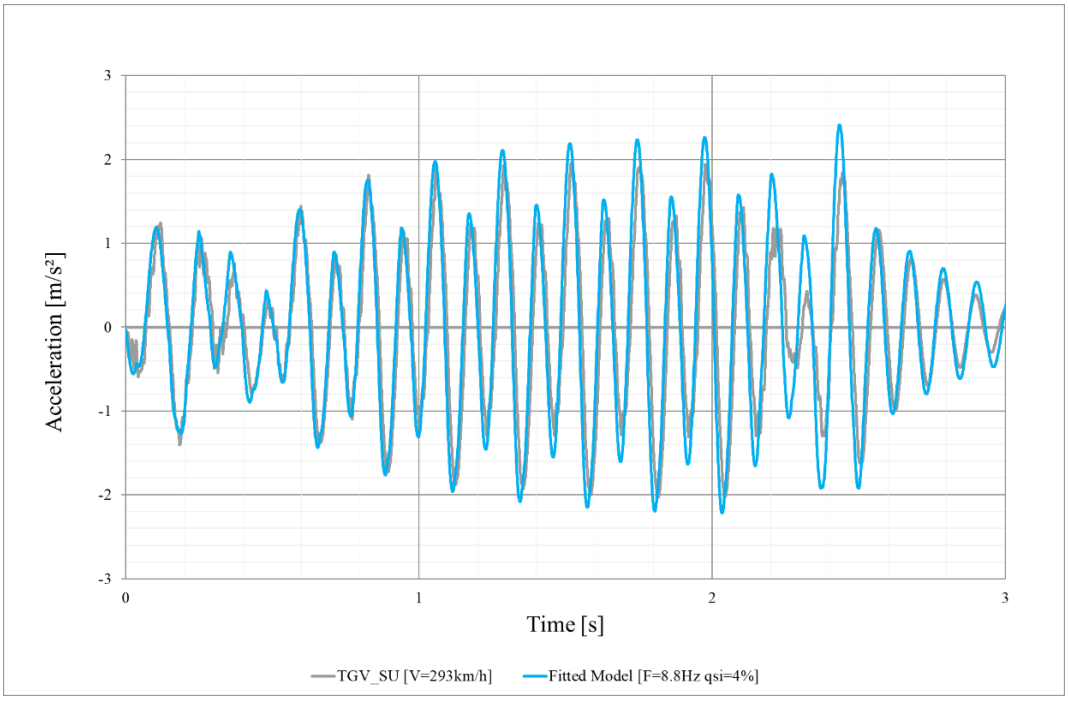


Figure 12: Comparison of the acceleration between measurement results and the digital twin for TGV SU at 293 km/h

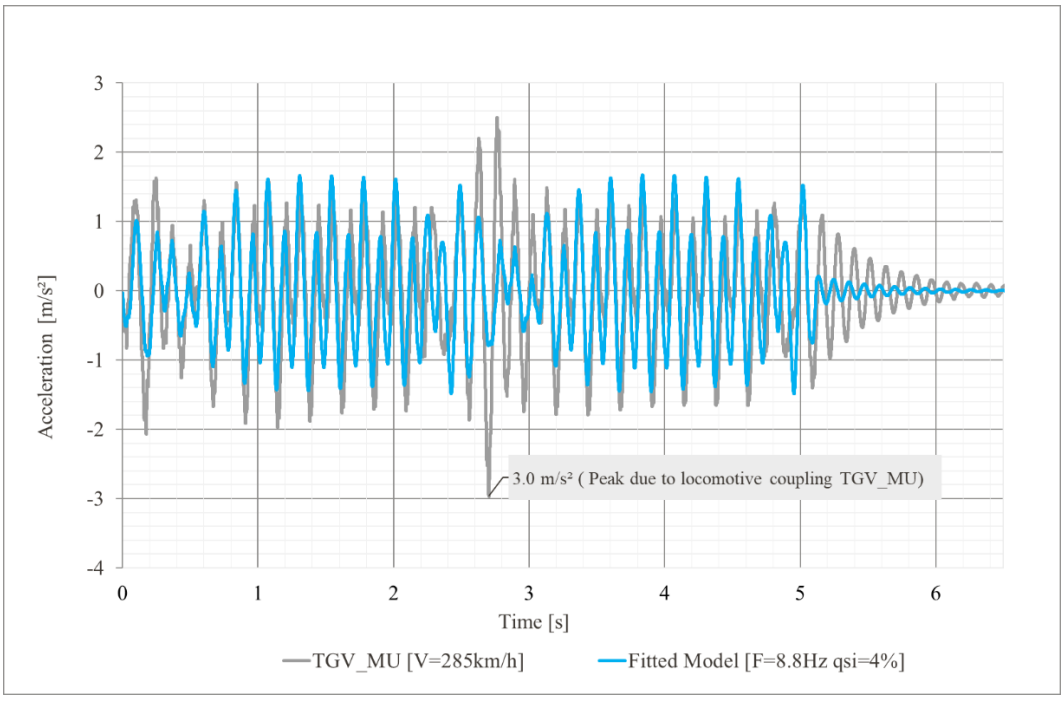


Figure 13: Comparison of the acceleration between measurement results and the digital twin for a TGV MU at 285 km/h.

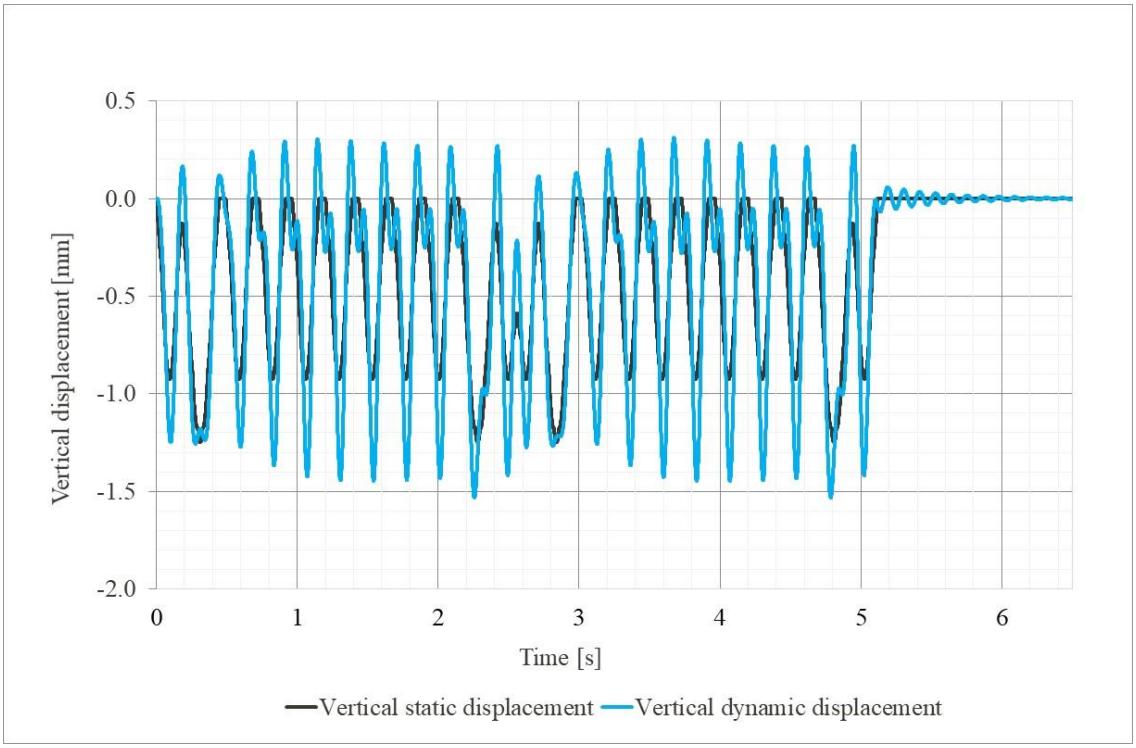


Figure 14: Comparison between the static and the dynamic vertical displacement for digital twin for a TGV MU at 285 km/h.

It can be noted that there is a very good correlation in acceleration and vertical displacement between the results of the measurements and the simulations of a TGV Simple Unit (TGV SU). The first natural frequency (8.8 Hz) corresponds to the one for a model with the stiffness of an uncracked concrete section. The critical damping is higher than the one recommended by the Eurocodes. However, in the figure 13, there is an acceleration peak caused by the coupling between 2 locomotives in a TGV Multiple Unit (TGV MU). The deck bends more under the overload of bogies of the 2 locomotives. The vertical displacement and the acceleration are close to values from a model with the stiffness of a cracked concrete section (figures 9 to 13). In this case, the 1$^{st}$ natural frequency is 8.0 Hz.

## 5 CONCLUSION

The monitoring of high-speed was like the monitoring presented in the article [5]. The keys differences on the monitoring part were that we instrument a greater number of bridges. And besides the measurement of the acceleration, we measure the vertical displacement. It required the development of a new measuring tool adapted to the constraints in the railway environment. It has been the subject of a patent [2].

Results of instrumentations and numerical simulations show that for concrete and coated beam constructions, the deck stiffness is almost always underestimated. The cracking assumptions adopted by the Eurocodes are relevant for verifications under heavy loads at low speeds (freight wagon at 22.5 tons per axle travelling at 100km/h) however they are too pessimistic in most cases studied for verifications under light loads at high speeds (fast train at 17 tons per axle travelling at 320km/h).

Similarly, the damping values obtained from the measurements are higher than those recommended by the Eurocode [4]. The latter are too pessimistic, especially for composite bridges whose span values lead to a very low damping in the order to 0.5%. This value leads to oversize

the structures and thus extra costs of construction. Consequently, a statistical analysis of all the data from the tests is underway to define optimized design rules.

## REFERENCES

[1] Université Gustave Eiffel & CEREMA, (n.d.), *Auscultation des ouvrages d'art*, from https://reflexscience.univ-gustave-eiffel.fr/lire/ouvrages/auscultation-des-ouvrages-dart

[2] Mathouraparsad, V. & Roy, A. (2018), *Système et procédé de surveillance d'une structure, notamment un ouvrage d'art ferroviaire*. (French Patent No. FR3077395). Institut national de la propriété industrielle (INPI), https://data.inpi.fr/brevets/FR3077395

[3] ERRI D 214/RP 9, 2000, *Rail bridges for speed > 200 km/h – final report*, European Rail Research Institute (ERRI)

[4] NF EN 1990/A1, Juillet 2006, *Eurocode 0 : Basis of structural design*. Association Française de Normalisation (AFNOR)

[5] Silva A, Ribeiro D, Montenegro PA, Ferreira G, Andersson A, Zangeneh A, Karoumi R, Calçada R. *New Contributions for Damping Assessment on Filler-Beam Railway Bridges Framed on In2Track EU Projects.* Applied Sciences. 2023; 13(4):2636. https://doi.org/10.3390/app13042636

COMPDYN 2023
9th ECCOMAS Thematic Conference on
Computational Methods in Structural Dynamics and Earthquake Engineering
M. Papadrakakis, M. Fragiadakis (eds.)
Athens, Greece, 12-–14 June 2023

# EXTENDED MODIFIED BRIDGE SYSTEM METHOD FOR VEHICLE-BRIDGE INTERACTION: TREATMENT OF ROTATIONAL DEGREES OF FREEDOM

**Hossein Homaei** [1], **Elias G. Dimitrakopoulos**[2]

[1] Department of Civil and Environmental Engineering, Hong Kong University of Science and Technology
Clear Water Bay, Kowloon, Hong Kong, China
e-mail: hhomaei@connect.ust.hk

[2] Department of Civil and Environmental Engineering, Hong Kong University of Science and Technology
Clear Water Bay, Kowloon, Hong Kong, China
e-mail: ilias@ust.hk

**Abstract.** *The extended modified bridge system (EMBS) method is a theoretically consistent approach to decouple the vehicle-bridge interaction (VBI) problem. The decoupling according to EMBS allows to solve the bridge independently of the vehicle by modifying the mechanical system of the bridge using additional (damping, stiffness, and loading) terms in the equation of motion. The EMBS method also identifies dominant coupling parameters, between the vehicle and the bridge, and their relative influence on the bridge response based on a dimensionless description of the VBI problem. The current study presents the EMBS method in the presence of rotational, in addition to translational, degrees of freedom (DOFs) in either the bridge or the vehicle subsystem. The analysis demonstrates in detail the procedure of making the multi-degree of freedom EOMs dimensionless by means of an example. Lastly, the study investigates the notion of physical similarity in VBI systems in order to highlight the significance of dimensionless parameters. Specifically, it demonstrates that two vehicle-bridge systems that possess the same dimensionless parameters will exhibit identical dimensionless response, regardless of their dimensional parameters.*

**Keywords:** Vehicle-bridge interaction, Railway bridges, Decoupled analysis, Rotational degrees of freedom.

## 1 INTRODUCTION

The Vehicle-Bridge Interaction (VBI) phenomenon has received greater attention in recent years primarily as a result of the global expansion of high-speed railway (HSR) networks [1–7]. HSR lines are characterized by a significant number and length of bridges, and trains traverse them at speeds reaching 300 to 350 km/h [8]. In this context, VBI is important from the perspective of bridge design and improving the safety and comfort of vehicle rides.

To accurately analyze the vehicle-bridge interaction problem, it is necessary to develop robust and high-fidelity VBI simulations that can capture the dynamic behavior of the coupled system (see [9–11]). Given that modeling such a complex VBI system is challenging, it is beneficial to simplify the problem by decoupling vehicle-bridge systems. The simplest decoupling approach is the well-known moving load approximation, which considers vehicles as moving loads on the supporting bridge [12, 13]. As an improvement, Eurocode suggests combining the moving load approximation with a damping ratio, in addition to the structural damping of the bridge, to account for the favorable damping effect of VBI [14–17]. However, both the moving load and Eurocode techniques have several well-documented limitations. For example, the moving load method does not consider the effect of irregularities, and the Eurocode approach underestimates this effect [18, 19]. To overcome these limitations, Stoura and Dimitrakopoulos ([20]) proposed the Extended Modified Bridge System (EMBS) method.

The EMBS method [20] is a systematic way to decouple the vehicle-bridge interaction (VBI) problem. The EMBS approach modifies the mechanical system of the bridge with additional damping, stiffness, and loading terms, and allows to solve the bridge and vehicle subsystems independently, producing however accurate results compared to a coupled solution. The EMBS method can tackle multi-degree of freedom (MDOF) vehicle-MDOF bridge systems including, for example, complicated bridge configurations such as continuous bridges and arch bridges. Furthermore, the EMBS method identifies dominant coupling parameters and their relative influence on the bridge response based on an asymptotic expansion analysis on the dimensionless equations of motion (EOMs).

The current study presents a generalization of the EMBS approach to systems with both rotational and translational degrees of freedom (DOFs) in either the bridge or the vehicle subsystem. Specifically, it presents the governing terms in those EOMs and demonstrates the procedure of making the (MDOF) EOMs dimensionless. Additionally, the study discusses the concept of physical similarity in coupled vehicle-bridge mechanical systems in order to illustrate the importance of dimensionless parameters.

## 2 FORMULATION OF THE VEHICLE-BRIDGE INTERACTION PROBLEM

The EOM of a coupled MDOF vehicle-MDOF bridge system can take the form [20, 21]:

$$\mathbf{m}\ddot{\tilde{\mathbf{u}}} + \mathbf{c}\dot{\tilde{\mathbf{u}}} + \mathbf{k}\tilde{\mathbf{u}} - \mathbf{W}\tilde{\boldsymbol{\lambda}} = \mathbf{f} \tag{1}$$

where $\tilde{\mathbf{u}}(t)$ is the displacement vector of the whole (coupled) system:

$$\tilde{\mathbf{u}}^{\mathrm{T}} = \begin{bmatrix} \tilde{\mathbf{u}}_V & \tilde{\mathbf{u}}_B \end{bmatrix} \tag{2}$$

Throughout this study, an overdot indicates differentiation with respect to the dimensional time $t$, while prime denotes differentiation with respect to the location of the vehicle $x$. Superscript $()^{\mathrm{T}}$ denotes the transpose of a vector or matrix, while the tilde is used to distinguish dimensional from the corresponding dimensionless quantities, when needed (later on). $\mathbf{m}$, $\mathbf{c}$ and $\mathbf{k}$ are the

corresponding mass, damping, and stiffness matrices of the entire system:

$$\mathbf{m} = \begin{bmatrix} \mathbf{m}_V & \mathbf{0} \\ \mathbf{0} & \mathbf{m}_B \end{bmatrix}, \ \mathbf{c} = \begin{bmatrix} \mathbf{c}_V & \mathbf{0} \\ \mathbf{0} & \mathbf{c}_B \end{bmatrix}, \ \mathbf{k} = \begin{bmatrix} \mathbf{k}_V & \mathbf{0} \\ \mathbf{0} & \mathbf{k}_B \end{bmatrix} \tag{3}$$

The subscript $()_B$ denotes the bridge subsystem, and the subscript $()_V$ indicates the vehicle subsystem. $\tilde{\boldsymbol{\lambda}}$ is the vector of the contact forces between the vehicle and bridge subsystems, $\mathbf{W}(x)$ is the contact direction matrix, and $\mathbf{f}$ is the external force vector of the entire system:

$$\mathbf{W} = \begin{bmatrix} \mathbf{W}_V \\ -\mathbf{W}_B \end{bmatrix}, \ \mathbf{f} = \begin{bmatrix} \mathbf{f}_V \\ \mathbf{f}_B \end{bmatrix} \tag{4}$$

To estimate the contact force $\tilde{\boldsymbol{\lambda}}$ we assume "rigid contact" between the wheels and the rails, and follow the calculation procedure of [21] which leads to:

$$\mathbf{m}\ddot{\tilde{\mathbf{u}}} + \bar{\mathbf{c}}\dot{\tilde{\mathbf{u}}} + \bar{\mathbf{k}}\tilde{\mathbf{u}} = \bar{\mathbf{f}} \tag{5}$$

with:

$$\begin{aligned} \bar{\mathbf{c}} &= [\mathbf{E} - \mathbf{W}\mathbf{G}^{-1}\mathbf{W}^{\mathrm{T}}\mathbf{m}^{-1}]\mathbf{c} + 2v\mathbf{W}\mathbf{G}^{-1}\mathbf{W}'^{\mathrm{T}}, \\ \bar{\mathbf{k}} &= [\mathbf{E} - \mathbf{W}\mathbf{G}^{-1}\mathbf{W}^{\mathrm{T}}\mathbf{m}^{-1}]\mathbf{k} + v^2\mathbf{W}\mathbf{G}^{-1}\mathbf{W}''^{\mathrm{T}}, \\ \bar{\mathbf{f}} &= [\mathbf{E} - \mathbf{W}\mathbf{G}^{-1}\mathbf{W}^{\mathrm{T}}\mathbf{m}^{-1}]\mathbf{f} + v^2\mathbf{W}\mathbf{G}^{-1}\mathbf{r}_c'' \end{aligned} \tag{6}$$

where $\mathbf{E}$ is the identity matrix, $\mathbf{G}^{-1}$ is the mass participating in the contact interaction between the wheels and the bridge where its inverse $\mathbf{G} = \mathbf{W}^{\mathrm{T}}\mathbf{m}^{-1}\mathbf{W}$, $\mathbf{r}_c(x)$ is the irregularities vector, and $v$ indicates the vehicle speed.

The EMBS method (Stoura and Dimitrakopoulos [20]) proceeds from Eq. (5) by partitioning Eq. (5) into the bridge and vehicle subsystems and further distinguishing the vehicle subsystem into the upper and wheel parts. Ultimately, the decoupling according to the EMBS method hinges on a dimensionless description of the vehicle-bridge EOM (Eq. (5)).

However, the first version of the EMBS method ([20]), did not distinguish between translational DOFs (or equivalently force equilibrium equations) and rotational DOFs (or equivalently moment equilibrium equations). Strictly speaking, the generic EOM (Eq. (5)) was dimensionalized only for translational DOFs ([20]). Here we extend the applicability of the EMBS method by explicitly considering rotational DOFs, in addition to translational DOFs, and dimensionalizing accordingly the different DOFs.

In particular, without loss of generality, we start from Eq. (5) and partition the original DOF vector $\tilde{\mathbf{u}}(t)$ into translational DOFs $\tilde{\mathbf{x}}$ and rotational DOFs $\tilde{\boldsymbol{\phi}}$:

$$\tilde{\mathbf{u}}^{\mathrm{T}} = \begin{bmatrix} \tilde{\mathbf{x}} & \tilde{\boldsymbol{\phi}} \end{bmatrix} \tag{7}$$

The EOM (Eq. (5)) of the whole (coupled) system becomes:

$$\begin{bmatrix} \mathbf{m}_x & \mathbf{0} \\ \mathbf{0} & \mathbf{m}_\phi \end{bmatrix} \begin{bmatrix} \ddot{\tilde{\mathbf{x}}} \\ \ddot{\tilde{\boldsymbol{\phi}}} \end{bmatrix} + \begin{bmatrix} \bar{\mathbf{c}}_x & \bar{\mathbf{c}}_{x,\phi} \\ \bar{\mathbf{c}}_{x,\phi}^{\mathrm{T}} & \bar{\mathbf{c}}_\phi \end{bmatrix} \begin{bmatrix} \dot{\tilde{\mathbf{x}}} \\ \dot{\tilde{\boldsymbol{\phi}}} \end{bmatrix} + \begin{bmatrix} \bar{\mathbf{k}}_x & \bar{\mathbf{k}}_{x,\phi} \\ \bar{\mathbf{k}}_{x,\phi}^{\mathrm{T}} & \bar{\mathbf{k}}_\phi \end{bmatrix} \begin{bmatrix} \tilde{\mathbf{x}} \\ \tilde{\boldsymbol{\phi}} \end{bmatrix} = \begin{bmatrix} \bar{\boldsymbol{f}}_x \\ \bar{\boldsymbol{f}}_\phi \end{bmatrix} \tag{8}$$

We dimensionalize the first of the matrix equations of Eq. (8) by dividing with a reference force $\mathscr{F}_{ref} = m_{ref} l_{ref} t_{ref}^{-2}$ and the second of Eq. (8) by dividing with a reference moment $\mathscr{M}_{ref} =$

$m_{ref} l_{ref}^2 t_{ref}^{-2}$ respectively:

$$\begin{aligned} \frac{1}{\mathscr{F}_{ref}}\left(\mathbf{m}_x\ddot{\tilde{\mathbf{x}}}+\bar{\mathbf{c}}_x\dot{\tilde{\mathbf{x}}}+\bar{\mathbf{c}}_{x,\phi}\dot{\tilde{\boldsymbol{\phi}}}+\bar{\mathbf{k}}_x\tilde{\mathbf{x}}+\bar{\mathbf{k}}_{x,\phi}\tilde{\boldsymbol{\phi}}\right) &= \frac{1}{\mathscr{F}_{ref}}\left(\bar{\mathbf{f}}_x\right) \\ \frac{1}{\mathscr{M}_{ref}}\left(\mathbf{m}_\phi\ddot{\tilde{\boldsymbol{\phi}}}+\bar{\mathbf{c}}_\phi\dot{\tilde{\boldsymbol{\phi}}}+\bar{\mathbf{c}}_{x,\phi}^{\mathrm{T}}\dot{\tilde{\mathbf{x}}}+\bar{\mathbf{k}}_\phi\tilde{\boldsymbol{\phi}}+\bar{\mathbf{k}}_{x,\phi}^{\mathrm{T}}\tilde{\mathbf{x}}\right) &= \frac{1}{\mathscr{M}_{ref}}\left(\bar{\mathbf{f}}_\phi\right) \end{aligned} \tag{9}$$

The specific expressions of the reference force $\mathscr{F}_{ref}$ and the reference moment $\mathscr{M}_{ref}$ depend on the problem at hand. In general, there are multiple eligible and meaningful ways to dimensionalize a physical problem depending on the perspective and the goal of the analysis. For instance, if the interest is on the bridge subsystem, we can adopt as reference mass, the generalized mass $m_B$ of the first mode of the bridge $m_{ref} = m_B$, as reference length the span of the bridge $l_{ref} = L_B$, and as reference time the first eigenfrequency $\omega_B$ of the bridge $t_{ref} = \omega_B^{-1}$ (Stoura and Dimitrakopoulos [18]). Another option is to define the dimensionless time with respect to the loading frequency $t_{ref} = (v/L_B)^{-1}$ (Dimitrakopoulos and Zeng [21]).

Regardless of the specific a choice of parameters $m_{ref}$, $l_{ref}$, and $t_{ref}$, it holds:

$$\begin{aligned} &\left(\frac{1}{m_{ref}}\mathbf{m}_x\right)\left(\frac{1}{l_{ref}t_{ref}^{-2}}\ddot{\tilde{\mathbf{x}}}\right)+\left(\frac{1}{m_{ref}t_{ref}^{-1}}\bar{\mathbf{c}}_x\right)\left(\frac{1}{l_{ref}t_{ref}^{-1}}\dot{\tilde{\mathbf{x}}}\right) \\ &+\left(\frac{1}{m_{ref}l_{ref}t_{ref}^{-1}}\bar{\mathbf{c}}_{x,\phi}\right)\left(\frac{1}{t_{ref}^{-1}}\dot{\tilde{\boldsymbol{\phi}}}\right)+\left(\frac{1}{m_{ref}t_{ref}^{-2}}\bar{\mathbf{k}}_x\right)\left(\frac{1}{l_{ref}}\tilde{\mathbf{x}}\right) \\ &+\left(\frac{1}{m_{ref}l_{ref}t_{ref}^{-2}}\bar{\mathbf{k}}_{x,\phi}\right)\left(\tilde{\boldsymbol{\phi}}\right)=\frac{1}{m_{ref}l_{ref}t_{ref}^{-2}}\left(\bar{\mathbf{f}}_x\right) \end{aligned} \tag{10}$$

$$\begin{aligned} &\left(\frac{1}{m_{ref}l_{ref}^2}\mathbf{m}_\phi\right)\left(\frac{1}{t_{ref}^{-2}}\ddot{\tilde{\boldsymbol{\phi}}}\right)+\left(\frac{1}{m_{ref}l_{ref}^2t_{ref}^{-1}}\bar{\mathbf{c}}_\phi\right)\left(\frac{1}{t_{ref}^{-1}}\dot{\tilde{\boldsymbol{\phi}}}\right) \\ &+\left(\frac{1}{m_{ref}l_{ref}t_{ref}^{-1}}\bar{\mathbf{c}}_{x,\phi}^{\mathrm{T}}\right)\left(\frac{1}{l_{ref}t_{ref}^{-1}}\dot{\tilde{\mathbf{x}}}\right)+\left(\frac{1}{m_{ref}l_{ref}^2t_{ref}^{-2}}\bar{\mathbf{k}}_\phi\right)\left(\tilde{\boldsymbol{\phi}}\right) \\ &+\left(\frac{1}{m_{ref}l_{ref}t_{ref}^{-2}}\bar{\mathbf{k}}_{x,\phi}^{\mathrm{T}}\right)\left(\frac{1}{l_{ref}}\tilde{\mathbf{x}}\right)=\frac{1}{m_{ref}l_{ref}^2t_{ref}^{-2}}\left(\bar{\mathbf{f}}_\phi\right) \end{aligned} \tag{11}$$

where each parenthesis represents accordingly a dimensionless response quantity or a dimensionless system parameter.

In matrix terms the dimensionless EOMs (Eqs. (10) and (11)) are:

$$\begin{aligned} \mathbf{M}_x\ddot{\mathbf{x}}+\bar{\mathbf{C}}_x\dot{\mathbf{x}}+\bar{\mathbf{C}}_{x,\phi}\dot{\boldsymbol{\phi}}+\bar{\mathbf{K}}_x\mathbf{x}+\bar{\mathbf{K}}_{x,\phi}\boldsymbol{\phi} &= \bar{\mathbf{F}}_x \\ \mathbf{M}_\phi\ddot{\boldsymbol{\phi}}+\bar{\mathbf{C}}_\phi\dot{\boldsymbol{\phi}}+\bar{\mathbf{C}}_{x,\phi}^{\mathrm{T}}\dot{\mathbf{x}}+\bar{\mathbf{K}}_\phi\boldsymbol{\phi}+\bar{\mathbf{K}}_{x,\phi}^{\mathrm{T}}\mathbf{x} &= \bar{\mathbf{F}}_\phi \end{aligned} \tag{12}$$

We can state the dimensionless EOM of the whole (coupled) system (Eq. 12) in the matrix form as:

$$\begin{bmatrix}\mathbf{M}_x & \mathbf{0}\\ \mathbf{0} & \mathbf{M}_\phi\end{bmatrix}\begin{bmatrix}\ddot{\mathbf{x}}\\ \ddot{\boldsymbol{\phi}}\end{bmatrix}+\begin{bmatrix}\bar{\mathbf{C}}_x & \bar{\mathbf{C}}_{x,\phi}\\ \bar{\mathbf{C}}_{x,\phi}^{\mathrm{T}} & \bar{\mathbf{C}}_\phi\end{bmatrix}\begin{bmatrix}\dot{\mathbf{x}}\\ \dot{\boldsymbol{\phi}}\end{bmatrix}+\begin{bmatrix}\bar{\mathbf{K}}_x & \bar{\mathbf{K}}_{x,\phi}\\ \bar{\mathbf{K}}_{x,\phi}^{\mathrm{T}} & \bar{\mathbf{K}}_\phi\end{bmatrix}\begin{bmatrix}\mathbf{x}\\ \boldsymbol{\phi}\end{bmatrix}=\begin{bmatrix}\bar{\mathbf{F}}_x\\ \bar{\mathbf{F}}_\phi\end{bmatrix} \tag{13}$$

or equivalently:

$$\mathbf{M}\ddot{\mathbf{u}}+\bar{\mathbf{C}}\dot{\mathbf{u}}+\bar{\mathbf{K}}\mathbf{u}=\bar{\mathbf{F}} \tag{14}$$

where $\mathbf{M} = \begin{bmatrix} \mathbf{M}_x & \mathbf{0} \\ \mathbf{0} & \mathbf{M}_\phi \end{bmatrix}$, $\bar{\mathbf{C}} = \begin{bmatrix} \bar{\mathbf{C}}_x & \bar{\mathbf{C}}_{x,\phi} \\ \bar{\mathbf{C}}_{x,\phi}^{\mathrm{T}} & \bar{\mathbf{C}}_\phi \end{bmatrix}$ and $\bar{\mathbf{K}} = \begin{bmatrix} \bar{\mathbf{K}}_x & \bar{\mathbf{K}}_{x,\phi} \\ \bar{\mathbf{K}}_{x,\phi}^{\mathrm{T}} & \bar{\mathbf{K}}_\phi \end{bmatrix}$ are the corresponding dimensionless mass, damping, and stiffness matrices of the entire system and $\mathbf{u}^{\mathrm{T}}(t) = \begin{bmatrix} \mathbf{x} & \boldsymbol{\phi} \end{bmatrix}$ denotes the dimensionless displacement vector of the (vehicle-bridge) system, with dimensionless translational DOFs:

$$\ddot{\mathbf{x}} = \frac{1}{L_B \omega_B^2} \ddot{\tilde{\mathbf{x}}};\ \dot{\mathbf{x}} = \frac{1}{L_B \omega_B} \dot{\tilde{\mathbf{x}}};\ \mathbf{x} = \frac{1}{L_B} \tilde{\mathbf{x}} \tag{15}$$

and dimensionless rotational DOFs:

$$\ddot{\boldsymbol{\phi}} = \frac{1}{\omega_B^2} \ddot{\tilde{\boldsymbol{\phi}}};\ \dot{\boldsymbol{\phi}} = \frac{1}{\omega_B} \dot{\tilde{\boldsymbol{\phi}}};\ \boldsymbol{\phi} = \tilde{\boldsymbol{\phi}} \tag{16}$$

Note that the time-derivatives of the dimensionless DOFs $x$ and $\phi$ emerge naturally for differentiation with respect to the dimensionless time $\tau = \omega_B t$.

The pertinent dimensionless system submatrices (partitioned according to the nature of the DOFs: translation vs rotation) are:

$$\begin{gathered} \mathbf{M}_x = \frac{1}{m_B} \mathbf{m}_x;\ \mathbf{M}_\phi = \frac{1}{m_B L_B^2} \mathbf{m}_\phi \\ \bar{\mathbf{C}}_x = \frac{1}{m_B \omega_B} \bar{\mathbf{c}}_x;\ \bar{\mathbf{C}}_{x,\phi} = \frac{1}{m_B L_B \omega_B} \bar{\mathbf{c}}_{x,\phi};\ \bar{\mathbf{C}}_\phi = \frac{1}{m_B L_B^2 \omega_B} \bar{\mathbf{c}}_\phi \\ \bar{\mathbf{K}}_x = \frac{1}{m_B \omega_B^2} \bar{\mathbf{k}}_x;\ \bar{\mathbf{K}}_{x,\phi} = \frac{1}{m_B L_B \omega_B^2} \bar{\mathbf{k}}_{x,\phi};\ \bar{\mathbf{K}}_\phi = \frac{1}{m_B L_B^2 \omega_B^2} \bar{\mathbf{k}}_\phi \\ \bar{\mathbf{F}}_x = \frac{1}{m_B L_B \omega_B^2} \bar{\mathbf{f}}_x;\ \bar{\mathbf{F}}_\phi = \frac{1}{m_B L_B^2 \omega_B^2} \bar{\mathbf{f}}_\phi \end{gathered} \tag{17}$$

Consequently, to dimensionalize the generic EOM (Eq. (5)) we need to partition degrees of freedom into translational and rotational DOFs and generate the diagonal matrix $\boldsymbol{\Delta}_{ref}$ accordingly:

$$\boldsymbol{\Delta}_{ref} = \begin{bmatrix} \frac{1}{\mathscr{F}_{ref}} \mathbf{E}_{x,x} & \mathbf{0}_{x,\phi} \\ \mathbf{0}_{\phi,x} & \frac{1}{\mathscr{M}_{ref}} \mathbf{E}_{\phi,\phi} \end{bmatrix} = \begin{bmatrix} \frac{1}{m_{ref} l_{ref} t_{ref}^{-2}} \mathbf{E}_{x,x} & \mathbf{0}_{x,\phi} \\ \mathbf{0}_{\phi,x} & \frac{1}{m_{ref} l_{ref}^2 t_{ref}^{-2}} \mathbf{E}_{\phi,\phi} \end{bmatrix} \tag{18}$$

where $\mathbf{E}$ is the identity matrix, subscript $x$ is the number of translational DOFs and subscript $\phi$ is the number of rotation DOFs. Multiplying both sides of the EOM (Eq. (5)) with the matrix $\boldsymbol{\Delta}_{ref}$ produces the dimensionless form of the EOMs pertinent to both translational and rotation DOFs:

$$\boldsymbol{\Delta}_{ref} \left( \mathbf{m} \ddot{\tilde{\mathbf{u}}} + \bar{\mathbf{c}} \dot{\tilde{\mathbf{u}}} + \bar{\mathbf{k}} \tilde{\mathbf{u}} \right) = \boldsymbol{\Delta}_{ref} \left( \bar{\mathbf{f}} \right) \tag{19}$$

Note that the proposed procedure for making the generic EOM (Eq. (5)) dimensionless is applicable to any equation of motion in matrix form for the VBI system.

## 3 ILLUSTRATION OF THE PROPOSED DIMENSIONLESS DESCRIPTION

This section illustrates the proposed procedure of making the vehicle-bridge EOMs dimensionless with reference to a generic bridge model and a generic vehicle model. To this end, consider the vehicle-bridge system of Figure 1, where the vehicle has 4 DOFs. Partition the DOFs of the vehicle into the upper part (i.e., non-contact) DOFs:

$$\tilde{\mathbf{u}}_u^{\mathrm{T}} = \begin{bmatrix} \tilde{z}_c & \tilde{\theta}_c \end{bmatrix} \tag{20}$$

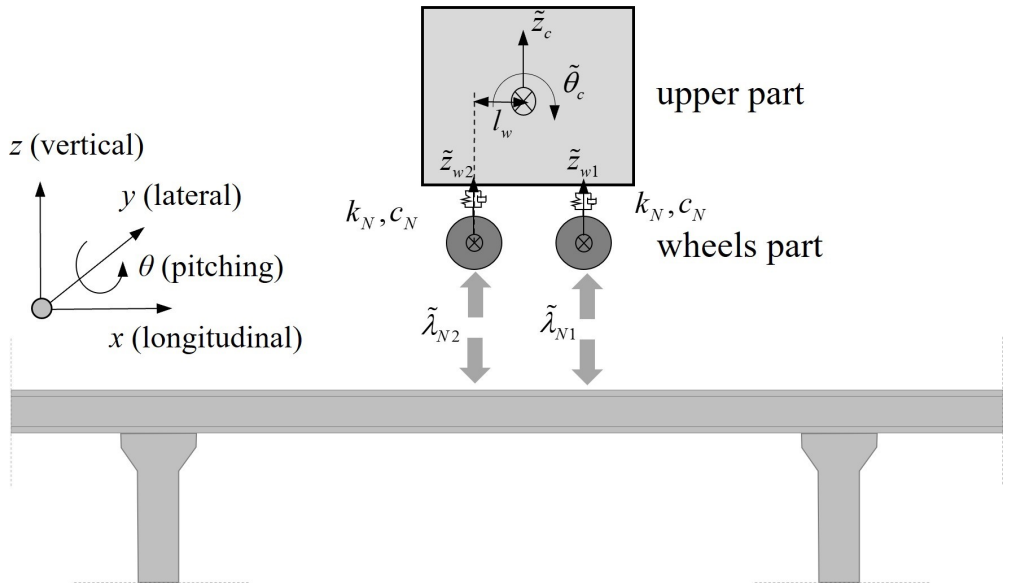


Figure 1: The vehicle-bridge interacting model

and the wheel part (i.e., contact) DOFs:

$$\tilde{\mathbf{u}}_w^{\mathrm{T}} = \begin{bmatrix} \tilde{z}_{w1} & \tilde{z}_{w2} \end{bmatrix} \tag{21}$$

Accordingly, we partition the mass, stiffness, and damping matrices of the vehicle as:

$$\mathbf{m}_V = \begin{bmatrix} \mathbf{m}_u & \mathbf{0} \\ \mathbf{0} & \mathbf{m}_w \end{bmatrix}, \ \mathbf{k}_V = \begin{bmatrix} \mathbf{k}_u & \mathbf{k}_{u,w} \\ \mathbf{k}_{w,u} & \mathbf{k}_w \end{bmatrix}, \ \mathbf{c}_V = \begin{bmatrix} \mathbf{c}_u & \mathbf{c}_{u,w} \\ \mathbf{c}_{w,u} & \mathbf{c}_w \end{bmatrix} \tag{22}$$

The pertinent mass submatrices for the vehicle system shown in Fig. 1 are:

$$\mathbf{m}_u = diag[m_c, I_{c\theta}], \ \mathbf{m}_w = diag[m_w] = m_w \mathbf{E} \tag{23}$$

The pertinent stiffness submatrices are:

$$\mathbf{k}_u = \begin{bmatrix} 4k_N & 0 \\ 0 & 4k_N l_w^2 \end{bmatrix}, \ \mathbf{k}_w = \begin{bmatrix} 2k_N & 0 \\ 0 & 2k_N \end{bmatrix}, \ \mathbf{k}_{u,w} = \mathbf{k}_{w,u}^{\mathrm{T}} = \begin{bmatrix} -2k_N & -2k_N \\ -2k_N l_w & -2k_N l_w \end{bmatrix} \tag{24}$$

The damping matrix and submatrices are similar to the stiffness ones if one replaces the stiffness constant with the damping constant:

$$\mathbf{c}_u = \begin{bmatrix} 4c_N & 0 \\ 0 & 4c_N l_w^2 \end{bmatrix}, \ \mathbf{c}_w = \begin{bmatrix} 2c_N & 0 \\ 0 & 2c_N \end{bmatrix}, \ \mathbf{c}_{u,w} = \mathbf{c}_{w,u}^{\mathrm{T}} = \begin{bmatrix} -2c_N & -2c_N \\ -2c_N l_w & -2c_N l_w \end{bmatrix} \tag{25}$$

The contact force vector and contact direction matrix are respectively:

$$\tilde{\boldsymbol{\lambda}} = \begin{bmatrix} \tilde{\lambda}_{\mathrm{N1}} \\ \tilde{\lambda}_{\mathrm{N2}} \end{bmatrix}, \ \mathbf{W}_w = \mathbf{E} = \begin{bmatrix} 1 & 0 \\ 0 & 1 \end{bmatrix} \tag{26}$$

If we model the bridge using shape functions (e.g., the fundamental mode):

$$\mathbf{W}_B = \begin{bmatrix} \psi^*_{\mathrm{BN}}(x_1) & \psi^*_{\mathrm{BN}}(x_2) \end{bmatrix} \tag{27}$$

where $\psi^*_{\mathrm{BN}}(x_i) = \psi_{\mathrm{BN}}(x_i)h(x_i)$ and $h(x_i) = H(x_i/v) - H((x_i - L)/v)$ in which $H(x)$ is the Heaviside step function, $L$ is length of the bridge, and $x_i$ indicates location of each contact point on the bridge. The function $h(x_i)$ activates the operation of each wheel on the bridge when it enters the bridge, and deactivates it when the wheel exits the bridge. $\psi_B(x)$ denotes the mode shape of the fundamental mode of the bridge. For example, $\psi_B(x)$ for a simply supported bridge is:

$$\psi_B(x) = sin\left(\frac{\pi x}{L}\right), \;\; 0 \le x \le L \tag{28}$$

The matrix $\mathbf{G}$ is given by:

$$\begin{aligned} \mathbf{G} = \mathbf{W}^{\mathrm{T}}\mathbf{m}^{-1}\mathbf{W} &= \begin{bmatrix} \begin{bmatrix} \mathbf{0} \\ \mathbf{W}_w \end{bmatrix} \\ -\mathbf{W}_B \end{bmatrix}^{\mathrm{T}} \begin{bmatrix} \begin{bmatrix} \mathbf{m}_u & \mathbf{0} \\ \mathbf{0} & \mathbf{m}_w \end{bmatrix} & \mathbf{0} \\ \mathbf{0} & \mathbf{m}_B \end{bmatrix}^{-1} \begin{bmatrix} \begin{bmatrix} \mathbf{0} \\ \mathbf{W}_w \end{bmatrix} \\ -\mathbf{W}_B \end{bmatrix} \\ &= \mathbf{W}_w^{\mathrm{T}}\mathbf{m}_w^{-1}\mathbf{W}_w + \mathbf{W}_B^{\mathrm{T}}\mathbf{m}_B^{-1}\mathbf{W}_B = \begin{bmatrix} \frac{1}{m_w} + \frac{\left(\psi^*_{\mathrm{BN}}(x_1)\right)^2}{M_{\mathrm{BN}}} & \frac{\left(\psi^*_{\mathrm{BN}}(x_1)\psi^*_{\mathrm{BN}}(x_2)\right)}{M_{\mathrm{BN}}} \\ \frac{\left(\psi^*_{\mathrm{BN}}(x_1)\psi^*_{\mathrm{BN}}(x_2)\right)}{M_{\mathrm{BN}}} & \frac{1}{m_w} + \frac{\left(\psi^*_{\mathrm{BN}}(x_2)\right)^2}{M_{\mathrm{BN}}} \end{bmatrix} \end{aligned} \tag{29}$$

Stoura and Dimitrakopoulos [20] presented the EOM of the upper part of the vehicle as:

$$\mathbf{m}_u\ddot{\tilde{\mathbf{u}}}_u + \mathbf{c}_u\dot{\tilde{\mathbf{u}}}_u + \mathbf{k}_u\tilde{\mathbf{u}}_u = -\mathbf{c}_{u,w}\mathbf{W}_w^{-\mathrm{T}}\left(v\mathbf{W}'^{\mathrm{T}}_B\tilde{\mathbf{u}}_B + \mathbf{W}_B^{\mathrm{T}}\dot{\tilde{\mathbf{u}}}_B + v\mathbf{r}'_c\right) - \mathbf{k}_{u,w}\mathbf{W}_w^{-\mathrm{T}}\left(\mathbf{W}_B^{\mathrm{T}}\tilde{\mathbf{u}}_B + \mathbf{r}_c\right) \tag{30}$$

Importantly, for such two-dimensional VBI problems $\mathbf{W}_w = \mathbf{E}$ and thus its inverse exists and is equal to $\mathbf{W}_w^{-\mathrm{T}} = \mathbf{E}$.

Substituting the mass (Eq. (23)), stiffness (Eq. (24)), and damping (Eq. (25)) matrices and degrees of freedom vector of the vehicle (Eq. (20)) into the EOM of the upper part of the vehicle (Eq. (30)) and considering the first mode of the bridge (Eq. (27)) gives:

$$\begin{aligned} &\begin{bmatrix} m_c & 0 \\ 0 & I_{c\theta} \end{bmatrix}\begin{bmatrix} \ddot{\tilde{z}}_c \\ \ddot{\tilde{\theta}}_c \end{bmatrix} + \begin{bmatrix} 4c_N & 0 \\ 0 & 4c_N l_w^2 \end{bmatrix}\begin{bmatrix} \dot{\tilde{z}}_c \\ \dot{\tilde{\theta}}_c \end{bmatrix} + \begin{bmatrix} 4k_N & 0 \\ 0 & 4k_N l_w^2 \end{bmatrix}\begin{bmatrix} \tilde{z}_c \\ \tilde{\theta}_c \end{bmatrix} = \\ &-\begin{bmatrix} -2c_N & -2c_N \\ -2c_N l_w & -2c_N l_w \end{bmatrix}\left(v\begin{bmatrix} \psi^{*\prime}_{\mathrm{BN}}(x_1) \\ \psi^{*\prime}_{\mathrm{BN}}(x_2) \end{bmatrix}\tilde{\mathbf{u}}_B + \begin{bmatrix} \psi^*_{\mathrm{BN}}(x_1) \\ \psi^*_{\mathrm{BN}}(x_2) \end{bmatrix}\dot{\tilde{\mathbf{u}}}_B + v\begin{bmatrix} r'_c(x_1) \\ r'_c(x_2) \end{bmatrix}\right) \\ &-\begin{bmatrix} -2k_N & -2k_N \\ -2k_N l_w & -2k_N l_w \end{bmatrix}\left(\begin{bmatrix} \psi^*_{\mathrm{BN}}(x_1) \\ \psi^*_{\mathrm{BN}}(x_2) \end{bmatrix}\tilde{\mathbf{u}}_B + \begin{bmatrix} r_c(x_1) \\ r_c(x_2) \end{bmatrix}\right) \end{aligned} \tag{31}$$

In other words, the EOM of the translational DOF of the vehicle is:

$$\begin{aligned} &m_c\ddot{\tilde{z}}_c + 4c_N\dot{\tilde{z}}_c + 4k_N\tilde{z}_c = \\ &2\left(c_N v\sum_{j=1}^{2}\psi^{*\prime}_{\mathrm{BN}}(x_j) + k_N\sum_{j=1}^{2}\psi^*_{\mathrm{BN}}(x_j)\right)\tilde{\mathbf{u}}_B + 2c_N\sum_{j=1}^{2}\psi^*_{\mathrm{BN}}(x_j)\dot{\tilde{\mathbf{u}}}_B + \\ &2\left(c_N v\sum_{j=1}^{2}r'_{\mathrm{c}}(x_j) + k_N\sum_{j=1}^{2}r_{\mathrm{c}}(x_j)\right) \end{aligned} \tag{32}$$

and the EOM of the rotational (pitching) DOF of the vehicle is:

$$I_{c\theta}\ddot{\tilde{\theta}}_c + 4c_N l_w^2 \dot{\tilde{\theta}}_c + 4k_N l_w^2 \tilde{\theta}_c = 2\left(c_N v l_w \sum_{j=1}^{2} \psi_{\mathrm{BN}}^{*'}(x_j) + k_N l_w \sum_{j=1}^{2} \psi_{\mathrm{BN}}^{*}(x_j)\right)\tilde{\mathbf{u}}_B + 2c_N l_w \sum_{j=1}^{2} \psi_{\mathrm{BN}}^{*}(x_j)\dot{\tilde{\mathbf{u}}}_B + 2\left(c_N v l_w \sum_{j=1}^{2} r_{\mathrm{c}}'(x_j) + k_N l_w \sum_{j=1}^{2} r_{\mathrm{c}}(x_j)\right) \tag{33}$$

As explained in section 2, to convert an equation of motion in matrix form into a dimensionless form, we need to partition the degrees of freedom into translational and rotational DOFs and create the matrix $\mathbf{\Delta}_{ref}$ for the system. Then, multiplying both sides of the equation with the matrix $\mathbf{\Delta}_{ref}$ produces dimensionless EOM. Given that the vehicle system in this example has one translational and one rotational DOF, the matrix $\mathbf{\Delta}_{ref}$ for this system is:

$$\mathbf{\Delta}_{ref} = \begin{bmatrix} \frac{1}{\mathscr{F}_{ref}}\mathbf{E}_{x,x} & \mathbf{0}_{x,\phi} \\ \mathbf{0}_{\phi,x} & \frac{1}{\mathscr{M}_{ref}}\mathbf{E}_{\phi,\phi} \end{bmatrix} = \begin{bmatrix} \frac{1}{\mathscr{F}_{ref}} & 0 \\ 0 & \frac{1}{\mathscr{M}_{ref}} \end{bmatrix} \tag{34}$$

Therefore, we need to multiply both sides of Eq. (31) with the matrix $\mathbf{\Delta}_{ref}$ (Eq. 34) to make it dimensionless. This leads to dividing both sides of the EOM corresponding to the translational DOF (Eq. (32)) with the reference force e.g., $\mathscr{F}_{ref} = m_B L_B \omega_B^2$, and the EOM corresponding to the rotational DOF (Eq. (33)) with the reference moment e.g., $\mathscr{M}_{ref} = m_B L_B^2 \omega_B^2$. Hence, dividing both sides of Eq. (32) with $\mathscr{F}_{ref} = m_B L_B \omega_B^2$ and grouping the dimensionless terms leads:

$$\frac{m_c}{m_B}\frac{\ddot{\tilde{z}}_c}{L_B\omega_B^2} + 4\frac{c_N}{m_B\omega_B}\frac{\dot{\tilde{z}}_c}{L_B\omega_B} + 4\frac{k_N}{m_B\omega_B^2}\frac{\tilde{z}_c}{L_B} = 2\left(\frac{c_N}{m_B\omega_B}\frac{v}{L_B\omega_B}\sum_{j=1}^{2} L_B\psi_{\mathrm{BN}}^{*'}(x_j) + \frac{k_N}{m_B\omega_B^2}\sum_{j=1}^{2}\psi_{\mathrm{BN}}^{*}(x_j)\right)\frac{\tilde{\mathbf{u}}_B}{L_B} + 2\frac{c_N}{m_B\omega_B}\sum_{j=1}^{2}\psi_{\mathrm{BN}}^{*}(x_j)\frac{\dot{\tilde{\mathbf{u}}}_B}{L_B\omega_B} + 2\left(\frac{c_N}{m_B\omega_B}\frac{v}{L_B\omega_B}\sum_{j=1}^{2} r'_{\mathrm{c}}(x_j) + \frac{k_N}{m_B\omega_B^2}\sum_{j=1}^{2}\frac{r_{\mathrm{c}}(x_j)}{L_B}\right) \tag{35}$$

Similarly, dividing both sides of Eq. (33) with $\mathscr{M}_{ref} = m_B L_B^2 \omega_B^2$ and grouping the dimensionless terms yields:

$$\frac{I_{c\theta}}{m_B L_B^2}\frac{\ddot{\tilde{\theta}}_c}{\omega_B^2} + 4\frac{c_N l_w^2}{m_B\omega_B L_B^2}\frac{\dot{\tilde{\theta}}_c}{\omega_B} + 4\frac{k_N l_w^2}{m_B L_B^2\omega_B^2}\tilde{\theta}_c = 2\left(\frac{c_N l_w}{m_B\omega_B L_B}\frac{v}{L_B\omega_B}\sum_{j=1}^{2} L_B\psi_{\mathrm{BN}}^{*'}(x_j) + \frac{k_N l_w}{m_B\omega_B^2 L_B}\sum_{j=1}^{2}\psi_{\mathrm{BN}}^{*}(x_j)\right)\frac{\tilde{\mathbf{u}}_B}{L_B} + 2\frac{c_N l_w}{m_B\omega_B L_B}\sum_{j=1}^{2}\psi_{\mathrm{BN}}^{*}(x_j)\frac{\dot{\tilde{\mathbf{u}}}_B}{L_B\omega_B} + 2\left(\frac{c_N l_w}{m_B\omega_B L_B}\frac{v}{L_B\omega_B}\sum_{j=1}^{2} r'_{\mathrm{c}}(x_j) + \frac{k_N l_w}{m_B\omega_B^2 L_B}\sum_{j=1}^{2}\frac{r_{\mathrm{c}}(x_j)}{L_B}\right) \tag{36}$$

Substituting dimensionless parameters from Eqs. (15), (16), and (17) and also using dimensionless speed parameter $S_v = v/(L_B\omega_B)$, scaled slope of irregularities vector $R'_{\mathrm{c}} = r'_{\mathrm{c}}$, and scaled

irregularities vector $R_c\left(x_j\right) = r_{\mathrm{c}}\left(x_j\right)/L_B$ in Eqs. (35) and (36) yields:

$$\begin{gathered} M_x\ddot{z}_c + 4C_x\dot{z}_c + 4K_x z_c = \\ 2\left(C_x S_v \sum_{j=1}^{2} L_B \psi_{\mathrm{BN}}^{*'}\left(x_j\right) + K_x \sum_{j=1}^{2} \psi_{\mathrm{BN}}^{*}\left(x_j\right)\right)\mathbf{u}_B + 2C_x \sum_{j=1}^{2} \psi_{\mathrm{BN}}^{*}\left(x_j\right)\dot{\mathbf{u}}_B + \\ 2\left(C_x S_v \sum_{j=1}^{2} R_c'\left(x_j\right) + K_x \sum_{j=1}^{2} R_c\left(x_j\right)\right) \end{gathered} \tag{37}$$

and:

$$\begin{gathered} M_\phi\ddot{\theta}_c + 4C_\phi\dot{\theta}_c + 4K_\phi\theta_c = \\ 2\left(C_{x,\phi} S_v \sum_{j=1}^{2} L_B \psi_{\mathrm{BN}}^{*'}\left(x_j\right) + K_{x,\phi} \sum_{j=1}^{2} \psi_{\mathrm{BN}}^{*}\left(x_j\right)\right)\mathbf{u}_B + 2C_{x,\phi} \sum_{j=1}^{2} \psi_{\mathrm{BN}}^{*}\left(x_j\right)\dot{\mathbf{u}}_B + \\ 2\left(C_{x,\phi} S_v \sum_{j=1}^{2} R'_c\left(x_j\right) + K_{x,\phi} \sum_{j=1}^{2} R_c\left(x_j\right)\right) \end{gathered} \tag{38}$$

where all variables and parameters in Eqs. (37) and (38) are dimensionless.

### 3.1 FEM description of the bridge

In this section, we discuss the differences in the EOMs that arise from using the finite element method instead of considering the first mode of the bridge. To this end, assume we model the bridge using the FEM, and consider the DOF vector of a typical bridge-deck element (two-node Euler-Bernoulli beam element with two DOFs at each node); for example:

$$\tilde{\mathbf{u}}_B^{\mathrm{T}} = \begin{bmatrix} \tilde{w}_1 & \tilde{\theta}_{y1} & \tilde{w}_2 & \tilde{\theta}_{y2} \end{bmatrix} \tag{39}$$

The corresponding direction matrix would be:

$$\mathbf{W}_B\left(x\right) = \begin{bmatrix} \psi_{\mathrm{BN1}}^{*}\left(x_1\right) & \psi_{\mathrm{BN1}}^{*}\left(x_2\right) \\ \psi_{\mathrm{BN2}}^{*}\left(x_1\right) & \psi_{\mathrm{BN2}}^{*}\left(x_2\right) \\ \psi_{\mathrm{BN3}}^{*}\left(x_1\right) & \psi_{\mathrm{BN3}}^{*}\left(x_2\right) \\ \psi_{\mathrm{BN4}}^{*}\left(x_1\right) & \psi_{\mathrm{BN4}}^{*}\left(x_2\right) \end{bmatrix} \tag{40}$$

where again, $\psi_{\mathrm{BN}}^{*}(x_i) = \psi_{\mathrm{BN}}(x_i)h(x_i)$ and $h(x_i) = H(x_i/v) - H((x_i - L_e)/v)$, but now $L_e$ is the length of the element. Function $h(x_i)$ here activates and deactivates the action of each wheel of the vehicle on the pertinent element of the bridge, when it enters and leaves the element, respectively. We can state shape functions $\psi_{\mathrm{BN}}(x)$ for a two-node Euler-Bernoulli beam element with two DOFs at each node as follows:

$$\begin{aligned} \psi_{\mathrm{BN1}}\left(x\right) &= 1 - 3\left(\frac{x}{L_e}\right)^2 + 2\left(\frac{x}{L_e}\right)^3 \\ \psi_{\mathrm{BN2}}\left(x\right) &= L_e\left(\frac{x}{L_e}\right) - 2L_e\left(\frac{x}{L_e}\right)^2 + L_e\left(\frac{x}{L_e}\right)^3 \\ \psi_{\mathrm{BN3}}\left(x\right) &= 3\left(\frac{x}{L_e}\right)^2 - 2\left(\frac{x}{L_e}\right)^3 \\ \psi_{\mathrm{BN4}}\left(x\right) &= -L_e\left(\frac{x}{L_e}\right)^2 + L_e\left(\frac{x}{L_e}\right)^3 \end{aligned} \tag{41}$$

The matrix **G** becomes:

$$\mathbf{G} = \mathbf{W}^T \mathbf{m}^{-1} \mathbf{W} = \mathbf{W}_w^{\mathrm{T}} \mathbf{m}_w^{-1} \mathbf{W}_w + \mathbf{W}_B^{\mathrm{T}} \mathbf{m}_B^{-1} \mathbf{W}_B = \begin{bmatrix} \frac{1}{m_w} & 0 \\ 0 & \frac{1}{m_w} \end{bmatrix} + \begin{bmatrix} g_{11} & g_{12} \\ g_{12} & g_{22} \end{bmatrix} \tag{42}$$

with:

$$\begin{aligned} g_{11} &= \frac{\left(\psi^*_{\mathrm{BN1}}(x_1)\right)^2}{m_{\tilde{w}_1}} + \frac{\left(\psi^*_{\mathrm{BN2}}(x_1)\right)^2}{m_{\tilde{\theta}_{y1}}} + \frac{\left(\psi^*_{\mathrm{BN3}}(x_1)\right)^2}{m_{\tilde{w}_2}} + \frac{\left(\psi^*_{\mathrm{BN4}}(x_1)\right)^2}{m_{\tilde{\theta}_{y2}}} \\ g_{12} &= \frac{\psi^*_{\mathrm{BN1}}(x_1)\,\psi^*_{\mathrm{BN1}}(x_2)}{m_{\tilde{w}_1}} + \frac{\psi^*_{\mathrm{BN2}}(x_1)\,\psi^*_{\mathrm{BN2}}(x_2)}{m_{\tilde{\theta}_{y1}}} + \frac{\psi^*_{\mathrm{BN3}}(x_1)\,\psi^*_{\mathrm{BN3}}(x_2)}{m_{\tilde{w}_2}} + \frac{\psi^*_{\mathrm{BN4}}(x_1)\,\psi^*_{\mathrm{BN4}}(x_2)}{m_{\tilde{\theta}_{y2}}} \\ g_{22} &= \frac{\left(\psi^*_{\mathrm{BN1}}(x_2)\right)^2}{m_{\tilde{w}_1}} + \frac{\left(\psi^*_{\mathrm{BN2}}(x_2)\right)^2}{m_{\tilde{\theta}_{y1}}} + \frac{\left(\psi^*_{\mathrm{BN3}}(x_2)\right)^2}{m_{\tilde{w}_2}} + \frac{\left(\psi^*_{\mathrm{BN4}}(x_2)\right)^2}{m_{\tilde{\theta}_{y2}}} \end{aligned} \tag{43}$$

where $m_{\tilde{w}_1}$, $m_{\tilde{\theta}_{y1}}$, $m_{\tilde{w}_2}$, and $m_{\tilde{\theta}_{y2}}$ are the bridge element masses corresponding to the element DOFs (Eq. 39). When we model the bridge with FEM, both translational and rotational DOFs are present in the bridge subsystem. Therefore, to convert the equations of motion of the bridge into a dimensionless form, we need to partition EOMs into translational and rotational DOFs and create the matrix $\mathbf{\Delta}_{ref}$ (Eq. (18)) for the system. By multiplying the equations of motion with the appropriate $\mathbf{\Delta}_{ref}$ matrix, we can obtain the dimensionless equations of motion for both translational and rotational degrees of freedom. Specifically, we can express $\mathbf{\Delta}_{ref}$ for the EOMs of a bridge when we model it with a two-node Euler-Bernoulli beam element and its DOF vector is given in Eq. (39) as:

$$\mathbf{\Delta_{ref}} = \begin{bmatrix} \frac{1}{\mathscr{F}_{ref}} & 0 & 0 & 0 \\ 0 & \frac{1}{\mathscr{M}_{ref}} & 0 & 0 \\ 0 & 0 & \frac{1}{\mathscr{F}_{ref}} & 0 \\ 0 & 0 & 0 & \frac{1}{\mathscr{M}_{ref}} \end{bmatrix} = \begin{bmatrix} \frac{1}{m_B L_B \omega_B^2} & 0 & 0 & 0 \\ 0 & \frac{1}{m_B L_B^2 \omega_B^2} & 0 & 0 \\ 0 & 0 & \frac{1}{m_B L_B \omega_B^2} & 0 \\ 0 & 0 & 0 & \frac{1}{m_B L_B^2 \omega_B^2} \end{bmatrix} \tag{44}$$

## 4 PHYSICAL SIMILARITY

This section investigates the concept of physical similarity to highlight the importance of dimensionless parameters in the vehicle-bridge interaction problem. The underlying notion behind physical similarity in VBI systems is that if the dimensionless terms of two mechanical systems are the same, regardless of whether the dimensional terms are different, the dimensionless response for two systems will be the same and the dimensional response will be proportional. To illustrate, we consider two (coupled) vehicle-bridge systems (A and B). Table 1 presents the dimensional and dimensionless properties of both systems. System A corresponds the Pioneer train and Skidträsk bridge (Pioneer - Skidträsk bridge) [7, 18]. Although the dimensional parameters of systems A and B differ, their dimensionless parameters are identical (Table 1). Hence, the two systems are physically similar.

Figure 2 depicts the dimensional and dimensionless displacement time history at the midspan of the bridge under the passage of a ten-vehicle train, as well as the dimensional and dimensionless acceleration of the pitching DOF of the first vehicle. Note that for obtaining the numerical results we model the bridge with the finite element method (FEM) and the vehicle with 10 degrees of freedom (DOFs). As expected according to the concept of physical similarity, the

Table 1: Dimensional and dimensionless properties of two systems

| Dimensional parameters | | |
|---|---|---|
| Description (unit) | System A | System B |
| Bridge length $L_B$ (m) | 36 | 54 |
| Mass of the bridge $m_B$ (kg) | 306,000 | 459,000 |
| Moment of inertia $I$ ($m^4$) | 0.82 | 2.77 |
| Young's modulus $E$ (GPa) | 210 | 210 |
| Fundamental frequency $f_B$ (Hz) | 3.86 | 3.15 |
| Damping ratio $\zeta_B$ (%) | 0.5 | 0.5 |
| Stiffness of the bridge $k_B$ (N/m) | $179.76 \cdot 10^6$ | $179.76 \cdot 10^6$ |
| Mass of the train $m_V$ (kg) | 58,000 | 87,000 |
| Mass moment of inertia of the train $I_{c\theta}$ ($kg \cdot m^2$) | 1,064,400 | 3,592,350 |
| Stiffness of the train $k_{V,i}$ (kN/m) | $2.08 \cdot 10^3$ | $2.08 \cdot 10^3$ |
| Damping of the train $c_{V,i}$ (kNs/m) | 60 | 73.8 |
| Length of the train $\tilde{d}$ (m) | 25 | 37.5 |
| Speed of the vehicle $v$ (km/h) | 250 | 307.5 |
| Dimensionless parameters | | |
| Description | Systems A and B | |
| Scaled distance $d_i = \tilde{d}/L_B$ | 0.69 | |
| Speed parameter $S_v = v/(\omega_B L_B)$ | 0.08 | |
| Mass ratio $M_x = m_V/m_B$ | 0.19 | |
| Mass ratio $M_\phi = I_{c\theta}/(m_B L_B^2)$ | 0.0027 | |
| Stiffness ratio $K_i = k_{V,i}/k_B$ | 0.012 | |
| Impedance ratio $C_i = c_{V,i}/(m_B \omega_B)$ | 0.008 | |
| Normalized vehicle weight $F_{B,i} = f_{B,i}/(k_B L_B)$ | $2.2 \cdot 10^{-5}$ | |

dimensional response (displacement and acceleration) for systems A and B, as shown in Figures 2a, 2b, 2d, and 2e, are different since the dimensional parameters of these two systems are different. More importantly though, Figs. 2c and 2f indicate that the dimensionless response for both systems is the same, since the dimensionless parameters for both systems are the same. This demonstrates that two VBI systems that are physically similar produce the identical dimensionless response, confirming the physical similarity concept.

## 5 CONCLUSIONS

The extended modified bridge system (EMBS) method offers a consistent way to decouple a coupled vehicle-bridge system. Ultimately, it allows to solve the bridge and vehicle subsystems independently, providing results that are comparable to a coupled solution. The present study focuses on the vertical plane of vehicle-bridge interaction (VBI), and considers a generic train-bridge system with multi-degree of freedom (MDOF), which can be applied to a wide range of train-bridge systems. The aim is to demonstrate the application of the EMBS method on systems that have both translational and rotational degrees of freedom. In this context, the study first provides a comprehensive description of the governing terms in the equations of motion (EOMs). Then, it illustrates the procedure of converting the multi-degree of freedom EOMs into a dimensionless form. In this context, the analysis explores the differences in the EOMs that arise from simulating the bridge using the finite element method, as opposed to using mode superposition (or merely the first mode of the bridge). Furthermore, the study

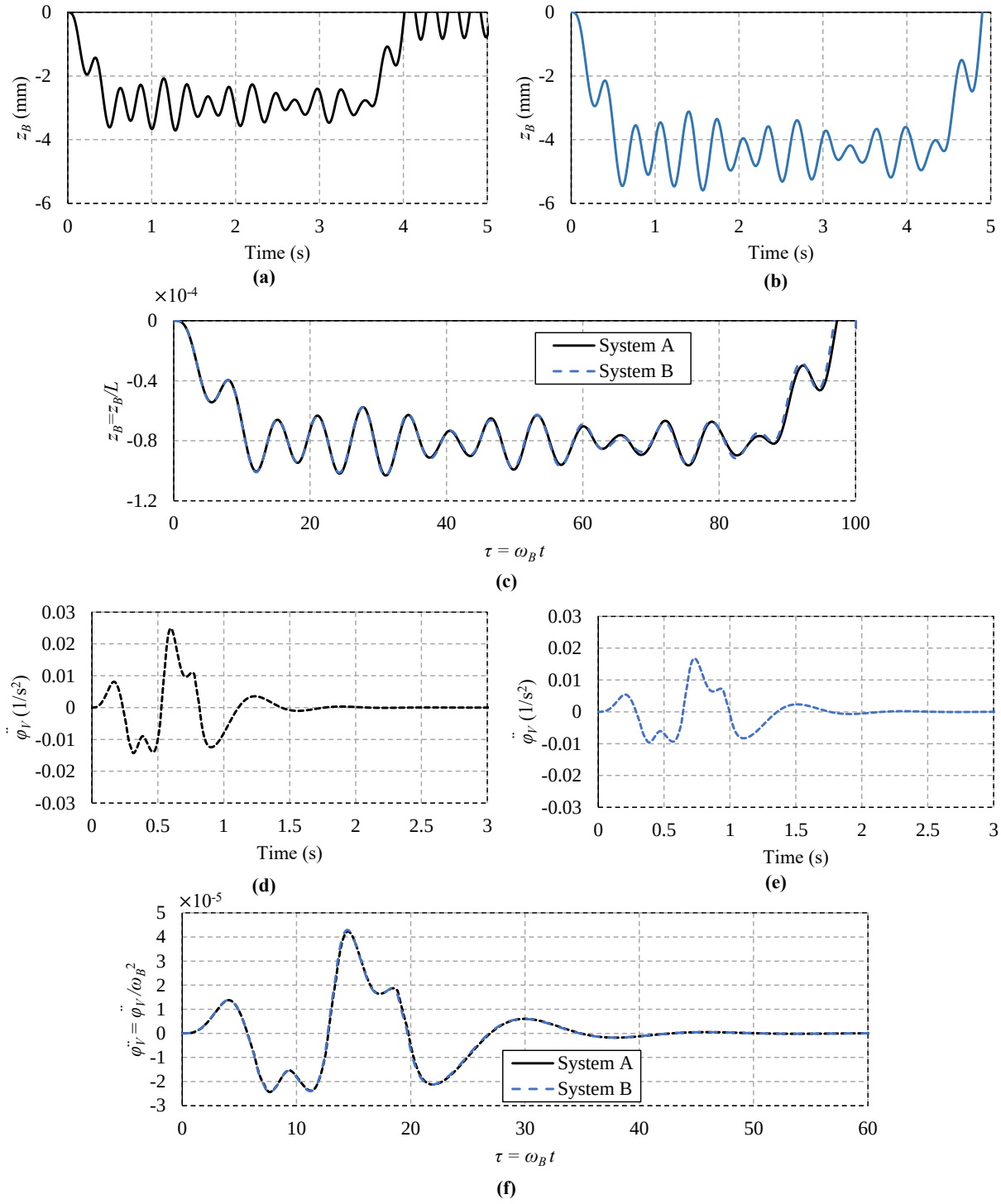


Figure 2: Time history of the displacement of the bridge midpoint (a) dimensional for system A (b) dimensional for system B (c) dimensionless for both systems A and B Time history of the acceleration of the pitching DOF of the vehicle (d) Dimensional for system A (e) dimensional for system B (f) dimensionless for both systems A and B

highlights the importance of a dimensionless description of the VBI problem by demonstrating the principle of physical similarity: the dimensionless response of two vehicle-bridge systems will be the same as long as their dimensionless terms are identical, even if two systems have varying dimensional parameters.

## 6 ACKNOWLEDGEMENTS

This work was supported by the University Grants Committee Research Grants Council of Hong Kong, under Grant Reference Number GRF 16212522.

## References

[1] H. Xia, N. Zhang, W. Guo, Dynamic interaction of train-bridge systems in high-speed railways. Springer, 2018.

[2] X. He, T. Wu, Y. Zou, Y.F. Chen, H. Guo, Z. Yu, Recent developments of high-speed railway bridges in China. *Structure and Infrastructure Engineering*, **13**, 1584–1595, 2017.

[3] Y.B. Yang, B.H. Lin, Vehicle-bridge interaction analysis by dynamic condensation method. *Journal of Structural Engineering*, **121**(11), 1636–1643, 1995.

[4] Y.B. Yang, J.D. Yau, Y.S. Wu, Vehicle-Bridge Interaction Dynamics: With Applications to High-Speed Railways. World Scientific, 2004.

[5] S.G.M. Neves, A.F.M. Azevedo, R. Calçada, A direct method for analyzing the vertical vehicle–structure interaction. *Engineering Structures*, **34**(1), 414–420, 2012.

[6] Q. Zeng, C.D. Stoura, E.G. Dimitrakopoulos, A localized lagrange multipliers approach for the problem of vehicle-bridge-interaction. *Engineering Structures*, **168**, 82–92, 2018.

[7] H. Homaei, E.G. Dimitrakopoulos, A. Bakhshi, Vehicle-bridge interaction and the tuned-mass damper effect on bridges during vertical earthquake excitation. *Acta Mechanica*, 2023 (DOI: 10.1007/s00707-023-03533-2).

[8] Q. Zeng, E.G. Dimitrakopoulos, Vehicle–bridge interaction analysis modeling derailment during earthquakes. *Nonlinear Dynamics*, **93**, 2315–2337, 2018.

[9] N. Zhang, H. Xia, Dynamic analysis of coupled vehicle-bridge system based on inter-system iteration method. *Computers and Structures*, **114**, 26–34, 2013.

[10] C.D. Stoura, E. Paraskevopoulos, E.G. Dimitrakopoulos, S. Natsiavas, A Dynamic Partitioning Method to solve the vehicle-bridge interaction problem. *Computers and Structures*, **251**, 1–12, 2021.

[11] S.P. Stefanidou, E.A. Paraskevopoulos, Seismic fragility analysis of railway reinforced concrete bridges considering real-time vehicle-bridge interaction with the aid of co-simulation techniques. *Earthquake Engineering and Structural Dynamics*, **51**(9), 1–25, 2022.

[12] S.P. Timoshenko, D.H. Young, Vibration Problems in Engineering. D. Van Nostrand, New York, 1955.

[13] L. Frýba, Dynamics of Railway Bridges. Thomas Telford, London, 1996.

[14] A. Doménech, P. Museros, M.D. Martínez-Rodrigo, Influence of the vehicle model on the prediction of the maximum bending response of simply-supported bridges under high-speed railway traffic. *Engineering Structures*, **72**, 123–139, 2014.

[15] T. Arvidsson, R. Karoumi, C. Pacoste, Statistical screening of modelling alternatives in train-bridge interaction systems. *Engineering Structures*, **59**, 693–701, 2014.

[16] J.D. Yau, M.D. Martínez-Rodrigo, A. Doménech, An equivalent additional damping approach to assess vehicle-bridge interaction for train-induced vibration of short-span railway bridges. *Engineering Structures*, **188**, 469–479, 2019.

[17] C.D. Stoura, E.G. Dimitrakopoulos, Additional damping effect on bridges because of vehicle-bridge interaction. *Journal of Sound and Vibration*, **476**, 1–16, 2020.

[18] C.D. Stoura, E.G. Dimitrakopoulos, A Modified Bridge System method to characterize and decouple vehicle–bridge interaction. *Acta Mechanica*, **231**(9), 3825-3845, 2020.

[19] P. Salcher, C. Adam, A. Kuisle, A stochastic view on the effect of random rail irregularities on railway bridge vibrations. *Structure and Infrastructure Engineering*, **1**, 1–16, 2019.

[20] C.D. Stoura, E.G. Dimitrakopoulos, MDOF extension of the Modified Bridge System method for vehicle–bridge interaction. *Nonlinear Dynamics*, **102**, 2103–2123, 2020.

[21] E.G. Dimitrakopoulos, Q. Zeng, A three-dimensional dynamic analysis scheme for the interaction between trains and curved railway bridges. *Computers and Structures*, **149**, 43–60, 2015.

COMPDYN 2023
9th ECCOMAS Thematic Conference on
Computational Methods in Structural Dynamics and Earthquake Engineering
M. Papadrakakis, M. Fragiadakis (eds.)
Athens, Greece, 12-14 June 2023

# AN INTERFACE FOR CHECKING DYNAMIC COMPATIBILITY OF ROLLING STOCK WITH EXISTING RAILWAY BRIDGES

**Muriel Ragueneau**[1], **Huyen Nguyen**[1], **and Vincent Mathouraparsad**[1]

[1] SNCF Reseau, Direction Générale Industrielle et Ingénierie
e-mail: (muriel.ragueneau, huyen.nguyen, vincent.mathouraparsad)@reseau.sncf.fr

## Abstract

*Since the application of the Directive (EU) 2016/797 of the European Parliament and of the Council [1] on the interoperability of the rail system within the European Union and the 4th railway package, for any new rolling stock, its Route Compatibility before being placed into service could be carried out by the railway undertakings (RU). However, the dynamic compatibility of a train with existing rail bridges is always a technically complicated subject. In order to ensure a high level of traffic safety and facilitate the studies carried out by the RUs, SNCF offers a simplified, reliable and efficient interface to the compatibility check between rolling stock and existing SNCF Réseau bridges. This article aims to explain the analytical approach to build this interface and a quick overview of its application. By using the sum of a geometric progression to describe the deflection at mid-span of a beam with 2 articulated supports under the repetitive passage of repeated loads, the maximum acceleration at the resonance expressed by two parameters $R_{dB}$ and $R_{z,n}$ depending on the parameters of the rolling stock. If the bridges respect their frequency domain and have standard damping values, the maximum acceleration of a bridge only depends on the axle load, the wheelbase of the bogies, the distances between the groups of bogies and the number of axles. All of these load and geometric criteria will define the frequency domain of the rolling stock for a required speed.*

**Keywords:** Existing bridges, railway, dynamic behavior, spectral approach

# 1 INTRODUCTION

The circulation of new rolling stock on the European rail network is only authorized after numerous checks have been carried out, in particular the compatibility checks between the Rolling Stock and the rail bridges. Previously these checks were made, except at high speeds, by using these quasi-static analyses: the effects of the vehicle's speed on the rail bridges were taken into account by means of an enhancement factor calibrated from experimental tests. This study is carried out on railway bridges in the 1960s by the Office for Research and Experimentation (ORE) et published in UIC leaflet 776-1R,1979 [2] by International Union of Railway (UIC). These quasi-static checks regulated by UIC 700 [3] and then by European standard EN15528 [4] are rather simple and allow to guarantee the safety of freight train traffic in Europe at speeds up to 120 km/h or even 100 km/h for heavy freight at 22,5 Tonnes per axle.

Nowadays, with fourth railway package for the open access for Rail passenger Services in Europe, the European directives impose through the Technical Specifications for Interoperability (TSIs) on RU to fulfill additional dynamic checks. This aims to guarantee the safety of traffic whose speed exceeds 100 km/h. These additional dynamic checks are required because of the high evolution of new passenger train's aggressivity at European level regarding new architectures, loads and higher design speeds than before:

- The length of the cars and the composition of the trains have diversified to adapt to the needs of passengers, particularly those with reduced mobility.
- The axle loads of passenger trains have increased from 17T to 20T or even 21.5T, in particular with the use of double decker trains to transport more passengers
- The design speed of passenger trains has increased from 160km/h to 200km/h to effectively compete with other modes of transport

These additional dynamic checks are essential for the safety of passenger traffic because they aim to exclude the risk of the bridge's resonance when the train passes over it. The resonance phenomenon occurs when the frequency of passage of the train's bogies on the rail bridge coincides perfectly with the bridge's natural frequency:

- The vertical vibrations at mid-span of the rail bridge deck are then amplified each time the bogie passes.
- The accelerations transmitted to the ballasted railway track, when they exceed a certain threshold, cause a loss of the ballast's cohesion which can cause a loss of rail-wheel contact or even a buckling of the track in hot weather.

Even if the probability of this risk is low but the severity is very high because the risk of the track buckling can cause the derailment of the train and the next one. It is absolutely imperative to exclude this risk in the compatibility checks of rolling stock with existing railway bridges before being placed into service. However, two problems arise for railway companies, slow down the open access competition trains in Europe:

- The number of existing railway bridges on a route is very high and the input data to perform the calculations are not easily accessible (there is no digitized database of rail bridge archives in Europe).
- There is no simplified method to check the dynamic compatibility between a train and a bridge. Dynamic calculations therefore require sufficient resources with the right skills for complex calculations.

Thereby SNCF RESEAU has developed a simplified spectral method to facilitate and secure dynamic compatibility studies between new passenger trains and the 15000 railway bridges on conventional lines in which the passenger train's speed exceeding 100 km/h.

## 2 THEORICAL ANALYSIS

### 2.1 Fundamental analysis of a single load

In this study, the bridges are considered as a beam with 2 simply articulated supports. We define by *y(x,t)* the dynamic deflection of an isostatic beam of span *L* (m) subjected to a moving point load of intensity noted *P*. The position of the moving load varies according to its speed (*v* in m/s) and time (*t* in seconds).

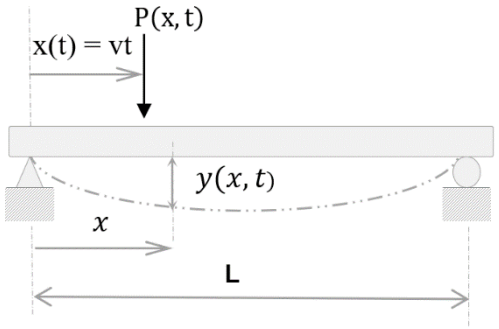


Figure 1: Deflection of an isostatic beam of span *L* under a mobile load *P* at *x(t)*

| *Parameter* | *Value* |
|---|---|
| Lengh | L [m] |
| Modulus of elasticity | E [N.m-2] |
| Moment of inertia | I [m4] |
| Linear mass | m [kg.m-1] |
| Damping rate | ζ (%) |

Table 1: Deck model as Bernouilli-Euler simply supported beam

For a moderate load *P*, the transverse displacement remains small compared to the transverse dimensions of the beam. And the equilibrium between the forces of inertia, the internal forces and the external force *P(x,t)* applied to the beam allow to write this following partial differential equation

$$P(x,t) = m\frac{\partial^2 y(x,t)}{\partial t^2} + EI\frac{\partial^4 y(x,t)}{\partial t^4} \quad (1)$$

In order to simplify the resolution of this equation, the dynamic deflection *y(x,t)* of the beam under a moving point load *P(x,t)* can be expressed as a function of its deflection at mid-span U(t) and of its first eigenmode called ϕ1(x):

$$y(x,t) = U(t)\phi_1(x) \quad (2)$$

Under a point load, the first eigenmode mode represents 99% of their global dynamic response with $\phi_1(x) = \sin(\pi x/L)$. Thus, the deflection of the beam can be expressed with very good precision as a function of its deflection at mid-span and of the first mode. Due to the independence of the two functions, one function of time *U(t)* and the other function of the

abscissa of the beam $\phi_1(x)$, a simplified equivalent model with one degree of freedom can be determined [5][6]. The equilibrium function can be written as follow, with $M^*$ and $K^*$ respectively the overall mass and stiffness of the equivalent 1 DOF

$$P(x,t) = m\frac{\partial^2 y(x,t)}{\partial t^2} + EI\frac{\partial^4 y(x,t)}{\partial t^4} \quad \equiv \quad M^*\ddot{U}(t) + K^*U(t) = P^*(t) \tag{3}$$

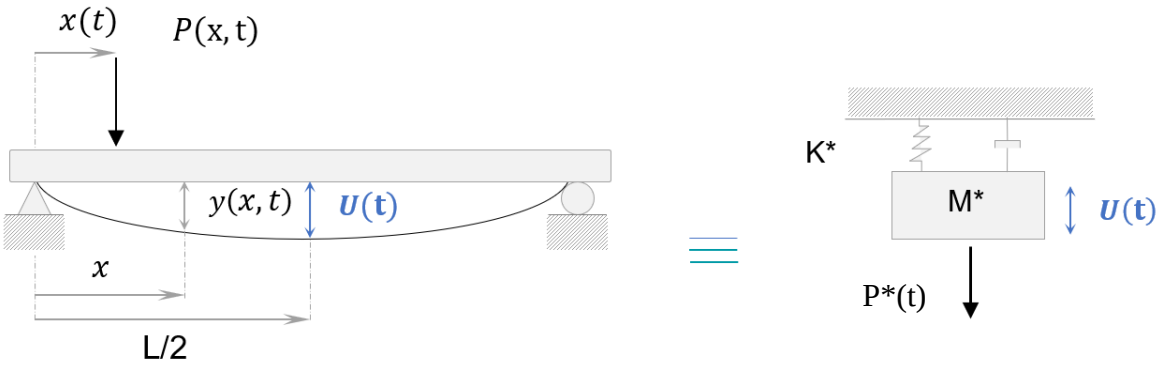


Figure 2: Transformation of a Bernouilli-Euler beam into 1 DOF oscillator

The parameters of this simplified model are determined by equalizing the kinetic and elastic potential energies of the two models. The equivalent load $P^*(t)$ is calculated to produce the same work identical to the load $P(x,t)$:

$$K^* = EI\frac{\pi^4}{L^4}\int_0^L \sin^2(\pi x/L) = EI\frac{\pi^4 EI}{L^3} = \frac{48{,}7EI}{L^3} \approx \frac{48{,}7EI}{L^3} \tag{4}$$

$$M^* = m\int_0^L \phi_1^2(\pi x/L)dx = m\int_0^L sin^2(\pi x/L)dx = mL/2 \tag{5}$$

$$P^*(t) = \int_0^L \mathrm{P}(\mathrm{x},\mathrm{t})\,\phi_1(x)\,dx = \int_0^L P\delta(x-vt)\phi_1(x)dx = P\phi_1(vt) = Psin\left(\frac{\pi}{L}vt\right) \tag{6}$$

The equivalent force depends on the parameters of the moving load (intensity and speed) but also on the span L of the beam. By introducing the pulsations of the beam ω and the mobile load ω̃, the differential equation of the equivalent simplified model is written:

$$\ddot{U}(t) + \omega^2 U_i(t) = \frac{P}{K^*}\omega^2 \sin(\tilde{\omega}t) \tag{7}$$

With

- $\omega = 2\pi F = \sqrt{\frac{K^*}{M^*}}$, the pulsation of the first natural frequency beam F in Hz
- $\tilde{\omega} = \frac{\pi}{L}v$, the pulsation of the moving load on the beam of span $L$ and speed $v$

By introducing the parameter β as the ratio between the two pulsations, the resolution of this equation helps to determine the maximum acceleration at mid-span of the beam in free oscillation under the action of a mobile load of intensity P according to few parameter [7]

$$\ddot{U} = \frac{P}{\mathrm{mL}} f(\beta) \tag{8}$$

Where

$$f(\beta) = \frac{4\beta}{(1-\beta^2)} \left|\cos\left(\frac{\pi}{2\beta}\right)\right| \text{ and } \beta = (v/2FL) \tag{9}$$

## 2.2 Influence of two-axle bogie

Actually, railway bridges are mostly solicited by passenger train with two-axles bogies. The resolution can be carried out with two moving loads spaced by a distance noted $d_B$. The analog resolution with two loads differs simply in the initial conditions of the second load which are imposed by the first load. The acceleration in this case can be expressed as a function of the acceleration obtained under a single load weighted by an enhancement factor called bogie coefficient $R_{dB}$

$$R_{dB} = 2 \left| cos(\frac{\pi d_B}{2\beta \mathrm{L}}) \right| \tag{10}$$

When the distance $d_B$ is equal to $2\beta L$, the coefficient $R_{dB}$ reaches 2. This phenomenon occurs while the frequency of passage of the second load ($v/d_B$) coincides perfectly with the natural frequency of the beam ($F$). From the equation (9)

$$F = \frac{v}{2\beta L} = \frac{v}{d_B} \tag{11}$$

Thus, for a beam of length $L$, we can define for each train's speed $v$ a critical distance between the moving loads worth $d_{critical} = 2\beta L = v/F$

## 2.3 Influence of repetitive loads - Coefficient $R_{\zeta,n}$ depending on the number of axle loads

When the frequency at which the axles or a group of axles pass over the bridge coincides with the natural frequency of the bridge, the dynamic free oscillation response of the second load joins to that of the first load and so on for the $n$ repetitive loads. Thus, without damping, the maximum acceleration obtained for $n$ repetitive loads will be multiply $n$ times the response under the first load determined above. Taking into account the damping of the bridge, we can determine the additional coefficient $R_{\zeta,n}$ which will be $n$ without damping decreases toward 1 if the damping is infinite [7]. At resonance while $F = v/d_{critical}$, with $d_{critical}$ the distance between the repetitive axles or group of axles, the coefficient of repetitive loads can be defined as

$$R_{\zeta,n} = \mathrm{e}^{-2\pi\zeta^0} + \mathrm{e}^{-2\pi\zeta^1} + \mathrm{e}^{-2\pi\zeta^2} + \cdots \mathrm{e}^{-2\pi\zeta^{\mathrm{i}-2}} + \mathrm{e}^{-2\pi\zeta^{\mathrm{n}-1}} = \frac{\left(1 - \mathrm{e}^{-2\pi\zeta^{\mathrm{n}}}\right)}{\left(1 - \mathrm{e}^{-2\pi\zeta}\right)} \tag{12}$$

The figure 3 illustrates the evolution of this coefficient under the number of train axles and the bridge's damping.

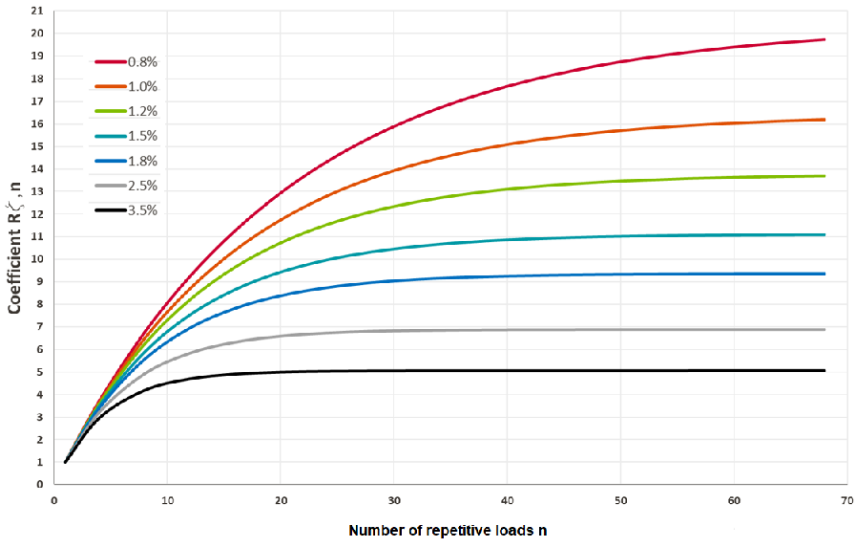


Figure 3: Variations of $R_{\zeta,n}$ as a function of the number of axles for different bridge's damping

## 2.4 Particular case of harmonic as double of load frequency

While the bridge's natural frequency is double that of the moving loads, $F=2v/d_{critical}$. The deck oscillates twice between two consecutive loads. The influence of damping can be defined by the coefficient $R_{2\zeta,v}$ as an analogue of the coefficient $R_{\zeta,v}$ at resonance (equation (12)).

$$R_{2\zeta,n} = \frac{\left(1 - e^{-4\pi\zeta^n}\right)}{\left(1 - e^{-4\pi\zeta}\right)} \; while \; F = 2v/d_{critical} \tag{13}$$

## 3 LAW OF BRIDGE'S NATURAL FREQUENCY AND ASSOCIATED SPEEDS

By analyzing the acceleration as a function of the parameter β, it is worth highlighting that when the pulsations of the beam and that of the single moving load are equal, the parameter β is equal to 1. A single moving load can therefore enter into resonance with the beam. However, thanks to the magnitude of the natural frequencies of all rail bridges (55/L at a minimum with L the length of the beam), it would be necessary for this single load to run at a speed greater than 400 km/h to cause this resonance.

The graph in the Figure 4 illustrates the impact of the natural frequency law of the bridge on the function *f(β)* which controls the acceleration response according to equation (8). We can note that the modification of the natural frequency law of the bridge only has the effect of translating the curves. The higher the F.L value, the more the acceleration peak will be shifted to a higher speed. We thus note that the acceleration increases quickly and exceeds the intermediate peaks for a speed:

- $v_{80/L} \approx$ 220 km/h ( = 61 m/s)
- $v_{65/L} \approx$ 180 km/h ( = 50 m/s)
- $v_{55/L} \approx$ 150 km/h ( = 42 m/s)

It's worth to highlight that for these bridge's frequencies and at these speeds, the critical distance $d_{critical}$ is similar and determined by :

$$d_{critical} = \frac{v}{F} = \frac{61}{80/L} \approx \frac{50}{65/L} \approx \frac{42}{55/L} = 0{,}76L \tag{14}$$

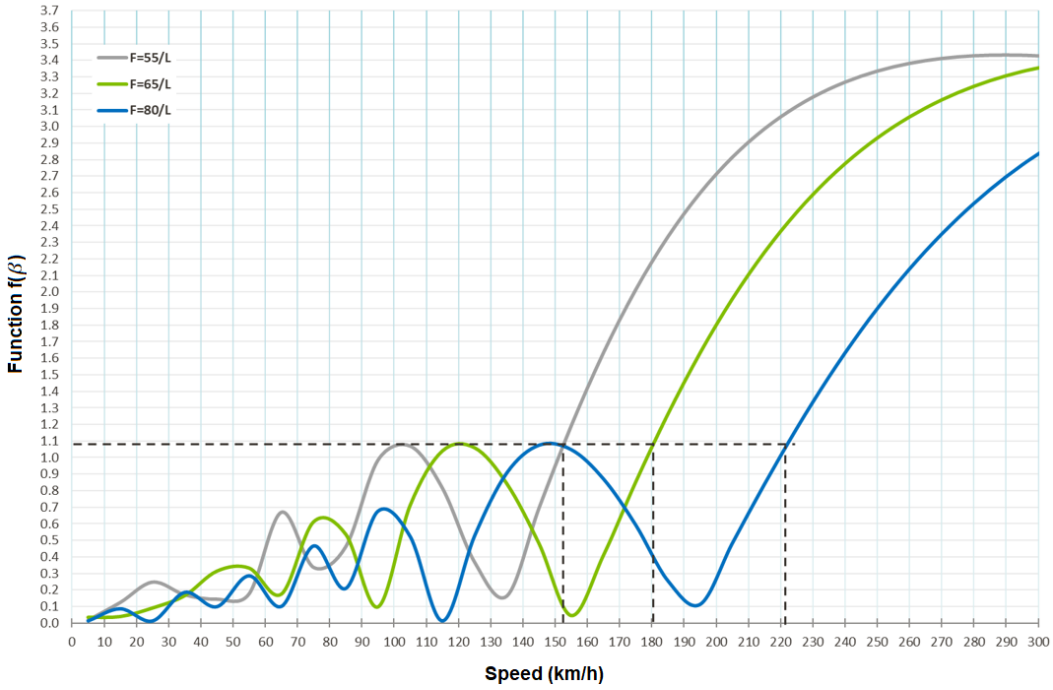


Figure 4: Acceleration of beam in function of the speed for different 1st frequency

The offset of this "limit" speed from which the acceleration under a single load increasing greatly is proportional to the frequency ratio because they occur at the same value of $d_{critical}$. It is possible to deduce for any frequency law the value of the limit speed from which the accelerations under a single load increase critically. It is also noted that the maximum of the function *f(β)* is approximately 1.07 when the speed of the mobile load remains lower than the limit speed determined for each natural frequency law.

In another hand, the intermediate peak is reached when $\beta$ is reaches 1/4 corresponding to the maximum of the $cos(\pi/2\beta)$ function (equation (10)). For any frequency law, we can thus determine the speed of the intermediate peak and the value of the associated critical distance between 2 loads:

$$\beta = \frac{v}{2LF} = 1/4 \rightarrow v \simeq \frac{LF}{2} \rightarrow d_{critical} = L/2 \quad (14)$$

We thus find the critical speed for the intermediate peak for the 3 laws studied, for example with $F = 80/L$

$$v \simeq \frac{LF}{2} = \frac{L \times 80/L}{2} = 40\ (m/s^2) \quad (15)$$

- $v_{80/L}$ = 40 m/s ≈145 km/h
- $v_{65/L}$ = 32,5 m/s ≈120 km/h
- $v_{55/L}$ = 27,5 m/s ≈100 km/h

The minimum law of *55/L* corresponds to a static design of the bridges. The *80/L* law corresponds to a design for speeds up to 200km/h.

# 4 VALIDATION AND APPLICATIONS IN COMPATIBILITY CHECKS

## 4.1 Comparison with numerical modeling

To illustrate this spectral approach, take the example of the 20m span bridge. The figure 5 shows the variation of the acceleration in m/s² at mid-span of a bridge according to the speed of a moving load of 200KN. The graphs are given in free and forced oscillation (when the load is on the bridge) according to the analytical method and by using of a numerical simulation software. This bridge respects the natural frequency law F=80/L and has the linear mass of 18370kg/ml and a damping of 1,8%.

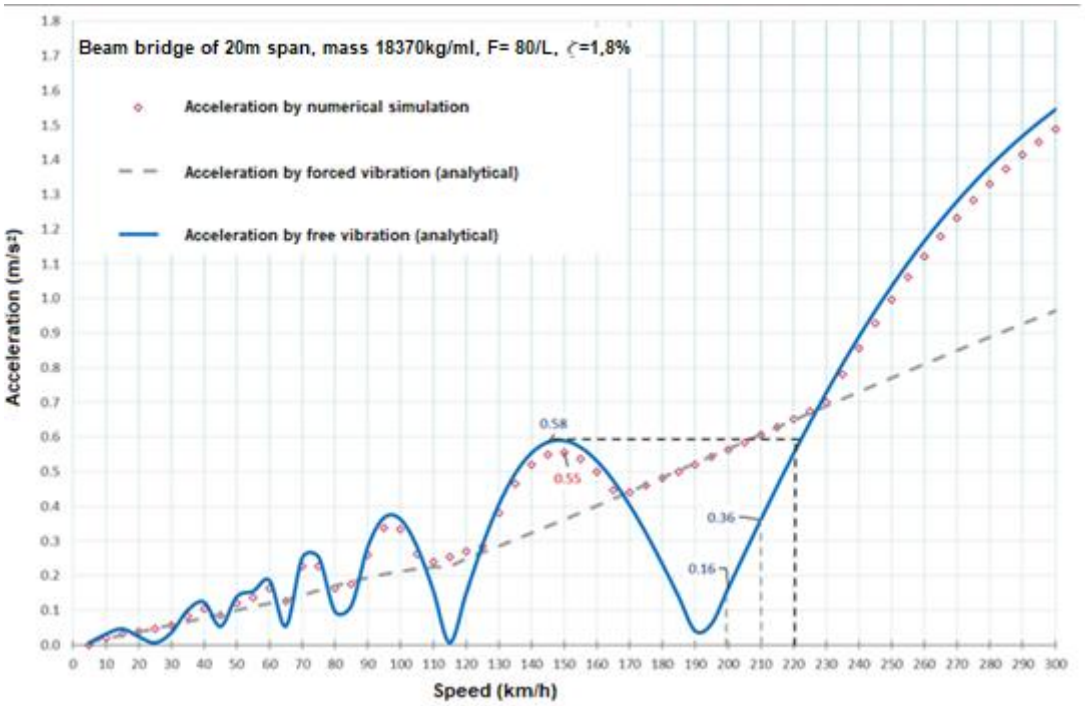


Figure 5: Comparison of acceleration in function of speed of bridge

The analysis 5 allows us to identify the speed range at risk which is indeed above 220km/h because the accelerations increase sharply over this speed. In the same way, the speed limits for the other frequency laws have also been adjusted.

The analytical solution without damping is very close to numerical simulations carried out with a damping of 1.8%. The influence of damping on the first load crossed the bridge is low, and this can be taken into account by a reducing factor $e^{-\zeta\pi/2\beta}$ (further demonstrations in [7]). With this value of damping, the coefficient $f(\beta)x\ e^{-\zeta\pi/2\beta}$ is approximately equal to 1. By using of the analytical formula, the maximum value of the acceleration for a speed not exceeding 220 km/h (speed limit for a frequency law F=80/L) can be found.

$$\ddot{U}max(v < 220km/h) = -200.10^3/(18370\text{x}20)\text{x}1.07 = -0.58 \text{ with } \zeta=0 \qquad (16)$$

$$\ddot{U}max\ (v < 220km/h) = -200.10^3/(18370\text{x}20)\text{x}1.0 = -0.54 \text{ with } \zeta=1{,}8\% \qquad (17)$$

The value of the acceleration obtained with the numerical simulation is 0.55 m/s², for an analytical value of 0.54m/s², meaning an approximately of 2%. The spectral method has a suitable estimation of acceleration and more accurate to deal with a high number of bridges of the network.

### 4.2 Repetitive axle loads

For the same bridge of 20m span, we can determine the maximum response for 200KN repetitive loads. For a damping of 1,8%, at resonance, the coefficient $R_{\zeta,n}$ is limited to 9,2 (see Figure 3). The maximum acceleration obtained is therefore 0,54×9,2≈5m/s² . This value of acceleration at 220km/h appears while distance between 2 consecutive axles of the rolling stock reaches *0,76L* (equation 14), so 15,2m. This distance can be found among the rolling stock which are authorized to operate in French network up to 200 km/h [8]. This peak is too high, the traffic speed for bridges with a natural frequency of 80/L will be reduced to 210km/h or 200km/h with a safety margin. Thus for a speed of 200km/h the acceleration will be limited to 1.5m/s2 (= 9,2×0,16m/s$^2$) or at 210km/h to 3,3m/s² (= 9,2×0,36m/s$^2$) (see Figure 5).

Focus now into the intermediate acceleration peak at $\beta=1/4$ occurs at the speed around 145km/h *(F=80/L)* which exited by the critical distance $d_{critical} = L/2$ = 10m (see equation 14). However, this distance between axles 10m doesn't correspond to any train authorized to run up to 145km/h. The rolling stock having this distance is actually limited to 100km/h on the network. Therefore, for this intermediate peak, the calculation must be carried out for a critical distance of 20m to cover the case in which the bridge's frequency is double of load frequency (see section 2.4)

$$F = \frac{2v}{d_{critical}} \rightarrow d_{critical} = L \tag{18}$$

The acceleration obtained is 0,54m/s² ×4,9 ≈2,65 m/s² because of maximum value of $R_{2\zeta,\nu=}\frac{\left(1-e^{-4\pi\zeta n}\right)}{\left(1-e^{-4\pi\zeta}\right)}$ is 4,9.

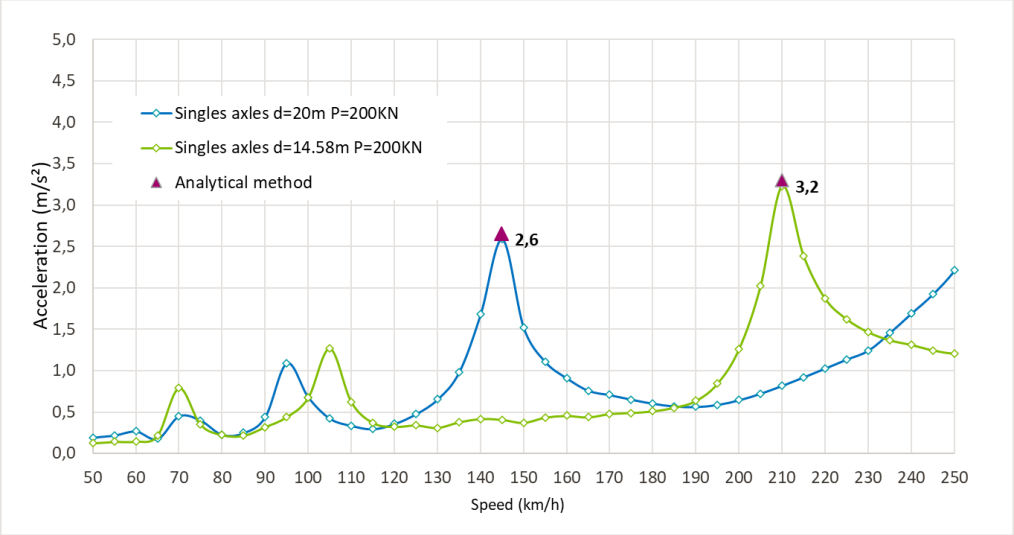


Figure 6: Validation of analytical method

The figure 6 illustrates the comparison between the analytical method and the results of the numerical calculations for the speeds of 210km/h and 145km/h (intermediate peak). We note that the results obtained with the analytical method are very similar with less than 3% deviation. However, the gain in time and simplicity is higher for the analytical approach. Because using of numerical method, for each speed, a vehicle must be modeled in order to evolve the distance between the axles in order to determine the resonance.

## 5 CONCLUSIONS

This spectral method has allowed to identify the main parameters that lead the dynamic response of bridges under repetitive loads. Speed limits and critical distances between repetitive axles have been defined for each railway bridge according to its natural frequency law. By using this approach to assess the existing bridges of the SNCF network for which the main characteristics as type, span and slenderness are known, numerous parametric studies are performed to figure out the sensible bridges. Among all bridges, 12000 bridges (80% of the national network) were validated without further dynamic calculations [8]. 3000 bridges were identified as having a dynamic risk under to the new rolling stock. For these bridges, traffic speed must be lower or equal to the limit speed corresponding to their natural frequency law. These 3000 bridges were consequently notified in the SNCF RESEAU infrastructure register (RINF) and will require specific controls by the railway undertakings.

## REFERENCES

[1] Directive (EU) 2016/797 of the European Parliament and of the Council on The interoperability of the rail system within the European Union. Mai 11, 2016.

[2] International Union of Railway UIC, Loads to be considered in railway bridge design. *UIC leaflet 776-R1*, 1979.

[3] International Union of Railway UIC, Classification of lines, Resulting load limits for wagons. *UIC leaflet 700*, 10th edition, November 2004.

[4] European Committee for Standardisation, F01-528, NF EN 15528, Railway applications - Line categories for managing the interface between load limits of vehicles and infrastructure, 2021

[5] L. Frýba, Dynamics of Railway Bridges, *Thomas Thelford Services*, Prague 1996

[6] E. Savin, Dynamic amplification factor and response spectrum for the evaluation of vibrations of beams under successive moving, *Journal of Sound and Vibration, Volume 248, Issue 2*, pp. 267-288, November 2001

[7] M. Gaio Resende, M. Ragueneau, Q. Jungers, Overhaul of the European normative interface to check dynamic compatibility of rolling stock with existing railway bridges, *The 12th World Congress on Railway Research*, Tokyo, November 2019

[8] M. Ragueneau, Procedures for compatibility check of vehicles with the railway bridges of SNCF network, *SNCF Procedure*, 2021

COMPDYN 2023
9th ECCOMAS Thematic Conference on
Computational Methods in Structural Dynamics and Earthquake Engineering
M. Papadrakakis, M. Fragiadakis (eds.)
Athens, Greece, 12-14 June 2023

# DYNAMIC AMPLIFICATION OF TRAFFIC LOADS ON ROAD BRIDGES EVALUATED USING PROBABILISTIC TRAFFIC SIMULATIONS

**Marian Ralbovsky[1], Maciej Kwapisz[1], Alois Vorwagner[1] and Stefan Lachinger[1]**

[1] AIT Austrian Institute of Technology
Center for Low-Emission Transport
Giefinggasse 4, 1210 Vienna, Austria
{marian.ralbovsky, maciej.kwapisz, alois.vorwagner, stefan.lachinger}@ait.ac.at

## Abstract

*The traffic loads on road bridges undergo long-term changes as the transport requirements and vehicle technologies develop over time. The current traffic load models of Eurocode were developed decades ago. With the growing database of available axle-load measurements, a re-evaluation seems technically possible. However, dynamic amplification factors need to be determined additionally to the quasi-static load effects.*
*The presented work is based on calculating the effects of simulated traffic flows on a set of chosen bridges. The traffic was generated using probabilistic traffic simulations, which consider different traffic intensities and a combination of probabilistic and deterministic traffic/vehicle parameters. In this work, 20 years of traffic flow was generated and applied on chosen simple bridge models of single-span bridges with spans ranging from 15 to 120 m. Dynamic Amplification Factors were calculated for all significant traffic events.*
*The results showed that DAF has a decreasing tendency with increasing quasi-static load effects, which was also observed in previous evaluations from monitoring data. Further observed tendencies were decreasing DAF with increasing span length and increasing DAF with decreasing bridge mass per unit length.*

**Keywords:** Road bridge, Dynamic amplification, Traffic simulation, Axle loads, DAF.

# 1 INTRODUCTION

The amplification of traffic-induced loads on road bridges occurs due to dynamic effects of the coupled bridge-vehicle system. The amplitude of the amplification is influenced by the vehicle dynamics, road roughness profile and most prominently by dynamic bridge properties and its resonance behavior. Unlike for railway bridges, the Eurocode [1] does not specify the values of the dynamic amplification on road bridges. Instead, the dynamic effects are already included in the load models for the ULS (Ultimate Limit State), which were established assuming medium pavement quality (road surface class C in [1], Annex B) and a pneumatic vehicle suspension. In case of fatigue load models, the Eurocode assumes pavement of good quality (road surface class B) for dynamic effects that are included in the load models and specifies an additional dynamic amplification factor $\Delta\varphi_{fat}$ to be taken into account near expansion joints. This additional factor reaches values up to 1.3 (at the joint) but diminishes quickly to value of 1.0 at 6 m distance from the joint.

In the last 10-20 years, the amount of available data on actual traffic loads increased significantly due to installation and operation of Weigh-In-Motion (WIM) systems, which measure axle loads and distances in flowing traffic at different locations across Europe. The new data cluster gives an opportunity for new evaluations of road traffic models. Further, future traffic scenarios are being considered. For example, the EU-project LEVITATE investigated the effects of automated driving. Among other aspects, the impacts of truck platooning on bridges were analyzed [2]. These new evaluations, which primarily concentrate on quasi-static load effects, need to additionally consider also the dynamic amplification of traffic loads.

For this purpose, the Dynamic Amplification Factor (DAF) is a widely used quantity. The DAF for a quantity X (which can be for example bending moment, shear force, stress) is defined as the ratio of the maximum of total response $X_{tot}$ and the maximum of quasi-static response $X_{stat}$ (1).

$$DAF(X) = \frac{max(X_{tot})}{max(X_{stat})} \tag{1}$$

It was observed, both in measurements and in simulation results, that the value of DAF has decreasing trend with increasing gross weight of passing vehicles. Kalin et.al. [3] presented evaluation of the DAF at different percentiles of the occurring vehicle weights on Slovenian motorways and state roads, as well as on US highways. In here, the linear regression of $DAF_p$ curves resulted in approx. halving of the value of DAF when comparing DAF at maximum recorded loading to mean DAF.

The evaluation of the DAF from measurements is often possible using simple signal-processing techniques, which filter-out the dynamic components. Figure 1 shows an evaluation of DAF from strain measurements acquired on an Austrian highway bridge. The strain gauge was placed in midspan of a concrete box-girder bridge with multiple spans. The figure displays data from more than 1 year of continuous monitoring, and each dot represents an evaluated DAF from one traffic event. In here, the weight of the passing vehicles was not evaluated, thus the horizontal axis represents the amplitude of the measured quasi-static strain (peak-to-peak) instead, which is a direct effect of axle weights on the bridge. The decreasing trend of the DAF is also here apparent.

The fact that values of DAF are lower for traffic events with high quasi-static load is beneficial for the evaluation of total load extremes.

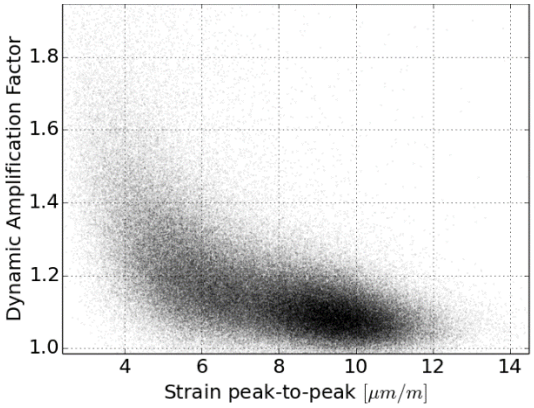


Figure 1: DAF of strain in midspan evaluated from measurements at an Austrian highway bridge

O'Brien et.at. [4] argued that the Assessment Dynamic Ratio (ADR) is a more representative quantity than DAF. The ADR is defined as the ratio of characteristic values of the total effect $\tilde{X}_{tot}$ and of the quasi-static effects $\tilde{X}_{stat}$ (2). While DAF can be evaluated for each traffic event separately, the ADR is evaluated only once for the whole traffic flow, because the statistical evaluation is included in the separate evaluations of $\tilde{X}_{tot}$ and $\tilde{X}_{stat}$.

$$ADR(X) = \frac{\tilde{X}_{tot}}{\tilde{X}_{stat}} \tag{2}$$

The research of comparing DAF and ADR was continued by Carey et.al. [5], concluding that ADR is a more reliable value, especially when evaluating extreme values of traffic loads.

The work presented here intends to investigate DAF using numerical simulations. It builds on the traffic load simulations, which were performed during the finished project LEVITATE, and further extended in the currently ongoing project REAL-LAST.

## 2 SIMULATION METHOD AND PARAMETERS

### 2.1 Traffic

Traffic flows were generated using existing traffic simulation algorithms. These result in a simulated sequence of vehicles and include a complete description of the vehicle sequences: vehicle types, their masses and distances, which are then decomposed into axle sequences for each lane. An axle sequence consists of axle forces and their distances. Although the traffic simulation algorithm contains also the formation of congestions, they are not relevant for dynamic amplification evaluations. Therefore, only flowing traffic was analyzed dynamically.

The traffic simulation adopted following assumptions:

- Traffic is a random stationary process and does not evolve over time
- Vehicle speed is constant and all vehicles in one lane share the same speed
- Vehicles do not change lanes while on the bridge
- Most vehicles comply with the prescribed limits of gross vehicle weight; violations of this limit are not excessive
- The distribution of the vehicle amount on a two-lane highway is assumed as 80%-20% until the capacity of the right lane is saturated.

Vehicle properties (Figure 2) as well as traffic composition (Table 1) were adopted from [6]. The traffic flows consists of personal cars and 5 truck types. The right lane is occupied by trucks

only, simulating an inter-city highway traffic. The truck types include two 5-axle trucks (types 41 & 98), two 4-axle trucks (types 33 & 97) and one 2-axle truck (type 8). Special vehicles, like a crane vehicle (mass of which is displayed in Figure 2 left) were not considered in the modelled traffic mix.

| Lane | Type 8 | Type 33 | Type 41 | Type 97 | Type 98 | Cars |
|---|---|---|---|---|---|---|
| Right | 11 % | 5 % | 17 % | 8 % | 59 % | 0 % |
| Left | 2.20 % | 1 % | 3.40 % | 1.60 % | 11.80 % | 80 % |

Table 1: Traffic composition

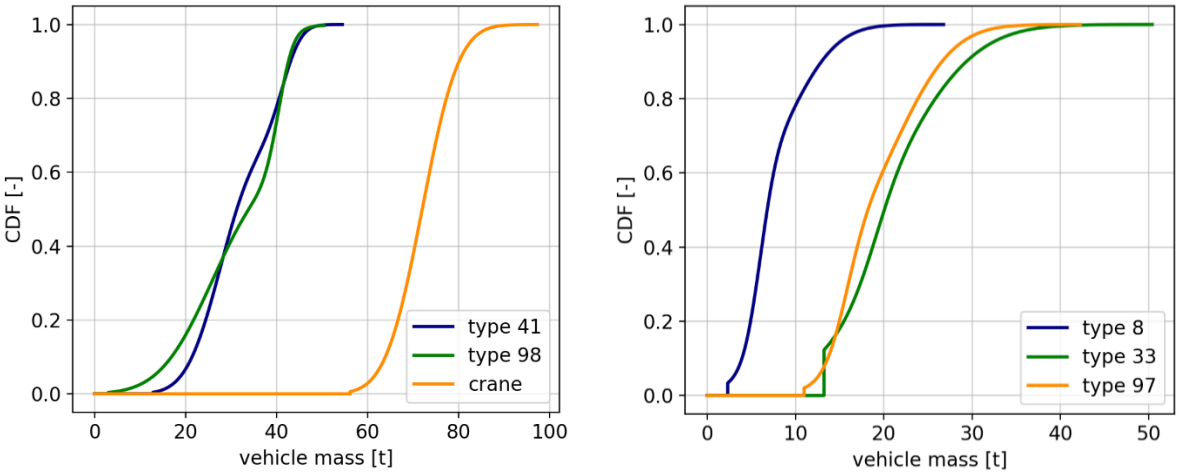


Figure 2: Cumulative distributions of gross vehicle masses for simulated truck types

The traffic was modelled to have two lanes. The generation of vehicle sequence is a random process with the above listed properties. Axle distances as well as the distribution of total vehicle weight to individual axles were assumed to be constant for each vehicle type. These vehicle properties were also adopted from [6].

Different traffic situations were simulated, with traffic volumes ranging from 12.000 vehicles/day to 120.000 vehicles/day. The initial assumption of having 80% of the vehicles in the right lane could be sustained up to a traffic volume of 38.000 vehicles/day. At this point, the right lane became saturated and part of the vehicles from right lane were assumed to start switching to the left lane, thus gradually changing composition of the left lane with increasing traffic volume.

The vehicle distances followed a lognormal distribution. The shape and scale of the distribution was fitted to match the modelled traffic volume, assuming a vehicle speed of 80 km/h.

In total, 20 years of traffic was generated.

## 2.2 Bridges

The population of simulated bridges consisted of 35 bridges, properties of which are listed in Table 2. The bridge set includes most common bridge types: reinforced-concrete slab, prestressed-concrete T-beam, prestressed-concrete box-girder, composite bridge with welded steel girders, composite bridge with steel box-girders, steel girder bridge with orthotropic deck, and steel box-girder bridge. The cross-section dimensions were estimated based on common construction and dimensioning rules. All bridges were assumed to carry a two-lane highway, thus the deck width was modelled with 10.5 m.

| Bridge type | Span [m] | μ [t/m] | $f_0$ [Hz] | Bridge type | Span [m] | μ [t/m] | $f_0$ [Hz] |
|---|---|---|---|---|---|---|---|
| RC slab | 15 | 29.4 | 5.65 | Comp.girder | 30 | 11.6 | 2.7 |
| RC slab | 15 | 22.8 | 4.17 | Comp.girder | 35 | 11.8 | 2.4 |
| RC slab | 20 | 38.2 | 4.3 | Comp.girder | 40 | 12 | 2.15 |
| RC slab | 20 | 29.4 | 3.18 | Comp.girder | 50 | 12.5 | 1.8 |
| PC T-beam | 20 | 16.8 | 5.83 | Comp.box-girder | 40 | 13.4 | 2.05 |
| PC T-beam | 20 | 14.9 | 3.77 | Comp.box-girder | 50 | 14 | 1.75 |
| PC T-beam | 25 | 19.2 | 4.78 | Comp.box-girder | 60 | 14.5 | 1.52 |
| PC T-beam | 25 | 16.7 | 3.17 | Comp.box-girder | 70 | 15 | 1.35 |
| PC T-beam | 30 | 21.6 | 4.04 | Steel girder | 35 | 6.1 | 2.61 |
| PC T-beam | 30 | 18.4 | 2.72 | Steel girder | 40 | 6.3 | 2.4 |
| PC T-beam | 35 | 24 | 3.49 | Steel girder | 50 | 6.6 | 2.08 |
| PC T-beam | 35 | 20.1 | 2.38 | Steel girder | 60 | 6.9 | 1.84 |
| PC T-beam | 40 | 26.4 | 3.07 | Steel box-girder | 70 | 7 | 1.73 |
| PC T-beam | 40 | 21.9 | 2.1 | Steel box-girder | 90 | 7.7 | 1.44 |
| PC box-girder | 40 | 21.1 | 3.2 | Steel box-girder | 120 | 9 | 1.14 |
| PC box-girder | 50 | 23.7 | 2.57 | | | | |
| PC box-girder | 60 | 26.8 | 2.12 | | | | |
| PC box-girder | 70 | 30.4 | 1.8 | | | | |
| PC box-girder | 90 | 37.1 | 1.38 | | | | |

Table 2: Basic properties of simulated bridges

Due to large amount of performed simulations, a simple bridge model was required in order to keep the calculation performant. Therefore, bridges were simulated as simply-supported single-span beams, effectively neglecting torsional effects of the two-lane traffic. Multi-span bridges are expected to produce lower dynamic amplifications, therefore this assumption is deemed to be conservative.

### 2.3 Calculation

The calculation was carried out by means of transient dynamic analysis using the mode superposition method. The traffic loads were modeled as moving axle forces. The analysis does not contain any vehicle dynamics, nor effects of road roughness. Each axle force is constant in time. Therefore, the dynamic behavior arises solely from the bridge structure.

To reduce the computational effort, the traffic flow was filtered for the largest traffic events. First, a quasi-static simulation was performed and for each month of traffic, 100 traffic events that produced the highest quasi-static bridge response were selected. This was done separately for the midspan bending moment and the shear force at the abutment. The selected traffic events were then used for transient dynamic analysis.

## 3 RESULTS

The results of the simulations were processed and DAF-value was evaluated for each traffic event. The DAF was evaluated separately for bending moment and shear force. In the next step, DAF-values of different quantiles were determined. In here, quantiles of 95%, 99% and 100% (the maximum) were evaluated from a group of traffic events. In order to capture the dependance between DAF and the magnitude of quasi-static load effects, the traffic events were first divided into 5 clusters based on the magnitude of quasi-static load effect. The cluster boundaries

were chosen on the basis of cluster size, with diminishing cluster size towards the high loading events. An example for one bridge is displayed in Figure 3, where the magnitude of quasi-static response is plotted on horizontal axis. $M_{q,st}/M_{Q,k}$ is the ratio between peak quasi-static bending moment during one traffic event to the bending moment due to load model LM1. Similarly, $V_{q,st}/V_{Q,k}$ is the ratio of peak shear force to the code-value. The green areas represent the magnitude of 95%-, 99%- and 100% DAF-quantiles of the respective cluster of simulated traffic events. In this example, which shows calculations on a reinforced-concrete slab with 15 m span, DAF-values in the highest cluster ($X_{q,st}/X_{Q,k} > 0.63$) reach values of $DAF_{95\%} = 1.082$ for bending moment and $DAF_{95\%} = 1.044$ for the shear force.

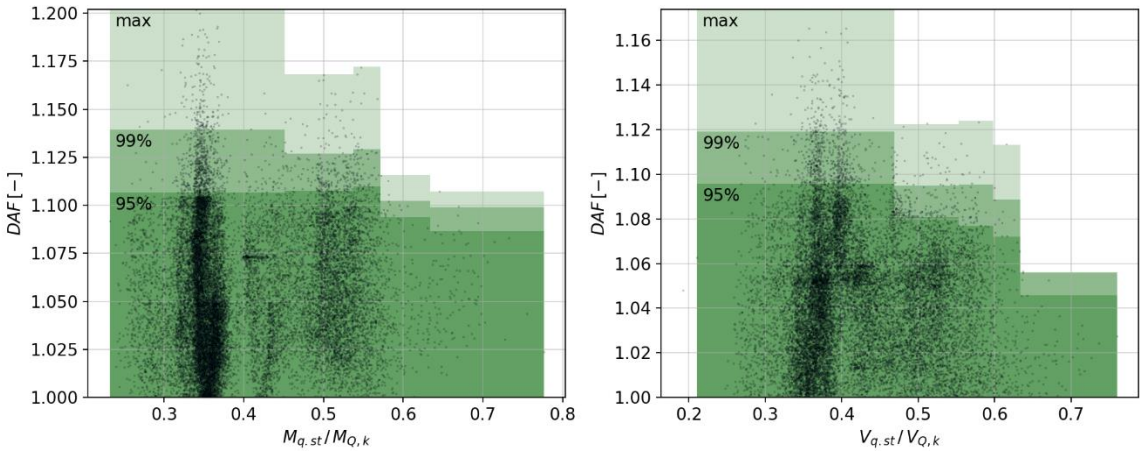


Figure 3: DAFs of traffic events on RC slab with 15 m span, μ=22.8 t/m, $f_0$=4.2 Hz. Bending moment (left) and shear force (right).

Figure 4 shows a similar evaluation on a composite bridge with welded steel girders with 50 m span. In here, the DAF-values in the highest cluster reach values of $DAF_{95\%} = 1.049$ for bending moment and $DAF_{95\%} = 1.04$ for the shear force.

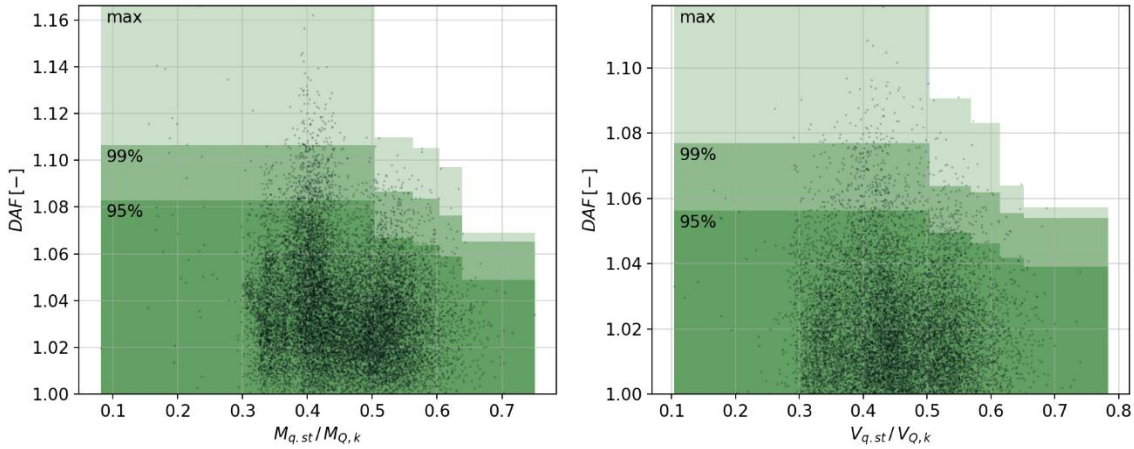


Figure 4: DAFs of traffic events on composite bridge with welded steel girders with 50 m span, μ=12.5 t/m, $f_0$=1.8 Hz. Bending moment (left) and shear force (right).

The lowest DAF values were achieved on long-span bridges. Figure 5 shows an evaluation on a steel box-girder bridge with 90 m span. In here, the DAF-values in the highest cluster reached values of $DAF_{95\%} = 1.021$ for bending moment and $DAF_{95\%} = 1.014$ for the shear force.

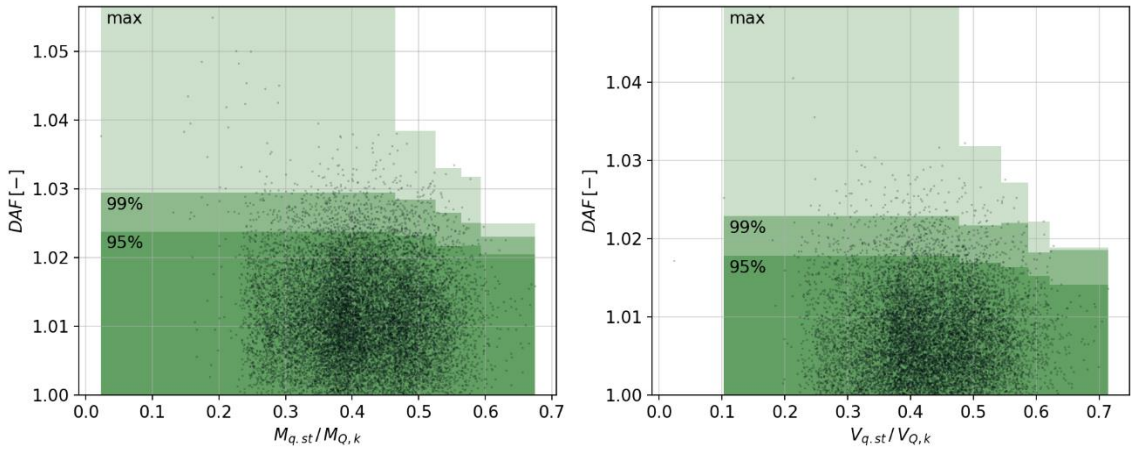


Figure 5: DAFs of traffic events on steel box-girder bridge with 90 m span, μ=7.7 t/m, $f_0$=1.4 Hz. Bending moment (left) and shear force (right).

A question that is not answered in this work is, which cluster of traffic events should be used and using which percentile of DAF-values of this cluster. The following figures show a different type of evaluation, which is considered to be a possible option for the choice of representative DAF-value. On the horizontal axis, portion of vehicles included in the evaluation is displayed. The vehicles are sorted by magnitude of the quasi-static bridge response, which means that for example in the portion of 0.001% (=$10^{-5}$), the highest 0.001% of all traffic events are included, in terms of the quasi-static bridge response. On the vertical axis, the maximum DAF (100%-quantile) within the respective group of events is plotted. The resulting curves show a step-wise characteristic, which is a natural consequence of evaluating the maxima of data with consecutively increasing group size. Figure 6 shows results of the same DAF-values that are also displayed in Figure 3.

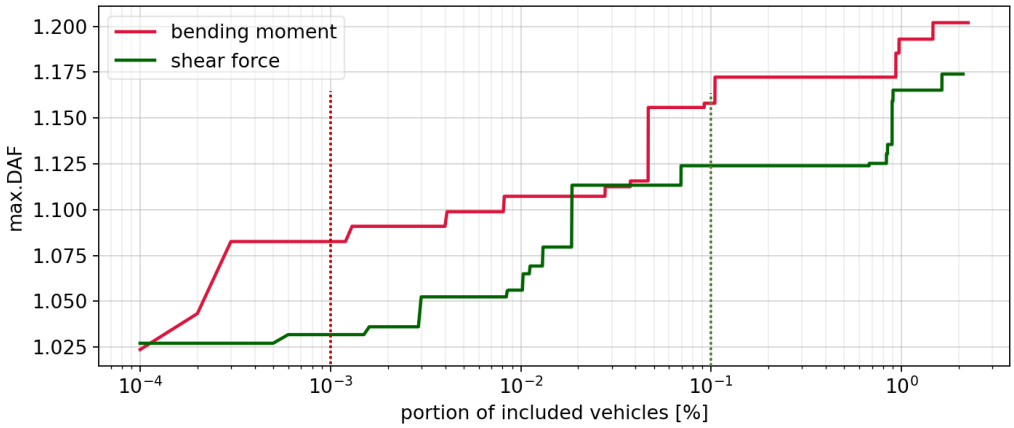


Figure 6: Maximum DAFs of traffic events on RC slab with 15 m span, μ=22.8 t/m, $f_0$=4.2 Hz with consecutively increasing size of traffic events group.

Figure 7 shows a similar evaluation of results on a steel bridge, which are also displayed in different form in Figure 5. In Figure 6 and Figure 7, two vertical dotted lines (one red, one green) are plotted. These mark the portions of vehicles, which were chosen for the results displayed in Figure 8. The red dotted line represents the portion of vehicles of q=$10^{-5}$; the green dotted line the portion of vehicles of q=0.001. These results are plotted in Figure 8 using red and green marks, respectively.

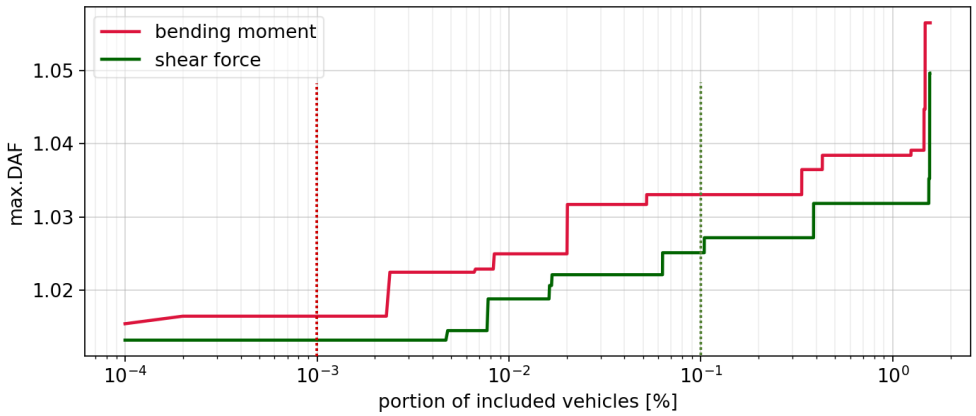


Figure 7: Maximum DAFs of traffic events on steel box-girder bridge with 90 m span, μ=7.7 t/m, $f_0$=1.4 Hz with consecutively increasing size of traffic events group.

Figure 8 summarizes results of evaluated maximum DAFs on all investigated bridges, using the portion of included vehicles of q=$10^{-5}$ and q=0.001.

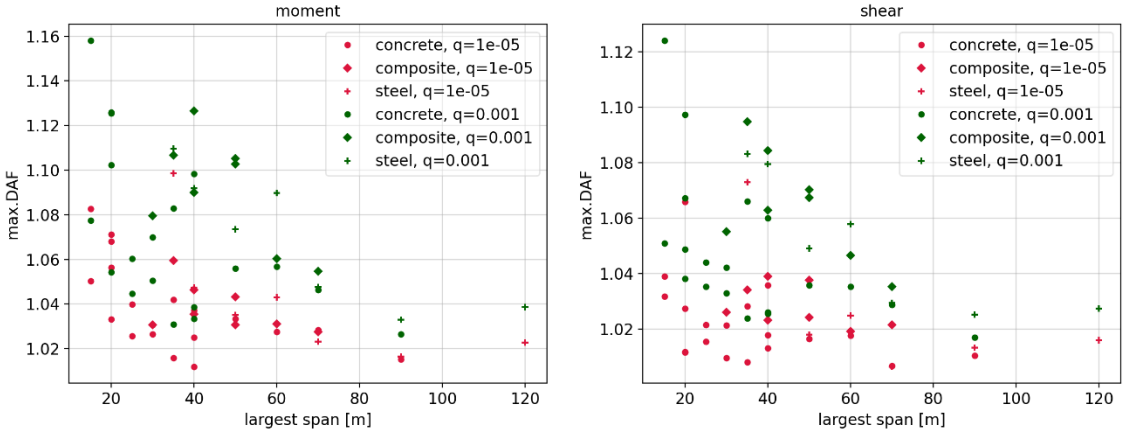


Figure 8: Maximum DAFs of traffic events on all investigated bridges, evaluated at portions of included vehicles of q=$10^{-5}$ and q=0.001.

## 4 CONCLUSION

This paper presented results of dynamic amplification factors (DAFs) calculated on a chosen set of bridges, using simulated traffic flows that encompass 20 years of operation. Comparison of the resulting DAFs confirm results of other research works in that the DAF decreases with increasing magnitude of the quasi-static load effect. Further dependencies that were observed are the decrease of DAF-values with increasing span length, and the general tendency for higher DAF-values on lighter bridges (e.g. steel compared to composite and concrete bridges).

The resulting DAFs were evaluated for different quantiles of traffic events sorted by their quasi-static magnitude. A question that remains unanswered in this work is, which quantile should be chosen for the representative DAF value. This will be a topic in continuation of this research, where further statistical evaluations are planned, as well as the comparison of the evaluated DAFs to the Assessment Dynamic Ratios (ADRs), which were proposed by other research groups.

## ACKNOWLEDGEMENTS

Authors thankfully acknowledge the funding of research projects LEVITATE within Horizon 2020 research and innovation programme under grant agreement No 824361; and research project REAL-LAST funded by FFG within Mobility of Future, project No FO999889387, which made this work possible.

## REFERENCES

[1] European Committee for Standardization, EN 1991-2, Actions on structures – Part 2: Traffic loads on bridges, 2012.

[2] B. Hu, G. Brandstätter, M. Ralbovsky, M. Kwapisz, A. Vorwagner, R.d. Zwart, C. Mons, W. Weijermars, J. Roussou, M. Oikonomou, Ziakopoulos, A. Chaudhry, S. Sha, R. Haouari, H.C. Boghani, Medium-term impacts of cooperative, connected, and automated mobility on freight transport, *Deliverable D7.3 of the H2020 project LEVITATE*, 2021.

[3] J. Kalin, A. Žnidarič, A. Anžlin, M. Kreslin, Measurements of bridge dynamic amplification factor using bridge weigh-in-motion data. *Structure and Infrastructure Engineering, p.1164-1176,* 2022.

[4] E.J. O'Brien, D. Cantero, B. Enright, A. González, Characteristic Dynamic Increment for extreme traffic loading events on short and medium span highway bridges. *Engineering Structures 32*, p. 3827–3835, 2010.

[5] C. Carey, E.J. O'Brien, A. Malekjafarian, M. Lydon, S. Taylor, Direct field measurement of the dynamic amplification in a bridge. *Mechanical Systems and Signal Processing 85*, p. 601–609, 2017.

[6] U. Freundt, S. Böning, et.al.: Anpassung von DIN-Fachberichten „Brücken" an Eurocodes (Adaptation of DIN technical reports "Bridges" to Eurocodes), *Berichte der Bundesanstalt für Straßenwesen (Reports of the Federal Highway Research Institute), Brücken- und Ingenieurbau Heft B 77 (Bridges and Engineering Construction issue B 77)*, ISBN 978-3-86918-108-0, Bergisch Gladbach, Germany, 2011.

COMPDYN 2023
9th ECCOMAS Thematic Conference on
Computational Methods in Structural Dynamics and Earthquake Engineering
M. Papadrakakis, M. Fragiadakis (eds.)
Athens, Greece, 12-14 June 2023

# IMPROVING RELIABILITY OF UZBEKISTAN'S TRANSPORT INFRASTRUCTURE FACILITIES UNDER IMPACT OF NATURAL HAZARDS BY ANALYSIS OF ITS VULNERABILITY, MONITORING AND MODELING

**Ulugbek Z. Shermukhamedov[1], Zukhritdin Z. Ergashev[1], Shakhzod M. Takhirov[2], and Abdurakhim A. Abdullaev[1]**

[1] Tashkent State Transport University: Tashkent, Uzbekistan
e-mail: ulugbeksermuxamedov@gmail.com
ergashev33@gmail.com
abdurahim4095@gmail.com

[2] University of California, Berkeley: Berkeley, California, USA
e-mail: takhirov@berkeley.edu

## Abstract

*The paper is focused on the analysis of the vulnerability of the transportation infrastructure of Uzbekistan based on monitoring and modeling. The paper provides detailed information about the railroads and railway bridges of Uzbekistan. It also summarizes major natural hazards, the impact of which can lead to failures of the transportation infrastructure. The paper aimed at improving the performance of railroads and railway bridges based on comprehensive monitoring, subsequent modeling, and predictions of performance. An example of the application of seismic protection for bridge design in Uzbekistan is discussed. The bridge was recently constructed in an area with a seismic intensity of 9 on the MSK scale. Both damping and bearing systems were used in the design and construction of the bridge. Due to the damping effect, it was possible to reduce the seismic forces in the piers. At the same time, the rigidity of the connection between the superstructure and the pier has increased. This is critical for railway bridges in ensuring small relative displacements as opposed to regular seismic isolation systems.*

**Keywords:** transport infrastructure facilities, natural hazards, vulnerability, railway bridge, earthquake engineering, seismic isolation, damping device.

## INTRODUCTION

A railway transportation infrastructure can be impacted by many natural hazards including but not limited to earthquakes, landslides, snowfalls, cave-ins, avalanches, mudflows, tsunamis, liquefaction, soil settlement, massive snowfalls, and many others. The consequences of train failures can be devastating and in the case of passenger trains, can lead to loss of life. For freight trains, failures can lead to significant environmental issues depending on the train's payload of the freight trains, as occurred in the recent train derailment in Ohio, USA [1]. Less severe natural disasters and hazards can lead to an interruption of transport services for the population and the economy, which results in productivity and monetary losses. Hence, continuous monitoring, modeling, and predictions of the railway infrastructure's performance under the impact of various natural hazards are important for ensuring the resiliency of the transportation network. The importance of this problem for Uzbekistan cannot be overestimated. Uzbekistan is one of only two doubly landlocked countries in the world. Hence, the resiliency of the railway infrastructure is a high priority. To mitigate the risk of failures, Uzbekistan focuses its attention on studying the vulnerability of the transport infrastructure under the impact of natural hazards during the design, construction, and usage phases.

## STATE OF UZBEKISTAN'S RAILWAY INFRASTRUCTURE

Railway passenger and freight transportation are one of the highest priorities in the transport sector worldwide. Railways play a significant role in ensuring international trade and economic relationships. Since all countries of Central Asia are landlocked, the railways have a significant effect on the international trade among these countries [2, 3].

The overall length of the railway track in countries of Central Asia is more than 26,185 thousand km, the density of the network is equal to 6.53 km/km$^2$. By using a number of countries, S.P. Pershin [4] introduced an empiric relationship between the railway network density and the country's overall area:

$$G_c = (\mathbf{23} + \mathbf{3,5} * \boldsymbol{S})/\boldsymbol{S} \quad (1)$$

where S is the country's overall area measured in millions of km$^2$.

For example, in Belarus this density is five times greater than that of Central Asia. In the case of Latvia the density is seven times greater than that of Central Asia. The low density of the railways is evidence of a significant lag in the development of the railway network. This lag is one of the reasons for the delay in growth of the region's wealth.

Table 1 shows the density of the railroad network of the Central Asian countries.

| № | Country | Area of the territory, S mln. km$^2$ | Operational length of railroads, L, thousand km | Density of the rail network | | $G_{cc}$ / $G_{ca}$ |
|---|---|---|---|---|---|---|
| | | | | Actual, $G_{cf}$ | Calculated, $G_{cc}$ | |
| 1 | Uzbekistan | 0,449 | 4,64 | 10,33 | 54,72 | 5,30 |
| 2 | Kazakhstan | 2,725 | 16,61 | 6,10 | 11,94 | 1,96 |
| 3 | Kyrgyzstan | 0,1999 | 0,424 | 2,12 | 118,56 | 55,90 |
| 4 | Tajikistan | 0,143 | 0,96 | 6,71 | 164,34 | 24,48 |
| 5 | Turkmenistan | 0,491 | 3,551 | 7,23 | 50,34 | 6,96 |
| | Central Asia | 4,008 | 26,185 | 6,53 | 9,24 | 1,41 |

Table 1. The density of the railroad network in the countries of Central Asia

Various engineering structures (ES) are being constructed on the railways of Central Asia, most of which are bridges. A large number of ES is located in seismically hazardous areas of Central Asia [6]. Figure 1 shows the railway network of Central Asia overlayed on a seismic hazard map expressed in earthquake magnitude (MSK scale).

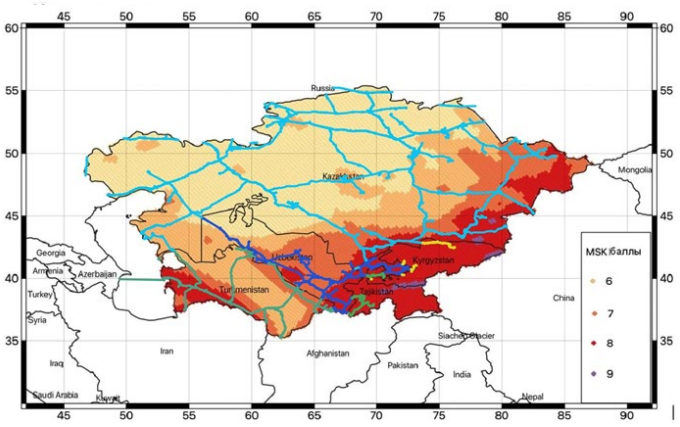


Figure 1. Seismic hazard map of Central Asia with railway network overlay

The railroad network of Uzbekistan is an integral part of the large railway network of the Central Asian countries. In recent years Uzbekistan has built a new railway network with a total length of more than 1,200 km, modernized and reconstructed more than 3,800 km of roads, and electrified almost 1,100 km of railways [3, 5]. Figure 2 shows a map of railways in Uzbekistan.




Figure 2. Map of railroads in Uzbekistan

Table 2 summarizes the railway network of Uzbekistan [5]. As presented in the table, the total length of the railroads is 9,925.8 km, of which 7,420.7 km are for general use.

| № | Indicators | Length, km |
|---|---|---|
| 1 | The total length of railroads | 9,925.8 |
| | of which are for public use | 7,420.7 |
| 2 | Operating length | 4,641.9 |
| 3 | Length of electrified sections | 3,728.6 |
| | of which operational length | 1,646.0 |
| | including high-speed sections | 718.6 |

Table 2. Network of railroads in Uzbekistan

Figure 3 shows a histogram of the development of construction and reconstruction of

railroads in Uzbekistan presented for four time periods. The first time period covers railways constructed from 1888 to 1920 (1,049 km or 17.65% of the total). The second time period covers railways constructed from 1920 to 1950 (1,245 km or 20.95% of the total). The third time period covers railways constructed from 1950 to 1991 (1,278 km or 21.51% of the total). The fourth time period covers railways constructed from 1991 to 2001 (2,370 km or 39.89% of the total) [5].

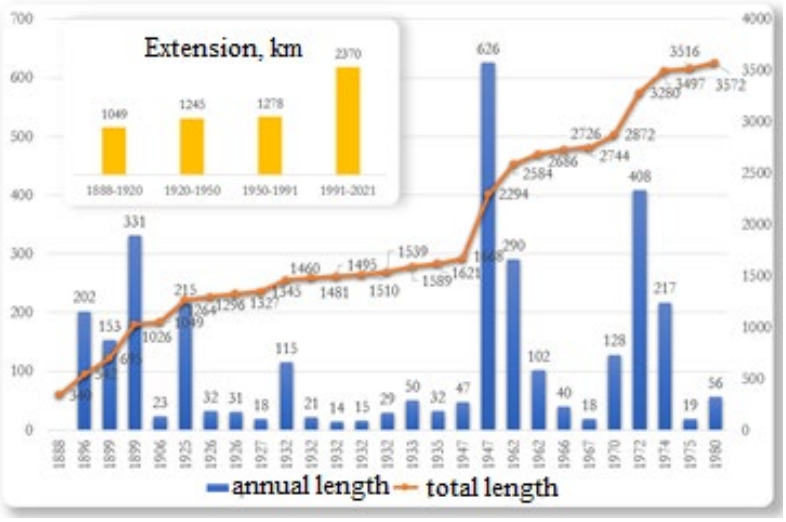


Figure 3. Development of the railroad network in Uzbekistan

As of 2019, there are 1,380 bridges on the main railway lines of Uzbekistan's railway company, Temir Yullari JSC. Of these 1,307 are reinforced concrete bridges, 48 are steel bridges, and 25 are combined or composite bridges. The engineering structures include: railway tunnels (2), pedestrian tunnels (10), footbridges (30), galleries (5), aqueducts (4), pipes (4420) pieces, flumes (386), and culverts (245). The total length of all bridges is approximately 41 km [7, 8]. Table 3 shows engineering structures classified by material and length. Figure 4 presents the same information in a graphical form.

| № | Name | | Quantity, pcs. | Length, p.m. |
|---|---|---|---|---|
| 1 | Total bridges on the main tracks including: | | 1,380 | 39,157 |
| | steel | | 48 | 599 |
| | reinforced concrete | | 1,307 | 30,014 |
| | combined or composite | | 25 | 3,144 |
| 2 | Total reinforced concrete spans | | 2,511 | - |
| Basic schemes of reinforced concrete bridges | | 5 x 6,0 m | 3x16,5 m, 11,5m+23,6m+11,5m | 7x23,6 m, 16,5m+4x23,6m+16,5m |

Table 3. Engineering structures on the railroads of the Republic of Uzbekistan

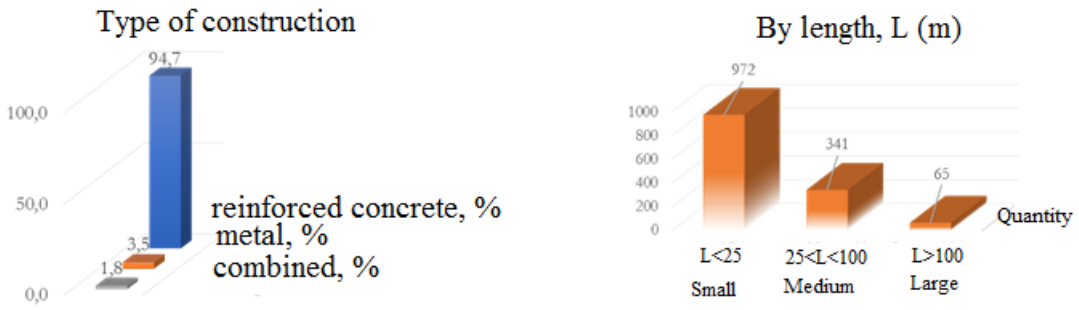


Figure. 4. Classification of engineering structures on the railroads of Uzbekistan

Since 1991, a large number of construction and rehabilitation projects have been conducted for the development of transportation and communication systems. Uzbekistan has ensured the independence of the transportation system and has created a national system linking all of the regions of Uzbekistan. The country's effective transportation system contributes to the development of international economic relations and strengthens integration with neighboring countries.

## VULNERABILITY OF RAILWAY INFRASTRUCTURE DUE TO EARTHQUAKES

Uzbekistan is located in a seismically active region. Thus the issue of seismic protection is relevant [9]. Figure 5 shows a map of the general seismic zoning of the territory of the Republic of Uzbekistan.

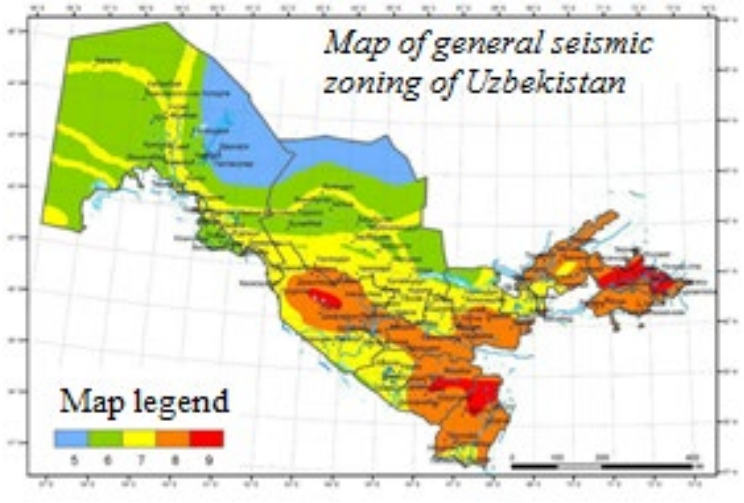


Figure 5. Seismic hazard map of Uzbekistan

Earthquakes are usually caused by tectonic strains in the earth's crust. These strains can accumulate over years. At some point, the tectonic plates slip in respect to each other, resulting in the sudden release of a large amount of strain energy. As a result, seismic waves propagate in all directions. When the waves reach the earth's surface, they cause vibrations in the upper part of the soil layer [10] and thus in all above-ground and underground buildings and structures.

The problem of seismic resistance of bridges and bridge structures is extremely important due to the fact that severe earthquakes can cause damage so they cannot function normally. Depending on the severity of the earthquakes and the construction design bridges can be even

destroyed. The bridges and bridge structures are constructed of many elements, the most important of which are piers and bearing parts [6, 10-12].

In Uzbekistan, there are a few natural hazards (related to earthquakes) that can cause the destruction of bridges. These include the discontinuous tectonic displacement of the crust, seismic ground vibrations, landslides, cave-ins, avalanches, mudflows, liquefaction, soil settlement, and many others.

Based on post-earthquake analysis of several severe earthquakes, a few mitigation measures were developed for incorporation into construction practice in order to improve the seismic stability of buildings and structures [13].

Analysis of various data allows us to distinguish two major groups of damage to bridge structures [11, 13-16]:

– *damage to span structures*: their shift on bridge seats, or falling from supports under relatively minor damage to the support.

– *destruction or severe damage to the supports*: resulting in the complete or partial collapse of the bridge.

Worldwide the field of seismic resistance of bridges is in a process of continuous development because humankind learns from each new earthquake, especially from those similar to the February 6, 2023 earthquake in Turkey [17]. The methods of seismic strengthening of bridges are being added to regulatory documents to ensure the bridges' seismic resistance, durability, and reliability. Uzbekistan is part of this worldwide development although its construction code is slightly lagging and does not contain the recent developments in this field (as does the US construction code, for example). This paper is focused on the utilization of seismic protection devices in bridge engineering to stimulate code development.

To facilitate the development of modern construction code and improve design and construction practices, a large research center in Uzbekistan is under consideration. The center will address the infrastructure resiliency in all major transportation-related fields of Uzbekistan: railways, automotive roads, and aviation. In addition to other issues, it will focus on improving the performance of railroads and railway bridges based on comprehensive monitoring, experimental studies, subsequent modeling, and performance predictions via computational simulations. The center will utilize the best practices worldwide, including US practices for the development and validation of measures improving seismic stability. To create a reliable numerical model, the seismic protection device and the design approaches need to be studied in experimental studies. Figure 6 shows an example of component testing of a damping device in the US being evaluated for use as seismic protection [18].

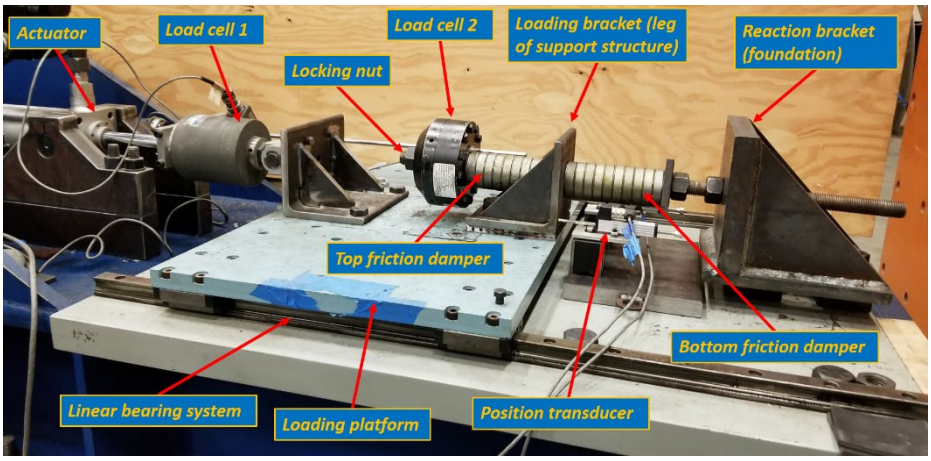


Figure 6. Example of experimental validation of damping device [18]

An example of full-scale component testing of a seismic isolator in the US to be utilized as a seismic protection device [19] is shown in Figure 7.

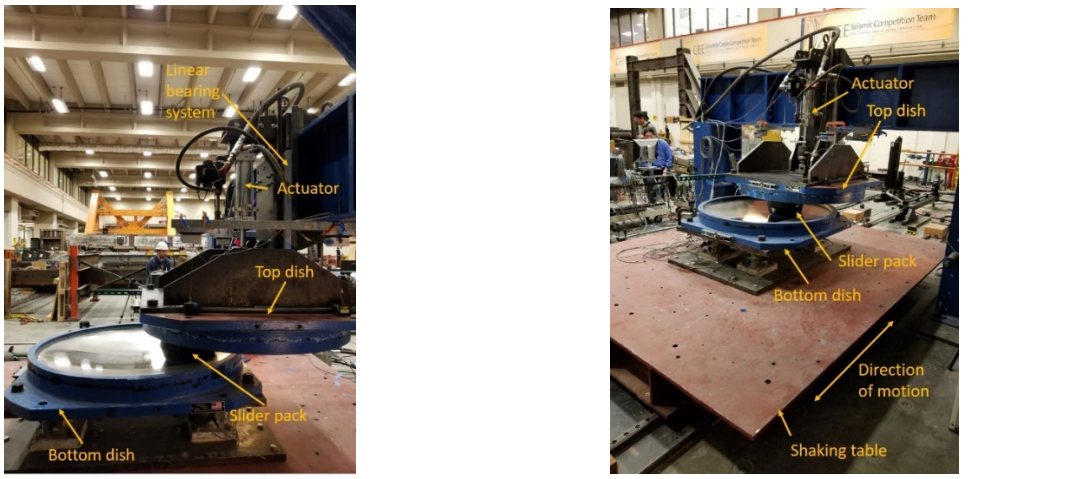


a) Testing at large displacement cycles

b) Weight of the superstructure is imposed by an actuator

Figure 7. Example of experimental validation of seismic isolation [19]

New damping devices for bridges are continuously being developed and they cannot be used in practice without a validation test (see [20] for example). The design approaches cannot be adopted to practice without rigorous testing to ensure their optimum performance (see [21] for example).

## SEISMIC ISOLATION SYSTEM

Seismic isolation is currently one of the main means of ensuring the seismic resistance of bridges, especially for an earthquake intensity of 8 and greater (MSK scale). In this case, compliant or sliding seismic isolation bearings are installed between the superstructure and the support. This solution is well known, however, its application is limited to road bridges at this time.

The limited application is related to concerns over the failure of the track structure on the bridge [12, 14] due to the high buckling of the support parts and the high horizontal forces of the braking load. Nevertheless, there are a few cases of the successful application of seismic insulation of railway bridges in bridge construction practice. Here we can highlight the seismic insulation of the Las Piedras Bridge in Spain and the Northern Railway Bridge in Budapest as well as the Maurer Sohnes Bridge in Greece [16]. Providing a railway bridge with seismic insulation leads to very significant savings in areas with seismic intensity of 8 or more, and the cost of the support construction can be reduced by 40-50 %.

In the bridge construction industry of Uzbekistan, the supports of railway bridges are designed to withstand seismic loads, which in turn leads to both increased loads and the expediency of applying special seismic protection methods. A typical example is the bridges on the Sochi-Adler line designed by OJSC "Transmost" with the seismic insulation system carried out by CJSC "Stroykompleks-5". This is the seismic isolation system considered here, which is represented by the photo and diagram of the supporting part (Figure 8) [6, 22, 23].

This paper examines the longitudinal behavior of a Stroycomplex-5 seismically insulated railway bridge against earthquakes of varying severity and recurrence.

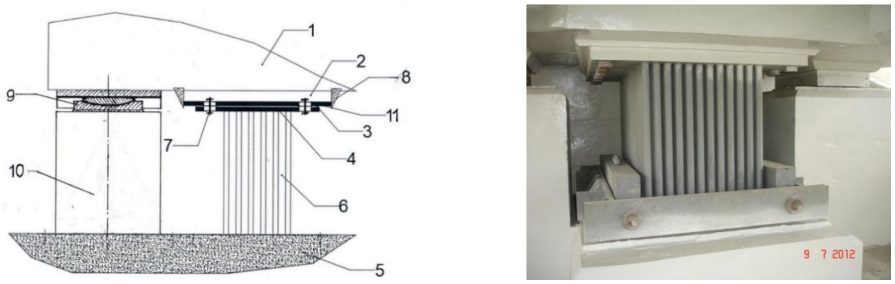


Figure 8: Stroycomplex-5 seismic isolation support system: left - placement of support elements on one of the bridges in Sochi; right - seismic isolation flexible rod package

A movable ball bearing element (9) is installed between the span structure (1) and the support (5) via the sub-bearer (10). Parallel to the support element (9), a seismic bar shock absorber (6), connected via a friction cover (FC), is installed. The complementary sheet (11), freely moving along the vertical axis of the sheet, is connected to the stops (8), which are mounted on the spanning structure (1). In doing so, there is a gap (2) between the seismic isolating element and the superstructure. This approach eliminates the transmission of the vertical load from the superstructure, which is fully absorbed by the movable support element [24].

The developed seismic isolation device provides three degrees of protection for the load-bearing structures of the bridge, shown in Figure 9.

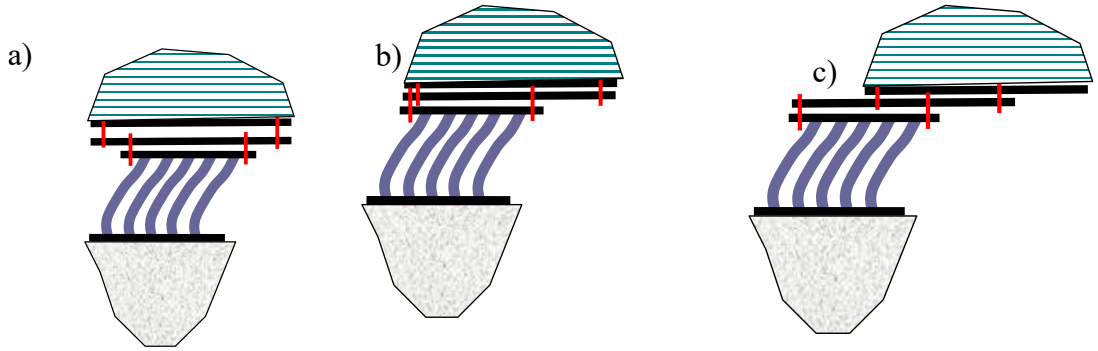


Figure 9: Behavior of seismic protection levels a) level one; b) level two; c) level three

The first level of protection ensures an elastic behavior of all bridge elements under the action of the design earthquake, while the second and third levels of protection do not work during the vibration of the structure. The flexibility of the rod spring can be specified with the guarantee of a limit displacement from the braking load of the rolling stock $T_{BRAKE}$, equal to $U_{lim}$. When the seismic load exceeds the elastic capacity (i.e. when plastic deformation takes place) of the rod spring, the second level of seismic protection is activated.

Seismic protection at the second and third levels of protection is provided by friction pendulum bearing connections in the form of bolted connections with oval bolt holes. The operation of these connections is described in detail in publications [25-27]. The difference between the second and third level of protection is the value of the bolt friction force [24]. The friction force of the second level of protection is less than the elastic limit of the stem spring and the support itself. If the seismic load is greater than the above-mentioned friction

force value, the bolts of the second level connection start to slide along the oval holes and reduce the peak accelerations in the structure.

## DESCRIPTION OF THE BRIDGE DESIGN. RESULTS AND DISCUSSION

This paper considers the technical implementation of a seismic protection for a bridge in the seismic regions of Uzbekistan. The 5-span (5x23,6m scheme) railway bridge with a total length of 128.9 m constructed in the Namangan region, an area with an estimated seismic intensity of 9 (MSK scale), is considered. The scheme of the bridge is shown in Figure 10. It has tall solid supports on a natural base and relatively small and light spans. Since the bridge is sectional, each column operates independently. The seismic protection of the supports in the most dangerous longitudinal direction is considered. In a conventional support solution, a significant horizontal load is transmitted to each support.

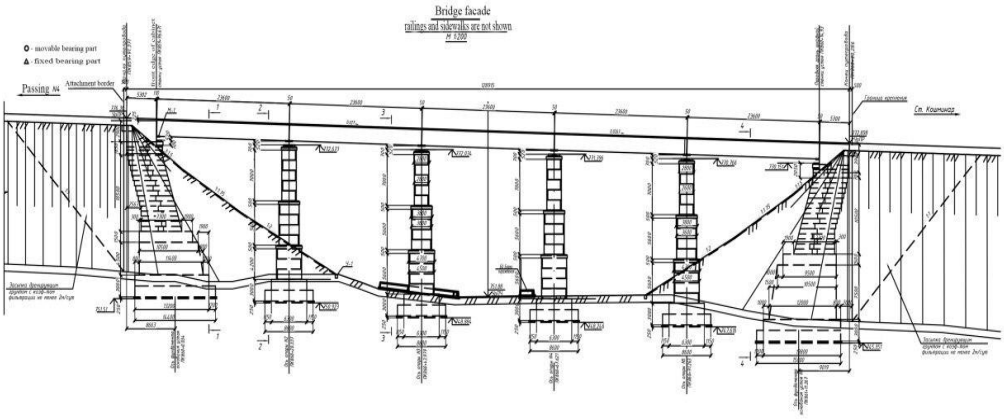


Figure. 10. General view of the bridge

The protection system is applied to the design of bridges with heavy spans [28]. It is impossible to use the superstructure as a dynamic vibration damper (DVD) for the piers because the superstructure's mass exceeds the critical value [14, 29], above which the dampening effect disappears. However, in many cases the DVD effect can be realized. Figure 11 shows the support of a small railway bridge in Uzbekistan under the span L=23 m and mass m=27.5 t.

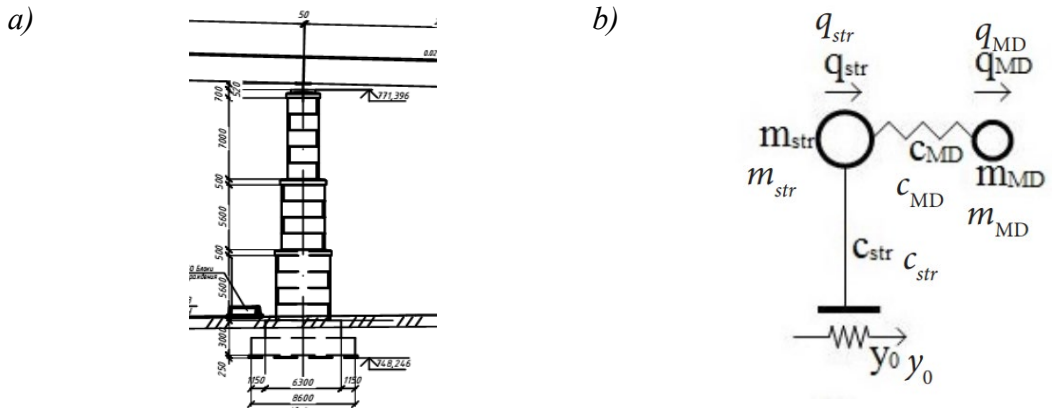


Figure 11. Diagram of railroad bridge support under span L=23,6 m: a) scheme; b) calculation scheme

Since the bridge consists of a few sections, each section works independently. Seismic protection of supports in the most dangerous longitudinal direction is considered. In a traditional bearing design, a significant horizontal load is transferred to each support. Some results of calculations by the linear spectral method (LSM) are given below. For the calculation, a version of the LSM was used which includes corrections to seismic loads due to modal damping [30-32].

The design of the seismic insulation was carried out at Stroykompleks-5 under the supervision of S.A. Shulman. The paper [24] describes the basic provisions of a seismic-isolated bridge design with calculations by the linear spectral method (LSM). Two options of seismic isolation are considered.

In the first type of seismic isolation, the optimum stiffness setting of the superstructure is ensured for its operation in the DVD mode. However, this stiffness setting violates the regulatory requirement limiting the displacement of the span ends from the operational load (braking).

$$u < 0.5\sqrt{L} \tag{2}$$

where $L$ is the span of the bridge in meters and $u$ is the offset of the span in centimeters.

In our case, the limit displacement is approximately 2.5 cm.

## SELECTION OF SEISMIC ISOLATION PARAMETERS

The selection of the seismic isolation parameters was carried out by varying the shear stiffness of the supporting part. The dependence of the moment along the foot of the support, calculated using the LSM by taking into account damping, is shown in Figure 12. A case of zero rigidity of the supporting part corresponds to a support without a superstructure. Alternatively in the case when the rigidity is infinitely high corresponds to a traditional support with a rigid supporting element. It is important to note that in this case the effect of dynamic damping of support oscillations occurs. As a result the superstructure acts as a dynamic vibration damper (DVD). The effect is achieved when GF is close to 1000 T. At the same time, the moment along the foot of the support decreases to 1494 Tm. For comparison, the moment M along the foot of the support free from the superstructure reaches 1940 Tm, and with a rigid supporting part, M = 2870 Tm.

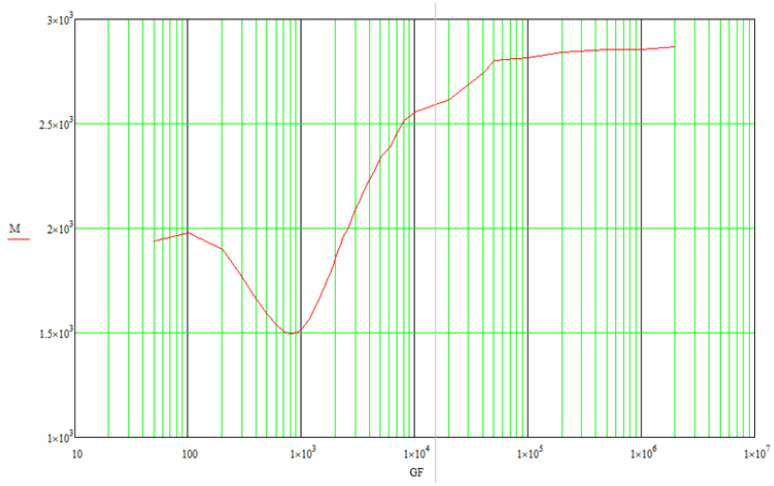


Figure 12. Dependence of the moment along the foot of the support on the shear stiffness of seismic isolation

The graph of the superstructure displacements relative to the support under operational loads are presented in Figure 13. The plot shows te relationship between these displacements and the period of the first fundamental mode of the support vibration.

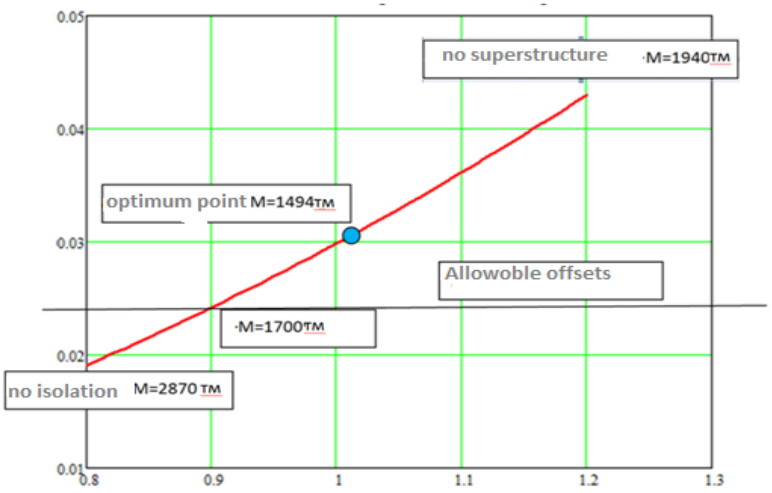


Figure 13. Dependence of the superstructure displacements on the braking load on the seismic isolation rigidity (period of fundamental mode)

Unfortunately, the displacements of the superstructure on the compliant support part exceed the permissible standards in accordance with formula (1). The calculations performed earlier [23, 31, 32] show that it is possible to safely increase the permissible displacement by a factor of two.

## CONCLUSION

At present, the worldwide practice of earthquake-resistant construction applies a multi-level approach to the design of seismic-resistant structures. In accordance with this approach, the structure is calculated for several levels of seismic impact at the corresponding limit states. This approach is adopted in Eurocode-8, where it is recommended to consider at least two levels of impact and two limit states: (1) an interruption of normal operation (serviceability limit state (SLS)) and (2) a collapse of the structure (ultimate limit state (ULS)).

The work performed herein shows that the use of seismic protection devices is very effective for railway bridge structures constructed in earthquake-prone areas. Based on the results of this paper it was concluded that for girder railway bridges the most effective seismic protection is a combination of elastic elements with friction pendulum bearings. In this case, the spans are supported by the friction pendulum bearings, and seismic elastic elements reduce the demand in both horizontal directions. Hence, due to the use of seismic isolation devices, it is possible to increase the reliability of the bridge under seismic impact. Moreover, the use of seismic isolation devices results in a reduction in use of basic building materials by about 30% and as such, can result in a reduction of the construction cost by about the same percentage.

## ACKNOWLEDGMENTS

The authors would like to acknowledge Ms. Holly Halligan of UC Berkeley for editing the paper.

## REFERENCES


[1] https://news.climate.columbia.edu/2023/02/20/the-ohio-toxic-train-wreck-and-governments-failure-of-regulation-and-response/.

[2] Ergashev Z.Z., Shermukhamedov U.Z., Abdukadyrov F.E. *Peculiarities of ensuring seismic resistance of railway bridges on high-speed lines // Scientific and Practical Journal "Vysshaya Shkola"*, Ufa, RF. 2016. No. 18. -– pp. 70-72.

[3] Shermuxamedov U.Z., Salikhanov S.S. *The current state and prospects for the construction of overpass high-speed railway lines in the seismic conditions of the Republic of Uzbekistan // Journal "TashIIT Bulletin*". Issue. No. 2. - Tashkent, 2020. – pp. 3-8.

[4] Pershin S.P. *Monitoring of network development/"Transport Construction"* 1992 .2 .p. 14-25.

[5] Resolution of the president of the Republic of Uzbekistan "On approval of the Strategy for the development of the transport system of the Republic of Uzbekistan for the period up to 2035".

[6] Shermuxamedov, U., Shaumarov, S., & Uzdin, A. *Use of seismic insulation for seismic protection of railway bridges. In E3S Web of Conferences* (Vol. 264, p. 02001). EDP Sciences. 2021. https://doi.org/10.1051/e3sconf/202126402001.

[7] *Information on artificial structures owned by the railways of Uzbekistan*. Uzbekistan Temir Yullari JSC Administration. 2019.

[8] U.Z. Shermuxamedov, Sh.Z. Nishonboyev, U.K. Abduraimov, F.Z. Zokirov. *Inspection and diagnostics of railway reinforced concrete bridge in Andijan-Khanabad peregon // Eurasian Journal of Engineering and Technology.* ISSN: 2795-7640. Volume 9. August, 2022. – p. 77-83.

[9] Shermukhamedov, U.Z. *Design of earthquake-resistant structures for the conditions of Uzbekistan // "In New technologies in bridge building" 2010.* – pp. 95-99.

[10] T.R. Rashidov, U.Z. Shermukhamedov, *Earthquake resistance of transport facilities. Textbook.* – T.:2020. – 406 p.

[11] Shermukhamedov, U.Z. *Damping of longitudinal seismic oscillations of beam bridge supports with seismic isolation bearing parts.* Moscow: MIIT, 2010. - 23 p.

[12] Ulugbek Shermukhamedov, Anora Karimova, Abdurakhim Abdullaev and Inobat Hikmatova. *Calculation of monolithic bridges taking into account seismic conditions of Republic of Uzbekistan // IV International Scientific Conference "Construction Mechanics, Hydraulics and Water Resources Engineering"* (CONMECHYDRO - 2022), E3S Web of Conf. Volume 365, 2023. EDP Sciences. https://doi.org/10.1051/e3sconf/202336502005.

[13] Shermukhamedov U.Z., Tayirov Sh.Sh. *Some features of damage to un-cut reinforced concrete bridges under severe earthquakes // "Science and innovation" international scientific journal.* Volume 2 Issue 1, JANUARY 2023. UIF-2022: 8.2 | ISSN: 2181-3337. – p. 54-62.

[14] Kuznetsova, I. O., & Shermukhamedov, U. Z. *Basic principles of multi-level design of bridges // Bulletin of TashIIT* №3, 2009. – 22 p.

[15] Wai-Fah Chen, Lian Duan. *Bridge Engineering Handbook. Second Edition: Seismic Design*. – NY.: 2014, – 722p.

[16] Huber Peter. *Realized projects of Isolation Systems for Railway Bridges in Spain, Hungary and Greece* / Peter Huber // PROCEEDINGS OF WORKSHOP "*Bridges seismic isolation and large-scale modeling*" Saint-Petersburg 29.06 - 03.07.2010. - pp. 37 – 50.

[17] https://www.usgs.gov/news/featured-story/m78-and-m75-kahramanmaras-earthquake-sequence-near-nurdagi-turkey-turkiye.

[18] Shakhzod Takhirov, Leon Kempner, Michael Riley, Eric Fujisaki and Brian Low (2019). *SEISMIC PROTECTION OF HIGH-VOLTAGE EQUIPMENT BY FRICTION DAMPERS: NUMERICAL MODELLING CORRELATED WITH FULL-SCALE COMPONENT TESTS*. COMPDYN-2019, 7th ECCOMAS Thematic Conference on Computational Methods in Structural Dynamics and Earthquake Engineering. M. Papadrakakis, M. Fragiadakis (eds.), Crete, Greece, 24–26 June 2019.

[19] Shakhzod Takhirov, Leon Kempner, Michael Riley, Eric Fujisaki, Brian Low (2020). *Component Testing of Full-Scale Friction Pendulum Bearing per IEEE693 for Seismic Isolation of High-Voltage Equipment*. In the Proceedings of 8th International Conference on Advances in Experimental Structural Engineering. Christchurch, New Zealand, 3-5 February 2020.

[20] K. M. Mosalam, S. Hao, Y. Wu, S. Günay, S. Takhirov, and P. Wong (2020). *SYSTEM-LEVEL HYBRID SIMULATION AND DESIGN OF HIGHWAY BRIDGES WITH INNOVATIVE CONNECTING DEVICES*. The 17th World Conference on Earthquake Engineering, 17WCEE, Sendai, Japan, September 13-18 2020.

[21] Daniel J Miller. (2019). *Ductile Behavior of Reinforced Concrete Arch Ribs*. A dissertation submitted in partial satisfaction of the requirements for the degree of Doctor of Philosophy in Engineering - Civil and Environmental Engineering in the Graduate Division of the University of California, Berkeley.

[22] Dolgaya A.A., Kuznetsova I.O., Uzdin A.M., Frese M.V., Shulman S.A. *Seismic resistance of railway bridges. Science and transport,* 2012, no. 4, p. 43-47.

[23] Zhgutova T.V., Kuznetsova I.O., Uzdin A.M., Shulman S.A. *Seismic isolation of railway bridges in Sochi. Proceedings of the meeting of the working group of the international society on seismic protection systems (ASSISi),* 2011, pp. 119-132.

[24] Zhgutova T.V. *Assessment of the track performance on bridges with seismic isolation and requirements for seismic isolation, taking into account the track performance* / Zhgutova T.V., Uzdin A.M. // *Bulletin of the Petersburg State University of Railways*. - №3.-2012.-C. 199-204.

[25] Berezantseva E.V., Sakharova E.V., Simkin A.Y., Uzdin A.M. *Friction-moving connections on high-strength bolts // International Colloquium "Bolt and special mounting connections in steel structures"*. M., 1989. T. 1. p. 73-76.

[26] Hashem A. M., Uzdin A. M. *The use of the friction movable braces for designing the seismic proof structures with predetermined parameters of ultimate conditions // 11 World Conference on Earthquake Eng*. 1996. Paper 51.

[27] Uzdin A.M., Eliseev O.N., Nikitin A.A., Pavlov V.E., Simkin A.Y., Kuznetsova I.O. *Elements of friction theory, calculation and technology of friction-moving connections*. SPb.: VITU, 2001. 75 p.

[28] SP 35.13330.2011 *"Bridges and pipes"*. Updated edition of SNiP 2.05.03-84 *.

[29] Shermuxamedov, U., & Shaumarov, S. Impact of configuration errors on the dynamic oscillation absorbers effectiveness of different masses on the seismic resistance of bridges. In E3S Web of Conferences (Vol. 97, p. 03017). EDP Sciences. – 2019.

[30] Uzdin A.M., Elizarov S.V., Belash T.A. Earthquake resistant structures of transport buildings and structures. Tutorial. FGOU "Educational and methodological center for education in railway transport", 2012-500 p.

[31] Uzdin A.M., Kuznetsova I.O. Seismic resistance of bridges. Saarbrücken (Germany), Palmarium, 2014, 450 p.

[32] Uzdin A.M. On the account of energy dissipation in assessing the seismic resistance of transport structures // Seismic resistance of transport and network structures / M., Nauka, 1986, pp. 35-44.

COMPDYN 2023
9th ECCOMAS Thematic Conference on
Computational Methods in Structural Dynamics and Earthquake Engineering
M. Papadrakakis, M. Fragiadakis (eds.)
Athens, Greece, 12-14 June 2023

# DESIGNING A LOW-COST WIRELESS SENSING SYSTEM FOR REAL TIME DAMAGE ASSESSMENT OF R/C BRIDGES

**Vassilis K. Papanikolaou[1], Konstantinos Mixios[1], Sotiria Stefanidou[1], and Olga Markogiannaki[2]**

[1] Aristotle University of Thessaloniki
School of Civil Engineering
e-mail: {billy, mixioske, ssotiria}@civil.auth.gr

[2] REDI Engineering Solutions
markogiannaki.olga@gmail.com

## Abstract

*This paper presents an overview of an ongoing project that aims to develop a low-cost system and software platform for real-time identification and evaluation of the damage state of reinforced concrete bridges, with a focus on extreme events such as earthquakes. The project includes the design and manufacturing of a portable, battery-powered, wireless acceleration streaming device, a software tool to optimize a parameterized finite element model, and an integrated methodology for damage identification and evaluation. The effectiveness of the proposed system will be tested on a typical existing R/C bridge in a region of high seismicity, with validation in both real field conditions and simulated experiments. The paper discusses the project methodology, current progress, and expected outcomes, including the potential to reduce the cost and time for bridge inspection and provide real-time safety information after an extreme event. This project presents a significant contribution to the field of structural health monitoring and has the potential to further enhance the application of SHM techniques in both academic and practical structural engineering communities.*

**Keywords:** Reinforced concrete bridges, real-time identification, acceleration, damage evaluation, structural health monitoring.

## 1 INTRODUCTION

Bridges play a pivotal role in transportation systems, acting as vital connections that enhance the economy, improve quality of life, and promote community integration. However, the current infrastructure is struggling to meet the growing demands, requiring both immediate measures to maintain existing structures in a satisfactory condition and long-range transformations using advanced technologies to boost their durability and resilience. Following a severe earthquake event, civil protection agencies and highway stakeholders are faced with critical decisions regarding the closure or continued operation of highway networks, with particular attention paid to bridges, which are often their most vulnerable components.

Bridge damage poses risks to road safety, causes traffic disruptions, and triggers significant direct and indirect economic losses. Past incidents, such as the collapse of the Mississippi River bridge, USA (2007), the Pinios (2016) and Kompsatos (2017) bridges in Greece, and the Morandi bridge in Genoa, Italy (2018), have highlighted the devastating consequences of bridge failures. Moreover, bridges are susceptible to multiple natural hazards, including earthquakes, and also environmental threats. Prompt inspection of critical road infrastructure becomes imperative in the aftermath of a strong earthquake. Motorway administrators face the challenge of making decisions, such as the precautionary closure of bridges pending post-seismic inspection, which can affect serviceability, rescue operations, and evacuation efforts. Conversely, leaving bridges operational without inspection poses significant risks, as subsequent earthquake events could compromise their stability, potentially leading to additional casualties. Therefore, administrators must decide whether the motorway network can continue to operate without restrictions. Insufficient coordination during such critical periods may also increase anxiety among motorway users.

Structural Health Monitoring (SHM) techniques have emerged as essential tools to address these challenges by facilitating the identification of structural characteristics and behaviors. SHM can involve continuous or periodic measurements, as well as assessments following severe loading events, to capture the static or dynamic mechanical response of bridges. Although SHM in its simplest form focuses on comparing measured responses to design model predictions, advanced strategies involve calibrating and updating theoretical bridge models to align with measured data. Although Finite Element (FE) model updating algorithms have been widely employed, a comprehensive and integrated approach that fully leverages SHM measurements for model verification, damage identification, and evaluation is still lacking. Recent research efforts [1,2] have begun to address this gap, but holistic methodologies considering the entire bridge system and employing highly accurate finite element models remain limited.

In response to these challenges, there is an urgent need for the development and implementation of systems capable of assessing the structural condition of bridges in real-time [3,4]. The present project, titled RISE (Real-time Identification and Evaluation of Damage in Reinforced Concrete Bridges), aims to provide a novel real-time assessment system specifically designed for reinforced concrete (R/C) bridges. The primary objective of this project is to develop an innovative low-cost sensing system and an integrated software platform to identify the damage state of R/C bridges in real-time conditions.

The suggested system encompasses the development of an integrated, low-cost solution to rapidly assess structural damage in existing bridges. This solution relies on vibration-based system identification procedures and features an innovative device along with appropriate control software to facilitate short-term multipoint acceleration recording on bridge structures. The monitoring device will be designed and manufactured based on a high precision MEMS acceleration sensor and will reduce the cost and time required for routine bridge inspections,

thereby offering an efficient solution for field researchers. The in-house production of these devices will enable their patenting and mass production, enabling broader applications within both academic/research and practical structural engineering communities.

Additionally, RISE is committed to developing a software platform capable of optimizing a parameterized finite element model as part of the SHM process. This platform, based on measurements of vehicle-induced bridge vibrations, will utilize signal processing and optimization algorithms to update the finite element model. In addition, the RISE project aims to surpass the current research forefront by integrating the process of finite element model updating into a software tool that utilizes a Functional Mockup Unit (FMU). This FMU-based tool will operate as a model exchange and co-simulation standard, allowing for future expansion and co-simulation purposes across a variety of solvers. An improved version of GID-OpenSees, a graphical user interface developed for OpenSees [5], will also be developed within the RISE project and will enable the export of parameterized finite element models.

Another key objective is the development of an integrated methodology for real-time damage identification and evaluation of the damage state of R/C bridges. This methodology will employ a damage identification process that uses measured data at different time intervals ($t_0 \ldots t_i$) to compare the initial and current response of the bridge. Information from this process will then be used to define suitable damage state criteria based on capacity curves of the structure. Finally, the project aims to apply the proposed system to a typical existing R/C bridge in a region of high seismicity, to identify structural damage states using monitoring data. This practical application of the system will provide valuable insights into the effectiveness and potential areas of improvement for the developed technologies and methodologies.

By addressing these critical aspects of the current state-of-the-art, the RISE project aims to enhance the utilization of structural health monitoring techniques in assessing bridge performance and providing real-time safety information following extreme events. This advancement will enable the identification and evaluation of bridge damage in a comprehensive manner, thus significantly contributing to the field of structural health monitoring. Fig. 1 shows a comprehensive chart of the project roadmap.

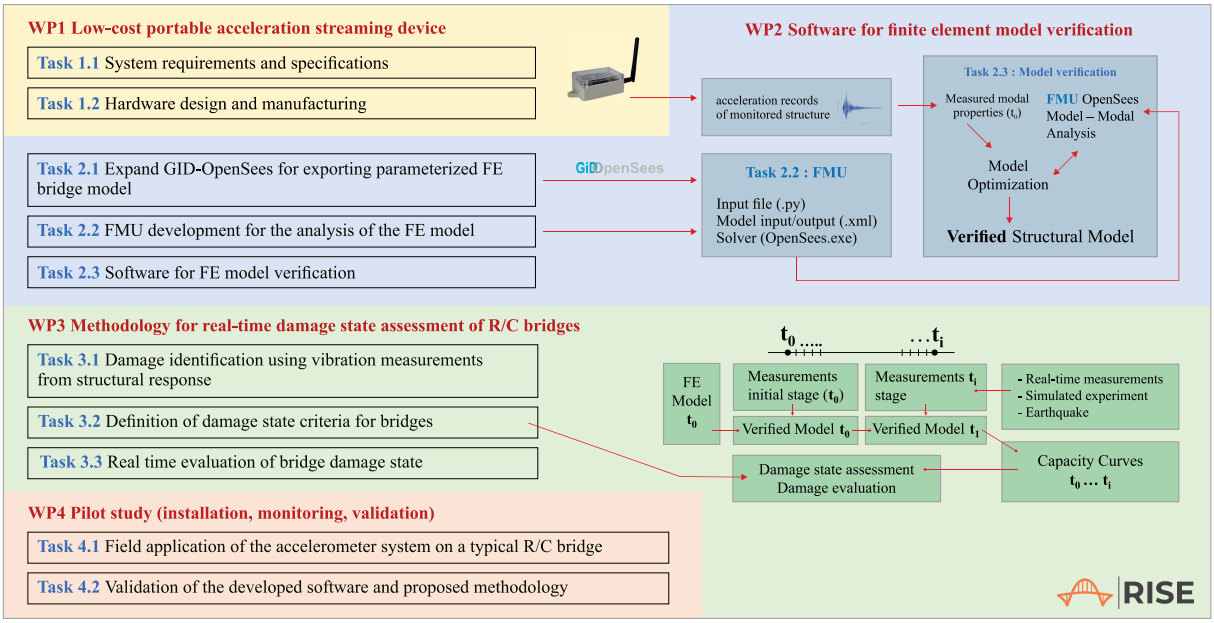


Fig. 1 : Overview of the RISE project roadmap.

During the current phase of the RISE project, primary attention is placed on establishing system requirements and initiating the design process for the required multi-point acceleration recording device, which is currently under development. This paper will concentrate on the decision-making process during its design phase, specifically the reasoning behind component selection, how these choices align with the overarching objectives of the project, and early decisions influencing the expected functionality of the device.

## 2 DESIGN REQUIREMENTS AND DECISIONS

In alignment with the project roadmap described in the previous section, the initial aim of the RISE project is to design an effective sensing system capable of short-term recording of vehicle-induced vibrational data from multiple points on the bridge deck. The collected time vs. acceleration data series (aka. accelerograms, acceleration records) will serve as the fundamental input for the subsequent signal processing and optimization algorithms. When combined with the FMU-based analysis, these data will facilitate the production of verified structural models for real-time damage assessment of bridge structures. The primary requirements for designing the acceleration sensors proposed herein, listed in descending order of importance, are as follows:

1. *Absolute Time Synchronization*: This feature is essential for accurate and efficient post-processing of acceleration data in the context of system identification procedures. It ensures that data from multiple sensors can be correctly aligned and compared, thereby enabling a comprehensive and accurate understanding of the bridge's dynamic behavior.
2. *Multi-Directional, High Resolution, and Low Output Noise Measurements:* A high-performance triaxial sensor capable of detecting vibrations in all three spatial dimensions at high resolution is preferable. This allows the sensor to capture small changes in acceleration accurately. Additionally, the sensor should produce low output noise to preserve the quality and integrity of the recorded data. Circuit design should also consider the potential for data interference and aim to minimize it to ensure the fidelity of the captured signals. However, these performance demands should be balanced with cost, which needs to remain within a reasonable range to keep the overall project budget manageable.
3. *Quick and Temporary Field Installation/Deinstallation and Data Collection*: The device should be compact, battery-powered, and capable of wireless data transmission to enable rapid deployment and retrieval in the field. Although establishing a sufficiently long wireless range without transmission latency or data loss issues can be challenging, wired connections, such as Ethernet, would significantly undermine the rapid assessment objective of the project by increasing setup and teardown times.
4. *Low Component and Manufacturing Costs*: Keeping the production cost low will facilitate the manufacture of a greater quantity of devices. This allows for measurements at a greater number of locations on a bridge concurrently and promotes a policy of direct unit replacement, rather than repair, in the unlikely event of hardware malfunction. However, it is critical to balance cost with the need for reliability and precision in data collection.
5. *Robustness and Durability*: Given the environment where these devices will be deployed (outdoors, on bridges, exposed to various weather and temperature conditions), they must be robust enough to withstand these conditions without failure or loss of accuracy.

6. *Data Management*: The device should be connected to a reliable remote storage system where data can be saved and accessed for analysis.
7. *Ease of Use*: The device should be user-friendly with easy installation, operation, and data collection processes. This can significantly save time and reduce the chances of errors during setup or use.

As outlined in the design requirements, *absolute time synchronization* is of utmost importance for the proposed acceleration sensor devices. This requirement becomes particularly crucial in a distributed sensing system, where accurate time alignment from multiple sensors is necessary. There are several methods to achieve this, including the Global Positioning System (GPS), Network Time Protocol (NTP), and synchronization pulse techniques. Each method comes with unique characteristics, rendering them suitable for certain applications while less optimal for others. In this context, GPS synchronization offers numerous advantages that make it a favorable choice for synchronizing acceleration sensors in a distributed system:

(a) GPS synchronization provides time accuracy within a few nanoseconds globally, significantly surpassing the millisecond accuracy offered by NTP.
(b) GPS synchronization does not depend on internet connectivity. This independence from the internet, which is a requirement for NTP, increases system robustness. It is particularly useful in remote locations where reliable internet service may not be available or in situations where the device needs to operate in an offline environment.
(c) GPS synchronization is independent of wired connections, compared to traditional sync pulse methods that require a physical connection. This independence allows greater flexibility in device placement and simplifies the installation process, a critical factor in scenarios involving temporary installations. Although the sync pulse method usually relies on a wired connection for the transmission of the common trigger signal, it can also be configured as a point-to-point wireless transmission within a local wireless network. However, this alternative requires careful setup to avoid potential latency and may only be used as an alternative when the GPS signal is weak due to weather conditions.
(d) GPS synchronization can support a virtually unlimited number of sensors, an important advantage when monitoring multiple points on a bridge. In contrast, the performance of systems using NTP might degrade as the number of devices in the network increases.

Taking all the above factors into account, GPS synchronization emerges as a robust, scalable, and flexible solution for time-synchronizing acceleration sensors for the proposed application.

Moving further into design considerations, another critical requirement for the proposed sensing system involves the quick and temporary field installation and data collection, which highlights the importance of *wireless connections* for data transmission. Wireless connectivity options vary, including cellular networks (4G/5G), Bluetooth, LoRaWAN, Zigbee, and WiFi, among others. Each of these technologies has its strengths and potential drawbacks, but for the proposed application of temporary, short-term acceleration data recording from multiple points, WiFi is the most suitable choice:

(a) WiFi maintains a balance between range and data rate that few other wireless technologies can match. While a typical WiFi network has a range of up to 100 meters, special high-gain antennas or WiFi range extenders can be utilized to extend this range beyond the usual limit, if required. This expanded range can cover a broad area on most bridge structures. Coupled with the high data rate that WiFi offers, the technology is well-suited for transmitting the large amounts of data generated by high-resolution triaxial accelerometers.

(b) While a pre-existing WiFi infrastructure may not always be available at a bridge site, establishing a local WiFi network using a gateway (e.g. WiFi access point or router) is a straightforward and cost-effective process. This characteristic of WiFi further facilitates quick and temporary installations and reduces setup time and costs.
(c) Compared to other wireless technologies, WiFi exhibits lower latency, which ensures real-time or near real-time transmission of acceleration. However, even if minor latency issues occur, the use of GPS synchronization ensures precise timestamping of the data, thus mitigating potential impacts on data alignment.
(d) WiFi supports a large number of devices connected concurrently, aligning well with the need to collect data from multiple sensors placed at various points on a bridge. Furthermore, with the WiFi gateway connected to a computer, easy and reliable data storage becomes feasible, enhancing the overall efficiency of data management.
(e) Devices equipped with WiFi capabilities, such as ESP8266 or ESP32 microcontrollers, are readily available and affordable. They offer a high level of integration, enabling compact device designs for quick deployment and retrieval in the field.

Considering various aspects such as range, data rate, availability, latency, and the capacity to support multiple devices, it becomes clear that WiFi stands out as the most suitable wireless connection option. Its capabilities align effectively with the requirements of rapid and temporary field installation and data collection for this specific application.

For the remaining design considerations, the following additional decisions align with the outlined requirements for the proposed acceleration sensor device:

(a) A rechargeable Lithium Polymer (LiPo) battery has been selected as the power source for the device, ensuring autonomous operation. This choice is particularly advantageous given the general scarcity of continuous power availability on bridge structures. LiPo batteries offer the advantage of high energy density in a compact and lightweight form, making them particularly suitable for this application. Their flexible form factors also facilitate seamless integration within the compact design of the device.
(b) Employing 3D printing technology, a compact and robust enclosure will be designed for a precise fit, ensuring the protection of electronic components from external elements. This enhances the durability and lifespan of the device. The enclosure is designed to house all components, including the necessary GPS and WiFi antennas. An additional design feature is the inclusion of a small OLED screen in the device. This screen provides real-time data and status information, offering immediate feedback and diagnostics. The advantage of this feature is that it eliminates the need to connect the device to a computer for status updates or troubleshooting.
(c) To expedite rapid field installations, a magnetic mounting system needs to be embedded in the enclosure to secure the sensors to the bridge, using a reusable metallic base plate. This system will provide a secure, non-invasive attachment method, eliminating the need for additional tools or hardware for installation. It simplifies the setup process while also reducing the time for both installation and removal.

In conclusion, each design consideration, from power source to physical construction to ease of use, has been carefully made to ensure the proposed sensing system fulfills the essential requirements while maximizing performance and user-friendliness. Fig. 2 illustrates a representative bridge installation, depicting sensor devices placed at key points on the bridge. Each of these devices is equipped with wireless connectivity and GPS, ensuring efficient data transmission and synchronized data timestamping, respectively. They are wirelessly connected to a central WiFi gateway, forming a comprehensive monitoring system for recording vehicle-induced vibrations.

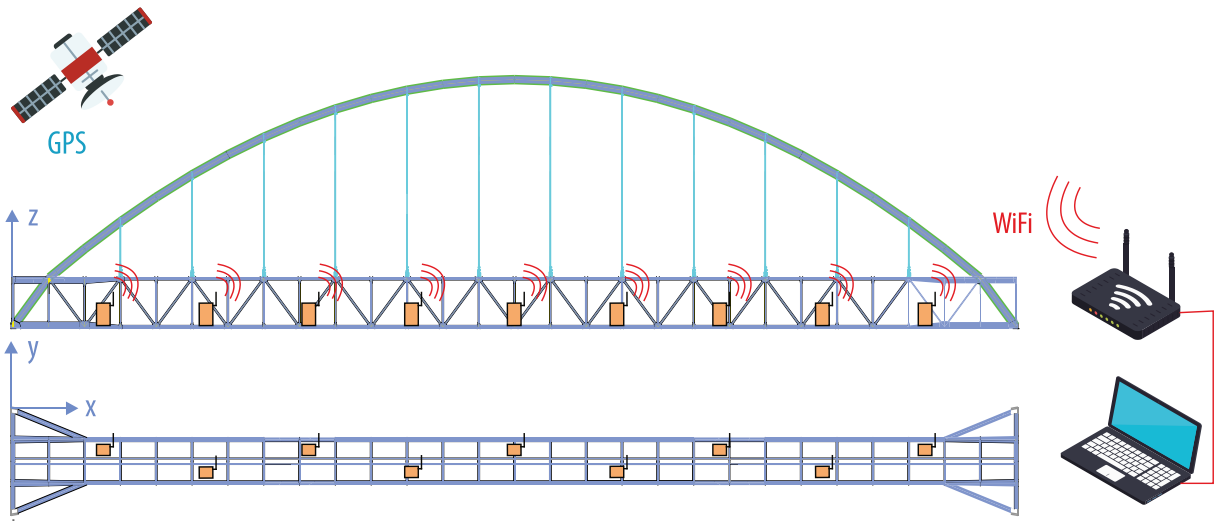


Figure 2: Distributed sensor network on a bridge structure.

## 3 COMPONENT IDENTIFICATION

Moving from general design considerations and system layout, this section turns attention to detailed component identification. Specifically, it focuses on the choice of the acceleration sensor, GPS module, and WiFi platform, discussing the particulars of each and their role in the overall system operation.

### 3.1 Acceleration sensor

In the process of selecting an appropriate acceleration sensor for this project, Micro-Electro-Mechanical Systems (MEMS) accelerometers emerge as a more favorable option in comparison to other types, such as Piezoelectric (PZT) sensors. Primarily, MEMS accelerometers gain recognition for their compact size, robustness, and lower power consumption, attributes that align well with the requirements of a portable and energy-efficient device for field applications. Their large-scale production in the consumer electronics industry further leads to competitive pricing, making them a cost-effective choice compared to other types of accelerometers.

MEMS accelerometers come with either analog or digital interfaces. For this project, a digital interface was chosen due to the simplification it brings to the system design. Specifically, it facilitates direct connection to microcontrollers, eliminating the need for additional costly analog-to-digital converters. Moreover, it is better shielded against electromagnetic interference, making it a superior choice for operation in noisy environments.

Key characteristics to consider when selecting a MEMS accelerometer include resolution and noise density. The resolution, expressed in bits, indicates the sensitivity of the sensor, with higher resolution enabling the detection of smaller accelerations. Noise density, expressed in $\mu g/\sqrt{Hz}$ or root mean square (RMS) noise (mg), is the most critical parameter that defines the smallest acceleration changes that can be distinctly detected by the sensor. A lower noise density, as well as a constant noise response across the frequency range of interest (e.g. DC to 30 Hz) is preferable as it ensures more accurate and reliable acceleration measurements.

Following a comparison of various low-cost MEMS accelerometers available in the market, the Analog Devices ADXL355 accelerometer was selected for the device. This decision was driven by its superior performance in terms of resolution and noise density, making it an op-

timal choice for capturing high-quality and precise acceleration data from bridge vibrations (Table 1). To further validate its performance, a pilot test was performed in which the accelerometer demonstrated an impressively low noise level (< 0.1 mg RMS), confirming its suitability for the task. Fig. 3 presents the measured noise floor in terms of power spectral density among the selected sensor, a lower-spec MEMS sensor [6], and a commercial grade force-balance accelerometer.

| Manufacturer | Model | Range (g) | Resolution (bits) | Noise density (μg/√Hz) | RMS noise[1] (mg) | Price[2] (€) |
|---|---|---|---|---|---|---|
| TDK InvenSense | MPU-6000 | ± 2,4,8,16 | 16 | 400 | 2.83 | 12.8 |
| STMicroelectronics | LIS331DLH | ± 2,4,8 | 16 | 218 | 1.54 | 4.1 |
| Analog Devices | ADXL313 | ± 0.5,1,2,4 | 10-13 | 150 | 1.06 | 11.2 |
| Bosch Sensortec | BMA456 | ± 2,4,8,16 | 16 | 120 | 0.85 | 2.6 |
| NXP | MMA8451Q | ± 2,4,8 | 14 | 99 | 0.70 | 3.7 |
| STMicroelectronics | LIS3DHH | ± 2.5 | 16 | 45 | 0.32 | 14.3 |
| Analog Devices | ADXL355 | ± 2,4,8 | 20 | 22.5 | 0.16 | 61.1 |

[1] calculated approximately as : noise density × √(bandwidth), for a typical 50 Hz bandwidth.
[2] price for one piece, extracted on 30/05/2023 from a major distributor.

Table 1: Characteristics of various digital MEMS accelerometers.

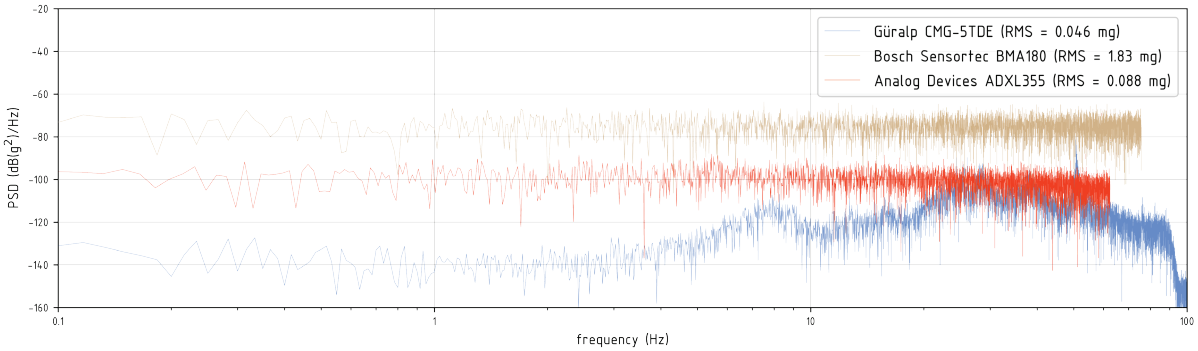


Figure 3: Noise performance (power spectral density) between the ADXL355 accelerometer compared to an obsolete 14-bit sensor and a commercial-grade accelerometer.

## 3.2 GPS module

The GPS module embedded in the device serves a crucial function by providing an absolute time reference. This is achieved through a Pulse-Per-Second (PPS) digital signal, enabling nanosecond-precise synchronization across all deployed devices. As explained in the previous section, this feature is essential for consistent data collection and subsequent analysis. Several GPS modules were examined during the selection process, the details of which can be found in Table 2.

Although spatial accuracy was considered, it was not the decisive factor in this selection. All modules under consideration offer spatial accuracy down to 2-3 meters, depending on the number of satellites locked and subject to varying weather conditions. However, the overall accuracy could potentially be improved through continuous monitoring and subsequent post-processing of the stationary device locations on the bridge during measurements. Other selection criteria included power consumption, form factor, and cost. All GPS modules also require a small active ceramic antenna for satellite signal acquisition. The choice of antenna depends

on factors such as its gain (dB) and size. Ultimately, the u-blox NEO-6M module was chosen for its comprehensive blend of features and performance.

| Module | PPS signal | Accuracy (m) | Tracking channels | Consumption (mA) | Form |
|---|---|---|---|---|---|
| u-blox NEO-6M Red | Yes | 2.5 | 22 | 45 |  |
| ATGM336H | Yes | 2.5 | 32 | 25 |  |
| Quectel L80 | Yes | 2.5 | 22 | 25 | 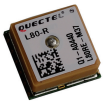 |
| Grove - GPS (Air530) | Yes | 2.5 | 22 | 60 |  |

Table 2: Characteristics of various GPS modules.

### 3.3 WiFi platform

In the process of choosing the most appropriate WiFi platform, various factors were evaluated. First, there was the need for a fast and reliable connection to a wireless gateway, which ensures efficient transmission of acceleration data. Additionally, interface compatibility of the platform with the selected MEMS accelerometer and GPS module was critical to ensure the seamless integration of these different components. Furthermore, cost effectiveness, energy efficiency, programming language, and the active engagement of its user community were all essential considerations in the decision-making process.

Various WiFi platforms were evaluated during the selection process, each offering a different combination of features and performance. Preference was given to platforms with an integrated development environment (IDE) that simplifies programming and debugging. Other key considerations included cost, power consumption, and availability of support resources, such as online tutorials and community forums. Furthermore, the option of an external antenna connection was deemed essential to ensure better signal reception. Several WiFi modules were examined during the selection process, the details of which can be found in Table 3.

From the pool of potential options, two WiFi platforms from Espressif Systems, ESP8266 and ESP32, stood out as promising candidates due to their affordability, performance and strong support community. After careful consideration, the ESP8266 platform was ultimately selected. This decision was primarily driven by its affordable cost, adequate number of input/output (I/O) pins, and the availability of standard communication protocols such as serial, SPI, and I2C for interfacing with other components. It is worth noting that while the ESP32 offers even more I/O pins and includes a Bluetooth feature, these added functionalities were not deemed necessary for this project. It should be mentioned that there are several variants of the ESP8266 and ESP32 platforms available on the market as different module implementations. In the context of this project, the selected variant of the ESP8266 included an onboard LiPo battery charging circuit. This added feature, beyond the fundamental capabilities of ESP8266, contributes to the operational efficiency of the device by providing an integrated power management solution.

| Platform | Processor | Programming | Price (€) | Form |
|---|---|---|---|---|
| ESP8266 | Tensilica L106<br>32-bit RISC | Arduino<br>C++<br>MicroPython | 3.5 to 27 |  |
| ESP32 | Xtensa LX6<br>32-bit Dual-Core | Arduino<br>C++<br>MicroPython | 8 to 32 |  |
| Arduino<br>MKR WiFi 1010 | SAMD21<br>Cortex-M0+ | Arduino | 42 |  |
| Raspberry Pi<br>Zero W | Broadcom<br>BCM2835 | Python<br>C++<br>Java | 20 | 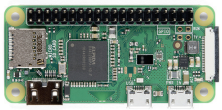 |
| NRF24L01 | nRF24L01+ | C/C++ | 2.5 to 5 |  |

Table 3: Characteristics of various WiFi platforms.

## 4 CONCLUSIONS

This paper provided an in-depth discussion on the design and development of a cost-effective, easily deployable, compact, and energy-efficient structural health monitoring (SHM) system intended for application in bridge structures, in the form of a distributed acceleration sensor network. The system relied on a high-performance MEMS accelerometer, GPS, and WiFi technology, which were described in detail throughout the paper.

A detailed presentation of the proposed system architecture was provided, including aspects such as synchronization, data transmission, and power management. Attention was turned to the selection process for each critical component of the system. MEMS accelerometers emerged as an optimal choice due to their compact size, robustness, and lower power consumption. Among several candidates, the Analog Devices ADXL355 accelerometer was selected for its superior resolution and low noise density. The GPS module, which serves as an absolute time reference for synchronization, was considered necessary, and the NEO-6M module was chosen for its combination of features and performance. Finally, the WiFi platform was selected based on the need for a fast and reliable connection to a wireless gateway, with the ESP8266 platform emerging as the optimal choice due to its affordability, performance, and strong support community. The robust integration and programming of the above components, mounted on a custom 3D printed enclosure, is expected to provide an efficient distributed acceleration recording solution.

This SHM system is a key component of the RISE project, which is dedicated to improving the utilization of structural health monitoring techniques for bridge performance assessment and real-time safety information provision, particularly after extreme events. Despite its compact and cost-effective design, the system is expected to deliver accurate acceleration data, indicating potential applicability in real-world situations. The project roadmap establishes the framework for ongoing system improvement, a rigorous assessment of its reliability and performance, and an exploration of potential enhancements to its existing capabilities. These efforts are expected to make a significant contribution to the progression of structural health monitoring.

## ACKNOWLEDGEMENT

The research project was supported by the Hellenic Foundation for Research and Innovation (H.F.R.I.) under the "2nd Call for H.F.R.I. Research Projects to support Faculty Members & Researchers" (Project Number: 4191).

## REFERENCES

[1] Iranmanesh, A. and Ansari, F. Energy-Based Damage Assessment Methodology for Structural Health Monitoring of Modern Reinforced Concrete Bridge Columns. Journal of Bridge Engineering, 19(8), 2014.

[2] Prendergast, L. J., Limongelli, M. P., Ademovic, N., Anžlin, A., Gavin, K., & Zanini, M. Structural Health Monitoring for Performance Assessment of Bridges under Flooding and Seismic Actions. Structural Engineering International, 28(3), 2018.

[3] Anastasopoulos, I. et al. Development of RApid REsponse (RARE) System for Motorway Bridges: Overview and Pilot Application to Attiki Odos Motorway. Int. J. Geoengin. Case Hist., 2018.

[4] Androutselis, T. et al. Real-Time Seismic Damage Assessment of Various Bridge Types Using a Nonlinear Three-Stage Least Squares Approach. J. Infrastruct. Syst. 26(3):04020019, 2020.

[5] Papanikolaou, V.K., Kartalis-Kaounis, T., Protopapadakis, E. and Papadopoulos, T. A New Graphical User Interface for OpenSees", OpenSees Days Europe, Porto, Portugal, June 2017.

[6] Papanikolaou, V.K and Karakostas, C.Z. A low cost MEMS-based accelerograph, Experimental Vibration Analysis for Civil Engineering Structures EVACES'13, Ouro Preto, Brazil, October 2013

COMPDYN 2023
9th ECCOMAS Thematic Conference on
Computational Methods in Structural Dynamics and Earthquake Engineering
M. Papadrakakis, M. Fragiadakis (eds.)
Athens, Greece, 12-14 June 2023

# A DAMAGE DETECTION APPROACH TO ASSESS THE PERFORMANCE LEVEL OF R/C BRIDGES USING VIBRATIONAL RESPONSE MEASUREMENTS

**K. Mixios[1], O. Markogiannaki[2], S. Stefanidou[1], V. Papanikolaou[1]**

[1] Aristotle University of Thessaloniki
Thessaloniki, Greece
e-mail: {mixioske, ssotiria, billy}@civil.auth.gr

[2] REDI Engineering Solutions PC
markogiannaki.olga@gmail.com

## Abstract

*Bridge damage presents risks to road safety and traffic flow, potentially resulting in significant economic losses, both direct and indirect. Therefore, there is an urgent need to develop and implement systems for evaluating the structural health of bridges. This study introduces a methodology that utilizes measured vibration data from initial and damaged responses of a monitored bridge system to identify damage. A highly detailed finite element model consistent with the measured data is employed for this purpose. The model parameters of the damaged structure are estimated using optimization algorithms to identify, localize, and quantify damage. Capacity curves for both the calibrated and the damaged bridge are developed to evaluate the effect of the damage on the global response of the bridge. The approach is applied to monolithic R/C bridge in a case study, and simulated experiments (e.g. damage scenarios) are conducted to demonstrate the proposed methodology.*

**Keywords:** capacity curves, damage detection, R/C bridges.

## 1 INTRODUCTION

The research topic of identifying structural damage in bridges has gained significant attention over the years. Its increased popularity can be primarily attributed to the aging road and rail infrastructure, which faces traffic loading conditions that far exceed the original design criteria. This unprecedented increase in loading speeds up structural fatigue, leading to a decrease in the service life of these bridges. Moreover, as the bridge infrastructure continues to age and deteriorate, it becomes necessary to increase the frequency of inspections to compensate for the reduced safety of these structures. However, this task is challenging due to its immense scale. Europe has approximately one million highway bridges, and 35% of its half a million rail bridges are over a century old [1]. Consequently, there has been a significant surge in research focused on effectively managing the maintenance and upkeep of these bridges [2]. One area of study that has gained prominence is the investigation of vibration-based techniques for detecting and identifying damage.

In the past few decades, the most extensively studied techniques for detecting damage in structures have been traditional modal-based methods. The concept of utilizing measured vibrations to identify structural damage has been employed for quite some time. Traditional modal parameters such as shifts in natural frequency and other modal properties like mode shapes, damping ratios, and modal curvatures have conventionally been utilized for damage detection [3]. Ideally, these properties should be obtained dynamically from a bridge prior to its initial opening, if feasible, using ambient and forced vibration. Mode shapes offer distinct advantages as they are less affected by environmental factors compared to natural frequencies. Additionally, they encompass both local and global information, making them valuable for damage localization. Over the years, several mode shape monitoring techniques have been developed. One such technique is the modal assurance criterion (MAC) [4], [5], which assesses changes in mode shapes across the entire structure by utilizing eigenvector orthogonality. Building upon MAC, Kim et al [6] introduced the coordinate modal assurance criterion (COMAC), which monitors modal node displacement to detect and pinpoint damage. COMAC can be applied to a node i by measuring the normalized difference between mode shape vectors under undamaged ($\varphi u_{i,j}$) and damaged ($\varphi d_{i,j}$) conditions. The application of MAC and COMAC in bridge structures revealed that these methods not only detected most structural changes and their locations but also identified instances of false or spurious damage [7]. Nevertheless, modal-based methods encounter limitations in terms of efficiency when local damage does not significantly alter the modal properties of the structure. This is particularly true when the severity of the damage has a minimal impact on the overall integrity of the structural system. As a result, damage indicators that rely on measured data directly come into play, encompassing various approaches such as frequency response functions (FRFs), operating deflection shapes, and transmittance functions, among others [8]. To address the limitations of conventional structural damage detection methods, various frameworks for structural monitoring have been developed, as highlighted by [8], [9].

This study introduces a novel framework for damage detection in reinforced concrete (R/C) bridges, focusing on the utilization of vibrational measurements and on the estimation of the severity of the identified damage. The computational framework employs the Dynamic Mode Decomposition method to detect potential damages in R/C bridges, and the results are validated using a reference finite element model with selected damage scenarios. The location and severity of the identified damage are determined through a model update process utilizing the Particle Swarm Optimization algorithm. Furthermore, the proposed approach involves comparing the capacity curves of the models towards an accurate estimation of the severity of the damage in relation to the bridge system. The framework is applied to a typical three-span

bridge, utilizing simulated acceleration recordings for the chosen damage scenarios. The results demonstrate the reliability of the proposed process, providing valuable information about the actual condition of the bridge to stakeholders.

## 2 METHODOLOGY

This research paper presents a detailed approach to identifying damage in reinforced concrete (R/C) bridges. The methodology places significant emphasis on localizing and quantifying the extent of damage within bridge components by utilizing vibrational measurements. The following outlines the specific stages of the methodology:

**Step 1:** A finite element model of the structure studied is created using appropriate finite element software (e.g., OpenSees [10]). Ensuring the simulation's accuracy with respect to the physical model is crucial for more precise damage calculations. The model of step 1 is the healthy model of the considered structure.

**Step 2:** A sensitivity analysis is conducted. The purpose of conducting a sensitivity analysis is to identify the crucial parameters in a model. This analysis helps in clustering the parameters of the bridge model, such as Young's modulus of elasticity and moment-curvature relationships of pier sections, based on the similarity of their effects on the model's response. The sensitivity analysis in this case utilizes the mode shapes as the objective function. Another commonly employed method in such applications is the frequency response function (FRF) [8].

**Step 3:** The capacity curve of the healthy bridge is estimated via pushover analysis of the bridge system [11]. To conduct the pushover analysis, a horizontal load is applied longitudinally along the bridge's span, specifically at the locations corresponding to the piers. This load distribution enables the evaluation of the structural response and performance under progressively increasing displacement demands, providing valuable insights into the behavior of the bridge.

**Step 4:** The development of damaged models involves considering various damage scenarios based on the reference model. Once the model parameters have been clustered, modified values are assigned to the variables within the most sensitive clusters to create the damaged models. The number of variables can vary depending on the complexity of the model simulation. In accordance with the structural bridge system, different damage scenarios are chosen for analysis.

**Step 5**: The damaged bridge response is measured by determining the locations for placing accelerometers on the bridge deck. These accelerometers are positioned at locations where a series of maximum eigen-displacements are expected to occur. One advantage of having a finite element model before conducting field investigations is that it provides valuable insights into the behavior of the structure. Installing multiple accelerometers can improve the accuracy of the results, as it allows for a more precise observation of the system's response. In on-site applications, it is recommended to attach the accelerometers to the center of the bridge deck to avoid any torsional effects.

**Step 6:** Damage detection using Dynamic Mode Decomposition (DMD) [12]. The acceleration data retrieved from the sensors are used in the procedure of Dynamic Mode Decomposition (DMD). DMD is data-driven by nature, and the first step is to collect snapshots pairs of a system's state as it develops over time. These snapshot pairings are designated as $\{(x(t_k), x(t_k'))\}_{k=1}^{m}$, where $t_k' = t_k + \Delta t$ and the time-step Δt in order to identify high frequencies A snapshot represents the state of a system, reshaped into a high-dimensional column vector. These snapshots can be depicted in two data matrices $\boldsymbol{X}, \boldsymbol{X'}$.

$$\boldsymbol{X} = [\, x(t_1) \quad x(t_2) \ \ldots \quad x(t_m)] \tag{1}$$

$$\boldsymbol{X'} = [\, x(t'_1) \quad x(t'_2) \ \ldots \quad x(t'_m)] \tag{2}$$

The DMD algorithm seeks the leading spectral decomposition of the most accurate fitted linear operator **A** that correlates the two snapshot matrices in the time domain.

$$\boldsymbol{X'} \approx \boldsymbol{AX} \tag{3}$$

Operator **A** then establishes a linear dynamic system that best advances snapshot measurements in time. The best-fit operator A is defined as:

$$A = argmin\left|\left|\boldsymbol{X'} - \boldsymbol{AX}\right|\right|_F \tag{4}$$

An ambient vibration is imposed to retrieve the damaged model's state due to the basic assumption of DMD. DMD provides a modal decomposition consisting of spatially correlated components that have the same linear behavior in time. Therefore, the state of the bridge is not changing over time.

The DMD procedure is summarized in the following steps:

- The singular value decomposition of **X** is computed.

$$\boldsymbol{X} \approx \widetilde{\boldsymbol{U}}\widetilde{\boldsymbol{\Sigma}}\widetilde{\boldsymbol{V}}^{*} \tag{5}$$

Where $\widetilde{\mathbf{U}} \in \mathbb{C}^{n\times r}, \widetilde{\mathbf{\Sigma}} \in \mathbb{C}^{r\times r}$, and $\widetilde{\mathbf{V}} \in \mathbb{C}^{m\times r}$, and $r \leq m$ denotes either the exact or the approximate rank of the data matrix **X**.

- A full matrix A is obtained, computing the pseudo-inverse of **X**.

$$\mathbf{A} = \mathbf{X'}\widetilde{\mathbf{V}}\widetilde{\mathbf{\Sigma}}^{-1}\widetilde{\mathbf{U}}^{*} \tag{6}$$

- The spectral decomposition of **A** is computed:

$$\widetilde{\mathbf{A}}\mathbf{W} = \mathbf{W}\boldsymbol{\Lambda} \tag{7}$$

- The high-dimensional DMD modes $\boldsymbol{\Phi}$ are reconstructed using the eigenvectors **W** of the reduced system and the time-shifted snapshot matrix $\boldsymbol{X'}$ according to

$$\boldsymbol{\Phi} = \mathbf{X'}\widetilde{\mathbf{V}}\widetilde{\mathbf{\Sigma}}^{-1}\mathbf{W} \tag{8}$$

- Remarkably, these DMD modes are eigenvectors of the high-dimensional **A** matrix corresponding to the eigenvalues in $\boldsymbol{\Lambda}$.

$$\begin{aligned}\mathbf{A}\boldsymbol{\Phi} &= \left(\mathbf{X'}\widetilde{\mathbf{V}}\widetilde{\mathbf{\Sigma}}^{-1}\underbrace{\widetilde{\mathbf{U}}^{*}\big)\big(\mathbf{X'}\widetilde{\mathbf{V}}\widetilde{\mathbf{\Sigma}}^{-1}}_{\widetilde{\mathbf{A}}}\mathbf{W}\right)\\ &= \mathbf{X'}\widetilde{\mathbf{V}}\widetilde{\mathbf{\Sigma}}^{-1}\widetilde{\mathbf{A}}\mathbf{W}\\ &= \mathbf{X'}\widetilde{\mathbf{V}}\widetilde{\mathbf{\Sigma}}^{-1}\mathbf{W}\boldsymbol{\Lambda}\\ &= \boldsymbol{\Phi}\boldsymbol{\Lambda}.\end{aligned} \tag{9}$$

The state of the model is finally defined utilizing the eigenvectors calculated above. The localization of the damage is the output of a model update process. The methodology followed for the model update is based on particle swarm optimization (PSO) described in Fig. 1 as proposed in [13] and is described in detail below.

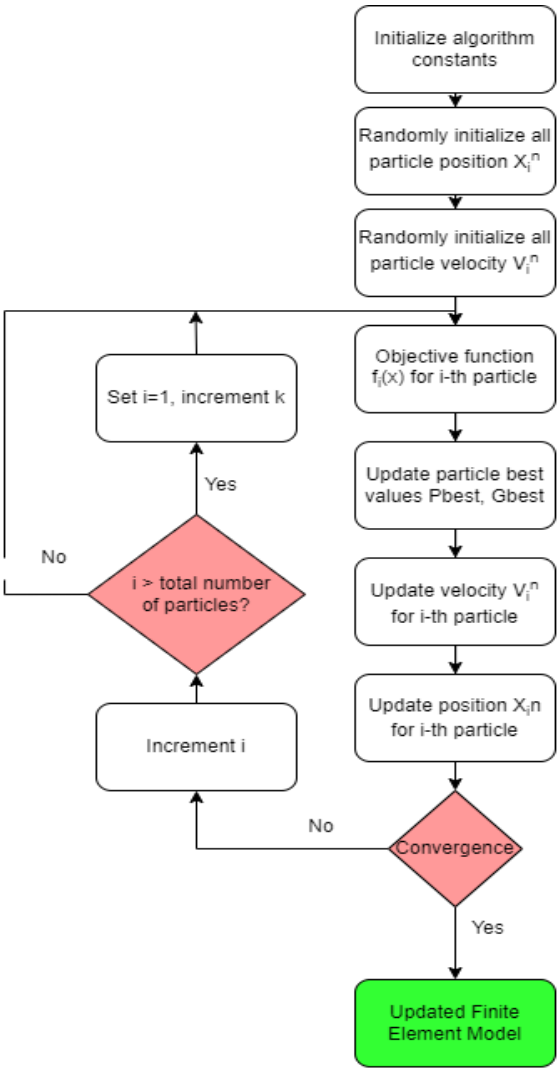


Figure 1. Workflow of the Particle Swarm Optimization procedure.

The main steps can be summarized as follows:

- Initialization of the algorithm constants (position and velocity vectors), definition of the number of particles. Definition of an objective function. Recording and updating the best particle position and the best position ever reached.
- Updating the velocity of each particle based on:

$$\boldsymbol{x}_{ij}^{n+1} = \boldsymbol{x}_{ij}^{n} + \boldsymbol{v}_{ij}^{n+1} \tag{10}$$

where $v_{ij}^{n+1}$ is the velocity vector and $x_{ij}^{n+1}$ is the position vector in the iteration n + 1, $\boldsymbol{x}_{ij}^{n}$ is the position vector in iteration n. The velocity vector of the particle swarm is calculated with the equation:

$$\boldsymbol{v}_{ij}^{n+1} = w\boldsymbol{v}_{ij}^{n} + C_1\text{rand}_1\left(\textbf{Pbest}_{ij} - \boldsymbol{x}_{ij}^{n}\right) + C_2\text{rand}_2\left(\textbf{Gbest}_{j} - \boldsymbol{x}_{ij}^{n}\right) \quad (11)$$

where C1 and C2 are the learning factors, and $\text{rand}_1$ and $\text{rand}_2$ the random values between 0 and 1. $\text{Pbest}_{ij}$ and $\text{Gbest}_{j}$ are the best positions that i-th particle achieved closest to the target since the start of the procedure.

- Update the position of every particle based on the behavior of the swarm.

The above method ends when the termination criteria are fulfilled. Fig. 1 depicts the particle swarm optimization method. PSO does not require any knowledge of the function formula or its derivatives and can investigate numerous potential solutions. Since it is a global approach, its performance is independent of the original population solutions.

**Step7:** Finally, a pushover analysis is performed on the updated model with damage in order to extract its capacity. The new capacity of the model is compared to the initial capacity of the model (healthy model) in terms of displacement ductility ($\delta_4/\delta_y$).

The workflow of the methodology proposed herein containing the steps described above is shown in Fig. 2.

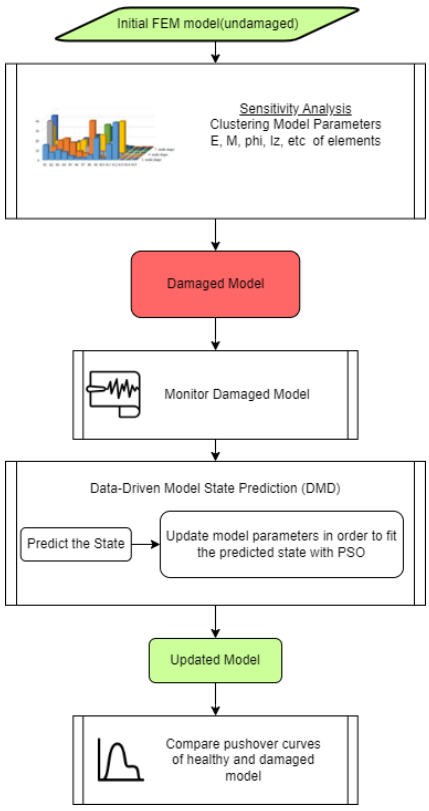


Figure 2. Workflow of the proposed methodology.

## 3 CASE STUDY

The described methodology is implemented on a typical three-span bridge located in Northern Greece. The bridge consists of three spans, with the outer spans measuring 27 m each and the central span measuring 45 m. The deck of the bridge is a prestressed concrete box girder section, 10 m wide. The piers have a solid circular reinforced concrete section with a diameter of 2.0 m and are connected monolithically to the deck. Figure 3 illustrates that the left pier has a height of 7.9 m, while the right pier has a height of 9.3 m due to the longitudinal slope of the bridge axis. The abutments of the bridge are seat-type, with a backwall height of 2.5 m [14], [15]. At the abutment positions, the deck is supported by two elastomeric bearings.

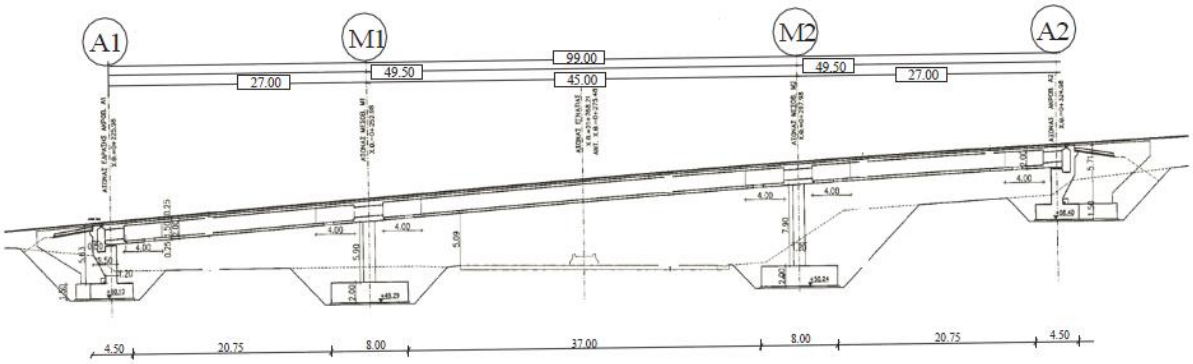


Figure 3. Longitudinal section of the bridge model.

| Parameters | | Lower Bound | Upper Bound | Nominal Values |
|---|---|---|---|---|
| Young Modulus E (right pier) [MPa] | 1 | 18733.20 | 43710.80 | 31222.00 |
| Young Modulus E (left pier) [kPa] | 2 | 18733.20 | 43710.80 | 31222.00 |
| Yielding Moment Top Section – My_top(left pier) [kNm] | 3 | 16770.8 | 39131.9 | 27951.4 |
| Yielding Moment – My_bottom (left pier) [kNm] | 4 | 16883.0 | 39393.6 | 28138.3 |
| Ultimate Moment Top Section – Mu_top(left pier) [kNm] | 5 | 17185.8 | 40100.2 | 28643.0 |
| Ultimate Moment Bottom Section – Mu_bottom (left pier) [kNm] | 6 | 17280.7 | 40321.6 | 28801.2 |
| Yielding Moment Top Section – Mu_top (right pier) [kNm] | 7 | 16735.6 | 39049.8 | 27892.7 |

| | | | | |
|---|---|---|---|---|
| Yielding Moment Bottom Section – My_bottom (right pier) [kNm] | 8 | 16895.3 | 39422.4 | 28158.9 |
| Ultimate Moment Top Section – Mu_top (right pier) [kNm] | 9 | 17153.22 | 40024.2 | 28588.7 |
| Ultimate Moment Bottom Section – Mu_bottom | 10 | 17287.1 | 40336.6 | 28811.9 |
| Yielding curvature Top Section – curvature_top (left pier) | 11 | 17287.1 | 40336.6 | 28811.9 |
| Yielding curvature Bottom Section – curvature_bottom (left pier) | 12 | 0.001706014 | 0.0039807 | 0.002843357 |
| Ultimate curvature Top section – curvature_top (left pier) | 13 | 0.00169238 | 0.00395789 | 0.002827064 |
| Ultimate curvature Bottom section – curvature_bottom (left pier) | 14 | 0.04416 | 0.10304 | 0.0736 |
| Yielding curvature Top section – curvature_top (right pier) | 15 | 0.001707499 | 0.003984163 | 0.002845831 |
| Yielding curvature Bottom Section – curvature_bottom (right pier) | 16 | 0.001695788 | 0.00395684 | 0.002826314 |
| Ultimate curvature Top Section – curvature_top (right pier) | 17 | 0.4416 | 0.10304 | 0.0736 |
| Ultimate curvature Bottom Section – curvature_bottom (right pier) | 18 | 0.04416 | 0.10304 | 0.0736 |
| Gaps | 19 | 0.01 | 0.10 | 0.10 |

**Table 1.** Parameters of cluster A grouped from the sensitivity analysis. Lower and Upper Bounds is also given for the sensitivity analysis.

The model was constructed using OpenSeesPy [16], which is a Python library serving as an interface to the OpenSees software. The bridge elements are modeled as elastic, while the piers incorporate a plastic hinge formulation at both ends. The applied loads on the bridge are limited to gravitational forces. To generate the damaged model, a sensitivity analysis and

clustering procedure were conducted. As mentioned earlier, the parameters were grouped based on their influence on the bridge's response, utilizing the unweighted multiple group method with arithmetic mean [17].

The results of the sensitivity analysis are summarized in Table 1. Two damage scenarios were executed to assess and validate the proposed methodology (Fig. 4). In the first scenario, a decrease in the yield moment and Young's modulus of elasticity was applied to the left pier. The same reduction was implemented for the right pier in the second scenario. Extended damage was represented by a 40% reduction in the properties of the pier elements. Furthermore, is assumed that the gaps between the deck and the abutments are effectively closed.

The locations for placing acceleration recorders on the bridge deck were determined based on where the maximum eigen displacements occur (Fig. 5). Modal analysis was performed on the reference model to obtain the eigenmodes and the model's response. To apply the proposed methodology, simulated damage scenarios were considered, and the Dynamic Mode Decomposition (DMD) process was implemented. Given the complexity of existing libraries, the authors developed a lightweight Python library for this purpose. The result of the DMD procedure is the state of the damaged model. Particle swarm optimization is employed to determine the values of the model parameters that correspond to the specific damage scenario being considered.

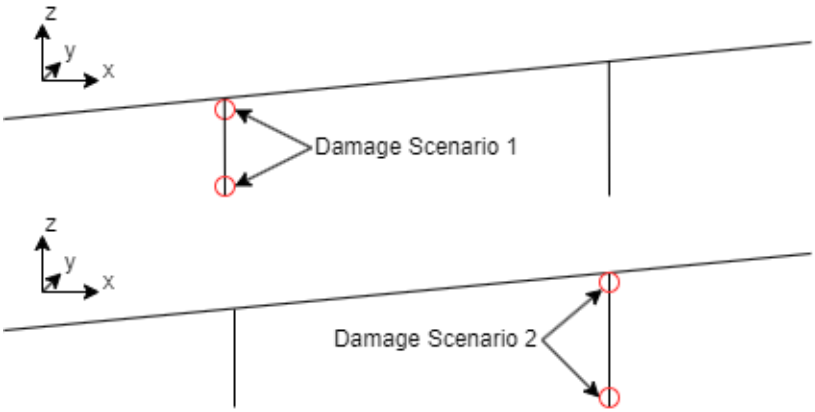


Figure 4. Locations of the damge scenarios implementation

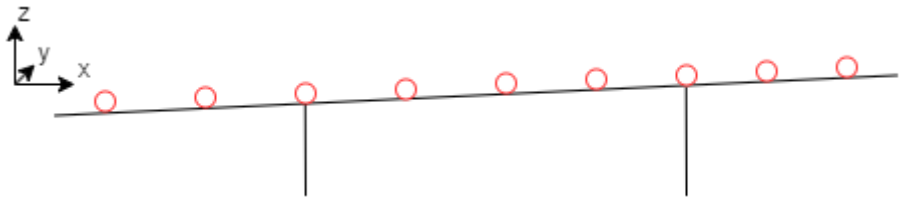


Figure 5. Acceleration recorder location on the bridge deck

## 4 RESULTS AND CONCLUSIONS

The efficiency of the proposed methodology is demonstrated in Figures 6-7. The predicted damaged model exhibits periods that are comparable to the initial model with damage in both scenarios. This indicates that the DMD process accurately captures the modal properties of the dynamic system. Figure 8 illustrates the changes in the model's behavior resulting from the damage scenarios in relation to the healthy model. The slight discrepancies can be attributed to the numerical assumptions and computational procedures of the solver used in the analysis. It is evident that these differences are marginal.

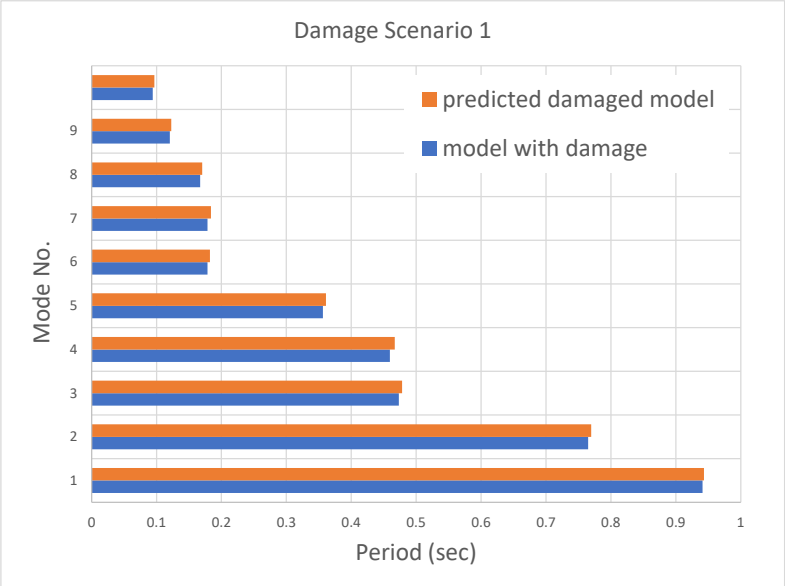


Figure 6. Comparison of the known damaged model and the predicted damaged model. (Scenario 1)

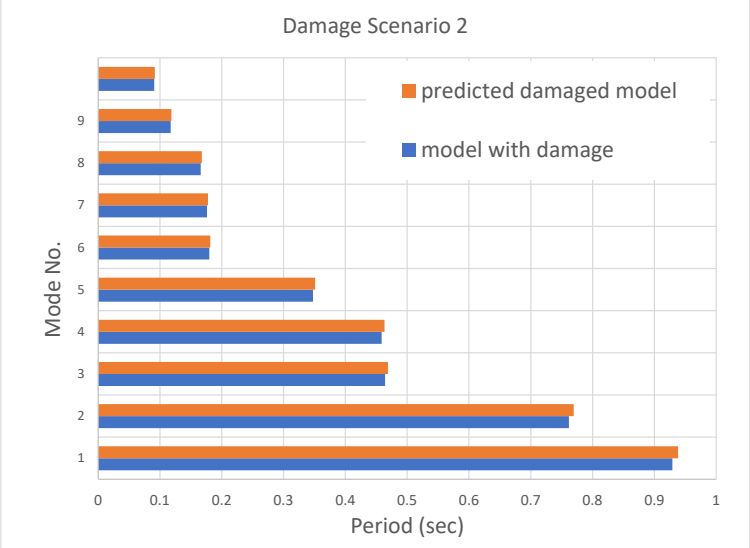


Figure 7. Comparison of the known model and the predicted damaged model. (Scenario 2)

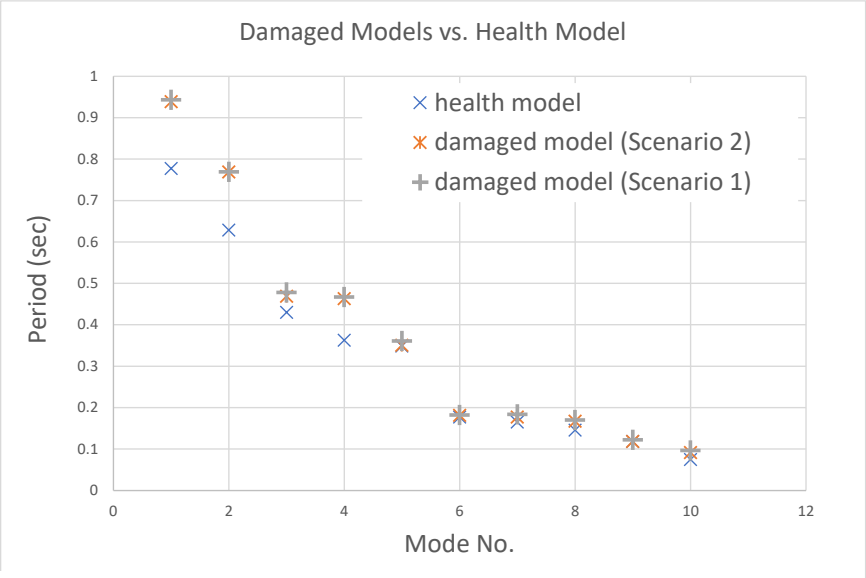


Figure 8. Comparison of Undamaged model and known damaged models.

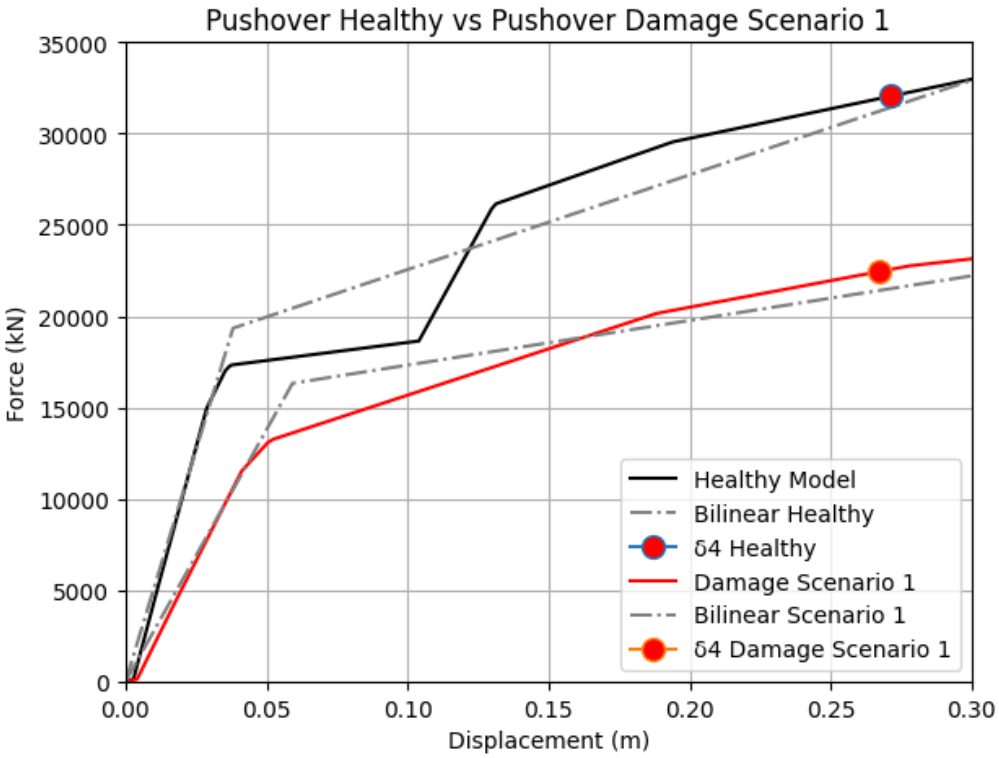


Figure 9. Pushover analysis of undamaged model and damaged model (Scenario 1)

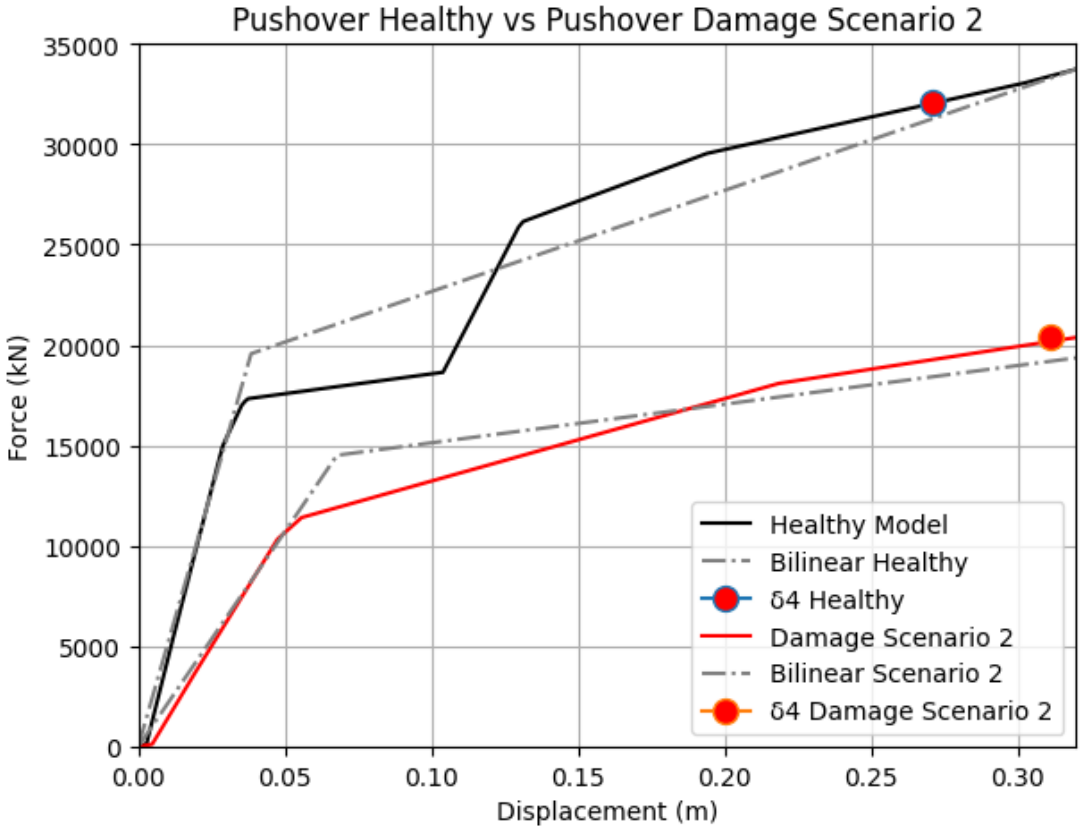


Figure 10. Pushover analysis of undamaged model and damaged model (Scenario 2)

Figure 9 and 10 show the pushover curves of the damaged model of Scenario 1 and Scenario 2, respectively, in comparison to the pushover curve of the undamaged model. By examining the pushover curves of the damaged model, it is evident that its load-carrying capacity has been decreased. Moreover, the comparison of the two pushover curves reveals a significant difference in stiffness, with the damaged model exhibiting a lower stiffness compared to the healthy one. In the healthy model's pushover curve, distinct stiffness changes (change of slope) are observed. The first change in slope occurs at the position corresponding to a lateral force of 17000 kN, coinciding with the occurrence of pier-yielding phenomena. Additionally, a second change in stiffness is observed at a displacement of 0.10 m, indicating the contribution of abutment stiffness after the closure of the gap. Based on an analysis of the pushover curves of the damaged models, notable variations in stiffness are evident. Specifically, a discernible change in stiffness can be observed in the pushover curves of damaged model 1 and damaged model 2. These changes occur at approximately 13000 kN and 12000 kN load magnitudes, respectively. Upon examining the pushover curves of the damaged models, it is evident that the initial slope of these curves reflects the combined stiffness originating from both the abutment and the piers. However, unlike the healthy model pushover curve, the activation mechanism of the abutment is not readily apparent in the damaged models' curves. As the piers yield, a notable alternation in stiffness occurs. Subsequently, the post yield behavior of the structure conforms to the moment-curvature

constitution law assigned to each pier. The aforementioned observations are applicable to both scenarios investigated in this research.

The data points illustrated in Figure 9 and Figure 10 correspond to the displacement at which a 10% reduction in moment occurs within the cross-section constitutive law (hinge) of piers. The displacement ductility ($\delta_4/\delta_y$) of each model is $\mu_{\delta,Healthy} = 6.675$, $\mu_{\delta,Damage1} = 4.5166$ $\mu_{\delta,Damage2} = 4.568$. In other words, the healthy model demostrates a higher ductility in comparison to the other two models.

Future investigations can be conducted into models with nonlinearities, such as active and passive damping systems. Examples include models incorporating elastomeric bearings connecting the deck to the piers or employing tuned mass dampers and base isolation techniques for vibration control. The accuracy and precision of the model updating process can be enhanced by applying diverse methodologies. Optimization algorithms like simulated annealing, grey-wolf optimization, colliding bodies optimization, and gravitational search algorithms offer distinct characteristics that can be tailored to meet specific model updating requirements. Furthermore, advanced data-driven methods and machine learning techniques can be explored to enhance damage detection and localization accuracy. Techniques such as artificial neural networks, support vector machines, and ensemble learning methods have shown promise in various structural health monitoring applications, contributing to the refinement of the proposed methodology.

## 5 AKNOWLEDGEMENTS

The research project was supported by the Hellenic Foundation for Research and Innovation (H.F.R.I.) under the “2nd Call for H.F.R.I. Research Projects to support Faculty Members & Researchers” (Project Number: 4191).

## REFERENCES

[1] L. Elfgren, Benchmark of new technologies to extend the life of elderly rail infrastructure: Deliverable D1. 1 of the MAINLINE Project. MAINLINE, 2013.

[2] J. Casas, “Assessment and monitoring of existing bridges to avoid unnecessary strengthening or replacement,” presented at the Bridge Maintenance, Safety, Management and Life-Cycle Optimization: Proceedings of the Fifth International IABMAS Conference, Philadelphia, USA, 11-15 July 2010, CRC Press, 2010, p. 444.

[3]J. R. Casas and A. C. Aparicio, “Structural damage identification from dynamic-test data,” Journal of Structural Engineering, vol. 120, no. 8, pp. 2437–2450, 1994.

[4] R. J. Allemang, “The Modal Assurance Criterion – Twenty Years of Use and Abuse,” SOUND AND VIBRATION, 2003.

[5] X. Q. Zhu and S. S. Law, “Structural Health Monitoring Based on Vehicle-Bridge Interaction: Accomplishments and Challenges,” Advances in Structural Engineering, vol. 18, no. 12, pp. 1999–2015, Dec. 2015, doi: 10.1260/1369-4332.18.12.1999.

[6] K.-C. Chang and C.-W. Kim, “Modal-parameter identification and vibration-based damage detection of a damaged steel truss bridge,” Engineering Structures, vol. 122, pp. 156–173, Sep. 2016, doi: 10.1016/j.engstruct.2016.04.057.

[7] O. S. Salawu and C. Williams, “Bridge Assessment Using Forced-Vibration Testing,” Journal of Structural Engineering, vol. 121, no. 2, pp. 161–173, Feb. 1995, doi: 10.1061/(ASCE)0733-9445(1995)121:2(161).

[8] O. Markogiannaki, A. Arailopoulos, D. Giagopoulos, and C. Papadimitriou, "Vibration-based Damage Localization and Quantification Framework of Large-Scale Truss Structures," Structural Health Monitoring, vol. 22, no. 2, pp. 1376–1398, Mar. 2023, doi: 10.1177/14759217221100443.
[9] H. S. Atamturktur, B. Moaveni, C. Papadimitriou, and T. Schoenherr, Eds., Model Validation and Uncertainty Quantification, Volume 3: Proceedings of the 33rd IMAC, A Conference and Exposition on Structural Dynamics, 2015. in Conference Proceedings of the Society for Experimental Mechanics Series. Cham: Springer International Publishing, 2015. doi: 10.1007/978-3-319-15224-0.
[10] F. McKenna, G. L. Fenves and M. H. Scott (2000). Open System for Earthquake Engineering Simulation. University of California, Berkeley, http://opensees.berkeley.edu.
[11] R. Pinho, C. Casarotti, and S. Antoniou, "A comparison of single-run pushover analysis techniques for seismic assessment of bridges," Earthquake Engineering & Structural Dynamics, vol. 36, no. 10, pp. 1347–1362, 2007, doi: 10.1002/eqe.684.
[12] J. H. Tu et al., "On dynamic mode decomposition: Theory and applications," Journal of Computational Dynamics, vol. 1, no. 2, pp. 391–421, 2014, doi: 10.3934/jcd.2014.1.391.
[13] M. O. Okwu, L. K. Tartibu, M. O. Okwu, and L. K. Tartibu, "Particle swarm optimisation," Metaheuristic Optimization: Nature-Inspired Algorithms Swarm and Computational Intelligence, Theory and Applications, pp. 5–13, 2021.
[14] I. G. Mikes and A. J. Kappos, "Optimization of the seismic response of bridges using variable-width joints," Earthquake Engineering & Structural Dynamics, vol. 52, no. 1, pp. 111–127, Jan. 2023, doi: 10.1002/eqe.3751.
[15] S. P. Stefanidou, A. G. Sextos, A. N. Kotsoglou, N. Lesgidis, and A. J. Kappos, "Soil-structure interaction effects in analysis of seismic fragility of bridges using an intensity-based ground motion selection procedure," Engineering Structures, vol. 151, pp. 366–380, 2017.
[15] M. Zhu, F. McKenna, and M. H. Scott, "OpenSeesPy: Python library for the OpenSees finite element framework," SoftwareX, vol. 7, pp. 6–11, Jan. 2018, doi: 10.1016/j.softx.2017.10.009.
[17] Li Yujian and Xu Liye, "Unweighted Multiple Group Method with Arithmetic Mean," in 2010 IEEE Fifth International Conference on Bio-Inspired Computing: Theories and Applications (BIC-TA), Changsha, China: IEEE, Sep. 2010, pp. 830–834. doi: 10.1109/BICTA.2010.5645232.

COMPDYN 2023
9th ECCOMAS Thematic Conference on
Computational Methods in Structural Dynamics and Earthquake Engineering
M. Papadrakakis, M. Fragiadakis (eds.)
Athens, Greece, 12-14 June 2023

# A 3D FRACTURE ENERGY-BASED SMEARED CRACK APPROACH FOR THE NONLINEAR BEHAVIOR OF REINFORCED CONCRETE STRUCTURES.

**Christos Mourlas[1], George Markou[2] and Manolis Papadrakakis[3]**

[1] Czech Technical University in Prague, Faculty of Civil Engineering, Thákurova 7, 166 29 Prague,Czech Republic
christos.mourlas@fsv.cvut.cz

[2] Department of Civil Engineering, University of Pretoria, South Africa
e-mail: george.markou@up.ac.za

[3] Department of Civil Engineering, National Technical University of Athens, Greece
e-mail: mpapadra@central.ntua.gr

## Abstract

*This research study presents a novel energy-based constitutive model of concrete in the framework of the smeared crack approach. The proposed model constitutes an extension to a previous numerical model [1,2] with an addition of a fracture energy-based algorithmic approach developed by [3]. The uncracked behavior of concrete is based on the experimental evidence of the triaxial behavior of concrete described in the literature [4]. The cracked behavior of concrete is modelled with a fracturing approach while cracking is treated with the smeared crack approach. The proposed modelling approach manages to capture the behavior of reinforced concrete (RC) structures with computational efficiency and numerical accuracy as it combines the experimental triaxial behavior of concrete in an algorithmic framework that can alleviate numerical issues of nonlinear concrete behavior such as cracking. The numerical simulation is implemented by using hexahedral isoparametric finite elements for discretizing the concrete domain and truss elements for the steel reinforcement. The proposed approach has been tested on two RC specimens focusing on structural members with insufficient shear reinforcement and high shear stresses. The numerical behavior has been validated by the comparison of the numerical with experimental data found in the international literature. The effect of choosing different approaches of the smeared crack method (fixed and rotated) is also investigated.*

**Keywords:** Cracking, Fracture, smeared crack approach, 3D FEM, Detailed modeling, Shear behavior.

## 1 INTRODUCTION

In the last few decades, many numerical models have been proposed to simulate the mechanical behavior of reinforced concrete (RC) structures. Many models can be found in the literature that can describe specific aspects of concrete behavior and their applications are limited to certain cases of little practical interest. These constitutive models emphasize the post-peak material by introducing several material parameters. The values of these parameters are usually calculated after a parametric investigation in an attempt to directly match the numerical and experimental results by reverse-engineering the problem. This approach leads to the loss of objectivity and the inability to use this approach to perform predictive analysis.

The constitutive model of the behavior of concrete must describe a realistic behavior of concrete under a generalized three-dimensional state of stress. The key features of every numerical approach must consider:

1. Nonlinear stress-strain behavior under a multiaxial state of stress.
2. Strain softening behavior and the anisotropic elastic degradation.
3. Progressive cracking caused by tensile stress and strains.

There are many models proposed for RC structures, in the literature [1-6]. Each model has its advantages and disadvantages resulting from its limitations. Many models combine plasticity formulations for concrete behavior under compression with fracture energy-based approaches for tension [3]. In addition, several models based on damage mechanics [7, 8] are proposed for the behavior of concrete under monotonic and cyclic loading conditions.

However, a numerical approach combined with a constitutive model for concrete behaviour that produces accurate and computationally efficient results for any RC structural member is still an open research topic. An accurate, objective, and computationally efficient approach will be a powerful tool for any professional civil engineer and scientist studying the seismic behavior of existing RC structures or performing the design of retrofit interventions for severely deteriorated RC structures.

The model proposed in [1], describes the triaxial behavior of concrete without the need of introducing numerous parameters of the concrete material. The proposed constitutive relations have been derived from the experimental and numerical work of Kotsovos and Pavlovic [4]. The only parameters required to be defined in their proposed algorithmic approach [4], are the uniaxial compressive strength, the tensile strength, Young's modulus, and Poisson's ratio. The model has been improved in [2] where damage factors have been introduced that they are being automatically defined according to the number of cycling loads and the number of cracks. The key features of this numerical approach are accuracy, numerical simplicity and stability, and computational efficiency. These features made the model attractive even for the analysis of large-scale structures [9].

The accuracy of the model is mainly based on the smeared crack approach and the algorithmic approach that has been applied for every stress state [2]. However, this approach can lead to excessive cracking in order to represent a severely damaged state. Although the model doesn't appear to have mesh sensitivity issues [10], it is difficult to prove with the current algorithmic approach. To control the smeared cracking, a crack band approach [11] must be applied.

In this article, a connection between two algorithmic approaches is proposed and tested in terms of computational stability and numerical accuracy. In addition, a discussion takes place in relation to the use of different smeared crack approaches and how every approach affects the behavior of the RC numerical model. Finally, the model is examined and its ability to model RC structures that are subjected to monotonic loading conditions is evaluated.

## 2 UNCRACKED CONCRETE MATERIAL CONSTITUTIVE MODEL

The stress-strain relationships are expressed by decomposing each state of strain and stress into hydrostatic and deviatoric components. Therefore, the normal and shear octahedral stresses ($\sigma_0$, $\tau_0$) and strains ($\varepsilon_0$, $\gamma_0$) are used. It is known that hydrostatic stresses $\sigma_0$ induce the variation of the volumetric strain $\varepsilon_{0(h)}$, while the application of deviatoric stresses $\tau_0$ cause both volumetric and deviatoric strains. The combined approach presented by Kotsovos and Pavlovic [4] is based on the use of the bulk modulus *K* and the shear modulus *G* which describe the non-linear $\sigma_0$-$\varepsilon_{0(h)}$ and $\tau_0$-$\gamma_{0(d)}$ behavior combined with the use of $\sigma_{id}$ to take into account the coupling effect of $\tau_0$-$\varepsilon_{0(d)}$ (*h* and *d* stand for hydrostatic and deviatoric components, respectively). The $\sigma_{id}$ is an equivalent external stress which can be added to the externally applied hydrostatic stress. The constitutive relations take the following form:

$$\varepsilon_0 = \varepsilon_{0(h)} + \varepsilon_{0(d)} = (\sigma_0 + \sigma_{id}) / (3K_s) \tag{1}$$

$$\gamma_0 = \gamma_{0(d)} = \tau_0 / (2G_s) \tag{2}$$

where $K_s$ and $G_s$ are the secant forms of bulk and shear moduli, respectively. An extensive experimental investigation in [4] led to the analytical expressions of the $\sigma_{id}$ and the secant and tangent forms of bulk and shear modulus as functions of the current state of stress ($\sigma_0$, $\tau_0$, $f_c$). The analytical expressions obtained by regression analysis, have this form:

$$K_s / K_e = 1/[1 + A(\sigma_0 / f_c)^{b-1}] \quad \text{for } \sigma_0 / f_c \le 2 \tag{3a}$$

$$K_s / K_e = 1/[1 + 2^{b-1}Ab - 2^b(b-1)A(\sigma_0 / f_c)^{-1}] \text{ for } \sigma_0 / f_c > 2 \tag{3b}$$

$$G_s / G_e = 1/[1 + C(\tau_0 / f_c)^{d-1}] \tag{4}$$

$$\sigma_{id} / f_c = M(\tau_0 / f_c)^n \tag{5}$$

where the parameters *A*, *b*, *C*, *d*, *M*, and *n* are calculated by the expressions (as a function of the uniaxial compressive strength $f_c$) in Table 1.

| | |
|---|---|
| $A = 0.516$ for $f_c \le 31.7$<br>$A = 0.516/[1 + 0.0027(f_c - 31.7)^{2.397}]$ for $f_c > 31.7$ | $M = k/[1 + l(\sigma_0 / f_c)^m]$ |
| | $k = 4/[1 + 1.087(f_c - 15)^{0.23}]$ |
| $d = 2.12 + 0.0183 f_c$ for $f_c \le 31.7$<br>$d = 2.7$ for $f_c > 31.7$ | $l = 0.222 + 0.01086 f_c - 0.000122 f_c^2$ |
| | $m = -2.415$ for $f_c \le 31.7$<br>$m = -3.531 + 0.0352 f_c$ for $f_c > 31.7$ |
| $C = 3.573$ for $f_c \le 31.7$<br>$C = 3.573/[1 + 0.0134(f_c - 31.7)^{1.414}]$ for $f_c > 31.7$ | $n = 1$ for $f_c > 31.7$<br>$n = 0.3124 + 0.0217 f_c$ for $f_c > 31.7$ |

Table 1 Expression of parameters *A*, *b*, *C*, *d*, *M*, and *n* as functions of $f_c$ that are used in the concrete material model.

The strains expressed in the global coordinate system are determined by the use of the expression in Eq. 1 and take the following equivalent form:

$$\varepsilon_{ij} = (\sigma_{ij} + \sigma_{id}\delta_{ij}) / (2G_s) - (3\nu_s / E_s)(\sigma_0 + \sigma_{id})\delta_{ij} \tag{6}$$

where $E_s$ ($\sigma_o$, $\tau_o$, $f_c$) and $\nu_s$ ($\sigma_o$, $\tau_o$, $f_c$) are the secant Young's modulus and Poisson's ratio, respectively, and are derived from $K_s$ and $G_s$ by the following standard formula of linear elasticity:

$$E_s = (9K_sG_s) / (3K_s + G_s),\ \nu_s = (3K_s - 2G_s) / (6K_s + 2G_s) \tag{7}$$

During the nonlinear procedure, the stress and strain increments are calculated using the tangent expressions $K_t$, $G_t$, $E_t$, and $\nu_t$ as presented in [4]. The expression of Eq. 6 is used in order to correct the stresses and strains taking into account stress $\sigma_{id}$ which represents the coupling effect between $\tau_0$ and $\varepsilon_{0(d)}$. The constitutive matrix of the proposed 3D material model can take the following form:

$$D = \begin{bmatrix} 2G_t + \mu & \mu & \mu & 0 & 0 & 0 \\ \mu & 2G_t + \mu & \mu & 0 & 0 & 0 \\ \mu & \mu & 2G_t + \mu & 0 & 0 & 0 \\ 0 & 0 & 0 & G_t & 0 & 0 \\ 0 & 0 & 0 & 0 & G_t & 0 \\ 0 & 0 & 0 & 0 & 0 & G_t \end{bmatrix} \tag{8}$$

where $\mu = K_t - 2G_t/3$ and $K_t = K_t(\sigma_0,\tau_0,f_c)$, $G_t = G_t(\sigma_0,\tau_0,f_c)$. It is assumed that the uncracked concrete behaves elastically at low-stress levels. Particularly, when the deviatoric stress of an uncracked Gauss Point (GP) of a concrete element, is less than 50% of the corresponding ultimate strength, then the elastic constitutive matrix is used [1]. Otherwise, the constitutive material matrix is updated using the tangent expressions of bulk and shear moduli.

## 3 CRITERION OF FAILURE

The value of ultimate deviatoric stress may be interpolated by the $\tau_{0e}$ and $\tau_{0c}$ stresses using the expressions of Willam and Warnke [12].

$$\begin{aligned} &\tau_{0u} = \{2\tau_{0c}(\tau_{0c}^2 - \tau_{0e}^2)\cos\theta + \tau_{0c}(2\tau_{0e} - \tau_{0c}) \\ &[4(\tau_{0c}^2 - \tau_{0e}^2)\cos^2\theta + 5\tau_{0e}^2 - 4\tau_{0c}^2\tau_{0e}^2]^{1/2}\} / [4(\tau_{0c}^2 - \tau_{0e}^2)\cos^2\theta + (2\tau_{0e} - \tau_{0c})^2] \end{aligned} \tag{9}$$

The $\tau_{0e}$ ($\theta$=0°) corresponds to the state of $\sigma_1 = \sigma_2 > \sigma_3$ (triaxial extension), while $\tau_{0c}$ ($\theta$ = 60°) correspond to the state of $\sigma_1 > \sigma_2 = \sigma_3$ (triaxial compression). It is also known that concrete's strength under tension is unaffected by triaxial phenomena. Therefore, it is considered that concrete fails in tension when a tensile stress $\sigma_{ij}$ exceeds the tensile strength of concrete $f_{ct}$. The schematic representation of the ultimate strength is shown in Fig. 1.

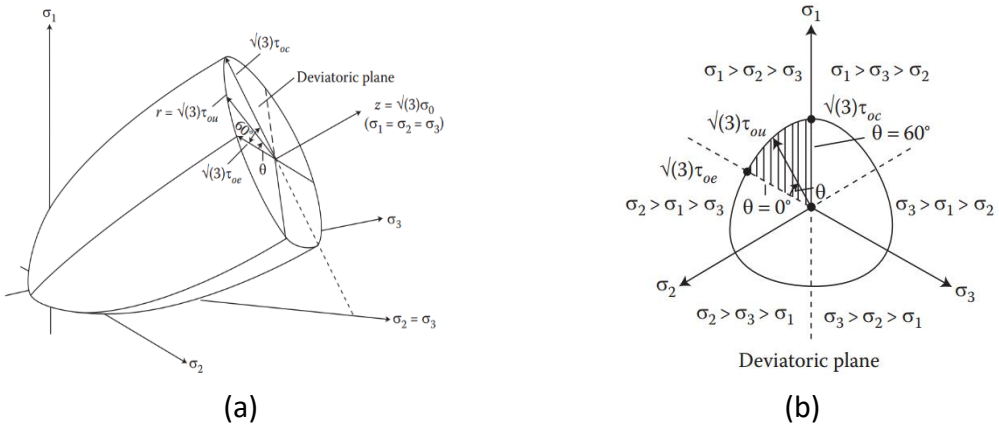


Figure 1 Schematic representation of the ultimate-strength surface : (a) general view in stress space, (b) typical cross-section of the strength envelope with a deviatoric plane (a plane of constant σ0, viewed along the axis $\sigma_1 = \sigma_2 = \sigma_3$).[4]

The expressions of $\tau_{0e}$ and $\tau_{0c}$ are derived by an experimental investigation as shown here:

$$\tau_{0c} / f_c = 0.944(\sigma_0 / f_c + 0.05)^{0.724} \quad (10)$$

$$\tau_{0e} / f_c = 0.633(\sigma_0 / f_c + 0.05)^{0.857} \quad (11)$$

## 4 FRACTURE MODELLING

The fracture modelling approach proposed by Cervenka et al. [3] is used in this work. When the criterion of failure is satisfied, then the fracture model is activated. The model assumes small strains and it can be written as:

$$\varepsilon_{ij} = \varepsilon_{ij}^{e} + \varepsilon_{ij}^{f} \quad (12)$$

Therefore, the stress development that shows the material degradation can be described by the following rate equations:

$$\sigma_{ij} = D_{ijkl} \cdot \left( \varepsilon_{kl} - \varepsilon_{kl}^{f} \right) \quad (13)$$

Also, the evolution of the fracture rate $\varepsilon_{kl}^{f}$ is governed by the following flow rule:

$$\varepsilon_{kl}^{f} = \lambda^{f} \cdot m_{ij}^{p}, m_{ij}^{p} = \frac{\partial g^{f}}{\partial \sigma_{ij}} \quad (14)$$

where $\lambda^{f}$ is the inelastic fracturing multiplier, and $g^{f}$ is the potential defining the direction of inelastic fracturing strains in the fracturing model.

It is considered that, when the criterion of failure is satisfied and the specimen is under tension, one of the principal stresses exceeds the tensile strength. Therefore, in tension, the failure surface is transformed into a Rankine failure surface. The principal stress (along the principal direction p) in the case of cracking under tension must satisfy the following equation:

$$f_p^{f} = {}^{t}\sigma_{ij}\, n_i^{p}\, n_j^{p} - D_{ijmn}\, d\varepsilon_{mn}^{f}\, n_i^{k}\, n_j^{k} - f_t = 0 \quad (15)$$

where ${}^{t}\sigma_{ij}$ is a trial elastic prediction that has been made taking into account the current stain state. Assuming an associated form ($g^f$=$f^f$) for the fracturing strain increment, Eq. 14 takes the following form:

$$d\varepsilon_{ij}^{fp} = d\lambda^p \cdot \frac{\partial f_p^f}{\partial \sigma_{ij}} = d\lambda^p \cdot n_i^p \cdot n_j^p \tag{16}$$

After substituting Eq. 16 into Eq. 15, the fracturing multiplier can be expressed in the following form:

$$d\lambda^p = \frac{{}^{t}\sigma_{ij}\, n_i^p\, n_j^p - f_t(w^p)}{D_{ijmn}\, n_i^p\, n_j^p\, n_m^p\, n_n^p} \tag{17}$$

where,

$$w^p = L_t\left(\hat{\varepsilon}_p + d\lambda^p\right) \tag{18}$$

Eqs. 17 and 18 must be solved iteratively since for softening materials the tensile strength is a function of crack opening $w^p$. The crack opening is defined by the following expression suggested by Hordijk [13]:

$$\frac{\sigma}{f_t} = \left[1 + \left(c_1 \frac{w}{w_0}\right)^3\right] e^{-c_2 \frac{w}{w_0}} - \frac{w}{w_0}(1 + c_1^3) e^{-c_2} \tag{19}$$

where σ is the tensile concrete stress normal to crack, $f_t$ is the concrete tensile strength, $c_1 = 3$, $c_2 = 6.93$, $w_0 = 5.14\, G_f / f_t$, and $G_f$ is the fracture energy of the material. In Eq. 18, the $L_t$ represents the characteristic length used as a crack band size introduced by Bazant and Oh (1983). The suggested limits for the values of the characteristic length related to the size of the finite elements from the work of Cervenka et al. [3], have been adopted for the needs of this work.

The local fracturing strains can be calculated by using the expression of Rots and Blaauwendraad [14]:

$$\varepsilon^f = (D + D^{cr})^{-1} D\, \varepsilon \tag{20}$$

where $D_{cr}$ is the stiffness inside the crack zone. It is defined by the following formulas:

- Mode I

$$D_{pppp}^{cr} = \frac{f_t(w^p)}{\hat{\varepsilon}_p^f} \tag{21}$$

- Mode II and III

$$D_{ijij}^{cr} = min\left(D_{iiii}^{cr}, D_{jjjj}^{cr}\right) \cdot r^g \tag{22}$$

where $r^g$ is the shear coefficient which is an input parameter of the model. For the above expressions, large penalty numbers $D_{pppp}^{cr} = \frac{f_t(0)}{e}$ (where $e$ is a small number) are used to avoid cases during the onset of cracking that they may lead the above expression to infinity. The secant constitutive matrix in the material directions can be derived from Eq. 13 using Eq. 20:

$$D_s = D - D \cdot \left(D^{cr} + D\right)^{-1} \cdot D \tag{23}$$

The model is further described by Cervenka et al., [3]. The flow chart that describes the algorithm through which the model has been applied for a single GP is shown in Fig. 2.

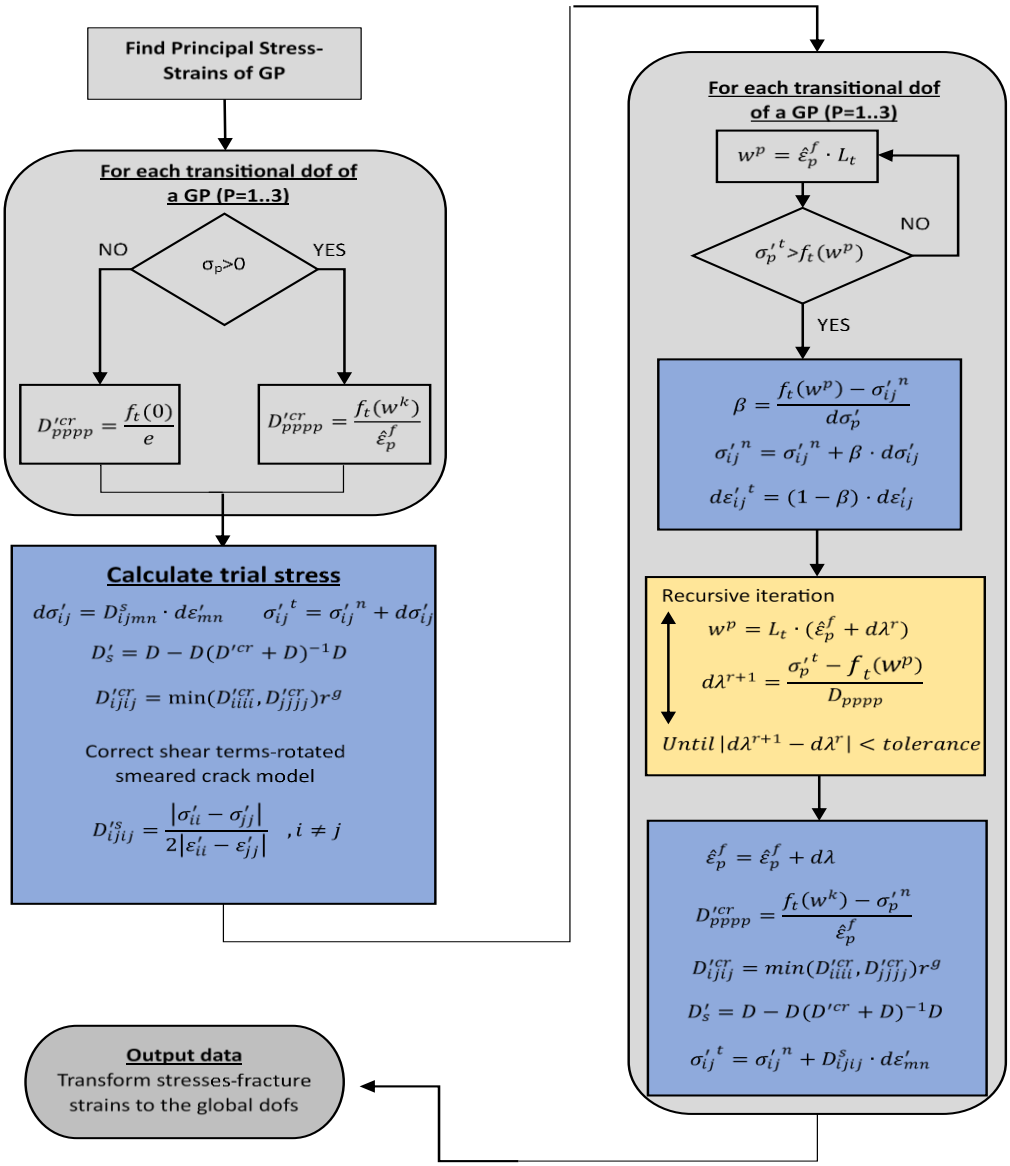


Figure 2 Flow chart of the fracture model of concrete (adapted from [3])

According to the above-described formulations of concrete behaviour of concrete under tension [3] and compression [4], the proposed concrete material model combines the two different theories in an attempt to derive a more accurate material model. This is evaluated through the use of experimental data that are used to assess the ability of the proposed material model in capturing the behaviour of RC specimens that develop significant shear deformation. The following section discusses a first set of numerically obtained results.

# 5 NUMERICAL APPLICATIONS

## *5.1 Leonhart's shear beam*

The well-known Leonhart's shear beam (Leonhardt and Walther [15]) is examined to validate the proposed constitutive approach using three-dimensional hexahedral isoparametric finite elements, where the steel reinforcement is modeled through the use of embedded truss elements. The shear beam does not have shear reinforcement (stirrups) and according to the experimental data [15], it develops a severe shear failure at the end of the test. The geometry of the RC specimen which was tested through a four-point bending test, is presented in Fig. 3. Due to symmetry, half of the beam is modelled herein using the appropriate boundary conditions, which also allows its modeling through ATENA software. It must be also noted here that for the case of the proposed material model, the analysis foresees a displacement control nonlinear analysis.

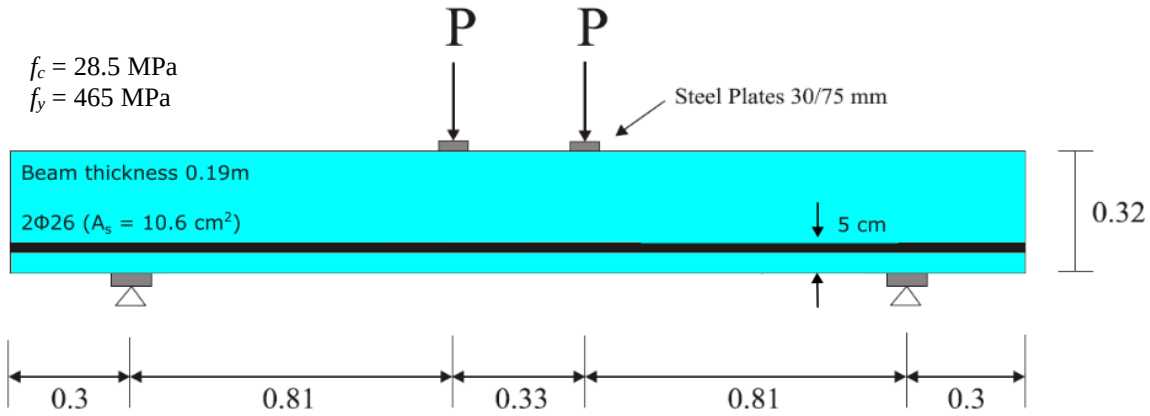


Figure 3 Leonhart's shear beam. Geometric and reinforcement details (adapted from [3]).

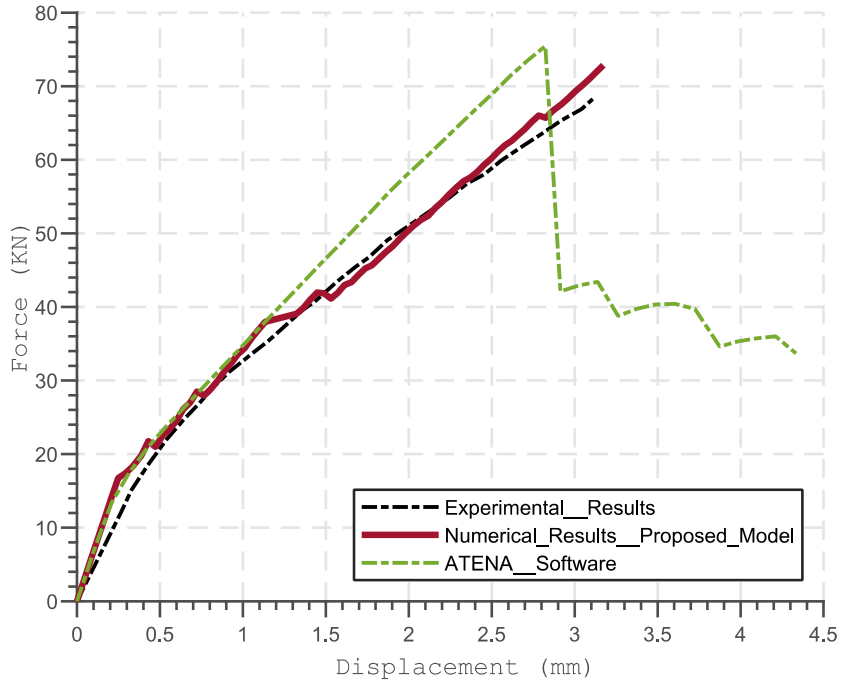


Figure 4 Leonhart's shear beam. Comparison of the numerical results with the experimental data.

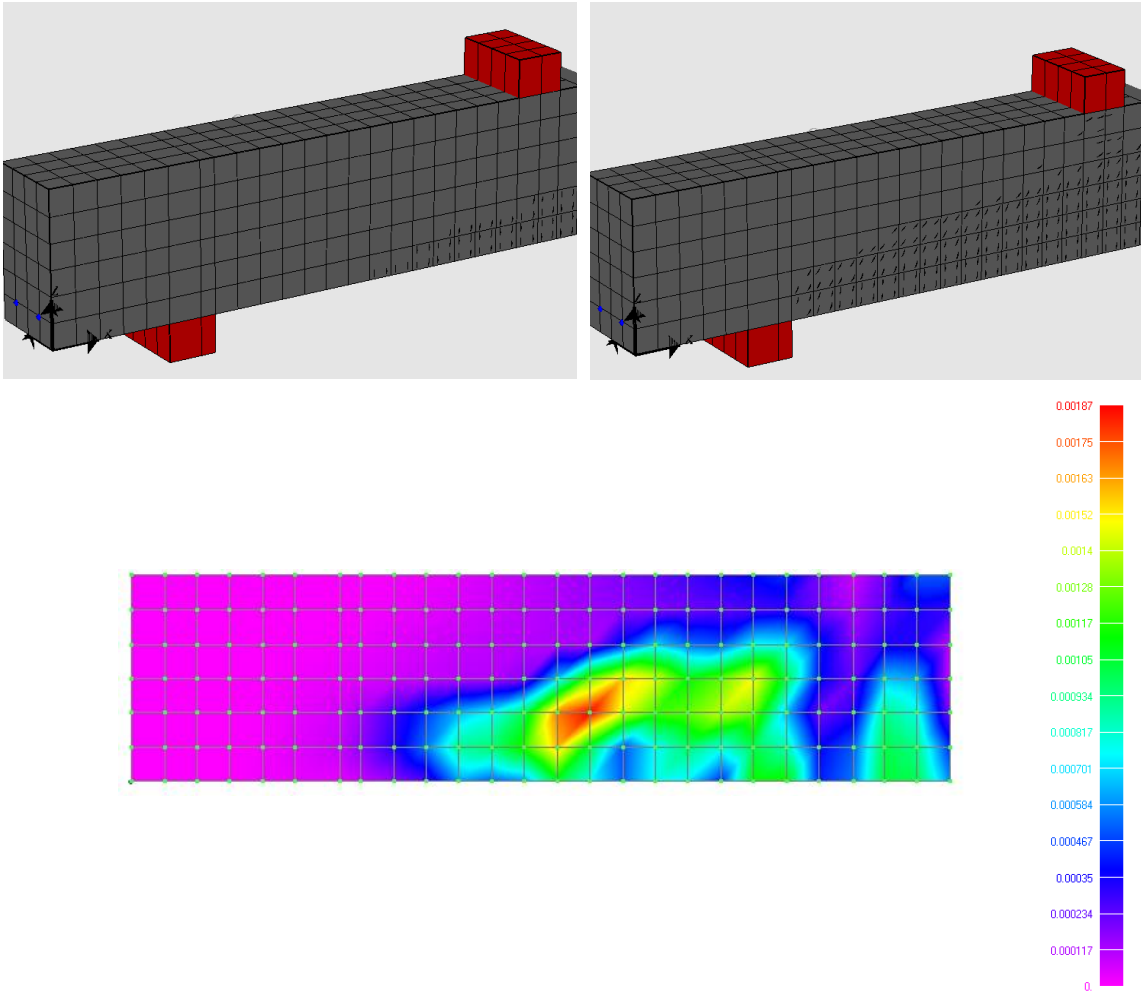


Figure 5 Crack pattern (Left) at first crack opening and (Right) prior to failure. (Down) Solid von Mises strain contour prior to failure.

As it was stated above, the concrete domain is modelled by 8-noded hexahedral finite elements, and the steel reinforcement is modelled by truss finite elements. The numerical results are compared with the experimental ones in Fig. 4. Additionally, the numerical results are compared with the numerical results obtained by ATENA software [16]. According to the curves in Fig. 4, it is easy to observe that the proposed constitutive model derives the best results when compared to the curve obtained by ATENA software that uses the model for both tension and compression of concrete as it was presented in [3]. It is also very interesting to note that the proposed material model manages to capture the concrete material deterioration in an almost perfect manner as the experiment evolves, while the model that adopts the material model proposed in [3] fails to do so. It is noteworthy to state here that ATENA was also used herein to perform a displacement control analysis. It is evident and undeniable that the overall RC response that derives from the ATENA software [16] that uses the Cervenka et al., [3] material model is not realistic in this regard since it fails to capture the basic mechanical response that RC structures usually exhibit, especially when the reinforcement ratio is low.

The crack patterns in Fig. 5 show that the crack development starts from small diffused flexural cracks near the midspan which eventually lead to a large shear crack between the point of the applied load and the support (see the crack pattern and solid von Mises contour in Fig. 5). This is in line with the crack formation reported in [15].

### *5.2 Lefas and Kotsovos shear wall*

The RC shear wall specimen which is investigated experimentally in Lefas and Kotsovos [17], is denoted as shear wall SW31 and numerically studied herein. The geometric details of the RC shear wall are illustrated in Fig. 6, where it can be seen that is 650 mm wide, 1300 mm height, and 70 mm thick. The uniaxial compressive strength ($f_c$) of SW31 was 35.2 MPa which is also the value defined within the proposed material model. The yielding stresses ($f_y$) of the steel reinforcement were 420, 520, and 470 MPa for the 4-, 6- and 8-mm diameter bars used, respectively. The shear wall was subjected to different cyclic loading conditions.

The concrete domain is modelled by 8-noded hexahedral finite elements, and the steel reinforcement is modelled with embedded truss finite elements. At the top and the bottom of the shear wall, 81 rigid 8-noded hexahedral elements are used to represent the rigid RC beams, while 50 concrete finite elements (130 mm x 130 mm x 65 mm) and 318 steel embedded elements are used to discretize the RC domain.

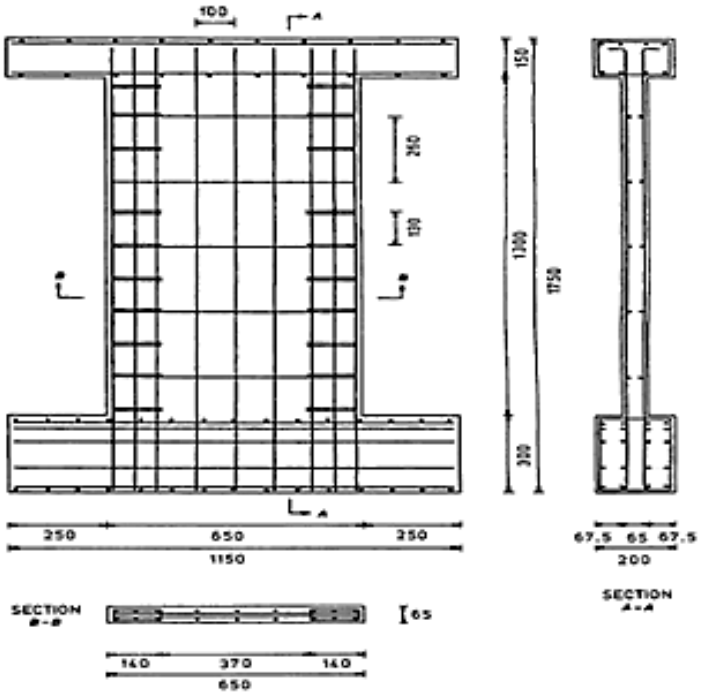


Figure 6 Geometric and reinforcement detail of the SW31 [17]

The numerical curves are compared with the corresponding experimental curve as can be depicted in Fig. 7. It is easy to observe that the numerical results are in good agreement with the experimental data in terms of stiffness and strength. The experimental results show that the specimens SW31 had a load-carrying capacity of 119 kN, respectively whereas the numerical predicted load-carrying capacity of the same specimens subjected to the same loading conditions is 121 kN. This is an error that is less than 2%.

The proposed model has used three approaches of smeared crack modelling for the needs of investigating the different available methods which are:

1. rotated (update crack plane for each iteration),
2. multidirectional (each crack can open in a different plane but remain fixed), and
3. fixed (cracks can open in certain crack planes and remain fixed) smeared crack model.

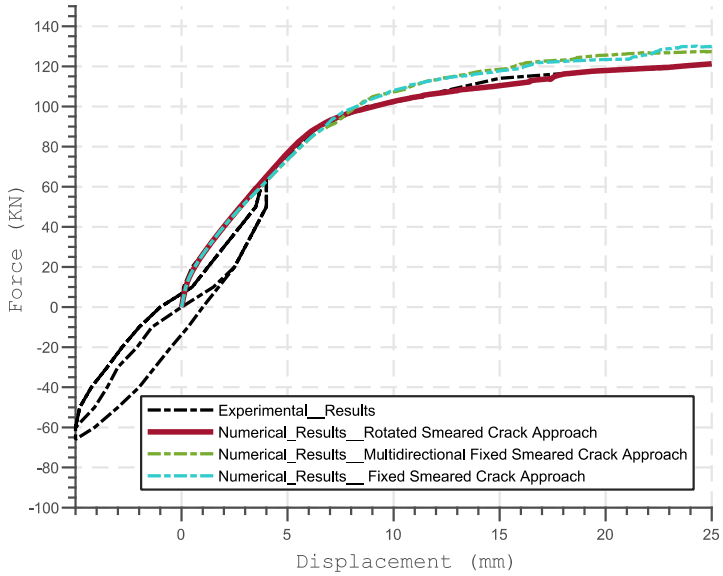


Figure 7 Comparison of the numerical results with the experimental data of the SW31.

The numerical results show that there is good agreement with the experimental data for all three crack approaches, thus similar responses are obtained. However, the model with the fixed approach (multidirectional and fixed smeared crack approach) derives a slightly stiffer behavior, especially in the post-cracking area.

The numerically obtained crack pattern of the RC shear wall specimen is illustrated in Fig. 8 when the maximum imposed displacement is reached. The cracks are formed within the areas of the section that are under tension due to the bending moment. Therefore, the cracks appear to be mainly horizontal. As the cracks form closer to the compressive zone of the section, they develop a relative inclination. Additionally, the figure shows a great concentration of cracks in the center of the shear wall which is dominated by a more complex state of stress due to triaxial phenomena attributed to the large normal and shear strains.

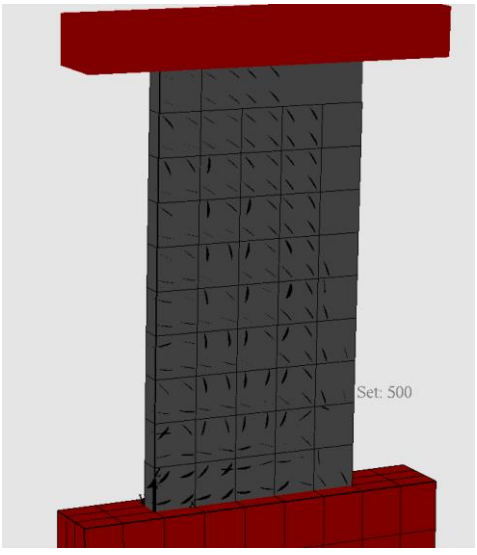


Figure 8 Crack pattern of the SW31 prior to failure.

## 6 CONCLUSIONS

This manuscript presents a conjunction of two constitutive modelling approaches for the simulation of concrete material in 3D. The modelling approach foresees that for the compressive behavior of the uncracked concrete, the material model proposed in [1] is used, whereas when the concrete is under tension, then it is modelled by using the constitutive material model as presented in [3]. The proposed material model which is a combination of a model derived from experimental data regression [1] and a model based on the thermodynamics law [3] was evaluated through the use of two experimental tests. According to the obtained numerical results, it was found that the combination of these two concrete material models produces a solid constitutive approach that can simulate accurately the nonlinear behavior of concrete when it develops extreme shear, which leads to a shear failure.

Future research work foresees the use of additional experimental data to be used for further validation of the proposed material model. In addition, the model will be expanded and integrated with the ability to capture the cyclic response of concrete. Further validation work will be performed in the case of cyclic loading conditions.

## REFERENCES

[1] C. Mourlas, G. Markou, and M. Papadrakakis. "Accurate and computationally efficient non-linear static and dynamic analysis of reinforced concrete structures considering damage fac-tors". Engineering Structures, Vol. 178, pp. 258–285, Jan. 2019.

[2] Markou G, Garcia R, Mourlas Ch., Maurizio Guadagnini, Pilakoutas K., Papadrakakis M. "A New Damage Factor For Seismic Assessment Of Deficient Bare and FRP-Retrofitted RC Structures", Engineering Structures, Vol. 248,2021,113152.

[3] J. Červenka and V. K. Papanikolaou, "Three dimensionalcombined fracture–plastic material model for concrete,"International Journal of Plasticity, vol. 24, no. 12, pp. 2192–2220, 2008

[4] Kotsovos M.D. and Pavlovic M.N. (1995), Structural concrete. Finite Element Analysis for Limit StateDesign, Thomas Telford, London.

[5] Lykidis GC, Spiliopoulos K V. "An efficient numerical simulation of the cyclic loading experiments on RC structures". Computers and Concrete, Vol. 13(3), pp. 343–59, 2014.

[6] Moharrami M, Koutromanos I. "Finite element analysis of damage and failure of reinforced concrete members under earthquake loading". Earthquake Engineering & Structural Dynamics, Vol. 46(15), pp. 2811–29, 2017.

[7] Jason L, Huerta A, Pijaudier-Cabot G, Ghavamian S. "An elastic plastic damage formulation for concrete: Application to elementary tests and comparison with an isotropic damage model". Computer Methods in Applied Mechanics and Engineering, Vol. 195(52), pp. 7077–92, 2006.

[8] Richard B, Ragueneau F. "Continuum damage mechanics based model for quasi brittle materials subjected to cyclic loadings: Formulation, numerical implementation and applications". Engineering Fracture Mechanics, Vol. 98(1), pp. 383–406, 2013.

[9] G. Markou, C. Mourlas, H. Bark, and M. Papadrakakis. "Simplified HYMOD non-linear simulations of a full-scale multistory retrofitted RC structure that undergoes multiple cyclic excitations – An infill RC wall retrofitting study". Engineering Structures, Vol. 176, pp. 892–916, Dec. 2018.

[10] Markou G, Roeloffze W. Finite element modelling of plain and reinforced concrete specimens with the Kotsovos and Pavlovic material model, smeared crack approach and fine meshes. International Journal of Damage Mechanics. 2021;30(6):845-871. doi:10.1177/1056789520986601

[11] Bažant, Z.P., Oh, B.H., 1983. Crack band theory for fracture of concrete. Materials and Structures, RILEM 16 (3), 155–177.

[12] Willam K, Warnke EP. "Constitutive model for the triaxial behavior of concrete". Seminar on concrete structures subjected to triaxial stresses, Instituto Sperimentale Modeli e Strutture, Bergamo, Paper III-1., 1974.

[13] Hordijk, D.A., 1991. Local approach to fatigue of concrete. Ph.D. Thesis, Delft University of Technology, The Netherlands

[14] Rots, J.G., Blaauwendraad, J., 1989. Crack models for concrete: discrete or smeared? Fixed, multi-directional or rotating? Heron 34 (1)

[15] Leonhardt, F., Walther, R., 1962. Schubversuche an einfeldrigen stahlbetonbalken mit und ohne schubbewehrung. Deutscher Ausschuss fu¨r Stahlbeton, 151, Berlin, West Germany.

[16] Cervenka Consulting, ATENA software, https://www.cervenka.cz

[17] Lefas ID, Kotsovos MD. "Strength and Deformation Characteristics of Reinforced Concrete Walls Under Load Reversals". ACI Structural Journal, Vol. 87(6), pp. 716–26, 1990.

COMPDYN 2023
9th ECCOMAS Thematic Conference on
Computational Methods in Structural Dynamics and Earthquake Engineering
M. Papadrakakis, M. Fragiadakis (eds.)
Athens, Greece, 12-14 June 2023

# MODELING THE INFLUENCE OF STRAIN-RATE IN SUPERELASTIC SHAPE MEMORY ALLOYS

**Maria I. Ntina**[1]

[1] Department of Civil Engineering, Aristotle University of Thessaloniki
Thessaloniki, GR-54124, Greece
e-mail: mntina@civil.auth.gr

## Abstract

*Shape Memory Alloys (SMAs) are materials with appealing properties. They have the ability to recover stress-induced strains performing the superelastic effect, ideally resulting in insignificant residual strain (re-centering capability). A dependency of their behavior, exhibiting different hysteresis loops, has been reported on temperature and loading rate variations, maximum deformation, material composition and treatments. Presenting a wide applicability potential, SMAs have been intensively investigated in various sectors possessing a considerable place in structural engineering. Studies have been published developing constitutive models to simulate their behavior presenting some drawbacks: the inability to capture the rate-dependent nature, the large number of parameters, complexity and difficulty of implementation. In this context, a uniaxial rate-dependent constitutive model based on Graesser and Cozzarelli model for superelastic SMAs, aimed at capturing their essential hysteretic response has been developed. After the verification of the model prediction comparing it with experimental data derived from literature, a comparison with the rate-independent model of Auricchio and Sacco (1997) is attempted to indicate the effect of the rate-dependency. Results showed that the proposed model managed to successfully simulate the influence of strain rate using a simple equation rendering feasible the potential implementation of a robust solution algorithm easy to program in commercial software constituting a valid and effective computational tool for the analysis of superelastic SMAs.*

**Keywords:** Shape Memory Alloys, Superelastic Effect, Rate-dependency, Hysteretic Behavior, Constitutive Modeling.

## 1 INTRODUCTION

Shape Memory Alloys (SMAs) are smart materials possessing attractive properties. They have the ability to recover apparently permanent strains through the martensitic phase transformations being solid-solid diffusionless phase transformations [1] between a high-symmetric, usually cubic, austenitic phase and a low-symmetric martensitic phase, brought about by temperature change performing the shape memory effect or by unloading following stress application performing the superelastic effect, ideally resulting in insignificant residual strain (re-centering capability). They exhibit different types of hysteresis depending on which effect is demonstrated. Experimental evidence shows a dependency of their behavior on temperature and loading rate variations, maximum deformation, material composition and treatments. SMAs have demonstrated energy dissipation capabilities, large elastic strain capacity, hysteretic damping, good high and low-cycle fatigue resistance, recentering capabilities and excellent corrosion resistance [2].

SMAs have been intensively investigated over the past decades through experimental and analytical studies illustrating their wide implementation ability in various sectors. In structural engineering, superelastic (stress-induced) SMA applications possess a considerable place as through the energy dissipation capacity and the re-centering capability constitute a potential candidate for replacing conventional materials setting the basis for innovative applications, mitigating permanent residual deformations and allowing for achieving demanding serviceability and safety requirements. In this context, the research interest has focused on the development of SMA-based energy-dissipation devices to achieve vibration control [3-6] demonstrating the efficiency of the proposed schemes. Another interesting research effort regarded the use of SMAs as structural connecting elements proving the enhancement of the performance of steel connections [7, 8]. SMA applications in framing systems as diagonal braces exploiting the superelastic effect showed the reduction both of interstory drift ratios and residual displacements [9-10] achieving the prescribed performance objectives [11]. SMAs have been employed in vibration mitigation in bridges by conducting experiments on an SMA device to be used as restrainer cable of in-span hinges of concrete bridges [12], analytical studies on the effectiveness of superelestic NiTi SMA reinforcing bars [13] and on a novel concept for bridge columns with SMA bars placed inside a plastic hinge element of rubber [14], proving the effectiveness of SMAs in eliminating damage. The potential use of SMAs in developing advanced seismic protective systems for structure retrofitting has been investigated proposing the deployment of SMA-based devices to increase the in-plane seismic resistance of masonry walls by exploiting the superelastic effect [15-17]. In [18, 19] Cu-based SMAs were employed to address the issues encountered with the use of conventional steel reinforcing bars and their inability to restrain residual deformations in structures during and after intense earthquakes.

Considering the growing research interest in superelastic SMAs, studies have been published developing constitutive models to simulate their behavior. The reported models present some drawbacks as for instance the inability to capture the rate-dependent nature, the large number of parameters, complexity and difficulty of implementation. To address these issues, a uniaxial rate-dependent model based on Graesser and Cozzarelli model [20] for superelastic SMAs has been developed. After the verification of the model prediction comparing it with experimental data derived from literature, a comparison with the rate-independent model of Auricchio and Sacco [21] is attempted to indicate the effect of the rate-dependency.

## 2 RATE-DEPENDENCY OF SUPERELASTIC SMAS

Superelasticity is the recovery of large deformations during mechanical loading-unloading cycles of an SMA in the austenitic state through the phase transformation from austenite to martensite, exhibiting the flag-shaped loop depicted in Figure 1. As reported, the austenite is stable at high temperatures and low values of the stress, while the martensite is stable at low temperatures and high values of the stress [22]. The austenitic alloy displays an elastic behavior upon the application of stress level up to the transformation stress $\sigma_s^{A-M}$, after which the stress-induced martensitic transformation occurs [23]. During transformation the stress-strain curve follows a stress plateau until the complete transformation to martensite at stress $\sigma_f^{M-A}$ with further straining causing its elastic loading. Upon unloading, since martensite is stable due to the presence of the applied stress, the reverse transformation takes place [20]. Due to defect generation mechanisms taking place during martensitic transformation, a residual strain, $\varepsilon_r$, can be induced in the material during deformation which will be carried over to the next stress cycle in case of incomplete recovery [23].

The hysteretic behavior of austenite SMAs depends on loading rate variations. The stress-induced phase transformations are associated with the release and absorption of latent heat, with the forward transformation increasing the temperature of the material (exothermic reaction) and with the reverse transformation consuming energy from the environment and reducing the temperature of the material (endothermic reaction) [24]. This heat alteration can affect the material temperature and consequently its response to mechanical stimuli. At low strain rates, the heat generated allows maintenance of a thermal balance as the exchange with the surroundings occurs sufficiently fast, which allows the SMA temperature to be identical with the ambient temperature and, as a result, such loading can be considered to be an isothermal process [25]. However, at high strain rates this thermal equilibrium is affected as the material cannot exchange heat with its surroundings and it experiences a gradual accumulation of heat, leading to an increase in the internal temperature due to the Clausius–Clapeyron law [24], working under adiabatic conditions [25]. This thermomechanical coupling is the cause of the strain rate dependence observed in SMAs [24]. Passing to frequencies of seismic interest, the hysteretic loop decreases in size and the loading and the unloading stresses increase, affecting the energy dissipation capacity of the material.

All the above were proved experimentally as this phenomenon engaged the special interest of the research community. Shaw and Kyriakides [26] conducted a series of experiments investigating the effects of latent heat and loading rate on the response of specimens at different temperatures. The uniaxial tensile tests on Ni-Ti wires at two different temperatures at isothermal (water) and non-isothermal (air) conditions indicated that the self-heating and cooling of the specimen that result from transformations increases the stress required for the forward transformation from austenite to martensite and reduces the stress required for the reverse transformation. The temperature evolution under the cyclic loading of different frequencies was investigated in [27] proving that the temperature rise becomes significant in the high-frequency range. Tests under various loading rates were also conducted in [28-29] indicating the self-heating of the specimens due to the loading rate increase.

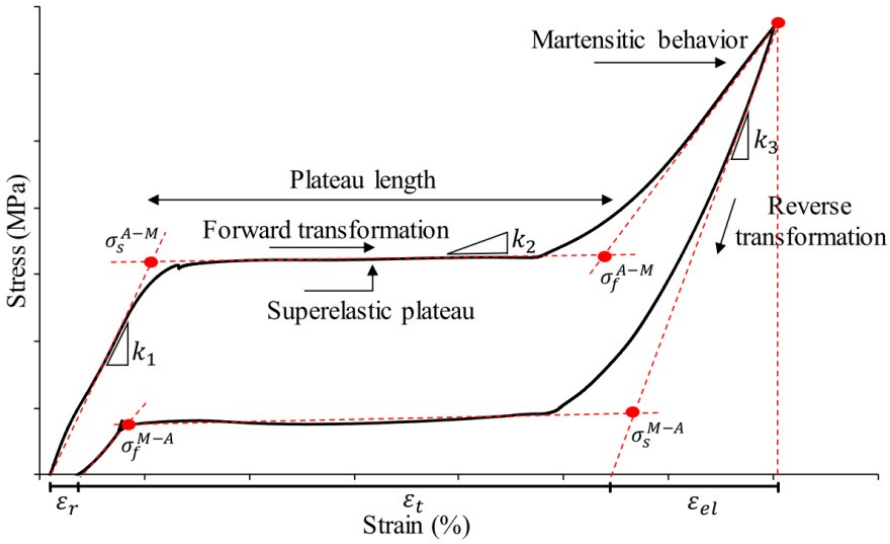


Figure 1: A typical superelastic stress-strain curve [23].

## 3 MODELING THE INFLUENCE OF STRAIN RATE

To simulate the superelastic behavior of SMAs various research efforts have been conducted. Auricchio et al. [1] formulated one- and three-dimensional thermomechanical constitutive models using an internal-variable inelastic framework able to describe solid-solid phase transformations considering an isothermal time-discrete formulation. In another study, [21] a superelastic beam model was presented based on the classical Euler-Bernoulli theory to allow the use of a reduced but significant set of kinematic parameters, not considering though the influence of strain rate. A few years later, Auricchio and his team [30] formulated a model for SMA behavior based on two scalar internal variables, the static martensite fraction and the dynamic martensite fraction to simulate rate phenomena. A limitation of the model is the increased number of parameters and the requirement of the advance knowledge of the maximum residual strain of the SMA. Another interesting effort in SMA modeling came from Graesser and Cozzarelli [20] who modified Özdemir's force-displacement relationship for a metallic damper [31] and specifically the equation describing the backstress, in order to capture the behavior of SMAs due to the shape memory as well as the superelastic effect, creating a rate-independent model.

To model the rate-dependent nature of superelastic SMAs, an extension of Graesser and Cozzarelli model [20] is presented. The expression of stress $\sigma$ is identical to the one of Graesser and Cozzarelli model, given in Equation (1), while the backstress $\beta$ given in Equation (2), involves the addition of one more term, namely stress $\sigma_2$, introduced to capture the rate-dependence, yielding Equation (3).

Aiming to determine the form of the stress equation, data from experiments conducted by DesRoches et al. [32] on 7.1 mm diameter bars under cyclic loading, which causes stable strain rate at frequencies of 0.025 Hz, 0.5 Hz and 1 Hz were used. The digitized stress-strain curves obtained from the experiment for these three frequencies are depicted in Figure 2, presented as full loops as only the continuous parts of the curves were reported. The formulation of Equation 3 is based on expressing the stress difference of the dynamic response of 0.5 Hz to the quasistatic response of 0.025 Hz as a rate-dependent function [33]. This is done by curve fitting on the stress difference data as shown in Figure 3, deriving Equation (4):

.

$$\dot{\sigma} = \mathrm{E}\left[\dot{\varepsilon} - \dot{\varepsilon}\left(\frac{\sigma-\beta}{\mathrm{Y}}\right)^{\eta}\right] \tag{1}$$

$$\beta = \mathrm{E}\alpha\left\{\varepsilon^{in} + f_t|\varepsilon|^{c}\, erf(a\varepsilon)\left[u(-\varepsilon\dot{\varepsilon})\right]\right\} \tag{2}$$

$$\beta_{tot} = \beta + \sigma_2 \tag{3}$$

$$\sigma_2 = \Delta\sigma_2 \cdot sign(\varepsilon)\left(|\varepsilon|\right)^{\left|\frac{\dot{\varepsilon}_0}{\dot{\varepsilon}}\right|} \tag{4}$$

Where $E$ is the Young's modulus of elasticity, $\dot{\varepsilon}$ is the strain rate, $\beta$ is the backstress, $Y$ is the "yield" stress and $\eta$ is a constant controlling the sharpness of transition from elastic to plastic states, $\alpha$ is a constant controlling the slope of the stress-strain curve, parameters $f_t$, $c$ and $a$ are material constants and notations $erf(\ )$ and $u(\ )$ are used to represent the error function and the unit step function respectively. $\Delta\sigma_2$ is the stress difference at maximum strain between the experimental response at a quasi-static frequency and at a dynamic frequency, $\dot{\varepsilon}_0$ is the strain rate produced at a quasi-static frequency and $\dot{\varepsilon}$ is the strain rate induced by the frequency in the dynamic range.

In order to verify the effectiveness of the proposed equation capturing the strain rate, data from experiments conducted by Dolce and Cardone [34] on 1.84 mm diameter austenitic wire were used. The frequencies of loading of the experimental data available were 0.02, 0.2 and 2 Hz presented as full loops in Figure 4, as only the continuous parts of the curves were reported. The fitted curve on the stress difference data is depicted in Figure 5.

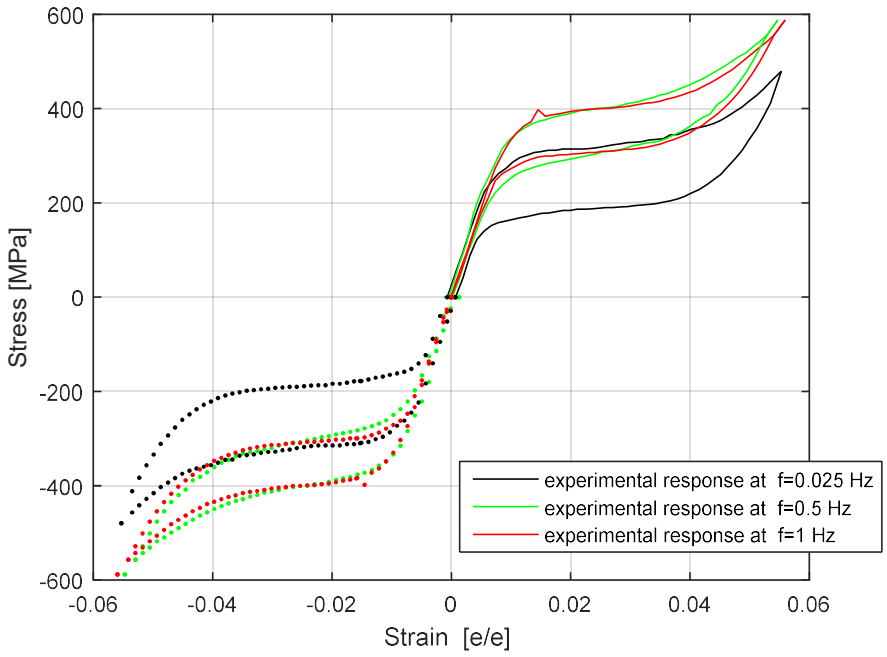


Figure 2: Comparison of the experimental responses at frequencies of 0.025, 0.5 and 1 Hz (data from [32]).

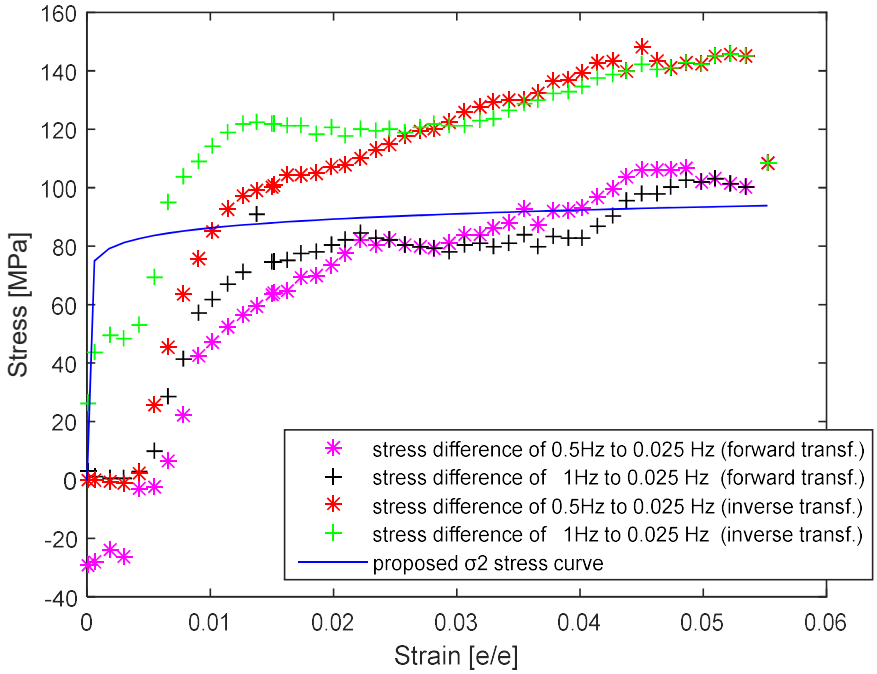


Figure 3: Comparison The fitted curve on the stress data from [32].

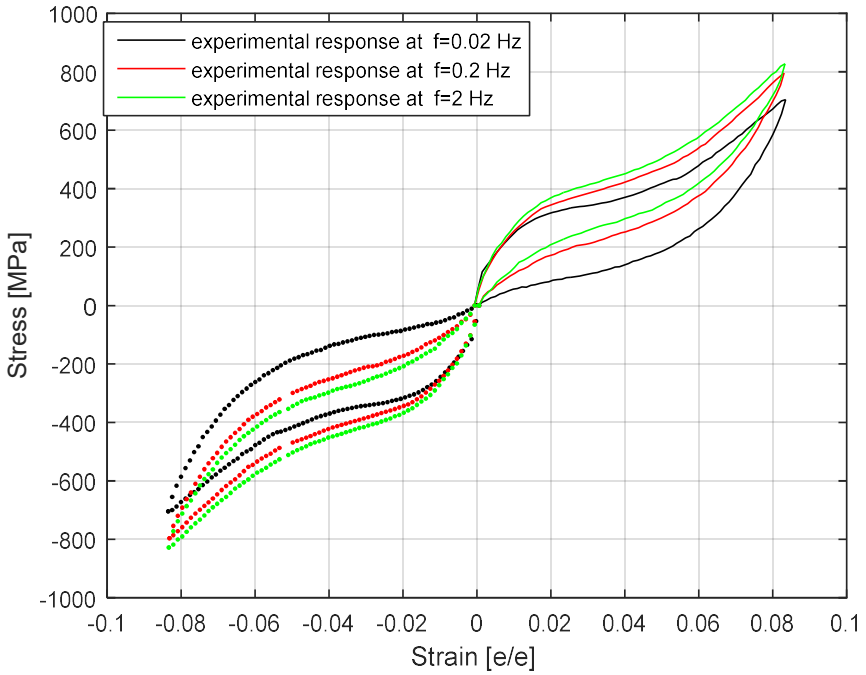


Figure 4: Comparison of the experimental responses of experiments conducted in [34] at frequencies of 0.02, 0.2 and 2 Hz.

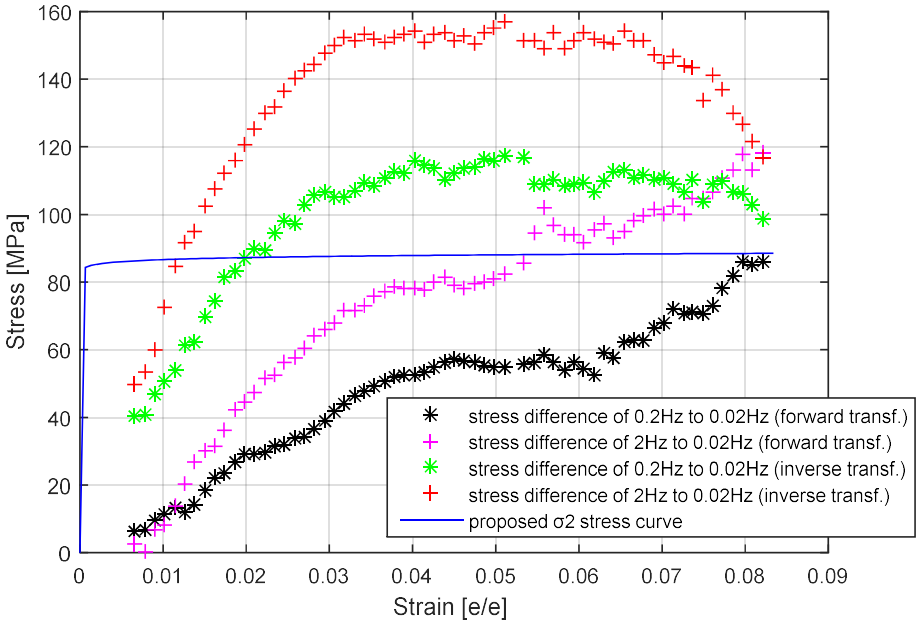


Figure 5: The fitted curve on the stress data from [34]

Comparison of the proposed model prediction to Graesser and Cozzarelli rate-independent model prediction and to the experimental responses from [32] at frequencies of 0.5 and 1 Hz (Figure 6), using the following model parameter values: $E = 35GPa$ , $Y = 300\,MPa$ , $\eta = 7$ , $\alpha = 0.0488$ , $f_t = 0.268$ , $c = 0.002$ and $a = 165$ , shows that the increase of the stresses attributed to heat exchanges especially when passing from quasi-static to dynamic conditions is well captured by the proposed model. The rate-independent Graesser and Cozzarelli model gives the same response prediction for the frequencies of 0.5 and 1 Hz. Comparison of the proposed model prediction to Graesser and Cozzarelli rate-independent model prediction and to the experimental responses from [34] at frequencies of 0.2 and 2 Hz (Figure 7) using the following model parameter values: $E = 30GPa$ , $Y = 250\,MPa$ , $\eta = 7$ , $\alpha = 0.16$ , $f_t = 0.05$ , $c = 0.002$ and $a = 165$ , denotes as well the stress alteration exhibited from the proposed model. Another characteristic of the SMA superelastic behavior the elastic loading of the fully transformed martensite at higher strains is also modeled in [33] adding another equation to backstress, an issue which is beyond the scope of this paper.

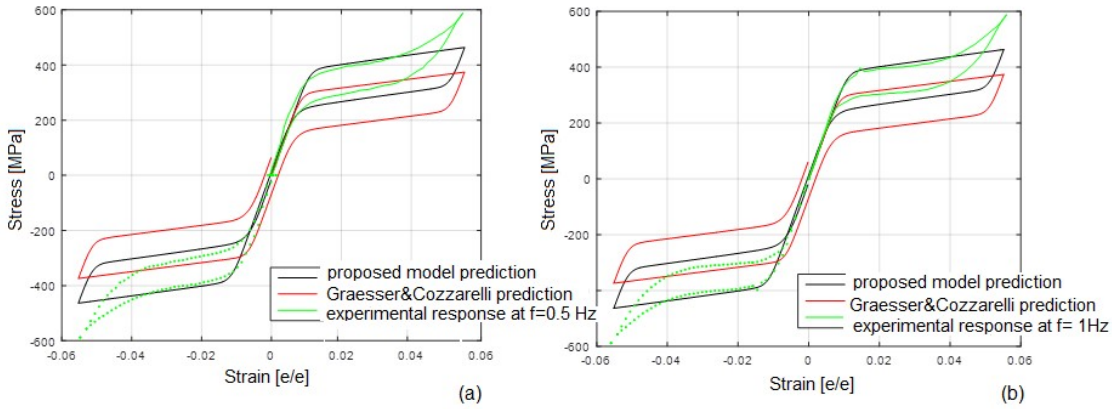


Figure 6: Comparison of the proposed model prediction to Graesser and Cozzarelli model and the experimental response (a) at a frequency of 0.5 Hz, (b) at a frequency of 1 Hz.

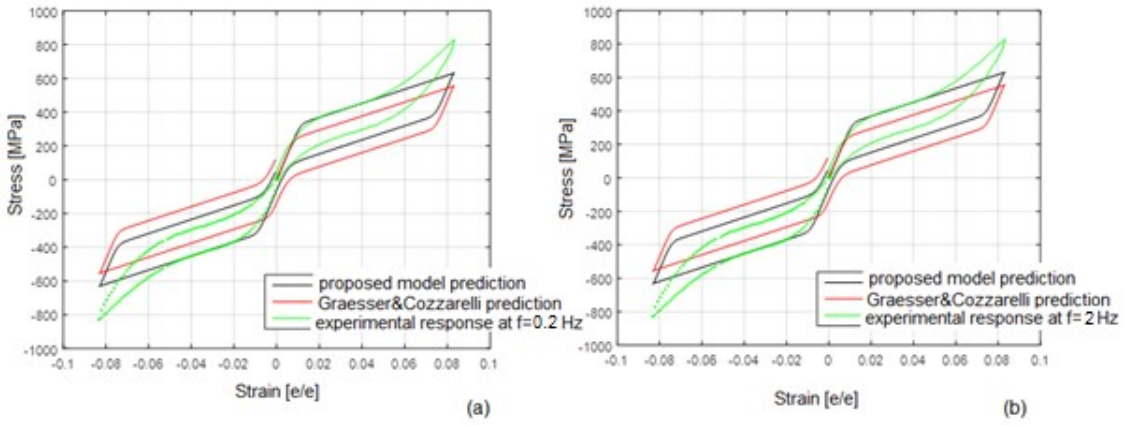


Figure 7: Comparison of the proposed model prediction to experimental response (a) at a frequency of 0.2 Hz, (b) at a frequency of 2 Hz.

To further evaluate the proposed model prediction, the performance of a single-storey Special Truss Moment Frame (STMF) with SMAs as X-diagonals incorporated in the pin-ended middle segment (Figure 8), conducting non-linear dynamic analysis in SeismoStruct software [35] was compared with the response of the same single-storey STMF simulated via a 4DOF model ($u_1, \phi_1, u_2, \phi_2$) consisting of two lumped masses (Figure 9), solved in MATLAB software [36] through the direct integration of the equations of motion. SeismoStruct embedded SMA model is rate-independent and uniaxial and follows the constitutive relationship proposed by Auricchio and Sacco [21] assuming a constant stiffness for both the fully austenitic and the fully martensitic behavior while the MATLAB model incorporated the proposed SMA model described herein. The two models' predictions are compared, comparing also the response of the left mass of the mechanical model with the response of node N1 of the SeismoStruct model incorporating 0.025 m and 0.035 m diameter SMA bars in each diagonal, under seven benchmark earthquakes [33]. Results for Northridge earthquake (NE) are presented herein (Figures 10 and 11). Response differences are justified, since the 4-DOF model is consisted of two rigid masses, while the model in SeismoStruct is a structure modeled with frame and truss elements, hence stiffer, analyzed with the finite element method. The comparison of the rate-independent SeismoStruct model with the proposed rate-dependent model indicates the stress increase. This was expected as the proposed model takes into consideration the influence of strain rate. Moreover, the loop derived from SeismoStruct model is of triangular shape that is not representative of the actual SMA loading-unloading loop while the loop generated form the proposed model resembles the "full" SMA curve. SeismoStruct analysis gives larger SMA deformations and this happened due to larger rotations derived than those of the 4-DOF model.

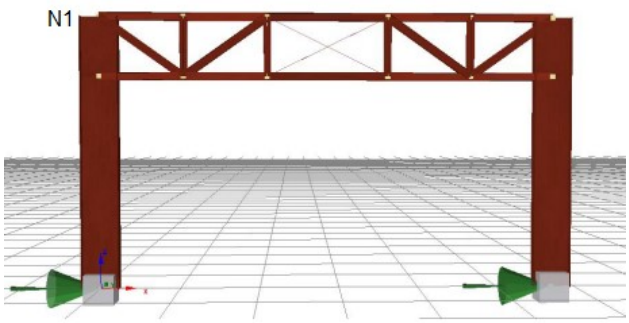


Figure 8: The SeismoStruct model of the STMF with X-diagonal SMA dampers in the special segment.

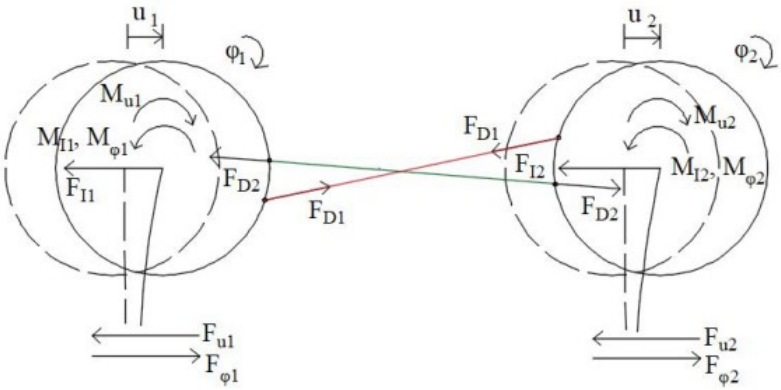


Figure 9: The free body diagram of the STMF with X-diagonal SMA dampers in the special segment.

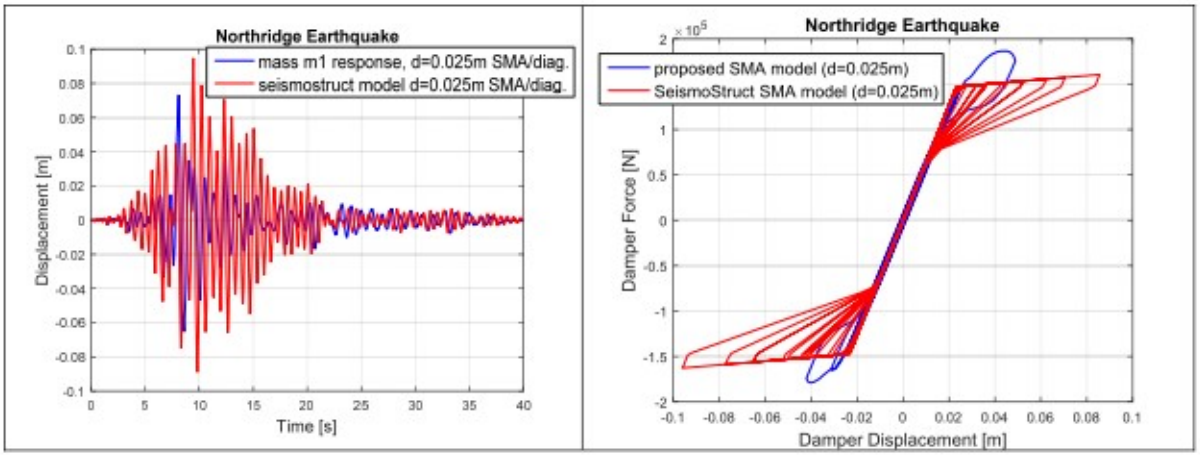


Figure 10: Comparison of frame response and damper force-deformation curve of the damper of the mechanical model and SeismoStruct (d=0.025 m) for Northridge Earthquake.

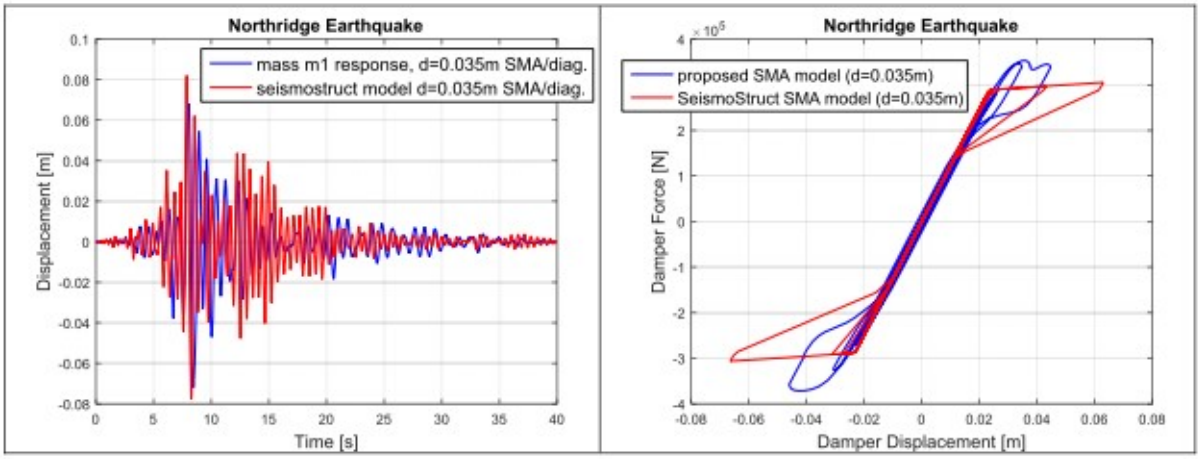


Figure 11: Comparison of frame response and damper force-deformation curve of the damper of the mechanical model and SeismoStruct (d=0.035 m) for Northridge Earthquake.

## 4 CONCLUSIONS

This work deals with the development of a constitutive model capturing the influence of strain rate in superelastic SMAs. The proposed model is an extension of Graesser and Cozzarelli rate-independent model that includes the addition of a rate-dependent function in the

equation describing the backstress, formulated from experimental data found in the literature. Comparison of the model prediction with the aforementioned data as well as with Auricchio and Sacco [21] rate-independent model showed that the proposed model managed to successfully reproduce the complex superelastic behavior using a simple equation for considering the influence of strain rate, rendering feasible the potential implementation of a robust solution algorithm easy to program in commercial software. The model can be applied for either wires or bars while material parameters can be obtained conducting simple uniaxial tests, constituting a valid and effective computational tool for the analysis of superelastic SMAs that will enhance the advancement of knowledge regarding their systematic use in civil structures.

## REFERENCES


[1] O.C. Zienkiewicz, R.C. Taylor, *The finite element method, Vol. I, 4th Edition*. McGraw Hill, 1989. [1] F. Auricchio, R. L. Taylor, J. Lubliner, Shape memory alloys: macro-modelling and numerical simulations of the superelestic behavior. *Comput. Methods Appl. Mech. Engrg*., **146,** 281-312, 1997

[2] G. Attanasi, F. Auricchio, M. Urbano, Theoretical and experimental investigation on SMA superelastic springs. *Journal of Materials Engineering and Performance,* **20**, 706–711, 2011.

[3] M. Dolce, D. Cardonne, R. Marnetto, Implementation and testing of passive control devices based on shape memory alloys. *Earthquake Engineering and Structural Dynamics*, **29**, 945-968, 2000.

[4] Y. Zhang, S. Zhu, A shape memory alloy-based reusable hysteretic damper for seismic hazard mitigation. *Smart Materials and Structures*, **16(5)**, 1603-1613, 2007.

[5] H. Qian, H. Li, G. Song, Experimental investigations of building structure with a superelastic shape memory alloy friction damper subject to seismic loads. *Smart Mater. Struct*., **25:125026**, 14 pages, 2016.

[6] A.M. Asfaw, O.E. Ozbulut, Characterization of shape memory alloy energy dissipators for earthquake-resilient structures. *Struct. Control Health Monit*., **28**, e26972021, 2021.

[7] J. Ocel, R. DesRoches, T. Leon, W.G. Hess, R. Krumme, J.R. Hayes, S. Sweeney, Steel Beam-column connections using shape memory alloys. *Journal of Structural Engineering*, **130(5)**, 732-740, 2004.

[8] C. Fang, W. Wang, C. He, Y. Chen, Self-centring behaviour of steel and steel-concrete composite connections equipped with NiTi SMA bolts. *Engineering Structures*, **150**, 390-408, 2017.

[9] M. Ghassemieh, R. Kargarmoakhar, Response modification factor of steel frames utilizing shape memory alloys. *Journal of Intelligent Material Systems and Structures*, **24(10)**, 1213–1225, 2013.

[10] D. Vafaei, R. Eskandari, Seismic performance of steel mega braced frames equipped with shape-memory alloy braces under near-fault earthquakes. *Struct. Design Tall Spec. Build.*, **25(3)**, 3–21, 2016

[11] C.-X. Qiu, S. Zhu, Performance-based seismic design of self-centering steel frames with SMA-based braces. *Engineering Structures*, **130**, 67-82, 2017.

[12] R. Johnson, E.J. Padgett, M.E. Maragakis, R. DesRoches, M.S. Saiidi, Large scale testing of nitinol shape memory alloy devices for retrofitting of bridges. *Smart Materials and Structures*, **17(3)**, 1-10, 2008.

[13] K.C. Shrestha, M.S. Saiidi, C.A. Cruz, Advanced materials for control of post-earthquake damage in bridges. *Smart Materials and Structures*, **24**, 1-16, 2015.

[14] S. Varela, M.S. Saiidi, A bridge column with superelastic NiTi SMA and replaceable rubber hinge for earthquake damage mitigation. *Smart Materials and Structures*, **25**, 1-18, 2016.

[15] M.G. Castellano, M. Indirli, A. Martelli, J.J. Azevedo, G.E. Sincraian, D. Tirelli, V. Renda, A. Bonci, A. Viskovic, Seismic protection of cultural heritage using shape memory alloy devices- An EC funded project (ISTECH). *International Post-SMiRT Conference Seminar on Seismic Isolation, Passive Energy Dissipation and Active Control of Vibrations of Structures,* Cheju, Korea, August 23-25, 1999.

[16] M. Indirli, B. Carpani, A. Martelli, M.G. Castellano, G. Croci, M. Biritognolo, A. Bonci, A. Viskovic, A. Viani, Experimantal Tests on masonry structures provided with shape memory alloy antiseismic devices. *12WCEE*, Auckland, New Zealand, 2000.

[17] M. G. Castellano, M. Indirli, A. Martelli, Progress of application, research and development and design guidelines for shape memory alloys devices for cultural heritage structures in Italy. *Proceedings of SPIE - The International Society for Optical Engineering*, 2001.

[18] K.C. Shrestha, Y. Araki, T. Nagae, T. Omori, Effectiveness of superelastic bars for seismic rehabilitation of clay-unit masonry walls. *Earthquake Engng Struct. Dyn*, **42**, 725–741, 2013.

[19] K.C. Shrestha, Y. Araki, T. Nagae, T. Omori, Y. Sutou, R. Kainuma, K. Ishida, Applicability of Cu-Al-Mn shape memory alloy bars to retrofitting of historical masonry constructions. *Earthquakes and Structures,* **2(3)**, 233-256, 2013.

[20] E.J. Graesser, F.A. Cozzarelli, Shape-memory alloys as new materials for aseismic isolation. *Journal of Engineering Mechanics*, **117(11)**, 2590-2608, 1991.

[21] F. Auricchio, E. Sacco, A superelastic shape-memory-alloy beam. *Journal of Intelligent Materials and Structures*, **8**, 489-501, 1997.

[22] F. Auricchio, R. L. Taylor, J. Lubliner, Shape memory alloys: macromodelling and numerical simulations of the superelestic behavior. *Comput. Methods Appl. Mech. Engrg*., **146,** 281-312, 1997.

[23] B. Duran, K. Can Atlı, Ö. Avşar, Superelastic Cyclic Properties of Cu-Al-Mn and Ni-Ti Shape Memory Alloys for Seismic Mitigation. *5th World Congress on Civil, Structural, and Environmental Engineering (CSEE'20)*, Lisbon, Portugal, Virtual Conference – October 2020.

[24] P. C. S. Silva, E. N. D. Grassi, C. J. Araújo, J. M. P. Q. Delgado, A. G. B. Lima, NiTi SMA superelastic micro cables: thermomechanical behavior and fatigue life under dynamic loadings. *Sensors*, **22**, 8045, 2022.

[25] S. Alazzawi, P. Filip, Modeling the transient behavior of the NiTi shape memory actuator using finite element analysis: Parametric study of the rate effects. *Results in Materials,* **1**, 2019.

[26] J.A. Shaw, S. Kyriakides, Thermomechanical aspects of Ni-Ti. *Journal of Mech. Phys. Solids*, **43(8)**, 1243-1281, 1995.

[27] Y. J. He, Q. P. Sun, Frequency-dependent temperature evolution in NiTi shape memory alloy under cyclic loading. *Smart Mater. Struct*., **19**, 9 pages, 2010.

[28] B. Gencturk, Y. Araki, T. Kusama, T. Omori, R. Kainuma, F. Medina, Loading rate and temperature dependency of superelastic Cu–Al–Mn alloys. *Construction and Building Materials*, **53**, 555-560, 2014.

[29] A. Falahian, P. Asadi, H. T. Riahi, M. Kadkhodaei, An experimental study on a self-centering damper based on shape-memory alloy wires. *Mechanics Based Design of Structures and Machines*, 2021.

[30] F. Auricchio, D. Fugazza, R. DesRoches, A 1D Rate-Dependent Viscous Constitutive Model for Superelastic Shape-Memory Alloys: Formulation and Comparison with Experimental Data. *Smart Materials and Structures*, **16**, 39-50, 2007.

[31] H. Özdemir, Nonlinear Transient Dynamic Analysis of Yielding Structures. PhD Dissertation, University of California, Berkeley, 1976.

[32] R. DesRoches, J. McCormick, M. Delemont, Cyclic properties of superelastic shape memory alloys wires and bars. *Journal of Structural Engineering*, **130 (1)**, 38-46, 2004.

[33] M.I Ntina, Analytical investigation of the seismic performance of special truss girder framing systems with new technologies. Ph.D. Dissertation, Department of Civil Engineering, University of Thessaly, Volos, Greece (in English), 2020.

[34] M. Dolce, D. Cardone, Mechanical behavior of shape memory alloys for seismic applications. 2. Austenite NiTi wires subjected to tension. *International Journal of Mechanical Sciences*, **43(11)**, 2657-2677, 2001.

[35] Seismosoft, (2018), "SeismoStruct 2018 – A computer program for static and dynamic nonlinear analysis of framed structures", available from https://seismosoft.com/

[36] MATLAB : https://www.mathworks.com/products/matlab.html.

COMPDYN 2023
9th ECCOMAS Thematic Conference on
Computational Methods in Structural Dynamics and Earthquake Engineering
M. Papadrakakis, M. Fragiadakis (eds.)
Athens, Greece, 12-14 June 2023

# MODELLING OF THE FULL-RANGE RESPONSE OF ABUTMENT-BACKFILL SYSTEMS

**Ioannis G. Mikes**[1,2], **Andreas J. Kappos**[2]

[1] City, University of London
London, United Kingdom
e-mail: ioannis.mikes@city.ac.uk

[2] Khalifa University
Abu Dhabi, United Arab Emirates
andreas.kappos@ku.ac.ae

## Abstract

*Over the last decades, the findings of numerous analytical studies, experiments and in-situ observations have highlighted the importance of the deck-abutment-backfill interaction on the seismic response of bridges. These findings have allowed various research groups to develop closed-form relationships that describe the nonlinear behaviour of the abutment-backfill system. Such relationships have been broadly used in research, reflected in modern seismic codes and guidelines, and incorporated in nonlinear analysis software.*

*However, the behaviour of the abutment-backfill systems after the attainment of peak strength has been neither studied to a sufficient extent from the analysis point of view nor included in the constitutive models of widely used nonlinear analysis software packages, such as OpenSees, even though large-scale tests have captured this critical phase of the response. The softening region of the response of the backfill has been addressed by some hardening/softening plasticity models that are not appropriate when simpler approaches (like Winkler springs) are used. Notably, the estimation of the abutment-backfill response at any level of seismic intensity is necessary for an appropriate fragility analysis of a bridge since the abutment-backfill component is almost always considered to affect at least some aspects of the bridge response and its failure is one of the possible failure modes that should be accounted for.*

*In the above context, the main aim of the work presented herein is to propose an extended version of the 'Hyperbolic Gap' OpenSees material, the so-called 'Hyperbolic Gap Softening' material, which allows the user to define a set of parameters that describe the softening branch of the backbone curve of an abutment-backfill system. In addition to tests of the new model using a simple configuration, results of response history analyses of a case study bridge with different abutment-backfill properties are also reported, with a view to verifying the applicability of the proposed model and investigating the importance of capturing the post-peak abutment-backfill behaviour on the estimation of the response of a bridge.*

**Keywords:** Hyperbolic gap, softening, OpenSees, post-peak response, abutment, backfill

## 1 INTRODUCTION

A large number of studies have been devoted to a better understanding of the behaviour of the abutment-backfill system in the longitudinal direction of the bridges, including full- and small-scale experiments of model walls and pile caps supporting backfill soil and analytical studies [1]. Most of these studies attempted to develop representative equivalent linear, bilinear, or other nonlinear estimations of the abutment-backfill lateral force ($F$) as a function of lateral displacement ($\delta$) that could be implemented in elastic, nonlinear static or nonlinear dynamic (response history) analyses of finite element models in the form of soil springs. One of the first proposed models was that in [2], a simplified model composed of bilinear springs and dashpots to study the response of skew bridges, while [3] used an approach based on the classical Rankine theory [4] to estimate the equivalent stiffness of a seat-type abutment-backfill system in the longitudinal direction that was incorporated in the finite element model of the bridge in the form of a vertical Winkler beam. The remarkable progress in nonlinear analysis methods that was marked in the years that followed, turned the research focus to the development of fully nonlinear models that were able to capture the behaviour of the abutment-backfill system more accurately, usually based on experimental results. Among the best known models of this category is that of Shamsabadi et al. ([1], [5]), who developed the 'Log-Spiral Hyperbolic' (LSH) stress-strain model by adopting a log-spiral passive failure surface in the backfill soil and coupling it with the hyperbolic stress-strain law proposed in [6]. Their model was validated against the results of large- and small-scale tests. Extending the LSH model, the same research group proposed several more practice-oriented, closed-form force-displacement relationships accounting for the dependence on the backwall height (Extended Hyperbolic Force-Displacement model or EHFD, [7]) and covering a broad range of cohesion values, friction angles and wall-soil interface friction angles (Generalized Hyperbolic Force-Displacement model or GHFD, [8]), being more appropriate to represent the various backfill soil types used in bridge construction. The development of these models focused solely on the behaviour of the so-called 'sacrificial' backwalls, i.e., backwalls that are assumed to shear off during a seismic event right after the collision with the deck to protect the substructure, as recommended by the Caltrans design guidelines [9]. However, lots of backwalls worldwide are stronger and have a more ductile behaviour, forming a plastic hinge at their bottom as they collide with the deck. Such behaviour is common in the seismic regions of Europe [10], [11] and also in bridges in seismic regions of the US that were designed before the implementation of the Caltrans guidelines [12]. Therefore, modelling methods that include nonlinear beam-column elements and soil springs to represent the structural parts of the abutment and the backfill soil, respectively, have been proposed (e.g. [10], [13]), while [14] developed a methodology that results in a simple single-spring model that is able to capture effectively the nonlinear behaviour of the entire abutment-backfill system with 'hinging' backwall.

Based on the hyperbolic relationship in [15] and the LSH model ([1], [5]), the 'Hyperbolic Gap Material' force-displacement model was developed by Dryden & Fenves [16] and was implemented in OpenSees [17]. Since its development, the 'Hyperbolic Gap Material' has been used widely in research works that consider the nonlinearity of the abutment-backfill system and its contribution to the dynamic response of bridges (e.g., [18]–[22]). This is a compression-only constitutive model that follows a hyperbolic backbone curve, which has been shown to properly capture the actual backfill soil behaviour found in experimental campaigns like [23]; it includes an initial zero-valued branch to represent the gap between the deck and the backwall allowing the user to avoid the implementation of separate gap elements, which are known to be prone to numerical difficulties (e.g. [14], [24]) and it is also able to capture the accumulated damage in the backfill soil. However, it has a number of drawbacks,

the most important arguably being that it does not offer the option of defining a post-peak softening behaviour, although this behaviour has been observed in pertinent tests (e.g. [25]–[27]) and hence, it may result in inaccuracies in the representation of the post-peak abutment-backfill behaviour in the case of ground motions of high intensity. These inaccuracies are important when the full-range response of the abutment-backfill system has to be taken into account, which is notably the case in vulnerability/fragility analysis.

The main aim of this paper is to present a new, improved version of the 'Hyperbolic Gap Material', the so-called 'Hyperbolic Gap Softening' model that was developed by the authors in the form of a new 'object' of the 'Uniaxial Material' class in OpenSees. The 'Hyperbolic Gap Softening' model allows the user to define a post-peak descending branch and a subsequent residual force branch to fully cover the response of the abutment-backfill system, according to available experimental results. In addition to tests of the new model using a simple configuration, indicative results are also shown of nonlinear response history analyses of a 3D bridge model that were conducted to verify the applicability of the new model and to compare its effect on the bridge response with that of the 'Hyperbolic Gap Material'.

## 2 FORMULATION OF THE PROPOSED MODEL

The compression-only backbone curve of the existing 'Hyperbolic Gap Material' model is described by Equation 1:

$$F(x) = \frac{x}{\frac{1}{K_{max}} + R_f \frac{x}{F_{ult}}} \tag{1}$$

where F(x) is the lateral force that develops at the backfill, x is the horizontal displacement, while the user-defined parameters are $K_{max}$, the initial stiffness of the backfill soil, which is the initial slope of the force – displacement curve, $F_{ult}$, the 'ultimate' passive resistance, and $R_f$, the 'failure ratio', i.e., the ratio of $F_{ult}$ to the strength corresponding to the asymptote of the hyperbola (eq. 1). The cyclic behaviour of the model is determined by $K_{ur}$, the stiffness during unloading and reloading, also defined by the user. As commented in [27], Equation 1 is meant to represent the passive force-displacement behaviour up to peak resistance and some sort of capping of the derived curve should be implemented if the behaviour beyond that point needs to be considered. The reason for this limitation is that in Equation 1 there is no displacement related to a maximum resistance value; hence, the resulting backbone curve extrapolates to infinity in terms of x as the corresponding F(x) tends to the asymptote of the hyperbola. An indicative example of the 'Hyperbolic Gap Material' presented in [28] is shown in Figure 1.

As already stated, the model proposed herein was mainly developed to offer the option of modelling the post-peak behaviour of the backfill soil in an effective, yet reasonably accurate, way, based on past research works that studied this behaviour. The results collected by field observations and the literature review of [26] showed that after reaching its peak, the passive resistance of a backfill drops until a level of residual passive force ($F_{res}$), which is about 60% to 70% of the maximum passive force $F_{ult}$, at a displacement $x_{res}$ that is approximately equal to 2.5 to 3 times the value of displacement at maximum passive force ($x_{max}$). The shape of the descending branch often resembles an exponential curve with an inflection point at about $2x_{max}$ according to [26]. However, the shape of the descending branch varies significantly in tests with different backfill soil materials and it depends on various parameters, such as the cohesion and the water content [26], [27]. The inflection point of the descending branch is also case-dependent. For instance, although the test results of [27] for soil confirm the assumption of [26] regarding the point of inflection of the descending branch, the results of the

same study for soil with higher water content indicate that there is no evident inflection before the onset of the branch of the residual force (Figure 2).

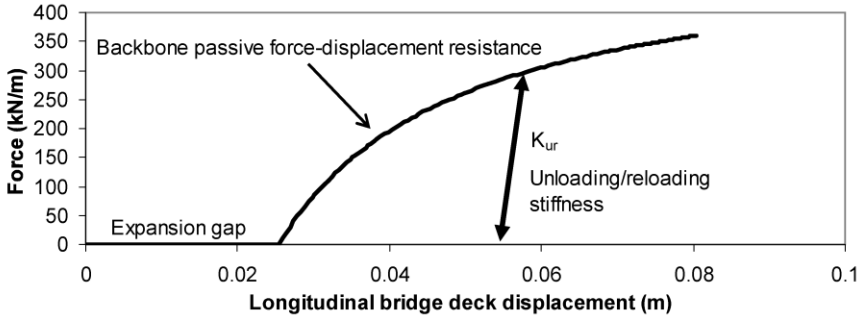


Figure 1. Force-displacement behaviour of the 'Hyperbolic Gap Material' [28]

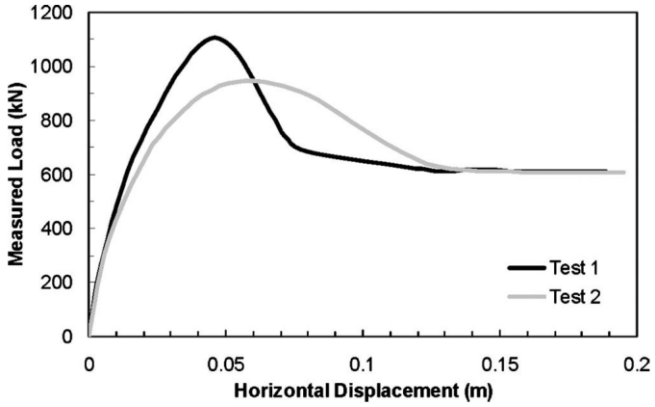


Figure 2. Experimentally derived force-displacement backbone relationships of engineered silty sand backfill. Test 1: Dry conditions. Test 2: Field water conditions [27]

Another ambiguous point in the formulation of the 'Hyperbolic Gap Material' is the use of the empirically defined $R_f$ parameter (Equation 1), whose value may vary significantly from case to case. For instance, [6] suggest a value range of 0.75 – 0.95, while [29] fitted their experimental results to Equation 1 with $R_f = 0.7$. The fact that other research works introduced modified versions of Equation 1 resulting in a different range of empirically defined $R_f$ values (e.g., Shamsabadi et al. [1] recommend values from 0.94 to 0.98 for their closed-form relationship) may also cause confusion. Moreover, $R_f$ does not have any direct physical meaning, while its accurate estimation is impossible without calibration against available test data, which are not always available. On the contrary, $x_{max}$ (the displacement at $F_{ult}$) has a clear physical meaning and it is also relevant in the assessment of the abutment-backfill performance since it defines a limit state of the abutment-backfill system. Furthermore, there are recommended $x_{max}$ values available in the literature (e.g., [1], [8], [26]) based on experiments with various backfill soil types. Therefore, it was decided to select $x_{max}$ instead of $R_f$ as an input parameter of the new 'Hyperbolic Gap Softening' OpenSees material. To this purpose, $R_f$ was expressed as a function of $K_{max}$, $F_{ult}$ and $x_{max}$ by solving Equation 1 for $R_f$ taking $x = x_{max}$ and $F(x) = F(x_{max}) = F_{ult}$:

$$R_f = 1 - \frac{F_{ult}}{K_{max}\, x_{max}} \tag{2}$$

In the light of the previous considerations, a simplified bilinear form was selected for the post-peak part of the backbone curve of the new 'Hyperbolic Gap Softening' material object of OpenSees. The two branches of this bilinear segment represent the softening and the residual force phases of the backfill. The 'Hyperbolic Gap Softening' model allows the user to select the values of the parameters that define these two new branches, in order to approximate the softening behaviour of a backfill with an acceptable level of accuracy. Namely, these parameters are 1) the displacement at $F_{ult}$, considering a closed gap between the deck and the backwall ($x_{max}$), 2) the displacement at the onset of the residual force branch of the backbone ($x_{res}$), and 3) the value of the residual force ($F_{res}$). The backbone of the 'Hyperbolic Gap Material' (Equation 1) was adopted as the behaviour of the new model up to the point of maximum passive force, while the way that the unloading/reloading stiffness $K_{ur}$ is defined was also kept the same. The sign conventions of the 'Hyperbolic Gap Material' were followed in the 'Hyperbolic Gap Softening', since it is also a compression-only model, and the signs of the newly introduced parameters were set accordingly. All user-defined input parameters, including those that were adopted from the 'Hyperbolic Gap Material', are summarised in Table 1. A typical backbone curve of the 'Hyperbolic Gap Softening' model is illustrated in Figure 3.

| *Input parameter* | *Description* |
|---|---|
| $K_{max}$ | Initial stiffness |
| $K_{ur}$ | Unloading/reloading stiffness |
| $x_{max}$ | Displacement at $F_{ult}$ (with closed gap) |
| $F_{ult}$ | Maximum passive resistance |
| $x_{gap}$ | Initial gap |
| $x_{res}$ | Displacement at the onset of the residual force branch |
| $F_{res}$ | Residual passive resistance |

Table 1: User defined input parameters of the 'Hyperbolic Gap Softening' OpenSees material

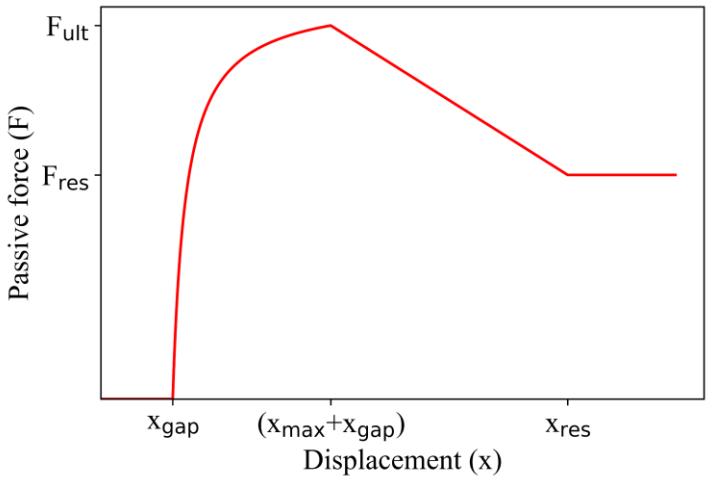


Figure 3. Typical backbone curve of the 'Hyperbolic Gap Softening' OpenSees material

Apart from the introduction of the softening and the residual force branches, the overshooting issues of the 'Hyperbolic Gap Material' that were noted occasionally in the reloading phase by the authors during their research (e.g. Figure 4a) were fixed in the 'Hyperbolic Gap Softening' material (Figure 4b). In the new material, the force is not allowed to exceed the backbone curve at any point. Whenever such an exceedance occurs at an iteration of an analy-

sis time step, the overshooting force is added to the residual force of the associated finite element (typically a uniaxial 'zero-length' element).

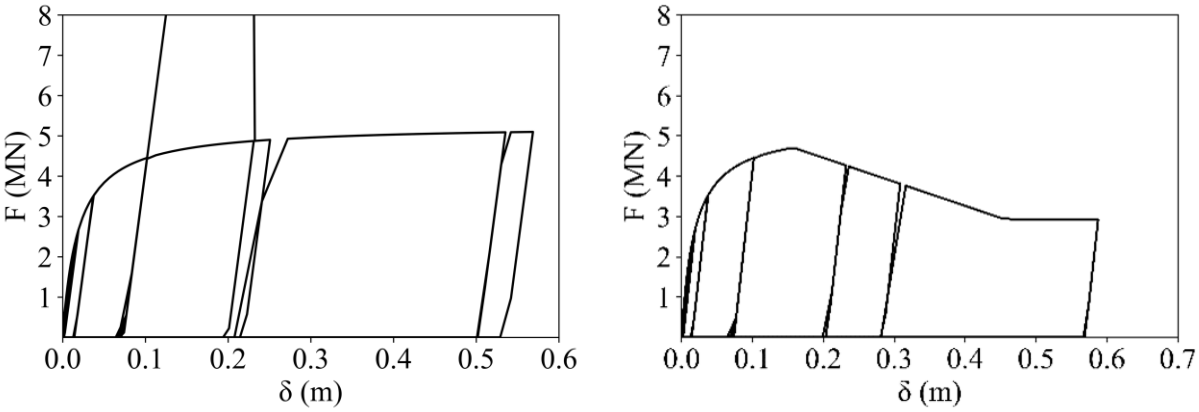


Figure 4. Force-displacement history diagrams of the abutment-backfill system of a bridge using (a) 'Hyperbolic Gap Material' and (b) 'Hyperbolic Gap Softening'

## 3 APPLICATION OF THE PROPOSED MODEL

The previously described model was used in an extensive set of parametric analyses to verify its applicability, identify any possible numerical issues, and compare the behaviour of systems that include it with those that include the existing 'Hyperbolic Gap Material'.

### 3.1 Verification using single-degree-of-freedom systems

First, the model was applied to various single-mass systems, which were subjected to a large number of response history analyses within a broad range of earthquake intensity levels. These SDOF systems consisted of a vertical beam-column element, which was fixed at its base and had an attached lumped mass to its top (the dynamic DOF was the horizontal displacement of the mass). A horizontal zero-length element was attached to the lumped mass. Half of the analyses were conducted using the 'Hyperbolic Gap Softening' constitutive law at the zero-length element; the other half used the 'Hyperbolic Gap Material'. Various stiffness and mass values of the SDOF were tried, while in some analyses a plastic hinge was assigned at its bottom. No numerical difficulties were noted when the 'Hyperbolic Gap Softening' uniaxial material was used, except for the cases where an elastic-perfectly plastic law (zero hardening) was used at the plastic hinge of the SDOF. In such cases, the analyses with both 'Hyperbolic Gap Softening' and 'Hyperbolic Gap Material' failed as a singular SDOF stiffness matrix was formed subsequent to yielding of the plastic hinge. Furthermore, no overshooting appeared during the analyses with 'Hyperbolic Gap Softening'. An example where the same SDOF and input ground motion were used and only the material law of the zero-length changed is shown in Figure 5. As can be noted in Figure 5, the two models resulted in notably different absorbed energies and maximum displacements.

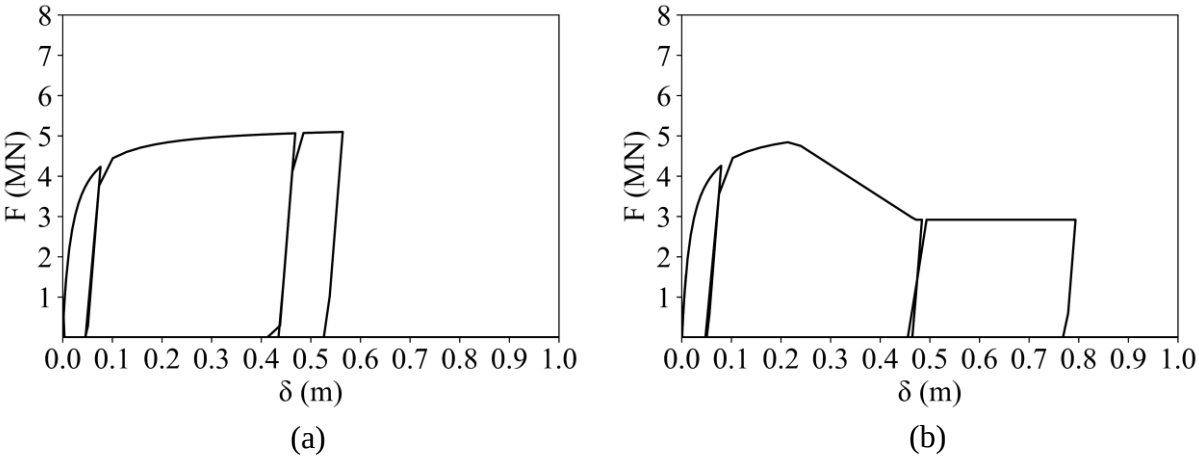


Figure 5. Force-displacement history diagrams of a zero-length element attached to the top of a single mass system using (a) 'Hyperbolic Gap Material' and (b) 'Hyperbolic Gap Softening'

### 3.2 Effect of softening backfill on the seismic response of bridges

A parametric study of the effect of using the 'Hyperbolic Gap Softening' in the seismic response of a typical 3-span overpass was carried out, in comparison with the response obtained using the 'Hyperbolic Gap Material' in the same model. The 99 m long reference bridge, which is a modification of an existing overpass of Egnatia Motorway in N. Greece, consists of a 45 m central and two 27 m outer spans. The 10 m wide box girder deck is monolithically connected to the two cylindrical piers, which have a diameter of 1.20 m and clear heights of 5.9 m and 7.9 m. The seat-type abutments are 5.6 m and 5.7 m high; they include 2.45 m high backwalls and each of them supports the deck through a pair of elastomeric bearings with dimensions (mm) 350 × 450 × 181 and total rubber thickness $t_r$ = 77 mm. The bridge rests on relatively firm cohesive soil that roughly corresponds to soil class C of Eurocode 8 [30] and thus, 6 m × 6 m × 1.50 m surface footings were found to be adequate for supporting the piers. All the structural and geotechnical components of the model bridge were designed and checked according to the pertinent Eurocodes, while soil-pier foundation-structure interaction was taken into account, following the relationships given in [31]. The layout of the bridge model is shown in Figure 6.

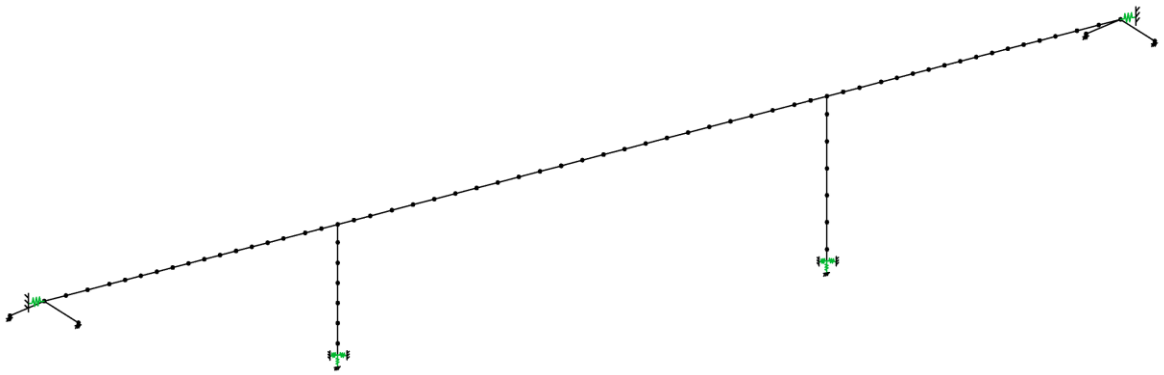

Figure 6. Structural model of the case study bridge

The case study bridge was subjected to a set of 7 spectrum-compatible artificial accelerograms parallel to its longitudinal direction, taken from a companion paper [11], scaled to vari-

ous amplitudes of the design spectrum. The lowest level of seismic intensity considered was at $PGA_{,rock}$ = 0.32 g and the highest was at $PGA_{,rock}$ = 0.96 g (six times the design earthquake $E_d$), as backfill softening was found to occur for high intensities only. Various initial deck-abutment joint gap sizes were used in the parametric analyses (0 to 300 mm). The nonlinear behaviour of the sacrificial abutment-backfill system was modelled using a single zero-length element, with properties corresponding to an engineered granular backfill. The backbone curve of the backfill soil until the point of maximum passive resistance was calculated according to [8] and $x_{max}$ was assumed to be equal to 3% of the backwall height, following an empirical recommendation for granular backfill soil found in [26]. The values of all the input parameters of the two hyperbolic gap models except the varying $x_{gap}$ are listed in Table 2. The backbone curves that were used in each backfill model are presented in Figure 7.

The average of the maximum absolute values of the displacements of the abutment-backfill springs subsequent to gap closure and the pier drifts derived from the nonlinear response history analyses for various intensity levels and initial gap sizes using the two hyperbolic constitutive models are shown in Tables 3 and 4. For relatively low seismic intensities, the two models yield the same results, as expected. Notable differences are observed at the highest examined intensity levels, where the maximum difference in the maximum pier drifts and abutment displacements was about 8%. This can be attributed to the reduced lateral force that the abutment carries after the point of peak resistance in the case of the 'Hyperbolic Gap Softening' model, as shown in Figure 8b. On the contrary, in the case of the 'Hyperbolic Gap Material', the passive force remains at the level of the maximum passive resistance throughout the analysis (Figure 8a) and hence, the abutment-backfill systems relieve the piers substantially even at very large displacements. As anticipated, the differences between the two models tend to be less important as the initial joint gap becomes larger.

| $K_{max}$ (kN/m) | $K_{ur}$ (kN/m) | $x_{max}$ (m) | $F_{ult}$ (kN) | $x_{res}$ (m) | $F_{res}$ (kN) |
|---|---|---|---|---|---|
| 375,570 | 206,564 | 0.073 | 5,415 | 0.219 | 3,249 |

Table 2: Values of the input parameters of the two hyperbolic gap models used in the case study

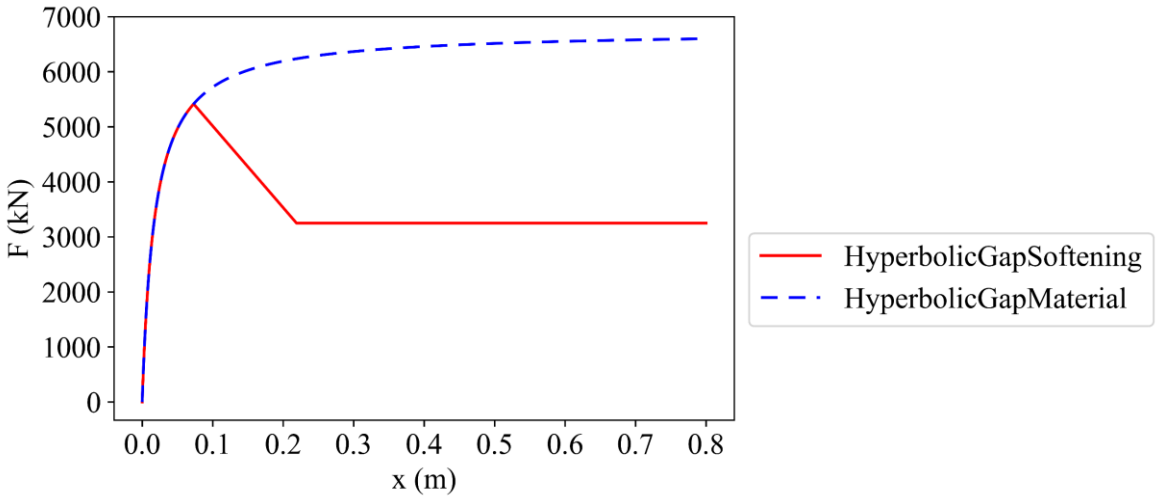


Figure 7. Backbone curves of the 'Hyperbolic Gap Softening' and 'Hyperbolic Gap Material' models used in the response history analyses with $x_{gap}$ = 0

| Gap size | Earthquake intensity (PGA,rock) | | | | | |
|---|---|---|---|---|---|---|
| | *0.32 g* | | *0.96 g* | | *1.28 g* | |
| | *HG* | *HGsoft* | *HG* | *HGsoft* | *HG* | *HGsoft* |
| ***0*** | 0.059 | 0.059 | 0.320 | 0.345 | 0.474 | 0.505 |
| ***25*** | 0.036 | 0.036 | 0.298 | 0.321 | 0.450 | 0.484 |
| ***50*** | 0.019 | 0.019 | 0.270 | 0.292 | 0.428 | 0.462 |
| ***75*** | - | - | 0.252 | 0.270 | 0.410 | 0.439 |
| ***100*** | - | - | 0.232 | 0.248 | 0.389 | 0.413 |
| ***150*** | - | - | 0.191 | 0.202 | 0.495 | 0.367 |
| ***300*** | - | - | 0.074 | 0.074 | 0.215 | 0.228 |

Table 3: Comparison of the average value of the maximum abutment-backfill displacement (in m) after gap closure for the 7 input motions using the two hyperbolic gap models (Hyperbolic Gap and Hyperbolic Gap Softening).

| Gap size | Earthquake intensity (PGA,rock) | | | | | |
|---|---|---|---|---|---|---|
| | *0.32 g* | | *0.96 g* | | *1.28 g* | |
| | *HG* | *HGsoft* | *HG* | *HGsoft* | *HG* | *HGsoft* |
| ***0*** | 1.08% | 1.07% | 5.30% | 5.61% | 7.80% | 8.30% |
| ***25*** | 1.12% | 1.12% | 5.31% | 5.60% | 7.82% | 8.36% |
| ***50*** | 1.17% | 1.17% | 5.27% | 5.56% | 7.87% | 8.40% |
| ***75*** | 1.31% | 1.31% | 5.35% | 5.60% | 7.98% | 8.43% |
| ***100*** | 1.36% | 1.36% | 5.42% | 5.65% | 8.00% | 8.42% |
| ***150*** | 1.36% | 1.36% | 5.60% | 5.74% | 8.13% | 8.50% |
| ***300*** | 1.36% | 1.36% | 6.09% | 6.10% | 8.48% | 8.70% |

Table 4: Comparison of the average value of the maximum pier drift after gap closure for the 7 input motions using the two hyperbolic gap models (Hyperbolic Gap and Hyperbolic Gap Softening)

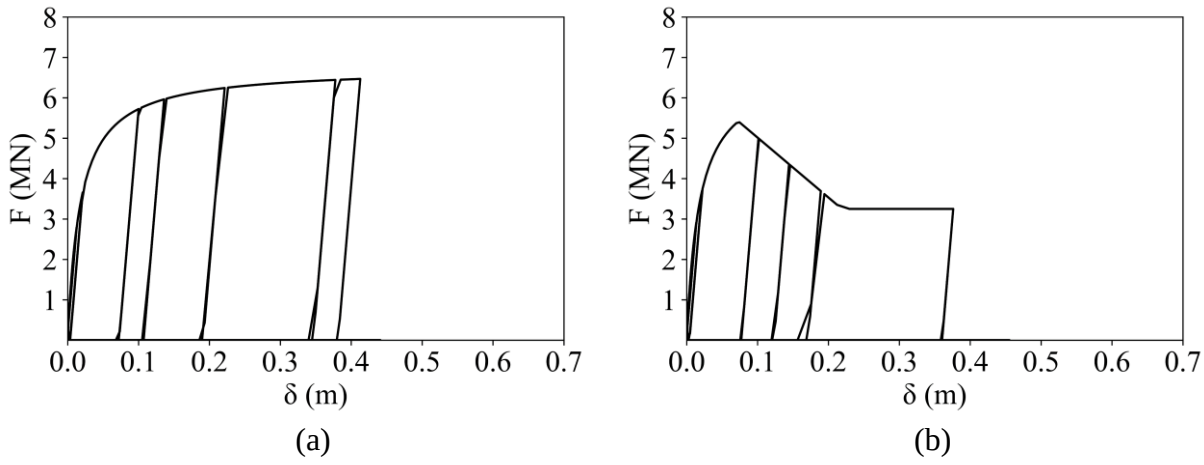


Figure 8. Force-displacement history diagrams of the abutment-backfill system (sacrificial backwall modelling) of the case study bridge subjected to a ground motion scaled to PGA = 1.28 g using (a) 'Hyperbolic Gap Material' and (b) 'Hyperbolic Gap Softening'

## 4 CONCLUSIONS

The present study highlighted the inadequacies of the 'Hyperbolic Gap Material' of OpenSees if it is used in nonlinear response history analyses when significant backfill displacement develop. The ensuing softening in the response of the abutment-backfill system may be relevant, especially when a proper fragility analysis has to be carried out. The new 'Hyperbolic Gap Softening' OpenSees material model that is proposed herein resolves this important issue by introducing a descending and a residual branch after the point of peak resistance, using parameter values available in the literature, while it attempts to remove any ambiguities in the definition of the constitutive model of the backfill soil spring by including input parameters with a direct physical meaning. The difference in the definition of the backbone curve of the backfill spring seems to lead to notable differences not only in the response of the abutment-backfill per se but also in the response of other seismically critical bridge components, such as the piers. In cases where only large joint gaps or low seismic intensities are considered, the existing 'Hyperbolic Gap Material' produces quite accurate results. However, the new model did not exhibit any numerical difficulties throughout the case studies wherein it was used; instead, it solved the overshooting problems that occur occasionally when the existing OpenSees material is used. Furthermore, its response under ground motions of low intensity is the same as the response of 'Hyperbolic Gap Material' when equivalent input parameters are used. Thus, in the authors' opinion, it is the preferred option when OpenSees is used in fragility analysis to capture the advanced damage states, especially when these are controlled by damage in the backfill.

Except for the joint gap size and seismic intensity, the importance of the accurate representation of the post-peak backfill behaviour seems to depend on the structural configuration of the entire bridge. This conclusion is based on the observation that the significant differences that the two compared models exhibited in the analysis of a single mass system were mitigated to some extent when the models were incorporated into the model of an entire bridge. For that reason, a large number of analyses considering a variety of bridge structural characteristics has to be carried out using both models, not only to further verify the applicability of the proposed model but also to draw reliable conclusions regarding the effect that the modelling of the full-range response of the abutment-backfill system has on the seismic response of bridges.

## REFERENCES

[1] A. Shamsabadi, K. M. Rollins, and M. Kapuskar, "Nonlinear soil–abutment–bridge structure interaction for seismic performance-based design," *J. Geotech. geoenvironmental Eng.*, vol. 133, no. 6, pp. 707–720, 2007.

[2] E. A. Maragakis and P. C. Jennings, "Analytical models for the rigid body motions of skew bridges," *Earthq. Eng. Struct. Dyn.*, vol. 15, no. 8, pp. 923–944, 1987.

[3] E. A. Maragakis and R. Siddharthan, "Estimation of inelastic longitudinal abutment stiffness of bridges," *J. Struct. Eng.*, vol. 115, no. 9, pp. 2382–2398, 1989.

[4] W. J. M. Rankine, "On the Stability of Loose Earth.," *Proc. R. Soc. London*, pp. 185–187, 1856.

[5] A. Shamsabadi, M. Ashour, and G. Norris, "Bridge abutment nonlinear force-displacement-capacity prediction for seismic design," *J. Geotech. geoenvironmental Eng.*, vol. 131, no. 2, pp. 151–161, 2005.

[6] J. M. Duncan and C.-Y. Chang, “Nonlinear analysis of stress and strain in soils,” *J. soil Mech. Found. Div. ASCE*, vol. 96, no. 5, pp. 1629–1653, 1970.

[7] A. Shamsabadi, P. Khalili-Tehrani, J. P. Stewart, and E. Taciroglu, “Validated simulation models for lateral response of bridge abutments with typical backfills,” *J. Bridg. Eng.*, vol. 15, no. 3, pp. 302–311, 2010.

[8] P. Khalili-Tehrani, A. Shamsabadi, J. P. Stewart, and E. Taciroglu, “Backbone curves with physical parameters for passive lateral response of homogeneous abutment backfills,” *Bull. Earthq. Eng.*, vol. 14, no. 11, pp. 3003–3023, 2016.

[9] Caltrans, “Seismic Design Criteria (version 2.0),” CA, USA, 2019.

[10] S. A. Mitoulis, “Seismic design of bridges with the participation of seat-type abutments,” *Eng. Struct.*, vol. 44, pp. 222–233, 2012.

[11] I. G. Mikes and A. J. Kappos, “Optimization of the seismic response of bridges using variable-width joints,” *Earthq. Eng. Struct. Dyn.*, 2023.

[12] Q. Zheng, C. W. Yang, Y. Xie, J. Padgett, R. DesRoches, and C. Roblee, “Influence of abutment straight backwall fracture on the seismic response of bridges,” *Earthq. Eng. Struct. Dyn.*, vol. 50, no. 7, pp. 1824–1844, 2021.

[13] S. P. Stefanidou, A. G. Sextos, A. N. Kotsoglou, N. Lesgidis, and A. J. Kappos, “Soil-structure interaction effects in analysis of seismic fragility of bridges using an intensity-based ground motion selection procedure,” *Eng. Struct.*, vol. 151, pp. 366–380, 2017, doi: 10.1016/j.engstruct.2017.08.033.

[14] I. G. Mikes and A. J. Kappos, “Simple and complex modelling of seat-type abutment-backfill systems,” in *Proceedings of the International Conference on Computational Methods in Structural Dynamics and Earthquake Engineering*, 2021, vol. 2021, pp. 5266–5282.

[15] J. M. Duncan and R. L. Mokwa, “Passive earth pressures: theories and tests,” *J. Geotech. Geoenvironmental Eng.*, vol. 127, no. 3, pp. 248–257, 2001.

[16] G. M. Dryden and G. L. Fenves, *The integration of experimental and simulation data in the study of reinforced concrete bridge systems including soil-foundation-structure interaction*. Rep. PEER 2009/03, University of California, Berkeley, 2009.

[17] F. McKenna, M. H. Scott, and G. L. Fenves, “Nonlinear Finite-Element Analysis Software Architecture Using Object Composition,” *J. Comput. Civ. Eng.*, vol. 24, no. 1, pp. 95–107, 2010, doi: 10.1061/(asce)cp.1943-5487.0000002.

[18] R. Omrani *et al.*, “Guidelines for Nonlinear Seismic Analysis of Ordinary Bridges: Version 2.0,” *Caltrans Final Rep. No. 15-65A0454*, no. December, p. 168, 2015.

[19] X. Chen and C. Li, “Seismic performance of tall pier bridges retrofitted with lead rubber bearings and rocking foundation,” *Eng. Struct.*, vol. 212, no. November 2019, p. 110529, 2020, doi: 10.1016/j.engstruct.2020.110529.

[20] A. R. Ghotbi, “Performance-based seismic assessment of skewed bridges with and without considering soil-foundation interaction effects for various site classes,” *Earthq. Eng. Eng. Vib.*, vol. 13, no. 3, pp. 357–373, 2014, doi: 10.1007/s11803-014-0248-7.

[21] Y. Wang, L. Ibarra, and C. Pantelides, “Seismic retrofit of a three-span RC bridge with buckling-restrained braces,” *J. Bridg. Eng.*, vol. 21, no. 11, p. 4016073, 2016.

[22] N. Xiang and M. S. Alam, “Comparative seismic fragility assessment of an existing isolated continuous bridge retrofitted with different energy dissipation devices,” *J. Bridg. Eng.*, vol. 24, no. 8, p. 4019070, 2019.

[23] A. Lemnitzer, E. R. Ahlberg, R. L. Nigbor, A. Shamsabadi, J. W. Wallace, and J. P. Stewart, “Lateral performance of full-scale bridge abutment wall with granular backfill,” *J. Geotech. Geoenvironmental Eng.*, vol. 135, no. 4, pp. 506–514, 2009.

[24] S.-H. Kim and M. Shinozuka, “Effects of Seismically Induced Pounding at Expansion Joints of Concrete Bridges,” *J. Eng. Mech.*, vol. 129, no. 11, pp. 1225–1234, 2003.

[25] R. T. Cole and K. M. Rollins, “Passive earth pressure mobilization during cyclic loading,” *J. Geotech. Geoenvironmental Eng.*, vol. 132, no. 9, pp. 1154–1164, 2006.

[26] A. Bozorgzadeh, S. A. Ashford, J. I. Restrepo, and N. Nimityongskul, “Experimental and Analytical Investigation on Stiffness and Ultimate Capacity of Bridge Abutments,” Report No. SSRP–07/12, UC San Diego, 2008.

[27] P. Wilson and A. Elgamal, “Large-Scale Passive Earth Pressure Load-Displacement Tests and Numerical Simulation,” *J. Geotech. Geoenvironmental Eng.*, vol. 136, no. 12, pp. 1634–1643, 2010, doi: 10.1061/(asce)gt.1943-5606.0000386.

[28] P. Wilson and A. Elgamal, “Bridge-abutment-backfill dynamic interaction modeling based on full scale tests,” in *9th US National and 10th Canadian Conference on Earthquake Engineering 2010, Including Papers from the 4th International Tsunami Symposium*, 2010, vol. 3, pp. 1736–1745.

[29] P. Wilson and A. Elgamal, “Full Scale Bridge Abutment Passive Earth Pressure Tests and Calibrated Models,” in *14th World Conference on Earthquake Engineering*, 2008, pp. 1–8.

[30] CEN, “Eurocode 8: Design of structures for earthquake resistance-part 1: general rules, seismic actions and rules for buildings,” *Brussels Eur. Comm. Stand.*, 2005.

[31] G. Mylonakis, S. Nikolaou, and G. Gazetas, “Footings under seismic loading: Analysis and design issues with emphasis on bridge foundations,” *Soil Dyn. Earthq. Eng.*, vol. 26, no. 9, pp. 824–853, 2006.

COMPDYN 2023
9th ECCOMAS Thematic Conference on
Computational Methods in Structural Dynamics and Earthquake Engineering
M. Papadrakakis, M. Fragiadakis (eds.)
Athens, Greece, 12-14 June 2023

# ON THE CALIBRATION OF UBCSAND CONSTITUTIVE MODEL AGAINST MONOTONIC & CYCLIC TRIAXIAL COMPRESSION DATA FOR BALLAST AGGREGATES

**Tadahiro Kishida**[1], **Rusul F. Aldulaimi**[1] **and George Mylonakis**[1]

[1] Khalifa University
UAE
{tadahiro.kishida, 100059665, george.mylonakis}@ku.ac.ae

## Abstract

*Understanding the mechanical behavior of ballast aggregates under multi-axial loading is key in railway foundation analysis and design. UBCSAND is an effective-stress constitutive model which can predict static and dynamic behavior of granular materials under combined shear and normal stresses. This study presents results from a suite of triaxial monotonic and cyclic compression tests for four different aggregates (gabbro, limestone, demolished concrete, steel slag) and discusses the applicability of UBCSAND model for simulating the relevant non-linear stress-strain curves. To this end, UBCSAND is integrated, for the first time, analytically for shear and volumetric strains, to facilitate calibration against experimental data. Four novel solutions are derived, expressed in terms of monomials and Gauss' hypergeometric functions (${}_2F_1$) of the stress ratio (q/p'). Variation in the calibrated parameters is discussed considering different loading conditions and types of aggregates.*

**Keywords:** UBCSAND, drained & undrained triaxial tests, analytical solution, numerical calibration

## 1 INTRODUCTION

Understanding drained monotonic and cyclic behavior of ballast aggregates is key in railway foundation design. The UBCSAND model [1-3] is often employed in such analyses, as a simple alternative to more complex constitutive formulations for predicting monotonic and cyclic response of granular soil under both drained and undrained conditions [4-23]. The specific model is employed in commercial finite difference and finite element software (e.g., [3, 24-26]) as it realistically simulates volumetric and deviatoric strains in granular soils under monotonic and cyclic loading.

The study at hand presents an analytical methodology for integrating the UBCSAND model that yields a set of four novel closed-form solutions for shear and volumetric strains. Contrary to numerical integration approaches, these solutions are free of numerical errors and, thereby, can provide insight on the role of the various model parameters and their calibration against experimental data. Three novel methodologies developed by the authors in a companion paper [27] for calibrating the model are compared: (1) a graphical "chart" solution based on results from forward numerical simulations; (2) a numerical approach based on minimization of residuals; (3) a trial-and-error graphical approach based on the analytical solution. These calibration procedures are applied to experimental data from drained strain- and stress-controlled triaxial compression tests carried out in the Geotechnical Materials Lab at Khalifa University on four types of aggregates: gabbro, limestone, demolished concrete and steel slag. The performance of the model with number of cycles is discussed against data from cyclic compression tests.

## 2 UBCSAND FORMULATION

The pressure-dependent, non-linear elastic shear and bulk moduli ($G^e$, $K^e$) can be established by means of Eqs. (1) and (2), as functions of the mean effective stress $p'$ and Poisson's ratio $\nu$ [30]

$$G^e = k_G^e \left(\frac{p'_M}{p_a}\right)^{ne} p_a \tag{1}$$

$$K^e = \frac{2(1+\nu)}{3(1-2\nu)} G^e \tag{2}$$

where $k_G^e$ is a dimensionless elastic shear modulus parameter, $p_a$ is the atmospheric pressure (usually taken equal to 100 kPa) and $p'_M = (\sigma'_1 + \sigma'_3)/2$ is the familiar MIT mean effective stress. In Eq. (1), the elastic shear modulus exponent *ne* is often taken equal to around 0.5 based on experimental observations of small-strain shear moduli (e.g., [31-33]).

The incremental elastic stress-strain relation can be cast in terms of $G^e$ and $K^e$ as shown in Eq. (3).

$$\begin{bmatrix} dp' \\ dq \end{bmatrix} = \begin{bmatrix} K^e & 0 \\ 0 & 2G^e \end{bmatrix} \begin{bmatrix} d\varepsilon_v^e \\ d\gamma^e \end{bmatrix} \tag{3}$$

where $p'$ and $q$ are the corresponding Cambridge stress invariants defined as $p' = (\sigma'_1 + \sigma'_2 + \sigma'_3)/3$, $q = \sigma'_1 - \sigma'_3$ under triaxial loading, and $d\varepsilon_v^e$, $d\gamma^e$ are the corresponding incremental volumetric and shear strains $d\varepsilon_v^e = d\varepsilon_a^e + 2d\varepsilon_r^e$, $d\gamma^e = d\varepsilon_a^e - d\varepsilon_r^e$. Since UBCSAND employs the MIT stress path parameters $p'_M = \frac{1}{2}(\sigma'_1 + \sigma'_3)$ and $q_M = \frac{1}{2}(\sigma'_1 - \sigma'_3)$, Equation (3) can be recast in the following equivalent forms:

$$\begin{bmatrix} dp'_M \\ dq_M \end{bmatrix} = \begin{bmatrix} K^e & G^e/3 \\ 0 & G^e \end{bmatrix} \begin{bmatrix} d\varepsilon_v^e \\ d\gamma^e \end{bmatrix} \tag{4a}$$

$$\begin{bmatrix} d\varepsilon_v^e \\ d\gamma^e \end{bmatrix} = \begin{bmatrix} 1/K^e & -1/3K^e \\ 0 & 1/G^e \end{bmatrix} \begin{bmatrix} dp'_M \\ dq_M \end{bmatrix} \tag{4b}$$

With reference to elastoplastic response, the yield surface is defined as

$$f = \eta - \eta_{mob} = 0 \tag{5}$$

where $\eta = q_M/p'_M$ is the dimensionless stress ratio. Yielding occurs when $\eta$ reaches the mobilized stress ratio $\eta_{mob}$.

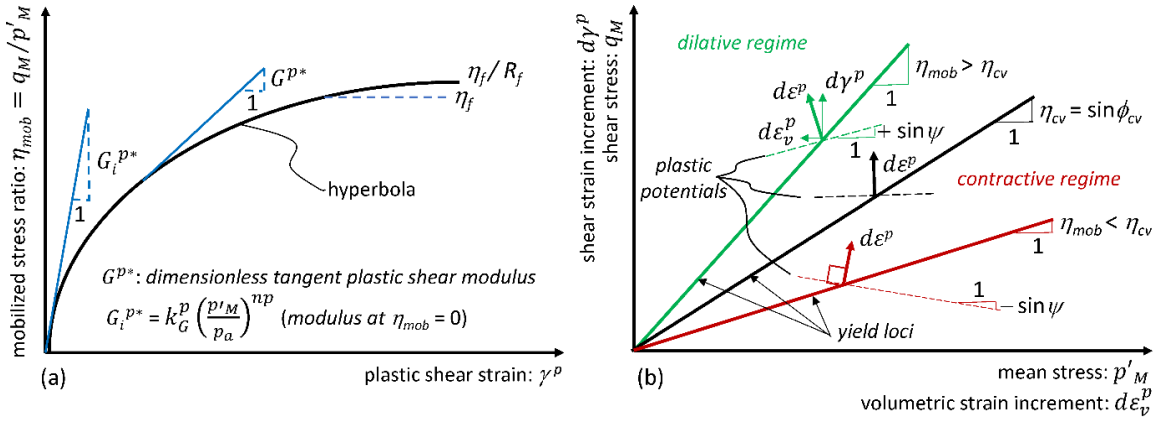


Figure 1. (a) Hardening rule; (b) Yield criterion and flow rule for UBCSAND model [27]

The hardening rule can be expressed in differential form using the total derivative:

$$d\gamma^p = \frac{1}{G^{p*}} d\eta_{mob} = \frac{1}{G^{p*} p'_M} \left(-\eta_{mob} dp'_M + dq_M\right) \tag{6}$$

where $G^{p*}$ is a dimensionless plastic shear modulus relating $d\gamma^p$ and $d\eta$. In the realm of the specific model, $G^{p*}$ is estimated from the empirical relation

$$G^{p*} = k_G^p \left(\frac{p'_M}{p_a}\right)^{np} \left(1 - \frac{\eta_{mob}}{\eta_f / R_f}\right)^2 \tag{7}$$

where $k_G^p$ is a dimensionless plastic shear modulus parameter (being equal to $G^{p*}$ at $p'_M = p_a$ and $\eta_{mob} = 0$), and $\eta_f$ is the stress ratio at failure. $R_f$ is the failure ratio adjustment for preventing the over-prediction of strength at failure [2, 34]. The plastic shear modulus exponent *np* is usually selected in the range 0.4 – 0.7 [29].

The flow rule is of the non-associative type and is given by the simple equation

$$\frac{d\varepsilon_v^p}{d\gamma^p} = \eta_{cv} - \eta_{mob} \tag{8}$$

where $\eta_{cv}$ is the stress ratio under constant volume. A graphical illustration of the UBCSAND hardening and flow rules, mathematically expressed by Eqs. (6) and (8) respectively, is provided in Figure 1.

By combining Eqs. (6) and (8), the plastic strain increment can be expressed as

$$\begin{bmatrix} d\varepsilon_v^p \\ d\gamma^p \end{bmatrix} = \frac{1}{G^{p*} p'_M} \begin{bmatrix} -\eta_{mob}(\eta_{cv} - \eta_{mob}) & \eta_{cv} - \eta_{mob} \\ -\eta_{mob} & 1 \end{bmatrix} \begin{bmatrix} dp'_M \\ dq_M \end{bmatrix} \tag{9}$$

Adding Eqs. (4b) and (9), the combined elastic and plastic volumetric and shear strain increments are obtained from the equation:

$$\begin{bmatrix} d\varepsilon_v \\ d\gamma \end{bmatrix} = \begin{bmatrix} C_{11} & C_{12} \\ C_{21} & C_{22} \end{bmatrix} \begin{bmatrix} dp'_M \\ dq_M \end{bmatrix} \tag{10}$$

where

$$C_{11} = \frac{1}{K^e} + \frac{-\eta_{mob}(\eta_{cv} - \eta_{mob})}{G^{p*} p'_M} \qquad C_{12} = \frac{-1}{3K^e} + \frac{\eta_{cv} - \eta_{mob}}{G^{p*} p'_M} \tag{11a,b}$$

$$C_{21} = \frac{-\eta_{mob}}{G^{p*} p'_M} \qquad C_{22} = \frac{1}{G^e} + \frac{1}{G^{p*} p'_M} \tag{11c, d}$$

are the elements of the compliance matrix ***C***. Explicit formulae obtained upon substituting Eq. (7) into Eqs (11) are provided in [27].

The stress increments are obtained from the stiffness formulation in Eq. (12):

$$\begin{bmatrix} dp'_M \\ dq_M \end{bmatrix} = \begin{bmatrix} D_{11} & D_{12} \\ D_{21} & D_{22} \end{bmatrix} \begin{bmatrix} d\varepsilon_v \\ d\gamma \end{bmatrix} \tag{12}$$

where $D_{11}, D_{12}, D_{21}$ and $D_{22}$ are the elements of the stiffness matrix ***D*** (inverse of matrix ***C*** in Eq. (10)). Explicit formulae obtained by substituting Eqs. (1) and (7) into Eqs (12) are provided in [27]. For stress-controlled drained triaxial compression $\delta q_M = \delta p'_M$ ; the overall volumetric strain increment can then be obtained from $d\gamma$ as follows:

$$d\varepsilon_v = \left(\frac{D_{22} - D_{12}}{D_{11} - D_{21}}\right) d\gamma \tag{13}$$

The initial shear modulus ($G_o$) of isotropically consolidated samples under triaxial drained compression ($dq_M = dp'$) can be obtained from the terms $C_{21}$ and $C_{22}$ in Eq. (10) as $G_o = dq_M/d\gamma = 1/(C_{21} + C_{22})$. This yields the following solution

$$G_o = \frac{k_G^e k_G^p}{k_G^p \left(\frac{p'_M}{p_a}\right)^{1-n^e} + k_G^e \left(\frac{p'_M}{p_a}\right)^{-n^p}} p'_M \tag{14}$$

where $p_M'$ ($= p_c'$) is the isotropic confining stress. Evidently, since $\eta_{mob}$ is assumed equal to 0, there is no purely elastic regime so that elastic and plastic strains coexist even at zero deviatoric stress. Accordingly, a combination of parameters $k_G^e$ and $k_G^p$ control the value of $G_o$. Setting $\eta_{mob} = 0^+$ allows for an elastic region in the limit sense, prohibiting plastic deformations ($k_G^P \rightarrow +\infty$). Imposing this condition to Eq. (14) yields the anticipated result $G_o = G^e$ according to Eq. (1).

## 3. ANALYTICAL INTEGRATION

The UBCSAND hardening and flow rule differential in Eqs. (6) and (8) can be integrated analytically for different stress paths. Considering triaxial compression and drained conditions, the mean effective stress can be expressed as $p'_M = p'_c + q_M$, where $p'_c$ is the effective confining pressure at zero deviatoric stress. As the stress ratio $\eta$ is equal to $q_M/p'_M$, the mean effective stress and the deviatoric stress at the plane of loading can be expressed as functions of $\eta$ via the equations:

$$p'_M = \frac{1}{1-\eta} p'_c \tag{15}$$

$$q_M = \frac{\eta}{1-\eta} p'_c \tag{16}$$

Combining Eq. (16) with Eqs. (1) and (4b), and after some trivial algebraic manipulations, the elastic shear strain increment can be expressed as

$$d\gamma^e = \frac{dq_M}{G^e} = \frac{1}{k_G^e(1-\eta)^{2-ne}} \left(\frac{p'_c}{p_a}\right)^{1-ne} d\eta \tag{17}$$

Integrating the above equation over $\eta$ yields the elastic shear strain in closed form

$$\gamma^e = \frac{-1}{k_G^e\ (1-ne)} \left[1 - \frac{1}{(1-\eta)^{1-ne}}\right] \left(\frac{p'_c}{p_a}\right)^{1-ne} \tag{18}$$

expressed as a function of five dimensionless parameters ($k_G^e$, $\eta$, $\nu$, $ne$ and $p'_c/p_a$).

In the same vein, using Eq. (15) and Eq. (7), Eq. (6) can be expressed in terms of $\eta$ to give the plastic shear strain increment

$$d\gamma^p = \frac{1}{k_G^p \left(\frac{p'_c}{p_a}\right)^{np} \left(1-\frac{\eta}{\eta_f/R_f}\right)^2} (1-\eta)^{np} d\eta \tag{19}$$

The above equation can be integrated analytically for the plastic shear strain

$$\gamma^p = \frac{1}{k_G^p \left(\frac{p'_c}{p_a}\right)^{np} (1-np)} \left[ \frac{(1-\eta)^{(1+np)}}{\left(1-\frac{\eta}{\eta_f/R_f}\right)^2} \ {}_2F_1\left[1,2,2-np, \frac{1-\frac{1}{\eta_f/R_f}}{1-\frac{\eta}{\eta_f/R_f}}\right] - \ {}_2F_1\left[1,2,2-np, 1-\frac{1}{\eta_f/R_f}\right] \right] \tag{20}$$

where ${}_2F_1$ is the Gaussian hypergeometric function [35]. The elastic volumetric strain can be obtained in a similar manner as the elastic shear strain, by combining Eqs. (15) and (16) with Eq. (4b) to get

$$d\varepsilon_v^e = \frac{dp'_M}{K^e} - \frac{dq_M}{3K^e} = \frac{2p'_c}{3K^e(1-\eta)^2} d\eta \tag{21}$$

Substituting Eqs. (1) and (2) in the above formula and integrating over $\eta$ yields

$$\varepsilon_v^e = \int_0^\eta \frac{1}{k_G^e(1-\eta)^{2-ne}} \frac{(1-2\nu)}{(1+\nu)} \left(\frac{p'_c}{p_a}\right)^{1-ne} d\eta = \frac{-1}{k_G^e\ (1-ne)} \left[1 - \frac{1}{(1-\eta)^{1-ne}}\right] \frac{(1-2\nu)}{(1+\nu)} \left(\frac{p'_c}{p_a}\right)^{1-ne} \tag{22}$$

which is a function of the same dimensionless parameters as $\gamma^e$ in Eq. (18).

Finally, the plastic volumetric strain can be derived analytically from the flow rule. Indeed, substituting Eq. (19) in Eq. (8) and integrating with respect to $\eta$, one gets

$$\varepsilon_v^p = \int_0^\eta \frac{a(1-\eta)^{np}(\eta_{cv}-\eta)}{k_G^p \left(\frac{p'_c}{p_a}\right)^{np} \left(1-\frac{\eta}{\eta_f/R_f}\right)^2} d\eta \tag{23}$$

where $a$ is a fitting parameter typically taken equal to 1. The solution to the above integral is

$$\varepsilon_v^p = \frac{a\ \eta_f/R_f}{k_G^P \left(\frac{p'_c}{p_a}\right)^{np}} (X_1 - X_2 - X_3) \tag{24}$$

where,

$$X_1 = -\frac{\left(1-\frac{\eta_{cv}}{\eta_f/R_f}\right)}{\left(1-\frac{1}{\eta_f/R_f}\right)}\left\{1-\left[1+\frac{\left(1-\frac{1}{\eta_f/R_f}\right)}{np\left(1-\frac{\eta_{cv}}{\eta_f/R_f}\right)}\right]{}_2F_1\left[1,1,1-np,1-\frac{1}{\eta_f/R_f}\right]\right\} \quad (25a)$$

$$X_2 = -\frac{\eta_f/R_f{}^{(1+np)}\left(1-\frac{\eta_{cv}}{\eta_f/R_f}\right)}{(1-np)\left(1-\frac{\eta}{\eta_f/R_f}\right)^{1-np}}\ {}_2F_1\left[1-np,-np,2-np,\frac{\left(1-\frac{1}{\eta_f/R_f}\right)}{\left(1-\frac{\eta}{\eta_f/R_f}\right)}\right] \quad (25b)$$

$$X_3 = -\frac{\eta_f/R_f{}^{(1+np)}}{np\left(1-\frac{\eta}{\eta_f/R_f}\right)^{-np}}\ {}_2F_1\left[-np,-np,1-np,\frac{\left(1-\frac{1}{\eta_f/R_f}\right)}{\left(1-\frac{\eta}{\eta_f/R_f}\right)}\right] \quad (25c)$$

are dimensionless functions. Like in the solution in Eq. (20), no general conclusions can be gleaned as to the behavior of functions $X_1$, $X_2$, $X_3$ without numerical evaluation of the series. A graphical illustration of Eqs. (25) is provided in [27]. The above analysis can be readily extended to other stress paths (such as triaxial extension), but this lies beyond the scope of this work.

As a final remark, integrating over $\eta$ implies a monotonic increase of $\eta$ from zero (or a finite value). This stress-controlled loading implies no $\eta$-softening with the analytical approximation. To account for such softening (which is a common trait of the response of dense sands under drained loading), modifications in the analysis would be required which lie beyond the scope of this work.

## 4. PARAMETER SELECTION

The dimensionless parameters involved in the model are: $k_G^p$, $k_G^e$, $\eta_f/R_f$, $\eta_{cv}$, $\nu$, *ne* and *np*. The last three, $\nu$, *ne* and *np*, are often selected empirically and for the purposes of these study we have assumed $\nu = 0.2$, $ne = 0.5$, $np = 0.4$ based on the following brief discussion.

The elastic Poisson's ratio $\nu$ is typically selected between 0 to 0.2 [2, 30] based on studies of small strain elastic response of sands [36]. Recent laboratory experiments have confirmed that $\nu$ ranges from 0.1 to 0.3 for different granular materials [37-38]. In this light, the value $\nu \approx 0.2$ seems reasonable.

In the ensuing, *np* has been taken equal to 0.4 based on the tested materials and stress conditions.

## 5. APPLICATION TO DRAINED MONOTONIC & CYCLIC TESTS

### 5.1 Test Materials

The experiments carried out in the Geotechnical Materials Lab at Khalifa University involved four different materials: (a) gabbro; (b) limestone; (c) demolished concrete; and (d) electric arc furnace (EAF) slag. Gabbro is a coarse grain igneous rock that is rich in iron, magnesium and calcium, and is extracted at the border between UAE and Oman. It is both strong and suitable for construction. Limestone is a sedimentary rock made of calcium carbonate, and is available throughout the UAE. It is weaker than gabbro, but also suitable for construction and provides excellent drainage when used as ballast. Demolished concrete is a recycled material - a mixture of cement and aggregates. The cement is weak and crushable. More than 29 million tons of cement are produced annually in the UAE [39]. Slag is a by-product of smelting

generated as industrial waste during steel-making process. Slag is stronger and more resilient than the other three materials. More than 800,000 tons of slag are annually produced in the UAE [40].

Gabbro and demolished concrete particles are rounded, whereas limestone and slag have sharp angular shapes. Table 1 presents a summary of the grain-size distribution and their characteristics. All materials show uniform gradations. The effective grain size ($D_{10}$) ranges from 4.6 to 12.8 mm, whereas the coefficient of uniformity ($C_u$) ranges from 1.3 to 1.7.

Table 1. Summary of tested materials [27]

| ***Material*** | ***$D_{10}$ (mm)*** | ***$C_u$*** | ***Particle shape*** | ***Mineralogy*** |
|---|---|---|---|---|
| Gabbro | 9.7 | 1.3 | Sub-rounded | Coarse-grained silicate |
| Limestone | 4.6 | 1.7 | Angular | Calcium carbonate |
| Demolished concrete | 6.7 | 1.4 | Sub-rounded | Calcium carbonate, silicate aggregate |
| EAF Slag | 12.8 | 1.3 | Sub-angular | Calcium and iron oxide |

### 5.2 Test Procedure

Triaxial tests were conducted using a GCTS Testing System device (Model No.: SSC-2K-0000). Details are provided in [27] The tests were conducted in three stages:

Stage 1) Isotropic consolidation under confining stress $\sigma'_c = 50\ kPa$.

Stage 2) Drained cyclic loading with $q_M = 50\ kPa$ with a loading frequency of 1 *Hz*. The applied number of cycles ($N$) varied from 50 to 200.

Stage 3) Triaxial compression under drained conditions.

### 5.3 Experimental Drained Cyclic and Monotonic Compression Measurements

Figure 2 shows the cyclic loading responses between $q_M$ and axial strain ($\varepsilon_a$) for each material from 1 to 50 cycles. The gabbro testing displayed stiff behavior, whereas slag demonstrated ratcheting. The residual $\varepsilon_a$ and volumetric strain ($\varepsilon_v$) against $N$, is presented in Figures 3(a) and (b). $\varepsilon_a$ and $\varepsilon_v$ gradually increase with $N$, where the slag and the gabbro show the largest and smallest strains, respectively. Limestone and demolished concrete exhibit an intermediate behavior. The accumulation of $\varepsilon_a$ and $\varepsilon_v$ is similar indicating that the radial strain is limited during cyclic compression. This observation is consistent with previous studies [41], where the radial strain was limited when the amplitude of cyclic load is less than 70% of the static peak strength. In fact, the amplitude of cyclic $q_M$ (Figure 2) applied in this study was approximately 40% of the static peak strength (Figure 14). Figure 14(a) shows a drained monotonic compression response in terms of deviatoric shear stress $q_M$ versus shear strain $\gamma$. Limestone exhibits the highest strength (~160 kPa), whereas the other three materials have similar strengths in the range 120-150 kPa. Figure 14(b) plots $\varepsilon_v$ versus $\gamma$. The largest and smallest dilatancies were observed in gabbro and demolished concrete, respectively.

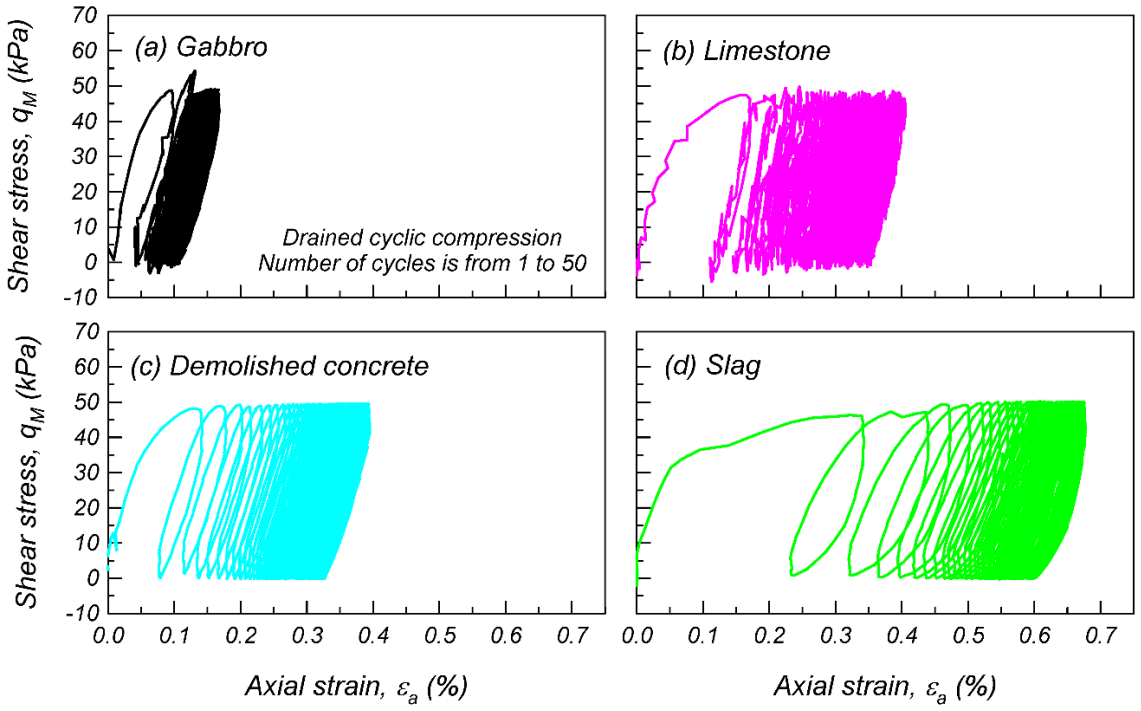


Figure 2. Drained cyclic compression test results: (a) Gabbro, (b) Limestone, (c) Demolished concrete, (d) Slag. In all tests $\sigma'_c$ = 50 kPa, $q_M$ = 50 kPa [27].

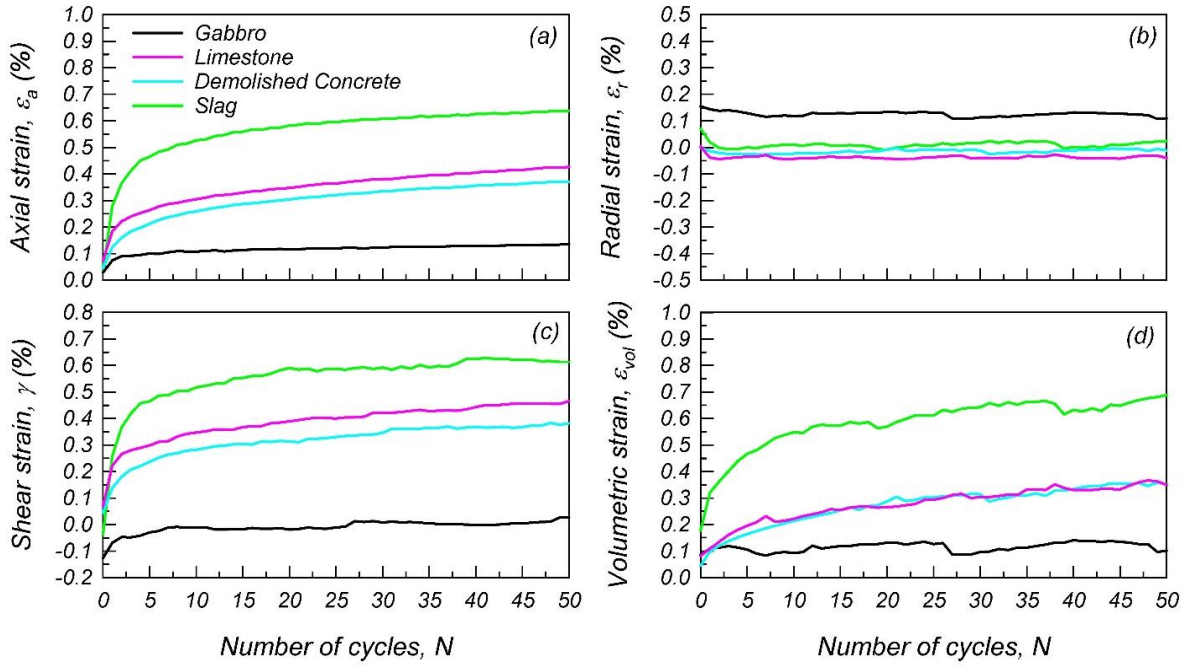


Figure 3. Cyclic drained compression test results for different materials: (a) $\varepsilon_a$ vs. $N$, (b) $\varepsilon_r$ vs. $N$ (d) $\gamma$ vs. $N$. In all tests $\sigma'_c$ = 50 kPa, $q_M$ = 50 kPa [27].

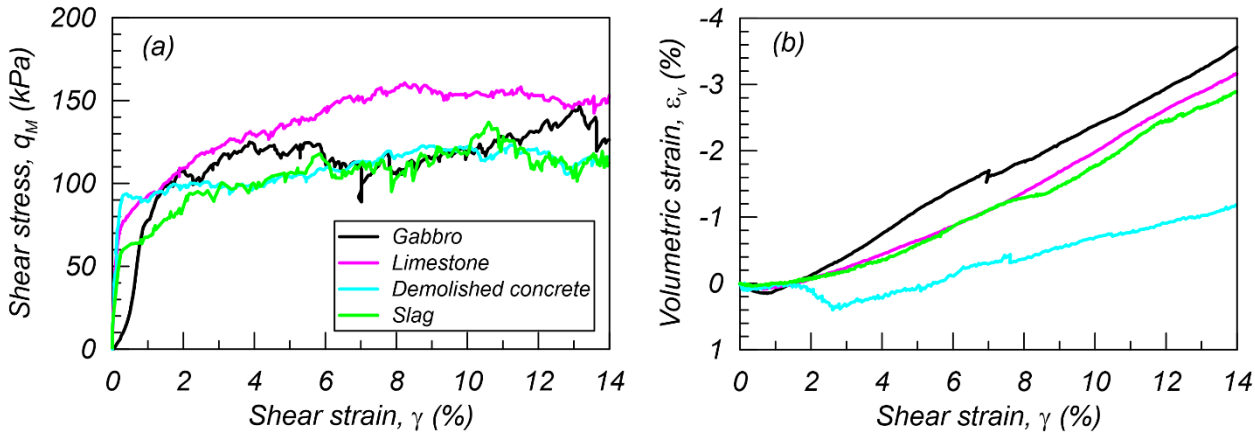


Figure 4. Monotonic drained compression test results for different materials (a) $q_M$ vs. $\gamma$ (b) $\varepsilon_v$ vs. $\gamma$ [27].

### 5.4 Calibration of UBCSAND Model to the Experimental Data

UBCSAND models were calibrated both numerically and analytically using the aforementioned experimental data from drained monotonic compression tests. The numerical and graphical 'chart' solutions for strain-controlled conditions follow the procedures described in detail in [27]. Table 2 provides UBCSAND parameters estimated by employing the three different calibration approaches presented in this study: analytical, chart solution, numerical. Figure 5(a)-(h) presents the calibrated responses of $\eta$ vs. $\gamma$ and $\varepsilon_v$ vs. $\gamma$ computed following these approaches. It is demonstrated that the main aspects of the drained monotonic compression response are reproduced adequately by all three methods relative to the experimental data in Figure 4. The analytical and numerical solutions work best for strains above 1% while the chart solution deviates from both and from the experimental data as well, except for strains less than 1%.

Table 2. Calibrated UBCSAND parameters against drained monotonic triaxial compression data for four different ballast aggregates using the three methods described in this paper ($\sigma'_c$ = 50 kPa) [27].

| Material | Method | $k_G^p$ | $k_G^p/k_G^e$ | $\eta_f/R_f$ | $\eta_{cv}$ |
|---|---|---|---|---|---|
| Gabbro | Analytical | 500 | 2.00 | 0.75 | 0.42 |
| | Chart | 234 | 2.00 | 0.73 | 0.36 |
| | Numerical | 620 | 2.77 | 0.74 | 0.41 |
| Limestone | Analytical | 400 | 0.10 | 0.77 | 0.50 |
| | Chart | 720 | 0.02 | 0.77 | 0.53 |
| | Numerical | 410 | 0.10 | 0.77 | 0.50 |
| Demolished concrete | Analytical | 1000 | 0.10 | 0.70 | 0.60 |
| | Chart | 1,640 | 0.02 | 0.71 | 0.55 |
| | Numerical | 980 | 0.05 | 0.68 | 0.59 |
| EAF Slag | Analytical | 300 | 0.50 | 0.68 | 0.42 |
| | Chart | 700 | 0.02 | 0.68 | 0.53 |
| | Numerical | 320 | 0.05 | 0.68 | 0.44 |

*ne*, *np*, and *v* values are fixed at 0.5, 0.4, and 0.2, respectively.

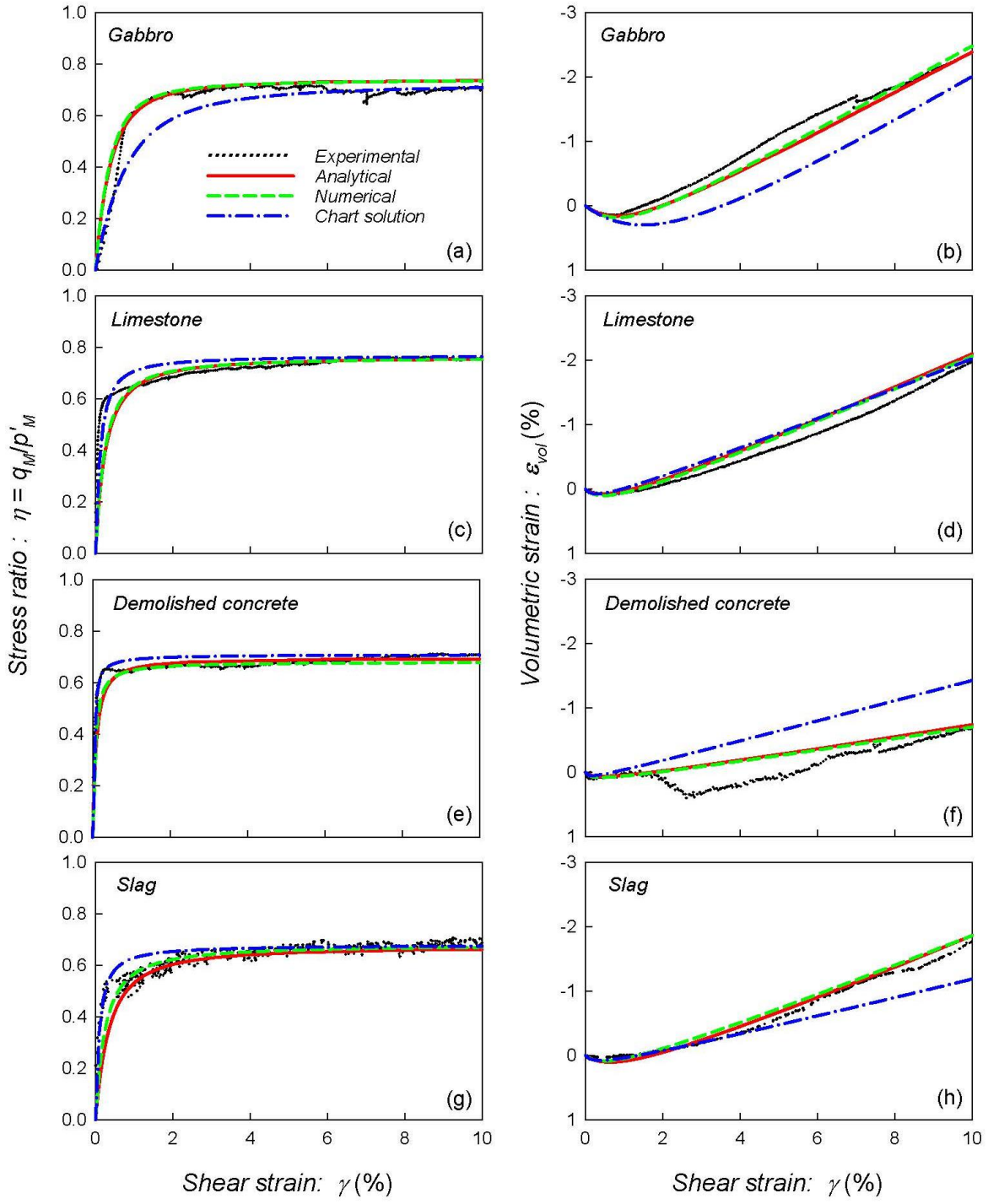


Figure 5. Calibrated monotonic drained compression tests for four different aggregate materials using the analytical, numerical and chart solutions. The UBCSAND parameters for each case are provided in Table 3. (a) $\eta$ vs. $\gamma$, (b) $\varepsilon_v$ vs. $\gamma$ for gabbro, (c) $\eta$ vs. $\gamma$, (d) $\varepsilon_v$ vs. $\gamma$ for limestone, (e) $\eta$ vs. $\gamma$, (f) $\varepsilon_v$ vs. $\gamma$ for demolished concrete, (g) $\eta$ vs. $\gamma$, (h) $\varepsilon_v$ vs. $\gamma$ for slag [27].

Figure 6 shows the example responses of UBCSAND for drained cyclic compression tests of gabbro and slag, using the parameters of numerical calibration in Table 2. The slag simulation exhibits the largest residual $\varepsilon_a$ compared to gabbro, which is consistent with the experimental observations in Figure 2. However, the rate of strain accumulation is constant for UBCSAND, which is different from the experimental findings. Figure 7 shows the residual

values of $\varepsilon_a$ and $\varepsilon_v$ for drained cyclic compression computed with UBCSAND using the parameters in Table 2. Comparing the results from Figures 3 and 7, it is fair to mention that the model parameters should be different for cyclic versus monotonic loading, which complicates its application for combinations of static and dynamic loads (a most common case in earthquake engineering).

Moreover, the rate of increase of volumetric and shear strains with number of cycles is linear, hence cannot realistically reproduce results for excess pore pressures under undrained loading. This is evident in Fig. 8 where different calibrations are needed for different number of cycles. These observations are important when trying to apply the specific model to dynamic problems – notably for soil liquefaction analysis.

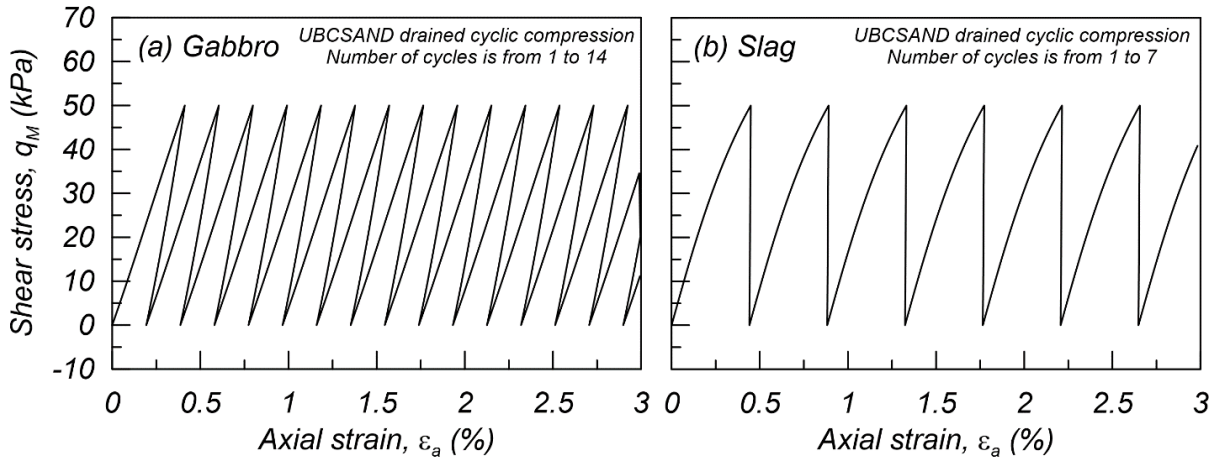


Figure 6. Example of $q_M$ vs. $\varepsilon_a$ cyclic drained response predicted using UBCSAND model based on the calibrated parameters in Table 3: (a) gabbro, (b) slag [27].

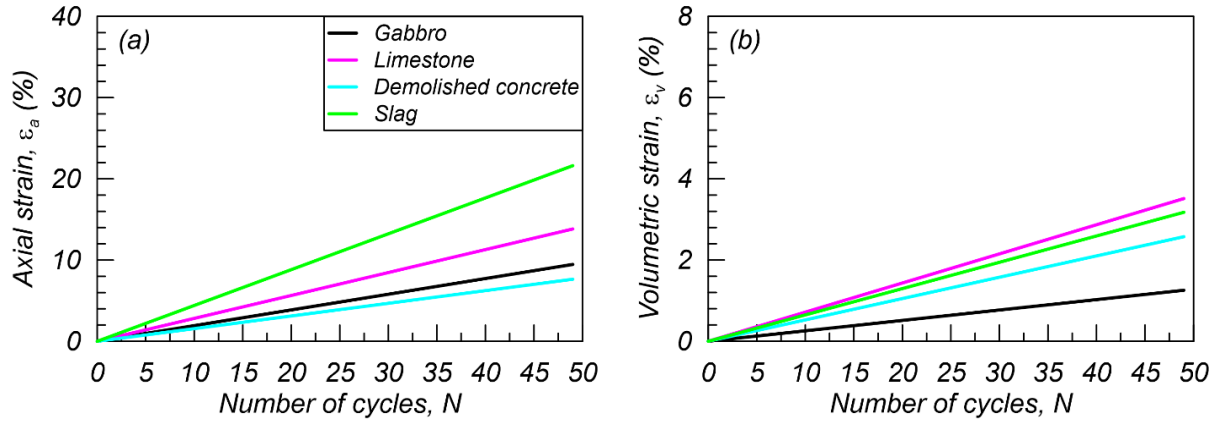


Figure 7. Examples of residual axial and volumetric strains predicted using UBCSAND for drained cyclic compression using the calibrated parameters in Table 2: (a) $\varepsilon_a$ vs. $N$; (b) $\varepsilon_v$ vs. $N$ ($\sigma'_c$ = 50 kPa, $q_M$ = 50 kPa) [27].

The UBCSAND model was calibrated against drained cyclic compression tests for different number of loading cycles. Table 3 shows the calibrated parameters for $N$ from 0 to 2, 0 to 10 and 0 to 50 cycles for different materials, respectively. The calibration procedure follows Figure 8 for stress-controlled conditions. The parameters $k_G^p/k_G^e$ and $\eta_f/R_f$ are fixed from Table 2 for drained monotonic conditions. The $k_G^p/k_G^e$ ratio was fixed because the calibrated value was very large (i.e. small $k_G^e$) due to the plastic deformations developing during successive unloading cycles. $\eta_f/R_f$ was fixed because it does not provide a reliable value due to the

low amplitude of cyclic loads to determine the failure parameters. Table 3 shows that the $k_G^p$ parameter increases as the number of cycles increases. $\eta_{cv}$ similarly increases as the number of cycles increases when the material exhibits contractive behavior.

Figure 8 shows the residual strains $\varepsilon_a$ and $\varepsilon_v$ for slag under drained cyclic tests compared with the calibrated UBCSAND for different loading conditions. The results suggest that the UBCSAND model can be reasonably fitted by adjusting the calibration range. The figure also shows that the calibrated parameters against drained monotonic compression tests only predict the cyclic compression responses well when *N* is not larger than 1 - 4 cycles. Evidently, there is no single set of parameters which can reproduce well both drained monotonic and cyclic conditions.

Table 3. Numerically calibrated UBCSAND parameters against drained cyclic compression tests ($\sigma'_c$ = 50 kPa, $q_M$ = 100 kPa) [27].

| Material | # of cycles *N* | $k_G^p$ | $k_G^p/k_G^e$ | $\eta_f/R_f$ | $\eta_{cv}$ |
|---|---|---|---|---|---|
| Gabbro | 0 – 2 | 5,400 | 2.77 | 0.74 | 0.61 |
| | 0 – 10 | 18,500 | 2.77 | 0.74 | 0.32 |
| | 0 - 50 | 69,600 | 2.77 | 0.74 | 0.36 |
| Limestone | 0 – 2 | 1,500 | 0.10 | 0.77 | 0.54 |
| | 0 – 10 | 4,800 | 0.10 | 0.77 | 0.74 |
| | 0 - 50 | 15,900 | 0.10 | 0.77 | 0.86 |
| Demolished concrete | 0 – 2 | 2,900 | 0.05 | 0.68 | 1.00 |
| | 0 – 10 | 7,700 | 0.05 | 0.68 | 1.00 |
| | 0 - 50 | 25,300 | 0.05 | 0.68 | 0.99 |
| EAF Slag | 0 – 2 | 760 | 0.05 | 0.68 | 0.50 |
| | 0 – 10 | 2,800 | 0.05 | 0.68 | 0.71 |
| | 0 - 50 | 11,900 | 0.05 | 0.68 | 0.83 |

*ne*, *np*, and *v* values are fixed at 0.5, 0.4, and 0.2, respectively. $k_G^p/k_G^e$ and $\eta_f/R_f$ values are fixed based on the monotonic compression tests

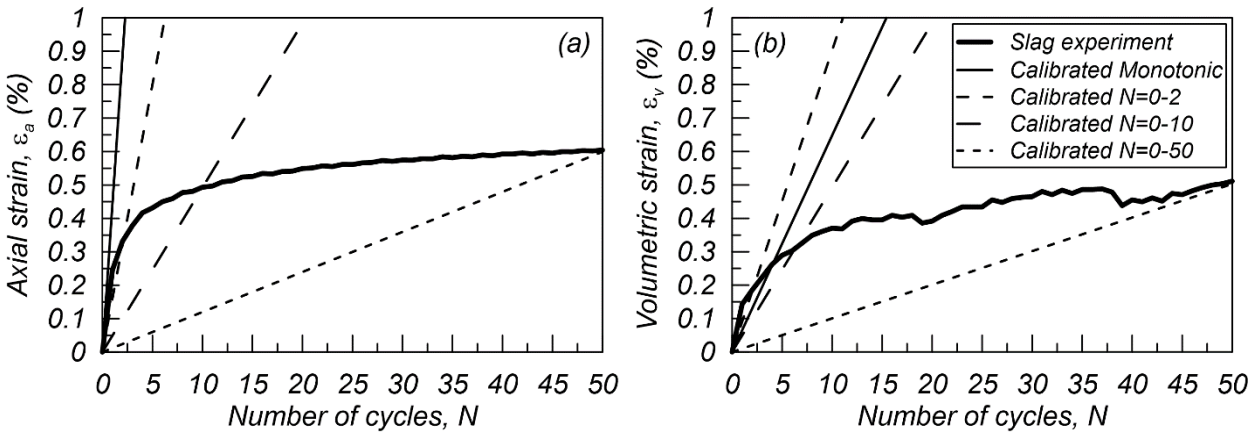


Figure 8. Comparison of residual strains of slag between experimental and UBCSAND models calibrated based on different loading conditions: (a) *N* vs. $\varepsilon_a$, (b) *N* vs. $\varepsilon_v$; $\sigma'_c$ = 50 kPa, $q_M$ = 50 kPa [27].

## 6. CONCLUSIONS

The popular UBCSAND constitutive model was reviewed and integrated analytically for monotonic and cyclic drained triaxial compression conditions. A novel closed form solution for the elastic and plastic shear and volumetric strains was presented. Three new methodologies for calibrating the model parameters to experimental data were compared: (1) a graphical "chart" solution; (2) a numerical approach based on minimization of residuals; and (3) a trial-and-error approach based on the analytical solution. It has been demonstrated that:

(1) The analytical solution provides an excellent tool, free of numerical errors, for calibrating the UBCSAND parameters against laboratory data.
(2) Results from the numerical calibration against both monotonic and cyclic test data show that the parameters of UBCSAND are different between monotonic and cyclic drained compression conditions. The calibrated parameters against monotonic tests only predict the cyclic compression responses well when $N$ is less than 1 - 4 cycles. Therefore, UBCSAND models should be calibrated against the target loading conditions and number of cycles.
(3) The model parameters should be different for cyclic versus monotonic loading, which makes its application for combinations of static and dynamic loads (a most common case in earthquake engineering) difficult.
(4) The rate of increase of volumetric and shear strains with number of cycles is always linear, hence cannot realistically reproduce results for excess pore pressures under undrained loading.

These observations are important when trying to apply the specific model to dynamic problems – notably in soil liquefaction analysis.

## 7. ACKNOWLEDGEMENTS

The work presented in this paper was funded by the Khalifa University of Science & Technology – Competitive Internal Research Award CIRA 2019-015 [Project Title: "SUPERTRACK: Superior Performance Railway TRACKS for the UAE"] and FSU 2021-028 [Project Title: "Next Generation Framework for Seismic Design of Quay Walls"]. The third author is supported by Khalifa University Combined Master's/Doctoral Research/Teaching Scholarship (CMDRTS). The authors are grateful to Saif Bin Darwish Crusher, Mawaad Environmental Services, Star International Waste Management LLC, and Al Dhafra Recycling Industries for providing the testing materials used in this study.

## 8. REFERENCES

[1] Beaty, M.H., Byrne, P.M. (1998). An effective stress model for predicting liquefaction behaviour of sand. *Geotechnical Earthquake Engineering and Soil Dynamics III ASCE Geotechnical Special Publication*, **75**(1):766-777.
[2] Beaty, M.H., Byrne, P.M. (2011). UBCSAND constitutive model: Version 904aR. *Documentation Report: UBCSAND Constitutive Model on Itasca UDM Web Site*; February 2011. http://www.itasca-udm.com/pages/UBCSand.html.
[3] Tsegaye, A. (2010). PLAXIS liquefaction model. *Report no. 1. PLAXIS knowledge base*.
[4] Schofield, A.N., Wroth P. (1968). *Critical State Soil Mechanics*. McGraw-Hill Book Company
[5] Prévost, J.H., Hoeg. K. (1975). Effective Stress-Strain-Strength Model for Soils. *Journal of Geotechnical Engineering-ASCE*. **101** (GT3, Proc. Paper 11157): 259-278.
[6] Nova, R., Wood, D.M. (1979). A constitutive model for sand in triaxial compression. *International journal for numerical and analytical methods in geomechanics.* **3**(3):255-278
[7] Manzari, M. T., Dafalias, Y. F. (1997). A critical state two-surface plasticity model for sands. *Géotechnique*, 47:2, 255-272. https://doi.org/10.1680/geot.1997.47.2.255

[8] Jefferies, M.G. (1993) Nor – Sand: a simple critical state model for sand. *Géotechnique*, **43**(1): 91-103
[9] Pestana, J. M., Whittle, A. J. (1995). Compression Model for Cohesionless Soils. *Géotechnique*, **45**(4): 611-631. doi:10.1680/geot.1995.45.4.611
[10] Papadimitriou, A.G. & Bouckovalas, G. (2002). Plasticity model for sand under small and large cyclic strains: A multiaxial formulation. *Soil Dyn. Earthquake Eng*., **22** (3): 191-204, 10.1016/S0267-7261(02)00009-X
[11] Been, K., Jefferies, M.G. (2004). Stress-dilatancy in very loose sand. *Canadian Geotechnical Journal.* **41**: 972-989. doi: 10.1139/T04-038
[12] Loukidis, D. and Salgado, R. (2009). Modeling sand response using two-surface plasticity. *Comput. Geotech.*, **36** (1–2):166-186, 10.1016/j.compgeo.2008.02.009
[13] Karamitros, D.K. (2010) *Development of a numerica:l algorithm for the dynamic elastoplastic analysis of geotechnical structures in two and three dimensions.* PhD Thesis, Dept of Civil Engineering, NTUA, Athens
[14] Diambra, A., Ibraim, E., Russell, A.R., Wood, D.M. (2013). Fibre reinforced sands: from experiments to modelling and beyond. *International Journal for Numerical and Analytical Methods in Geomechanics*. **37**(15): 2427-2455.
[15] Boulanger, R.W., Ziotopoulou K. (2015). PM4Sand (Version 3): A sand plasticity model for earthquake engineering applications. *Report No. UCD/CGM-15/01, Center for Geotechnical Modeling Department of Civil and Environmental Engineering University of California Davis*.
[16] Cubrinovski, M., Ishihara, K. (1998). State Concept and Modified Elastoplasticity for Sand Modelling, *Soils and Foundations*, **38**(4): 213-225
[17] Hashiguchi, K., Mase, T., Yamakawa, Y. (2021). Elaborated subloading surface model for accurate description of cyclic mobility in granular materials, *Acta Geotechnica*, 17:699–719, https://doi.org/10.1007/s11440-021-01203-y
[18] Yang, M., Seidalinov, G., Taiebat, M. (2019). Multidirectional cyclic shearing of clays and sands: Evaluation of two bounding surface plasticity models, *Soil Dynamics and Earthquake Engineering*, 124: 230-258
[19] Barrero, A. R., Taiebat, M., Dafalias, Y. F. (2020). Modeling cyclic shearing of sands in the semifluidized state, *Int J Numer Anal Methods Geomech*; 44:371–388
[20] Yang, M., Taiebat, M. and Dafalias, Y. F. (2020). SANISAND-MSf: a sand plasticity model with memory surface and semifluidised state, *Géotechnique*, https://doi.org/10.1680/jgeot.19.P.363
[21] Duque, J., Yang, M., Fuentes, W., Mas, D., Taiebat, M. (2021). Characteristic limitations of advanced plasticity and hypoplasticity models for cyclic loading of sands, *Acta Geotechnica*, https://doi.org/10.1007/s11440-021-01418-z
[22] Asaoka, A. Noda, T., Yamada, E., Kaneda, K. and Nakano, M. (2002). An Elasto-Plastic Description of Two Distinct Volume Change Mechanisms of Soils, *Soils and Foundations*. **42**(5): 47-57.
[23] Corti, R., Diambra, A., Wood, D. M., Escribano, D. E., Nash, D. F. T. (2016). Memory Surface Hardening Model for Granular Soils under Repeated Loading Conditions, *J. Eng. Mech*., **142**(12): 04016102.
[24] Itasca (2011). FLAC, Fast Lagrangian Analysis of Continua, Version 7.0. Itasca Consulting Group, Minneapolis, MN; 2011. http://www.itascacg.com/.
[25] Shriro, M., Bray, J.D. (2013). Calibration of numerical model for liquefaction-induced effects on levees and embankments. *Seventh International Conference on Case Histories in Geotechnical Engineering*. 29 April – 3 May, Chicago
[26] PLAXIS (2018). Computer aided geotechnical analysis software. Bentley Systems, https://www.bentley.com/en/products/brands/plaxis.
[27] Voyagaki E., Kishida T., Aldulaimi R.F., Mylonakis G. (2023). Integration and calibration of UBCSAND model for drained monotonic and cyclic triaxial compression of aggregates, *Soil Dynamics & Earthquake Engineering*. 171 107978, https://doi.org/10.1016/j.soildyn.2023.107978

[28] Puebla, H., Byrne, P.M., Phillips, R. (1997). Analysis of CANLEX liquefaction embankments: Prototype and centrifuge models. *Canadian Geotechnical Journal*, **34**: 641–657.
[29] Petalas, A., Galavi, V. (2013). PLAXIS Liquefaction Model UBC3D-PLM. Available online: https://communities.bentley.com/cfs-file/__key/communityserver-wikis-components-files/00-00-00-05-58/UBC3D_2D00_PLM_2D00_REPORT.June2013.pdf.
[30] Beaty, M.H. (2018). Application of UBCSAND to the LEAP centrifuge experiments. *Soil Dynamics and Earthquake Engineering*, **104**: 143-153.
[31] Seed and Idriss. (1970). Soil Moduli and Damping Factors for Dynamic Response Analyses. *Report EERC70-10, Earthquake Engineering Research Center*, University of California, Berkeley.
[32] Hardin, B.O., Drnevich, V.P. (1972). Shear modulus and damping in soils: Design equations and curves. *Journal of the Soil Mechanics and Foundations Division, ASCE*. SM7: 667-692
[33] Darendeli, M.B. (2001). *Development of a new family of normalized modulus reduction and material damping curves.* PhD Thesis. The University of Texas at Austin
[34] Duncan, J.M., Chang, C.Y. (1970). Nonlinear analysis of stress and strain in soils. *Journal of the Soil Mechanics and Foundations Division, ASCE*, **96**(5): 1629-1653.
[35] Abramowitz, M., Stegun, I. (1970). *Handbook of Mathematical Functions with Formulas*. Graphs, and Mathematical Tables, Dover Publications, ISBN: 0486612724.
[36] Hardin, B.O. (1978). The Nature of Stress-Strain Behaviour for Soils. *Proceedings of Earthquake Engineering and Soil Dynamics, ASCE*, Pasadena, 19-21 June 1978, 3-89.
[37] Hoque, E. & Tatsuoka, F. (1998). Anisotropy in Elastic Deformation of Granular Materials, *Soils and Foundations.* **38** (1): 163-179.
[38] Suwal, L. P. & Kuwano, R. (2018). Statically and Dynamically Measured Poisson's Ratio of Granular Soils on Triaxial Laboratory Specimens, *Geotechnical Testing Journal*, **36**(4): 493-505.
[39] Global Cement. (2015). *The growing cement industry of the UAE*. https://www.globalcement.com/magazine/articles/917-the-growing-cement-industry-of-the-uae. (Last accessed, November 2022)
[40] Emirates Steel. (2022). *Emirates Steel signs slag management agreement with Finnish company ECOFER Technologies – Emirates Steel*.
https://www.emiratessteelarkan.com/press/emirates-steel-signs-slag-management-agreement-with-finnish-company-ecofer-technologies/. (last accessed November 2022)
[41] Sun, Q.D., Indraratna, B., Nimbalkar, S. (2016). Deformation and Degradation Mechanisms of Railway Ballast under High Frequency Cyclic Loading. *Journal of Geotechnical & Geoenvironmental Engineering*, **142**(1): 04015056.

COMPDYN 2023
9th ECCOMAS Thematic Conference on
Computational Methods in Structural Dynamics and Earthquake Engineering
M. Papadrakakis, M. Fragiadakis (eds.)
Athens, Greece, 12-14 June 2023

# INVESTIGATION OF FAILURE OCCURRENCE MECHANISM OF HISTORIC MASONRY BUILDINGS AND PERFORMANCE OF REINFORCEMENT MEASURES USING DEM

**J. Kiyono**[1] **and A. Furukawa**[2]

[1] Department of Urban Management, Kyoto University
Kyotodaigaku-katsura, Nishikyo-ku, Kyoto 615-8540, JAPAN
e-mail: kiyono.junji.5x@kyoto-u.jp

[2] Department of Urban Management, Kyoto University
Kyotodaigaku-katsura, Nishikyo-ku, Kyoto 615-8540, JAPAN
e-mail: furukawa.aiko.3w@kyoto-u.ac.jp

## Abstract

*There are many historic masonry buildings worldwide. Some types of masonry buildings have particularly low earthquake resistance. Such structures collapse even at low-ground motion intensities and rapidly at high intensities. Therefore, improving the earthquake resistance of these primarily weak masonry buildings is necessary to prevent their damage and leave them for posterity. However, knowledge is still limited on how the failure begins and proceeds, how buildings collapse, and how earthquake resistance can be improved effectively. With this background, this study aims to investigate the seismic behaviors of masonry buildings and compare the effectiveness of reinforcement measures by numerical simulations.*

**Keywords:** Masonry building, Failure behavior, Reinforcing measures, Distinct element method, Earthquake.

## 1 INTRODUCTION

There are many historic masonry buildings worldwide. Due to their low earthquake resistance [1], they get damaged even at low intensities of ground motion and collapse rapidly at high intensities [2][3][4]. Therefore, improving the earthquake resistance of these primarily weak masonry buildings is necessary to prevent their damage and leave them for posterity. However, knowledge is still limited on how the failure begins and proceeds, how buildings collapse, and how earthquake resistance can be improved effectively. With this background, this study aims to investigate the seismic performance of masonry buildings and compare the effectiveness of reinforcement measures by numerical simulations.

The finite element method (FEM) is the most common numerical analysis method. It has been used for the analysis of masonry structures [5][6][7][8]. The FEM can deal with both elastic and plastic behaviors, but it has difficulty solving failure and collapse phenomena since it is based on the mechanics of the continuum. A method based on the mechanics of the dis-continuum is more suitable for analyzing failure and collapse phenomena. An example of a numerical method for a dis-continuum is the distinct element method (DEM) [9]. However, the DEM also has disadvantages. A way of determining the spring constant from the material properties has not been established in the DEM, and the values need to be quantified experimentally [10][11]. Therefore, the reliability of the results is not high.

As an alternative, the present paper uses a refined DEM [12][13], which simulates a series of seismic behaviors in three-dimension—from elastic to failure to collapse behaviors. This method still cannot handle Poisson's effect like the original DEM, but unlike the original DEM, the spring constant of each spring is theoretically determinable. Using the refined DEM, this paper simulates the seismic behavior of historical masonry buildings and compares the performances of reinforcement measures.

## 2 REFINED DEM

This study employs a refined DEM [12] to simulate a series of structural dynamic behaviors from elastic to failure to collapse phenomena. A structure is modeled as an assembly of rigid elements, and interaction between the elements is modeled with multiple springs and dashpots attached to the elements' surfaces. The elements are rigid, but the method allows the simulation of structural deformation by allowing penetration between elements.

Fig. 1 (a) shows a spring for computing the restoring force (restoring spring), which models the elasticity of elements. The restoring spring is set between continuous elements. Structural failure is modeled as the breakage of the restoring spring, at which time the restoring spring is replaced with a contact spring and a contact dashpot (Fig. 1 (b)). Fig. 1 (b) shows the spring and dashpot for computing the contact force (contact spring and dashpot) and modeling the contact, separation and recontact between elements. The dashpots are introduced to express energy dissipation due to the contact. Structural collapse behavior is obtained using these springs and dashpots. The elements shown in Figs. 1 (a) and (b) are rectangular parallelepipeds, but the method does not limit the geometry of the elements.

The surface of an element is divided into small segments, as shown in Fig. 1 (c). The segment in the figure is rectangular, but the method does not limit the geometry of the segment. The black points indicate the representative point of each segment, and the relative displacement or contact displacement between elements is computed for these points. Such points are referred to as contact points or master points in this study. One restoring spring and one combination of contact spring and dashpot are attached to one segment (Fig. 1 (d)) at each of the representative points in Fig. 1 (c). The spring constant for each segment is derived based on the stress-strain relationship of the material and the segment area.

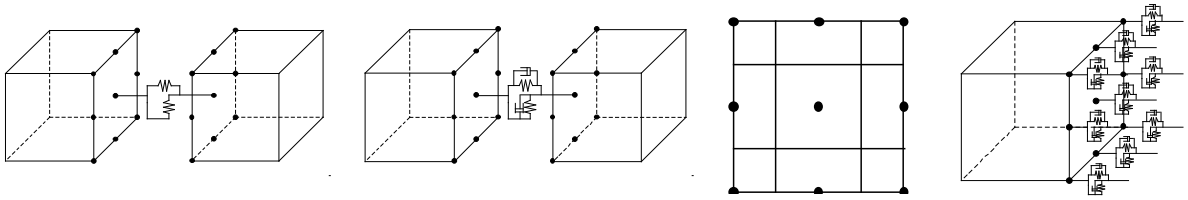

(a) Restoring spring (b) Contact spring and dashpot (c) Segments and contact points (d) Multiple springs and multiple dashpots

Figure 1: Basic concept of the analysis method [12]

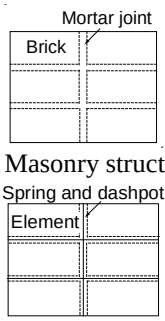


(a) Masonry structure

(b) Analytical model

Figure 2 Analytical modeling of masonry structures

Table 1 Material properties

| Variable | Adobe brick | Mortar | Wood | FRP |
|---|---|---|---|---|
| Mass density (kg/m$^3$) | $1.8 \times 10^3$ | $1.8 \times 10^3$ | $7.0 \times 10^2$ | $1.8 \times 10^3$ |
| Young's modulus (N/m$^2$) | $9.8 \times 10^7$ | $9.8 \times 10^7$ | $6.3 \times 10^8$ | $2.5 \times 10^{10}$ |
| Poisson's ratio | 0.25 | 0.25 | 0.3 | 0.3 |

Table 2 Strength of mortar, wood, and FRP

| Variable | Mortar | Wood | FRP |
|---|---|---|---|
| Tensile strength $f_t$ (N/m$^2$) | $4.6 \times 10^3$ | $1.1 \times 10^7$ | $1.27 \times 10^5$ |
| Shear strength $c$ (N/m$^2$) | $2.9 \times 10^3$ | $9.0 \times 10^6$ | $3.04 \times 10^4$ |
| Friction angle $\phi$ | 32° | 0° | 32° used |
| Compressive strength (N/m$^2$) | $4.9 \times 10^5$ | $4.5 \times 10^7$ | $4.9 \times 10^5$ |

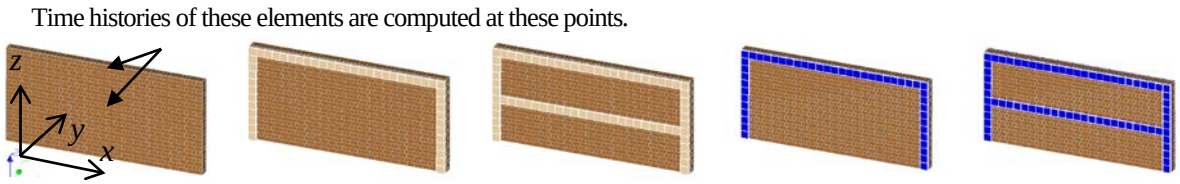


(a)Non-reinforced model (b)Reinforced model with timbers (T1) (c)Reinforced model with timbers (T2) (d) Reinforced model with FRP strips (F1, F3) (e) Reinforced model with FRP strips (F2, F4)

Figure 3 Analytical masonry wall models

The behavior of an element consists of translational and rotational behaviors. Each element's translational and rotational behaviors are computed explicitly by solving Newton's law of motion and Euler's equation of motion. Forces acting on each element are obtained by summing the restoring force, contact force, and other external forces, such as the gravitational force and the earthquake's inertial force.

## 3 ANALYSIS OF MASONRY WALL

### 3.1 Modeling Strategy of Masonry

In this study, individual components of the masonry structure shown in Fig. 2 (a) (i.e., brick and mortar joints) are modeled as shown in Fig. 2 (b). The bricks are modeled with rigid elements, and the mortar joint between elements is modeled with multiple springs and dashpots. The size of one element is the sum of the brick size and mortar thickness. The multiple springs and dashpots interact with the surfaces of adjacent elements. The elements are modeled with rigid rectangular parallelepipeds. Faces surrounding the elements are divided into segments. The size of the segments is set to 1/4 of the shortest edge length, according to a past study [12].

### 3.2 Analytical Masonry Wall Models

As shown in Fig. 3, one masonry wall model without reinforcement, 2 reinforcement models with timbers, and 4 reinforcement models with FRP strips were considered. The directions ($x$, $y$, $z$) are also shown in Fig. 3(a). Reinforcement using timbers is frequently used where timber materials are easily available at a reasonable price. The reinforcement using FRP strips is recently gathered much attention due to its high performance.

The non-reinforced model has a width of 5m, a height of 2.4m, and a thickness of 0.2m. The walls are mainly composed of bricks with dimensions of 0.2 m × 0.1 cm × 0.1 m. There are mortar joints with a thickness of 0.01 m between the bricks.

There are two reinforced models using timbers. Model T1 has two vertical columns and one horizontal beam on the top, and the reinforcement is one-sided. Model T2 has an additional horizontal beam in the middle height of the wall. Both columns and beams have 0.2m width and 0.1m thickness and are divided into many elements of 0.2m length to express the deformation and breakage. Therefore, the size of timber elements is 0.2 m × 0.1 cm × 0.1 m.

Four reinforced models use FRP strips. Model F1 is a one-sided reinforcement model with two vertical strips and one horizontal strip on the top. Model F2 is a model with an additional horizontal strip in the middle height of the wall. Model F3 has a reinforcement of F1 on both sides of the wall. Model F4 has a reinforcement of F2 on both sides of the wall. The FRP strips have 0.2m width and 0.02m thickness and are divided into many elements of 0.2m length to express the deformation and breakage. Therefore, the size of FRP elements is 0.2 m × 0.02 cm × 0.1 m.

### 3.3 Material Properties and Strength

Table 1 presents the material properties. The mass density and Young's modulus of adobe bricks are chosen based on experimental results for adobe bricks [14]. The mass density and Young's modulus of the mortar are assumed to be the same as those for the adobe bricks. The material properties of the timber and FRP elements are listed in Table 1.

Ghannand et al. [14] conducted a laboratory experiment to measure the strength of the adobe bricks used in rural regions in Iran. The results are shown in Table 2. Since the friction angle was not given, the value of a damaged adobe building during a reconnaissance survey of the Bam earthquake in Iran [3] is used.

General values shown in Table 2 are used for the timber and FRP elements.

### 3.4 Input Ground Motion

The Building and Housing Research Center in Iran recorded the main shock of the Bam earthquake [2]. The maximum accelerations of the two horizontal ($T$, $L$) and vertical ($V$) components of the earthquake after correction were 6.23 m/s$^2$ ($T$), 7.78 m/s$^2$ ($L$), and 9.80 m/s$^2$ ($V$) (Figs. 4 (a)–(c)). The direction of the accelerometer for the $L$ component is N278E. The vertical component is very large. For the horizontal components, the peak ground acceleration of the $L$ component is greater than that of the $T$ component. The $T$, $L$, and $V$ components are input in the $x$, $y$, and $z$ directions.

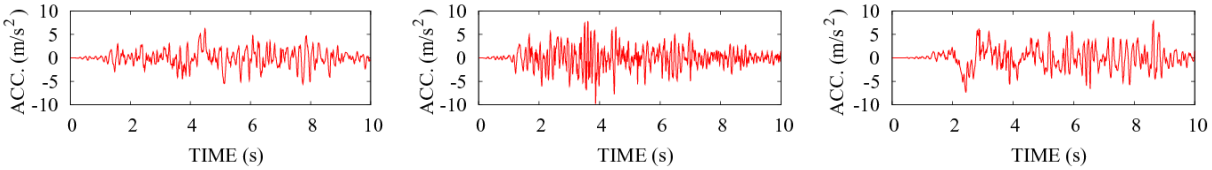


(a) $T$ componentt (b) $L$ component (c) $V$ component

Figure 4 Time histories of input ground motion

### 3.5 Seismic Behavior of Masonry Wall Models

The seismic behavior is shown in Fig. 5. The non-reinforced model vibrated in the out-of-plane direction, a horizontal crack was generated at the middle height, and the wall fell.

Both reinforced models with timbers (T1, T2) successfully prevented the collapse, but diagonal cracks can be seen in the wall.

Two single-sided reinforced models with FRP strips (F1, F2) could not prevent the wall from falling. On the contrary, double-sided reinforced models with FRP strips (F3, F4) did not fall. This outcome does not mean that reinforcement from both sides is always necessary. In the case of the building, walls are connected with the adjacent walls, reducing the walls' out-of-plane deformation. In this case, the single-sided reinforcement is sufficient to prevent the wall from collapsing. T1 and T2 are also single-sided reinforced models, but the timbers are thicker than FRP strips, which may be why the T1 and T2 models did not fall. No clear difference can be seen between models T1 and T2, F1 and F2, and F3 and F4. This outcome indicates that one horizontal timber or FRP strip is sufficient for this model.

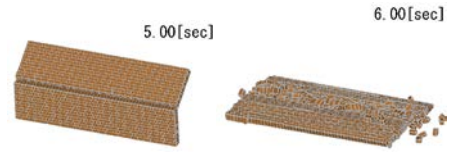


(a) Non-reinforced model (Front view)




(b)Reinforced model with timbers (T1)
(left: front view, right: rear view)

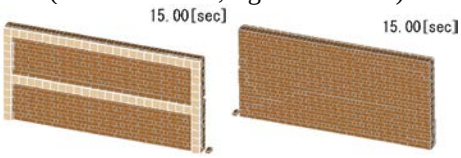


(c)Reinforced model with timbers (T2)
(left: front view, right: rear view)

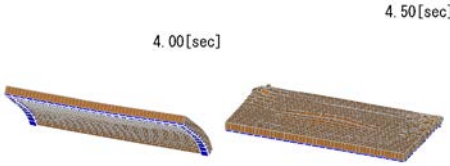


(d) Single-sided reinforced model with FRP strips (F1)

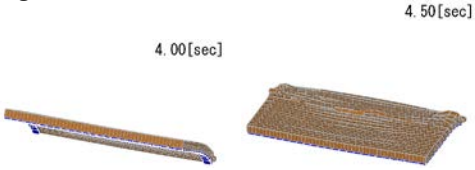


(e) Single-sided reinforced model with FRP strips (F2)

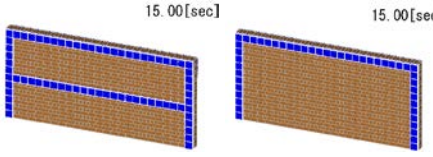


(f) Double-sided reinforced model with FRP strips (F3)
(g) Double-sided reinforced model with FRP strips (F4)

Figure 5 Seismic behavior of masonry wall models

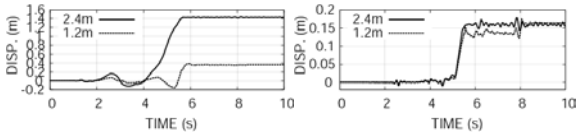


(a) Non-reinforced model

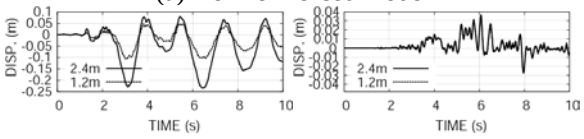


(b) Reinforced model with timbers (T1)

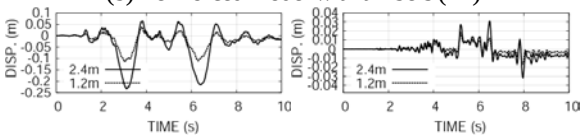


(c) Reinforced model with timbers (T2)

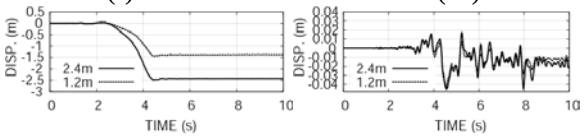


(d) Single-sided reinforced model with FRP strips (F1)

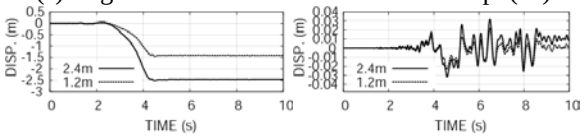


(e) Single-sided reinforced model with FRP strips (F2)

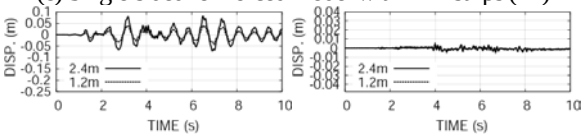


(f) Double-sided reinforced model with FRP strips (F3)

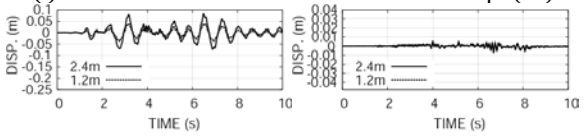


(g) Double-sided reinforced model with FRP strips (F4)

Figure 6 Displacement history of masonry walls
(left: x-direction, right: y-direction)

### 3.6 Displacement History of Masonry Wall Models

Next, displacement histories at two points (shown in Fig.3(a)) are compared. Fig. 6 shows the displacement history in the *x*- and *y*-direction. From the comparison among Figs. 6(a), (d), and (e), it is found that reinforced models F1 and F2 collapsed earlier than the non-reinforced model. The reason for this is considered as follows. The non-reinforced model moves in both directions during vibration. However, the single-sided reinforced models tend to move in a single direction and start tilting earlier than the non-reinforced model. The analyzed model is a single wall with thin FRP strips, which may be why the FRP strips could not prevent the wall from falling down. Even though the wall fell, the effect of FRP strips can be seen. At least, the single-sided FRP reinforcement could prevent the wall from scattering. The displacements of F3 and F4 are much smaller than those of T1 and T2 (Fig.6 (b)(c)(f)(g)). The FRP is stiffer and largely reduces the deformation than the timbers so that fewer cracks can be seen in F3 and F4 compared to T1 and T2. The models with one and two horizontal reinforcing elements showed almost the same displacement level.

## 4 ANALYSIS OF MASONRY BUILDINGS

### 4.1 Analytical Models

Fig. 7 illustrates the masonry building model with a flat roof made of wooden beams. The direction (*x, y, z*) is also shown in Fig. 7. The walls facing the *y* direction support the roof, so these walls are referred to as bearing walls, and the other two walls are referred to as nonbearing walls. The external width of the building is 5.4 m × 3.4 m. The internal width is 5.0 m × 3.0 m. The height of the walls is 2.4 m. The depth of the walls is 0.2 m. The walls are composed of bricks with dimensions of 0.2 m × 0.1 cm × 0.1 m. There are mortar joints with a thickness of 0.01 m between the bricks.

One bearing wall has a door and a window opening. The size of the door is 1.2 m (width) × 2.0 m (height). The size of the window is 1.0 m × 1.0 m and the height of the lower side of the window is 1.0 m. There are wooden beams above the openings that support the elements above the openings. The dimensions of the beams above the openings are 0.2 m × 0.1 m × 1.4 m (in length). These beams are divided into segments with a length of 0.2 m to express their deformation and separation. The roof consists of 27 beams that run in the *y* direction. The beams' dimensions are 0.2 m × 0.2 m × 3.4 m (in length). These roof beams are divided into segments with a length of 0.2 m to express their deformation and separation. The roof beams rest on the walls, and there are mortar joints between the beams and walls.
In this section, the *L*, *T*, and *V* components are input in the *x*, *y*, and *z* directions.

### 4.2 Seismic Behavior of Non-Reinforced Model

The seismic behavior is shown in Fig. 8. The elements with a red area mean that the tensile failure occurred in this area. Only tensile failure occurred, and neither shear nor compressive failure could be seen. The diagonal cracks can be seen around the wall and door openings. The structure collapsed in the *y*-direction due to the out-of-plane deformation of the bearing walls. The seismic behavior is summarized as follows. Diagonal and horizontal cracks in the bearing wall with openings are generated at 2.0 s. Vertical cracks in the bearing wall were generated before 3.6 s. The bearing wall then deformed in the out-of-plane direction at 6.0 s and fell in this direction. The roof collapsed with the failure of the bearing wall with the openings.

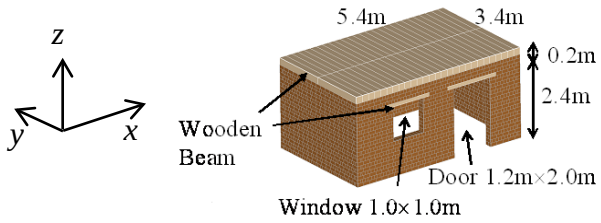


Figure 7 Analytical masonry building models

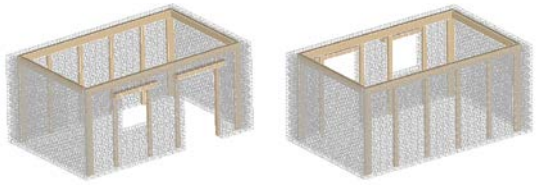

(a) front view (b) rear view

Figure 9 Analytical model of reinforced building

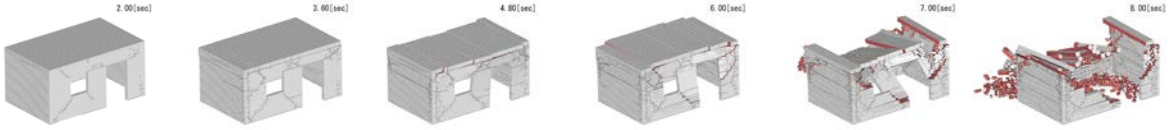

Figure 8 Seismic behavior of non-reinforced building

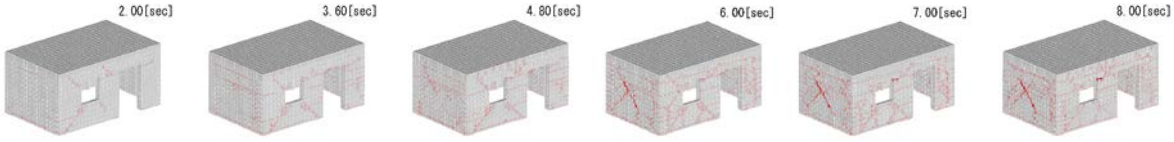


Figure 10 Seismic behavior of reinforced building with timbers

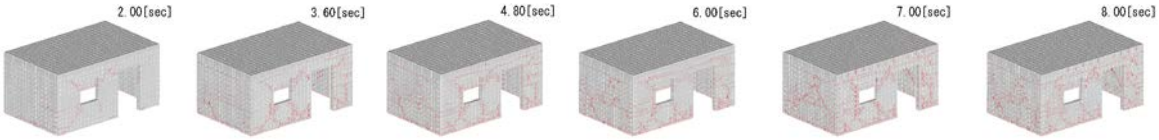


Figure 11 Seismic behavior of reinforced building with FRP strips

### 4.3 Reinforced Models

Two reinforced models with timbers and FRP strips are considered, as shown in Fig.9. Each bearing wall is reinforced with 6 vertical and 1 horizontal timbers or FRP strips. The vertical columns in the edge and horizontal beams have a width of 0.2m. The other columns have a width of 0.1m. The thickness of all timber columns and beams is 0.1m. The FRP strips have the same width as the timbers but have a thickness of 0.02m. Reinforcement was done inside the structure not to ruin the value of a historic structure.

### 4.4 Seismic Behavior of Reinforced Models

The seismic behaviors of the reinforced models are shown in Figs. 10 and 11. Both reinforced models did not collapse. The tensile failure occurred in both models, but the reinforced model with timbers has clearer diagonal cracks in the walls than the reinforced model with FRP strips since the FRP has a larger stiffness.

## 5 CONCLUSIONS

The seismic behavior of masonry walls and building models are analyzed, and the effectiveness of the reinforcement measures using timbers and FRP strips are compared. Since the FRP strips have larger stiffness than the timbers, FRP strips reduced the structural deformation and the number of cracks more effectively than the timbers.

## REFERENCES

[1] R.R. Parajuli, A. Furukawa, D. Gautam, Experimental characterization of monumental brick masonry in Nepal. *Structures*, **28**, 1314-1321, 2020. https://doi.org/10.1016/j.istruc.2020.09.065

[2] BHRC, The very urgent preliminary report on Bam earthquake of Dec 26, 2003, 2003. http://www.bhrc.gov.ir.

[3] J. Kiyono, A. Kalantari, Collapse mechanism of adobe and masonry structures during the 2003 Iran Bam earthquake. *Bulletin of Earthquake Research Institute, University of Tokyo*, **79**, 157-161, 2004.

[4] A. Furukawa, J. Kiyono, R.R. Parajuli, H.R. Parajuli, K. Toki, Evaluation of damage to a historic masonry building in Nepal through comparison of dynamic characteristics before and after the 2015 Gorkha Earthquake. *Frontiers in Built Environment*, **3:62**, 2017. doi:10.3389/fbuil.2017.00062.

[5] P.B. Lourenco, Analysis of masonry structures with interface elements, theory and applications. The Delft University of Technology, Faculty of Civil Engineering, TU-DELFT report no.03-21-22-0-01, 1994.

[6] H.R. Parajuli, J. Kiyono, H. Taniguchi, K. Toki, A. Furukawa, P.N. Maskey, Parametric study and dynamic analysis of a historical masonry building of Kathmandu. *Journal of Disaster Mitigation of Cultural Heritage and Historic Cities*, **4**, 149-156, 2010.

[7] H.R. Parajuli, J. Kiyono, M. Tatsumi, Y. Suzuki, H. Umemura, H. Taniguchi, K. Toki, A. Furukawa, P.N. Maskey, Dynamic characteristic investigation of a historical masonry building and surrounding ground in Kathmandu. *Journal of Disaster Research*, **6(1)**, Dr6-1-4522, 2011. doi: 10.20965/jdr.2011.p0026

[8] A. Furukawa, J.J. Prasetyo, J. Kiyono, Performance of interlocking brick walls against out-of-plane excitation. *International Journal of GEOMATE*, **22(89)**, 100-105, 2022. https://doi.org/10.21660/2022.89.gxi413

[9] P.A. Cundall, O.D.L Strack, A discrete numerical model for granular assemblies. *Geotechnique*, **29**, 47-65, 1979.

[10] A. Furukawa, Y. Ohta, Failure process of masonry buildings during earthquake and associated casualty risk evaluation. *Natural Hazards*, 49(1), 25-51, 2009. http://dx.doi.org/10.1007/s11069-008-9275-x

[11] A. Furukawa, R. Spence, Y. Ohta, E. So, Analytical study on vulnerability functions for casualty estimation in the collapse of adobe buildings induced by earthquake, *Bulletin of Earthquake Engineering*, **8(2)**, 451-479, 2010. http://dx.doi.org/10.1007/s10518-009-9156-z

[12] A. Furukawa, J. Kiyono, K. Toki K, Proposal of a numerical simulation method for elastic, failure and collapse behaviors of structures and its application to masonry walls. *Journal of Disaster Research*, **6(1)**, Dr6-1-4524, 2011. doi: 10.20965/jdr.2011.p0051

[13] A. Furukawa, J. Kiyono, K. Toki, Numerical simulation of the failure propagation of masonry buildings during an earthquake, *Journal of Natural Disaster Science*, **33(1)**, 11-36, 2012, http://dx.doi.org/10.2328/jnds.33.11

[14] M.A. Ghannad, A. Bakhshi, E.S.E. Mousavi, A. Khosravifar, Y. Bozorgnia, B.A.A. Taheri, A study on seismic vulnerability of rural houses in Iran. *Proceedings of the 1st European Conference on Earthquake Engineering and Seismology*, No. 680, 2006.

COMPDYN 2023
9th ECCOMAS Thematic Conference on
Computational Methods in Structural Dynamics and Earthquake Engineering
M. Papadrakakis, M. Fragiadakis (eds.)
Athens, Greece, 12-14 June 2023

# PERFORMANCE COMPARISON OF MASONRY WALLS WITH RECTANGULAR BRICKS AND INTERLOCKING BRICKS – STATIC LOADING TEST AND DYNAMIC ANALYSIS USING DEM –

**A. Furukawa**[1] **and J. Kiyono**[2]

[1] Department of Urban Management, Kyoto University
Kyotodaigaku-katsura, Nishikyo-ku, Kyoto 615-8540, JAPAN
e-mail: furukawa.aiko.3w@kyoto-u.ac.jp

[2] Department of Urban Management, Kyoto University
Kyotodaigaku-katsura, Nishikyo-ku, Kyoto 615-8540, JAPAN
e-mail: kiyono.junji.5x@kyoto-u.jp

## Abstract

*Masonry structures are commonly used in developing countries due to their inexpensiveness and material availability. Masonry structures are strong in resisting gravitational force but vulnerable to lateral forces such as earthquakes. Therefore, reinforcement for masonry structures in earthquake-prone areas is necessary. This paper considers using interlocking bricks instead of regular rectangular bricks as a reinforcement measure for masonry structures as it does not require extra material and is easy to implement. The effectiveness of interlocking bricks instead of regular rectangular bricks is examined by comparing the performance against static loading test and dynamic analysis results using DEM. The static loading test compares the load-displacement relationship of the masonry wall with rectangular bricks and the wall with interlocking bricks. The dynamic analysis results compare the collapse behavior against sinusoidal input between the masonry wall with rectangular bricks and the wall with interlocking bricks in both in-plane and out-of-plane directions. The performance of rectangular bricks and interlocking bricks are compared, and the effectiveness of using interlocking bricks instead of rectangular bricks is discussed.*

**Keywords:** Masonry wall, Rectangular brick, Interlocking brick, Static loading test, Distinct element method.

# 1 INTRODUCTION

It is reported that 75% of the deaths caused by earthquakes are due to collapsed buildings and that most of the deaths caused by collapsed buildings are due to collapsed masonry structures with low earthquake resistance, often constructed in developing regions [1]. Although masonry structures are extremely vulnerable to seismic shaking, they are still being built worldwide today, especially in developing regions [2][3], because of their inexpensive materials, easy construction, and excellent heat and moisture insulation properties. There is a need for inexpensive and easy-to-construct seismic retrofitting methods for masonry structures.

Some of the existing studies on seismic strengthening methods for masonry structures have proposed the use of steel rods [4], reinforced fiber plastic [5], scrap tires [6], and PP-band, a polypropylene cord used for packing [7]. All of these are expected to be possible due to the tensile resistance of the materials. PP-band has already been introduced in developing regions because the materials are readily available worldwide, and the construction is easy.

All of the above methods require reinforcement. In contrast, one method that does not require reinforcement is the use of interlocking blocks/bricks [8][9][10]. This reinforcement method is expected to have higher seismic performance than conventional masonry walls, simply by using interlocking blocks/bricks without using reinforcement materials. However, experimental and numerical verification of reinforcement methods using interlocking blocks/bricks are still limited.

Based on the above, this study compares the result of the static loading test and dynamic analysis of masonry walls consisting of rectangular bricks and interlocking bricks and discusses the performance of interlocking bricks. In the dynamic analysis, this study used the refined DEM (distinct element method) [11] rather than the conventional FEM (finite element method) [12].

The FEM is the most common numerical analysis method. It has been used for the analysis of masonry structures [10][12][13][14]. The FEM can deal with both elastic and plastic behaviors, but it has difficulty solving failure and collapse phenomena since it is based on the mechanics of the continuum. A method based on the mechanics of the dis-continuum is more suitable for analyzing failure and collapse phenomena. An example of a numerical method for a dis-continuum is the DEM [15]. However, the DEM also has disadvantages in that the spring constant cannot be determined from the material properties, and the values need to be quantified experimentally [16][17]. Therefore, the reliability of the results is not high. As an alternative, the present paper uses a refined DEM [11][18], where the spring constant of each spring is theoretically determinable. Using the refined DEM, this paper simulates the dynamic behavior of masonry walls consisting of rectangular and interlocking bricks.

# 2 STATIC LOADING TEST

## 2.1 Overview

A static loading test of two rectangular brick walls and two interlocking brick walls was conducted to investigate the performance of the interlocking bricks against rectangular bricks.

## 2.2 Rectangular and interlocking masonry walls

Masonry structures are generally constructed by stacking rectangular bricks, as shown in Fig. 1(a). Failure generally occurs and propagates at joints in rectangular brick walls. When a joint fails, the joint loses resistance other than frictional force and becomes very vulnerable, as shown in Fig. 1(a).

In order to improve the bearing capacity of masonry structures, the use of interlocking bricks has been studied. Assuming that the bricks do not fracture, even if the fracture occurs at joints, the interlocking generates resistant force in addition to friction force, as shown in Fig. 1(b). This resistant force may improve the overall bearing capacity of the masonry structure.

### 2.3 Masonry wall test specimen

This study considered four types of masonry walls, shown in Fig. 2. Three samples are made for each type. The width, height, and depth of each masonry wall are shown in Table 1. The four types of masonry walls were set to be as close to a square as possible, and the length of one side was as equal as possible. Most of the mortar thickness was 10 mm. However, to keep the masonry walls close to squares, the horizontal joint width was set to 7 mm for the rectangular type 1 and 8 mm for the interlocking types 1 and 2.

Figure 3 shows the dimension of bricks stacked in each type of masonry wall. As shown in Fig. 2, the bricks at the left and right ends of the odd-numbered rows were cut in half. The fabrication errors of several millimeters were observed in the bricks and mortar thickness.

Table 2 shows the material properties and strength obtained by element tests. All elemental tests were conducted three times, and the values were averaged.

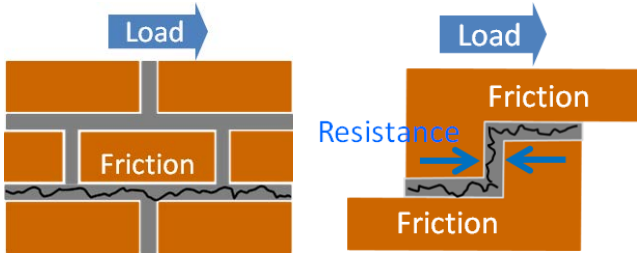


(a)Rectangular brick wall (b)Interlocking brick wall

Figure 1: Rectangular and interlocking brick walls

Table 1: Dimension of masonry walls (unit: mm)

| Name | Width | Height | Depth |
|---|---|---|---|
| Rectangular type 1 | 590 | 596 | 100 |
| Rectangular type 2 | 590 | 590 | 100 |
| Interlocking type 1 | 590 | 588 | 100 |
| Interlocking type 2 | 590 | 588 | 100 |

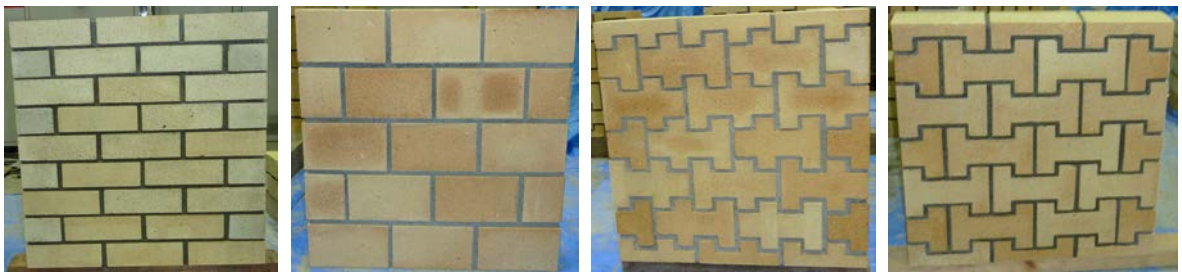

(a) Rectangular type 1 (b) Rectangular type 2 (c) Interlocking type 1 (d) Interlocking type 2

Figure 2: Photographs of masonry walls

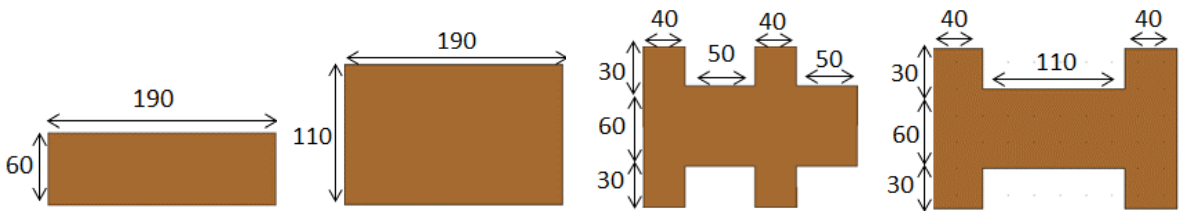


(a) Rectangular type 1 (b) Rectangular type 2 (c) Interlocking type 1 (d) Interlocking type 2

Figure 3: Dimensions of bricks (unit: mm, depth: 10mm)

Table 2: Material properties and strength obtained by element test

(a) Brick and mortar

| | Young's modulus ($N/m^2$) | Poisson's ratio | Compressive strength ($N/m^2$) | Tensile strength ($N/m^2$) |
|---|---|---|---|---|
| Brick (rectangular type 1) | $2.04\times10^{10}$ | 0.33 | $2.41\times10^{7}$ | $8.84\times10^{6}$ |
| Brick (except rectangular type 1) | $1.69\times10^{10}$ | — | $1.69\times10^{7}$ | $8.92\times10^{6}$ |
| Mortar | $8.00\times10^{8}$ | 0.18 | $1.69\times10^{7}$ | $1.28\times10^{6}$ |

(b) Interface between bricks and mortar

| Tensile strength ($N/m^2$) | Bond strength ($N/m^2$) | Friction coefficient |
|---|---|---|
| $9.69\times10^{5}$ | $1.68\times10^{5}$ | 1.25 |

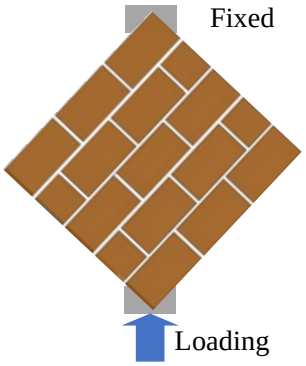


Figure 4: Loading condition

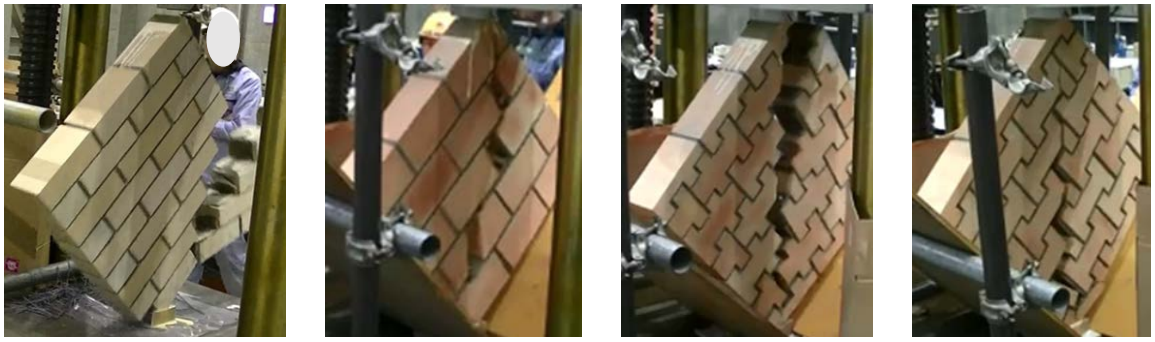

(a) Rectangular type 1 (b) Rectangular type 2 (c) Interlocking type 1 (d) Interlocking type 2

Figure 5: Photographs of masonry walls during loading

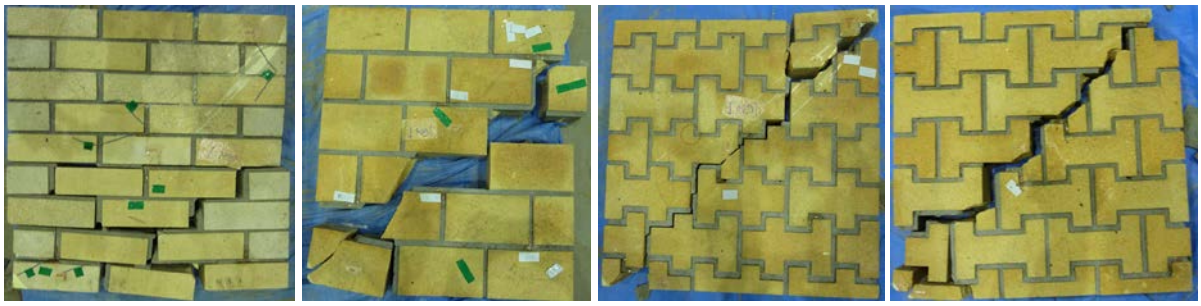

(a) Rectangular type 1 (b) Rectangular type 2 (c) Interlocking type 1 (d) Interlocking type 2

Figure 6: Photographs of masonry walls after loading

## 2.4 Loading method

Static loading tests were conducted on the four types of masonry wall test specimens. Three specimens of each of the four types were tested. As shown in Fig. 4, M-shaped jigs were attached to the upper and lower loading plates of the universal material testing machine, and the specimen was placed between the jigs.

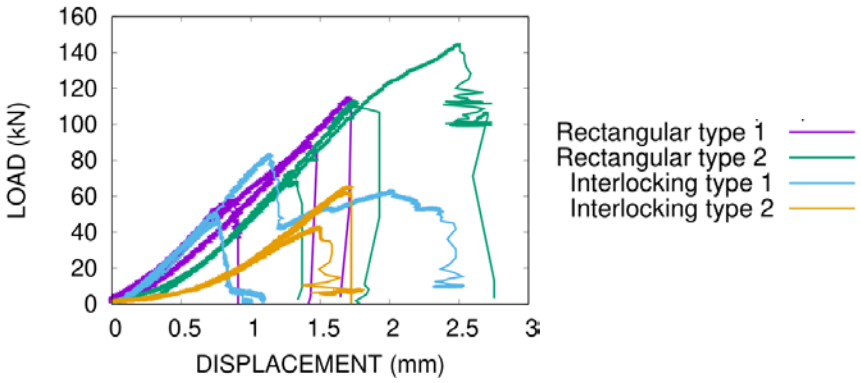


Figure 7: Load-displacement relationship

## 2.5 Result (Failure pattern)

Three tests were conducted on each of the four different masonry wall models. Photographs of the test specimen during loading are shown in Fig. 5. Photographs of the test specimen after loading are shown in Fig. 6.

In the case of rectangular type 1, the fracture developed on the brick/mortar interface in a stair-step manner. The failure did not occur inside the brick. However, the entire wall collapsed due to the propagation of a fracture on the brick/mortar interface.

In the case of rectangular type 2, the failure propagated in a stair-step manner. Three bricks, one on the bottom and two on the top, got fractured inside the bricks, and the others got fractured in a stair-step manner at the brick/mortar interface (red line). The failure surfaces occurred in the loading direction that connects the upper and lower loading points.

In interlocking types 1 and 2, the failure surface occurred in the loading direction, connecting the upper and lower loading points. The failure occurred at the brick/mortar interface and inside the brick.

## 2.6 Result (Load-displacement relationship)

The load-displacement relationship is shown in Fig. 7. Three specimens were tested for each type of masonry wall model, shown in the same color.

The three test specimens for the same type have almost the same slope of the load-displacement relationships but different maximum loads. The variation in the maximum load was probably caused by variations in the strength of the bricks and mortar, variations in the strength of the brick-mortar interface, and variations in the setting of the test apparatus.

The maximum load of both interlocking types is smaller than that of both rectangular types.

## 2.7 Discussion

In the case of the rectangular types, the failure surface mainly developed on the brick/mortar interface. In the case of the interlocking types, the failure surface developed in bricks and on the brick/mortar interface.

The maximum load tended to be lower for the interlocking types than for the rectangular types. The reason for the lower maximum loads in the interlocking types is assumed to be the stress concentration in the bricks in the interlocking area, which facilitates failure.

# 3 DYNAMIC ANALYSIS

## 3.1 Overview

Next, the dynamic analysis of the two rectangular brick walls and two interlocking brick walls is performed by the refined DEM to investigate the performance of the interlocking brick walls over the rectangular brick walls.

## 3.2 Refined DEM

This study employs a refined DEM [11] to simulate a series of structural dynamic behaviors from elastic to failure to collapse phenomena. A structure is modeled as an assembly of rigid elements, and interaction between the elements is modeled with multiple springs and dashpots attached to the elements' surfaces. The elements are rigid, but the method allows the simulation of structural deformation by allowing penetration between elements.

Fig. 8 (a) shows a spring for computing the restoring force (restoring spring), which models the elasticity of elements. The restoring spring is set between continuous elements. Structural failure is modeled as the breakage of the restoring spring, at which time the restoring spring is replaced with a contact spring and a contact dashpot (Fig. 8 (b)). Fig. 8 (b) shows the spring and dashpot for computing the contact force (contact spring and dashpot) and modeling the contact, separation, and recontact between elements. The dashpots are introduced to express energy dissipation due to the contact. Structural collapse behavior is obtained using these springs and dashpots. The elements shown in Figs. 8 (a) and (b) are rectangular parallelepipeds, but the method does not limit the geometry of the elements.

The surface of an element is divided into small segments, as shown in Fig. 8 (c). The segment in the figure is rectangular, but the method does not limit the geometry of the segment. The black points indicate the representative point of each segment, and the relative displacement or contact displacement between elements is computed for these points. Such points are referred to as contact points or master points in this study. One restoring spring and one combination of contact spring and dashpot are attached to one segment (Fig. 8 (d)) at each of the representative points in Fig. 8 (c). The spring constant for each segment is derived based on the stress-strain relationship of the material and the segment area.

The behavior of an element consists of translational and rotational behaviors. Each element's translational and rotational behaviors are computed explicitly by solving Newton’s law of motion and Euler’s equation of motion. Forces acting on each element are obtained by summing the restoring force, contact force, and other external forces, such as the gravitational force and the earthquake’s inertial force.

## 3.3 Analytical model

The analytical model is shown in Fig. 9. A 70 kg weight is placed on the top of each masonry wall. Figure 10 shows how the brick is modeled in each type of masonry wall. Each brick consists of smaller rectangular elements to account for brick failure. The failure of brick occurs between the element boundary. The failure of mortar occurs between bricks. Figure 11 shows the arrangement of bricks in each model.

The material properties of the rectangular brick type 1 and the material properties of mortar shown in Table 2(a) are used in the analysis. In order to investigate the effect of interlocking mechanisms on the dynamic response, the same material properties of bricks and mortar are used for all the masonry wall models.

As for damping, mass-proportional damping was assumed, and the damping constant was set to 0.03 for the first mode.

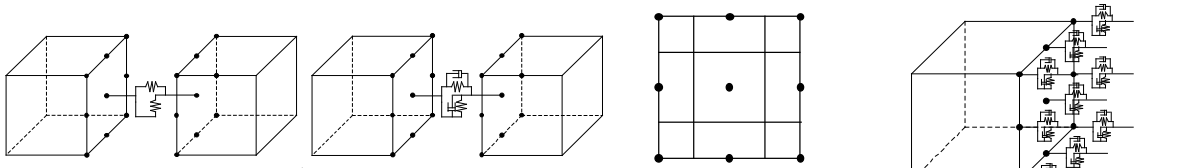

(a) Restoring spring (b) Contact spring/dashpot (c) Segments and contact points (d) Multiple springs/dashpots

Figure 8: Basic concept of the analysis method [11]

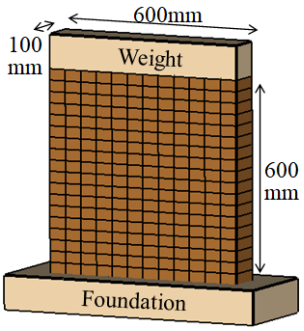


Figure 9: Numerical model

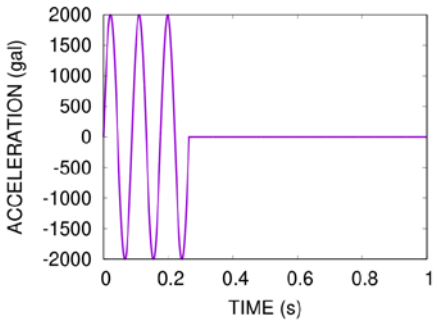


Figure 12: Input acceleration

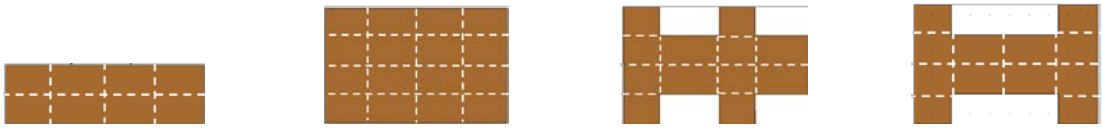

(a) Rectangular type 1 (b) Rectangular type 2 (c) Interlocking type 1 (d) Interlocking type 2

Figure10: Brick model

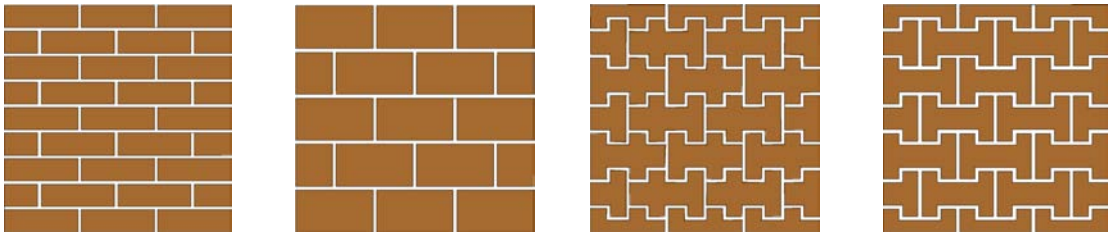

(a) Rectangular type 1 (b) Rectangular type 2 (c) Interlocking type 1 (d) Interlocking type 2

Figure 11: Masonry wall model

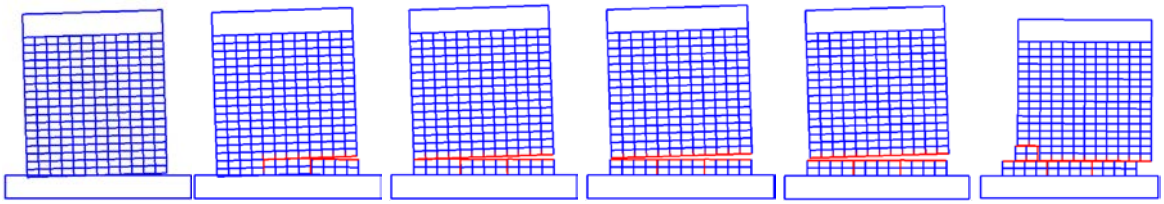

Figure 13: Dynamic behavior of rectangular type 1 (0.22s, 0.23s, 0.24s, 0.25s, 0.26s, 1.0s, from the left)

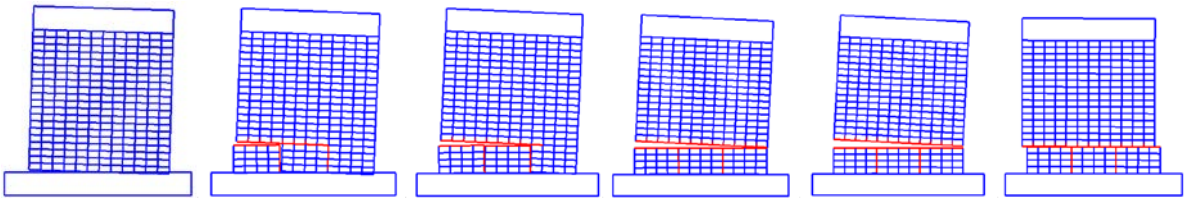

Figure 14: Dynamic behavior of rectangular type 2 (0.26s, 0.27s, 0.28s, 0.29s, 0.30s, 1.0s, from the left)

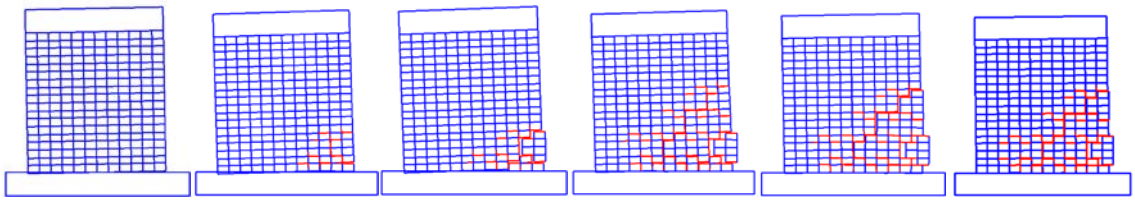

Figure 15: Dynamic behavior of interlocking type 1 (0.21s, 0.22s, 0.23s, 0.24s, 0.25s, 1.0s, from the left)

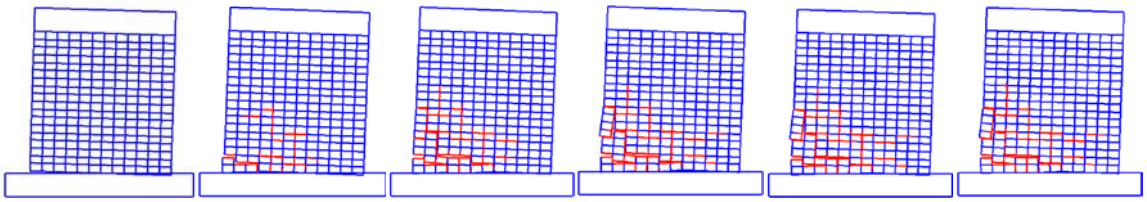

Figure 16: Dynamic behavior of interlocking type 2 (0.26s, 0.27s, 0.28s, 0.29s, 0.30s, 1.0s, from the left)

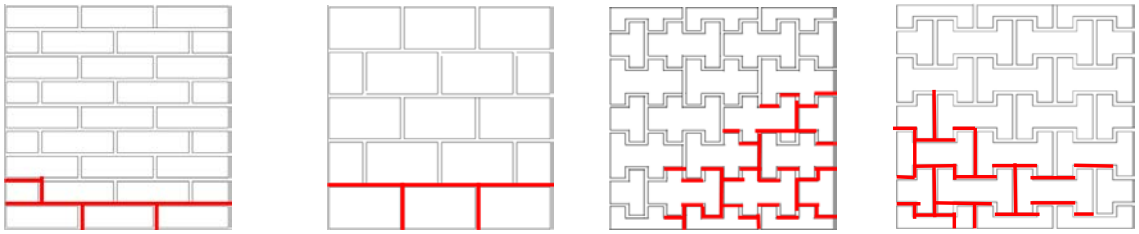

(a) Rectangular type 1 (b) Rectangular type 2 (c) Interlocking type 1 (d) Interlocking type 2

Figure 17: Location of failure after dynamic loading

### 3.4 Input acceleration

The first mode natural frequency of the analytical model in the in-plane direction was found to be 11.328 Hz through the dynamic analysis of the free vibration. Therefore, three cycles of a sine wave with an amplitude of 2000 gal and a frequency of 11.328 Hz, as shown in Fig.12, were input as ground acceleration in the in-plane direction.

### 3.5 Result

The process of failure propagation during dynamic loading is shown in Figs. 13-16. The failure location after the dynamic loading is shown in Fig. 17. The red lines indicate where the tensile failure occurred.

In the case of rectangular type 1 (Fig. 13), the failure occurred at 0.23 s at the brick/mortar interface between the lowest and the second lowest bricks on the right side and propagated in the left direction. The failure progressed along the horizontal joints and completely penetrated at 0.24 s. As shown in Fig.17(a), the failure only occurred at the brick/mortar interface, and no failure occurred inside the brick.

In the case of rectangular type 2 (Fig. 14), the failure occurred at 0.27 s at the brick/mortar interface between the lowest and the second lowest bricks on the left side. The failure propagated along the horizontal joints and completely penetrated at 0.29 s. As shown in Fig.17(b), the failure only occurred at the brick/mortar interface, and no failure occurred inside the brick.

In the case of interlocking type 1 (Fig. 15), the failure occurred at 0.22 s at the brick/mortar interface on the right bottom side. The failure then progressed in the wider range compared to rectangular types 1 and 2. As shown in Fig.17(c), the failure occurred at the brick/mortar interface and inside the bricks. Even though the failure occurred in the wider

range and both the brick/mortar interface and the brick itself got failure, the failure propagation stopped during the loading, and the failure surface did not penetrate the brick wall.

In the case of interlocking type 2 (Fig. 16), the failure occurred at 0.27 s on the brick/mortar interface and inside the brick on the left bottom side. Then failure propagated a wider range. Even though the failure occurred in the wider range and both the brick/mortar interface and the brick itself got failure, the failure propagation stopped during the loading, and the failure surface did not penetrate the brick wall, as shown in Fig. 17(d).

Interlocking bricks effectively prevented the cracks from penetrating the masonry wall, although cracking occurs over a wide area of the masonry wall. The interlocking bricks allowed the wall to retain its full shape after the end of the excitation.

## 4 CONCLUSIONS

This study considered using interlocking bricks as a reinforcement measure for masonry structures as it does not require extra material and is easy to implement. The effectiveness of interlocking bricks instead of regular rectangular bricks is examined by comparing the performance against static loading test and dynamic analysis results using the refined DEM. The static loading test compared the failure behavior and the load-displacement relationship of the masonry walls. The dynamic analysis compared the collapse behavior of the masonry walls against sinusoidal input in the in-plane directions.

The static loading test found that the failure occurred on the brick/mortar interface in the rectangular brick walls, while the failure occurred both on the brick/mortar interface and inside bricks in the interlocking brick walls. It was also found that the interlocking brick walls have a lower maximum load than the rectangular brick walls. The reason is the stress concentration at the interlocking part. The effectiveness of interlocking bricks over rectangular bricks could not be seen in the static loading test.

The dynamic loading analysis observed that the failure only occurred on the brick/mortar interface in the rectangular brick walls. In contrast, the failure occurred in the brick/mortar interface and inside bricks in the interlocking walls. The rectangular brick wall underwent a horizontal crack that penetrated the entire wall and was divided into two pieces. However, the interlocking brick wall suffered cracks in the wider range, but no crack penetration occurred, and the wall was never divided into two parts. The effectiveness of interlocking bricks over rectangular bricks could be seen in the dynamic analysis.

## REFERENCES

[1] OCHA: www.unocha.org. [Accessed February 27, 2023].

[2] R.R. Parajuli, A. Furukawa, D. Gautam, Experimental characterization of monumental brick masonry in Nepal. *Structures*, **28**, 1314-1321, 2020. https://doi.org/10.1016/j.istruc.2020.09.065

[3] H.R. Parajuli, J. Kiyono, M. Tatsumi, Y. Suzuki, H. Umemura, H. Taniguchi, K. Toki, A. Furukawa, P.N. Maskey, Dynamic characteristic investigation of a historical masonry building and surrounding ground in Kathmandu. *Journal of Disaster Research*, **6(1)**, Dr6-1-4522, 2011. doi: 10.20965/jdr.2011.p0026

[4] A. Darbhanzi, S. Marefat, M. Khanmohammadi, Investigation of in-plane seismic retrofit of unreinforced masonry walls by means of vertical steel ties, *Construction and Building Materials*, **52**, 122-129, 2014.

[5] G. Marcari, G. Manfredi, A. Prota, M. Pecce, In-plane shear performance of masonry panels strengthened with FRP. *Composites: Part B,* **38**, 887-901 , 2007.

[6] A. Turer, M. Golalm, Scrap tire as low-cost post-tensioning material for masonry strengthening. *Materials and Structures*, **41**, 1345-1361, 2011.

[7] N. Sathiparan, K. Sakurai, K. Meguro, Experimental study of PP-band retrofitted masonry structure made of shapeless stone. *SEISAN-KENKYU,* **61(6)**, 1051-1054, 2009.

[8] A. Furukawa, K. Masuda, J. Kiyono, Diagonal compression test of mortar interlocking masonry wall with various block shapes and different support conditions. *Frontiers in built environment,* **6:579366**, 2020. https://doi.org/10.3389/fbuil.2020.579366

[9] A. Furukawa, J.J. Prasetyo, J. Kiyono, Failure process and load-displacement relationship of rectangular block and interlocking block walls during in-plane lateral loading. *Journal of Japan Society for Natural Disaster Science,* **38**, 25-41, 2019. https://doi.org/10.24762/jndsj.38.S06_25

[10] A. Furukawa, J.J. Prasetyo, J. Kiyono, Performance of interlocking brick walls against out-of-plane excitation. *International Journal of GEOMATE,* **22(89)**, 100-105, 2022. https://doi.org/10.21660/2022.89.gxi413

[11] A. Furukawa, J. Kiyono, K. Toki K, Proposal of a numerical simulation method for elastic, failure and collapse behaviors of structures and its application to masonry walls. *Journal of Disaster Research*, **6(1)**, Dr6-1-4524, 2011. doi: 10.20965/jdr.2011.p0051

[12] P.B. Lourenco, Analysis of masonry structures with interface elements, theory and applications. The Delft University of Technology, Faculty of Civil Engineering, TU-DELFT report no.03-21-22-0-01, 1994.

[13] H.R. Parajuli, J. Kiyono, H. Taniguchi, K. Toki, A. Furukawa, P.N. Maskey, Parametric study and dynamic analysis of a historical masonry building of Kathmandu. *Journal of Disaster Mitigation of Cultural Heritage and Historic Cities*, **4**, 149-156, 2010.

[14] A. Furukawa, J. Kiyono, R.R. Parajuli, H.R. Parajuli, K. Toki, Evaluation of damage to a historic masonry building in Nepal through comparison of dynamic characteristics before and after the 2015 Gorkha Earthquake. *Frontiers in Built Environment*, **3:62**, 2017. doi:10.3389/fbuil.2017.00062.

[15] P.A. Cundall, O.D.L Strack, A discrete numerical model for granular assemblies. *Geotechnique*, **29**, 47-65, 1979.

[16] A. Furukawa, Y. Ohta, Failure process of masonry buildings during earthquake and associated casualty risk evaluation. *Natural Hazards*, 49(1), 25-51, 2009. http://dx.doi.org/10.1007/s11069-008-9275-x

[17] A. Furukawa, R. Spence, Y. Ohta, E. So, Analytical study on vulnerability functions for casualty estimation in the collapse of adobe buildings induced by earthquake, *Bulletin of Earthquake Engineering*, **8(2)**, 451-479, 2010. http://dx.doi.org/10.1007/s10518-009-9156-z

[18] A. Furukawa, J. Kiyono, K. Toki, Numerical simulation of the failure propagation of masonry buildings during an earthquake, *Journal of Natural Disaster Science*, **33(1)**, 11-36, 2012, http://dx.doi.org/10.2328/jnds.33.11

COMPDYN 2023
9th ECCOMAS Thematic Conference on
Computational Methods in Structural Dynamics and Earthquake Engineering
M. Papadrakakis, M. Fragiadakis (eds.)
Athens, Greece, 12-–14 June 2023

# VULNERABILITY ASSESSMENT OF BUILDINGS BASED ON THE PSEUDO-DYNAMIC TESTING METHOD WITH SUB-STRUCTURING: APPLICATION TO PROGRESSIVE COLLAPSE

**Jean-Baptiste Charrié[1], David Bertrand[1], Cédric Desprez[1], Stéphane Grange[1]**

[1]Univ Lyon, INSA Lyon, GEOMAS, EA7495
69621 Villeurbanne, France
e-mail: {jean-baptiste.charrie, david.bertrand, cedric.desprez, stephane.grange}@insa-lyon.fr

**Abstract.** *Due to various natural or anthropogenic hazards, buildings' structural members can lose their bearing capacities which can lead to the building's progressive collapse. The latter subject is of growing interest regarding the socio-economic context [1]. Academic research on progressive collapse took off in the early 2000s, with the 9/11 attacks on the Twin Towers (NY, 2001) [1]. Analyses on large structures are mainly done numerically. On the other side, most experiments are lead on smaller structural elements. Until now, these experiments have been limited by dimensions, dynamic forces and real-time control capabilities. In earthquake engineering, the pseudo-dynamic method (PsD) is often used [2]. Experimental tests are performed quasi-statically on a structural part, while the inertial forces are computed within a time integration scheme. An extension of the method is the sub-structured PsD trials, which consists of inserting the tested part in a larger finite element mesh. Sub-structuring enables accounting for the whole structure's effect on the tested part [3]. The paper presents a first experimental campaign, which validated the interest of the approach on a simple structural part. Another experimental campaign is underway, on larger structural members to further comfort the method's validity to study progressive collapse.*

**Keywords:** Progressive collapse, Pseudo-dynamic testing, Sub-structuring, Reinforced concrete modeling, Dynamic behavior

# 1 INTRODUCTION

The paper aims at studying the sudden loss of bearing capacity in civil engineering structures. Loss of bearing capacity has been of growing interest for the past two decades, especially after the terrorist attacks on the World Trade Center (NY, 2001)[1]. The phenomenon leads to partial or complete structural collapse. Origins are diverse, from gas explosions to natural or anthropogenic risks, including design defects, building decay, *etc*.

New knowledge is still needed to propose new structures capable of mitigating damages due to such events, whilst maintaining structural and/or functional integrity, as well as retro-fitting real-estate to prolong existing buildings' lives. Approaches to characterize structural integrity remains largely experiment based, to validate numerical models. To guarantee representative results, full scale experiments are needed. This point is often a limiting factor due to the scale of civil engineering structures; logistics, costs and dynamic solicitation of large masses are all drawbacks to this approach. This is all the more true for larger structures, and when the damaged zone is limited.

For those reasons, a novel approach is proposed to tackle those problems, taking advantage of the Pseudo-Dynamic (PsD) method. The latter is largely used in earthquake engineering, to test dynamic responses of building in a *quasi*-static manner [2]. Combined with a sub-structuring approach, the resulting tests will resolve scale, resulting forces and logistical problems to some extent [3]. Sub-structured PsD testing has never been used in progressive collapse experiments. This paper presents this promising alternative to currently used methods. As well as greatly reducing costs, experimental implementation is simplified. From an experimental point of view, the structure's static response is needed, whereas the dynamic behavior is accounted for numerically. Thus, testing is simpler, with smaller forces, lower data acquisition, and time dilation. Better control during trials yield more repeatability, and should enable parametric studies with a high confidence degree in the results.

Foremost, the PsD testing approach with sub-structuring is presented. Then, the two experimental campaigns, representing accidental loss of bearing scenarios are proposed. The first campaign is a proof-of-concept to demonstrate the method's legitimacy to investigate progressive collapse events. The second experimental campaign's aim is to further validate the method, with larger, more intricate structural members, and better boundary conditions (BCs). Additional phenomenons will be highlighted, such as Tensile Catenary Action (TCA) and Compressive Arch Action (CAA) [1]. The first campaign's results are compared and validated using a non-linear, Finite Element (FE), multi-fiber model. Finally, results are discussed, and the second experimental campaigns objectives and perspectives are presented.

# 2 METHODOLOGY

## 2.1 Pseudo-Dynamic testing algorithm

### 2.1.1 Classic Pseudo-Dynamic method

The algorithm used is an $\alpha$ Operator-Splitting ($\alpha$-OS). It is particularly suited as it is implicit and non-iterative [2]. Eq. (1) gives the relationship at time $t_{n+1} = t_n + \Delta t$, with $n$ being the time increment index.

$$\mathbb{M}\boldsymbol{a}^{n+1} + \mathbb{C}\boldsymbol{v}^{n+1} + \boldsymbol{R}(\boldsymbol{d}^{n+1}) = \boldsymbol{F}_{ext}^{n+1} \tag{1}$$

$\mathbb{M}$ and $\mathbb{C}$ are respectively the mass and damping matrices. $\boldsymbol{d}$, $\boldsymbol{v}$ and $\boldsymbol{a}$ are the nodal displacements, velocities and accelerations. $\boldsymbol{F}_{ext}$ are the external forces and $\boldsymbol{R}$ the restoring forces,

measured statically on the tested structure.

The $\alpha$-OS scheme is based on a predictor-corrector procedure. The prediction step is given by Eq. (2) :

$$\text{Prediction} \begin{cases} \tilde{\boldsymbol{d}}^{n+1} & = \boldsymbol{d}^n + \Delta t\, \boldsymbol{v}^n + \frac{\Delta t^2}{2}(1-2\beta)\boldsymbol{a}^n \\ \tilde{\boldsymbol{v}}^{n+1} & = \boldsymbol{v}^n + \Delta t\,(1-\gamma)\boldsymbol{a}^n \end{cases} \tag{2}$$

The coefficients $\beta$ and $\gamma$ depend on $\alpha$, the scheme's parameter: $\beta = \frac{(1-\alpha)^2}{4}$ and $\gamma = \frac{1-2\alpha}{2}$. Once the desired predicted displacements $\tilde{\boldsymbol{d}}^{n+1}$ have been imposed, the experimental system fetches the measured displacements and forces: $\tilde{\boldsymbol{d}}_m^{n+1}$ and $\tilde{\boldsymbol{R}}_m^{n+1}$. The acceleration vector is then computed (Eq. (3) using the pseudo-mass matrix $\hat{\mathbb{M}}$ (Eq. (4)) and the $\alpha$-shifted pseudo-force vector $\hat{\boldsymbol{f}}^{n+1+\alpha}$ (Eq. (5)).

$$\boldsymbol{a}^{n+1} = \hat{\mathbb{M}}^{-1}\,\hat{\boldsymbol{f}}^{n+1+\alpha} \tag{3}$$

$$\hat{\mathbb{M}} = \mathbb{M} + \gamma\,\Delta t\,(1+\alpha)\mathbb{C} + \beta\,\Delta t^2\,(1+\alpha)\mathbb{K}^{\mathbb{I}} \tag{4}$$

$$\begin{aligned} \hat{\boldsymbol{f}}^{n+1+\alpha} = {} & (1+\alpha)\,\boldsymbol{F}_{ext}^{n+1} - \alpha\,\boldsymbol{F}_{ext}^{n} + \alpha\,\tilde{\boldsymbol{R}}^n - (1+\alpha)\tilde{\boldsymbol{R}}^{n+1} + \dots \\ & \dots + \alpha\,\mathbb{C}\,\tilde{\boldsymbol{v}}^n - (1+\alpha)\,\mathbb{C}\,\tilde{\boldsymbol{v}}^{n+1} + \alpha(\gamma\,\Delta t\,\mathbb{C} + \beta\,\Delta t^2\,\mathbb{K}^I)\boldsymbol{a}^n \end{aligned} \tag{5}$$

To guarantee the algorithm's convergence, the stiffness matrix $\mathbb{K}^{\mathbb{I}}$ used to compute $\hat{\mathbb{M}}$ must be as close as possible to the initial elastic stiffness matrix, and greater than the current tangent matrix [2]. To compensate for measurement errors without iterating, the restoring forces are estimated from the imposed predicted displacement (eq. (6)).

$$\tilde{\boldsymbol{R}}^{n+1} \approx \tilde{\boldsymbol{R}}_m^{n+1} + \mathbb{K}^I\left[\tilde{\boldsymbol{d}}_m^{n+1} - \tilde{\boldsymbol{d}}^{n+1}\right] \tag{6}$$

Once $\tilde{\boldsymbol{R}}^{n+1}$ is computed, $\hat{\boldsymbol{f}}^{n+1+\alpha}$ can be calculated to get $\boldsymbol{a}^{n+1}$. Finally, the kinematic field is corrected (eq. (7))

$$\text{Correction} \begin{cases} \boldsymbol{d}^{n+1} & = \tilde{\boldsymbol{d}}^{n+1} + \beta\Delta t^2\,\boldsymbol{a}^{n+1} \\ \boldsymbol{v}^{n+1} & = \tilde{\boldsymbol{v}}^{n+1} + \gamma\Delta t\,\boldsymbol{a}^{n+1} \end{cases} \tag{7}$$

### 2.1.2 Sub-Structuring method

Sub-structuring allows for part of the structure to be simulated ($S$), while only the critical part is physically tested ($T$) under *quasi*-static conditions. A domain decomposition is done on the equations presented above to separate the simulated and tested parts. The resolution process is based on [3], and can be written as:

$$\begin{bmatrix} {}^S\hat{M}_{ij} & {}^S\hat{M}_{i\theta} & 0 \\ {}^S\hat{M}_{\delta j} & {}^S\hat{M}_{\delta\theta} + {}^T\hat{M}_{\delta\theta} & {}^T\hat{M}_{\delta J} \\ 0 & {}^T\hat{M}_{I\theta} & {}^T\hat{M}_{IJ} \end{bmatrix} \begin{bmatrix} a_j^{n+1} \\ a_\theta^{n+1} \\ a_J^{n+1} \end{bmatrix} = \begin{bmatrix} {}^S\hat{f}_i^{n+1+\alpha} \\ {}^S\hat{f}_\delta^{n+1+\alpha} + {}^T\hat{f}_\delta^{n+1+\alpha} \\ {}^T\hat{f}_I^{n+1+\alpha} \end{bmatrix} \tag{8}$$

Indices $I$ and $J$ (resp. $i$ and $j$) refer to tested (resp. simulated) Degrees of Freedom (DOFs). Interface DOFs are index $\delta$ and $\theta$. To treat simulated and tested parts in parallel, a static condensation is performed. The pseudo-mass matrix is generated, then accelerations of the modeled part's DOFs are condensed onto the tested part (Eq. (9) using the first line of Eq.(8)).

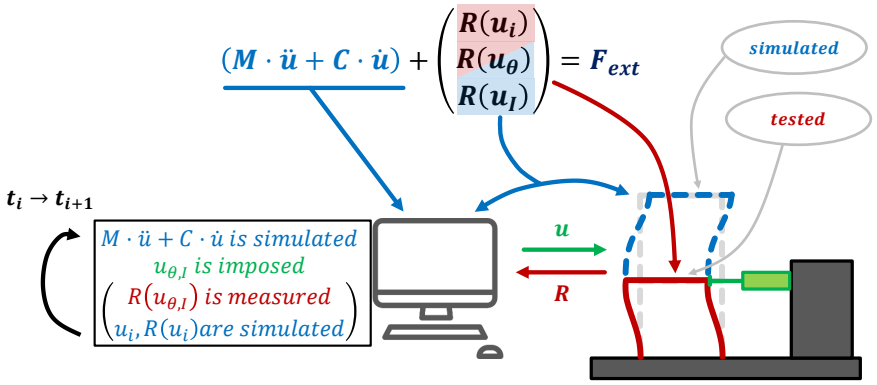


Figure 1: Principle of the sub-structured PsD tests' procedure. Red part is tested, blue part is modeled using FEM. Actuators are represented in green.

$$ {}^{S}\hat{M}_{ij} a_j^{n+1} = {}^{S}\hat{f}_i^{n+1+\alpha} - {}^{S}\hat{M}_{i\theta} a_\theta^{n+1} \tag{9} $$

Then, Eq. (9) is injected onto Eq. (8)'s second and third line:

$$ \begin{bmatrix} {}^{T}\hat{M}_{\delta\theta} + {}^{SC}\hat{M}_{\delta\theta} & {}^{T}\hat{M}_{\delta J} \\ {}^{T}\hat{M}_{I\theta} & {}^{T}\hat{M}_{IJ} \end{bmatrix} \begin{bmatrix} a_\theta^{n+1} \\ a_J^{n+1} \end{bmatrix} = \begin{bmatrix} {}^{T}\hat{f}_\delta^{n+1+\alpha} + {}^{SC}\hat{f}_\delta^{n+1+\alpha} \\ {}^{T}\hat{f}_I^{n+1+\alpha} \end{bmatrix} \tag{10} $$

With ${}^{SC}\hat{M}_{\delta\theta} = {}^{S}\hat{M}_{\delta\theta} - {}^{S}\hat{M}_{\delta j} {}^{S}\hat{M}_{ji}{}^{-1} {}^{S}\hat{M}_{i\theta}$ and ${}^{SC}\hat{f}_\delta^{n+1+\alpha} = {}^{S}\hat{f}_\delta^{n+1+\alpha} - {}^{S}\hat{M}_{\delta j} {}^{S}\hat{M}_{ji}{}^{-1} {}^{S}\hat{f}_i^{n+1+\alpha}$.

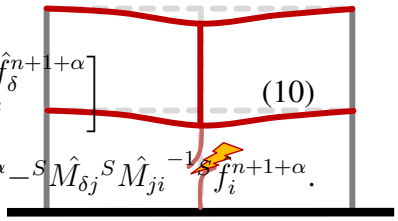

## 2.2 Experimental setups

### 2.2.1 Campaign 00 - 2021

As a proof of concept for PsD based progressive collapse trials, four Reinforced Concrete (RC) beams were made. For the sake of simplicity, boundary conditions and geometry were as simple as possible. The beams' responses were characterized by two pushovers tests done at different loading rates to validate that the static response is independent of load rate. A first, classic PsD test was conducted, serving as a reference trial. The last beam was tested using a sub-structured PsD test. Results will be discussed in this section.

**RC beam characteristics** Beams were poured using $C25/30$ concrete, along with $HA500\,B$ steel rebars. Reinforcements were designed according to Eurocode 2 recommendations, for a $20kN$ ultimate load in a three points bending test configuration. Dimensions and details are depicted in Figure (2).

Trials were conducted after 28 days of curing or more. Compression and Brazilian tests on $11 \cdot 22cm$ cylindrical samples yielded the following results: $f_{cm} = 29.75MPa$ and $f_{ctm} = 2.79MPa$.

**Experimental setup** Each beam is simply supported at each end, with a $2.12m$ span. An hydraulic actuator controls the beam's mid-span displacement. A force sensor is bolted on the actuator's head, in contact with a steel plate located on the beam's upper surface at mid-span. A diffuse light device shines on the freckled center zone of the beam. A camera captures the zone of interest during the test, for Digital Image Correlation (DIC) measurements. The setup is shown in Figure (3).

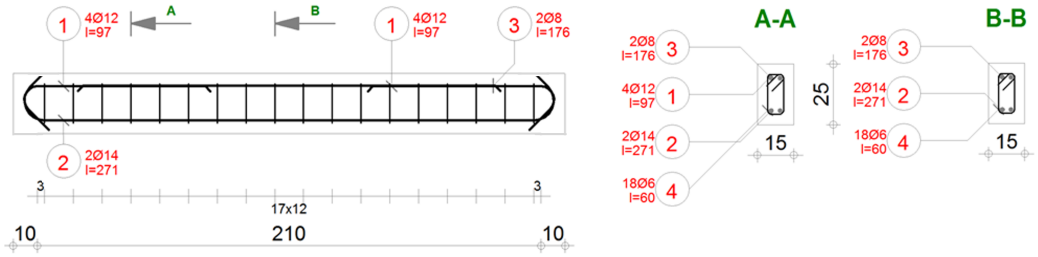


Figure 2: Beam and reinforcement dimensions ($cm$) - Campaign 00, 2021

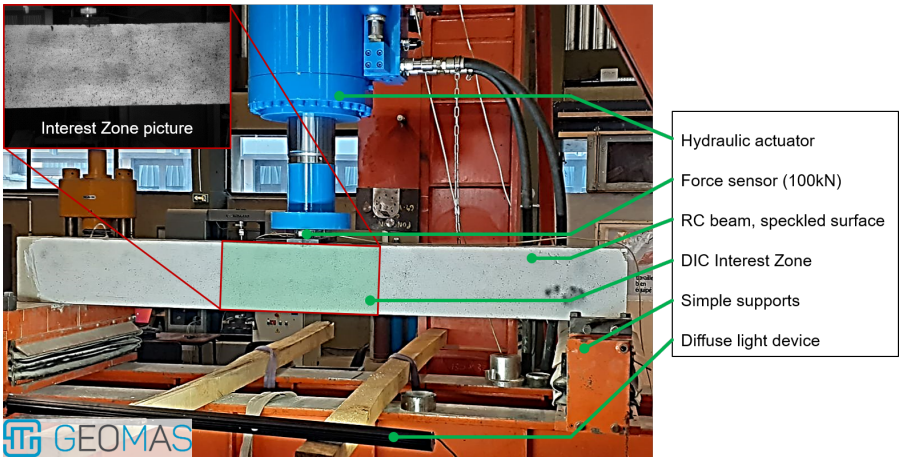


Figure 3: Experimental setup - Campaign 00, 2021

**Pushover tests** Two beams are subjected to a pushover test in three points bending conditions. To assess load rate dependency, two settings are used: 10mm/s for `Beam1P0` and 0.032 mm/s for `Beam2P0`.

**Classic PsD test** The classic PsD test is done on beam `Beam4PsDB`. Its response is that of a simply supported beam, carrying $M_p = 4500kg$, a *virtual* load taken into account using the PsD method. At time $t = 0s$, gravity is applied, simulating a bearing loss at mid-span. The system responses as a single DOF, and viscous damping is considered : $c = 2\xi\sqrt{K^I M_p}$; with $\xi = 5\%$, and $K^I = 5.7 \cdot 10^6 N.m^{-1}$ the averaged initial stiffness of beams `Beam1PO` and `Beam2PO`. The experimental setup is described in Figure (3).

**Sub-structured PsD test** PsD using sub-structuring is done on `Beam3PsDSS`: the experimental beam is part of a larger numerical model. The structure is meshed and modeled using 2D, *Euler-Bernoulli* kinematic Finite Elements, with 3 FEs along each post and beam. Only the lower beam is not modeled, as it corresponds to the experimental sub-structure. The full model is described in Figure (4).

For the sake of simplicity, the simulated part is considered elastic. Furthermore, the response is assumed symmetrical as the bearing loss happens on the central post. The following numerical values are used: a *Young*'s modulus of $21GPa$, a density of $2500kg$, and $5\%$ Rayleigh damping (applied on the $1^{st}$ and $5^{th}$ eigenmodes). Using those values, the numerical beams have stiffness values equivalent to those of the experimental ones.

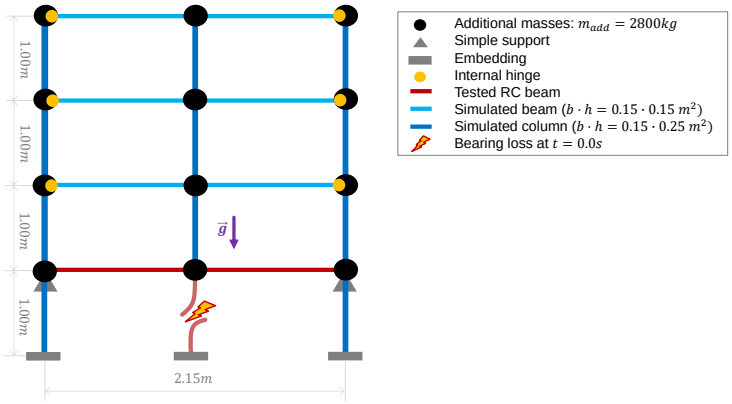


Figure 4: Diagram for the simple PsD test (`Beam4PsDB`)

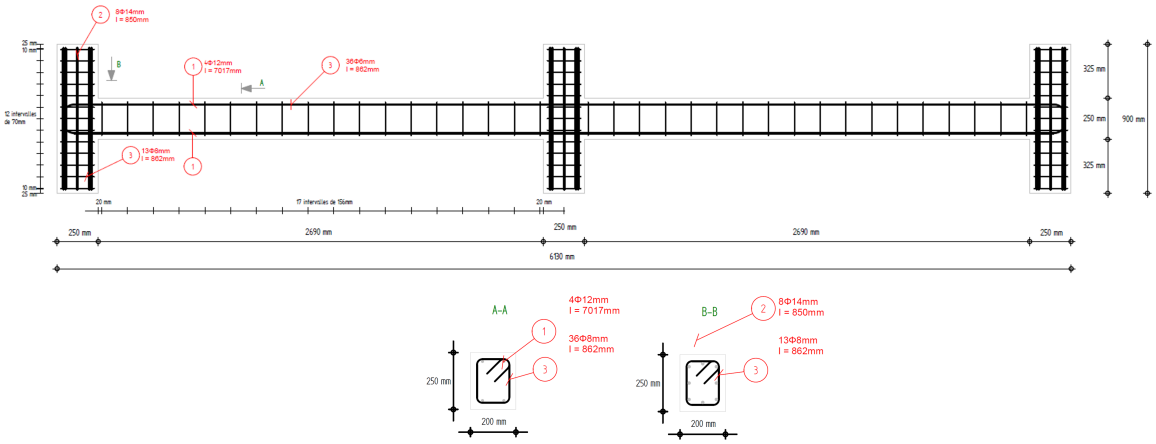


Figure 5: Beam and reinforcement dimensions - Campaign 01, 2023

### 2.2.2 Campaign 01 - 2023

This campaign features better controlled, more realistic boundary conditions, as well as representative RC beam size, geometry and design. Mechanical effects such as Tensile Catenary Action (TCA) and Compressive Arch Action (CAA) should be observed. The latters greatly influence a building's response during progressive collapse [1].

**RC beam characteristics** Beams feature specifically designed beam-column nodes. Dimensions are described in Figure (5). They are designed according to Eurocode 2 recommendations, regarding Service Limit State (SLS) and Ultimate Limit State (ULS). Variable design load is a $4.50 \cdot 10^3 N.m^{-2}$ surface load (which corresponds to a $26.4 \cdot 10^3 N.m^{-1}$ linear load). The concrete used is *C25/30-XC1-S3*, with *CEM I 52.5 N* cement. Steel rebars are *HA500 B*.

All beams will be tested after more than 28 days of curing. $16 \cdot 32cm^2$ cylindrical samples will be tested along with each beams. Steel reinforcement samples will also be tested, equipped with strain-gauges.

**Experimental setup** Ten structural members will be tested. Specific Boundary Conditions (BCs) have been developed, coming as close as possible to ideal embeddings. BCs will be instrumented to get transiting efforts. The hydraulic actuator will press on the central node's

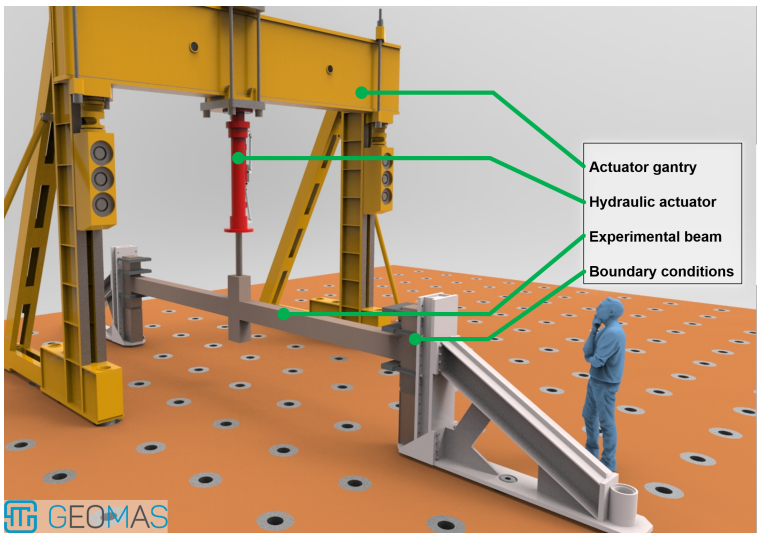


Figure 6: Experimental setup - Campaign 01, 2023

post, with force and displacement measured. 8 strain-gauges are glued on each beam's steel reinforcements. Lasers and LDVT displacement sensors, as well as speckled surfaces and camera with Digital Image Correlation (DIC) will complete the measuring apparatus. The general setup is represented in Figure(6).

## 3 RESULTS

### 3.1 Campaign 00 - 2021

#### 3.1.1 Multi-fiber FEM comparison model

A full numerical FE model has been used to validate the proposed approach. Multi-fiber FEs were used for the numerical comparison to the experiments. The *ATL4S* platform was used[4]. *Timoshenko* kinematics [5], concrete behavior based on the works of Laborderie [6], steel behavior based on a 1D model from Menegotto and Pinto [7]), and a *Newmark* integration scheme were used. For the sub-structured PsD test comparison, the numerical part remains modeled by *Euler-Bernoulli* kinematics with a linear behavior. Details of the numerical model can be found in [8].

#### 3.1.2 Pushovers

In total, 4 curves are obtained, as the PsD tests on `Beam4PsDB` and `Beam3PsDSS` also give force-displacement graphs. Mean stiffness and yield force are as follow: $K^I = 5.37 \cdot 10^6 N.m^{-1}$ ($\pm 20\%$) and $F_y = 57.5 \cdot 10^3 N$ ($\pm 5\%$). Figure (7) shows the force-displacements curves for all four beams. Those results were used to calibrate the numerical model described above.

#### 3.1.3 Classic PsD

Very good agreement between numerical and experimental results can be observed in Figure (8). Although the beam suffers significant damage, the beam's behavior is well depicted by the model. Slightly larger displacements and vibration period can be explained by the lower numerical stiffness (calibrated using the pushovers results). In terms of efforts, the yield plateau is very well reproduced.

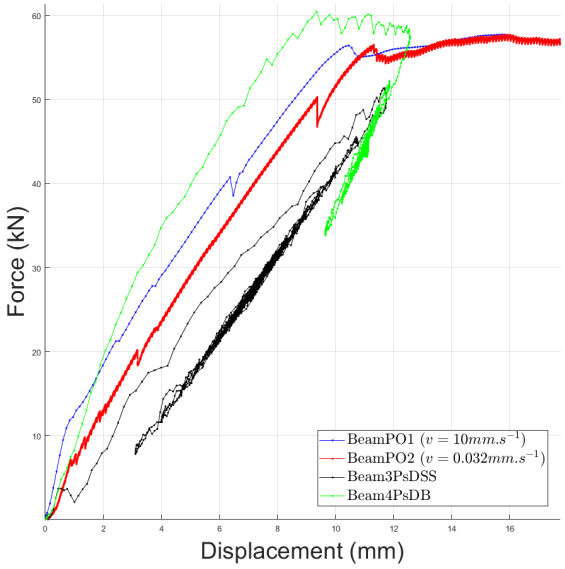


Figure 7: Force displacement curves of all beams

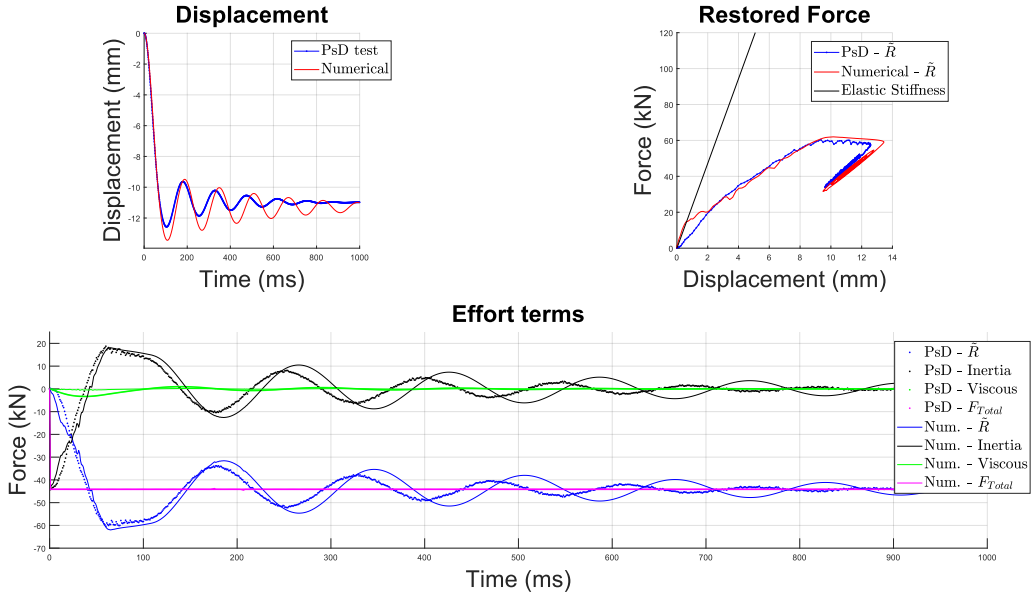


Figure 8: Experimental and numerical results, classic PsD test (`Beam4PsDB`)

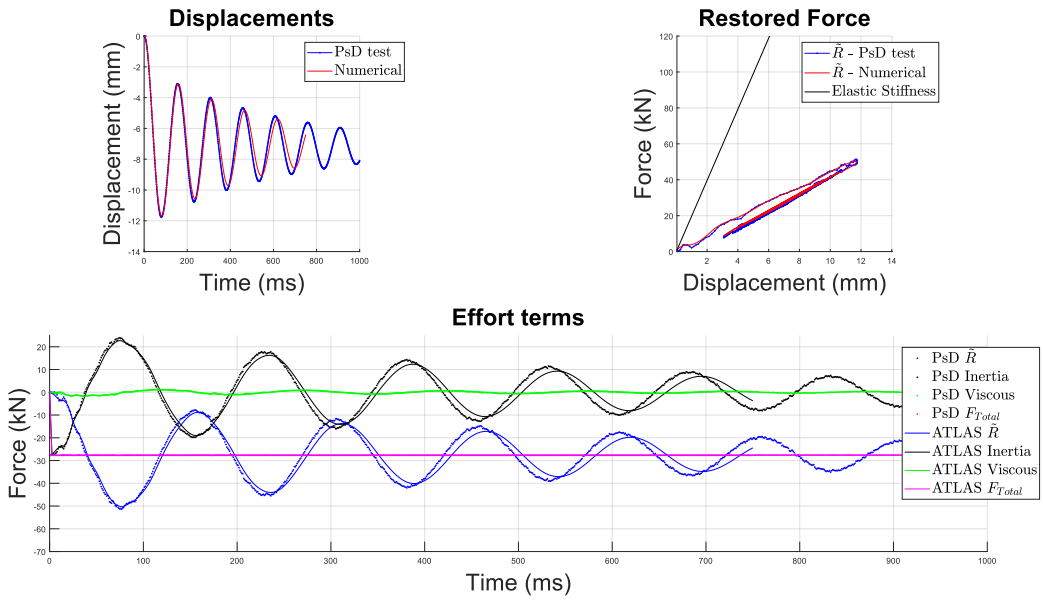


Figure 9: Experimental and numerical results, sub-structured PsD test (`Beam3PsDSS`)

### 3.1.4 Sub-structured PsD

Once again, the agreement between the model and the tested beam is very satisfactory, as shown in Figure (9). Displacements and vibration period are precisely represented by the numerical model. Furthermore, the internal efforts redistribution due to sub-structuring can be noted, as plastic damages on the beam are much lower than for the classic PsD test.

## 4 CONCLUSION AND PERSPECTIVES

### 4.1 Conclusion

A new way to assess the effect of loss of bearing capacity on civil engineering structures is proposed. The method is based on sub-structured Pseudo-Dynamic testing.

A very good agreement between non-linear multi-fiber models and experimental data is observed. Indeed, once calibrated, the same set of parameters is sufficient to describe the two different PsD tests (classical and sub-structured methods). In addition, pushover tests have shown that the structure's response is strain-rate independent. This legitimates the use of PsD testing, proving its robustness and showing its interest.

One of the method's main advantage is the setup's reduced cost and complexity. Physical tests are done only on the most affected parts, whilst still accounting for the remaining structure's influence. Sub-structured PsD tests on critical parts allows for a better capture of the non-linear response, compared to complex numerical models, which can prove tricky to calibrate when depicting severe non-linearities.

Another very important aspect is the methods' ability to numerically account for the and inertial forces. Thus, the dynamic response's analysis for full scale buildings is feasible using mainstream instrumentation rather than high-speed, high efforts, and high acquisition rate equipment. Tests' safety and control are improved, allowing for reproducible experiments.

### 4.2 Campaign 01's perspectives

As of the redaction of this paper, Campaign 01 is still underway. However, experimental results should yield answers regarding the method's ability to reproduce progressive collapse events on reinforced concrete civil engineering structures.

Larger experimentally tested sub-structured, with improved geometry and well designed beam-post integration will better represent real-life structures. Work on the boundary conditions' designs will also depict more realistically interactions between the tested sub-structure and the rest of the building. Physical phenomena such as Compressive Arch Action (CAA) and Tensile Catenary Action (TCA) should be observed. Futhermore, attention has been put on the beams' design following Eurocode 2 recommendations. The latter is driven by a realistic Service Limit State (SLS). The beams' properties come as close as possible to those of structural parts encountered in real estate.

Moreover, work on the simulated part will be done, as extension to non-linear numerical response is rather straight-forward for moderate damage representation. More extensive testing on concrete and steel samples should enable for good numerical calibration.

Finally, more instrumentation has been put in place: strain-gauges on reinforcements and boundary conditions, cameras, and a wider array of laser and LVDT displacement sensors.

## REFERENCES

[1] J. Adam, F. Parisi, J. Sagaseta, and X. Lu. Research and practice on progressive collapse and robustness of building structures in the 21st century. *Engineering Structures*, 173:122–149, 2018.

[2] D. Combescure and P. Pegon. $\alpha$-operator splitting time integration technique for pseudo-dynamic testing : Error propagation analysis. *Soil Dynamics and Earthquake Engineering,*, 1997.

[3] P. Pegon and A. Pinto. Pseudo-dynamic testing with substructuring at the elsa laboratory. *Earthquake Engng Struct. Dyn.*, 29:905–925, 2000.

[4] S. Grange. Atl4s plateform (a tool and language for simplified structural solution strategy). Technical report, INSA Lyon, 2009-2021.

[5] P. Kotronis and J. Mazars. Simplified modelling strategies to simulate the dynamic behaviour of rc walls. *Journal of Earthquake Engineering*, 9 (2):285 – 306, 2005.

[6] C. LaBorderie. *Phenomenes unilateriaux dans un materiau endommageable modélisation et application á l'analyse de structures en béton*. PhD thesis, Université Pierre et Marie Curie, 1991.

[7] M. Menegotto and P. Pinto. Method of analysis of cyclically loaded rc plane frames including changes in geometry and non-elastic behavior of elements under normal force and bending. Technical Report 13, Preliminary Report IABSE, 1973.

[8] D. Bertrand, S. Grange, and J.-B. Charrié. Progressive collapse analysis of rc frame building based on pseudo-dynamic (psd) testing with sub-structuring. *Journal of Building Engineering*, 52:104420, 2022.

COMPDYN 2023
9th ECCOMAS Thematic Conference on
Computational Methods in Structural Dynamics and Earthquake Engineering
M. Papadrakakis, M. Fragiadakis (eds.)
Athens, Greece, 12-–14 June 2023

# MODELING OF FRAMES WITH HYBRIDFEM, A PSEUDO-DISCRETE-FINITE MODEL INCLUDING NONLINEAR GEOMETRIC EFFECTS AND NONLINEAR MATERIALS

**Igor Bouckaert[1*], Michele Godio[2], João Pacheco de Almeida[1]**

[1]Institute of Mechanics, Materials and Civil Engineering, UCLouvain
Louvain-la-Neuve, Belgium
e-mail: {igor.bouckaert,joao.almeida}@uclouvain.be

[2] RISE Research Institutes of Sweden
Brinellgatan 4, 504 62 Boras, Sweden
e-mail: michele.godio@ri.se

**Abstract.** *In this paper, a novel numerical method for strucural analysis, called the Hybrid Discrete-Finite Element Method (HybriDFEM), is presented. In this method, a structure is modeled as an assembly of rigid blocks in contact. All the deformation is concentrated at the interfaces, which are modeled as series of distributed nonlinear multidirectional springs. The method shares similarities with the Discrete Element Methods (DEM) in its ability to account for contact interfaces and/or block deformability, and with the Applied Element Method (AEM) in the representation of interfaces as a series of normal and shear springs. However, it is close to the FEM in the way it is formulated, which offers the possibility to readily link both methods for potential hybrid applications. This paper focuses on the modeling of continuous and discontinuous frames with the HybriDFEM. It is shown how the model can do so with a nonlinear material model, and considering (or not) nonlinear geometric effects through large nodal displacements. Different nonlinear solution procedures implemented in HybriDFEM are demonstrated, such as load-control and various displacement-controlled methods. This model is able to simulmate contacts between rigid or deformable units, an important feature when it comes to the modeling of, e.g., unreinforced masonry structures, with a reasonable computational cost and a formulation that is cast within the framework of the classical FEM.*

**Keywords:** Hybrid modelling, Discrete Element Methods, Applied Element Method, $P-\Delta$ effects, masonry, frames, piers, spandrels

# 1 INTRODUCTION

In structural mechanics, accurately modeling interfaces is crucial when analyzing structures that present discontinuities, either for masonry (URM) structures that are discontinuous by nature, for cracked reinforced concrete (RC) members or for soil-structure interactions. The Finite Element Method (FEM) [5, 14], which is the most widely-used modeling technique amongst practitioners, is commonly used to model structures as a continuous medium. When discontinuities arise, FEM-based modeling techniques can use homogenization techniques to average the discontinuous behaviour over the element, or use micro-modeling approaches to account explicitly for discontinuous behavior [13, 11]. The former comes with an increased computational efficacy but at the price of a loss of precision in the results and representation of the physical response, whereas the latter requires a lot of computational power.

The Discrete Element Method (DEM) [4, 9, 1] is a family of modeling techniques that can represent more accurately the discontinuous nature of material assemblies but requires more computational resources. It models a structure as an assembly of rigid elements connected through deformable contact interfaces. All DEM formulations share the characteristic that a numerical time-stepping algorithm is required, resulting in a drastically higher computational time, and the incapacity to handle static or buckling problems. Other methods treat the problem as an assembly of rigid units interconnected by deformable interfaces modeled as distributed nonlinear multidirectional springs, making it suitable for analyzing large structures in static or dynamic problems. Various formulations, such as the Rigid Block model (RB) [12], the Rigid-Body-Spring Model (RBSM) [3], the Applied Element Method (AEM) [10] and the Fiber Contact Element Method (FCEM) [7, 6], are proposed to model discontinuities with this approach. These methods are interesting because they model the structure with a limited number of degrees of freedom (DoFs) considered at the structural level [15]. This paper introduces a new method called the Hybrid Discrete-Finite Element Method (HybriDFEM), which is capable of handling discontinuities in structures. This method extends the existing FCEM method by incorporating nonlinear geometric and material models. The HybriDFEM involves a collection of rigid rectangular blocks (how block deformability can be taken into account will be explained after) interacting with each other through interfaces composed of distributed nonlinear springs, similarly to the AEM. In Section 2, some theoretical developments of the method will be covered. Then, a first benchmark problem will be introduced in Section 3, showing the ability of the HybriDFEM to model the behaviour of a continuous frame, including $P-\Delta$ effects. The results of this benchmark problem will be compared against classical FEM formulations. In Section 4, a simple masonry portal frame composed of multiple discontinuous, rigid blocks, will be simulated. The failure mechanism and the collapse load multiplier of the frame will be compared against analytical solutions from limit analysis.

# 2 THEORETICAL DEVELOPMENTS

## 2.1 Block discretisation

In the HybriDFEM method, a planar structure is modeled as a series of rigid blocks in contact through contact faces (CFs). The discretisation of the structure in $n_b$ blocks defines the total number of DoFs considered at the global level. The motion of a block is described by three kinematic variables, two translations and one rotation, which are stored in the vector of nodal displacements $\mathbf{U}$. The kinematic variables of a generic block $i$ are the displacements $U_{3i-2}$, $U_{3i-1}$ and $U_{3i}$, expressed in the global reference system $(X, Y)$. The block discretisation of a beam is shown in Figure 1.

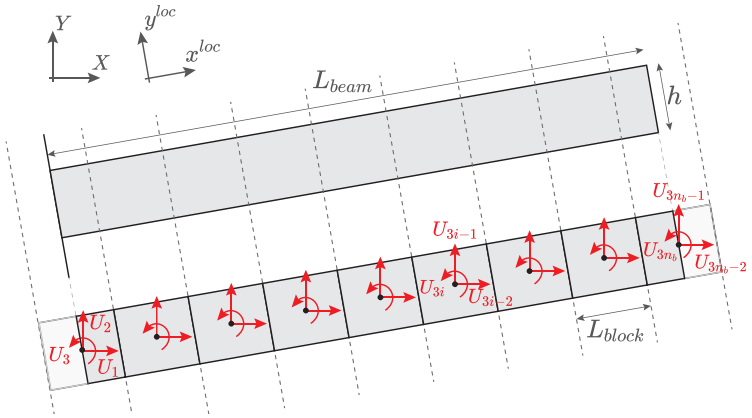


Figure 1: Block discretisation and kinematic variables of a beam at the structural level [2].

## 2.2 Contact pair discretisation

Each CF is further subdivided into a series of $n_c$ contact pairs (CPs) evenly distributed along the interface between two blocks (Figure 2b). One CP consists of three points $A$, $B$ and $C$. The two first are respectively fixed to the edge of the first and second block. A nonlinear spring is attached to point $A$ and connected to another nonlinear spring attached to point $B$ through a hinged contact point $C$ (Figure 2c). The kinematics of the contact pair is described by eight DoFs in total. The three first refer to the displacement of point $A$ and its spring's orientation, which follows the orientation of the block to which it is attached. Similarly, the three next DoFs of the CP refer to the displacement of point $B$ and its spring's orientation. The last two DoFs refer to the displacement of point C and will be condensed for the computations at the structural level.

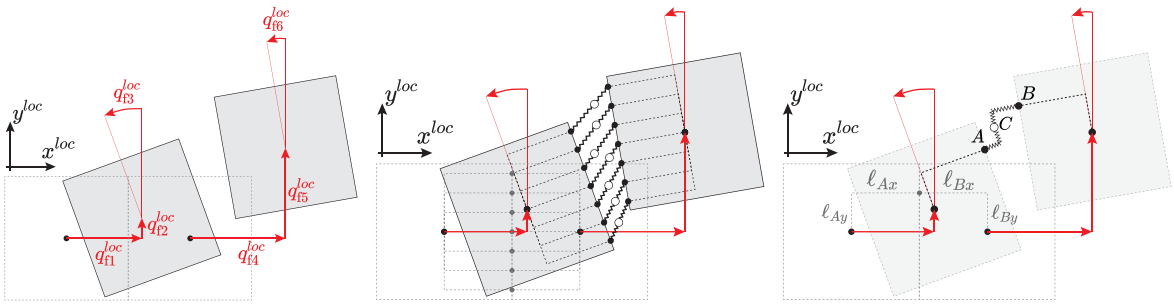


(a) (b) (c)

Figure 2: (a) Block kinematics in the local reference system (b) contact pair discretisation of the contact face (c) Isolated contact pair [2].

The kinematics of the six first DoFs of the CP can be derived solely through compatibility relations, since the position of $A$ and $B$ with respect to their respective blocks does not change, and the blocks are rigid. These first six DoFs of each CP can be directly related with the six DoFs of the adjacent blocks, $q_1^{loc}$ to $q_6^{loc}$, represented in Figure 2a. To derive the position of point $C$ (i.e., the last two DoFs of each CP), however, the relative elongations of the two pairs

of springs need to be known. They can be derived through a set of two linear equations relative to compatibility and two possibly nonlinear equations relative to equilibrium. The former states that the total CP deformation must be equal to the sum of elongation of the first and second spring, both in the normal and tangential directions (Figure 3a). By isolating the deformation of the CP without considering its rigid-body motion, nonlinear geometry is accounted for. The equations relative to equilibrium state that the forces through spring $A$ must be equal to the forces through spring $B$ (Figure 3b). These forces depend on the constitutive relations assigned to the springs, relating the spring elongation with the spring forces. The constitutive relations can represent either the behaviour at the contact between the two blocks (e.g. when modeling assemblies of rigid blocks) or can be scaled to represent the behaviour of a continuous material, where the deformation of the block is concentrated at each CF. By assigning a nonlinear constitutive relation to the springs, nonlinear material effects can be included.

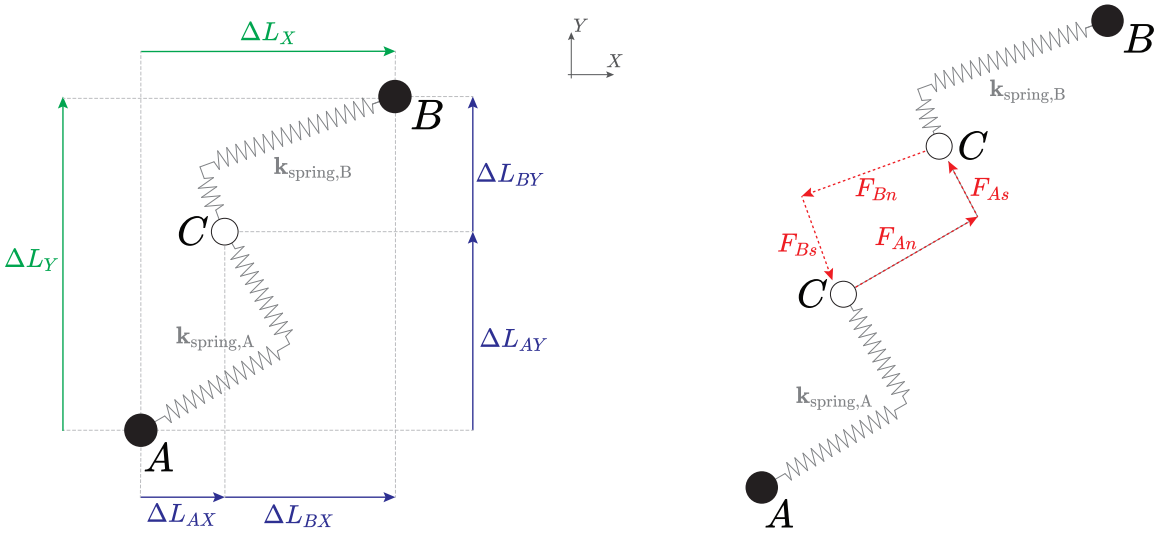


Figure 3: (a) Compatibility relation of the CP and (b) equilibrium of spring forces used to determine the position of point $C$, the relative spring elongations, and the spring forces [2].

The set of nonlinear equations relative to compatibility and equilibrium is solved by means of a Newton-Raphson solution procedure, at the end of which the forces through the springs attached to $A$ and $B$ are known, along with their relative elongations and the displacement of point $C$. This nonlinear solution procedure is referred to as the internal solution procedure, as opposed to the external solution procedure at the global level, common to the nonlinear FEM, which will be described in section 2.3.

From the spring forces, the resisting forces of each CP can be derived by equilibrium in the deformed configuration, which allows to account for nonlinear geometric effects. Finally, the resisting forces of each CF can be computed by assembling the resisting forces of all of its CPs, and the resisting forces $\mathbf{P}_r$ of the structure can be computed by assembly of the resisting forces of all CFs.

### 2.3 Solution procedure at the structural level

The steps described hereabove can be used to derive the resisting forces $\mathbf{P}_r$ of the structure associated to a given set of nodal displacements $\mathbf{U}$. From the constitutive relation assigned to the springs, an incremental relation between the spring forces and spring elongations can be derived, which corresponds to the tangent stiffness matrix of the springs. The tangent stiffness matrices of the two springs composing one CP can be used to assemble the tangent stiffness matrix of the CP, which can then be assembled into the tangent stiffness matrix of the contact face. Finally, the tangent stiffness matrix of the structure can be assembled from the stiffness matrices of all the CFs. In the case of linear elastic structures, this stiffness matrix can be used to relate directly the nodal displacements stored in $\mathbf{U}$ to the global resisting forces $\mathbf{P}_r$, and equilibrium with a given set of applied forces $\mathbf{P}$ can be found by inverting such tangent stiffness matrix (or, computationally, any solution method for linear equations). When nonlinear effects are considered, however, the nodal displacements equilibrating the resisting forces with the applied forces cannot be computed by matrix inversion, and an incremental solution procedure is required. Such incremental-iterative solution procedure, which can be for instance a Newton-Raphson (load-control), displacement-control, or work-control procedure [5], computes the tangent stiffness matrix of the structure at each iteration to achieve quadratic convergence. This solution procedure, as well as a detailed account of all the equations expressing the operations described in this Section 2, can be found elsewhere [2].

## 3 MODELING OF A CONTINUOUS FRAME WITH $P-\Delta$ EFFECTS

In this benchmark, the capacity of the HybriDFEM to approximate the behaviour of continuous structures despite its discontinuous nature, is demonstrated. This example also shows how it can capture nonlinear material and geometric effects, and how it can be coupled with classical finite elements to increase its computational efficacy.

this example consists of a one-storey one-bay $3$ m$\times 3$ m frame, in which the flexural stiffness of the columns equals twice the flexural stiffness of the beam, which is assumed to have a square cross-section of $h \times b = 0.2$ m$\times 0.2$ m. The two columns are simply supported. The material law assigned to both the column and the beam is an elastic-perfectly plastic law of the type

$$\begin{cases} \sigma = \varepsilon E_0 & \text{when} \quad \mid \varepsilon \mid \leq \varepsilon_y \\ \sigma = f_y & \text{when} \quad \mid \varepsilon \mid > \varepsilon_y \\ \tau = \gamma G_0 \end{cases}, \tag{1}$$

where $E_0 = 30$ GPa, $G_0 = 15$ GPa and $f_y = 20$ MPa.

The response of the frame is evaluated with three different models:

(a) A simple FEM model built with three Timoshenko beam elements (Figure 4a) for which nonlinear geometric effects can be included, but restricted to linear elastic response;

(b) A coupled FEM-HybriDFEM model where the columns are modeled with one such Timoshenko beam element each and the beam is modeled with one HybriDFEM element, with 40 blocks and 30 CPs per block (Figure 4b);

(c) A full HybriDFEM model where both the columns and the beams are modeled with 40 blocks and 30 contact pairs at each interface (Figure 4c).

At its current state of development, the HybriDFEM code can only handle beam-like members (one-directional members), which can be connected through rigid-node connections. Therefore, the beam and the columns are each modeled as three distinct beam-like members, and the centroid of their extremity blocks are connected through a rigid-node connection.

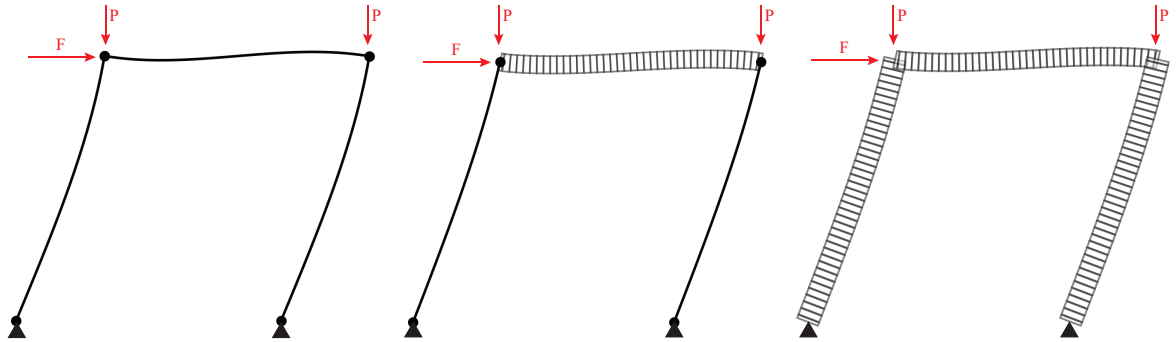


Figure 4: (a) full FEM model (b) coupled HybridFEM (beam)- FEM (columns) model (c) full HybriDFEM model at a horizontal displacement of 5 cm. The deformations are magnified by a factor of 20.

The lateral capacity of the frame is evaluated by applying a horizontal force $F$ at the centroid of the block located at the top left corner. The value of the applied force is controlled by means of a displacement-control monitoring the horizontal displacement $\Delta$ of the top left corner, with increments of $1$ mm up to $65$ mm. The additional weight of possible upper storeys is represented by two constant vertical downward forces of $P = 100$ kN applied at the top left and top right corners of the frame.

At first, the pushover curves of the three models are computed neglecting $P - \Delta$ effects, i.e. assuming linear geometry. For an Euler-Bernoulli beam, the horizontal force at which the material will start yielding, $F_y = 17.8$ kN can be derived analytically. Using the beam plastic moment, it is also possible to derive the maximal capacity of the frame, $F_{max} = 26.7$ kN (Figure 5a). The response of the frame in the linear range is compared with the linear FEM model, and the pushover curve of the full HybriDFEM model can be compared with the coupled FEM-HybriDFEM model, under the observation that with the HybriDFEM plastification occurs in the beam and not in the columns.

The deformed shapes of the three models at the end of the simulation, magnified by a factor of 20, are visible in Figure 4. The force-displacement response associated to the three models is visible in Figure 5a. The curves of the coupled and the full HybriDFEM model plateau at $27.3$ kN, which corresponds to a $2.3\%$ increase in maximal capacity with respect to the analytical value. The first yielded CP appears at a displacement of $21$ mm, at which the applied force equals $18.43$ kN, corresponding to a $3.5\%$ relative error with respect to the analytical value. The stresses in the beam and its deformed shape at a displacement of $\Delta = 50$ mm (Figure 6) highlight the formation of the plastic hinges at the extremities of the beam. No yielding was observed in the columns with the full HybriDFEM model, as expected. The three models show excellent agreement in the linear range. Beyond yielding, the linear FEM model can evidently not be compared with the two others. However, the pushover curve obtained with the coupled model matches very well the curve obtained with the full HybriDFEM model, since the columns

continue to behave elastically throughout the entire response. The computational time necessary to run the coupled model is 3.5 times less than that required to run the full HybriDFEM model, which illustrates one of the computational advantages of the present proposal.

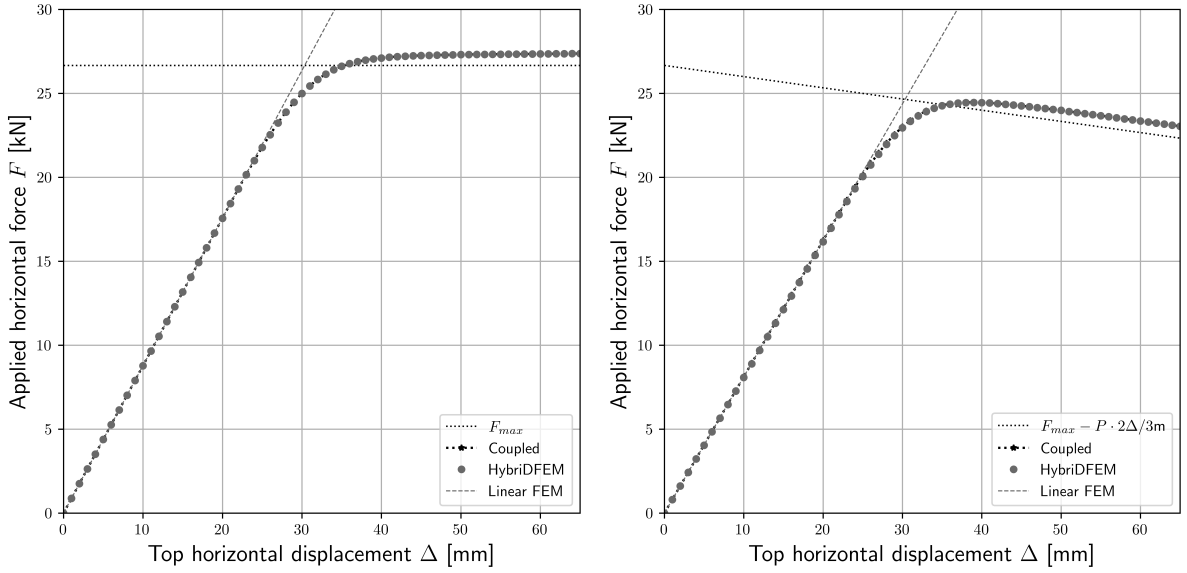


(a) (b)

Figure 5: Force-displacement curves of the frame (a) neglecting $P - \Delta$ effects, and (b) considering $P - \Delta$ effects .

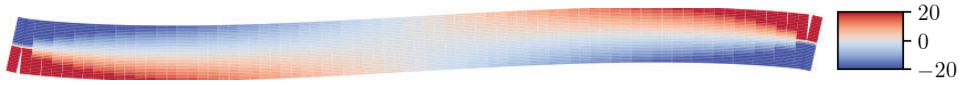


Figure 6: Stresses in the beam, in MPa, highlighting the presence of plastic hinges at the extremities of the beam.

The same three models are run considering nonlinear geometric effects. In that case, the descending branch of the pushover curve, after the plastic hinges have formed, can be derived analytically and corresponds to a horizontal line of equation $F = F_{max} - P \cdot 2\Delta/3$ m in the $F - \Delta$-plane. The responses of the three models in the linear material range, before the material yields, once again compare very well. As expected, the slope of the ascending branch is slightly lower than when nonlinear geometric effects were neglected due to the $P-\Delta$ effects. After the peak, when the plastic hinges have formed, the pushover curves of the coupled and full HybriDFEM model descend along a line parallel to the analytical one, with an error comparable to the linear case, displaying a slightly higher capacity than the analytical value. Again, the two pushover curves of the coupled and HybriDFEM model show negligible difference.

This benchmark highlights the capacity of the HybriDFEM to capture nonlinear geometric effects, with accurate simulation of the $P - \Delta$ effects in the frame, and nonlinear material effects with the appearance of plastic hinges in the beam modeled with the HybriDFEM. It also highlights the possibility to straightforwardly couple the HybriDFEM with classical FEM

formulations in zones of the structure that remain linear-elastic, making the simulation computationally more efficient. Finally, it shows that the HybriDFEM can model accurately frames made of a continuous material, despite the discontinuous nature of its formulation.

## 4 MASONRY FRAMES

This benchmark is taken from Giordano et al. [8], in which analytical formulae to determine the collapse load multiplier of a heavy masonry frame are derived through kinematic analysis. The collapse load multiplier $\alpha$ is defined as the ratio between $F_{max}$ and $W_{tot}$, where the former is the horizontal force leading to collapse and applied at the top left corner of the frame, and the latter is the total weight of the masonry frame (Figure 7): $W_{tot} = W_1 + W_2 + W_3 + W_4 + W_5$, where $W_1$,...,$W_5$ refer to the weight of each of the blocks. The geometry of the frame and the considered forces are visible in Figure 7. The analytical formulae have been derived under the assumptions that cracks can only occur at the pier-to-spandrel connections (dashed lines in Figure 7), no tensile strength, infinite compression strength transferable across the cracks, and no sliding between blocks is allowed. Finally, the blocks are considered as rigid units and undergo only small displacements.

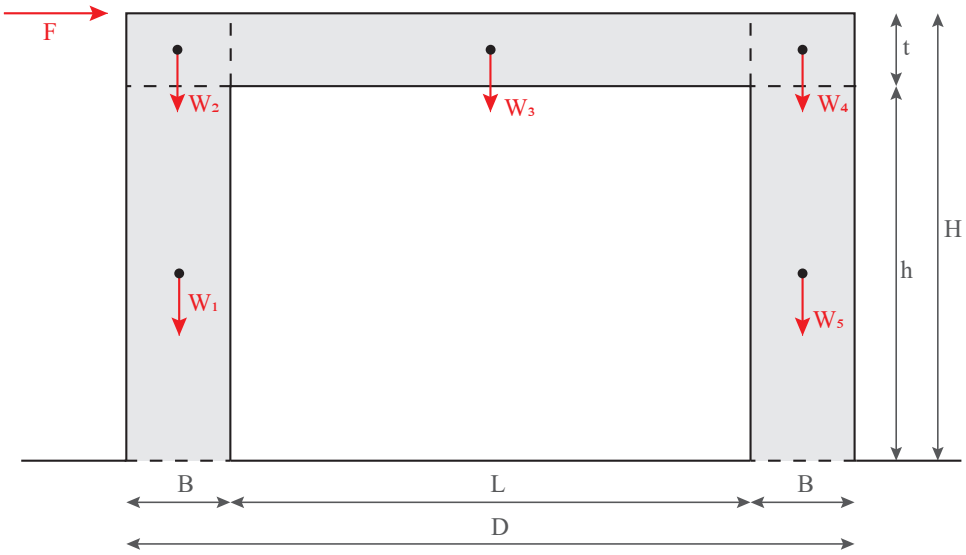


Figure 7: Geometry of the masonry frame with the applied forces. The possible crack lines are indicated with a dashed line.

Under these assumptions, the frame behaves as a rigid-block assembly of 5 macroblocks, and the collapse of the frame occurs by the formation of at least four hinges located on interfaces between rigid blocks. Since there are six interfaces, the total number of possible collapse mechanisms is 15. In [8], the analytical expression of the collapse load multiplier has been derived for only four of these 15 possible mechanisms, which are shown in Figure 8.

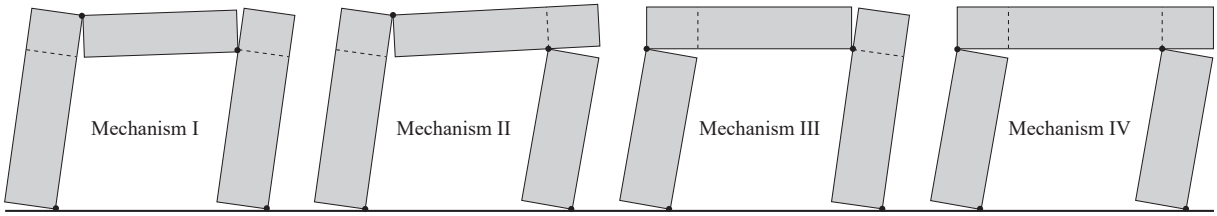


Figure 8: Collapse mechanisms considered in Giordano et al. [8].

The same frame has been implemented in the HybriDFEM code, with a height-to-width ratio $H/D$ equal to 1. The model is composed of seven blocks in total: the five macroblocks composing the frame, and one block under each pier representing the supports. These two base blocks are fixed in the three directions. The interface between each of the blocks is modeled as a no-tension interface, by assigning the following contact law to the contact faces:

$$\begin{cases} \sigma = 0 \quad \text{and} \quad \tau = 0 & \text{when} \quad \varepsilon > 0 \\ \sigma = \varepsilon E_0 & \text{when} \quad \varepsilon \leq 0 \end{cases}, \tag{2}$$

in which $E_0$ is set to a very large value in order to approximate a rigid interface in compression. The self-weight of each macroblock is applied at its centroid, and the horizontal force $F$ is applied at the top left corner of the frame. This force is controlled by means of a displacement-control procedure on the horizontal displacement of the spandrel block. Considering that the collapse of the structure occurs when the program is not able to converge to an equilibrium solution, the collapse load multiplier $\alpha_{Num}$ of the frame is computed as the force $F$ applied at the last converged step divided by the total weight. Since this value of load multiplier corresponds to a structure on the brink of collapse, but still in equilibrium, it is expected to be slightly lower than the value of collapse load multiplier computed analytically.

Table 1 gives the collapse load multipliers obtained with the HybriDFEM model, and compares them with the ones obtained with kinematic analysis [8], for a ratio $B/D$ ranging from 0.1 to 0.4 and a ratio $t/H$ ranging from 0.1 to 0.3. The percentage error between both values, which corresponds to the difference between the numerical and analytical value, divided by the analytical one, is also provided. The load multipliers obtained with the HybriDFEM compare well with the analytical ones, with a maximal error of -2.45%. As expected and discussed, the numerical load multiplier is always slightly smaller than the analytical one. All simulations with $B/D = 0.4$ triggered the collapse mechanism III (Figure 9a), which corresponds to what was predicted analytically [8]. However, while the expected collapse mechanism for all other values of $B/D$ was mechanism I, the HybriDFEM model triggered a fifth collapse mechanism (Figure 9b) that was not taken into account in the original paper. These frames were run again with only three macroblocks in order to force mechanism I, and the associated value of $\alpha_{num}$ was always slightly higher than the one triggering mechanism V, but still lower than the analytical collapse load multiplier associated to mechanism I. This tends to indicate that the choice to consider only four mechanisms out of the 15 possible was not always conservative, even if the load multiplier associated to the fifth mechanism was never less than 2% lower than the one associated with Mechanism I.

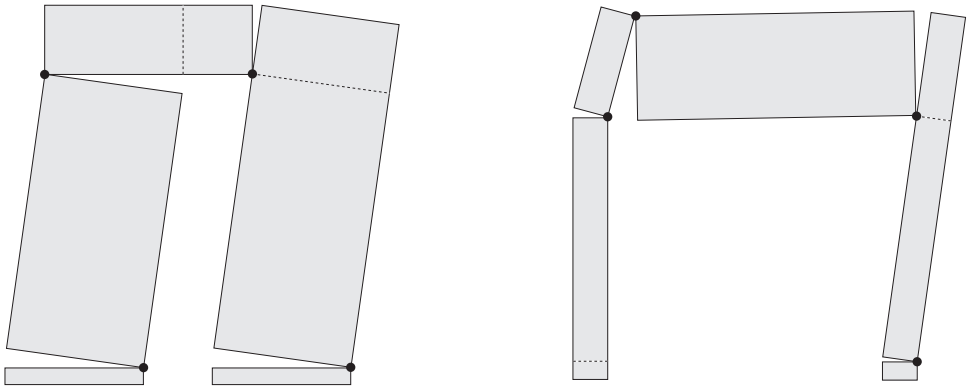

(a) (b)

Figure 9: (a) Mechanism III triggered for $t/H = 0.2$ and $B/D = 0.4$ and (b) Mechanism V triggered for $t/H = 0.3$ and $B/D = 0.1$ with the HybriDFEM.

| $t/H$ $\downarrow$ | $B/D$ $\rightarrow$ | 0.1 | 0.2 | 0.3 | 0.4 |
|---|---|---|---|---|---|
| 0.1 | $\alpha_{LA}$ | 0.054 | 0.109 | 0.165 | 0.238 |
| | $\alpha_{Num}$ | 0.053 | 0.107 | 0.167 | 0.235 |
| | Err. [%] | -1.98 | -1.56 | -1.20 | -1.26 |
| 0.2 | $\alpha_{LA}$ | 0.06 | 0.122 | 0.195 | 0.286 |
| | $\alpha_{Num}$ | 0.059 | 0.121 | 0.193 | 0.282 |
| | Err. [%] | -2.45 | -1.13 | -1.09 | -1.40 |
| 0.3 | $\alpha_{LA}$ | 0.07 | 0.144 | 0.247 | 0.346 |
| | $\alpha_{Num}$ | 0.069 | 0.142 | 0.245 | 0.342 |
| | Err. [%] | -0.98 | -1.10 | -1.10 | -1.15 |

Table 1: Collapse load multipliers obtained analytically from [8] ($\alpha_{LA}$) and numerically with the HybriDFEM ($\alpha_{Num}$).

## 5 CONCLUSIONS

The HybriDFEM method presented in this paper as an extension of the Fibre Contact Element Method (FCEM) [7], models a structure as an assembly of rigid blocks. This method shares similitudes with the Applied Element Method (AEM) in that the deformation is concentrated at the block interfaces, which are modeled as distributed nonlinear springs. But it also differs from it in the measure that it can include springs connected in series at the interfaces, allowing to differentiate, for instance, the relative deformations of two blocks made of a different material. The HybriDFEM, which is discontinuous by nature, can be used as a proxy to model continuous structures through the use of scaled spring constitutive models [2]. Here it was shown that several members can be connected through rigid-node connections in order to model discontinuous frames.

After a brief overview of the theoretical developments of the method, two benchmark problems have been implemented and compared with classical FEM or analytical solutions. The first benchmark, which consisted of a frame made of a continuous material, highlighted the capacity

of the method to capture nonlinear geometric effects (here $P - \Delta$ effects) and to use nonlinear material models (here an elastic-perfectly plastic material). It was shown that the HybriDFEM could be coupled with a classical Timoshenko beam element accounting for nonlinear geometric effects. The second benchmark consisted of a masonry portal frame in which the crack lines were pre-defined at the pier-to-spandrel connections. The frame has been modeled as an assembly of five rigid blocks assembled through rigid no-tension interfaces. The horizontal capacity of the masonry frame with different geometries has been computed with the HybriDFEM and compared with analytical values from the literature. The results showed a maximum relative error of -2.45% between the HybriDFEM and the analytical values, and expanded the number of possible collapse mechanisms to include those that were not considered in [8].

Ongoing developments of the HybriDFEM include the extension to dynamic problems, the modeling of reinforced concrete (RC) beams and the extension to two-directionally spread members. The formulation is developed with the intention to resemble that of a classical FEM, allowing hybrid simulations to be carried out with small computational demand, while simultaneously and explicitly modelling discontinuities.

## 6 Acknowledgements

The first author is thankful for the financial support given by UCLouvain.

## REFERENCES

[1] D. Baraldi, E. Reccia, and A. Cecchi. In plane loaded masonry walls: Dem and fem/dem models. a critical review. *Meccanica*, 53(7):1613–1628, 2017.

[2] I. Bouckaert, M. Godio, and J. Almeida. A hybrid discrete-finite element method for modeling continuous and discontinuous beam-like members including nonlinear geometric and material effects. *Under review*, 2023.

[3] S. Casolo and G. Uva. Nonlinear analysis of out-of-plane masonry façades: full dynamic versus pushover methods by rigid body and spring model. *Earthquake Engineering Structural Dynamics*, 42(4):499–521, 2013.

[4] P. A. Cundall. A computer model for simulating progressive large scale movements in blocky rock systems. In *Symposium of the International Society for Rock Mechanics*, volume II-8. Society for Rock Mechanics (ISRM).

[5] R. de Borst, M. A. Crisfield, J. J. C. Remmers, and C. V. Verhausel. *Non-Linear Finite Element Analysis of Solids and Structures*. Wiley Series in Computational Mechanics. Chichester, 2 edition, 2012.

[6] J. M. C. Estêvão and A. S. Carreira. Using the new fibre contact element method for dynamic structural analysis. *Engineering Structures and Technologies*, 7(1):24–38, 2015.

[7] J. M. C. Estêvão and C. S. Oliveira. A new analysis method for structural failure evaluation. *Engineering Failure Analysis*, 56:573–584, 2015.

[8] A. Giordano, A. De Luca, E. Mele, and A. Romano. A simple formula for predicting the horizontal capacity of masonry portal frames. *Engineering Structures*, 29(9):2109–2123, 2007.

[9] J. Lemos. Discrete element modeling of the seismic behavior of masonry construction. *Buildings*, 9(2):43, 2019.

[10] K. Meguro and H. Tagel-Din. Simulation of buckling and post-buckling behavior of structures using applied element method. *Bull. ERS*, 32, 1999.

[11] A. Munjiza and J. P. Latham. Computational challenge of large scale discontinua analysis. *Third International Conference on Discrete Element Methods*, 2002.

[12] F. P. A. Portioli. Rigid block modelling of historic masonry structures using mathematical programming: a unified formulation for non-linear time history, static pushover and limit equilibrium analysis. *Bulletin of Earthquake Engineering*, 18(1):211–239, 2020.

[13] P. Roca, M. Cervera, G. Gariup, and L. Pela'. Structural analysis of masonry historical constructions. classical and advanced approaches. *Archives of Computational Methods in Engineering*, 17(3):299–325, 2010.

[14] W. Rust. *Non-Linear Finite Element Analysis in Structural Mechanics*. 2015.

[15] H. Tagel-Din and K. Meguro. Applied element simulation for collapse analysis of structures. *Bull. ERS*, 32, 1999.

COMPDYN 2023
9th ECCOMAS Thematic Conference on
Computational Methods in Structural Dynamics and Earthquake Engineering
M. Papadrakakis, M. Fragiadakis (eds.)
Athens, Greece, 12-14 June 2023

# ADVANCES IN 3D NUMERICAL SIMULATION OF SEISMIC RESPONSE OF SAFETY-RELATED NUCLEAR STRUCTURES

**Fernando Rastellini[1,2], Junior Ramirez[1], José Manuel Gonzalez[2], Alex H. Barbat[2], Cuauhtémoc Escudero[1], Yeudy F. Vargas[2] and Luis G. Pujades[2]**

[1] Centre Internacional de Metodes Numerics a l'Enginyeria (CIMNE)
Gran Capitan s/n, 08034, Barcelona, Spain.
e-mail: frastellini@cimne.upc.edu, {jramirez, cuauhtemoc}@cimne.upc.edu

[2] Universitat Politecnica de Catalunya (UPC)
Jordi Girona 1-3, 08034, Barcelona, Spain.
{fernando.rastellini, jose.manuel.gonzalez, alex.barbat, yeudy.felipe.vargas, lluis.pujades}@upc.edu

## Abstract

*In the event of an earthquake at a nuclear power plant, it is vitally important to ensure the survival of personnel and the integrity of high-value equipment. The objective of this study is to analyze the dynamic response of a safety-related nuclear structure subjected to near-margin seismic signals and to calculate the corresponding in-structure response spectra. A set of seed signals conveniently extracted from databases are selected to generate seismic signals compatible with the target spectrum. These signals are translated to the bedrock level using an iterative deconvolution process. The numerical modeling considers the non-linearities coming from the structural behavior and from the sliding and rocking at the soil-structure interface. The FEM model includes the soil layers up to the bedrock and cyclic symmetry conditions at the lateral boundaries. Reinforced concrete is modeled using the mixture theory that allows combining non-linear constitutive models of damage and plasticity. The floor spectra are calculated in the positions corresponding to the equipment. Finally, the results show how the non-linearity of the material hardly affects the global response of the analyzed structure. However, the sliding nonlinearity significantly affects the response spectrum of the structure, reducing maximum acceleration peaks.*

**Keywords:** Seismic Hazard Analysis, Equipment Safety, Safety-related Nuclear Structure, Material Non-linear Analysis, Sliding Contact Interface.

## 1 INTRODUCTION

After the "Fukushima I NPP" event on March-2011, a reassessment of the current nuclear facilities, in the face of demanding earthquakes, appeared to be necessary, incorporating non-linearities in the structural analysis. Modifications have been also proposed in the calculation standards to include non-linearities [1].

A safety-related structure of a NPP is studied herein. Since its analysis involves non-linearities, a complete time integration is carried out, what allows capturing the entire seismic response of the structure. For this reason, a FEM code with explicit integration is chosen.

As input data, the geometry of the structure discretized in finite elements is required, including the properties of its materials and the profile of the underlying soil layers. A set of seed signals are adjusted to target spectrum. These seismic signals are deconvolutioned to the bedrock and applied to the computational model.

The main result is the seismic response of the structure in terms of displacements, velocities, accelerations, and also the levels of damage or plastic strains in each material point of the structure. These first results are post-processed to obtain in-structure response spectra (ISRS), also called floor spectra.

## 2 GENERATION OF SEISMIC ACCELEROGRAMS

The reference seismic signal is defined as the Seismic Margin Earthquake (SME). The target spectrum corresponds to the UHS spectrum calculated, using the probabilistic seismic hazard method [2], at the foundation base level with the seismic parameters at the location of the building. A seismic source identified as near-field signal with a magnitude of 6.3 and an epicentral distance of 2km. Existing acceleration time histories (seed signals) are selected from the database of the *Pacific Ocean Earthquake Research Center (PEER)*[1]. These signals are fitted to the target spectrum for the nuclear construction site, using a spectral matching technique that modifies the frequency content of the seed signal. For this calculation, the wavelets algorithm proposed by Abrahamson [3, 4] or the algorithm proposed by Al-Atik [5] may be employed.

A family of seven acceleration time histories defined for the three spatial directions {X, Y, Z} is defined to account for the variability and uncertainty of ground motion. Satisfactory adjustments to the target spectrum is obtained in all of them. In near-field motions, the directionality of the signal is determined by the short distance to the seismic source. To consider this variability, the following directionality factors have been considered: {0.81, 0.89, 0.94, 1.0, 1.06, 1.13, 1.23} and applied to the family of seven signals employed in this analysis. It should be noted that these signals are defined at the surface level, at the level of the foundation of the structure. Subsequently, they must be deconvolutioned to the bedrock of the soil model, also considering the uncertainty of the soil properties.

The soil profile below the structure's foundation is obtained from the existing geological data. To address the uncertainty of the mechanical characteristics of the soil layers, a statistical dispersion study is carried out on the geological soil profile. In this way, a sample of 1000 soil profiles has been generated following a correlation according to the Toro model [6] and considering the following criteria:

- Geophysical properties, such as shear wave velocity (Vs), damping, and layers density, follow a log-normal distribution with a median value equal to the base profile and a dispersion coefficient of 0.35.

[1]PEER Database Website: https://ngawest2.berkeley.edu/ (last accessed 04/07/2021)

- The thicknesses of the soil layers are considered to be invariant, and are not subject to statistical dispersion. This simplifies the subsequent geometric modeling of soil layers.

Three different soil profiles are extracted, thus: Upper Bound (UB), Best Estimate (BE) and Lower Bound (LB), corresponding to percentiles 16%, 50% and 84% of the sample population, respectively. In this way, the three representative profiles are defined by the shear wave velocity (Vs), the damping ratio (ξ) and the density (ρ). Figure 1 shows the shear wave velocity and damping ratio for these profiles. The Young's modulus for each soil layer is calculated as a function of the shear wave velocity [7, 8]. Consequently, the Poisson's ratio is obtained from the elastic relationship between Young and shear modulus.

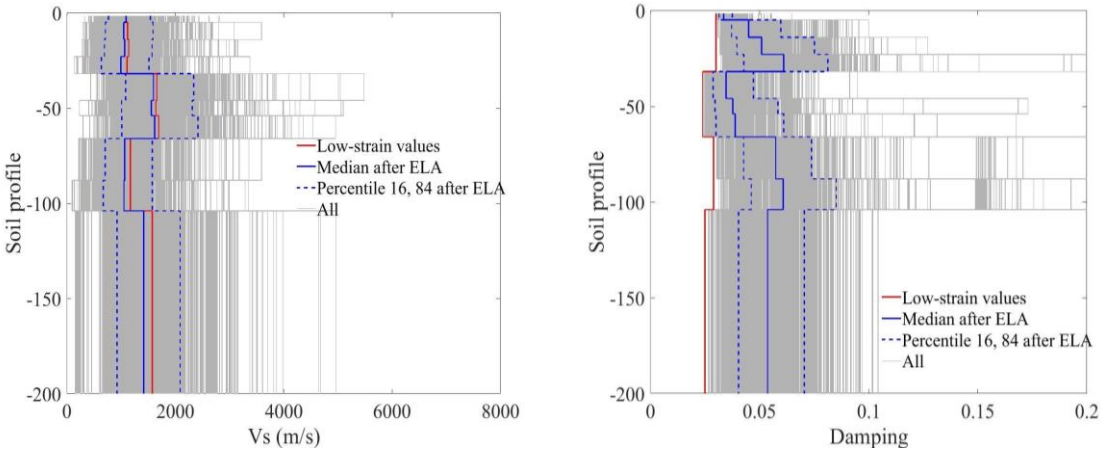


Figure 1. Soil profiles LB, BE and UB. - Shear wave velocity (left) and damping ratio (right).

The numerical analysis requires the seismic signal to be applied at the bedrock, its deconvolution is performed by using an iterative procedure of wave propagation [9]. To take into account the non-linear properties of the soil, the equivalent linear method is employed to obtain the degraded layers' properties for the three soil profiles: LB, BE, UB. [10, 11].

## 3 MODELLING OF THE SOIL-STRUCTURE INTERACTION PROBLEM

The finite element method (FEM), combined with an explicit strategy of time integration, is used to calculate the effect produced by each seismic signal on the studied building. This methodology allows taking into account the non-linearities, not only in the materials but also in the soil-structure interface. Two sub-models of different nature are defined: one, to model the behavior of the structural part, and the second, to model the free field behavior of the soil. Finally, both models are conveniently combined with a contact algorithm that allows capturing the non-linear effects happening at the interface. The structural sub-model includes all the reinforced concrete components from the foundation to the roof, also including the layer of lean concrete used to level the foundation base. The soil sub-model includes all the layers from the foundation base the bedrock, where the deconvolutioned accelerograms are applied. Each sub-model is described henceforward.

### 3.1 Modelling of the structure

An existing nuclear structure where auxiliary and control tasks are carried out, is studied herein. It has an almost square shape with a semi-circular cut on the south façade, due to the presence of the containment building. The structure presents a plane of symmetry with respect to the Y direction, while a lack of symmetry is observed in X direction, as it can be seen in Figure 2 (left). This figure shows a schematic view of the plan (64.3 m long and 61.9 m

wide, with a semi-circular cutout of 22.5 m radius). Figure 2 (right) shows an elevation view of the structure. The foundation level is at level +91.00. Above, the building has five floors with levels: +96.0 (intermediate floor), +100.0, +108.0 and +114.5, and +120.7 (roof level).

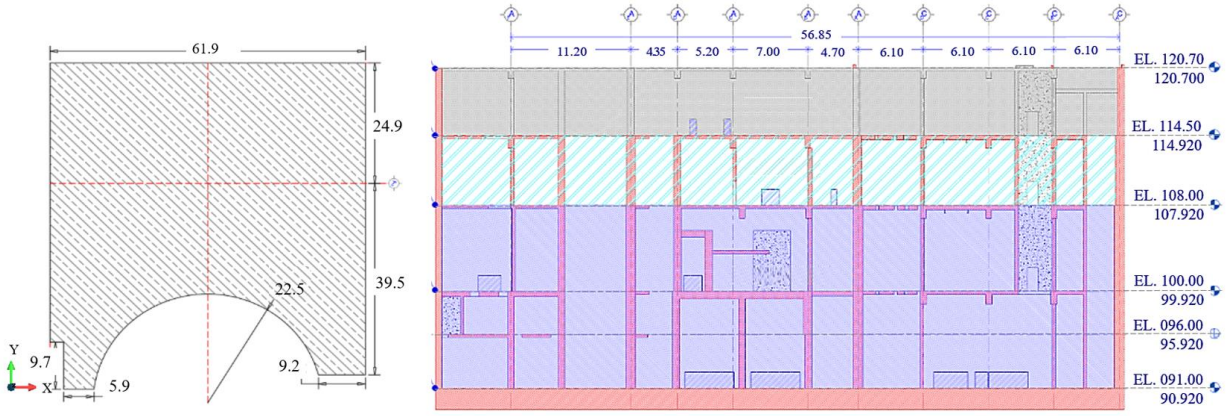


Figure 2. Geometry of the structural sub-model. Plan view (left) and elevation view (right).

The structural elements of the building are: shear walls, columns, beams and slabs. Various types of reinforced concrete sections are identified for each element depending on the arrangement and quantity of the steel bars, according to the reinforcement project. The structure is discretized with finite elements of shell type, known as 3-node rotation-free shell elements [12]. These elements have an adequate flexural behavior and simplify the assembly with the solid hexahedral elements used to model the foundation and the lean concrete, since both element types only have translational degrees of freedom.

The constitutive law that governs the material behavior of reinforced concrete is approached through the theory of serial-parallel rule of mixtures proposed by Rastellini [13]. This theory allows obtaining the behavior of the composite material by taking into account the appropriate sum of the non-linear constitutive models of its constituent materials. An isotropic damage model is used for the concrete, and an elastoplastic model for the structural steel in each section. The effect of the material non-linearity is one of the aspects analyzed. The reinforcement steel is modeled with an elastoplastic model, while an isotropic damage model with exponential hardening is selected for the structural concrete. The fracture energy parameter for the damage model is taken from previous works [14-15]. Since the original concrete has aged over the years, the characteristic strength of the concrete is considered to have increased by 25% and the stiffness by 11.8%.

| **Properties** | **Structural concrete (H-375)** | **Structural steel** | **Foundation concrete (H-375)** | **Lean concrete (H-150)** |
|---|---|---|---|---|
| Constitutive model | isotropic damage | elasto-plasticity | elastic | elastic |
| Density | 2400 kg/m3 | 7850 kg/m3 | 2500 kg/m3 | 2300 kg/m3 |
| Young's modulus | 28.7 GPa | 210.0 GPa | 28.7 GPa | 18.14 GPa |
| Poisson 's Ratio | 0.2 | 0.3 | 0.2 | 0.17 |
| Yield strength (fc, ft) | 36.8 Mpa, 3.8 MPa | 470.9 MPa | - | - |

Table 1. Properties of the materials of the elements of the reinforced concrete roof in the building.

The foundation slab is also made of reinforced concrete, with dimensions 61.0x63.6 m and 2 m thick. Its irregular geometry has been discretized with a structured mesh of 8-node linear hexahedrons. Below, it rests on a layer of lean concrete with a similar geometry and dimensions. Although the original thickness was variable, a uniform thickness geometry of 4m has been modeled for simplicity. Likewise, linear hexahedrons with 8 nodes are used. Both parts, the foundation and the lean concrete layer, are assumed to behave within the elastic range.

Material properties are briefly described in Table 1 for the concrete and steel fraction, for all structural elements of the building (aged mechanical properties for concrete are shown). The damping has been set at 10% for all the structural elements following the normative recommendations [16].

The possible interactions with the adjoining buildings have been dismissed since they are separated from the building under study by means of joints. However, there are adjacent soil layers that do interact with the building. The effect of the soil pressure on the walls is considered in those parts where the structure is effectively exposed to contact with the surrounding soil. In order to address the problem of the boundary constraints caused by the surrounding soil, a simplified approach based on springs is developed. Thus, a rigid frame was considered to replicate the shape of the building's silhouette and to apply the elastic constraints imposed by the surrounding soil. This rigid frame copies the movement of the upper layers of the soil by means of multi-point constraints. Then the structure is linked this frame, by means of elastic springs, in order to replicate the lateral soil restraint. The stiffness of the horizontal springs is based on a ballast coefficient of 40 MN/m3, which is a conservative value for the type of existing soil. Figure 3 shows a scheme of the horizontal constraint due to boundary conditions.

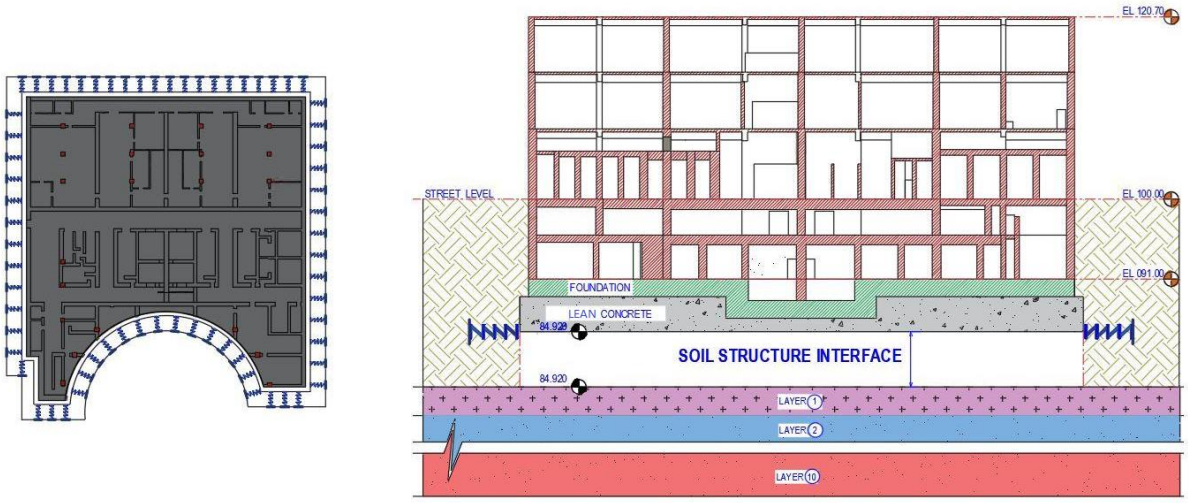


Figure 3. Horizontal constraint due to lateral boundary conditions.

## 3.2 Modelling of the soil

The thicknesses of the soil layers correspond to the profile identified by existing geotechnical surveys. Ten layers of soil are taken with their best estimation of thickness and mechanical properties. The bedrock was identified as the depth at which shear wave velocities exceeded 2,500 m/s, resulting in a model depth of 198.30 m.

The horizontal dimension of the soil model is defined by the distance between the limits of the foundation and the boundary of the soil. This length must be 3 times the foundation size, which leads us to a minimum dimension of 600 m x 600 m, to prevent that waves could be reflected from the model boundaries to the structure generating disturbances in the records, and, subsequently, altering the response spectra.

Cyclic symmetry boundary conditions are applied to the lateral faces in order to assume that the soil domain radiates the ground motion to infinity [17]. In this way, all pairs of points on opposing faces are rigidly linked, as master and slave, in terms of displacements, velocities and accelerations.

### 3.3 Full soil-structure model

The full numerical model is created by joining the structure and soil models. An interface has to be defined between both models. Figure 4 shows the location of the soil-structure interface. This interface is located just below the lean concrete layer in contact with the first layer of soil. Between these two surfaces, a contact algorithm is defined that uses penalty parameters to counteract the possible penetrations at the interface level. The present study considers three types of models, with different hypotheses for this interface:

- fixed base (FB), which assumes that the structure does not interact with the soil in any way, so no contact exists and the structure base is considered fixed to bedrock (surface signals are applied in this case).
- fixed contact (FC), which assumes that both sides of the interface move together without relative motion.
- sliding contact (SC), which allows relative displacements of gapping and horizontal sliding with a friction coefficient of 0.5 (and null cohesion).

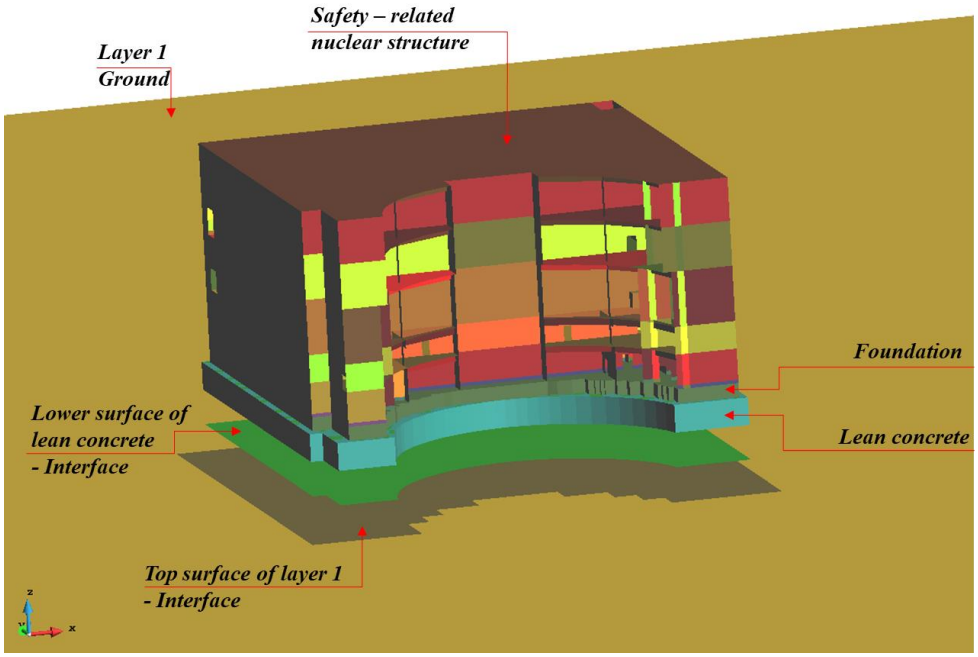


Figure 4. Interface location scheme for soil-structure contact.

The structure model is discretized with 324,150 3-node shell elements. In addition, 59,796 8-node linear hexahedral elements are employed to discretize the foundation and the lean concrete layer. The minimum side of the shell elements is 34 cm in order to reduce the computational cost by maximizing the time step of the explicit integration procedure, without losing resolution in the response. A critical time step of $0.23 \cdot 10^{-3}$ seconds has been set.

The soil model is discretized with 1.43M linear hexahedral elements, considering that the vertical size of soil elements must be conveniently chosen in order to properly reproduce the dynamic response, especially the high frequencies, guaranteeing that the propagation of waves is capable of reproducing frequencies up to 100 Hz [16]. Consequently, the maximum vertical

sizes of each layer of soil are established according to the shear wave velocity, requiring elements of 2.20 m for some layers and of 3.40 m for others.

The FEM kernel employed is PLCD[2], an in-house CIMNE[3] code with explicit scheme. This code can solve structural dynamic problems with several constitutive material formulations and finite element typologies. The capabilities and accuracy of the PLCD code for the structural analysis of nuclear facilities has been thoroughly validated using experimental data [15] and has been widely used in other similar works on nuclear buildings [18] and by analyzing composite structures [19]. In addition, the GID[4] software, also developed by CIMNE, is employed as pre- and post-processor.

## 4 STRUCTURAL ANALYSIS

The main objective of the present work is to calculate the in-structure response spectra (ISRS) of safety-related nuclear structures with special emphasis on considering the non-linearities coming from the material and from the soil-structure contact interface.

The numerical simulation is performed in two calculation phases. In the first phase, the gravitational loads are applied, such as the self-weight of the structure, permanent loads and 25% of use loads. In the second phase, the seismic action is applied to the bedrock of the model. The acceleration is calculated at each of the predefined control points, enabling the calculation of ISRS. These results are carried out in order to examine two different aspects:

- The first aspect is the effect of material non-linearity. With this aim, the fixed base case (FB) is compared with the sliding-contact case (SC).
- The second aspect is the effect of non-linearity coming from the sliding on the interface. For this, three contact scenarios are compared, namely: only structure with fixed base (FB), soil-structure with fixed contact (FC), and soil-structure with sliding contact (SC). ISRS are calculated for 5% damping.

The effect of the mechanical uncertainty of the soil column is also analyzed by comparing ISRS obtained for three soil columns: LB, BE, UB. In the comparisons, the response spectra obtained is the average of seven seismic actions. Each record-keeping point is located in the position of singular security-related equipment.

Summing up, the calculations are performed for 7 accelerograms generated for near field earthquakes, considering 3 scenarios for the soil-structure interface (FB, FC, SC) and 3 soil columns (LB, BE, UB). Thus, 49 numerical calculations are to be performed.

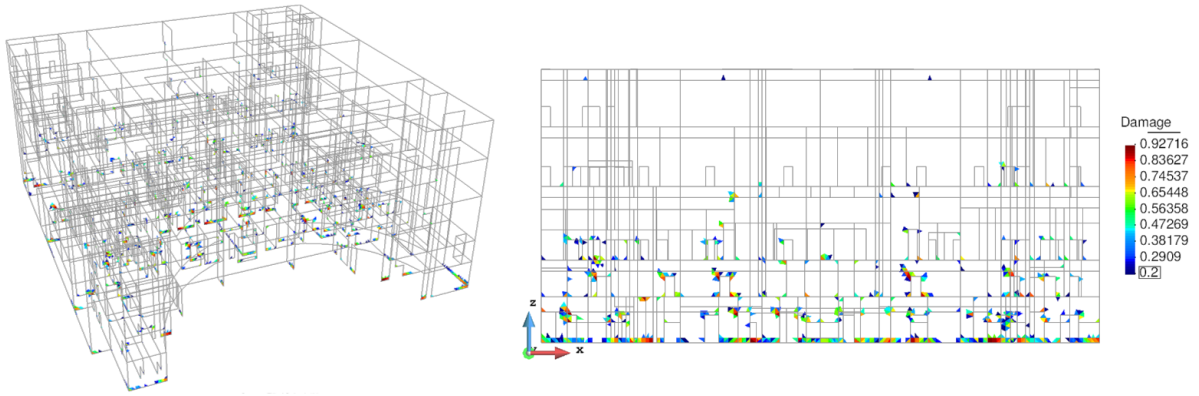


Figure 5. Structural damage for FB case. General 3D view (left), and cross-sectional view (right).

[2]PLCD home page: www.cimne.com/PLCd
[3]CIMNE - International center for numerical methods in engineering: www.cimne.com
[4]GID home page: www.gidsimulation.com

## 5 RESULTS

When a material point of the structure exceeds the elastic limit, the concrete begins to crack, what produces a decrease in stiffness and the possible plastification of the structural steel. The evolution of microcracks in concrete is described with a mechanical damage model where its main internal variable varies between 0 (no damage) and 1 (completely damaged). Figure 5 shows that the level of damage recorded is remarkably low in all cases, and appears in much localized areas due to local stress concentration effects.

Two extreme scenarios are compared: the fixed base case (FB) versus the sliding-contact case (SC). Results are generated for the BE soil profile, considered as representative. Figure 6 shows the effect of non-linearity on the structural response spectrum obtained for fixed base (FB) and sliding-contact (SC), at three elevations of the building {+91.00, +108.00 and +120.70}, for the linear elastic and non-linear material models, in Y direction.

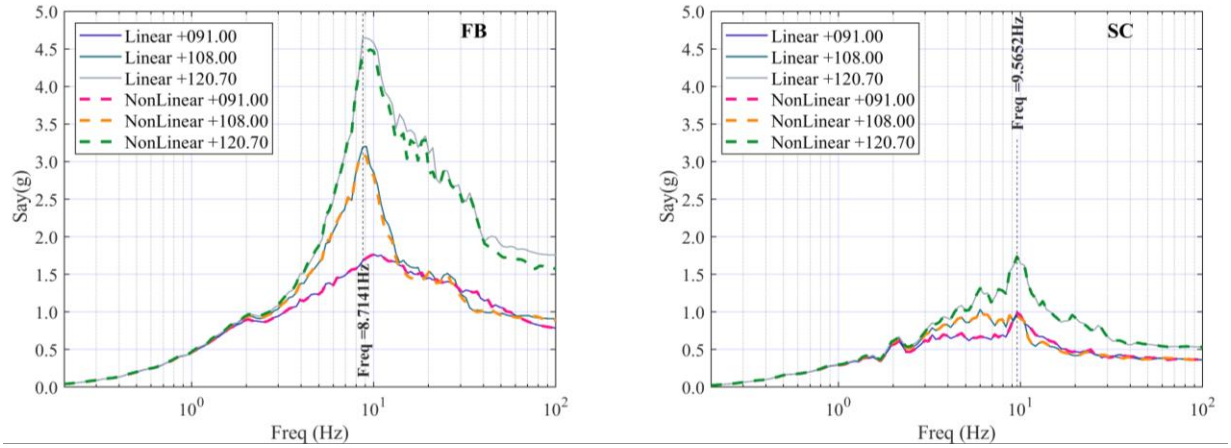


Figure 6. Response spectra in Y direction. FB case (left) and SC case (right).

The effects of the material non-linearity on the ISRS of the studied nuclear structure are insignificant due to its mechanical characteristics. However, the effects of the non-linearity in the soil-structure interface is crucial as it is shown in Figure 6. In the case of the sliding contact (SC), the spectral ordinates reduce drastically if compared with the fixed base case (FB).

One of the sources of uncertainty in the structural analysis of a structure is the underlying soil and its mechanical and dynamic properties. A statistical approach is considered in order to quantify the effect of uncertainty arising from the mechanical properties of the soil column.

Figure 7 shows the ISRS obtained in the structure at the foundation level (+91.00) and at the roof level (+120.7) for three columns {LB, BE, UB} corresponding to the percentiles 18%, 50% and 86% respectively, and two scenarios for the soil-structure interaction {FC, SC}.

The effect of soil uncertainty is noticed when comparing the PSA ratio with respect to the most representative case: the Best Estimate (BE) soil column. The resulting spectra show that the improvement of the mechanical properties of the column (UB) leads to higher ISRS curves and higher values of the PSA ratio with respect to the degraded soil (LB). Movements at interface (SC) significantly reduce the PSA to a remarkably low value. The sliding interface acts as an "isolator unit" for the structure with respect to the mechanical properties of the soil, which highlights the relevance of soil-structure interface nonlinearity in the analysis. The ISRS in the horizontal direction (X, Y) show a very similar behavior while the ISRS in the vertical direction present some peculiarities. The frequency range is extended with respect to the horizontal direction spectra in all cases, and the peak frequency ($f^{psa}$) reaches higher values when the mechanical properties of the soil improve. This fact becomes more evident in the case with fixed-contact (FC) and it softens in the case of sliding-contact (SC).

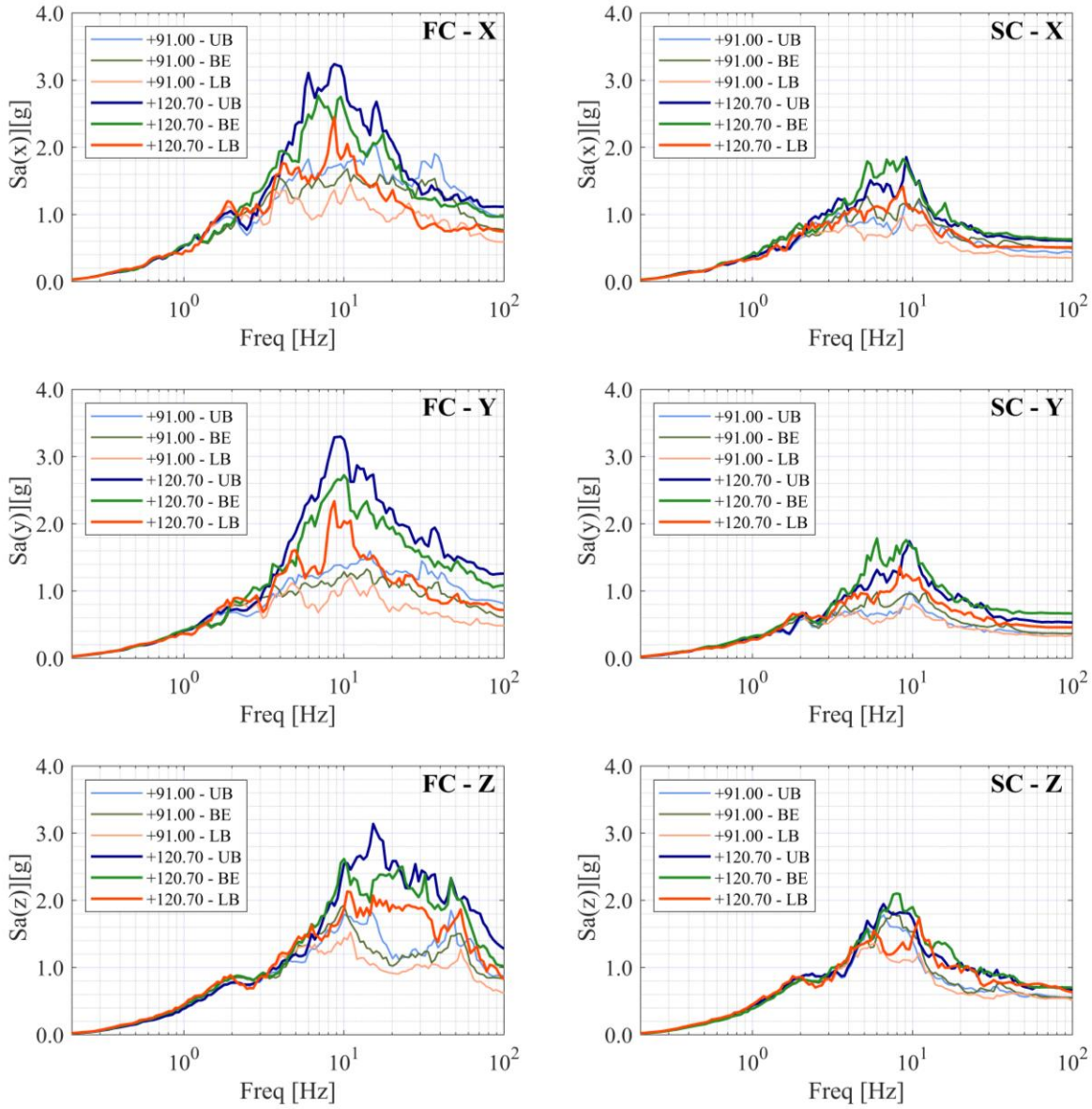


Figure 7. In-structure response spectra in X, Y, Z directions for the three soil columns (UB, BE, LB), and two soil-structure interface scenarios: FC fixed-contact (above). SC sliding-contact (below).

The effects of the non-linearity of the soil-structure interface is analyzed by observing the obtained response spectra. This evaluation is carried out through the ISRS of the movement measured at several floors: at the level of the ground surface (FF), at the foundation level (+91.00), at the level of the third floor in the structure (+108.00) and at the roof level (+120.70), for three soil-structure interface scenarios and three directions {X, Y, Z}.

The analysis of the ISRS allows extracting the maximum spectral acceleration (PSA) and the corresponding maximum frequency ($f^{psa}$). Figure 8 shows an ISRS matrix for soil-structure interaction (horizontal X, Y) and top-bottom direction (vertical, Z) cases. Table 2 summarizes the main results of the ISRS obtained, to allow the comparison in terms of peak spectral acceleration (PSA) and peak frequency ($f^{psa}$).

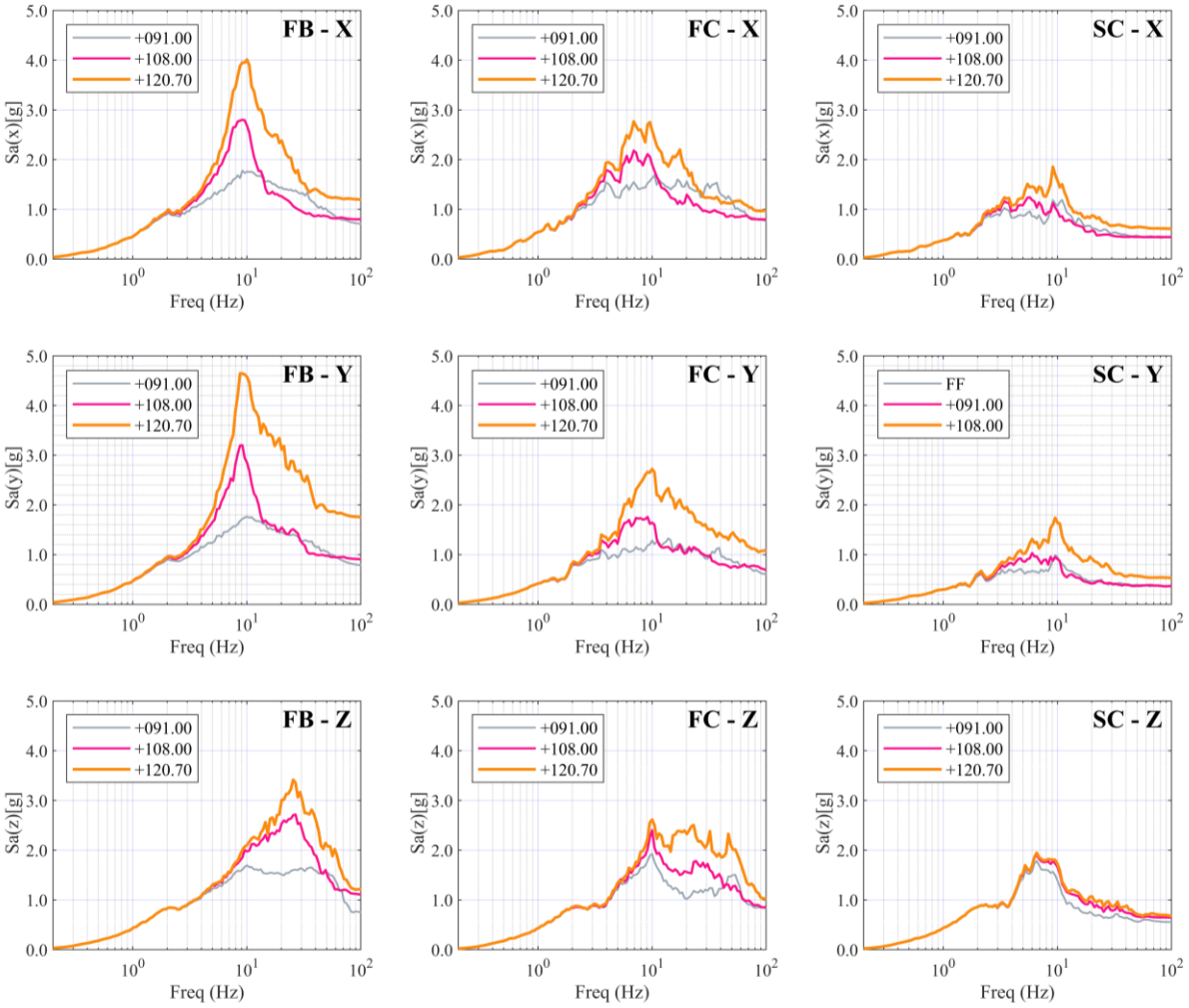


Figure 8. In-structure response spectra for three scenarios: FB (left), FC (center), SC (right).

| Dir | FB | | | | FC | | | | SC | | | |
|---|---|---|---|---|---|---|---|---|---|---|---|---|
| | Base | | Roof | | Base | | Roof | | Base | | Roof | |
| | Freq (Hz) | PSA (g) | Freq (Hz) | PSA (g) | Freq (Hz) | PSA (g) | Freq (Hz) | PSA (g) | Freq (Hz) | PSA (g) | Freq (Hz) | PSA (g) |
| X | 9.13 | 1.78 | 10.02 | x | 10.50 | 1.68 | 6.90 | 2.77 | 11.00 | 1.19 | 9.13 | 1.85 |
| Y | 10.02 | 1.76 | 8.71 | 4.65 | 13.89 | 1.33 | 10.02 | 2.72 | 9.57 | 0.99 | 9.57 | 1.74 |
| Z | 10.02 | 1.69 | 25.45 | 3.41 | 10.02 | 1.93 | 10.02 | 2.62 | 6.59 | 1.78 | 6.59 | 1.95 |

Table 2. Summary of the ISRS features for three contact scenarios.

## 6 CONCLUSIONS

This work studies the dynamic structural response of an existing safety-related nuclear structure subjected to near-field seismic actions. It evaluates how floor spectra is influenced by including in the analysis the non-linearities coming from the material and the soil-structure interface.

The methodology to determine the seismic action applied to the structure is based on a set of representative seed signals obtained from public databases. Using seismic factors of the area and directionality parameters, a set of seven floors of ground movement in the foundation

is defined. These signals are fitted and validated against the target spectra and translated, through a deconvolution process, to the bedrock level where they are applied to the entire model.

The structural scheme is defined with a high degree of realism to capture the structural behavior. The structural typologies involved are specifically modeled: shear walls, slabs, beams and columns. Likewise, the model considers the irregularities existing in the structure. The foundations and the underlying layers of lean concrete are also considered in detail.

In the FEM soil model, specific boundary conditions are carefully considered, such as cyclic symmetry at the edges of the soil domain and the interaction of the structure with dynamic forces due to the surrounding ground and adjacent buildings.

The results show how the non-linearity of the material barely affects the global response of the structure and floor spectra. However, the non-linearity due to sliding at the soil-structure interface significantly affects the response spectra of the structure, reducing the maximum spectral acceleration peaks. Additionally, the ISRS registered at each equipment location would allow a subsequent analysis to assess the integrity of critical equipment in case of a margin near-field earthquake.

## ACKNOWLEDGEMENTS

The authors are grateful for the financial support of the Ministry of Science and Innovation of Spain, through the *Severo Ochoa Program for Centers of Excellence in R&D (2019-2013)* under the grant CEX2018-000797-S financed by MCIN/ AEI/10.13039/501100011033.

## REFERENCES

[1] Coleman, JL, Bolisetti, C., Whittaker, A. (2016) *"Time-domain soil-structure interaction analysis of nuclear facilities"* Nuclear Engineering and Design 298 pp: 264-270.

[2] Cornell, CA (1968) *"Engineering seismic risk analysis"* Bulletin of the Seismological Society of America, 58(5): 1583–1606.

[3] Abrahamson NA (1992) *"Non-stationary spectral matching"*, Seismol. Res. Lett. 63, 30.

[4] Hancock, J., Watson-Lamprey, J., Abrahamson, NA, Bommer, JJ, Markatis, A., McCoy, E., and Mendis, R. (2006). *"An improved method of matching response spectra of recorded earthquake ground motion using wavelets"*, J. Earthquake Eng. 10, 67–89.

[5] Al-Atik, LY and Abrahamson, N (2010) *"An improved method for non-stationary spectral matching"*. Earthquake Spectra, vol. 26-33, p. 601-617.

[6] Toro, GR, (1996) *"Probabilistic Models of Site Velocity Profiles for Generic and Site-Specific Ground Motion Amplification Studies"*, Report submitted to Brookhaven National Laboratory, Contract No, 770573, Upton, New York.

[7] Kramer, Steven L. (1996) *"Geotechnical Earthquake Engineering"* - Prentice Hall.

[8] Lazcano, S. (2012). *"Shear wave velocity profiles and analysis of the seismic behavior of the soil in western Guadalajara"*, Jal. Memo XXVI National Meeting of Soil Mechanics and Geotechnical Engineering.

[9] Electric Power Research Institute. (1991) *"A Methodology for Assessment of Nuclear Power Plant Seismic Margin"*. EPRI Report NP-6041-SL, Rev. 1, Palo Alto, California.

[10] Kumar, A., and Mondal, JK (2017). *"Newly developed MATLAB based code for equivalent linear site response analysis"*. Geotechnical and Geological Engineering, 35(5), 2303-2325.

[11] Hashash, YMA, Musgrove, MI, Harmon, JA, Ilhan, O., Xing, G., Numanoglu, O., Groholski, DR, Phillips, CA, and Park, D. (2020). *"DEEPSOIL 7, Software"*. Urbana, IL, Board of Trustees of the University of Illinois at Urbana-Champaign.

[12] Flores FG, Oñate E. (2005), *"Applications of a Rotation-Free Triangular Element for Finite Strain Analysis of Thin Shells and Membranes"*. In: Oñate E., Kröplin B. (eds) Textile Composites and Inflatable Structures. Computational Methods in Applied Sciences, vol 3. Springer, Dordrecht.

[13] Rastellini, FG; Oller, S.; Salomón, RO; Oñate, E. (2008) *"Composite materials nonlinear modeling for long fiber-reinforced laminates: continuum basis, computational aspects and validations"* Computers and structures, 86(9): 879-896.

[14] Jiménez, S., Cornejo, A., Barbu, LG, Oller, S., Barbat, AH (2020) *"Analysis of the mock-up of a reactor containment building: Comparison with experimental results"*, Nuclear Engineering and Design, 359, 110454.

[15] Jiménez, S., A. Cornejo, LG Barbu, AH Barbat, S. Oller, (2021) *"Failure pressure analysis of a nuclear reactor prestressed concrete containment building"*, Engineering Structures, 236, 112052.

[16] American Society of Civil Engineers, ASCE (2017). "*Seismic Analysis of Safety – Related Nuclear Structures"* ASCE 4-16.

[17] Valadés Rodríguez, JD (2019). *"Boundary conditions for problems in semi -infinite means using the MEF: Perfectly matched Layers and Infinite Elements applied to soil-structure interaction problems"*. (in Spanish, unpublished final degree project). University of Seville, Seville, Spain.

[18] Cornejo, A., LG Barbu, C. Escudero, X. Martínez, S. Oller, AH Barbat, (2018) *"Methodology for the analysis of post-tensioned structures using a constitutive serial-parallel rule of mixtures"*, Composite Structures, 200: 480-497.

[19] Barbu, LG, A. Cornejo, X. Martínez, S. Oller, AH Barbat (2019). *"Methodology for the analysis of post-tensioned structures using a constitutive serial-parallel rule of mixtures: Large scale non-linear analysis"*, Composite Structures, 216: 315-330.

COMPDYN 2023
9th ECCOMAS Thematic Conference on
Computational Methods in Structural Dynamics and Earthquake Engineering
M. Papadrakakis, M. Fragiadakis (eds.)
Athens, Greece, 12-14 June 2023

# ENERGY LOSS MECHANISMS OF ROCKING BLOCKS: EXPERIMENTAL OBSERVATIONS

**Georgios Vlachakis[1], Carla Colombo[1], Anastasios I. Giouvanidis[2], Nuno Mendes[1], Nathanaël Savalle[3], Paulo B. Lourenço[1]**

[1] University of Minho, ISISE, ARISE, Department of Civil Engineering, 4800-058 Guimarães, Portugal
E-mail: carla.colombo95@gmail.com, giorgovlachaki@gmail.com, nunomendes@civil.uminho.pt, pbl@civil.uminho.pt

[2] Department of Civil Engineering, University of Nottingham, University Park, NG7 2RD Nottingham, United Kingdom
E-mail: anastasios.giouvanidis@nottingham.ac.uk

[3] Université Clermont Auvergne, Clermont Auvergne INP, CNRS, Institut Pascal
F-63000 Clermont-Ferrand, France
E-mail: nathanael.savalle@uca.fr

## Abstract

*A variety of different structures experience rocking motion when subjected to dynamic actions, making rocking dynamics a fundamental problem of earthquake engineering. Rocking motion presents peculiar dynamic characteristics, such as negative stiffness during pivoting and non-smooth phenomena during impacts. Hence, modelling of the rocking problem faces significant challenges. One of the most significant is related to the energy losses that occur during impacts, commonly represented by the coefficient of restitution. Despite the numerous theoretical attempts to accurately estimate the coefficient of restitution, it is apparent that experimental observations are essential in providing a direct insight into the complex and non-smooth phenomena of rocking motion. To this end, the present work conducts an extended experimental campaign on the free-rocking motion of limestone blocks. More specifically, a total of 36 blocks are tested, corresponding to 12 different geometrical aspect ratios. The free-rocking motion is thoroughly analysed, while attention is also given to three-dimensional effects. Finally, the coefficient of restitution is experimentally quantified and compared with both previous theoretical and experimental results gathered from the literature.*

**Keywords:** Rocking Motion, Coefficient of Restitution, Experimental Campaign, Free-rocking, Masonry, Digital Image Correlation

## 1 INTRODUCTION

The dynamic behaviour of a block rocking freely on its base constitutes a fundamental, yet challenging, problem of nonlinear dynamics and earthquake engineering, as it reflects the basic dynamic response of a variety of structures, such as buildings [1,2], bridges [3–8], classical monuments [9,10], non-structural elements [11], statues [12,13] etc. In particular, with respect to masonry structures, rocking behaviour becomes evident when the façades experience out-of-plane deformations due to lack of sufficient (or preliminarily fractured) connections with the adjacent walls [14,15]. In fact, such a collapse mechanism has been observed to be the most decisive and recurrent type of failure for masonry buildings after actual seismic events [16,17].

In general, the dynamics of a rocking block differs from the classical single-degree-of-freedom oscillator and present peculiar characteristics [18,19]. In essence, the rocking motion is composed of two phases: i) the pivoting over each corner, and ii) the impacts with the base when alternating the corners of pivoting. Firstly, the pivoting phase is smooth (although nonlinear due to the negative stiffness of the system), while impacts are non-smooth, impulsive and lead to energy losses. As a result, the pivoting phase is usually adequately described when using geometrically nonlinear models [20], while impacts are burdensome to model explicitly [21–23]. Therefore, impacts are commonly treated in a phenomenological sense by studying the time instants immediately before and after each impact, while considering the energy losses with the Coefficient of Restitution (CoR) [24].

Clearly, the CoR has a crucial role when modelling the rocking motion numerically, though its estimation is non-trivial. It may be estimated by using either theoretical assumptions or experimental observations [25]. In more detail, the first theoretical approach to compute the CoR was proposed by Housner [24], who assumed pure rocking motion (i.e. no sliding or bouncing), and computed the CoR using the conservation of angular momentum. Later, the research provided significant contributions in this theoretical framework by alleviating most assumptions [26–29]. Nevertheless, the general formulation of the problem appears to introduce undefined parameters that need to be experimentally or geometrically specified. On the contrary, experimental investigations of the CoR allow its direct quantification [30]. In this case, assumptions are omitted while the physical complexities of the problem are revealed. Indicatively, experimental investigations have shown the importance of bouncing [31], sliding [32], three-dimensional motion [33], the role of interface and material properties [34–37], and/or the influence of geometrical imperfections and irregularities [38]. Nevertheless, experimental studies are notably sparse, usually limited to few geometrical aspect ratios, while three-dimensional recording is often lacking.

The objective of this study is to provide an experimental insight into the energy losses of rocking motion and investigate the impact of three-dimensional effects on the global rocking response. To this end, a total of 36 free-rocking tests are conducted and analysed using 36 different limestone blocks of 12 different geometrical aspect ratios, i.e. height over width ratios. Attention is also given to the three-dimensional response of the rocking blocks, which is measured with a state-of-the-art contactless technique. Furthermore, the dependence of the CoR on the rocking amplitude and aspect ratio is presented and discussed.

The paper is structured as follows: the present section (Section 1) introduces the research significance and objectives of the work. Section 2 presents the theoretical framework of rocking dynamics, while Section 3 describes the experimental campaign. Section 4 first provides a detailed discussion of the outcomes of a representative free-rocking test, which is followed by the illustration of the CoR results for all the 36 tests. Finally, Section 5 concludes the work by highlighting the main observations.

## 2 THEORETICAL ROCKING DYNAMICS

Consider a block with height $H$ and width $B$ that experiences planar rocking motion on its base (Figure 1a). The rocking motion may be described using rigid body dynamics. Thus, the equation of motion writes [24]:

$$\ddot{\theta}_{xx} = -p^2\left[\sin(\pm\alpha - \theta_{xx}) + \frac{\ddot{u}_g}{g}\cos(\pm\alpha - \theta_{xx})\right] \tag{1}$$

where $\theta_{xx}$ describes the rocking rotation, $\alpha$ is the critical slenderness angle of the block (i.e. $\alpha = \tan^{-1}(H/B)$), $p$ is the frequency parameter of the block, defined as $p = \sqrt{mgR/I_0}$, with $m$ representing the mass, $I_0$ the rotational moment of inertia with respect to the pivot points and $R$ the diagonal distance of the centre of mass to the pivot points, $g$ is the acceleration of gravity and $\ddot{u}_g$ is the base (ground) acceleration. Finally, the signum $\pm$ refers to the sign of the rocking angle $\theta_{xx}$ with the upper sign corresponding to clockwise and the bottom to counter-clockwise rotations. Note that Eq. (1) is non-linear and thus the period $T$ of rocking motion is amplitude dependent [24]:

$$T = \frac{4}{p}\cosh^{-1}\left[1\Big/\left(1 - \frac{\theta_{xx,0}}{\alpha}\right)\right] \tag{2}$$

where $\theta_{xx,0}$ is the amplitude of the rocking angle $\theta_{xx}$.

Furthermore, assuming pure rocking behaviour (i.e. no sliding and bouncing), the two energy components of rocking motion, i.e. the Potential $E_{\text{POTENTIAL}}$ and Kinetic $E_{\text{KINETIC}}$ energies, compose the Total energy $E_{\text{TOTAL}}$ that read respectively:

$$E_{\text{POTENTIAL}} = mgR\left[\cos\left(\alpha - |\theta_{xx}|\right) - \cos\alpha\right] \tag{3}$$

$$E_{\text{KINETIC}} = \frac{1}{2}I_0\dot{\theta}_{xx}^2 \tag{4}$$

$$E_{\text{TOTAL}} = E_{\text{POTENTIAL}} + E_{\text{KINETIC}} \tag{5}$$

Equation (1) represents the smooth part of rocking motion, i.e. when pivoting, while non-smooth impacts occur when the block changes pivot point, i.e. when $\theta_{xx} = 0$. Those impacts occur over finite, but extremely short, time periods and result in energy losses. An accurate description of the impacts is commonly omitted, in favour of a phenomenological treatment using the CoR [39]. More specifically, the post-impact angular velocity $\dot{\theta}^+$ is related to the pre-impact $\dot{\theta}^-$ using the CoR: $e = \dot{\theta}^+/\dot{\theta}^-$. Assuming no bouncing or sliding, Housner [24] estimated the CoR using the conservation of angular momentum before and after impact, yielding:

$$e = 1 - \frac{3}{2}\sin^2\alpha \tag{6}$$

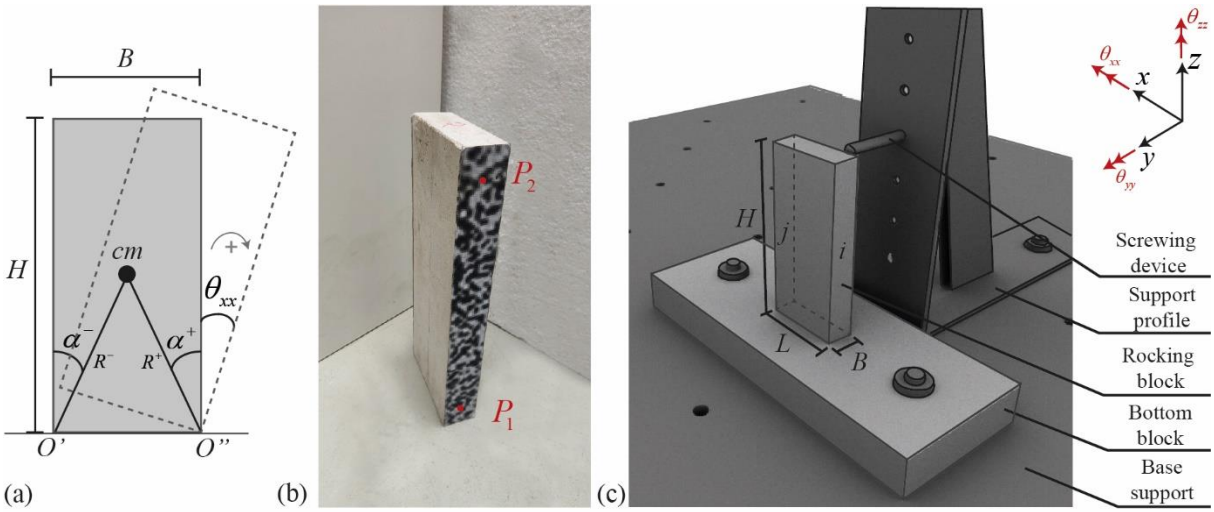


Figure 1: (a) Schematic view of the planar asymmetric rocking block, (b) limestone block with the speckle pattern used by the Digital Image Correlation (DIC) system, and (c) schematic 3D drawing of the free-rocking experimental setup.

Note that according to Housner's theory [24], the CoR (Eq. (6)) depends solely upon the geometry of the block, and thus the material properties are assumed irrelevant to the overall damping of the system.

## 3 FREE-ROCKING EXPERIMENTAL CAMPAIGN

The free-rocking tests are performed on limestone parallelepiped blocks (Figure 1b) of density $\rho = 2238$ kg/m$^3$ and elastic modulus $E = 32.7$ GPa [40]. All the blocks have common nominal dimensions in plan ($B = 50$ mm and $L = 150$ mm, $L/B = 3$), while their height $H$ spans from 200 mm to 750 mm with steps of 50 mm, resulting in 12 groups with aspect ratios $H/B$ ranging from 4 to 15. More specifically, 3 different blocks for each of the 12 $H/B$ aspect ratios are investigated, yielding a total of 36 specimens. Due to material irregularities and geometrical imperfections, the blocks' actual geometrical dimensions might slightly differ from the nominal ones. Such incongruity, especially if occurring at the edges [38], could cause an asymmetric response behaviour between the two rocking signs of rotation. In order to take into account such effects, the experimental parameters describing the actual properties of the system (i.e. $p$ and $\alpha$) are herein extracted distinctly for each sign of rotation by leveraging the relationship between the amplitude and the period of motion (Eq. (2)) [30].

Figure 1c schematically shows the main components of the free-rocking experimental setup. More specifically, it consists of a bottom block fixed on a rigid base, and a top block standing free on the former constitutes the structure under investigation. The free-rocking motion is activated in two steps. Firstly, an initial positive rotation $\theta_{xx}$ larger than the critical slenderness angle $\alpha^+$ is imposed on the block (Figure 1a). Secondly, a threaded rod, which is locally in contact with the top of the block, is screwed, triggering the initiation of free-rocking motion with an initial condition of almost zero angular velocity [25]. The free-rocking motion is recorded by a Digital Image Correlation (DIC) system. The DIC is a contactless optical technique that allows the recording of the displacement field over time, with the advantage of avoiding any physical interference that might affect the dynamics of the system. Four cameras record the motion of the two faces of the block in the $yz$ plane (Figure 1c), with a sampling frequency of 145 Hz. Figure 1b illustrates the preliminary preparation of the block surfaces,

which is characterised by a speckle pattern made of randomly distributed dots in greyscale and of uniform size (calibrated with respect to the camera's field of view). From each surface i and j shown in Figure 1c, the displacement time histories of two vertically aligned points (P1 and P2) are extracted (Figure 1b). Assuming rigid body motion, the displacement over time of the four points allows the estimation of the three rotations over the x-x, y-y and z-z axes as follows.

The rocking rotation over the x-x axis $\theta_{xx}$ is estimated as:

$$\theta_{xx,i} = \sin^{-1}\left(\frac{y_{i,top} - y_{i,bottom}}{dH}\right) \tag{7}$$

where $y_{i,top}$ and $y_{i,bottom}$ are the displacements in the y direction of the top and bottom points of the surface $i$, and $dH$ is their relative vertical distance. Similarly, $\theta_{xx}$ is calculated for the surface $j$, while the final $\theta_{xx}$ is the average of the rotations of the two surfaces.

The rotation over the y-y axis $\theta_{yy}$ is estimated as:

$$\theta_{yy,top} = \sin^{-1}\left(\frac{z_{i,top} - z_{j,top}}{L}\right) \tag{8}$$

where $z_{i,top}$ and $z_{j,top}$ are the displacements in z direction of the top points of surface $i$ and $j$, respectively, whereas $L$ is the length of the block. Similarly, $\theta_{yy}$ is estimated for the bottom points, while the final $\theta_{yy}$ is the average of the top and bottom points.

The rotation over the z-z axis $\theta_{zz}$ is estimated as:

$$\theta_{zz,top} = \sin^{-1}\left(\frac{x_{i,top} - x_{j,top}}{L}\right) \tag{9}$$

where $x_{i,top}$ and $x_{j,top}$ are the displacements in x direction of the top points of surface $i$ and $j$, respectively. Similarly, $\theta_{zz}$ is evaluated using the bottom points, and the final $\theta_{zz}$ is estimated as the average of the top and bottom points.

Finally, the energy loss during the free-rocking motion is quantified using the CoR. Experimentally, the CoR is preferably estimated using the energy balance of Eqs. (3-5), rather than directly using the ratio of angular velocities after and before each impact. More specifically, assuming that energy is preserved during the pivoting (i.e. smooth rocking) phase, the kinetic energy at impact (Eq. (4)) can be equated with the potential energy at the peak response of the corresponding half cycle (Eq. (3)), as they are alternatively nullified. This deliberate choice stems from two main reasons [25,30,35]: i) the DIC acquisition system directly measures displacements, which are consequently experimentally more reliable than velocities (which are computed as the gradient of displacements), and ii) instances of maximum rotations are captured with higher fidelity than instances of impacts, considering a constant sampling acquisition frequency of 145 Hz, and the high velocities of the system around impact. For the general case of asymmetric response, the results of each sign of rotation are preferably analysed. Therefore, the CoR is estimated as:

$$e = \sqrt{\sqrt{\frac{E_{\text{POTENTIAL, peak,i}}}{E_{\text{POTENTIAL, peak,i+2}}}}} \tag{10}$$

where $E_{\text{POTENTIAL, peak,i}}$ and $E_{\text{POTENTIAL, peak,i+2}}$ are the potential energies at time instances of peak responses $i$ and $i+2$. In Eq. (10), the first square root derives from the squared angular velocity (Eq. (4)), while the second one is introduced since two impacts separate the peak responses $i$ and $i+2$.

## 4 RESULTS

Figure 2 presents the response time history of a representative free-rocking test performed with a block of aspect ratio $H/B=5$. In detail, Figure 2a shows the rotational response over the x-x axis $\theta_{xx}$, which constitutes the preeminent rocking response. $\theta_{xx}$ starts from an initial rotation equal to the critical slenderness angle, while the end of the motion is assumed to occur when an uncertainty threshold is reached, displayed in Figure 2 with a dashed line. Such threshold aims to delineate the boundary of reliable acquired response and it is defined

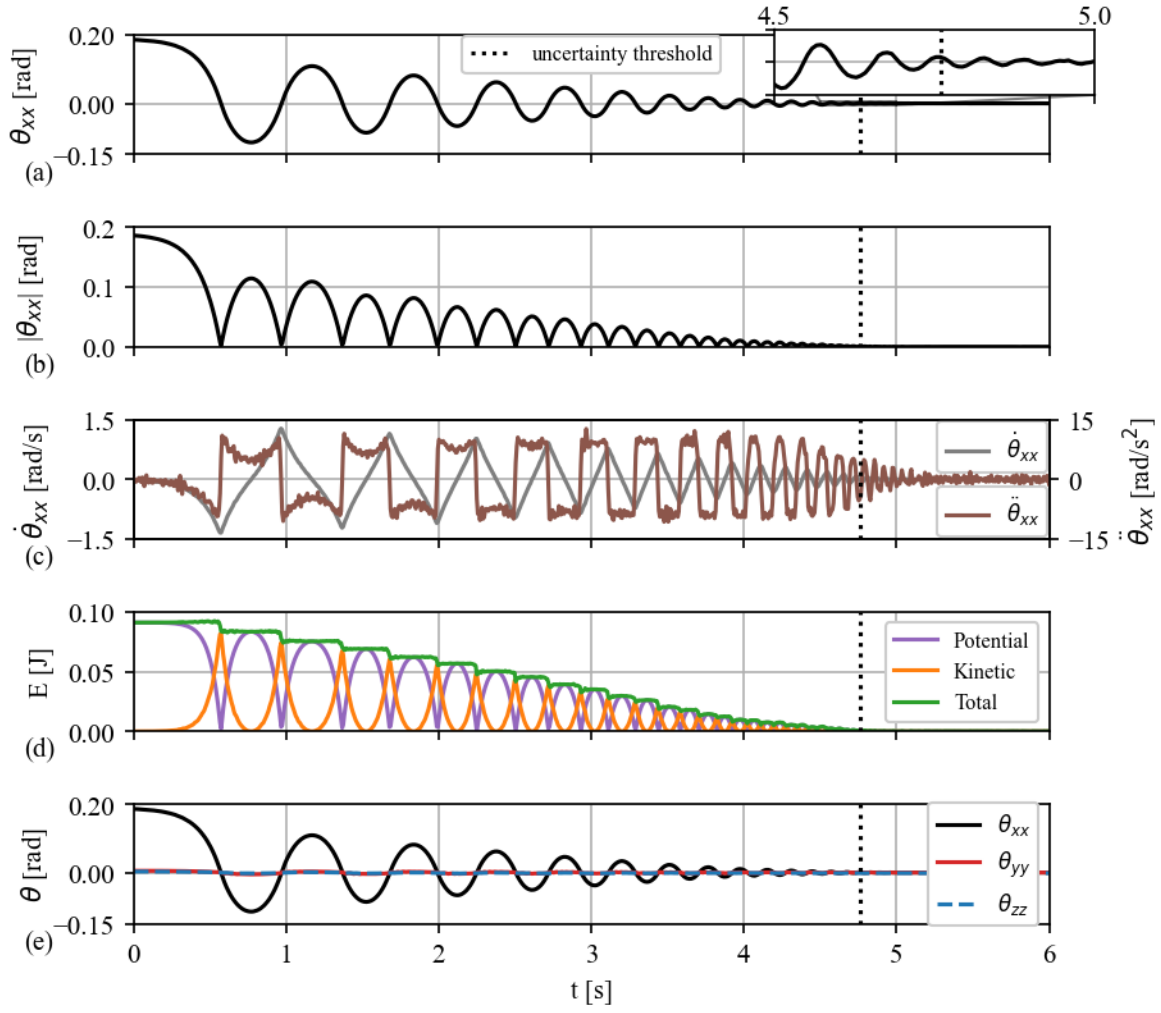


Figure 2: Response time histories in terms of (a) rotation over the x-x axis, (b) absolute rotation over the x-x axis, (c) angular velocity and angular acceleration over the x-x axis, (d) potential, kinetic and total energies, and (e) rotation over the x-x, y-y, and z-z axes.

assuming the ratio between the uncertainty value, recorded by the DIC system, and the amplitude of the rotation $\theta_{xx}$ to be less than 10%. Figure 2b plots the absolute value of the rocking angle $\theta_{xx}$, where a modest asymmetric response can be observed. This phenomenon may be attributed to one or a combination of several factors, such as the presence of irregular contact interfaces, geometrical defects, a non-centred centre of mass, inclination of the bottom block etc. Figure 2c reports the angular velocity $\dot{\theta}_{xx}$ and angular acceleration $\ddot{\theta}_{xx}$ response time histories, obtained from the first and second numerical derivatives of the rotation $\theta_{xx}$, respectively. The angular velocity $\dot{\theta}_{xx}$ shows a rather linear trend, which gradually decreases its amplitude over time. Its value becomes zero when the rotation $\theta_{xx}$ becomes maximum, while its maximum value occurs during impact. The angular acceleration $\ddot{\theta}_{xx}$ response is approximately constant during the pivoting (smooth rocking) phase, except for an internal oscillation caused by the cumulative noise introduced by the double derivatives, while it changes its sign suddenly at each impact. Figure 2d shows the experimentally measured energy balance of rocking motion (Eqs (3-5)). For each cycle, the $|\theta_{xx}|$ amplitude peaks correspond to a maximum potential energy and zero kinetic energy, with the latter reaching its maximum during impact. Overall, the total energy reduces with a stepwise fashion, i.e. being constant during the pivoting and experiencing abrupt reductions during impacts, thus being perfectly in line with the theoretical rocking dynamics [24]. Importantly, as the total energy remains constant during the pivoting (smooth rocking) phase, it appears reasonable to compute the CoR using the potential energy as per Eq. (10). Finally, Figure 2e depicts the rotations of the block in all three axes, x-x, y-y and z-z, where it is clearly shown that the $\theta_{xx}$ is the main component of motion, while $\theta_{yy}$ and $\theta_{zz}$ present negligible values.

Figure 3 illustrates with dots the experimental maximum amplitude $|\theta_{xx}|$ of each half cycle versus the corresponding period for the representative test of Figure 2, separately for positive and negative oscillations. Note that the first half cycle is omitted since it might include small interferences triggered by the screwing device. The experimental parameters $p$ and $\alpha$ are estimated as the best fit resulting from the minimisation of the error between the amplitude-period law (Eq. (2)) and the experimental data. The outcomes of the fitted $p$ and $\alpha$ parameters are shown in Table 1 and plotted in Figure 3, together with the values for nominal

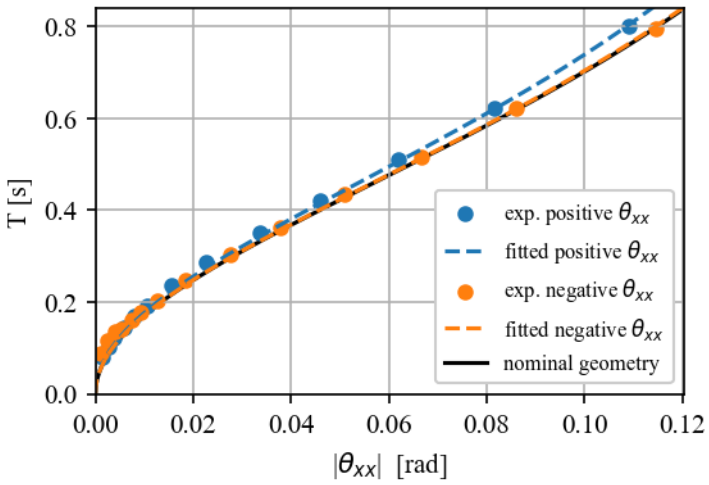


Figure 3: Period-amplitude dependency: experimental versus nominal geometry.

Table 1: Nominal and experimental parameters $\alpha$ and $p$.

| | $\alpha$ [rad] | diff. [%] | $p$ [Hz] | diff [%] |
|---|---|---|---|---|
| Nominal | 0.197 | - | 7.597 | - |
| Experimental positive $\theta_{xx}$ | 0.187 | 5.5 | 7.595 | 0.0 |
| Experimental negative $\theta_{xx}$ | 0.197 | 0.3 | 7.597 | 0.0 |

(i.e. ideal) geometry. Table 1 indicates that the experimentally computed frequency parameter $p$ perfectly resembles its nominal value for both signs of rotation, with a maximum difference of 0.02 % for the positive sign, while the slenderness angle $\alpha$ shows a minor difference of 5.5 % and 0.3 % for the positive and negative signs, respectively. Overall, the experimental period-amplitude data appears to follow closely the form of Eq. (2) and indicates a small asymmetry of the block between its two signs of rotation.

Figure 4a illustrates the experimentally estimated CoR values versus the maximum angular velocity $\dot{\theta}_{xx}$ of each corresponding cycle, for the representative test previously presented. Note that Figure 5a shows the evolution of the test starting from the right side of the graph and evolves towards the left side, following the reduction of the angular velocity. Moreover, Figure 4a plots the CoR given by Eq. (6), which is based on the assumption of conservation of angular momentum and is constant throughout the response time history. However, Figure 4a shows a non-constant trend of the experimental CoR that rather presents a gradual decrease over time with a scattered distribution at the end of the response. Nevertheless, the experimental CoR does not differ significantly from the theoretical CoR of Eq. (6). Finally, Figure 4b plots the experimental CoR values coming from all the 36 free-rocking tests performed herein. In addition, Figure 4b collects the experimentally measured CoR values found in the literature [20,26,30,31,34,36,41–46], together with the theoretical CoR computed using Eq. (6). Overall, Figure 4b shows that the 36 free-rocking tests follow the theoretical prediction of Eq. (6) up to an aspect ratio $H/B$ of 12, while for higher aspect ratios the experimental outcomes indicate a smaller CoR. This discrepancy probably arises

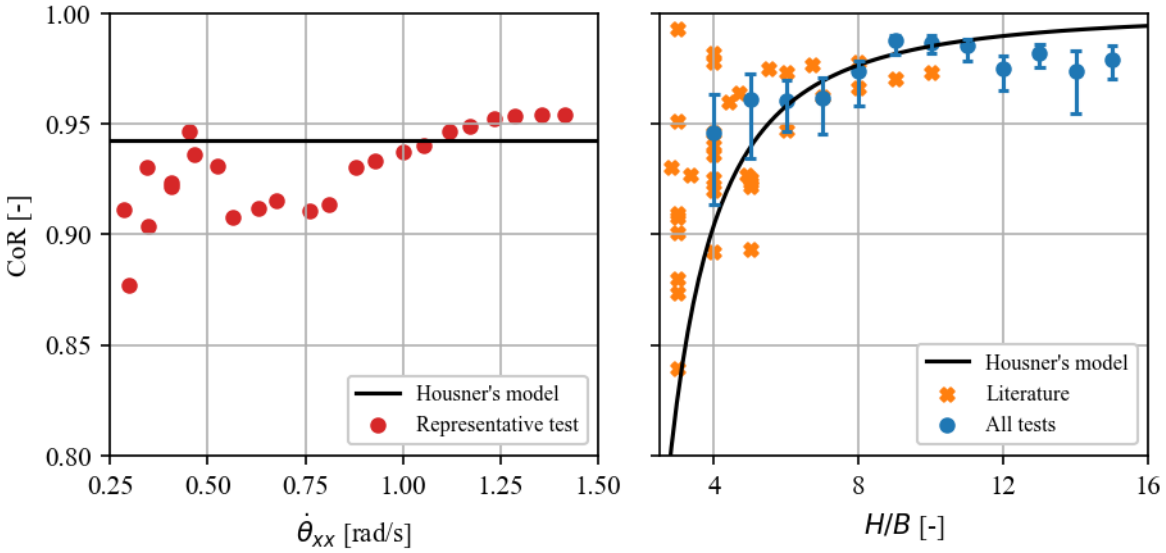


Figure 4: (a) Experimental versus Housner's theoretical CoR values for a representative free-rocking test, and (b) comparison of the CoR values estimated for all the 36 free-rocking tests with pertinent values from the literature [20,26,30,31,34,36,41–46] and Housner's model of Eq. (6) [13].

either due to the violation of the assumption of elastic impact behind Eq. (6) (i.e. no plastic deformation occurs at the surface asperities) or due to the presence of three-dimensional motion. Furthermore, the experimental results show a higher scatter for lower aspect ratios, with Eq. (6) providing a lower bound estimation. One potential explanation for this divergence has been provided by previous theoretical research [26–29] that highlighted that the impulsive forces during impact might not be concentrated solely at the corner pivot points. Nonetheless, the experimental CoR outcomes of this work lie within the scatter of the existing literature results for lower aspect ratios, while they provide novel experimental indications for higher aspect ratios, currently lacking from literature.

## 5 CONCLUSIONS

This paper presents an experimental characterisation of the free-rocking response of free-standing limestone blocks. The experimental campaign includes the investigation of 36 blocks, grouped into 12 aspect ratios (i.e. from 4 to 15) with three blocks for each group. Special attention is given to the energy dissipation mechanism at impacts, which is quantified via the coefficient of restitution (CoR), while the three-dimensional response, which is captured by a four-camera digital image correlation system, is also investigated.

The time history response of a representative test is firstly introduced and thoroughly discussed. The results show an oscillatory free-rocking behaviour, featured by modest asymmetry between the positive and negative rotations. Such an aspect is attributed to several sources of imperfection, which, however, are found to be of negligible interest given the very close resemblance between the nominal and experimental geometrical parameters, i.e. $p$ and $\alpha$. Overall, the planar rocking rotation $\theta_{xx}$ dominates the response compared to the other rotations ($\theta_{yy}$, $\theta_{zz}$), reinforcing the common assumption of planar rocking response.

Furthermore, particular emphasis is given to the experimental estimation of the energy losses during free-rocking motion through quantification of the CoR. The CoR values of a representative test appear to gradually decrease over time characterised by scattered values for small angular velocities − in contrast with Housner's assumption of constant CoR throughout the response time history. Finally, a comprehensive comparison is made among the CoR values extracted from all the 36 free-rocking tests conducted herein, the experimental results gathered from the literature, and the theoretical CoR of Housner's model. In general, the experimentally estimated CoR values follow the trend of the theoretical Housner's model prediction. Specifically, the experimental results verify the high scatter of the CoR values observed in the literature for lower aspect ratios, while the CoR is underestimated for higher aspect ratios. Nevertheless, the results shown herein are part of a wider experimental investigation currently in progress aiming to provide a deeper insight into the estimation of the energy dissipation throughout the response time history and the complex nonlinear rocking phenomena.

## REFERENCES

[1] S. Lagomarsino, Seismic assessment of rocking masonry structures, Bull. Earthq. Eng. 13 (2015) 97–128. https://doi.org/10.1007/s10518-014-9609-x.

[2] M. Aghagholizadeh, N. Makris, Seismic Response of a Yielding Structure Coupled with a Rocking Wall, J. Struct. Eng. 144 (2018) 1–13. https://doi.org/10.1061/(asce)st.1943-541x.0001894.

[3] A.I. Giouvanidis, Y. Dong, Seismic loss and resilience assessment of single - column rocking bridges, Bull. Earthq. Eng. (2020). https://doi.org/10.1007/s10518-020-00865-5.

[4] E.G. Dimitrakopoulos, A.I. Giouvanidis, Seismic response analysis of the planar rocking frame, J. Eng. Mech. 141 (2015) 04015003. https://doi.org/10.1061/(ASCE)EM.1943-7889.0000939.

[5] A. Agalianos, A. Psychari, M.F. Vassiliou, B. Stojadinovic, I. Anastasopoulos, Comparative assessment of two rocking isolation techniques for a motorway overpass bridge, Front. Built Environ. 3 (2017) 1–19. https://doi.org/10.3389/fbuil.2017.00047.

[6] A.I. Giouvanidis, E.G. Dimitrakopoulos, Seismic Performance of Rocking Frames with Flag-Shaped Hysteretic Behavior, J. Eng. Mech. 143 (2017). https://doi.org/10.1061/(ASCE)EM.1943-7889.0001206.

[7] I.M. Thomaidis, A.J. Kappos, A. Camara, Dynamics and seismic performance of rocking bridges accounting for the abutment-backfill contribution, Earthq. Eng. Struct. Dyn. (2020) 1–19. https://doi.org/10.1002/eqe.3283.

[8] N. Reggiani Manzo, M.F. Vassiliou, Cyclic tests of a precast restrained rocking system for sustainable and resilient seismic design of bridges, Eng. Struct. 252 (2022). https://doi.org/10.1016/j.engstruct.2021.113620.

[9] I.N. Psycharis, M. Fragiadakis, I. Stefanou, Seismic reliability assessment of classical columns subjected to near-fault ground motions, Earthq. Eng. Struct. Dyn. 42 (2013) 2061–2079. https://doi.org/10.1002/eqe.2312.

[10] S. Diamantopoulos, M. Fragiadakis, Modeling, fragility and risk assessment of ancient freestanding columns and colonnades, Eng. Struct. 275 (2023). https://doi.org/10.1016/j.engstruct.2022.115273.

[11] L. Sorrentino, L. Liberatore, D. Liberatore, R. Masiani, The behaviour of vernacular buildings in the 2012 Emilia earthquakes, Bull. Earthq. Eng. 12 (2014) 2367–2382. https://doi.org/10.1007/s10518-013-9455-2.

[12] A. Mehrotra, M.J. DeJong, The influence of interface geometry, stiffness, and crushing on the dynamic response of masonry collapse mechanisms, Earthq. Eng. Struct. Dyn. 47 (2018) 2661–2681. https://doi.org/10.1002/eqe.3103.

[13] A. Di Egidio, A. Contento, Base isolation of slide-rocking non-symmetric rigid blocks under impulsive and seismic excitations, Eng. Struct. 31 (2009) 2723–2734. https://doi.org/10.1016/j.engstruct.2009.06.021.

[14] A. Mauro, G. de Felice, M.J. DeJong, The relative dynamic resilience of masonry collapse mechanisms, Eng. Struct. 85 (2015) 182–194. https://doi.org/10.1016/j.engstruct.2014.11.021.

[15] O. Al Shawa, G. De Felice, A. Mauro, L. Sorrentino, Out-of-plane seismic behaviour of rocking masonry walls, Earthq. Eng. Struct. Dyn. 41 (2012) 949–968. https://doi.org/10.1002/eqe.1168.

[16] G. Vlachakis, E. Vlachaki, P.B. Lourenço, Learning from failure: Damage and Failure of Masonry Structures, after the 2017 Lesvos Earthquake (Greece), Eng. Fail. Anal. 117 (2020) 104803. https://doi.org/10.1016/j.engfailanal.2020.104803.

[17] L. Sorrentino, S. Cattari, F. da Porto, G. Magenes, A. Penna, Seismic behaviour of

ordinary masonry buildings during the 2016 central Italy earthquakes, Bull. Earthq. Eng. 17 (2019) 5583–5607. https://doi.org/10.1007/s10518-018-0370-4.

[18] N. Makris, A half-century of rocking isolation, Earthq. Struct. 7 (2014) 1187–1221. https://doi.org/10.12989/eas.2014.7.6.1187.

[19] A.I. Giouvanidis, E.G. Dimitrakopoulos, P.B. Lourenço, Chattering: An overlooked peculiarity of rocking motion, Nonlinear Dyn. 109 (2022) 459–477. https://doi.org/10.1007/s11071-022-07578-1.

[20] J.A. Bachmann, M. Strand, M.F. Vassiliou, M. Broccardo, B. Stojadinović, Is rocking motion predictable?, Earthq. Eng. Struct. Dyn. 47 (2018) 535–552. https://doi.org/10.1002/eqe.2978.

[21] M.N. Chatzis, A.W. Smyth, Robust Modeling of the Rocking Problem, J. Eng. Mech. 138 (2012) 247–262. https://doi.org/10.1061/(ASCE)EM.1943-7889.0000329.

[22] G. Vlachakis, A.I. Giouvanidis, A. Mehrotra, P.B. Lourenço, Numerical block-based simulation of rocking structures using a novel universal viscous damping model, J. Eng. Mech. 147 (2021) 04021089. https://doi.org/10.1061/(ASCE)EM.1943-7889.0001985.

[23] A.I. Giouvanidis, E.G. Dimitrakopoulos, Nonsmooth dynamic analysis of sticking impacts in rocking structures, Bull. Earthq. Eng. 15 (2017) 2273–2304. https://doi.org/10.1007/s10518-016-0068-4.

[24] G. Housner, The behavior of inverted pendulum structures during earthquakes, Bull. Seismol. Soc. Am. 53 (1963) 403–417. https://doi.org/10.1017/CBO9781107415324.004.

[25] L. Sorrentino, O. AlShawa, L.D. Decanini, The relevance of energy damping in unreinforced masonry rocking mechanisms. Experimental and analytic investigations, Bull. Earthq. Eng. 9 (2011) 1617–1642. https://doi.org/10.1007/s10518-011-9291-1.

[26] D. Kalliontzis, S. Sritharan, A. Schultz, Improved Coefficient of Restitution Estimation for Free Rocking Members, J. Struct. Eng. (2016) 1–7. https://doi.org/10.1061/(ASCE)ST.1943-541X.0001598.

[27] T. Ther, L.P. Kollar, Refinement of Housner's model on rocking blocks, Bull. Earthq. Eng. 15 (2017) 2305–2319. https://doi.org/10.1007/s10518-016-0048-8.

[28] M.N. Chatzis, M.G. Espinosa, A.W. Smyth, Examining the Energy Loss in the Inverted Pendulum Model for Rocking Bodies, J. Eng. Mech. 143 (2017). https://doi.org/10.1061/(ASCE)EM.1943-7889.0001205.

[29] H. Zhu, M.N. Chatzis, S. Acikgoz, A new impact model for the flexible rocking oscillator, Earthq. Eng. Struct. Dyn. 51 (2022) 1819–1839. https://doi.org/10.1002/eqe.3639.

[30] F. Peña, P.B. Lourenço, A. Campos-Costa, Experimental dynamic behavior of free-standing multi-block structures under seismic loadings, J. Earthq. Eng. 12 (2008) 953–979. https://doi.org/10.1080/13632460801890513.

[31] P.R. Lipscombe, S. Pellegrino, Free Rocking of Prismatic Blocks, J. Eng. Mech. 119 (1993) 1387–1410. https://doi.org/10.1061/(ASCE)0733-9399(1993)119:7(1387).

[32] D. Konstantinidis, N. Makris, Experimental and analytical studies on the response of

freestanding laboratory equipment to earthquake shaking, Earthq. Eng. Struct. Dyn. 38 (2009) 827–848. https://doi.org/10.1002/eqe.871.

[33] P.L. Várkonyi, M. Kocsis, T. Ther, Rigid impacts of three-dimensional rocking structures, Nonlinear Dyn. 107 (2022) 1839–1858. https://doi.org/10.1007/s11071-021-06934-x.

[34] M. ElGawady, Q. Ma, J. Butterworth, J. Ingham, Effects of interface material on the performance of free rocking blocks, Earthq. Eng. Struct. Dyn. 40 (2011) 375–392. https://doi.org/10.1002/eqe.1025.

[35] A.A. Costa, A. Arêde, A. Penna, A. Costa, Free rocking response of a regular stone masonry wall with equivalent block approach: experimental and analytical evaluation, Earthq. Eng. Struct. Dyn. 42 (2013) 2297–2319. https://doi.org/10.1002/eqe.2327.

[36] P.D. Spanos, A. Di Matteo, A. Pirrotta, M. Di Paola, Rocking of rigid block on nonlinear flexible foundation, Int. J. Non. Linear. Mech. 94 (2017) 362–374. https://doi.org/10.1016/j.ijnonlinmec.2017.06.005.

[37] D. Kalliontzis, S. Sritharan, Characterizing dynamic decay of motion of free-standing rocking members, Earthq. Spectra. 34 (2018) 843–866. https://doi.org/10.1193/011217EQS013M.

[38] C. Mathey, C. Feau, I. Politopoulos, D. Clair, L. Baillet, M. Fogli, Behavior of rigid blocks with geometrical defects under seismic motion: an experimental and numerical study, Earthq. Eng. Struct. Dyn. 45 (2016) 2455–2474. https://doi.org/10.1002/eqe.2773.

[39] P. Flores, Contact mechanics for dynamical systems: a comprehensive review, Multibody Syst. Dyn. 54 (2021) 127–177. https://doi.org/10.1007/s11044-021-09803-y.

[40] G. Vlachakis, C. Colombo, A.I. Giouvanidis, N. Savalle, P.B. Lourenco, Experimental characterisation of dry-joint masonry structures: Interface stiffness and interface damping, Constr. Build. Mater. (2023). https://doi.org/10.1016/j.conbuildmat.2023.130880.

[41] M. Aslam, W.G. Godden, D.T. Scalise, Earthquake Rocking Response of Rigid Bodies, 1978.

[42] M.J.N. Priestley, R.J. Evison, A.J. Carr, Seismic Response of Structures free to rock on their foundations, Bull. New Zeal. Soc. Earthq. Eng. 11 (1978) 141–150.

[43] C.M. Wong, W.K. Tso, Steady state rocking response of rigid blocks part 2: Experiment, Earthq. Eng. Struct. Dyn. 18 (1989) 107–120. https://doi.org/10.1002/eqe.4290180110.

[44] N. Ceh, G. Jelenic, B. Nenad, Analysis of restitution in rocking of single rigid blocks, Acta Mech. 229 (2018) 4623–4642. https://doi.org/10.1007/s00707-018-2246-8.

[45] K. Muto, H. Umemura, Y. Sonobe, Study of the overturning vibration of slender structures, in: Proc. Second World Conf. Earthq. Eng., Japan, 1960.

[46] N. Ogawa, A study on rocking and overturning of rectangular column, Rep. Natl. Res. Cent. Disaster Prev. 18 (1977).

COMPDYN 2023
9th ECCOMAS Thematic Conference on
Computational Methods in Structural Dynamics and Earthquake Engineering
M. Papadrakakis, M. Fragiadakis (eds.)
Athens, Greece, 12-14 June 2023

# DYNAMIC BEHAVIOUR OF A STRENGTHENED POINTED ARCH TESTED ON SHAKING TABLE

**Paulo Šćulac[1], Nina Čeh[1], and Matei Cukarić[2]**

[1] University of Rijeka, Faculty of Civil Engineering
Radmile Matejčić 3, 51000 Rijeka
e-mail: {paulo.sculac,nina.ceh}@uniri.hr

[2] Koning Projekt d.o.o
Spinčićeva 4, 52100 Pula
matei.cukaric@gmail.com

## Abstract

*This paper presents an experimental study of a strengthened pointed arch subjected to horizontal sinusoidal excitation on a shaking table. The geometry of the arch was selected to represent the geometry of typical Gothic vaults found in small single-nave village churches in Istria with preserved medieval wall paintings. The arch model was constructed from identical timber blocks with dry joints, while the reinforcement (duct tape) was applied either at extrados or at intrados of the arch. The aim of this study was to document the dynamic behaviour of pointed arches strengthened with composites, since there is a lack of experimental tests on this type of geometry. Contactless optical measuring system was used to monitor the openings between the blocks, since conventional sensors are difficult to apply. Two high-speed cameras made it possible to record the formation and closure of hinges between the blocks. Due to strengthening some hinges were hindered and consequently the seismic capacity of the arch was significantly improved.*

**Keywords:** Masonry, Pointed Arch, Strengthening of Arches, DIC, Shaking Table Test, Collapse Mechanisms.

## 1 INTRODUCTION

Strengthening of existing masonry buildings is a topic that is increasingly being researched in order to extend the design life of structures and preserve historic buildings. At present, researches are mostly dealing with methods that use steel, carbon or glass fibers in fiber-reinforced polymers (FRP) and textile-reinforced mortar (TRM) systems, as well as steel ties or other fibrous materials that could be used as reinforcing materials for masonry arches and vaults [1, 2, 3, 4, 5]. According to the principles from ISCARSAH recommendations for the structural restoration of protected architectural heritage special attention must be given to the selection of the appropriate retrofitting method in order to satisfy compatibility with existing materials, reversibility and lowest impact criteria (keeping interventions to the minimum to guarantee safety and durability) [6]. This especially applies to strengthening methods regarding new composite materials.

The behaviour of arches is usually analyzed on a four-link model with three rigid blocks (consisting of multiple masonry stone or brick blocks) interconnected by four hinges occurring alternately at the extrados and at intrados of the arch [7]. The collapse of an arch depends on its geometry rather than on its material properties (masonry strength), i.e. the collapse will occur due to loss of stability without material failure.

In case of composite reinforcement applied at extrados or/and at intrados of the arch the failure mode is changed significantly: due to reinforcement the formation of the fourth hinge will usually be prevented. This means that the collapse will not occur due to transformation of the arch into a mechanism but due to other failure mechanisms related to reinforcement, such as composite rupture and composite detachment (bond failure), shear sliding of blocks or due to masonry crushing [1, 4].

Pointed arches and vaults give smaller values of thrust than circular arches and can be made thinner than circular arches for large angles of embrace [8]. Although they are quite widespread (they are essential both in the Islamic architecture and in the architecture from the Gothic period) there is still a lack of numerical and experimental studies of strengthening on this type of geometry.

To date, only few shaking table tests have been conducted on strengthened arches and vaults (only with circular geometry). Castellano et al. [9] performed dynamic tests on a full-scale tuff masonry semi-circular arch strengthened at extrados with a 5 mm thick glass fabric reinforced cementitious matrix. As expected, the reinforcement prevented the opening of hinges at the intrados and a substantial increase of the seismic capacity of the arch. Giamundo et al. [10] conducted shaking table tests of a full-scale clay brick masonry segmental barrel vault. Tests have been first performed on the unreinforced vault; the vault was then strengthened with inorganic matrix applied at the extrados of the vault and tested again to investigate the effects of the retrofitting.

Tilting tests are often used as a static approximation of the shaking table tests (see e.g. [11, 12]). In this simplified alternative, the base with the scaled model is gradually tilted up until the collapse of the model. The tangent of the angle at which the collapse occurs corresponds to the base acceleration at which the model is transformed into a mechanism. In case of arch with dry joints strengthened at extrados or at intrados, it is not possible to use the tilt tests to obtain the base acceleration. Instead of one hinge, the crack opening is smeared over a greater area (i.e. several narrow hinges will open in adjacent blocks interconnected by reinforcement) and unrealistic large results are obtained.

This paper summarizes some preliminary results of a pointed arch model with dry joints tested on shaking table. Arch was strengthened either at extrados or at intrados and subjected to sinusoidal base excitation with fixed amplitude and increasing frequency.

## 2 EXPERIMENTAL SETUP

The geometry of the arch was selected to represent the geometry of pointed barrel vaults found in more than 15 small single-nave Gothic churches in Istria with preserved medieval wall paintings, which are protected as cultural heritage (Figure 1). Churches with wall paintings are an essential part of the Istrian cultural identity; so far, more than 140 sites with fresco paintings dating from the 8th to the 17th century have been investigated and documented [13].



Figure 1: Single-nave churches with pointed vaults in Istria.

A rather simple experimental model has been designed, due to the fact that the collapse of an arch depends on its geometry rather than on material strength. The model was made of timber blocks – beech was chosen because it has sufficient strength in order to perform multiple tests without damaging the blocks. The arch was composed of 23 blocks: 22 blocks had the same trapezoidal form, while the keystone was cut in a triangular form and glued to the neighboring trapezoidal blocks thus making a three-block unit (Figure 2). In order to make the friction coefficient closer to dry-joint stone arches a sandpaper with grit size P150 was glued on the upper surface of each block. The total mass of the arch model was equal to 5207 g (mean mass value of a unit block was 207 g, while the three-block keystone had 653 g). Thickness orthogonally to the plane of the arch was 8 cm.

To allow rotation at the base and formation of hinges L-shaped aluminum profiles were used as supports, fastened to the timber base plank with open side placed downwards. The timber base was attached to the shaking platform *Quanser ST-III* (Figure 3).

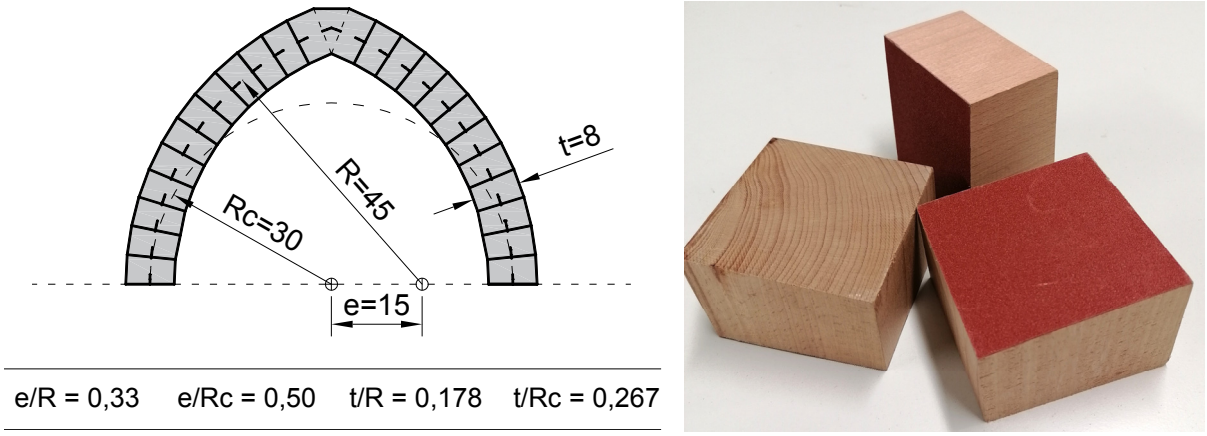


Figure 2: Geometry of the pointed arch (dimensions in cm) and timber blocks.

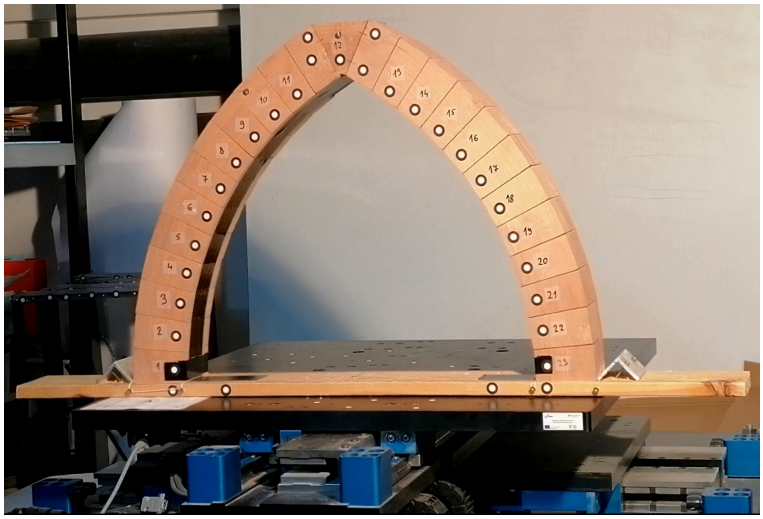

Figure 3: Experimental setup: arch model on the shaking platform.

Duct tape (*TEXO American Duct Tape*) was used as reinforcement, thereby trying to simulate the FRP or TRM strengthening system. One layer of tape, 50 mm wide and 0.19 mm thick, was applied either at extrados or at intrados of the arch. Mechanical properties of the tape were: tensile strength 31.6 N/cm, adhesion to steel 4.8 N/cm. The tape was made of PVC, PE and a fabric layer. Detail of tape anchorage to timber base is presented in Figure 4.

The model was monitored with a system for contactless optical measurement of 3D displacements and strains *GOM Aramis 4M* using a digital image correlation approach (DIC), which consisted of two high-speed cameras with a resolution of 2400×1728 pixels. Round point markers were attached to the front side of each block in order to detect any displacement change occurring at the contacts between the blocks. The experiment was tracked with 100 frames per second.

The base displacement of the platform was defined as a sinusoidal function:

$$d_{\text{base}}(t) = d_0 \cdot \sin(\omega t) \tag{1}$$

and the base acceleration was:

$$a_{\text{base}}(t) = -d_0 \cdot \omega^2 \cdot \sin(\omega t) \tag{2}$$

where $d_0$ is the maximum displacement of the base, $\omega$ is the natural frequency related to shaking table's frequency ($f = \omega/2\pi$) while $t$ is time. The displacement amplitude of 2.5 cm was kept constant, while the frequency was increased starting from 0.25 Hz with steps of 0.25 Hz, and held piecewise constant throughout the experiment.

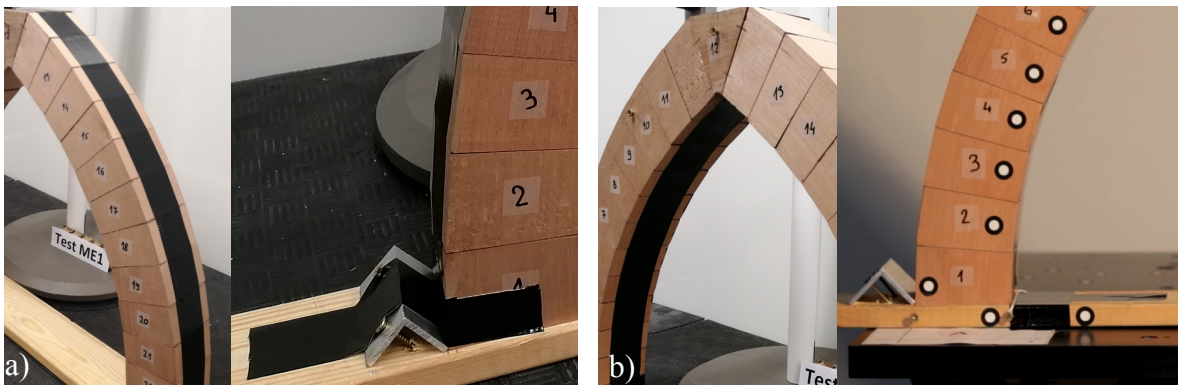


Figure 4: Reinforcement applied a) at extrados or b) at intrados of the arch and detail of anchorage.

# 3 RESULTS AND DISCUSSION

## 3.1 Un-strengthened arch

First, the results for the un-strengthened arch are presented. Figure 5 displays the base displacement and base acceleration time-history graphs. The peak acceleration in the final part of the experiment was 3.0 m/s$^2$.

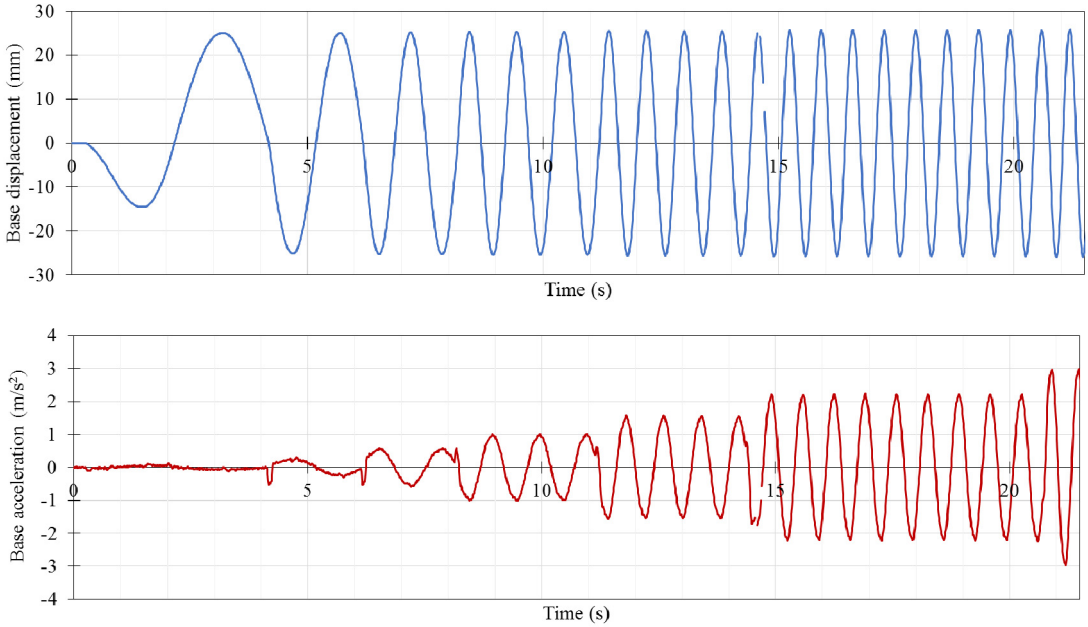


Figure 5: Base displacement and base acceleration time-history for un-strengthened arch ($f_{max}$ = 1.75 Hz).

High speed cameras made it possible to record the formation of hinges and failure of the arch (Figure 7). Arch initially behaved as a rigid body, and there were no hinges visible to the naked eye until t = 15 s. At about t = 20 s four hinges formed alternately at extrados and intrados of the arch. Due to base platform movement in the reverse direction, this hinges then closed but were soon followed by formation of four hinges in an alternate position (i.e. almost mirror symmetric). Note that the location of the hinges is not fixed during the base movement – closure of initial hinges followed by relocation may be observed. A more detailed discussion on the behaviour of a pointed arch tested on a shaking table is given in [14].

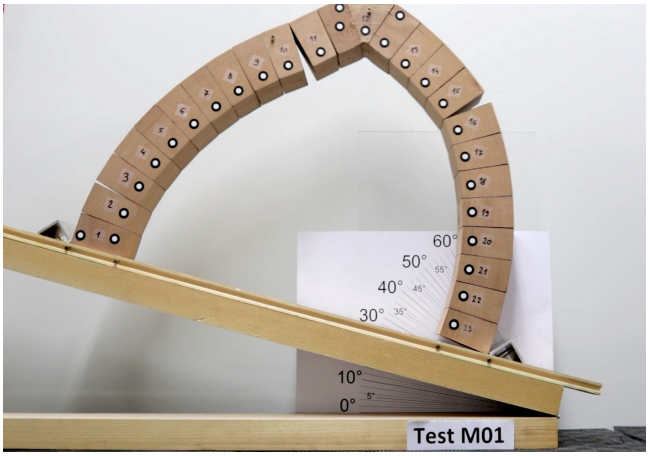


Figure 6: Tilting test (un-strengthened arch)

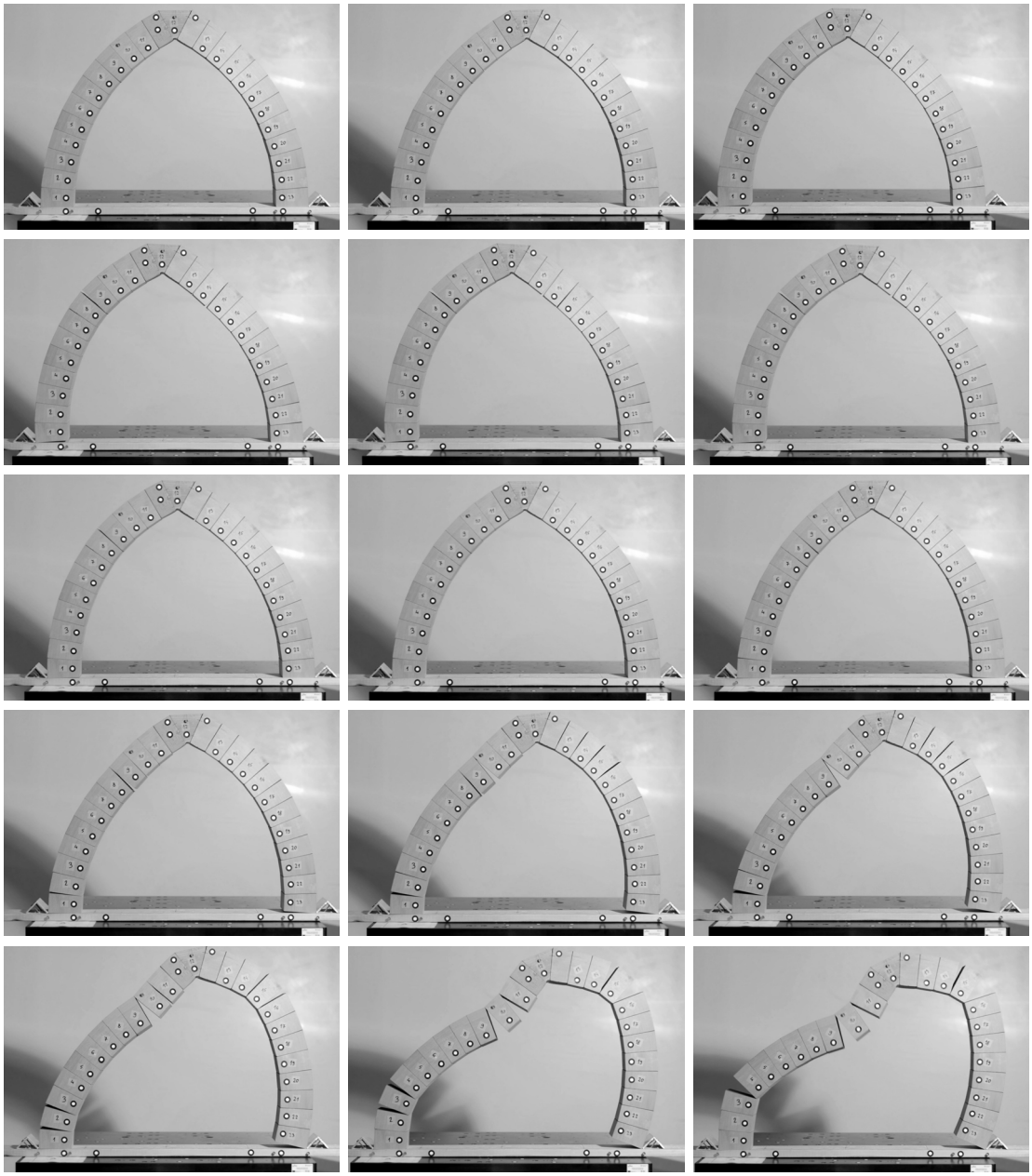

Figure 7: Series of photos documenting hinge formation in un-strengthened pointed arch.

Tilting tests were also conducted (Figure 6). Angle at which the arch transformed into a mechanism was between 16° and 18°, what corresponds to base acceleration 0.29g to 0.32g, and is in good correlation with the maximum acceleration obtained on the shaking table test.

### 3.2 Arch strengthened at extrados

Figure 8 presents the base displacement and base acceleration time-history graphs for arch strengthened at extrados. Part of data that is missing on the graph is due to low quality of images (DIC wasn't able to provide data). The maximum base acceleration recorded was 4.9 $m/s^2$ – a notable increase with respect to the unreinforced arch. Note that the number of cycles that the arch could withstand prior to failure also increased.

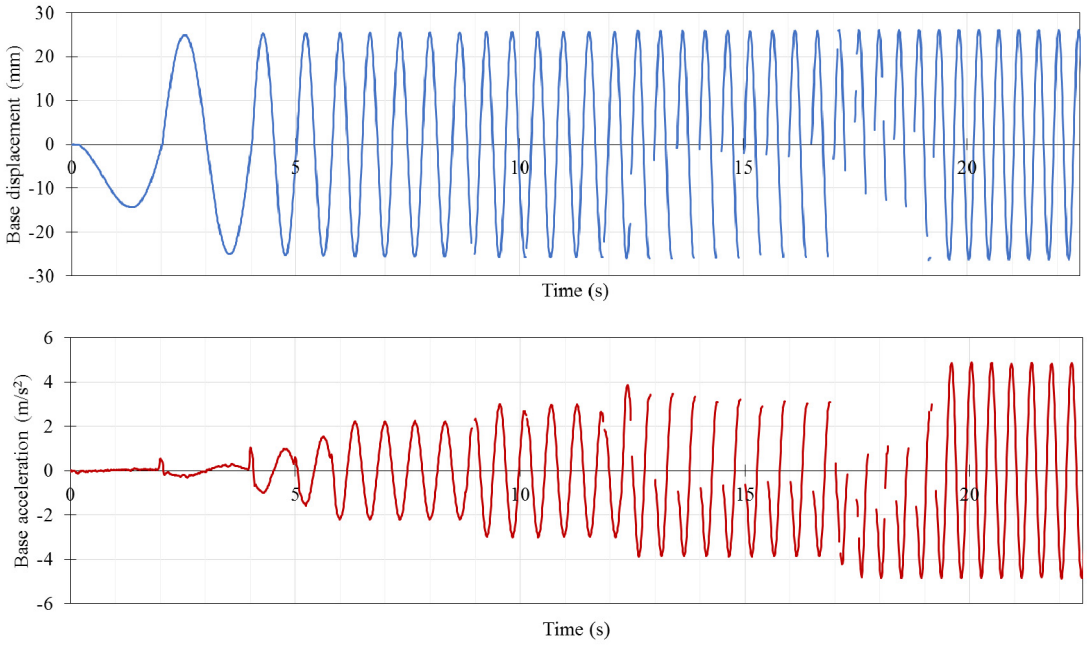


Figure 8: Base displacement and base acceleration time-history for arch strengthened at extrados ($f_{max}$ = 2.25 Hz).

The opening of some hinges is presented in Figure 9, where data series numbers denote the block numbers (for block numeration see Figure 3), while "B" is the base (for example "distance 6-7" denotes the distance between the round point markers located on blocks 6 and 7). Opening and closing of hinges follow the sinusoidal movement of the shaking table.

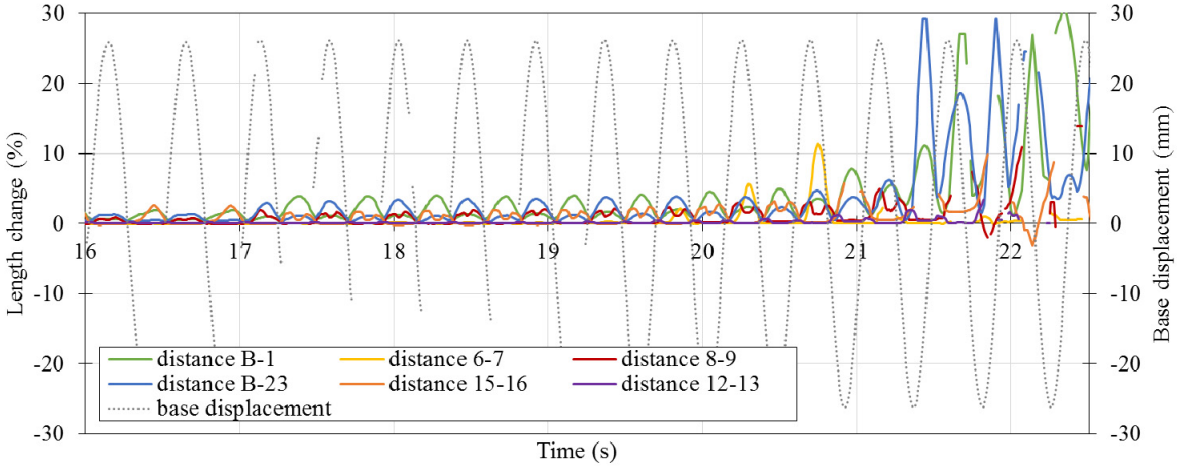


Figure 9: Tracking of openings between blocks via DIC (arch strengthened at extrados).

Figure 10 reports the shaking table testing of arch strengthened at extrados. The failure mechanism differs from the model without reinforcement - the reinforcement applied at extrados prevented opening of hinges at intrados and caused rocking. Finally, the failure occurred due to loss of anchorage at supports, debonding of the tape and shear sliding. The tensile strength of the reinforcement was actually improperly too high selected so that no rupture occurred.

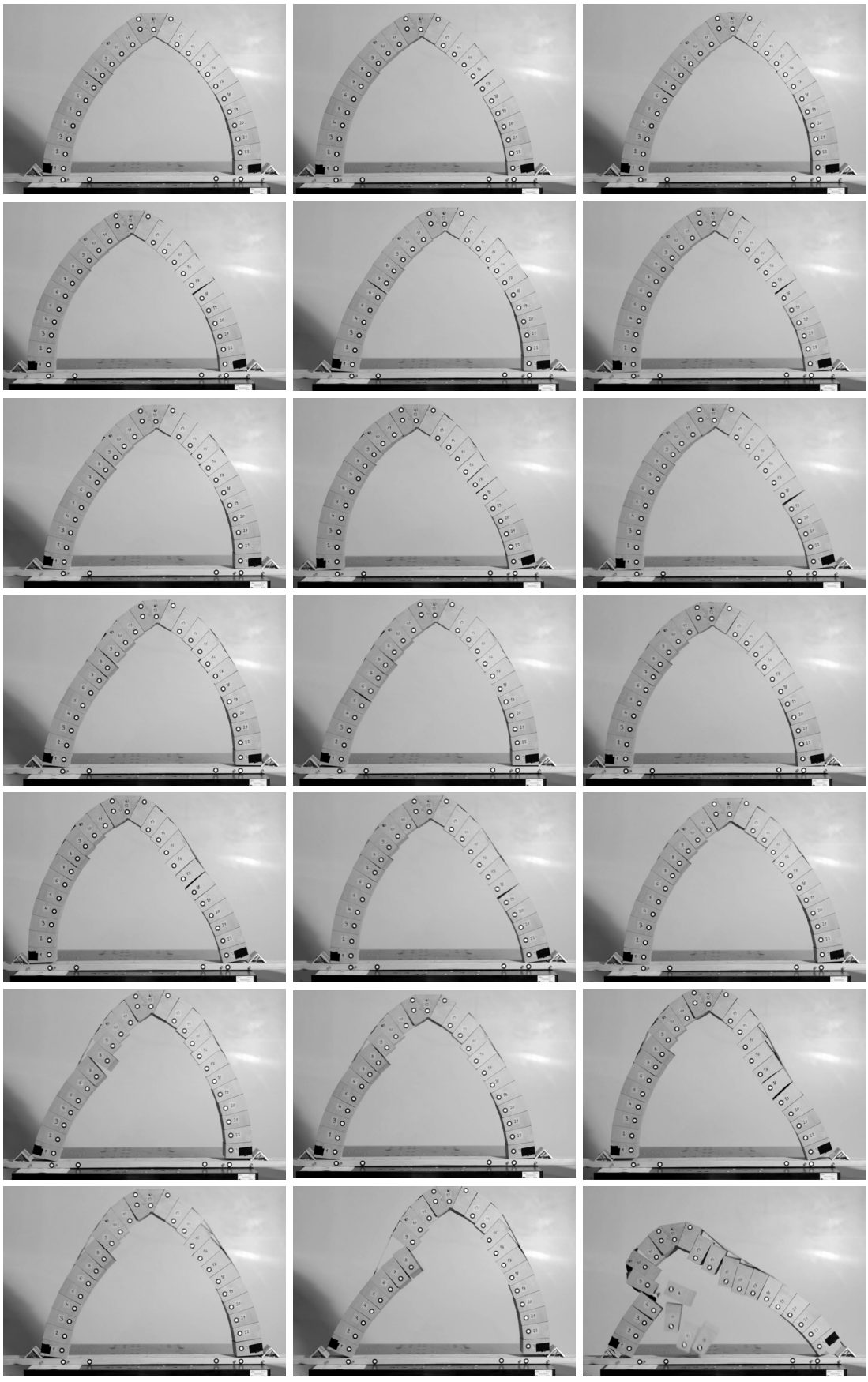

Figure 10: Series of photos documenting testing of pointed arch strengthened at extrados.

### 3.3 Arch strengthened at intrados

Figure 11 presents the base displacement and base acceleration time-history graphs for arch strengthened at intrados. Again, the reinforcement prevented opening of hinges - in this case at the extrados, since the reinforcement is applied at intrados.

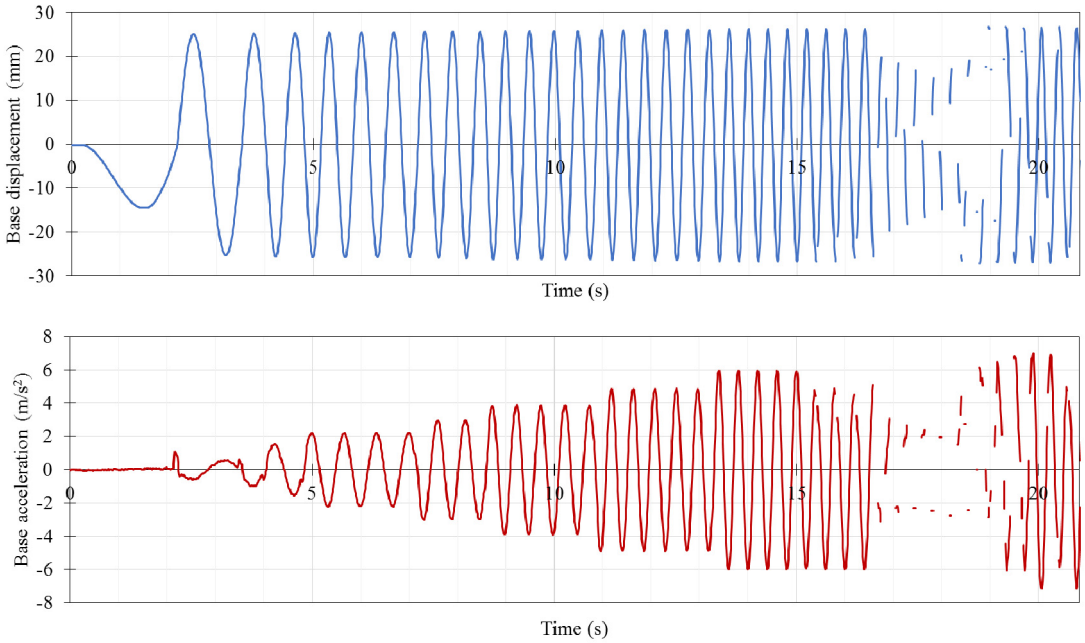


Figure 11: Base displacement and base acceleration time-history for arch strengthened at intrados ($f_{max}$= 2.75 Hz).

The maximum base acceleration recorded was 7.15 m/s$^2$, which is a significant increase when compared with un-strengthened arch, but also with arch strengthened at extrados. This can be attributed to better anchorage of the duct tape to the base plank – in case of intrados strengthening an additional string has been added at the model-base plank joint to hold the tape tightly connected to the base. In the end, it was this string that actually caused the tape to break (the string cut the tape).

Tracking of some hinges is presented in Figure 12, while Figure 13 documents the failure of the arch.

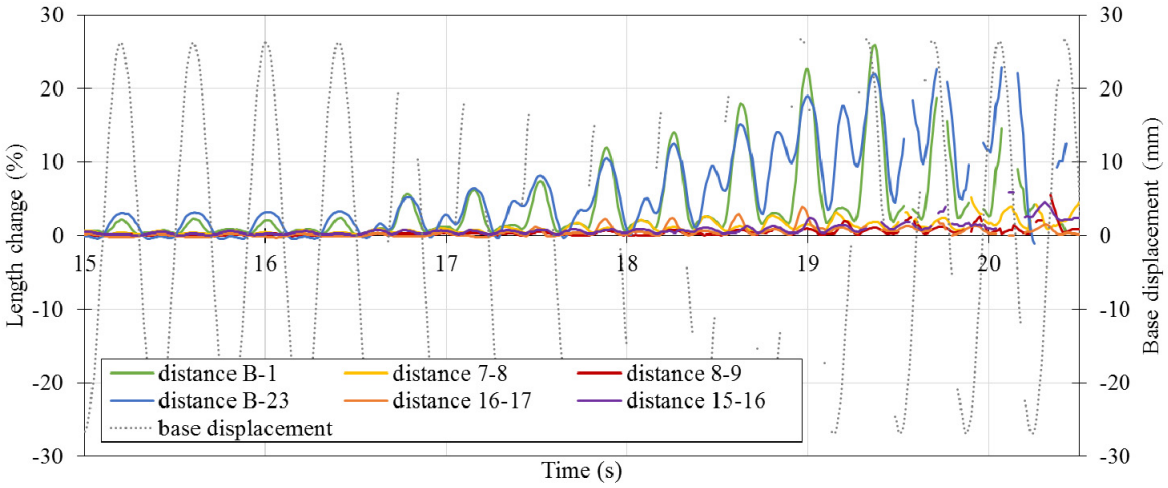


Figure 12: Tracking of openings between blocks via DIC (arch strengthened at intrados).

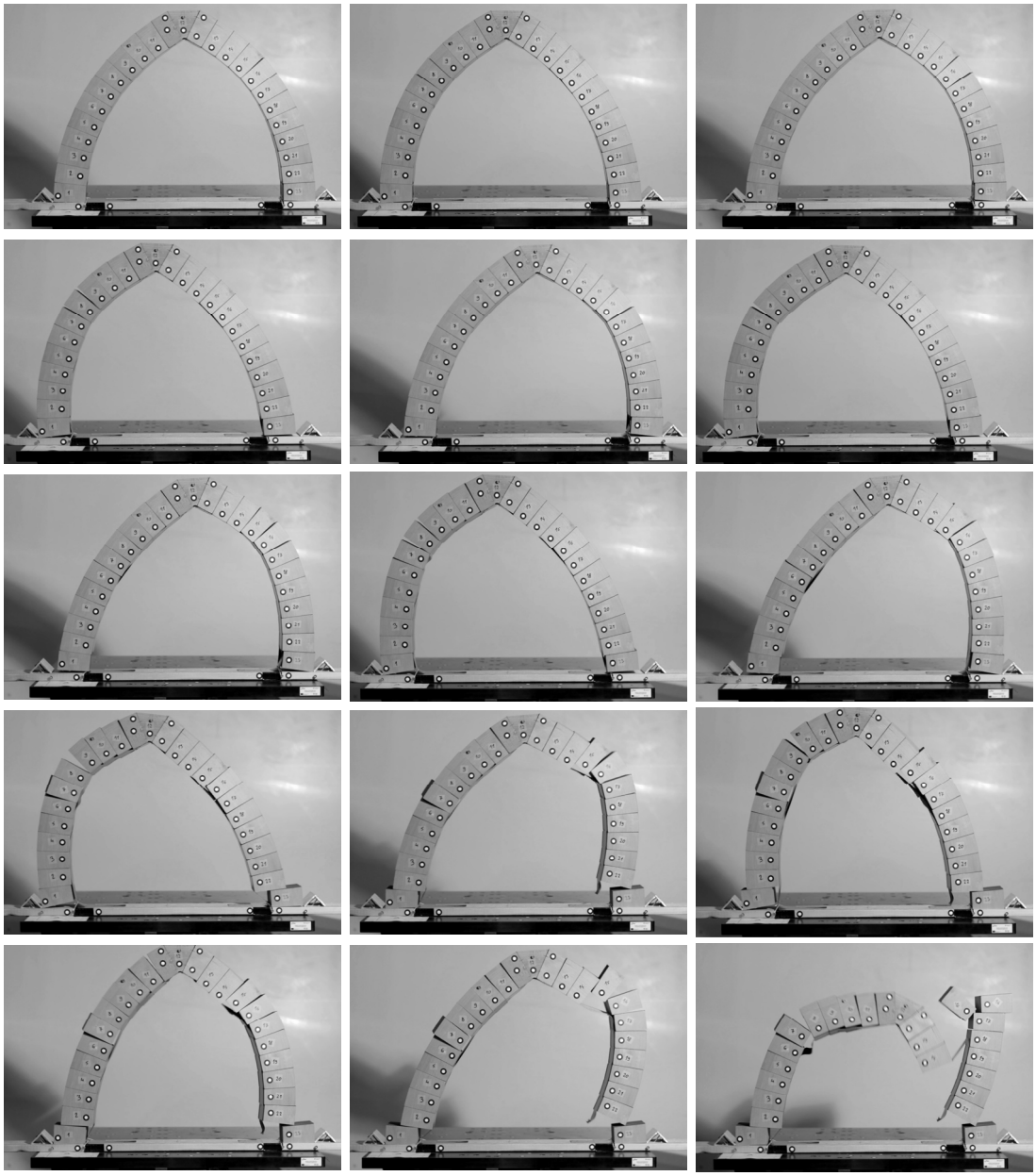

Figure 13: Series of photos documenting testing of pointed arch strengthened at intrados.

## 4 CONCLUSIONS

- In this paper we presented pre-collapse dynamic behaviour of a strengthened pointed arch. To date, shaking table tests haven't been conducted on strengthened pointed arches.
- The arch model was constructed from identical timber blocks with dry joints and subjected to a sinusoidal excitation. Duct tape was used as the strengthening material, simulating FRP/TRM reinforcement, applied either at extrados or intrados of the arch. Although the model is rather simple and low-cost, it can still provide valuable results.
- Due to effect of reinforcement some hinges were hindered, and the seismic capacity was significantly increased for both reinforcing types. The collapse was due to debonding and shear sliding. Arch reinforced at intrados was able to withstand greater base acceleration what is attributed to better anchorage of the reinforcing tape to the base plank.

## 5 ACKNOWLEDGEMENTS

The Authors thank the University of Rijeka for supporting the publication of this paper through grants *ZIP-UNIRI-1500-3-20*, *uniri-mladi-tehnic-20-41 2645* and *uniri-tehnic-18-127*.

## REFERENCES

[1] P. Zampieri, N. Simoncelo, C.D. Tetougueni, C. Pellegrino, A review of methods for strengthening of masonry arches with composite materials. *Engineering Structures*, **171**, 154-169, 2018.

[2] G. Misseri, L. Rovero, G. Stipo, S. Barducci, V. Alecci, M. De Stefano, Experimental and analytical investigations on sustainable and innovative strengthening systems for masonry arches. *Composite Structures*, **210**, 526-537, 2019.

[3] F.G. Carozzi, C. Poggi, E. Bertolesi, G. Milani, Ancient masonry arches and vaults strengthened with TRM, SRG and FRP composites: Experimental evaluation. *Composite Structures*, **187**, 466-480, 2017.

[4] A. Borri, P. Casadei, G. Castori, J. Hammond, Strengthening of brick masonry arches with externally bonded steel reinforced composites. *Journal of Composites for Construction (ASCE)*, **13**, 468-475, 2009.

[5] C. Chisari, D. Cacace, G. De Matteis, Parametric Investigation on the Effectiveness of FRM-Retrofitting in Masonry Buttressed Arches. *Buildings*, **11**, 406, 2021.

[6] P. Roca, P.B. Lourenço, A. Gaetani, *Historic Construction and Conservation: Materials, Systems and Damage*. Routledge, 2019.

[7] F. Di Carlo, S. Coccia, M. Piedigrossi, Dynamics of masonry pointed arches under base motion. *International Journal of Masonry Research and Innovation.* **2**(4), 335-354, 2017.

[8] A. Romano, J.A. Ochsendorf, The mechanics of gothic masonry arches. *International Journal of Architectural Heritage*, **4**(1), 59-82, 2010.

[9] A. Castellano, A. Fraddosio, J. Scacco, G. Milani, M.D. Piccioni, Dynamic Response of FRCM Reinforced Masonry Arches. *Key Engineering Materials*, **817**, 285-292, 2019.

[10] V. Giamundo, G.P. Lignola, G. Maddaloni, F. da Porto, A. Prota, G. Manfredi, Shaking table tests on a full-scale unreinforced and IMG-retrofitted clay brick masonry barrel vault. *Bulletin of Earthquake Engineering*, **14**, 1663–1693, 2016.

[11] G. Misseri, M.J. DeJong, L. Rovero, Experimental and numerical investigation of the collapse of pointed masonry arches under quasi-static horizontal loading. *Engineering Structures*, **173**, 180-190, 2018.

[12] A. Gaetani, P.B. Lourenço, G. Monti, M. Moroni, Shaking table tests and numerical analyses on a scaled dry-joint arch undergoing windowed sine pulses. *Bulletin of Earthquake Engineering*, **15**, 4939-4961, 2017.

[13] Ž. Bistrović, *Colourful trail of Istrian frescoes*. Istria County, Pula, 2011.

[14] P. Šćulac, N. Čeh, Experimental test on a pointed arch model monitored by contactless optical system. *International Journal of Masonry Research and Innovation*, 1-16, 2023.

COMPDYN 2023
9th ECCOMAS Thematic Conference on
Computational Methods in Structural Dynamics and Earthquake Engineering
M. Papadrakakis, M. Fragiadakis (eds.)
Athens, Greece, 12-14 June 2023

# MATERIAL TESTING OF MICRO-CONCRETE AND 3D-PRINTED REINFORCEMENT FOR USE IN SMALL-SCALE SEISMIC TESTING OF RC STRUCTURES

**Medhat Elmorsy[1,2*], Rafal Wrobel[3], Christian Leinenbach[3], Michalis F. Vassiliou[1]**

[1]Chair of Seismic Design and Analysis, Institute of Structural Engineering (IBK),
ETH Zürich Stefano-Franscini-Platz 5 8093 Zürich, Switzerland
{medhat.elmorsy, vassiliou}@ibk.baug.ethz.ch

[2]Structural Engineering Department, Mansoura University, Mansoura, Egypt

[3]EMPA, Swiss Federal Laboratories for Materials Science and
Technology Überlandstrasse 129, CH-8600 Dübendorf
{rafal.wrobel, christian.leinenbach}@empa.ch

## Abstract

*A framework for small scale modeling of RC structures that helps understanding their seismic behavior is discussed in this paper. The framework includes testing of small scale RC buildings manufactured using micro concrete and additively manufactured (3D printed) reinforcement cages on a shake table mounted on a geotechnical centrifuge. This paper presents material level testing of micro-concrete and 3D printed reinforcement that are to be used in the proposed framework. Mechanical properties of the 3D printed rebars are first discussed and compared to full scale rebar mechanical properties. A Concept Laser M2 Laser Powder Bed Fusion (LPBF) printer is used for printing the rebars. In addition, the compressive and tensile behavior of micro-concrete are studied using small scale cylinders and beams (for four-point bending tests), respectively. The results of this paper reveal that the mechanical properties of 3D printed submillimeter rebars can be adjusted by modulating the printing parameters. Moreover, concrete mechanical properties that are suitable for the discussed framework can be achieved.*

**Keywords:** 3D printed reinforcement, Global level assumptions, Small scale modeling, Reinforced concrete structures.

## 1 INTRODUCTION: THE NEED FOR SMALL SCALE TESTING

Experimental testing has always played a vital role in pushing the limits imposed on structural design by modelling uncertainties. Moncarz and Krawinkler [1] identified three basic objectives for which experimental testing is generally conducted; (1) develop or verify component-level force deformation relationships (2) establish loading criteria for environmental effects such as wind and earthquakes (3) study of the structure-level behavior. Structure-level tests are necessary for the validation of the global level (system level) assumptions. Examples of global level assumptions are the ones related to boundary conditions, interaction of components, damping model, numerical integration scheme. In an opinion paper by Bradley [2], these global level assumptions have been identified as a major source of error in numerical modeling of earthquake engineering problems. Uncertainty in earthquake engineering can be categorized into two main classes; ground motion uncertainty (e.g., [3], among others) and modeling uncertainty (e.g., [4-6], among others). Currently, time history analysis is considered as the state of the art in modeling the seismic response of RC structures at the system level. Its most widespread validation procedure is the test of predicting the response of a RC structure tested on a shaking table. However, blind prediction contests show that the contestants fail in predicting the response of the tested specimens with reasonable accuracy, even for structures much simpler than the ones constructed in practice, and even when the structural properties and the measured excitation are given to the contestants [7].

For instance, the simple RC column shown in Figure 1 (left) was tested on the shaking table of UCSD in 2010 under 6 ground motions [8, 9]. A total of 41 expert teams were invited to predict the response. The measured response and the predictions for the maximum top displacement are indicatively shown in Figure 1 (middle). There is a large dispersion in the numerical results and many predictions grossly underestimate or overestimate displacements. Interestingly, after the test series of the six earthquakes, the column did not appear to have failed. However, only 14 out of 41 contestants predicted non-failure, while the rest predicted failure. Within the group that predicted failure, there was a large dispersion related to the mode of failure (Figure 1, right). Similar observations were also seen in the blind prediction contest for a shear wall building slice tested by Panagiotou et al. [10].

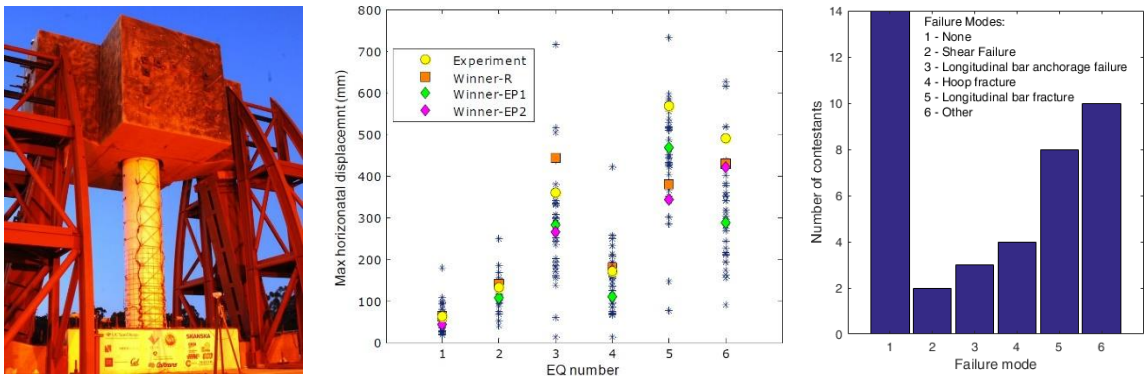


Figure 1: Left: Bridge column tested in UCSD [9]. Middle: Maximum top displacements predicted by the blind prediction contest contestants [8]. Right: Number of predictions for each of the six suggested failure modes [4].

This lack of match between mathematical modeling and experiments happened despite the fact that in such contests, the material level uncertainty is reduced by providing to the contestants the material properties. Moreover, blind prediction contests for cyclic component-

level tests show much better results than the system-level ones [11, 12]. These observations emphasis the importance of validation of the global level assumption.

In parallel, conventional validation test of numerically reproducing the experimentally obtained response to a particular ground motion with acceptable accuracy is too strict of a validation test for structural models [13, 14]. The Earthquake Engineering design problem involves predicting the statistics of the response to an ensemble of ground motions characterizing a given seismic hazard; not to a single ground motion. This is a weaker model validation test that requires that the structural model only be unbiased and introduce less uncertainty than the uncertainty introduced by the excitation itself. In other words, models that can be designated "good", in the scope of earthquake engineering, should introduce less uncertainty than the already-existing motion-to-motion variability [15, 16]. Such statistical procedure is possible at a material or component level, but it is currently impossible at a system level due to the prohibitive cost of performing multiple shake table tests with virgin identical specimens. Moreover, this lack of adequate data has led to very different approaches in modelling, without the experimental tools to create enough data to statistically accept or reject the hypotheses behind them. It is this lack of experimental tools that has led to disagreements between major figures of structural earthquake engineering, in terms of modelling approaches. We believe that this lack of consensus in modelling approaches and the degree of structural modelling accuracy constitutes a major research gap. Therefore, there is a need to develop a methodology to perform low cost system-level seismic testing of RC structures, so that it can be performed multiple times and increase the datasets that we have to calibrate our models on.

To this end, this paper illustrates a framework for small scale (on the order of 1:30 – 1:40) testing of RC structures. The framework is explained in detail in the next section. After illustrating the proposed framework, this paper offers a brief summary of the efforts done as a feasibility study of this framework. Consequently, this paper presents material level testing of micro-concrete and 3D printed reinforcement that are to be used in the proposed framework. Mechanical properties of the 3D printed rebars are first discussed and compared to full scale rebar mechanical properties. In addition, the compressive and tensile behavior of micro-concrete are studied via testing small scale cylinders and beams (for four-point bending tests), respectively.

## 2 PROPSED FRAMEWOEK

This section outlines the framework to validate the global level assumptions that was outlined in the previous section. The framework has two main goals: (1) to develop a methodology for physical modelling of RC at a very small scale. The methodology will be based on 3D printing. We focus on modern (i.e. of the last 30-40 years) ductile buildings to avoid issues related to scaling of shear strength and of bonding behavior (2) to use this approach to statistically evaluate some major assumptions that the structural engineering research community makes to scale up from component-level cyclic behavior to system-level dynamic behavior.

To this end, scaled models (on the order of 1:30) will be constructed and tested both statically and dynamically using a shake table mounted on a geotechnical centrifuge. The scaled reinforcement will be 3D printed using a metal 3D printer, to make the construction of multiple specimens timewise feasible – something that was not possible before 3D printing. Material and component level tests will be performed at the model scale, so that values directly obtained at the scale of the shake table tests are used as input in the numerical models. Although efforts are made to avoid model distortions, it should be acknowledged that scaled models may have some degree of distortion, as concrete properties scale with size, even when scaled aggregates

are used. However, our specimens will serve for numerical model validation of the global level assumptions for given (tested) material and component properties.

## 3 FEASIBILITY STUDY

Recently, as a feasibility study, compression tests of micro-concrete (gypsum and fine silica sand) cylindrical specimens and bending tests of micro-RC beams were performed [17] (Figure 3a). The concrete had a compression strength ranging from 15 to 25 MPa (obtained from tests on 50 x 112 mm cylinders, depending on the mixture ratio and on the type of gypsum) and a tension strength of 2 to 8 MPa obtained from 4-point bending tests on 10 x 10 x 80 mm plain concrete beams). In addition, 3D printed reinforcement was provided for 12.5 x 12.5 x 70 mm beams using Laser Powder Bed Fusion (LPBF) printing technology. The stirrups had a diameter of 0.35 mm and the longitudinal reinforcement a diameter of 0.6 mm (1:40 scaled models of Φ14 and Φ24). The yield strength of the reinforcement was around 400 MPa. The force-deformation curve of the small-scale reinforced concrete beam agreed well with preliminary numerical results obtained with Opensees software platform (using Mander et al. [18] concrete material model).

In addition, Del Giudice et al. [19] performed cyclic tests on 5 small scale micro-concrete beams reinforced with 3D printed stainless steel reinforcement cages (Figure 3b). Concrete with cement/sand/water ratio of 1/1/0.5 by weight was used. All the tested beams failed in bending mode in which fracture of the longitudinal reinforcement was observed. According to their test campaign, the construction of small-scale models was feasible and the behavior of the tested beams resembled the full-scale behavior in terms of strengths and stiffness. Moreover, their numerical models (using Opensees) captured most of the cyclic behavior of the concrete beams. However, there were some limitations: (a) the setup could not apply axial load on the specimens, so only beams (not columns) could be tested (b) there was high variability in steel mechanical properties (c) the numerical analysis performed could not capture the post-peak degradation behavior (d) no characterization of bond behavior between micro-concrete and 3D printed steel was performed. These limitations are to be addressed in this paper.

## 4 3D PRINTED STEEL TENSILE TESTING

In order to study the mechanical properties of the 3D reinforcing bars, two batches of steel rebars were manufactured by Laser Powder Bed Fusion (LPBF) using a Concept Laser M2 printer that is able to manufacture various types of metal. A gas-atomized stainless steel 316L powder with with a mean powder diameter of ~ 32 μm was used as a feedstock material. The printing parameters of each batch are shown in Table 1. Two rebar diameters were tested; 0.8 mm and 0.4 mm, corresponding to 24 mm and 12 mm reinforcing bars in the prototype scale, if a 1:30 scale is assumed. Six rebars were tested for each diameter to evaluate the dispersion among similar rebars. Two different rib configurations were tested; plain rebars (P) and ribbed rebars (D1) with rib parameters as shown in Table 2 according to EN:10080 standard [20]. The rebar with 0.4 mm diameter was only tested with plain surface (without ribs) for two reasons: a) when printing the rebar with ribs, the ribs were barely printed due to the lower accuracy of the printer for such small details b) the 0.4 mm rebar was intended to be used as shear reinforcement (stirrups) in the proposed framework where ribs are not significant. An optical microscope was used to measure the actual diameter of the rebars and to check the general surface deformation of the rebars.

A 200 kN Universal Testing Machine (UTM) at the ETH Zurich was used to perform the tensile tests. Figure 3 shows the test setup used to perform the tests. A pair of 1 kN tension grips were attached to the machine. The specimens were tested under monotonically increasing

displacement with strain rate of 0.015 (1.5%) mm/mm/minute according to [21] until fracture occurs. The strain rate was controlled by the movement of the cross head of the UTM. Strain was also measured using an extensometer attached to the rebar. A 10 kN load cell was used to measure the applied load.



(a)

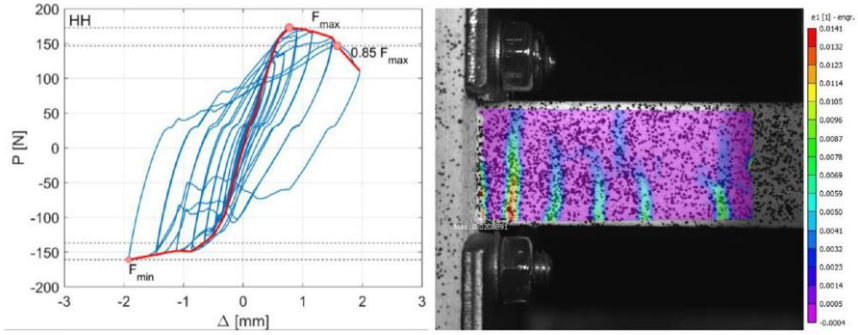


(b)

Figure 2: (a) Four-point bending tests on 3D printed steel reinforced micro-concrete beams [17] (b) Lateral cyclic loading tests on 3D printed steel reinforced micro-concrete columns [19].

| Batch | Laser power [W] | Scanning speed [mm/s] | Hatch spacing [mm] | Layer thickness [mm] | Printing orientation [°] | Number of contours | Contour distance [mm] |
|---|---|---|---|---|---|---|---|
| I | 110 | 300 | 0.01 | 0.03 | 45 | 1 | 0.075 |
| II | 110 | 300 | 0.01 | 0.03 | 45 | 2 | 0.06 |

Table 1: Printing characteristics of the tensile test specimen batches.

| Category | *h* | *c* | *β* |
|---|---|---|---|
| EN:10080 [20] recommended range | 0.03d:0.15d* | 0.40d:1.20d | 35°:75° |
| D1 | 0.10d | 1.00d | 63.43° |

*d is the rebar diameter.

Table 2: Transverse rib parameters for the tested rib configuration.

## 5 CONCRETE COMPRESSION AND FOUR-POINT BENDING TESTS

Two concrete mixes were used to identify favorable concrete mechanical properties that are comparable to prototype scale properties. Two binders were tried according to Table 3. The water binder ratio (W/B) was 0.5 and 0.7 for the mix with cement (mix A) and gypsum (mix B)

binder, respectively. For the two mixes, the sand binder (S/B) ratio was kept constant at 1.0 based on studies by [19, 22]. The sand used in all mixes was Perth silica sand (Crystaline silica $SiO_2$). The testing of the cement concrete mix had been previously tested by Del Giudice et al. [19]. However, since the cement concrete compressive strength, tensile strength, and bond behavior was not comparable to that of the prototype ones as discussed later in this paper, the gypsum mix was manufactured and tested.

Cylinders of 15 mm diameter and 30 mm height were tested under uniaxial compression. For the four-point bending test, beams with 15 mm x 15 mm cross section and 80 mm length (shear span was equal to 20 mm). For each mix, six cylinders and six beams were tested to evaluate the dispersion of flexural and compression strength. A PLA (Polylactic acid) 3D printer was used to print the beam molds while for the cylinder molds, PVC pipes with 15 mm inner diameter were used as molds and then the specimens were cut into 30 mm high pieces.

The same 200 kN UTM with the appropriate attachments was used to perform the compression and the four-point bending on concrete samples. The loading was applied with displacement-controlled increments corresponding to a strain rate of $1\times10^{-5}$ mm/mm/second until failure. Such a strain rate was chosen according to [18] so that strain rate does not affect the behavior of the tested samples.

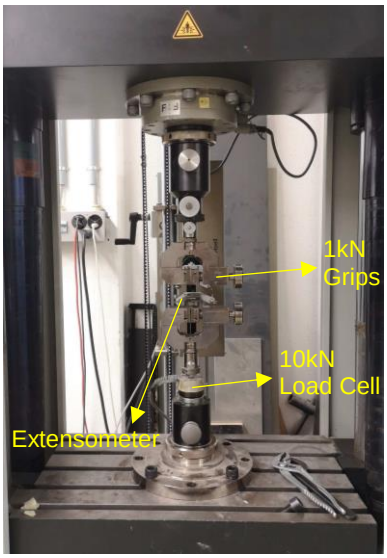


Figure 3: Test Setup for the performed tensile tests.

| Mix | Binder | Binder Commercial name | S/B | W/B | Additives |
|---|---|---|---|---|---|
| A | Cement | Holcim CEM I 42.5N (Normo 4) | 1.0 | 0.5 | 1.0g of Master MasterGlenumACE30 (Superplasticizer) |
| B | Gypsum | Prestia Tradition Plaster | 1.0 | 0.7 | - |

Table 3: Concrete mix details

## 6 TEST RESULTS

### 6.1 Tensile test of reinforcing bars

The stress strain relationship of the 3D printed steel is shown in Figures 4 and 5 for batches I and II, respectively. The average (AVG) and the variability of the data measured by the

coefficient of variation (COV) of the main features of the stress strain relationships is summarized in Table 4. These main features are: a) Elastic modulus ($E_s$) b) Yield strength ($f_y$) c) Ultimate strength ($f_u$) d) Ratio of ultimate to yield strength ($T/Y$) e) Ratio of post yield modulus to elastic modulus ($\alpha$) f) Maximum strain ($\varepsilon_{su}$). Yield Strength value was calculated using the offset of 3‰ as suggested by ASTM E8/E8M-21. In addition, the characteristic parameter values according to the Eurocode for design of concrete structures EC2 [23] are shown in Table 4. These values correspond to 5%, 10%, and 10% percentiles for $f_y$, $T/Y$, and $\varepsilon_{su}$ parameters and are reported to evaluate the resemblance of the small-scale 3D printed rebars to their prototype scale counterparts and the related design code requirements.

According to the Eurocode (EC2), reinforcing bars are divided into three classes according to ductility; A, B, and C with A being the least ductile and C being the most ductile. The requirements for ductility of reinforcing bars in EC2 are as follows:

1. Characteristic yield strength should be in the range of 400 – 500 MPa for all the three ductility classes. The upper limit of the code is imposed for ensuring enough ductility since high yield strength can significantly reduce ductility. The deformed rebars (D1) in the two batches satisfied this requirement. However, the larger diameter plain rebars had yield strength which is lower than the lower limit of the code range of 400 MPa (97.5% and 88.9% of the code minimum for batches I and II, respectively).
2. The ratio of characteristic ultimate strength to the characteristic yield strength ($T/Y$ ratio) should be at least 1.05, 1.08, 1.15 for ductility classes A, B, and C, respectively. The $T/Y$ ratio is mainly responsible for the distribution of plastic deformation over larger distance and avoiding local strain concentrations [24]. Larger $T/Y$ ratios can increase member ductility by increasing the distance over which plastic deformations are distributed [24, 25]. For batch I, all the tested 3D printed bar batches had $T/Y$ ratios of more than 1.21, satisfying the requirements of ductility class C indicating good ductility properties of the rebars from the T/Y point of view. For batch II, only the 0.4 mm bar satisfied class C requirements – while the other rebars satisfied class B requirements.
3. The characteristic ultimate elongation (strain), $\varepsilon_{suk}$, should be at least 2.5%, 5%, and 7.5% for ductility classes A, B, and C, respectively. Along with lower yield strength and high $T/Y$ ratio, increasing the ultimate strain capacity can significantly affect reinforced concrete member ductility. Hassan and Elmorsy [24], based on parametric section analysis, showed that increasing the ultimate steel strain capacity increases the section ductility by up to 100%. Increasing the ultimate steel strain capacity from 0.05 to 0.10 yielded about 100% increase in section curvature ductility [24]. For batch I, the tested rebars had high strain capacities ranging from 6.33% (0.4 mm plain rebar) to 14.06% (0.8 mm plain rebar) indicating high ductility and satisfying ductility class B (for the 0.4 mm plain rebar) and ductility class C (for other rebars) requirements. On the other hand, for batches II, the deformed bars had higher strain capacities (3.28%) than plain rebars. The 0.8 mm defamed rebars in batches II lied between the requirements of the ductility classes A and B. Taking into consideration that the 0.4 mm plain rebars are intended to model stirrups in the proposed framework, the ductility of these rebars are typically not important, especially for modern structures that are mainly designed to fail in flexural hinging mode. The 0.8 mm plain rebars had low maximum strain capacity - $\varepsilon_{suk}$ was 2.32 for batches II, which is below the limit of the least ductile reinforcing bars class of ductility (class A).

On a different note, the variability of the yield strength, ultimate strength, and, accordingly, the $T/Y$ ratio was small (the COV was 6.1% as a maximum value among the three parameters). On the other hand, the variability of the elastic modulus and maximum strain was generally higher. This high variability of the maximum strain capacity contributed to the low characteristics maximum strain compared to the mean/median values.

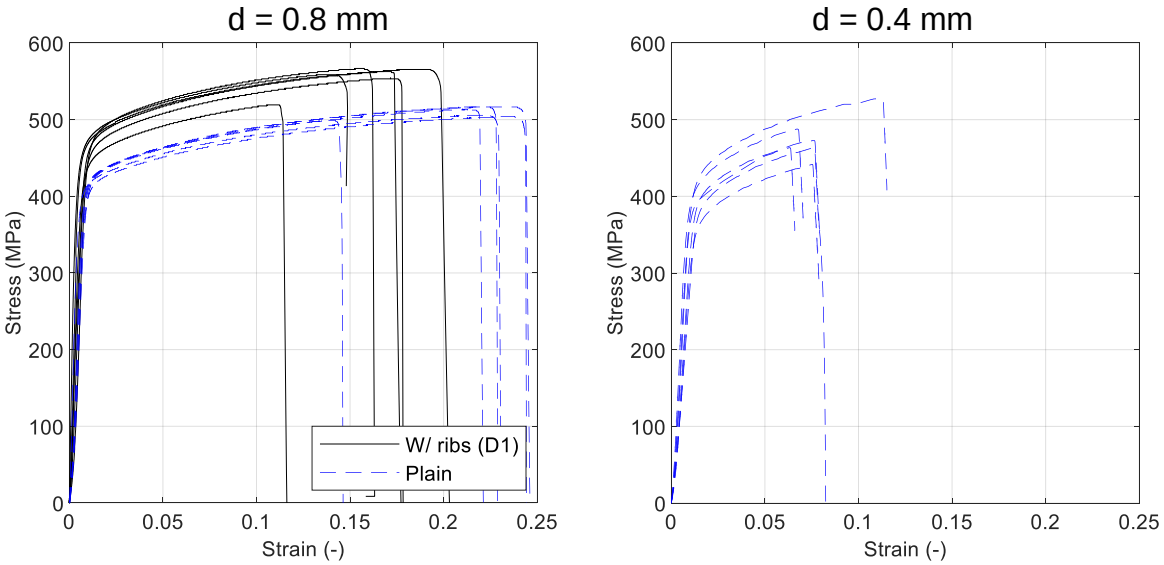


Figure 4: Stress strain relationships of rebars from Batch I.

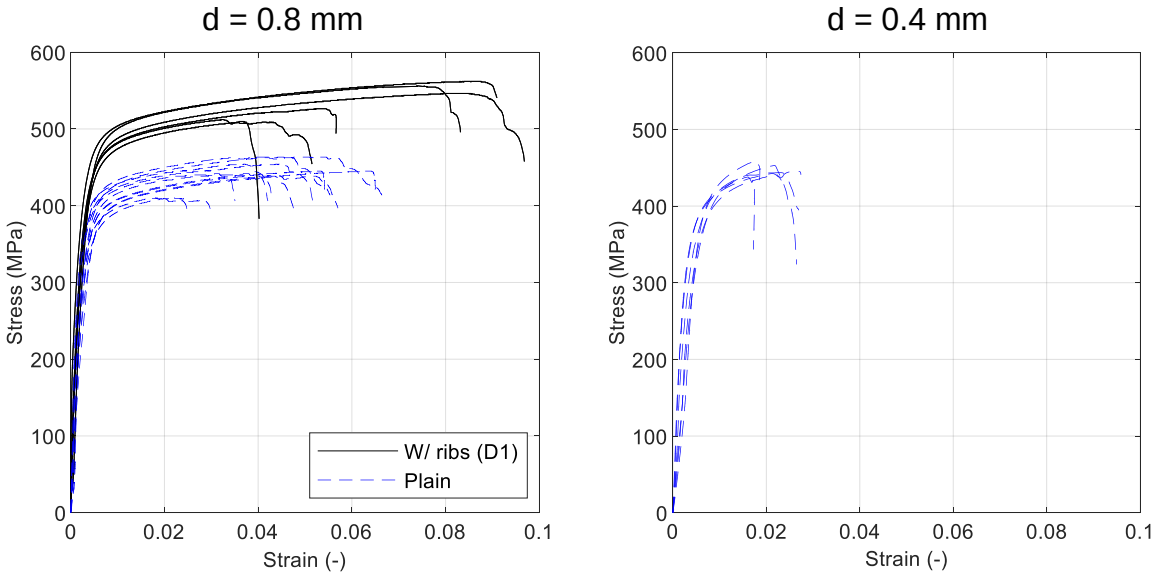


Figure 5: Stress strain relationships of rebars from Batch II.

## 6.2 Concrete compression and four-point bending tests

This section discusses the compressive ($f_c$) and tensile strength (represented by the modulus of rupture, $f_r$) of the two mixes tried in this paper. The cement concrete was left to cure for 28 days before testing while the gypsum concrete was left for only 14 days. The cement concrete mix had average compressive strength 41.04 MPa and the modulus of rupture was 10.38 MPa The measured modulus of rupture is 250% larger than what ACI 318-19 code [26] predicts ($f_r = 0.62\sqrt{f_c} = 3.97$ MPa). While the compressive strength is typical and is frequently encountered in full scale structures, the tensile strength is much higher than the prototype strength which is intelligible because of size effects [27]. The tensile strength of concrete is an important parameter affecting the concrete strength in diagonal tension and resistance to shear, bond strength with bars, and cracking load levels and crack patterns [27]. Therefore, the proper scaling of tensile strength is vital for replication of failure modes and cracking pattern. This

observation motivated the use of other gypsum as a binder instead of cement since it was observed to be less prone to scale effects in previous studies [22, 27, 28].

| Batch | Nominal Diameter [mm] | Actual Diameter [mm] | Rib configuration | | $E_s$ [MPa] | $f_y$ $(Y)$ [MPa] | $f_{yk}$ [MPa] | $f_u$ $(T)$ [MPa] | $T/Y$ | $(T/Y)_k$ | $\alpha$ [%] | $\varepsilon_{su}$ [%] | $\varepsilon_{suk}$ [%] |
|---|---|---|---|---|---|---|---|---|---|---|---|---|---|
| I | 0.80 | 0.75 | P | *AVG* | 71375 | 396.9 | 390.2 | 509.3 | 1.28 | 1.26 | 0.71 | 20.0 | 14.06 |
| | | | | *COV* | 0.203 | 0.011 | - | 0.014 | 0.014 | - | 0.193 | 0.167 | - |
| | 0.80 | 0.75 | D1 | *AVG* | 82848 | 440.3 | 411.6 | 554.5 | 1.26 | 1.21 | 0.68 | 15.0 | 10.8 |
| | | | | *COV* | 0.270 | 0.048 | - | 0.032 | 0.048 | - | 0.281 | 0.178 | - |
| | 0.40 | 0.33 | P | *AVG* | 40226 | 381.9 | 344.8 | 476.0 | 1.25 | 1.21 | 2.91 | 7.8 | 6.33 |
| | | | | *COV* | 0.183 | 0.052 | - | 0.061 | 0.033 | - | 0.179 | 0.212 | - |
| II | 0.80 | 0.96 | P | *AVG* | 198725 | 371.7 | 355.6 | 442.3 | 1.19 | 1.14 | 0.57 | 4.2% | 2.32 |
| | | | | *COV* | 0.101 | 0.053 | - | 0.041 | 0.043 | - | 0.142 | 0.313 | - |
| | 0.80 | 0.96 | D1 | *AVG* | 193637 | 452.4 | 450.9 | 535.4 | 1.18 | 1.12 | 0.54 | 6.0 | 3.28 |
| | | | | *COV* | 0.056 | 0.032 | - | 0.042 | 0.026 | - | 0.095 | 0.357 | - |
| | 0.40 | 0.56 | P | *AVG* | 174340 | 363.3 | 339.0 | 450.9 | 1.25 | 1.16 | 1.88 | 2.1 | 1.62 |
| | | | | *COV* | 0.310 | 0.068 | - | 0.017 | 0.069 | - | 0.459 | 0.177 | - |

Table 4: Tensile test results summary.

For mix B, the average compressive strength was much lower reaching 19.93 MPa. Moreover, the COV for the compressive strength and modulus of rupture were 0.08 and 0.04, respectively. Comparing to prototype scale, the modulus of rupture of mix B was 4.14, which makes it only 49% larger than what ACI 318-19 code [26] predicts ($f_r = 0.62\sqrt{f_c}$ = 2.77 MPa) – indicating an improvement compared to mix A.

| Mix | Binder | S/B | W/B | $f_c$ (AVG) [MPa] | $f_c$ (COV) | $f_r$ (AVG) [MPa] | $f_r$ (COV) | $f_r/f_c$ (AVG) |
|---|---|---|---|---|---|---|---|---|
| A | Cement | 1.0 | 0.5 | 41.04 | 0.11 | 10.38 | 0.14 | 0.25 |
| G | Gypsum | 1.0 | 0.7 | 19.93 | 0.08 | 4.14 | 0.04 | 0.21 |

Table 5: Results of compression and four-point bending tests.

## 7 CONCLUSIONS

This paper illustrated a framework for small scale (on the order of 1:30 – 1:40) testing of RC structures. Moreover, this paper presents material level testing of micro-concrete and 3D printed reinforcement that are to be used in the proposed framework. Mechanical properties of the 3D printed rebars are first discussed and compared to full scale rebar mechanical properties. In addition, the compressive and tensile behavior of micro-concrete are studied via testing small scale cylinders and beams (for four-point bending tests), respectively. Through the test results of the material tests performed in this paper, the following conclusions can be drawn:

- The mechanical properties of 3D printed submillimeter rebars can be adjusted by modulating the printing parameters. Moreover, concrete mechanical properties that are suitable for the discussed framework can be achieved.
- Obtaining mechanical properties of 3D printed submillimeter bars that are comparable to full scale prototype rebars seems feasible.
- Attention should be paid to scaling effects of concrete in tension and bonding since these both properties control cracking pattern and failure mode. Using gypsum as a binder produced closer concrete mechanical properties as compared to full scale concrete.

## ACKNOWLEDGEMENTS

This work was supported by the ETH Zurich under grant ETH-11 21-1.

## REFERENCES

[1] P. Moncarz, H. Krawinkler. Theory and Application of Experimental Model Analysis in. Earthquake Engineering, John A Blume Earthquake Engineering Center, Department of Civil Engineering, Stanford, Calif. 1981.

[2] B.A. Bradley. A critical examination of seismic response uncertainty analysis in earthquake engineering. *Earthquake engineering & structural dynamics*. 2013;42(11):1717-29.

[3] M. Elmorsy, M.F. Vassiliou. Effect of ground motion processing and filtering on the response of rocking structures. *Earthquake Engineering & Structural Dynamics*. 2023.

[4] M. Elmorsy. Nonlinear Modeling Parameters for Beam-Column Joints in Seismic Analysis of Concrete Buildings: Master Thesis, University of Alaska Anchorage; 2020.

[5] W.M. Hassan, M. Elmorsy. Probabilistic Beam–Column Joint Model for Seismic Analysis of Concrete Frames. *Journal of Structural Engineering*. 2022;148(4):04022011.

[6] W.M. Hassan WM, M. Elmorsy. Cyclic nonlinear modeling parameters for unconfined beam-column joints. *ACI Struct J*. 2022;119(1):89-104.

[7] P. Fajfar. Analysis in seismic provisions for buildings: past, present and future. Recent Advances in Earthquake Engineering in Europe: *16th European Conference on Earthquake Engineering*-Thessaloniki 2018; 2018: Springer.

[8] V. Terzic, M.J. Schoettler, J.I. Restrepo, S.A. Mahin. Concrete column blind prediction contest 2010: outcomes and observations. *PEER Report*. 2015;1(2015):1-145.

[9] M.J. Schoettler, J.I. Restrepo, G. Guerrini, D.E. Duck, F. Carrea. A full-scale, single-column bridge bent tested by shake-table excitation. Center for Civil Engineering Earthquake Research, Department of Civil Engineering, University of Nevada. 2012.

[10] M. Panagiotou, J.I. Restrepo, J.P. Conte. Shake-table test of a full-scale 7-story building slice. Phase I: Rectangular wall. *Journal of Structural Engineering*. 2011;137(6):691-704.

[11] M. Trüb. Numerical modeling of high-performance fiber reinforced cementitious composites. *IBK Bericht*. 2011;333.

[12] X. Lin, X. Lu. Numerical models to predict the collapse behavior of RC columns and frames. *The Open Civil Engineering Journal*. 2017;11(1).

[13] J. Bachmann, M. Strand M, M.F. Vassiliou, M. Broccardo, B. Stojadinovic. Is rocking motion predictable? *Earthquake Engineering & Structural Dynamics*. 2018;47(2):535-52.

[14] J. Bachmann, M. Strand M, M.F. Vassiliou, M. Broccardo, B. Stojadinovic. Modelling of rocking structures: Are our models good enough? *Online Proceedings: 2nd International Conference on Natural Hazards & Infrastructure (ICONHIC 2019)*; 2019: National Technical University of Athens.

[15] A.A. Katsamakas, M.F. Vassiliou. Finite element modeling of free‐standing cylindrical columns under seismic excitation. Earthquake Engineering & Structural Dynamics. 2022;51(9):2016-35.

[16] A.A. Katsamakas, M.F. Vassiliou. Experimental parametric study and phenomenological modeling of a deformable rolling seismic isolator. Earthquake Engineering and Structural Dynamics (accepted for publication). 2022.

[17] L. Del Giudice, R. Wróbel, C. Leinenbach, M.F. Vassiliou. Static testing of additively manufactured microreinforced concrete specimens for statistical structural model validation at a small scale. *8AESE Abstract Book*. 2020:78-85.

[18] J.B. Mander, M.J. Priestley, R. Park. Theoretical stress-strain model for confined concrete. *Journal of structural engineering*. 1988;114(8):1804-26.

[19] L. Del Giudice, R. Wróbel, A.A. Katsamakas, C. Leinenbach, M.F. Vassiliou. Physical modelling of reinforced concrete at a 1: 40 scale using additively manufactured reinforcement cages. *Earthquake Engineering & Structural Dynamics*. 2022;51(3):537-51.

[20] EN:10080, Steel for reinforcement of concrete – weldable reinforcing steel – general. 2021.

[21] Standard test methods for tension testing of metallic materials: ASTM international; 2016.

[22] J. Knappett, C. Reid, S. Kinmond, K. O'Reilly. Small-scale modeling of reinforced concrete structural elements for use in a geotechnical centrifuge. *Journal of Structural Engineering*. 2011;137(11):1263-71.

[23] Eurocode 2: Design of concrete structures—. Part. 2004;1(1):230.

[24] W.M. Hassan W, M. Elmorsy. Database trends and critical review of seismic performance tests on high strength steel reinforced concrete components. *Engineering Structures*. 2021; 239:112092.

[25] D. Sokoli. Fracture of high-strength bars in concrete frame members under earthquake loads: PhD Thesis, The University of Texas at Austin; 2018.

[26] H.G. Harris, G. Sabnis. Structural modeling and experimental techniques: CRC press; 1999.

[27] M. Loli, J.A. Knappett, M.J. Brown, I. Anastasopoulos, G. Gazetas. Centrifuge modeling of rocking‐isolated inelastic RC bridge piers. *Earthquake engineering & structural dynamics*. 2014;43(15):2341-59.

[28] Building code requirements for structural concrete (ACI 318-19) and commentary, 2019: American Concrete Institute.

COMPDYN 2023
9th ECCOMAS Thematic Conference on
Computational Methods in Structural Dynamics and Earthquake Engineering
M. Papadrakakis, M. Fragiadakis (eds.)
Athens, Greece, 12-14 June 2023

# VERIFICATION OF MATERIAL MODELS FOR MASONRY WALLS IN NONLINEAR PUSHOVER ANALYSIS

**H. He**[1] **and S. J. H. Meijers** [2]

[1 2]Advanced Technology and Research, Industry & Buildings, HaskoningDHV Nederland B.V., Rotterdam, the Netherlands
[1]e-mail: huan.he@rhdhv.com; [2]e-mail: sander.meijers@rhdhv.com

## Abstract

*Masonry material model used in the non-linear pushover (NLPO) analysis plays an important role for the building responses. Different material models based on the smeared failures for unreinforced masonry (URM) wall are tested and compared in the in-plane nonlinear pushover analysis in this study. Special attentions are paid on the base shear versus displacement curves and the failure modes (crack pattern) in the analysis. Influences by the geometric shape ratio (i.e. height/width), the overburden level, boundary conditions and masonry type are discussed in the paper. Meanwhile, numerical results of selected URM walls with different material models are compared to the analytical ones based on the codes. Eventually, the most suitable material model for masonry walls in NLPO analysis is identified in the paper.*

**Keywords:** Unreinforced masonry walls, Nonlinear pushover analysis, Engineering masonry model, FEM.

## 1 INTRODUCTION

The seismic risk in Groningen area of the Netherlands is induced by the gas extraction. The frequency of the shallow earthquakes is generally increased year by year (over 80 times per year in the recent decade), which received a great concern by the Dutch society. Therefore, a framework for the seismic assessment and retrofitting design of structures in the Groningen region, called VIIA, was initiated and developed from 2015. Different approaches have been used for the purpose of seismic analysis, *e.g.* modal response spectrum (MRS) analysis, nonlinear pushover (NLPO) analysis, nonlinear time-history (NLTH) analysis and reference approach, *etc*.

NLPO analysis is a simple static seismic technique, which is therefore commonly used for the evaluations of existing buildings. In the NLPO analysis, the determination of a global base shear versus displacement curve (called the pushover curve) is fundamental for the assessment. Meanwhile, unreinforced masonry (URM) wall is one of the most vulnerable structural elements for the buildings in the area. The selection of material models of masonries can directly influence the performances of buildings in NLPO analysis. Therefore, it is crucial to identify the performances of different material models for masonry in the NLPO analysis using a FEA software, *i.e.* DIANA[1].

The global behavior of building in NLPO analysis is largely influenced by the in-plane response of individual components in the structure system such as the piers and spandrels. Accordingly, in-plane pushover tests on single unreinforced masonry (URM) walls with different material models are performed in DIANA software in the study. The base shear versus displacement curves and the failure modes (crack pattern) will be focused in the analysis. For URM walls, the maximum shear capacity and the expected failure modes are influenced by the geometric shape ratio (height/width, H/L), the overburden level, boundary conditions and masonry types. It can also be estimated based on formulas from codes, e.g. NPR 9998:2017[2], Eurocode 6[3]. Therefore, selected URM walls with different material model are tested in NLPO analysis and the results are compared to the analytical ones. The most suitable material model for masonry walls in NLPO analysis is, therefore, identified.

## 2 MASONRY MATERIAL MODEL

Masonry is one of the oldest but still popular construction materials. Its properties largely depend on the components and the arrangement. Generally, there are two modelling methods used for the simulation of masonry, *i.e.* micro-modelling and macro-modelling[4]. Every component of masonry is separately modelled by the micro-modelling method. Therefore, the crack propagation and failure mechanism can be realistically simulated detailly by this method. However, this method is not feasible for the structural assessment of large masonry buildings due to the computational consumption. Therefore, macro-modelling method is a good alternative. It considers masonry as a composite material. Generally, continuum and homogeneous properties are assumed for the masonry by this method.

Total Strain Crack Model (TSCM) is one of the continuum constitutive models, which can be used for the simulation of masonry. It follows a smear approach for the fracture energy[1]. Regarding its evaluation of stress-strain relationship, one method is following the principal direction of strain vector, which is called the rotating crack model (TSCM-rotating). Another method is using the fixed coordination system, which is called the fixed crack model (TSCM-fixed) [1]. Both of these two approaches use a secant-based loading-unloading curve. Therefore, it underestimates the energy dissipation of masonry under the cyclic loading compared to the experimental references[5]. Meanwhile, TSCM is developed for the isotropic materials, which is not the case for masonry.

Therefore, a comprehensive masonry material model *i.e.* Engineering Masonry Model (EMM) has been developed in DIANA, which can consider the orthotropic mechanical properties (in tension, compression and shear) and hysteresis damping effects[5]. The new developed model has been verified by the comparison with quasi-static experimental references both under in-plane and out-of-plane (OOP) loadings[5]. One example comparison was done with a OOP pushover test[6,7], shown in Figure 1. Moreover, a comparison study has been done with the dynamic one-way out-of-plane shaking table tests[8], which validated the EMM parameters.

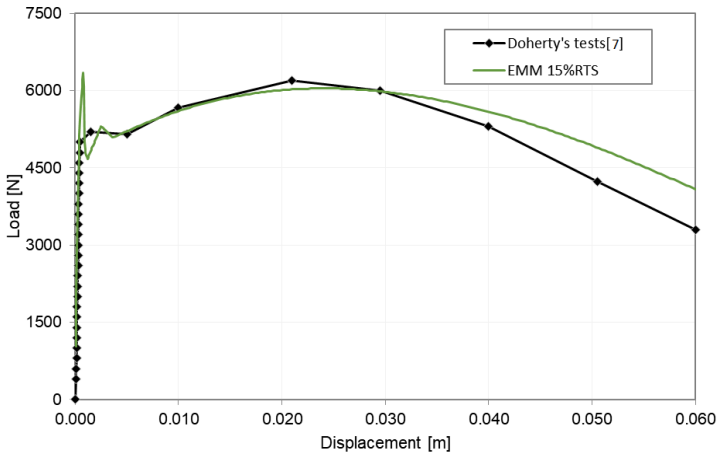


Figure 1: Static pushover comparison under OOP loading[6]

## 3 TESTING MODELS

The material models tested in this report are the Engineering Masonry Model (EMM) and the two Total Strain-based Crack Models, *i.e.* TSCM-rotating and TSCM-fixed. For the application of the incremental load, a simple top (whole edge tied) horizontal displacement-controlled pushover method is used in the test. There are two vertical constrain conditions for the top edge: free and entirely fixed, which will be discussed separately later in the study. The masonry walls are all 2.76 m high and 0.102 m thick, but with different width (the different shape ratio H/Ls, see Figure 2). Three types of Groningen masonries made by clay bricks, defined in NPR 9998:2017[2], *i.e.* normal clay brickwork pre 1945 (BKv), poor clay brickwork pre 1945 (BKvl) and clay brickwork post 1945 (BKn), are used in the tests (listed Table 1). Other materials parameters of masonries can be referred by Table F2 of NPR 9998:2017[2]

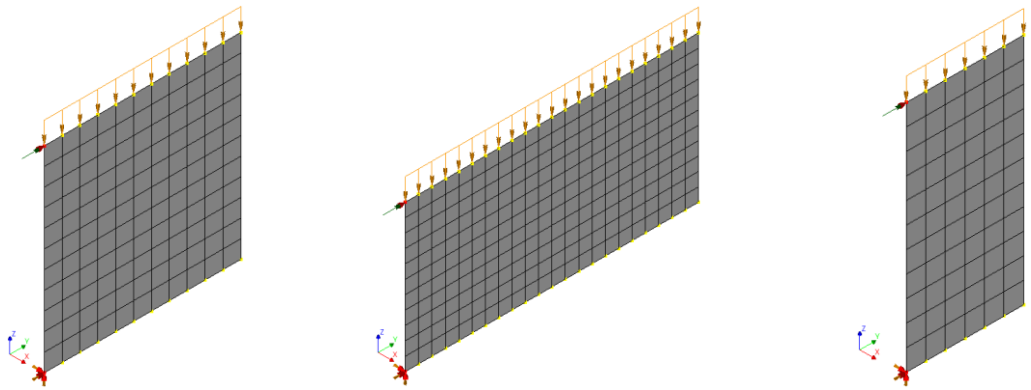

(a) (b) (c)

Figure 2: Three models used in the study with different shape ratios: (a)H/L=1; (b) H/L=1:2; (c) H/L=2:1

| Masonry | $f_c$ (N/m$^2$) | L (m) | H/L (-) | R_OB1 (-) | OB1 force (N/m) | R_OB2 (-) | OB2 force (N/m) | Visualization |
|---|---|---|---|---|---|---|---|---|
| BKv | 8.50E+06 | 2.76 | 1 | 0.2 | 1.73E+05 | 0.02 | 1.73E+04 | 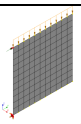 |
| BKvl | 5.10E+06 | 2.76 | 1 | 0.2 | 1.04E+05 | 0.02 | 1.04E+04 | |
| BKn | 1.00E+07 | 2.76 | 1 | 0.2 | 2.04E+05 | 0.02 | 2.04E+04 | |
| BKv | 8.50E+06 | 5.52 | 0.5 | 0.2 | 1.73E+05 | 0.02 | 1.73E+04 | 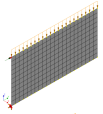 |
| BKvl | 5.10E+06 | 5.52 | 0.5 | 0.2 | 1.04E+05 | 0.02 | 1.04E+04 | |
| BKn | 1.00E+07 | 5.52 | 0.5 | 0.2 | 2.04E+05 | 0.02 | 2.04E+04 | |
| BKv | 8.50E+06 | 1.38 | 2 | 0.2 | 1.73E+05 | 0.02 | 1.73E+04 | 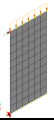 |
| BKvl | 5.10E+06 | 1.38 | 2 | 0.2 | 1.04E+05 | 0.02 | 1.04E+04 | |
| BKn | 1.00E+07 | 1.38 | 2 | 0.2 | 2.04E+05 | 0.02 | 2.04E+04 | |

*Note: $f_c$: compressive strength of masonry; OB: overburden load; R_OB: ratio of overburden load to the compressive strength of the masonry, $P_{OB}/f_c$;*

Table 1: Specifications of tested models.

## 4 ANALYTICAL ESTIMATION

NPR9998:2017[2] specifies different failure mechanisms and the corresponding shear capacities. Diagonal tensile capacity failure occurs when the principal stress is exceeding diagonal tensile strength. Toe crushing failure should also be considered for the shear loading. Rocking failure occurs commonly when wall is slender and mortar strength is relatively good. Bed-joint sliding is a stable mode of failure, which should be considered in the evaluation. Different capacities due to different mechanisms are specified in Table 2 following NPR 9998:2017[2]. Moreover, Eurocode 6 specifies shear capacities of walls with similar but simpler formulas[3].

| Failure mechanism | *Capacity* formula | Explanation |
|---|---|---|
| Diagonal tensile capacity (DTC) $V_{dt}$ | $V_{dt} = f_{dt} \times A_n \times \beta \times \sqrt{1 + \frac{f_a}{f_{dt}}}$<br>$f_{dt} = 0.5 \times c + f_a \times \mu_f$ | $\beta$ is a nonlinear corrector factor, which is 0.67 if H/L>1.5 and 1.0 if H/L<0.5;<br>$A_n$ is the net area of mortared/grouted section;<br>$f_{dt}$ is the masonry tensile strength;<br>$f_a$ is the axial compressive stress at mid-height;<br>$c$ is the bed-joint cohesion;<br>$\mu_f$ is the frictional coefficient;<br>$\alpha$ is a boundary factor, which equals 0.5 for fix-free cantilever and equals 1 for fixed-fixed case;<br>$P$ is the overburden load at top of wall;<br>$P_w$ is the self-weight of wall;<br>$t_{norm}$ is the nominal thickness of masonry brick excluding pointing. |
| Toe crushing $V_{tc}$ | $V_{tc} = (\alpha \times P + 0.5 \times P_w)(\frac{L}{H})(1 - \frac{f_a}{f_c})$ | |
| Rocking strength $V_r$ | $V_r = 0.9 \times [(\alpha \times P) + (0.5 \times P_w)] \times (\frac{L}{H})$ | |
| Bed-joint sliding (BJS) $V_s$ | $V_s = 0.7 \times [t_{norm} \times L \times c + \mu_f (P + P_w)]$ | |

Table 2: Different capacity formulas based on the failure mechanisms in NPR9998:2017[2].

## 5 RESULTS AND DISCUSSION

Based on the above specifications, different wall models are tested in in-plane NLPO analysis by DIANA. Only some selected results are presented in the paper due to the space limitation. The pushover curves and corresponding crack patterns at the peak force with different material models are shown for the different cases. Figure 3 and Figure 4 are for the case with H/L=1.0, BKv material, overburden OB1 and the fixed-free boundary condition. Figure 5 and Figure 6 are for the case with H/L=1.0, BKv material, overburden OB2 and the fixed-free boundary condition. Figure 7 and Figure 8 are for the case with H/L=0.5, BKv material, overburden OB1 and the fixed-free boundary condition. Figure 9 and Figure 10 are for the case with H/L=2.0, BKv material, overburden OB1 and the fixed-free boundary condition. Figure 11 and Figure 12 are for the case with H/L=1.0, BKv material, overburden OB1 and the fixed-fixed boundary condition.

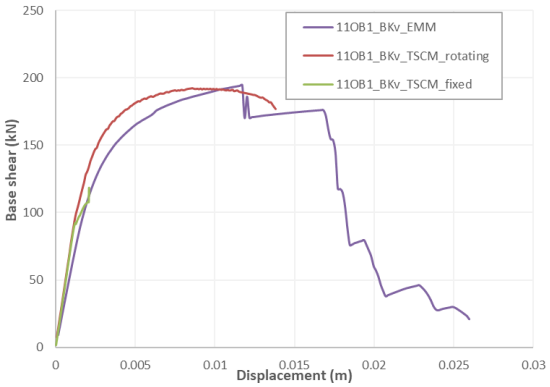


Figure 3: Base shear-displacement curves for walls with H/L=1.0, BKv material, overburden OB1, fixed-free boundary condition and different material models

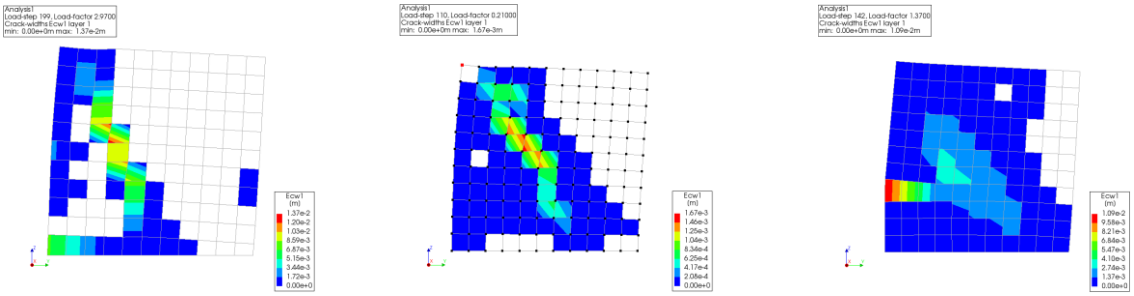

(a) (b) (c)

Figure 4: Crack width patterns of masonry walls at the peak force with condition of Figure 3: (a) EMM; (b)TSCM-fixed; (c)TSCM-rotating.

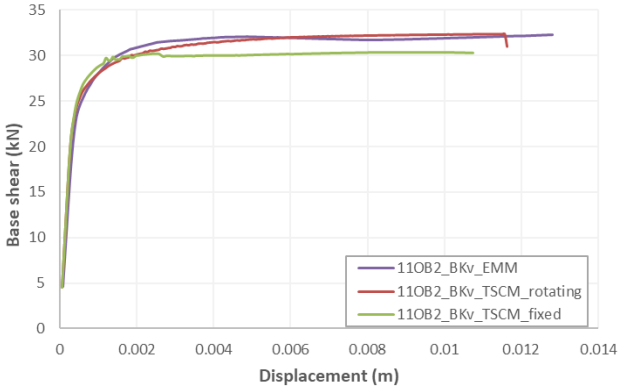


Figure 5: Base shear-displacement curves for walls with H/L=1.0, BKv material, overburden OB2, fixed-free boundary condition and different material models

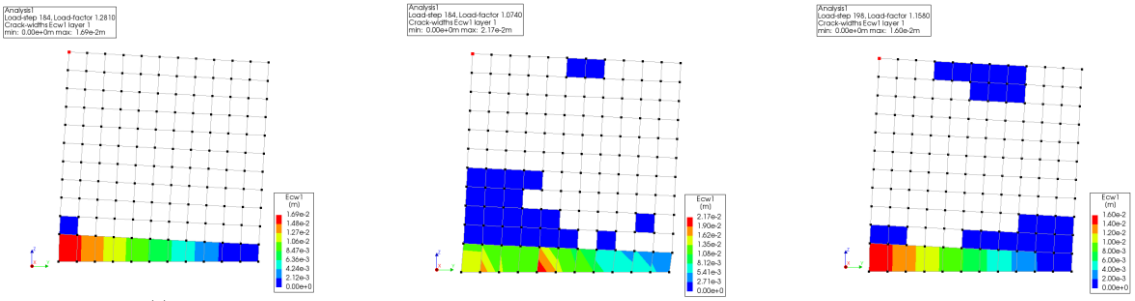

(a) (b) (c)

Figure 6: Crack width patterns of masonry walls at the peak force with condition of Figure 5: (a) EMM; (b)TSCM-fixed; (c)TSCM-rotating.

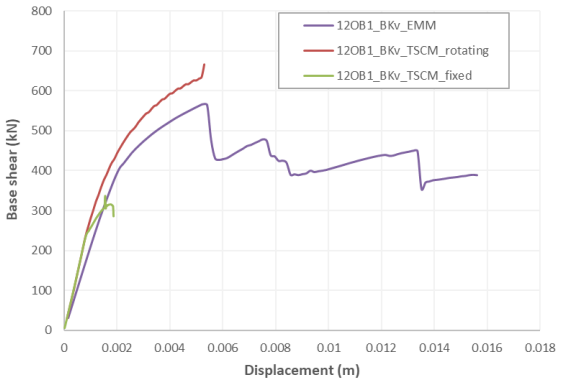


Figure 7: Base shear-displacement curves for walls with H/L=0.5, BKv material, overburden OB1, fixed-free boundary condition and different material models

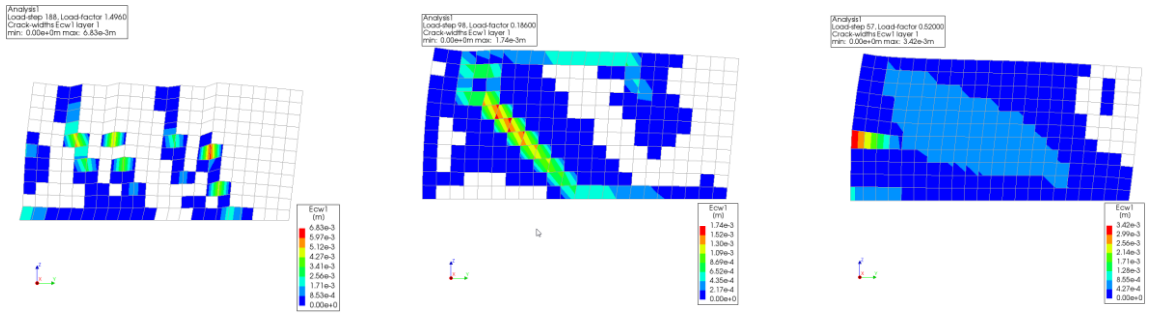

(a) (b) (c)

Figure 8 Crack width patterns of masonry walls at the peak force with condition of Figure 7: (a) EMM; (b)TSCM-fixed; (c)TSCM-rotating.

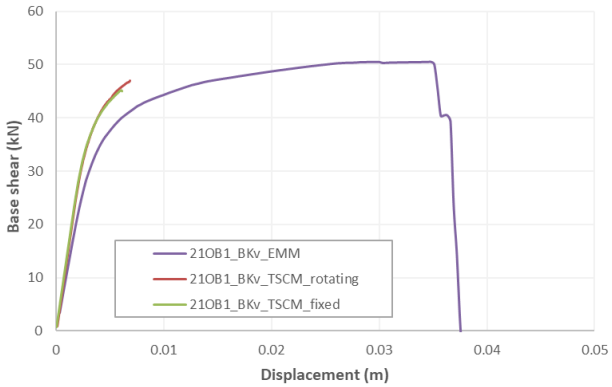


Figure 9: Base shear-displacement curves for walls with H/L=2, BKv material, overburden OB1, fixed-free boundary condition and different material models

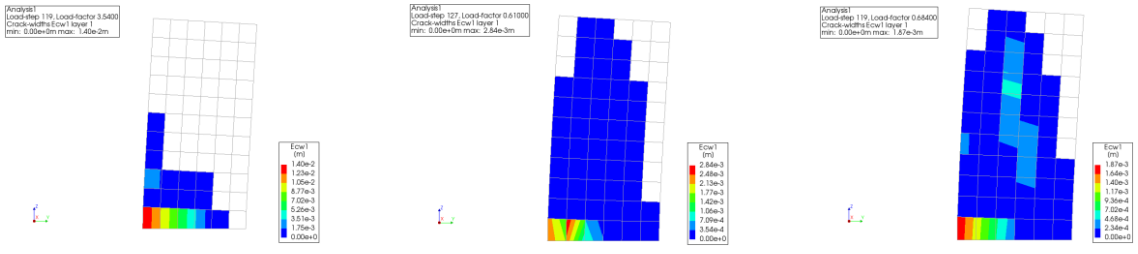

(a) (b) (c)

Figure 10: Crack width patterns of masonry walls at the peak force with condition of Figure 9: (a) EMM; (b)TSCM-fixed; (c)TSCM-rotating.

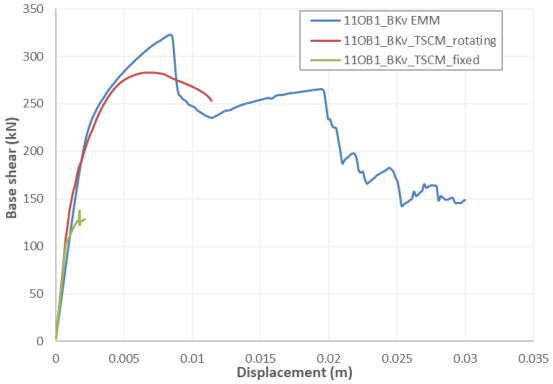


Figure 11: Base shear-displacement curves for walls with H/L=1, BKv material, overburden OB1, fixed-fixed boundary condition and different material models

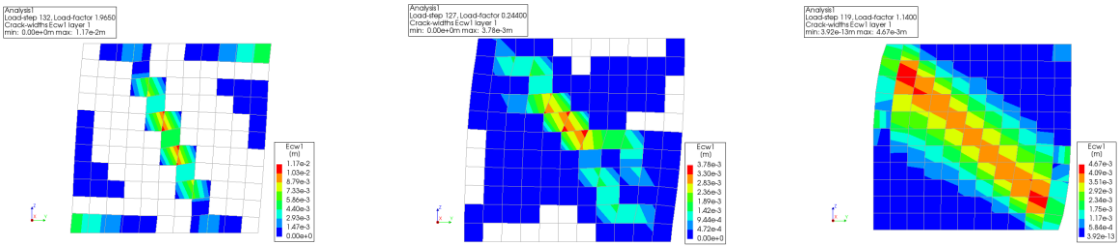

(a) (b) (c)

Figure 12: Crack width patterns of masonry walls at the peak force with condition of Figure 11: (a) EMM; (b)TSCM-fixed; (c)TSCM-rotating.

Above results show that model with TSCM-rotating has a closer response to the model with EMM compared to the TSCM-fixed. Meanwhile, models with EMM present generally a more stable post-peak behavior, which means that a higher ductility can be observed in push-over curves. This is especially true for cases with a higher overburden load. Moreover, models with the vertically free top edges and a lower overburden load are more stable for all material models. Models with a higher overburden and fixed top boundary condition have higher in-plane shear capacities.

Following the methods described in Section 4, shear capacities of masonry walls are estimated based on different failure mechanisms by NPR 9998:2017[2] and Eurocode 6 (EC6) [3], listed in Table 3 and Table 4 for cases with fixed-free and fixed-fixed boundary conditions, respectively. Meanwhile, the capacities with different material models revealed by the numerical results are also listed in the table for the comparison purpose. The results shows that the prediction method based on NPR 9998: 2017[1] provides more detailed information based on the different mechanisms than one based on the Eurocode 6[3]. In general, the results by NPR 9998:2017 correlate well with the numerical results obtained in this study, especially those with EMM and TSCM-rotating.

| H/L | $P_{OB}/f_c$ (-) | Masonry | EC6[3] moment based (kN) | EC6[3] shear based (kN) | NPR[2] DTC (kN) | NPR[2] toe crush (kN) | NPR[2] rocking (kN) | NPR[2] BJS (kN) | NPR[2] Min. (kN) | EMM peak (kN) | TSCM-fixed peak (kN) | TSCM-rotating peak (kN) |
|---|---|---|---|---|---|---|---|---|---|---|---|---|
| 1 | 0.2 | BKv | 190.8 | 370.4 | 503.3 | 175.2 | 222.2 | 318.4 | 175.2 | 195 | 118 | 192 |
| | | BKvl | 130.1 | 136.1 | 211.0 | 106.9 | 136.1 | 121.5 | 106.9 | 89 | 77 | 116 |
| | | BKn | 212.1 | 433.7 | 596.8 | 205.4 | 260.2 | 382.4 | 205.4 | 224 | 180 | 228 |

| H/L | $P_{OB}/f_c$ (-) | Masonry | EC6[3] moment based (kN) | EC6[3] shear based (kN) | NPR[2] DTC (kN) | NPR[2] toe crush (kN) | NPR[2] rocking (kN) | NPR[2] BJS (kN) | NPR[2] Min. (kN) | EMM peak (kN) | TSCM-fixed peak (kN) | TSCM-rotating peak (kN) |
|---|---|---|---|---|---|---|---|---|---|---|---|---|
| 0.5 | 0.02 | BKv | 30.6 | 47.3 | 90.2 | 22.4 | 28.4 | 92.2 | 22.4 | 32 | 30 | 32 |
| | | BKvl | 21.5 | 33.0 | 46.2 | 15.5 | 19.8 | 48.0 | 15.5 | 22 | 21 | 22 |
| | | BKn | 34.6 | 53.7 | 110.6 | 25.4 | 32.2 | 116.4 | 25.4 | 38 | 37 | 38 |
| | 0.2 | BKv | 269.2 | 740.7 | 1205.6 | 701.0 | 888.9 | 636.8 | 636.8 | 566 | 337 | 635 |
| | | BKvl | 218.2 | 272.2 | 505.4 | 427.4 | 544.3 | 243.0 | 243.0 | 229 | 198 | 371 |
| | | BKn | 270.3 | 867.4 | 1429.6 | 821.6 | 1040.9 | 764.9 | 764.9 | 680 | 462 | 775 |
| 2 | 0.02 | BKv | 59.4 | 94.7 | 216.2 | 89.6 | 113.6 | 184.5 | 89.6 | 123 | 83 | 84 |
| | | BKvl | 42.2 | 65.9 | 110.7 | 62.1 | 79.1 | 96.0 | 62.1 | 73 | 50 | 64 |
| | | BKn | 66.8 | 107.3 | 264.8 | 101.7 | 128.8 | 232.8 | 101.7 | 144 | 120 | 143 |
| | 0.2 | BKv | 109.4 | 185.2 | 201.9 | 43.8 | 55.6 | 159.2 | 43.8 | 51 | 45 | 47 |
| | | BKvl | 70.3 | 68.0 | 84.7 | 26.7 | 34.0 | 60.8 | 26.7 | 30 | 27 | 27 |
| | | BKn | 125.3 | 216.9 | 239.5 | 51.4 | 65.1 | 191.2 | 51.4 | 60 | 59 | 59 |
| | 0.02 | BKv | 15.5 | 23.7 | 36.2 | 5.6 | 7.1 | 46.1 | 5.6 | 9 | 8 | 8 |
| | | BKvl | 10.9 | 16.5 | 18.5 | 3.9 | 4.9 | 24.0 | 3.9 | 6 | 5 | 6 |
| | | BKn | 17.6 | 26.8 | 44.4 | 6.4 | 8.0 | 58.2 | 6.4 | 10 | 10 | 10 |

Table 3: Peak base shears of different models and the corresponding analytical predictions[7,8], with the fixed-free boundary condition.

| H/L | $P_{OB}/f_c$ (-) | Masonry | EC6[3] moment based (kN) | EC6[3] shear based (kN) | NPR[2] Tensile-diagonal (kN) | NPR[2] toe crush (kN) | NPR[2] rocking (kN) | NPR[2] BJS (kN) | NPR[2] Min. (kN) | EMM peak (kN) | TSCM-fixed peak (kN) | TSCM-rotating peak (kN) |
|---|---|---|---|---|---|---|---|---|---|---|---|---|
| 1 | 0.2 | BKv | 190.8 | 370.4 | 503.3 | 345.1 | 437.6 | 318.4 | 318.4 | 323 | 138 | 283 |
| | | BKvl | 130.1 | 136.1 | 211.0 | 208.3 | 265.3 | 121.5 | 121.5 | 118 | 76 | 171 |
| | | BKn | 212.1 | 433.7 | 596.8 | 405.4 | 513.6 | 382.4 | 382.4 | 386 | 212 | 337 |
| | 0.02 | BKv | 30.6 | 47.3 | 90.2 | 39.4 | 49.9 | 92.2 | 39.4 | 59 | 41 | 41 |
| | | BKvl | 21.5 | 33.0 | 46.2 | 25.7 | 32.7 | 48.0 | 25.7 | 38 | 25 | 25 |
| | | BKn | 34.6 | 53.7 | 110.6 | 45.4 | 57.5 | 116.4 | 45.4 | 71 | 60 | 69 |
| 0.5 | 0.2 | BKv | 269.2 | 740.7 | 1205.6 | 1380.3 | 1750.3 | 636.8 | 636.8 | 704 | 369 | 845 |
| | | BKvl | 218.2 | 272.2 | 505.4 | 833.3 | 1061.2 | 243.0 | 243.0 | 268 | 204 | 509 |
| | | BKn | 270.3 | 867.4 | 1429.6 | 1621.6 | 2054.4 | 764.9 | 764.9 | 831 | 464 | 1001 |
| | 0.02 | BKv | 59.4 | 94.7 | 216.2 | 157.5 | 199.7 | 184.5 | 157.5 | 157 | 96 | 175 |
| | | BKvl | 42.2 | 65.9 | 110.7 | 102.7 | 130.8 | 96.0 | 96.0 | 94 | 59 | 106 |
| | | BKn | 66.8 | 107.3 | 264.8 | 181.7 | 230.1 | 232.8 | 181.7 | 206 | 152 | 203 |
| 2 | 0.2 | BKv | 109.4 | 185.2 | 201.9 | 86.3 | 109.4 | 159.2 | 86.3 | 107 | 44 | 47 |
| | | BKvl | 70.3 | 68.0 | 84.7 | 52.1 | 66.3 | 60.8 | 52.1 | 48 | 26 | 29 |
| | | BKn | 125.3 | 216.9 | 239.5 | 101.4 | 128.4 | 191.2 | 101.4 | 126 | 71 | 69 |
| | 0.02 | BKv | 15.5 | 23.7 | 36.2 | 9.8 | 12.5 | 46.1 | 9.8 | 16 | 14 | 17 |
| | | BKvl | 10.9 | 16.5 | 18.5 | 6.4 | 8.2 | 24.0 | 6.4 | 10 | 9.3 | 10.9 |
| | | BKn | 17.6 | 26.8 | 44.4 | 11.4 | 14.4 | 58.2 | 11.4 | 19 | 19 | 20 |

Table 4: Peak base shears of different models and the corresponding analytical predictions[7,8], with the fixed-fixed boundary condition.

## 6 CONCLUSIONS

In this study, URM walls with different Groningen masonries of clay brickwork are numerically tested by the NLPO method using different material models. The influences of other factors, *e.g.* overburden loads, shape ratio, boundary conditions, etc. are also discussed in the study. Furthermore, numerical results are compared with the theoretical estimations by NPR 9998:2017[2] and Eurocode 6[3]. Based on the in-plane NLPO test results, some conclusions are drawn as follows.

- Compared to the model with TSCM-fixed, model with TSCM-rotating has closer responses to the one with EMM.
- Models with EMM present generally a more stable post-peak behavior, which reveals a higher ductility. This is especially true for cases with a higher overburden load.
- In general, the prediction method based on NPR 9998: 2017[2] provides more detailed information based on the different mechanisms than one based on the Eurocode 6[3]. The results based on NPR 9998:2017 correlate well with the numerical results obtained in this report, especially those with EMM and TSCM-rotating.
- There are a few cases that capacities of models with EMM is higher than the ones based on NPR 9998: 2017[2]. This may be due to the more comprehensive definitions of masonry material by EMM, which could be studied in the future.
- Based on the comparison study, the EMM presents a better behavior than the other options. Hence it is recommended to select this material model as the preferable default masonry model for the NLPO analysis in DIANA for the URM objects.

## REFERENCES

[1] DIANA FEA, *Finite Element Analysis*: *release 10.5*, DIANA FEA BV, Delft, the Netherlands, 2020

[2] NEN, *NPR 9998: 2017, Beoordeling van de constructieve veiligheid van een gebouw bij nieuwbouw, verbouw en afkeuren – Grondslagen voor aardbevingsbelastingen: geïnduceerde aardbevingen*, NEN. 2018.

[3] European Committee for Standardization, *Eurocode 6: design of masonry structures—part 1-1: general rules for reinforced and unreinforced masonry structures.* European Committee for Standardization, Brussels, Belgium, 2006

[4] F.J. Noortman, *Applicability of the pushover method for the seismic assessment of URM structures in Groningen: a case study of a low-rise building*, Master thesis, TU Delft, 2019.

[5] G.M.A. Schreppers, A. Garofano, F. Messali, J.G. Rots, *DIANA Validation Report for Engineering Masonry Model*, TNO DIANA report 2016-DIANA-R1601, TU Delft Structural Mechanics CITG report CM-2016-17. 2016.

[6] H. He, *Out-of-plane Performance of EMM: Validation by the Static and Seismic tests*, VIIA report, 2016.

[7] K.T. Doherty, *An investigation of the weak links in the seismic load path of unreinforced masonary buildings*. PhD Thesis, University of Adelaide, Australia. 2000.

[8] H. He, S.J.H. Meijers, R.A. Vonk, F.H. Middelkoop, Numerical study on the seis-mic out-of-plane performance of URM walls, J. Kubica, A. Kwiecień & Ł. Bednarz (Eds),

*Proceeding of 17th International Brick and Block Masonry Conference (17IB2MaC)*, Krakow, Poland in July 5-8, 2020. 916-923, Taylor & Francis Group, 2020.

COMPDYN 2023
9th ECCOMAS Thematic Conference on
Computational Methods in Structural Dynamics and Earthquake Engineering
M. Papadrakakis, M. Fragiadakis (eds.)
Athens, Greece, 12-14 June 2023

# STRUCTURAL PERFORMANCE AND HUMAN COMFORT ASSESSMENT OF RC CANTILEVER GRANDSTANDS: THE CASE OF THE SECOND RING OF SAN SIRO MEAZZA STADIUM IN MILAN

**Martina Cogliano[1], Nicola Scattarreggia[2], Matteo Moratti[3], and Gian Michele Calvi**

[1] University School for Advanced Studies IUSS Pavia, Pavia, Italy
Piazza della Vittoria, 15, Pavia 27100, Italy
e-mail: martina.cogliano@iusspavia.it

[2] University School for Advanced Studies IUSS Pavia
Piazza della Vittoria, 15, Pavia 27100, Italy
{nicola.scattarreggia, gm.calvi}@iusspavia.it

[3] Studio Calvi Ltd
Via S. Severino Boezio, 10, Pavia 27100, Italy
matteo.moratti@studiocalvi.eu

## Abstract

*Reports from all over the world highlight that several stadiums with cantilever grandstand have shown problems due to excessive vibrations during soccer matches, requiring a more detailed and careful evaluation of the actual structural performances with the aim of assessing both human comfort and structural safety. As a matter of fact, many of the stadiums currently used have been designed and built neglecting some phenomena (e.g., dynamic load of spectators), because of the limited knowledge and computational resources. This work intends to examine the San Siro Meazza reinforced concrete Stadium, located in Milan; in particular, the analysis focuses on the study of a portion of the second sector, for which observed acceleration values could disturb the spectators according to literature's reference. The dynamic behavior of the structure has been evaluated under different conditions of dynamic loads in terms of frequency and synchronous/asynchronous motion of people through a linear finite element model (FEM). The model has been calibrated on experimental dynamic data. The studies have highlighted the importance of the dynamic characterization of the structure for both human comfort and structural safety; under certain load conditions, numerical results are consistent with those obtained experimentally.*

**Keywords:** reinforced concrete, stadium, dynamic analysis, human comfort, Finite Element Method.

## 1 INTRODUCTION

Nowadays stadiums are multifunctional facilities, being used not only for sport events but also, for instance, for concerts. During these events, people may jump following music's beat, with the consequence of generating a strong dynamic periodic load on the structure. Typically, old stadiums have not been designed for this type of dynamic excitation, therefore different matters may arise, among which excessive level of vibrations, which can disturb audience or even generate panic, with the extreme possibility of endangering human life; and excessive level of demand on the structure, in terms of both stress and strain, that can compromise the structural safety. With the purpose of studying these issues, different load models have been considered to represent a dynamic crowd acting on the grandstand of the Giuseppe Meazza Stadium in Milan. It is a reinforced concrete stadium, characterized by a peculiar construction history, as illustrated in section 3. The study takes advantage of the several experimental data available for this structure acquired by the monitoring system handled by Politecnico di Milano. The availability of the acceleration (and displacement) time-histories recorded during several events, mainly soccer games, has allowed the authors to better calibrate numerical assumptions, obtaining a robust structural model. Indeed, structural modelling plays a significant role in evaluating the realistic response of the structure; as a matter of fact, both two-dimensional and three-dimensional models have been developed in order to find a balance between computational demand and model accuracy. Consequently, sensitivity analyses have been performed to calibrate each model, by varying those parameters which may affect the static and dynamic properties of the structure, as shown in section 5.1. Once proved the model feasibility with respect to experimental results, the dynamic response of the structure has been studied, first through steady-state analysis, followed by time-history analysis. Two different jumping load models in combination with the synchronism and asynchronism of the crowd have been used to characterize the structure response at significant frequencies.

## 2 HUMAN ACTIVITIES AND COMFORT

Grandstands are susceptible to human-induced movements; particularly when they are sustained by slender cantilever structures. Depending on the stadium employment and occupancy, human activities can significantly vary, as described in [1]: from a predominantly seated crowd for classical concerts and regular sport events, to excited crowd during more extreme events, such as important football matches and rock concerts, where fans may bob and jump following the music beat. Dynamic loads characterizing intense events might be much higher than the static ones, thus inducing concerns for both structure safety and serviceability.

An important issue is the mutual effect of people movement and structure response; it has been shown [2] that the human body does not simply represent a mass, but can adsorb and release energy due to its flexibility. Consequently, it will interact with the structure depending on its response. A distinction between two extreme cases is useful, i.e., considering a stationary and a moving crowd. A stationary crowd will affect the structural behavior, altering its frequencies and possibly increasing its damping properties; a moving crowd can be considered solely as a load hence the "empty" structure properties remain intact [3].

A very severe condition is represented by the entire crowd jumping at a frequency resonant with one of the structure main response frequencies, a possible consequence of a music recurring rhythm [4].

### 2.1 Load models

Possible models of the vertical loads considered to represent the human crowd dynamic loading are those proposed in [5], [6] and [7].

Two independent numerical loads, experimentally calibrated, are described by periodic functions defined as a function of different parameters, e.g.:

- The average weight of each person;
- The jumping period (or frequency);
- Duration of the contact between the jumping person and the structure, i.e. how long a jumping person is in contact with the structure between two consecutive jumps.

In addition, a parameter that accounts for different levels of synchronism between persons needs to be considered, for instance as proposed by [7] as function of the number of people involved in the activity. Indeed, most likely the asynchronism increases while the number of people increases. However, this study refers to two different jumping crowds:

- *Synchronous crowd*, assuming all people jumping in perfect synchronicity;
- A*synchronous crowd*, assuming 3 persons per square meter, according to [5, 6] the multiplier factor reduces the load of the synchronous crowd of about 34% for the load model proposed in [5] and 60% for the one proposed in [6].

Figure 1 illustrates the difference in shape between the two load models, for each of which a representation for both synchronous and asynchronous crowd is given for frequency equal to 2.14 Hz.

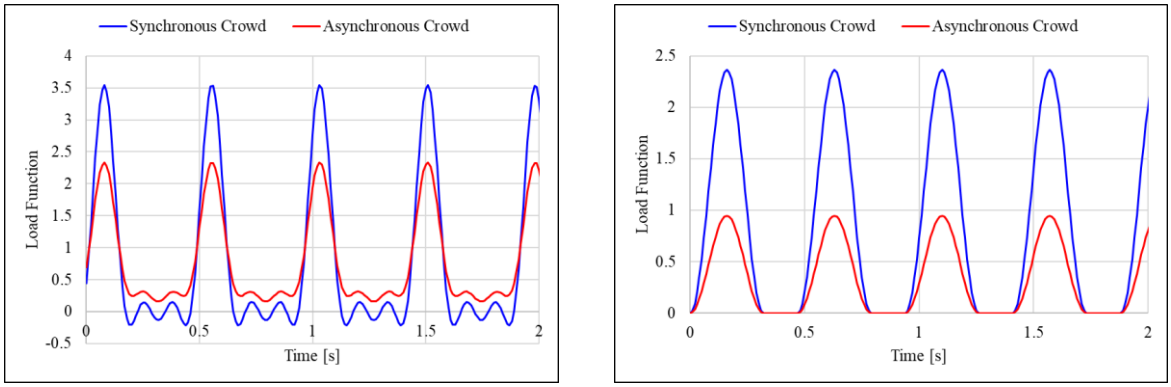


**(a)** **(b)**

Figure 1: Load model 1 a) and 2 b) representation with frequency equal to 2.14 Hz for both synchronous and asynchronous crowd.

## 2.2 Comfort

An excessive level of vibrations may annoy the audience, especially those not participating in generating the excitations, or even generate panic. There are different methods to assess whether an acceleration level is disturbing or not, based on different definition of intensity measures, as illustrated in [8], among which peak acceleration, root mean square of acceleration (arms), which represents the square root of the mean square of the acceleration history, and the vibration dose values (VDVs), which combines amplitude and duration of vibrations. For simplicity, the peak acceleration approach has been followed. The maximum vertical acceleration recorded during the analyses has been compared with the vibration limits proposed in [9] and shown in Table 1.

| Vibration level | Reaction |
|---|---|
| < 5% *g* | Reasonable limit for passive person |
| < 18% *g* | Disturbing |
| < 35% *g* | Unacceptable |
| > 35% *g* | Probably causing panic |

Table 1: Peak vertical acceleration limits

## 3 THE SAN SIRO MEAZZA STADIUM CASE STUDY

The Giuseppe Meazza stadium, also known as *San Siro* from the name of the neighborhood that hosts it, was built in Milan in 1925, and is the largest sport arena in Italy. Initially it consisted of four straight concrete stands, with a capacity of 35,000 spectators; the extension work, begun in 1935, led to the realization of the connecting curved corners, shaping what nowadays is the first ring and increasing the maximum number of spectators up to 55,000 [10].

Later, a new concrete structure, which embraces the existing one, was built in 1955, with the aim of supporting a second tier, the so called second ring, which surrounds and partially covers the first ring. The total capacity raised to 80,000 people, of which 60,000 seated.




Figure 2: San Siro Stadium a) and section view of the three rings b) ([11]).

On the occasion of the 1990 World Cup, the need of a larger capacity and a more reasonable distribution of spectators for safety purposes induced the municipality of Milan to decide to further expand the stadium. A new structure was again added: eleven towers, with helicoidal-shaped ramps, were erected as supports for the third ring, which develops only on three sides. This third grandstand is characterized by post-tensioned concrete box girders, each of them carrying two cantilever tiers. Four red truss beams, supported by the corner towers, form the roof structure covering all the 80,000 seats.

The Meazza Stadium has undergone several reinforcement and restoration interventions; in particular, seismic retrofitting was necessary to adapt the structure to modern standards in 2014.

As described in detail in [11, 12], the stadium is subjected to permanent continuous monitoring, in consideration of its complexity and relevance.

### 3.1 The second ring

The subject of this study is the second ring, built in the 1950s, whose structure is made of 132 reinforced concrete frames, perpendicular to the soccer field, about 20 m tall; they are grouped in 14 sections that can be considered as independent structures. Each frame comprises the main following elements:

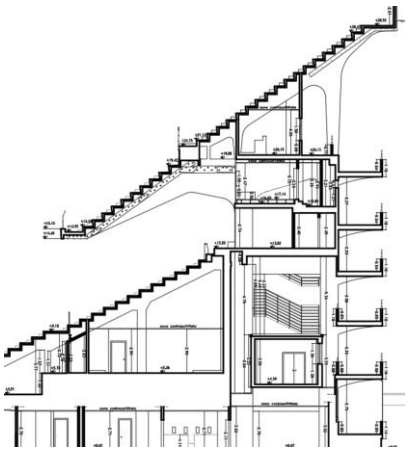

Figure 3: Section view of the second ring.

- Two columns with different heights (about 16 m and 18 m high) and same rectangular cross-section 1.20 x 0.70 m;
- A beam with variable depth (from 0.25 m to 2.90 m), 0.70 m wide, characterized by supported and cantilevered portions;
- Two beams with rectangular cross-section of 1.90 x 0.70 m, located at intermediate heights of the frame to link the columns.

In the direction parallel to the field, the frames are connected at a height of about 20 m by concrete slabs, transverse beams and outer ramps.

Each frame of the second ring has been strengthened applying two continuous plates, laterally bolted to the cantilever beam.

The interest in the second ring of San Siro stadium arises from vibration levels higher than usual recorded during some recent football events, particularly in areas where organized supporters are located. The maximum accelerations attained were about 2.5 m/s$^2$ in the vertical direction and 1.2 m/s$^2$ in the horizontal one. These values were recorded at the knee of the cantilever beam. These occurrences induced to investigate how a dynamic crowd load may affect and interact with the structure.

## 4 STRUCTURAL DYNAMIC AND HUMAN COMFORT ANALYSIS

### 4.1 Dynamic identification from experimental tests

Dynamic identification tests performed by Politecnico di Milano in 2006 show that the dynamic behavior is governed by few harmonics:

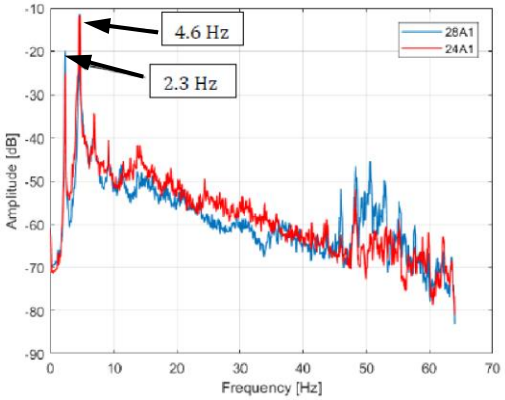


Figure 4: Dynamic identification for the Second Ring of San Siro Stadium

- A first mode with frequency of 2.2-2.3 Hz, related to the horizontal movement of the second ring's main frames;
- A second mode with frequency of 4.4-4.6 Hz, related to the vertical movement of the cantilever portion of the beam.

Tests have also indicated that the structural damping coefficient is between 1.9% and 2.2%; consequently, the numerical models adopt a damping coefficient equal to 2%.

### 4.2 Structural modelling

Two different models have been developed using SAP2000 software [13]:

- A 3D-model of eight frames, which corresponds to sector of the second ring mainly interested by the vibration phenomena event mentioned in 3.1, shell elements have been added to consider the grandstands effects. This model is meant to be used for the numerical calibration of 2D-model.
- A 2D-model of a single internal frame, with loads derived considering an area of influence equal to 5 m (distance between two consecutive frames in the direction parallel to the field).

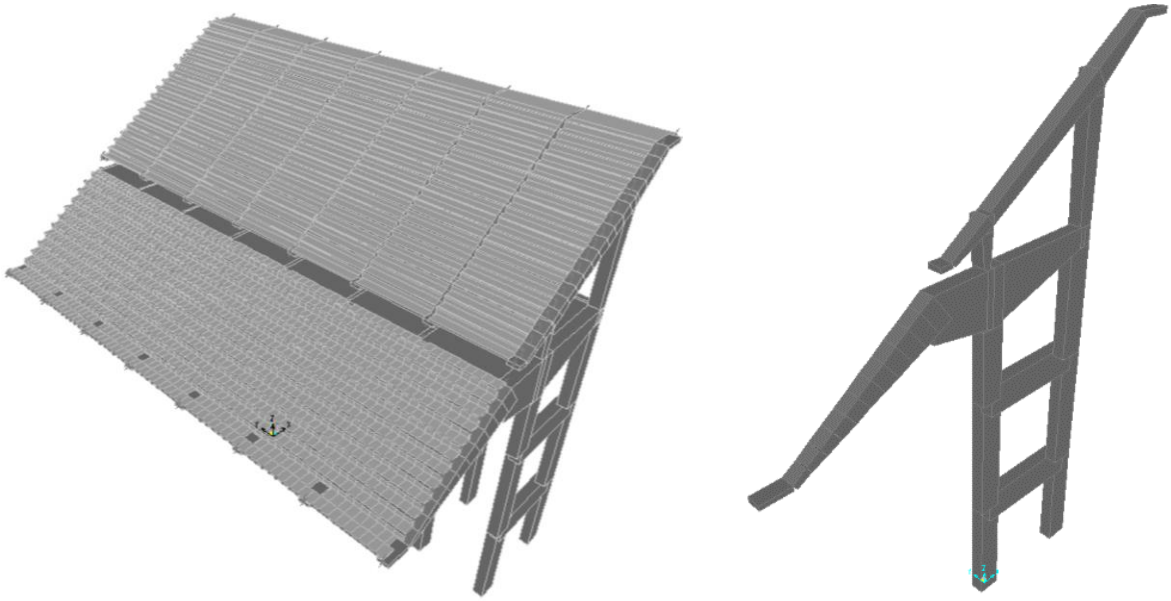

**(a)** **(b)**

Figure 5: Numerical models of the Second Ring of San Siro Stadium built within SAP2000: 3D-model a) and 2D-model b).

## 5 DYNAMIC STRUCTURAL PERFORMANCE ASSESSMENT

Four different types of analysis have been performed to reconstruct the system response:

- An Eigenvalue analyses of the empty structure on both 3D- and 2D-models;
- A steady state analyses on the 2D-model;
- A linear Time-History analyses on the 2D-model.

### 5.1 Analysis assumptions

The variability of parameters not fully known has been taken into account by performing parametric analyses that included:

- A Young modulus calibration with respect to the first two periods of vibration;

- Various assumptions on the grandstands – frames connection;
- Various levels of the live loads acting on tiers;

The aim of these sensitivity analyses was to better approximate the dynamic behavior experimentally captured.

The dynamic live load represented by the crowd is located on the cantilever grandstand with a load distribution of 3 persons per square meter.

## 5.2 Eigenvalue analyses results

The first modelling validation has been obtained by comparing the eigen properties of the numerical 3D-model with the ones obtained experimentally.

The differences in terms of eigen frequencies, shown in Table 2, between tests results and numerical modelling are always lower than 10%.

| Mode Case | Test result | 3D model | Difference |
|---|---|---|---|
| Horizontal movement | 2.2 - 2.3 Hz | 2.14 Hz | 2.7% - 7% |
| Vertical movement | 4.4 - 4.6 Hz | 4.38 Hz | 0.45% - 4.8% |

Table 2: Comparison of first two natural frequencies of the structure obtained by experimental tests and numerical modelling.

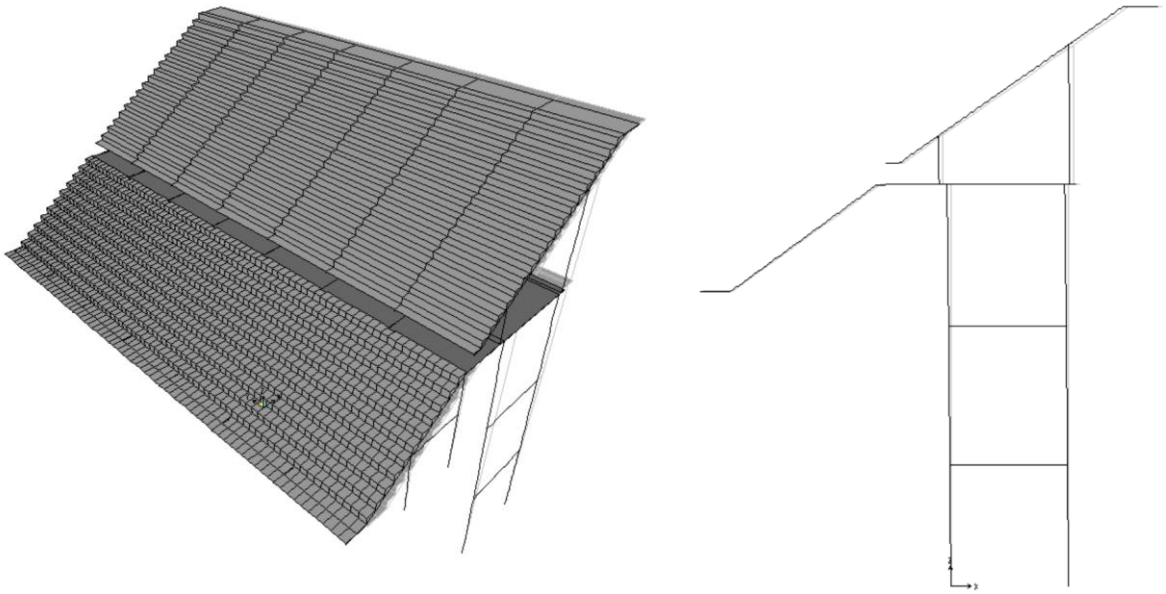

**(a)** **(b)**

Figure 6: First modal shape related to the horizontal movement of the entire frame of the 3D-model: 3D view a) and 2D view b).

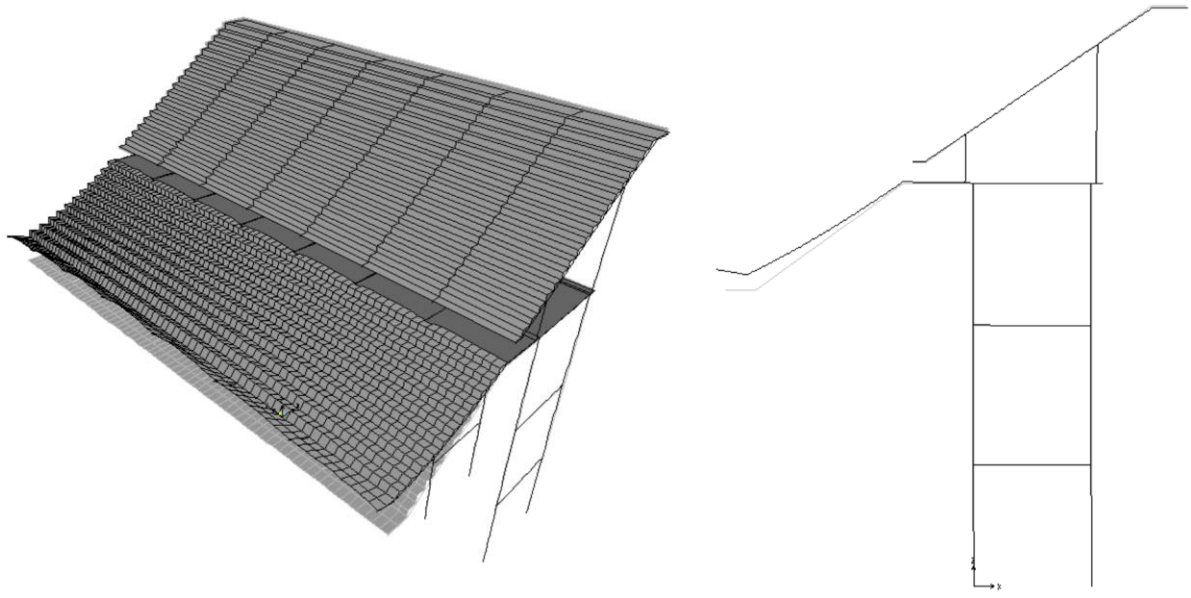

**(a)** **(b)**

Figure 7: Second modal shape related to the vertical movement of the cantilever grandstand of the 3D-model: 3D view a) and 2D view b).

Relying on these results, the 2D-model has been calibrated to obtain the same dynamic properties of the 3D-model, as Table 3 shows. Successively, a steady state analysis has been performed to identify the frequencies that amplify the structural response to a larger extent.

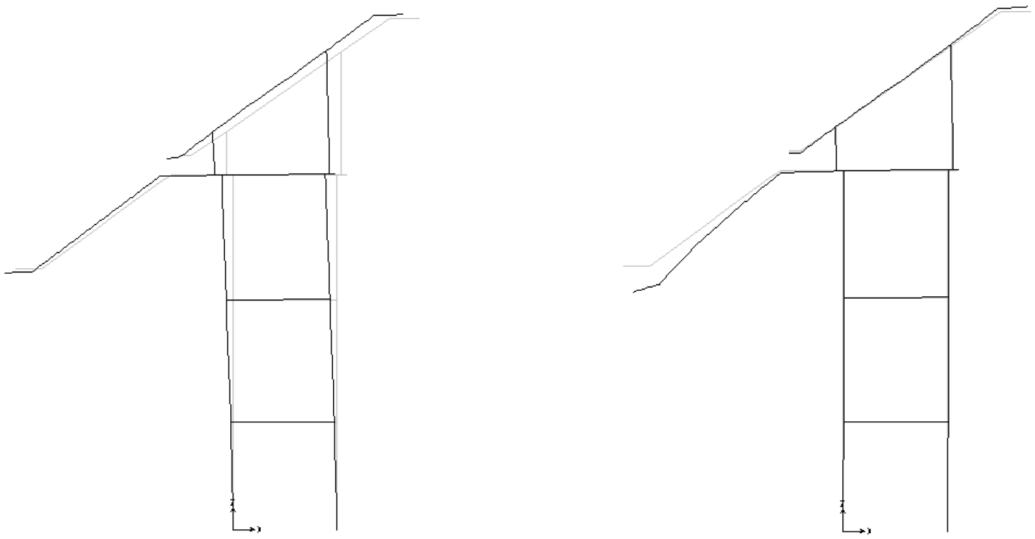

**(a)** **(b)**

Figure 8: Modal shapes of the first two vibrational modes for the 2D-model: horizontal mode of the entire frame a) and vertical mode of the cantilever grandstand b).

| Mode Case | Model | T [s] | f [Hz] |
|---|---|---|---|
| Horizontal movement | 3D | 0.466 | 2.14 |
| | 2D | 0.466 | 2.14 |
| Vertical movement | 3D | 0.228 | 4.39 |
| | 2D | 0.228 | 4.39 |

Table 3: Eigen properties of both 3D- and 2D-models

## 5.3 Steady-state analyses results

The steady state analysis allows determining the probabilistic response of a structure subjected to a cyclic load (harmonic, sinusoidal) included within a specific range of frequencies and is useful for studying the vibrational behavior of the structures.

Results of the steady state analysis, reported in Figure 9, highlights that in correspondence with the natural frequencies of the system, 2.14 Hz and 4.39 Hz, there a considerable amplification of the structural response may occur. The largest acceleration is attained for a dynamic excitation close to the frequency of 4.39 Hz, i.e., the first vertical mode of the tier.

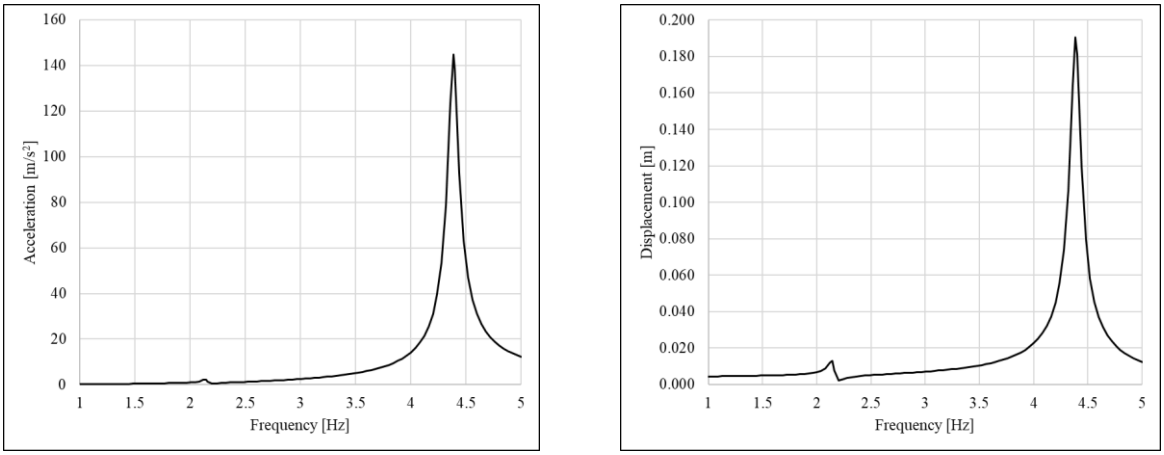


**(a)** **(b)**

Figure 9: Vertical acceleration a) and vertical displacement b) response spectra derived from the steady state analysis

The experimental measurements during an intense event are about 1/45 of the theoretical maximum in terms of acceleration and 1/4 as in terms of vertical displacement. As previously specified, this type of analysis is conducted using a harmonic, sinusoidal forcing, which however is not perfectly representative of the type of load acting on the structure. However, this analysis has been carried out to support that maximum amplifications of the response are obtained when the forcing load is applied with a frequency close to or equal to those of the structure itself. For the evaluation of the effects on the structure of a dynamic load, reference is made to time history analyses conducted with the load models described in section 2.1.

## 5.4 Time-histories analyses results

The linear time history analysis allows studying the structural response to a vertical dynamic load, simulating the jumping crowd, varying its frequency, in order to determine a frequency response spectrum, with a procedure similar to that of the steady state analyses.

Figure 10 and Figure 11 show response time histories in terms of both vertical acceleration and vertical displacement recorded at the knee of the cantilever grandstand for the two load models, when the load frequency is equal to that of the horizontal movements of the structure.

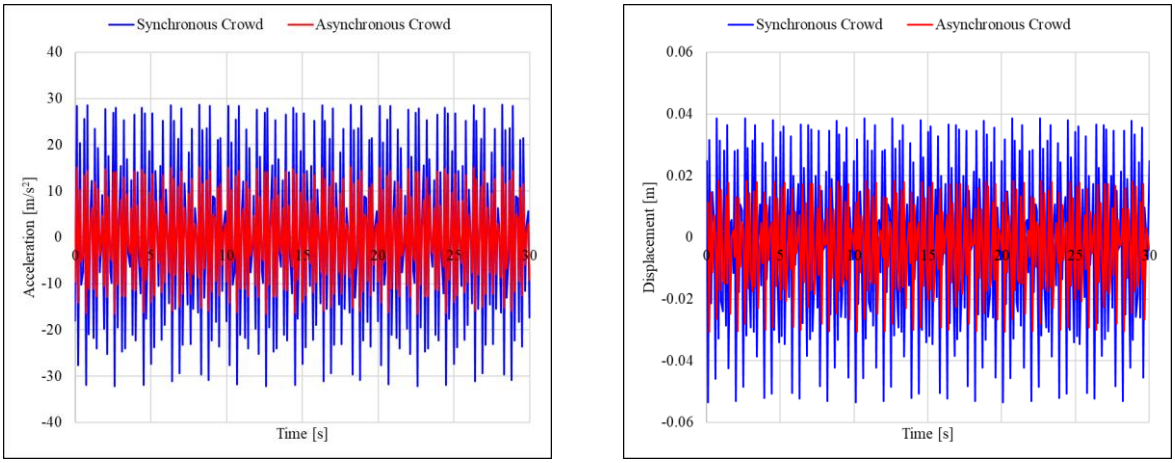


**(a)** **(b)**

Figure 10: Vertical acceleration a) and vertical displacement b) time histories for load model 1 with load frequency = 2.14 Hz (i.e. first mode of vibration)

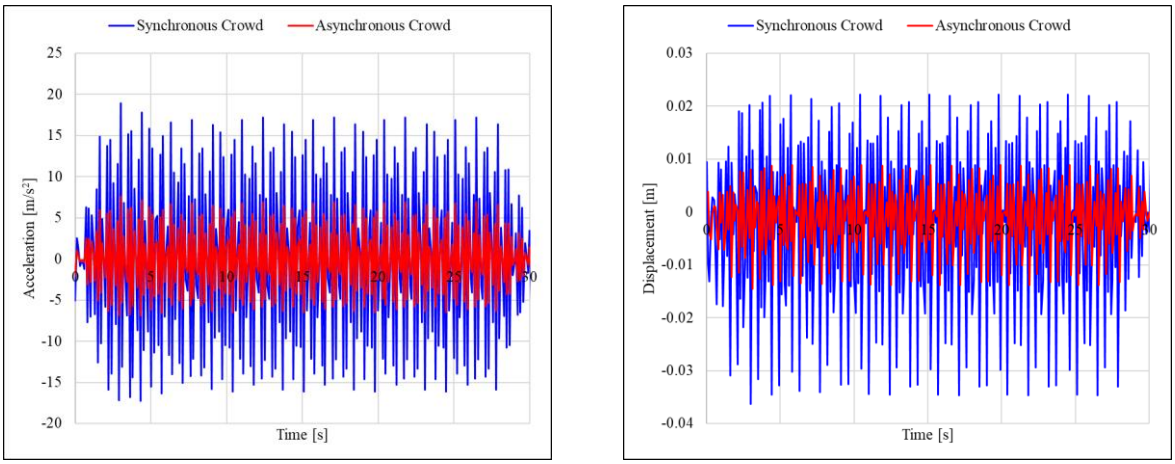


**(a)** **(b)**

Figure 11: Vertical acceleration a) and vertical displacement b) time histories for load model 2 with load frequency = 2.14 Hz (i.e. first mode of vibration)

Recording the peak responses by varying the load frequency in order to match the fundamental ones of the structure, few points of frequency response spectra have been identified in Figure 12. Results underline how important is the synchronism of the crowd: if the spectators move in a perfectly synchronous way, peak response might be 35% - 60% higher.

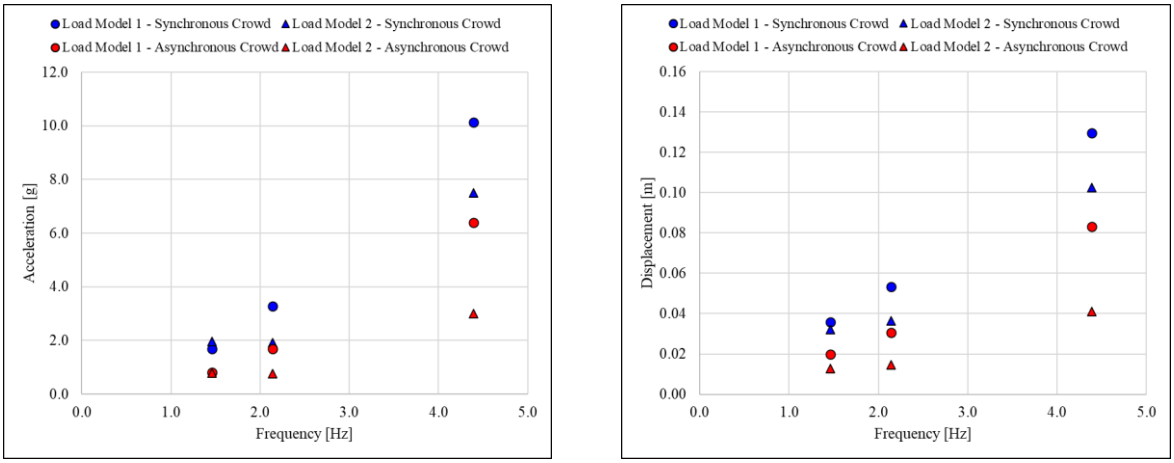


**(a)** **(b)**

Figure 12: Peak vertical accelerations a) and peak vertical displacements b) obtained from linear time history analyses

| Crowd Type | Load Model | Peak Vertical Acceleration [m/s²] | | |
|---|---|---|---|---|
| | | $f_1$=1.46 Hz | $f_2$=2.14 Hz | $f_3$=4.39 Hz |
| Synchronous | 1 | 1.7 | 3.3 | 10.1 |
| | 2 | 2.0 | 1.9 | 7.5 |
| Asynchronous | 1 | 0.8 | 1.7 | 6.4 |
| | 2 | 0.8 | 0.8 | 3.0 |

Table 4: Peak vertical accelerations obtained from linear time history analyses

| Crowd Type | Load Model | Peak Vertical Displacement [m] | | |
|---|---|---|---|---|
| | | $f_1$=1.46 Hz | $f_2$=2.14 Hz | $f_3$=4.39 Hz |
| Synchronous | 1 | 0.036 | 0.053 | 0.130 |
| | 2 | 0.032 | 0.036 | 0.103 |
| Asynchronous | 1 | 0.020 | 0.031 | 0.083 |
| | 2 | 0.013 | 0.015 | 0.041 |

Table 5: Peak vertical displacements obtained from linear time history analyses

Results of the steady state analysis, reported in Figure 9, highlight a peak in vertical response at both the first frequency of vibration (horizontal movement of the frame) and the second frequency of vibration (vertical movement of the cantilever).

Furthermore, as [2] report, the achievable frequency for a jumping crowd is between 1.5 Hz – 3.5 Hz; jumping at frequency equal to 4.39 Hz is unrealistic for a group of people. This implies that the vertical mode can be actually excited when the activity matches a submultiple of the vertical mode (e.g., 1.46 Hz).

For what concerns human comfort assessment, according to the acceleration limits reported in Table 1, the acceleration recorded during time history analyses is always above 35% g, which means that it might cause panic. This consideration should be associated to the investigated load frequencies, which are the closest to the natural frequencies of the structure; consequently, they represent the worst-case scenario for the cantilever assessment.

## 6 CONCLUSIONS

- Cantilever grandstands are sensitive to dynamic load, which should be taken into account during both design and assessment process. In this study, only the vertical response has been investigated; consequently, further evaluations are needed to assess the structural behavior along the horizontal direction, also considering the potential coupling.
- When experimental data are available, a Finite Element approach is efficient in terms of computational demand and the results reasonably accurate for studying the structural dynamic behavior. The dynamic identification allowed to adequately calibrate the numerical model.
- The nonlinear behavior of the grandstand has not been taken into account. The structure will enter in the nonlinear field when subjected to significant load conditions, implying changes in its dynamic properties; consequently, further evaluations are needed to consider how it affects the response, especially for what concerns assessment up to collapse.
- Different load conditions and configurations might be of interest in order to assess human comfort during more frequent events, not only for the worst-case scenario.
- Studying the response of the grandstand by varying the frequency of the excitation allows to build acceleration and displacement response spectra, that might be advantageous to assess the structural behavior.

## REFERENCES

[1] Institution of Structural Engineers (Great Britain), Great Britain. Department for Communities and Local Government., and M. and Sport. Great Britain. Department for Culture, *Dynamic performance requirements for permanent grandstands subject to crowd action : recommendations for management, design and assessment*.

[2] B. R. Ellis, T. Ji, and J. D. Littler, "The response of grandstands to dynamic crowd loads," *Proceedings of the Institution of Civil Engineers: Structures and Buildings*, vol. 140, no. 4, 2000, doi: 10.1680/stbu.2000.140.4.355.

[3] B. R. Ellis and T. Ji, "Human-structure interaction in vertical vibrations," *Proceedings of the Institution of Civil Engineers: Structures and Buildings*, vol. 122, no. 1, 1997, doi: 10.1680/istbu.1997.29162.

[4] B. R. Ellis and T. Ji, "Loads generated by jumping crowds: Numerical modelling," *Structural Engineer*, vol. 82, no. 17. 2004.

[5] T. Ji and B. R. Ellis, "Floor vibration. Floor vibration induced by dance-type loads. Theory," *Structural engineer London*, vol. 72, no. 3, 1994.

[6] R.G. Faísca, "Characterization of Dynamic Loads due to Human Activities", PhD Thesis (In Portuguese) Civil Engineering Department, COPPE/UFRJ, Rio de Janeiro/RJ, Brazil, pp. 1-240, 2003

[7] D. F. Campista, J. G. S. da Silva, and A. C. C. F. Sieira, "Dynamic Analysis and Human Comfort Evaluation of Soccer Stadium Grandstands," *Int J Eng Res Appl*, vol. 11, no. 05, 2016, doi: 10.9790/9622-0611052331.

[8] N. T. Do, M. Gül, O. Abdeljaber, and O. Avci, "Novel Framework for Vibration Serviceability Assessment of Stadium Grandstands Considering Durations of Vibrations," *Journal of Structural Engineering*, vol. 144, no. 2, 2018, doi: 10.1061/(asce)st.1943-541x.0001941.

[9] B. R. Ellis and J. D. Littler, "Response of cantilever grandstands to crowd loads. Part 1: serviceability evaluation," *Proceedings of the Institution of Civil Engineers: Structures and Buildings*, vol. 157, no. 4, 2004, doi: 10.1680/stbu.157.4.235.41176.

[10] Silvana Sermisoni (a cura di), *San Siro. Storia di uno stadio*, Milano, Electa, 1989, p. 5.

[11] A. Cigada, G. Moschioni, M. Vanali, and A. Caprioli, "The measurement network of the san siro meazza stadium in milan: Origin and implementation of a new data acquisition strategy for structural health monitoring: Dynamic testing of civil engineering structures series," *Exp Tech*, vol. 34, no. 1, 2010, doi: 10.1111/j.1747-1567.2009.00536.x.

[12] A. Cigada and G. Moschioni, "The system for structural measurement diagnosis and surveillance in Meazza stadium in Milan," in *Conference Proceedings of the Society for Experimental Mechanics Series*, 2007.

[13] CSI, "SAP2000. Analysis Reference Manual," *CSI: Berkeley (CA, USA): Computers and Structures INC*, no. July, 2016.

COMPDYN 2023
9th ECCOMAS Thematic Conference on
Computational Methods in Structural Dynamics and Earthquake Engineering
M. Papadrakakis, M. Fragiadakis (eds.)
Athens, Greece, 12-–14 June 2023

# NUMERICAL MODELLING OF POORLY DETAILED EXISTING RC BEAM-COLUMN JOINTS

**Angiolilli M.[1], Gregori A.[2], Bizzarri L.[2], D'Agostino C.[2], Ciuffetelli E.[2], Peditto A.[2], Gualtieri P.[2]**

[1] National Institute for Nuclear Physics (INFN) -Gran Sasso Laboratory (LNGS)
Via G. Acitelli, 67100 L'Aquila, Italy
e-mail: michele.angiolilli@lngs.infn.it

[2] Department of Civil, Construction and Environmental Engineering, University of L'Aquila
Monteluco di Roio 67100 L'Aquila, Italy
e-mail: amedeo.gregori@e-univaq.it, lorenzo.bizzarri@graduate.univaq.it,
caterina.dagostino@graduate.univaq.it, edoardo.ciuffetelli@univaq.it, alfredo.peditto@univaq.it,
pasqualino.gualtieri@univaq.it

**Abstract.**

*The catastrophic collapse of existing reinforced concrete (RC) structures in areas with low to high seismic risk was often caused by the failure of beam-column joints, which are essential in transporting stresses and moments between those two main elements. Indeed, post-earthquake observations highlighted that most of the 1960s-70s Italian RC buildings, suffering significant damage levels during the last seismic sequences, were characterized by insufficient transverse reinforcing of the joints. In some cases, stirrups were even absent since were not prescribed by old design codes. Numerical three-dimensional finite element (FE) model for simulating crack propagation and fracture in concrete utilizing the smeared crack approach is used in this study to simulate an experimental test (part of a larger experimental campaign conducted by the University of L'Aquila) on exterior (i.e. façade) beam-column RC joint. In particular, according to the experimental assumptions, the FE model was developed to emphasize the vulnerability of the joints and, therefore, to achieve shear failure in the joint panel prior to yielding of both beam and column reinforcements. The model made it possible to examine specific assumptions on the mechanical performance of the RC joints. Numerical tests investigated the performance of the RC frame at different stage of the analysis (attainment of the first cracks as well as collapse condition) under both monotonic and cyclic tests aiming to investigate possible damage accumulation phenomena, that in turn, could affect the main mechanical properties of the sample. The results showed that the model well predicted the experimental outcomes, especially in terms of shear strength and crack propagation, and provided critical insight into the calibration of the numerical model under cyclic loads, mainly trough the investigation of a material property regulating the shear stiffness reduction after cracks.*

**Keywords:** Cyclic, Reinforced Concrete, Earthquake Engineering, Damage accumulation, Energy dissipation, Nonlinear Analysis, Crack pattern, Shear retention factor

## 1 INTRODUCTION

Based on previous and recent earthquakes or studies, reinforced-concrete (RC) buildings demonstrated severe structural damage at both the local and global levels due to the potential brittle failure of vertical members, such as columns ( (e.g., [1, 2]), whereas usability preventing and loss-providing damages are more frequent and primarily associated with the damage of nonstructural elements (e.g., [1, 3, 4, 5]). The behavior of beam-column intersections, or the so-called beam-column joint (BCJ) panel, on which this work is focused, is another significant factor that seems to have a significant impact on the seismic performance of existing frames, particularly in non-conforming buildings. Deficiencies mostly resulting from poor material qualities, insufficient or no transverse reinforcement at the BCJ panel, inappropriate anchor length/detail, among others, may cause catastrophic brittle failures linked to poor energy dissipation and sudden strength and stiffness degradation. Even under moderate seismic actions, such an adverse seismic behavior evidently affects the structural integrity of the entire system.

Reliable quantification of BCJ of non-conforming RC frames is critical for seismic vulnerability assessment. Therefore, the experimental performance of deficient joints has attracted considerable research interest especially for retrofitting purposes (e.g. [6, 7, 8, 9]). In the last two decades, several theoretical and empirical models have been proposed for evaluating the shear capacity of BCJ. A comprehensive overview of capacity models for shear strength of exterior RC joints is presented in [10], where uncertainties were also quantified by probabilistic procedures.

Those constitutive models are in general implemented in computer programs (e.g. [11, 12]) by which is still a challenge getting reliable simulations due to the general complexity of concrete behaviour associated with the crushing in compression, characterized by pronounced nonlinear behaviour also in the pre-peak stage, and quasi-brittle cracking in tension, with a decay of tensile capacity with the widening of the cracking process that, in turn, is followed by a decrease of crack shear stress transfer due to the deterioration of aggregate interlock. Furthermore, bar-slip phenomena and flexure-shear interaction in the members framing into the BCJ as well as various uncertainty sources (e.g. [9, 13]) strongly affect the simulations. The behavior of BCJ has been replicated numerically by using a variety of techniques, from straightforward to sophisticated finite or discrete element models [14, 15, 16]. Recent research has benefited from the advancement of computer-aided nonlinear analysis, which has been utilized to replicate the behavior of BCJ in multiaxial stress fields. The authors suggest to interested readers referring to [17] for a comprehensive overview of the various numerical approaches.

Furthermore, due to relatively scarce information based on experimental tests on gravity-load-designed frame systems and subassemblies, there is a general lack of appropriate modelling solutions for poorly designed beam-column joint system.

In this paper, an experimental test performed on a full-scale RC façade sub-assembly, tested under cyclic load up to its failure, is replicated through the use of a numerical three-dimensional model based on the concrete smeared crack (CSC) approach. A comparison between monotonic and cyclic numerical responses is provided. In particular, the effect of the shear stiffness reduction during cyclic loads (the so-called shear retention factor) is here investigated.

## 2 BRIEF DESCRIPTION OF THE RC FRAME EXPERIMENTALLY TESTED

A RC beam-column frame, representing an exterior subassembly isolated at the mid-points of members of a multi-storey building, was constructed and tested under the collaboration between the University of L'Aquila (Italy) and Tonelli Consulting company (Avezzano, Italy).

The beams with a cross-section of 300 x 500 mm$^2$ had an extension of 2,000 mm from the column face, whereas the columns had a cross-section of 300 x 500 mm$^2$ and a total height of 3,200 mm. A 300 x 500 mm $^2$ transversal beam extending 300 mm from the column face was also realized to better replicate the real geometry of existing RC frames.

Longitudinal reinforcement on both the two short sides of the column consisted of four steel rebars with 24 mm in diameter. Longitudinal reinforcement of the beams (both on top and bottom position) consisted of two bars of 24 mm in diameter plus three bars of 20 mm in diameter. The short transversal beam was reinforced by four bars with 16 mm in diameter, one in each of the corners. Transversal reinforcement for both columns and beams consisted of 10 mm in diameter and steel stirrups spaced 100 mm. It is noteworthy that stirrups were appositely not inserted in the joint panel, as justified above.

Specimens were tested imposing a precise sequence of increasing amplitude quasi-static cyclic displacements to a column-end (to simulate the seismic inter-floor drifts) in combination with null external forces applied to the column.

The load $V$ was applied at the head column using an actuator with 500 kN capacity based on a displacement-controlled regime. Loading history details for all specimens were based on ACI 374.1 [18] and included several series of force sets, each one consisting of three fully reversed cycles (except the last three cycles, for which only one fully reversed cycles were applied for them). The drift ratio values were selected to evaluate the performance of the joints at different loading stages such as elastic response, before and beyond yielding, and failure. Here, the drift ratio was defined as the ratio between head column displacement and the length of the column by also considering the encumbrance of the support frames (i.e., total length of 3,340 mm). Note that [18] recommends that the end of the test should be at a drift ratio that equals or exceeds 3.5%. The diagonal deformation in the joint was measured by linear variable displacement transducers (LVDTs). Other LVDTs were also used to measure displacements of the head column and the two beam ends.

The experimental result showed an almost symmetrical cyclic behavior among the two load directions up to the attainment of the maximum strength $V_{max}$ of 218 kN (for an imposed displacement $d$ =177.4 mm). The initial hairline cracking in the BCJ panel started at 61.2 kN corresponding to about 0.4% of $\theta$. For more details on the experimental campaign, the reader is referred to [19], where it was also provided a comparison in terms of $V_{max}$ with the results of NTC2018 [20] and ACI-352R [21] prescriptions and other literature formulations (discussed in [10]). In particular, it was highlighted that the experimental test led to lower values with respect to the ones obtained by the various formulations (in some cases, the difference was pretty consistent).

## 3 DETAIL OF THE NUMERICAL MODEL

In this study, a numerical model was developed using the concrete smeared crack (CSC) model (implemented in the MIDAS FEA NX v1.1 software; release version: Nov 22 2022), which has been already successfully employed to simulate RC members under seismic loads (e.g. [22, 23, 24]).

With respect to the discrete models, in which the cracks are explicitly modelled merely through the separation of particles when tensile strength is reached, in the CSC approach, the extension of cracks is predicted by using the concept of fracture mechanics and studying the stress concentrations at the crack tip. Constitutive calculations are performed independently at each integration point of the finite element model. In the CSC model, the initiation of cracking process at any location happens when the concrete stresses reach one of the failure surfaces

either in the biaxial tension region or in a combined tension-compression region.

The CSC is used to simulate plain concrete and assumes that the monotonic load is applied to concrete under low confining pressure. The low confining pressure corresponds to the stress less than 1/5 to 1/4 of the maximum compressive strength of concrete. and it simulates the compression part of concrete using a typical isotropic elasto-plastic model, and the tensile part of concrete is simulated using a smeared crack model. The latter is a method of simulating the crack by adjusting the stress and stiffness at the integration point, without reconfiguring the mesh. In the CSC, the band-width obtained based on the size of the element is reflected in the crack behavior to avoid mesh dependencies ([11]). For a three-dimensional element, the cubic root of a volume is the crack width of the element. The compressive and tensile uniaxial behavior of the CSC model is shown in Fig. 1.

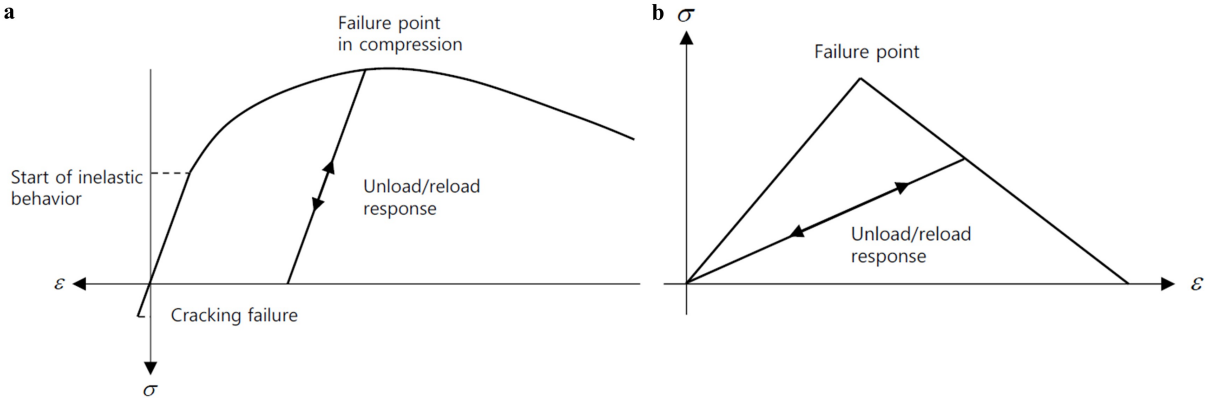


Figure 1: a) Uniaxial behavior of SCS; b) Tensile behavior of CSC.

Cracks occur when the stress is outside the crack detection surface, a type of yield function. If a crack occurs, the stress is returned using an implicit backward Euler method, and the direction of the maximum principal strain is the direction of the crack. This direction is stored to simulate the anisotropy by cracking in subsequent analyses. Since the orthogonal fixed crack model is used in this study, the subsequent crack shall be in a direction orthogonal to the existing crack direction and up to three in the case of the 3D model. If the elastic strain in the direction of the crack is tensile after the crack has occurred, it has behaved as damaged elastic and it is considered that the crack is closed when it is compressed.

In this study, the compression behavior of the plain concrete was modeled by the Thorenfeldt's law [26]. Note that in the preliminary calibration of the model [19], another constitutive model, namely JSCE-2017[27] was adopted (see an application in [28]). The compressive strength of concrete ($f_c$) was assumed according to the equivalent cylindrical compressive strength of tests performed on three samples, with an average value of 29.3 MPa.

The tensile behavior was instead modeled by the Hordijik's law [29] characterized by a linear hardening branch followed by a nonlinear softening branch. The area under the stress-strain curve should be equal to the fracture energy ($G_f$) divided by the equivalent length (according to the different size mesh adopted for the elements). According to CEB-FIP MC90, the concrete tensile strength $f_t$ was defined as $0.3f_c^{(2/3)} = 2.85$MPa and $G_f$ was assumed equal to 0.05 N/mm. The concrete elastic modulus was set as $E_{cm} = 22,000(0.1f_c)^{0.3} = 30,373$ MPa. Furthermore, concrete density $\gamma_c = 2.5e-3$ N/mm$^3$ and Poisson modulus $\nu_c$ =0.2.

In order to obtain the best balance between simulation accuracy and computational burden

as well as to thoroughly explore in particular the nonlinear behavior of the BCJ, following sensitivity analysis, it was decided to employ a different discretization of the RC sample.

In particular, eight-node solid brick elements with a maximum mesh size of 20 mm were specifically used to represent the joint up to an extension of 200 mm from its edges. Instead, the maximum mesh size at the beam and column ends, which extended respectively 1,200 mm and 770 mm, was 80 mm. The remaining center portion of the beam and column, with an extension respectively of 600 mm and 380 mm, had a maximum mesh size of 40 mm.

The steel rebars and ties are modelled as two-node one-dimensional embedded truss elements (do not require node sharing and are hence more convenient with respect to the conventional truss elements) which ignore flexural behavior. The tensile and compressive strengths were assumed according to B450C steel property defined in NTC2018 and characterized by yield strength $f_y = 450$ MPa, ultimate strength $f_u = 540$ MPa, elastic modulus $E_s = 210,000$ MPa, ultimate strain $\varepsilon_{s,u} = 0.75\%$, steel density $\gamma_s = 7.85e-5$ N/mm$^3$ and Poisson modulus $\nu_c$ =0.29. The embedded method with a perfect bond between reinforcement and surrounding concrete is adopted to simulate the reinforcement-concrete bonding interaction. It is notable that the effects usually associated with reinforcement-concrete interface, such as bond slip and dowel action cannot be directly modeled.

The stiffening effect provided by the steel plates at both the beam and column ends was simulated by introducing rigid links. In particular, a master node was applied in correspondence with the actuator's center of action at the top head column, whereas their respective slave nodes were located on the mesh nodes belonging to the top face of the column. Three further master nodes were applied in correspondence with the centre of the pinned support (at the base-column) and that of the roller supports at the two beam ends. Their respective slave nodes were applied to the mesh nodes belonging to the interested faces.

Regarding constraints: i) fixed translations along X and Z and fixed rotation along Y and Z were applied to the master nodes at the two beam ends; ii) fixed translations along X, Y, and Z and fixed rotations along Y and Z were applied to the master node at the base-column; iii) fixed translation along X was assumed to the master node at the head-column (note that this constraint was specifically introduced in this paper aiming to better represent the real cyclic behavior of the sample avoiding deflection along the gravitational direction after the joint failure).

Finally, note that the displacement $d$ was applied in the master node at the top head column along Y direction, whereas gravitational loads were applied to all mesh nodes along negative X direction.

Fig. 2 shows the FE model and some details of both steel reinforcements and rigid-links simulating the steel plate stiffening.

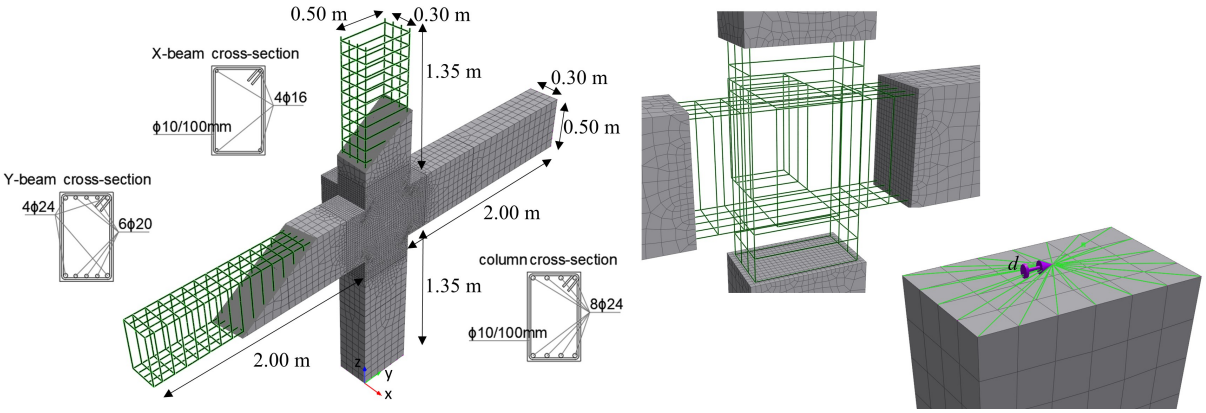


Figure 2: Numerical model with details of the geometry, the steel rebars and the rigid links at the column head

### 3.1 Effect of the cyclic shear reduction

A key feature of the cracking model is that, unlike crack initiation, which only considers Mode I fracture (tensile stress parallel to the crack plane), post-cracked behavior considers both Mode I and Mode II fracture (shear stress acting parallel to the plane of the crack and perpendicular to the crack front). The amount of crack opening, also function of the friction between the two surfaces of a crack and therefore very complex to predict in any damage model, determines the Mode II shear behavior. The dependence is that the shear modulus decreases as the crack expands. The post-cracked shear stiffness can therefore be calculated by the so-called shear retention model. Shear retention should theoretically decrease for large crack strains as less shear stress is capable of being transmitted across the crack. This phenomenon depends not only on the crack width but also on the transverse reinforcement ratio since the reinforcement provides additional strength.

Within smeared crack approach one can adopt rotating crack models (RCM) or fixed crack models (FCM). In contrast to RCM, which alters its orientation during loading in accordance with the principal stress directions, FCM used in the smeared crack technique maintains a stable crack orientation during the whole computational process. The RCM provides acceptable stress/strain rotations and a better prediction of model stiffness because of the shear retention function that provides coaxially between the principal stresses and strains. Acceptable FCM results can only be achieved when a near zero shear retention factor $\beta$ is employed. In particular, $\beta$=0 refers to no aggregate interlock, whereas $\beta$=1 represents a full aggregate interlock. If the value of the shear retention factor is specified near to 1, there is a possibility of stress locking.

In [30] it was highlighted that the use of a variable shear retention factor (decreasing for increasing crack opening) allowed for the best fitting between numerical and experimental results (beams tested under 4-point bending). On the contrary, the use of a constant shear retention factor may result in a stiffer post-peak response and too little structural softening [31]. A study [32] recommended that an average value of 0.40 is to be taken into account in RC beams analysis, whereas other studies (e.g. [33]) suggest values between 0.2 and 0.3. However, the sensitivity of deformability and damage evolution as a function of constant $\beta$ was explored in [30] finding out that the results are almost identical for values of $\beta$ greater than 0.2 while lower values are ineffective. Finally, several studies (e.g. [34, 35]) showed that post-peak behavior could be satisfactorily simulated by assuming a very low $\beta$ value (e.g., 0.001). Thereby, it can be concluded that the shear retention factor is an important parameter to be calibrated case by case depending on the loading and structure types based on which one should make a judgment in selecting this

parameter.

The model adopted in this study allows considering a shear retention factor. Hence, a parametric investigation was performed in terms of $\beta$, assuming for it constant values of 0.05, 0.2 or 0.4 as well as variable values through the relation developed in [36], for which shear stiffness decreases as a function of the normal total strain $\varepsilon_{nn}$, as follows: $\beta = 0.4(f_t/(E\varepsilon_{nn}))$.

The following results are presented by using labels in which the first letter indicates the type of test (E=experimental; N=numerical), the second letter indicates the compressive constitutive law (J for JSCE-2017 or T for Thorenfeldt [26]). Then, it is specified the value assumed for the shear retention factor $\beta$.

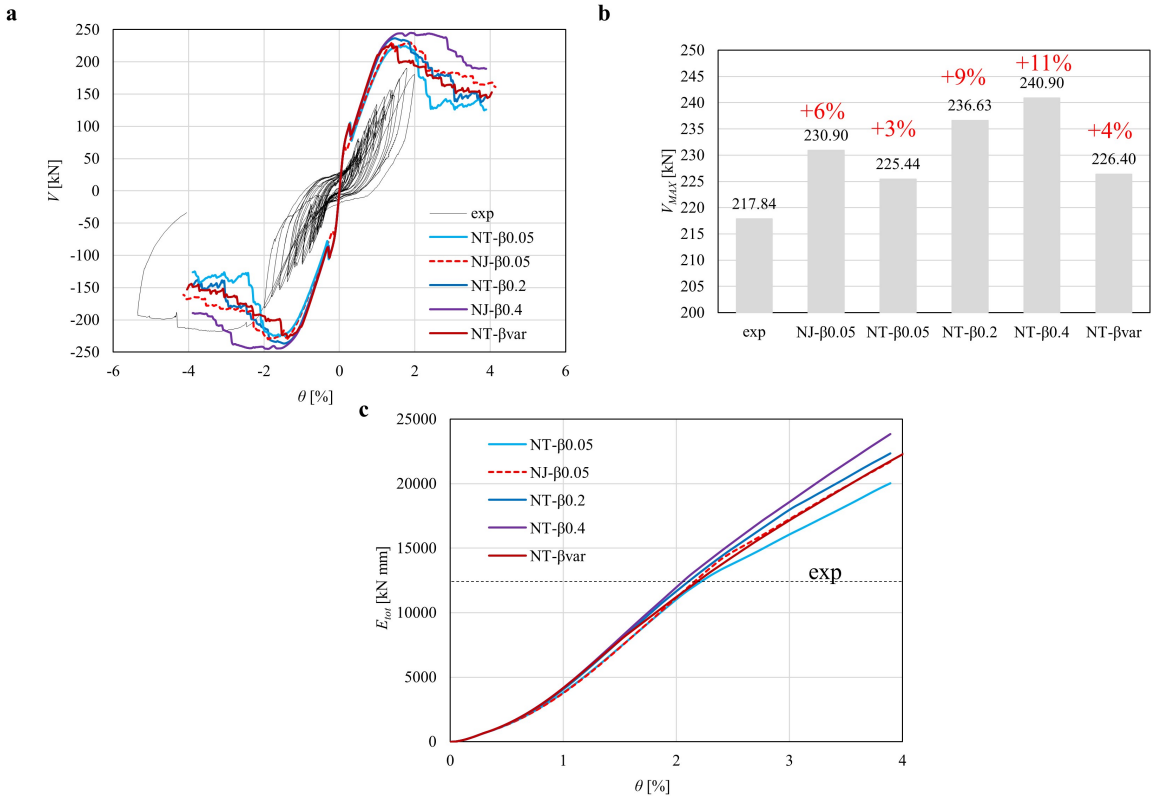


Figure 3: Comparison between cyclic experimental curve and monotonic numerical curves in terms of: a) $V - \theta$ curves; (b) shear strength values; c) Energy dissipation $E_{tot}$.

In particular, Fig. 3a shows the $V - \theta$ responses obtained numerically under monotonic load-condition as well as experimentally under cyclic test. It is important to highlight that also the response obtained in the initial calibration phase of the model [19] (i.e. the NJ-$\beta$0.05 case) is reported in Fig. 3a, noting that it was obtained by assuming JSCE-2017 constitutive law in compression, constant $\beta$ value equal to 0.05, and through a different software version (v1.1, release: Oct. 23 2020). The different law in compression adopted in the present study was mainly due to the instability issue that occurred during numerical cyclic analysis (described later).

First of all, the main difference with respect to the experimental response regards the slope of the numerical curve, which is higher as compared to the experimental one. This could be depending on possible bar-slip phenomenon, which cannot be captured in the present model, as already commented in [19]. Among the numerical curves of Fig. 3a, one can see a slight

difference in terms of maximum strength and a more consistent difference in the post-peak behavior. In general, results suggest that the lower the constant value assumed for $\beta$, the lower the strength and load-bearing capacity according also to the literature studies described above. For all cases, a first stress drop is seen close to 100 kN and caused by the onset of cracks in the BCJ panel (as proven in [19]).

In Fig. 3b, a comparison in terms of shear strength $V_{max}$ is shown. In particular, one can see that the best matching of the experimental value is obtained for the case with the lower $\beta$ constant value (i.e., NT-$\beta$0.05) as well as with variable one (i.e., NT-$\beta$var).

To further aid the evaluation of specimen performance under different $\beta$ assumptions, the cumulative energy dissipation $E_{tot}$, was computed as the area enclosed by the global response, in terms of $V - d$ relationship. The comparison of the results was computed up to the same imposed displacement ($d = 130$mm). Specifically, also the value reported for the experimental case (about 12,000 kN mm) was computed for the envelope curve in the negative direction of the test (i.e., Y -, for which collapse occurred) and referred to a maximum value of $d = 130$mm. It is important to note that this specific imposed value allowed stable results avoiding numerical instability for all the investigated cases.

The simulation of cyclic tests was also carried out in quasi-static regime, in line with the experimental procedure (acceleration was almost negligible due to the comparatively slow applied load).In particular, only the initial sequence of the experimental test is presented in this study, as depicted in Fig. 4a where it can be observed the imposed $d$ during the test (not symmetric between the positive and negative load direction). The experimental response of the first phase is shown in Fig. 4b, whereas the crack pattern is depicted in Fig. 4c, noting that only a few hair crack lines in the BCJ occurred in this preliminary phase. Then, in Fig. 4d is reported the measurement of the shear strain $\gamma$ as the sum of the two strains $\varepsilon$ (in absolute terms) measured along the two LVTDs mounted to the BCJ panel.

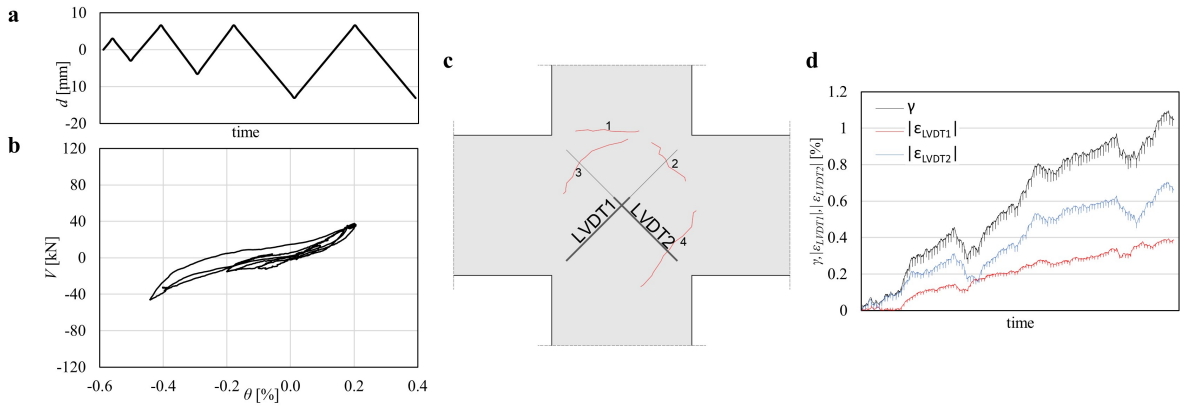


Figure 4: Details of the first cycles of the experimental test: a) imposed $d$ during the test-time; b) $V - \theta$ curve; c) crack pattern at the BCJ; deformation of the BCJ

The numerical capacity curves are reported in Fig. 5a, where it can be observed that the lower the constant value of $\beta$, the higher the shear strength degradation achieved at the various cycles. Moreover, for all the investigated cases, one can observe a slight stiffness reduction at the various cycles.

In Fig. 5b, the numerical shear strain is reported as a function of the step analysis, showing a slightly lower value of $\gamma$ achieved with respect to the experimental one (for which $\gamma$ was about 1% at the end of the investigated phase, also taking into account possible erroneous movements

of the LVTDs). The case that better reproduced the experimental outcome is the NT-$\beta$var one. In Fig. 5c it is shown the crack pattern of the only BCJ panel plotted up to 0.01 mm in crack width. In particular, one can see that for NT-$\beta$0.4 and NT-$\beta$var cases, a more concentration of cracks occurs in the center of the BCJ, in line with the experimental evidence. This propensity can be observed also in Fig.6, where the crack pattern, Von Mises stress, and strain rebars are depicted. Indeed, from that figure it is pretty clear that the outcomes referred to low constant $\beta$ values (i.e. NT-$\beta$0.05 and NT-$\beta$0.2) wrongly reproduced the experimental evidence since, unlike to that case, stress concentration and crack propagation interested also columns and beams of the RC frame as well as the rebar strain also exceeded the yield value and it was close to the ultimate condition.

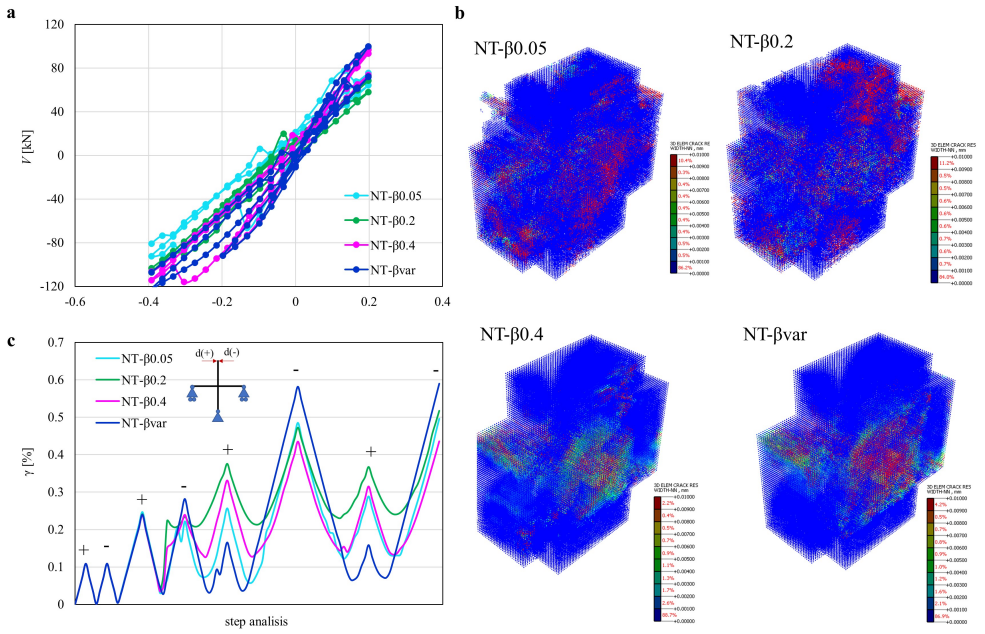


Figure 5: a) $V-\theta$ numerical curve; b) Crack pattern of the only BCJ panel; c) numerical shear strain

Therefore, despite a good match of the experimental outcome (especially in terms of shear strength) was obtained by assuming very low constant $\beta$ values through numerical monotonic tests (see Fig. 3a), this assumption led to a completely wrong prediction of cyclic tests. On the contrary, by assuming variable $\beta$ value (as a function of the normal total stain) a good prediction of both monotonic and cyclic tests was performed. Hence, future numerical studies performed by the Authors and focusing on the mechanical behavior of different typologies of RC beam-column joints under both unreinforced and reinforced conditions will consider this assumption for the shear retention factor.

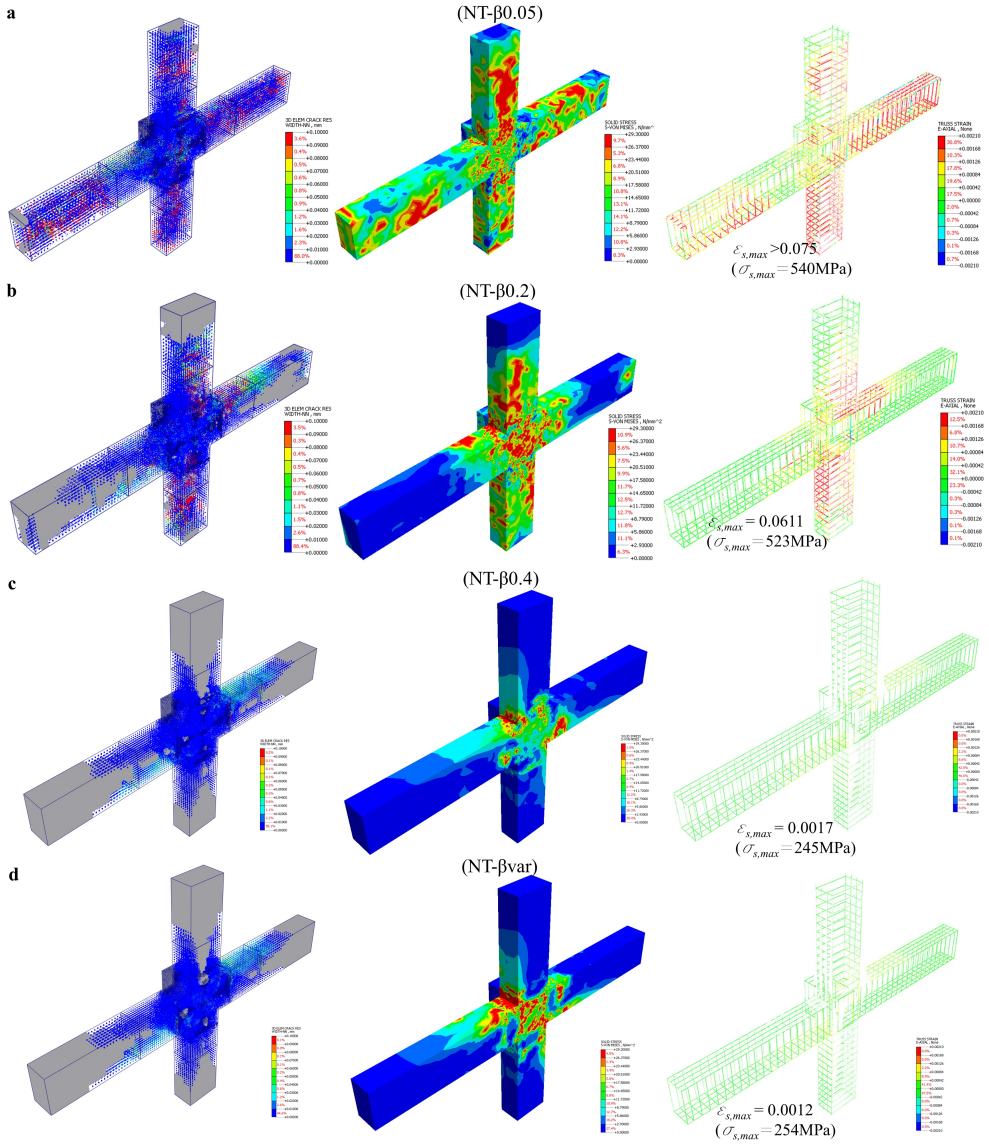


Figure 6: Crack pattern (right), Von Mises Stress (centre) and rebar strain (left) for the different investigated cases: NT-$\beta$0.05 (a), NT-$\beta$0.2 (b), NT-$\beta$0.4 (c), NT-$\beta$var (d)

## 4 CONCLUSIONS

The numerical results of an RC beam-column joint connection are described in the current work. The joints' brittleness—typical of Italian reinforced concrete buildings from the 1960s to the 1970s—was emphasized to cause shear failure only in the junction panel before yielding both the beam and column reinforcements (differently from other tests described in the current literature). To simulate crack propagation and fracture in concrete as well as to comprehend some physical principles, a three-dimensional model utilizing the smeared crack technique was employed. A parametric numerical study was carried out to show how a particular parameter, the shear retention factor, affects both monotonic and cyclic tests. Indeed, it is worth noting that, despite the fact that very low constant values assumed for the shear retention factor, in monotonic tests, lead to the best matching of the experimental test, also in line with numerous literature findings, it is essential to assume variable values for it (as a function of the normal total strain of the elements or, in general, also in terms of crack wide) to properly simulate cyclic

tests. Indeed, apart from the increased numerical stability of the simulation, the best benefit in assuming variable values for it in cyclic tests is related to the very accurate simulation of stress concentration and fracture propagation in plane concrete as well as the good distribution of the stress to the rebars.

## REFERENCES

[1] P. Ricci P., F. De Luca, G. M. Verderame, 6th April 2009 L'Aquila earthquake, Italy: Reinforced concrete building performance. *Bulletin of Earthquake Engineering* **9**(1), 285–305, 2011

[2] P. Ricci, M. Di Domenico, and G. M. Verderame, Empirical-based out-of-plane URM infill wall model accounting for the interaction with in-plane demand. *Earthquake Engineering & Structural Dynamics* **47**(3) 802–27, 2018

[3] F. Braga, , V. Manfredi, A. Masi, A. Salvatori, M. Vona, Performance of non-structural elements in RC buildings during the L'Aquila, 2009 earthquake. *Bulletin of Earthquake Engineering* **9**(1), 307-24, 2011

[4] R. Vicente, H. Rodrigues, H. Varum, A. Costa, J. A. R. Mendes da Silva, Performance of masonry enclosure walls: Lessons learned from recent earthquakes. *Earthquake Engineering and Engineering Vibration* **11**(1), 23–24, 2012

[5] M. Angiolilli, M. E. Minkada, M. Di Domenico, S. Cattari, A. Belleri, G. M. Verderame, Comparing the Observed and Numerically Simulated Seismic Damage: A Unified Procedure for Unreinforced Masonry and Reinforced Concrete Buildings. *Journal of Earthquake Engineering*, 1–37, 2022

[6] C. Del Vecchio, M. Di Ludovico, A. Balsamo, A. Prota, G. Manfredi, M. Dolce, Experimental investigation of exterior RC beam-column joints retrofitted with FRP systems. *Journal of Composites for Construction* **18**(4), 04014002, 2014

[7] C. Del Vecchio, M. Di Ludovico, A. Balsamo, A. Prota, Seismic retrofit of real beam-column joints using fiber-reinforced cement composites. *Journal of Structural Engineering* **144**(5) 04018026, 2018

[8] O. Yurdakul, O. Avsar, Strengthening of substandard reinforced concrete beam-column joints by external post-tension rods. *Engineering Structures* **107**, 9–22, 2016

[9] O. Yurdakul, C. Del Vecchio, M. Di Ludovico, O. Avsar, Numerical simulation of substandard beamcolumn joints with different failure mechanisms. *Struct Concrete* **21**(6), 2515–2532, 2020

[10] C. Lima, E. Martinelli, C. Faella, Capacity models for shear strength of exterior joints in RC frames: state-of-the-art and synoptic examination. *Bulletin of Earthquake Engineering* **10**, 967–983, 2012

[11] Z. Bažant, B. H. Oh, Crack band theory for fracture of concrete. *Matériaux et construction* **16**, 155–177, 1983

[12] A. Hillerborg, M. Modéer, P. E. Petersson, Analysis of crack formation and crack growth in concrete by means of fracture mechanics and finite elements. *Cement and concrete research* **6**(6), 773–781, 1976

[13] A. Rimkus, V. Cervenka, V. Gribniak, J. Cervenka, Uncertainty of the smeared crack model applied to RC beams. *Engineering Fracture Mechanics* **233**,107088, 2020

[14] S. J. Pantazopoulou, J. F. Bonacci, On earthquake-resistant reinforced concrete frame connections. *Canadian Journal of Civil Engineering*, **21**(2), 307–328, 1994.

[15] M. Youssef, A. Ghobarah, Modelling of RC beam-column joints and structural walls. *Journal of earthquake engineering*, **5**(01), 93–111, 2001

[16] G. Calvi, G. Pampanin, Experimental test on a three storey RC frame designed for gravity only. *12th European Conference on Earthquake Engineering* London, paper n. 727, 2002

[17] A. E. Behbahani, J. A. Barros, A. Ventura-Gouveia, Plastic-damage smeared crack model to simulate the behaviour of structures made by cement based materials. *International Journal of Solids and Structures* **73** 20–40, 2015

[18] ACI 374.1, Acceptance Criteria for Moment Frames Based on Structural Testing and Comm. *American Concrete Institute*, Farmington Hills, 2005.

[19] M. Angiolilli, A. Gregori, R. Tonelli, C. Tonelli, E. Ciuffetelli, A. Peditto, Structural performance of unreinforced full-scale façade concrete beam-column joint under cyclic load. *Procedia Structural Integrity* **44**, 870–877, 2023

[20] NTC, Norme tecniche per le costruzioni in zone sismiche, in Italian, Ministerial Decree DM; 2018.

[21] ACI 352R-02, Recommendations for Design of Beam-Column Connections in Monolithic Reinforced Concrete Structures, ACI-ASCE Committee, 2002

[22] M. Asgarpoor, A. Gharavi, S. Epackachi, A simplified model for concrete at low confining pressures. *Structures* **29**, 1322–1351, 2021

[23] F. Di Carlo, A. Meda, Z. Rinaldi, Numerical cyclic behaviour of un-corroded and corroded RC columns reinforced with HPFRC jacket. *Composite Structures* **163**, 432–443, 2017

[24] A. Earij, G. Alfano, K. Cashell, X. Zhou, Nonlinear three–dimensional finite–element modelling of reinforced–concrete beams: Computational challenges and experimental validation. *Engineering Failure Analysis* **82** 92–115, 2017

[25] H. D. Hibbitt, A simplified model for concrete at low confining pressures. *Nuclear engineering and design* **104**, 313–320, 1987

[26] E. Thorenfeldt, A. Tomaszewicz, J. J. Jensen, Mechanical properties of highstrength concrete and applications in design. *In Proc. Symp. Utilization of HighStrength Concrete, Stavanger, Norway*, 1987

[27] JSCE, Guideline on Design and Application Methods of Silicate-based Surface Penetrants used for Concrete Structures. *Japan Society of Civil Engineers*, Concrete Library 137, 2017

[28] Fu, L., Nakamura H., Yamamoto Y., M. Taito, Effect of various structural factors on shear strength degradation after yielding of RC members under cyclic loads. *Journal of Advanced Concrete Technology* **18**, 211–226, 2020

[29] D. A. Hordijk, Local approach to fatigue of concrete. *Delft University of Technology, The Netherlands*, 1991

[30] R. Scotta, R. Vitaliani, A. Saetta, E. Oñate, A. Hanganu, A scalar damage model with a shear retention factor for the analysis of reinforced concrete structures: theory and validation. *Computers & structures* **79**(7), 737–755, 2001

[31] J. G. Rots, R. De Borst, Analysis of mixed-mode fracture in concrete. *Journal of engineering mechanics* **113**(11), 1739–1758, 1987

[32] S. Khalfallah, A. Charif, N. Mohammed, Nonlinear analysis of reinforced concrete structures using a new constitutive model. *Revue Européenne des Eléments* **13**(8), 841–856, 2004

[33] L. Dahmani, A. Khennane, S. Kaci, Crack identification in reinforced concrete beams using ANSYS software. *Strength Mater* **42**(2), 232–240, 2010

[34] N. Mitra, L. N. Lowes, Factors influencing analytical continuum simulation of three-point bend test of a concrete notched beam. *14th World Conference on Earthquake Engineering*, Beijing, China, October, 2008.

[35] J. G. Rots, P. Nauta, G. M. A. Kuster,J. Blaauwendraad, Smeared crack approach and fracture localization in concrete. *HERON* **30**(1), 1985

[36] R. S. H. Al-Mahaidi, Nonlinear Finite Element analysis of reinforced concrete deep members. *Cornell University*, 1978

[37] T. Paulay, M.J.N. Priestley, Seismic design of reinforced concrete and masonry building. *John Wiley & Sons, inc.*, New York, 1992

[38] M. J. N. Priestley, Myths and fallacies in earthquake engineering, revisited. *The Mallet Milne Lecture. IUSS Press: 58 Pavia, Italy*, 2003

COMPDYN 2023
9th ECCOMAS Thematic Conference on
Computational Methods in Structural Dynamics and Earthquake Engineering
M. Papadrakakis, M. Fragiadakis (eds.)
Athens, Greece, 12-14 June 2023

# DYNAMIC CHARACTERIZATION OF THE CIRCUS MAXIMUS ARCHEOLOGICAL SITE

**Amir Reza Elahi[1], Alessandro Cardoni[1], Cosimo Pellecchia[1], Marialetizia Buonfiglio[2], Federica Michela Rossi[2], Elena Federico[2,] Fabio Pacciani[2] and Gian Paolo Cimellaro[1]**

[1] Department of Structural, Geotechnical and Building Engineering, Politecnico di Torino, Corso Duca degli Abruzzi 24, 10129 Turin, Italy.
e-mail: {alessandro.cardoni, cosimo.pellecchia, gianpaolo.cimellaro}@polito.it
e-mail: {amirreza.elahi}@studenti.polito.it

[2] Sovrintendenza Capitolina Beni Culturali, Direzione Interventi su Edilizia Monumentale, Via Ostiense 106, 00154 Rome, Italy.

e-mail:{marialetizia.buonfiglio, federicamichela.rossi, elena.federico, fabio.pacciani}@comune.roma.it

## Abstract

*Monumental structures and archeological sites are often exposed to intense ambient and anthropic vibrations which might compromise their structural integrity. Monitoring these precious assets allows to assess their overall conditions and highlight possible changes in the behavior of the structure. In this paper, the effects of vibrations on the Circus Maximus archeological area are investigated. A wireless structural health monitoring system was used to record accelerations from July 2022 to January 2023. During this period, several concerts and events were held in the area. The acceleration records were used to perform dynamic characterizations of the site. Different numbers of sensors and configurations were used to assess the influence of spatial resolution. The modal properties were obtained through the frequency domain decomposition technique and compared to those from previous studies. Overall, a reduction of the modal frequencies has been observed which requires further investigations.*

**Keywords:** Monumental Structures, Towers, Anthropic Vibrations, Dynamic Characterization, Operational Modal Analysis.

# 1 INTRODUCTION

Most historical built heritage, such as ancient palaces, monuments, and churches are complex masonry structures whose preservation against degradation and extreme vibration is of primary concern in Europe. In the Italian territories, the vast majority were architected during the Renaissance and extended in different regions, hosting large crowds on occasion. To propose a preservation plan, evaluate the impact of extraordinary excitations, and ensure the safety of them, various Structural Health Monitoring (SHM) strategies are utilized.

Among existing SHM strategies, vibration-based systems are one of the emerging non-invasive technologies to address safety concerns and propose restoration plans for monumental assets by means of system identification schemes. System identification is defined as the evolution of models from experimental studies that can be employed to calibrate numerical simulations, and damage identification algorithms. The usual parameters determined through the experimental studies are the modal properties (i.e., frequency, mode shapes, and damping ratios). They are directly dependent on the inherent characteristics of a structure, such as the stiffness, mass, and material type, which modification results in distinct response of a system. However, the damping ratio is set aside from the damage indicators since its estimation can be largely biased using the conventional techniques [1].

Experimental Modal Analysis (EMA) and Operational Modal Analysis (OMA) are popular tools for structural identification. The former involves recording the input and output, while in the latter, the identification is entirely carried out based on the response. In addition, the former scheme is neither feasible nor practical for built heritage due to the complexity in proper excitation levels and boundary conditions. Thus, the output-only identification methods are the optimal solution in which the infrastructure's service is not halted during the process.

There are several studies on the dynamic identification of historical sites using OMA techniques. In a recent study, the Sant'Agata del Mugello church was densely instrumented to evaluate the spatial resolution impacts on the derived modal properties. The modal anomalies, captured during two experimental campaigns using Enhanced Frequency Domain Decomposition (EFDD) [2], were applied to establish a relation between the dynamic response and the history of restorations. The study disclosed the effect of sensor placement on the extracted modal properties [3].

As a part of the seismic vulnerability assessment of Esfahan Shah mosque, the dynamic identification was performed response using Stochastic Subspace Identification (SSI) [4] and EFDD technique. The modal properties were applied in the calibration of the FE model to perform nonlinear analysis and obtain a relation between the simulated damages and the monument. The study suggested improving the stiffening walls and the two domes connection for better global performance [5].

Saint Torcato church is another historical complex under a hybrid static and dynamic monitoring system. The hybrid SHM monitoring documented the evolution of specific parameters such as cracks width and frequencies before, during, and after the restoration planes. The study took into consideration the impact of environmental agents, namely, temperature variation and humidity, on the specific parameters by long-term monitoring of the asset [6].

As mentioned, in the vibration-based techniques, the damage indicative parameters are mostly natural frequencies and corresponding mode shapes. However, the change in the identified values does not necessarily imply the degradation of physical properties. In fact, the variability of modal properties can be associated with environmental agents [7].

In a study on the Consoli Palace in Gubbio, the role of environmental agents in the accuracy of early damage detection was highlighted. A hybrid SHM system was employed to discard the environmental effects of the damage caused by material degradation and earthquake

excitation. The modal properties were identified using FDD, EFDD, and SSI, while the impact of freeze and thaw cycles was quantified. During the long-term monitoring, nonlinear trends for crack widths and frequencies were derived in contrast with previous studies [8].

A similar study was carried out on the renowned masonry monuments, Milan Cathedral, utilizing electrodynamic, temperature and humidity, and tilt measurement sensors. The continuous monitoring was performed using the automated cov-SSI to extract sensitive modal features. The long-term monitoring revealed the negligible effect of relative humidity on the crack width and natural frequencies. In addition, a distinctive correlation was observed between the natural frequencies and temperature fluctuation. The study suggests the use of mode shape geometries and their associated mode complexity as a monitoring parameter due to fewer deviations toward environmental agents [9].

This study aims at the modal identification of the Circo Massimo archeological site in Italy. The historical site is characterized by three sensor placement strategies to record ambient vibration response. Since the major international festivals of Italian capitals are held on this site, the acquired modal properties are compared with their counterparts derived in 2019 to detect anomalies [10]. Additionally, due to the inherent vulnerability of modal parameters against thermal variation, long-term SHM monitoring is carried out to evaluate their impact.

## 2 METHODOLOGY

In the frequency domain, the general peak picking and Frequency Domain Decomposition (FDD) [11] techniques are widely applied for identification purposes due to high interaction with users. The general peak-picking method assumes the contribution of one mode to the dynamic response at resonance leading to the misidentification of closely spaced modes. On the contrary, the FDD technique has a superior ability to estimate these modes.

In the FDD technique, the first step is the estimation of Power Spectral Density (PSD) from the recorded ambient vibration response. PSD is determined by taking the Fourier transform of correlation between sensor outputs besides assuming the input as a white noise signal. The relation of PSD is summarized below, where the power density function of output is obtained from the input counterpart:

$$G_{yy}(i\omega) = \sum_{k=1}^{n}\sum_{s=1}^{n}\left[\frac{R_k}{(i\omega-\lambda_k)} + \frac{R^*_k}{(i\omega-\lambda^*_k)}\right] C \left[\frac{R_s}{(i\omega-\lambda_s)} + \frac{R^*_s}{(i\omega-\lambda^*_s)}\right] \quad (1)$$

Then, the PSD is decomposed using the Singular Value Decomposition technique as follow:

$$G_{yy}(i\omega_i) = U_i S_i V_i^H \quad (2)$$

The SVD forms two matrices, namely singular values and corresponding singular vectors. The former matrix is diagonal, where the system's natural frequencies are ordered. Furthermore, their associated modes are placed column-wise in the latter matrix. Once the PSD matrix is determined, each peak of the SVD spectrum indicates the relevant frequency of the system [12].

In addition to the FDD method, an automated version is introduced to implement in online SHM monitoring systems. The method is based on the identification of a modal domain at the vicinity of each peak in the SV spectrum by establishing a criterion. The number of modes, domain width, and the criterion to identify them directly affect the specifying physical modes of vibration [13]. The method was developed for the identification of various infrastructures and details can be found on [14], [15], [16].

In the current study, two separate scripts are developed in MATLAB [17] based on the above formulation to perform the analysis in the next sections.

## 3 CIRCO MASSIMO

The Italian capital is renowned for its ancient elliptical monument, Colosseum, the largest amphitheater ever built. In the southeast of this asset, the Circo Massimo, an ancient chariot-racing stadium, is located where many international gatherings take place. Its wooden perimeters were constructed in the sixth century BC when the "ludi romani" Italian ceremonies were held. Starting from the year of 46 BC, the evolution of masonry elements had initiated, and many retrofits over the years were carried out. Just after the last festival in 549 AD, the site was given up, and numerous natural disasters caused the accumulation of 9-meter debris on the current track. The ancient stadium, the Torre della Moletta, and the circus ruins are depicted in Figure 1.

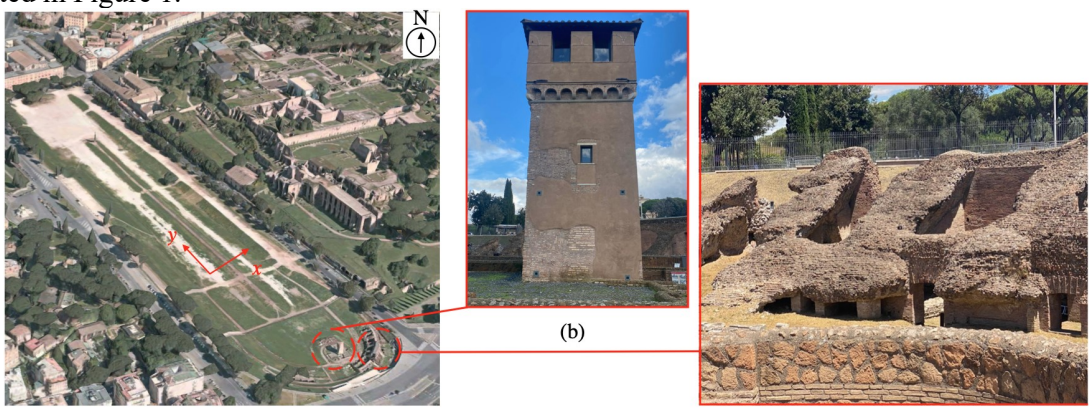


Figure 1: The Circo Massimo. (a) the general view, (b) Torre della Moletta, (c) circus ruins.

As indicated in the Figure 1, the Torre della Moletta is located in the southern part of the circus. The tower can be regarded as an extraordinary case study since the abundant sediment accumulations increase the uncertainty in the soil-structure interaction response. During the last restoration, steel frames connected to the spiral staircase were added to the structure. They are schematized in the following figure:




Figure 2: (a) The steel frame, (b) the spiral staircase.

As mentioned, the structure is exposed to intense ambient vibration due to numerous concert events. Thus, it is necessary to evaluate the impact of such excitation on the health of this archeological site.

## 4 HEALTH MONITOING SYSTEM

The historical complex is instrumented through the establishment of an extensive monitoring plan. Different locations, such as the circus ruins, the Mithraeum temple, and the Moletta tower, were instrumented, from which a part is on the scope of the current study.

The first sensor layout is labeled as configuration A, carried out on July 9, 2022. The circus ruins and Torre della Moletta are instrumented, as indicated in Figure 3.

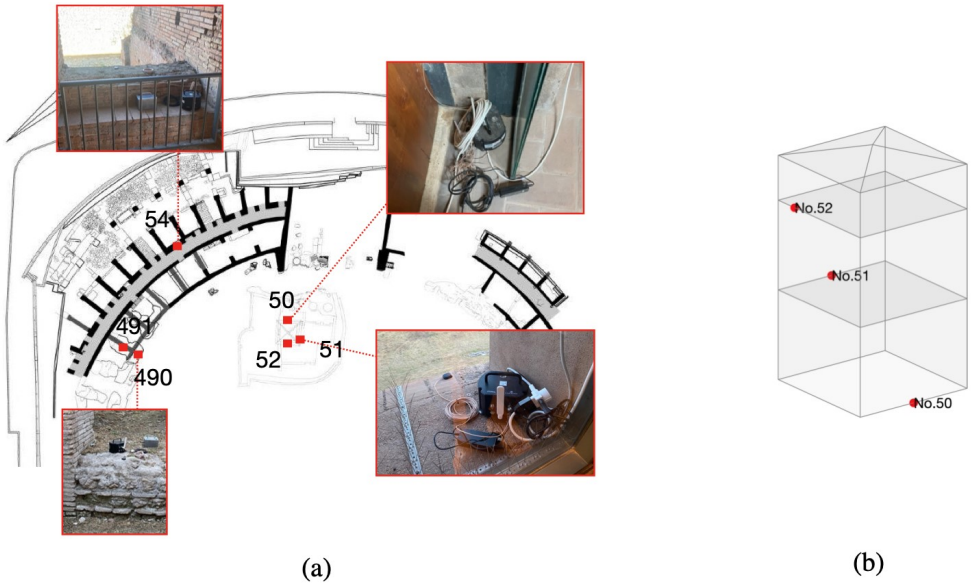


Figure 3: Sensor Configuration A, (a) Circo Massimo, (b) Torre della Moletta.

In sensor configuration B, five sensors are placed exclusively on the tower, and their layout are plotted below:

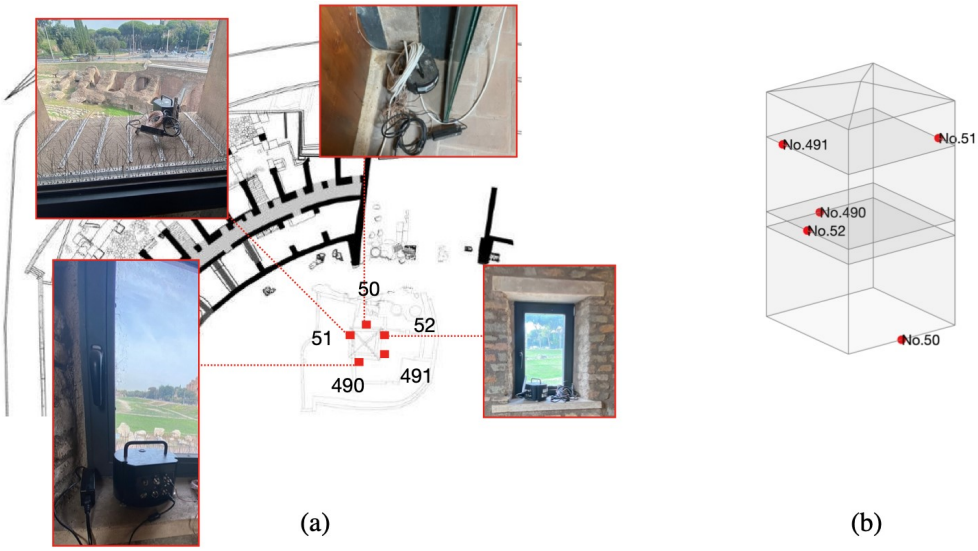


Figure 4: Sensor Configuration B, (a) Circo Massimo, (b) Torre della Moletta.

In the final layout, again, the focus is on the tower by instrumentation on four sensors which are illustrated in Figure 5.

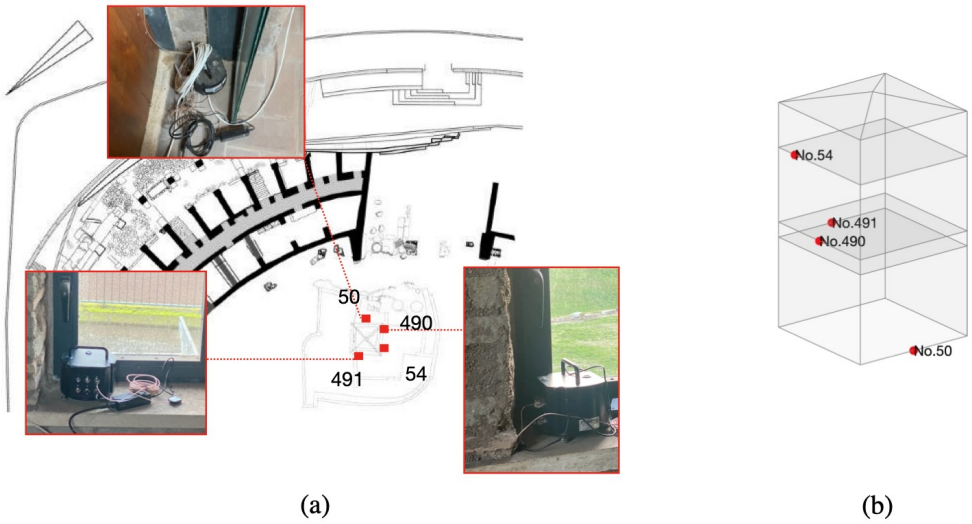


Figure 5: Sensor Configuration C, (a) Circo Massimo, (b) Torre della Moletta.

It is important to mention in section (b) of each figure imaginary rectangular floors are schemed to indicate the sensor's location. However, there is no floor or any kind of diaphragm there.

## 5 IDENTIFICATION OF MODAL PARAMETERS FROM AMBIENT VIBRATION

In this section, the ambient vibration response for each sensor configuration is set as the input of FDD analysis to extract natural frequencies and their corresponding mode of vibration. In the analysis of sensor configuration A, the data is related to July 9, 2022, from 9:15 to 10:15 UTC. The identified peaks in the SV spectrum using the manual FDD analysis for the Torre della Moletta are plotted in Figure 6.

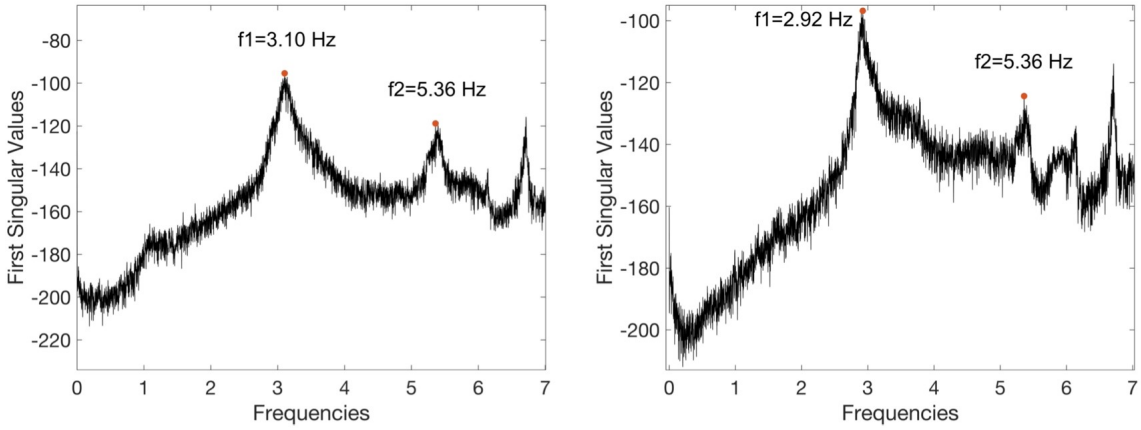


Figure 6: The selected peaks of the SV spectrum for configuration A. (a) x-direction, (b) y-direction.

It is observed that the first mode of vibration in the *x* and *y* direction is 3.10 and 2.92 Hz, respectively. Additionally, the same frequency is obtained for the second mode in both direc-

tions, indicating a simultaneous mode. The acquired mode shapes are plotted in MATLAB using spline interpolation to smoothen the deformed shape and better depiction in Figure 7.

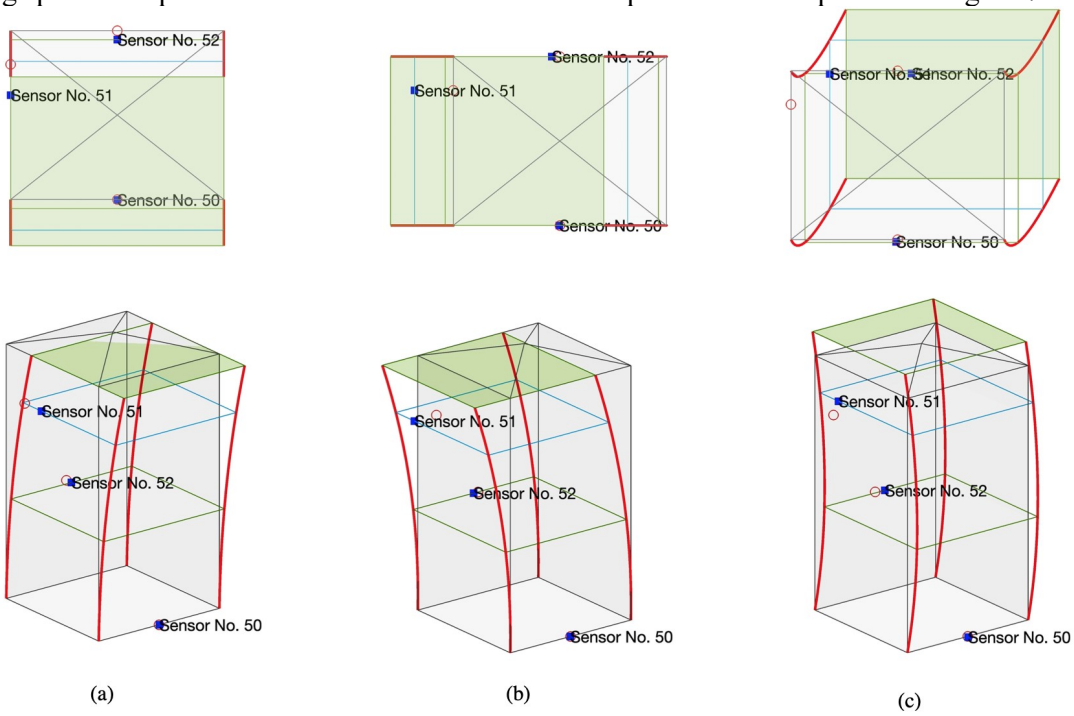


Figure 7: The 3D mode shapes of sensor configuration A. (a) mode in the *x* direction, (b) mode in the *y* direction, (c) mode in both directions.

Following the same scheme, the ambient vibration response of circus ruins related to the interval of 11:00-12:00 are analyzed and the SV spectrum is obtained. The extracted frequencies are compared with the result of similar investigation on 2019 in Table 1.

Table 1: Comparison of extracted frequencies for configuration A.

| Torre della Moletta | | | | Circus | | | |
|---|---|---|---|---|---|---|---|
| Puzzilli et al. (2019) | | Politecnico di Torino 09.07.22 | | Puzzilli et al. (2019) | | Politecnico di Torino 09.07.22 | |
| X-dir | Y-dir | X-dir | Y-dir | X-dir | Y-dir | X-dir | Y-dir |
| 3.25 | 3.00 | 3.10 | 2.92 | 2.5 | 2.5 | 2.22 | 2.22 |
| 5.80 | 5.80 | 5.36 | 5.36 | - | - | 4.42 | 4.56 |

A remarkable reduction in the system's natural frequencies is highlighted by comparing the results of current and former campaigns. This decrease can be induced by damage or interaction with various parameters like temperature variations. Thus, further study is carried out to determine the source of frequency reduction.

To capture the mode shapes of the tower more accurately, configuration B of the sensor's layout was proposed. By performing the manual FDD analysis, the natural frequency of the system is obtained as seen in Figure 8.

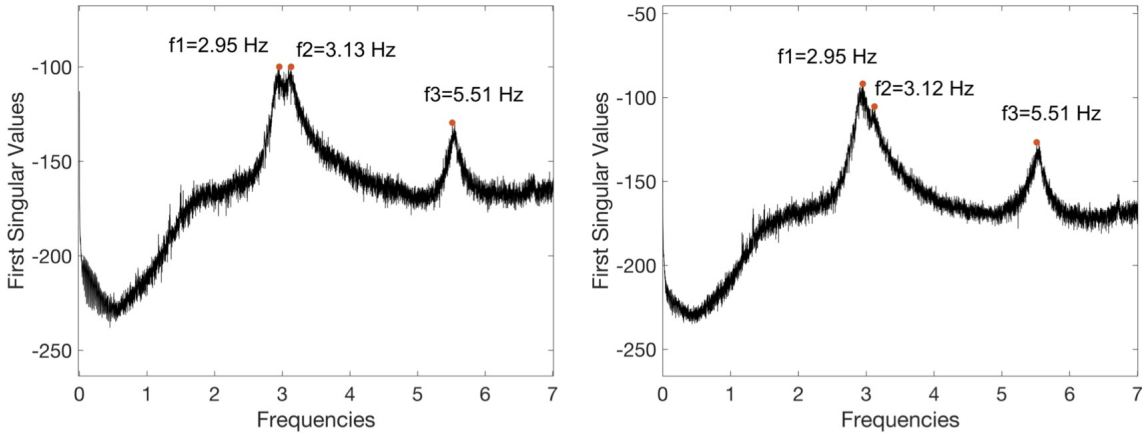


(a) (b)

Figure 8: The selected peaks of the SV spectrum for configuration B. (a) x-direction, (b) y-direction.

The new findings are summarized in Table 2.

Table 2: Comparison of extracted frequencies for configuration B.

| Puzzilli et al. (2019) | | Politecnico di Torino 09.07.22 | | Politecnico di Torino 21.10.22 | |
|---|---|---|---|---|---|
| X-dir | Y-dir | X-dir | Y-dir | X-dir | Y-dir |
| 3.25 | 3.00 | 3.10 | 2.92 | 2.95 | 2.95 |
| 5.80 | 5.80 | 5.36 | 5.36 | 3.13 | 3.12 |
| - | - | - | - | 5.51 | 5.51 |

Analyzing the new data indicates the presence of novel mode shapes in addition to an increase in the natural frequencies concerning July 9. In this part, the role of spatial resolution in the accurate capturing of modes is highlighted. The frequencies in the *x* and *y* directions are equal, implying the presence of simultaneous modes with the probable diagonal movement of the tower.

The 3D mode shapes are plotted in Figure 9.

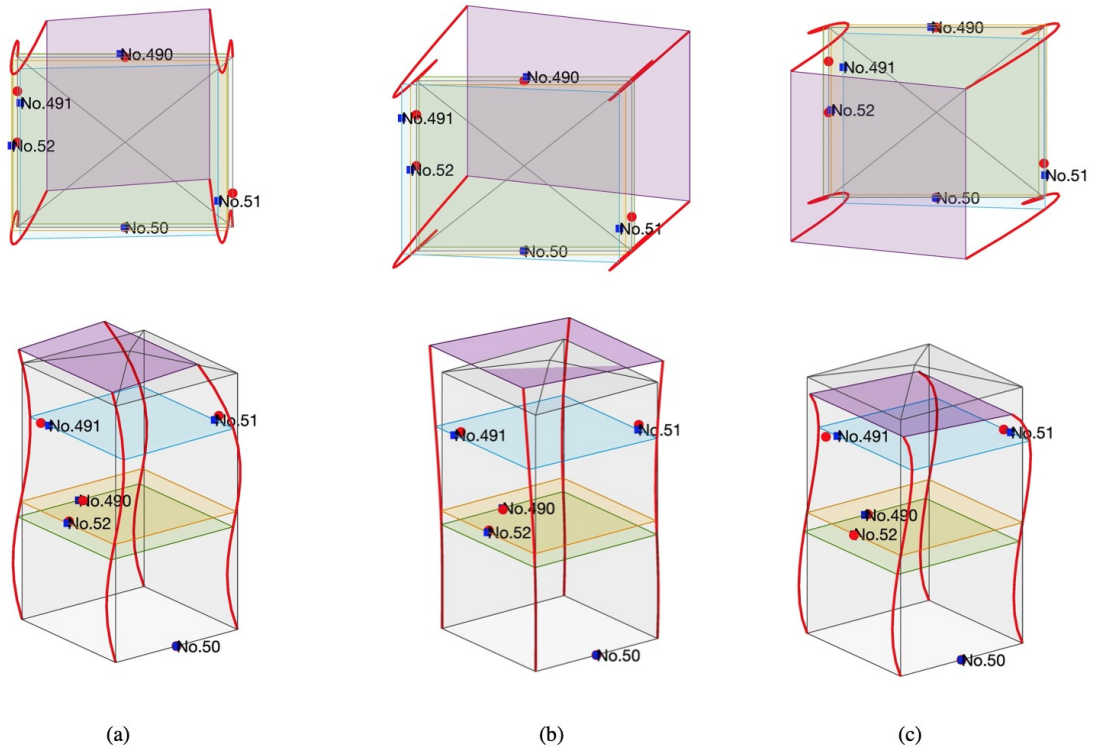


Figure 9: The 3D mode shapes of sensor configuration B. (a) mode 1, (b) mode 2, (c) mode 3.

Figure 9 is significant since the rotation of the tower sides is evident for all acquired modes of vibration on the top level. The twisting phenomenon on the tower can be due to its interaction with the spiral staircase. Thus, it is necessary to perform a further investigation on providing a restoration plan to prevent it.

In the last configuration, the data of December 30 with the similar duration are analyzed. Following the same scheme, the SV plots are not presented for the sake of brevity. The attained modal parameters of configuration C confirm the presence of new mode shapes contradicting the study on July 9. Moreover, there is an increasing trend in the acquired frequencies from July 9 to December 30, raising the hypothesis of environmental impacts on the system.

Table 3: Summary of the extracted frequencies for all configuration.

| Puzzilli et al. (2019) | | Politecnico di Torino 09.07.22 | | Politecnico di Torino 21.10.22 | | Politecnico di Torino 30.11.22 | |
|---|---|---|---|---|---|---|---|
| X-dir | Y-dir | X-dir | Y-dir | X-dir | Y-dir | X-dir | Y-dir |
| 3.25 | 3.00 | 3.10 | 2.92 | 2.95 | 2.95 | 3.01 | 3.01 |
| 5.80 | 5.80 | 5.36 | 5.36 | 3.13 | 3.12 | 3.22 | 3.22 |
| - | - | - | - | 5.51 | 5.51 | 5.89 | 5.89 |

In the final part of this section, the 3D modes are presented. Since there are not two sensors at the same level, the rotation of the tower is not captured.

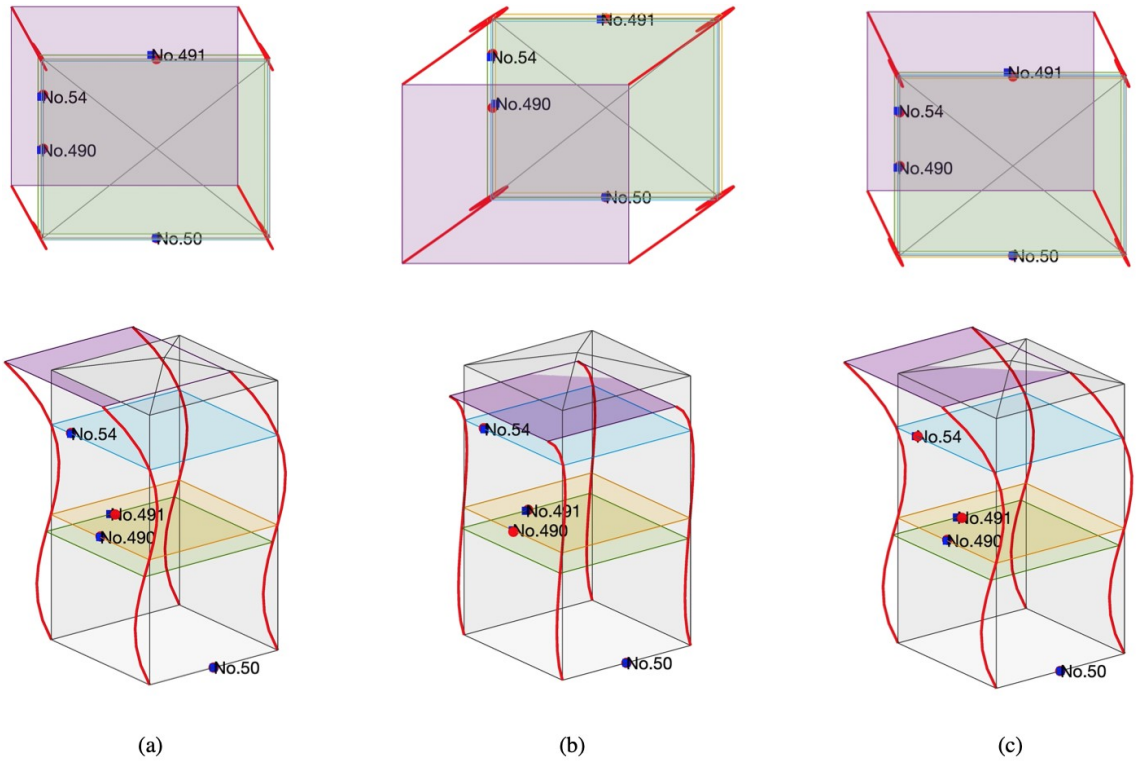


Figure 10: The 3D mode shapes of sensor configuration B. (a) mode 1, (b) mode 2, (c) mode 3.

## 6 CONTINOUS MONITORING OF THE TOWER

This section aims to assess the effect of temperature variation on the natural frequencies of the tower. For this regard, the AFDD method is employed to analyze the recorded structural response from July 9 to October 20 for sensor configuration A. The analysis for each date is divided into two intervals:

- Daily analysis for 60 minutes acceleration in the interval of 12:30-13:30 UTC;
- Nightly analysis for 60 minutes acceleration in the interval of 2:30-3:30 UTC.

The temperature records pertaining to the CIAMPINO station in the Rome are considered as the thermal variation of the site during the analysis. Before selecting the above intervals, the initial analysis indicated the highest and lowest temperature documented within these intervals.

After extracting the modal properties using the AFDD, the frequencies for daily and nightly intervals are presented in Figure 11. In addition, to prove the efficiency of the modal tracking approach and the fact that all frequencies are related to a certain mode of vibration, the Modal Assurance Criterion (MAC) is implemented. The MAC between the extracted mode shapes is calculated with respect to the one corresponding to July 9 and plotted on the top in Figure 11.

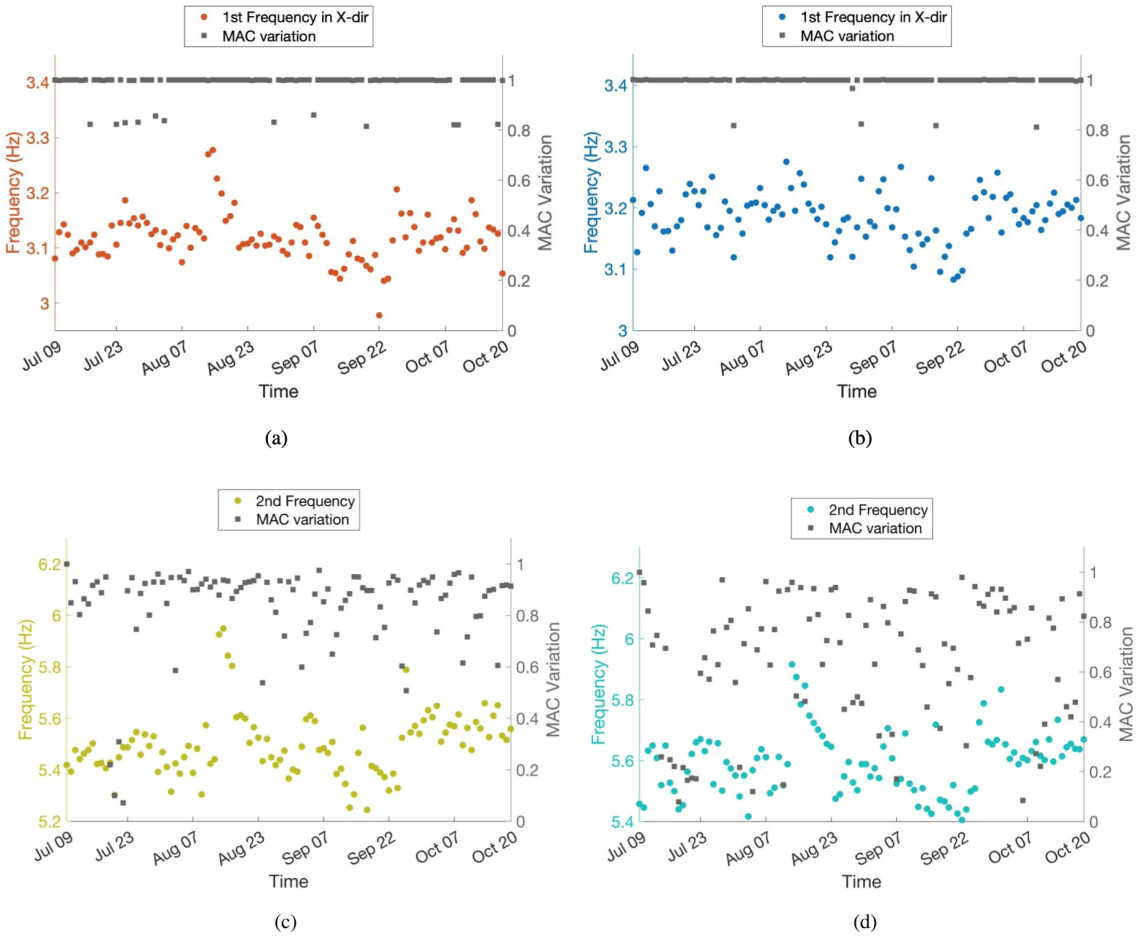


Figure 11: Obtained frequencies, (a) Daily 1st frequency in the *x*-direction, (b) Nightly 1st frequency in the *x*-direction, (c) Daily mutual frequency, (d) Nightly mutual frequency.

In the above figure, the similar observation is made for the first mode in the *y*-direction. According to the figures, it is observed that the acquired data for the second mode during the night has unstable MAC variation, which may originate from the noise made during the time interval. Although it is expected to have some variation of MAC in the higher modes due to environmental effects, it is better to take into consideration some measurements in this regard. As a result, the frequencies with a MAC less than 0.6, indicated in Figure 11 (d), are discarded.

To evaluate the effect of temperature, the determined frequencies for each mode of vibration are plotted against the corresponding temperature in Figure 12. The variation of natural frequencies aligns with the expectation in the masonry structures where the lower the temperature the higher the stiffness. Conducting a statistical analysis, linear regression is performed to correlate the thermal variation with the change of modal frequencies.

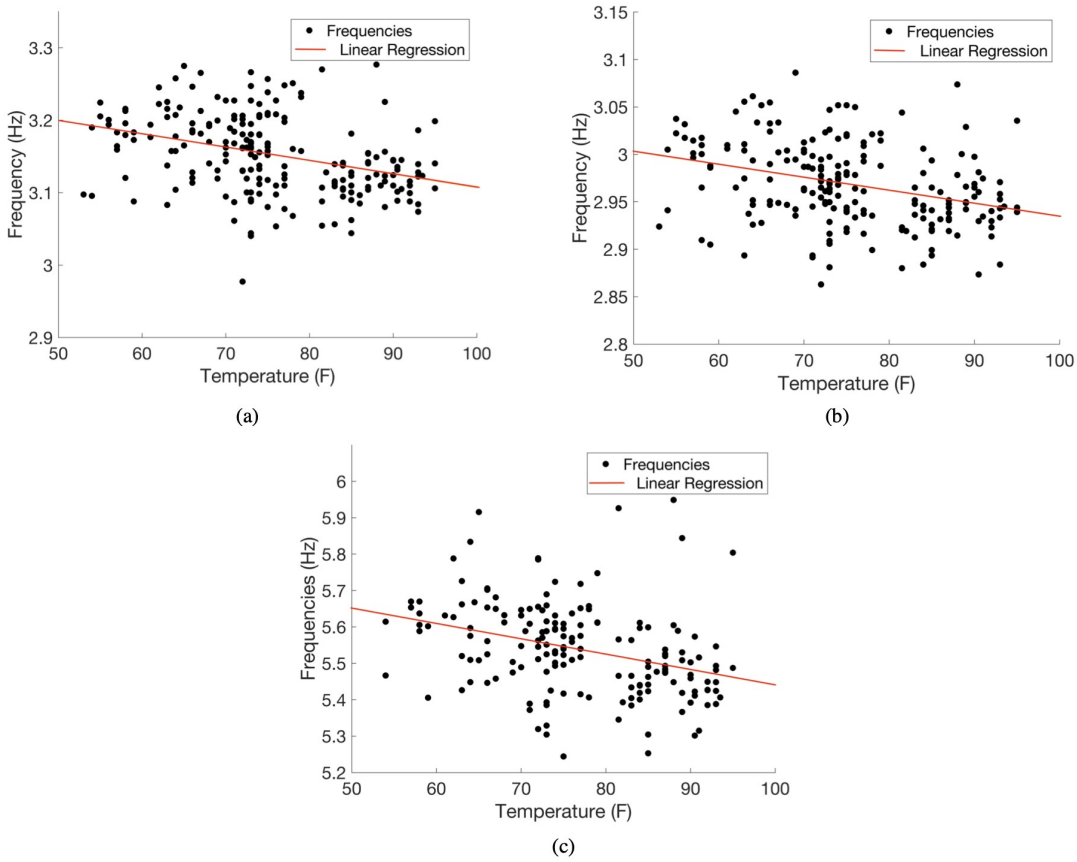


Figure 12: Frequency changes versus temperature variations: (a) Mode 1 in *x*-dir, (b) Mode 1 in the *y*-dir, (c) The mutual mode.

The linear regression is performed since a linear trend in the variation of frequencies is observed on the larger scale, which aligns with previous works, as well. The established relations are:

$$F_{1x} = 3.293 - 0.001862T \qquad R^2 = 0.127 \tag{3}$$

$$F_{1y} = 3.071 - 0.001366T \qquad R^2 = 0.108 \tag{4}$$

$$F_{2x} = F_{2y} = 5.863 - 0.004215T \qquad R^2 = 0.116 \tag{5}$$

In the establishment of the frequency-temperature relation, it is evident that the natural frequencies were highly susceptible to change. Besides, identical frequencies with the previous study in 2019 are observed during the continuous monitoring. On September 30, for the interval duration of 23:30-24:00 UTC, the resultant SV spectrum from FDD analysis are derived.

In which, the frequencies are:

Table 4: comparison of frequencies between July 9 and September 30.

| Puzzilli et al. (2019) | | Politecnico di Torino 09.07.22 | | Politecnico di Torino 30.09.22 | |
|---|---|---|---|---|---|
| X-dir | Y-dir | X-dir | Y-dir | X-dir | Y-dir |
| 3.25 | 3.00 | 3.10 | 2.92 | 3.24 | 3.01 |
| 5.80 | 5.80 | 5.36 | 5.36 | 5.79 | 5.79 |

It can be suggested that the main reason behind the frequency reduction on July 9 was the thermal variation since the 2019 analysis was performed in September too. This suggestion aligns with the continuous monitoring of frequencies.

## 7 CONCLUSION

An innovative SHM campaign was designed for monitoring Circo Massimo and Torre della Moletta. Three separate sensor configurations have been defined for the dynamic characterization to evaluate the effect of spatial distribution on modal properties. In addition, the thermal influence on modal parameters was assessed through establishing continuous long-term monitoring. The FDD and AFDD were applied to derive natural frequencies and mode shapes. Moreover, the correlation between natural frequencies and temperature variation has been acquired by statistical analysis. The following concluding remarks are drawn:

- The analysis of ambient vibration response on July 9 captured natural frequencies below the previous campaign in 2019. Conventionally, the frequency reduction could be regarded as a damage warning if the proper environmental conditions are available.
- The sensor configurations B and C highlighted the presence of three modes of vibration in each direction with the same natural frequency. This finding underlines the significance of spatial resolution in dynamic identification.
- For sensor layout B, two sensors were placed on the same level to identify torsional modes by plotting 3D mode shapes from FDD analysis. The surprising outcome was the depiction of torsion in all acquired modes. This critical finding could be initiated by interaction with the spiral staircase and needs further elaboration in future works.
- Long-term monitoring indicated the high susceptibility of natural frequencies toward thermal variation. The statistical analysis revealed the decreasing trend of frequencies with the increase in temperature. There is a possibility that the reduction of frequency was related to temperature rather than damage.

## REFERENCES

[1] C.-X. Qu, Y.-F. Liu, T.-H. Yi, and H.-N. Li, "Structural Damping Ratio Identification through Iterative Frequency Domain Decomposition," *J. Struct. Eng.*, vol. 149, no. 5, p. 04023042, May 2023, doi: 10.1061/JSENDH.STENG-11837.

[2] R. Brincker, C. Ventura, and P. Andersen, "Damping estimation by Frequency Domain Decomposition," in *Proceedings of the International Modal Analysis Conference - IMAC*, Jan. 2001, vol. 1.

[3] A. Montabert, E. D. Mercerat, J. Clément, P. Langlaude, H. Lyon-Caen, and M. Lancieri, "High resolution operational modal analysis of Sant'Agata del Mugello in light of its building history," *Engineering Structures*, vol. 254, p. 113767, Mar. 2022, doi: 10.1016/j.engstruct.2021.113767.

[4] P. Van Overschee and B. De Moor, Subspace Identification for Linear Systems. *Kluwer Academic Publishers*, 1996. doi: 10.1007/978-1-4613-0465-4_6.

[5] A. T. Dinani, G. Destro Bisol, J. Ortega, and P. B. Lourenço, "Structural Performance of the Esfahan Shah Mosque," *J. Struct. Eng.*, vol. 147, no. 10, p. 05021006, Oct. 2021, doi: 10.1061/(ASCE)ST.1943-541X.0003108.

[6] M.-G. Masciotta, L. F. Ramos, and P. B. Lourenço, "The importance of structural monitoring as a diagnosis and control tool in the restoration process of heritage structures: A case study in Portugal," *Journal of Cultural Heritage*, vol. 27, pp. 36–47, Oct. 2017, doi: 10.1016/j.culher.2017.04.003.

[7] R. M. Azzara, M. Girardi, V. Iafolla, D. M. Lucchesi, C. Padovani, and D. Pellegrini, "Ambient Vibrations of Age-old Masonry Towers: Results of Long-term Dynamic Monitoring in the Historic Centre of Lucca," *International Journal of Architectural Heritage*, vol. 15, no. 1, pp. 5–21, Jan. 2021, doi: 10.1080/15583058.2019.1695155.

[8] A. Kita, N. Cavalagli, and F. Ubertini, "Temperature effects on static and dynamic behavior of Consoli Palace in Gubbio, Italy," *Mechanical Systems and Signal Processing*, vol. 120, pp. 180–202, Apr. 2019, doi: 10.1016/j.ymssp.2018.10.021.
[9] C. Gentile, A. Ruccolo, and F. Canali, "Long-term monitoring for the condition-based structural maintenance of the Milan Cathedral," *Construction and Building Materials*, vol. 228, p. 117101, Dec. 2019, doi: 10.1016/j.conbuildmat.2019.117101.
[10] L. M. Puzzilli, G. Bongiovanni, P. Clemente, V. Di Fiore, and V. Verrubbi, "Effects of Anthropic and Ambient Vibrations on Archaeological Sites: The Case of the Circus Maximus in Rome," *Geosciences*, vol. 11, no. 11, p. 463, Nov. 2021, doi: 10.3390/geosciences11110463.
[11] R. Brincker, L. Zhang, and P. Andersen, "Modal identification of output-only systems using frequency domain decomposition," *Smart Mater. Struct.*, vol. 10, no. 3, pp. 441–445, Jun. 2001, doi: 10.1088/0964-1726/10/3/303.
[12] R. Brincker, "Introduction to Operational Modal Analysis," John Wiley & Sons, 2015. doi: 10.1002/9781118535141.
[13] R. Brincker, P. Andersen, and N.-J. Jacobsen, "Automated Frequency Domain Decomposition for Operational Modal Analysis," *IMAC-XXIV : A Conference & Exposition on Structural Dynamics*, Jan. 2007.
[14] F. Magalhães, Á. Cunha, and E. Caetano, "Dynamic monitoring of a long span arch bridge," *Engineering Structures*, vol. 30, no. 11, pp. 3034–3044, Nov. 2008, doi: 10.1016/j.engstruct.2008.04.020.
[15] A. Elahi, A. Cardoni, M. Domaneschi, and G. Cimellaro, "Automating the Frequency Domain Decomposition Technique Using the Modal Assurance Criterion," 2023, pp. 1063–1073. doi: 10.1007/978-3-031-21187-4_92.
[16] G. P. Cimellaro, S. Piantà, and A. De Stefano, "Output-Only Modal Identification of Ancient L'Aquila City Hall and Civic Tower," *J. Struct. Eng.*, vol. 138, no. 4, pp. 481–491, Apr. 2012, doi: 10.1061/(ASCE)ST.1943-541X.0000494.
[17] MATLAB R2022, last accessed 2016/11/21.

COMPDYN 2023
9th ECCOMAS Thematic Conference on
Computational Methods in Structural Dynamics and Earthquake Engineering
M. Papadrakakis, M. Fragiadakis (eds.)
Athens, Greece, 12-14 June 2023

# SENSITIVITY ANALYSIS FOR DERIVATION OF 1D $V_S$ PROFILES USING INVERSE QUARTER-WAVELENGTH THEORY

**Mehmet Ozışın[1], Zehra Cagnan[2*]**

[1] Graduate student, Middle East Technical University
Engineering Sciences Department, Ankara, Turkey, 06800
e-mail: ozisin.mehmet@metu.edu.tr

[2] Associate Professor, Middle East Technical University
Engineering Sciences Department, Ankara, Turkey, 06800
zehrae@metu.edu.tr

## Abstract

*It is possible to convert median response spectra estimated based on a selected Ground-motion Prediction Equation (GMPE) to its corresponding Fourier amplitude spectrum (FAS) by using the inverse vibration theory (IRVT). The IRVT uses extreme value statistics, properties of single-degree-of-freedom oscillator transfer functions, and spectral ratio correction to develop FAS that are compatible with input median response spectra. After obtaining a linear site amplification function in frequency domain corresponding to a specific site condition from analysis of FAS, the quarter-wavelength approximation (QWL) can be employed inversely and a 1D shear wave profile ($V_S$ profile) as well as a host kappa value representative of the site condition and GMPE under consideration can be derived. kappa is the spectral-decay parameter which is often used to account for the reduction of the high-frequency amplitude of ground-motion caused by attenuation within the site profile. As part of the first step, when the IRVT is used to compute FAS, utilized peak-factor model and duration of motion model influences the results. Likewise, as part of the second step, when a linear site amplification function is derived based on FAS in hand, a reference $V_S$ profile is employed that influences the linear site amplification function computed. And lastly as part of the third step, in computation of 1D $V_S$ profile and host kappa value from linear site amplification function representing the site condition and the GMPE under consideration by employing the inverse quarter-wavelength theory, the density model utilized influences the computed $V_S$ profile. Main objective of this study is to derive GMPE compatible $V_S$ profiles and host kappa values for the recent Turkish GMPE of [1]. In doing so, different peak factor models; duration models; randomly generated reference $V_S$ profiles and different density models were used. This allowed investigating the degree of effect of peak factor model, duration model, reference $V_S$ profile and density model on computed 1D $V_S$ profiles and host kappa values.*

**Keywords:** Inverse Random Vibration Theory, Quarter-wavelength approximation, $V_s$ profile, kappa.

## 1 INTRODUCTION

[1] ground-motion prediction equation (GMPE) estimates the median and standard deviation of the ground motion as a function of source, path, and site parameters such as earthquake magnitude (i.e., moment magnitude, $M_w$), source-to-site distance (i.e., Joyner and Boore distance, $R_{JB}$), style of faulting, and local site conditions. This GMPE is based on abundant empirical ground-motion data from Turkey. [1] GMPE uses the nonlinear site function developed by [2] for the broader Europe to account for local site conditions. Local site conditions in this GMPE are characterized by the time-averaged shear-wave velocity over the top 30 m of the site profile ($V_{S30}$). Other parameters such as depth to a shear-wave velocity of 1.0 or 2.5 km/s horizon ($Z_{1.0}$ and $Z_{2.5}$) are not used hence effect of deeper part of the shear wave velocity ($V_S$) profile that controls long-period amplification and reflects basin effects are not taken into account. [1] study justify applicability of [2] site amplification model to the Turkish strong-motion data by carrying out detailed residual analyses. [1] reports no observable trends with changing $V_{S30}$ values. In [3], the inverse quarter-wavelength (QWL) method proposed by [4] is used to estimate GMPE compatible host 1D $V_S$ profiles and kappa values, $\kappa$ for the [1] GMPE for different site conditions with corresponding $V_{S30}$ values of 360 m/s, 490 m/s, 620 m/s and 760 m/s. In this manuscript, the study of [3] is extended and influence of peak-factor models, duration models, reference 1D $V_S$ profiles and density models on computed 1D GMPE compatible $V_S$ profiles and host kappa values are investigated.

## 2 INVERSE RANDOM VIBRATION THEORY

In this study, the inverse random vibration theory (IRVT) based method first proposed by [5] then modified by [6] is used to convert median response spectra estimated based on a selected GMPE to corresponding FAS. The IRVT uses extreme value statistics, properties of single-degree-of-freedom oscillator transfer functions, and spectral ratio correction to develop FAS that are compatible with input response spectra ([6]). The IRVT procedure approximates the Fourier amplitude [A(f_n)] at the oscillator natural frequency $f_n$ as:

$$[A(f_n)]^2 \approx \frac{1}{f_n\left(\frac{\pi}{4\xi}-1\right)}\left(\frac{T_d}{2}\frac{Sa^2}{pf^2} - \int_0^{f_n}|A(f)|^2 df\right) \quad (1)$$

where $\xi$ represents the critical damping ratio, Sa represents the spectral acceleration, pf represents the peak factor, and $T_d$ represents the duration of the ground motion.

While it is generally straightforward to convert an FAS to a corresponding response spectrum using random vibration theory, converting a response spectrum to a corresponding FAS using IRVT is not so simple. The fact that a spectral acceleration at a given period is influenced by a range of frequencies in the FAS making it impossible to relate the spectral acceleration at a given period merely to its FAS counterpart at the same period complicates the calculation of the Fourier amplitude [A(f_n)]. This problem is addressed in [6] using the properties of single-degree-of-freedom transfer functions that are narrow banded for lightly damped systems going to zero for frequencies greater than the natural frequency, $f_n$. This property limits the frequency range that contributes to the spectral acceleration at a certain period. The fact that the peak factor pf, which is needed to estimate the FAS cannot be determined a priori introduces another complication to the calculation of the Fourier amplitude [$A(f_n)$]. [6] suggests first assuming a peak factor value to develop an initial estimate of the FAS and then updating this assumed value using the generated FAS in later iterations.

As part of the IRVT procedure, Equation 1 is successively applied from lower frequencies to higher frequencies allowing for the calculation of the integral term in Equation 1. As the last

step of the IRVT procedure, [6] suggests modifying the derived FAS based on the spectral ratio of the target to calculated response spectra. This correction process ensures a better match between the target response spectrum and the calculated response spectrum based on the IRVT-generated FAS.

In this study, the IRVT-generated FAS of response spectra that are computed by employing the recent Turkish GMPE of [1] is used for two purposes: (1) as the required input for the inverse QWL method which is outlined in the subsequent section, (2) as the required input for the calculation of host $\kappa$ values by following the [7] approach.

For the calculation of host $\kappa$ values, [7] suggests firstly computing response spectra at short distances for rock type site condition by employing a GMPE. Scenarios with short distances are suggested in order to minimize the impact of anelastic attenuation on the high-frequency part of the response spectrum and FAS. Scenarios with high $V_{S30}$ values are suggested in order to avoid over-whelming $\kappa$ with soil damping. In the [7] approach, response spectra are then converted to their corresponding FAS by employing the IRVT procedure summarized above. [7] suggests estimating $\kappa$ values based on slope of FAS after converting FAS to log-linear space by following the [8] approach. According to [8], FAS in log-linear space follows the function $A_o \exp(-\pi\kappa f)$ between frequencies $f_1$ and $f_2$, where $f_1$ and $f_2$ are selected based on visual inspection such that ln(A[f]) versus f relationship is linear in the selected range. The [7] approach assumes that the crustal amplification function corresponding to the subsurface profile is constant in the frequency range used to estimate $\kappa$ and that the FAS at high frequency is only controlled by $\kappa$. If the crustal amplification is not near constant at high frequencies, then [7] recommends that FAS is divided by the crustal amplification before estimating $\kappa$ from the slope of the FAS.

## 3 INVERSE QWL METHOD

The QWL approximation to linear site amplification was first introduced by [9]. This method is based on computing the FAS linear site amplification at a particular frequency, A[f(z)] based on Equation 2: the square root of the ratio between the local seismic impedance (shear-wave velocity times density) and the seismic impedance at the source depth. Frequently, it is used to estimate linear site amplification given a reference $V_S$ profile. Equation 2 is applicable for shear-waves with zero angle of incidence with respect to the vertical direction. $\rho_R$ and $V_{SR}$ represent the density and shear-wave velocity at the source depth. The local shear-wave velocity and density are averaged over a depth corresponding to one quarter of a wave-length for the frequency under consideration. Based on the work of [10], $\rho_R$ and $V_{SR}$ are adopted as 2.8 g/cm3 and 3.7 km/s, respectively, in this study. The linear relationship between density and $V_S$ is employed as given in Equation 4, which is based on [11].

$$A[f(z)] = \sqrt{\frac{\rho_R V_{SR}}{\overline{\rho(z)}\,\overline{V_S(z)}}} \tag{2}$$

$$\overline{V_S(z)} = z \times 4f(z) \tag{3}$$

$$\rho = 1.742 + 0.2875 V_S \tag{4}$$

The inverse QWL method proposed by [4], which enables development of a 1D $V_S$ profile given a linear site amplification function in FAS domain, is also based on Equations 2 and 3. For a given FAS linear site amplification function, when the approach outlined below is applied sequentially from high to low frequencies, the corresponding 1D $V_S$ profile can be computed from shallow to deeper layers:

**Step 1:** Express Equation 2 only in terms of $V_S$ after substituting Equation 4 into Equation 2. For the highest frequency and shallowest layer: $\overline{V_S(z)} = V_s$ and $\overline{\rho(z)} = \rho$. Using the FAS

linear site amplification corresponding to the largest available frequency, $V_S$ for the shallowest layer can be derived based on Equation 2.

**Step 2:** $V_S$ value of step 1 can be used together with largest available frequency to estimate depth z of the shallowest layer of the $V_S$ profile based on Equation 3.

**Step 3:** For each subsequent frequency ($f_i$) in the given site amplification function sorted in descending order, the shear-wave velocity, $V_S(i)$ of the corresponding profile layer, i, can be analytically solved for using Equation 5.

$$0.2875\Delta tt V_S(i)^2 + 1.742\Delta tt V_S(i) + z(i-1)\overline{\rho(\imath-1)} - \frac{\rho_R V_{SR} tt(i)}{A(i)^2} = 0 \quad (5)$$

The travel time to depth i, tt(i), can be related to frequency based on Equation 6. The difference in travel time between subsequent layers, Δtt, can then be written as given in Equation 7. Equation 8 illustrates that depth of a layer, Δz, and Δtt can be related through $V_S(i)$. Using these basic definitions, it is possible to express time averaged shear-wave velocity and density for layer i as given in Equations 9 and 10. After substituting Equations 9 and 10 into Equation 2, it is possible to derive the quadratic function of Equation 5, in which the only unknown is $V_S(i)$.

$$tt(i) = 1/(4f_i) \quad (6)$$

$$\Delta tt = tt(i) - tt(i-1) \quad (7)$$

$$\Delta z = V_S(i)\Delta tt \quad (8)$$

$$\overline{V_S(\imath)} = \frac{z(i-1)+\Delta z}{tt(i)} \quad (9)$$

$$\overline{\rho(\imath)} = \frac{\left[z(i-1)\overline{\rho(\imath-1)}+\Delta z\rho(i)\right]}{z(i-1)+\Delta z} \quad (10)$$

## 4 APPLICATION OF THE INVERSE QWL METHOD TO RECENT TURKISH GMPE

The inverse QWL method of [4] as described in the previous section is employed to derive GMPE compatible $V_S$ profiles for the recent Turkish GMPE of [1] that will be referred to as KAAH15 throughout the rest of this manuscript. Main objective of this work was to derive host $V_S$ profiles and $\kappa$ values for the KAAH15 GMPE for $V_{S30}$=760 m/s site condition and to study influence of peak factor model, duration model, reference $V_S$ profile and density model on the computed 1D $V_S$ profile. As linear site response in GMPEs does not distinguish between site amplification and small-strain damping ($\kappa$), GMPE-specific host $V_S$ profiles and companion $\kappa$ values are derived together for the studied $V_{S30}$=760 m/s site condition. This required slight modification of the inverse QWL method as proposed by [4]. This will be discussed below.

Firstly, median response spectra for strike-slip scenarios with $M_w$: 5, 6, and 7; $R_{JB}$: 5, 10, and 20 km; and $V_{S30}$: 760 and 1000 m/s are computed for Turkey by employing the KAAH15 GMPE. Nonlinear site response is disabled in the calculation of median response spectra to isolate the linear site response. As strike-slip scenarios are chosen, ground-motion recordings from Northwestern Turkey govern median response spectra of KAAH15 GMPE. The derived $V_S$ profiles and $\kappa$ values are, therefore, specifically applicable for this region of Turkey.

The IRVT method is used to convert median response spectra to corresponding FAS. In this study, the computer program pyrvt ([12]) is employed for the conversion of median response spectra to corresponding FAS. Duration, $T_d$, is calculated using the [13] significant duration model D5-75, [14] total duration model, [15] significant duration model D5-95. Increase of duration due to oscillatory response is also considered according to [16] and [17] models.

Another parameter necessary for this conversion is the peak factor, pk. In this study, the peak factor models of [18], [19], [20], [21] and [22] are used in conversion of response spectra to FAS. The [18] peak factor model is consistent with the [19] model the most; [20], [21] and [22] deviate from the [18] models in the high frequency range and are listed in order of increasing deviation. The peak factor calculations are known to have higher sensitivity to higher frequency values ([23]).

For KAAH15, the ratio of FAS for each of the nine scenarios at a specific $V_{S30}$ relative to the FAS of the same earthquake scenario with $V_{S30}$ of 1000 m/s is computed. The FAS site response relative to $V_{S30}$ of 1000 m/s is then computed by averaging those of the scenarios with $M_w$ 6 and 7 and $R_{JB}$ distance 5, 10, and 20 km. Relative FAS site response computed for the $M_w$ 5 scenarios are not employed because they exhibit the largest deviation from the rest of the scenarios at high frequencies.

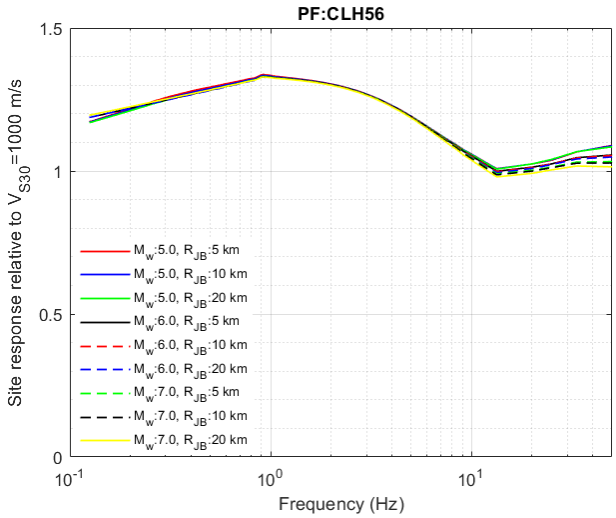


Figure 1: Linear site response in FAS domain relative to $V_{S30}$ of 1000 m/s for KAAH15 ([1]) for scenarios with $M_w$ 5, 6, and 7 and $R_{JB}$ of 5, 10, and 20 km. The [18] peak factor model and [14] duration model are utilized.

Figure 1 illustrates the ratio of FAS for the nine scenarios corresponding to a $V_{S30}$ value of 760 m/s relative to those at 1000 m/s for KAAH15. This ratio approximates the FAS linear site response of the GMPE relative to the selected reference site condition. Figure 1 indicates that the computed FAS site response relative to the reference site conditions is generally stable for the nine scenarios considered. In the high frequency range, deviations among the scenarios are observed for frequencies exceeding 25 Hz. This behavior of IRVT-based FAS is described as saturation of the response spectrum at high frequencies by [7] and linked to high regional $\kappa$ values. To make sure that this behavior does not have any effect on the results: (1) the relative FAS site response is computed by averaging those of the scenarios with $M_w$ 6 and 7 and distance of 5, 10, and 20 km, excluding those with $M_w$ 5 as they exhibit the largest deviation from rest of the scenarios at high frequencies, (2) the relative FAS site response values corresponding to frequencies up to 20 Hz are used in the derivation of GMPE compatible host $V_S$ profiles and $\kappa$ values.

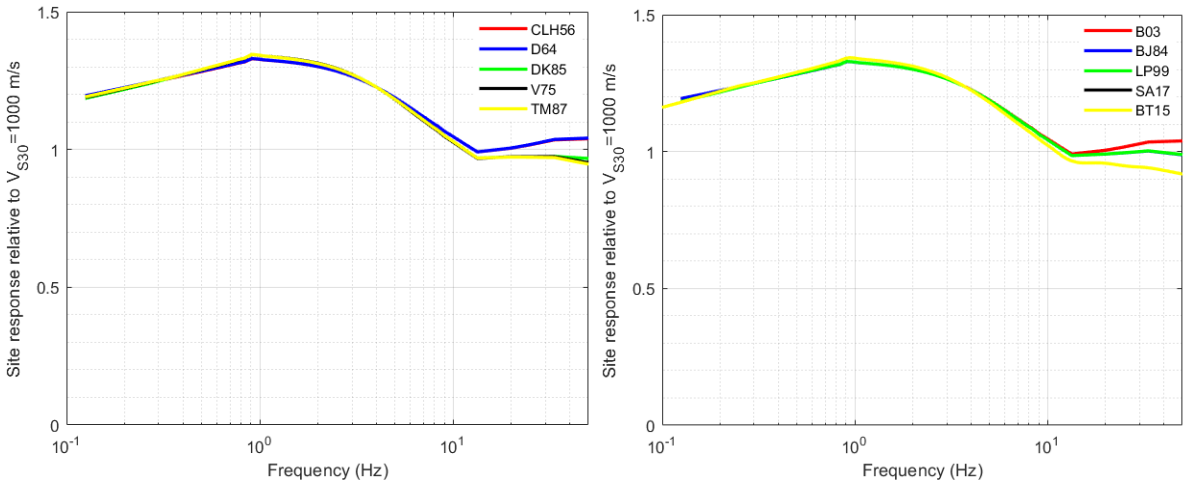


Figure 2: (a) Linear site response in FAS domain relative to $V_{S30}$ of 1000 m/s for KAAH15 ([1]) by utilizing the CLH56 ([18]), D64 ([19]), DK85 ([20]), V75 ([21]) and TM87 ([22]) peak factor models with [14] duration model and (b) Linear site response in FAS domain relative to $V_{S30}$ of 1000 m/s for KAAH15 ([1]) by utilizing the B03 ([14]), BJ84 ([16]), LP99 ([17]), SA17 ([13]), BT15 ([15]) duration models. In FAS computations together with all duration models listed, the CLH56 peak factor model was used; except for the BT15 duration model which was used together with the V75 peak factor model.

Figure 2a illustrates the average relative linear FAS site response functions for the KAAH15 for $V_{S30}$ value of 760 m/s computed by utilizing five different peak factor models together with the [14] duration model. These functions represent the combined relative effects of linear site amplification and relative $\kappa$ scaling.

The relative linear FAS site response functions given in Figure 3 are converted into total FAS site response functions by multiplying them with the FAS site amplification model of the corresponding reference Vs profile (i.e., for $V_{S30}$ value of 1000 m/s for the KAAH15 GMPE) including corresponding kappa attenuation. In computation of a reference $V_S$ profile for $V_{S30}$ of 1000 m/s, the generic rock and generic very hard rock velocity models of [11] are used together with the interpolation method of [24] as $V_S$ profiles specifically suggested for Turkey are not available especially up to required depths and required $V_{S30}$ values. For the obtained reference $V_S$ profile corresponding linear site amplification values are then calculated using the QWL method with zero angle of incidence by using the computer program site_amp ([25]). The host $\kappa$ for the reference site condition is also calculated. The FAS of the nine scenarios with $M_w$ 5, 6, and 7; $R_{JB}$ distances of 5, 10 and 20 km and $V_{S30}$ of 1000 m/s are used to calculate $\kappa$. The IRVT based approach suggested by [7], which is described above is followed for this purpose. The average $\kappa$ value derived from studying FAS of these nine scenarios is 0.0376. The computed FAS site amplification model for the $V_{S30}$ value of 1000 m/s is illustrated in Figure 3.

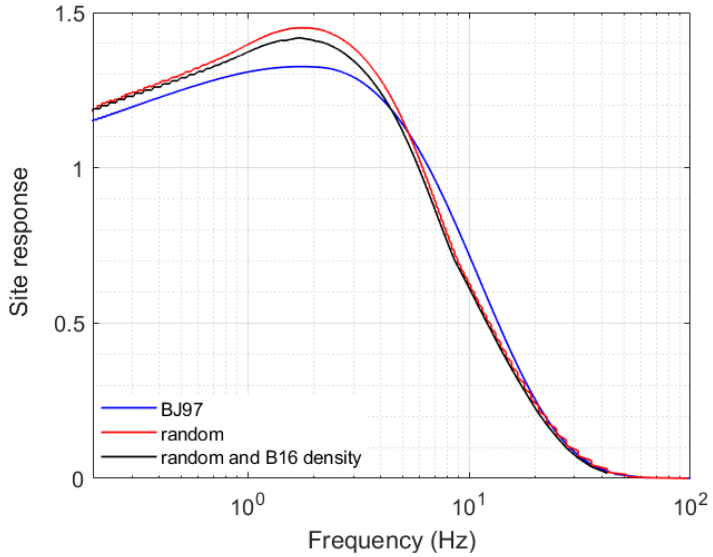


Figure 3: FAS site amplification models of reference $V_S$ profiles (Both random and B16 based). For the KAAH15 ([1]) GMPE, the reference $V_S$ profile corresponds to a $V_{S30}$ value of 1000 m/s. Two separate density models are used in derivation of these amplification models: BJ97 and B16.

The total FAS site response functions computed for $V_{S30}$ value of 760 m/s by multiplying the relative linear FAS site response functions of Figure 2 with the FAS site amplification model of reference $V_S$ profile (Figure 3) are given in Figure 4.

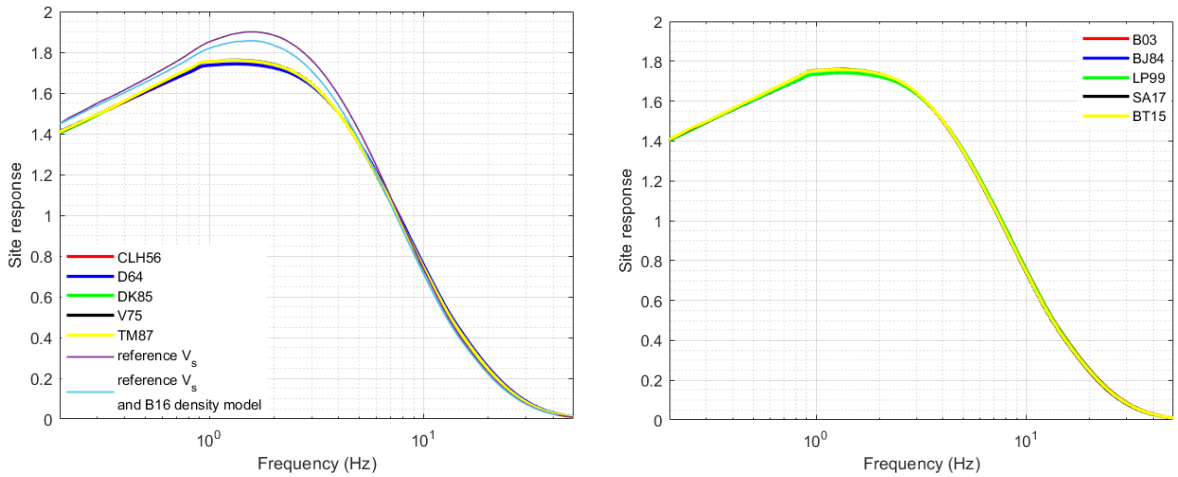


Figure 4: Total linear site response in FAS domain for KAAH15 ([1]) and for $V_{S30}$ value of 760 m/s (a) by utilizing the CLH56 ([18]), D64 ([19]), DK85 ([20]), V75 ([21]) and TM87 ([22]) peak factor models with [14] duration model and (b) by utilizing the B03 ([14]), BJ84 ([16]), LP99 ([17]), SA17 ([13]), BT15 ([15]) duration models.

As mentioned above, relative FAS site responses computed for different scenarios deviate from one another for frequencies exceeding 20 Hz. To eliminate effect of these deviations on computed $V_S$ profiles FAS site response functions are not used for frequency values exceeding 20 Hz. However, the frequency range of 20-100 Hz is necessary for derivation of host $V_S$ profiles. As a solution of this problem, [4] suggests representing the top 30m of the Vs profile with

a power function and obtains the analytical model of total FAS site response as given in Equation 11, which is applicable for the top 30m. Selecting a frequency range such as $f_{30}$-100 Hz, $f_{30}$ representing the frequency corresponding to a 30m depth of a profile and fitting Equation 11 for estimation of unknown parameters b and $\kappa$ in this range, allows estimation of $\kappa$ values for different peak factor and duration models considered as well as computation of total FAS site response for frequencies in the range 20-100 Hz. Estimated $\kappa$ values in this manner represent GMPE compatible host $\kappa$ values and are listed in Table 1 for $V_{S30}$ value of 760 m/s.

$$SR(f) = \left[ \frac{\rho_R V_{SR} 0.03^b / V_{S30}}{\left( 1.742 - \frac{V_{S30} * 0.2875 * \left( 4f * \frac{0.03^b}{V_{S30}} \right)^{\frac{b}{b-1}}}{0.03^b * (b^2 - 1)} \right) * \left( \frac{4f * 0.03^b}{V_{S30}} \right)^{b/(b-1)}} \right]^{1/2} * \exp(-\pi \kappa f) \tag{11}$$

| Peak-factor and duration models | $\kappa$ (s) |
|---|---|
| pf: CLH56, d: B03 | 0.0393 |
| pf: D64, d: B03 | 0.0393 |
| pf: DK85, d: B03 | 0.0397 |
| pf: V75, d: B03 | 0.0398 |
| pf: TM87, d: B03 | 0.0399 |
| pf: V75, d: BT15 | 0.0398 |
| pf: CLH56, d: SA17 | 0.0400 |
| pf: CLH56, d: LP99 | 0.0394 |
| pf: CLH56, d: BJ84 | 0.0394 |
| pf: CLH56, d: B03 random $V_S$ profile | 0.0385 |
| pf: CLH56, d: B03 random $V_S$ profile and B16 density model | 0.0400 |

Table 1: Derived host $\kappa$ (s) values for the KAAH15 ([1]) for $V_{S30}$ of 760.

Based on the inverse QWL approach of [4] and IRVT approach of [7], the estimated $\kappa$ values are not $\kappa_0$ (i.e. $\kappa$ estimated at zero epicentral distance) but $\kappa_1$ (i.e. average $\kappa$ estimated for scenarios at short distances) instead. [4] studied the relationship between short-distance kappa, $\kappa_1$ and zero-distance kappa, $\kappa_0$ for Western United States and reached the conclusion that $\kappa_0$ is smaller than $\kappa_1$ with a constant shift of 0.005s for different scenarios considered.

The modified total FAS site response obtained by following above explained approximation in the frequency range of 20-100 Hz is then divided by the $\kappa$ operator term to obtain the FAS linear site amplification for different site conditions considered. The inverse QWL approach is applied to the FAS linear site amplification obtained to derive the GMPE specific host $V_S$ profiles for $V_{S30}$ value of 760 m/s. The derived $V_S$ profiles are constrained to attain the $V_S$ value of 2500 m/s at depths consistent with the [26] suggested depth-to-bedrock model (Z2.5).

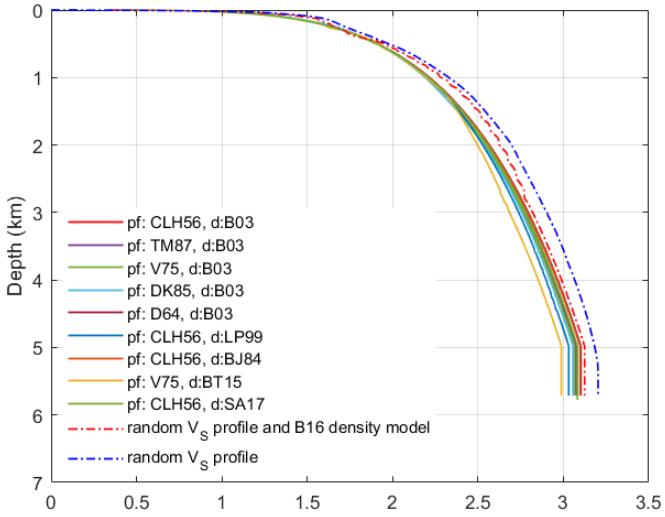


Figure 5. GMPE compatible host $V_S$ profiles for KAAH15 corresponding to $V_{S30}$= 760 m/s.

In order to observe sensitivity of computed 1D Vs profile and host kappa value to adopted density model, using peak factor model of CLH56 and duration model of B03, density model of [24] is used instead of [11]. Also, in order to observe sensitivity of computed 1D Vs profile and host kappa value to adopted reference $V_S$ profile for $V_{S30}$ value of 1000 m/s, a reference $V_S$ profile is randomly generated as 4 power law functions such that in the top 30m depth average value is 1000 m/s, at 0.443km $V_S$ value is 2500 m/s (default $Z_{2.5}$ value of NGAWest2 for Western United States) and 3500 m/s is not exceeded for deeper layers (velocity at the source). Results are shown in Figure 5 and Table 1.

## 5 CONCLUSIONS

In this study, GMPE compatible 1D host $V_S$ profiles and $\kappa$ value are derived for Turkey. [1] GMPE is selected to represent regional ground-motion attenuation for Turkey. GMPE compatible $V_S$ profiles are derived for site condition with $V_{S30}$ value of 760 m/s up to 6km depth. Host $\kappa$ values are also computed for site condition with $V_{S30}$ values of 760 and 1000 m/s. In doing so, the peak factor models suggested by [18], [19], [20], [21] and [22]; the duration models suggested by [13], [14], [15], [16] and [17]; randomly generated reference $V_S$ profiles and density models suggested by [11] and [24] were used. This allowed investigating the degree of effect of peak factor model, duration model, reference $V_S$ profile and density model on computed 1D $V_S$ profiles and host $\kappa$ values. Results indicate that computed 1D $V_S$ profiles and host $\kappa$ values are quite stable and adopted reference $V_S$ profile influences the computed 1D $V_S$ profiles and host $\kappa$ values the most.

## REFERENCES

[1] Kale O, Akkar S, Anooshiravan A, Hamzehloo H (2015). A ground-motion predictive model for Iran and Turkey for horizontal PGA, PGV and 5%-Damped response spectrum: investigation of possible regional effects. Bull. Seismol. Soc. Am., 105(2A): 963–980.

[2] Sandıkkaya M A, Akkar S, Bard P Y (2013). A nonlinear site amplification model for the new pan-European ground-motion prediction equations. Bull. Seismol. Soc. Am., 103(1): 19–32.

[3] Cagnan Z (2023). 1D reference Vs profiles compatible with ground motion prediction equations developed for Turkey. Bull. Earthquake Eng., 21: 1775–1792.

[4] Atik L A, Abrahamson N (2021). A methodology for the development of 1D reference VS profiles compatible with ground-motion prediction equations: application to NGA-West2 GMPEs. Bull. Seismol. Soc. Am., 111(4): 1765–1783.

[5] Gasparini D A, Vanmarcke E H (1976). SIMQKE: Simulated earthquake motions compatible with prescribed response spectra, Mass. Institute of Tech., Cambridge, Massachusetts.

[6] Rathje E M, Kottke A R, Ozbey M C (2005). Using inverse random vibration theory to develop input Fourier Amplitude Spectra for use in site response. Proceedings of 16th International Conference on Soil Mechanics and Geotechnical Engineering: TC4 Earthquake Geotechnical Engineering Satellite Conference, Osaka, Japan, 160-166.

[7] Al Atik L, Kottke A, Abrahamson N, Hollenback J (2014). Kappa (κ) scaling of ground-motion prediction equations using an inverse random vibration theory approach. Bull. Seismol. Soc. Am., 104(1): 336–346.

[8] Anderson J, Hough S (1984). A model for the shape of the Fourier amplitude spectrum of acceleration at high frequencies. Bull. Seismol. Soc. Am., 74:1969–1993.

[9] Joyner W B, Warrick R E, Fumal T E (1981). The effect of Quaternary alluvium on strong ground motion in the Coyote Lake, California, earthquake of 1979. Bull. Seismol. Soc. Am. 71(4): 1333–1349.

[10] Askan A, Sisman F N, Pekcan O (2014). A regional near-surface high frequency spectral attenuation (kappa) model for northwestern Turkey. Soil Dynamics and Earthquake Engineering, 65: 113-125.

[11] Boore D, Joyner W (1997). Site amplifications for generic rock sites. Bull. Seismol. Soc. Am., 87(2): 327-341.

[12] Kotke A (2020). https://github.com/arkottke/pyrvt.

[13] Sandıkkaya M A, Akkar S (2017). Cumulative absolute velocity, Arias intensity and significant duration predictive models from a pan-European strong-motion dataset. Bull. Earth. Eng., 15: 1881-1898.

[14] Boore D M (2003). Simulation of ground motion using the stochastic method. Pure Appl. Geophys., 160(3-4): 635-676.

[15] Boore DM and Thompson EM (2015). Revisions to some parameters used in stochastic-method simulations of ground motion. Bull. Seismol. Soc. Am. 105(2A): 1029–1041.

[16] Boore DM, Joyner WB (1984). A note on the use of random vibration theory to predict peak amplitudes of transient signals. Bull Seismol Soc Am 74(5):2035–2039.

[17] Liu L and Pezeshk S (1999). An improvement on the estimation of pseudo response spectral velocity using RVT method. Bull. Seismol. Soc. Am. 89(5): 1384–1389.

[18] Cartwright, D E, Longuet-Higgins M S (1956). The statistical distribution of the maxima of a random function. Proc. Roy. Soc. London, A237: 212-223.

[19] Davenport AG (1964). Note on the distribution of the largest value of a random function with application to gust loading. Proceedings of the Institution of Civil Engineers 28(2): 187–196.

[20] Der Kiureghian A (1980). Structural response to stationary excitation. Journal of the Engineering Mechanics Division 106(6): 1195–1213.

[21] Vanmarcke, EH (1975). On the distribution of the first-passage time for normal stationary random processes. J. Appl. Mech. 42(1): 215–220.

[22] Toro GR and McGuire RK (1987). An investigation into earthquake ground motion characteristics in eastern north America. Bull. Seismol. Soc. Am. 77(2): 468–489.

[23] Kottke A R, Rathje E M (2009). Technical manual for Strata. PEER Report 2008/10, Pacific Earthquake Engineering Research Center, College of Engineering, University of California, Berkeley.

[24] Boore D (2016). Determining generic velocity and density models for crustal amplification calculations with an update of the Boore and Joyner (1997) generic site amplification for VS(z)= 760 m/s. Bull. Seismol. Soc. Am., 106 (1): 316-320.

[25] Boore D (2005). SMSIM - Fortran Programs for Simulating Ground Motions from Earthquakes: Version 2.3 - A Revision of OFR 96-80-A, U.S. Geological Survey Open-File Report 00-509, revised 15 August 2005, 55 pp.

[26] Akkar S, Yenier E (2009). Assessment of point-source stochastic simulations using recently derived ground-motion prediction equations. Bull. Seismol. Soc. Am., 99(6): 3172–3191.

COMPDYN 2023
9th ECCOMAS Thematic Conference on
Computational Methods in Structural Dynamics and Earthquake Engineering
M. Papadrakakis, M. Fragiadakis (eds.)
Athens, Greece, 12-14 June 2023

# EFFECT OF THE SOIL PILE STRUCTURE INTERACTION IN A DYNAMIC ANALYSIS CONSIDERING A LINEAR BEHAVIOR

**Amar Alyaman[1], Fernando Lopez Caballero[2], Daniel Dias[3], Hussein Mroueh[4], Marwan Sadek[5] and Eric Antoinet[6]**

[1,6] Antea Group, F-92160 Antony, France
e-mail: Amar.alyaman@anteagroup.fr
e-mail: Eric.antoinet@anteagroup.fr

[1,4,5] Univ. Lille, Laboratoire LGCgE, F-59000 Lille, France
e-mail : Hussein.mroueh@polytech-lille.fr
e-mail : Marwan.sadek@polytech-lille.fr

[2] Univ. Paris Saclay, Laboratoire LMPS, F-91190 Gif-Sur-Yvette, France
e-mail : Fernando.lopez-caballero@centralesupelec.frr

[3] Univ. Grenoble Alpes, Laboratoire 3SR, F-38401 Grenoble, France
e-mail : Daniel.dias@3sr-grenoble.fr

## Abstract

*The present work aims to evaluate the kinematic interaction effects of a rigid inclusion reinforced soil mass under seismic waves. In order to understand the seismic behaviour of the system, a three-dimensional finite element code (FEM) is used (code Aster). Two numerical studies are presented. The first is a simple case study of a single Rigid Inclusion (RI), carried out to evaluate the influence of the RI modelling taking into account a beam element or a pile void element (called hybrid method). This technique consists of modelling the vertical reinforcements as void elements with the introduction of a beam element in their central axis. The use of this method makes it easier to determine the internal forces in the vertical reinforcements, taking into account the element rigid section. The second numerical work is a parametric study to highlight the effect of parameters such as the soil stiffness, mattress stiffness and RI diameter on the seismic response of a 5x5 rigid inclusion group considering a linear elastic behaviour.*

**Keywords:** Rigid inclusions; dynamic analysis; numerical modelling; Kinematic interaction, Hybrid method

## INTRODUCTION

Soils with low bearing capacity can cause problems in the construction of civil engineering works due to differential settlements. Reinforcement of compressible soils by vertical rigid inclusions (RI) is a technique used to improve the soil quality by combining a network of inclusions with a mattress made up of granular soil (Figure 1). The various elements of this system interact in a complex manner, and a particular attention should be paid to the response of soils reinforced by rigid inclusions under complex and dynamic loads [1,2]. Compared to pile foundations, this technology represents a good compromise between an effective settlement reduction and a reduced construction cost.

Previous studies, in particular the ASIRI national project, have focused on the behaviour of compressible soils reinforced by rigid inclusions, subjected to uniform static loadings, leading to practical recommendations for the profession. A smaller attention has been paid to the study of the behavior of this type of foundation under seismic loading. Therefore, this paper proposes to quantify the response of a group of RI under dynamic loading. This work is supported by National Project ASIRI+.

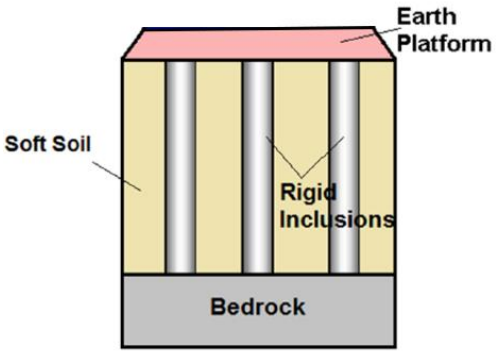


*Figure 1: Rigid inclusion system [3]*

The use of a rigid inclusion in a seismic zone is an interesting concept, and in terms of seismic stresses this reinforcement system is similar to the isolation system at the structure base . A load transfer platform (LTP) represents an energy dissipation zone that is transferred between the structure and the rigid elements, reducing the inertial effects of the structure [4-6]. This type of reinforcement has been implemented in the Rion-Antirion bridge [7].

This study is aimed at analyzing the kinematic interaction of a soil-mattress-inclusion-structure system. The analysis consists in calculating the response of all the elements of the system to the seismic loads. It is conducted using a three-dimensional finite element code (Code Aster). Particular attention is paid to studying the effect of the presence of RI on the modification of response of the system.

### 1. Kinematic interaction

Kinematic interaction is a soil-structure interaction mechanism related to the stiffness contrast between the soil and the foundation elements it contains. In particular, for soils reinforced by rigid inclusions, it can influence the seismic wave propagation and modify the incident seismic action on structures (amplitude and frequency content). It can also induce

additional stresses (bending, shear) in the rigid inclusions in addition to the vibration stresses inherent in the supported structure.

In order to understand this phenomenon, this paper study is based on a dynamic model covering different configurations and aims to understand the effect of dynamic interaction between the inclusions and the soil.

## 2. Three-dimensional rigid inclusion modelling.

In order to study the influence of the rigid inclusion modelling on the response of the system, a special analysis is performed where the inclusion is modelled as a solid element combined with beam elements, which we call the "hybrid method", and only the beam element connected to the ground is considered.

### 2.1. Hybrid method

This technique consists of modelling the vertical reinforcements as void elements with the introduction of a beam element in their central axis. For each depth, connection conditions are defined between the inclusion nodes and the nodes of the boundary of the void, as shown in (Figure 2a). The use of this method makes it easy to determine the internal forces in the vertical reinforcements, taking into account the rigid element section [8].

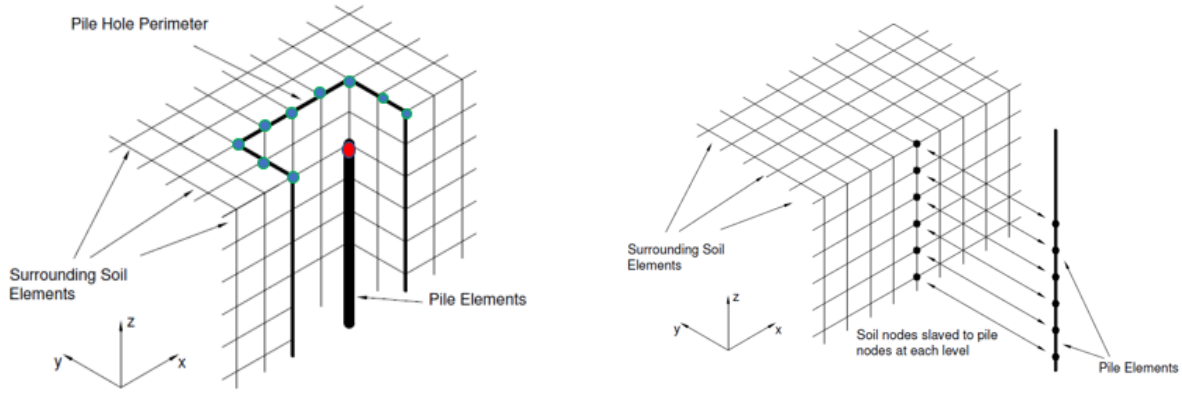


*Figure 2:Isometric view a) Hybrid model, b) Beam element model*

### 2.2. Beam element modeling

This technique, (Figure 2b), consists of representing the inclusions by beam elements, which are later rigidly connected to the soil. Loads were transferred between the inclusions and the soil through the nodes connected at different depths. The advantage of this method is that the internal forces can be easily determined without considering the solid element.

### 2.3. Geometry of the one inclusion Model

The first analyzes focused on a simple model 3mx3mx15m containing one rectangular rigid inclusion of dimensions 0.3mx0.3m and a length L=10 m placed in the centre of the model figure 3. This analysis considers a damping ratio of 5% under the Friuli earthquake, (Figure 7), applied as an imposed velocity at the model base.

The soil is modelled with 8-node hexahedral elements and the inclusion is modelled with both the beam element method and hybrid method. The soil Elastic modulus is Es = 97.6 MPa, Poisson's ratio $\upsilon$= 0.35 and density $\rho$= 1610 kg/m$^3$. The inclusion has the following properties: Elastic modulus Em = 30 MPa, Poisson's ratio $\upsilon$ = 0.2, density $\rho$ = 2500 kg/m3.

The fundamental frequency of the soil is 2.5 Hz, and the soil and rigid support is assumed to behave elastic.

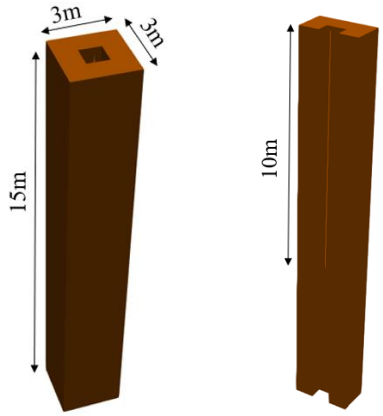


a)Basic geometry b)Longitudinal section

*Figure 3: Basic geometry of the numerical model*

(Figure 4) shows the variation of the normalized bending moment for different pile dimension 0.3mx0.3m, 0.6mx0.6m and 0.9mx0.9m with depth.

$$M\ normalized = \frac{M\ "beam\ element"}{M\ "Hybrid\ method"} \quad (1)$$

$$Displacement\ normalized = \frac{d\ "beam\ element"}{d\ "Hybrid\ method"} \quad (2)$$

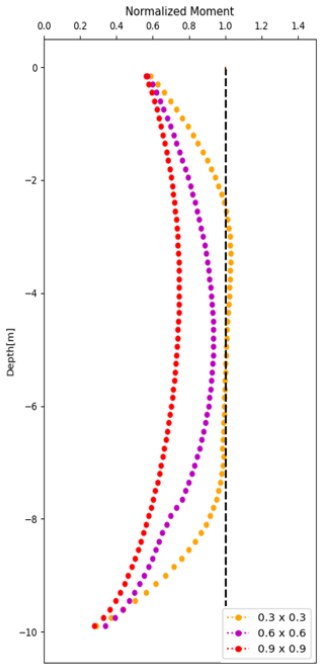


*Figure 4: Normalized bending moment*

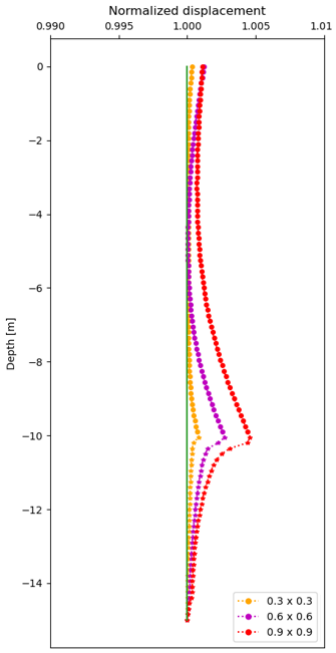


*Figure 5: Normalized horizontal displacement*

The results show that there is no significant difference, between the moment derived from the beam element method and the hybrid one for the depth between 2m and 8m where the moment is maximum, for a small dimension of 0.3m. The Results show that this variation increases as the inclusion dimension increases. For dimensions 0.6 x 0.6 and 0.9 x 0.9 there is a difference of 20 % and 50% respectively with the 0.3 x 0.3 dimension. Therefore, for large inclusion dimensions the modelling method should be taking into account.

(Figure 5) shows a small influence of the modelling method on the normalised displacement at the top and the base of the inclusion. However, this different is still negligible and does not exceed 0.5%.

In this case study, modelling the inclusions with beam elements or hybrid elements has little effect on the response of the inclusion for a dimension less than 0.4m, but it should be considered for larger dimensions.

## 3. NUMERICAL MODEL

The numerical method used in this study is the Finite Element Method (FEM) with code Aster. A full FEM 3D model is proposed. The geometry of the domain is provided by the software Salome-Meca, where we can define the external boundaries of the domain, the soil properties, the pile diameter, and the pile length.
In terms of finite elements, the model consists of 3D 8-node hexahedral elements representing the soil and the mattress, and beam elements representing the inclusions.
The particular choice of beam elements to represent the inclusion behaviour is based on the previous analysis which showed no difference between the two modelling methods for the small

inclusion dimension of 0.4m. And because the beam element facilitates the calculation of internal forces in the inclusion, compared to 3D volumetric elements.

### 3.1.Case study description

The dimensions of the soil volume considered in this study are 35 m x 35 m x 15 m. The model studied concerns a group of 5x5 rigid inclusions of length L=9.5 m, in a layer of soil with uniform mechanical properties. The diameter of the inclusions is 40 cm. They are floating inclusions modelled by beam elements. The spacing between inclusions is S = 2 m (S/D = 5, D is the inclusion diameter). A 0.5m thick load transfer platform (LTC) is placed directly above the rigid inclusions. The rigid inclusions are not connected to the LTP Figure 6. The cover ratio α is expressed as the ratio of the area of the rigid inclusion to the area of the reinforcing soil. Boundary conditions, called "paraxial elements" [9], are considered at the bottom and lateral boundaries of the model.

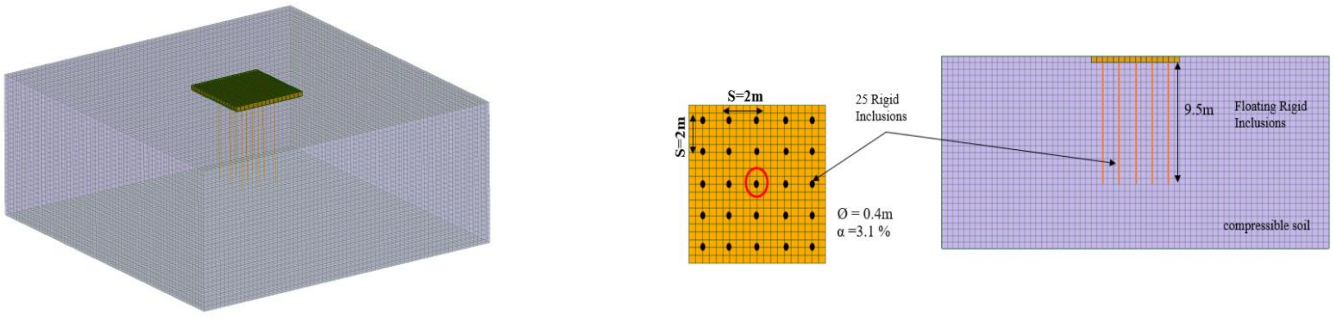


a)3D Model b) Plan view of the mattress and cross section

*Figure 6: Basic geometry of the numerical model*

The soil, the mattress and the rigid inclusions are assumed to behave in a linear elastic manner. The properties of the different element constituting the model are summarized in table 1. A Rayleigh damping ratio of 5% was assigned to the soft soil.

| Parameters | Rigid inclusion | LTP | Soft soil |
|---|---|---|---|
| **Young Modulus E (MPa)** | 40000 | 200 | 97.6 |
| **Volumetric weight (kg/m³)** | 2500 | 1800 | 1610 |
| **Poisson's ratio** | 0.2 | 0.3 | 0.35 |

*Table 1 : Parameters used for the numerical model.*

### 3.2.Dynamic loading

The load was applied as an imposed velocity at the base of the soil mass. Calculation is performed using the record of the Friuli earthquake that occurred in Italy, with maximum acceleration = 0.25g. (Figure 7) gives the details of this record. The fundamental frequency of

the soil layer is 2.5 Hz. The earthquake is applied in the form of velocity to the base of the model.

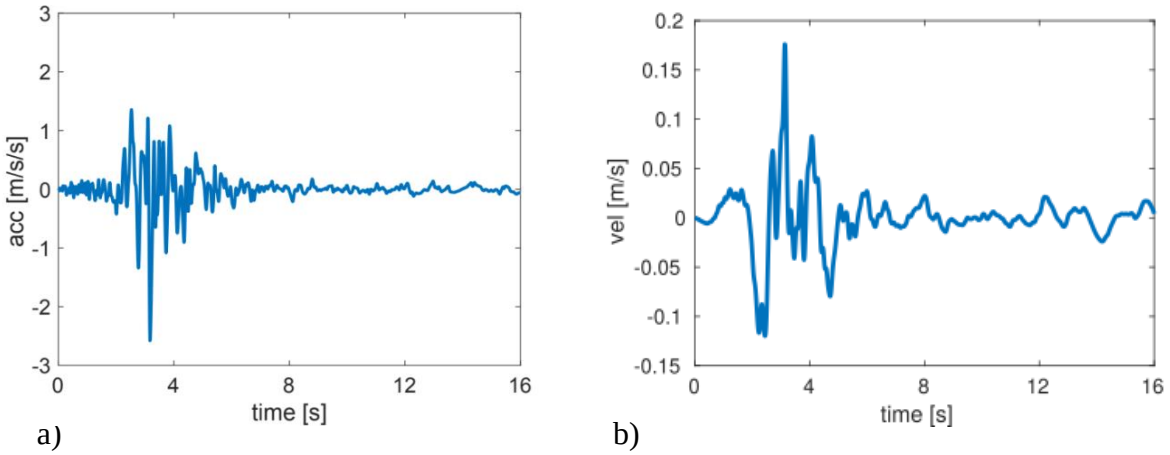


a) b)

*Figure 7: Dynamic input motion: a) Acceleration time history record, b) Velocity time history record for Friuli Earthquake*

### 3.3.Case studies

In order to highlight the effect of some parameters on the response of the reinforcement system, a parametric study was initiated for the RI diameter, the soil and mattress parameters, the RI length and the group effect.

#### 3.3.1. Influence of the Diameter of the RI

The diameter of rigid inclusions is known to be an important parameter for the load transfer mechanisms. (Figure 8a) shows the variation of the horizontal displacement of the central rigid inclusion starting from a depth of 0.5m to 10m normalised to the free field displacement as a function of depth. At depths greater than 10 m (ie. under the inclusion), it represents the horizontal normalized displacement of the soil. The displacement within the inclusion follows a linear relationship, with a maximum at the head and then decreasing to a minimum at the end. The values obtained from the displacement show the influence of the diameter on the variation of the displacement. The displacement of the inclusion head increases as the diameter of the RI increases. The results show that there is no significant variation of the displacement of the rigid inclusion. However, this isn't the case for the bending moment. (Figure 8b) shows the envelope of the bending moment which reaches its maximum of 12 kN.m for the reference case of $\Phi$ = 0.4m at depth = 4m. The results show that with increasing the diameter, the moment increases by approximately 4 times the reference case for $\Phi$ = 0.6m to reach 50 kN.m. The bending moment graph starts at depth -0.5m corresponding to the position of the inclusion in the model.

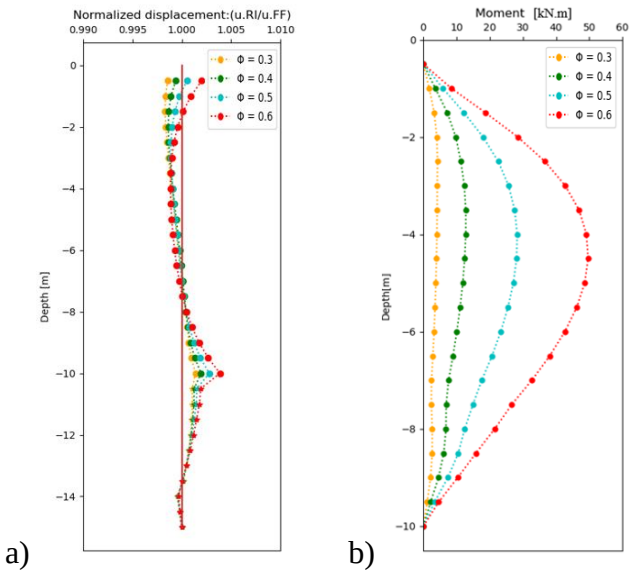


*Figure 8: Influence of the diameter of the inclusion on a) the normalized displacement and b) the normalized bending moment along the rigid vertical elements.*

### 3.3.2. Influence of the soil parameters

(Figure 9) shows the bending moment distribution of RI with two different young's modulus. It is noted that the bending moment presents a classic profile with a maximum near the central part of the inclusion reaching 13 kN.m for the reference case of E = 98 MPa. This result decreases to reach the value of 9kN.m for E = 174MPa because of the stiffer soil surrounded the inclusions which provides lateral support.

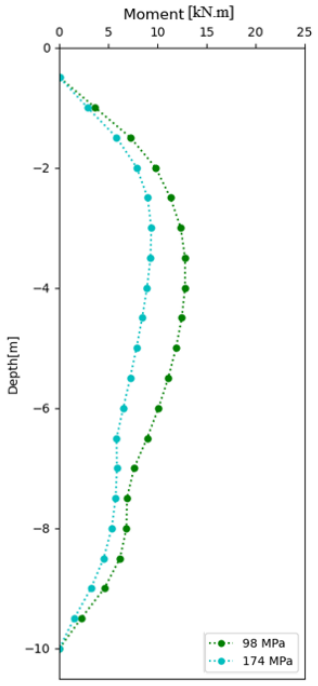


*Figure 9: Influence of the soil property on the normalized bending moment along the rigid vertical elements.*

### 3.3.3. Influence of the mattress stiffness

(Figure 10) compares the moments for three different mattress properties. Results show that, as the properties of the mattress increase, the moment experienced in the first three meters increases. Varying the elastic modulus from 200 MPa to 400 MPa induces an increase in the bending moment from 9 to 10.5 kN.m respectively at depth of 2m.

This result indicates that the mechanical properties of the mattress have an important effect on the response of the system.

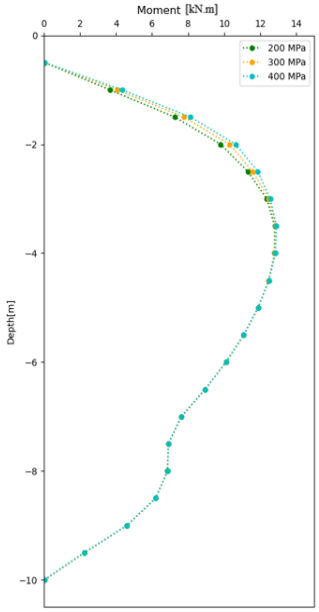


*Figure 10 : Influence of the mattress property on the normalized bending moment along the rigid vertical elements.*

### 3.3.4. Influence of the inclusion's position

In fact, the distribution of seismic forces between different rigid inclusions is not regular as it depends on the position of the elements within the group. (Figure 11) shows the bending moment envelopes for the center and outer inclusions. The RI are spaced by 5D. The results show that the corner inclusion experiences a greater moment, so it's more exposed to damage than the central inclusion, which has the least bending moment and is better protected (shadow effect).

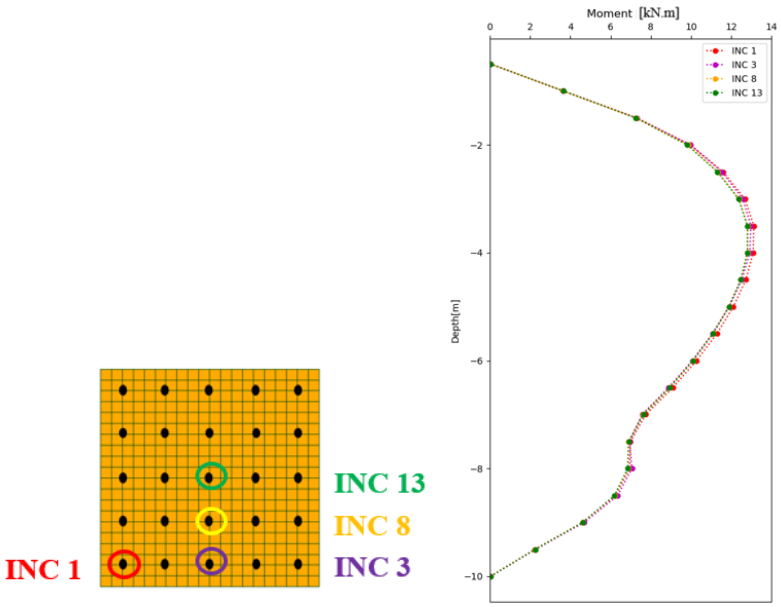


*Figure 11: Influence of the RI position on the normalized bending moment.*

## Conclusion

A numerical study is presented to evaluate the effect of the kinematic interaction for a soil reinforced by reinforced by rigid inclusions under the passage of seismic waves. The calculations were performed using a 3D FEM.

The results obtained show that considering a beam element for the rigid inclusion gives similar results to the hybrid method in terms of horizontal displacements and bending moments in the RI for a pile dimension lower than 0.4m. The results become different when the diameter is greater than 0.4m. The results of the parametric study show that inclusions modify the seismic ground response and that the RI system "diameter and position", soil and mattress characteristics have a great influence on the efforts and displacements of the rigid elements.

The research will continue by investigating the soil non-linearity considering more complex constitutive models.

## REFERENCES

[1] Jenck O., “Le renforcement des sols compressibles par des inclusions rigides verticales. Modélisation des sols par inclusions rigides ». Symp. Int. Sur l'Amélioration des Sols en Place. ASEP-GI, 9-10 septembre 2004, Paris, Presses de l’Ecole Nationale des Ponts et Chaussées, 2004, pp 15-44

[2] Briançon L., Kastner R., Simon B., Dias D. “Etat des connaissances - Amélioration des sols par inclusions rigides ”. Symp. Int. Sur l'Amélioration des Sols en Place. ASEP-GI, 9-10 septembre 2004, Paris, Presses de l’Ecole Nationale des Ponts et Chaussées, 2004, pp 15-44.

[3] LOPEZ JIMENEZ G.A., “Static and dynamic behavior of pile supported structures in soft soil” PHD thesis 2019. Université Grenoble Alpes.

[4] Dobry R., Pecker A., Mavroeidis G., Zeghal M., Gohl B., Yang D., "Damping/Global Energy Balance in FE Model of Bridge Foundation Lateral Response", J. of Soil Dynamics and Earth.Eng, 23(6), (2003), 483-495

[5] Pecker A., Garnier J. (1999). "Use of Centrifuge Tests for the Validation of Innovative Concepts in Foundation Engineering". Proc. 2nd Int. Conf. on Earthq. Geotech. Eng., Lisbon, 433-439.

[6] Pecker A, Salençon J. (1999). "Ground Reinforcement in Seismic Area". Proc. of the XI Panamerican Conf. on Soil Mech. and Geotech. Eng., Iguasu, 799-808.

[7] Pecker A., Teyssandier J.P. 1998, "Seismic design for the foundation of the Rion-Antirion bridge", Geotechnical Engineering, vol.131, p.4-11

[8] L.M. Wotherspoon. "Three-dimensional pile finite element modelling using OpenSees". 2006 NZSEE Conference.

[9] Code Aster: [R4.02.05] Absorbing boundary elements

COMPDYN 2023
9th ECCOMAS Thematic Conference on
Computational Methods in Structural Dynamics and Earthquake Engineering
M. Papadrakakis, M. Fragiadakis (eds.)
Athens, Greece, 12-14 June 2023

# INVESTIGATING THE SOIL STRESS LEVELS FOR DIFFERENT PILE GEOMETRIES UNDER DIFFERENT LOADING CONFIGURATIONS

**Daniel Rademan**[1], **and George Markou**[2]

[1] University of Pretoria
cnr Lynwood Road and Roper Street, Hatfield, South Africa
u18049037@tuks.co.za

[2] University of Pretoria
cnr Lynwood Road and Roper Street, Hatfield, South Africa
george.markou@up.ac.za

## Abstract

*The high complexity of investigating the mechanical response of reinforced concrete pile foundations embedded in different soil domains is well known, thus not allowing a deep understanding of the overall structural and geotechnical response of the foundation system. This study investigates the Soil-Structure-Interactions (SSI) and the development of stress levels for different pile configurations under different imposed lateral displacements and superstructural loads.*

*SSI has a significant effect on the lateral resistance of pile groupings that assume two or more piles. The state-of-the-art 3D detailed numerical investigation performed in this research work foresaw an investigation of the effects that pile groupings under imposed lateral displacement have on soil stresses and the overall response of the soil and foundation system. An in-depth study of the resulting stress regions and levels in the soil medium was performed for different loading configurations.*

*The study concluded that the base reaction is proportional to the imposed displacement and the number of piles in the grouping, while the geometry of the foundation system significantly affects the soil stress development. Finally, when torsion is developed at the level of the foundation system, a significantly complicated deformation field derives that requires an advanced modelling approach to objectively and accurately investigate the overall mechanical response of the soil and foundation domains.*

**Keywords:** Soil-structure-interactions, finite element method, numerical investigation, pile groupings, reinforced concrete.

## 1 INTRODUCTION

In industry and the academic scene, engineers make use of software to model large and complex reinforced concrete (RC) structures. The majority of these software packages make use of the Finite Element Method (FEM) to compute how the structure and in some cases how the founding material would react to various loading scenarios. When analyzing the mechanical behavior between the structure and the founding soil it can be challenging to visualize or study what is occurring below the structure as the soil does not provide indicators of stresses or strains that other materials such as steel would. By attempting to model conditions that the built structure would be experiencing in-situ, the engineer can visually represent results and develop a better understanding of factors that are affecting the capacity of a structure.

Structures are typically built on top of foundations, which serve as anchors and support the structure while allowing reactions to be transferred and loads to be distributed into the soil. Pile foundations are one of the many different types of foundations that interface between the soil and the structure. Pile foundations are generally used where the soil conditions are poor, this could be expansive soils or weak, collapsible, and compressive soils that extend below the base of the structure. Occasionally single piles act as foundations for parts of a larger structure but most commonly piles are closely spaced, grouped, and tied together by a pile cap to support structural members.

When pile foundations are grouped the total capacity of the group is not equal to the sum of the capacity of the individual piles. When the spacing between piles is small the stress regions around each pile overlap according to the load applied at the pile cap. The overlapping stress regions reduce the load-bearing capacity of the individual pile and thus in turn the capacity of the pile grouping. Factors such as the soil type, the method of pile construction, pile geometry, and the load application and direction also affect the stress regions around the pile foundation.

The reaction of soil when loads or displacements are applied, and stresses are induced is relatively complex to model as the soil does not exhibit a definite elastic stress region. There are many non-linear material models of soil that each have their own unique relationships between the stress and strain of soils. The behavior of soils is sometimes simplified to a model with an elastic and plastic region defined by a "yield point" which is classified as the failure point of the soil. If the critical stresses were to be reached in the soil that surrounds the foundations, the structure would develop a large settlement or even collapse due to the loss of support. Therefore, engineers need to understand both structural and soil mechanics, this knowledge provides insight into the interaction between the structure and the soil, and how the stress regions form in the soil around foundations. The implementation of FEM in large-scale construction jobs could lead to a reduction in the occurrence of structural failures and in turn, provide engineers with safer designs.

## 2 SOIL REACTION AROUND LATERALLY LOADED PILES

Applied loads on piles can be axial, either having a tensile or compressive component, lateral or moment. Although horizontal loads are minor in comparison to vertical loads in the majority of foundations, there are some cases, such as retaining structures piles and harbor constructions that are subjected to large lateral loads. Furthermore, significant lateral loads occur in the event of an earthquake and other seismic actions.

Horizontal soil displacement in front of laterally loaded piles was researched and presented in [1]. It was concluded that horizontal displacements are often greater than vertical displacements and that both values reduce exponentially as the distance from the pile surface increases. Using a Strain Wedge (SW) model, [2] examined the strain induced in front of a laterally loaded pile. They concluded that using the SW model to solve the problem of a laterally loaded pile is

a robust method. In several experimental tests using a pile model, [3] found that spacing greater than six times the pile diameter had no group impact. The group impact rises when the pile gap is reduced by 5.65 pile diameters, according to [4]. X-ray computed tomography was used to analyze 3D failure patterns in the sand caused by a laterally loaded pile [5]. The failure zones stretch, and the volume and angle of the failure zone rise as the pile loading level increases, although there is an ultimate value at some loading levels, according to the findings. In addition, as the depth along the pile increases, the area of the failure zone reduces. The 3D form of the failure zone is near conical as shown in Figure 1.

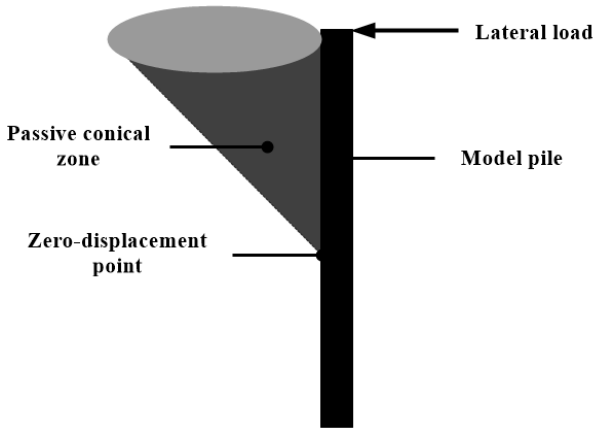


Figure 1: Conical passive zone of a laterally loaded pile.

## 3 NUMERICAL MODELLING OF PILE FOUNDATIONS

The pile foundations assessed herein are groupings commonly used in the construction of bridges, piers, and building foundations. The founding soil medium is assumed to be uniform in composition and stiffness. The soil modelled can be classified as a non-expansive, medium stiff to hard clay and there is no layer of soil or rock for the pile to be embedded into. For this reason, the pile foundations modelled are considered friction piles. Induced stresses and strains in the soil caused by pile driving or other installation methods were not considered in this investigation as this phenomenon was outside the scope of this research work. It is important to note at this point that the piles that will be modelled are vertical, thus battered piles will not be considered in this study [6].

The modelled piles have a diameter of 40 cm and an embedded depth of 7 m. The pile cap has a depth of 60 cm leaving a gap of 10 cm which allows the pile cap to decouple from the soil surface, thus allowing the piles to transfer all the imposed loading into the soil medium. Piles are spaced at 3.5 times the pile diameter (1.4 m spacing). The average hexahedral element size is 10 cm. The formulation of the isoparametric hexahedral finite elements that were used in this research work is based on the elements used in [7]. The pile cap system consists of modules (1.4 m by 1.4 m by 0.6 m deep) that are meshed together to form a single pile cap that tied the pile foundations together. The pile caps increased in size as the number of pile foundations increased.

All the pile foundations assumed the same reinforcing layout being 1% longitudinal reinforcing (12Y36) and (Y10) stirrups spaced at 100 mm intervals with 30 mm of concrete cover. The reinforcing in the pile cap varies from the traditional cage structures. To reduce the model's complexity a simplified layout was used. It is important to note at this point that the

reinforcement was modeled as embedded rebar elements and the discretization and embedded rebar mesh generation were performed according to [8].

The soil geometry for each pile grouping was unique. As the number and rows of piles increased, the soil geometry needed to be increased accordingly. The edge distance for the perimeter piles remained constant for all pile groupings, 2.8 m in the direction of the imposed displacement (x-direction) and 2.1 m in the y-direction (see Figure 2).

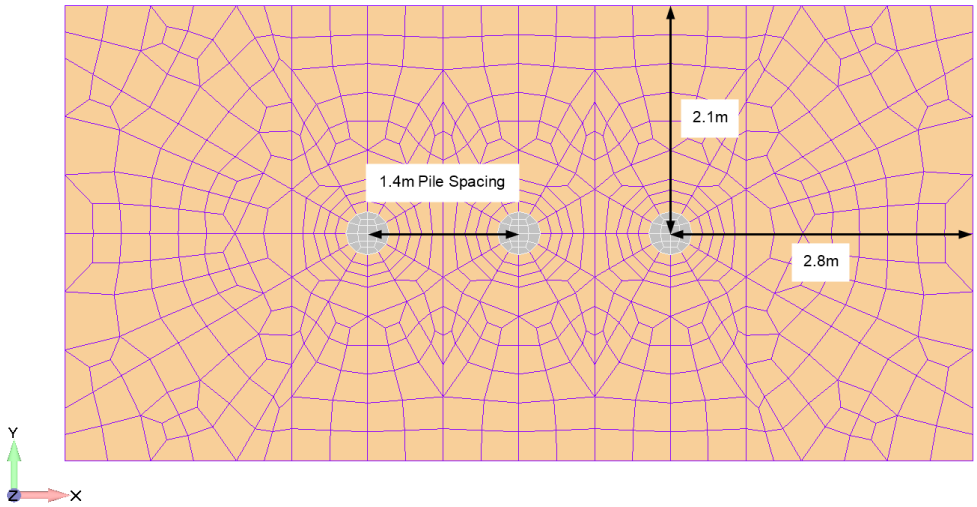


Figure 2: Hexahedral mesh and soil geometry of a 3-pile grouping (G3)

As illustrated below in Figure 3, all models had a constant soil domain depth of 9 meters with translational fixity in the x and y directions on the vertical perimeter planes and complete fixity in x, y, and z on the horizontal base plane.

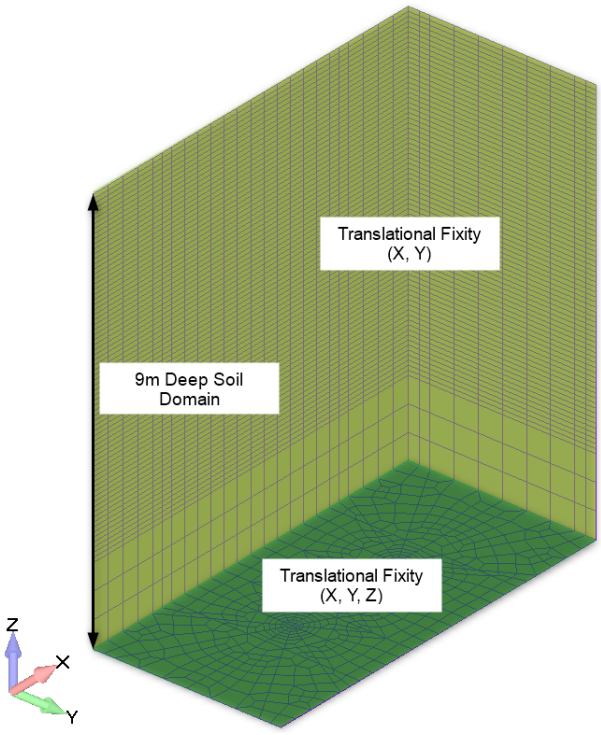


Figure 3: Boundary conditions of soil domain (Fixed DOFs)

For the needs of this research work, two different imposed displacements were assumed. The first foresaw a horizontal imposed displacement that was solved by using a displacement control problem [9], whereas the second assumed the imposition of displacements that would lead to the development of pure torsion at the level of the pile grouping.

For this experiment, uniform material properties were chosen for all models, based on engineering judgment (as shown in Table 1). The soil modeling employed a von Mises yielding criterion, in line with the approach adopted in [6]. For the needs of the nonlinear numerical modeling of the RC domain of the piles, the 3D detailed approach presented in [7] was adopted. This approach foresees the simulation of cracking through the use of the smeared crack approach, where the microcracking effect is also accounted for [7].

| Material | Modulus of Elasticity (MPa) | Poisson's ratio | Compressive/Tensile Strength (MPa) |
|---|---|---|---|
| Clay Soil | 100 | 0.3 | 0.25 |
| Concrete | 30,000 | 0.2 | 60 |
| Steel | 200,000 | 0.3 | 450 |

Table 1: Material properties of all models

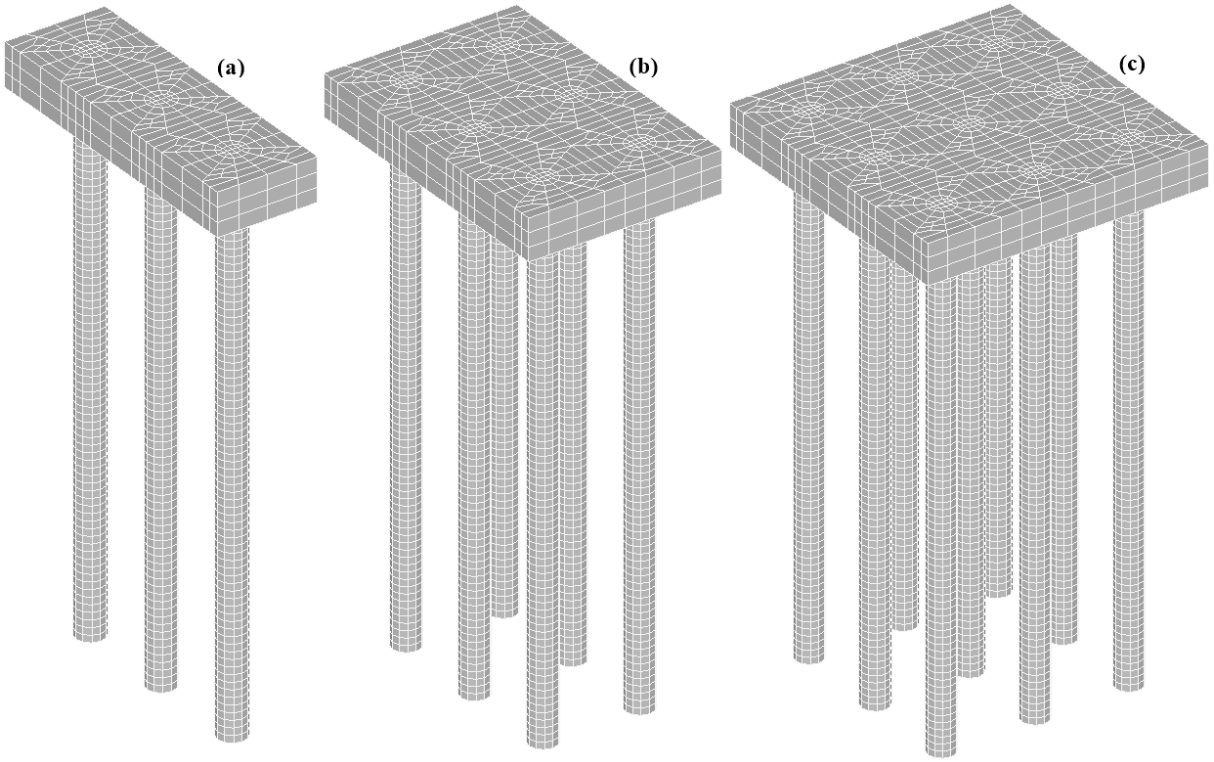


Figure 4: Pile and pile cap system. (a) G3 pile grouping, (b) G2x3 group and (c) G3x3 group

As this study investigates the grouping effects of pile foundations, multiple numerical models were created. The pile group models are denoted based on their arrangement, characterized by the group (G) and the number of rows (y-direction) by the number of piles in the x-direction. Three representative pile group models are depicted in Figure 4. Figure 4a portrays a single group of three piles (G3). Figure 4b showcases a group of piles comprising two rows, each containing three piles (G2x3). Figure 4c illustrates a group of piles consisting of three rows,

each with three piles (G3x3). These models serve as a comprehensive representation of the pile group arrangements under investigation.

## 4 IMPOSED DISPLACEMENTS AND LOADING PROCEDURE

### 4.1 Push over analysis

Push-over analysis (POA) was conducted by imposing 10 mm (2.5% of the pile diameter) of uniform horizontal displacement (see Figure 5) to the pile caps using 10 or 20 displacement increments depending on the size of the mesh as can be seen in Figure 6. Furthermore, a vertical static load equal to 10% of the ultimate capacity of the RC pile or pile grouping was applied to each of the pile caps to simulate the superstructural loads.

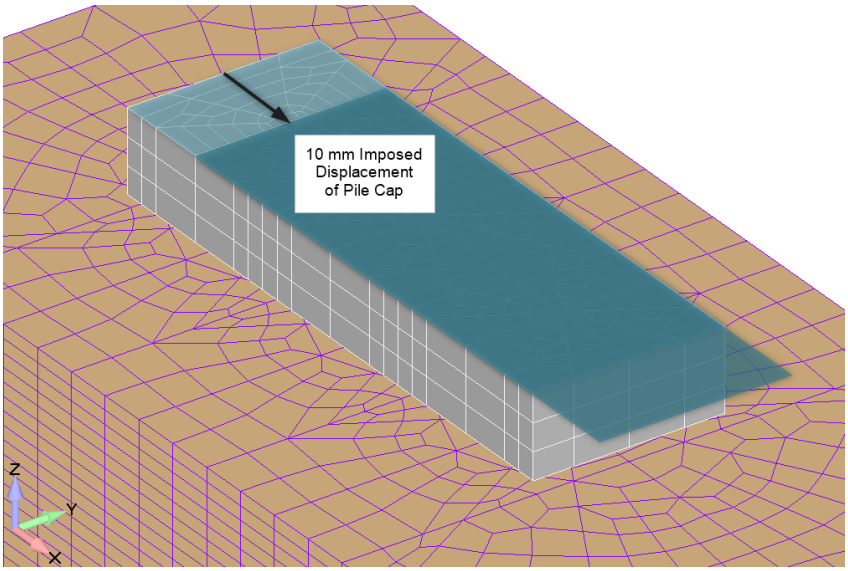


Figure 5: Graphical representation of the imposed displacement at the pile cap.

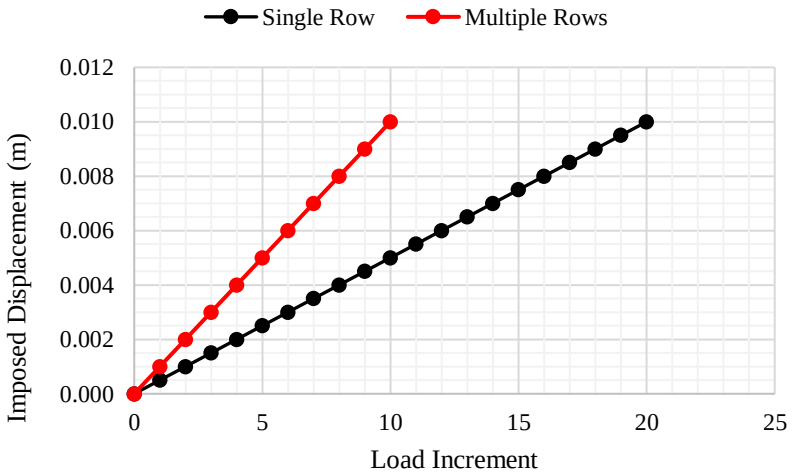


Figure 6: Loading of Pushover Analysis for smaller (Single Row) and larger models (Multiple Rows).

Pile groupings that consisted of a single row of piles (G1, G3, and G4) were not as computationally demanding as the larger groupings with two (G2x3, G2x4, G2x6) or three rows (G3x3, G3x4, G3x6) of piles. For this reason, it was decided to load the simpler models to the maximum

imposed displacement in 20 load increments (see Figure 6 Single Row) and the larger models in 10 load increments (see Figure 6 Multiple Rows). The effect of changing the number of load increments does not affect the structure and how the model reacts to loading, it does however influence the refined representation of the numerically obtained P-δ curve [6].

### 4.2 Torsional Imposed Deformation

The Torsional Imposed Deformation (TID) was conducted by imposing a total 10 mm uniform displacement to two opposing faces of the pile caps using the same loading increments. The 10% vertical static load was also applied to these tests during analysis. Figure 7 shows the imposed rotation applied to the pile cap during the TID of the models.

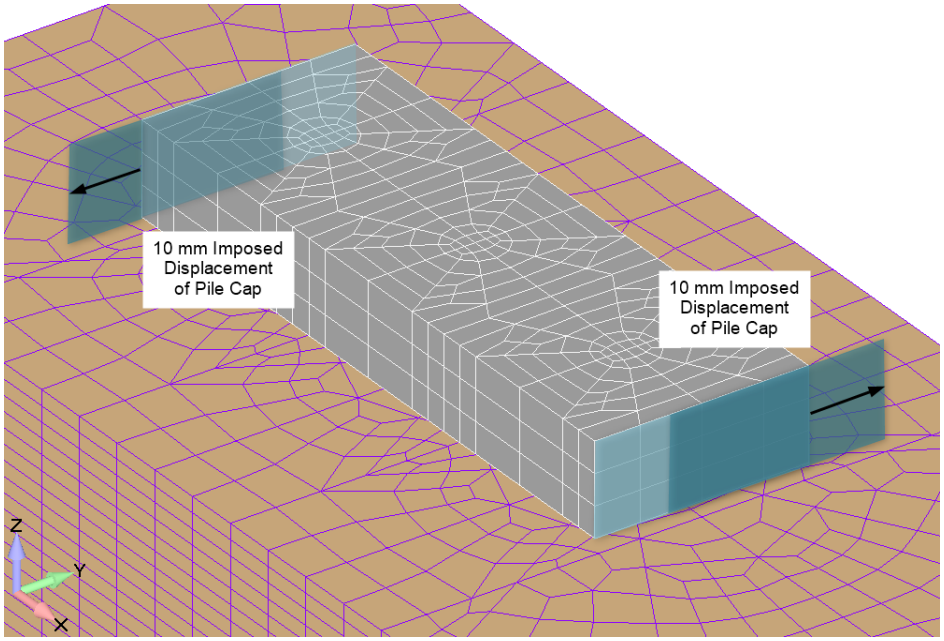


Figure 7: Imposed Rotation of the pile cap.

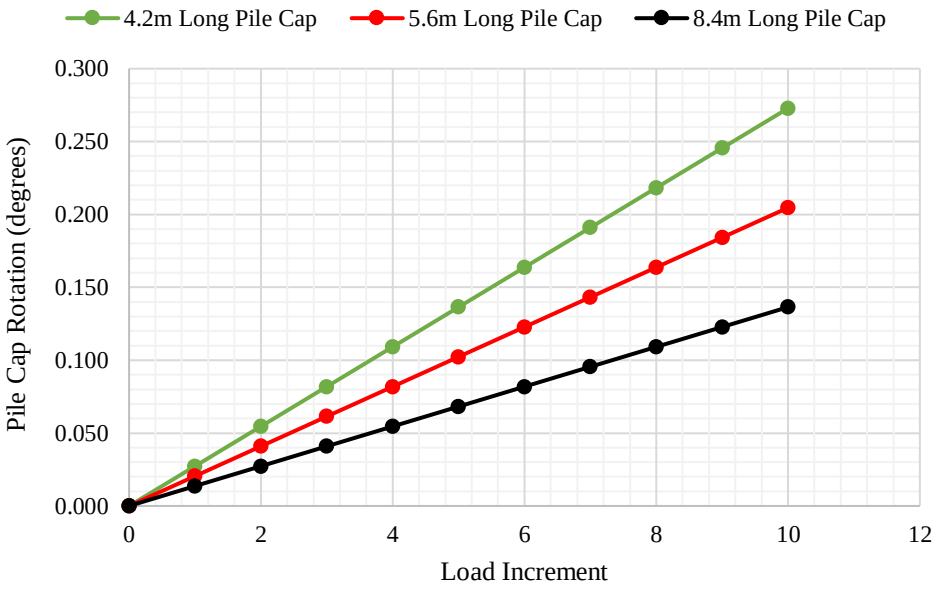


Figure 8: Loading of Torsional Imposed Deformation.

All the pile groupings underwent the same level of imposed displacement on each opposing pile cap edge, however as the length of the pile cap increased the rotation of the system decreased. Pile groupings with three piles in a row (4.2 m long pile cap) had a smaller rotational lever arm than the pile groupings with four (5.6 m long pile cap) or six (8.4 m long pile cap) piles in a row (see Figure 8).

## 5 PUSH-OVER ANALYSIS RESULTS

Failure in pile foundations can occur in multiple ways, most commonly being the failure of the surrounding soil (bearing failure, excessive lateral deformation, etc.) or the pile foundation itself could fail (pile plastic hinge, reinforcement rupture due to excessive bending, etc.). During the investigation conducted herein, it was discovered that the embedded rebar elements would fail when higher displacements were imposed upon the pile groupings due to excessive tension.

For the needs of this research work, the investigation of stress development in the soil domain was conducted by selecting three critical points along the pile length. These critical points can be seen in Figure 9, where the solid von Mises (SVM) stress development was plotted against the base shear reaction for every pile in the groupings studied. For pile groupings that consisted of two or three rows of piles (i.e., G2x3 and G3x3, etc.) the average of the stresses in each row was plotted against the base shear reaction as the percentage difference between the curves was low (less than 10%).

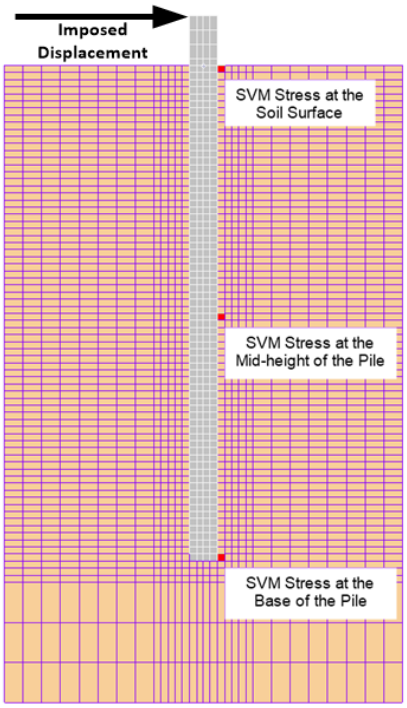


Figure 9: Points monitored for the development of the stress curves.

### 5.1 Single pile

When investigating the result from loading a single pile (see Figure 10), the soil elements at the surface layer reach the set maximum ultimate compressive stress (250 kPa) quite rapidly after a few load increments. The stress level at the base of the pile is usually higher than the stresses at the mid-height of the pile. This phenomenon is predominantly caused by the distribution of bearing stress at the base of the pile. When studying Figure 11 it is evident that there are relatively large increases in the SVM stresses in early load increments until a point where

the stress growth rate stabilizes. At the mid-height of the pile, there is little to no growth in the SVM stress levels (this changes based on the grouping configuration). Near the base of the individual pile, it can be seen that there are effects of bearing stress that increase the SVM stresses surrounding the pile base, which is possibly caused by the applied vertical static load. This phenomenon becomes more complex when pile groupings are analyzed and will be discussed. These trends can be seen in pile groupings with some degree of variation.

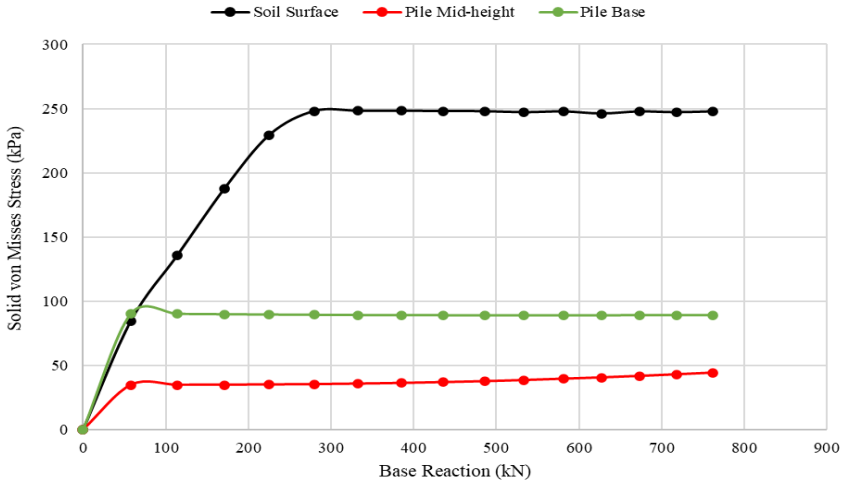


Figure 10: SVM stress development for a single pile G1.

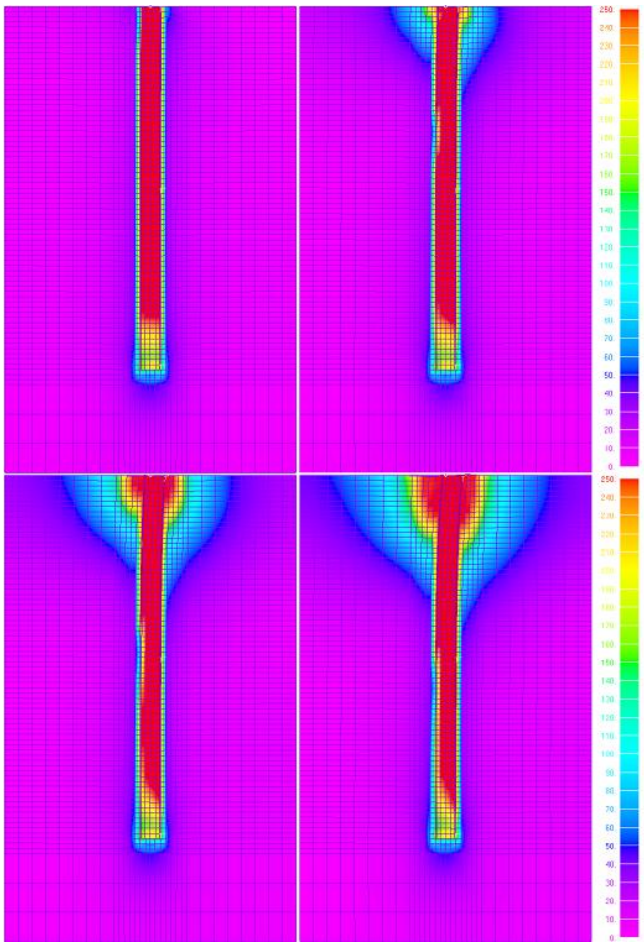

Figure 11: SVM stress distribution around a single pile (kPa) with increasing imposed displacements.

## 5.2 Pile groupings

As an imposed displacement is applied to the pile groupings a shear reaction develops in the soil medium. The shear reaction is directly proportional to the imposed displacement and the size of the pile grouping. As the number of piles in the pile grouping increase so does the base rection (shear reaction) of the foundation. In Figure 12 it can be seen that increasing the group size results in a higher base reaction and subsequently a higher lateral resistance. The orientation of the pile grouping with respect to the applied load or displacement also influences the lateral resistance of the pile foundations. The development of the shear resistance for pile groupings G2x6 and G3x4 are similar. Both groupings have the same number of piles (12) and the only factor contributing to the difference in lateral resistance is the orientation of the group. Pile groups with a longer group length in the direction of the applied force or displacement will have higher lateral resistances.

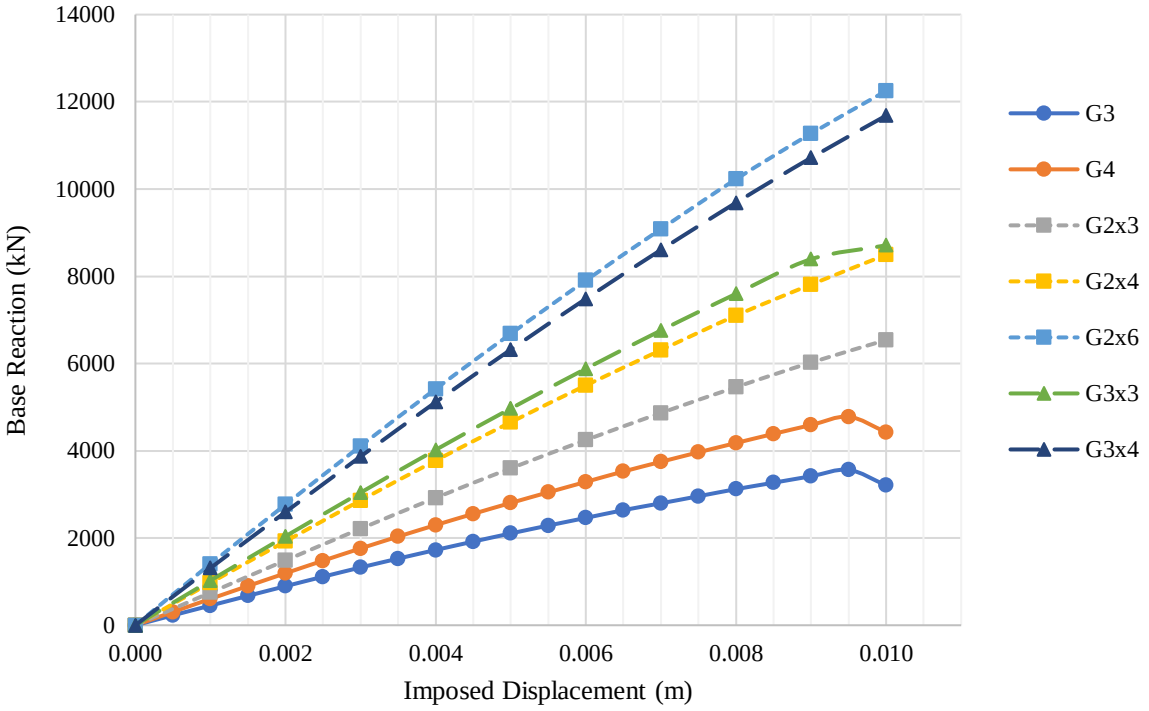


Figure 12: Combined P-δ curves for various pile groupings.

It should be noted that for pile groupings G3, G4, and G3x3 there is a slight decrease in the shear reaction near the end of the loading procedure. This is caused by cracks developing and propagating in the concrete at the base of the pile cap combined with reinforcement yielding. This failure first occurs in the last pile (due to high soil compression) and spreads to the rest of the piles eventually reaching the leading pile (first pile).

When considering soil elements that surround the piles at the soil surface level, it can be seen that the stress around the individual piles in the group reaches the ultimate compressive resistance of the soil (250 kPa). The soil around the leading pile in the group reaches the maximum stress and plateau quite fast when compared to the subsequent piles. The trailing piles in the group have soil-stress development curves that are almost parallel with a small degree of difference. These relationships can be seen in Figure 13.

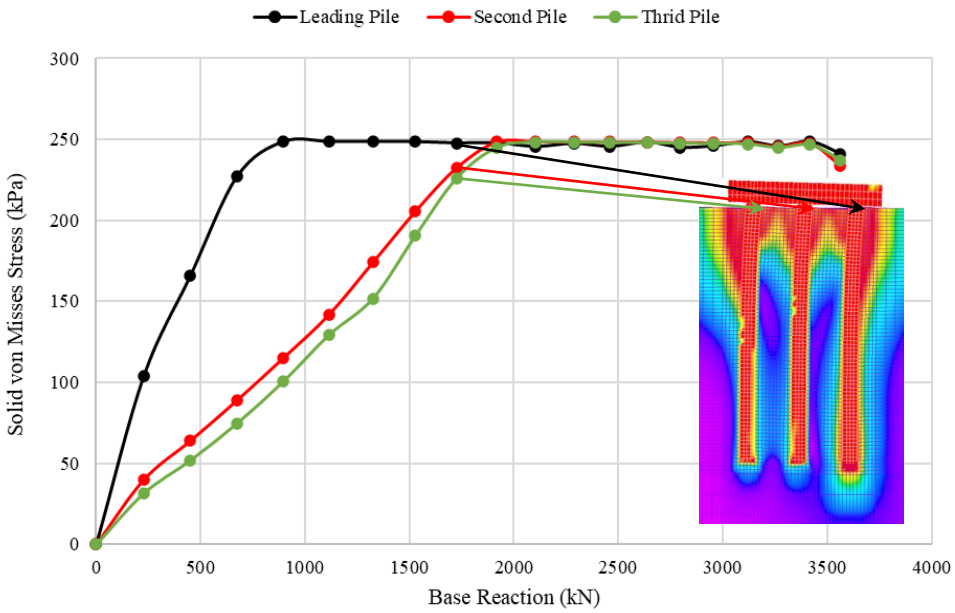


Figure 13: Stress development curve of pile grouping G3 at the soil surface.

When assessing the soil elements that surround the piles at the mid-height of the pile foundation, the stress around the individual piles in the group gradually increases but does not reach the ultimate compressive resistance of the soil. The leading pile in the group is found to develop a higher soil-stress increase rate than the subsequent piles. On the other hand, the trailing piles in the group have soil-stress development curves that are relatively similar to the third (last pile) deriving a slight decrease and then a higher increase rate in stress levels. This mechanical response is depicted in Figure 14.

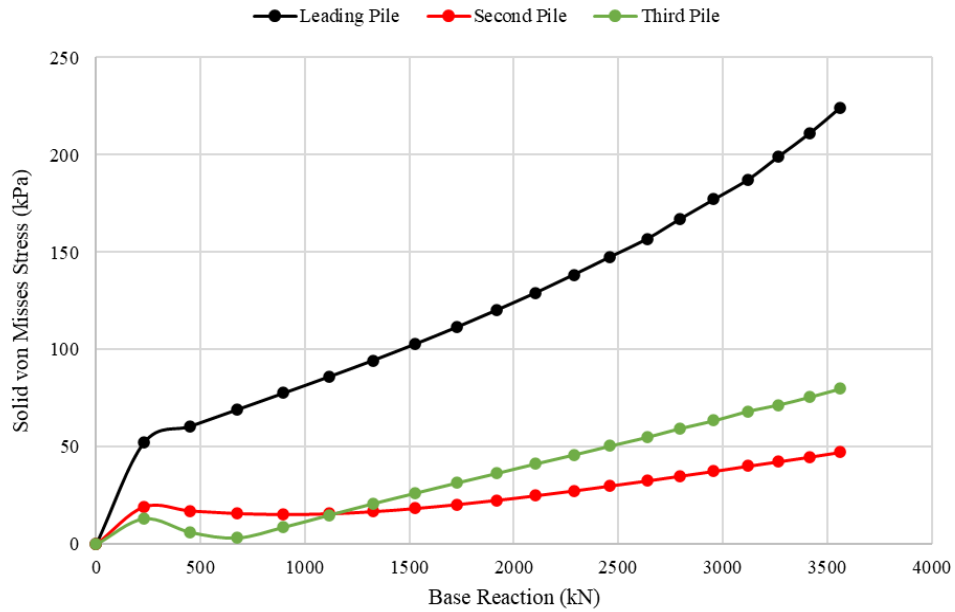


Figure 14: Stress development curve of pile grouping G3 at the mid-height of the pile.

The soil elements that surround the piles at the base have more complex reactions to lateral loading. Stress in the soil elements around the pile base of the leading pile increase until the ultimate compressive force is reached, where this happens near the midpoint of the loading stage as seen in Figure 15. The middle pile or piles in the group have a steady decrease in soil-stress levels in the front of the pile and an increase in stress at the rear of the pile. This effect is attributed to the movement of the pile in the opposite direction to the applied displacement (see Figure 16). The movement of the pile grouping in the negative x-direction occurs when the system experiences out-of-plane clockwise rotation.

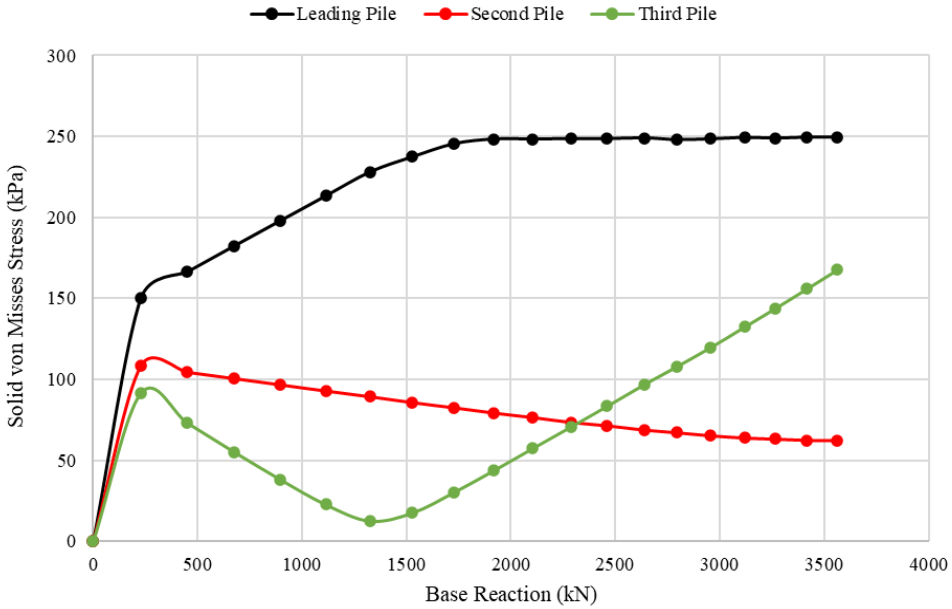


Figure 15: Stress development curve of pile grouping G3 at the pile base.

The deformation shape of the soil elements with increasing displacement steps (DS) can be seen in Figure 16, where the deformation has been scaled by 50 times. It is easy to observe that the high initial vertical displacement of elements under the leading pile is evident. The soil elements surrounding the leading and second pile deform downwards (settlement), while there seems to be some degree of heave of elements surrounding the third pile foundation. These effects cause the pile group to rotate about the out-of-plane axis in a clockwise manner and if the rotation were to become excessive it would result in the cracking or failure of the pile cap, buckling failure of the pile, or reinforcement failure.

In Figure 15 it can be seen that the last pile in the group experiences a rapid decrease in soil stress until a turning point on the curve is reached. Following this, there is a rapid increase in stress levels, whereas the total rotation of the system eventually causes a decrease in stress. The stress increase at the base of the pile occurs when the rotation of the pile grouping is resisted by an increasing bearing stress in the soil surrounding the last pile. These phenomena can be seen in Figure 17. The SVM stress development in the soil domain and the discussed phenomena can be seen in Figure 18.

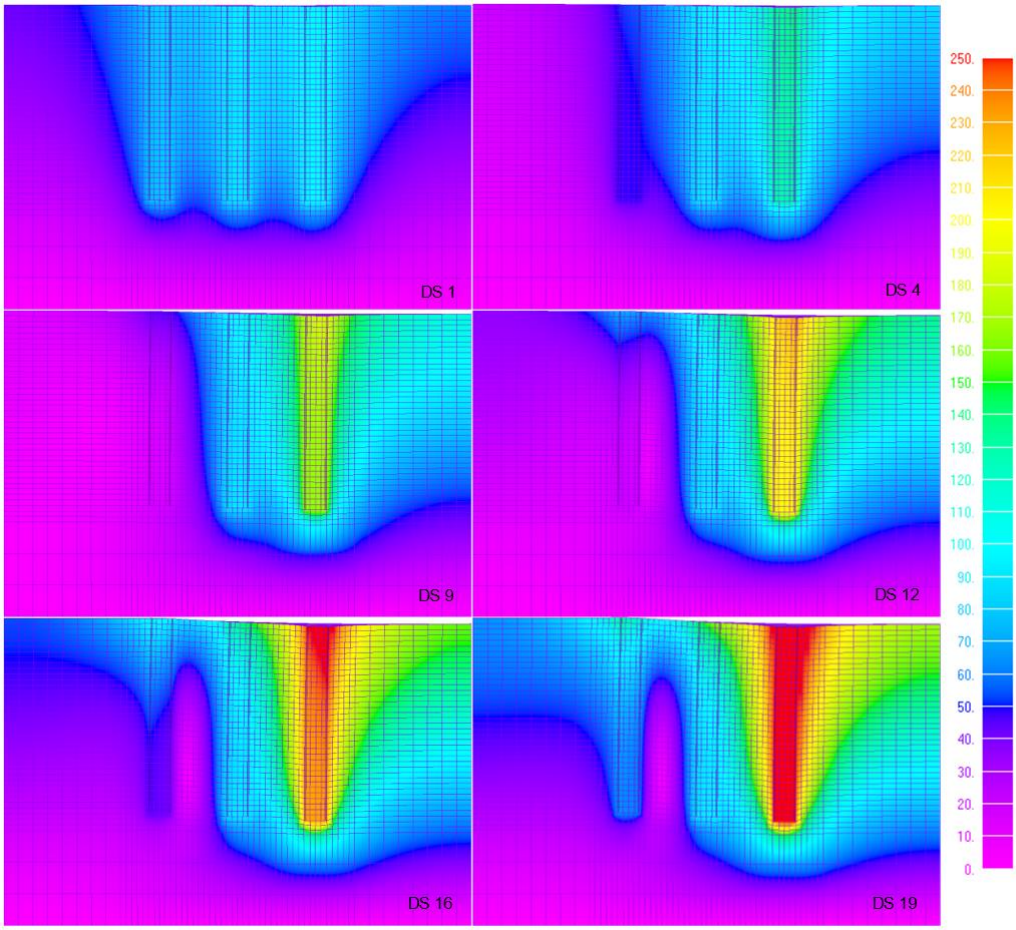


Figure 16: 50x scaled total translation in the bottom half of the soil domain (G3).

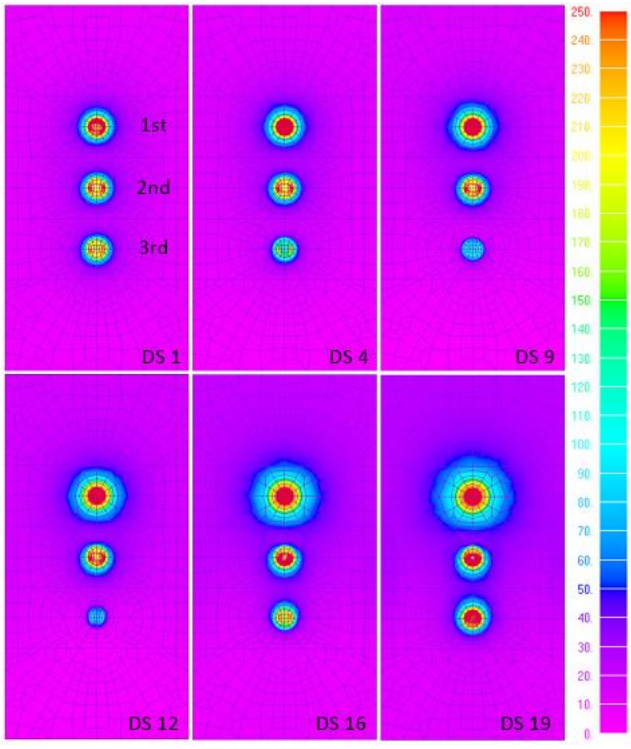


Figure 17: Bearing stress under the leading (top), second (middle), and third (bottom) pile foundation (G3).

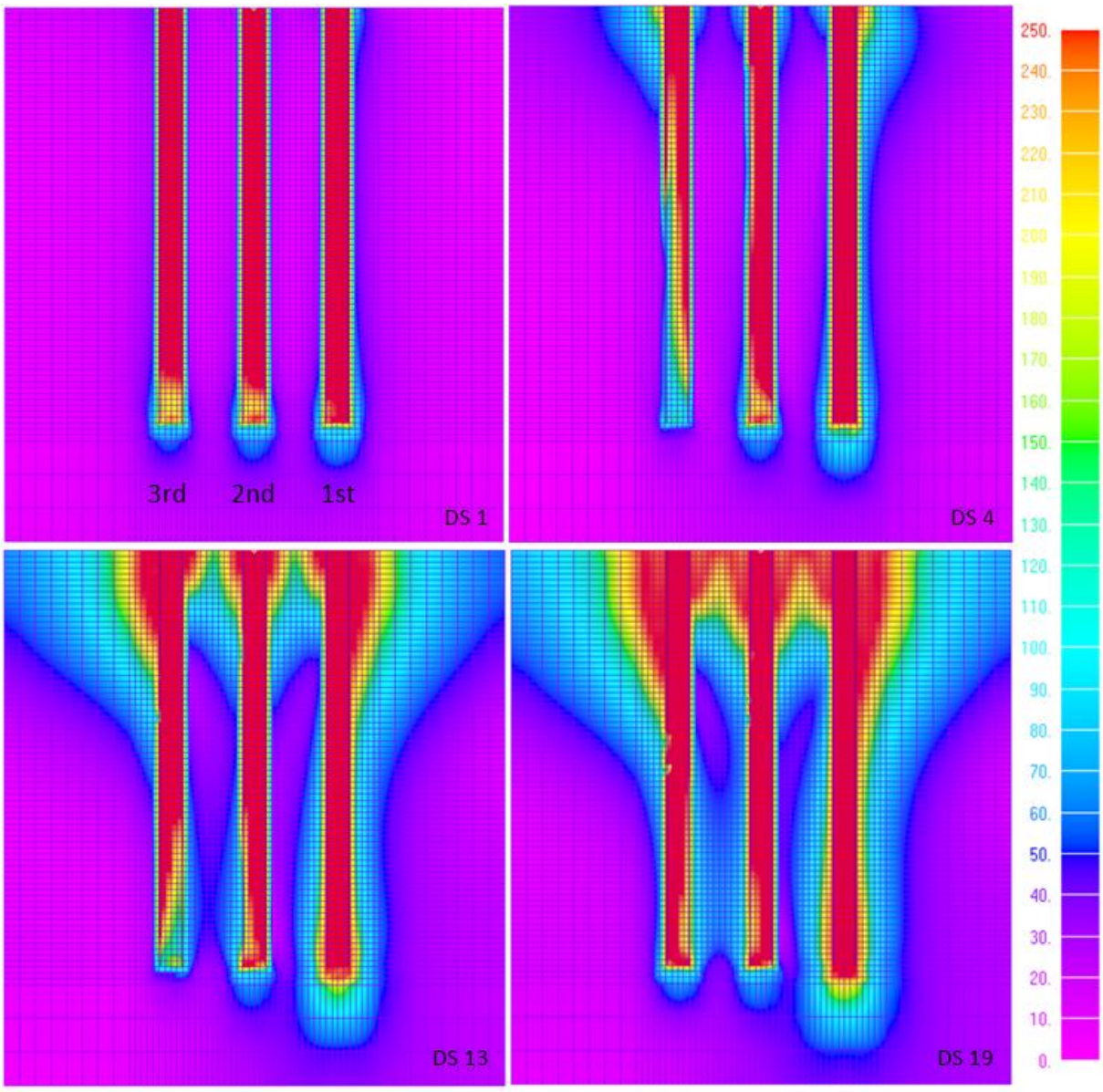


Figure 18: SVM stress contours for pile group G3 at different displacement levels.

The overlapping of stress regions in the soil surrounding the pile foundation can result in the plastification of the soil and consequently the failure of the pile system. The stress within the elements at the soil surface can be seen in Figure 19a. High stresses surround the pile and accumulate where the stress bulbs overlap, an effect that results in a block of elements with the same stress magnitude. In Figure 19b and Figure 20, the stress isosurfaces can be seen (predominantly the leading and the second pile) in a region of equal stresses. These high stresses surrounding the leading pile were explained previously by the rotation of the pile cap and the overall deformation of the foundation system when pushed horizontally. It is also important to note that the vertically applied superstructure load also contributes to the development of the field within the soil domain. It is noteworthy to state here that the vertical load also decreases the overall horizontal rotation of the piling foundation system, as it was found from the parametric investigation, thus acts as a stabilizing mechanism.

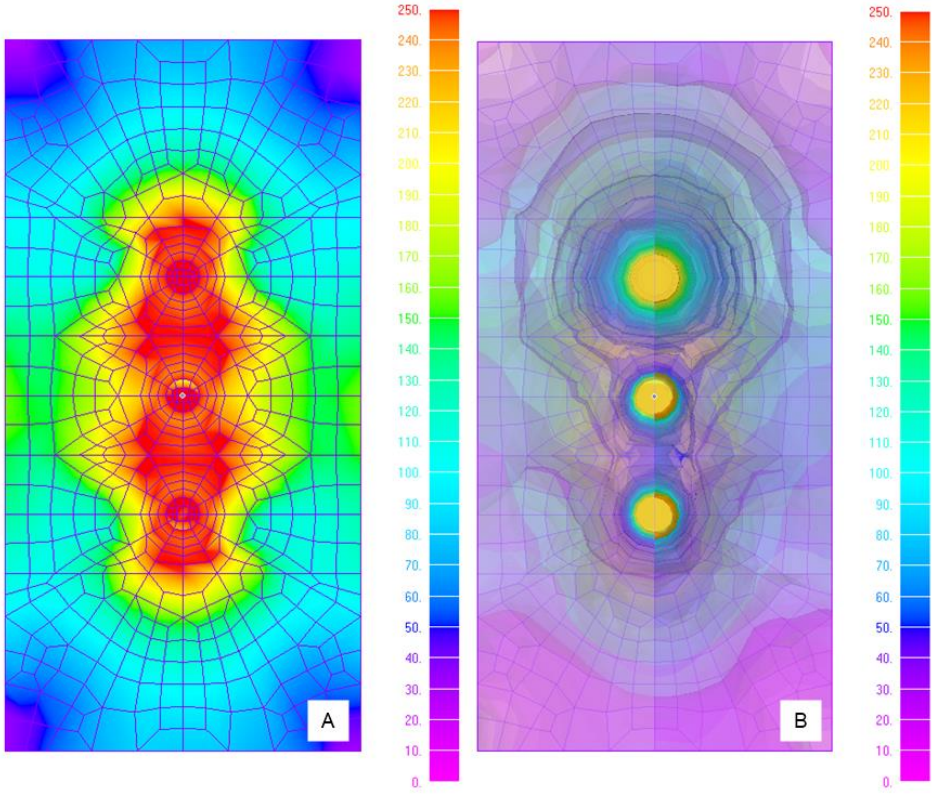


Figure 19: Top view of soil domain (G3) illustrating (a) soil stress distribution and (b) overlapping stress isosurfaces in kPa.

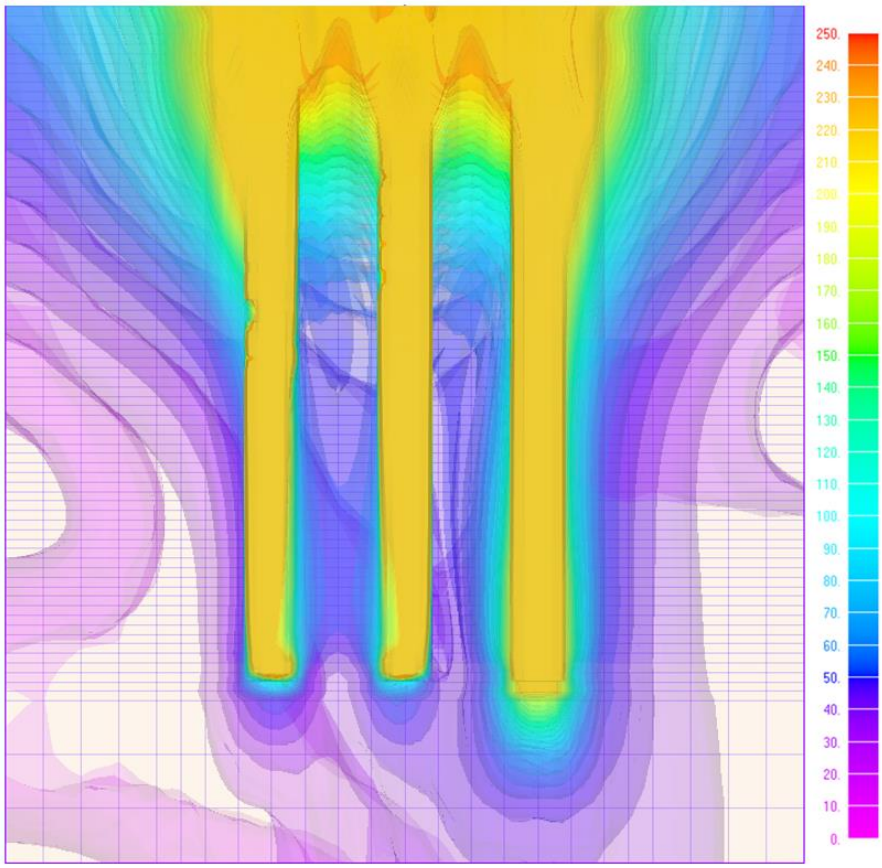


Figure 20: Section view illustrating stress isosurfaces in the soil around model G3 in kPa (DS 19).

The relationships discussed for the pile grouping G3 can be applied to the larger pile groupings analyzed for the needs of this research work. The SSI and phenomena were observed in all the subsequent pile groupings. The figures below serve to validate the previously discussed behaviors. Larger pile groupings show the intermediate curves in the stress development of the pile groupings under imposed horizontal displacements and vertical superstructural loads. The validation of the above statement can be seen below using the pile groupings G4 (see Figure 21 through Figure 24) and G2x6 (Figure 25 through Figure 28).

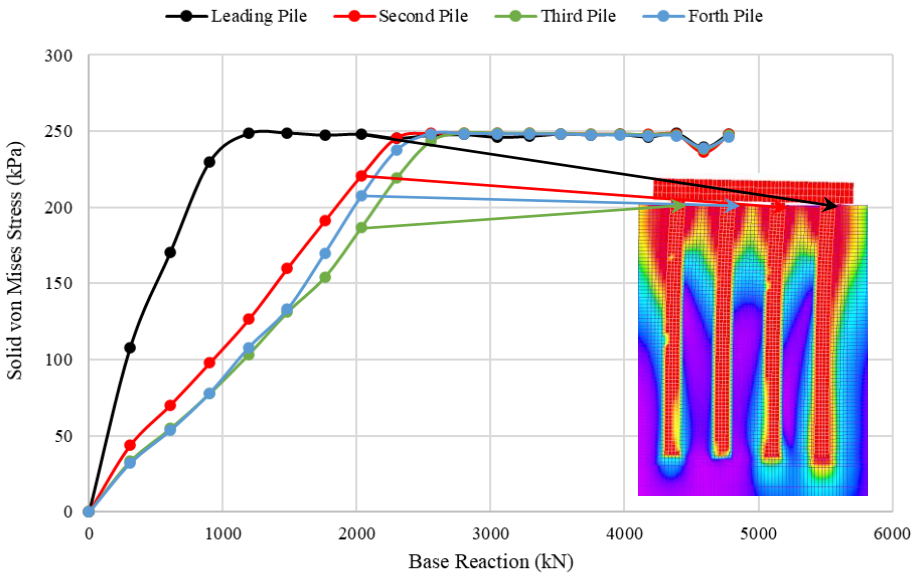


Figure 21: Stress development curve of pile grouping G4 at the soil surface.

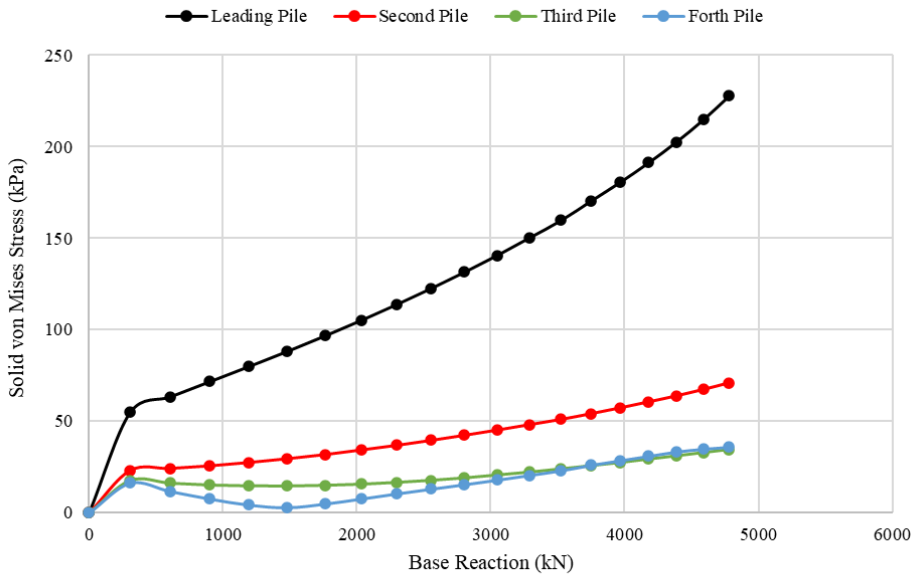


Figure 22: Stress development curve of pile grouping G4 at the mid-height of the pile.

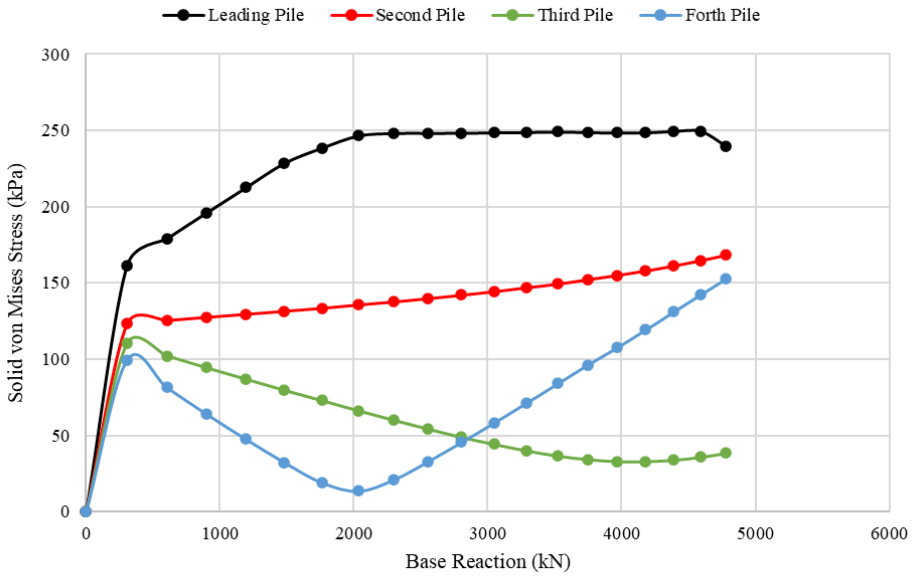


Figure 23: Stress development curve of pile grouping G4 at the pile base.

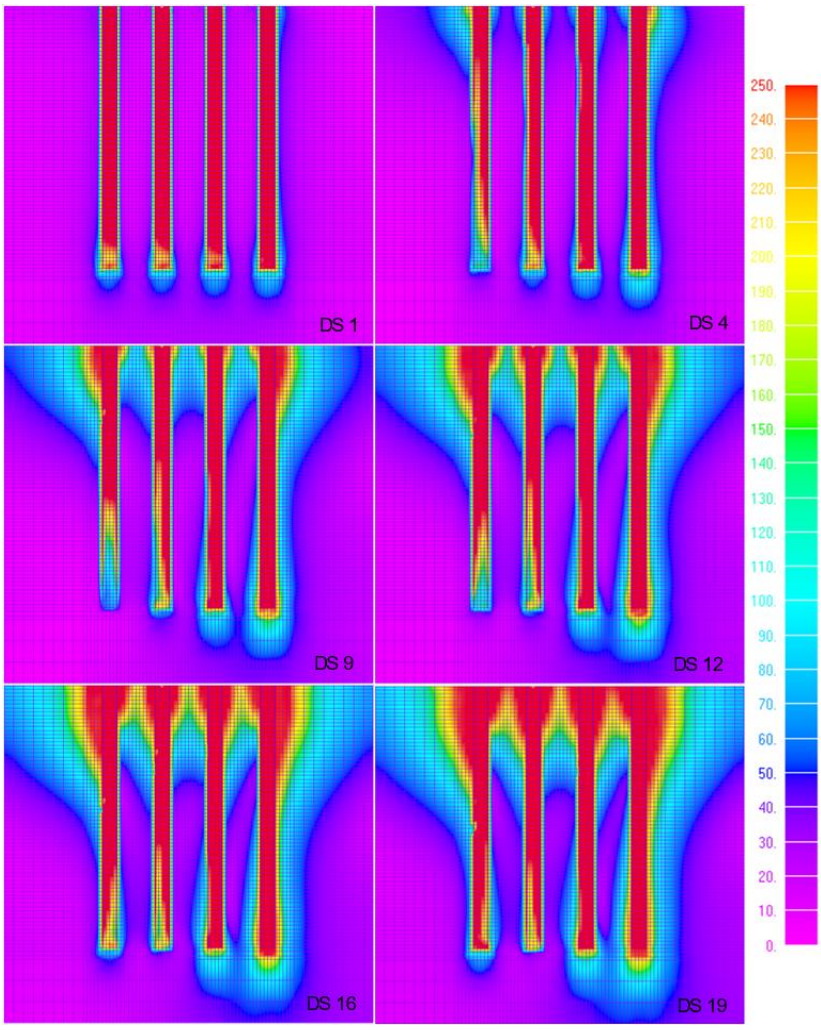


Figure 24: Stress development (kPa) in pile grouping G4 at increasing imposed displacements. Number of displacement increments imposed: max DS = 20.

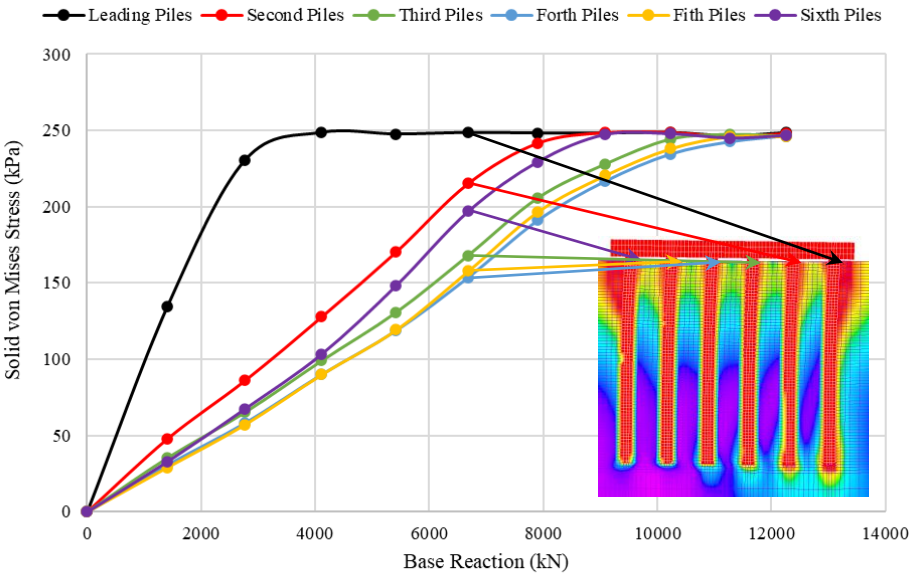


Figure 25: Stress development curve of pile grouping G2x6 at the soil surface.

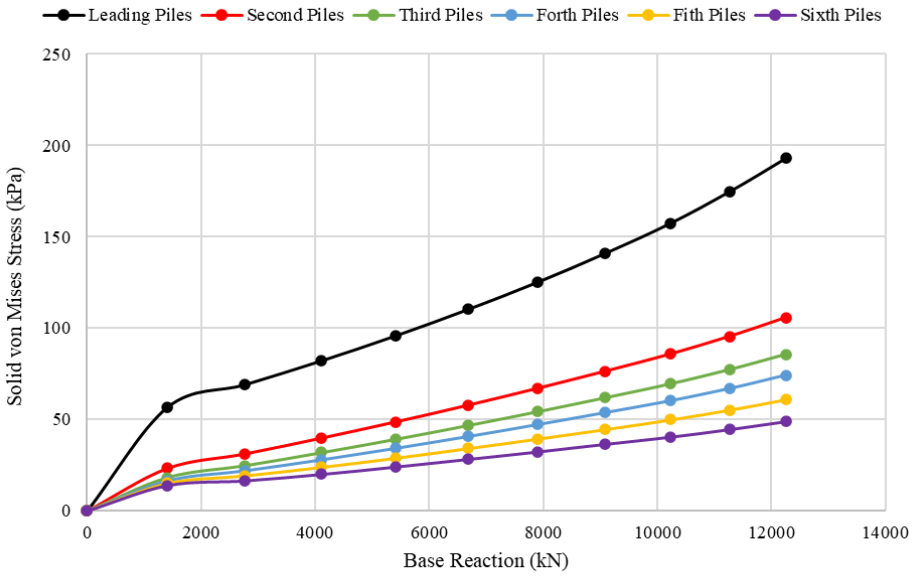


Figure 26: Stress development curve of pile grouping G2x6 at the mid-height of the pile.

Figure 27 shows that the effect of soil stress decreases at the last pile's base which is more visible since the geometry of the pile foundation system G2x6 is larger and more complicated (see Figure 28) compared to the G3 group series. The overall rotation of the foundation requires a larger horizontal displacement to fully develop, significantly affecting this way the soil stress development as noted from the graphs in Figure 27. This finding also highlights the complexity of the SSI problem that in this study only accounts for a monotonic loading condition, neglecting the more complicated phenomena that will derive when a cyclic load is applied.

Furthermore, it is also easy to observe that the stresses within the soil domain increase significantly under the base of the leading piles (see Figure 28). This is attributed to the overall rotation of the pile cap as it is being pushed along the x-axis. This mechanical response was found to develop for all groupings investigated in this research work.

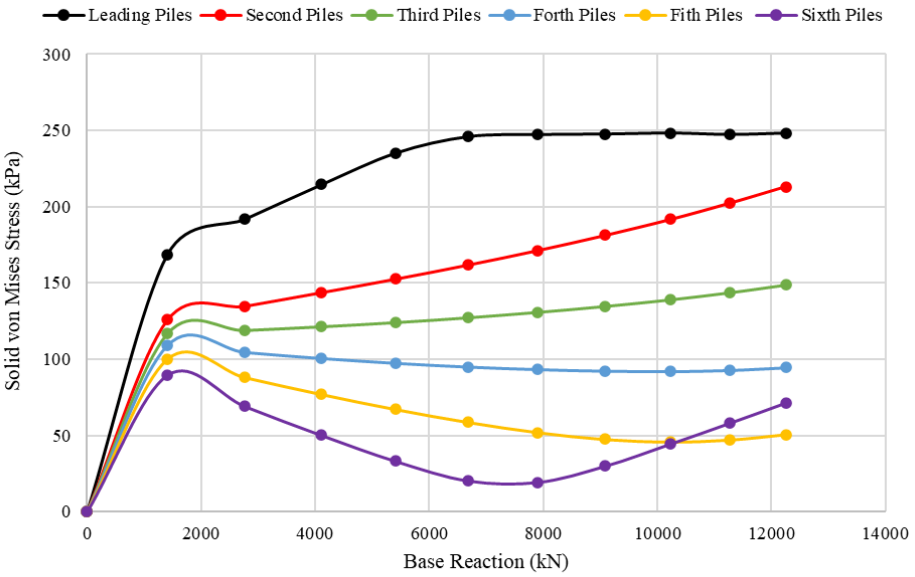


Figure 27: Stress development curve of pile grouping G2x6 at the pile base.

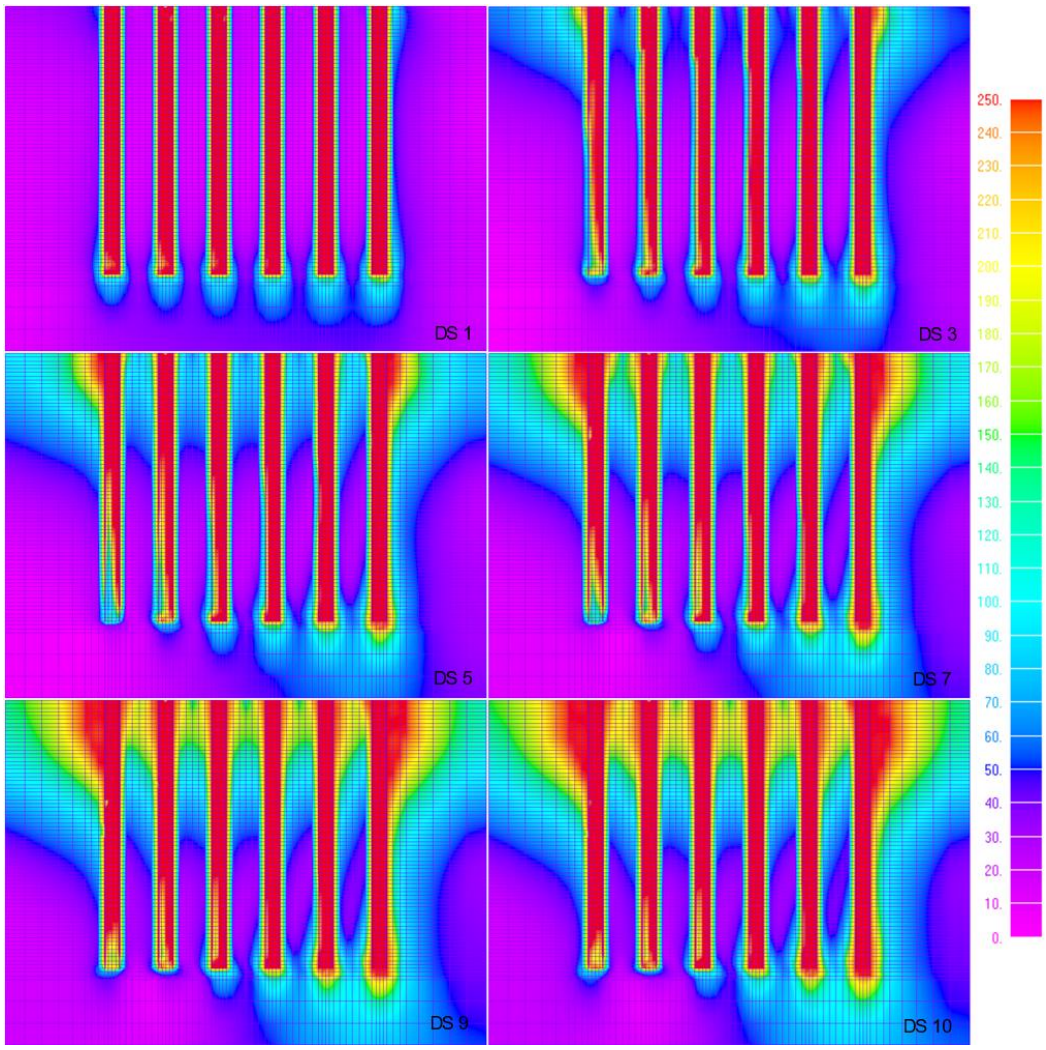


Figure 28: Stress development (kPa) in pile grouping G2x6 at increasing imposed displacements. Number of displacement increments imposed: max DS = 10.

## 6 TORSIONAL IMPOSED DEFORMATION

Similarly, to the POA, larger pile groupings were more susceptible to developing soil failure due to the overlapping 3D stress regions. Larger pile group systems exhibited stiffer behavior than the smaller groupings and this caused the embedded rebar elements in pile groupings G2x6, G3x3, and G3x4 to fail at the maximum imposed torsion.

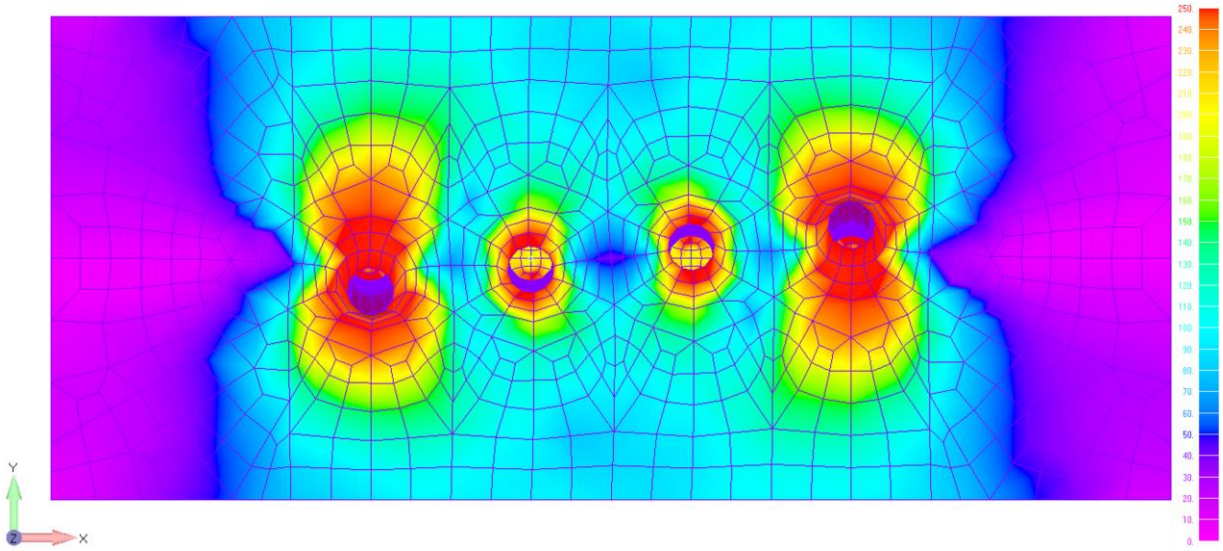

Figure 29: Scaled deformed top view showing the SVM stress distribution around group G4 (kPa) under imposed torsion (DS 20).

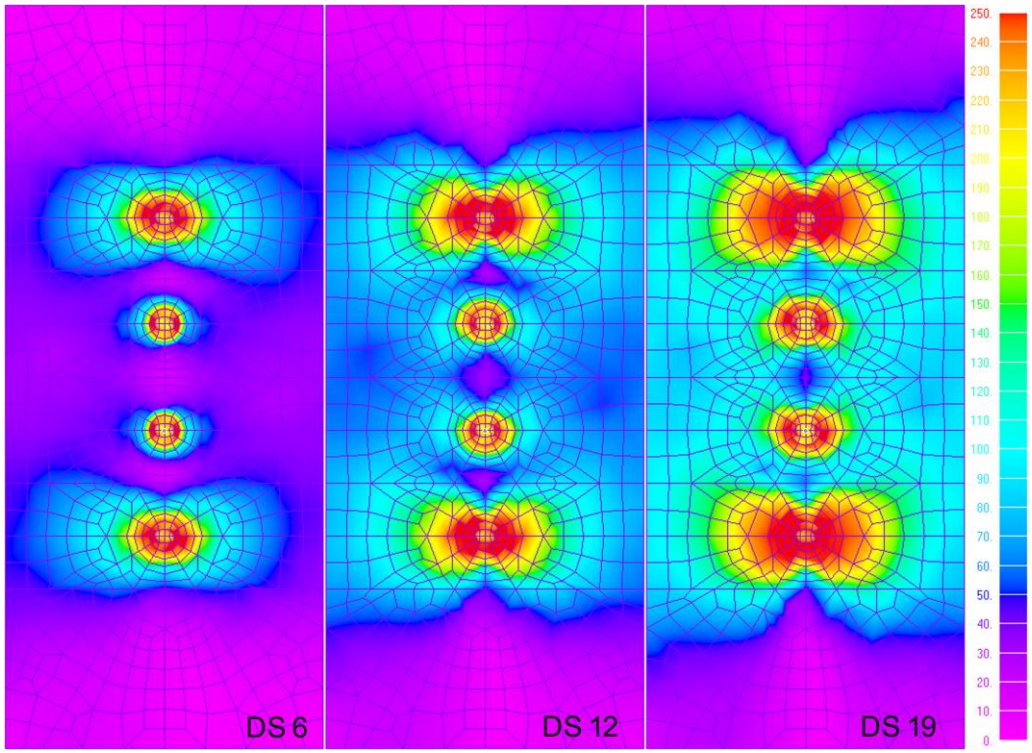


Figure 30: Top view of SVM stress development (kPa) for displacement steps 6, 12, and 19 for group G4. Number of displacement increments imposed: max DS = 20.

As an imposed rotation is applied to the pile groupings, stress develops in the soil medium. Accordingly, the developed stress is proportional to the imposed angle of twist on each pile group. The stress development of pile systems experiencing torsion is symmetrical, the soil elements around the first and last pile had equal stresses both in front and behind the pile and the stress development of the soil elements around the central piles was also mirrored. This mechanical phenomenon can be seen in Figure 29. It is also worth noting that the soil surrounding the central piles, experiences lower stresses than around the piles positioned at the ends, a phenomenon attributed to the lower relative deformation (see Figure 30).

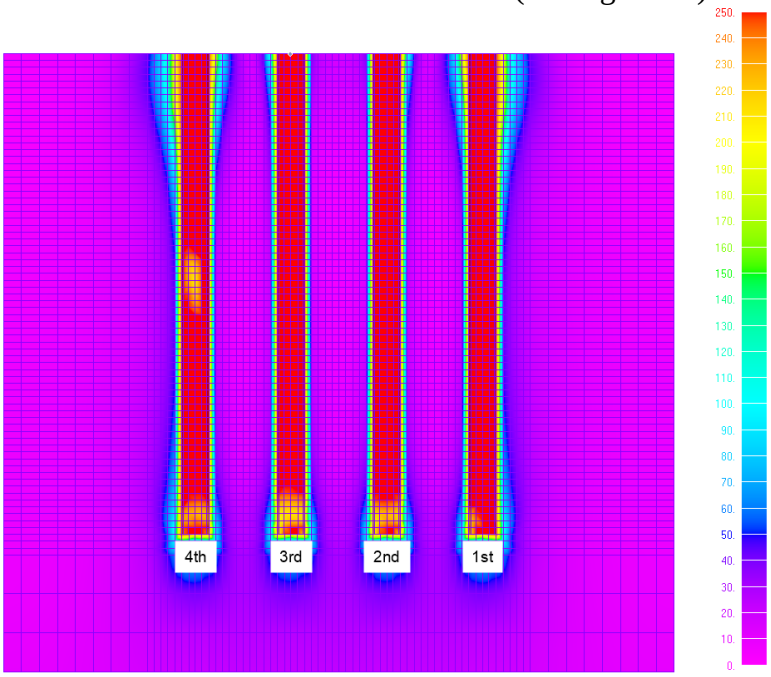


Figure 31: SVM stress contours (kPa) for group G4 at DS 6. Number of displacement increments imposed: max DS = 20.

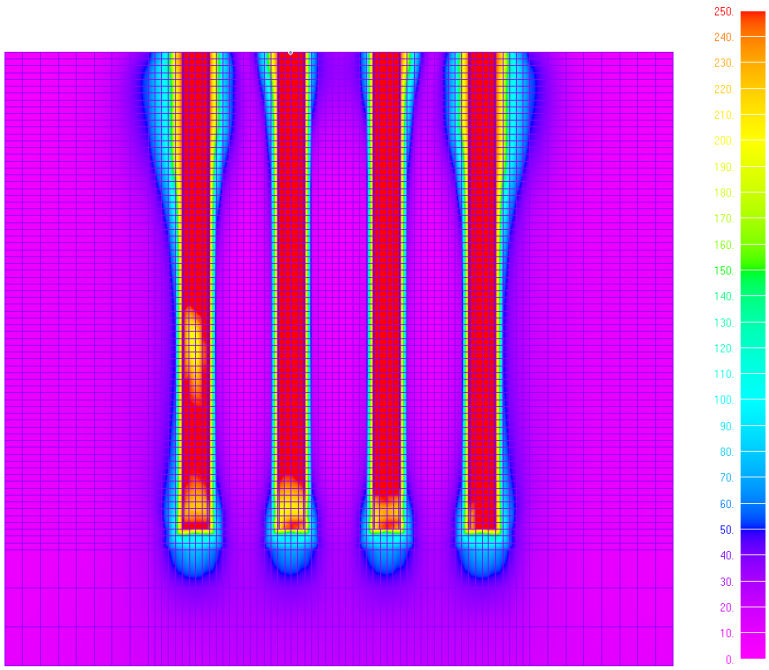


Figure 32: SVM stress contours (kPa) for group G4 at DS 12. Number of displacement increments imposed: max DS = 20.

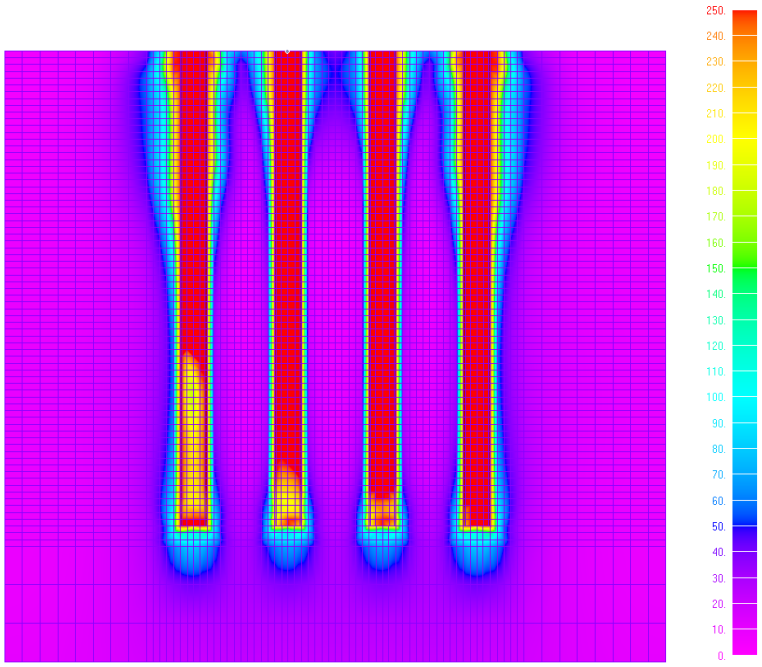


Figure 33: SVM stress contours (kPa) for group G4 at DS 19. Number of displacement increments imposed: max DS = 20.

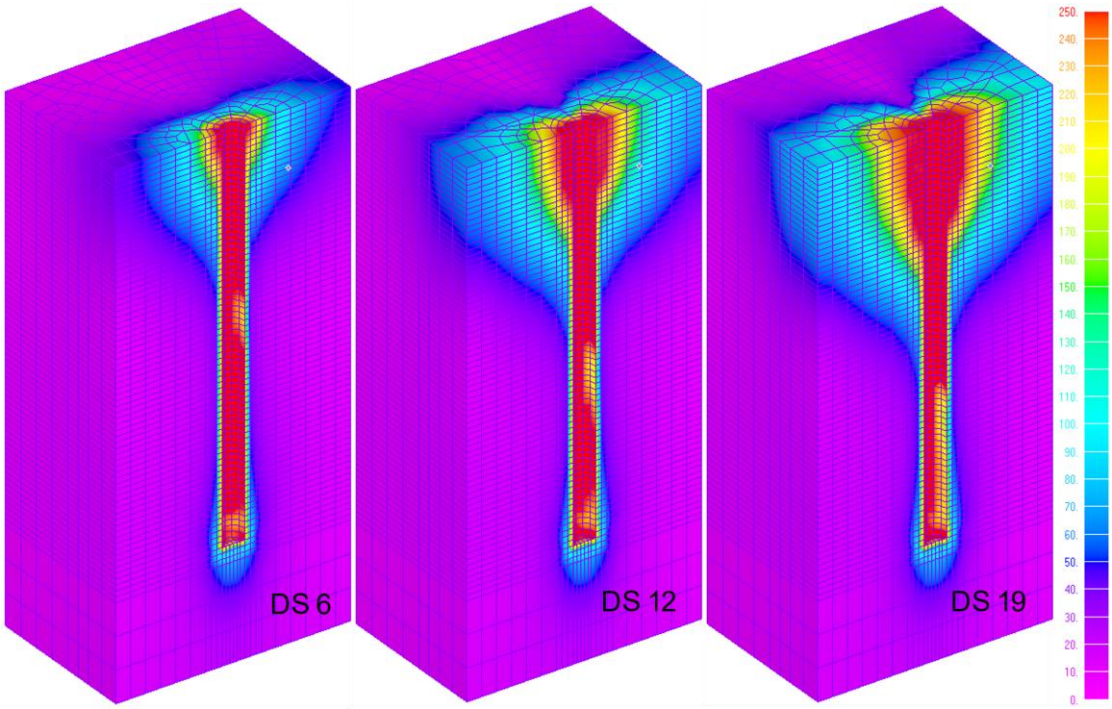


Figure 34: Dimetric view of SVM stress development (kPa) for displacement steps 6, 12, and 19 for group G4. Number of displacement increments imposed: max DS = 20.

Figure 31 through Figure **33** show how the first and fourth piles have identical stress development in the soil medium under increasing torsion for the case of model G4. The same applies to the second and the third pile. As torsion increases, the soil elements near the soil surface develop higher stresses, thus, the corresponding stress bulb increases in size and the pile foundation experiences bending at the pile level. The bending of the pile foundation results in compressive stresses in front of each pile and lower stresses behind the pile foundation. This can be

seen when studying the stress development of the soil elements around the middle of the fourth pile that have lower stresses than the surrounding elements. This region of reduced stress increases in size as the applied torsion and in turn the bending of the pile increases (see Figure 34), a phenomenon that was found to be mirrored behind the first pile. It is worth noting that this behavior also occurs in the soil elements around the central piles but with significantly reduced effects, attributed to their position that is close to the center of rotation.

In Figure 35 the rapid increase in the soil stress of the first and fourth piles can be seen. For the case of the G4 model the central, second, and third piles, were found to have a lower rate of increase in soil stress. The soil elements around all the piles at the soil surface level reach the maximum compressive stress and plateau. This trend is visible for all pile groupings with some small degree of variation.

Figure 36 shows the stress development at the mid-height of the pile and indicates the rapid increase of the soil stress for the outer piles. There is a gradual increase in the soil stress at the soil elements that surround the central piles. At the base of the piles (see Figure 37) the soil elements of the outer first and fourth piles experience a gradual increase in the soil stress and the central pile elements experience a gradual reduction in the soil stress. Both above-mentioned trends are visible for all of the pile groupings studied in this experiment given that for all cases the outer piles are found to be the critical ones.

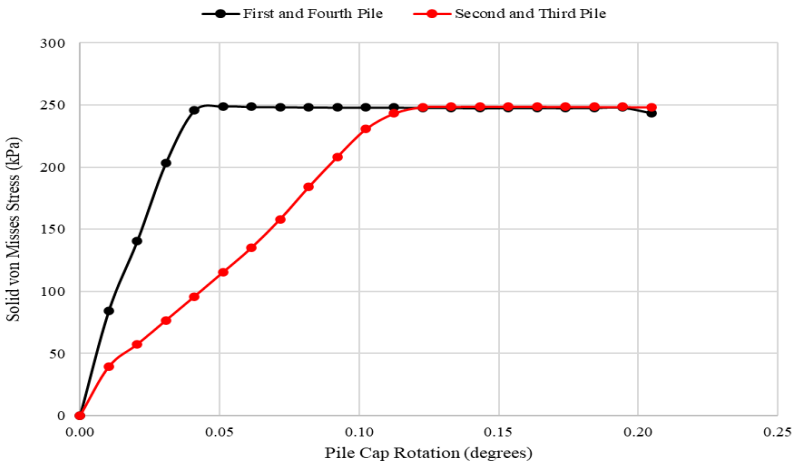


Figure 35: Stress development at the soil surface of pile group G4 under torsion.

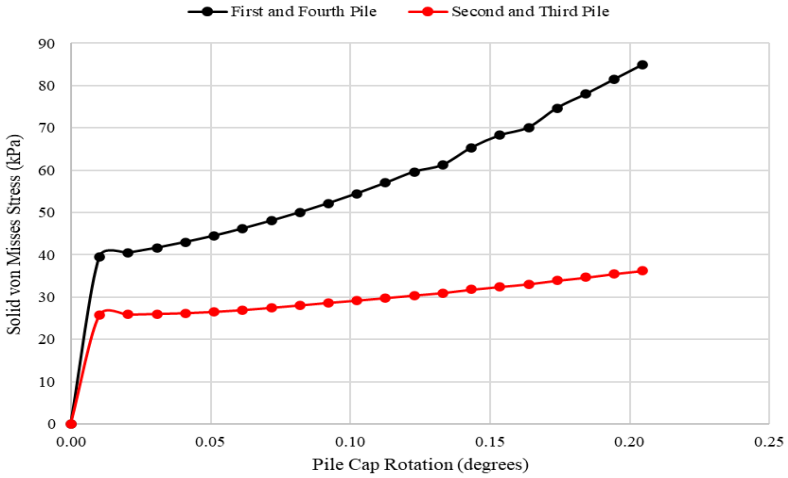


Figure 36: Stress development at the mid-height of the pile of group G4 under torsion.

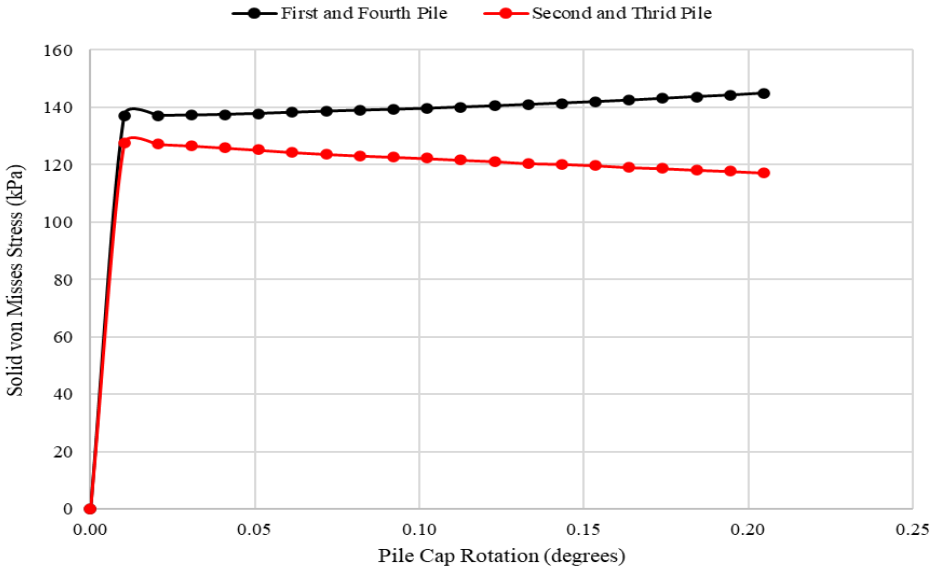


Figure 37: Stress development at the pile base of group G4 under torsion.

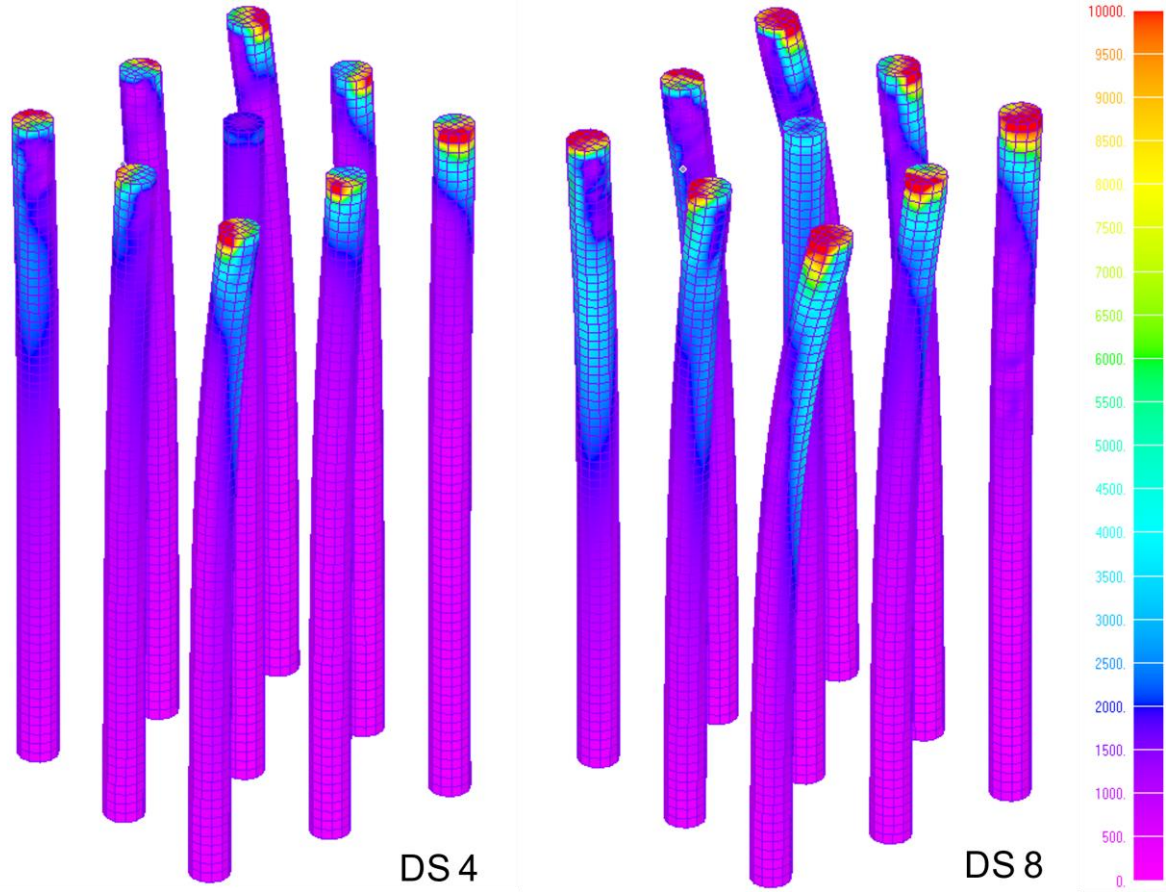


Figure 38: Bending development and SVM contours of pile foundations in pile group G3x3 with increasing torsion (kPa). Number of displacement increments imposed: max DS = 10.

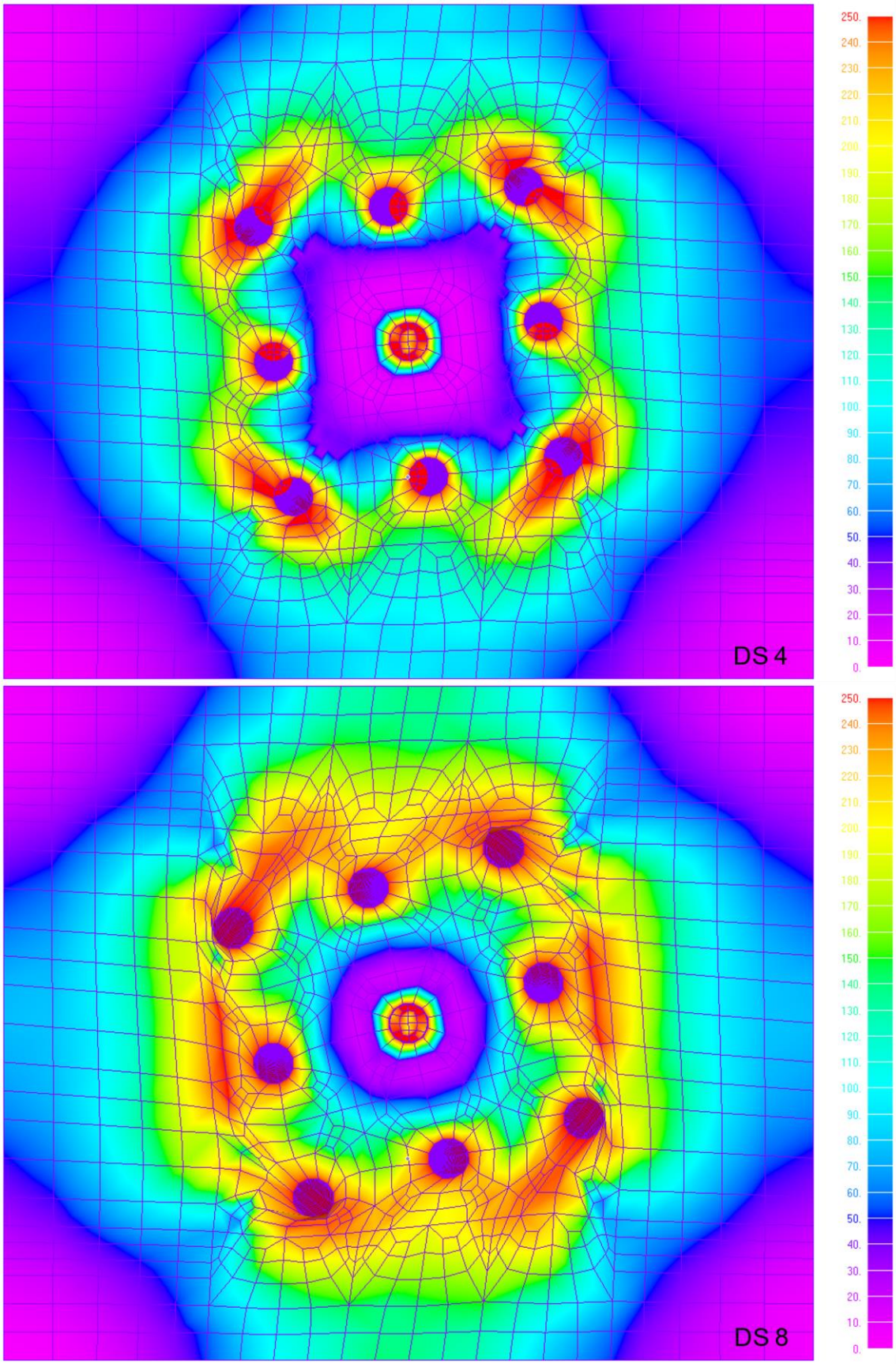


Figure 39: Scaled deformed view of the soil domain around pile group G3x3 with increasing torsion (kPa). Number of displacement increments imposed: max DS = 10.

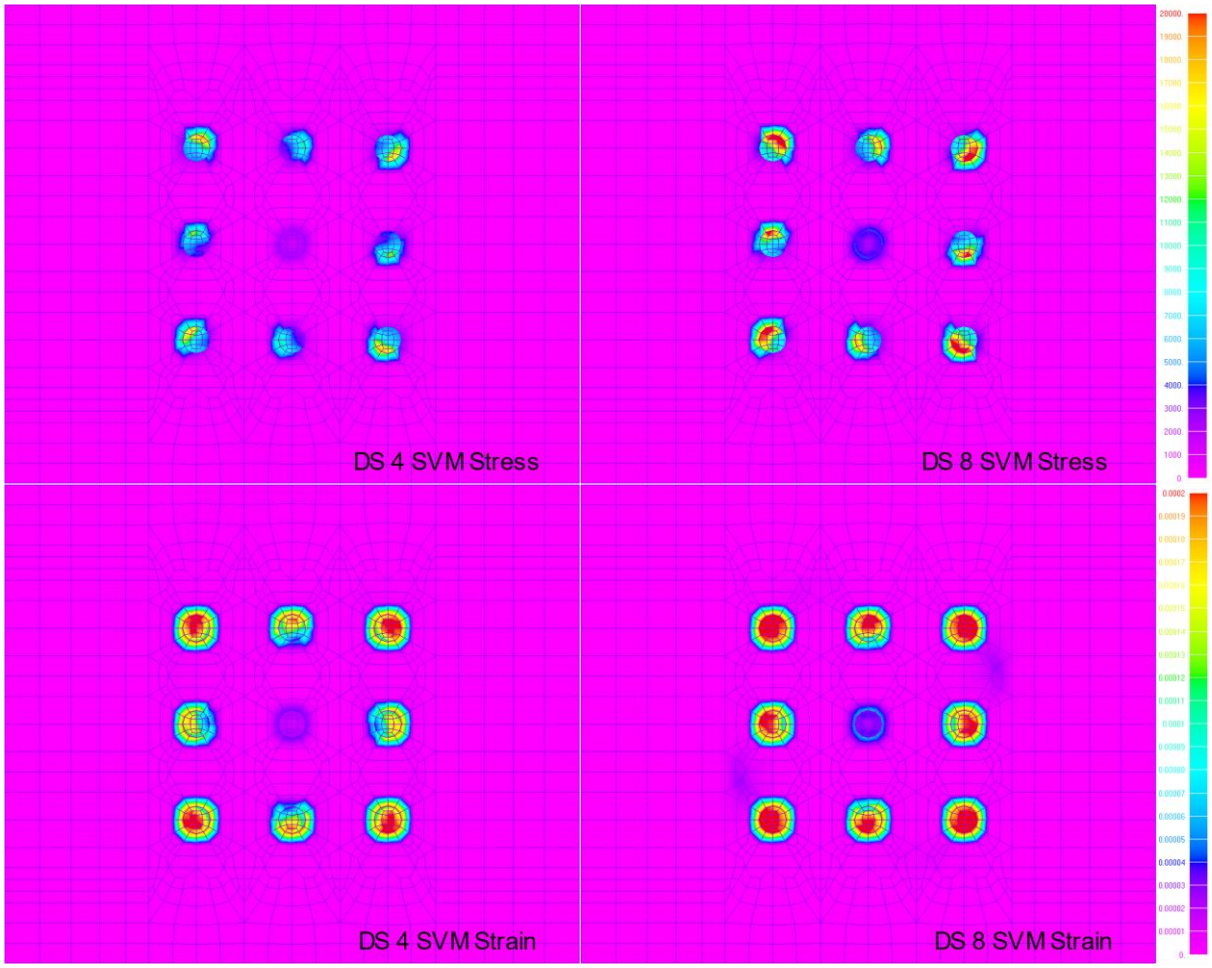


Figure 40: Crack propagation in pile foundation with increasing torsion (G3x3). Number of displacement increments imposed: max DS = 10.

Square pile groupings with odd numbers of piles in the group (3x3, 5x5, 7x7, etc.) have a central pile that lies on the rotational axis. As the central pile has no lever arm to experience bending, the pile undergoes pure torsion (see Figure 38). Because the central pile experiences no bending there is low-stress development in the soil medium around this pile as illustrated in Figure 39. The base of this central pile experiences some stress development which is caused by the vertical nominal load as opposed to imposed torsion. An interesting occurrence that was also observed during this experiment was the crack development and propagation in the pile foundations at the base of the pile cap. Cracks started forming on the tension side of the piles experiencing bending and these cracks developed along the circumference of the pile foundation. This behavior can be seen in Figure 38 through Figure 40.

The large variation in the stress of the soil elements around the central pile is visible in Figure 41 through Figure 43. The SVM stress curves represent the stress development of the soil elements around the second pile (central pile in three rows of model G3x3). At the soil surface and mid-height of the pile, the soil elements around the second pile in the first and second rows have identical stress development curves (<1% difference), while the central pile develops much lower soil stress levels.

Near the base of the pile, the behavior of the soil differs slightly, where is a gradual decrease in the stress of the soil elements around the base of the central pile. The relatively higher stresses around the base of the central pile are a result of bearing pressures under the pile foundation.

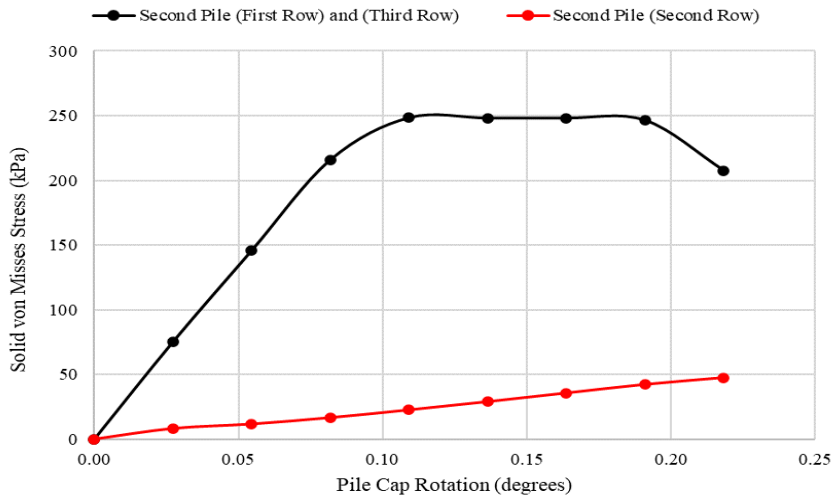


Figure 41: Stress development at the soil surface of pile group G3x3 under torsion.

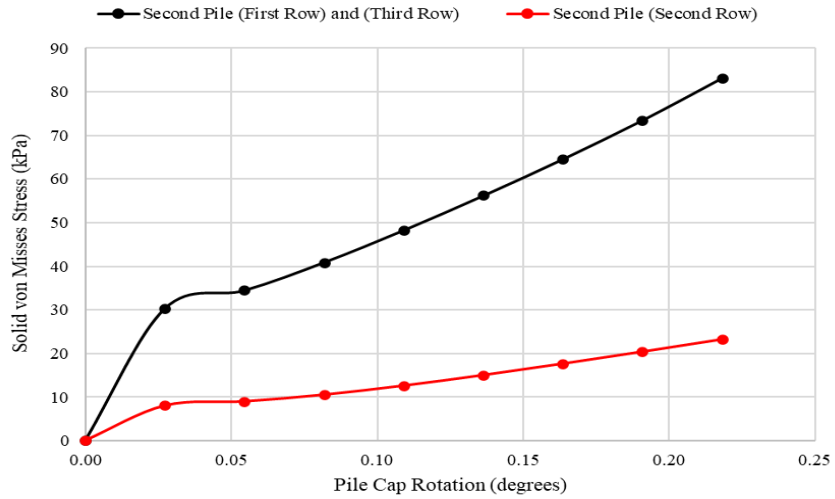


Figure 42: Stress development at the mid-height of the pile of group G3x3 under torsion.

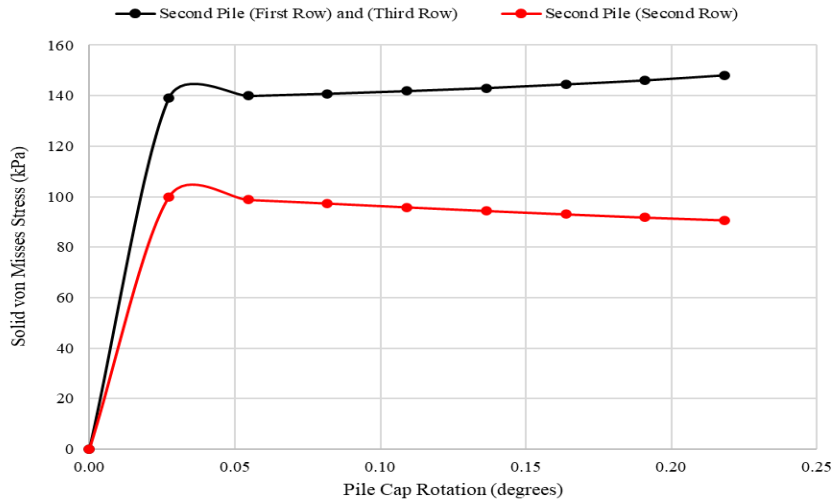


Figure 43: Stress development at the pile base of group G3x3 under torsion.

## 7 CONCLUSIONS

A numerical parametric investigation was presented in this manuscript, where the investigation of the stress level development of different pile foundations was performed. According to the numerical findings, the following conclusions can derive:

- As an imposed displacement is applied to a pile grouping, a base reaction develops in the soil medium that is proportional to the imposed horizontal displacement at the pile cap. The base reaction is not only directly proportional to the imposed displacement, but also to the number of piles in the grouping. Increasing the pile group size results in higher lateral resistance. The orientation of the pile grouping with respect to the applied load or displacement also influences the lateral resistance of the pile foundations. According to the parametric investigation, it was found that the pile groups with a longer group length in the direction of the applied force or displacement will have higher lateral resistances.

- Stress levels at the base of a single pile foundation are usually higher than the stresses surrounding the mid-height of the pile. This is predominantly caused by the distribution of bearing stress at the base of the pile which is a result of the applied load. There are high increases in the SVM stresses at the soil surface during the early loading stages of imposed displacements followed by a point where the stress magnitude remains constant. At the mid-height of the pile, there is little to no increase in the SVM stress levels, however, this effect changes when piles are grouped.

- For grouped pile foundations the soil that surrounds the leading pile reaches maximum stress and plateaus quite rapidly when compared to subsequent piles in the group. The trailing piles in the group have soil-stress development curves that are almost parallel to each other. This is attributed to the deformation that develops during the displacement control analysis that is controlled by the geometry of the foundation system.

- When investigating the soil that surrounds the piles at the mid-height of the pile foundation, the stress around the individual piles in the group gradually increases but does not reach the ultimate compressive resistance of the soil. It was found that the leading pile in the group has a higher soil-stress increase rate than the subsequent piles. The trailing piles in the group have soil-stress development curves that are relatively similar with the last pile having a slight initial decrease followed by an increase in stress levels. This phenomenon is attributed to the overall rotation of the foundation system due to the horizontal displacement of the pile-cap.

- Stresses in the soil around the base of the leading pile increase until the ultimate compressive force is reached. The middle pile(s) derive a steady decrease in soil-stress levels in the front soil domain of the pile. The last pile within the group experiences a rapid decrease in soil stress immediately followed by a rapid increase in the stress levels. Movement of the pile in the positive z-direction (uplift) and total rotation of the system causes a decrease in soil stress. Whereas the increase in stress at the pile base occurs when the rotation of the pile system is resisted by an increasing bearing stress in the soil surrounding the last pile

- The leading pile in a foundation system experiences relatively large vertical displacements due to the vertically imposed static load (superstructure loads) and the clockwise rotation of the foundation system. The soil surrounding the leading and second piles forces a rotation that pushes the piles downwards, whereas the soil around the trailing pile experiences heave. If this rotation were to become excessive, it would cause the pile system to fail either by a failure of the pile cap, bending and shear of the pile which occurs due to

reinforcement rupture, or concrete crushing due to excessive compression and shear deformation.

- Stress regions in the soil surrounding pile foundations were found to overlap, which may result in the failure of the soil if these levels reach a critical point. Therefore, the minimum spacing between piles should always be implemented during design.
- Soil-foundation interaction has a significant effect on the lateral resistance of the pile groupings. Numerical investigations are crucial as the knowledge obtained from these investigations gives insight into the interaction between the structure and the soil, and how the stress regions form around foundations. The implementation of 3D detailed modeling could lead to a reduction in the occurrence of structural failures and thus safer and more sustainable designs.

## REFERENCES

[1] Tominaga, K., Yamagata, K., Kishida, H., Horizontal displacement of soil in front of laterally loaded piles, *Soils and Foundations*, 1983.

[2] Ashour, M., Norris, G., Pilling, P., Lateral loading of a pile in layered soil using the strain wedge model, *Journal of Geotechnical and Geoenvironmental Engineering ASCE,* 1998.

[3] Patra, N., Pise, P., Ultimate lateral resistance of pile groups in sand, *Journal of Geotechnical and Geoenvironmental Engineering ASCE,* 2001.

[4] Egbert, J., Garrett, B., Jensen, D., Olsen, K., Olsen, R., Rollins, K., Pile spacing effects on lateral pile group behavior, *Analysis Journal of Geotechnical and Geoenvironmental Engineering ASCE,* 2006.

[5] Otani, J., Pham, K., Sano, J., Investigation of failure patterns in sand due to laterally loaded pile using X-ray CT, *Soils and Foundations,* 2006.

[6] Gravett, D. Z., Markou, G., State-of-the-art investigation of wind turbine structures founded on soft clay by considering the soil-foundation-structure interaction phenomenon - Optimization of battered RC piles, *Engineering Structures*, 2021.

[7] Markou, G., Papadrakakis, M., Accurate and Computationally Efficient 3D Finite Element Modeling of RC Structures, *Computers & Concrete*, 12 (4), pp. 443-498, 2013.

[8] Markou, G., Computational performance of an embedded reinforcement mesh generation method for large-scale RC simulations, *International Journal of Computational Methods*, 12(3), 1550019-1:48, 2015.

[9] Markou, G., Mourlas, C., Bark, H., Papadrakakis, M., Simplified HYMOD Non-Linear Simulations of a Full-Scale Multistory Retrofitted RC Structure that Undergoes Multiple Cyclic Excitations – An infill RC Wall Retrofitting Study, *Engineering Structures*, 176, pp. 892–916, 2018.

COMPDYN 2023
9th ECCOMAS Thematic Conference on
Computational Methods in Structural Dynamics and Earthquake Engineering
M. Papadrakakis, M. Fragiadakis (eds.)
Athens, Greece, 12-14 June 2023

# FRAGILITY CURVES FOR BRIDGES SUBJECTED TO THREE-DIMENSIONAL SEISMIC ENVIRONMENTS

**Jimena Rosas[1], Juan M. Mayoral[1*], and Mauricio Anaya[1]**

[1] Institute of Engineering National University of Mexico, Mexico City, Mexico

*email: JMayoralV@iingen.unam.mx

## Abstract

*Bridges built on soft soils, such as highly compressible plastic clays, may present a greater seismic vulnerability due to the low shear strength, high compressibility, low stiffness, small damping increment with shear strain, and high plasticity index, which can lead to large amplifications of the seismic movements. These factors entail a greater probability of experiencing failures in the foundation or structure, which result in the loss of functionality and interruption of the transport network. Therefore, the design of urban bridges built on soft soils and located in densely populated cities requires using numerical models to establish the probability of reaching or exceeding a given damaged state in a seismic event. This paper presents a vulnerability assessment of an urban bridge built on the typical soft soils found in Mexico* City. *The evaluations were carried out considering both normal and subduction fault events expressed in uniform hazard spectra for several return periods (i.e., 125, 187.5, 250, 362.5, 475, 1475, and 2475 years), assuming a three-dimensional seismic environment. Site response analyses and site-specific numerically derived fragility curves were used to assess the critical supports probability of reaching or exceeding a given damage state. The system's seismic response was characterized using a series of three-dimensional numerical models developed with the software FLAC3D. The effect of both soil conditions and ground motion characteristics on the soil-structure system response was accounted for in the analyses. The damage index was defined in terms of earthquake-induced transversal, longitudinal, and vertical upper deck displacements associated with column cracking and potential loss of support of the upper deck beam. The vulnerability of the analyzed bridge was established.*

**Keywords:**
Damage in bridges
Soil-structure interaction
Fragility curves
Damage index

## 1 INTRODUCTION

The failures of bridges and urban overpasses during earthquakes [1-10] have demonstrated the importance of defining an adequate approach to evaluate and improve the performance of these systems against extreme events.

Fragility curves have been developed using two-dimensional seismic environments with frequency domain analysis [11,12], without considering the effect of vertical ground motion on the seismic response of the system. Limited studies have developed dynamic analyzes for bridges integrating the vertical ground motions without considering the effect of soil-foundation-structure interaction, site effects and frequency content [13-16]. In this regard, it has been seen that the use of three-dimensional seismic environments realistically considers the behavior of the structures. In addition, taking into account the vertical component of movement implies inducing changes in the magnitude of the axial load of structural elements, which is a factor that determines their capacity [17, 18].

For seismic design, the vertical component acceleration has been considered as a fraction of the magnitude of horizontal movement. Rosenblueth (1975) [19] identified that the relationship between the vertical and horizontal components is not constant and depends on the structure period. Newmark (1979) [20] determines that the vertical component should be estimated as 2/3 of the peak value of the horizontal component of movement. In turn, Bozorgnia (1995) [21] observed that the main characteristic of the Loma Prieta (1989) and Taiwan (1999) earthquakes was the V/H relationship since it was notably exceeded with a value much higher than 2/3, so it is shown that the relationship between the vertical and horizontal movement V/H depends on the distance to the place where the earthquake originated.

Currently, there are no seismic fragility curves for bridges that consider the three-dimensional seismic environment and soil-foundation-structure interaction in soft soils like those found in Mexico City. The fragility curves derived from this research work will be based on the PGA, which will be applied in the evaluation of bridges located on soft soils.

## 2 METHODOLOGY

The proposed methodology (figure 1) consists of five main stages: 1) selection of the site study, 2) characterization of the seismic environment in terms of uniform hazard spectra, UHS. In our case study, synthetic acceleration time histories were developed for normal and subduction events considering seven return periods, 3) identification of failure modes and damage intervals for the most common types of bridges built on soft soils. For this case study, the damage index was considered in terms of longitudinal, transversal, and vertical displacements of the pier induced by the earthquake, which are associated with column cracking and loss of support of the upper deck of the bridge, 4) generation of three-dimensional numerical models of finite differences to simulate and evaluate the effects of the soil-foundation-structure seismic interaction and, 5) generation of fragility curves to assess the probability that the critical supports reach or exceed a given damage state, through a parametric study for different return periods.

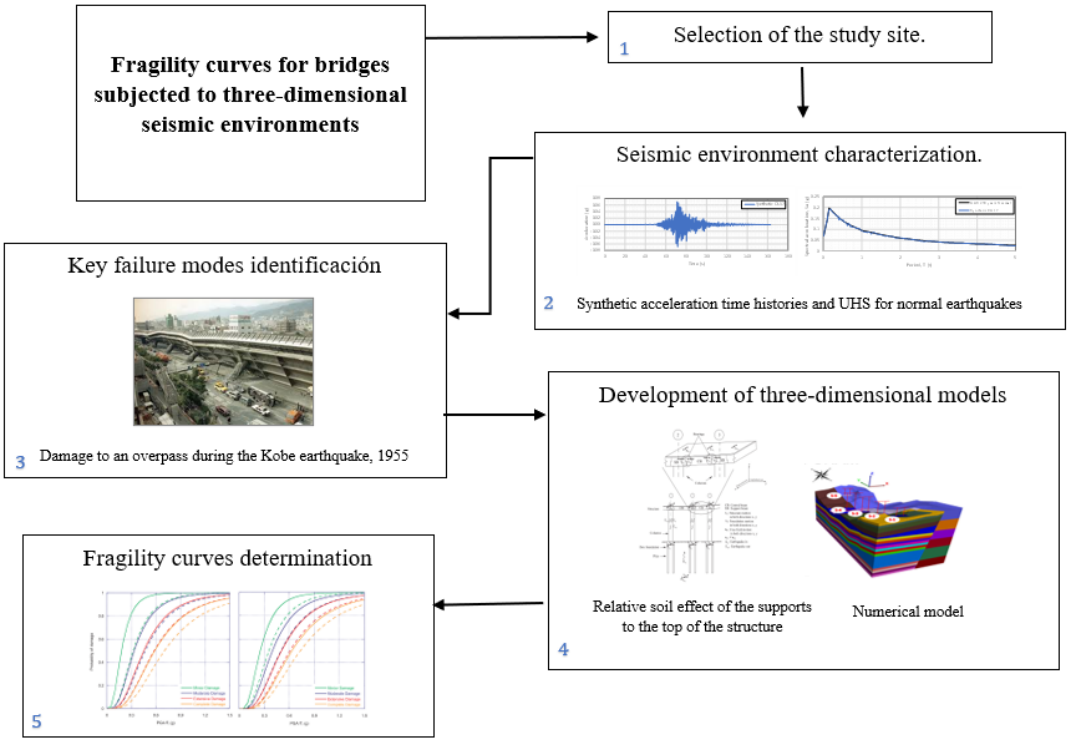


Figure 1: Proposed methodology to develop fragility curves for bridges. (Modified from [11]).

## 2.1 Derivation of fragility curves

Fragility curves were developed for the longitudinal, transversal, and vertical directions using a typical bridge typology of Mexico City. The different ground motions depend on amplitude, frequency content, and duration. The damage level was estimated in terms of the maximum lateral displacement of the column normalized by its average height, and it is related to the peak ground acceleration in the free field, $PGA_{ff}$. Equation 1 calculates the probability of reaching or exceeding different damage states for a ground motion level. Each fragility curve is characterized by a mean value of soil movement and an associated dispersion factor (lognormal standard deviation). Ground motion is estimated in terms of the peak ground acceleration, PGA, or spectral acceleration, $S_a$, and ground failure is quantified in terms of permanent ground deformations, PGD [22].

$$P_f\left(ds \geq ds_i \middle| PGA_{ff}\right) = \emptyset\left[\frac{1}{\beta_{tot}} In\left(\frac{PGA_{ff}}{PGA_{ffmi}}\right)\right] \quad (1)$$

where $P_f(\cdot)$ denotes the probability of reaching or exceeding a particular damage state, *ds*, for a given seismic intensity level defined by the seismic intensity measure (i.e., $PGA_{ff}$), Φ is the standard cumulative distribution, $PGA_{ffmi}$ is the median threshold value of the earthquake intensity measurement required to cause the i-th damage, and $\beta_{tot}$ is the total logarithmic standard deviation.

This last parameter is estimated from the following expression $\beta_{tot} = \sqrt{\beta ds^2 + \beta C^2 + \beta D^2}$, where $\beta_{tot}$ includes three sources of uncertainty: the definition of damage states (βds), the response and resistance (capacity) of the element (βC), and the variability in the earthquake input motion (demand) (βD).

Following the HAZUS [23] approach, βds is set equal to 0.4, βC is considered equivalent to 0.4 as presented by Franchetti et al. [4], and βC is calculated based on the variability of the different ground motions. The median threshold value of the seismic parameter, mi, is obtained

for each damage state as a function of the evolution of the damage with the increase in the earthquake's intensity.

Based on the criteria shown by Franchetti [4] and considering the damage states proposed by Jin-Hak [24], five different damage states were established. These damage states are none, ds1, slight/minor, ds2, moderate, ds3, extensive, ds4, and complete, ds5.

### 2.2 Damage index and damage states

Slight bridge damage, ds2, is identified by the appearance of minor cracks and detachments in the abutment, cracks in the abutment key, little detachments in the hinges, a minor detachment in the column, or by minor cracking in the spine. Moderate damage, ds3, is defined by any column that shows shear cracks, moderate movements in the abutment (<2"), connections that have broken shear keys or bent bolts, bearing failure, etc. Extensive damage, ds4, is seen for any column that degrades short of collapse (shear or flexural failure), significant residual movement at connections, vertical displacement at the abutment, differential column displacements, and settlements. Complete damage, ds5, is defined by any column that collapses and the connection loses all bearing support, which can lead to the imminent collapse of the deck or tilting of the sub-structure due to foundation failure.

## 3 CASE STUDY

The case study was located in the soft soil of Mexico City, where it is common to find highly compressible plastic clays. The typology of this overpass is similar to the Viaducto Bicentenario and the North and South Urban Highways of Mexico City [25]. These bridges are single-deck prestressed concrete precast structures with bearing surfaces ranging from 2 to 6 lanes.

The overpass typology comprises hollow central beams with a trapezoidal section 40 m long, precast in high-resistance prestressed concrete, and on which lies a 9 m wide platform of the same material. Above the platform, a structural firm forms a rigid diaphragm and increases the resistance of the same platform, and the asphalt layer acts as a rolling surface (figure 6a).

In the same way, the 12 m high column has a hollow rectangular section, it is a precast element of high-resistance prestressed concrete. The union of the column and the bridge platform is connected with a head made of the same material as that of the column. In this way, all the elements are structurally attached.

The support foundation is made up of a compensated reinforced concrete square box placed (width 12.5 m) at a depth of 6 m. The cushion slab's top, bottom, and walls are 40 cm thick (figure 3). Below the foundation box are nine reinforced concrete piles, each 9 m long and with a square cross-section of 0.50 m on each side. Therefore, the total depth of the foundation is 15 m, contemplating the foundation box and the piles as shown in figure 6a. In this type of foundation, it is sought that the piles mitigate the settlements [26-28] improve the seismic design [29-31], and mitigate problems related to subsidence [32]. Both lie the offset box will distribute the load capacity of the substructure.

### 3.1 Soil profile

The bridge studied is located in the Lake Zone of Mexico City [33]. The study site was analyzed by Mayoral and Mosqueda [34].

Figure 2 shows the stratigraphic profile and the shear wave velocity distribution of the analyzed site. Typically, the stratigraphic profile in this area exhibits a desiccated clay crust on top, extending to a depth of 5.0 m, which is underlain by a layer of soft clay approximately 30.0 m thick, with interbedded lenses of sandy silts and silty sands. Beneath the clay is a layer 5.0 m thick, on average, of very dense sandy silt, which rests on a layer of rigid clay that descends to a depth of 40.0 m. Below this elevation is found a competent layer of very dense sandy silt.

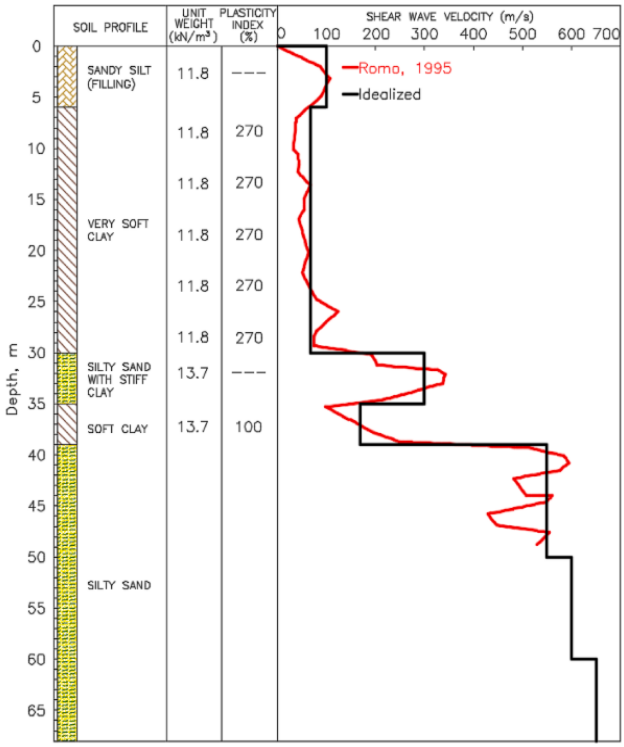


Figure 2: Soil profile and shear wave velocity distribution of the analyzed site.

Normalized modulus degradation and damping curves for sands were estimated by Seed and Idriss [35]. To characterize the degradation of the stiffness and the increase in damping of the clays during the seismic event, the Gonzalez and Romo [36] model was used, see figure 3. The shear wave velocity distribution was obtained by Seed et al. [37] using the down-hole and P-S suspension logging techniques and is also included in figure 3.

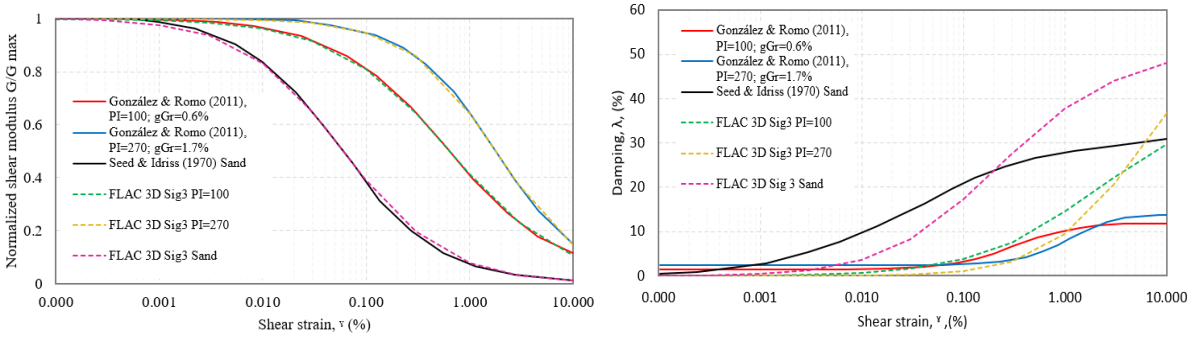


(a) (b)

Figure 3. Normalized (a) shear stiffness degradation, $G/G_{max}$, and (b) damping λ curves.

## 3.2 Seismic environment

The seismic hazard of Mexico City is controlled by interplate earthquakes along the subduction zone on the Pacific coast, such as the September 19, 1985 earthquake; as well as intra-plate earthquakes in the subducted Cocos plate [5, 32].

The seismic environment was established through uniform hazard spectra developed for seven return periods considering normal and subduction events. The soil-foundation-bridge seismic interaction was analyzed with six ground motions, as shown in Table 1.

| Seismo-genic Zone | Earthquake name | Location | Year | Moment magnitude [Mw] | Epicentral distance, Ed [km] | PGA [g] | Duration [s] |
|---|---|---|---|---|---|---|---|
| Normal | Umbria | Umbria Marche, Italy | 1998 | 4.8 | 10 | 0.223 | 40 |
| | Montenegro | Montenegro, Yugoslavia | 1979 | 6.9 | 21 | 0.251 | 48 |
| | CU17 | Puebla, Mexico | 2017 | 7.1 | 122 | 0.059 | 281 |
| Subduc-tion | CU85 | Michoacan, Mexico | 1985 | 8.1 | 419 | 0.033 | 73 |
| | Chile | Maule, Chile | 2010 | 8.8 | 109 | 0.638 | 120 |
| | Japan | Honshu, Japan | 2011 | 9 | 283 | 0.939 | 300 |

Table 1: Ground motions used in the analysis.

Synthetic ground motions were developed so that their 5% damped response spectrum reasonably matches the design response spectrum, using the method proposed by Lysmer [38], and modified by Abrahamson [39]. In this way, the signals induced in the three-dimensional model of the bridge represent a realistic design condition for the site.

According to Newmark [20], horizontal accelerations were considered complete, and 60 and 30% were in the vertical component of movement for normal and subduction earthquakes, respectively.

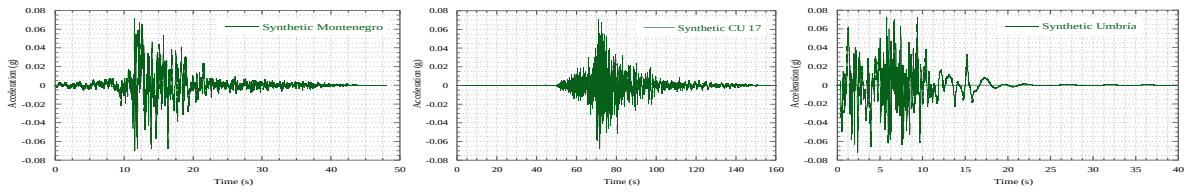


(a)

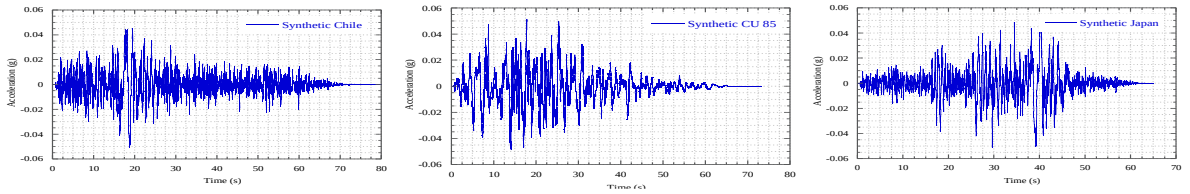


(b)

Figure 4: Synthetic time histories, for (a) normal, and (b) subduction events for a return period of 250 years.

The adjusted synthetic acceleration time histories for the normal and subduction earthquakes for TR=250 years are shown, respectively, in figure 4. The acceleration time histories were adjusted for each earthquake event and each return period (125, 187.5, 362.5, 475, 1475, and 2475 years) considered in the analysis (figure 5).

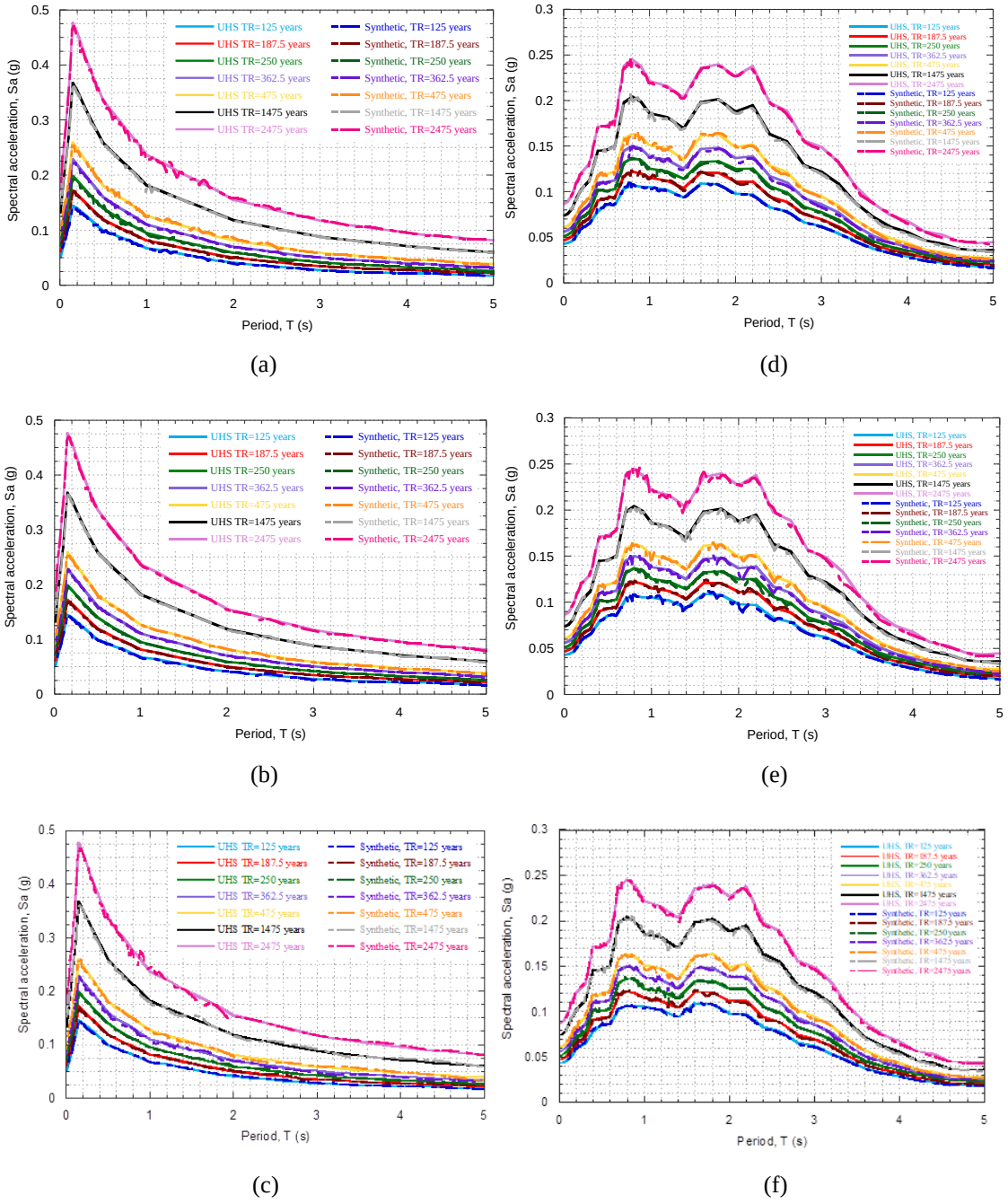


Figure 5: Uniform hazard spectra and adjusted ground motion response spectra for normal and subduction events: (a) CU 17, (b) Montenegro, (c) Umbria, (d) Chile, (e) CU 85 y (f) Japan.

## 3.3 Numerical model

To evaluate the seismic response of the system, a series of three-dimensional finite difference numerical models were developed using the FLAC3D software [40] considering the non-linearity of the soil in clayey materials.

A non-linear elastic behavior model was used, which tries to characterize the transient ground response in each load cycle as a function of the evolution of shear strains during ground shaking, rather than the steady state response established in the resonant column and cyclic triaxial test, from which modulus degradation and damping curves (figure 3). The free field

boundaries implemented in FLAC3D were used along the edges of the model, to avoid energy reflexing at the model edges, and represent free field conditions.

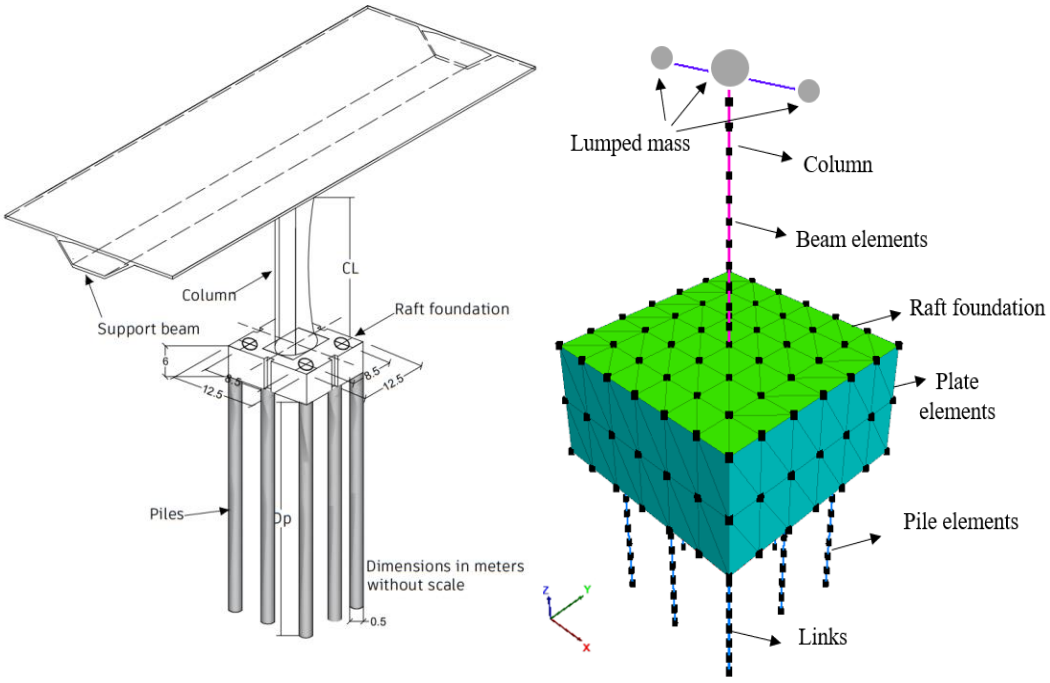


Figure 6: Schematic representation of (a) urban overpass y (b) three-dimensional model of finite differences.

The soil-structure system was divided into three stages: soil, foundation, and structure. The structure was modeled with three-dimensional beam elements and lumped masses, a foundation with plate elements, and piles with three-dimensional pile elements, which take into account the effects of diameter and the interaction between the pile and the surrounding soil (figure 6b).

### 3.4 Site response analyses

Initially, the free field condition was established from the results obtained from the one-dimensional analysis using the SHAKE software [41].

The free field boundaries implemented in FLAC$^{3D}$ were used along the edges of the model, and a flexible base was considered at the bottom.

To consider the variation of the modulus stiffness degradation with the shear strain during the seismic event, the "Sig3" hysteretic model available in FLAC$^{3D}$ [38] was used. The free field finite difference model is shown in figure 7. This model considers an ideal soil, in which the stress depends only on the deformation and not on the number of cycles. So, an incremental constitutive relationship of the degradation curve can be described by $\tau_n/\gamma = G/G_{max}$, where $\tau_n$ is the normalized shear stress, $\gamma$ is the shear strain, and $G/G_{max}$ the normalized secant modulus. The Sig3 model is defined by equation 2.

$$\frac{G}{G_{max}} = \frac{a}{1+\exp\left(-\frac{L-x_0}{b}\right)} \tag{2}$$

where L is the logarithmic deformation defined as L = log10 (g), and the parameters a, b and $x_0$, used by the Sig3 model, were obtained through an iterative approach, in which the modulus degradation curves were fitted with the model equations. The corresponding damping is given directly by the hysteresis loop during cyclic loading. For the cases studied herein, the parameters "a", "b" and "$x_0$" vary from 1 to 1.0035, -0.428 to -0.0559 and, 0.250 to -1.222, respectively.

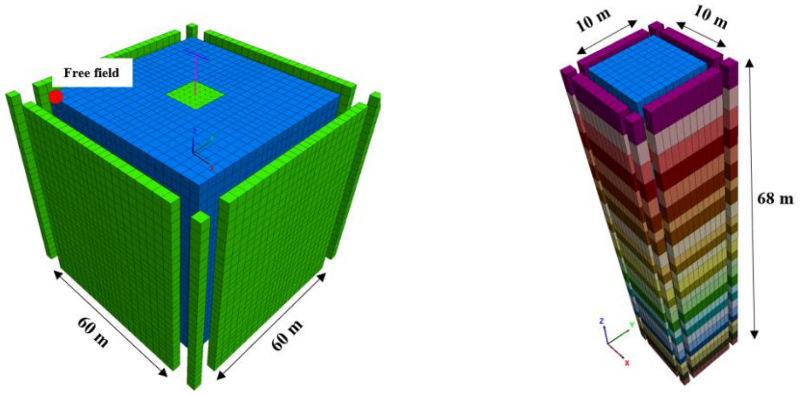


(a) (b)

Figure 7: Three-dimensional finite difference model, and soil column finite difference model.

Numerical distortion of the propagating wave can occur in a dynamic analysis depending on the modeling conditions. Both the input wave's frequency content and the system's wave velocity characteristics will affect the wave transmission's numerical precision. These lateral limits should be placed at sufficient distances to minimize propagating wave distortion and achieve free field conditions. For this case, the recommendation of Kuhlemeyer and Lysmer (1973) [38] was considered, where for an accurate representation of the transmission of waves through a model, the size of the spatial element, Δl, should be smaller. to one-fifth of the wavelength associated with the highest frequency component of the input wave containing appearing energy, fmax (for example, $\Delta l \leqslant \lambda/5$). In this case, the smallest average shear wave velocity Vs of the studied site in the soft clays ranges between 70 and 100 m/s, as shown in figure 3 and the highest significant frequency of excitation where the energy is concentrated is around 4.6 Hz. Therefore, the wavelength varies between 15 and 21 m, so it is appropriate to consider an Δl of 3 m. Models developed by Mayoral (2015) [42] have shown good agreement between finite difference models developed with FLAC3D and SHAKE for low to moderate levels of movement, using meshes with similar element sizes.

### 3.5 Soil-foundation-structure seismic interaction

The connection between the foundation box and the piles was considered embedded, although in practice the union of these two elements is at a joint, as can be seen in figure 6b. Said connection is designed to transmit loads axially to the pile and avoid perforation of the bottom slab. The characteristics of the elements for modeling the bridge are presented in Table 2.

| Element | Model | Young's modulus (GPa) | Poisson ratio | Unit weight ($kN/m^3$) |
|---|---|---|---|---|
| Bridge superstructure | Beam elements | 31.82 | 0.30 | 24 |
| Square box | Plate elements | 22.14 | 0.20 | 24 |
| Piles | Pile elements | 24.25 | 0.20 | 24 |

Table 2: Properties of the structural model.

For the dynamic analysis, the synthetic ground motions were applied in three directions x, y, and z (longitudinal, transversal, and vertical), considering 100% of the movement in the horizontal components and 60% and 30% in the vertical direction for normal earthquakes and subduction earthquakes, respectively.

For this case study, the damage index, DI see table 3, was established based on the lateral displacement of the column normalized by an average column height (i.e., 12 m), and in turn, in table 4, damage indices are shown for a two-dimensional seismic event [11].

| Damage state (dsi) | ds1. None | ds2.Minor/ Slight | ds2. Moderate | ds4. Extensive | ds5. Complete |
|---|---|---|---|---|---|
| Range of damage index | DI ≤ 0.007 | 0.007< DI ≤ 0.015 | 0.015< DI ≤ 0.025 | 0.025< DI ≤ 0.050 | DI> 0.050 |

Table 3: Damage state estimation for the urban overpass

| Damage state (dsi) | ds1. None | ds2.Minor/ Slight | ds2. Moderate | ds4. Extensive | ds5. Complete |
|---|---|---|---|---|---|
| Range of damage index | DI ≤ 0.0025 | 0.0025< DI ≤ 0.0035 | 0.0035< DI ≤ 0.0045 | 0.0045< DI ≤ 0.006 | DI> 0.006 |

Table 4: Damage state estimation for the urban overpass [11]

Figures 8 and 9 show the evolution of DI concerning the peak ground acceleration in free field, $PGA_{ff}$, in the transverse and longitudinal directions, along with an average exponential regression that fits the data set. Meanwhile, figure 10 show the fragility curves for normal and subduction earthquakes in both directions (transversal and longitudinal).

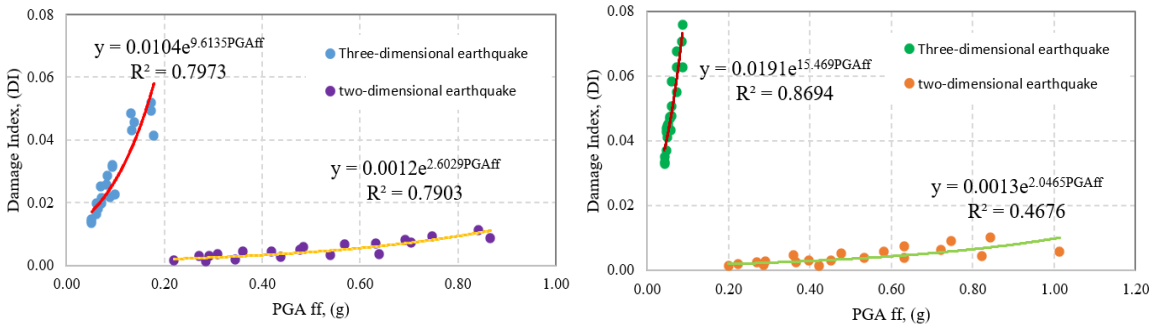


(a) (b)

Figure 8: Evolution of the DI (a) normal earthquakes (b) subduction earthquakes (Transversal direction).

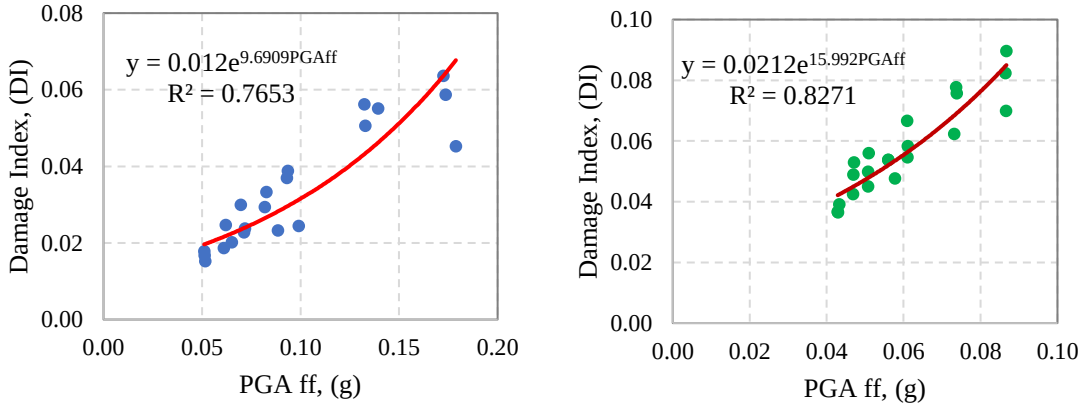


(a) (b)

Figure 9: Evolution of the DI (a) normal earthquakes (b) subduction earthquakes (longitudinal direction).

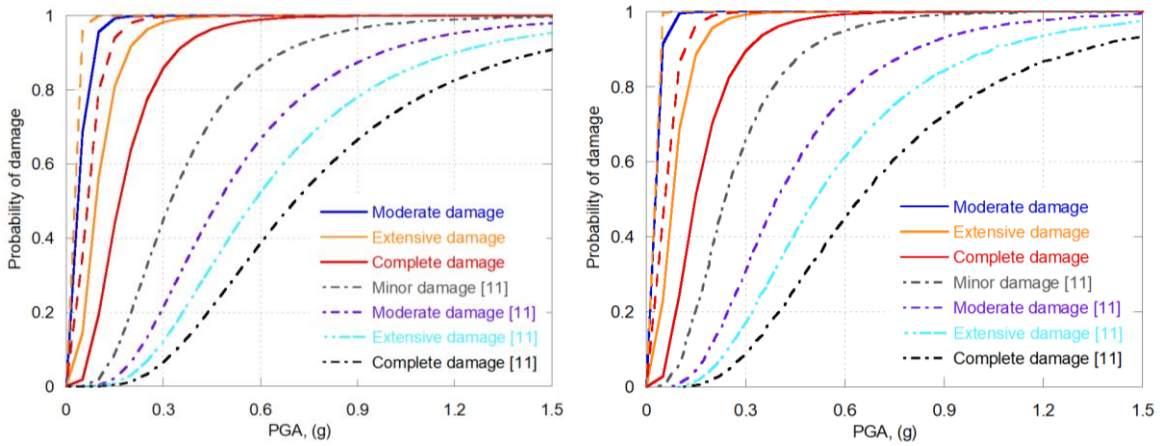


(a) (b)

Figure 10: Fragility curves for normal (solid lines) and subduction (dashed lines) events for (a) transversal and (b) longitudinal direction.

The fragility curves generated were compared with those obtained by Mayoral et al., [11], which were developed in rigid soils and with two-dimensional seismic environments. It can be observed that the probability of reaching a damage state is higher considering a three-dimensional seismic environment. Likewise, the probability of reaching a damage state increases due to the properties of soft soils that induce increased displacements of the structure, partially caused by the rocking effect. Therefore, the fragility curves are presented starting from a moderate damage state for normal and subduction earthquakes, respectively.

Comparing the two fragility curves, it can be seen that the greatest damage occurred in the bridge transversal direction (figure 11a). Complete damage is achieved with a PGA greater than 0.25 g for subduction earthquakes (dashed line) and 0.50 g for normal earthquakes (solid line).

Complete damage state was achieved first for subduction earthquakes due to most of the energy is concentrated in periods around 1 and 2 s, leading to large amplifications and lengthening of the duration of ground movements [33, 43] caused by high plasticity clay deposits. Likewise, a modification of the frequency content is produced, which in turn leads to a resonance effect, between the movements of the ground and the structure, as occurred during the Mw 8.1 09/19/1985 subduction fault earthquake, where the predominant period of the soil was found between 0.9 and 1.2 s, which coincides with the period of the structure (1.01 s), resulting

in a resonance effect. This was also accentuated due to the concentration of energy in the high frequency range (low period range of 0.15–1.0 s) [44].

Currently, the construction regulations for Mexico City consider a return period of 250 years. This implies that the index damage for this return period is extensive for both normal and subduction earthquakes. On the other hand, major return periods (362.5, 475, 1475, and 2475 years) present a complete damage state for normal and subduction events.

## 4 CONCLUSIONS

Fragility curves were generated for urban bridges located in densely populated urban areas, through a series of three-dimensional numerical models considering the site response, soil-foundation-structure interaction effects, and frequency content. It was observed that the probability of reaching a damage state is greater with the use of a three-dimensional seismic environment, because vertical movement increases the level of response and the amount of damage on a bridge. According to the site-specific fragility curves developed in this article, and the results obtained from the probabilistic analysis of site response, as well as the probability of reaching or exceeding a given damage state of the urban overpass, it can be noted that the highest probability of failure is reached with subduction events. Likewise, the probability of reaching a damage state increases due to the properties of soft soils that induce increased displacements of the structure, partially caused by the rocking effect.

## REFERENCES

[1] M. Torres y M. Rodríguez, Capacidad de desplazamiento lateral de columnas para puentes de concreto reforzado y presforzado en zonas sísmicas. *XIX Congreso Nacional de Ingeniería Sísmica*, Veracruz, México, 2013.

[2] J. Bray y D. Frost, *Geo-engineering reconnaissance of the 2010 Maule, Chile earthquake*. Report of the NSF sponsored GEER association team No. GEER-022, 2010.

[3] D. Rivera y R. Meli, Procedimiento de diseño sísmico de columnas de puentes urbanos de concreto reforzado, *Revista de Ingeniería Sísmica*, nº 79, pp. 1-23, 2008.

[4] P. Franchetti, M. Grendence, C. Modena, D. Slejko y F. Bergo, Evaluation of seismic risk: application to bridges and viaducts in veneto (Italy), 13th *World Conference on Earthquake Engineering*. Vancouver, B. C., Canada. August, nº 2791, pp. 1-6, 2004.

[5] J. M. Pestana, R. B. Sancio, J. D. Bray, M. P. Romo, M. J. Mendoza, R. E. S. Moss, J. M. Mayoral Villa y R. B. Seed, Geotechnical engineering aspects of the June 1999 Central México earthquakes, *Journal Earthquake SPECTRA*, vol. 18, nº 3, pp. 481-499, 2002.

[6] R. Zelinski, *Post Earthquake Investigation Team Report for the Loma Prieta Earthquake*. California Department of Transportation. Division of Structures, Sacramento, Sacramento, 1994.

[7] M. Yashinsky, R. Oviedo, S. Ashford, L. Fargier-Gabaldon y M. Hube, *Performance of highway and railway structures during the February 27, 2010 Maule, Chile earthquake*, Maule, Chile, 2010.

[8] G. Housner, Competing against time. Report to Governor George Deukmejian from the Governor's Board of Inquiry on the 1989 Loma Prieta Earthquake. *Office of Planning and Research*, State of California, Mayo, p. 264, 1990.

[9] K. Kawashima , Damage of bridges resulting from fault rupture in the 1999 Kocaeli and duzce, Turkey earthquakes and the 1999 Chi-Chi, Taiwan earthquake, *Proceedings of Seismic Fault-induced Failures*, Tokyo, 2001, pp. 171-190.

[10] M. J. Priestley y Y. Uang, *Damage Analysis of Selected Freeway Bridges*, University of California, San Diego, Structural Systems Research, vol. 06, nº SSRP-94, 1994.

[11] J. M. Mayoral Villa, A. Badillo y J. M. Alcaráz Barranco, Vulnerability and recovery time evaluation of an enhanced urban overpass foundation, *Journal of Soil Dynamics and Earthquake Engineering*, vol. 100, nº ISSN 0267-7261, pp. 1-15, 2017.

[12] C. Gomez Soberon y I. Soria Rodriguez, Curvas de fragilidad para tres puentes carreteros típicos de concreto., Universidad Autonoma Metropolitana Azcapotzalco, Mexico., vol. 4, nº 2, pp. 15-11, 2013.

[13] A. J. Papazoglu y A. S. Elnashai, Analytical and field evidence of the damaging effect of vertical earthquake ground motion., *Journal Earthquake Eng Struct Dyn*, vol. 25, nº 10, pp. 1109-37, 1996.

[14] M. A. Saadeghvariri y D. A. Foutch, Dynamic behavior of R/C highway bridges under the combined effect of vertical and horizontal earthquake motions, Journal Earthquake Eng Struc Dyn , vol. 20, nº 6, pp. 535-49, 1991.

[15] C. P. Yu, Effect of vertical earthquake components on bridge responses., Ph. D. thesis, University of Texas at Austin, Austin., 1996.

[16] M. R. Button , C. J. Cronin y R. L. Mayes, Effect of vertical motions on seismic response of bridges., Journal Struct Eng, vol. 128, nº 12, pp. 1551-64, 2002.

[17] S. J. Jong, S. Abdollah, H. L. Do, C. Eunsoo y D. Reginald, Damage Assessment of older highway bridges subjected to three-dimensional ground motions: Characterization of shear-axial force interaction on seismic fragilities, Engineering Structures, vol. 87, pp. 47-57, 2015.

[18] E. Erduran y A. Yakut, Drift based damage functions for reinforced concrete columns, Computers & Structures, vol. 82, pp. 121-130, 2004.

[19] E. Rosenblueth y H. Contreras, Approximate design for multicomponent earthquakes, ASCE Journal of Engineering Mechanics, vol. 103, pp. 895- 911.

[20] N. M. Newmark y W. J. Hall, Earthquake spectra and design, Earthquake Engineering Research Institute, Berkeley, California, 1982.

[21] Y. Bozorgnia y N. Mansour, Characteristics of Free Field Vertical Ground Motion During the Northridge Earthquake, Earthquake Spectra, vol. 11, nº 4, pp. 515-525, 1995.

[22] K. Pitilakis, H. Crowley y A. M. Kaynia, SYNER-G:Typology Definition and Fragility Functions for Physical Elements at Seismic Risk, Springer.

[23] M. H. Hazus, Technical manuals, Washington, DC., 2004.

[24] Y. Jin-Hak, K. Sang-Hoon y K. Shigeru, PDF interpolation technique for seismic fragility analysis of bridges, Engineering Structures, vol. 29, pp. 1312-1322, 2007.

[25] M. J. Mendoza Lopez, E. Ibarra Razo, M. P. Romo Organista, M. Rufiar Jarquin, J. M. Mayoral Villa, W. P. Paniagua Zavala y E. Garces Camara, Pruebas de carga axial a compresión y extracción en pilas de cimentación instrumentadas del Viaducto Bicentenario, Estado de México, de XXV Raunion Nacional de Mecanica de suelos e ingenieria geotecnica., Acapulco,Guerrero, Mexico, 2010.

[26] M. J. Mendoza y G. Auvinet, The Mexico earthquake of September 19, 1985- behavior of biulding foundations in Mexico City, Journal, Earthq Spectra, vol. 4, nº 4, pp. 53-835, 1998.

[27] G. Auvinet, Seismic response of subsoil and building foundations in Mexico City (1985-2017), ISSMGE Touring Lecture, 2018.

[28] N. Riordan, A. Canavate, S. Kumar y F. Ciruela, Analysis of Friction Piles in Consolidating Soil., de NUMGE 2018 9th. European Conference on Numerical Methods in Geotechnical Engineering, 2018.

[29] M. Mendoza, Comportamiento de una cimentacion con pilotes de friccion, Ciudad de Mexico: Programa de maestria y doctorado en ingenieria, UNAM, 2004.

[30] J. M. Mayoral Villa y J. Ramirez, Site response effects on an urban overpass., Journal of Soil Dynamics and Earthquake Engineering, nº ISSN 0267-7261, 2011.

[31] J. M. Mayoral Villa y M. P. Romo, Seismic response of bridges with massive foundations, Journal of Soil Dynamics and Earthquake Engineering, vol. 71, pp. 88-99, 2015.

[32] J. M. Mayoral Villa, S. Tepalcapa, A. Roman, C. S. Mohtar y R. Rivas, Ground Subsidence and its implication on building seismic performance, Journal of Soil Dynamic Earthq Eng, vol. 126, 2019.

[33] J. M. Mayoral Villa y G. Mosqueda, Tunnelling and Underground Space Technology incorporating Trenchless Technology Research, Journal of Soil Dynamics and Earthquake Engineering, 2021.

[34] J. M. Mayoral Villa y G. Mosqueda, Seismic interaction of tunnel-building systems on soft clay, Journal Soil Dynamics and Earthquake Engineering, vol. 139, 2020.

[35] H. B. Seed y I. M. Idriss, Soil moduli and damping factors for dynamic response analysis, vol. 70, nº 10, 1970.

[36] M. P. Romo, Clay behavior, soil response and soil structure interaction studies in Mexico City, de Proceedings of the third international conference on recent advances in geotechnical earthquake engineering and soil dynamics, San Luis Missouri, USA, 1995.

[37] H. B. Seed, I. M. Idriss , J. Sun , A. Jaime y J. Lysmer, Relationships between soil conditions and earthquake ground motions, Journal Earthq Spectra, vol. 4, nº 2, pp. 687-730, 1988.

[38] J. Lysmer, Analytical Procedures in soil dynamics, University of California, vol. 29, nº ReportNo.EERC78, 1978.

[39] N. Abrahamson, State of the practice of seismic hazard evaluation, de International Conference on Geotechnical & Geological Engineering, Australia, 2000.

[40] I. C. Group, FLAC3D, fast Lagrangian analysis of continua in 3 dimensions.

[41] P. B. Schnabel, J. Lysmer y H. B. Seed, SHAKE: a computer program for earthquake response analysis of horizontally layered sites, College of Engineering, CA., 1972.

[42] J. M. Mayoral Villa, Seismic response of bridges with massive foundations, Soil Dynamics and Earthquake Engineering, vol. 71, pp. 88-99, 2015.

[43] J. M. Mayoral Villa, K. W. Franke y T. Hutchinson, The September 19, 2017 Mw 7.1 Puebla-Mexico city earthquake: Important findings from the field – Overview of Special Edition, Journal Soil Dynamics and Earthquake Engineering, vol. 123, pp. 520-524, 2019.

[44] J. M. Mayoral Villa, D. Asimaki, S. Tepalcapa, S. Wood, A. Roman, T. Hutchinson, K. Franke y G. Montalva, Site effects in Mexico City basin: Past and present, Journal, Soil Dynamics and Earthquake Engineering, vol. 121, pp. 369-382, 2019. O.C. Zienkiewicz, R.C. Taylor, *The finite element method, Vol. I, 4th Edition*. McGraw Hill, 1989.

COMPDYN 2023
9th ECCOMAS Thematic Conference on
Computational Methods in Structural Dynamics and Earthquake Engineering
M. Papadrakakis, M. Fragiadakis (eds.)
Athens, Greece, 12-14 June 2023

# EVALUATION OF SEISMIC SITE EFFECTS IN A REAL SLOPE THROUGH 2D FE NUMERICAL ANALYSES

**Annamaria di Lernia**[1], **Carmela Buono**[2] **and Gaetano Elia**[1]

[1] Department of Civil, Environmental, Land, Building Engineering and Chemistry (DICATECh),
Technical University of Bari
via Orabona 4, 70125 Bari, Italy
e-mail: {annamaria.dilernia, gaetano.elia}@poliba.it

[2] Sigma Ingegneria s.r.l.
via della Libertà, 201, 90143 Palermo, Italy
carmenbuono100196@gmail.com

## Abstract

*The seismic site effects are the result of wave amplification processes related to the topographic irregularities, the sequence of soil layers, the morphology of the stratigraphic contacts, the dynamic properties of the soils and the input motion features. These local effects may be responsible for damages to structures and infrastructures located in different portions of the urban area, as well as they may be the trigger for landslide instability processes. In the present paper, the numerical simulations of the site effects occurring in a real natural slope have been performed through 2D finite element (FE) linear visco-elastic analyses, aiming at investigating and quantifying the influence of both the topography and the buried stratigraphy on the seismic amplification at the ground surface. The considered case study is the western slope of Chieuti, in the south of Italy, location of a deep landslide instability mechanism mainly related to static actions. After an earthquake occurred in August 2018, a worsening of the landslide-related damages affecting buildings and roads has been observed, thus requiring further investigations on the effects of the dynamic loading. Therefore, a detailed seismic geotechnical model has been developed for this case study, based on a suite of in-situ investigations, including MASW and down-hole tests. The site response analyses have been conducted with reference to three longitudinal sections and one transversal section, crossing the crest of the hillslope. The numerical results are illustrated in terms of topographic and stratigraphic amplification factors, quantifying the effect of the slope topography and the buried stratigraphy, respectively. The results show that, for this specific case study, the stratigraphic effects are predominant with respect to the topographic ones, due to the strong subsoil heterogeneity characterizing the upper portion of the slope. However, topographic effects are relevant at the crest of the hillslope, inducing further amplification of the motion.*

**Keywords:** Seismic site response analysis, Topographic effect, Stratigraphic effect, Natural slopes, FE modelling

## 1 INTRODUCTION

It is well-known that the topographic irregularities, the sequence of soil layers, the morphology of the stratigraphic contacts and the dynamic properties of the soils, affecting the wave propagation processes, are responsible for seismic site effects [1–5]. The modification of the input motion due to the soil dynamic properties and the heterogeneity of the deposit is referred to as "stratigraphic amplification". It is related to the filtering processes of the seismic waves propagating through a medium of certain dynamic characteristics in terms of stiffness and dissipative capacity. The seismic motion may be also modified by the surface topography, giving rise to the so called "topographic amplification". These local effects may be responsible for damages to structures and infrastructures located in different portions of the urban area, as well as they may trigger or reactivate landslide instability processes [6–9].

The estimation of site effects represents a crucial issue, especially for old towns located on hilltops, characterized by urban aggregates of old masonry buildings, and for existing landslides which can be reactivated by earthquakes. In this context, an increase of the seismic demand due to topographic effects may be important in the assessment of the seismic risk of existing buildings in historical centers [10,11].

The numerical evaluation of stratigraphic effects is usually performed through one-dimensional (1D) simulations, implementing the sequence and the thickness of the soil layers and the dynamic properties of the soils [12–15]. The topographic effects are, instead, evaluated decoupling them from the stratigraphic effects, by comparing the results of two- or three-dimensional site response analyses, accounting for both stratigraphic and topographic amplification, with the output of 1D simulations, affected by the soil stratigraphy only. Numerous studies have been published in the literature on the effect of topographic amplification on the dynamic response of slopes [1,3,6,11]; most of them refers to parametric analyses of ideal case studies, assuming simplified site conditions [16–20].

In the present paper, site response analyses have been carried out through a two-dimensional (2D) FE modelling approach to investigate and quantify the influence of both the topography and the buried stratigraphy on the seismic amplification occurring at the ground surface along the western slope of Chieuti. Chieuti is a little historical hamlet in the south of Italy, location of a deep landslide instability mechanism mainly related to static actions, affecting the urban area on the crest of the hillslope [21,22]. After an earthquake of low intensity occurred on the 16$^{th}$ of August 2018, the landslide-related damages affecting buildings and roads have been observed to be aggravated, which has required a deeper investigation on the effects of the wave propagation processes into the slope.

The numerical simulations have been carried out with reference to a detailed subsoil model, developed on the basis of bespoke in-situ geotechnical and geophysical tests. The acceleration time history of the Montecilfone earthquake, recorded on the 16$^{th}$ of August 2018 at the Melanico-Santa Croce di Magliano station close to Chieuti, has been adopted in the simulations. The results have been interpreted separating the topographic effects from the stratigraphic ones, through the evaluation of appropriate amplification factors based on peak ground accelerations.

## 2 THE CHIEUTI CASE STUDY AND DYNAMIC CHARACTERIZATION

Chieuti (Foggia) is a small town located in the north of the Apulia region. Founded in the XV century, the old town is perched on a hilltop at 221 m a.s.l, characterized by a historic urban center with short masonry buildings and narrow alleys. The western side of the site, bounded by the Taverna stream to the north and the Fico stream valley to the west, is currently interested by an ancient landslide phenomenon, affecting the urban center since 1800 and

causing the collapse or demolition of several buildings suffering from important vertical downward displacements [21–23].

The spatial-temporal characterization of the ground displacement field has already allowed to identify the active retrogression of a progressive failure within the rear scarp of a large landslide [22]. In particular, the landsliding is characterized by multiple rotational mechanisms affecting two different bodies nested in the same toe along the Fico stream with a retrogressive evolution in time [21]. The genesis of the deep landsliding has been deemed to be related to geological processes, as demonstrated by FE hydro-mechanical simulations of the first failure corroborating the phenomenological interpretation. Indeed, the deep and retrogressive failure mechanism affecting the Chieuti area has been related to both the asymmetrical river valley erosion of the Bivento river and the surface erosion along the slope [23].

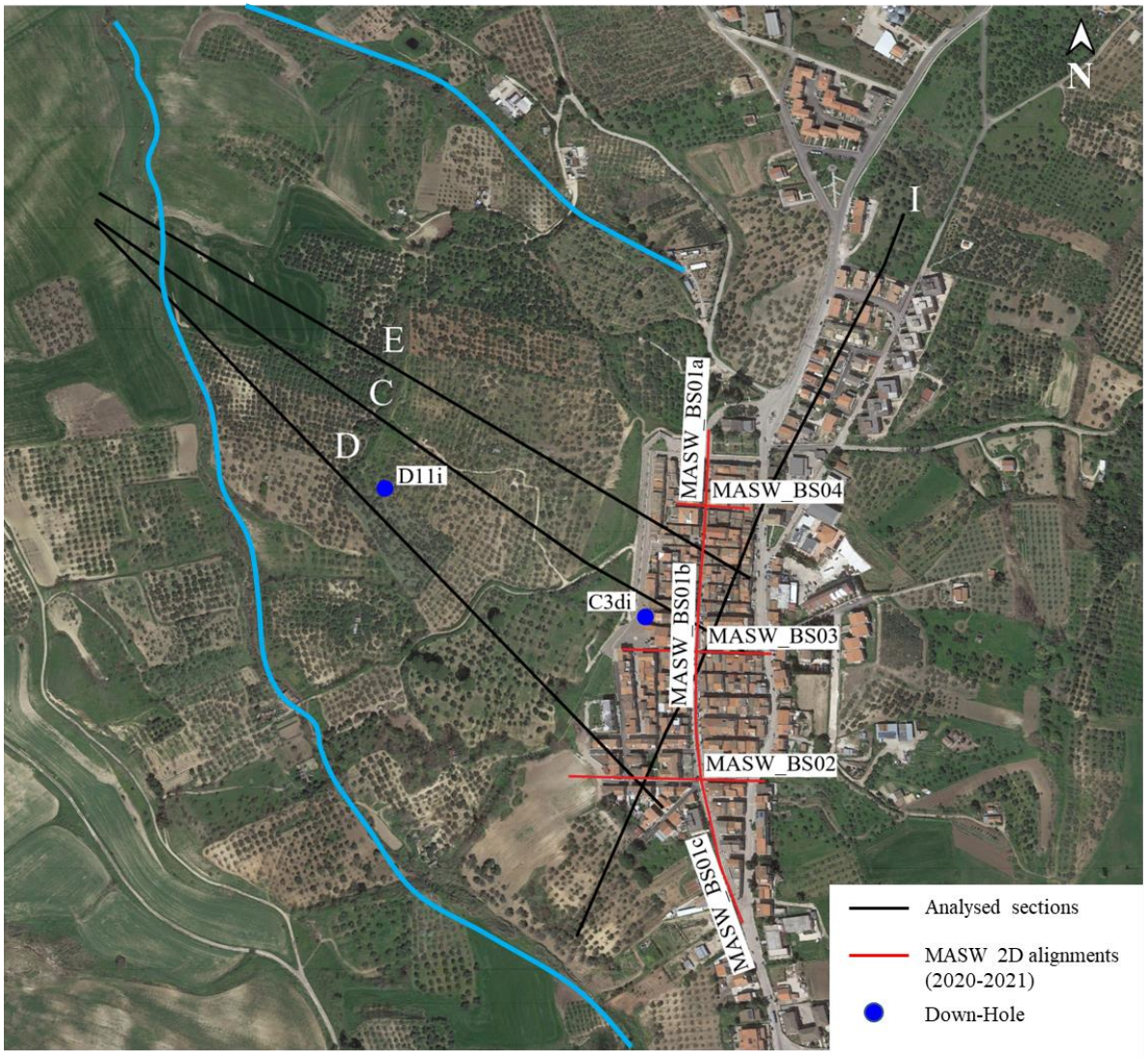


Figure 1: Orthophoto of the western slope of Chieuti and location of the in-situ geophysical tests.

From a seismic point of view, Chieuti is characterized by medium-to-high seismicity, due to the proximity to different strike-slip faults, such as the Apricena and Mattinata faults [24], which make the impact of earthquake events on slopes, buildings and infrastructures non-negligible. According to the Italian seismic hazard map [26], the Chieuti area is characterized by a PGA between 0.175g and 0.225g on the outcropping rock for a return period of 475

years. The analysis of the historical seismicity of Chieuti reveals that the site has been rarely struck by high intensity seismic events [25], among which the most important are the San Severo earthquake (30/07/1627), grade VII of the MCS, and the 2002 Molise earthquake, with 5.9 $M_w$.

The Chieuti hillslope is formed by a foredeep marine succession overlain by continental deposits [27,28]. The historical center is built above a top-hill thinner continental layer (*Campomarino Conglomerates* formation), made of gravel, silty, sandy and clayey intervals, deposited in an alluvial environment. The continental layer is underlain by the marine succession represented by the *Serracapriola Sands* and the *Montesecco Clay* formations. The *Serracapriola Sands* can be subdivided into two units, i.e. the lower silty-sandy unit and the upper sandy unit including local intercalation of gravel bodies, while the *Montesecco Clay* formation consists of grey marine clays with silty-sandy levels [21].

The geotechnical characterization of the slope soils has been based on the available in-situ and laboratory tests, carried out during several geotechnical campaigns, among which the last one has been conducted between December 2020 and March 2021 [21]. The analysis and the interpretation of the geotechnical characterization has allowed to identify four different materials corresponding to the sedimentary successions, i.e. Unit 1 representing the *Campomarino Conglomerates*, Unit 2a and Unit 2b associated to the upper sandy portion and the lower silty-sands portion of the *Serracapriola Sands* and Unit 3 representing the stiff marine clays belonging to the *Montesecco Clay* formation [21].

The dynamic subsoil characterization has been based on in-situ geophysical tests, including down-hole (DH) and seismic surface waves tests. Specifically, two DH tests have been carried out along the C3di (48 m deep) and D11di (70 m deep) boreholes, located within the town and in the middle of the western slope, respectively. Additionally, 2D Multi-channel Analyses of Surface Waves (MASW 2D) tests have been conducted along one longitudinal MASW_BS01 alignment and three transversal alignments, i.e. MASW_BS02, MASW_BS03 and MASW_BS04, crossing the urban center of Chieuti (Figure 1). The long MASW_BS01 test has been split along three consecutive alignments, named, from south to north, BS01c, BS01b and BS01a.

The joint interpretation of the DH and MASW 2D tests, supported by the stratigraphic information derived from the closest boreholes, has allowed to identify and to characterize the subsoil layers. The results of the DH tests are reported in Figure 2, together with the corresponding stratigraphic logs obtained from the analysis of the continuous coring performed in the C3di and C11p boreholes, the latter very close to the D11di down-hole test. Along the C3di borehole (Figure 2a), the first 18 m, where the Units 1 and 2a are encountered, are characterised by a gradual increase of velocity; the transition between the second and the third layer, i.e. Units 2a and 2b, is not significantly pronounced. This is probably due to the strong heterogeneity of the soil deposit in the upper portion of the slope, already recognised by other stratigraphic logs in the area. Along the D11di borehole (Figure 2c), the wave velocity profiles show an overall increasing trend with depth, except between 12.2 and 16.8 m of depth, where an inversion of wave velocity profile is observed at the sandy silt portion of the Unit 2b. This inversion might be associated either to the presence of inclusions of stiffer materials in the upper layer or to disturbance processes localised where the material becomes less stiff, likely due to the presence of a shear band at this depth.

Normalising the corresponding shear stiffness modulus $G_0$ profiles by the confining pressure $p'$ (Figure 2b, d), it can be observed that the soils in the D11di borehole are overall stiffer than those present along the C3di vertical. With reference to the D11di stratigraphic profile, the sandy member of the Unit 2b (between 7 and 12.2 m depth) is characterised by a ratio $G_0/p'$ significantly higher than the value evaluated along the C3di profile in the same layer

(between 18 m and 25 m). Moreover, the normalized stiffness of the silty member of Unit 2b alongside C3di (between 25 and 30 m depth) results to be higher than that obtained for the same soil layer in D11di (between 12.2 and 16.8 m depth). This indicates that, on one side, the sandy member of Unit 2b in the borehole D11di is significantly stiffer with respect to the underlaying silt member; on the other side, the silty member in D11di is particularly less stiff than the same material along the C3di profile. This circumstance might be justified by the concurrence of two effects, i.e. the strong lithological heterogeneity discovered between 7 and 12.2 m during the stratigraphic analysis and the possible presence of a shear band at a depth between 12.2 and 16.8 m, which contributes to reduce the stiffness of the material.

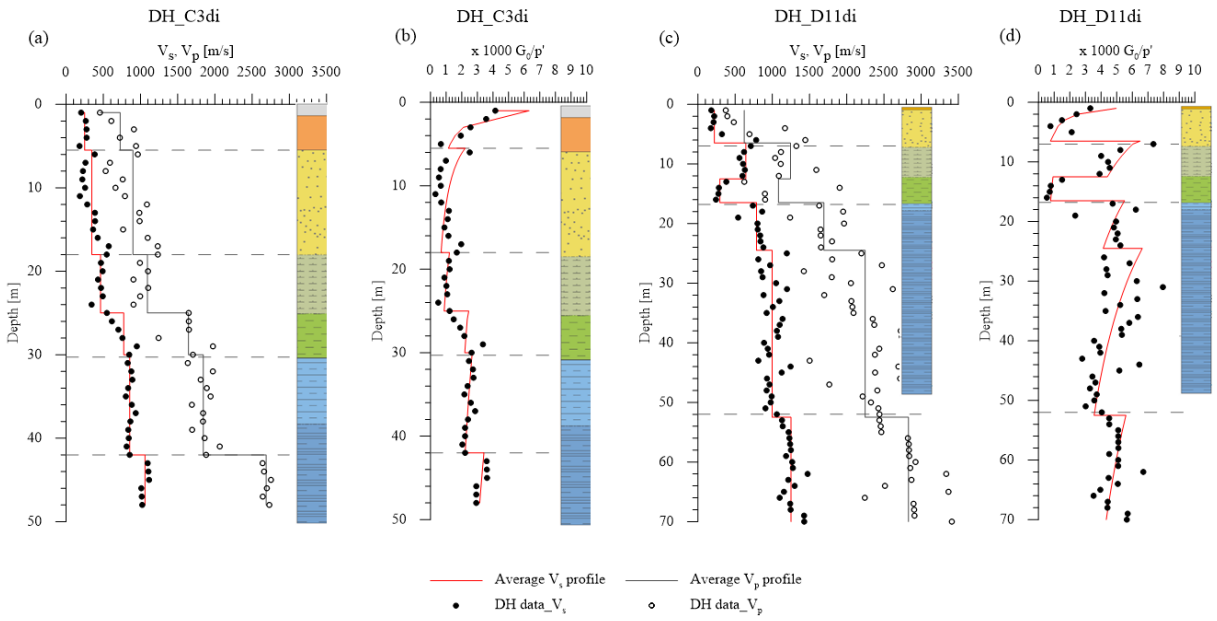


Figure 2: S- and P-wave velocity profiles and normalized shear stiffness modulus $G_0/p'$ along the (a, b) C3di and (c, d) D11di boreholes obtained from down-hole seismic tests.

The MASW 2D tests consisted in using multiple equally-spaced receivers, placed along linear survey alignments and acquiring signals from an active impulsive source, in order to obtain 7 or 15 shear wave velocity $V_s$ profiles along each section. The results of the MASW 2D elaboration are reported in Figure 3, together with the average $V_s$ profile for each alignment. The detailed analysis of the $V_s$ profiles highlights that the stiffness tends to increase with depth, starting from values of about 200 m/s, referable to the man-made material layer, and achieving values of about 800-1000 m/s for the deeper layers, coherently with the DH S-wave velocity profiles. Below the first layer, a material characterised by $V_s$ equal to 300-400 m/s can be detected, which is ascribable to the Unit 1, followed by a stratum of 400-500 m/s of $V_s$, associated to the sub-unit 2a. Below this, a material with $V_s$ of 600-700 m/s is encountered, referable to the Unit 2b, overlaying a soil layer characterised by S-wave velocity higher than 800 m/s, as expected for the deeper Unit 3 layer.

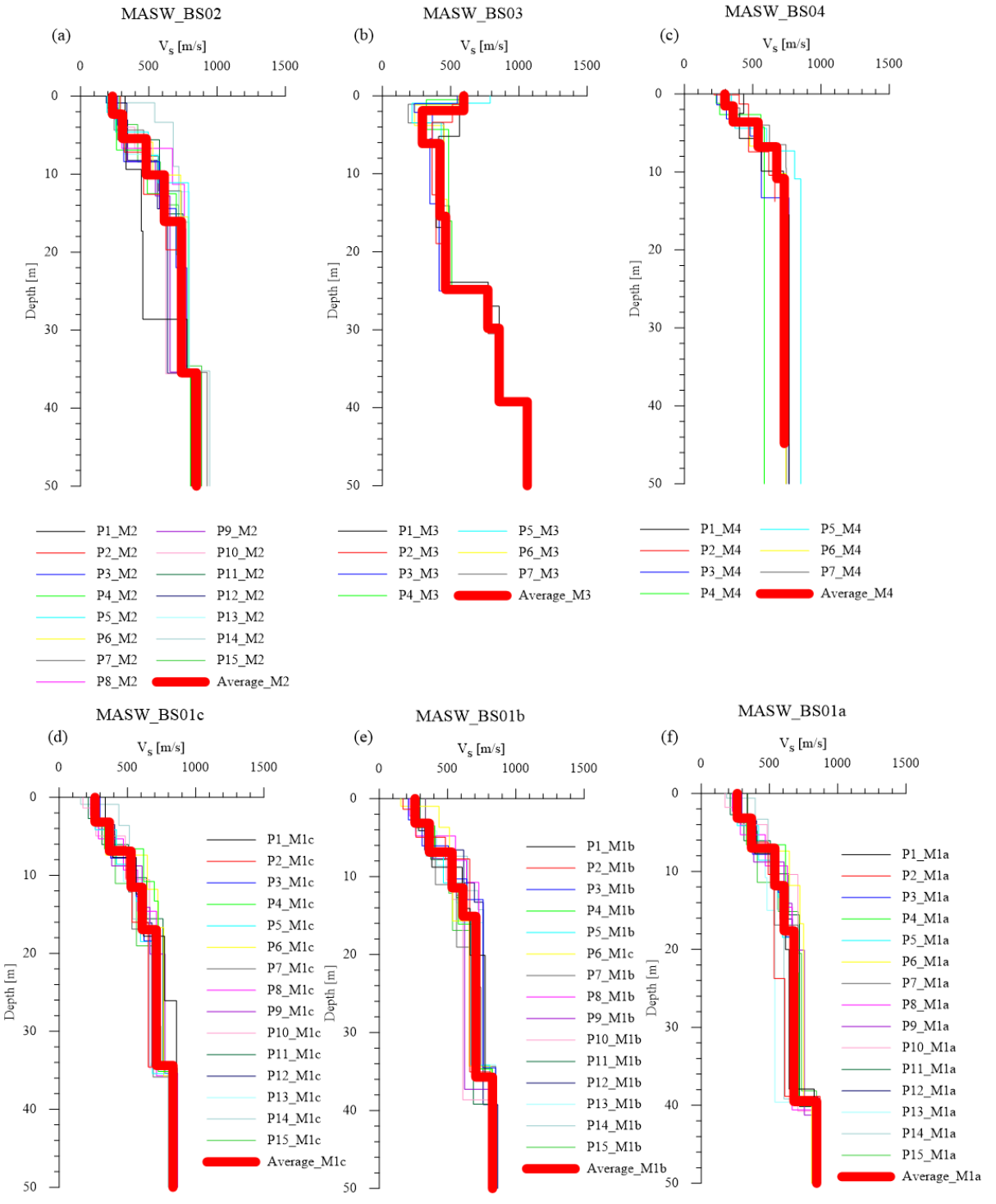


Figure 3: S-wave velocity profiles obtained from MASW2D tests along the (a) BS02; (b) BS03; (c) BS04; (d) BS01c; (e) BS01b and (f) BS01a alignments.

Using the results of these seismic in-situ investigations, the dynamic geotechnical model of the western slope of Chieuti has been constructed. Each lithological unit has been characterized by a constant value of the S-wave velocity, determined as an average value of the available measured data. The resulting model is reported in Table 1, in terms of S-wave velocity associated to each lithological unit.

| Soil layer | $V_s$ (m/s) |
|---|---|
| Man-made soil | 200 |
| Unit 1 | 317 |
| Unit 2a | 491 |
| Unit 2b | 627 |
| Unit 3 | 871 |
| Seismic bedrock | 1250 |

Table 1. Dynamic geotechnical model adopted for the site response analyses.

## 3 NUMERICAL MODELS FOR SEISMIC RESPONSE ANALYSES

The dynamic simulations of the seismic site effects have been conducted with reference to three longitudinal sections (sections C, D and E in Figure 1) and one transversal section (section I in Figure 1) crossing the western slope of Chieuti, using the FE software PLAXIS 2D [29].

The 2D plane strain FE models are illustrated in Figure 4, only with reference to the longitudinal section C and the transversal section I, for the sake of brevity. Each investigated section is characterized by a different slope length, $L_{slope}$. The longitudinal sections cross the western slope of Chieuti from the highest elevation at the crest to the toe, where the impluvium is encountered. Thus, the horizontal extension of the investigated models is 771 m for section C, 806 m for section D and 745 m for section E, while the length of section I is 782 m. The average inclination of each slope model is about 9° for Section C, 8.5° for section D and 8.8° for section E. The maximum height of each longitudinal slope section, $H_{right}$, is 170.3 m for section C, 170 m for section D and 170 m for section E. All the geometrical models have been laterally extended by 8 times the height of the vertical sides, i.e. $H_{left}$ and $H_{right}$, in order to avoid any interference of the vertical boundaries with the area of interest along the slope.

Each slope section is characterized by a sequence of Unit 1, 5 to 7 m thick, outcropping in the upper portion of the slope and overlaying the Unit 2a layer, of thickness between 15 and 20 m, in turn underlain by Unit 2b of about 8-10 m thickness. This succession overlays the Unit 3 clay soil layer. An important issue to be dealt with is the choice of the position of the top of the seismic bedrock, defined as the stratigraphic contact identifying the soil layer with $V_s$ greater than 1200 m/s. In this case, the top of the seismic bedrock has been identified based on the DH seismic tests. Specifically, the down-hole D11di detected a material with $V_s$ greater than 1200 m/s at a depth of 52 m b.g.l., while the seismic test identified a shear wave velocity of about 1000 m/s at a depth of 40 m under the urban center along the C3di. Thus, the subsoil under the town is most likely characterized by $V_s$ greater than 1000 m/s at depth greater than 40 m. Therefore, the top of the seismic bedrock has been defined parallel to the sloping ground surface at a depth of 50 m b.g.l. The shear wave velocity values implemented in the FE models are summarized in Table 1 for each soil layer.

The soil behavior has been simulated with a linear visco-elastic model, characterized by a constant unit weight of 19 kN/m$^3$, Poisson's ratio equal to 0.33, at-rest earth pressure coefficient $K_0$ equal to 0.5. The damping ratio has been implemented through the Rayleigh formulation [30], where the control frequencies $f_m$ and $f_n$ have been selected equal to 1 Hz and 12 Hz with a target damping $D^*$ of 5%, ensuring that an average damping ratio of 3%, representative of the dissipative capacity of the involved soils in the 0.001% - 0.01% strain range, is implemented in the model.

The 2D soil domain of each slope model has been discretized with 15-node triangular elements, distributed such that a greater refinement is obtained approaching the ground surface. Specifically, Section C has been discretized with 18154 elements, Section D consists of

19571 elements, Section E is composed of 22114 elements, while Section I is characterized by 19770 elements. On the top surface of each model, the nodes have a maximum distance equal to the predominant wavelength of the Rayleigh waves ($\lambda_R \cong 0.94 \cdot V_s/f_{max}$), to capture the frequency content of the travelling surface waves. In the vertical direction, the node distance has been set equal to one eighth of the wavelength ($\lambda_S \cong V_s/f_{max}$) associated to the maximum frequency of the seismic excitation (assumed equal to 20 Hz), in order to capture the frequency content of the seismic excitation [31].

During the static stage, performed with the $K_0$-procedure, standard boundary conditions have been applied to the slope models, consisting in imposing total fixities to the nodes at the bottom of the mesh and horizontal fixities to the nodes at the lateral sides of the models. After the initial static stage, the dynamic simulations have been conducted by adopting the *free field* boundary conditions at the vertical sides of the model, simulating the free field conditions, and the *compliant base* boundary [32] at the bottom of the mesh, simulating the dissipation of the waves into the deep soil layers with minimum reflection at the bottom boundary. In this case, the input motion is applied to the main domain in terms of normal and shear stress time histories. Since only the upward propagating waves should be considered in the signal applied at the *compliant base*, only half of the input motion is prescribed at the base of the FE model.

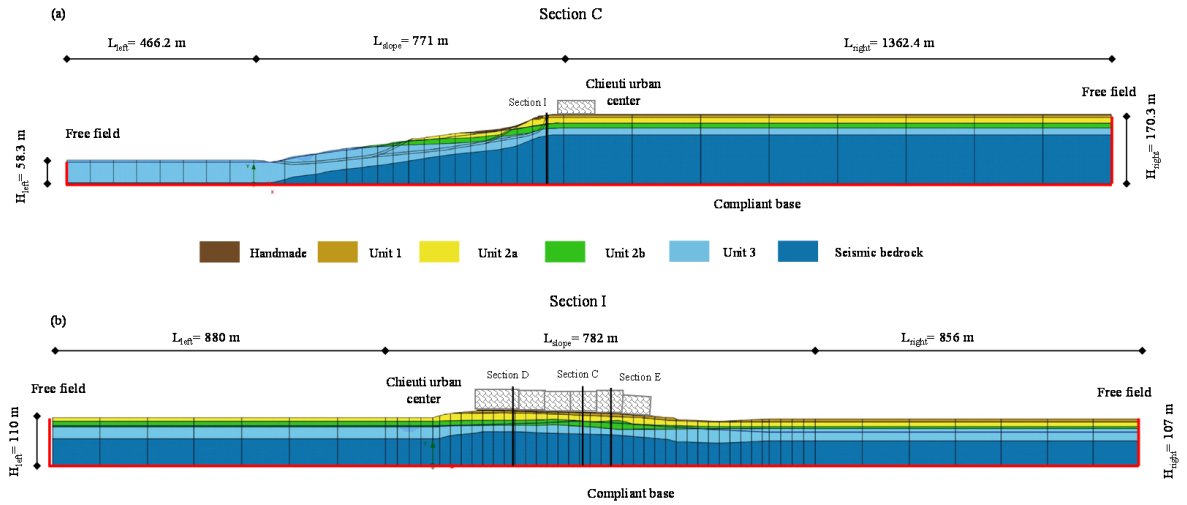


Figure 4: 2D FE models of the longitudinal section C and the transversal section I.

The seismic motion adopted in the dynamic simulations refers to the earthquake occurred at Montecilfone (Campobasso, Molise) on the 16$^{th}$ of August 2018, characterised by $M_w$ equal to 5.2 and epicentral depth of 20 km. The acceleration time history (Figure 5a), recorded at the Melanico-Santa Croce di Magliano station (MELA station), is characterized by a duration of 50 s, a peak ground acceleration (PGA) of 0.022g and a high frequency content covering a range up to 20 Hz (Figure 5b). The predominant period $T_p$ of the input motion has been identified to be equal to almost 0.1 s (Figure 5c).

All the dynamic analyses have been carried out under the assumption of fully undrained conditions. The Generalized Newmark method has been employed as time integration scheme during the dynamic stage, with Newmark parameters $\alpha_N$ and $\beta_N$ equal to 0.25 and 0.5, respectively, which implies that no numerical damping is introduced in the FE simulations. A time step of 0.01 s has been adopted, largely fulfilling the required constrain suggested by Bathe [31].

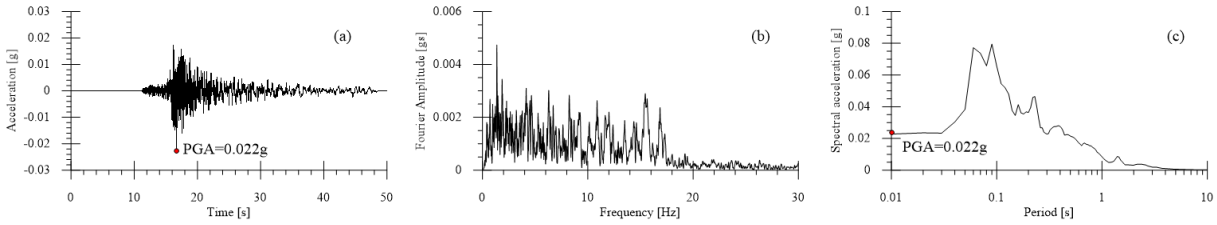


Figure 5: Seismic event occurred on the 16th of August 2018 recorded at the Melanico-Santa Croce di Magliano station: (a) acceleration time history, (b) Fourier spectrum and (c) response spectrum.

## 4 EVALUATION OF THE TOPOGRAPHIC AND STRATIGRAPHIC EFFECTS

The computed 2D site response is presented here in terms of total amplification factor *AF*, defined as the ratio between the absolute value of the peak ground acceleration $a_{\max,s}$ recorded at a given observation point on the ground surface of each 2D slope model and the maximum acceleration of the input motion, $a_{\max,i}$, i.e. 0.022g:

$$AF = \frac{a_{\max,s}(2D)}{a_{\max,i}} \tag{1}$$

The distribution of the amplification factors *AF* at the ground surface for each slope section (Figure 6) highlights that the seismic input motion is significantly amplified at the crest of the slope and in its middle portion at the distance between 300 m and 640 m for section C (Figure 6a), between 300 m and 710 m for section D (Figure 6b) and between 300 m and 610 m for section E (Figure 6c). Conversely, a typical valley effect is observed at the topographic impluvium, as expected, where the propagating input motion suffers from a de-amplification at the ground surface. A similar and unexpected de-amplification of the input motion is also detected in the upper portion of the slope at the distance between 640 m and 700 m for section C (Figure 6a), between 710 m and 750 m for section D (Figure 6b) and between 610 m and 660 m for section E (Figure 6c). The maximum amplification factors, attaining values between 2.1 and 1.7, are detected at the crest of the longitudinal sections. The minimum values of *AF* for each longitudinal section are between 0.8-0.9, highlighting a de-amplification of the input motion both at the toe and in the upper portion of the slope.

With the aim of separating the topographic from the stratigraphic amplification effects and quantifying how much the total amplification is due to either the stratigraphy of the buried subsoil or the topographic profile of the slope, stratigraphic and topographic amplification factors have been computed. To this purpose, additional numerical simulations have been carried out with reference to 1D models, accounting for the soil layer amplification only, built with reference to the stratigraphic conditions of each 2D longitudinal section.

Specifically, the stratigraphic amplification factor $AF_S$ is defined as the ratio of the peak ground acceleration at the top of the 1D model and the maximum acceleration of the input motion, $a_{\max,i}$, i.e. 0.022g:

$$AF_S = \frac{a_{\max,s}(1D)}{a_{\max,i}} \tag{2}$$

The topographic amplification factor $AF_T$ is, instead, defined as the ratio between 2D and 1D peak ground accelerations:

$$AF_T = \frac{a_{\max,s}(2D)}{a_{\max,s}(1D)} \tag{3}$$

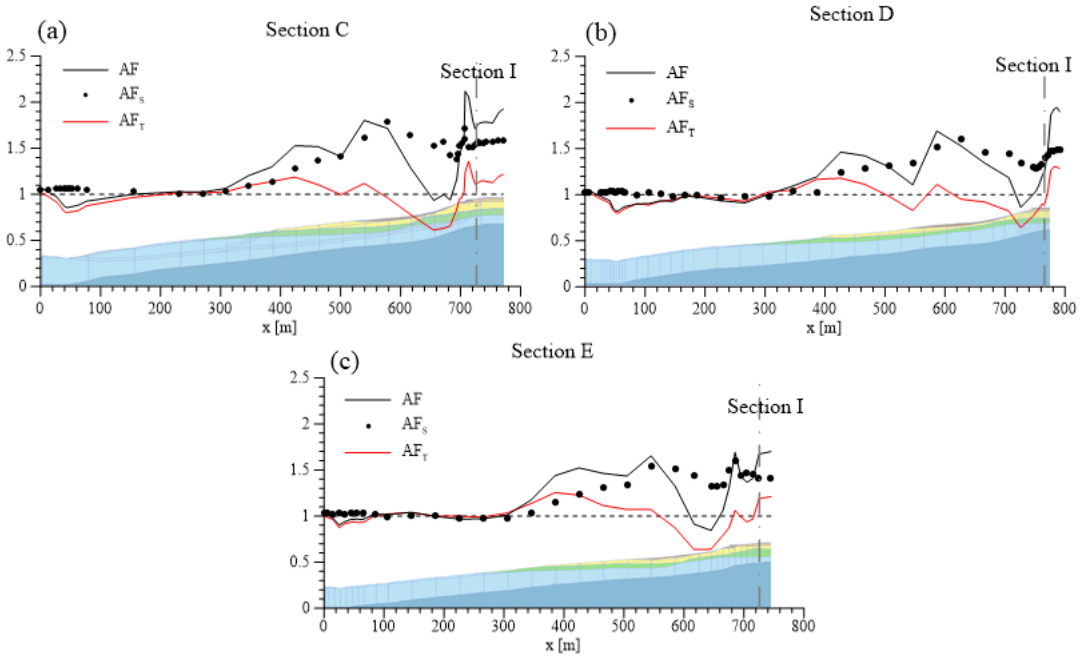


Figure 6: Distribution of the total amplification *AF*, topographic amplification $AF_T$ and stratigraphic amplification $AF_S$ factors for (a) section C, (b) section D and (c) section E.

The distributions of the amplification factors along each slope section are illustrated in Figure 6. For all the examined longitudinal sections, the $AF_T$ distribution shows fluctuations around the unit value. Moreover, the $AF_T$ factors are always lower than the $AF_S$ values, highlighting the more pronounced influence of the soil stratigraphy with respect to the slope topography on the seismic amplification processes. However, the effects due to the topography should not be neglected. Indeed, while the $AF_S$ achieves maximum values between 1.6 and 1.8 in the middle portion of the slope, the topographic amplification factor $AF_T$ reaches maximum values between 1.2 and 1.4 at the crest of the slope. Therefore, the high values of the total amplification factors observed at the crest of the slope are related not only to the subsoil heterogeneous stratigraphy, but also to the focalization of the seismic waves due to the topographic profile. The de-amplification of the seismic motion at the impluvium is clearly due to the presence of the valley, as confirmed by the $AF_T$ distribution reducing to values lower than 1, where $AF_S$ attains values around 1.

As previously observed, the computed 2D response shows an unexpected seismic de-amplification in the upper portion of the slope, i.e. between 600 m and 750 m depending on the considered longitudinal section, which is clearly not an effect of the soil stratigraphy as revealed by the $AF_S$ distribution. In fact, this could be due to either the topography of the slope or to the morphology of the buried subsoil, non-horizontally layered in these parts of the slope.

To quantify the influence of the subsoil heterogeneity and the morphology of the stratigraphic contacts of the soil layers on the ground amplification, further 2D numerical simulations have been performed implementing an equivalent homogeneous soil layer resting on the seismic bedrock, whose dynamic properties are representative of the average behavior of the examined subsoil. Thus, an equivalent shear wave velocity value has been defined according to Eq. 4:

$$V_{S,eq} = \frac{H}{\sum_{i=1}^{n} \frac{h_i}{V_{s,i}}} \tag{4}$$

where $H$ is the thickness of the homogeneous soil layer resting on the seismic bedrock, i.e. 50 m in the present case study, $h_i$ and $V_{s,i}$ are the thickness and the shear wave velocity of the soil layer, respectively, constituting the soil stratigraphy along each longitudinal section. It should be noted that, since the subsoil stratigraphy is not horizontally layered and variable thickness of soil units are detected along each slope section, different values of the equivalent shear wave velocity for each slope section can be expected, as reported in Table 2.

| Section | $V_{s.eq}$ (m/s) |
|---|---|
| C | 491 |
| D | 471 |
| E | 478 |
| I | 480 |

Table 2. Values of the equivalent shear wave velocity adopted for the homogeneous slope models.

The heterogeneity amplification factor $AF_H$ may well be defined as the ratio between the peak ground acceleration of the 2D heterogenous model, $a_{\max,s}$ (2D), and the peak ground acceleration of the 2D equivalent homogeneous model, $a_{\max,s,eq}$ (2D):

$$AF_H = \frac{a_{\max,s}(2D)}{a_{\max,s,eq}(2D)} \tag{5}$$

The distributions of the total amplification factor, computed for both the heterogenous ($AF$) and the homogeneous ($AF_{eq}$) slope models, are illustrated in Figure 7 for each slope section, together with the heterogeneity $AF_H$ amplification factor. The 2D homogeneous models of the longitudinal sections (Figure 7a-c) are characterized by total amplification factors $AF_{eq}$ attaining values close to 1, especially between 300 m and 650 m (depending on the considered section), clearly indicating a small amplification if the slope is assumed homogeneous. Furthermore, the valley and the canyon effects are emphasized in correspondence of the impluvium and at the crest of the slope, respectively, where $AF_{eq}$ reaches values between 0.7 and 0.8 at the toe of the slope and between 1.1 and 1.2 at the crest. Indeed, the $AF_H$ profile clearly shows the predominant influence of the subsoil heterogeneity in amplifying the seismic motion on the ground surface between 300 m and about 650 m. Conversely, in the upper portion of the slope between 600 m and 750 m, the de-amplification of the seismic motion is related more to the slope topography than to the buried subsoil features. Indeed, in these portions the heterogeneity amplification factors $AF_H$ along each longitudinal section are characterized by values of about 0.7-0.8. The reason for this response lies in the morphology of the slope profile, characterized by a local variation in the surface inclination, forming a sort of valley. In particular, the sloping surface changes its inclination from 8° to 21° along section C, from 9° to 20° along section D and from 10° to 16° along section E where the minimum $AF_H$ is attained. At the crest of the slope, a combination of stratigraphic and topographic effects might be detected, as confirmed by the $AF_H$ profiles along the longitudinal sections.

With reference to the transversal section I (Figure 7d), the $AF_{eq}$ profile shows a flat pattern characterized by values between 0.8 and 1. Conversely, the $AF_H$ profile attains the minimum value of 1.5 in the southern area (left side of the 2D model), where the Unit 2a outcrops, and the maximum value of 2.4 in the middle portion of the section, between the intersection with

sections C and D, where the Unit 1 is outcropping. Thus, the heterogeneity characterizing the subsoil at the crest of the slope might be deemed to be responsible for the seismic amplification at the ground surface, although the topographic irregularities are also contributing to the wave propagation process, as revealed by the comparison between *AF* and $AF_S$, reported in the figure at the intersection with the longitudinal sections only.

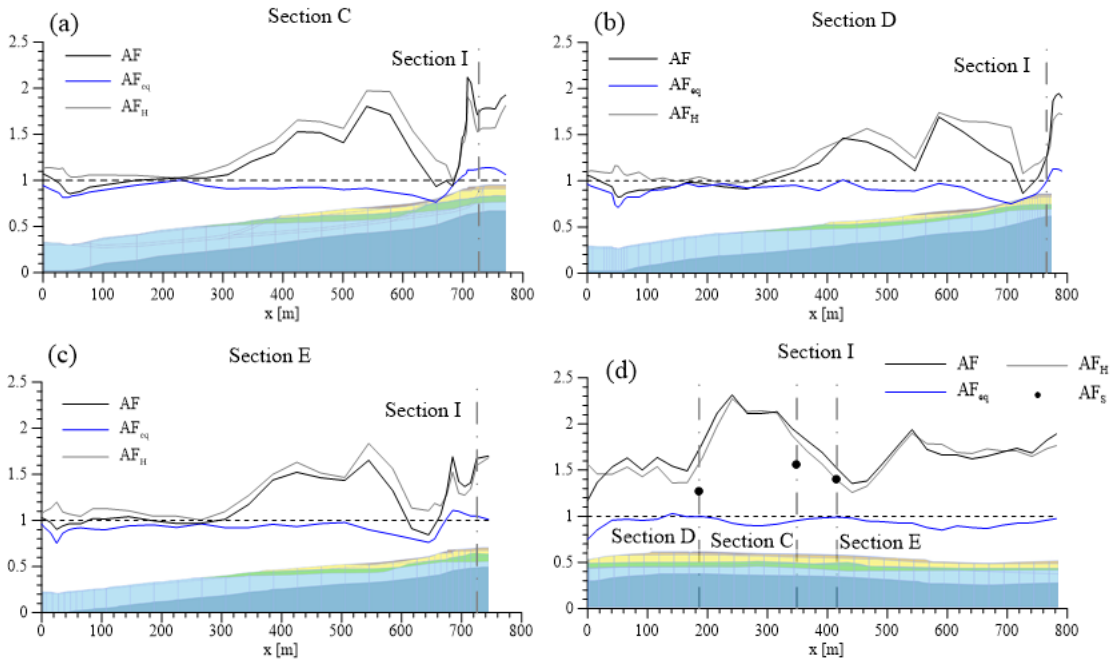


Figure 7: Distribution of the total amplification factors evaluated for the heterogeneous (*AF*) and equivalent homogeneous ($AF_{eq}$) slope models and the heterogeneity amplification factor $AF_H$ for (a) section C, (b) section D, (c) section E and (d) section I.

## 5 CONCLUSIONS

The present paper is aimed at evaluating and identifying the seismic site effects affecting a real natural slope, the western slope of Chieuti in the south of Italy, using a 2D FE numerical approach. The topographic effects have been decoupled from the stratigraphic effects through the separate evaluation of the topographic and stratigraphic amplification factors.

The numerical simulations revealed that the stratigraphic effects are predominant for most of the slope, while the topographic effects play a significant role in its upper portion, where the focalization of the seismic waves occurs. Indeed, the strong heterogeneity characterizing the subsoil of Chieuti is mostly responsible for the seismic ground surface amplification affecting the urban area. Although the topographic amplification factors are not significantly high for the specific case study, the topographic effects can also play an important role in the wave propagation process, as the input motion is amplified by 1.2-1.4 at the crest, where the buildings are located. Thus, neglecting these topographic effects, as suggested by the Italian Building code [33] for slope angles lower than 15°, could be detrimental for a proper assessment of the seismic vulnerability of the structures.

The analyses of the seismic site response of different slope sections allowed to identify the area of the hillslope mostly affected by the seismic amplification phenomena. Indeed, the slope portion characterized by high amplification factors is the crest of the slope, as a result of the combination of the topographic irregularities and the heterogeneity of the buried subsoil.

Moreover, the highest amplification factors are detected in the southern part of the slope crest between sections C and D.

## ACKNOWLEDGEMENTS

The research has been supported by the PON-AIM project (AIM1871082) and the PON-MITIGO project (ARS01_00964). The third author is grateful for the financial support received by the project "National Centre for HPC, Big Data and Quantum Computing – Spoke 5: Environment and Natural Disasters" (CN_00000013) funded by the National Recovery and Resilience Plan (NRRP), M4_C2_1.4 – NextGenerationEU.

## REFERENCES

[1] D. Assimaki, G. Gazetas, E. Kausel, Effects of local soil conditions on the topographic aggravation of seismic motion: parametric investigation and recorded field evidence from the 1999 Athens earthquake. *Bulletin of the Seismological Society of America*, **95**(3), 1059–1089, 2005.

[2] L. Geli, P.Y. Bard, B. Jullien, The effect of topography on earthquake ground motion: A review and new results. *Bulletin of the Seismological Society of America*, **78**(1), 42–63, 1988

[3] G.A. Athanasopoulos, P.C. Pelekis, E.A. Leonidou, Effects of surface topography on seismic ground response in the Egion (Greece) 15 June 1995 earthquake. *Soil Dynamics and Earthquake Engineering*, **18**(2), 135–149, 1999.

[4] G. Biondi, M. Maugeri, Seismic response analysis of the Monte Po hill (Catania). In *Seismic prevention of damage. A case study in a Mediterranean City*, Southampton, UK, 2005.

[5] Y. Fukushima, K. Irikura, T. Uetake, H. Matsumoto, Characteristics of Observed Peak Amplitude for Strong Ground Motion from the 1995 Hyogoken Nanbu (Kobe) Earthquake. *Bulletin of the Seismological Society of America*, **90**(3), 545–565, 2000.

[6] G. Gazetas, P.V. Kallou, P.N. Psarropoulos, Topography and Soil Effects in the MS 5.9 Parnitha (Athens) Earthquake: The Case of Adámes. *Natural Hazards*, **27**, 133–169, 2002.

[7] K.O. Cetin, A.G. Papadimitriou, S. Altun, P. Pelekis, B. Unutmaz, E. Rovithis, et al, The role of site effects on elevated seismic demands and corollary structural damage during the October 30, 2020, M7.0 Samos Island (Aegean Sea) Earthquake. *Bulletin of Earthquake Engineering*, **20**(14), 7763–7792, 2022.

[8] Y. Yin, F. Wang, P. Sun, Landslide hazards triggered by the 2008 Wenchuan earthquake, Sichuan, China. *Landslides*, **6**, 139–152, 2009.

[9] E. Bertrand, A.M. Duval, J. Régnier, R.M. Azzara, F. Bergamaschi, P. Bordoni, et al, Site effects of the Roio basin, L'Aquila. *Bulletin of Earthquake Engineering*, **9**, 809–823, 2011.

[10] F. Sabetta, G. Fiorentino, F. Bocchi, M. Sinibaldi, G. Falcone, A. Mendicelli, Influence of local site effects on seismic risk maps and ranking of Italian municipalities. *Bulletin of Earthquake Engineering*, 1–28, 2023.

[11] A. Pagliaroli, G. Lanzo, B. D'Elia, Numerical Evaluation of Topographic Effects at the Nicastro Ridge in Southern Italy. *Journal of Earthquake Engineering*, **15**(3), 404–432, 2011.

[12] J. Régnier, L. Bonilla, P. Bard, E. Bertrand, F. Hollender, H. Kawase, et al, International Benchmark on Numerical Simulations for 1D, Nonlinear Site Response (PRENOLIN): Verification Phase Based on Canonical Cases. *Bulletin of the Seismological Society of America*, **106**(5), 2112-2135, 2016.

[13] A. di Lernia, A. Amorosi, D. Boldini, A multi-directional numerical approach for the seismic ground response and dynamic soil-structure interaction analyses. *7ICEGE. VII International Conference on Earthquake Geotechnical Engineering*, Rome, Italy, 2019.

[14] G. Falcone, D. Boldini, A. Amorosi, Site response analysis of an urban area: A multi-dimensional and non-linear approach. *Soil Dynamics and Earthquake Engineering*, **109**, 33–45, 2018.

[15] J. Régnier, L. Bonilla, P. Bard, E. Bertrand, F. Hollender, H. Kawase, et al, PRENOLIN: International Benchmark on 1D Nonlinear Site‐Response Analysis—Validation Phase Exercise. *Bulletin of the Seismological Society of America*, **108**(2), 876‐900, 2018.

[16] G.D. Bouckovalas, A.G. Papadimitriou. Numerical evaluation of slope topography effects on seismic ground motion. *Soil Dynamics and Earthquake Engineering*, **25**(7–10), 547–558, 2005.

[17] A.G. Papadimitriou, S.A. Paraskevopoulos, A.N. Lamprakopoulos, Aggravation of spectral acceleration along 2D symmetrical trapezoidal valleys. *16th European Conference on Earthquake Engineering*, Thessaloniki, Greece, 2018.

[18] A.G. Papadimitriou. An engineering perspective on topography and valley effects on seismic ground motion. *7ICEGE. VII International Conference on Earthquake Geotechnical Engineering*, Rome, Italy, 2019.

[19] S. Rizzitano, E. Cascone, G. Biondi, Coupling of topographic and stratigraphic effects on seismic response of slopes through 2D linear and equivalent linear analyses. *Soil Dynamics and Earthquake Engineering*, **67**, 66–84, 2014.

[20] Z. Zhang, J.A. Fleurisson, F. Pellet, The effects of slope topography on acceleration amplification and interaction between slope topography and seismic input motion. *Soil Dynamics and Earthquake Engineering*, **113**, 420–431, 2018.

[21] F. Santaloia, A. di Lernia, S. Guglielmi, L. Pisano, A. Sonnessa, M. Stragapede, et al, Phenomenological analysis and monitoring of a slow-moving paleo-landslide affecting an urban area. *Engineering Geology*, in prep.

[22] A. Sonnessa, A. di Lernia, D.O. Nitti, R. Nutricato, E. Tarantino, F. Cotecchia, Integration of Multi-sensor MTInSAR and ground-based geomatic data for the analysis of non-linear dis-placements affecting the urban area of Chieuti, Italy. *International Journal of Applied Earth Observation and Geoinformation*, **117**, 103194, 2023.

[23] V. Tagarelli, F. Santaloia, G. Elia, F. Cotecchia, Numerical modelling of the geological processes responsible for mid-Pleistocene landslide inception: an insight into possible factors for the current landslide activity. *10th European Conference on Numerical Methods in Geotechnical Engineering*, London, UK, 2023.

[24] E. Patacca, P. Scandone, The 1627 Gargano earthquake (Southern Italy): Identification and characterization of the causative fault. *Journal of Seismology*, **8**(2), 259–273, 2004

[25] M. Locati, R. Camassi, A. Rovida, E. Ercolani, F. Bernardini, V. Castelli, et al, DBMI15, the 2015 version of the Italian Macroseismic Database. *Istituto Nazionale Di Geofisica e Vulcanologia*, 2016.

[26] M. Stucchi, C. Meletti, V. Montaldo, H. Crowley, G.M. Calvi, E. Boschi, Seismic Hazard Assessment (2003-2009) for the Italian Building Code. *Bulletin of Seismological Society of America*, **101**(4), 1885–1911, 2011.

[27] A. Amorosi, V. Bracone, V. Di Donato, C.M. Rosskopf, P.P.C. Aucelli, The Plio–Pleistocene succession between Trigno and Fortore rivers (Molise and Apulia Apennines): stratigraphy and facies characteristics. *GeoActa*, **8**, 1–12, 2009.

[28] V. Bracone, A. Amorosi, P.P.C. Aucelli, C.M. Rosskopf, F. Scarciglia, V. Di Donato, et al, The Pleistocene tectono-sedimentary evolution of the Apenninic foreland basin between Trigno and Fortore rivers (Southern Italy) through a sequence-stratigraphic perspective. *Basin Research*, **24**(2), 213–233, 2012.

[29] PLAXIS 2D CE V20, *PLAXIS CONNECT Edition V20. Reference manual*, 2020.

[30] J. Rayleigh, *The theory of sound*. New York, Dover, 1945.

[31] K.J. Bathe, *Finite Element Procedures*. 2nd ed. Upper Saddle River, Prentice Hall, 1996.

[32] W.B. Joyner, A.T.F. Chen, Calculation of nonlinear ground response in earthquake. *Bulletin of Seismological Society of America*, **65**(5), 1315–1336, 1975.

[33] CS.LL.PP. Norme tecniche per le costruzioni. *Gazzetta Ufficiale della Repubblica Italiana*, 2018.

COMPDYN 2023
9th ECCOMAS Thematic Conference on
Computational Methods in Structural Dynamics and Earthquake Engineering
M. Papadrakakis, M. Fragiadakis (eds.)
Athens, Greece, 12-–14 June 2023

# MODELLING OF RIGID INCLUSIONS REINFORCED FOUNDATIONS TO INVESTIGATE THE FAILURE ENVELOPE IN THE V-M-H SPACE (COMPDYN 2023)

**Ramon Alcala-Ochoa**[*,1], **Zheng Li**[2], **Panagiotis Kotronis**[1] **and Giulio Sciarra**[1]

[1] Nantes Université, École Centrale Nantes, CNRS, Institut de Recherche en Génie Civil et Mécanique (GeM), UMR 6183, F-44000 Nantes, France.
e-mail: {ramon.alcala-ochoa,panagiotis.kotronis,giulio.sciarra}@ec-nantes.fr

[2] Laboratoire Centrifugeuses Géotechniques, Département GERS, Université Gustave Eiffel Campus de Nantes
Allée des Ponts et Chaussées, 44340 Bouguenais, France
e-mail: zheng.li@univ-eiffel.fr

**Abstract.** *The technique of ground reinforcement using Rigid Inclusions (RIs) is known to reduce settlements and enhance bearing capacity in soft soils. This approach leads to significant nonlinear interactions among the load transfer platform, piles, and the surrounding soil. The main objective of this paper is to identify the failure envelope of a shallow foundation on soft soil reinforced by RIs. This is a critical step in the safety assessment of this combined foundation system under static and dynamic (seismic) loading. The failure envelope, defined in the vertical force (V), bending moment (M) and horizontal force (H) space, is constructed using swipe tests from numerical simulations. A simple analytical formula is proposed to describe the failure envelope in V-M-H space. The failure envelope described by the proposed equation is the key ingredient for the macro-element modeling for the analysis of Soil-Structure Interaction of RIs foundation systems.*

**Keywords:** Shallow foundations, Reinforced soils, Ground improvement, Failure envelope

## 1 INTRODUCTION

As the demand for infrastructure grows, construction on soft ground becomes increasingly necessary. Consequently, it is crucial to design a reinforced foundation system with great care. Rigid Inclusions (RIs) are one of the soil improvement techniques for structures founded on compressible soils, as they can increase the soil-bearing capacity and limit the settlement of the superstructure. A RI reinforced foundation is composed of a shallow foundation, a compacted sand or gravel layer (Load Transfer Platform (LTP)) and vertical rigid inclusions. RI foundations are not only subject to vertical loads, but also to overturning moments and horizontal loads caused by wind or earthquake actions. Therefore, for an efficient design, understanding the coupling of vertical forces, $V$, bending moments, $M$, and horizontal forces, $H$, is mandatory. A failure envelope offers directly the bearing capacity that the foundation can provide. Multiple finite element method (FEM) simulations are carried out to investigate the complete failure locus of rigid inclusion reinforced foundations in the $V-M-H$ space. An analytical formula for the 3D failure surface is finally introduced.

## 2 NUMERICAL MODEL FOR A RI REINFORCED FOUNDATION

The numerical simulation is performed using the general purpose finite element code Cast3M [1]. The model is composed of a shallow foundation, a LTP, seven vertical rigid inclusions and a stiff soil layer based in the experimental model from a static centrifuge test conducted at the University Gustave Eiffel (Centrif−UGE) in the framework of the French national project − ASIRIplus-SDS [2]. The LTP layer is a mix of five Hostun sand fractions (HN38, HN34, HN31, HN04/08, HN06/1), according to [3] and is 1 m thick. The groundwater level is below the LTP at $-1$ m. A mixture of 80% Speswhite kaolin clay and 20% Fontainebleau sand serves as the compressible soil. This soft soil is 9.5 m thick, pre-consolidated at 120 kPa. The stiff soil bottom layer has a thickness of 4 m and is prepared with saturated dense Hostun (HN31) sand. The dimensions are given in the Figure 1.

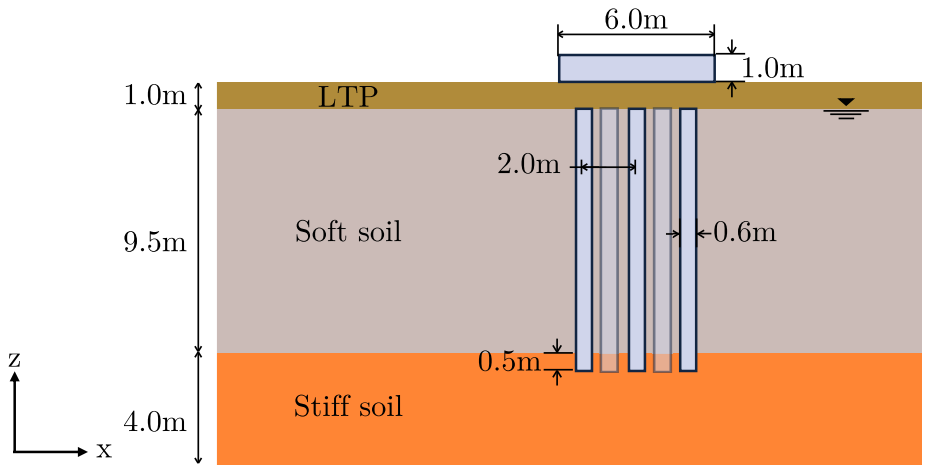


Figure 1: Centrifuge model of a circular shallow foundations with rigid inclusions (right): Geometry and soil stratigraphy, (prototype scale).

## 2.1 Calibration and validation of the soil characteristics

A linear elastic (EL) behavior is adopted for the footing and the RIs. To account for the sand nonlinearities in the LTP and stiff soil layers, a perfect elastoplastic Drucker-Prager (DP) constitutive model with a non-associated flow rule ($\psi \neq \varphi$) is considered. The DP parameters are closely matched to reproduce the classical Mohr–Coulomb model. The constitutive law is calibrated and validated using experimental triaxial tests from [3], with a relative density $I_{\mathrm{d}} = 0.9$, a friction angle $\varphi = 36°$ and a dilatancy angle $\psi = 2.5 - 4°$, see Figure 2 (a) and (b).

The compressible soil layer is numerically simulated using the critical state theory elastoplastic strain hardening Modified Cam-Clay model (MCC). The values of the normal consolidation, $\lambda = C_c/\ln(10)$, and swelling, $\kappa = C_s/\ln(10)$, slopes are determined from the compression, $C_c = 0.269$, and rebound, $C_s = 0.048$, indexes from the oedometer test S03 [4]. As shown in Figure 2 (c), a fair agreement of the numerical and experimental results is observed.

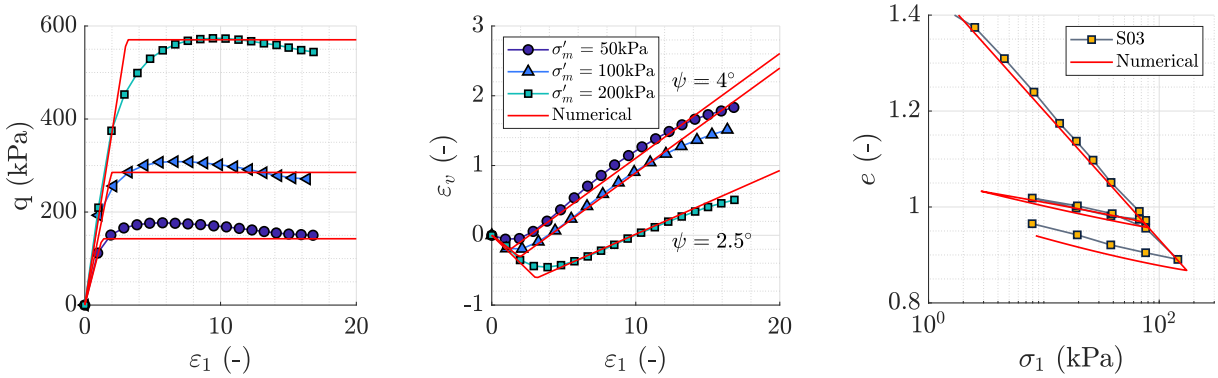


Figure 2: Experimental results (dots) and numerical calibration (red lines) (a) triaxial compression (b) triaxial extension test of Hostun mix sand, with a relative density $I_{\mathrm{d}} = 0.9$, from [3]; (c) experimental oedometric test results to stress vertical load increment, $\sigma_a$ versus void ratio, $e$, from [4].

## 2.2 Finite element mesh and boundary conditions

The numerical simulation is performed using the general purpose finite element code Cast3M [1] respecting the dimensions of Figure 1. The dimensions of the mesh are 8B × 4B × 2.5B, (B= 6.0 m, the width of the foundation), and the number of elements is 148775. Due to symmetry, only half of the domain is considered. Preliminary analyses illustrated the areas of significant plastic strains, leading to a local mesh refinement at the vicinity of the piles and the footing edges, see Figure 3. Boundary conditions are applied by fixing the nodal displacements in the $x$, $y$ and $z$ directions at the base of the finite element model. The displacements at the other lateral boundaries are blocked in normal directions. No slippage is allowed between the soil and the RIs, because of the overconsolidation ratio $OCR > 1$, which leads to significant soil-pile confinement.

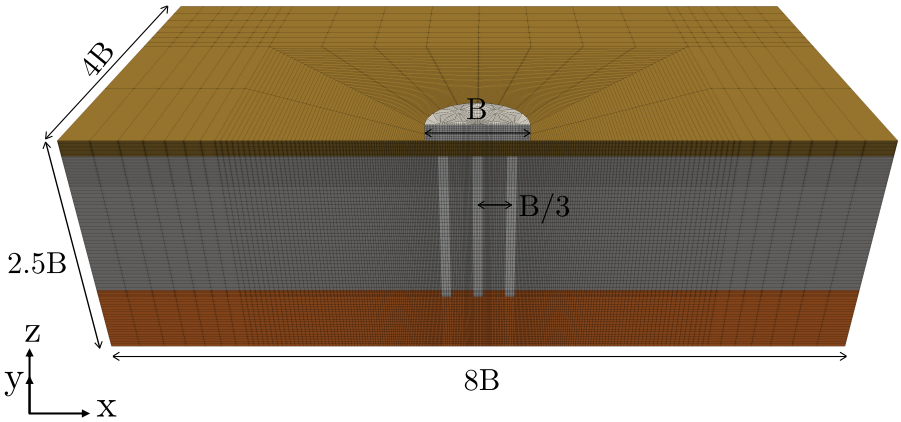


Figure 3: Finite element mesh and geometry for the foundation with RIs.

## 3 NUMERICAL STUDY OF THE 3D FAILURE ENVELOPE

### 3.1 Swipe tests

In order to determine the ultimate combined resistance of a shallow foundation reinforced by RIs, the displacement-controlled *swipe test* methodology is adopted. The fundamental idea comes from analogies with the hardening plasticity theory applied in critical state soil mechanics [5], in which the result is a load path that tracks along with the failure envelope (e.g., discussed in [6, 7, 8]). The sign conventions and the example of a load sweep in the $V - H$ space are shown in Figure 4. By assuming the maximum vertical displacement, $w_0$, and tracking the load paths generated by multiple combinations of horizontal displacements, $u$, and rotations, $\theta$, the final 3D failure envelope can be numerically obtained.

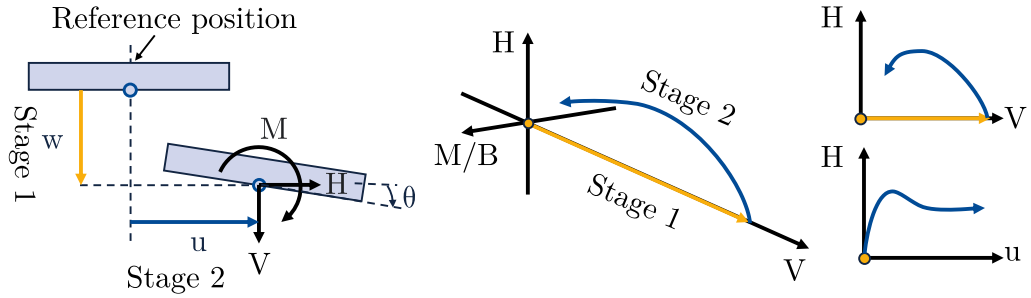


Figure 4: Swipe tests: stages, sign conventions, vertical and horizontal applied displacements, adapted from [9].

### 3.2 Vertical bearing capacity

First, a vertical displacement test is conducted to retrieve the vertical bearing capacity, $V_0$, and the corresponding vertical displacement, $w_0$. From the results shown in Figure 5 (a), the parameters can not be established, since the apparent failure is not observed. The tangent intersection method [10] is therefore adopted to approximate the maximal vertical bearing capacity, $V_0$ (red dot), calculated as the intersection of two tangents (black lines), the first corresponding to the initial slope and the second to the steeper portion of the final part of the curve. The final values are $V_0 = 4583$ kN and $w_0 = 0.09$ m.

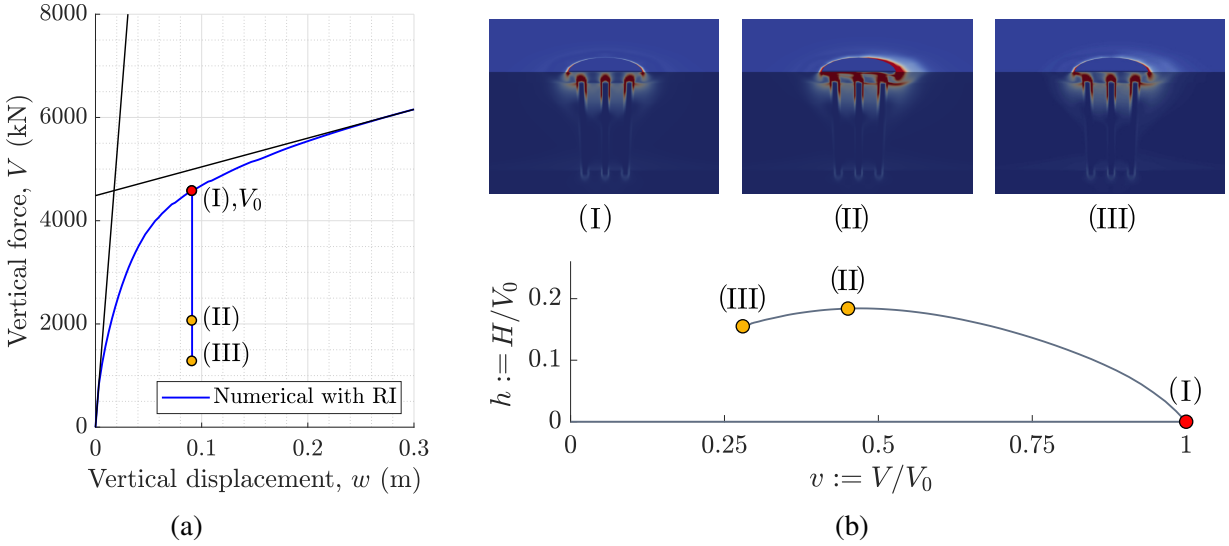


Figure 5: (a) Vertical displacement-load curve (blue line). Calculation of the maximal bearing capacity, $V_0$ (red dot), by the tangent intersection method (black lines) [10]. (b) Collapse mechanism in the normalized $v-h$ plane at (I) maximum vertical bearing capacity, (II) maximum horizontal normalized force and (III) end of the swipe test. The top part shows the plastic shear strain, $\gamma^p$, where the nonlinearities are concentrated in the red areas.

### 3.3 Numerical 3D failure envelope

The procedure described in subsection 3.1 is employed to find the full failure envelope. As mentioned, by assuming the maximum vertical displacement, $w_0$, the technique can generate a complete yield locus with only a few tests as the displacement combination tracks along with the failure envelope.

For an example of a purely horizontally driven swipe test, the evolution of the corresponding collapse mechanism can be visualized by plotting the plastic shear strain, $\gamma^p$, at specific load steps. This is illustrated in the top part of Figure 5 (b) for three steps zones in the normalized $v-h$ plane: (I) at maximum vertical bearing capacity, (II) at maximum horizontal normalized force and (III) at the end of the swipe test. From the figure is observed that the load is transferred to the piles through the LTP by the arching effect, and simultaneously, the vertical force applied to the RIs is transferred to the stiff soil layer. It can be drawn that the collapse mechanism is mainly developed in the LTP layer.

The numerical 3D failure envelope, resulting from sixty-two numerical swipe tests, is shown (in grey) in the $v-h-m$ normalized space in Figure 6 (a). The representation of a cut in the $m-h$ plane is shown in yellow for $v = 0.5$.

## 4 ANALYTICAL 3D FAILURE ENVELOPE OF RI REINFORCED FOUNDATIONS

This section aims to approximate the failure envelope of subsection 3.3, found using numerically reproduced swipe tests, with an appropriate closed-form mathematical formulation. It can be concluded from Figure 6 (a) that:

- $h-m$ plane: results have the form of an inclined ellipse centred at the origin.
- $v-h$ plane: the failure envelope has a parabolic form. Starting from $V_0$, its size increases with the decreasing of vertical force $v$. In this plane, the maximum is reached at a critical

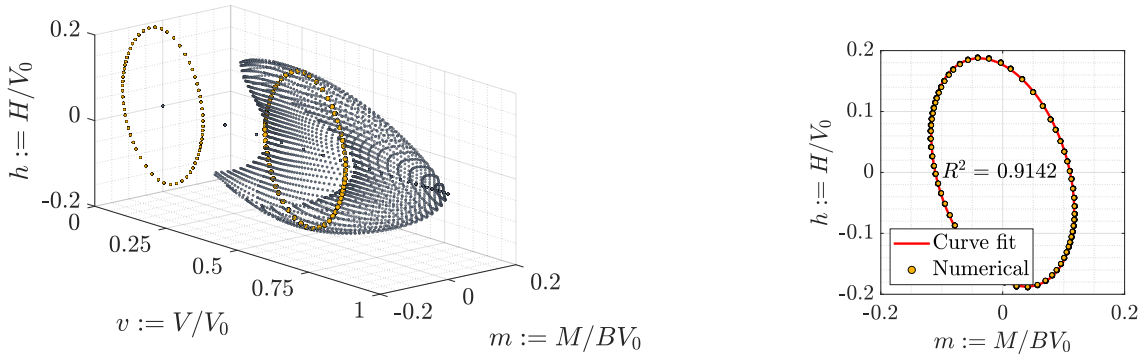


(a) (b)

Figure 6: (a) Failure envelope obtained from sixty-two numerical swipe tests. The representation of a cut in the $m - h$ plane is shown in yellow for $v = 0.5$ (b) Curve fitting of the numerical data using the direct least square fitting of ellipses [11].

point close to $v = 0.45 - 0.5$ (also observed in Figure 5 (b)). A decreasing trend is observed afterwards for lower values of $v$.

The main idea to find the analytical formula is i) to calibrate the three parameters $(a, b, c)$ of the inclined ellipse general equation $ay^2 + bz^2 + cyz - a^2b^2 = 0$ with the numerical results corresponding to the critical point of the vertical forces, taken hereafter equal to $v = 0.5$; and then ii) to use the parabola of the form $4x(1 - x) = 0$ (that has a peak value equal to 1 at 0.5 and being 0 at 0 and 1) to automatically control the different ellipses' size.

The 'cigar shape' parabolic ellipsoid envelope, used in the literature for shallow foundations on sand, see [7, 12, 13, 14], among others, is therefore again adopted hereafter. The complete expression, in terms of normalized loads, can be expressed as:

$$f(v, m, h) = \frac{m^2}{m_0^2} + \frac{h^2}{h_0^2} - 2a_0\frac{mh}{m_0 h_0} - [4v(1 - v)]^2 = 0 \tag{1}$$

where $m_0$ and $h_0$ determine the failure envelope shape and size and represent the intersection of each ellipse in the normalized $v - m$ and $v - h$ planes, respectively. $a$ represents the cross-section tilt angle in the $m - h$ plane, measured from the $h$ axis.

In order to calibrate the ellipse, the direct method for least square fitting of ellipses is employed [11], see Figure 6 (b). The three parameters are found to be

$$h_0 = 0.1766 \quad m_0 = 0.1105 \quad a_0 = -0.3325 \tag{2}$$

The final parabolic ellipsoid representation of Equation 1 is shown in yellow, together with the numerical swipe test results as grey dots, in Figure 7. A high correlation is obtained ($R^2 = 0.9142$), evidencing that the suggested formula is suitable for design purposes and the development of simplified modelling strategies, such as novel macro-elements.

## 5 CONCLUSIONS

This paper presents a 3D finite element model to numerically reproduce the ultimate combined resistance of RIs foundations using swipe tests. The analytical formula defined by Equation 1 and Equation 2 is proposed for the failure envelope of a rigid inclusion reinforced foundation

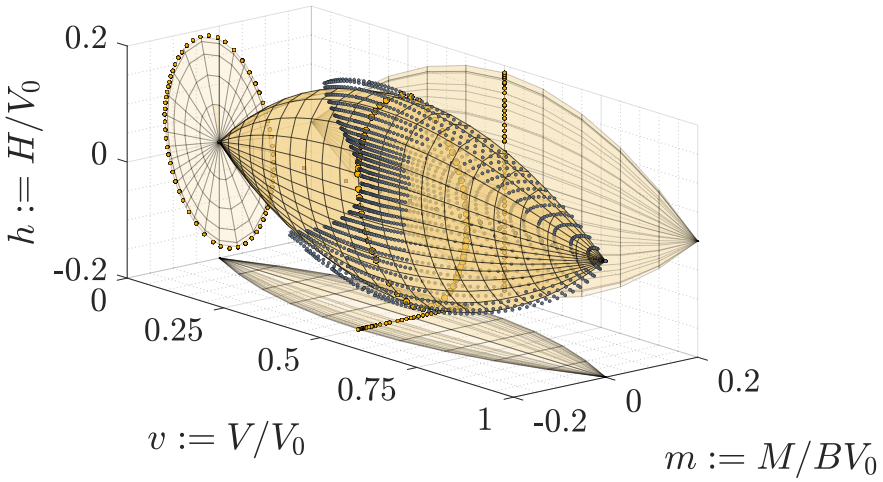


Figure 7: Normalized failure envelope in $v-m-h$ space. Proposed analytical formula (yellow) and numerical swipe test results (gray dots).

on soft soil. Practitioners can use the proposed analytical equation of the failure envelope to quantify the bearing capacity under complex 3D loading and researchers to develop novel macroelements. More details on this work can be found in [15].

## REFERENCES

[1] CEA, "Cast3m," 2001. http://www-cast3m.cea.fr/.

[2] ANR, "Soil improvement by rigid inclusions: Seismic and dynamic loading – ASIRIplus-SDS," 2020.

[3] G. Baudouin, *Sols renforcés par inclusions rigides : modélisation physique en centrifugeuse de remblais et de dallage*. PhD thesis, Université de Nantes. Faculté des sciences et des techniques, 2010. 2010NANT2046.

[4] S. Escoffier, Z. Li, and C. Soriano, "Data Report no. 2 ASIRI+ Project amélioration des sols par inclusions rigides: sollicitations dynamiques et sismiques," tech. rep., Université Gustave Eiffel, 9 2022.

[5] A. Schofield and P. Wroth, "Critical state soil mechanics," *McGraw Hill, London*, 1968.

[6] F. Tan, *Centrifuge and theoretical modelling of conical footings on sand*. PhD thesis, University of Cambridge, Cambridge, UK, 1990.

[7] G. Gottardi and R. Butterfield, "On the bearing capacity of surface footings on sand under general planar loads," *Japanese Society of Soil Mechanics and Foundation Engineering*, vol. 33, pp. 68–79, 9 1993.

[8] S. Grange, *Modélisation simplifiée 3D de l'interaction sol-structure: application au génie parasismique.* PhD thesis, Institut National Polytechnique de Grenoble - INPG, June 2008.

[9] R. Butterfield, G. T. Houlsby, and G. Gottardi, "Standardized sign conventions and notation for generally loaded foundations," *Geotechnique*, vol. 47, pp. 1051–1054, 1997.

[10] A. Hirany and F. H. Kulhawy, "Conduct and interpretation of load tests on drilled shaft foundations: Volume 1, detailed guidelines: Final report," tech. rep., Cornell University, 7 1988.

[11] A. Fitzgibbon, M. Pilu, and R. B. Fisher, "Direct least square fitting of ellipses," *IEEE Trans. Pattern Analysis and Machine Intelligence*, vol. 21, pp. 987–996, 5 1999.

[12] R. Nova and L. Montrasio, "Settlements of shallow foundations on sand," *Géothecnique*, vol. 41, pp. 243–256, 1991.

[13] M. J. Cassidy, *Non-linear analysis of jack-up structures subjected to random waves*. PhD thesis, University of Oxford, 1999.

[14] G. Gottardi, G. T. Houlsby, and R. Butterfield, "Plastic response of circular footings on sand under general planar loading," 6 1999.

[15] R. Alcala-Ochoa, Z. Li, P. Kotronis, and G. Sciarra, "3D failure envelope of RI foundations," 2023. Unpublished, to be submitted to Géotechnique.

COMPDYN 2023
9th ECCOMAS Thematic Conference on
Computational Methods in Structural Dynamics and Earthquake Engineering
M. Papadrakakis, M. Fragiadakis (eds.)
Athens, Greece, 12-14 June 2023

# FRAGILITY CURVES FOR A SMALL ZONED EARTH DAM

**M. Tretola**[1], **S. Sica**[1]

[1] Department of Civil Engineering, University of Sannio
Benevento, Italy
martretola@unisannio.it

## Abstract

*The paper presents a suite of fragility curves to evaluate the seismic vulnerability of a small earth dam. The goal is to provide a user-friendly tool to estimate the expected damage of this type of barrages that, since classified as small, are typically subjected to less restricting controls than large dams with the consequent increase of their vulnerability. In this study, the incremental dynamic analysis method (IDA) was applied to a prototype of small zoned earth dam. To perform nonlinear dynamic analyses through the finite element software Plaxis2D, an advanced soil constitutive model combined to a three-phase formulation was adopted. To develop the fragility curves for each damage type relevant for the seismic performance of the dam, ten representative accelerometric signals were selected. Four damage measures (DMs) were considered, namely the settlement ratio at the dam crest, the lateral displacements of the dam crest, the freeboard reduction and the maximum plastic shear strain of the watertightness element. These damage indicators were later related to three intensity measures (IMs), i.e. PGA, PGV and the Arias Intensity. As outcome of the study, the fragility curves for different limit states of the identified DMs were obtained.*

**Keywords:** Zoned earth dam, fragility curve, damage index, intensity measure

## 1 INTRODUCTION

Dam safety assessment has always been a challenging task for civil engineers due to the high risk generally associated with these structures. Actually, the direct and indirect consequences of any uncontrolled release of water from the reservoir can be catastrophic for the downstream population.

In the case of existing earth dams, the problem is further complicated by the inherent difficulty in achieving a detailed knowledge on recent and past loading history of the dam, on properties of the soil materials and their possible modification during the life of the dam.

The lack of reliable information on the original design of the structure combined to that of a thorough monitoring activity is even more critical for small earth dams, i.e. those characterized by embankments of lower height and limited reservoir capacity ($H \leq 15$ m or water storage $\leq 1$ million $m^3$). Despite their size, the risk associated with small dams could be comparable or even higher than that associated to larger dams. In Italy most of the existing dams (small and large) are located in areas characterized by high seismic hazard. Moreover, most of them dating back to the middle of the last century, were built without taking seismic actions into account or underestimating the seismic hazard at the dam site.

Actually, the seismic performance of these dams needs to be evaluated using more advanced analytical approaches. It is also advisable to provide the dam owners (mostly private) or the local authority in charge of the dam operation with the results of the study carried out, organized in suitable tables or charts to assess the dam safety immediately after the earthquake.

A useful tool, which is increasingly emerging in the field of earth dams as a valid alternative to the traditional deterministic methods, is represented by fragility curves. These are obtained by means of a probabilistic approach that allows the uncertainties associated with the input motion and/or soil properties to be overcome. In addition, the fragility curves represent the anticipated tool that ensures a rapid assessment of the probable damage caused by an earthquake and, in particular, the probability that a certain damage index (DI) exceeds a limit state threshold for a given intensity measure (IM) of the seismic event.

Nowadays, fragility curves have mostly been obtained for concrete and arch dams [1, 2, 3, 4]. A few studies, recently published, refer to large earth dams, mainly concrete-faced rockfill dams (CFRDs) [5, 6, 7], earth-rockfill dams [8], rockfill dams with concrete core [9, 10] and just one study (in the authors' knowledge) concerns tailing dams [11].

In this study, fragility curves were developed for a small zoned earth dam assumed to be placed in an area of medium-high seismic hazard. It represents the prototype of many small dams widespread in Italy and worldwide.

The seismic performance of the dam prototype was evaluated basing on different damage indicators computed through the incremental dynamic analysis method (IDA) using the finite element code Plaxis2D. Peak ground acceleration (PGA), peak ground velocity (PGV) and Arias intensity (AI) were selected as intensity measures (IMs). The failure likelihood for the dam prototype has been researched for the three limit states of minor, moderate, and severe damage.

## 2 MODELING OF THE CASE STUDY

The case study concerns an ideal 13m-high zoned earth dam, composed of sandy shells and a clayey core founded on a rigid foundation (Figure 1). At this stage of the work, this simple configuration of the small dam was selected to avoid site effects and foundation-soil compliance.

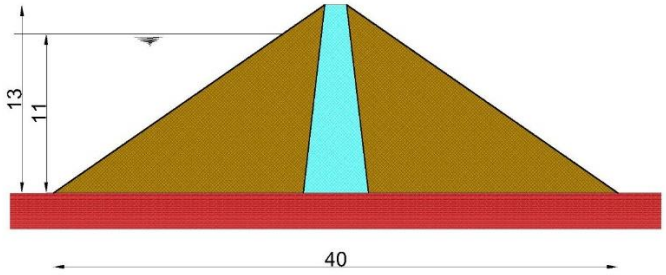


Figure 1: Geometry of the small earth dam.

The dam prototype was modeled in 2D assuming plane strain conditions. To perform the nonlinear dynamic analyses for computing the fragility curves, an elastoplastic constitutive law, defined *Hardening Soil with Small Strain Stiffness* (HS small) implemented in Plaxis2D, was assigned to the different materials of the dam body. It is an advanced constitutive law that is able to describe with sufficient accuracy the non-linear, hysteretic and plastic response of the soil from the small to the high strain levels. To account for the partial saturation of the dam soils, a three-phase formulation was adopted by assigning suitable water retention curves to the core and the shell materials through the *Van Genuchten* formulation (1980) [12]. The static analysis of the dam was preliminarily carried out by simulating the construction of the embankment and the first filling of the reservoir.

The dynamic stage was simulated considering the impounding level fixed at its maximum height ($H_w$=11 m) and by applying the input signal in the horizontal direction along the bottom boundary of the model. In addition to the hysteretic damping provided by the HS-small constitutive law, a small amount of material damping $\xi$ = 1% (initial damping) was attributed to the dam soils through the Rayleigh formulation. The coefficients $\alpha$ and $\beta$, which are respectively proportional to the mass [M] and stiffness [K] matrix, were computed in correspondence of two target frequencies, $f_1$ and $f_2$, as proposed by Hudson et al. [13] or Hash and Park [14]. In this case, $f_1$ was set equal to 5 Hz (almost equal to the first fundamental frequency of the dam body) and $f_2$=3$f_1$. Table 1 summarizes the physical and mechanical parameters attributed to the dam core and shells.

| Parameters | Unit | Clayey core | Sandy shells |
|---|---|---|---|
| $\gamma_{sat}$ | *[kN/m$^3$]* | 22 | 19.6 |
| $\gamma_{unsat}$ | *[kN/m$^3$]* | 21 | 16.3 |
| e | *[-]* | 0.4 | 0.6 |
| $k_{sat}$ | *[m/s]* | 2.8E-10 | 3.5E-5 |
| c’ | *[kPa]* | 14 | 1 |
| φ' | *[°]* | 36 | 41 |
| ψ | *[°]* | 0 | 0 |
| $k_0$ | *[-]* | 0.4 | 0.34 |
| $E_{50}^{ref}$ | *[MPa]* | 8.5 | 19.8 |
| $E_{oed}^{ref}$ | *[MPa]* | 5.5 | 14. |
| $E_{ur}^{ref}$ | *[MPa]* | 25.5 | 59.4 |
| m | *[-]* | 0.98 | 0.5 |
| $G_0^{ref}$ | *[MPa]* | 95 | 165 |
| $\gamma_{0.7}$ | *[-]* | 1.7E-4 | 1.7E-4 |

Table 1: HS-small parameters used in the numerical analysis.

## 3 INPUT SIGNAL SELECTION

To estimate the dam vulnerability against earthquakes, it is necessary to find the relationship between the seismic motion intensity and the structural response so that the probability of exceeding a given limit state may be calculated.

| Signal ID | PGA [g] | IA [m/s] | $T_p$ [s] | $D_{5\text{-}95}$ [s] |
|---|---|---|---|---|
| #Signal_1 | 0.110 | 0.12 | 0.10 | 12.7 |
| #Signal_2 | 0.110 | 0.21 | 0.32 | 16.2 |
| #Signal_3 | 0.140 | 0.46 | 0.16 | 17.5 |
| #Signal_4 | 0.150 | 0.23 | 0.38 | 6.5 |
| #Signal_5 | 1.390 | 0.18 | 0.22 | 14.8 |
| #Signal_6 | 0.069 | 0.21 | 0.20 | 10.0 |
| #Signal_7 | 0.181 | 0.38 | 0.50 | 12.2 |
| #Signal_8 | 1.392 | 0.27 | 0.18 | 34.8 |
| #Signal_9 | 1.800 | 0.25 | 0.11 | 24.6 |
| #Signal_10 | 0.072 | 0.13 | 0.34 | 17.3 |

Table 2: Main parameters of the input signals used for the IDA.

For this purpose, a set of 10 representative acceleration time-histories were selected such that their predominant frequencies include the first natural frequency of the dam (estimated approximately around 5 Hz). Figure 2 shows the amplitude Fourier spectrum of the selected input signals. For computing the fragility curves of the dam, each natural accelerogram was scaled in magnitude from a peak acceleration of 0.11g to 0.44g, trying to avoid scale factors too high for not modifying the signal nature. Considering all waveforms in Table 2 and the 7 scale factors adopted, a total amount of 70 dynamic analyses were performed.

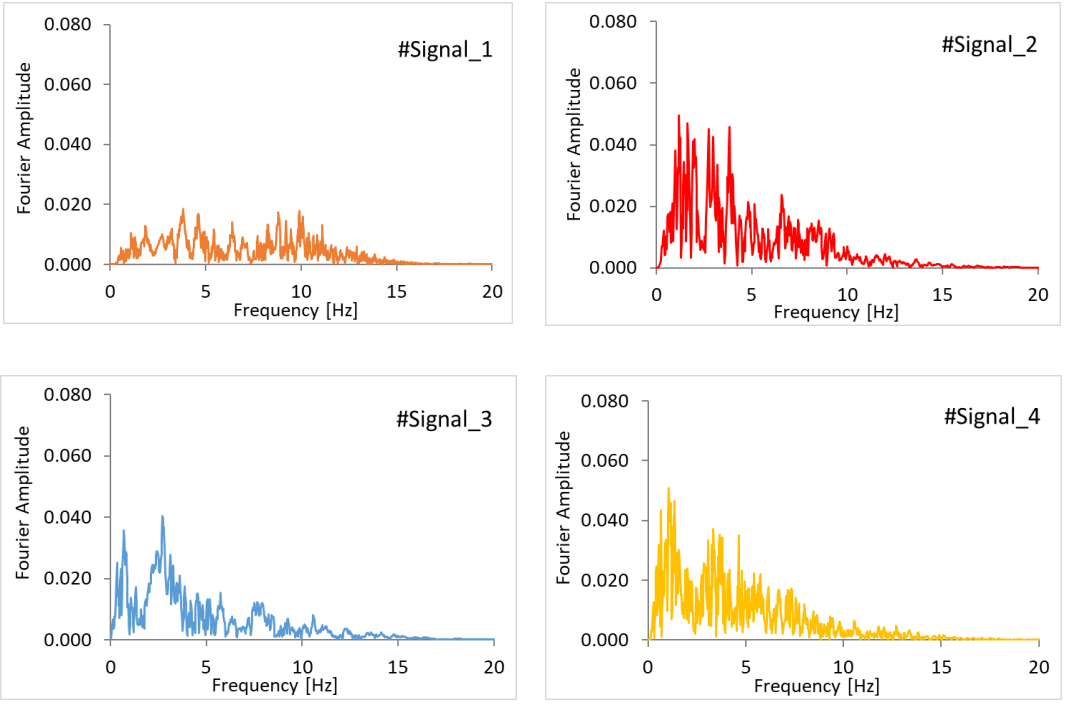

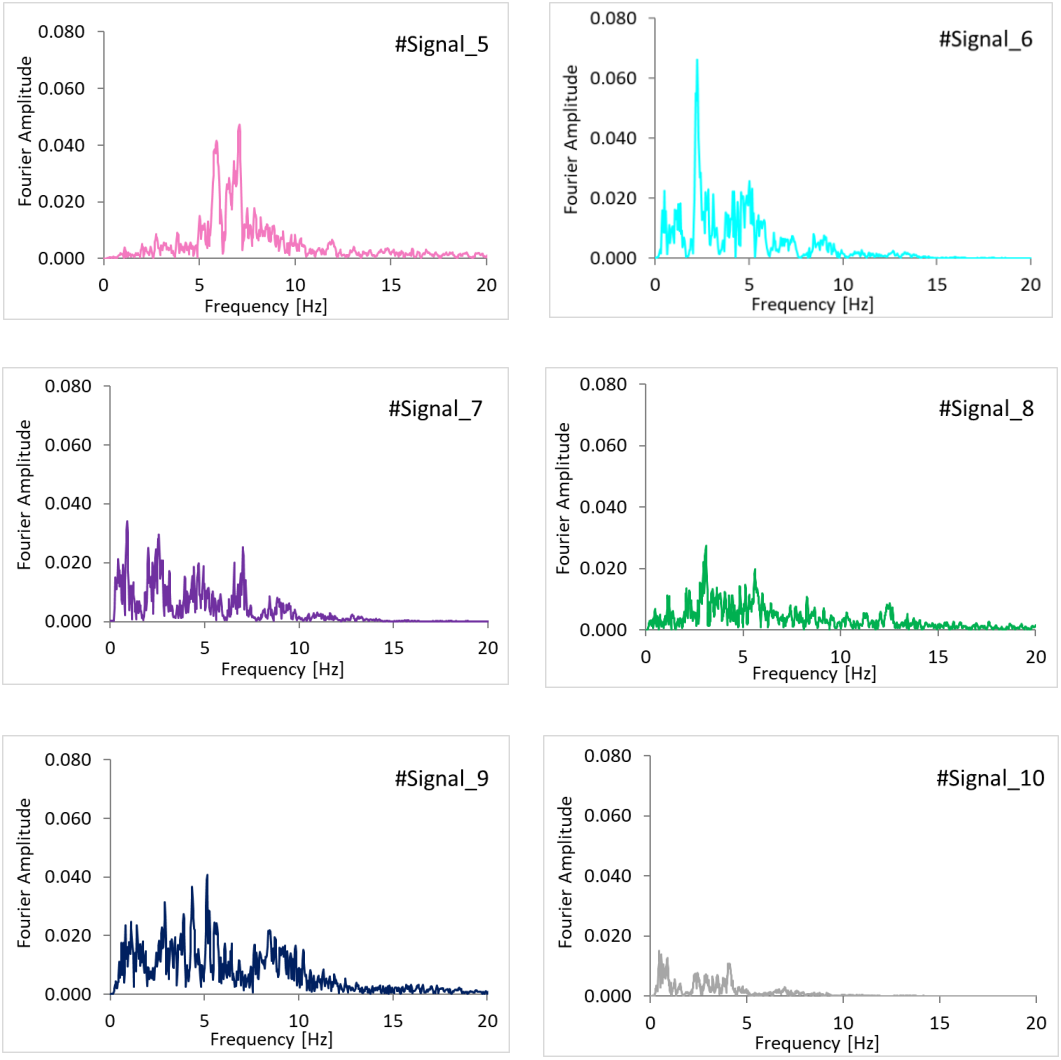


Figure 2: Fourier amplitude spectrum for all the adopted input signals.

As an example, Figure 3 shows the typical deformed configuration of the small dam at the end of the dynamic stage with the input accelerogram #Signal_1, while Figure 4 provides for the corresponding contours of vertical ($u_y$) and horizontal ($u_x$) permanent displacements. Higher displacements were computed on the upstream shell of the dam with a maximum vertical displacement of about 0.16 m and a maximum horizontal displacement of about 0.13 m. The core, instead, denotes a less deformable response.

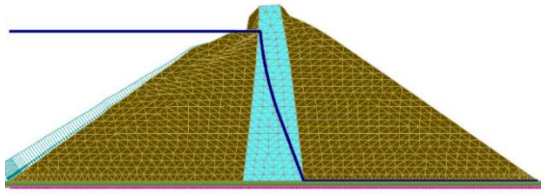

Figure 3: Deformed configuration at the end of the dynamic stage for the representative input #Signal_1.

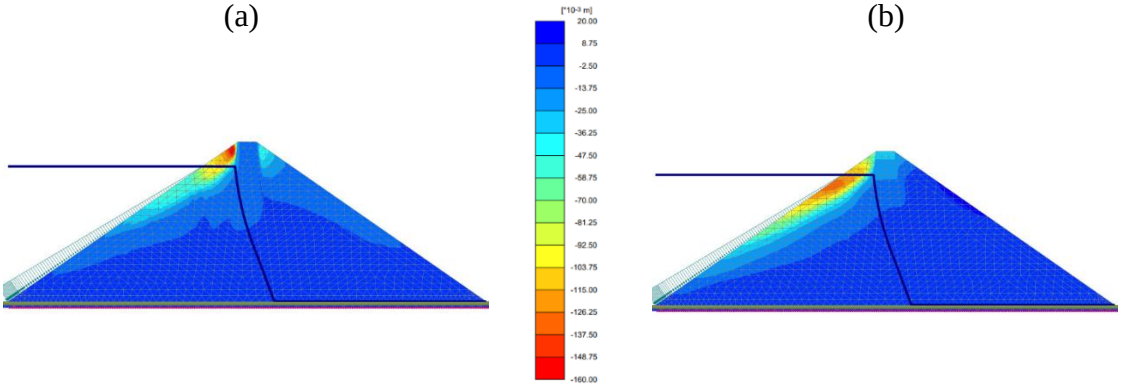


Figure 4: Contour of the (a) vertical and (b) horizontal displacements computed at the end of input #Signal_1.

## 4 FRAGILITY CURVES

### 4.1 Overview of the methodology

The fragility of a structure may be described using the statistical expression of conditional probability. Given two events A and B, it represents the probability of A occurring, knowing that B has happened:

$$P[A|B] \tag{1}$$

In the field of civil engineering, fragility is represented by the probability of exceeding a certain damage measure (DM) given the occurrence of a particular intensity measure (IM):

$$P[d > DM \mid IM=x] \tag{2}$$

In this study, the probability has been mathematically expressed through a log-normal cumulative distribution function, as given by the following equation:

$$P[d > DM \mid IM=x] = 1 - \Phi\left(\frac{\ln x - \ln \theta}{\beta}\right) \tag{3}$$

where $\Phi$ is the standard normal cumulative distribution function; $x$ is the variable of the intensity measure; $\theta$ is the median value of the intensity measure and $\beta$ is the standard deviation of the natural logarithm of the intensity measure.

In particular, the mean value was obtained from the linear regression analysis of the 70 data points obtained through the performed nonlinear time-history analyses using the equation stated below:

$$\theta = A + B \cdot \ln x \tag{4}$$

while the standard deviation of the natural logarithm was obtained as:

$$\beta = \sqrt{\sum_{i=1}^{n} (d_i - \theta_i)^2 / (n-2)} \tag{5}$$

### 4.2 Limit states

For earth dams, different limit states relating to different collapse modes of the dam embankment may be identified. In this study, four damage measures (DMs) were considered to perform the IDA procedure and obtain the fragility curves (Table 3):

- Dimensionless settlement ratio in correspondence of the dam crest (DSR), i.e. the ratio of the vertical displacement of the dam crest to the total height of the dam body. According to the popular classification suggested by Swaisgood [15, 16, 17] or Pells and

Fell [18], three limit states were considered, i.e. 0.2% as minor damage, 0.5% as moderate damage and 1.0% as severe damage;
- the lateral displacements of the dam crest, with the damage thresholds proposed by Idriss [19], namely 15 cm as minor damage, 30 cm as moderate damage and 90 cm as severe damage;
- the freeboard reduction, i.e. the settlement of the upstream vertex of the crest divided by the initial freeboard. Damage thresholds equal to 25% as minor damage, 50% as moderate damage, and 65% as severe damage were considered;
- the maximum plastic shear strain of the watertightness element. This study refers to the classification proposed by Pang et al. [5], who considered three limit states equal to 1.5%, 2.5% and 3.5%, corresponding to minor, moderate and severe damage levels, respectively.

| **Damage measures** | **Threshold** | | |
|---|---|---|---|
| | **Minor** | **Moderate** | **Severe** |
| Settlement ratio (DSR) | 0.2% | 0.5% | 1.0% |
| Lateral displacement (LD) | 15 cm | 30 cm | 90 cm |
| Freeboard reduction (FR) | 25% | 50% | 65% |
| Plastic shear strain (PSS) | 1.5% | 2.5% | 3.5% |

Table 3: Threshold values of the three limit states considered for the damage measures of the small dam.

### 4.3 Results

Figures 5, 6 and 7 shows the fragility curves of the small zoned earth dam on rock foundation, obtained for three intensity measures (PGA, PGV and AI) and the four damage measures mentioned above.

As highlighted in the previous sections, the advantage of these curves is the possibility to obtain an expedited estimation of the possible damage suffered by the structure, once the intensity of the earthquake at the dam site has been estimated. This tool provides for an effective support to identify the critical response or weakness of the structure, which requires a prompt decision by the dam owner.

From all the fragility curves computed (Figures 5 - 7), it emerges that the damage mechanism likely to be mostly overcome is the dimensionless settlement ratio at the dam crest (DSR), followed by the plastic deformation of the watertightness element (PSS) for all the IMs considered (PGA, PGV and AI). Conversely, at first glance, the fragility curve corresponding to the freeboard reduction (FR) does not seem to be as representative as the others DMs. Such a noticeable difference between DSR and FR may be attributed to the damage thresholds that have been identified in literature for the FR measure, being these values not consistent with those assumed for DSR. This aspect has further been investigated in this study by regenerating the fragility curves corresponding to FR with lower thresholds than those listed in Table 3, that is 2% for minor, 6% for moderate and 10% for severe damage.

In Figure 8, the fragility curves of all DMs corresponding to minor and severe damage have been compared. This provides useful information on the probability of exceeding the serviceability or collapse state of the dam for a given value of the IM, provided for example by the seismic stations placed at the dam site.

Among the different intensity measures, it was observed that a lower standard deviation is associated to AI rather than PGA and PGV, as already highlighted in Sica et al. [20]. This supports the use of the Arias Intensity as primary IM for developing fragility curves of earth

dams as it is widely ascertained that AI correlates better with the predicted damage of the dam embankment.

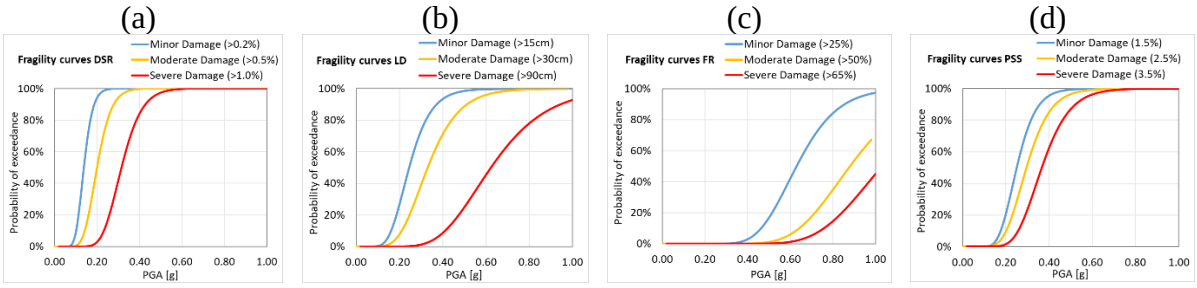


Figure 5: Fragility curves with PGA as intensity measure: (a) settlement ratio at the dam crest (DSR), (b) lateral displacement (LD), (c) freeboard reduction (FR) and (d) plastic shear strain of the watertightness element (PSS)

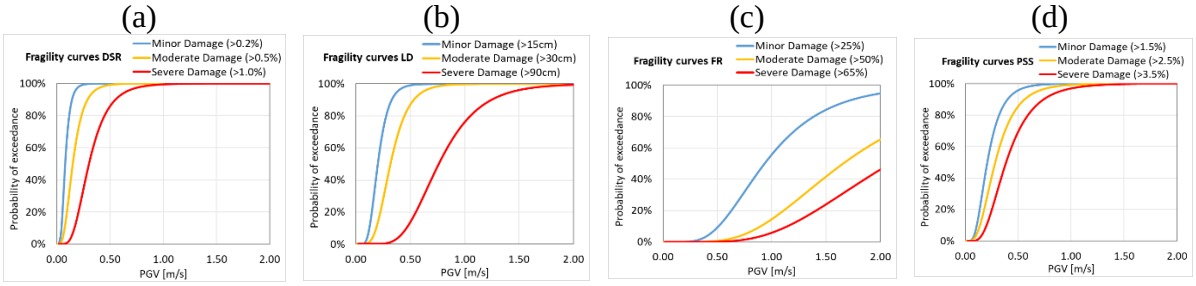


Figure 6: Fragility curves with PGV as intensity measure: (a) settlement ratio at the dam crest (DSR), (b) lateral displacement (LD), (c) freeboard reduction (FR) and (d) plastic shear strain of the watertightness element (PSS)

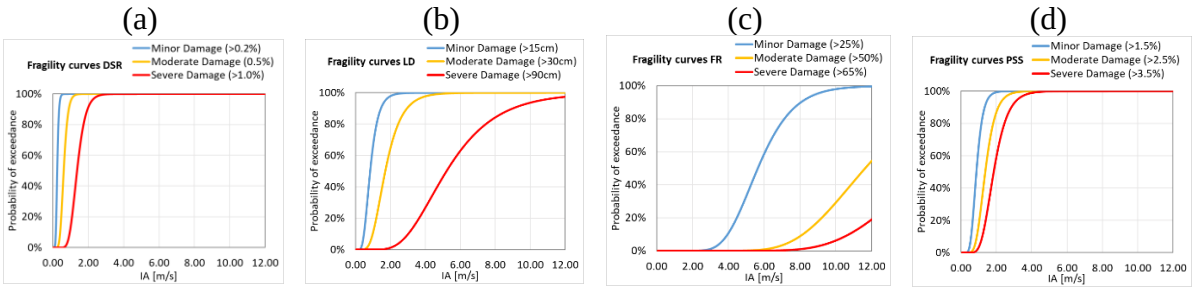


Figure 7: Fragility curves with AI as intensity measure: (a) settlement ratio at the dam crest (DSR), (b) lateral displacement (LD), (c) freeboard reduction (FR) and (d) plastic shear strain of the watertightness element (PSS)

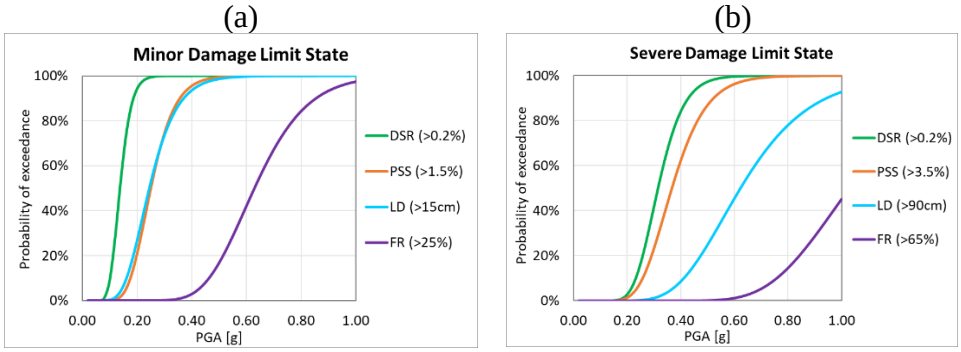


Figure 8: Comparison among the fragility curves for all the DMs considered in this study in case of minor (a) and severe (b) damage limit state.

As a further consideration, the probability of exceeding a certain damage level was evaluated for the limit states prescribed by the Italian technical code for dams [21, 22], assuming that the ideal small dam considered in this work is located on a rock outcrop in a zone characterized by medium-high seismic hazard. For a dam with a reference period $V_R$=75 years, the limit states imposed by the current Italian standards [21, 22] are listed in Table 4, with the corresponding probability of exceeding $P_{VR}$, return period $T_R$ and PGA.

| Limit state | $P_{VR}$ [%] | $T_R$ [years] | PGA [g] |
|---|---|---|---|
| OLS | 81 | 45 | 0.066 |
| DLS | 63 | 75 | 0.085 |
| VLS | 10 | 710 | 0.223 |
| CLS | 5 | 1460 | 0.282 |

Table 4: Limit states, return periods and maximum rock accelerations at the dam site.

Considering the dimensionless settlement ratio at the dam crest as the most sensitive damage measure, the probability of exceedance is almost null for all the damage levels corresponding to DLS. Conversely, for the CLS, there is the almost complete possibility of exceeding minor and moderate damage (100% and 85% respectively) and the 32% of probability of reaching the condition of severe damage. If the fragility curves provided in literature for large zoned earth dams are considered for comparison, it emerges a lower exceedance probability of the same limit states considered in this paper for the small dam on a rigid base. It is worth pointing out that the published fragility curves refer to large dams founded on deformable soil deposits. Therefore, as future perspective of the present study, fragility curves for small earth dams founded on non-rocky soils will be computed.

## 5 CONCLUSIONS

The paper proposed a suite of fragility curves to evaluate the seismic vulnerability of small earth dams. The selected case study is representative of a wider category of tailing or small earth dams, which are often disregarded in control activity, irrespectively of their generally high vulnerability. Fragility curves may be useful tools for a rapid post-earthquake damage assessment and also for planning future repair interventions. The obtained fragility curves indicate the probability that a certain damage level will be exceeded, given the occurrence of an intensity measure. To develop the fragility curves, the randomness of the input ground motion was taken into account and the seismic performance of the reference dam was assessed through finite element analyses considering four damage measures, i.e. the settlement ratio and the lateral displacements at the dam crest, the freeboard reduction and the maximum plastic shear strain of the watertightness element. As an outcome of the study, the Arias Intensity revealed to be the most sensitive intensity measure to assess dam damage. For the small dam considered in this study, among the different damage mechanisms considered, the settlement ratio at the dam crest and the plastic shear strain of the watertightness element presented the higher probability of being exceeded. As future perspective of this research study, additional parametric analyses accounting for the uncertainty related to soil properties and subsoil layer setting will be carried out.

## REFERENCES


[1] Alembagheri, M., & Ghaemian, M. Seismic assessment of concrete gravity dams using capacity estimation and damage indexes. *Earthquake Engineering & Structural Dynamics, 42*(1), 123-144, 2013.

[2] Alembagheri, M., & Ghaemian, M. Damage assessment of a concrete arch dam through nonlinear incremental dynamic analysis. *Soil Dynamics and Earthquake Engineering, 44*, 127-137, 2013.

[3] Hariri-Ardebili, M. A., & Saouma, V. E. Collapse fragility curves for concrete dams: comprehensive study. *Journal of Structural Engineering, 142*(10), 04016075, 2016.

[4] Bernier, C., Padgett, J. E., Proulx, J., & Paultre, P. Seismic fragility of concrete gravity dams with spatial variation of angle of friction: case study. *Journal of Structural Engineering, 142*(5), 05015002, 2016.

[5] Pang, R., Xu, B., Kong, X., & Zou, D. Seismic fragility for high CFRDs based on deformation and damage index through incremental dynamic analysis. *Soil Dynamics and Earthquake Engineering, 104*, 432-436, 2018.

[6] Pang, R., Xu, B., Zou, D., & Kong, X. Seismic performance assessment of high CFRDs based on fragility analysis. *Science China Technological Sciences, 62*, 635-648, 2019.

[7] Pang, R., Xu, B., Zhou, Y., Zhang, X., & Wang, X. Fragility analysis of high CFRDs subjected to mainshock-aftershock sequences based on plastic failure. *Engineering Structures, 206*, 110152, 2020.

[8] Jin, C., & Chi, S. Seismic fragility analysis of high earth-rockfill dams considering the number of ground motion records. *Mathematical Problems in Engineering, 2019*, 1-12, 2019.

[9] Ayati Ahmadi, A., Noorzad, A., MohammadNezhad, H., & Mirghasemi, A. A. Seismic Fragility of Rockfill Dams with Asphaltic Concrete Core. *Iranian Journal of Science and Technology, Transactions of Civil Engineering*, 1-14, 2022.

[10] Khalaj, O., Ayati Ahmadi, A., Abedin Nejad, S., Mašek, B., Štadler, C., & Skála, J. Evaluation of the effect of varying the angle of asphaltic concrete core on the behavior of the meijaran rockfill dam. *Coatings*, 12(6), 720, 2022.

[11] Boada, G., Pasten, C., & Heresi, P. Analytical fragility curves for abandoned tailings dams in North-Central Chile. *Soil Dynamics and Earthquake Engineering, 164*, 107637, 2023.

[12] Brinkgreve, R.B.J. PLAXIS 2D Manuals. General Information. Tutorial Manual. Reference Manual. Ma-terial Models Manual. Scientific Manual. Delft Univer-sity of Technology & PLAXIS. ISBN13.978(90). 76016, 2018.

[13] Hudson, M. A. R. T. I. N., Idriss, I. M., & Beikae, M. QUAD4M: a computer program to evaluate the seismic response of soil structures using finite element procedures and incorporating a compliant base. Center for Geotechnical Modeling, Department of Civil and Environmental Engineering, University of California, Davis, 1994.

[14] Hashash, Y. M., & Park, D. Viscous damping formulation and high frequency motion propagation in non-linear site response analysis. *Soil Dynamics and Earthquake Engineering, 22*(7), 611-624, 2002.

[15] Swaisgood, J. R. Embankment dam deformations caused by earthquakes. In *Pacific conference on earthquake engineering* (Vol. 14), 2003.

[16] Swaisgood J. R. Seismically-induced deformation of embankment dams. *In proceedings of sixth national conference on earthquake engineering. Seattle, Washington, U. S. A.*, 1998.

[17] Swaisgood, J. R., & Au-Yeung, Y. Behavior of dams during the 1990 Philippines earthquake. In *ASDSO Annual Conference*, 1991.

[18] Pells, S., & Fell, R. Damage and cracking of embankment dams by earthquakes and the implications for internal erosion and piping. University of New South Wales, School of Civil and Environmental Engineering, 2002.

[19] Idriss, I. M. Evaluating seismic risk in engineering practice. Proceedings of the eleventh international conference on soil mechanics and foundation engineering, San Francisco, 12-16. *Publication of: Balkema (AA)*, 1985.

[20] Sica, S. & Pagano, L. Performance-based analysis of earth dams: Procedures and application to a sample case. *Soils and Foundations* 49(6), pp. 921-939, 2009.

[21] MIT, Ministero delle Infrastrutture e dei Trasporti 2014. Norme tecniche per la progettazione e la costruzione degli sbarramenti di ritenuta (dighe e traverse). Decreto del Ministro 26 giugno 2014, Gazzetta Ufficiale n°156 del 08.07.2014 (in Italian), 2014.

[22] NTC2018, Norme tecniche per le costruzioni, D.M. 17/01/2018, Gazzetta Ufficiale n. 35 del 20.02.2018, Suppl. Ord. n.42, 2018. 2018.

COMPDYN 2023
9th ECCOMAS Thematic Conference on
Computational Methods in Structural Dynamics and Earthquake Engineering
M. Papadrakakis, M. Fragiadakis (eds.)
Athens, Greece, 12-14 June 2023

# EFFECT OF SOIL-STRUCTURE INTERACTION ON THE DYNAMIC IDENTIFICATION OF A PRESTRESSED CONCRETE BRIDGE

**Ambrosino A.**[1], **De Angelis A.**[1], **Pecce M.R.**[2], **and Sica S.**[1]

[1] Department of Engineering, University of Sannio, Benevento-Italy
e-mail: anambrosino@unisannio.it

[2] Department of Structures for Engineering and Architecture
University of Naples Federico II, Naples

## Abstract

*In recent years, safety assessment of existing bridges is becoming an urgent and critical issue in light of the increased number of collapses observed worldwide, most of which related to the high vulnerability of the structure itself due to material (concrete or steel) degradation over the years. In seismically-active areas, vulnerability of existing bridges might combine to the high seismic hazard of the site. The fatal consequence is that after a strong earthquake, total or partial interruption of the road infrastructure could occur with the bridge behaving as the weakest component of the chain. In order to shed light on the seismic response of existing r.c. bridges, the paper illustrates the numerical procedure developed by the authors to investigate the dynamic response of a pre-stressed reinforced concrete bridge placed in the highly seismic area of Benevento (IT). The paper investigates the effect of soil-structure interaction on the dynamic behavior of the bridge. A detailed 3D model representing the structure and the soil deposit was developed and solved through the finite element method with the software MIDAS FEA NX. The use of a 3D continuum approach also for the subsoil was motivated by the huge stratigraphic and topographical variability characterizing the soil deposit. After the calibration of the soil model, the bridge was added. At this stage of the work, the structure was modelled through solid elements and a perfect contact was imposed between the piers and the soil. A modal analysis was conducted on the complete model made of both soil and bridge to get the natural oscillation frequencies and mode shapes of the coupled system. These results were later compared to those provided by the analyses in which the superstructure was modelled with a fixed base or a compliant base with springs.*

**Keywords:** Soil Structure Interaction, Finite element analysis, Modal Analysis, Pre-stressed concrete bridge.

## 1 INTRODUCTION

In the last few years, there have been a high number of bridges collapsed both in Italy and abroad. This is due to the lack of inspections and maintenance of the road infrastructure, which has led to widespread deterioration of materials, especially for reinforced concrete bridges. Therefore, there is an increasingly urgent need for an assessment of the health condition of bridges [1], particularly in Italy. This urgency is enhanced by the fact that bridges and viaducts constitute infrastructure networks of strategic importance for the management of seismic and post-seismic emergencies in consideration of the high seismicity of large part of the Italian territory. As well as providing an escape route for the local population, they are also part of the main arteries for the arrival of emergency vehicles.

The dynamic identification of bridges has become an increasingly widespread technique, supported by numerous studies and research [4], to implement accurate and reliable models to perform later more complex analyses. Indeed, a common practice is to perform Ambient Vibration Testing (AVT) to assess the dynamic properties of existing structures within the elastic domain, simply using natural vibrations (e.g., micro-vibrations, wind, and anthropogenic activity). The obtained experimental dynamic properties in terms of vibration frequencies, damping and modal shapes are then used for the calibration of numerical models, which will be useful for design purposes. It is common practice to update the numerical model by changing the material properties in order to match the experimental dynamic response to that provided by the numerical model. This is usually assumed to be fixed based [5].

Reinforced concrete bridges are generally characterized by a strong development in length (hundreds of meters up to kilometers). Therefore, the analysis of the structure alone, even schematized with fixed constraints at its base, could not always correctly and exhaustively represent the real dynamic response of the structure. In fact, the dynamic response of the superstructure may significantly be modified if soil-structure-interaction (SSI) phenomena between the superstructure, the underlying foundation and the lateral soil take place. For long span bridges and viaducts, SSI effects may combine to ground motion asynchrony due to soil heterogeneity at the pier foundations [7].

Several studies accounting for soil-structure interaction in case of bridges can be found in literature [10]. Most studies use the simplified sub-structure approach, in which ground response, kinematic interaction (for defining input motion, FIM) and inertial interaction are analyzed separately. Complete three-dimensional models [18] are not yet widespread due to the complexity of modelling real morphological and soil layering setting (valleys, slopes, high stratigraphic variability) and the difficulty in solving complex numerical models with the available commercial softwares [21].

Developing numerical models including SSI is challenging, especially for existing bridges. It is well known that SSI could lead to a reduction of the fundamental frequency of the coupled system and, hence, to a modification of the seismic action at the base of the piers [22].

The aim of this work is to quantify the role of SSI on the dynamic behavior of a prestressed concrete bridge, strategic for the city of Benevento. The bridge is characterized by piers also working as abutments (pier-abutment). For this reason, a detailed three-dimensional model of the overall superstructure (deck and piers), with the foundations and the subsoil interacting with the bridge has been developed. Finally, the modal shapes and natural frequencies of the bridge were computed numerically and compared with those obtained experimentally during the investigation works detailed in [27].

## 2 SAN NICOLA BRIDGE

The San Nicola bridge, located in the city of Benevento (Italy), connects the Capodimonte area with the upper part of the city, known as Cretarossa district (Figure 1). The structure was designed in between 1952 and 1955 by the engineer Riccardo Morandi, who also designed the much more famous bridge over the Polcevera River in Genoa, collapsed in 2018. A detailed analysis of the San Nicola bridge can be found in the previous studies [27], the most important data of which are recalled hereinafter.



(a) (b)

Figure 1 : Side view (a) and detail of the abutment (b) of the San Nicola Bridge

The bridge deck is made of pre-stressed concrete, cast in situ, while the piers and foundations are made of reinforced concrete. As shown in Figure 2, the deck consists of 80 m-long main span and two 20 m-long side cantilevers. The deck has a variable depth across the spans (beam with curved intrados), providing for a beneficial arch effect. It consists of four pre-stressed box girders whose thickness varies from a minimum of 13cm in the center to a maximum of 30cm at the supports. A lower slab, forming a multi-cell box section with 8 cells, completes the section in the negative moment zone. The total width of the bridge is 9 m with a deck of 7 m.

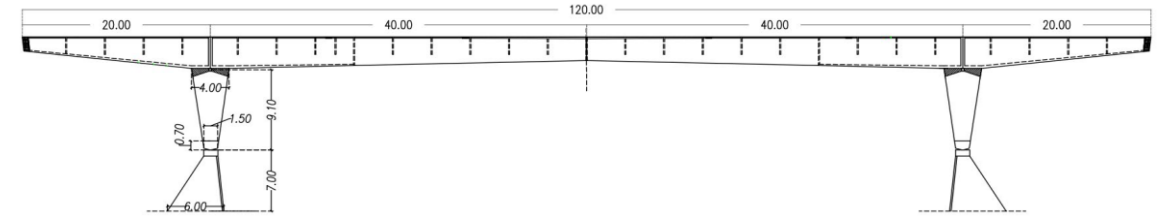


(a)

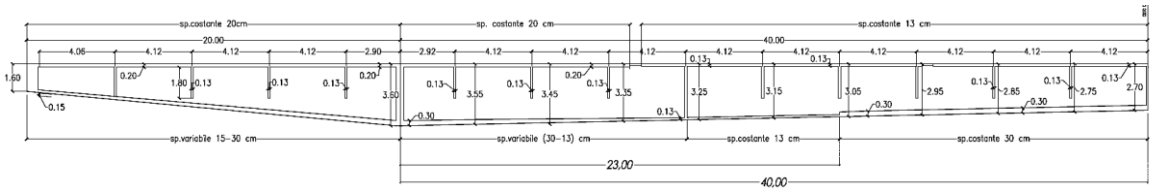


(b)

Figure 2: (a) Longitudinal scheme of the bridge and (b) detail of the deck

The two 9.40 m-high piers are connected to the foundations by steel hinges (see Figure 3b). The piers consist of eight rectangular columns, 40.0 cm-thick and variable in width from 1.50 m at the base to 4.00 m at the top. They are connected at the base and top by a transverse beam (see Figure 3a).

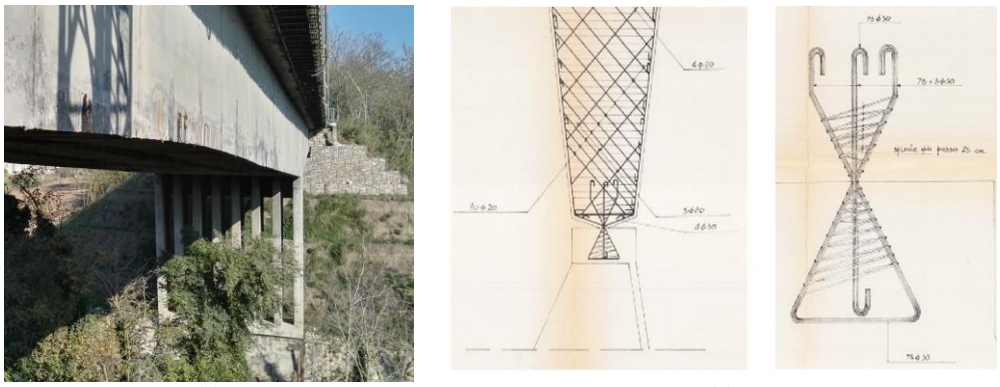

(a) (a)

Figure 3: Transversal view of the pier (a) and original detail of the hinges (b).

The structure is very complex and innovative for its time, also in terms of foundation geometry (Figure 4). Furthermore, the San Nicola Bridge is a rare case of a bridge with a pier-abutment, unlike other cases where the main structural elements of the bridge (deck, pier, and abutment) are clearly identified. The foundation is very similar to the structure of the pier itself, with eight columns, each one 40 cm thick, connected at the top by a rigid transverse element. As an outcome of several tests carried out on the foundation structure in 2020, it was discovered that the laminae are filled with sandy soils.

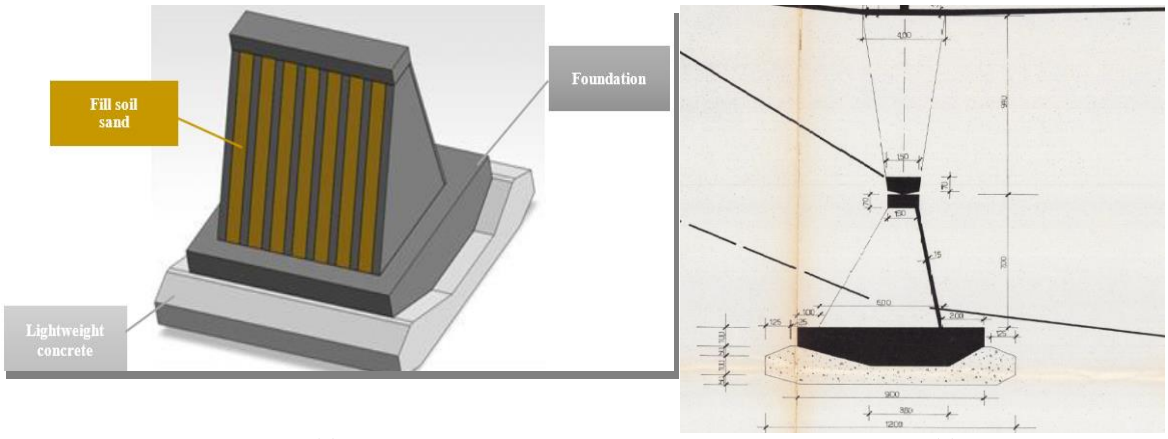


(a) (a)

Figure 4: 3D detail (a) and the original scheme (b) of the foundation – abutment.

## 3 GEOPHYSICAL AND GEOTECHNICAL SITE DATA

For the geotechnical characterization of the site in correspondence of the bridge piers, two different experimental campaigns were performed, the former carried out in 2015 for the stabilization of the right slope and the latter in 2020. Three boreholes with Standard Penetration Test (SPT) were carried out together with laboratory tests (oedometer test and triaxial tests)

on the fine-grained materials. The characterization of the soil shear wave velocity in correspondence of the right pier was achieved through a downhole test (DH) and a Multichannel Analysis of Surface Waves (MASW) test while for identifying the fundamental frequencies of the subsoil close to the pier base Horizontal-to-Vertical Spectral Ratio (HVSR) analyses were carried out. The location of above-mentioned tests is schematically shown in Figure 5.

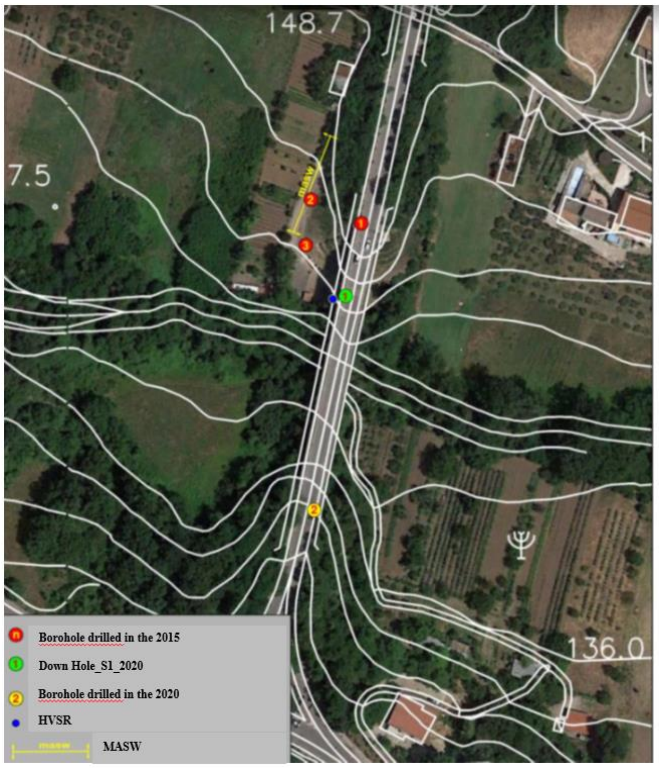


Figure 5: Overview of the bridge valley with location of the geotechnical investigations carried out in 2015 and 2020.

The performed investigations lead to the 2D geotechnical model shown in Figure 6. In the same figure the schematic location of the boreholes and the bridge have been overlapped.

The following soil layers have been identified: an artificial fill (AF), alluvial deposits consisting of sand and gravel (YS), fluvial colluvial deposits (FC), alluvial deposits consisting of sandy silt to clayey places (LS), and blue-grey clayey silt (BGC). The rigid bedrock formation, represented by the bottom blue-grey clay layer, was detected at a depth of 65 m from the ground level in correspondence of the east pier (borehole S1-2020). The main physical and mechanical parameters for each soil layer are reported in Table 1.

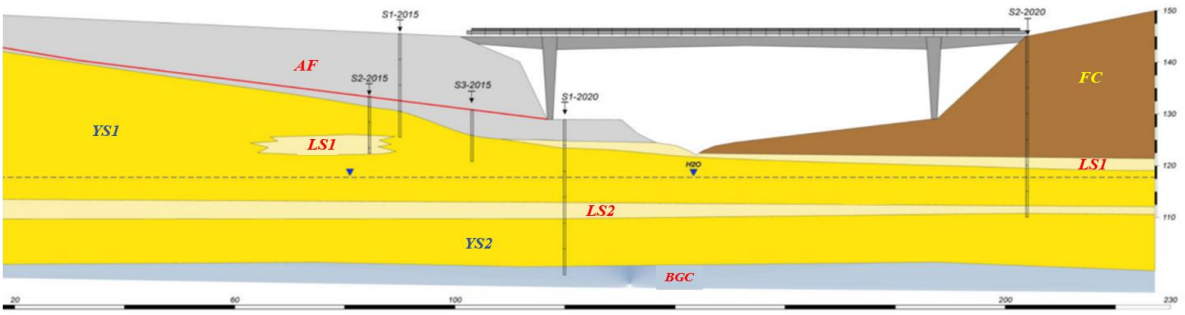


Figure 6: Longitudinal section of the valley with a superimposed sketch of the bridge

| Layer | $\gamma$ [kN/m$^3$] | $V_s$ [m/s] | $G_0$ [MPa] | $D_0$ [%] |
|---|---|---|---|---|
| AF | 18 | 370 | 256 | 2 |
| FC | 18 | 185 - 225 | 63 - 94 | 2 |
| LS 1 | 18 | 320 | 198 | 2 |
| YS 1 | 21 | 300 - 640 | 192 - 903 | 2 |
| LS 2 | 18 | 660 | 822 | 2 |
| YS 2 | 21 | 680 | 1004 | 2 |
| BGC | 19 | 650 | 815 | 2 |
| Bedrock | 19 | 800 | 1200 | 2 |

Table 1: Physical and mechanical parameters assigned to the soil layers

## 4 NUMERICAL MODELS

For the dynamic characterization of the bridge, a 3D finite element model was developed with the software MIDAS FEA NX [29]. As stated above, two numerical models were built: a fixed base model (FB) with the superstructure only and a complete model (SSI) with the bridge structure, the foundations and the soil. The FB model is the reference one for evaluating the soil contribution to the overall dynamic response of the structure.

### 4.1 Fixed base model (FB)

The geometry of the structure was determined according to the results of the geometric surveys and in-situ inspections, as detailed in [27]. The various components of the structure were modeled considering their real geometry with three-dimensional (solid) finite elements, obtaining the 3D model of the structure (deck+piers) shown in the Figure 7. This model was restrained at the base by means of hinges. The steel sidewalk, added after the construction of the bridge, was modelled by the insertion of a longitudinal beam (frame element) with transverse stiffness equivalent to the sidewalk-guard-rail-parapet system that runs along the entire deck. In particular, the bridge was modeled as a continuous homogeneous material using a tetrahedral mesh with a size of 0.3 m. At this stage of the work, a linear-elastic constitutive model was attributed to the bridge material, with the mechanical properties listed in Table 2. The assigned parameters were derived from a previously developed and tuned f.e. model [27].

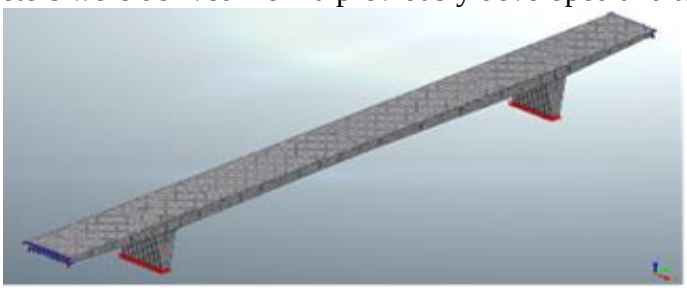

Figure 7: Fixed-base model of the San Nicola Bridge in MIDAS FEA-NX

| Element | $f_{cm}$ [MPa] | E [MPa] |
|---|---|---|
| Deck | 46.1 | 32965 |
| Piers | 33.8 | 2400 |

Table 2: Mechanical parameters for the bridge

The in-situ dynamic tests [27] showed that the lateral cantilevers of the San Nicola Bridge in its current state are constrained horizontally (due to the filling of the expansion joint with concrete) and vertically, due to retaining walls (gabions) built a few decades after the bridge construction. Consequently, in the structural model fixed horizontal constraints and vertical springs were inserted at the ends of the bridge cantilevers consistently with the previous study [27]. In summary, the constraint conditions adopted in the FB model of the bridge are as follows: fixed longitudinal hinge-type constraints; vertical and lateral elastic constraints at the ends of the two bridge cantilevers for representing the interaction with the road abutments and gabions, and hinges at the base of the piers.

### 4.2 Full model (SSI)

The full model was obtained by adding the foundation below each pier and the soil volume interacting with the bridge itself. One of the most complex aspects of the overall modelling procedure was to reproduce the real morphology of the valley. For this purpose, the photogrammetric survey of the Municipality of Benevento was used, and the 3D digital elevation model of the strait was generated.

The overall soil domain corresponds to a volume with a plan of 250m x 200m and a height of 67 m (Figure 8a). This soil domain, made of solid tetrahedral elements with the size respecting the Kuhlemeyer and Lysmer's (1973), contains the different soil layers described in section 3. All soil layers were assumed to have a linear elastic behavior, with the physical and mechanical properties listed in Table 1. To improve model accuracy, the f.e. mesh was made denser close to the bridge foundations. Solid elements with a tetrahedral mesh size of 0.3 m were also used for the abutments. In this first stage of the work, a perfect contact between the pier foundations and the surrounding soil was considered. The same constraints of the FB model at the boundaries between the soil and the bridge lateral cantilevers were adopted.

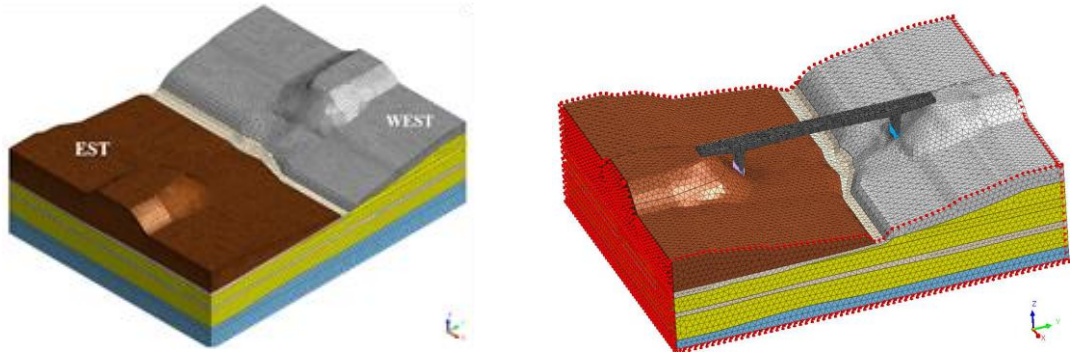


(a) (b)

Figure 8: Ground domain (a) and full model (b) in MIDAS FEA-NX

## 5 RESULTS

To investigate the influence of soil compliance on the dynamic response of the bridge in the linear field, only modal analyses were performed on the two numerical models described above, FB and SSI. The calibration of the numerical model on the experimental data is the first step to perform later on more complex analyses, such as the seismic analysis of the bridge. For this reason, the numerical results (num) obtained by modal analysis were compared to the experimental results (exp) obtained from the in-situ test [27], in terms of frequency discrepancy, $D_f$, through eq. (1) and modal assurance criterion MAC [30], defined in eq. (2).

$$D_f = \frac{\left(f_{num} - f_{exp}\right)}{f_{exp}} \tag{1}$$

$$MAC = \frac{\left(\{\varphi_{num}^T\}\cdot\{\varphi_{exp}\}\right)^2}{\left(\{\varphi_{num}^T\}\cdot\{\varphi_{exp}\}\right)\cdot\left(\{\varphi_{num}^T\}\cdot\{\varphi_{exp}\}\right)} \tag{2}$$

## 5.1 Modal Analysis for the FB model

The results of the modal analysis on the FB model in terms of fundamental frequencies and modal shapes are summarized in Figure 10 and Table 3. It is worth to note that a good match between the experimental and the numerical modal shapes (see the MAC values in Table 3) was obtained, especially for the first two vibration modes of the bridge. Higher frequency discrepancies of 40% and 14% were respectively obtained for the transverse bending mode (first mode) and the vertical torsional mode (third mode) while the value is acceptable for the vertical bending mode (second mode).

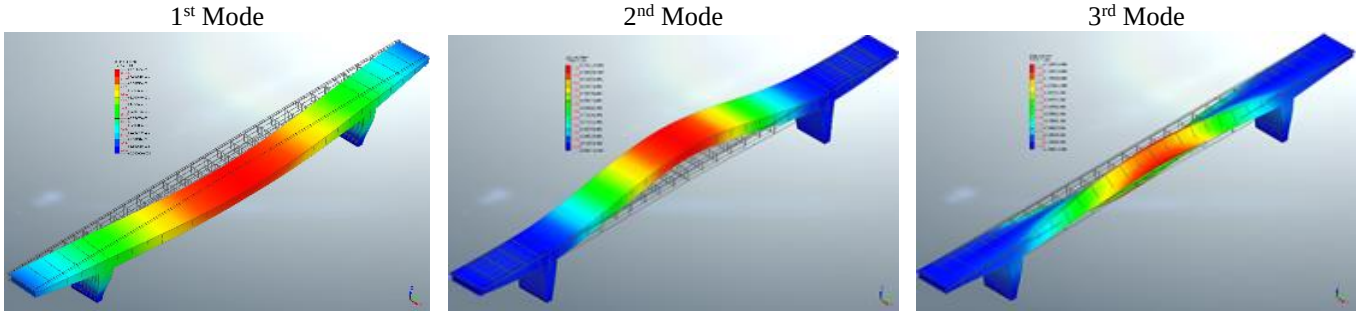


Figure 9: Numerical modal shapes of the FB model

| Mode N. | Mode Type | $f_{exp}$ [Hz] | $f_{num}$ [Hz] | $D_f$ [%] | MAC [-] |
|---|---|---|---|---|---|
| 1 | Transverse bending mode | 1.19 | 1.97 | 40 | 95 |
| 2 | Vertical bending mode | 2.12 | 2.22 | 5 | 94 |
| 3 | Vertical torsional mode | 5.64 | 6.61 | 14 | 88 |

Table 3: Comparison between experimental and numerical results for the FB model

Figure 10 shows the almost perfect overlapping between the numerical and experimental mode shapes along the two lanes of the bridge.

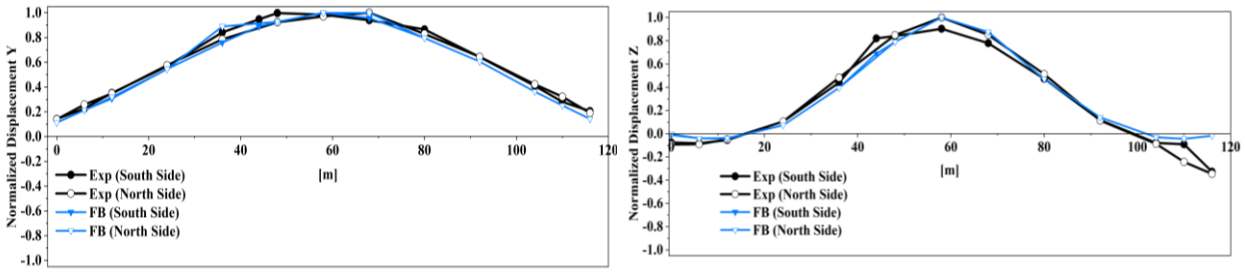


(a) Transverse bending mode

(b) Vertical bending mode

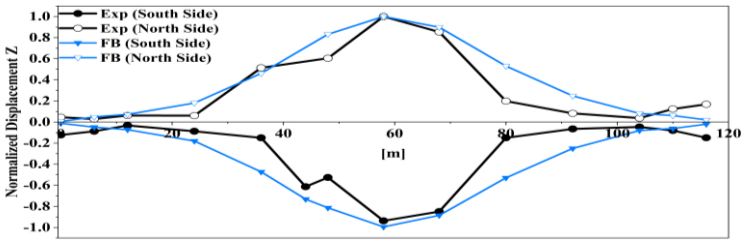


(c) Vertical torsional mode

Figure 10: Comparison of the experimental and the numerical modal shapes: (a) transverse bending mode; (b) vertical bending mode; (c) vertical torsional mode

## 5.2 Modal Analysis for the SSI model

To identify the dynamic response of the compliant base model (SSI), a preliminary model containing only the soil below the bridge valley was firstly validated [31]. In short, the modal analysis procedure, typically used in the structural field, was also extended to the soil in order to identify the fundamental frequencies of the soil deposit and the corresponding modal shapes. For the soil, a more complex frequency response was predicted as more exhaustively described in [31].

Once the soil model was validated, the modal analysis was then carried out on the full model encompassing the bridge and the soil. For such an aim, fixed constraints along the base and free-field elements along the lateral boundaries of the soil domain were adopted.

Figures 11 and Table 4 show the results of the modal analysis on the SSI model in terms of fundamental frequencies and modal shapes. In Figure 12 the comparison between the experimental and the numerical results is also provided. Due to soil contribution, the SSI model gives lower eigenfrequencies (more flexible) than the fixed-base model. From Table 4, a closer agreement between the numerical and experimental data may be observed. Compared to the fixed base model, the SSI contribution appears stronger on the third mode of vibration.

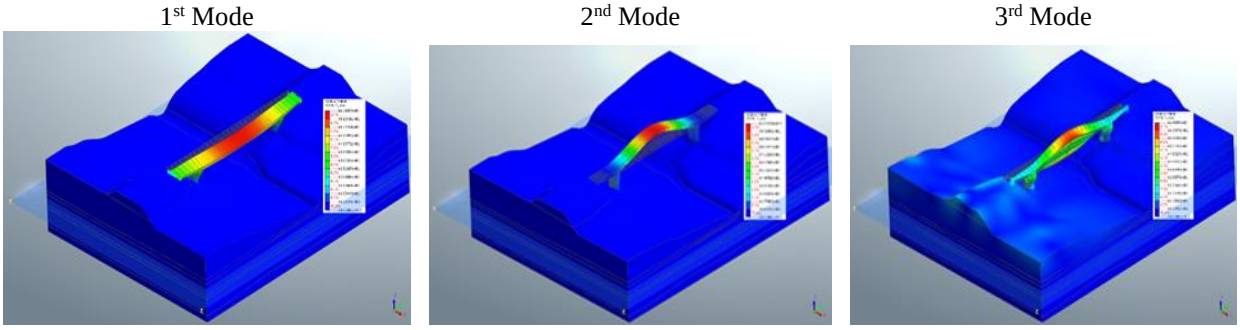


Figure 11: Numerical modal shapes for the SSI model

| Mode Type | $f_{exp}$ [Hz] | Fixed-Based model (FB) | | | Full Model (SSI) | | |
|---|---|---|---|---|---|---|---|
| | | $f_{num}$ [Hz] | $D_f$ [%] | MAC [-] | $f_{num}$ [Hz] | $D_f$ [%] | MAC [-] |
| Transversal bending mode | 1.18 | 1.97 | 40 | 95 | 1.56 | 24 | 99 |
| Vertical bending mode | 2.12 | 2.22 | 5 | 94 | 2.08 | -2 | 96 |
| Vertical torsional mode | 5.69 | 6.61 | 14 | 88 | 6.02 | 5 | 92 |

Table 4 Comparison between experimental and numerical results for the FB and SSI models

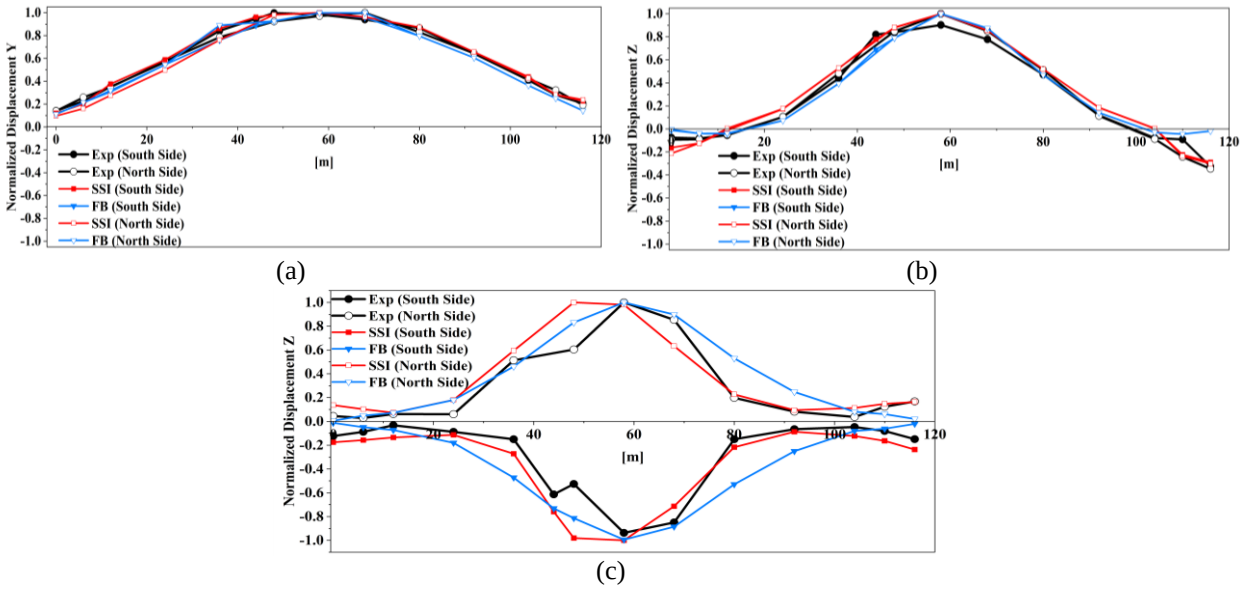


Figure 12: Comparison between experimental and numerical modal shapes for the SSI model: (a) transverse bending mode; (b) vertical bending mode; (c) vertical torsional mode

## 6 CONCLUDING REMARKS

This paper describes the first results of a more comprehensive numerical study aimed at evaluating the effect of soil-structure interaction on the dynamic behavior of a pre-stressed reinforced concrete bridge built in the 1950s. The objective of the study is the definition of an accurate model including the structure and the soil, which is propaedeutic to investigate the seismic performance of the bridge through advanced analyses. Based on the results of these preliminary analyses, the following main conclusions may be drawn:

- The fixed base model of the bridge allows modal shapes to be properly reproduced but the corresponding frequencies are significantly different from those obtained experimentally with values of frequency discrepancy ($D_f$) factor up to 40% .
- The contribution of soil compliance in the numerical model allows the best-fitting of both experimental frequencies and modal shapes of the bridge. The frequency discrepancy ($D_f$) is significantly reduced, especially for the last two modes. The values of the MAC also improved, especially for the higher-order torsional mode.

The outcomes of the performed study highlight the limits of the common practice of updating the fixed-base numerical model of a bridge to match the experimental results of environmental vibration tests by modifying only the mechanical properties of the construction materials. Accurate numerical models, which include also soil contribution, may turn to be essential to perform also advanced seismic analyses, to properly reproduce ground motion asynchronism in correspondence of the bridge piers and abutments.

## REFERENCES


[1] Van der Auweraer, H., & Peeters, B. International research projects on structural health monitoring: an overview. *Structural Health Monitoring*, 2(4), 341-358. 2003.

[2] Zonta, D., Glisic, B., & Adriaenssens, S. Value of information: impact of monitoring on decision-making. *Structural Control and Health Monitoring*, *21*(7), 1043-1056. 2014.

[3] Morassi, A., & Tonon, S. Dynamic testing for structural identification of a bridge. *Journal of bridge engineering*, *13*(6), 573-585. 2008.

[4] Wilson, J. C., & Liu, T. Ambient vibration measurements on a cable-stayed bridge. *Earthquake engineering & structural dynamics*, *20*(8), 723-747. 1991.

[5] Mottershead, J. E., & Friswell, M. I. Model updating in structural dynamics: a survey. *Journal of sound and vibration*, *167*(2), 347-375. 1993.

[6] Zárate, B. A., & Caicedo, J. M. Finite element model updating: Multiple alternatives. *Engineering Structures*, *30*(12), 3724-3730. 2008.

[7] Capatti, M. C., Tropeano, G., Morici, M., Carbonari, S., Dezi, F., Leoni, G., & Silvestri, F. Implications of non-synchronous excitation induced by nonlinear site amplification and of soil-structure interaction on the seismic response of multi-span bridges founded on piles. *Bulletin of Earthquake Engineering*, *15*, 4963-4995. 2017.

[8] Conțiu, M., Ghiocel, D. M., Crețu, D., & Botiș, M. F. A Step-by-Step Probabilistic Seismic Soil–Structure Interaction Analysis with Ground Motion Incoherency for a Bridge Pier on Bored Pile Foundations. *Applied Sciences*, *12*(4), 1828. 2022.

[9] Chouw, N., & Hao, H. Significance of SSI and nonuniform near-fault ground motions in bridge response I: Effect on response with conventional expansion joint. *Engineering Structures*, *30*(1), 141-153. 2008.

[10] Carbonari, S., Morici, M., Dezi, F., Gara, F., & Leoni, G. Soil-structure interaction effects in single bridge piers founded on inclined pile groups. *Soil Dynamics and Earthquake Engineering*, *92*, 52-67. 2017.

[11] Dezi, F., Carbonari, S., Tombari, A., & Leoni, G. Soil-structure interaction in the seismic response of an isolated three span motorway overcrossing founded on piles. *Soil Dynamics and Earthquake Engineering*, *41*, 151-163. 2012.

[12] De Angelis, A., Mucciacciaro, M., Pecce, M.R., Sica, S. Influence of SSI on the Stiffness of Bridge Systems Founded on Caissons. Journal of Bridge Engineering 2017; 22(8): 04017045.

[13] Kappos, A. J., Manolis, G. D., & Moschonas, I. F. Seismic assessment and design of R/C bridges with irregular configuration, including SSI effects. *Engineering Structures*, *24*(10), 1337-1348. 2002.

[14] Elgamal, A., Yan, L., Yang, Z., & Conte, J. P. Three-dimensional seismic response of Humboldt Bay bridge-foundation-ground system. *Journal of structural engineering*, *134*(7), 1165-1176. 2008.

[15] Zani, G., Martinelli, P., Galli, A., Gentile, C., & di Prisco, M. Seismic assessment of a 14th-century stone arch bridge: role of soil–structure interaction. *Journal of Bridge Engineering*, *24*(7), 05019008. 2019.

[16] Mucciacciaro, M., Gerolymos, N., & Sica, S. Seismic response of caisson-supported bridge piers on viscoelastic soil. *Soil Dynamics and Earthquake Engineering*, *139*, 106341. 2020.

[17] Wang, Z., Dueñas-Osorio, L., & Padgett, J. E. Seismic response of a bridge–soil–foundation system under the combined effect of vertical and horizontal ground motions. *Earthquake Engineering & Structural Dynamics*, *42*(4), 545-564. 2013.

[18] Gara, F., Regni, M., Roia, D., Carbonari, S., & Dezi, F. Evidence of coupled soil-structure interaction and site response in continuous viaducts from ambient vibration tests. *Soil Dynamics and Earthquake Engineering*, *120*, 408-422. 2019.

[19] Güllü, H., & Jaf, H. S. Full 3D nonlinear time history analysis of dynamic soil–structure interaction for a historical masonry arch bridge. *Environmental Earth Sciences*, *75*, 1-17. 2016.

[20] Güllü, H., & Özel, F. Microtremor measurements and 3D dynamic soil–structure interaction analysis for a historical masonry arch bridge under the effects of near-and far-fault earthquakes. *Environmental Earth Sciences*, *79*, 1-29. 2020.

[21] Ouanani, M., & Tiliouine, B. Effects of foundation soil stiffness on the 3-D modal characteristics and seismic response of a highway bridge. *KSCE Journal of Civil Engineering*, *19*, 1009-1023. 2015.

[22] Wolf, J. P., & Obernhuber, P. Non-linear soil-structure-interaction analysis using dynamic stiffness or flexibility of soil in the time domain. *Earthquake engineering & structural dynamics*, *13*(2), 195-212. 1985.

[23] Gazetas, G., & Mylonakis, G. Seismic soil-structure interaction: new evidence and emerging issues. *Geotechnical special publication*, (75 II), 1119-1174. 1998.

[24] Mylonakis, G., & Gazetas, G. Seismic soil-structure interaction: beneficial or detrimental?. *Journal of earthquake engineering*, *4*(3), 277-301. 2000.

[25] Vlassis, A. G., & Spyrakos, C. C. Seismically isolated bridge piers on shallow soil stratum with soil–structure interaction. *Computers & structures*, *79*(32), 2847-2861. 2001.

[26] Saiidi, M., & Douglas, B. M. Effect of design seismic loads on a highway bridge. *Journal of Structural Engineering*, *110*(11), 2723-2737. 1984.

[27] De Angelis, A.; Pecce, M.R. (2023). Model assessment of a bridge by load and dynamic tests. Eng. Struct., 275, 115282

[28] Pecce, M. R., Santamato, F., Ciampa, E., & Cosenza, E. The design approach of a prestressed concrete bridge constructed in 1950s in Italy. In *Proceedings of the International fib Symposium on Conceptual Design of Structures* (pp. 105-112). 2019.

[29] MIDAS FEA-NX – Midas Engineering Software – Manual.

[30] Allemang RJ, Brown DL. A correlation coefficient for modal vector analysis. *Proceedings of the 1st International Modal Analysis Conference*. Orlando, USA, 1982.

[31] Ambrosino A., Sica S. Calibration of a 3D numerical model to perform modal analysis of coupled systems of soil and structure. *Proceedings 10th European Conference on Numerical Methods in Geotechnical Engineering*, Zdravković L, Konte S, Taborda DMG, Tsiampousi A (eds), NUMGE 2023.

COMPDYN 2023
9th ECCOMAS Thematic Conference on
Computational Methods in Structural Dynamics and Earthquake Engineering
M. Papadrakakis, M. Fragiadakis (eds.)
Athens, Greece, 12-14 June 2023

# SHEAR RATE EFFECT ON GRAIN CRUSHING OF SANDS. A LABORATORY STUDY BY THE BROOMHEAD APPARATUS

**P. Sidiropoulos, Dipl. Civil Eng. M.S., MBA, Ph.D. cand.[1], C. A. Stamatopoulos, Ph.D.[2], V.P. Panoskaltsis Professor[3]**

[1,3] Department of Civil Engineering, Demokritos University of Thrace
University Campus Xanthi-Kimmeria, Xanthi, 67100, GREECE
[1]psidirop@civil.duth.gr, [3]vpanoska@civil.duth.gr

[2] Hellenic Open University
Isavron 5, Athens, 11471, GREECE
k.stam@saa-geotech.gr

## Abstract

*Large scale landslides have been related to the dramatic decrease of the undrained shear strength of sands along the slip surface. This decrease of shear strength has been attributed to the crushing of sand grains. Landslides may appear to have a wide spectrum of speeds from extremely low (0.3 meters every 5 years) to moderately fast (1.5 meters per month), to extremely rapid. This paper studies the influence of the shear rate on grain crushing of sands, experimentally. It is reported in the literature that even significant changes in shear rate usually play an insignificant role in the shear stress paths of samples, as long as the tests are kept drained. Nevertheless, according to new studies when the changes in shear rates become very large the changes in grain crushing may be of importance. In order to study the effect of shear rate on grain crushing, a new series of tests was performed. The tests were conducted in the Bromhead Ring Shear device at the Soil Mechanics and Foundation Engineering Laboratory of the Department of Civil Engineering at the Demokritos University of Thrace. The specimens used were of the same geometry, from the same materials (with the same density). They were sheared under equal normal stresses at variable shear rates by taking full advantage of the Bromhead apparatus capabilities. These tests were stopped at increasing displacements up to the final point (1m). This way, the study of progress of the grain crushing phenomenon was possible for each speed as well as the comparison of the grain crushing phenomenon for variable speeds.*

**Keywords:** Bromhead, Ring Shear Apparatus, Sands, Landslides, Grain Crushing.

## 1 INTRODUCTION

Landslides occur every year somewhere in the world due to earthquakes, rainfall, and other agencies such as engineering activities [1].The impact of landslides can be extensive as it may include loss of lives, destruction of infrastructure, damage to land, destruction of farmer's livelihoods [2]. Although many parameters affect landslides, grain crushing of sand layers within the shear zone formed is often considered key to rapid motion. In fact, since 1996 Sassa et al [3] proposed the concept of sliding surface liquefaction in which grain crushing was considered to have an important effect on excess pore pressure generation.

In order to study landslides that usually involve large displacements of materials, the most appropriate apparatus is found to be the Ring Shear Device. The Ring Shear Device uses a ring shaped cell which rotates around its central axis, thus eliminating to some degree shear displacement limitations and it is mainly used to find residual shear strength. It was initially developed by Hvorslev [4] and [5]. La Gatta [6] Bishop et al [7] and Bromhead [8] also contributed later on with changes to the initial design. Sassa since 1984 [9] has developed a low stress high speed ring shear apparatus for the research of motion of debris flow. Later on, he made several variations to his initial design. Nevertheless, today the only two types that are commercially available are the Bishop and the Bromhead type. The Bromhead type of ring shear apparatus is today more widely used in laboratories around the world because of its lower cost and ease of use, when compared to the more sophisticated apparatus developed by the Norwegian Geotechnical institute and Imperial College [7] aka the Bishop apparatus. Despite this, it has been showed that drained residual strength values measured at the Bromhead apparatus are in good agreement with those calculated at the Bishop apparatus [10], while similar values coincide with those found by back-calculated analysis for landslides at Warden Point and South California [11] , and the Wenallt slip [12].

The main factor that differentiates the Bromhead apparatus from the Bishop device is the dimensions and mechanism of the cell. The Bromhead apparatus uses a rather shallow ring shape cell, 5 mm deep, and a similar ring shape cap. Torque is applied to the cell and while it rotates, shear stress is measured by measuring the force necessary to keep the cap immobile. Because of the limited dimensions of the cell the Bromhead apparatus is mainly used to test the shear strength of silts, as there is the fear that sands may form a shear zone when tested that is obstructed by the cell's limited depth and the results taken compromised. Nevertheless, it was found that under certain conditions of initial granulometry of the materials tested, normal stress and length of the shear displacement, the Bromhead apparatus is able to provide reliable results for sands [13]. It deserves mentioning that the manuals of the apparatus do not refer any limitation as far as the materials to be tested.

## 2 SHEAR RATE IN BROMHEAD RING SHEAR APPARATUS TESTS AND ITS INFLUENCE ON THE GRAIN CRUSHING PHENOMENON IN SANDS.

In this paper the influence of shear rate in the Bromhead Ring shear apparatus is studied with tests executed at the Soil Mechanics and Foundation Engineering Laboratory of the Department of Civil Engineering at the Demokritos University of Thrace. A new series of tests was executed with variable shear rates and progressive shear displacements by using three types of sand, silica, calcareous and quartzitic and applying the same Normal stress. The purpose was to determine if the shear displacement rate variance, (faster vs slower) influences the grain crushing phenomenon.

We know by the bibliography that as long as a drained behavior is achieved "within reasonable limits, then, the rate at which a cohesionless soil is sheared is not important" [14]. Nevertheless at the same source, Lambe, we find at the triaxial testing for cohesionless soils section that "Tests on one type of dry sand indicated only a 10% increase in strength when the elapsed time from the start of loading to the time of maximum compressive stress was decreased from 1000 seconds to 0.01 second". So it is recognized that when the time of loading is decreased substantially, thus the shearing speed is increased, there is a noticeable increase in strength. Shear strength or resistance is the fraction $\tau/\sigma$ so for the fraction to increase, by keeping the normal stress $\sigma$ constant, $\tau$ increases. In triaxial testing the displacements are minimal when compared to those achieved in the Ring Shear apparatus, thus a small increase may alter significantly the end result in large deformations.

The first study found from our bibliographical research to point differences in shear stress when different shear speeds are applied to the Ring Shear apparatus was Fukuoka et al [15]. As can be seen in Figure 1 and Figure 2 differences in shear speed caused differences in shear stresses, although grain crushing percentages were not considered changed.

On the contrary a more recent paper by Okada, Sassa, Fukuoka of 2004 [16] as can be seen on Figure 3 reports an increased grain crushing percentage in sands in relation to the increased shear stress caused when high shear speeds are applied to Ring Shear tests.

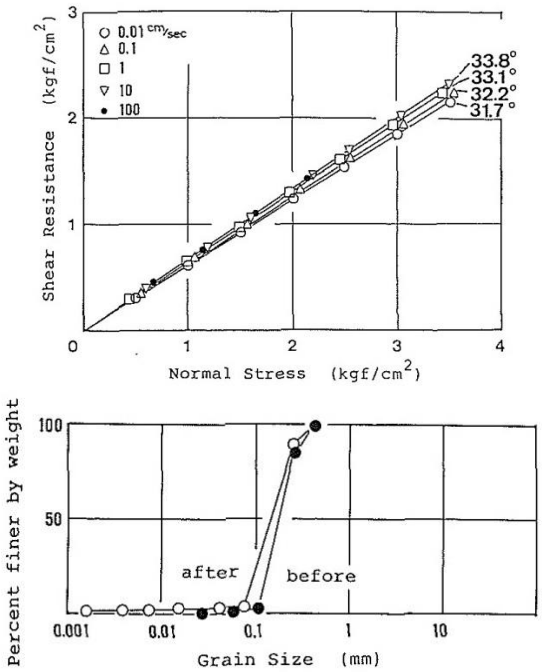


Figure 1. When Ring Shear tests for Toyoura sand executed with different shear rates are compared, it seems that the shear stress increases with the increase of the shear speed, the granulometry was not found, to differ among the various speeds [15]

The increase in shear stress may very well alter the grain crushing phenomenon as "Grain crushing depends, in addition to the load and time, on the stress path if exposed to more intensive gradient of shearing, the extent of crushing increases" [17] Another paper [18] mentions that "Under relatively high shear velocity conditions (i.e., >100 mm/sec), the grain crushing

effect is more significant and results in rapid mass movements" strengthening the hypothesis that higher shear speeds may mean higher grain crushing percentages.

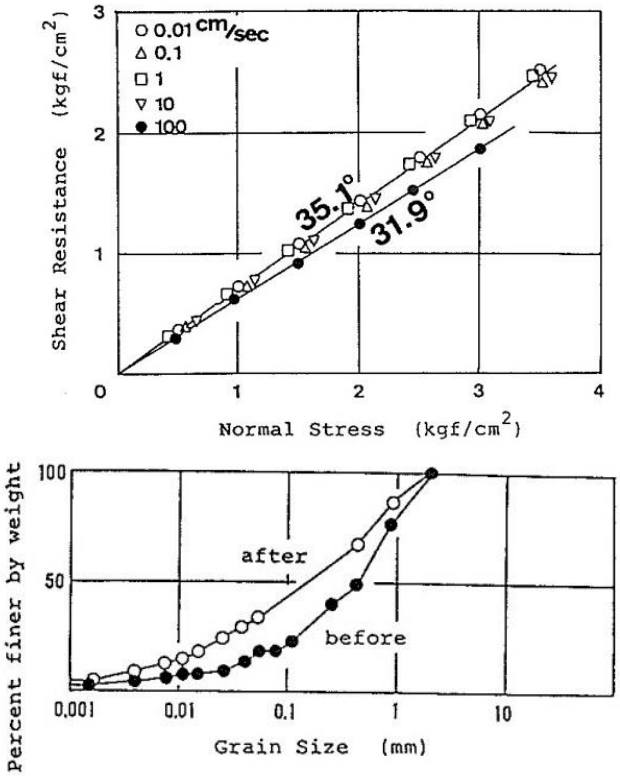


Figure 2. On the other hand when Ring Shear tests with plain tennis court sands executed with different shear rates are compared, the faster ones seem to present slightly lower shear stress. In both comparisons of Figure 2 and 3 the grain crushing phenomenon is reported as constant

Other researchers agree on the fact that changes in shear speed lead to changes in the shear strength but disagree on the effect that the increase in shear strength has on grain crushing "Shear strength is a function of shear velocity and normal stress. Generally, shear strength increases with increasing shear velocity", [19]" but then proceed to find different results as illustrated in Figure 4. In fact Jiang et al measure higher grain crushing percentages for lower shear rates which attribute to "greater time available for particle crushing during the slower tests", [19] among other factors.

The fact of the matter is that a paper that studies the influence of shear displacement rates on grain crushing in cohesionless soils for the Bromhead apparatus was not found in the bibliography available. As changes in grain crushing due to changes in the shear rate are probably not very intense, such an influence may not be predicted easily as results from studies can be controversial.

| | Test no. | Sample | $\sigma_0$ (kPa) | $e_0$ | $B_D$ | Shear speed (mm/s) | Sample preparation | Drainage condition |
|---|---|---|---|---|---|---|---|---|
| $S_1$ | | Silica sand no. 8 | 50 | 1.13 | 0.95 | 56 | NC | Naturally drained |
| $S_2$ | | | 198 | 1.09 | 0.95 | 56 | NC | |
| $S_3$ | | | 472 | 0.96 | 0.96 | 58 | NC | |
| $S_4$ | | | 471 | 0.97 | 0.96 | 3 | NC | |
| $S_5$ | | | 472 | 0.97 | 0.96 | 5 | NC | |
| $S_6$ | | | 473 | 0.97 | 0.96 | 100 | NC | |

Table 1. Test identification numbers and specimen characteristics [16]

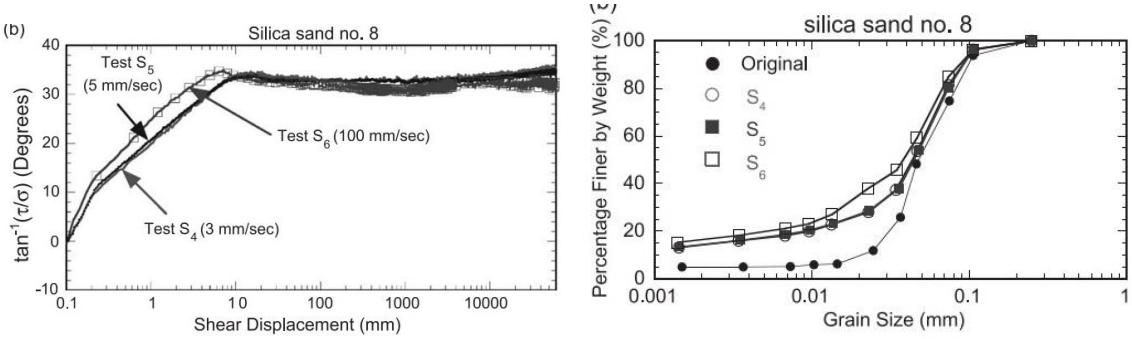


Figure 3. Here a comparison of similar tests executed with different speeds is reported, the test executed with the higher shear rate displacement seems to present greater shear stress values at the initial stage of the test and the same test seems to present a greater grain crushing percentage. The other two tests with similar shear speeds presented same shear stress values and same grain crushing percentages [16]

.

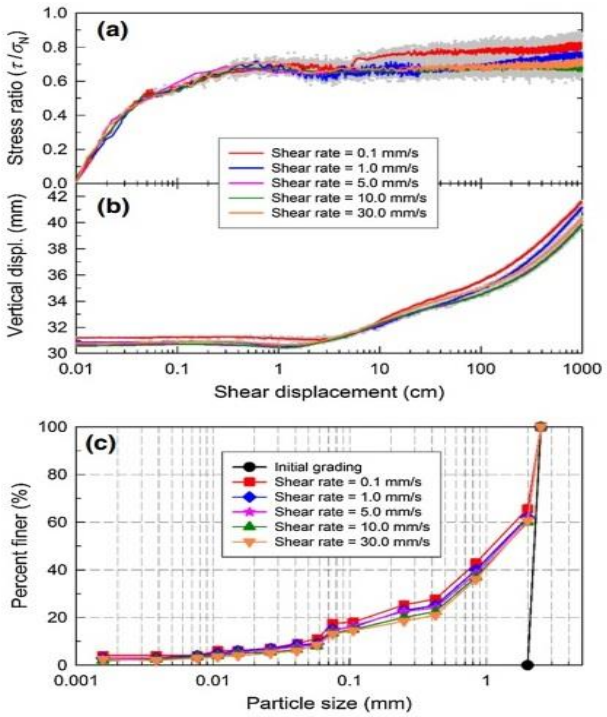


Figure 4. In the study of Jiang et al, the slower the shear speed the higher the shear stress and the grain crushing phenomenon, it can be seen that researchers who study different shear speeds in Ring Shear tests find different results [19]

## 3 NEW TESTS EXECUTED ON SILICA SAND WITH VARIABLE SHEAR RATES

In order to study accurately the phenomenon of grain crushing in relation to shear speed, a series of new tests was executed using silica sand, a material already used in the past in research, known to present grain crushing when tested, quite easily. The initial granulometry of this material was between 300-150 μm, a granulometry that allowed for the grain crushing phenomenon to develop freely by forming a shear zone to the relatively shallow Bromhead cell [13] and [20] but at the same time it allowed for the phenomenon to be clearly monitored and measured by sieving the remaining sample material.

The densities of the samples in all the tests executed for this study were in the range of 1,60-1,65 gr/cm$^3$. The densities were achieved as uniformly as possible by following this procedure: initially the sample was placed in the cell with a small spoon, then the ring shape cap was placed appropriately above the cell and 40 kg of dead weight were applied on the loading pin of the apparatus. This weight on the loading pin is equivalent to 1200 KPa of pressure. After that, there enough time was left for the sample to compact, and that was controlled by the vertical displacement gauge. When the vertical displacement gauge stopped moving, the weight of 40 kg was put down. After the loading pin was released, 2 kg of dead weight, equivalent to 75 KPa of pressure, were loaded to the pin. The sample was again left to consolidate and then the tests could begin. The parameters of the tests apart the shear rate, mainly the compaction process, the vertical stress σN and the initial granulometry, were chosen so as to achieve reliable results for the maximum shear displacement possible in the Bromhead apparatus [13].

The time scale used on the recorder was that of the Logarithmic type because it offers more measurements at the initial part of the test when the shear stress increases where the differences in shear stress may or may not affect the shear stress-strain response. Later on, when the shear stress reaches a constant value as can be expected by the bibliography, the need for many measurements becomes less important. The tests were stopped when the proper shear displacement was reached according to the program established earlier, as shown in Table 2. The rotation was converted to linear displacement according to the formula mentioned in the Bromhead apparatus manual [21]. Practically degrees per minute are multiplied by 0.742 to be converted in mm/min and then as shear speed is constant it is easy to calculate the duration of the tests by dividing shear displacement with time.

When the tests reached the proper shear displacements, the apparatus was stopped, the cell emptied, the content was dried and the granulometries taken. Then results were reported to picture 6 so as to establish a timeline of the grain crushing phenomenon for each shear rate applied.

As can be seen in Figure 5 all tests arrived at the same shear stress value after shear displacement arrived at 0.01 meters and remained almost constant until the end of the tests. At the initial stages of the tests though, the shear stress-stress responses differ somewhat. Before analyzing the differences of the stress-strain responses, the different number of values taken for the different tests especially at the initial stages of the tests, must be taken into account and justified. In fact the logarithmic scale model measures the majority of values during the initial stages of a test, that is why it is used in this paper. Since differences among tests occur at the initial stages, then measurements need to be more precise, but the time needed for the tests to be finished differs vastly. Thus in order for the fastest test of 60 deg/min to arrive at 1 meter of shear displacement it takes 22.5 min to be completed, for the slowest of 1.80 deg/min it takes 750 min (that is 12.5 hours!). So it is obvious that as the tests become faster less values are reported at the initial stage, something that may alter somewhat the natural

curve of the stress-strain response until it reaches constant values. Unfortunately the instruments at our disposal do not predict a faster measuring protocol than the logarithmic one used.

Nevertheless it can be seen that the slower test of 1.8 deg/min arrives at the constant values by a path that reports smaller values, that is less steep than all the others. On the contrary one of the faster tests executed at 30 deg/min not only arrives much more steeply but is also presenting a pseudo dense behavior with a small peak at the shear stress-strain response graph. There is reason to believe of course that the shear stress-strain response of the test executed at 60 deg/min is steep as the one executed at 30 deg/min, but the recorder measured the second value when the test had already reached the constant shear stress status, thus no curve is represented but rather a line.

| Name | Type of sand | Moisture % | Density in gr/cm3 | Type of shear behavior | Speed of shear in deg/min | Shear Displacement in m |
|---|---|---|---|---|---|---|
| S1 | Silica | 10 | 1.61 | Drained | 1.8 | 0.3 |
| S2 | Silica | 12 | 1.65 | Drained | 1.8 | 0.5 |
| S3 | Silica | 11 | 1.6 | Drained | 1.8 | 0.7 |
| S4 | Silica | 9 | 1.62 | Drained | 1.8 | 1 |
| S5 | Silica | 11 | 1.63 | Drained | 6 | 0.3 |
| S6 | Silica | 12 | 1.65 | Drained | 6 | 0.5 |
| S7 | Silica | 10 | 1.64 | Drained | 6 | 0.7 |
| S8 | Silica | 10 | 1.63 | Drained | 6 | 1 |
| S9 | Silica | 9 | 1.64 | Drained | 15 | 0.3 |
| S10 | Silica | 12 | 1.62 | Drained | 15 | 0.5 |
| S11 | Silica | 11 | 1.61 | Drained | 15 | 0.7 |
| S12 | Silica | 10 | 1.61 | Drained | 15 | 1 |
| S13 | Silica | 12 | 1.65 | Drained | 30 | 0.3 |
| S14 | Silica | 9 | 1.6 | Drained | 30 | 0.5 |
| S15 | Silica | 11 | 1.65 | Drained | 30 | 0.7 |
| S16 | Silica | 11 | 1.64 | Drained | 30 | 1 |
| S17 | Silica | 10 | 1.63 | Drained | 60 | 0.3 |
| S18 | Silica | 9 | 1.64 | Drained | 60 | 0.5 |
| S19 | Silica | 11 | 1.62 | Drained | 60 | 0.7 |
| S20 | Silica | 12 | 1.61 | Drained | 60 | 1 |

Table 2. The principal parameters of the tests. All the samples had the same initial granulometry of 300-150 μm so as to achieve clear objective measurements of the grain crushing phenomenon as it evolved. The tests also were subjected to vertical stress σN 75 KPa which was found by previous research at the Soil Mechanics and Foundation Engineering Laboratory of the Department of Civil Engineering at the Demokritos University of Thrace enough to provoke grain crushing but also help to maintain a stable shear stress path for a maximum of 1 meter of shear displacement

In Figure 6 there is the comparison of the grain crushing percentages measured after the tests were finished. Naturally by the compaction process a certain percentage of grain crushing already occurs and for the parameters used in these tests it was found to be 4,83%. This percentage was subtracted by the final grain crushing percentages measured. Obviously since only the compaction process was responsible for this percentage, thus no shear movement had happened yet, it was the same for all tests executed.

It can be seen a noticeable difference in the grain crushing for the two faster tests, the series executed at 60 deg/min and 30 deg/min while no distinct difference was found for the other tests.

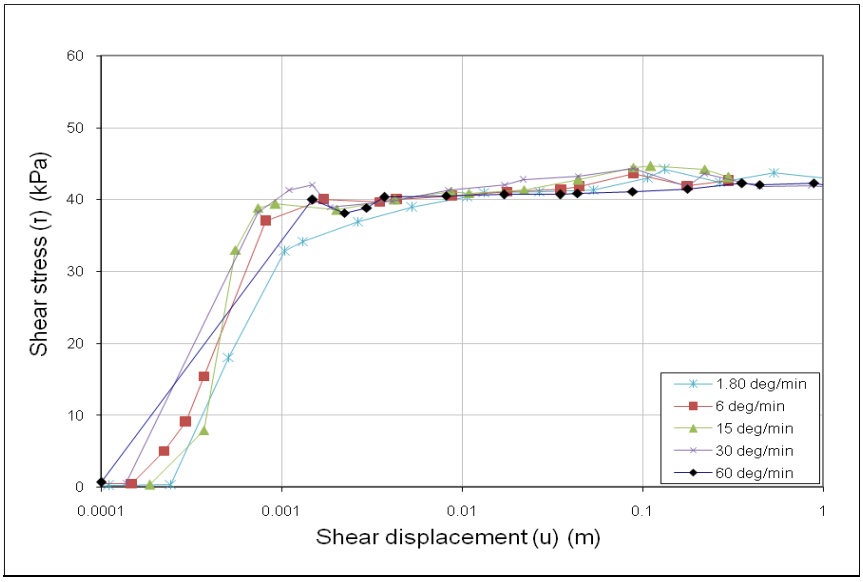


Figure 5. Results from Silica sand tests that arrived up to 1 meter of shear displacement, i.e. S4, S8, S12, S16, S20. Similar graphs could be made for tests that arrived shear displacements of 0.3 m, 0.5 m, 0.7 m but it seemed superfluous as this graph is representative of the others

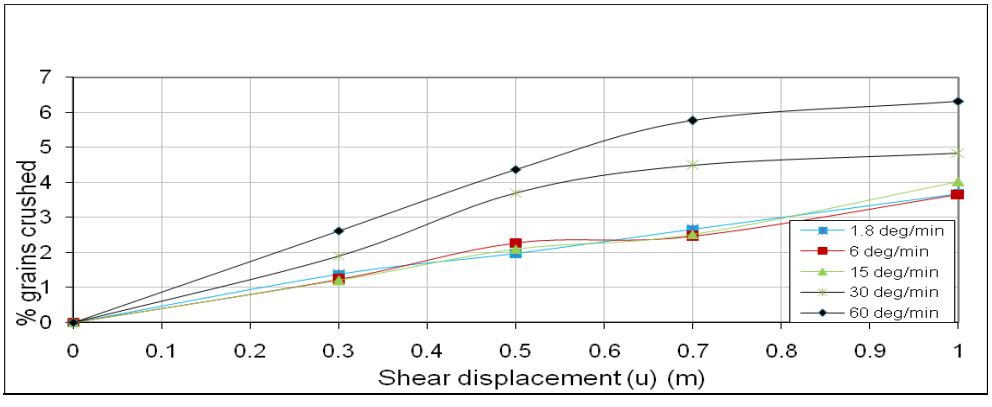


Figure 6. Percentages of the crushed grains in relation to the shear displacement and the shear rates used for the execution of the tests. The two series of tests executed faster i.e. with 60 deg/min and 30 deg/min present larger percentages of crushed grains in relation to the slower ones executed with 15, 6 and 1.8 deg/min of shear rate. The three slower ones in fact seem to not present considerable differences in crushed grains

## 4 NEW TESTS EXECUTED ON CALCAREOUS SAND WITH VARIABLE SHEAR RATES

The methodology of examining Calcareous sand was identical with the one previously used to examine Silica sand. The initial granulometry was kept between 300-150 μm, the densities of the samples were in the range of 1.60-1.65 gr/cm3 achieved by following the preloading procedure as described previously, the Normal pressure applied during the tests was 75 KPa, and the shear rates and displacements were kept the same so as to make comparisons easier. The test parameters are shown in more detail in Table 3.

| Name | Type of sand | Moisture % | Density in gr/cm3 | Type of shear behavior | Speed of shear in deg/min | Shear Displacement in m |
|---|---|---|---|---|---|---|
| C1 | Calcareous | 11 | 1.63 | Drained | 1.8 | 0.3 |
| C2 | Calcareous | 10 | 1.62 | Drained | 1.8 | 0.5 |
| C3 | Calcareous | 10 | 1.61 | Drained | 1.8 | 0.7 |
| C4 | Calcareous | 10 | 1.61 | Drained | 1.8 | 1 |
| C5 | Calcareous | 11 | 1.6 | Drained | 6 | 0.3 |
| C6 | Calcareous | 12 | 1.64 | Drained | 6 | 0.5 |
| C7 | Calcareous | 11 | 1.65 | Drained | 6 | 0.7 |
| C8 | Calcareous | 10 | 1.6 | Drained | 6 | 1 |
| C9 | Calcareous | 12 | 1.61 | Drained | 15 | 0.3 |
| C10 | Calcareous | 11 | 1.62 | Drained | 15 | 0.5 |
| C11 | Calcareous | 11 | 1.63 | Drained | 15 | 0.7 |
| C12 | Calcareous | 10 | 1.61 | Drained | 15 | 1 |
| C13 | Calcareous | 9 | 1.64 | Drained | 30 | 0.3 |
| C14 | Calcareous | 10 | 1.62 | Drained | 30 | 0.5 |
| C15 | Calcareous | 9 | 1.64 | Drained | 30 | 0.7 |
| C16 | Calcareous | 10 | 1.63 | Drained | 30 | 1 |
| C17 | Calcareous | 10 | 1.62 | Drained | 60 | 0.3 |
| C18 | Calcareous | 10 | 1.61 | Drained | 60 | 0.5 |
| C19 | Calcareous | 12 | 1.63 | Drained | 60 | 0.7 |
| C20 | Calcareous | 11 | 1.6 | Drained | 60 | 1 |

Table 3. Main parameters of the Calcareous sand tests as executed in the Bromhead apparatus. The initial granulometry of all the samples was 300-150 μm, while the vertical stress applied was 75 KPa for reasons explained previously

In Figure 7 are reported the shear stresse-stress responses of the Ring Shear tests that were left to arrive up to 1 meter of shear displacement. It can be seen that five shear rates were used, starting from the slowest, 1,80 deg/min, up to the fastest that the Bromhead apparatus may permit, 60 deg/min. It can be noticed that although the residual stresses are nearly the same in all shear speeds, the stress-strain responses at the initial phases of the tests differ somewhat. The slower tests present an increase at the shear stress in smaller shear displacements, although the shear stress strains response measured is less steep. It is rather interesting that the

initial values of the shear stresses present themselves in order from the slower to the fastest and on the graph there is a clear distinction.

The shear stress-strain responses as reported on Figure 7 show certain differences that concern not only the initial phase of the tests but also the constant shear stress phase. It can be noticed that the initial phases of the tests differ in relation to the shear rate used. The slower the test, the shear test shows increases for smaller displacements. On the other hand the faster tests present the same residual shear stresses for larger shear displacements and their shear stress-strain response is much steeper but it reaches constant shear stress phase in lower displacements when compared to the slower tests. For example the 60 deg/min test reaches constant shear stress at 0,002 m while the 1,8 deg/min at more than 0,01 m of shear displacement, thus more than five times the shear displacement of the faster test.

The constant shear stress phase of the tests also seems related to the shear rate as can be seen at the graph in Figure 7. In fact the faster tests seem to present slightly higher shear stresses than the slower ones, a behavior also found bibliographically [15], [19].

On Figure 8 are reported the percentages of the crushed grains caused only by the Ring Shear tests as the initial quantity of crushed grains caused by the compaction process on the samples (the preloading as previously reported) which was found to be 7.56%, was subtracted.

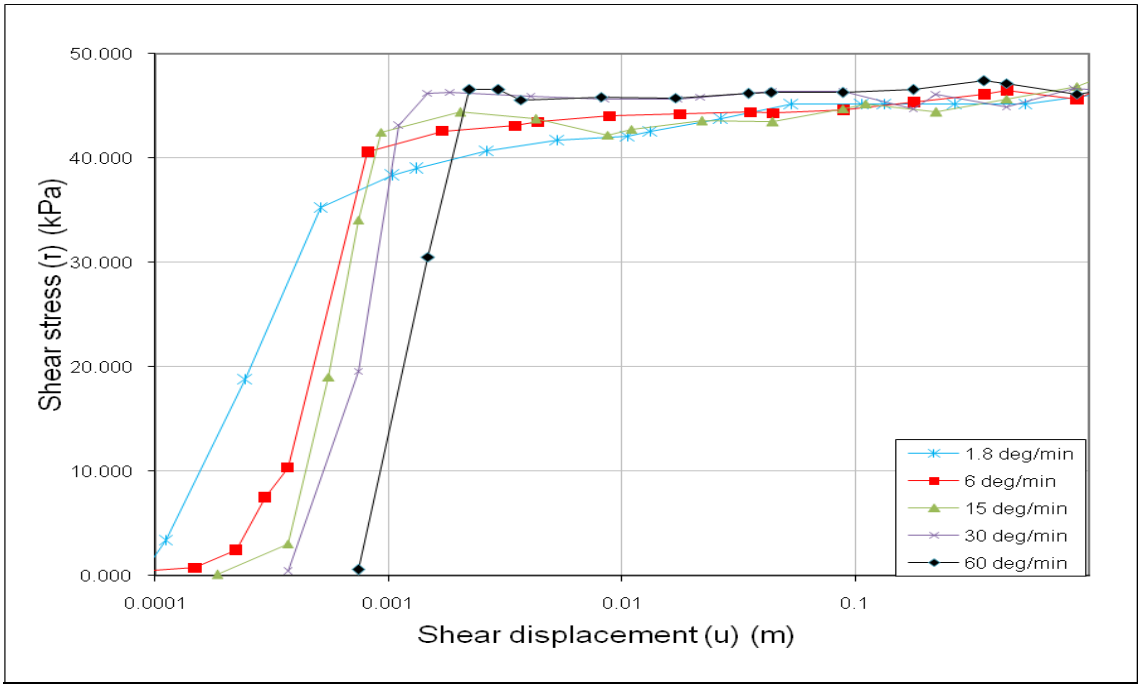


Figure 7. . Results from Rings Shear tests on the Bromhead apparatus that arrived up to 1 meter of shear displacement, i.e. C4, C8, C12, C16, C20. It can be seen that the shear rate plays a certain role to the initial shear stress path of the tests, in fact the slower tests present an increase in shear stress for shorter shear displacements

As can be seen in this series of tests, the fastest test of 60 deg/min presented a rather smaller percentage of crushed grains for the final displacement of 1 meter. The other tests although present grain crushing differences at the progression of the shear displacement, their final percentages of grain crushing share nearly the same values. It is to be noticed though that despite the minor differences in grain crushing at the final displacements, the order of shear rates correlates negatively to the grain crushing percentage, that is, the faster the test, the lower the

grain crushing percentage. As far as the progression of the grain crushing phenomenon is concerned, the slower shear rates had slightly larger grain crushing percentages which decreased with the increase of shear speed.

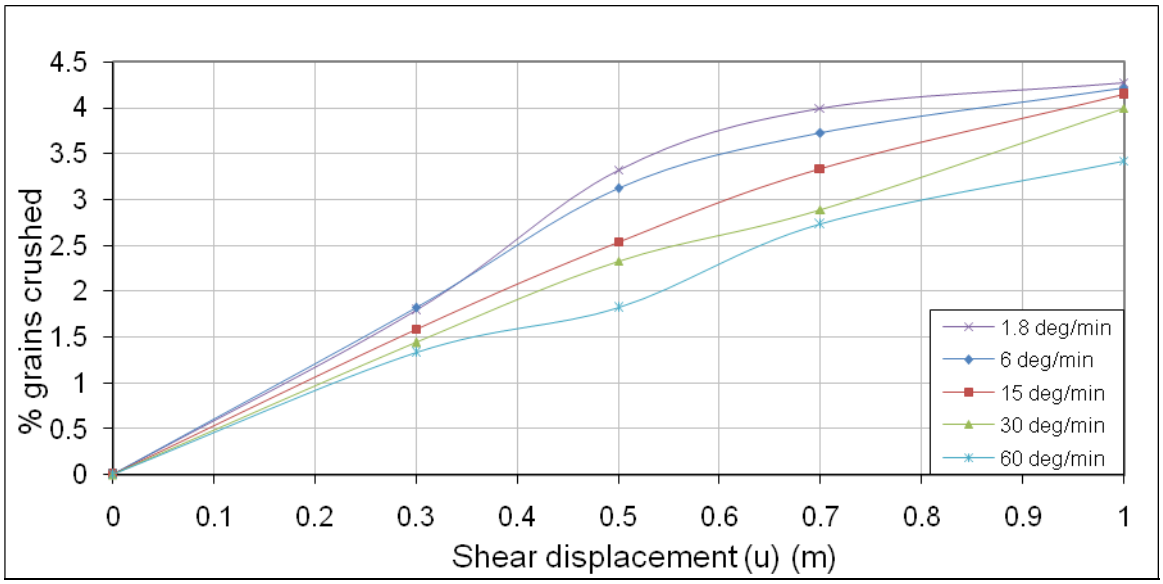


Figure 8. Percentages of the crushed grains of Calcareous sand after the Ring Shear tests executed in relation to the shear displacement and the shear rates used for the execution of the tests. The series of tests executed faster i.e. with 60 deg/min present a smaller percentage of crushed grains in relation to the slower ones executed with 30, 15, 6 and 1.8 deg/min of shear rate. The trend though for the Calcareous Sand used in these tests at the Bromhead Ring Shear apparatus was that the slower the test the more increased the grain crushing percentage

## 5 NEW TESTS EXECUTED ON QUARTZITIC SAND WITH VARIABLE SHEAR RATES

A series of Ring Shear tests on the Bromhead apparatus was executed using Quartzitic sand. This sand has the characteristic that presents very limited grain crushing as measured by similar experiments [22] and [13]. Six tests were executed ending at 1 m of shear displacement by using the same test parameters as previously, granulometry of 300-150 μm, 10% of moisture, 75 Kpa of normal stress, density of 1,60-1,65 gr/cm$^3$ and variable shear rates of 60, 30, 15, 6 and 1,8 deg/min. Test parameters can be seen on Table 4.

The compaction process was as reported previously and the initial grain crushing percentage caused solely by the compaction process was found to be 1,85%. This percentage was subtracted by the final granulometries found at the end of the tests. In this way only the grain crushing percentages caused by the rotational movement of the Ring Shear Apparatus were reported in Figure 10.

On Figure 9 are reported the shear stresses in relation to the shear displacements for the six shear rates used. As can be seen the faster shear rates follow a steeper path towards the residual stress values which remain constant. On the other hand the shear stresses begin to increase for smaller displacements as the shear rates are slower. All shear stress paths begin the residual shear stress phase for nearly the same shear displacement as can be seen on Figure 9.

| Name | Type of sand | Moisture % | Density in gr/cm3 | Type of shear behavior | Speed of shear in deg/min | Shear Displacement in m |
|---|---|---|---|---|---|---|
| Q1 | Quartzitic | 10 | 1.61 | Drained | 1.8 | 1 |
| Q2 | Quartzitic | 11 | 1.61 | Drained | 6 | 1 |
| Q3 | Quartzitic | 10 | 1.60 | Drained | 15 | 1 |
| Q4 | Quartzitic | 10 | 1.63 | Drained | 30 | 1 |
| Q5 | Quartzitic | 11 | 1.61 | Drained | 60 | 1 |

Table 4. Main parameters of the Quartzitic sand tests as executed in the Bromhead apparatus. The initial granulometry of all the samples was 300-150 μm, while the vertical stress applied was 75 KPa

The residual stresses remain constant but the two slower tests, (1,8 and 6 deg/min) present slightly lower values in shear stress than the others. The two slower tests and the three faster tests present among themselves no noticeable difference in values.

Grain crushing percentage as expected is lower than the other two sands tested. There seems to be a negative correlation between shear rate and grain crushing percentage i.e. the faster tests seem to cause lower grain crushing and as the tests become slower the grain crushing increases.

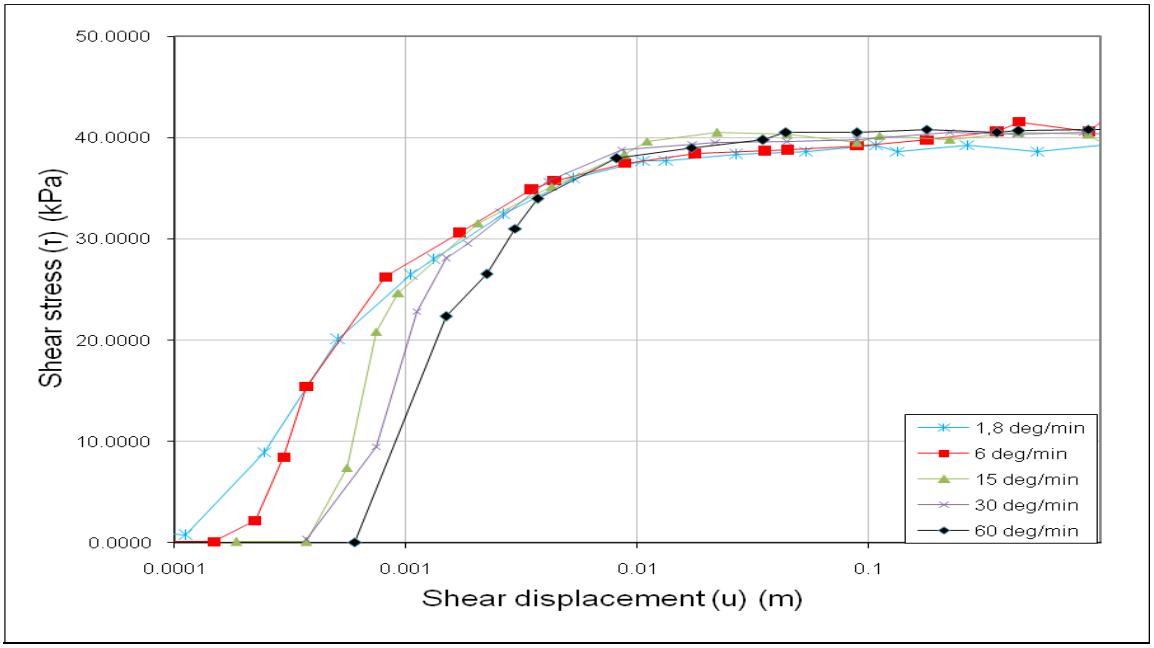


Figure 9. Results from the tests executed on the Bromhead apparatus with quartzitic sand that arrived up to 1 meter of shear displacement, i.e. Q1, Q2, Q3, Q4, Q5. In the case of quartzitic sand It can also be seen how the shear rate plays a certain role to the initial shear stress path of the tests. In fact the slower tests present an increase in shear stress for shorter shear displacements and their path is less steep

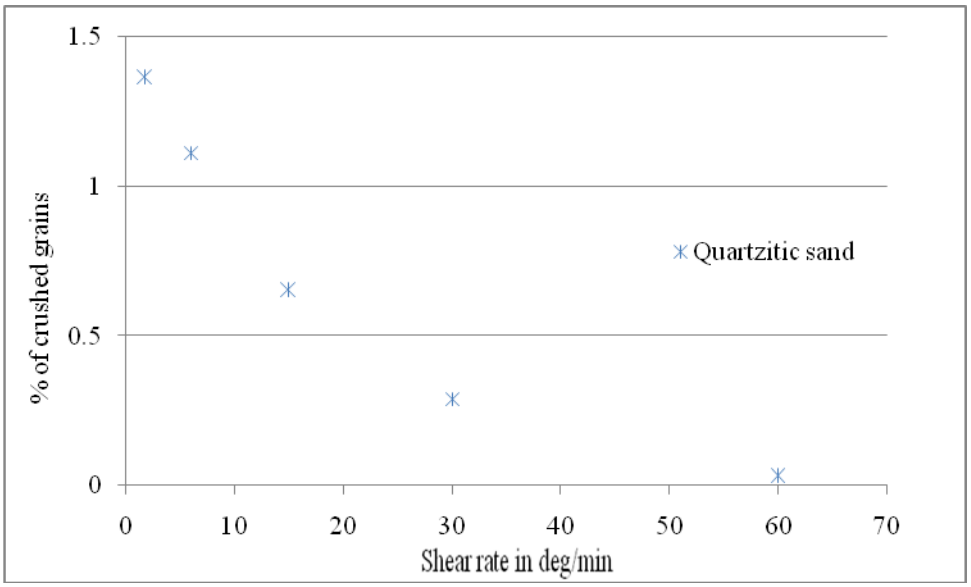


Figure 10. Percentages of the crushed grains of Quartzitic sand in relation to the shear displacement and the shear rates used. The series of tests executed faster i.e. with 60 deg/min present a smaller percentage of crushed grains in relation to the slower ones executed with 30, 15, 6 and 1.8 deg/min of shear rate

## 6 COMPARISONS BETWEEN THE THREE SANDS TESTED ON THE BROMHEAD APPARATUS

Testing three different types of sand by using the same test parameters permits us to evaluate the element of material diversity to the results of the Ring Shear tests at the Bromhead apparatus. As can be seen on Figure 11 where shear stress paths are reported for same test parameters, different sand types present similar shear stress paths, but do show some differences.

For this comparison the shear speed of the 15 deg/min was chosen as it is in the middle of the shear rates used and provides a fairly representative picture of the whole phenomenon. Quartzitic sand presents lower values of shear stress throughout the entire test when compared to Silica and Calcareous and its initial phase is less steep. Silica Sand presents higher constant shear stress values when compared to Calcareous and Quartzitic. Silica and Calcareous sand arrive at the constant shear stress values rather abruptly when compared to quartzitic and at nearly the same displacements in relation to quartzitic.

The main differences of sand material diversity to the Bromhead Ring Shear tests though seem to lie on the effect it has on the grain crushing phenomenon. As can be seen in Figures 12, 13, 14 higher shear rates lead to higher grain percentages for Silica sand, while the inverse happens for Calcareous and Quartzitic sands. On Figures 12, 13, 14 are reported the grain crushing percentages measured at 1 meter of shear displacements and the formulas that emerge from the graphs that relate shear rate to grain crushing percentage. The different crushing percentages seem to correlate to the variance of shear rates when all other test parameters are kept the same. Correlation, negative and positive between shear rates and grain crushing is mentioned in the relative literature as already mentioned.

In order to determine why diverse shear rates have the inverse effect on grain crushing in relation to the sand type, the diverse breaking propensity of sands to normal and shear stress

must be considered. On table 4 the percentages of the crushed grains caused by the compaction process i.e. normal stress, the ring shear test process i.e. shear stress, and their fraction which delimit the importance of one over the other. In Calcareous and Quartzitic sand where the fraction of percentage of crushed grains caused by Normal stress, divided by the percentage of crushed grains caused by shear stress is superior to the unit, the slower tests present more intense grain crushing. Thus when the vertical stress is more influential than the shear stress to the totality of the grain crushing phenomenon, time under normal stress plays a key role to higher grain crushing percentages. On the other hand when the aforementioned fraction is below the unit, such as in Silica sand, higher shear rates cause higher grain crushing percentages.

| Type of sand | % of crushed grains caused by compaction | % of crushed grains caused by Ring Shear Test | Fraction of compaction/Ring shear test |
|---|---|---|---|
| Silica | 4.83 | 6.3 | 0.77 |
| Calcareous | 7.56 | 4.5 | 1.68 |
| Quartzitic | 1.85 | 1.4 | 1.32 |

Table 5. Main parameters of the Quartzitic sand tests as executed in the Bromhead apparatus. The initial granulometry of all the samples was 300-150 μm, while the vertical stress applied was 75 KPa

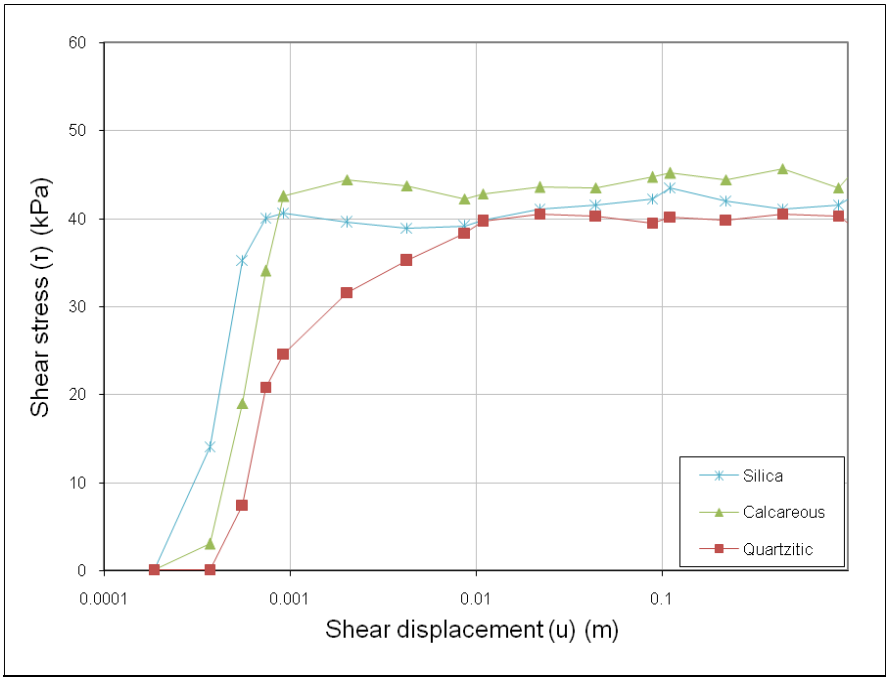


Figure 11. Shear stress-strain responses of the three sands tested on the Bromhead apparatus for 1 m and 15 deg/min of shear speed. The differences at the initial phase of the tests and at the constant phase of residual shear stress are noticeable

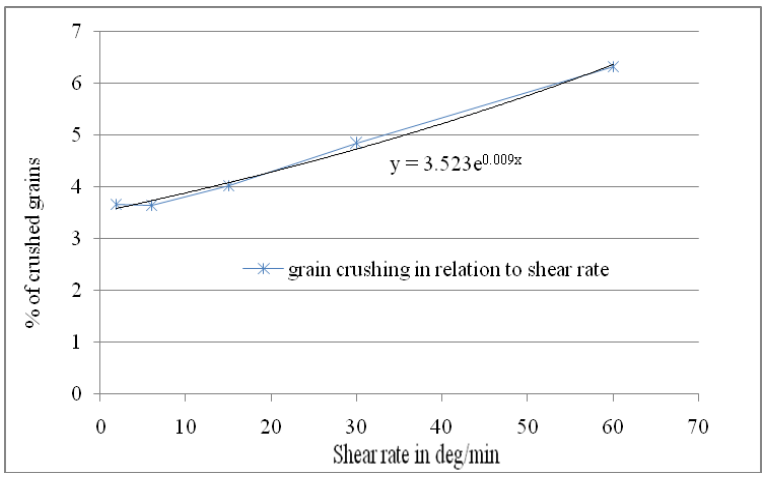


Figure 12. Percentages of the crushed grains of Silica sand in relation to the shear displacement. It can be seen that there although the relation extracted is an exponential function the graph is almost linear between the grain crushing percentage and the shear speed of the tests

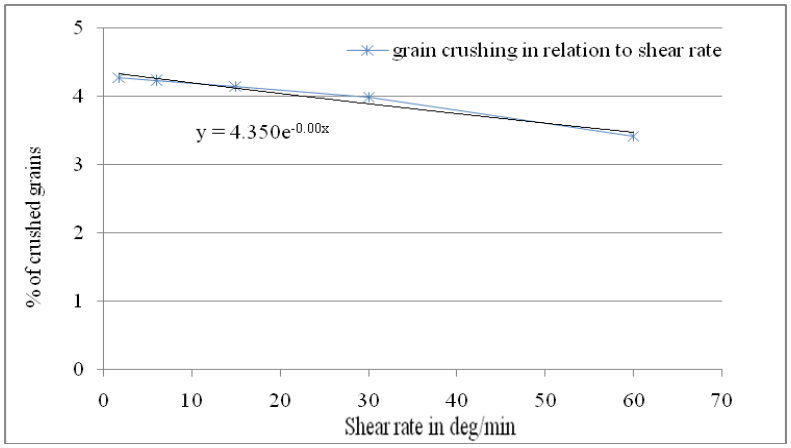


Figure 13. Percentages of the crushed grains of Calcareous sand in relation to the shear displacement, the polyonimic function extracted by the values measured lead to an exponential function. Of course the limits are because of the non negative values and the limits to shear speed

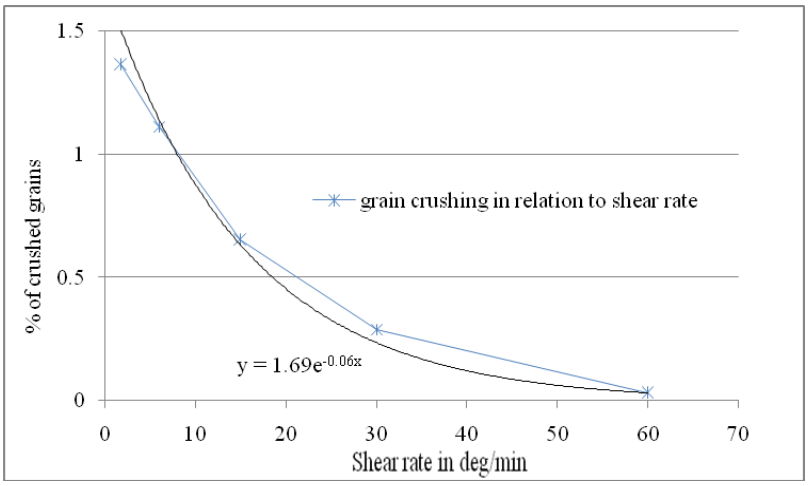

Figure 14. Percentages of the crushed grains of Quartzitic sand in relation to the shear displacement lead to an exponential function

## 7 CONCLUSIONS – PROPOSALS FOR FUTURE STUDY

In order to determine the effect variation of shear rates plays over the grain crushing phenomenon of sands over large shear displacements, three series of new tests were executed on three different types of sand. The tests were executed on the Bromhead apparatus of the Soil Mechanics and Foundation Engineering Laboratory of the Department of Civil Engineering at the Demokritos University of Thrace. The parameters of these tests i.e. the initial granulometry, the compaction process, moisture contained, vertical stress applied and the lengths of shear displacements were determined at previous papers and taken so as to ensure reliable results. [13] and [20]

Conclusions over differences of the shear stress paths measured in relation to the shear rates are in general agreement to bibliographical references. Grain crushing percentages seem to correlate with shear rates, positively when shear stresses cause more grain crushing than normal stresses, negatively when the inverse happens. In fact when Normal stress is more important than shear stress for the grain crushing phenomenon, (at least for the parameters tested in this paper) then time under load is of paramount importance for the grain crushing phenomenon.

The grain crushing phenomenon is rather complex and needs to be studied further as it proves quite important to landslide behavior. A future research could involve the study of grain crushing in relation to different normal stresses. It is found that higher normal stresses accentuate the grain crushing phenomenon but the phenomenon should be studied further to see if it is possible to extract any relative formulas.

The grain crushing phenomenon could be studied for different fractions of moisture from air dry to saturated, and by using diverse types of sand or mixtures of the sand types already used. Also it would be interesting to see how different granulometries of sands, after the Bromhead apparatus has been validated to ensure reliable results for such granulometries, affect the grain crushing phenomenon.

## REFERENCES

[1] Wang F., Sassa K., Relationship between grain crushing and excess pore pressure generation by sandy soils in ring-shear tests, *Journal of Natural Disaster Science*, Volume 22, number 2, pp 87-96, 2001.

[2] Food and Agricultural Organization of the United Nations, *FAO in emergencies, Landslides, available at: https://www.fao.org/emergencies/emergency-types/landslides/en/* (accessed 8/11/2021), 2021.

[3] Sassa K., Fukuoka H., Mugnozza G.S., Evans St., Earthquake induced landslides motion and mechanisms, *Special issue of soils and foundations* pp. 53-64, Japanese Geotechnical Society, 1996.

[4] Hvorslev M. J., Conditions of Failure for Remoulded Cohesive Soil. *Proceedings of the 1st International Conference on Soil Mechanics and Foundation Engineering*, Cambridge, 22-26 June 1936, 51-53, 1936.

[5] Hvorslev M. J., Torsion shear tests and their place in the determination of the shearing resistance of soils, *Symposium on the shear testing of soils,* ASTM, Vol. 39, pp. 999-1022, 1939.

[6] La Gatta D. P., Residual strength of clay and clay shales by rotation shear tests. *Army corps of engineers*, 1970.

[7] Bishop A.W., Green G.E., Garga V.K., Andresen A., and Brown J.D.. A new ring shear apparatus and its application to the measurement of residual strength. *Geotechnique*, Vol. 21, No 4 pp. 273-328, 1971.

[8] Bromhead E. M., A simple ring shear apparatus, *Ground Engineering*, Vol 12, No 5, pp. 40-44, 1979.

[9] Sassa K., Shima M., Hiura H., Nakagawa A., Suemine A., Development of Ring Shear type Debris flow Apparatus: Report of a grant-in-aid for scientific research from the Japanese Ministry of Education, *Science and Culture*, No 57860028, 1984.

[10] Bromhead E. N. Dixon N., The field residual strength of London clay and its correlation with laboratory measurements, especially ring shear tests, *Geotechnique*, Vol. 36, No. 4, pp.449-452, 1986.

[11] Stark T.D., Eid H.T., Comparison of of field and laboratory residual strengths, *Proceedings,ASCE Specialty Conference stability and performance of slopes and embankments 2*, University of California Berkeley, 1992.

[12] Newberry J., Baker D. A. B., The stability of cuts on the M4 North of Cardiff, *Quarterly journal of Engineering Geology*, Vol. 26, pp. 195-205, 1981.

[13] Sidiropoulos P., Stamatopoulos C., Panoskaltsis V., Markou I., Laboratory study of grain crushing of three sands in the Bromhead ring shear apparatus, *ICONHIC convention*, Athens, Greece, 2022.

[14] Lambe T.W., Soil testing for engineers, *John Wiley and Sons Inc*, pp. 88-95, 1951.

[15] Fukuoka H., Sassa K., High speed high stress ring shear tests on granular soils and clavey soils, *USDA Forest Service Gen, Tech, Rep. PSW* GTR-130: 33-42, 1991.

[16] Okada Y., Sassa K., Fukuoka H., Excess pore pressure and grain crushing of sands by means of undrained and drained ring shear tests, *Engineering Geology* 75: 325-343, Elsevier, 2004.

[17] Feda J., Notes on the effect of grain crushing on the granular soil behaviour, *Engineering Geology* 63: 93-98, Elsevier, 2002.

[18] Jeong S.W., Park S. S., Fukuoka H., Shear behavior of waste rock materials in drained and undrained ring shear tests, *Geosciences Journal*, Vol. 18, No 4:459-468, The Association of Korean Geoscience Societies and Springer, 2014.

[19] Jiang Y., Wang G., Toshitaka K., Fast shear behavior of granular materials in ring shear tests and implications for rapid landslides, *Acta Geotechnica* 12: 645-655, Springer, 2017.

[20] Sidiropoulos P. Stamatopoulos C. A., Panoskaltsis V. P., Laboratory tests for the study of grain crushing of sands under shear stress and the demonstration of its consequences at causing avalanches through proper numerical modeling, *IV International Congress of Antiseismic Mechanics and Technical Seismology*, Athens, Greece, 2019.

[21] Buhl & Faubel, Anular shear apparatus manual, *Buhl & Faubel*, 1989.

[22] Luzzani L. Coop M. R. On the relationship between particle breakage and the critical state of sands. *Soils and foundations*, Vol. 35, No 1, pp 71-82, 2002.

COMPDYN 2023
9th ECCOMAS Thematic Conference on
Computational Methods in Structural Dynamics and Earthquake Engineering
M. Papadrakakis, M. Fragiadakis (eds.)
Athens, Greece, 12-14 June 2023

# MULTISCALE MODELING OF COUPLED THERMO-HYDRO-MECHANICAL ANALYSIS OF HETEROGENEOUS POROUS MEDIA WITH MICRO-DYNAMIC EFFECTS

**Amir R. Khoei and Saeed Saeedmonir**

Center of Excellence in Structures and Earthquake Engineering, Department of Civil Engineering,
Sharif University of Technology, P.O. Box. 11365-9313, Tehran, Iran
e-mail: arkhoei@sharif.edu

## Abstract

*This paper presents a computational multiscale model for analysis of the transient heat and fluid flow in deformable porous media. Because of the heterogeneity in the porous media, the direct numerical simulation (DNS) of the micro-structures leads to high computational costs. Hence, the multiscale technique is developed to provide an efficient computational procedure. Accordingly, the first-order computational homogenization method is applied for two-scale simulation of THM problems. The Hill-Mandel theory is extended to capture the presence of micro-dynamic effects. The governing equations of the THM problem include the stress equilibrium equation, the mass continuity equation, and the advection-diffusion equation in a fully coupled manner. The weak forms of governing equations are then obtained as a bridging stage between the scales. Different boundary conditions of the microscopic domain are defined in terms of the macroscopic information to fulfill the averaging constraints. In order to consider the transient dynamic effects, the micro-inertial terms are involved in the micro-scale analysis, and the microscopic boundary conditions are improved to evaluate the accuracy of the analysis. The macroscopic properties including the homogenized tangent material property tensor and equivalent quantities, such as stress tensors, are determined from the microscopic solution through the appropriate mathematical approaches. Moreover, an upwind finite element squared method is employed for highly advective heat transfer to achieve the accurate spatial results. Finally, the numerical example of 2D heterogeneous medium is simulated to study the efficiency and validity of the proposed computational algorithm.*

**Keywords:** Computational homogenization, THM analysis, Micro-dynamic effects, Heterogeneous porous media, Advection-diffusion.

## 1 INTRODUCTION

There are several engineering problems that include the coupling of different physics, such as hydraulic fracturing, cold and hot water injection in reservoirs, oil and gas reservoirs, radioactive waste disposal, geothermal reservoirs, ground energy storage systems and etc. There are various numerical methods developed in the literature to simulate the coupled thermo-hydro-mechanical (THM) problems in steady-state and transient conditions [1–6], the multi-phase flow systems [7, 8], and the fractured thermo-hydro-mechanical media [9–12]. In real engineering problems, the case studies are generally constructed from complex micro-heterogeneities, resulting in high computational cost for modeling the micro-structures in details. Hence, the multiscale techniques have been developed by researchers to reduce the computational cost of numerical simulation without the compensation of accuracy. Among all multiscale approaches, the computational homogenization technique is found efficient and applicable to various problems. Computational homogenization approach is an interesting method in study of complex problems. In this method, the two scale levels are considered as the micro-scale and macro-scale levels, in which the constitutive behavior and equivalent quantities of each scale is determined through the solution of the lower scale. Since the heterogeneities are not directly modeled in the coarse-scale domain, this procedure reduces the computational cost as the analysis is performed distinctly for each micro-scale domain; hence, the high CPU and memory storage are not crucial in this approach.

In the computational homogenization method, the micro-scale and macro-scale are solved simultaneously with the finite element method, called the $FE^2$, with the information transferring between the two scales continuously. In the micro-scale level, a sample domain, called as the Representative Volume Element (RVE), is determined and simulated subject to specific boundary conditions, developed from the macro-scale level [13]. Basically, selection of the RVE is a significant step in the multiscale analysis and has been one of the major concerns by researchers [14, 15]. In fact, the micro-scale characteristic length for the RVE must be much smaller than the macro-scale level of the continuum model, which is an important assumption in the multiscale analysis, which is called the principle of separation of scales. However, the size and configuration of a RVE must be defined according to the distribution and arrangement of heterogeneities in the natural system. Moreover, the RVE size should be defined in a manner that an increase in the RVE size causes no change in the overall results of the simulation [16]. The RVE must represent even the smallest heterogeneity, so selection of the RVE is a significant step in the multiscale analysis.

In the present paper, a two-scale model is developed for the thermo-hydro-mechanical analysis of heterogeneous porous media. The transient dynamic effects of micro-structures are taken into account. The computational homogenization technique is developed based on the finite element squared method ($FE^2$), in which a Representative Volume Element is associated with each Gauss point of a macroscopic domain as the microscopic domain. For micro-scale analysis of the RVE, the appropriate boundary conditions are considered including the periodic and linear boundary conditions. In order to take the micro-inertial terms into account, additional constraints are coupled with the conventional periodic boundary conditions. Note that in the advection-diffusion equation coupled with the hydro-mechanical equations, the transient behavior of the micro-scale domain is not similar to the pure conduction problem. In fact, the presence of the convection (advection) heat transfer leads to numerical errors when the fluid velocity takes a large value. Thus, the Petrov-Galerkin finite element method is employed in the micro-scale domain instead of the conventional Galerkin FE method for the

weak formulation of the advection-diffusion equation. However, there are alternative techniques, such as the artificial diffusion method that lead to the same solution. It is demonstrated that on the contrary to the single-scale simulation, often called the Direct Numerical Simulation (DNS), the multiscale analysis does not lead to oscillating behavior in the spatial discretization of temperature field in highly convective problems.

## 2 GOVERNING EQUATIONS OF THM PROBLEM

The governing equations of THM problem are derived for two continuum scales of the multiscale analysis, in which the micro-scale, which is called the microscopic level, contains the heterogeneities of the medium, and the macroscopic scale is assumed as the homogenized domain of the physical problem. The governing equations are solved at the micro-scale level according to the specific boundary conditions, which is derived from the macroscopic level. In fact, a microscopic domain is associated with each material point of the macroscopic domain, where the macroscopic data are downscaled to the micro-scale level. The required data are then upscaled to the macro-scale level through the well-known Hill-Mandel principle of macro-homogeneity. In this study, the first order homogenization method is adopted, so the macroscopic main variables and their gradient fields are downscaled to the microscopic level. It must be noted that the classical separation of scales may need some reconsiderations in the case of transient loading [17, 18]. In such case, the full separation of scales cannot be considered anymore and the transient terms in the micro-scale level have significant influence on the overall transient behavior of the macroscopic problem. In this manner, the transient computational homogenization should be utilized to capture the micro-dynamic effects. In what follows, the governing equations of the thermo-hydro-mechanical analysis are presented.

In this study, the macroscopic quantities and mathematical operations with respect to the macroscopic coordinates are indicated by a bar, e.g. $\overline{\Theta}$. Hence, a quantity without a bar represents a microscopic quantity or operation with respect to microscopic coordinates. In addition, quantities with a tilde sign on top, e.g. $\tilde{\Theta}$, show the fluctuation field in the RVE. The volume average of a quantity in a specific domain in the RVE is defined as

$$\langle \Xi \rangle_{\Omega_0} = \frac{1}{|\Omega_0|} \int_{\Omega_0} \Xi \, d\Omega \tag{1}$$

In order to model the non-isothermal flow in a saturated deformable porous medium, the coupled governing equations are presented based on the force equilibrium equation, momentum balance equation, and energy balance equation. Based on the $u-p$ formulation, the primary variables are chosen as the displacement field $u$, fluid pressure $p$, and temperature of the mixture $\theta$ [19–21]. In this study, the instantaneous thermal equilibrium is considered between the fluid and solid, i.e. $\theta_S = \theta_f$; thus, only one energy balance equation is evaluated. The strong form of the mentioned equations can be expressed as

$$\begin{aligned}
&\boldsymbol{\nabla}.\boldsymbol{\sigma} + \mathbf{f}_{\text{Int}} = \mathbf{0} && \text{with} && \mathbf{f}_{\text{I}} = \rho\mathbf{b} - \rho\ddot{\mathbf{u}} \\
&\boldsymbol{\nabla}.\dot{\mathbf{w}} + \dot{\zeta} = 0 && \text{with} && \dot{\zeta} = \alpha\boldsymbol{\nabla}.\dot{\mathbf{u}} + \frac{\dot{p}}{Q} - \beta_f\dot{\theta} \\
&\nabla.\boldsymbol{J} + \dot{\eta}' = 0 && \text{with} && \boldsymbol{J} = \boldsymbol{J}_{\text{adv}} + \boldsymbol{J}_{\text{dif}} \quad \text{and} \quad \eta' = \rho c\theta
\end{aligned} \tag{2}$$

in which $\boldsymbol{\sigma}$ is the total stress tensor defined as $\boldsymbol{\sigma} = \boldsymbol{\sigma}' - \alpha p\mathbf{I}$, with $\boldsymbol{\sigma}'$ denoting the effective stress tensor, $\mathbf{f}_{\text{int}}$ is the inertial force vector, and $\mathbf{b}$ is the body force vector. In above, $\boldsymbol{\sigma}'$ is

defined as $\boldsymbol{\sigma}' = \mathbf{C} : (\boldsymbol{\varepsilon} - \boldsymbol{\varepsilon}_T)$ in the presence of thermal strain, with $\mathbf{C}$ indicating the elasticity tensor. Moreover, $\dot{\mathbf{w}}$, $\dot{\varsigma}$, $\alpha$, $Q$ and $\beta$ denote the Darcy velocity vector of the fluid with respect to the solid skeleton, the fluid content per volume, the Biot coefficient, the compressibility coefficient of the mixture, and the thermal expansion of the bulk, respectively. Also, it can be stated $\alpha = 1 - K_T / K_S$, $1/Q = (\alpha - n)/K_S + n/K_f$ and $\beta = (\alpha - n)\beta_s + n\beta_f$, in which $K_T$, $K_S$ and $K_f$ stand for the bulk modulus of the mixture, solid grains and fluid, respectively, and $n$ is the porosity of the soil. It is noteworthy that $\beta_s$ and $\beta_f$ are the thermal expansion coefficients of the solid and fluid, respectively. For plane strain problems, $\beta_s$ should be replaced by $\beta_s' = \beta_s(1+\nu)$, with $\nu$ denoting the Poisson ratio. In above equations, the average density of the mixture is defined as $\rho = (1-n)\rho_s + n\rho_f$. The term $\dot{\varsigma}$ in the 2nd equation of governing equations (2) can be obtained from the change of fluid density, which is described as $\rho_f = \rho_{f_0} \exp\left[-\beta_f \theta + 1/K_f (p - p_0)\right]$ [22]. In addition, $\boldsymbol{J}$, $\dot{\eta}'$ and $c$ are respectively the total heat flux vector, heat content per volume and specific heat capacity. For a solid-fluid mixture, the average heat capacity is defined as $\rho c = (1-n)(\rho c)_s + n(\rho c)_f$. The 3rd equation of governing equations (2) is the Divergence form of the advection-diffusion equation [23]. Due to the presence of the fluid flow, the heat is transferred by both conduction (diffusion) and convection (advection) regimes. It should be noted that the total energy balance equation is derived from the combination of the energy balance equation for each phase. Applying the Fourier law of thermal conduction, the advective and diffusive heat fluxes can be obtained as

$$\begin{aligned} \boldsymbol{J}_{\text{adv}} &= (\rho c)_f \dot{\mathbf{w}} \theta \\ \boldsymbol{J}_{\text{dif}} &= -\lambda \boldsymbol{\nabla} \theta \end{aligned} \tag{3}$$

where $\lambda$ is the average conductivity (diffusivity) of the mixture, defined as $\lambda = (1-n)\lambda_s + n\lambda_f$. Expanding the 3rd equation of governing equations (2) and applying equation (3) and the mass continuity equations of the solid and fluid phases, the convective form of the energy balance equation can be extracted as

$$\boldsymbol{\nabla}.(\boldsymbol{J}_{\text{dif}}) + \eta = 0 \qquad \text{with} \qquad \eta = (\rho c)_f \dot{\mathbf{w}} \boldsymbol{\nabla} \theta + \rho c \dot{\theta} \tag{4}$$

where $\boldsymbol{J}_{\text{dif}} = -\lambda \nabla \theta$. It should be noted that in the convective form, $\eta$ cannot be taken as the previously defined heat content and the effect of advection must be included. The fluid relative velocity $\dot{\mathbf{w}}$ can be obtained from the generalized Darcy law by $\dot{\mathbf{w}} = \mathbf{k}(-\nabla p + \rho \mathbf{b} - \rho \ddot{\mathbf{u}})$, with $\mathbf{k}$ denotes the permeability tensor of the porous medium. It is noted that the convective form of the advection-diffusion equation neglects the explicit dependency of the equation to the displacement and pressure fields, while in the Divergence form, all the main variables are included in the equation.

## 3 MULTISCALE FORMULATION OF THM PROBLEMS

In order to perform the multiscale analysis of THM problem, the method of multiple scales is carried out, in which a macroscopic domain is considered as the homogenized medium and a micro-scale domain is assigned to each material point. In this manner, the homogenized quantities are extracted from the micro-scale domain at each material point employing the two scale transitions within the multiscale analysis; first downscaling the macroscopic solution to the micro-scale and then, upscaling the homogenized quantities to the macro-scale problem.

### 3.1 Downscaling technique

Let $\Omega$ and $\Gamma$ denote the domain and the boundary of the Representative Volume Element (RVE) at the micro-scale domain, respectively. The primary fields at the RVE can be described as

$$\begin{aligned}
&\mathbf{u}(\mathbf{x}) = \bar{\mathbf{u}} + \bar{\boldsymbol{\nabla}}\bar{\mathbf{u}}.\mathbf{x} + \tilde{\mathbf{u}} \equiv \bar{\mathbf{u}} + \mathbf{H}^{\mathrm{T}}\bar{\boldsymbol{\epsilon}} + \tilde{\mathbf{u}} \qquad \text{with} \qquad \mathbf{H} = \begin{bmatrix} x_1 & 0 & x_2/2 \\ 0 & x_2 & x_1/2 \end{bmatrix} \\
&p(\mathbf{x}) = \bar{p} + \mathbf{x}^{\mathrm{T}}\,\bar{\boldsymbol{\nabla}}\bar{p} + \tilde{p} \\
&\theta(\mathbf{x}) = \bar{\theta} + \mathbf{x}^{\mathrm{T}}\,\bar{\boldsymbol{\nabla}}\bar{\theta} + \tilde{\theta}
\end{aligned} \tag{5}$$

in which $\mathbf{x} \in \Omega$ is the position vector of a point in the RVE, measured from the centroid of the RVE. It should be noted that the first two terms of the above relations are known as the smooth part of the microscopic fields, which vary linearly inside the RVE, and the third terms, which are known as the fluctuation fields, play the role of higher order terms in the Taylor expansion of the functions. These terms are the variable parts of the solution defined through the micro-scale analysis. In addition, it is noteworthy that for displacement field, the Voigt notation can be exploited for the simplicity of the finite element formulation as an alternative to the general formulation in terms of displacement gradient (or deformation gradient). As a basic assumption in the homogenization framework, the average of gradient fields should be equal to the macroscopic gradients. Hence, the following constraints can be written as

$$\begin{aligned}
&\bar{\boldsymbol{\epsilon}} = \frac{1}{|\Omega|}\int_{\Omega} \boldsymbol{\epsilon}\, d\Omega \\
&\bar{\boldsymbol{\nabla}}\bar{p} = \frac{1}{|\Omega|}\int_{\Omega} \boldsymbol{\nabla} p\, d\Omega \\
&\bar{\boldsymbol{\nabla}}\bar{\theta} = \frac{1}{|\Omega|}\int_{\Omega} \boldsymbol{\nabla}\theta\, d\Omega
\end{aligned} \tag{6}$$

As a result of equations (5) and (6), it can be stated that

$$\begin{aligned}
&\int_{\Gamma} \boldsymbol{\mathcal{N}}\tilde{\mathbf{u}}\, d\Gamma = \mathbf{0} \qquad \text{with} \qquad \boldsymbol{\mathcal{N}} = \begin{bmatrix} n_1 & 0 & n_2 \\ 0 & n_2 & n_1 \end{bmatrix}^{T} \\
&\int_{\Gamma} \tilde{p}\,\mathbf{n}\, d\Gamma = 0 \\
&\int_{\Gamma} \tilde{\theta}\,\mathbf{n}\, d\Gamma = 0
\end{aligned} \tag{7}$$

where $\mathbf{n}$ is the outward normal vector at the boundary of the RVE. It must be noted that in the above procedure, the Green theorem is employed to transform the domain integral equation to a boundary integral equation. In order to satisfy the aforementioned constraints, various techniques have been proposed in the literature, such as the Taylor model, linear boundary condition, periodic boundary condition, minimally constrained boundary condition, and Reuss methods. Among all these approaches, the periodic boundary condition is known to exhibit the closest response to the exact ones in comparison to the other techniques. Hence, the periodic boundary condition is chosen here to study the proposed computational algorithm. In this method, the fluctuation fields at the opposite boundaries of the RVE are set to be equal, which

results in anti-periodic tractions and fluxes. Moreover, to maintain the magnitude of volume average of the field variables to the macroscopic solution, four corner points are constrained such that the fluctuation fields vanish in these points.

### 3.2 Upscaling technique

In order to perform the multiscale analysis, the required variables should be extracted from the micro-scale solution and utilized in the macro-scale solution. To this end, an extended form of the Hill-Mandel principle of macro-homogeneity is adopted [24, 25]. According to this principle, the volume average of the virtual power in the microscopic domain should be equal to the macroscopic virtual power at the associated point. From the weak form of the governing equations (2) and (4), the volume average of the virtual work can be expressed in the microscopic domain as

$$\begin{aligned}
\langle \delta \mathcal{W}^u \rangle &:= \frac{1}{|\Omega|}\int_\Omega (\delta \boldsymbol{\nabla}\mathbf{u}\colon \boldsymbol{\sigma} - \delta \mathbf{u}.(\rho \mathbf{b} - \rho \ddot{\mathbf{u}}))\, d\Omega \\
\langle \delta \mathcal{W}^f \rangle &:= \frac{1}{|\Omega|}\int_\Omega \Big( -\delta \boldsymbol{\nabla} p.\dot{\mathbf{w}} + \delta p\, \alpha\, \boldsymbol{\nabla}.\dot{\mathbf{u}} + \delta p \frac{\dot{p}}{Q} - \delta p\, \beta_f \dot{\theta}\Big)\, d\Omega \\
\langle \delta \mathcal{W}^\theta \rangle &:= \frac{1}{|\Omega|}\int_\Omega \big( -\delta \boldsymbol{\nabla}\theta.\boldsymbol{J}_{\text{dif}} + \delta\theta(\rho c)_f \dot{\mathbf{w}}.\boldsymbol{\nabla}\theta + \delta\theta\, \rho c \dot{\theta}\,\big) d\Omega
\end{aligned} \tag{8}$$

in which for the corresponding material point in the macroscopic domain, the virtual work relations can be described as

$$\begin{aligned}
\delta \bar{\mathcal{W}}^u &:= \delta \bar{\boldsymbol{\nabla}}\bar{\mathbf{u}}\colon \bar{\boldsymbol{\sigma}} - \delta \bar{\mathbf{u}}.\big(\bar{\rho}\bar{\mathbf{b}} - \bar{\rho}\ddot{\bar{\mathbf{u}}}\big) = \delta \bar{\boldsymbol{\nabla}}\bar{\mathbf{u}}\colon \bar{\boldsymbol{\sigma}} - \delta \bar{\mathbf{u}}.\bar{\mathbf{f}}_{\text{Int}} \\
\delta \bar{\mathcal{W}}^f &:= -\delta \bar{\boldsymbol{\nabla}}\bar{p}.\dot{\bar{\mathbf{w}}} + \delta \bar{p}\, \bar{\alpha}\, \bar{\boldsymbol{\nabla}}.\dot{\bar{\mathbf{u}}} + \delta \bar{p}\frac{\dot{\bar{p}}}{\bar{Q}} - \delta \bar{p}\, \overline{\beta_f}\dot{\bar{\theta}} = -\delta \bar{\boldsymbol{\nabla}}\bar{p}.\dot{\bar{\mathbf{w}}} + \delta \bar{p}\dot{\bar{\zeta}} \\
\delta \bar{\mathcal{W}}^\theta &:= -\delta \bar{\boldsymbol{\nabla}}\bar{\theta}.\bar{\boldsymbol{J}} + \delta\bar{\theta}(\bar{\rho}\bar{c})_f \dot{\bar{\mathbf{w}}}.\boldsymbol{\nabla}\theta + \delta\bar{\theta}\, \bar{\rho}\bar{c}\dot{\bar{\theta}} = -\delta \bar{\boldsymbol{\nabla}}\bar{\theta}.\bar{\boldsymbol{J}} + \delta\bar{\theta}\bar{\eta}
\end{aligned} \tag{9}$$

In order to perform the macro-homogeneity principle, the macroscopic virtual power should be derived from the average of virtual powers in the micro-scale domain. Hence, it can be concluded from equations (8) and (9) that

$$\begin{aligned}
\delta \bar{\boldsymbol{\nabla}}\bar{\mathbf{u}}\colon \bar{\boldsymbol{\sigma}} - \delta \bar{\mathbf{u}}.\bar{\mathbf{f}}_{\text{Int}} &= \frac{1}{|\Omega|}\int_\Omega (\delta \boldsymbol{\nabla}\mathbf{u}\colon \boldsymbol{\sigma} - \delta \mathbf{u}.\mathbf{f}_{\text{Int}})\, d\Omega \\
-\delta \bar{\boldsymbol{\nabla}}\bar{p}.\dot{\bar{\mathbf{w}}} + \delta \bar{p}\dot{\bar{\zeta}} &= \frac{1}{|\Omega|}\int_\Omega \big( -\delta \boldsymbol{\nabla} p.\dot{\mathbf{w}} + \delta p\, \dot{\zeta}\,\big) d\Omega \\
-\delta \bar{\boldsymbol{\nabla}}\bar{\theta}.\bar{\boldsymbol{J}} + \delta\bar{\theta}\bar{\eta} &= \frac{1}{|\Omega|}\int_\Omega \big( -\delta \boldsymbol{\nabla}\theta.\boldsymbol{J}_{\text{dif}} + \delta\theta\, \eta\,\big) d\Omega
\end{aligned} \tag{10}$$

in which the right-hand sides in above equations are expressed in the forms given in equations (2) and (4). Applying the downscaling relations defined in (5), considering the variations of macroscopic terms, i.e. $\delta\bar{\mathbf{u}}$, $\delta\bar{p}$, and $\delta\bar{\theta}$, as the constant functions within the RVE, and substituting the above relations into the right-hand side of equations (3), it leads to

$$\begin{aligned}
\delta \bar{\boldsymbol{\nabla}}\bar{\mathbf{u}}\colon \bar{\boldsymbol{\sigma}} - \delta \bar{\mathbf{u}}.\bar{\mathbf{f}}_{\text{Int}} = \delta \bar{\boldsymbol{\nabla}}\bar{\mathbf{u}}\colon &\left(\frac{1}{|\Omega|}\int_\Omega (\boldsymbol{\sigma} - \mathbf{f}_{\text{Int}} \otimes \mathbf{x})\, d\Omega\right) \\
&-\delta \bar{\mathbf{u}}.\left(\frac{1}{|\Omega|}\int_\Omega \mathbf{f}_{\text{Int}}\, d\Omega\right) + \left(\frac{1}{|\Omega|}\int_\Omega (\delta \tilde{\boldsymbol{\nabla}}\tilde{\mathbf{u}}\colon \boldsymbol{\sigma} - \delta \tilde{\mathbf{u}}.\mathbf{f}_{\text{Int}})\, d\Omega\right)
\end{aligned}$$

$$
\begin{aligned}
-\delta\bar{\boldsymbol{\nabla}}\bar{p}.\dot{\bar{\mathbf{w}}}+\delta\bar{p}\dot{\bar{\zeta}} &= -\delta\bar{\boldsymbol{\nabla}}\bar{p}.\left(\frac{1}{|\Omega|}\int_{\Omega}\left(\dot{\mathbf{w}}-\mathbf{x}\,\dot{\zeta}\right)d\Omega\right)\\
&\quad+\delta\bar{p}.\left(\frac{1}{|\Omega|}\int_{\Omega}\dot{\zeta}\;d\Omega\right)+\left(\frac{1}{|\Omega|}\int_{\Omega}\left(-\delta\boldsymbol{\nabla}\tilde{p}.\dot{\mathbf{w}}+\delta\tilde{p}\;\dot{\zeta}\right)d\Omega\right)\\
-\delta\bar{\boldsymbol{\nabla}}\bar{\theta}.\bar{\boldsymbol{J}}+\delta\bar{\theta}\bar{\eta} &= -\delta\bar{\boldsymbol{\nabla}}\bar{\theta}.\left(\frac{1}{|\Omega|}\int_{\Omega}\left(\boldsymbol{J}_{\mathrm{dif}}-\mathbf{x}\,\eta\right)d\Omega\right)\\
&\quad+\delta\bar{\theta}.\left(\frac{1}{|\Omega|}\int_{\Omega}\eta\;d\Omega\right)+\left(\frac{1}{|\Omega|}\int_{\Omega}\left(-\delta\boldsymbol{\nabla}\tilde{\theta}.\boldsymbol{J}_{\mathrm{dif}}+\delta\tilde{\theta}\;\eta\right)d\Omega\right)
\end{aligned}
\tag{11}
$$

Applying the Divergence theorem to the third terms at the right-hand side of above equations, it can be concluded that these terms can be vanished by applying the appropriate boundary conditions, e.g. the periodic boundary conditions and linear boundary conditions. These equations can be considered as the variational form of governing equations in the microscopic scale. In fact, the weak forms of the micro-scale problem are recovered directly from the generalized Hill-Mandel principle, which should be solved under the mentioned boundary conditions. On the other hand, by noting the fact that functions $\delta\bar{\boldsymbol{\nabla}}\bar{\mathbf{u}}$, $\delta\bar{\mathbf{u}}$, $\delta\bar{\boldsymbol{\nabla}}\bar{p}$, $\delta\bar{p}$, $\delta\bar{\boldsymbol{\nabla}}\bar{\theta}$, and $\delta\bar{\theta}$ are arbitrary functions, the following results can be achieved from (11) as

$$
\begin{aligned}
\bar{\boldsymbol{\sigma}} &= \frac{1}{|\Omega|}\int_{\Omega}\left(\boldsymbol{\sigma}-\mathbf{f}_{\mathrm{Int}}\otimes\mathbf{x}\right)d\Omega & \bar{\mathbf{f}}_{\mathrm{Int}} &= -\frac{1}{|\Omega|}\int_{\Omega}\mathbf{f}_{\mathrm{Int}}\,d\Omega\\
\dot{\bar{\mathbf{w}}} &= -\frac{1}{|\Omega|}\int_{\Omega}\left(\dot{\mathbf{w}}-\mathbf{x}\,\dot{\zeta}\right)d\Omega & \dot{\bar{\zeta}} &= \frac{1}{|\Omega|}\int_{\Omega}\dot{\zeta}\;d\Omega\\
\bar{\boldsymbol{J}} &= -\frac{1}{|\Omega|}\int_{\Omega}\left(\boldsymbol{J}_{\mathrm{dif}}-\mathbf{x}\,\eta\right)d\Omega & \bar{\eta} &= \frac{1}{|\Omega|}\int_{\Omega}\eta\;d\Omega
\end{aligned}
\tag{12}
$$

Obviously, it can be observed from relations (12) that the macroscopic quantities are extracted from the microscopic solution. However, the classical averaging approach does not hold in the current formulation due to presence of the transient terms.

## 4 FINITE ELEMENT MODELING OF THM MULTISCALE ANALYSIS

### 4.1 FE discretization of macro-scale domain

In order to derive the FE discretization of macro-scale governing equations, the weak forms of the macro-scale domain are defined on the basis of information upscaled from the microscopic model. To this end, the variational forms of the macroscopic governing equations can be expressed as

$$
\begin{aligned}
&\int_{\bar{\Omega}}\left(\delta\bar{\boldsymbol{\nabla}}\bar{\mathbf{u}}:\bar{\boldsymbol{\sigma}}-\delta\bar{\mathbf{u}}.\bar{\mathbf{f}}_{\mathrm{Int}}\right)d\Omega-\int_{\bar{\Gamma}}\delta\bar{\mathbf{u}}^{\mathrm{T}}\bar{\mathbf{t}}\;d\Gamma\;=0\\
&\int_{\bar{\Omega}}\left(-\delta\bar{\boldsymbol{\nabla}}\bar{p}.\dot{\bar{\mathbf{w}}}+\delta\bar{p}\dot{\bar{\zeta}}\right)d\Omega+\int_{\bar{\Gamma}}\delta\bar{p}\;\bar{q}_{f}\;d\Gamma=0\\
&\int_{\bar{\Omega}}\left(-\delta\bar{\boldsymbol{\nabla}}\bar{\theta}.\bar{\boldsymbol{J}}+\delta\bar{\theta}\bar{\eta}\right)d\Omega+\int_{\bar{\Gamma}}\delta\bar{\theta}\;\bar{q}_{T}\;d\Gamma=0
\end{aligned}
\tag{13}
$$

Applying the finite element discretization, the weak forms of the macro-scale domain can be discretized as

$$\begin{aligned}
\bar{\boldsymbol{\psi}}_u &= \int_{\bar{\Omega}} \left(\bar{\mathbf{B}}_u^{\mathrm{T}}\ \underline{\boldsymbol{\sigma}} - \bar{\mathbf{N}}_u^{\mathrm{T}}\ \bar{\mathbf{f}}_{\mathrm{Int}}\right) d\Omega - \int_{\bar{\Gamma}} \bar{\mathbf{N}}_u^{\mathrm{T}}\ \bar{\mathbf{t}}\ d\Gamma\ = 0 \\
\bar{\boldsymbol{\psi}}_p &= \int_{\bar{\Omega}} \left(-\bar{\mathbf{B}}_p^{\mathrm{T}}\ \dot{\bar{\mathbf{w}}} + \bar{\mathbf{N}}_p^{\mathrm{T}}\ \dot{\bar{\zeta}}\right) d\Omega + \int_{\bar{\Gamma}} \bar{\mathbf{N}}_p^{\mathrm{T}}\ \bar{q}_f\ d\Gamma = 0 \\
\bar{\boldsymbol{\psi}}_T &= \int_{\bar{\Omega}} \left(-\bar{\mathbf{B}}_\theta^{\mathrm{T}} \dot{\bar{\boldsymbol{J}}} + \bar{\mathbf{N}}_\theta^{\mathrm{T}}\ \dot{\bar{\eta}}\right) d\Omega + \int_{\bar{\Gamma}} \bar{\mathbf{N}}_\theta^{\mathrm{T}}\ \bar{q}_T\ d\Gamma = 0
\end{aligned} \tag{14}$$

where $\bar{\mathbf{N}}_u$, $\bar{\mathbf{N}}_p$ and $\bar{\mathbf{N}}_\theta$ are the global shape functions corresponding to the primary variables and $\bar{\mathbf{B}}_u$, $\bar{\mathbf{B}}_p$ and $\bar{\mathbf{B}}_\theta$ denote the gradients of the shape functions. In above, the underbar '_" is utilized to represent the vector form of the symmetric 2nd order tensors, such as the stress tensor. Due to the general nonlinearity of equations (14), the Newton-Raphson scheme is adopted in order to linearize and solve the discretized system of governing equations as

$$\bar{\boldsymbol{\mathcal{F}}}_n^{i+1} = \bar{\boldsymbol{\mathcal{F}}}_n^i + \bar{\boldsymbol{\mathcal{J}}}_n^i . d\bar{\boldsymbol{\mathcal{X}}}_n^i \quad , \quad \bar{\boldsymbol{\mathcal{F}}} = \begin{Bmatrix} \bar{\boldsymbol{\psi}}_u \\ \bar{\boldsymbol{\psi}}_p \\ \bar{\boldsymbol{\psi}}_T \end{Bmatrix} \quad , \quad \bar{\boldsymbol{\mathcal{X}}} = \begin{Bmatrix} \bar{\mathbf{U}} \\ \bar{\mathbf{P}} \\ \bar{\boldsymbol{\Theta}} \end{Bmatrix} \tag{15}$$

where $\bar{\boldsymbol{F}}$ is the nodal values of residual vector, $\bar{\boldsymbol{X}}$ denotes the nodal values of the primary variables, and $\bar{\boldsymbol{J}}$ represents the Jacobian matrix defined as

$$\bar{\boldsymbol{\mathcal{J}}} = \begin{bmatrix} \dfrac{\partial \bar{\boldsymbol{\psi}}_u}{\partial \bar{\mathbf{U}}} & \dfrac{\partial \bar{\boldsymbol{\psi}}_u}{\partial \bar{\mathbf{P}}} & \dfrac{\partial \bar{\boldsymbol{\psi}}_u}{\partial \boldsymbol{\Theta}} \\ \dfrac{\partial \bar{\boldsymbol{\psi}}_p}{\partial \bar{\mathbf{U}}} & \dfrac{\partial \bar{\boldsymbol{\psi}}_p}{\partial \bar{\mathbf{P}}} & \dfrac{\partial \bar{\boldsymbol{\psi}}_p}{\partial \boldsymbol{\Theta}} \\ \dfrac{\partial \bar{\boldsymbol{\psi}}_T}{\partial \bar{\mathbf{U}}} & \dfrac{\partial \bar{\boldsymbol{\psi}}_T}{\partial \bar{\mathbf{P}}} & \dfrac{\partial \bar{\boldsymbol{\psi}}_T}{\partial \boldsymbol{\Theta}} \end{bmatrix} \tag{16}$$

In relation (15), the subscripts and superscripts, denoted by $n$ and $i$, represent the number of increment and iteration, respectively. In equation (16), the components of the Jacobian matrix can be obtained by taking the variations of (13) with respect to the primary variables.

### 4.2 FE discretization of micro-scale domain

In order to derive the FE discretization of micro-scale governing equations, the weak forms of the micro-scale domain are derived to determine the response of the RVE. The variational formulations of microscopic governing equations can be obtained as

$$\begin{aligned}
&\int_\Omega \left(\delta\boldsymbol{\nabla}\tilde{\mathbf{u}} : \boldsymbol{\sigma} - \delta\tilde{\mathbf{u}} . (\rho\mathbf{b} - \rho\ddot{\mathbf{u}})\right) d\Omega = 0 \\
&\int_\Omega \left( -\delta\boldsymbol{\nabla}\tilde{p} . \dot{\mathbf{w}} + \delta\tilde{p}\ \alpha\ \boldsymbol{\nabla} . \dot{\mathbf{u}} + \delta\tilde{p}\,\frac{\dot{p}}{Q} - \delta\tilde{p}\ \beta_f \dot{\theta}\right) d\Omega = 0 \\
&\int_\Omega \left( - \delta\boldsymbol{\nabla}\tilde{\theta} . \boldsymbol{J}_{\mathrm{dif}} + \delta\tilde{\theta}(\rho c)_f \dot{\mathbf{w}} . \boldsymbol{\nabla}\theta + \delta\tilde{\theta}\ \rho c\dot{\theta}\ \right) d\Omega = 0
\end{aligned} \tag{17}$$

Applying the finite element discretization, the weak forms of the micro-scale domain can be discretized as

$$\begin{aligned}
\boldsymbol{\psi}_u &= \mathbf{M}_u\ddot{\mathbf{U}} + \mathbf{K}\mathbf{U} - \mathbf{Q}\mathbf{P} - \mathbf{W}\boldsymbol{\Theta} - \mathbf{F}_u = \mathbf{0} \\
\boldsymbol{\psi}_p &= \mathbf{M}_f\ddot{\mathbf{U}} + \mathbf{Q}^{\mathrm{T}}\dot{\mathbf{U}} + \mathbf{H}\,\mathbf{P} + \mathbf{S}\,\dot{\mathbf{P}} + \mathbf{R}\,\dot{\boldsymbol{\Theta}} - \mathbf{F}_p = \mathbf{0} \\
\boldsymbol{\psi}_T &= \mathbf{L}\,\dot{\boldsymbol{\Theta}} + \mathbf{C}\,\boldsymbol{\Theta} - \mathbf{F}_\theta = \mathbf{0}
\end{aligned} \tag{18}$$

in which the complete definition of the matrices and vectors can be found in references [26, 27]. Implementation of the Newton-Raphson linearization method, the system of algebraic equations can be described as

$$\boldsymbol{\mathcal{F}}_n^{i+1} = \boldsymbol{\mathcal{F}}_n^i + \boldsymbol{\mathcal{J}}_n^i . d\boldsymbol{\mathcal{X}}_n^i \quad , \quad \boldsymbol{\mathcal{F}} = \begin{Bmatrix} \boldsymbol{\psi}_u \\ \boldsymbol{\psi}_p \\ \boldsymbol{\psi}_T \end{Bmatrix} \quad , \quad \boldsymbol{\mathcal{X}} = \begin{Bmatrix} \mathbf{U} \\ \mathbf{P} \\ \boldsymbol{\Theta} \end{Bmatrix} \tag{19}$$

Applying the Newmark method for the time domain discretization in equations (18), in which the time derivative variables are expressed in terms of the known variables given in the previous increment and unknown current variables, the microscopic Jacobian matrix can be obtained as

$$\boldsymbol{\mathcal{J}} = \begin{bmatrix} a_0\mathbf{M}_u + \mathbf{K} & -\mathbf{Q} & -\mathbf{W} \\ a_0\mathbf{M}_f + \mathbf{Q}^{\mathrm{T}} & \mathbf{H} + a_6\mathbf{S} & a_6\mathbf{R} \\ \mathbf{0} & \mathbf{0} & a_6\mathbf{L} + \mathbf{C} \end{bmatrix} \tag{20}$$

where $a_0 = 1/(\alpha_2 \Delta t^2)$ and $a_6 = 1/(\alpha_3 \Delta t)$ with $\alpha_2$ and $\alpha_3$ denoting the Newmark parameters.

The multiscale analysis is performed using the $FE^2$ technique, in which the initial and boundary conditions of the real problem are considered for the macro-scale domain. The macro-scale domain is discretized by the finite element method and the relevant matrices are obtained for the medium. An RVE is associated with each Gauss point of an element, as a micro-scale domain, and the field variables are transferred to the discretized micro-scale domain. The nonlinear transient micro-scale problem is solved using the appropriate initial and boundary conditions through the iterative Newton-Raphson method, and the macroscopic variables and tangent operators are extracted from the resultant solution. The quantities are then transferred to the macro-scale domain and utilized in the Newton-Raphson procedure. While the data corresponding to all Gauss integration points in the macro-scale domain are extracted from the micro-scale analyses, the linearized macro-scale equations are solved and the field variables are updated. The above iterative procedure is continued until the convergence is achieved at the macro-scale domain.

## 5 NUMERICAL SIMULATION RESULTS

In order to demonstrate the efficiency and accuracy of the proposed multiscale algorithm, the coupled thermo-hydro-mechanical analysis is performed for a 2D heterogeneous medium. A square domain of $6 \times 6\,\mathrm{m}^2$ is constructed from two different materials, called the matrix and particle, as shown in Figure 1. The material properties of the matrix and particle are given in Table 1. The particles are considered as a circular shape with the radius of $0.35\,\mathrm{m}$. The geometry and boundary conditions of the problem are presented in Figure 1. The medium is restricted to horizontal displacement at the left and right edges, while the top and bottom edges are constrained against the vertical displacement. In fact, the problem is assumed as one-quarter of an injection-production system, in which the fluid is injected from its center and the production occurs at the corners (see Figure 1). On the other hand, on the virtue of symmetry the above boundary conditions are appropriate for the injection-production problem. It must be noted that the displacement field is not zero within the domain since there are the fluid flow and temperature changes that can affect the displacement field. Moreover, the temperature of $100\,^{\circ}\mathrm{C}$ is applied at the region A, while the temperature of region B is set to zero.

Table 1: Material properties of the square heterogeneous medium

| Property | Material 1 (Matrix) | Material 2 (Particle) |
|---|---|---|
| Elasticity modulus | $E = 6$ MPa | $E = 3000$ MPa |
| Poisson ratio | $\nu = 0.4$ | $\nu = 0.4$ |
| Biot coefficient | $\alpha = 1$ | $\alpha = 0.65$ |
| Porosity | $n = 0.3$ | $n = 0.1$ |
| Solid density | $\rho_s = 2000$ Kg/m$^2$ | $\rho_s = 20000$ Kg/m$^2$ |
| Water density | $\rho_w = 1000$ Kg/m$^2$ | $\rho_w = 1000$ Kg/m$^2$ |
| Bulk modulus of solid | $K_s = 10^7$ MPa | $K_s = 10^8$ MPa |
| Bulk modulus of fluid | $K_f = 10^3$ MPa | $K_f = 10^3$ MPa |
| permeability | $k = 1.1 \times 10^{-9}$ m$^4$/Pa. s | $k = 3.8 \times 10^{-11}$ m$^4$/Pa. s |
| Thermal conductivity of mixture | $\lambda = 837$ W/m C° | $\lambda = 16.74$ W/m C° |
| Heat capacity of solid | $c_s = 878$ J/kg C° | $c_s = 1369.7$ J/kg C° |
| Heat capacity of fluid | $c_f = 4184$ J/kg C° | $c_f = 4184$ J/kg C° |
| Thermal expansion coefficient | $0.9 \times 10^{-6}$ | $0.3 \times 10^{-6}$ |

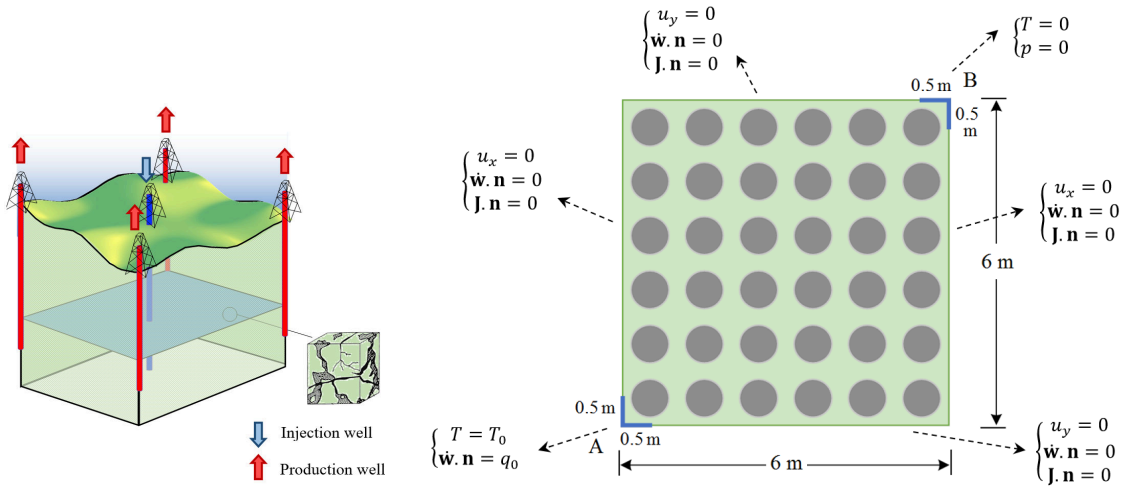


Figure 1: A heterogeneous square domain; The geometry and boundary conditions

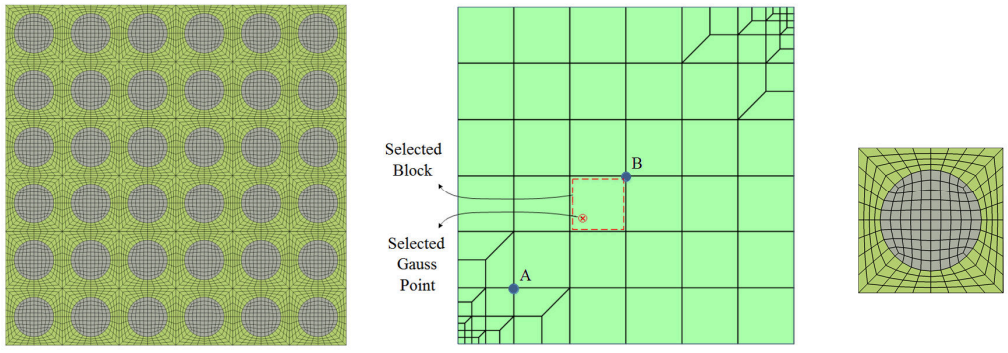


(a) (b) (c)

Figure 2: A heterogeneous square domain; a) Finite element mesh of DNS model, b) FE mesh of macro-scale model, c) the RVE of the micro-scale model

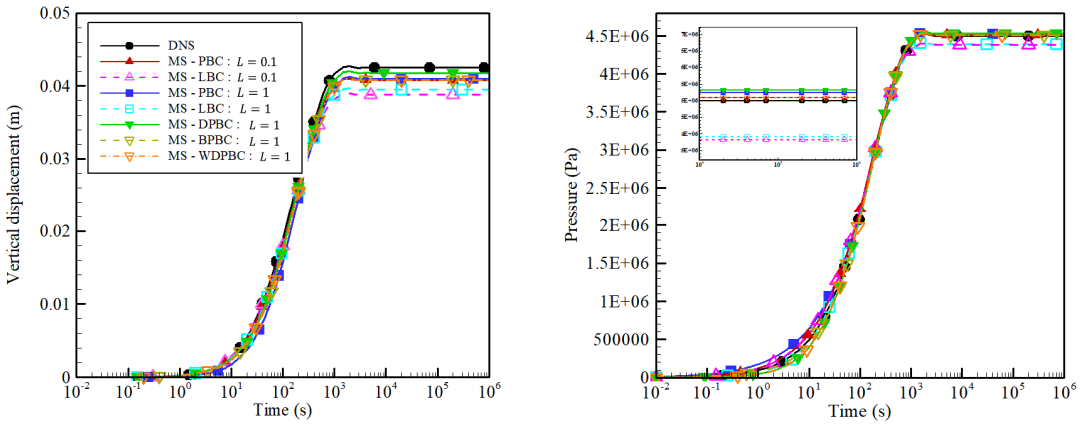


Figure 3. The variations with time of the vertical displacement and fluid pressure for the THM analysis of a heterogeneous square domain at point A; A comparison between the DNS model and multi-scale analysis with different RVE boundary conditions and length scales

The fluid is injected with a rate of $q = 10^{-4}\ \mathrm{m}^2/\mathrm{s}$ from the region A uniformly distributed in $1\,\mathrm{m}$ length ($0.5\,\mathrm{m}$ along each side). Similarly, the pressure is set to zero at the region B as the production area. Other boundaries are insulated to the fluid and heat exchange. The DNS model is performed to compare the results of the multiscale analysis with a very fine FE mesh and to illustrate the accuracy of the method. The FE mesh of DNS model is constructed from 8064 bilinear elements with 8161 nodes, as shown in Figure 2. In this figure, the FE meshes of macro-scale and micro-scale analyses are presented. The macro-scale domain consists of 78 bilinear elements with 103 nodes, and the RVE comprises of 224 elements with 241 nodes. In the multiscale analysis, different aspects of micro-scale boundary conditions are studied, including the typical periodic boundary condition with corner nodes constraints (PBC), periodic boundary condition with domain integral constraint (D–PBC), periodic boundary condition with boundary integral constraint (B–PBC), periodic boundary condition with weighted domain integral constraint (WD–PBC), and linear boundary condition (LBC) using two RVE length sizes of $L = 0.1$ and $1\,\mathrm{m}$.

In Figure 3, the variations with time of the vertical displacement and fluid pressure are plotted for the heterogeneous square domain at point A. Obviously, the results of multiscale analysis using various micro-scale boundary conditions are in good agreement with that obtained from the DNS model. However, a slight discrepancy can be seen in the displacement field using the LBC model with the RVE length sizes of $L = 0.1$ and $1\,\mathrm{m}$ at the steady state condition. In Figure 4, the variations with time of the temperature are plotted for a heterogeneous square domain at points A and B. It can be observed that the results of multiscale analysis with different micro-scale boundary conditions are close to that of DNS model at point B. However, significant discrepancies can be observed for the RVE size of $L = 0.1$ and WD–PBC model at point B. On the other hand, the results of typical PBC with $L = 0.1$ and $1\,\mathrm{m}$ as well as the LBC with $L = 0.1\,\mathrm{m}$, and WD–PBC model are completely unacceptable for point A due to substantial deviations even in large time steps. Unlikely, D–PBC, B–PBC and LBC with $L = 1\,\mathrm{m}$ present a reasonable agreement with the DNS model. Since the idea of boundary integral periodic boundary condition is taken from the linear boundary condition, appropriate results can be expected from these approaches.

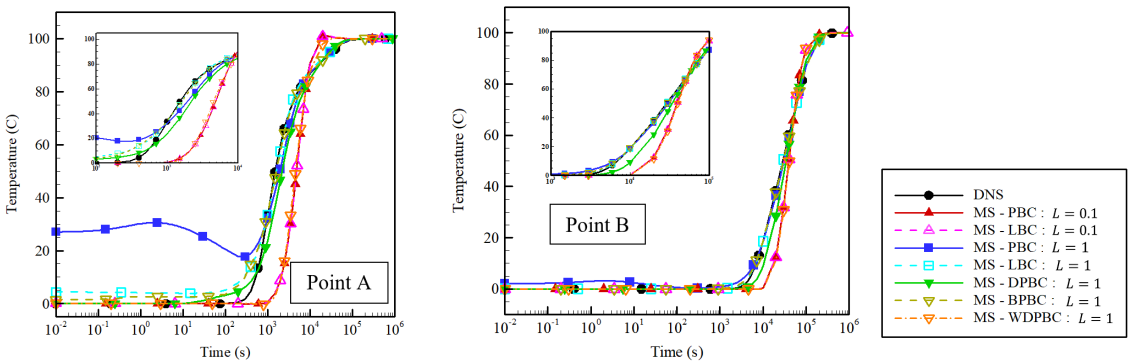


Figure 4. The variations with time of the temperature for the THM analysis of a heterogeneous square domain at points A and B; A comparison between the multiscale analysis with different RVE boundary conditions and RVE length scales

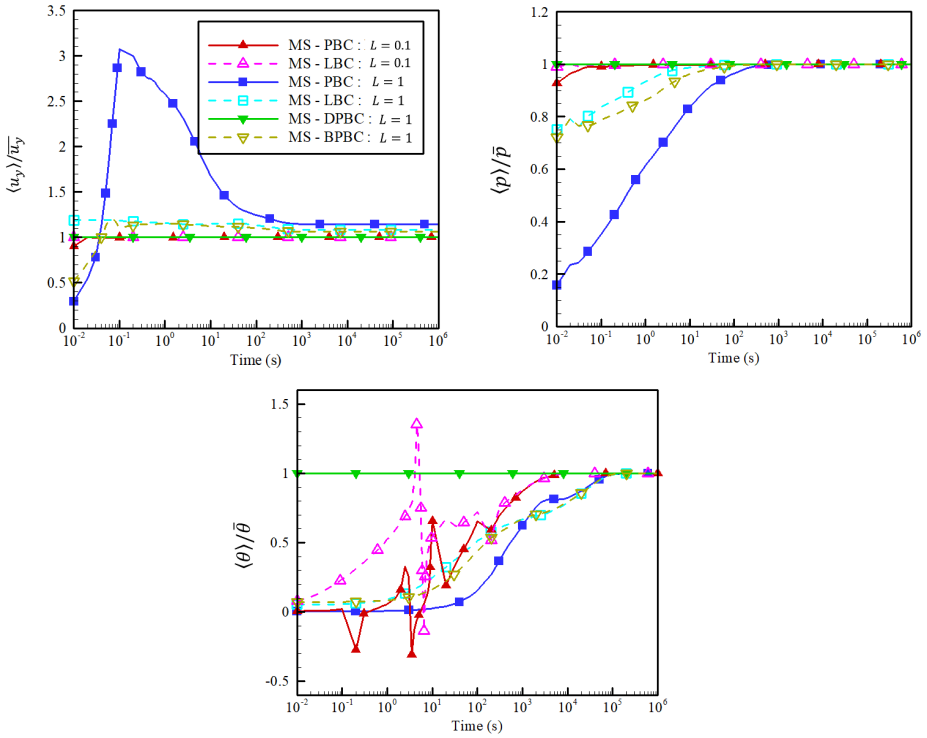


Figure 5. The variations with time of the ratio of average micro-scale field variables to the macro-scale solution at the selected Gauss integration point

In Figure 5, the variations with time of the ratio of average micro-scale field variables to the macro-scale solution are plotted at the selected Gauss integration point. It can be observed that the ratio of average micro-scale to macro-scale solution for the displacement and pressure fields are close to each other for the most micro-scale boundary conditions except the typical PBC model with $L = 1\,\mathrm{m}$. However, the typical PBC experiences deviation from the unity that alerts the possible discrepancy in highly transient problems. Moreover, the ratio of average micro-scale to macro-scale of the thermal field demonstrates completely improper behavior for all micro-scale boundary conditions except the D–PBC model.

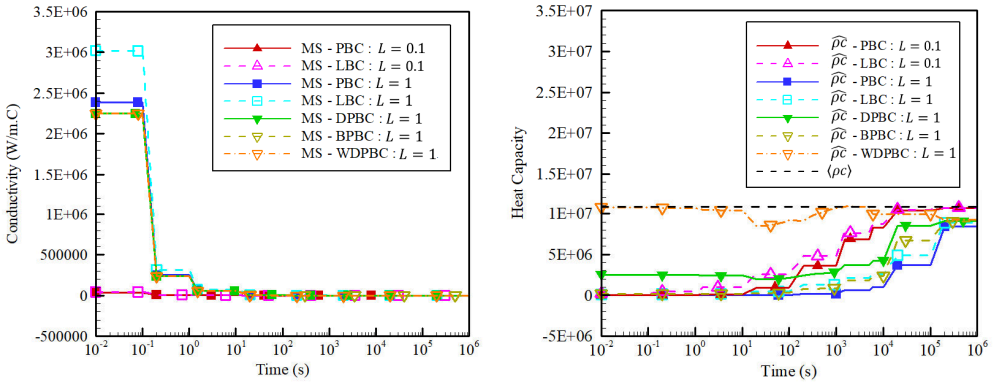


Figure 6. The variations with time of the homogenized conductivity and the heat capacity for the THM analysis of a heterogeneous square domain using multiscale analysis using different RVE boundary conditions and RVE length scales

The oscillating behavior can be even seen in Figure 5 for the LBC and PBC models with $L = 0.1\text{m}$. Although the LBC with $L = 1\text{m}$ and the B–PBC model are far from the unity, the solution is still desirable. It is noteworthy that this ratio explains how the microscopic fluctuation fields vary over the RVE. As the transient terms become larger, the variation of fluctuation fields become intensive, and as a result, the first order homogenization approach fails to yield to the desirable solution. In fact, the larger size of the RVE results in the violation of the principle of separation of scales in transient problems in the case of typical PBC model. In Figure 6, the variations with time of the homogenized conductivity and the heat capacity are plotted for the THM analysis of a heterogeneous square domain using the multiscale analysis with different RVE boundary conditions and RVE length scales. It can be observed that the heat capacity of the LBC and PBC models with $L = 0.1\text{m}$ approach the volume average of corresponding material property, while the other RVE boundary conditions converge to a different value in the steady state condition. In fact, it confirms that the classical assumption of the equivalent heat capacity in the steady-state microscopic solution can be chosen as the volume average of the heat capacity. Moreover, a comparison between the results of homogenized conductivity of the conduction-convection case and the only conduction case reveals that the LBC and PBC models with $L = 0.1\text{m}$ are not affected by the convection phenomenon, while the other RVE boundary conditions except the LBC with $L = 1\text{m}$ converge to the value of 760 W/m.C in the steady state condition. In addition, the WD–PBC model presents the oscillating behavior in both the homogenized conductivity and heat capacity. Moreover, the LBC model represents a larger conductivity than the PBC model at early time steps, which is rational due to overestimation manner of the LBC. However, in the steady state condition, the resultant conductivity of PBC model becomes greater than the LBC model. This behavior is the result of convection heat transfer that affects the homogenized conductivity.

## 6 CONCLUSIONS

In the present paper, a multiscale $FE^2$ framework was developed for two-scale simulation of the thermo-hydro-mechanical analysis of heterogeneous porous media. The governing equations was presented based on the classical Biot theory of porous media in combination with the advection-diffusion equation as the energy balance equation. The first order homoge-

nization method was applied, in which the main macroscopic field variables and their gradients were downscaled to the micro-scale level. In order to satisfy the Hill-Mandel principle of macro-homogeneity, the proper virtual power relations were defined based on the variational forms of the governing equations as the bridging of the micro- to macro-scale level. The weak forms of the micro-scale governing equations were derived and solved according to the appropriate boundary conditions. Moreover, the transient dynamic terms were included in the micro-scale formulations by defining several additional constraints to the conventional periodic boundary conditions, in order to achieve accurate results in the presence of micro-inertial terms. It was described that the transient effects cannot be captured through the conventional periodic boundary conditions. Furthermore, the Petrov-Galerkin $FE^2$ method was applied for the advection dominant heat transfer to restrict inaccurate solutions, although the resultant macroscopic field cannot reveal oscillatory behavior. Finally, the capability and accuracy of the proposed computational multiscale algorithm was presented through the coupled thermo-hydro-mechanical analysis of a 2D heterogeneous medium. It was demonstrated that in transient problems, the principle of separation of scales cannot be applied in the computational homogenization method, while the micro-inertial terms were neglected in small RVEs and the inconsistency can be observed with the exact solution. Even more, the inaccuracy of the results was obvious when the convection heat transfer was incorporated. In addition, the D–PBC and B–PBC models illustrate the most promising results comparing to the DNS model.

## REFERENCES


[1] R.W. Lewis, C. Majorana, B. Schrefler, A coupled finite element model for the consolidation of nonisothermal elastoplastic porous media. *Transport in Porous Media* **1**, 155–178, 1986.

[2] S. Seetharam, H. Thomas, P.J. Cleall, Coupled thermo/hydro/chemical/mechanical model for unsaturated soils – Numerical algorithm. *International Journal for Numerical Methods in Engineering* **70**, 1480–1511, 2007.

[3] R. Liu, M. Wheeler, C. Dawson, R. Dean, Modeling of convection-dominated thermoporomechanics problems using incomplete interior penalty Galerkin method. *Computer Methods in Applied Mechanics and Engineering* **198**, 912–919, 2009.

[4] A.R. Khoei, T. Mohamadnejad, Numerical modeling of multiphase fluid flow in deforming porous media; A comparison between two- and three-phase models for seismic analysis of earth and rockfill dams. *Computers and Geotechnics* **38**, 142–166, 2011.

[5] W. Cui, K. Gawecka, D. Taborda, D. Potts, L. Zdravković, Time-step constraints in transient coupled finite element analysis. *International Journal for Numerical Methods in Engineering* **106**, 953–971, 2016.

[6] A.R. Khoei, S.M.S. Mortazavi, Thermo-hydro-mechanical modeling of fracturing porous media with two-phase fluid flow using X-FEM technique. *International Journal for Numerical and Analytical Methods in Geomechanics* **44,** 2430–2472, 2020.

[7] J. Rutqvist, L. Börgesson, M. Chijimatsu, A. Kobayashi, et al., Thermo-hydro-mechanics of partially saturated geological media: governing equations and formulation of four finite element models. *International Journal of Rock Mechanics and Mining Sciences* **38**, 105–127, 2001.

[8] A.R. Khoei, D. Amini, S.M.S. Mortazavi, Modeling non-isothermal two-phase fluid flow with phase change in deformable fractured porous media using extended–FEM. *International Journal for Numerical Methods in Engineering* **122**, 4378–4426, 2021.

[9] M. Duflot, The extended finite element method in thermoelastic fracture mechanics. *International Journal for Numerical Methods in Engineering* **74**, 827–847, 2008.

[10] A.R. Khoei, S. Moallemi, E. Haghighat, Thermo-hydro-mechanical modeling of impermeable discontinuity in saturated porous media with X-FEM technique. *Engineering Fracture Mechanics* **96**, 701–723, 2012.

[11] A.R. Khoei, B. Bahmani, Application of an enriched FEM technique in thermo-mechanical contact problems. *Computational Mechanics* **62**, 1127–1154, 2018.

[12] S. Mortazavi, P. Pirmoradi, A.R. Khoei, Numerical simulation of cold and hot water injection into naturally fractured porous media using XFEM and an equivalent continuum model. *International Journal for Numerical and Analytical Methods in Geomechanics* **46**, 617–655, 2022.

[13] M.V. Júnior, E.A. de Souza Neto, P.A. Munoz-Rojas, *Advanced Computational Materials Modeling: from Classical to Multiscale Techniques*. John Wiley 2011.

[14] V.P. Nguyen, O. Lloberas-Valls, M. Stroeven, L.J. Sluys, On the existence of representative volumes for softening quasi-brittle materials – a failure zone averaging scheme. *Computer Methods in Applied Mechanics and Engineering* **199**, 3028–3038, 2010.

[15] A.R. Khoei, M.R. Hajiabadi, Fully coupled hydro-mechanical multiscale model with micro-dynamic effects. *International Journal for Numerical Methods in Engineering* **115**, 293–327, 2018.

[16] M.G. Geers, V.G. Kouznetsova, W. Brekelmans, Multiscale computational homogenization: Trends and challenges. *Journal of Computational Applied Mathematics* **234**, 2175–2182, 2010.

[17] A. Waseem, T. Heuze, L. Stainier, M. Geers, V. Kouznetsova, Model reduction in computational homogenization for transient heat conduction. *Computational Mechanics* **65**, 249–266, 2020.

[18] K. Pham, V. Kouznetsova, M.G. Geers, Transient computational homogenization for heterogeneous materials under dynamic excitation. *Journal of the Mechanics and Physics of Solids* **61**, 2125–2146, 2013.

[19] R.W. Lewis, B. Schrefler, *The Finite Element Method in the Static and Dynamic Deformation and Consolidation of Porous Media*. John Wiley 1998.

[20] O.C. Zienkiewicz, R.L. Taylor, P. Nithiarasu, *The Finite Element Method for Fluid Dynamics*. Elsevier 2014.

[21] A.R. Khoei, *Extended Finite Element Method, Theory and Applications*. John Wiley 2015.

[22] A. Waseem, T. Heuzé, L. Stainier, M. Geers, V. Kouznetsova, Two-scale analysis of transient diffusion problems through a homogenized enriched continuum. *European Journal of Mechanics A. Solids* **87**, 104212, 2021.

[23] H.J.G. Diersch, *FEFLOW: Finite Element Modeling of Flow, Mass and Heat Transport in Porous and Fractured Media*. Springer 2013.

[24] I. Özdemir, W. Brekelmans, M. Geers, Computational homogenization for heat conduction in heterogeneous solids. *International Journal for Numerical Methods in Engineering* **73**, 185–204, 2008.

[25] E. de Souza Neto, P. Blanco, P. Sánchez, R. Feijóo, An RVE-based multiscale theory of solids with micro-scale inertia and body force effects. *Mechanics of Materials* **80**, 136–144, 2015.

[26] A.R. Khoei, S. Saeedmonir, Computational homogenization of fully coupled multiphase flow in deformable porous media. *Computer Methods in Applied Mechanics and Engineering* **376**, 113660, 2021.

[27] S. Saeedmonir, A.R. Khoei, Multiscale modeling of coupled thermo-hydro-mechanical analysis of heterogeneous porous media. *Computer Methods in Applied Mechanics and Engineering* **391**, 114518, 2022.

COMPDYN 2023
9th ECCOMAS Thematic Conference on
Computational Methods in Structural Dynamics and Earthquake Engineering
M. Papadrakakis, M. Fragiadakis (eds.)

# MODEL CALIBRATION AND NONLINEAR SITE RESPONSE ANALYSIS FOR MEDIUM COMPACTED SATURATED VOLCANIC SAND

**S. J. Fattahi[1], Y. Jafarian[2,3], M. Konstadinou[2], E. A. Olafsdottir[1], S. Erlingsson[1], B. Bessason[1], and R. Rupakhety[1]**

[1] Faculty of Civil and Environmental Engineering, University of Iceland
Reykjavík, Iceland
e-mail: sjf7@hi.is

[2] Deltares
Delft, Netherlands
yaser.jafarian@deltares.nl , maria.konstadinou@deltares.nl

[3] International Institute of Earthquake Engineering and Seismology, Tehran, Iran

## Abstract

*Site response analyses on saturated sand from Iceland have been performed with nonlinear (NL) and equivalent-linear (EL) methods. An advanced constitutive model was calibrated to simulate the nonlinear (NL) behavior of the sand by means of a monotonic Direct Simple Shear (DSS) test conducted in this study. The DSS test was conducted on dry sand under a constant volume conditions. In such a procedure, the change in vertical stress during shearing is assumed to be equal to the excess pore water pressure. In this study, the computed equivalent blow count ($N_{1,60}$) is limited to the top four meters, and a relative density of* 60% *has been considered. An average shear wave velocity ($V_s$) profile has been measured through the Multichannel Analysis of Surface Waves (MASW) technique. The calibrated model is employed in the nonlinear site response analysis, and the results are compared with those of the equivalent linear method. The EL and NL analyses in DEEPSOIL and PLAXIS, respectively, predicted liquefaction at the site and aligned with surface evidence and prior researches.*

**Keywords:** Liquefaction, Site response analysis, DSS, Non-linear analysis, Constitutive model, Equivalent-linear analysis, Python

## 1 INTRODUCTION

The seismic activity in Iceland is concentrated in two complex fracture zones, namely the South Iceland Seismic Zone (SISZ) and the Tjörnes Fracture Zone (TFZ), which are associated with the Mid-Atlantic plate boundary. Over the past three centuries, about 30 earthquakes with a magnitude greater than six have been recorded in these regions [1]. In the SISZ, destructive earthquakes often occur in sequences.

Iceland has the highest seismic hazard in Northern Europe, comparable to that in Southern Europe. The two main seismic zones in the country have a Peak Ground Acceleration (PGA) of 0.5g with a mean return period of 475 years. Since 2000, three destructive earthquakes have struck the largest agricultural region in South Iceland, with earthquakes with moment magnitudes ($M_w$) of 6.5 and 6.4 occurring in 2000 and one $M_w$ 6.3 earthquake in 2008. These events caused significant damage to the area's buildings, farms, power plants, bridges, and other infrastructure. However, no serious injuries or fatalities occurred due to these events [2].

The soil in Iceland is mainly composed of Holocene soils that are typically normally consolidated and have basaltic origins. Additionally, postglacial sediments are present in a large portion of the island and are considered geologically young and rapidly built up. This results in local soils typically consisting of coarse silty particles, including coarser grains, often loosely compacted [3, 4].

Loose, partially, or fully saturated soils may lose strength substantially during earthquake shaking or sudden changes in stress conditions, a phenomenon referred to as liquefaction. The effects of liquefaction can vary, including sudden or gradual lateral deformations, ground oscillations, vertical settlements, and the development of sand boils, depending on soil and site characteristics [5]. Structures resting on or buried in liquefied soil are at risk of severe damage. Hence, assessing soil site liquefaction hazards is crucial in seismically active regions.

The study aims to evaluate liquefaction at the Arnarbaeli site by the Ölfus river in south Iceland by comparing site response analysis results from DEEPSOIL's equivalent linear (EL) method and PLAXIS' nonlinear (NL) simulation. It also seeks to calibrate the NL model by minimizing differences between numerical and experimental shear strength values. Hence, the study determines if both methods accurately predicted liquefaction and if the results aligned with surface evidence and previous studies.

## 2 SOIL CHARACTERISTICS AT THE SITE

Less than 10 km from the epicenter of the $M_w$ 6.3 Ölfus earthquake in 2008, liquefaction was observed at the Arnarbaeli site, which is situated on the banks of the estuary of the Ölfus river and consists of a thick layer of silty sand. The earthquake had a PGA of 0.88g, affecting approximately 5000 low-rise residential buildings [6]. The occurrence of liquefaction can be attributed to the site's soil characteristics, combined with the strong shaking caused by the earthquake. The event highlights the potential hazards in SISZ of earthquake-induced liquefaction in areas with similar soil conditions and seismic activity. The most notable surface indications of liquefaction, including ground settlements and sand boil, were observed at the Arnarbaeli site. Arnarbaeli is comprised of volcanic sand deposits that are relatively uniform. Table 1 and 2 summarize the tested sand's geotechnical characteristics, the soil layers' shear wave velocity ($V_s$), and the equivalent blow count ($N_{1,60}$) for down to 100 m depth. This information was obtained from various sources [7–10]. The SPT equivalent values up to a depth of 4 m were determined by Green et al. [7] using DCP field test results. However, for the depth range between 4 and 100 m, this study extrapolated the $N_{1,60}$ values.

Table 1 Physical properties of the tested sand [7]. Soil properties represented in the table include specific gravity ($G_s$), minimum and maximum dry unit weight ($\gamma_{d,min}$, $\gamma_{d,max}$), saturated unit weight ($\gamma_{sat}$), and uniformity coefficient ($C_u$).

| Soil | Classification symbol | $G_s$ [-] | $\gamma_{d,min}$ [g/cm$^3$] | $\gamma_{d,max}$ [g/cm$^3$] | $\gamma_{sat}$ [g/cm$^3$] | $C_u$ [-] | *Fines content* [%] |
|---|---|---|---|---|---|---|---|
| Arnarbaeli sand | SW-SM | 2.84 | 11.6 | 16.4 | 18.2 | 9 | 7 |

Table 2 Soil layers properties, [7–10].

| Layer no | Thickness [m] | $V_s$ [m/s] | $N_{1,60}$ [-] |
|---|---|---|---|
| 1 | 2 | 75 | 3.0 |
| 2 | 3 | 115 | 10.6 |
| 3 | 5 | 230 | 32.1 |
| 4 | 10 | 330 | 94.8 |
| 5 | 20 | 420 | 321.1 |
| 6 | 30 | 480 | 1177.4 |
| 7 | 30 | 530 | 3470.6 |

## 3 UNDRAINED MONOTONIC DSS TEST

This study's sample was taken from a shallow depth (0.5 meters) at the Arnarbaeli site. The results of the monotonic direct simple shear (DSS) test are presented in Figure 1, which includes the shear stress ($\tau$) versus shear strain ($\gamma$) on the left and the pore-water pressure (PWP) buildup against $\gamma$, on the right side of the picture. The figure provides essential information on the behavior of the sand under constant volume conditions. The DSS test was performed under a vertical stress level of 100 kPa and a relative density of ($D_r$) 60%.

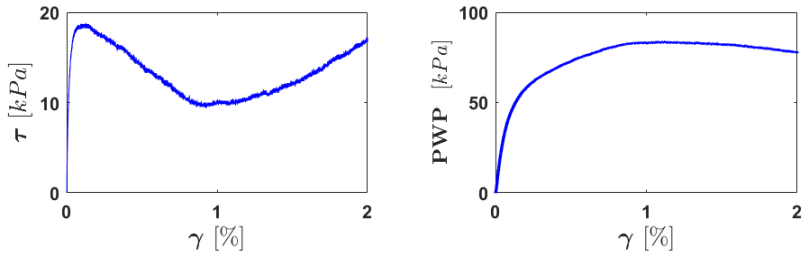


Figure 1 Shear stress and PWP against shear strain. Monotonic direct simple shear test performed under constant volume conditions.

Jaky's equation was used to determine the coefficient of lateral earth pressure at rest ($K_0$) [11]. Table 3 summarizes the test specifications of the monotonic DSS test conducted in this study.

Table 3 Summary of monotonic DSS test.

| Test | Loading type | Void ratio | $K_0$ | $D_r$ [%] | Vertical pressure [kPa] | Friction angle [degree] |
|---|---|---|---|---|---|---|
| DSS - 60 - 100 | Monotonic | 1.08 | 0.425 | 60 | 100 | 31.3 |

## 4 SITE RESPONSE ANALYSIS

In evaluating the soil effects on ground motion, three main approaches are typically used: the attenuation relationship approach, the soil coefficient approach, and the site response analysis [12]. However, the first two approaches are limited in their applicability since they

oversimplify the actual soil distribution. Site response analysis offers more detailed results, such as the variation of seismic waves in terms of amplitude, duration, and frequency at different depths of the soil deposit.

In this study, the liquefaction potential of the Arnarbaeli site was evaluated using one-dimensional site response analysis with two different methods and software. The DEEPSOIL software was used for the EL approximation, while PLAXIS was used for the NL approach.

### 4.1 Equivalent linear analysis

The EL model iteratively selects shear modulus and damping ratio based on soil parameters, Table 1 and 2. The model uses the Pressure-Dependent Modified Kondner-Zelasko (MKZ) soil model and a Non-Masing Re/Unloading hysteretic loading and unloading formulation. The Darendeli reference curve and reduction factor [13, 14] have been utilized to calibrate the tested sand. Figure 2 illustrates the shear modulus reduction, material damping, and shear strength curves based on Darendeli's empirical formulas [13]. The 'Current' term reflects the behavior of a soil layer used in the analysis, adjusted with the 'Fit Curve' to match field measurements and observations. The 'Fit Curve' adjusts the soil layer's properties to align with the field measurements, while the 'Reference Curve' serves as a basis for defining the properties of the layered soil profile.

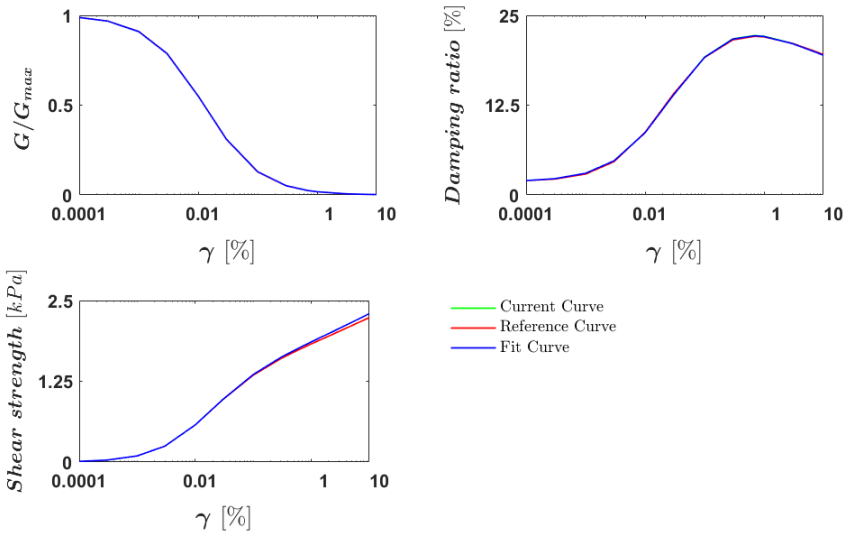


Figure 2 Plot generated for the first soil layer illustrating the iteration procedure towards a strain compatible normalized shear modulus ($G/G_{max}$), material damping, and shear strength curves based on DEEPSOIL [14].

Green et al. [7] determined the SPT equivalent values for a depth down to 4 m using DCP field test results. In this study, $N_{1,60}$ values were extrapolated to a depth of 100 m. The cyclic resistance ratio (*CRR*) for a $M_w$ 6.3 event over the same depths was then estimated using the correlation proposed by Youd et al. [15]. The cyclic stress ratio (*CSR*), which represents the cyclic loading level on the soil caused by an earthquake, was determined using EL analysis.

### 4.2 Calibration of UBC3D model

The UBC3D-PLM model is an advanced method for simulating liquefaction behavior in dynamic situations [16]. This model utilizes two yield surfaces for a smooth transition near the mobilized friction angle and employs the Mohr-Coulomb yield condition with a hardening

law similar to the Hardening Soil model. The input parameters for this model are based on commonly used tests such as drained triaxial tests or standard penetration tests. The UBC3D-PLM model is beneficial for undrained dynamic calculations where the evolution of excess pore pressures in sandy soils needs to be accurately modeled. The parameters of the model [16] and their calibrated values are summarized in Table 4.

The manual [16] suggests a set of equations for determining the model parameters based on the normalized $N_{SPT}$. In this study, the suggested equations for obtaining the initial values of the soil model's parameters were found to be unsuitable due to several limitations. The lack of field data and other restrictions associated with the suggested equations posed barriers to this approach. Therefore, to ensure accurate modeling, a calibration process was undertaken. In this calibration, a wide range of values for each variable of the model was considered. By taking these steps, it was possible to develop a more accurate and reliable model for the soil.

The parameters in the list (Table 4) are calibrated through trial and error with a script that runs the PLAXIS DSS simulator using Python. This iterative process continues until the difference between the numerically computed and experimentally obtained shear strength is less than 10%.

Table 4 Parameters of the UBC3D-PLM model with their corresponding calibrated values.

| Function | Symbol | Definition | Calibrated value | Unit |
|---|---|---|---|---|
| Stiffness Parameters | $k^{*e}_B$ | Elastic bulk modulus factor | 1150 | [-] |
| | $k^{*e}_G$ | Elastic shear modulus factor | 350 | [-] |
| | $k^{*p}_G$ | Plastic shear modulus factor | 150 | [-] |
| | $me$ | Rate of stress-dependency of elastic bulk modulus | 0.35 | [-] |
| | $ne$ | Rate of stress-dependency of elastic bulk modulus | 0.45 | [-] |
| | $np$ | Rate of stress-dependency of plastic shear modulus | 0.45 | [-] |
| | $p_{ref}$ | Reference pressure | 101.32* | [kN/m$^2$] |
| Strength Parameters | $\varphi_{cv}$ | Constant volume friction angle | 31.3* | [°] |
| | $\varphi_p$ | Peak friction angle | 32.5* | [°] |
| | $C$ | Cohesion | 0* | [kN/m$^2$] |
| Advanced Parameters | $R_f$ | Failure ratio | 0.9 | [-] |
| | $N_{1,60}$ | Corrected SPT value | 12 | [-] |
| | $f_{dens}$ | Densification factor | 1.0* | [-] |
| | $f_{Epost}$ | Post-liquefaction factor | 1.0* | [-] |

* These parameters were kept constant during the calibration process.

The UBC3D-PLM model is capable of reproducing the buildup of PWP. In this study, the excess pore pressure ratio ($R_u$) was used to differentiate between liquefied and non-liquefied soil layers. $R_u$ represents the normalized pore water pressure to initial effective vertical stress. A zone is considered to be liquefied if it has a maximum $R_u$ greater than 0.7. A $R_u$ value of 1.0 indicates that the corresponding layer is in a completely liquefied state [12].

### 4.3 Performance of the model

The UBC3D-PLM model is used to perform a numerical reproduction of an undrained monotonic DSS test. The Soil Test Tool from the finite element program PLAXIS is employed for the numerical simulation of the test. Figure 3 illustrates the performance of the UBC3D-PLM model.

## 5 RESULTS AND DISCUSSION

In this study, site response analyses were used to predict liquefaction occurrence at the Arnarbaeli site. The EL site response analysis in DEEPSOIL and the NL simulation in PLAXIS were compared. The NL model was calibrated using a trial and error iterative code

in Python to reduce the differences between the shear strength of the soil in both the numerical (UBC3D-PLM constitutive soil model) and experimental (DSS) test. The differences were kept below 10%. The trends of pore water generation and shear stress over the DSS test are similar, as shown in Figure 3. While the study attempted to keep the simulated and experimental shear strength values close, comparing pore water generation between the two methods demonstrates a better match.

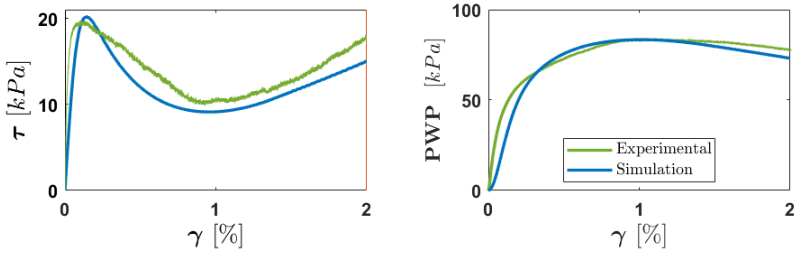


Figure 3 Comparison between experimental results and the UBC3D-PLM model's simulation of a monotonic DSS test with $D_r$ = 60% and vertical pressure of 100 kPa by PLAXIS SoilTest simulator tool; (left) shear stress and (right) pore water pressure generation.

Figure 4 shows a liquefaction resistance curve ($N_{1,60}$ - *CRR*) scaled to the $M_w$ 6.3 Ölfus earthquake.

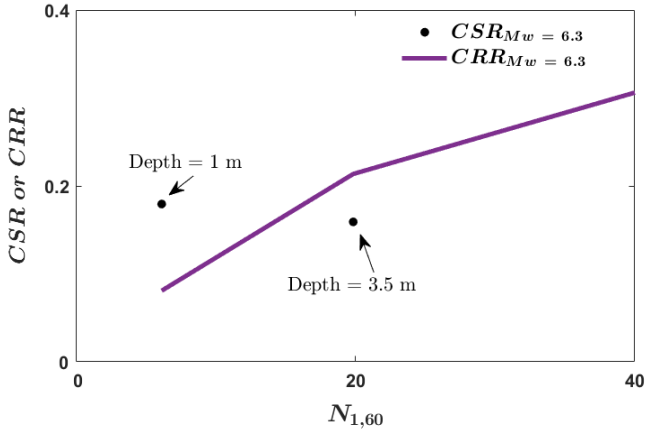


Figure 4 Graph displaying liquefaction evaluation results for the Arnarbaeli soil obtained through EL site response analysis.

Figure 4, 5, and 6 show that the first soil layer (with a thickness of 2 m) underwent complete liquefaction, while the NL analysis showed liquefaction also occurring in deeper layers. In other words, the second and third layers were also liquefied, as indicated by $R_u$ values greater than or equal to 0.9 (Figure 6).

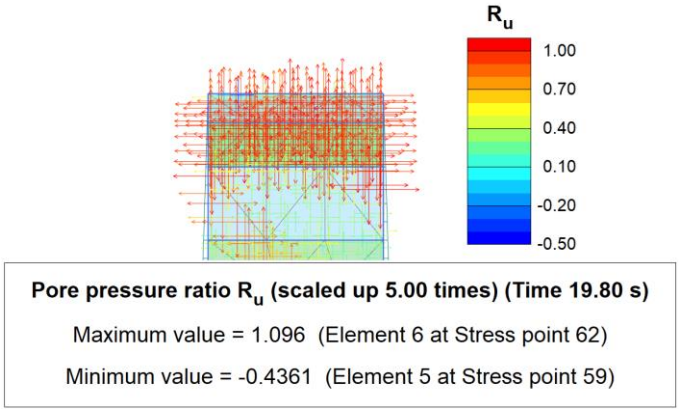


Figure 5 $R_u$ distribution obtained with PLAXIS for the top 3 soil layers. The red arrows represent $R_u$ values greater than 0.8.

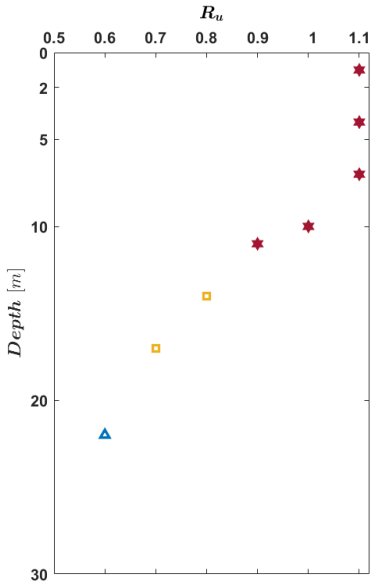


Figure 6 PLAXIS-derived $R_u$ values plotted against depth for the top five layers. Red pentagrams indicate $R_u$ values greater than or equal to 0.9, orange diamonds represent $R_u$ values between 0.7 and 0.8, and blue triangles represent non-liquefied layers with $R_u < 0.7$.

## 6 SUMMARY AND CONCLUSIONS

In conclusion, this study successfully predicted liquefaction occurrence at the Arnarbaeli site. Both the EL site response analysis in DEEPSOIL and the NL simulation in PLAXIS predicted liquefaction and were consistent with surface evidence of liquefaction at the site and in previous studies. The differences in shear strength between the numerical and experimental tests were kept below 10% through Python calibration of the NL model. The advanced constitutive model provided more detailed results than the equivalent linear analysis and *CSR* vs. $N_{1,60}$ graph. The NL analysis indicated liquefaction of the top three soil layers down to a depth of 10 meters. In contrast, the EL analysis showed liquefaction occurring only in the first layer.

## ACKNOWLEDGEMENTS

Funding for this study was provided by the Icelandic Research Fund (Rannis) under Grant numbers 206793-053 and 218149-051. The first author would like to acknowledge that this project was completed during his Erasmus Plus internship at Deltares Geotechnical Laboratory under the guidance and expertise of their professionals.

## REFERENCES

[1] P. Einarsson, "Plate boundaries, rifts and transforms in Iceland," *Jokull*, vol. 58, no. 12, pp. 35–58, 2008.

[2] K. Jonasson *et al.*, "A harmonised instrumental earthquake catalogue for Iceland and the northern Mid-Atlantic Ridge," *Nat. Hazards Earth Syst. Sci.*, vol. 21, no. 7, pp. 2197–2214, 2021.

[3] S. Erlingsson, "Geotechnical challenges in Iceland," in *17th European Conference on Soil Mechanics and Geotechnical Engineering, ECSMGE 2019, 1 September 2019 through 6 September 2019*, Reykjavík, Iceland, 2019, pp. 27–51. doi: 10.32075/17ECSMGE-2019-1109.
[4] B. Bessason and A. M. Kaynia, "Site amplification in lava rock on soft sediments," *Soil Dyn. Earthq. Eng.*, vol. 22, no. 7, pp. 525–540, 2002.
[5] S. L. Kramer, *Geotechnical earthquake engineering*. Pearson Education India, 1996.
[6] B. Bessason, J. O. Bjarnason, A. Gudmundsson, J. Solnes, and S. Steedman, "Analysis of damage data of low-rise buildings subjected to a shallow Mw6. 3 earthquake," *Soil Dyn. Earthq. Eng.*, vol. 66, pp. 89–101, 2014.
[7] R. A. Green, B. Halldorsson, A. Kurtulus, H. Steinarsson, and O. Erlendsson, "A unique liquefaction case study from the 29 May 2008, Mw6. 3 Olfus earthquake, southwest Iceland," in *Proceedings of the 15th World Conference on Earthquake Engineering, Lisbon, Portugal*, 2012, pp. 24–28.
[8] E. A. Olafsdottir, B. Bessason, and S. Erlingsson, "Application of MASW in the South Iceland Seismic Zone," in *Proceedings of the International conference on Earthquake Engineering and Structural Dynamics*, 2019, pp. 53–66.
[9] E. A. Olafsdottir, S. Erlingsson, and B. Bessason, "Tool for analysis of multichannel analysis of surface waves (MASW) field data and evaluation of shear wave velocity profiles of soils," *Can. Geotech. J.*, vol. 55, no. 2, pp. 217–233, 2018.
[10] E. A. Olafsdottir, B. Bessason, and S. Erlingsson, "MASW for assessing liquefaction of loose sites," in *Proceedings of the XVI European Conference on Soil Mechanics and Geotechnical Engineering (XVI ECSMGE)*, Edinburgh, 13-17 September, 2015, pp. 2431–2436.
[11] J. Jaky, "Pressure in silos," in *Proc. 2nd Int. Conf. Soil Mech.*, 1948, vol. 1, pp. 103–107.
[12] Micha van der Sloot, "Site response analysis and liquefaction evaluation." Bentley. [Online]. Available: https://communities.bentley.com/products/geotech-analysis/w/wiki/46050/site-response-analysis-and-liquefaction-evaluation
[13] M. B. Darendeli, *Development of a new family of normalized modulus reduction and material damping curves*. The university of Texas at Austin, 2001.
[14] Y. M. A. Hashash, M. I. Musgrove, J. A. Harmon, D. R. Groholski, C. A. Phillips, and D. Park, "' DEEPSOIL 7.0, User Manual'. Urbana, IL, Board of Trustees of University of Illinois at Urbana-Champaign," *Erişim Adresi Httpdeepsoil Cee Ill. Edu-FilesDEEPSOILUserManualv6 Pdf*, 2016.
[15] T. L. Youd and I. M. Idriss, "Liquefaction resistance of soils: summary report from the 1996 NCEER and 1998 NCEER/NSF workshops on evaluation of liquefaction resistance of soils," *J. Geotech. Geoenvironmental Eng.*, vol. 127, no. 4, pp. 297–313, 2001.
[16] "PLAXIS Material models manual." Bentley, Aug. 26, 2022. [Online]. Available: https://communities.bentley.com/cfs-file/__key/communityserver-wikis-components-files/00-00-00-05-58/PLAXIS2D_2D00_CE_2D00_V22.00_2D00_1_2D00_Tutorial.pdf
[17] S. J. Fattahi, E. A. Olafsdottir, S. Erlingsson, B. Bessason, and R. Rupakhety, "Liquefaction Assessment of a Loose Silty Sand Site in the 2008 Mw 6.3 Ölfus Earthquake," Sep. 2022, Accessed: Feb. 26, 2023. [Online]. Available: https://opinvisindi.is/handle/20.500.11815/3826

COMPDYN 2023
9th ECCOMAS Thematic Conference on
Computational Methods in Structural Dynamics and Earthquake Engineering
M. Papadrakakis, M. Fragiadakis (eds.)
Athens, Greece, 12-14 June 2023

# PRELIMINARY STUDY FOR SEISMIC ASSESSMENT OF THE UNDERGROUND FACILITIES AT POINT 5 OF THE LARGE HADRON COLLIDER (LHC) AT CERN

**Ugo Carmando[1], Ahmed Mubarak[2], Antonio Bilotta[1], Emilio Bilotta[3], Jonathan Knappett[2], Saverio La Mendola[4], Martin Gastal[4], Pieter Mattelaer[4], Luca Sironi[4], Davide Merlini[5], Matteo Falanesca[5], Gianluca Bella[5], Filippo Gianelli[5], Marco Andreini[4]**

[1] University of Napoli Federico II
Department of Structures for Engineering and Architecture
via Claudio, 21 - Naples, Italy
ugo.carmando@unina.it; antonio.bilotta@unina.it

[2] University of Dundee
School of Science and Engineering
Dundee, United Kingdom
a.mubarak@dundee.ac.uk; j.a.knappett@dundee.ac.uk

[3] University of Napoli Federico II
Department of Civil, Architectural and Environmental Engineering
via Claudio, 21 - Naples, Italy
emilio.bilotta@unina.it

[4] CERN - European Organisation for Nuclear Research
Geneva, Switzerland
saverio.la.mendola@cern.ch; martin.gastal@cern.ch; pieter.mattelaer@cern.ch; luca.sironi@cern.ch; marco.andreini@cern.ch

[5]Pini Group SA
Switzerland
matteo.falanesca@pini.group; filippo.gianelli@pini.group; gianluca.bella@pini.group; davide.merlini@pini.group

**Abstract**

*The European Organisation for Nuclear Research (CERN) is continuously upgrading its extensive underground facilities to cope with the need for new and more complex experiments. The Large Hadron Collider (LHC) houses the Compact Muon Solenoid (CMS) detector at its Point 5, where there are two large shafts, two 100 m deep major parallel caverns, with a total span of 50 m, separated by a 7 m wide and 28 m high concrete pillar, and a system of secondary tunnels and caverns. Such a complex underground infrastructure lies in a sedimentary rock formation (red molasse) of the Geneva basin, with a low rock cover of about 20 m to the overlying 50 m thick layer of water bearing moraine. The site is classified as a zone of moderate seismicity and the underground structures were designed against a "standard" seismic risk, that corresponds to the importance category II according to Eurocode 8. To study the dynamic response of the caverns to seismic waves, a series of Finite Element (FE) full dynamic analyses have been carried out, where the non-linear behavior of the underground layers has been carefully modelled. A suite of input signals that comply with the design spectrum has been applied to the model. The preliminary results are commented in the paper to define the seismic safety requirement for the sensitive infrastructures and installations located inside the tunnels and caverns.*

**Keywords:** Finite Element Model, Underground Tunnels, Seismic Input Motion, Damping, Dynamic Analyses.

## 1 INTRODUCTION

In recent years, several researchers carried out analytical and numerical studies concerning various aspects of the behavior of underground structures under seismic excitations in different ground conditions. In parallel, there is a need to properly quantify the structural safety and operativity of the underground facilities of CERN (European Organisation for Nuclear Research), an international research laboratory site at the Franco – Swiss border, in the Geneva basin: more specifically, consisting of linear and circular accelerators, including the Large Hadron Collider (LHC), representing particle physics experiments of international relevance.
This paper shows the preliminary results of a study aiming to model and simulate the behavior of two deep caverns of the LHC Point 5, hosting the Compact Muon Solenoid (CMS) experiment, under plane-strain conditions. Stratigraphic and lithological profiles have been simplified on the basis of previous studies [1]. Different seismic input motions were applied to the bedrock.

This study aims to assess the amplification of the ground shaking through the layers up to ground level, as well as to identify the effect of seismic excitations on the cavities' boundaries, to provide a tool to check the seismic safety of the sensitive equipment and installations located inside the mentioned tunnels and caverns.

## 2 SITE LOCATION AND RELATED SEISMIC HAZARD

The Geneva basin is characterized by crystalline basement rocks and formations of Triassic, Jurassic and Cretaceous ages. It is filled with sedimentary deposits, the so called Molasse, which is overlain by Quaternary glacial moraines. The Molasse comprises horizontally bedded sedimentary deposits layers of marls, limestones, sandstones, sandy marls and marly sandstones, with varying strengths, material properties and layer thickness. The moraine deposits essentially comprise gravels and sands, with varying amount of silt and clay [2]. Located on the border between France and Switzerland, the seismic classification of the site is based on the indications given in the "*Décret no 2010-1254 du 22 octobre 2010 relatif à la prévention du risque sismique*" [3], which subdivides French territory into five seismic zones from very low seismicity (zone 1) to strong seismicity (zone 5). According to the "*Arrêté du 22 octobre 2010 relatif à la classification et aux règles de construction parasismique applicables aux bâtiments de la classe dite 'à risque normal*" [4], LHC point 5 is in zone 3 ("*sismicité modérée*"), Figure 1, and the seismic action, defined in terms of reference peak ground acceleration on type A ground, is about 0.090g, 0.112g, 0.135g and 0.159g respectively for return periods of 243, 475, 821 and 1303 years.

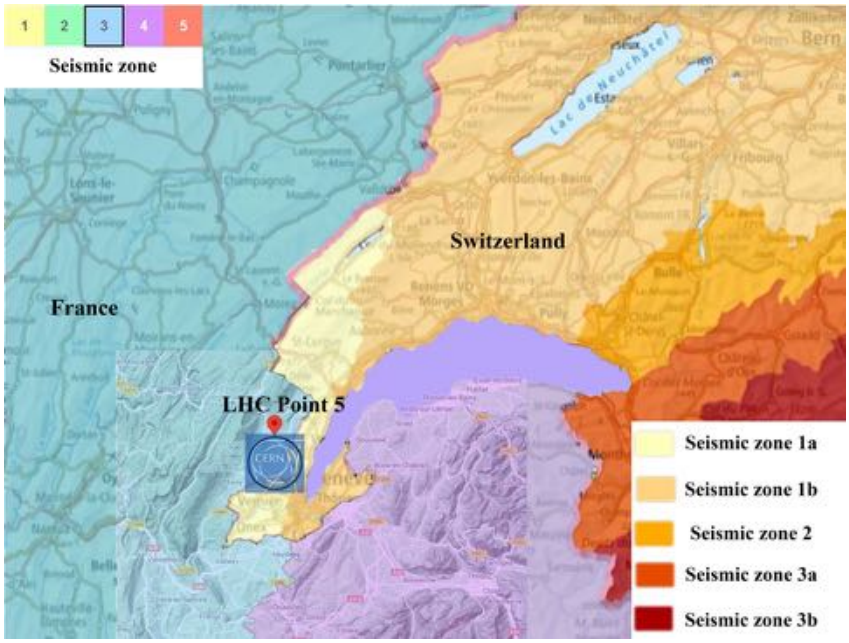


Figure 1. LHC ring: seismic classification and identification of Point 5 where CMS experiment is located.

## 3 DESCRIPTION OF THE NUMERICAL MODEL

To estimate the response of the large underground cavities under seismic excitations, several fully dynamic analyses have been carried out through the software PLAXIS v20 [5], where non-linear material properties for each soil layer were assigned. The caverns' lining was modelled with elastic plate elements. The vertical boundaries of the model were set at five times the caverns' depth to reduce the effect of boundary wave reflection in the area of interest [6]. This leads the total width of the model to 1 km.

The seismic input signals were retrieved from the Engineering Strong-Motion Database (ESM) [7], in order to be compatible with the horizontal design spectrum foreseen by the Eu-

rocode 8 for a type-A ground, assuming nominal life of 100 years. Hence, the reference peak ground acceleration was scaled to 0.15g.

Once the materials models were defined, a mesh of 15-noded elements was generated (Figure 3) in conformity with the most common element sizing criteria [8]. Five preliminary plastic calculation stages were computed to achieve a realistic stress state in the ground, which included cavities excavation and supports, simulated according to the available documentation (Figures 2a-2b).

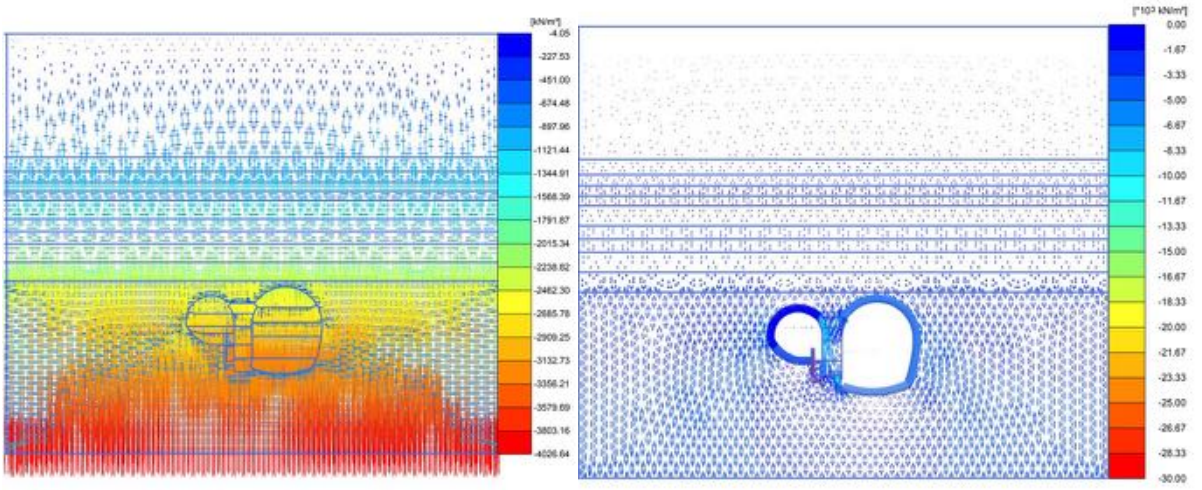

a) b)

Figure 2. Stress state in the ground: a) free-field lithostatic conditions and b) post cavities excavation.

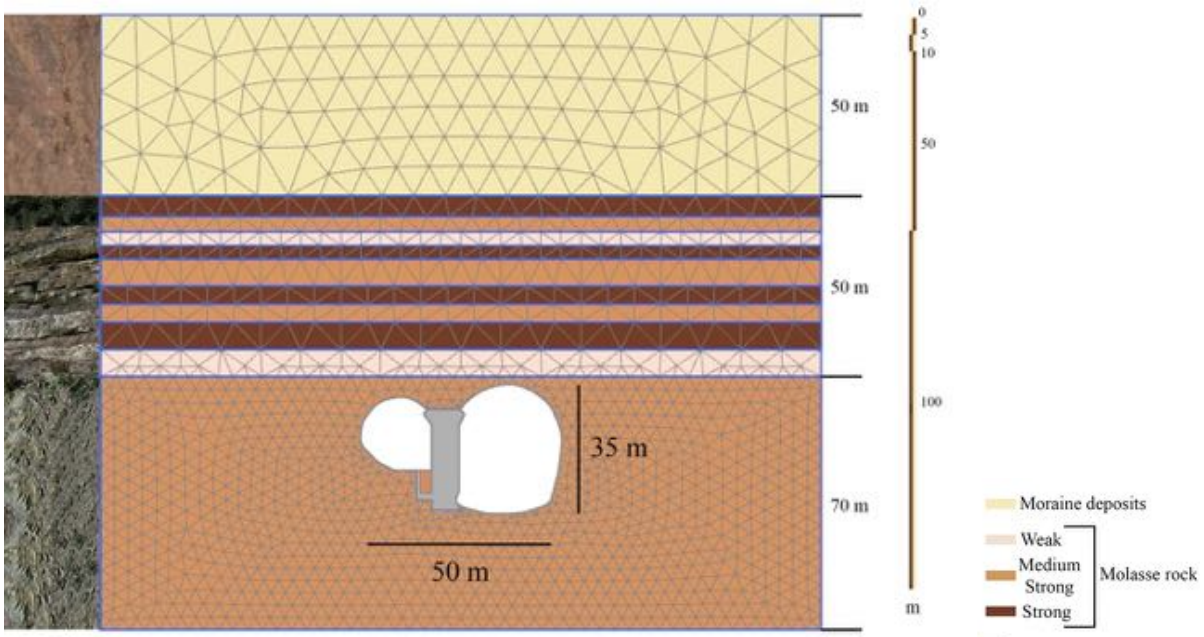


Figure 3. LHC Point 5: stratigraphic and mesh layout.

### 3.1 FE Model Description

The model is ideally divided into three major layers, starting from the top: a Moraine deposits layer, extending from ground level to 50 m depth; an underlying Molasse rock layer, extending to 100 m depth, divided into sublayers by stiffness; and a medium stiff Molasse rock layer extending a further 50 m to the base of the model. Static boundary conditions were defined restraining the horizontal and vertical displacements at the base and the horizontal displacements at both sides. During the dynamic stages, the input acceleration time history was applied at the base of the model and the lateral boundary conditions were set as equivalent to a free-field condition. The stress-strain behavior of the various materials was modeled using the non-linear elasto-plastic isotropic hardening hysteretic model, known as Hardening Soil model with small strain stiffness (HS small) [9]. HS small model parameters used for the different geotechnical units are: $\gamma_{sat}$ ,the saturated unit weight; $E_{50}^{ref}$, $E_{oed}^{ref}$ , $E_{ur}^{ref}$ the reference secant normal, oedometer and unloading-reloading stiffness moduli respectively, defined at mean effective reference confining pressure of 100 kPa; $G_o^{ref}$, the reference shear modulus; $\gamma_{0,7}$, the shear strain at $G = 0.7\ G_o$; ν, the Poisson's ratio; *m*, the exponent for stress – level dependency of stiffness; $c'_{ref}$, the cohesion; φ', the friction angle; ψ, the dilatancy angle. The model incorporates the increase of damping ratio with strain, D(γ) through its hysteretic formulation, while the damping at very small strain level ($D_0$) has been modelled using a Rayleigh approach with double frequency control. Tables 1 – 2 report the adopted on the basis of available ground investigation data of previous studies [1].

| Parameter | Unit | Moraine | Molasse rock | | |
|---|---|---|---|---|---|
| | | | Weak | Med.-strong | Strong |
| $\gamma_{sat}$ | kN/m$^3$ | 23 | 24 | 24 | 24 |
| $E_{50}^{ref}$ | kN/m$^2$ | 30 x 10$^3$ | 340 x 10$^3$ | 1.2 x 10$^6$ | 2.42 x 10$^6$ |
| $E_{oed}^{ref}$ | kN/m$^2$ | 30 x 10$^3$ | 340 x 10$^3$ | 700 x 10$^3$ | 1.8 x 10$^6$ |
| $E_{ur}^{ref}$ | kN/m$^2$ | 60 x 10$^3$ | 680 x 10$^3$ | 2.4 x 10$^6$ | 4.84 x 10$^6$ |
| $G_0^{ref}$ | kN/m$^2$ | 92 x 10$^3$ | 2.24 x 10$^6$ | 2.72 x 10$^6$ | 4.1 x 10$^6$ |
| $\gamma_{0.7}$ | [-] | 0.09 x 10$^{-3}$ | 1.2 x 10$^{-3}$ | 1.2 x 10$^{-3}$ | 1.2 x 10$^{-3}$ |
| $c'_{ref}$ | kN/m$^2$ | 0 | 140 | 792 | 1660 |
| φ' | [°] | 35 | 18 | 50 | 53 |
| ψ | [°] | 0 | 0 | 0 | 0 |
| ν | [-] | 0.3 | 0.25 | 0.25 | 0.25 |
| m | [-] | 0.5 | 0 | 0.7 | 0.7 |

Table 1. LHC Point 5: mechanical properties and model parameters for the different layers.

| Parameter | Unit | Shotcrete C35/45 | Concrete C50/60 |
|---|---|---|---|
| γ | kN/m$^3$ | 25 | 25 |
| E | kN/m$^2$ | 34.63 x 10$^6$ | 37.24 x 10$^6$ |
| EA | kN/m | 45 x 10$^6$ | 230 x 10$^6$ |
| EI | kN m$^2$/m | 6.34 x 10$^6$ | 739 x 10$^6$ |

Table 2. LHC Point 5: mechanical properties for UXC55 cavity walls.

### 3.2 Seismic Input Motion and Analyses Setup

Table 3 lists the five accelerograms selected from the ESM database. The Newmark time integration scheme was used in the simulations where the time step was constant. A critical time step for dynamic analyses was estimated in order to accurately model wave propagation and reduce the error due to the integration of time history functions, based on the material properties and the element size [5]. The calculation time step is adjusted to this value through sub-stepping. As an example, the first adopted input time history is shown in Figure 4a and the related Fourier spectrum in Figure 4b.

| Accelerogram | Event date | Accelerometer registration component | Peak Ground Acceleration [g] | Arias Intensity [m/s] | Bracketed Duration [s] |
|---|---|---|---|---|---|
| Friuli | 15/09/1976 | HNN | 0.128 | 0.095 | 2.85 |
| Centre Italy | 30/10/2016 | HNE | 0.146 | 0.183 | 7.255 |
| Iceland_1 | 17/06/2000 | HN2 | 0.123 | 0.165 | 3.595 |
| Iceland_2 | 17/06/2000 | HN3 | 0.155 | 0.192 | 3.795 |
| Iceland_5 | 29/05/2008 | HN2 | 0.13 | 0.112 | 3.935 |

Table 3. Selected seismic records.

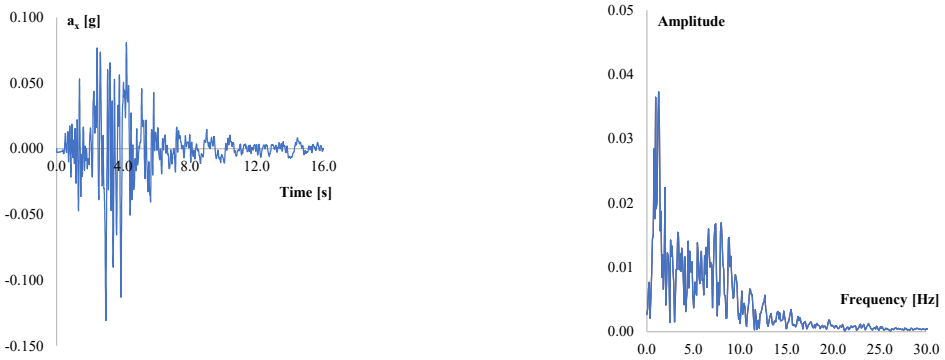


a) b)

Figure 4. Friuli earthquake input signal: a) time history of the acceleration and the related b) Fourier spectrum.

## 4 RESULTS

For the sake of brevity, we set a limit herein in presenting the details of the first seismic input considered in this study (i.e., Friuli earthquake of 1976) in Section 4.1. A comparison with the results obtained using the other inputs is presented in Section 4.2.

### 4.1 Friuli earthquake (1976)

Figure 5 shows a comparison in terms of Pseudo-Spectral Acceleration (PSA) computed along three vertical axes: across the main experimental cavern, 90 m away and 300 m away from it. Acceleration amplification, compared to the bedrock, is calculated towards the ground surface, within the underlying molasse layer (see “Bottom border molasse-molasse”), the layered molasse sequence (see “Upper border moraine-molasse”) and the uppermost moraine layer (see “Ground level). The two central axes (0 and 90m) are affected by the presence of the caverns. The basement of the UXC55 cavern shows larger amplification than the surrounding rock at very low periods (peak at 0.15s). Comparing with the point at the roof of UXC55 it seems clear that the response spectra change with the position along the perimeter of the cavern cross-section.

Figure 6 shows the PSA along horizontal axes (ground level, upper border of the layered molasses, bottom border of the layered molasses). It confirms that amplifications larger than

under free-field conditions are generally computed around the cavities, within a horizontal distance from the cavern wall of at least two times the value of the cavity height.

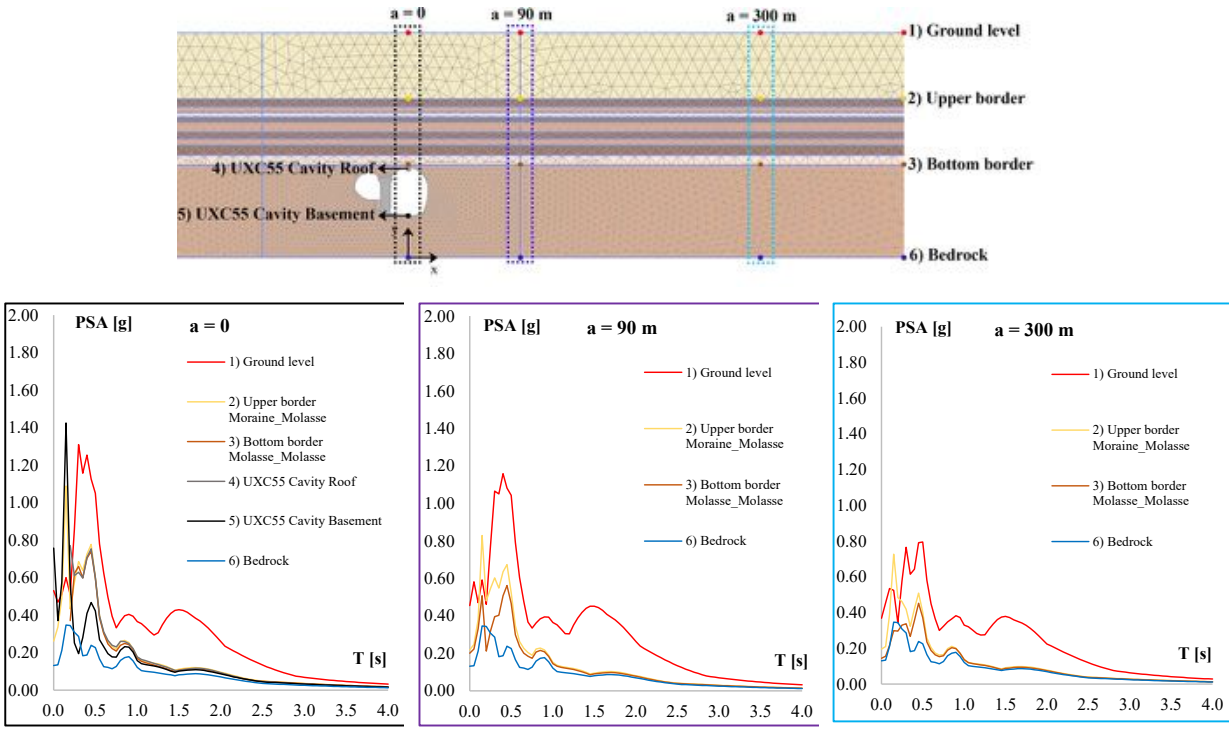


Figure 5. PSA values along vertical arrays, related to Friuli signal, in significative points of the model.

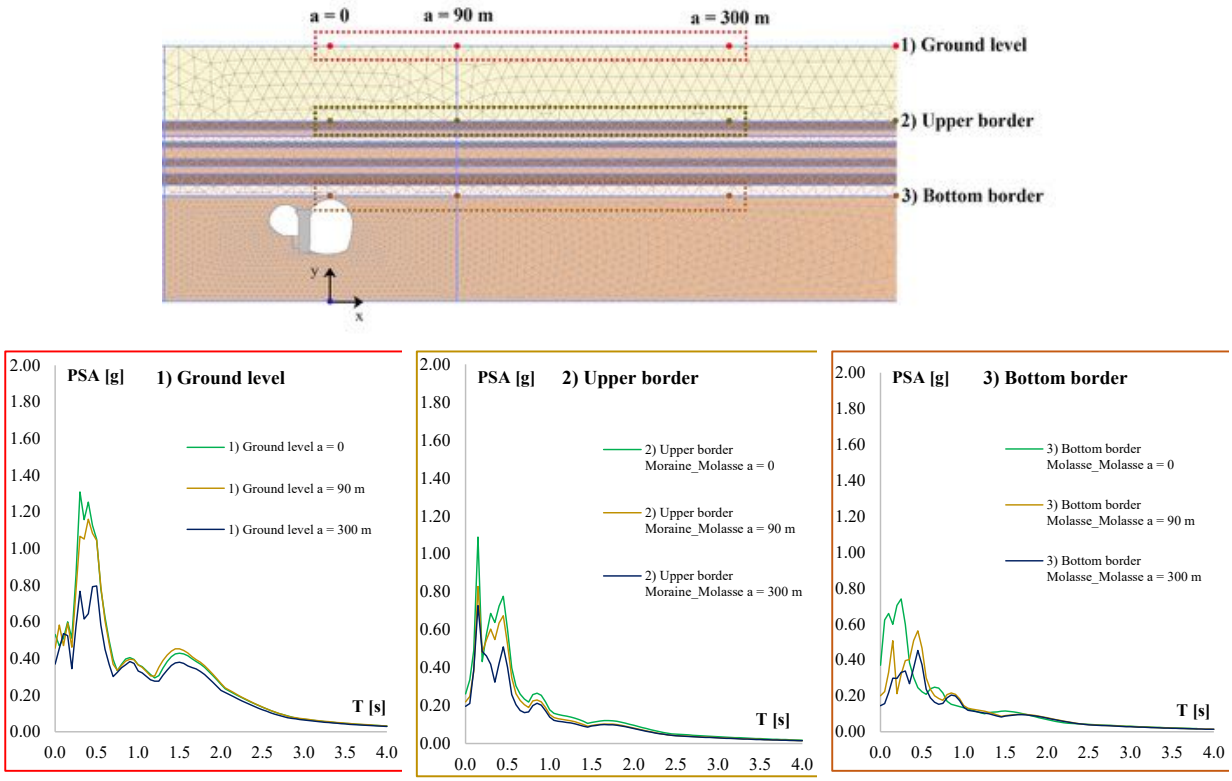


Figure 6. Friuli earthquake PSA values along horizontal axes, computed in significative points of the model.

## 4.2 Other input motions

The results using the whole set of input signals are plotted in Figure 7 in terms of response spectra. On the cavity perimeter (both basement and roof) the response spectra show a larger peak at around 0.15s, which corresponds to the predominant period of the input signals; a second peak, around 0.5s, appears predominant in the response of the rock layers ('upper border' and 'bottom border'). This seems to indicate a rather rigid response of the cavern system, that could be influenced by the stiff behavior of the 7 m wide / 28 m high concrete pillar that separates the two cavities.

A direct comparison between the mean spectra for the cavity basement and the cavity roof confirms that the spectral response is affected by the position along the perimeter of the cavity cross-section.

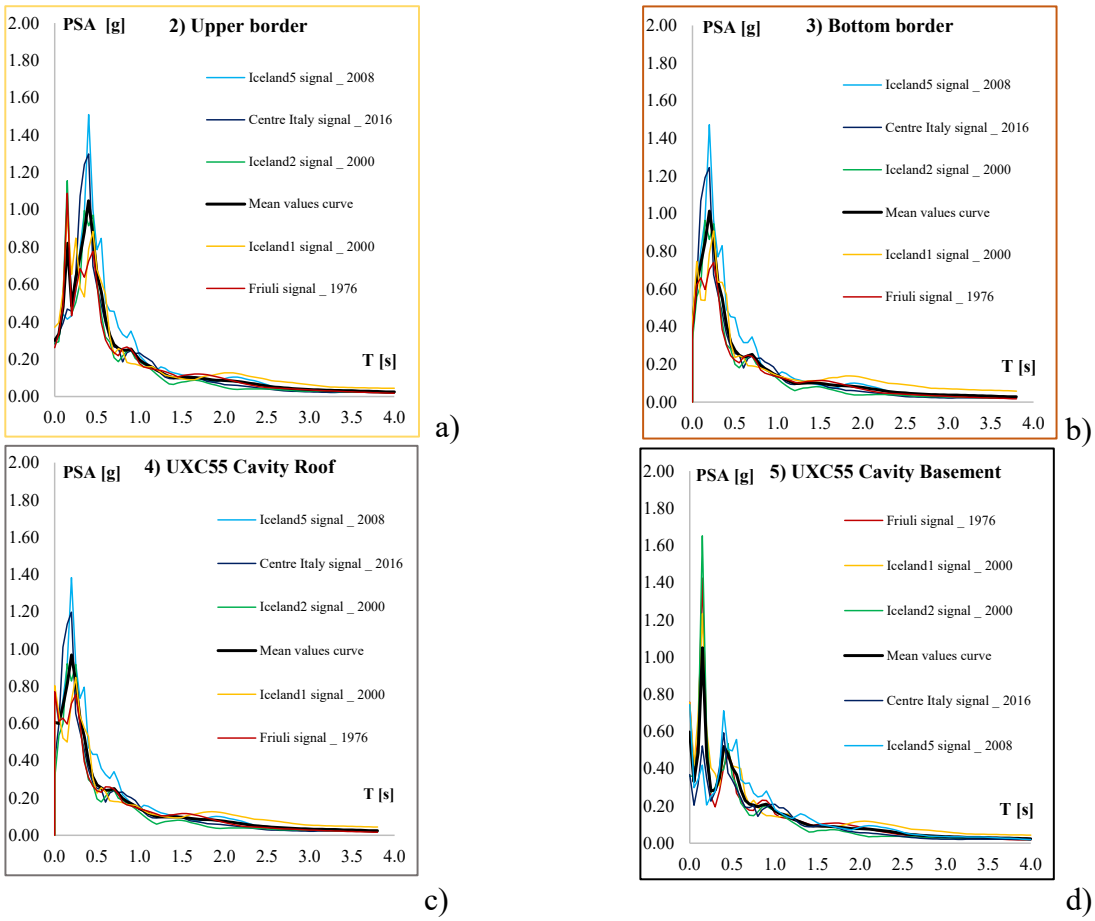


Figure 7. PSA values for the considered seismic inputs at different locations.

## 5 CONCLUSIONS

The application of a numerical methodology to the main LHC Point 5 underground infrastructures is presented. Several seismic inputs were applied to the bedrock and propagated up to ground level. The effects on the underground cavities in terms of plane-strain conditions have been assessed.

The results of non-linear dynamic analyses show how the seismic response may vary along the perimeter of the cavern cross-sections. Therefore, a thorough assessment of the seismic

response of the underground cavities contributes to more accurate estimations of the structural safety and the functional integrity requirements of the hosted equipment and installations, which are unique in their kind and permit a continuous improvement of the human understanding of how the nature of the universe works. Future developments will consider the use of a larger number of input signals to take in due consideration the uncertainties of the seismic hazard in the area. Furthermore, three-dimensional FE analyses will be carried out to investigate possible non-uniform response of the cavities along the longitudinal axis.

## 6 REFERENCES

[1] Mubarak A. Numerical simulation of large tunnel systems under seismic loading conditions: CERN infrastructure as a case study, *Doctoral dissertation*, University of Dundee (UoD), UK, 2022.

[2] Kurzweil H. C. The LHC-Project of CERN – Large Caverns in Soft Rock. A Challenge for Scientists and Engineers, *GEOCONSULT Consulting Engineers*, 2004

[3] "*Décret no 2010-1254 du 22 octobre 2010 relatif à la prévention du risque sismique*" (in French), 2010

[4] "*Arrêté du 22 octobre 2010 relatif à la classification et aux règles de construction parasismique applicables aux bâtiments de la classe dite 'à risque normal*" (in French), 2010

[5] Plaxis. Material Models Manual and Reference Manual - Plaxis CONNECT Edition V22.02. Bentley, 2022.

[6] Visone C., Bilotta E., De Magistris F. S., One – Dimensional Ground Response as a Preliminary Tool for a Dynamic Analyses in Geotechnical Earthquake Engineering. *Journal of Earthquake Engeneering,* **14**, 131 – 162, 2010.

[7] Luzi L., Lanzano G., Felicetta C., D'Amico M. C., Russo E., Sgobba S., Pacor, F., & ORFEUS Working Group 5. *Engineering Strong Motion Database* (ESM) (Version 2.0). Istituto Nazionale di Geofisica e Vulcanologia (INGV). *https://doi.org/10.13127/ESM.2,* 2020

[8] Kuhlemeyer R.L., Lysmer J. "Finite Element Method Accuracy for Wave Propagation Problems". *Journal of Soil Mechanics & Foundations*. Div. ASCE. **99(5)**:421–427, 1973.

[9] Benz T., Vermeer P.A., Schwab, R., A small – strain overlay model. *Int. J. Numer. Anal. Meth. Geomach*. **33(1)**, 25 – 44, 2009.

COMPDYN 2023
9th ECCOMAS Thematic Conference on
Computational Methods in Structural Dynamics and Earthquake Engineering
M. Papadrakakis, M. Fragiadakis (eds.)
Athens, Greece, 12-14 June 2023

# DYNAMIC RESPONSE OF TREES SUBJECT TO A LANDSLIDE-INDUCED AIR BLAST: IMPLICATIONS FOR AIR BLAST RISK ASSESSMENTS

**Yu Zhuang[1,2*], Perry Bartelt[1,3], Aiguo Xing[2], Alexander Bast[1,3]**

[1] WSL Institute for Snow and Avalanche Research SLF
Flüelastrasse 11, 7260 Davos Dorf, Switzerland
e-mail: Yu.Zhuang@slf.ch, bartelt@slf.ch, alexander.bast@slf.ch

[2] State Key Laboratory of Ocean Engineering, Shanghai Jiao Tong University
Shanghai, 200240, PR China
Yu.Zhuang@slf.ch, xingaiguo@sjtu.edu.cn

[2] Climate Change, Extremes and Natural Hazards in Alpine Regions Research Center CERC
Flüelastrasse 11, 7260 Davos Dorf, Switzerland
bartelt@slf.ch, alexander.bast@slf.ch

## Abstract

*Large landslides are known to generate powerful air blasts capable of causing damage far beyond the landslide runout. In many cases, observations of tree destruction are the only evidence to quantify the air blast danger. In this study, we proposed an approach to assess the air blast power using the tree breakage information, including the eigenfrequency prediction, tree motion calculation and breakage conditions. The tree is modelled as a flexible beam with elastic support at the tree base. Large tree deflection is accounted for when calculating the air blast loading and two failure modes (bending and overturning) are defined. Modelling results illustrated that tree eigenfrequency is always close to the air blast frequency, leading to a dynamic magnification for tree deformation. This magnification effect is greatly influential in a weak air blast case, but the large tree inclination resulting from strong air blast loading would weaken the effect. Additionally, both failure modes are likely to occur and the exact failure mode of trees depends heavily on their bending and anchorage resistance. Therefore, further measurements need to be conducted on the biometric and mechanical characteristics of trees, which will improve the accuracy of air blast hazard assessment.*

**Keywords:** Landslide-induced air blast, Tree eigenfrequency, Dynamic response, Tree breakage.

## 1 INTRODUCTION

Long runout landslides are characterized by their high mobility, long moving distance and possible chain disasters [1]. A moving landslide with a large volume can generate powerful air blasts that are capable of breaking trees and even flattening buildings [2,3]. In recent years, destructive air blasts that caused mass casualties and damages are frequently recorded worldwide [4-6]. Understanding their destructive force is of great importance for landslide disaster prevention in mountainous regions.

Monitoring equipment has been proved to be a great approach to determine the air blast dynamics [7,8]. However, most cases occurred in the mountainous regions without a warning, and no monitoring equipment was settled in advance [9]. Therefore, very few air blast cases were measured in history. The occurrence of air blasts can be identified through the suspended powder cloud and geological evidence. In many cases, observations of tree breakage are the only data to quantify the air blast power [10]. Geologists can assess the air blast hazard using forest destruction and tree breakage information [11,12]. Snapped stems and uprooted/overturned trees outlined the impact area of air blasts and their falling direction could indicate the primary movement of the landslide. Any information on forest damage is valuable to help evaluate the air blast hazard.

The problem with using information of tree breakage for air blast risk assessment is that a simple relationship between air blast pressure and tree failure is hard to establish. Bending and overturning are two common tree failure modes caused by strong winds. Bending failure occurs when the bending stress exerted by the air blast exceeds the wood strength [13, 14], while the uprooting will occur when the applied torque overcomes the anchorage resistance [15-16]. Occurrence of the specific failure mode depends heavily on both the tree strength and air blast loading. Accounting for the minor destructive force of air blasts relative to the landslide, though long recognized that flowing sliding mass can easily break trees, tree destruction results from air blast loading has received less attention [17]. Existing models quantifying the air blast-induced tree breakage are mostly static [11] or proposed based on the small-deflection theory [10]. These approaches help the rapid evaluation of air blast power, but further research is needed to focus on the dynamic response of trees subjected to a strong wind loading.

Here we developed a simple mechanical model to calculate the natural frequency of trees and their dynamic response subject to an air blast loading. The tree is assumed as a multi-degree-of-freedom beam with variable diameters and the impacts of large deflection and root anchorage are accounted for. Furthermore, both bending and overturning failure modes are involved in the proposed model. Our work is expected to provide insights into the destructive force of landslide-induced air blasts and offers an applicable method for air blast hazard assessment.

## 2 MODEL DESCRIPTION

Landslide-induced air blasts are known of short duration, large impact area and can reach an extremely high velocity [7, 18]. The impact of this impulse wave on trees is similar to strong wind gusts, producing large bending stress/moments in the stem and root system, forcing trees to get deformation. To describe the dynamic response and failure of trees subject to the air blast loading, we proposed a dynamic tree-swaying model that accounts for the large tree deflection, including the eigenfrequency prediction method, tree motion equations and the breakage conditions.

## 2.1 Eigenfrequency prediction

The tree is modelled as a flexible cantilever beam that is hinged at the ground surface using elastic support (Fig. 1). Considering the decreasing diameter of stems and crown from bottom to top, the beam diameter is assumed to linearly decrease with height. Additionally, the tilt of tree base in response to the moment is described by the anchorage stiffness ($K$) of the root system [19]. In the eigenfrequency prediction model, the tree beam is split into two segments with a splitting point at the crown base. We assume that the tree crown shows minor impacts on elastic modulus and is accounted for through the crown mass.

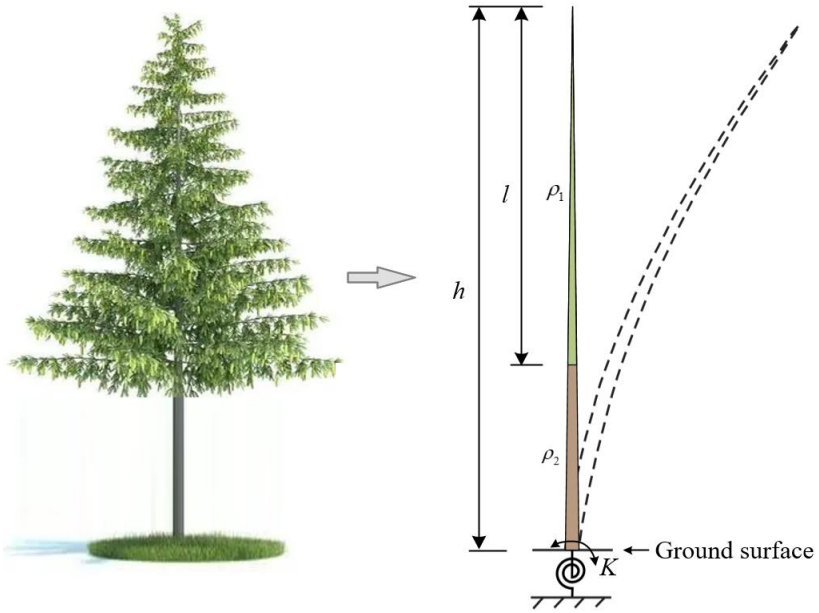


**Fig. 1** Diagrammatic sketch of the eigenfrequency prediction model.

The governing equation for the dynamic bending of a nonuniform Euler-Bernoulli beam can be written as [20]:

$$z^2\frac{\partial^4 u}{\partial z^4}+8z\frac{\partial^3 u}{\partial z^3}+12\frac{\partial^2 u}{\partial z^2}-\frac{16\rho\omega^2 u}{E\mu^2}=0 \tag{1}$$

where $u$ is the tree displacement, $\rho$ is the material density, $\omega$ is the eigenfrequency, $E$ is the elastic modulus, $z$ is the position variable along the beam length. The original point ($z$=0) is set at the treetop to simplify the calculation, so that the beam diameter $d(z)$ at position $z$ can be easily described by a gradient coefficient ($\mu$): $d(z)=\mu z$. The general solution of Eq. 2 can be expressed as:

$$u(z)=\frac{1}{z}\left[A_1J_2(2\sqrt{\lambda z})+A_2Y_2(2\sqrt{\lambda z})+A_3J_2(2i\sqrt{\lambda z})+A_4Y_2(2i\sqrt{\lambda z})\right] \tag{2}$$

where $\lambda=\sqrt{\frac{16\rho\omega^2}{E\mu^2}}$, $J_2$ and $Y_2$ represent the Bessel functions of the first and send kind, respectively. $A_1$-$A_4$ are coefficients that need to be calculated according to the boundary and continuity conditions.

According to Eq. (2), the deformation of the upper crown segment and the lower trunk segment can be similarly expressed as:

$$u_1(z)=\frac{1}{z}\left[A_1J_2\left(2\sqrt{\lambda_1 z}\right)+A_2Y_2\left(2\sqrt{\lambda_1 z}\right)+A_3J_2\left(2i\sqrt{\lambda_1 z}\right)+A_4Y_2\left(2i\sqrt{\lambda_1 z}\right)\right] \quad 0\leqslant z<l \tag{3}$$

$$u_2(z)=\frac{1}{z}\left[B_1J_2\left(2\sqrt{\lambda_2 z}\right)+B_2Y_2\left(2\sqrt{\lambda_2 z}\right)+B_3J_2\left(2i\sqrt{\lambda_2 z}\right)+B_4Y_2\left(2i\sqrt{\lambda_2 z}\right)\right] \quad l\leqslant z\leqslant h \quad (4)$$

where $l$ represents the crown length, $h$ is the tree height, $\lambda_1=\sqrt{\frac{16\rho_1\omega^2}{E\mu^2}}$ and $\lambda_2=\sqrt{\frac{16\rho_2\omega^2}{E\mu^2}}$ are the single-valued function of eigenfrequency, $\rho_2$ is the wood density, $\rho_1$ is the equivalent density attributes by both tree crown and trunk, $B_1$-$B_4$ are coefficients of the tree deflection equation, which are the same to $A_1$-$A_4$ in Eq. (2).

Regarding the boundary condition at the treetop ($z$=0) is the free end, Eq. (4) can be simplified as:

$$u_1(z)=\frac{1}{z}\left[A_1J_2\left(2\sqrt{\lambda_1 z}\right)+A_3J_2\left(2i\sqrt{\lambda_1 z}\right)\right] \qquad 0\leq z<l \quad (5)$$

According to the boundary conditions at the tree base ($z$=$h$) and the continuity conditions at the splitting points of two segments, following constraints are determined: $u_1(l)=u_2(l)$ , $u_1'(l)=u_2'(l)$ , $u_1''(l)=u_2''(l)$ , $u_1'''(l)=u_2'''(l)$ , $u_2(h)=0$ , and $Ku_2'(h)+EI(h)u_2''(h)=0$ . Introducing the constraints into Eqs. (4-5), these six equations can be written in a matrix format:

$$\left[F\left(\lambda_1,\lambda_2\right)\right]_{6\times6}\cdot\left[A_1 \quad A_3 \quad B_1 \quad B_2 \quad B_3 \quad B_4\right]^T=0 \quad (6)$$

where $\left[F\left(\lambda_1,\lambda_2\right)\right]_{6\times6}$ is the matrix that is composed of the eigenfrequency ($\omega$). The orders of eigenfrequency and the corresponding vibration mode are calculated by solving the equation: the determinant of matric $\left|F(\lambda_1,\lambda_2)\right|=0$ .

## 2.2 Dynamic response of trees

Dynamic response of trees subject to an air blast loading is calculated using a modified multi-degree-of-freedom tree swaying model [21]. To calculate the air blast loading, the size of tree crown here refers to its real frontal area distribution, which is different from the simplification in the eigenfrequency prediction mode. The tree beam is divided into a set of segments and the tree deflection is calculated using linear modal analysis. According to numerical works performed by Sellier et al. (2008)[22] and Pivato et al. (2014) [23], for trees with a slender shape, the contribution of the first vibration mode is far ahead of the others. The present work only used the first vibration mode and the corresponding eigenfrequency to calculate the tree response. Furthermore, the modelling of the air blast loading accounts for the large tree deflection and wind-tree relative motion through regarding the beam velocity and geometric nonlinearities led by the inclination of beam segments ($\theta_i$) (Fig. 2). With respect to the large tree deflection, the impact of eccentric gravity is also involved in the model. Considering that damaged trees often fall in the direction of landslide motion and have little time to sway, the maximum response is suggested to be reached before the damping forces act [10]. The impact of damping is therefore neglected. Equations for tree motion and the air blast loading are expressed as:

$$m\frac{\partial^2 y}{\partial t^2}+ky=\int_0^h F_i\phi\mathrm{d}s+\int_0^h G_i\phi\mathrm{d}s \quad (7)$$

$$F_i=0.5\rho C_{\mathrm{d}}A_{\mathrm{f}}\left|v\cos\theta_i-\frac{\partial y}{\partial t}\cos\theta_i\right|\left(v\cos\theta_i-\frac{\partial y}{\partial t}\cos\theta_i\right)\cos\theta_i \quad (8)$$

$$G_i=m_i g\cdot\sin\theta_i\cdot\cos\theta_i \quad (9)$$

where $\phi$, $w$, $m = \int_0^h \overline{m}\phi^2 \mathrm{d}s$, $k = 4\pi^2 m\omega^2$ represent the first mode shape, the first eigenfrequency, modal mass and stiffness, respectively. $\overline{m}$ is the mass distribution, $F_i$ and $G_i$ represent the air blast loading and eccentric gravity acting on the $i$th beam segment, $h$ is the tree height, $C_\mathrm{d}$ is the drag efficient, $A_\mathrm{f}$ is the frontal area, $\rho$ and $v$ are the density and velocity of the air blast, respectively.

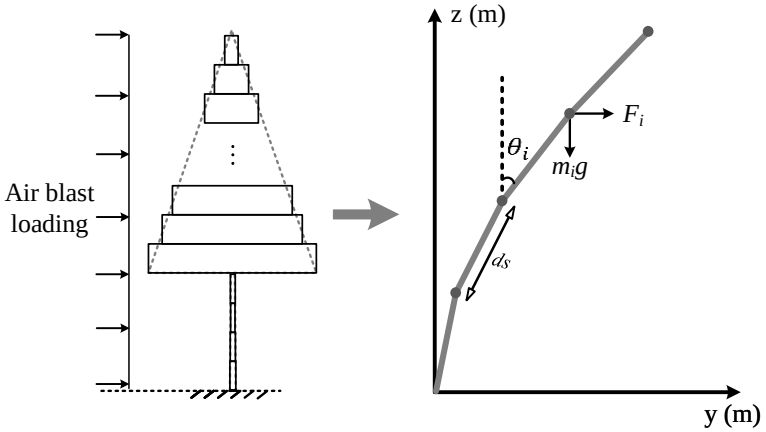


**Fig. 2** Modeling the tree as a multi-degree-of-freedom flexible beam to calculate the dynamic response of trees subjected to an air blast.

In this study, the velocity of landslide-induced air blasts is characterized as a sine wave impulse with a short duration $t_0$:

$$v = v_{\max}\sqrt{\sin \varpi t} \tag{10}$$

where $v_{\max}$ represents the maximum air blast velocity and $\varpi$ is treated as the circular frequency of the air blast loading $\varpi = \pi / t_0$ (wind force is linked to the square of its velocity). The dynamic response and deformation of trees subject to an air blast loading are determined by introducing the wind velocity (according to Eq. 10) into Eqs. 7-9, and then solving the tree motion equations using the central finite-difference scheme [21].

## 2.3 Tree breakage conditions

The present work involves two common failure modes caused by powerful air blasts: bending and overturning [14].

For the bending failure, tree breakage will occur when the maximum bending stress ($\sigma_{\max}$) reaches the bending strength ($\sigma_{\mathrm{crit}}$):

$$\sigma_{\max} = \left[\frac{M(t,z)\cdot d(z)/2}{I(z)}\right]_{\max} \geq \sigma_{\mathrm{crit}} \tag{11}$$

where $M(t,z)$ is the bending moment, which is calculated at different positions during the air blast loading:

$$M(t,z) = EI(z)\frac{\mathrm{d}\theta}{\mathrm{d}s} \tag{12}$$

where $\theta$ represents the inclination between the beam segment with the vertical direction and $\frac{\mathrm{d}\theta}{\mathrm{d}s}$ is the local beam curvature.

For the cases of overturning, tree breakage will occur at the basement when the moment ($M_{\mathrm{base}}(t)$) exceeds the anchorage resistance ($M_{\mathrm{crit}}$):

$$M_{\text{base}}(t) \geq M_{\text{crit}} \tag{13}$$

## 3 APPLICATION

We consider the problem proposed by Bartelt et al. (2018)[10] to illustrate the air blast power: a landslide-induced air blast enters a forest of tall spruce (25-30 m). The short-duration air blast has a maximum velocity of 20 m/s and lasts a few seconds with a frequency $\varpi$. The sliding mass stopped before entering the forests and only the air blast acted on trees.

**Table 1** Model parameters used in the numerical simulations of the tree response. Parameters are derived from data contained in Kantola and Mäkelä (2004) and Bartelt et al. (2018).

| Height $h$(m) | Crown height $l$(m) | Crown width $w$(m) | Diameter at trunk base $D$(m) | Wood density $\rho_2$ (kg/m$^3$) | Branch mass $m$(kg) | Drag coefficient $C_d$ | Elastic modulus $E$(GPa) |
|---|---|---|---|---|---|---|---|
| 27 | 18 | 5 | 0.4 | 480 | 540 | 0.4 | 10 |

Using the tree-related parameters shown in Table 1, we set the crown mass of a single tree to be 540 kg. The crown is assumed to have a cone shape with a length of 18 m ($\frac{2}{3}h$) and a width of 5 m. Neild and Wood (1999) [19] performed many in-situ measurements on spruce anchorage stiffness ($K$), showing a large value variation of 80-1200 kN·m. In this study, $K$ values of 100-1200 kN·m are applied in the eigenfrequency calculation.

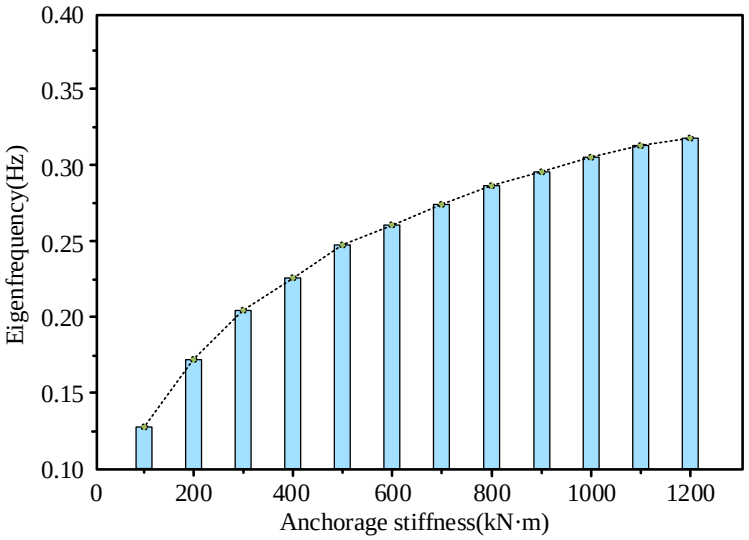


**Fig. 3** Impact of anchorage stiffness on the tree eigenfrequency.

The eigenfrequency ranging from 0.13 Hz ($K$=100 kN·m) to 0.32 Hz ($K$=1200 kN·m) is calculated using the above parameters (Fig. 3), which is basically consistent with measurements performed by Jonsson et al. (2007)[24]. The good agreement between the calculated eigenfrequency and the measurement validates the proposed eigenfrequency prediction method. Notably, though the tree eigenfrequency varies significantly with the anchorage stiffness, the calculated values are always in the same order of magnitude with the air blast frequency, necessitating further research on the potential effect of resonance.

To investigate the potential dynamic magnification effect on tree deformation, we designed cases using the tree eigenfrequency of 0.26 Hz ($K$=600 kN·m) and the associated vibration mode. We character this effect using the ratio of the maximum dynamic deformation ($u_{\text{d,max}}$) to the static deformation ($u_{\text{sta}}$):

$$D = \frac{u_{\mathrm{d,max}}(\beta)}{u_{\mathrm{sta}}} = \frac{u_{\mathrm{d,max}}(\beta)}{\int_0^h F_{\mathrm{s,max}}\phi \mathrm{d}s / k} = \frac{u_{\mathrm{d,max}}(\beta)}{\int_0^h \rho C_{\mathrm{d}} A_{\mathrm{f}} v_{\mathrm{max}}^2 \phi \mathrm{d}s / k} \tag{14}$$

where $F_{\mathrm{s,max}}$ represents the maximum static wind force and $\beta = \dfrac{\varpi}{\omega}$ is the ratio between the air blast frequency ($\varpi$) and the tree eigenfrequency ($\omega$). Regarding that dust mixed in the air blast would increase the fluid density, $\rho = 5\mathrm{kg/m}^3$ is utilized here [11]. In this case, the static tree deformation $u_{\mathrm{sta}}$ is calculated to be 9.8 m.

Fig. 4 shows the impact of dynamic magnification on tree deformation. Consider first an air blast duration of 1.6 s ($\beta = 1.2$), the maximum dynamic displacement $u_{\mathrm{d,max}}$ reaches 10.7 m, corresponding to the magnification factor *D* of 1.09. The air blast frequency is higher than that of trees, thus the maximum deformation reaches after the loading time. For a longer air blast lasting 3.2 s ($\beta = 0.6$), the magnification factor *D* is calculated to be 1.34, a high value. The maximum tree displacement happens during the air blast loading. In this scenario, an air blast with a velocity of 20 m/s can cause similar tree breakage as a long-duration wind travels at 25 m/s. Although the large tree deflection (tree inclination) decreases the wind load acting on trees, the impulse air blast will increase the risk of tree breakage because of the dynamic magnification effect.

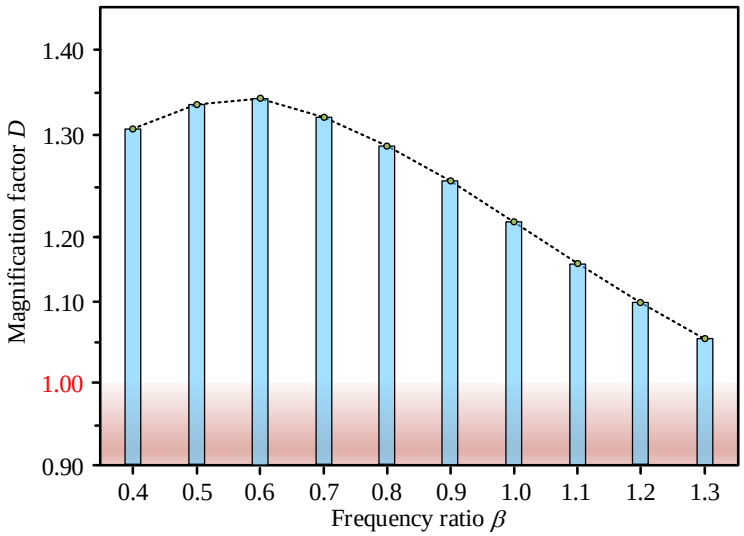


**Fig. 4** Magnification factor change with various frequency ratios.

Using the proposed model, further simulations were conducted on the air blast-induced tree breakage. The air blast is assumed to have a maximum velocity of 20 m/s and lasts 3.2 s. In this case, the maximum bending stress is calculated to be 35 Mpa, located at 9 m height (crown base), while the maximum moment is identified at the tree base with a value of 192 kN·m. In natural forests, it is known that the bending strength and anchorage resistance of trees depend heavily on tree species, soil characteristics and climates, etc. In-situ measurements performed by Peltola et al. (1999) [13] indicated that the bending stress to destroy mature trees should exceed a minimum value of 30 Mpa, and anchorage resistance of mature spruces could reach up to 100-400 kN·m. Therefore, bending and overturning failure will both likely happen for the case performed in this study.

## 4 DISCUSSION

Evaluation of air blast hazards is an important issue of landslide risk assessment in mountainous regions. Compared with existing models, one improvement of our model is to involve the impact of anchorage and treat trees as beams with a variable cross-section. This improvement allows trees to sway as their natural vibration and make the bending failure more realistic. The failure position can be simulated using the proposed model. In previous models that describe the air blast-tree interaction, trees are modelled as beams with a constant diameter [11], and thus the maximum bending stress always reaches at the tree base. This failure feature is greatly different from the field observations.

Another improvement of the proposed model is to involve the large tree deflection. A comparative analysis is designed to investigate its impact on tree response. We simplified the tree motion equation of Eq. 7 without accounting for the large tree deflection. The simplified model is similar to that proposed by Bartelt et al. (2018) [10]:

$$m\frac{\partial^2 y}{\partial t^2}+ky=\int_0^h 0.5\rho C_d A_f v_{max}^2\phi ds\cdot\sin\varpi t=\int_0^h F_{s,max}\phi ds\cdot\sin\varpi t \tag{15}$$

The displacement at the tree top can be written as:

$$\begin{cases} u(t)=\dfrac{\int_0^h F_{s,max}\phi ds}{k}\dfrac{1}{1-\beta^2}(\sin\varpi t-\beta\sin\omega t) & 0\le t\le t_0 \\ u(t)=\dfrac{u'(t_0)}{\omega}\sin\omega(t-t_0)+u(t_0)\cos\omega(t-t_0) & t>t_0 \end{cases} \tag{16}$$

The magnification factor $D$ for both scenarios can be expressed as:

$$\begin{cases} D=\dfrac{1}{1-\beta^2}[\sin(\dfrac{2\pi\beta}{\beta+1})-\beta\sin\dfrac{2\pi}{\beta+1}] & \beta\le 1 \\ D=\dfrac{2\beta}{\beta^2-1}\cos\dfrac{\pi}{2\beta} & \beta>1 \end{cases} \tag{17}$$

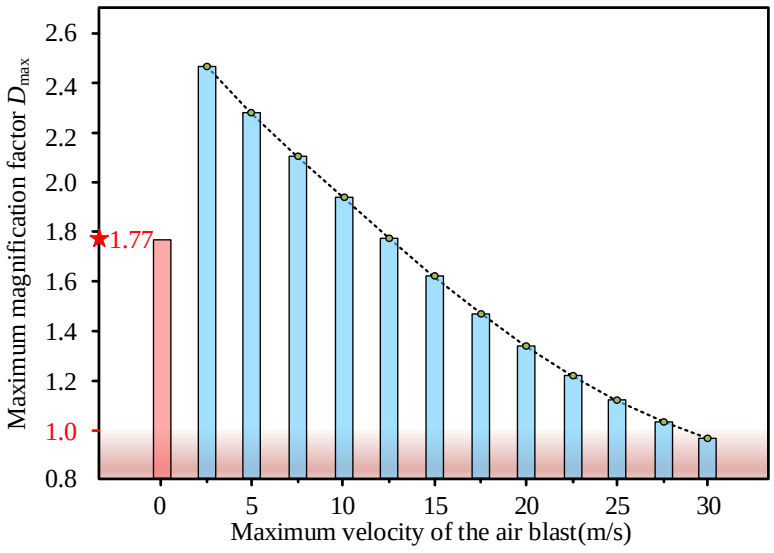


**Fig. 5** Impact of large tree deflection on the maximum magnification factor $D_{max.}$ The red star represents the $D_{max}$ calculated from Eq. 17. The red bar represents the $D_{max}$ corresponding to the scenario with a very low air blast velocity (maximum velocity of 0.1m/s) and the eccentric gravity is not considered.

The impact of large tree deflection on the magnification effect is shown in Fig. 5. In the case of a very low wind velocity (maximum velocity of 0.1m/s) and in the absence of eccen-

tric gravity, the $D_{max}$ value is calculated to be 1.77, which is in agreement with the analytical solution from Eq. 17. This scenario ignores the impact of large tree deflection. The tree displacement is small when subjected to such a weak air blast loading, and the comparison result validates the proposed model. Further calculations accounting for the impact of large tree deflection show different results. In the cases of a low wind velocity, the eccentric gravity is significantly influential, leading to a rather high magnification factor (>2). Nevertheless, $D_{max}$ greatly decreases in the cases of a larger wind velocity. The dynamic response and eccentric gravity amplify the tree deflection, but the tree inclination reduces the frontal area and the associated air blast loading. This special mechanism is rarely considered in previous air blast risk assessments. The modelled tree deflection subjected to a strong air blast might be overestimated without accounting for the large tree deflection.

The mechanical response and failure of trees subject to a powerful air blast are complex, depending on the biometric characteristics of trees. Some biomass changes can be represented through modifying parameters in the proposed model. For example, for leafless trees, air blasts only act on the branch, leading to a smaller wind load [25]. A small drag efficient $C_d$ will provide better performance. Due to the shielding effect of forests, single trees are always subject to a larger wind loading than trees in dense forest stand [11]. A reduction of the frontal area $A_t$ is needed in such a condition. Additionally, the anchorage characteristic is also influential as it greatly contributes to the tree eigenfrequency and the likely failure mode. For now, though many efforts have been paid to mechanical properties of trunks, little information is available about the anchorage stiffness and resistance of trees. A reliable test value of anchorage resistance and bending strength is of utility to help the tree failure prediction and clarify which failure mode will occur. In the future, regional databases for the mechanical and biometric properties of trees are suggested to be established. This would provide reliable information for geologists during the risk assessment of landslide-induced air blasts.

## 5 CONCLUSIONS

Landslide-induced air blasts are short-duration impulses and can cause damage far beyond the sliding mass. Tree breakage in situ provides the opportunity to quantify the air blast power. In this study, we proposed a framework to assess the air blast danger using the tree breakage information, including the eigenfrequency prediction method, tree motion equations and breakage conditions. Trees are modelled as a flexible variable cross-section beam hinged at ground using elastic support. The impacts of anchorage and large tree deflection are involved in the model. We draw several conclusions from the analysis.

Though the anchorage property is greatly influential to the tree eigenfrequency, the tree eigenfrequency is always in the same order of magnitude as the air blast frequency. The associated dynamic response amplifies the tree deflection and leads to a higher risk of tree breakage. Short-duration air blasts travelling at 20 m/s can cause similar damage as a long-duration wind moves at 25 m/s. Notably, this magnification effect results from dynamic loading and eccentric gravity is significant in a weak wind case, while large tree deflection (tree inclination) caused by powerful air blasts would weaken the effect. Additionally, bending and overturning are two likely failure modes for trees, but what kind of failure will occur for a specific forest depends heavily on tree properties. In the future, more measurements are needed to be conducted on the mechanical and biometric properties of trees, which will help the prediction of air blast danger.

## REFERENCES


[1] De Blasio FV, Crosta GB (2015) Fragmentation and boosting of rock falls and rock avalanches. Geophysical Research Letters, 42, 8463-8470.

[2] Yin YP (2014) Vertical acceleration effect on landsides triggered by the Wenchuan earthquake, China. Environmental Earth Sciences, 71, 4703-4714.

[3] Penna IM, Hermanns RL, Nicolet P, Morken OA, Jaboyedoff M (2021) Airblasts caused by large slope collapses. Geological Society of America Bulletin, 133, 939-948.

[4] Bartelt P, Buser O, Vera Valero C, Bühler Y (2016) Configurational energy and the formation of mixed flowing/powder snow and ice avalanches. Annals of Glaciology, 57(71), 179-188.

[5] Zhuang Y, Xu Q, Xing AG (2019) Numerical investigation of the air blast generated by the Wenjia valley rock avalanche in Mianzhu, Sichuan, China. Landslides, 16, 2499-2508.

[6] Zhuang Y, Xu Q, Xing AG, Bilal M, Gnyawali KR (2022a) Catastrophic air blasts triggered by large ice/rock avalanches, Landslides. Doi: 10.1007/s10346-022-01967-8.

[7] Sukhanov G (1982) The mechanism of avalanche air blast formation as derived from field measurements, Data Glaciology Student, 44, 94-98.

[8] Caviezel A, Margreth S, Ivanova K, Sovilla B, Bartelt P (2021) Powder snow impact of tall vibrating structures. Eccomas Proceedia Compdyn, 5318-5330.

[9] Yin YP, Xing AG (2012) Aerodynamic modeling of the yigong gigantic rock slide-debris avalanche, Tibet, China. Bulletin of Engineering Geology and the Environment, 71, 149-160.

[10] Bartelt P, Bebi P, Feistl T, Buser O, Caviezel A (2018) Dynamic magnification factors for tree blow-down by powder snow avalanche air blasts. Natural Hazards Earth System Sciences, 18, 759-764.

[11] Feistl T, Bebi P, Christen M, Margreth S, Diefenbach L, Bartelt P (2015) Forest damage and snow avalanche flow regime. Natural Hazards and Earth System Sciences, 15, 1275-1288.

[12] Fujita K, Inoue H, Izumi T, Yamaguchi S, Sadakane A, Sunako S, Nishimura K, Immerzeel WW, Shea JM, Kayastha RB, Sawagaki T, Breashears DF, Yagi H, Sakai A (2017) Anomalous winter-snow-amplified earthquake-induced disaster of the 2015 Langtang avalanche in Nepal, Natural Hazards Earth System Sciences. 17, 749-764.

[13] Peltola H, Kellomäki S, Väisänen H, Ikonen V (1999) A mechanistic model for assessing the risk of wind and snow damage to single trees and stands of scots pine, norway spruce, and birch. Canadian Journal of Forest Research, 29, 647-661.

[14] Gardiner B, Peltola H, Kellomäki S (2000) Comparison of two models for predicting the critical wind speeds required to damage coniferous trees. Ecological Modelling, 129, 1-23.

[15] Jonsson MJ, Foetzki A, Kalberer M, Lundström T, Ammann W, Stöckli V (2006) Root-soil rotation stiffness of norway spruce (Picea abies (L.) Karst) growing on subalpine forested slopes, Plant Soil, 285, 267-277.

[16] Nicoll BC, Gardiner BA, Rayner B, Peace AJ (2006) Anchorage of coniferous trees in relation to species, soil type, and rooting depth. Canadian Journal of Forest Research, 36, 1871-1883.

[17] Bartelt P, Stöckli V (2001) The influence of tree and branch fracture, overturning and debris entrainment on snow avalanche flow. Annals of Glaciology, 32, 209-216.

[18] Grigoryan S, Urubayev N, Nekrasov I (1982) Experimental investigation of an avalanche air blast. Data Glaciology Student, 44, 87-93.

[19] Neild AS, Wood CJ (1999) Estimating stem and root-anchorage flexibility in trees. Tree Physiology, 19, 141-151.

[20] Keshmiri A, Wu N, Wang Q (2018) Free Vibration Analysis of a Nonlinearly Tapered Cone Beam by Adomian Decomposition Method. International Journal of Structural Stability and Dynamics, 18(7), 1850101.

[21] Zhuang Y, Xing AG, Jiang YH, Sun Q, Yan JK, Zhang YB (2022b) Typhoon, rainfall and trees jointly cause landslides in coastal regions. Engineering Geology, 298, 106561.

[22] Sellier D, Brunet Y, Fourcaud T (2008) A numerical model of tree aerodynamic response to a turbulent airflow. Forestry, 81(3), 279-297.

[23] Pivato D, Dupont S, Brunet Y (2014) A simple tree swaying model for forest motion in windstorm conditions. Trees, 28, 281-293.

[24] Jonsson MJ, Foetzki A, Kalberer M, Lundström T, Ammann W, Stöckli V (2006) Root-soil rotation stiffness of norway spruce (Picea abies (L.) Karst) growing on subalpine forested slopes. Plant Soil, 285, 267-277.

[25] Schelhaas MJ, Kramer K, Peltola H, Werf DC, Wijdeven SMJ (2007) Introducing tree interactions in wind damage simulation. Ecological Modelling, 207(2-4), 197-209.

COMPDYN 2023
9th ECCOMAS Thematic Conference on
Computational Methods in Structural Dynamics and Earthquake Engineering
M. Papadrakakis, M. Fragiadakis (eds.)
Athens, Greece, 12-–14 June 2023

# A NEW PHYSICS-GUIDED DATA ASSIMILATION FRAMEWORK FOR ONLINE STRUCTURAL MONITORING: APPLICATION TO SHAKING-TABLE TESTS

**Matthieu Diaz[1*], Pierre-Étienne Charbonnel[2] and Ludovic Chamoin[1,3]**

[1] Université Paris-Saclay, CentraleSupélec, ENS Paris-Saclay, LMPS - Laboratoire de Mécanique Paris-Saclay, 91190 Gif-sur-Yvette, France
e-mail: {matthieu.diaz,ludovic.chamoin}@ens-paris-saclay.fr

[2] SEMT - Service d'Études Mécaniques et Thermiques (SEMT), CEA, Université Paris-Saclay, 91191 Gif-sur-Yvette, France
e-mail: pierreetienne.charbonnel@cea.fr

[3] Institut Universitaire de France (IUF), 1 rue Descartes, 75231 Paris CEDEX 5, France

**Abstract.** *The modified Constitutive Relation Error (mCRE) is a model updating functional whose physics-based construction avoids the explicit dependency into a priori user's expertise. Its robustness to measurement noise and remarkable convexity properties make it a credible alternative to classical model updating methods. In recent works, the authors developed an automated mCRE-based model updating framework for the offline update of finite element models of structures submitted to ground motion inputs, before deriving it to data assimilation with the development of the Modified Dual Kalman Filter (MDKF). In the latter, we addressed sequential data assimilation by integrating the mCRE as new observer within a dual Kalman filter. Contrary to classical Kalman filters, the comparison between measurements and model predictions is achieved through the mCRE functional itself, in which the data-to-model distance is enriched with a model error term with strong mechanical content (the CRE).*

*In this contribution, we focus on MDKF numerical improvements to achieve real-time data assimilation for structural health monitoring applications where an extensive number of parameters may need to be tracked with a few amount of data, which makes the identification process ill-posed and prone to instabilities. Using (i) parallelized mCRE computation and sigma-points propagation, (ii) the Scaled Spherical Simplex Kalman filter structure and (iii) a CRE-based clustering pre-step, CPU requirements are reduced by partial state update without loss of accuracy. The MDKF methodology and the novel key ingredients for efficient (near-optimal) data assimilation are illustrated throughout (simulated) earthquake engineering examples of growing complexity.*

**Keywords:** Data assimilation, Kalman filtering, modified Constitutive Relation Error, Shaking-table experiments, Earthquake Engineering.

# 1 Introduction

## 1.1 Earthquake engineering context

Earthquake engineering problems are no exception to the need of using experimental data to build, validate and operate robust numerical models, in particular when it comes to monitor and predict the structural state of civil engineering structures [5]. Such a data-to-model interaction is commonly referred to as digital twin [25] or Dynamic Data-Driven Application System (DDDAS) [8] as the updated model somehow impacts the response or the behavior of experimental device. The problem that motivates the present contribution is the control of hydraulic actuators of the CEA/TAMARIS shaking-tables when performing experiments on damaging specimens. If the control of electro-hydraulic shaking-tables for seismic replication is a well-identified issue [23], most of the proposed strategies do not consider the fact that sudden damage occurence in the tested specimen may lead to unstable experiments. Actually, because the actuators, the shaking-table and the tested specimen are physically strongly coupled, the controllability of the full device particularly depends on the modal signature of the specimen. When damage propagates, the modal signature suddenly changes, which may turn the control strategy inappropriate, the test unstable, and put the safety of the facility at risk. To avoid such situations, an alternative lies in the above-mentioned DDDAS paradigm in which a close dialog between the experimental device and a digital twin is performed in real-time (see Fig. 1).

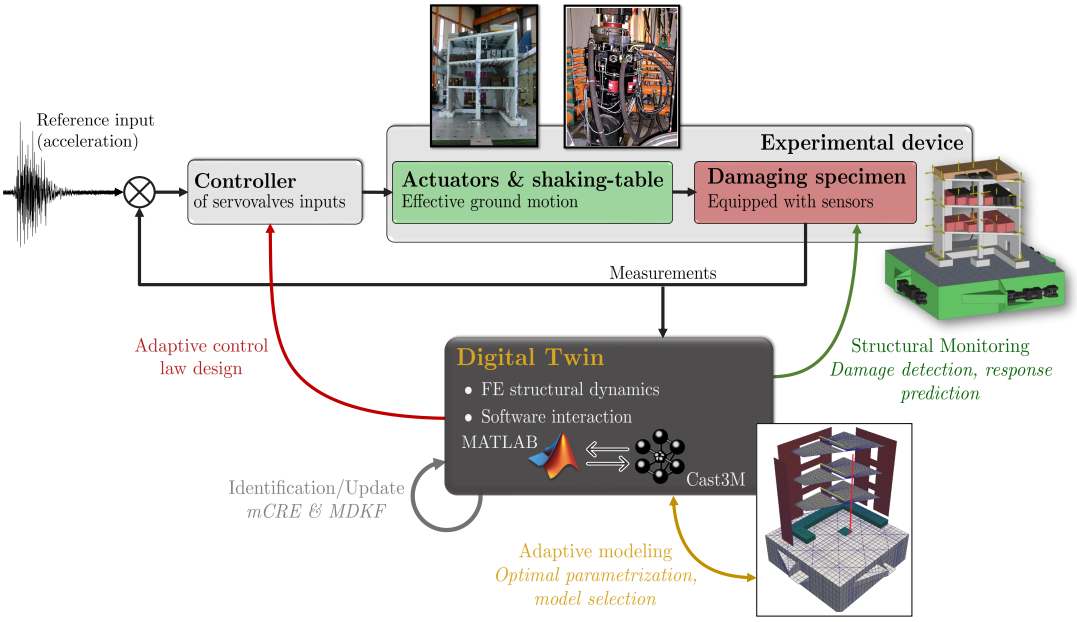


Figure 1: DDDAS framework for enhanced monitoring and control of shaking-table experiments.

## 1.2 Data assimilation and Kalman filtering

The feasibility of Dynamic Data Driven Application Systems (DDDAS) lies (among others) in efficient data assimilation schemes able to update model predictions from acquired data. In particular, such algorithms must be able to operate in real-time whereas the computational burden carried by recursive calls to model predictions can be prohibitive. With the extended availability of data and the difficulties of validating complex nonlinear full order models, last

decades have seen the emergence of hybrid approaches, often described as *data-driven* techniques. They systematically involve a reduced order model and the correction of model predictions (due to mismodeling or unanticipated phenomena) by a data-based enrichment step. Data assimilation techniques then differ according to the (reduced order) model structure and the way data are integrated and exploited to update model predictions.

For the sake of conciseness, we will mostly focus on sequential data assimilation by Kalman filtering (KF) in this contribution. Initially presented as an optimal linear unbiased quadratic estimator for linear dynamic systems under Gaussian assumptions [15], the KF algorithm is structured as a recursive prediction-correction scheme, where model predictions are sequentially corrected based on newly assimilated measurements. The KF has been massively derived and extended to process nonlinear systems. Among them, the *Extended Kalman Filter* (EKF) is based on the principle of operator linearization [14], whereas the *Unscented Kalman Filter* (UKF) [21] and the *Scaled Spherical Simplex Filter* (S3F) [22] are alternative algorithms based on statistical regularization: these techniques are based on the fact that sampling points (called $\sigma$-points) transformed by nonlinear operators allow for a better approximation of state statistics when nonlinearities are hardly linearizable. The *Ensemble Kalman Filter* (EnKF) [13] and the *Particle Filter* (PF) [6] use the same principle with much more propagated sampling-points as they aim to reconstruct the full probability density of the estimated state.

In addition, parameter estimation techniques using the Dual or Joint extensions of nonlinear KFs have also been developed to allow the simultaneous identification of mechanical state and structural parameters.

Of course, all the performance of these different KF have been extensively compared [2, 17, 20], highlighting that UKF is often more efficient than EnKF and PF in terms of CPU time, and is more accurate than EKF for an equivalent computational cost. Finally, it is worth noticing that the recent S3F outperforms UKF: S3F can be used in all applications where UKF can be involved, achieving the exact same numerical performance in terms of accuracy. However, by sampling $n+2$ sigma-points instead of $2n+1$ ($n$ being the state space dimension), S3F preserves all the important features of UKF with the minimal amount of sampling points to propagate and significant CPU time savings (see Fig. 2).

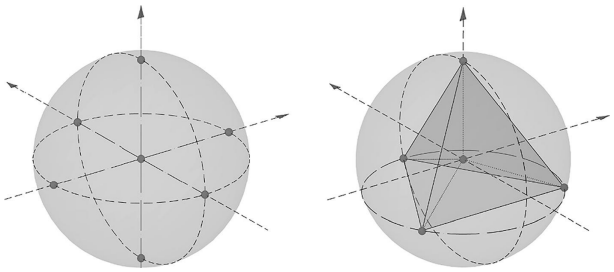

Figure 2: Sigma-points locations around the current mean state estimate ($n = 3$) for UKF (spread over a hypersphere - left) and S3F (corners of a simplex - right) - from [22].

### 1.3 The modified Constitutive Relation Error

Initially proposed for model updating in dynamics [7, 9] by Ladevèze and co-workers, an alternative to standard deterministic/stochastic model updating techniques consists in using the concept of *modified Constitutive Relation Error* (mCRE). The mCRE functional is defined as a quadratic model-to-measurements distance enriched with a term based on the concept of *Constitutive Relation Error* (CRE) [16]. The idea behind this enrichment is to improve the ellipticity

properties of the functional by adding a term which has a strong mechanical content and relaxes the most unreliable parts of the model description. This energy-based residual offers interesting advantages. First, it improves local convexity properties compared to a classical least-square functional [1]. Besides, the CRE part of the residual, computed over the whole structure, allows to select the most erroneous areas in order to restrain the updating process to a few parameters [11]. The numerous applications of mCRE for model updating during the last two decades have proven its robustness and efficiency throughout a wide range of applications. Recently, a mCRE-based model updating algorithm has been fully automated in low-frequency dynamics, with enhanced robustness with respect to measurement noise and a dedicated formulation when dealing with random inputs [10, 11].

Although dedicated to model updating, this functional has been combined to model order reduction for real-time data assimilation, leading to the Modified Kalman Filter in quasi-statics [18, 19] and to the Modified Dual Kalman Filter (MDKF) in low-frequency dynamics [12].

### 1.4 Main contributions

In this paper, following the work initiated in [12], we will essentially focus on the Modified Dual Kalman Filter algorithm and enhance its numerical performance. First, we compare and assess several Kalman filters that integrate the mCRE as observation operator in order to exhibit which KF structure is most appropriate for real-time data assimilation, with effort paid to optimize the numerical performance of the MDKF. Despite a well-chosen algorithmic structure, it cannot still be enough to reach real-time constraints when the parameter space under study is of high dimension. It is particularly the case when it comes to detect damage from linear FE models [11]. A solution may lie in using at best the information stored in the Constitutive Relation Error term. We thus propose to add a clustering step in the recursive KF-loop to generate and propagate an optimal number of $\sigma$-points at each data assimilation step (in the CRE sense), with corrections focused on parameters that are identified as erroneous.

The remainder of the paper is structured as follows: Section 2 recalls the fundamentals of mCRE and MDKF for FE stiffness model updating in low-frequency dynamics. Improvements for enhanced numerical performance are presented in Section 3 before being compared on an academic earthquake-engineering-inspired example in Section 4. Conclusions and prospects are finally drawn in Section 5.

## 2 The Modified Dual Kalman Filter for FE stiffness updating in low-frequency dynamics

This section intends to briefly recall the fundamentals of the mCRE-based model updating framework for low-frequency dynamics, starting from a linear finite element (FE) problem written in the frequency domain. The interested reader is respectively referred to [9, 10] and [12] for additional information about mCRE and MDKF.

### 2.1 FE framework, measurements and stiffness parametrization

Let us consider the general case of an elastic structure $\Omega$ spatially discretized in $E$ (non-overlapping) finite elements such that $\Omega = \cup_{e=1}^{E} \Omega_e$ subjected to a given dynamical excitation $F$. We denote by $K, D, M$ the stiffness, damping and mass FE matrices, respectively. $F_\omega$ and $U_\omega$ are the frequency counterparts of nodal loading conditions and displacement field. With these notations, the dynamical equilibrium written in the frequency domain at a given angular frequency $\omega$ reads:

$$\left[-\omega^2 M + i\omega D + K\right] U_\omega = F_\omega \tag{1}$$

In addition to the dynamic equilibrium, a set of sensors is used to measure the magnitude of certain kinematic quantities (displacement, velocity and/or accelerations). In the frequency domain, assuming measurements are perfect, such information can be written without loss of generality as:

$$\Pi U_\omega = Y_\omega \tag{2}$$

where $Y_\omega$ refers to the frequency counterpart of measurements at angular frequency $\omega$ and $\Pi$ denotes a projection matrix that allows to extract the components of $U_\omega$ that are measured.

As one can interpret damage as local stiffness loss, a convenient manner to parametrize a linear FE problem for damage detection is to parametrize the stiffness matrix. Doing so, in this contribution, the $n_\theta$ parameters to update $\theta \in \Theta \subset \mathbb{R}^{n_\theta}$ only affect the stiffness matrix $K$. More precisely, the stiffness FE matrix is decomposed in $n_\theta$ non-overlapping subdomains and parametrized as follows:

$$K(\theta) = \sum_{i=1}^{n_\theta} \frac{\theta_i}{\theta_{0,i}} K_{0,i} \quad \text{with} \quad K(\theta_0) = \sum_{i=1}^{n_\theta} K_{0,i} \tag{3}$$

Note that the subdomains can perfectly match with finite elements or gather some of them to reduce the number $n_\theta$ of parameters to identify.

### 2.2 The modified CRE: a physics-regularized approach for inverse problems

Originally intended to perform model validation [16], the key idea for the construction of the CRE residual lies into the distinction between reliable and unreliable information on the reference mechanical problem. The mCRE concept extends this distinction to the experimental data as well. Indeed, the redundant information gathered in equations (1) and (2) means all equations cannot be exactly verified. Some of them must be considered less reliable, and thus relaxed as they will be only verified at best by minimizing the so-called mCRE functional.

At a given angular frequency $\omega$, the mCRE for stiffness identification is defined as:

$$\begin{aligned} e_\omega^2(s_\omega, \theta;\, Y_\omega) \;&\triangleq\; \zeta_\omega^2(s_\omega, \theta) \;+\; \frac{\alpha}{2}\left\|\Pi U_\omega - Y_\omega\right\|_G^2 \\ \text{with } \zeta_\omega^2(s_\omega, \theta) = \frac{1}{2}(U_\omega - V_\omega)^H K(\theta)(U_\omega - V_\omega) &= \frac{1}{2}\left\|U_\omega - V_\omega\right\|_{K(\theta)}^2 \text{ and } s_\omega = (U_\omega, V_\omega) \end{aligned} \tag{4}$$

- The CRE $\zeta_\omega^2(s_\omega, \theta)$ measures the closeness of the mechanical displacement fields $(U_\omega, V_\omega)$ in the sense of the stiffness matrix. $U_\omega$ verifies the reliable kinematic equations of the problem (boundary conditions, closeness to measurements as involved in the data-to-model distance) and $V_\omega$ is constrained to satisfy the dynamic equilibrium of the problem. In practice, $s_\omega$ is obtained by solving an optimization problem for all $\omega$ (for a given parameter set $\theta$):

$$s_\omega(\theta;\, Y_\omega) \;=\; \arg\min \left[e_\omega^2(s_\omega, \theta;\, Y_\omega)\right] \text{ s.t. } [-\omega^2 M + i\omega D]U_\omega + K(\theta)V_\omega = F_\omega \tag{5}$$

  which is equivalent to solve the following matrix system:

$$AX = b \text{ with } \begin{cases} A &= \begin{bmatrix} [K(\theta) + i\omega D - \omega^2 M]^H & \frac{r}{1-r}\Pi^H G \Pi \\ -K^H(\theta) & [K(\theta) + i\omega D - \omega^2 M] \end{bmatrix} \\ X &= \begin{Bmatrix} U_\omega - V_\omega & U_\omega \end{Bmatrix}^T \\ b &= \begin{Bmatrix} \frac{r}{1-r}\Pi^H G Y_\omega & F_\omega \end{Bmatrix}^T \end{cases} \tag{6}$$

- The data-to-model distance is a Hermitian norm of the gap between model predictions $U_\omega$ with measurements $Y_\omega$. $G$ is a symmetric positive-definite matrix guaranteeing that $\|\square\|_G$ is homogeneous to $\zeta_\omega^2$ and equivalent in level. The choice of $G$ is not critical: herein, $G$ is taken proportional to the identity matrix and weighted by the strain energy stored in the first (involved) eigenmodes. The tuning factor $\alpha \in \mathbb{R}^+$ enables one to give more or less confidence to the measurements; large values can be specified when measurements are considered reliable whereas close-to-zero values are better suited to corrupted or noisy recordings. The choice of $\alpha$ is therefore crucial for providing relevant parameter estimates. Its optimal calibration has been deeply studied in [10, 11], with attention paid to its dependency into the measurement noise level if known.

As the model updating procedure is conducted on a given frequency bandwidth $D_\omega$ which contains the essential information about the response of the structure, the mCRE functional $\mathcal{J}$ to be minimized is thus obtained by direct integration over $D_\omega$:

$$\mathcal{J}(\theta,\, Y) = \int_{D_\omega} z(\omega) e_\omega^2(s(\theta,\, Y_\omega), \theta,\, Y_\omega)\, \mathrm{d}\omega \tag{7}$$

where $z(\omega)$ is a frequency weighting function such that $\int_{D_\omega} z(\omega)\, \mathrm{d}\omega = 1$ allowing to modulate the importance of specific frequencies of $D_\omega$. Indeed, a frequency weighting function derived from the experimental frequency content enables to automatically favor the vicinity of the experimental eigenfrequencies; this enhances the robustness of the functional to measurement noise in low-frequency dynamics [10].

### 2.3 The MDKF: integration of the mCRE as a nonlinear observer

As previously mentioned in the introduction, nonlinear KFs are relevant tools to update on-the-fly FE models of dynamical (and evolutive) systems. They permit to track and identify accurately structural parameters from sparse and noisy measurements. The starting point of the KF theory is the definition of a dynamical system under state-space discrete form. Considering the evolution with time of structural parameters alongside the physical state of the system, the full dynamical system reads:

$$\begin{cases} \theta_{k+1} &= \theta_k + w_{\theta,k} \\ x_{k+1} &= \mathcal{M}_k(x_k, \theta_k, e_k) + w_{x,k} \\ y_{k+1} &= \mathcal{H}_{k+1}(x_{k+1}, e_{k+1}) + v_{k+1} \end{cases} \tag{8}$$

In terms of notations, $x_k \in \mathbb{R}^{n_x}$ is the state vector at time point $t_k$. $y_k$ is the vector of observations. $w_x \sim \mathcal{N}(0, Q_x)$ and $v \sim \mathcal{N}(0, R)$ are zero-mean Gaussian white-noise accounting for additive model and measurement errors respectively. The dynamical system is based on two (possibly nonlinear) operators, namely the model operator $\mathcal{M}$ and the observation operator $\mathcal{H}$. The latter classically extracts partial information regarding the predicted state $x_k$ or inputs $e_k$. Without any *a priori* knowledge on parameters $\theta_k \in \mathbb{R}^{n_\theta}$, one can formulate a simple stationary evolution law. As it remains a restrictive hypothesis (*e.g.* damage is not), the stationarity assumption is then relaxed with the addition of a last zero-mean Gaussian white-noise $w_{\theta,k} \sim \mathcal{N}(0, Q_\theta)$ so as to model uncertainty on parameters and enable their evolution during the data assimilation process.

Although the common definition of a projection matrix as observer seems rather intuitive since sensors directly collect measurements to be compared to model predictions, the choice

of the observation metric (and thus the way measurements are processed) can be reconsidered for enhanced robustness with respect to measurement noise. From a dual KF viewpoint, one can choose to replace the dual observation operator (classically being a state prediction Kalman filter composed of the last two equations of (8)) with another functional able to quantify the closeness between model predictions and assimilated measurements.

The Modified Dual Kalman Filter (MDKF) derives the mCRE as new observation operator in a dual Kalman filter framework [12]. Practically, in a similar manner as one would compute optimal parameters minimizing the functional $\mathcal{J}$ from (7), the observation equation of the MDKF will reinvest the mCRE gradient $\nabla_\theta \mathcal{J}$ in order to guarantee the stationarity of the cost function. Please note that no additional numerical error is made with the call to the mCRE gradient as its analytical expression can be explicitly derived from the constrained minimization problem (6) (see *e.g.* [4] for complementary details). The MDKF dynamical system thus reads:

$$\begin{cases} \theta_{k+1} &= \theta_k + w_{\theta,k} \\ 0 &= \nabla_\theta \mathcal{J}(\theta_k,\, Y_k) + v_k \end{cases} \tag{9}$$

This new framework thus differs from classical KFs as measurements are indirectly compared with model predictions through the mCRE functional. Parameter estimates are then sought as minimizers of the mCRE (according to current measurements). The doubt put on the mCRE gradient (with the observation noise $v$) then quantifies the authorized proximity of estimates to the optimal set of parameters that minimizes the mCRE at each time step.

### 2.3.1 Algorithmic subtleties about MDKF

The use of MDKF raises several questions, in particular regarding its robustness with respect to measurement noise, the calibration of internal parameters and the achievable numerical performance.

It is worth noticing that the coupling between mCRE and dual Kalman filtering avoids the calibration of process and measurement covariance matrices for state estimation. However, mCRE internal parameters should be well-tuned if one intends to obtain relevant data assimilation results. It can be realistically assumed that the mCRE functional can be calibrated using the rules given in [11] after a first training stage involving a low-level non-damaging random input before performing data assimilation. Besides, the selection of filtering parameters, *i.e.* noise covariance matrices, is made easier by several user-friendly guidelines that have been proposed and validated to calibrate $Q_\theta$ and $R$ in [12].

If complete explanations are available in [12], let us finally recall that MDKF implies time-frequency domains nested interaction when mixing sequential data assimilation (in time) and mCRE (written in the frequency domain). Compared to classical KF approaches, updating parameters for all new data points does not seem relevant as the observer operates on data in the frequency domain. A sliding window technique is thus proposed for handling the time-frequency nested interaction. The overlapping rate between two consecutive windows defines the amount of new assimilated data at each time step. Note that it also fully conditions the real-time prospects of the MDKF algorithm to the extent that one considers data is assimilated in real-time if the necessary CPU time per iteration is lower than the time between two consecutive data assimilation time steps.

## 3 MDKF improvements for real-time data assimilation

To prove the relevance of MDKF to perform data assimilation efficiently, the last point to address concerns the numerical performance, in particular when the parameter set $\theta$ and/or the number of degrees-of-freedom of the FE problem become important. This section is dedicated to present several improvements that allowed to enhance numerical performance of MDKF.

### 3.1 Efficient mCRE computation

The most consuming operations of the MDKF algorithm are the frequency domain data preprocessing and the computation of the mCRE for each set of $\sigma$-points and frequency of $D_\omega$. Even if the call to Fast Fourier Transforms is unavoidable, several actions can be made to reduce the computational burden due to mCRE computations:

- The computation of the mCRE value for all $\sigma$-points per iteration can be drastically shortened using reduced basis to decrease the size of the system (6) [9, 10].
- The gradient of the mCRE functional $\mathcal{J}$ with respect to parameters can be expressed analytically and obtained after a low-cost post-processing operation once system (6) is solved. It can be shown that:

$$\forall k \in [\![1; n_\theta]\!],\ \frac{\mathrm{d}e_\omega^2}{\mathrm{d}\theta_k} = \frac{1}{2}\left[U_r^T K_{0,k} U_r + U_i^T K_{0,k} U_i - V_r^T K_{0,k} V_r - V_i^T K_{0,k} V_i\right] \tag{10}$$

  with $U_r = \Re(U_\omega), U_i = \Im(U_\omega), V_r = \Re(V_\omega)$, and $V_i = \Im(V_\omega)$.
- Parallelization techniques can be used to propagate $\sigma$-points so as to overcome the computational burden of sampling-based KF, whose CPU time significantly increases with the dimension of the parameter vector to update. In particular, the solution of system (6) for all frequencies in $D_\omega$ can be parallelized easily using new in-core page-wise left matrix divide function `pagemldivide` (available since MATLAB© 2022a release).

### 3.2 Nonlinear Kalman filter structure

The system (9) is not constrained to be used in an UKF framework as originally presented in [12]. As mentioned earlier, the S3F is an alternative sigma-point Kalman Filter that has proved to have the same numerical performance than UKF with almost 50% CPU time reduction. Indeed, the latter samples only $(n_\theta + 2)$ $\sigma$-points whereas UKF needs $(2n_\theta + 1)$. Fundamentally, the S3F and UKF algorithms do only differ in the way $\sigma$-points (and associated weights) are declared. The algorithmic modifications from UKF to S3F are therefore limited to a few code lines.

Besides, UKF was preferred to EKF in the initial MDKF due to its better accuracy in higher order statistical moments. However, from the computational viewpoint, EKF avoids the (costly) propagation of $\sigma$-points, which implies it should be quicker without being much inaccurate as the analytical expression of the mCRE gradient is available.

MDKF based on dual EKF, dual UKF and dual S3F structures will be compared in terms of accuracy and CPU time in the next section of this contribution.

### 3.3 CRE-based clustering for partial state-update

The CPU performance of sampling-based KFs remains directly proportional to $n_\theta$. Therefore, the processing of data in real-time may not be possible in cases where $n_\theta \gg 1$, which can be the case in realistic monitoring applications on large-scale structures. A possible way

to improve numerical performance without loss of accuracy is to use the full potential of the mCRE within the MDKF. The CRE term provides a direct insight regarding the validity of the model itself, making it a relevant tool for identifying erroneous parts of the model as all finite element contributions to CRE can be computed independently. If stiffness parameters affect group of elements (*i.e.* subdomains of the FE model), the CRE per subdomain $S_i$ then reads:

$$\forall\, i \in [\![1; n_\theta]\!], \quad \zeta^2_{\omega,i}(s_\omega, \theta) = \sum_{e \subset S_i} \frac{1}{2} \left\| U_\omega - V_\omega \right\|^2_{K_e(\theta)} \tag{11}$$

Thus, if the CRE can be a convenient local model indicator, one can imagine exploiting it so that only most erroneous parts of the model should be corrected. To do so in an automated way, a CRE-based clustering technique can be used. Briefly, clustering techniques allow to partition a space in subsets (the so-called clusters) in the sense of a given distance: within a cluster, the distance between objects of a cluster remains small, whereas a distance between objects of different clusters is larger (see [24] for further details). Among the wide range of clustering techniques, a fuzzy $k$-means clustering algorithm developed in [3] is reinvested in this work. Originally intended for separating the physical modes from the spurious modes produced by a growing model-order identification algorithm in modal analysis, its robustness with respect to non-convex, poorly dissociated and heterogeneous clusters makes it a relevant tool to define parameter distributions from the CRE map. Starting from the initial model, the key idea is to identify a cluster of most erroneous elements through the computation of the model error (CRE) map per element which naturally emphasizes on the damaged area if the initial parameter guess is well determined. In other words, we perform a two-cluster distinction from

$$X = \left\{ \int_{D_\omega} z(\omega) \zeta^2_{\omega,i} \mathrm{d}\omega \right\}_{i=1}^{n_\theta} \tag{12}$$

and forthcoming correcting actions can be focused on the cluster of most erroneous elements in the CRE sense. Note that this is not a computationally expensive procedure as it is a (vectorizable) post-processing operation once mechanical fields solution of (6) has been obtained. Note that in an offline model updating context, it was shown that the clustering step works as a form of regularization (in the Tikhonov sense) of the mCRE functional. An illustration of the CRE-based clustering potentialities to update a large number of parameters from a few amount of acceleration data is given in Fig. 3.

As a complement, the pseudo-code of the MDKF coupled to the CRE-based clustering is given in Alg. 1.

## 4 Application to stiffness parameter tracking from sparse accelerometer data

### 4.1 Plane frame submitted to random ground motion

In this section, we intend to validate and compare MDKF structures (EKF, UKF, S3F) and the benefits of the CRE-based clustering approach with a typical earthquake engineering academic example. Let us consider the plane frame structure shown in Fig. 4, whose stiffness distribution is assumed unknown. This structure is clamped to a rigid moving support (*e.g.* a shaking-table) and submitted to a $120$ s random bi-axial ground motion input. The reference stiffness field presents a defect that suddenly appears in the wall W10 while the initial guess does not perfectly correspond to the healthy reference configuration (10% underestimation). The FE model is made of elastic beam elements and built with the CEA FE simulation software

**Algorithm 1:** Clustered Modified Dual Kalman Filter (for a sampling-based KF structure)

**Initialization:**

- Sliding window, data assimilation time steps $\{t_k\}$
- mCRE tuning parameters: $D_\omega, \alpha, z(\omega)$ and reduced basis
- Initial statistics on parameters: mean $\widehat{\theta}_0$ and covariance $P_0^\theta$
- Noise process and measurements covariance matrices: $Q_\theta, R$

**for** $k = 0 : \infty$ **do**

0) **CRE-based clustering**

Computes the CRE map at the current estimate: $\zeta_i^2(\widehat{\theta}_k)\ \forall\, i \in [\![1; n_\theta]\!]$
Identification of a restricted subset in need of correction $\theta_{R,k},\ R \subset [\![1; n_\theta]\!]$

1) **Generation of samples**

Computation of $\sigma$-points for the restricted parameter set $\theta_{R,k}$

2) **Prediction step**

Computation of *a priori* mean and covariance for $\theta_{R,k}$

3) **Processing new data in the frequency domain**

Extraction of the new data block with the sliding window: $y_k(t)$
Fast Fourier transform for mCRE analysis: $Y_k(\omega)\ \forall \omega \in D_\omega$

4) **Correction step**

Propagation of the $\sigma$-points through the mCRE functional and gradient computation
Correction of predictions to compute *a posteriori* statistics of $\theta_R$
The statistics of $\theta_{R^C,k+1}$ remain unchanged compared to $\theta_{R^C,k}$.

**end**

**Result:** Successive estimates of the parameter vector statistics $(\widehat{\theta}_k, P_k^\theta)$

CASTEM. Following (3), the updated stiffness FE matrix is decomposed in $n_\theta = 6$ or $n_\theta = 12$ non-overlapping subdomains. They follow an intuitive wall/slab decomposition (see Fig. 4).

In order to assess the robustness of the data assimilation algorithms with respect to measurement noise, a white noise of known standard deviation is added to the synthetic measurements. The noise level $\delta$ (in $\%$) is then defined according to the magnitude of the input ground acceleration $\ddot{U}_d$ such that noisy synthetic acceleration data is obtained as follows:

$$\ddot{y}_{noisy}(t) = \ddot{y}(t) + \delta\ \text{std}\left(\ddot{U}_d(t)\right)\eta(t) \tag{13}$$

where $\eta(t)$ is a random Gaussian vector of zero mean and unitary standard deviation.

### 4.2 Comparative study between mCRE-based Kalman filters - procedure, results and discussion

The first objective of this study is to assess which of nonlinear KF structures (UKF, EKF, S3F) is the most appropriate to perform stiffness parameter tracking with MDKF accurately in real-time from discrete acceleration measurements. Various levels of noise are considered $\delta = \{0; 5; 15\}\%$ to assess the robustness to measurement noise. For the sake of conciseness and clarity, we will only present in the forthcoming figures the probability density function

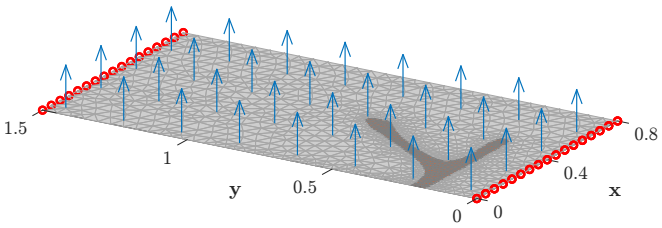


(a) Plane wall with damage defect to identify from sparse acceleration measurements.

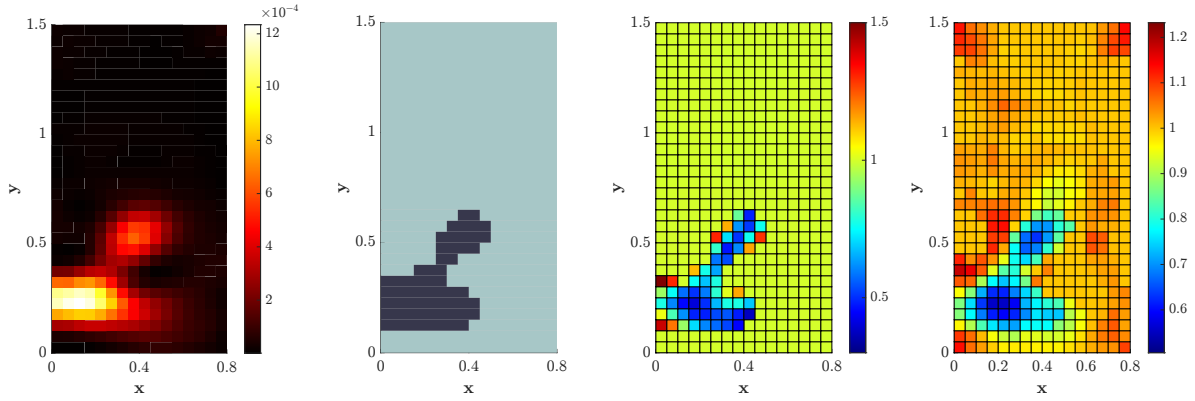

(b) Initial CRE map. (c) CRE-based clustering. (d) Parameter estimate. (e) Parameter estimate without clustering.

Figure 3: Regularizing effect of CRE-based clustering for stiffness identification of a non-convex defect on a plane wall submitted to random ground motion. Acceleration noisy measurements are processed, and CRE-based clustering allows for better parameter estimation with 75% of unchanged parameters - from [11].

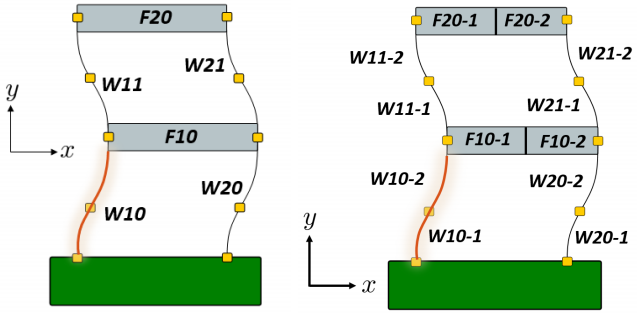


(a) Subdomains labelling and sensors location.

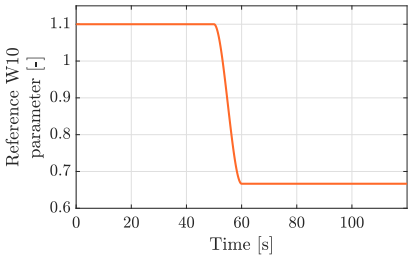


(b) W10 reference stiffness parameter evolution.

Figure 4: Two-story plane frame problem with sensors location (yellow dots) and subdomains.

of subdomain W10, even if all parameters are updated alltogether. A $L_2$-norm misfit error on parameters allows to properly assess the different KFs in terms of accuracy. It is denoted $\epsilon_\theta$ is defined as, :

$$\epsilon_\theta = \frac{\int \left(\widehat{\theta}(t) - \theta^*(t)\right)^2 \mathrm{d}t}{\int \theta^*(t)^2 \mathrm{d}t} \tag{14}$$

| **MDKF framework** | **Reference value** | | |
|---|---|---|---|
| Data sampling frequency | $f_s$ | $=$ | $1000$ Hz |
| Overlapping rate for MDKF windows | $\alpha_{\text{ovlp}}$ | $=$ | $95\%$ |
| mCRE frequency interval | $D_\omega$ | $=$ | $[1\text{ Hz}; 20\text{ Hz}]$ |
| mCRE frequency sampling step | $\Delta f$ | $=$ | $0.1$ Hz |
| Amount of new data per window | $(1-\alpha_{\text{ovlp}})/\Delta f$ | $=$ | $0.1$ s |
| Covariance on parameter state | $Q_\theta$ | $=$ | $10^{-3}I$ |
| Covariance on mCRE | $R$ | $=$ | $10^{-8}$ |
| Initial covariance on parameters | $P_0^\theta$ | $=$ | $0.01I$ |

Table 1: Reference setting parameters of MDKF.

with $\theta^*$ the reference parameter value and $\widehat{\theta}$ the mean estimate provided by KFs. The key results of this study are all stored in Tab. 2, and illustrated in Figure 5. For the reader information, they have been obtained on a standard personal laptop (Intel i5-10310, 8Go RAM).

| | $\delta = 0\%$ (perfect data) | | | $\delta = 5\%$ (noisy) | | | $\delta = 15\%$ (highly-noisy) | | |
|---|---|---|---|---|---|---|---|---|---|
| KF basis | UKF | S3F | EKF | UKF | S3F | EKF | UKF | S3F | EKF |
| $\epsilon_{\text{W10}}$ | 0.0052 | 0.0052 | 0.0083 | 0.0054 | 0.0054 | 0.0111 | 0.0069 | 0.0070 | 0.0198 |
| $\epsilon_{\text{W11}}$ | 0.0001 | 0.0001 | 0.0001 | 0.0005 | 0.0005 | 0.0004 | 0.0017 | 0.0017 | 0.0011 |
| $\epsilon_{\text{W20}}$ | 0.0002 | 0.0002 | 0.0002 | 0.0004 | 0.0004 | 0.0005 | 0.0004 | 0.0004 | 0.0005 |
| $\epsilon_{\text{W21}}$ | 0.0001 | 0.0001 | 0.0001 | 0.0009 | 0.0009 | 0.0015 | 0.0009 | 0.0009 | 0.0015 |
| $\epsilon_{\text{F10}}$ | 0.0004 | 0.0004 | 0.0003 | 0.0007 | 0.0007 | 0.0006 | 0.0007 | 0.0007 | 0.0006 |
| $\epsilon_{\text{F20}}$ | 0.0001 | 0.0001 | 0.0000 | 0.0003 | 0.0003 | 0.0004 | 0.0003 | 0.0003 | 0.0004 |
| Average CPU time per step [s] | 0.22303 | 0.16379 | 0.13590 | 0.21300 | 0.16154 | 0.13137 | 0.21424 | 0.16375 | 0.12753 |

Table 2: Comparison of mCRE-based KFs for stiffness parameter tracking from several datasets. All filters perform in real-time as new assimilated data per iteration last 0.5 seconds.

Several remarks can be made from these results:

- Whatever the KF structure in which the mCRE has been integrated, the tracking of parameters is successfully performed in real-time, with always more than 50% of data assimilation step remaining time to perform other operations online. Even for highly-noisy measurements, the mCRE-based data assimilation framework provides a correct parameter tracking, particularly the well captured fall of W10 stiffness.
- From the error indicator values $\epsilon_\bullet$ displayed in Tab. 2, one can consider the identification of correct quality. The fact that $\epsilon_{\text{W10}}$ is one order of magnitude higher is due to the slight delay at the identification of the sudden change in W10. This delay is not abnormal as it is a direct consequence of the sliding window technique [12].
- Owing to the fact that UKF and S3F produce the exact same estimates [22], Fig. 5a-5c and Fig. 5d-5f are identical. As almost half sigma-points are required for S3F compared to UKF, the analysis of CPU times in Tab. 2 confirms that using S3F $\sigma$-points allows a significant gain on this academical example (30% faster, 8 $\sigma$-points instead of 13 in that case). There is no doubt that this CPU gain will be higher in problems where the parameter space dimension $n_\theta$ is larger. The author thus strongly recommend the systematic use of S3F instead of UKF, as it is as accurate for a lower computational cost.

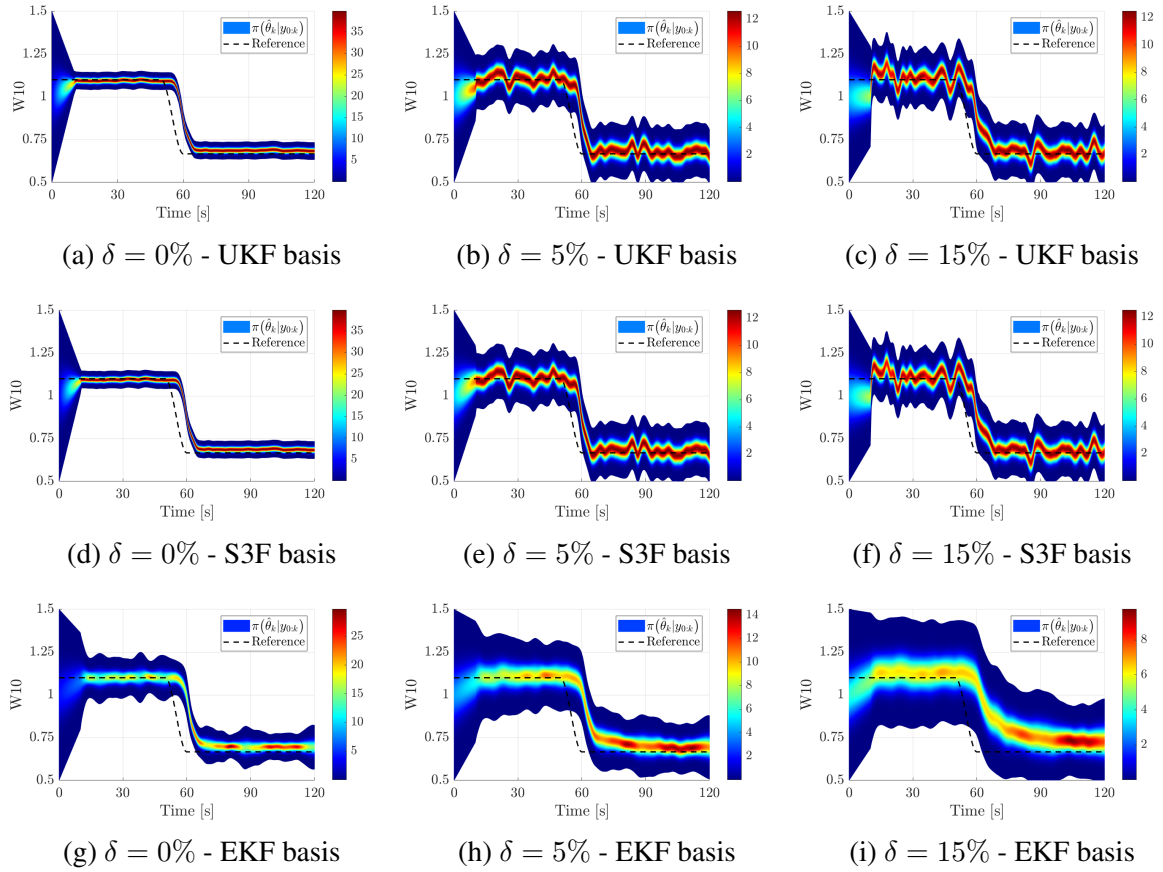


(a) $\delta = 0\%$ - UKF basis (b) $\delta = 5\%$ - UKF basis (c) $\delta = 15\%$ - UKF basis

(d) $\delta = 0\%$ - S3F basis (e) $\delta = 5\%$ - S3F basis (f) $\delta = 15\%$ - S3F basis

(g) $\delta = 0\%$ - EKF basis (h) $\delta = 5\%$ - EKF basis (i) $\delta = 15\%$ - EKF basis

Figure 5: On-the-fly update of W10 stiffness parameter using several mCRE-based KFs.

- EKF-based MDKF benefits from the simplicity of EKF and the parallel computation of mCRE computations to process data faster than $\sigma$-points-based MDKF. However, it also naturally carries the limitations of EKF in terms of accuracy, with the loss of tracking reactivity that appears at high measurement noise levels. Therefore, if EKF-based MDKF is faster, it is also less accurate than mCRE-based sigma-points KFs.

In the end, it appears that S3F-based MDKF is the best compromise between computational cost and accurate estimates. It will thus be chosen as reference mCRE-based KF algorithm.

### 4.3 A proof of concept for the relevance of the clustered MDKF

In this last paragraph, we intend to complete the case study with the validation of the clustered MDKF when trying to update the frame parametrization described by $n_\theta = 12$ non-overlapping subdomains. Having "too numerous" subdomains (as it is the case for damage detection problems) will allow to present a proof of concept of the relevance of the clustered MDKF for large dimensional parameter tracking problems. More specifically, the objective of this study is to assess the ability to recover the expected parameters from simulated acceleration measurements acquired by discrete sensors scattered over the structure (yellow dots in Fig. 4), with particular attention paid to accuracy and CPU time savings compared to standard MDKF. The internal parameters of MDKF used to obtain the forthcoming results are still the ones specified in Tab. 1. In order to avoid falling into local minimas as the initial guess does not match correctly with the expected parameters (10% gaps), the first 10 iterations (over 110) are forced

to update the full set of parameters. Afterwards, the CRE-based clustering automatically drives which parameters have to be updated.

The clustered MDKF is applied to assimilate the same data that has been processed to obtain the results displayed in Fig. 6. Parameter identification results are shown in Fig. 7 and the comparison between CPU times is summarized in Tab. 3.

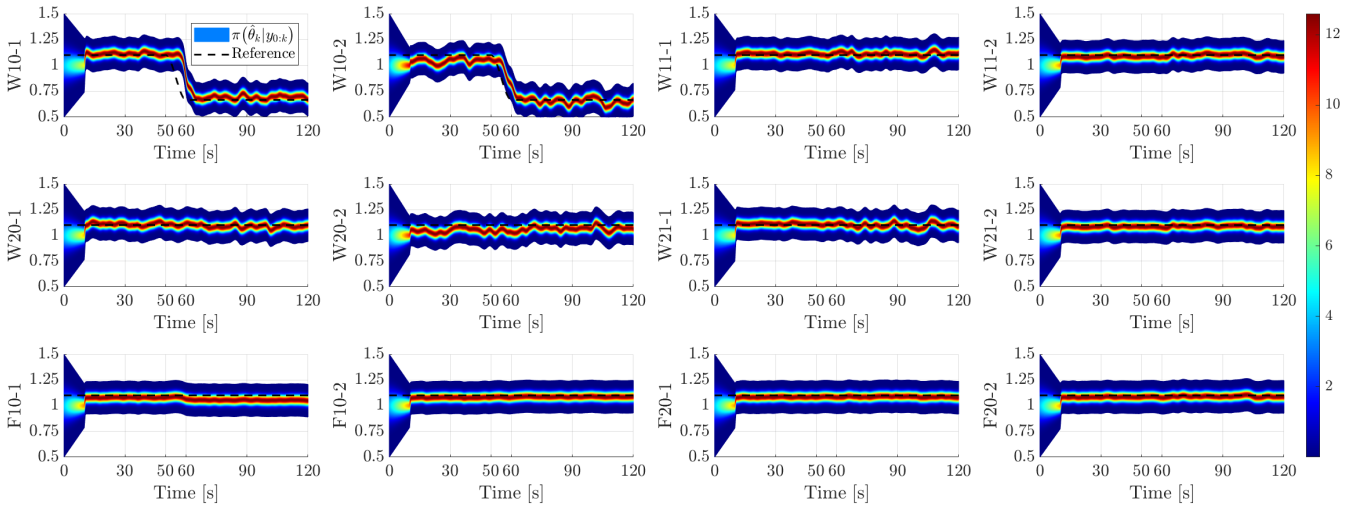


Figure 6: MDKF results of the frame model from noisy measurements ($\delta = 2\%$). Probability density functions are plotted for each of the $n_\theta = 12$ parameters with expected values.

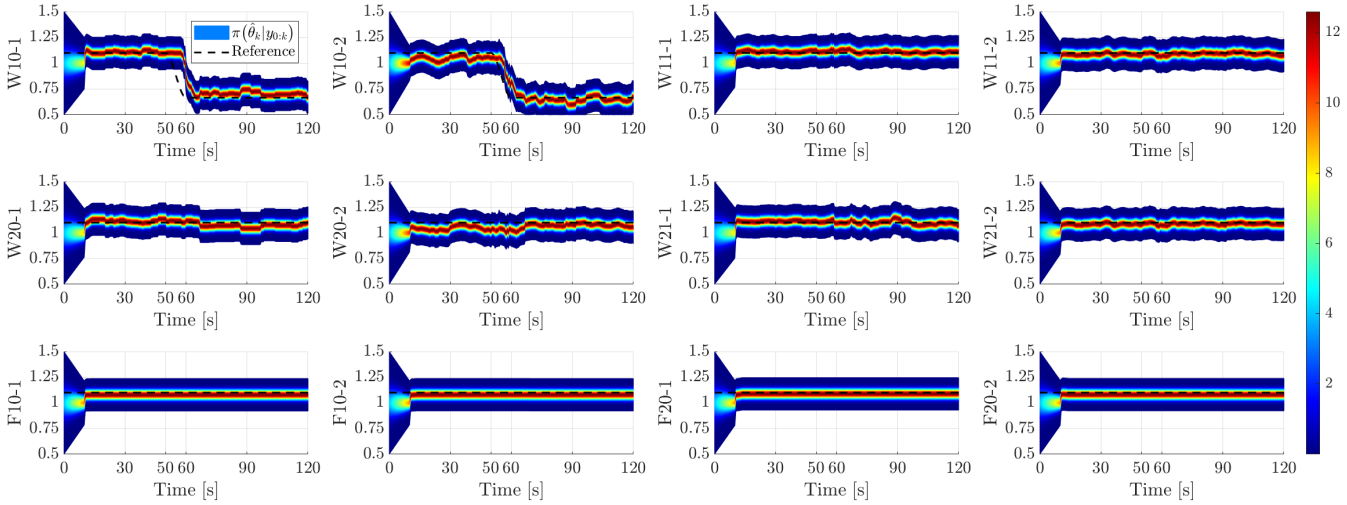


Figure 7: Clustered MDKF results of the frame model from noisy measurements ($\delta = 2\%$). Probability density functions are plotted for each of the $n_\theta = 12$ parameters with expected values.

The analysis of these results allow to conclude that clustered MDKF does not have significant effects on the identification quality of the results by respectively comparing Fig.6-7. Indeed, the noise level and MDKF internal parameters still condition accuracy results, whether the clustering step is present or not.

| **Algorithm** | $n_\theta$ | Average CPU time per iteration |
|---|---|---|
| UKF-based MDKF | 6 | $0.33$ s |
| S3F-based MDKF | 6 | $0.16$ s |
| UKF-based MDKF | 12 | $0.76$ s |
| S3F-based MDKF | 12 | $0.44$ s |
| Clustered UKF-based MDKF | 12 | $0.48$ s (including $0.02$ s for the clustering step) |
| Clustered S3F-based MDKF | 12 | $0.35$ s (including $0.02$ s for the clustering step) |

Table 3: Comparison of CPU time per iteration between MDKF and clustered MDKF to assimilate the same amount of data.

In terms of computational times, it is undeniable that the clustering step is not a time-consuming procedure: only $0.02$ s on the $0.5$ s allowed to process data in real-time. However, it provides a significant speed-up according to the results given in Tab. 3: in most time steps only half of the clusters (the ones located at the bottom of the frame) are updated. The remaining saved time can therefore be spent for DDDAS purposes instead of trying to update low-sensitive or already well-identified parameters (with respect to the CRE). Besides, one should note that only 12 parameters were updated here and that the value of $n_\theta$ does not explictly affect much the required CPU time for clustering. The speedup one can expect when $n_\theta \gg 1$ may thus be even larger than the one observed in this case study.

As a last remark, CPU time comparisons between UKF-based MDKF and S3F-based MDKF have also been done in Tab. 3 in order to show that when combining (i) a KF in which the number of sigma-points is optimized and (ii) an adaptive parametrization of the problem, considerable gains can be made for substantially equivalent precision.

## 5 Conclusion and prospects

In this paper, a new sequential data assimilation method, using the mCRE as an alternative metrics for observations, has been presented and several improvements has been proposed to improve its performance. We discussed and fairly compared possible variants of the MDKF according to the KF structure in which the mCRE functional is embedded, with the conclusion that the mCRE-based S3F is the best compromise between computational cost and estimation accuracy. Finally, an extension of MDKF for partial state update without loss of accuracy was presented. An additional (low-cost) CRE-based clustering step was included in the data assimilation scheme so as to exploit at best the information carried by the model error term of the mCRE observer. The clustering step permits to restrain the amount of updated parameters per iteration, which allows to achieve real-time constraints without losing accuracy, and to save extra-time for post-processing operations in a DDDAS context. A proof of concept from an academic earthquake engineering example allowed to validate the relevance of the proposed MDKF extension and to draw first limitations that are (unsurprisingly) inherent to the mCRE ones.

The MDKF algorithm will be soon reinvested to perform adaptive model-based control in the context illustrated in Fig. 1 to enhance the control of time-evolving systems (*e.g.* damaging structures). The clustered MDKF would be particularly relevant when considering rich/full-field measurements and damage detection problems such as the ones that can occur in structural health monitoring.

## REFERENCES


[1] AQUINO, W., AND BONNET, M. Analysis of the error in constitutive equation approach for time-harmonic elasticity imaging. *SIAM Journal on Applied Mathematics 79*, 3 (Dec. 2019), 822–849. arXiv:1812.03653.

[2] ASTROZA, R., EBRAHIMIAN, H., AND CONTE, J. P. Performance comparison of Kalman-based filters for nonlinear structural finite element model updating. *Journal of Sound and Vibration 438* (Jan. 2019), 520–542.

[3] CHARBONNEL, P.-E. Fuzzy-driven strategy for fully automated modal analysis: Application to the SMART2013 shaking-table test campaign. *Mechanical Systems and Signal Processing 152* (May 2021), 107388.

[4] CHARBONNEL, P.-E., LADEVÈZE, P., LOUF, F., AND LE NOAC'H, C. A robust CRE-based approach for model updating using in situ measurements. *Computers & Structures 129* (Dec. 2013), 63–73.

[5] CHATZI, E. N., CHATZIS, M. N., AND PAPADIMITRIOU, C., Eds. *Robust Monitoring, Diagnostic Methods and Tools for Engineered Systems*. Frontiers Research Topics. Frontiers Media SA, Lausanne, 2020.

[6] CHATZI, E. N., AND SMYTH, A. W. The unscented Kalman filter and particle filter methods for nonlinear structural system identification with non-collocated heterogeneous sensing. *Structural Control and Health Monitoring 16*, 1 (Feb. 2009), 99–123.

[7] CHOUAKI, A. T., LADEVÈZE, P., AND PROSLIER, L. Updating Structural Dynamic Models with Emphasis on the Damping Properties. *AIAA Journal 36*, 6 (1998), 1094–1099. Publisher: American Institute of Aeronautics and Astronautics.

[8] DAREMA, F. Dynamic Data Driven Applications Systems: A New Paradigm for Application Simulations and Measurements. In *Computational Science - ICCS 2004* (Berlin, Heidelberg, 2004), M. Bubak, G. D. van Albada, P. M. A. Sloot, and J. Dongarra, Eds., Lecture Notes in Computer Science, Springer, pp. 662–669.

[9] DERAEMAEKER, A., LADEVÈZE, P., AND LECONTE, P. Reduced bases for model updating in structural dynamics based on constitutive relation error. *Computer Methods in Applied Mechanics and Engineering 191*, 21-22 (Mar. 2002), 2427–2444.

[10] DIAZ, M., CHAMOIN, L., AND CHARBONNEL, P.-E. Robust energy-based model updating framework for random processes in dynamics: application to shaking-table experiments. *Computers and Structures 264*, 106746 (Jan. 2022), 40.

[11] DIAZ, M., CHARBONNEL, P.-E., AND CHAMOIN, L. Fully automated physics-regularized model updating algorithm for vibration-based damage detection from sparse data. *Under review* (2023).

[12] DIAZ, M., CHARBONNEL, P.-E., AND CHAMOIN, L. A new kalman filter approach for structural parameter tracking: Application to the monitoring of damaging structures tested on shaking-tables. *Mechanical Systems and Signal Processing 182* (2023), 109529.

[13] EVENSEN, G. The Ensemble Kalman Filter: theoretical formulation and practical implementation. *Ocean Dynamics 53*, 4 (Nov. 2003), 343–367.

[14] HOSHIYA, M., AND SAITO, E. Structural Identification by Extended Kalman Filter. *Journal of Engineering Mechanics 110*, 12 (Dec. 1984), 1757–1770.

[15] KALMAN, R. E. A New Approach to Linear Filtering and Prediction Problems. *Journal of Basic Engineering 82*, 1 (Mar. 1960), 35–45.

[16] LADEVÈZE, P., AND LEGUILLON, D. Error Estimate Procedure in the Finite Element Method and Applications. *SIAM Journal on Numerical Analysis 20*, 3 (June 1983), 485–509. Publisher: Society for Industrial and Applied Mathematics.

[17] LEFEBVRE, T., BRUYNINCKX, H., AND DE SCHUTTER, J. Kalman filters for non-linear systems: a comparison of performance. *International Journal of Control 77*, 7 (May 2004), 639–653.

[18] MARCHAND, B., CHAMOIN, L., AND REY, C. Real-time updating of structural mechanics models using Kalman filtering, modified constitutive relation error, and proper generalized decomposition: Real-time updating of structural mechanics models. *International Journal for Numerical Methods in Engineering 107*, 9 (Aug. 2016), 786–810.

[19] MARCHAND, B., CHAMOIN, L., AND REY, C. Parameter identification and model updating in the context of nonlinear mechanical behaviors using a unified formulation of the modified Constitutive Relation Error concept. *Computer Methods in Applied Mechanics and Engineering 345* (Mar. 2019), 1094–1113.

[20] MARIANI, S., AND CORIGLIANO, A. Impact induced composite delamination: state and parameter identification via joint and dual extended Kalman filters. *Computer Methods in Applied Mechanics and Engineering 194*, 50-52 (Dec. 2005), 5242–5272.

[21] MARIANI, S., AND GHISI, A. Unscented Kalman filtering for nonlinear structural dynamics. *Nonlinear Dynamics 49*, 1-2 (May 2007), 131–150.

[22] PAPAKONSTANTINOU, K. G., AMIR, M., AND WARN, G. P. A Scaled Spherical Simplex Filter (S3F) with a decreased n + 2 sigma points set size and equivalent 2n + 1 Unscented Kalman Filter (UKF) accuracy. *Mechanical Systems and Signal Processing 163* (Jan. 2022), 107433.

[23] SHEN, G., ZHU, Z., LI, X., LI, G., TANG, Y., AND LIU, S. Experimental evaluation of acceleration waveform replication on electrohydraulic shaking tables: A review. *International Journal of Advanced Robotic Systems 13*, 5 (Sept. 2016), 172988141666253.

[24] VON LUXBURG, U. A tutorial on spectral clustering. *Statistics and Computing 17*, 4 (Dec. 2007), 395–416.

[25] WAGG, D. J., WORDEN, K., BARTHORPE, R. J., AND GARDNER, P. Digital Twins: State-of-the-Art and Future Directions for Modeling and Simulation in Engineering Dynamics Applications. *ASCE-ASME Journal of Risk and Uncertainty in Engineering Systems Part B Mech. Engrg. 6*, 3 (Sept. 2020), 030901.

COMPDYN 2023
9th ECCOMAS Thematic Conference on
Computational Methods in Structural Dynamics and Earthquake Engineering
M. Papadrakakis, M. Fragiadakis (eds.)
Athens, Greece, 12-14 June 2023

# OPTIMISED STRUCTURAL MODELLING FOR INVERSE ANALYSIS PARAMETER IDENTIFICATION RELYING ON DYNAMIC MEASUREMENTS

**Aram Cornaggia[1], Tomasz Garbowski[2], Giuseppe Cocchetti[3], Rosalba Ferrari[1], and Egidio Rizzi[1]**

[1]Department of Engineering and Applied Sciences, Università degli studi di Bergamo
viale G. Marconi 5, 24044 Dalmine (BG), Italy
e-mail: {aram.cornaggia,rosalba.ferrari,egidio.rizzi}@unibg.it

[2] Department of Biosystems Engineering, Poznań University of Life Sciences
Wojska Polskiego 50, 60-627 Poznań, Poland
e-mail: tomasz.garbowski@up.poznan.pl

[3] Department of Civil and Environmental Engineering, Politecnico di Milano
piazza Leonardo da Vinci 32, 20133 Milano (MI), Italy
e-mail: giuseppe.cocchetti@polimi.it

**Abstract.** *In the context of Inverse Analysis in Civil Engineering, parameter identification and model calibration, of a structural system, relying on dynamic measurements, are subjects of a growing research interest. In the present contribution, the topic is tackled with reference both to simplified structural numerical examples and to a specific case study, namely a historical road three-span reinforced concrete arched bridge, with vibrational data previously acquired by standard wired accelerometers on the deck, under operational traffic conditions. In particular, the present work aims at focussing on the identification issues, concerning the definition of a maximum allowable threshold number of sought material parameters (e.g., Young's moduli and mass densities of different structural components), with respect to the amount of available measurement data, and the investigation of the inverse analysis discrepancy function to be optimised, in order to set the intrinsic issue of multiple "realizations", in case of a plain use of modal properties, and in view of forming a well–posed optimisation problem. Structural modelling, sensitivity analysis and numerical optimisation approaches are herein combined toward a robust and efficient identification strategy, to be effectively employed in structural assessment and diagnosis, also with respect to originally available or enriched sets of experimental data. The proposed methodology, and collected results, shall outline an efficient identification procedure, in view of automated inverse analysis, practically oriented to the dynamic assessment and structural diagnosis in the Civil Engineering context, as applied e.g. to strategic bridge infrastructures.*

**Keywords:** Inverse Analysis, Parameter Identification, Structural Identification, Structural Optimisation, Dynamic Modal Measurements, Historic Reinforced Concrete Bridge.

## 1 INTRODUCTION

Inverse Analysis approaches assumed, since several years, a significant role in scientific and engineering research, as a reliable methodology toward parameter identification and model calibration (see, e.g., [1, 2]). Nowadays, a growing interest, supported by computational advancements, is exhibited in the context of both Solid and Structural Mechanics, fostering engineering problem–oriented developments (see, e.g., [3, 4, 5, 6, 7]).

Within such a framework, a complete Inverse Analysis setup may be devised in eight main steps, as described in the following.

- Selection of the parameters to be estimated in the investigated problem, namely choice of the sought quantities to be identified, toward assessment and calibration of the specific behaviour and model.
- Design of the experiment, as the best suitable experimental procedure to collect response data as source of information for a subsequent identification phase.
- Test simulation, by computational modelling, to effectively reproduce the experimental phenomena, in a reliable manner, to evaluate numerical counterparts of experimental measurements.
- Definition of a feasible "search domain", namely of a constrained space of the underlying system parameters, with limits possibly suggested by experts or guidelines, to be adopted within the identification procedure.
- Sensitivity analysis (see, e.g., [8]) of the investigated problem, with respect to the sought parameters, in order to efficiently understand the specific influence of the selected parameters (possibly, to be reduced) on the system behaviour and, specifically, on the observed quantities.
- Formulation of an appropriate "discrepancy function", to be minimised, as a scalar norm between measured and computed quantities, therefore forming a function of the input sought parameters, possibly also accounting for sources of uncertainty.
- Selection and implementation of a minimisation algorithm, in order to handle, in a robust and efficient manner, the foreseen optimisation problem of inverse identification, selecting for instance among mathematical programming methods, evolutive methods or artificial intelligence methods.
- Validation and accuracy checks, developed to test and confirm the effectiveness of the specific devised approach, either on pseudo–experimental (necessary validation condition) or real experimental measurement data.

The current state of the art, in the context of aforementioned Inverse Analysis approaches, presents several contributions, particularly within Industrial Engineering applications, e.g., for material characterisation and diagnosis of metallic structural components [9, 10, 11, 12, 13], for mechanical characterisation of advanced materials [14, 15], and for biomechanical identification [16]. With shared methodologies, in recent years, a growing interest has been exerted for Inverse Analysis also in Civil Engineering context, as, e.g., in material characterisation of concrete structures [17, 18], in bridge and infrastructure analysis [19, 20, 21], and in structural identification [22, 23, 24].

Such a renewed research branch displays significant advantages, by the adoption of the Inverse Analysis methodology, in experimental or operational state measurements of the structure, toward the estimation of modal properties of a structure, specifically by Operational Modal Analysis, as proposed, e.g., in [25, 26, 27, 28, 29, 30, 31]. Pursuing the goals of this research branch, the present paper sets an Inverse Analysis problem based on modal properties, first on a simple archetypal structure and, then, on a specific case study, namely a historical reinforced concrete arched bridge, that is Brivio bridge (1917) [32], located in Northern Italy. The bridge, given its still crucial infrastructural role and historical value, has been subjected, in recent years, to monitoring experimental campaigns and to subsequent response signal processing (see, e.g., [33, 34, 35, 36]) and structural modelling and identification (see, e.g., [37, 38]), as also enquired in the present contribution and in companion work [39].

Within the subject of Inverse Analysis relying on dynamic measurements, the present investigation aims at defining and developing a robust parameter identification procedure, supported by a proper selection of the sought model parameters, the measurement data and the discrepancy function formulation. The main goals of the contribution shall point out to a general guideline procedure, numerically applied on an archetypal structure, to be further investigated on the specific real case study of Brivio bridge, for structural validation, particularly toward understanding the current structural behaviour, and reassuring the associated model calibration/updating, in view of diagnosis and Structural Health Monitoring (SHM) goals.

The article is organised in two main sections, as follows. Section 2 sets the Inverse Analysis problem on a characteristic structural example, analysing the most effective selection of input parameters, measured data and discrepancy function. In subsequent Section 3, account taken of the previously discussed methodological results, an optimised structural modelling and consistent Inverse Analysis approach is investigated with reference to the specific case study of Brivio bridge, toward SHM aims. Furthermore, Section 4 collects closing global observations, highlighting the central role of Inverse Analysis as a reliable general methodology for model calibration and structural assessment, then proposing possible future developments in the context of dynamic modal measurements and processing.

## 2 PARAMETER IDENTIFICATION RELYING ON DYNAMIC MEASUREMENTS: PROBLEM SETUP

According to the implementation stages of an Inverse Analysis problem described in the Introduction, in the current section, the problem setup is first devised and investigated with reference to an archetypal structure, namely a pinned-pinned beam, relying on dynamic modal pseudo–experimental measurements. Advantageously exploiting the basic structural configuration, the reference pseudo–experimental solution and the identification analyses are developed by standard methods of Structural Dynamics, both for uniform beams [40, 41, 42] and stepped beams [42, 43, 44], i.e., with varying material, or geometrical, parameters along the beam axis.

The selection of the discrepancy function, $\omega(\boldsymbol{\theta})$, as the objective function measuring the discrepancy between the description of the numerical model and the real object, to be minimised in order to estimate the sought parameters ($\boldsymbol{\theta}$) of the model, is operated in accordance with previous choice [37], also adopted in companion paper [39]. Consistently, the dynamic modal properties of the structure are considered as mode shapes $\boldsymbol{u}(\boldsymbol{\theta})^i$ and mode frequencies $f(\boldsymbol{\theta})^i$, while the model parameters are selected, for diverse structural elements, as material Young's moduli and/or densities ($\boldsymbol{\theta} = [E_1, \ldots, E_N; \rho_1, \ldots, \rho_N]$). Consequently, the discrepancy function may be written, in vectorial form, by the following equation:

$$\omega(\boldsymbol{\theta}) = \frac{\left(\sum_{i=1}^{n} \left\| \boldsymbol{u}(\boldsymbol{\theta})_{num}^{i} - \boldsymbol{u}_{exp}^{i} \right\|^2\right)^{1/2}}{\|\boldsymbol{u}_{exp}\|} + \frac{\left(\sum_{i=1}^{n} \left( f(\boldsymbol{\theta})_{num}^{i} - f_{exp}^{i} \right)^2\right)^{1/2}}{\|\boldsymbol{f}_{exp}\|} \tag{1}$$

where experimental quantities may equivalently be substituted by pseudo–experimental counterparts.

The investigation of the objective function and Inverse Analysis problem on the archetypal structure is developed either in a two–dimensional parameter space (i.e. uniform beam, parameters $\boldsymbol{\theta} = [E, \rho]$) and in a four–dimensional parameter space (i.e. stepped beam, parameters $\boldsymbol{\theta} = [E_1, E_2, \rho_1, \rho_2]$), leading to the following observations.

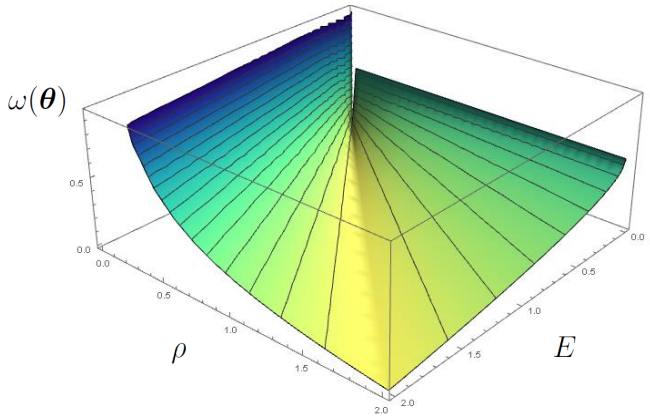


Figure 1: Normalised plot of the objective function, for the archetypal structure, in a 2D parameter space.

- The adoption of modal properties, as a unique source of measurement data, intrinsically brings in a "non–well posedness" condition, in terms of multiple "realisations", in terms of ratios between stiffness and mass properties of a structural system, namely leading to the identification of the correlated parameters, as also shown by the "valley" of minima in the discrepancy function plot for a two–dimensional parameter space (see Figure 1).

- Uniqueness of the optimisation problem may be found, in a two–dimensional parameter space, fixing either one of the two constitutive parameters or their ratio. Therefore, in a practical application case study, additional evaluations or measurements shall be required, to possibly estimate specific mechanical parameters at the local scale (e.g., by material testing) or from global scale measurements devised by experimentally controlled static or dynamic testing of the structure.

- The enlargement of the parameter space size further exhibits a correlation between parameters, namely a possible balancing effects or multiple mathematically equivalent "realisations". Such an observation is graphically depicted in Figure 2, where three–dimensional cross sections of the discrepancy function, analysed in a four–dimensional parameter space, reveal possible "valleys" of minima, also in terms of ratios between stiffness or mass density parameters (Figure 2a and 2b, respectively).

- Therefore, a robust Inverse Analysis procedure shall require complemented measurement data, suitable to assess the behaviour of diverse structural components and capable to estimate, possibly in a sequential procedure, both stiffness and mass density properties, for instance also considering experimental static or dynamic loading tests on the structure.

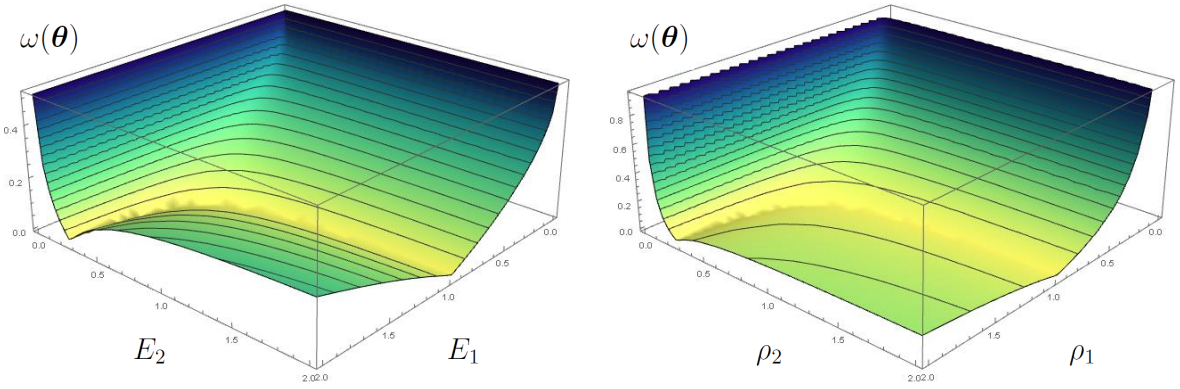


(a) (b)

Figure 2: Three–dimensional cross sections of the objective function, for the archetypal structure, in a 4D parameter space.

## 3 OPTIMISED STRUCTURAL MODELLING ON THE CASE STUDY OF A HISTORICAL CONCRETE BRIDGE

After the prodromal investigation of the Inverse Analysis problem on a simplified archetypal structure, as briefly delineated in Section 2, one aim of the present work is to extend the validity of the methodology toward real application case studies. Therefore, in the current section a specific case study is considered, namely a historical reinforced concrete three–span arched road bridge, namely Brivio bridge (1917) [32]. Such an infrastructure, completed around the end of World War I, still holds nowadays an important role and historical value, while also keeping its key traffic infrastructural functionality, in connecting the provinces of Lecco (Brivio territory) and Bergamo (Cisano Bergamasco territory), in the Lombardia region, Northern Italy, over the Adda river.

The following brief description of Brivio bridge structure (Figures 3 and 4) is here intended for a proper understanding of relevant numerical modelling, sensitivity analysis and Inverse Analysis stages. Detailed information may be found in references [32, 33, 34, 35, 37] and in companion paper [39].

The reinforced concrete road bridge consists of three arched spans, coupled to twin parabolic arches and with tied hanging underneath straight deck. The structure shows full symmetry, with respect to its mid–longitudinal plane, with the following characteristic lengths: average height of the deck above water level equal to 8 m; central span length equal to 44 m; lateral spans pairing to 43.4 m; total length of 130.8 m. Lateral spans (“Span 1” toward Brivio, “Span 3” toward Cisano Bergamasco) are connected to the river banks, while the central one (“Span 2”) is supported by two pillars within the river bed, with pier foundation system set on reinforced concrete piles. The twin parabolic arches of the bridge are designed on a geometry with a 42.80 m span and a 8.00 m rise, being the whole profile symmetric with respect to the vertical axis at half



(a)

(b)

Figure 3: Brivio bridge (1917): (a) downstream view of the road three–span arched bridge crossing the Adda river; Brivio (Lecco) right bank (left), Cisano Bergamasco (Bergamo) left bank (right); (b) zoomed upstream view of Span 1 (toward Brivio). Pictures taken by author E.R. on 7 July and 9 May 2022, respectively.

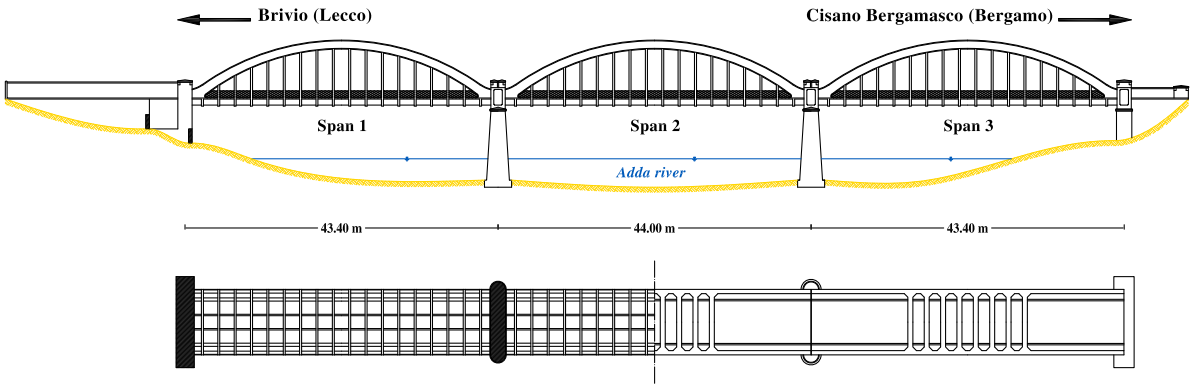


Figure 4: Brivio bridge (1917): schematic representations of downstream front and bottom section–top views.

span. The upper central part of each arch is connected to the respective corresponding one by eight transverse beams, while the bridge deck is linked to the arches, at each side, at each span, through a system of sixteen reinforced concrete hangers. The road deck, 9.2 m wide, provided with two roadway lanes and two cantilever sidewalks, is built by two main longitudinal girders, joined by secondary beam elements and transverse grid beam connections, and completed by a reinforced concrete slab at the deck level.

In order to analyse, for sensitivity and Inverse Analysis, the bridge structure, a linear elastic FEM model of Brivio bridge (single span, referring to Span 1, see Figure 5, originally developed in [37]) is employed, within the software environments of Abaqus finite element code and Python and Matlab self–implemented routines.

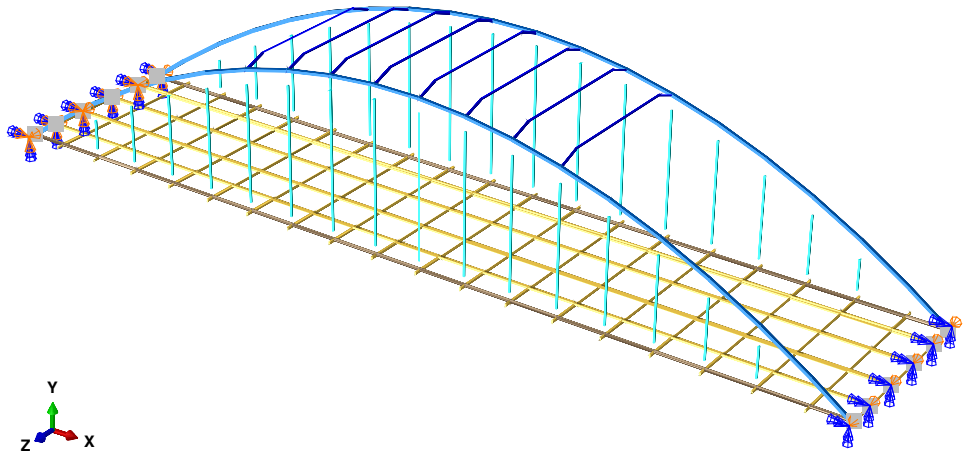


Figure 5: FEM model of Brivio bridge (single span); diverse elements of the structure for sought material parameters identified by colours, boundary conditions by symbols.

The model is developed as a three–dimensional frame structure built by beam finite elements, practically composed as an assembly of five principal structural components: deck, main longitudinal deck girders, arches, hangers and upper transverse beams. Consistently, a constitutive material is associated to each structural type, with regard to Young's moduli and mass densities, as reported in Table 1 and also highlighted in Figure 5. The geometrical characteristics of the FEM model are adopted as in [37] and companion paper [39]. The global computational size and cost of the FEM model is kept rather limited, in view of repetitive runs in Inverse Analysis optimisation loops, summing up to 380 beam elements and 1680 degrees of freedom (254 beam elements for the deck grid, 70 beam elements for the arches, 24 beam elements for the upper beams, deck–hanger and hanger–arch joints modelled by rigid links, added non–structural mass components). The boundary conditions are realised by a simply supported deck configuration, with combined elastic supports (linear spring elements), implemented by two $z$–axis rotational springs, at both extremities, and two translational springs (at $x$–axis, horizontal, and $y$–axis, vertical, respectively set at the second edge (reference coordinate system: $x$ for the longitudinal axis, $y$ for the vertical axis and $z$ for the transverse horizontal axis of the bridge, as also depicted in Figure 5).

To the aim of properties identification, the sought parameters and search domain are selected, according to previous work in [37], as in Table 1, while measured quantities are considered

| Parameter | Lower bound | Upper bound | Reference value |
|---|---|---|---|
| Deck elastic modulus, $E_1$ [GPa] | 24.4 | 45.4 | 34.9 |
| Main longitudinal girders elastic modulus, $E_2$ [GPa] | 24.4 | 45.4 | 34.9 |
| Parabolic arches elastic modulus, $E_3$ [GPa] | 25.0 | 46.4 | 35.7 |
| Hangers elastic modulus, $E_4$ [GPa] | 25.0 | 46.4 | 35.7 |
| Upper transverse beams elastic modulus, $E_5$ [GPa] | 25.0 | 46.4 | 35.7 |
| Deck mass density, $\rho_1$ [kg/m$^3$] | 1710 | 3170 | 2440 |
| Main longitudinal girders mass density, $\rho_2$ [kg/m$^3$] | 1710 | 3170 | 2440 |
| Parabolic arches mass density, $\rho_3$ [kg/m$^3$] | 1710 | 3170 | 2440 |
| Hangers mass density, $\rho_4$ [kg/m$^3$] | 1710 | 3170 | 2440 |
| Upper transverse beams mass density, $\rho_5$ [kg/m$^3$] | 1710 | 3170 | 2440 |
| I–support translational ($x$–axis) spring stiffness, $k_1$ [kN/m] | $10^{-7}$ | $10^{-3}$ | $10^{-5}$ |
| I–support translational ($y$–axis) spring stiffness, $k_2$ [kN/m] | $10^{8}$ | $10^{12}$ | $10^{10}$ |
| I–support rotational spring stiffness, $k_3$ [kNm] | $10^{-7}$ | $10^{-3}$ | $10^{-5}$ |
| II–support rotational spring stiffness, $k_4$ [kNm] | $10^{-7}$ | $10^{-3}$ | $10^{-5}$ |

Table 1: Material input parameters and search domain for the sensitivity analysis and Inverse Analysis problem, based on the FEM model, after [37].

relying on dynamic modal measurements (also consistently with aforementioned discrepancy function, Equation 1), namely investigating structural vibration modes and natural frequencies.

With reference to the base FEM model, in Figure 6, it is possible to observe the first sixteen structural vibration modes of Brivio bridge, clearly involving the whole set of structural components, particularly at deck and arch levels. Such an observation highlights the quest of complete measurements, for several modes, considering both deck beams and arches, in order to fully characterise the current structural behaviour of the bridge and to reliably estimate the associated material parameters. For each vibration mode, the relevant natural frequency, evaluated at the reference parameter values, is reported in Table 2, second column.

Further analyses, developed on the numerical model of Brivio bridge, allow for first additional guidelining observations, as in the following.

- Among the selected modelling parameters, for material and boundary condition standpoints, with reference to the selected measurements and discrepancy function, a major role is assumed by nine mechanical constitutive parameters, namely Young's moduli ($E_1, \ldots, E_5$) and mass densities ($\rho_1, \ldots, \rho_4$) of the structural components, as pointed out by previous sensitivity analyses in [37].

- Global property measurement, such as for natural frequency, may suffer reduced sensitivity effects, causing significant difficulties in specific parameter identification. This particular condition can be observed from the numerical results in Table 2, third and fourth columns, where the global frequency variation is computed for a 30% range variation on parabolic arches elastic modulus ($E_3$) and mass density ($\rho_3$), with variation gain on the results approximately reduced by one order of magnitude.

- According to the previous point, in order to ensure a robust and reliable parameter identification procedure, specific requirements are expected in the measuring stages, namely

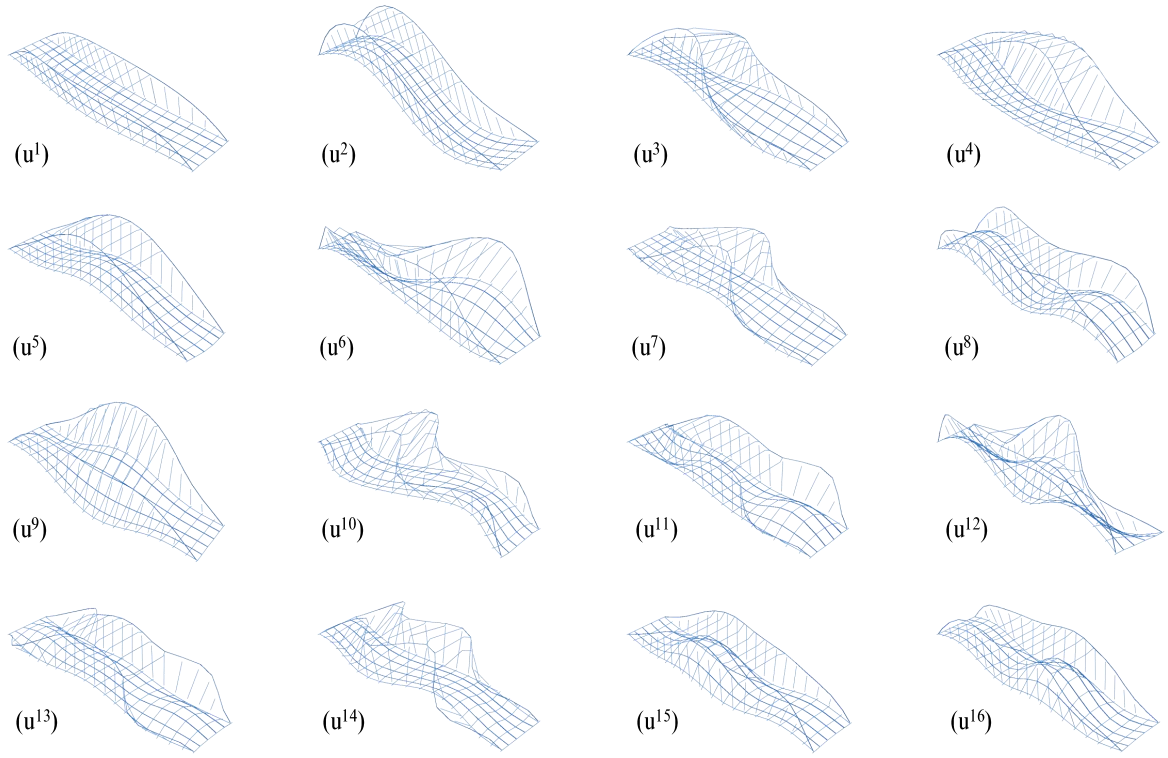


Figure 6: First sixteen vibration modes of the FEM base model (parameters set at reference value) of the bridge.

| Frequency [Hz] | Reference parameter values | $E_3$ +30% | $\rho_3$ +30% | $k_2$ +30% |
|---|---|---|---|---|
| $f^1$ | 2.5312 | +1.28% | −4.22% | +0.07% |
| $f^2$ | 3.7908 | +3.53% | −2.91% | +0.01% |
| $f^3$ | 3.9781 | +4.41% | −5.30% | +0.06% |
| $f^4$ | 5.4889 | +1.52% | −1.42% | +0.08% |
| $f^5$ | 5.8677 | +3.72% | −1.77% | +0.30% |
| $f^6$ | 6.4903 | +1.63% | −4.26% | +0.00% |
| $f^7$ | 7.7809 | +4.66% | −6.00% | +0.18% |
| $f^8$ | 7.8392 | +4.08% | −2.36% | +0.15% |
| $f^9$ | 8.8131 | +2.41% | −2.80% | +0.16% |
| $f^{10}$ | 10.311 | +1.84% | −5.40% | +0.01% |
| $f^{11}$ | 10.325 | +4.03% | −2.99% | +0.10% |
| $f^{12}$ | 10.672 | +3.73% | −4.45% | +0.28% |
| $f^{13}$ | 10.888 | +4.45% | −5.72% | +0.23% |
| $f^{14}$ | 12.139 | +1.38% | −4.10% | +0.06% |
| $f^{15}$ | 12.160 | +4.05% | −1.55% | +0.01% |
| $f^{16}$ | 12.490 | +2.43% | −1.46% | +0.09% |

Table 2: First sixteen natural frequencies of the FEM base model (parameters set at reference values) of the bridge, and percentage variations for possible parameter variations.

significantly reducing noise effects and providing complete structural observations, possibly complemented by local detailing measurements and estimations.

- As a complementary global source of measurement information, vibration modes can carry similar observations, as the above–mentioned for natural frequencies, both on sensitivity effects and complete measurement requirements. As an example, the results reported in Figure 7 graphically represent the numerical results for the second vibration mode of the bridge at the base configuration and for a 30% range variation of various specific parameters, without, however, structurally meaningful mode shape variations.

- The effect of boundary conditions on the mode shapes and natural frequencies appears to be less sensitive with respect to material parameters of bridge structural components (see, also, sensitivity analysis in [37]). However, the influence of mechanical parameters of elastic boundary conditions can rule a contribution approximately of one order of magnitude lower, though not negligible on a global scale structural behaviour (see, for an example, Table 2, fifth column). Therefore, particular attention is required in setting numerical model definition also regarding the boundary conditions, in order to produce a reliable numerical instrument, avoiding biased parameter fitting, in Inverse Analysis methodology for structural assessment and diagnosis.

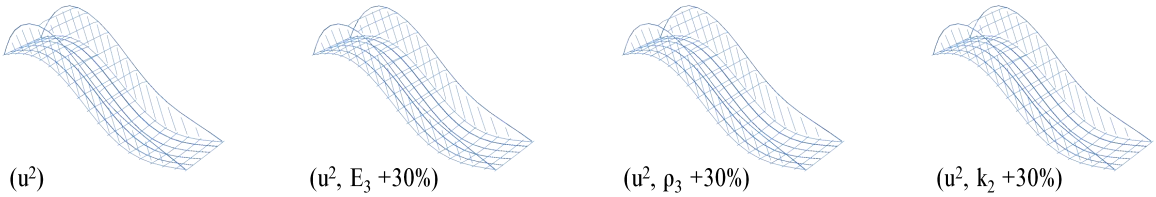


Figure 7: Second vibration mode of the FEM model of the bridge, with parameters set at reference values and with possible variations.

## 4 CONCLUSIONS

In the present paper, an Inverse Analysis methodology for structural parameter identification, relying on dynamic modal measurements, is investigated. The problem has been tackled, by analytical and numerical tools, first on a simplified archetypal structure, for problem setup and understanding, then on a specific application case study, regarding a reinforced concrete historical road arched bridge, Brivio bridge (1917). The global aim of such a research work is the definition of a robust, efficient and reliable methodology, supported by Inverse Analysis approaches, toward parameter identification, structural assessment and diagnosis in Structural Health Monitoring contexts, possibly in automatised operational conditions, for Civil Engineering structures and infrastructures.

In particular, the analysis of an archetypal simplified structure has highlighted the intrinsic "non–well posedness" condition, in terms of multiple "realisations", of the identification problem relying only on dynamic modal measurements, with respect to the estimation of both stiffness and mass density properties. The correlation effect between sought parameters, therefore the non–uniqueness of the solution, has been observed also in a larger size parameter space,

highlighting ratio compensation effects among stiffness values and mass density values of diverse structural parts/components.

Such conditions would consistently require, in order to develop a robust and reliable identification methodology, two specific interventions at experimental design: the introduction of local measurements on material properties, as additional source of information within the discrepancy function; the adoption of a specifically conceived experimental structural testing, either in static or dynamic configurations, under controlled loading conditions, suitable for direct or stepwise identification of structural properties and assessment of current structural behaviour.

The investigation conducted on an archetypal simplified structure has then been extended to the real case study of Brivio bridge (1917), with the adoption of a numerical FEM model, as more case–oriented specifically considered in companion paper [39]. The consideration of dynamic modal measurements, namely vibration structural modes and natural frequencies, further than the features observed on the archetypal structure, has highlighted the reducing sensitivity of global measurements at increasing model complexity and parameter space size. Moreover, the effect of the boundary conditions has presented a strict requirement in the level of refinement and accuracy for the numerical model of the structure, in a high–fidelity detailing, in order to avoid biased parameter fitting, toward, instead, reliable estimation of parameters characteristic of the complete current behaviour of the structure under investigation.

Consistently, in view of a thorough and reliable application of such an Inverse Analysis methodology to a practical case study (i.e. with further investigation on Brivio bridge or to other similar structures), several hints may be proposed as guidelines: the adoption of high precision and reduced noise experimental measurements; the introduction of complete measurements, suitable to observe the full structural behaviour, in particular for non–principal structural elements (e.g. arches, secondary beams and hangers); the definition of an optimised and detailed numerical model, also with respect to the number of selected sought parameters; the enrichment of the identification procedure by introduction of local material testing and/or global measurements under experimentally load controlled conditions, in a static or, preferably, dynamic regime.

The proposed methodology, results and observation of the present paper gather a first insight on the structural identification problem relying on dynamic modal measurements, both from a conceptual point of view and for a preliminary application standpoint on Brivio bridge, specific subject of investigation in companion paper [39]. In future developments, the highlighted hints may lead to subsequent researches, particularly focussing on the "well–posedness" conditions of the Inverse Analysis problem, on the optimisation of the modelling stages, and on the development of a thorough and reliable methodology for parameter estimation within the current context of Structural Dynamics for infrastructures. Such a perspective may, therefore, aim at defining a guideline approach, particularly suitable for identification and prognosis stages in an innovative Structural Health Monitoring framework, supported by algorithmic tools of Inverse Analysis.

## Acknowledgements

The financial support by "*Fondi di Ricerca d'Ateneo ex 60%*", "*STaRs – Azione 2 Visiting e Fellow*" and "*PRIN Life–long optimized structural assessment and proactive maintenance with pervasive sensing techniques*" at the University of Bergamo is gratefully acknowledged.

## REFERENCES


[1] A. Tarantola, *Inverse Problem Theory*. Siam, 2005.

[2] R.C. Aster, B. Bochers, C.H. Thurber, *Parameter Estimation and Inverse Analysis*. Elsevier, 2013.

[3] H.D. Bui, *Inverse Problems in the Mechanics of Materials: An Introduction*. CRC Press, 1994.

[4] Z. Mróz, G.E. Stavroulakis eds., *Parameter Identification of Materials and Structures*. Springer, 2005.

[5] V. Buljak, *Inverse Analysis with Model Reduction*. Springer, 2012.

[6] T. Garbowski, Stochastic model reduction applied to inverse analysis. J.P.M. de Almeida, P. Díez, C. Tiago, N. Parés eds. *VI International Conference on Adaptive Modeling and Simulation (ADMOS 2013)*, Lisbon, Portugal, June 3-5, 2013.

[7] V. Buljak, G. Cocchetti, A. Cornaggia, T. Garbowski, G. Maier, G. Novati, Materials Mechanical Characterizations and Structural Diagnoses by Inverse Analyses. G.Z. Voyiadjis ed. *Handbook of Damage Mechanics*, Springer, 619–642, 2015.

[8] M. Kleiber, H. Antúnez, T.D. Hien, P. Kowalczyk, *Parameter Sensitivity in Nonlinear Mechanics*. Wiley, 1997.

[9] M. Bocciarelli, V. Buljak, C.K.S. Moy, S.P. Ringer, G. Ranzi, An inverse analysis approach based on a POD direct model for the mechanical characterization of metallic materials. *Computational Materials Science*, **95**, 302–308, 2014.

[10] F. Arizzi, E. Rizzi, Elastoplastic parameter identification by simulation of static and dynamic indentation tests. *Modelling and Simulation in Materials Science and Engineering*, **22**, 035017, 2014.

[11] V. Buljak, G. Cocchetti, A. Cornaggia, G. Maier, Assessment of residual stresses and mechanical characterization of materials by "hole drilling" and indentation tests combined and by inverse analysis. *Mechanics Research Communications*, **68**, 18–24, 2015.

[12] V. Buljak, G. Cocchetti, A. Cornaggia, G. Maier, Estimation of residual stresses by inverse analysis based on experimental data from sample removal for "small punch" tests. *Engineering Structures*, **136**, 77–86, 2017.

[13] V. Buljak, G. Cocchetti, A. Cornaggia, G. Maier, Parameter identification in elastoplastic material models by Small Punch Tests and inverse analysis with model reduction. *Meccanica*, **53**, 3815–3829, 2018.

[14] G. Cocchetti, M.R. Mahini, G. Maier, Mechanical characterization of foils with compression in their planes. *Mechanics of Advanced Materials and Structures*, **21**, 853–870, 2014.

[15] V. Buljak, S. Bavier–Romero, A. Kallel, Calibration of Drucker–Prager cap constitutive model for ceramic powder compaction through inverse analysis. *Materials*, **14**, 4044, 2021.

[16] K. Zaborowicz, T. Garbowski, B. Biedziak, M. Zaborowicz, Robust estimation of the chronological age of children and adolescents using tooth geometry indicators and POD–GP. *International Journal of Environmental Research and Public Health*, **19**, 2952, 2022.

[17] T. Garbowski, G. Maier, G. Novati, Diagnosis of concrete dams by flat–jack tests and inverse analyses based on proper orthogonal decomposition. *Journal of Mechanics of Materials and Structures*, **6**, 181–202, 2011.

[18] T. Gajewski, T. Garbowski, Calibration of concrete parameters based on digital image correlation and inverse analysis. *Archives of Civil and Mechanical Engineering*, **14**, 170–180, 2014.

[19] D. Ribeiro, R. Calçada, R. Delgado, M. Brehm, V. Zabel, Finite element model updating of a bowstring–arch railway bridge based on experimental modal parameters. *Engineering Structures*, **40**, 413–435, 2012.

[20] C. Bendon, M. Dilena, A. Morassi, Ambient vibration testing and structural identification of a cable–stayed bridge. *Meccanica*, **51**, 2777–2796, 2016.

[21] T. Garbowski, A. Pożarycki, Multi–level backcalculation algorithm for robust determination of pavement layers parameters. *Inverse Problems in Science and Engineering*, **25**, 674–693, 2017.

[22] B. Miller, Application of neural networks for structure updating. *Computer Assisted Mechanics and Engineering Sciences*, **18**, 191–203, 2011.

[23] F. Shabbir, P. Omenzetter, Model updating using genetic algorithms with sequential technique. *Engineering Structures*, **120**, 166–182, 2016.

[24] M. Crognale, V. Gattulli, A. Paolone, F. Potenza, A damage identification procedure for steel truss. A. Carcaterra, A. Paolone, G. Graziani eds. *Proceedings of XXIV AIMETA Conference 2019 (AIMETA 2019)*, Roma, Italy, September 15-19, 2020.

[25] J.E. Mottershead, M.I. Friswell, Model updating in structural dynamics: A survey. *Journal of Sound and Vibration*, **167**, 347–375, 1993.

[26] E. Reynders, System identification methods for (Operational) Modal Analysis: Review and comparison. *Archives of Computational Methods in Engineering*, **19**, 51–124, 2012.

[27] C. Rainieri, G. Fabbrocino, *Operational Modal Analysis of Civil Engineering Structures*. Springer, 2014.

[28] F. Pioldi, R. Ferrari, E. Rizzi, Output–only modal dynamic identification of frames by a refined FDD algorithm at seismic input and high damping. *Mechanical Systems and Signal Processing*, **68–69**, 265–291, 2016.

[29] F. Pioldi, R. Ferrari, E. Rizzi, Earthquake structural modal estimates of multi–storey frames by a refined Frequency Domain Decomposition algorithm. *JVC/Journal of Vibration and Control*, **23**, 2037–2063, 2017.

[30] F. Pioldi, R. Ferrari, E. Rizzi, Seismic FDD modal identification and monitoring of building properties from real strong–motion structural response signals. *Structural Control and Health Monitoring*, **24**, e1982, 2017.

[31] R. Cardoso, A. Cury, F. Barbosa, A robust methodology for modal parameters estimation applied to SHM. *Mechanical Systems and Signal Processing*, **95**, 24–41, 2017.

[32] L. Santarella, E. Miozzi, *Ponti Italiani in Cemento Armato (in Italian)*. Hoepli, 1948.

[33] R. Ferrari, D. Froio, E. Chatzi, C. Gentile, F. Pioldi, E. Rizzi, Experimental and numerical investigations for the structural characterization of a historic RC arch bridge. M. Papadrakakis, V. Papadopoulos, V. Plevris eds. *5th ECCOMAS Thematic Conference on Computational Methods in Structural Dynamics and Earthquake Engineering*, Crete Island, Greece, May 25-27, 2015.

[34] R. Ferrari, F. Pioldi, E. Rizzi, C. Gentile, E. Chatzi, R. Klis, E. Serantoni, A. Wieser, Heterogeneous sensor fusion for reducing uncertainty in structural health monitoring. M. Papadrakakis, V. Papadopoulos, G. Stefanou eds. *1st ECCOMAS Thematic Conference on Uncertainty Quantification in Computational Sciences and Engineering (UNCECOMP 2015)*, Crete Island, Greece, May 25-27, 2015.

[35] R. Ferrari, F. Pioldi, E. Rizzi, C. Gentile, E. Chatzi, E. Serantoni, A. Wieser, Fusion of wireless and non-contact technologies for the dynamic testing of a historic RC bridge. *Measurement Science and Technology*, **27**, 124014, 2016.

[36] A. Cornaggia, R. Ferrari, M. Zola, E. Rizzi, C. Gentile, Signal processing methodology of response data from a historical arch bridge toward reliable modal identification. *Infrastructures*, **7**, 74, 2022.

[37] R. Ferrari, D. Froio, E. Rizzi, C. Gentile, E. Chatzi, Model updating of a historic concrete bridge by sensitivity and global optimization–based Latin hypercube sampling. *Engineering Structures*, **1**, 139–160, 2019.

[38] G. Zonno, C. Gentile, Assessment of similar reinforced concrete arch bridges by Operational Modal Analysis and model updating. *Lecture Notes in Civil Engineering*, **156**, 853–868, 2021.

[39] T. Garbowski, G. Cocchetti, A. Cornaggia, R. Ferrari, E. Rizzi, Inverse analysis investigation by Gaussian Processes optimisation of a historical concrete bridge relying on dynamic modal measurements. M. Papadrakakis, M. Fragiadakis eds. *9th ECCOMAS Thematic Conference on Computational Methods in Structural Dynamics and Earthquake Engineering (COMPDYN 2023)*, Athens, Greece, June 12-14, 2023.

[40] R.W. Clough, J. Penzien, *Dynamics of Structures*. Computer & Structures, Inc., 1995.

[41] A.K. Chopra, *Dynamics of Structures*. Prentice Hall, 2012.

[42] C.Y. Wang, C.M. Wang, *Structural vibration*. CRC Press, 2014.

[43] N.J. Taleb, E.W. Suppiger, Vibration of stepped beams. *Journal of the Aerospace Sciences*, **28**, 295–298, 1961.

[44] S.K. Jang, C.W. Bert, Free vibration of stepped beams: exact and numerical solutions. *Journal of Sound and Vibration*, **130**, 342–346, 1989.

COMPDYN 2023
9th ECCOMAS Thematic Conference on
Computational Methods in Structural Dynamics and Earthquake Engineering
M. Papadrakakis, M. Fragiadakis (eds.)
Athens, Greece, 12-14 June 2023

# INVERSE ANALYSIS INVESTIGATION BY GAUSSIAN PROCESSES OPTIMISATION OF A HISTORICAL CONCRETE BRIDGE RELYING ON DYNAMIC MODAL MEASUREMENTS

**Tomasz Garbowski[1], Giuseppe Cocchetti[2], Aram Cornaggia[3], Rosalba Ferrari[3], and Egidio Rizzi[3]**

[1]Department of Biosystems Engineering, Poznań University of Life Sciences
Wojska Polskiego 50, 60-627 Poznań, Poland
e-mail: tomasz.garbowski@up.poznan.pl

[2] Department of Civil and Environmental Engineering, Politecnico di Milano
piazza Leonardo da Vinci 32, 20133 Milano (MI), Italy
e-mail: giuseppe.cocchetti@polimi.it

[3] Department of Engineering and Applied Sciences, Università degli studi di Bergamo
viale G. Marconi 5, 24044 Dalmine (BG), Italy
e-mail: {aram.cornaggia,rosalba.ferrari,egidio.rizzi}@unibg.it

**Abstract.** *In the broad field of Inverse Analysis and Structural Identification, it is nowadays of a large interest the study of Gaussian Processes, as a reliable and efficient optimisation method, particularly helpful toward the identification of a global optimum point, under the conditions of complicated functions to be optimised. In the present contribution, a specific case study is considered, focusing on a historical road reinforced concrete arched bridge, located in Northern Italy, employing dynamic modal properties, deciphered from in-situ measurements, previously acquired under operational traffic conditions, by a standard wired accelerometer system, placed at the deck level. Aiming at the identification and diagnosis of the bridge structure, three main methodological steps are herein considered: the adoption of a FEM model of the structure (in the linear dynamic framework), the definition of an appropriate discrepancy function, based on measured and numerically computed quantities (natural frequencies and mode shapes of the bridge), and the investigation of such a discrepancy function, toward a consistent selection of an optimisation strategy for the identification of sought parameters (Young's moduli and mass densities of diverse elements of the structure). The presented developments, within the framework of methodological optimisation approach by Gaussian Processes, and achieved results display a rather efficient perspective, with reference to the considered case study, toward inverse analysis for structural diagnosis, in the context of strategic (historical) infrastructures.*

**Keywords:** Inverse Analysis, Structural Identification, Gaussian Processes Optimisation, Dynamic Modal Measurements, Historic Reinforced Concrete Bridge.

## 1 INTRODUCTION

In a Structural Identification context, it is nowadays of a large and growing interest the possibility to effectively estimate model parameters, starting from experimental measurements, toward reliable model calibration, for subsequent employment and predictions. Within general and various approaches (see, e.g., [1, 2]), a significant relevance is assumed by Gaussian Processes, employable toward the Inverse Analysis goal as optimisation tools, particularly advantageous, from a computational and robustness point of view, to tackle complicated identification problems featuring local minima difficulties (see, e.g.,[3, 4, 5, 6, 7]). Such approaches have been proven to be particularly efficient in various analyses, regarding different engineering application fields, such as Environmental Engineering (see, e.g., [8]) and Biomechanical Engineering (see, e.g., [9]).

Classical Inverse Analysis problems are usually tackled also in Civil Engineering research and applications, e.g. toward the identification of mechanical properties of structural elements, for design or diagnosis purposes. In this field, the suitable adoption of in situ testing and consistent computational modelling, and their reliable combination, represent a fundamental step together with numerical optimisation for robust and high quality parameter estimations (see, e.g., at a local structural scale [10, 11] or at a global structural scale [12, 13, 14]). Within Civil Engineering application fields, the dynamic testing of structures in regular operative conditions plays a significant role toward Structural Health Monitoring purposes. Such research branch strictly correlates Inverse Analysis and Structural Identification during vibration experiments or operational state measurements of the structure, aiming at the estimation of modal properties of a structure by Operational Modal Analysis, as proposed, e.g., in [15, 16, 17, 18, 19, 20, 21, 22, 23].

In combination of innovative Inverse Analysis, based on Gaussian Processes optimisation, and dynamic modal input measurements, the present paper develops an investigation toward model calibration in a Structural Dynamics context for a Reinforced Concrete bridge. Specifically, the considered case study focuses on a historical reinforced concrete arched bridge, Brivio bridge, located in Northern Italy [24]. The bridge, both for hits historical value and its crucial, currently active, infrastructural role, has recently been the subject of a thorough study supported by experimental campaigns, followed by response signal processing and deciphering (see, e.g., [25, 26, 27, 28]) and by property identification, model calibration and structural diagnosis (see, e.g., [29, 30, 31, 32]).

The main goals of the present work aim at defining a complete and robust Inverse Analysis procedure able to efficiently tackle a complex structural identification problem relying on dynamic modal measurements only, taking advantage of a global optimisation approach, as provided by Gaussian processes. With specific reference to the considered case study, the investigation is devised for an efficient and automated methodology toward structural diagnosis or current operative condition assessment. Moreover, from a more general standpoint, the analysis procedure may be extended, either as a methodological guideline and application approach, to related structures in Civil Engineering research fields, combined to Structural Health Monitoring purposes.

The paper is organised as follows. In Section 2 the methodological approach adopted for Inverse Analysis is presented, focusing both on the Gaussian Processes strategy (Section 2.1) and on the specific selection of objective function to be investigated (Section 2.2). Section 3 describes the selected case study, namely Brivio bridge, from the structural, modelling and experimental testing standpoints. As an application of the proposed approach to the specific case

study, in Section 4, the main results of the developed analyses are collected and discussed, providing relevant comments. Furthermore, general remarks are outlined in Section 5, gathering global observations and proposing possible future research perspectives, toward achieving effective Inverse Analysis procedures.

## 2 INVERSE ANALYSIS INVESTIGATION RELYING ON DYNAMIC MODAL MEASUREMENTS

According to the aims aforementioned in the Introduction, in the current section, the proposed methodology is discussed from a general point of view, both for the selected optimisation approach, namely Gaussian Processes (Section 2.1), and for a proper choice of the objective function, to be minimised within an Inverse Analysis strategy, specifically conceived to rely only on dynamic modal measurements, toward structural mechanical parameter estimation (Section 2.2).

### 2.1 Methodological optimisation approach by Gaussian Processes

Gaussian Processes represent a reliable and efficient optimisation method, particularly helpful toward the identification of a global minimum point, under conditions of severely complicated functions to be optimised. In the current section, a brief theoretical introduction to the approach is provided; further details may be found, e.g., in [3, 4, 5, 6], also illustrated by applications, e.g., in [8, 9].

Gaussian Processes can be illustrated by a linear regression model, which consists of a combination between a linear function of model parameter vector $\boldsymbol{w}$ and a non–linear function of input data vector $\boldsymbol{x}$:

$$y(\boldsymbol{w}, \boldsymbol{x}) = \sum_{m=1}^{M} w_m \varphi_m(\boldsymbol{x}) \tag{1}$$

where $\varphi_m(\boldsymbol{x})$ is a fixed set of basis functions of the input data variables (e.g., polynomial or radial basis functions [33, 34]).

For $N$ given learning training patterns $(\boldsymbol{x}_n, t_n)$, being $\boldsymbol{x}_n$ the input vector and $t_n$ the observation response value for $n = 1, \ldots, N$, model parameter vector $\boldsymbol{w}$ of the linear combination may be obtained by the penalised least–squares method, namely:

$$\boldsymbol{w} = (\boldsymbol{\Phi}^{\mathrm{T}}\boldsymbol{\Phi} + \alpha \boldsymbol{I})^{-1}\boldsymbol{\Phi}^{\mathrm{T}}\boldsymbol{t} \tag{2}$$

where $\boldsymbol{\Phi}_{N\times M}$ is a method design matrix, with elements defined as $\varphi_m(\boldsymbol{x}_n)$, and $\boldsymbol{I}$ is the identity matrix of order $M$. Regularisation parameter $\alpha$ (usually called hyperparameter, in the process jargon) can be computed by using a validation set or by maximising the evidence of dataset $p(\boldsymbol{t}|\alpha)$, with respect to $\alpha$, within a Bayesian inference framework [5].

The Gaussian Process model shall consistently be derived by reformulating the linear model in terms of a dual representation, where the learning process is achieved by a minimisation of a regularised error, defined through a $N \times N$ symmetric Gram matrix:

$$\boldsymbol{K} = \boldsymbol{\Phi}\boldsymbol{\Phi}^{\mathrm{T}} = \boldsymbol{k}(\boldsymbol{x}, \boldsymbol{x}') \tag{3}$$

where elements of the matrix correspond to a kernel function $k(\boldsymbol{x}, \boldsymbol{x}')$. Such definition allows for a prediction associated to a new input vector $\boldsymbol{x}^*$, namely:

$$GP(\boldsymbol{x}^*|\boldsymbol{x}, \boldsymbol{t}, \alpha) = \boldsymbol{k}_*(\boldsymbol{x}, \boldsymbol{x}^*)^{\mathrm{T}}(\boldsymbol{K} + \alpha \boldsymbol{I})^{-1}\boldsymbol{t} \tag{4}$$

where $\boldsymbol{k}_*(\boldsymbol{x}, \boldsymbol{x}^*)$ holds the role of a covariance vector between a new input $\boldsymbol{x}^*$ and the whole set of other inputs.

Therefore, a Gaussian Process approach may be interpreted, according to Bayesian theory, as a dual representation of a linear combination model, while the kernel function may be conceived as a covariance function. Consistently, the regression model allows for the prediction of target variable $y(\boldsymbol{x}^*)$, for each new input vector $\boldsymbol{x}^*$. The evaluation of conditional distribution $p(y|\boldsymbol{t})$, associated to Gaussian Process, requires the definition of relevant mean and covariance, as:

$$\bar{\boldsymbol{x}^*} = \boldsymbol{k}^{\mathrm{T}}\boldsymbol{C}{-}1\boldsymbol{t} \tag{5}$$

$$\sigma^2(\boldsymbol{x}^*) = \bar{\boldsymbol{x}^*} - \boldsymbol{k}^{\mathrm{T}}\boldsymbol{C}{-}1\boldsymbol{k} \tag{6}$$

$$\boldsymbol{C}(\boldsymbol{x}, \boldsymbol{x}') = \boldsymbol{K} + \frac{1}{\beta}\boldsymbol{I} \tag{7}$$

where $\beta$ is the variance parameter of the target distribution and $\boldsymbol{C}_{N\times N}$ is the covariance matrix, defining likelihood of input $\boldsymbol{x}$ and $\boldsymbol{x}'$, which should give rise to strongly correlated values of $y(\boldsymbol{x})$ and $y(\boldsymbol{x}')$ in the output space.

Any function suitable to generate a specific non–negative covariance matrix can be used as a covariance kernel function for any ordered set of input vectors; a stationary, non–isotropic squared exponential covariance function may be selected, as given by:

$$k(\boldsymbol{x}, \boldsymbol{x}') = \nu \exp\left(-\frac{1}{2}\sum_{m=1}^{M}\gamma_m(x_m - x'_m)^2\right) + b \tag{8}$$

where $\nu$ controls the vertical scale of the problem, $\gamma_m$ provides a different scaling factor for each $m$–th dimension, $b$ represents the deviation control factor. Such hyperparameters display a rather important role, directly related to the model sensitivity with respect to the input parameters, therefore allowing to measure the importance of the input parameters.

The definition of a covariance function allows for the Gaussian Process prediction of new input vectors, provided that hyperparameters are effectively calibrated, e.g. by the maximisation of a log–likelihood function:

$$\boldsymbol{\delta} = [\beta, \nu, \gamma_1, \ldots, \gamma_M, b]^{\mathrm{T}} \tag{9}$$

$$\log p(\boldsymbol{t}|\boldsymbol{\delta}) = \frac{1}{2}\log|\boldsymbol{C}| - \frac{1}{2}\boldsymbol{t}\boldsymbol{C}^{-1}\boldsymbol{t} - \frac{N}{2}\log 2\pi \tag{10}$$

as possibly efficiently optimised by gradient based algorithms (e.g., a Levenberg–Marquart Algorithm or a Trust Region Algorithm).

### 2.2 Study on the objective function

In a Inverse Analysis approach, a fundamental step is the proper selection of an objective function $f(\boldsymbol{\theta})$, as a measure of the discrepancy between the numerical model and the real object; therefore, the minimisation of such a function shall lead to obtain the sought parameters ($\boldsymbol{\theta}$) of the model.

In the present study, according to a previous selection [29], the objective function is based on dynamic modal properties of the structure under consideration (mode shapes $\boldsymbol{u}(\boldsymbol{\theta})^i$ and mode frequencies $\omega(\boldsymbol{\theta})^i$), while the sought parameters are selected as material Young's moduli and densities of diverse structural elements ($\boldsymbol{\theta} = [E_1, \ldots, E_N, \rho_1, \ldots, \rho_M]$). Consequently, the discrepancy function consists of a vector of differences between the calculated eigenvectors, i.e. mode shapes of the structure ($\boldsymbol{u}(\boldsymbol{\theta})^i_{num}$), and eigenvalues, i.e. related to modal frequencies ($\omega(\boldsymbol{\theta})^i_{num}$), of the model and, respectively, eigenvectors ($\boldsymbol{u}^i_{exp}$) and eigenvalues ($\omega^i_{exp}$) obtained from experiments on a real object, namely in one possible mathematical form:

$$f(\boldsymbol{\theta}) = \frac{\left(\sum_{i=1}^{n} \left\| \boldsymbol{u}(\boldsymbol{\theta})^i_{num} - \boldsymbol{u}^i_{exp} \right\|^2\right)^{1/2}}{\|\boldsymbol{u}_{exp}\|} + \frac{\left(\sum_{i=1}^{n} \left(\omega(\boldsymbol{\theta})^i_{num} - \omega^i_{exp}\right)^2\right)^{1/2}}{\|\boldsymbol{\omega}_{exp}\|} \tag{11}$$

The proper matching correspondence for eigenvectors and eigenvalues with real counterparts may be found by Modal Assurance Criterion (MAC) computations [35], also improved by a priori (i.e., before objective function evaluation) pairing, ensuring a regularisation effect:

$$\mathrm{MAC}_{ij} = \left(\frac{\boldsymbol{u}(\boldsymbol{\theta})^i_{num}}{\|\boldsymbol{u}(\boldsymbol{\theta})^i_{num}\|}\right)^{\mathrm{T}} \left(\frac{\boldsymbol{u}^j_{exp}}{\|\boldsymbol{u}^j_{exp}\|}\right) \tag{12}$$

In order to further deepen the study on the objective function, to allow for better computational performance of the minimisation algorithm, in view of adoption of Gaussian Processes, a second definition of discrepancy function is conceived, providing an additional contribution to Equation (11), namely:

$$f^*(\boldsymbol{\theta}) = f(\boldsymbol{\theta}) + F \left| \frac{\sum_{j=1}^{m} v_j \rho_j}{\bar{\rho}} - 1 \right| \tag{13}$$

where $F$ acts as a penalty coefficient, $v_j$ is the ratio of the volume for a given material structural element to the volume of the entire structure, and $\bar{\rho}$ is an average reference material mass density.

In following Section 4, the results of the study on the objective function are presented, highlighting the differences and advantages with respect to each choice of the discrepancy function, either by Equation (11) or Equation (13), with the aim to achieve an effective adoption of Gaussian Processes as an Inverse Analysis optimisation approach.

## 3 CASE STUDY: A HISTORICAL CONCRETE BRIDGE

The case study considered in the present work refers to a specific road infrastructure: Brivio bridge, a historical reinforced concrete three–span arched bridge [24]. The bridge, built in 1917, displays a significant historical and structural value, and currently preserves its full daily



Figure 1: Brivio bridge (1917): downstream view of the road three–span arched bridge crossing the Adda river; Brivio (Lecco) right bank (left), Cisano Bergamasco (Bergamo) left bank (right). Picture taken by author E.R. on 7 July 2022.

traffic infrastructural functionality, then keeping a key role in the local territory, between Brivio (province of Lecco) and Cisano Bergamasco (province of Bergamo), in the Lombardia region, Northern Italy, over the Adda river (Figure 1).

In the current section, brief descriptions of Brivio bridge (Figure 2) from a structural standpoint, of the developed FEM model (Figure 3) and of a previously carried out experimental campaign are provided, for a proper understanding of the Inverse Analysis procedure (source reference and detailed information may be found in [24, 25, 26, 27, 29]).

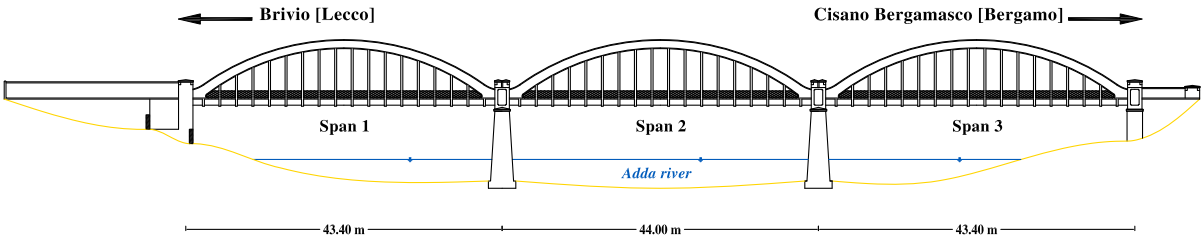


Figure 2: Brivio bridge (1917): schematic representation of downstream front.

The reinforced concrete road bridge consists of three arched spans, supported by characteristic twin parabolic arches and with hanging underneath straight deck. The structure shows full symmetry, with respect to its mid–longitudinal plane. The average height of the deck is about 8 m above water level (Adda river, flowing out of the Lecco branch of Como lake and going down toward the Po valley). The central span, supported by two pillars in the bed of the river, is 44 m long, while the lateral spans, connected to the river banks, are 43.4 m long, summing up to a total length of 130.8 m (in the sequel, for the sake of simplicity: “Span 1” for the lateral span toward Brivio, “Span 2” for the central one, “Span 3” for the lateral span toward Cisano Bergamasco, as also shown in Figure 2). The twin parabolic arches of the bridge are designed on a geometry with a 42.80 m span and a 8.00 m rise. The cross section of each arch structural element displays a rectangular shape, built with a constant width (0.60 m) and a variable height (from 1.37 m, at the impost, to 1.25 m, at the crown), being the whole profile of each arch symmetric, with respect to the vertical axis at half span. Each arch is connected to the corresponding other, on their upper central part, by eight transverse beams, and to the bridge

deck through a system of sixteen reinforced concrete hangers (at each side, at each span), with a rectangular cross section (0.32 m × 0.60 m). The road deck is 9.2 m wide, as designed for two roadway lanes, contoured by two sidewalks (each 0.8 m wide), built as cantilevers. Two main longitudinal girders (section 0.45 m × 1.00 m) are placed in each span of the bridge, at a respective transverse distance of 8.60 m, and are joined by further secondary beam elements (section 0.20 m × 0.55 m) installed at a distance equal to 2 m, symmetrically located with respect to the vertical longitudinal plane of the bridge; between this girder system, transverse grid beam connections (section 0.30 m × 0.75 m) are employed, approximately every 2.30 m. Such grid substructure is completed, at the deck level, by a reinforced concrete slab, with a thickness of 0.15 m. The intermediate supports of the spans, inside the river bed, are constituted by two concrete piers, built with a tapered cross section (maximum dimensions, at the base, equal to 12.8 m × 3.8 m, respectively in the transverse and longitudinal directions). The pier foundation system is set on forty–eight reinforced concrete piles (square cross section with a 0.35 m side), with a driving depth ranging from 13 m to 16 m. Supporting reinforced concrete slabs (height equal to 1 m) are placed above both the intermediate piers and the abutments.

Consistently with the above–provided synoptic technical description, a linear elastic FEM model of Brivio bridge (single span, referring to Span 1, see Figure 3) is adopted, as originally developed in [29], employing the Abaqus finite element code, then combined with Python and Matlab self–implemented routines.

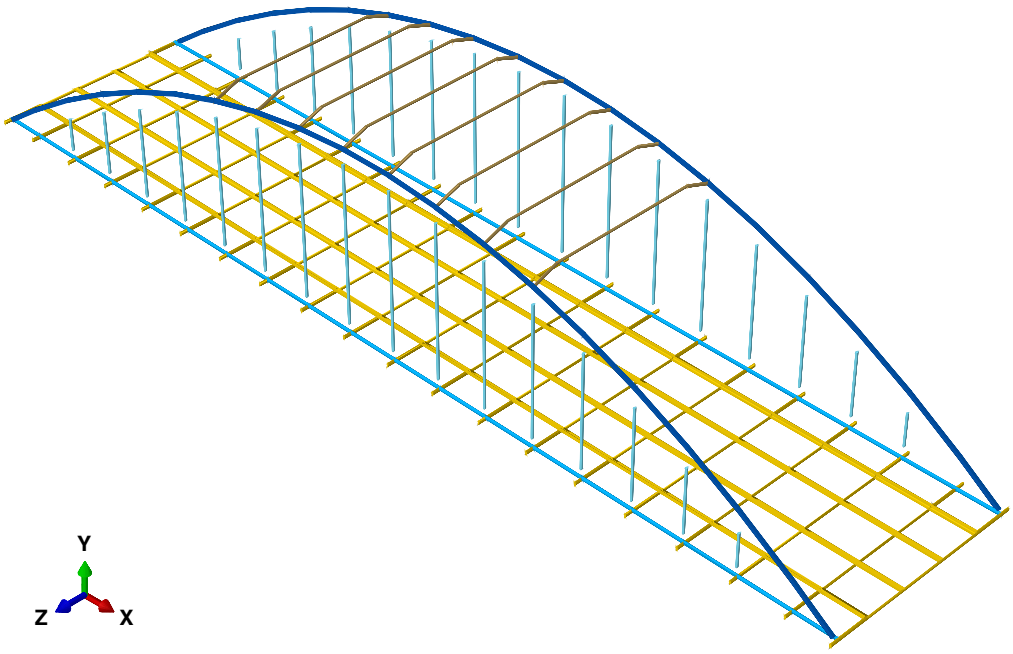


Figure 3: FEM model of Brivio bridge (single span); colours identify diverse elements of the structure for sought material parameters.

The model is conceived as a three–dimensional frame structure composed by beam finite elements, realised as an assembly of five principal structural components: deck, longitudinal deck girders, arches, hangers and upper transverse beams, as also highlighted in Figure 3, together with the reference coordinate system ($x$ for the longitudinal axis, $y$ for the vertical axis and $z$ for the transverse horizontal axis of the bridge). The mechanical constitutive parameters are

selected consistently with the five underlying structural components, although only nine parameters (five Young's moduli and four mass densities) are finally adopted as sought parameters in the Inverse Analysis problem, according to a sensitivity analysis study previously developed in [29] and as reported in Tables 1 and 2. The geometrical features of the FEM model are carefully assumed as in [29]. The deck is modelled by a meshing grid of 254 beams, the arches are built by 70 elements, whereas 24 elements are employed for the upper beams. Moreover, the deck–hanger and the hanger–arch joints are reproduced by the implementation of rigid link models. Globally, the FEM model of the bridge sums up to 380 beam elements and 1680 degrees of freedom, keeping a significantly reduced size for the computational model, in view of the computational burden for repetitive runs within the Inverse Analysis optimisation. Further, non–structural mass components, e.g. referring to the asphalt layer, are also included in the model. In defining the boundary conditions, the model is implemented as simply supported at the deck with combined elastic supports (linear spring elements), namely with two $z$–axis rotational springs at both extremities and two translational springs (at $x$–axis, horizontal, and $y$–axis, vertical, respectively), set at the second edge.

| Parameter | Lower bound | Upper bound | Reference value |
|---|---|---|---|
| Deck elastic modulus, $E_1$ [GPa] | 24.4 | 45.4 | 34.9 |
| Main longitudinal girders elastic modulus, $E_2$ [GPa] | 24.4 | 45.4 | 34.9 |
| Parabolic arches elastic modulus, $E_3$ [GPa] | 25.0 | 46.4 | 35.7 |
| Hangers elastic modulus, $E_4$ [GPa] | 25.0 | 46.4 | 35.7 |
| Upper transverse beams elastic modulus, $E_5$ [GPa] | 25.0 | 46.4 | 35.7 |
| Deck mass density, $\rho_1$ [kg/m$^3$] | 1710 | 3170 | 2440 |
| Main longitudinal girders mass density, $\rho_2$ [kg/m$^3$] | 1710 | 3170 | 2440 |
| Parabolic arches mass density, $\rho_3$ [kg/m$^3$] | 1710 | 3170 | 2440 |
| Hangers mass density, $\rho_4$ [kg/m$^3$] | 1710 | 3170 | 2440 |

Table 1: Material input parameters and search domain for the Inverse Analysis problem, based on the FEM model.

| Parameter | Reference value |
|---|---|
| Upper transverse beams mass density, $\rho_5$ [kg/m$^3$] | 2440 |
| I–support translational ($x$–axis) spring stiffness, $k_1$ [kN/m] | $10^{-5}$ |
| I–support translational ($y$–axis) spring stiffness, $k_2$ [kN/m] | $10^{10}$ |
| I–support rotational spring stiffness, $k_3$ [kNm] | $10^{-5}$ |
| II–support rotational spring stiffness, $k_4$ [kNm] | $10^{-5}$ |

Table 2: Base FEM model parameters, at fixed values, not included in the Inverse Analysis search domain.

In order to feed the optimisation procedure in the Inverse Analysis methodology, the numerical counterparts computed on the FEM model are compared with experimentally obtained quantities (i.e., identified experimental mode shapes and modal frequencies). Operational experimental campaigns were performed on Brivio bridge between 11 and 13 June 2014 (see details reported in [25, 26, 27]). Several instrumentation systems were adopted during the test phases, in particular: ten uniaxial wired piezoelectric accelerometers, seven wireless sensors,

four QDaedalus system total stations and a laser scanner; simultaneous dynamic testing and measurement of the structure, under regular operational traffic loading conditions, were defined also according to diverse setups. In the present work, experimentally identified quantities are acquired from previously processed data, while details on experimental identification and response signal processing may be found, respectively, in [29] and [28], with reference both to single span and whole bridge analysis.

## 4 ANALYSIS RESULTS

In the current section, the computed results are presented, as based on the previously described methodology, objective function choice and FEM model. In particular, as a key term in understanding and solving the Inverse Analysis problem, the discrepancy function is analysed according to four configurations:

1. 9D search domain, based on the complete set of parameters,
   $\boldsymbol{\theta} = [E_1, E_2, E_3, E_4, E_5, \rho_1, \rho_2, \rho_3, \rho_4]$;
2. 5D search domain, based on a reduced set of parameters, limited to Young's moduli,
   $\boldsymbol{\theta} = [E_1, E_2, E_3, E_4, E_5]$;
3. 2D search domain, based on a reduced set of parameters, limited to averaged Young's modulus and mass density,
   $\boldsymbol{\theta} = [\bar{E}, \bar{\rho}]$;
4. 4D search domain, based on a simplified beam model characterised by two structural components, respectively associated to Young's modulus and mass density values,
   $\boldsymbol{\theta} = [E_1, E_2, \rho_1, \rho_2]$.

By limiting the problem to a two–parameter space (configuration 3), it is possible to observe that a mode adjustment in the modal pairing, as inner loop in the objective function evaluation, leads to a very irregular and discontinuous objective function (see Figure 4a). On the contrary, by selecting a priori the appropriate modes, without the possibility of changing them in the fitting process, namely by introducing a MAC regularisation as proposed in Section 2.2, a continuous target function may effectively be obtained (see Figure 4b).

Therefore, on the basis of such preliminary analyses, the introduction of a regularisation procedure turns out to be a necessary step in view of the application of Gaussian Processing, to reduce abrupt function discontinuities. However, also in such a regularised approach (see Figure 4b), the employment of Gaussian Processes still appears to be less feasible, due to the intrinsic "ill–posedness" condition of the objective function, linked to the identification based just on modal properties, as displayed by the "valley" of possible "realisations", i.e. by the couple of parameters equally satisfying the minimisation problem. Therefore, such an issue may lead to an impractical or misleading application of Gaussian Processing optimisation, suggesting for an improvement of objective function definition toward achieving an automated identification method.

In a further step, adopting a 5D parameter space (configuration 2), Young's moduli of diverse structural components are considered as model parameters to be calibrated, while mass densities are assumed at a fixed value, as previously estimated in [29], aiming at temporarily excluding the "realisation valley" issue. In order to prepare the appropriate number of learning points, required for Gaussian Processes implementation, numerical evaluations of the FEM

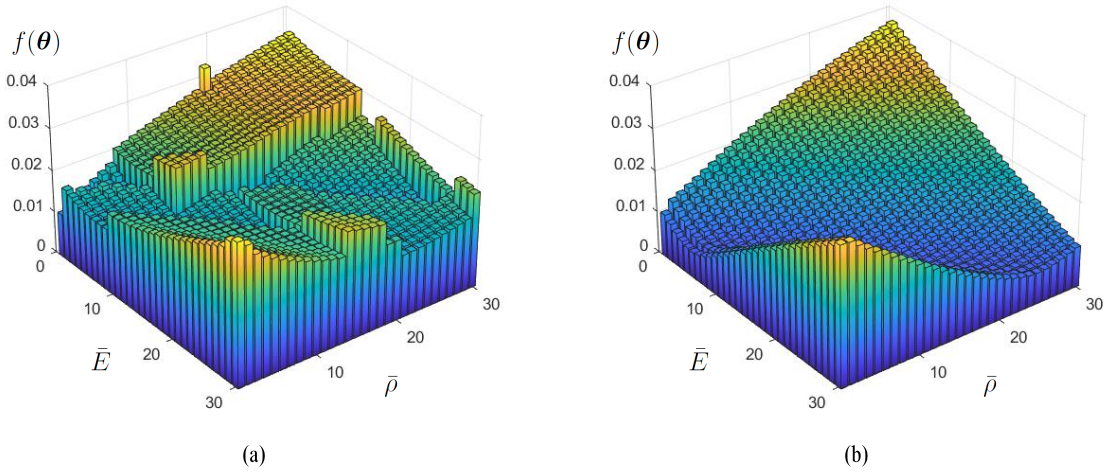


Figure 4: Normalised bar plot of the objective function in the 2D parameter space (configuration 3): (a) without MAC regularisation, (b) with MAC regularisation.

model and of the discrepancy function are produced over a regular grid in the search domain for $5^7$ = 16,807 points (i.e., for 7 scanning values, for each of the 5 sought parameters). Such an investigation of the objective function highlights non–satisfactory minima conditions, such as minimum points in non–feasible parameter space locations and equivalent minimum points, namely for a negligible variation of discrepancy function value, associated to significantly different parameter vector estimations (see Table 3). The highlighted behaviour may be interpreted as a lack of observed quantities (e.g., for missing data about mode shapes of other parts of the bridge, as bridge arches) in the objective function and/or as a reduced sensitivity, with respect to the sought parameters. The issue can further be confirmed by investigating the shape of the objective function, for example through cross section representations, where several irregularities and local minima may be observed (see the example cross sections collected in Figure 5).

| $f(\boldsymbol{\theta})$ [-] | 0.005990 | 0.006053 | 0.006098 | 0.006114 | 0.006118 | 0.006184 | 0.006210 |
|---|---|---|---|---|---|---|---|
| $E_1$ [GPa] | 45.2 | 45.2 | 45.2 | 45.2 | 45.2 | 45.2 | 45.2 |
| $E_2$ [GPa] | 24.4 | 34.8 | 24.4 | 27.9 | 27.9 | 27.9 | 45.2 |
| $E_3$ [GPa] | 35.7 | 32.1 | 35.7 | 35.7 | 35.7 | 35.7 | 28.6 |
| $E_4$ [GPa] | 46.4 | 42.8 | 42.8 | 42.8 | 39.3 | 46.4 | 42.8 |
| $E_5$ [GPa] | 35.7 | 42.8 | 35.7 | 46.4 | 46.4 | 42.8 | 39.3 |

Table 3: Seven best values of the objective function, by grid search, and corresponding parameters in the 5D search domain (configuration 2).

Similar results are obtained in the original 9D parameter space (configuration 1), analysed with a regular grid of $3^9$ = 19,638 points (i.e., for 3 scanning values, for each of the 9 sought parameters), as depicted in Figure 6 with four sample cross sections of the objective function, also highlighting non–feasible locations for minimum points at the search domain boundaries.

In consideration of the observed features of the employed objective function, in view of a proper choice of the minimisation algorithm to tackle the identification problem, it is worth to mention that the selection of "local algorithms" to find the global minimum (rather related to the "best" minimum within the possible combination of sought parameters) exhibits practical

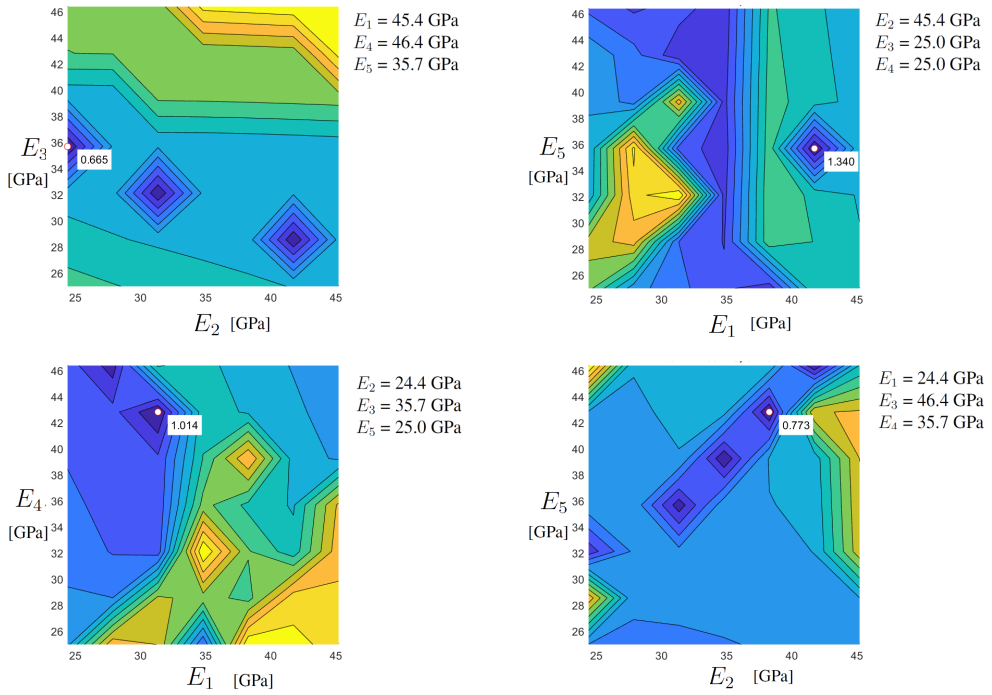


Figure 5: Selected cross sections of the objective function in the 5D parameter space (configuration 2).

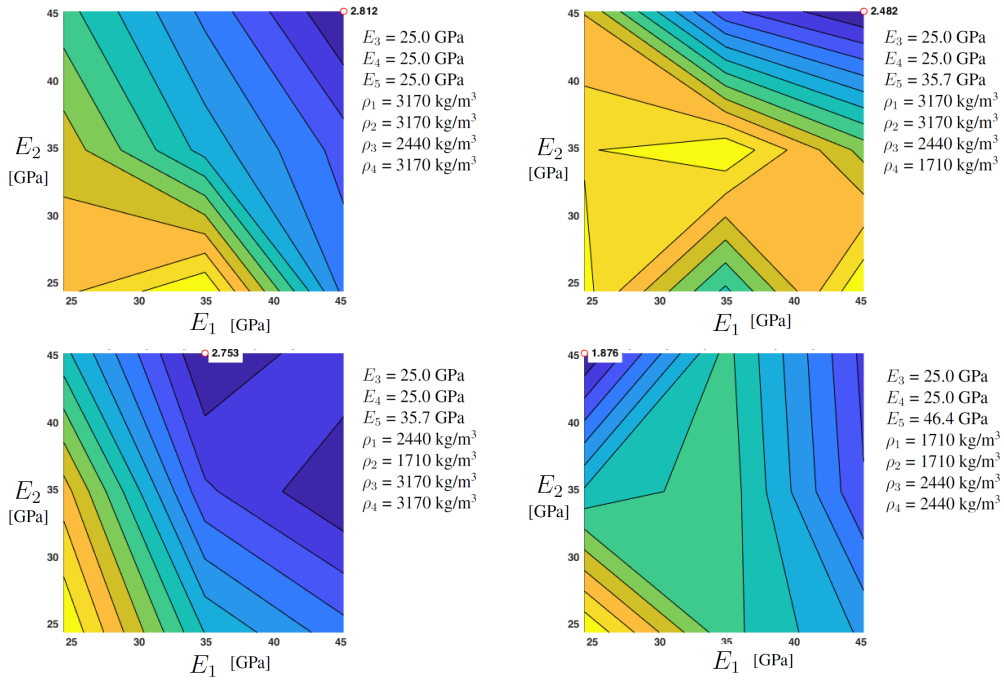


Figure 6: Selected cross sections of the objective function in the 9D parameter space (configuration 1).

difficulties, while the use of "global algorithms" (including Gaussian Processes), associated with a large computational cost, may not guarantee the estimation of parameters at feasible values, due to a possible mismatch between "global" numerical minimum and "best" parameter combination from a structural standpoint.

An attempt to improve the identification behaviour of the objective function is developed by introducing a penalty term related to the mass densities of the structural components, as proposed in Section 2.2. In order to validate the novel approach, a pseudo–experimental configuration is developed in a 4D parameter space, on a simplified beam model (configuration 4), namely by adopting two beam structural components, each characterised by an associated Young's modulus and mass density. Consistently, Figure 7 displays an example of the modification effect produced on the objective function shape by the introduction of the mass density penalty term.

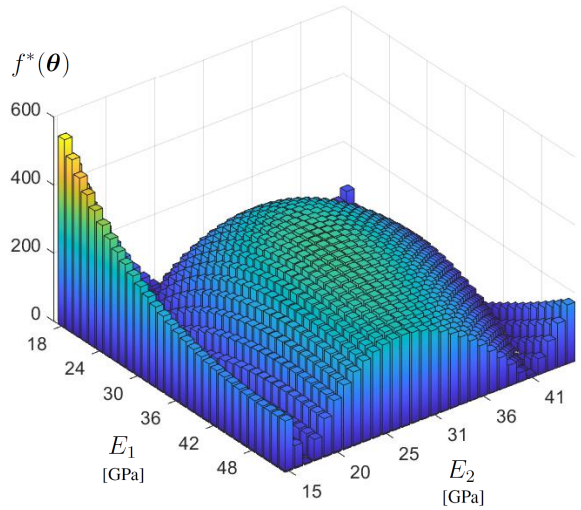


Figure 7: Three–dimensional cross section of the objective function in the 4D parameter space (configuration 4), with penalty mass density factor $F$ = 1000.

For testing the numerical procedure, within the validation scheme, one parameter value (specifically $\rho_2$) is kept at a fixed value, while the other three parameters are estimated, using pseudo–experimental data, at varying penalty coefficient $F$. For two diverse reference structural configurations, four identification tests are conducted, as respectively reported in Table 4 and Table 5. However, the computed results, even for elevated penalty coefficient values, do not allow to ensure for correct parameter estimations neither for a robust identification procedure. Therefore, the modified formulation of the objective function may be deemed as only partially improved, although not effective in defining a fully reliable automated calibration methodology in the present context, at this stage of development.

## 5 CONCLUSIONS

In the present paper, a methodology for model calibration relying on dynamic modal measurements is sought. The Inverse Analysis problem has been tackled in an application case study devoted to a reinforced concrete road arched bridge, Brivio bridge (1917), of a significant historical and infrastructural interest for Structural Health Monitoring assessment in the present operative conditions.

| | Reference | Test 1 | Test 2 | Test 3 | Test 4 |
|---|---|---|---|---|---|
| $f^*(\boldsymbol{\theta})$ [–] | – | 0.4901 | 0.8349 | 2.8628 | 13.2080 |
| $F$ [–] | – | 0 | 10 | 100 | 1000 |
| $E_1$ [GPa] | 33.74 | 38.02 | 38.02 | 36.81 | 36.81 |
| $E_2$ [GPa] | 28.38 | 31.55 | 31.55 | 31.55 | 31.55 |
| $\rho_1$ [kg/m$^3$] | 2235 | 2524 | 2524 | 2441 | 2441 |
| $\rho_2$ [kg/m$^3$] | 2147 | 2400 | 2400 | 2400 | 2400 |

Table 4: First test case for effectiveness of mass density penalty term in objective function, evaluated in 4D parameter space (configuration 4).

| | Reference | Test 1 | Test 2 | Test 3 | Test 4 |
|---|---|---|---|---|---|
| $f^*(\boldsymbol{\theta})$ [–] | – | 0.3955 | 0.9702 | 5.5767 | 18.2130 |
| $F$ [–] | – | 0 | 10 | 100 | 1000 |
| $E_1$ [GPa] | 38.00 | 36.81 | 36.81 | 38.02 | 39.22 |
| $E_2$ [GPa] | 29.00 | 27.41 | 27.41 | 27.41 | 27.41 |
| $\rho_1$ [kg/m$^3$] | 2300 | 2193 | 2193 | 2276 | 2359 |
| $\rho_2$ [kg/m$^3$] | 2500 | 2400 | 2400 | 2400 | 2400 |

Table 5: Second test case for effectiveness of mass density penalty term in objective function, evaluated in 4D parameter space (configuration 4).

In particular, within the general framework of Inverse Analysis approaches, an optimisation strategy based on Gaussian Processes has been selected and discussed, as an innovative method to tackle a demanding identification problem, both from computational efficiency and capability in searching for a "global" minimum. The choice of a promising optimisation approach has been coupled with multiple and improving definitions of a suitable objective function, as a central element in an Inverse Analysis problem. Moreover, considering the specific case study, particular attention has been devoted in the adoption of a FEM model apt to computationally generate numerical counterparts of the dynamic modal properties of the bridge structure, previously acquired out of an experimental campaign.

Further, with reference to the case study of Brivio bridge and, at the same time, providing observations of a more general validity, the investigation has been focused on the peculiar features and behaviour of the objective function, with possible regularisations and modifications, also at varying size of the parameter optimisation space. From the analysis results some main comments may be derived:

- in relying on dynamic modal measurements, as experimental data for identification problem, a regularisation criterion (e.g., by a fixed Modal Assurance Criterion) is required to reduce abrupt discontinuity jumps in the discrepancy function shape;
- the exploitation of modal properties, as a unique experimental source, intrinsically exhibits a "non–well posedness" condition, in terms of multiple "realisations", in aiming at a joint estimation of stiffness and mass properties of a structural system, namely leading to the identification of the correlated parameters;
- incomplete modal dynamic measurements (e.g. just at the deck level) may lead to a non–effective and non–robust identification procedure, consequently difficult to be tackled by

optimisation algorithms, also including Gaussian Processes;

- the introduction of penalty and regularisation terms in the discussed objective functions may lead to improved computational performances, however not sufficiently effective to provide a robust approach to be adopted in an automated identification procedure, toward structural assessment and diagnosis.

Despite the computational difficulties highlighted by the on–going analysis, the deepening and improved understanding on the objective function behaviour, for the tackled problem, confirm the validity of Inverse Analysis approaches toward Structural Identification and Structural Health Monitoring, with possible extensions, in future developments, to the insertion of additional sources of measurements.

Moreover, additional and corroborating studies, which may act just on the pure modelling side, based on pseudo–experimental results, relying on a full control of the underlying FEM modelling, for a digital replication of the infrastructure, may help in guidelining appropriate optimisation paths and variable choices, and needed measurement data, in the identification process, to investigate the role of "well-posedness", of the scheduled optimisation task, and associated reliability of the optimisation algorithm that is being employed. This is concomitantly under current research investigation, as separately reported for first encouraging outcomes in companion paper [36].

**Acknowledgements**

The financial support by "*Fondi di Ricerca d'Ateneo ex 60%*", "*STaRs – Azione 2 Visiting e Fellow*" and "*PRIN Life–long optimized structural assessment and proactive maintenance with pervasive sensing techniques*" at the University of Bergamo is gratefully acknowledged.

## REFERENCES

[1] A. Tarantola, *Inverse Problem Theory*. Siam, 2005.

[2] G. Maier, V. Buljak, T. Garbowski, G. Cocchetti, G. Novati, Mechanical characterization of materials and diagnosis of structures by inverse analyses: Some innovative procedures and applications. *International Journal of Computational Methods*, **11**, 1343002, 2014.

[3] C.E. Rasmussen, C.K.I. Williams, *Gaussian Processes for Machine Learning*. MIT Press, 2006.

[4] D. Sivia, J. Skilling, *Data Analysis: A Bayesian Tutorial, 2nd Edition*. Oxford Science Publications, 2006.

[5] C.M. Bishop, *Pattern Recognition and Machine Learning*. Springer, 2007.

[6] M. Alvarez, N. Lawrence, Sparse Convolved Gaussian Processes for Multi–Output Regression. D. Koller, D. Schuurmans, Y. Bengio, L. Bottou eds. *Twenty–Second Annual Conference on Neural Information Processing Systems (NIPS)*, Vancouver, Canada, December 8-10, 2008.

[7] T. Garbowski, Stochastic model reduction applied to inverse analysis. J.P.M. de Almeida, P. Díez, C. Tiago, N. Parés eds. *VI International Conference on Adaptive Modeling and Simulation (ADMOS 2013)*, Lisbon, Portugal, June 3-5, 2013.

[8] M. Adamski, M. Czechlowski, K. Durczak, T. Garbowski, Determination of the Concentration of Propionic Acid in an Aqueous Solution by POD–GP Model and Spectroscopy. *Energies*, **14**, 8288, 2021.

[9] K. Zaborowicz, T. Garbowski, B. Biedziak, M. Zaborowicz, Robust Estimation of the chronological age of children and adolescents using tooth geometry indicators and POD–GP. *International Journal of Environmental Research and Public Health*, **19**, 2952, 2022.

[10] T. Garbowski, G. Maier, G. Novati, Diagnosis of concrete dams by flat–jack tests and inverse analyses based on proper orthogonal decomposition. *Journal of Mechanics of Materials and Structures*, **6**, 181–202, 2011.

[11] T. Gajewski, T. Garbowski, Calibration of concrete parameters based on digital image correlation and inverse analysis. *Archives of Civil and Mechanical Engineering*, **14**, 170–180, 2014.

[12] D. Ribeiro, R. Calçada, R. Delgado, M. Brehm, V. Zabel, Finite element model updating of a bowstring–arch railway bridge based on experimental modal parameters. *Engineering Structures*, **40**, 413–435, 2012.

[13] C. Bendon, M. Dilena, A. Morassi, Ambient vibration testing and structural identification of a cable–stayed bridge. *Meccanica*, **51**, 2777–2796, 2016.

[14] F. Shabbir, P. Omenzetter, Model updating using genetic algorithms with sequential technique. *Engineering Structures*, **120**, 166–182, 2016.

[15] J.E. Mottershead, M.I. Friswell, Model updating in structural dynamics: A survey. *Journal of Sound and Vibration*, **167**, 347–375, 1993.

[16] C.P. Fritzen, D. Jennewein, T. Kiefer, Damage detection based on model updating methods. *Mechanical Systems and Signal Processing*, **12**, 163–186, 1998.

[17] E. Reynders, System identification methods for (Operational) Modal Analysis: Review and comparison. *Archives of Computational Methods in Engineering*, **19**, 51–124, 2012.

[18] F. Ubertini, C. Gentile, A.L. Materazzi, Automated modal identification and its application to bridges. *Engineering Structures*, **46**, 264–278, 2013.

[19] C. Rainieri, G. Fabbrocino, *Operational Modal Analysis of Civil Engineering Structures*. Springer, 2014.

[20] F. Pioldi, R. Ferrari, E. Rizzi, Output–only modal dynamic identification of frames by a refined FDD algorithm at seismic input and high damping. *Mechanical Systems and Signal Processing*, **68–69**, 265–291, 2016.

[21] F. Pioldi, R. Ferrari, E. Rizzi, Earthquake structural modal estimates of multi–storey frames by a refined Frequency Domain Decomposition algorithm. *JVC/Journal of Vibration and Control*, **23**, 2037–2063, 2017.

[22] F. Pioldi, R. Ferrari, E. Rizzi, Seismic FDD modal identification and monitoring of building properties from real strong–motion structural response signals. *Structural Control and Health Monitoring*, **24**, e1982, 2017.

[23] R. Cardoso, A. Cury, F. Barbosa, A robust methodology for modal parameters estimation applied to SHM. *Mechanical Systems and Signal Processing*, **95**, 24–41, 2017.

[24] L. Santarella, E. Miozzi, *Ponti Italiani in Cemento Armato (in Italian)*. Hoepli, 1948.

[25] R. Ferrari, D. Froio, E. Chatzi, C. Gentile, F. Pioldi, E. Rizzi, Experimental and numerical investigations for the structural characterization of a historic RC arch bridge. M. Papadrakakis, V. Papadopoulos, V. Plevris eds. *5th ECCOMAS Thematic Conference on Computational Methods in Structural Dynamics and Earthquake Engineering*, Crete Island, Greece, May 25-27, 2015.

[26] R. Ferrari, F. Pioldi, E. Rizzi, C. Gentile, E. Chatzi, R. Klis, E. Serantoni, A. Wieser, Heterogeneous sensor fusion for reducing uncertainty in structural health monitoring. M. Papadrakakis, V. Papadopoulos, G. Stefanou eds. *1st ECCOMAS Thematic Conference on Uncertainty Quantification in Computational Sciences and Engineering (UNCECOMP 2015)*, Crete Island, Greece, May 25-27, 2015.

[27] R. Ferrari, F. Pioldi, E. Rizzi, C. Gentile, E. Chatzi, E. Serantoni, A. Wieser, Fusion of wireless and non-contact technologies for the dynamic testing of a historic RC bridge. *Measurement Science and Technology*, **27**, 124014, 2016.

[28] A. Cornaggia, R. Ferrari, M. Zola, E. Rizzi, C. Gentile, Signal Processing Methodology of Response Data from a Historical Arch Bridge toward Reliable Modal Identification. *Infrastructures*, **7**, 74, 2022.

[29] R. Ferrari, D. Froio, E. Rizzi, C. Gentile, E. Chatzi, Model updating of a historic concrete bridge by sensitivity and global optimization–based Latin hypercube sampling. *Engineering Structures*, **1**, 139–160, 2019.

[30] G. Zonno, C. Gentile, Assessment of Similar Reinforced Concrete Arch Bridges by Operational Modal Analysis and Model Updating. *Lecture Notes in Civil Engineering*, **156**, 853–868, 2021.

[31] P. Borlenghi, C. Gentile, G. Zonno, Monitoring Reinforced Concrete Arch Bridges with Operational Modal Analysis. *Lecture Notes in Civil Engineering*, **200**, 361–371, 2022.

[32] P. Borlenghi, C. Gentile, M. Pirrò, Continuous Dynamic Monitoring and Automated Modal Identification of an Arch Bridge. *Lecture Notes in Civil Engineering*, **254**, 166–176, 2023.

[33] J. Nocedal, S.J. Wright, *Numerical Optimization*. Springer, 1999.

[34] M.D. Buhmann, *Radial Basis Functions*. Cambridge University Press, 2003.

[35] R.J.Allemang, The Modal Assurance Criterion – Twenty Years of Use and Abuse. *Sound and Vibration*, **2003**, 14–21, 2003.

[36] A. Cornaggia, T. Garbowski, G. Cocchetti, R. Ferrari, E. Rizzi, Optimised structural modelling for Inverse Analysis parameter identification relying on dynamic measurements. M. Papadrakakis, M. Fragiadakis eds. *9th ECCOMAS Thematic Conference on Computational Methods in Structural Dynamics and Earthquake Engineering (COMPDYN 2023)*, Athens, Greece, June 12-14, 2023, submitted.

COMPDYN 2023
9th ECCOMAS Thematic Conference on
Computational Methods in Structural Dynamics and Earthquake Engineering
M. Papadrakakis, M. Fragiadakis (eds.)
Athens, Greece, 12-14 June 2023

# SENSITIVITY TO DAMPING IN NONLINEAR DYNAMIC ANALYSIS

**Terje Haukaas**[1]

[1] Professor, Dept. of Civil Engineering, The University of British Columbia, Vancouver
6250 Applied Science Lane, Vancouver, BC, V6T 1Z4, Canada
e-mail: terje@civil.ubc.ca

## Abstract

*Exact response sensitivities are derived and calculated for nonlinear dynamic analysis with Rayleigh damping formulated in terms of the current tangent stiffness matrix. The derivations show that the third-order tensor formed by the derivative of the tangent stiffness matrix with respect to the displacement vector is required. That quantity is non-zero only for material models that feature nonlinearity in at least a portion of their stress-strain curve. Bilinear models do not have that characteristic. The Bouc-Wen material model is selected in this paper to verify the implementations. That model exhibits a smooth transition between the elastic and the yield state. In order to obtain correct response sensitivities, it is necessary to let the third-order tensor amend the coefficient matrix of the system of equations that produce the sensitivity results. This paper also presents exact response sensitivities for modal damping and Rayleigh damping with coefficients implicitly specified as a target damping at two natural frequencies. Eigenvalue derivatives are implemented in order to calculate results for those cases. The amendment of the coefficient matrix is then asymmetric. Examples are presented to show the sensitivity of the displacement response with respect to four groups of parameters: material properties, cross-section geometry, mass, and parameters of the damping model.*

**Keywords:** Response sensitivity analysis, Direct differentiation method, Nonlinear dynamic structural analysis, Rayleigh damping, Modal damping, Bouc-Wen material model.

# 1 INTRODUCTION

Nonlinear dynamic analyses are computationally demanding. That is one reason why it is desirable to learn as much as possible from every analysis. One instrument for adding insight beyond the response is the calculation of response sensitivities. Response sensitivities have value even when the confidence in the response is low. For example, the response derivatives may reveal that the response is highly sensitive to an input parameter that is associated with substantial uncertainty. That would prompt caution, as well as investigations related to that parameter. The fundamental objective in this paper is to derive, implement, and calculate exact response sensitivities in an efficient manner. Pioneered at the University of Iowa [1][2][3][4][5] and extended at the University of California at Berkeley[6][7][8], the direct differentiation method is adopted in this paper. It facilitates the efficient calculation of response sensitivities in parallel with the calculation of the response. The results from the direct differentiation method are exact once the derivative equations are correctly implemented on the computer.

Three specific objectives are addressed in this paper. First, exact response sensitivities are derived, implemented, and calculated for situations where the damping matrix is formulated in terms of the current tangent stiffness and, hence, the current displacement. Second, response sensitivities are obtained for situations where the user specifies the target damping on selected natural frequencies. One example is the use of Rayleigh damping with a target damping ratio specified at two natural frequencies. Another example addressed in this paper is the modal damping matrix, which entails the specification of a target damping on some or all of the natural frequencies. In both cases, it is necessary to differentiate the dynamic eigenvalue problem for the structure. The third objective is to visualize and verify the response sensitivity results, and to present applications other than gradient-based reliability and optimization analysis.

The scope of this paper includes displacement-based frame elements with fiber-discretized sections and one uniaxial material model in each fiber. Derivatives of the displacement response are calculated with respect to nodal masses, material parameters, and cross-section shape parameters. Shape sensitivities associated with nodal coordinates are not included here. The scope of the paper also includes the differentiation of the response equations for a specific Bouc-Wen material model. That model is employed because it exhibits smooth transitions from elastic to yield. That is significant because the derivations in this paper show that the derivative of the tangent stiffness of the material with respect to the strain is required in the response sensitivity calculations. Based on work by Baber and Noori [9], the author implemented a somewhat complex Bouc-Wen model featuring degradation in OpenSees [10] in the early 2000s. A more transparent model was later implemented in OpenSees by Schellenberg et al. [11] based on work by Casciati [12]. That implementation is extended in the present work. The Bouc-Wen model was originally formulated by Wen [13], who referenced a 1967 conference paper by R. Bouc. Early work on this model was also presented by Baber and Wen [14].

This paper is organized in the manner that the actual derivation & implementation work progressed. Starting with developments for the Bouc-Wen material model, followed by its use in static then dynamic analysis, this paper tours the lessons learned to establish the implementation of correct response sensitivity calculations.

# 2 ELEMENTS, SECTIONS, MATERIALS

A modest but transparent finite element model is employed to demonstrate the developments presented in this paper. The steel column shown in Figure 1 is utilized, discretized into five displacement-based nonlinear frame elements. Each element has five integration points, formulated as wide-flange sections, located along the element according to the Lobatto quadrature rule. As shown in Figure 1, each cross-section has two integration points in each flange, and

eight integration points in the web. The results presented in this paper are obtained with $L$=15m, $h_w$=355mm, $t_w$=11mm, $b_f$=365mm, $t_f$=18mm, and $M=(A\rho)L/5$=392.1kg, where $A$ is the section area and $\rho$=7,850kg/m$^3$ is the mass density. Combined with the initial stiffness value given in the next paragraph, this gives the column a first natural period of 0.52 sec.

Each integration point in each section contains a hysteretic uniaxial material model. As mentioned earlier, the Bouc-Wen model is selected in order to highlight issues related to the direct differentiation method for Rayleigh damping with the current tangent stiffness. That material model takes six input parameters: $E$, $f_y$, $\alpha$, $\gamma$, $\beta$, and $\eta$. Specifically, $E$ is the modulus of elasticity, here set to 200GPa; $f_y$ is the yield stress, here set to 350MPa; $\alpha$ is the strain hardening, here set to 2%. The two "Bouc-Wen parameters" $\gamma$ and $\beta$ are set equal to 0.5. The integer $\eta$ governs the sharpness of the transition from elastic to yield. The value $\eta$=3 is used throughout this paper, except in the next paragraph.

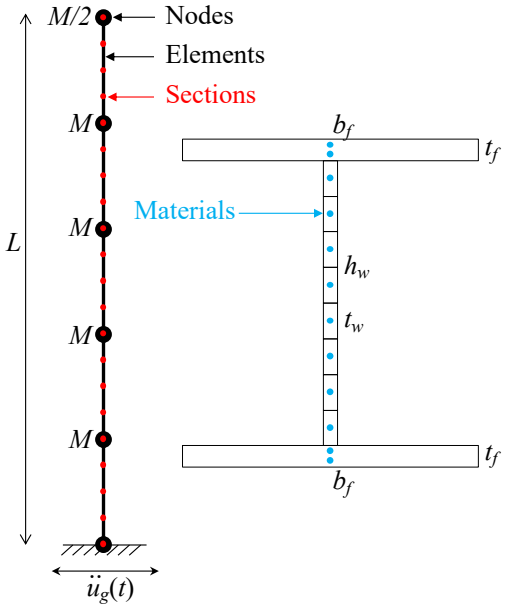


Figure 1: Structural model.

Figure 2 shows stress-strain curves for different values of $\eta$. The smooth transition from the elastic state to plastic flow is clearly visible. The higher value of $\eta$, the sharper the transition is. The stress-strain curves shown in Figure 2 are obtained by recording the stress when the strain is varied as a sine-function with 1% amplitude. For that to be achieved, only the stress response is required. That is insufficient for the calculation of response sensitivities. In fact, it is insufficient even for nonlinear static and dynamic analysis, because the algorithmically consistent tangent, i.e., the derivative of the stress with respect to the strain is missing. That issue and others are addressed in the implementations made in this work.

The two previously mentioned implementations of the Bouc-Wen model are made in the open-source framework OpenSees [10]. That object-oriented software framework created in C++ was spearheaded in the late 1990s by Dr. Fenves and his then PhD student Dr. McKenna. Around the same time, Dr. Fenves taught a course on nonlinear structural analysis, for which he developed a miniature version of OpenSees in Matlab, which labelled G2, because OpenSees was then called G3. The author of the present paper took that course and recently translated G2 into the Python programming language. It is an extended Python version of G2 that is employed

to obtain the results presented in this paper. The extended Python version of G2 is posted on the author's research website, terje.civil.ubc.ca, along with notes and examples.

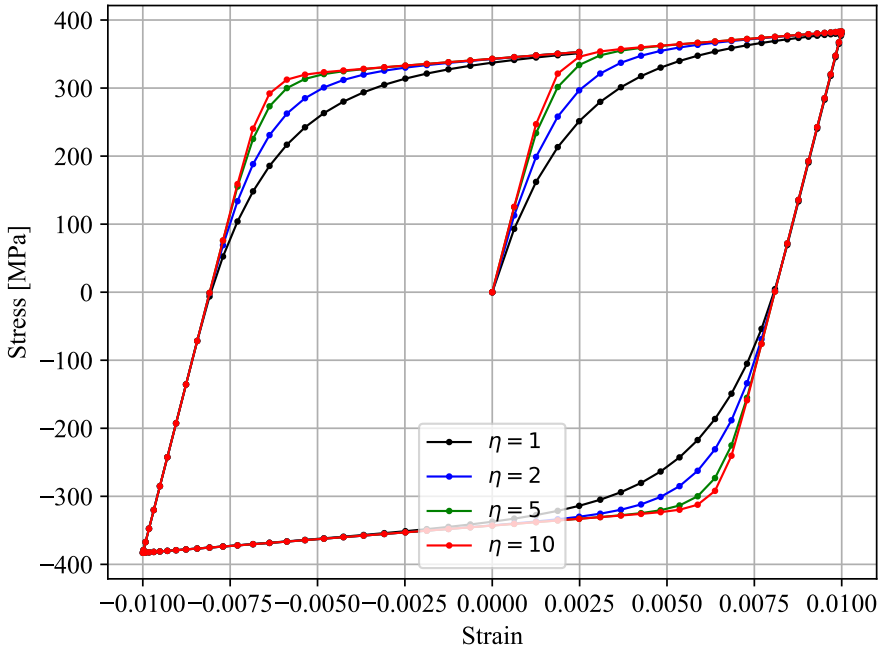


Figure 2: Material model.

## 3 CONSISTENT TANGENT

In nonlinear analysis, static and dynamic, an accurate tangent stiffness ensures optimal convergence towards equilibrium in the Newton-Raphson algorithm. Errors in the tangent leads to slow convergence, or no convergence at all. In this paper it is stressed that the tangent stiffness also appears in the system of equations that govern the response sensitivities. As a result, an inaccurate tangent stiffness leads to inaccurate response sensitivity results.

It is not only bugs in the implementation that can cause accuracy problems in the sensitivity results, associated with the tangent stiffness. The use of the "continuum tangent" instead of the algorithmically consistent tangent leads to slower convergence and also inaccurate response sensitivity results. An example, suppose the cantilever column in Figure 1 is subject to a uniformly distributed lateral load with intensity 10kN/m. Tracking the top tip displacement as the load increases produces a distinctly nonlinear load-displacement curve, not shown here for brevity. Significant yielding occurs after the load increases beyond 6kN/m. The derivative of that tip displacement with respect to the modulus of elasticity is shown in Figure 3. In that figure, and throughout this paper, black dots identify sensitivity results obtained by the finite difference method. That method entails the rerunning of each analysis with a perturbed parameter value in order to estimate, in an approximate manner, the derivative of the displacement with respect to the input value. The black dots in Figure 3 are obtained by rerunning the nonlinear static analysis with the value of the modulus of elasticity perturbed by $10^{-8}$ times its original value. The maximum difference between that approximate result and the blue line, which is obtained by the direct differentiation implementations in this work, is $2.3 \cdot 10^{-18}$ m/Pa. That is reasonable accuracy, because Figure 3 shows that the response sensitivity is in the order of $1.5 \cdot 10^{-11}$ m/Pa. Notice that the response sensitivity result obtained with the *continuum* tangent, shown as a red line in Figure 3 and derived shortly, exhibits significant error. Adding to the appeal of the algorithmically consistent tangent is that the number of iterations of the

Newton-Raphson algorithm in the ten load increments is 3, 5, 5, 6, 6, 7, 7, 7, 7, 7 with the algorithmically consistent tangent and 5, 7, 11, 14, 17, 22, 31, 32, 19 with the continuum tangent.

To understand the difference between the continuum tangent and the consistent tangent, consider the stress of the Bouc-Wen model, written

$$\sigma = \alpha \cdot E \cdot \varepsilon + (1-\alpha) \cdot f_y \cdot z \tag{1}$$

where $z$ varies during the analysis and governs the hysteretic response. The sought tangent is

$$\frac{d\sigma}{d\varepsilon} = \alpha \cdot E + (1-\alpha) \cdot f_y \cdot \frac{dz}{d\varepsilon} \tag{2}$$

The differential equation that governs the evolution of $z$ is

$$\dot{z} = \frac{1}{\varepsilon_y} \cdot (\dot{\varepsilon} - \gamma \cdot \dot{\varepsilon} \cdot |z|^\eta - \beta \cdot |\dot{\varepsilon}| \cdot z^\eta) \tag{3}$$

where $\varepsilon_y = f_y/E$=yield strain, and $\gamma$, $\beta$, and $\eta$ are material parameters. Implemented by Schellenberg et al. [11], $\varepsilon_y$ here serves as a scaling factor to provide a transition from elastic to yielding at appropriate strain values. When the sum of $\gamma$ and $\beta$ equal unity then $z$ varies between –1 and 1. The choice $\gamma = \beta = 0.5$ is appropriate for a bilinear material with smooth transitions; examples with other values are shown in the first figure in the paper by Wen [13] and elsewhere.

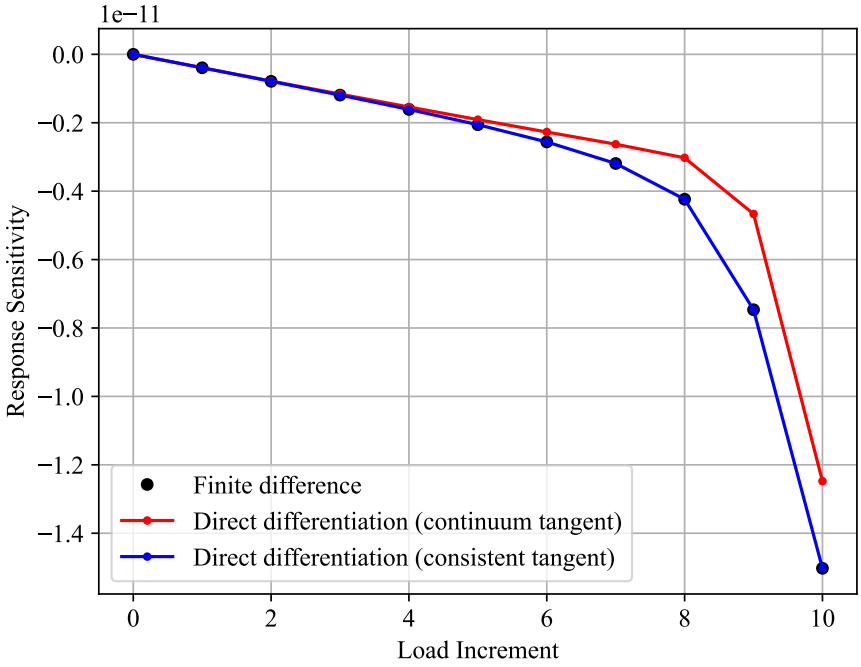


Figure 3: Derivative of tip displacement with respect to modulus of elasticity.

The Backward Euler algorithm, generically written $z_{n+1} = z_n + \Delta t\, r(z_{n+1})$, where $r$ is the right-hand side, is utilized to solve the differential equation in Eq. (3). The relevant right-hand side, i.e., that of Eq. (3), is first reorganized by pulling the strain rate outside the parenthesis:

$$\dot{z} = \frac{1}{\varepsilon_y} \cdot \left(1 - \left(\gamma + \beta \cdot \text{sign}(\dot{\varepsilon} \cdot z)\right) \cdot |z|^\eta\right) \cdot \dot{\varepsilon} \tag{4}$$

That right-hand side is then substituted into the Backward Euler algorithm, which then reads

$$z_{n+1} = z_n + \frac{1}{\varepsilon_y} \cdot \left(1 - \left(\gamma + \beta \cdot \text{sign}(\dot{\varepsilon}_{n+1} \cdot z_n)\right) \cdot |z_{n+1}|^\eta\right) \cdot (\varepsilon_{n+1} - \varepsilon_n) \tag{5}$$

because $\Delta t$ cancels. To solve Eq. (5) for $z_{n+1}$, which appears on both sides of the equal sign, the Newton algorithm, generically written $x_{j+1}=x_j-f(x_j)/f'(x_j)$ is employed. The function $f$ is the right-hand side of Eq. (5), once $z_{n+1}$ is moved to that side, and prime means derivative with respect to $z_{n+1}$.

Once the Newton algorithm that determines $z_{n+1}$ converges, the tangent is sought. For reference, the continuum version of the derivative $dz/d\varepsilon$ in Eq. (2) is obtained by first using the chain rule of differentiation to state the basic fact that

$$\dot{z} = \frac{dz}{dt} = \frac{dz}{d\varepsilon}\frac{d\varepsilon}{dt} = \frac{dz}{d\varepsilon}\dot{\varepsilon} \tag{6}$$

A comparison between Eq. (4) and Eq. (6) immediately reveals the expression for $dz/d\varepsilon$, which is substituted into Eq. (2) to produce the continuum tangent. The consequence of using that tangent is inaccurate response sensitivity results, as suggested by the red line in Figure 3.

The algorithmically consistent version of $dz/d\varepsilon$ can be obtained in two ways. First, recognize that any change in $z_{n+1}$ results from a change in the fraction $f/f'$ that appears in the Newton algorithm. As a result, the differentiation of $f/f'$ with respect to $\varepsilon_{n+1}$ yields the correct derivative to be substituted into Eq. (2). Another approach is to differentiate Eq. (5) with respect to $\varepsilon_{n+1}$ and solving for $dz_{n+1}/d\varepsilon_{n+1}$. Both approaches give the same result, but the latter approach is preferred in this paper. That is because the repeated differentiation of Eq. (5) is adopted when additional derivatives are sought later in the paper.

## 4 THE DIRECT DIFFERENTIATION METHOD

Let the lateral displacement at the top of the cantilevered column in Figure 1 be denoted by $u(t)$, where $t$ is time. Furthermore, let one of the input parameters, for example $M$, $E$, $f_y$, $\alpha$, or a cross-section dimension, be denoted by the generic symbol $\theta$. The objective of the direct differentiation method is to calculate $du(t)/d\theta$ in an exact and efficient manner. In order to do so, consider the system of governing equilibrium equations

$$\mathbf{M}\ddot{\mathbf{u}} + \mathbf{C}\dot{\mathbf{u}} + \tilde{\mathbf{F}}(\mathbf{u}) = \mathbf{F} \tag{7}$$

where $\mathbf{M}$=mass matrix, $\mathbf{C}$=damping matrix, $\tilde{\mathbf{F}}$=internal resisting forces, $\mathbf{F}$=external loads, and $\mathbf{u}$ is the displacements vector, which contains the tracked displacement $u$. Each superimposed dot means one derivative with respect to time. The nonlinear dependence of $\tilde{\mathbf{F}}$ on $\mathbf{u}$ is shown; subsequent derivations address the situation where $\mathbf{C}$ is also a function of $\mathbf{u}$. Eq. (7) represents a spatial discretization of the structural boundary value problem in terms of elements connected to degrees of freedom collected in the vector $\mathbf{u}$. A temporal discretization of the initial value problem is introduced by means of the following generic time-stepping scheme:

$$\ddot{\mathbf{u}}_{n+1} = a_1\mathbf{u}_{n+1} + a_2\mathbf{u}_n + a_3\dot{\mathbf{u}}_n + a_4\ddot{\mathbf{u}}_n \tag{8}$$

$$\dot{\mathbf{u}}_{n+1} = a_5\mathbf{u}_{n+1} + a_6\mathbf{u}_n + a_7\dot{\mathbf{u}}_n + a_8\ddot{\mathbf{u}}_n \tag{9}$$

where $a_i$ are constants. In the analyses behind this paper, the Newmark algorithm with $\gamma$=0.5 and $\beta$=0.25 is employed. Here, the symbols $\gamma$ and $\beta$ must not be confused with the identical symbols used in the Bouc-Wen model. The selected discretization implies that $a_1=1/(\beta\,\Delta t^2)$, $a_2=-a_1$, $a_3=-1.0/(\beta\,\Delta t)$, $a_4=1-1/(2\beta)$, $a_5=\gamma/(\beta\,\Delta t)$, $a_6=-a_5$, $a_7=1-\gamma/\beta$, and $a_8=\Delta t\,(1-\gamma/(2\beta))$. In order to obtain $du(t)/d\theta$, Eqs. (8) and (9) are substituted into Eq. (7) followed by the differentiation of the result with respect to $\theta$. Before embarking on those steps, special attention is given to the differentiation of $\tilde{\mathbf{F}}$. The reason is that $\tilde{\mathbf{F}}$ depends on $\theta$ implicitly via $\mathbf{u}$ and also potentially explicitly via the algorithm that calculates and assembles $\tilde{\mathbf{F}}$. This is symbolically written $\tilde{\mathbf{F}}(\mathbf{u}(\theta),\theta)$ and the chain rule of differentiation yields [6]

$$\frac{\partial \tilde{\mathbf{F}}}{\partial \mathbf{u}} \cdot \frac{\partial \mathbf{u}}{\partial \theta} + \left.\frac{\partial \tilde{\mathbf{F}}}{\partial \theta}\right|_{\mathbf{u}\text{ fixed}} = \frac{\partial \mathbf{F}}{\partial \theta} \tag{10}$$

For hysteretic problems it is necessary to calculate all components of the vector $d\mathbf{u}/d\theta$ in order to calculate $du/d\theta$. The vector $d\mathbf{u}/d\theta$ appears in Eq. (10). This is kept in mind when Eqs. (8) and (9) are now substituted into Eq. (7), followed by differentiation and reorganization of the result to obtain, at time step $n$+1:

$$\left(a_1\mathbf{M} + a_5\mathbf{C} + \frac{\partial \tilde{\mathbf{F}}_{n+1}}{\partial \mathbf{u}_{n+1}}\right)\frac{\partial \mathbf{u}_{n+1}}{\partial \theta} =$$

$$\frac{\partial \mathbf{F}_{n+1}}{\partial \theta} - \frac{\partial \mathbf{M}}{\partial \theta}(a_1\mathbf{u}_{n+1} + a_2\mathbf{u}_n + a_3\dot{\mathbf{u}}_n + a_4\ddot{\mathbf{u}}_n) - \mathbf{M}\left(a_2\frac{\partial \mathbf{u}_n}{\partial \theta} + a_3\frac{\partial \dot{\mathbf{u}}_n}{\partial \theta} + a_4\frac{\partial \ddot{\mathbf{u}}_n}{\partial \theta}\right) -$$
$$\frac{\partial \mathbf{C}}{\partial \theta}(a_5\mathbf{u}_{n+1} + a_6\mathbf{u}_n + a_7\dot{\mathbf{u}}_n + a_8\ddot{\mathbf{u}}_n) - \mathbf{C}\left(a_6\frac{\partial \mathbf{u}_n}{\partial \theta} + a_7\frac{\partial \dot{\mathbf{u}}_n}{\partial \theta} + a_8\frac{\partial \ddot{\mathbf{u}}_n}{\partial \theta}\right) - \left.\frac{\partial \tilde{\mathbf{F}}(\mathbf{u}_{n+1})}{\partial \theta}\right|_{\mathbf{u}_{n+1}\text{ fixed}} \tag{11}$$

where ground motion loading means that the load vector derivative is

$$\frac{\partial \mathbf{F}_{n+1}}{\partial \theta} = -\frac{d\mathbf{M}}{d\theta} \cdot \boldsymbol{\Gamma} \cdot \ddot{u}_{g,n+1} \tag{12}$$

where $\ddot{u}_g$ is the ground acceleration in the horizontal direction, at time $t_{n+1}$, and $\boldsymbol{\Gamma}$ is the mass participation vector. After convergence of the Newton-Raphson algorithm at each time increment, the linear system of equations in Eq. (11) is solved for $d\mathbf{u}/d\theta$. The coefficient matrix in that system is $a_1\mathbf{M} + a_5\mathbf{C} + \left(\partial \tilde{\mathbf{F}}_{n+1}/\partial \mathbf{u}_{n+1}\right) \equiv a_1\mathbf{M} + a_5\mathbf{C} + \mathbf{K}_{n+1}$, which is identical to the effective tangent stiffness employed in the iterations of the Newton-Raphson algorithm. Eq. (11) is implemented in G2, leading to the results presented in this paper. What is presented thus far leads to the following summary of the direct differentiation method:

1) The method is associated with a one-time cost to implement Eq. (11) in the nonlinear finite element analysis code. The derivation and correct implementation of $\partial \tilde{\mathbf{F}}_{n+1}/\partial \theta$ for fixed current displacements can be demanding; that task is addressed in subsequent sections. The differentiation of the damping matrix, $\mathbf{C}$, may also require careful attention; that task is also addressed in subsequent sections.

2) The method gives exact and algorithmically consistent results. No approximations are involved in the derivations and implementations.

3) The method is efficient because Eq. (11) is a linear system of equations. Solvers that factorize the coefficient matrix once, followed by solutions for different right-hand sides, further reduces the computational cost. Nonetheless, it is noted that Eq. (11) must be solved for each parameter, $\theta$, at every time increment when hysteretic material models are present.

4) The method benefits from avoiding the Modified Newton-Raphson approach, characterized by not updating the stiffness during the iterations. In the proper Newton-Raphson algorithm, the tangent stiffness is recalculated in each iteration, benefitting the direct differentiation method because it requires the current tangent stiffness after convergence, in order to solve Eq. (11). Developments presented in this paper produce amendments to that coefficient matrix before Eq. (11) is solved.

5) The method requires two calls to each hysteretic material instance, at every time step, beyond the ordinary state determination of the Newton-Raphson algorithm. As stressed by Zhang & Der Kiureghian [6], the calculation of $\partial\tilde{\mathbf{F}}_{n+1}/\partial\theta$ for fixed current displacements, stemming from Eq. (10), prompts two "phases" of the sensitivity calculations. In Phase 1 the elements, sections, and materials are called to produce contributions to $\partial\tilde{\mathbf{F}}_{n+1}/\partial\theta\big|_{\mathbf{u}_{n+1}\text{ fixed}}$ in order to form the right-hand side of Eq. (11). Because the calculations are for fixed displacements at increment $n$+1 but *not* at increment $n$ and earlier, it is necessary to store the unconditional derivative of the history variables of the materials *without* the assumption of fixed displacements. That is referred to as Phase 2, conducted after Eq. (11) is solved for $d\mathbf{u}_{n+1}/d\theta$. The storage of unconditional derivatives of history variables must accommodate one entry for every $\theta$.

The method requires care when calculating $\partial\tilde{\mathbf{F}}_{n+1}/\partial\theta\big|_{\mathbf{u}_{n+1}\text{ fixed}}$, for at least two reasons. First, the algorithm for the material state determination may be intricate, with bug-prone sensitivity implementations as a result. Second, the requirement for the conditional derivative is that $\mathbf{u}_{n+1}$ is fixed, not that $\varepsilon_{n+1}$ is fixed. This is emphasized because when $\theta$ represents a cross-section dimension, which is relevant in this paper, then the strain changes with $\theta$ even when $\mathbf{u}_{n+1}$ is fixed. This point is elaborated upon in subsequent sections.

6) The method requires the following amendment to the Newton-Raphson algorithm of nonlinear analysis:

Upon convergence, at each time increment, $n$+1, before committing the state:
- Ensure that the algorithmically consistent tangent stiffness is up-to-date
- Loop over the $\theta$-variables for which response sensitivities are sought
  - Phase 1: Assemble the right-hand side of Eq. (11) for the relevant $\theta$ by calculating the conditional derivative of the stress and other internal forces for fixed displacement $\mathbf{u}_{n+1}$ but *not* fixed $\mathbf{u}_n$ and not necessarily fixed $\varepsilon_{n+1}$
  - Solve Eq. (11) for $\partial\mathbf{u}_{n+1}/\partial\theta$
  - Phase 2: Send $\partial\mathbf{u}_{n+1}/\partial\theta$ to elements, sections, and materials in order to calculate the unconditional derivative of all hysteretic history variables for the relevant $\theta$
- Commit the converged state, i.e., store history variables, as well as their unconditional derivatives calculated in Phase 2

## 5 BOUC-WEN DERIVATIVES, PART I

At this stage, before damping is addressed, it is clear that each material instance must at least be able to produce the conditional derivative $d\sigma/d\theta|_{\varepsilon_{n+1}\text{ fixed}}$ and store the unconditional derivative of the history variables, once $\partial\varepsilon_{n+1}/\partial\theta$ is available. For the Bouc-Wen model, this is accomplished by differentiating Eqs. (1) and (5). The first reads

$$\left.\frac{d\sigma_{n+1}}{d\theta}\right|_{\varepsilon_{n+1}\text{ fixed}} = \frac{d\alpha}{d\theta}\cdot E\cdot\varepsilon_{n+1} + \alpha\cdot\frac{dE}{d\theta}\cdot\varepsilon_{n+1}$$
$$-\frac{d\alpha}{d\theta}\cdot f_y\cdot z_{n+1} + (1-\alpha)\cdot\frac{df_y}{d\theta}\cdot z_{n+1} + (1-\alpha)\cdot f_y\cdot\left.\frac{dz_{n+1}}{d\theta}\right|_{\varepsilon_{n+1}\text{ fixed}} \quad (13)$$

Differentiation of Eq. (5) with respect to $\theta$ yields a somewhat lengthy expression with $dz_{n+1}/d\theta$ on both sides of the equal sign. As an example of the derivatives that appear is $d|z_{n+1}|^{\eta}/d\theta$, which evaluates to $\eta\,|z_{n+1}|^{\eta-1}\cdot\text{sign}(z_{n+1})\cdot dz_{n+1}/d\theta$. In the end, solving for $dz_{n+1}/d\theta$ yields the result required in Eq. (13). That result is implemented in G2 and its correctness is verified in Figure 3. Its correctness is also verified in subsequent plots because it serves as a foundation for the developments presented later.

## 6 SECTION DERIVATIVES, PART I

The result presented for $du/d\theta$ in Figure 3, for $\theta=E$, carries the simplicity that $E$ is a parameter of the material model. An additional point is now made for situations where $\theta$ is one of the cross-section parameters, i.e., $h_w$, $b_f$, $t_f$, or $t_w$. To that end, consider the section integration

$$\widetilde{\boldsymbol{F}}_s = \sum_{j=1}^{N_{\text{fib}}}(\mathbf{T}_{ms}\cdot A\cdot\sigma) \tag{14}$$

where the section force vector, $\widetilde{\boldsymbol{F}}_s=[M,\ N]^{\text{T}}$, contains the bending moment, $M$, and the axial force, $N$, $N_{\text{fib}}$ is the number of fibers in the cross-section, and $\mathbf{T}_{ms}=[-y,\ 1]^{\text{T}}$ is the kinematic transformation between the material level and the section level, entering the relationship $\varepsilon=\mathbf{T}_{ms}\mathbf{u}_s$. The symbol $y$ denotes the location of the fiber relative to the centroid. The cross-section parameters $h_w$ and $t_f$ affect $y$. In that case, the complete derivative of the section forces, sought in Eq. (11), reads

$$\left.\frac{\partial\widetilde{\boldsymbol{F}}_s(\mathbf{u}_{s,n+1})}{\partial\theta}\right|_{\mathbf{u}_{s,n+1}\text{ fixed}} = \sum_{j=1}^{N_{\text{fib}}}\left(\frac{\partial\mathbf{T}_{ms}}{\partial\theta}\cdot A\cdot\sigma_{n+1}+\mathbf{T}_{ms}\cdot\frac{\partial A}{\partial\theta}\cdot\sigma_{n+1}+\mathbf{T}_{ms}\cdot A\cdot\left(\frac{\partial\sigma_{n+1}}{\partial\varepsilon_{n+1}}\cdot\frac{\partial\varepsilon_{n+1}}{\partial\theta}+\left.\frac{\partial\sigma_{n+1}}{\partial\theta}\right|_{\varepsilon_{n+1}\text{ fixed}}\right)\right) \tag{15}$$

where $d\sigma_{n+1}/d\varepsilon_{n+1}$ is the stiffness of the material. The derivative $d\varepsilon_{n+1}/d\theta$ is carefully observed to be $(d\mathbf{T}_{ms}/d\theta)\mathbf{u}_s$, which involves the derivative of $y$ with respect to the cross-section parameter. For that reason, the implicit dependence of the stress via the strain in the last parenthesis in Eq. (15) is important for the accuracy of response derivatives calculated with respect to $h_w$ and $t_f$. Figure 4 included to emphasize that point; it shows the derivative of the tip displacement with respect to $h_w$. When $d\varepsilon_{n+1}/d\theta=d\mathbf{T}_{ms}/d\theta\,\mathbf{u}_s$ is included in Eq. (15), leading to the result shown as a blue line in Figure 4, then the result matches the finite difference results shown by black dots. In contrast, omitting $d\varepsilon_{n+1}/d\theta$ leads to the inaccurate result shows as a red line in Figure 4.

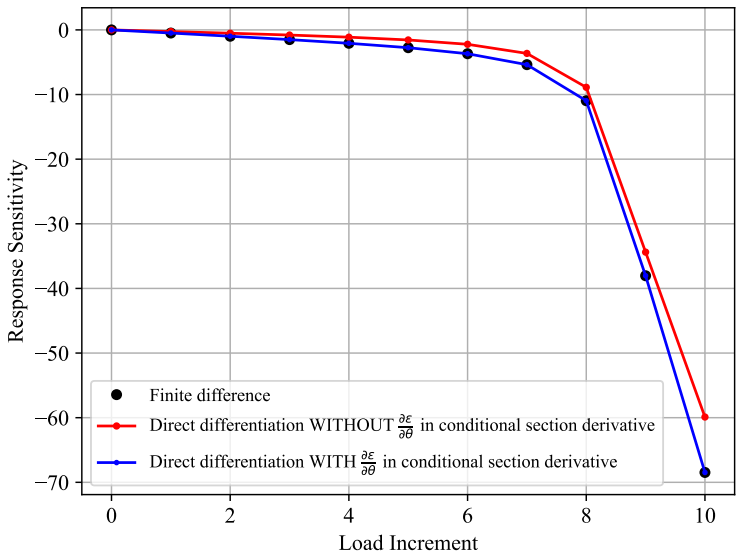


Figure 4: Inaccuracy in response sensitivity result when missing the chain rule of differentiation in Eq. (15).

The derivations presented thus far facilitate the plot of response sensitivities shown in Figure 5, obtained from the same nonlinear static analysis that produced Figure 3. Figure 5 shows the derivative of the tip displacement for three material parameters and four cross-section parameters. As before, black dots are finite difference results, provided to check the accuracy of the direct differentiation implementation, which product the colored lines. A scaling is conducted to facilitate the plotting of all results in one figure. Specifically, each variable is assigned at 10% coefficient of variation, which means that its standard deviation is 10% of the values provided earlier. Figure 5 shows the derivatives $du/d\theta$ multiplied by its respective standard deviation. The choice of a uniform coefficient of variation equal to 10% is made in order to provide transparent results. If the reader wishes to apply a smaller coefficient of variation to the geometry parameters, for instance, then that is achieved by scaling the relevant lines in Figure 5. With the uniform coefficient of variation, the web height is the most important parameter, followed by the flange width. The yield stress also ranks high. Note also that all parameters featured in Figure 5 are "resistance parameters," in the sense that increasing their value decreases the displacement response. The remainder of the paper deals with dynamic analysis.

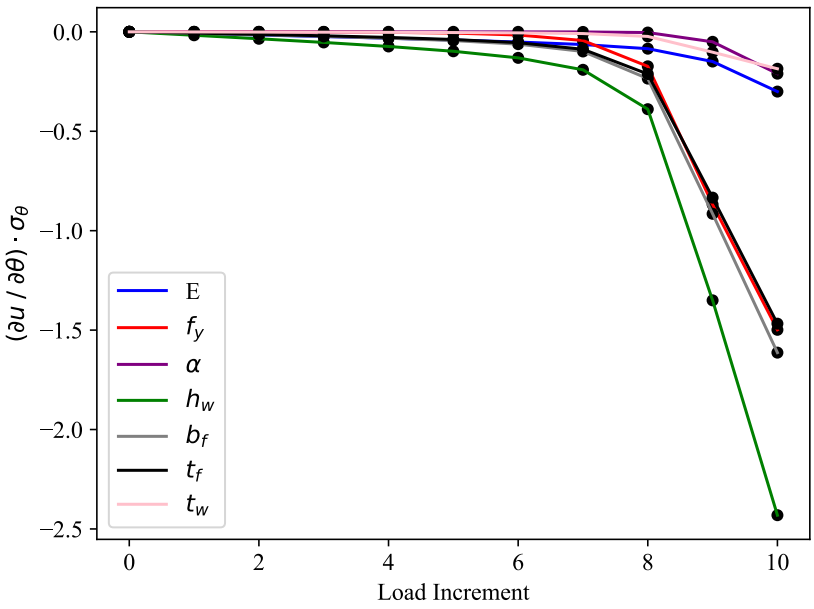


Figure 5: Derivatives $du/d\theta$ multiplied by the respective standard deviation of $\theta$.

To demonstrate the items presented already, in the context of dynamics, the cantilevered column in Figure 1 is subjected to an artificial impulse-type ground motion. It consists of a single sine-wave lasting from $t$=0 to $t$=0.5sec. with maximum amplitude 7g at $t$=0.25sec. The ground acceleration is zero after $t$=0.5sec. That ground motion is intended to cause significant yielding, thereby testing the derivations and implementations of the direct differentiation method. Several challenges disappear when the analysis is linear. In the analyses conducted in this section, the Rayleigh damping matrix $\mathbf{C}=c_M\mathbf{M}+c_K\mathbf{K}$ is employed with 5% damping ratio specified for the first two natural frequencies of the column. As a result, $c_M$=1.033 and $c_K$=0.001185 when the initial stiffness matrix is employed in the damping matrix. Figure 6 shows the displacement response at the top of the column, with colors identifying the degree of nonlinearity. The red color identifies increments where the first natural frequency is larger than 4.0 times the initial frequency; the magenta color identifies increments with that ratio above 2.0; the blue color identifies increments with that ratio above 1.01. The black line identifies

increments with little yielding. Figure 6 shows that significant yielding is taking place when the aforementioned ground motion is applied.

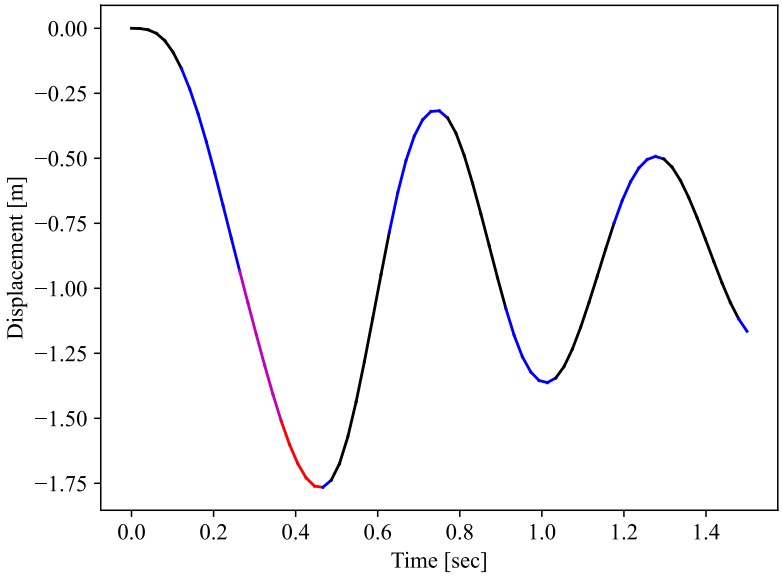


Figure 6: Displacement at the tip due to sine-wave pulse for Rayleigh damping using the initial stiffness.

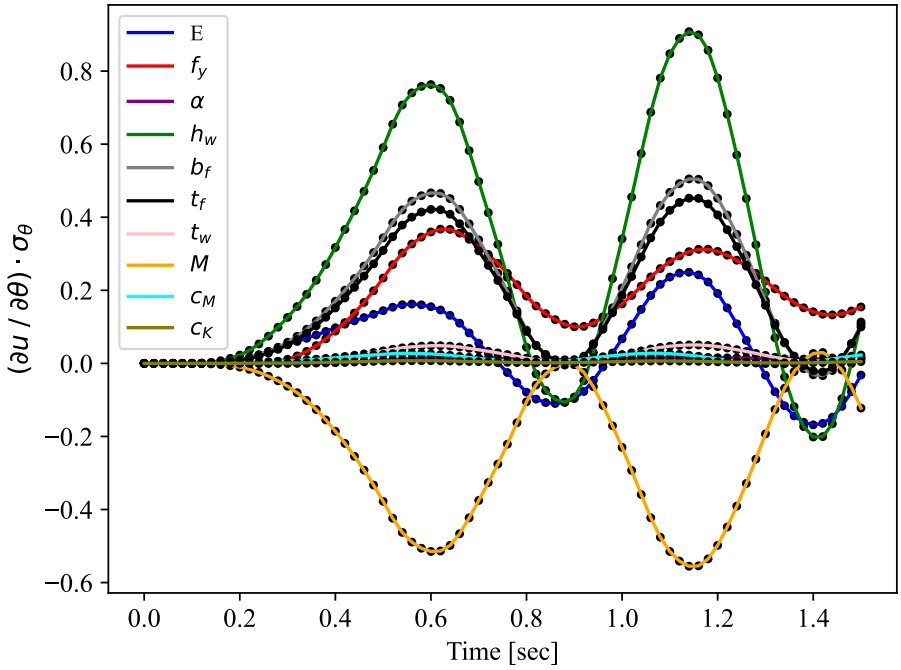


Figure 7: Response sensitivities $du/d\theta$ times $\sigma_\theta$ for initial-stiffness-damping and given $c_M$, $c_K$.

Figure 7 shows the displacement sensitivity results obtained for the seven parameters included in Figure 5, plus $M$, $c_M$, and $c_K$. As was done for the results in Figure 5, each response derivative is multiplied by the standard deviation of the respective parameter, with a 10% coefficient of variation assigned to all variables. With that scaling, the mass and the cross-section height are the two most important parameters; the former serves as a load variable; the latter serves as a resistance variable. Also, notice that $c_M$ and $c_K$ do not show up as important input parameters, with the given coefficients of variation. Finally, notice that Figure 7 reveal high

sensitivity of the response to parameter changes. Keeping in mind the caveat that those results are essentially local derivatives, not capturing nonlinearity, a 10% change in the value of the mass or the cross-section height would lead to a change in the response by more than 0.5m.

Figure 7 is also intended as a verification of the implementations of the direct differentiation method for nonlinear dynamic problems. As before, the black dots show results obtained by rerunning the analysis with perturbed parameter values, followed by finite difference estimation of the response derivatives. Figure 7 suggests an excellent match between the finite difference approximation and the exact results. That fact is confirmed in the analyses conducted as background work for this paper; the difference between the results obtained from the implementation of the direct differentiation method and the finite difference approximations are at least six orders of magnitude smaller than the sensitivity result. In this paper, the parameter perturbation in the finite difference analyses is set equal to $10^{-8}$ times the original parameter value.

## 7 RAYLEIGH COEFFICIENT DERIVATIVES

The derivative $d\mathbf{C}/d\theta$ appears in the right-hand side of Eq. (11). With the Rayleigh damping matrix $\mathbf{C}=c_M\mathbf{M}+c_K\mathbf{K}$, utilizing the initial stiffness matrix, that derivative reads

$$\frac{\partial \mathbf{C}}{\partial \theta} = \frac{\partial c_M}{\partial \theta}\mathbf{M} + c_M\frac{\partial \mathbf{M}}{\partial \theta} + \frac{\partial c_K}{\partial \theta}\mathbf{K} + c_K\frac{\partial \mathbf{K}}{\partial \theta} \tag{16}$$

Suppose $c_M$ and $c_K$ are implicitly specified by the analyst as a target damping ratio, $\zeta_{\text{target}}$, at two natural frequencies $\omega_1$ and $\omega_2$. In that case [15]

$$c_M = \omega_1 \cdot \omega_2 \cdot \frac{2\cdot\zeta_{\text{target}}}{\omega_1+\omega_2} \tag{17}$$

and

$$c_K = \frac{2\cdot\zeta_{\text{target}}}{\omega_1+\omega_2} \tag{18}$$

As a result, the derivatives required in Eq. (16) are

$$\frac{\partial c_M}{\partial \theta} = \frac{\partial \omega_1}{\partial \theta}\cdot\omega_2\cdot\frac{2\cdot\zeta_{\text{target}}}{\omega_1+\omega_2} + \omega_1\cdot\frac{\partial \omega_2}{\partial \theta}\cdot\frac{2\cdot\zeta_{\text{target}}}{\omega_1+\omega_2} - \omega_1\cdot\omega_2\cdot\frac{2\cdot\zeta_{\text{target}}}{(\omega_1+\omega_2)^2}\cdot\left(\frac{\partial \omega_1}{\partial \theta}+\frac{\partial \omega_2}{\partial \theta}\right) \tag{19}$$

and

$$\frac{\partial c_K}{\partial \theta} = -\frac{2\cdot\zeta_{\text{target}}}{(\omega_1+\omega_2)^2}\cdot\left(\frac{\partial \omega_1}{\partial \theta}+\frac{\partial \omega_2}{\partial \theta}\right) \tag{20}$$

The derivatives $d\omega_1/d\theta$ and $d\omega_2/d\theta$ are obtained from the derivative of the eigenvalues $\gamma_1$ and $\gamma_2$ from the eigenvalue problem $[\mathbf{K}-\gamma\mathbf{M}]\boldsymbol{\phi}=\mathbf{0}$, where $\boldsymbol{\phi}$ is an eigenvector. Because $\omega$ is the square root of $\gamma$, the result is

$$\frac{\partial \omega}{\partial \theta} = \frac{1}{2}\cdot\frac{1}{\sqrt{\gamma}}\cdot\frac{\partial \gamma}{\partial \theta} \tag{21}$$

Before embarking on the calculation of $d\gamma/d\theta$, it is noted that the eigenvectors are scaled to unit length. As a result, the norm $||\boldsymbol{\phi}||$ equals unity and the derivative $\mathrm{d}||\boldsymbol{\phi}||/d\theta$ is zero. It can be shown that $\mathrm{d}||\boldsymbol{\phi}||/d\theta$ equals the dot product $\boldsymbol{\phi}^{\mathrm{T}}(\mathrm{d}\boldsymbol{\phi}/d\theta)$, and the fact that $\boldsymbol{\phi}^{\mathrm{T}}(\mathrm{d}\boldsymbol{\phi}/d\theta)=0$ is employed in the following. The derivative of the eigenvalues are derived by differentiating $[\mathbf{K}-\gamma\mathbf{M}]\boldsymbol{\phi}=\mathbf{0}$ with respect to $\theta$, which yields [16]

$$\frac{d\mathbf{K}}{d\theta}\boldsymbol{\phi} - \frac{d\gamma}{d\theta}\mathbf{M}\,\boldsymbol{\phi} - \gamma\frac{d\mathbf{M}}{d\theta}\boldsymbol{\phi} + [\mathbf{K}-\gamma\,\mathbf{M}]\,\frac{d\boldsymbol{\phi}}{d\theta} = \mathbf{0} \tag{22}$$

Multiplying through by $\boldsymbol{\phi}^{\mathrm{T}}$ from the left, observing that $\boldsymbol{\phi}^{\mathrm{T}}(\mathrm{d}\boldsymbol{\phi}/d\theta)=0$, and solving for $d\gamma/d\theta$ yields

$$\frac{d\gamma}{d\theta} = \frac{\boldsymbol{\phi}^{\mathrm{T}}\frac{d\mathbf{K}}{d\theta}\boldsymbol{\phi} - \gamma\boldsymbol{\phi}^{\mathrm{T}}\frac{d\mathbf{M}}{d\theta}\boldsymbol{\phi}}{\boldsymbol{\phi}^{\mathrm{T}}\mathbf{M}\,\boldsymbol{\phi}} \tag{23}$$

Figure 8 is offered to verify that result, with black dots representing finite difference results, and to gain insight into the importance of the target damping. Again, an excellent match between direct differentiation and finite difference results are observed in the figure and in the background analyses for this paper. As observed earlier for $c_M$ and $c_K$, the target damping does not appear as an important variable for the 10% coefficient of variation that is assigned uniformly to all parameters.

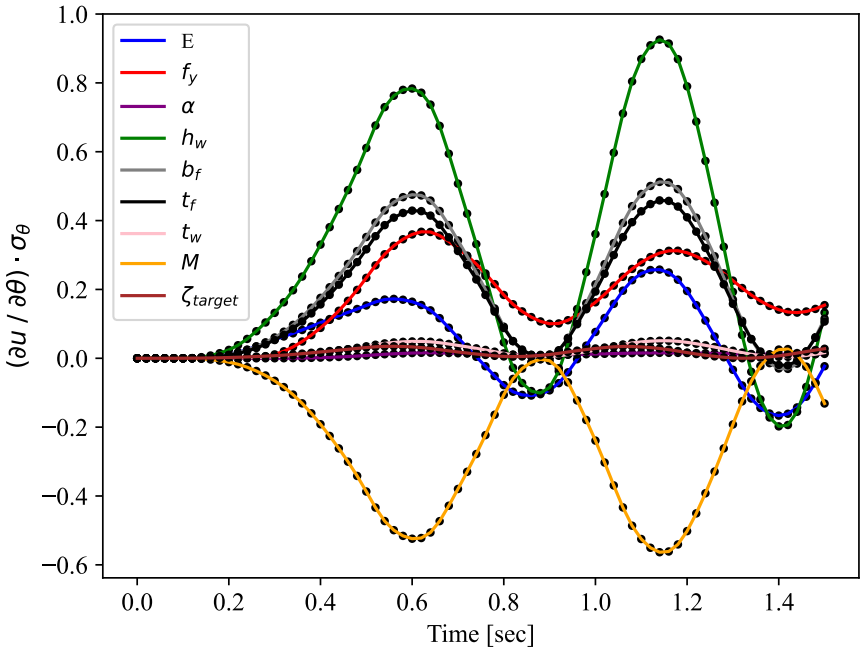


Figure 8: $du/d\theta \cdot \sigma_\theta$ for initial-stiffness-damping and use of eigenvalues to calculate $c_M$ and $c_K$.

## 8 RAYLEIGH MATRIX DERIVATIVES, PART I

Now consider the case where the Rayleigh damping matrix is formulated in terms of the current tangent stiffness matrix:

$$\mathbf{C} = c_M\mathbf{M} + c_K\mathbf{K}(\mathbf{u}(\theta),\theta) \tag{24}$$

where the implicit dependence on $\theta$ via $\mathbf{u}$ is highlighted, together with the potential explicit dependence on $\theta$ via the algorithm that forms $\mathbf{K}$. Before proceeding, the displacement response with that damping scheme is displayed in Figure 9. As expected, the maximum displacement is now somewhat larger than what is displayed in Figure 6. That is the result of the lower damping associated with the lower current tangent stiffness. Differentiation of the damping matrix in Eq. (24) yields

$$\frac{\partial\mathbf{C}}{\partial\theta} = \frac{\partial c_M}{\partial\theta}\mathbf{M} + c_M\frac{\partial\mathbf{M}}{\partial\theta} + \frac{\partial c_K}{\partial\theta}\mathbf{K} + c_K\left(\frac{\partial\mathbf{K}}{\partial\mathbf{u}_{n+1}}\frac{\partial\mathbf{u}_{n+1}}{\partial\theta} + \left.\frac{\partial\mathbf{K}(\mathbf{u}_{n+1})}{\partial\theta}\right|_{\mathbf{u}\text{ fixed}}\right) \tag{25}$$

The appearance of the third-order tensor $d\mathbf{K}/d\mathbf{u}$ is unusual in structural analysis. It appears because of the implicit dependence on $\theta$ via $\mathbf{u}$. In fact, Eq. (25) shows that the elements, sections, and materials must produce $d\mathbf{K}/d\mathbf{u}$, in addition to the conditional derivative $d\mathbf{K}/d\theta$. That

challenge is addressed in the next section for the Bouc-Wen model; the presence of $d\mathbf{K}/d\mathbf{u}$ is the primary reason why that material model is selected for this paper. For a bilinear model, the result would be $d\mathbf{K}/d\mathbf{u}=\mathbf{0}$ because the displacement would not affect the stiffness in the infinitesimal vicinity of any strain value, whether the response is elastic or plastic. Conversely, a material model with a nonlinear stress-strain curve, such as the Bouc-Wen model, will have $d\mathbf{K}/d\mathbf{u}\neq\mathbf{0}$.

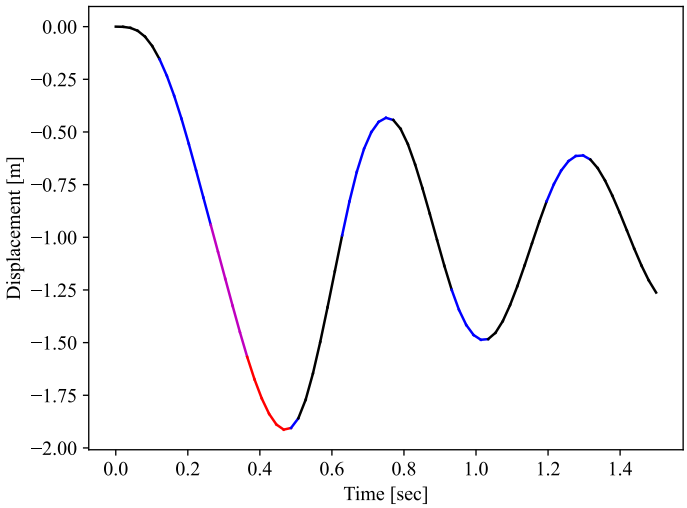


Figure 9: Displacement response for Rayleigh damping with current tangent stiffness.

Eq. (25) raises another issue; the sought response sensitivity $d\mathbf{u}/d\theta$ appears in $d\mathbf{C}/d\theta$, and therefore in the right-hand side of Eq. (11). Recall that Eq. (11) is a system of equations intended to be solved for exactly $d\mathbf{u}/d\theta$. This means that the portion of Eq. (25) with $d\mathbf{u}/d\theta$ must be moved to the left-hand side of Eq. (11). To accomplish that, two steps are taken. First, the part of Eq. (25) that contains $d\mathbf{u}/d\theta$ is substituted into the relevant term in the right-hand side of Eq. (11). That term is a vector here denoted by the symbol $\mathbf{b}$:

$$\mathbf{b} = -c_K \frac{\partial \mathbf{K}}{\partial \mathbf{u}_{n+1}} \frac{\partial \mathbf{u}_{n+1}}{\partial \theta} (a_5 \mathbf{u}_{n+1} + a_6 \mathbf{u}_n + a_7 \dot{\mathbf{u}}_n + a_8 \ddot{\mathbf{u}}_n) \tag{26}$$

Index notation is helpful when isolating $d\mathbf{u}/d\theta$ in order to have the remainder serve as the modification to the coefficient matrix in Eq. (11):

$$b_i = -c_K \left(\frac{\partial \mathbf{K}}{\partial \mathbf{u}_{n+1}}\right)_{imj} \left(\frac{\partial \mathbf{u}_{n+1}}{\partial \theta}\right)_j (a_5 \mathbf{u}_{n+1} + a_6 \mathbf{u}_n + a_7 \dot{\mathbf{u}}_n + a_8 \ddot{\mathbf{u}}_n)_m =$$

$$= -\left[c_K \left(\frac{\partial \mathbf{K}}{\partial \mathbf{u}_{n+1}}\right)_{imj} (a_5 \mathbf{u}_{n+1} + a_6 \mathbf{u}_n + a_7 \dot{\mathbf{u}}_n + a_8 \ddot{\mathbf{u}}_n)_m\right] \left(\frac{\partial \mathbf{u}_{n+1}}{\partial \theta}\right)_j \tag{27}$$

The square bracket contains the amendment to the effective stiffness, i.e., the coefficient matrix in Eq. (11). Importantly, Eq. (27) shows that the parenthesis $(a_5 \mathbf{u}_{n+1} + a_6 \mathbf{u}_n + a_7 \dot{\mathbf{u}}_n + a_8 \ddot{\mathbf{u}}_n)$ is contracted with the middle index of the third-order tensor $\partial\mathbf{K}/\partial\mathbf{u}$. That amendment is implemented in G2, together with the derivations in the next section, in order to obtain correct response sensitivities in nonlinear dynamics with Rayleigh damping specified in terms of the current tangent stiffness. In passing, it is noted that this development also amends a somewhat imprecise statement made by the author near Eq. (24) in [17]. Rayleigh damping with current tangent stiffness does not lead to a nonlinear system of equations for the response sensitivities; rather, the coefficient matrix must be adjusted as described above.

## 9 BOUC-WEN DERIVATIVES, PART II

The previous section reveals the need for $d\mathbf{K}/d\mathbf{u}$ and $d\mathbf{K}/d\theta$, the latter conditional on fixed current displacements. At the material level, this prompts the calculation of the derivative of the stiffness, $d\sigma_{n+1}/d\varepsilon_{n+1}$, and therefore $dz_{n+1}/d\varepsilon_{n+1}$, with respect to $\varepsilon_{n+1}$ and also with respect to $\theta$, the latter for fixed $\varepsilon_{n+1}$. Earlier in this paper, Eq. (5) was differentiated with respect to $\varepsilon_{n+1}$ in order to obtain the algorithmically consistent tangent stiffness. That derivative is now differentiated again, separately with respect to $\varepsilon_{n+1}$ and $\theta$. The resulting expressions for $d(dz_{n+1}/d\varepsilon_{n+1})/d\varepsilon_{n+1}$ and $d(dz_{n+1}/d\varepsilon_{n+1})/d\theta$ are implemented in G2 in order to obtain the results presented shortly.

## 10 SECTION DERIVATIVES, PART II

The point made earlier in regards to the differentiation of the section integration in Eq. (14) is here reiterated for the calculation of $d\mathbf{K}/d\theta$. The importance of this point relates to situations where $\theta$ is a cross-section parameter that affects the transformation $\varepsilon = \mathbf{T}_{ms}\mathbf{u}_s$. The section integration to calculate the section stiffness reads

$$\mathbf{K}_s = \sum_{j=1}^{N_{\text{fib}}} (\mathbf{T}_{ms}^{\text{T}} \mathbf{T}_{ms} \cdot A \cdot \sigma) \tag{28}$$

The derivative sought in the last term in Eq. (25) is, when $\theta$ is a section parameter:

$$\left.\frac{\partial \mathbf{K}_s}{\partial \theta}\right|_{\mathbf{u}_{s,n+1}\text{ fixed}} = \sum_{j=1}^{N_{\text{fib}}} \left( \begin{array}{c} \frac{\partial \mathbf{T}_{ms}}{\partial \theta} \mathbf{T}_{ms} \cdot A \cdot \frac{\partial \sigma_{n+1}}{\partial \varepsilon_{n+1}} + \mathbf{T}_{ms} \frac{\partial \mathbf{T}_{ms}}{\partial \theta} \cdot A \cdot \frac{\partial \sigma_{n+1}}{\partial \varepsilon_{n+1}} \\ + \mathbf{T}_{ms} \cdot \frac{\partial A}{\partial \theta} \cdot \frac{\partial \sigma_{n+1}}{\partial \varepsilon_{n+1}} + \mathbf{T}_{ms}^{\text{T}} \mathbf{T}_{ms} \cdot A \cdot \left( \frac{\partial \left(\frac{\partial \sigma_{n+1}}{\partial \varepsilon_{n+1}}\right)}{\partial \varepsilon_{n+1}} \cdot \frac{\partial \varepsilon_{n+1}}{\partial \theta} + \left.\frac{\partial \left(\frac{\partial \sigma_{n+1}}{\partial \varepsilon_{n+1}}\right)}{\partial \theta}\right|_{\varepsilon_{n+1}\text{ fixed}} \right) \end{array} \right) \tag{29}$$

where the derivative of the stiffness with respect to the strain, an unusual quantity in structural analysis, appears. Figure 10, the result of nonlinear dynamic analysis, shows displacement derivatives with respect to $h_w$. The figure highlights the importance of including the somewhat unusual derivatives $d(d\sigma_{n+1}/d\varepsilon_{n+1})/d\varepsilon_{n+1}$ and $d(d\sigma_{n+1}/d\varepsilon_{n+1})/d\theta$ in order to calculate correct response sensitivities. With those quantities included, the blue line in Figure 10 matches perfectly the finite difference result, shown as black dots. Conversely, missing the aforementioned derivatives in Eq. (29) yields the erroneous red line in Figure 10.

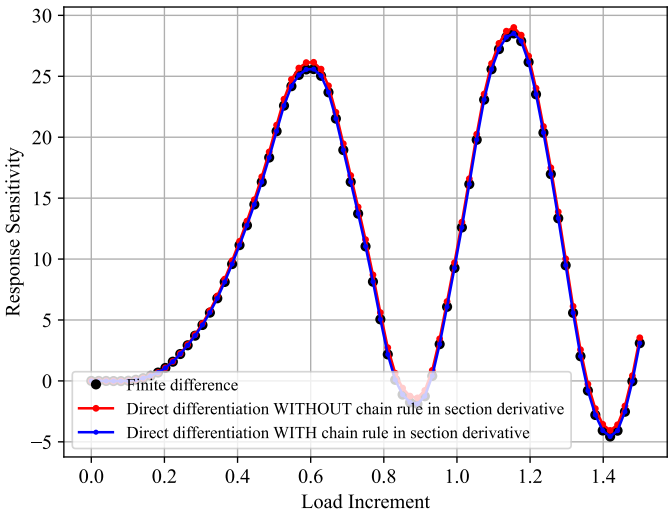


Figure 10: Inaccuracy in response sensitivity result when missing the chain rule of differentiation in Eq. (29).

## 11 RAYLEIGH MATRIX DERIVATIVES, PART II

The use of the current tangent stiffness in Rayleigh damping has an additional consequence when $c_M$ and $c_K$ are implicitly specified as a target damping ratio, $\zeta$, at two natural frequencies $\omega_1$ and $\omega_2$. The earlier derivations are now extended to include the implicit dependence of $\theta$ via the displacement vector. Differentiation of $c_M$ yields

$$\frac{\partial c_M}{\partial \theta} = \left(\frac{\partial c_M}{\partial \omega_1}\cdot\frac{\partial \omega_1}{\partial \gamma_1}\cdot\frac{\partial \gamma_1}{\partial \mathbf{K}} + \frac{\partial c_M}{\partial \omega_2}\cdot\frac{\partial \omega_2}{\partial \gamma_2}\cdot\frac{\partial \gamma_2}{\partial \mathbf{K}}\right)\cdot\frac{\partial \mathbf{K}}{\partial \mathbf{u}}\cdot\frac{\partial \mathbf{u}}{\partial \theta} + \left.\frac{\partial c_M}{\partial \theta}\right|_{\mathbf{u}\text{ fixed}} \tag{30}$$

and differentiation of $c_K$ yields

$$\frac{\partial c_K}{\partial \theta} = \left(\frac{\partial c_K}{\partial \omega_1}\cdot\frac{\partial \omega_1}{\partial \gamma_1}\cdot\frac{\partial \gamma_1}{\partial \mathbf{K}} + \frac{\partial c_K}{\partial \omega_2}\cdot\frac{\partial \omega_2}{\partial \gamma_2}\cdot\frac{\partial \gamma_2}{\partial \mathbf{K}}\right)\cdot\frac{\partial \mathbf{K}}{\partial \mathbf{u}}\cdot\frac{\partial \mathbf{u}}{\partial \theta} + \left.\frac{\partial c_K}{\partial \theta}\right|_{\mathbf{u}\text{ fixed}} \tag{31}$$

All derivatives required in Eqs. (30) and (31) are presented earlier, except the derivative of the eigenvalues with respect to the current stiffness matrix, i.e., $d\gamma/d\mathbf{K}$. In fact, the conditional derivatives in the last term of Eqs. (30) and (31) are presented earlier in Eqs. (19) and (20). In order to obtain $d\gamma/d\mathbf{K}$, it is again helpful to employ index notation. The eigenvalue problem then reads

$$\left[K_{ij} - \gamma M_{ij}\right]\phi_j = 0 \tag{32}$$

Differentiating through with respect to the stiffness matrix yields

$$\frac{d}{dK_{kl}}\left(\left[K_{ij} - \gamma M_{ij}\right]\phi_j\right) = \left[\frac{dK_{ij}}{dK_{kl}} - \frac{d\gamma}{dK_{kl}}M_{ij} - \gamma\frac{dM_{ij}}{dK_{kl}}\right]\phi_j + \left[K_{ij} - \gamma M_{ij}\right]\frac{d\phi_j}{dK_{kl}} = 0 \tag{33}$$

Multiplying from the left by the transpose of the eigenvector causes the last term to vanish, as before, with the result

$$\phi_i\frac{dK_{ij}}{dK_{kl}}\phi_j - \phi_i\frac{d\gamma}{dK_{kl}}M_{ij}\,\phi_j - \phi_i\gamma\frac{dM_{ij}}{dK_{kl}}\phi_j = 0 \tag{34}$$

where the "identity matrix" is recognized in the first term:

$$\phi_i I_{ij,kl}\phi_j - \phi_i\frac{d\gamma}{dK_{kl}}M_{ij}\,\phi_j - \phi_i\gamma\frac{dM_{ij}}{dK_{kl}}\phi_j = 0 \tag{35}$$

The derivative of the mass with respect to stiffness, in the last term, is zero in practical situations. The product $\phi_i I_{ij,kl}\phi_j$ results in a matrix formed by the outer product of the eigenvector with itself. Solving for the sought derivative yields

$$\frac{d\gamma}{dK_{kl}} = \frac{\phi_k\phi_l}{\phi_i M_{ij}\,\phi_j} \tag{36}$$

In vector-matrix notation, that result reads

$$\frac{d\gamma}{d\mathbf{K}} = \frac{\boldsymbol{\phi}\boldsymbol{\phi}^{\mathrm{T}}}{\boldsymbol{\phi}^{\mathrm{T}}\mathbf{M}\,\boldsymbol{\phi}} \tag{37}$$

Eqs. (30) and (31) represent yet another case where the sought response sensitivity, $d\mathbf{u}/d\theta$, appears in the right-hand side of Eq. (11). Index notation is again employed, albeit not shown here for brevity, to demonstrate the following: 1) The amendment to the coefficient matrix of the response sensitivity system is the outer product of two vectors; 2) The first vector is obtained by a contraction of the first two indices of $d\mathbf{K}/d\mathbf{u}$ with the two indices of $d\gamma/d\mathbf{K}$; 3) The second vector is obtained from the matrix-vector product of the mass matrix with the parenthesis that contains $a_5$, presented earlier. Interestingly, the resulting correction of the coefficient matrix in the system of equations for $d\mathbf{u}/d\theta$ is asymmetric. This fact is verified in the background analyses

for this paper, with a perfect match obtained with finite difference results once the previous equations are correctly implemented. Figures are not included here because they look very similar to Figure 7 and Figure 8.

## 12 MODAL DAMPING

Several problems are associated with the use of Rayleigh damping in nonlinear dynamic analysis. That is the case regardless of whether the initial stiffness or the current tangent stiffness is included [18][19][20]. Chopra and McKenna [20] identify the benefits of employing the modal damping matrix instead, which reads

$$\mathbf{C} = \mathbf{M}\left(\sum_{j=1}^{N} \frac{2\zeta_j \omega_j}{m_j} \boldsymbol{\phi}_j \boldsymbol{\phi}_j^{\mathrm{T}}\right)\mathbf{M} \tag{38}$$

where $N$ is here the number of modes, $\zeta_j$ is the imposed damping ratio at mode $j$, $\omega_j$ is the natural frequency of vibration in mode $j$, $\boldsymbol{\phi}_j$ is the corresponding mode shape, and $m_j$ is the modal mass, i.e., $\boldsymbol{\phi}_j^{\mathrm{T}}\mathbf{M}\boldsymbol{\phi}_j$. The objective now is to calculate the derivative $\partial\mathbf{C}/\partial\theta$, where $\theta$ is an input parameter to the finite element model. The product rule of differentiation yields

$$\begin{aligned}\frac{d\mathbf{C}}{d\theta} &= \frac{d\mathbf{M}}{d\theta}\left(\sum_{j=1}^{N} \frac{2\zeta_j \omega_j}{m_j} \boldsymbol{\phi}_j \boldsymbol{\phi}_j^{\mathrm{T}}\right)\mathbf{M} \\ &+\mathbf{M}\left(\sum_{j=1}^{N} \frac{2\zeta_j \frac{d\omega_j}{d\theta}}{m_j} \boldsymbol{\phi}_j \boldsymbol{\phi}_j^{\mathrm{T}}\right)\mathbf{M} - \mathbf{M}\left(\sum_{j=1}^{N} \frac{2\zeta_j \omega_j}{m_j^2} \cdot \frac{dm_j}{d\theta} \cdot \boldsymbol{\phi}_j \boldsymbol{\phi}_j^{\mathrm{T}}\right)\mathbf{M} \\ &+\mathbf{M}\left(\sum_{j=1}^{N} \frac{2\zeta_j \omega_j}{m_j} \cdot \frac{d\boldsymbol{\phi}_j}{d\theta} \boldsymbol{\phi}_j^{\mathrm{T}}\right)\mathbf{M} + \mathbf{M}\left(\sum_{j=1}^{N} \frac{2\zeta_j \omega_j}{m_j} \boldsymbol{\phi}_j \frac{d\boldsymbol{\phi}_j^{\mathrm{T}}}{d\theta}\right)\mathbf{M} \\ &+\mathbf{M}\left(\sum_{j=1}^{N} \frac{2\zeta_j \omega_j}{m_j} \boldsymbol{\phi}_j \boldsymbol{\phi}_j^{\mathrm{T}}\right)\frac{d\mathbf{M}}{d\theta}\end{aligned} \tag{39}$$

where $dm_j/d\theta = (d\boldsymbol{\phi}_j/d\theta)^{\mathrm{T}}\mathbf{M}\boldsymbol{\phi}_j + \boldsymbol{\phi}_j^{\mathrm{T}}(d\mathbf{M}/d\theta)\boldsymbol{\phi}_j + \boldsymbol{\phi}_j^{\mathrm{T}}\mathbf{M}(d\boldsymbol{\phi}_j/d\theta)$. The derivative of the mass matrix is usually trivial and the derivative of eigenvalues and eigenvectors are developed in previous sections. Plots are not presented in this section for brevity, but Eq. (39) is implemented in G2 and the results are verified by means of finite difference calculations. The reason why plots are omitted is that, when the initial stiffness matrix is employed in the eigenvalue problem to determine $\gamma$ and $\boldsymbol{\phi}$, the displacement response is essentially the same as in Figure 6, presented earlier. Furthermore, the sensitivity results are essentially the same as in Figure 8.

## 13 APPLICATIONS

Gradient-based algorithms, employed in design optimization and the first-order reliability method, are direct applications of the response sensitivities derived in this paper. However, one may argue that all nonlinear dynamic analyses should be accompanied by considerations of response sensitivities. A few examples are suggested in the following sections.

### 13.1 Importance Ranking of Input Parameters

One obvious application of response sensitivity results is displayed in Figure 5, Figure 7, and Figure 8. Those plots show the evolution in the response sensitivities with time, or pseudo-time for static analysis. However, in those plots, the choice of 10% coefficient of variation for all parameters is not realistic. Denoting a coefficient of variation by the symbol $\delta$, the somewhat

more realistic choices $\delta_E$=10%, $\delta_{fy}$=20%, $\delta_\alpha$=20%, $\delta_{hw}$=2%, $\delta_{bf}$=2%, $\delta_{tf}$=2%, $\delta_{tw}$=2%, $\delta_M$=20%, and $\delta_{targetDamping}$=20% give a new version of Figure 8, shown in Figure 11. The analysis is continued until 3 seconds, for the same sine pulse as described earlier, for the sake of this illustration. As explained on Page 39 of the book by Der Kiureghian [21], $(du/d\theta)\sigma_\theta$, displayed in Figure 11 and earlier, is a basic importance measure for the ranking input parameters. Figure 11 reveals that the mass and the yield stress are the most important input parameters, with opposite effect on the displacement. Also note that even parameters such as the modulus of elasticity and the cross-section height rank above the target damping in importance.

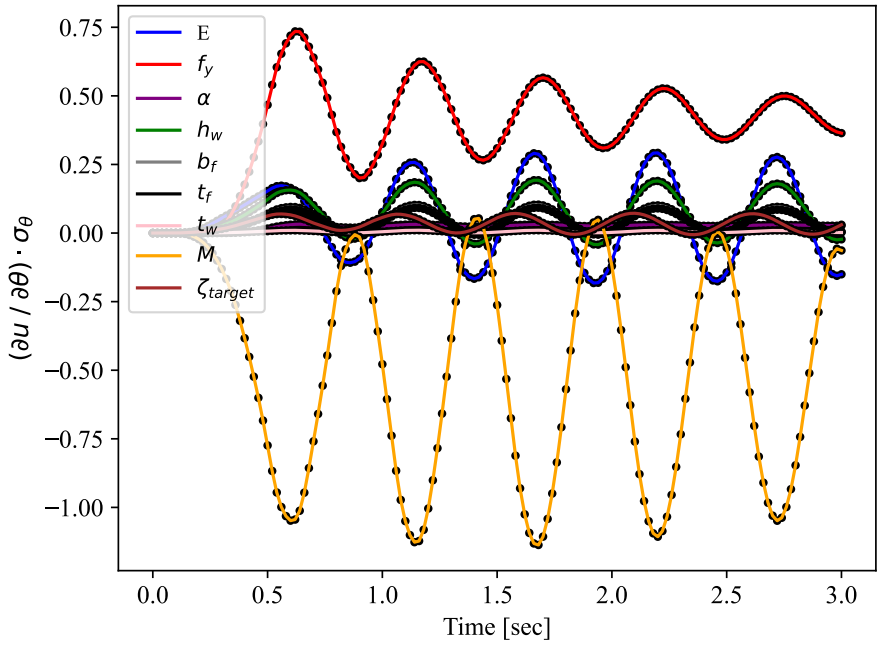


Figure 11: New version of Figure 8 with updated $\sigma_\theta$-values.

## 13.2 Response Standard Deviation

Another application of response sensitivities calculated alongside the response is the estimation of the standard deviation of the response. In the absence of correlation, an approximation of the standard deviation based on a Taylor linearization of the displacement is the square root of the sum of squared values in Figure 11. See for example Section 2.9 in [21]. The result is shown in Figure 12. The result in Figure 12 is produced with Rayleigh damping with the initial stiffness, and the uniform 10% coefficients of variation for all parameters. In Figure 6, presented earlier, the average displacement is roughly 0.8m with a maximum displacement of 1.75m. Considering uncertainty in all of $E$, $f_y$, $\alpha$, $h_w$, $b_f$, $t_f$, $t_w$, $M$, and $\zeta_{target}$ the resulting standard deviation of the response is displayed in Figure 12. The average standard deviation of the response, as well as the maximum standard deviation, are near the average and maximum displacement. That high value of the standard deviation stems from the high sensitivity remarked below Figure 7.

## 13.3 Actual Ground Motion

A comment related to the coefficient of variation of the response is added by subjecting the column in Figure 1 to the well-known El Centro ground motion, here scaled to a peak ground acceleration of 3g in order to observe nonlinear structural behaviour. Repeating the analysis setup with 10% coefficient of variation for all nine uncorrelated input parameters, plus Rayleigh damping with the initial stiffness matrix, produces the displacement response shown in Figure

13. If that response is considered as a stochastic process, then its standard deviation is varying at levels below approximately 0.2m. However, that standard deviation is not what is discussed in the previous section. Rather, the coefficient of variation gleaned from Figure 13 is a result of the energy, i.e., variance of the ground motion. Conversely, the coefficient of variation discussed in the previous section and plotted in Figure 14 for the El Centro ground motion is the standard deviation of the function $u(\mathbf{x})$, where $\mathbf{x}$ is the vector containing the nine input random variables. Figure 14 matches the observation made in the previous section, showing response standard deviations of the same order of magnitude as the response.

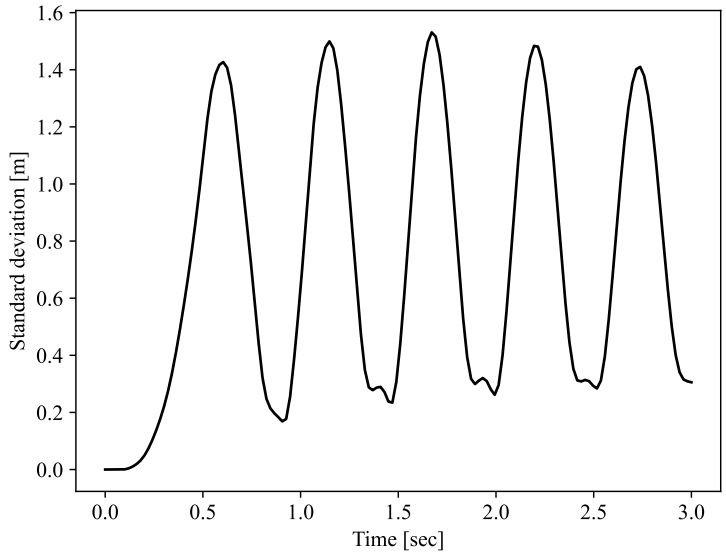


Figure 12: Standard deviation of the displacement, as a function of time, using the values in Figure 11.

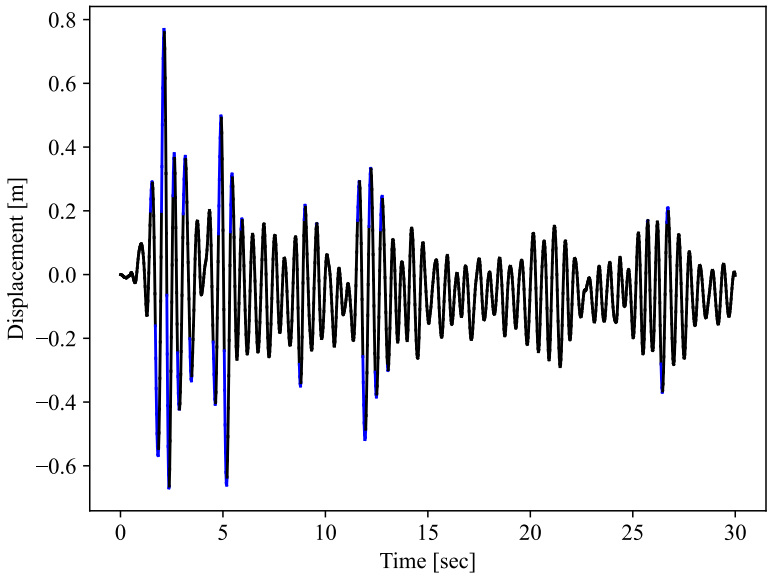


Figure 13: Displacement at the tip of the column subjected to the scaled El Centro ground motion.

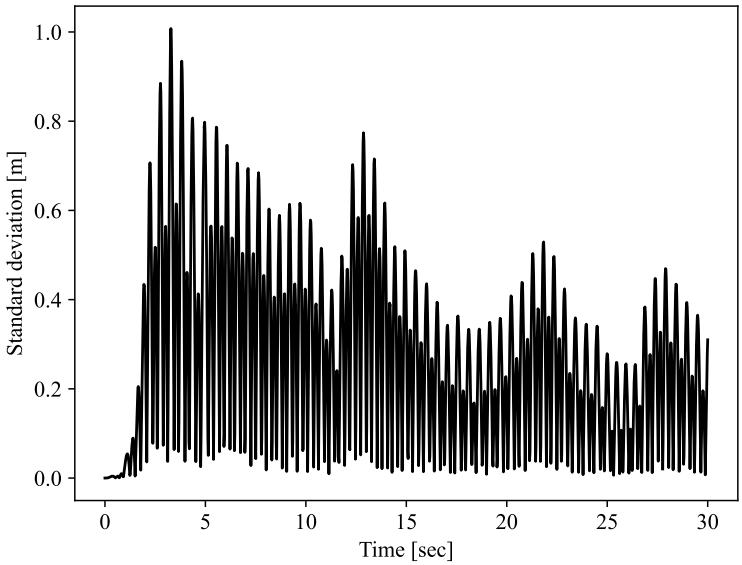


Figure 14: Standard deviation of the displacement for the scaled El Centro ground motion.

## 14 CONCLUSIONS

A viscous damping matrix is needed in nonlinear dynamic analysis of structures. Several options exist. A common choice is Rayleigh damping, in which the damping matrix is a weighted sum of the mass matrix and either the initial stiffness matrix or the current stiffness matrix. The modal damping matrix serves as yet another alternative. This paper presents derivations, implementations, and calculations of exact response sensitivities when any of the those damping models are employed. The direct differentiation method is adopted; that means the governing response equations are analytically differentiated and implemented alongside the response algorithm. The three-dimensional tensor formed by differentiation of the stiffness matrix with respect to the displacement vector appear in the derivations. So does the derivative of the eigenvalues with respect to the input parameters. Results are presented in this paper to verify the response sensitivity implementations and to suggest applications for such results.

## REFERENCES

[1] Choi, K. K., Santos, J. L. T., Yao, T.-M. (1988). “Recent advances in design sensitivity analysis and its use in structural design process.” SAE Transactions, 97(5), 181-197.

[2] Arora, J. S. & Cardoso, J. B. (1989). “A design sensitivity analysis principle and its implementation into ADINA.” Computers & Structures, 43(3/4), 691-705.

[3] Tsay, J. J. & Arora, J. S. (1990). “Nonlinear structural design sensitivity analysis for path dependent problems. Part 1: General Theory.” Computer Methods in Applied Mechanics and Engineering, 81, 183-208.

[4] Tsay, J. J. & Arora, J. S. (1990). “Nonlinear structural design sensitivity analysis for path dependent problems. Part 2: Analytical Examples.” Computer Methods in Applied Mechanics and Engineering, 81, 209-228.

[5] Cardoso, J. B. & Arora, J. S. (1992). "Design sensitivity analysis of nonlinear dynamic response of structural and mechanical systems." Structural Optimization, 4, 37-46.

[6] Zhang, Y. & Der Kiureghian, A. (1993). "Dynamic response sensitivity of inelastic structures." Computer Methods in Applied Mechanics and Engineering, 108, 23-36.

[7] Haukaas, T. & Der Kiureghian, A. (2003). "Finite element reliability and sensitivity methods for performance-based earthquake engineering" Pacific Earthquake Engineering Research (PEER) Center Report No. 2003/14.

[8] Scott, M. H., Franchin, P., Fenves, G. L., Filippou, F. C. (2004). "Response sensitivity for nonlinear beam-column elements." ASCE Journal of Structural Engineering, 130(9), 1281-1288.

[9] Baber, T. T. & Noori, M. N. (1985). "Random vibration of degrading, pinching systems." ASCE Journal of Engineering Mechanics, 111(8), 1010–1026.

[10] McKenna, F., Scott, M. H., Fenves, G. L. (2010). "Nonlinear finite-element analysis software architecture using object composition." ASCE Journal of Computing in Civil Engineering, 24(1), 95-107.

[11] Schellenberg, A. H, Sarebanha, A., Schoettler, M. J., Mosqueda, G., Benzoni, G., Mahin, S. A. (2015). "Hybrid simulation of seismic isolation systems applied to an APR-1400 nuclear power plant." Pacific Earthquake Engineering Research (PEER) Center Report No. 2015/05.

[12] Casciati, F. (1989). "Stochastic dynamics of hysteretic media." Structural Safety, 6, 259-269.

[13] Wen, Y.-K. (1976). "Method for random vibration of hysteretic systems." ASCE Journal of Engineering Mechanics, 102(2), 249–263.

[14] Baber, T. T. & Wen, Y.-K. (1981). "Random vibration of hysteretic degrading systems." ASCE Journal of Engineering Mechanics, 107(6), 1069-1087.

[15] Chopra, A. K. (1995). Dynamics of structures: Theory and applications to earthquake engineering." Prentice Hall.

[16] Magnus, J. (1985). "On differentiating eigenvalues and eigenvectors." Econometric Theory, 1, 1790191.

[17] Haukaas, T. & Der Kiureghian, A. (2005). "Parameter sensitivity and importance measures in nonlinear finite element reliability analysis." ASCE Journal of Engineering Mechanis, 131(10), 1013-1026.

[18] Hall, J. F. (2006). "Problems encountered from the use (or misuse) of Rayleigh damping." Earthquake Engineering & Structural Dynamics, 35, 525-545.

[19] Carney, F. A. (2008). "Unintended consequences of modeling damping in structures." ASCE Journal of Structural Engineering, 134(4), 581-592.

[20] Chopra, A. K. & McKenna, F. (2016). "Modeling viscous damping in nonlinear response history analysis of buildings for earthquake excitation." Earthquake Engineering & Structural Dynamics, 45, 193-211.

[21] Der Kiureghian, A. (2022). "Structural and System Reliability." Cambridge University Press.

COMPDYN 2023
9th ECCOMAS Thematic Conference on
Computational Methods in Structural Dynamics and Earthquake Engineering
M. Papadrakakis, M. Fragiadakis (eds.)
Athens, Greece, 12-14 June 2023

# GROUND MOTION PROCESSING IN ROCKING STRUCTURES

**Medhat Elmorsy[1, 2] and Michalis F. Vassiliou[1]**

[1]Chair of Seismic Design and Analysis, Institute of Structural Engineering (IBK), ETH Zürich

[2]Structural Engineering Department, Mansoura University, Mansoura, Egypt

{medhat.elmorsy, vassiliou}@ibk.baug.ethz.ch

## Abstract

*Recorded ground motions require filtering and baseline correction to remove noise that results in unrealistic velocity and displacement time histories. The effect of ground motion processing is well studied for elastic and inelastic oscillators; however, it has not been studied for the rocking oscillator. The behavior of the rocking oscillator is used to describe a wide range of systems; such as masonry structures, unanchored equipment, and ancient Greco Roman and Chinese temples. This paper investigates the effect of ground motion processing on the response of the rocking oscillator. Different types of digital ground motions (pulse like and non pulse like) and different processing schemes and scheme parameter values are presented to illustrate this effect on the displacement spectra for planar rocking blocks. Based on the results of this paper, on a single ground motion basis, ground motion processing has an effect on the rocking spectra which is basically similar to the elastic oscillator. However, when treating the problem in a statistical way (by comparing the statistics of the response to sets of ground motions, not to a single ground motion - as seismic design typically requires), the effect is significantly reduced. In fact, as long as the system is not close to overturning (failure), the rocking spectra only loosely depend on the processing scheme.*

**Keywords:** Near-field ground motions, Ground motion processing, Rocking, Digital filtering, Uplifting structures.

## 1 INTRODUCTION

Starting with Housner's seminal paper in 1963 [1], the study of the rocking oscillator has gained an increasing attention due to its ability to describe a wide range of systems that cannot be adequately described by the elastic oscillator [2-12]. Moreover, rocking motion can be used as a seismic isolation mechanism [13-19]. Interestingly, rocking has been used since more than 40 years as a seismic isolation method in the former USSR countries via intentionally designing a soft rocking story that limits the force transmitted to the super structure [20].

The use of ground motion records for time history analysis is a cornerstone in earthquake engineering. However, these recorded motions are often plagued by diverse sources of noise. Noise can be defined as any distortion in the record that lead to physically unrealistic velocity or displacement traces. The velocity trace should show zero values at the end of the record. On the other hand, the displacement trace should reflect the residual displacement (often referred to as the fling step) at the recording site, acquired from geodetic data. Practically, many ground motion processing schemes (including the procedure adopted by the widely-used NGA West 2 [21] ground motion database) neglect the effect of the fling step, mainly due to the lack of geodetic data or lack of interest in the fling step effect (e.g., in the case of far-field motions). Therefore, the use of processing and noise filtration schemes is inevitable.

Processing of strong ground motions typically starts with removing the mean value of the pre-event buffer (or the mean of the whole record in case pre-event data are not available, which is the case in analog ground motion records). The next step, which is the essential part, is to apply a low and high pass Butterworth filters, of which, the most important is the high-pass filter (low-cut filter) which aims to remove the long period noise that exists in both analog and digital records. Two types of digital filters are typically used; causal and acausal (zero-phase) filters. Causal filters result in shifted filtered ground motion signal in contrary to acausal filters. Acausal filters is the state of the art within ground motion processing context. NGA West 1 project used causal filtered ground motions, while acausal filters were used in the updated version of the project, NGA West 2 [21]. Moreover, the use of time domain baseline corrections is often combined with the use of filters. The choice of filter parameters (order and corner frequency) involves some degree of subjective judgement since the noise source is not well understood, especially the long period noise [22]. Boore and Bommer [22] claimed that there is no way to identify a best processing technique for an individual ground motion and that the uncertainty of the whole procedure should be appreciated by the end users of the processed record.

In this study, a procedure based on the procedure adopted by PEER NGA West 2 database was implemented with variations in the low-cut filter corner frequency. The variations in the cut-off frequency, being the most important parameter in ground motion processing, are aimed at simulation of the uncertainty and subjectivity in that choice. In addition, the effect of filter causality is also discussed. These variations of ground motion filtering are used to quantify the effect of ground motion processing on the response of rocking structures. As a proxy for understanding the behavior of rocking structures, the rocking displacement spectra is used, as discussed in Section 2 of this paper.

## 2 ROCKING DISPLACEMENT SPECTRA

This section briefly describes the rocking oscillator and underline some of its properties that will facilitate the study of the dependence of its response on ground motion correction methods. The equation of in-plane motion for a rigid rectangular rocking block (Figure 1a) with slenderness ratio $\alpha$ and a semi-diagonal length $R$ is:

$$\ddot{\theta} = -p^2(\sin[\pm\alpha - \theta] + \frac{\ddot{u}_g}{g}\cos[\pm\alpha - \theta]) \quad (1)$$

where $p = \sqrt{(3g)/(4R)}$ is the frequency parameter of the rocking column. The upper and the lower sign in front of $\alpha$ corresponds to a positive and a negative rocking angle $\theta$, respectively, with respect to the defined coordinate system in Figure 1a. It is assumed that energy is only dissipated during impact. Housner [1] assumed that (a) the impact is instantaneous and (b) the impact forces are concentrated on the impacting corner (Point O in Figure 1a). Based on these assumptions, the ratio of post to pre-impact rotational velocities (coefficient of restitution) is:

$$r = 1 - \frac{3}{2}\sin^2\alpha \quad (2)$$

Inspecting equation (1), one can conclude that the rotational response of a rocking block to a given ground motion is a function of $\alpha$ and $R$. Similarly, for the elastic oscillator, the response is a function of the eigen period, $T$, and damping ratio $\zeta$ [23]. One difference between the rocking and the elastic oscillator is that in the case of the former, both $R$ and $\alpha$ strongly influence the rotational response whereas in the latter one parameter ($T$) is more influential than the other ($\zeta$). Manzo and Vassiliou [23] suggested that using displacement response instead of rotational response will further reduce the dimensionality of the rocking oscillator problem. The top displacement, $u$, of the rocking block can be obtained by a one-to-one mapping of rotation, $\theta$, (see Figure 1a):

$$u = 2R\sin(\pm\alpha) - 2R\sin(\pm\alpha - \theta) \quad (3)$$

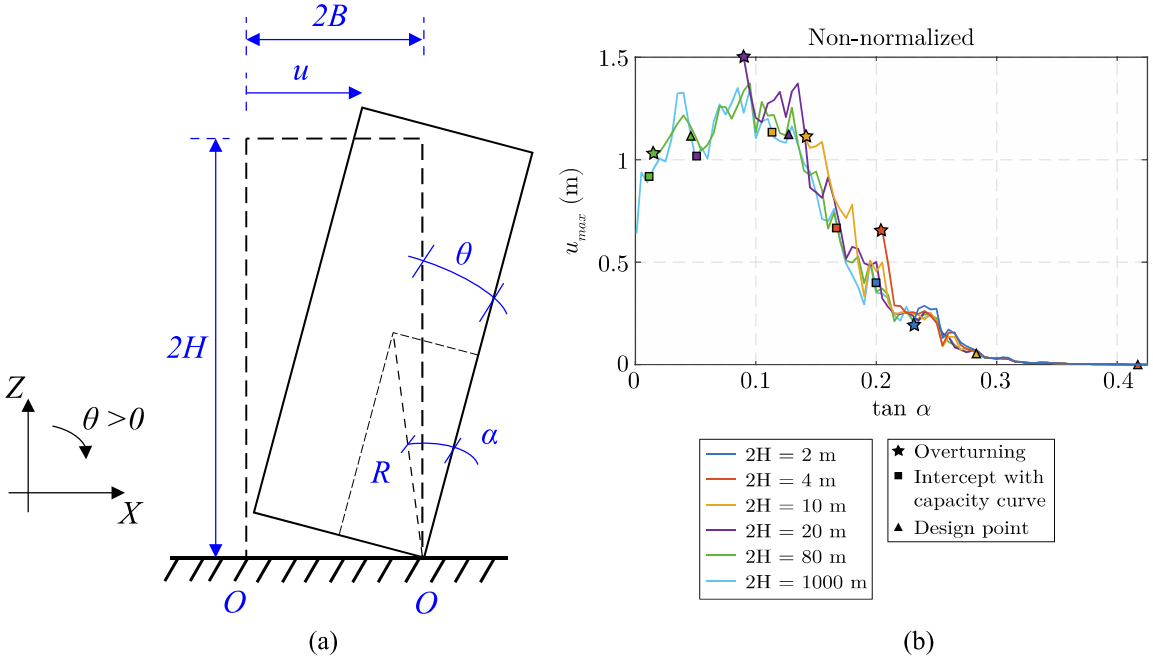


Figure 1: Displacement-based analysis of rocking blocks: (a) geometry of the rigid rocking block showing angle of rotation (θ) and horizontal displacement (u) (b) median rocking displacement spectra median for different sizes for a set of near-field pulse-like records [23].

They concluded that a large and a small rocking block of the same slenderness will have the same top displacement, given that both are away from overturning (they named this conclusion:

"*equal displacement rule of rocking structures*"). They obtained the same result using analytical pulses and actual ground motion records (FEMA P695 [24] ground motion sets) as input excitations. The condition that the blocks are not close to overturning is a design requirement, so practically, slenderness is the only parameter affecting the displacement response, not the block size. Vassiliou et al. [25] have proven that rigid rocking blocks with the same height ($H$) attached to massless foundations of the same size behave identically, no matter what their actual column width is. Therefore, it is more meaningful to use $H$ as a size parameter instead of $R$, even if the former does not explicitly appear in the equation of motion. Figure 1b depicts the median rocking displacement spectra for different sizes (expressed in terms of height $2H$) for a set of near-field pulse-like records. The rocking spectrum throughout this paper refers to the relationship between the tangent of the slenderness angle on the horizontal axis and the maximum displacement response due to the ground excitation on the vertical axis. The figure shows the equal displacement rule and also shows some deviation when the block is near overturning (see block with size $2H$ = 20 m).

Accordingly, in this paper, a block with height ($2H$) of 2000 meters was used to study the effect of different processing/filtering variations on the displacement response of rocking structures. A height of 2000 m represent the case when $2H \rightarrow \infty$ which is being studied for mathematical completeness (having spectrum ordinates at very low tangent of the slenderness angle).

## 3 GROUND MOTIONS SELECTION

In total, 12 digital ground motions were selected and split into two groups (near field pulse-like and near field non pulse-like) as described in FEMA P695 [24]. The nature of noise and baseline tilts in analog records are very distinct from digital records [22]. A discussion of this different nature is offered in [22, 26]. In digital records, the velocity trace noise typically appears to have a linearly increasing baseline offset. This paper focuses on digital records.

A source-site distance (defined as the Joyner-Boore distance [27]) of 10 km was used to separate near- and far-field records. Only strong motions (magnitude > 6.5) were considered. For each ground motion, the two horizontal components were treated as different records, resulting in 24 records in total. The vertical component of the ground motion was not used in this study, as it seems that it does not significantly influence the response of the rocking oscillator [28, 29]. The ground motions were classified as pulse- or non pulse-like based on the classification of PEER NGA West 2 database, if the ground motion is available there. Otherwise, the methodology and the code developed by [30, 31] are used to classify the records.

Tables 1 summarizes the ground motion database. The PGA, PGV, and PGD values in Tables 1 and 2 are calculated using the records corrected using acausal filtering (discussed later in the paper) with a high-pass filter corner frequency 0.1 Hz. These values are taken as the maximum of the temporal maximum of each of the two horizontal components of each record, i.e. $PGA=\max(PGA_x,PGA_y)$.

## 4 GROUND MOTION PROCESSING PARAMETERS

The adopted processing scheme comprised a baseline correction and an application of a causal or acausal filter. Figure 2 depicts the adopted processing schemes for acausal filtering. The scheme was based on the NGA West 2 processing methodology [21, 32]. It starts by removing the pre-event buffer mean. Then the start and the end of the signal are tapered using cosine tapers with a length equal to 1% of the trace length [33]. The next step is to apply zero pads at the end of the record so that the number of points in the time series is a power of two since the filtering is conducted in the frequency-domain using the Fast Fourier transform (FFT) [34].

| Event | *M* | Station | Network | $R_{jb}$ (km) | PGA ($m/s^2$) | PGV (m/s) | PGD (m) | Pulse/No-Pulse |
|---|---|---|---|---|---|---|---|---|
| 2008 Wenchuan, China | 7.90 | Mianzuqing-ping | NSMONS[1] | 0.00 | 7.127 | 0.905 | 0.565 | Pulse-like |
| 1999 Chi-Chi, Taiwan | 7.62 | TCU049 | TSMIP[2] | 3.76 | 2.658 | 0.625 | 0.348 | Pulse-like |
| | | TCU068 | TSMIP | 0.00 | 5.014 | 1.560 | 1.401 | Pulse-like |
| | | TCU102 | TSMIP | 1.49 | 2.909 | 0.829 | 0.728 | Pulse-like |
| | | TCU082 | TSMIP | 5.16 | 2.119 | 0.431 | 0.378 | Pulse-like |
| | | TCU065 | TSMIP | 0.57 | 7.750 | 1.158 | 0.710 | Pulse-like |
| 2016 Kaikoura | 7.80 | KEKS | GeoNet[3] | 3.00 | 10.909 | 1.054 | 0.453 | No-pulse |
| | | WDFS | GeoNet | 8.50 | 12.232 | 0.922 | 0.348 | No-pulse |
| | | WTMC | GeoNet | 0.70 | 10.345 | 1.064 | 0.367 | No-pulse |
| 2015 Nepal | 7.80 | KATNP | CESMD[4] | 0.10 | 1.655 | 0.983 | 0.843 | No-pulse |
| 2016 Kumamoto | 7.00 | KMM004 | K-NET, KiK-net, and JMA[5] | 3.90 | 3.439 | 0.777 | 0.457 | No-pulse |
| | | KMMH16 | | 0.50 | 11.574 | 1.343 | 0.455 | No-pulse |

[1]NSMONS: National Strong-Motion Observation Network System of China.
[2]TSMIP: Taiwan Strong Motion Instrumentation Program.
[3] GeoNet: The New Zealand GeoNet project.
[4]CESMD: Center for Engineering Strong Motion Data [35], with stations that belong to different networks including coast and geodetic survey (C&GS), California Strong Motion Instrumentation Program (CSMIP), and United States National Strong-Motion Network (NSMP).
[5]K-NET, KiK-net: Japan network of strong-motion seismographs, JMA: Japan Meteorological Agency.

Table 1: Details of the selected digital records used in this paper.

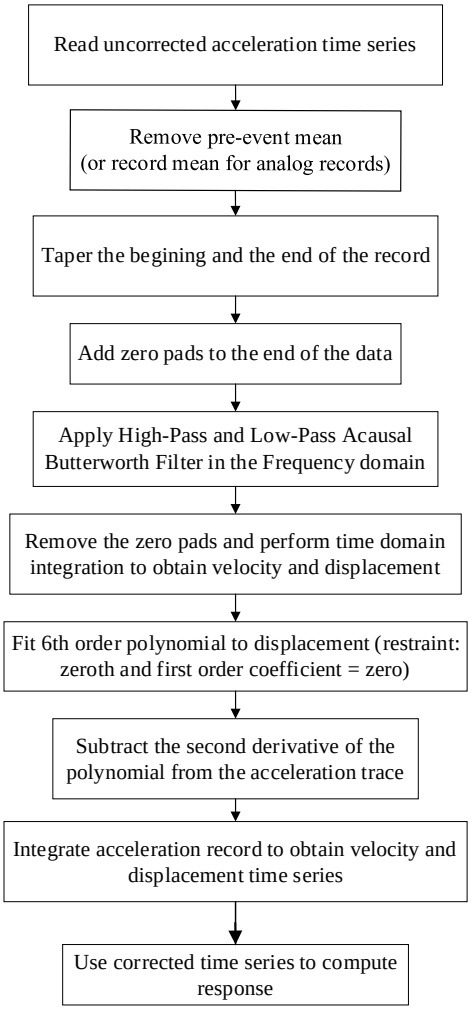


Figure 2: The adopted processing algorithm for acausal filtering based on the PEER NGA West 2 processing scheme [21, 32].

Thereafter, high pass and low pass acausal Butterworth filters are applied to the acceleration time series in the frequency domain. Then, the zero pads are removed and a 6$^{th}$ order polynomial is fitted to the displacement trace (obtained by double integration of the acceleration trace) and the second derivative of the polynomial is subtracted from the acceleration time history. A similar procedure was used for the causal filtering scheme with a causal Butterworth filter (Figure 3). For causal filters the tapering and zero padding steps are not included since they are only needed for the acausal filtering [32, 36].

Apart from the baseline correction and filtering, the time series for all ground motion records were checked for non-standard noise (e.g., unrealistic spikes) on a single record basis. The MATLAB code used in this study was based on the codes of Akkar [21, 32] and Abrahamson [32]. The used corner periods of the high-pass filters were 10, 15, 20, 30, 40, and 60 seconds, with longer periods corresponding to more relaxed filtering and shorter periods corresponding to more intense filtering. The chosen high-pass corner periods range was based on [37] in which the effects of long-period processing on structural collapse predictions of steel moment frames was investigated. The low-pass filter (causal and acausal) corner frequency was chosen to be 25 Hz (i.e. corner period equal to 0.04 seconds).

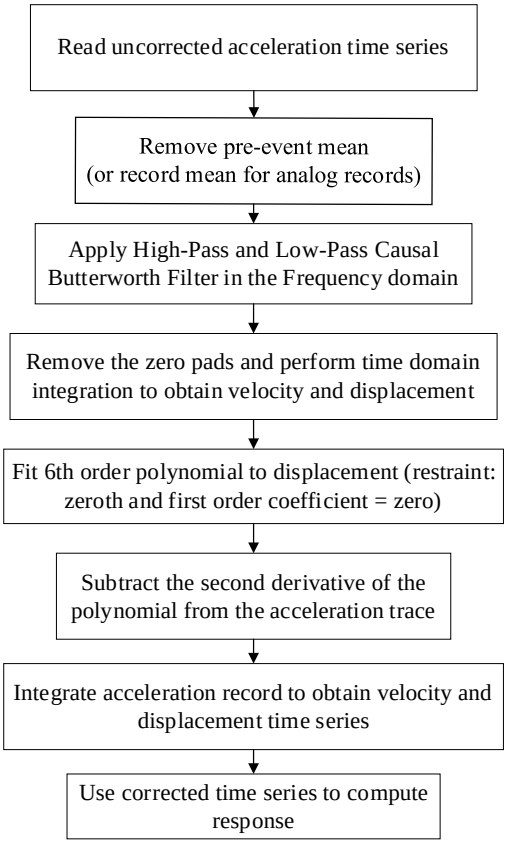


Figure 3: The adopted processing algorithm for causal filtering.

Figure 4 shows the filter frequency response function (magnitude and phase) for the adopted causal and acausal (zero phase) filters with 8 poles for different cut-off periods. The figure depicts the difference in phase shifts between causal and acausal filters as discussed earlier. It is also worth mentioning that discussions about usable spectral periods (often expressed relative to the filter corner period) are irrelevant to the rocking oscillator since its "period" is amplitude dependent and can take values from zero to infinity [1]. Verification of the adopted processing

scheme is presented in [26]. Notably, in this study, the Zero Order Corrected (ZOC) record refers to the record with mean removed (mean of the pre-event portion as discussed earlier).

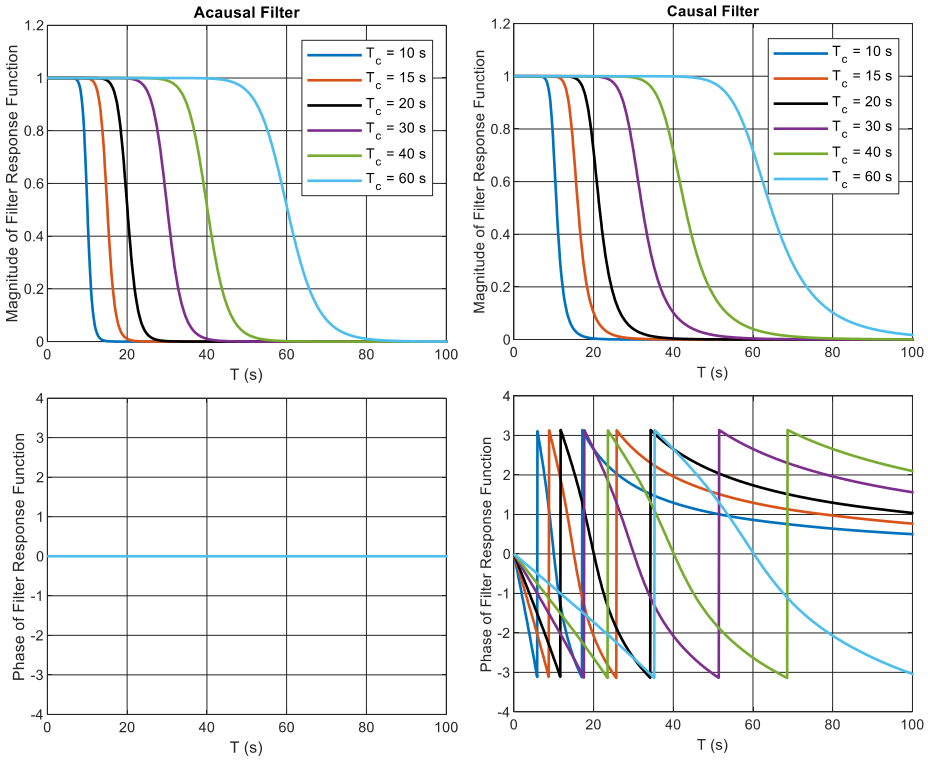


Figure 4: Filter response function (magnitude and phase in radian) of the adopted acausal (zero phase) and causal high-pass filters (number of poles = 8).

## 5 RESULTS

As discussed earlier, the rocking spectra presented in this study plot the maximum top displacement of a rigid block versus the tangent of the slenderness angle. Accordingly, the rocking spectrum is not to be confused with the linear elastic oscillator spectrum (elastic spectrum). The rocking spectrum is highly non-linear and is not correlated to the elastic spectrum [7]. For reasons that will be discussed later in this section, all ground motions were scaled to have a PGV of 50 cm/s. As the raw ground motion results in unrealistically high PGVs, the scaling factor for different corner periods and for the same component was kept constant and equal to the one needed to scale the record that was processed with the 10 seconds cut off period and an acausal filter to a PGV of 50 cm/s. As the number of analyses was high, the ETH Zurich scientific computing cluster (Euler) was used for performing the analysis.

Figure 5 shows some indicative rocking spectra for causal and acausal filtering. To develop Figure 5, the recordings at the following stations were used: El Centro for El Mayor Cucapah earthquake and WTMC for Kaikoura earthquake. One can observe that causal filtering resulted in higher variability than acausal filtering, an observation that agrees with previous studies for elastic systems [36]. In addition, in all cases in Figure 5, the variability of the spectrum due to the choice of different cut-off frequencies decreases with increasing tangent of the slenderness angle $\alpha$. There is a physical reason for this: As the slenderness angle decreases, the rocking

block tilts to larger angles. Larger tilt angles lead to larger periods [1], where the variability due to high-pass filtering typically is expected to increase, as in elastic systems [36].

The discussion up till this point only focused on the spectra on a single ground motion basis. As rocking is a very sensitive problem to all the parameters that define it, Yim et al. [38], as early as 1980, have suggested that a sensitivity analysis of the rocking oscillator should be performed in a statistical sense, namely by comparing the statistics of the response to an ensemble of ground motions, rather than to individual excitations [39]. Such a statistical approach is not only applied to rocking structures: Riddell and Newmark [40] produced inelastic spectra for yielding structures based on statistics on ensembles of excitations. In fact, this approach is consistent with the fundamental seismic design problem, which involves computing the response to a set of ground motions, rather than to an individual one [41, 42].

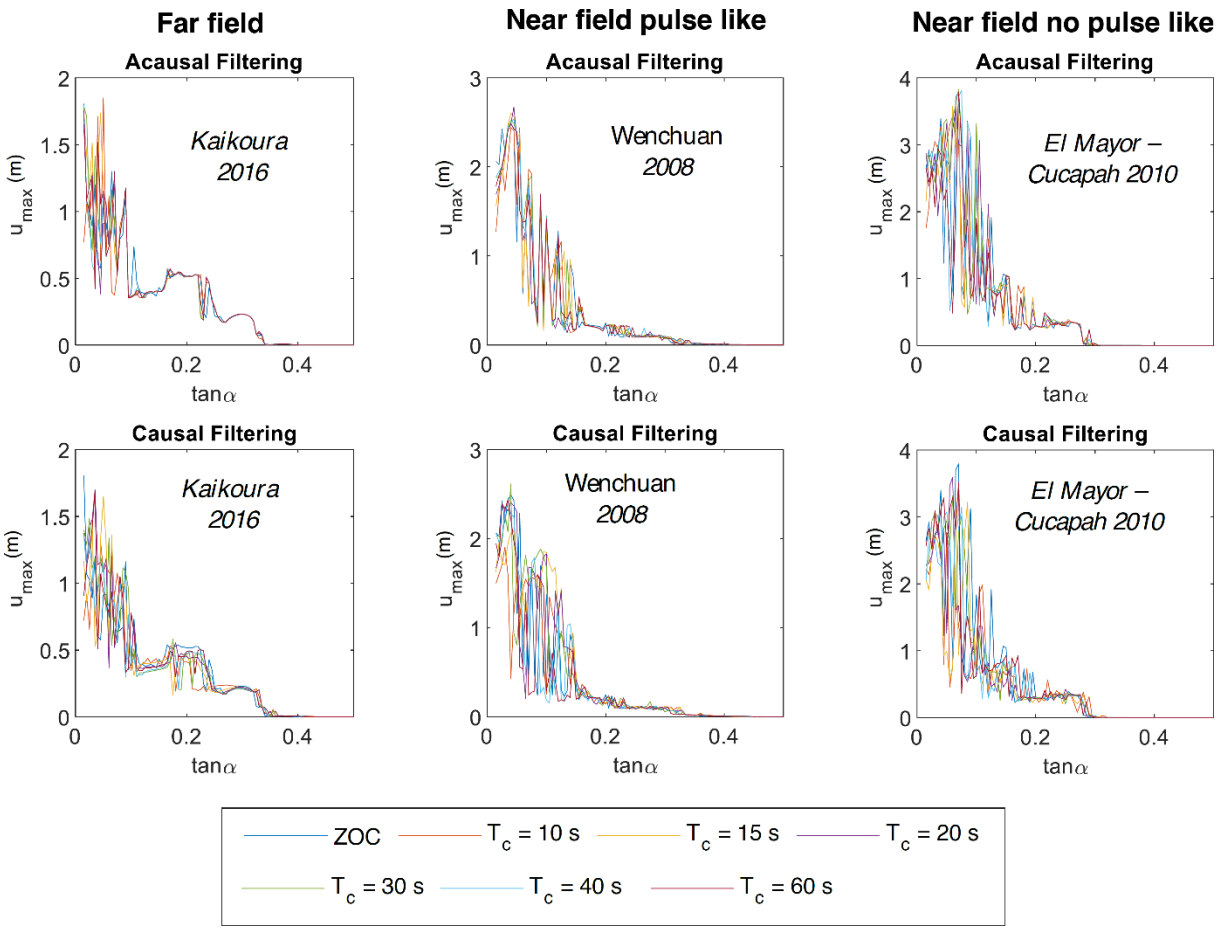


Figure 5: Example rocking spectra for different categories of filtering schemes and ground motions for digital ground motion records (left: far field, middle: near field pulse like, right: near field non pulse-like).

For an ensemble of ground motions to be useful, in this paper all ground motions were scaled to the same PGV. PGV was used as an intensity measure, as it performs better than PGA or PGD for rocking structures [43, 44].

Figures 6 and 7 show the median rocking spectra for the near-field pulse-like and near-field non pulse-like record bins, derived for different processing schemes. As stated earlier, all the rocking spectra in this paper are derived for size (2H) of 2000 meters which represent the case when $2H \rightarrow \infty$ that is being studied for mathematical completeness. Then, these rocking spectra

could be used to determine the response of rocking blocks of finite size. Moreover, Figures 6 and 7 show the 95% confidence interval of the median (over the ground motions of each set) response for the zero-order corrected case (ZOC), i.e. of the case were only the mean of the record was removed. The 95% confidence interval (CI) was constructed using the bootstrap method [45] by taking 1000 response samples for each value of tanα. Taking 10,000 response samples did not seem to change the CIs.

Based on the median rocking spectra (Figures 6 and 7), one can observe that for larger tan$\alpha$ (resulting into smaller displacements) the rocking spectra only loosely depend on the processing scheme, as it can also be observed on an individual motion base (Figure 5). For smaller tan$\alpha$, there seems to be some non-negligible influence of the response on the processing scheme, but in most cases, the curves for the different processing schemes fall within the 95% confidence interval of the rocking spectrum of the zero-order corrected (ZOC) case, indicating that the motion-to-motion variability is larger than the variability caused by the different correction schemes. Moreover, there is not trend of the response with respect to increasing or decreasing corner period or with respect to causal or acausal filtering. Therefore, even if the different processing schemes do influence the rocking response, the bias of this influence seems negligible – at least for the parameter values examined. The above conclusion seems to be independent of whether the ground motion is pulse like or non pulse like.

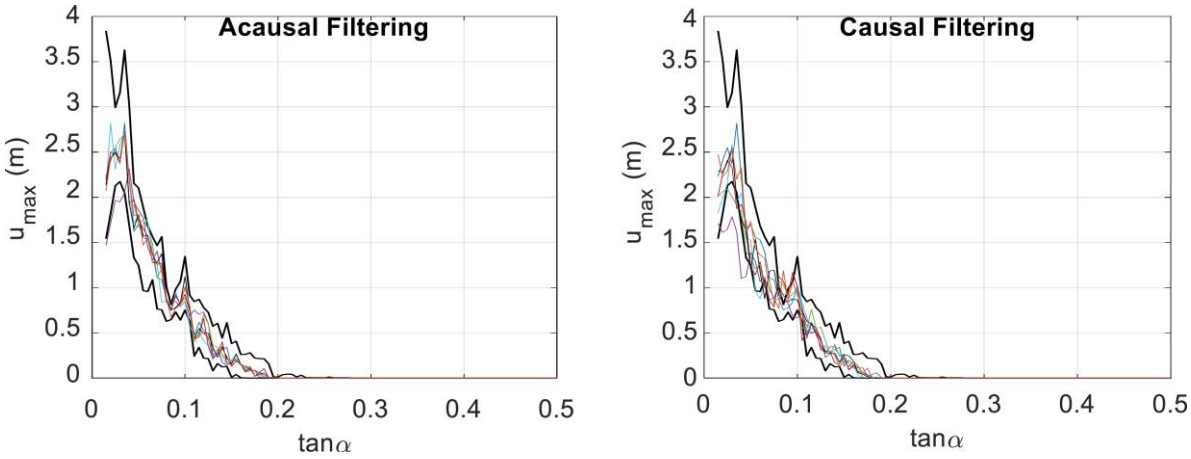


Figure 6: Median estimates of the rocking spectra for different correction schemes for the near-field pulse-like record set (the confidence interval is derived for the ZOC spectrum).

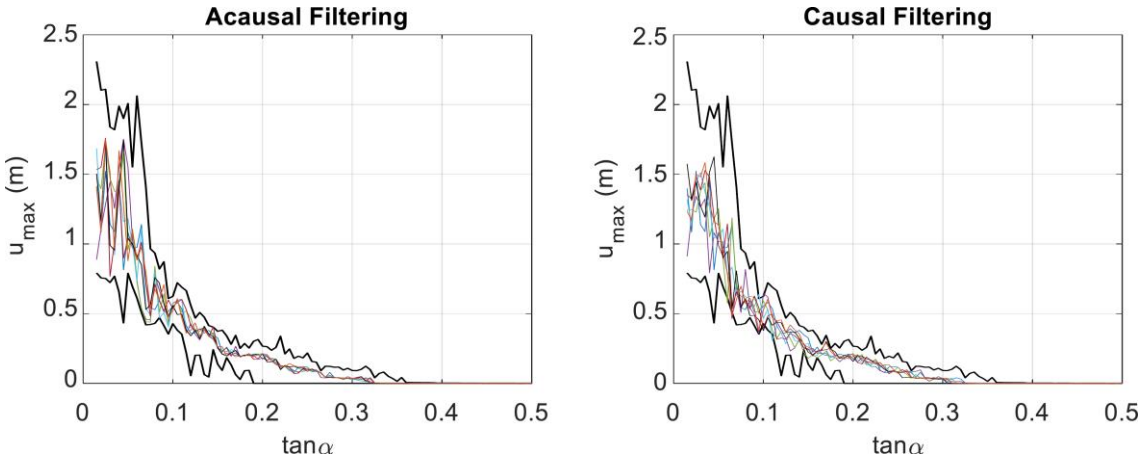


Figure 7: Median estimates of the rocking spectra for different correction schemes for the near-field non pulse-like record set (the confidence interval is derived for the ZOC spectrum).

Figure 8 shows the standard deviation and the coefficient of variation (COV, calculated as the standard deviation divided by the mean value) of the median estimates of the rocking spectra (Figures 6 and 7) for the cases presented in this study. The standard deviation values decrease for all the cases with increasing tanα, confirming that the variability decreases with tanα. For higher tangent of the slenderness angle, the COV reaches large values (on the order of 250%), but this only because in this region the mean tends to zero. Notably, for all the cases, the COV for the lower values of the tangent of the slenderness angle had almost a constant value of less than 0.2 on average.

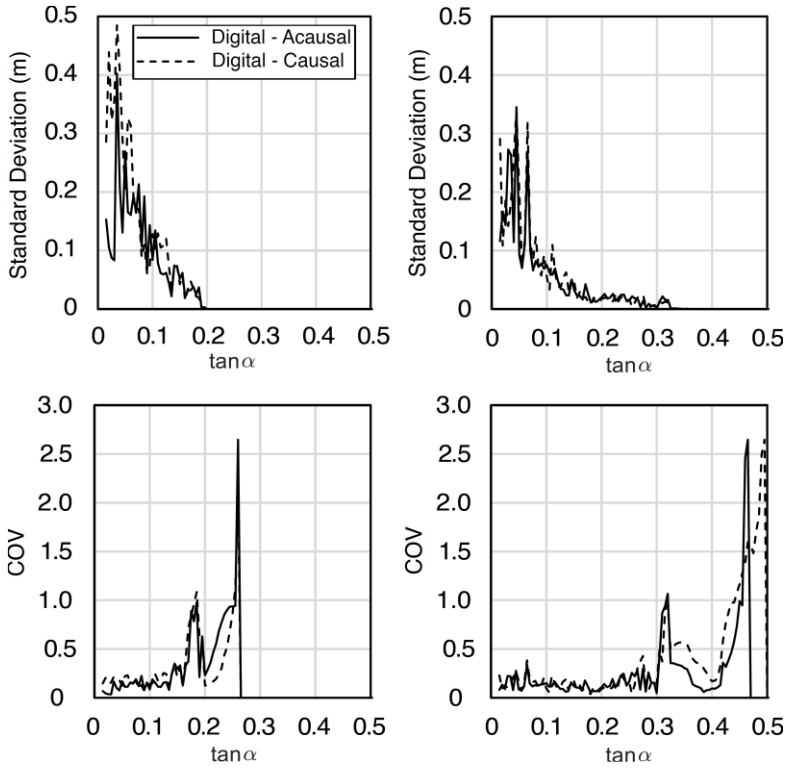


Figure 8: Variability (standard deviation and coefficient of variation) of the median estimates of the rocking spectra for different processing schemes derived for the studies sets of ground motions (left: near field pulse like, right: near field non pulse-like).

## 6 CONCLUSIONS

This paper studies the influence of ground motion filtering on the response of the rocking isolator. To this end, different kinds of ground motions and variations of processing schemes were used to explore their effect on the rocking displacement spectra for planar rocking blocks. On a single ground motion basis, it can be concluded that:

- Causal filtering results in higher variability than acausal filtering; agreeing with previous studies on the elastic oscillator.
- The variability of the spectrum due to the choice of different cut-off frequencies decreases with increasing tangent of the slenderness angle.

However, the seismic design problem does not involve the response to an individual ground motion but the statistics of the responses to a set of ground motions that characterize the seismic hazard. Therefore, this paper has argued that the influence of processing schemes should be evaluated statistically, essentially by evaluating whether they induce bias in the spectra. This work followed such an approach and showed that the median rocking displacement spectra to sets of ground motions are not significantly sensitive to the ground motion processing scheme.

In most cases, the curves for the different processing schemes fall within the 95% confidence interval of the rocking spectrum of the zero-order corrected (ZOC) case. Therefore, the motion-to-motion variability was more important than the processing scheme. This conclusion holds for filter cut off periods larger than or equal to 10 seconds and applies to both causal and acausal filters, and to all near field pulse like and near field non pulse like records.

## ACKNOWLEDGEMENTS

This work was supported by the ETH Zurich under grant ETH-11 21-1.

## REFERENCES

[1] G.W. Housner. The behavior of inverted pendulum structures during earthquakes. *Bull Seismol Soc Am*. 1963; 53(2): 403-417.

[2] A.K. Chopra, S.C-S. Yim. Simplified earthquake analysis of structures with foundation uplift. *J Struct Eng*. 1985; 111(4): 906-930.

[3] I.N. Psycharis. Effect of base uplift on dynamic response of SDOF structures. *J Struct Eng*. 1991; 117(3): 733-754.

[4] G. Oliveto, I. Calio, A. Greco. Large displacement behaviour of a structural model with foundation uplift under impulsive and earthquake excitations. *Earthq Eng Struct Dyn*. 2003; 32(3): 369-393.

[5] D. D'Angela, G. Magliulo, E. Cosenza. Seismic damage assessment of unanchored non-structural components taking into account the building response. *Structural Safety*. 93, 102126, 2021. https://doi.org/10.1016/j.strusafe.2021.102126

[6] D. D'Angela, G. Magliulo, E. Cosenza. Towards a reliable seismic assessment of rocking components. *Engineering Structures*. 230, 111673. 2021. https://doi.org/10.1016/j.engstruct.2020.111673

[7] A.I. Giouvanidis, E.G. Dimitrakopoulos, P.B. Lourenço. Chattering: an overlooked peculiarity of rocking motion. *Nonlinear Dynamics*. 109, 459–477. 2022

[8] M. Kohrangi, K. Bakalis, G. Triantafyllou, D. Vamvatsikos, P. Bazzurro. Hazard consistent record selection procedures accounting for horizontal and vertical components of the ground motion: Application to liquid storage tanks. *Earthquake Engng Struct Dyn*. 2023;52:1232–1251.https://doi.org/10.1002/eqe.3813

[9] J. Wang, W. Chen, K. Dai, T. Li, S. Tesfamariam, Y. Lu. Seismic damage evaluation of unanchored nonstructural components under combined effects of horizontal and vertical near-fault ground motions. *Earthquake Engng Struct Dyn*. 2023;1-21.https://doi.org/10.1002/eqe.3846

[10] Q.T.M Ma. The mechanics of rocking structures subjected to ground motion. 2010, ResearchSpace@ Auckland.

[11] S. Acikgoz, M.J. DeJong. The interaction of elasticity and rocking in flexible structures allowed to uplift. *Earthq Eng Struct Dyn*. 2012; 41(15): 2177-2194.

[12] N. Makris, D. Konstantinidis. The rocking spectrum and the limitations of practical design methodologies. *Earthq Eng Struct Dyn*. 2003; 32(2): 265-289.

[13] S.I. Reyes, J.L. Almazán. A novel device for a vertical rocking isolation system with uplift allowed for industrial equipment and structures. *Engineering Structures*. 2020; 214:110595.

[14] K. Zhang, J. Junfeng, L. Ning, j. Zhao, Y. Bai. Analytical model for evaluating lateral force capacity of precast concrete-filled steel tube column. *Engineering Structures*. https://doi.org/10.1016/j.engstruct.2022.115106

[15] S. Li, H-Ho. Tsang, N. Lam. Seismic protection by rocking with superelastic tendon restraint. *Earthquake Engng Struct Dyn*. 2022; 51:1718–1737. https://doi.org/10.1002/eqe.3635

[16] J. Yang, Z. Yang, Y. Chen, Y. Lv, N. Chouw. Finite element simulation of an upliftable rigid frame bridge under earthquakes: Experimental verification. *Soil Dynamics and Earthquake Engineering*. 2023. https://doi.org/10.1016/j.soildyn.2022.107716

[17] C.G. Lachanas, D. Vamvatsikos, E.G. Dimitrakopoulos. Intensity measures as interfacing variables versus response proxies: The case of rigid rocking blocks. *Earthquake Engng Struct Dyn*. 2023;1-18.https://doi.org/10.1002/eqe.3838

[18] C.G. Lachanas, D. Vamvatsikos, E.G. Dimitrakopoulos. Statistical property parameterization of simple rocking block response. *Earthquake Engineering and Structural Dynamics*. 2023;52:394-414. https://doi.org/10.1002/eqe.3765

[19] S.I. Reyes, J.L. Almazán, M.F. Vassiliou, N.F. Tapia, J.I. Colombo, J.C. de la Llera. Full‐scale shaking table test and numerical modeling of a 3000‐liter legged storage tank isolated with a vertical rocking isolation system. *Earthquake Engineering & Structural Dynaics*. 2022;51(6):1563-85.

[20] J. Bachmann, M.F. Vassiliou, B. Stojadinović. Dynamics of rocking podium structures. Earthquake Engineering & Structural Dynamics. 2017. 46(14): p. 2499-2517.

[21] T.D. Ancheta, R.B. Darragh, J.P. Stewart, E. Seyhan, W.J. Silva, B.S-J. Chiou, K.E. Wooddell, R.W. Graves, A.R. Kottke, D.M. Boore, T. Kishida, J.L. Donahue. *PEER NGA-West2 Database*. 2013; Pacific Earthquake Engineering Research Center, University of California, Berkeley, CA. p. 134.

[22] D.M. Boore, J.J. Bommer. Processing of strong-motion accelerograms: needs, options and consequences. *Soil Dyn Earthquake Eng*. 2005; 25(2): 93-115.

[23] N. Reggiani Manzo, M.F. Vassiliou. Displacement-based analysis and design of rocking structures. *Earthq Eng Struct Dyn*. 2019; 48(14): 1613-1629.

[24] FEMA P695. *Quantification of Building Seismic Performance Factors*. Washington, D.C: Rep. FEMA P695, Federal Emergency Management Agency; 2009.

[25] M.F. Vassiliou , K.R. Mackie, B. Stojadinović. Dynamic response analysis of solitary flexible rocking bodies: modeling and behavior under pulse‐like ground excitation. *Earthquake engineering & structural dynamics*. 2014. **43**(10): p. 1463-1481.

[26] M. Elmorsy, M.F. Vassiliou . Effect of ground motion processing and filtering on the response of rocking structures. *Earthquake Engineering & Structural Dynamics*. 2023.

[27] N.A. Abrahamson, K.M. Shedlock. Overview. *Seismological Research Letters*. 1997; 68(1): 9-23.

[28] C.G. Lachanas, D. Vamvatsikos, M.F. Vassiliou. The influence of the vertical component of ground motion on the probabilistic treatment of the rocking response of free-standing blocks. *Earthq Eng Struct Dyn*. 202; 51(8): 1874-1894.

[29] N. Makris, G. Kampas, Size Versus Slenderness: Two Competing Parameters in the Seismic Stability of Free‐Standing Rocking Columns Size Versus Slenderness: Two Competing Parameters in the Seismic Stability of Free‐Standing Rocking Columns. *Bulletin of the Seismological Society of America*, 2016. 106(1): p. 104-122.

[30] S.K. Shahi, J.W. Baker. An efficient algorithm to identify strong-velocity pulses in multicomponent ground motions. *Bull Seismol Soc Am*. 2014; 104(5): 2456-2466.

[31] S.K. Shahi, J.W. Baker . *Pulse classification algorithm*. 2012. http://www.jackwbaker.com/pulse-classification.html (last accessed 2nd December 2022).

[32] D.M. Boore, A. Azari Sisi, S. Akkar. Using pad-stripped acausally filtered strong-motion data. *Bull Seismol Soc Am.* 2012; 102(2): 751-760.

[33] C.A. Goulet, et al. PEER NGA-east database. *Earthquake Spectra*. 2021. 37(1_suppl): p. 1331-1353.

[34] D.M. Boore. On pads and filters: Processing strong-motion data. *Bull Seismol Soc Am*. 2005; 95(2): 745-750.

[35] CESMD, Center for Engineering Strong-Motion Data (CESMD) https://www.strongmotioncenter.org/ (last accessed 2nd December 2022).

[36] D.M. Boore, S. Akkar. Effect of causal and acausal filters on elastic and inelastic response spectra. *Earthq Eng Struct Dyn*. 2003; 32(11): 1729-1748.

[37] K. Buyco, B. Roh, T.H. Heaton. Effects of long-period processing on structural collapse predictions. *Earthquake Spectra*. 2021; 37(1): 204-234.

[38] C.S. Yim, A.K. Chopra, J. Penzien. Rocking response of rigid blocks to earthquakes. *Earthq Eng Struct Dyn*. 1980; 8(6): 565-587.

[39] A.A. Katsamakas, M.F. Vassiliou. Finite element modeling of free‐standing cylindrical columns under seismic excitation. *Earthquake Engineering & Structural Dynamics*. 2022;51(9):2016-35.

[40] R. Riddell. *Statistical analysis of the response of nonlinear systems subjected to earthquakes*. 1979: University of Illinois at Urbana-Champaign.

[41] J.A. Bachmann, M. Strand, M.F. Vassiliou , Broccardo M, Stojadinović B. Is rocking motion predictable?. *Earthq Eng Struct Dyn*. 2018; 47(2): 535-552.

[42] M.F. Vassiliou , M. Broccardo, C. Cengiz, M. Dietz, L. Dihoru, S. Gunay, K.M. Mosalam, G. Mylonakis, A. Sextos, B. Stojadinovic. Shake table testing of a rocking podium: Results of a blind prediction contest. *Earthq Eng Struct Dyn*. 2021; 50(4): 1043-1062.

[43] N. Reggiani Manzo, C.G. Lachanas, M.F. Vassiliou , D. Vamvatsikos. Uniform risk spectra for rocking structures. *Earthq Eng Struct Dyn*. 2022; 51(11): 2610-2626.

[44] A. Pappas, A. Sextos, Da Porto F, Modena C. Efficiency of alternative intensity measures for the seismic assessment of monolithic free-standing columns. *Bull Earthquake Eng*. 2017;15(4):1635-1659.

[45] B. Efron, R.J. Tibshirani. *An introduction to the bootstrap*. 1994: CRC press.

COMPDYN 2023
9th ECCOMAS Thematic Conference on
Computational Methods in Structural Dynamics and Earthquake Engineering
M. Papadrakakis, M. Fragiadakis (eds.)
Athens, Greece, 12-14 June 2023

# EQUAL DISPLACEMENT CONCEPT FOR INELASTIC ANALYSIS OF STRUCTURES

**Johnn P. Judd**[1]

[1] Brigham Young University
430 EB, Provo, Utah, 84602, USA
e-mail: johnn@byu.edu

## Abstract

*In this paper, the equal displacement concept is applied to inelastic analysis of structures subjected to symmetric and asymmetric excitation. Numerical analyses of inelastic single-degree-of-freedom (SDOF) systems were conducted to determine the effect of symmetric and nonsymmetric excitation on the nonlinear response history of the structure. The results show that for elastoplastic structures, the equal displacement rule holds for symmetric loading. For nonsymmetric loading, the rule breaks down for lateral systems with a yield strength that is less than half of the corresponding elastic system. The results of this study explain why the displacements are approximate in earthquake engineering: application of the equal displacement rule for asymmetric excitations generally does not hold and depends on the strength reduction compared to the elastic system.*

**Keywords:** Structural Dynamics, Earthquake Engineering, Wind Engineering.

# 1 INTRODUCTION

## 1.1 Equal Displacement Rule

A fundamental notion in modern earthquake engineering is that ductility, not strength, is the key to economically design a structure to withstand a strong earthquake. The importance of ductility was determined by Veletsos and Newmark in a landmark study [1] which showed that the displacement of an inelastic structure subjected to a seismic ground motion is approximately equal to the displacement of the same structure responding elastically.

To illustrate, consider the response of a single-degree-of-freedom (SDOF) system with a period of vibration ($T$) of 1.0 s and 2% viscous damping ($\zeta$) subjected to the horizontal ground acceleration recorded during the 1940 El Centro earthquake at the Imperial Valley Irrigation District station [2], shown in Figure 1(a). The displacement history, normalized by the peak elastic displacement ($\Delta_e$), is shown in Figure 1(b) for an elastic system. The effect of the yield strength ($F_y$) for an elastoplastic system on the displacement history is shown for $F_y$ equal to 1/2, 1/4, and 1/8 of the minimum yield strength ($F_e$) required for the system to remain elastic.

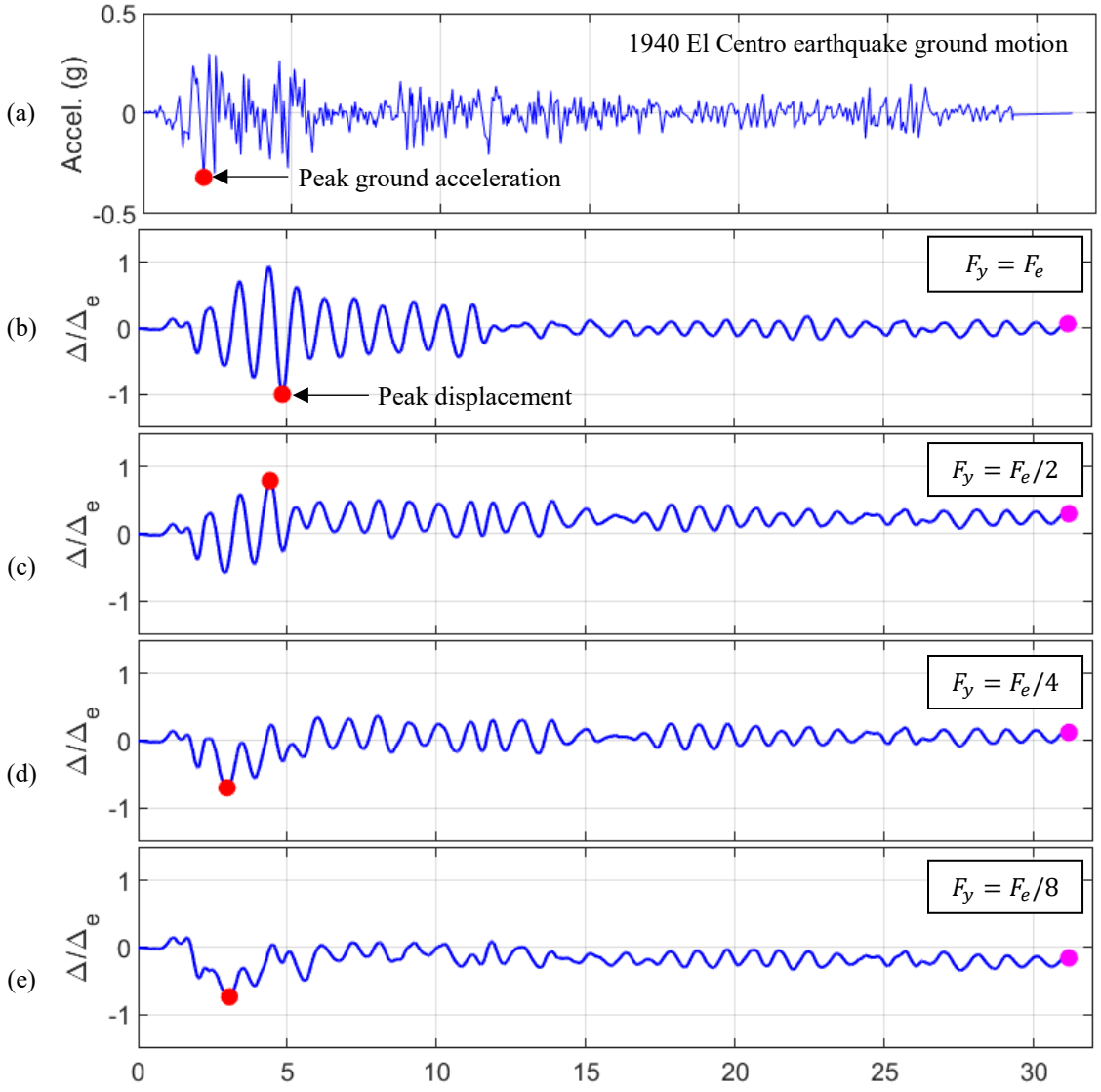


Figure 1: Displacement history (s) for SDOF system ($T$ = 1.0, $\zeta$ = 2%): (a) ground acceleration record, (b) normalized displacement for elastic system, and (c), (d), and (e) normalized displacements for elastoplastic systems.

The response in Figure 1 shows that as the yield strength of the system decreases, the peak displacement is somewhat constant. Thus, the displacement of an elastoplastic structure is essentially independent of the yield strength of the lateral system. This concept is commonly known as the "equal displacement rule."

The equal displacement rule has had a major impact on seismic design of buildings worldwide because it postulates that a structure can be designed for significantly reduced forces, provided that (1) the lateral system has the capability to deform (ductility) proportional to that reduction, (2) the lateral system can undergo a high number of inelastic cycles without fatigue, and (3) the strength and stiffness of the lateral system is preserved (no degradation of stiffness and strength). Additionally, the rule is conditioned on a large-strain but small displacement response, such that second-order ("P-Delta") effects are negligible.

It is well-known that the peak inelastic displacement is only roughly equal to the peak elastic displacement. For example, compare the peak displacement in Figure 1(b) with the peak displacements in Figure 1(c). It is also well known that the peak inelastic displacement is not constant. For example, note the variation in peak displacements in Figure 1(c) to Figure 1(e). However, to the author's knowledge, the approximate and variable nature of the equal displacement rule in earthquake engineering has not been explained previously.

### 1.2 Application to Wind Engineering

The equal displacement rule is also important for wind design of buildings. Since the 1960s, inelastic structural dynamics has evolved beyond earthquake engineering to consideration of other hazards, windstorms in particular [3]. One reason for this is that rare, large-magnitude windstorms, such as thunderstorms, tornadoes, derechos, and hurricanes cannot always be mitigated economically using elastic resistance. For example, consider a structure in Chicago. The 3-s average wind speed used for design ranges from 47.8 m/s for ordinary buildings up to 53.2 m/s for buildings that are considered essential facilities (https://asce7hazardtool.online/ [4]). However, if tornados are considered in the design, the wind speed jumps to 116 m/s, depending on the effective plan area of the structure and the mean recurrence interval. Since wind pressure is proportional to the square of the wind speed, an elastic design could require a lateral system with nearly five times the strength to resist tornado wind pressures. That would be similar to requiring a building in San Francisco to remain elastic under the Maximum Consider Earthquake (MCE) ground motions. In both cases, an elastic approach may not be economical. Nevertheless, although several frameworks for performance-based wind design have been proposed, e.g., [5,6,7], application of inelastic behavior to wind loads is still undeveloped.

Lateral wind loads differ from seismic loads in two key aspects:

- First, lateral wind loads are generated by air pressures exerted on the structure (force excitation). Seismic loads are generated by inertial forces as the structure moves relative to the ground (ground excitation). As a result, wind loads depend on the building shape, but seismic loads depend on the building mass. Moreover, seismic excitation is essentially symmetric (it moves the building in both positive and negative directions), whereas wind loads can be either asymmetric (i.e. along-wind direction) or symmetric (cross-wind direction).
- Second, the temporal variation of wind pressure varies greatly on the type of wind event. Synoptic wind events caused by pressure differences over large distances, such as hurricanes, tend to be very long duration excitations measured in hours. Non-synoptic wind events, such as thunderstorms and tornadoes, tend to be long duration events measured in minutes. Both types of wind events are at least an order of magnitude longer in duration than earthquakes, which are generally last a matter of seconds. As a result, wind records are longer and involve many more cycles compared to ground motion records.

### 1.3 Objective

The objective of this study is to the examine the approximate nature of the equal displacement rule and determine if the rule is applicable to wind engineering. The hypothesis is that the equal displacement rule depends primarily on the symmetry of the excitation. To test the hypothesis, inelastic SDOF systems were analyzed using excitations with varying degrees of symmetry (equal motion in the positive and negative directions).

## 2 METHODOLOGY AND RESULTS

Wavelet-based excitations were used to determine the effect of symmetry. Unlike a sine wave, which is symmetric but has unlimited duration, a wavelet is a symmetric or asymmetric waveform with a limited duration. A wavelet provides a way to emulate both the degree of symmetry and the non-stationary characteristics (duration) of an "ideal" ground motion, defined in this paper as a ground motion without stochastic features.

For this study a wavelet-based excitation was generated using a complex frequency wavelet that was constructed using a basis-spline (B-Spline) function [8]. The complex frequency B-Spline wavelet used in this study is defined in Equation 1:

$$\psi(t) = \sqrt{f_b}\left[\sin\left(\frac{f_b t}{m}\right)\right]^m e^{2i\pi f_c t} \tag{1}$$

where $\psi$ is the complex wavelet of order $m$, $f_c$ is the center frequency of the wavelet, and $f_b$ is the bandwidth parameter. A ground acceleration history was generated by taking the real component of the wavelet, as defined in Equation 2:

$$a_g(t) = Re(\psi) \tag{2}$$

For purposes of comparison with the El Centro ground motion, the ground acceleration in Equation 2 was normalized to match the peak ground acceleration in Figure 1. The resulting excitation is shown in Figure 2 for a wavelet center frequency of 2 Hz, a bandwidth parameter of 0.5, and a wavelet order of 3. In Figure 2, the upper and lower bounds of the waveform duration are 10 s. The wavelet was computed using wavelet toolbox in MATLAB [9].

The response of a an elastic SDOF system with $T$ equal to 1.0 s and $\zeta$ equal to 2% is shown in Figure 3. The displacement history is normalized by the peak elastic displacement ($\Delta_e$), and the force is normalized by the minimum yield strength ($F_e = F_y$) that is required for the system to remain elastic.

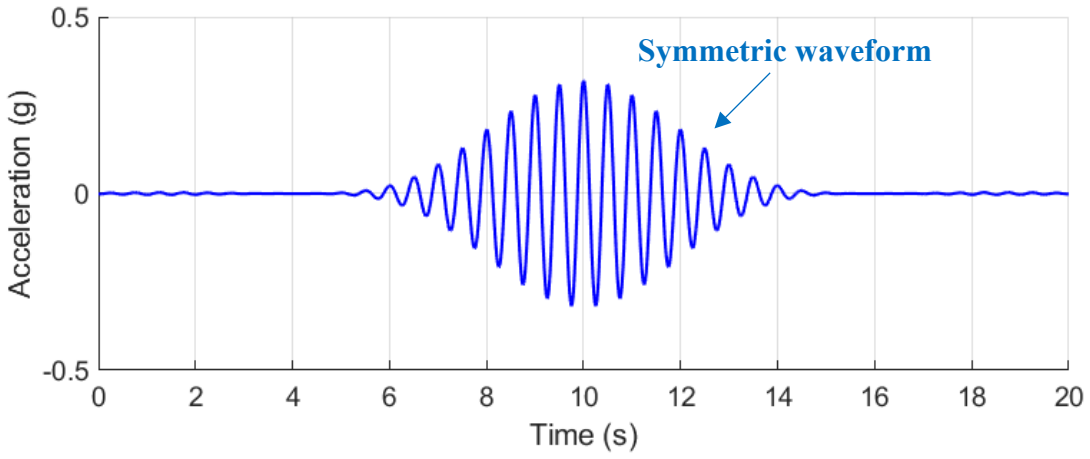


Figure 2: Symmetric ground excitation generated using a B-Spline function complex wavelet.

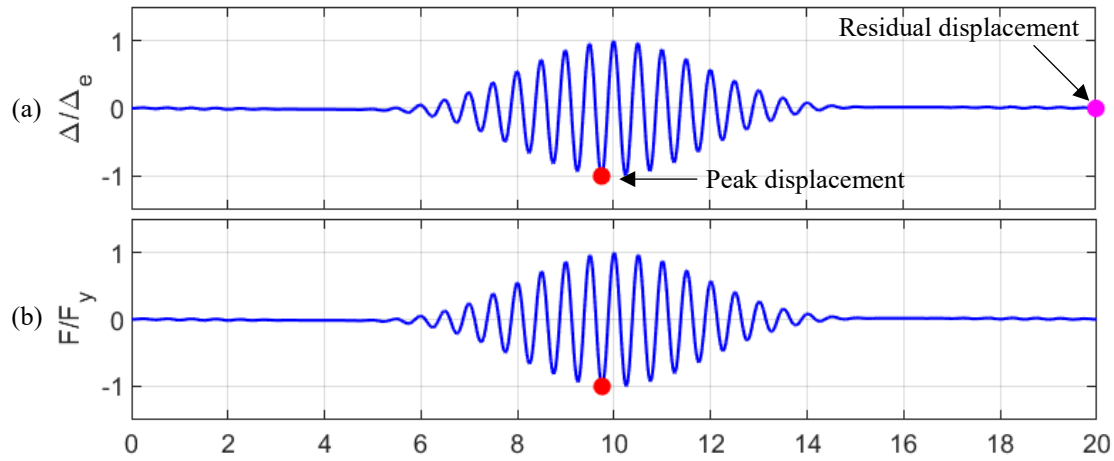


Figure 3: Response history (s) for elastic SDOF system ($T$ = 0.5, $\zeta$ = 2%) subjected to wavelet excitation: (a) normalized displacement, and (b) normalized force.

The nonlinear equation of motion was solved iteratively using implicit direct-time integration. A constant average acceleration (Newmark's method) was used with Newton-Raphson iterations until force convergence within a tolerance of $10^{-8}$. Newmark's method is relatively efficient compared to explicit integration methods, unconditionally stable for linear analysis, and is generally effective for nonlinear analysis of simple constitutive models, including the elastoplastic model used in this study.

Figure 4 shows the nonlinear response history for the elastoplastic SDOF system with $F_y$ equal to 1/2 of $F_e$ when subjected to a symmetric wavelet excitation. Figure 4(a) and Figure 4(b) show the displacement and force histories. Note that the peak inelastic displacement is exactly equal to the peak elastic displacement. Figure 4(c) shows yield events (in this case, 18 inelastic excursions).

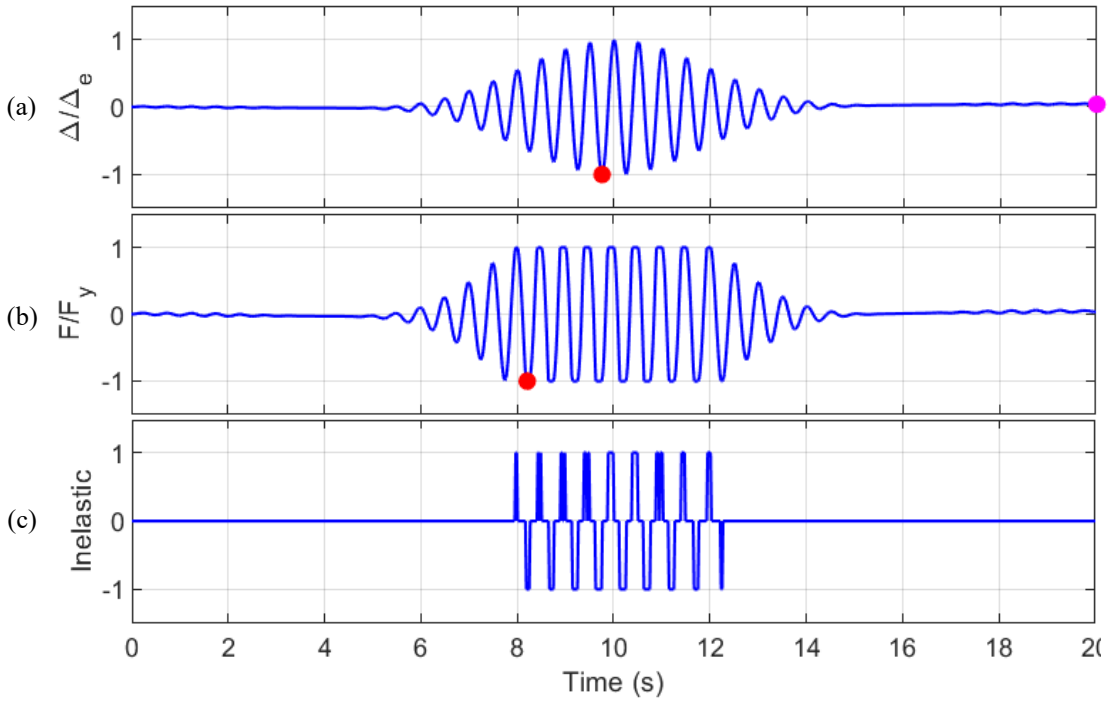


Figure 4: Response history (s) for elastoplastic SDOF system ($T$ = 0.5, $\zeta$ = 2%) subjected to wavelet excitation: (a) normalized displacement, (b) normalized force, and (c) yield events (1 = inelastic excursion).

Nonlinear response history analyses were then run using the symmetric waveform applied across a range of strength reduction ratios ($F_e/F_y$). The resulting ratio of the normalized peak inelastic displacement ($\Delta/\Delta_e$) versus the strength reduction ratio is shown in Figure 5. For purposes of comparison, nonlinear response history analyses were also run using the El Centro ground motion. The results clearly show that for an ideal symmetric excitation, the peak displacements are constant, but for a ground motion record, the peak displacements are only approximately constant. To explore the effect of other analysis parameters, additional analyses, not shown here, were run using a range of periods of vibration, damping, and other symmetric waveforms. The results confirm the observation that the equal displacement rule holds for symmetric excitation for other periods, damping, and waveforms.

The effect of the waveform symmetric was examined by subjecting the system to an asymmetric complex frequency B-Spline wavelet excitation. Asymmetry was introduced by amplitude-scaling the positive half of the signal by 50%. The resulting excitation is shown in Figure 6. The nonlinear response history analyses were then run again using the asymmetric waveform. Figure 5 shows that the asymmetric waveform has a large effect on the peak displacements. The results confirmed the hypothesis that the equal displacement rule depends primarily on the symmetry of the excitation.

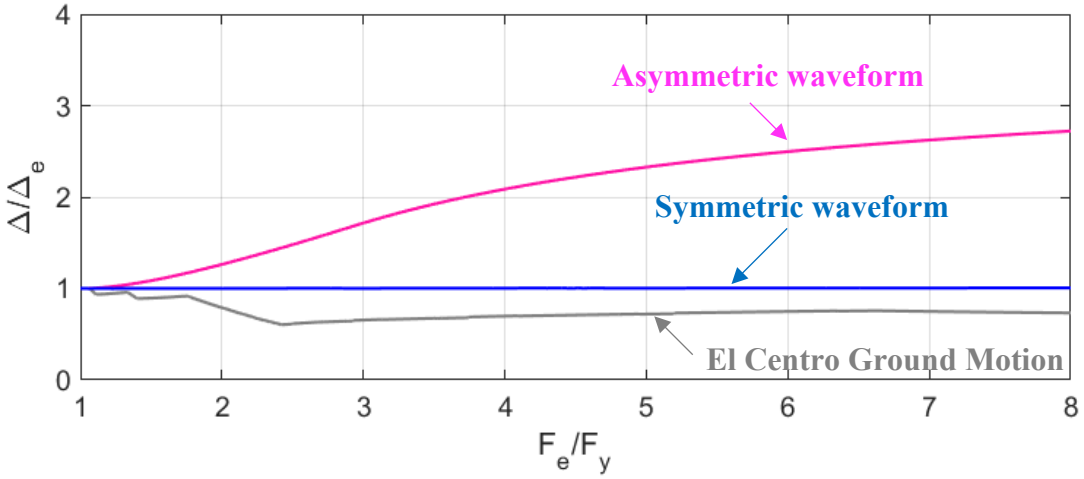


Figure 5: Ratio of normalized peak inelastic displacement versus strength reduction ratio.

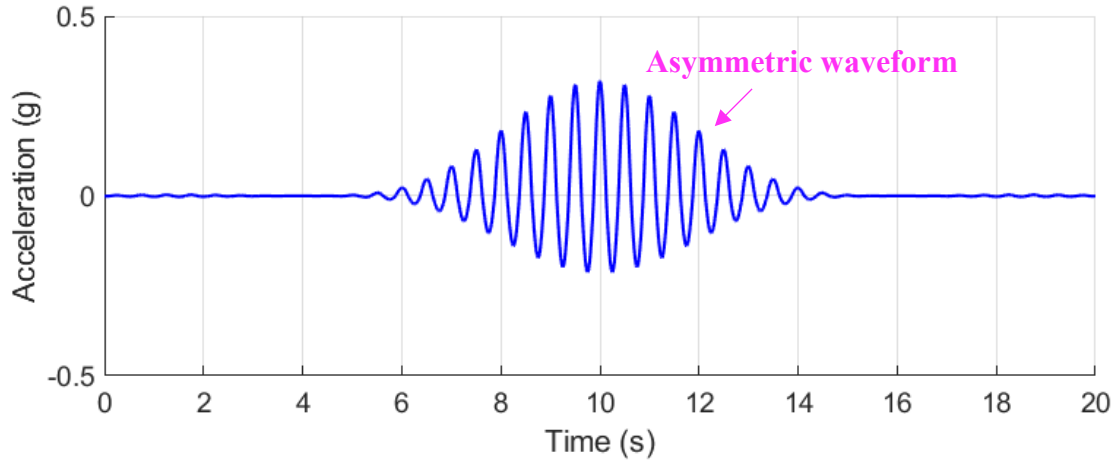


Figure 6: Asymmetric ground excitation generated using a B-Spline function complex wavelet.

## 3 CONCLUSIONS

Elastoplastic SDOF systems were subject to both symmetric and asymmetric excitations. The nonlinear response history results show that the peak inelastic displacement is exactly equal to the peak displacement for the corresponding elastic system if the excitation is symmetric. The equal displacement rule does not hold for asymmetric excitations. Peak inelastic displacements increase for elastoplastic systems with larger strength reduction ratios. For pseudo-symmetric excitations, including typical ground motion records, the equal displacement rule is approximate.

The results indicate that the equal displacement concept is conditional upon the symmetry of the excitation. As a consequence, the peak inelastic displacements for asymmetric excitations, including non-stationary stochastic wind loads, are not constant and depend on the strength reduction. The implication for wind engineering is that only a limited strength reduction may be justified for rare large-magnitude windstorms, and additional studies are warranted to determine the effect of duration on the response of non-elastoplastic systems and the application of the equal displacement rule to multi-degree of freedom systems and systems with gravity load effects.

## REFERENCES

[1] A.S. Veletsos, N.M. Newmark. 1960. Effect of inelastic behavior on the response of simple systems to earthquake motions. *Second World Conference on Earthquake Engineering*, Tokyo, Japan, **2**, 895-912, 1960.

[2] A.K. Chopra, Dynamics of structures: theory and applications to earthquake engineering, 6th edition. Pearson, 2022.

[3] American Society of Civil Engineers (ASCE). *Prestandard for performance-based wind design*. ASCE, Reston, Virginia, 2019.

[4] American Society of Civil Engineers (ASCE). *ASCE 7-22 Minimum Design Loads and Associated Criteria for Buildings and Other Structures*. ASCE, Reston, Virginia, 2022.

[5] S.M.J. Spence, W.C. Chuang, P. Tabbuso, E. Bernardini, A. Kareem, L. Palizzolo, A. Pirrotta. Performance-based engineering of wind excited structures: a general methodology. *Structures Congress*, Phoenix, Arizona, 2016.

[6] L. Griffis, V. Patel, S. Muthukumar, S. Baldava. A framework for performance-based wind engineering. *Advances in Hurricane Engineering*, 1205-1216, 2012.

[7] A. Kareem, S.M.J. Spence, E. Bernardini. *Performance-based design of wind-excited tall and slender structures*. NatHaz Modeling Laboratory, University of Notre Dame, South Bend, Illinois, September, 2013.

[8] A. Teolis. *Computational signal processing with wavelets.* Birkhäuser, 1998.

[9] The Math Works Inc, MATLAB, version R2021b, Update 2, Natick, Massachusetts, 2021.

COMPDYN 2023
9th ECCOMAS Thematic Conference on
Computational Methods in Structural Dynamics and Earthquake Engineering
M. Papadrakakis, M. Fragiadakis (eds.)
Athens, Greece, 12-–14 June 2023

# STEADY-STATE RESPONSE OF A HIGH-STRENGTH MOMENT-RESISTING STEEL FRAME-SELF-CENTERING STEEL PLATE SHEAR WALL SYSTEM

**Chuandong Xie[1], Xiantie Wang[1], and George Vasdravellis[2]**

[1]School of Civil Engineering, Xi'an University of Architecture and Technology, Xi'an, 710055, China
e-mail: {chuandongxie,wangxtgm}@xauat.edu.cn

[2] School of Energy, Geoscience, Infrastructure and Society, Institute for Infrastructure & Envi-ronment, Heriot-Watt University, Edinburgh, EH14 4AS, UK
e-mail: G.Vasdravellis@hw.ac.uk

**Abstract.** *A resilient system comprised of a high-strength moment-resisting steel frame (HS-MRF) and self-centering steel plate shear walls (SC-SPSWs) has been proposed to address the issue of frame expansion. The system's steady-state dynamic responses were analysed using an analytical solution of a single-degree-of-freedom nonlinear oscillator under harmonic excitation, solved via the method of slowly varying parameters. A stability analysis was also conducted to assess the behaviour of singular points. The hysteretic model for the proposed structure is a combination of validated bilinear, self-centering, and pinching hysteresis, representing the high-strength frame, self-centering frame, and steel plate shear wall, respectively. The results indicate that increasing the proportion of bilinear hysteresis has minimal impact on resonance but can decrease nonlinearity for lower excitation intensities. However, for higher intensities, increasing the bilinear hysteresis can significantly decrease peak responses and reduce both the jump and unbounded phenomena. Most of the unstable responses can be divided into four zones, and the unstable regions are greatly influenced by the ratio of hysteretic models. This steady-state dynamic analysis suggests that a well-designed mixture of high-strength moment-resisting steel frames and self-centering steel plate shear walls can bring a favourable seismic performance.*

**Keywords:** Resilient structure, Nonlinear dynamics, Frequency response, Stability analysis, Frame-wall system

## 1 INTRODUCTION

Recent developed self-centering structural systems are designed to manage the structural damage through the introduction of the rocking connections, easy-to-replace energy-dissipating elements and post-tensioned (PT) system. During a strong earthquake, gap openings occurs in the rocking connections, elongating the PT elements which provides the restoring force and brings the buildings back to their origin position. The energy is dissipated by the elements that are across the rocking connections and will be replaced after the earthquake [1–4]. However, the frame will expand due to the elongation of the beams since the beam rotate at their flanges, and the expansion beyond a certain level can induce failure in the perimeter self-centering frame and excessive cracks in the slabs [5,6]. As an alternative solution, an innovative dual frame-wall resilient system consisting of a high-strength moment-resisting steel frame (HS-MRF) and self-centering steel plate shear walls (SC-SPSWs) is proposed [7], as shown in Fig. 1. The HS-MRF provide large elastic deformation capability due to the use of high-strength steel (e.g. Q460), and all the SC-SPSWs are located at the outside bays and use composite columns, steel beams, steel plates, PT strands in the beams and PT bars in the columns. The steel plates serve as energy-dissipating elements and are connected to the boundary elements by bolt work, so that the plates are easy to replace. The slot connections between HS-MRF and SC-SPSWs allow frame expansion and enable the continuous slab free from damage. Four performance levels are designed, including immediate occupancy (IO), damage control (DC), life safety (LS) and collapse prevention (CP), corresponding to the peak inter-storey drifts of 0.4%, 1.0%, 2.0% and 4.0%, respectively. The HS-MRF work provides larger resistance to lateral forces but remains elastic during both IO and DC levels, and the SC-SPSW ensures recentering capability at the DC level by using the PT elements. More details can be found in the previous paper [7].

Experimental and numerical studies have effectively characterized the mechanical behaviour and dynamic responses of self-centering systems, as evidenced by recent research [8–11]. However, obtaining a complete picture can be both time-consuming and costly, and the results are often not continuous. To overcome these limitations, the steady-state analysis of the system under harmonic motion can explore suitable designs and perform parameter investigations, optimizations, and statistical model updating. Nonetheless, obtaining closed-form solutions for the dynamic response of the systems is a challenging task due to the continuous but non-differentiable properties of hysteretic models. This can be solved by the method of averaging, which has been implemented into flag-shaped hysteresis [12] and flag-shaped hysteresis with viscous damping [13]. For the self-centering systems without considering damping, Christopoulos (2004) [12] finds that both stable solution branches can be achieved depending on the nature of the excitation, and an amplitude jump phenomenon is also found when increasing frequency and decreasing frequency sweeps. Kitayama and Yang (2021) [13], considering the self-centering hysteresis with viscous damping, and with or without elasto-plastic hysteresis, finds that the self-centering systems may have large displacement demand due to the potentially limited energy dissipation. However, the performance levels in the dual frame-wall resistant system present a complicated task to determine the resonant responses. At the IO level, the energy is absorbed by viscous damping only, but by viscous damping and infill web plate which exhibits pinching behaviour at the DC level. While at the LS level, more energy is dissipated by the HS-MRF and the web plate will fail, and then at the CP level the energy is mainly absorbed by the HS-MRF. Therefore, more research is required to address the issue of resonant responses of the proposed dual frame-wall system.

To this end, this paper first summarised the hysteresis and proposed the analytical expressions

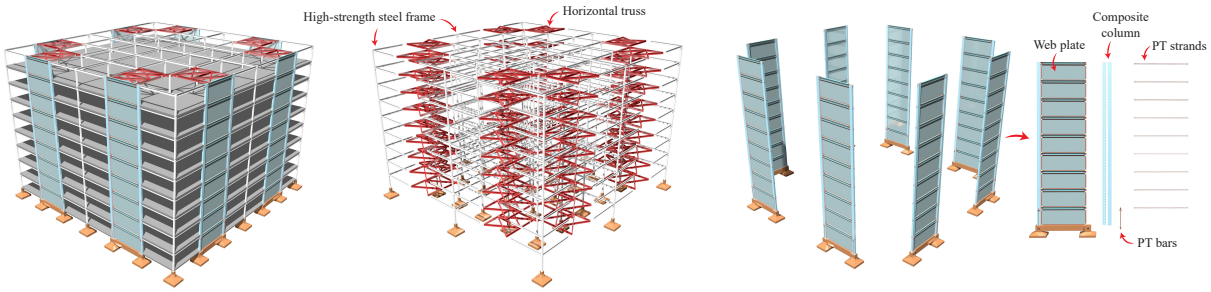


(a) frame-wall system (b) HS-MRF (c) SC-SPSWs

Figure 1: Dual frame-wall resilient system [7]

for the steady-state response and the corresponding stability of a nonlinear oscillator subjected to harmonic excitation considering viscous damping, followed by the discussion of dynamic behaviour of the dual frame-wall system. The findings shed light on the inherent dynamic properties of the dual frame-wall system and suggest that a reasonable combination can achieve a favourable seismic performance. This research is based on previous work [**?**] where more details can be found.

## 2 HYSTERETIC MODELS

The proposed dual frame-wall system consists of a HS-MRF and SC-SPSWs. Due to the use of high-strength material, the HS-MRF can keep elastic up to the LS level, and then present beam-hinge ductile response [14]. Recently developed hinge techniques that are easy to replace [15–17] can also be employed. All these studies show that the HS-MRF exhibit bilinear hysteretic responses. Fig. 2a shows the bilinear hysteresis, where $k_{\mathrm{iH}}$, $f_{\mathrm{yH}}$ and $\alpha_{\mathrm{H}}$ are the initial stiffness, yielding strength and post-yielding stiffness ratio of the model, respectively. The SC-SPSW is composed of a pure self-centering frame and infill-thin web plates, as shown in Fig. 1c. During IO level, the system work elastically. After that, the interfaces in the rocking connection detach, elongating the PT elements and the energy is dissipated by the infill-thin web plates. Available investigations on self-centering frame [5, 7, 18–21] show that the prestressed design provides recentering ability, and the pure self-centering frame exhibit trilinear hysteretic relationship. Studies on the infill-thin web plates [22–25] also find that due to the buckling and plastic deformation, the shear plate shows pinching effect in hysteretic curves. Since the coupling effect between thin web plates and self-centering frame are negligible, the hysteretic behaviour of SC-SPSW is assumed by a trilinear relationship superposed by a pinching relationship. Fig. 2b shows the hysteretic model of self-centering system, where $k_{\mathrm{iS}}$, $f_{\mathrm{yS}}$ and $\alpha_{\mathrm{S}}$ are the initial stiffness, yielding strength and decompressed stiffness ratio of the model, respectively. Fig. 2c shows the hysteretic model of web plate, which is modified from Pinching 4 material [26]. The model consists of response envelopes ($m$ path), unload-reload paths ($p$ and $n$ path) and damage rules. Details of the first and third rules can be found in [26]. Since the kinematic hardening plays a domain role in thin web plate, and in order to be compatible with bilinear hysteresis, the pinching rules are modified from the previous study [26], as shown in Fig. 2d. The unloading-reloading rule is defined by unloading and reloading points. Taking the positive-negative branch as example, $n_{\mathrm{u}}$ is defined from $n_{\mathrm{u},0}$ and $n_{\mathrm{u},1}$ by a parameter $\beta_{\mathrm{uf}}$, and $n_{\mathrm{r}}$ is defined by two parameters, $\beta_{\mathrm{rd}}$ and $\beta_{\mathrm{rf}}$, which control the displacement and force portion, respectively. The modified pinching hysteresis has been implemented in OpenSees [27] as an uniaxial material, named Pinching4M.

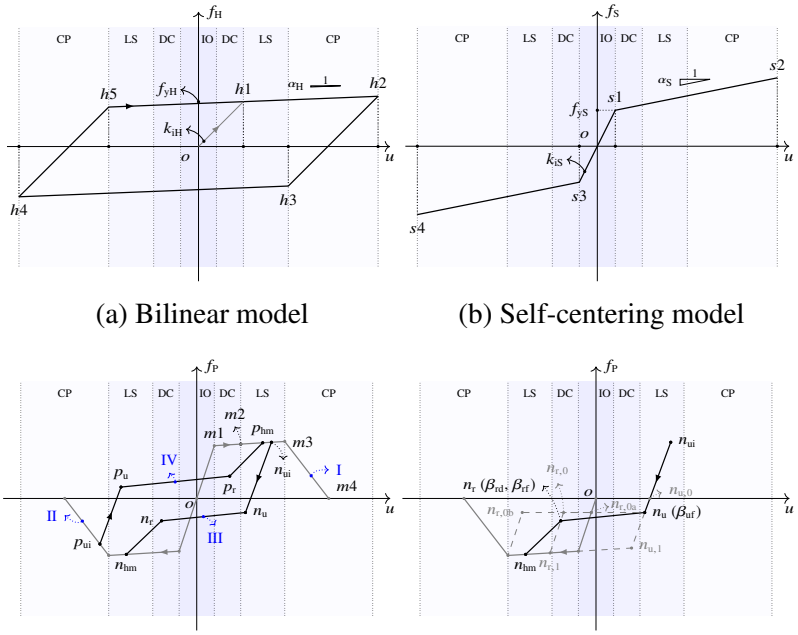


(a) Bilinear model (b) Self-centering model

(c) Pinching model (d) Pinching rulel

Figure 2: Hysteretic models

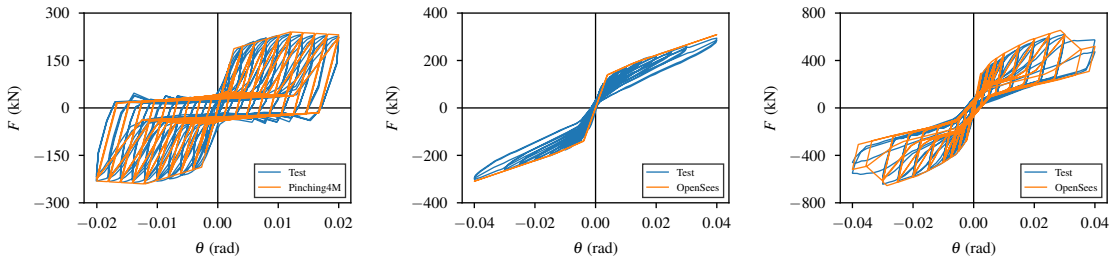


(a) Pinching hysteresis [24] (b) Self-centering hysteresis [7] (c) SC-SPSW [7]

Figure 3: Verification of hysteretic models

The validation of pinching and self-centering hysteresis is shown in Fig. 3a, based on the experiment carried by Yu et al. (2011) [24], and it is found that the modified pinching hysteresis can well predict the hysteretic responses. The self-centering hysteresis and SC-SPSW model are verified through the specimens of SC-SPSW-1 and SC-SPSW-4 in Reference [7]. Again both hysteretic responses can be well matched by the self-centering hysteresis and the combination of self-centering and pinching hysteresis, respectively.

## 3 HARMONIC FREQUENCY RESPONSE

### 3.1 Derivation of closed-form frequency response

The equation of a general nonlinear single-degree-of-freedom oscillator subjected to a steady harmonic excitation can be written as

$$m\frac{\mathrm{d}^2u(t)}{\mathrm{d}t^2}+c\frac{\mathrm{d}u(t)}{\mathrm{d}t}+k\bar{f}(u)=-mA_{\mathrm{g}}\cos\omega_{\mathrm{g}}t \tag{1}$$

where $m$ is the mass; $u(t)$ is the relative displacement; $c$ is the damping constant; $k$ is the initial stiffness of structure; $\bar{f}(u)$ is normalised restoring force; $A_{\mathrm{g}}$ and $\omega_{\mathrm{g}}$ are amplitude and the circular frequency of the base excitation, respectively.

Let

$$\omega_0 = \sqrt{\frac{k}{m}}; \qquad \tau = \omega_0 t; \qquad \zeta = \frac{c}{2m\omega_0}; \qquad \sigma = \frac{\omega_{\mathrm{g}}}{\omega_0}; \qquad u_{\mathrm{s}} = -\frac{mA_{\mathrm{g}}}{k} \tag{2}$$

where $\omega_0$ is the initial natural circular frequency of the system; $\tau$ is the nondimensional time; $\zeta$ is the damping ratio; $\sigma$ is the excitation frequency ratio.

Eq. (1) can be written as

$$\frac{\mathrm{d}^2 u}{\mathrm{d}\tau^2} + 2\zeta\frac{\mathrm{d}u}{\mathrm{d}\tau} + \bar{f}(u) = u_{\mathrm{s}}\cos\sigma\tau \tag{3}$$

Assuming that the steady-state response of the system exists, the solution of Eq. (3) can be written as

$$u(\tau) = a\cos(\sigma\tau + \beta) \tag{4}$$

where $a$ and $\beta$ are slowly varying parameters. Letting $\theta = \sigma\tau + \beta$ and using the method of averaging [28], we have

$$-2\zeta\sigma a_0 + S(a_0) = u_{\mathrm{s}}\sin\beta_0 \tag{5}$$

$$-\sigma^2 a_0 + C(a_0) = u_{\mathrm{s}}\cos\beta_0 \tag{6}$$

in which

$$S(a) = \frac{1}{\pi}\int_0^{2\pi} \bar{f}(a\cos\theta)\sin\theta\mathrm{d}\theta \tag{7}$$

$$C(a) = \frac{1}{\pi}\int_0^{2\pi} \bar{f}(a\cos\theta)\cos\theta\mathrm{d}\theta \tag{8}$$

and $a_0$ and $\beta_0$ are the amplitude and the phase during steady-state response, respectively. Let

$$\bar{S} = \frac{S(a_0)}{a_0}; \qquad \bar{C} = \frac{C(a_0)}{a_0} \tag{9}$$

Substituting Eq. (9) for Eqs. (5) and (6), squaring each equation and summing them, we obtain

$$R_{\mathrm{u}} - \frac{R_{\mathrm{a}}}{\sqrt{\left(\bar{S} - 2\zeta\sigma\right)^2 + \left(\bar{C} - \sigma^2\right)^2}} = 0 \tag{10}$$

in which

$$R_{\mathrm{u}} = \frac{a_0}{u_{\mathrm{s}}}; \qquad R_{\mathrm{a}} = \frac{A_{\mathrm{g}}}{A_{\mathrm{s}}}; \qquad A_{\mathrm{s}} = \frac{ku_{\mathrm{y}}}{m} \tag{11}$$

where $R_{\mathrm{u}}$ is the normalised amplitude response; $R_{\mathrm{a}}$ is the normalised excitation.

Noting that no specific hysteresis has been taken into account, Eq. (10) can be applied for the non-time sensitive nonlinear structural systems.

### 3.2 Derivation of stability

The stability of the different portions of the response curves can be identified by investigating the nature of the singular points of Eq. (10). Let

$$a = a_0 + \mu_0 e^{\lambda t}; \qquad \beta = \beta_0 + \nu_0 e^{\lambda t} \tag{12}$$

where $\mu$, $\nu$ are constants.

Considering the results of frequency response, we have

$$\begin{bmatrix} -2\sigma\lambda + \frac{\partial S}{\partial a} - 2\zeta\sigma & \sigma^2 a_0 - C(a_0) \\ \frac{\partial C}{\partial a} - \sigma^2 & S(a_0) - 2\sigma a_0 \lambda - 2\zeta\sigma a_0 \end{bmatrix} \begin{bmatrix} \mu_0 \\ \nu_0 \end{bmatrix} = \begin{bmatrix} 0 \\ 0 \end{bmatrix} \tag{13}$$

Taking the determinant of Eq. (13) gives the following

$$(2\sigma\lambda)^2 + 2\sigma\lambda P + Q = 0 \tag{14}$$

where

$$P = 4\zeta\sigma - \bar{S} - \frac{\partial S}{\partial a} \tag{15}$$

$$Q = \left(\bar{C} - \sigma^2\right)\left(\frac{\partial C}{\partial a} - \sigma^2\right) + 2\zeta\sigma\left(2\zeta\sigma - \frac{\partial S}{\partial a} - \bar{S}\right) + \frac{\partial S}{\partial a}\bar{S} \tag{16}$$

The solutions for Eq. (14) are

$$\lambda_{1,2} = \frac{-P \pm \sqrt{P^2 - 4Q}}{4\sigma} \tag{17}$$

The stability of singular points depends on the sign of solutions, which can be determined by the sign of $P$ and $Q$. Reference [28] shows that only when both $P > 0$ and $Q > 0$, the singular points are stable. Noting that no hysteresis is specified in Eq. (14), again the conclusion can be used for non-time sensitive nonlinear structural systems.

### 3.3 Dual frame-wall system

For the dual frame-wall resilience system, the $\bar{f}(u)$ can be written as

$$\bar{f}(u) = \bar{f}(u)_{\mathrm{H}} + \bar{f}(u)_{\mathrm{S}} + \bar{f}(u)_{\mathrm{W}} \tag{18}$$

where $\bar{f}(u)_{\mathrm{H}}$, $\bar{f}(u)_{\mathrm{S}}$ and $\bar{f}(u)_{\mathrm{W}}$ are the normalised restoring force of bilinear, self-centering and pinching hysteretic models and can be calculated by Eqs. (19) to (21), respectively.

$$\bar{f}_{\mathrm{H}}(u) = \begin{cases} \bar{f}_{\mathrm{H1}} = \bar{k}_{\mathrm{iH}}\left(u - (1-\alpha_{\mathrm{H}})\left(a - u_{\mathrm{yH}}\right)\right) & u \in (u_{\mathrm{H1}}, u_{\mathrm{H2}}) \quad (19a) \\ \bar{f}_{\mathrm{H2}} = \bar{k}_{\mathrm{iH}}\left(\alpha_{\mathrm{H}} u - u_{\mathrm{yH}}\left(1-\alpha_{\mathrm{H}}\right)\right) & u \in (u_{\mathrm{H2}}, u_{\mathrm{H3}}) \quad (19b) \\ \bar{f}_{\mathrm{H3}} = \bar{k}_{\mathrm{iH}}\left(u + (1-\alpha_{\mathrm{H}})\left(a - u_{\mathrm{yH}}\right)\right) & u \in (u_{\mathrm{H3}}, u_{\mathrm{H4}}) \quad (19c) \\ \bar{f}_{\mathrm{H4}} = \bar{k}_{\mathrm{iH}}\left(\alpha_{\mathrm{H}} u + u_{\mathrm{yH}}\left(1-\alpha_{\mathrm{H}}\right)\right) & u \in (u_{\mathrm{H3}}, u_{\mathrm{H4}}) \quad (19d) \end{cases}$$

$$\bar{f}_{\mathrm{S}}(u) = \begin{cases} \bar{f}_{\mathrm{S1}} = \bar{k}_{\mathrm{iS}}\left(\alpha_{\mathrm{S}} u + u_{\mathrm{y}}\left(1-\alpha_{\mathrm{S}}\right)\right) & u \in (u_{\mathrm{S1}}, u_{\mathrm{S2}}) \quad (20a) \\ \bar{f}_{\mathrm{S2}} = \bar{k}_{\mathrm{iS}} u & u \in (u_{\mathrm{S2}}, u_{\mathrm{S3}}) \quad (20b) \\ \bar{f}_{\mathrm{S3}} = \bar{k}_{\mathrm{iS}}\left(\alpha_{\mathrm{S}} u - u_{\mathrm{y}}\left(1-\alpha_{\mathrm{S}}\right)\right) & u \in (u_{\mathrm{S3}}, u_{\mathrm{S4}}) \quad (20c) \end{cases}$$

$$\bar{f}_{\mathrm{W}}(u)=\begin{cases}\bar{f}_{\mathrm{W1}}=\bar{k}_{\mathrm{iW}}\left(u+\left(1-\alpha_{\mathrm{W}}\right)\left(u_{\mathrm{y}}-a\right)\right) & u\in\left(u_{\mathrm{W1}},u_{\mathrm{W2}}\right) \quad (21a)\\ \bar{f}_{\mathrm{W2}}=\bar{k}_{\mathrm{iW}}\dfrac{\left(\beta_{\mathrm{uf}}-\beta_{\mathrm{rf}}\right)u+\beta_{\mathrm{rf}}\gamma_2+\beta_{\mathrm{rd}}\beta_{\mathrm{uf}}a}{\gamma_2+a\beta_{\mathrm{rd}}} & u\in\left(u_{\mathrm{W2}},u_{\mathrm{W3}}\right) \quad (21b)\\ \bar{f}_{\mathrm{W3}}=\bar{k}_{\mathrm{iW}}\dfrac{\left(\frac{1-\beta_{\mathrm{rf}}}{a}u+\beta_{\mathrm{rd}}-\beta_{\mathrm{rf}}\right)\gamma_1}{1-\beta_{\mathrm{rd}}} & u\in\left(u_{\mathrm{W3}},u_{\mathrm{W4}}\right) \quad (21c)\\ \bar{f}_{\mathrm{W4}}=\bar{k}_{\mathrm{iW}}\left(u-\left(1-\alpha_{\mathrm{W}}\right)\left(u_{\mathrm{y}}-a\right)\right) & u\in\left(u_{\mathrm{W4}},u_{\mathrm{W5}}\right) \quad (21d)\\ \bar{f}_{\mathrm{W5}}=\bar{k}_{\mathrm{iW}}\dfrac{\left(\beta_{\mathrm{uf}}-\beta_{\mathrm{rf}}\right)u-\beta_{\mathrm{rf}}\gamma_2-\beta_{\mathrm{rd}}\beta_{\mathrm{uf}}a}{\gamma_2+a\beta_{\mathrm{rd}}} & u\in\left(u_{\mathrm{W5}},u_{\mathrm{W6}}\right) \quad (21e)\\ \bar{f}_{\mathrm{W6}}=\bar{k}_{\mathrm{iW}}\dfrac{\left(\frac{1-\beta_{\mathrm{rf}}}{a}u-\beta_{\mathrm{rd}}+\beta_{\mathrm{rf}}\right)\gamma_1}{1-\beta_{\mathrm{rd}}} & u\in\left(u_{\mathrm{W6}},u_{\mathrm{W7}}\right) \quad (21f)\end{cases}$$

where

$$\gamma_1=u_{\mathrm{y}}+a\alpha_{\mathrm{W}}-\alpha_{\mathrm{W}}u_{\mathrm{y}} \quad (22)$$

$$\gamma_2=\left(1-\alpha_{\mathrm{W}}\right)\left(a-u_{\mathrm{y}}\right)-\beta_{\mathrm{uf}}\gamma_1 \quad (23)$$

Thus, we have

$$\begin{aligned}\bar{S}&=\frac{1}{\pi a}\int_0^{2\pi}\bar{f}\sin\theta\mathrm{d}\theta=\frac{1}{\pi a}\int_0^{2\pi}\left(\bar{f}_{\mathrm{H}}+\bar{f}_{\mathrm{S}}+\bar{f}_{\mathrm{W}}\right)\sin\theta\mathrm{d}\theta\\&=\bar{S}_{\mathrm{H}}+\bar{S}_{\mathrm{S}}+\bar{S}_{\mathrm{W}}\end{aligned} \quad (24)$$

$$\begin{aligned}\bar{C}&=\frac{1}{\pi a}\int_0^{2\pi}\bar{f}\cos\theta\mathrm{d}\theta=\frac{1}{\pi a}\int_0^{2\pi}\left(\bar{f}_{\mathrm{H}}+\bar{f}_{\mathrm{S}}+\bar{f}_{\mathrm{W}}\right)\cos\theta\mathrm{d}\theta\\&=\bar{C}_{\mathrm{H}}+\bar{C}_{\mathrm{S}}+\bar{C}_{\mathrm{W}}\end{aligned} \quad (25)$$

## 4 HARMONIC FREQUENCY RESPONSE OF THE DUAL FRAME-WALL SYSTEM

### 4.1 Steady-state dynamic response

The steady-state responses of the dual frame-wall system can be evaluated using Eq. (10), which requires calculating $\bar{S}$ and $\bar{C}$ using Eqs. (24) and (25). Fig. 4 presents the responses for different stiffness ratios ($k=\bar{k}_{\mathrm{iH}}:\bar{k}_{\mathrm{iS}}:\bar{k}_{\mathrm{iW}}$) for bilinear, self-centering, and pinching hysteresis systems, where $\alpha_{\mathrm{H}}$, $\alpha_{\mathrm{S}}$, and $\alpha_{\mathrm{W}}$ are 0.0, 0.1, and 0.0, respectively and under the same viscous damping of 0.02. When the bilinear system stiffness is low (0.1), as shown in Fig. 4a, the higher self-centering hysteresis causes larger resonance, but the response levels remain at the DC and LS levels for $R_{\mathrm{a}}=0.2$. Since the self-centering hysteresis cannot provide hysteretic damping, the pinching system plays an important role in energy dissipation and reducing resonance. However, when $R_{\mathrm{a}}=0.6$ (Fig. 4b), the response becomes unbounded when the pinching system dominates, making the self-centering building hazardous if the hysteretic damping system deteriorates. After increasing the bilinear system stiffness ratio to 0.5, the resonant responses change significantly. As shown in Fig. 4c, under low excitation intensity ($R_{\mathrm{a}}=0.2$), the peak response for the systems remains around 2.5, despite the different stiffness ratios between the self-centering and pinching systems. Increasing the pinching system stiffness ratio can further decrease the peak value. When $R_{\mathrm{a}}=0.6$ (Fig. 4d), the maximum response increases to approximately 3.6 for $k=0.5:0.5:0.0$. Increasing the stiffness ratio of the pinching system can decrease the peak value. Figs. 4e and 4f compare the steady-state responses of

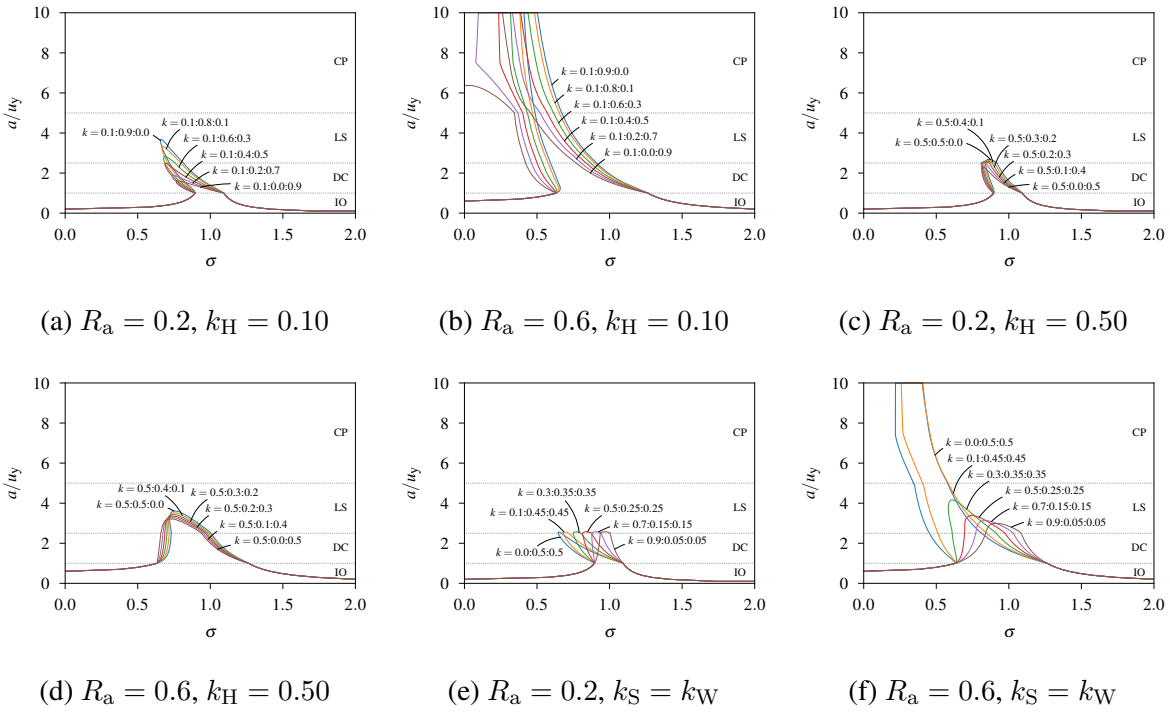


(a) $R_{\mathrm{a}} = 0.2$, $k_{\mathrm{H}} = 0.10$ (b) $R_{\mathrm{a}} = 0.6$, $k_{\mathrm{H}} = 0.10$ (c) $R_{\mathrm{a}} = 0.2$, $k_{\mathrm{H}} = 0.50$

(d) $R_{\mathrm{a}} = 0.6$, $k_{\mathrm{H}} = 0.50$ (e) $R_{\mathrm{a}} = 0.2$, $k_{\mathrm{S}} = k_{\mathrm{W}}$ (f) $R_{\mathrm{a}} = 0.6$, $k_{\mathrm{S}} = k_{\mathrm{W}}$

Figure 4: Steady-state response of dual frame-wall system under different stiffness ratios

systems with the same stiffness ratio of self-centering and pinching systems ($k_{\mathrm{S}} = k_{\mathrm{W}}$) but different stiffness ratios of the bilinear system. Similar to Fig. 4c, the peak response is around 2.5 under low excitation intensity ($R_{\mathrm{a}} = 0.2$), but the higher self-centering and pinching systems bring more nonlinearity and increase the unstable zone. After increasing the excitation intensity ($R_{\mathrm{a}} = 0.6$), the peak responses increase significantly for the system with decreasing bilinear system stiffness (Fig. 4f). Thus, the stiffness ratio between the bilinear, self-centering, and pinching systems controls the dynamic responses of the dual frame-wall system.

The response of dual frame-wall systems with a stiffness ratio of $\bar{k}_{\mathrm{iH}} : \bar{k}_{\mathrm{iS}} : \bar{k}_{\mathrm{iW}} = 0.5 : 0.25 : 0.25$ is presented in Fig. 5, under varying excitation amplitude and damping ratio. Fig. 5a shows that the resonance of the system is initially at the DC level, and then progresses to the LS level as the excitation amplitude increases. At $R_{\mathrm{a}} = 1.0$, the peak response reaches 5.0, indicating that a bilinear system with a stiffness ratio of 0.5 can effectively control the maximum response. Jump phenomena are also observed in these cases. Increasing the damping ratio can significantly decrease the peak response under both low ($R_{\mathrm{a}} = 0.2$, Fig. 5b) and high ($R_{\mathrm{a}} = 0.6$, Fig. 5c) excitation intensities. In the former case, the resonance is brought back to the DC level, where the bilinear system remains elastic, while in the latter case, the viscous damping plays a key role since only half of the bilinear system contributes to the lateral resistance. These results demonstrate that a well-designed dual frame-wall system can exhibit favourable dynamic behaviour.

## 4.2 Stability analysis

Fig. 6 shows the edges of the solutions of Eq. (16) of the proposed system. In 6a, where $k_{\mathrm{H}} = 0.1$, most of the responses are divided into four zones, corresponding to $R_{\mathrm{u}}$ values of 1.0, 2.5, 5.0, and 7.5. Both self-centering and pinching hysteresis have a normalized yielding value of 1.0, and the pinching hysteresis starts to fail at 5.0 and completely fails at 7.5, as shown

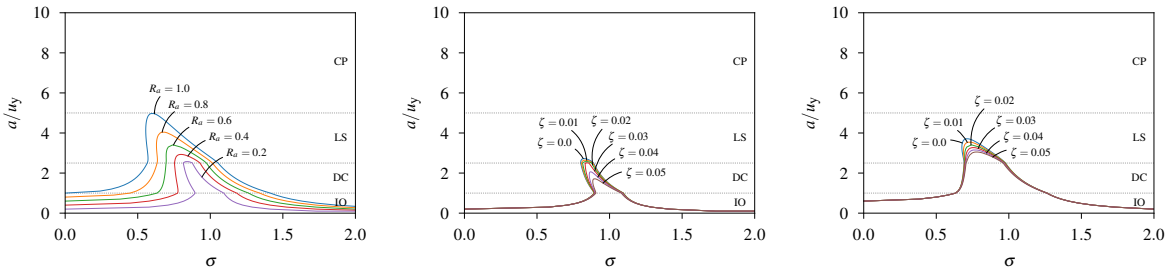


(a) $\zeta = 0.02$ (b) $R_{\mathrm{a}} = 0.2$ (c) $R_{\mathrm{a}} = 0.6$

Figure 5: Steady-state response of dual frame-wall system ($\bar{k}_{\mathrm{iH}} = 0.5$, $\bar{k}_{\mathrm{iS}} = 0.25$, $\bar{k}_{\mathrm{iW}} = 0.25$)

in Figure 2. However, an extra value of 2.5 is contributed from the yielding of the bilinear hysteresis. This indicates that although the stability of the standalone bilinear hysteresis is always stable, the stability behaviour cannot be obtained by summing all the responses in a nonlinear oscillator. For the system where $k = 0.1 : 0.9 : 0.0$ and only bilinear and self-centering hysteresis are combined, the $Q < 0$ zone is bounded and starts at the (1.0,1.0) point and is necking when $R_{\mathrm{u}} = 2.5$. Thus, the corresponding steady-state responses in 4a and 4b are divided into three branches. When $k = 0.1 : 0.8 : 0.1$, pinching hysteresis is introduced, resulting in additional separations of the $Q < 0$ zone at the CP level. However, the pinching system fails at the CP level, bringing a highly nonlinear problem. Further research is required for collapse-prevent behaviour and design. With an increase in the pinching hysteresis, the $Q < 0$ zone shifts to the left, and the area is increased. In the case of $k = 0.1 : 0.1 : 0.9$, the unstable area is unbounded. Therefore, a higher stiffness of the pinching system increases the nonlinearity of the oscillator.

In the results presented in Fig. 6b, it can be seen that as $k_{\mathrm{H}}$ is increased to 0.5, the solutions for $Q < 0$ are divided into two zones: a lower zone at the DC level and an upper zone across LS and CP levels. The lower unstable zones are initially formed by the self-centering and pinching hysteresis. By comparing the steady-state responses shown in Figs. 4c and 4d with Fig. 6b, it is apparent that the monotonic decreasing solutions in the steady-state are unstable. The upper zone is bounded at the LS level, but left-bounded at the CP level when $R_{\mathrm{u}} < 7.5$. The bilinear hysteresis contributes to the discontinuity of the zones, and the gap between them is increased with the stiffness of the pinching hysteresis. Fig. 6c presents the overall stability map under different $k_{\mathrm{H}}$ values when $k_{\mathrm{S}} = k_{\mathrm{W}}$. When only self-centering and pinching hysteresis are present in the system (i.e., $k = 0.0 : 0.5 : 0.5$), the unstable zone is continuous and left-bounded between $R_{\mathrm{u}} = 5.0$ and $R_{\mathrm{u}} = 7.5$. As $k_{\mathrm{H}}$ is increased to 0.1, and $k_{\mathrm{S}} = k_{\mathrm{W}} = 0.45$, necking occurs around $R_{\mathrm{u}} = 2.5$. With further increases in $k_{\mathrm{H}}$, the unstable zone becomes divided. When $k_{\mathrm{H}} = 0.9$, the previous upper unstable zone vanishes. The unstable behaviour of the singular points is, therefore, a result of the self-centering and pinching hysteresis.

6d presents the results of the dual frame-wall system ($k = 0.50 : 0.25 : 0.25$, $\alpha_{\mathrm{H}} = 0.1$) under different viscous damping ratios. The increase in viscous damping does not have a significant effect on the unstable zone at the DC level, where the bilinear system remains elastic and the self-centering and pinching systems behave nonlinearly. However, at the LS and CP levels, it is found that increasing the viscous damping ratio can reduce the unstable zone. The reason for this is mainly due to the coupling of hysteretic damping and viscous damping, as the yielding of a bilinear system provides a large amount of hysteretic damping. However, the exact coupling mechanism remains unclear, and further investigation is needed. The post-yielding

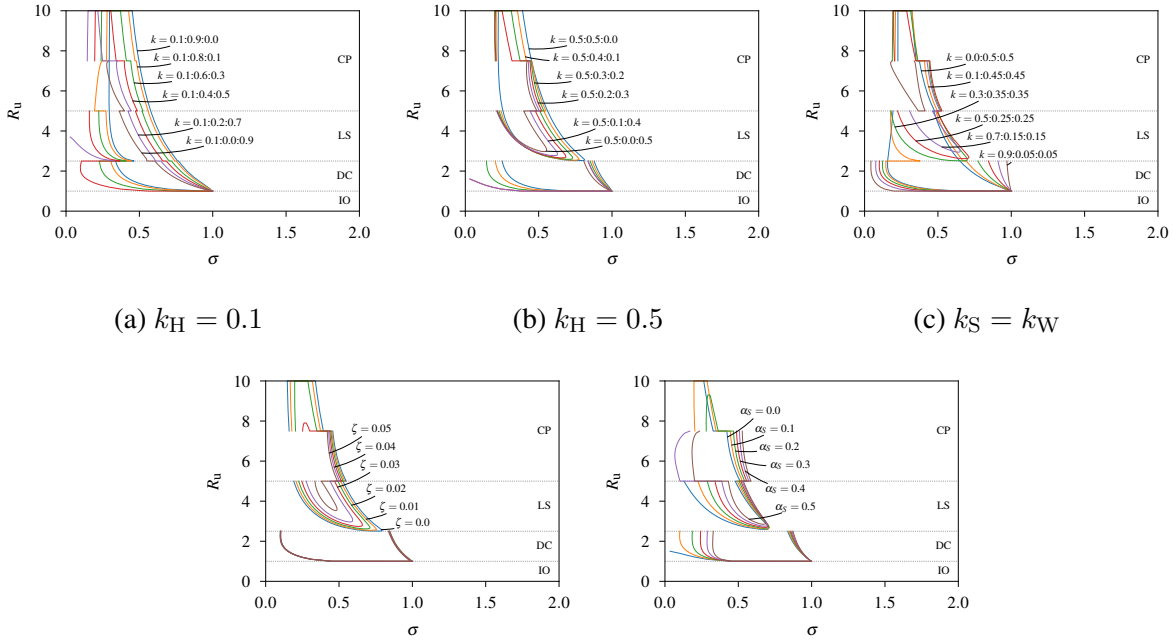


(a) $k_{\mathrm{H}} = 0.1$ (b) $k_{\mathrm{H}} = 0.5$ (c) $k_{\mathrm{S}} = k_{\mathrm{W}}$

(d) $k = 0.50 : 0.25 : 0.25$, $\alpha_H = 0.1$ (e) $k = 0.50 : 0.25 : 0.25$, $\zeta = 0.02$

Figure 6: Stability of dual frame-wall system

stiffness ratio of self-centering hysteresis is an important factor in the nonlinearity of the system. 6e shows the map of $Q < 0$ of the oscillator ($k = 0.50 : 0.25 : 0.25$, $\zeta = 0.02$) under different $\alpha_{\mathrm{H}}$. Increasing the value of $\alpha_{\mathrm{H}}$ can shift the unstable zone to the right and decrease its area. Since only 0.25 of self-centering hysteresis is present here, the unstable zone is still able to separate the steady-state responses, leading to the jump phenomenon.

## 5 CONCLUSIONS

The main focus of this paper is to investigate the nonlinear dynamic behaviour of a mixed dual frame-wall resilient system, comprising of a high-strength moment-resisting steel frame (HS-MRF) and self-centering steel plate shear walls (SC-SPSWs). The hysteretic model employed in this system includes bilinear, self-centering, and pinching hysteresis that represent the HS-MRF, self-centering frame, and steel plate shear wall, respectively. The study utilizes the method of averaging to obtain the analytical solution for a single-degree-of-freedom nonlinear oscillator under harmonic excitation. Based on the analysis, the following conclusions can be drawn.

1. The method of averaging was used to obtain analytical solutions for a single-degree-of-freedom nonlinear oscillator subjected to harmonic excitation and incorporating viscous damping. The stability of the system was also studied by analysing the nature of the singular points. This analysis did not consider any specific hysteresis model, making the solutions applicable to non-time-sensitive nonlinear structural systems.

2. This study on the dual frame-wall system reveals that increasing the proportion of bilinear hysteresis has little impact on resonance but can decrease nonlinearity for lower excitation intensities. However, for higher intensities, an increase in bilinear hysteresis

can notably lower peak responses and reduce both the jump and unbounded phenomena. Most of the unstable responses can be divided into four zones, and the unstable regions are greatly influenced by the ratio of hysteretic models. This steady-state dynamic analysis suggests that a well-designed mix of HS-MRF and SC-SPSW can bring a favourable seismic performance.

## ACKNOWLEDGEMENTS

The research described in this paper was financially supported by the National Natural Science Foundation of China (51678474, 52278213), the Natural Science Basic Research Plan in Shaanxi Province of China (2022JM-189), and the China Scholarship Council (202108610187). Any options, findings, conclusions, or recommendations expressed in this publication are those of the authors and do not necessarily reflect the views of the sponsors.

## REFERENCES

[1] N. Chancellor, M. Eatherton, D. Roke, and T. Akbaş, "Self-Centering Seismic Lateral Force Resisting Systems: High Performance Structures for the City of Tomorrow," *Buildings*, vol. 4, pp. 520–548, Sept. 2014.

[2] D. Sun, Y. Yang, Y. Ma, Y. Xue, Y. Yu, and S. Feng, "Seismic behavior of self-centering column base with replaceable stiffener angle steels," *Thin-Walled Structures*, vol. 181, p. 110113, Dec. 2022.

[3] S. Feng, Y. Yang, Y. Xue, and Y. Yu, "A post-tensioned hybrid beam-column connection with a web friction device: Experimental study and theoretical analysis," *Journal of Building Engineering*, vol. 43, p. 103105, Nov. 2021.

[4] G. Xu, T. Guo, and A. Li, "Self-Centering Rotational Joints for Seismic Resilient Steel Moment Resisting Frame," *Journal of Structural Engineering*, vol. 149, p. 04022245, Feb. 2023.

[5] C.-C. Chou and J.-H. Chen, "Development of floor slab for steel post-tensioned self-centering moment frames," *Journal of Constructional Steel Research*, vol. 67, pp. 1621–1635, Oct. 2011.

[6] C. Fang, W. Wang, and W. Feng, "Experimental and numerical studies on self-centring beam-to-column connections free from frame expansion," *Engineering Structures*, vol. 198, p. 109526, Nov. 2019.

[7] C. Xie, X. Wang, and G. Vasdravellis, "Mechanical behaviour and experimental evaluation of self-centring steel plate shear walls considering frame-expansion effects," *Journal of Building Engineering*, vol. 72, p. 106636, Aug. 2023.

[8] Y. Zhang and L.-H. Xu, "Cyclic loading tests of a resilient hinged self-centering RC wall," *Engineering Structures*, vol. 270, p. 114920, Nov. 2022.

[9] X. Wang, C. Xie, Z. Jia, and G. Vasdravellis, "Seismic behaviour of post-tensioned beam-to-column connection using slender energy-dissipating rectangles," *Engineering Structures*, vol. 250, p. 113444, Jan. 2022.

[10] P. Mottier, R. Tremblay, and C. Rogers, "Shake table test of a two-story steel building seismically retrofitted using gravity-controlled rocking braced frame system," *Earthquake Engineering & Structural Dynamics*, vol. 50, no. 6, pp. 1576–1594, 2021.

[11] X. Li, F. Zhang, Z. Wang, K. Tian, J. Dong, and L. Jiang, "Shaking table test of a frame structure retrofitted by externally-hung rocking wall with SMA and disc spring self-centering devices," *Engineering Structures*, vol. 240, p. 112422, Aug. 2021.

[12] C. Christopoulos, "Frequency Response of Flag-Shaped Single Degree-of-Freedom Hysteretic Systems," *Journal of Engineering Mechanics*, vol. 130, pp. 894–903, Aug. 2004.

[13] S. Kitayama and C. Yang, "Steady-state dynamic response analysis of self-centering structural systems with viscous damping," *Soil Dynamics and Earthquake Engineering*, vol. 150, p. 106926, Nov. 2021.

[14] F. Hu, G. Shi, and Y. Shi, "Experimental study on seismic behavior of high strength steel frames: Global response," *Engineering Structures*, vol. 131, pp. 163–179, Jan. 2017.

[15] S. Ramhormozian, G. C. Clifton, G. A. MacRae, G. P. Davet, and H.-H. Khoo, "Experimental studies on Belleville springs use in the sliding hinge joint connection," *Journal of Constructional Steel Research*, vol. 159, pp. 81–94, Aug. 2019.

[16] J.-p. Wei, L.-m. Tian, Y. Guo, H.-y. Qiao, Y. Bao, Z.-a. Jiao, and X.-j. Shi, "Numerical study of the seismic performance of a double-hinge steel frame joint," *Journal of Constructional Steel Research*, vol. 187, p. 106963, Dec. 2021.

[17] A.-L. Zhang, X. Chen, Z.-Q. Jiang, Y.-T. Kang, and X.-F. Yang, "Experiment on seismic behavior of earthquake-resilience prefabricated cross hinge column foot joint," *Journal of Constructional Steel Research*, vol. 189, p. 107056, Feb. 2022.

[18] A. I. Dimopoulos, T. L. Karavasilis, G. Vasdravellis, and B. Uy, "Seismic design, modelling and assessment of self-centering steel frames using post-tensioned connections with web hourglass shape pins," *Bulletin of Earthquake Engineering*, vol. 11, pp. 1797–1816, Oct. 2013.

[19] A. S. Tzimas, A. I. Dimopoulos, and T. L. Karavasilis, "EC8-based seismic design and assessment of self-centering post-tensioned steel frames with viscous dampers," *Journal of Constructional Steel Research*, vol. 105, pp. 60–73, Feb. 2015.

[20] X. Huang, Z. Zhou, Q. Xie, R. Xue, and D. Zhu, "Force distribution analysis of self-centering coupled-beams for moment-resisting-frames without floor elongation," *Engineering Structures*, vol. 147, pp. 328–344, Sept. 2017.

[21] X. Guan, H. Burton, and S. Moradi, "Seismic performance of a self-centering steel moment frame building: From component-level modeling to economic loss assessment," *Journal of Constructional Steel Research*, vol. 150, pp. 129–140, Nov. 2018.

[22] P. M. Clayton, T. B. Winkley, J. W. Berman, and L. N. Lowes, "Experimental Investigation of Self-Centering Steel Plate Shear Walls," *Journal of Structural Engineering*, vol. 138, pp. 952–960, July 2012.

[23] M. Dastfan and R. Driver, "Test of a Steel Plate Shear Wall with Partially Encased Composite Columns and RBS Frame Connections," *Journal of Structural Engineering*, vol. 144, p. 04017187, Feb. 2018.

[24] J. Yu, J. Huang, B. Li, and X. Feng, "Experimental study on steel plate shear walls with novel plate-frame connection," *Journal of Constructional Steel Research*, vol. 180, p. 106601, May 2021.

[25] Y. Shi, Z. Luo, Y. Xu, Y. Zou, L. Xu, and Q. Ma, "Experimental study on the seismic behavior of high-performance cold-formed steel plate shear walls," *Engineering Structures*, vol. 251, p. 113552, Jan. 2022.

[26] L. N. Lowes, N. Mitra, and A. Altoontash, "A Beam-Column Joint Model for Simulating the Earthquake Response of Reinforced Concrete Frames," Technical Report PEER Report 2003-10, Pacific Earthquake Engineering Research Center, University of California, Berkeley, CA., Feb. 2003.

[27] F. McKenna, M. H. Scott, and G. L. Fenves, "Nonlinear Finite-Element Analysis Software Architecture Using Object Composition," *Journal of Computing in Civil Engineering*, vol. 24, pp. 95–107, Jan. 2010.

[28] A. H. Nayfeh and D. T. Mook, *Nonlinear Oscillations (Pure and Applied Mathematics: A Wiley - Interscience Series of Texts, Monographs and Tracts)*. New York: John Wiley & Sons, 1979.

COMPDYN 2023
9th ECCOMAS Thematic Conference on
Computational Methods in Structural Dynamics and Earthquake Engineering
M. Papadrakakis, M. Fragiadakis (eds.)
Athens, Greece, 12-14 June 2023

# THE SEISMIC RESPONSE OF MIXED REINFORCED CONCRETE–STEEL LOW-RISE BUILDINGS UNDER NEAR-FAULT EARTHQUAKES

**Paraskevi K. Askouni**[1] **and George A. Papagiannopoulos**[2]

[1] Department of Civil Engineering, University of Patras,
26504 Rio Patras, Greece
askounie@upatras.gr

[2] School of Science and Technology, Hellenic Open University,
18 Parodos Aristotelous St, 263 35 Patras, Greece
papagiannopoulos@eap

## Abstract

*This work investigates the seismic behaviour of a group of mixed reinforced concrete-steel low-rise buildings, a structural type that is often met in engineering praxis. Specifically, the considered mixed buildings consisting of reinforced concrete (r/c) lower story/ies and a structural steel upper story, are analysed by examining their seismic non-linear response characteristics. Considering the small number of existing research literature for this type of mixed low-rise building frames, as well as the lack of specific recommendations of the current seismic codes for the latter, the investigation of the seismic response of this structural building type appears important. A comparison of the two cases of support condition, i.e. fixed or pinned, of the upper steel story upon the lower r/c story/ies is performed. Near-fault seismic motions are used in the current time-history analyses to force the investigated mixed buildings to exhibit strong nonlinear responses. The conclusions drawn from these non-linear dynamic analyses provide helpful guidelines for the seismic performance design of mixed r/c-steel low-rise frames.*

**Keywords:** Mixed Buildings, Reinforced Concrete, Steel, Non-linear time-history analysis, Near-fault Earthquakes, Seismic Response.

## 1 INTRODUCTION

According to the current design codes [1], the same structural material is considered for the construction of a whole building frame throughout all stories. Seismic codes usually refer to structures made from one material, such as reinforced concrete (r/c) [2], or steel [3]. However, the case of a steel story added upon an r/c building is often found in everyday construction practice. Neglecting the consideration of the added steel story as a secondary structure [4], i.e. a smaller in mass and weight added steel structure upon an r/c one, the resulting mixed r/c steel building type is examined here, assuming the same size in-plan of the steel and the underlying r/c stories. This paper presents selected the response results of the investigated seismic behaviour of mixed r/c-steel low-rise frames subjected to near-fault earthquakes.

## 2 DESCRIPTION OF CASE STUDIES AND ANALYSIS

In this work, two-, three- and four-story 3D mixed r/c steel building frames are examined, as shown in Fig. 1, where the lower story/ies are considered to be constructed by r/c and the upper story by steel. The mixed buildings have a square plan with $15.0 \times 15.0 m^2$ dimension consisting of three equal spans of 5.0m in each horizontal direction, X and Y. The r/c bottom story has a height of 4.0m and the upper r/c or steel stories have a height of 3.0m. The diaphragm action of each floor is considered due to r/c and composite slabs on each floor with a thickness of 0.15m.

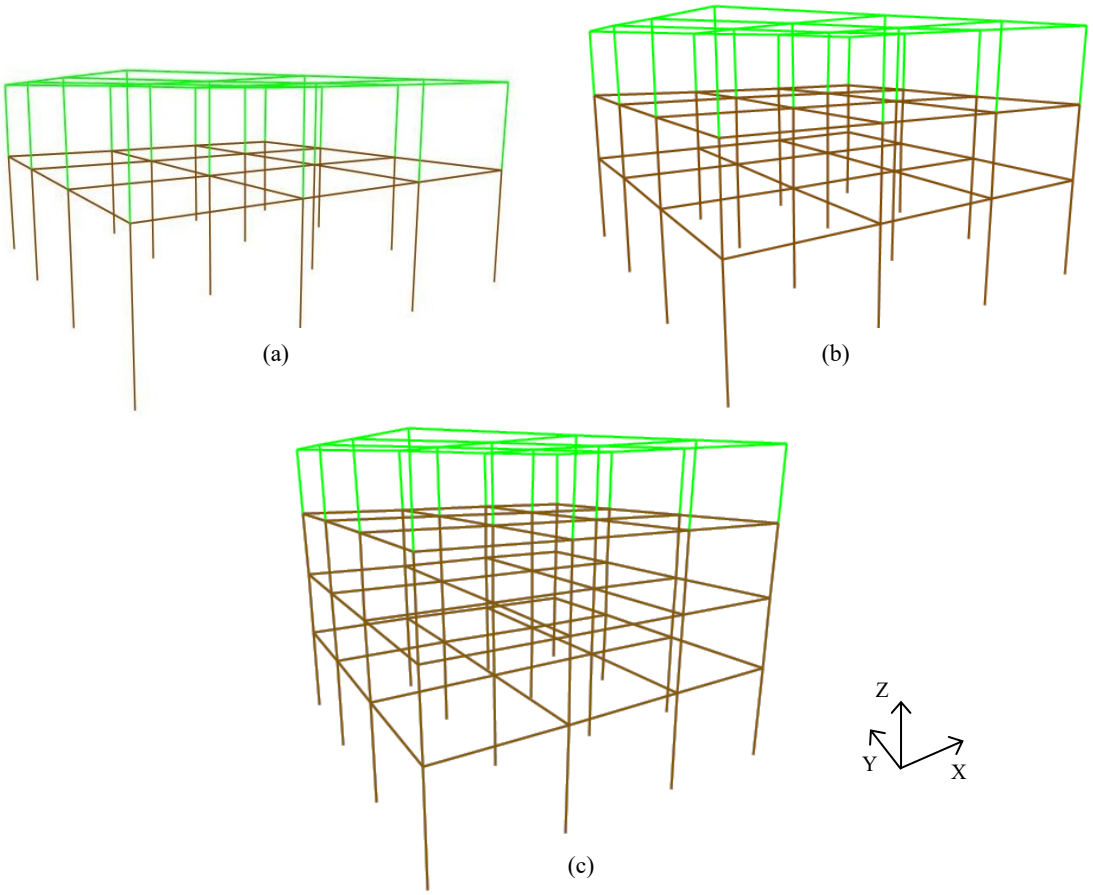


Figure 1: (a) Two-, (b) three- and (c) four-story mixed r/c-steel 3D frames under study (lower r/c stories and upper steel story with brown and green colours respectively) with the global coordinate system.

In all mixed frames, the material assumed for the r/c part is concrete C25/30 with steel reinforcement B500c, and for the steel part is structural steel S355. A dead load of 5.0 kN/m$^2$ is applied on the floors and 3.0 kN/m on walls [5]. A live load of 2.5 kN/m$^2$ is applied on r/c or composite slabs [5]. The mixed building frames are dimensioned according to the current seismic codes [1] for medium ductility class (DCM) using the typical rigid soil assumption with the following design spectrum considerations: zone ground acceleration 0.36g, importance factor 1.0, viscous damping ratio 5% and soil type C. The maximum values of the behaviour factor according to [1] for DCM are considered as 3.9 for the r/c part and 4.0 for the steel part of the mixed frames. The combination rule of 30% [1] is followed in the seismic loading calculations in both horizontal directions, considering as well an accidental eccentricity of 5%. The seismic design calculations are performed separately for the r/c part and the steel one by the aforementioned assumptions, considering the damage limits for non-structural elements of brittle materials [1]. The final dimensioned sections for beams and columns of the mixed buildings are shown in Table 1. The orientation of the steel columns is shown in Fig. 2, selected to form a strong perimetrical steel frame.

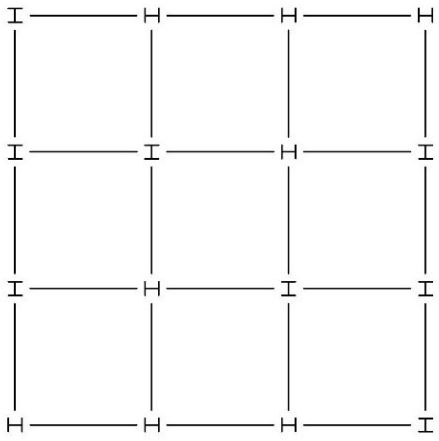

Figure 2: The in-plane orientation of the steel columns of the steel story.

| Two-story mixed building | | | | Columns | | | Beams | |
|---|---|---|---|---|---|---|---|---|
| story number | story height (m) | material | cross-section dimensions (cm/cm) | longitudinal reinforcement | stirrups | cross-section dimension (cm/cm) | longitudinal reinforcement | stirrups |
| 1 | 4.0 | r/c | 50/50 | 8Φ22 | Φ8/10 | 25/60 | 8Φ18 | Φ8/10 |
| 2 | 3.0 | steel | | HEA 360 | | | IPE 270 | |
| Three-story mixed building | | | | Columns | | | Beams | |
| story number | story height (m) | material | cross-section dimensions (cm/cm) | longitudinal reinforcement | stirrups | cross-section dimension | longitudinal reinf/ment | stirrups |
| 1 | 4.0 | r/c | 55/55 | 16Φ20 | Φ8/10 | 25/60 | 8Φ20+8Φ10 | Φ8/10 |
| 2 | 3.0 | r/c | 50/50 | 8Φ20+8Φ10 | Φ8/10 | 25/60 | 8Φ18 | Φ8/10 |
| 3 | 3.0 | steel | | HEA 360 | | | IPE 270 | |
| Four-story mixed building | | | | Columns | | | Beams | |
| story number | story height (m) | material | cross-section dimensions (cm/cm) | longitudinal reinforcement | stirrups | cross-section dimensions (cm/cm) | longitudinal reinforcement | stirrups |
| 1 | 4 | r/c | 60/60 | 16Φ20 | Φ8/10 | 25/70 | 8Φ20+8Φ10 | Φ8/10 |
| 2 | 3 | r/c | 60/60 | 8Φ20+8Φ16 | Φ8/10 | 25/70 | 8Φ20+8Φ10 | Φ8/10 |
| 3 | 3 | r/c | 50/50 | 8Φ20+8Φ10 | Φ8/10 | 25/60 | 8Φ18 | Φ8/10 |
| 4 | 3 | steel | | HEA 360 | | | IPE 270 | |

Table 1: Dimensioning of columns and beams of the mixed building two-, three- and four-story frames.

Regarding the support of the steel story upon the r/c part of the mixed buildings, the following two boundary conditions are considered: (a) a fixed support of the steel columns leading essentially to biaxial moment excursions, (b) a called as "fixed-pinned" support of the steel columns, indicating a fixed behaviour in the cross-section major axis and a pinned behaviour in the cross-section minor axis. These (a) and (b) boundary conditions represent the design of the column-base connection in terms of the base plate, anchor rods, and embedment into the concrete column. In both examined supporting conditions, the dimensioning of the mixed buildings is the same for comparison reasons.

The mixed frames are investigated by non-linear time history (NLTH) analysis by SAP2000 software [6] under the near-fault ground motions described in Table 3 as downloaded by [7]. In Table 3, the name, location, year, moment magnitude $M_w$ and the peak ground acceleration (PGA) of each earthquake are provided, where more relevant information is available in [7]. As shown by various literature works, indicatively mentioned Refs. [8-9], the earthquake incidence angle may affect the structural response. In the current work, the considered angles of the ground motions are along the major horizontal axes, as shown in Figure 1, which are $0^o$ and $90^o$. The elastoplastic behaviour or r/c and steel elements is considered in the current NLTH analyses through the application of point hinges at the ends of all elements ends following the recommendations of ASCE 41-17 [10].

| Name and Year of each earthquake | Earthquake name in response plots | $M_w$ | PGA (g) |
|---|---|---|---|
| Landers, 1992 | LANDERS | 7.3 | 0.81/0.73 |
| San Fernando, 1971 | PACO | 6.6 | 1.17/1.08 |
| Cape Mendocino, 1992 | PETROLIA | 6.9 | 0.66/0.59 |
| Loma Prieta, 1989 | LOS GATOS | 7.0 | 0.56/0.61 |
| Chi-Chi, 1999 | TAIWAN | 7.6 | 0.50/0.36 |
| Kefalonia, 2014 | KEFALONIA | 6.1 | 0.67/0.60 |
| Tabas, Iran, 1978 | TABAS | 7.1 | 0.93/1.10 |
| Superstition Hills, 1987 | HILLS | 6.5 | 0.45/0.38 |
| Northridge, 1994 | SYLMAR | 6.7 | 0.37/0.58 |
| Kobe, 1995 | KOBE | 6.9 | 0.61/0.62 |
| Imperial Valley, 1979 | ARRAY | 6.5 | 0.34/0.46 |

Table 2: Earthquakes used in the NLTH analyses of the mixed frames.

A selected one value of the damping ratio of the whole mixed frame is necessary for the NLTH analyses [11], however, this value is not provided for mixed buildings by the current regulations [1-3]. Following the procedure proposed by Sivandi-Pour et al. [12], a uniform value of damping ratio is calculated here for each mixed building considering the first few modes of modal analysis, as shown in next Table 3.

| Mixed frame | Damping ratio |
|---|---|
| Two-story | 4.57 % |
| Three-story | 4.33 % |
| Four-story | 3.63 % |

Table 3: Uniform damping ratio values used in the NLTH analyses of the mixed frames shown in Figure 1.

## 3 NUMERICAL RESULTS AND DISCUSSION

In this section, the numerical results of the mixed frames NLTH analyses under the ground motions of Table 2 are shown and discussed. Due to space limitations selected plots are presented here concerning the maximum interstory drift ratio (IDR) for each earthquake of the mixed frames of Figure 1 on the two horizontal axes, X and Y, along the building height. For evaluation purposes, the following IDR plots are compared to the IDR limit values for the seismic performance levels of [13], as mentioned here for convenience. Regarding moment resisting frames (MRFs) by r/c or steel, the IDR value of 0.5% corresponds to the limit of Fully Operational (FO) performance level, 1.5% refers to the Immediate Occupancy/operational (IO) performance level, 2.5% refers to Life Safety (LS) performance level, and 3.8% refers to Near Collapse (NC) performance level [13]. In the presented IDR plots, each earthquake label is followed by 0 or 90 referring to the earthquake incidence angle of 0º and 90º, respectively, for brevity reasons.

Concerning the two-story mixed building with the fixed connection of the steel story on the r/c one, as in Figure 3, the maximum IDR values are within the limit of LS performance level in the X axis, and, respectively, within the NC level in the Y axis. The maximum values of IDR are observed at the top of the 1st story in both axes, such as up to 1.82% for the X axis and 2.35% for the Y axis (Fig. 3).

Regarding the fixed-pinned connection of the steel story on the r/c one of the two-story mixed building, greater values of IDR are observed in both X and Y axes, (Fig. 4) as compared to the respective plots for the fixed connection in Fig. 3. In Fig. 4a, the maximum IDR values are observed at the top of the steel story, even up to 4.11% within the limit of NC level [13]. In Fig. 4b, the maximum IDR values are observed on the Y axis at the top of the 1st story, up to 2.98%.

Comparing the IDR plots of the two-story mixed frame in both axes (Figs. 3-4), the IDR values in the X axis are greater for the considered earthquakes with incidence angle 0º, than for the angle of 90º for the same earthquakes. Respectively, the IDR values in the Y axis are greater for these earthquakes with incidence angle 90º, than for the angle 0º.

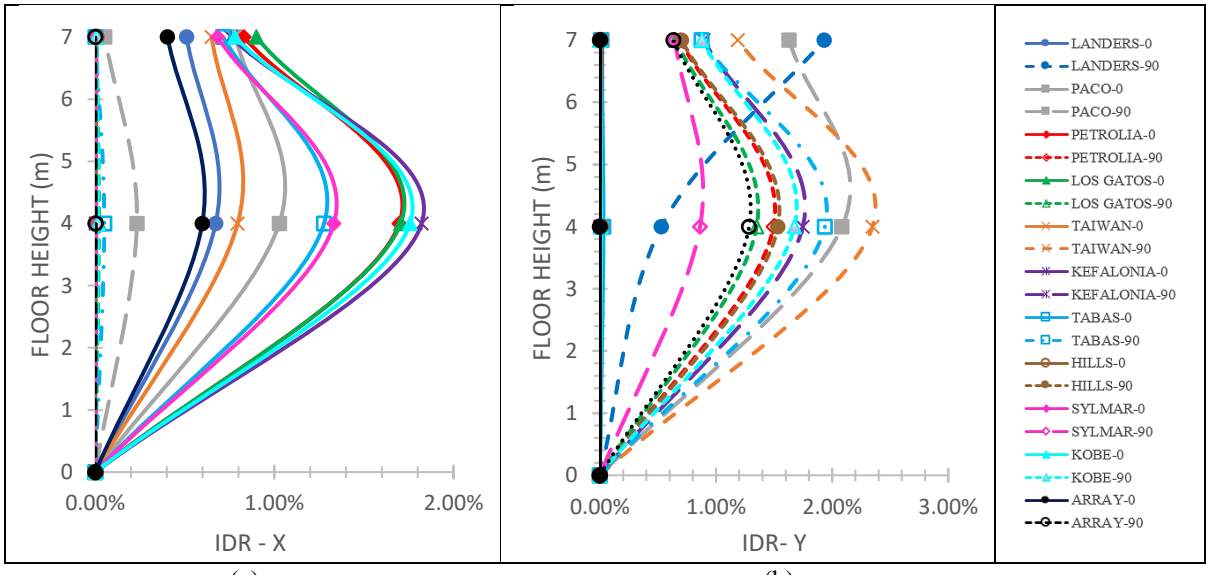


(a) (b)

Figure 3: IDR on the (a) X and (b) Y axes for the fixed connection of the steel story on the r/c one of the two-story mixed building.

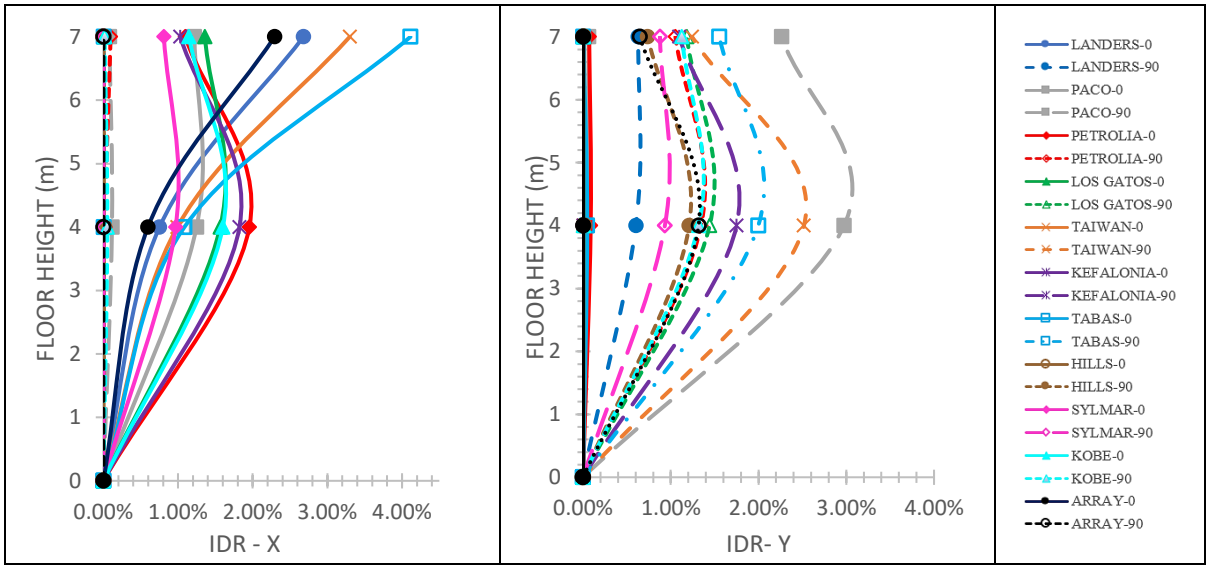


(a) (b)

Figure 4: IDR on the (a) X and (b) Y axes for the fixed-pinned connection of the steel story on the r/c one of the two-story mixed building.

At the three-story mixed building for the fixed connection of the steel story on the r/c ones, as in Fig. 5a, the values of IDR in the X axis are within the limit of LS performance level, with a maximum value of 2.22%. Respectively, as observed in Fig. 5b, the values of IDR in the Y axis are within the limit of NC performance level with a maximum value of 2.92%. In Figs, 5a-b, the data for the seismic motions "Los Gatos" with angle 90º and "Array" with angle 0º are not shown due to IDR values greater than the limits of [13] indicating building failure.

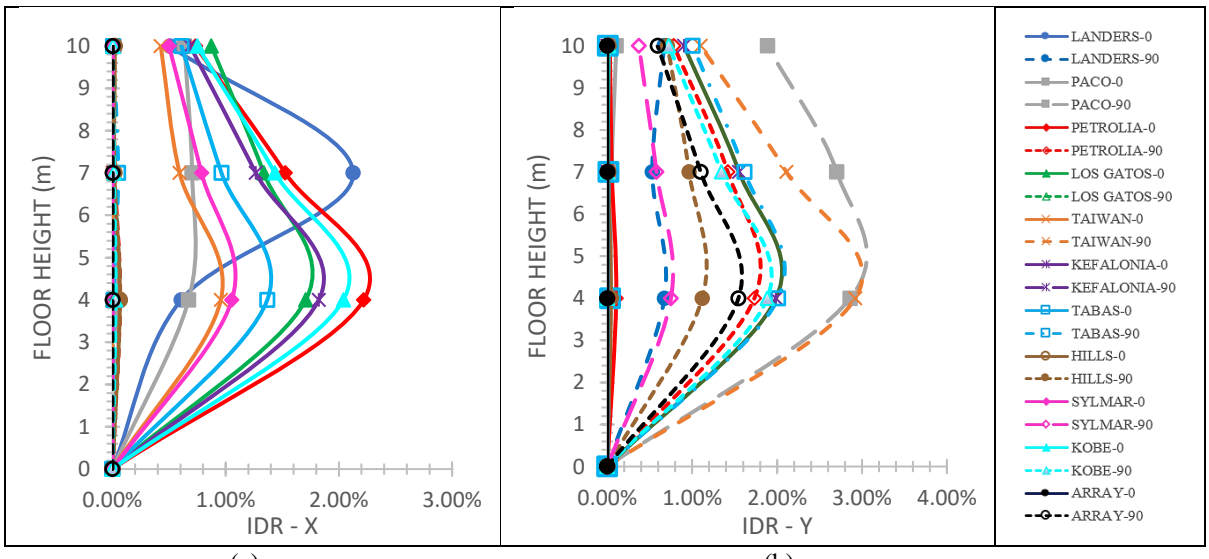


(a) (b)

Figure 5: IDR on the (a) X and (b) Y axes for the fixed connection of the steel story on the r/c ones of the three-story mixed building.

Concerning the fixed-pinned connection for the three-story mixed building, the values of IDR on the X axis are within the limit of LS performance level up to 2.2%, as in Fig. 6a, where the maximum values for each earthquake are observed at the top of the 1st story. Respectively, the values of IDR on the Y axis are observed to be within the limits of NC performance level

in Fig. 6b, up to 2.93%. Similar maximum IDR values are observed in Figs. 5-6 for both support types of the steel story on the r/c ones, while more building failures due to large IDR values are observed for the fixed support, as compared to the fixed-pinned support.

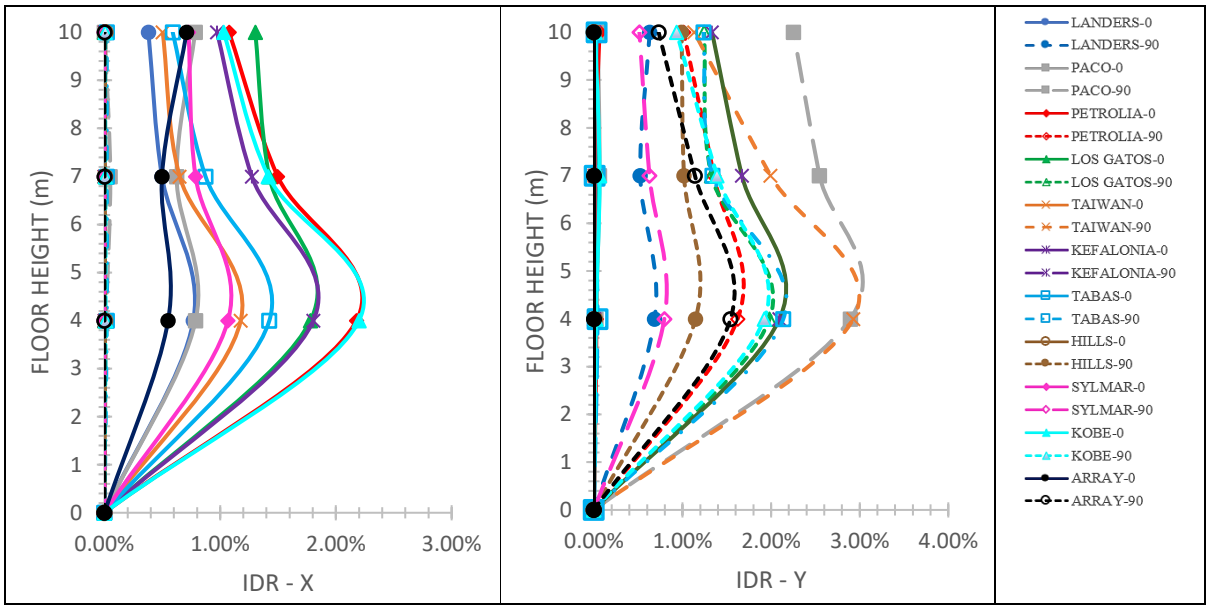


(a) (b)

Figure 6: IDR on the (a) X and (b) Y axes for the fixed-pinned connection of the steel story on the r/c ones of the three-story mixed building.

At the four-story mixed building, as shown in Figs. 7-8, the greater IDR values in both X and Y axes are observed at the top of the 1st story, in the range value of NC performance level. Considering the fixed support of the steel story on the r/c ones, as in Fig. 7, the maximum IDR observed is 3.45% on the X axis and 2.42% on the Y axis. At the building top, the maximum IDR is 1.18% on the X axis (Fig. 7a), and 1.47% on the Y axis (Fig. 7b). In Fig. 7, concerning the four-story mixed buildings with the fixed supporting condition, due to IDR values beyond the limit of NC performance level [13], the IDR plots for the seismic motions "Landers" with incidence angle 0º, "Los Gatos" with angle 90º and "Kefalonia" with angle 90º are not shown.

As shown in Fig. 8 for the fixed-pinned support of the steel story on the r/c part, the maximum IDR is 3.32% in the X axis and 2.43% in the Y axis, with similar values as for the fixed support as in Fig. 7. At the building top, the maximum IDR values, as observed in Fig. 8, are 1.39% in the X axis and 1.21% in the Y axis. In the four-story mixed buildings with the fixed-pinned support (Fig. 8), due to exceedance of the IDR limits of NC performance level [13], there are left out the IDR response data of the seismic motions "Landers" with incidence angle 0º, "Los Gatos" with angle 90º, "Kefalonia" with angle 90º and "Paco" with angle 90º. Thus, more damage and building failures are observed for the fixed-pinned support condition, compared to the fixed support of the steel story on the r/c part of the mixed building. Similarly to the previous Figs. 5-8, greater values of IDR are observed in the X axis for the ground motions with incidence angle 0º, and respectively in the Y axis for these ground motions with incidence angle 90º.

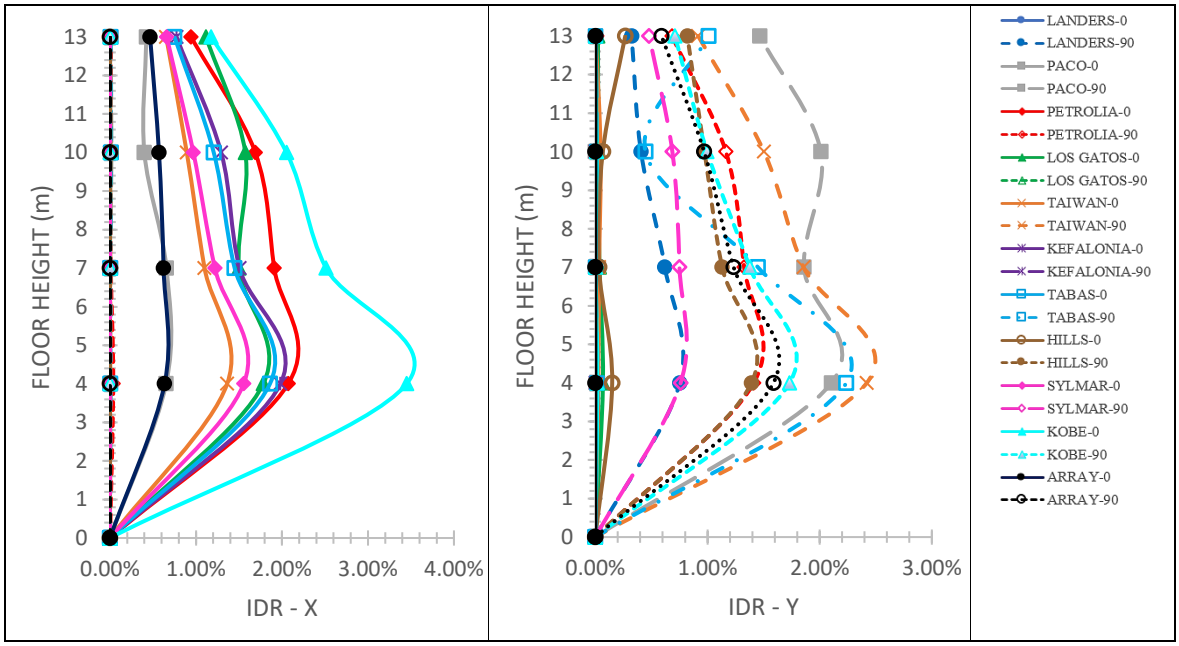


(a) (b)

Figure 7: IDR on the (a) X and (b) Y axes for the fixed connection of the steel story on the r/c ones of the four-story mixed building.

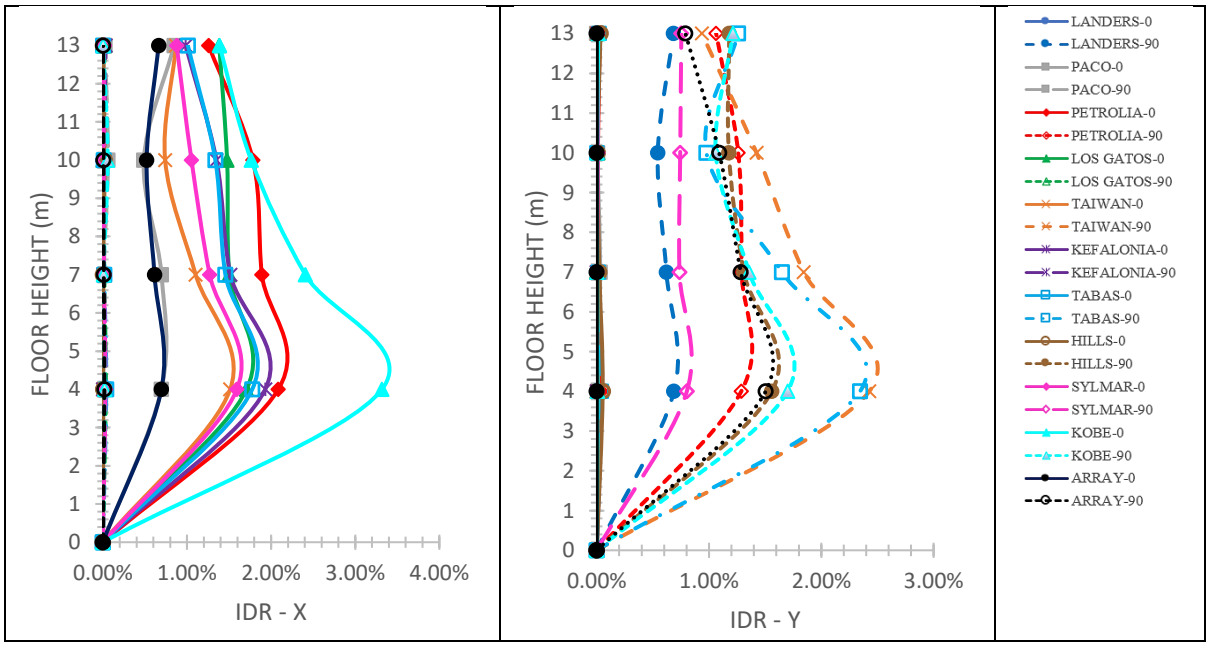


(a) (b)

Figure 8: IDR on the (a) X and (b) Y axes for the fixed-pinned connection of the steel story on the r/c ones of the four-story mixed building.

## 4 CONCLUSIONS

This work aims to investigate the seismic response of simple mixed r/c-steel building structures under near-fault seismic motions. The presented IDR plots have general values over the Fully Operational performance level [13] leading to a strong inelastic response of

the mixed buildings being observed from the NLTH analyses of the selected strong ground motions. From the presented response IDR plots of the mixed r/c-steel 3D frames in comparison to the seismic performance levels [13], the following conclusions can be stated.

- The consideration of the fixed-pinned support of the steel story on the r/c part of the mixed building tends to result either in an increased IDR range of values (for either one or both r/c and steel parts) or in a greater number of building failures, as compared to the fixed support condition. Thus, the fixed-pinned support appears as more detrimental to the seismic structural response of the mixed building, as compared to the fixed support.
- At the level of the interconnection of the steel story on the r/c part, a greater IDR range of values by 18~40% is observed for the fixed connection still within the limit of LS performance level, as compared to the fixed-pinned support, respectively.
- The mixed buildings present general IDR values within the limits of the NC performance level, which indicates a general structural behaviour within the guidelines of the current seismic codes.
- The steel story of the mixed buildings tends to exhibit elastic behaviour with smaller IDR values, while the r/c part is stressed more showing greater IDR values at the top of the 1st story, as compared to the whole mixed building. This indicates that the usual addition of a steel story upon an r/c part burdens the r/c part of the resulting mixed building.

## REFERENCES

[1] Eurocode 8 (EC8). Design of Structures for Earthquake Resistance - Part 1-1: General rules, seismic actions and rules for buildings; *European Committee for Standardization (CEN):* Brussels, 2004.

[2] Eurocode 2 (EC2). Design of concrete structures - Part 1-1: General rules and rules for buildings; *European Committee for Standardization (CEN):* Brussels, 2004.

[3] Eurocode 3 (EC3). Design of Steel Structures - Part 1-1: General rules and rules for Buildings; *European Committee for Standardization (CEN):* Brussels, Belgium, 2009.

[4] R. Villaverde. Seismic design of secondary structures: state of the art. *Journal of structural engineering*, *123*(8), pp.1011-1019, 1997

[5] Eurocode 1 (EC1). Actions on structures - Part 1-1: General actions, Densities, self-weight, imposed loads for buildings. *European Committee for Standardization (CEN)*: Brussels, 2001.

[6] SAP 2000. Static and Dynamic Finite Element Analysis of Structures: Version 19.0; *Computers and Structures (CSI):* Berkeley, CA, USA, 2016

[7] Pacific Earthquake Engineering Research Center. PEER strong motion database. http:www.peer.berkeley.edu/smcat (accessed on January 2022).

[8] P.K. Askouni, D.L. Karabalis. The Modification of the Estimated Seismic Behaviour of R/C Low-Rise Buildings Due to SSI. *Buildings.* **12,** 975, 2022.

[9] P.K. Askouni, D.L. Karabalis. SSI influence on the seismic response of asymmetrical small, low-rise R/C buildings. *Structures*, **32**, 1355-1373, 2021.

[10] ASCE 41-17. Seismic Evaluation and Retrofit of Existing Buildings. *American Society of Civil Engineers (ASCE):* Reston, VA, USA, 2017.

[11] A.V. Papageorgiou, C. J. Gantes. Equivalent modal damping ratios for concrete/steel mixed structures. *Computers and Structures,* **88,** 1124-1136, 2010.

[12] A. Sivandi-Pour, M. Gerami, D. Khodayarnezhad. Equivalent modal damping ratios for non-classically damped hybrid steel concrete buildings with transitional storey. *Structural Engineering and Mechanics,* **50**(3), 383-401, 2014.

[13] SEAOC. Recommended Lateral Force Requirements and Commentary, 7th Edition; *Structural Engineers Association of California*, Sacramento, USA, 1999.

COMPDYN 2023
9th ECCOMAS Thematic Conference on
Computational Methods in Structural Dynamics and Earthquake Engineering
M. Papadrakakis, M. Fragiadakis (eds.)
Athens, Greece, 12-14 June 2023

# INVESTIGATION OF THE SEISMIC BEHAVIOR OF BUILDINGS WITH U-BOOT SLABS

**Denise-Penelope N. Kontoni**[1,2,*], **Ali Ghamari**[3], **and Mojtaba Noorolahi**[4]

[1] Department of Civil Engineering, School of Engineering, University of the Peloponnese, GR-26334 Patras, Greece
e-mail: kontoni@uop.gr (* *corresponding author*)

[2] School of Science and Technology, Hellenic Open University, GR-26335 Patras, Greece
e-mail: kontoni.denise@ac.eap.gr

[3] Department of Civil Engineering, Ilam Branch, Islamic Azad University, Ilam, Iran
e-mail: aghamari@alumni.iust.ac.ir

[4] Department of Architectural Engineering, Ilam Branch, Islamic Azad University, Ilam, Iran
e-mail: mojtaba.noorollahi@gmail.com

## Abstract

*Since U-boot slabs can cover a large area without the need for columns, they are known as a favorable option for architects. On the other hand, from the point of view of the structural and earthquake engineer, reducing the number of columns can lead to the reduction of the additional resistance factor of the structure, which may lead structures to risks during an earthquake. Considering that published comprehensive studies in this field are limited, therefore, in this paper, the nonlinear dynamic behavior of concrete structures with U-boot slabs will be investigated. For this purpose, the behavior of short to medium-order structures will be investigated. Correspondingly, based on the obtained results, the necessary recommendations in this field will be proposed to improve this system. These recommendations are proposed with the approach of architectural requirements as well as structural requirements.*

**Keywords:** Concrete building; U-boot slab; Flexural; Seismic behavior; Pushover.

# 1 INTRODUCTION

Generally, architects are always looking for a solution to reduce the number of columns and use more space, especially for commercial uses and parking. Reducing the number of columns improves the architectural aspects which are usually in conflict with the structural engineering approach, especially for Reinforced Concrete (RC) buildings. Till now, several methods such as special truss frames [1], staggered trusses system [2], tube framing for perimeter columns [3], and the use of waffle slabs have been introduced to improve the use of space by reducing the number of columns. Among the proposed methods, using waffle slabs can be considered as a practical and economical use for RC buildings. The U-boot slabs as a waffle slab system introduced by Robert-II Grande, an Italian engineer, who developed and patented a new system of hollow former to reduce transport vehicles [4]. It is the recycled polypropylene formwork technology used for construction purposes. One of the important barriers with constructions, in the instance of horizontal slabs, is the soaring weight, which ceiling the span. Figure 1 shows an example of an industrial U-boot and the schematic view of the U-boot slab system. In U-boot automation, slabs are fabricated with large spans a contract floor thinner by depleting the weight while keeping the advance of reinforced concrete technology.

Although the use of the U-boot slab increases the useful space of the architecture, due to the reduction of the number of columns and also the lack of use of middle beams, comprehensive studies should be done regarding its seismic behavior. In fact, the RC frames as conventional seismic resisting rely on the hinge formation at two ends of beams to dissipate imposed seismic energy. Since the beams as a part of the main frame at the moment resisting frame (MRF) has the task of bearing gravity loads in addition to lateral loads, it is difficult to repair it after a severe earthquake. Consequently, in this paper, the behavior of structure with U-boot slabs is considered.



U-Boot®
*U-Boot® Beton void box for two-way lightened slabs*
*(https://www.daliform.com)*

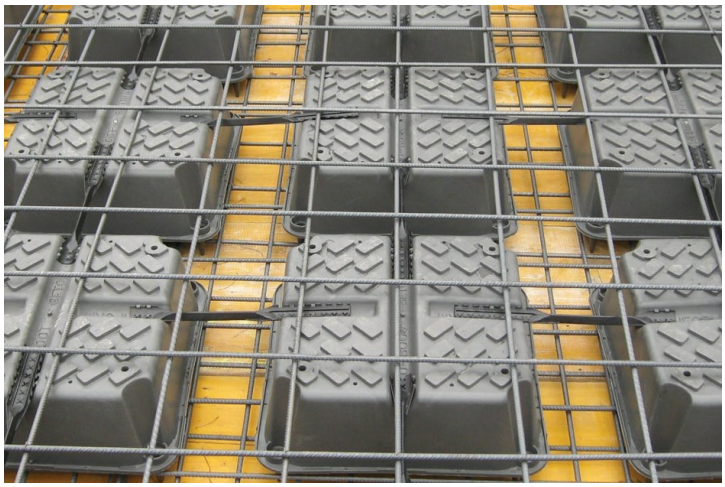

Figure 1: An example of a U-boot and the U-boot slab system.

# 2 NUMERICAL STUDY

## 2.1 Modeling approach

To analyze the numerical models, ETABS [5] software was used. The structural elements are modeled as nonlinear frame elements with lumped plasticity by defining plastic hinges at both ends of the beams and columns. Figure 2 depicts the hinge type and location. ETABS [5]

incorporates the plastic hinge properties described in FEMA 356 [6] and as shown in Figure 3 [6], the points labeled A, B, C, D, and E define the force-deformation behavior of a plastic hinge. Once the structure is modeled and the section properties, steel content, and applied loads are specified, the plastic hinges are assigned to the structural elements (P-M and V for columns, M and V for beams, and M and V for shear links), where V stands for shear plastic hinge, M represents flexural plastic hinge, and P-M stands for the axial-flexural hinge.

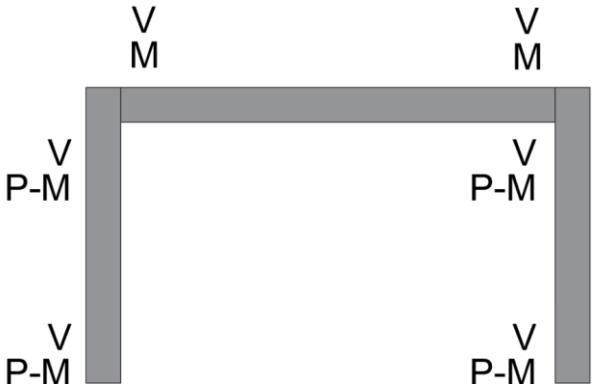


Figure 2: The hinge type and location.

The user-defined hinge properties are obtained via moment-curvature analysis of each element. The modified Park model [7] for confined concrete and the typical stress-strain model with strain hardening for steel are implemented in moment-curvature analyses. The sensitivity of a plastic-damage-based structural damage index on mesh density was studied by Kang and Lee [8]. The moment-curvature analysis is carried out for each column, considering the section properties and constant axial loads on the elements. All actions shall be classified as either deformation controlled, or force-controlled using the component force versus deformation curves based on FEMA 440 [9]. Since columns are controlled as force control components, this rule is applied to columns. In Figure 3, points B and C are related to yield and ultimate curvatures, respectively. Point B is obtained from ETABS using an approximate value for the component's initial effective stiffness according to ATC-40 [10] (i.e., 0.5EI and 0.70EI for beams and columns, respectively). Also, the ultimate curvature is described as the smallest values of a) reduced moment equal to 80% of the maximum moment determined from the moment-curvature analysis, b) extreme compression fiber reaching the ultimate compressive strain of concrete based on FEMA 440 [9], and the longitudinal steel reaching a tensile strain equal to 50% of the ultimate strain capacity that corresponds to the monotonic fracture strain.

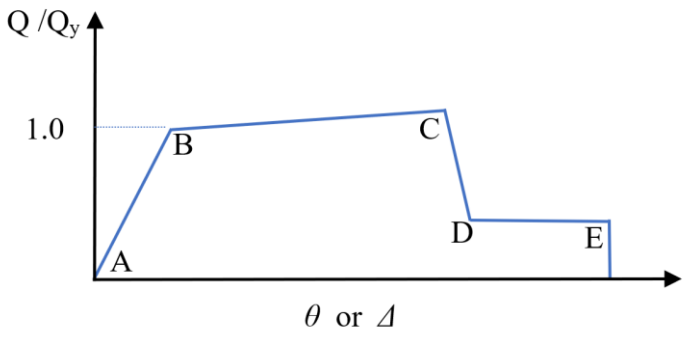


Figure 3: Generalized force-deformation relation.

All models are subjected to lateral loads that are gradually increased from zero to a magnitude beyond the system's capacity. The maximum displacement limit is considered to occur at a drift angle of 2.5% per ASCE 7-16 [11]. Also, based on the ASCE [11] and FEMA 440 [9], the maximum ultimate strength degradation is considered as 20%. Therefore, the final acceptable amount of the system bearing will be calculated as the minimum amount of 2.5% drift or 80% of ultimate strength degradation.

## 2.2 Numerical models

To evaluate the behavior of the buildings when the U-boot is used for the slab, a plan with the dimension of 10m×14m is considered, Figure 4. Accordingly, the placement of the columns as well as the framing plan is shown in Figure 5. For buildings with two-way slabs, a thickness of 150mm was designed for the slab. Also, the thickness of U-boots was designed according to the distance of the boots and the slab's rebar.

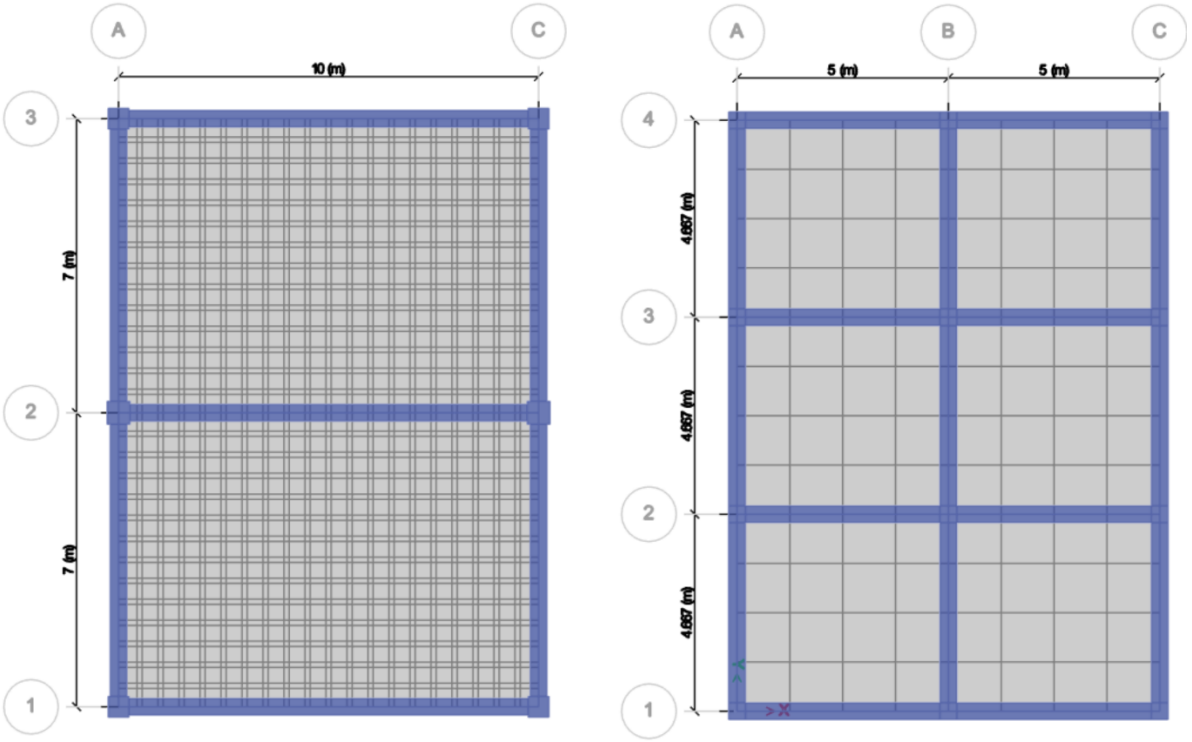


(a) (b)

Figure 4. The plan view of structures with a) U-boot slab, and b) two-way slab.

Also, three types of structures including structures with 3 stories, 6 stories, and 9 stories are investigated which are shown in Figure 5. The structures were designed based on the ACI [12]. For the design of the structures, the dead and live load equals, respectively, 105 and 200 kg/m$^2$ were considered. Also, the weight of slabs was considered using the capability of the software. Also, a load of 800 Kg/m for each story and 300 Kg/m on the premises of structures was applied to the structures as equivalent to walls.

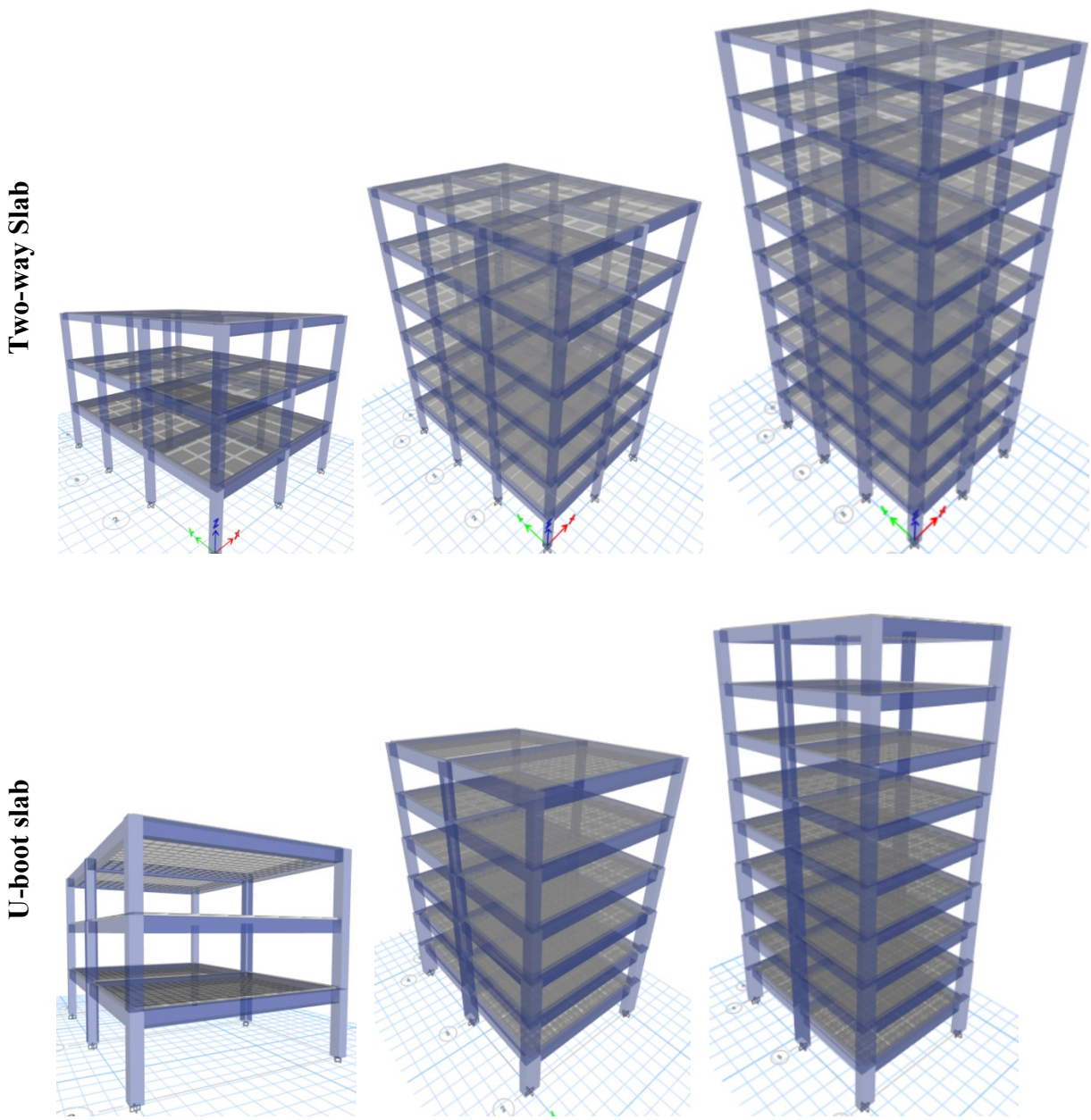


Figure 5: The view of the studied structures.

Moreover, to determine the lateral load imposed on the structures, a spectrum analysis was used. To do so, the spectrum as shown in Figure 6 according to the Iranian Code 2800 [13] was used for this purpose. It was assumed that these buildings are built on type II soil in an area with high seismic risk.

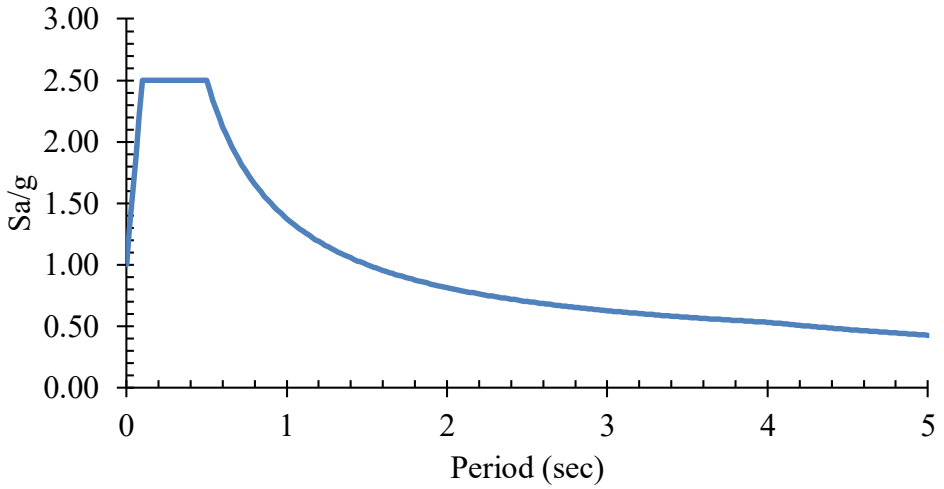


Figure 6: The spectrum used in the design of structures.

## 3 RESULTS AND DISCUSSIONS

### 3.1 Fundamental period

As the fundamental period, T, for each structure is accounted as an important parameter in the design of structures as well as in predicting the behavior of structures, the T of structures in two directions is listed in Table 1. Referring to the results of this table, in low-rise structures (three stories), by changing the floor from a two-way slab to a U-boot slab, the fundamental period of the structure decreases, but in 9-story structures, this trend is reversed. The main reason can be stated that by changing the floor and reducing the number of columns, columns with huge dimensions are inevitably used, which has a significant effect on the fundamental period. So, a comprehensive study with a wide number of structures must be accomplished to consider the effect of changing the floor from a two-way slab to a U-boot slab, on the fundamental period. By the way, in low-rise structures, the U-boot reduces the fundamental period.

| Model | $T_x$ | $T_y$ | U/RC | |
|---|---|---|---|---|
| | | | $T_x$ | $T_y$ |
| RC-3 | 0.574 | 0.51 | | |
| RC-6 | 0.951 | 0.84 | | |
| RC-9 | 1.081 | 1.07 | | |
| U-3 | 0.562 | 0.52 | 0.98 | 1.02 |
| U-6 | 0.812 | 0.75 | 0.85 | 0.90 |
| U-9 | 1.33 | 1.17 | 1.23 | 1.09 |

Table 1: Comparing the fundamental period of structures.

### 3.2 Pushover curves

Pushover curves give valuable information about the behavior of the structure. The general features of each system can be realized by an overall review of the diagram. Therefore, the pushover curves of the system are compared in Figure 7. Results indicated that systems with U-boot slabs have a failure before reaching the maximum allowed drift. Therefore, it is ex-

pected to fail the structure with low ductility. Therefore, it is susceptible to damage in high-risk seismic zones. The structural parameters obtained from the curves are investigated in the next section.

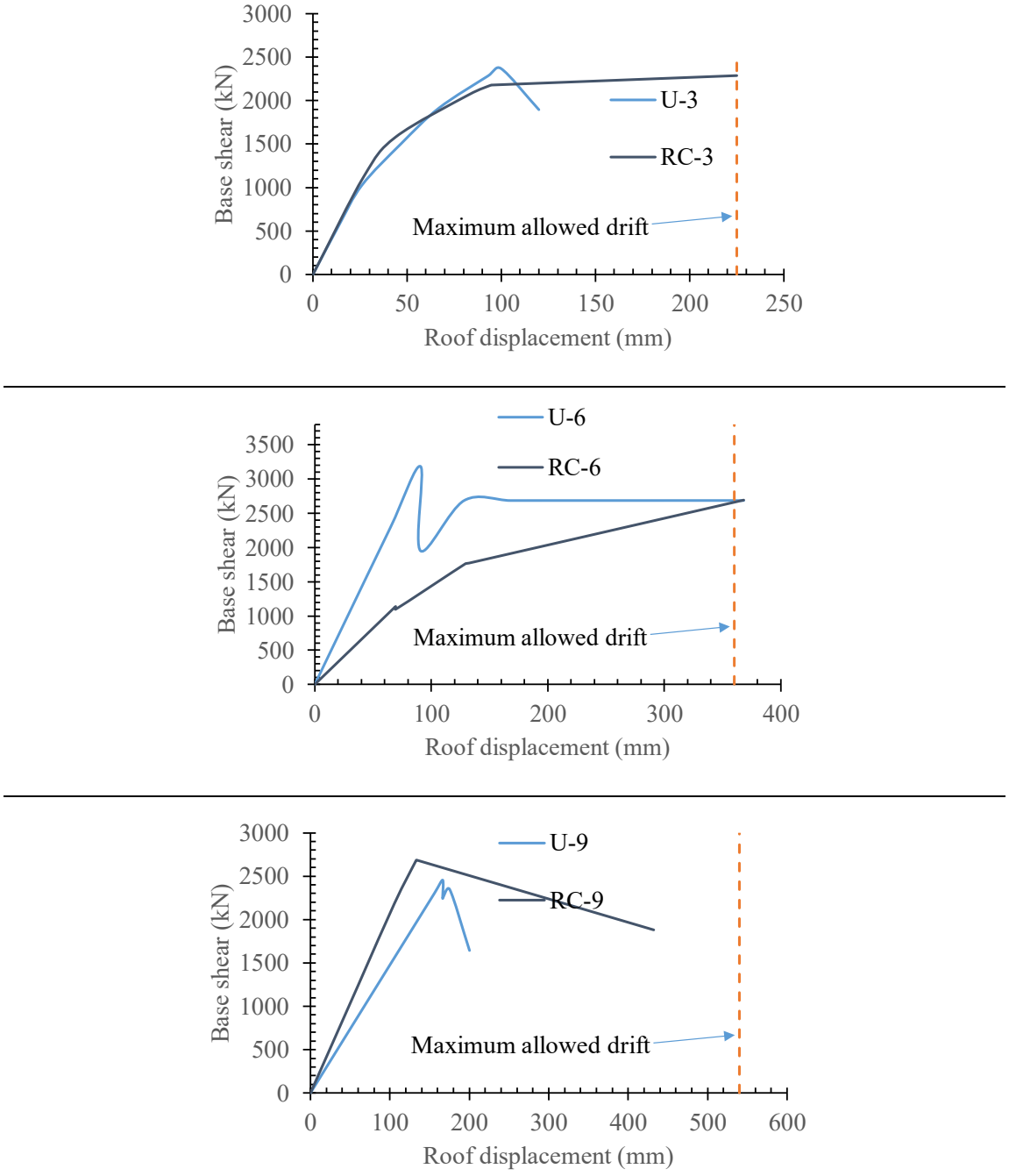


Figure 7: The pushover curves.

### 3.3 Structural parameters

In Table 2, the structural parameters of the models are listed. Results indicate that using U-boot slabs the displacement corresponding to the yielding, $\Delta_y$, is reduced for low-rise structures although it increased in higher structures. But, it causes a reduction in the ultimate displacement, $\Delta_u$, by 36%, 63%, and 22%, respectively, for structures with 3, 6, and 9 stories.

In the 6-story structure, although the pushover curve reaches the maximum allowed drift, the ultimate displacement is measured at the point of the dropped curve corresponding to the 80% ultimate strength. This result causes a reduction in the ductility, μ, by 0.52%, 0.46%, and 0.48%, respectively, for structures with 3, 6, and 9 stories. This reduction in μ is considerable. Comparing the ultimate lateral strength of the structures indicated that the system with two-way slabs and U-boots shows a close outcome together with differences between 4% to 19% that is despond of the dimensions of the columns. But, the remarkable finding regarding the overstrength, Ω, is that the use of U-boots has increased it in three-story structures, but it has decreased by 48% and 15% in 6-story and 9-story buildings, respectively.

| Model | $\Delta_y$ (mm) | $\Delta_u$ (mm) | $V_y$ (kN) | $V_u$ (kN) | μ | Ω |
|---|---|---|---|---|---|---|
| RC-3 | 35.06 | 225.00 | 1464.16 | 2288.73 | 6.42 | 1.56 |
| RC-6 | 66.28 | 225.00 | 1087.81 | 2689.67 | 3.39 | 2.47 |
| RC-9 | 105.58 | 225.00 | 2183.67 | 2685.68 | 2.13 | 1.23 |
| U-3 | 32.35 | 99.84 | 1299.32 | 2371.07 | 3.09 | 1.82 |
| U-6 | 70.45 | 128.06 | 2502.06 | 3188.11 | 1.82 | 1.27 |
| U-9 | 158.26 | 175.08 | 2335.72 | 2452.65 | 1.11 | 1.05 |
| | 0.92 | 0.44 | 0.89 | 1.04 | 0.48 | 1.17 |
| U/RC | 1.06 | 0.57 | 2.30 | 1.19 | 0.54 | 0.52 |
| | 1.50 | 0.78 | 1.07 | 0.91 | 0.52 | 0.85 |

Table 2: Structural parameters.

## 4 CONCLUSIONS

In this paper, the effect of U-boot slabs on the behavior of RC frames was numerically investigated. The findings are summarized in the following:

- The U-boot gives a better architectural aspect than the two-way slab. It is due to the long span used and the greater spaces when the U-boots are used.
- In low-rise structures, by changing the floor from a two-way slab to a U-boot, the fundamental period of the structure decreases, but in 9-story structures, this trend is reversed.
- Pushover curves results indicated that systems with U-boot slabs have a failure before reaching the maximum allowed drift.
- Using U-boot slabs the displacement corresponding to the yielding, $\Delta_y$, is reduced for low-rise structures although it increased in higher structures. But, it causes a reduction in the ultimate displacement, $\Delta_u$, by 36%, 63%, and 22%, respectively, for structures with 3, 6, and 9 stories. In the 6-story structure, although the pushover curve reaches the maximum allowed drift, the ultimate displacement is measured at the point of the dropped curve corresponding to the 80% ultimate strength.
- Since the systems with U-boot slabs show a lower ductility, they are susceptible to damage in high-risk seismic zones. U-boot slabs cause a reduction in the ductility, μ, by 0.52%, 0.46%, and 0.48% %, respectively, for structures with 3, 6, and 9 stories. This reduction in μ is considerable.

- Comparing the ultimate lateral strength of the structures indicated that the system with two-way slabs and U-boots shows a close outcome together with differences between 4% to 19% that is despond of the dimensions of the columns.
- Regarding the overstrength, Ω, the use of U-boots has increased Ω in 3-story structures, but it has decreased Ω by 48% and 15% in 6-story and 9-story buildings, respectively.

## REFERENCES


[1] R. Kumar, D.R. Sahoo, Seismic fragility of steel special truss moment frames with multiple ductile vierendeel panels. *Soil Dynamics and Earthquake Engineering*, **143**, 106603, 2021. https://doi.org/10.1016/j.soildyn.2021.106603.

[2] Y. Yin, F. Huang, N. Chu, X. Liu, Study on application of staggered truss system. *Proceedings of the Fourth International Conference on Advances in Steel Structures*, Shanghai, China, June 13-15, Volume II, pp. 1323-1328, 2005. https://doi.org/10.1016/B978-008044637-0/50196-7.

[3] J.K. Makam, S.M. Gupta, Behaviour of Outrigger and Tube in Tube Structural Systems: A Review. J.A. Fonseca de Oliveira Correia, S. Choudhury, S. Dutta (eds), *Advances in Structural Mechanics and Applications, ASMA 2021*. Structural Integrity, vol. 26., Springer, Cham., pp. 318–326, 2023. https://doi.org/10.1007/978-3-031-05509-6_26.

[4] S.K.T. Khan, A Review Paper on "U-Boot Beton: The Concrete Saver". *International Journal of Scientific and Research Publications*, **10**(7), 756-757, 2020. http://dx.doi.org/10.29322/IJSRP.10.07.2020.p10383.

[5] ETABS v. 2015, *Integrated building design software*. Computers and Structures, Inc. (CSI), Berkeley, U.S.A., 2015.

[6] FEMA 356, *Prestandard and Commentary for the Seismic Rehabilitation of Buildings*. American Society of Civil Engineers (ASCE) for the Federal Emergency Management Agency (FEMA), Washington, D.C., U.S.A., 2000.

[7] B.D. Scott, R. Park, M.J.N. Priestley, Stress-strain behavior of concrete confined by overlapping hoops at low and high strain rates. *ACI Journal Proceedings*, **76**(1), 13-27, 1982. https://doi.org/10.14359/10875.

[8] J.W. Kang, J. Lee, A correction method for objective seismic damage index of reinforced concrete columns. *Computers and Concrete*, **21**(6), 741-748, 2018. http://dx.doi.org/10.12989/cac.2018.21.6.741.

[9] FEMA 440, *Improvement of Nonlinear Static Seismic Analysis Procedures*. Applied Technology Council (ATC) for the Federal Emergency Management Agency (FEMA), Washington, D.C., U.S.A., 2005.

[10] ATC-40, *Seismic Evaluation and Retrofit of Concrete Buildings*. Applied Technology Council (ATC), California, U.S.A., 1996.

[11] ASCE 7-16, *Minimum Design Loads and Associated Criteria for Buildings and Other Structures (ASCE/SEI 7-16)*. American Society of Civil Engineers (ASCE), Reston, Virginia, U.S.A., 2017.

[12] ACI-318, *Building Code Requirements for Structural Concrete and Commentary*. American Concrete Institute (ACI), Farmington Hills, MI, U.S.A., 2022.

[13] Iranian Code 2800, *Iranian Code of Practice for Seismic Resistant Design of Buildings, Standard No. 2800-05, 3rd edition*. Building and Housing Research Center (BHRC), Tehran, Iran, 2005.

COMPDYN 2023
9th ECCOMAS Thematic Conference on
Computational Methods in Structural Dynamics and Earthquake Engineering
M. Papadrakakis, M. Fragiadakis (eds.)
Athens, Greece, 12-–14 June 2023

# A NEW MULTISCALE STEEL-CONCRETE BOND MODEL FOR STRUCTURAL DYNAMICS APPLICATIONS

**Maryam Trad[1,2], Ibrahim Bitar[1], Stéphane Grange[2], and Benjamin Richard[1]**

[1]Institut de Radioprotection et de Sûreté Nucléaire (IRSN), PSN-EXP/SES/LMAPS
B.P. 17 - 92262 Fontenay-aux-Roses Cedex, France
e-mail: {maryam.trad, ibrahim.bitar, benjamin.richard}@irsn.fr

[2] Univ Lyon, INSA Lyon, GEOMAS, EA7495
69621 Villeurbanne, France
e-mail: {maryam.trad, stephane.grange}@insa-lyon.f

**Abstract.** *The robust characterization of the mechanical behavior for some reinforced concrete structures, such as the auxiliary buildings of nuclear plants, can be a major challenge. Therefore, it is necessary to identify the different energy dissipation sources: viscous dissipation, numerical dissipation due to the temporal integration scheme, and material dissipation that includes the interaction between concrete and steel reinforcement bars. Indeed, the energy dissipation along the steel-concrete interface may account up to* $15\%$ *of the total material energy dissipation [1]. In addition, the consideration of this steel-concrete interface in numerical modeling has a notable importance in the realistic estimation of the cracking process and stress redistribution. The various numerical strategies proposed in the literature are not sufficient to provide an accurate cracking prediction at the local level of the interface (cracks spacing and opening) [2]. Furthermore, applying these methodologies for large scale structures is time consuming and has a high numerical cost [3]. Therefore, the main objective of this study is to propose an original modeling strategy to take into account the behavior of the steel-concrete bond for structural applications. A multi-scale approach with internal degrees of freedom is proposed. It consists in using a macro-element capable of reproducing the behavior of steel and steel-concrete interface connected by means of interface stresses. This macro-element is inspired by an initial formulation proposed in [4] to model a rigid inclusion encased in a soil volume. In the present work, this initial formulation is further developed and adapted to the steel-concrete interface problematic. Cyclic bond laws are considered, which allows a representation of the interface for cyclic and dynamic structure applications. Structural case studies are performed, showing a good reproduction of the experimental behavior of reinforced concrete elements.*

**Keywords:** Steel-concrete interface, Reinforced concrete, Macro-element, Static condensation, Multiscale model, Kinematic relations.

## 1 INTRODUCTION

In reinforced concrete structures, the stress transfer between steel and concrete occurs along the interface between these materials, playing a crucial role in their mechanical functioning. As soon as the first cracks appear in concrete, the tensile properties of steel are used, provided that the steel-concrete interface transmits the corresponding internal forces. Hence, the consideration of this interface in numerical modeling has a significant importance on the cracking process of reinforced concrete structures and on the spatial distribution of cracks. In addition, the energy dissipation within the steel-concrete interface constitutes about $15\%$ of the total material energy dissipation [1].

Several models are proposed in the literature within different methodological frameworks (interface elements [5], enhanced elements [6]) to describe the interface between steel and concrete. These models are often integrated into detailed 2D and 3D analyses to improve the prediction of the behavior of a structural element. Taking into account the steel-concrete interface at the scale of an industrial building with these types of approaches remains impractical.

This work aims to propose a representative modeling strategy for the steel-concrete interface that has the lowest possible numerical cost. For this, a multi-scale approach is proposed. This approach consists in defining a macro-element capable of reproducing the behavior of the steel and the steel-concrete interface connected by means of a density of adhesive forces. The macro-element of [4] initially developed to link a rigid inclusion to a surrounding soil domain is developed here and adapted to the problematic of the steel-concrete interface. This approach is integrated into 2D/3D structural calculations. The formulation of the macro-element is described in this article. A validation example is performed by modeling a pull-out test under a cyclic load path, showing the capability of the macro-element of reproducing the interface behavior. An application example of a reinforced concrete tie-rod test is then presented. This application demonstrates the model's ability to replicate the experimental cracking behavior of a reinforced concrete structural element.

## 2 THEORETICAL BACKGROUND

The considered multi-scale approach consists in defining a macro-element at two distinct scales: a global scale and a local one. The global scale is at the level of the studied reinforced concrete structure, where the macro-element is considered as a four-node element. At the local level, one macro-element is an assembly of different biphasic elements representing each a steel bar, an interface zone, and bond stresses acting between the steel and the interface. Two complementary Newton-Raphson resolution algorithms are adopted at the two levels. The coupling between the two levels is done by means of a static condensation technique.

### 2.1 Global scale: reinforced concrete structure

At this scale, the classical finite elements method is adopted. The reinforced concrete structure is discretized into two types of elements: 2D/3D concrete elements and four-node macro-elements. A classical Newton Raphson algorithm is adopted for the resolution.

### 2.2 Local scale: macro-element

The four-node macro-element is an assembly of several biphasic elements. The formulation of one biphasic element is here described.

One biphasic element represents a steel bar element and an interface domain linked with bond stresses. Let $H$ be the length of one biphasic element. $(E_i, S_i)$ and $(E_s, S_s)$ are the

Young's modulus and the cross-section of the steel and the interface zone, respectively. Virtual strain fields $\varepsilon_s$ and $\varepsilon_i$ are associated to the steel and the interface.

Friction stresses $\tau_i(y_s - y_i) = -\tau_s(y_s - y_i)$ are considered between the two domains. $\tau_s$ represents the adhesion stresses applied to the steel and $\tau_i$ are the stresses applied to the interface zone. These stresses are linear or nonlinear functions of the relative displacement $(y_s - y_i)$ between the steel and the interface. $y_s$ and $y_i$ are the longitudinal displacements along the steel and the interface. Additional external forces may be applied whose associated virtual work is here called $P^*_{ext}$.

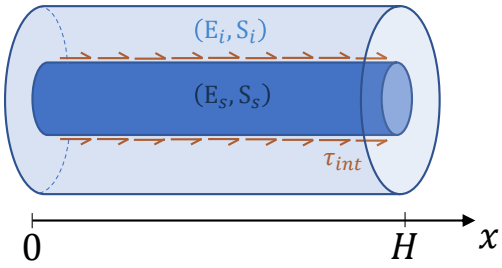


Figure 1: Two domains of the biphasic element with bond stresses $\tau_{int}$ in between.

The principle of virtual power is expressed as:

$$\int_0^H \left(\varepsilon_s^* \sigma_s(\varepsilon_s)\mathrm{S}_s + \varepsilon_i^* \mathrm{E}_i \varepsilon_i \mathrm{S}_i\right) dx + \int_0^H \left(y_s^* - y_i^*\right) \tau_i \left(y_s - y_i\right) \mathrm{P} dx = P^*_{ext} \tag{1}$$

P is the perimeter of the steel bar. In the current version of the macro-element model, and in the sake of simplicity, a linear constitutive law is associated to the interface. Hence, the stress of this zone, denoted $\sigma_i$, is expressed in equation 1 as $\mathrm{E}_i\varepsilon_i$, which represents a linear relationship with the value of $\varepsilon_i$. However, affecting a nonlinear constitutive law for the interface zone remains possible. The stress of the steel is given by $\sigma_s(\varepsilon_s)$, which is a function that is either linear or nonlinear, dependent on the constitutive law of the steel.

The first term in equation 1 represents the virtual internal power:

$$P^*_{int} = \int_0^H \left(\varepsilon_s^* \sigma_s(\varepsilon_s)\mathrm{S}_s + \varepsilon_i^* \mathrm{E}_i \varepsilon_i \mathrm{S}_i\right) dx + \int_0^H \left(y_s^* - y_i^*\right) \tau_i \left(y_s - y_i\right) \mathrm{P} dx \tag{2}$$

### 2.2.1 Discretization procedure

A spatial discretization is done in order to resolve equation 1. Three-node bar elements are used in parallel connected via adhesive forces. This discretization makes it possible to express the displacements of a node $i$ belonging to the interface and a node $s$ belonging to the steel according to the elementary displacement vectors $\boldsymbol{u_i}$ and $\boldsymbol{u_s}$.

$$y_s(x) = \boldsymbol{N}(x)\boldsymbol{u}_s \tag{3}$$

$$y_i(x) = \boldsymbol{N}(x)\boldsymbol{u}_i \tag{4}$$

The strains $\varepsilon_s$ and $\varepsilon_i$ are calculated as:

$$\varepsilon_s = \boldsymbol{B}(x)\boldsymbol{u}_s \tag{5}$$

$$\varepsilon_i = \boldsymbol{B}(x)\boldsymbol{u}_i \tag{6}$$

$\boldsymbol{B}$ is the matrix of the derivatives of the interpolation functions $\boldsymbol{N}(x)$. Therefore, equation 2 is expressed as follows:

$$P^*_{int} = \int_0^H \boldsymbol{u}_s^{*T}\boldsymbol{B}^T \mathrm{S}_s\sigma_s(\boldsymbol{B}\boldsymbol{u}_s) + \boldsymbol{u}_i^{*T}\boldsymbol{B}^T \mathrm{E}_i\mathrm{S}_i\boldsymbol{B}\boldsymbol{u}_i dx + \int_0^H \left(\boldsymbol{u}_i^* - \boldsymbol{u}_s^*\right)^T \boldsymbol{N}^T \tau_i \left(y_i - y_s\right) \mathrm{P} dx \tag{7}$$

$T$ is the transpose operator. $\boldsymbol{u}_i^*$ and $\boldsymbol{u}_s^*$ are defined as two independent virtual displacement vectors. The internal force vector $\boldsymbol{p^{el}}$ of a biphasic element is composed of the contributions of the two three-node bar elements (steel and interface) and the internal friction forces.

$$\boldsymbol{p^{el}} = \begin{bmatrix} \int_0^H \boldsymbol{B}^T \mathrm{S}_s\sigma_s(\boldsymbol{B}\boldsymbol{u}_s)dx \\ \int_0^H \boldsymbol{B}^T \mathrm{E}_i\mathrm{S}_i\boldsymbol{B}\boldsymbol{u}_i dx \end{bmatrix} + \begin{bmatrix} \int_0^H -\boldsymbol{N}^T \tau_i \left(y_i - y_s\right) \mathrm{P} dx \\ \int_0^H \boldsymbol{N}^T \tau_i \left(y_i - y_s\right) \mathrm{P} dx \end{bmatrix} \tag{8}$$

The subtraction of equations 3 and 4 gives:

$$y_i - y_s = \begin{bmatrix} -\boldsymbol{N} & \boldsymbol{N} \end{bmatrix} \begin{bmatrix} \boldsymbol{u}_s \\ \boldsymbol{u}_i \end{bmatrix} = \begin{bmatrix} -\boldsymbol{N} & \boldsymbol{N} \end{bmatrix} \boldsymbol{u^{el}} \tag{9}$$

The derivation of equation 8 with respect to the elementary degrees of freedom vector $\boldsymbol{u^{el}}$ gives:

$$\frac{\partial \boldsymbol{p^{el}}}{\partial \boldsymbol{u^{el}}} = \int_0^H \begin{bmatrix} \boldsymbol{B}^T C_s \mathrm{S}_s \boldsymbol{B} & 0 \\ 0 & \boldsymbol{B}^T \mathrm{E}_i \mathrm{S}_i \boldsymbol{B} \end{bmatrix} dx + \int_0^H \begin{bmatrix} -\boldsymbol{N}^T \\ \boldsymbol{N}^T \end{bmatrix} \frac{\partial \tau_i}{\partial \left(y_i - y_s\right)} \begin{bmatrix} -\boldsymbol{N} & \boldsymbol{N} \end{bmatrix} \mathrm{P} dx \tag{10}$$

$\frac{\partial \boldsymbol{p^{el}}}{\partial \boldsymbol{u^{el}}}$ is the elementary stiffness matrix of one biphasic element. $C_s$ is the steel constitutive law matrix. $\frac{\partial \tau_i}{\partial (y_i - y_s)}$ is calculated due to the expression of the steel-interface constitutive bond law which links the stress value $\tau_i$ to the steel-concrete slip $y_s - y_i$. The number of biphasic elements constituting one macro-element is an input parameter.

### 2.3 Coupling between the global and the local scales

At the global scale, the macro-element (seen as a four-node element) is assembled with 2D/3D concrete elements. Kinematic relations are defined to link the degrees of freedom of the macro-elements to degrees of freedom of the concrete elements.

#### 2.3.1 Connection between the macro-elements and the concrete elements meshes

The interface part of the macro-element is perfectly connected to the concrete. The steel is perfectly connected to the concrete in the normal directions, using kinematic relationships. Along the longitudinal direction with respect to the macro-element, the steel can slide relatively to the interface (while interacting with the interface via the bond stresses). The meshes of the macro-elements and the concrete elements may be non-coincident. In this case, shape functions $N_i$ are used to establish kinematic relationships of displacements as shown in figure 2 to link the interface to concrete. In the same way steel is linked to concrete in the normal directions. It is important to note here that the interface and the steel nodes have the same initial position. Two distinct nodes are illustrated in figure 2 for clarification.

Incorporating the kinematic relations to link steel, interface, and concrete nodes while resolving the global Newton Raphson algorithm is possible by applying classical methodologies such as the penalty method [7] [8] and the single or double Lagrange multipliers method [9].

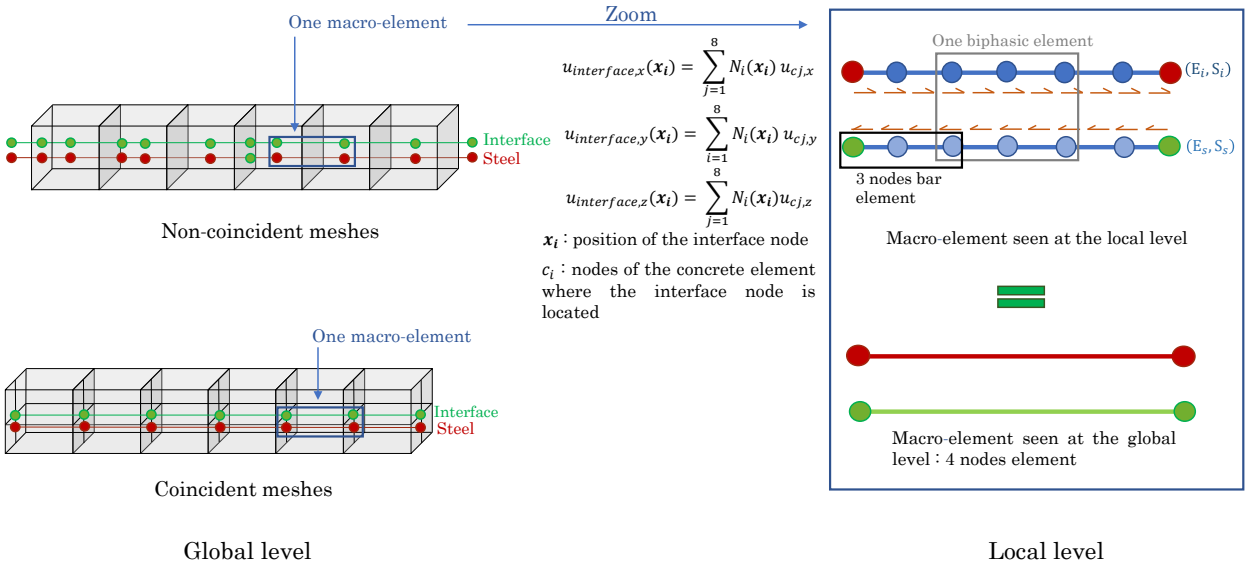


Figure 2: Global and local levels.

There are however some drawbacks to these classical approaches. Indeed, the penalty method efficiency depends on the choice of a penalty parameter incorporated in the resolution [10]. In parallel, the Lagrange method, even though it is widely used to add kinematic relations to a finite elements resolution system, adds additional unknowns to be calculated (the Lagrange multipliers) [11]. Using these classical approaches is convenient when considering Dirichlet boundary conditions (which are technically kinematic relations). In contrast, linking steel and interface zones to concrete adds kinematic relations for all the steel and the interface nodes. An alternative method is proposed here to incorporate steel/interface-concrete kinematic relations in the resolution. This approach based on a kinematic projection principle is here described.

Let $\boldsymbol{F}$ and $\boldsymbol{F_{tot}}$ be the internal and the external forces vectors of the reinforced concrete structure that take into account the Dirichlet boundary conditions, using the double Lagrange multipliers method. The global resolution algorithm aims to resolve the following equation:

$$\boldsymbol{F}(\boldsymbol{U_{tot}}) = \boldsymbol{F_{tot}} \tag{11}$$

$\boldsymbol{U}_{tot}$ is the vector assembling the total degrees of freedom of the structure and the Lagrange multipliers to be determined. In a more detailed form, equation 11 is written as:

$$\begin{bmatrix} \boldsymbol{F_{int}}(\boldsymbol{u}) + \boldsymbol{L}^T\boldsymbol{\lambda^1} + \boldsymbol{L}^T\boldsymbol{\lambda^2} \\ \boldsymbol{Lu} - \alpha\boldsymbol{\lambda^1} + \alpha\boldsymbol{\lambda^2} \\ \boldsymbol{Lu} + \alpha\boldsymbol{\lambda^1} - \alpha\boldsymbol{\lambda^2} \end{bmatrix} = \begin{bmatrix} \boldsymbol{F_{ext}} \\ \boldsymbol{U}_d \\ \boldsymbol{U}_d \end{bmatrix} \tag{12}$$

With:

$$\boldsymbol{U_{tot}} = \begin{bmatrix} \boldsymbol{u} \\ \boldsymbol{\lambda^1} \\ \boldsymbol{\lambda^2} \end{bmatrix}, \boldsymbol{F_{tot}} = \begin{bmatrix} \boldsymbol{F_{ext}} \\ \boldsymbol{U}_d \\ \boldsymbol{U}_d \end{bmatrix} \tag{13}$$

$\boldsymbol{u}$ is the vector of the degrees of freedom of the studied structure. The value of $\alpha$ is a parameter of the double Lagrange method to be optimized. $\boldsymbol{L}$ is the matrix of blocking used to express the Dirichlet boundary conditions as:

$$\boldsymbol{Lu} = \boldsymbol{U_d} \tag{14}$$

Where $\boldsymbol{U_d}$ is the imposed boundary degrees of freedom values vector. Equation 11 takes into account the Dirichlet boundary conditions. Considering, in addition to these Dirichlet conditions, the steel and interface- concrete links can be done using the kinematic projection method. The kinematic projection approach is proposed to incorporate the kinematic relations that link steel and interface nodes to concrete into the resolution. It consists of classifying the total degrees of freedom $\boldsymbol{U_{tot}}$ into two complementary vectors such as:

$$\boldsymbol{U_{tot}} = \begin{bmatrix} \boldsymbol{U_c} & \boldsymbol{U_i} \end{bmatrix}^T \tag{15}$$

Where:

- $\boldsymbol{U_c}$ is the vector of the dependent degrees of freedom.
- $\boldsymbol{U_i}$ is the vector of the independent degrees of freedom.

The kinematic relations impose that the values of the displacements of the steel and the interface nodes are dependent of the values of the displacements of the surrounding concrete nodes, which allows to define $\boldsymbol{U_c}$ as the vector of the displacements of the interface nodes in the three dimensions of the space and the displacements of the steel nodes in the normal directions with respect to the steel bars directions.

By deriving the kinematic relations equations, the vectors of the incremental values of the total degrees of freedom and the independent ones can be linked with a kinematic projection matrix $\boldsymbol{P}$:

$$\boldsymbol{\delta U_{tot}} = \boldsymbol{P \delta U_i} \tag{16}$$

The projection matrix here $\boldsymbol{P}$ holds the sets of the derivatives of the kinematic relations. Multiplying equation 11 by the transpose of the vector $\boldsymbol{\delta U_{tot}}$ gives:

$$\delta \boldsymbol{U_i^T P^T F(U_{tot})} = \delta \boldsymbol{U_i^T P^T F_{tot}} \tag{17}$$

So,

$$\boldsymbol{P^T F(U_{tot})} = \boldsymbol{P^T F_{tot}} \tag{18}$$

Equation 18 is the equilibrium equation to be resolved. The residue $R$ associated with the equilibrium equation is defined as:

$$\boldsymbol{R} = \boldsymbol{P^T F_{tot}} - \boldsymbol{P^T F(U_{tot})} \tag{19}$$

The iterative resolution of the global Newton Raphson algorithm aims to minimise the value of the residue $R$. It incorporates the derivation of the residue calculated as:

$$\frac{\partial \boldsymbol{R}}{\partial \boldsymbol{U_i}} = \frac{\partial \left( \boldsymbol{P^T F_{tot}} \right)}{\partial \boldsymbol{U_i}} - \frac{\partial \left( \boldsymbol{P^T F(U_{tot})} \right)}{\partial \boldsymbol{U_i}} \tag{20}$$

The residue $\boldsymbol{R}$ is derived with respect to $\boldsymbol{U_i}$. The advantage of this kinematic projection approach is that only $\boldsymbol{U_i}$ is calculated at each resolution iteration. $U_c$ is deduced using the kinematic relations. Equation 20 is developed as:

$$\frac{\partial \boldsymbol{R}}{\partial \boldsymbol{U_i}} = - \left[ \boldsymbol{P^T} \frac{\partial \boldsymbol{F(U_{tot})}}{\partial \boldsymbol{U_{tot}}} \frac{\partial \boldsymbol{U_{tot}}}{\partial \boldsymbol{U_i}} \right] \tag{21}$$

Knowing that the linear expressions of the used kinematic relations impose that $\frac{\partial \boldsymbol{P}}{\partial \boldsymbol{U_i}}$ is equal to zero. $\frac{\partial \boldsymbol{U_{tot}}}{\partial \boldsymbol{U_i}}$ is equal to the projection matrix $\boldsymbol{P}$ (see equation 16), so:

$$\frac{\partial \boldsymbol{R}}{\partial \boldsymbol{U_i}} = -\left[\boldsymbol{P}^T \frac{\partial \boldsymbol{F}(\boldsymbol{U_{tot}})}{\partial \boldsymbol{U_{tot}}} \boldsymbol{P}\right] \tag{22}$$

$\frac{\partial \boldsymbol{R}}{\partial \boldsymbol{U_i}}$ is the tangent operator of the nonlinear global Newton Raphson resolution (where the Dirichlet boundary conditions and the kinematics relations that link the steel/interface displacements to the concrete nodes displacements are taken into account).

### 2.3.2 Inner resolution of the macro-element equilibrium

A local Newton Raphson algorithm aims to resolve the local inner equilibrium at the level of one macro-element. The coupling between the two levels is done by adopting a static condensation technique.

In the global resolution, four degrees of freedom are considered for each macro-element (the longitudinal displacements of the four outer nodes of the inner local discretization). $\boldsymbol{u_{tot}^T} = \begin{bmatrix} \boldsymbol{u_r} & \boldsymbol{u_b} \end{bmatrix}^T$ is the total degrees of freedom vector of the biphasic elements consituting one macro-element. $\boldsymbol{r}$ and $\boldsymbol{b}$ subscripts refer to internal and external degrees of freedom. $\boldsymbol{u_b}$ represents the degrees of freedom of the four outer nodes, and $\boldsymbol{u_r}$ is the internal degrees of freedom vector of the inner nodes.

The resistant forces vector $\boldsymbol{f_{tot}}$ of a macro-element is an assembly of the elementary internal forces vectors $\boldsymbol{p^{el}}$ (see equation 8). Let $\boldsymbol{f_r}$ be the forces vector at the level of the inner nodes of a macro-element, and $\boldsymbol{f_b}$ be the forces at the level of the outer nodes. Hence, it is possible to define $\boldsymbol{f_{tot}}$ such that $\boldsymbol{f_{tot}^T} = \begin{bmatrix} \boldsymbol{f_r} & \boldsymbol{f_b} \end{bmatrix}^T$. The inner resolution at the local level of the macro-element consists in resolving the following equation:

$$\boldsymbol{f_r} = 0 \tag{23}$$

Equation 23 states the inner equilibrium at the level of the inner discretization of the macro-element. Let $\boldsymbol{k_{bp}}$ be the assembly of the elementary stiffness matrices of biphasic elements constituting one macro-element (see equation 10). It is possible to state that:

$$\boldsymbol{df_{tot}} = \boldsymbol{k_{bp}} \boldsymbol{du_{tot}} \tag{24}$$

Where $\boldsymbol{du_{tot}}$ represents the vector of the incremental values of the total degrees of freedom of the inner discretization of the macro-element. $\boldsymbol{du_{tot}^T} = \begin{bmatrix} \boldsymbol{du_r} & \boldsymbol{du_b} \end{bmatrix}^T$ where $\boldsymbol{du_r}$ and $\boldsymbol{du_b}$ are the vectors of the incremental values of $\boldsymbol{u_r}$ and $\boldsymbol{u_b}$. According to these degrees of freedom subscripts $\boldsymbol{r}$ and $\boldsymbol{b}$ (internal and external degrees), the matrix $\boldsymbol{k_{bp}}$ is composed of four parts: $\boldsymbol{k_{rr}}$, $\boldsymbol{k_{rb}}$, $\boldsymbol{k_{br}}$, and $\boldsymbol{k_{bb}}$. In order to calculate the algorithmic tangent operator, it is necessary to differentiate $\boldsymbol{f_b}$ according to $\boldsymbol{u_b}$. Hence, the differentiation of the internal efforts vector $\boldsymbol{f_b}$ gives:

$$\begin{bmatrix} \boldsymbol{k_{bb}} & \boldsymbol{k_{br}} \\ \boldsymbol{k_{rb}} & \boldsymbol{k_{rr}} \end{bmatrix} \begin{bmatrix} \boldsymbol{du_b} \\ \boldsymbol{du_r} \end{bmatrix} = \begin{bmatrix} \boldsymbol{df_b} \\ 0 \end{bmatrix} \tag{25}$$

A static condensation provides a link between the incremental vectors $\boldsymbol{du_b}$ and $\boldsymbol{df_b}$ as:

$$\left(\boldsymbol{k_{bb}} - \boldsymbol{k_{br}} \boldsymbol{k_{rr}^{-1}} \boldsymbol{k_{rb}}\right) \boldsymbol{du_b} = \boldsymbol{df_b} \tag{26}$$

In a more condensed form, equation 26 is written as:

$$\boldsymbol{k}_{em}\boldsymbol{du}_b = \boldsymbol{df}_b \tag{27}$$

Where $\boldsymbol{k}_{em}$ is the condensed elementary stiffness matrix of one macro-element returned to the global resolution algorithm at the level of the whole reinforced concrete structure.

## 3 VALIDATION TEST: PULL-OUT MODEL

In this section, the pull-out experimental test of [12] is modeled as a validation test of the macro-element formulation. A simplified 1D simulation is done where one macro-element represents the whole test. In other terms, for this simplified pull-out model, the macro-element model itself represents the steel, the concrete, and the steel-concrete bond stresses. The interface part of the macro-element represents the whole concrete volume. A cyclic loading configuration is studied.

### 3.1 Description of the test

The experimental test geometry is composed of a concrete cube crossed by a single steel reinforcement bar. The translation of the concrete cube is blocked by a metal plate. The concrete-steel slip is measured by an LVDT (Linear Variable Differential Transformer) sensor located at the unloaded edge of the reinforcement. The contact length is equal to five times the steel bar diameter which is denoted $d_a$. The adhesion value $\tau$ is supposed to be constant along the steel bar and is calculated as follows:

$$\tau = \frac{F}{d_a l \pi} \tag{28}$$

Where $F$ is the measured reaction and $l$ is the steel-concrete contact length. The experimental bond law is defined as the evolution of the calculated bond stress value $\tau$ with respect to the steel-concrete slip.

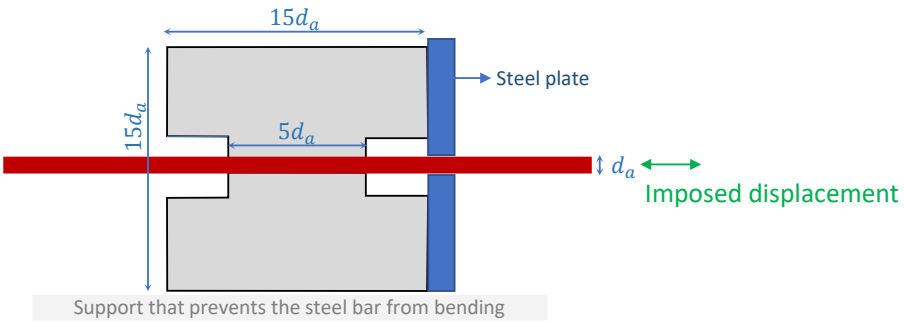


Figure 3: Pull-out test geometry and boundary conditions.

### 3.2 Simulation

A simplified 1D model of the pull-out test is here performed. Only the central part of the pull-out test where a bond contact links steel and concrete is represented (with a bond length equal to five times the bar diameter). One macro-element represents the test. This macro-element is discretized into three biphasic elements.

For this 1D model, the cross-section of the interface part of the macro-element is taken equal to the section of the concrete cube specimen of the pull-out test, which is equal to $15d_a \times 15d_a$, where $d_a$ is the steel bar diameter equal to 12 mm.

Linear elastic constitutive laws are affected to steel and concrete (the interface zone of the macro-element here). There is only one source of non-linearity in the problem, which arises from the non-linear expression of the bond stress law at the steel-concrete interface.

The cyclic bond law of [13] is here used. It is defined by three parameters: the maximum bond strength $\tau_1$, the slip $g_1$ for which $\tau_1$ is reached, and the slip $g_3$. For slip values bigger than $g_3$, the total stress of the monotonic version of the law remains constant. For the monotonic initial envelope curve of the law, the bond stress is assumed to be the sum of two types of stresses: the friction stress $\tau_f$ and the bearing stress $\tau_b$. This envelope curve is reduced due to the unloading/reloading cycles. The cyclic law is defined with no additional input parameters with respect to the monotonic envelop (see [13] for the detailed bond law formulation).

A Cyclic load configuration is tested. Boundary conditions are modified between the two configurations of figure 4 every time the imposed displacement is equal to zero.

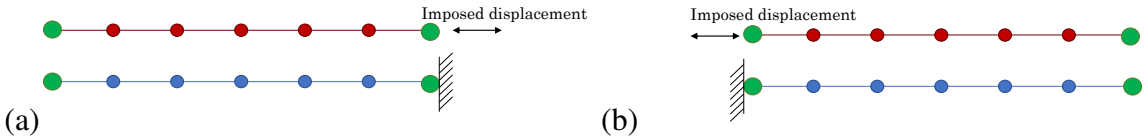


Figure 4: Configurations (a) and (b) for the cyclic 1D pull-out model.

Table 1 sums up the material properties used for the 1D pull-out model. These parameters are chosen to match the experimental material properties given by [12].

| Parameter | Description | Value | Unit |
|---|---|---|---|
| $E_c$ | Concrete Young's modulus | 28 | GPa |
| $E_s$ | Steel Young's modulus | 200 | GPa |
| $\tau_1$ | Input parameter of the bond law | 22.5 | MPa |
| $g_1$ | Input parameter of the bond law | 1.45 | mm |
| $g_3$ | Input parameter of the bond law | 10 | mm |

Table 1: Material properties for the 1D pull-out model.

Figure 5 illustrates an imposed cyclic displacement scheme with the corresponding reaction curve.

The reaction force curves show that the constitutive expression of a pullout-test that links the force $F$ to the bond stress $\tau$ (equation 28) is fullfilled. The 1D pull-out model is a simplified yet representative model of the pull-out test where one macro-element is capable of reproducing the experimental pull-out test behavior.

## 4 APPLICATION: TIE-ROD MODEL

The macro-element formulation is used here to model a reinforced concrete tie-rod. The experimental test of [14] is considered (see figure 6).

This test has been modeled by [12] and [15]. The aim here is to test the possibility of reproducing the experimental behaviour of the tie-rod with the macro-element model. Two

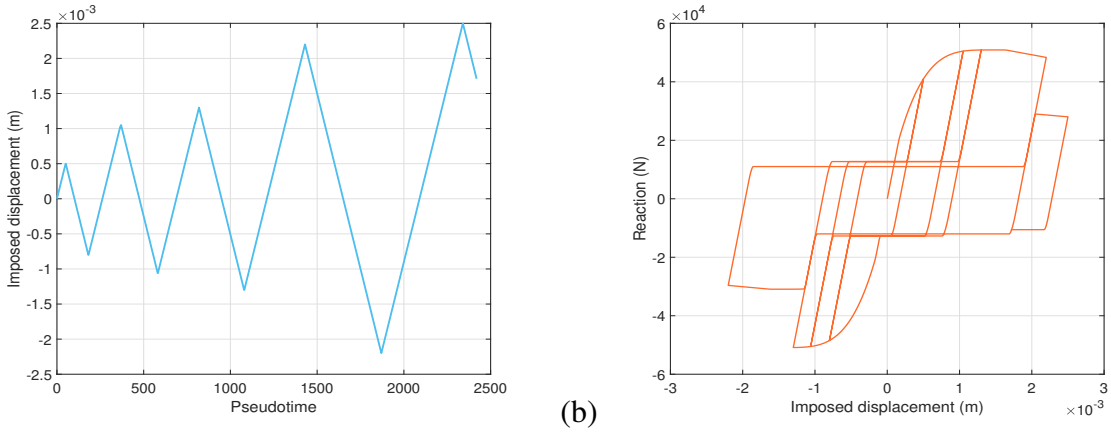


(a) (b)

Figure 5: Cyclic 1D pull-out model: imposed displacement (a) and reaction curves.

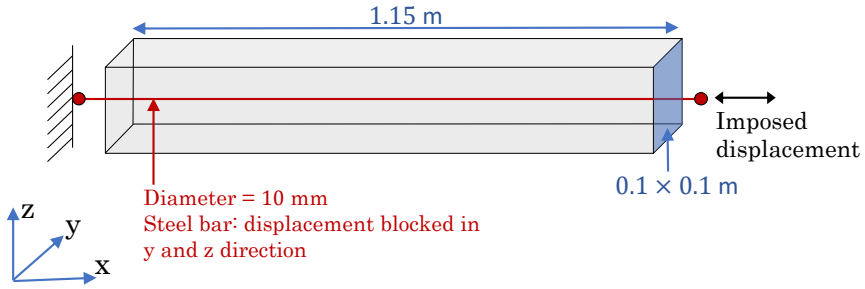


Figure 6: Presentation of the tie-rod test.

types of simulations are performed: one with a linear behavior assigned to concrete and a second one with a non-linear concrete behavior. For each type of simulation, the options of perfect steel-concrete bond and nonlinear bond behavior are tested.

## 4.1 Linear concrete behavior simulations

For this type of simulation, a linear behavior is associated to concrete, the aim being to focus the study on the consideration (or not) of a non-linear behavior of the interface. The mesh shown in figure 7 is considered. Each macro-element is discretized into two biphasic elements.

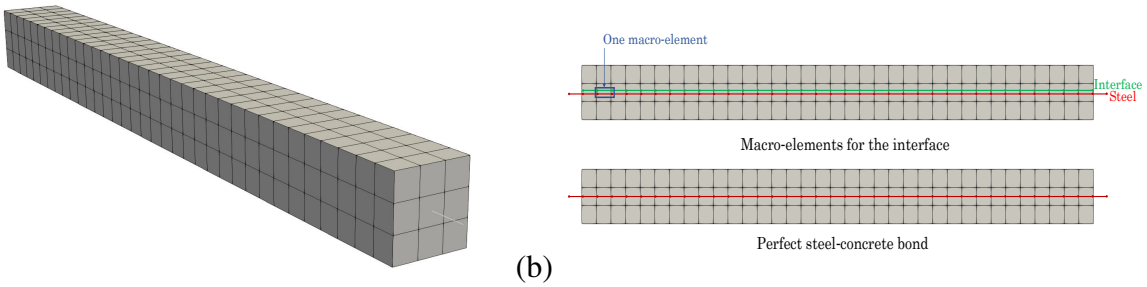


(a) (b)

Figure 7: Tie-rod test mesh: 3D mesh view (a); 2D cut-section view.

For the perfect bond simulation option, bar elements are used to mesh the steel. Kinematic relationships impose a perfect steel-concrete adhesion. The interface non-linear behavior option

is achieved by connecting macro-elements to concrete volumetric elements.

Experimentally, the steel is plasticizes at the end of the tie-rod test. The interest here is to study the phase of concrete cracking during which the steel behavior remains linear. A linear behavior law is associated to steel with a Young's module equal to $200$ GPa. For concrete, a linear law with a Young's module of $30.4$ GPa and a Poisson's ratio of $0.22$ is used (for linear concrete simulations).

In order to study the influence of the interface model rigidity on the resulting reaction curve, figure 8 shows reactions curves with linear bond laws compared to the perfect bond curve. When increasing the slope of the linear bond law, the reaction curve gets closer to the perfect bond curve. In other terms, the perfect bond case is equivalent to a infinitely rigid interface.

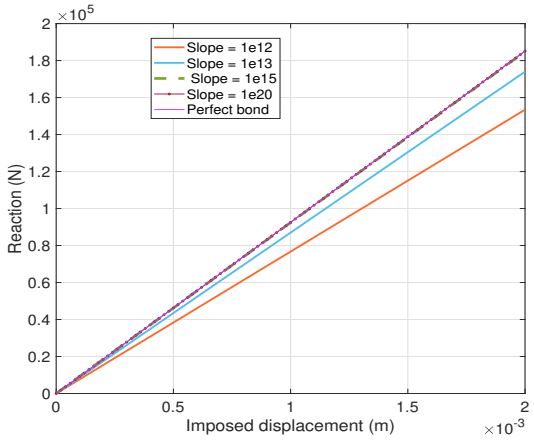


Figure 8: Reaction curves with linear bond laws compared to the perfect bond reaction curve.

## 4.2 Nonlinear concrete behavior simulations

For the nonlinear concrete behavior simulations, the Mazars' damage behavior law is used(see [16] for the description of the law). Hillerborg method [17] is used for the energy regularization of the Mazar's law, in tension. Table 2 resumes the regularized law parameters.

| Parameter | Description | Value | Unit |
|---|---|---|---|
| $f_t$ | Tensile strength | 2.6 | MPa |
| $\varepsilon_{d0}$ | Damage threshold | $\frac{f_t}{E_c} = 8.5526 \times 10^{-5}$ | - |
| $A_t$ | Local Mazars' model input | Not used - the law is regularized | - |
| $B_t$ | Mazars' model input | Regularized | - |
| $A_c$ | Mazars' model input | 1.2 | - |
| $B_c$ | Mazars' model input | 700 | - |
| $\beta$ | Mazars' model input | 1.06 | - |
| $G_f$ | Fracture energy | 150 | J/m$^3$ |

Table 2: Concrete properties used for the concrete nonlinear simulations.

The parameter $A_t$ that characterizes the local Mazars' law is not used for the regularized law (where an exponential expression is used for the damage evolution). The non-linear bond law of the interface is the one shown in figure 9. The different slip - bond stress values indicated in figure 9 are linked with linear expressions.

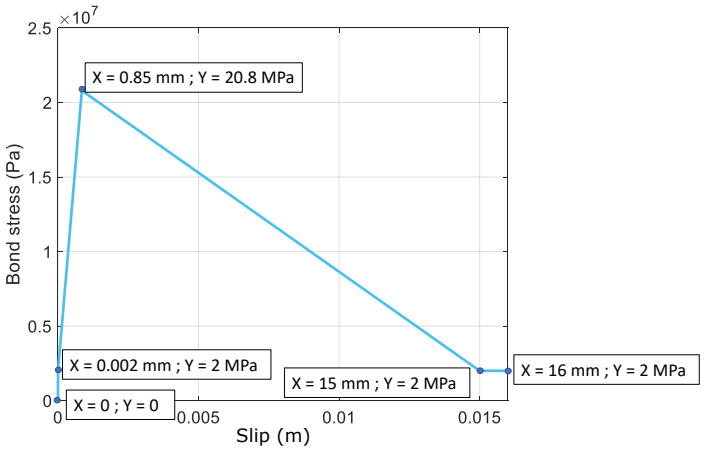


Figure 9: Nonlinear bond law used for the tie-rod model.

The finite elements mesh is identical to the one used for the linear concrete simulations. An aleatory strain-based damage threshold distribution is affected to concrete elements. This distribution follows an average Gaussian law with a mean value equal to the ratio of the tensile strength of the concrete to its Young's modulus (value indicated in table 2) and a coefficient of variation of $5\%$. An isotropic correlation is used with a correlation length equal to the size of the concrete elements. The turning bands method is used to generate the damage threshold distribution [18].

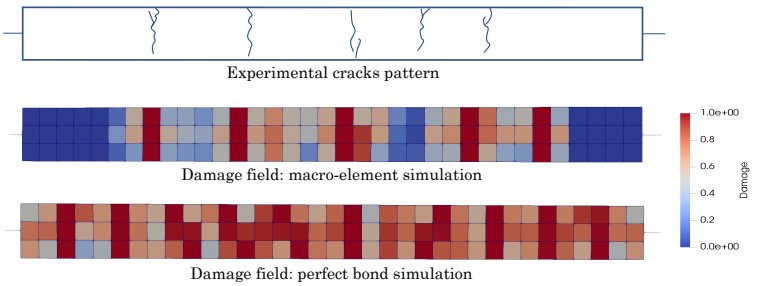


Figure 10: Concrete damage field compared to the experimental cracks pattern.

Figure 10 compares the experimental cracking path with the numerical damage distribution result. It demonstrates the importance of taking into account the behaviour of the steel-concrete interface in the simulations of reinforced concrete elements to better estimate the number of cracks and their spacing. Indeed, the distribution of the damage in the concrete volume better represents the experimental cracking pattern for the simulation where the non-linear behavior of the interface is taken into account.

Visualizing the horizontal strain instead of the damage field in concrete makes it easier to count the total number of cracks (see figure 11).

## 5 CONCLUSIVE REMARKS AND PERSPECTIVES

In this work, a modeling approach of the steel-concrete interface is proposed. This multi-scale strategy consists of defining macro-elements capable of representing the behavior of the steel, an interface zone and the bond stresses between the steel and the interface. The macro-element is defined at the global scale of the reinforced concrete structure. A local scale is

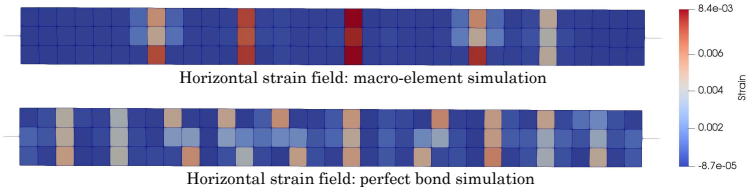


Figure 11: Horizontal concrete strain.

defined to perform internal discretization at the macro-element level, regardless of the size of the global mesh. A static condensation technique is used to couple the two scales. A more detailed presentation of the proposed modeling strategy is done in [19]. A validation test of a 1D pull-out model is performed using the macro-element formulation. The model is able to reproduce the interface behavior. An application is presented where a tie-rod test is modeled. This application justifies the importance of considering this interface behavior in reproducing the cracking phase of concrete in a reinforced concrete structural element. From the perspective of enhancing the current version of the macro-element formulation, an alternative approach is to use beam elements for discretizing the steel and interface areas of the macro-element, rather than selecting bar elements. By incorporating a behavior law that characterizes normal stresses as a function of relative displacement in the normal direction, it becomes feasible to introduce stresses between the two domains that are perpendicular to the direction of the macro-element. With this extension, numerical simulations of reinforced concrete structures can incorporate a more accurate depiction of the wedging action caused by steel bar ribs (see [20]). In addition, since cyclic bond laws are easily introduced in the macro-element formulation, using this interface model is possible to perform complex dynamic applications. This can be useful to assess the energy dissipation at the level of the steel-concrete interface for different loading configurations and to study the importance of taking into account the interface behavior to accurately simulate the dynamic behavior of reinforced concrete structures.

## REFERENCES

[1] M.H. Aguilera, Un modèle global homogénéisé pour la fissuration des voiles en béton armé sous chargements sismiques, *Ecole centrale de Nantes*, PhD thesis, 2016.

[2] T. S. Phan, P. Rossi, J.L. Tailhan, Numerical modelling of the concrete/rebar bond, *Cement and Concrete Composites*, **192**, 1-9, 2015.

[3] C. Mang, L. Jason, and L. Davenne, A new bond slip model for reinforced concrete structures: Validation by modelling a reinforced concrete tie, *Engineering Computations*, 2015.

[4] A. Sahyouni, S. Grange, L. Briançon, P. Burtin, J. Racinais, F. Prunier, B. Quandalle, Développement d'un macro-élément pour modéliser un massif renforcé par des inclusions rigides – étape 1, essai de chargement , *11èmes journées nationales de géotechnique et de géologie de l'ingénieur*, 2022.

[5] B. Richard, F. Ragueneau, C. Cremona, L. Adelaide, J.L. Tailhana, A three-dimensional steel/concrete interface model including corrosion effects, *Engineering Fracture Mechanics*, **77(6)**, 951-973, 2010.

[6] R. Gutiérrez, L. Stempniewski, W. Fleming, Modelling steel-concrete interaction using the extended finite element method, *Obras y Proyectos*, **24**, 6–12, 2018.

[7] I. Babuška, The Finite Element Method with Penalty. *Mathematics of computation*,**27**, 122, 1973.

[8] J. Chessa, P. Smolinski, T. Belytschko, The extended finite element method (xfem) for solidification problems. *International Journal for Numerical Methods in Engineering* , **53(8)**, 1959–1977, 2002.

[9] P. Verpeaux, T. Charras, Multiplicateur de Lagrange, Condensation Statique et Conditions Unilatérales, *10ème colloque national en calcul des structures*, 2011.

[10] M. Moumnassi, La représentation implicite des volumes pour l'analyse par éléments finis avec XFEM et Level-sets *Université Paul Verlaine-Metz*, PhD thesis, 2011.

[11] B. Richard, G. Rastiello, C. Giry, F. Riccardi, R. Paredes, E. Zafati, S. Kakarla, C. Lejouad, CastLab: an object-oriented finite element toolbox within the Matlab environment for educational and research purposes in computational solid mechanics, *Advances in Engineering Software*, **128**, 136–151, 2019.

[12] A. Casanova, Prise en compte de la liaison acier-béton pour le calcul de structures industrielles, *École normale supérieure de Cachan-ENS Cachan*, PhD thesis, 2012.

[13] J. Murcia-Delso, A. Stavridis, B. Shing, Modeling the bond-slip behavior of confined large-diameter reinforcing bars, *III ECCOMAS thematic conference on computational methods in structural dynamics and earthquake engineering*, 25-28, 2011.

[14] B. Farra, Influence de la résistance du béton et de son adhérence avec l'armature sur la fissuration, *Thèse, Ecole polytechnique fédérale de Laussanne* PhD thesis, 1995.

[15] C. Mang, Modélisation de la liaison acier-béton dans le calcul de structures en béton armé, *Université Paris Ouest*, PhD thesis, 2015.

[16] J. Mazars, Application de la mécanique de l'endommagement au comportement non linéaire et à la rupture du béton de structure, *Université pierre et marie curie-paris 6*, PhD thesis, 1984.

[17] A. Hillerborg , M. Modéer, P.E. Petersson. Analysis of crack formation and crack growth in concrete by means of fracture mechanics and finite elements, *Cement and Concrete Research*, **6(6)**, 773-781, 1976.

[18] A. Mantoglou, J.L. Wilson, The Turning Bands Method for Simulation of Random Fields Using Line Generation by a Spectral Method, *Water Resources Research*, **18(5)**, 1379–1394, 1982.

[19] M. Trad, I. Bitar, S. Grange, B. Richard, A multiscale steel-concrete interface model for structural applications, 2023 (paper under submission).

[20] J. Murcia-Delso, P. Benson Shing, Bond-slip model for detailed finite-element analysis of reinforced concrete structures, *Journal of Structural Engineering*, **141(4)**, 04014125, 2015.

COMPDYN 2023
9th ECCOMAS Thematic Conference on
Computational Methods in Structural Dynamics and Earthquake Engineering
M. Papadrakakis, M. Fragiadakis (eds.)
Athens, Greece, 12-–14 June 2023

# WAVE FINITE ELEMENT METHOD FOR THE DYNAMICS OF STRUCTURES WITH CYCLIC SYMMETRY

**T. Hoang[1], D. Duhamel[1], G. Foret[1], and L-H. Tran[2]**

[1]Laboratoire Navier, Ecole des Ponts, CNRS, Uni Gustave Eiffel
Champs-sur-Marne, France
e-mail: {tien.hoang,denis.duhamel,gilles.foret}@enpc.fr

[2]Faculty of Civil Engineering - VNU Hanoi
University of Engineering and Technology, Hanoi, Vietnam
e-mail: hungtl@vnu.edu.vn

**Abstract.** *The finite element method for axisymmetric and cyclic symmetric structures has been developed and integrated in numerous commercial FEM codes. Based on the periodicity of the geometry and loads, the dynamics of a 3D structure can be solved by considering only its section or one period, which permits to reduce the calculation time. However, this method cannot be used easily when the boundary conditions and loads are not symmetric. This article presents a new approach of the wave finite element method (WFE) to calculate the dynamic responses of such a structure in a general case: non-symmetric loads and boundary conditions. Based on the WFE for periodic structures, we can determine the wave decomposition of a substructure's responses in the cylindrical coordinate system. The loads on the substructure can be represented as waves added to the response. Then, we apply the wave decomposition to all substructures until getting the first one and this results a relation between the wave amplitudes and the external loads. This relation is simple and can be applied for arbitrary boundary conditions via the reaction forces. The numerical results show the advantage of this methods in the calculation time in comparing with FEM.*

**Keywords:** Wave finite element, dynamics, periodic structure, axisymmetry, cyclic symmetry, reduced model.

## 1 INTRODUCTION

Many engineering structures are axisymmetric or cyclic symmetric. Some techniques of the finite element method can deal with this type of structure without any difficulty when the loads and boundary condition are also symmetric [1]. However, when the "perfect" symmetry is not respected, the classical FEM and some reduced models can be applied but they have sometimes disadvantage because of the heavy calculation due to the great number degree of freedom or the model construction cost [2, 3]. This article presents a new technique of the wave finite element method (WFE) for such a structure in general case: non-symmetric loads and boundary conditions.

The wave finite element method was developed originally for the wave propagation in periodic structure [4]. This method permits to calculate the dynamic responses of a period structure by using the wavemodes of one period of the structure with different approaches [5, 6, 7, 8, 9, 10, 11, 12, 13]. Recently, this method has been applied for cyclic symmetric structures in several researches. Mencik [14] has used the force response and dynamic flexibility modes of cyclic symmetric structures. This technique is also applied to compute the free and forced vibration of a tire [15]. Reno et al. [16] proposed a the wave decomposition in angular and axis directions for calculating the forced response of cylinder and cylindrical shells. However, these methods can not applied easily when the periodic structure presents boundary conditions.

This article proposes a new and simple expression (see equation 21) to compute the response of a cyclic symmetric structures with WFE. By rewriting the dynamic equation of one period of the structure in the frequency domain, we can obtain the wavemodes which propagate in the two circumstantial directions of the structure. The loads on a period appear in this relation as an additive term. On the other side, the boundary of the last substructure is also a boundary of the first one. This characteristic leads to a simple expression of the wave amplitudes of the responses according to the external loads on the structure. When the structure has some non-symmetric boundary conditions, this method can be applied by calculating via the reaction forces. For applications, the first example of a 2D gear subjected to forces at a teeth and a fix boundary condition shows a time reduction of 90.4%. The second example is a cooling tower which is represented by a shell model and the calculation shows that the new technique allows a reduction of of 30% computing time compared to the FEM.

## 2 BASIC FRAMEWORKS

We consider a cyclic symmetric structure which is composed of $N$ substructures. Each substructure is subjected to external loads which can be different for each substructure. By using the finite element method, the dynamic equation of a substructure can be written as follows

$$\tilde{\mathbf{D}}\mathbf{q} = \mathbf{F} \tag{1}$$

where $\mathbf{q}$ and $\mathbf{F}$ are the DOF and nodal loads; $\tilde{\mathbf{D}}$ is the dynamic stiffness matrix of the cell.

*Change of the coordinate system:* In order to take into account of the geometric symmetry, equation(1) needs to be established in the cylindrical coordinate system. If it is in a Cartesian coordinate, we can change the system by using the rotation matrix. For each node of the substructure, we have the element rotation matrix for a vector $q^T = [q_x \quad q_y \quad q_z]$ given by

$$\begin{bmatrix} q_x \\ q_y \\ q_z \end{bmatrix} = \begin{bmatrix} \cos\theta & -\sin\theta & 0 \\ \sin\theta & \cos\theta & 0 \\ 0 & 0 & 1 \end{bmatrix} \begin{bmatrix} q_r \\ q_\theta \\ q_z \end{bmatrix} \tag{2}$$

where $\theta$ is the angle coordinate of the node. Then, the rotation matrix $\mathbf{R}$ is the diagonal block matrix of all element matrix. Finally, the dynamic stiffness matrix in the cylindrical system is given by $\mathbf{R}^T\tilde{\mathbf{D}}\mathbf{R}$.

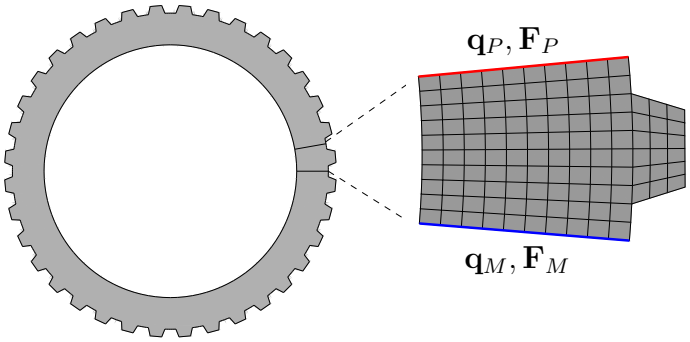


Figure 1: A cyclic symmetric structure presented by a substructure

Each substructure connects to the other ones by its boundaries in counter-clockwise (P) and clockwise (M) directions (see figure 1). Thus, we can rewrite equation (1) as follows

$$\begin{bmatrix} \tilde{\mathbf{D}}_{II} & \tilde{\mathbf{D}}_{IM} & \tilde{\mathbf{D}}_{IP} \\ \tilde{\mathbf{D}}_{MI} & \tilde{\mathbf{D}}_{MM} & \tilde{\mathbf{D}}_{MP} \\ \tilde{\mathbf{D}}_{PI} & \tilde{\mathbf{D}}_{PM} & \tilde{\mathbf{D}}_{PP} \end{bmatrix} \begin{bmatrix} \mathbf{q}_I \\ \mathbf{q}_M \\ \mathbf{q}_P \end{bmatrix} = \begin{bmatrix} \mathbf{F}_I \\ \mathbf{F}_M \\ \mathbf{F}_P \end{bmatrix} \tag{3}$$

where $I$ denote for the inner nodes. We can reduce the inner nodes $\mathbf{q}_I$ from the first row of equation (3) as follows

$$\mathbf{q}_I = \tilde{\mathbf{D}}_{II}^{-1}\left[\mathbf{F}_I - \tilde{\mathbf{D}}_{IM}\,\mathbf{q}_M - \tilde{\mathbf{D}}_{IP}\mathbf{q}_P\right] \tag{4}$$

Then, by substituting the aforementioned equation into equation (3), we obtain

$$\begin{bmatrix} \mathbf{D}_{MI}\mathbf{F}_I \\ \mathbf{D}_{PI}\mathbf{F}_I \end{bmatrix} + \begin{bmatrix} \mathbf{D}_{MM} & \mathbf{D}_{MP} \\ \mathbf{D}_{PM} & \mathbf{D}_{PP} \end{bmatrix} \begin{bmatrix} \mathbf{q}_M \\ \mathbf{q}_P \end{bmatrix} = \begin{bmatrix} \mathbf{F}_M \\ \mathbf{F}_P \end{bmatrix} \tag{5}$$

where

$$\begin{aligned} \mathbf{D}_{MI} &= \tilde{\mathbf{D}}_{MI}\tilde{\mathbf{D}}_{II}^{-1} & \mathbf{D}_{PI} &= \tilde{\mathbf{D}}_{PI}\tilde{\mathbf{D}}_{II}^{-1} \\ \mathbf{D}_{MM} &= \tilde{\mathbf{D}}_{MM} - \tilde{\mathbf{D}}_{MI}\tilde{\mathbf{D}}_{II}^{-1}\tilde{\mathbf{D}}_{IM} & \mathbf{D}_{PP} &= \tilde{\mathbf{D}}_{PP} - \tilde{\mathbf{D}}_{PI}\tilde{\mathbf{D}}_{II}^{-1}\tilde{\mathbf{D}}_{IP} \\ \mathbf{D}_{MP} &= \tilde{\mathbf{D}}_{MP} - \tilde{\mathbf{D}}_{MI}\tilde{\mathbf{D}}_{II}^{-1}\tilde{\mathbf{D}}_{IP} & \mathbf{D}_{PM} &= \tilde{\mathbf{D}}_{PM} - \tilde{\mathbf{D}}_{PI}\tilde{\mathbf{D}}_{II}^{-1}\tilde{\mathbf{D}}_{IM} \end{aligned} \tag{6}$$

We see that equation (5) presents a relation between the nodal loads and DOF at the counterclockwise and clockwise boundaries of the substructure. For the two consecutive substruc-

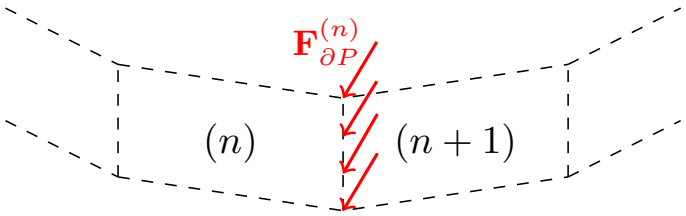


Figure 2: Two consecutive substructures

tures as shown in Figure 2, the counterclockwise boundary of $(n)$ is the clockwise boundary of

$(n+1)$. Therefore, we have

$$\begin{aligned} \mathbf{q}_P^{(n)} &= \mathbf{q}_M^{(n+1)} \\ \mathbf{F}_P^{(n)} + \mathbf{F}_M^{(n+1)} &= -\mathbf{F}_{\partial P}^{(n)} \end{aligned} \tag{7}$$

where $\mathbf{F}_{\partial P}^{(n)}$ are the external nodal loads at the counterclockwise boundary $P$ of the cell $(n)$ as shown in Figure 2. By combining equations (5) and (7), we obtain

$$\begin{bmatrix} \mathbf{q}_M^{(n+1)} \\ -\mathbf{F}_M^{(n+1)} \end{bmatrix} = \begin{bmatrix} -\mathbf{D}_{MP}^{-1}\mathbf{D}_{MI}\mathbf{F}_I^{(n)} \\ \left(\mathbf{D}_{PI} - \mathbf{D}_{PP}\mathbf{D}_{MP}^{-1}\mathbf{D}_{MI}\right)\mathbf{F}_I^{(n)} + \mathbf{F}_{\partial P}^{(n)} \end{bmatrix} + \mathbf{S} \begin{bmatrix} \mathbf{q}_M^{(n)} \\ -\mathbf{F}_M^{(n)} \end{bmatrix} \tag{8}$$

where

$$\mathbf{S} = \begin{bmatrix} -\mathbf{D}_{MP}^{-1}\mathbf{D}_{MM} & -\mathbf{D}_{MP}^{-1} \\ \mathbf{D}_{PM} - \mathbf{D}_{PP}\mathbf{D}_{MP}^{-1}\mathbf{D}_{MM} & -\mathbf{D}_{PP}\mathbf{D}_{MP}^{-1} \end{bmatrix}, \tag{9}$$

We can also rewrite equation (6) as follows

$$\mathbf{u}^{(n+1)} = \mathbf{S}\mathbf{u}^{(n)} + \mathbf{b}^{(n)} \tag{10}$$

where

$$\mathbf{u}^{(n)} = \begin{bmatrix} \mathbf{q}_M^{(n)} \\ -\mathbf{F}_M^{(n)} \end{bmatrix}, \quad \mathbf{b}^{(n)} = \begin{bmatrix} -\mathbf{D}_{MP}^{-1}\mathbf{D}_{MI}\mathbf{F}_I^{(n)} \\ \left(\mathbf{D}_{PI} - \mathbf{D}_{PP}\mathbf{D}_{MP}^{-1}\mathbf{D}_{MI}\right)\mathbf{F}_I^{(n)} + \mathbf{F}_{\partial P}^{(n)} \end{bmatrix} \tag{11}$$

Equation (10) presents a relation between the response (DOF and nodal loads) of the substructures $(n)$ and $(n+1)$. Here $\mathbf{b}^{(n)}$ presents the external loads on the substructure $(n)$ (when the cell is free, $\mathbf{b}^{(n)} = 0$). In the periodic structure of $N$ substructures, this equation presents a recurrent relation with regard to $n$, which can be reduced to the following results

$$\mathbf{u}^{(n)} = \mathbf{S}^n\mathbf{u}^{(0)} + \sum_{k=1}^{n} \mathbf{S}^{n-k}\mathbf{b}^{(k-1)} \tag{12}$$

Equation (11) gives the relations between the responses at the substructre $(n)$ and $\mathbf{u}^{(0)}$. We note that $\mathbf{u}^{(0)}$ can be chosen at any substructure because the structure is periodic.

## 3 WAVE DECOMPOSITION

The matrix $\mathbf{S}$ given by equation (9) is a linear transformation which yields complex eigenvalues and eigenvectors $\{\mu_j, \phi_j\}_j$ defined by $\mathbf{S}\phi_j = \mu_j\phi_j$. Due to the symplectic nature of the matrix $\mathbf{S}$ (see [5]), we can put the eigenvalues in pair $(\mu_j, \mu_j^\star)$ with $\mu_j^\star = 1/\mu_j$ which correspond to the pair of eigenvectors $(\phi_j, \phi_j^\star)$. We call $\phi_i$ the wave from the left to right with eigenvalue $\|\mu_j\| \leq 1$ and $\phi_i^\star$ the wave from the right to left with eigenvalue $\|\mu_j^\star\| \geq 1$.

The set of $\phi_j$ and $\phi_j^\star$ forms a base of the vectorial space of $\mathbf{u}^{(n)}$ and $\mathbf{b}^{(n)}$ defined by equation (10). This base is symplectic orthogonal in the meaning of $\phi_j^T\mathbf{J}\phi_i = \phi_j^{\star T}\mathbf{J}\phi_i^\star = 0$ $(\forall i, j)$ and $\phi_j^{\star T}\mathbf{J}\phi_i = \phi_j^T\mathbf{J}\phi_i^\star = 0$ $(\forall i \neq j)$(see [8]). We can normalize this wave base in the meaning of $\phi_i^{\star T}\mathbf{J}\phi_i = -\phi_i^T\mathbf{J}\phi_i^\star = 1$.

If we note $\mathbf{\Phi} = [\phi_1 \cdots \phi_n]$ and $\mathbf{\Phi}^\star = [\phi_1^\star \cdots \phi_n^\star]$, we can decompose each vector of equation (9) in this wave base as follows

$$\begin{aligned} \mathbf{u}^{(n)} &= \mathbf{\Phi}\mathbf{Q}^{(n)} - \mathbf{\Phi}^\star\mathbf{Q}^{\star(n)} \\ \mathbf{b}^{(n)} &= \mathbf{\Phi}\mathbf{Q}_E^{(n)} - \mathbf{\Phi}^\star\mathbf{Q}_E^{\star(n)} \end{aligned} \tag{13}$$

where $\mathbf{Q}^{(n)}, \mathbf{Q}^{\star(n)}$ are the wave amplitudes of $\mathbf{u}^{(n)}$ and $\mathbf{Q}_E^{(k)}, \mathbf{Q}_E^{\star(k)}$ are the wave amplitudes of the external loads on the intermediate substructures $\mathbf{b}^{(n)}$.

The wave decomposition in equation (13) is different from usual expression for WFE by the minus sign on the right to left waves. The advantage of this expression is that we can calculate directly the wave amplitudes by using the symplectic orthogonality of the wave basis as the following

$$\begin{aligned} \mathbf{Q}^{(n)} &= \mathbf{\Phi}^{\star T}\mathbf{J}\mathbf{u}^{(n)}, \quad \mathbf{Q}^{\star(n)} = \mathbf{\Phi}^{T}\mathbf{J}\mathbf{u}^{(n)} \\ \mathbf{Q}_E^{(n)} &= \mathbf{\Phi}^{\star T}\mathbf{J}\mathbf{b}^{(n)}, \quad \mathbf{Q}_E^{\star(n)} = \mathbf{\Phi}^{T}\mathbf{J}\mathbf{b}^{(n)} \end{aligned} \tag{14}$$

By substituting equation (11) into equation (14), we obtain (see A)

$$\begin{aligned} \mathbf{Q}_E^{(k)} &= \left(\boldsymbol{\mu}\mathbf{\Phi}_q^{\star T}\mathbf{D}_{MI} + \mathbf{\Phi}_q^{\star T}\mathbf{D}_{PI}\right)\mathbf{F}_I^{(k)} + \mathbf{\Phi}_q^{\star T}\mathbf{F}_{\partial P}^{(k)} \\ \mathbf{Q}_E^{\star(k)} &= \left(\boldsymbol{\mu}^{\star}\mathbf{\Phi}_q^{T}\mathbf{D}_{MI} + \mathbf{\Phi}_q^{T}\mathbf{D}_{PI}\right)\mathbf{F}_I^{(k)} + \mathbf{\Phi}_q^{T}\mathbf{F}_{\partial P}^{(k)} \end{aligned} \tag{15}$$

Equation (15) shows that the loads on each substructure creates two waves which propagate to the counterclockwise and clockwise directions of the structures.

Now we will calculate the responses of a substructure in function of the wave amplitudes. By replacing equation (13) with $n = 0$ into equation (12), we obtain

$$\mathbf{u}^{(n)} = \mathbf{S}^n\left(\mathbf{\Phi}\mathbf{Q} - \mathbf{\Phi}^{\star}\mathbf{Q}^{\star}\right) + \sum_{k=1}^{n}\mathbf{S}^{n-k}\left(\mathbf{\Phi}\mathbf{Q}_E^{(k-1)} - \mathbf{\Phi}^{\star}\mathbf{Q}_E^{\star(k-1)}\right) \tag{16}$$

where $\mathbf{Q}, \mathbf{Q}^{\star}$ are the wave amplitudes of $\mathbf{u}^{(0)}$. In addition, we have by definition of the wave bases

$$\mathbf{S}^n\mathbf{\Phi} = \mathbf{\Phi}\boldsymbol{\mu}^n, \quad \mathbf{S}^n\mathbf{\Phi}^{\star} = \mathbf{\Phi}^{\star}\boldsymbol{\mu}^{\star n} \tag{17}$$

Thus, we can rewrite equation (16) as follows

$$\mathbf{u}^{(n)} = \mathbf{\Phi}\boldsymbol{\mu}^n\mathbf{Q} - \mathbf{\Phi}^{\star}\boldsymbol{\mu}^{\star n}\mathbf{Q}^{\star} + \sum_{k=1}^{n}\mathbf{\Phi}\boldsymbol{\mu}^{n-k}\mathbf{Q}_E^{(k-1)} - \mathbf{\Phi}^{\star}\boldsymbol{\mu}^{\star n-k}\mathbf{Q}_E^{\star(k-1)} \tag{18}$$

Because $\boldsymbol{\mu}^{\star} = \boldsymbol{\mu}^{-1}$, we have

$$\mathbf{u}^{(n)} = \mathbf{\Phi}\boldsymbol{\mu}^n\left(\mathbf{Q} + \sum_{k=1}^{n}\boldsymbol{\mu}^{\star k}\mathbf{Q}_E^{(k-1)}\right) - \mathbf{\Phi}^{\star}\boldsymbol{\mu}^{\star n}\left(\mathbf{Q}^{\star} + \sum_{k=1}^{n}\boldsymbol{\mu}^{k}\mathbf{Q}_E^{\star(k-1)}\right) \tag{19}$$

On the other side, the counterclockwise boundary of the substructure $N$ is also the clockwise boundary of the substructure $0$, we have $\mathbf{u}^{(N)} = \mathbf{u}^{(0)}$. In addition, the wave decomposition of a boundary in the wave base $\{\mathbf{\Phi}, \mathbf{\Phi}^{\star}\}$ is unique. Thus, we have

$$\mathbf{Q} = \left[\mathbf{I} - \boldsymbol{\mu}^N\right]^{-1}\sum_{k=1}^{N}\boldsymbol{\mu}^{N-k}\mathbf{Q}_E^{(k)}, \quad \mathbf{Q}^{\star} = \left[\boldsymbol{\mu}^N - \mathbf{I}\right]^{-1}\sum_{k=1}^{N}\boldsymbol{\mu}^{k}\mathbf{Q}_E^{\star(k)} \tag{20}$$

Finally, we obtain the expression of the response by substituting the aforementioned equation into equation (13)

$$\mathbf{u}^{(0)} = \mathbf{\Phi}\left[\mathbf{I} - \boldsymbol{\mu}^N\right]^{-1}\sum_{k=1}^{N}\boldsymbol{\mu}^{N-k}\mathbf{Q}_E^{(k)} + \mathbf{\Phi}^{\star}\left[\mathbf{I} - \boldsymbol{\mu}^N\right]^{-1}\sum_{k=1}^{N}\boldsymbol{\mu}^{k}\mathbf{Q}_E^{\star(k)} \tag{21}$$

Equation (21) presents the response at the boundary of each substructure and the external loads on the structure. For the inner nodes of the substructures, we can use equation (4) to compute the response. We note that this method needs to calculate only once the wave amplitudes of the external loads on each substructure and we don't need to inverse any matrix as in the classical FEM.

### Remarks

*Non-symmetric boundary conditions*: We see that the structure's responses can be calculated from the external loads via their wave amplitudes given in equation (15). However, if the boundary condition is given instead of the forces, we can use use this method by calculating via the reaction force. Firstly, we write the relation between the displacement of the boundary condition in function of the reaction forces and external loads. Then, we can write the boundary condition to obtain an equation on the reaction forces. Once the reaction forces are calculated, we can compute the responses of the structure.

*Symmetric loads*: When the loads on the structure is symmetric, we have $\mathbf{Q}_E^{(k)} = \mathbf{Q}_E$ and $\mathbf{Q}_E^{\star(k)} = \mathbf{Q}_E^{\star}$ for all substructures. We obtain the following result from equation (21)

$$\mathbf{u}^{(0)} = \mathbf{\Phi} \left[\mathbf{I} - \boldsymbol{\mu}\right]^{-1} \mathbf{Q}_E + \mathbf{\Phi}^{\star} \left[\mathbf{I} - \boldsymbol{\mu}\right]^{-1} \mathbf{Q}_E^{\star} \tag{22}$$

It is remarkable that this result does not depend on the number of substructures.

## 4 NUMERICAL APPLICATIONS

Let's consider a 2D gear with 36 teeth as shown in Figure 1.The structure is subjected to a load at the tooth of the substructure number 1 and a fixed constrain at the radius of the substructure number 10. We use the finite element method with the element type S4 in Abaqus to obtain the dynamic stiffness matrix of a substructure. Then, the calculation is performed with FEM and WFE methods in Matlab. Figure 3 shows the results obtained by the two methods. The results agrees well and the calculation times are 17.7s and 1.7s for FEM and WFE respectively, which means 90.4% of time reduction.

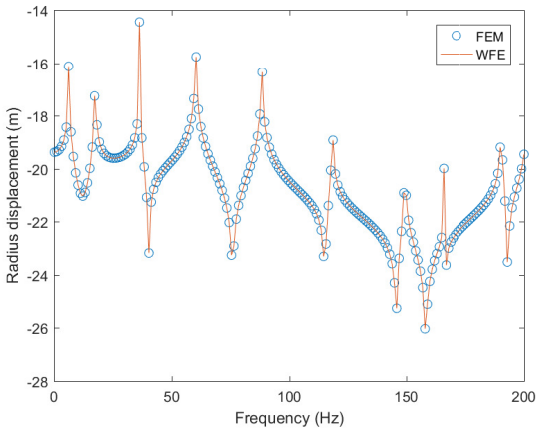


Figure 3: Result example 1

We take another example of a hyperbolic cooling tower in a nuclear center. The dimensions of the tower are given by [17] with height of 138m, the fixed base is of 108m in diameter. The

tower is subjected to a pressure in a rectangular domain of 10x5m with the center at the height of 100m. This tower has an axisymmetric geometry but the load is not symmetric. Therefore, we can not use the axisymmetric element in FEM code. We use the shell element S4 to compute the dynamic stiffness of the whole tower and its substructure which composes only 1 element in the tangent direction, corresponding to an arc of 5°. Thus, the number of substructures is $\frac{360}{5} = 72$. It is remarkable that each node contains 6 degrees of freedom corresponding to the displacements and rotations in 3 directions. Therefore, the rotation matrix of one node contains not only the matrix $3 \times 3$ in equation (2) but a $6 \times 6$ matrix with 2 diagonal blocks of this $3 \times 3$ matrix. Figure 5 shows the results obtained by FEM and the new method. The two results agree

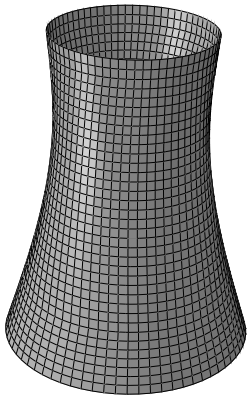

Figure 4: Example of a cooling tower

well and the calculation times are 102.2s for FEM and 70.7 for WFE.

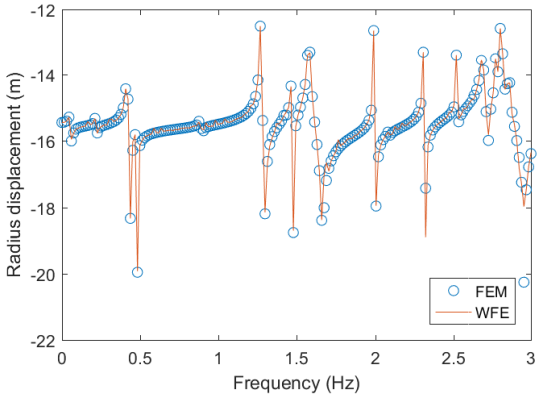


Figure 5: Example of a cooling tower

## 5 CONCLUSIONS

By using the wave finite element method, we demonstrate that the dynamic response of a cyclic symmetric structure is a sum of all waves generated by external loads in each substructure. This method permits to reduce the DOF of the structure to only one substructure and therefore reduce the calculation times.

## A CALCULATION OF WAVE AMPLITUDES OF EXTERNAL LOADS

Because the vector $\mathbf{u}^{(n)}$ contains two components corresponding to the displacements and forces, we can separate the components of the wave base as follows

$$\mathbf{\Phi} = \begin{bmatrix} \mathbf{\Phi}_q \\ \mathbf{\Phi}_F \end{bmatrix} \quad \mathbf{\Phi}^\star = \begin{bmatrix} \mathbf{\Phi}_q^\star \\ \mathbf{\Phi}_F^\star \end{bmatrix} \tag{23}$$

By substituting equation (11) into equation (14), we obtain

$$\begin{aligned} \mathbf{Q}_E^{(n)} &= \mathbf{\Phi}_q^{\star T}\left(\mathbf{F}_{\partial P}^{(n)} + \left(\mathbf{D}_{PI} - \mathbf{D}_{PP}\mathbf{D}_{MP}^{-1}\mathbf{D}_{MI}\right)\mathbf{F}_I^{(n)}\right) + \mathbf{\Phi}_F^{\star T}\mathbf{D}_{MP}^{-1}\mathbf{D}_{MI}\mathbf{F}_I^{(n)} \\ &= \mathbf{\Phi}_q^{\star T}\mathbf{F}_{\partial P}^{(n)} + \left(\left(\mathbf{\Phi}_F^{\star T} - \mathbf{\Phi}_q^{\star T}\mathbf{D}_{PP}\right)\mathbf{D}_{MP}^{-1}\mathbf{D}_{MI} + \mathbf{\Phi}_q^{\star T}\mathbf{D}_{PI}\right)\mathbf{F}_I^{(n)} \\ \mathbf{Q}_E^{\star(n)} &= \mathbf{\Phi}_q^{T}\left(\mathbf{F}_{\partial P}^{(n)} + \left(\mathbf{D}_{PI} - \mathbf{D}_{PP}\mathbf{D}_{MP}^{-1}\mathbf{D}_{MI}\right)\mathbf{F}_I^{(n)}\right) + \mathbf{\Phi}_F^{T}\mathbf{D}_{MP}^{-1}\mathbf{D}_{MI}\mathbf{F}_I^{(n)} \\ &= \mathbf{\Phi}_q^{T}\mathbf{F}_{\partial P}^{(n)} + \left(\left(\mathbf{\Phi}_F^{T} - \mathbf{\Phi}_q^{T}\mathbf{D}_{PP}\right)\mathbf{D}_{MP}^{-1}\mathbf{D}_{MI} + \mathbf{\Phi}_q^{T}\mathbf{D}_{PI}\right)\mathbf{F}_I^{(n)} \end{aligned} \tag{24}$$

In addition, we have the relation between the $\mathbf{\Phi}_q$ and $\mathbf{\Phi}_F$ as follows (see [8])

$$\begin{aligned} \mathbf{\Phi}_F &= \mathbf{D}_{PP}\mathbf{\Phi}_q + \mathbf{D}_{PM}\mathbf{\Phi}_q\boldsymbol{\mu}^\star \\ \mathbf{\Phi}_F^\star &= \mathbf{D}_{PP}\mathbf{\Phi}_q^\star + \mathbf{D}_{PM}\mathbf{\Phi}_q^\star\boldsymbol{\mu} \end{aligned} \tag{25}$$

By substituting equation (25) into (24), we obtain

$$\begin{aligned} \mathbf{Q}_E^{(k)} &= \mathbf{\Phi}_q^{\star T}\mathbf{F}_{\partial P}^{(k)} + \left(\boldsymbol{\mu}\mathbf{\Phi}_q^{\star T}\mathbf{D}_{MI} + \mathbf{\Phi}_q^{\star T}\mathbf{D}_{PI}\right)\mathbf{F}_I^{(k)} \\ \mathbf{Q}_E^{\star(k)} &= \mathbf{\Phi}_q^{T}\mathbf{F}_{\partial P}^{(k)} + \left(\boldsymbol{\mu}^\star\mathbf{\Phi}_q^{T}\mathbf{D}_{MI} + \mathbf{\Phi}_q^{T}\mathbf{D}_{PI}\right)\mathbf{F}_I^{(k)} \end{aligned} \tag{26}$$

If we note

$$\mathbf{F}_E^{(k)} = \begin{bmatrix} \mathbf{F}_I^{(k)} \\ \mathbf{F}_{\partial P}^{(k)} \end{bmatrix}, \qquad \begin{aligned} \mathbf{\Phi}_E &= \begin{bmatrix} \boldsymbol{\mu}\mathbf{\Phi}_q^{\star T}\mathbf{D}_{MI} + \mathbf{\Phi}_q^{\star T}\mathbf{D}_{PI} & \mathbf{\Phi}_q^{\star T} \end{bmatrix} \\ \mathbf{\Phi}_E^\star &= \begin{bmatrix} \boldsymbol{\mu}^\star\mathbf{\Phi}_q^{T}\mathbf{D}_{MI} + \mathbf{\Phi}_q^{T}\mathbf{D}_{PI} & \mathbf{\Phi}_q^{T} \end{bmatrix} \end{aligned} \tag{27}$$

Equation (26) becomes

$$\mathbf{Q}_E^{(k)} = \mathbf{\Phi}_E\mathbf{F}_E^{(k)} \quad \text{and} \quad \mathbf{Q}_E^{\star(k)} = \mathbf{\Phi}_E^\star\mathbf{F}_E^{(k)} \tag{28}$$

On the other side, $\mathbf{F}_E^{(k)}$ is the vector of the external loads applying on the substructure $k$. Equation (28) presents a simple relation between the external loads and its wave amplitudes.

## REFERENCES


[1] D. Thomas, Dynamics of rotationally periodic structures, *International Journal for Numerical Methods in Engineering*, **14** (1979) 81–102.

[2] P. Vargiu, C. Firrone, S. Zucca, M. Gola, A reduced order model based on sector mistuning for the dynamic analysis of mistuned bladed disks, *International Journal of Mechanical Sciences*, **53** (8) (2011) 639 – 646.

[3] D.-M. Tran, Reduced models of multi-stage cyclic structures using cyclic symmetry reduction and component mode synthesis, *Journal of Sound and Vibration*, **333** (21) (2014) 5443 – 5463.

[4] D. Mead, A general theory of harmonic wave propagation in linear periodic systems with multiple coupling, *Journal of Sound and Vibration*, **27** (2) (1973) 235 – 260.

[5] D. Duhamel, B. R. Mace, M. J. Brennan, Finite element analysis of the vibrations of waveguides and periodic structures, *Journal of Sound and Vibration*, **294** (1-2) (2006) 205–220.

[6] Y. Waki, B. Mace, M. Brennan, Numerical issues concerning the wave and finite element method for free and forced vibrations of waveguides, *Journal of Sound and Vibration*, **327** (1) (2009) 92 – 108.

[7] M. Ichchou, J.-M. Mencik, W. Zhou, Wave finite elements for low and mid-frequency description of coupled structures with damage, *Computer Methods in Applied Mechanics and Engineering*, **198** (15) (2009) 1311 – 1326.

[8] J. M. Mencik, D. Duhamel, A wave-based model reduction technique for the description of the dynamic behavior of periodic structures involving arbitrary-shaped substructures and large-sized finite element models, *Finite Elements in Analysis and Design*, **101** (2015) 1–14.

[9] J. M. Renno, B. R. Mace, On the forced response of waveguides using the wave and finite element method, *Journal of Sound and Vibration*, **329** (26) (2010) 5474 – 5488.

[10] J.-M. Mencik, D. Duhamel, A wave finite element-based approach for the modeling of periodic structures with local perturbations, *Finite Elements in Analysis and Design*, **121** (2016) 40–51.

[11] J.-M. Mencik, M. Ichchou, A substructuring technique for finite element wave propagation in multi-layered systems, *Computer Methods in Applied Mechanics and Engineering*, **197** (6) (2008) 505 – 523.

[12] W. Zhou, M. Ichchou, Wave propagation in mechanical waveguide with curved members using wave finite element solution, *Computer Methods in Applied Mechanics and Engineering*, **199** (33) (2010) 2099 – 2109.

[13] A. Kessentini, M. Taktak, M. B. Souf, O. Bareille, M. Ichchou, M. Haddar, Computation of the scattering matrix of guided acoustical propagation by the wave finite element approach, *Applied Acoustics*, **108** (2016) 92 – 100, applied Acoustics in Multiphysic systems.

[14] J.-M. Mencik, A wave finite element approach for the analysis of periodic structures with cyclic symmetry in dynamic substructuring, *Journal of Sound and Vibration*, **431** (2018) 441 – 457.

[15] Y. Waki, B. Mace, M. Brennan, Free and forced vibrations of a tyre using a wave/finite element approach, *Journal of Sound and Vibration*, **323** (3) (2009) 737 – 756.

[16] J. M. Renno, B. R. Mace, Calculating the forced response of cylinders and cylindrical shells using the wave and finite element method, *Journal of Sound and Vibration*, **333** (21) (2014) 5340 – 5355.

[17] J. Tang, H. Wu, S. Ke, Q. Fang, Numerical simulations of a large-scale cooling tower against the impact of commercial aircrafts, *Thin-Walled Structures*, **144** (2019) 106367.

COMPDYN 2023
9th ECCOMAS Thematic Conference on
Computational Methods in Structural Dynamics and Earthquake Engineering
M. Papadrakakis, M. Fragiadakis (eds.)
Athens, Greece, 12-–14 June 2023

# COMPUTATION OF THE RESPONSE OF DAMAGED RAILWAY TRACKS SUBJECTED TO CONSTANT MOVING LOADS: NUMERICAL RESULTS OBTAINED WITH THE WAVE FINITE ELEMENT METHOD AND ANALYTICAL RESULTS.

**Benjamin Claudet[1], Denis Duhamel[1], Gilles Foret[1], Tien Hoang[1], Francis Sabatier[2], Bertrand Findinier[2], and Hervé Lenglin[2]**

[1]Navier Laboratory, UMR8205
École des Ponts ParisTech
Champs-sur-Marne, France
e-mail: {benjamin.claudet,denis.duhamel,gilles.foret,tien.hoang}@enpc.fr

[2] GETLINK
Coquelles, France
e-mail: {francis.sabatier,bertrand.findinier,herve.lenglin}@eurotunnel.com

**Abstract.** *Railway tracks are subjected to heavy repeated loads due to the train traffic. These loads can damage the track and especially its supports. To compute the behavior of railway tracks, many authors used a periodicity hypothesis, which is broken by the presence of a damaged zone. Researchers proposed different analytical or numerical methods to compute the dynamics of such structures. Analytical methods permit low numerical cost computations of the track dynamics, but are limited to very simple representations of the track, whereas numerical methods allow the use of much more detailed representations of the track but with higher numerical cost.*

*In most regions, railway tracks can be modeled as periodic structures. Several methods take advantage of this periodicity to limit the numerical cost for the computation of the track dynamics. Among these methods, the Wave Finite Element (WFE) method was initially created to compute free vibrations in periodic structures. This method was improved to compute the dynamic response of periodic structures subjected to any kind of loads. In recent development, the authors adapted the WFE method to compute the response of structures composed of two semi infinite periodic zones linked by a central zone with different mechanical properties.*

*In this paper, the results obtained with an analytical method will be compared to results obtained with the WFE method for the computation of the dynamic responses of different ballastless railway tracks such as healthy and damaged tracks. In these computations, the tracks will be subjected to constant moving loads representing the load applied by a train wheel. In the WFE results, the rail, the supports, and the supporting concrete slabs are represented with a three-dimensional model. A special focus will be made on the state of stress of the different*

**Keywords:** Wave Finite Element Method, Railway, Dynamics, Moving loads, Transition zones, Damaged and reinforced tracks.

*materials which constitute the tracks. A failure criterion will be computed at components scale for the different tracks simulated. This criterion can then be used to compute the likeliness of long-term fatigue of the track components.*

## 1 Introduction

During their exploitation, railway tracks are subjected to heavy repeated loads leading to fatigue damages. Numerical simulations can be conducted to understand the mechanical behavior of railway tracks and to anticipate their degradation. To limit the cost of this computation, several authors modeled railway tracks as periodic structures. With this periodicity hypothesis, authors proposed both analytical [1–4] and numerical [5–8] models for computing railway tracks dynamics.

In many cases the track contains portions with different mechanical properties, which breaks its periodicity. These different mechanical properties can come from transition between portions with different natures – like ballasted to ballastless tracks – but also from local damage or reinforcement of the track. To simulate such tracks, one have to use tools which takes into account the periodicity breakage.

In 2017, Hoang *et al.* [9] proposed an analytical model to compute the response of a railway track resting on a non-uniform foundation subjected to constant moving loads. In this model, the rail is represented by a Euler beam and its supports by mass-spring-dampers systems. This model was then reused by Tran *et al.* [10]. Claudet *et al.* [11] developed a similar model representing the rail by a Timoshenko beam.

In recent years, several authors proposed numerical models of railway tracks containing periodicity breaks [5, 12–16]. Among them, Claudet *et al.* [16], in COMDYN 2021, proposed a method to compute the mechanical response of structures constituted of two semi-infinite periodic structures linked by a central part and subjected to moving or fixed loads. To do so, the authors combined the Wave Finite Element (WFE) method – for the periodic zones – and classical Finite Element Method (FEM) – for the central zone. In this method, the WFE method enables taking into account the infinite nature of the geometry. In the presented example, this method was used to simulate a damaged railway track using a one dimensional model.

In the present article, the mechanical behavior of tracks containing one damaged support is studied. A special focus is done on evaluating the level of stresses in the tracks' components depending on the level of degradation of the damaged support. For this study, analytical results will be compared to numerical ones. The analytical results are obtained with the method proposed by Hoang *et al.* [9] and improved by Claudet *et al.* [11]. The numerical model uses the WFE method proposed by Claudet *et al* [16] in COMDYN 2021. These numerical results uses a fine three-dimensional model of the damaged tracks.

## 2 Methods used

This section briefly describes the two methods used in the present article to compute the dynamical response of damaged railway tracks. In the considered tracks, each support is constituted of a reinforced concrete block linked to the rail and the underlying concrete slab by two elastic stages. The first elastic stage is situated between the rail and the concrete block and is called rail pad. The second one, situated between the concrete bloc and the slab, is called undersleeper pad.

### 2.1 Analytical method

In the analytical method proposed by Claudet *et al.* [11], in healthy zone, the track is represented by a periodically supported Timoshenko beam. The beam represents the rail and the supports are modeled by mass-springs-dampers systems (see figure 1).

Claudet *et al.* supposed the track contains a finite number of supports with varying spacings

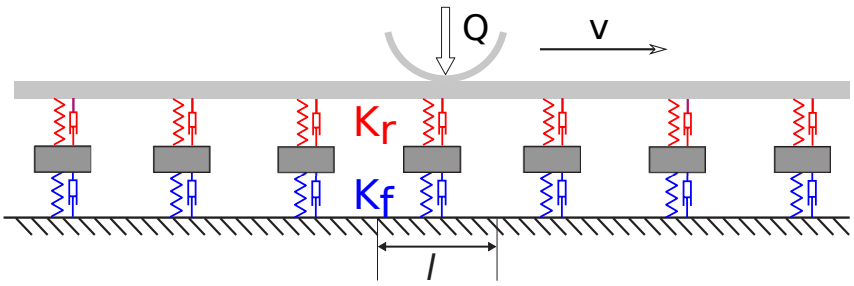


Figure 1: Periodically supported beam model.

or dynamic stiffnesses. This structure is subjected to constant loads $Q_j$ situated at $x = -D_j$ at $t = 0$. These loads are moving at a constant speed $v$. To compute the response of this structure, the authors considered an auxiliary problem of the response of a beam resting on a repetition of a set of $m$ supports. The length of the structure's pattern is noted $L$. Figure 2 gives a representation of the true problem and the auxiliary problem (with $m = 5$) for a track containing one damaged support.

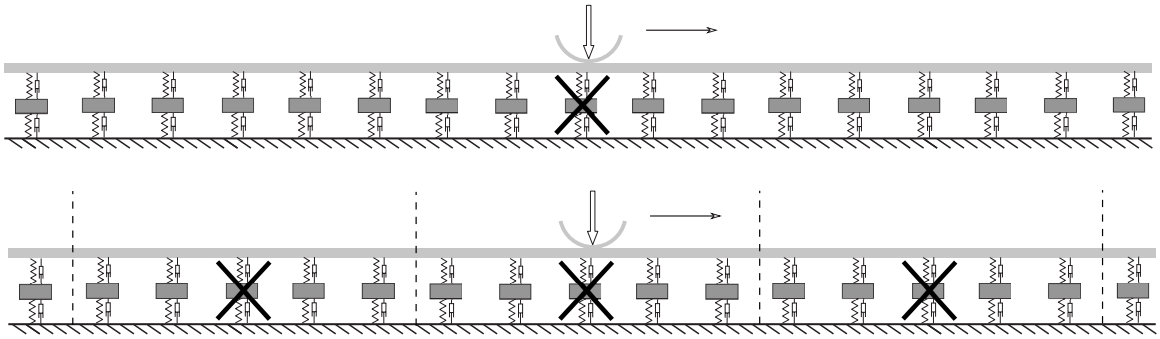

Figure 2: Railway track containing one damaged support. True problem (top), auxiliary problem with $m = 5$ (bottom).

The authors proved that, at a given frequency $\omega$ and a given position $x$, denoting $\hat{R}_p(\omega)$ the force applied by the support $p$, the rail deflection $\hat{w}$ is given by:

$$\hat{w}(x,\omega) = \sum_{p=0}^{m-1} \hat{R}_p(\omega) \mathrm{e}^{\mathrm{i}\omega\frac{pl-x}{v}} \eta(pl-x,\omega) - \eta(0,\omega)\mathcal{Q}(\omega)\mathrm{e}^{-\mathrm{i}\frac{\omega x}{v}} \tag{1}$$

Where,

$$\eta(x,\omega) = \frac{\mathrm{e}^{\mathrm{i}\frac{\omega x}{v}}}{2EI\,(\lambda_1^2+\lambda_2^2)} \left[ \frac{C_1}{\lambda_1} \frac{\sin\lambda_1(L-x) + \mathrm{e}^{-\mathrm{i}\frac{\omega L}{v}}\sin\lambda_1 x}{\cos L\lambda_1 - \cos\frac{\omega L}{v}} - \frac{C_2}{\lambda_2} \frac{\sinh\lambda_2(L-x) + \mathrm{e}^{-\mathrm{i}\frac{\omega L}{v}}\sinh\lambda_2 x}{\cosh L\lambda_2 - \cos\frac{\omega L}{v}} \right]$$

$$\mathcal{Q}(\omega) = \frac{\widetilde{p}_0 L}{v} \eta(0,\omega)^{-1} \sum_{j=1}^{K} Q_j \mathrm{e}^{-\mathrm{i}\omega\frac{D_j}{v}}$$

With,

$$C_{1,2} = 1 - \frac{\rho I\omega^2 \mp EI\lambda_{1,2}^2}{\kappa SG}$$

$$\lambda_{1,2}^2 = \sqrt{\frac{\omega^4}{4}\left(\frac{\rho I}{EI} - \frac{\rho S}{\kappa SG}\right)^2 + \frac{\rho S\omega^2}{EI}} \pm \frac{\omega^2}{2}\left(\frac{\rho I}{EI} + \frac{\rho S}{\kappa SG}\right)$$

$$\widetilde{p}_0 L = \frac{\kappa SG - \rho I\omega^2 + EI\frac{\omega^2}{v^2}}{\kappa SG\left(EI\frac{\omega^4}{v^4} - \rho S\omega^2\right) - \rho SI\left(\kappa G + E - \rho v^2\right)\frac{\omega^4}{v^2}}$$

With $I$ the beam's inertia, $G$ its shear modulus and $S$ its section, $\kappa$ its Timoshenko shear coefficient and $E$ the Young modulus of the beam's material, $\rho$ its density.

This leads to the following system:

$$\begin{pmatrix} \eta_0 & \eta_1 & \cdots & \eta_{m-1} \\ \eta_{m-1} & \eta_0 & \cdots & \eta_{m-2} \\ \vdots & \vdots & \ddots & \vdots \\ \eta_1 & \eta_2 & \cdots & \eta_0 \end{pmatrix} \begin{pmatrix} \hat{\mathbf{R}}_0 \\ \hat{\mathbf{R}}_1 \\ \vdots \\ \hat{\mathbf{R}}_{m-1} \end{pmatrix} = \eta_0 \mathcal{Q} \begin{pmatrix} 1 \\ 1 \\ \vdots \\ 1 \end{pmatrix} + \begin{pmatrix} \hat{\mathbf{w}}_0 \\ \hat{\mathbf{w}}_1 \\ \vdots \\ \hat{\mathbf{w}}_{m-1} \end{pmatrix} \tag{2}$$

Which can be rewritten in the following matricial form:

$$\underline{\underline{\mathbf{C}}}\,\underline{\hat{\mathbf{R}}} = \eta_0 \mathcal{Q}\underline{\mathbf{1}} + \underline{\hat{\mathbf{w}}} \tag{3}$$

The problem is then closed using the dynamic stiffness $k_p(\omega)$ of each support of the pattern, giving: $-k_p(\omega)\hat{w}(x_p,\omega) = \hat{R}_p(\omega)$. Using $\underline{\underline{\mathbf{D}}} = -diag(1/k_0, \ldots, 1/k_{m-1})$, one can write:

$$\underline{\hat{\mathbf{R}}} = \mathcal{Q}\underline{\underline{\mathbf{A}}}^{-1}\underline{\mathbf{1}} \tag{4}$$

Where $\underline{\underline{\mathbf{A}}} = \eta_0^{-1}\left(\underline{\underline{\mathbf{C}}} + \underline{\underline{\mathbf{D}}}\right)$.

To solve the auxiliary problem, one can directly use Eq. (4) or the iterative procedure presented in [11]. It is considered that, if $m$ (respectively $L$) is large enough, then, the solution on one pattern in the auxiliary problem is close to the solution on the same $m$ supports in the real problem.

### 2.2 Numerical method

Being based on a very simplified representation of the track, the previous model can not give access to stresses and strains at a fine scale. In this aim, in the present article, the numerical method proposed by Claudet *et al.* [16] is used to compute the mechanical response of railway transition zones. In this method, the structure is divided into two semi-infinite periodic zones – called right zone and left zone – and a central finite zone with no special property – called transition zone. The obtained geometry is represented in Figure 3.

To compute the mechanical behavior of the obtained structure, the authors combined the Wave Finite Element (WFE) method in the periodic zones with a Finite Element dynamic equilibrium relationship in the transition zone.

#### 2.2.1 The Wave Finite Element (WFE) method

The WFE method consists in reducing the computation of the mechanical behavior of a periodic structure to a much smaller wave problem at one boundary of one of its patterns. The main steps of this method are described in the following.

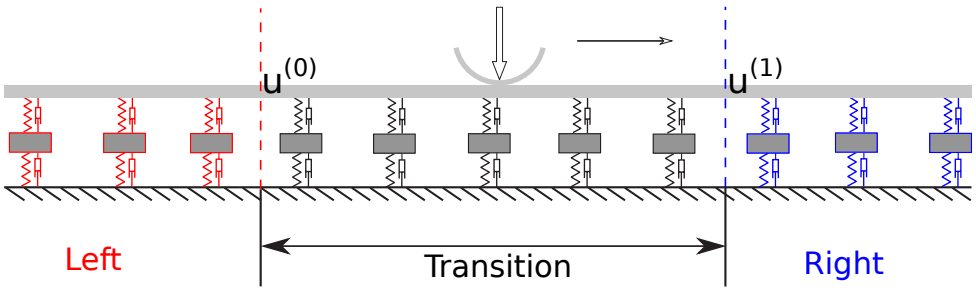


Figure 3: Transition zone between two semi-infinite periodic railway tracks.

In the frequency domain, using the Finite Element Method, the dynamic equilibrium of one pattern can be written. Denoting $\underline{\mathbf{q}}^{(n)}$ the degrees of freedom of the pattern, $\underline{\mathbf{F}}^{(n)}$ the external forces applied on this pattern and $\underline{\underline{\mathbf{D}}}$ its dynamic stiffness matrix, the following equation is obtained:

$$\begin{bmatrix} \underline{\underline{\tilde{\mathbf{D}}}}_{II} & \underline{\underline{\tilde{\mathbf{D}}}}_{IL} & \underline{\underline{\tilde{\mathbf{D}}}}_{IR} \\ \underline{\underline{\tilde{\mathbf{D}}}}_{LI} & \underline{\underline{\tilde{\mathbf{D}}}}_{LL} & \underline{\underline{\tilde{\mathbf{D}}}}_{LR} \\ \underline{\underline{\tilde{\mathbf{D}}}}_{RI} & \underline{\underline{\tilde{\mathbf{D}}}}_{RL} & \underline{\underline{\tilde{\mathbf{D}}}}_{RR} \end{bmatrix} \begin{bmatrix} \underline{\mathbf{q}}_I \\ \underline{\mathbf{q}}_L \\ \underline{\mathbf{q}}_R \end{bmatrix} = \begin{bmatrix} \underline{\mathbf{F}}_I \\ \underline{\mathbf{F}}_L \\ \underline{\mathbf{F}}_R \end{bmatrix} \tag{5}$$

Where the subscripts $_{I}$, $_{L}$ and $_{R}$ respectively stand for inner nodes, left boundary and right boundary nodes.

In the WFE method this equation is transformed into the following propagation equation:

$$\underline{\mathbf{u}}^{(n+1)} = \underline{\underline{\mathbf{S}}}\,\underline{\mathbf{u}}^{(n)} + \underline{\mathbf{b}}^{(n)} \tag{6}$$

Where

$$\underline{\mathbf{u}}^{(n)} = \begin{bmatrix} \underline{\mathbf{q}}_L^{(n)} \\ -\underline{\mathbf{F}}_L^{(n)} \end{bmatrix}, \quad \underline{\mathbf{b}}^{(n)} = \begin{bmatrix} \underline{\underline{\mathbf{D}}}_{qI}\,\underline{\mathbf{F}}_I^{(n)} \\ \underline{\underline{\mathbf{D}}}_{fI}\,\underline{\mathbf{F}}_I^{(n)} - \underline{\mathbf{F}}_{\partial R}^{(n)} \end{bmatrix}$$

$\underline{\underline{\mathbf{S}}}, \underline{\underline{\mathbf{D}}}_{qI}, \underline{\underline{\mathbf{D}}}_{FI}$ and $\underline{\mathbf{F}}_{\partial R}^{(n)}$ are defined in the works of Hoang *et al.* [17] or Claudet *et al.* [8, 16].

Making use of the propagation equation (6) to compute the mechanical response of a periodic structure, power of $\underline{\underline{\mathbf{S}}}$ matrix appears. To compute the power of $\underline{\underline{\mathbf{S}}}$ matrix, authors compute the eigenvectors of $\underline{\underline{\mathbf{S}}}$. They usually separate eigenvectors $\left\{\underline{\phi}_j\right\}$ corresponding to eigenvalues $\{\mu_j\}$ whose modulus are smaller than 1 and eigenvectors $\left\{\underline{\phi}_j^\star\right\}$ corresponding to eigenvalues $\left\{\mu_j^\star\right\}$ whose modulus are greater than 1.

Then the basis $\left\{\underline{\underline{\mathbf{\Phi}}}\,\underline{\underline{\mathbf{\Phi}}}^\star\right\}$ is defined as: $\underline{\underline{\mathbf{\Phi}}} = [\underline{\phi}_1 \dots \underline{\phi}_n]$ and $\underline{\underline{\mathbf{\Phi}}}^\star = [\underline{\phi}_1^\star \dots \underline{\phi}_n^\star]$. Using the subscript "$_q$" (respectively "$_F$") for the components corresponding to the degrees of freedom (DoF) (resp. the loads), leads to Eq. (7).

$$\underline{\underline{\mathbf{\Phi}}} = \begin{bmatrix} \underline{\underline{\mathbf{\Phi}}}_q \\ \underline{\underline{\mathbf{\Phi}}}_F \end{bmatrix} \quad \underline{\underline{\mathbf{\Phi}}}^\star = \begin{bmatrix} \underline{\underline{\mathbf{\Phi}}}_q^\star \\ \underline{\underline{\mathbf{\Phi}}}_F^\star \end{bmatrix} \tag{7}$$

Using the same sign convention as in [6, 8, 16], $\mathbf{u}^{(n)}$ and $\mathbf{b}^{(n)}$ can be written in this wave basis:

$$\begin{aligned} \underline{\mathbf{u}}^{(n)} &= \underline{\underline{\mathbf{\Phi}}}\,\underline{\mathbf{Q}}^{(n)} - \underline{\underline{\mathbf{\Phi}}}^\star\,\underline{\mathbf{Q}}^{\star(n)} \\ \underline{\mathbf{b}}^{(n)} &= \underline{\underline{\mathbf{\Phi}}}\,\underline{\mathbf{Q}}_E^{(n)} - \underline{\underline{\mathbf{\Phi}}}^\star\,\underline{\mathbf{Q}}_E^{\star(n)} \end{aligned} \tag{8}$$

With this notations, Hoang *et al.* [6] proved:

$$\begin{aligned}\underline{\mathbf{Q}}_E^{(k)} &= \left[\left(\underline{\underline{\boldsymbol{\mu}}}\,\underline{\underline{\boldsymbol{\Phi}}}_q^{\star T}\,\underline{\underline{\mathbf{D}}}_{LI} + \underline{\underline{\boldsymbol{\Phi}}}_q^{\star T}\,\underline{\underline{\mathbf{D}}}_{RI}\right)\underline{\mathbf{F}}_I^{(k)} - \underline{\underline{\boldsymbol{\Phi}}}_q^{\star T}\,\underline{\mathbf{F}}_{\partial R}^{(k)}\right] \\ \underline{\mathbf{Q}}_E^{\star(k)} &= \left[\left(\underline{\underline{\boldsymbol{\mu}}}^{\star}\,\underline{\underline{\boldsymbol{\Phi}}}_q^{T}\,\underline{\underline{\mathbf{D}}}_{LI} + \underline{\underline{\boldsymbol{\Phi}}}_q^{T}\,\underline{\underline{\mathbf{D}}}_{RI}\right)\underline{\mathbf{F}}_I^{(k)} - \underline{\underline{\boldsymbol{\Phi}}}_q^{T}\,\underline{\mathbf{F}}_{\partial R}^{(k)}\right]\end{aligned} \tag{9}$$

### 2.2.2 Problem closure

In the previous paragraph, the basic WFE equations were reminded. These equations allow to reduce the mechanical behavior of a periodic structure to a wave problem at one of its boundaries. To close the problem, Claudet *et al.* used the equilibrium relationship of the transition zone. Using the same notations as before, this equilibrium relationship of this zone can be written:

$$\underline{\underline{\tilde{\mathbf{D}}}}_T \begin{bmatrix} \underline{\mathbf{q}}_I \\ \underline{\mathbf{q}}_L \\ \underline{\mathbf{q}}_R \end{bmatrix} = \begin{bmatrix} \underline{\mathbf{F}}_I \\ \underline{\mathbf{F}}_L \\ \underline{\mathbf{F}}_R \end{bmatrix} \tag{10}$$

Lets denote $(0)$ the left boundary of the transition zone and $(1)$ its right boundary – see Fig. 3. Then, denoting with "$_R$" subscript the right zone and "$_L$" subscript the left zone, the following propagation equations are obtained:

$$\begin{cases} \forall n \geqslant 1,\ \underline{\mathbf{u}}_R^{(n+1)} = \underline{\underline{\mathbf{S}}}_R\,\underline{\mathbf{u}}^{(n)} + \underline{\mathbf{b}}^{(n)} \\ \forall n \leqslant 0,\ \underline{\mathbf{u}}_L^{(n-1)} = \underline{\underline{\mathbf{S}}}_L^{-1}\,\underline{\mathbf{u}}^{(n)} - \underline{\underline{\mathbf{S}}}_L^{-1}\,\underline{\mathbf{b}}^{(n-1)} \end{cases} \tag{11}$$

Writing,

$$\begin{aligned}\underline{\mathbf{u}}^{(0)} &= \underline{\underline{\boldsymbol{\Phi}}}_L\,\underline{\mathbf{Q}}_L - \underline{\underline{\boldsymbol{\Phi}}}_L^{\star}\,\underline{\mathbf{Q}}_L^{\star} \\ \underline{\mathbf{u}}^{(1)} &= \underline{\underline{\boldsymbol{\Phi}}}_R\,\underline{\mathbf{Q}}_R - \underline{\underline{\boldsymbol{\Phi}}}_R^{\star}\,\underline{\mathbf{Q}}_R^{\star}\end{aligned} \tag{12}$$

Claudet *et al.* proved that the dynamics of the structure is ruled by Eq. (13):

$$\left(\underline{\underline{\tilde{\mathbf{D}}}}_T\,\underline{\underline{\mathbb{C}}}_q - \underline{\underline{\mathbb{C}}}_F\right)\underline{\tilde{\mathbf{q}}} = \underline{\tilde{\mathbf{F}}} \tag{13}$$

Where,

$$\begin{aligned}\underline{\tilde{\mathbf{q}}} &= \begin{bmatrix} \underline{\mathbf{q}}_I \\ \underline{\mathbf{Q}}_L^{\star} \\ \underline{\mathbf{Q}}_R \end{bmatrix},\ \underline{\underline{\mathbb{C}}}_q = \begin{bmatrix} \underline{\underline{\mathbf{I}}} & \underline{\underline{\mathbf{0}}} & \underline{\underline{\mathbf{0}}} \\ \underline{\underline{\mathbf{0}}} & -\underline{\underline{\boldsymbol{\Phi}}}_{L,q}^{\star} & \underline{\underline{\mathbf{0}}} \\ \underline{\underline{\mathbf{0}}} & \underline{\underline{\mathbf{0}}} & \underline{\underline{\boldsymbol{\Phi}}}_{R,q} \end{bmatrix},\ \underline{\underline{\mathbb{C}}}_F = \begin{bmatrix} \underline{\underline{\mathbf{0}}} & \underline{\underline{\mathbf{0}}} & \underline{\underline{\mathbf{0}}} \\ \underline{\underline{\mathbf{0}}} & \underline{\underline{\boldsymbol{\Phi}}}_{L,F}^{\star} & \underline{\underline{\mathbf{0}}} \\ \underline{\underline{\mathbf{0}}} & \underline{\underline{\mathbf{0}}} & \underline{\underline{\boldsymbol{\Phi}}}_{R,F} \end{bmatrix} \\ \underline{\tilde{\mathbf{F}}} &= \begin{bmatrix} \underline{\mathbf{F}}_I \\ -\underline{\underline{\boldsymbol{\Phi}}}_{L,F} \sum_{k=1}^{\infty} \underline{\underline{\boldsymbol{\mu}}}_L^{k-1}\,\underline{\mathbf{Q}}_E^{(-k)} \\ \underline{\mathbf{F}}_{\partial R} + \underline{\underline{\boldsymbol{\Phi}}}_{R,F}^{\star} \sum_{k=1}^{\infty} \underline{\underline{\boldsymbol{\mu}}}_R^{k}\,\underline{\mathbf{Q}}_E^{\star(k)} \end{bmatrix} - \underline{\underline{\tilde{\mathbf{D}}}}_T \begin{bmatrix} \underline{\mathbf{0}} \\ \underline{\underline{\boldsymbol{\Phi}}}_{L,q} \sum_{k=1}^{\infty} \underline{\underline{\boldsymbol{\mu}}}_L^{k-1}\,\underline{\mathbf{Q}}_E^{(-k)} \\ \underline{\underline{\boldsymbol{\Phi}}}_{R,q}^{\star} \sum_{k=1}^{\infty} \underline{\underline{\boldsymbol{\mu}}}_R^{k}\,\underline{\mathbf{Q}}_E^{\star(k)} \end{bmatrix}\end{aligned} \tag{14}$$

In this equation, vector $\underline{\tilde{\mathbf{q}}}$ contains the unknown of the problem. For known loads, the series $\sum_{k=1}^{\infty} \underline{\underline{\boldsymbol{\mu}}}_L^{k-1}\,\underline{\mathbf{Q}}_E^{(-k)}$ and $\sum_{k=1}^{\infty} \underline{\underline{\boldsymbol{\mu}}}_R^{k}\,\underline{\mathbf{Q}}_E^{\star(k)}$ can be computed using Eq. (9).

## 3 Results

In this section, the previous models are applied to the computation of the dynamic responses of ballastless railway tracks containing a single damaged support.

To simplify interpretation and the comparison between the two models, we assumed that the structure is subjected to a single constant load $Q = 100\,\mathrm{kN}$ moving at a constant speed $v$. Due to the support degradation, the neighboring supports tend to be overloaded. The aim of this section is to estimate the overload.

In the presented results, the damage level is represented by a decrease in the support dynamic stiffness. More precisely, the dynamic stiffness of the two elastic stages of the damaged support is multiplied by a coefficient lower than one. This choice is justified by the low stiffness of the elastic stages compared to the other components in the studied track. This choice also eases the comparison between both models.

Five levels of degradation of the damaged support are considered: $0\%$ – healthy track –, $25\%$, $50\%$, $75\%$ et $99\%$ – almost completely broken support. For both methods, the computation is made with a maximal frequency of $300\,\mathrm{Hz}$ and a $1\,\mathrm{Hz}$ frequency step.

In the numerical model, the rail, the reinforced concrete block, the two elastic pads and the underlying concrete slab are finely modeled in three dimensions. The used geometry and mesh are represented in figure 4. The same mesh is used in the three zones. Only the stiffness of each elastic pad is changed in the transition zone.

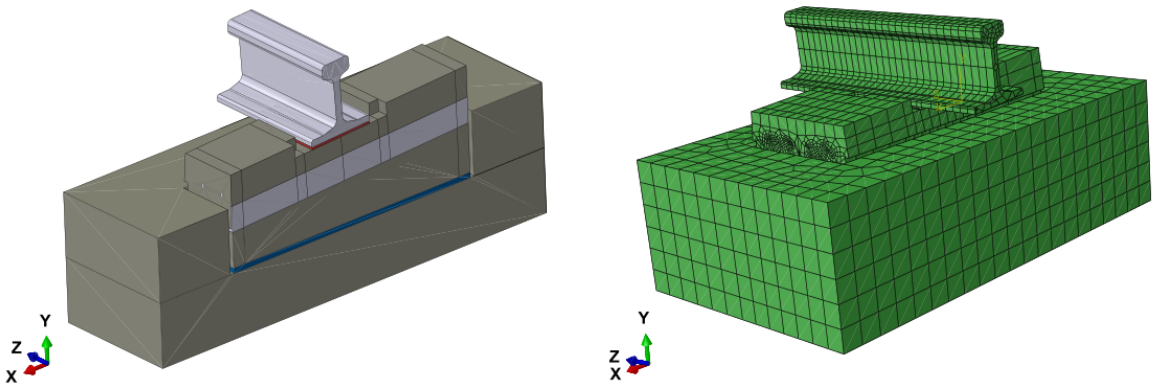


Figure 4: Cross-sectional view of the geometry and mesh of one pattern.

The parameters used to describe the tracks in the analytical and numerical models are given in table 1.

### 3.1 Analytical results

In this computation, the damaged support is numbered support $0$. In Figure 5, the maximal force applied on each support is plotted against the support number for the different damage states of support $0$. As expected, the more the central support is damaged, the more the neighboring supports are loaded. In every case, the overload is mainly distributed to supports $-1$ and $+1$.

Table 2 gives the maximum force applied on supports $-2$ to $2$ and on support $20$ which is supposed to be far enough from the damage to be independent of the damage level. These results are given for the different damage levels of the damaged support. The small asymmetry between supports before and after the damaged one is due to damping in the under-sleeper and under-rail pads.

| Parameter | Value |
|---|---|
| Steel density | $7.8\,\mathrm{kg/dm^3}$ |
| Steel Young modulus | $210\,\mathrm{GPa}$ |
| Rail inertia | $3.038 \times 10^{-5}\,\mathrm{m^4}$ |
| Timoshenko coefficient | $0.4$ |
| Rail section | $7.64 \times 10^{-3}\,\mathrm{m^3}$ |
| Shear modulus | $8.077\,\mathrm{GPa}$ |
| Train speed | $37\,\mathrm{m \cdot s^{-1}}$ |
| Support spacing | $0.6\,\mathrm{m}$ |
| Concrete Young modulus | $50\,\mathrm{GPa}$ |
| Concrete density | $2.4\,\mathrm{kg/dm^3}$ |
| Under-rail pad Young modulus | $20\,\mathrm{MPa}$ |
| Under-rail pad stiffness | $192\,\mathrm{MN \cdot m^{-1}}$ |
| Under-rail pad density | $1\,\mathrm{kg/dm^3}$ |
| Under-rail pad dampening | $1.97\,\mathrm{MN \cdot s \cdot m^{-1}}$ |
| Under-sleeper pad Young modulus | $20\,\mathrm{MPa}$ |
| Under-sleeper pad stiffness | $26.4\,\mathrm{MN \cdot m^{-1}}$ |
| Under-sleeper pad density | $1\,\mathrm{kg/dm^3}$ |
| Under-sleeper pad dampening | $0.17\,\mathrm{MN \cdot s \cdot m^{-1}}$ |

Table 1: Mechanical parameters of the track components.

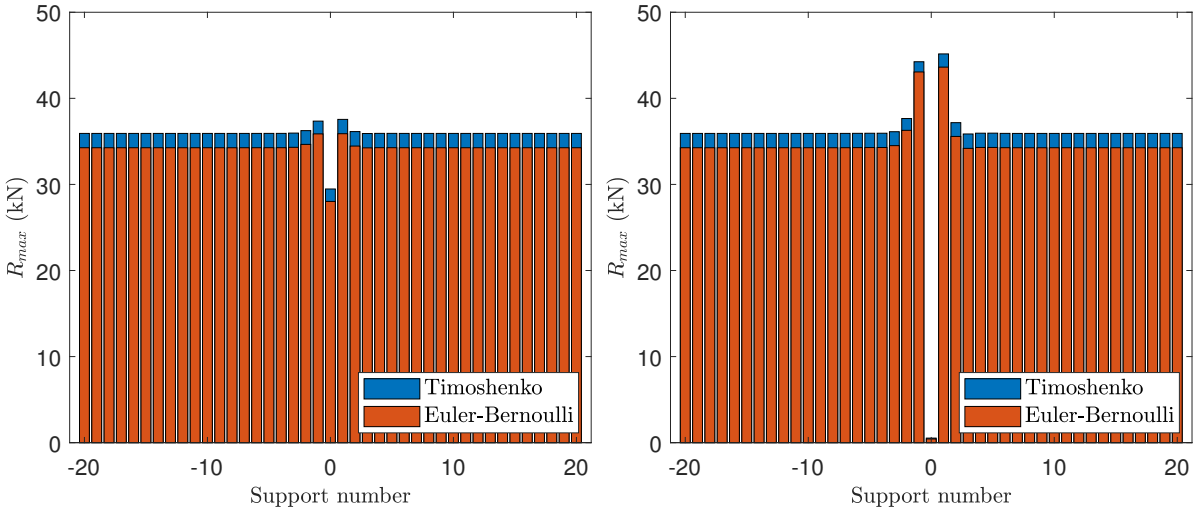


Figure 5: Maximum load applied on each support for a damage level of $0.25$ (left) and $0.99$ (right).

### 3.2 Numerical results

The numerical method developed by Claudet *et al.* [16] gives access to the displacements at every nodes in the mesh. These displacements are numerically derived to compute the strains in each element. Then, using Hooke law, the stress tensor is computed. Finally, this stress is used to compute a failure criterion in every element of the mesh. As the concrete has different strengths in tension $\sigma_t$ and compression $\sigma_c$, the Drucker-Prager yield criterion was chosen. This

| Damage level | Support number | | | | | |
|---|---|---|---|---|---|---|
| | $-2$ | $-1$ | $0$ | $1$ | $2$ | $20$ |
| $0$ | $36.1$ | $36.1$ | $36.1$ | $36.1$ | $36.1$ | $36.1$ |
| $0.25$ | $36.5$ | $37.6$ | $29.7$ | $37.7$ | $36.3$ | $36.1$ |
| $0.50$ | $36.9$ | $39.4$ | $21.8$ | $39.7$ | $36.6$ | $36.1$ |
| $0.75$ | $37.4$ | $41.5$ | $12$ | $42.1$ | $36.9$ | $36.1$ |
| $0.99$ | $37.9$ | $44.5$ | $0.5$ | $45.3$ | $37.2$ | $36.1$ |

Table 2: Maximal loads (kN) applied on each support in function of the damage level.

criterion can be expressed as follows:

$$C = \left(\sqrt{3J_2} - BI_1\right)/A \tag{15}$$

Where $J_2$ and $I_1$ are the usual stress tensor invariants and $A$ and $B$ are defined by:

$$\begin{aligned} A &= 2\frac{\sigma_c\sigma_t}{\sigma_c + \sigma_t} \\ B &= \frac{\sigma_t - \sigma_c}{\sigma_c + \sigma_t} \end{aligned} \tag{16}$$

This failure criterion compares the stress computed in each element to the strenghts of their constitutive material. A value of $1$ means the material will experience plastic yield in one cycle.

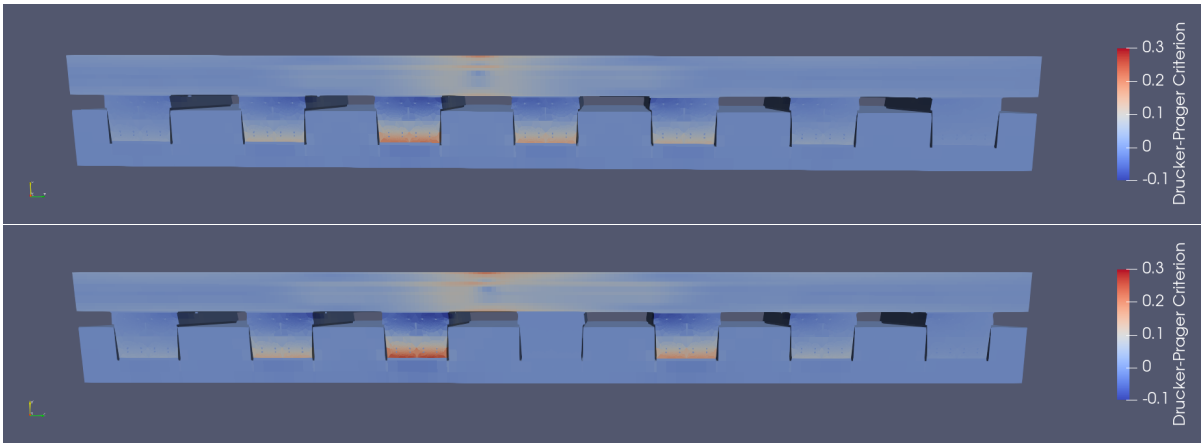


Figure 6: Drucker-Prager failure criterion at $t = 0$ for a damage level of $0.25$ (top) and of $0.99$ (bottom).

Figure 6 gives a cutted view of the computed Drucker-Prager criterion at $t = 0$ for different damage levels of the damaged support. The localization of the maximum of this criterion shows a strong agreement with damages observed in real track supports. As expected, more loaded supports experience a higher Drucker-Prager criterion. This phenomenon can lead to early fatigue damage and, therefore, damages propagation along the track.

As previously, we numbered the different supports with number $0$ corresponding to the damaged support. Table 3 gives the maximum value of the Drucker-Prager criterion in function of the support number and the damage level of the damaged support. Once again, the overload seems to be mainly supported by the two closest supports. This overload grows with the damage level.

| Damage level | Support number | | | | | | |
|---|---|---|---|---|---|---|---|
| | $-3$ | $-2$ | $-1$ | 0 | 1 | 2 | 3 |
| 0 | 0.173 | 0.173 | 0.174 | 0.173 | 0.174 | 0.173 | 0.173 |
| 0.25 | 0.173 | 0.175 | 0.181 | 0.141 | 0.182 | 0.175 | 0.173 |
| 0.5 | 0.173 | 0.177 | 0.191 | 0.103 | 0.192 | 0.177 | 0.173 |
| 0.75 | 0.173 | 0.179 | 0.204 | 0.057 | 0.204 | 0.179 | 0.174 |
| 0.99 | 0.173 | 0.182 | 0.219 | 0.004 | 0.221 | 0.182 | 0.174 |

Table 3: Maximum value of Drucker-Prager criterion in function of support number and damage level.

### 3.3 Comparison of the results given by the two methods

The analytical method allows a rapid computation of the maximal force applied on each support. On the other hand, with a much higher cost, the numerical can give access to the Drucker-Prager failure criterion at components scale. In Figure 7, the maxima of Drucker-Prager failure criterion for each support are plotted in function of the maxima of forces computed with the analytical model. These two values show a strong linear correlation with a regression coefficient $R^2 = 0,998$. This result proves that, in the case a a track containing a single damaged support, the analytical method can be a good method with low cost to assess the stresses in the supports.

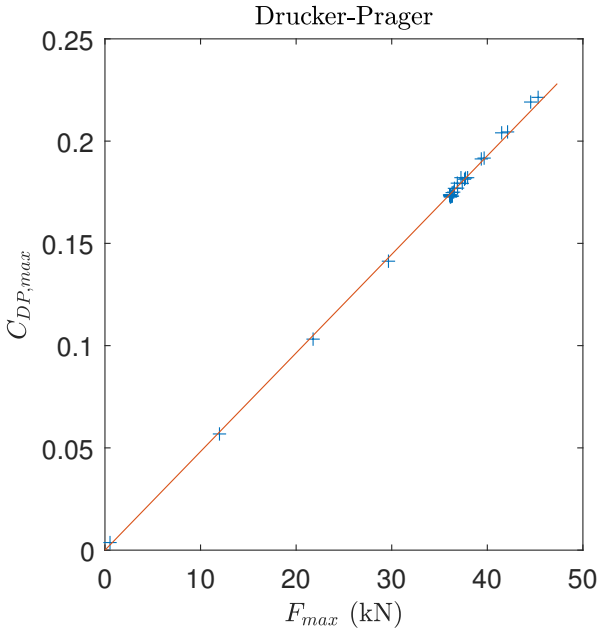


Figure 7: Temporal maximum Drucker-Prager failure criteria computed with the numerical method in function of maximum loads computed with the analytical one. Results and linear regression.

## 4 Conclusion

In this article, we studied the load level of the different supports in a ballastless railway track containing one damaged support. To compute these load levels, two different methods were used. The first one is based on a very simplified representation of the track whose response is computed analytically. Being analytical, this method allows very quick computation of the

track behavior. To access finer results – such as stresses and strains at the component scale – we used a numerical method. With this method, the use of a fine three-dimensional representation of the track implies a much higher numerical cost.

With the numerical method, the Drucker-Prager failure criterion was computed at the component scale with a three-dimensional geometry. The localization of the maxima of this criterion was in strong agreement with the damages observed in real tracks.

In the final section, the analytical results were compared with the numerical ones. We found that the maximum loads per support analytically computed are in strong linear correlation with the maximum Drucker-Prager criterion numerically computed. This correlation demonstrates the analytical method's usefulness in providing a quick assessment of stresses in the different materials of the supports.

## References

[1] P.M. Belotserkovskiy. "On The Oscillation of infinite periodic beams subjected to a moving concentrated force". In: *Journal of Sound and Vibration* 193.3 (June 1996), pp. 705–712. ISSN: 0022-460X. DOI: 10.1006/JSVI.1996.0309. URL: https://www.sciencedirect.com/science/article/pii/S0022460X96903090.

[2] A. Nordborg. "Vertical Rail Vibrations: Parametric Excitation". In: *ACUSTICA· acta acustica* 84 (1998), pp. 289–300. URL: http://www.soundview.de/wp-content/uploads/2015/04/A-Nordborg-Vertical-Rail-Vibrations-Parametric-Excitation.pdf.

[3] T. Hoang et al. "Calculation of force distribution for a periodically supported beam subjected to moving loads". In: *Journal of Sound and Vibration* 388 (Feb. 2017), pp. 327–338. ISSN: 10958568. DOI: 10.1016/j.jsv.2016.10.031. URL: http://dx.doi.org/10.1016/j.jsv.2016.10.031%20https://www.sciencedirect.com/science/article/pii/S0022460X1630565X.

[4] T. Hoang, D. Duhamel, and G. Foret. "Dynamical response of a Timoshenko beams on periodical nonlinear supports subjected to moving forces". In: *Engineering Structures* 176 (Dec. 2018), pp. 673–680. ISSN: 0141-0296. DOI: 10.1016/J.ENGSTRUCT.2018.09.028. URL: https://www.sciencedirect.com/science/article/pii/S014102961832995X.

[5] Elodie Arlaud, S Costa D'aguiar, and E Balmes. "Receptance of railway tracks at low frequency: Numerical and experimental approaches". In: *Transportation Geotechnics* 9 (2016), pp. 1–16. DOI: 10.1016/j.trgeo.2016.06.003. URL: http://dx.doi.org/10.1016/j.trgeo.2016.06.003.

[6] T. Hoang et al. "Wave finite element method for the dynamic analysis of railway tracks". In: *13th World Congress on Computational Mechanics (WCCM XIII) 2nd Pan American Congress on Computational Mechanics (PANACM II)*. New York City, NY, USA, 2018.

[7] Xianying Zhang, David Thompson, and Xiaozhen Sheng. "Differences between Euler-Bernoulli and Timoshenko beam formulations for calculating the effects of moving loads on a periodically supported beam". In: *Journal of Sound and Vibration* 481 (2020), p. 115432. ISSN: 10958568. DOI: 10.1016/j.jsv.2020.115432. URL: https://doi.org/10.1016/j.jsv.2020.115432.

[8] B Claudet et al. "Application of the Wave Finite Element method to the computation of the response of a ballastless railway track, comparison with on-site measurements". In: *Proceedings of The Fifth International Conference on Railway Technology: Research,*

*Development and Maintenance*. Ed. by J. Pombo. Vol. 1. Civil-Comp Press, Edinburgh, UK, 2022. DOI: 10.4203/ccc.1.8.1.

[9] T. Hoang et al. "Computational method for the dynamics of railway tracks on a non-uniform viscoelastic foundation". In: *Procedia Engineering*. Vol. 199. 2017, pp. 354–359. DOI: 10.1016/j.proeng.2017.09.034. URL: www.sciencedirect.comwww.sciencedirect.com.

[10] Le-hung Tran et al. "Calculation of the dynamic responses of a railway track on a non-uniform foundation". In: *Journal of Vibration and Control* May (May 2022), p. 107754632210993. ISSN: 1077-5463. DOI: 10.1177/10775463221099353. URL: http://journals.sagepub.com/doi/10.1177/10775463221099353.

[11] Benjamin Claudet et al. "A comparison of beam models for the dynamics of railway tracks on a non-uniform viscoelastic foundation". In: *ICSV2021*. 2021, pp. 1–8.

[12] Mojtaba Shahraki, Chanaka Warnakulasooriya, and Karl Josef Witt. "Numerical study of transition zone between ballasted and ballastless railway track". In: *Transportation Geotechnics* 3 (2015). ISSN: 22143912. DOI: 10.1016/j.trgeo.2015.05.001. URL: http://dx.doi.org/10.1016/j.trgeo.2015.05.001.

[13] José Nuno Varandas, Paul Hölscher, and M. A.G. Silva. "Three-dimensional track-ballast interaction model for the study of a culvert transition". In: *Soil Dynamics and Earthquake Engineering* (2016). ISSN: 02677261. DOI: 10.1016/j.soildyn.2016.07.013.

[14] T Gras et al. "On a coupling between the Finite Element (FE) and the Wave Finite Element (WFE) method to study the effect of a local heterogeneity within a railway track". In: *Journal of Sound and Vibration* 429 (2018), pp. 45–62. ISSN: 10958568. DOI: 10.1016/j.jsv.2018.05.011. URL: https://doi.org/10.1016/j.jsv.2018.05.011.

[15] André Paixão et al. "Numerical simulations to improve the use of under sleeper pads at transition zones to railway bridges". In: *Engineering Structures* 164 (June 2018), pp. 169–182. ISSN: 0141-0296. DOI: 10.1016/J.ENGSTRUCT.2018.03.005. URL: https://www.sciencedirect.com/science/article/pii/S014102961733078X?via%3Dihub.

[16] Benjamin Claudet et al. "Wave Finite Element Method for Computing the Dynamic Response of Railway Transition Zones". In: *Proceedings of the 7th International Conference on Computational Methods in Structural Dynamics and Earthquake Engineering (COMPDYN 2015)*. Vol. 3. Crete, Greece: Institute of Structural Analysis and Antiseismic Research School of Civil Engineering National Technical University of Athens (NTUA) Greece, 2019, pp. 4538–4547. ISBN: 978-618-82844-5-6. DOI: 10.7712/120119.7247.18688. URL: www.eccomasproceedia.org%20https://www.eccomasproceedia.org/conferences/thematic-conferences/compdyn-2019/7247.

[17] T. Hoang et al. "Wave finite element method for vibration of periodic structures subjected to external loads". In: *6th European Conference on Computational Mechanics (ECCM 6)*. June. 2018, pp. 11–15. URL: http://www.eccm-ecfd2018.org/admin/files/filePaper/p218.pdf.

COMPDYN 2023
9th ECCOMAS Thematic Conference on
Computational Methods in Structural Dynamics and Earthquake Engineering
M. Papadrakakis, M. Fragiadakis (eds.)
Athens, Greece, 12-14 June 2023

# TEST OF AN IDEA FOR SETTING THE NONLINEARITY TOLERANCE IN NONLINEAR RESPONSE HISTORY ANALYSES ACCORDING TO PROCEDURES ORIGINATED IN THE SEISMIC CODE OF NEW ZEALAND NZS 1170.5:2004

**Aram Soroushian**

[1] International Institute of Earthquake Engineering and Seismology (IIEES)
No. 21, West Arghavan St., North Dibajee St., S. Lavasani St., Tehran 19537, Iran
e-mail: a.soroushian@iiees.ac.ir

## Abstract

*Nonlinear response history analysis using an integration scheme and an iterative nonlinear solution method is a versatile tool for analyzing structural systems subjected to earthquakes. Nevertheless, the resulting responses are inexact and the analyses are generally complicated and computationally expensive. In a recent study, a slight change is applied to the continuation/end of the nonlinear solutions' iterations and the probable stop of the analysis. As a result, the simplicity and efficiency of the analysis according to the seismic code of New Zealand NZS 1170.5:2004 is enhanced, without negative effects on the response accuracy. In this paper, in order to simplify the analysis further, and under the assumption of piecewise linear behavior, three simple suggestions for setting the nonlinearity tolerance are tested. Consequently, when the response history analysis is based on repetition of time integration analysis, as it is in the seismic code of New Zealand, NZS 1170.5:2004, the nonlinearity tolerance can be simply set and reduced with each new repetition. Such selections not only simplify the analysis by eliminating the concerns on the nonlinearity tolerance, but also may reduce the computational effort. The reduction in computational effort may be considerable specifically when the behavior is highly nonlinear. The added simplicity can increase the interest in using response history analysis in earthquake engineering practice, as well.*

**Keywords:** Seismic Nonlinear Response History Analysis, Nonlinearity Tolerance, Seismic Code of New Zealand NZS 1170.5:2004, Response Accuracy, Analysis Simplicity, Analysis efficiency.

## 1 INTRODUCTION

Nonlinear response history analysis is one of the most versatile analysis tools for studying the behaviors of structural systems, irreplaceable in many real analyses [1, 2]. The computed responses are however approximations and the analysis is generally time-consuming [2-4]. The probability of stop of analysis because of failure of nonlinear solutions iteration exists, as well [5-7]. In addition, for computing the response, nonlinear response history analysis generally uses a time integration method combined with an iterative nonlinear solution method [2]; accordingly, various analysis parameters should be set prior to the analysis. Considering these, there is little interest in using nonlinear response history analysis in the earthquake engineering practice especially in regions where advanced computational facilities are hardly available. Many researchers have reported studies on the above-mentioned problems, e.g. see [2, 8-15], and also on the efforts to reduce these problems, e.g. see [15-25]. Unresolved problems still exist, e.g. see [2, 7, 26, 27]. One of these problems, in view of an established legalized analysis procedure introduced in the seismic code of New Zealand, NZS 1170.5:2004 [28, 29], is the selections of the integration method, the iterative nonlinear solution method, and the nonlinearity tolerance. The concentration here is on the nonlinearity tolerance.

Analysis of structures' seismic nonlinear dynamic behaviors typically starts with discretizating the mathematical models in space and defining the behavior in the framework of the solution of the resulting ordinary initial value problem, stated below (see [2]):

$$\mathbf{M}\,\ddot{\mathbf{u}}(t)+\mathbf{f}_{\text{int}}(t)=-\mathbf{M}\Gamma\ddot{u}_g(t) \qquad 0\le t\le t_{\text{end}}$$

$$\text{Initial Conditions}: \quad \left|\begin{array}{l}\mathbf{u}(t=0)=\mathbf{u}_0\\ \dot{\mathbf{u}}(t=0)=\dot{\mathbf{u}}_0\\ \mathbf{f}_{\text{int}}(t=0)=\mathbf{f}_{\text{int}_0}\end{array}\right. \quad . \tag{1}$$

$$\text{Additional Constraints}: \ \mathbf{Q}$$

In Eq. (1), which is in some cases directly available under assumptions, like shear frame behavior [30-32], $t$ and $t_{\text{end}}$ imply the time and the analysis time interval; $\mathbf{M}$ is the mass matrix; $\mathbf{f}_{\text{int}}$ is the vector of the internal force, because of the elastic forces and damping (in linear problems, generally $\mathbf{f}_{\text{int}}=\mathbf{K}\mathbf{u}+\mathbf{C}\dot{\mathbf{u}}$, where $\mathbf{K}$ and $\mathbf{C}$ stand for the matrices of stiffness and viscous damping, respectively); $\ddot{u}_g(t)$ implies the single-component ground acceleration, and $\Gamma$ is a vector with the size of the degrees of freedom, needed for matrix multiplication and considering spatial changes of $\ddot{u}_g(t)$; $\mathbf{u}(t)$, $\dot{\mathbf{u}}(t)$, and $\ddot{\mathbf{u}}(t)$, denote the vectors of displacement, velocity, and acceleration, relative to the ground; $\mathbf{u}_0$, $\dot{\mathbf{u}}_0$, and $\mathbf{f}_{\text{int}_0}$, define the initial status, and $\mathbf{Q}$ implies the limiting conditions due to nonlinearity. (When the ground motion is multi-component, $\Gamma$ and $\ddot{u}_g(t)$ will change to a matrix and a vector, respectively.) The typical approach for analysis of Eq. (1) is to use a time integration method and a method for nonlinear solution; see Fig. 1. Accordingly, the integration method, the nonlinear solution method, and the related parameters, e.g. the nonlinearity tolerance should be set in advance. Focusing on nonlinearity tolerance, $10^{-4}$ is a conventional value for the tolerance to control the errors occurring in modeling the nonlinearities; see [2, 33]. Meanwhile, although it is conventional to use a single value for the tolerance, the tolerance can change for the nonlinearities at different parts of the structural system and at different time instants. Even more, for the analyses that are based on repetition of time integration (recommended in the literature, [30, 34], and legalized in the seismic code of New Zealand NZS 1170.5:2004 [28, 29]), the

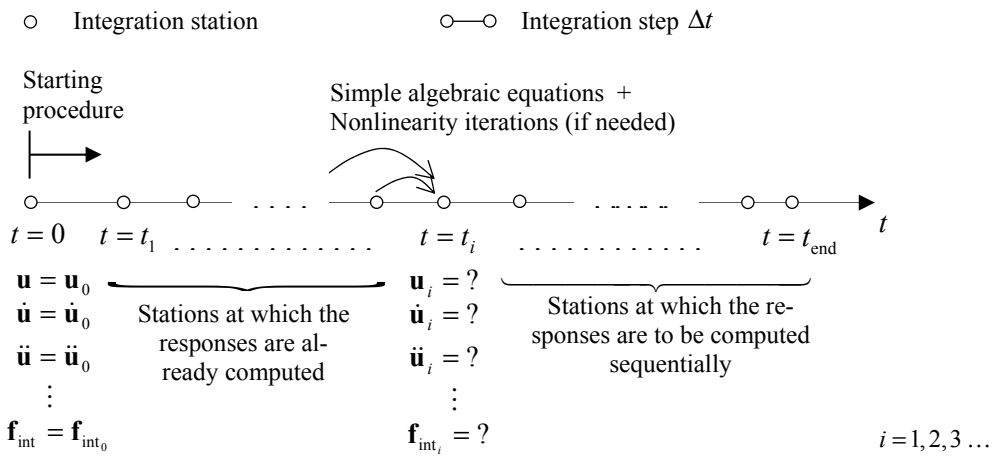


Figure 1: Brief description of the process of time history analysis using a time integration method [2].

tolerance can change with each repetition of the time integration. Theories and suggestions exist for reduction of the nonlinearity tolerance with each new time integration analysis, e.g. see [35, 36]. Since the procedure in the seismic code of New Zealand, NZS 1170.5:2004 [28, 29], is the only legalized procedure for seismic nonlinear response history analysis [7, 37], it is reasonable to consider this procedure as a basis for studying the analysis performance. Accordingly, attention is paid to sequential time integration analyses. Furthermore, the theories defining changes of the tolerance in sequential time integration analyses are based on the most important necessity of numerical computations, i.e. convergence of the approximate response to the exact response [38, 39]. Considering these issues, it is reasonable to pay attention to the convergence-based theories in changing the tolerance from an analysis to the next analysis, while, for the sake of simplicity, keep the tolerance constant throughout the structure and total time interval.

Returning to the analysis procedure, a slight change is recently proposed [7, 40, 41] in the analysis procedure of NZS 1170.5:2004 [28, 29]. The change is very effective in the analysis simplicity and efficiency [7], and hence is in complete consistence with the objectives of this paper, stated in the first paragraph. Accordingly, the procedure introduced in [7, 41] will be the analysis procedure to which the suggestions in this paper will be applied. For the change of the nonlinearity tolerance, though the suggestion based on responses convergence [35, 36] is considerably effective [42-45], it is hardly practical in view of its complexity and dependence to some new parameters. In this paper, three simplifications of this suggestion is introduced for the analysis of structural systems with piecewise linear behavior (a conventional nonlinearity in earthquake engineering [30, 31, 46]) and their performances are tested in seismic analysis of a structural system considering different earthquake records and different severities of nonlinear behavior. In continuation, after reviewing the main concepts on nonlinear time integration analysis, the existing suggestion on reducing the nonlinearity tolerance [35, 36] is explained. The new simplified suggestions are stated discussed and tested numerically, and after brief discussions, the paper is concluded with a set of the conclusions.

## 2 THEORY

### 2.1 The main Concepts

Regardless of the static or dynamic behavior of structural systems, and even in applications different from structural and earthquake engineering, a broadly accepted relation governing the iterations of nonlinear solutions is as follows; see [5, 6, 25, 26, 35, 47-50]:

$$\begin{aligned} &\|\delta_k\| > \bar{\delta} \text{ and } k < \bar{k}: \text{ Continue the iterations} \\ &\|\delta_k\| \le \bar{\delta} \text{ and } k \le \bar{k}: \text{ Stop the iterations and continue the analysis} \\ &\|\delta_k\| > \bar{\delta} \text{ and } k = \bar{k}: \text{ Stop the iterations and stop the analysis} \\ &k = 1,2,3,\ldots k' \quad , \quad k' \le \bar{k} \quad , \quad \bar{k} < \infty \end{aligned} \qquad (2)$$

In Eq. (2), $\|\delta_k\|$ denotes the inaccuracy in modeling the nonlinearity after the $k$ th iteration of the nonlinear solution, $\bar{\delta}$ implies the tolerance (maximum acceptable inaccuracy in modeling the nonlinearity), and $\bar{k}$ is the maximum acceptable number of the iterations representing the available computational facility. The definition of $\|\delta_k\|$ and $\bar{\delta}$ can be in terms of displacement, force, energy, etc., and there are many methods for iterative nonlinear solution; see [6, 25, 47-56]. It is also notable that the case $k = \bar{k}$ may be unavailable due to the divergence of the response and very large values of the response, e.g. when using the Newton Raphson at values of the dynamics stiffness close to zero (see [30, 31, 51]), at which case the analysis is automatically stopped. This case is rarely probable in dynamic problems due to the difference between static and dynamic stiffness in time integration analyses (see [30, 31]), and when using iterative methods like modified Newton Raphson [51] and fractional time stepping [56, 57].

Recently, the following simple change is proposed in the above formulation [7, 40, 41, 58]:

$$\begin{aligned} &\|\delta_k\| > \bar{\delta} \text{ and } k < \bar{k}: \text{ Continue the iterations} \\ &\|\delta_k\| \le \bar{\delta} \quad \text{or } k = \bar{k}: \text{ Stop the iterations and continue the analysis} \\ &k = 1,2,3,\ldots k' \quad , \quad k' \le \bar{k} \quad , \quad \bar{k} < \infty \end{aligned} \qquad (3)$$

Application of this change in the analysis procedure of NZS 1170.5:2004 results in a procedure for nonlinear response history analysis that is simpler and more efficient compared to using Eq. (2) in the procedure of NZS 1170.5:2004 [28, 29]. The brief reason is the no stop of analysis when the iterations of nonlinear solution fails, which can cause less time integration analyses and more analysis efficiency; see also [7]. The resulting procedure is considered as the analysis procedure in this paper, and the nonlinearity tolerances are to be set for use in this procedure.

In view of the definition of piecewise linear systems [36], the nonlinear behaviors of structural systems in earthquake engineering are mostly of the piecewise linear type; see [28, 29, 46]. Besides, the details of the existing suggestion on changes of nonlinearity tolerance in sequential time integration analyses consider nonlinear behaviors of piecewise linear type [35, 36]. Considering these, in this paper, the nonlinear behaviors are of the piecewise linear type, and for simplicity fractional time stepping [56, 57] is used for nonlinear solution.

### 2.2 The existing suggestion on changes of nonlinearity tolerance

The suggestion for the nonlinearity tolerance in sequential analyses [35, 36] is set such that the response obtained from the time integration analysis converges properly [2, 59] with respect to the integration step (see Fig. 2, where $E$ and $\Delta t$ represent the response error [60] and the integration step [2-4], respectively). The main relation is as follows:

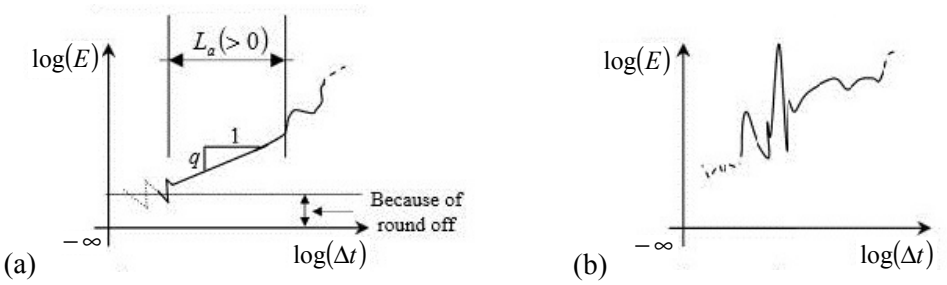


Figure 2: Typical changes of computational errors with respect to the integration step: (a) proper convergence, improper convergence [59].

$$ {}_{l+1}\bar{\delta}_{\Omega_p} = \left[ \underset{j=1,2,\ldots {}_lJ_p}{\text{Min}} \left( {}_l\delta_j \right) \right] \left( \frac{{}_{l+1}\Delta t}{{}_l\Delta t} \right)^q \quad , \quad {}_l\delta_j \text{ occurs in } \Omega_p \quad p=1,2,\ldots P \quad , \quad l=1,2,\ldots \tag{4} $$

where, $q$ denotes the rate of convergence with respect to the integration step in absence of nonlinearity (generally equal to the integration method's order of accuracy and equal to two [3, 4, 61, 62]), $l$ is an indicator for the sequence of time integration analysis, ${}_l\Delta t$ stands for the integration step of the $l$ th time integration analysis, $\Omega_P$ implies the total space of probable nonlinearity, briefly defined in Fig. 3, $p$ is an indicator for the subspace of probable nonlinearity under consideration (see Fig. 3), ${}_i\delta_j$ represents the final $\|\delta_k\|$ in Eqs. (2) or (3) at the $j$ th nonlinearity detected in the $l$ th time integration analysis in $\Omega_p$, ${}_l\bar{\delta}_{\Omega_p}$ denotes the nonlinearity tolerance to be used in $\Omega_p$ in the $l$ th time integration analysis, and ${}_lJ_p$ stands for the number of nonlinearities detected in $\Omega_p$ in the $l$ th time integration analysis. Evidently, Eq. (4) increases the complicatedness of nonlinear response history analysis; specifically, the initial study needed to determine $\Omega_P$ and to select the subspaces $\Omega_p$, and the computation of Eq. (4) itself are notable. Therefore, Eq. (4) can hardly be acceptable in the practice of nonlinear response history analysis. Simplification of Eq. (4) is studied in the next section.

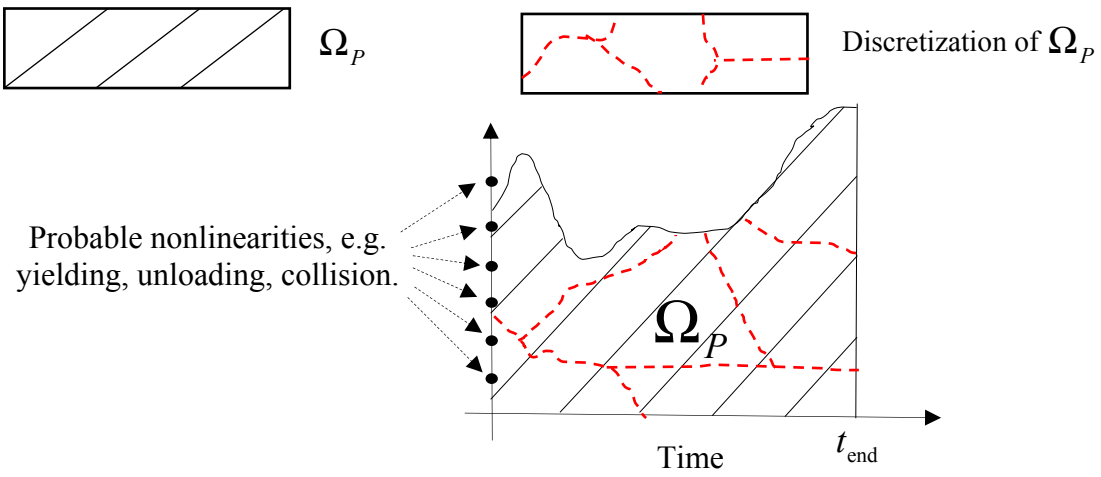


Figure 3: Typical space of probable nonlinearity in response history analysis of piecewise linear systems and the typical discretization.

### 2.3 Three new suggestions for the nonlinearity tolerances

From Eqs. (2)-(4), we can deduce that nonlinearity tolerance is to decrease when repeating the time integration analysis with smaller steps, i.e. when $l$ in Eq. (4) increases. Besides, generally and as recommended in [4, 61],

$$q = 2 \tag{5}$$

and as stated in [28, 29]:

$$\frac{{}_{l+1}\Delta t}{{}_{l}\Delta t} = 0.5 \tag{6}$$

and finally the discretization of $\Omega_P$ is arbitrary, and we can select:

$$P = 1 \tag{7}$$

Considering these, we can simplify Eq. (4) to

$${}_{l+1}\bar{\delta} = \frac{1}{4}\left[\underset{j=1,2,\ldots {}_{l}J}{\text{Min}}\left({}_{l}\delta_j\right)\right] \quad , \quad {}_{l}\delta_j \text{ occurs in } \Omega_P \qquad l = 1,2,\ldots \tag{8}$$

and practically eliminate the need to determine $\Omega_P$, by using the following equation instead of Eq. (8):

$${}_{l+1}\bar{\delta} = \frac{1}{4}\left[\underset{j=1,2,\ldots {}_{l}J}{\text{Min}}\left({}_{l}\delta_j\right)\right] \quad , \quad l = 1,2,\ldots \tag{9}$$

In simplification of Eq. (9), attention is paid to:

1. In view of Eqs. (2) and (3), it is reasonable to expect that in most of the nonlinearity detections:

$${}_{l}\delta_j \cong \leq {}_{l}\bar{\delta} \tag{10}$$

2. In view of the theory leading to Eq. (4) (see [35, 36]), the minimization in Eq. (4) causes the resulting tolerances to be conservative from the viewpoint of the responses proper convergence.
3. The selection in Eq. (7) highlights the previous point and makes the resulting tolerance even more conservative.
4. According to the nature of sequential time integration analyses, the number of the analyses is two or more, and hence in view of the conventional value of the tolerance, i.e. 1.0E-4 [33], it is reasonable to consider the nonlinearity tolerance of the second analysis around the conventional tolerance.
5. Both as conventional in practice and academia and tolerable by structural analysts the maximum number of sequential analyses would rather be not more than around six.
6. In view of hardware capabilities and round off errors, it sounds reasonable to consider lower bounds for the nonlinearity tolerance around 1.0E-12.
7. In view of Eqs. (2), (3) and (8), the reduction of nonlinearity tolerance from a time integration analysis to its next analysis should be more than four times. With this in mind, for simplicity, the nonlinearity tolerance in a time integration analysis will be obtained by dividing the tolerance in the previous analysis by a power of ten.

Considering Eq. (9) and the above points, three suggestions are stated in Table 1. The next section is dedicated to testing the performance of analyses using these three suggestions in comparison to the procedure introduced in [7, 41].

| Analysis Sequence | Suggestion 1 | Suggestion 2 | Suggestion 3 |
|---|---|---|---|
| 1 | 1.0E-1 | 1.0E-2 | 1.0E-1 |
| 2 | 1.0E-3 | 1.0E-4 | 1.0E-4 |
| 3 | 1.0E-5 | 1.0E-6 | 1.0E-7 |
| 4 | 1.0E-7 | 1.0E-8 | 1.0E-10 |
| 5 | 1.0E-9 | 1.0E-10 | 1.0E-13 |
| 6 | 1.0E-11 | 1.0E-12 | 1.0E-13 |
| 7 and more | 1.0E-13 | 1.0E-12 | 1.0E-13 |

Table 1: Suggestions for nonlinearity tolerance in sequential nonlinear time integration analyses.

## 3 NUMERICAL INVESTIGATION

### 3.1 Preliminary notes

Since this is a first test on the suggested nonlinearity tolerances (see Table 1), in order to better understand and interpret the changes, in this section, one structural system with piecewise linear behavior is taken into account. Two different earthquake records are considered as the excitations in two separate studies (see Fig. 4; where, $_f\Delta t$ is the step of digitization), and three severities of nonlinear behavior [7, 63-65] are considered in three separate studies, by applying the following three scales to the two excitations:

$$S = 1, 2, 5 \tag{11}$$

Therefore, totally six tests are carried out for each of the suggestions in Table 1. Using either of the suggestions in Table 1 eliminates the selection of appropriate values to be assigned to the nonlinearity tolerance. Meanwhile, similar to the analysis procedure in NZS 1170.5:2004 [28, 29], the analysis procedure proposed in [7, 41] is equipped with some control on the accuracy of the target response in the last steps of the analysis procedures. Therefore, the main purpose of the above-mentioned tests is to study the computational effort needed to implement the suggestions in Table 1 in the procedure introduced in [7, 41]. In view of the fact that the procedure in [7, 41] is consisted of sequential time integration computations, using or not using the suggestion in Table 1 does not affect the computer in-core memory, and the study of computational effort can be based on the analysis run-time.

With regard to the integration methods, in view of the suggestions existing for nonlinear analysis [5], the Newmark's average acceleration method [66] is used for all of the analyses. For the nonlinearity solution, in view of the system's piecewise linear behavior, and for the sake of simplicity, the selection is to use the fractional time stepping method with the conventional value for maximum number of iteration, i.e. $\bar{k} = 5$ [56, 57]. Based on this selection, the analysis run-time can be simple studied in view of the total number of integration steps; see [2].

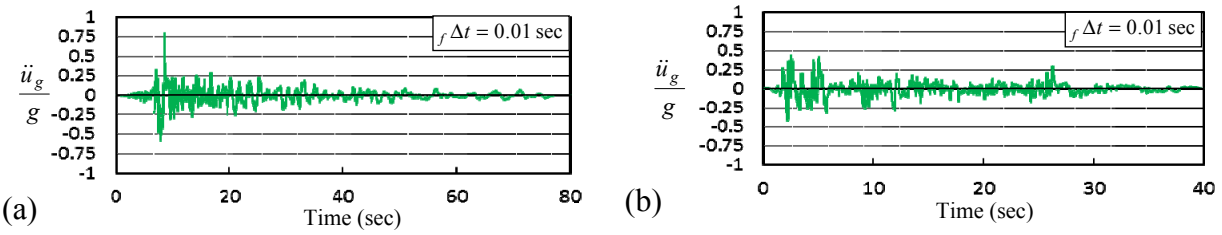


Figure 4: The two earthquake records under consideration in the numerical investigation.

### 3.2 The example

Taken from [7], the structural system is a preliminary model of a tall building; see Fig. 5 and Table 2. The target response is the top displacement, for which the exact responses are reported in Fig. 6, in correspondence to the six models defined by Fig. 4, and Eq. (11) (Num stands for the total number of stiffness change representing the severity of nonlinear behavior).

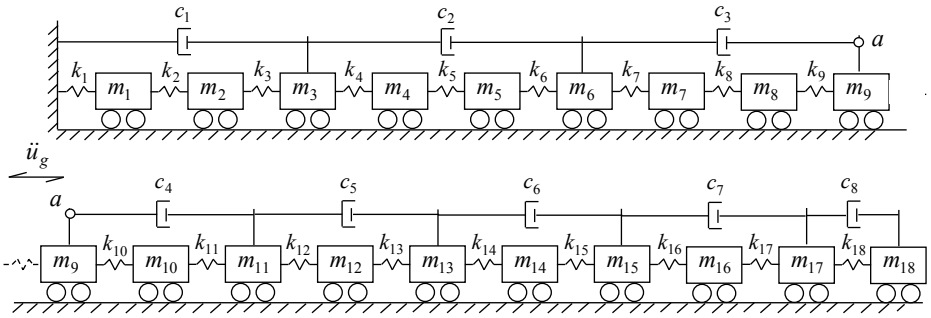


Figure 5: The structural model in the numerical investigation [7].

| Property | $i$ | | | | | | | | | | | | | | | | | |
|---|---|---|---|---|---|---|---|---|---|---|---|---|---|---|---|---|---|---|
| | 1 | 2 | 3 | 4 | 5 | 6 | 7 | 8 | 9 | 10 | 11 | 12 | 13 | 14 | 15 | 16 | 17 | 18 |
| $10^{-9}\times m_i$ (Kg) | 3 | 3 | 3 | 3 | 3 | 3 | 3 | 3 | 1.5 | 1.5 | 1.5 | 1.5 | 1.5 | 1.5 | 0.5 | 0.5 | 0.5 | 0.5 |
| $10^{-12}\times k_i$ (N/m) | 2 | 2 | 2 | 2 | 1.2 | 1.2 | 1.2 | 1.2 | 0.6 | 0.6 | 0.6 | 0.6 | 0.6 | 0.6 | 0.1 | 0.1 | 0.1 | 0.1 |
| $10^{-8}\times c_i$ (N sec/m) | 12 | 8 | 6 | 2.5 | 2.5 | 1.5 | 0.5 | 0.2 | | | | | | | | | | |
| $10^{2}\times u_{y_i}$ (m) | 8 | 8 | 8 | 8 | 8 | 8 | 5 | 5 | 5 | 5 | 5 | 5 | 5 | 5 | 3 | 3 | 3 | 3 |

Table 2: Main properties of the structural model in Fig. 5 [7, 32].

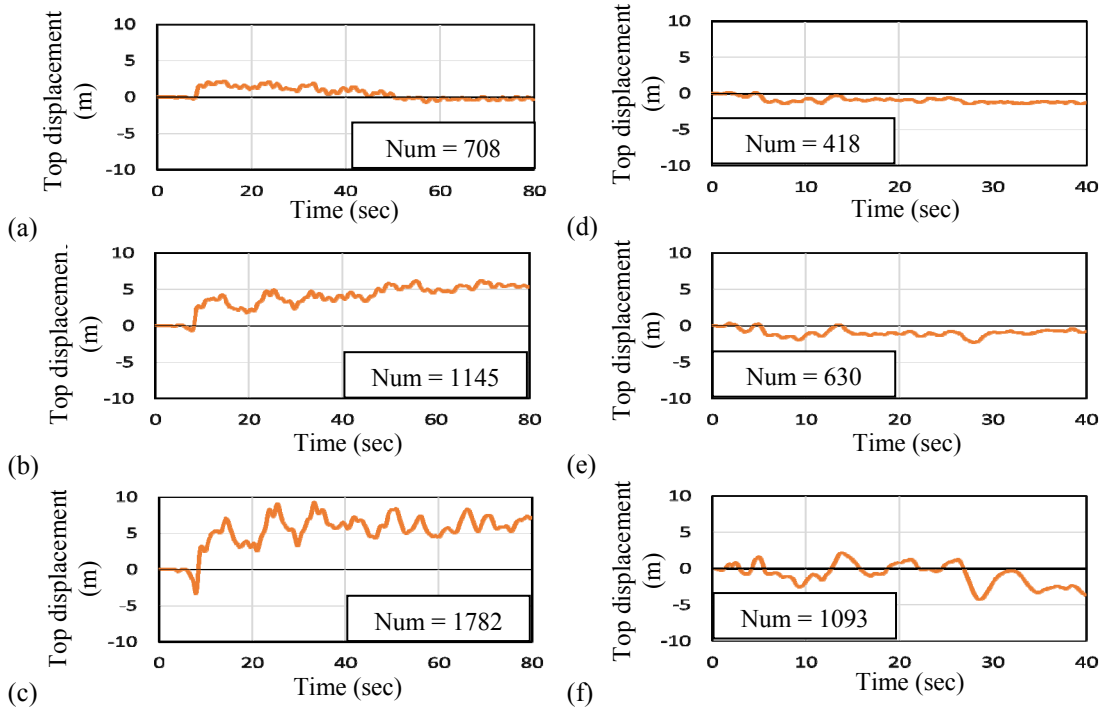


Figure 6: Exact top displacements for the structural system introduced in Figs. 4 and 5, Table 2, and Eq. (11), when the excitation is represented with: (a) Fig. 4(a), (b) Fig. 4(a) scaled by $S = 2$, (c) Fig. 4(a) scaled by $S = 5$, (d) Fig. 4(b), (e) Fig. 4(b) scaled by $S = 2$, (f) Fig. 4(b) scaled by $S = 5$.

In view of the three suggestions in Table 1, for arriving at approximations of the target responses displayed in Fig. 6, the procedure introduced in [7, 41] is carried out 18 times; all starting with time integration analyses with steps equal to 0.01 sec (according to the analysis procedure). The approximations are achieved in the price of the total number of steps and total number of time integration analyses reported in Tables 3-8. As expected, with more severe nonlinear behavior the computational effort is more. However the interesting point is that the differences between the computational efforts corresponding to the three suggestions decrease when the severity of nonlinear behavior increases. To have a better study on the computational efforts, the analyses are carried out without implementing the suggestions in Table 1 several times (with constant nonlinearity tolerances equal to 1.E-2, 1.E-4, and 1.E-6). The average total number of integration steps and the average total number of analyses are reported in Table 9. In view of Table 9, the suggestions in Table 1 not only simplify the nonlinear response

| Feature | Suggestion 1 | Suggestion 2 | Suggestion 3 |
|---|---|---|---|
| Number of Analyses | 3 | 3 | 3 |
| Number of steps | 68851 | 76032 | 76726 |

Table 3: Total numbers of the analyses and integration steps when using the suggestions in Table 1, for Fig. 6(a).

| Feature | Suggestion 1 | Suggestion 2 | Suggestion 3 |
|---|---|---|---|
| Number of Analyses | 4 | 3 | 3 |
| Number of steps | 161176 | 88243 | 90106 |

Table 4: Total numbers of the analyses and integration steps when using the suggestions in Table 1, for Fig. 6(b).

| Feature | Suggestion 1 | Suggestion 2 | Suggestion 3 |
|---|---|---|---|
| Number of Analyses | 5 | 5 | 5 |
| Number of steps | 337808 | 365998 | 380398 |

Table 5: Total numbers of the analyses and integration steps when using the suggestions in Table 1, for Fig. 6(c).

| Feature | Suggestion 1 | Suggestion 2 | Suggestion 3 |
|---|---|---|---|
| Number of Analyses | 3 | 3 | 3 |
| Number of steps | 35519 | 39859 | 40207 |

Table 6: Total numbers of the analyses and integration steps when using the suggestions in Table 1, for Fig. 6(d).

| Feature | Suggestion 1 | Suggestion 2 | Suggestion 3 |
|---|---|---|---|
| Number of Analyses | 3 | 3 | 3 |
| Number of steps | 39597 | 45945 | 47148 |

Table 7: Total numbers of the analyses and integration steps when using the suggestions in Table 1, for Fig. 6(e).

| Feature | Suggestion 1 | Suggestion 2 | Suggestion 3 |
|---|---|---|---|
| Number of Analyses | 3 | 3 | 3 |
| Number of steps | 47930 | 59728 | 60576 |

Table 8: Total numbers of the analyses and integration steps when using the suggestions in Table 1, for Fig. 6(f).

| Feature | Table 3 | Table 4 | Table 5 | Table 6 | Table 7 | Table 8 |
|---|---|---|---|---|---|---|
| Number of analyses | 2.3333 | 3 | 6 | 2.3333 | 3.3333 | 4 |
| Number of steps | 49168.3 | 90964 | 5604098 | 25236.67 | 57624.67 | 370546.33 |

Table 9: Average numbers of the analyses and integration steps when not using the suggestions in Table 1.

history analysis but also may reduce the computational effort especially when the nonlinearity is more severe. And more that: (1) the three suggestions seem not very different in analysis efficiency especially when the severity of nonlinear behavior is more, (2) the enhancement in analysis efficiency may be considerable; in view of Table 9, see the 94% and 87% reduction in computational effort for Suggestion 1 in Tables 5 and 8, respectively. Though, the number of the tests is small, the resulting analysis simplicity, with no negative effect on accuracy in the sense of the analysis procedure [7, 28, 29, 41], and besides the observed effects on the efficiency, explains much further study on suggestions like those presented in Table 1. The next section briefly presents an effort to explain the observed effects on analysis efficiency.

### 3.3 Brief explanation of the observed analysis efficiency

In view of the analysis procedure stated in [7, 41], the minimum number of time integration analyses is two (essential for the error control in the end of the procedure). Besides, in view of the discussions presented in [35, 36] and as reasonable, the changes of the computational errors of nonlinear analyses when using/not using the suggestions in Table 1 is as typically displayed in Fig. 7. As an evident result, when using similar integration steps and close nonlinearity tolerances in the first time integration analyses of the procedure introduced in [7, 41], without and with applying the reductions proposed in Table 1, the total number of time integration analyses is equal or more when not using the suggestions in Table 1 (this is also observed in the studied example and details of Table 9, not reported for the sake of brevity). Considering this along with the fact that in analysis of piecewise linear systems the contribution of nonlinearity solutions in the computational effort reduces when using smaller integration steps (see [2]), the higher number of time integration analyses when not using the suggestions in Table 1 implies the more computational effort when not applying the suggestions compared to when applying the suggestions. The case when the total numbers of time integration analyses are equal in applying/not applying the suggestions mostly occurs when the total number of the analyses is small, i.e. two, three, or four, the nonlinearity tolerances of the first analysis in applying/not applying the suggestions are not equal, and the two graphs in Fig. 7 are not completely separated. As implied in Tables 3-8, this happens when the severity of nonlinear behavior is low. It is interesting that in these cases the computational effort is generally low and the additional efforts because of the suggestions in Table 1 worth the achieved simplicity. In cases with more severity of nonlinear behavior however the computational efforts are high and the suggestions in Table 1 reduce these high computational effort during a simple analysis, as desired.

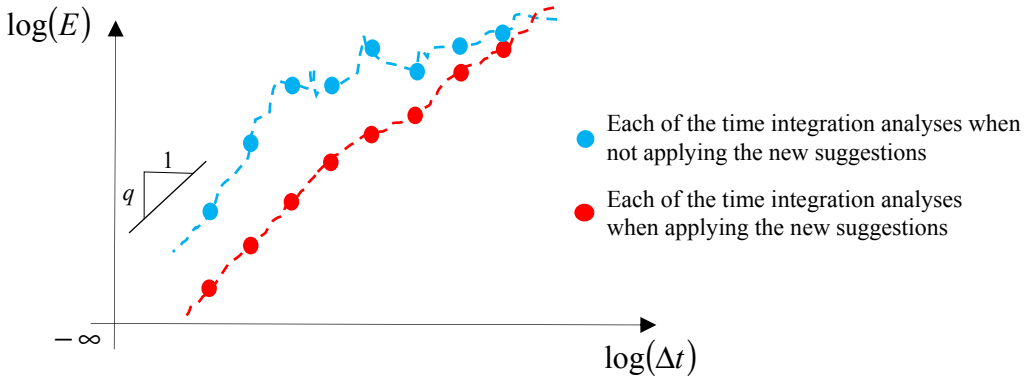


Figure 7: Typical trend of computational errors in the analyses according to the procedure introduced in [7, 41].

## 4 DISCUSSION

The observation and explanation presented in the previous sections, implies considerable simplification in seismic nonlinear response history analysis of piecewise linear systems, along with the possibility of more analysis efficiency when the severity of nonlinear behavior is considerable. Much further study is essential before counting on these statements. However, the simplicity and the considerable probable reduction in the computational effort can explain the further study. Even more, the following observations:

1. Elimination of the concern on nonlinearity tolerance is a considerable simplification of nonlinear response history analysis.
2. The simplicity and analysis efficiency because of implementation of the suggestions in Table 1 depend on the selected suggestion, only slightly (the first suggestion seems slightly better). The dependence is less when the severity of nonlinear behavior is more.
3. The enhancement in analysis efficiency is more when the severity of nonlinear behavior is more.

can simply cause considerable increase in the structural analysts' interest in nonlinear response history analysis. This can be true, especially when large and fast computer systems are not simply available and reducing the analysis effort is attractive, e.g. in less developed countries with low income and large structural projects. The secondary consequence can be better seismic structural analysis and safer buildings and infrastructures. Consequently, more effort to establish some idea about the nonlinearity tolerances in nonlinear response history analysis of piecewise linear systems is reasonably essential, both from a pure academic point of view, as well as considering the practical aspects. Some of the issues that should be included in an extended study are:

1. Many examples should be studied.
2. The sizes of the examples from the point of view of the numbers of degrees of freedom would rather be completely different.
3. The effect of the computational facility (the $\bar{k}$ in Eqs. (2) and (3)) should be studied.
4. The effect of the integration method, and specifically the numerical damping, would rather be studied.
5. Considering the important role of pounding in seismic damages [67-69], different types of nonlinearities should also be studied.
6. More detailed attention would rather be paid to the concept of severity of nonlinear behavior.

## 5 CONCLUSUION

In order to simplify the procedure of seismic nonlinear response history analysis, according to a recent procedure [7, 41] (slightly different from that in [28, 29]), three suggestions on nonlinearity tolerance are tested in analysis of six piecewise linear structural cases. The observations are briefly explained, as well.

Because of the simplicity of the rules suggested for selection of the nonlinearity tolerance (see Table 1), the simplification of the analysis is evident. Besides, it is observed that:

1. There is no specific difference between the analyses considering the three suggestions. It is only needed to take into account the seven points addressed in Section 2.3. Still, the performance of the first suggestion (see Table 1), i.e.

$$_{l}\bar{\delta} = \begin{cases} 10^{-(2l+1)} & l \le 6 \\ 10^{-13} & l > 6 \end{cases} \tag{12}$$

was in overall slightly better ($l$ is the number of sequential time integration analysis).

2. The reduction in computation effort because of the suggestions in Table 1 appears when the nonlinear behavior is sufficiently severe.
3. The amount of the reductions in computational effort can be considerable, e.g. 94% (see Section 3.2)

Because of the significance of the observations and the probable influence of the enhancements in analysis simplicity and efficiency on practical seismic response history analysis, further studies specifically on issues discussed in Section 4 are strongly recommended.

## ACKNOWLEDGMENTS

The author acknowledges the financial assistance of the International Institute of Earthquake Engineering and Seismology (IIEES) in relation to the Projects 7420 and 7528.

## REFERENCES

[1] P. Fajfar, Analysis in seismic provisions for buildings: past, present and future. *Bulletin of Earthquake Engineering*, **16**, 2567–2608, 2018.

[2] A. Soroushian, Integration step size and its adequate selection in analysis of structural systems against earthquakes. M. Papadrakakis, V. Plevris, N.D. Lagaros, eds. *Computational Methods in Earthquake Engineering Vol 3*, Springer, USA, pp. 285-329, 2017.

[3] T. Belytschko, T.J.R. Hughes, *Computational methods for transient analysis*. Elsevier, 1983.

[4] W.L. Wood, *Practical time stepping schemes*. Oxford, 1990.

[5] K.J. Bathe, *Finite element procedures*. Prentice-Hall, 2006.

[6] T. Belytschko, W.K. Liu, B. Moran, *Non-linear finite elements for continua and structures*. John Wiley & Sons, 2000.

[7] A. Soroushian, P. Wriggers, Elimination of the stops because of failure of nonlinear solutions in nonlinear seismic time history analysis. *Journal of Vibration Engineering and Technologies*, (in Press). https://doi.org/10.1007/s42417-023-00968-8.

[8] Y.M. Xie, G.P. Steven, Instability, chaos, and growth and decay of energy of time-stepping schemes for nonlinear dynamic equations. *Communications in Numerical Methods in Engineering*, **10**, 393-401, 1994.

[9] S. Rashidi, M.A. Saadeghvaziri, Seismic modeling of multispan simply supported bridges using Adina. *Computers & Structures*, **64**, 1025-1039, 1997.

[10] A. Cardona, M. Geradin, Time integration of the equations of motion in mechanism analysis. *Computers &* Structures, **33**, 801-820, 1989.

[11] W.L. Wood, M.E. Oduor, Stability properties of some algorithms for the solution of nonlinear dynamic vibration equation. *Communications in Applied Numerical Methods*, **4**, 205-212, 1988.

[12] K.H. Low, Convergence of the numerical methods for problems of structural dynamics. *Journal of Sound and Vibration*, **150**, 342-349, 1991.

[13] A. Soroushian, J. Farjoodi, Convergence of the responses that time integration generates for contact problems. M. Ghafory-Ashtiany, M. Mokhtari eds. *4th International Conference on Seismology and Earthquake Engineering (SEE4)*, Tehran, Iran, May 12-14, 2003 (in Persian).

[14] A. Hernandez, C.H. Pinto, E. Amezua, H. Fernandez, Analysis of the components of discretization error in nonlinear structural problems. *Finite Elements in Analysis and Design*, **39**, 835-864, 2003.

[15] T. Belytschko, D.F. Schoeberle, On the unconditional stability of an implicit algorithm for structural dynamics. *Journal of Applied Mechanics*, **42**, 865-869, 1975.

[16] P. Hauret, P. Le Tallec, Energy-controlling time integration methods for nonlinear elastodynamics and low-velocity impact. *Computer Methods in Applied Mechanics and Engineering*, **195**, 4890-4916, 2006.

[17] D. Kuhl, M.A. Crisfield, Energy-conserving and decaying algorithms in nonlinear structural dynamics. *International Journal for Numerical Methods in Engineering*, **45**, 569-599, 1999.

[18] T.A. Laursen, V. Chawla, Design of energy conserving algorithms for frictionless dynamic contact problems. *International Journal for Numerical Methods in Engineering*, **40**, 863-886, 1997.

[19] J.C. Simo, N. Tarnow, The discrete energy-momentum methods: conserving algorithms for nonlinear elastodynamics. *Zeitschrift für Angewandte Mathematik und Physik ZAMP*, **43**, 757-792, 1992.

[20] O.A. Bauchau, G. Damilano, N.J. Theron, Numerical integration of nonlinear elastic multi-body systems. *International Journal for Numerical Methods in Engineering*, **38**, 2727-2751, 1995.

[21] P. Betsch, P. Steinmann, Conservation properties of a time FE method-part II: Time-stepping schemes for non-linear elastodynamics. *International Journal for Numerical Methods in Engineering*, **50**, 1931-1955, 2001.

[22] P.B. Bornemann, U. Galvanetto, M.A. Crisfield, Some remarks on the numerical time integration of non-linear dynamical systems. *Journal of Sound and Vibration*, **252**, 935-944, 2002.

[23] X. Chen, K.K. Tamma, D. Sha, Virtual-pulse time integral methodology: A new approach for computational dynamics. Part 2. Theory for nonlinear structural dynamics. *Finite Elements in Analysis and Design*, **20**, 195-204, 1995.

[24] J. Chung, J.M. Lee, A new family of explicit time integration methods for linear and non-linear structural dynamics. *International Journal for Numerical Methods in Engineering*, **37**, 3961-3976, 1994.

[25] M.A. Crisfield, G. Jelenic, Y. Mi, H.J. Zhong, Z. Fan, Some aspects of the non-linear finite element method. *Finite Elements in Analysis and Design*, **27**, 19-40, 1997.

[26] M. Trcala, I. Němec, A. Gálová, On the nonlinear transient analysis of structures. W. Salazar, ed. *Earthquakes*, *Recent Advances, New Perspectives and Applications*, IntechOpen, 2023. Available from: http://dx.doi.org/10.5772/intechopen.108446

[27] S. Cao, Z. Li, B. Liu, Nonlinear time history analysis of a large-scale complex connected structure base on an explicit friction pendulum element. *工程力学* , **36**, 128–137, 2019.

[28] NZS 1170. Structural Design Actions, Part 5: Earthquake Actions-New Zealand. New Zealand, 2004.

[29] NZS 1170.5 Supp 1. Structural Design Actions - Part 5: Earthquake Actions. Standards New-Zealand, New Zealand, 2004.

[30] R.W. Clough, J. Penzien, *Dynamics of structures*. McGraw-Hill, 1993.

[31] A.K. Chopra, *Dynamics of structures: theory and application to earthquake engineering*. Prentice Hall, 1995.

[32] A. Soroushian, A.S. Moghadam, A. Sabzei, S. Amiri, A. Saaed, A. Yahyapour, An engineering comment for simply accelerating seismic response history analysis of mid-rise steel-structure buildings. *Journal of Architectural and Engineering Research*, (in Press). https://doi.org/10.54338/27382656-2023.4-001.

[33] E.L. Wilson, A. Habibullah, *SAP2000, structural analysis program*. Computers & Structures, Inc., Berkeley, 1995.

[34] E. Hairer, G. Wanner, *Solving ordinary differential equations II: stiff and differential-algebraic problems*. Springer, 1996.

[35] A. Soroushian, *New methods to maintain responses' convergence and control responses' errors in analysis of nonlinear dynamic models of structural systems*. Ph.D. Thesis, University of Tehran, Iran, 2003. (in Persian)

[36] A. Soroushian, P. Wriggers P, J. Farjoodi, Practical integration of semidiscretized nonlinear equations of motion: proper convergence for systems with piecewise linear behavior. *Journal of Engineering Mechanics*, **139**, 114–145, 2013.

[37] S. Amiri, A. Soroushian, A brief review on building structural analysis regulations in different seismic codes. *Research Bulletin of Seismology and Earthquake Engineering*, **20**, 1–24 (in Persian).

[38] P. Henrici, *Discrete variable methods in ordinary differential equations*. Prentice-Hall, 1962.

[39] J.C. Strikwerda, *Finite difference schemes and partial differential equations*. Wadsworth & Books/Cole, Pacific Grove, 1989.

[40] A. Soroushian, P. Wriggers, J. Farjoodi, From the notions of nonlinearity tolerances towards a deficiency in commercial Transient Analysis softwares and its solution. M. Papadrakakis, V. Papadopoulos, V. Plevris eds. 5th *ECCOMAS Thematic Conference on Computational Methods in Structural Dynamics and Earthquake Engineering (COMPDYN 2015)*, Crete, Greece, May 25-27, 2015.

[41] A. Soroushian, P. Wriggers, Test of an idea for improving the efficiency of nonlinear time history analyses when implemented in seismic analysis according to NZS 1170.5:2004. Dimitrovová Z, Biswas P, Gonçalves R, Silva T eds. *10th International Conference on Wave Mechanics and Vibrations (WMVC 2022)*, Lisbon, Portugal, July 4-6, 2022.

[42] J. Farjoodi, A. Soroushian, Roobust convergence for the dynamic analysis of MDOF elastoplastic systems. A. Zingoni ed. *1st International Conference on Structural Engineering Mechanics and Computation (SEMC 2001)*, Cape Town, South Africa, April 2-4, 2001.

[43] A. Soroushian, J. Farjoodi, Responses convergence in time integration of nonlinear semi-discrete equations of motion. M. Brennan ed. *8th International Conference on Recent Advances in Structural Dynamics (RASD 2003)*, Southampton, UK, July 14-16, 2003

[44] A. Soroushian, J. Farjoodi, P. Wriggers, Reliable convergence for dynamic linearly-elastic/perfectly-plastic systems analyzed with different time integration methods. A. Nilson, H. Boden eds. *10th International Congress on Sound and Vibration (ICSV 10)*, Stockholm, Sweden, July 7-10, 2003.

[45] A. Soroushian, A.M. Kermani, K. Chavan, A. Ivanian, Responses' convergence for time integration analyses involved in linearly-elastic/perfectly-plastic behaviour and impact. Z.H. Yao, M.W. Yuan, W.X. Zhong eds. *6th World Conference on Computational Mechanics (WCCM VI in conjunction with APCOM'04)*, Beijing, China, September 5-10, 2004.

[46] F. Naeim, S. Zhogzhi, *The seismic design handbook*. Kluwer, 2001.

[47] P. Wriggers, *Nonlinear finite element methods*. Springer, 2008.

[48] S.L. Richter, R.A. Decarlo, Continuation methods: theory and applications. *IEEE Transactions on Systems, Man, and Cybernetics*, vol. SMC-13, no. 4, 459-464, July-Aug. 1983.

[49] W.C. Rheinboldt, Numerical continuation methods: a perspective. *Journal of Computational and Applied Mathematics*, **124**, 229-244, 2000.

[50] E.L. Allgower, K. Georg, *Numerical continuation methods, an introduction*. Springer, 1990.

[51] R.D. Cook, D.S. Malkus, M.E. Plesha, R.J. Witt, *Concepts and applications of finite element analysis*. Wiley, 2002.

[52] R. De Borst, M.A. Crisfield, J.J. Remmers, C.V. Verhoosel, *Nonlinear finite element analysis of solids and structures*. Wiley, 2012.

[53] Y.S. Yang, W. Wang, J.Z. Lin, Direct-iterative hybrid solution in nonlinear dynamic structural analysis. *Computer Aided Civil and Infrastructure Engineering*, **32**, 397–411, 2017.

[54] K.J. Bathe, A.P. Cimento, Some practical procedures for the solution of nonlinear finite element equations. *Computer Methods in Applied Mechanics and Engineering*, **22**, 59–85, 1980.

[55] M. Geradin, S. Idelsohn, M. Hogge, Nonlinear structural dynamics via Newton and quasi-Newton methods. *Nuclear Engineering and Design*, **58**, 339–348, 1980.

[56] J.M. Nau, Computation of inelastic spectra. *Journal of Engineering Mechanics*, **109**, 279–288, 1983.

[57] S.A. Mahin, J. Lin, *Construction of inelastic response spectra for single degree-of-freedom systems, Report UCB/EERC-83/17*. Earthquake Engineering Research Center (EERC), Univ. of California, Berkeley, USA, 1983.

[58] A. Soroushian, S. Amiri, A comment on nonlinear time history analysis regulations of seismic code of New Zealand applicable in Eurocode 8 and many other seismic codes. K.D. Pitilakis ed. *16th European Conference on Earthquake Engineering (ECEE 2018)*, Thessaloniki, Greece, June 18-21, 2018.

[59] A. Soroushian, Proper convergence, a concept new in science and important in engineering. D.T. Tsahalis ed. *4th International Conference From Scientific Computing to Computational Engineering (IC-SCCE 2010)*, Athens, Greece, July 7-10, 2010.

[60] A. Ralston, P. Rabinowitz, *First course in numerical analysis*, McGraw Hill, 1978.

[61] T.J.R. Hughes, *The finite element method: linear static and dynamic finite element analysis*. Prentice-Hall, 1987.

[62] S.N. Penry, W.L. Wood. Comparison of some single-step methods for the numerical solution of the structural dynamic equation. *International Journal for Numerical Methods in Engineering*, **21**, 1941-1955, 1985.

[63] A. Soroushian, J. Farjoodi, H. Mehrazin, A new measure for the nonlinear behavior of piece-wisely linear structural dynamic models. J. Eberhardsteiner, H.A. Mang, H. Waubke eds. *13th International Congress on Sound and Vibration (ICSV13)*, Vienna, Austria, July 2-6, 2006.

[64] A. Soroushian, G. Ahmadi, S. Amiri, A class of synchronized nonlinear two-dof systems with closed form solution. *Scientia Iranica*, **25** (6: Special Issue Dedicated to Professor Goodarz Ahmadi), 3258-3273, 2018.

[65] V.I. Babitsky, V.L. Krupenin, *Vibration of strongly nonlinear discontinuous systems*. Springer, 2001.

[66] N.M. Newmark, A method of computation for structural dynamics. *Journal of Engineering Mechanics*, **85**, 67-94, 1959.

[67] N.I. Basoz, A.S. Kiremidjian, S.A. King, K.H. Law, Statistical analysis of bridge damage data from the 1994 Northridge, CA California. *Earthquake Spectra*, **15**, 25-53, 1999.

[68] V. Jeng, W.L. Tzeng, Assessment of seismic pounding hazard for Taipei city. *Engineering Structures*, **22**, 459-471, 2000.

[69] A. Taghinia, A. Vasseghi, M. Khanmohammadi, A. Soroushian, Development of seismic fragility functions for typical Iranian multi-span RC bridges with deficient cap beam–column joints. *International Journal of Civil Engineering*, **20**, 305–321, 2022.

COMPDYN 2023
9th ECCOMAS Thematic Conference on
Computational Methods in Structural Dynamics and Earthquake Engineering
M. Papadrakakis, M. Fragiadakis (eds.)
Athens, Greece, 12-14 June 2023

# ML-BASED PUNCHING STRENGTH ESTIMATIONS OF FLAT SLABS WITHOUT TRANSVERSE REINFORCEMENT UNDER LATERAL LOADING

**H. Panahi**[1], **A. S. Genikomsou**[2]

[1] Ph.D. Candidate, Department of Civil Engineering, Queen's University, Kingston, ON, K7L 2N6, Canada
e-mail: Hadi.panahi@queensu.ca

[2] Assistant Professor, Department of Civil Engineering, Queen's University, Kingston, ON, K7L 2N6, Canada
ag176@queensu.ca

## Abstract

*Reinforced concrete flat plate systems are commonly used in North America due to their advantages such as the versatile architectural arrangements, ease of construction; however, these systems can be susceptible to brittle punching shear failure. As there is no other potential loading path after the occurrence of punching shear, this failure can lead to a progressive collapse of the structure. However, current design code provisions for punching shear are associated with high discrepancies for the punching shear strength estimation as they account for limited independent variables in their simple formulations and are mostly based on empirical equations derived from experimental data. Consequently, there is a need for proper numerical assessment of slab-column connections that can potentially lead to modifications to the design provisions. Due to the available uncertainties, a precise predictive tool is of great requirement. This study aims at applying machine-learning-based algorithms in the determination of punching shear capacity of slab-column connections without transverse reinforcement under both concentric vertical gravity forces and unbalanced moments due to lateral loadings. Herein, a Multilayer Perceptrons neural network model is trained using gradient descent and backpropagation algorithms. The performance of the developed model is further investigated by comparing its strength prediction with those of the available code provisions in which it is noted that the trained neural network showed higher accuracy.*

**Keywords:** Flat Plate System, Machine Learning Technique, Unbalanced Moments, Drift, Code Provisions.

## 1 INTRODUCTION

The seismic performance-based design approach aims to accurately estimate the seismic functionality of structures and their advanced post-earthquake behavior for a wide range of earthquake scenarios. To achieve this, performance-based earthquake engineering requires the detection of various damage stages in structural elements, allowing for appropriate rehabilitation methods for existing structures or economically efficient design of new structures by predicting their hysteretic responses during earthquakes. One critical component in two-way flat plate systems is the reinforced concrete (RC) slab-column connection, as its integrity dictates the overall performance and global structural stability of the plate systems under lateral load demands. The governing brittle failure mode limiting the lateral deformation capacity of connections in flat plate systems is pure punching shear or flexural-punching failure, with potential for progressive collapse of the whole frame system. This study focuses on the behavior of slab-column connections under seismic loads using available experimental data and design provisions to determine their ultimate moment and drift capacities for seismic performance assessment.

Recent computational advancements have made machine learning (ML) techniques increasingly beneficial in structural and earthquake engineering. ML uses programming algorithms to optimize a performance index, based on available data. In structural engineering, researchers have applied ML models for strength regression, failure mode classification, damage assessment, and fragility curve regression (e.g., [1-7]). However, while these models can provide more accurate predictions than existing empirical formulations in flat plate systems, they are limited to slabs under monotonic vertical loading. A gap has also been identified in using ML methods to capture the limit states of RC slab-column connections subjected to unbalanced moments. Additionally, due to the lack of an adequate dataset on slabs under lateral loading, ML models are crucial in accurately predicting the drift capacity of slabs. Therefore, ML algorithms are used to fit models for estimating the ultimate moment strength and drift capacity of slab-column connections at the failure point under lateral cyclic loading.

Currently, non-linear parameters available in ASCE 41-17 [8], empirically defined equations such as the bilinear equation in ACI 318-19 [9], the hyperbolic equation in CSA A23.3-19 [10], or the double bilinear equations proposed by Zhou and Hueste [11], and mechanical models proposed by Drakatos et al. [12], Setiawan et al. [13], Broms [14], and Muttoni et al. [15], can be used to determine the drift-based backbone response as the limit state of slab-column connections for numerical analysis. However, empirically defined equations have limited independent variables and provide lower or average bounds for the design drift. Furthermore, code provisions are mostly based on limited experimental data obtained from small-scale isolated interior slab-column connections, making them less reliable for numerical analysis. Therefore, the derivation of a precise regression that can be employed for failure recognition in numerical analysis/design requires intricate solutions.

Predicting the unbalanced moment resistance and contribution of each lateral-load resisting mechanism (i.e., flexure, torsion, and eccentric shear) to the overall strength of slab-column connections is complex due to their non-linear behavior. In ACI 318-19 [9] design code, a fraction of column side lengths is adopted to relate the contribution of shear ($\gamma_v$) and flexural ($\gamma_f$) mechanisms, and the torsion mechanism is neglected. While the column is square, the eccentric shear and flexure mechanism coefficients are 0.4 and 0.6, respectively. ACI 318-19 [9] recommends a formula for unbalanced moment resistance, which is a function of initial vertical loading, the fraction of resisting mechanism coefficients, the polar moment of inertia, and the punching shear strength of the connection. The unbalanced moment resistance determined by EC2-2004 [16] includes different mechanism contribution coefficients, punching shear

strength with various variables, and a different polar moment of inertia. CSA A23.3-19 [10] provides an equation for unbalanced moment prediction of slabs similar to ACI 318-19 [9]; however, the punching shear capacity of concrete is with different coefficients. The available design codes include several shortcomings. The contribution of eccentric shear force and flexure mechanisms considered in all design provisions are constant for any drift limits; however, the actual behavior of the slab connections subjected to lateral loading represents variable mechanism coefficients. Moreover, the design provisions are based on experimental and empirical research while neglecting the contribution of the torsion mechanism. Furthermore, the existing design practices assume a linear distribution of shear stresses on the critical perimeter while it is non-linear in reality.

Therefore, this paper aims to propose more accurate formulations for estimating the unbalanced moment and drift capacities of slabs under lateral loading, taking into account the variable nature of the flat slab design procedure, performance requirements, and various geometric and material properties. To achieve this, 105 interior moment-resisting slab-column specimens without shear reinforcement under (monotonic or cyclic) lateral loading are analyzed using different ML models, including decision trees, random forests, support vector machines (SVMs), and deep neural network (NN) algorithms. The proposed models correlate slab moment and drift capacities with ten independent parameters, including slab side lengths ($l_1$ and $l_2$), column side lengths ($c_1$ and $c_2$), slab thickness ($h$), average effective depth ($d$), flexural reinforcement ratio ($\rho$), compressive strength of concrete ($f_c'$), the initial vertical gravity load ($V_g$), and the lateral loading type ($LT$). Results show that the deep NN model is the most suitable for estimating drift limit and moment capacity.

## 2 DATA COLLECTION

The present study compiled a database of 105 RC two-way flat slab specimens subjected to lateral loading, sourced from various research articles and dissertations. These specimens included small-scale or full-scale experiments and frame assemblies of interior slabs or interior continuous connections without transverse reinforcement under gravity and lateral (monotonic or uniaxial/biaxial cyclic) loadings. Pearson's method was used to estimate the standard correlation coefficient of the dataset, as shown in Figure 1, which demonstrates the strong correlation between the moment and drift values at the failure of the slab-column connection and the slab and column geometry, material properties, and loading parameters. The input features considered in this study comprise a 10-dimensional vector, including slab dimensions, slab thickness, average effective depth, column sides, concrete compressive strength, flexural reinforcement ratio, initial vertical gravity load, and lateral loading type. Table 1 shows the mean and standard deviation of each model feature, while Figure 2 displays the distributions of the key parameters selected to characterize the drift and moment capacities of the two-way flat slabs.

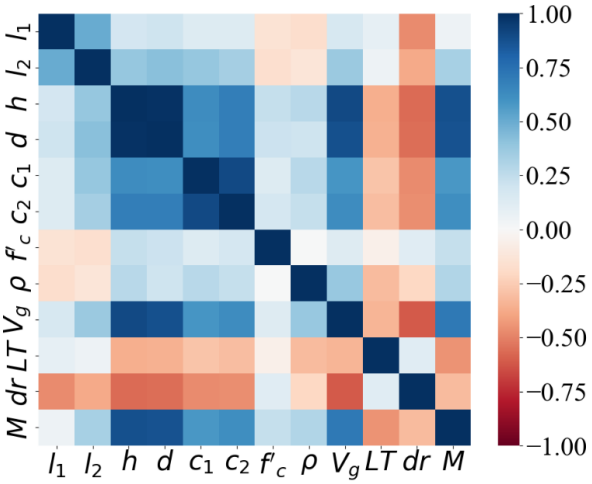


Figure 1. Correlation heat map between the features.

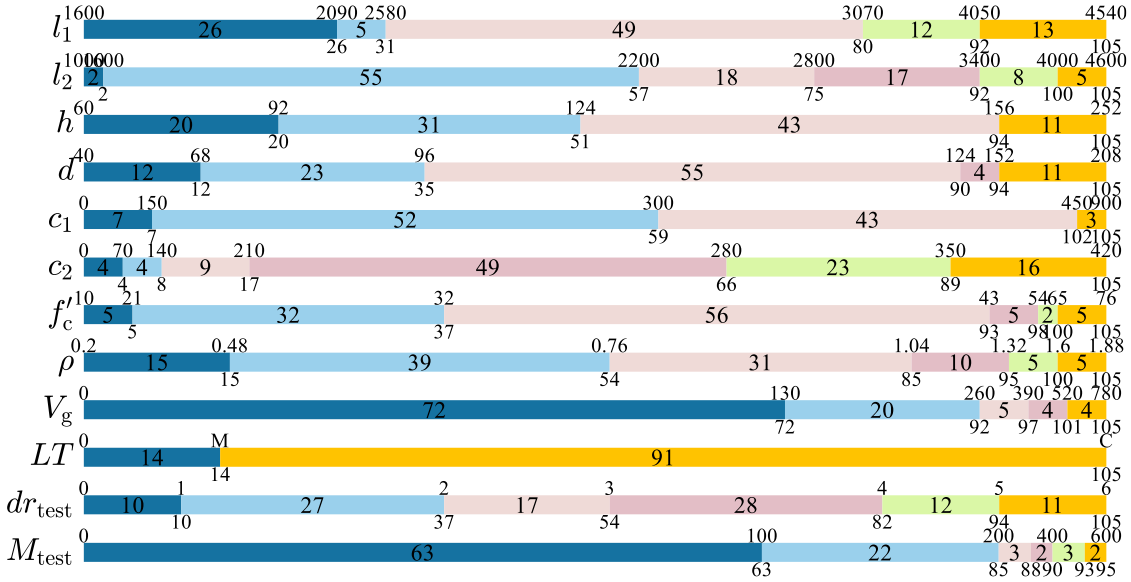


Figure 2. Distribution of features. The number inside the bars shows the number of specimens in each range, the top number shows the value of each range for the relevant feature, and the bottom number indicates the accumulated number of specimens until that value.

Table 1. Mean and standard deviation of model features.

| Feature/Output | Notation | Mean/Count | Standard Deviation |
|---|---|---|---|
| Slab length parallel to loading dir. (mm) | $l_1$ | 2910 | 804 |
| Slab length normal to loading dir. (mm) | $l_2$ | 2433 | 733 |
| Slab thickness (mm) | $h$ | 137 | 47 |
| Average effective depth (mm) | $d$ | 109 | 37 |
| Column side parallel to loading dir. (mm) | $c_1$ | 290 | 130 |
| Column side normal to loading dir. (mm) | $c_2$ | 265 | 80 |
| Concrete compressive strength (MPa) | $f'_c$ | 34.98 | 11.21 |
| Flexural reinforcement ratio (%) | $\rho$ | 0.794 | 0.345 |
| Initial vertical gravity load (kN) | $V_g$ | 143.96 | 160.23 |
| Lateral loading type: monotonic/cyclic | LT | 91/14 | - |
| Drift ratio at punching failure (%) | $dr$ | 2.77 | 1.45 |
| Moment at punching failure (kN.m) | M | 106.14 | 113.27 |

## 3 PREDICTIONS BY AVAILABLE EQUATIONS

### 3.1 Drift Prediction

The scatter plot in Figure 3 shows the relationship between the drift limit state of the collected database and GSR, along with the predicted drift values by the empirical equations provided by ACI 318-19 [9], ASCE 41-17 [8], CSA A23.3-19 [10], and Zhou and Hueste [11]. Drakatos et al. [12] and Muttoni et al. [15] are excluded from the figure as their mechanical models do not have a specific shape concerning GSR values. The empirically defined equations have limited independent variables and give lower or average bounds for the design drift. Figure 3 also shows that while the increase of initial gravity load leads to a degradation of the lateral load resisting capacity of the connections and vice versa, the experimental test data of interior slab-column connections without transverse reinforcement subjected to lateral monotonic or seismic actions demonstrate that the deformation capacity of the connections is not perfectly correlated with GSR. As a result, it is not possible to accurately estimate the drift capacity of slabs with a simple equation and requires a point-prediction method such as ML algorithms.

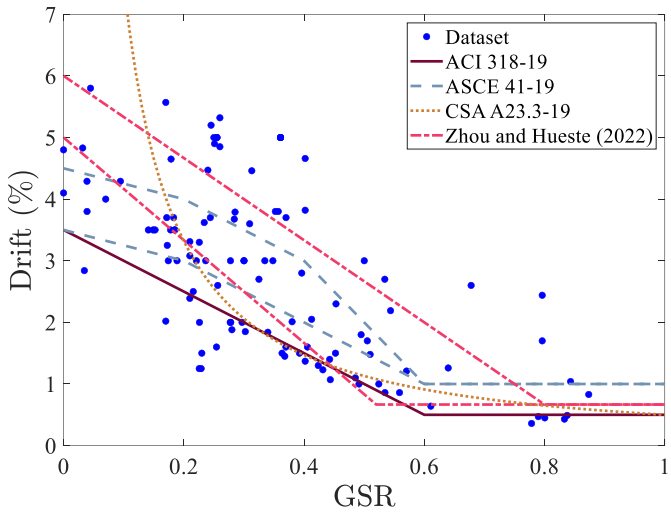


Figure 3. Accumulated dataset and its comparison to the design codes and empirical predictions.

Figure 4 compares the design code provisions with available empirical and mechanical equations in terms of predicted and experimental drift capacity values. The accuracy indices such as coefficient of determination, $R^2$, mean absolute error, $MAE$, the root of mean square error, $RMSE$, and the coefficient of variation values, $COV$ are used for comparison. The $R^2$ for ACI 318-9 and CSA A.23.3-19 [9, 10] are negative values, and for estimations by Muttoni et al., Zhou and Heuste, and ASCE 41-17 [8, 11, 15] are 2%, 43%, and 45%, respectively. The shortcoming of available empirical models in identifying accurate lateral drift limit of slab-column connections is conspicuous. As the mechanical model of Drakatos et al. [12] requires maximum aggregate size and the yield stress capacity of tensile flexural reinforcements, which are not available for 72 specimens of the dataset, these data are excluded, as shown in Figure 4-f, and the accuracy indices are among just 33 specimens. As shown in Figure 4-a, b, and d, since ACI 318-19, ASCE 41-17, and Zhou and Hueste [8, 9, 11] restrain the drift values as a lower bound at 0.5, 1.0, and 0.67%, respectively, the predicted drift capacities could not go lower than these values. Conversely, there are five slabs that failed at drift lower than 0.5% and 11 slabs at lower than 1.0%.

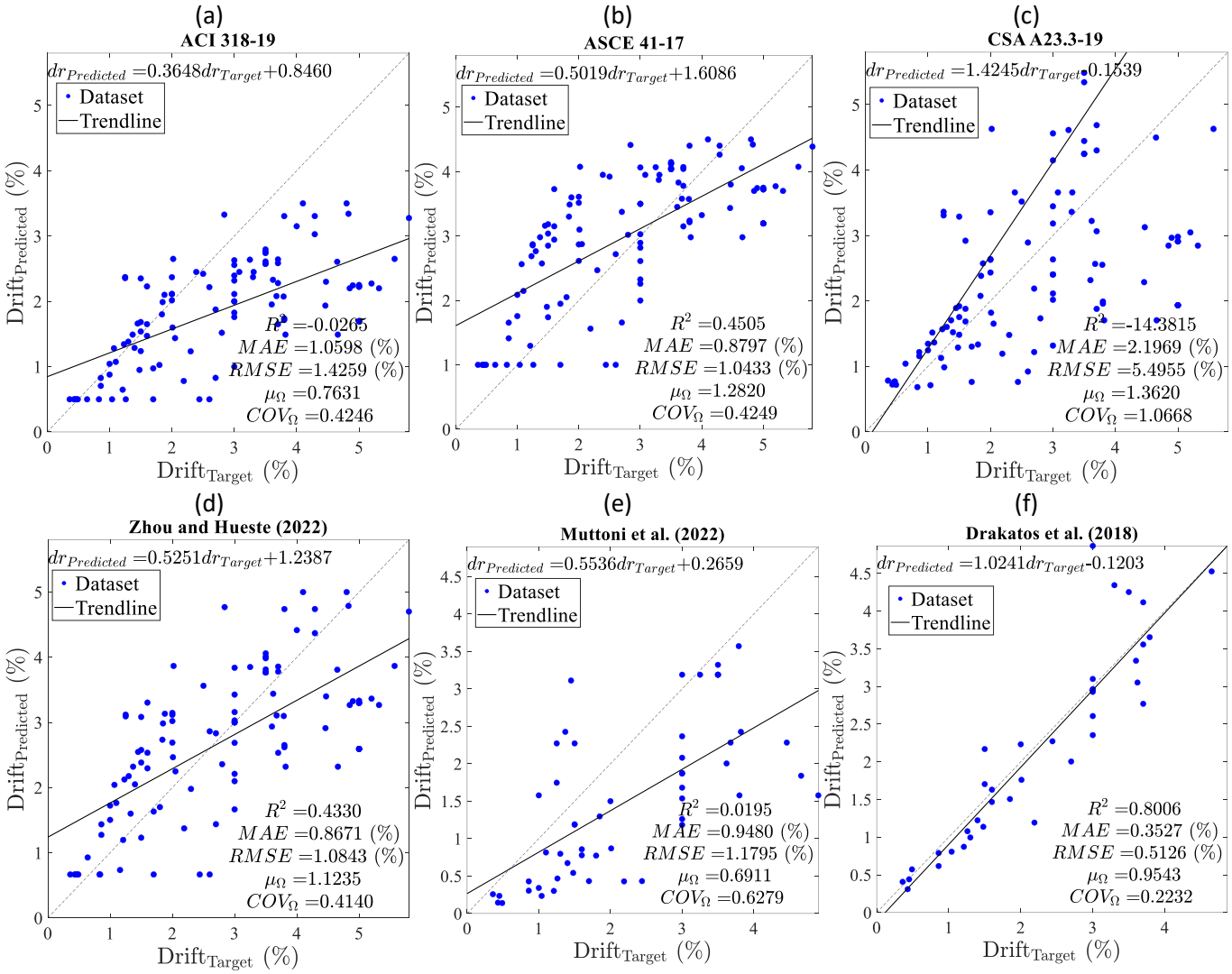


Figure 4. Comparison of the prediction model results versus actual experimental data for drift at punching failure: a) ACI 318-19 [9], b) ASCE 41-17 [8], c) CSA A.23.3-19 [10], d) Zhou and Hueste [11], e) Muttoni et al. [15], and f) Drakatos et al. [12].

## 3.2 Unbalanced Moment Prediction

Figure 5 compares the prediction and experimental target values for unbalanced moments of the collected data among different design codes. It is observed that EC2-2004 [16] performs better in terms of $R^2$, $MAE$ and $RMSE$ indices for the capacity of connections regarding the unbalanced moment, followed by CSA A23.3-19 and ACI 318-19, respectively. This difference may be attributed to the inclusion of the flexural reinforcement effect in EC2-2004's punching shear strength equation, which is not considered in ACI 318-19 and CSA A23.3-19.

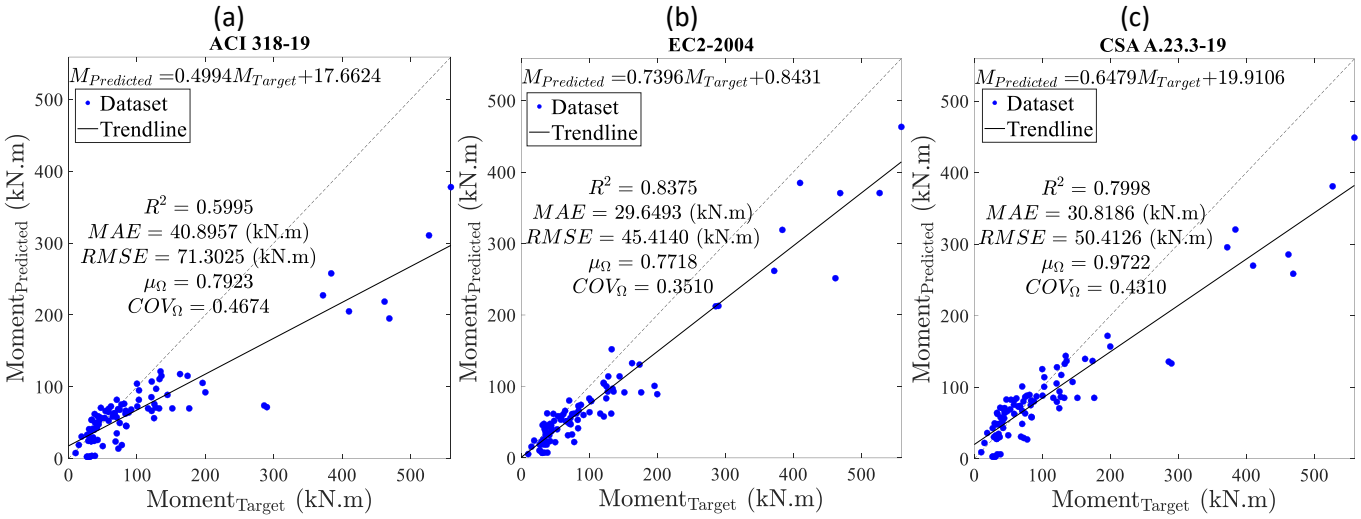


Figure 5. Comparison of the prediction model results versus actual experimental data for the unbalanced moment at punching failure: a) ACI 318-19 [9], b) EC2-2004 [16], and c) CSA A.23.3-19 [10].

## 4 MACHINE LEARNING METHODS

In this section, various ML algorithms are used to assess their performance regarding drift and unbalanced moment strengths prediction of the collected data.

### 4.1 Decision Trees

Decision trees are versatile ML algorithms that can perform regression fitting of complex datasets. These are fundamental components of the random forests model, which are among the most powerful ML models available today. One of the qualities of decision trees is that they do not require special preprocessing and feature scaling. The CART optimization algorithm is adopted to train growing trees. This greedy algorithm works by first splitting the training dataset in a way to minimize the MSE. This model is often called a non-parametric model, not because it does not require any parameters but because the number of parameters is not determined prior to the training. Thereby, the structure of the model is free to stick to the data, and they are prone to overfitting. Hence, it is needed to set some hyperparameters, such as the minimum number of samples of a leaf node that is set to 2 and the maximum depth of the tree, which is tuned to five.

### 4.2 Random Forests

The random forests algorithm is mainly an ensemble of many decision trees on a random subset of features in which each tree is grown by a random bootstrap sample of a training dataset and then averaged out their prediction. At each node of the tree, a randomly chosen subset of features is used to generate the best partitioning. The training procedure continues until each point in the sample is assigned to a terminal node from previously partitioned nodes and is repeated until the desired number of trees has been grown. The trained model includes 100 trees in the forest with the maximum depth of the tree equal to five. The minimum number of samples required to be at a leaf node is set to 2 in order to overcome overfitting.

### 4.3 Support Vector Machines

SVMs for regression (known as support vector regression, SVR) is a kind of ML algorithm capable of linear and non-linear regression for small to medium-sized datasets. SVR tries to

fit as many samples as possible on the street while limiting margin violations. Since it is prone to overfitting L2 regularization is adopted. The non-linear SVR model is trained with the RBF kernel with degree of the polynomial kernel function equal to 10.

### 4.4 Deep Neural Network

NNs are versatile, powerful, and ideal to tackle large and highly complex ML tasks. Thereby, a deep NN, which is heavily used today, is established to fit a non-linear regression for the deformation capacity of RC two-way flat slabs without transverse reinforcement. NN models are comprised of weights and biases (i.e., unknown model parameters) in which these values have been calculated so that the model best fits the training set by optimizing a cost function. In this study, a deep NN module is developed using the Nadam optimization algorithm in a deep network, as Nadam optimization outperforms in this regard. The hyperparameters of the model, including the number of hidden layers, the number of neurons in each layer, the learning rate, and activation functions, are tuned after multiple trials and errors. The developed NN architecture, as shown in Figure 6, includes ten neurons in the input layer, 128, 256, 256, 256, 128, and 64 neurons in six hidden layers, and a neuron in the output layer as the estimated value for the lateral drift or unbalanced moment capacity of slabs. The value of each neuron in hidden and output layers is determined by the activation of neurons in the previous layer using the activation function. Herein, the *ReLU function* is adopted as an activation function for neurons. Since the range of input features is different, it is needed to standardize all the input and output features of the dataset by Equation (1).

$$x_j = (x - x_{\min})/(x_{\max} - x_{\min}) \tag{1}$$

Where, $x_{\max}$ and $x_{\min}$ are the maximum and minimum values among all values of feature $x$ in the training set or test set.

Mean squared error (MSE) formulation, as expressed in Equation (2), is adopted as a cost function, $C$, of the network to evaluate the accuracy of the model in each iteration (epoch).

$$C(w,b) = \mathrm{MSE}(y,a) = \frac{1}{n}\sum_{j=1}^{n}\left\|y_j(x) - a_j\right\|^2 \tag{2}$$

Here, $w$ denotes the collection of all weights in the network, $b$ presents all the biases, $n$ is the total number of training inputs, $y$ is the desired target drift capacity (from test data), $a$ is the vector of outputs from the network when $x_j$ is input, and the sum is over all training inputs, $x$. The training of weights and biases of the artificial network is carried out using the Nadam algorithm in Python. The training procedure is monitored after each epoch to avoid underfitting the model, and the L2 regularization penalty is applied to the model to avoid overfitting.

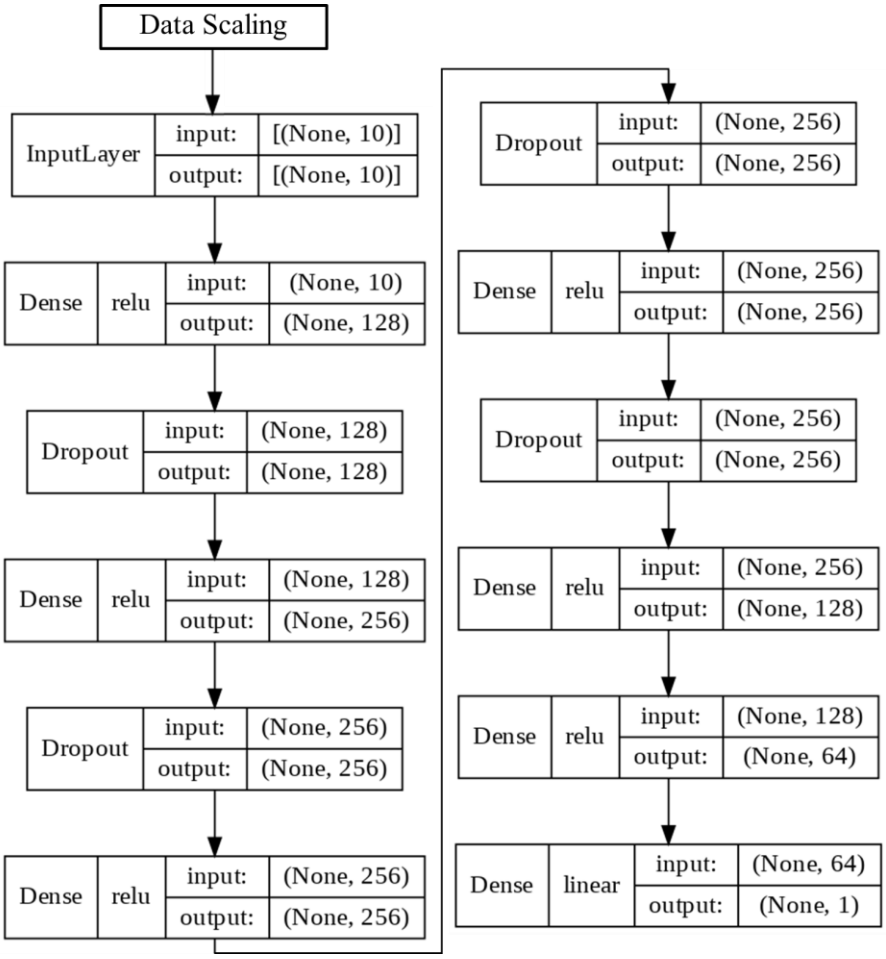


Figure 6. Assumed architecture for the deep NN model.

### 4.5 Training of the Accumulated Dataset

To assess which ML method is suited for the training of data, a preliminary analysis is conducted in which linear regression, decision tree, linear SVR, SVR, and random forests algorithms, as well as a deep neural network, were tested using Tensorflow and Scikit-learn modules available in Python programming language and by applying a k-fold cross validation of 12 splits. The dataset is split into 70% as a training set (for fitting the model) and 30% as a test set (to evaluate the trained model) that are randomly sampled. Table 2 lists the models tested along with their performance measures. Based on Table 2, the deep neural network model achieved the highest performance in $R^2$, $MAE$, and mean square error, $MSE$, values followed by the decision trees and random forests models, respectively, while the remaining models showed less suitable performance regarding predicting drift or moment estimation.

The fitted data along with the actual experimental drift and moment values are compared in Figure 7-a and -b, respectively, for the deep NN model. According to Figure 7, Figure 4, and Figure 5, the trained deep NN estimated the drift capacity of the connections with 41% and 42% higher accuracy than ASCE 41-17 [8] and Zhou and Hueste's model [11], respectively, and the unbalanced moment capacity with 31% and 22% higher precision than CSA A23.3-19 and EC2-2004.

Table 2. ML regression models results.

| *ML Regression Model* | *Total Data* | | | | | |
|---|---|---|---|---|---|---|
| | *Drift* | | | *Moment* | | |
| | $R^2$ | *MAE* | *MSE* | $R^2$ | *MAE* | *MSE* |
| Linear regression | 0.530 | 0.81 | 0.97 | 0.642 | 29.18 | 602.10 |
| Decision trees | 0.854 | 0.36 | 0.30 | 0.884 | 27.78 | 502.90 |
| Linear SVR | 0.356 | 0.90 | 1.34 | 0.501 | 33.20 | 607.89 |
| SVR | 0.799 | 0.30 | 0.42 | 0.834 | 21.95 | 502.42 |
| Random forests | 0.840 | 0.43 | 0.33 | 0.878 | 34.10 | 510.67 |
| Deep neural network | 0.856 | 0.38 | 0.30 | 0.961 | 22.40 | 501.58 |

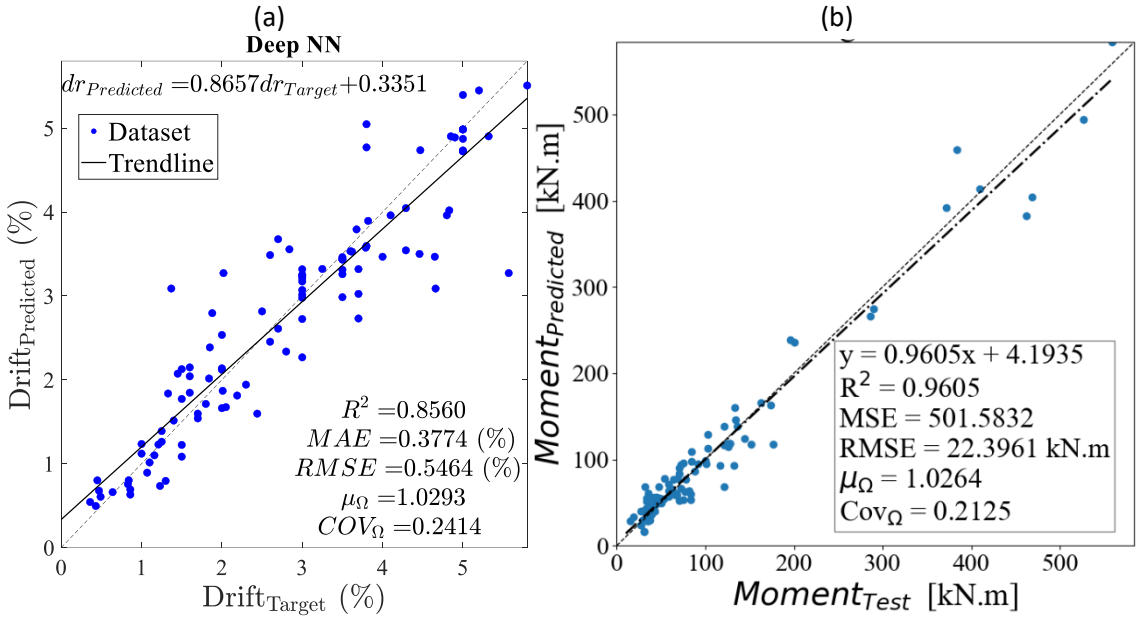


Figure 7. Comparison of the accumulated experimental data with predicted values by the developed deep NN model for a) drift at the punching failure and b) moment at the punching failure.

## 5 CONCLUSIONS

Based on the collected data and the machine learning analysis results, the following conclusions can be drawn:

- Available design code equations are conservative for assessing the seismic performance of these connections regarding unbalanced moment or drift capacities.
- The various empirical models to estimate the drift limit states of the connections are not precise for the seismic assessment of buildings with flat plate systems.
- A dataset of 105 experimental test results of small-scale and full-scale, as well as frame assemblies of interior slabs without transverse reinforcement under both gravity and lateral (monotonic or uniaxial/biaxial cyclic) loadings was collected.
- Various machine learning algorithms are trained, and the deep neural network model outperformed in predicting slab drift limit states and moment strengths under lateral loading.

## REFERENCES


1. Chetchotisak, P., et al., *Punching shear strengths of RC slab-column connections: Prediction and reliability*. KSCE Journal of Civil Engineering, 2018. **22**(8): p. 3066-3076.
2. Mangalathu, S. and J.-S. Jeon, *Classification of failure mode and prediction of shear strength for reinforced concrete beam-column joints using machine learning techniques.* Engineering Structures, 2018. **160**: p. 85-94.
3. Abambres, M. and E.O. Lantsoght, *Neural network-based formula for shear capacity prediction of one-way slabs under concentrated loads.* Engineering Structures, 2020. **211**: p. 110501.
4. Chen, P.-Y., Z.Y. Wu, and E. Taciroglu, *Classification of Soft-Story Buildings Using Deep Learning with Density Features Extracted from 3D Point Clouds.* Journal of Computing in Civil Engineering, 2021. **35**(3): p. 04021005.
5. Tran, V.-L. and S.-E. Kim, *A practical ANN model for predicting the PSS of two-way reinforced concrete slabs.* Engineering with Computers, 2021. **37**(3): p. 2303-2327.
6. Mangalathu, S., et al., *Explainable machine learning models for punching shear strength estimation of flat slabs without transverse reinforcement.* Journal of Building Engineering, 2021. **39**: p. 102300.
7. Asteris, P.G., et al., *Predicting the shear strength of reinforced concrete beams using Artificial Neural Networks.* Computers and Concrete, An International Journal, 2019. **24**(5): p. 469-488.
8. ASCE/SEI. *Seismic evaluation and retrofit of existing buildings*. 2017. American Society of Civil Engineers.
9. ACI. *ACI CODE-318-19: Building Code Requirements for Structural Concrete and Commentary*. 2019. American Concrete Institute.
10. CSA. *CSA A23.3-19: Design of Concrete Structures*. 2019. Canadian Standards Association.
11. Zhou, Y. and M.B.D. Hueste, *Nonlinear Modeling Parameters and Acceptance Criteria for Interior Slab-Column Connections.* ACI Structural Journal, 2022. **119**(1): p. 145-154.
12. Drakatos, I.-S., A. Muttoni, and K. Beyer, *Mechanical model for drift-induced punching of slab-column connections without transverse reinforcement.* ACI Structural Journal, 2018. **115**(2): p. 463-474.
13. Setiawan, A., R.L. Vollum, and L. Macorini, *Numerical and analytical investigation of internal slab-column connections subject to cyclic loading.* Engineering Structures, 2019. **184**: p. 535-554.
14. Broms, C., *Structural Model for Interstory Drift Capacity of Flat Slabs without Shear Reinforcement.* ACI Structural Journal, 2020. **117**(3).
15. Muttoni, A., et al., *Deformation capacity evaluation for flat slab seismic design.* Bulletin of Earthquake Engineering, 2022: p. 1-36.
16. Européen, C., *Eurocode 2: Design of concrete structures—Part 1-1: General rules and rules for buildings.* London: British Standard Institution, 2004.

COMPDYN 2023
9th ECCOMAS Thematic Conference on
Computational Methods in Structural Dynamics and Earthquake Engineering
M. Papadrakakis, M. Fragiadakis (eds.)
Athens, Greece, 12-–14 June 2023

# SEMI-ANALYTICAL CHARACTERIZATION OF A SLOSHING FLUID MASS USING A SMOOTHED PARTICLE HYDRODYNAMIC BASED METHOD

**Giorgia C. GOURSAND-PARENTE[1], Bonaventura TAGLIAFIERRO[2], Salvatore CAPASSO[1], Alejandro CRESPO[3], Giacomo VICCIONE[1]**

[1]Department of Civil Engineering, University of Salerno
Salerno, Italy
e-mail: g.goursandparente@studenti.unisa.it;

[2] Universitat Politècnica de Catalunya, Barcelona Tech
Barcelona, Spain

[3] Environmental Physics Laboratory, CIM-UVIGO, Universidade de Vigo
Ourense, Spain

**Abstract.** *Sloshing phenomena regard the dynamic excitation of a partially filled tank which leads to the motion of the fluid within. The dynamic effects, especially if the excitation frequency approaches the natural frequency of the tank (near resonance), may compromise the structure stability. Amplification of motion may be either pursued or avoided, depending on the design purposes; regardless, it is important to predict the coupled effects generated by the tank interacting with the contained liquid. The present study aims to offer a simplified approach along with valid parameters that link the filling level of the tank to the sloshing mode of vibration. The parameterization procedure is numerically supported by a Computational Fluid Dynamics (CFD) solver based upon the Smoothed Particles Hydrodynamics (SPH) meshless method. Within the proposed framework, a parametric sloshing tank is simulated and validated using experimental data as a test-rig, therefore used to perform a wide sensitivity study by changing the filling ratio. The numerical results interpretation leads to a method which can synthetically predict the characterizing frequency of the phenomenon using a semi-analytical fitting, with improved accuracy over previous literature methods. This procedure is established within the open-source SPH-based DualSPHysics, and provides a reliable alternative to traditional approaches, proving that validated numerical methods can directly support the design of sloshing tanks, with all the advantages related: quickness, affordability and reproducibility.*

**Keywords:** Sloshing, free-surface, Fluid-Structure Interaction, CFD, Smoothed Particle Hydrodynamics, DSPH

## 1 INTRODUCTION

The motion of the liquid in partially filled tanks subject to dynamic excitation, or to any sort of disturbance, is called sloshing [1]. The free-surface displacement, depending on the container shape and on the external forcing condition, may range from planar to chaotic. The following dynamic effects are of great interest in various fields of engineering: likewise physics is recognized, among others, in soil-fixed tanks subject to extreme events (i.e. earthquakes), fuel or propellant tanks of crafts and vehicles in motion, transportation of liquid fuels (i.e. liquid natural gas – LNG), and offshore petroleum factories (Floating Production Storage and Offloading – FPSO) - an extensive consultation is referred in [2]. The present craft industry trend, in particular, advances with increasingly bigger models. Global demand of trade of commercial products and fuel requests greater cargo ships. Parallel to that, increasing demand for commercial trips is leading air-craft industry to enlarge its capacities producing bigger models - an article entitled 'Big Jets Fly Again As Long-Haul Travel Picks Up' was issued on the February $6^{th}$, 2023 edition of the Wall Street Journal ([3]).

Hence, the comprehension of the dynamics involved and its effects are of current practical interest. The sloshing topic is therefore widely investigated, to the point of recognizing the need to establish reference conditions for experimental tests: in 2012, a benchmark on sloshing model tests was held with the participation of world-wide universities and research institutes [4] and other experimental rigs were conducted in order to provide useful information for further sloshing tests in various conditions and still capture experimental uncertainties [5]. Even though experimental tests remain crucial for the comprehension of the sloshing mechanics, analytical and numerical approaches developed upon the consistent experimental background can provide useful alternatives or completions of the field campaigns. In order to obtain the response spectrum of the liquid motion, analytical equations with rigorous solution may be used [6]. Nonetheless, when describing non-linear phenomena, their handling may thoroughly outcome too complex, as closed explicit solutions are feasible only for a few special cases such as upright cylindrical and rectangular containers [1].

In the latter case, an alternative to the costly physical tests to investigate non-linear dynamics is offered by numerical methods, within which it is possible to vary dimensions and conditions of the fluid-tank system. Generally, Computational Fluid Dynamics (CFD) methods are preferred when studying extreme phenomena with significant nonlinearities, as it may be in sloshing near resonance, and mesh-less approaches are likely more feasible than mesh-based ones when dealing with free-surface flows and considerable displacements. In mesh-based procedures, in fact, the relative position of the lattice nodes is predetermined and difficulties arise when simulating large deformations, discontinuities or even phase transformations [7]. Mesh-less methods, on the other hand, do not require any fixed grid to connect the computational nodes, which, hence, develop their own physical evolution, including changes of position, according to governing equations.

Nevertheless, mesh-based methods have been extensively used to investigate weakly non-linear phenomena and with very accurate results [8]. The re-meshing computational cost, however, may turn them into less efficient solution when compared to mesh-less methods for FSI studies, having to couple different meshing procedures between fluid and structure phases, especially for deformable structures [9]. Further methods, such as Arbitrary Lagrangian-Eulerian (ALE), were proposed in attempt to capture deformations, but their efficiency is limited for small deformations [10], and still require another Lagrangian mesh to discretize the structure [8].

In particle methods [11] the domain can be discretized in nodes (particles) carrying their own assigned information about the physical properties. Among the particle methods, the Smoothed Particles Hydrodynamic (SPH) method is used for this investigation.

The SPH is a meshless discretization technique that has been widely used to CFD applications [12]. The inherent suitability of this approach for reproducing the physics featured in sloshing problems greatly helped in divulging the SPH method as a real alternative to traditional grid-based solvers [13]. Even the aforementioned issue of sloshing in LNG tankers was investigated through SPH simulations [14]. It was recognized to be a promising tool, so further optimized application matured. Specifically regarding sloshing, benchmark experiments aimed to inquire the SPH simulation suitability: Vorobyev et al. [15] validated a 3-D Weakly Compressible formulation for central sloshing, whereas Zhang et al. [16] implemented a Riemann-based SPH solver with dissipation limiter (in order to restrain dissipation for violent free-surface phenomena) and applied it to violent sloshing phenomena. Generally, free-surface motion and impact pressure showed great accordance with experimental data.

The SPH implementation in DualSPHysics [17] provides several tools and features that make the code ready for engineering applications, and very efficient when fluid phases are relevant [more in 18]. During the last few years, the code has seen an increase in availability of functionalities that are very apt for the simulation of Fluid-Structure Interaction in different engineering fields, ranging from renewable energy device [19, 20, 21] to hydroelasticity problems [22, 23, 24, 25]. The code, moreover, proved its reliability for nearly any kind of free-surface flow interacting with rigid structures: dambreak-induced violent flows on downhill structures [26, 27], coastal breakwaters [28, 29] or floating objects [30, 31, 32]. Sloshing simulations as well have been performed using DualSPHysics. Green et al., 2021 [33] recently tackled complex 3-D cases of long duration sloshing in tanks, and Kotsarinis et al. 2023 [34] modeled sloshing damping for spacecrafts; a traditional sloshing problem, indeed, is utilized in English et al. 2022 [35] to assess the performance of the newly developed modified Dynamic Boundary Conditions (mDBC).

Undertaken this premise, we propose an analytical simplified approach, whose parameters are retrieved from numerical simulations. Our research consists in numerically simulating the fluid sloshing response induced by tank motion considering different filling ratios, i.e. the ratio between water level $d$ and the tank's semi-base $l$ - $(d/l)$. The tank is initially displaced using a smooth sinusoidal function that lasts one cycle and then the tank is kept still and the fluid motion is observed. The sloshing natural frequency is computed using an analytical relationship. The SPH solutions are validated against the reference solution for sloshing parametrization, and the results are compared with the outcomes obtained from other CFD approaches.

## 2 SPH DISCRETIZATION

In the Smoothed Particle Hydrodynamics (SPH) method, the value of the particle's properties derives from the interpolation, through a weighting function and its derivatives, of the neighboring particles' values. Hereupon, the hydrodynamic of fluid particles is calculated with the locally averaged Navier-Stokes equations, with conservation of mass and linear momentum [11].

The interpolation takes place within an established domain of influence (of the single particle) defined upon the so-called smoothing length ($h$). This interpolation is weighted by the smoothing function or kernel function (Figure 1), which corresponds to the discrete Dirac delta

function at a continuous level. The continuous SPH interpolation of a generic function reads:

$$< f(\mathbf{r}) >= \int_{\Omega} f(\mathbf{r'}) W(\mathbf{r'} - \mathbf{r}, h)\, d\Omega \tag{1}$$

where $f$ is the interpolation function (expressed in its integral average), $\Omega$ is the compact support, **r** and **r'** the position vectors of two different particles in space.

In discrete form, the function is approximated by summing up the values of the nearest neighbor particles that possess fixed mass $m_b$, density $\rho_b$, and volume $V_b$. The discrete form of Equation (2) for a particle $a$, being $b \in [1, N_p]$ part of its support domain is:

$$< f(\mathbf{r}_a) >= \sum_{b=1}^{N_p} \frac{m_b}{\rho_b} f(\mathbf{r}_b) W_{ab} \tag{2}$$

The smoothing length must be well-determined in order to maintain a compact support of the kernel - that is, to guarantee convergence. The latter kernel must satisfy several properties, like positivity on the compact support, normalization, and monotonically decreasing with distance. Kernel functions may assume different forms, which derive from the original Gaussian function; Gaussian kernels, however, are deprecated because of the heavy computational cost they require. The weighting function used in this work, hence, is defined by a piecewise polynomial expression, known as the Quintic Wendland kernel [36].

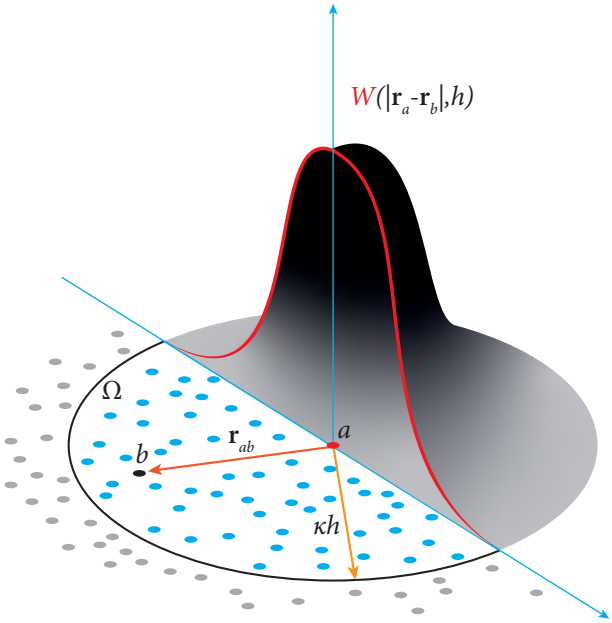


Figure 1: Example of a kernel function (reproduced from [26]).

DualSPHysics uses the so-called modified Dynamic Boundary Condition (or mDBC) to implement solid geometry discretizations within the SPH domain [35]. They overcome some issues of the former implementation, Dynamic Boundary Condition (DBC) – Crespo et al. [37]. The novel procedure is able to avoid the nonphysical gap between boundary and fluid particles that occur in dry boundary-wet boundary transition phases even using coarse resolution; this makes the mDBC perfectly suitable for the purpose of this work especially for the modeling of

sloshing fluid masses. Details about their implementation are in [35] in which a sloshing tank with very energetic motion is validated; other application can be found in Capasso et al. [38] and Ruffini et al. [39].

## 3 SLOSHING FLUID EQUIVALENT MODEL

The present investigation was done on a prismatic tank, and the motion imposed to it is purely horizontal: likewise, the sloshing motion is assumed to be horizontal. This premise allows us to study through a linearized two-dimensional model, as the flow motion does not present relevant three-dimensional features. By means of linearization, the motion is studied via the combination of the $m$ harmonic motions that compose it. Moreover, the fluid is considered to be irrotational and inviscid. Boundary conditions are withal inferred.

### 3.1 Fundamental assumptions

The liquid contained in the tank is considered to be incompressible, giving rise to the continuity equation:

$$\nabla \cdot \mathbf{u} = 0 \tag{3}$$

with $\mathbf{u} = \{u, w\}$ being the velocity field. The fluid is also inviscid, and its motion can be assumed irrotational, so that the velocity may be deduced from a velocity potential $\phi = \phi(x, z)$. In this case, the velocity is given by the spatial derivative of the defined potential, known as Laplace equation:

$$\nabla^2 \phi = 0 \tag{4}$$

Previous studies demonstrated that the moving fluid may be partitioned in an impulsive and a convective portion [40]. The former moves along with the tank whilst the latter oscillates relatively to it. The velocity potential, likewise, may be split into impulsive and convective:

$$\phi = \phi_i + \phi_c \tag{5}$$

The boundary conditions for the velocity potentials with respect to tank walls are:

$$\frac{\delta \phi_i}{\delta n} = V; \frac{\delta \phi_c}{\delta n} = 0 \tag{6}$$

where $V$ is the velocity of the tank in the direction of the imposed motion, and $n$ the direction orthogonal to the tank walls, retained undeformable [6]. This condition indicates that the motion of the particles near the tank wall is reconducted to the sole motion of the tank wall, that is, near the boundary, the motion is exclusively given by the impulsive portion of fluid.

As mentioned before, the sloshing phenomenon can be represented by $m$ modes of vibration. Of particular interest are the anti-symmetric modes, which horizontally shift the liquid's center of gravity position (Figure 2) producing lateral motion in order to re-establish equilibrium [41]. The convective oscillation also discloses free-surface phenomena which can often be nonlinear, except for small amplitude waves under weak oscillation.

### 3.2 Linearized flow equations

Our study proposes the numerical simulation of a sloshing problem included in the group of cases that have explicit solution by pure analytical methods, as the sloshing is purely horizontal and the tank has rigid upright walls with rectangular geometry. The latter cases are also feasible

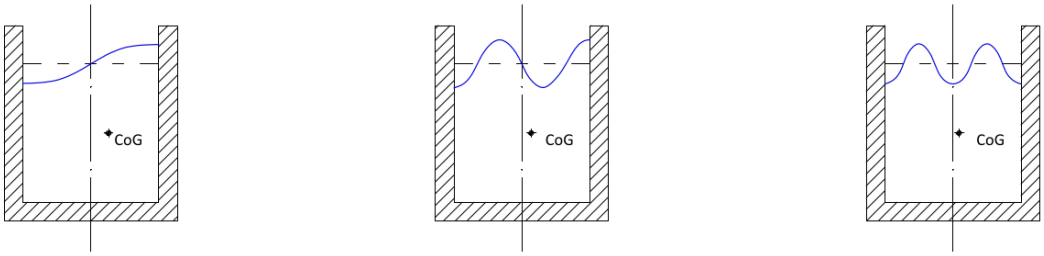


Figure 2: center of gravity shift in the first three anti-symmetric modes of vibration.

for mesh-based simulation. We are thus able to compare results from all three methods. The setup was arranged as illustrated in Figure 3. In order to analytically compare the results, the case must be linearized following the hypothesis hereunder exposed.

Inflicting a horizontal impulse to the tank, the displacement in time $X(t)$ may be written as:

$$X(t) = -iX_0 e^{i\omega t} \tag{7}$$

where $X_0$ is the initial position of the tank and $\omega$ is the angular frequency. Deriving $X(t)$ in time, we obtain the horizontal velocity of the tank $u(t)$:

$$u(t) = iX_0 \omega e^{i\omega t} \tag{8}$$

Given the system's geometrical and forcing conditions, waves generated with a single impulse tend to be regular. The free-surface elevation description is, hence, explicited by a sinusoidal function $\eta$:

$$\eta(x,t) = Asin(\omega t - kx) \tag{9}$$

being $A$ the amplitude of the wave, $k = 2\pi/\lambda$ the wave number (where $\lambda$ is the wave length). Moreover, the motion is considered to be smooth, so particles outlining the free-surface are always the same. At the same time, given the reference system as per Figure 3, with $x_1$ and $x_2$ being two consecutive positions of the same particle and $t_1$ and $t_2$ the respective instants observed ($\Delta t = t_2 - t_1$), we may linearly describe the free-surface as:

$$\eta|_{(x_2,t_2)} = \eta|_{(x_1,t_1)} + w\Delta t \tag{10}$$

At the same time, assuming that the elevation may be described as a harmonic function (sinusoidal), it can be explicited as a Taylor series. In our case, the series may be trimmed at its first order differential without considerable error; rewriting (10) as so, bringing $v\Delta t$ to the left term and dividing by $\Delta t$ gives:

$$w = \frac{\delta\eta}{\delta t} \tag{11}$$

namely, the kinematic free-surface boundary condition assuming small amplitudes ($\delta\phi/\delta x$ is negligible). The second fundamental assumption, as mentioned before, is that fluid is inviscid, that is, with no internal friction, so no dissipation is computed inside the system. The Bernoulli equation, hence describes the system's equilibrium. The kinematic term $u^2$+$w^2$ can

be considered negligible. Knowing that the fluid pressure at the surface ($z = 0$) is equal to the atmospheric pressure, we can set the dynamic free-surface boundary condition:

$$\frac{\delta\phi}{\delta t} + g\eta = 0 \tag{12}$$

where $g$ is the gravitational acceleration.

The velocity potential $\phi$, must then obey the two aforementioned boundary conditions, and may be written in the form:

$$\phi(x, z, t) = [C_1 \cosh k(z + d)] \sin(\omega t - kx + \phi_i) \tag{13}$$

in which $C_1$ is a case-dependent constant and $d$ is the water depth.

This potential description is suitable for our purpose of study, given that we aim to characterize the motion with a dispersion relation. In fact, fitting curves were proposed in literature with the angular frequency depending on the sole filling ratio ($d/l$). This means that for a tank of determined dimensions (semi-base $l$), $d$ becomes the only variable of the curve's equation. The curves previously proposed were obtained by the parametrization of the wave number, which is substituted by a fitting scalar. The fitting outcomes from data obtained with experimental tests, analytical solution or mesh-based simulation. We propose a further parametrization through data obtained in meshless simulation. Hereafter, comparison of our solution with the ones proposed in literature is done, aiming to optimize the fitting parameters.

In order to describe the free-surface, we recall that for our reference system the latter is located at $z = 0$ (Figure 3); hence, Equations (9) and (13) are substituted in Equation (12). We note that $w = \delta\eta/\delta t$, and at the same time, $w = \delta\phi/\delta z$. By these means, we conclude that:

$$\omega^2 = gk \tanh kd \tag{14}$$

which is an example of dispersion relation.

## 4 VALIDATION

The numerical setup is implemented in DualSPHysics according to Figure 3. The geometry of the tank is used throughout the testing phase, and only the water level ($d$) changed according to the specific test. The four walls are discretized using the mDBC technique and as such, they comprise seven layers of particles. As in Figure 3, two numerical gauges were positioned at a small distance $\delta$ from the two lateral solid boundaries to capture the dynamic evolution of the free-surface ($\eta$) during the simulation. The water is set into motion by an initial translation along the $x$-axis.

Aiming at the characterization of the fluid motion through its free-surface profile, which in pure horizontal motion may be approximated with the sole first mode shape, we simulated a decay test in DualSPHysics. The test consists in imposing to the tank a single horizontal sinusoidal impulse with determined amplitude and period. Next, the external impulse is ceased and the liquid is left to slosh without any external addition of energy. Using data sampled by the two wave gauges, the peak heights were identified, and eventually used to identify the period $T$ of the waves, as explained in the following. Specifically, the time series of the wave peaks was processed using a properly developed software routine, that purged the initial noise by backtracking data with circular shift. Using the up-zero-crossing method, we obtained the wave height referred to the undisturbed free-surface level.

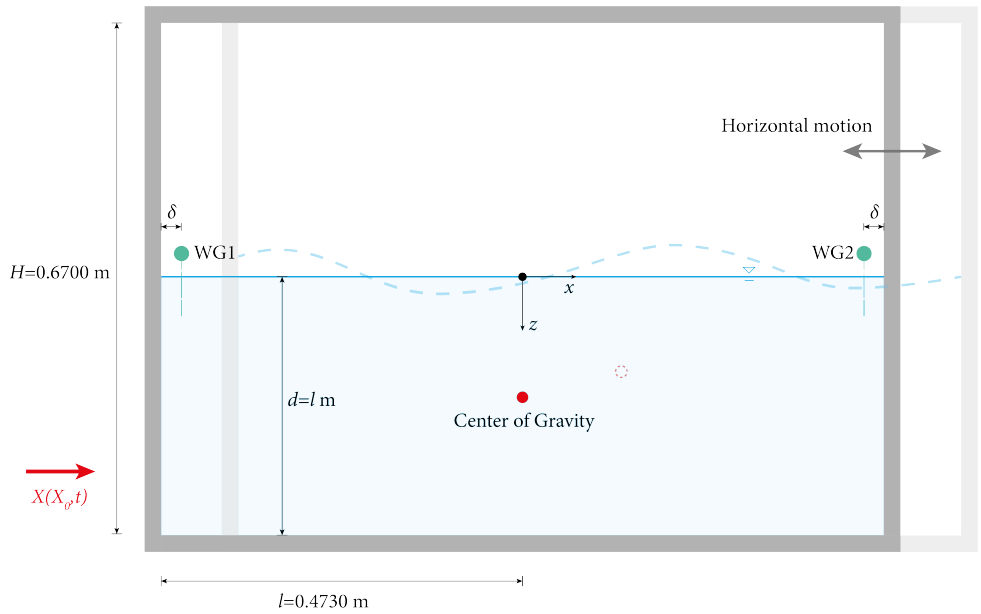


Figure 3: Sketch of the numerical setup implemented in DualSPHysics.

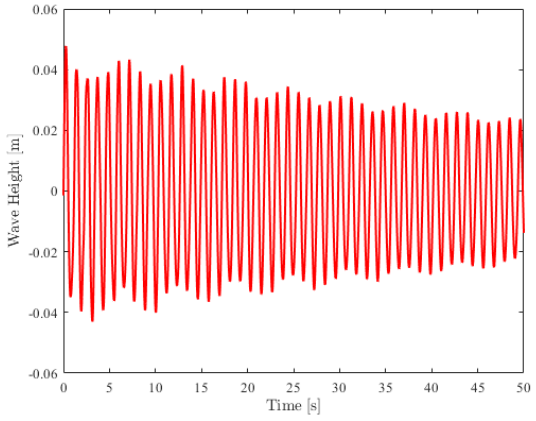


(a) Wave height measurements at WG1 for $d/l$ = 1.0.

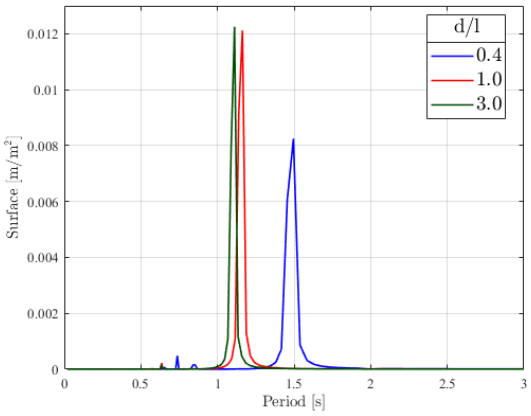


(b) Period spectrum for different filling ratios.

Figure 4: Transformation of the wave height signal from decay test simulations in DSPH.

The graphic Figure 4a shows the free surface time history gauged nearby the fixed wall of the tank. It can be observed that no substantial noise affects the decaying behavior of the fluid mass. Therefore, it is valid to determine the wave period as the interval between two subsequent peaks. We thus obviate the direct computation of $\lambda$.

The convolution of the period signal towards the the liquid was transferred through the Fast Fourier Transform (FFT) analysis tool, which operates with sinusoidal functions as basis. The period spectrum is respectively restored through sine functions [42].

Reading the period spectrum in Figure 4, whither the higher peak corresponds to the natural period ($T_1$) of the sloshing (higher density value of the spectrum). At this point, the natural

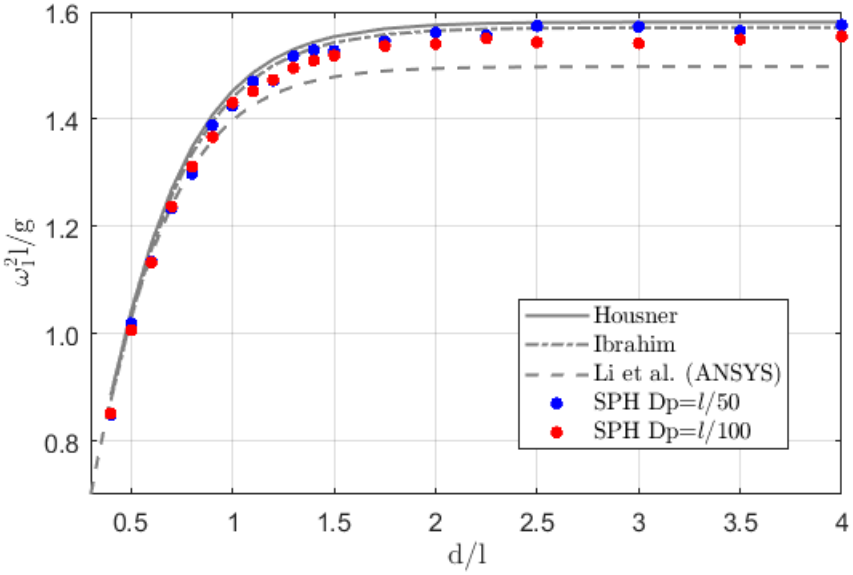


Figure 5: Comparison between results from simulations in DSPH ($Dp = l/50$ and $Dp = l/100$) and frequency curves previously proposed in literature ($Housner$ and $Ibrahim$).

frequency ($\omega_1$) is quantified using the following relationship:

$$\omega_1 = \frac{2\pi}{T_1} \tag{15}$$

The natural frequencies obtained, each regarding a specific filling ratio, were likewise charted. As previously mentioned, fitting curves linking $\omega$ to the filling ratio $d/l$ appear in literature. Specifically for the first mode of vibration, Housner (1963) [40], with an analytical-experimental method, proposed:

$$\omega_1^2 = \sqrt{2.5}.\frac{g}{l}.\tanh\sqrt{2.5}\frac{d}{l} \tag{16}$$

Further, finer research, headed by Ibrahim [1], explicited the equation with a purely analytical approach on different tank geometries (as a combination of primary geometry solutions). For anti-symmetric modes in a rectangular tank, it follows:

$$\omega_1^2 = \frac{g\pi}{2l}\tanh\frac{d\pi}{2l} \tag{17}$$

The approach was later optimized by Li et al. [43] with a simpler method using the CFD-based solver available in ANSYS, whose data was analytically synthesized by means of a least square fitting curve, giving the following equation:

$$\omega_1^2 = 1.498\frac{g}{l}\tanh 1.681\frac{d}{l} \tag{18}$$

We notice that all the proposed equations are parameter calibrations of Equation (14). Our numerical simulation was carried out in two different resolutions of discretization for the initial inter-particle distance ($Dp$). In particular, since $Dp = l/100$ showed good accordance with the

fitting curves mentioned above, an ulterior simulation was processed with $Dp = l/50$, and good accordance persisted (see Figure 5).

As a matter of fact, comparison between our results and the equations proposed in literature, even when simulation was carried out in low resolution ($Dp = l/50$ and $Dp = l/100$), shows that the natural frequency obtained was comprised between the curves delineated by equations by Li [43], Housner [40], and Ibrahim [1]. We may then conclude that great accordance was observed even for low resolution simulation (as for $Dp = l/50$ in Figure 5). This is an important result in an SPH simulation, given that high resolutions demand greater computational effort - thus, we were able to characterize a free-surface phenomenon with minor computational demand and no economical cost. Charting the solution equations proposed by Housner and Ibrahim, we observe that they are almost superimposed, whereas the simplification proposed by Li et al. addresses an underestimated value of $\omega_1$. In order to illustrate our considerations, we took the example of the simulation conducted for a $1.0$ filling ratio. Transforming the data from gauges through the FFT, we had a natural period $T_1$ of 1.163 s, consequently, a natural frequency $\omega_1$ of 5.403 rad/s. For the same filling ratio, results from literature were: 5.489 rad/s (Equation (16)); 5.466 rad/s (Equation (17)); 5.384 rad/s (Equation (18)).

Another available option for analyzing the simulation is an optical approach. By identifying frames with the same free-surface profile, the time interval between two consecutive matching profiles corresponds to the wave period. As illustrated above, wave periods may be computed based on the free-surface profile. A decay test was launched imposing a 0.040 m amplitude and 1.133 s period impulse to the partially filled tank with $d/l$ = 1.0.

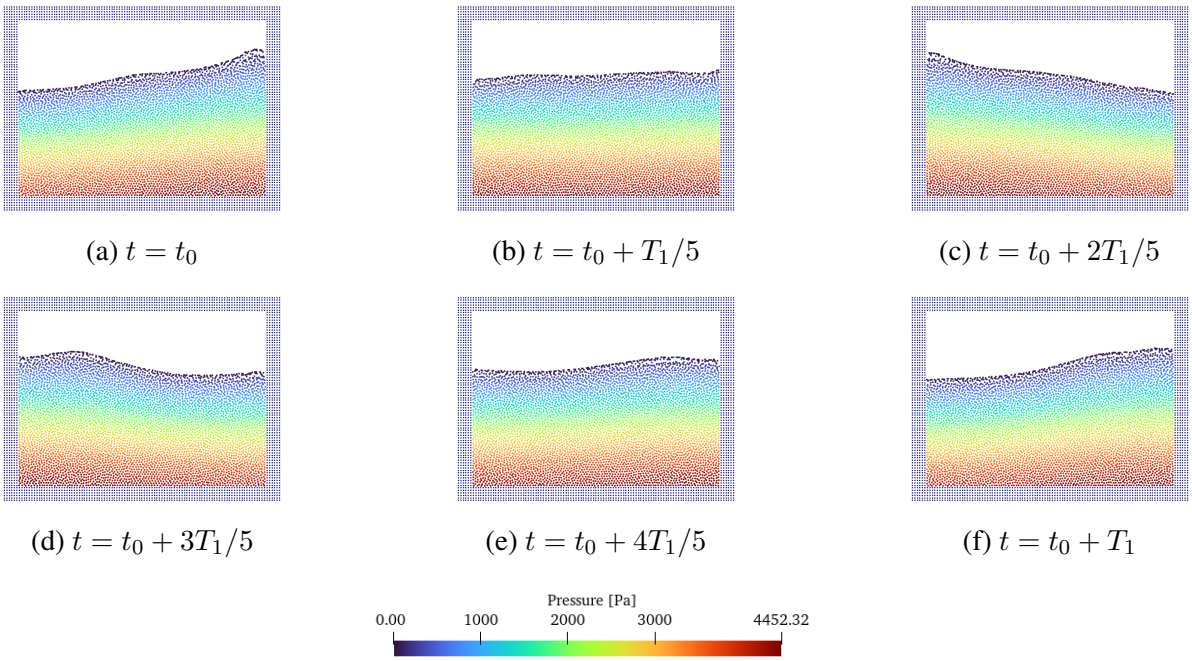


(a) $t = t_0$ (b) $t = t_0 + T_1/5$ (c) $t = t_0 + 2T_1/5$

(d) $t = t_0 + 3T_1/5$ (e) $t = t_0 + 4T_1/5$ (f) $t = t_0 + T_1$

Figure 6: Post-process visualization of the decay test simulation launched in DSPH during a time-lapse of $1.16s$.

In Figure 6, frames were captured in a time-lapse corresponding to the natural period $T_1$ obtained through the FFT of the wave signal captured. Even though profiles at the first (Figure 6a) and last (Figure 6f) frame are similar, they do not exactly correspond to each other, as we would expect for a regular wave at the completion of its period. A part from the fact that post-process

filter for the free-surface was not applied, other explanations may be seized: the waves are not purely regular; in the FFT the energy dissipation by collision with the tank wall is not computed; moreover, in the spectrum itself we notice that other than the higher density value there is a second minor peak at the left indicating another mode that still interferes (Figure 4).

## 5 CONCLUSIONS

The present study aimed to characterize the sloshing motion in a partially filled tank within a simplified method, that could nonetheless well capture free-surface outline and relative non-linearities. A numerical meshless approach was undertaken to avoid drawbacks observed in other methods – despite the accuracy, purely analytical solutions are not explicit if not in simple cases, such as rectangular rigid tank. Experimental tests offer indisputable reference data, though less affordable insight of economical costs and facilities needed. We thus proceeded with CFD simulations using the open-source code DualSPHysics. Depicting a case that could be described by explicit analytical formulae, numerical results were compared to theoretical solutions in sight of validating the use of SPH method.

Simulations consisted in imposing a force of determined amplitude ($A_t$) and period ($T_t$) to the tank through a horizontal thrust kept for a single cycle. Hence, ceased the motion, liquid was left to slosh and settled gauges measured the wave height at fixed points. The signal read was transformed into a spectrum, giving back the natural period of the fluid's motion. Once the natural period is known, we immediately calculate the natural frequency $\omega_1$. Our results, at that point, were compared to the ones proposed in literature so to assure that the method was valid. Accordingly, the numerical simulation results were actually close to that of other methods, and differently from the mesh-based model proposed by Li et al., in our case $w_1$ was not much underrated if compared to experimental results. The underestimation of the motion, indeed, could be a dangerous imprecision when foreseeing its effects on structures.

Once the motion is thus properly characterized, apropos of the specific filling ratio, sloshing may be tuned towards or against the natural frequency of the structure depending on the purpose of interest. By that premise, given the validation of the method and its potential to solve non-linear phenomena, it could represent a solution tool for further cases of study in which explicit analytical solving is not possible.

## References

[1] R. Ibrahim. *Liquid Sloshing Dynamics*. 2005.

[2] O. Faltinsen and A. Timokha. *Sloshing*. Cambridge University Press, 2009. ISBN: 9780521881111.

[3] B. Katz. "The World's Biggest Planes Are Finding Their Way Back Into the Skies." In: *Wall Street Journal* (2023).

[4] T. Loysel, S. Chollet, E. Gervaise, L. Brosset, and P.-E. Seze. "Results of the First Sloshing Model Test Benchmark." In: *Proceedings of the International Offshore and Polar Engineering Conference* (2012).

[5] A. Souto-Iglesias, E. Botia-Vera, A. Martín, and F. Pérez-Arribas. "A set of canonical problems in sloshing. Part 0: Experimental setup and data processing." In: *Ocean Engineering* 38.16 (2011), pp. 1823–1830. ISSN: 0029-8018.

[6] F. Dodge. *THE NEW "DYNAMIC BEHAVIOR OF LIQUIDS IN MOVING CONTAINERS"*. 2000.

[7] S. Garg and M. Pant. "Meshfree Methods: A Comprehensive Review of Applications." In: *International Journal of Computational Methods* 15 (2017).

[8] Z. Ozdemir, M. Moatamedi, Y. Fahjan, and Y. Soulie. "ALE and Fluid Structure Interaction for Sloshing Analysis." In: *The International Journal of Multiphysics* 3 (2009), pp. 307–336.

[9] J. Xu and Y. Soulie. "SPH and ALE formulations for sloshing tank analysis." In: *The International Journal of Multiphysics* 9 (2015), pp. 209–224.

[10] M. Rakhsha, C. Kees, and D. Negrut. "Lagrangian vs. Eulerian: An Analysis of Two Solution Methods for Free-Surface Flows and Fluid Solid Interaction Problems." In: *Fluids* 6 (2021), p. 460.

[11] G. Liu and M. Liu. *Smoothed Particle Hydrodynamics*. WORLD SCIENTIFIC, 2003.

[12] J. Monaghan. "Smoothed Particle Hydrodynamics." In: *Annual Review of Astronomy and Astrophysics* 30.1 (1992), pp. 543–574.

[13] M. Liu and G. Liu. "Smoothed Particle Hydrodynamics (SPH): an Overview and Recent Developments." In: *Archives of Computational Methods in Engineering* 17 (2010), pp. 25–76.

[14] L. Delorme, A. Souto-Iglesias, and S. Pérez. "Sloshing loads simulation in LNG tankers with SPH." In: (2005).

[15] A. Vorobyev, V. Kriventsev, and W. Maschek. "Simulation of central sloshing experiments with smoothed particle hydrodynamics (SPH) method." In: *Nuclear Engineering and Design - NUCL ENG DES* 241 (2011).

[16] C. Zhang, Y. Zhu, D. Wu, N. Adams, and X. Hu. "Smoothed Particle Hydrodynamics: Methodology development and recent achievement." In: (2022).

[17] J. M. Domínguez et al. "DualSPHysics: from fluid dynamics to multiphysics problems." In: *Computational Particle Mechanics* 9.5 (2022), pp. 867–895. ISSN: 2196-4386.

[18] C. Altomare, J. M. Domínguez, and G. Fourtakas. "Latest developments and application of SPH using DualSPHysics." In: *Computational Particle Mechanics* 9.5 (2022), pp. 863–866.

[19] B. Tagliafierro et al. "A new open source solver for modelling fluid-structure interaction: case study of a point-absorber wave energy converter with a power take-off unit." In: *Proceedings of the 11$^{th}$ International Conference on Structural Dynamics, Athens, Greece*. 2020.

[20] B. Tagliafierro, P. Ropero-Giralda, A. J. C. Crespo, J. Coe Ryan G.and Domínguez, G. Bacelli, and M. Gómez-Gesteira. "DualSPHysics: a Numerical Tool to Design Point-Absorbing WECs." In: *14th European Wave and Tidal Energy Conference (EWTEC), Plymouth, UK*. 2021.

[21] B. Tagliafierro, I. Martínez-Estévez, J. M. Domínguez, A. J. Crespo, M. Göteman, J. Engström, and M. Gómez-Gesteira. "A numerical study of a taut-moored point-absorber wave energy converter with a linear power take-off system under extreme wave conditions." In: *Applied Energy* 311 (2022), p. 118629. ISSN: 0306-2619.

[22] S. Capasso et al. "On the development of a novel approach for simulating elastic beams in DualSPHysics with the use of the Project Chrono library." In: vol. 2021-June. National Technical University of Athens, 2021.

[23] S. Capasso, B. Tagliafierro, I. Martínez-Estévez, J. M. Domínguez, A. J. C. Crespo, and G. Viccione. "A DEM approach for simulating flexible beam elements with the Project Chrono core module in DualSPHysics." In: *Computational Particle Mechanics* 9.5 (2022), pp. 969–985. ISSN: 2196-4386.

[24] J. O'Connor and B. D. Rogers. "A fluid–structure interaction model for free-surface flows and flexible structures using smoothed particle hydrodynamics on a GPU." In: *Journal of Fluids and Structures* 104 (2021), p. 103312. ISSN: 0889-9746.

[25] I. Martínez-Estévez, B. Tagliafierro, J. El Rahi, J. Domínguez, A. Crespo, P. Troch, and M. Gómez-Gesteira. "Coupling an SPH-based solver with an FEA structural solver to simulate free surface flows interacting with flexible structures." In: *Computer Methods in Applied Mechanics and Engineering* 410 (2023), p. 115989. ISSN: 0045-7825.

[26] S. Capasso et al. "A Numerical Validation of 3D Experimental Dam-Break Wave Interaction with a Sharp Obstacle Using DualSPHysics." In: *Water* 13.15 (2021). ISSN: 2073-4441.

[27] G. Ruffini et al. "MESH-IN: A MESHed INlet offline coupling method for 3-D extreme hydrodynamic events in DualSPHysics." In: *Ocean Engineering* 268 (2023). ISSN: 0029-8018.

[28] C. Altomare, A. Crespo, B. Rogers, J. Dominguez, X. Gironella, and M. Gómez-Gesteira. "Numerical modelling of armour block sea breakwater with smoothed particle hydrodynamics." In: *Computers & Structures* 130 (2014), pp. 34–45. ISSN: 0045-7949.

[29] F. Zhang, A. Crespo, C. Altomare, J. Domínguez, A. Marzeddu, S.-p. Shang, and M. Gómez-Gesteira. "DualSPHysics: A numerical tool to simulate real breakwaters." In: *Journal of Hydrodynamics* 30 (2018).

[30] J. Domínguez et al. "SPH simulation of floating structures with moorings." In: *Coastal Engineering* 153 (2019), p. 103560. ISSN: 0378-3839.

[31] B. Tagliafierro, M. Karimirad, I. Martínez-Estévez, J. M. Domínguez, G. Viccione, and A. J. C. Crespo. "Numerical Assessment of a Tension-Leg Platform Wind Turbine in Intermediate Water Using the Smoothed Particle Hydrodynamics Method." In: *Energies* 15.11 (2022). ISSN: 1996-1073.

[32] C. Salvatore et al. "Numerical Simulation of a Moored Wave-Buoy in Waves and Current by Smoothed Particle Hydrodynamics." In: *Proceedings of 42$^n$d International Conference on Offshore Mechanics and Arctic Engineering - OMAE*. 2023.

[33] M. D. Green, Y. Zhou, J. M. Dominguez, M. G. Gesteira, and J. Peiró. "Smooth particle hydrodynamics simulations of long-duration violent three-dimensional sloshing in tanks." In: *Ocean Engineering* 229 (2021), p. 108925. ISSN: 0029-8018.

[34] K. Kotsarinis, M. Green, A. Simonini, O. Debarre, T. Magin, and A. Tafuni. "Modeling sloshing damping for spacecraft: A smoothed particle hydrodynamics application." In: *Aerospace Science and Technology* 133 (2023), p. 108090. ISSN: 1270-9638.

[35] A. English et al. "Modified dynamic boundary conditions (mDBC) for general-purpose smoothed particle hydrodynamics (SPH): application to tank sloshing, dam break and fish pass problems." In: *Computational Particle Mechanics* 9.5 (2022), pp. 1–15.

[36] H. Wendland. "Piecewise polynomial, positive definite and compactly supported radial basis functions of minimal degree." In: *Advances in Computational Mathematics* 4.1 (1995), pp. 389–396.

[37] A. Crespo, M. Gómez-Gesteira, and R. Dalrymple. "Boundary conditions generated by dynamic particles in SPH methods." In: *Computers, Materials and Continua* 5.3 (2007), pp. 173–184. ISSN: 1546-2218.

[38] S. Capasso et al. "A numerical validation of 3d experimental dam-break wave interaction with a sharp obstacle using dualsphysics." In: *Water (Switzerland)* 13.15 (2021). ISSN: 2073-4441.

[39] G. Ruffini, R. Briganti, P. De Girolamo, J. Stolle, B. Ghiassi, and M. Castellino. “Numerical Modelling of Flow-Debris Interaction during Extreme Hydrodynamic Events with DualSPHysics-Chrono.” In: *Applied Sciences* 11.8 (2021). ISSN: 2076-3417.

[40] G. W. Housner. “The dynamic behavior of water tanks.” In: *Bulletin of the Seismological Society of America* 53.2 (1963), pp. 381–387. ISSN: 0037-1106.

[41] F. Angeletti, A. Stolfi, and P. Gasbarri. “Learning-based Control of a Spacecraft with Sloshing Propellant.” In: *Aerotecnica Missili & Spazio* 99 (2020).

[42] P. S. Heckbert. “Fourier Transforms and the Fast Fourier Transform ( FFT ) Algorithm.” In: (1998).

[43] Y.-C. Li and H.-L. Gou. “Modeling Problem of Equivalent Mechanical Models of a Sloshing Fluid.” In: *Shock and Vibration* 2018 (2018), pp. 1–13.

COMPDYN 2023
9th ECCOMAS Thematic Conference on
Computational Methods in Structural Dynamics and Earthquake Engineering
M. Papadrakakis, M. Fragiadakis (eds.)
Athens, Greece, 12-14 June 2023

# SEISMIC NUMERICAL MODELLING OF ELECTRICAL CABINETS

**D. Rodriguez[1], S. Peloso[2], E. Brunesi[2], D. Perrone[1,3] and A. Filiatrault[1]**

[1] University School for Advanced Studies IUSS Pavia
Piazza della Vittoria, n.15, Pavia, Italy
e-mail: derek.rodriguez@iusspavia.it, daniele.perrone@iusspavia.it, andre.filiatrault@iusspavia.it

[2] European Centre for Training and Research in Earthquake Engineering
Via A. Ferrata, n.1, Pavia, Italy
email: simone.peloso@eucentre.it, emanuele.brunesi@eucentre.it

[3] University of Salento
Piazza Tancredi, n.7, Lecce, Italy

## Abstract

*The seismic performance of non-structural elements, such as electrical cabinets, has been proven to be of crucial importance when assessing the global performance of modern code-compliant facilities. The seismic performance of several typologies of electrical cabinets was recently assessed in a shake table testing campaign conducted in the 6DLAB laboratory of the Eucentre Foundation, located in Pavia, Italy. Using the experimental data obtained from the testing campaign, numerical models were calibrated to reproduce the hysteretic response of the electrical cabinets. Three different criteria were considered for the calibration of the numerical models: i) absorbed energy time-history, ii) relative displacement time-history, and iii) force-relative displacement hysteretic response. The developed numerical models can approximate the seismic response of the electrical cabinets when subjected to the seismic testing protocols of increasing intensity used during the testing campaign. Furthermore, the developed numerical models are useful to generalize the experimental results obtained in the testing campaign and can be used to conduct additional numerical studies on the seismic performance of other configurations of electrical cabinet systems.*

**Keywords:** Non-structural elements, electrical cabinets, hysteretic response, numerical modelling, absorbed energy.

## 1 INTRODUCTION

Non-structural elements (NSEs) became a crucial aspect of earthquake engineering after the introduction of performance-based seismic design by the Pacific Earthquake Engineering Research Center in the early 2000's [1]. The necessity of improving the global seismic performance of code-compliant facilities shed some light into previously overlooked issues, as for example the higher vulnerability exhibited by NSEs in comparison to their structural counterpart, especially at lower seismic intensities [2,3].

In order to improve the seismic performance of NSEs, such as electrical cabinets, several experimental and numerical studies have been conducted during the last two decades by the earthquake engineering community. As part of these efforts, a shake table experimental campaign was conducted recently to assess the seismic performance of several typologies of electrical cabinets in the 6DLAB laboratory of the Eucentre Foundation, located in Pavia, Italy [4]. During this experimental campaign, seven different specimens of electrical cabinets were tested using two different loading protocols, namely the Telcordia-GR-63-CORE loading [5] and the protocol developed recently as part of a proposed seismic classification procedure for NSEs in Italy [4, 6]. The installed instrumentation consisted of an array of accelerometers to measure the acceleration response of the specimens, and horizontal and vertical potentiometers to measure the horizontal displacement and uplift of the specimens, respectively. Details on the experimental campaign can be found in Merino et al. [4].

While comprehensive testing is a necessary process to characterize the seismic response of non-structural systems, due to economic and functional limitations it is usually not possible to test every possible geometrical and material configuration of a given non-structural system typology. Therefore, the calibration of numerical models based on experimental data is often conducted to generalize the results obtained from experimental campaigns to be used in different geometrical and material configurations than the ones tested. It should be noted that when using numerical models calibrated based on experimental results, attention should be paid to the characteristics of the specimen (i.e., geometry, type of profiles, connections between the load bearing elements, etc.), given that different constructive solutions could lead to NSEs apparently similar but characterized by different seismic responses. Analogously to the case of structural systems, the detailing adopted for the seismic design of a NSE can play a critical role, deeply influencing the ductility and energy dissipation capacity.

In order to generalize the results obtained from the experimental campaign conducted by Merino et al. [4], this paper develops numerical models based on one of the tested cabinet specimens. The developed numerical models were calibrated based on the relative displacement time-history, absorbed energy time-history, and force-relative displacement hysteretic response. The objective was to generate calibrated models that are able to approximate the response of the electrical cabinets when subjected to the loading protocols used in the experimental campaign and that can be used to conduct additional numerical studies on the seismic performance of other configurations of electrical cabinets.

## 2 TEST SPECIMEN SELECTED FOR THE CALIBRATION

The seven electrical cabinets specimens tested during the experimental campaign were divided in two groups. Group 1 consisted of four different electrical cabinet specimens mounted on the surface of the shake table and tested at the same time. On the other hand, Group 2 consisted of three electrical cabinet specimens, one mounted on a rigid steel frame rigidly attached to the surface of the shaking table to simulate a wall-mounted cabinet, while the other two specimens were mounted on the surface of the shake table, as the specimens of Group 1. The

Specimen 4 of Group 1 was selected to conduct the calibration of the numerical models, given that during the shake table tests this specimen experienced progressive damage as the intensity of the loading protocols increased, therefore allowing for a proper calibration of the response along the complete range of elastic and inelastic response. Figure 1 shows a photograph and the geometry of the selected specimen for the calibration of the numerical models.

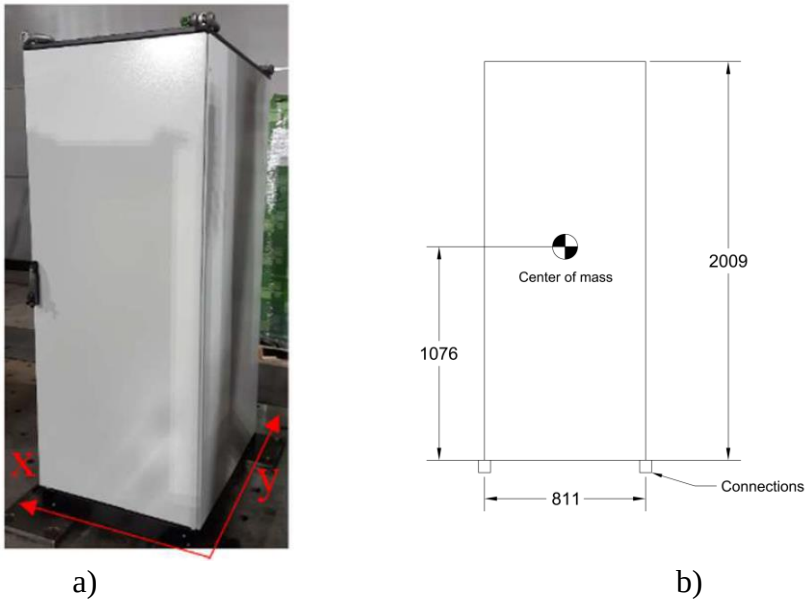


a) b)

**Figure 1. Specimen selected for the calibration of the numerical models: a) Photograph of the specimen, and b) its respective geometry along the shorter direction (x direction). Units in millimeters.**

## 3 NUMERICAL MODELS

Two different modelling approaches were followed to recreate numerically the response of the electrical cabinets documented during the experimental campaign: i) a single-degree-of-freedom (SDOF) system calibrated to match the relative displacement time-history, absorbed energy time-history, and force-relative displacement hysteretic response obtained during the experimental campaign, and ii) a mechanics-based multiple-degree-of-freedom (MDOF) system in which the calibration of the response of the specimen attachments and the specimen internal support structure were conducted separately, based on proper decomposition of the recorded experimental response. The separately calibrated degrees of freedom of the MDOF were then combined to recreate the relative displacement time-history, absorbed energy time-history, and force-relative displacement hysteretic response observed during the experimental tests. In the following sections, each of the modelling approaches is described in detail. The absorbed energy was defined as the integration over time of the force experienced by the specimen integrated through its displacement.

### *3.1 Single-degree-of-freedom model*

The first numerical model, calibrated with the experimental shake-table test data consisted in a SDOF damped system with a non-linear spring ($K_c$), and a dashpot ($C$) supplying additional energy dissipation beyond the hysteretic energy dissipated by the yielding of the non-linear spring. Figure 2 shows a schematic view of the proposed SDOF modelling approach. The calibration of the model was conducted by using the open-source platform OpenSees [7]. The *Hysteretic* tri-linear material from the OpenSees material library [9] was used to calibrate the non-linear spring $K_c$ (Figure 2). A damping ratio equal to 4.5% was considered for the definition of the dashpot element in order to improve the match of the absorbed energy time history.

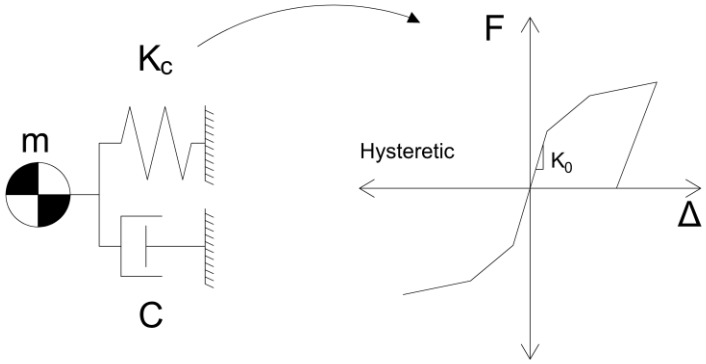


**Figure 2. Modelling approach selected for the SDOF numerical model of the electrical cabinets.**

### *3.2 Multiple-degree-of-freedom model*

The second model consisted in a mechanics-based MDOF model, which has a pair of non-linear springs to capture the response of the base connections of the electrical cabinet specimens, and another non-linear spring to capture the lateral response of the internal support structure of the electrical cabinet. For the calibration of this model, the response of the base connections and the internal support structure of the electrical cabinet specimen were decoupled and calibrated independently. Figure 3 shows a schematic view of the modelling and calibration approach considered for the MDOF model of the electrical cabinets. The developed MDOF model was inspired by the model proposed by Feinstein and Moehle [8]. Note that no additional damping was applied to this model beyond the hysteretic damping provided by the yielding of the non-linear springs. As for the case of the SDOF model, the open-source platform OpenSees was used for the calibration of the numerical model. A *Hysteretic* tri-linear material was used for the calibration of the base non-linear springs ($K_a$) that are meant to simulate the response of the electrical cabinet attachments to the ground slab, while a *SelfCentering* (flag-shaped) material was selected to calibrate the non-linear spring meant to simulate the response of the internal support structure of the electrical cabinet ($K_c$) [9]. The calibration of $K_a$ and $K_c$ was conducted by decoupling the numerical modelling, as shown in Figure 3a and Figure 3b. The force-relative displacement hysteretic response, absorbed energy time-history, and the relative displacement time-history of the specimen obtained at the lower intensity range of the experimental campaign were used for the calibration of the $K_c$ non-linear spring, given that, at the lower intensity range, the response of the electrical cabinets was strongly dominated by the response of the internal support structure, with no rocking of the specimen occurring. On the other hand, the non-linear springs $K_a$ were calibrated by using the response of the specimen at the higher intensity range, where the response of the specimen was mainly driven by the non-linear response of the base attachments, with significant rocking of the specimen being mobilized. The calibration process was completed by integrating the independently calibrated non-linear springs $K_a$ and $K_c$ in a single numerical model, as shown in Figure 3c, and adjusting the calibrated parameters of the non-linear spring $K_a$ in order to match the response of the numerical model to that of the specimen across the complete intensity range of the experimental campaign.

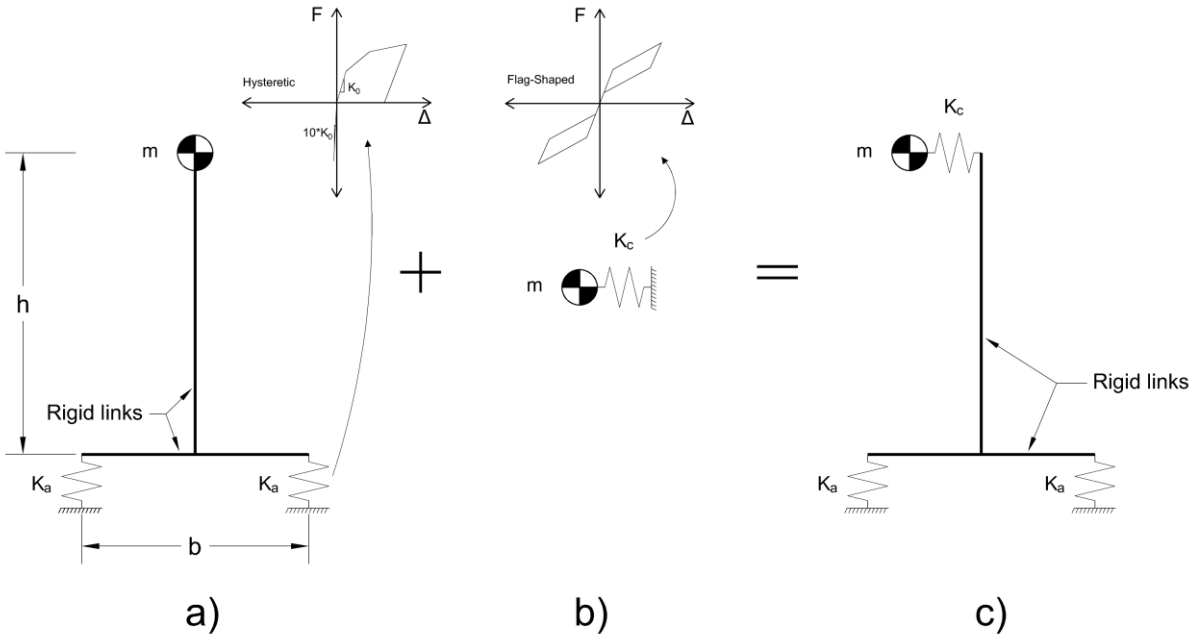


**Figure 3. Modelling and calibration approach considered for the MDOF numerical model of the electrical cabinets.**

For the calibration of the $K_a$ non-linear springs, a compression stiffness one order of magnitude higher than the tension stiffness was considered, in order to simulate the vertical constraint provided by the base slab at which the specimens are connected. Rigid links are used to locate the mass *m* of the specimen at its center of gravity at a height *h* and a width *b/2* and recreate the overturning moment produced by the electrical cabinet mass distribution.

## 4 RESULTS

### *4.1 Single-degree-of-freedom model*

The SDOF model was calibrated using 15 shake table tests of increasing intensity conducted during the experimental campaign. The input demand on the model consisted in the acceleration time-histories recorded at the base level of the shake table for each of the considered tests. The calibration was conducted individually for each of the selected tests, thus the damage accumulation experienced by the electrical cabinets due to the sequence of tests is not considered within this numerical model. Figure 4, Figure 5, and Figure 6 show the comparison between the absorbed energy time-history, the hysteretic response, and the relative displacement time-history documented for each of the selected tests from the experimental campaign against the prediction of the calibrated SDOF numerical model. The identification number assigned to each of the tests during the experimental campaign along with the corresponding peak test acceleration (PTA) are indicated for each of the tests used for the calibration of the numerical models. The numerical model is able to approximate accurately the absorbed energy and relative displacement time-histories. With respect to the hysteretic response, the numerical model underestimates the force experienced by the electrical cabinet during the selected tests from the experimental campaign. It is worth mentioning that applying a low-pass filter (at about 8Hz) to

remove the high frequency content shown by the recorded acceleration time-histories, but absent in the recorded displacement time-histories, improves the accuracy of the inertial force estimate. The final calibrated parameters for the hysteretic material of the SDOF numerical model are listed in Table 1.

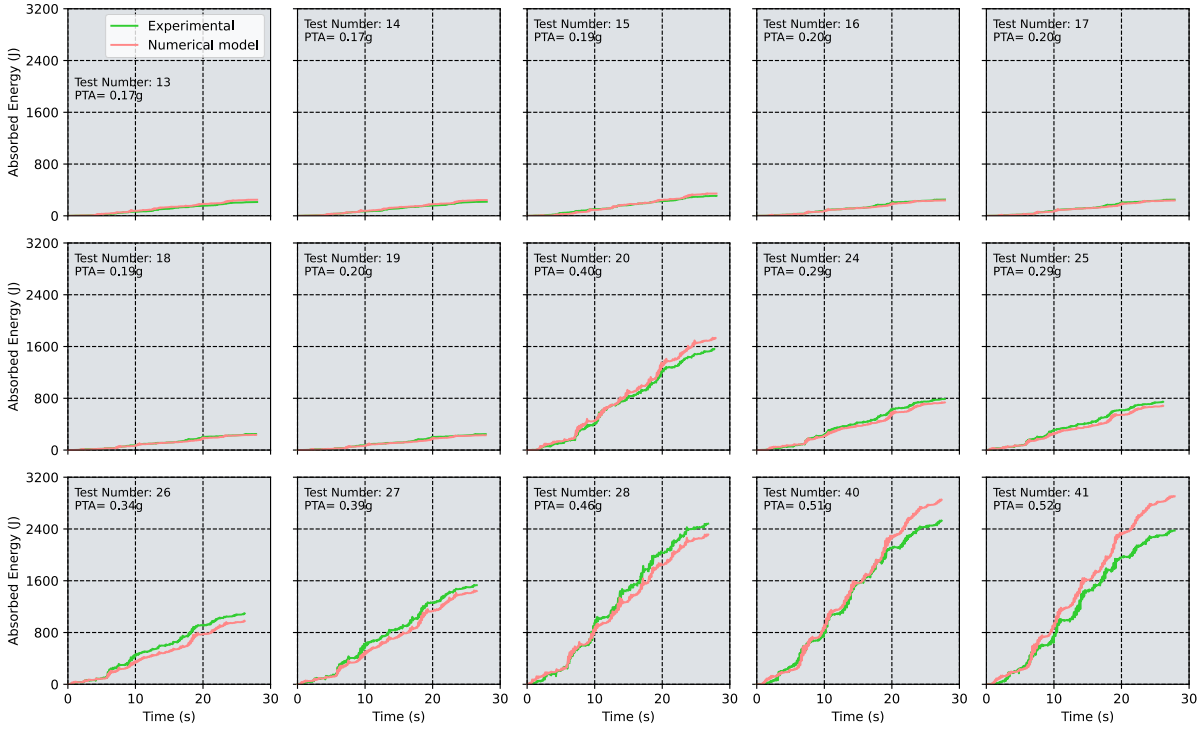


**Figure 4. Comparison of the absorbed energy time-history of the electrical cabinet obtained during the experimental campaign against the prediction of the calibrated SDOF numerical model**

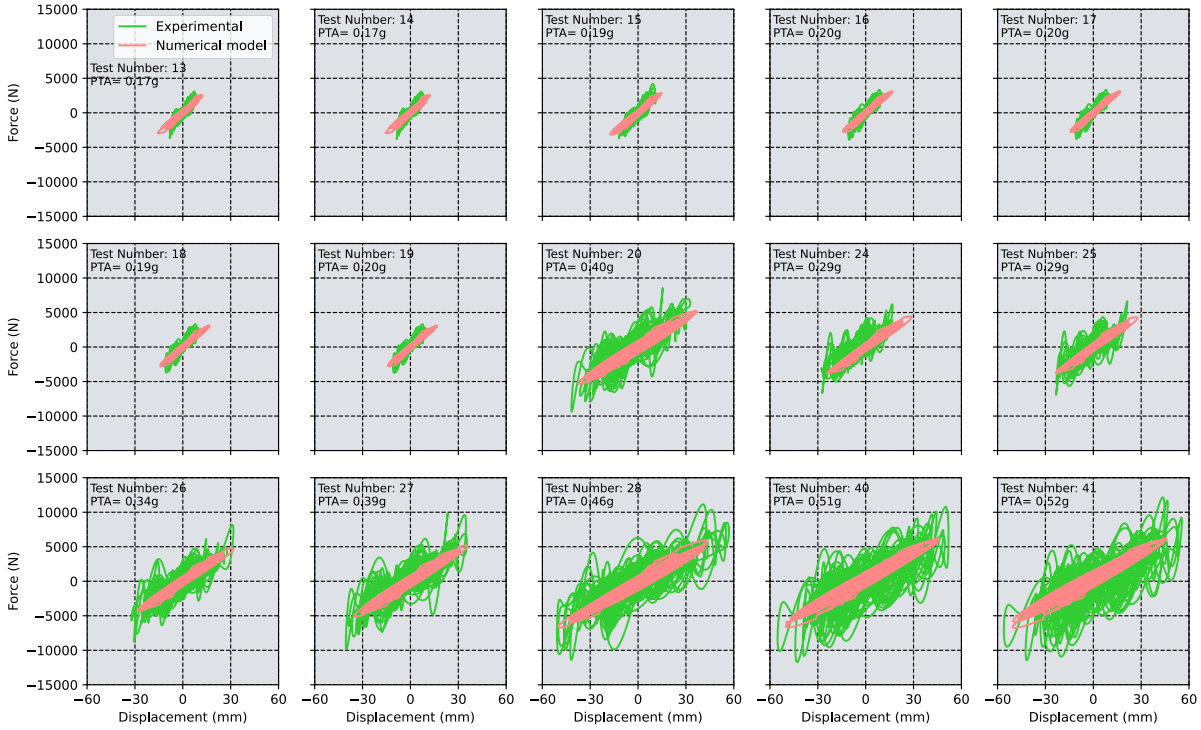


**Figure 5. Comparison of the hysteretic response of the electrical cabinet obtained during the experimental campaign against the prediction of the calibrated SDOF numerical model**

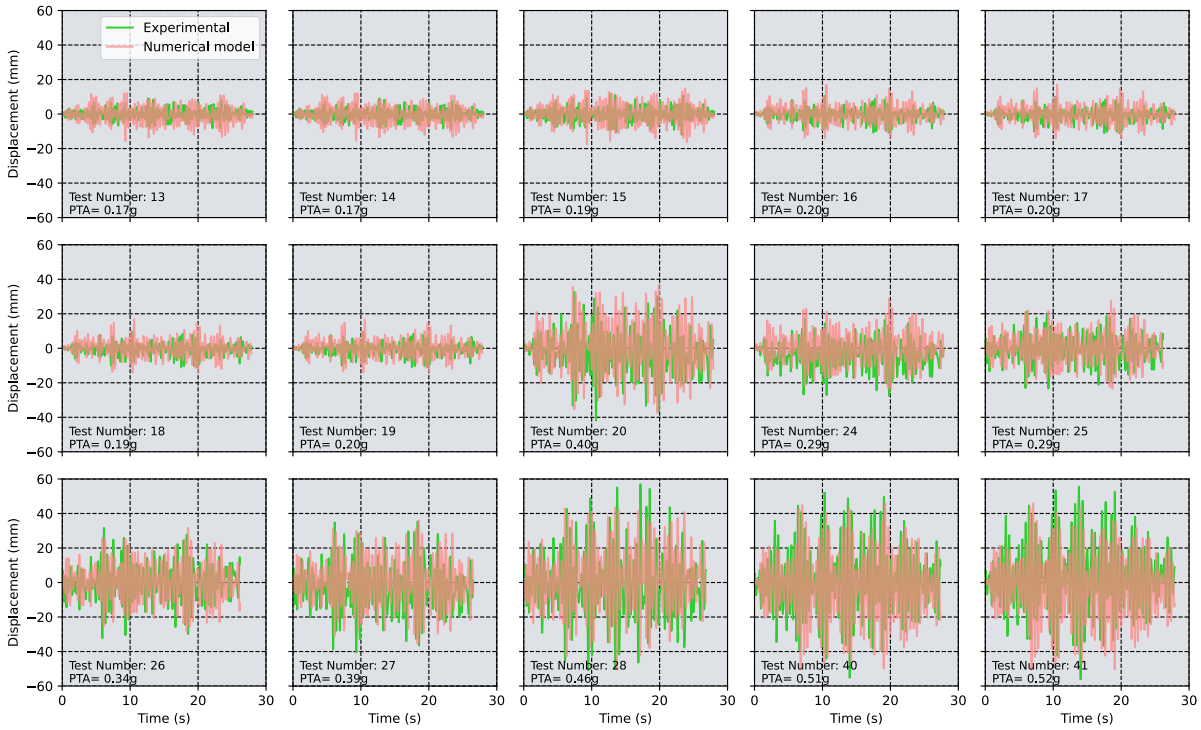


**Figure 6. Comparison of the relative displacement time-history of the electrical cabinet obtained during the experimental campaign against the prediction of the calibrated SDOF numerical model**

**Table 1. Calibrated parameters for the *Hysteretic* material of the SDOF numerical model**

| ***Hysteretic ($K_c$)*** | |
|---|---|
| ***Parameter*** | ***Value*** |
| $s_{1p}$ | 0.35 |
| $e_{1p}$ | 0.7 |
| $s_{2p}$ | 2 |
| $e_{2p}$ | 7 |
| $s_{3p}$ | 6.68 |
| $e_{3p}$ | 50.9 |
| $s_{1n}$ | -0.35 |
| $e_{1n}$ | -0.7 |
| $s_{2n}$ | -2 |
| $e_{2n}$ | -7 |
| $s_{3n}$ | -6.68 |
| $e_{3n}$ | -50.9 |
| *pinchx* | 1 |
| *pinchy* | 0.2 |
| *damage1* | 0 |
| *damage2* | 0 |
| $\beta_H$ | 0.33 |
| $x_{Damp}$ | 4.50E-02 |

### *4.2 Multiple-degree-of-freedom-model*

For the calibration of the MDOF numerical model, the same 15 shake table tests used for the calibration of the SDOF numerical model were considered. In this case, the calibration was conducted by using the final state of the MDOF numerical model after each of the selected shake table tests, as initial conditions for the following shake table test, thus considering explicitly the damage accumulation in the electrical cabinets. Figure 7, Figure 8 and Figure 9 show the comparison between the absorbed energy time-history, the hysteretic response, and the relative displacement time-history documented for each of the selected tests from the experimental campaign against the prediction of the calibrated MDOF numerical model. The identification number assigned to each of the tests during the experimental campaign along with the corresponding peak test acceleration (PTA) are indicated for each of the tests used for the calibration of the numerical models. As for the case of the SDOF numerical model, the MDOF numerical model is also able to approximate accurately the absorbed-energy and relative displacement time-histories, while for the case of the hysteretic response, the force experienced by the electrical cabinets is underestimated. An improvement in the accuracy of the inertial force estimates is also observed for the MDOF numerical model when applying a low-pass filter (at about 8Hz) to the recorded acceleration time-histories. The final calibrated parameters for the *Hysteretic* and *SelfCentering* (flag-shaped) materials of the MDOF numerical model are listed in Table 2.

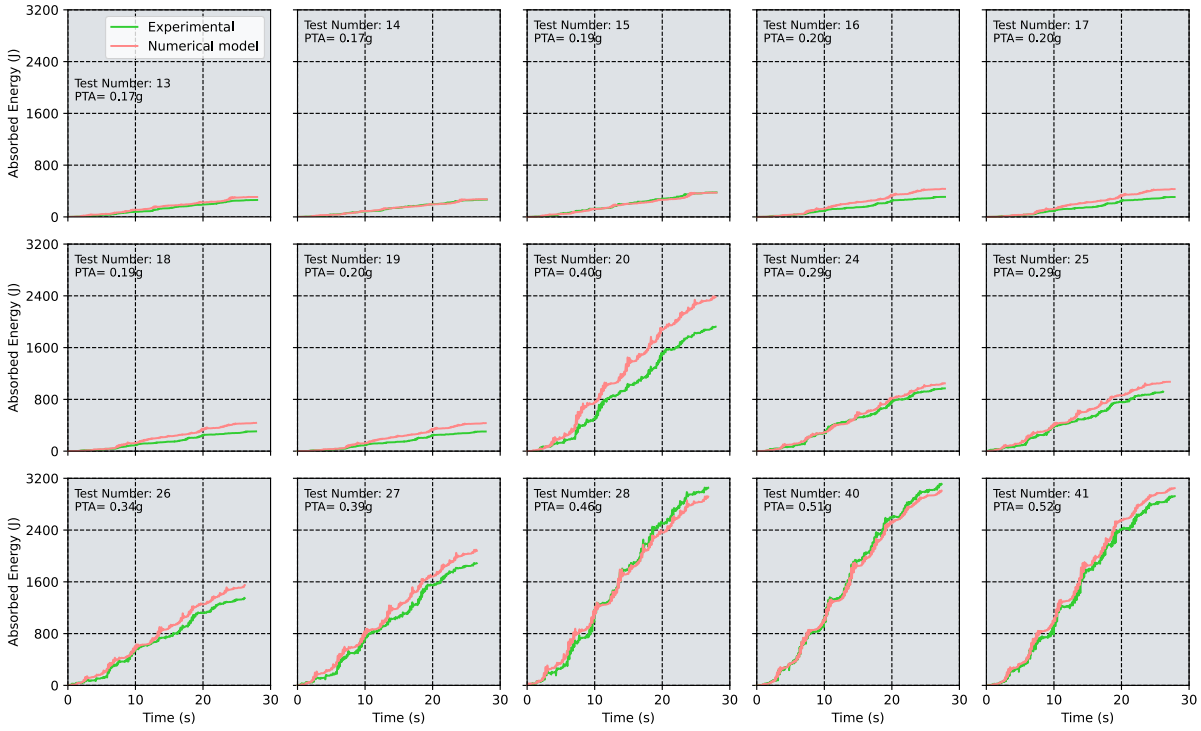


**Figure 7. Comparison of the absorbed energy time-history of the electrical cabinet obtained during the experimental campaign against the prediction of the calibrated MDOF numerical model**

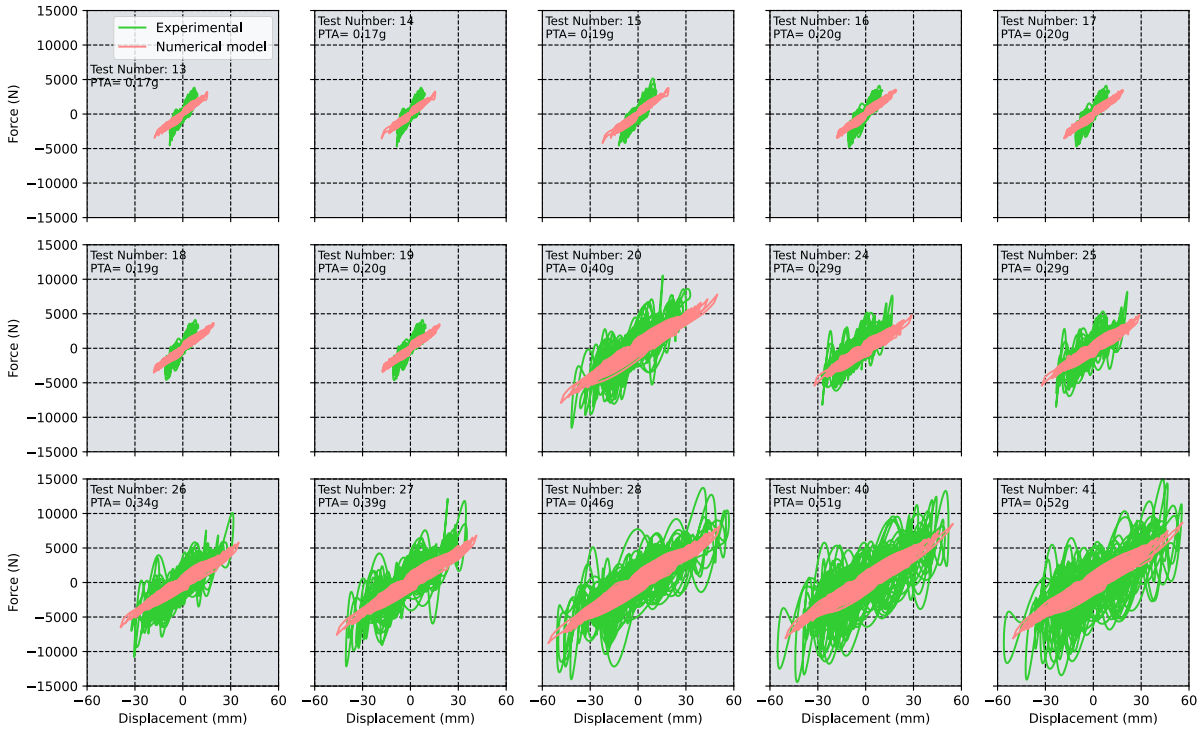


**Figure 8. Comparison of the hysteretic response of the electrical cabinet obtained during the experimental campaign against the prediction of the calibrated MDOF numerical model**

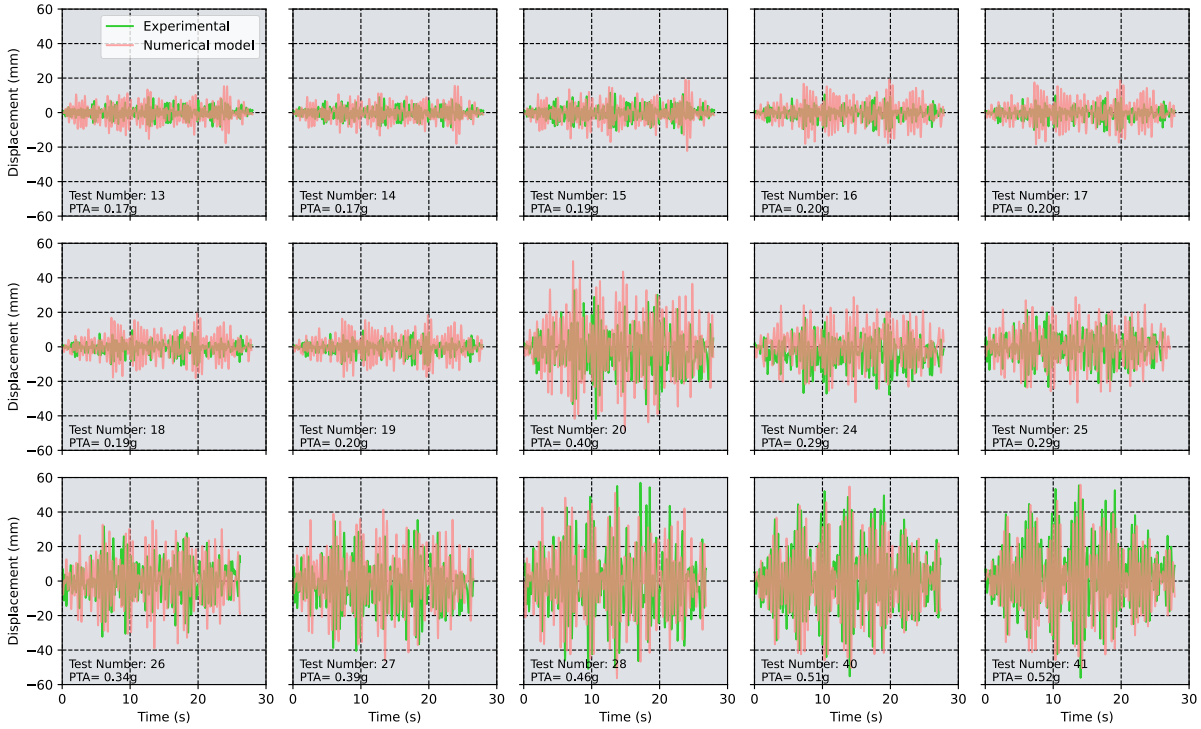


**Figure 9. Comparison of the relative displacement time-history of the electrical cabinet obtained during the experimental campaign against the prediction of the calibrated MDOF numerical model**

**Table 2. Calibrated parameters for the hysteretic and self-centering (flag-shaped) materials of the MDOF numerical model**

| *Hysteretic ($K_a$)* | | *SelfCentering ($K_c$)* | |
|---|---|---|---|
| ***Parameter*** | ***Value*** | ***Parameter*** | ***Value*** |
| $s_{1p}$ | 2.16 | $k_1$ | 0.8 |
| $e_{1p}$ | 2.2 | $k_2$ | 0.3 |
| $s_{2p}$ | 6.48 | *sigAct* | 0.85 |
| $e_{2p}$ | 11 | *beta* | 1.3 |
| $s_{3p}$ | 25.2 | | |
| $e_{3p}$ | 60.5 | | |
| $s_{1n}$ | -21.6 | | |
| $e_{1n}$ | -2.2 | | |
| $s_{2n}$ | -64.8 | | |
| $e_{2n}$ | -11 | | |
| $s_{3n}$ | -252 | | |
| $e_{3n}$ | -60.5 | | |
| *pinchx* | 0.21 | | |
| *pinchy* | 0.02 | | |
| *damage1* | 0 | | |
| *damage2* | 0 | | |
| $\beta_H$ | 0 | | |

## 5 CONCLUSIONS

In this paper, numerical models were developed to predict the response of electrical cabinets based on the results from a shake table experimental campaign conducted in the 6DLAB laboratory of the Eucentre Foundation. One specimen from the experimental campaign was selected for the calibration of the models. Two different numerical models were calibrated: i) a single-degree-of-freedom (SDOF) system calibrated to match the relative displacement time-history, absorbed energy time-history, and force-relative displacement hysteretic response obtained during the experimental campaign, and ii) a mechanics-based multiple-degree-of-freedom (MDOF) system in which the calibration of the response of the specimen attachments and the specimen internal support structure were conducted separately, and then combined to recreate the relative displacement time-history, absorbed energy time-history, and force-relative displacement hysteretic response observed during the experimental tests. By comparing the experimental results with the numerical predictions, it was shown that the developed numerical models are able to accurately approximate the absorbed energy and relative displacement time-histories of the electrical cabinets when subjected to the input base accelerations from the shake table tests, while for the case of the hysteretic response, the inertial force experienced by the electrical cabinets is underestimated. Furthermore, the MDOF numerical model is able to capture the damage accumulation in the electrical cabinet as a result of the applied sequence of shake table tests.

The calibrated numerical models are useful to generalize the results obtained during the experimental campaign, and can be used to conduct additional numerical studies on the seismic performance of other configurations of electrical cabinets.

## 6 REFERENCES

[1] G.G. Deierlein, H. Krawinkler, C.A. Cornell, A framework for performance-based earthquake engineering. *2003 Pacific Conference on Earthquake Engineering*, 2003.

[2] G.J. O'Reilly, D. Perrone, M. Fox, R. Monteiro, A. Filiatrault, Seismic assessment and loss estimation of existing school buildings in Italy. *Engineering Structures*, 168(1): 142-162, 2018.

[3] L. Sousa, R. Monteiro, Seismic retrofit options for non-structural building partition walls: impact on loss estimation and cost-benefit analysis. *Engineering Structures*, 161: 8-27, 2018.

[4] R.J. Merino, F. Dacarro, P. Dubini, F. Graziotti, L. Grottoli, I. Lanese, D. Perrone, M. Rota, R. Nascimbene, A. Filiatrault, A Shake Table Testing Campaign of Electrical Cabinets, *XIX ANIDIS Conference*, Seismic Engineering in Italy, 2022.

[5] Telcordia-GR-63-CORE, *NEBSTM Requirements: Physical Protection*, Telcordia Technologies Generic Requirements, Piscataway, New Jersey, USA, 2006.

[6] R.J. Merino, D. Perrone, A. Filiatrault, R. Nascimbene, A Seismic Classification Procedure for Non-Structural Building Elements based on Shake-Table Qualification Testing. *Proceedings of the 3rd European Conference on Earthquake Engineering and Seismology*, Bucharest, Romania, 2022.

[7] F. McKenna, G.L. Fenves, M.H. Scott, *Open System for Earthquake Engineering Simulation*, University of California, Berkeley, http://opensees.berkeley.edu, 2000.

[8] T. Feinstein, J.P. Moehle, Mechanics Based Numerical Modelling of Floor-Anchored Nonstructural Components. *Journal of Structural Engineering*, 149(1): 04022213, 2023.

[9] S. Mazzoni, F. McKenna, M.H. Scott, G.L. Fenves, *OpenSees Command Language Manual*. University of California, Berkeley, http://opensees.berkeley.edu/manuals/usermanual, 2006.

COMPDYN 2023
9th ECCOMAS Thematic Conference on
Computational Methods in Structural Dynamics and Earthquake Engineering
M. Papadrakakis, M. Fragiadakis (eds.)
Athens, Greece, 12-14 June 2023

# INVESTIGATING THE IMPACT OF POROSITY DISTRIBUTION AND GRADING PARAMETER ON THE FREE VIBRATION OF FUNCTIONALLY GRADED BEAMS

**Lazreg Hadji[1], Vagelis Plevris[2] and Royal Madan[3]**

[1] Department of Civil Engineering, University of Tiaret
BP 78 Zaaroura, Tiaret 14000 Tiaret, Algeria
e-mail: lazreg.hadji@univ-tiaret.dz

[2] Department of Civil and Architectural Engineering, Qatar University
Doha P.O. Box 2713, Qatar
e-mail: vplevris@qu.edu.qa

[3] Department of Mechanical Engineering, G H Raisoni Institute of Engineering and Technology, Nagpur 440016, India
e-mail: royalmadan6293@gmail.com

## Abstract

*This study focuses on investigating the free vibration of porous functionally graded (FG) beams and the impact of porosity distribution on the properties and performance of materials. To achieve this, the study assumes that the beam's material characteristics vary continuously along its thickness direction. The volume fraction of constituents is specified using the modified rule of the mixture, which includes porosity volume fraction with changed porosity patterns across the cross-section. The study uses the hyperbolic shear deformation theory without shear correction factors to derive the equations of motion by applying Hamilton's principle. The study employs Navier's method to obtain analytical results for the free vibration of porous/non-porous FG beams under simply supported boundary conditions at both ends. To verify the proposed formulation, the study compares the results with relevant findings from the literature. The study also examines the relationship between frequency of vibration and grading parameter in homogeneous porosity distributions, as well as the frequency of vibration in beam structures with different porosity patterns. Additionally, numerical examples are provided to investigate the impact of parameters like power-law index, span to depth ratio, porosity distribution pattern, and porosity volume fraction on the natural frequencies of FG beams. The analysis provides significant insights into the behavior of different porous materials and can be useful for designing and selecting materials with porosities.*

**Keywords:** Free Vibration, Functionally Graded Materials, Porosity, Hyperbolic Shear Deformation Theory, Navier Solution.

## 1 INTRODUCTION

Composite materials are materials that are made up of two or more different materials that are combined together to form a single material with unique properties. The different materials used in a composite material are called constituents, and they can be selected based on their specific properties, such as strength, stiffness, durability, and others. In most cases, composites exhibit consistent material properties throughout their structure, meaning that the properties do not change significantly in any direction [1]. On the other hand, functionally graded materials (FGMs) are advanced materials that have a continuously varying composition or structure, typically from one end of the material to the other. This variation can be controlled to produce specific functional properties in different regions of the material. FGMs are typically designed to have properties that vary gradually from one region to another, rather than abruptly changing at a boundary. This gradual change in properties can result in improved performance and durability compared to homogeneous materials, making them more suitable for applications where the properties of the material need to vary to achieve optimal performance [2]. To prevent delamination caused by differences in thermo-mechanical properties, FGMs are fabricated in a way that ensures a gradual transition of material properties from one layer to another. This gradual transition helps to reduce the mismatch in the thermal expansion coefficients of different layers and minimizes the formation of interfacial stresses that can cause delamination [3].

The differential quadrature method (DQM), a numerical method used to approximate the solution of differential equations, was used to calculate the frequencies of FG plates with different boundary conditions (BCs) [4]. This technique was later applied to other studies, such as analyzing the free vibration of micro circular plates under thermal loads and 3D free vibration analysis [5, 6]. In the work of Alipour et al. [7], the free vibration behavior of 2D FGMs under various boundary conditions was investigated. The authors found that clamped boundary conditions resulted in the highest frequency, simply supported conditions resulted in the lowest frequency, and free-free conditions resulted in intermediate frequencies. Nie and Batra [8] used a semi-analytical numerical method to analyze the bending behavior of 2D FG circular and annular plates and the bending and thermal deformations of FG beams with various end conditions. Additionally, an impact analysis using a similar numerical method was performed [9].

The distribution of porosity in a structure can be uniform or non-uniform depending on how it is fabricated. To avoid negative effects on performance, researchers are exploring ways to eliminate porosity [10]. Pores may form in powder metallurgy due to improper sintering and different reinforcement shapes, with irregular shapes leading to more pores than rounded or elliptical ones. The elastic modulus of a material also depends on the reinforcement shape, with spherical particles having the highest elastic modulus. Improper solidification during centrifugal casting and rapid heating and solidification during additive manufacturing may also lead to porosity, as noted in several studies [11-14].

The free vibration behavior of functionally graded beams was investigated by utilizing the finite element method. The findings suggest that alterations in material distribution along the axial direction can affect the stiffness of the beam, leading to changes in mode shapes and frequencies. The fundamental frequencies and mode shapes were not impacted by the slenderness ratio due to the limitations of the Euler-beam theory. Moreover, the natural frequencies either increased or decreased with a change in the power exponent, depending on the material distribution [15]. Apart from these, various methods have been employed by researchers to study the free vibration of FG beams such as dynamic stiffness method [16], Rayleigh–Ritz method [17], higher-order shear deformation beam theories [18], among others.

A detailed dynamic analysis of a functionally graded beam can pose significant computational challenges [19]. In a previous work, the authors attempted a static and free vibration

analysis of porous FG beams [20]. The main objective of the present research work is to investigate how the distribution of voids affects the free vibration characteristics of FGM beams by utilizing an advanced shear deformation model. This model takes into account the impact of voids by employing a modified mixture law that incorporates void phases introduced by previous studies from [21, 22]. The study also investigates the effects of various parameters on the free vibration of FGM beams. These parameters include the power index, pore volume fraction (amount and distribution of voids or pores), geometry ratio (dimensions of the FGM beam), porosity distribution pattern, and thickness ratio. By studying the effects of these parameters, the study aims to understand the behavior of FGM beams under free vibration conditions. The variation of material properties in the FGM beam is assumed to follow a power-law distribution of the volume fraction of the constituents. To derive the equation of motion for FGM beams, Hamilton's principle is used. The results of the study can be useful in designing FGM structures that results in higher frequency.

## 2 GEOMETRIC CONFIGURATION AND MATERIAL PROPERTIES

An FG beam is considered with geometry dimensions as shown in Figure 1. The material properties vary in a graded manner in the thickness direction (along $h$). In this study, we investigate an imperfect functionally graded beam that contains a specific volume fraction of porosity $\alpha$ ($\alpha \ll 1$), which is distributed differently between the metal (denoted as $m$) and ceramic ($c$) components. To account for this porosity distribution, we utilize the modified mixture rule developed by Wattanasakulpong and Ungbhakorn [23].

$$P(z) = P_m\left(V_m - \frac{\alpha}{2}\right) + P_c\left(V_c - \frac{\alpha}{2}\right) \tag{1}$$

The assumed relationship for the volume fraction of ceramic is a power law, as shown below:

$$V_c = \left(\frac{z}{h} + \frac{1}{2}\right)^k \tag{2}$$

The relation obtained can be written as:

$$P(z) = (P_c - P_m)\left(\frac{z}{h} + \frac{1}{2}\right)^k + P_m - (P_c + P_m)\frac{\alpha}{2} \tag{3}$$

where $k$ is the power law index. The FGM beam can transform into a fully ceramic or fully metal beam, depending on the value of $k$. If $k$ is zero, then the beam is fully ceramic, while for large values of $k$, it becomes fully metal. The elastic modulus $E$ for porous FG plate can be written as [24, 25].

$$E(z) = (E_c - E_m)\left(\frac{z}{h} + \frac{1}{2}\right)^k + E_m - (E_c + E_m)\frac{\alpha}{2} \tag{4}$$

To determine the material properties of a perfect functionally graded beam, the volume fraction of porosity, $\alpha$, is assumed to be zero. Since the Poisson ratio, $v$, only varies slightly, it can be considered constant. The current study investigates various forms of porosity, including the patterns "O", "V", and "X", as shown in detail in Table 1.

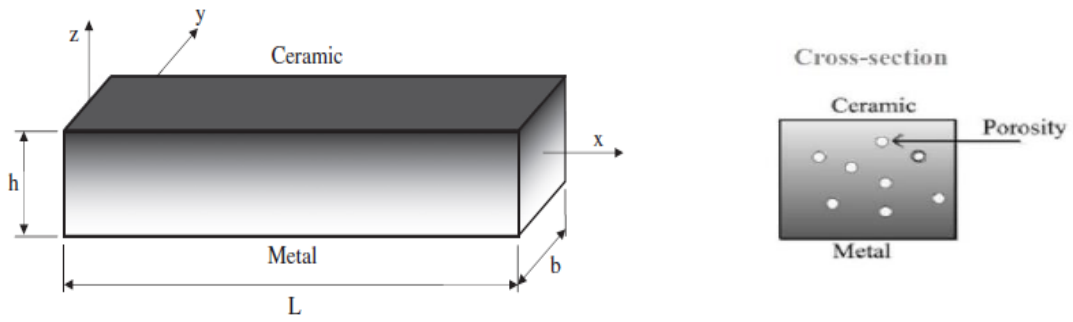


(a) (b)

Figure 1. Geometry of the FG beam: (a) 3D view, (b) Cross section.

## 3 KINEMATIC, STRAIN AND STRESS RELATIONS

The displacement field of the present higher order shear deformation model is given by the following expression [26]:

$$u(x,z,t) = u_0(x,t) - z\frac{\partial w_b}{\partial x} - f\left(z\right)\frac{\partial w_s}{\partial x} \tag{5}$$

$$w(x,z,t) = w_b(x,t) + w_s\left(x,t\right) \tag{6}$$

The study uses a refined shear deformation theory where the axial displacement of a point on the mid-plane of the beam is represented by $u_0$, and the bending and shear components of transverse displacement are $w_b$ and $w_s$, respectively. The theory employs a shape function, $f(z)$, to determine the distribution of transverse shear strain and shear stress throughout the beam depth, while satisfying stress-free boundary conditions.

$$f(z) = z\left[1+\frac{3\pi}{2}\text{sech}\left(\frac{1}{2}\right)^2\right] - \frac{3\pi}{2}h\tanh\left(\frac{z}{h}\right) \tag{7}$$

The strains associated with the displacements in Eqs (5) and (6) are

$$\varepsilon_x = \varepsilon_x^0 + z\ k_x^b + f(z)\ k_x^s \tag{8}$$

$$\gamma_{xz} = g(z)\ \gamma_{xz}^s \tag{9}$$

where

$$\varepsilon_x^0 = \frac{\partial u_0}{\partial x}, \quad k_x^b = -\frac{\partial^2 w_b}{\partial x^2}, \quad \gamma_{xz}^s = \frac{\partial w_s}{\partial x} \tag{10}$$

$$g(z) = 1 - f'(z) \quad \text{and} \quad f'(z) = \frac{df(z)}{dz} \tag{11}$$

The generalized Hooke's law expresses the state of stress present in the beam in the following manner:

$$\sigma_x = Q_{11}(z)\ \varepsilon_x \quad \text{and} \quad \tau_{xz} = Q_{55}(z)\ \gamma_{xz} \tag{12}$$

where

$$Q_{11}(z) = E(z) \quad \text{and} \quad Q_{55}(z) = \frac{E(z)}{2(1+\nu)} \tag{13}$$

## 4 EQUATIONS OF MOTION

In order to obtain the equations of motion, the method of Hamilton's principle is applied, as shown in the following equation [27].

$$\delta \int_{t_1}^{t_2} (U - T)\,\mathrm{d}t = 0 \tag{14}$$

The variables used in this equation are the time, $t$, the time instances $t_1$, $t_2$, representing the initial and final times, respectively, the potential strain energy, $U$, and the kinetic energy, $T$. The strain energy variation of the beam can be expressed as:

$$\begin{aligned} \delta U = & \int_0^L \int_{-\frac{h}{2}}^{\frac{h}{2}} \left(\sigma_x \delta\varepsilon_x + \tau_{xz}\delta\gamma_{xz}\right)\mathrm{d}z\mathrm{d}x = \\ & \int_0^L \left( N \frac{d\delta\, u_0}{dx} - M_b \frac{d^2\delta\, w_b}{dx^2} - M_s \frac{d^2\delta\, w_s}{dx^2} + Q \frac{d\delta\, w_s}{dx} \right)\mathrm{d}x \end{aligned} \tag{15}$$

where $N_x$, $M_b$, $M_s$ and $Q_{xz}$ are the stress resultants defined as

$$(N, M_b, M_s) = \int_{-h/2}^{h/2} (1,\, z,\, f)\,\sigma_x \mathrm{d}z \quad \text{and} \quad Q_{xz} = \int_{-h/2}^{h/2} g\,\tau_{xz}\mathrm{d}z \tag{16}$$

The change in the kinetic energy can be stated as:

$$\begin{aligned} \delta T = & \int_0^L \int_{-h/2}^{h/2} \rho(z)\left[\dot{u}\delta\dot{u} + \dot{w}\delta\dot{w}\right]\,\mathrm{d}z\mathrm{d}x = \\ & \int_0^L \left\{ I_1\left[\dot{u}_0\delta\dot{u}_0 + \left(\dot{w}_b + \dot{w}_s\right)\left(\delta\dot{w}_b + \delta\dot{w}_s\right)\right] - I_2\left(\dot{u}_0 \frac{\mathrm{d}\delta\dot{w}_b}{dx} + \frac{\mathrm{d}\dot{w}_b}{dx}\delta\dot{u}_0\right) \right. \\ & + I_4\left(\frac{\mathrm{d}\dot{w}_b}{\mathrm{d}x}\frac{\mathrm{d}\delta\dot{w}_b}{\mathrm{d}x}\right) - I_3\left(\dot{u}_0 \frac{\mathrm{d}\delta\dot{w}_s}{\mathrm{d}x} + \frac{\mathrm{d}\dot{w}_s}{\mathrm{d}x}\delta\,\dot{u}_0\right) + I_6\left(\frac{\mathrm{d}\dot{w}_s}{\mathrm{d}x}\frac{\mathrm{d}\delta\dot{w}_s}{\mathrm{d}x}\right) \\ & \left. + I_5\left(\frac{\mathrm{d}\dot{w}_b}{\mathrm{d}x}\frac{\mathrm{d}\delta\dot{w}_s}{\mathrm{d}x} + \frac{\mathrm{d}\dot{w}_s}{\mathrm{d}x}\frac{\mathrm{d}\delta\dot{w}_b}{\mathrm{d}x}\right)\right\}\mathrm{d}x \end{aligned} \tag{17}$$

where the dot-superscript convention indicates the differentiation with respect to the time variable $t$; $\rho(z)$ is the mass density; and ($I_1$, $I_2$, $I_3$, $I_4$, $I_5$, $I_6$) are the mass inertias defined as

$$\left(I_1, I_2, I_3, I_4, I_5, I_6\right) = \int_{-h/2}^{h/2} \left(1, z, f, z^2, zf, f^2\right)\rho(z)\mathrm{d}z \tag{18}$$

By plugging in the equations for $\delta U$ and $\delta T$ from Eqs (15) and (17) into Eq. (14), and performing integration by parts with respect to both spatial and temporal variables, while grouping together the coefficients of $\delta u_0$, $\delta w_b$, and $\delta w_s$, we can obtain the equations of motion for the functionally graded beam:

$$\delta u_0: \quad \frac{\mathrm{d}N_x}{\mathrm{d}x} = I_1\ddot{u}_0 - I_2\frac{\mathrm{d}\ddot{w}_b}{\mathrm{d}x} - I_3\frac{\mathrm{d}\ddot{w}_s}{\mathrm{d}x} \tag{19}$$

$$\delta w_b: \quad \frac{\mathrm{d}^2M_b}{\mathrm{d}x^2} = I_1(\ddot{w}_b + \ddot{w}_s) + I_2\frac{\mathrm{d}\ddot{u}_0}{\mathrm{d}x} - I_4\frac{\mathrm{d}^2\ddot{w}_b}{\mathrm{d}x^2} - I_5\frac{\mathrm{d}^2\ddot{w}_s}{\mathrm{d}x^2} \tag{20}$$

$$\delta w_s: \quad \frac{\mathrm{d}^2M_s}{\mathrm{d}x^2} + \frac{\mathrm{d}Q_{xz}}{\mathrm{d}x} = I_1(\ddot{w}_b + \ddot{w}_s) + I_3\frac{\mathrm{d}\ddot{u}_0}{\mathrm{d}x} - I_5\frac{\mathrm{d}^2\ddot{w}_b}{\mathrm{d}x^2} - I_6\frac{\mathrm{d}^2\ddot{w}_s}{\mathrm{d}x^2} \tag{21}$$

The equations of motion in relation to the displacement can be obtained by replacing the stress resultants from Eq. (16) into Eqs (19), (20), (21) ($u_0$, $w_b$, $w_s$) as follows:

$$A_{11}\frac{\partial^2 u_0}{\partial x^2} - B_{11}\frac{\partial^3 w_b}{\partial x^3} - B^s_{11}\frac{\partial^3 w_s}{\partial x^3} = I_1\ddot{u}_0 - I_2\frac{\mathrm{d}\ddot{w}_b}{\mathrm{d}x} - I_3\frac{\mathrm{d}\ddot{w}_s}{\mathrm{d}x} \tag{22}$$

$$B_{11}\frac{\partial^3 u_0}{\partial x^3} - D_{11}\frac{\partial^4 w_b}{\partial x^4} - D^s_{11}\frac{\partial^4 w_s}{\partial x^4} = I_1(\ddot{w}_b + \ddot{w}_s) + I_2\frac{\mathrm{d}\ddot{u}_0}{\mathrm{d}x} - I_4\frac{\mathrm{d}^2\ddot{w}_b}{\mathrm{d}x^2} - I_5\frac{\mathrm{d}^2\ddot{w}_s}{\mathrm{d}x^2} \tag{23}$$

$$B^s_{11}\frac{\partial^3 u_0}{\partial x^3} - D^s_{11}\frac{\partial^4 w_b}{\partial x^4} - H^s_{11}\frac{\partial^4 w_s}{\partial x^4} + A^s_{55}\frac{\partial^2 w_s}{\partial x^2} = I_1(\ddot{w}_b + \ddot{w}_s) + I_3\frac{\mathrm{d}\ddot{u}_0}{\mathrm{d}x} - I_5\frac{\mathrm{d}^2\ddot{w}_b}{\mathrm{d}x^2} - I_6\frac{\mathrm{d}^2\ddot{w}_s}{\mathrm{d}x^2} \tag{24}$$

where the terms $A_{11}$, $D_{11}$, etc., denote the beam stiffness, defined by

$$\left(A_{11}, B_{11}, D_{11}, B^s_{11}, D^s_{11}, H^s_{11}\right) = \int_{-h/2}^{h/2} Q_{11}\left(1, z, z^2, f(z), z\,f(z), f^2(z)\right)\mathrm{d}z \tag{25}$$

$$A^s_{55} = \int_{-h/2}^{h/2} Q_{55}\left[g(z)\right]^2\mathrm{d}z \tag{26}$$

## 5 ANALYTICAL SOLUTION

Assuming certain variations, the variables $u_0$, $w_b$, $w_s$ can be expressed, and these equations of motion can lead to Navier solutions for simply supported beams.

$$\begin{Bmatrix} u_0 \\ w_b \\ w_s \end{Bmatrix} = \sum_{m=1}^{\infty} \begin{Bmatrix} U_m \cdot \cos(\lambda x)\cdot e^{i\omega t} \\ W_{bm} \cdot \sin(\lambda x)\cdot e^{i\omega t} \\ W_{sm} \cdot \sin(\lambda x)\cdot e^{i\omega t} \end{Bmatrix} \tag{27}$$

Here, $U_{\mathrm{m}}$, $W_{bm}$, and $W_{sm}$ are undetermined parameters that need to be calculated, while $\omega$ represents the eigenfrequency corresponding to the eigenmode. By substituting the expansions of Eq. (27) into the equations of motion (Eqs (22), (23), (24)), we obtain analytical solutions through the following equations where $\omega$ is the eigenfrequency associated with the $m^{\mathrm{th}}$ eigenmode, and $\lambda = m\pi / L$, as follows:

$$\left(\begin{bmatrix} a_{11} & a_{12} & a_{13} \\ a_{12} & a_{22} & a_{23} \\ a_{13} & a_{23} & a_{33} \end{bmatrix} - \omega^2 \begin{bmatrix} m_{11} & m_{12} & m_{13} \\ m_{12} & m_{22} & m_{23} \\ m_{13} & m_{23} & m_{33} \end{bmatrix}\right)\begin{Bmatrix} U_m \\ W_{bm} \\ W_{sm} \end{Bmatrix} = \begin{Bmatrix} 0 \\ 0 \\ 0 \end{Bmatrix} \tag{28}$$

where

$$a_{11} = A_{11}\lambda^2, \quad a_{12} = -B_{11}\lambda^3, \quad a_{13} = -B^s_{11}\lambda^3 \tag{29}$$

$$a_{22} = D_{11}\lambda^4, \quad a_{23} = D_{11}^s\lambda^4, \quad a_{33} = H_{11}^s\lambda^4 + A_{55}^s\lambda^2 \tag{30}$$

$$m_{11} = I_1, \quad m_{12} = -I_2\lambda, \quad m_{13} = -I_3\lambda \tag{31}$$

$$m_{22} = I_1 + I_4\lambda^2, \quad m_{23} = I_1 + I_5\lambda^2, \quad m_{33} = I_1 + I_6\lambda^2 \tag{32}$$

## 6 RESULTS AND DISCUSSION

### 6.1 Different porosity distribution patterns

Table 1 presents a comparison of various porosity distributions that occur as a result of different fabrication techniques. Porosity refers to the amount of void space or empty volume within a material. It is a measure of how much of the material is made up of empty spaces or pores, relative to the total volume of the material. The distribution of porosity can have a significant impact on the properties and performance of the material, such as strength, durability, and permeability. As shown in Table 1, different fabrication techniques can result in different porosity distributions, and these distributions may be uncertain or difficult to achieve.

| Porosity distribution form | Elastic Modulus Expression | Schema |
|---|---|---|
| Homogeneous ("H") | $E(z)=(E_c-E_m)\left(\frac{z}{h}+\frac{1}{2}\right)^k+E_m-(E_c+E_m)\frac{\alpha}{2}$ |  |
| "O" shape | $E(z)=(E_c-E_m)\left(\frac{z}{h}+\frac{1}{2}\right)^k+E_m-(E_c+E_m)\frac{\alpha}{2}\left(1-2\frac{\lvert z\rvert}{h}\right)$ | 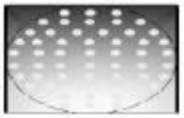 |
| "X" shape | $E(z)=(E_c-E_m)\left(\frac{z}{h}+\frac{1}{2}\right)^k+E_m-(E_c+E_m)\frac{\alpha}{2}\left(2\frac{z}{h}\right)$ | 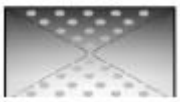 |
| "V" shape | $E(z)=(E_c-E_m)\left(\frac{z}{h}+\frac{1}{2}\right)^k+E_m-(E_c+E_m)\frac{\alpha}{2}\left(\frac{1}{2}+\frac{z}{h}\right)$ | 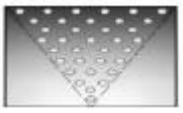 |

Table 1: Different distribution forms of porosity.

The porosity distribution in powder metallurgy depends on several factors such as sintering time, sintering temperature, and reinforcement distribution. Sintering is the process of heating the compacted metal powders to a temperature below the melting point of the metal to fuse the particles together and form a solid, dense component. Sintering time, the duration for which the metal powder is heated at a specific temperature during sintering, is an important parameter as it can affect the microstructure, mechanical properties, and dimensional accuracy of the sintered component. Similarly, sintering temperature can affect the microstructure, mechanical properties, and dimensional accuracy of the sintered component. Porosity can be controlled by adjusting the sintering time and temperature. Longer sintering times and higher sintering temperatures typically lead to lower porosity, while shorter times and lower temperatures result in higher porosity.

The distribution of reinforcement particles can also affect porosity, as the particles can create channels or voids in the material. In centrifugal casting, porosity can occur due to incomplete or improper solidification of the material due to a number of factors. This can happen when the

material cools too quickly, or when there is uneven cooling or solidification due to variations in the casting geometry or mold design.

### 6.2 Validation of the study

Table 2 represents the relationship between frequency and grading parameter *k* for a homogeneous porosity distribution, for the case *L*/*h* = 5. The *L*/*h* parameter refers to the length-to-height ratio of the beam structure. In this context, the grading parameter refers to the degree of variation in the material's composition, with higher values of *k* indicating a greater variation in composition. The results show that as a general trend, as *k* increases, the frequency decreases. This is because metal is stiffer than ceramic and larger values of *k* mean that the metal part of material increases over the ceramic part. The method used to generate the results is accurate compared to the results obtained using other methods published in the literature. Table 3 demonstrates the corresponding results for the case *L*/*h* = 20.

| **Theory** | $\alpha$ | $k = 0$ | $k = 0.2$ | $k = 0.5$ | $k = 1$ | $k = 5$ | $k = 10$ |
|---|---|---|---|---|---|---|---|
| **CBT*** | 0 | 5.3953 | 5.0206 | 4.5931 | 4.1484 | 3.5949 | 3.4921 |
| **FSDBT*** | 0 | 5.1525 | 4.8066 | 4.4083 | 3.9902 | 3.4312 | 3.3134 |
| **ESDBT*** | 0 | 5.1542 | 4.8105 | 4.4122 | 3.9914 | 3.4014 | 3.2813 |
| **PSDBT*** | 0 | 5.1527 | 4.8092 | 4.4111 | 3.9904 | 3.4012 | 3.2816 |
| | 0 | 5.1529 | 4.8082 | 4.4108 | 3.9906 | 3.4001 | 3.2812 |
| **Present** | 0.1 | 5.2225 | 4.8499 | 4.4044 | 3.9071 | 3.1465 | 3.0284 |
| | 0.2 | 5.3050 | 4.8998 | 4.3929 | 3.7866 | 2.6946 | 2.5700 |

* Results from Şimşek [28].

Table 2: Variation of fundamental frequency $\bar{\omega}$ with the power-law index for FG beam for *L*/*h* = 5 (Homogeneous distribution form).

| **Theory** | $\alpha$ | $k = 0$ | $k = 0.2$ | $k = 0.5$ | $k = 1$ | $k = 5$ | $k = 10$ |
|---|---|---|---|---|---|---|---|
| **CBT*** | 0 | 5.4777 | 5.0967 | 4.6641 | 4.2163 | 3.6628 | 3.5546 |
| **FSDBT*** | 0 | 5.4603 | 5.0827 | 4.6514 | 4.2051 | 3.6509 | 3.5415 |
| **ESDBT*** | 0 | 5.4604 | 5.0829 | 4.6516 | 4.2051 | 3.6483 | 3.5389 |
| **PSDBT*** | 0 | 5.4603 | 5.0829 | 4.6516 | 4.2050 | 3.6485 | 3.5389 |
| | 0 | 5.4603 | 5.0815 | 4.6511 | 4.2051 | 3.6484 | 3.5389 |
| **Present** | 0.1 | 5.5341 | 5.1244 | 4.6413 | 4.1118 | 3.3775 | 3.2808 |
| | 0.2 | 5.6215 | 5.1755 | 4.6254 | 3.9776 | 2.8855 | 2.8019 |

* Results from Şimşek [28].

Table 3: Variation of fundamental frequency $\bar{\omega}$ with the power-law index for FG beam for *L*/*h* = 20 (Homogeneous distribution form).

### 6.3 Effect of different porosity distributions on natural frequency

It is also worth noting that the presence of porosity in a material can increase the frequency of vibration by providing a cushioning effect. This is because the presence of pores reduces the effective stiffness of the material, which in turn can increase the frequency of vibration. Table 4 presents the results of a frequency analysis for different porosity patterns in a beam structure. The results show that the highest frequency is observed for the homogeneous ("H") type porosity pattern, followed by the "O", "V", and "X" type patterns. Interestingly, for the "X" type pattern, the frequency is higher than for a perfect, non-porous beam. It is important to note that a perfect beam has the lowest frequency in all cases except for the "X" type pattern. This is because a

non-porous beam has no voids or openings for energy to dissipate, resulting in a lower frequency of vibration. The results also indicate that the grading parameter and the *L*/*h* ratio have an impact on the frequency of the beam structure. The grading parameter refers to the variation in porosity within each porosity pattern.

| | | | Porosity distribution patterns | | | |
|---|---|---|---|---|---|---|
| ***k*** | ***L/h*** | **Perfect** ($\alpha = 0$) | **"H"** ($\alpha = 0.2$) | **"O"** ($\alpha = 0.2$) | **"X"** ($\alpha = 0.2$) | **"V"** ($\alpha = 0.2$) |
| 0 | 5 | 5.1529 | 5.3050 | 5.2888 | 5.1425 | 5.2196 |
| | 10 | 5.3933 | 5.5525 | 5.5469 | 5.3812 | 5.4627 |
| | 20 | 5.4603 | 5.6215 | 5.6193 | 5.4477 | 5.5305 |
| 1 | 5 | 3.9905 | 3.7866 | 4.0216 | 4.1574 | 4.0227 |
| | 10 | 4.1586 | 3.9364 | 4.2003 | 4.3438 | 4.1954 |
| | 20 | 4.2050 | 3.9776 | 4.2499 | 4.3957 | 4.2432 |
| 5 | 5 | 3.4001 | 2.6946 | 3.2814 | 3.6526 | 3.3603 |
| | 10 | 3.5933 | 2.8431 | 3.5035 | 3.8839 | 3.5721 |
| | 20 | 3.6483 | 2.8855 | 3.5683 | 3.9506 | 3.6333 |
| 10 | 5 | 3.2812 | 2.5700 | 3.1520 | 3.4641 | 3.2039 |
| | 10 | 3.4814 | 2.7493 | 3.4063 | 3.6920 | 3.4289 |
| | 20 | 3.5389 | 2.8019 | 3.4823 | 3.7580 | 3.4947 |

Table 4: Effect of the shape of porosity distribution on the fundamental frequency $\bar{\omega}$.

Figure 2 shows the trend of variation of the frequency with *L/h* for different porosity patterns. The porosity pattern refers to the arrangement of the voids within the porous layer, which can greatly affect the properties of the material. The graph shows that for $L/h > 8$, the variation in the frequency is not so significant. This means that the material properties have reached a point of saturation and further increasing the *L/h* ratio does not significantly affect the frequency. In addition, the "O" and "V" shapes yield very similar results, as shown by the red and blue lines which overlap for most of the graph. This suggests that these two patterns have similar acoustic properties in terms of sound wave frequency variation. Overall, the analysis provides important insights into the behavior of different porous materials and can be useful for designing and selecting materials with porosities.

In both composite materials and FGMs, achieving a uniform distribution of reinforcement material or composition can be difficult. This is because the reinforcement material or composition can have a tendency to clump together or settle out during the manufacturing process. This can result in regions of the material with higher or lower concentrations of reinforcement material or composition, which can have a significant impact on the overall properties of the material. To address this issue, various manufacturing techniques and processes have been developed to ensure a more uniform distribution of reinforcement material or composition. For example, in composite materials, the use of high shear mixing processes, such as ultrasonication or high-speed mixing, can help to disperse the reinforcement material more evenly throughout the matrix material.

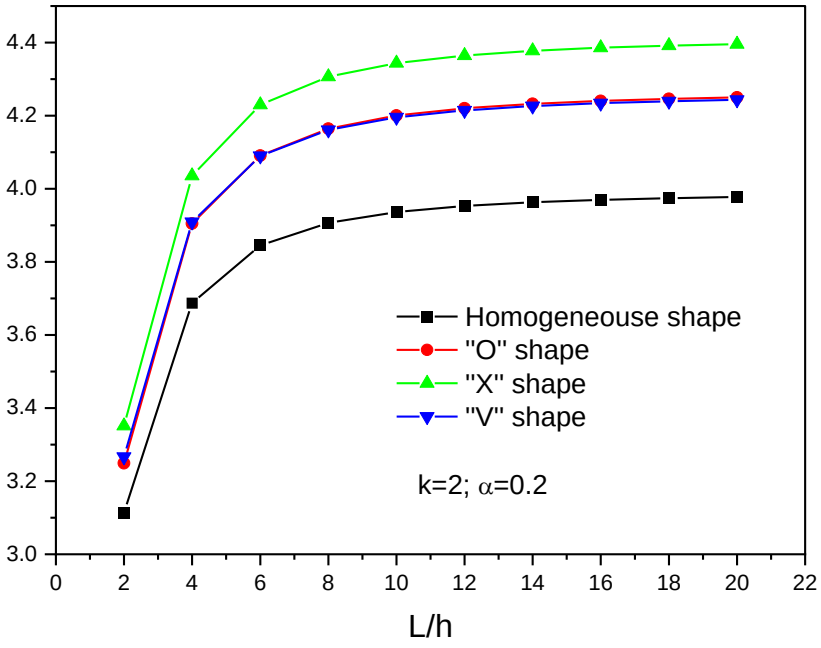


Figure 2. Effect of the shape of porosity distribution on the non-dimensional fundamental frequency $\overline{\omega}$ versus length-to-thickness ratio $L/h$ of an $Al/Al_2O_3$ FGM beam.

## 7 CONCLUSIONS

In composite materials and FGMs, achieving a uniform distribution of reinforcement material or composition can be challenging. Nevertheless, there are various techniques and processes that can be used to improve the uniformity and consistency of these advanced materials. Understanding these factors is important for achieving the desired porosity distribution and ensuring the material has the desired properties and performance. The conducted analysis highlights the importance of porosity distribution and its impact on the properties and performance of materials. The porosity distribution can vary depending on the fabrication technique used and may be difficult to control. The grading parameter and $L/h$ ratio also affect the frequency of vibration in materials and beam structures, with higher values leading to a decrease in frequency. Porosity can increase the frequency of vibration by providing a cushioning effect, while the arrangement of voids within the porous layer can greatly affect the properties of the material. These findings provide valuable insights into the behavior of different porous materials and can inform the design and selection of materials with specific porosity requirements.

## REFERENCES

[1] Dev Singh, D., S. Arjula, and A. Raji Reddy, *Functionally Graded Materials Manufactured by Direct Energy Deposition: A review*. Materials Today: Proceedings, 2021. **47**: p. 2450-2456 DOI: https://doi.org/10.1016/j.matpr.2021.04.536.

[2] Jamshidi, M. and J. Arghavani, *Optimal material tailoring of functionally graded porous beams for buckling and free vibration behaviors*. Mechanics Research Communications, 2018. **88**: p. 19-24 DOI: https://doi.org/10.1016/j.mechrescom.2018.01.006.

[3] Suresh, S. and A. Mortensen, *Functionally graded metals and metal-ceramic composites: Part 2 Thermomechanical behaviour.* International Materials Reviews, 1997. **42**(3): p. 85-116 DOI: https://doi.org/10.1179/imr.1997.42.3.85.

[4] Nie, G. and Z. Zhong, *Dynamic analysis of multi-directional functionally graded annular plates.* Applied Mathematical Modelling, 2010. **34**(3): p. 608-616 DOI: https://doi.org/10.1016/j.apm.2009.06.009.

[5] Kermani, I.D., M. Ghayour, and H.R. Mirdamadi, *Free vibration analysis of multi-directional functionally graded circular and annular plates.* Journal of Mechanical Science and Technology, 2012. **26**(11): p. 3399-3410 DOI: https://doi.org/10.1007/s12206-012-0860-2.

[6] Yas, M.H. and N. Moloudi, *Three-dimensional free vibration analysis of multi-directional functionally graded piezoelectric annular plates on elastic foundations via state space based differential quadrature method.* Applied Mathematics and Mechanics, 2015. **36**(4): p. 439-464 DOI: https://doi.org/10.1007/s10483-015-1923-9.

[7] Alipour, M.M., M. Shariyat, and M. Shaban, *A semi-analytical solution for free vibration of variable thickness two-directional-functionally graded plates on elastic foundations.* International Journal of Mechanics and Materials in Design, 2010. **6**(4): p. 293-304 DOI: https://doi.org/10.1007/s10999-010-9134-2.

[8] Nie, G.J. and R.C. Batra, *Stress analysis and material tailoring in isotropic linear thermoelastic incompressible functionally graded rotating disks of variable thickness.* Composite Structures, 2010. **92**(3): p. 720-729 DOI: https://doi.org/10.1016/j.compstruct.2009.08.052.

[9] Shariyat, M. and R. Jafari, *A micromechanical approach for semi-analytical low-velocity impact analysis of a bidirectional functionally graded circular plate resting on an elastic foundation.* Meccanica, 2013. **48**(9): p. 2127-2148 DOI: https://doi.org/10.1007/s11012-013-9729-4.

[10] Eltaher, M.A., et al., *Modified porosity model in analysis of functionally graded porous nanobeams.* Journal of the Brazilian Society of Mechanical Sciences and Engineering, 2018. **40**(3): p. 141 DOI: https://doi.org/10.1007/s40430-018-1065-0.

[11] Abdalla, H.M.A. and D. Casagrande, *An Intrinsic Material Tailoring Approach for Functionally Graded Axisymmetric Hollow Bodies Under Plane Elasticity.* Journal of Elasticity, 2021. **144**(1): p. 15-32 DOI: https://doi.org/10.1007/s10659-021-09822-y.

[12] Bobbio, L.D., et al., *Analysis of formation and growth of the σ phase in additively manufactured functionally graded materials.* Journal of Alloys and Compounds, 2020. **814**: p. 151729 DOI: https://doi.org/10.1016/j.jallcom.2019.151729.

[13] Verma, R.K., D. Parganiha, and M. Chopkar, *A review on fabrication and characteristics of functionally graded aluminum matrix composites fabricated by centrifugal casting method.* SN Applied Sciences, 2021. **3**(2): p. 227 DOI: https://doi.org/10.1007/s42452-021-04200-8.

[14] Mallick, A., S. Gangi Setti, and R.K. Sahu, *Centrifugally cast A356/SiC functionally graded composite: Fabrication and mechanical property assessment.* Materials Today: Proceedings, 2021. **47**: p. 3346-3351 DOI: https://doi.org/10.1016/j.matpr.2021.07.155.

[15] Alshorbagy, A.E., M.A. Eltaher, and F.F. Mahmoud, *Free vibration characteristics of a functionally graded beam by finite element method.* Applied Mathematical Modelling, 2011. **35**(1): p. 412-425 DOI: https://doi.org/10.1016/j.apm.2010.07.006.

[16] Banerjee, J.R., *Dynamic Stiffness Formulation and Free Vibration Analysis of Centrifugally Stiffened Timoshenko Beams.* Journal of Sound and Vibration, 2001. **247**(1): p. 97-115 DOI: https://doi.org/10.1006/jsvi.2001.3716.

[17] Pradhan, K.K. and S. Chakraverty, *Generalized power-law exponent based shear deformation theory for free vibration of functionally graded beams.* Applied Mathematics and Computation, 2015. **268**: p. 1240-1258 DOI: https://doi.org/10.1016/j.amc.2015.07.032.

[18] Vu, T.-V., et al., *Buckling analysis of the porous sandwich functionally graded plates resting on Pasternak foundations by Navier solution combined with a new refined quasi-3D hyperbolic shear deformation theory.* Mechanics Based Design of Structures and Machines, 2022: p. 1-27 DOI: https://doi.org/10.1080/15397734.2022.2038618.

[19] Plevris, V. and G. Tsiatas, *Computational Structural Engineering: Past Achievements and Future Challenges.* Frontiers in Built Environment, 2018. **4**(21): p. 1-5 DOI: https://doi.org/10.3389/fbuil.2018.00021.

[20] Hadji, L., V. Plevris, and R. Madan, *A Static and Free Vibration Analysis of Porous Functionally Graded Beams*, in *2nd International Conference on Civil Infrastructure and Construction (CIC 2023)*. 2023: Doha, Qatar.

[21] Wattanasakulpong, N. and A. Chaikittiratana, *Flexural vibration of imperfect functionally graded beams based on Timoshenko beam theory: Chebyshev collocation method.* Meccanica, 2015. **50**(5): p. 1331-1342 DOI: https://doi.org/10.1007/s11012-014-0094-8.

[22] Demirhan, P.A. and V. Taskin, *Bending and free vibration analysis of Levy-type porous functionally graded plate using state space approach.* Composites Part B: Engineering, 2019. **160**: p. 661-676 DOI: https://doi.org/10.1016/j.compositesb.2018.12.020.

[23] Wattanasakulpong, N. and V. Ungbhakorn, *Linear and nonlinear vibration analysis of elastically restrained ends FGM beams with porosities.* Aerospace Science and Technology, 2014. **32**(1): p. 111-120 DOI: https://doi.org/10.1016/j.ast.2013.12.002.

[24] Atmane, H.A., et al., *A computational shear displacement model for vibrational analysis of functionally graded beams with porosities.* Steel and Composite Structures, 2015. **19**(2): p. 369-385 DOI: https://doi.org/10.12989/scs.2015.19.2.369.

[25] Hadj, B., B. Rabia, and T.H. Daouadji, *Influence of the distribution shape of porosity on the bending FGM new plate model resting on elastic foundations.* Structural Engineering and Mechanics, 2019. **72**(1): p. 61-70 DOI: https://doi.org/10.12989/sem.2019.72.1.061.

[26] Hadji, L., T.H. Daouadji, and E.A. Bedia, *A refined exponential shear deformation theory for free vibration of FGM beam with porosities.* Geomechanics and Engineering, 2015. **9**(3): p. 361-372 DOI: https://doi.org/10.12989/gae.2015.9.3.361.

[27] Reddy, J.N., *Energy Principles and Variational Methods in Applied Mechanics*. 3rd ed. 2017: Wiley, ISBN: 978-1-119-08737-3.

[28] Şimşek, M., *Fundamental frequency analysis of functionally graded beams by using different higher-order beam theories.* Nuclear Engineering and Design, 2010. **240**(4): p. 697-705 DOI: https://doi.org/10.1016/j.nucengdes.2009.12.013.

COMPDYN 2023
9th ECCOMAS Thematic Conference on
Computational Methods in Structural Dynamics and Earthquake Engineering
M. Papadrakakis, M. Fragiadakis (eds.)
Athens, Greece, 12-14 June 2023

# RAILWAY TRACK STRUCTURAL DYNAMICS VIA PERIODIC APPROACHES

**Angie C. Lamprea-Pineda[1], Alexandre Castanheira-Pinto[2], Pedro Alves Costa[2], Peter K. Woodward[1], Mohammed F.M. Hussein[3], and David P. Connolly[1]**

[1] Institute for High Speed Rail and System Integration, University of Leeds
LS29JT, Leeds, UK
e-mail: {cnaclp@leeds.ac.uk, D.Connolly@leeds.ac.uk, P.K.Woodward@leeds.ac.uk}

[2] Construct-FEUP, University of Porto
4099-002, Porto, Portugal
e-mail: {amgcpinto@fe.up.pt, pmbcosta@reit.up.pt}

[3] Department of Civil and Architectural Engineering, Qatar University
2713 Doha-Qatar
e-mail: {mhussein@qu.edu.qa}

## Abstract

*Periodicity can be defined as the repetitive character of a structure's features. In railway track systems, periodicity can be found in the geometrical and material properties in the train passage direction. For example, the repeating pattern of sleepers, rail seats or slab track units. To take advantage of this, this paper employs the direct periodic method, a novel numerical method which exploits the invariant nature of the railway track structure. Instead of simulating the total track domain, the direct periodic method studies a discrete portion of the track, often known as the reference cell, which captures its repetitive pattern and provides the total track response. First, the cell response is obtained by enforcing compatibility conditions within its system of equations of motion in the wavenumber-frequency domain. Then, the total space response is retrieved by replicating the cell's solution via a combination of periodic conditions and Fourier transformations. It is combined with perfectly matched layers to simulate infinite depth soil boundary conditions. Thus, this paper employs the direct periodic method in combination with perfectly matching layers to analyze track-ground dynamic interaction.*

**Keywords:** Periodic Modelling, Ballasted Track, Vibration Problems, Vibration Modes, Wave Propagation, Frequency Response.

## 1 INTRODUCTION

Vibration issues in railway systems are a result of the intricate dynamic relationship between the train, the track, and the supporting soil. As the need for transportation increases, so does the severity of these problems, requiring an in-depth comprehension of the dynamic behavior of the system components, improved design, and efficient solutions to reduce future maintenance and replacement costs. Consequently, assessing the condition of the entire system and its components is essential.

Often, this characterization is accomplished through empirical, analytical, semi-analytical, and numerical methods that enable the simulation and assessment of vibration issues associated with railway systems. The first approach is usually limited to specific conditions and is based on experience, numerical data, and field results for its formulation [1,2]. Perhaps the most comprehensive studies on railway track components' behavior have been conducted using analytical methods involving beam-on elastic foundation (BOEF) formulations. These studies have a straightforward definition which simplifies the components of the track system into beams, elastic elements, and lumped masses. Thus, allowing for a broad range of analyses – see for instance [2,3,4,5].

However, analytical approaches find it challenging to represent wave propagation in complex geometries. To overcome this limitation, the soil behavior is approximated using stiffness and flexibility matrices defined in the frequency domain. Examples of this are the domain transformation (DT) by Sheng [6,7] and the thin-layer method (TLM) [8]. Despite their accuracy, analytical and semi-analytical approaches cannot represent complex geometries. This has led to the development of numerical methods such as finite element methods (FEM), which provides a more flexible description of railway system behavior (e.g. complex railhead geometries, transition zones, etc. [9,10,11]). However, these methods require significant computational capacity due to the need for large domains.

Alternatively, periodic methods are implemented to reduce the computational effort while still providing accurate approximations of the structure's behavior. These methods exploits the periodic or repetitive characteristics of the structure (e.g. material and geometrical properties), allowing for a reduction of the domain under consideration and consequently, providing lower computational times [12,13,14,15]. In railway systems, the behavior is observed in both ballast and slab tracks. For instance, in ballasted tracks, the pattern is given by the repeated sleeper arrangement [16,17]; whereas in slab tracks, this is generated by the discrete rail-seats or repeating slab units [18,19,20,21]. Among the various periodic approaches, the 2.5D FEM has been extensively used for train-track-ground simulations in recent years [22,23,24,25,26,27]. Typically, this method is coupled with BE or PML (perfectly matching layers [28]) to account for the wave propagation response. However, the 2.5D FE only defines the structure's cross-section and assumes a homogenous behavior in the longitudinal direction, which makes it unable to represent the discrete support effect.

The periodic approach proposed by [29], known as the direct periodic method (DM), can address the limitation of computing the response of discretely supported structures. This method obtains the system's response via a direct inversion of a modified equilibrium formulation in the wavenumber-frequency domain. By combining it with PML, the DM allows to simulate infinite depth soil boundary conditions and further improving the efficiency of the overall computation.

Thus, this paper employs the direct periodic approach in combination with perfectly matching layers in order to study the dynamic behavior of a periodic ballasted track resting on a homogeneous ground.

## 2 MODELLING APPROACH

The direct periodic method (DM) defined by [29], in combination with 3D finite elements and perfectly matching layers (3D FE-PML), is employed in the simulation of the train-track-ground interaction response. By enforcing the periodic characteristic of the ballasted tracks, the DM allows to retrieve the behavior of the total domain (Ω) via the analysis of a restricted domain of length $d$ – also referred to as the unit or reference cell ($\widetilde{\Omega}$), which is assumed to infinitely repeat itself in the longitudinal or direction $x$ – see Figure 1. This allows for the formulation and solution of the system of equations of motions, in the wavenumber and frequency domain ($k_1, \omega$), in terms of $\widetilde{\Omega}$. Then, by enforcing periodic conditions and Fourier transformations, the response of Ω is retrieved in the space domain.

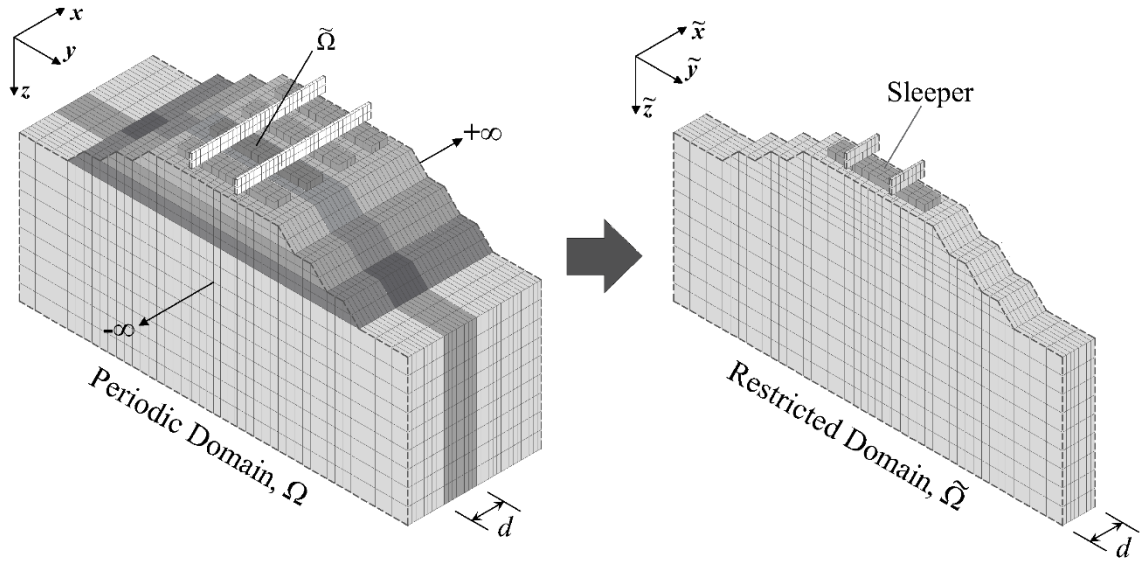


Figure 1: Periodic ballasted track domain infinitely extending in the longitudinal direction and its reference cell of length *d*.

### 2.1 Reference cell definition

The track and the ground behavior are included in the reference cell's formulation – as shown in Figure 1. In the first case, FE are employed. In contrast, PML are used to define the wave propagation effect of the ground. Then, both are coupled within a dynamic stiffness matrix (DSM) which allows for the definition of the system of equations of motion of $\widetilde{\Omega}$ - as described in Equation (1):

$$\left[\widetilde{D}_{n=0}\right]\{\tilde{u}_{n=0}\} = \{\tilde{F}_{n=0}\} \tag{1}$$

where $\{\tilde{u}_{n=0}\}$ and $\{\tilde{F}_{n=0}\}$ are the vectors of displacements and forces of $\widetilde{\Omega}$, respectively. The DSM, $\left[\widetilde{D}_{n=0}\right]$ (Equation (2)), is defined by the matrices of mass $[M_{n=0}]$ and complex stiffness $[K_{n=0}]$, the latter accounting for a hysteretic damping model (Equation (3)).

$$\left[\widetilde{D}_{n=0}\right] = [K_{n=0}] - \omega^2[M_{n=0}] \tag{2}$$

$$[K_{n=0}] = [k_{n=0}](1 + i\eta) \tag{3}$$

where $[k_{n=0}]$ is the matrix of stiffness and $\eta$ is the damping loss factor. Note that when accounting for the ground representation, the PML uses complex stretching coordinates, which

are defined upon complex stretching functions $\tilde{\lambda}_{\tilde{s}}$. Thus, the matrices in Equations (2)-(3) are also complex and described by:

$$\begin{aligned}\left[k_{n=0}^{PML}(\tilde{x},\tilde{\lambda}_{\tilde{y}},\tilde{\lambda}_{\tilde{z}})\right] &= \int_{\tilde{x}}\int_{\tilde{y}}\int_{\tilde{z}}\tilde{\lambda}_{\tilde{y}}\tilde{\lambda}_{\tilde{z}}\left[\check{B}(\tilde{x},\tilde{\lambda}_{\tilde{y}},\tilde{\lambda}_{\tilde{z}})\right]^{T}[D]\left[\check{B}(\tilde{x},\tilde{\lambda}_{\tilde{y}},\tilde{\lambda}_{\tilde{z}})\right]d\tilde{x}d\tilde{y}d\tilde{z}\\ \left[M_{n=0}^{PML}(\tilde{x},\tilde{\lambda}_{\tilde{y}},\tilde{\lambda}_{\tilde{z}})\right] &= \int_{\tilde{x}}\int_{\tilde{y}}\int_{\tilde{z}}\tilde{\lambda}_{\tilde{y}}\tilde{\lambda}_{\tilde{z}}\left[\check{N}(\tilde{x},\tilde{\lambda}_{\tilde{y}},\tilde{\lambda}_{\tilde{z}})\right]^{T}\rho\left[\check{B}(\tilde{x},\tilde{\lambda}_{\tilde{y}},\tilde{\lambda}_{\tilde{z}})\right]d\tilde{x}d\tilde{y}d\tilde{z}\end{aligned} \quad (4)$$

where $\left[\check{B}(\tilde{x},\tilde{\lambda}_{\tilde{y}},\tilde{\lambda}_{\tilde{z}})\right]$ is the complex matrix of partial derivatives of the shape functions $\left[\check{B}(\tilde{x},\tilde{\lambda}_{\tilde{y}},\tilde{\lambda}_{\tilde{z}})\right]$, and $[D]$ is the material matrix. Note that in the case of FEM, $\tilde{\lambda}_{\tilde{s}} = 1$.

## 2.2 Compatibility conditions and solution

To allow for continuity of the displacements and equilibrium of forces between each repeated cell, periodic conditions, formulated upon the Floquet's theorem [30], must be enforced within the reference cell boundaries:

$$\tilde{u}_n(x,y,z,k_1,\omega) = \tilde{u}_{n=0}(\tilde{x},\tilde{y},\tilde{z},k_1,\omega)e^{ik_1nd} \quad (5)$$

in where $\tilde{u}_n$ and $\tilde{u}_{n=0}$ are the displacements of the complete and discretized domain, respectively. Similarly, the space vectors in $\Omega$ and $\tilde{\Omega}$ are defined by $s = \{x,y,z\}$ and $\tilde{s} = \{\tilde{x},\tilde{y},\tilde{z}\}$, respectively; the cell number is defined by n, being *n=0* and *n≠0* the reference and the remaining cells. Overall, the tilde notation '~' represents the transformed domain ($k_1$,ω), corresponding to the wavenumber $k_1$ and angular frequency ω. To impose Equation (5), the reference cell's displacements at its front ($\tilde{u}_{n=0}^{front}$) and back face ($\tilde{u}_{n=0}^{back}$) must be related through the exponential term $e^{ik_1d}$:

$$\tilde{u}_{n=0}^{front}(\tilde{x}=d,\tilde{y},\tilde{z},k_1,\omega) = \tilde{u}_{n=0}^{back}(\tilde{x}=0,\tilde{y},\tilde{z},k_1,\omega)e^{ik_1d} \quad (6)$$

where $\tilde{u}_{n=0}^{front}$ and $\tilde{u}_{n=0}^{back}$ refer to the front and back border displacements of the reference cell, respectively – see Figure 2. Equation (6) ensures continuity at the boundaries of every $n^{th}$ cell.

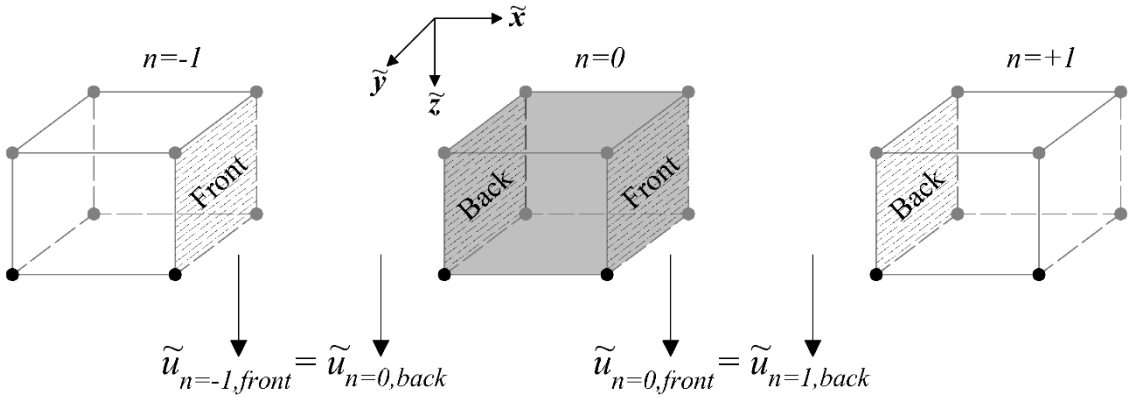


Figure 2: Continuity of displacements at the boundaries of the cells.

Once the displacements in all cells have been retrieved, Fourier transformations and employed to compute the response of the complete domain in space domain:

$$\hat{u}(x,y,z,\omega) = \frac{1}{2\pi}\int_{-\infty}^{\infty}\tilde{u}_n(x,y,z,k_1,\omega)e^{ik_1x}dk_1 \quad (7)$$

in where $\hat{u}$ is the displacement of the complete domain, and the notation '^' describes the space-frequency domain $(x,\omega)$.

## 3 APPLICATION

The combined DM and 3D FE-PML are employed to simulate the dynamic track-ground behavior. To do so, a ballasted track resting on a semi-infinite soil is considered. Table 1 shows the main properties of the various track components, including the material and dimensions of the rail section, railpad, sleeper, ballast, sub-ballast, and the subgrade. The reference cell of length *d=0.6m* is defined through 8-node solid elements.

| Component | Parameter | Value |
|---|---|---|
| Track | Gauge | 0.7175m |
| Rail | Section | CEN60/60E2 |
| | Height | 0.218m |
| | Width | 0.035m |
| | Density | 7850kg/m$^3$ |
| | Young's modulus | 210GPa |
| Railpad | Height | 0.01m |
| | Density | 1000kg/m$^3$ |
| | Young's modulus | 300MPa |
| | Poisson's ratio | 0.45 |
| | Loss factor | 0.15 |
| Sleeper | Material | Concrete |
| | Depth | 0.2m |
| | Thickness | 0.2m |
| | Length | 1.3m |
| Ballast | Depth | 0.3m |
| | Length (top) | 1.6m |
| | Length (bottom) | 2.1m |
| | Density | 1700kg/m$^3$ |
| | Young's modulus | 220MPa |
| | Poisson's ratio | 0.3 |
| | Loss factor | 0.4 |
| Sub-ballast | Depth | 0.2m |
| | Length | 2.7m |
| | Density | 1900kg/m$^3$ |
| | Young's modulus | 200MPa |
| | Poisson's ratio | 0.3 |
| | Loss factor | 0.1 |
| Subgrade | Depth | ∞ |
| | Density | 1800kg/m$^3$ |
| | Young's modulus | 80MPa |
| | Poisson's ratio | 0.35 |
| | Loss factor | 0.1 |

Table 1: Track properties.

In addition, the reference cell is subject to a stationary impulse force $F$ of unit magnitude, $P = 1N$, excited at frequency $\omega$:

$$F(x) = P\delta(x - x_o)e^{i\omega t} \tag{8}$$

where $\delta$ is the Dirac delta function defining the impulse, $t$ is the time, and $x_o$ is the observation point. $F$ is applied on the rail above the sleeper support and deflections and velocities are obtained at different positions of the track (see Figure 3):

- the rail on support – i.e. same position of the force,
- the rail at mid-span – i.e. between two sleepers, and
- at the middle of the sleeper.

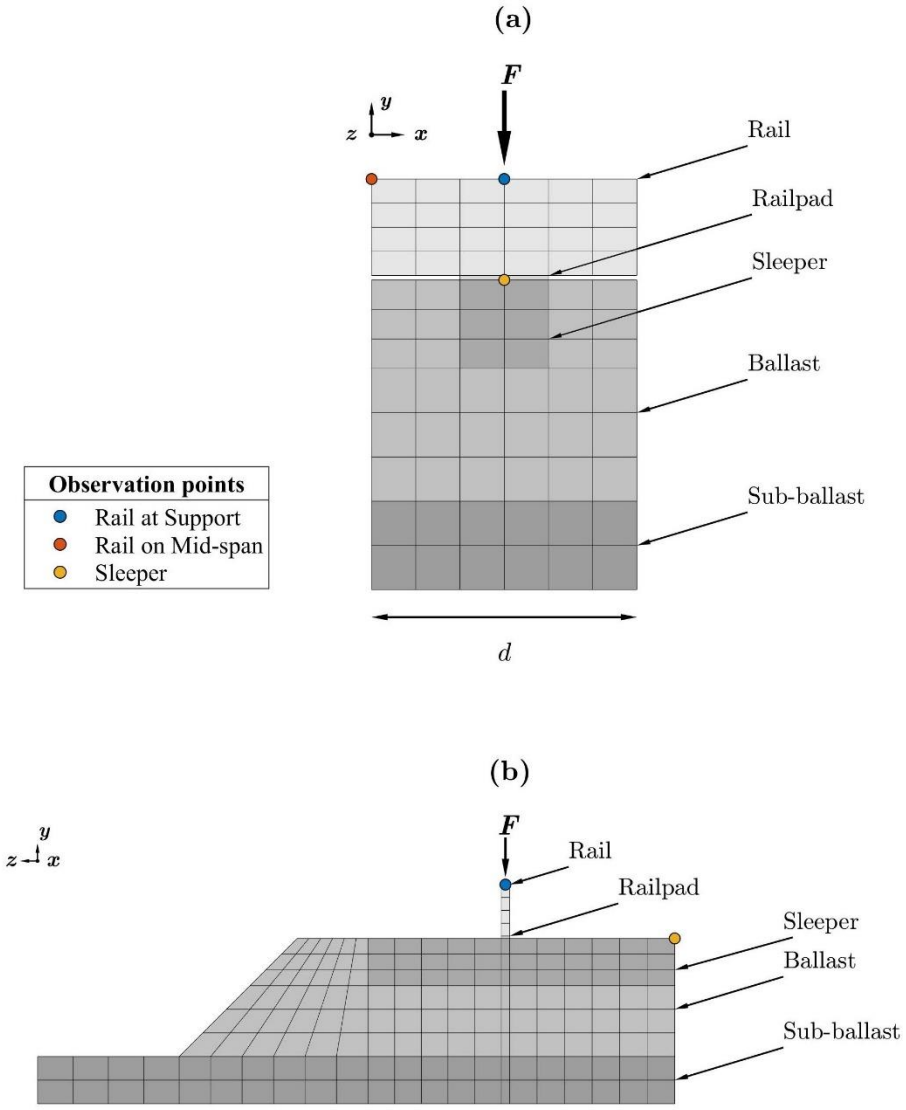


Figure 3: Excitation and observation locations within the model: (a) $x-y$ view, and (b) $y-z$ view. Subgrade layer omitted for visibility.

## 4 RESULTS

Figure 4 presents the absolute deflection, in the space-frequency domain, at different track positions due to a unit harmonic excitation. Three main regions, corresponding to the frequencies of resonances describe the vibration modes of the total structure: the full-track ($f_{\text{full-track}}$), the railpad ($f_{\text{railpad}}$) and the pin-pin ($f_{\text{pin-pin}}$) resonant frequencies. The first one, corresponding to $f_{\text{full-track}}$, occurs below 20Hz. It can be seen that regardless of the observation point, the maximum deflection is achieved around this frequency. This is consequence of the soft subgrade supporting the much stiffer ballasted track. The soil properties effect decreases with the

frequency until reaching $f_{\text{railpad}}$. At this frequency, the railpad behavior dominates the response. Note that, besides the highlighted frequencies, some other maximum peaks are observed, however, they are result of the wave propagation of the subgrade. Finally, the peak occurring around 1000Hz corresponds to $f_{\text{pin-pin}}$. Since the excitation is applied on the rail above the sleeper support, the peak is downward, resulting in an anti-resonance.

Similar results are observed in the velocity curves of Figure 5. Again, the three main frequencies are visible; however, the response is computed in terms of velocity rather than displacements, leading to a maximum response occurring at high-frequency ranges.

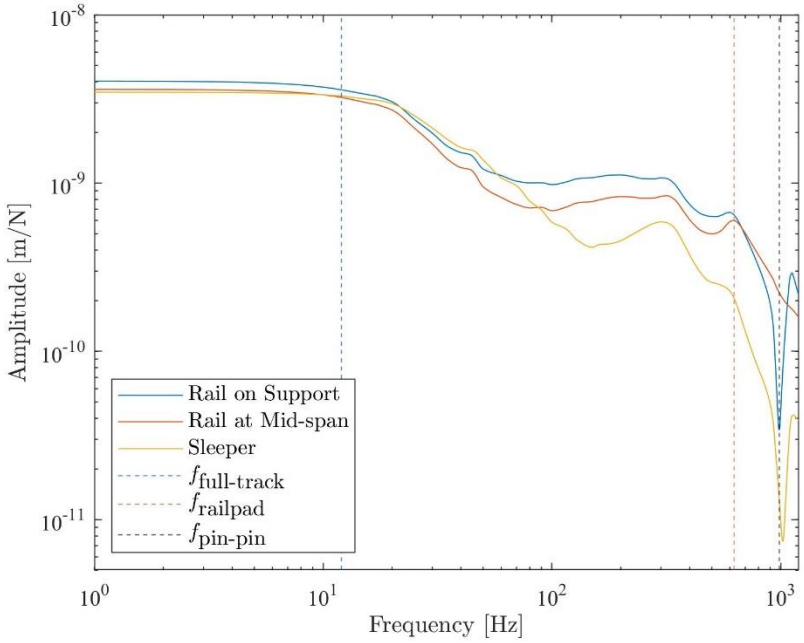


Figure 4: Track deflections due to unit harmonic force *F*.

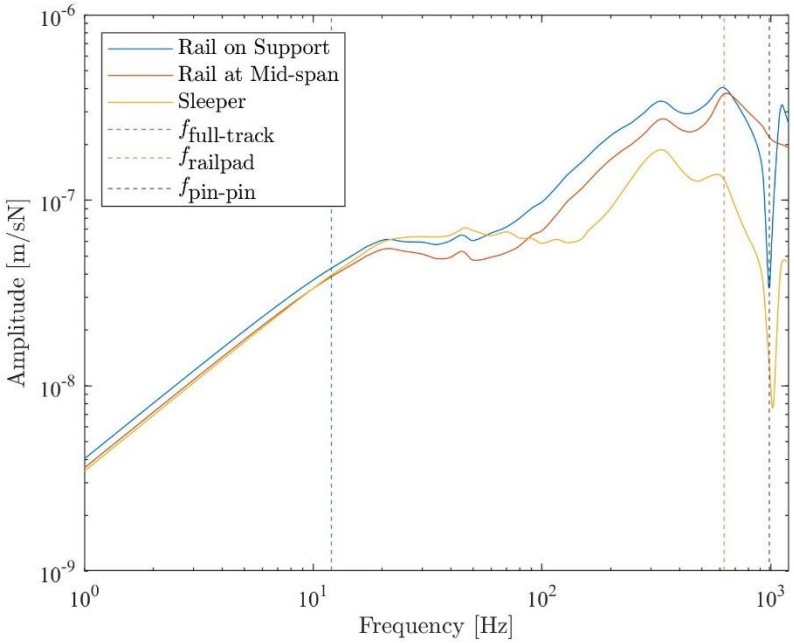


Figure 5: Track velocities due to unit harmonic force *F*.

Figure 6 shows the vibration modes of the track at the tree main frequencies. Figure 6(a) shows that at $f_{\mathrm{full-track}}$, the rail and the sleeper mass move vertically, and in phase, over the ballast. In contrast, in the track behavior corresponding to $f_{\mathrm{railpad}}$, both the rail and the sleeper move in antiphase on the railpad – see Figure 6(b). Similarly, at $f_{\mathrm{pin-pin}}$, the rail and the sleeper are moving in antiphase; however, the wavelength of the rail is described by the support spacing– see Figure 6(c). Overall, in both $f_{\mathrm{railpad}}$ and $f_{\mathrm{pin-pin}}$, the rail is vibrating on the supports.

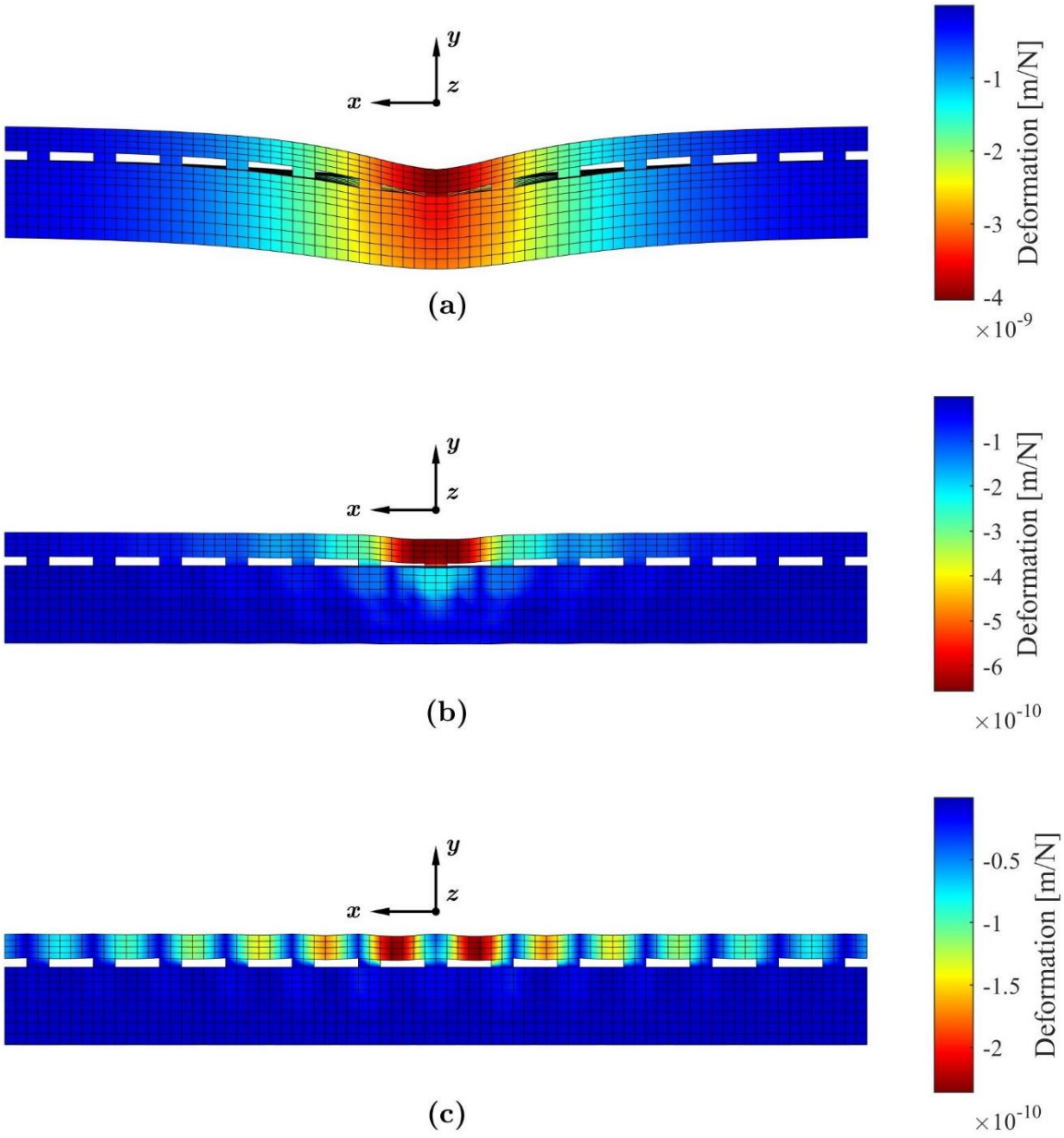


Figure 6: Absolute track response at: (a) full-track resonance (b) railpad resonance, and (c) pin-pin resonance – railpad dimensions and deflections magnified for visibility.

Alternatively, Figure 7(a) and Figure 7(b) present the structure's response, including the subgrade's, around 100 and 325Hz, respectively. It can be noted that although maximum values occur around these frequency values, they do not correspond to the main three resonant frequencies. In both cases, wave propagation is observed within the soil, indicating its properties' influence on the response. However, in the latter, the soil effect reduces since the frequency is

high and closer to the railpad frequency of resonance. In addition, the lower track layers (i.e. ballast and sub-ballast) also affect the total response at 325Hz – see Figure 7(b). It should be noted that, for improved visibility, the railpad dimensions and the deflection values have been magnified in Figures 6 and 7. Additionally, only 13 cells are displayed, i.e. $n = -6{:}\,6$.

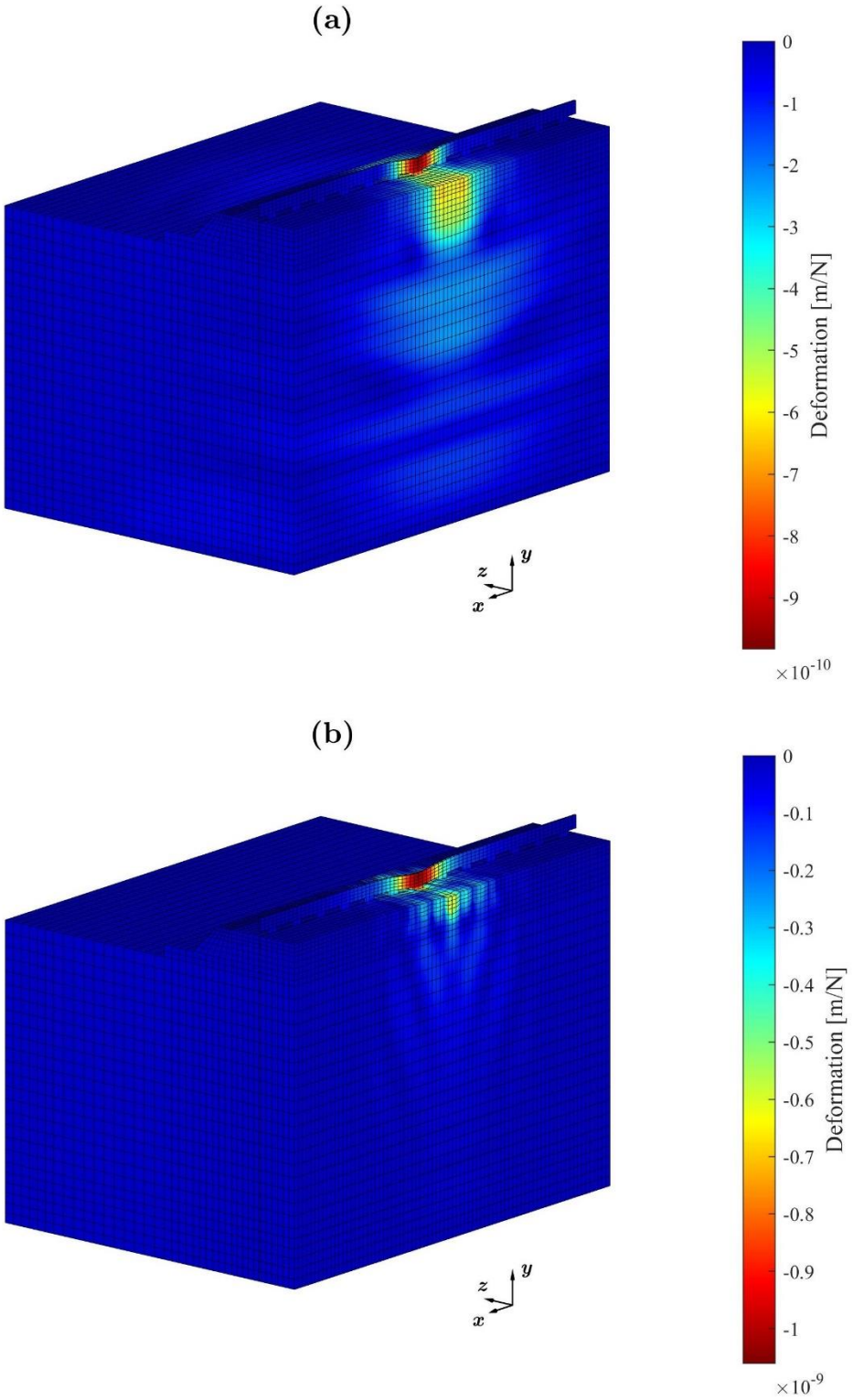


Figure 7: Absolute track response at: (a) 100Hz, and (b) 325Hz – railpad dimensions and deflections magnified for visibility.

## 5 CONCLUSIONS

Vibration issues in railway systems are caused by the complex dynamic interactions between the train, the track, and the underlying soil. With the growing demand for transportation, so is the severity of these problems, resulting in faster track deteriorations and higher maintenance costs. This has led to the development of simulation techniques to approximate the system's behavior and asses this vibration issues. Thus, this paper employs a direct periodic strategy combined with 3D FE and PML to study a ballasted track resting on a homogeneous soil. The periodic nature of the track is exploited, resulting in a computationally efficient method that only requires the discretization of a slice, which can retrieve the total response.

It can be seen that the DM successfully captures the main resonant frequencies exciting the railway system, including the full-track, railpad and the pin-pin. Since the pin-pin frequency can be simulated, so is its discrete support. Similarly, by combining it with PML, the DM can retrieve the wave propagation effect as described by the vibration modes of the structure. Overall, the obtained results, show that the soil properties play an important role in the track response at lower frequencies. In contrast, higher frequencies results are mostly affected by the track behavior.

## REFERENCES

[1] A.P. de Man, Pin-pin resonance as a reference in determining ballasted railway track vibration behaviour. *HERON*, **45**, 35-51, 2000.

[2] A.C. Lamprea-Pineda, D.P. Connolly, M.F.M. Hussein, Beams on elastic foundations – A review of railway applications and solutions. *Transportation Geotechnics*, **33**, 100696, 2022.

[3] K.L. Knothe, S.L. Grassie, Modelling of Railway Track and Vehicle/Track Interaction at High Frequencies. *Vehicle System Dynamics*, **22**, 209-262, 1993.

[4] S.L. Grassie, R.W. Gregory, D. Harrison, K.L. Johnson. The Dynamic Response of Railway Track to High Frequency Vertical Excitation. *Journal of Mechanical Engineering Science*, **24**, 77-90, 1982.

[5] D. Thompson, *Railway Noise and Vibration, 1st Edition.* Elsevier, 2009.

[6] X. Sheng, C.J.C. Jones, M. Petyt, Ground vibration generated by a harmonic load acting on a railway track. *Journal of Sound and Vibration*, **225**, 3–28, 1999.

[7] X. Sheng, C.J.C. Jones, M. Petyt, Ground vibration generated by a load moving along a railway track. *Journal of Sound and Vibration*, **228**, 129–56, 1999.

[8] E. Kausel, Thin-layer method: Formulation in the time domain. *International Journal for Numerical Methods in Engineering*, **37**, 927–941, 1994.

[9] Y. Ma, V.L. Markine, A.A. Mashal, M. Ren, Effect of wheel–rail interface parameters on contact stability in explicit finite element analysis. *Proceedings of the Institution of Mechanical Engineers, Part F: Journal of Rail and Rapid Transit*, **232**, 1879–1894, 2018.

[10] H. Wang, V. Markine, Modelling of the long-term behaviour of transition zones: Prediction of track settlement. *Engineering Structures*,**156**, 294–304, 2018.

[11] P. Chumyen, D.P. Connolly, P.K. Woodward, V. Markine. The effect of soil improvement and auxiliary rails at railway track transition zones. *Soil Dynamics and Earthquake Engineering*, **155**, 107200, 2022.

[12] E. Arlaud, S. Costa D'Aguiar, E. Balmes, Receptance of railway tracks at low frequency: Numerical and experimental approaches. *Transportation Geotechnics*, **9**, 1–16, 2016.

[13] M, Germonpré, G, Degrande, G, Lombaert, A track model for railway-induced ground vibration resulting from a transition zone. *Proceedings of the Institution of Mechanical Engineers, Part F: Journal of Rail and Rapid Transit*, **232**, 1703–1717, 2018.

[14] P. Ferreira, Modelling and prediction of the dynamic behaviour of railway infrastructures at very high speeds. *Universidade Técnica de Lisboa, Instituto Superior Técnico*, 1-432, 2010.

[15] B.R. Mace, D. Duhamel, M.J. Brennan, L. Hinke, Finite element prediction of wave motion in structural waveguides. *The Journal of the Acoustical Society of America*, **117**, 2835–2843, 2005.

[16] M. Sadri, T. Lu, M. Steenbergen, Railway track degradation: The contribution of a spatially variant support stiffness - Local variation. *Journal of Sound and Vibration*, **455**, 203–20, 2019.

[17] M. Sadri, T. Lu, M. Steenbergen, Railway track degradation: The contribution of a spatially variant support stiffness - Global variation. *Journal of Sound and Vibration*, **464**, 114992, 2020.

[18] S. Gupta, G. Degrande, H. Chebli, D. Clouteau, M.F.M. Hussein, H.E.M. Hunt. A coupled periodic FE-BE model for ground-borne vibrations from underground railways. *III European Conference on Computational Mechanics (ECCM-2006)*, Lisbon, Portugal, June 5–9, 2006.

[19] H. Chebli, R. Othman, D. Clouteau, M. Arnst, G. Degrande, 3D periodic BE–FE model for various transportation structures interacting with soil. *Computers and Geotechnics*, **35**, 22–32, 2008.

[20] M.F.M. Hussein, H.E.M. Hunt, Modelling of Floating-Slab Track with Discontinuous Slab: Part 1: Response to Oscillating Moving Loads. *Journal of Low Frequency Noise, Vibration and Active Control*, 25, 23–39, 2006.

[21] J.A. Forrest, Modelling of Ground Vibration from Underground Railways. *University of Cambridge*, 1999.

[22] P. Alves Costa, R. Calçada, A. Silva Cardoso, Track–ground vibrations induced by railway traffic: In-situ measurements and validation of a 2.5D FEM-BEM model. *Soil Dynamics and Earthquake Engineering*, **32**,111–28, 2012.

[23] P. Alves Costa, R. Calçada, A. Silva Cardoso, Ballast mats for the reduction of railway traffic vibrations, Numerical study. *Soil Dynamics and Earthquake Engineering*, **42**, 137–50, 2012.

[24] C. Charoenwong, D.P. Connolly, P.K. Woodward, P. Galvín, P. Alves Costa, Analytical forecasting of long-term railway track settlement. *Computers and Geotechnics*, **143**, 104601, 2022.

[25] C. Charoenwong, D.P. Connolly, K. Odolinski, P. Alves Costa, P. Galvín, A. Smith, The effect of rolling stock characteristics on differential railway track settlement: An engineering-economic model. *Transportation Geotechnics*, **37**, 100845, 2022.

[26] C. Charoenwong, D.P. Connolly, A. Colaço, P. Alves Costa, P.K. Woodward, A. Romero, P. Galvín, Railway slab vs ballasted track: a comparison of track geometry degradation. *Construction and Building Materials*, 2023.

[27] J. Fernández Ruiz, P.J. Soares, P. Alves Costa, D.P. Connolly, The effect of tunnel construction on future underground railway vibrations. Soil Dynamics and Earthquake Engineering, 125, 105756, 2019.

[28] D.P. Connolly, A. Giannopoulos, M.C. Forde, A higher order perfectly matched layer formulation for finite-difference time-domain seismic wave modeling. *GEOPHYSICS*, **80**, T1–16, 2015.

[29] A. Castanheira-Pinto, A. Colaço, J.F. Ruiz, P. Alves Costa, L. Godinho, Simplified approach for ground reinforcement design to enhance critical speed. *Soil Dynamics and Earthquake Engineering*, **153**, 107078, 2022.

[30] P. Gómez García, J.P. Fernández-Álvarez, Floquet-Bloch Theory and Its Application to the Dispersion Curves of Nonperiodic Layered Systems. *Mathematical Problems in Engineering*, **2015**, 1–12, 2015.

COMPDYN 2023
9th ECCOMAS Thematic Conference on
Computational Methods in Structural Dynamics and Earthquake Engineering
M. Papadrakakis, M. Fragiadakis (eds.)
Athens, Greece, 12-–14 June 2023

# NUMERICAL INVESTIGATION ON STABILITY OF COLUMNS UNDER DYNAMIC LOADS WITH TWO FREQUENCIES

**Jian Deng**[1]

[1]Department of Civil Engineering, Lakehead University, Ontario P7B 5E1, Canada
e-mail: jdeng2@lakeheadu.ca

**Abstract.** *Investigation of stability of structures under dynamic loads with a single frequency leads to differential equations with periodic coefficients, i.e., Mathieu-Hill equations. In many cases of civil engineering, however, the dynamic force is not periodic with a single frequency but quasi-periodic with multiple frequencies. This paper proposes a new numerical method to study the stability of columns under dynamic loads with two frequencies. The equation of motion for columns with fixed-fixed connections under parametric loads is derived and decoupled into an ordinary differential equation with variable coefficients. The first step of the numerical method is to approximate the system with two frequencies by a system with a single frequency (or period) as closely as possible. A numerical method is proposed to calculate the state transition matrix on one period through which the dynamic stability can be determined. As a verification of the proposed numerical method, a system under parametric excitation with two incommensurate frequencies is studied and compared to existing results in the literature. The efficiency and accuracy of the proposed numerical method are demonstrated. As an application example, dynamic stability of a column under parametric loads with two frequencies is investigated through instability diagrams and vibration responses. Vibration responses provide partial validation of the instability diagrams. The numerical results for instability diagrams can serve as a calibration of other approximate results. The proposed method can also be extended to multiple degrees of freedom systems under arbitrary parametric excitations with multiple frequencies.*

**Keywords:** Columns, Dynamic stability, Numerical simulation, Multiple frequencies, Instability diagrams.

## 1 INTRODUCTION

Investigation of structural stability under dynamic loads leads to a governing partial differential equation, which is usually converted into ordinary differential equations with periodic coefficients, i.e., Mathieu-Hill equations [1]. This dynamical system is called parametrically excited system and the instability is known as parametric resonance. The traditional method for parametric resonance is from Floquet theory. Bolotin developed harmonic balance in terms of Hill infinite determinants [1] to obtain a hierarchy of instability boundaries. Mathieu-Hill equations are also solved by approximate methods such as the method of perturbation [2] and the method of averaging [3], but these methods are only applicable for small periodic excitations.

In many cases, however, the dynamic force is not periodic with a single frequency but quasi-periodic with multiple frequencies. In civil engineering, for example, parametric resonance occurs when a pile foundation is subjected to vertical earthquake excitations. If one assumes that the vertical earthquake excitation is a periodic force, the equation of motion of the file foundation turns out to be a Mathieu-Hill equation. In reality, however, earthquake excitations are not periodic; instead, they consist of different waves and contain many different frequencies. Another example is a ship sailing in longitudinal sea waves where parametric resonance often occurs because the equation of motion of the ship is a Mathieu-Hill equation [6]. However, sea waves are not periodic with a single frequency in nature; instead, sea waves contain multiple incommensurate frequencies. Unfortunately, the classical methods [1, 4] are only applicable to systems under a parametric excitation with only a single frequency. Zhang et al. [5] recently investigated dynamic stability of an axially transporting beam with two-frequency parametric excitation and internal resonance. There is no complete theory for Mathieu-Hill equations with multiple frequencies. Sharma and Sinha proposed an approximate analysis of quasi-periodic systems via Floquet theory [6]. The present paper attempts to present a numerical investigation on stability of columns under dynamic loads with two frequencies. The numerical results on dynamic stability are consolidated by vibration responses.

## 2 FORMULATION

The column with fixed-fixed ends in Fig. 1(a) is excited by a longitudinal dynamic force $P(t)$. Transverse vibration $v(x,t)$ occurs in the $xv$ plane. This column may be a model of deep pile foundation under earthquake excitations. To study the dynamics of the column, an element $\mathrm{d}x$ is analyzed: the axial force $P$, the shear force $S$, the moment $M$, the external damping force $\beta_0 \mathrm{d}x\frac{\partial v}{\partial t}$, and the inertia force $(\rho A \mathrm{d}x)\frac{\partial v}{\partial t}$, where $\beta_0$ is the damping coefficient per unit length, $\rho$ is the density, $A$ is the cross-sectional area, and $EI$ is the flexural rigidity.

Applying equations of equilibrium

$$\mathrm{d}S + (\rho A \mathrm{d}x)\ddot{v}(x,t) + \beta_0 \mathrm{d}x\dot{v}(x,t) = 0, \tag{1}$$

$$\mathrm{d}M(x,t) - S\mathrm{d}x + P(t)\mathrm{d}xv(x,t) = 0, \tag{2}$$

$$M(x,t) = EI\frac{\partial^2 v(x,t)}{\partial x^2}, \tag{3}$$

results in the equation of motion of the column

$$EI\frac{\partial^4 v(x,t)}{\partial x^4} + \rho A\frac{\partial^2 v(x,t)}{\partial x^2} + \beta_0\frac{\partial v(x,t)}{\partial x} + P(t)\frac{\partial^2 v(x,t)}{\partial x^2} = 0. \tag{4}$$

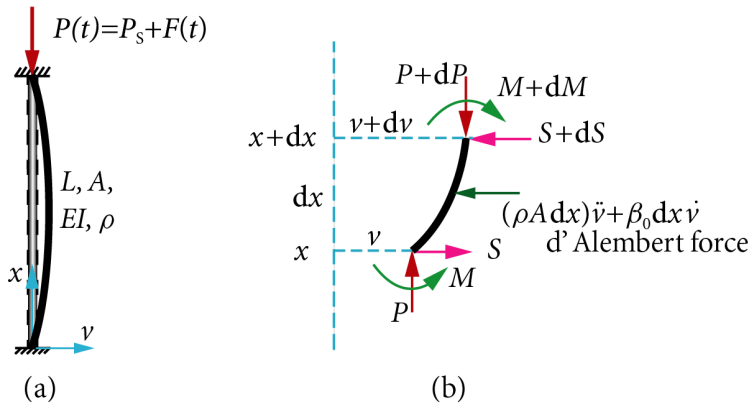


Figure 1: A column under a dynamic force (a) the column; (b) forces on the element d$x$.

The fixed-fixed boundary conditions are given by

$$\text{at } x = 0, v(0,t) = \frac{\partial v(0,t)}{\partial x} = 0; \text{ at } x = L, v(L,t) = \frac{\partial v(L,t)}{\partial x} = 0. \tag{5}$$

The method of separation of variables is used in Eq. (4)

$$v(x,t) = \sum_{n=1}^{\infty} q_n(t) \left[1 - \cos\frac{2n\pi x}{L}\right], \tag{6}$$

and the equation of motion in terms of the lateral deflection $q_n(t)$ is

$$\rho A \left[1 - \cos\frac{2n\pi x}{L}\right] \ddot{q}_n(t) + \beta_0 \left[1 - \cos\frac{2n\pi x}{L}\right] \dot{q}_n(t) + P(t) \left(\frac{2n\pi}{L}\right)^2 \cos\frac{2n\pi x}{L} q_n(t) - EI \left(\frac{2n\pi}{L}\right)^4 \cos\frac{2n\pi x}{L} q_n(t) = 0. \tag{7}$$

Performing a differentiation on Eq. (7) with respect to $x$ and taking the first mode ($n = 1$) yield

$$\ddot{q}(t) + \frac{\beta_0}{\rho A}\dot{q}(t) + \omega_0^2 \left[1 - \frac{P(t)}{P_0}\right] q(t) = 0, \tag{8}$$

where

$$\omega_0^2 = \frac{EI}{\rho A}\left(\frac{2\pi}{L}\right)^4, P_0 = EI\left(\frac{2\pi}{L}\right)^2. \tag{9}$$

By assuming that the dynamic force is composed of a static component and multiple dynamic components of multiple frequencies

$$P(t) = P_s + \sum_{i=1}^{m} \left(P_{di} \cos\theta_i t\right), \theta_i = \frac{2\pi}{T_i}, \tag{10}$$

where $m$ is the number of frequencies in the dynamic force and also the number of dynamic component forces, $P_s$ is the static component force, $P_{di}$ is the amplitude of the $i$-th dynamic component force, $\theta_i$ is the $i$-th angular frequency, and $T_i$ is the $i$-th period.

Eq. (8) can be transformed into

$$\ddot{q} + 2\beta\dot{q} + \omega_0^2 \left[1 - \frac{P_s}{P_0} - \sum_{i=1}^{m} \left(\frac{P_{di}}{P_0}\cos\theta_i t\right)\right] q = 0, \beta = \frac{\beta_0}{2\rho A}, \tag{11}$$

$$\ddot{q} + 2\beta\dot{q} + \left[\omega_0^2 \left(1 - \frac{P_s}{P_0}\right) - \omega_0^2 \sum_{i=1}^{m} \left(\frac{P_{di}}{P_0}\cos\theta_i t\right)\right] q = 0. \tag{12}$$

By changing the variable $q(t) = e^{-\beta t}u(t)$, Eqs. (11-12) can be transformed to an equivalent undamped equation, respectively,

$$\ddot{u} + \omega_0^2 \left[1 - \frac{\beta^2}{\omega_0^2} - \frac{P_s}{P_0} - \sum_{i=1}^{m} \left(\frac{P_{di}}{P_0}\cos\theta_i t\right)\right] u = 0, \tag{13}$$

$$\ddot{u} + \left[\omega_0^2 \left(1 - \frac{P_s}{P_0}\right) - \beta^2 - \omega_0^2 \sum_{i=1}^{m} \left(\frac{P_{di}}{P_0}\cos\theta_i t\right)\right] u = 0. \tag{14}$$

## 3 NUMERICAL METHOD FOR DYNAMIC STABILITY

Eq. (13) or (14) is an ordinary differential equation with a variable coefficient of multiple frequencies (quasi-periodic), which is hard to solve by directly using the Bolotin's method [1]. The idea of our numerical method is to convert the quasi-periodic equation to an equation with a periodic coefficient of a single frequency, i.e., a Mathieu-Hill equation, then one can divide period $T$ into sufficient time intervals, approximate the equation with variable coefficients by an equation with constant coefficients on each interval, and accumulate the responses on each time interval in one period $T$. So, the key step is to approximate the system with multiple frequencies by a system with a single frequency.

### 3.1 Approximation of multiple frequencies by a single frequency

The idea is to approximate the system with multiple frequencies by a system with a single frequency as closely as possible.

Consider a system with two frequencies in the dynamic force. Take $m = 2$ with angular frequency $\theta_1$ and $\theta_2$ as an example. The approximate single period can be determined in the following minimization search process.

$$\min_{i=1\ldots h} \min_{j=1\ldots h} \left| i\frac{2\pi}{\theta_1} - j\frac{2\pi}{\theta_2} \right|, \tag{15}$$

where $h$ is an appropriate positive integer that is used to decide which combination of $(i, j)$ will lead to a minimum value of $\left|i\frac{2\pi}{\theta_1} - j\frac{2\pi}{\theta_2}\right|$. In order to approximate the system with two frequencies by a system with a single frequency as closely as possible, the value of $\left|i\frac{2\pi}{\theta_1} - j\frac{2\pi}{\theta_2}\right|$ should be as small as possible, say, less than a very small specified real number such as $10^{-2}$. If this small number is not satisfied during the search process, then one should increase $h$ and search again. If $\theta_1$ is commensurate with $\theta_2$, i.e., their ratio $\theta_1/\theta_2$ is a rational number, the final period is accurate, $T = i\frac{2\pi}{\theta_1} = j\frac{2\pi}{\theta_2}$. A rational number is the ratio of two integers. On the contrary, if $\theta_1$ is incommensurate with $\theta_2$, i.e., their ratio $\theta_1/\theta_2$ is not a rational number, the final period is only approximate, $T = i\frac{2\pi}{\theta_1} \approx j\frac{2\pi}{\theta_2}$.

Take $m = 3$ with circular frequency $\theta_1$, $\theta_2$, and $\theta_3$ as another example. The search process for a single period is as follows.

$$\min_{i=1\cdots h}\min_{j=1\cdots h}\min_{k=1\cdots h}\left\{\left|i\frac{2\pi}{\theta_1}-j\frac{2\pi}{\theta_2}\right|+\left|i\frac{2\pi}{\theta_1}-k\frac{2\pi}{\theta_3}\right|+\left|j\frac{2\pi}{\theta_2}-k\frac{2\pi}{\theta_3}\right|\right\}. \tag{16}$$

Locate the combination of $(i, j, k)$ that will lead to a minimum value of $\left\{\left|i\frac{2\pi}{\theta_1}-j\frac{2\pi}{\theta_2}\right|+\left|i\frac{2\pi}{\theta_1}-k\frac{2\pi}{\theta_3}\right|+\left|j\frac{2\pi}{\theta_2}-k\frac{2\pi}{\theta_3}\right|\right\}$. If $\theta_1$, $\theta_2$, and $\theta_3$ are commensurate, the final period is accurate, $T = i\frac{2\pi}{\theta_1} = j\frac{2\pi}{\theta_2} = k\frac{2\pi}{\theta_3}$. On the contrary, if $\theta_1$, $\theta_2$, and $\theta_3$ are incommensurate, the final period is only approximate, $T = i\frac{2\pi}{\theta_1} \approx j\frac{2\pi}{\theta_2} \approx k\frac{2\pi}{\theta_3}$.

Consider a system with an excitation of two frequencies which is shown in Fig. 2(a): $\theta_1 = \frac{\pi}{2}(T = 4)$ and $\theta_2 = \frac{\pi}{3}(T = 6)$. Taking $h = 10$, minimization of Eq. (15) leads to $i = 3$ and $j = 2$ which make $\left|i\frac{2\pi}{\theta_1}-j\frac{2\pi}{\theta_2}\right| = 0$. Since $\theta_1 = \frac{\pi}{2}$ is commensurate with $\theta_2 = \frac{\pi}{3}$, the system with two frequencies can be accurately represented by a system with a single frequency: the single period $T = 3\frac{2\pi}{\theta_1} = 2\frac{2\pi}{\theta_2} = 12$ and the single angular frequency is $\theta = \frac{2\pi}{T} = \frac{\pi}{6}$.

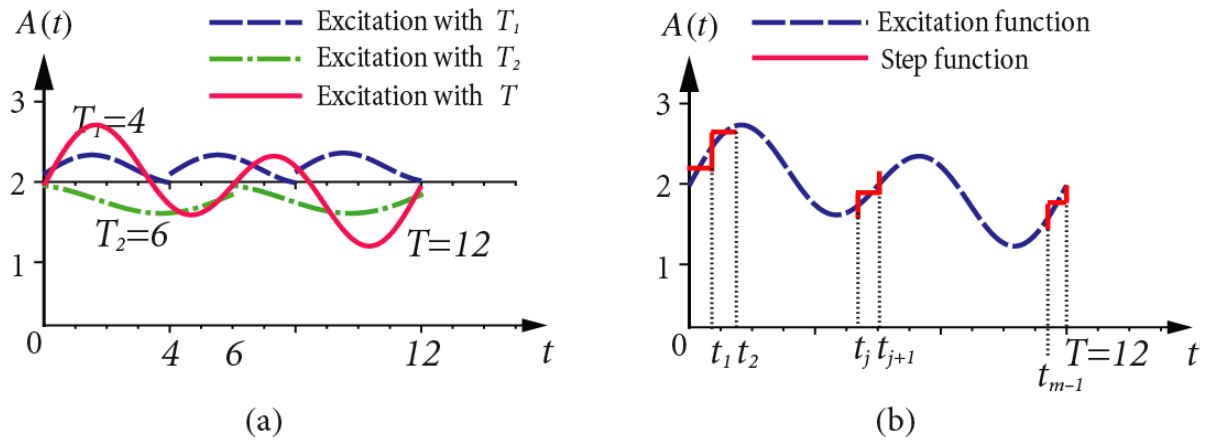


Figure 2: Approximation of two frequencies by a single frequency.

### 3.2 Numerical method for dynamic stability

After approximation of multiple frequencies by a single frequency, Eq. (11) is approximated by

$$\ddot{q}+2\beta\dot{q}+\omega_0^2[1-S(t)]q=0, S(t)=\frac{P_s}{P_0}+\sum_{i=1}^{m}\left(\frac{P_{di}}{P_0}\cos\theta_i t\right), S(t)\approx S(t+T)\quad 0<t\leq T, \tag{17}$$

one can use the following numerical method to construct the instability diagram [7, 8, 9].

Divide the period $T$ into $m$ equal time intervals, as shown in Fig. 2(b). On interval $[t_j, t_{j+1}]$, the step function is determined by the average of the real excitation function,

$$h_j^2=\frac{1}{t_{i+1}-t_j}\int_{t_j}^{t_{j+1}}\omega^2\left[1-\frac{\beta^2}{\omega_0^2}-S(t)\right]dt, t_{j+1}-t_j=\frac{T}{m}, j=0,1,\cdots m-1. \tag{18}$$

The equation of motion in Eq. (17) is approximated by a differential equation with constant coefficients on the time interval $[t_j, t_{j+1}]$,

$$\frac{d^2q(t)}{dt^2} + {h_j}^2 q = 0, \quad t_j \le t \le t_{j+1}. \tag{19}$$

The solution of Eq. (19) is given by

$$\begin{bmatrix} q(\tau) \\ \dot{q}(\tau) \end{bmatrix} = \boldsymbol{G}(\tau) \begin{bmatrix} c_1 \\ c_2 \end{bmatrix}, \boldsymbol{G}(\tau) = \begin{bmatrix} \sin(h_j\tau) & \cos(h_j\tau) \\ h_j\cos(h_j\tau) & -h_j\sin(h_j\tau) \end{bmatrix}, \tau = t - t_j, \tag{20}$$

where constants $C_1$ and $C_2$ are determined by the local initial conditions, $q(t_j)$ and $\dot{q}(t_j)$,

$$\begin{bmatrix} q(t=t_j) \\ \dot{q}(t=t_j) \end{bmatrix} = \begin{bmatrix} \sin(0) & \cos(0) \\ h_j\cos(0) & -h_j\sin(0) \end{bmatrix} \begin{bmatrix} C_1 \\ C_2 \end{bmatrix} = \begin{bmatrix} 0 & 1 \\ h_j & 0 \end{bmatrix} \begin{bmatrix} C_1 \\ C_2 \end{bmatrix}, \tag{21}$$

$$\begin{bmatrix} C_1 \\ C_2 \end{bmatrix} = \boldsymbol{G}^{-1}(0) \begin{bmatrix} q(t=t_j) \\ \dot{q}(t=t_j) \end{bmatrix} = \frac{1}{-h_j} \begin{bmatrix} 0 & -1 \\ -h_j & 0 \end{bmatrix} \begin{bmatrix} q(t=t_j) \\ \dot{q}(t=t_j) \end{bmatrix}, \tag{22}$$

$$\boldsymbol{G}^{-1}(0) = \begin{bmatrix} 0 & 1 \\ h_j & 0 \end{bmatrix}^{-1} = \frac{1}{-h_j} \begin{bmatrix} 0 & -1 \\ -h_j & 0 \end{bmatrix} = \begin{bmatrix} 0 & \frac{1}{h_j} \\ 1 & 0 \end{bmatrix}. \tag{23}$$

The solution at $t = t_{j+1}$ is determined by

$$\begin{bmatrix} q(t=t_{j+1}) \\ \dot{q}(t=t_{j+1}) \end{bmatrix} = \boldsymbol{G}(t_{j+1} - t_j)\boldsymbol{G}^{-1}(0) \begin{bmatrix} q(t=t_j) \\ \dot{q}(t=t_j) \end{bmatrix} = [M]_j \begin{bmatrix} q(t=t_j) \\ \dot{q}(t=t_j) \end{bmatrix}, \tag{24}$$

$$[M]_j = \boldsymbol{G}(t_{j+1} - t_j)\boldsymbol{G}^{-1}(0) = \boldsymbol{G}(T_0)\boldsymbol{G}^{-1}(0) = \begin{bmatrix} \cos(h_jT_0) & \frac{\sin(h_jT_0)}{h_j} \\ -h_j\sin(h_jT_0) & \cos(h_jT_0) \end{bmatrix}, \tag{25}$$

with $T_0 = t_{j+1} - t_j = \frac{T}{m}$.

Accumulating all responses in one period

$$\begin{bmatrix} q(t=T) \\ \dot{q}(t=T) \end{bmatrix} = [\mathcal{M}] \begin{bmatrix} q(t=t_0) \\ \dot{q}(t=t_0) \end{bmatrix}, [\mathcal{M}] = [M]_{m-1} \cdots [M]_1[M]_0 = \begin{bmatrix} \mathcal{M}_{11} & \mathcal{M}_{12} \\ \mathcal{M}_{21} & \mathcal{M}_{22} \end{bmatrix}, \tag{26}$$

where $[\mathcal{M}]$ is the state transition matrix whose eigenvalues ($\kappa_{1,2}$) can decide the stability of Eq.(17)

$$\begin{vmatrix} \mathcal{M}_{11} - \kappa & \mathcal{M}_{12} \\ \mathcal{M}_{21} & \mathcal{M}_{22} - \kappa \end{vmatrix} = 0, \tag{27}$$

$$\kappa^2 - (\mathcal{M}_{11} + \mathcal{M}_{22})\kappa + 1 = 0, \tag{28}$$

$$\kappa_{1,2} = \frac{\mathcal{M}_{11} + \mathcal{M}_{22}}{2} \pm \sqrt{\left(\frac{\mathcal{M}_{11} + M_{22}}{2}\right)^2 - 1}. \tag{29}$$

When $\left|\frac{\mathcal{M}_{11}+\mathcal{M}_{22}}{2}\right| > 1$, without loss of generality, one may suppose $\kappa_1 < 1$ then $\kappa_2 > 1$, the system is unstable if $\frac{1}{T}\log|\kappa_2| > \beta$. When $\left|\frac{\mathcal{M}_{11}+\mathcal{M}_{22}}{2}\right| < 1$, $\kappa_{1,2}$ are complex numbers, the system is stable. When $\left|\frac{\mathcal{M}_{11}+\mathcal{M}_{22}}{2}\right| = 1$, the system is in the critical state between unstable and stable, i.e., the boundaries.

# 4 DYNAMIC STABILITY ANALYSIS

## 4.1 A system with two incommensurate frequencies

Consider a system with two incommensurate frequencies:

$$\ddot{q} + d\dot{q} + [a + b_1 \cos(\pi t) + b_2 \cos(7t)]\, q = 0. \tag{30}$$

As stated in Section 3, to study the stability, the first step is to convert the system with two frequencies $\theta_1 = \pi$ and $\theta_2 = 7$ to an equivalent system with a single frequency. Four cases are listed in Table 1 with an increasing accuracy but a decreasing calculation efficiency.

Case I is for $h = 120$. The minimum value of $\left| i\frac{2\pi}{\theta_1} - j\frac{2\pi}{\theta_2} \right| = 0.012636$ is relatively large, so one can increase $h$ such that a smaller $\left| i\frac{2\pi}{\theta_1} - j\frac{2\pi}{\theta_2} \right|$ can be achieved.

In Case II, $h = 350$ is supposed, minimization of Eq. (15) locates $i = 57$ and $j = 127$ which make $\left| i\frac{2\pi}{\theta_1} - j\frac{2\pi}{\theta_2} \right| = 0.0050665 < 10^{-2}$. So the system with two frequencies can be approximated by an equivalent system with a single frequency: the single period $T = 57\frac{2\pi}{\theta_1} \approx 127\frac{2\pi}{\theta_2} \approx 114$ and the single angular frequency is $\theta = \frac{2\pi}{T} = 0.05512$.

If more accuracy is needed, one can suppose $h = 700$ as in Case III of Table 1. Minimization of Eq. (15) leads to $i = 149$ and $j = 332$ which make $\left| i\frac{2\pi}{\theta_2} - j\frac{2\pi}{\theta_2} \right| = 0.0025033 < 10^{-2}$, then the single period $T = 149\frac{2\pi}{\theta_1} \approx 332\frac{2\pi}{\theta_2} \approx 298$ and the single angular frequency is $\theta = \frac{2\pi}{T} = 0.02108$.

If further accuracy is needed, one can suppose $h = 800$ as in Case IV of Table 1. Minimization of Eq. (15) leads to $i = 355$ and $j = 791$ which make $\left| i\frac{2\pi}{\theta_1} - j\frac{2\pi}{\theta_2} \right| = 0.00005999 < 10^{-4}$, then the single period $T = 355\frac{2\pi}{\theta_1} \approx 791\frac{2\pi}{\theta_2} \approx 710$ and the single angular frequency is $\theta = \frac{2\pi}{T} = 0.008849$.

It can be seen that $T = 114$ is already accurate enough, this paper takes the single frequency/period $T = 114$. Using the numerical method in Section 3.2, the instability diagram is obtained in Fig. 3(a) for an undamped system and in Fig. 3(b) for a damped system with $d = 0.1$, where the blue shaded areas indicate stability and the blank areas represent instability. The same system has been studied by Sharma and Sinha [6] by taking $b_1 = b_2 = b$. It can be seen that the numerical results in Fig. 3(a) and Fig. 3(b) are almost identical to Fig. 3(f) and Fig. 12(i) in [6], respectively. So our numerical method is correct and accurate enough.

| Case | $h$ | $i$ | $j$ | $i\frac{2\pi}{\theta_1}$ | $j\frac{2\pi}{\theta_2}$ | $T$ |
|---|---|---|---|---|---|---|
| I | 120 | 35 | 78 | 70 | 70.012636 | 70 |
| II | 350 | 57 | 127 | 114 | 113.9949335 | 114 |
| III | 700 | 149 | 332 | 298 | 298.0025033 | 298 |
| IV | 800 | 355 | 791 | 710 | 709.9999400 | 710 |

Table 1: Equivalent single period ($\theta_1 = \pi$, $\theta_2 = 7$)

## 4.2 A column under parametric loads with multiple frequencies

Consider a column with fixed connections: Length $L = 800$ mm, width $W = 25$ mm, thickness $t = 1$ mm, Young's modulus $E = 2 \times 10^{11}$ N/m$^2$, mass density $\rho = 7.8 \times 10^3$ kg/m$^3$. The minimum moment of inertia is $I = \frac{0.025 \times 0.001^3}{12} = 2.0833 \times 10^{-12}$ m$^4$.

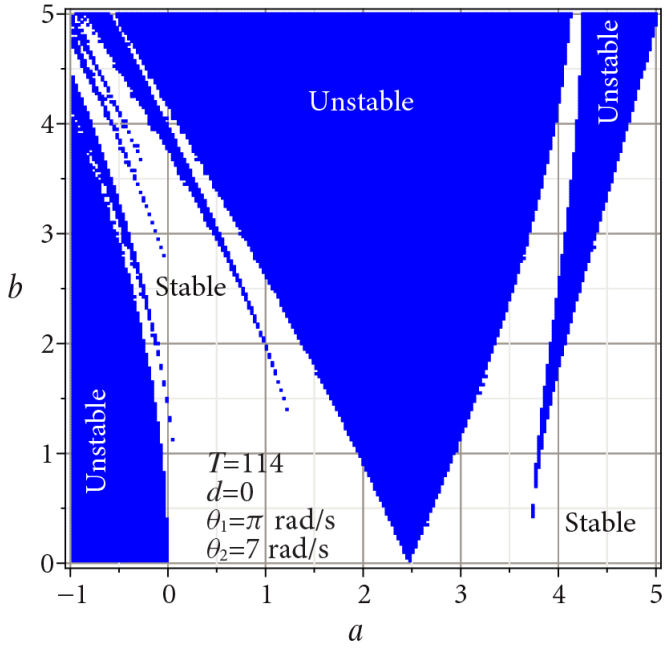


(a)

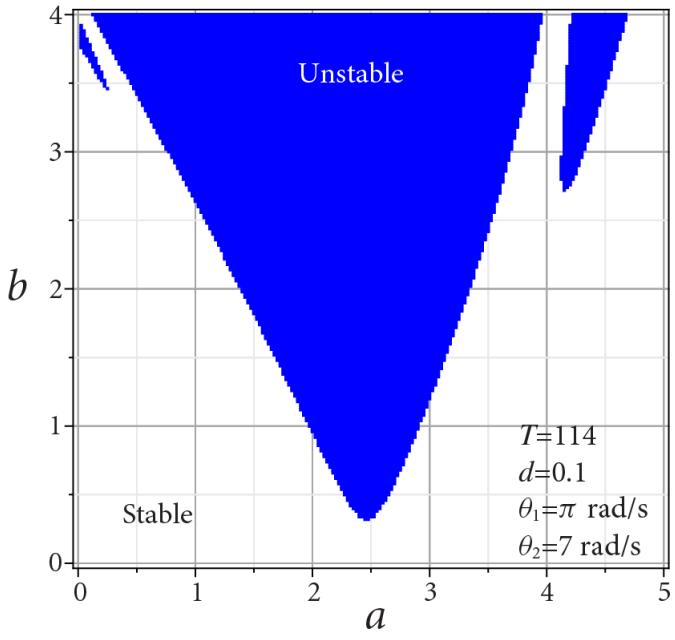


(b)

Figure 3: Instability diagrams for a system with two incommensurate frequencies. (a) undamped; (b) damped with $d = 0.1$.

From Eq. (9), the fundamental frequency is $\omega_0 = 90.2$ rad/s or $14.4$ Hz and the Euler's load is $P_0 = 102.81$ N.

$$\omega_0 = \left(\frac{2\pi}{L}\right)^2 \sqrt{\frac{EI}{\rho A}} = \left(\frac{2 * \pi}{0.8}\right)^2 \sqrt{\frac{2 \times 10^{11} * 2.0833 \times 10^{-12}}{7.8 \times 10^3 (0.001)(0.025)}} = 90.2 \frac{\text{rad}}{\text{s}} \text{ or } 14.2 \text{ Hz}, \quad (31)$$

$$P_0 = \mathrm{EI}\left(\frac{2\pi}{L}\right)^2 = 2\times 10^{11} * 2.0833\times 10^{-12} * \left(\frac{2*\pi}{0.8}\right)^2 = 25.7\ \mathrm{N}. \tag{32}$$

The equation of motion for the column is given by

$$\ddot{q} + 2\beta\dot{q} + 8130.3\left[1 - \frac{p_s}{p_0} - \sum_{i=1}^{m}\left(\frac{p_{di}}{p_0}\cos\theta_i t\right)\right] q = 0. \tag{33}$$

By assuming $\theta_1 = \frac{2\pi}{0.13} = 48.3\frac{\mathrm{rad}}{\mathrm{s}}$ [10], $\theta_2 = \frac{2\pi}{0.03} = 209.4\frac{\mathrm{rad}}{\mathrm{s}}$, and

$$P(t) = P_s + P_d(\cos 48.3t + \cos 209.4t), \lambda_s = \frac{P_s}{P_n}, \lambda_d = \frac{P_d}{P_n}. \tag{34}$$

Eq. (33) can be transformed into

$$\ddot{q} + 2\beta\dot{q} + 8130.3\left[1 - \lambda_s - \lambda_d(\cos 48.3t + \cos 209.4t)\right] q = 0. \tag{35}$$

Eq. (35) is a dynamic system under a parametric excitation with two frequencies, $\theta_1 = 48.3\frac{\mathrm{rad}}{\mathrm{s}}$ and $\theta_2 = 209.4\frac{\mathrm{rad}}{\mathrm{s}}$. This system is converted to an equivalent parametric excitation with a single frequency. Three cases are listed in Table 2 with an increasing accuracy but a decreasing calculation efficiency.

In Case I, $h = 30$ is supposed, minimization of Eq. (15) locates $i = 3$ and $j = 13$ which make $\left|i\frac{2\pi}{\theta_1} - j\frac{2\pi}{\theta_2}\right| = 0.0001863 < 10^{-3}$. So the system with two frequencies can be approximated by a system with a single frequency: the single period $T = 3\frac{2\pi}{\theta_1} \approx 13\frac{2\pi}{\theta_2} \approx 0.39$ and the single angular frequency is $\theta = \frac{2\pi}{T} = 16.1107$.

If more accuracy is needed, one can suppose $h = 700$ as in Case II of Table 2. Minimization of Eq. (15) leads to $i = 161$ and $j = 698$ which make $\left|i\frac{2\pi}{\theta_1} - j\frac{2\pi}{\theta_2}\right| = 2.9999967\times 10^{-9}$, then the single period $T = 161\frac{2\pi}{\theta_1} \approx 698\frac{2\pi}{\theta_2} \approx 0.29$ and the single angular frequency is $\theta = \frac{2\pi}{T} = 21.6662$.

Even if one supposes $h = 4000$, minimization of Eq. (15) remains unchanged as in Case II of Table 2. It can be seen that $T = 0.29$ is already accurate enough. Using the numerical method in Section 3.2, the instability diagram is obtained in Fig. 4 for a damped system with $\beta_0 = 0.1$, where the blue shaded areas indicate stability and the blank areas represent instability. From this diagrams, one can decide the stability for a specific system. For example, system A with $\lambda_s = 0.6$ and $\lambda_d = 0.3$ is stable, but system B with $\lambda_s = 0.7$ and $\lambda_d = 0.3$ is unstable, as shown in Fig. 4. This is confirmed by the bounded responses of point A and unbounded responses of point B in Fig. 5(a) and Fig. 5(b), respectively. The numerical algorithm for vibration responses is given in next section.

| Case | $h$ | $i$ | $j$ | $i\frac{2\pi}{\theta_1}$ | $j\frac{2\pi}{\theta_2}$ | $T$ |
|---|---|---|---|---|---|---|
| I | 30 | 3 | 13 | 0.3902599572 | 0.3900735865 | 0.39 |
| II | 700 | 161 | 698 | 20.94395104 | 20.943951043 | 0.29 |
| III | 4000 | 161 | 698 | 20.94395104 | 20.943951043 | 0.29 |

Table 2: Equivalent single period ($\theta_1 = 48.3$, $\theta_2 = 209.4395$)

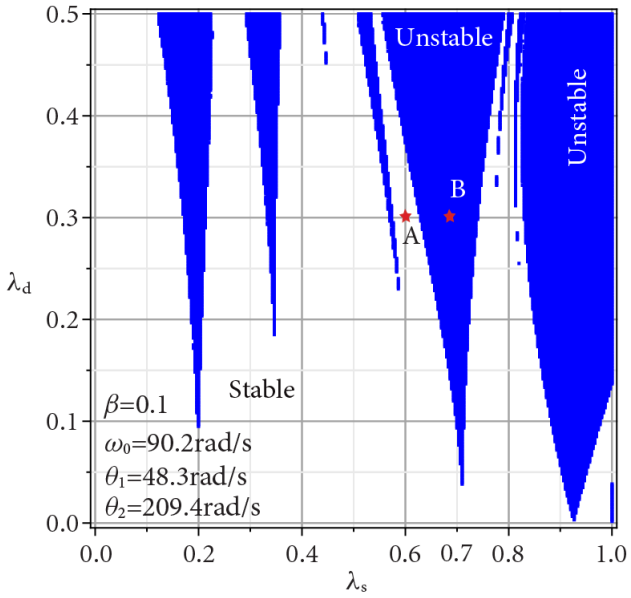


Figure 4: Instability diagrams for a column under parametric load.

### 4.3 Numerical solutions of vibration responses

The vibration responses in Eq. (17) can be calculated by numerical solutions of differential equations, such as the Runge-Kutta method [11]. Letting $y_1 = q$, $y_2 = \dot{q}$, one can obtained from Eq. (17)

$$\dot{y}_2 = -2\beta y_2 - \omega_0^2[1 - S(t)]y_1, \tag{36}$$

or in the matrix form,

$$\left\{ \begin{array}{c} \dot{y}_1 \\ \dot{y}_2 \end{array} \right\} = \left\{ \begin{array}{c} y_2 \\ -2\beta y_2 - \omega_0^2[1 - S(t)]y_1 \end{array} \right\} = \left\{ \begin{array}{c} f_1\left(t; y_1, y_2\right) \\ f_2\left(t; y_1, y_2\right) \end{array} \right\}. \tag{37}$$

By taking point A ($\lambda_s = 0.6, \lambda_d = 0.3$) in Fig. 4 as an example, the equation of motion is given by, from Eq. (35),

$$\ddot{q} + 0.2\dot{q} + 8130.3[0.4 - 0.3(\cos 48.3t + \cos 209.4t)]q = 0, \tag{38}$$

$$f_1\left(t; y_1, y_2\right) = y_2, f_2\left(t; y_1, y_2\right) = -0.2y_2 - 8130.3[0.4 - 0.3(\cos 48.3t + \cos 209.4t)]y_1. \tag{39}$$

Based on the initial conditions $q(t_0 = 0) = 0$ and $\dot{q}(t_0 = 0) = 0.01$ at point A, Eq. (38) can be numerically solved by the fourth-order Runge-Kutta method, which is implemented by MATLAB functions. The vibration responses at point A and point B is shown in Fig. 5(a) and Fig. 5(b), respectively. The parameters at point B are $\lambda_s = 0.7, \lambda_d = 0.3$, and the initial conditions are $q(t_0 = 0) = 0$ and $\dot{q}(t_0 = 0) = 0.00001$. It is seen that the responses at point A are bounded so the system is stable; on the contrary, the responses at point B are unbounded so the system is unstable. The vibration responses in Fig. 5 provide partial validation of the instability diagram in Fig. 4.

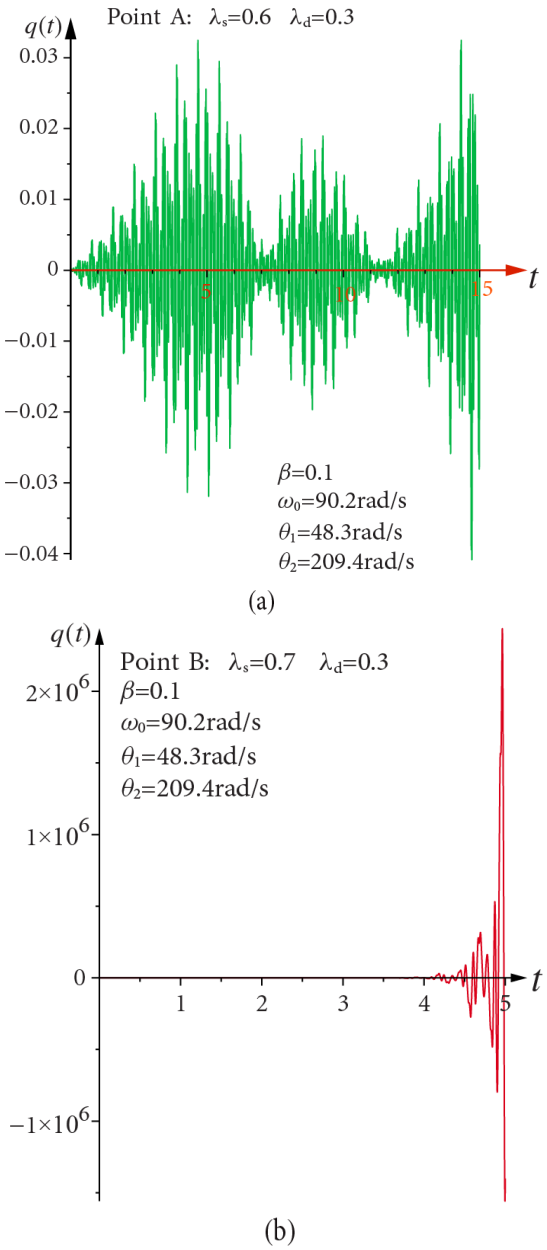


Figure 5: Responses of a column. (a) Point A; (b) Point B.

## 5 CONCLUSIONS

This paper proposes a new numerical method to study the stability of columns under dynamic loads with multiple frequencies. The equation of motion for columns with fixed-fixed connections under parametric load is derived and decoupled into an ordinary differential equation with variable coefficients of multiple frequencies. The first step of the numerical method is to approximate the system with multiple frequencies by an equivalent system with a single frequency (or period $T$) as closely as possible. Then divide the period $T$ into enough equal time intervals. On each interval, the system is approximated by an equation of motion with constant coefficients which can be readily solved. Responses on each interval in one period $T$ are accumulated. The stability can be investigated by the state transition matrix.

As a verification of the proposed numerical method, a system under parametric excitation

with two incommensurate frequencies is studied and compared to existing results in the literature. The efficiency and accuracy of the proposed numerical method are demonstrated. As an application example, dynamic stability of a column under parametric load with two frequencies is investigated through instability diagrams and vibration responses. The vibration responses can provide partial validation of the instability diagrams.

The numerical results for instability diagrams can serve as a calibration of approximate results. The proposed method can be extended to multiple degrees of freedom systems under arbitrary parametric excitations with multiple frequencies.

## 6 ACKNOWLEDGEMENTS

We acknowledge the support in part by funding from the Government of Canada's New Frontiers in Research Fund (NFRF) [NFRFR-2021-00262] and in part by the Natural Sciences and Engineering Research Council of Canada through discovery grant.

## REFERENCES

[1] V. Bolotin, *The Dynamic Stability of Elastic Systems*. San Francisco: Holden Day Inc., 1964.

[2] A.H. Nayfeh and D.T. Mook, *Nonlinear Oscillations*. New York: Wiley, 1979.

[3] J.A. Sanders and F. Verhulst, *Averaging Methods in Nonlinear Dynamical Systems*. New York: Springer, 1985.

[4] W-C. Xie, *Dynamic Stability of Structures*. Cambridge: Cambridge University Press, 2006.

[5] D. Zhang , Y. Tang , R. Liang, L. Yang, and L. Chen, Dynamic stability of an axially transporting beam with two-frequency parametric excitation and internal resonance. *European Journal of Mechanics / A Solids*. **85**, 104084, 2021.

[6] A. Sharma and S.C. Sinha, An approximate analysis of quasi-periodic systems via Floquet theory. *Journal of Computational and Nonlinear Dynamics*, **13(2)**, 021008, 2018.

[7] J. Deng, Analytical and numerical investigations on pillar rockbursts induced by triangular blasting waves. *International Journal of Rock Mechanics and Mining Sciences*, **138**, 104518, 2021.

[8] J. Deng, N.S. Kanwar, M.D. Pandey, and W-C. Xie, Dynamic buckling mechanism of pillar rockbursts induced by stress waves. *Journal of Rock Mechanics and Geotechnical Engineering*, **11**, 944–953, 2019.

[9] J. Deng, M. Shahroudi, and K. Liu, Dynamic stability and responses of beams on elastic foundations under a parametric load. *International Journal of Structural Stability and Dynamics*, **23(02)**, 2350018, 2023.

[10] D. Liu, *Dynamic Stability Analysis of Frame Systems by Application of The Finite Element Method (Doctoral thesis)*. University of Louisville, USA, 2001

[11] W-C. Xie, *Differential Equations for Engineers*. Cambridge: Cambridge University Press, 2010.

COMPDYN 2023
9th ECCOMAS Thematic Conference on
Computational Methods in Structural Dynamics and Earthquake Engineering
M. Papadrakakis, M. Fragiadakis (eds.)
Athens, Greece, 12-–14 June 2023

# THE EVALUATION OF THE OPTIMAL COLLISION CONDITIONS BETWEEN FOLDED PAPER STRUCTURES

**Gyehee Lee**[1]

[1] Dept. of Ocean Eng. , Mokpo National Maritime University
91 HaeYangDaeHagRo, Mokpo, 58628, S. KOREA
e-mail: lghlsk@mmu.ac.kr

**Abstract.** *In this study, the modeling of the folded paper structures used in a traditional Korean game and the optimal collision conditions to win the game were studied. The 3-stage folding process was used to construct the paper structure. In the analysis, the nonlinear behavior of the paper material was considered, but the frictional behavior and gravitational acceleration were ignored in the folding process. A 2-stage process, involving moving and impacting, was used in the collision analysis. Genetic algorithms were used to search for the optimal collision conditions, such as overlapping ratio, impact speed, and impact angle. Direction cosines were used as the fitness for intermediate analysis, and the inverse of impact speed was used as the final fitness. Various approaches were applied to improve the efficiency of the analysis.*

**Keywords:** Instructions, ECCOMAS Thematic Conference, Structural Dynamics, Earthquake Engineering, Proceedings.

# 1 INTRODUCTION

In this study, it was analyzed a traditional Korean game with a rule that the player who causes a overturn in the struck folded paper structure by striking it with a folded paper structure wins. Nonlinear collision analysis scheme was used for the study. The whole analyses in these study were performed by ABAQUS/Explicit.[1]

# 2 FOLDING PROCESS

## 2.1 Folded Paper Structure

The material used to construct the folded paper structure, which is the subject of the analysis, was set to A4 paper (297mm x 210mm), which is commonly used as office paper. The folding method involves folding one sheet of A4 paper in half vertically using two folds, and then placing the folded paper with the center overlapped, followed by folding the unoverlapped parts diagonally. In this paper, the parts folded diagonally are referred to as ”wing”, and the overlapped central part is referred to as the ”base”.

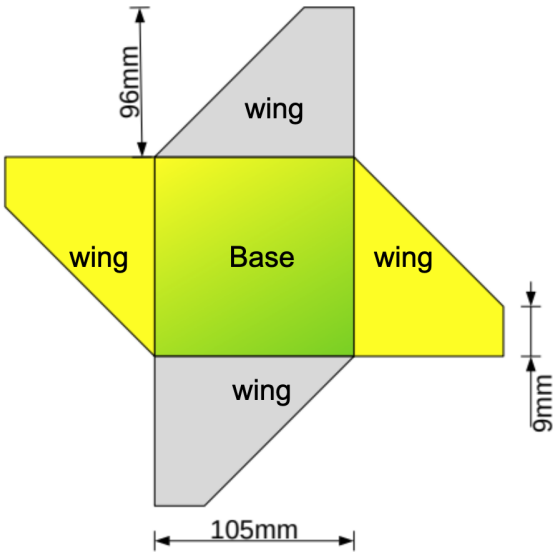


Figure 1: Development figure of paper structure

In this state, the base is composed of four layers, and the wing part is also composed of four layers of paper. The thickness of currently used office paper is typically managed between 0.1 and 0.14mm, with a mass of 80g ($80g/m^2$) per square meter. In this study, the thickness of one layer of office paper was assumed to be 0.12mm. The material stiffness of the paper material is anisotropic, defined in two directions along the fibers of the paper. In this study, the properties of the machine direction (MD) in the stress-strain material curve, as shown in Figure 2, were used.

## 2.2 Folding Analysis

In the model used to analyze the folding process of the paper structure under the given conditions, the multiple layers of paper overlap that occur during the folding process were modeled as a single layer without modeling each layer separately. The structural effect due to

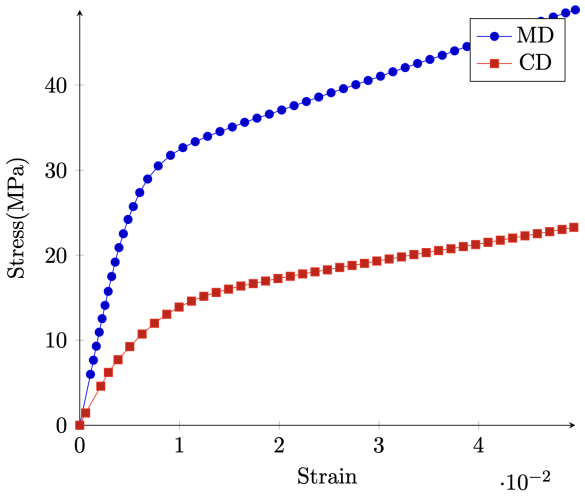


Figure 2: Stress-strain Relation of Paper[2]

the overlap will be manifested as inertial forces caused by the stiffness and mass of the paper with respect to bending. Among these, the inertial force was considered by taking into account the thickness of the overlap between the base and wings. The effect on bending is expected to be dominant at the point where the base and wings meet, where the curvature radius is relatively small compared to other parts during the folding process. Therefore, this part was assumed to behave as a solid body with the greatest frictional force, made up of multiple layers of paper. The initial structure used to analyze the folding process was modeled as a shell element with the shape shown in Figure 3, based on these assumptions. (Figure 3)

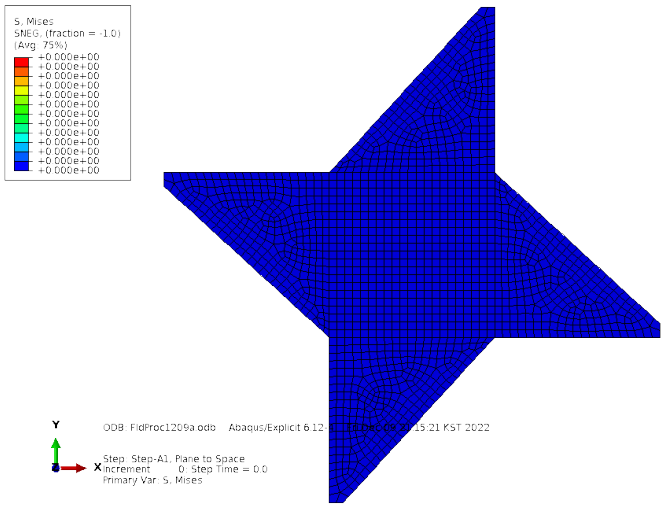


Figure 3: Element mesh of paper structure

The final shape of the paper structure is determined by the frictional forces between the wings in their twisted position, supporting the restoring forces due to bending in the wings and the base. Therefore, frictional forces must be introduced at the twisted wing position. To create this state, the following steps were taken:

1. Perform a deformation analysis by using displacement boundary conditions to move the

end of the wing from the flat position to the twisted position. (Figure 4a))

2. Apply compression to the upper part of the wing in the twisted position using a rigid plate. (Figure 4b))

These two steps are used as the process of folding the actual paper structure, and they have been implemented through structural analysis.

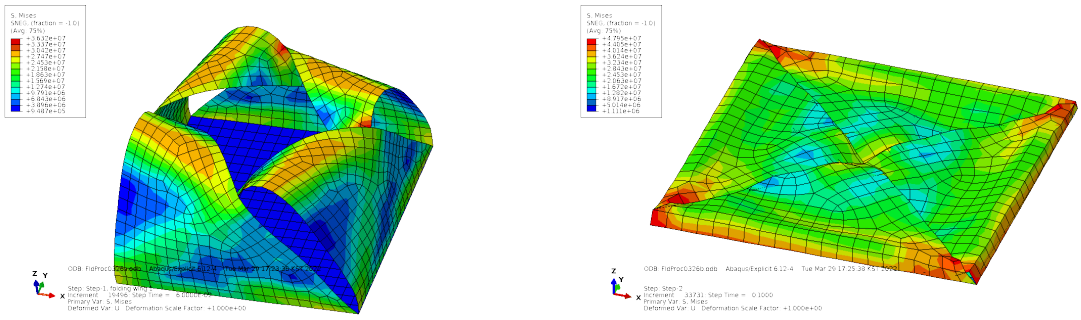

a) Twisted b) Pressed

Figure 4: Deformed shape of struture in the folding process

However, in the first step, if the end of the wing is displaced to the desired position in a straight line, excessive displacement occurs in the element where interference occurs with the adjacent wing part, resulting in a divergence in the analysis. This corresponds to the case where the paper tears during the actual folding process. In this study, to prevent this phenomenon, the wing part was first deformed to an angle of 80 degrees from the plane while maintaining the wing in a flat position, and then deformed to the final twisted position. If the angle at which the wing is standing exceeds 90 degrees, the aforementioned interference phenomenon occurs when deforming the wing to the final twisted position, leading to a divergence in the analysis.

After positioning the wing's end at the twisted position, an frictionless rigid plate is placed on the upper part of the wing, and the paper structure is compressed by applying a boundary condition of forced displacement. The compression thickness is set to 5mm. In the paper structure studied here, the base consists of 4 layers, and the wings consist of 4 layers each. Taking into account the overlapping at the twisted position, the total number of layers is generally 12. Therefore, if the paper structure is completely pressed, the thickness of the structure would be at least about 1.5mm.

After applying compression, the structure is subjected to gravitational loads and placed on the plate for dynamic relaxation analysis. During this process, the folded structure undergoes a restoration deformation. The final deformed shape resembles a flattened pyramid shape with no vertex at the top. (See Figure 6)

As discussed earlier, in the second stage of the folding process, which is the compression stage, the connection between the base and the wings undergoes significant plastic deformation compared to other parts. After the folding process is completed, the final stress distribution is shown in Figure 7. As expected, the stress distribution is highest at the corner where the smallest curvature radius deformation occurs, while other parts exhibit relatively low stress distribution.

## 3 COLLISION ANALYSIS

The collision analysis process consists of two steps: moving the striking structure to meet the given collision conditions, and estimating the behavior of the structure resulting from the

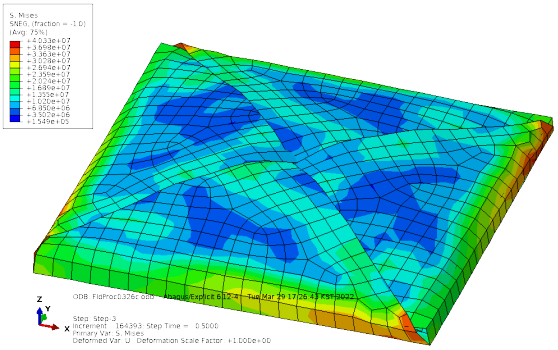

Figure 5: Deformed shape after dynamic relaxation

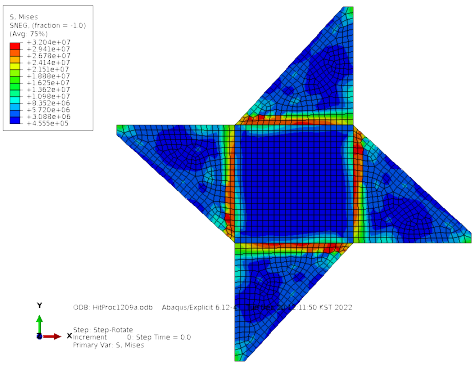

Figure 6: Stress distribution at the end of folding process

collision. The collision conditions considered in the analysis are as follows:

1. Overlap in the x direction (0.1 0.9)
2. Overlap in the y direction (0.1 0.5)
3. Collision angle (0 1.0 rad)
4. Collision velocity (5m/s 15m/s).

In actual games, it is difficult for the striking structure to perfectly overlap with the hit structure, and intentional eccentricity is common due to the nature of the game. Therefore, the degree of overlap was assumed as a collision condition. Similarly, the collision angle cannot be expected to remain perfectly horizontal during collision. The collision speed refers to the speed of the hitting structure when it approaches the struck structure, and the horizontal and vertical forces of this speed are calculated using the collision angle.

### 3.1 Moving Analysis

Moving analysis is the process of positioning the striking structure at the actual location and angle of collision. This was performed by imposing forced displacements at the boundary conditions. To satisfy the two conditions of collision location and angle, a rotational displacement was generated based on the edge of the striking structure's bottom, and then the analysis was performed to generate horizontal displacement.

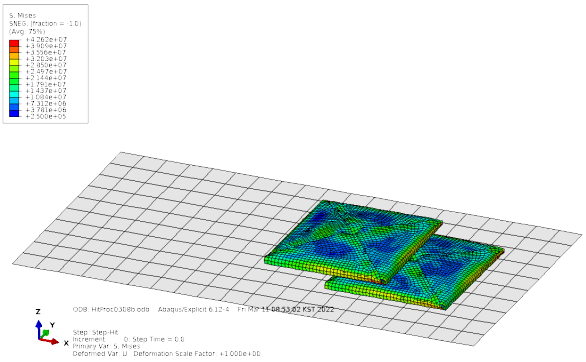

Figure 7: Example of striking position

### 3.2 Rebounding Analysis

Rebounding analysis is the step where the striking structure causes a recoil behavior to the passivestructure during an actual collision. The striking structure is in contact with the passive structure for a short period of time before it causes a recoil behavior with the ground. The struck structure absorbs the kinetic energy transmitted from the striking structure and generates motion with strain energy. After the two structures fall off the support surface, they vibrate locally but move overall like a thrown object according to the gravitational force. Therefore, it is possible to estimate the behavior after this by using simple motion equations, but since there are cases where secondary collisions occur between the two structures in air, the motion equation of the rigid body was not applied overall.

## 4 SEARCHING WINNING CONDITIONS

The winning condition of this game is that the struck structure must end up in a final overturned state and the motion must end at the moment of landing after collision. To achieve this final winning condition, the goal of the analysis is to determine the collision location, angle, and velocity. However, since there can be several collision conditions that satisfy the final winning condition for the struck structure, this study defines the optimal collision condition as the one with the lowest kinetic energy, i.e., the lowest collision speed. To find this optimal collision condition, optimization using a genetic algorithm[3] was performed.

### 4.1 Consist of Collision Analysis

Performing optimization using a genetic algorithm typically requires repeated analyses of various collision conditions. Therefore, both the moving and collision analyses described in the previous section need to be performed repeatedly. However, the rebounding analysis, which involves performing nonlinear dynamic analysis until the struck structure comes to rest due to the kinetic energy transferred from the striking structure, is computationally expensive. Therefore, it was aimed to efficiently perform this process to obtain efficient analysis results. To achieve this, the recoil analysis was conducted in two stages as follows.

#### 4.1.1 Rising Phase

The initial stage of collision behavior is the phase where the struck structure rises due to the impact from the striking structure. In most cases where there is a secondary collision with

the striking structure, it occurs in this stage. Based on various analyses, this stage has been set as the first 0.1 seconds after the collision. If the final behavior of the struck structure in this stage does not lead to a reversal, the analysis is terminated in the first stage. The termination condition for the analysis is as follows:

- If the direction cosine of the normal vector of the struck structure's bottom surface is below a certain threshold, and
- if the direction cosine of the normal vector of the struck structure's bottom surface is decreasing.

If the normal direction cosine of the struck structure's bottom surface is less than or equal to the threshold value, and it is decreasing, the analysis is terminated at the end of the first stage. When the bottom of the struck structure is perpendicular to the ground, the direction cosine of the normal is 0, and it is 1.0 when it is overturned. Thus, the above conditions indicate a state where the struck structure is falling downward with its bottom facing down, without overturning, at the time of termination of the first-stage analysis. In general, about three-quarters of the analyses fail to satisfy this condition and terminate during the rising phase.

#### 4.1.2 Falling Phase

This stage is the period of analysis during the collision where the struck structure interacts with the ground in the downward phase, if the termination condition for the rising phase is not met. Similar to the rising phase, the time interval for this phase has been determined through empirical rules based on analysis results, and set at 0.3 seconds.

### 4.2 Fitness Function

The rising and falling phases each require a fitness function for performing the genetic algorithm. The overall optimization goal should be evaluated in the falling phase, but since about 3/4 of the analysis only involves the rising phase, if the analysis is only performed in the rising phase, a different optimization needs to be performed from the overall optimization. In this study, the optimization goals of the rising and falling phases were defined differently and analyzed accordingly.

1. Raising
$$f_u = \cos \vec{n} \tag{1}$$
where, $\vec{n}$ is normal vector of base.

2. Falling
$$f_d = \frac{10}{V_{imp}} \tag{2}$$
where $V_{imp}$ is collision speed. However, this fitness function is only used in the case of a overturn, and in other cases, the same fitness function as the rising phase was used.

The changes in fitness by generation obtained from performing optimization under the above conditions are shown in Figure 10. The difference between case 1 and case 2 is the phase of the target structure (strike in the inverted state). In both interpretations, successful collision conditions were found to satisfy the winning condition. In this graph, the first occurrence of

finding the winning condition is the point where the fitness suddenly increases because the fitness becomes positive when a reversal occurs. In the case of case 1 shown in Figure 10, the winning condition found initially did not improve during repeated analyses, while in the case of case 2, there was one improvement. Such improvements or discoveries of solutions are expected to increase as the number of analysis generations increases.

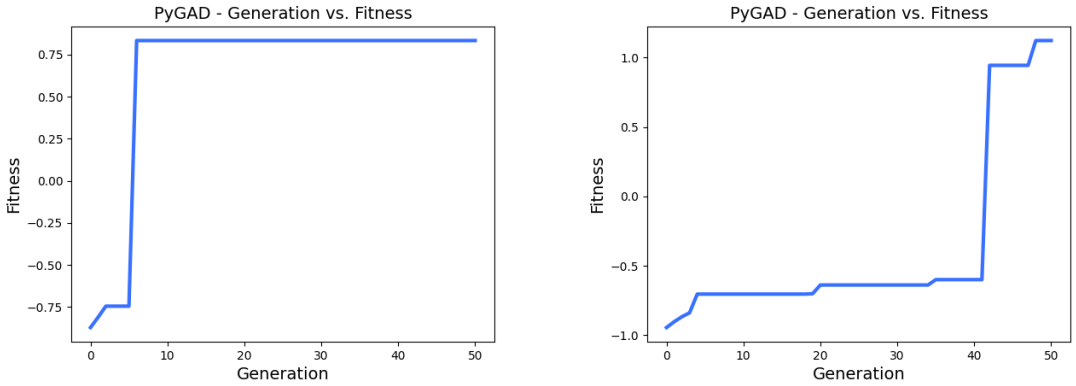


a) case1 b) case2

Figure 8: Changes of Fitness as Generations

## 5 CONCLUSIONS

In this study, the folding and collision processes of paper structures used in traditional Korean games were implemented through nonlinear dynamic analysis. Using the folded paper structures, the winning conditions of the game were explored through an optimization process using a genetic algorithm. As a result, it was possible to successfully search for collision conditions that can win the game within the given collision conditions.

## ACKNOWLEDGEMENT

This work was supported by the National Research Foundation of Korea(NRF) grant funded by the Korea government(MSIT) (No. 2021R1F1A1060204)

## REFERENCES

[1] SIMULIA, *Abaqus 6.12 Analysis User's Manual*, SIMULIA, 2012

[2] Mikael Nygards, Magnus Just, Nils Hallbäck, and Johan Tryding. A finite element model for simulations of creasing and folding of paper- board. *In 2005 ABAQUS Users' Conference*, 2005.

[3] Ahmed Fawzy Gad, *PyGAD:An Intuitive Genetic Algorithm Python Library*, arXiv, 2106.06158, 2021

COMPDYN 2023
9th ECCOMAS Thematic Conference on
Computational Methods in Structural Dynamics and Earthquake Engineering
M. Papadrakakis, M. Fragiadakis (eds.)
Athens, Greece, 12-–14 June 2023

# A NOVEL FINITE ELEMENT FORMULATION FOR THE DYNAMIC ANALYSIS OF DAMPED EULER-BERNOULLI BEAMS UNDER MOVING LOADS

**Hugo A.F.A. Santos**

Departamento de Engenharia Mecânica,
Instituto Superior de Engenharia de Lisboa,
Rua Conselheiro Emídio Navarro 1, 1959-007 Lisboa, Portugal
e-mail: hugo.santos@isel.pt

**Abstract.** *A novel finite element formulation for the dynamic analysis of linear-elastic damped Euler-Bernoulli beams subjected to moving loads is proposed. The formulation is consistent with a complementary form of the well known Hamilton's variational principle, and will be used to address some numerical tests in both frequency and time domains. The effectiveness and accuracy of the formulation will be assessed and discussed by comparison between the obtained results and those rendered by the standard displacement-based finite element formulation. As it will be demonstrated, the proposed formulation not only renders continuous bending moment and shear-force distributions, a desired feature in the structural design field, but also has a superior accuracy than that provided by the displacement formulation that uses the same number of nodal degrees-of-freedom.*

**Keywords:** Structural Dynamics, Euler-Bernoulli Beams, Moving Loads, Finite Element Analysis.

## 1 INTRODUCTION

Moving loads are commonly found in practical civil, mechanical, and aerospace engineering problems. For example, moving train wheels over a railway track, a moving vehicle on a bridge, a roller coaster moving on its track, an overhead crane used either for manufacturing or maintenance applications, a sliding robot manipulator, a span morphing aircraft wing, etc. Early studies highlighted the fact that moving loads on structures may induce significantly higher dynamic deflections and stresses than those observed in the static case. Therefore, it is crucial to conceive structural models in which the dynamic effects are taken into account and, hence, to develop effective and accurate methods that can be used to analyse such models.

In fact, the dynamics of structures under moving loads has been an active research area, particularly in the past decades, with the focus on the numerical analysis and modelling [1], mainly due to the rapidly increasing computer performance which has allowed the development of highly robust and sophisticated computational and numerical methods.

In moving load type problems, the applied load changes its position on the structure in a time-dependent way. The numerical discretization of time-dependent problems involves the following two stages: (i) spatial discretization and (ii) temporal discretization. Several methods have been employed for the spatial discretization, such as the finite difference, finite element, boundary element, and differential quadrature methods. Among these, the finite element method has been the most adopted one, due to its versatility, capability to handle complex geometries, etc. The application of the finite element method results in a set of ordinary differential equations in time for the finite element variables. The resulting system of equations needs, thus, to be further discretized in time, often using finite difference schemes for the time derivatives, such as Newmark's, Wilson's or Runge-Kutta schemes.

Among the various formulations of the finite element method, its displacement-based formulation has been the most adopted one. In this formulation, the displacements are taken as the fundamental unknowns, selected such that only those patterns which satisfy compatibility requirements are to be admitted as possible solutions. Examples of this formulation applied to the dynamics of beams can be found in [2, 3, 4]. However, this formulation leads to bending moment and shear-force distributions that are discontinuous between elements and that do not satisfy, in general, the equilibrium boundary conditions. As a result, and since for many structural engineering purposes the 'stress' distribution is, very often, the paramount information needed, applications of this formulation usually involve an averaging procedure to obtain continuous 'stress' distributions for design calculations. Formulations that avoid the need for these averaging procedures are the so-called equilibrium-based formulations, which are capable of producing equilibrated solutions, *i.e.*, solutions satisfying in strong form the equilibrium differential equations, as well as the equilibrium boundary conditions. Examples of these formulations applied to one-dimensional beam problems were proposed in, *e.g.*, [5, 6, 7, 8], but all of them are limited to statics.

The standard displacement-based finite element formulations for structural dynamics may be derived from the well known Hamilton's variational principle. However, attempts to formulate dual, or complementary, forms of the Hamilton's principle are very scarce in the literature. A few exceptions in the framework of the free vibration analysis of beams can be found in [9, 10].

To the best of the author's knowledge, equilibrium-based finite element formulations for the dynamic analysis of beams under moving loads have not yet been proposed in the literature. It is the goal of the present work to introduce a novel finite element formulation, which relies on a complementary variational principle, in conjunction with a Newmark's time discretization

scheme, for the dynamic analysis of linear-elastic damped Euler-Bernoulli beams subjected to moving loads. The formulation will be used to address some numerical tests in both frequency and time domains, and its effectiveness and accuracy will be assessed and discussed by comparison between the obtained results and those rendered by the standard two-node displacement-based finite element formulation. As it will be shown, the proposed formulation not only can produce continuous bending moment and shear-force distributions, a desired feature in the field of structural design, but also has a superior accuracy than that given by the displacement-based formulation.

## 2 DYNAMICS OF EULER-BERNOULLI BEAMS UNDER MOVING LOADS: BVP

Let us consider a beam traversed by a moving load, assumed as a concentrated load with constant speed $v$ and amplitude $g(t)$. The following assumptions will be adopted in this study: (1) The beam is homogeneous and of constant cross-section; (2) plane cross-sections remain plane after deformation; (3) the Euler-Bernoulli hypothesis holds; (4) only a single moving load is considered to travel on the beam at a time; (5) the damping of the beam is of the viscous (external) type; and (6) the beam is initially at rest before the load moves in.

The moving load may be represented in terms of a distribution over the beam domain as

$$f(x,t) = g(t)\delta(x - vt) \tag{1}$$

where $\delta$ represents the Dirac delta function, with $vt$ the load position at time $t$.

We shall use $w(x,t)$ to denote the beam deflection along the $y$ axis at position $x$ and time $t$. $L$ is the length of the beam, $m$ the mass of the beam per unit length, $c$ the viscous damping coefficient per unit length, $E$ the Young's modulus, and $I$ the moment of inertia of the beam. Based on the aforementioned assumptions, the governing equation of motion of the beam can be written as

$$EIw'''' + m\ddot{w} + c\dot{w} = f(x,t) \tag{2}$$

where primes ( $'$ ) and dots ( $\dot{}$ ) denote differentiation with respect to coordinate $x$ and time $t$, respectively.

The response of the beam is said to be a forced response for

$$0 \leq \frac{vt}{L} \leq 1 \tag{3}$$

and a free response for

$$\frac{vt}{L} > 1 \tag{4}$$

The boundary conditions depend on the beam supports. Considering, for instance, a clamped-hinged beam, as illustrated in Figure 1, the following conditions must hold

$$w(0,t) = 0 \tag{5a}$$
$$w(L,t) = 0 \tag{5b}$$
$$w'(0,t) = 0 \tag{5c}$$
$$EIw''(L,t) = 0 \tag{5d}$$

Equations (5a-5c) represent kinematical boundary conditions, whereas equation (5d) stands for an equilibrium boundary condition.

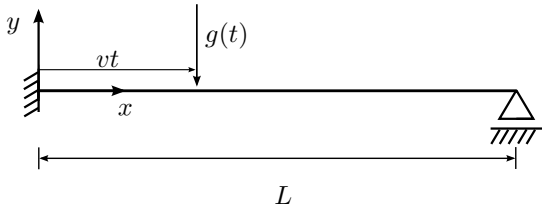


Figure 1: Clamped-Hinged Beam.

The initial conditions are

$$w(x,0) = 0 \tag{6a}$$

$$\dot{w}(x,0) = 0 \tag{6b}$$

as the beam is assumed to be at rest prior to the arrival of the moving load.

Noting that both the impulse per unit length, $p$, and the bending moment, $M$, can be related with the beam deflection, $w$, as

$$p = m\dot{w} \tag{7}$$

and

$$\frac{M}{EI} - w'' = 0 \tag{8}$$

the governing equation (2) can be rewritten in the following form

$$M'' + \dot{p} + \frac{c}{m}p = f \tag{9}$$

which is known as the equilibrium differential equation of the beam.

The shear-force acting on the beam, $Q$, is related with the bending moment, $M$, as follows

$$M' - Q = 0 \tag{10}$$

## 3 VARIATIONAL SETTING

### 3.1 Primal (or Hamilton's type) Variational Principle

Based on the classical variational approach, the Lagrangian of an undamped ($c = 0$) beam is defined as the following one-field energy functional

$$L(w, \dot{w}) = T(\dot{w}) - V(w) \tag{11}$$

with $T$ and $V$ the kinetic and potential energies of a beam element, respectively, given by

$$T(w) = \frac{1}{2}\int_0^L m\dot{w}^2 \, dx \tag{12}$$

and

$$V(w) = \frac{1}{2}\int_0^L EIw''^2 \, dx - \int_0^L fw \, dx \tag{13}$$

The Hamilton's principle states that the motion of the undamped beam element during the time interval $t_0 < t < t_1$ is such that the time integral of the energy $L$ is stationary. In other words, it states

$$\int_{t_0}^{t_1} \delta L \, dt = 0, \text{ subject to } \delta w = 0 \text{ at } t = t_0, t_1 \tag{14}$$

This condition leads to the governing equation (2), considering $c = 0$, and, additionally, to the following boundary conditions at $x = 0, L$

$$\text{either } EIw'' = 0 \Rightarrow w'' = 0 \text{ (Natural B.C.)} \tag{15a}$$
$$\text{or } \delta w' = 0 \Rightarrow w' \text{ is specified (Geometric B.C.)} \tag{15b}$$

and

$$\text{either } EIw''' = 0 \Rightarrow w''' = 0 \text{ (Natural B.C.)} \tag{16a}$$
$$\text{or } \delta w = 0 \Rightarrow w \text{ is specified (Geometric B.C.)} \tag{16b}$$

When non-conservative systems are considered, there is no longer an energy functional that is conserved in time. However, a separate functional can be introduced to account for non-conservative systems within the framework of Hamilton's principle, well known as Rayleigh's dissipation functional, which can be defined, in this case, as

$$D = \frac{1}{2}\int_0^L c\dot{w}^2 \, dx \tag{17}$$

Making use of Rayleigh's dissipation functional, an extended version of the Hamilton's principle states that the motion of the damped beam element during the time interval $t_0 < t < t_1$ is such that the following condition holds

$$\int_{t_0}^{t_1} \left(\delta L + \frac{\partial D}{\partial \dot{w}}\right) \delta w \, dt = 0, \text{ subject to } \delta w = 0 \text{ at } t = t_0, t_1 \tag{18}$$

which leads to the complete governing equation (2) and to the set of boundary conditions (15,16). This variational statement is, therefore, herein taken as the primal variational principle.

### 3.2 Two- and One-Field Dual Variational Principles

An alternative, or complementary, form of the primal variational principle presented above can be formulated. Consider the following two-field complementary energy functional of the undamped beam

$$L_c^*(p, M) = T_c(p) - U_c(M) \tag{19}$$

with $T_c$ and $U_c$ the complementary kinetic and complementary strain energies, respectively, given by

$$T_c(p) = \frac{1}{2}\int_0^L \frac{p^2}{m} \, dx \tag{20}$$

and

$$U_c(M) = \frac{1}{2}\int_0^L \frac{M^2}{EI} \, dx \tag{21}$$

A solution for the bending moment field that satisfies equation (9) can be decomposed as

$$M = M_h + M_p \tag{22}$$

with $M_h$ a solution to the homogeneous form of the equation and $M_p$ a particular solution to the equation, *i.e.*

$$M_h'' + \dot{p} + \frac{c}{m}p = 0 \tag{23a}$$

$$M_p'' = f \tag{23b}$$

Considering the following variable transformation

$$r'' = -p \tag{24}$$

yields

$$\dot{r}'' = -\dot{p} \tag{25}$$

which, taking into account the decomposition assumed for the bending moment, gives

$$M_h = \dot{r} + \frac{c}{m}r \tag{26}$$

This shows that the introduced variable $r$ represents a bending-moment impulse.

As for $M_p$, double integration of the moving load $f$ with respect to $x$ gives

$$M_p(x,t) = g(t)H(x-vt)x + c_1(t)x + c_2(t) \tag{27}$$

Making use of equation (8), the deflection of the beam associated with the particular solution comes out as

$$w_p(x,t) = \int\int \frac{M_p}{EI}\, dx\, dx + c_3(t)x + c_4(t) \tag{28}$$

which gives

$$w_p(x,t) = \frac{1}{EI}\left(\frac{1}{6}g(t)(x-vt)^2(x+2vt)H(x-vt) + \frac{c_1(t)}{6}x^3 + \frac{c_2(t)}{2}x^2\right) + c_3(t)x + c_4(t) \tag{29}$$

The associated cross-section rotation results, therefore, as

$$w_p'(x,t) = \frac{1}{EI}\left(\frac{1}{2}g(t)(x^2 - v^2t^2)H(x-vt) + \frac{c_1(t)}{2}x^2 + c_2(t)x\right) + c_3(t) \tag{30}$$

The integration functions $c_1(t)$, $c_2(t)$, $c_3(t)$ and $c_4(t)$ are obtained from the boundary conditions of the specific problem under analysis. It is worth mentioning that this particular solution, $w_p$, is the solution to the corresponding static beam problem, *i.e.*, the problem for which both the velocity , $\dot{w}$, and the acceleration, $\ddot{w}$, are null.

The variable transformation (24) allows to rewrite the two-field functional $L_c^*(p, M)$ for the undamped beam case as the following one-field, or pure, energy functional

$$L_c(r, \dot{r}) = \frac{1}{2}\int_0^L \frac{r''^2}{m}\, dx - \frac{1}{2}\int_0^L \frac{(\dot{r} + M_p)^2}{EI}\, dx \tag{31}$$

This energy functional resembles the one derived in [9] for the free vibrations of Euler-Bernoulli beams.

The stationarity condition of $L_c$ reads

$$\int_{t_0}^{t_1} \delta L_c\, dt = 0, \text{ subject to } \delta r = 0 \text{ at } t = t_0, t_1 \tag{32}$$

and leads to equation (8) and, additionally, to the following boundary conditions at $x = 0, L$

$$\text{either } \frac{r''}{m} = 0 \Rightarrow r'' = 0 \text{ (Natural B.C.)} \tag{33a}$$

$$\text{or } \delta r' = 0 \Rightarrow r' \text{ is specified (Geometric B.C.)} \tag{33b}$$

and

$$\text{either } \frac{r'''}{m} = 0 \Rightarrow r''' = 0 \text{ (Natural B.C.)} \tag{34a}$$

$$\text{or } \delta r = 0 \Rightarrow r \text{ is specified (Geometric B.C.)} \tag{34b}$$

For the damped beam element, the following condition is required

$$\int_{t_0}^{t_1} \left( \delta L_c + \int_0^L \frac{M}{EI} \frac{c}{m} \delta r \, dx \right) dt = 0, \text{ subject to } \delta r = 0 \text{ at } t = t_0, t_1 \tag{35}$$

It can be shown that, under the subsidiary condition of equilibrium (9), this variational statement leads to equation (8) and to the boundary conditions (33,34). It is, therefore, taken herein as the dual variational principle.

## 4 DUAL FINITE ELEMENT FORMULATION AND IMPLEMENTATION ASPECTS

A new numerical approach based on a novel finite element formulation for space discretization together with an unconditionally Newmark's scheme for time integration is herein proposed. The novel finite element formulation is based on the dual variational principle presented above (35). The approach can be applied to the dynamic analysis of either simple or continuous linear-elastic planar beams subjected to a single or a series of either moving or fixed time-dependent loads. The approach was implemented in Wolfram Mathematica® for both frequency- and time-domain analyses.

### 4.1 Space Discretization: Dual Finite Element Formulation

A new two-node beam element is herein proposed. The element is derived within the framework of a novel finite element formulation for space discretization, which is based on the dual variational principle presented above (35).

Since $C^1$ continuity is required (*i.e.*, approximations that are continuous and have continuous first-order derivatives), the bending-moment impulse and its $x$-derivative (or shear-force) are taken as the nodal degrees-of-freedom. Hermite cubic polynomials are, therefore, adopted for $r$. It is worth noting that, the standard displacement-based (or primal) finite element formulation also requires a $C^1$ interpolation for the beam deflection $w$. The simplest primal finite element formulation is also based on a two-node beam element with two degrees-of-freedom per node, which are the transverse displacement and its $x$-derivative (or rotation).

The approximation of the bending-moment impulse at the element level, $r_e$, is written as

$$r_e^h(x,t) = \boldsymbol{N}_r(x)\boldsymbol{r}_e(t) \tag{36}$$

with $\boldsymbol{N}_r$ the matrix that contains the approximation functions, taken as mentioned above as Hermite cubic polynomials, and $\boldsymbol{r}_e$ the vector that collects the element degrees-of-freedom for $r_e$.

The derivatives of $r_e$ can be written, therefore, as

$$r_e^{h\prime\prime} = \boldsymbol{N}_r'' \boldsymbol{r}_e, \quad \dot{r}_e^h = \boldsymbol{N}_r \dot{\boldsymbol{r}}_e \tag{37}$$

The discrete form of the Euler-Lagrange equations associated with the dual variational principle (35) come out as the following governing system of equations defined at the element level

$$\boldsymbol{\mathcal{M}}_e \ddot{\boldsymbol{r}}_e + \boldsymbol{\mathcal{C}}_e \dot{\boldsymbol{r}}_e + \boldsymbol{\mathcal{F}}_e \boldsymbol{r}_e = \boldsymbol{d}_e \tag{38}$$

with

$$\boldsymbol{\mathcal{M}}_e = \int_0^{L_e} \frac{\boldsymbol{N}_r^T \boldsymbol{N}_r}{EI}\, dx \tag{39a}$$

$$\boldsymbol{\mathcal{C}}_e = \int_0^{L_e} \frac{c\boldsymbol{N}_r^T \boldsymbol{N}_r}{mEI}\, dx \tag{39b}$$

$$\boldsymbol{\mathcal{F}}_e = \int_0^{L_e} \frac{\boldsymbol{N}_r''^T \boldsymbol{N}_r''}{m}\, dx \tag{39c}$$

$$\boldsymbol{d}_e = -\int_0^{L_e} \frac{\boldsymbol{N}_r^T \dot{M}_p}{EI}\, dx \tag{39d}$$

The element matrices $\boldsymbol{\mathcal{M}}_e$, $\boldsymbol{\mathcal{C}}_e$ and $\boldsymbol{\mathcal{F}}_e$ are $(4 \times 4)$ matrices, and the element vector $\boldsymbol{d}_e$ is a $(4 \times 1)$ vector.

Assembling the element equations (38), gives the following governing system of global equations

$$\boldsymbol{\mathcal{M}} \ddot{\boldsymbol{r}} + \boldsymbol{\mathcal{C}} \dot{\boldsymbol{r}} + \boldsymbol{\mathcal{F}} \boldsymbol{r} = \boldsymbol{d} \tag{40}$$

The eigenfrequencies of the proposed dual model, $\omega_i$, can be obtained from the following condition

$$det(\boldsymbol{\mathcal{M}}\omega - \boldsymbol{\mathcal{F}}) = 0 \tag{41}$$

### 4.2 Time Integration: Newmark's Method

The governing system of global equations (40) is transformed into a set of algebraic equations by means of Newmark's method. In particular, the approximated bending-moment impulse and its first time derivative are taken at the end of the time step $t_{n+1}$ as

$$\boldsymbol{r}_{n+1} = \boldsymbol{r}_n + \dot{\boldsymbol{r}}_n \Delta t + \big((\frac{1}{2} - \beta)\ddot{\boldsymbol{r}}_n + \beta \ddot{\boldsymbol{r}}_{n+1}\big)\Delta t^2 \tag{42a}$$

$$\dot{\boldsymbol{r}}_{n+1} = \dot{\boldsymbol{r}}_n + \big((1-\gamma)\ddot{\boldsymbol{r}}_n + \gamma \ddot{\boldsymbol{r}}_{n+1}\big)\Delta t \tag{42b}$$

where $\Delta t$ is the time step given by

$$\Delta t = t_{n+1} - t_n \tag{43}$$

and $\beta$ and $\gamma$ are the control parameters of the algorithm. It is required that $2\beta \geq \gamma \geq 1/2$ to ensure an unconditionally stable numerical scheme. For $\beta = 1/4$ and $\gamma = 1/2$, which is the combination adopted within the framework of the proposed formulation, the algorithm corresponds to the average acceleration method.

The governing system of global equations at the time step $t_{n+1}$ reads

$$\boldsymbol{\mathcal{M}} \ddot{\boldsymbol{r}}_{n+1} + \boldsymbol{\mathcal{C}} \dot{\boldsymbol{r}}_{n+1} + \boldsymbol{\mathcal{F}} \boldsymbol{r}_{n+1} = \boldsymbol{d}_{n+1} \tag{44}$$

Hence, on insertion of (42) into (44) yields

$$\ddot{\boldsymbol{r}}_{n+1} = \boldsymbol{\mathcal{M}}^{*-1}\boldsymbol{d}^{*}_{n+1} \tag{45}$$

with

$$\boldsymbol{\mathcal{M}}^{*} = \boldsymbol{\mathcal{M}} + \boldsymbol{\mathcal{C}}\gamma\Delta t + \boldsymbol{\mathcal{F}}\beta\Delta t^2 \tag{46a}$$

$$\boldsymbol{d}^{*}_{n+1} = \boldsymbol{d}_{n+1} - \boldsymbol{\mathcal{C}}\Big(\dot{\boldsymbol{r}}_n + \big((1-\gamma)\ddot{\boldsymbol{r}}_n\big)\Delta t\Big) - \boldsymbol{\mathcal{F}}\Big(\boldsymbol{r}_n + \dot{\boldsymbol{r}}_n\Delta t + \big((\frac{1}{2}-\beta)\ddot{\boldsymbol{r}}_n\big)\Delta t^2\Big) \tag{46b}$$

The homogeneous part of the element bending-moment solutions, $M^h_h$, can be retrieved from the obtained bending-moment impulses $\boldsymbol{r}$. The total bending-moment solutions of the beam elements arise from $M^h = M_p + M^h_h$. The element shear-forces, $Q^h$, are computed from equation (10). The resulting element bending-moments, $M^h$, and shear-forces, $Q^h$, satisfy all equilibrium conditions. The obtained solutions are, therefore, said to be equilibrated solutions.

The associated element deflections, $w^h_h$, can be computed from equation (8), which requires double integration of $M^h_h$ with respect to $x$. The resulting integration constants, two per element, are obtained by setting the kinematical boundary conditions $w^h_h(0,t) = w^h_h(L,t) = 0$ and the interlement compatibility conditions $[\![w^h_h]\!]_{int} = 0$. The total deflections of the beam elements are obtained from $w^h = w_p + w^h_h$.

It is worth mentioning that, although it appears that the proposed dual (equilibrium-based) finite element formulation has the ability to produce the exact solutions, since the obtained bending-moments are continuous as well as satisfy all equilibrium boundary conditions, and the obtained deflections are continuous as well as satisfy all kinematical boundary conditions, this is not the case, since equation (7) is not satisfied in strong form at the element level. In fact, the displacement fields that would arise from integration in time of equation (7) differ from the ones computed from the integration is space of equation (8).

## 5 NUMERICAL TESTS

To validate and assess the accuracy and effectiveness of the proposed finite element formulation, a clamped-hinged (CH) beam as illustrated in Figure 1 was considered. The beam was analysed using both the primal and dual finite element formulations. Uniform meshes of 2, 4, 8 and 16 two-node finite elements with Hermite cubic polynomials were adopted within the framework of both formulations. All the required integrations were performed exactly.

The beam parameters were set as: length $L = 2\,m$, bending stiffness $EI = 1000\,Nm^2$, mass per unit length $m = 100\,kg/m$, and viscous damping coefficient $c = 100\,Ns/m^2$. The loading parameters were taken as: speed $v = 5\,m/s$ and amplitude $g = 100\,N$.

Within the framework of Newmark's method, the following parameters were considered: $\beta = 1/4$ and $\gamma = 1/2$. The assumed time step was $\Delta t = 1/2000\,s$.

A frequency-domain analysis, with $c = 0$, was first considered. The numerical results obtained using both primal and dual formulations for the first five eigenfrequencies of the beam are displayed in Table 1. As it can be observed, the dual formulation leads to more accurate solutions than the primal one, despite the fact that both formulations make use of the same number of degrees-of-freedom. Also, both formulations lead to approximate eigenfrequencies that converge from above with respect to their corresponding exact solutions.

A time-domain analysis was afterwards considered, in which approximate bending-moment, shear-force and deflection solutions were computed using both formulations in the time range $t \in [0,2]s$.

| $n_e$ | | $\omega_1$ | $\omega_2$ | $\omega_3$ | $\omega_4$ | $\omega_5$ |
|---|---|---|---|---|---|---|
| 2 | P | 12.301909 | 46.174026 | 123.043485 | | |
| | D | 12.265060 | 44.131810 | 107.169201 | 197.034079 | |
| 4 | P | 12.196863 | 39.747105 | 84.272284 | 158.252902 | 258.009925 |
| | D | 12.196275 | 39.711429 | 83.835978 | 155.809214 | 247.605731 |
| 8 | P | 12.189651 | 39.517097 | 82.560694 | 141.639528 | 217.449063 |
| | D | 12.189641 | 39.516534 | 82.553323 | 141.591539 | 217.240958 |
| 16 | P | 12.189193 | 39.501732 | 82.424433 | 140.981199 | 215.223318 |
| | D | 12.189192 | 39.501723 | 82.424317 | 140.980444 | 215.220008 |

Table 1: CH beam - Primal (P) and dual (D) eigenfrequencies $(rad/s)$.

The mid-span bending-moment solutions were first computed within the framework of the time-domain analysis considering the time range $t \in [0, 2]s$ using both formulations on the 2- and 8-finite element meshes. As it can be observed from Figure 2, the dual formulation produces more accurate solutions than the primal one. The solution that would be obtained on a static analysis is also represented in Figure 2 for comparison purposes and, as it can be seen, the maximum dynamic bending-moment is higher than the static one.

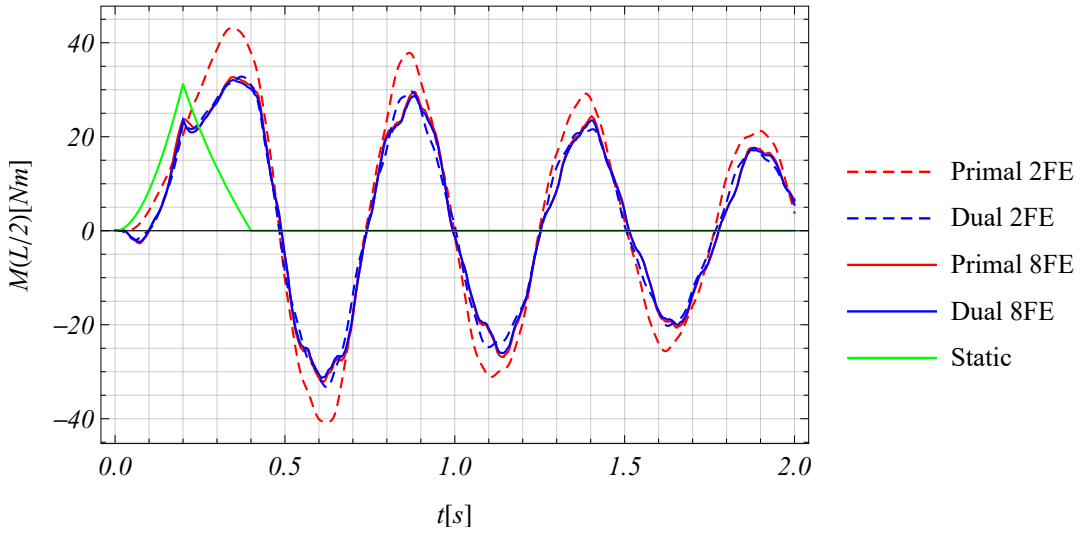


Figure 2: CH beam - Mid-span bending-moment solutions in the time range $t \in [0, 2]s$.

The bending-moments at $x = L$ were also computed using both formulations on the 2- and 8-finite element meshes. The obtained results are depicted in Figure 3. As it can be observed, while the dual formulation leads to bending-moment fields that exactly satisfy the equilibrium boundary condition $M(L) = 0$ on both meshes, the primal one does not. The same conclusion would arise for finer meshes as well.

Also the mid-span deflections were computed using both formulations on the 2-finite element mesh. The obtained solutions are represented in Figure 4, which shows that both formulations provide similar accuracies for the deflections. This was expected, since both formulations provide approximate solutions for the deflections that are continuous as well as satisfy all kinematical boundary conditions.

Finally, the bending-moment and shear-force distributions obtained on the 4-finite element

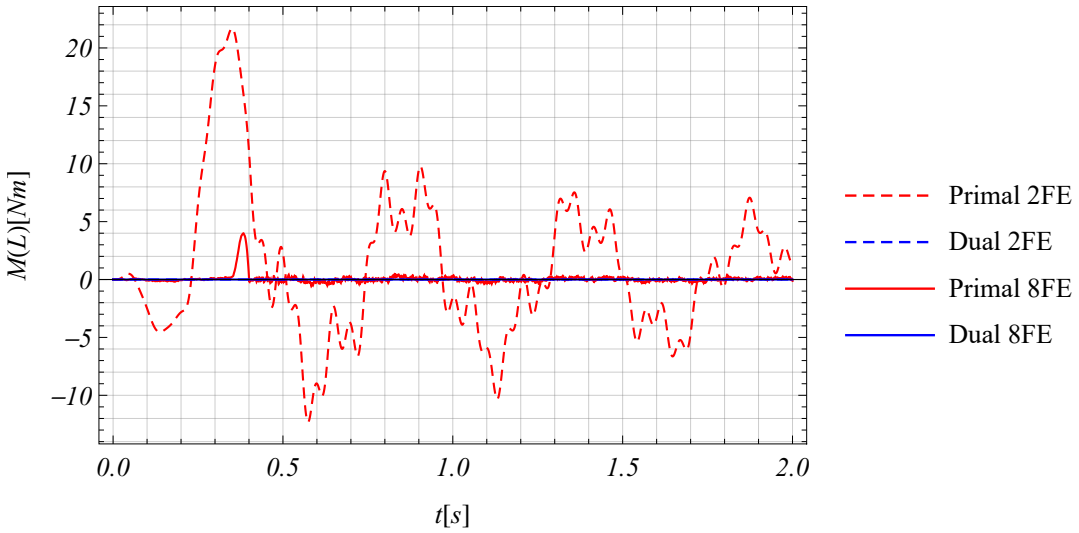


Figure 3: CH beam - Bending-moment solutions at $x = L$ in the time range $t \in [0, 2]s$.

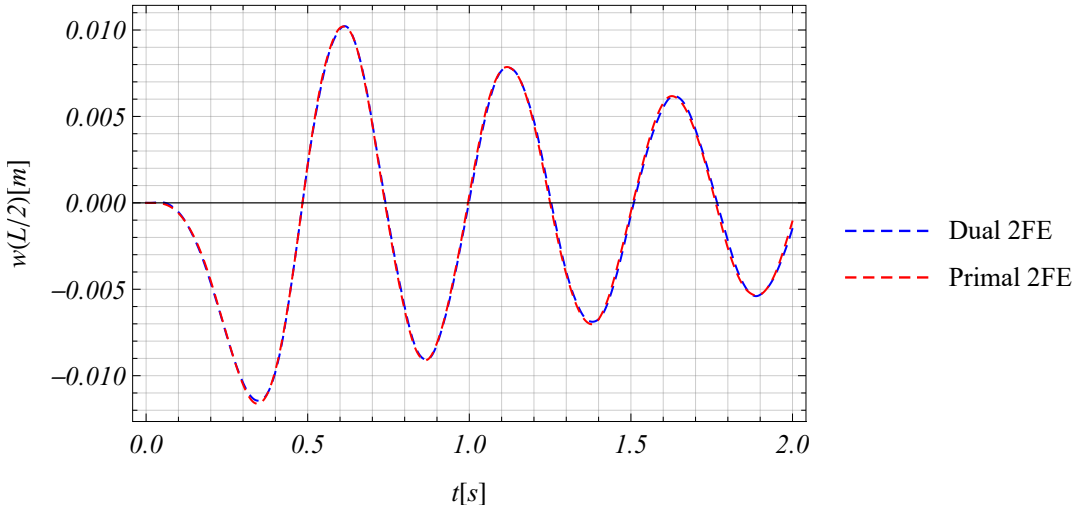


Figure 4: CH beam - Mid-span deflection solutions in the time range $t \in [0, 2]s$.

mesh for $t = 0.08s$ and $t = 0.18s$ are shown in Figures 5 and 6, respectively. Clearly, in contrast to the results provided by the primal formulation, the dual formulation produces continuous bending-moment and shear-force distributions that automatically satisfy the equilibrium boundary conditions. As shown in Figure 6, the discontinuities of the shear-force distributions produced by the dual formulation only occur at $x = vt$, the position of the applied load for the considered instant of time, and match exactly the magnitude of the applied load. On the contrary, the primal formulation is not able to represent the exact shear-force discontinuity resulting from the applied concentrated load.

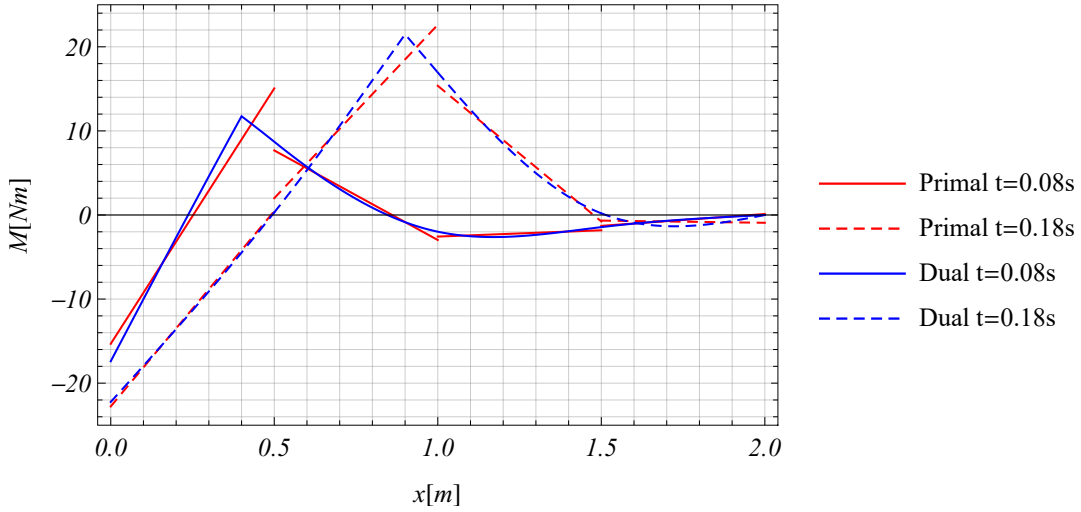


Figure 5: CH beam - Bending-moment distributions on the 4-finite element mesh for $t = 0.08s$ and $t = 0.18s$.

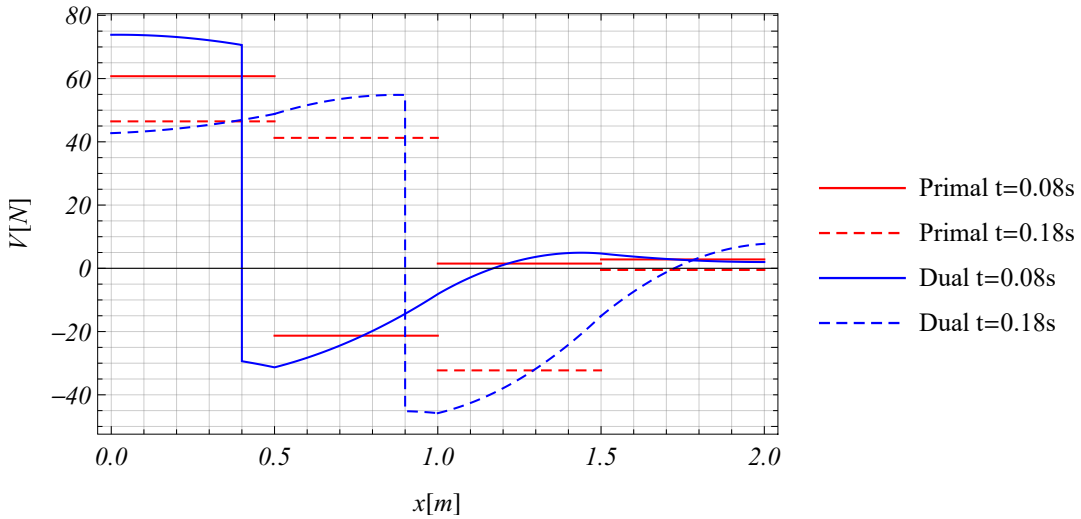


Figure 6: CH beam - Shear-force distributions on the 4-finite element mesh for $t = 0.08s$ and $t = 0.18s$.

## 6 CONCLUSIONS

The dynamic analysis of Euler-Bernoulli linear-elastic beams with internal viscous damping under moving loads was numerically addressed by resorting to a new finite element formulation. The proposed formulation was derived from a complementary variational principle, which can be viewed as the dual principle of the well known Hamilton's principle. Based on this formulation, a novel two-node beam element was derived in which the bending-moment impulse and its $x$-derivative were taken as the fundamental nodal degrees-of-freedom. The accuracy and effectiveness of the formulation were numerically assessed in both frequency and time domains by comparison of the obtained results with those provided by the standard two-node displacement-based formulation with the same number of nodal degrees-of-freedom. Integration in time was carried out by adopting an unconditionally stable version of Newmark's method. In the frequency-domain, it was numerically demonstrated that both formulations produce approximate eigenfrequencies that converge from above with respect to their corresponding exact solutions, as well as more accurate solutions were obtained by resorting to the proposed for-

mulation. In the time-domain, the new formulation proved capable of not only rendering continuous bending-moment and shear-force distributions, a desired feature in the structural design field, but also demonstrated a superior accuracy than that provided by the standard two-node displacement-based formulation.

## REFERENCES

[1] D. Froio, L. Verzeroli, R. Ferrari, et al., On the numerical modelization of moving load beam problems by a dedicated parallel computing FEM implementation. *Archives of Computational Methods in Engineering*, **28**, 2253–2314, 2021.

[2] F.V. Filho, Finite element analysis of structures under moving loads. *Shock and Vibration Digest*, **10**, 27–35, 1978.

[3] W.H. Lin and M.W. Trethewey, Finite element analysis of elastic beams subjected to moving dynamic loads. *Journal of Sound and Vibration*, **136 (2)**, 323–342, 1990.

[4] J.R. Rieker, Y.H. Lin, and M.W. Trethewey, Discretization considerations on moving load finite element beam models. *Finite Elements in Analysis and Design*, **21 (3)**, 129–144, 1996.

[5] H.A.F.A. Santos, Complementary-energy methods for geometrically non-linear structural models: an overview and recent developments in the analysis of frames. *Archives of Computational Methods in Engineering*, **18**, 405–440, 2011.

[6] H.A.F.A. Santos, Variationally consistent force-based finite element method for the geometrically non-linear analysis of Euler-Bernoulli framed structures. *Finite Elements in Analysis and Design*, **53**, 24–36, 2012.

[7] H.A.F.A. Santos, A novel updated Lagrangian complementary energy-based formulation for the elastica problem: force-based finite element model. *Acta Mechanica*, **226 (4)**, 1133–1151, 2015.

[8] H.A.F.A. Santos, Buckling analysis of layered composite beams with interlayer slip: A force-based finite element formulation. *Structures*, **25**, 542–553, 2020.

[9] B.H. Karnopp, Duality relations in the analysis of beam oscillations. *Zeitschrift für Angewandte Mathematik und Physik (ZAMP)*, **18**, 575–580, 1967.

[10] B. Tabarrok, and B.H. Karnopp, Analysis of the oscillations of the Timoshenko beam. *Zeitschrift für Angewandte Mathematik und Physik (ZAMP)*, **18**, 580–587, 1967.

COMPDYN 2023
9th ECCOMAS Thematic Conference on
Computational Methods in Structural Dynamics and Earthquake Engineering
M. Papadrakakis, M. Fragiadakis (eds.)
Athens, Greece, 12-–14 June 2023

# EXPLORATION OF DYNAMIC LOADING STRUCTURAL TOPOLOGY OPTIMIZATION AND APPLICATION TO BUILDING LATERAL LOAD RESISTING FRAME

**Arya Prakash Padhi[1],Vaibhav Bhandari[1], Anupam Chakrabarti[2] and Rajib Chowdhury[3]**

[1]Research Scholar, IIT Roorkee
Roorkee, UK, India-247667
e-mail: apadhi@ce.iitr.ac.in. vaibhavb@ce.iitr.ac.in

[2] Professor, Department of Civil Engg., IIT Roorkee
Roorkee, UK, India-247667

[3] Associate Professor, Department of Civil Engg., IIT Roorkee
Roorkee, UK, India-247667

**Abstract.** *The dynamic response topology optimization problems are usually computationally expensive, especially for time domain solution scheme involving additional iterations of Newmark beta time integration. In our work, frequency domain solution scheme as well model order reduction techniques for time domain strategy have been explored. Structural optimization for minimizing dynamic compliance has been studied for several standard examples. Application of this strategy to lateral load resisting system of a building subjected to earthquake ground excitation has been studied. The effect of geometric nonlinearity has also been studied for better accuracy of the solution.*

**Keywords:** Dynamic Structural Optimization, Bracing layout, Geometric non linearity

## 1 INTRODUCTION

Dynamic response topology optimization has gained significant attention in recent years due to its potential to design lightweight and durable structures that can withstand dynamic loads and vibrations. The objective of dynamic response topology optimization is to optimize the distribution of material in a structure to minimize its weight while maintaining its perfor-mance under dynamic loads. This is achieved by incorporating dynamic loading and vibration considerations into the optimization process. The optimization can be performed using various techniques such as mathematical programming, level set, and evolutionary algorithms. Several research studies have investigated the optimization of different types of structures, including trusses, plates, and shells. Constraints such as natural frequency, stress, and displacement can be considered in the optimization process to ensure the optimal design satisfies performance requirements. The resulting optimized structures can offer several benefits, including reduced weight, improved performance, and reduced manufacturing costs. However, dynamic re-sponse topology optimization remains a complex and challenging problem due to the high computational cost and the difficulties in dealing with geometric nonlinearities and material uncertainties. Therefore, further research is required to develop efficient and effective optimi-zation techniques that can handle these challenges.

Geometric nonlinear dynamic loading topology optimization is a technique used to optimize the shape of a structure subjected to dynamic loads, considering geometric nonlinearities. Geometric nonlinearity refers to the changes in shape of a structure that can occur under load, which can significantly affect its behaviour. Dynamic loading refers to loads that change over time, such as the impact of a moving object or the effect of wind on a structure. These types of loads can cause a structure to vibrate, leading to potential failure if the design is not optimal.

In [1] a method for dynamic response topology optimization of structures with contact constraints using the level set method has been developed. The proposed method is applied to optimize the design of a brake disc under dynamic loading, and the results demonstrate that the method is effective in finding an optimized design that can withstand dynamic loads and vibrations. In [2] approximate analysis techniques for topology optimization under multifrequency harmonic excitation has been studied. Use of model order reduction techniques for computational efficiency has been shown in [3]. Structural design of building components using spectral approach has been proposed in [4] for earthquake excitation and optimitum topology has been obtained.. Ran-dom vibration and uncertainties have been considered in [5, 6] for dynamic response topology optimization. Geometric nonlinear analysis for topology optimization has been presented in [7] for structures subjected to dynamic loading using equivalent static loads. Solutions for structures involving nonlinearity has been performed in [8] using moving morphable components. Several researches have studied geometric nonlinear topology optimization including SIMP, BESO, energy interpolation and other techniques [9, 10, 11, 12]. From literature, it has been observed that dynamic loading topology optimization studies have been explored only recently and optimizations considering finite deformation are rare.

The goal of this paper is to explore the dynamic loading topology optimization of structures subjected to dynamic excitation including sinusoidal wave and earthquake ground motion and use it for optimizing lateral bracing. Also, the effect of geometric nonlinearity is briefly summarized.

## 2 TOPOLOGY OPTIMIZATION

The well-known density-based method [13] is used in this study for the dynamic response topology optimization problem. Using a modified solid isotropic material with penalization (SIMP) interpolation scheme, the density-based topology optimization approach interpolates each element's Young's modulus $E_e$ and structural density (or mass density) $\rho$ with element $e$. This polynomial interpolation model [14], which helps avoiding localized modes in dynamic analysis is as follows:

$$\begin{aligned} E_e &= E_0\left(\alpha\eta_e^p + (1-\alpha)\eta_e\right) \\ \rho_e &= \rho_0\eta_e \end{aligned} \tag{1}$$

where $p$ is a penalization number to prevent intermediate densities and $E_0$ and $\rho_0$ are the Young's modulus and structural density of the solid material, $\alpha$ is a positive real number smaller than $1.0$. For dynamic loading, the objective function considered here (as in [3]) is the mean dynamic compliance given by:

$$c(u,\eta) = \frac{1}{t_f}\int_0^{t_f} f^T(t)u(t)dt \tag{2}$$

where $f(t)$ is the applied force vector and $u(t)$ is the displacement response vector. Finally the optimization problem [3] is configured as:

$$\begin{array}{ll} \min_\eta & c(u,\eta) \\ \text{s.t.} & \boldsymbol{M}\ddot{\boldsymbol{u}}(t) + \boldsymbol{C}\dot{\boldsymbol{u}}(t) + \boldsymbol{K}\boldsymbol{u}(t) = \boldsymbol{f}(t), t \in [0, t_f] \\ & g(\eta) = V(\eta) - V_{\max} = \sum_{\mathrm{e}=1}^{N} \eta_e v_e - V_{\max} \leq 0 \\ & \mathbf{0} < \eta_{\min} \leq \eta \leq \mathbf{1} \end{array} \tag{3}$$

where $M$, $C$, and $K$ are matrices representing the global mass, damping, and stiffness, respectively. The number of elements in the structure is denoted by $N$. The volume of each individual element is represented by $v_e$, while $V_{max}$ is the total prescribed volume of material. To prevent singularity of the stiffness matrix during the topology optimization process, a positive lower bound vector $\eta_{min}$ is assigned to $\eta$. The displacement vector $u(t)$, velocity vector $\dot{u}(t)$, and acceleration vector $\ddot{u}(t)$ can be determined by solving the dynamic equilibrium equation, given the value of the design variable vector $\eta$ and the initial conditions $u(0) = u_0$ and $\dot{u}(0) = \dot{u}_0$.

### 2.1 Sensitivity Analysis

Considering $J_d$ as the objective function and adding dynamic equilibrium equation multiplied by lagrange multiplier, we can compute adjoint sensitivity [3] which brings huge computational efficiency compared to direct sensitivity. And this is very much essential in case of dynamic topology optimization problems as the finite element solution of the equilibrium equation itself involves iterative Newmark Beta algorithm.

$$\begin{aligned} \frac{\partial J_d}{\partial \eta_e} &= \frac{\partial J_d}{\partial \eta_e} + \int_0^{t_f} \lambda^T \frac{\partial}{\partial \eta_e}(\boldsymbol{M}\ddot{\boldsymbol{u}} + \boldsymbol{C}\dot{\boldsymbol{u}} + \boldsymbol{K}\boldsymbol{u} - \boldsymbol{f})dt \\ &= \int_0^{t_f} \left(\frac{\partial c}{\partial \eta_e} + \frac{\partial c}{\partial \boldsymbol{u}}\frac{\partial \boldsymbol{u}}{\partial \eta_e}\right) dt \\ &+ \int_0^{t_f} \lambda^T \frac{\partial}{\partial \eta_e}(\boldsymbol{M}\ddot{\boldsymbol{u}} + \boldsymbol{C}\dot{\boldsymbol{u}} + \boldsymbol{K}\boldsymbol{u})dt \end{aligned} \tag{4}$$

$$\begin{aligned}\frac{\partial J_d}{\partial \eta_e} = &\int_0^{t_f} \left( \boldsymbol{\lambda}^T \frac{\partial \boldsymbol{M}}{\partial \eta_e} \ddot{\boldsymbol{u}} + \lambda^T \frac{\partial \boldsymbol{C}}{\partial \eta_e} \dot{\boldsymbol{u}} + \lambda^T \frac{\partial \boldsymbol{K}}{\partial \eta_e} \boldsymbol{u} + \frac{\partial c}{\partial \eta_e} \right) dt \\ &+ \int_0^{t_f} \left( \frac{\partial \boldsymbol{u}}{\partial \eta_e} \right)^T \left( \boldsymbol{M} \ddot{\boldsymbol{\lambda}} - \boldsymbol{C} \dot{\boldsymbol{\lambda}} + \boldsymbol{K} \boldsymbol{\lambda} + \frac{\partial c}{\partial \boldsymbol{u}} \right) dt \\ &+ \left[ \left( \frac{\partial \boldsymbol{u}}{\partial \eta_e} \right)^T (-\boldsymbol{M} \dot{\boldsymbol{\lambda}} + \boldsymbol{C} \boldsymbol{\lambda}) + \left( \frac{\partial \dot{\boldsymbol{u}}}{\partial \eta_e} \right)^T \boldsymbol{M} \boldsymbol{\lambda} \right] \Bigg|_{t=t_f}\end{aligned} \tag{5}$$

Choosing $\lambda$ in a way to eliminate derivatives of state variable $u$ with respect ro design variable $\eta_e$ leads to computation of $\lambda$ and finally the adjoint sensitivity analysis.

### 2.2 Frequency Domain Approach

Here, a frequency domain method has been used for computational efficiency and is adopted from [15]. Assuming a response excitation under a single harmonic excitation, $\mathbf{f}(t) = \mathbf{F}e^{i\omega t}$ , where $\mathbf{F}$ is the maximum amplitude and $\omega$ is the forcing frequency of the harmonic response. The maximum displacement is the solution of the state equation $\mathbf{F} = \mathbf{SU}$ where $\mathbf{U}$ is the peak amplitude of the displacement response and the dynamic stiffness is $\mathbf{S} = (\mathbf{K} + i\omega\mathbf{C} - \omega^2\mathbf{M})$.

The formulation of topology optimization for dynamic compliance minimization under a forcing frequency $\omega$ using the dynamic state equation is as follows:

$$\begin{array}{lll} \text{minimize} & \Phi_D(\rho, \mathbf{U}) = \left| \mathbf{F}^T \mathbf{U}(\rho) \right| & \\ \text{subject to:} & \int_\Omega \rho dV - \bar{V} 0 & \\ & 0 \leq \rho_e \leq 1, & \forall e \in \Omega \\ \text{with:} & \mathbf{F} = \mathbf{SU} & \end{array}$$

where $\Phi_D$ is the objective function and $|.|$ stands for the complex modulus. The aforementioned topology optimization formulation is essentially equivalent to the standard static compliance topology optimization. The important feature is the introduction of the complex state equation and displacement vector $\mathbf{U}$. in the dynamic compliance. When the dynamic stiffness becomes closer to the structural stiffness matrix $\mathbf{S}(\omega = 0) = \mathbf{K}$, the challenge is reduced to topology optimization for minimising of static compliance. As the input driving frequency approaches one of the inherent frequencies of the structure, i.e. resonance, the dynamic compliance dramatically increases. Furthermore take note that several definitions of the dynamic compliance have been put forward, such as average power of the excitation $\Phi_D = \left| \mathrm{F}^T \mathrm{U}_{\mathbf{I}} \right|$ and total response $\Phi_D = \mathbf{U}^T \overline{\mathrm{U}}$ , where $\mathbf{U}$ is the conjugate of the displacement vector, among others.

Extension to multi-frequency input excitations, such as earth-quake ground motions, by representing the excitation as a linear superposition of harmonics can be performed as follows:

$$\Phi_{TD}(\rho, \mathbf{U}) = \int_{\omega_a}^{\omega_b} \left| \mathbf{F}^T \mathbf{U} \right| d\omega \tag{6}$$

### 2.3 Nonlinear Dynamic Topology Optimization

In case of geometric non linear structures the stiffness matrix $K$ will also depend upon the current sate of displacement in addition to the density design variable. So the equation now

becomes:

$$\begin{array}{ll} \min_{\eta} & J_d \\ \text{s.t.} & \boldsymbol{M}(\boldsymbol{\rho})\ddot{\boldsymbol{u}}(t) + \boldsymbol{C}(\boldsymbol{\rho})\dot{\boldsymbol{u}}(t) + \boldsymbol{K}(\rho, u)\boldsymbol{u}(t) = \boldsymbol{f}(t), t \in [0, t_f] \\ & g(\eta) = V(\eta) - V_{\max} = \sum_{e=1}^{N} \eta_e v_e - V_{\max} \leq 0 \\ & \mathbf{0} < \eta_{\min} \leq \eta \leq \mathbf{1} \end{array} \tag{7}$$

The equilibrium equation is expressed in terms of residual as:

$$R = F_{ext} - F_{int} = 0 \tag{8}$$

## 3 RESULTS

Here a building shear wall subjected to lateral loading is considered for structural optimization ([15]) as shown in Fig. 1(a). Modal compliance in frequency domain is optimized to obtain the efficient layout subjected to volume fraction of 0.2. The building is fixed in the bottom. Three base to height ratio (1:3, 1:4, 1:5) have been studied to see the output shapes. The shapes are shown in Fig. 1(b), 1(c) and 1(d). The bracing system comes similar to eccentric bracing. Next a time domain analysis (adopted from [16]) has been conducted and output shape is shown in Fig. 2 for a three storey building, with masses concentrated in three storeys. It is to be noted that the blue colour space is actually void i.e. free of any material. Figure 3 shows a small comparison of linear analysis and geometric non linear optimization results. The difference is minimal for considered earthquake loading although it is being investigated further.

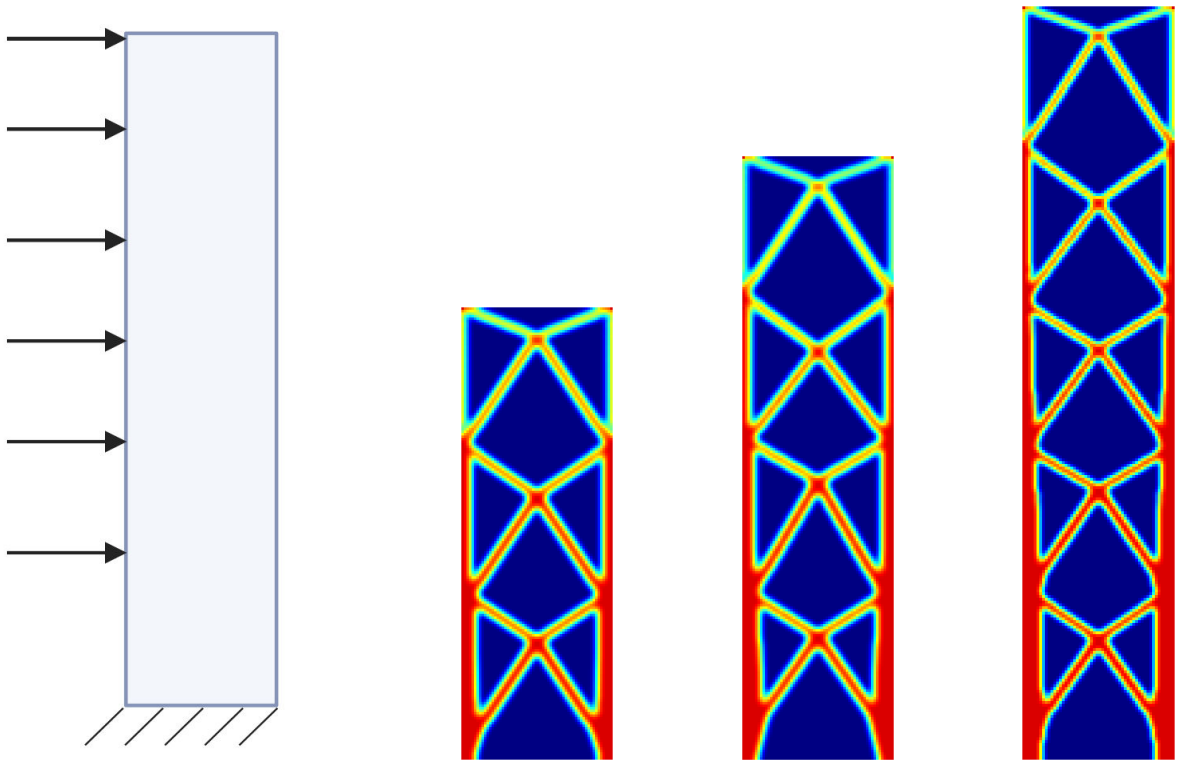

(a) (b) (c) (d)

Figure 1: Configuration of building lateral load resisting frame subjected to lateral loading

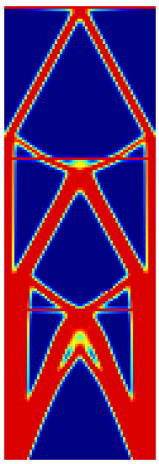

Figure 2: Configuration of building lateral load resisting frame subjected to lateral loading

## 4 CONCLUSIONS

In this paper dynamic response topology optimization using SIMP approach has been studied for dynamic compliance minimization subjected to volume fraction in time and frequency domain. Time domain analysis using Newmark-Beta algorithm takes significantly large time compared to frequency domain analysis. The output shapes are more or less same. The case study (taken from literature) of a building shear wall frame subjected to earthquake ground motion has been studied. Incorporation of geometric non linearity. The incorporation of geometric non linearity has shown minimal changes in the output layout for the considered earthquake loading although change of loading might have majot impact and needs further study.

## REFERENCES

[1] R. Picelli, A. Neofytou, and H. A. Kim, "Topology optimization for design-dependent hydrostatic pressure loading via the level-set method," *Structural and Multidisciplinary Optimization*, vol. 60, pp. 1313–1326, 2019.

[2] S. Zheng, X. Zhao, Y. Yu, and Y. Sun, "The approximate reanalysis method for topology optimization under harmonic force excitations with multiple frequencies," *Structural and Multidisciplinary Optimization*, vol. 56, pp. 1185–1196, 2017.

[3] J. Zhao and C. Wang, "Dynamic response topology optimization in the time domain using model reduction method," *Structural and Multidisciplinary Optimization*, vol. 53, pp. 101–114, 2016.

[4] W. Gao, X. Lu, and S. Wang, "Seismic topology optimization based on spectral approaches," *Journal of Building Engineering*, vol. 47, p. 103781, 2022.

[5] J. H. Rong, Z. L. Tang, Y. M. Xie, and F. Y. Li, "Topological optimization design of structures under random excitations using sqp method," *Engineering Structures*, vol. 56, pp. 2098–2106, 2013.

[6] F. Valentini, O. M. Silva, and E. L. Cardoso, "Robust topology optimization for harmonic displacement minimization of structures subjected to uncertainty in the excitation fre-

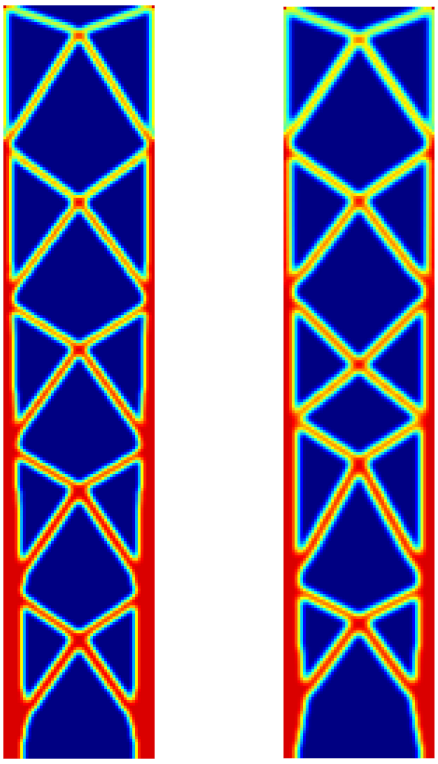

(a) (b)

Figure 3: (a) Linear (b) Non-linear analysis

quency," *Computer Methods in Applied Mechanics and Engineering*, vol. 379, p. 113767, 2021.

[7] H.-A. Lee and G.-J. Park, "Nonlinear dynamic response topology optimization using the equivalent static loads method," *Computer Methods in Applied Mechanics and Engineering*, vol. 283, pp. 956–970, 2015.

[8] S. Lu, Z. Zhang, H. Guo, G.-J. Park, and W. Zuo, "Nonlinear dynamic topology optimization with explicit and smooth geometric outline via moving morphable components method," *Structural and Multidisciplinary Optimization*, vol. 64, pp. 2465–2487, 2021.

[9] T. Buhl, C. B. Pedersen, and O. Sigmund, "Stiffness design of geometrically nonlinear structures using topology optimization," *Structural and Multidisciplinary Optimization*, vol. 19, pp. 93–104, 2000.

[10] F. A. Gomes and T. A. Senne, "An algorithm for the topology optimization of geometrically nonlinear structures," *International Journal for Numerical Methods in Engineering*, vol. 99, no. 6, pp. 391–409, 2014.

[11] Y. Han, B. Xu, and Y. Liu, "An efficient 137-line matlab code for geometrically nonlinear topology optimization using bi-directional evolutionary structural optimization method," *Structural and Multidisciplinary Optimization*, vol. 63, pp. 2571–2588, 2021.

[12] H. Lin, A. Xu, A. Misra, and R. Zhao, "An ansys apdl code for topology optimization of structures with multi-constraints using the beso method with dynamic evolution rate (der-beso)," *Structural and Multidisciplinary Optimization*, vol. 62, pp. 2229–2254, 2020.

[13] M. P. Bendsøe, "Optimal shape design as a material distribution problem," *Structural optimization*, vol. 1, pp. 193–202, 1989.

[14] J. Zhu, X. Zhang, and Z. Wang, "Backward interpolation architecture for algebraic soft-decision reed–solomon decoding," *IEEE transactions on very large scale integration (VLSI) systems*, vol. 17, no. 11, pp. 1602–1615, 2009.

[15] A. Martin and G. G. Deierlein, "Structural topology optimization of tall buildings for dynamic seismic excitation using modal decomposition," *Engineering Structures*, vol. 216, p. 110717, 2020.

[16] S. Allahdadian and B. Boroomand, "Topology optimization of planar frames under seismic loads induced by actual and artificial earthquake records," *Engineering Structures*, vol. 115, pp. 140–154, 2016.

COMPDYN 2023
9th ECCOMAS Thematic Conference on
Computational Methods in Structural Dynamics and Earthquake Engineering
M. Papadrakakis, M. Fragiadakis (eds.)
Athens, Greece, 12-14 June 2023

# COMPARISON OF POD-UDEIM AND POD-ECSW MODEL ORDER REDUCTION IN THE CASE OF DAMAGING RC STRUCTURES SUBJECTED TO EARTHQUAKES

**B. Bodnar[1, 2], W. Larbi[1], M. Titirla[1], J.-F. Deü[1], F. Gatuingt[2] and F. Ragueneau[2, 3]**

[1] Conservatoire National des Arts et Métiers, Laboratoire de Mécanique des Structures et des Systèmes Couplés
292 rue Saint-Martin, 75141 Paris cedex 03, France
{bastien.bodnar, walid.larbi, magdalini.titirla, jean-francois.deu}@lecnam.net

[2] Université Paris-Saclay, Centrale Supélec, ENS Paris-Saclay, CNRS, Laboratoire de Mécanique Paris-Saclay
91190, Gif-sur-Yvette, France
{bastien.bodnar, fabrice.gatuingt, frederic.ragueneau}@ens-paris-saclay.fr

[3]EPF École d'Ingénieurs
{frederic.ragueneau}@epf.fr
55 av. Président Wilson, F-94230, Cachan, France

## Abstract

*This paper uses Hyper-Reduced Order Models (HROMs) to accelerate parametric and sensitivity analyses on reinforced concrete structures subjected to earthquakes. The number of Degrees Of Freedom (DOFs) is reduced using a Proper Orthogonal Decomposition (POD) reduced basis. The nonlinear terms of the matrix system are approximated using an Unassembled Discrete Empirical Interpolation Method (UDEIM) or an Energy Conserving with Sampling and Weighting procedure (ECSW). Both strategies are compared regarding accuracy and time-savings on a L-shaped three-story building modeled by damaging multifibre beam elements. The efficiency of the HROMs is assessed in the case of parametric analyses about the external loading (e.g., ground motions) or mechanical properties (e.g., elastic modulus, or tensile strength). Results (1) show that both methods correctly model the nonlinear response of the structure with a strain energy error of less than 0.5 % and a speed-up factor between 20 and 32 during the online phases, and (2) prove that the POD-ECSW is more accurate than the POD-UDEIM despite an offline phase that requires more CPU time.*

**Keywords:** Earthquake Engineering, Reinforced Concrete, Multifibre Beam Elements, Model Order Reduction, Proper Orthogonal Decomposition, Unassembled Discrete Empirical Interpolation Method, Energy Conserving with Sampling and Weighting.

## 1 INTRODUCTION

An important part of Reinforced Concrete (RC) structures design is the capability to withstand dynamic loadings (e.g., earthquakes, or wind). Accurately assessing such structural responses requires 3D nonlinear dynamic Finite Element (FEM) analyses. However, it is not easy since it can be costly in Central Processing Unit (CPU) time. As a result, knowing that FEM analyses usually do not exceed 12 hours in a civil engineering design office, other approaches are used instead for design purposes. Among them, the widespread quasi-static "push-over" method allows computing the loading demand on each structural component (e.g., column, or beam) for several earthquakes without performing dynamic FEM analyses ([1], [2]). This approach is well suited for design but is limited compared to dynamic FEM analyses since the higher eigenmodes and the earthquake-induced cyclic loading are not considered. As a result, torsional effects or local collapse mechanisms cannot be modeled correctly, as well as hysteretic energy dissipations (e.g., frictional sliding) or stiffness recovery when the cracks are closing. To consider all these phenomena, nonlinear dynamic FEM analyses must be repeated with several ground motions coming from one or several directions. Reducing the computational cost of such sensitivity analyses is thus useful in an industrial context. The development of pseudo-dynamic and real-time hybrid tests over the last decades also pushed forward the need for nonlinear numerical models of RC structures that can be run in quasi-real time ([3], [4]). As the commands of the actuators are based on the response of a nonlinear numerical model, the CPU time must be less than 10 ms per time step in real-time. Lower values can sometimes be required depending on the delays related to the components of the experimental setup (e.g., actuators, sensors, or controller boards). Hyper-Reduced Order Models (HROMs) can be used to reach these goals.

In the case of nonlinear systems, *a posteriori* data-driven methods are commonly applied. Training FEM analyses are first run on the nonlinear high dimensional system to generate relevant snapshots. Offline post-processing is then carried out to produce modes that best represent the nonlinear response of the model. The modal basis can be computed using a "greedy" fixed point algorithm or a Proper Orthogonal Decomposition (POD) method to build orthogonal modes incrementally or simultaneously ([5], [6], [7]). Several researchers successfully used the POD over the last decades to identify coherent structures [8], perform FEM analyses involving turbulent flows ([9], [10]), control dynamic systems [11], detect damage [12], update finite element models [13], and reduce structural dynamics models ([14], [15]). This approach drastically reduces the computational cost required to solve nonlinear matrix systems. However, it is limited since the computational cost related to the nonlinear terms (e.g., restoring forces) is still very high.

Using hyper-reduction methods avoids this drawback. They consist of approximating the nonlinear terms based on samples assessed on a set of elements belonging to a Reduced Integration Domain (RID). The Discrete Empirical Interpolation Method (DEIM) and its variants allow for achieving this purpose [16]. They rely on the "gappy" POD used to reconstruct facial images [17], hyper-reduce nonlinear systems in the fluid dynamics framework ([18], [19]), or perform process simulations [20]. DEIM approaches can be seen as an improvement of this method since a "greedy" algorithm is added to the offline phase to identify the best RID. As it is used with the POD to perform FEM analyses, no additional CPU time is required to build force snapshots. The procedure also remains the same regardless of the physics since the snapshots consider all the nonlinearities (e.g., damage, plasticity, or large deformations). Several collocation techniques allow using all the components belonging to the RID, improving the stability and the accuracy of the HROM [21]. The unassembled force snapshots (i.e., computed

element per element) can also be used to build the force basis [22]. As each collocation component refers to an element instead of a node, the elements belonging to the RID are directly selected when the greedy algorithm runs, making the unassembled DEIM (UDEIM) more suitable to perform FEM analyses. Better accuracy can thus be reached with smaller RIDs [21]. Other improvements were developed over the last decade, such as a localized DEIM ([23], [24]), an adaptation to parametric systems ([25], [26]), improved strategies to choose the collocation components [27], or applications to geometrically nonlinear static and dynamic systems involving nonlinear elastic material laws ([28], [21]). The DEIM and its variants are efficient but come with a huge drawback since they destroy the symmetry of the matrix system. The approximated DEIM reduced tangent operator is not entirely symmetric, which leads to a possible loss of stability, variational consistency, and underlying energy function fitting into the Lagrangian framework [21]. As a result, only the nonlinear part of the nonlinear terms can be interpolated. Other approaches, such as the Energy Conserving Mesh Sampling and Weighting (ECSW), need to be used instead to keep the symmetry of the matrix system. It consists of finding the smallest number of positive non-null weights applied to a reduced set of elements (belonging to the RID) so that the sum of their contribution is equal to the reduced restoring force vector up to a tolerance usually lower than 1 %. Contrary to the DEIM, the nonlinear terms are directly approximated on a reduced basis. The contribution of each element is computed separately according to the available unassembled force snapshots. A greedy Sparse Non-Negative Least Square (SNNLS) solver is then used during the offline phase to compute the weights applied to the elements belonging to the RID. The ECSW was initially developed in the framework of computer graphics [29] and later extended to the finite element framework to solve structural dynamics problems ([30], [31]). Several researchers worked later on improvements to reduce the computational cost due to the sparse SNNLS solver [32], or to selectively evaluate the nonlinearities at the Gauss point level instead of the element scale [33]. The ECSW proved to be more efficient than the DEIM approaches in the case of dynamic FEM analyses involving geometrical nonlinearities and nonlinear elastic materials [21].

This paper uses hyper-reduction methods to accelerate earthquake engineering parametric and sensitivity analyses on a reinforced concrete structure. To do so, both UDEIM and ECSW are compared in terms of accuracy and time-saving. The POD and the UDEIM procedures are detailed in Section 2, while the ECSW is described in Section 3. Hyper-reduced models are used in Section 4 to accelerate parametric analyses about the external loading (i.e., ground motion) and material properties (i.e., elastic modulus, tensile strength, and compressive strength of concrete) on a L-shaped three-story building made of multi-fiber beam elements.

## 2 REDUCED ORDER MODELING USING A POD-UDEIM APPROACH

Using nonlinear material laws increases the CPU time necessary to compute the nonlinear restoring force vector at each time step. In addition, performing all the matrix operations on a full basis can be time-consuming, especially if the structure has many DOFs. To reduce the computational cost of the Full Order Model (FOM), a POD-UDEIM hyper-reduced order modeling approach is proposed.

The key idea of the POD is to first perform a small number of nonlinear FEM analyses (e.g., by using earthquakes having different peak ground accelerations, frequency, strong motion phase duration, or oriented in different directions) on the FOM made of $N_{DOFs}$ free DOFs. Displacement snapshots are then used as training data to compute $N$ nonlinear POD modes by carrying out a Singular Value Decomposition (SVD). The $n$ first POD modes are next selected according to the criterion (1) to build a reduced modal basis:

$$1 - \frac{\sum_{i=1}^{n} \lambda_i}{\sum_{j=1}^{N} \lambda_j} \leq \varepsilon \tag{1}$$

where $\lambda_i$ is the $i^{th}$ singular value, $N$ is the number of POD modes, $n \ll N$ is the number of POD modes in the truncated modal basis, and $\varepsilon$ is the tolerance used to truncate the modal basis.

A tolerance $\varepsilon$ of $10^{-2}$ is recommended to ensure that approximately 99 % of the data quantified by the singular values is considered in the POD basis [15]. This *a posteriori* approach reduces the number of DOFs as well as the computational cost of the matrix operations. The displacement vector $\boldsymbol{u} \in \mathbb{R}^{N_{DOFs}}$ can thus be expressed in a new basis $\boldsymbol{\Phi} \in \mathbb{R}^{N_{DOFs} \times n}$ as described in (2):

$$\boldsymbol{u} \approx \boldsymbol{\Phi} \cdot \boldsymbol{q} \qquad \text{with} \qquad \boldsymbol{\Phi} = [\boldsymbol{\varphi}_1 \quad \cdots \quad \boldsymbol{\varphi}_n] \tag{2}$$

where $\boldsymbol{q} \in \mathbb{R}^n$ is the displacement vector in the reduced basis $\boldsymbol{\Phi}$, and $\boldsymbol{\varphi}_{i=1,\dots,n} \in \mathbb{R}^{N_{DOFs}}$ is the $i^{th}$ POD mode computed using a SVD procedure.

In addition, a UDEIM operator is added to the solving process. To do so, a second SVD is performed on the snapshots related to the nonlinear parts of the unassembled restoring force vector (i.e., computed element per element) (3). $N_e$ is the number of finite elements, and $N_c$ is the number of force components per element:

$$\boldsymbol{r}^{\mathrm{NL,u}}(\boldsymbol{u}) = \boldsymbol{r}^{\mathrm{u}}(\boldsymbol{u}) - \boldsymbol{K}_{\mathrm{E}}^{\mathrm{u}} \cdot \boldsymbol{B} \cdot \boldsymbol{u} \tag{3}$$

where $\boldsymbol{K}_{\mathrm{E}}^{\mathrm{u}} \in \mathbb{R}^{N_e \cdot N_c \times N_e \cdot N_c}$ is the unassembled elastic stiffness matrix, $\boldsymbol{B} = \left[\boldsymbol{L}_1^T \quad \cdots \quad \boldsymbol{L}_{N_e}^T\right]^T \in \mathbb{R}^{N_e \cdot N_c \times N_{DOFs}}$ is a Boolean assembly matrix, and $\boldsymbol{L}_{i=1,\dots,N_e} \in \mathbb{R}^{N_c \times N_{DOFs}}$ is a collocation matrix used to select the displacements of the nodes connected to the $i^{th}$ finite element (4):

$$\boldsymbol{r}^{\mathrm{u}} = \begin{pmatrix} \boldsymbol{r}_1^{\mathrm{u}} \\ \vdots \\ \boldsymbol{r}_{N_e}^{\mathrm{u}} \end{pmatrix} \quad \& \quad \boldsymbol{K}_{\mathrm{E}}^{\mathrm{u}} = \begin{pmatrix} \boldsymbol{K}_{\mathrm{E},1}^{\mathrm{u}} & \dots & \boldsymbol{0} \\ \vdots & \ddots & \vdots \\ \boldsymbol{0} & \dots & \boldsymbol{K}_{\mathrm{E},N_e}^{\mathrm{u}} \end{pmatrix}. \tag{4}$$

The $m$ first UDEIM modes are then selected according to (1) to build a second truncated modal basis $\boldsymbol{\Psi} \in \mathbb{R}^{N_e \cdot N_c \times m}$. So $\boldsymbol{r}^{\mathrm{NL,u}} \cong \boldsymbol{\Psi} \cdot \boldsymbol{c}$ where $\boldsymbol{c} \in \mathbb{R}^m$ is the vector containing the scalar weights associated with the truncated modal basis $\boldsymbol{\Psi} = [\boldsymbol{\psi}_1 \quad \cdots \quad \boldsymbol{\psi}_m]$. Algorithm 1 is next used to find for each UDEIM mode $\boldsymbol{\psi}_i \in \mathbb{R}^{N_e \cdot N_c}$ the best collocation component.

Algorithm 1: DEIM algorithm.

Input: A set of DEIM modes $\boldsymbol{\Psi} = [\boldsymbol{\psi}_1 \quad \cdots \quad \boldsymbol{\psi}_m]$
Output: Index of the interpolation DOFs $\boldsymbol{ID} = [ID_1 \quad \cdots \quad ID_m]$ and partition matrix $\boldsymbol{P} = [\boldsymbol{p}_1 \quad \dots \quad \boldsymbol{p}_m]$

Set $ID_1$ = index of the maximum component of $|\boldsymbol{\psi}_1|$
Set $\boldsymbol{I}_d = [\boldsymbol{e}_1 \quad \dots \quad \boldsymbol{e}_{N_e \cdot N_c}]$ the identity matrix of size $N_e \cdot N_c \times N_e \cdot N_c$
Initiate matrices : $\boldsymbol{V} = [\boldsymbol{\psi}_1]$, $\boldsymbol{P} = \left[\boldsymbol{e}_{ID_1}\right]$, $\boldsymbol{ID} = [ID_1]$

For $i = 2, \dots, m$ do
  Solve $\boldsymbol{P}^{\mathrm{T}} \cdot \boldsymbol{V} \cdot \boldsymbol{c}_i = \boldsymbol{P}^{\mathrm{T}} \cdot \boldsymbol{\psi}_i$
  Compute residual $\boldsymbol{res} = |\boldsymbol{\psi}_i - \boldsymbol{V} \cdot \boldsymbol{c}_i|$
  Set $ID_i$ = index of the maximum component of $\boldsymbol{res}$
  Augment $\boldsymbol{V} \leftarrow [\boldsymbol{V} \quad \boldsymbol{\psi}_i]$, $\boldsymbol{P} \leftarrow [\boldsymbol{P} \quad \boldsymbol{e}_{ID_i}]$, $\boldsymbol{ID} \leftarrow [\boldsymbol{ID} \quad ID_i]$
End

The $m$ components belonging to the RID are selected using a Boolean partition matrix $\boldsymbol{P} \in \mathbb{R}^{N_e \cdot N_c \times m}$. To improve the accuracy of the interpolation operator, the unused components of the RID are added to $\boldsymbol{P}$. The number of collocation components $k$ is thus higher than the number $m$ of UDEIM modes (i.e., $k > m$). Considering a new partition matrix $\boldsymbol{P} \in \mathbb{R}^{N_e \cdot N_c \times k}$ leads to an overdetermined matrix system $\boldsymbol{P}^{\mathrm{T}} \cdot \boldsymbol{\psi} \cdot \boldsymbol{c} \approx \boldsymbol{P}^{\mathrm{T}} \cdot \boldsymbol{r}^{\mathrm{NL,u}}$. The scalar weights $\boldsymbol{c} \in \mathbb{R}^m$ are thus computed in the least square sense using a Monroe-Penrose pseudo-inverse $(\cdot)^+$ so that the residual is minimized in the $L^2$-norm, leading to $\boldsymbol{c} \approx (\boldsymbol{P}^{\mathrm{T}} \cdot \boldsymbol{\psi})^+ \cdot \boldsymbol{P}^{\mathrm{T}} \cdot \boldsymbol{r}^{\mathrm{NL,u}}$. It should be noted that the selection of the collocation components could be improved by directly adding the additional components to $\boldsymbol{P}$ when Algorithm 1 runs [21]. Unfortunately, the CPU time related to the offline phase drastically increases since the size of the matrix system to solve at each iteration is $N_c$ times higher. In addition, the accuracy of the interpolation operator does not change significantly. As a result, the additional components are here added to $\boldsymbol{P}$ *a posteriori* (i.e., when the RID is already defined).

When the $k$ collocation components are set, the online phases proceed. The material laws are only updated on the elements belonging to the RID (i.e., where the nonlinear part of the unassembled restoring force vector needs to be computed). The $k$ collocation components stored in $\boldsymbol{r}_{\mathrm{RID}}^{\mathrm{NL,u}} = \boldsymbol{P}^{\mathrm{T}} \cdot \boldsymbol{r}^{\mathrm{NL,u}} \in \mathbb{R}^k$ are then used as samples to build the reduced vector $\overline{\boldsymbol{r}} \in \mathbb{R}^n$ in basis $\boldsymbol{\Phi}$, as described in (5):

$$\overline{\boldsymbol{r}}(\boldsymbol{\Phi} \cdot \boldsymbol{q}) = \boldsymbol{\Phi}^{\mathrm{T}} \cdot \boldsymbol{B}^{\mathrm{T}} \cdot \left( \boldsymbol{K}_{\mathrm{E}}^{\mathrm{u}} \cdot \boldsymbol{B} \cdot \boldsymbol{\Phi} \cdot \boldsymbol{q} + \boldsymbol{A} \cdot \boldsymbol{r}_{\mathrm{RID}}^{\mathrm{NL,u}}(\boldsymbol{\Phi} \cdot \boldsymbol{q}) \right) \quad \text{with} \quad \boldsymbol{A} = \boldsymbol{\Psi} \cdot (\boldsymbol{P}^{\mathrm{T}} \cdot \boldsymbol{\Psi})^+ \tag{5}$$

where $\boldsymbol{K}_{\mathrm{E}}^{\mathrm{u}} \in \mathbb{R}^{N_e \cdot N_c \times N_e \cdot N_c}$ is the unassembled elastic stiffness matrix, $\boldsymbol{\Phi} \in \mathbb{R}^{N_{DOFs} \times n}$ is the basis of POD modes, $\boldsymbol{q} \in \mathbb{R}^n$ is the displacement vector in basis $\boldsymbol{\Phi}$, $\boldsymbol{\Psi} \in \mathbb{R}^{N_e \cdot N_c \times m}$ is the basis of UDEIM modes, $\boldsymbol{P} \in \mathbb{R}^{N_e \cdot N_c \times k}$ is the partition matrix, and $\boldsymbol{A} \in \mathbb{R}^{N_e \cdot N_c \times k}$ is the UDEIM interpolation operator. As a result, according to (3), (5) becomes:

$$\overline{\boldsymbol{r}}(\boldsymbol{\Phi} \cdot \boldsymbol{q}) = \boldsymbol{\Phi}^{\mathrm{T}} \cdot \boldsymbol{B}^{\mathrm{T}} \cdot \left( (\boldsymbol{I}_{\mathrm{d}} - \boldsymbol{A} \cdot \boldsymbol{P}^{\mathrm{T}}) \cdot \boldsymbol{K}_{\mathrm{E}}^{\mathrm{u}} \cdot \boldsymbol{B} \cdot \boldsymbol{\Phi} \cdot \boldsymbol{q} + \boldsymbol{A} \cdot \boldsymbol{r}_{\mathrm{RID}}^{\mathrm{u}}(\boldsymbol{\Phi} \cdot \boldsymbol{q}) \right) \tag{6}$$

where $\boldsymbol{I}_{\mathrm{d}} \in \mathbb{R}^{N_e \cdot N_c \times N_e \cdot N_c}$ is an identity matrix, and $\boldsymbol{r}_{\mathrm{RID}}^{\mathrm{u}}(\boldsymbol{\Phi} \cdot \boldsymbol{q}) \in \mathbb{R}^k$ is the unassembled restoring force vector assessed on the $k$ collocation components belonging to the RID. The reduced tangent stiffness matrix $\overline{\boldsymbol{K}}_{\mathrm{T}} \in \mathbb{R}^{n \times n}$ can thus be approximated by derivation of (6) with respect to $\boldsymbol{q}$ (7):

$$\overline{\boldsymbol{K}}_{\mathrm{T}} = \frac{\partial \overline{\boldsymbol{r}}(\boldsymbol{q})}{\partial \boldsymbol{q}} \approx \boldsymbol{\Phi}^{\mathrm{T}} \cdot \boldsymbol{B}^{\mathrm{T}} \cdot \left( (\boldsymbol{I}_{\mathrm{d}} - \boldsymbol{A} \cdot \boldsymbol{P}^{\mathrm{T}}) \cdot \boldsymbol{K}_{\mathrm{E}}^{\mathrm{u}} + \boldsymbol{A} \cdot \boldsymbol{K}_{\mathrm{T,RID}}^{\mathrm{u}} \right) \cdot \boldsymbol{B} \cdot \boldsymbol{\Phi} \tag{7}$$

where $\boldsymbol{K}_{\mathrm{T,RID}}^{\mathrm{u}} = \frac{\partial \boldsymbol{r}_{\mathrm{RID}}^{\mathrm{u}}(\boldsymbol{\Phi} \cdot \boldsymbol{q})}{\partial \boldsymbol{B} \cdot \boldsymbol{\Phi} \cdot \boldsymbol{q}} = \boldsymbol{P}^{\mathrm{T}} \cdot \frac{\partial \boldsymbol{r}^{\mathrm{u}}(\boldsymbol{\Phi} \cdot \boldsymbol{q})}{\partial \boldsymbol{B} \cdot \boldsymbol{\Phi} \cdot \boldsymbol{q}} \in \mathbb{R}^{k \times N_e \cdot N_c}$ is the unassembled tangent stiffness matrix related to the $k$ collocation components belonging to the RID, computed when iterating and used as a sample to approximate $\overline{\boldsymbol{K}}_{\mathrm{T}}$ during the online phase.

## 3 REDUCED ORDER MODELING USING A POD-ECSW APPROACH

The ECSW is a hyper-reduction method that preserves the virtual work of the reduced restoring force vector $\overline{\boldsymbol{r}}(\boldsymbol{\Phi} \cdot \boldsymbol{q}) \in \mathbb{R}^n$ according to a set of training snapshots. It consists of finding an approximation of $\overline{\boldsymbol{r}}(\boldsymbol{\Phi} \cdot \boldsymbol{q})$ by summing the contributions of $m$ elements belonging to a reduced integration domain (RID). The contribution of each element of the RID (indexed $e$) is weighted by a nonzero positive factor $\xi_e \geq 0$ to match the energy of the full system and ensure positiveness. As a result, the reduced internal forces can be directly approximated in basis $\boldsymbol{\Phi}$ as described in (8):

$$\overline{\boldsymbol{r}}(\boldsymbol{\Phi}\cdot\boldsymbol{q}) \approx \sum_{e\,\in\,\widetilde{\Omega}}^{m} \xi_e \boldsymbol{\Phi}^{\mathrm{T}}\cdot\boldsymbol{L}_{\mathrm{e}}^{\mathrm{T}}\cdot\boldsymbol{r}_e(\boldsymbol{L}_{\mathrm{e}}\cdot\boldsymbol{\Phi}\cdot\boldsymbol{q}) \tag{8}$$

where $\boldsymbol{r}_e(\boldsymbol{L}_{\mathrm{e}}\cdot\boldsymbol{\Phi}\cdot\boldsymbol{q}) \in \mathbb{R}^{N_c}$ is the restoring force vector related to the $e^{th}$ finite element, $\boldsymbol{L}_e \in \mathbb{R}^{N_c \times N_{DOFs}}$ is a collocation matrix used to select the displacements of the nodes connected to the $e^{th}$ finite element, and $\widetilde{\Omega}$ is the reduced set of elements belonging to the RID (9):

$$\widetilde{\Omega} \in \{e \in \{1,\dots,N_e\} \mid \xi_e \geq 0\}. \tag{9}$$

The weighting factors $\xi_e$ are defined according to $n_s$ snapshots of $\boldsymbol{r}^{\mathrm{u}}(\boldsymbol{u}) \in \mathbb{R}^{N_e \cdot N_c}$ computed in the high dimensional full basis, while the displacement basis $\boldsymbol{\Phi}$ is built using snapshots of $\boldsymbol{u} \in \mathbb{R}^{N_{DOFs}}$ as described in Section 2. Contrary to the UDEIM, the ECSW does not require splitting the restoring force vector into linear and nonlinear parts to ensure stability. The balance equation (8) can be written as a matrix system for the $n_s$ snapshots according to (10):

$$\boldsymbol{Y}\cdot\boldsymbol{\xi} = \boldsymbol{b} \quad \text{with} \quad \boldsymbol{b} = \begin{pmatrix} \overline{\boldsymbol{r}}_1 \\ \vdots \\ \overline{\boldsymbol{r}}_{n_s} \end{pmatrix} = \begin{pmatrix} \sum_{e=1}^{N_e} \boldsymbol{\Phi}^{\mathrm{T}}\cdot\boldsymbol{L}_e^{\mathrm{T}}\cdot\boldsymbol{r}_e^{\mathrm{u}}(\boldsymbol{L}_e\cdot\boldsymbol{u}_1) \\ \vdots \\ \sum_{e=1}^{N_e} \boldsymbol{\Phi}^{\mathrm{T}}\cdot\boldsymbol{L}_e^{\mathrm{T}}\cdot\boldsymbol{r}_e^{\mathrm{u}}(\boldsymbol{L}_e\cdot\boldsymbol{u}_{n_s}) \end{pmatrix} \tag{10}$$

where $\boldsymbol{\xi} \in \mathbb{R}^{N_e}$ is a vector containing the weighting factors $\xi_{e\,=\,1,\dots,N_e}$, $\boldsymbol{b} \in \mathbb{R}^{n \cdot n_s}$ is a vector containing the reduced restoring force vectors $\overline{\boldsymbol{r}}_{j\,=\,1,\dots,n_s}$ (10), and $\boldsymbol{Y} \in \mathbb{R}^{n \cdot n_s \times N_e}$ is a matrix containing the contribution of each finite element in the reduced basis $\boldsymbol{\Phi}$ (11):

$$\boldsymbol{Y} = \begin{pmatrix} \boldsymbol{\Phi}^{\mathrm{T}}\cdot\boldsymbol{L}_1^{\mathrm{T}}\cdot\boldsymbol{r}_1^{\mathrm{u}}(\boldsymbol{L}_1\cdot\boldsymbol{u}_1) & \dots & \boldsymbol{\Phi}^{\mathrm{T}}\cdot\boldsymbol{L}_{N_e}^{\mathrm{T}}\cdot\boldsymbol{r}_{N_e}^{\mathrm{u}}(\boldsymbol{L}_{N_e}\cdot\boldsymbol{u}_1) \\ \vdots & \ddots & \vdots \\ \boldsymbol{\Phi}^{\mathrm{T}}\cdot\boldsymbol{L}_1^{\mathrm{T}}\cdot\boldsymbol{r}_1^{\mathrm{u}}(\boldsymbol{L}_1\cdot\boldsymbol{u}_{n_s}) & \dots & \boldsymbol{\Phi}^{\mathrm{T}}\cdot\boldsymbol{L}_{N_e}^{\mathrm{T}}\cdot\boldsymbol{r}_{N_e}^{\mathrm{u}}(\boldsymbol{L}_{N_e}\cdot\boldsymbol{u}_{n_s}) \end{pmatrix}. \tag{11}$$

The matrix system (10) is exactly fulfilled if each finite element is weighed with one, leading to $\boldsymbol{\xi} = (1 \quad \dots \quad 1)^{\mathrm{T}}$ so that all the elements belong to the RID. To achieve a reduction, (10) is approximated up to a tolerance $\tau$ with a sparse weighting vector $\boldsymbol{\xi}^* \in \mathbb{R}^{N_e}$ containing as many zero entries as possible. Each entry of $\boldsymbol{\xi}^*$ is constrained to be positive to ensure the positive definiteness of the virtual work. The constrained optimization problem to solve is written in (12):

$$\arg\min \#(e \mid \xi_e^* \neq 0) \quad \text{subject to} \quad \|\boldsymbol{Y}\cdot\boldsymbol{\xi}^* - \boldsymbol{b}\|_2 \leq \tau\|\boldsymbol{b}\|_2 \quad \text{and} \quad \boldsymbol{\xi}^* \geq \boldsymbol{0}. \tag{12}$$

Despite being Nondeterministic Polynomial time (NP) hard to solve, a solution of (12) can be computed using a SNNLS solver as described in Algorithm 2. It uses a greedy method seeking iteratively for a solution fitting the positivity constraint [34]. Note that the matrix $\boldsymbol{Y}_{\widetilde{\Omega}}$ is a submatrix of $\boldsymbol{Y}$ obtained by taking only the columns corresponding to the index set $\widetilde{\Omega}$.

Once the SNNLS problem is solved, the $m$ nonzero positive weighting factors $\xi_e^*$ are used to approximate $\overline{\boldsymbol{r}}(\boldsymbol{\Phi}\cdot\boldsymbol{q})$ (8) according to the reduced set of elements defined in (9). The reduced tangent stiffness matrix $\overline{\boldsymbol{K}}_{\mathrm{T}}$ is computed by derivation of (8) with respect to $\boldsymbol{q}$ as described in (13):

$$\overline{\boldsymbol{K}}_{\mathrm{T}} = \frac{\partial \overline{\boldsymbol{r}}(\boldsymbol{q})}{\partial \boldsymbol{q}} \approx \sum_{e \in \tilde{\Omega}}^{m} \xi_e \boldsymbol{\Phi}^{\mathrm{T}} \cdot \boldsymbol{L}_{\mathrm{e}}^{\mathrm{T}} \cdot \boldsymbol{K}_{\mathrm{T,e}}(\boldsymbol{L}_{\mathrm{e}} \cdot \boldsymbol{\Phi} \cdot \boldsymbol{q}) \cdot \boldsymbol{L}_{\mathrm{e}} \cdot \boldsymbol{\Phi} \tag{13}$$

where $\boldsymbol{K}_{\mathrm{T,e}}(\boldsymbol{L}_{\mathrm{e}} \cdot \boldsymbol{\Phi} \cdot \boldsymbol{q}) \in \mathbb{R}^{N_c \times N_c}$ is the tangent stiffness matrix related to the $e^{th}$ finite element. Contrary to the UDEIM, the ECSW preserves desirable properties like passivity, stability, symmetry, and variational consistency since $\overline{\boldsymbol{K}}_{\mathrm{T}}$ is symmetric. However, its accuracy still depends on the choice of the training dataset for which the equality of the virtual work is enforced. The tolerance $\tau$ also depends on the case study since its value is worth between $10^{-4}$ and $10^{-2}$ in the literature ([32], [35]).

Algorithm 2: Sparse Non-Negative Least Square (sNNLS) solver.

Input: Matrix $\boldsymbol{Y}$, vector $\boldsymbol{b}$, and tolerance $\tau \in ]0,1[$
Output: Index set $\tilde{\Omega}$ and sparse vector $\boldsymbol{\xi}^*$

Initiate the index set of entries where $\xi_e^* > 0$: $\tilde{\Omega} = \{\ \ \}$
Initiate the sparse vector: $\boldsymbol{\xi}^* = \boldsymbol{0}$
Initiate the residual: $\boldsymbol{res} = \boldsymbol{b}$

While $\|\boldsymbol{res}\|_2 > \tau \|\boldsymbol{b}\|_2$
  Compute error measure: $\boldsymbol{\mu} = \boldsymbol{Y}^{\mathrm{T}} \cdot \boldsymbol{res}$
  $e$ = index of the maximum component of $\boldsymbol{\mu}$
  Augment $\tilde{\Omega} = \tilde{\Omega} \cap e$
  Initiate Boolean: $\kappa = True$
  While $\kappa = True$
    Initiate trial solution satisfying the positivity constraint: $\boldsymbol{\zeta} = \boldsymbol{0}$
    Solve on the index set $\tilde{\Omega}$: $\boldsymbol{\zeta}_{\tilde{\Omega}} = (\boldsymbol{Y}_{\tilde{\Omega}})^{+} \cdot \boldsymbol{b}$
    If $\min(\boldsymbol{\zeta}) > 0$
      Positivity constraint fulfilled: $\boldsymbol{\xi}^* = \boldsymbol{\zeta}$
      Update Boolean: $\kappa = False$
    Else
      Define the index set $\tilde{\Pi}$ where the positivity constraint is not fulfilled:
      $\tilde{\Pi} = \{e \in \tilde{\Omega} \mid \zeta_e < 0\}$
      Compute the step width $\alpha$ to set the maximum violation to zero:
      $\alpha = \min\{\xi_e^*/(\xi_e^* - \zeta_e) | e < \tilde{\Pi}\}$
      Correct constraint violation: $\boldsymbol{\xi}^* = \boldsymbol{\xi}^* + \alpha(\boldsymbol{\zeta} - \boldsymbol{\xi}^*)$
      Update the index set $\tilde{\Omega}$: $\tilde{\Omega} = \{e \mid \xi_e \neq 0\}$
    End
  Update residual: $\boldsymbol{res} = \boldsymbol{b} - \boldsymbol{Y}_{\tilde{\Omega}} \cdot \boldsymbol{\xi}^*_{\tilde{\Omega}}$
  End
End

The ECSW is compared to the UDEIM in Section 4 in the case of parametric analyses on a RC structure subjected to earthquakes. One online phase was repeated with an increasing number of elements in the RID. Analyses about the properties of the external loading (e.g., earthquakes) and material properties were carried out.

# 4 APPLICATIONS

## 4.1 Numerical modeling of RC structure

The global kinematics of the case study was modeled using Timoshenko multi-fiber beam elements (see Figure 1) defined by quadratic and cubic shape functions [36].

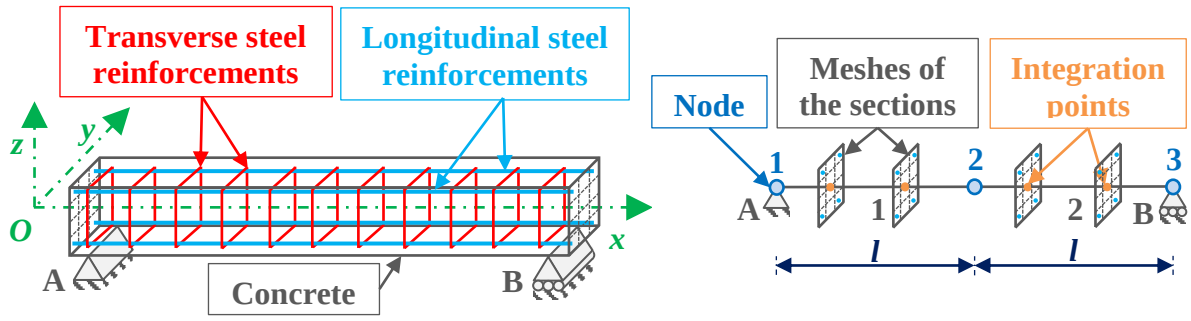


(a) (b)

Figure 1: Simply supported reinforced concrete beam (a), and multifibre mesh with two Timoshenko beam elements (b).

Knowing that the length/height ratio of the structural components (e.g., beams, or columns) is usually higher than 10 in civil engineering structures, the damage was assumed to be mainly due to bending. A "unilateral" damage law with frictional sliding developed to model quasi-brittle materials under dynamic or cyclic loadings [37] was used for concrete fibers (see Figure 2 (a) & (b)), while the steel rebars were modeled using a bilinear elastic-plastic law (see Figure 2 (c)).

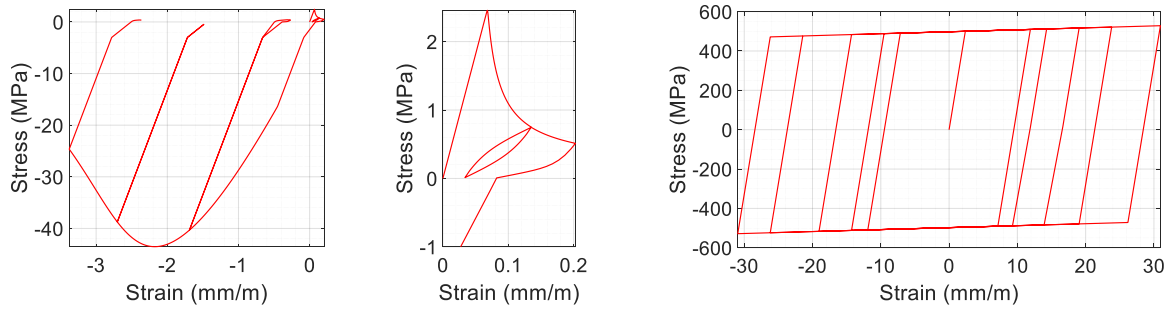


(a) (b) (c)

Figure 2: Uniaxial damage law for concrete with opening/closing of cracks (a) and frictional sliding (b), and uniaxial bilinear elastic-plastic law with kinematic hardening for steel rebars subjected to cyclic loadings (c).

## 4.2 Case study

The case study was a L-shaped three-story reinforced concrete building defined by 2383 nodes linked by 2866 multifibre beam elements (see Figure 3 (a)). All the columns were embedded to the floor level, and 14292 free DOFs modeled the structure. All stories were 3 m high, and each span was 3 m long. Two stairwells occupying areas of 2 × 2 m² were located at the ends of the building. Both were modeled by adding three columns to locally increase the stiffness. A mass per unit area of 400 kg/m² was applied to both floors via the longitudinal beams, whereas the masses of the stairwells were neglected.

The columns had a 15 × 15 cm square cross-section, and the beams had a 15 × 25 cm rectangular one. The diameter of each longitudinal steel rebar was set at 12 mm, and the steel coating was 20 mm (*cf.* Figure 3 (b)). The cross-sections of beams and columns were divided into 3 × 5 and 3 × 3 surface elements, respectively. The concrete fibers were located at the integration points of the surface elements (grey dots), while the steel fibers (blue dots) were located at 34 mm from the corners of the cross-sections (*cf.* Figure 3 (c)).

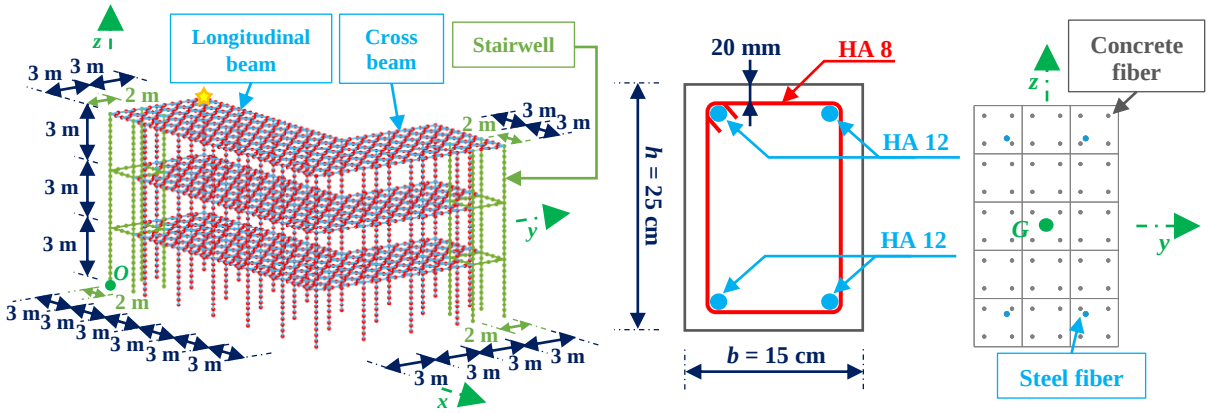


(a) (b) (c)

Figure 3: Mesh of the building (a), cross-section of the beams (b), and mesh of the cross-section of the beams (c).

The main eigenmodes and percentages of effective modal mass are summarized in Table 1. The structure weighed 255 tons and was mainly affected by the six first eigenmodes along the ***x*** and ***y***-axes, with a cumulative modal mass reaching 253 tons (i.e., 99.6 % of the total mass). A Rayleigh viscous damping ratio modeled the structural damping due to the viscosity of air and materials as well as discontinuities at junctions with respect to this frequency range. It was set at $\xi$ = 2 % at $f_1$ = 1.10 Hz (first eigenfrequency) and $f_6$ = 3.96 Hz (sixth eigenfrequency) so that its value reached a minimum around the main eigenmodes [38]. To induce torsional effects at floor level, 0.50 in the x-direction, 0.87 in the y-direction, and 0.30 in the z-direction weighed the ground motions. The dead and live loads were applied statically before entering the time step loop.

| Eigenfrequency | % of effective modal mass | | |
|---|---|---|---|
| (Hz) | ***x***-axis | ***y***-axis | ***z***-axis |
| 1.10 | 17.5 | 71.6 | ~ 0 |
| 1.11 | 72.6 | 18.3 | ~ 0 |
| 1.38 | 1.15 | 1.10 | ~ 0 |
| 3.15 | 1.08 | 7.35 | ~ 0 |
| 3.18 | 7.29 | 1.05 | ~ 0 |
| 3.96 | 0.09 | 0.12 | ~ 0 |

Table 1: Main eigenfrequencies and percentages of effective modal mass of the model.

### 4.3 Vulnerability analysis involving several ground motions

The POD-UDEIM and the POD-ECSW hyper-reduced order modeling (HROM) methods were applied to compute the response of the L-shaped three-story building under earthquake

conditions. Several natural ground motions fitting the design spectrum of the "Rhonetal" microzoning area around Visp in Switzerland (available here) modeled the seismic hazard. POD-UDEIM and POD-ECSW HROMs were first built according to 3088 snapshots based on the full order model (FOM) responses related to the ground motions in Figure 4 (a) & (b). Both HROMS were then used to approximate the response related to the ground motion in Figure 4 (c). All signals were of the same order of magnitude (with peak ground acceleration between 2.4 m/s² and 2.6 m/s²) and sampled at 100 Hz. Still, their frequency, strong motion duration, and number of aftershocks differed.

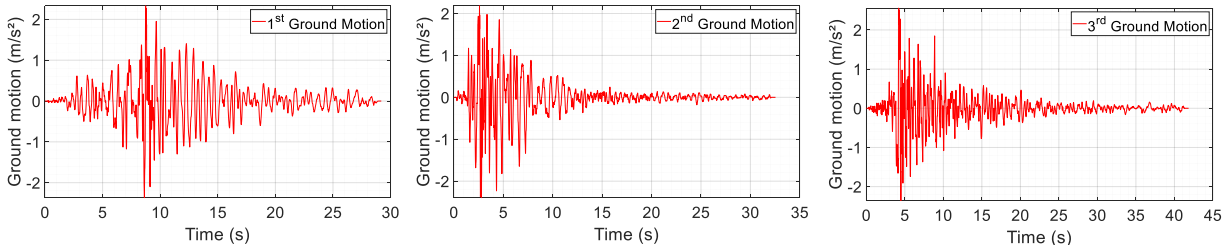


(a) (b) (c)

Figure 4: Ground motions used to compute snapshots (a) & (b), and ground motion used to approximate the response of the building using HROMS (c).

The displacement component $u_x$ of the northwest corner (see yellow star in Figure 3 (a)) is plotted in Figure 5 for each ground motion. All calculations were carried out on an Intel® Core™ i9-10900K CPU @ 3.70 GHz and 64 GB RAM personal computer using custom procedures implemented in MATLAB© software. The FEM analyses were performed using an implicit Newmark method ($\beta = 0.25$ and $\gamma = 0.50$) with a time step $\Delta t$ equal to 10 ms. A relative tolerance of $10^{-6}$ controlled the convergence of the Newton-Raphson algorithm. Results show that both responses were highly affected in amplitude and frequency by the material nonlinearities.

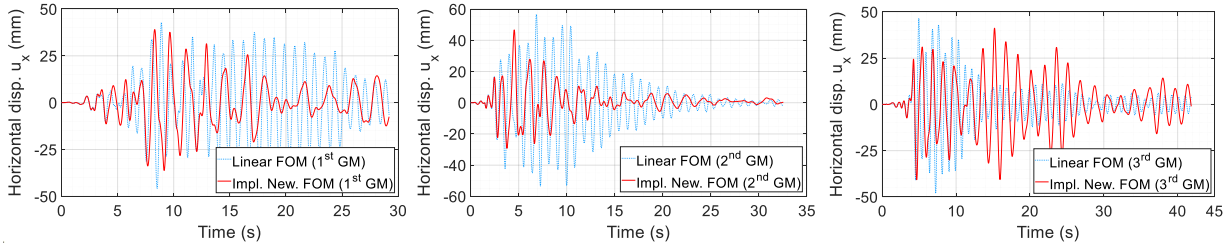


(a) (b) (c)

Figure 5: Displacement component $u_x$ of the northwest corner related to the 1st (a), 2nd (b), and 3rd (c) ground motions.

The snapshots used to build the HROMs were selected every two-time steps (i.e., every 20 ms) to avoid redundancy of the input data. As a result, 1460 snapshots were related to the first ground motion, and 1628 to the second.

A SVD was performed on the displacement snapshots to build the modal basis $\boldsymbol{\Phi}$. A number $n$ of 35 POD modes fulfilled the criterion (1) considering a tolerance $\varepsilon$ equal to $10^{-2}$ [15] (see Figure 6 (a)). The three main POD modes drawn in Figure 6 (b), (c), and (d) show that bending and torsion mainly affect the nonlinear response of the L-shaped three-story building. The first POD mode ($R_1$ = 1.15 Hz) is close to the first eigenmodes of bending along the $\boldsymbol{x}$ and $\boldsymbol{y}$-axes ($f_1$ = 1.10 Hz and $f_2$ = 1.11 Hz). The second ($R_2$ = 3.31 Hz) refers to the second eigenmodes of

bending along the ***x*** and ***y***-axes ($f_4$ = 3.15 Hz and $f_5$ = 3.18 Hz). The third ($R_3$ = 2.08 Hz) models torsional effects about the ***z***-axis and could be compared to the third eigenmode ($f_3$ = 1.38 Hz).

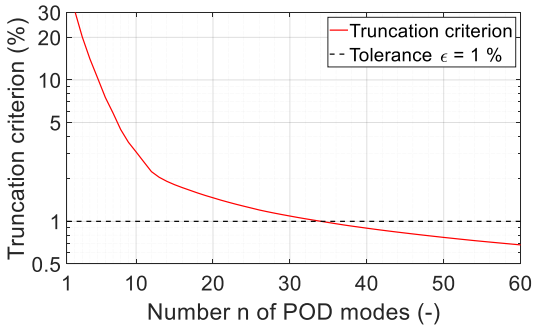


(a)

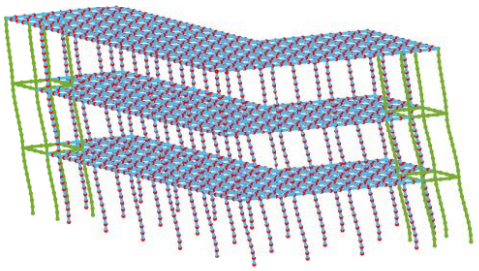

$R_1$ = 1.15 Hz

(b)

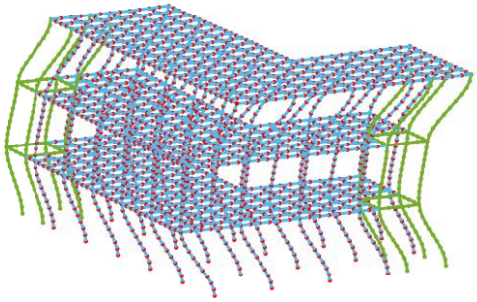

$R_2$ = 3.31 Hz

(c)

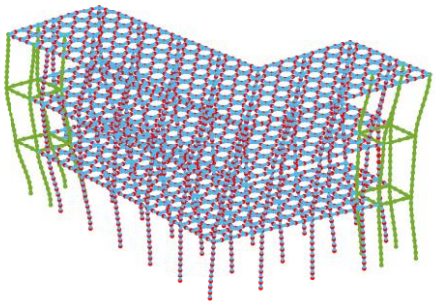

$R_3$ = 2.08 Hz

(d)

Figure 6: Criterion used to truncate the POD modal basis (a), and shapes and Rayleigh quotients of the first (b), second (c), and third (d) POD modes.

Knowing that the efficiency of UDEIM and ECSW hyper-reduction procedures highly depends on the snapshots, the nonlinear material laws, and the number $m$ of element in the RID, a sensitivity analysis compares the accuracy of both methods with a value of $m$ between 50 and 1000. The online and offline CPU times, the error, and the number of iterations in Figure 7 quantify the reliability of the HROMs to compute the nonlinear response related to the third ground motion. The solutions $(\boldsymbol{u}, \boldsymbol{r})$ are compared to the FOM $(\boldsymbol{u}^{\mathrm{FOM}}, \boldsymbol{r}^{\mathrm{FOM}})$ using the strain energy error $\varepsilon_{\mathrm{Ed}}$ defined in (14):

$$\varepsilon_{\mathrm{E_d}} = \frac{\|\Delta E_{\mathrm{d}}\|}{\left\|E_{\mathrm{d}}^{\mathrm{FOM}}\right\|} 100\ \% \quad \text{with} \quad \|\Delta E_{\mathrm{d}}\| = \frac{1}{2N_t \Delta t} \int_0^{N_t \cdot \Delta t} \left|\boldsymbol{\Delta u}^{\mathrm{T}}(t) \cdot \boldsymbol{\Delta r}(t)\right| dt \tag{14}$$

where $E_{\mathrm{d}}^{\mathrm{FOM}}$ is the strain energy of the implicit Newmark FOM, $\Delta E_{\mathrm{d}}$ is the difference in strain energy, $N_t$ is the number of time intervals, $\Delta t$ is the time step, $\boldsymbol{\Delta u} = \boldsymbol{u} - \boldsymbol{u}^{\mathrm{FOM}}$ is the difference in displacements, and $\boldsymbol{\Delta r} = \boldsymbol{r} - \boldsymbol{r}^{\mathrm{FOM}}$ is the difference in restoring forces.

Errors in Figure 7 (a) show that the POD-UDEIM is more accurate than the POD-ECSW when the RID is less than 250 elements since only the nonlinear part of the restoring forces are approximated. This is clearly visible in Figure 8 (a) where only 100 elements are required to ensure that the displacement component $u_x$ of the northwest corner agrees well in frequency with the FOM, while at least 200 are necessary with the POD-ECSW (see Figure 8 (b)). However, the later becomes more efficient when new elements are added to the RID, leading to a residual error approximately equal to 0.15 % when $m$ is higher than 350. This value is twice as

high with the POD-UDEIM as it stabilizes at 0.32 %. Knowing that the error is equal to 0.12 % with the POD reduced order model, the POD-ECSW is almost as accurate in the present case study.

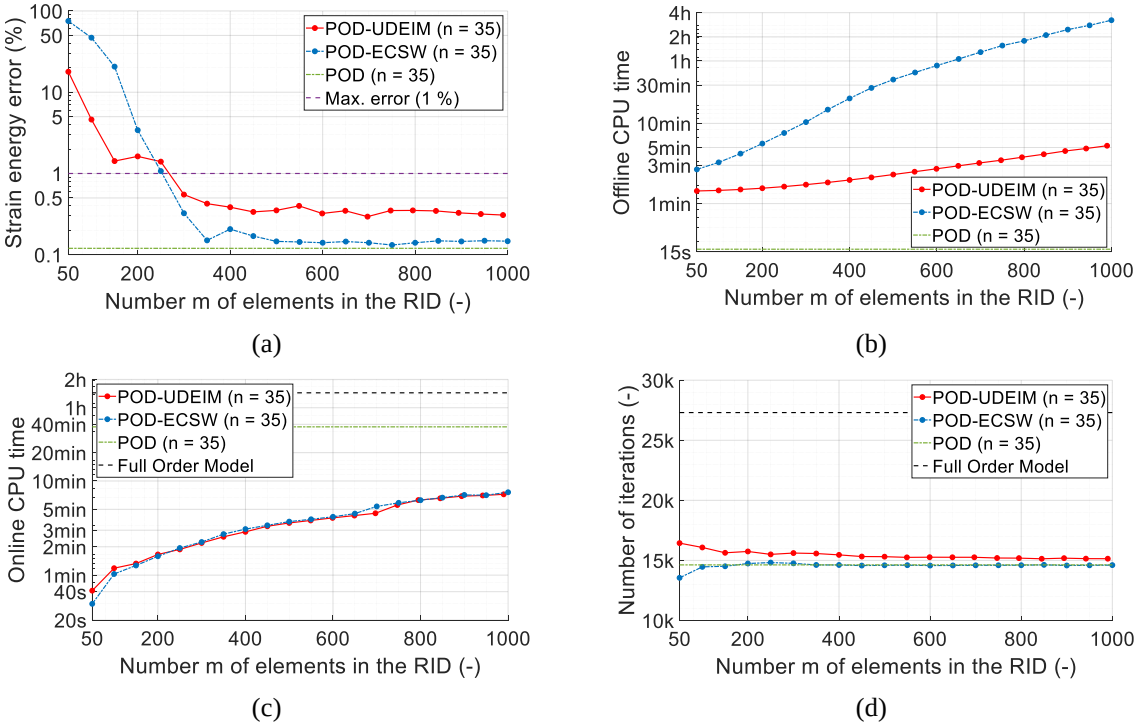


Figure 7: Strain energy error (a), offline CPU time (b), online CPU time (c), and number of iterations (d) with respect to the number of elements in the RID (comparison using the third ground motion with 35 POD modes).

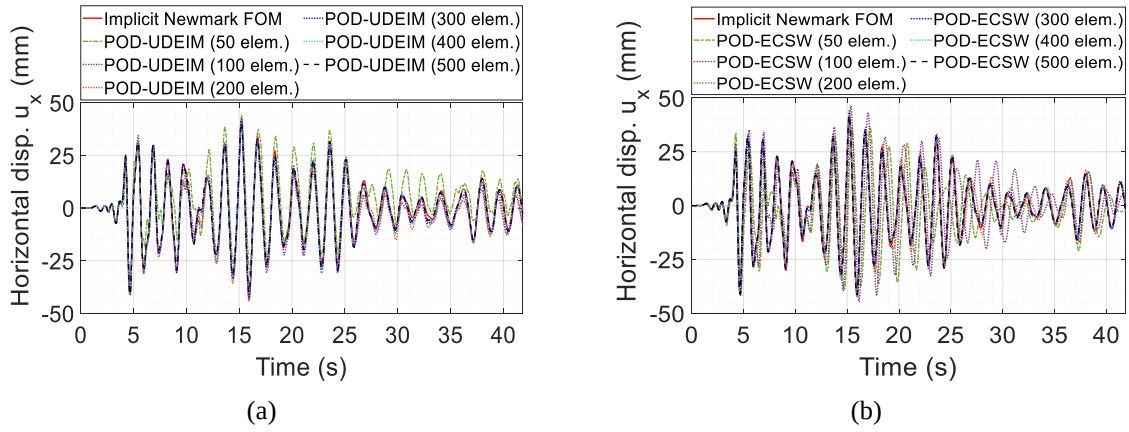


Figure 8: Displacement component $u_x$ of the northwest corner computed with the third ground motion using POD-UDEIM (a) and POD-ECSW (b) HROMs (with 35 POD modes).

Unfortunately, Figure 7 (b) shows that the ECSW is limited since the computational cost of the SNNLS solver ensuring the positivity of the weighting factors (see Algorithm 2) increases drastically with respect to the number $m$ of elements. In comparison, the DEIM algorithm (see Algorithm 1) runs faster considering that it involves only one iterative loop, and that unused components can be added *a posteriori* (as explained in Section 2). As a result, the time necessary to build a RID including 350 elements (i.e., when the residual error is reached) is 8 times

higher with the ECSW (lasting 16 min) than with the UDEIM (lasting 2 min). The POD-ECSW is thus more efficient than the POD-UDEIM provided that the HROM accelerates a large number of FEM analyses (i.e., online phases).

The online CPU times in Figure 7 (c) show that the speed-up factor is approximately the same with both methods, as well as the number of iterations required to solve the problem (see Figure 7 (d)). Using HROMs with a RID including 350 elements allows computing accurately the response of the building in 2 min 45 s, which is 13.8 and 31.6 times faster compared to the POD (~ 38 min) and to the FOM (~ 1 h 27 min), respectively. In addition, less iterations are required when using reduced or hyper-reduced order models since the nonlinearities are directly taken into account in the shape of the POD modes, which further decreases the CPU time. Knowing that it is necessary to iterate 27 k times to solve the equation of motion using the FOM, the number of iterations is approximately 1.7 times lower using the ROMs, with a value that does not exceed 16 k (see Figure 7 (c)). The number of iterations is the same with the POD and the POD-ECSW (~ 14.6 k) but its value slightly increases with the POD-UDEIM (~ 15.2 k) since the approximated tangent stiffness matrix is not fully symmetric, as explained in Section 1.

RIDs including 350 elements built using the UDEIM and the ECSW hyper-reduction methods are drawn in Figure 9 (b) & (c), respectively. Both are compared to the maximal damage index distribution related to the third earthquake (see Figure 9 (a)).

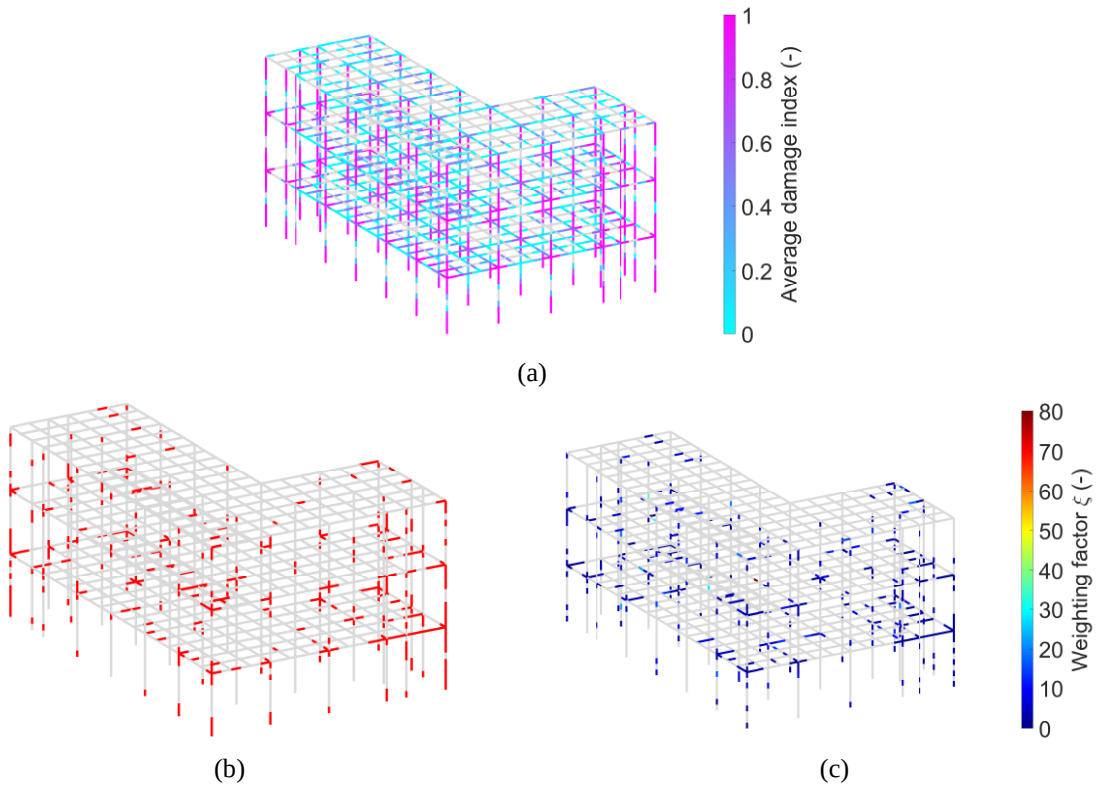


Figure 9: Damage index distribution on the FOM with the third earthquake (1845 damaged beam elements) (a), and RIDs with 35 POD modes and 350 elements: UDEIM (b) and ECSW with weighting factors (c).

In the present case study, 19 % of the 1845 elements where damage appears (i.e., 69 % of the whole structure) are required to correctly approximate the restoring force vector during the online phase. Many of them are located close to the stairwells, where the stiffness increases locally (see the colored elements in Figure 9 (b) and Figure 9 (c)). This shows that both hyper-

reduction methods can approximate strong nonlinearities (e.g., damage) distributed on a large number of elements, as it is commonly the case in the earthquake engineering framework.

### 4.4 Vulnerability analysis about the material properties

In Section 4.3, the POD-UDEIM and the POD-ECSW hyper-reduction methods proved their efficiency in accelerating vulnerability analyses involving several ground motions. Both methods were next applied to a parametric analysis about the concrete properties under earthquake conditions. The dynamic response related to the ground motion in Figure 10 (a) was computed considering that three different concretes can be used to model the L-shaped three-story building (see Figure 10 (b) & (c)). Table 2 gives the elastic modulus $E$, the tensile strength $f_t$, and the compressive strength $f_c$ of each one of them.

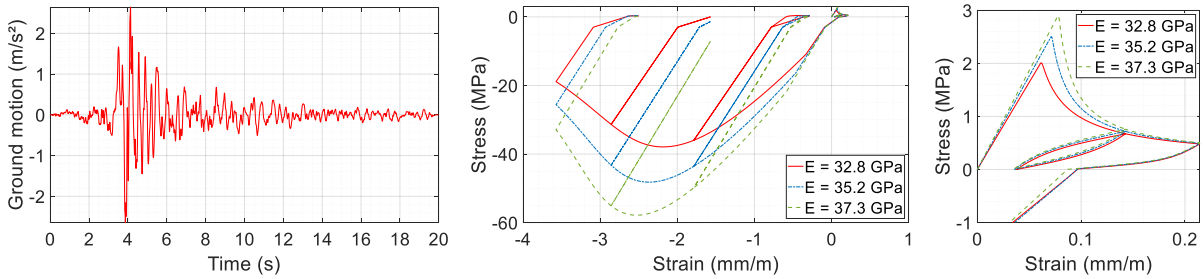


Figure 10: Ground motion used for the parametric analysis (a), uniaxial damage laws for each concrete with opening/closing of cracks (b), and frictional sliding (c).

| Concrete # (-) | $E$ (GPa) | $f_t$ (MPa) | $f_c$ (MPa) |
|---|---|---|---|
| 1 | 32.8 | 2.0 | 38.0 |
| 2 | 35.2 | 2.5 | 48.0 |
| 3 | 37.3 | 2.9 | 58.0 |

Table 2: Properties of the concretes used in the parametric analysis.

A set of 3000 snapshots was built using the first and third concretes responses, defined by elastic modules of 32.8 GPa and 37.3 GPa, respectively. The response of the second, defined by an elastic modulus of 35.2 GPa, was then approximated using HROMs. The displacement component $u_x$ plotted in Figure 11 (a) shows that the higher the tensile strength, the higher the energy dissipated by frictional sliding. As a result, differences in amplitude and frequency appear as damage increases.

The snapshots were selected every two-time steps (i.e., every 20 ms) from the results of dynamic analyses related to the ground motion in Figure 10 (a). A set of 1000 snapshots also came from the results of static analyses to be sure that the reduced order model was able to apply the dead and the live loads before entering the time step loop regardless of the concrete properties. According to Figure 11 (b), a basis $\boldsymbol{\Phi}$ of 20 POD modes fulfills the criterion (1) when a tolerance of 1 % is used.

The error and the online CPU times in Figure 12 (a) & (c) quantify the efficiency of the POD-UDEIM and the POD-ECSW to approximate the nonlinear response of the L-shaped three-story building in the case the second concrete is used. Each online phase includes a static analysis that apply the dead and the live loads using a POD ROM, and a dynamic analysis that

models the effects of the earthquake using HROMs. As in Section 4.3, both methods are compared with respect to the number $m$ of elements in the RID. Results shows that the POD-ECSW is very accurate since only 175 elements are required to reach an error close to 0.30 %. The response of the building (see Figure 12 (d)) can thus be accurately computed in 2 min 15 s, which is 8.4 and 24.0 times faster compared to the POD reduced order model (~ 19 min) and to the FOM (~ 55 min), respectively.

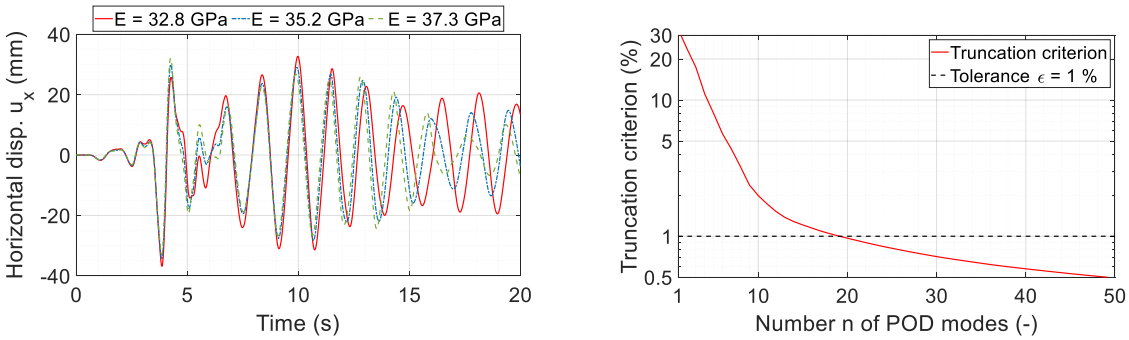


(a) (b)

Figure 11: Displacement component $u_x$ of the northwest corner computed using the FOMs (a), and criterion used to truncate the POD modal basis used to perform the parametric analysis (b).

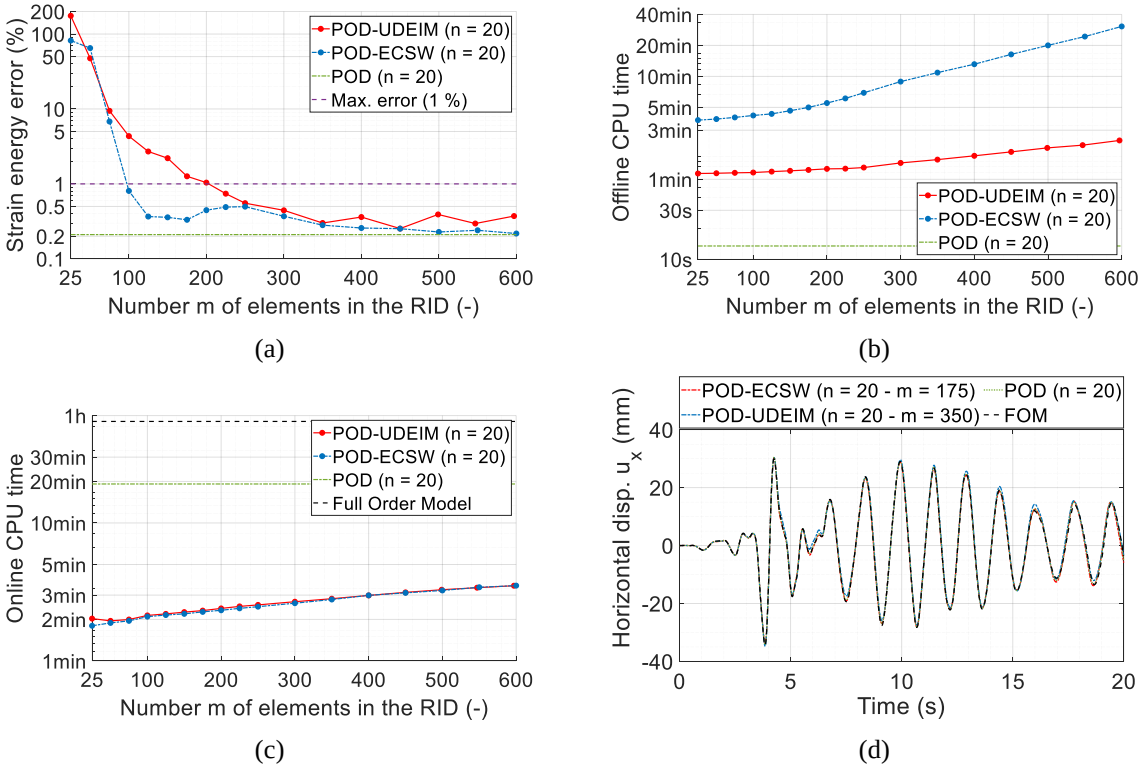


(a) (b)

(c) (d)

Figure 12: Strain energy error (a), offline CPU time (b), online CPU time (c), and displacement $u_x$ of the northwest corner when the residual error is reached (d) (comparison using the second concrete with 20 POD modes).

The POD-UDEIM is less efficient since 350 elements are necessary to guarantee the same residual error, leading to an online CPU time of 2 min 47 s. As a result, the online speed-up factors are lower, with values equal to 6.9 (POD) and 20.2 (FOM). The error stabilizes well with both methods even if slight variations may appear since time-dependent internal variables

are involved. Note that the offline CPU time of the POD-ECSW ($m$ = 175) is 3.2 times higher compared to the POD-UDEIM ($m$ = 350) in the present case study (see Figure 12 (b)). Still, the hyper-reduction method needs to be chosen wisely according to the number of online phases required to complete the parametric analysis, as suggested in Section 4.3.

The damage index distribution in Figure 13 (a) shows that nonlinearities appear in 1673 beam elements (i.e., 58 % of the whole structure) according to the FOM response. The RID achieving the residual error is thus 4.8 and 9.6 times smaller using the UDEIM and the ECSW, respectively (see Figure 13 (b) & (c)). As in Section 4.3, both methods are thus able to approximate solutions in the case damage appears on a large number of elements, making them suitable for analyses using the concrete properties as parameters.

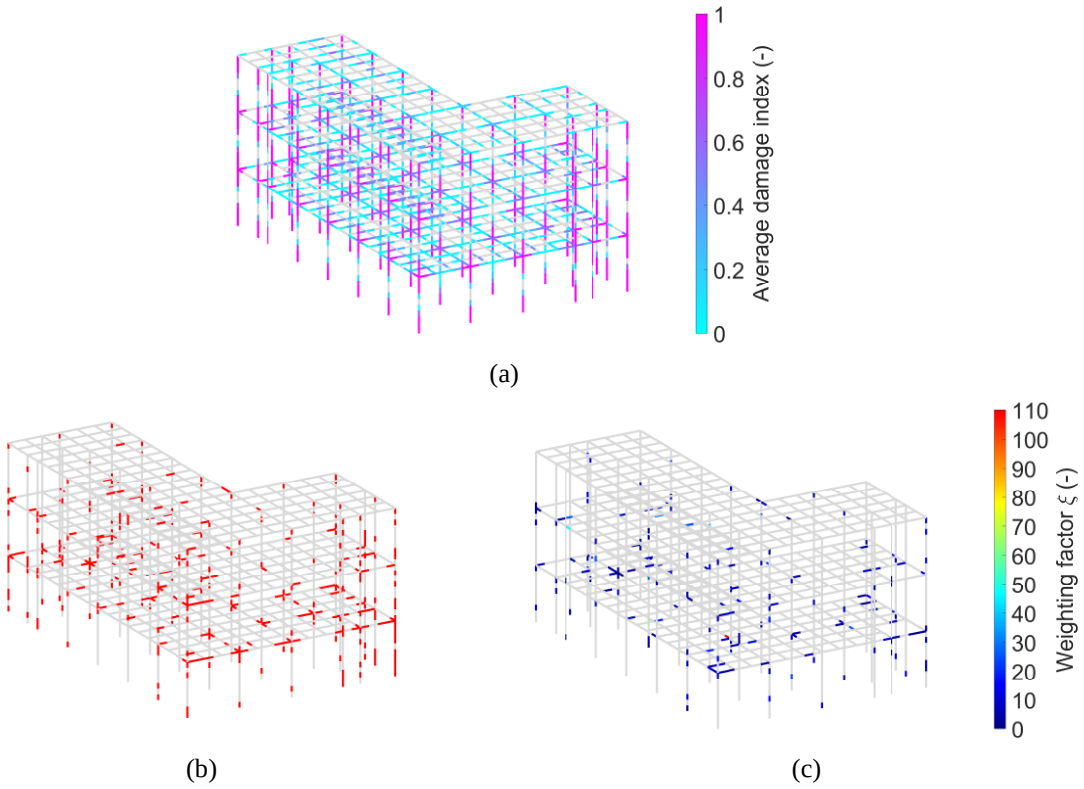


Figure 13: Damage index distribution of the FOM using the second concrete (1673 damaged beam elements) (a), and RIDs with 20 POD modes: UDEIM with 350 elements (b) and ECSW with 175 elements (c).

## 5 CONCLUSIONS

This paper compared the efficiency of two data-driven hyper-reduced order modeling methods, the POD-UDEIM and the POD-ECSW, to accelerate vulnerability analyses on reinforced concrete structures subjected to earthquakes. Both methods were applied to parametric analyses about the ground motions and the concrete properties. Applications on a L-shaped three-story building made of multi-fiber beam elements showed that both methods can successfully approximate solutions in the case damage appears on a large number of elements. Using HROMs made it possible to perform online FEM analyses from 20 and 32 times faster with errors lower than 0.5 %. The POD-ECSW revealed to be more efficient than the POD-UDEIM during the online phases, allowing for smaller errors, online CPU times, and reduced integration domains. However, the computational cost of the SNNLs solver used during the offline phase remains significantly higher than the DEIM algorithm, especially with high dimensional systems. As a

result, the POD-ECSW saves more CPU time only if the number of online FEM analyses is high enough.

Despite RIDs 5 to 10 times smaller than the high dimensional systems, both methods proved accurate enough to correctly model strong distributed nonlinearities (e.g., damage) involving time-dependent internal variables. Their reliability when applied to vulnerability analyses (e.g., fragility curves) involving earthquakes of differing orders of magnitude (e.g., with peak ground acceleration ranging from 0.5 m/s² to 7 m/s²) is still an open question. Additionally, extending the method to structures modeled by multilayer shells is relevant since these elements are commonly used to model slabs and walls in the earthquake engineering framework. Sensitivity or stochastic analyses about the dimensions (e.g., area of the sections) could also be achieved using HROMs.

## REFERENCES

[1] Saidi M., Sozen M. A. Simple nonlinear seismic analysis of R/C structures. *J. Struct. Div., ASCE, 107(5),* 937-52, 1981.

[2] Kilar V., Fazfar P. Simple push-over analysis for asymmetric buildings. *Earthquake Engng. Struct. Dyn., 26,* 233-49, 1997.

[3] Nakashima M., Kato H., Takaoka E. Development of real-time pseudo dynamic testing. *Earthquake Engineering and Structural Dynamics 21(1),* 79-92, 1992.

[4] Moutoussamy L. (2013). Essais hybrides en temps réel sur structures de Génie Civil. *ENS Cachan Phd-thesis,* 2013.

[5] Kosambi D. D. Statistics in function space. *Journal of Indian Mathematical Society 7,* 76-88, 1943.

[6] Karhunen K. Über lineare Methoden in der Wahrscheinlichkeitsrechnung. *Annals of Academic Science Fennicae, Series A1 Mathematics and Physics 37,* 3-79, 1946.

[7] Loève M. Fonctions aléatoires du second ordre. Processus Stochastiques et Mouvement Brownien, 1948.

[8] Sirovich L. Turbulence and the dynamics of coherent structures. I. Coherent structures. *Quarterly of applied mathematics 45.3,* 561-571, 1987.

[9] Hall K. C., Thomas J. P., Dowell E. H. Proper orthogonal decomposition technique for transonic unsteady aerodynamic flows. *AIAA Journal 38.10,* 1853-1862, 2000.

[10] Epureanu B. A parametric analysis of reduced order models of viscous flows in turbomachinery. *Journal of fluids and structures 17.7,* 971-982, 2003.

[11] Ravindran S. S. A reduced-order approach for optimal control of fluids using proper orthogonal decomposition. *International journal for numerical methods in fluids 34.5,* 425-448, 2000.

[12] De Boe P., Golinval J.-C. Principal component analysis of a piezosensor array for damage localization. *Structural health monitoring 2.2,* 137-144, 2003.

[13] Hemez F. M., Doebling S. W. Review and assessment of model updating for non-linear, transient dynamics. *Mechanical Systems and Signal Processing 15.1,* 45-74, 2001.

[14] Azeez M. F. A., Vakakis A. F. Numerical and experimental analysis of a continuous overhung rotor undergoing vibro-impacts. *International journal of non-linear mechanics 34.3*, 415-435, 1999.

[15] Ayoub N., Deü J.-F., Larbi W., Pais J., Rouleau L. Application of the POD method to nonlinear dynamic analysis of reinforced concrete frame structures subjected to earthquakes, *Engineering Structures, 270*, 114854 (9 pages), 2022.

[16] Chaturantabut S., Sorensen D.C. Nonlinear model reduction via discrete empirical interpolation. *SIAM J. Sci. Comput. 32 (5)*, 2737-2764, 2010.

[17] Everson R., Sirovich L. Karhunen-Loève procedure for gappy data. *Journal of the Optical Society of America A 12.8*, 1657-1664, 1995.

[18] Bui-Thanh T., Damodaran M., Willcox K. Proper orthogonal decomposition extensions for parametric applications in compressible aerodynamics. *AIAA paper 4213*, 2003.

[19] Willcox K. Unsteady flow sensing and estimation via the gappy proper orthogonal decomposition. *Computers & fluids 35.2*, 208-226, 2006.

[20] Astrid P. Reduction of process simulation models: a proper orthogonal decomposition approach. *Technische Universiteit Eindhoven PhD-thesis*, 2004.

[21] Rutzmoser J. B. Model order reduction for nonlinear structural dynamics: simulation-free approaches. *Technischen Universität München PhD-thesis*, 2017.

[22] Tiso P., Rixen D. J. Discrete empirical interpolation method for finite element structural dynamics. *Nonlinear Modelling and Applications, Volume 2. Springer*, 53-65, 2013.

[23] Peherstorfer B., Butnaru D., Willcox K., Bungartz H.-J. Localized discrete empirical interpolation method. *SIAM Journal on Scientific Computing 36.1, A168-A192*, 2014.

[24] Ghavamian F., Tiso P., Simone A. POD-DEIM model order reduction for strain-softening viscoplasticity. *Comput. Methods Appl. Mech. Engrg. 317*, 458-479, 2017.

[25] Antil H., Heinkenschloss M., Sorensen D. C. Application of the discrete empirical interpolation method to reduced order modeling of nonlinear and parametric systems. *Reduced order methods for modeling and computational reduction. Springer*, 101-136, 2014.

[26] Benner P., Gugercin S., Willcox K. A Survey of Projection-based Model Reduction Methods for Parametric Dynamical Systems. *SIAM Review 57.4*, 483-531, 2015.

[27] Drmac Z., Gugercin S. A new selection operator for the discrete empirical interpolation method - Improved a priori error bound and extensions. *SIAM Journal on Scientific Computing 38.2*, A631-A634, 2016.

[28] Radermacher A., Reese S. POD-based model reduction with empirical interpolation applied to nonlinear elasticity. *International Journal for Numerical Methods in Engineering 107.6*, 425-448, 2016.

[29] An S. S., Kim T., James D. L. Optimizing cubature for efficient integration of subspace deformations. *ACM Transactions on Graphics (TOG) 27.5*, No. 165, 2008.

[30] Farhat C., Avery P., Chapman T., Cortial J. Dimensional reduction of nonlinear finite element dynamic models with finite rotations and energy-based mesh sampling and weighting for computational efficiency. *International Journal for Numerical Methods in Engineering 98*, 625-662, 2014.

[31] Farhat C., Chapman T., Avery P. Structure-preserving, stability, and accuracy properties of the energy-conserving sampling and weighting method for the hyper reduction of nonlinear finite element dynamics models. *International Journal for Numerical Methods in Engineering 102.5*, 1077-1110, 2015.

[32] Chapman T., Avery P., Collins P, Farhat C. Accelerated mesh sampling for the hyper reduction of nonlinear computational models. *International Journal for Numerical Methods in Engineering 109.12*, 1623-1654, 2017.

[33] Hernandez J. A., Caicedo M. A., Ferrer A. Dimensional hyper-reduction of nonlinear finite element models via empirical cubature. *Computer Methods in Applied Mechanics and Engineering 313*, 687-722, 2017.

[34] Lawson C. L., Hanson R. J. Solving least square problems. Vol. 15. *SIAM*, 1995.

[35] Farhat C., Chapman T., Avery P. ECSW: An energy-based structure-preserving method for the hyper reduction of nonlinear finite element reduced-order models. *International Journal for Numerical Methods in Engineering 00*, 1-33, 2013.

[36] Davenne L., Ragueneau F., Mazars J., Ibrahimbegovic A. Efficient approaches to finite element analysis in earthquake engineering. *Computers and Structures 81*, 1223–1239, 2003.

[37] Richard B., Ragueneau F. Continuum damage mechanics based model for quasi brittle materials subjected to cyclic loadings: Formulations, numerical implementation and applications. Engineering Fracture Mechanics 98, 383-406, 2013.

[38] Chambreuil C. Modelling of damping in nonlinear dynamic analyses of reinforced concrete structures: constitutive formulations and experimental identification. ENS Paris-Saclay PhD-thesis, 2022.

[39] https://www.vs.ch/documents/315040/2787090/Karte_MSS_Visp.pdf/b52cae9a-a1bf-4b19-922c-1d0bfc080b1b

COMPDYN 2023
9th ECCOMAS Thematic Conference on
Computational Methods in Structural Dynamics and Earthquake Engineering
M. Papadrakakis, M. Fragiadakis (eds.)
Athens, Greece, 12-14 June 2023

# FINITE ELEMENT MODELING OF SUSPENDED CEILING SYSTEMS BASED ON EXTENSIVE COMPONENT TESTING AND MODEL EVALUATION VIA SHAKING TABLE TESTS: POP RIVET AND SEISMIC CLIP PERIMETER CONNECTIONS

**Shakhzod M. Takhirov**[1] **and Yelena Straight**[2]

[1] Dept. of Civil and Environmental Engineering, University of California, Berkeley,
337 Davis Hall, Berkeley, California, 94720, USA
e-mail: takhirov@berkeley.edu

[2] Building Codes and Standards Manager, USG Corporation
550 West Adams Street, Chicago, IL 60661, USA
e-mail: YStraight@usg.com

## Abstract

*This paper is focused on a finite element (FE) modeling of suspended ceiling systems. It is well-known that for installation in regions with high seismic activity, these non-structural systems need to pass seismic evaluation tests on a shaking table. Using a shaking table can be expensive, especially when developing new components and systems might require a few iterations. The goal of this modeling paper is to develop an approach that can be used as a cost-effective alternative for the development of new components and systems. A numerical model can predict the performance of the newly developed system, identify its weak links (if any), and help to develop solutions that address any shortcomings. This paper presents an approach based on developing a FE model, the performance of which closely correlates to that of the actual system. It is based on a series of component tests that are less expensive than shaking table testing. The results of the component testing are used in modeling components of the FE model. The evaluation of the model's performance at the system level is conducted by comparing its performance to that of the actual system in a seismic evaluation test via shaking table testing. The actual system was extensively instrumented for the shaking table tests. The instrumentation included position transducers, accelerometers, and strain gages. This paper discussed this approach in detail and summarized the results of the experimental and numerical studies.*

**Keywords:** Non-structural Components, Suspended Ceiling Systems, Component Testing, Shaking Table Testing, Finite Element Modeling, Seismic Evaluation.

# 1 INTRODUCTION

This paper is focused on suspended ceiling systems built with the USG's DX components. A pop riveted connection was selected for the fixed sides and a seismic clip was chosen for the perimeter connections of the floating sides. The extensive experimental program focused both on component testing of the system and on shaking table tests of the system constructed from these components. Based on the results of the component testing program, a finite element model was generated. The model's seismic performance was compared to the results of the shaking table tests.

# 2 COMPONENT TESTING

Failures of suspended ceiling systems usually occur at the connection points. This section of the paper is focused on component testing of the major connections of the suspended ceiling system. For the suspended ceiling studied in this paper, the following connections were studied in component testing. First, a main tee or a cross tee to the perimeter molding on the fixed sides was evaluated in quasi-static cyclic loading. Second, a cross tee to a cross tee connection was tested in quasi-static cyclic loading. Third, a main tee to a main tee connection was also evaluated during this experimental program. The latter two connection tests are referenced as joint tests in this paper.

## 2.1 Experimental Setups for Component Testing

The purpose of all component tests was to evaluate the overall performance of each connection along with its ultimate capacity. At least three tests per connection were conducted. The test samples were randomly selected. A list of tests is provided in Table 1. The conducted tests were part of a multiyear extensive program with the results summarized in the technical test reports [1-2].

| Connection | MT/CT name | Specimen name | Note | Reference |
|---|---|---|---|---|
| MT to M7 via PR | DX24 | USG2015-Sp01 | Perimeter at fixed side | [1] |
| CT to M7 via PR | DX424 | USG2015-Sp03 | Perimeter at fixed side | [1] |
| CT to M7 via PR | DX424 | USG2015-Sp04 | Perimeter at fixed side | [1] |
| CT to M7 via PR | DX424 | USG2015-Sp10 | Perimeter at fixed side | [1] |
| MT to MT joint | DX26 to DX26 | USG2021-Sp47 | Joint | [2] |
| CT to CT joint | DX424 to DX424 | USG2021-Sp44 | Joint | [2] |
| CT to CT joint | DX424 to DX424 | USG2021-Sp45 | Joint | [2] |
| CT to CT joint | DX424 to DX424 | USG2021-Sp48 | Joint | [2] |
| CT to CT joint | DX424 to DX216 | USG2021-Sp40 | Joint | [2] |
| CT to CT joint | DX424 to DX216 | USG2021-Sp41 | Joint | [2] |
| CT to CT joint | DX424 to DX216 | USG2021-Sp50 | Joint | [2] |
| CT to CT joint | DX216 to DX216 | USG2021-Sp35 | Joint | [2] |
| CT to CT joint | DX216 to DX216 | USG2021-Sp37 | Joint | [2] |
| CT to CT joint | DX216 to DX216 | USG2021-Sp38 | Joint | [2] |

Table 1: Summary of the component tests (all connections were tested in cyclic loading except USG2015-Sp01).

In Table 1 MT stands for a main tee, CT stands for a cross tee, and PR stands for a pop rivet. These abbreviations will be used herein. In addition, the following USG components are listed in Table 1: M7 is USG's wall molding, DX24 and DX26 are USG's main tees, DX424 and DX216 are USG's cross tees.

The connections were tested in two major configurations. The first configuration was developed for testing perimeter connections as presented in Figure 1. As shown in Figure 1a, the experimental setup consisted of an actuator applying the load to one side of the connection, with a reaction frame attached to the opposite side of the connection. In the case of the perimeter connection, the reaction frame was installed at 90 degrees to the axis of loading whereas for the joint connection, the loading and the reacting sides were in-line with the actuator. To ensure that the force is always applied along the same axis, the actuator was guided by a linear bearing system as presented in Figure 1b. The second configuration was developed for testing joints as presented in Figure 2.

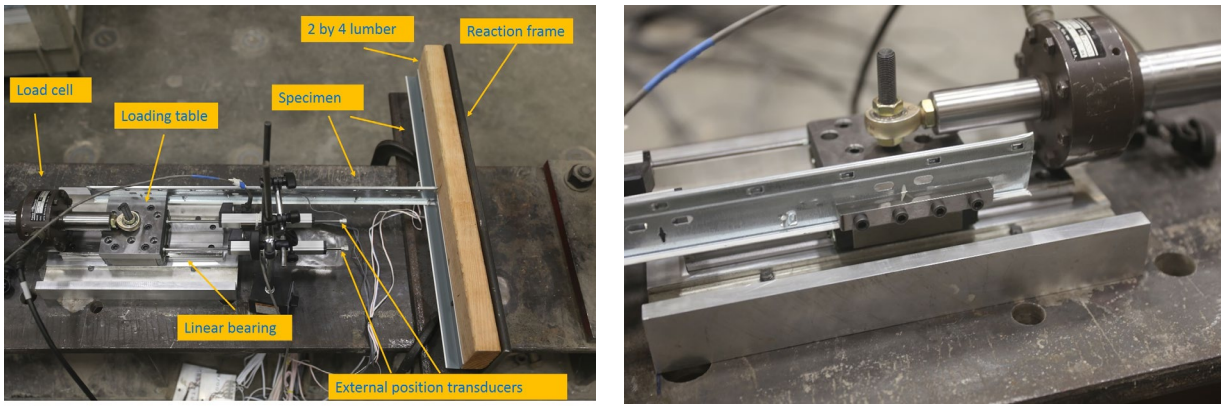


a) Major components b) Actuator guided by a linear bearing system

Figure 1: Experimental setup for component testing of perimeter connections.

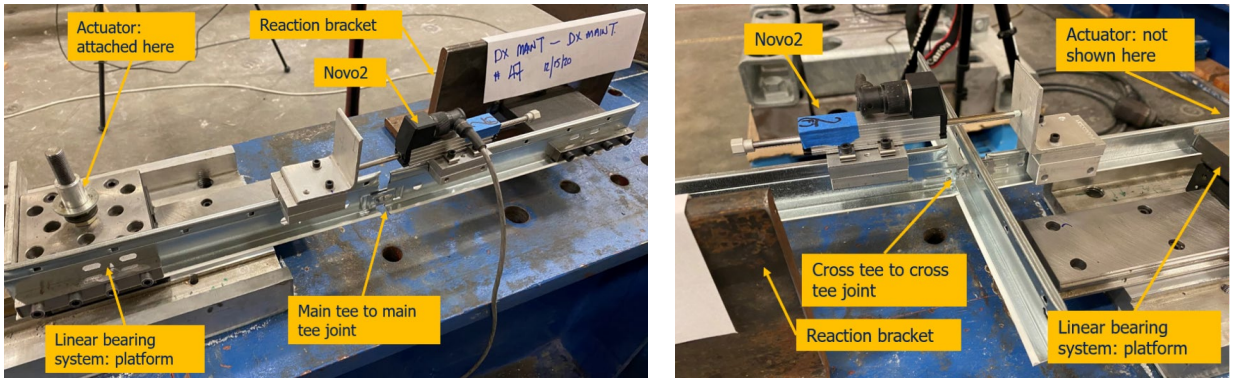


a) MT to MT b) CT to CT with MT at 90 degrees

Figure 2: Experimental setup for component testing of joints.

## 2.2 Tested Configurations and Test Results

Almost all component tests were conducted by imposing a cyclic loading as presented in Figure 3a. The test protocol consisted of groups of three cycles at the same amplitude, which were then incrementally increased. The response of the test specimens was monitored by a few position transducers as presented in Figure 1 and Figure 2. In addition, a tri-axial strain gage was installed at the wall molding, adjacent to the pop rivet, as presented in Figure 3b.

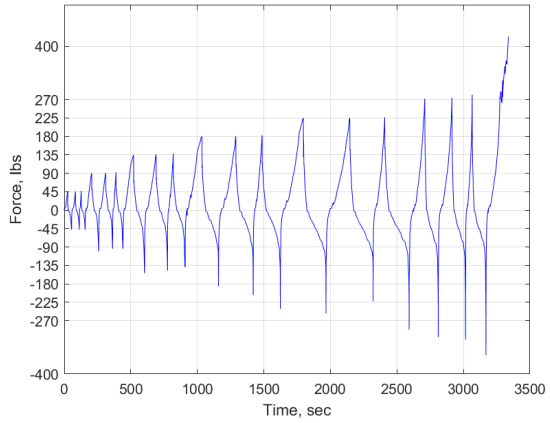


a) Typical loading protocol (1 lb = 4.4 N)

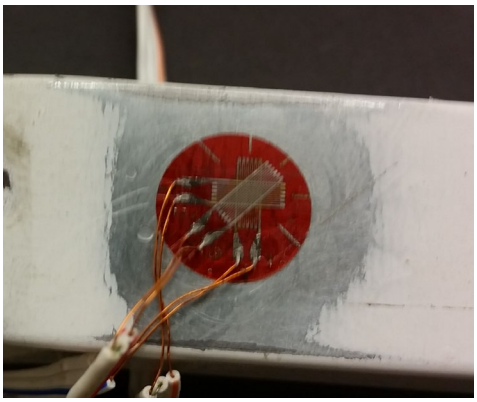

b) Tri-axial strain gage installed adjacent to the pop rivet location

Figure 3: Test protocol and additional instrumentation.

Typical test results are presented in Figure 4a. In this case a cyclic performance of USG2015-Sp10 (noted as Sp10 in the plot) is compared to a monotonic pull test conducted on USG2015-Sp01 (noted as Sp01 in the plot). The failure of the connection is related to the tear failure of the hole in the cross tee as shown in Figure 4b. As can be seen from Figure 4a a main tee in monotonic testing has a larger capacity than the cross tee in cyclic loading. This result can be explained by the fact that the flange of the main tee is thicker than that of the cross tee. In addition, it was evident that an ultra-low cycle loading fatigue affects the capacity of the cross tee in a significant way.

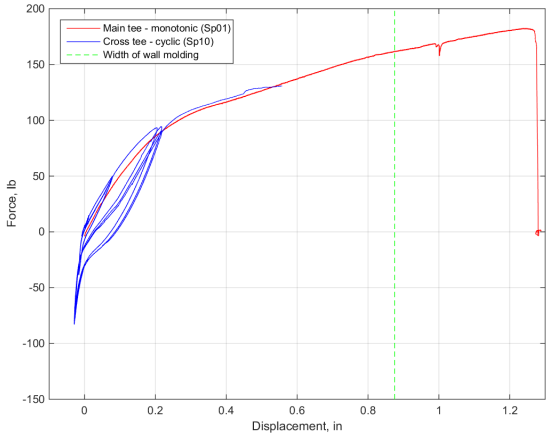


a) Typical test result (1 lb = 4.4 N; 1 in = 25.4 mm)

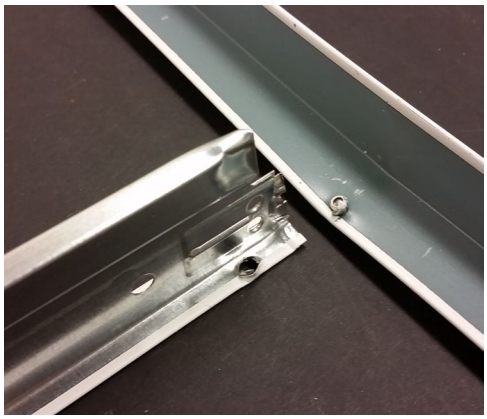

b) Typical failure mode (USG2015-Sp10 is shown)

Figure 4: Typical test result and failure mode.

## 3 SHAKING TABLE TESTING

A shaking table test was conducted in a 6.1 m by 6.1 m (20 ft by 20 ft) test frame specially designed and built at the University of California, Berkeley for testing suspended ceiling systems [3].

### 3.1 Test Frame and Test Time History

The test frame [3] enables the installation of suspended ceiling systems at an elevated position in order to be tested via shaking table tests. The shaking table was controlled by a test time history which was developed earlier [4] by following the requirements of ICC-ES AC156 [5]. This time history accounts for the amplification of the seismic demand over the elevation of buildings. To avoid any additional amplifications, the test frame is designed to be very stiff with frequencies greater than 20 Hz in all three principal axes. The frame is bolted to the top of the shaking table. Figure 5a shows the major components of the test frame. A typical view of the suspended ceiling installed into the frame is presented in Figure 5b.

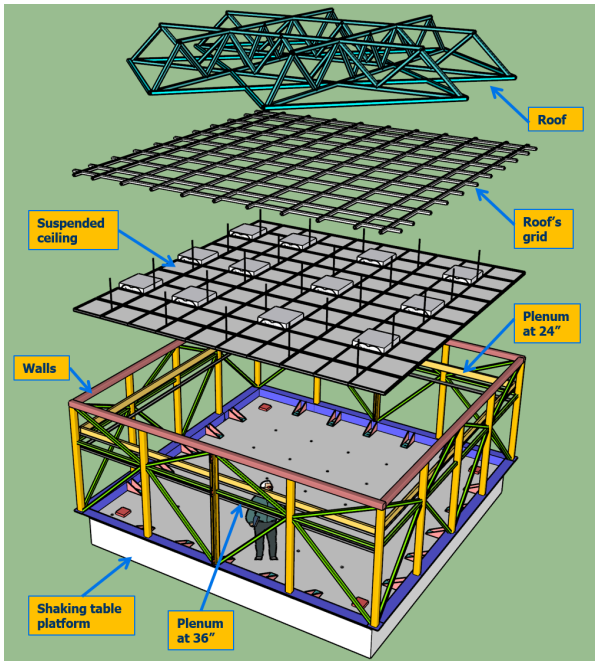


a) Major components

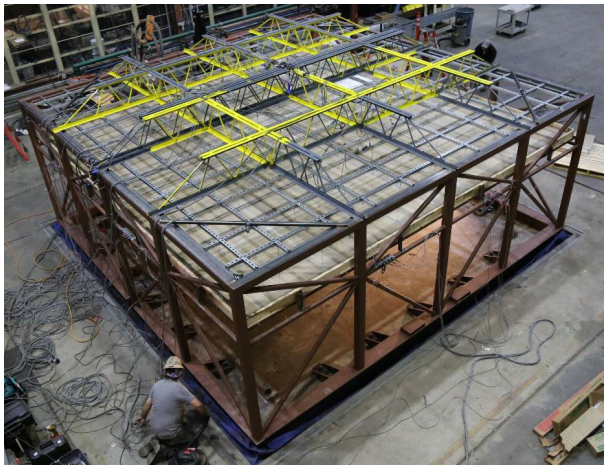

b) Typical view with ceiling installed

Figure 5: 6.1 m by 6.1 m test frame for testing suspended ceiling systems.

Prior to the time history testing a resonance search was conducted by imposing a white noise signal to the suspended ceiling system via the shaking table. The time history testing procedure was based on a value of spectral acceleration at short periods, $S_S$ [6], which controls the level of shaking [5]. The first time history test was conducted at $S_S = 2.0$ g, which was incrementally increased by 0.25g for the following tests up to $S_S = 2.75$ g.

### 3.2 Suspended Ceiling System Tested

The suspended ceiling tested via the shaking table tests is summarized in Table 2.

| Description | Characteristics or value |
|---|---|
| USG system identifier (duty rating) | USG DXT26 (heavy) |
| Main tee (USG ID) | DXT26 |
| Cross tee (USG ID) | DXT 424, DXT 222 |
| Wall molding (USG ID) | M7 |
| Panels (USG ID) | GLIP 3260 (two layers) |
| System weight (including grid weight), kg/m$^2$ (lb/ft$^2$) | 19.5 (4.0) |
| Perimeter wires | Yes (all 4 sides) |
| Stabilizer bars | None |
| 2 adjacent floating sides | ACM7 Clip |
| 2 adjacent fixed sides - tight no gap | Pop rivet |
| Floating wall clearance, mm (in) | 19.1 (3/4) |
| Compression post | At 1.83 m (6 ft) from floating sides |

Table 2: Suspended ceiling system tested via shaking table tests.

### 3.3 Instrumentation

The suspended ceiling, the test frame, and the shaking table were extensively instrumented. In addition to position transducers and accelerometers commonly used for testing suspended ceiling systems, a few strain gages were installed at critical locations. This extensive instrumentation was aimed at a detailed analysis of the performance of critical components. Figure 6a shows the schematic of the instrumentation. In this image "A" stands for accelerometer, "DA" stands for position transducers measuring displacement at the perimeter, "DR" stands for position transducers measuring displacement across the joints, "S" stands for uniaxial strain gages, and "R" stands for tri-axial strain gages. Typical instrumentation around the main tee's joint is presented in Figure 6b.

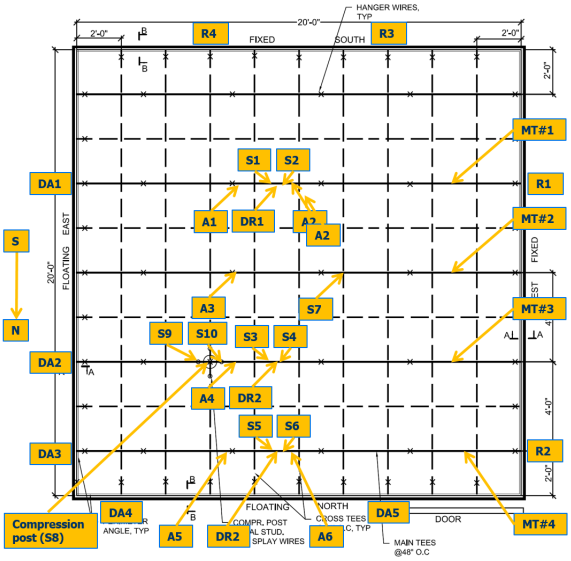


a) Schematic of instrumentation

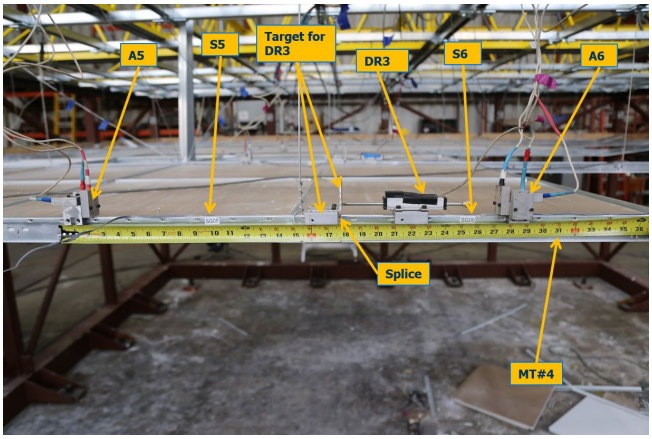


b) Example of main tee joint (splice) instrumented with position transducers, strain gages, and accelerometers

Figure 6: Instrumentation.

### 3.4 Shaking Test Results: Overall Performance

The spectral accelerations generated from the accelerations recorded on top of the shaking table enveloped the required response spectra specified by the AC156 document [5]. Typical

results are presented in Figure 7 for $S_S$ = 2.25 g. As presented in these images, the spectral plots enveloped the required response spectra shown by the red dashed line.

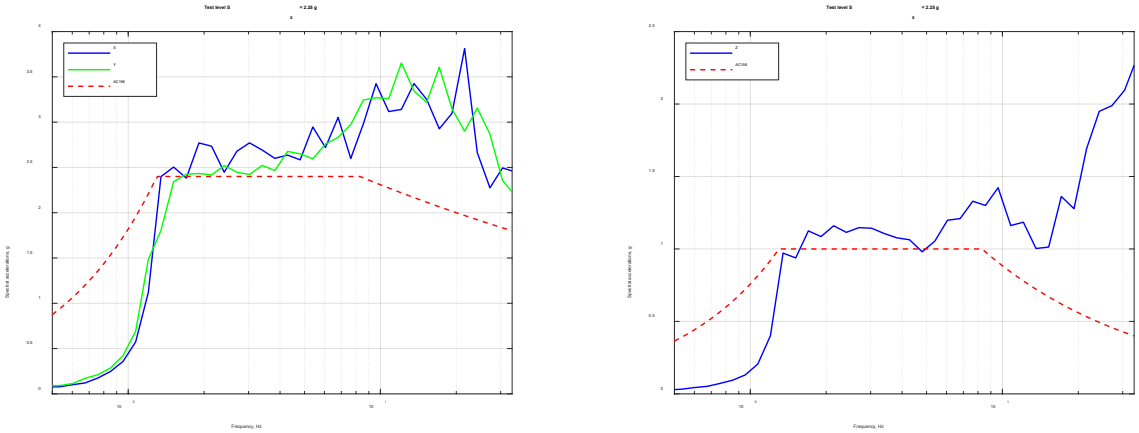

a) Spectral accelerations in X&Y axes b) Spectral accelerations in Z axis

Figure 7: Typical spectral plots ($S_S$ = 2.25 g is shown).

Overall performance of the system is summarized in Table 3.

| $S_S$, g | Description of anomaly or failure if any |
|---|---|
| 2.0 | No failure of the system was observed |
| 2.25 | No failure of the system was observed |
| 2.5 | Six 0.6 m x 0.6 m (2 ft x2 ft) panels dropped; integrity of the grid somewhat compromised |
| 2.75 | Cross tees disengaged from the wall angles with less than 50% of the tiles dropped |

Table 3: Overall performance of the system in the shaking table tests

## 4 NUMERICAL MODELING AND ANALYSIS

A suspended ceiling system is a complex structure consisting of many components and joints and it performs in a nonlinear manner. To make it realistic, a number of components must be modeled as nonlinear elements with some of the representative examples listed below. First, each panel is free to slide within the grid and when the gap between the grid and the panel is closed, the panels engage in a stiff planar system producing a diaphragm stiffness in the horizontal plane. As a result, the fully engaged grid-panel system prevents distortion of the grid. Second, all hanger wires can develop restraining forces only in tension and they have low stiffness in compression. Hence, the hanger wires need to be modeled as nonlinear tension-only members. Third, the components on both the floating and fixed sides perform in different ways depending on tension or compression. The connections on the fixed side have much larger stiffness in compression than that in tension. In addition, the connection on the fixed side can yield at high levels of seismic excitation. Fourth, the travel of the system on the floating side can exceed a gap (typically 19 mm or ¾ in) and as such, these elements have to be modeled as nonlinear gap elements.

It is always a challenge to incorporate all these nonlinearity effects into a finite element model. A few attempts at developing a finite element model of a suspended ceiling system were conducted earlier (see [7,8], as representative examples).

## 4.1 Grid modeling

The main tees, cross tees, and the compression post were modeled by elastic frames (in SAP2000 [9] terminology). The hanger and splay wires were modeled as nonlinear links that work in tension only. The stiffness of the wire was estimated based on its cross section and the material properties of mild steel. A view of the grid modeled in SAP2000 is presented in Figure 8. The main tees are presented in blue and the cross tees are shown in red. The system consists of five main tees and the rest of the system is assembled from cross tees. A model of the compression post with splay wires and cross-sections of the main grid components are presented in Figure 9.

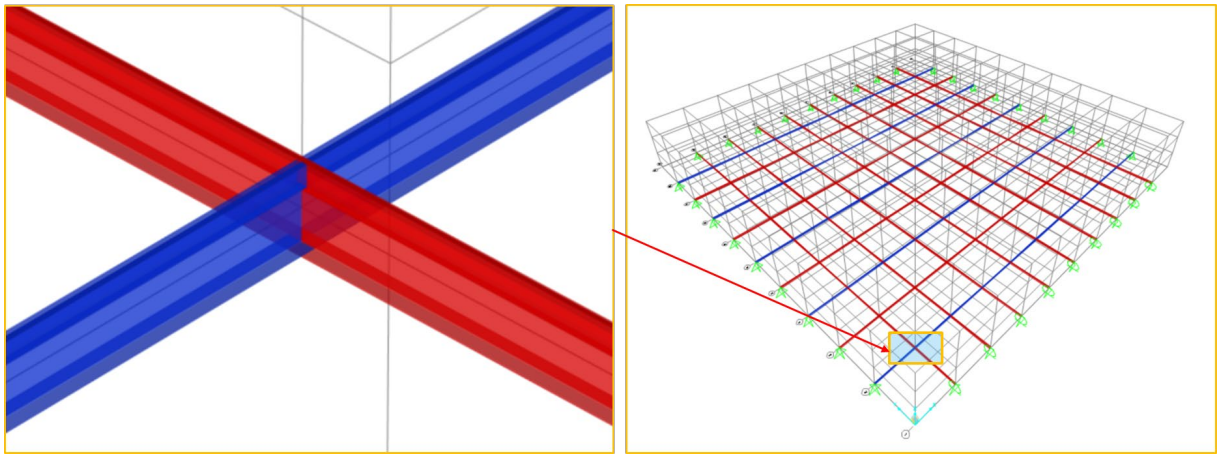

Figure 8: Grid model: overall view on the right and closeup view of MT to CT connection on the left.

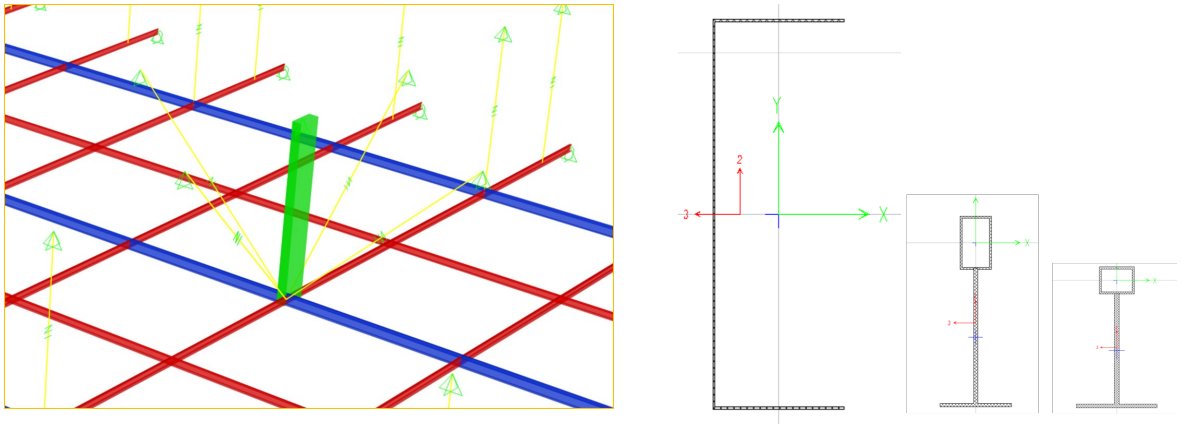

a) Compression post modeling b) Cross sections of post, MT, and CT

Figure 9: Details of grid model.

## 4.2 Modeling panels

The 0.6 m by 0.6 m (24 in by 24 in) panels were modeled as rigid elements with the weight of the panel lumped at its middle. Based on the tolerances of the grid and the panel, the clearance between the panel and the grid is 2.74 mm (0.108 in) on each side. To model this clearance, gap elements were introduced at each corner of the panel as presented in Figure 10. The accumulated weight of the panels and the grid is equal to 19.5 kg/m$^2$ (4 psf) distributed weight multiplied by the area of the system (37. 21 m$^2$ or 400 ft$^2$). The gaps in both horizontal directions are 2.74 mm (0.108 in), whereas the gap in the vertical direction is equal to zero.

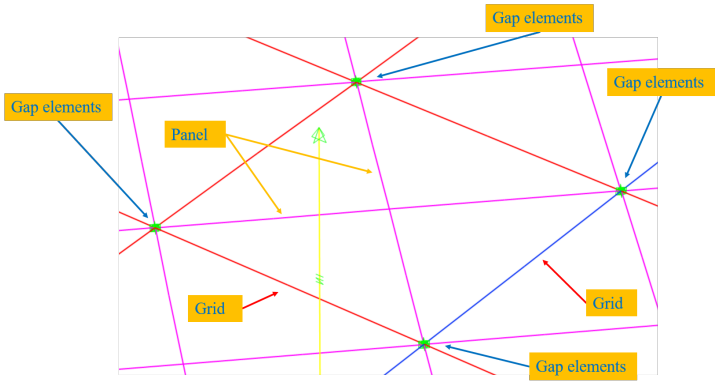


Figure 10: Details of panel modeling.

### 4.3 Modeling of perimeter connections

Figure 4a shows a typical performance of a perimeter connection that displays two major performance behaviors. First, the performance of the connection is direction dependent. The stiffness of the connection in the direction toward the wall (compression that corresponds to the negative force and displacement in the plot) is much higher than that in the opposite direction (tension). Second, the connection can undergo plastic deformation in tension.

This performance was modeled by combining two nonlinear links (SAP2000 terminology). The first link was a gap element and the second was a nonlinear link with the Wen plastic model as presented in Figure 11.

The floating side is modeled by friction elements in the papers reviewed earlier. This model does not reflect the actual performance of the system because the hanger wires work as a set of pendulum systems that result in lifting the grid on the floating side. Therefore, the effect of friction on the floating side is most likely negligible. Therefore, the floating side connections were modeled as frictionless sliders.

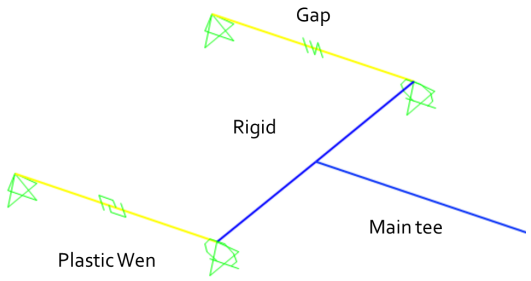


Figure 11: Details of perimeter connection modeling: fixed side.

### 4.4 Overall performance of the model

Based on the experimental data and observations during the shaking table tests, the failures usually occur at the cross tee connection when a tension force exceeding its capacity is applied. Although the tension capacity of the main tee is greater than that of the cross tee, it can also be a location for failure. Therefore, the main critical parameter to monitor during finite element analysis is the tension axial force in the tees. Typical results for one of the tees are presented in Figure 12.

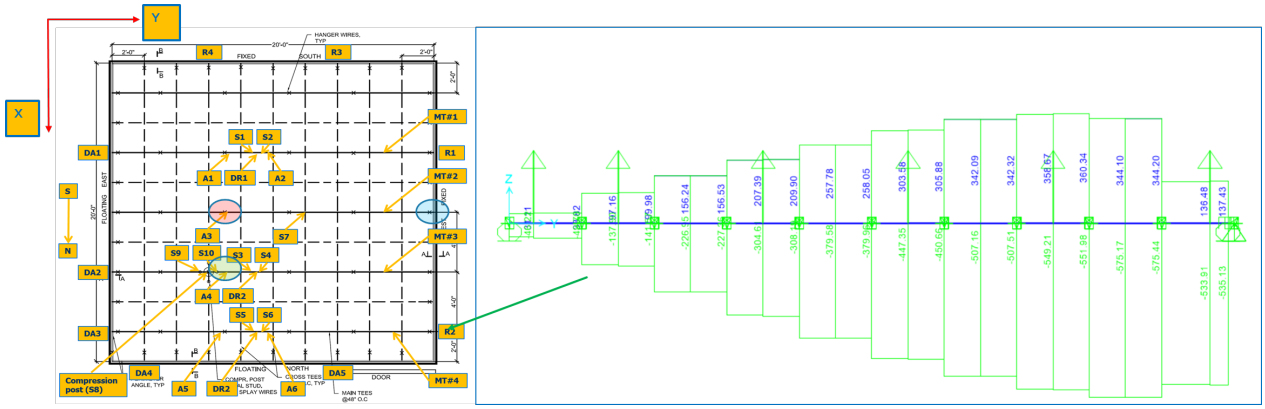


Figure 12: Results of FEA: tension forces in tees.

The same analysis can be done from tee to tee, but it can be less obvious where the tension forces are experiencing a maximum. To make the process of analyzing the numerical results more efficient, a special code was developed in the Matlab environment [10], that shows all tension forces in all cross tees. Figure 13 shows the result in 3D and Figure 14 shows the same result in the plane. In the latter plot, the color of the dot at the middle of each frame depends on the value of the tension force.

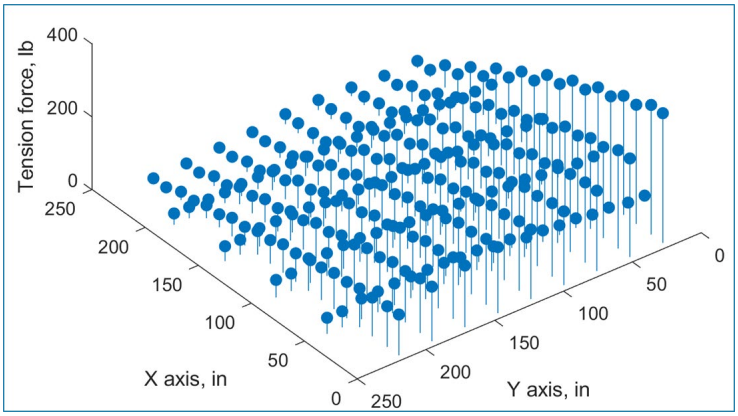


Figure 13: Maximum axial tension forces in cross tees (3D).

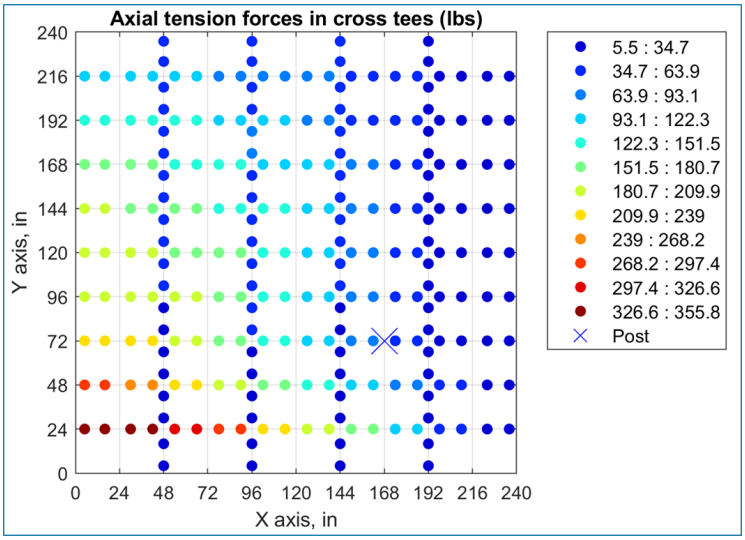


Figure 14: Maximum axial tension forces in cross tees.

## 5 CONCLUSIONS

Based on the extensive component test data a finite element model of the USG system was developed. The model closely replicate the system failures observed during the shaking table tests. The developed model will be used for the following optimization studies of the ceiling's performance: (1) the effect of the post's location or the removal of the post; (2) the effect of having an additional screw through the wall molding; (3) the optimization of light fixture locations; (4) the effect of a plenum depth; (5) the correlation seismic performances in 20'x20' test frame to that in large partitions; (6) the effect of seismic joints in large partitions and many others. The numerical modeling will help find solutions for future product development and performance simulations of suspended ceilings at larger scales.

## ACKNOWLEDGMENTS

Special thanks are due to the USG Corporation for funding the project. The authors would like to acknowledge Ms. Holly Halligan of UC Berkeley for editing the paper. A part of numerical modeling was conducted by Sensor Fusion and Monitoring Technologies, LLC.

## REFERENCES

[1] Shakhzod M. Takhirov. Evaluation of Wall Connections of USG Suspended Ceiling's Grid in Monotonic and Cyclic Testing. Report No. CEE-SL-STI/2015-01. Department of Civil and Environmental Engineering, University of California, Berkeley, July 2015.

[2] Shakhzod M. Takhirov and Amir Gilani. Component Tests of USG's Wall Perimeter Connections and Joints. Structures Laboratory Report 2021/02, Department of Civil and Environmental Engineering, University of California, Berkeley, April 2021.

[3] Shakhzod M. Takhirov and Amir Gilani. Development of 20' by 20' Test Frame for Experimental Seismic Evaluation of Large Suspended Ceiling Systems on Shaking Table: Design and Dynamic Analysis. Structures Laboratory Report 2018/01, Department of Civil and Environmental Engineering, University of California, Berkeley, January 2018.

[4] Amir Gilani and Shakhzod Takhirov. Current U.S. practice of seismic qualification of suspended ceilings by means of shake table tests, INGEGNERIA SISMICA journal, Italy: Vol. XXVIII, No. 1, pp. 26-42, 2011.

[5] International Code Council Evaluation Service Inc. (ICC-ES). Acceptance Criteria for Seismic Qualification by Shake-Table Testing of Nonstructural Components and Systems, AC156, ICC-ES, 2015.

[6] American Society of Civil Engineers, ASCE. Minimum Design Loads and Associated Criteria for Buildings and Other Structures (ASCE7-16). 800 pp. 2 volume set. 2017.

[7] Arash E. Zaghi, Siavash Soroushian, Alicia Echevarria Heiser, Manos Maragakis and Amvrossios Bagtzoglou (2016). Development and Validation of a Numerical Model for Suspended-Ceiling Systems with Acoustic Tiles, Journal of Architectural Engineering, 2016, Vol. 22, No3, pp. 04016008-04016008-13, DOI: 10.1061/(ASCE)AE.1943-5568.0000213.

[8] A. A. Echevarria, A. E. Zaghi, S. Soroushian and E. M. Maragakis (2012). Seismic Fragility of Suspended Ceiling Systems. Proceedings of 15th World Conference on Earthquake Engineering, September 24-28 2012, Lisbon, Portugal.

[9] SAP2000 (2011). Computers and Structures, Inc.

[10] MathWorks. Matlab Version R2020a. 2020.

COMPDYN 2023
9th ECCOMAS Thematic Conference on
Computational Methods in Structural Dynamics and Earthquake Engineering
M. Papadrakakis, M. Fragiadakis (eds.)
Athens, Greece, 12-14 June 2023

# PARAMETRIC ANALYSIS AND REDUCED ORDER MODEL OF RESULTING WIND LOADING ON STRUCTURAL COMPONENTS THROUGH CFD SIMULATIONS

**Sotiria Stefanidou**[1], **Olga Markogiannaki**[1], **and Elias Paraskevopoulos**[1]

[1] SURE Competence Center
Koila Kozanis, Greece
emails: sotiria.stefanidou@gmail.com, markogiannaki.olga@gmail.com, eapcivil@gmail.com

## Abstract

*Properly describing the interaction between a structure and an internal or surrounding fluid flow, known as Fluid-Structure Interaction (FSI), is of utmost importance for accurately predicting the resulting loading on the structure. This work provides a framework for accurately and computationally efficient describing the structure's wind-induced loading. More specifically, a parametric analysis for calculating the resulting forces at the interface through a series of three-dimensional (3D) CFD simulations is initially presented. In particular, two independent parameters are employed in this work, namely the dimensions of the structure and the wind velocity. Furthermore, the methodology for building reduced order models and, thus, more computationally efficient models of the resulting wind loading on the structure is introduced. Finally, these methods are applied in a real-life case study application in Greece. Specifically, a 40 [m] tall chimney is examined in this work, and the extracted numerical results demonstrate the effectiveness and applicability of the proposed techniques in large-scale engineering problems.*

**Keywords:** Fluid-Structure Interaction, Parametric analysis, Reduced order model, Vortex-induced vibrations, CFD, Chimney.

# 1 INTRODUCTION

The engineering field of Fluid-Structure Interaction (FSI)is defined as the mutual interaction between a movable or deformable structure and an internal or surrounding fluid flow [1]. More specifically, the core idea in FSI applications is that, due to the presence of the fluid, forces are exerted on the structure which results in the deformation or the movement of the structure. Subsequently, the produced structural deformation/movement will, in turn, affect the fluid flow.

Within this work, a simplified FSI approach is followed in order to study the fluid flow around structural components and, thus, the resulting wind loading. More specifically, slender structures, such as chimneys [2, 3], are of particular interest due to the vortex-induced vibrations (VIVs) [4]. Therefore, the focus is placed on such slender structures and, more specifically, on a real-life case study of a chimney within this work.

Based on this, the general framework for the parametric wind loading analysis is initially proposed. Specifically, two independent parameters are used in this work, namely the dimensions of the structure and the wind velocity. In particular, the chimney's dimensions are appropriately scaled to examine the influence of the resulting fluid flow around the structure and, thus, on the phenomena involved. Furthermore, wind velocity constitutes a free parameter of the aforementioned parametric analysis. Consequently, it varies in the range of 5-20 [m/s] such that the effect of the vortex-induced vibrations can be properly resolved.

Following that, the procedure for building reduced order models and, thus, more computationally efficient models of the resulting wind loading on the structure is presented. A series of 3D CFD simulations is initially performed, based on the above-presented parametric analysis. It is well known that wind tunnel testing accurately reproduces the atmospheric boundary layer (ABL) and the flow around structures. The proposed framework can be applied utilizing the results from extensive wind tunnel tests and on-site measurements, which is the ultimate goal. Building aerodynamics took place in the ABL where turbulence closure models are crucial. A simple logarithmic law can describe the mean velocity profile. Generally, international standards and building codes define the parameters entering the logarithmic law according to the surrounding surface. It should be noted that log law is strictly valid for flow over uniform rough terrain and not for flow around individual objects. Therefore, an accurate CFD model should always be calibrated with experimental data from wind tunnels or field experiments and on-site measurements. In the case of CFD simulations, a closure model for the turbulence closure model is selected. Subsequently, based on the results of these analyses, the reduced-order model is identified using the sparse identification of nonlinear dynamics (SINDy) [5, 6] to create an interpretable model. The prior knowledge of the system properties and behavior drives the selection of the test functions dictionary. Also, machine learning techniques could be implemented based on computational and experimental results.

Finally, a real-life case study application is examined in this work. More specifically, the model of a 40 [m] tall chimney is examined herein. Using this model, the above-mentioned techniques, including the parametric analysis and the model order reduction, are employed. The extracted numerical results demonstrate the effectiveness and applicability of the proposed methods in real-life and large-scale engineering problems.

## 2 FLUID FLOW ANALYSIS

Within this paper, a CFD approach is followed in order to calculate the fluid flow around the chimney and, thus, to extract the forces at the interface. Therefore, a detailed description of the computational model used throughout this work is provided in this section. For the case of an incompressible flow, the continuity and Navier-Stokes equations are derived in the form

$$\nabla \cdot \underline{V} = 0 \tag{1}$$

$$\frac{D\underline{V}}{Dt} = \frac{\partial \underline{V}}{\partial t} + \underline{V} \cdot \nabla \underline{V} = -\frac{1}{\rho} \nabla p + \nu \nabla^2 \underline{V} + \underline{g} \tag{2}$$

where $\underline{V}$ and p denote the unknown velocity and pressure fields, respectively. In addition, $\rho$is the fluid density, v denotes the fluid kinematic viscosity, while the vector $\underline{g}$ corresponds to the gravitational acceleration.

Concerning the turbulence modeling, a Reynolds-averaged simulation is performed by using the open-source CFD software, OpenFOAM [7]. Furthermore, the two-equation k-ω Shear Stress Transport (SST) model for the turbulence kinetic energy k and turbulence-specific dissipation rate ω [8, 9] is employed in order to achieve closure. This model uses the k-ω model to estimate turbulence in the near-wall region and k-ε outside the boundary layer, while a blending function is utilized in order to connect these two models. Inlet flow conditions are consistent with the ABL for a terrain category II according to Eurocodes. It should be noted that wall function roughness is appropriately modified to be compatible with the inlet wind profile and minimize horizontal inhomogeneity problems. Also, a grid independence test was performed to find the appropriate optimal grid.

Concerning the fluid domain, the corresponding dimensions are chosen based on the chimney's height, as shown in Fig. 1. More specifically, the length of the domain is selected as 6H, where H is the structure's height. Moreover, the flow inlet is located 3H upstream from the center of the chimney. In addition, the width of the fluid domain is 6H, while the corresponding height is equal to 4H.

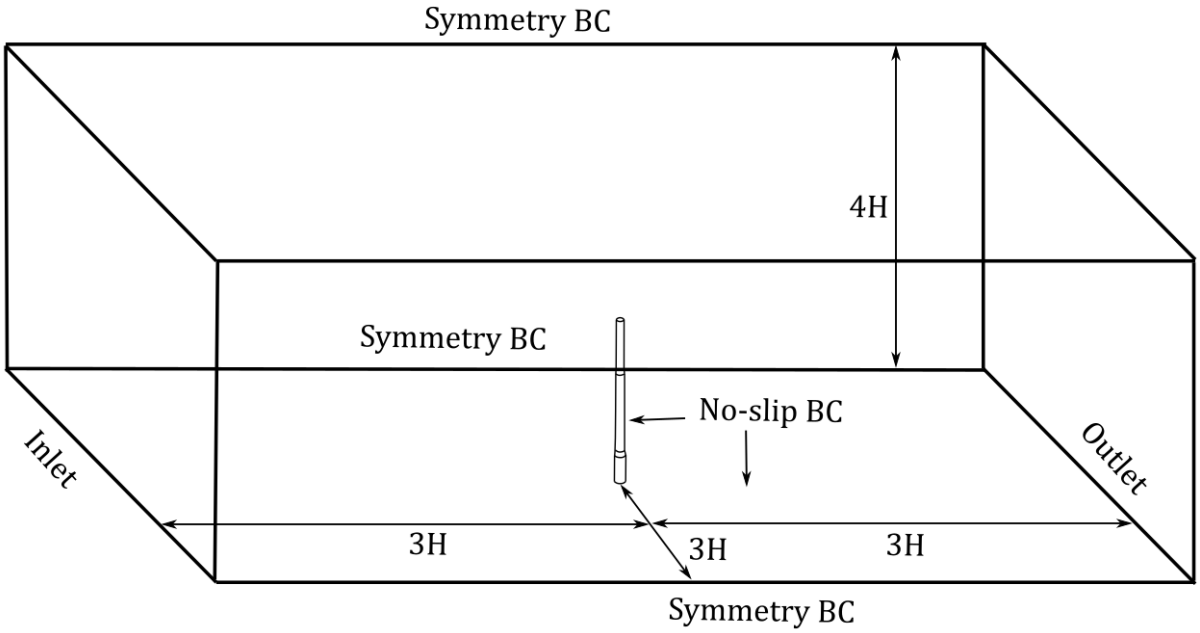


Figure 1 Fluid domain dimensions and boundary conditions

Furthermore, the numerical model's boundary conditions (BCs) are illustrated in Fig. 1. In particular, symmetry boundary conditions are applied to the top and side boundaries of the domain. Therefore, the fluid can slide freely along these boundaries of the domain but cannot penetrate or pull away. Moreover, no-slip boundary conditions are imposed at the chimney's surfaces, while a pressure outlet condition is specified at the outlet.

## 3 PARAMETRIC ANALYSIS

In the proposed methodology, the fluid flow around the chimney and, thus, the resulting forces at the interface need to be examined under various flow conditions. Consequently, it is necessary to define the dependent and independent parameters of the parametric analysis and calculate their numerical values in advance based on the expected flow conditions for the case study application.

In this paper, the wind velocity and the dimensions of the structure are chosen as the two independent parameters. More specifically, the wind velocity varies in the range of 5-20 [m/s] with an increment of 0.5 [m/s] such that the effect of the vortex-induced vibrations is properly resolved. Furthermore, the dimensions of the chimney severely influence the resulting fluid flow and, thus, the involved phenomena. Therefore, concerning the dimensions of the structure, three different cases have been examined in this work. That is, a case with the original dimensions of the chimney and two cases where the baseline diameters have been scaled by 0.8 and 1.2, respectively. Consequently, a total of twentyone (3x7=21) CFD simulations have been carried out in this work.

Finally, the resulting wind pressures at the structure are calculated at several positions. Namely, pressures are calculated at 24 control sections (along the height) and 12 points at each section were used to capture the in section variation of the pressures (24x12=288 points). In every part of the structure (Base, Middle, Top) Fig 2. at least five(5) control section were used.

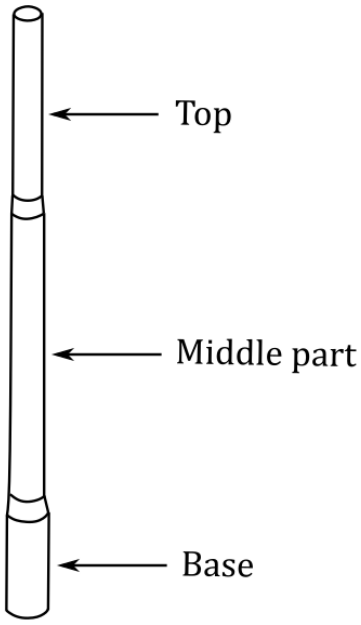


Figure 2 Resulting forces at the three distinct regions of the chimney

## 4 REDUCED ORDER MODEL

In order to derive a reduced-order dynamical model for the pressure variation, the SINDy method with controls (6) was applied.

$$\frac{\mathrm{d}p}{\mathrm{d}t} = f(p; v, k, t) \tag{3}$$

$$p(0) = p_0 \tag{4}$$

This concept is based on the method of snapshots and sparse regression. The evolution of pressure is described in terms of a selected set of parameters. The selected parameters are wind reference velocity (v), the geometric parameters of the structure **(k)** and time.

The library of candidate nonlinear functions **Θ(p,v,k)** contains any function that may describe the data. The choice of these members is crucial, and any knowledge of the system's behavior should be utilized.

After collecting the snapshots the system of equations (Eq. 3) can be written as

$$\dot{P} = \Theta(p, v, k)\, \Xi \tag{5}$$

The coefficients Ξ are mostly sparse and the final set of active (nonzero) coefficients is obtained solving the following optimization problem (sparse regression):

$$\xi_\kappa = \underset{\bar{\xi}_\kappa}{\operatorname{argmin}} \frac{1}{2} \left\| \dot{P}_k - \Theta(\mathrm{p}, \mathrm{v}, \mathbf{k})\, \bar{\xi}_\kappa \right\|_2^2 + \lambda \left\| \bar{\xi}_\kappa \right\|_0 \tag{6}$$

The term $\|*\|_0$promotes sparsity in the coefficient vector $\xi_\kappa$, although leads to nonconvex formulation. The primary outcome is an interpretable model, with only a few terms from the library **Θ**(sparse regression) in contrast to classical least square regressions.

## 5 NUMERICAL RESULTS AND DISCUSSION

Herein, the model of a 40 [m] tall chimney is examined in order to ensure the validity of the proposed techniques. In particular, all necessary dimensions of the structure are illustrated in Fig. 3. It should be noted that these are the baseline dimensions of the chimney model. Therefore, the corresponding diameters of the model are scaled by 0.8 and 1.2 during the parametric analysis in order to examine the influence on the resulting fluid flow around the structure and, thus, on the phenomena involved.

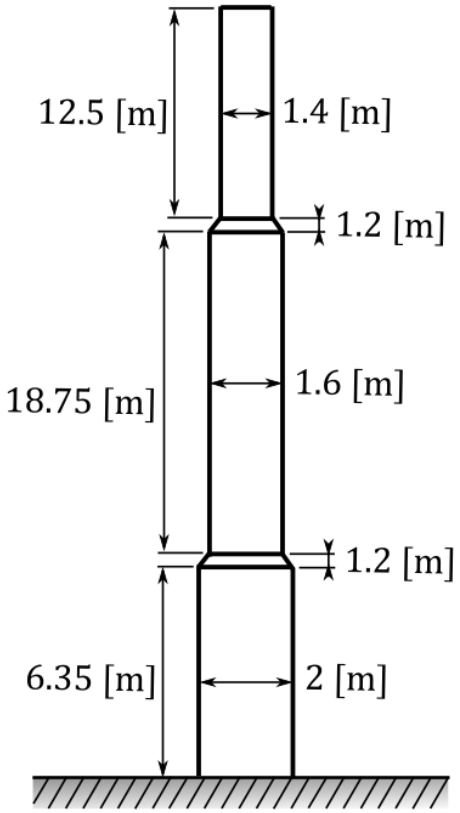


Figure 3 Chimney model and baseline dimensions

Using the above-presented model of the structure, the pressures at the interface are calculated for all twentyone (21) cases described previously in the section of the parametric analysis. More specifically, the case with the original dimensions of the chimney is initially examined, while the two cases where the baseline diameters have been scaled by 0.8 and 1.2, respectively, are studied next. In all cases, the second independent parameter, namely the wind velocity, varies in the range of 5-20 [m/s].

Proceeding with the extracted numerical results, the resulting forces at the structure for the case with the original dimensions are shown in Fig. 4 as functions of the wind velocity. These results computed from the reduced order model (for the pressures) obtained in section 4. For this, the last five (5) seconds of each (transient) simulation are utilized in order to get a representative value for the resulting forces of each case. In particular, the root mean square (RMS) value is employed in this work. It should be noted that a similar treatment is also employed in the cases where the baseline diameters have been scaled. Furthermore, in the same graph, the drag force calculated by using the analytical expression

$$F_x = \frac{1}{2} c_d \rho A v^2 \tag{7}$$

is also included, where A denotes the frontal area of the chimney and ρ the density of air. In addition, the drag coefficient $c_d$ is taken equal to 0.7.

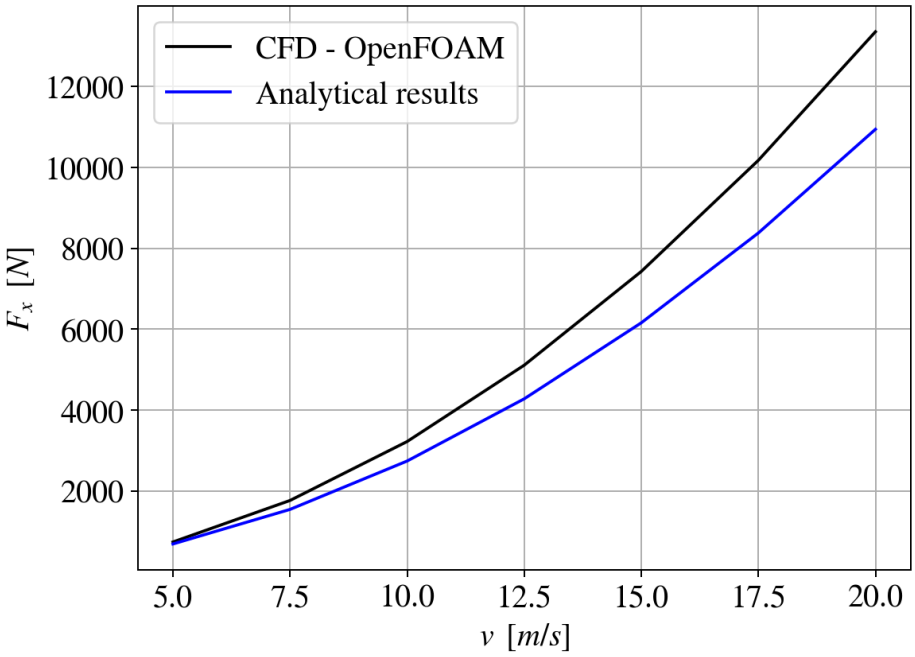


Figure 4 Total drag force as function of wind velocity for the case with the original dimensions

Obviously, the drag force calculated by utilizing the analytical expression is in good agreement with the results derived by the CFD software, due to the geometrical simplicity of the examined case. Moreover, the FFT analysis of the lift force in the middle part of the chimney is illustrated in Fig. 5 for the case where the baseline diameters have been scaled by 1.2 and the wind velocity is 10 [m/s]. As can be seen, the frequency of oscillating the resulting lift force, due to vortex shedding is 0.99. In addition, the expected (theoretical) value resulting from the analytical expression

$$n = St \frac{v}{D} \tag{8}$$

where D is the corresponding diameter of the chimney and St is the Strouhal number. Using the numerical values D=1.2*1.6=1.92 [m] and St=0.18, according to international standards [10], the theoretical value of the frequency is

$$n = 0.9375 \tag{9}$$

which is very close to the value calculated by utilizing the CFD software.

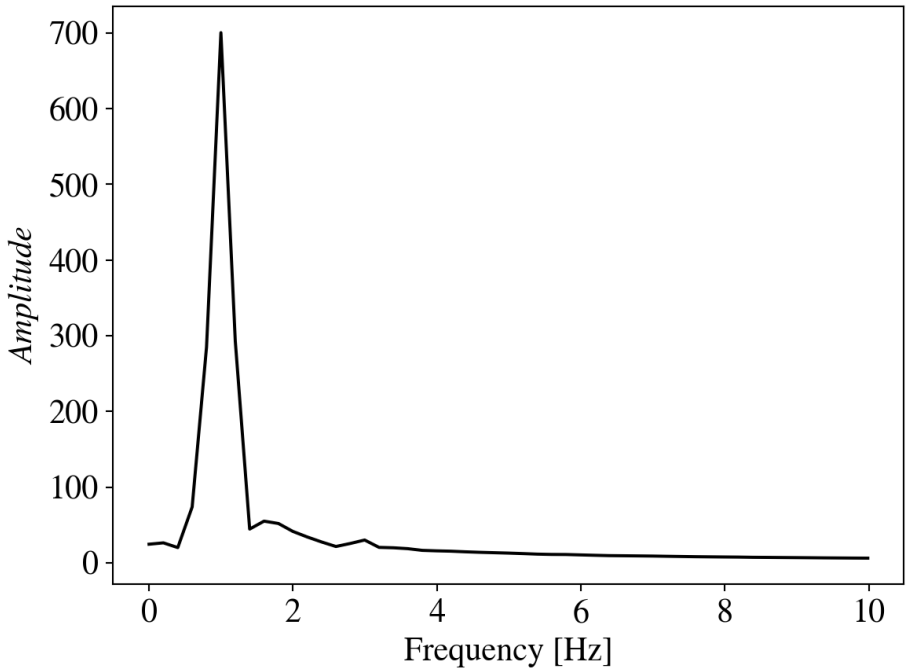


Figure 5 FFT analysis for the lift force in the middle part of the chimney. Baseline diameters scaled by 1.2 and wind velocity v=10 [m/s]

## 6 SYNOPSIS AND FUTURE WORK

Within this work, the focus is placed on adequately estimating the resulting wind loading on a structure, under various flow conditions, in a computationally efficient way. More specifically, a parametric analysis is initially employed to describe the structure's wind-induced loading as a function of two independent parameters, namely the dimensions of the structure and the wind velocity. For this, a series of three-dimensional CFD simulations is initially performed by utilizing the open-source CFD software, OpenFOAM. The proposed framework can be applied utilizing the results from extensive wind tunnel tests and on-site measurements, which is the ultimate goal. Furthermore, the methodology for building reduced order and, thus, more computationally efficient models of the resulting wind loading on the structure is presented next by employing the sparse identification of nonlinear dynamics (SINDy with control).

Finally, these methods are applied in a real-life case study application in Greece. Specifically, a 40 [m] tall chimney is examined in this work. As can be seen, both the total drag force and the frequency of the vortex shedding are in good agreement with the respective analytical (theoretical) values. Therefore, the extracted numerical results demonstrate the effectiveness and applicability of the proposed techniques in large-scale engineering problems.

## ACKNOWLEDGMENTS

This research is co-financed by Greece and the European Union (European Social Fund-ESF) through the Operational Programme "Competitiveness Entrepreneurship Innovation 2014-2020" in the action «Competence Centers» in the context of the project "Competence Center for a Sustainable and Resilient Built Environment using smart technologies" (MIS 5130744).

## REFERENCES

[1] Bungartz, H.-J., Schäfer, M.: Fluid-Structure Interaction: Modelling, Simulation, Optimization. Springer Science & Business Media, 2006.

[2] Belver, A. V., Ibán, A. L., Martín, C. E. L.: Coupling between structural and fluid dynamic problems applied to vortex shedding in a 90 m steel chimney. Journal of Wind Engineering and Industrial Aerodynamics, 100(1), 30-37, 2012.

[3] Black, C. J. M., Barrios, H. H., López, A. L.: A comparison of crosswind response evaluation for chimneys following different international codes. In Proc. 11th Americas Conference on Wind Engineering, Puerto Rico, San Juan, 2009.

[4] Williamson, C. H., Govardhan, R.: Vortex-induced vibrations. Annu. Rev. Fluid Mech., 36, 413-455, 2004.

[5] Brunton, S. L., Proctor, J. L., Kutz, J. N.: Discovering governing equations from data by sparse identification of nonlinear dynamical systems. Proceedings of the national academy of sciences, 113(15), 3932-3937, 2016.

[6] Brunton, S. L., Proctor, J. L., Kutz, J. N.: Sparse identification of nonlinear dynamics with control (SINDYc). IFAC-PapersOnLine, 49(18), 710-715, 2016.

[7] Weller, H.G., Tabor, G., Jasak, H., Fureby, C.: A tensorial approach to computational continuum mechanics using object-oriented techniques. Computers in Physics. 12, 620, https://doi.org/10.1063/1.168744, 1998.

[8] Menter, F.R.: Two-equation eddy-viscosity turbulence models for engineering applications. AIAA Journal. 32, 1598–1605, https://doi.org/10.2514/3.12149, 1994.

[9] Menter, F.R., Kuntz, M., Langtry, R.: Ten years of industrial experience with the SST turbulence model. Turbulence, heat and mass transfer. 4, 625–632, 2003.

[10] Standard, British. Eurocode 1: Actions on structures. General actions. Actions during execution, 2006.

COMPDYN 2023
9th ECCOMAS Thematic Conference on
Computational Methods in Structural Dynamics and Earthquake Engineering
M. Papadrakakis, M. Fragiadakis (eds.)
Athens, Greece, 12-14 June 2023

# DAMAGE ASSESSMENT OF CLASSICAL MONUMENTS USING NONLINEAR DYNAMIC SIMULATIONS

**Konstantina Mastrodimou, Vasiliki Kalogerakou, Vicky Dimakopoulou and Michalis Fragiadakis**

School of Civil Engineering, National Technical University of Athens
e-mail: mfrag@mail.ntua.gr

## Abstract

*The assessment of the seismic vulnerability of classical monuments is the aim of the present study. For this purpose, nonlinear dynamic analysis using the Discrete Element Method (DEM) was used in order to determine the seismic behavior and estimate the displacement profile for three common structural assemblies that are typically found in classical monuments, such as single columns and colonnades. More specifically, the paper examines the behavior of a column on the Parthenon's Pronaos and two colonnades one forming a straight line and another with a corner arrangement. Nine seismic excitations, specifically chosen for the site of the Athens Acropolis, thus being compatible with geological and tectonic criteria at the site, were applied in one and in two horizontal directions. The dynamic numerical simulations are a non-invasive tool with low computational cost and sufficient accuracy that can be used in order to take measures for cultural heritage preservation.*

**Keywords:** Seismic vulnerability of monuments, Parthenon, dynamic analysis, Discrete Element Method.

## 1 INTRODUCTION

Among the monuments perched on the rock of the Acropolis is the temple of the Parthenon. The most imposing building of the ancient Greek world was studied in the context of this work as it is the most important cultural heritage monument of Greece. It is a full-marble temple of Doric style that includes relief fronts, a pavilion with eight columns on the east and west side and seventeen columns on the north and the south side. The inner rectangular core of the temple, the cella, also surrounded by a colonnade, has the form of an amphitheater following the Ionic standards, with columns arranged only along the small sides. There are four spaces in the cloister: the pronaos, the nave, the opisthodromos and the opisthonaos (Figure 1).

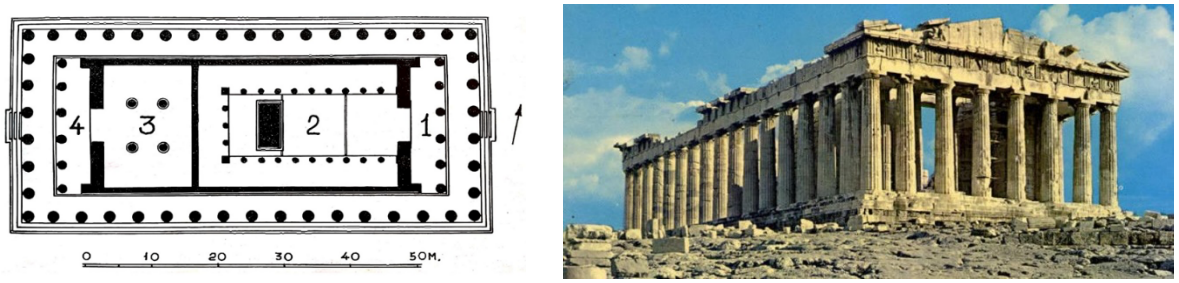


(a) (b)

Figure 1: (a) Plan of the Parthenon and numbering of the rooms of the cella: 1 pronaos, 2. nave, 3. opıshthodromos, 4. Opishthonaos, (b) northwestern view of the Parthenon.

For a more accurate assessment of the current condition of the Parthenon, it is useful to make a historical review of the existing damage and the factors that led the monument to the condition that it survives in our days. The temple was preserved in its original form until 267 AD, when parts of it were destroyed due to the burning of the temple by the Erulians. In 529, 1205, and 1456 AD the temple was transformed to a Christian church, first a cathedral for the Frankish conquerors and then a mosque for the Turkish invaders, respectively. The most destructive event in the monument's lifetime occurred in 1687 AD by the Venetian army of Morosini, who during their fight against the Turks blew up the building and destroyed large parts of it. In addition to the explosion, damage was caused during the attempt to loot the monument. In a similar attempt in 1801 AD, extensive damage was caused by the sawing and removal of a large number of sculptures by Thomas Bruce [1]. However, in addition to human-induced damage, various mechanisms of deterioration and erosion such as physical, chemical, mechanical, biochemical, and more generally environmental conditions, and seismic events are equally important causes of damage. Over the last decades, extensive restoration works were carried out and are about to be concluded in the near future.

## 2 SEISMIC RESPONSE OF THE PARTHENON

### 2.1 Damage due to past earthquakes

Many earthquakes have struck the Parthenon during its long lifetime that spans thousands of years. Three are the major factors that have determined the seismic behavior of the monument: the seismicity of Attica, the composition of the Acropolis rock and the way that the Parthenon was constructed [2,3,4]. There is a consensus among structural engineers, that the structural materials, the structural system and the excellent quality of the marble architectural elements have also given the temple an extraordinary structural capacity.

The most important seismic event that has struck the monument on the Acropolis hill, was the 1981 Alcyonides earthquake. During this earthquake, deformations were observed starting

from the lower drum of the columns up to the thrigos. The modular construction of the monument causes the rocking and sliding of its marble drums during an earthquake, resulting in permanent displacements that threaten its capacity to future seismic events.
The table below (Table 1) summarizes some major historical earthquakes that have struck the Parthenon [1,5]. This summary is attributed to Kalogeras and Egglezos [6] who compilation the listed information, while the peak ground accelerations were calculated according to the ground motion prediction relation of Skarlatoudis *et al.* [7].

Table 1: Major earthquakes that affected the Parthenon monument.

| Number | Magnitude (Richter) | Location | Distance (km) | Date | PGA ($cm/sec^2$) |
|---|---|---|---|---|---|
| 1 | - | Atalanti | 140 | 426 B.C. | - |
| 2 | - | Oropos | 40 | 1805 | 40 |
| 3 | 6.9 | Atalanti | 100 | 1894 | 30 |
| 4 | 6.7 | Korinthos | 77 | 1981 | 30 |

## 2.2 Seismic scenaria considered

The study of the seismic history of Athens and the most important earthquakes that have hit the Acropolis is an important step in the assessment of the seismic behavior of the monument. In the present work, accelerograms that are compatible with the seismotectonic environment of the Acropolis area and cover a wide range of frequency content have been selected. The ground motion selection, significantly affects the seismic response of such modular structures, as discussed by Psycharis *et al.* [8]. The ground motion selection was based on the report of Psycharis [9], where it is noted that the influence of the dynamic response of the Acropolis rock on the seismic motion at the top of the hill was taken into account approximately, using the topographic amplification factor of Eurocode 8.

In the seismic hazard study for the Athens area conducted by Ambraseys [10], it was shown that the ground acceleration that can occur with an annual probability of exceeding $5\times10^{-5}$ is about 0.19g. This acceleration corresponds to strong earthquake, but, usually, is not strong enough to collapse the monument.

Considering parameters that have a decisive impact on the dynamic response of ancient monuments, are the maximum ground velocity and the predominant period of the ground motion as well as directivity effects in the case of proximity to active seismic faults. Nine seismic excitations of surface earthquakes of normal faults were selected from the European and NGA Strong Motion Strong Motion Data Base. The ground motions have moment magnitudes in the range: $5.9 < M_w < 7.0$ and have been recorded in bedrock or rocky/stiff soil.

Table 2 summarizes the characteristics of the nine seismic excitations selected. The table includes the recording of the 1999 Athens earthquake at the Syntagma Metro Station, that was recorded at a distance less than 1km from the Acropolis hill. Also, among the two signals recorded at the Metro Station of Syntagma, recording B was chosen. This signal was recorded at a depth of 11 km and is considered that it has not been affected by the dynamic response of the station building, as opposed to the other recording at the same site (recording A).

Although in the case of the Acropolis hill there are no indications of seismic faults at a distance of up to 10 km, in the selection of the accelerograms for the analyses of the Acropolis monuments, seismic movements recorded at shorter distances from the fault (Cascia and Bagnoli-Irpino records) were taken into account. This selection was due to the estimate that similar ground motions with strong directivity effects can occur in Athens due to historical

earthquakes that were caused by faults located at distances greater than 10 km and contained directivity pulses.

Table 2: Seismic ground motions selected.

| A/A | Moment Magnitude $M_w$ | Location | Epicentral Distance (km) | Date | PGA (g) |
|---|---|---|---|---|---|
| 1 | 5.9 | Valnerina, Italy - Cascia | 1 | 1979 | 0.203 |
| 2 | 6.9 | Campano Lugano, Italy - Bisaccia | 19 | 1980 | 0.092 |
| 3 | 6.9 | Campano Lugano, Italy – Bagnoli Irpino | 6 | 1980 | 0.181 |
| 4 | 6.7 | Northridge, California, USA – Lake Hughes 9 | 27 | 1994 | 0.217 |
| 5 | 6.7 | Northridge, California, USA – San Gabriel E. Grand | 42 | 1994 | 0.256 |
| 6 | 6.7 | Northridge, California, USA – Los Angeles Wonderland Ave. | 23 | 1994 | 0.172 |
| 7 | 6.5 | Kozani, Greece – Kozani Prefecture Blg. | 14 | 1995 | 0.208 |
| 8 | 6.0 | Umbria Marche, Italy – Assisi Stallone | 14 | 1997 | 0.188 |
| 9 | 5.9 | Athens, Greece – Syntagma Metro B | 10 | 1989 | 0.109 |

## 3 DYNAMIC SIMULATIONS

In this study, the simplest assembly of the Parthenon temple was first examined, and two more assemblies have been considered. This simplest assembly was a column of the Pronaos and more specifically the sixth in a row and at full height restored southeastern column. This part of the Parthenon has been severely damaged due to the explosion that occurred in 1687AD. More recent investigations have focused on the identification of the original position of the scattered marble members. In this way, the columns were restored to their original position, but they are of various heights and only the column studied preserves its original height with repositioned drums, reinforced with iron and brass. The column height has been measured and found equal to 10.081 m and the total lower diameter of the drum is equal to 1.649 m. The detailed distribution of the marble drums along the height is shown in detail in Figure 3(b). The structural damage that occurred in this column were primarily thermal fractures in the form of peeling and ruptures. Fractures along the edges due to static and dynamic stresses on the fourth and the sixth drum was also observed. Destruction of surfaces due to the use of heavy tools during looting is also visible, together with fragmentation of the stones with gunpowder. In the ten dislocated drum cracks can be seen due to the swelling of oxidized iron that has been used during the reconstructions. From previous analyses of columns of Pronaos, it has been deducted that the above damage can considerably impair the stability of the column.

The column was first simulated without damage ("intact model") and then also a model that considers damage ("damaged model") was created. The geometric data were obtained exclusively from drawings that are available in the literature [11]. The twelve drums of the column were simulated in 3DEC software as "polydrums" with different lower and upper diameters, while the capital was simulated as a single piece. In addition, a rectangular base with dimensions 1.724 × 1.876 m has been placed below the lower drum in order to simulate the solid base on top which the column is standing. Any material losses on the inner side have been ignored and no account has been taken for the fasteners and the seals that were installed during the restorations. The structural system made of drums placed on top of the other, makes the behavior of ancient monuments strongly nonlinear and sensitive even to subtle changes of their geometry or the base movement.

A colonnade that consists of three columns in line arrangement that are connected at their top with an epistyle (architrave) is modelled as shown in Fig. 4 using 3DEC software. The axes

of the columns are 4 m apart. In order to exactly model the epistyle as it found in the Parthenon, it is three zones as shown in Figure 5 rather than a simple block; giving a height of 1.35 m, a width of each block equal to the distance between the column axes, i.e., 4m, and thicknesses of 0.426, 0.491 and 0.443m, from the outer to the inner zone of the epistyle, respectively. Initially, the colonnade was simulated as "intact" (without damage) following exactly the same geometry for the three columns, as discussed for the intact single column of the Pronaos, but in this case using "poly prism" command of 3DEC. The same colonnade is also tested in a "damaged" configuration. The central (middle) column is taken to be the SE column of the Pronaos with the damages already discussed, while for the side columns a random damage distribution was assumed but being compatible with the damage of the middle column (Fig.4). Specifically, the 2nd and 7th column drums were considered intact, as well as the rectangular base, while, in the other drums, damage were considered, from 1 to 3 in number, i.e., there are indentations ranging from 0.015 to 0.200 m. The epistyle is always considered intact, i.e., without any damage.

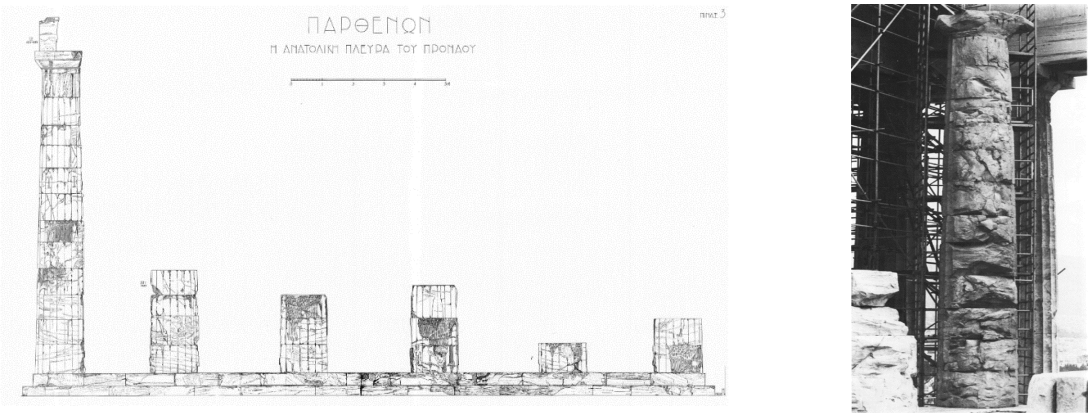


(a) (b)

Figure 2: (a) East side of Pronaos [12], (b) The 6th column of Pronaos [12].

The colonnade assembly was also considered by positioning the three columns in a corner arrangement and the corresponding corner epistyle was modelled as shown in Figs. 7 and 8. The axes of the columns are again 4m apart. The epistyle consists of three zones and the geometry is similar with that of the line arrangement, as shown in Figure 8. Therefore, the height of the epistyle is 1.35 m, the width of each piece such that the composition is achieved, and the thicknesses of the zones are 0.426, 0.491 and 0.443m, from the outer to the inner (Fig. 8). Initially, the colonnade is simulated intact (without damage) following the same geometry for the three columns. The same colonnade is then tested by applying damages. The corner column is taken to be the column of the previous section, with the damages already noted, while for the other two columns a random, same distribution of damages was assumed for both of them, exactly the same as the distribution assumed in the corresponding case of the damaged colonnade in a line arrangement. The epistyle is again considered intact.

Nine seismic scenarios were used in order to investigate the seismic behavior of the columns and the colonnades and to evaluate its deformation along the height under the influence of different seismic intensity records. The seismic excitations were applied in one and two horizontal directions accordingly. More specifically, the N-S direction is considered as the X direction of the model, while the E -W direction is the Y direction of the model.

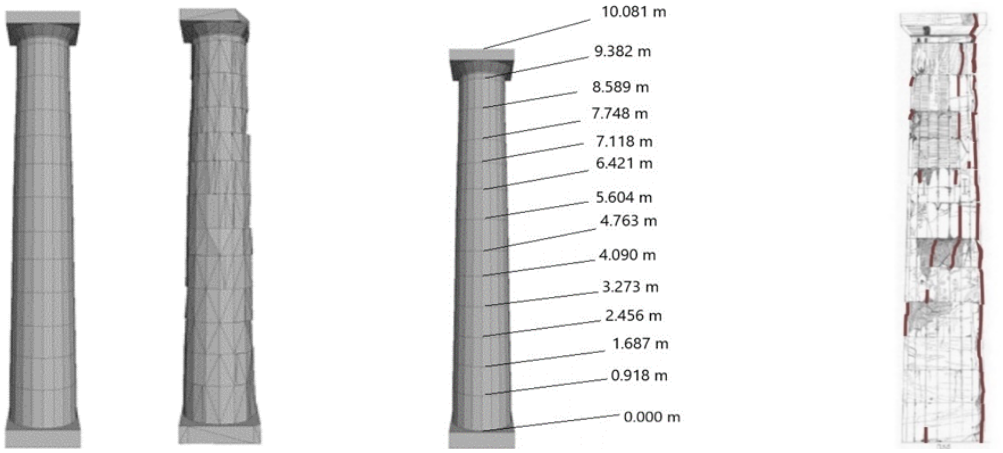


Figure 3: (a) Presentation of two models (with and without damage), (b) illustration of the heights of each drum, (c) illustration of a column with damage [11, 12].

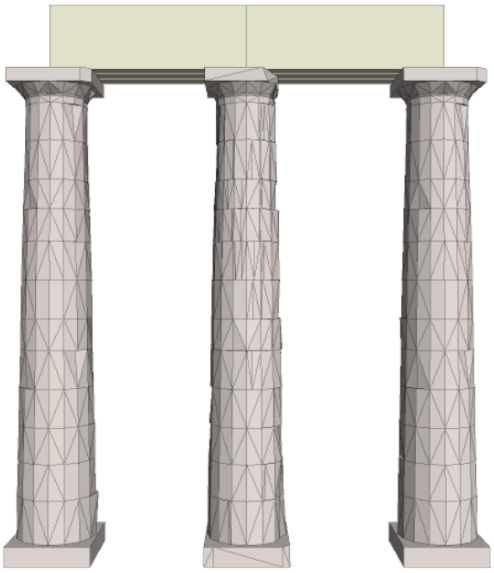

Figure 4: Simulation of the damaged 3-column colonnade in a line arrangement with epistyles (architraves).




Figure 5: (a) Top view of column drums of the intact 3-column colonnade in a line arrangement; (b) Top view of the 3-zone epistyle of the colonnade in a line arrangement.

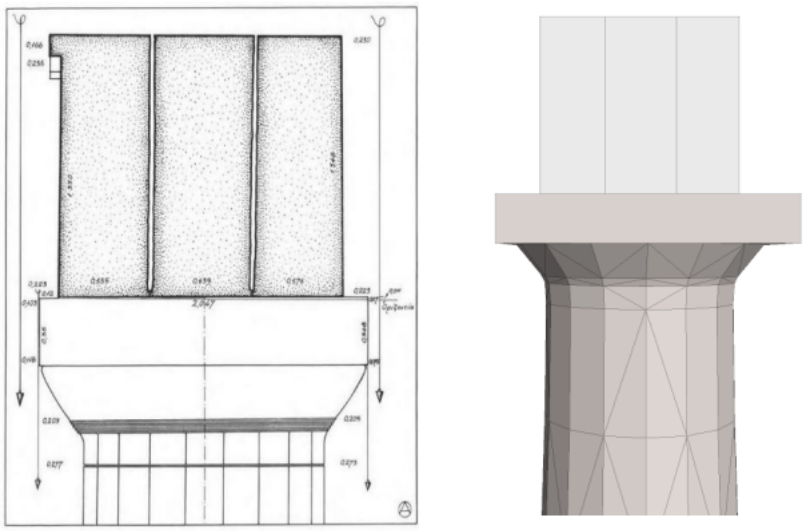

Figure 6: (left) Section of an epistyle of the Parthenon, (right) View of the analogically dimensioned epistyle

To investigate the behavior of the column under seismic excitation and to perform the dynamic analyses, the 3DEC software from ITASCA, which applies the Discrete Element Method (DEM), was adopted. The DEM method is an iterative method that allows calculating the body motions taking into account the interfacial forces at each step of the solution. It is characterized as hybrid as it combines elements of continuous and discontinuous behavior, it is suitable for solving dynamic problems as the bodies are considered as rigid or as deformable pieces interacting at their point of contact, thus allowing shear motion, rotation and detachment. The generalized Mohr-Coulomb model is used in the analysis to simulate the joints. According to reports by Zampas [13], the results of investigating the seismic behavior of columns using 3DEC were satisfactorily verified through experiments at the seismic table of the NTUA, making the program suitable for dynamic analyses of ancient columns despite the complexity and the large sensitivity of such systems.

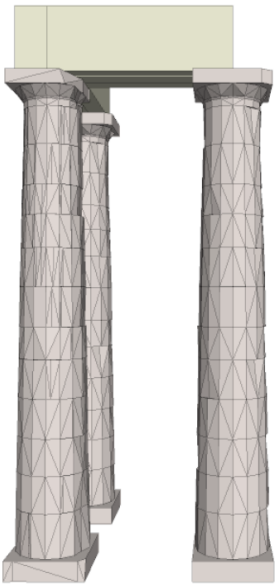

Figure 7: Simulation of the damaged 3-column colonnade in a corner arrangement with epistyles (architraves).

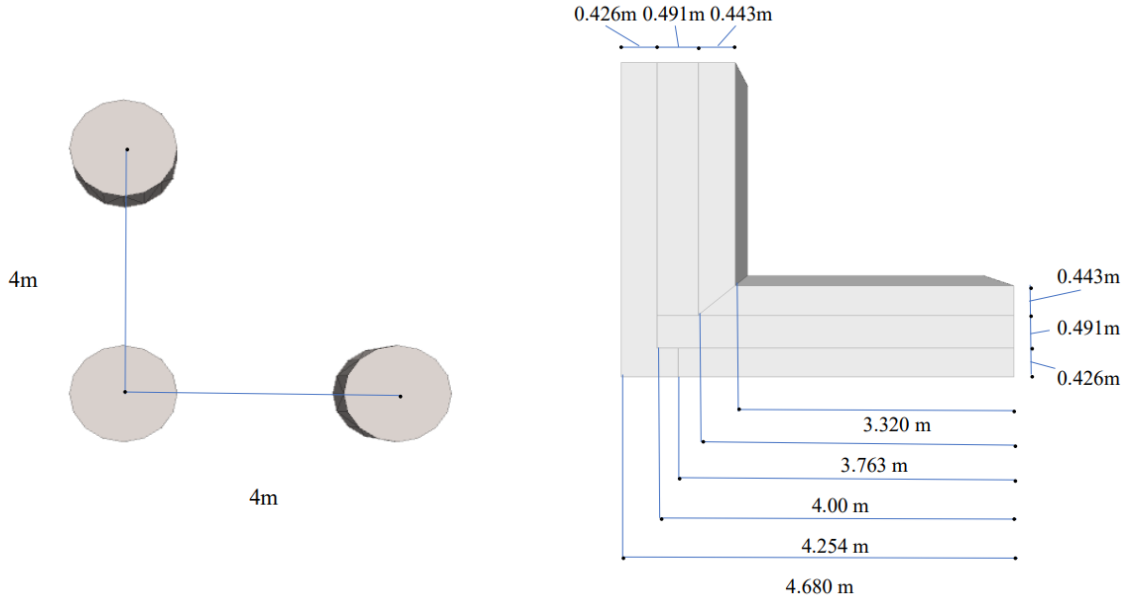


Figure 8: (a) Top view of column drums of the intact 3-column colonnade in a corner arrangement; (b) Top view of the 3-zone epistyle of the colonnade in a corner arrangement.

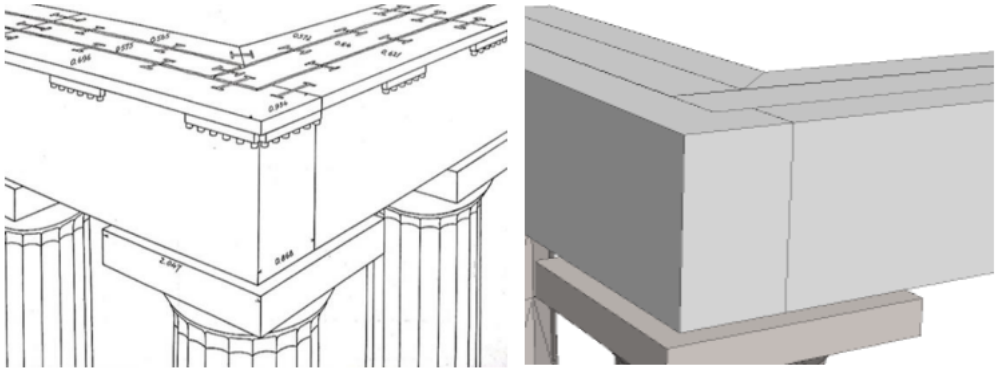

Figure 9: (left) Composition of corner epistyles [14], (right) View of the epistyle.

## 4 NUMERICAL RESULTS

A total of 108 analyses were performed for two conditions of the assembly considered, i.e. intact and damaged. Furthermore, 18 seismic scenarios were considered, i.e. nine seismic records along the X direction and nine in the X+Y direction. Figure 10 shows the plots of maximum absolute displacement in X and Y axis for the Bagnoli Irpino record applied along the X and X+Y direction for the two models of the single column assembly (intact and damaged) as well as the geometric mean of the displacements in X and Y axis for the two models both for earthquake in X direction and in X+Y direction. From the observation of the diagrams, it becomes evident that larger displacements in both the X and Y axes are presented when the earthquake is applied to the two horizontal axes simultaneously compared to the application of a single horizontal seismic component to the X axis. The higher values of displacements can be seen in the capital of the column both for intact and for damaged model, in both axes and for earthquake in X and in X+Y direction. The intact model displays a sightly worse behaviour in comparison with the damaged model fact that it may confirm that existing damage in some

cases can be beneficial for the column response in seismic excitation, depending on the direction of the earthquake.

Figure 11 and 12 show, as in Figure 10, the comparative plots of absolute maximum displacements and the geometric mean for earthquake both in X direction and in X+Y direction of the Bagnoli Irpino record for the central column of the colonnade in line and in corner arrangement respectively. In both figures as in Figure 10 the maximum values of displacement can be spotted at the capital of the studied columns as well as larger values are recorded when the seismic excitation is applied in two horizontal axes simultaneously. In the case of the line arrangement the damaged central columns' behavior is slightly worse in comparison with the intact model while in the corner arrangement as in the case of the single column, the damaged model behavior is better than the intact ones.

The effect of each arrangement is also compared for each condition for the Bagnoli Irpino record (intact or damaged model, for earthquake in X and in X + Y direction, for displacement in X and in Y axis) in Figure 13. In the case of earthquake applied in X axis, the corner column of the colonnade in corner arrangement has the larger displacement values while for the case of the seismic excitation applied in two horizontal axes simultaneously, the single column has the worst behavior. In the second case the existence of epistyles acts beneficially in the seismic response of the colonnade especially for the corner arrangement which has the lower displacement values.

Figures 14 to 16 compare all the seismic scenarios considered for the three assemblies (single column, central column of the colonnade in line and in corner arrangement). More specifically, it provides the mean distribution of the displacements along the height of the column when it is studied as a single column or as part of colonnade in the two arrangements considered. Thus, for the majority of the structural arrangements that are included in classical monuments, it can be estimated the displacement profile in case of a possible earthquake with a non-invasive analytical method. The diagrams of maximum relative displacements in the X direction are presented, their mean value separately marked and subsequently normalized to half the mean diameter of each column drum and then to the maximum value in height of each arrangement both for the intact and the damaged model. For the single column the values of relative displacement are higher both for the intact and the damaged model in comparison with the columns of the two colonnades considered. The capital of the column has the maximum displacement in the case of the single column while in the case of colonnades the maximum relative displacement can be found either among the three lowest drums or among the two highest drums and the capital of the column.

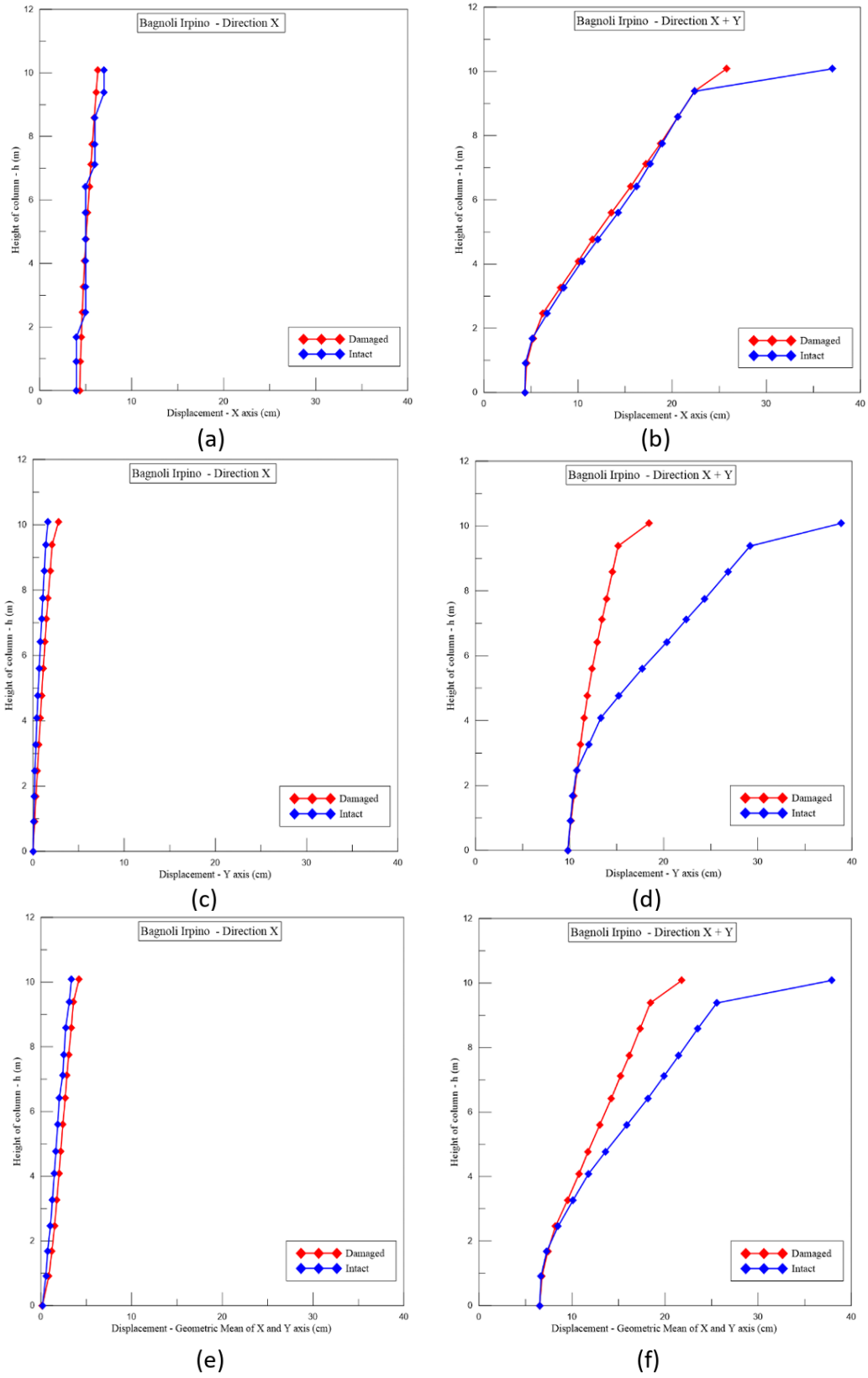


Figure 10: Single column assembly: diagrams of absolute maximum displacement of the Bagnoli Irpino record: (a) X direction displacements, earthquake in X direction, (a) X direction displacements, earthquake in X+Y direction, (c) Y direction displacements, earthquake in X direction, (D) Y direction displacements, earthquake in X+Y direction, (e) geometric mean of displacements, earthquake in X direction, (f) geometric mean of displacements. earthquake in X+Y direction.

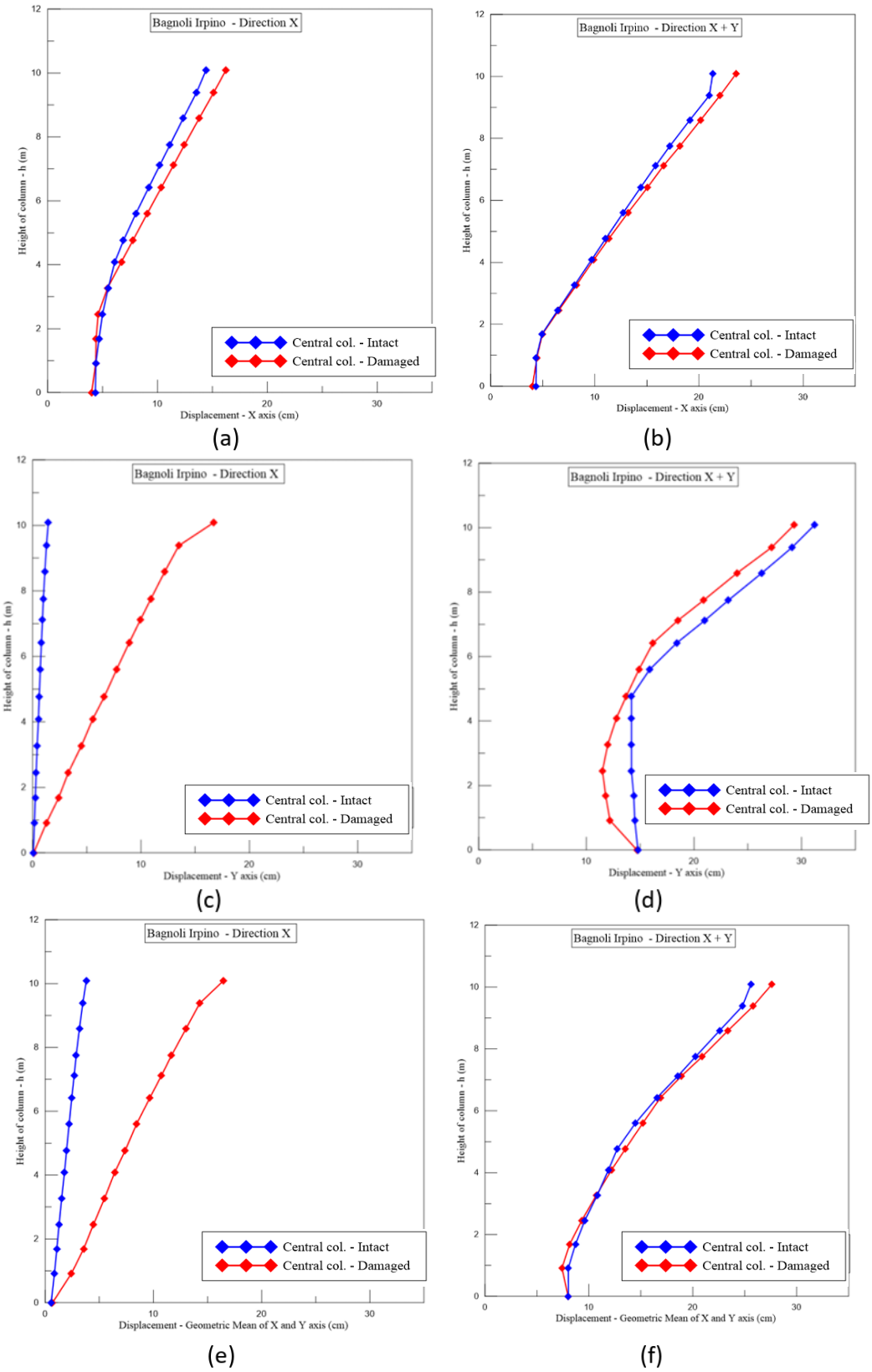


Figure 11: Colonnade in a line arrangement assembly - the central column: diagrams of absolute maximum displacement of the Bagnoli Irpino record: (a) X direction displacements, earthquake in X direction, (a) X direction displacements, earthquake in X+Y direction, (c) Y direction displacements, earthquake in X direction, (D) Y direction displacements, earthquake in X+Y direction, (e) geometric mean of displacements, earthquake in X direction, (f) geometric mean of displacements. earthquake in X+Y direction.

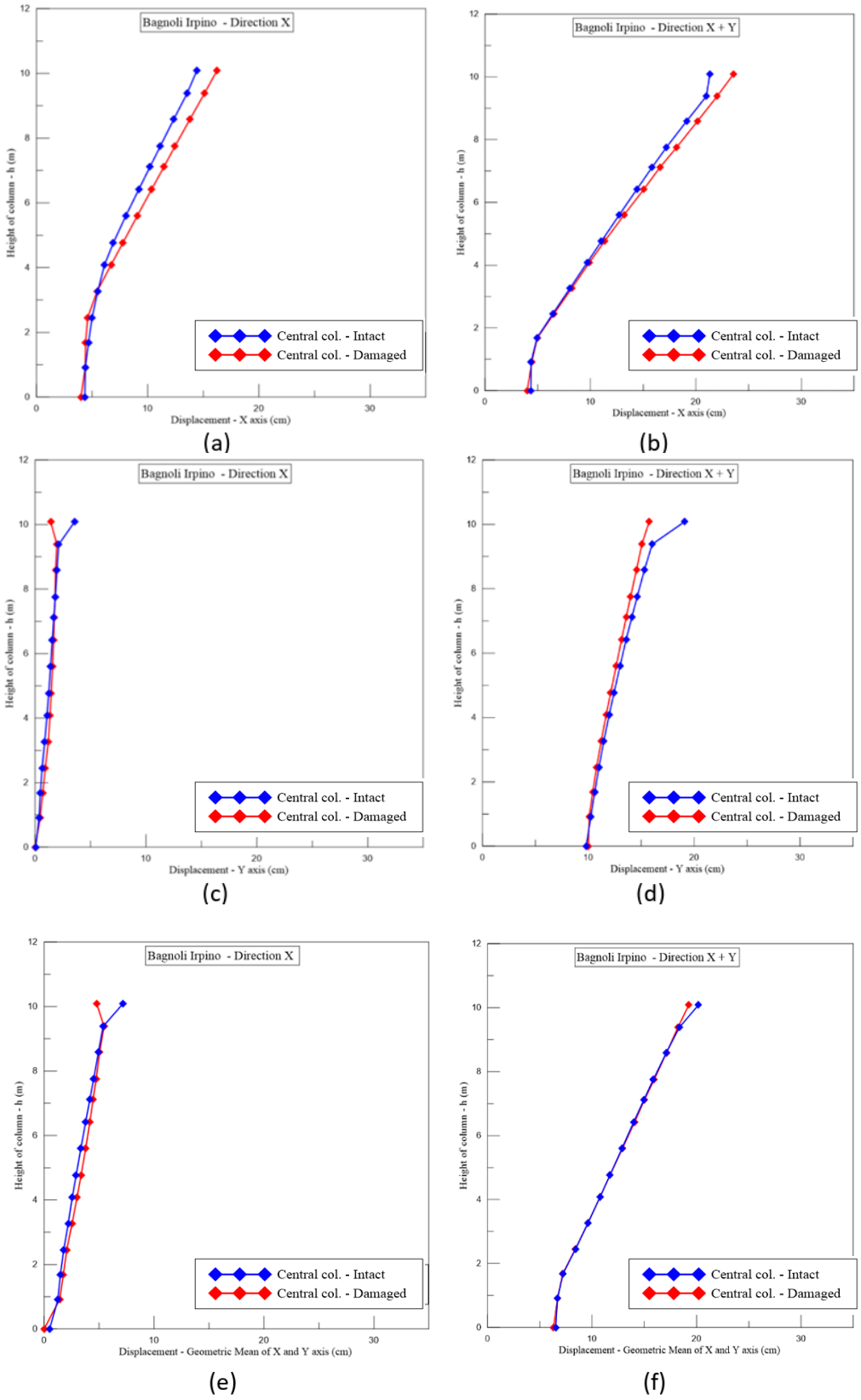


Figure 12: Colonnade in a corner arrangement assembly - the central column: diagrams of absolute maximum displacement of the Bagnoli Irpino record: (a) X direction displacements, earthquake in X direction, (a) X direction displacements, earthquake in X+Y direction, (c) Y direction displacements, earthquake in X direction, (D) Y direction displacements, earthquake in X+Y direction, (e) geometric mean of displacements, earthquake in X direction, (f) geometric mean of displacements. earthquake in X+Y direction.

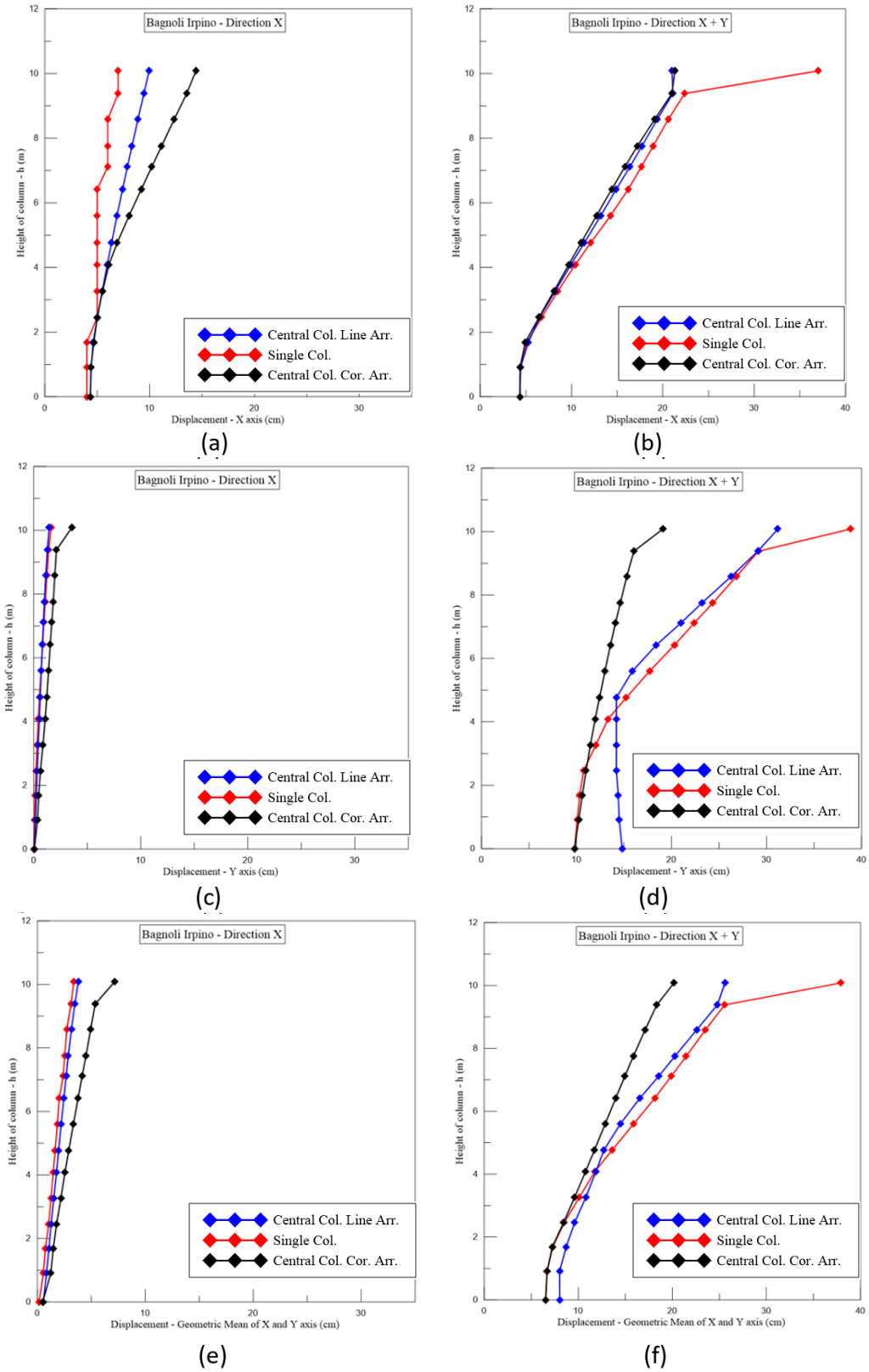


Figure 13: Diagrams of absolute maximum displacement of the Bagnoli Irpino record for single column and for the central column of the colonnades in line and in corner arrangement: (a) X direction displacements, earthquake in X direction, (a) X direction displacements, earthquake in X+Y direction, (c) Y direction displacements, earthquake in X direction, (D) Y direction displacements, earthquake in X+Y direction, (e) geometric mean of displacements, earthquake in X direction, (f) geometric mean of displacements. earthquake in X+Y direction.

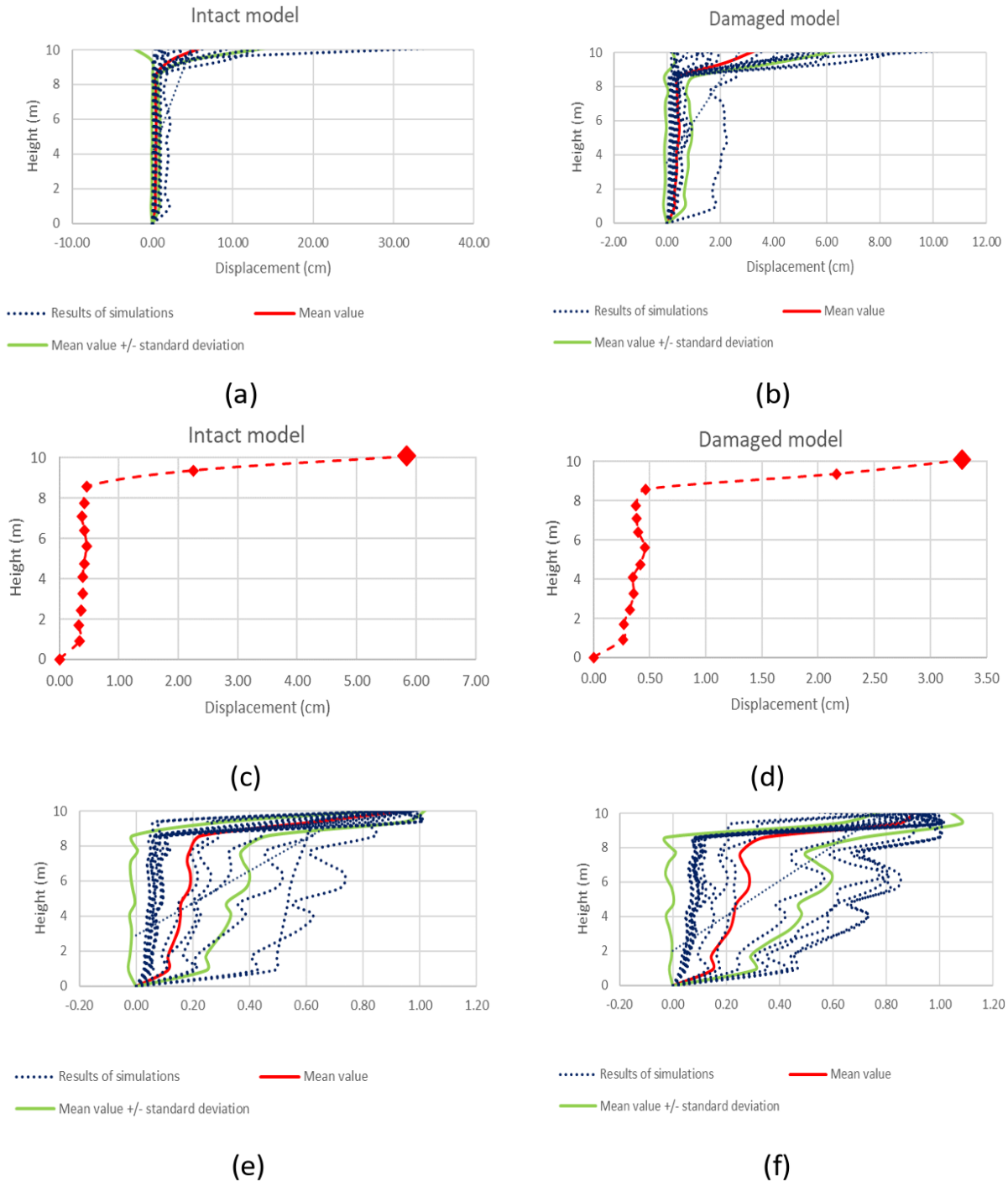


Figure 14: Plots of maximum relative displacements, mean value and standard deviations in X axis for earthquake in X direction from all the analyses of the single column for intact (a) and damaged model (b), only the mean value of intact (c) and damaged model (d) and further the (a) and (b) plots normalized to half the mean diameter of each drum and then to the maximum value in height (e and f respectively).

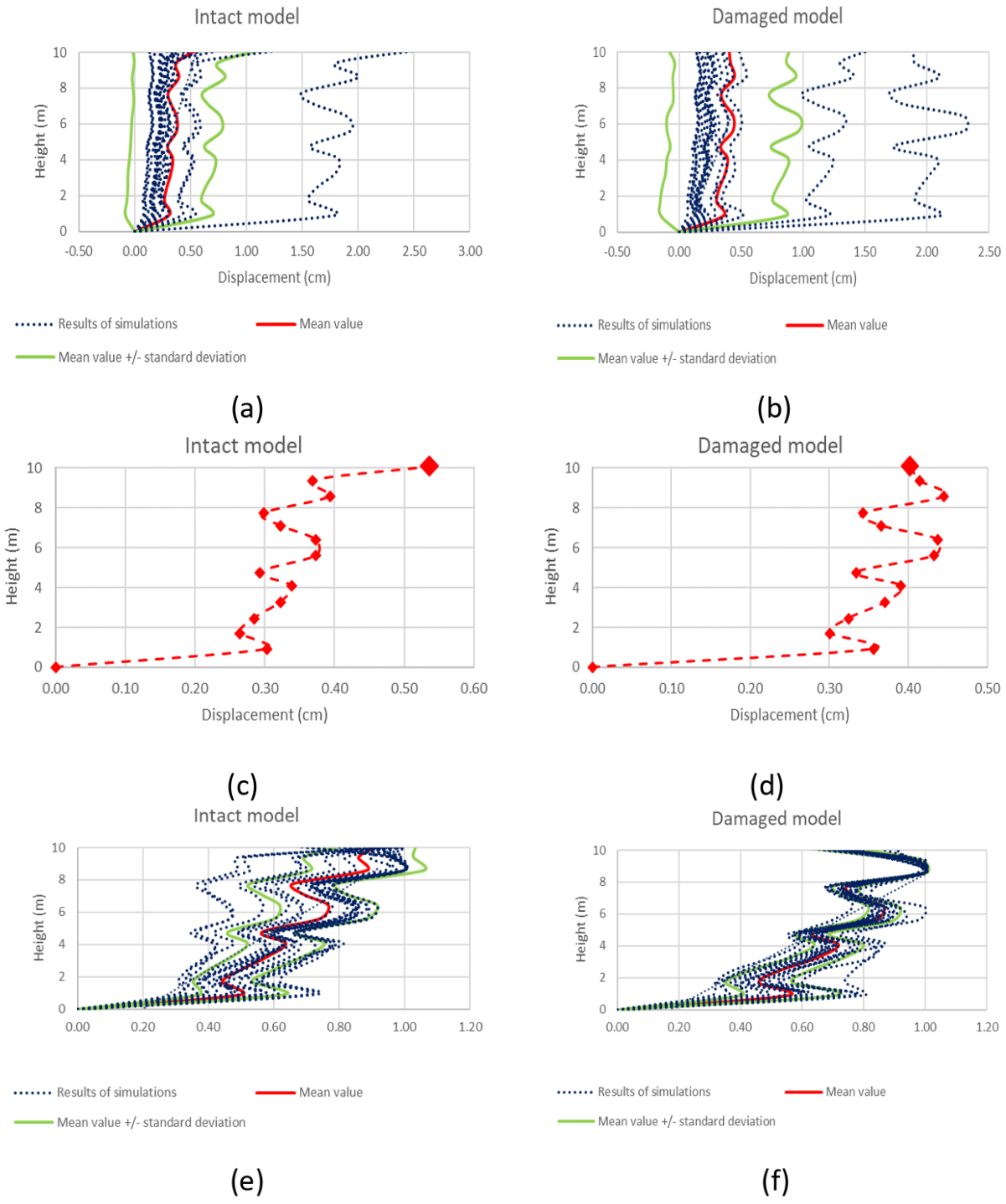


Figure 15: Plots of maximum relative displacements, mean value and standard deviations in X axis for earthquake in X direction from all the analyses of the central column of the colonnade in line arrangement for intact (a) and damaged model (b), only the mean value of intact (c) and damaged model (d) and further the (a) and (b) plots normalized to half the mean diameter of each drum and then to the maximum value in height (e and f respectively).

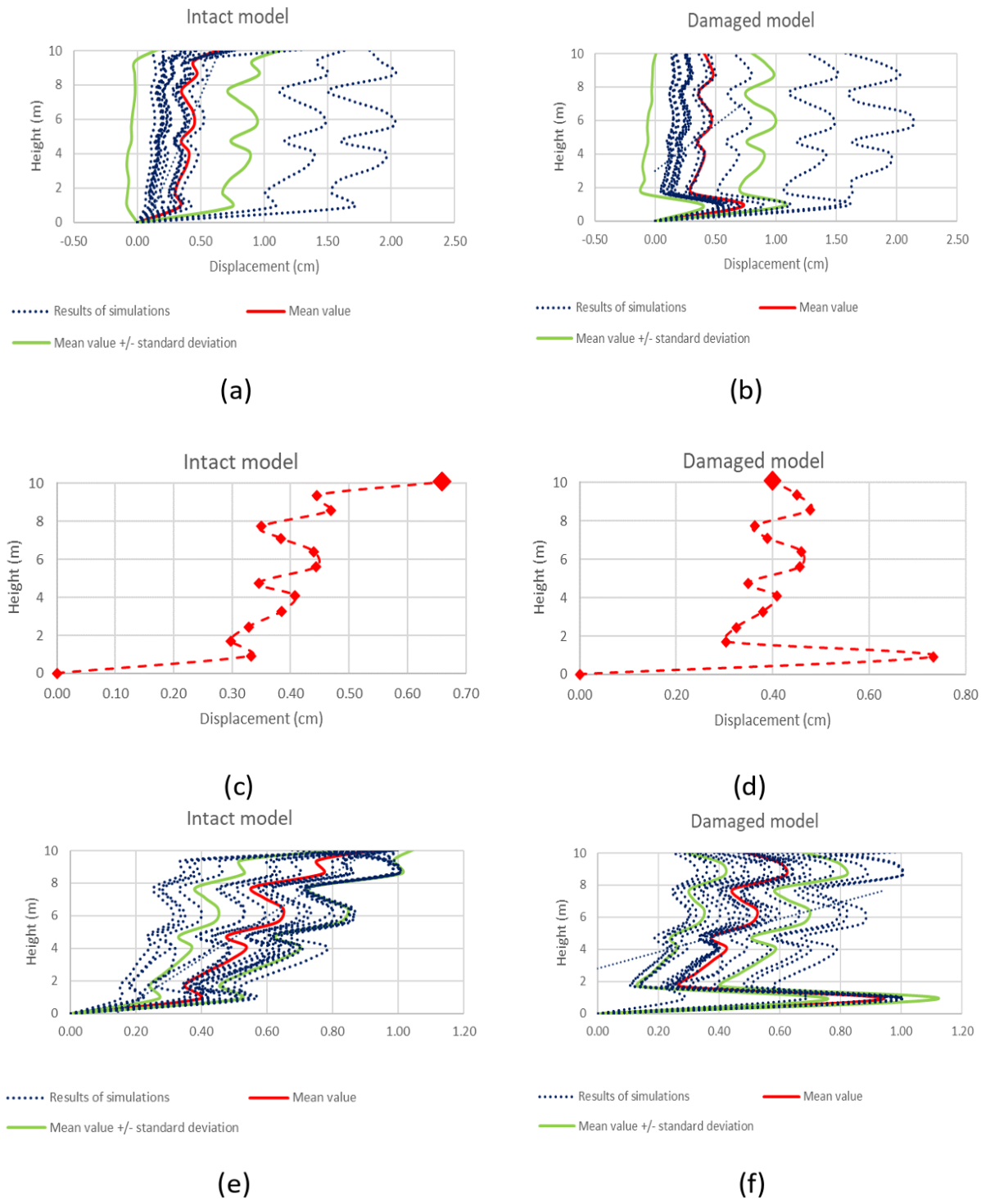


Figure 16: Plots of maximum relative displacements, mean value and standard deviations in X axis for earthquake in X direction from all the analyses of the central column of the colonnade in corner arrangement for intact (a) and damaged model (b), only the mean value of intact (c) and damaged model (d) and further the (a) and (b) plots normalized to half the mean diameter of each drum and then to the maximum value in height (e and f respectively).

## 5 CONCLUSIONS

Based on the numerical simulations performed, for the representative selected seismic intensities, collapses are very rare, at least for the configurations considered. Therefore, our

numerical simulations have confirmed that these structures are characterized by stability. The dynamic simulations where the records are applied simultaneously in the X+Y direction produced the most severe results, in both X and Y direction. By the observation of the absolute maximum X and Y displacements and relative maximum X displacements along the height, it becomes noticeable that the single column shows the maximum (relative) displacement in X (but also in Y) at the column capital. The corresponding column in the colonnade models often show maximum (relative) X-displacements in the 1st drum as well as at intermediate (7th, 8th) ones, in the damaged models, while in the original (intact) models it shows high relative X displacements and higher, e.g., in the capitals, as well.

The damaged models do not show systematically worse behavior compared to the intact ones; on the contrary, they sometime exhibit smaller displacements. Assemblies created by existing damage in the corresponding models may be beneficial for the columns, depending on the direction of the seismic excitation. Larger displacements are observed in the single column, while the other two arrangements show similar behavior with the line arrangement being more vulnerable. The architraves (epistyles) act, in general, as stabilizers. It has been observed that as the size of such structures increases, stability increases [9].

Ground motions with strong directivity effects combined with large earthquake magnitude and duration and long dominants periods, such as the example of the Bagnoli Irpino record, can have a significant impact and cause extremely increased displacements. Another interesting point that arises is that in such cases there are differences in the behavior of the three columns of each arrangement, especially in the Y direction. Thus, variations in kinematic behavior are observed depending on the position of a column in a colonnade.

All in all, special attention should be paid to the geometry and the problem parameters of the analysis due to the significant sensitivity and complexity of the assessment of the seismic vulnerability of classical monuments.

## ACKNOWLEDGMENTS

This research was funded by European structural and investment funds, Partnership Agreement 2014–2020, and is supervised by the General Secretariat for Research and Technology in the context of national action for bilateral cooperation between Greece–China. SCIENCE—Interferometry with Radar satellite data as a non-invasive tool for vulnerability assessment in cultural heritage areas (MIS 5050729) with code 68139800 implemented under the Operational Program COMPETITIVENESS, ENTREPRENEURSHIP and INNOVATION.

## REFERENCES

[1] YSMA (2018a), Web page of the Acropolis Restauration Service: https://www.ysma.gr/en/monuments/parthenon/

[2] Constantinou, C. M. (1994). Seismic Isolation Development in Europe. Passive and Active Structural Vibration Control in Civil Engineering. Vienna: Springer-Soong and Constantinou.

[3] Kapogianni, E., Psarropoulos, P. N., Kokoris, D., Kalogeras, I., Michalopoulou, D., Eleftheriou, V., & Sakellariou, M. (2021). Impact of Local Site Conditions on the Seismic Response of the Athenian Acropolis Hill. *Geotech Geol Eng*, pp. 1817-1830.

[4] Stiros, S. C. (199). Archeological evidence of antiseismic constructions in antiquity, *Annali di Geofisica*, pp. 725-736.

[5] Papazachos V., Papazachos C. (2003). The Earthquakes of Greece. Thessaloniki, Ziti Publications (in Greek).

[6] Kalogeras, I., Egglezos, D. (2013). Strong motion record processing for the Athenian Acropolis seismic response assessment. In Geotechnical Engineering for the Preservation of Monuments and Historic Sites (pp. 483–492). CRC Press.

[7] Skarlatoudis, C. B., Papazachos, B. N., Margaris, N., Theodoulidis, C., Papaioannou, I., Kalogeras, I. S., Karakostas, V. (2003). Empirical peak ground-motion predictive relations for shallow earthquake in Greece. *Bulletin of the Seismological Society of America*, 93(6), pp. 2591-2603.

[8] Psycharis, IN, Fragiadakis, M., Stefanou, I. (2013). Seismic reliability assessment of classical columns subjected to near-fault ground motions, Earthquake Engineering & Structural Dynamics 42(14), pp: 2061-2079.

[9] Psycharis I., (2015) Selection of suitable accelerometers for dynamic analyses of the Acropolis monuments, Technical Report, Hellenic Ministry of Culture, YSMA, NTUA, Athens.

[10] Ambraseys N. (2010) Assessment of the seismic vulnerability of free-standing columns and statues of the Academy of Athens. *Annual Report Eng. Seism. Res*. *Office 2008*, The Academy of Athens.

[11] Korres M. (1989). Restoration study of the Parthenon, Vol 2b. Ministry of Culture, ΕΣΜΑ, Athens (in Greek).

[12] Korres M., Toganidis N., Zambas, K. Skoulikidis, Th. (1989). Vol 2a. Ministry of Culture, ΕΣΜΑ, Athens (in Greek).

[13] Zambas K. (2002). Study of structural restauration ot the North Side of the Parthenon. Ministry of Culture, ΕΣΜΑ, Athens (in Greek).

[14] Orlandos K.A. (1977). The architecture of the Parthenon, *The Archeological Society at Athens* (in Greek).

COMPDYN 2023
9th ECCOMAS Thematic Conference on
Computational Methods in Structural Dynamics and Earthquake Engineering
M. Papadrakakis, M. Fragiadakis (eds.)
Athens, Greece, 12-14 June 2023

# SEISMIC PROTECTION OF NON-STRUCTURAL ELEMENTS IN RC BUILDINGS

**Saraswati Setia[1] Gurkirat Singh[2]**

[1]Professor :- Dept of Civil Engineering,
NIT Kurukshetra, India
ssetia@nitkkr.ac.in

[2]M. Tech :- Dept of Civil Engineering,
NIT Kurukshetra, India
gurkiratsingh974@gmail.com

## Abstract

*Seismic performance of Non-structural elements (NSEs) is a very crucial aspect in the safety of existing and new buildings. Non-structural elements are mainly free standing simply supported objects present in a structure that do not take part in the load-resistance. It has been observed from the past earthquakes that critical buildings such ass hospitals and fire stations, etc have suffered significant losses in the NSEs after an earthquake, thus hampering their usage post seismic event. During an earthquake, ground accelerations are the input at the base of a structure, which would thus lead to different accelerations at various floor levels and these floor accelerations are the input at the base of these non-structural elements. Hence, the study of floor accelerations is of prime importance to keep their functional requirement intact after a seismic event. This study deals with the development of floor response spectra and the variation of peak floor accelerations (PFA) along the height of RC framed building with varying plan shapes. Special Moment Resisting frame buildings in Seismic Zone V, importance factor of 1.5 in medium stiff soil. All the configurations have been subjected to fourteen recorded near-field ground motions. Linear Time history analysis has been performed in ETABS 2017. From the study of the above configurations, it has been observed that the variation in the Peak floor acceleration along with height is not linear as mentioned by many of the international standards (ASCE7-10, EC 8-2004). No definite trend in the variation of PFA is observed in the study. There is a significant amount of contribution in the higher modes and this contribution is more prominent in the lower stories.*

**Keywords**: Non-structural elements, floor response spectra, near field, FEMAP695.

## 1. INTRODUCTION

Nowadays in almost every structure 60-70% of the total construction cost of new buildings in urban India is of the non-structural elements (NSEs). Even if the structure is safe post a seismic event, person's safety may be at risk by the lack of safety in the building's items that directly cater to human needs. Building safety during earthquakes has gotten a lot of attention, but the safety of NSEs has attracted minimal attention. It has been evident from the past earthquakes that there is significant damage to the operational and the architectural equipments of a structure during the earthquake. Generally, in critical structures, functionality of the non-structural elements is at risk due to improper seismic assessment of these elements. Still, there are very few countries that have seismic design provisions for the safety of NSEs against earthquakes. This tells us that lessons are still not learnt worldwide from the losses that have occurred due to NSEs failure during previous seismic events. In most of the countries the losses due to the failure of the buildings and structures is so extreme that NSEs haven't been able to receive the much-needed attention. To satisfy the architectural demands the buildings are more often than not, irregular. The layout and type of structural elements of any building have a significant impact on its reaction. One of the major things affecting the response as a whole is the configuration of the structure. A building subjected to ground motion has the resultant acceleration different at its various floor levels and acceleration at a specific floor level is the input at base of NSEs kept on that floor level just like the ground accelerations due to an earthquake are the input at the base of building as shown in the Fig 1.1. Thus, by this we can conclude that identical NSEs kept on different floor levels experience different acceleration at their base, so the study of output acceleration at various floor levels is very important for the safe design of NSEs. NSEs are basically classified into three categories, namely 1)- Acceleration-sensitive, 2)- Displacement- sensitive 3)-Acceleration-displacement sensitive.

Acceleration sensitive NSEs oscillate during earthquake shaking and if they are not properly localized in a building and if the seismic assessment is not done, then it could lead to its damage which in turn would risk the life of the occupants in the building. Thus, its necessary to study the acceleration response of the buildings for safeguarding the non-structural elements in a structure.

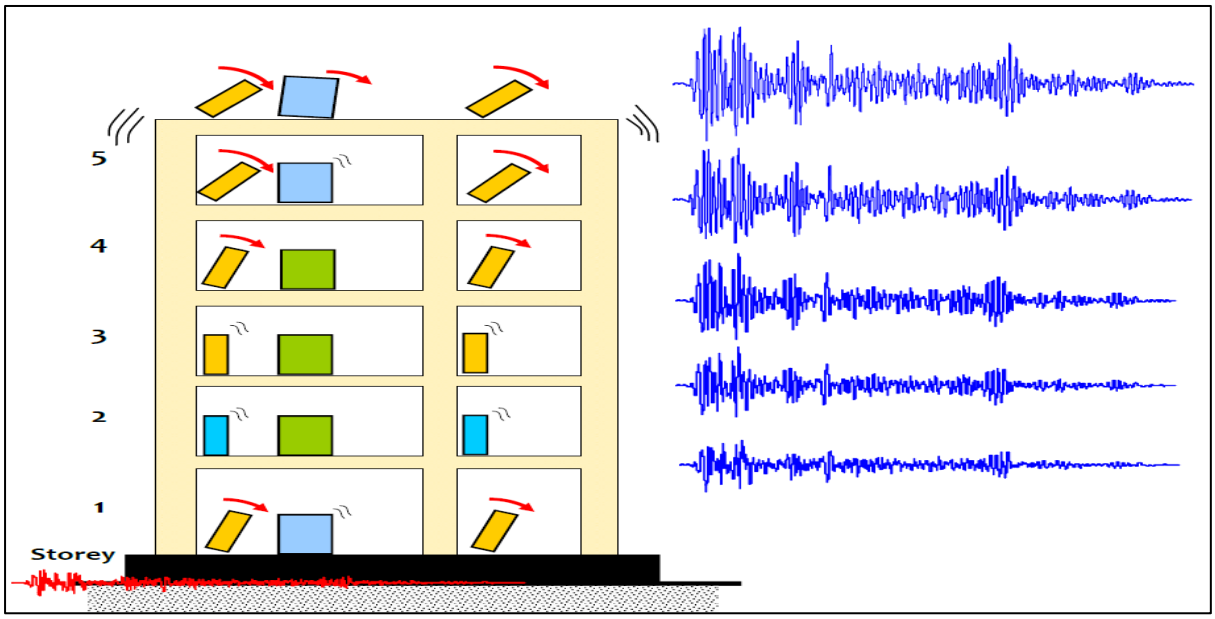


Figure 1. 1 Variation of Floor accelerations in a building (Murty, et al. 2012)

## 2. Literature Review

Previous earthquakes have shown that there is significant damage to the operational equipments of the structure. In many cases it is noted that there is minimum loss to the structure but the critical equipments have undergone irreparable damage. In USA, the financial losses due to the failure of non-structural components (NSEs) during a seismic event is alone US$2-0-4.5 billion per year over the past three decades (Murty,2012). Equipment failure especially in critical lifeline structures such as hospitals, fire stations can critically affect the performance and also put the life of patients in severe danger in the hospitals. Several prominent hospitals were evacuated during the 1994 Northridge earthquake, not only due to structural damage, but also due to the breakdown of power systems, air-conditioning units, ceilings, and light fixtures. The Saguenay earthquake in 1988 which was one of the strongest events to be recorded within the last 50 years in the eastern North America, caused almost no structural damage but the NSE damage was immense (M. Saatcioglu 2008). It is a fact that maximum injuries, damage to property and financial losses are caused by the damage of the operational and functional components (OFC) in buildings. If in hospital oxygen cylinders topple as happened in 1971 San Fernando earthquake as shown in Fig 2.1 and their pipelines to operation theatres and wards were broken, it could lead to secondary hazards i.e., damage to one element can lead to yet another disaster which would involve the safety of the people's live and the building contents occurred. During the 1971 San Fernando earthquake there was chemical spill in a laboratory which caused huge loss of life. Furthermore, suppose the X-ray machine topples during a seismic event, sensitive parts inside would become useless after the earthquake, and its function to provide the most essential services would be

affected, not to mention the human and financial loss that would occur as a result. The seismic fragility of NSEs mounted on hillside buildings was recently exposed by the SIKKIM earthquake, which resulted in considerable damage to hospital equipments thus, halting medical services (Report 2012). In many cases, the financial losses because of the damage of NSEs has even exceeded the cost that would be required to replace the building (EERI, 1984).



Figure 2. 1 Gas cylinders toppling during San Fernando Earthquake (1971) (Rupen and CVR 2012)

## 3. Objectives and Methodology

Based on the review of limited literature, the objective is to study the effect of various ground motions on building with varying configurations and perform a comparative study of the floor response spectra of these buildings.

The methodology is worked out to achieve the objectives mentioned above and for such purpose bi-directional linear time history analysis is performed on a finite element software package ETABS-2017. Time history analysis is a step-by-step study of a structure's response to a dynamic loading that varies over time. In this method the seismic response of a building is determined using recorded ground motions from a representative earthquake. Time history analysis is based on the appropriate recorded ground motion that is compatible with the design acceleration spectrum for a defined natural period and is carried out using the accepted principles of earthquake structural dynamics (1893 2016). In the present study a set of G+6 buildings with different structural configurations namely moment resisting frames, flat slab buildings, T-shaped buildings, L-shaped buildings, Y-shaped buildings along with a building on sloping ground has been considered. The peak floor acceleration values and the floor response spectra has been noted and developed respectively and compared for all the above cases. To investigate the floor response linear bi-directional

time history analysis is performed using the suite of 14 near field recorded ground motions obtained from FEMA P695. Floor response spectrum is an acceleration time history of a particular floor at a particular damping. It shows the greatest acceleration experienced by the NSEs versus their natural time period. It is obtained when number of NSEs with varying natural time periods but having similar damping are subjected to the similar accelerations at that floor. This eliminates the need for each NSE to undergo dynamic analysis.

## 4. Results and Discussions

The variation in the plan shapes could lead to significant variation in the mode shapes of the structure especially in T-shaped building where in the fundamental mode shape torsion comes along with translation. The peak floor acceleration values are more in L-shaped building as compared to T-shaped building. The maximum values are in the Y-direction as compared to X-direction for both the buildings. The mode shapes for the considered buildings are shown below: -

| Mode | T-shaped | L-shaped | Y-shaped |
|---|---|---|---|
| 1 | X-translation with torsion | X-translation | Torsion |
| 2 | Y-translation with torsion | Y-translation | X-translation |
| 3 | Torsion | Torsion | Y-translation |

Table 4. 1 Mode shapes of T, L and Y-shaped buildings

When there is a lack of symmetry in the plan shape of structures along the sides, certain undesired (diagonal translation and torsional) modes emerge. In typical buildings, the first few modes of oscillation determine the total motion; the fundamental mode (corresponding to the biggest natural period) usually contributes the most, followed by the second mode, third mode, and so on. In the above buildings with irregular plan shapes both T and Y shaped buildings are experiencing torsion in their fundamental mode itself. So, there is high amount of stress concentration which could lead to structural damage and in turn affect the safety of NSEs.

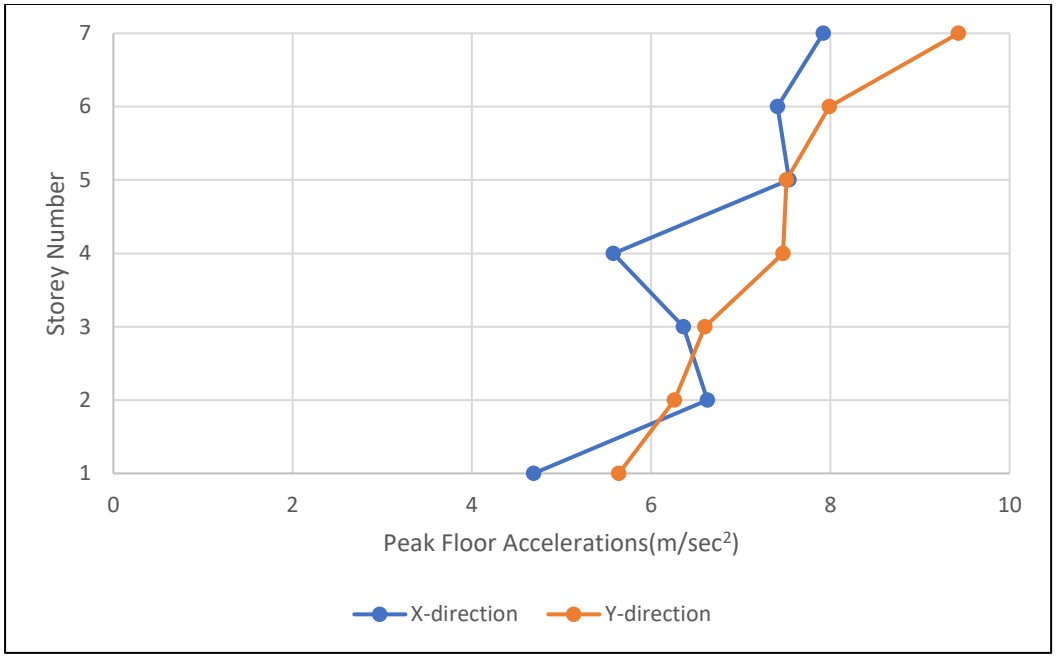


Fig 4. 1 PFA vs Storey No for T shaped building

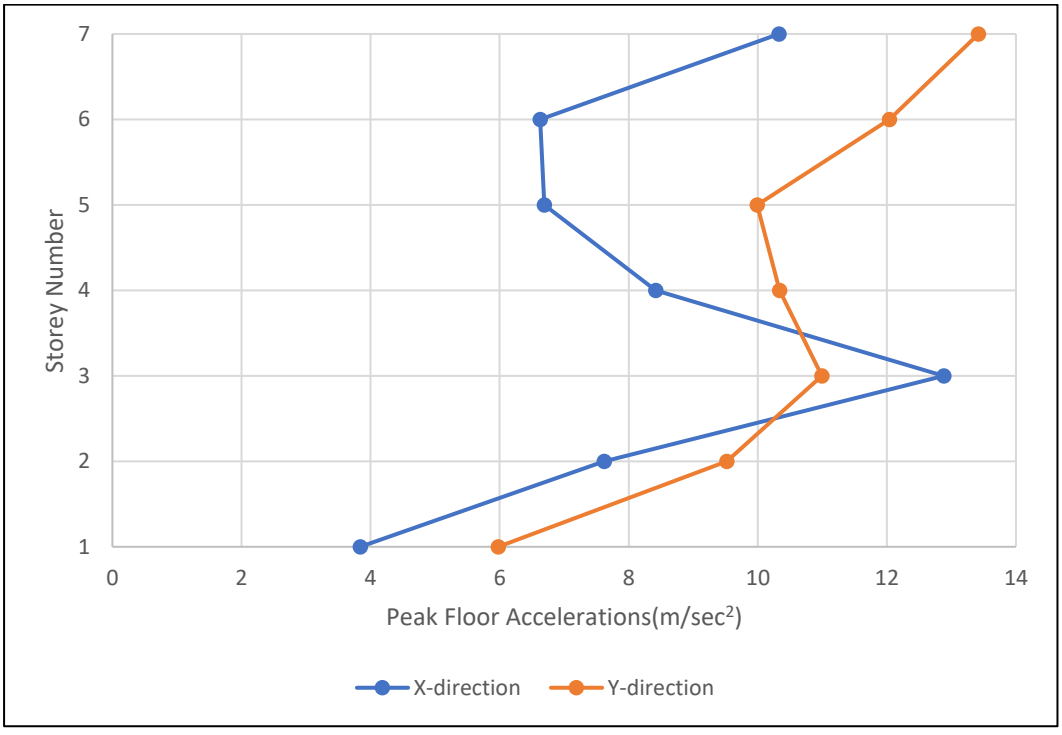


Fig 4. 2 PFA vs Storey No for L shaped building

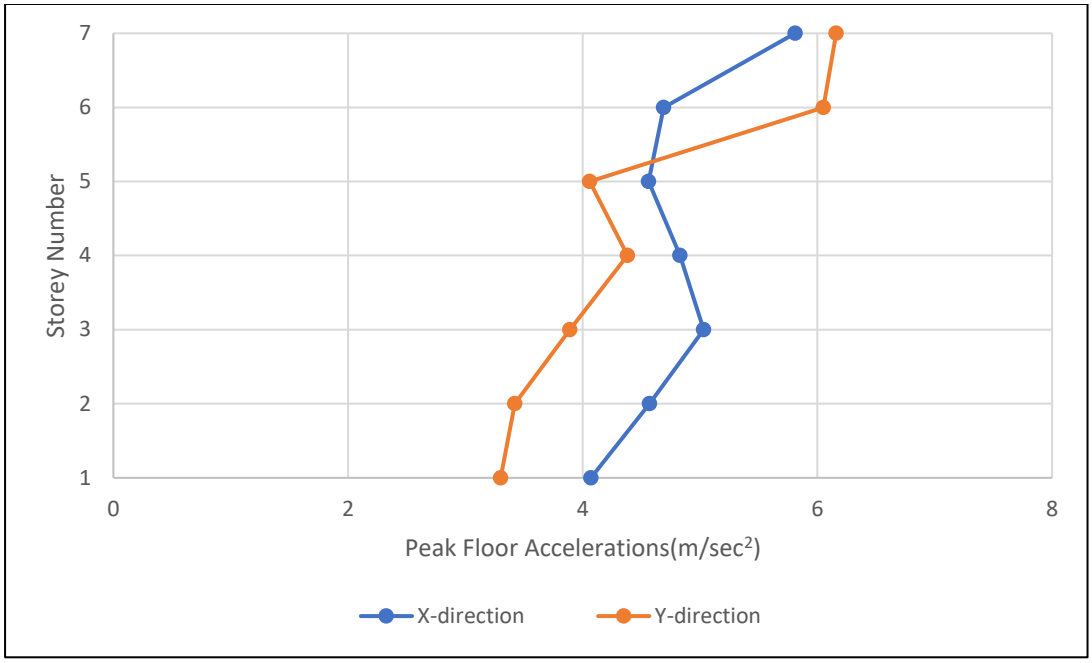


Fig 4. 3 PFA vs Storey No for Y shaped building

The floor response spectra for T, L and Y shaped buildings are shown in the Fig 4.4-Fig 4.6 respectively. It can be observed from the floor response spectra of L-shaped building that the elastic spectral acceleration corresponding to the fundamental time period($T_1$) is higher than that for the next two time periods ($T_2$ and $T_3$) for the story 7. For story 7 in T-shaped building there is not much of major difference between the elastic spectral acceleration of the first two time periods whereas when comparing the spectral accelerations for both T and L shaped buildings for story 7, T shaped plan experiences more accelerations at the story 7. For the story 5, there is not much of major difference between the floor accelerations for the first two natural periods in L-shaped buildings whereas for T-shaped building the second and the third time periods give more floor accelerations when compared to the fundamental time period. For the story 3 the elastic spectral accelerations are greater for the T-shaped building as compared to L-shaped building. The contribution of higher modes is more prominent in the story 3 and story 1 for L-shaped building as compared to T-shaped building.

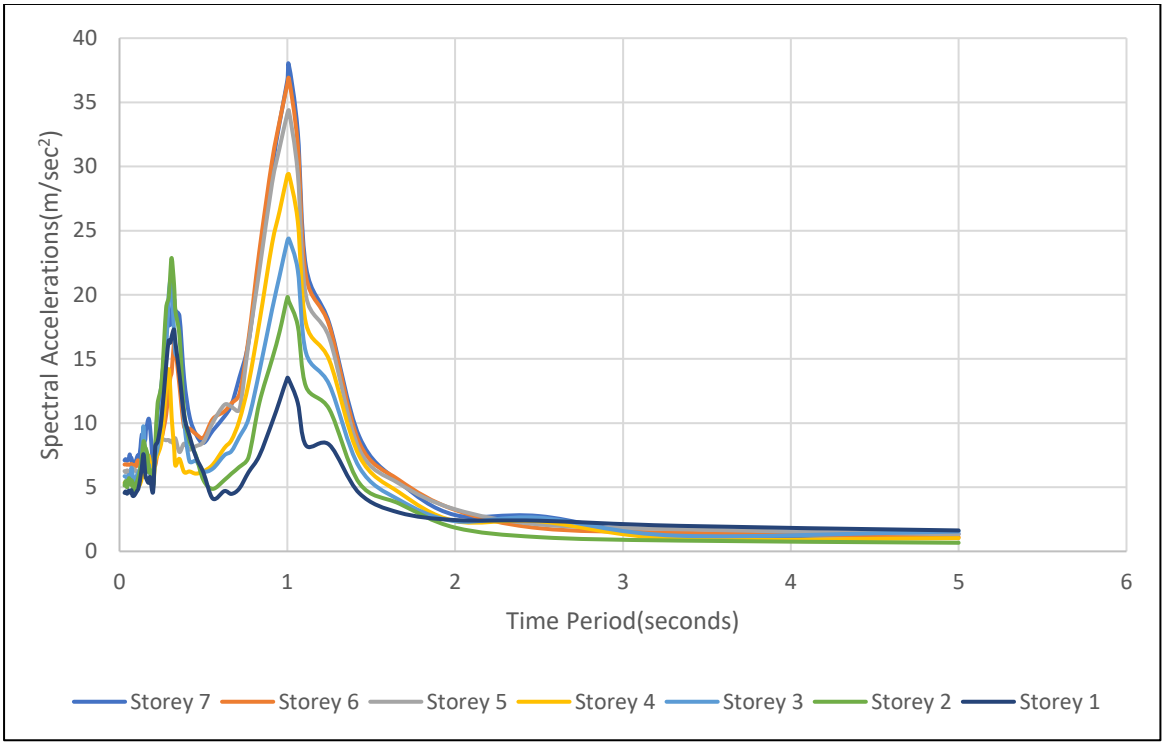


Fig 4. 4 Floor Response Spectra of T shaped Building

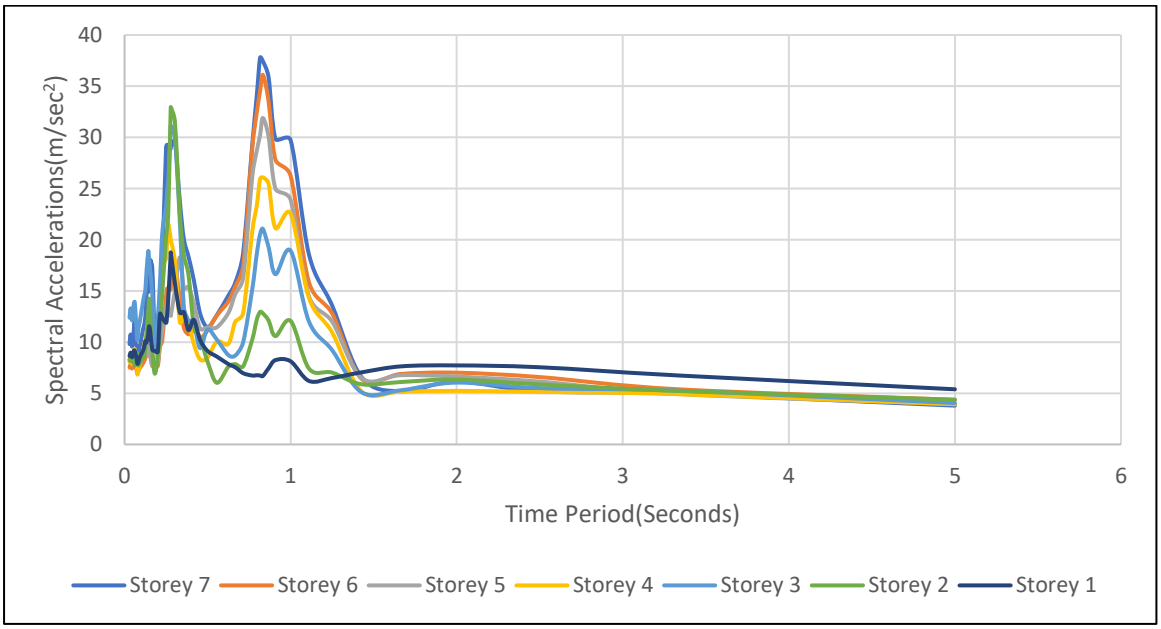


Fig 4. 5 Floor Response Spectra of L shaped Building

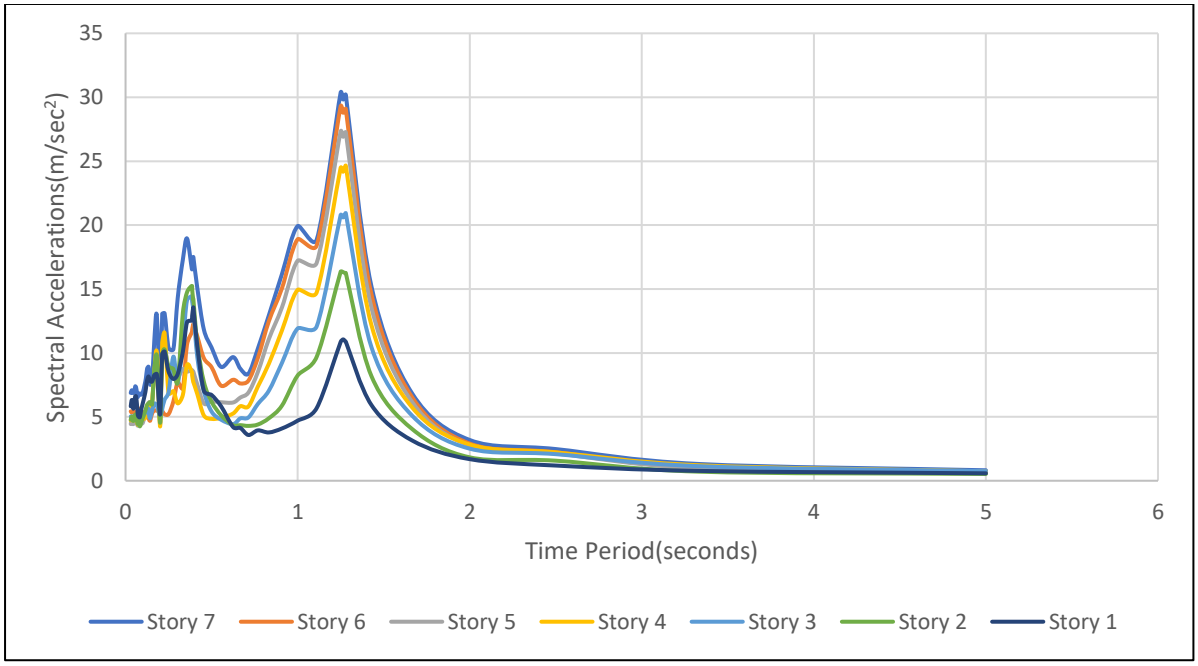


Fig 4. 6 Floor Response Spectra of Y shaped Building

## 5. CONCLUSIONS

There is no linear variation of Peak floor accelerations along the storey height as mentioned by most of the international standards (ASCE 7-10 n.d., EC-8 2004, FEMA P750 2009). All the configurations under consideration have shown different variations of PFA along the storey height and no common trend in the variation is drawn. Stability charts are generated in this study in the form of floor response spectra and the variation of PFA for different stories. These stability charts are beneficial for studying the overturning and rocking criteria of NSEs and estimating the maximum floor level of a particular NSE to attain stability in the building. It is noted from the floor response spectra of all the configurations considered that there is significant amount of contribution in the higher modes especially in the lower stories which is maybe due to structural deformability and the different ground motion inputs. It is important to note that the NSEs should not be protected only in case of strong earthquakes but also in case of low moderate ones where the vulnerability of the elements with short vibration periods would come into picture and thus can be a danger for them.

## 6. REFERENCES

[1] 1893, IS. 2016. *Criteria for earthquake resistant design of structures.* NEW DELHI.

[2] ASCE 7-10, 2010. n.d. *Minimum design loads for buildings and other structures,*. Reston, Virginia, United States.: ASCE Standard.

[3] Earthquake Engineering Research Institute (EERI). 1984. *Nonstructural issues of seismic design and construction.* , CA, USA.

[4] Earthquake Engineering Research Institute (EERI). 1984. *Nonstructural issues of seismic design and construction.* , CA, USA,.

[5] EC-8. 2004. • . *Design of structures for earthquake Resistance—part 1: general rules, Seismic Actions and Rules for Buildings,*. Brusells.

[6] FEMA P750. 2009. *NEHRP recommended seismic provisions for new buildings and other structures,*. Washington, D.C.

[7] FEMAP695. 2009. *Quantification of seismic performance factors.* Washington.

[8] M. Saatcioglu, M. Shooshtari, N. Naumoski and S. Foo,. 2008. "Development of floor response spectra for operational and functional componenets of concrete buildings in canada." *The 14th World conference on Earthuake Engineering.* Beijing,China.

[9] Murty, C. V. R., Rupen Goswami, A. R. Vijayanarayanan, R. Pradeep Kumar, and Vipul V. Mehta. 2012. *Some concepts in earthquake behaviour of buildings.*

[10] Report, EERI. 2012. *The Mw 6.9 Sikkim-Nepal border earthquake of September 18, 2011.* Oakland,United Stated,2012: EERI Report, Earthquake.

[11] Rupen, Goswami, and CVR Murty. 2012. *Introduction to Earthquake Protection of Non-Structural Elements in Buildings.* Gujarat.

COMPDYN 2023
9th ECCOMAS Thematic Conference on
Computational Methods in Structural Dynamics and Earthquake Engineering
M. Papadrakakis, M. Fragiadakis (eds.)
Athens, Greece, 12-14 June 2023

# CONTROL OF STRUCTURES SUBJECTED TO DYNAMIC LOADS USING MAGNETORHEOLOGICAL DAMPERS

**Verónica Valencia-Valencia[1], Mariana Castro-Osorio[2], Daniela Vallejo-Paniagua[2], Sebastián Echavarría- Montaña[2], and Luis A. Lara-Valencia[2]**

[1] Universidad Nacional de Colombia sede Medellín
Carrera 80 N.º65-223, Núcleo Robledo. Medellín, Colombia.
vvalenciav@unal.edu.co

[2] Universidad Nacional de Colombia sede Medellín
Carrera 80 N.º65-223, Núcleo Robledo. Medellín, Colombia.
{mcastroos, dvallejo, sechavarriam, lualarava}@ unal.edu.co

## Abstract

*In order to mitigate vibrations in structures subjected to dynamic loads, some control devices have been studied to reduce the forces and deformations caused by these loads. One of these control devices is the magnetorheological (MR) damper, a semi-active control device that consists of a controllable fluid, called magnetorheological fluid, that can change its rheological properties quickly in the presence of a magnetic field. This damper gives the structure robustness, reliability, and high stability. MR dampers have a strong nonlinear behavior, so it is necessary to work on non-linear control algorithms, which are methods derived from mathematical formulations or intelligent methods, to achieve optimal control forces to reduce the response of the controlled structures. This paper figures out how to reduce the response of a building equipped with MR dampers subjected to different seismic loads using a classic fuzzy logic controller. The proposed controller aims to find the adequate voltage that must be applied to the damper to generate damping forces that reduce the lateral displacements and velocities generated after the dynamic load has been applied. The results show that the use of an MR damper with the fuzzy logic controller decreases the response of the structure, demonstrating that the implementation of these devices is appropriate to control structures subjected to earthquake loads.*

**Keywords:** Structural control, magnetorheological damper, fuzzy logic, damping, optimization.

## 1 INTRODUCTION

In recent years, researchers have been focused on finding ways to mitigate the effects of dynamic loads on structures. Environmental loads, such as earthquakes, wind, or waves, can cause significant damage to structures if not properly addressed. The challenge for engineers is to develop effective methods to protect structures from these loads reducing the forces and deformations that occur because of them [1 – 4]. A potential solution to mitigate the effects caused by dynamic loads on structures is the use of control devices such as dampers [5 – 7]. These devices can be used to reduce the vibrations thereby decreasing the damage to the structure. Additionally, structural control systems can also be employed to decrease and dissipate the energy generated by these loads [8 – 10]. By actively controlling the structural motion, these systems can greatly reduce the forces and deformations experienced by the structure as well as improve its performance and safety during a seismic event.

Semi-active control systems have been gaining attention in the academic community. These systems offer a balance because use less energy than active control systems and have the dependability of passive control systems [11 – 13]. Unlike active controllers, which require a constant energy source to operate, semi-active systems usually use the movement of the structure to generate control forces. This is achieved using response sensors that measure the excitation of the structure and can be adjusted by an external power source. This allows for a more energy-efficient system while still providing the necessary control forces to mitigate the effects of dynamic loads. Furthermore, these systems can adapt to changes in the structure or the load, making them more reliable than passive control systems [14, 15].

A magnetorheological (MR) damper is a semi-active device that uses the properties of the MR fluids to control the vibrations of the structure. This fluid changes its viscosity when it is exposed to a magnetic field. When a magnetic field is present, the fluid behaves like a semi-solid and can provide significant resistance to motion. Conversely, when the magnetic field is absent, the fluid behaves like a liquid and offers very little resistance to motion. This property allows MR dampers to adjust to vibrations quickly and efficiently in real-time, providing precise control of the structural response under dynamic loads [16, 17]. The viscosity of the MR fluid can be adjusted by varying the intensity and duration of the magnetic field, providing a fast and efficient means of controlling vibrations in structures, making it a powerful tool for seismic protection and vibration control [18, 19]. Spencer *et al.* [20] developed a non-linear phenomenological model for MR dampers in 1997, which incorporates a modified Bouc-Wen hysteresis model that is numerically manageable and can exhibit hysteretic behaviors. This model allows for the accurate prediction of MR damper behavior under various loading conditions and can be used to optimize the design of MR dampers for specific applications [21, 22].

The use of MR dampers in structural control presents a significant challenge due to their strong nonlinear behavior. It is crucial to develop a suitable controller that can generate maximum force with minimal power supply [23, 24]. Therefore, research on non-linear control algorithms is necessary to effectively utilize MR dampers in structural control systems, these algorithms can help to improve the performance of the device and therefore, the safety of structures that implement it [25, 26].

In this context, some researchers have also been investigating ways to design and optimize the performance of MR dampers. One promising method that has been studied is the use of Fuzzy logic. This approach offers several advantages, such as reducing the difficulties associated with modeling and analyzing complex systems, and the ability to incorporate qualitative aspects of human experience into its mapping laws. Fuzzy logic is made up of four main components: fuzzification, a fuzzy inference engine, a fuzzy rule base, and defuzzification.

Overall, the use of Fuzzy logic in MR dampers has the potential to significantly enhance their performance in structural control systems [27, 28]. The fuzzification interface takes in crisp data and transforms it into fuzzy data that can be used by the inference system. The inference system then uses the knowledge base and the fuzzy data to make decisions and generate control actions. Finally, the defuzzification interface transforms the fuzzy control action back into a real control action (crisp output) that can be implemented in the system. These components form the backbone of fuzzy logic control and work together to take decisions in a robust and efficient manner [29, 30]. In 2012, Diptesh *et al.* [31] developed a new algorithm for controlling building frames under seismic excitation. The algorithm is based on fuzzy logic, which involves the fuzzification of the MR damper characteristics.

The objective of this research is to use fuzzy logic control to optimize the forces to reduce the structural response in terms of displacement and velocity of a 25-story building under different seismic excitations. This approach aims to improve the overall performance and safety of the building during seismic events.

## 2 MATHEMATICAL MODELS

### 2.1 Space-state representation of the problem

When analyzing a shear building with *n* degrees of freedom, equation (1) describes the motion of the building in terms of mass, damping, and stiffness matrix represented by $\boldsymbol{M}$, $\boldsymbol{C}$, and $\boldsymbol{K}$ respectively. The relative displacement, velocity, and acceleration of the structure are defined by the vectors $\boldsymbol{x}$, $\dot{\boldsymbol{x}}$, and $\ddot{\boldsymbol{x}}$ respectively. The applied loads are represented by the vector $\boldsymbol{f}$, and $\boldsymbol{u}$ is the vector of control forces applied to the building. $\boldsymbol{E}$ is the matrix that represents the location of the external forces, and $\boldsymbol{D}$ is the matrix that represents the location of the control forces.

$$\boldsymbol{M}\ddot{\boldsymbol{x}}(t) + \boldsymbol{C}\dot{\boldsymbol{x}}(t) + \boldsymbol{K}\boldsymbol{x}(t) = \boldsymbol{D}\boldsymbol{u}(t) + \boldsymbol{E}\boldsymbol{f}(t) \tag{1}$$

The above formulation is transformed into a space-state equation for ease of use, as shown in equation (2). This allows for a more streamlined approach to solving the problem and simplifies the process of analyzing and understanding the system.

$$\dot{\boldsymbol{z}}(t) = \boldsymbol{A}\boldsymbol{z}(t) + \boldsymbol{B}\boldsymbol{u}(t) + \boldsymbol{H}\boldsymbol{f}(t) \tag{2}$$

Matrix $\boldsymbol{A}$, $\boldsymbol{B}$, and $\boldsymbol{H}$ are presented in equation (3):

$$\begin{aligned} \boldsymbol{A} &= \begin{bmatrix} \mathbf{0} & \mathbf{I} \\ -\boldsymbol{M}^{-1}\boldsymbol{K} & -\boldsymbol{M}^{-1}\boldsymbol{C} \end{bmatrix} \\ \boldsymbol{B} &= \begin{bmatrix} \mathbf{0} \\ \boldsymbol{M}^{-1}\boldsymbol{D} \end{bmatrix} \\ \boldsymbol{H} &= \begin{bmatrix} \mathbf{0} \\ \boldsymbol{M}^{-1}\boldsymbol{E} \end{bmatrix} \end{aligned} \tag{3}$$

### 2.2 Phenomenological model of the MR damper.

The force generated by the MR damper can be represented by the modified Bouc-Wen model [20] illustrated in Figure 1. This model considers the hysteretic behavior of the damper and describes it in terms of a hysteresis loop. In this model, a damper is placed in series with a parallel spring. The force generated by the damper is represented by equation (4).

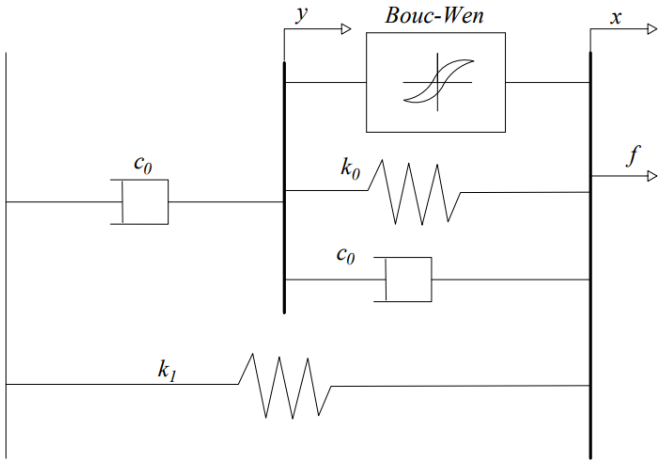


Figure 1: Phenomenological model for MR damper.

$$f = \alpha z + c_0\,(\dot{x} - \dot{y}) + k_0\,(x - y) + k_1\,(x - x_0) \tag{4}$$

Where $c_0$ and $c_1$ represent the viscous damping at long and low speeds respectively, $k_0$ is the stiffness of the damper at high speeds, $k_1$ represents the stiffness of the damper, $x_0$ is the initial displacement of the spring, $x$ is the relative displacement at one end of the MR damper, $\dot{x}$ is the speed of the damper, $y$ is the internal displacement of the damper, and $z$ is the evolutionary variable calculated with the equation (5):

$$z = -\gamma|\dot{x} - \dot{y}||z|^{n-1} - \beta(\dot{x} - \dot{y})|z|^{n} + A\,(\dot{x} - \dot{y}) \tag{5}$$

In the model, parameters $\gamma$, $\beta$, and $A$ affect the shape of the hysteresis cycles, while $\alpha$ and $n$ control the internal state $z$ and its relation to the force $f$ and its progression. $\dot{y}$ is defined by the following equation (6):

$$\dot{y} = \frac{1}{(c_0 + c_1)}\left[\alpha z + c_0\dot{x} + k_0\,(x - y)\,\right] \tag{6}$$

In the equation, the parameter $y$ represents the internal displacement of a MR damper. Despite its appearance in the equation, this parameter is purely fictitious and does not correspond to any actual physical displacement within the MR damper [32]. Parameters $\alpha, c_0$ and $c_1$ depend on the applied voltage and are calculated using the following equations (7).

$$\begin{aligned} \alpha &= \alpha_a + \alpha_b u \\ c_0 &= c_{0a} + c_{0b} u \\ c_1 &= c_{1a} + c_{1b} u \\ \dot{u} &= -\eta(u - v)\,u \end{aligned} \tag{7}$$

Where $\alpha_a$, $\alpha_b$, $c_{0a}$, $c_{0b}$, $c_{1a}$, and $c_{1b}$ are fixed parameters, determined by experimental results that connect the force of the damper with the voltage and $u$, $v$, and $\eta$ are the input voltages, output voltages, and the time constant for the first-order filter, respectively.

Table 1 presents the parameters used in the phenomenological model in this paper. The MR damper voltage ranges from 0 V to 10 V.

| Parameters used in the phenomenological model | | | |
|---|---|---|---|
| $c_{0a}$ | 110 kN·s/m | $\alpha_a$ | 46.2 kN/m |
| $c_{0b}$ | 114.3 kN·s/m/V | $\alpha_b$ | 41.2 kN/m/V |
| $c_{1a}$ | 8359 kN·s/m | $\gamma$ | 164 1/m$^2$ |
| $c_{1b}$ | 7482.9 kN·s/m | $\beta$ | 164 1/m$^2$ |
| $k_0$ | 0.01 kN/m | $A$ | 1107.2 |
| $k_1$ | 0.485 kN/m | $n$ | 2 |
| $x_0$ | 0 | $\eta$ | 100 1/s |

Table 1: Parameter of the model.

## 3 CONTROLLER BASED ON FUZZY LOGIC

The fuzzy logic was introduced by Zadeh [33] in 1965, this classical model uses linguistic control rules to connect fuzzy implication and compositional inference rules through a fuzzy logic controller (FLC). This approach contemplates the modeling of systems with imprecise or uncertain information. It allows for the representation of human thought processes and decision-making and is widely used in control systems, artificial intelligence, and expert systems. The FLC is a rule-based system that can handle ambiguity and uncertainty, making it suitable for complex and dynamic systems.

The main components of an FLC are:

- A knowledge base that holds the linguistic control rules.
- A fuzzification interface that converts real data into fuzzy data.
- An inference system that uses the knowledge base to make decisions.
- A defuzzification interface that transforms the fuzzy control action into a real control action.

Fuzzy systems behavior is determined using membership functions and fuzzy control rules. Membership functions are used to indicate how well an element fits into a particular set and can take on various shapes. Fuzzy control rules form the reasoning system of the controller and are typically written in the format of "if... then." If certain conditions are met, a set of outcomes can be inferred. The configuration of a conventional FLC is often illustrated in a diagram, such as shown in Figure 2.

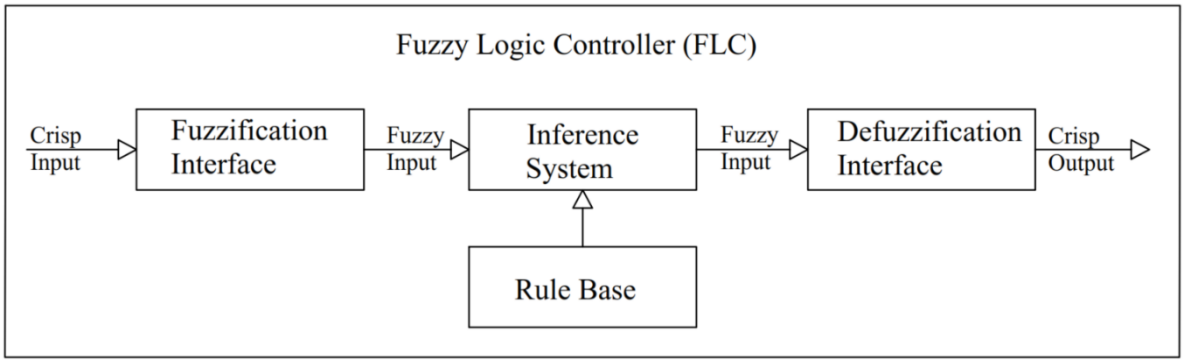


Figure 2: Configuration of a FLC.

The goal of this controller, which is based on the principles stated by Liu *et al.* [34] is to maintain the structure in a fixed position. If the structure moves away from this point, the controller increases the voltage to enhance damping and stabilize the structure. Nevertheless, if the structure is moving towards the equilibrium point, the controller decreases or stops applying a voltage as it is not necessary.

In the fuzzification interface, seven triangular membership functions are employed to define the displacement and velocity within the range [-1, 1]. These functions are used to assign a degree of membership to each value of displacement and velocity, based on their proximity to the defined linguistic variables. Scale factors, $n_d$ for displacement and $n_v$ for velocity, are also needed. Equations (8) provide the formulas for calculating these parameters:

$$n_d = k_d x$$
$$n_v = k_v \dot{x} \tag{8}$$

These equations consider the scaling factors $k_d$ for displacement and $k_v$ for velocity and use input values $x$ and $\dot{x}$ for displacement and velocity on the first floor of the building. The output voltage is determined by using four triangular membership functions defined in the range [0,1]. These functions calculate a voltage value using the centroid method. The transformation of the output voltage from a fuzzy control action to a real control action [0, 10] is carried out by using equation (9) [35].

$$V = 10\left(\frac{5}{3}s - \frac{1}{3}\right) \tag{9}$$

Where $V$ is the voltage to be applied to the damper and $s$ is the output value using the centroid method in the FLC.

The controller's inference system, as presented in Table 2, is made up of seven fuzzy rules that use linguistic parameters such as NL (negative large), NM (negative medium), NS (negative small), ZO (zero), PS (positive small), PM (positive medium), and PL (positive large).

| Vel / Dis | NL | NM | NS | ZO | PS | PM | PL |
|---|---|---|---|---|---|---|---|
| NL | PL | PL | PL | PM | ZO | ZO | ZO |
| NM | PL | PL | PL | PS | ZO | ZO | PS |
| NS | PL | PL | PL | ZO | ZO | PS | PM |
| ZO | PL | PM | PS | ZO | PS | PM | PL |
| PS | PM | PS | ZO | ZO | PL | PL | PL |
| PM | PS | ZO | ZO | PS | PL | PL | PL |
| PL | ZO | ZO | ZO | PM | PL | PL | PL |

Table 2: Inference system.

## 4 CASE OF STUDY

### 4.1 Structure

In this paper, was considered a 25-floor building as a case of study. The building is in an urban area, and it provides the characteristics of a medium-rise building. In Figure 3, is presented the elevation configuration and the plant of the building under study.

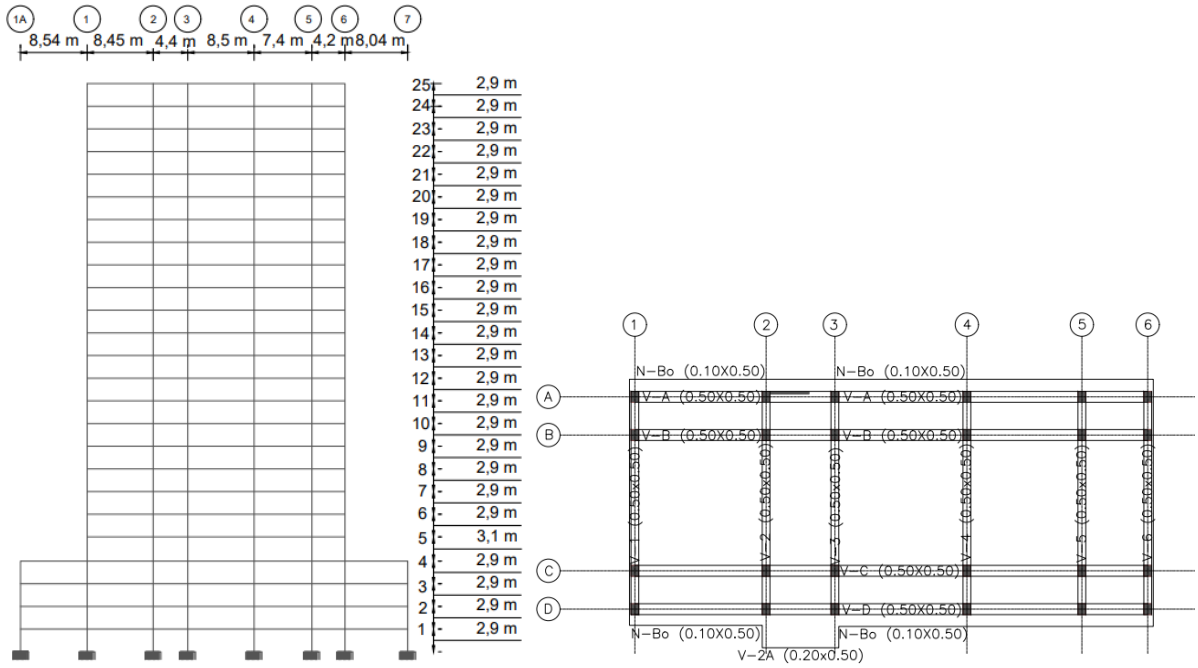


Figure 3: Building configuration.

The structural analysis for this project was conducted by reducing the stiffness matrix to a single degree of freedom for each floor of the building, this is obtained by assuming that the floor diaphragms are infinitely rigid and using static condensation to eliminate the rotational degrees of freedom. This allowed for a more detailed examination of the behavior of the structure during different ground accelerations. The mass matrix is represented as a diagonal matrix, where the entries in the diagonal represent the mass of each floor, and the matrix is used in conjunction with the stiffness matrix to calculate the dynamic response of the structure. The damping matrix was determined through the application of Rayleigh damping, with 5.0% of critical damping ($\xi$) assigned to the initial and final structural modes of the building. Below

in equation (10), it is presented the general form of the mass, stiffness, and damping matrix of the structure.

$$\boldsymbol{M} = \begin{bmatrix} m_1 & 0 & \cdots & \cdots & \cdots \\ 0 & m_2 & 0 & \ddots & \cdots \\ \vdots & 0 & m_3 & \ddots & \cdots \\ \vdots & \ddots & \ddots & \ddots & 0 \\ \vdots & \vdots & \vdots & 0 & m_n \end{bmatrix}$$

$$\boldsymbol{C} = \begin{bmatrix} c_1 + c_2 & -c_2 & 0 & \cdots & \cdots \\ -c_2 & c_2 + c_3 & c_3 & \ddots & \ldots \\ 0 & c_3 & \ddots & \ddots & \cdots \\ \vdots & \ddots & \ddots & \ddots & -c_{n-1} \\ \vdots & \vdots & \vdots & -c_{n-1} & c_{n-1} + c_n \end{bmatrix} \tag{10}$$

$$\boldsymbol{K} = \begin{bmatrix} k_1 + k_2 & -k_2 & 0 & \cdots & \cdots \\ -k_2 & k_2 + k_3 & -k_3 & \ddots & \ldots \\ 0 & -k_3 & \ddots & \ddots & \cdots \\ \vdots & \ddots & \ddots & \ddots & -k_{n-1} \\ \vdots & \vdots & \vdots & -k_{n-1} & k_{n-1} + k_n \end{bmatrix}$$

### 4.2 Seismic excitations

In this work, four different seismic excitations are used to demonstrate and validate the effectiveness of the damper. By conducting experiments with various levels of seismic activity, the study aims to provide a comprehensive assessment of the damper's performance and its ability to reduce structural vibrations. The results obtained from the different excitations will be analyzed and compared to establish the damper's effectiveness in reducing structural vibrations and improving the overall stability of the structure.

Table 3 presents the seismic excitations used in this study, which were obtained from the Center for Engineering Strong Motion Data [36]. The table includes information such as the location, year, and magnitude of the seismic event, as well as the component (direction), peak ground acceleration, and duration of each excitation.

| Seismic record | Event | Year | Station | Component | Magnitude | PGA [g] | Duration [s] |
|---|---|---|---|---|---|---|---|
| 1 | El Centro | 1940 | El Centro | S90W | 6.9 | 0.348 | 53.70 |
| 2 | Central Chile | 1985 | Melipilla | 0 | 7.8 | 0.686 | 79.36 |
| 3 | Mexico | 1985 | La Union | S00E | 8.1 | 0.169 | 62.90 |
| 4 | Morgan Hill | 1984 | USGS | 250 | 6.1 | 0.640 | 28.91 |

Table 3: Seismic excitations.

## 5 RESULTS

In-house MATLAB routines are used to simulate the behavior of the structure and generate the results presented in this study. Fulfilling the proposed goal, control forces are generated to reduce the displacement and velocity caused by the earthquake by using fuzzy logic for an MR damper. The decision to implement three dampers in the structure, located on the first floor, tenth floor, and twentieth floor, was made after a thorough iterative process. The results of the process showed that using three dampers on those floors was one of the most effective

ways to reduce the response of the structure, resulting in a significant improvement in its overall performance and optimization.

For each seismic excitation, a comparative analysis was conducted to evaluate the maximum displacement and velocity on the last floor. The analysis also included the maximum voltage required and the maximum force, which provided a comprehensive understanding of the system's response to different seismic events.

Figure 4 and Figure 5 display the graphical results of the displacement and velocity on the highest floor, respectively. The figures provide a clear illustration of the behavior of the system, with the blue line representing the response of the structure without control and the orange line representing the response with control.

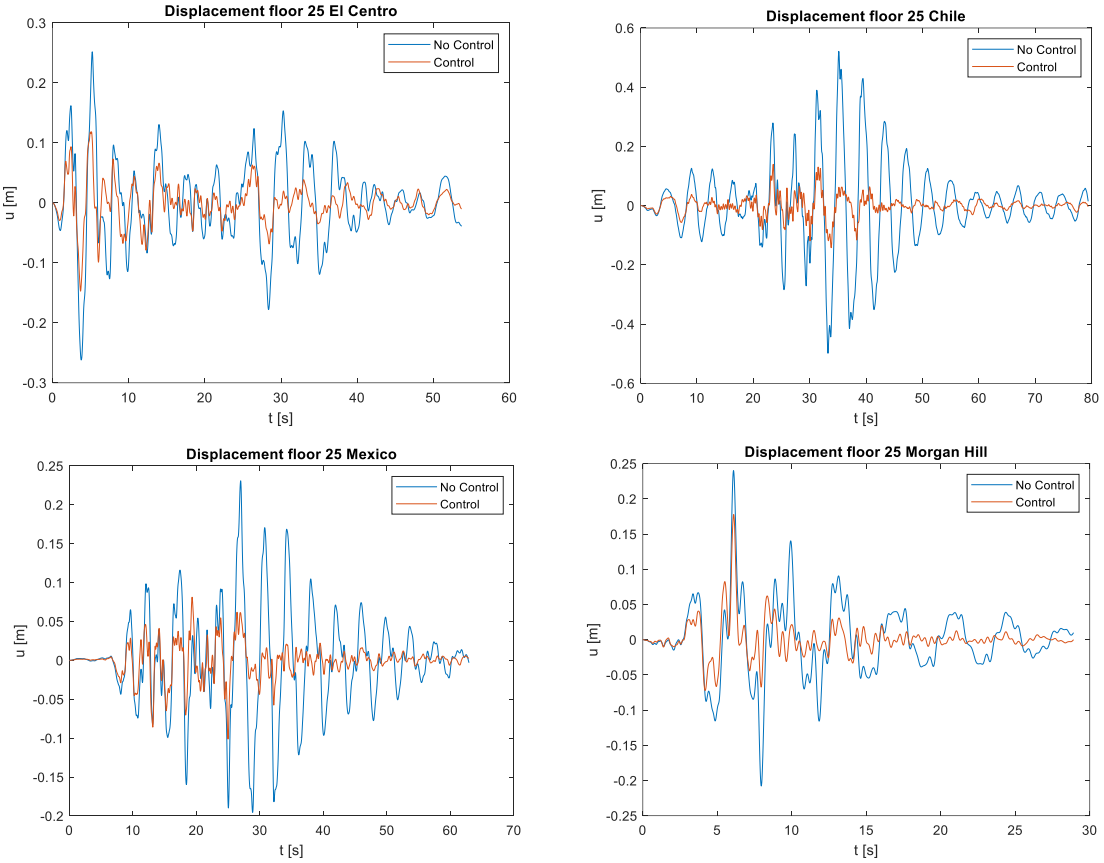


Figure 4: Displacements on the last floor.

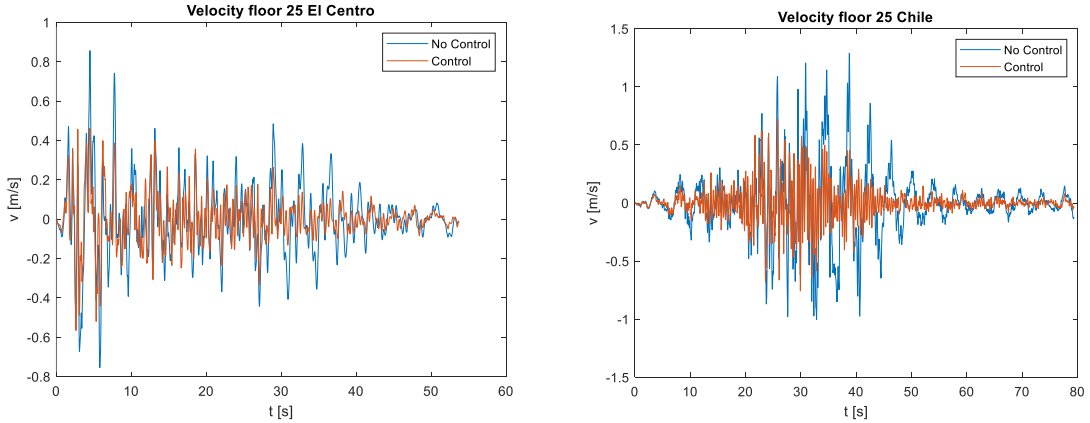

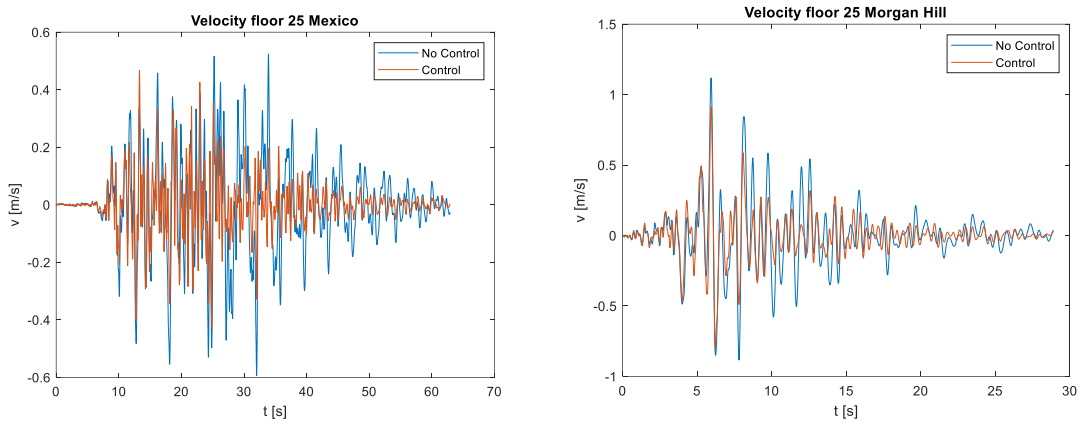


Figure 5: Velocities on the last floor.

Table 4 and Table 5 presents the results for the maximum displacement and the maximum velocity of the system in each excitation, respectively. The controller had an average reduction of 49.67% in the displacement and an average reduction of 28.8% in the velocity values compared to the values obtained without the controller.

| Maximum Displacements | | | |
|---|---|---|---|
| Event | Uncontrolled [m] | Controlled [m] | Reduction [%] |
| El Centro | 0.2619 | 0.1472 | 43.80 |
| Central Chile | 0.5210 | 0.1418 | 72.78 |
| Mexico | 0.2308 | 0.1012 | 56.15 |
| Morgan Hill | 0.2401 | 0.1778 | 25.95 |

Table 4: Maximum displacements.

| Maximum Velocities | | | |
|---|---|---|---|
| Event | Uncontrolled [m/s] | Controlled [m/s] | Reduction [%] |
| El Centro | 0.8562 | 0.5657 | 33.93 |
| Central Chile | 1.2898 | 0.7554 | 41.43 |
| Mexico | 0.5934 | 0.4672 | 21.27 |
| Morgan Hill | 1.1186 | 0.9110 | 18.56 |

Table 5: Maximum velocities.

Figure 6 displays the necessary voltage that must be applied to the damper in order to generate the forces required to control the structure. The results indicate that the maximum voltages are necessary to achieve the maximum responses without control.

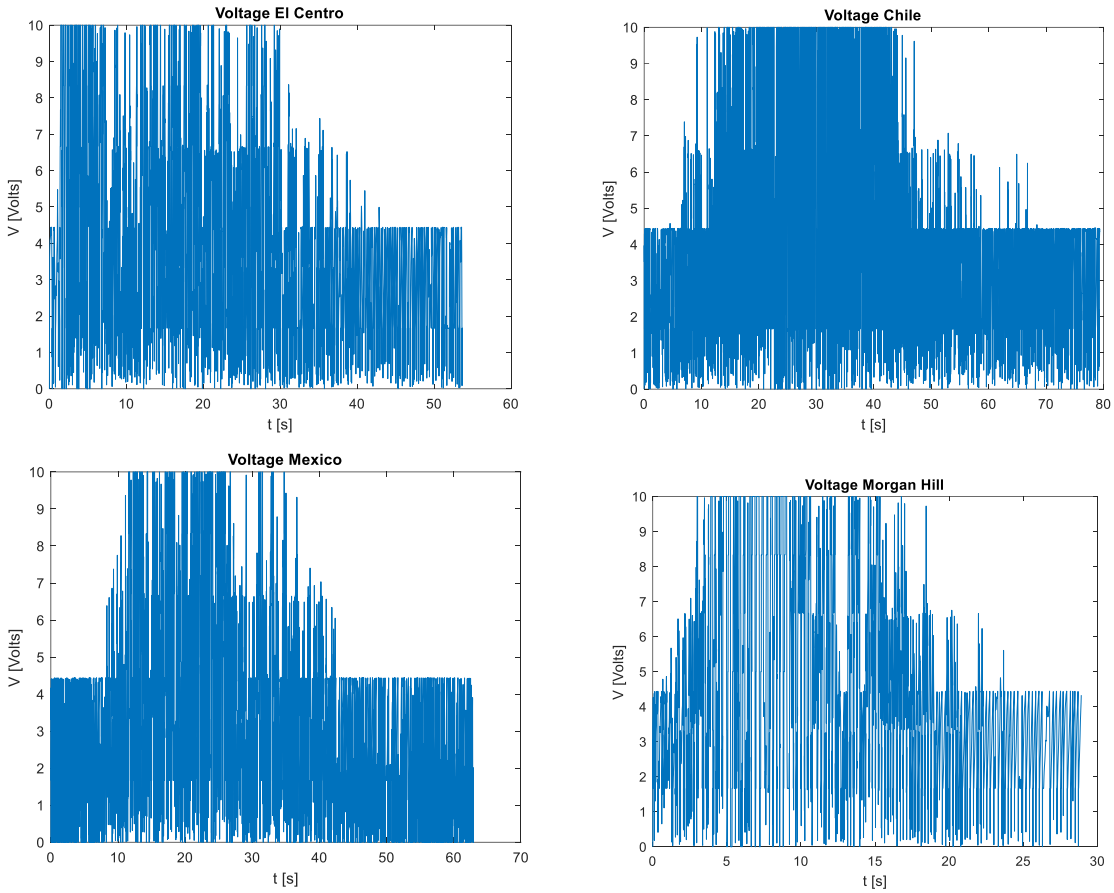


Figure 6: Voltage needed to reduce the response of the system.

The results of the study also showed that the force generated by the voltage shown above, exhibited the same behavior as the response of the structure when no control was present. According to Figure 7, the highest levels of the force applied occurred when the system experienced the highest levels of velocity and displacement showing a correlation between them.

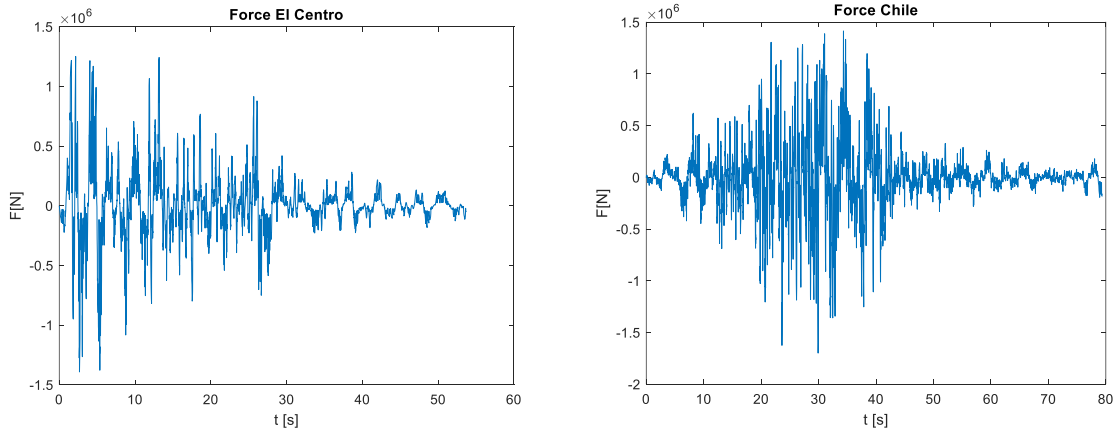

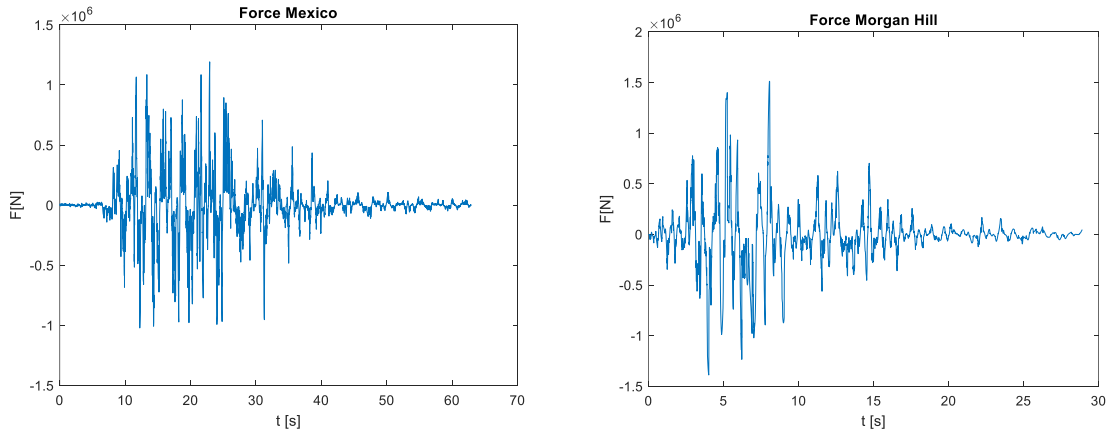


Figure 7: Force generated for each seismic record.

## 6 CONCLUSIONS

- Using fuzzy logic, the control forces are optimized to minimize the displacement and velocity induced by the seismic excitations. This methodology enables real-time modifications to the control forces, adapting to the fluctuating seismic conditions, leading to enhanced safety and performance of the structure. Incorporating fuzzy logic control for magnetorheological dampers in seismic design has the potential to greatly enhance the structural performance during earthquakes and provide a more efficient approach to mitigate the effects of seismic loads.

- The reduction in the system shows the effectiveness of the controller regulating the behavior of the system. By using the controller, the system has been able to achieve improved performance while ensuring that the maximum responses remain within acceptable limits. This is a clear indication that the controller has been successful in maintaining the stability of the system by limiting its response to external disturbances. As a result, the system can function reliably and predictably, and its performance can be optimized to meet the desired requirements.

- The ability of the damper to produce the necessary forces that keep a structure stable and balanced is dependent on the voltage, which serves as the driving force. Without the correct voltage, the damper would not be able to effectively regulate the structure, leading to potential instability and structural damage. Therefore, it is crucial to ensure that the right voltage is applied to the damper to guarantee its proper function and the safety of the structure.

- Effective control techniques are essential for optimizing the performance of dampers in various applications. When the structure faced with a maximum response with no control, it is necessary to apply the maximum voltage to the controller and implement advanced control algorithms to minimize displacement and velocity.

## REFERENCES


[1] V. Umachagi, K. Venkataramana, G. R. Reddy, and R. Verma, "APPLICATIONS OF DAMPERS FOR VIBRATION CONTROL OF STRUCTURES: AN OVERVIEW," 2013. [Online]. Available: http://www.ijret.org

[2] C. C. Lin, C. L. Chen, and J. F. Wang, "Vibration control of structures with initially accelerated passive tuned mass dampers under near-fault earthquake excitation," *Computer-Aided Civil and Infrastructure Engineering*, vol. 25, no. 1, pp. 69–75, Jan. 2010, doi: 10.1111/j.1467-8667.2009.00607.x.

[3] K. A. Al-Saif, K. A. Aldakkan, and M. A. Foda, "Modified liquid column damper for vibration control of structures," *Int J Mech Sci*, vol. 53, no. 7, pp. 505–512, Jul. 2011, doi: 10.1016/j.ijmecsci.2011.04.007.

[4] M. Abdel-Rohman, M. J. John, and M. F. Hassan, "Compensation of time delay effect in semi-active controlled suspension bridges," *JVC/Journal of Vibration and Control*, vol. 16, no. 10, pp. 1527–1558, Sep. 2010, doi: 10.1177/1077546309106518.

[5] Q. P. Ha, M. T. Nguyen, J. Li, and N. M. Kwok, "Smart structures with current-driven MR dampers: Modeling and second-order sliding mode control," *IEEE/ASME Transactions on Mechatronics*, vol. 18, no. 6, pp. 1702–1712, 2013, doi: 10.1109/TMECH.2013.2280282.

[6] S. Thenozhi and W. Yu, "Advances in modeling and vibration control of building structures," *Annual Reviews in Control*, vol. 37, no. 2. pp. 346–364, Dec. 2013. doi: 10.1016/j.arcontrol.2013.09.012.

[7] L. Marian and A. Giaralis, *Optimal design of inerter devices combined with TMDs for vibration control of buildings exposed to stochastic seismic excitations*. 2013.

[8] T. E. Saaed, G. Nikolakopoulos, J. E. Jonasson, and H. Hedlund, "A state-of-the-art review of structural control systems," *JVC/Journal of Vibration and Control*, vol. 21, no. 5. SAGE Publications Inc., pp. 919–937, Apr. 15, 2015. doi: 10.1177/1077546313478294.

[9] M. A. Lackner and M. A. Rotea, "Structural control of floating wind turbines," *Mechatronics*, vol. 21, no. 4, pp. 704–719, 2011, doi: 10.1016/j.mechatronics.2010.11.007.

[10] S. Korkmaz, "A review of active structural control: Challenges for engineering informatics," *Computers and Structures*, vol. 89, no. 23–24. pp. 2113–2132, Dec. 2011. doi: 10.1016/j.compstruc.2011.07.010.

[11] O. El-Khoury and H. Adeli, "Recent Advances on Vibration Control of Structures Under Dynamic Loading," *Archives of Computational Methods in Engineering*, vol. 20, no. 4. pp. 353–360, Dec. 2013. doi: 10.1007/s11831-013-9088-2.

[12] Spencer Jr and S. Michael K, "Controling Buildings A new frontier in Feedback," 1997.

[13] N. R. Fisco and H. Adeli, "Smart structures: Part I - Active and semi-active control," *Scientia Iranica*, vol. 18, no. 3 A. Sharif University of Technology, pp. 275–284, 2011. doi: 10.1016/j.scient.2011.05.034.

[14] S. M. Hasheminejad, A. H. Rabiee, and M. Jarrahi, "Semi-Active Vortex Induced Vibration Control of an Elastic Elliptical Cylinder with Energy

Regeneration Capability," *International Journal of Structural Stability and Dynamics*, vol. 17, no. 9, Nov. 2017, doi: 10.1142/S0219455417501073.

[15] K. I. Gkatzogias and A. J. Kappos, "Semi-active control systems in bridge engineering: A review of the current state of practice," *Structural Engineering International*, vol. 26, no. 4. Int. Assoc. for Bridge and Structural Eng. Eth-Honggerberg, pp. 290–300, 2016. doi: 10.2749/101686616X14555429844040.

[16] A. Yanik, J.-P. Pinelli, and H. Gutierrez, "CONTROL OF A THREE-DIMENSIONAL STRUCTURE WITH MAGNETO-RHEOLOGICAL DAMPERS," 2013.

[17] F. Weber, "Semi-active vibration absorber based on real-time controlled MR damper," *Mech Syst Signal Process*, vol. 46, no. 2, pp. 272–288, Jun. 2014, doi: 10.1016/j.ymssp.2014.01.017.

[18] A. K-Karamodin and H. H-Kazemi, "Semi-active control of structures using neuro-predictive algorithm for MR dampers," *Struct Control Health Monit*, vol. 17, no. 3, pp. 237–253, Apr. 2010, doi: 10.1002/stc.278.

[19] M. J. L. Boada, J. A. Calvo, B. L. Boada, and V. Díaz, "Modeling of a magnetorheological damper by recursive lazy learning," *Int J Non Linear Mech*, vol. 46, no. 3, pp. 479–485, Apr. 2011, doi: 10.1016/j.ijnonlinmec.2008.11.019.

[20] B. B. F Spencer Jr, S. J. Dyke, A. Member, M. K. Sain, and J. D. Carlson, "PHENOMENOLOGICAL MODEL FOR MAGNETORHEOLOGICAL DAMPERS." [Online]. Available: http://www.rheonetic.com/mrfluid/

[21] S. Talatahari, A. Kaveh, and N. Mohajer Rahbari, "Parameter identification of Bouc-Wen model for MR fluid dampers using adaptive charged system search optimization," *Journal of Mechanical Science and Technology*, vol. 26, no. 8, pp. 2523–2534, Aug. 2012, doi: 10.1007/s12206-012-0625-y.

[22] G. R. Peng, W. H. Li, H. Du, H. X. Deng, and G. Alici, "Modelling and identifying the parameters of a magneto-rheological damper with a force-lag phenomenon," *Appl Math Model*, vol. 38, no. 15–16, pp. 3763–3773, Aug. 2014, doi: 10.1016/j.apm.2013.12.006.

[23] A. Bahar, F. Pozo, L. Acho, J. Rodellar, and A. Barbat, "Hierarchical semi-active control of base-isolated structures using a new inverse model of magnetorheological dampers," *Comput Struct*, vol. 88, no. 7–8, pp. 483–496, 2010, doi: 10.1016/j.compstruc.2010.01.006.

[24] M. Zapateiro, H. R. Karimi, N. Luo, and B. F. Spencer, "Real-time hybrid testing of semiactive control strategies for vibration reduction in a structure with MR damper," *Struct Control Health Monit*, vol. 17, no. 4, pp. 427–451, Jun. 2010, doi: 10.1002/stc.321.

[25] M. Bitaraf, O. E. Ozbulut, S. Hurlebaus, and L. Barroso, "Application of semi-active control strategies for seismic protection of buildings with MR dampers," *Eng Struct*, vol. 32, no. 10, pp. 3040–3047, Oct. 2010, doi: 10.1016/j.engstruct.2010.05.023.

[26] A. Sarrafan, S. H. Zareh, A. A. A. Khayyat, and A. Zabihollah, "Neuro-fuzzy control strategy for an offshore steel jacket platform subjected to wave-induced forces using magnetorheological dampers," *Journal of Mechanical Science and Technology*, vol. 26, no. 4, pp. 1179–1196, Apr. 2012, doi: 10.1007/s12206-012-0212-2.

[27] K. C. Schurter and P. N. Roschke, "FUZZY MODELING OF A MAGNETORHEOLOGICAL DAMPER USING ANFIS."

[28] A. Bathaei, S. M. Zahrai, and M. Ramezani, "Semi-active seismic control of an 11-DOF building model with TMD+MR damper using type-1 and -2 fuzzy algorithms," *JVC/Journal of Vibration and Control*, vol. 24, no. 13, pp. 2938–2953, Jul. 2018, doi: 10.1177/1077546317696369.

[29] M. M. Algazar, H. Al-Monier, H. A. El-Halim, and M. E. E. K. Salem, "Maximum power point tracking using fuzzy logic control," *International Journal of Electrical Power and Energy Systems*, vol. 39, no. 1, pp. 21–28, Jul. 2012, doi: 10.1016/j.ijepes.2011.12.006.

[30] M. Rafie and F. Samimi Namin, "Prediction of subsidence risk by FMEA using artificial neural network and fuzzy inference system," *Int J Min Sci Technol*, vol. 25, no. 4, pp. 655–663, Jul. 2015, doi: 10.1016/j.ijmst.2015.05.021.

[31] D. Das, T. K. Datta, and A. Madan, "Semiactive fuzzy control of the seismic response of building frames with MR dampers," *Earthq Eng Struct Dyn*, vol. 41, no. 1, pp. 99–118, 2012, doi: 10.1002/eqe.1120.

[32] M. Boreiry, S. Ebrahimi-Nejad, and J. Marzbanrad, "Sensitivity analysis of chaotic vibrations of a full vehicle model with magnetorheological damper," *Chaos Solitons Fractals*, vol. 127, pp. 428–442, Oct. 2019, doi: 10.1016/j.chaos.2019.07.005.

[33] M. M. Gupta, "Forty-five years of fuzzy sets and fuzzy logic-A tribute to professor Lotfi A. Zadeh (the father of fuzzy logic)," *Scientia Iranica*, vol. 18, no. 3 D. Sharif University of Technology, pp. 685–690, 2011. doi: 10.1016/j.scient.2011.04.023.

[34] Y. Liu, F. Gordaninejad, C. A. Evrensel, and G. Hitchcock, "An Experimental Study on Fuzzy Logic Vibration Control of a Bridge Using Fail-Safe Magneto-Rheological Fluid Dampers," 2001. [Online]. Available: http://Web.me.unr.edu/ciml

[35] L. A. Lara-Valencia, Y. Valencia-Gonzalez, J. Luis Vital De Brito, L. Augusto, and L. Valencia, "Uso de lógica difusa para la administración de un sistema disipador de energía en estructuras compuesto por amortiguadores magnetoreológicos Use of fuzzy logic for the administration of a structural control system based on magnetorheological dampers," 2015.

[36] "Center for engineering strong-motion data (CESMD)." www.strongmotioncenter.org. (accessed Dec. 25, 2022).

COMPDYN 2023
9th ECCOMAS Thematic Conference on
Computational Methods in Structural Dynamics and Earthquake Engineering
M. Papadrakakis, M. Fragiadakis (eds.)
Athens, Greece, 12-14 June 2023

# CONTROL OF THE STRUCTURAL RESPONSE OF A HIGH-RISE BUILDING UNDER WIND LOAD USING A TUNED MASS DAMPER INERTER (TMDI)

**Daniela Vallejo-Paniagua[1], Mariana Castro-Osorio[2], Verónica Valencia-Valencia[2], Luis A. Lara-Valencia[2], and John J. Blandón-Valencia[2].**

[1] Universidad Nacional de Colombia sede Medellín
Carrera 80 N.º65-223, Núcleo Robledo. Medellín, Colombia.
dvallejo@unal.edu.co

[2] Universidad Nacional de Colombia sede Medellín
Carrera 80 N.º65-223, Núcleo Robledo. Medellín, Colombia.
{mcastroos, vvalenciav, lualarava, jjblandon}@unal.edu.co

## Abstract

*Several studies have been done on structural control over the last few decades, with the intent to reduce the structural response of buildings under environmental loads. Generally, the purpose of these works is to mitigate the accelerations and displacements that are generated and compromise the safety of people and the stability of the structure itself. To achieve the desired controlled behavior of the structure, a control device can be used. Among the different existing control alternatives, passive control devices have proven to be very effective and convenient for a structure because they use their own mass to generate inertial forces that counteract the external forces acting on the system. This paper explores the numerical design of a TMDI using a nature-like metaheuristic to find the optimal parameters of the device to implement it in a high-rise building under wind load. For this purpose, the grey wolf optimizer (GWO) is used to reduce the objective functions related to peak displacement and root mean square (RMS) value of acceleration. The results show an important improvement in the response of the building, meaning the displacements and accelerations were mitigated, proving that the TMDI is a suitable device for structural control.*

**Keywords:** Structural control, tuned mass damper inerter, Grey Wolf Optimizer, wind load.

## 1 INTRODUCTION

The effort to reduce vibrations caused by seismic or wind loads in buildings is especially important, as these loads can result in significant displacements and acceleration forces on the structure, compromising its stability and putting the safety of its inhabitants at risk. Therefore, the implementation of control strategies to mitigate their effects is essential for ensuring the safety of the building and its users [1].

Several methods have been investigated to reduce the structural response under dynamic loads such as increasing the inertia of the structure by modifying its mass or stiffness. However, the use of control devices has been gaining more popularity for their effectiveness in a wide range of applications and the variety of available devices [2]. Some control devices, known as active devices, work by applying an external counterforce. Others, known as passive devices, use the properties of the structure and the device to generate forces that counteract external loads.

Passive control devices have been widely studied to mitigate vibrations benefiting from the fact that they do not need an external source of energy and they are able to generate great damping [3]. Passive devices such as Adding Damper and Stiffness (ADAS), Tuned Liquid Column Damper (TLCD), and Viscoelastic Dampers have been shown to effectively improve the response of structures under environmental loads [4–6]. Another passive device, which has been studied in numerous research is a tuned mass damper (TMD), a concept that was first proposed by Den Hartog [7] and consists of a mass, a spring, and a damper tuned to the fundamental frequency of the structure. It is typically placed on the top floor of a building, where it helps to mitigate the most severe response to wind or seismic loads [8, 9]. This is achieved by redirecting the vibrations of the structure to the device, where they are then dissipated through the damping [10]. However, its ability to reduce the response of buildings to wind and seismic loads is limited due to construction constraints to place a device of a large mass on the top floor. Therefore, the mass of the device is selected with a typical upper limit of 5% of the total mass of the structure being controlled [11].

As an improvement of a TMD, a tuned mass damper inerter (TMDI) was proposed by Marian and Giaralis [12]. The TMDI consists of a traditional TMD with an attached inerter device. An inerter is a mechanical device with two terminals that links the TMD with the previous level it is located on. The most favorable feature of the inerter is amplifying its own small mass, a characteristic that allows it to have a significant impact. Since the inerter was proposed by Smith [13] many studies have been done, concluding that it is an effective mechanism to enhance passive devices to mitigate the structural response of buildings [14–16].

Despite the similarities of both devices (TMD and TMDI), and the positive performance of the first, a TMDI becomes a better option to reduce displacements and accelerations generated by environmental loads because nowadays, structures tend to grow vertically and slimmer. Therefore, the mass needed by the device to work adequately in a high-rise building is greater than the one needed for lower structures. Furthermore, these kinds of structures need to undergo an analysis of the wind load effect which they are very susceptible to, due to their slenderness [17, 18]. Research on buildings exposed to wind vibrations using a TMDI has yielded promising results [19, 20].

The optimal design of a TMDI depends on the structure it is intended for, as the parameters that govern the device must be adjusted to match the fundamental frequency of the building [21]. To find these parameters, metaheuristics optimization algorithms have proven to be a reliable method to use while being simple and applicable to a wide range of problems [22, 23]. In a metaheuristic approach, a set of possible solutions is randomly generated, and a function is used to evaluate the quality of each solution. The best solutions are then used to generate new solutions through a

process of exploration. This process is repeated until a satisfactory solution is found or a stopping criterion is met.

In this work, the Grey Wolf Optimizer (GWO) will be used to obtain the parameters needed to optimally design the TMDI. GWO is a nature-inspired, metaheuristic algorithm that is used to optimize solutions to a problem [24, 25]. The algorithm is inspired by the hunting behavior of a pack of wolves and replicates the hierarchy and cooperation present in a wolf pack. GWO has been shown to be an effective optimization technique while considering the constraints and limitations of the problem.

This paper aims to develop a TMDI that can minimize the structural impact of wind on high-rise buildings, specifically reducing maximum displacements and acceleration. The device will be located on the top floor of a 37$^{th}$ -story building and the inerter will be attached one floor below it. Finally, the GWO will be used and is expected to provide an efficient optimization process to find the optimal parameters for the TMDI: the frequency and damping ratio. The use of a TMDI optimized with the GWO optimization technique provides a reliable and efficient means to reduce the dynamic response of a high-rise building, being able to reduce up to 37% of the displacements suffered during a wind gust. Overall, the TMDI system provides a promising approach to addressing the challenges posed by dynamic wind loads and can help to enhance the resilience and reliability of structures.

## 2 MATHEMATICAL MODEL OF A TUNED MASS DAMPER INERTER (TMDI) IN A MULTI-DEGREE OF FREEDOM BUILDING

The mathematical model is presented for a plane frame with *n*-degrees of freedom, related to the horizontal translation per level of the frame subjected to an external force.

### 2.1 The inerter

The inerter, as presented in Figure 1, is a small mechanical element with two terminals which main characteristic is that the relative acceleration that the device experience at the terminals is also proportional to the applied force on them, in this case, the dynamic load. The internal force ($F_b$) resisting in each terminal can be written as shown in equation (1):

$$F_b = b(\ddot{u}_2 - \ddot{u}_1) \tag{1}$$

Where $\ddot{u}_1$ y $\ddot{u}_2$ are the accelerations on terminals 1 and 2, respectively, and *b* is the inerter proportionality constant that defines the device.

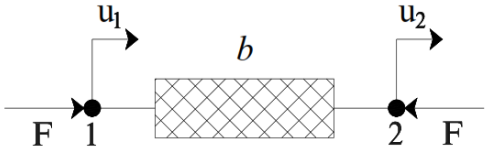


Figure 1: Outline of an inerter device.

An inerter can enhance the performance of passive control devices such as a TMD. TMDs have been successful in reducing building vibrations, however, their efficacy is restricted by the amount

of mass that can be located on the top floor. This not only reduces the inertial force that the device can produce but also restricts its impact to only one frequency since the mass of the device is fixed. This becomes increasingly difficult as buildings become taller. The inerter, on the other hand, is installed on the top floor and adds a minimal amount of mass while providing a resisting force of up to 200 times the added mass [26].

## 2.2 Equation of motion for an *n* degree of freedom system equipped with a TMDI

The equation of motion developed herein considers a multi-degree of freedom 2D frame equipped with a TMDI as shown in Figure 2. For each level of the frame, the properties such as stiffness, damping, and mass are represented with the spring constant of stiffness $k_i$, the viscous damper with damping constant $c_i$, and a concentrated mass $m_i$, respectively, where *i* stands for each level of the frame.

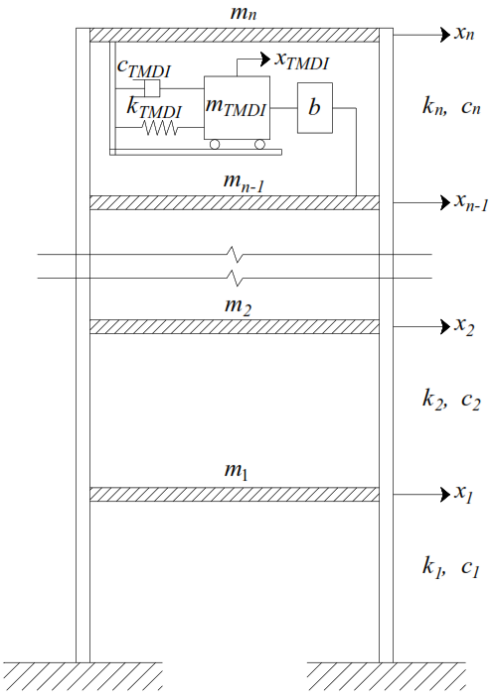


Figure 2: A *n* degrees of freedom system equipped with a TMDI.

Note the TMDI located in the upper level of the frame resembles a traditional TMD with an added inerter connecting the TMD and level *n-1*. The properties that characterized the device are almost the same as those for each level of the frame, therefore the mass is represented by $m_{TMDI}$ and the stiffness and damping of the device are $k_{TMDI}$ and $c_{TMDI}$, respectively. The only new parameter implemented is the constant *b* which refers to the inertance of the TMDI, and it provides information about the device's ability to resist changes in its motion.

The motion for the frame of *n+1* degrees of freedom specified above is described by equation (2) where $\ddot{\boldsymbol{x}}(t)$, $\dot{\boldsymbol{x}}(t)$ and $\boldsymbol{x}(t)$ are the *n+1* acceleration, velocity, and displacement vectors respectively and $\boldsymbol{F_{ext}}$ is the external force applied to the structure.

$$\boldsymbol{M}\ddot{\boldsymbol{x}}(t) + \boldsymbol{C}\dot{\boldsymbol{x}}(t) + \boldsymbol{K}\boldsymbol{x}(\boldsymbol{t}) = \boldsymbol{F_{ext}}(t) \tag{2}$$

In equation (2), ***M, C,*** and ***K*** represent the structure's mass, damping, and stiffness matrix, respectively of order *(n+1)* x *(n+1)* considering the degrees of freedom of the structure itself and the control device. They can be calculated as follows:

$$\boldsymbol{M} = \begin{bmatrix} m_1 & 0 & 0 & 0 & \cdots & \cdots & 0 \\ 0 & m_2 & 0 & 0 & \ldots & \cdots & 0 \\ 0 & 0 & m_3 & 0 & \cdots & \cdots & 0 \\ \vdots & \vdots & \vdots & \ddots & \cdots & \cdots & \vdots \\ \vdots & \vdots & \vdots & \vdots & m_{n-1}+b & 0 & -b \\ \vdots & \vdots & \vdots & \vdots & 0 & m_n & 0 \\ 0 & 0 & \cdots & \cdots & -b & 0 & m_{TMDI}+b \end{bmatrix} \tag{3}$$

$$\boldsymbol{C} = \begin{bmatrix} c_1+c_2 & -c_2 & 0 & 0 & \cdots & \cdots & 0 \\ -c_2 & c_2+c_3 & c_3 & 0 & \ldots & \cdots & 0 \\ 0 & c_3 & c_3+c_4 & c_4 & \cdots & \cdots & 0 \\ \vdots & \vdots & \vdots & \ddots & \cdots & \cdots & \vdots \\ \vdots & \vdots & \vdots & -c_{n-1} & c_{n-1}+c_n & -c_n & 0 \\ \vdots & \vdots & \vdots & 0 & -c_n & c_n+c_{TMDI} & -c_{TMDI} \\ 0 & 0 & \cdots & 0 & 0 & -c_{TMDI} & c_{TMDI} \end{bmatrix} \tag{4}$$

$$\boldsymbol{K} = \begin{bmatrix} k_1+k_2 & -k_2 & 0 & 0 & \cdots & \cdots & 0 \\ -k_2 & k_2+k_3 & -k_3 & 0 & \ldots & \cdots & 0 \\ 0 & -k_3 & k_3+k_4 & -k_4 & \cdots & \cdots & 0 \\ \vdots & \vdots & \vdots & \ddots & \cdots & \cdots & \vdots \\ \vdots & \vdots & \vdots & -k_{n-1} & k_{n-1}+k_n & -k_n & 0 \\ \vdots & \vdots & \vdots & 0 & -k_n & k_n+k_{TMDI} & -k_{TMDI} \\ 0 & 0 & \cdots & 0 & 0 & -k_{TMDI} & k_{TMDI} \end{bmatrix} \tag{5}$$

## 3 TMDI OPTIMIZATION

In order to design a properly functioning TMDI device, it is necessary to optimize the parameters that govern its performance. This optimization process involves finding the optimal values for the frequency and damping ratio of the device, which will ensure that it is able to effectively reduce the structural response of the building to wind.

### 3.1 Parameters that govern a TMDI

To design a TMDI it is necessary to define the parameters that are going to govern the device and therefore need to be optimized to mitigate the displacements and accelerations experienced by the structure. In equations (6) and (7) the critical damping ratio, $\xi_{TMDI}$ and frequency ratio, $\nu_{TMDI}$ are described where $m_{TMDI}$, $c_{TMDI}$, $k_{TMDI}$, and $b$ are the properties of the TMDI defined in the mathematical model and $\omega_1$ is the fundamental frequency of the structure.

$$\nu_{TMDI} = \frac{\omega_{TMDI}}{\omega_1} = \frac{\sqrt{\dfrac{k_{TMDI}}{m_{TMDI}+b}}}{\omega_1} \tag{6}$$

$$\xi_{TMDI} = \frac{c_{TMDI}}{2(m_{TMDI}+b)\omega_{TMDI}} \tag{7}$$

In addition to the natural frequency and critical damping ratio, there are two other parameters that define the TMDI. They are not intended to be optimized but kept constant throughout the process. They are the device mass ratio, $\mu$, and the inertance ratio, $\beta$, defined in equations (8) and (9), respectively, where $Ms$ represents the total mass of the structure.

$$\beta = \frac{b}{Ms} \tag{8}$$

$$\mu = \frac{m_{TMDI}}{Ms} \tag{9}$$

As the optimization problem involves two parameters, it is considered a two-dimensional problem, and it is necessary to establish the limits within which the optimal values can be found. This is done by defining the range of possible values for each of the parameters to be optimized that has been further investigated [27–30].

$$0.00 \leq \zeta_{\text{TMDI}} \leq 0.50 \tag{10}$$

$$0.50 \leq \nu \leq 2.00 \tag{11}$$

To find the optimal parameters for the TMDI device, it is essential to define the objective functions that the optimization algorithm will work on. These objective functions are used to evaluate the performance of the device and determine how well it is able to reduce the structural response of the building. The optimization algorithm then searches through different combinations of parameter values to find the combination that results in the best performance as defined by the objective functions.

In this particular case of study, the objective functions are defined as the minimization of the maximum peak displacement ($x_{i\,peak}$) and minimizing the root mean square (RMS) value of acceleration ($RMS(\ddot{x}_i)$) of the structure as shown in equations (12) and (13), respectively.

$$J_1 = \min\left(max\left(\left|x_{i\,peak}\right|\right)\right) \tag{12}$$

$$J_2 = \min\left(max\left(\left|RMS(\ddot{x}_i)\right|\right)\right) \tag{13}$$

### 3.2 Grey wolf optimizer (GWO) algorithm

The Grey Wolf Optimizer algorithm is a swarm intelligence method proposed by Mirjalili *et al.* [24] and was inspired by the hunting behavior of grey wolves. It is a nature-inspired metaheuristic algorithm used to optimize solutions for a problem by mimicking the hierarchy and cooperation of a pack of grey wolves when hunting for prey. GWO is a simple, fast, and efficient optimization algorithm that has been applied to a wide range of optimization problems. It has been shown to be a powerful tool for solving complex optimization problems. The wolf that has the most optimal

solution is the alpha (α), and the one with the second and third best solution is the beta (β) and delta (δ), respectively. Other candidate solutions are omega (ω). The advantage of the algorithm over others is that omegas keep searching and updating its position depending on the best solution found. The optimization process can be described as follows [24, 31] :

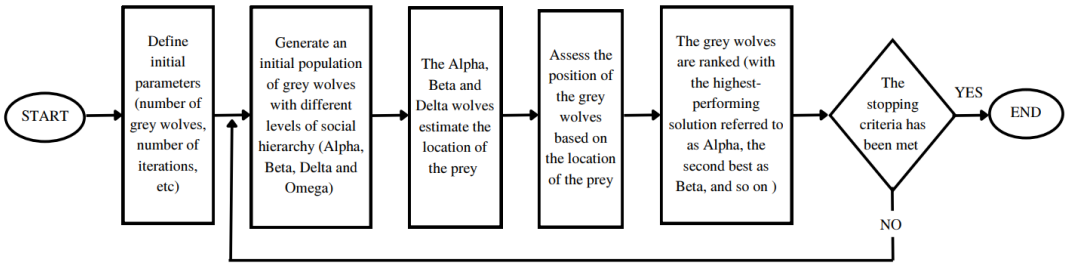


Figure 3: Grey wolf flowchart.

## 4 WIND LOAD

To analyze the dynamic wind load, the procedure proposed by Franco [32] will be applied. The approach consists of transforming the power spectrum of wind into fluctuating pressures represented by a number of harmonic functions. The procedure proposed by Franco provides an efficient and reliable method to generate the dynamic wind load, considering the different modes of vibration of the structure [33].

Important data such as the location and the topographic characteristics of where the structure of interest is located, need to be considered to find the basic parameters of wind speed. For the case of study in this paper, the Colombian earthquake-resistant design code, Normas Colombianas de Diseño y Construcción Sismoresistente NSR-10 [34], will be applicable due to the location of the building analyzed.

Figure 4 and Figure 5 demonstrate the results of the wind load analysis for the building. Figure 4 shows the fluctuating pressure of the wind over time, while Figure 5 illustrates the wind load acting on the 37$^{th}$ level. These results were obtained by using the methodology described above to simulate a dynamic wind load. These figures provide important information about the wind loads that the building will be subjected to and will be used to evaluate the structural response of the building and to determine the effectiveness of different control strategies.

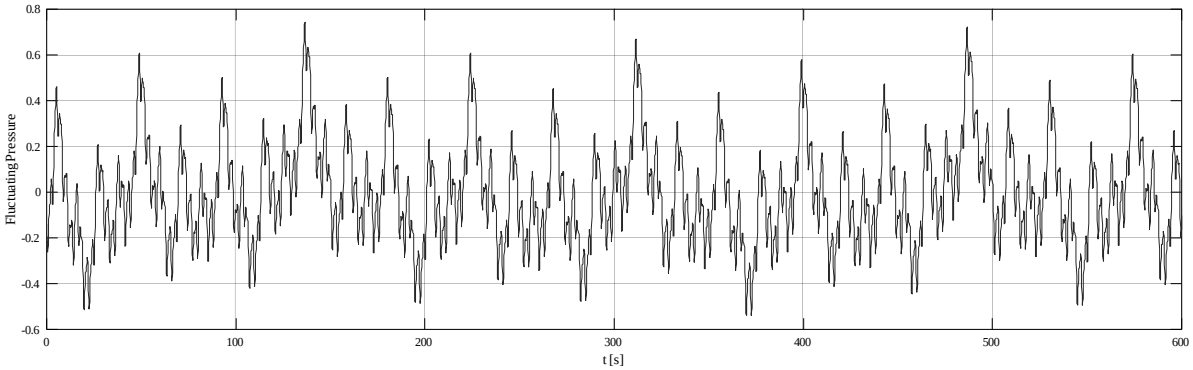


Figure 4: Fluctuating pressures of the wind.

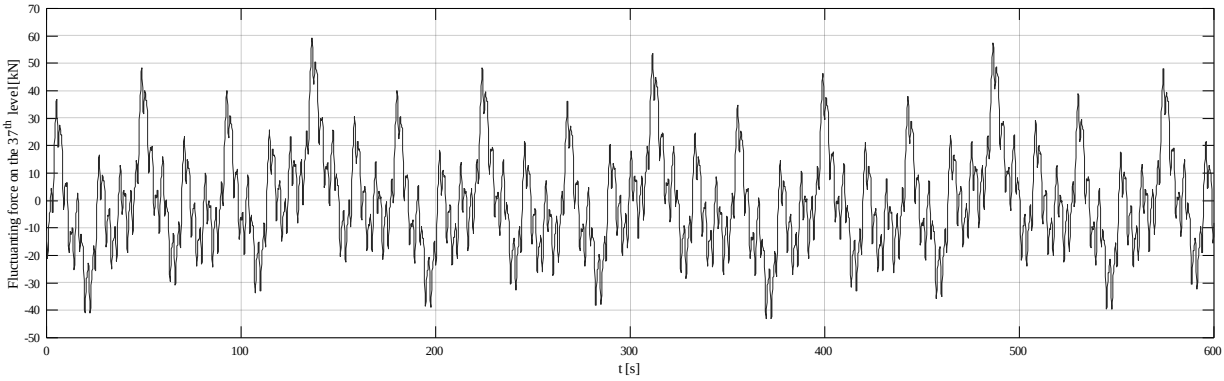


Figure 5: Wind load in the 37th level through time.

## 5 CASE OF STUDY

The mathematical model of a TMDI-controlled system is implemented in a real structure modeled as a plane frame, to evaluate its performance when it is subjected to wind load. The structure that was modeled and used in this case of study is *Cantagirone Tre Piú*, a residential building located in Medellín, Colombia. This building has 37 levels, with a height of 3.9 m per level. The total height is 144 m above ground level and the structure is 38 m wide where the modeled frame is. The building has a structural system that consists of reinforce concrete resisting frames alongside structural walls in the corners to improve the stiffness of the building. In Figure 6 the typical plan view and elevation of the building are shown.

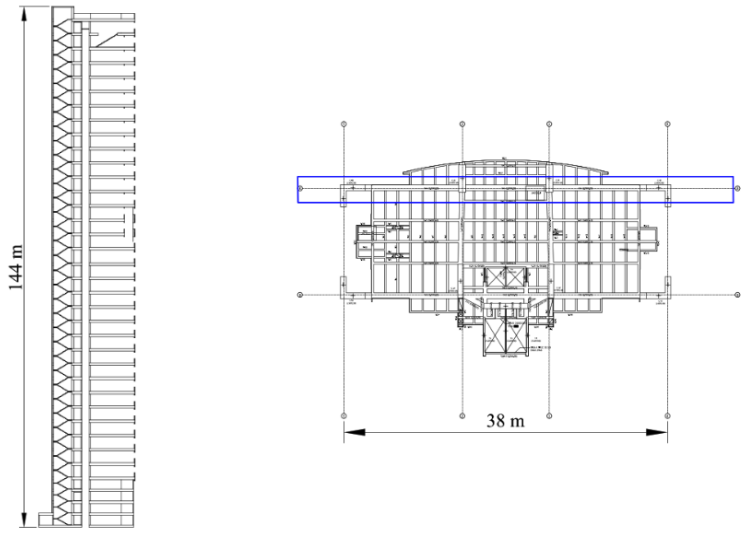


Figure 6: Elevation and plan view of *Cantagirone Tre Piú* building.

The analysis was made by reducing the plane frame to a single degree of freedom per level. To achieve this, a rigid floor diaphragm was assumed to obtain one degree of freedom for all horizontal translational nodes per level. Also, the columns were assumed axially infinitely rigid to eliminate all vertical translational degrees of freedom. Lastly, the rotational degrees of freedom were expressed in terms of the remaining horizontal translational degrees using static condensation. After

these assumptions the matrices of mass and stiffness of order *37* x *37* could be found. The damping matrix was determined by applying the Rayleigh method, using a structural damping value of 5% in the first and last modes of vibration. In Table 1, the result of the modal analysis performed in the structure is presented for the first six modes.

| Mode | T [s] | F [Hz] | ω [rad/s] |
|---|---|---|---|
| 1 | 0.8705 | 0.1828 | 1.1488 |
| 2 | 0.2614 | 0.6088 | 3.8254 |
| 3 | 0.1317 | 1.2083 | 7.5917 |
| 4 | 0.0801 | 1.9869 | 12.4838 |
| 5 | 0.0535 | 2.9722 | 18.6752 |
| 6 | 0.0385 | 4.1385 | 26.0030 |

Table 1: Modal properties of the plane frame.

## 6 RESULTS

The results obtained from the controlled response are categorized into two groups: the response of the controlled structure with the aim of reducing the highest peak displacement, represented by objective function $J_1$; and the controlled structural response with the objective of minimizing the RMS value of acceleration, represented by objective function $J_2$.

### 6.1 Algorithm Calibration

To calculate the controlled response, a calibration process was carried out in which the best combination of search inputs was sought so that the algorithm would search for the optimal parameters for the TMDI. The final selections for the optimization process resulted in 100 wolves and 20 iterations for the first objective function $J_1$ and 25 wolves with 10 iterations for the second objective function $J_2$. In order to select the wolf and iteration combinations that resulted in the best outcome, a trial-and-error process was carried out. Several combinations were tested to observe which one resulted in the maximum reduction while still optimizing time and computational efficiency. Through this process, an understanding of the problem was gained, which allowed decisions to be made regarding the selection of the best wolves and iteration combinations. Additionally, values were chosen to remain constant throughout the procedure, including the device mass ratio, $\mu$, and the inertance ratio, $\beta$, both of which were fixed at 5% based on satisfactory results shown in previous research [16, 21].

### 6.2 Uncontrolled response

To have a better understanding of how the structure behaves under wind load, Table 2 summarizes the behavior of some levels in the building. It can be observed that the maximum displacement of each floor increases as the level increases, as does the acceleration. In both cases, the most critical value is on the last floor, where the peak displacement is 0.416 m, and the peak acceleration is 0.3047 m/s$^2$. This behavior is also reflected in the RMS values of displacement and acceleration, which are at their highest on the last floor reaching 0.1482 m and 0.1741 m/s$^2$ respectively. This trend is expected and demonstrates the importance of effectively controlling the response of the structure, especially at higher levels.

| Level | Maximum uncontrolled displacement [m] | RMS value of uncontrolled displacement [m] | Maximum uncontrolled acceleration [m/s$^2$] | RMS value of uncontrolled acceleration [m/s$^2$] |
|---|---|---|---|---|
| 1 | 0.0012 | 0.0004 | 0.0306 | 0.0005 |
| 5 | 0.0264 | 0.0092 | 0.0583 | 0.0103 |
| 10 | 0.1024 | 0.0361 | 0.0739 | 0.0414 |
| 15 | 0.1899 | 0.0675 | 0.1363 | 0.0782 |
| 20 | 0.2718 | 0.0972 | 0.1929 | 0.1131 |
| 25 | 0.3373 | 0.1211 | 0.2401 | 0.1412 |
| 30 | 0.3836 | 0.1380 | 0.2777 | 0.1616 |
| 35 | 0.4083 | 0.1470 | 0.3014 | 0.1727 |
| 37 | 0.4116 | 0.1482 | 0.3047 | 0.1741 |

Table 2: Uncontrolled response of the structure under wind load.

### 6.3 Controlled response

The response of the controlled structure can be viewed in Table **3**, when the objective function used during the optimization process was $J_1$. For this scenario, the parameters that govern the device were found to be 0.001 for the damping ratio and 0.995 for the frequency ratio.

| Level | Maximum controlled displacement under $J_1$ [m] | RMS value of controlled displacement under $J_1$ [m] | Maximum controlled Acceleration under $J_1$ [m/s$^2$] | RMS value of controlled acceleration under $J_1$ [m/s$^2$] |
|---|---|---|---|---|
| 1 | 0.0008 | 0.0003 | 0.0306 | 0.0002 |
| 5 | 0.0174 | 0.0056 | 0.0583 | 0.0030 |
| 10 | 0.0666 | 0.0215 | 0.0669 | 0.0120 |
| 15 | 0.1221 | 0.0393 | 0.0922 | 0.0228 |
| 20 | 0.1728 | 0.0557 | 0.1237 | 0.0317 |
| 25 | 0.2124 | 0.0687 | 0.1359 | 0.0384 |
| 30 | 0.2400 | 0.0780 | 0.1672 | 0.0448 |
| 35 | 0.2547 | 0.0831 | 0.1940 | 0.0495 |
| 37 | 0.2565 | 0.0839 | 0.2210 | 0.0502 |

Table 3: Controlled response of the structure under $\boldsymbol{J_1}$.

The displacement and acceleration of level 37$^{th}$ are displayed in Figure **7**.a and Figure **7**.b respectively. The RMS value of displacement and acceleration for each level is shown in Figure **7**.c and Figure **7**.d respectively. It can be noted that peak displacement on the top level had a reduction of 37.67% going from 0.4116 m to 0.2565 m after the device is implemented. In the case of acceleration, a reduction is also observed, with a decrease from 0.3047 m/s$^2$ to 0.2210 m/s$^2$, resulting in a reduction of 27.47%. In a similar manner to the behavior of peak displacement and acceleration, the value of the RMS for both displacement and acceleration experiences a reduction of 43.40% and 71.17%, respectively.

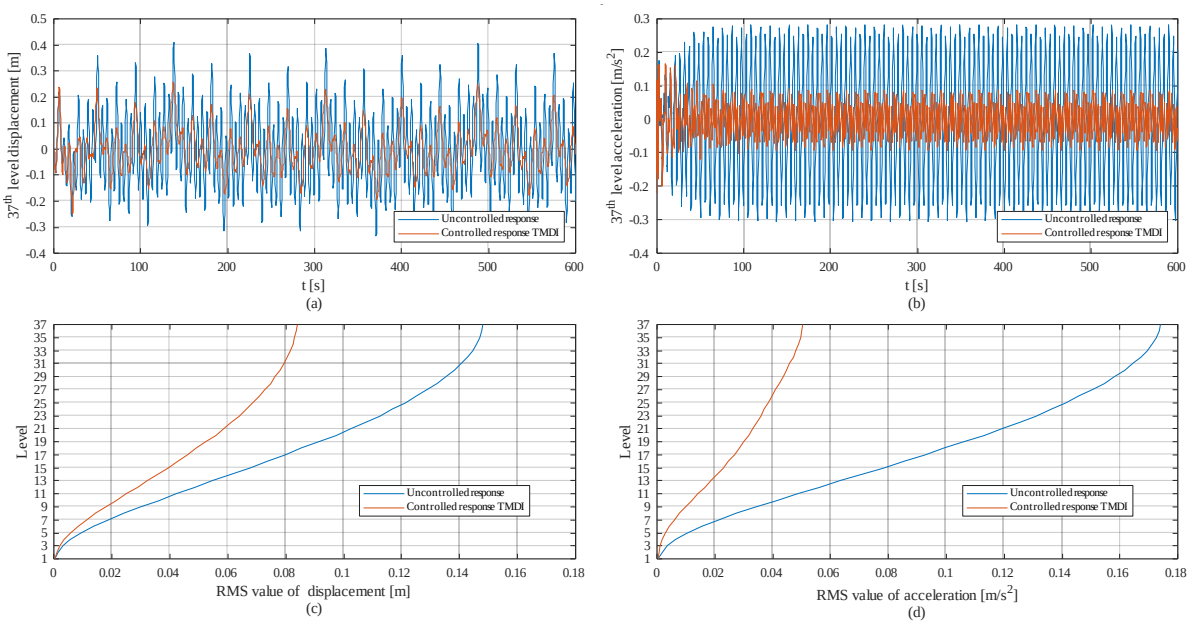


Figure 7. Structural controlled response using $J_1$. (a) Uncontrolled and controlled displacements on the 37th level. (b) Uncontrolled and controlled accelerations on the 37th level. (c) Uncontrolled and controlled RMS value of displacement. (d) Uncontrolled and controlled RMS value of acceleration.

In the optimization process, the second objective function tried was $J_2$, aimed to decrease the RMS value of acceleration. Satisfactory results were obtained and the controlled response at various levels of the structure can be seen in Table 4. This response was achieved once the design parameters of the device were found to be 0.01 for the damping ratio and 1.03 for the frequency ratio.

| Level | Maximum controlled displacement under $J_2$ [m] | RMS value of controlled displacement under $J_2$ [m] | Maximum controlled Acceleration under $J_2$ [m/s$^2$] | RMS value of controlled acceleration under $J_2$ [m/s$^2$] |
|---|---|---|---|---|
| 1 | 0.0008 | 0.0003 | 0.0306 | 0.0002 |
| 5 | 0.0167 | 0.0057 | 0.0583 | 0.0031 |
| 10 | 0.0641 | 0.0217 | 0.0669 | 0.0127 |
| 15 | 0.1199 | 0.0399 | 0.0921 | 0.0244 |
| 20 | 0.1732 | 0.0567 | 0.1232 | 0.0346 |
| 25 | 0.2171 | 0.0701 | 0.1476 | 0.0428 |
| 30 | 0.2498 | 0.0799 | 0.1682 | 0.0504 |
| 35 | 0.2687 | 0.0854 | 0.1950 | 0.0559 |
| 37 | 0.2718 | 0.0862 | 0.2209 | 0.0568 |

Table 4: Controlled response of the structure under $J_2$.

Figure 8 displays the controlled response of the building when $J_2$ was used. Figure 8.a and Figure 8.b shows the controlled displacements and accelerations respectively alongside the uncontrolled

response for comparison purposes. Similarly, Figure 8.c and Figure 8.d show the RMS value of displacement and acceleration respectively. The displacement has reduced from 0.4116 m to 0.2718 m, exhibiting a reduction of 33.95%. For the case of the acceleration, the value decreased from 0.3047 m/s$^2$ to 0.2209 m/s$^2$, resulting in a reduction of 27.51%. Finally, the reductions experienced by the RMS value of displacement and acceleration were of 41.80% and 67.36%, respectively.

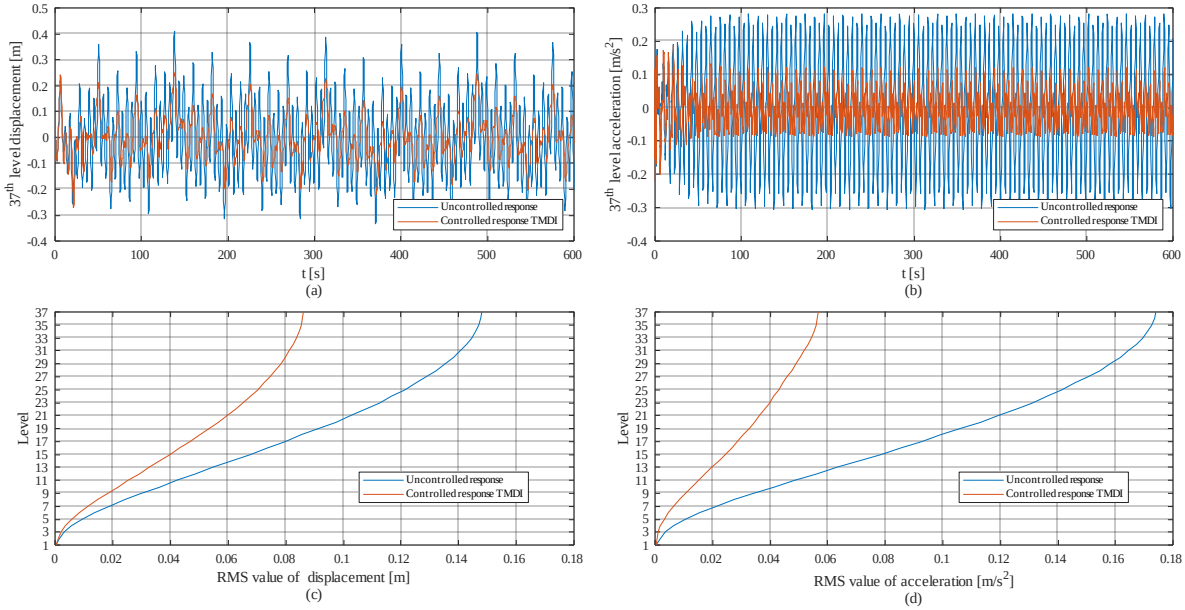


Figure 8. Structural controlled response using $J_2$. (a) Uncontrolled and controlled displacements on the 37$^{th}$ level. (b) Uncontrolled and controlled accelerations on the 37$^{th}$ level. (c) Uncontrolled and controlled RMS value of displacement. (d) Uncontrolled and controlled RMS value of acceleration.

## 7 CONCLUSIONS

- The optimization process carried out in this study involved searching for the optimal variables of the GWO that could identify the TMDI parameters resulting in the highest possible controlled response reduction. To accomplish this, the process was tried multiple times with various input variables to select the optimal combination. The selection criteria for identifying the best option were not solely based on achieving the maximum reduction but also on ensuring efficient use of computational resources. These findings highlight the importance of optimizing both computational resources and system performance in order to achieve the best results.

- Despite obtaining similar results with both objective functions, the response obtained was better when the objective function used for optimization was to reduce peak displacement. This may be because the response of a dynamic system subjected to wind load starts with calculating displacements, so when these are the target to be manipulated, the process is more direct and better results are obtained. In the case of the objective function that aimed to reduce the RMS of the acceleration, it can be said that it works in a similar way, since reducing the RMS requires decreasing some peaks and thereby achieving a more uniform response.

- The optimization resulting from the use of the objective function $J_1$ is governed by the following parameters, 0.001 for the damping ratio, and 0.995 for the frequency ratio. It can be observed that the value of the damping ratio is close to zero, indicating that the device requires a very small damper since the most influential factor in reducing the response is the inertial force generated by the inerter. This finding can provide insight into how to optimize the system for better performance, as a smaller damper can lead to reduced costs and greater efficiency.

- For this case of study, the TMDI system works optimally when the damping ratio is small. This finding is consistent with the understanding that the inerter provides a significant contribution to the reduction of dynamic response, and that the damping plays a less critical role in this process. However, it is important to note that the specific values for damping ratio that are considered small or optimal may depend on the specific characteristics of the structure and the loads it is subjected to.

## REFERENCES

[1] B. F. Spencer Jr Nathan M Newmark Professor and S. Nagarajaiah Associate Professor, "State of the Art of Structural Control."

[2] Y. M. Parulekar and G. R. Reddy, "passive response control systems for seismic response reduction: a state-of-the-art review," 2009. [Online]. Available: www.worldscientific.com

[3] T. E. Saaed, G. Nikolakopoulos, J. E. Jonasson, and H. Hedlund, "A state-of-the-art review of structural control systems," *JVC/Journal of Vibration and Control*, vol. 21, no. 5. SAGE Publications Inc., pp. 919–937, Apr. 15, 2015. doi: 10.1177/1077546313478294.

[4] S. Masoud, S. Alehashem, A. Keyhani, and H. Pourmohammad, "Behavior and Performance of Structures Equipped With ADAS & TADAS Dampers (a Comparison with Conventional Structures)," 2008. [Online]. Available: https://www.researchgate.net/publication/311641178

[5] F. Mazza and A. Vulcano, "Control of the earthquake and wind dynamic response of steel-framed buildings by using additional braces and/or viscoelastic dampers," *Earthq Eng Struct Dyn*, vol. 40, no. 2, pp. 155–174, 2011, doi: 10.1002/eqe.1012.

[6] Y. Bigdeli and D. Kim, "Damping effects of the passive control devices on structural vibration control: TMD, TLC and TLCD for varying total masses," *KSCE Journal of Civil Engineering*, vol. 20, no. 1, pp. 301–308, Jan. 2016, doi: 10.1007/s12205-015-0365-5.

[7] J. P. den Hartog, *Mechanical Vibrations*. New York: McGraw-Hill, 1956.

[8] B. G. W Housner *et al.*, "Structural control: past, present, and future," 1997.

[9] A. Kaveh *et al.*, "Optimum parameters of tuned mass dampers for seismic applications using charged system search," 2015. [Online]. Available: https://www.researchgate.net/publication/273115251

[10] C. L. Lee, Y. T. Chen, L. L. Chung, and Y. P. Wang, "Optimal design theories and applications of tuned mass dampers," *Eng Struct*, vol. 28, no. 1, pp. 43–53, Jan. 2006, doi: 10.1016/j.engstruct.2005.06.023.

[11] A. Kaveh, M. Fahimi Farzam, H. Hojat Jalali, and R. Maroofiazar, "Robust optimum design of a tuned mass damper inerter," *Acta Mech*, vol. 231, no. 9, pp. 3871–3896, Sep. 2020, doi: 10.1007/s00707-020-02720-9.

[12] L. Marian and A. Giaralis, "Optimal design of a novel tuned mass-damper-inerter (TMDI) passive vibration control configuration for stochastically support-excited structural systems," *Probabilistic Engineering Mechanics*, vol. 38, pp. 156–164, Oct. 2014, doi: 10.1016/j.probengmech.2014.03.007.

[13] M. C. Smith, "Synthesis of mechanical networks: The inerter," *IEEE Trans Automat Contr*, vol. 47, no. 10, pp. 1648–1662, Oct. 2002, doi: 10.1109/TAC.2002.803532.

[14] A. Giaralis and A. A. Taflanidis, "Optimal tuned mass-damper-inerter (TMDI) design for seismically excited MDOF structures with model uncertainties based on reliability criteria," *Struct Control Health Monit*, vol. 25, no. 2, Feb. 2018, doi: 10.1002/stc.2082.

[15] A. Giaralis and L. Marian, "Use of inerter devices for weight reduction of tuned mass-dampers for seismic protection of multi-story building: the Tuned Mass-Damper-Interter (TMDI)," in *Active and Passive Smart Structures and Integrated Systems 2016*, Apr. 2016, vol. 9799, p. 97991G. doi: 10.1117/12.2219324.

[16] L. A. Lara-Valencia, Y. Farbiarz-Farbiarz, and Y. Valencia-González, "Design of a Tuned Mass Damper Inerter (TMDI) Based on an Exhaustive Search Optimization for Structural Control of Buildings under Seismic Excitations," *Shock and Vibration*, vol. 2020, 2020, doi: 10.1155/2020/8875268.

[17] A. Giaralis and F. Petrini, "Wind-Induced Vibration Mitigation in Tall Buildings Using the Tuned Mass-Damper-Inerter," *Journal of Structural Engineering*, vol. 143, no. 9, p. 04017127, Sep. 2017, doi: 10.1061/(asce)st.1943-541x.0001863.

[18] K. T. Tse, ; K C S Kwok, Y. Tamura, and M. Asce, "Performance and Cost Evaluation of a Smart Tuned Mass Damper for Suppressing Wind-Induced Lateral-Torsional Motion of Tall Structures," 2012, doi: 10.1061/(ASCE)ST.

[19] Z. Zhu, W. Lei, Q. Wang, N. Tiwari, and B. Hazra, "Study on wind-induced vibration control of linked high-rise buildings by using TMDI," *Journal of Wind Engineering and Industrial Aerodynamics*, vol. 205, Oct. 2020, doi: 10.1016/j.jweia.2020.104306.

[20] J. Dai, Z. D. Xu, and P. P. Gai, "Tuned mass-damper-inerter control of wind-induced vibration of flexible structures based on inerter location," *Eng Struct*, vol. 199, Nov. 2019, doi: 10.1016/j.engstruct.2019.109585.

[21] D. Caicedo, L. Lara-Valencia, J. Blandon, and C. Graciano, "Seismic response of high-rise buildings through metaheuristic-based optimization using tuned mass dampers and tuned mass dampers inerter," *Journal of Building Engineering*, vol. 34, Feb. 2021, doi: 10.1016/j.jobe.2020.101927.

[22] G. Bekdaş and S. M. Nigdeli, "Metaheuristic based optimization of tuned mass dampers under earthquake excitation by considering soil-structure interaction," *Soil Dynamics and Earthquake Engineering*, vol. 92, pp. 443–461, Jan. 2017, doi: 10.1016/j.soildyn.2016.10.019.

[23] M. Abdel-Basset, L. Abdel-Fatah, and A. K. Sangaiah, "Metaheuristic algorithms: A comprehensive review," in *Computational Intelligence for Multimedia Big Data on the Cloud with Engineering Applications*, Elsevier, 2018, pp. 185–231. doi: 10.1016/B978-0-12-813314-9.00010-4.

[24] S. Mirjalili, S. M. Mirjalili, and A. Lewis, "Grey Wolf Optimizer," *Advances in Engineering Software*, vol. 69, pp. 46–61, 2014, doi: 10.1016/j.advengsoft.2013.12.007.

[25] M. Panda and B. Das, "Grey Wolf Optimizer and Its Applications: A Survey," in *Lecture Notes in Electrical Engineering*, 2019, vol. 556, pp. 179–194. doi: 10.1007/978-981-13-7091-5_17.

[26] W. Fu-Cheng, C. Cheng-Wei, L. Min-Kai, and H. Min-Feng, "Performance Analyses of Building Suspension Control with Inerters," 2007.

[27] G. Bekdaş and S. M. Nigdeli, "Metaheuristic based optimization of tuned mass dampers under earthquake excitation by considering soil-structure interaction," *Soil Dynamics and Earthquake Engineering*, vol. 92, pp. 443–461, Jan. 2017, doi: 10.1016/j.soildyn.2016.10.019.

[28] J. Salvi and E. Rizzi, "Optimum tuning of tuned mass dampers for frame structures under earthquake excitation," *Struct Control Health Monit*, vol. 22, no. 4, pp. 707–725, Apr. 2015, doi: 10.1002/stc.1710.

[29] F. Petrini, A. Giaralis, and Z. Wang, "Optimal tuned mass-damper-inerter (TMDI) design in wind-excited tall buildings for occupants' comfort serviceability performance and energy harvesting," *Eng Struct*, vol. 204, Feb. 2020, doi: 10.1016/j.engstruct.2019.109904.

[30] D. De Domenico and G. Ricciardi, "An enhanced base isolation system equipped with optimal tuned mass damper inerter (TMDI)," *Earthq Eng Struct Dyn*, vol. 47, no. 5, pp. 1169–1192, Apr. 2018, doi: 10.1002/eqe.3011.

[31] H. Rezaei, O. Bozorg-Haddad, and X. Chu, "Grey wolf optimization (GWO) algorithm," in *Studies in Computational Intelligence*, vol. 720, Springer Verlag, 2018, pp. 81–91. doi: 10.1007/978-981-10-5221-7_9.

[32] M. Franco, "Direct Along-Wind Dynamic Analysis of Tall Structures," 1993.

[33] H. H. Barrios, N. M. Santacruz, and I. H. Ríos, "Respuesta eólica de estructuras tipo punto ante viento sintético," 2019.

[34] Ministerio de Ambiente Vivienda y Desarrollo Territorial, *Reglamento Colombiano de Construcción Sismo Resistente "NSR-10" Bogotá*. Asociación Colombiana de Ingeniería Sísmica: Bogotá, Colombia, 2010.

COMPDYN 2023
9th ECCOMAS Thematic Conference on
Computational Methods in Structural Dynamics and Earthquake Engineering
M. Papadrakakis, M. Fragiadakis (eds.)
Athens, Greece, 12-14 June 2023

# OPTIMAL DESIGN OF A TUNED MASS DAMPER INERTER USING A WHALE OPTIMIZATION ALGORITHM FOR THE CONTROL OF BUILDINGS SUBJECTED TO GROUND ACCELERATIONS

**Mariana Castro-Osorio[1], Daniela Vallejo-Paniagua[2], Verónica Valencia-Valencia[2], Luis A. Lara-Valencia[2], and John J. Blandón-Valencia[2]**

[1,] Universidad Nacional de Colombia
Carrera 80 N.°65-223, Núcleo Robledo. Medellín, Colombia
mcastroos@unal.edu.co

[2] Universidad Nacional de Colombia sede Medellín
Carrera 80 N.º65-223, Núcleo Robledo. Medellín, Colombia.
{dvallejo, vvalencia, lualarava, jjblandon}@unal.edu.co

## Abstract

*Control devices, also known as protection systems, have been proposed to reduce undesirable vibrations, dissipate the input energy, and preserve the integrity of structures subjected to ground motion. The Tuned Mass Damper Inerter (TMDI) is a passive control device that integrates a classical Tuned Mass Damper (TMD) with an inerter mechanism that induces inertial resisting forces to the controlled system and consequently provides a mass equivalent amplification effect, also known as inertance, with the advantage that it demands less attached mass to achieve suitable vibration control of structures subjected to dynamic loads. This paper presents the implementation and optimal design of a TMDI on a mid-rise building in which the structural model is simplified as a two-dimensional shear frame subjected to different ground motion-induced vibrations, intending to reduce the lateral displacements of the structure. Moreover, for the tunning process of the device, the design parameters have been optimized using a natural-based metaheuristic algorithm known as the whale optimization algorithm (WOA). The objective function to be optimized is a linear combination of the maximum peak displacement and the root mean square (RMS) response for the displacement. The obtained results show remarkable reductions in the dynamic response of the structure, thus demonstrating the effectiveness of TMDI for structural control and damage reduction.*

**Keywords:** Structural control, tuned mass damper inerter, Whale Optimization Algorithm, ground motion-induced vibrations.

## 1 INTRODUCTION

In recent years, there has been a significant focus on developing and researching control devices implemented in structures. The purpose of these devices is to minimize damage and dissipate energy caused by dynamic environmental loads in civil structures. These control methods can be classified into four groups: passive control, active control, semi-active control, and hybrid control [1-3].

Passive devices are designed to modify the stiffness or the structural damping of a system without requiring an external power source to develop forces that counteract the motion of the structure. These devices present an attractive alternative to other types of controllers due to their mechanical simplicity, lower cost, ease of operation, and maintenance [4, 5].

The Tuned Mass Damper (TMD) is a passive system proposed by Frahm in 1909 [6] to attenuate vibrations in single-degree-of-freedom (SDOF) systems subjected to harmonic motion. Subsequent applications [7-9] have demonstrated that the device is capable of preventing damage, discomfort, and structural failure by employing inertial forces to dissipate energy and suppress undesired vibrations during seismic events. The TMD incorporates a secondary mass, a damper, and a spring linked to the structure in some strategic points, to improve the dynamic response [10]. TMDs have proven efficiency in damage reduction when are optimally tuned to one of the fundamental frequencies of the structure to be protected [11, 12]. These devices operate by transferring vibration energy from the main structure to the secondary mass, which then dissipates the energy by vibrating out of phase with the structural motion [4], resulting in a reduction of the motion amplitude.

Considering the limitations of TMDs in achieving optimal seismic performance, the Tuned Mass Damper Inerter (TMDI) was proposed by Marian and Giaralis [13]. This device consists of a classical linear TMD attached to the structure with the spring-damper system and linked to the floor via an inerter [14]. The inerter, which is a mechanical two-node device, induces an inertial force of resistance that is proportional to the relative acceleration of the two nodes, resulting in a mass-equivalent amplification effect, also known as inertance [15]. The addition of the inerter in the TMDs offers a lightweight passive vibration alternative that significantly improves the damping properties of the device. Numerous investigations have been carried out to optimally design the TMDIs. For instance, Brzeski *et al.* [16] investigated a TMDI featuring a specialized inerter that allows for precise inertance modifications, thus facilitating a wider range of applications. Pietrosanti *et al.* [17] proposed a methodology for achieving optimal TMDI performance in multi-degree-of-freedom (MDOF) structures, considering two TMDI configurations: grounded and ungrounded. Additionally, Lara-Valencia *et al.* [18] explored the optimal tuning and design of TMDIs employing various performance indices to minimize structural response.

One of the most effective methods for tuning control devices is through the use of meta-heuristic optimization algorithms because of their simplicity, flexibility, and local optima avoidance [19]. To obtain the optimal design parameters that ensure the best performance of the TMDI it will be used the Whale Optimization Algorithm (WOA) [20] which mimics the behavior of humpback whales in nature and the bubble-net hunting strategy, first encircling the prey, and then creating bubble nets for the final attack.

The current study presents a procedure for the design of TMDIs located on the upper storey of a mid-rise building subject to seismic excitations. The tunning process aims to minimize the dynamic response of the structure using a linear combination of two parameters which are the maximum peak displacement and the root mean square (RMS) value for displacements. The design parameters are the critical damping ratio, $\zeta_{TMDI}$, and frequency ratio, $\upsilon_{TMDI}$, which are computed via WOA. Finally, the seismic performance is evaluated considering the attached mass of 5%, and inertance added of

5% with respect to the total mass of the structure. The present study demonstrates that the TMDI can achieve substantial reductions in the structural response, covering key parameters such as peak displacements, RMS value of displacement, peak acceleration, RMS value of acceleration, and interstorey drift. This improved performance can be attributed to the inerter device, which amplifies the mass and stiffness of the structure, thereby enhancing its behavior while preserving its stability and functionality.

## 2 TUNNED MASS DAMPER INERTER MODEL

### 2.1 TMDI configuration for a multi-degree-of-freedom (MDOF) structure subjected to ground acceleration

To obtain a mathematical model that describes the performance of the TMDI, it is considered a linear damped multi-degree-of-freedom (MDOF) dynamical system as shown in Figure 1, which is a two-dimensional frame modeled as a shear beam building with $n$ degrees of freedom associated to the horizontal displacements on each storey and subjected to a ground acceleration $\ddot{u}_g(t)$. The structure is supplied with a TMDI attached to the last two storeys. Considering the structure shown in Figure 1, the properties of each storey $i$ $(i = 1, 2, \dots\ n)$ are represented with a spring of stiffness constant $k_i$, viscous damper with damping constant $c_i$, and concentrated mass $m_i$. Moreover, the TMDI is modeled as the combination of a classical TMD located in the upper level of the frame and an inerter that connects the conventional TMD and the level $n-1$ of the structure. The properties of the idealized device are $m_{TMDI}$, $k_{TMDI}$, $c_{TMDI}$, and $b$ that refers to the mass, stiffness, damping, and inertance coefficients respectively.

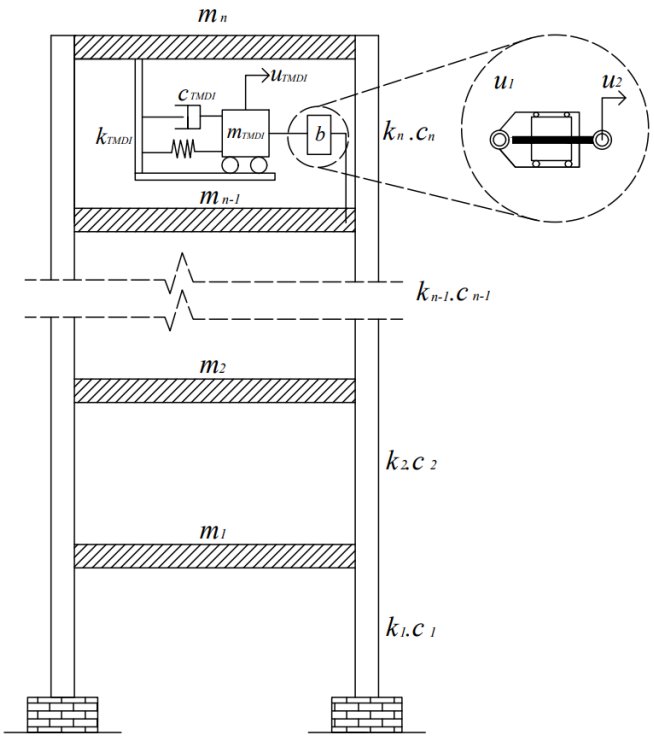


Figure 1: MDOF system integrated with TMDI.

## 2.2 The inerter device

Several analogies between electrical and mechanical systems have led to the development of the inerter [14] which is an element linked to two nodes and free to move independently as shown in Figure 2. This device has a small mass in comparison to the structure and has the property that the force that it generates is proportional to the relative acceleration between its nodes [21]. Its proportionality constant, $b$, is the inertance that characterizes the behavior of the device and is measured in terms of mass, furthermore, $b$ can be two hundred or more orders of magnitude greater than the real inerter mass. [15]. The resisting force produced by an inerter is given by the equation (1) as follows:

$$F = b(\ddot{u}_j - \ddot{u}_i) \tag{1}$$

Where $\ddot{u}_i - \ddot{u}_j$ represents the relative acceleration of the nodes $i$ and $j$ of the device.

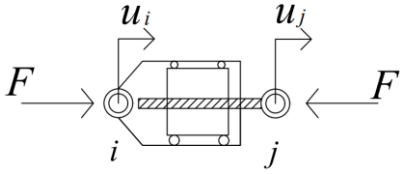


Figure 2: Inerter device.

## 2.3 Governing equations of motion for MDOF structure equipped with a TMDI

The $n + 1$ governing equations of motion that describe the behavior of the structure showed in Figure 1 subjected to ground acceleration, can be modeled in matrix form with the equation (2):

$$\boldsymbol{M}\ddot{\boldsymbol{U}}(t) + \boldsymbol{C}\dot{\boldsymbol{U}}(t) + \boldsymbol{K}\boldsymbol{U}(t) = -\boldsymbol{M}\,\{\mathbf{1}\}\,\ddot{u}_g(t) \tag{2}$$

Where $\boldsymbol{U}(t), \dot{\boldsymbol{U}}(t)$ and $\ddot{\boldsymbol{U}}(t)$ are respectively the relative displacement, velocity, and acceleration system vectors as a function of time with dimensions $(n + 1) \times 1$. On the other hand, $\ddot{u}_g(t)$ is a scalar representing the induced ground acceleration which also depends on the time, and $\{\mathbf{1}\}$ is a unitary vector of order $(n + 1) \times 1$.

The matrices $\boldsymbol{M}, \boldsymbol{K}$, and $\boldsymbol{C}$ with dimensions $(n + 1) \times (n + 1)$ respectively associated with the mass, stiffness, and damping of the structure, are proposed to include the effect of the TMDI. The mentioned matrices can be calculated with the expressions (3 – 5).

$$\boldsymbol{M} = \begin{bmatrix} m_1 & 0 & 0 & 0 & 0 & \dots & \dots & 0 \\ 0 & m_2 & 0 & 0 & 0 & \dots & \dots & 0 \\ 0 & 0 & m_3 & 0 & 0 & \dots & \dots & 0 \\ 0 & 0 & 0 & m_4 & 0 & \dots & \dots & 0 \\ \vdots & \vdots & \vdots & \vdots & \ddots & \dots & \dots & \vdots \\ \vdots & \vdots & \vdots & \vdots & \vdots & m_{n-1} + b & 0 & -b \\ \vdots & \vdots & \vdots & \vdots & \vdots & 0 & m_n & 0 \\ 0 & 0 & \dots & \dots & \dots & -b & 0 & m_{TMDI} + b \end{bmatrix} \tag{3}$$

$$\boldsymbol{K} = \begin{bmatrix} k_1+k_2 & -k_2 & 0 & 0 & 0 & \dots & \dots & 0 \\ -k_2 & k_2+k_3 & -k_3 & 0 & 0 & \dots & \dots & 0 \\ 0 & -k_3 & k_3+k_4 & -k_4 & 0 & \dots & \dots & 0 \\ 0 & 0 & -k_4 & k_4+k_5 & -k_5 & \dots & \dots & 0 \\ \vdots & \vdots & \vdots & \vdots & \ddots & \dots & \dots & \vdots \\ \vdots & \vdots & \vdots & \vdots & \vdots & k_{n-1} & -k_n & 0 \\ \vdots & \vdots & \vdots & \vdots & \vdots & -k_n & k_n & -k_{TMDI} \\ 0 & 0 & \dots & \dots & \dots & 0 & -k_{TMDI} & k_{TMDI} \end{bmatrix} \tag{4}$$

$$\boldsymbol{C} = \begin{bmatrix} c_1+c_2 & -c_2 & 0 & 0 & 0 & \dots & \dots & 0 \\ -c_2 & c_2+c_3 & -c_3 & 0 & 0 & \dots & \dots & 0 \\ 0 & -c_3 & c_3+c_4 & -c_4 & 0 & \dots & \dots & 0 \\ 0 & 0 & -c_4 & c_4+c_5 & -c_5 & \dots & \dots & 0 \\ \vdots & \vdots & \vdots & \vdots & \ddots & \dots & \dots & \vdots \\ \vdots & \vdots & \vdots & \vdots & \vdots & c_{n-1} & -c_n & 0 \\ \vdots & \vdots & \vdots & \vdots & \vdots & -c_n & c_n & -c_{TMDI} \\ 0 & 0 & \dots & \dots & \dots & 0 & -c_{TMDI} & c_{TMDI} \end{bmatrix} \tag{5}$$

Further, the natural frequency and the critical damping ratio of the TMDI can be expressed as:

$$\omega_{TMDI} = \sqrt{\frac{k_{TMDI}}{m_{TMDI}+b}} \tag{6}$$

$$\zeta_{TMDI} = \frac{c_{TMDI}}{2(m_{TMDI}+b)\omega_{TMDI}} \tag{7}$$

It is convenient for the analysis and design of systems equipped with TMDIs to consider the mass ratio ($\mu$), inertance ratio ($\beta$), and frequency ratio ($v$):

$$\mu = \frac{m_{TMDI}}{M_s} \tag{8}$$

$$\beta = \frac{b}{M_s} \tag{9}$$

$$v = \frac{\omega_{TMDI}}{\omega_s} = \frac{\sqrt{\frac{k_{TMDI}}{m_{TMDI}+b}}}{\omega_s} \tag{10}$$

Where $M_s$ is the total mass of the structure and $\omega_s$ will be assumed as the angular frequency of the structural first mode of vibration.

## 3 TMDI OPTIMIZATION METHODOLOGY

### 3.1 Parameters to be optimized

The optimization process is based on finding the optimal values of $k_{TMDI}$ and $c_{TMDI}$, equivalent to the dimensionless parameters $v$ and $\zeta_{TMDI}$ calculated with equations (7) and (10). The objective

of the tuning process is to optimize the variables under consideration, in such a way as to minimize the response of the structure under the induced ground acceleration.

The domain of the search is defined between:

$$0.50 \leq v \leq 2.00 \tag{11}$$

$$0.10 \leq \zeta_{\mathrm{TMDI}} \leq 0.50 \tag{12}$$

The limits mentioned above were established following recommendations found in the literature and common practice mainly in TMD devices, which have been further investigated [22, 23].

### 3.2 Objective function

The objective function ($OF$) proposed in the present research seeks to minimize the dynamic response of the structure when it is subjected to seismic excitations, this is measured using the minimum values of two response parameters: the maximum peak displacements $U_{ipeak}$, and the RMS response of the displacements $RMS(U_i)$. The final $OF$ is set up as a linear combination, and the weight of each term is established according to the desired reduction for each parameter.

$$OF = 0.6\frac{max(|(U_{ipeak(controlled)})|)}{max(|(U_{ipeak(uncontrolled)})|)} + 0.4\frac{max(|RMS(U_{i(controlled)})|)}{max(|RMS(U_{i(uncontrolled)})|)} \tag{13}$$

### 3.3 Whale optimization algorithm (WOA)

The Whale Optimization Algorithm (WOA) is a nature-inspired meta-heuristic algorithm proposed by Mirjalili and Lewis in 2016 [20]. They were inspired by the social behavior of humpback whales and their special hunting method known as the bubble-net feeding strategy. In recent investigations, other researchers have used this algorithm for the optimization of different engineering problems for example Kaveh and Ghazaan [24, 25] studied the sizing optimization of skeletal structures, Azizi *et al.* [26] upgraded the WOA for fuzzy logic-based vibration control of nonlinear steel structures, and Huang M *et al.* [27] developed a damage identification method based on the WOA.

For the application of the optimization process, the authors' first strategy is to define a population of whales which is the equivalent of a set of random solutions where each solution is thought to be a whale that tries to occupy a new place in the searching space, taking as a reference the best whale of the group. Two strategies are used for the hunting process of the prey (exploration) and the attack (exploitation).

#### 3.3.1 Bubble-net attacking method (exploitation phase)

Two approaches are used for the mathematical model that simulates the bubble-net behavior of humpback whales, the first one is encircling and the other one is the bubble-net creation via spiral updating. After the selection of the initial best search agent of the set of random solutions, the whales update their position for either a random agent or the best solution obtained at the moment.

The hunting mechanism of humpback whales is a combination of swimming around the prey within a shrinking circle and along a spiral-shaped path [29], thus, the probability of using one of the two mentioned mechanisms is the same.

### 3.3.2 Search for prey (exploration phase)

In this phase, the whale position is upgraded based on a randomly selected search agent and not on the best solution obtained so far, to make it possible, the current whale can search far away from the best solution and the WOA can achieve a global search avoiding local optima [29]. Figure 3 shows the flowchart of the WOA with the steps that this method requires.

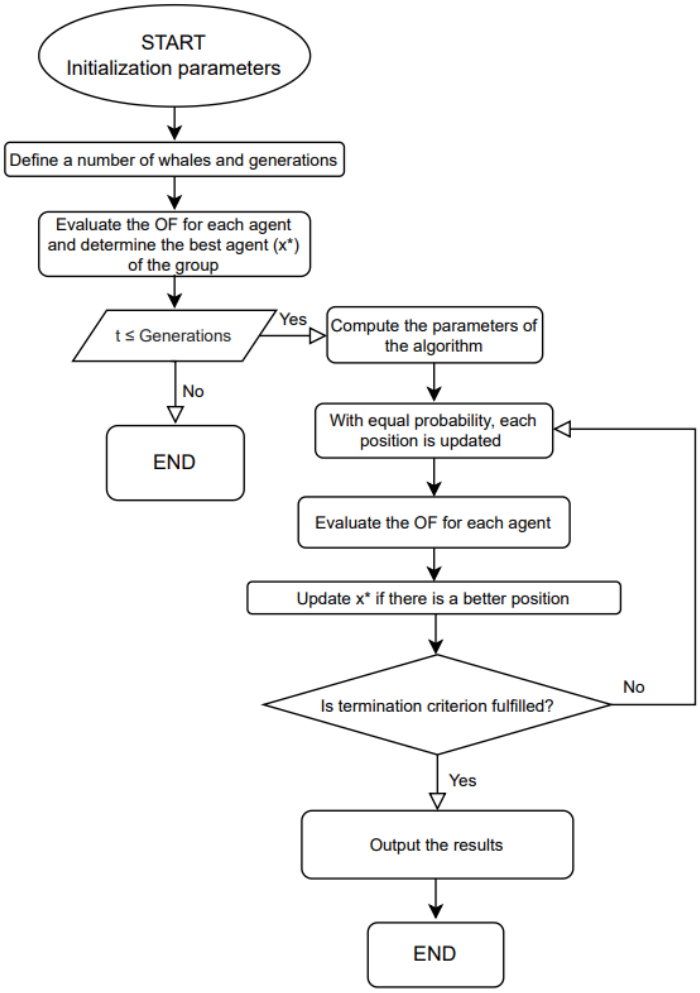


Figure 3: Flow chart of the WOA.

## 4 NUMERICAL EXAMPLE

The suggested methodology is applied to a 12-storey reinforced concrete (RC) residential building in Medellín, Colombia. The structure has a total height of 30 m, and the lateral force-resisting system of the structure consists of resistant moment frames combined with structural walls. Figure 4 shows an elevation view of the building and the selected frame for the study.

The mass matrix $\boldsymbol{M}$ and stiffness matrix $\boldsymbol{K}$, have dimensions of 12 × 12 considering only the horizontal degrees of freedom of the structure (one at each level), this is derived by assuming rigid floor diaphragms and applying static condensation of the rotational degrees of freedom and

elimination of the vertical degrees of freedom. On the other hand, the resulting damping matrix $\boldsymbol{C}$ of dimensions 12 × 12 was calculated using Rayleigh´s method for 5% damping in the first and second vibration modes. The calculation of the modal analysis was performed with Matlab [32] and the results are shown in Table 1.

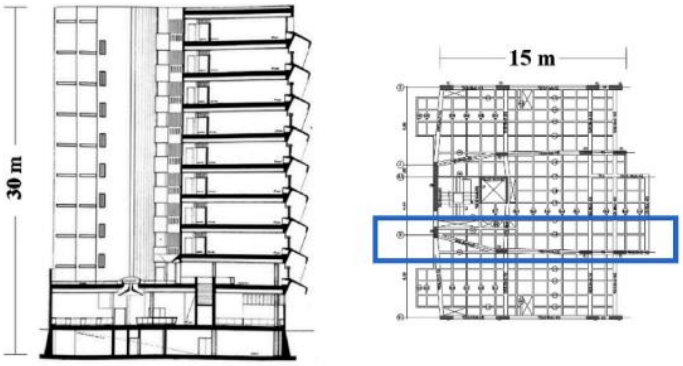


Figure 4: Building and frame used for the study.

| Mode | 1 | 2 | 3 | 4 | 5 | 6 | 7 | 8 | 9 | 10 | 11 | 12 |
|---|---|---|---|---|---|---|---|---|---|---|---|---|
| T [s] | 1.68 | 0.51 | 0.27 | 0.17 | 0.11 | 0.08 | 0.06 | 0.05 | 0.04 | 0.03 | 0.03 | 0.03 |
| F [Hz] | 0.59 | 1.96 | 3.69 | 5.85 | 8.70 | 12.11 | 16.06 | 20.63 | 25.52 | 29.46 | 31.89 | 34.94 |
| ω [rad/s] | 3.73 | 12.35 | 23.19 | 36.76 | 54.65 | 76.09 | 100.93 | 129.60 | 160.37 | 185.11 | 200.39 | 219.56 |

Table 1: Modal properties of the 2D frame.

The seismic-induced accelerations are represented by four ground motion records with different dynamic characteristics between them. The accelerograms were taken from the Pacific Earthquake Engineering Research (PEER) Centre database [30] and the Center for engineering strong-motion data [31], the information related to these events is summarized in Table 2.

| Seismic record | Event name | Year | Station | Component | Magnitude | PGA [g] | Duration |
|---|---|---|---|---|---|---|---|
| 1 | Mexico | 1985 | La Unión | S00E | 8.1 | 0.169 | 62.90 |
| 2 | Chile | 1985 | Melipilla | 0 | 7.8 | 0.686 | 79.36 |
| 3 | Petrolia | 1992 | Cape Mendocino, CA | 90 | 7.0 | 1.039 | 59.98 |
| 4 | Christchurch | 2011 | Christchurch Resthaven | S88E | 6.3 | 0.710 | 81.90 |

Table 2: Acceleration records.

The purpose of the numerical example is to test and prove the effectiveness of the WOA in determining the best parameters for the design of TMDIs, which improve the performance of structures subjected to ground motion, this is achieved using actual records of accelerograms as input seismic excitations and only elastic analysis were carried out.

## 5 RESULTS

The design parameters of the TMDI are obtained through the optimization of equation (13) via WOA. The objective function aims to minimize the structural response, specifically in terms of displacements. This is why it is formulated as a linear combination of peak displacements and RMS value of displacements, rather than utilizing other variables such as accelerations or interstorey drifts to optimize the dynamic response. This section presents a comparison between the controlled and uncontrolled structural response of a mid-rise building subjected to ground motion to evaluate the effectiveness of the TMDI in enhancing the dynamic behavior of the system. The analysis is conducted in the linear range, where the displacements are assumed to be part of the elastic behavior of the structure. As a result, plastic deformations and any potential damage are not taken into consideration. The primary goal of the controller device is to keep the structural response within the linear range. If that is not possible, the controller device aims to minimize the displacements in the non-linear range to prevent structural damage.

### 5.1 Uncontrolled response

Table 3 summarizes the response of the last four storeys of the uncontrolled frame subjected to the four different seismic records.

| Seismic record | Storey | Peak displacement [m] | RMS of the displacement [m] | Peak acceleration [m/s$^2$] | RMS of the acceleration [m/s$^2$] | Peak interstorey drift [m] |
|---|---|---|---|---|---|---|
| 1 | 9 | 0.1118 | 0.0285 | 4.8654 | 0.7895 | 0.0168 |
| | 10 | 0.1206 | 0.0315 | 3.7083 | 0.7715 | 0.0165 |
| | 11 | 0.1311 | 0.0341 | 5.6530 | 1.0354 | 0.0150 |
| | 12 | 0.1430 | 0.0363 | 8.5393 | 1.4855 | 0.0127 |
| 2 | 9 | 0.1346 | 0.0305 | 10.3952 | 1.7635 | 0.0307 |
| | 10 | 0.1496 | 0.0339 | 10.4644 | 1.5027 | 0.0347 |
| | 11 | 0.1640 | 0.0372 | 14.4649 | 2.1241 | 0.0338 |
| | 12 | 0.1767 | 0.0403 | 24.6003 | 3.4506 | 0.0286 |
| 3 | 9 | 0.1956 | 0.0420 | 12.4658 | 1.2861 | 0.0264 |
| | 10 | 0.2134 | 0.0462 | 14.2340 | 1.0170 | 0.0257 |
| | 11 | 0.2299 | 0.0497 | 14.9989 | 1.3822 | 0.0250 |
| | 12 | 0.2500 | 0.0528 | 17.6687 | 2.2355 | 0.0218 |
| 4 | 9 | 0.5600 | 0.0916 | 15.8605 | 1.6193 | 0.0868 |
| | 10 | 0.6322 | 0.1008 | 17.9111 | 1.8869 | 0.0776 |
| | 11 | 0.6956 | 0.1087 | 20.4108 | 2.3096 | 0.0657 |
| | 12 | 0.7490 | 0.1154 | 22.9834 | 2.8371 | 0.0547 |

Table 3: Dynamic response of the last four storeys of the uncontrolled structure under the seismic records.

According to the numerical results presented in Table 3, the uncontrolled frame exhibited a maximum peak displacement of 0.75 m in the 12$^{th}$ storey during the "Christchurch" earthquake, which is 5.24 times higher than the peak displacement observed in the same storey during the

"Mexico" earthquake. Furthermore, the 12th storey also had the highest RMS value for displacement during the "Christchurch" earthquake with a value of 0.12 m. The maximum peak acceleration and the maximum RMS value for acceleration occurred under the "Chile" seismic record in the top storey of the building, with values of 24.60 m/s$^2$ and 3.45 m/s$^2$, respectively.

The maximum displacement of 0.75 m may be enough for the structure to reach the inelastic range. However, the focus of this study is solely on the linear behavior of the structure, as stated earlier. Additionally, it is crucial to acknowledge that the building was modeled as a 2D shear frame, and if the total stiffness of the structure were considered, the displacements of both the controlled and uncontrolled structures would likely be reduced.

### 5.2 TMDI optimization process

For the calibration of the algorithm, values of 5% are set for both mass ratio ($\mu$) and inertance ratio ($\beta$), since recent investigations [2, 18] have shown that the results obtained with these values achieve a significant response reduction. Besides, considering that one of the advantages of implementing a TMDI is to reduce the amount of mass used on a classic TMD, it is reasonable to use this percentage which allows the device to be physically viable. Consequently, the values of $m_{TMDI}$ and $b$ are 54.20 Mg.

During the execution of the WOA, different combinations of whales and generations were tested, including 30, 50, 100, and 300 whales and 20, 30, 50, and 100 generations. The results showed that using a higher number of whales led to more precise optimization of the TMDI design parameters, as it helped to avoid the limits of the searching space and local optima. Moreover, it was found that the controlled response could be significantly reduced by using a combination of 100 whales and 50 generations. Table 4 presents the optimized critical damping ratio ($\zeta_{TMDI}$) and frequency ratio ($v$) founded using the WOA for each seismic record.

| Seismic record | Number of whales | Generation | $\zeta_{TMDI}$ | $v$ |
|---|---|---|---|---|
| 1 | 100 | 50 | 0.2683 | 0.7690 |
| 2 | 100 | 50 | 0.2396 | 1.1286 |
| 3 | 100 | 50 | 0.1368 | 0.7794 |
| 4 | 100 | 50 | 0.1000 | 1.0872 |

Table 4: WOA combinations and design parameters of the TMDI for each seismic record.

### 5.3 TMDI-controlled response

Table 5 presents the response of the last four storeys of the controlled structure subjected to each earthquake. First, the maximum peak displacement and the maximum RMS value of the displacement were obtained on the last storey under the “Christchurch” seismic record with values of 0.5094 m and 0.0799 m respectively, showing reductions of 31.99% and 30.78% for each response parameter. Then, the maximum peak acceleration and the maximum RMS value of the acceleration occurs on the 12th storey of the structure when the structure was subjected to the ”Chile” earthquake, decreasing from 24.60 m/s$^2$ to 18.05 m/s$^2$ and from 3.45 m/s$^2$ to 2.68 m/s$^2$, these decreases represent reduction percentages of 26.62% and 22.24% respectively. Finally, the maximum interstorey drift was observed in the 9th storey of the structure under the “Christchurch”

earthquake, with a value of 0.0635 m and a reduction of 26.86%. However, the structure exhibits its highest reduction in the interstorey drift on the 10th storey under the "Chile" earthquake, with a value of 30.15%.

| Seismic record | Storey | Peak controlled displacement [m] | Controlled RMS of the displacement [m] | Peak controlled acceleration [m/s$^2$] | Controlled RMS of the acceleration [m/s$^2$] | Controlled peak interstorey drift [m] |
|---|---|---|---|---|---|---|
| 1 | 9 | 0.0854 | 0.0209 | 4.8141 | 0.6932 | 0.0163 |
| | 10 | 0.0973 | 0.0233 | 3.5152 | 0.6602 | 0.0160 |
| | 11 | 0.1096 | 0.0254 | 4.7987 | 0.9064 | 0.0145 |
| | 12 | 0.1200 | 0.0273 | 8.1623 | 1.3042 | 0.0119 |
| 2 | 9 | 0.0904 | 0.0230 | 10.1056 | 1.5612 | 0.0229 |
| | 10 | 0.1027 | 0.0257 | 9.3688 | 1.2544 | 0.0243 |
| | 11 | 0.1131 | 0.0285 | 10.3111 | 1.6458 | 0.0242 |
| | 12 | 0.1223 | 0.0311 | 18.0521 | 2.6832 | 0.0202 |
| 3 | 9 | 0.1984 | 0.0316 | 11.8323 | 1.1061 | 0.0248 |
| | 10 | 0.2126 | 0.0348 | 13.4717 | 0.8679 | 0.0269 |
| | 11 | 0.2344 | 0.0376 | 14.2771 | 1.1084 | 0.0268 |
| | 12 | 0.2567 | 0.0400 | 16.6028 | 1.8020 | 0.0231 |
| 4 | 9 | 0.4088 | 0.0611 | 15.9374 | 1.1962 | 0.0635 |
| | 10 | 0.4453 | 0.0681 | 15.6906 | 1.3648 | 0.0572 |
| | 11 | 0.4780 | 0.0743 | 16.1852 | 1.7247 | 0.0481 |
| | 12 | 0.5094 | 0.0799 | 17.4830 | 2.2064 | 0.0389 |

Table 5: Dynamic response of the last four storeys of the TMDI-controlled structure under the seismic records.

Figure 5 to Figure 8 presents simultaneously the controlled response with the blue line, and the uncontrolled response with the orange one. The structural response is plotted in terms of peak displacements in the 12th storey, RMS values of the displacement per storey, peak accelerations in the 12th storey, RMS values of the acceleration per storey, and peak interstorey drift for the structure subjected to the four ground motions. The figures offer a clear representation of the dynamic behavior of the system.

Table 5 shows the results for the "Petrolia" earthquake, indicating that the controlled maximum peak displacements increase for the last four storeys in comparison to the uncontrolled results. This increase occurs during the first peak of the earthquake at 2.98 seconds, which has a relatively high PGA value of 1.039 g and is outside the trend observed in this seismic record as it is shown in Figure 7. If the algorithm attempts to estimate parameters for the TMDI that reduces this peak, it may not result in proper behavior for the rest of the time, as it is presented in Figure 7. Therefore, the parameters are established to achieve an optimal overall response. Taking into consideration that earthquakes are an unpredictable phenomenon, this type of condition can easily occur. Additionally, due to the increase in displacements, the maximum peak interstorey drifts are not

successfully reduced. However, for future research, it may be possible to optimize the objective function by including the peak interstorey drift as a parameter of the linear combination.

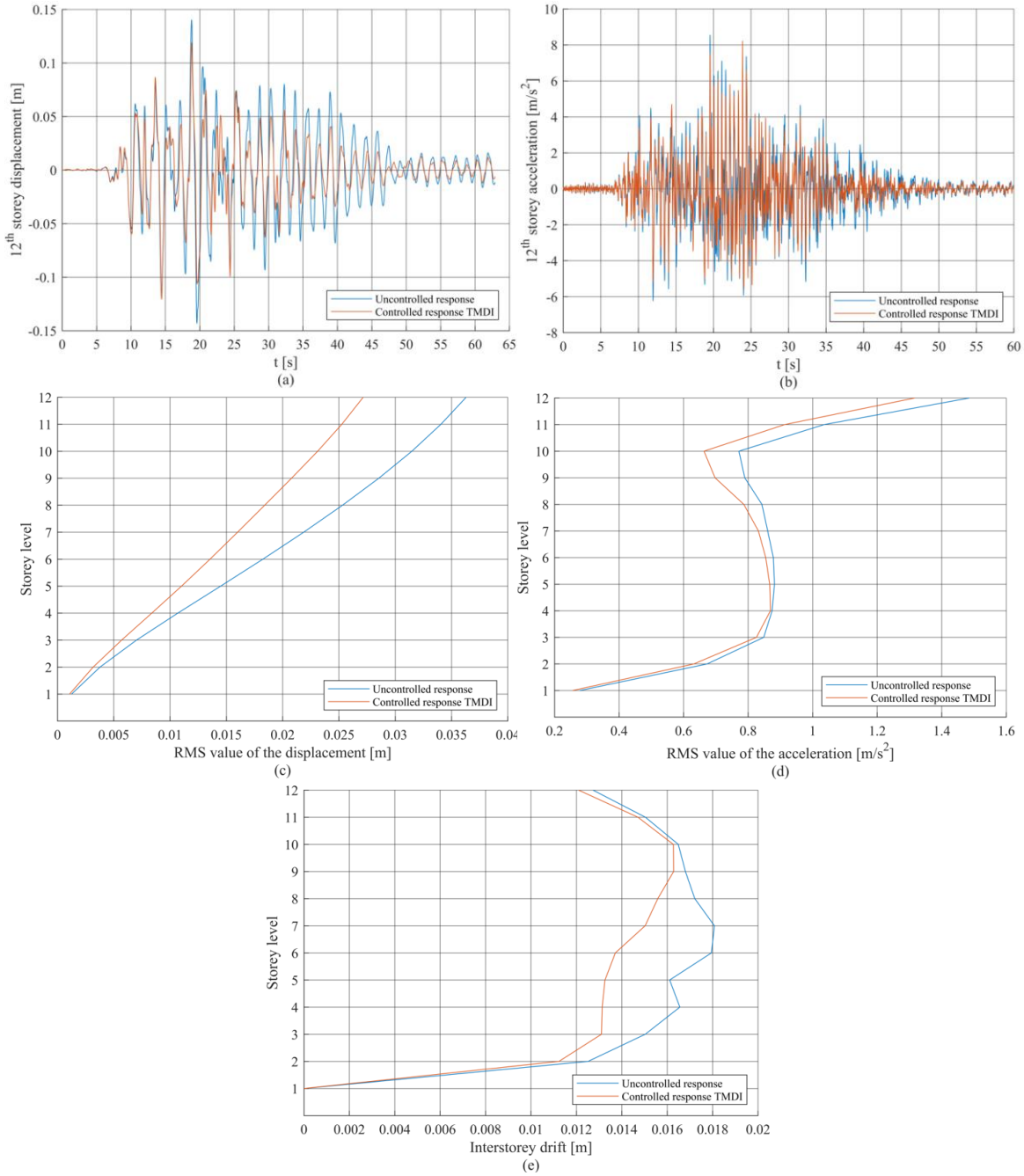


Figure 5: Response of the structure subjected to "Mexico" Seismic record. (a) 12th-storey maximum displacements. (b) 12th-storey maximum accelerations. (c) RMS value of the displacements per storey. (d) RMS value of the accelerations per storey. (e) Interstorey drift.

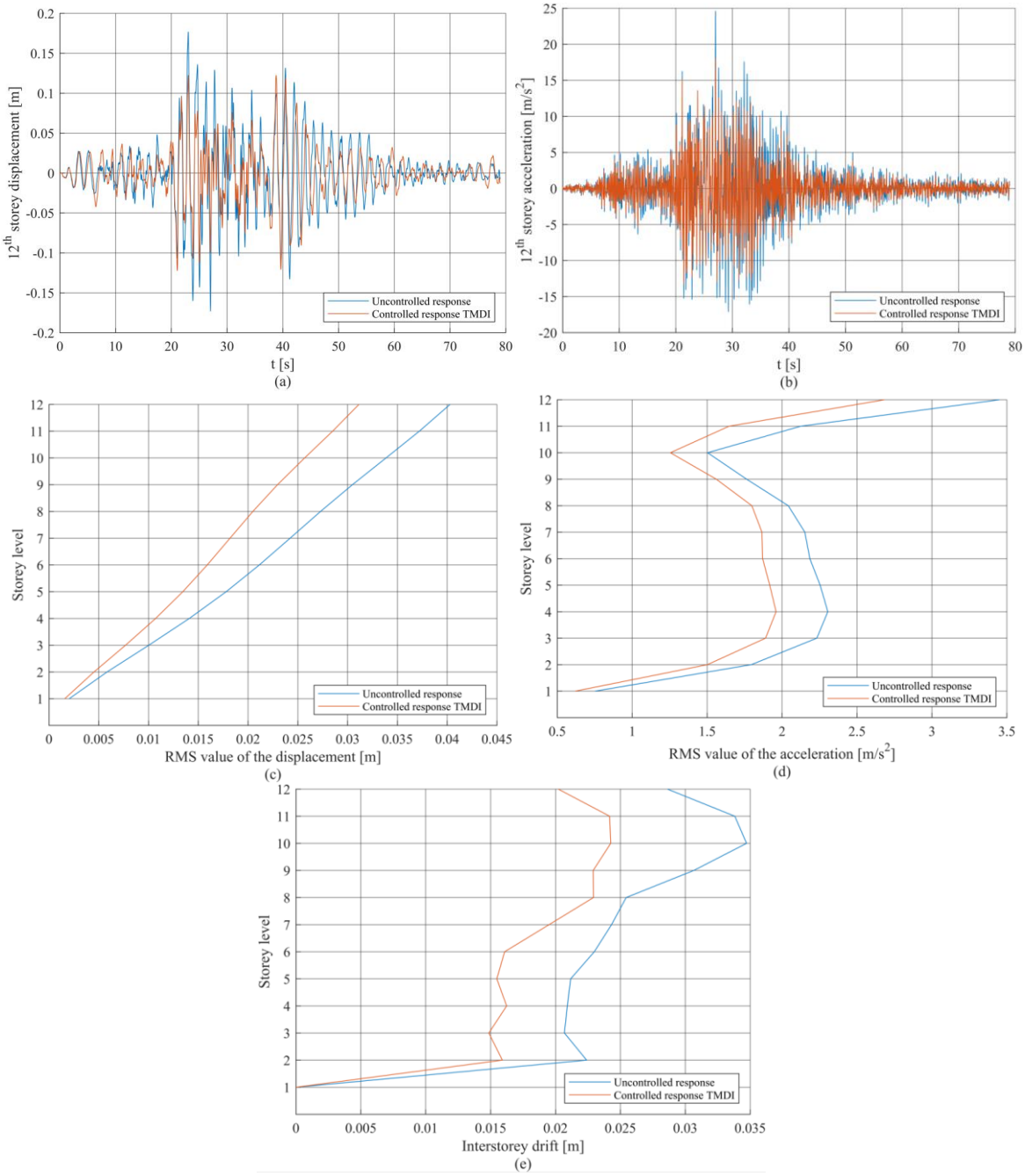


Figure 6: Response of the structure subjected to "Chile" Seismic record. (a) 12th-storey maximum displacements. (b) 12th-storey maximum accelerations. (c) RMS value of the displacements per storey. (d) RMS value of the accelerations per storey. (e) Interstorey drift.

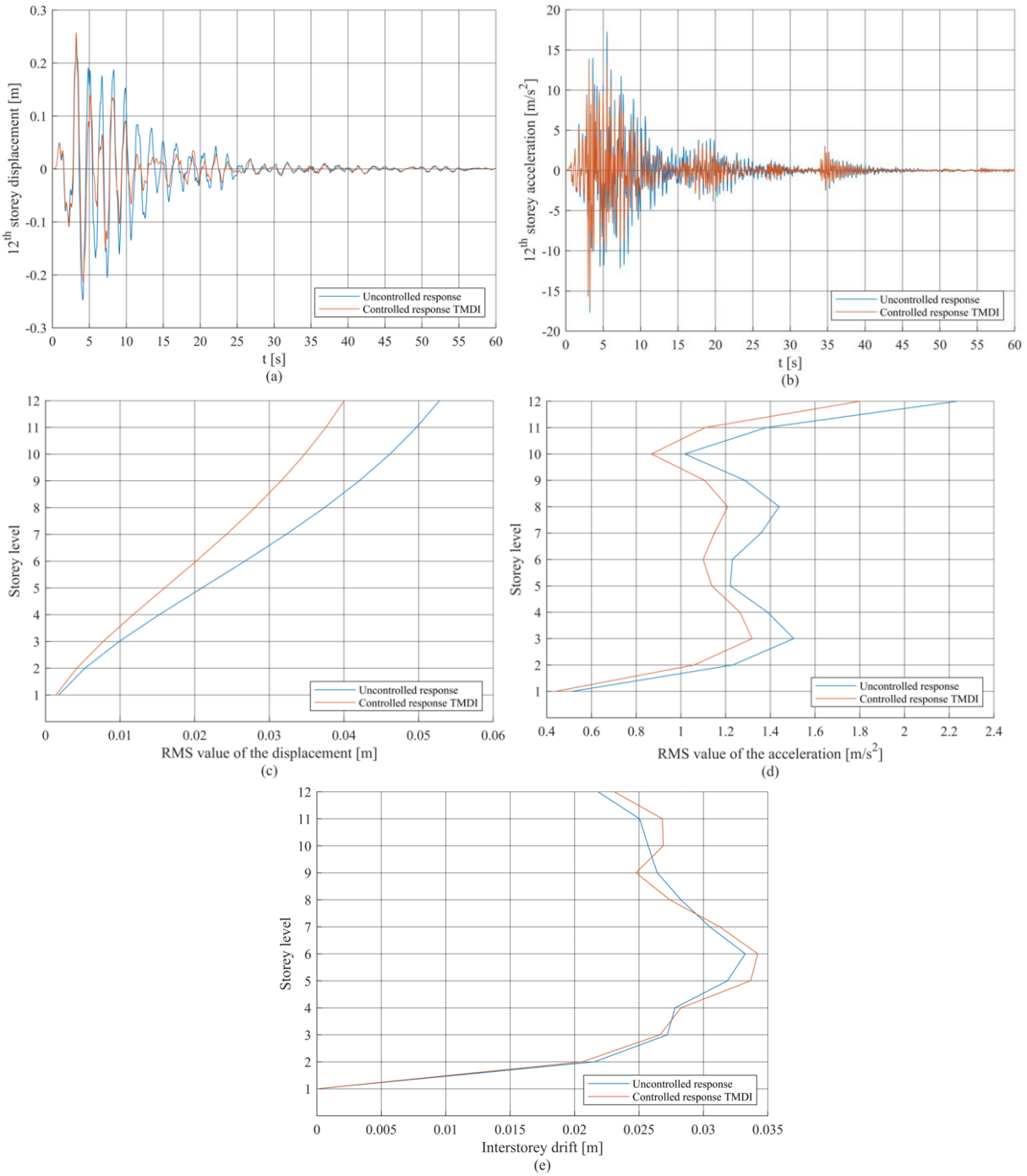


Figure 7: Response of the structure subjected to "Petrolia" Seismic record. (a) 12th-storey maximum displacements. (b) 12th-storey maximum accelerations. (c) RMS value of the displacements per storey. (d) RMS value of the accelerations per storey. (e) Interstorey drift.

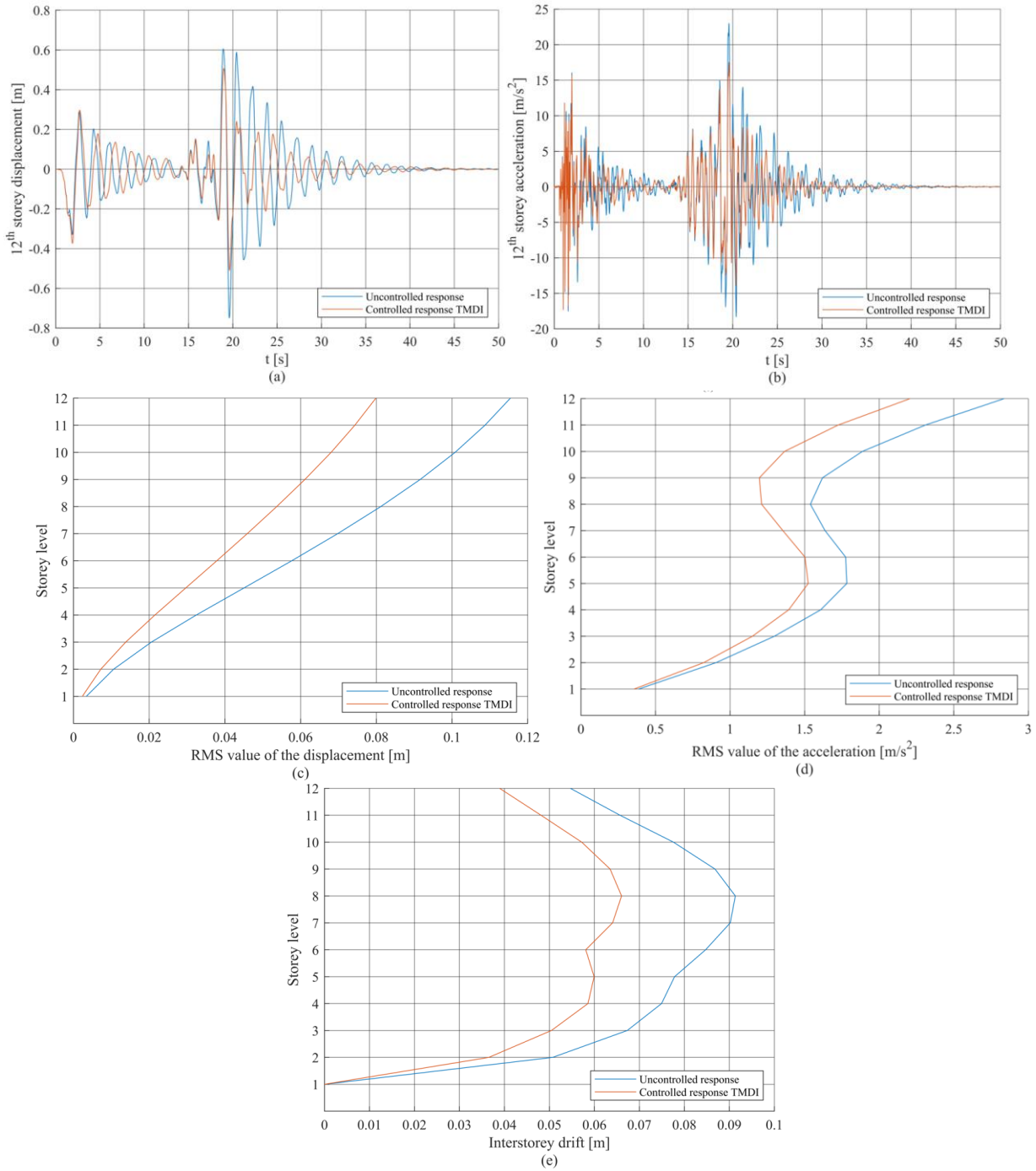


Figure 8: Response of the structure subjected to "Christchurch" Seismic record. (a) 12th-storey maximum displacements. (b) 12th-storey maximum accelerations. (c) RMS value of the displacements per storey. (d) RMS value of the accelerations per storey. (e) Interstorey drift.

## 6 CONCLUSIONS

- This study demonstrates the effectiveness of the TMDI device for the structural control and reduction of the dynamical response of a 12-storey building subjected to four different seismic records. The parameters of the devices were optimized via WOA, with the objective function proposed as a linear combination that aims to reduce both peak displacements and the RMS value of displacements. The maximum reduction percentages obtained for these parameters are 31.99% and 26.60% respectively proving the effectiveness of the objective function in the optimization process. Besides, reductions for peak accelerations, RMS value for acceleration, and peak interstorey drift are achieved for most of the analyzed earthquakes. The success of the controller in regulating the behavior of the structure is evident from the reduction achieved in its response.
- The TMDI is a modified version of the classical TMD that includes an inerter device. This addition induces a mass amplification effect that enables the device to dissipate the energy caused by an earthquake instead of the structure. TMDI is an attractive alternative for improving structural behavior while preserving its stability and functionality, thus, the use of this control device can reduce the risk of collapse under extreme seismic conditions.
- The WOA algorithm is a novel meta-heuristic technique that mimics the behavior of humpback whales in nature and showed to be a compelling alternative among the other state-of-art meta-heuristic methods available. Notably, the WOA is distinguished by its simplicity, efficiency, and fast-converging properties, making it a robust and versatile optimization algorithm that has shown to be highly effective in finding the optimal parameters of the TMDI that ensures to improve in the dynamic response. To guarantee optimal outcomes in the control of the structure is important to optimize both dynamic response and computational power, therefore the optimization process focused on obtaining the maximum reduction of the response and enhancing computational cost.

## REFERENCES

[1] J. Y. Xu, J. Tang, and Q. S. Li, “Semi-active control devices in structural control implementation,” *Structural Design of Tall and Special Buildings*, vol. 14, no. 2, pp. 165–174, 2005, doi: 10.1002/tal.270.

[2] P. Cristian and L. Septimiu, “Structural Control Systems Implemented in Civil Engineering,” no. January, 2005.

[3] D. Caicedo, L. Lara-Valencia, J. Blandon, and C. Graciano, “Seismic response of high-rise buildings through metaheuristic-based optimization using tuned mass dampers and tuned mass dampers inerter,” *Journal of Building Engineering*, vol. 34, no. September, 2021, doi: 10.1016/j.jobe.2020.101927.

[4] D. Pietrosanti, “Optimal design and performance evaluation of systems with Tuned Mass Damper Inerter ( TMDI ),” no. January, pp. 1367–1388, 2017, doi: 10.1002/eqe.2861.

[5] M. C. Constantinou, T. T. Soong, and G. F. Dargush, *Design and Retrofit*. 1986.

[6] Hermann Frahm, “Device for damping vibrations of bodies,” 1911.

[7] C. Lee, Y. Chen, L. Chung, and Y. Wang, "Optimal design theories and applications of tuned mass dampers," vol. 28, pp. 43–53, 2006, doi: 10.1016/j.engstruct.2005.06.023.

[8] F. Rahimi, R. Aghayari, and B. Samali, "Application of Tuned Mass Dampers for Structural Vibration Control : A State-of-the-art Review," vol. 6, no. 8, pp. 1622–1651, 2020.

[9] T. E. Saaed, G. Nikolakopoulos, J. E. Jonasson, and H. Hedlund, "A state-of-the-art review of structural control systems," *JVC/Journal of Vibration and Control*, vol. 21, no. 5, pp. 919–937, 2015, doi: 10.1177/1077546313478294.

[10] G. P. Cimellaro and S. Marasco, *Introduction to Dynamics of Structures and Earthquake Engineering*, vol. 45. 2018. [Online]. Available: https://doi.org/10.1007/978-3-319-72541-3_20%0Ahttp://link.springer.com/10.1007/978-3-319-72541-3

[11] John R. Sladek and Richard E. Klingner, "EFFECT OF TUNED-MASS DAMPERS ON SEISMIC RESPONSE By John R. Sladek 1 and Richard E. Klingner, 2 M. ASCE," vol. 109, no. 8, pp. 2004–2009, 2009.

[12] D. Ambrosini, "Single and multiple TMD optimization to control seismic response of nonlinear structures," vol. 252, no. September 2021, 2022, doi: 10.1016/j.engstruct.2021.113667.

[13] L. Marian and A. Giaralis, "Optimal design of a novel tuned mass-damper – inerter ( TMDI ) passive vibration control con fi guration for stochastically support-excited structural systems," *Probabilistic Engineering Mechanics*, pp. 1–9, 2014, doi: 10.1016/j.probengmech.2014.03.007.

[14] M. C. Smith, "Synthesis of Mechanical Networks : The Inerter," vol. 47, no. 10, pp. 1648–1662, 2002.

[15] C. Papageorgiou and M. C. Smith, "Laboratory experimental testing of inerters," pp. 3351–3356, 2005.

[16] P. Brzeski, T. Kapitaniak, and P. Perlikowski, "Novel type of tuned mass damper with inerter which enables changes of inertance," *J Sound Vib*, vol. 349, pp. 56–66, 2015, doi: 10.1016/j.jsv.2015.03.035.

[17] D. Pietrosanti, M. de Angelis, and M. Basili, "A generalized 2-DOF model for optimal design of MDOF structures controlled by Tuned Mass Damper Inerter (TMDI)," *Int J Mech Sci*, p. 105849, 2020, doi: 10.1016/j.ijmecsci.2020.105849.

[18] L. A. Lara-Valencia, Y. Farbiarz-Farbiarz, and Y. Valencia-González, "Design of a Tuned Mass Damper Inerter (TMDI) Based on an Exhaustive Search Optimization for Structural Control of Buildings under Seismic Excitations," *Shock and Vibration*, vol. 2020, 2020, doi: 10.1155/2020/8875268.

[19] S. Mirjalili, S. M. Mirjalili, and A. Lewis, "Grey Wolf Optimizer," *Advances in Engineering Software*, vol. 69, pp. 46–61, 2014, doi: 10.1016/j.advengsoft.2013.12.007.

[20] S. Mirjalili and A. Lewis, "The Whale Optimization Algorithm," *Advances in Engineering Software*, vol. 95, pp. 51–67, 2016, doi: 10.1016/j.advengsoft.2016.01.008.

[21] I. F. Lazar, "Using an inerter-based device for structural vibration suppression," no. November 2013, pp. 1129–1147, 2014, doi: 10.1002/eqe.

[22] S. Pal, D. Singh, and V. Kumar, "Hybrid SOMA: A tool for optimizing TMD parameters," in *Advances in Intelligent Systems and Computing*, 2017, vol. 546, pp. 35–41. doi: 10.1007/978-981-10-3322-3_4.

[23] A. Y. T. Leung, H. Zhang, C. C. Cheng, and Y. Y. Lee, "Particle swarm optimization of TMD by non-stationary base excitation during earthquake," *Earthq Eng Struct Dyn*, vol. 37, no. 9, pp. 1223–1246, Jul. 2008, doi: 10.1002/eqe.811.

[24] A. Kaveh, "Sizing Optimization of Skeletal Structures Using the Enhanced Whale Optimization Algorithm," in *Applications of Metaheuristic Optimization Algorithms in Civil Engineering*, Springer International Publishing, 2017, pp. 47–69. doi: 10.1007/978-3-319-48012-1_4.

[25] A. Kaveh and M. I. Ghazaan, "Enhanced whale optimization algorithm for sizing optimization of skeletal structures," *Mechanics Based Design of Structures and Machines*, vol. 45, no. 3, pp. 345–362, Jul. 2017, doi: 10.1080/15397734.2016.1213639.

[26] M. Azizi, R. G. Ejlali, S. A. Mousavi Ghasemi, and S. Talatahari, "Upgraded Whale Optimization Algorithm for fuzzy logic based vibration control of nonlinear steel structure," *Eng Struct*, vol. 192, pp. 53–70, Aug. 2019, doi: 10.1016/j.engstruct.2019.05.007.

[27] M. Huang, Z. Wan, X. Cheng, Z. Xu, Y. Lei, and D. Pan, "Two-stage damage identification method based on fractal theory and whale optimization algorithm," *Advances in Structural Engineering*, vol. 25, no. 11, pp. 2364–2381, Aug. 2022, doi: 10.1177/13694332221095629.

[28] H. Chen, Y. Xu, M. Wang, and X. Zhao, "A balanced whale optimization algorithm for constrained engineering design problems," *Appl Math Model*, vol. 71, pp. 45–59, Jul. 2019, doi: 10.1016/j.apm.2019.02.004.

[29] F. S. Gharehchopogh and H. Gholizadeh, "A comprehensive survey: Whale Optimization Algorithm and its applications," *Swarm Evol Comput*, vol. 48, pp. 1–24, Aug. 2019, doi: 10.1016/j.swevo.2019.03.004.

[30] Pacific Earthquake Engineering Research Center: Ground motion database. Available: http://peer.berkeley.edu/peer_ground_motion_database.

[31] Center for engineering strong-motion data (CESMD) www.strongmotioncenter.org.

[32] The MathWorks Inc, MATLAB R2019a, Natick, MA, USA, 2019.

COMPDYN 2023
9th ECCOMAS Thematic Conference on
Computational Methods in Structural Dynamics and Earthquake Engineering
M. Papadrakakis, M. Fragiadakis (eds.)
Streamed from Athens, Greece, 12–14 June 2023

# VARIATION STUDY OF THE CONSTRUCTION COST OF A 15-STORY R/C BUILDING BASED ON THE SEISMIC RISK ZONE

**Maria N. Kalaitzi**[1], **Theodoros A. Chrysanidis**[1*]

[1] International Hellenic University
P.O. Box 141, P.C. 57400, Sindos, Thessaloniki, Greece
theodoros_gr@yahoo.com

## Abstract

*Greece is divided into three seismic hazard zones ZI, ZII, ZIII. In the present research work, the same building in the three seismic zones of Greece is modeled, analysed and dimensioned and then the construction cost of its structural body is estimated. The building modeling was performed in SAP2000 using linear finite elements. The analysis of the building was performed by dynamic spectral analysis methods using the design spectrum of EC8. A fifteen-storey building with a standard floor plan per floor was used. The dimensioning of the building took place based on the results of the ground floor. The purpose of this research paper is to study the possible influence of seismicity, based on which the dimensioning takes place, on the construction cost of the load-bearing structure of a fifteen-storey building with a standard floor plan per floor. The degree of influence is studied by estimating the quantities of materials required depending on the seismic hazard zone. Interesting comparisons take place between the results for the three different seismic hazard zones. Useful conclusions are drawn regarding the influence of seismicity on the construction cost of the load-bearing structure of reinforced concrete buildings.*

**Keywords:** Cost of construction, Seismicity, Seismic hazard zone

## 1 INTRODUCTION

A catalytic role for the success of a project is played by an accurate construction cost estimation [1]–[7]. Construction cost means the cost made up of the purchase value of the materials and the labor fee that can be offered directly or through a subcontractor. For construction cost management to be considered successful, it is necessary to process certain processes such as resource planning, cost estimation, cost budgeting and its control. These processes aim to provide a construction cost estimate to guide a budget in order to complete the project within the given budget timeframe [8]. The size, construction area, density of columns and beams, the seismicity of the area and the type of foundation are some of the factors that affect the final construction cost [9]–[18]. As can be understood from the title, the present research work has as its main object of interest the seismicity and its influence on the construction cost, which is why special emphasis is placed on the term "seismicity". In more detail, an earthquake is a phenomenon, which usually occurs without any warning, it is an inevitable phenomenon and despite the fact that it lasts a short period of time, it is capable of causing significant material damage to human infrastructure, resulting in serious injuries and even loss of human life [19]. The term seismicity has no specific definition. It can be rendered as an increasing function of both the magnitudes and the frequency of them in an area during a certain period of time. Still, it depends on the size interval for which it is considered. The term seismic hazard is defined as the maximum expected value of a seismic parameter for a given recurrence period or for a specific probability of non-exceedance and a specific period of time [20]–[23].

The Map of Seismic Hazard Zones of Greece that is valid today was designed in the period 1986-1989 and started to be implemented in 1995. Its revision, almost 15 years after its preparation, was deemed necessary for many factors that have intervened since then. With the new map, the Greek area is divided into three zones of seismic risk, in contrast to the four zones, depending on the seismic risk, into which it was divided until now, as the smaller one is removed (Figure 1) [24]. The design ground acceleration values are 0.16g (percent of the acceleration of gravity g) for the first zone, 0.24g for the second zone and 0.36g for the third zone (Table 1) [24]. According to statistics, in terms of seismicity, Greece ranks first in the Mediterranean and in Europe, as well as sixth globally. Each earthquake has its own identity defined by physical characteristics, induced phenomena and effects. The physical characteristics of an earthquake are its magnitude, point (epicenter) and time of occurrence, as well as the extent to which it was felt locally. The two main regulations with which the dimensioning of the building of this research work complies are the Greek Seismic Code [24] and the Eurocodes [25]–[27]. More specifically, starting with the first one as its primary objectives, the regulation sets the protection of human life in the case of high intensities, the limitation and even the avoidance of economic losses in the case of moderate intensities. Finally, the assurance of a minimum level of operations of the projects. The projects covered by the regulation are the so-called "normal risk", i.e., projects whose potential damage is limited to the project itself, its contents and its immediate vicinity. The regulation consists of the basic provisions, design criteria, seismic actions and provisions related to the soil and supports applied to buildings and other structures in seismic areas. For projects such as bridges, silo tanks as well as the strengthening of existing buildings, additional provisions are necessary [28]–[31]. The same is provided for projects involving partial or complete anti-seismic insulation. This regulation offers options to the practitioner who is willing to implement more precise calculations than those required in everyday practice applications.

| Zone of seismic risk | Ground acceleration values (g) |
|---|---|
| Z1 | 0,16 |
| Z2 | 0,24 |
| Z3 | 0,36 |

Table 1: Ground acceleration values [24].

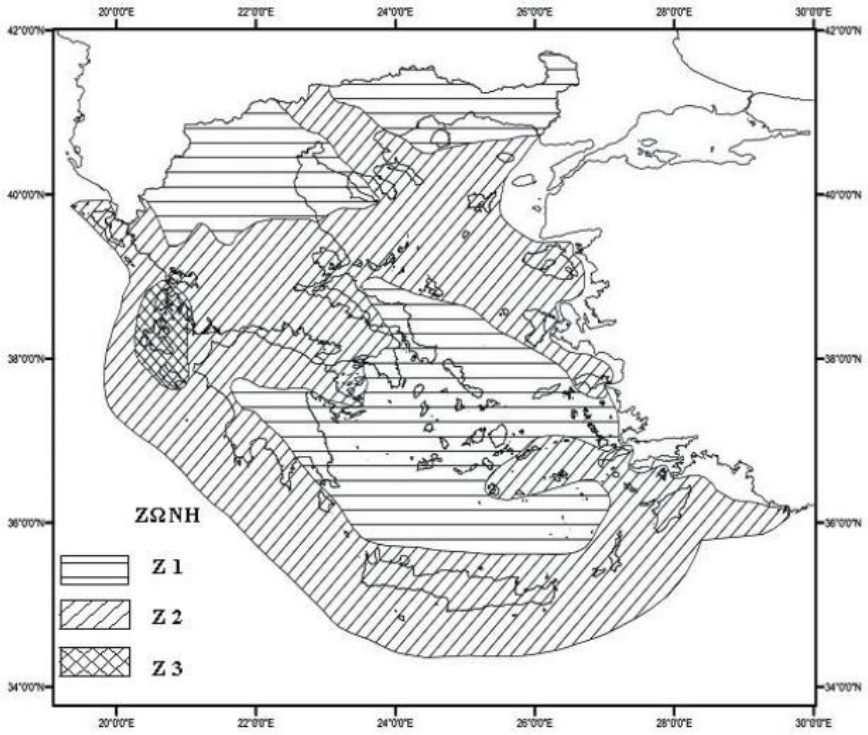


Figure 1: Seismic hazard map of Greece [24].

It is important to emphasize that in order to accept the application of the most accurate methods, it is necessary to satisfy certain conditions, to be accompanied by sufficient proofs that make them reliable and to ensure a level of safety at least commensurate with that intended by this regulation and in any case subject to the approval of their use by the competent public authority. Seismic risk is considered to be adequately addressed by the design, construction and use of a structure. This means that the elements of the load-bearing body under the design earthquake ensure minor and repairable damages [32]–[38]. Furthermore, they minimize the damages for earthquakes of lower intensity and with a higher probability of occurrence, when imposing the "design" seismic actions with an acceptably small probability of exceeding them during the life of the structure [39], [40]. With the flexural yielding of critical areas, i.e., the formation of plastic joints, the load-bearing body is able to turn into an elasto-plastic mechanism, which continues to respond to the peaks of seismic movements with prac-

tically constant intensity, releasing in each cycle a significant part of the seismic energy it has absorbed [20], [32], [34], [41]–[44]. The reduction of the calculated seismic action to a fraction 1/q of that corresponding to an elastic response is achieved by this capacity of the load-bearing body ("ductility"). This has the effect of limiting the resulting economic burden from seismic design to a reasonable framework. At the same time, it makes less pronounced the consequences of the various uncertainties arising from the seismic design. In order to achieve sufficient ductility of the load-bearing body, a reliable plastic mechanism without risks of cracking or chain collapse and a minimum degree of local ductility of the critical areas must be ensured through competent design with appropriate concrete confinement [20], [34], [45], [46]. At this point it is important to clarify the term "ductility", by the term ductility, it is meant the ability of the structure to absorb seismic energy and develop plastic deformations without significant loss of lateral strength and axial load carrying capacity (not to collapse).

As already mentioned, one of the regulations that this research work focuses on is the Eurocodes. The Eurocodes consist of a series of ten European Standards for the design of structures developed by the European Committee for Standardization. In this paper, a more extensive reference will be made to Eurocode 8 [25], as its subject is the anti-seismic design of load-bearing structures. The first part of Eurocode 8 presents the general requirements for seismic behavior as well as the rules for determining the seismic action for the design of any type of project. It mainly focuses on the compliance criteria and special rules for steel, reinforced concrete, wood or load-bearing masonry, composite (steel and concrete) buildings, as well as seismically insulated buildings. An extreme scenario is the case where the load-bearing body is required to remain elastic to the imposed deformations based on its strength alone. This results in a requirement of at least equal strength to the horizontal forces introduced by the earthquake into the elastic load-bearing body, based on its mass and elastic stiffness. In the Greek area, these forces receive values of 40% to 90% of the total weight of the project. Even if it is technically possible to design the load-bearing body in such a way that it is able to remain elastic under these forces, it is an extremely uneconomical solution for the load-bearing body and its foundation.

In the Greek region, it was fully embraced for buildings with concrete supports, that it is allowed to design the support for an elastic response to the design seismic action and indeed by dividing the elastic horizontal forces with a behavior factor of q=1.5 instead of q=1.0 which corresponds to elastic behavior. This is done by taking into account overstrength, such as margins between average design values and design values of material strengths, overstrength offered by minimum reinforcements or design for non-seismic actions. According to Eurocode 8 [25], the basic method of anti-seismic design and the only one accepted in the Greek area for buildings with concrete structures, is based on ductility. In Eurocode 8 [25], certain guiding principles are recorded and analyzed, from which it is necessary to shape the body of the building, in order to satisfy the basic behavior requirements at an acceptable cost. Indicative of some of these principles are the static simplicity, the uniformity and symmetry of the load-bearing body.

## 2 ANALYTICAL RESEARCH

### 2.1 Building data

The object of this work is the study of a 15-story reinforced concrete structure for all three seismic hazard zones. In more detail, the construction is doubly symmetrical, it has a rectangular floor plan measuring 25×25m with no basement (Figure 2). Additionally, in the center of the floor plan is a strong core, which is made up of a total of eight walls of different dimensions (six along the Y-axis and two along the X-axis). Finally, there are two walls at the pe-

rimeter of the plan along the Y-axis, whose edges have hidden columns. The cross-sections of the building's columns remain constant for the 1st floor (ground floor) and the 2nd, while the rest of the cross-sections of the columns are reduced by 5 cm per floor. At the same time, the cross-sections of the beams remain constant at all floors, in contrast to the cross-sections of the walls, which vary throughout the height of the building and, more specifically, they decrease by 12.5 cm every five floors. The load-bearing body's modelling has been performed with the usage of SAP2000 analysis software. The construction materials of the load-bearing body, which are C30/37 for the concrete and B500C for the reinforcement steel, are included in the program. According to the EC2 regulation [26] for concrete class C30/37, the modulus of elasticity is taken as $E_{cm}$=32 GPa, the self-weight of concrete $\gamma_c$=25 kN/m$^3$, the value of Poisson's ratio is taken as zero according to the specifications of the code for cracked concrete sections ν=0. From the sequence of commands in the program, the materials and the cross-sections of the structural elements (beams, columns, walls) are defined.

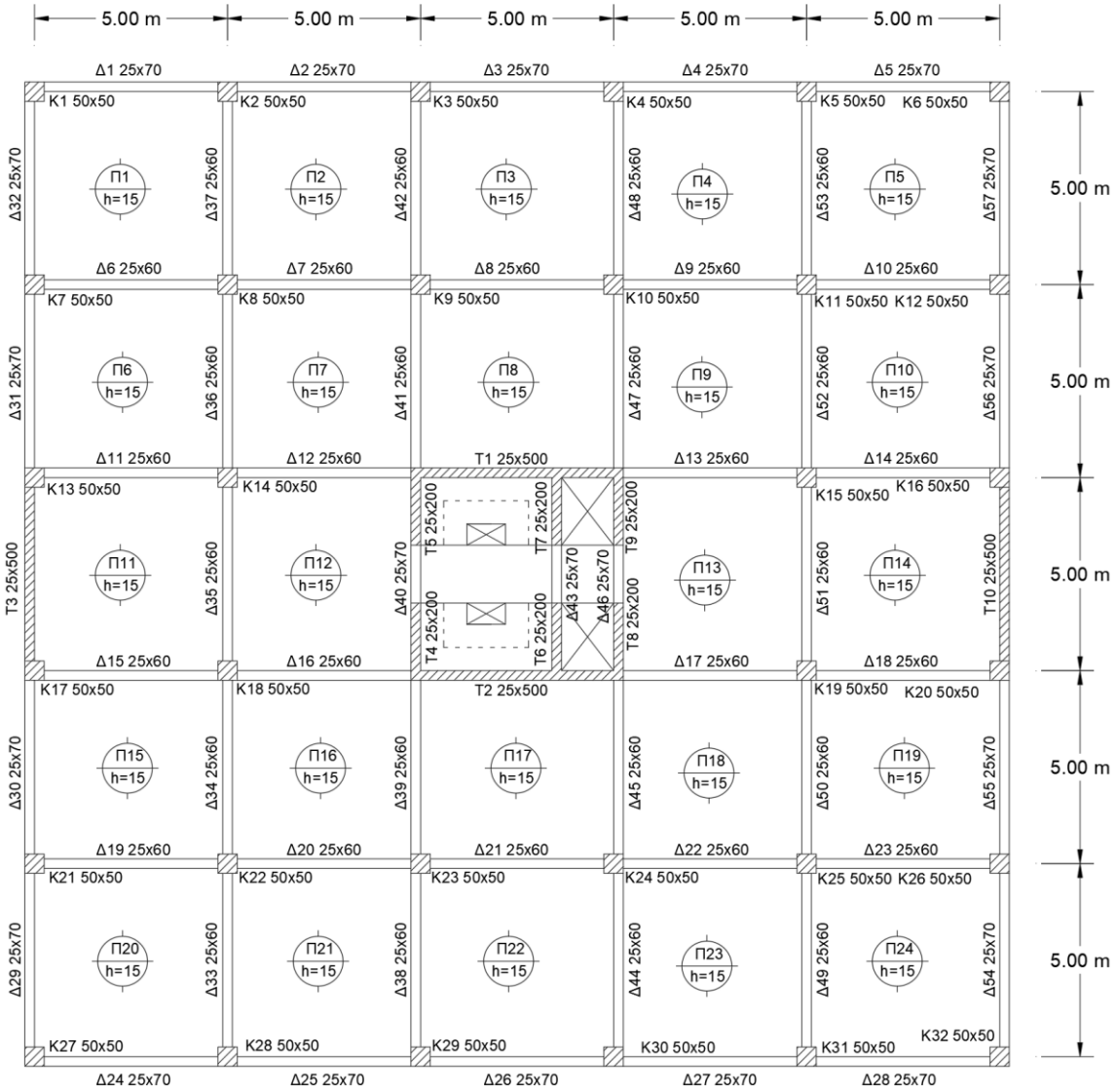


Figure 2: Typical floor plan.

| Floor | Height (m) | Beam dimensions (cm) | | Wall thickness (cm) | Column dimensions (cm) |
|---|---|---|---|---|---|
| | | Perimetric | Internal | | |
| **1st (Ground floor)** | 4.50 | 25×70 | 25×60 | 50 | 100×100 |
| **2** | 3.00 | 25×70 | 25×60 | 50 | 100×100 |
| **3** | 3.00 | 25×70 | 25×60 | 50 | 95×95 |
| **4** | 3.00 | 25×70 | 25×60 | 50 | 90×90 |
| **5** | 3.00 | 25×70 | 25×60 | 50 | 85×85 |
| **6** | 3.00 | 25×70 | 25×60 | 37.5 | 80×80 |
| **7** | 3.00 | 25×70 | 25×60 | 37.5 | 75×75 |
| **8** | 3.00 | 25×70 | 25×60 | 37.5 | 70×70 |
| **9** | 3.00 | 25×70 | 25×60 | 37.5 | 65×65 |
| **10** | 3.00 | 25×70 | 25×60 | 37.5 | 60×60 |
| **11** | 3.00 | 25×70 | 25×60 | 25 | 55×55 |
| **12** | 3.00 | 25×70 | 25×60 | 25 | 50×50 |
| **13** | 3.00 | 25×70 | 25×60 | 25 | 45×45 |
| **14** | 3.00 | 25×70 | 25×60 | 25 | 40×40 |
| **15** | 3.00 | 25×70 | 25×60 | 25 | 35×35 |

Table 2: Dimensions of the structural elements.

## 2.2 Loads

For the building in question, the loads are shown in Table 3.

| **PERMANENT LOADS** | | |
|---|---|---|
| **N/A** | **Type** | **Value** |
| **1** | Flooring | 1.40 kN/m$^2$ |
| **2** | Partition brick structures | 1.00 kN/m$^2$ |
| **3** | Perimeter brick structures | 8.00 kN/m |
| **4** | Roofing | 3.50 kN/m$^2$ |
| **5** | Parapet roof load | 3.60 kN/m$^2$ |
| **LIVE LOADS** | | |
| **N/A** | **Type** | **Value** |
| **1** | Ground floor | 2.00 kN/m$^2$ |
| **2** | Typical floors | 2.00 kN/m$^2$ |
| **3** | Roof | 2.00 kN/m$^2$ |
| **SPECTRUM DATA EC8** | | |
| **N/A** | **Type** | **Data** |
| **1** | Spectrum type | Horizontal design spectrum type 1 |
| **2** | Soil category | B |
| **3** | Factor β | 0.20 |
| **4** | Seismic acceleration factor α | For the three categories: α =0.16, 0.24, 0.36 |
| **5** | Gravity acceleration g | 9.81 m/sec$^2$ |
| **6** | Coefficient behavior q | Calculation based on EC8 |

Table 3: Building loads.

## 2.3 3D Modelling

The 3D modelling of the building is presented at Figure 3. The display takes place both for linear finite elements and the sections of the building.

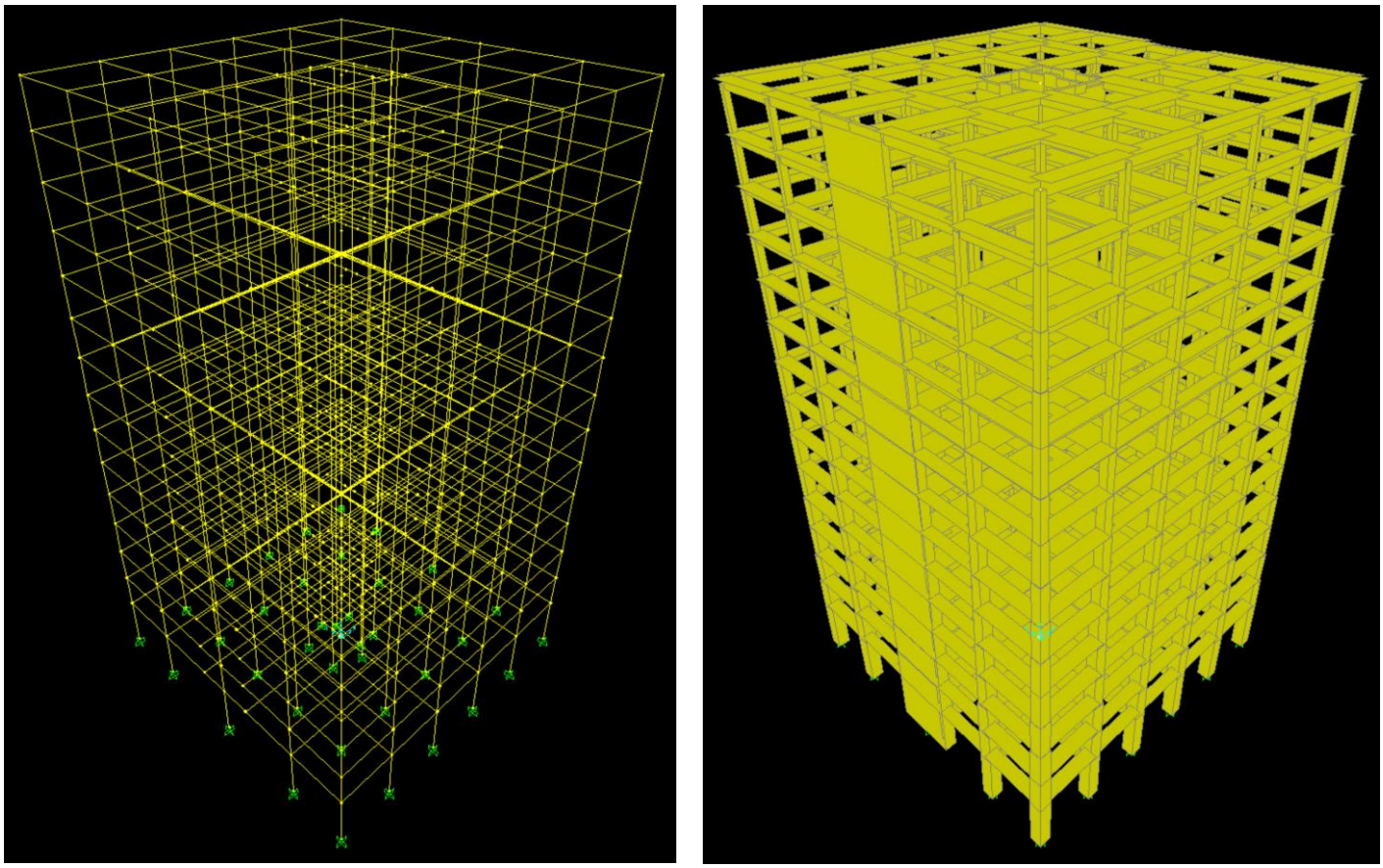

(a) (b)

Figure 3: Views of the 3D building model: (a) Linear finite elements (b) Sections.

## 2.4 Measurements of building materials

Based on the data obtained from the program for all three seismic hazard zones (stresses) the dimensioning of the load-bearing body for the structural elements of the ground floor was carried out. After a series of calculations, tables were formed with the bending and shear reinforcements for all three seismic hazard zones, for the structural elements (slabs, beams, columns, walls).

As already pointed out, the pre-measurement of the materials required for the construction of the project is an effective method in order to obtain as accurate a cost estimate as possible in order for the project to be successful. After all the necessary elements from the dimensioning have been gathered, the pre-measurement takes place. Initially, the pre-measurement of the concrete was carried out in all three zones, which were studied. It was observed that the amount of concrete remains constant for the three seismic zones, due to the fixed dimensions of the structural elements.

| CONCRETE MEASUREMENT | | | | | |
|---|---|---|---|---|---|
| **STOREY** | **SLABS ($m^3$)** | **BEAMS ($m^3$)** | **COLUMNS ($m^3$)** | **WALLS ($m^3$)** | **TOTAL (STOREY) ($m^3$)** |
| 1 | 90 | 33.08 | 139.2 | 63.08 | 325.36 |
| 2 | 90 | 33.08 | 91.2 | 41.33 | 255.61 |
| 3 | 90 | 33.92 | 82.31 | 41.61 | 247.84 |
| 4 | 90 | 34.72 | 73.87 | 41.90 | 240.49 |
| 5 | 90 | 35.55 | 65.89 | 42.18 | 233.62 |
| 6 | 90 | 36.35 | 58.37 | 31.85 | 216.57 |
| 7 | 90 | 37.19 | 51.3 | 32.06 | 210.55 |
| 8 | 90 | 37.99 | 44.69 | 32.28 | 204.96 |
| 9 | 90 | 38.82 | 38.53 | 32.49 | 199.84 |
| 10 | 90 | 39.62 | 32.83 | 32.7 | 195.15 |
| 11 | 90 | 40.46 | 27.59 | 21.95 | 180.00 |
| 12 | 90 | 41.26 | 22.8 | 22.09 | 176.15 |
| 13 | 90 | 42.09 | 18.47 | 22.23 | 172.79 |
| 14 | 90 | 42.89 | 14.59 | 22.37 | 169.85 |
| 15 | 90 | 43.69 | 11.17 | 22.52 | 167.38 |
| | | | | **TOTAL** | **3196.16** |

Table 4: Concrete measurement.

## 3 RESULTS ANALYSIS

Below are pie charts where the results were analyzed with their help (Figure 4, Figure 5).

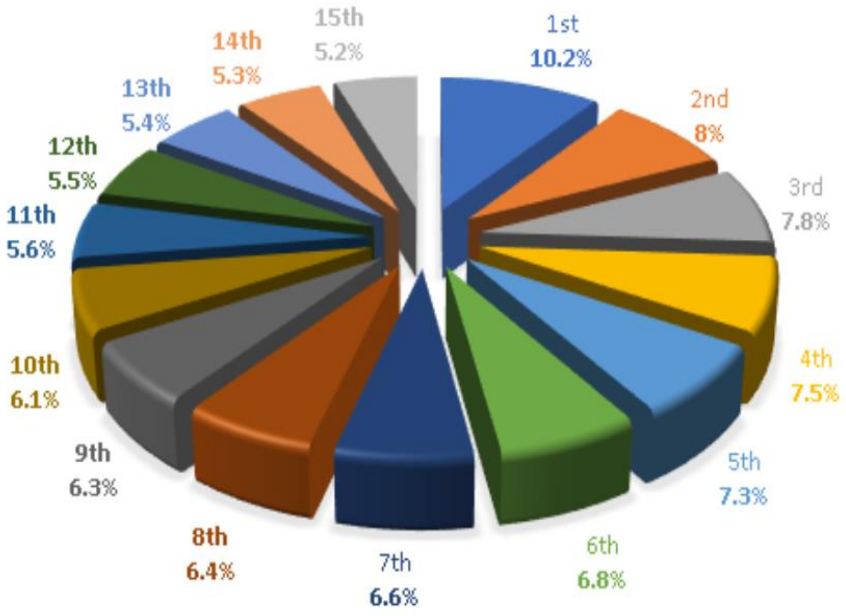


Figure 4: Percentage of concrete per floor (%).

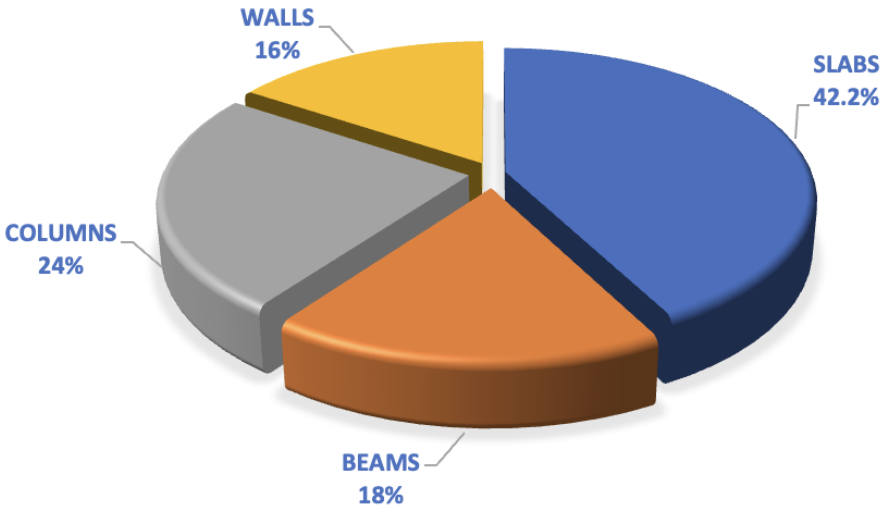


Figure 5: Percentage of structural elements in total concrete (%).

According to the pie diagram of Figure 4, it can be seen that the 1st floor occupies a larger percentage of concrete, compared to the other floors. On the contrary, the percentage of the remaining floors decreases from floor to floor (Figure 4). Still, the slabs are the ones that occupy the largest percentage of the total concrete with a percentage of 42.2%, followed by the columns with a percentage of 24%, the beams with a percentage of 18% and finally the walls with a percentage of 16% (Figure 5). Continuing with the analysis of the ground floor structural element reinforcement results for all three seismic zones, a diagram of the structural element reinforcement weight follows (Figure 6).

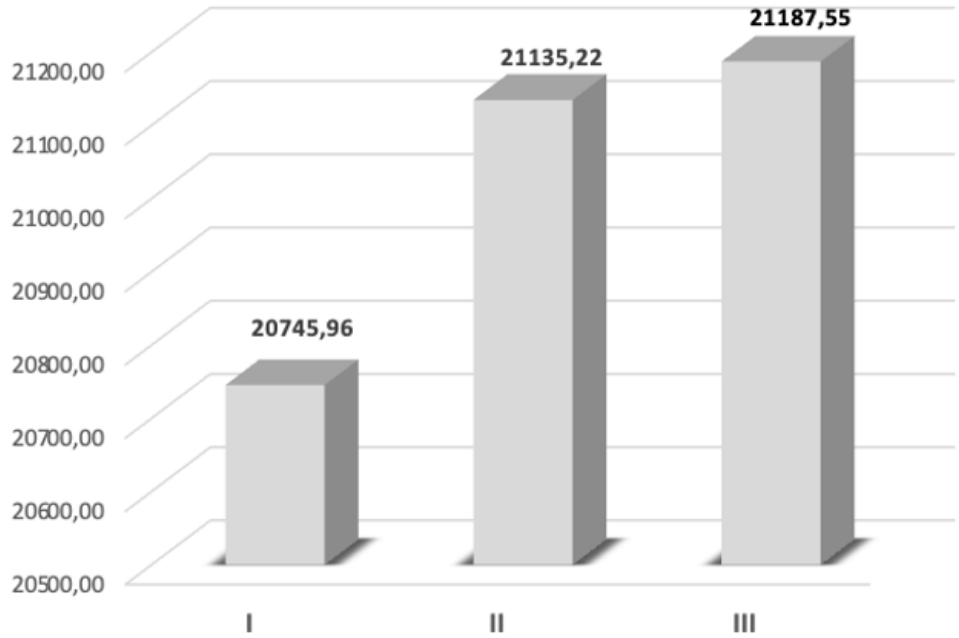


Figure 6: Total steel weight of ground floor structural elements for each seismic zone.

Then, a diagram was formed with the percentage increase in the total steel weight of the structural elements (Figure 7).

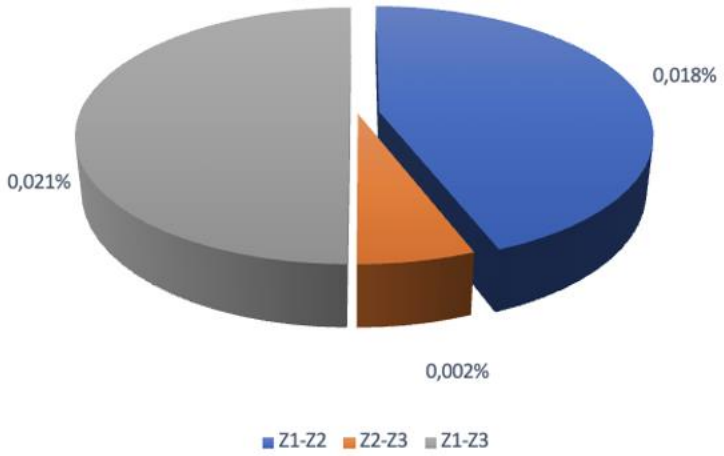


Figure 7: Percentage increase in total steel weight of ground floor structural elements between zones.

Through the preceding diagrams, the following emerges:

1. The transition of the structure from Zone I seismic acceleration $\alpha_g$ = 0.16g to Zone II seismic acceleration $\alpha_g$ = 0.24g results in:
   - 1.8% increase in the total steel weight of all structural elements
   - 0.3% increase in column steel weight
   - 1% increase in beam steel weight
   - 1.1% increase in wall steel weight
2. The transition of the structure from Zone II seismic acceleration $\alpha_g$ = 0.24g to Zone III seismic acceleration $\alpha_g$ = 0.36g results in:
   - 0.2% increase in the total steel weight of all structural elements
   - 0.29% increase in column steel weight
   - 0.59% increase in beam steel weight
   - 0.2% increase in wall steel weight
3. The transition of the structure from Zone I of seismic acceleration $\alpha_g$ = 0.16g to Zone III of seismic acceleration $\alpha_g$ = 0.36g results in:
   - 2.1% increase in the total steel weight of all structural elements
   - 0.6% increase in column steel weight
   - 1.57% increase in beam steel weight
   - 1.1% increase in wall steel weight
4. The increase in seismic acceleration by:
   - Zone I to Zone II: ((0.24-0.16)/0.16)*100 = 50 => 50% increment
   - Zone II to Zone III: ((0.36-0.24)/0.24)*100 = 50 => 50% increment
   - Zone I to Zone III: ((0.36-0.16)/0.16)*100 = 125 => 125% increment
5. There is an increase in the percentage of the weight of the individual structural elements of the structure (columns, beams and walls) from Zone I to Zone II and Zone III, except for the percentage of slabs, which remains constant for all three zones. This results in an increase in the total weight of the ground floor steel considered. More specifically:

- The slabs occupy certain percentages in steel, e.g. in Zone I: 44%, then in Zone II: 43% and lastly in Zone III: 43.5%.
- The beams occupy certain percentages in steel, e.g. in Zone I: 30%, in Zone II: 30% and in Zone III: 30%.
- The columns occupy certain percentages in steel, e.g. in Zone I: 12.3%, in Zone II: 12.4% and in Zone III: 12.4%.
- The walls occupy certain percentages in steel, e.g. in Zone I: 12%, in Zone II: 13.6% and in Zone III: 13.6%.

6. Also, it appears that during the transition from one zone to another for all three seismic zones:

➢ While the beams keep their longitudinal reinforcement constant, the transverse reinforcement shows some increments.
➢ The columns also keep their longitudinal reinforcement constant, while the transverse reinforcement shows some increments.
➢ Finally, the walls show increments in their transverse reinforcement, while at the same time the T3-T10 walls also show increments in their longitudinal reinforcement.

## 4 CONCLUSIONS

The building of the present study consists of 15 floors, is made of reinforced concrete with no basement and has a rectangular conventional floor plan in the three seismic zones Z1, Z2, Z3.

The conclusions reached in summary are the following:

1. Beams show the largest percentage increase in steel weight with increasing seismic acceleration.

Specifically during the transition:

➢ From Zone I (0.16g) → Zone II (0.24g): Increases 1%
➢ From Zone II (0.24g) → Zone III (0.36g): Increases 0.6%
➢ From Zone I (0.16g) → Zone III (0.36g): Increases 1.57%

2. In walls steel increases less than beams:

➢ From Zone I (0.16g) →Zone II (0.24g): Increases 1.1%
➢ From Zone II (0.24g) → Zone III (0.36g): Increases 0.2%
➢ From Zone I (0.16g) → Zone III (0.36g): Increases 1.1%

3. In columns the steel increases even less than in walls:

➢ From Zone I (0.16g) →Zone II (0.24g): Increases 0.3%
➢ From Zone II (0.24g) →Zone III (0.36g): Increases 0.29%
➢ From Zone I (0.16g) →Zone III (0.36g): Increases 0.6%

4. So, it follows that the dominant position in our structure is occupied by the beams.

5. The increase in seismic acceleration $\alpha_g$:

- From Zone I → Zone II it is of the order of 50%, while the percentage increase in the total amount of materials quantifies to only 1.8%.
- From Zone II → Zone III is of the order of 50%, while the percentage increase in the total amount of materials is only 0.2%
- From Zone I →Zone III is of the order of 125%, while the percentage increase in the total amount of materials quantifies to only 2.1%.

6. Therefore, the percentage increase in total steel demand is quite small.
7. According to all the above, it comes to the conclusion that for a fifteen-story reinforced concrete building, with a strong wall core arrangement, the influence of the seismic risk on the construction cost of the building is not an important factor, since the percentage increase of the materials required is quite smaller compared to the large percentage increases of the corresponding seismic accelerations.

## REFERENCES

[1] T. Chrysanidis and I. Tegos, "Cost Comparison and Parametrical Investigation of the R/C Shear Wall Core of a Tall Building," *International Journal of Engineering Research and Technology*, vol. 5, no. 09, pp. 592–595, 2016.

[2] T. Chrysanidis, V. Panoskaltsis, and I. Tegos, "Preliminary design and analysis of cost parameters of a high-rise building: Braced shear wall core system," *International Journal of Civil Engineering and Technology*, vol. 7, no. 5, pp. 137–152, 2016.

[3] M. Srivastava and V. Kumar, "The methods of using low cost housing techniques in India," *Journal of Building Engineering*, vol. 15, pp. 102–108, 2018, doi: 10.1016/j.jobe.2017.11.001.

[4] A. Jasvi and D. Bera, "Sustainable use of low cost building materials in the rural India," *International Journal of Research in Engineering and Technology*, vol. 4, no. 13, pp. 534–547, 2015, doi: 10.15623/ijret.2015.0425077.

[5] T.-E. Makris and T. Chrysanidis, "Does the seismicity of the area have an impact on the construction cost of the load-bearing structure of R/C buildings?," in *Proceedings of the 8th ECCOMAS Thematic Conference on Computational Methods in Structural Dynamics and Earthquake Engineering (COMPDYN 2021)*, 2021, pp. 4535–4546. doi: https://doi.org/10.7712/120121.8805.19134.

[6] T. Chrysanidis and M. Stergiou, "Cost study of construction of a 10-storey building in different seismic zones according to modern seismic codes," in *Lecture Notes in Civil Engineering (2022), Proceedings of the 4th International Conference on Civil Engineering and Architecture (ICCEA 2021)*, 2021, pp. 85–94. doi: https://doi.org/10.1007/978-981-16-6932-3_8.

[7] P. Tselempi and T. Chrysanidis, "Differentiation of the construction cost of a fifteen-storey R/C building depending on the seismic hazard zone," in *Proceedings of the 8th*

*ECCOMAS Thematic Conference on Computational Methods in Structural Dynamics and Earthquake Engineering (COMPDYN 2021)*, 2021, pp. 4520–4534. doi: https://doi.org/10.7712/120121.8804.19133.

[8] T. Chrysanidis, D. Mousama, E. Tzatzo, N. Alamanis, and D. Zachos, "Study of the Effect of a Seismic Zone to the Construction Cost of a Five-Story Reinforced Concrete Building," *Sustainability (Switzerland)*, vol. 14, no. 16, 2022, doi: 10.3390/su141610076.

[9] N. Alamanis and P. Dakoulas, "Effects of spatial variability of soil properties and ground motion characteristics on permanent displacements of slopes," *Soil Dynamics and Earthquake Engineering*, vol. 161, no. June, p. 107386, 2022, doi: 10.1016/j.soildyn.2022.107386.

[10] N. Alamanis and P. Dakoulas, "Investigation on the effect of spatial variability of soil properties on permanent seismic displacements of slopes in load," 2020.

[11] N. Alamanis, "Influence of random soil strength properties on the earthquake vulnerability of slopes with embedded oil and natural gas pipelines," *Energy Systems*, 2020, doi: 10.1007/s12667-020-00394-9.

[12] T. Chrysanidis and I. Tegos, "Axial and transverse strengthening of R/C circular columns: Conventional and new type of steel and hybrid jackets using high-strength mortar," *Journal of Building Engineering*, vol. 30, no. January, p. 101236, 2020, doi: 10.1016/j.jobe.2020.101236.

[13] T. Chrysanidis, "Evaluation of Out-of-Plane Response of R/C Structural Wall Boundary Edges Detailed with Maximum Code-Prescribed Longitudinal Reinforcement Ratio," *International Journal of Concrete Structures and Materials*, vol. 14, no. 1. 2020. doi: 10.1186/s40069-019-0378-4.

[14] T. Chrysanidis, "Influence of elongation degree on transverse buckling of confined boundary regions of R/C seismic walls," *Construction and Building Materials*, vol. 211, pp. 703–720, Jun. 2019, doi: 10.1016/J.CONBUILDMAT.2019.03.271.

[15] T. Chrysanidis and I. Tegos, "Does reinforcement ratio affect displacements due to lateral buckling behavior of concrete walls?," *International Journal of Applied Engineering Research*, vol. 12, no. 3, pp. 382–388, 2017.

[16] T. Chrysanidis and I. Tegos, "Displacements and mode of failure of medium high reinforced walls due to transverse buckling," *International Journal of Engineering Development and Research*, vol. 4, no. 3, pp. 628–634, 2016.

[17] D. S. Vijayan, P. Devarajan, and A. Sivasuriyan, "A review on eminent application and performance of nano based silica and silica fume in the cement concrete," *Sustainable Energy Technologies and Assessments*, vol. 56, no. February, p. 103105, 2023, doi: 10.1016/j.seta.2023.103105.

[18] D. S. Vijayan *et al.*, "A State of Review on Instigating Resources and Technological Sustainable Approaches in Green Construction," *Sustainability (Switzerland)*, vol. 15, no. 8, pp. 1–25, 2023, doi: https://doi.org/10.3390/su15086751.

[19] C. L. Segura and J. W. Wallace, "Seismic performance limitations and detailing of slender reinforced concrete walls," *ACI Structural Journal*, vol. 115, no. 3, 2018, doi: 10.14359/51701918.

[20] T. Chrysanidis and V. Panoskaltsis, “Experimental investigation on cracking behavior of reinforced concrete tension ties,” *Case Studies in Construction Materials*, vol. 16, no. June 2022, p. e00810, 2022, doi: 10.1016/j.cscm.2021.e00810.

[21] T. Chrysanidis, I. Tegos, and N. Alamanis, “Experimental Research on Improvement of the Ductility of R/C Seismic Walls Through Slip Prevention With the Use of Steel Rhs,” *Ingegneria Sismica*, vol. 39, no. 1, pp. 1–29, 2022.

[22] T. Chrysanidis, “The effect of longitudinal reinforcement ratio on the lateral buckling behavior of R/C walls modelled using prism elements,” *Journal of Building Engineering*, vol. 42, no. 102456, 2021, doi: 10.1016/j.jobe.2021.102456.

[23] T. Chrysanidis, “A Case of Lateral Buckling Under Seismic Action Using a Prism Column Specimen,” *Structural Engineering International*, 2021, doi: 10.1080/10168664.2021.2003741.

[24] Ministry of Environment Planning and Public Works, “Greek Earthquake Resistant Design Code,” Athens, Greece, 2003, p. . (In Greek).

[25] European Committee for Standardization, “EN 1998-1:2004, Eurocode 8: Design of structures for earthquake resistance - Part 1: General rules, seismic actions and rules for buildings,” Brussels, Belgium, 2004.

[26] European Committee for Standardization, “EN 1992-1-1:2004, Eurocode 2: Design of concrete structures - Part 1-1: General rules and rules for buildings,” Brussels, Belgium, 2004.

[27] E. C. for Standardization, “EN 1991-1-1:2002, Eurocode 1: Actions on structures - Part 1-1: General actions - Densities, self-weight, imposed loads for buildings,” Brussels, Belgium, 2002.

[28] I. Tegos, N. Giannakas, and T. Chrysanidis, “Serviceability cracking check of circular section piers,” *Bridge Structures*, vol. 7, no. 1, pp. 43–52, 2011, doi: 10.3233/BRS-2011-018.

[29] A. Astaneh-Asl, “Seismic behavior and design of steel shear walls,” *2001 SEAONC Seminar*. Structural Engineers Association of Nothern California, San Francisco, California, U.S., pp. 1–18, 2001.

[30] M. Fintel, “Shear walls - An Answer for Seismic Resistance?,” *Concrete International*, vol. 13, no. 7. pp. 48–53, 1991.

[31] F. J. Perez, S. Pessiki, and R. Sause, “Seismic Design of Unbonded Post-Tensioned Precast Concrete Walls with Vertical Joint Connectors,” *PCI Journal*, vol. 49, no. 1, pp. 58–79, 2014, doi: 10.15554/pcij.01012004.58.79.

[32] T. Chrysanidis and V. Panoskaltsis, “Analytical study on the effect of extreme seismic strains on the transverse buckling of ultra- reinforced seismic walls and their environmental design,” in *IOP Conference Series: Earth and Environmental Science, 2nd International Conference on Environmental Design (ICED 2021)*, 2021, p. 899. doi: 10.1088/1755-1315/899/1/012033.

[33] T. Chrysanidis and V. Panoskaltsis, “Experimental investigation of the influence of tensile strain on the cracking of R/C vertical structural elements,” in *Proceedings of the XI International Conference on Structural Dynamics (EURODYN 2020)*, 2020, pp. 3174–3185. doi: 10.47964/1120.9259.18582.

[34] T. Chrysanidis and V. Panoskaltsis, “Does the degree of tensile strain have an impact on the cracking behavior of vertical structural elements?,” in *IOP Conference Series: Materials Science and Engineering, 2020 5th International Conference on Civil Engineering and Materials Science (ICCEMS 2020)*, 2020, vol. 897. doi: 10.1088/1757-899X/897/1/012004.

[35] T. Chrysanidis, S. Tegou, I. Tegos, and S. Spyridonidou, “Analytical and experimental research on improvement of the ductility of buildings’ R/C seismic walls through slip prevention with the use of stoppers,” in *Proceedings of the 6th ECCOMAS Thematic Conference on Computational Methods in Structural Dynamics and Earthquake Engineering (COMPDYN 2017)*, 2017. doi: 10.7712/120117.5426.18266.

[36] T. Chrysanidis and I. Tegos, “The influence of the degree of elongation to the displacements and mode of failure of medium-reinforced ductile structural walls,” 2013.

[37] T. Chrysanidis and I. Tegos, “The influence of the longitudinal reinforcement ratio of R/C walls to their displacements due to failure of transverse instability under extreme seismic loads,” in *Proceedings of the Vienna Congress on Recent Advances in Earthquake Engineering and Structural Dynamics (VEESD 2013)*, 2013.

[38] T. Chrysanidis and I. Tegos, “Size of seismic tensile strain and its influence on the displacements due to transverse buckling of ultra-highly reinforced structural walls,” *ARPN Journal of Engineering and Applied Sciences*, vol. 11, no. 23, pp. 13884–13890, 2016.

[39] D. S. Vijayan *et al.*, “A Comprehensive Analysis of the Use of SFRC in Structures and Its Current State of Development in the Construction Industry,” *Materials*, vol. 15, no. 19, 2022, doi: 10.3390/ma15197012.

[40] D. S. Vijayan, L. R. Ayyasamy, A. S. Sharma, A. Mohan, P. Devarajan, and A. Sivasuriyan, “Finite element analysis of behavior and ultimate strength of composite column,” *Science and Engineering of Composite Materials*, vol. 29, no. 1, pp. 176–182, 2022, doi: 10.1515/secm-2022-0017.

[41] A. Rosso, J. P. Almeida, and K. Beyer, “Stability of thin reinforced concrete walls under cyclic loads: state-of-the-art and new experimental findings,” *Bulletin of Earthquake Engineering*, vol. 14, no. 2, pp. 455–484, 2016, doi: 10.1007/s10518-015-9827-x.

[42] T. Chrysanidis and V. Panoskaltsis, “Numerical study of the tensile experiments modelling the elongation degree of highly-reinforced extreme edges of seismic walls for studying the transverse buckling phenomenon,” in *Lecture Notes in Civil Engineering (2022), Proceedings of the 4th International Conference on Civil Engineering and Architecture (ICCEA 2021)*, 2021, pp. 119–130. doi: https://doi.org/10.1007/978-981-16-6932-3_11.

[43] T. Chrysanidis and V. Panoskaltsis, “Analytical investigation of the tensile experiments modeling the elongation degree of R/C walls for studying the lateral buckling phenomenon,” in *Proceedings of the 8th ECCOMAS Thematic Conference on Computational Methods in Structural Dynamics and Earthquake Engineering (COMPDYN 2021)*, 2021, pp. 2718–2729. doi: https://doi.org/10.7712/120121.8669.18668.

[44] T. Chrysanidis and V. Panoskaltsis, “Analytical investigation of the tensile experiments

to prisms with varying longitudinal ratio for studying the lateral buckling of R/C walls," in *Proceedings of the 8th ECCOMAS Thematic Conference on Computational Methods in Structural Dynamics and Earthquake Engineering (COMPDYN 2021)*, 2021, pp. 2730–2743. doi: https://doi.org/10.7712/120121.8670.18669.

[45] T. Chrysanidis and V. Panoskaltsis, "Cracking for low-reinforced RC members under uniaxial tension," in *Emerging Trends in Engineering Research and Technology Vol. 3*, L. Salisu, Ed. London, UK: Book Publisher International, 2020, pp. 43–54. doi: http://dx.doi.org/10.9734/bpi/etert/v3.

[46] T. Chrysanidis and V. Panoskaltsis, "Evaluation of cracking behavior of R/C vertical components reinforced with varying longitudinal reinforcement ratios," in *Proceedings of the XI International Conference on Structural Dynamics (EURODYN 2020)*, 2020, pp. 3186–3197. doi: 10.47964/1120.9260.18887.

COMPDYN 2023
9th ECCOMAS Thematic Conference on
Computational Methods in Structural Dynamics and Earthquake Engineering
Hamid Nikzad and Shinta Yoshitomi
Athens, Greece, 12-14 June 2023

# OPTIMAL PLACEMENT METHOD OF OUTRIGGER WITH BRB IN A CORE WALL SYSTEM STRUCTURE

**Hamid Nikzad**[1] **and Shinta Yoshitomi**[2]

Ritsumeikan University
1-1-1 Noji-higashi, Kusatsu Shiga 525- 0058 Japan
hamid.nikzada@gmail.com, yositomi@fc.ritsumei.ac.jp

## Abstract

*The outrigger system has shown to be an effective structural lateral load resisting system in super-tall buildings and provides significant lateral stiffness under seismic loading conditions. The optimal placement of outrigger along with optimal combination of energy dissipation devices have major influence on seismic performance of super-tall buildings. In this paper, the power optimization procedure is performed to determine the optimal number and optimal location of outriggers by controlling Buckling Restrained Braces (BRBs) stiffness installed at perimeter column and outrigger connection zone. A 9-zone Finite Element (FE) model is developed in MATLAB programing and is subjected to a series of nonlinear time history analyses. The number of outrigger and BRB stiffness is considered as design variables, and the inter-story drift response of the model is to be minimized as objective functions. The results indicate that the optimization solution with different BRB grouping has almost the same solution and increasing of BRB stiffness does not significantly affect the optimal placement solution of outriggers. Therefore, this method of optimization solution shown to be an effective and practical optimal solution of optimal placement of outriggers with BRB for improving the seismic performance of outrigger system structure.*

**Keywords:** Outrigger, Energy Dissipation Devices, Power Optimization, Time History Analysis.

## 1 INTRODUCTION

The outrigger system has been proved to be an affective lateral load resisting system to improve the seismic performance of high-rise building structures. The outriggers and perimeter columns work together as a further restrain to the core wall to resists the part of overturning moment resulting from the lateral loading [1]. The setting of outriggers will lead to the rapid changes of the story stiffness and causing the abrupt changes of the story shear force, thus resulting in forming the weak stories under strong earthquakes [2]. The conventional outrigger system can be upgraded by attaching energy dissipation devices at the outrigger connection zone to absorb the vibrations caused by winds or earthquakes. Supplemental passive, active, hybrid and semi active damping strategies offer attractive means to protect structures against natural hazards, and are widely accepted by engineering community for improving seismic response of the structures [3].

The optimal placement of outrigger along with supplemental energy dissipation devices have major influence on seismic performance of super-tall buildings and have been the focus of many researchers. A multi-objective genetic algorithm was applied on a mathematical model of outrigger braced structures to achieve the optimal number and placement of outrigger under wind excitation to reduce the top drift and core base moment [4]. Their study concluded that the optimal solution for the minimum top drift of the structure is two outriggers. Finite Element (FE) models were developed to simulate the specimen of the shaking table test to determine the optimal number and optimal locations of outriggers in a 9-zone model based on response spectrum analysis [5]. They further extended their studies by modifying the conventional outrigger into energy dissipation outriggers to determine the most effective combination of energy dissipation outriggers along the structure using time history analysis. Furthermore, a study on optimal quantity and placement of outriggers for a super-tall building based on simple sensitive vector algorithm optimization method reported that the optimal outrigger scheme relates to both the quantity and placement rather than simply proportional to the quantity [6]. The optimal single damped-outrigger elevation shown to be approximately 70% to 80% of the building height, and placing a conventional and damped-outrigger at elevation of 70% and 50% height, respectively, are effective in reducing the structural damages [7]. Additionally, an inter-story drift parameter analysis for optimal location of outrigger in tall building reported that under earthquake load, the optimal elevation of outrigger is slightly lower compare to that of wind load [8]. Optimum outrigger position using the dynamic time history analysis reported that the optimal location of outriggers depends on the type of earthquake records [9]. They also concluded that it is more effective to locate the single outrigger at the upper part of the tall building to reduce the lateral displacement at the top of the building. Most of the optimal placement of outrigger elevations in the past studies rely on a huge number of constraints and analytical model which are leading to maximum computational efforts and analysis cost.

This study reports a simple and practical power optimization approach for optimal placement of outrigger by controlling BRB stiffness attached vertically at perimeter column and outrigger connection zones. A 3D 9-zone FE model is developed in Matlab to simulate the shaking table tests specimen which was carried out at Guangzhou University [10]. The aim of this study is to propose a simple method to evaluate the seismic response of multiple outrigger system to minimize the inter-story drift of the structure. The method presented in this study significantly reduces the computational efforts and analysis cost, and itis an effective method to determine the number and location of outriggers in a tall building structure.

## 2 MODEL DESCRIPTIONS

The structure model used in this study rely on the model structure used for the shaking table tests [10]. The dimension of the model is 1600 mm by 400 mm in each horizontal direction respectively. All materials used in this study is steel of 345 MPa nominal yield strength. The size of core tube is 200 mm by 400 mm and the thickness of steel tube is 8 mm. The size of column is 50mm×50mm with thickness of 5 mm. Each zone has two L-section steel beams of 30 mm by 30 mm and with thickness of 3 mm to connect the column in Y-direction. The outriggers are steel channels with a cross-section of 120 mm by 40 mm and 8 mm thick. An additional mass of 280 kg is added on each story. There are two outriggers with Viscus Damper (VD) attached at zone 4 and 8 representing damped outriggers in the original model of figure 1.

In the original model, the overall height of the structure is 7200 mm in height. However, in this study, the total height of the structure is modified to 8100 mm resulting in a 9-zone model with the height of 900 mm for each zone as shown in figure 2. The outriggers are installed in zone 2 to zone 9 and the BRBs are attached at each outrigger level. The outriggers are installed 150 mm above the floor levels and it is fixed at the core wall and they are attached with BRBs at the column side. There is 100 mm gap between outriggers and column to provide space for the BRBs. The BRBs are attached between outrigger and column with i-end attached to the outrigger at the outrigger level, and the j-end at column with 50 mm height from the floor level. Our aim is to find the optimal number and optimal location of outrigger by controlling BRB stiffness at each outrigger location as will be discussed in the next section.



Figure 1: Original model on a shaking table test [10]

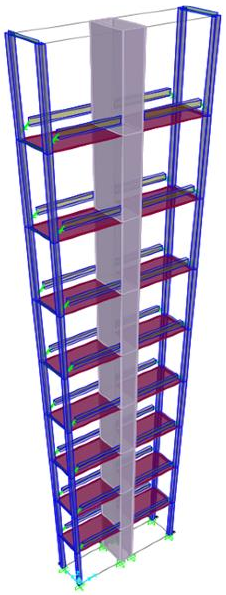

Figure 2: Perspective view of target model

## 3 OPTIMIZATION PROCEDURES

A 9-zone structural model is developed in Matlab programming and the Power Optimization procedure is applied using time history analysis of 1940 El Centro seismic waves. The number of outriggers and stiffness of BRB is considered as design variable and the objective function to be minimized is the maximum inter-story drift response of the model. The BRBs are attached into outriggers and column at each zone level of 2 to 9 to represent damped outrigger with BRB based on random placement. A simple algorithm is used to solve the optimi-

zation problem. This procedure continuously traces the most effective placement of outrigger by increasing the total stiffness of BRB from zero based on figure 3 as follows:

a- Consider N-story structure model and set the yield displacements of the structure and BRB and the incremental stiffness of the BRB (Δk).

b- Consider N candidate models. In this example, the total optimization step number is set to 8, one for each outrigger level with BRB. As for the i-th candidate model, BRB with stiffness Δk is added to the i-th story of the model with optimal outrigger with BRBs obtained in the previous optimization step.

c- Compute the time history responses of the N candidate models in (b) for input ground acceleration and evaluate the maximum response as an objective function.

d- Find the candidate model with the lowest objective function among the N candidate models.

e- Update the stiffness of BRBs and return to (b) until the total stiffness of BRBs reaches the specified value.

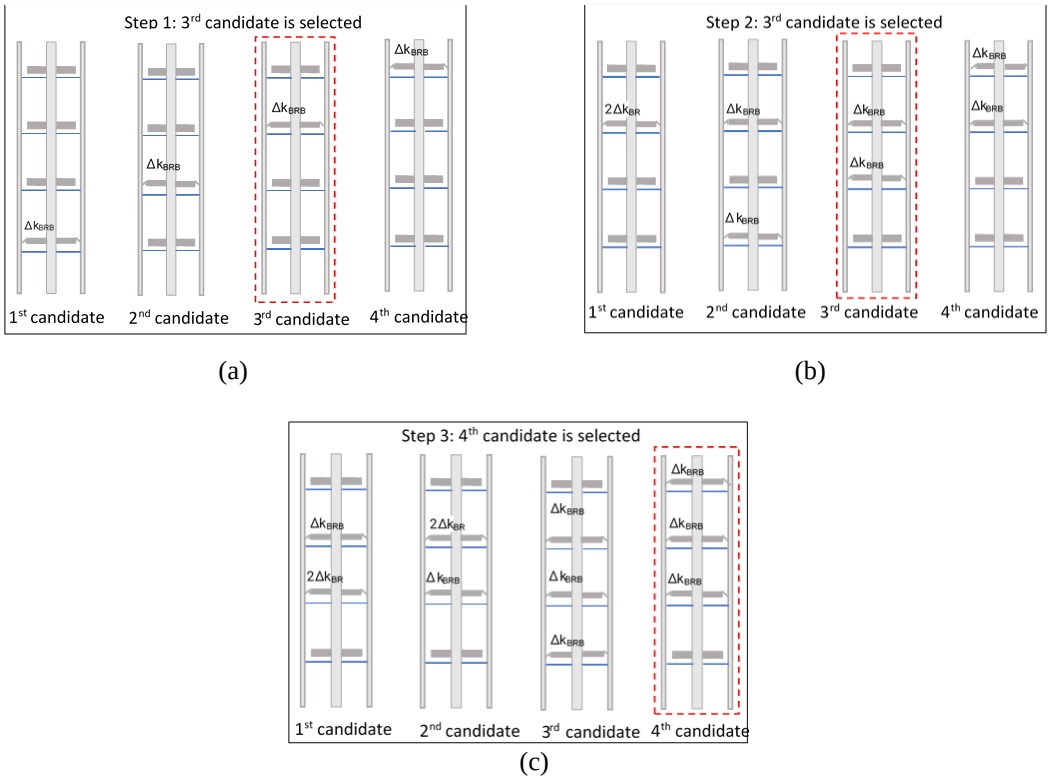


Figure 3: Schematic model of outrigger BRB placement using power optimization method: (a) 1st step, (b) 2nd step, and (c) 3rd step

This method of optimization requires only N-candidate numbers at each optimization step which is equal to the number of stories. Figure 3 above compares only four candidate number corresponding to the smallest maximum inter-story drifts; however, there are 8 candidate solutions which are equal to the total number of stories in which the outriggers are to be installed. During the optimization procedure, the outrigger is installed at each designated zone first, then, the BRBs are installed at each outrigger level, and the optimal story with the smallest maximum story responses is selected based on procedure (b). Then, the obtained op-

timal story is considered constant and the second BRB is installed to the outrigger in the story with the smallest maximum story responses. This procedure is continued until the nth optimal story is obtained.

The optimization procedure is examined with 6 different BRB stiffnesses or grouping. First, one BRB is installed at each outrigger level and the time history analysis is performed. In order to validate the accuracy of proposed method and the effect of BRB stiffness, the number of BRB is increased from 1 to 2, 3, 4, 5, and 10 BRBs referred to BRB groups of 1 to 6 at each outrigger level and the analysis is performed for each case separately. The maximum inter-story drift response of the model is obtained at each optimization step. This method of optimization does not require complicated analytical procedure and significantly reduces the computational efforts of analysis cost and time.

## 4 RESULTS

The results of optimization solution are presented in figure 4. Our aims are to obtain the optimal placement of outrigger by controlling BRB stiffness. From the results of analysis and figure 4, it can be seen that the method proposed in this study can identify the optimal placement and the optimal number of outriggers with BRBs. This method of optimization can also predict and identify the outrigger placement with minor or no effects on the performance of the structure. As discussed earlier, this method of optimization requires total of 8 optimization steps which is equal to the total number of outrigger placement in the model. The first four optimization steps corresponding to zones 7, 9, 5 and 3 shows the optimal placement of outrigger in the model.

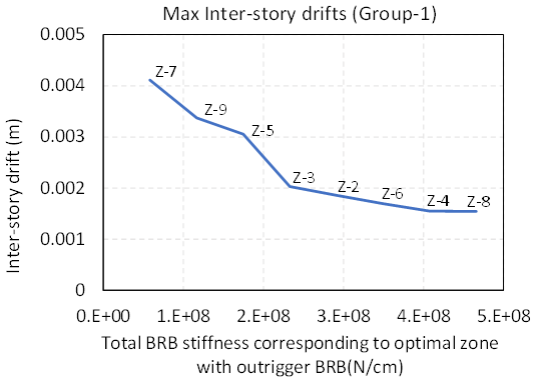


(a)

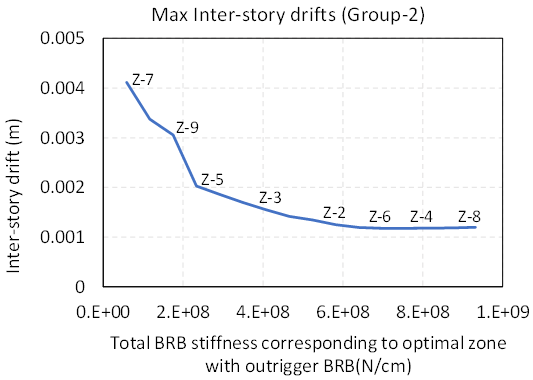


(b)

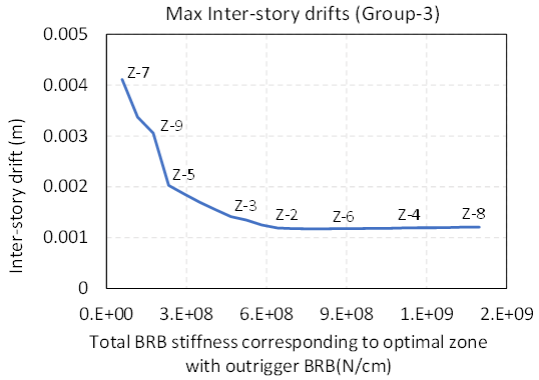


(c)

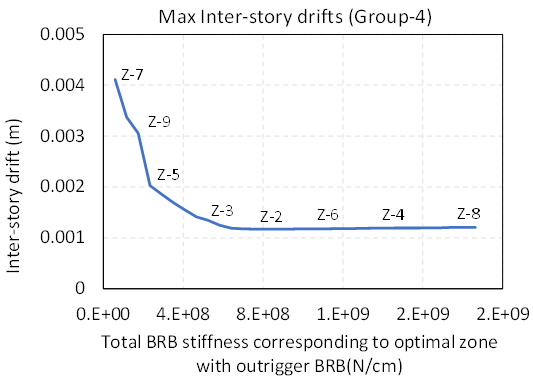


(d)

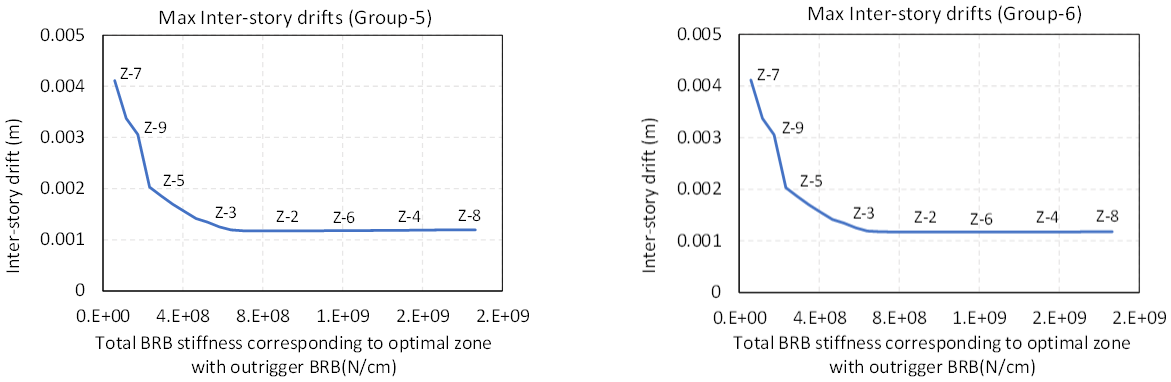


(e) (f)

Figure 4: Effect of BRB stiffness on optimal placement of outrigger BRB: (a) 1 BRB, (b) 2 BRBs, (c) 3 BRBs, (d) 4 BRBs, (e) 5 BRB, (f) 10 BRBs

However, the last four optimization steps corresponding to zones 2, 6, 4 and 8 have minor or no effects on the performance of the structure. Figure 4 (a) and (b) shows that when smaller stiffness is used, the optimal placement with minor effect on the performance of the structure is predicted and the story response of the model is slightly different compare to larger BRB stiffness. However, with larger BRB stiffness, the inter-story drift response of the model remains unchanged with outrigger at zones 2, 6, 4 and 8, indicating that the outrigger placement at these zones does not have any effects on performance of the structure. Figure 5 compares the response of the model with different groups of BRBs.

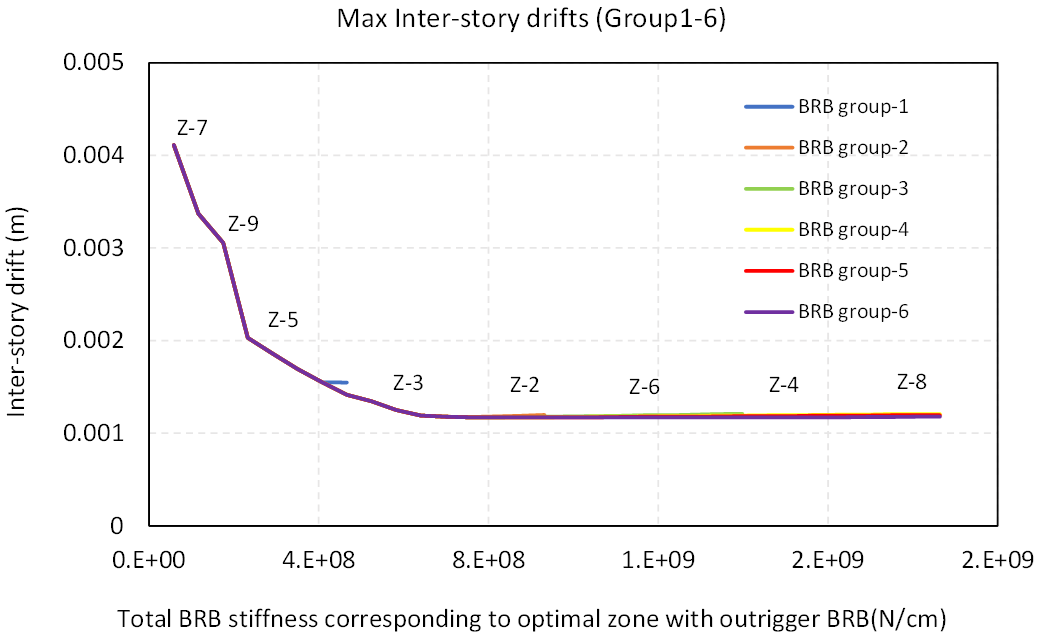


Figure 5: Comparison of optimal placement of outriggers with different BRB grouping

Figure 5 indicates that the optimization solution with different BRB grouping has almost the same solution and changing of BRB stiffness does not significantly affect the optimal placement solution of outriggers. Therefore, this method of optimization solution shown to be an effective and practical optimal solution of optimal placement of outriggers with BRB for improving the seismic performance of outrigger system structure.

| Optimal location of outrigger | Number of BRB at each outrigger end in each optimal step | | | | | |
|---|---|---|---|---|---|---|
| | Group-1 | Group-2 | Group-3 | Group-4 | Group-5 | Group-6 |
| Zone-7 | 1 | 2 | 3 | 4 | 4 | 1 |
| Zone-9 | 1 | 2 | 3 | 4 | 5 | 5 |
| Zone-5 | 1 | 2 | 3 | 4 | 5 | 10 |
| Zone-3 | 1 | 2 | 3 | 4 | 2 | 2 |
| Zone-2 | 1 | 2 | 3 | 4 | 1 | 1 |
| Zone-6 | 1 | 2 | 3 | 4 | 5 | 10 |
| Zone-4 | 1 | 2 | 3 | 4 | 5 | 2 |
| Zone-8 | 1 | 2 | 3 | 4 | 5 | 1 |
| Total | 8 | 16 | 24 | 32 | 32 | 32 |

Table 1: Maximum number of BRBs at each outrigger end in each optimal step of optimization solution

Table 1 compares the maximum number of BRBs at each outrigger end corresponding to optimal step of optimization with different BRB grouping. According to the table, the order of optimal placement of outrigger under different grouping of BRBs remains the same. When smaller stiffness of BRBs (group 1 to 4) are installed at the outrigger end, the BRBs are distributed equally within the outrigger connection zone, however, with larger BRB stiffness (group 5 and 6), the BRBs are distributed unevenly within the outrigger connection zone. In both cases, the inter-story drift response of the model does not change significantly. From figures 4 and 5, and the distribution of BRBs of table 1, it can be judged that the BRB stiffness does not affect the optimal placement of outrigger and that of the performance of the structure.

## 5 CONCLUSION

A simple and practical approaches of optimal placement of outrigger by controlling BRB stiffness was proposed to improve the seismic performance of outrigger system structure. The number of outriggers and BRB stiffness was considered as design variables, and the smallest maximum inter-story drift response of the model was considered as objective function. Time history analysis was performed using 1940 El Centro seismic waves in Matlab programing. According to optimization solutions, four outriggers at zones (3-5-7-9) at the height of 0.2407H, 0.463H, 0.685H and 0.9074H of a structure with 9-zones are the optimal solutions for the minimum inter-story drift requirements. This solution is only a local solution since the outrigger location is fixed at 150mm height above the floor levels of zones 2-9, and not all possible zone combinations and scenarios are considered for the optimization solution. In order to achieve the global solution for the optimal number and optimal placement of outrigger, the possibility of outrigger at different height within the zone of the structure along with all possible combination shall be studied, which will be investigated in the future study.

## REFERENCES

[1] B.S. Smith, and I. Salim, Parameter study of outrigger-braced tall building structures, *Journal of Structural Division, ASCE,* **6**, 2001-2014, 1981.

[2] F. F. Sun, G. Yang, and Z. bin Hu, A single step seismic optimal design method for damped outrigger structure with BRB, *Engineering Structures*, **249**, 2021

[3] B. G. Kavyashree, S. Patil, and V. S. Rao, Evolution of outrigger structural system: A state-of-the-art review, *Arabian Journal for Science and Engineering*, **46**, 10313–10331, 2021.

[4] Y. Chen and Z. Zhang, Analysis of outrigger numbers and locations in outrigger braced structures using a multiobjective genetic algorithm, *Struct Design Tall Spec Build*. **27**, 2017.

[5] L. Xing, Y. Zhou, and M. Aguaguiña, Optimal vertical configuration of combined energy dissipation outriggers, *Struct Design Tall Spec Build*, **28**, 2018.

[6] L. Wang and X. Zhao, Fast optimization of outriggers for super-tall buildings using a sensitivity vector algorithm, *Journal of Building Engineering*, **43**, 2021.

[7] M. Morels-Beltran, G. Turan, O. Dursun, and R. Nijsse, Energy dissipation and performance assessment of double damped outrigger in tall buildings under strong earthquake, *Struct Design Tall Spec Build*, **28**, 2019.

[8] Y. Zhou, C. Zhang and X. Lu, An inter-story drift-based parameter analysis of the optimal location of outriggers in tall buildings, *Struct Design Tall Spec Build*, **58**, 2015-2031, 2015

[9] I. Inam, S. Çeribas, and I. Karapınar, Determining the optimum outrigger locations for steel tall buildings by using time history analyses, *Struct Design Tall Spec Build*, **30**, 2021.

[10] P. Tan, C. J. Fang, W. R. Tu, F. L. Zhou, Y. Wang, M. Jiang, Experimental study on the outrigger damping system for high-rise building, Proceedings in the 15th World Conference on Earthquake Engineering, Lisbon, Portugal 2012.

## ACKNOWLEDGMENTS

This work was supported by JST SPRING, Grant Number JPMJSP2101.

COMPDYN 2023
9th ECCOMAS Thematic Conference on
Computational Methods in Structural Dynamics and Earthquake Engineering
M. Papadrakakis, M. Fragiadakis (eds.)
Athens, Greece, 12-14 June 2023

# INDOOR TRACKING USING UNMANNED AERIAL VEHICLES

**Alessandro Cardoni[1], Raffaele Tarantini[1], Gian Paolo Cimellaro[1]**

[1] Department of Structural, Geotechnical and Building Engineering, Politecnico di Torino, Corso Duca degli Abruzzi 24, 10129, Turin (TO), Italy
e-mail: {alessandro.cardoni, raffaele.tarantini, gianpaolo.cimellaro}@polito.it

## Abstract

*Search and rescue operations during emergencies are complex missions that put at risk the life of first responders. The main challenge is to detect the trapped and injured people inside buildings damaged by different hazards. With a tool showing on a map the number, location and health status of victims, first responders would be able to significantly reduce the evacuation time and save more lives. In this paper, an innovative real-time indoor localization system using Unmanned Aerial Vehicles (UAVs) is proposed. The system includes anchor nodes (antennas) that are mounted on three UAVs flying outside the building and can track the position of people wearing a smart bracelet (tags). The system allows measuring both the absolute and relative location between groups of nodes in 3D without relying on any fixed communication infrastructure that could fail because of the disruptive event. In addition, vital parameters such as heart rate and body temperature can be monitored for each victim and rescuer wearing the bracelet. Each UAV collects, processes, and transfers the data to a portable gateway. A software application with a graphical user interface was developed to display the real-time position of the UAVs and tags with a color-coded indication of the accuracy. Preliminary results of the on-field tests of the systems are presented and discussed.*

**Keywords:** Indoor tracking, First responders, Emergency management, Search and rescue, Structural health monitoring.

## 1 INTRODUCTION

Natural and man-made disasters such as earthquakes, floodings, fires are often responsible of disproportionate human and economic losses. The main challenge in these situations is finding trapped and injured people inside damaged buildings. Localization and indoor tracking systems of first responders and victims would allow for safer and more rapid search and rescue operations.

Indoor tracking systems are generally classified according to signal type, measurement metrics, and dependency on existing infrastructure [1]. Several applications adopting different types of techniques, such as infrared, Bluetooth, WiFi, Radio Frequency Identification (RFID), Ultrawide Band (UWB), and Micro-Electro-Mechanical Sensors (MEMS), have been developed. Rantakokko et al. (2011) [2] proposed a positioning system using multiple sensors such as GPS receivers. Inokuchi et al. [3] proposed a method that allows first responders to create an indoor/outdoor map using range scanners, GPS and Wi-Fi wearable devices. The system can detect obstacles with different confidence levels depending on different scenarios and environments. Another study was done by Li et al. (2014) [4] who proposed an environment-aware beacon deployment algorithm integrated with Building Information Modeling (BIM) and metaheuristics. In this system, smartphones are used as mobile sensing platforms carried by first responders and building occupants to localize them. Yoon et al. (2015) [5] presented a smartphone-based system for indoor emergency response assistance. The system includes both a victim positioning system, which uses Wi-Fi signals from multiple access points, and a victim assessment system based on 3D acceleration changes by the status of a victim. UWB has shown solid performance in this field of application. For instance, Grazzini et al. [6] tested an UWB radar for buried victim detection, while Sachs et al. [7] presented a system to detect breathing motion that can be used to find earthquake and avalanche survivors.

The main shortcomings of these tools are related to range of functioning, battery life, accuracy, costs, and durability of the materials that make it difficult to use them extensively. Moreover, they require a certain level of automation and technology integration which is usually expensive to install into existing buildings. Innovative approaches are the use of chemical sensors to detect breath and skin emitted metabolic tracers [8] as well as the deployment of robots [9, 10]. Even though tangible progress has been done towards the use of robots in dangerous environments, there are still many challenges to overcome before robots can perform most of the routine tasks during emergencies.

This article describes a new real-time indoor localization system of people following catastrophic events (e.g., earthquakes, fires, etc.). This system is proposed as a fast, reliable, and low-cost solution to optimize the rescue operations carried out by firefighters and any other operator in the emergency sector. The purpose is to create a link between injured and/or unconscious occupants of damaged buildings and rescue teams, for faster and more efficient rescue operations. The system consists of three unmanned aerial vehicles (UAVs) equipped with UWB antennas (anchors) flying outside a building and are used to track the position of wearable devices (tags). The UAVs are placed in a predefined configuration based on the geometry of the building. Then they are moved simultaneously at different elevations to scan all the floor levels. The system was tested on-field on a case study to evaluate its performance. The results of these preliminary tests are presented and discussed in this work. Sensitivities analyses were carried out to evaluate the precision of the indoor tracking varying the UAV elevation, their distance from the building, and the distance of occupants from the UAVs.

## 2 DESCRIPTION OF THE PROPOSED INDOOR TRACKING SYSTEM

The new aspect of this research is to install the needed infrastructure for the real-time indoor tracking on UAVs that are flying outside the structures. This represents a cheaper and more reliable solution since it does not depend on any existing fixed infrastructure that might fail during the disruptive event.

The technology chosen for the localization system is based on UWB, which offers a higher level of accuracy than other technologies, such as WiFi and passive radio frequency identification. The technology allows measuring the absolute position of the wearable devices (tags) in three dimensions and the relative distance between them. The system can identify tags both outdoor and indoor providing an indication of the level of accuracy. Obviously, the presence of walls and internal partitions has an impact on the system precision. Nonetheless, the proposed technology is promising, and drones can be strategically positioned in configurations that maximize the signal strength. For instance, they can be placed closer to transparent and thin elements such as windows and openings. The possibility of installing UWB antennas on drones has been verified to guarantee a good compromise between payload, flight duration, and power consumption. Indeed, power banks needed to be mounted onboard to power the antennas and the transmission module. The transmission module is a Raspberry Pi, which gathers the data about the tags collected by the antennas and sends it to a localization engine implemented on a mini pc. The data can then be processed and visualized on a map from a laptop. The map shows the indoor location and health state (e.g., dead/alive and conscious/unconscious) depending on the data collected by the wearable devices.

Figure 1 shows the system architecture, while a picture of fully equipped UAVs is shown in in Figure 2. In the next subsections more details about the main components of the system are provided.

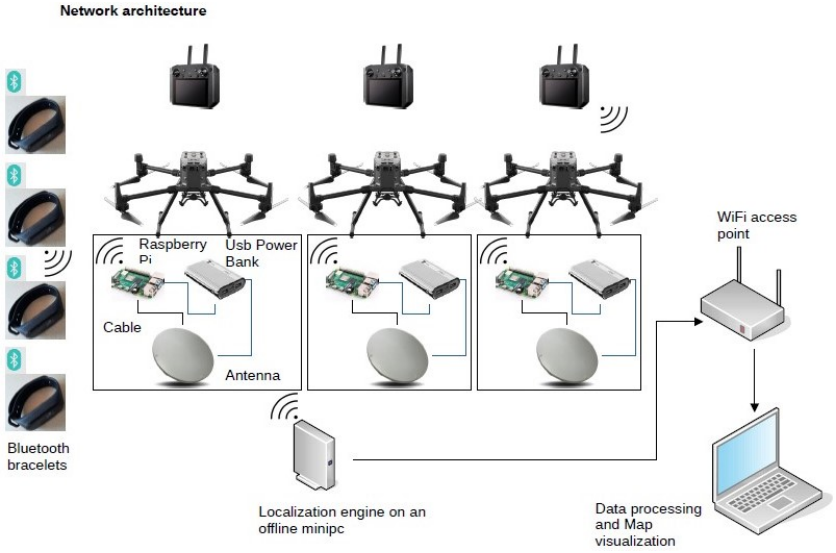


Figure 1: System architecture.



Figure 2: UAVs equipped with antenna, Raspberry Pi, and power bank.

## 2.1 Unmanned Aerial Vehicles (UAVs)

A swarm of three drones "DJI MATRICE 300 RTK" (Figure 3) was used to deploy the tracking system. It is the most recent commercial drone platform from DJI that draws design cues from complex aviation systems. It provides up to 55 minutes of flying time, powerful AI capabilities, 6 Directional sensing and positioning, and more. AES-256 encryption ensures safe data transmission, and real-time auto-switching between 2.4 GHz and 5.8 GHz allows for more stable flight in high-interference environments. To maximize flight safety and reliability, the MATRIC300 RTK platform has been developed with multiple system and sensor redundancies. The following redundancies and safety features are included: redundant obstacle sensor systems, dual flight control system sensors, redundant control signal connections, dual intelligent batteries, redundant transmission links, and three-propeller emergency landing. Dual-vision and Time-of-Flight (ToF) sensors are present on all six sides of the aircraft to improve in-flight safety and aircraft stability. These sensors have a maximum detection range of up to 40 meters and allow the DJI Pilot App user to adjust the aircraft's sensing behavior. This six-direction sensing and positioning technology aids in maintaining the safety of the aircraft and the mission even in challenging operating circumstances. It has a maximum payload of 2.7 kg, which was almost reached as the weight of the mounted components is about 2 kg.



Figure 3: DJI MATRICE 300 RTK.

### 2.2 Tracking antennas

A “Quuppa Q35 Locator” (Figure 4) antenna, is mounted on each of the three UAVs. It is a transceiver operating at 2.4 GHz, that enables the location and tracking of any object or person equipped with tags. Both indoor and outdoor environments are suitable for the Q35, making it possible an accurate tracking in even the most difficult circumstances. It has a high data throughput and a sub-meter accuracy.



Figure 4: Quuppa Q35 Locator.

### 2.3 Wearable devices

Tags are mobile devices that are designed to be worn by the person being tracked. Tags gather data on the monitored person's location and vital parameters (e.g., heart rate). The device conducts a trilateration and calculates the person's position based on the distance from the anchors. The tags use a rechargeable battery that can be powered by any device with a USB port. The “LandingSite eBand LS-B1” tags were selected (Figure 5). They are smart wearable devices fully compatible with the Quuppa Locator. Their main features are indoor localization, date/time synchronization, integrated heart rate sensor, QR code identification, and long-lasting battery.




Figure 5: LandingSite eBand LS-B1.

## 3 CASE STUDY AND SYSTEM PERFORMANCE

On field testing has been conducted in the hangar of the airfield “Pegasus” (Busano, Italy). Tags have been placed inside the hangar, while three equipped UAVs on the open field outside it. The objective of the tests was to evaluate the system performance considering the effects of case study specific characteristics and three variables, namely the UAV elevation, their distance from the building, and the distance of occupants from the UAVs. The environment and building’s characteristics may have a significant impact on the system coverage. For instance, material and thickness of the obstacles standing between the anchors and the tags can alter the accuracy of the indoor tracking.

Figure 6 shows an aerial view of the airfield and a scheme of the positioning of the UAVs, indicated by the letters A, B, C, and the tags (1, 2, 3, 4). The flight formation was an equilateral triangle shape (ABC) with a side of 15m that was fixed during all the tests. The UAVs were then moved at different elevations (2m, 4m, 6m, 8m, 10m) for three distances from the hangar entrance (2m, 6m, 10m). Since the hangar gate is only about 6m, this means that UAVs B and C were shielded by the hangar walls and gate (Figure 7).




Figure 6: Aerial view of the testing site showing a scheme of the UAVs and tag positioning.



Figure 7: View of the test building.

Four people were provided with tags and asked to walk from the gate towards the opposite wall of the hangar. Their position and vital parameters were continuously monitored and recorded in real time. For visualization purposes, the results obtained for six distances from the hangar gate are reported, i.e., 2m, 4m, 6m, 8m, 10m, 12m. Tag no. 1 was constantly shielded

by a wall and never had direct visibility with the three UAVs. Tags no. 2 and no. 3, while moving towards the center of the building, were separated by helicopters, simulating metal obstacles. Tag no. 4 was the only one to keep constant visibility of the drones.

Figures 8-10 show the results of the sensitivity analyses. They show the accuracy of the indoor position of each tag varying the UAV elevation and the distance between tags and hangar gate when the UAVs B and C are at a distance of 2m, 6m, 10m from the hangar. The position accuracy was categorized into four levels: 0 - Bad (Target not detected), 1 - Poor (>3m), 2 - Good (<3m), 3 - Excellent (<1m).

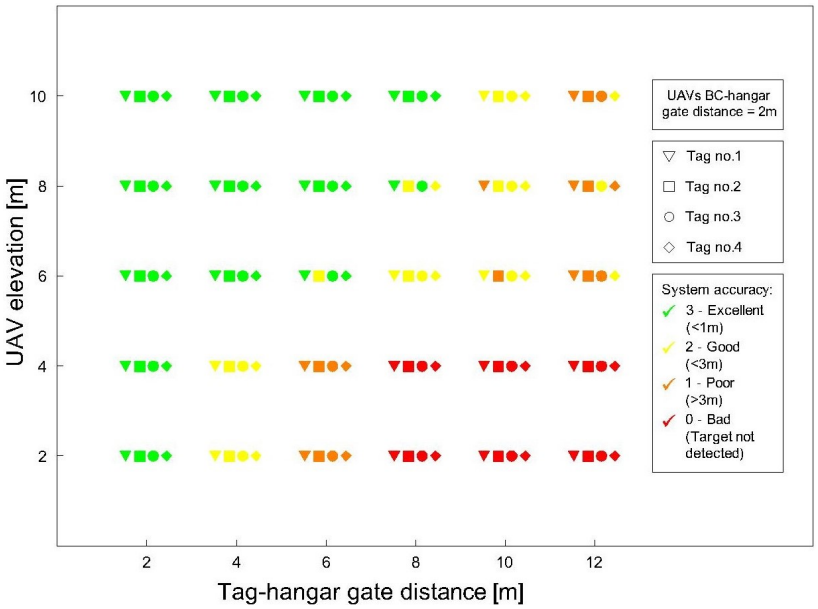


Figure 8: Indoor position accuracy for a distance UAVs BC-hangar gate = 2m.

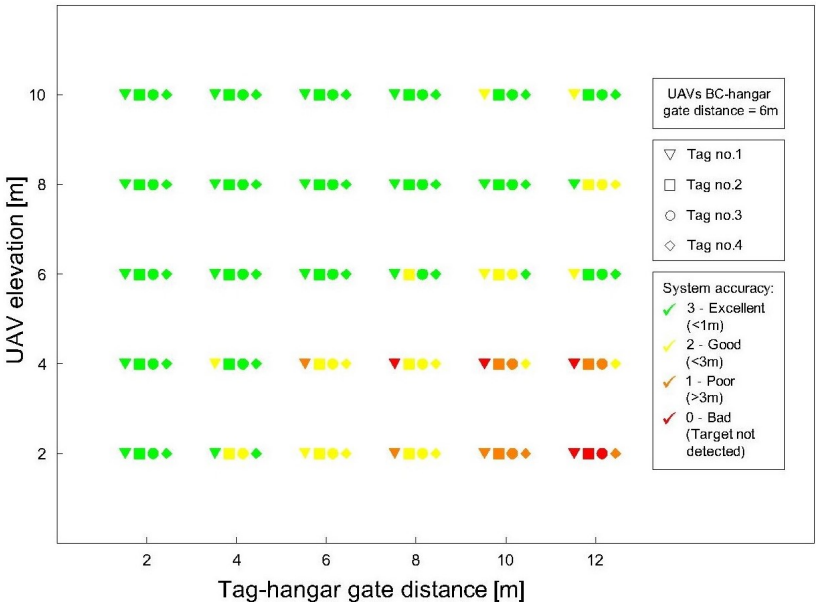


Figure 9: Indoor position accuracy for a distance UAVs BC-hangar gate = 6m.

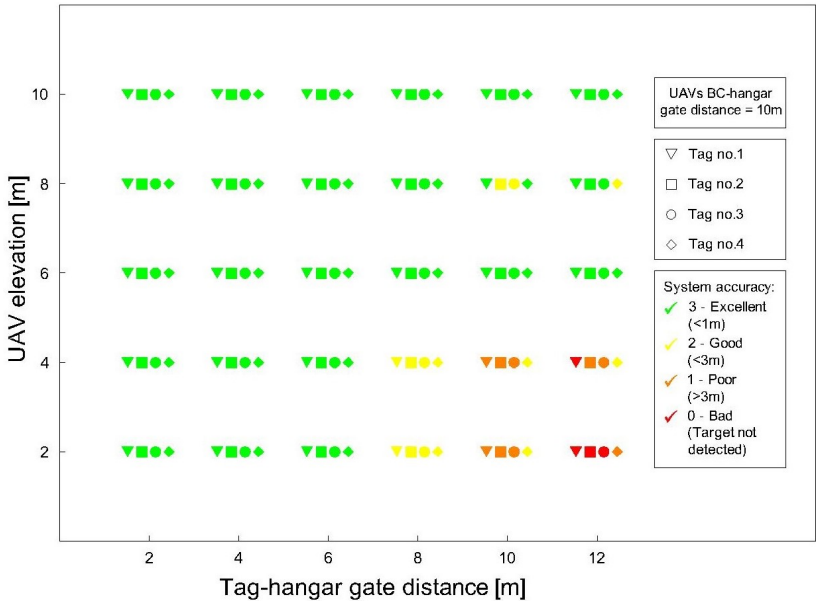


Figure 10: Indoor position accuracy for a distance UAVs BC-hangar gate = 10m.

The graphs show that increasing the UAVs elevation has a positive effect on the system accuracy. This is due to the fact that the area covered by the antennas increases with the elevation. As expected, increasing the tag-hangar gate distance the indoor tracking accuracy decreases until the tags are no longer detected. On the other hand, the performance improves by increasing the distance between the UAVs BC and the hangar. This means that when the UAVs are too close to the walls the signal suffers from reflection and interference phenomena.

## 4 CONCLUSIONS

This work presented an innovative system that can be used during emergencies to track the presence of injured and unconscious people inside damaged buildings. It is also intended to be used to monitor and guide first responders in search and rescue operations. The main components of the system are UWB antennas mounted on UAVs that are deployed outside a building to detect the position and vital parameters of the people inside. This data is collected by simple wearable devices and transferred to a positioning engine. Information about position and health status can be visualized on a map from a laptop connected to an access point.

The proposed technology for real time indoor tracking using UAVs showed promising results and is innovative compared to other technologies because: (i) it does not rely on power and telecommunication networks (WiFi, GPS, GPRS, etc.), that might not be available after a disaster; (ii) it allows data transfer related to vital parameters and tracking of both rescuers and victims in real time; (iii) it does not require pre-installed fixed nodes (anchors) in the buildings. These features would allow first responders to act more rapidly and in safer conditions during search and rescue operations.

## ACKNOWLEDGEMENTS

The research leading to these results has received funding from the European Research Council under the ERC-2019 Proof of Concept Grant n. 875183 of the project IDEAL DRONE - Use of drones for Emergency Management.

## REFERENCES


[1] Bastos, A. S., Vieira, V., and Apolinário Jr, A. L. *Indoor location systems in emergency scenarios-A Survey*. Proceedings of the annual conference on Brazilian Symposium on Information Systems: Information Systems: A Computer Socio-Technical Perspective, 34.

[2] Rantakokko, J., Rydell, J., Strömbäck, P., Händel, P., Callmer, J., Törnqvist, D., Gustafsson, F., Jobs, M., and Grudén, M. 2011. *Accurate and reliable soldier and first responder indoor positioning: multisensor systems and cooperative localization*. IEEE Wireless Communications, 18(2), 10-18.

[3] Inokuchi, M., Higuchi, T., Yamaguchi, H., & Higashino, T. (2012, November). *Autonomous recognition of emergency site by wearable sensors.* In 2012 IEEE International Conference on Green Computing and Communications (pp. 400-409). IEEE.

[4] Liu, H., Gan, Y., Yang, J., Sidhom, S., Wang, Y., Chen, Y., and Ye, F. *Push the limit of WiFi based localization for smartphones.* Proceedings of the 18th annual international conference on Mobile computing and networking, 305-316.

[5] Yoon, H., Shiftehfar, R., Cho, S., Spencer Jr, B. F., Nelson, M. E., and Agha, G. 2015. *Victim localization and assessment system for emergency responders.* Journal of Computing in Civil Engineering, 30(2), 04015011.

[6] Grazzini, G., Pieraccini, M., Parrini, F., Spinetti, A., Macaluso, G., Dei, D., & Atzeni, C. (2010, June). *An ultra-wideband high-dynamic range GPR for detecting buried people after collapse of buildings.* In Proceedings of the XIII Internarional Conference on Ground Penetrating Radar (pp. 1-6). IEEE.

[7] Sachs, J., Helbig, M., Herrmann, R., Kmec, M., Schilling, K., & Zaikov, E. (2014). *Remote vital sign detection for rescue, security, and medical care by ultra-wideband pseudo-noise radar.* Ad Hoc Networks, 13, 42-53.

[8] Güntner, A. T., Pineau, N. J., Mochalski, P., Wiesenhofer, H., Agapiou, A., Mayhew, C. A., & Pratsinis, S. E. (2018). *Sniffing entrapped humans with sensor arrays.* Analytical chemistry, 90(8), 4940-4945.

[9] Kruijff, G. J. M., Pirri, F., Gianni, M., Papadakis, P., Pizzoli, M., Sinha, A., ... & Priori, F. (2012, November). *Rescue robots at earthquake-hit Mirandola, Italy: A field report.* In 2012 IEEE international symposium on safety, security, and rescue robotics (SSRR) (pp. 1-8). IEEE.

[10] Trevelyan, J., Hamel, W. R., & Kang, S. C. (2016). *Robotics in hazardous applications.* In Springer handbook of robotics (pp. 1521-1548). Springer, Cham.

[11] Cimellaro GP, Domaneschi M, Zamani Noori A. *Improving post-earthquake emergency response using indoor tracking.* Earthquake Spectra. 2020;36(3):1208-1230. doi:10.1177/8755293020911163

COMPDYN 2023
9th ECCOMAS Thematic Conference on
Computational Methods in Structural Dynamics and Earthquake Engineering
M. Papadrakakis, M. Fragiadakis (eds.)
Athens, Greece, 12-14 June 2023

# NUMERICAL INVESTIGATIONS ON DYNAMIC BEHAVIOUR OF LUMPED MASS MODEL OF NON-STRUCTURAL ELEMENTS & 3D RC BUILDINGS

**S. Saranya*** **and Palissery Sunitha**
EARTHQUAKE ENGINEERING RESEARCH CENTRE
INTERNATIONAL INSTITUTE OF INFORMATION TECHNOLOGY
PROFESSOR C R RAO ROAD, GACHIBOWLI, HYDERABAD, INDIA -500032
saranya.s@research.iiit.ac.in, sunitha.palissery@iiit.ac.in

## Abstract

*This study considers simple acceleration sensitive Non-structural elements (NSEs) with fundamental period $T_S \leq 0.07$seconds, modelled as a rigid cantilever with lumped mass at the top (stick model). Numerical modelling of building and NSE together (complete model) and nonlinear time history analyses using 11 natural ground motions are performed in commercial software PERFORM 3D. Parametric studies of NSEs with lumped mass of 1-10 percent total seismic weight of building (in increments of 1 percent) for each fundamental period of NSE (in increments of 0.01s) is carried out, using spectrally scaled ground motions. Variations in: (a) lateral force demand on NSE, (b) Component Amplification Factor (CAF), and (c) Floor Amplification Factor (FAF), are monitored. Results are compared with the values of above parameters estimated as per EAK (2000), Eurocode 8 (1998 (1):2004), ASCE 07 (2016), NZS 4219 (2009), and NZS 1170 (5) (2004). It is observed that FAF varies nonlinearly across the floors (and significantly in the lower floors), as against linear variation stipulated in the above codes. The average CAF for the ground motions considered ranged between 1 and 2 up to $T_s \leq$ 0.06s. However, it increased significantly for $T_s$ = 0.07s, thereby complementing ASCE 07 stipulation of 0.06s limit for rigid NSEs. The value of 2 is consistent with NZS 1170(5):2004 and 1 with ASCE 07 and EAK (2000). Further, as the NSE weight increased, the fundamental period of the building increased, and the average CAF marginally decreased. And, seismic force demand imposed on all NSEs during nonlinear time history analysis exceeded code recommended seismic design force under most ground motions.*

**Keywords:** Non-structural elements, stick model, design lateral force, Component Amplification Factor, Floor Amplification Factor

## 1 INTRODUCTION

Non-structural elements (*NSEs*) are secondary structures of *architectural, mechanical* and *electrical components*, mounted on primary structures (buildings), with seismic weight less than 25% of effective seismic weight of the structure [1]. Past earthquake experience demonstrated participation of *NSEs* in the lateral load resistance and even alteration in the load paths of primary structures. Particularly, the architectural NSEs triples the lateral stiffness of building and reduce inter-storey drift by more than 2 times. [2]. Failure of acceleration sensitive NSEs occurs frequently after an earthquake because the dynamic features of the supporting structure are disregarded while calculating the seismic demand on NSEs [3]. Thus, modelling approaches of acceleration sensitive NSEs (Figure 1) are gaining prominence, to minimize *NSE* damages. There are mainly two modelling approaches of acceleration sensitive NSEs in buildings, namely (a) coupled or complete model and (b) decoupled model [4].



Figure 1 : Examples for acceleration sensitive NSEs [5]

While in coupled models, NSEs are modelled together with the primary structure, they are not in decoupled models. Despite permitted use of decoupled model in the absence of sufficient data during preliminary structural analysis of buildings, it leads to significant error especially in seismic demands on vertical lateral load resisting elements [6]. One of the primary inputs to calculate the force on *NSEs* is *Acceleration Floor Response Spectra* (*AFRS*) of the buildings obtained from dynamic analysis of buildings [7]. Several numerical studies had been carried out to understand the behaviour of NSEs under seismic loads using coupled and uncoupled models [7, 8, 9, 10, 11, 12, 13, 14, 15]. In some studies, benefits of coupled model over decoupled model were investigated; amplification of the displacement response (especially at top floor) were observed in coupled model when the fundamental frequency of the primary structure and the secondary structure are equal [16]. On the other hand, experimental investigations on decoupled model reported underestimation of actual acceleration experience by the NSE [17]. Further, behaviour studies of light subsystems supported on nonlinear structures using floor spectra of decoupled model without considering building-NSE interaction, torsion in buildings, and inelastic actions in buildings were also carried out [18, 19]. Torsion in supporting structures, in particular, amplifies response of the NSE depending on its location [20]. And, presence of large openings in the façade leads to torsional effects in supporting structure [21]. Also, contribution of higher modes depends on the characteristics of

ground motion and the associated flexural overstrength of each mode [22]. An expression was also proposed considering nonlinear variation of FAF for a decoupled model [23]

Thus, there is an urgent need to complement the ongoing research using coupled model to predict building-NSE interaction. This paper presents numerical studies in this direction; complete (–coupled) modelling of rigid NSEs ($T_S \leq 0.06$s) is adopted in commercial software PERFORM 3D, to capture the seismic behaviour of NSEs and its interaction with the supported study building [1, 24]. The design parameters considered in this study are: (a) floor amplification factor at base of NSE, (b) component amplification factor at top of NSE, and (c) lateral force demand on NSE.

## 2 DESIGN SEISMIC LATERAL FORCE ON NSE

Expressions to estimate design seismic lateral force enunciated in international codes are summarized in Table 1. In general, *demand* and *performance* factors are used to determine the design seismic lateral force on *NSEs* [25]. When considered together, these factors constitute the *seismic coefficient* of NSE. While demand factor constitutes hazard factor, Component Amplification Factor (CAF) and Floor Amplification Factor (FAF), importance/risk factor and ductility Factor of the component are part of performance factor. Hazard factor represents the design acceleration of the site considered and CAF and FAF are empirical. Importance factor depends on the component functions, and ductility factor decides level of inelasticity allowed in the NSE under a seismic event. But, performance factors are mostly judgemental [25].

| **Codes** | **Design horizontal lateral force** |
|---|---|
| ASCE 7:2016[1] | $F_p=(1+2z/h)0.4a_p I_p S_{DS} W_P /R_p$ ; $S_{DS}$ = 2/3 $F_a S_{S;} 0.3S_{DS} I_p W_p < F_p < 1.6S_{DS} I_p W_p$ |
| EAK 2000[26] | $H_p =(\varepsilon W_p \gamma_p)/q_p$ ; $\varepsilon = \alpha\beta$ (1+z/H) ; $\beta$ = 2/(1+(1-$T_\pi/T)^2$ ) ≥1 |
| EN 1998.1:2004[27] | $F_p = S_a W_a \gamma_a /q_a$ ; $S_a = \alpha S$ [3(1 + z/H)/(1 + (1 –$T_a/T_1)^2$ - 0.5] ≥$\alpha S$ |
| NZS 1170.5:2004[28] | $F_{ph} = C_p (T_p) C_{ph} R_p W_p \leq 3.6 W_p$; $C_p(T_p) = C(0) C_{Hi} C_i(T_p)$ ; $C(0) = C_h (0) Z R N (T,D)$ |
| NZS 4219:2009[29] | $F_p = CW$; $C = 2.7 C_H Z C_p R_c < 3.6$ |

*Note :* $a_p$ component amplification factor; $q_a$ behaviour factor of NSE; $q_p$ reduction factor; *z* point of attachment of NSE above the base level; *C* lateral force coefficient; *C(0)* site hazard coefficient for T = 0; $C_h(0)$ spectral shape factor; $C_i(T_p)$ component spectral shape factor at level *i;* $C_p$ performance factor; $C_{ph}$ part horizontal response factor; $C_p(T_p)$ horizontal design coefficient of the *NSE*; $C_{H,}$ $C_{Hi}$ floor amplification factor; $F_a$ short-period site coefficient at 0.2s; H, h height of the building; $I_p, \gamma_a, \gamma_p$ Importance factor of the NSE; *N(T,D)* Near fault factor; *R* Return period factor; $R_c$ component risk factor; $R_p$ part risk factor/component response modification factor; *S* soil factor; $S_a$ seismic coefficient; $S_{DS}$ spectral acceleration at short periods; $S_s$ spectral response acceleration parameter at short periods; *T*, $T_1$ fundamental period of the building; $T_a, T_p, T_\pi$ fundamental period of the *NSE;* $W_a, W_p$ NSE weight; *Z* hazard /zone factor; $\alpha$ ratio of the design ground acceleration on to the acceleration of gravity; $\varepsilon$ seismic factor

Table 1: Summary of code formulations

# 3 NUMERICAL STUDY

## 3.1 Details of the 3D RC building

The study Reinforced Concrete Special Moment Frame building modelled in commercial software PERFORM 3D is 7-storey tall with typical storey height 3.7m, 5 bays with bay length 5m in *X*—direction and 3 bays with bay length 3m in *Y*— direction, founded on medium stiff soil. Importance factor considered is 1.5, live load 3kN/m$^2$, steel and concrete grade Fe415 and M30, respectively. Buildings are designed to resist PGAs (Zone factors) 0.2g, 0.36g and 0.72g, following IS1893:2016 and IS13920:2016 provisions [30, 31]. Slab loads and brick masonry infill loads are distributed on beams, and rigid diaphragm action is enabled. Mander's confinement model is used for defining confinement effects of building elements [32]. Fibre modelling of inelasticity is used in select members in select locations of buildings.

## 3.2 Details of the NSE

In general, NSEs have weight less than 25% of effective seismic weight of supporting structure [1]. This study considers simple acceleration sensitive *NSEs* with fundamental period $T_S \leq 0.07$seconds, modelled as a rigid cantilever with lumped mass at the top (stick model). NSE is located at the roof of the RC building (Figure 2), and is assumed to behave elastically. The equivalent height of NSE considered is 0.5 m. Parametric studies of NSEs with lumped mass of 1-10 percent total seismic weight of building (in increments of 1 percent) for each fundamental period of NSE (in increments of 0.01s) is carried out. Stiffness of the NSE is varied according to the required percentage of seismic weight of the building and desired fundamental period of the NSE.

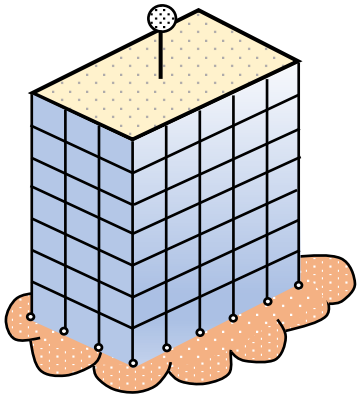

Figure 2: Schematic of *complete model* of NSE

## 3.3 Nonlinear Time History Analysis

Nonlinear time history analyses are performed of the complete model using 11 natural Ground Motions (GM) (Table 2) as per ASCE 07 and corresponding to 5% damped response spectrum presented in Figure 3 [1]. Spectral amplitude scaling is carried out at elastic natural period of the building designed for each design PGA [33]. A total of 2, 343 nonlinear time history analyses are performed to investigate the behaviour of NSEs and buildings under ground motions.

| *GM No.* | *Event* | *Station* | *Year* | $M_w$ | *PGA (g)* | *Epicentral distance (km)* |
|---|---|---|---|---|---|---|
| 1 | Kobe | Nishi-Akashi | 1995 | 6.9 | 0.483 | 7.08 |
| 2 | Loma Prieta | Hollister-South Pine | 1989 | 6.9 | 0.370 | 28.80 |
| 3 | Imperial Valley | Delta | 1979 | 6.5 | 0.351 | 43.60 |
| 4 | Chi Chi | TCU 047 | 1999 | 7.6 | 0.298 | 35.00 |
| 5 | Hectormine | Hector | 1999 | 7.1 | 0.265 | 11.66 |
| 6 | Northridge | Downey- Co Maint Bldg | 1994 | 6.7 | 0.229 | 47.60 |
| 7 | San Fernando | Palmdale Fire Station | 1971 | 6.6 | 0.133 | 25.40 |
| 8 | Sikkim | Gangtok | 2011 | 6.8 | 0.160 | 58.00 |
| 9 | Uttarkashi | Bhatwari | 1991 | 6.8 | 0.253 | 36.00 |
| 10 | Fruili | Tolmezzo | 1976 | 6.4 | 0.351 | 28.00 |
| 11 | Peru | ICA | 2007 | 7.9 | 0.278 | 140.00 |

Table 2: Characteristics of Ground Motions (GMs) considered in the study [34, 35, 36, 37, 38]

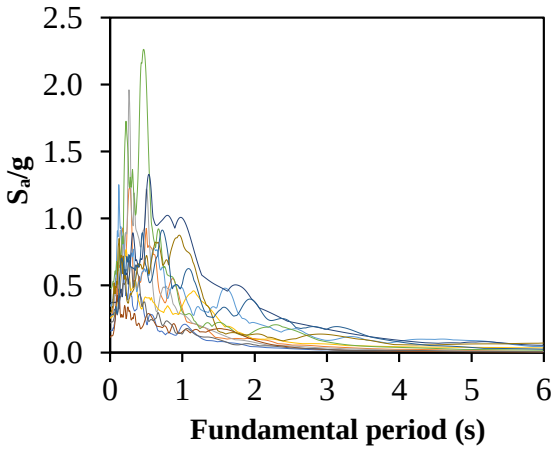


Figure 3: Elastic acceleration response spectra of ground motions considered in the study

## 4 DISCUSSION OF RESULTS

### 4.1 Floor Amplification Factor of the building

Floor Amplification Factor (FAF) is defined as the ratio of Peak Floor Acceleration (PFA) to the Peak Ground Acceleration (PGA). FAF represents the dynamic amplification of acceleration from ground to the floor location of interest where the NSE is attached, but without considering NSE. FAF is largely influenced by: (a) lateral load resisting system, (b) modal and damping properties of building, (c) structural configuration of building, (d) diaphragm rigidity, (e) stiffness, strength, and ductility of the building, and (f) the vertical location of NSE across the height of the building [39]. Variation of FAF across the floors of the designed buildings without NSE is presented (Figure 4). In Figure 4, for brevity, GM refers to ground motion whose numbers are represented in Table 2.

Investigation of results demonstrate less amplification of floor acceleration in buildings designed for 0.72g (stiff building) (Figure 4 (c)) compared to buildings designed for 0.20g (less stiff building) (Figure 4 (a)). It is observed that FAF (a) is nonlinear across the floors, (b) not a constant 3 for all the floors, and (c) is higher in lower floors. This behaviour is a departure from the provisions in design standards [ASCE 07:2016, EAK 2000, NZS 1170.52004, NZS 4219:2009]. Further, characteristics of earthquakes significantly alter the seismic behaviour of

the building; of the 11 ground motions considered, amplification under Sikkim earthquake is more prominent (Figure 4). Amplification observed on the first floor exceeds the factor 3 of New Zealand code under Sikkim earthquake in building designed for 0.2g (Figure 4 (a)). Further, amplification in the third and fourth floor is more than on the second floor, and reduces towards top under most earthquakes. Furthermore, in all 3 buildings, at lower floors, FAF is significantly higher than the linear variation recommended by some international design codes.

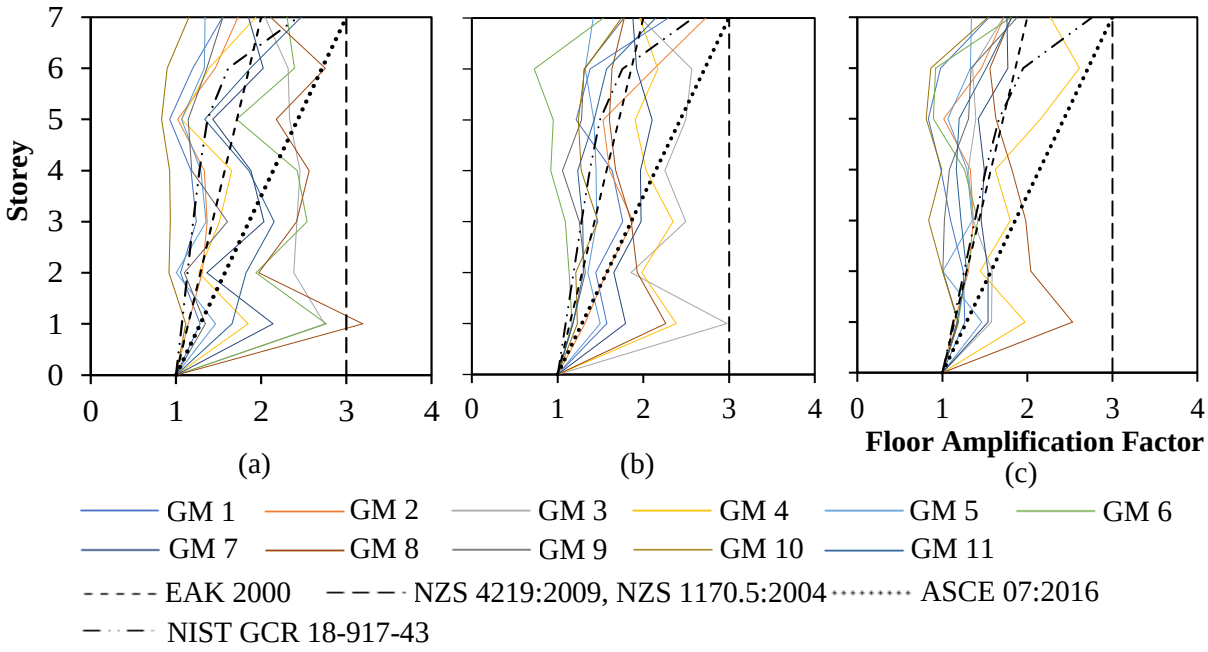


Figure 4: Variation of FAF in buildings designed for PGA: (a) 0.2g, (b) 0.36g, and (c) 0.72g

### 4.2 Roof response spectrum of the complete model

Roof response of complete model or system (both NSE and building modelled) represents the dynamic amplification of acceleration from ground to the roof where NSE is attached. Roof response spectrum of complete model, with NSE of fundamental period 0.04s and designed for 5% of seismic weight of building is presented in Figure 5. It is observed that spectral amplification increases at lower periods for all ground motions, and this increase is more prominent in buildings designed for higher PGAs. Maximum spectral amplification is about 8 for Sikkim earthquake at very low period (Figure 5 (c)); similar characteristics of Sikkim ground motion is observed in FAF also, thereby confirming the influence of ground motion characteristics on seismic behaviour of structural and non-structural elements. In particular, seismic resistance and behaviour of rigid NSEs with fundamental period less than 0.06 seconds are crucial and critically affected by ground motion characteristics.

### 4.3 Component Amplification Factor from the complete model

Component Amplification Factor (CAF) is defined as ratio of Peak Component Acceleration to Peak Floor Acceleration. CAF represents the dynamic amplification of acceleration from floor to the top of the NSE (Figure 6), and *average Component Amplification Factor* is average CAF under all considered ground motions. And, seismic weight ratio of NSE is the weight of NSE as percentage of seismic weight of the building.

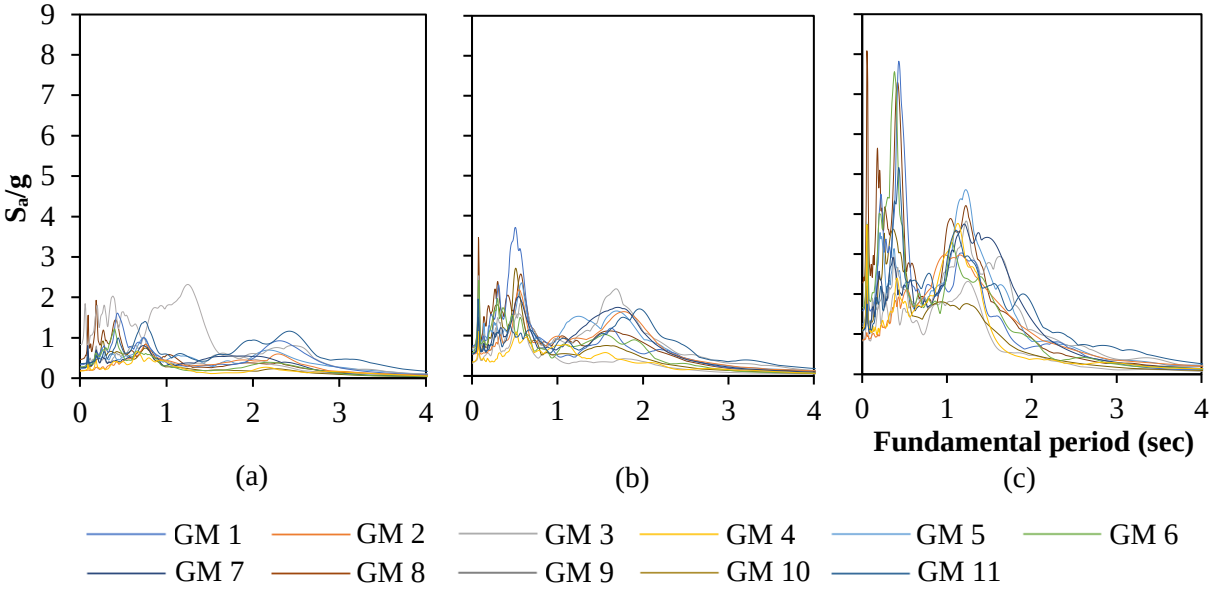


Figure 5: Roof response spectrum of system with buildings designed for PGA (a) 0.2g, (b) 0.36g, and (c) 0.72g

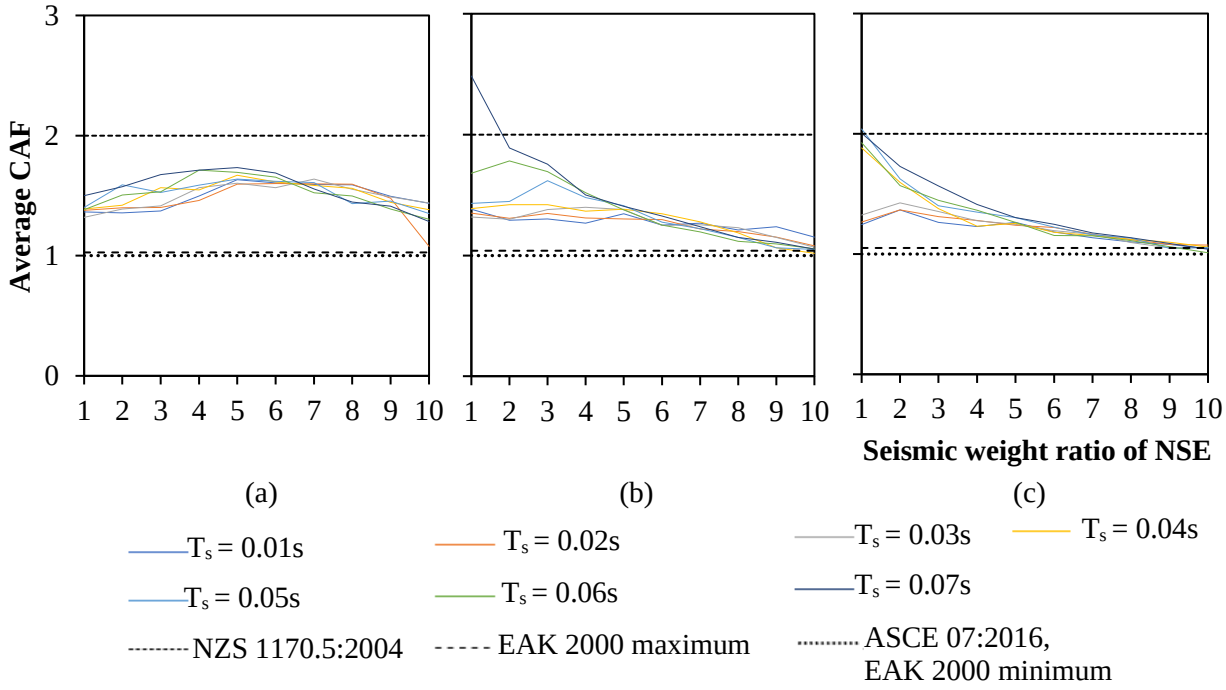


Figure 6: Variation of CAF in buildings designed for PGA (a) 0.2g, (b) 0.36g, and (c) 0.72g

It is observed that CAF increases marginally with increase in seismic weight ratio and reduces after 5% seismic weight ratio in building designed for 0.2g (Figure 6 (a)). Nevertheless, CAF is about 1.5 in all NSEs. And, CAF reduces significantly and approaches one rapidly in buildings designed for higher PGAs and more prominently in building designed for 0.72g (Figure 6 (c)). Also, NSEs with fundamental period 0.04s and above achieve CAF of about 2 for very stiff NSEs in building designed for 0.72g (Figure 6 (c)), and NSE with fundamental period 0.07s demonstrate a different behaviour with CAF above 2 in building designed for 0.36g

(Figure 6 (b)). This is complementing the ASCE 07 definition of rigid NSEs to be those with fundamental period less than 0.06s, because impending behaviour change is observed for the NSE considered above this range, in this study.

### 4.4 Design lateral force from complete model

Seismic coefficients for design of NSEs are first estimated using design code recommended equations (Table 3). And, the average lateral force demand on NSEs under 11 ground motions from the PERFORM 3D results, and seismic coefficient using the above average lateral force demand, are also estimated for comparison with Table 3 values (Figure 7). Eurocode and Greece code estimates minimum seismic coefficient for NSE with fundamental period 0.01s, and maximum value for NSE with fundamental period 0.06s (Table 3). For further comparison in this study, maximum values are used.

| *Codes* | *Parameter* / *Design PGA (g)* | *FAF* | *CAF* | *Component response factor* | *Importance Factor* | *Lateral Force demand ($W_p$)* |
|---|---|---|---|---|---|---|
| *ASCE 07:2016* | 0.20<br>0.36<br>0.72 | 3 | 1 | 1.5 | 1.5 | 0.26<br>0.44<br>0.71 |
| *EAK 2000* | 0.20<br>0.36<br>0.72 | 2 | 1.005-1.028<br>1.006-1.040<br>1.008-1.050 | 2.5 | 1.5 | 0.24-0.25<br>0.43-0.45<br>0.87-0.90 |
| *EC8 EN 1998.1:2004* | 0.20<br>0.36<br>0.72 | 0.578<br>1.041<br>2.091 | | 2.0 | 1.5 | 0.43-0.47<br>0.78-0.81<br>1.57-1.65 |
| *NZS 1170.5:2004* | 0.20<br>0.36<br>0.72 | 3 | 2 | 0.85 | 1.0 | 0.36<br>0.64<br>1.29 |
| *NZS 4219:2009* | 0.20<br>0.36<br>0.72 | 3 | --- | 0.85 | 1.0 | 1.38<br>2.48<br>3.60 |

Table 3 : Lateral force estimate using international design standards

Due to comparable component response factor and the format of seismic coefficient estimate, ASCE 07 and EAK values are close and lesser than values estimated for other codes (Table 3). Further, it is observed that lateral force demand under actual ground motions decreases with increase in seismic weight ratio, but increases at a particular seismic weight ratio and increasing design PGA (Figure 7). This decrease with increase in seismic weight ratio is significant for NSEs with seismic weight ratio 5% and above. In addition, for 9% seismic weight ratio and above, lateral force demand is within NZS 1170.5:2004 in buildings designed for 0.72g (Figure 7 (c)), but exceeds in buildings designed for lower PGAs (Figure 7 (a) and (b)). On the other hand, NZS 4219:2009 values are not exceeded in any case. Similarly, seismic demand is lower than Eurocode estimate only in NSEs with 7% seismic weight and above in building designed for 0.2g, 6% seismic weight ratio and above in building designed for 0.36g, and 5% seismic weight ratio and above in building designed for 0.72g. And, in NSEs with

fundamental period 0.04s and above, lateral force demand increases significantly in building designed for 0.72g (Figure 7 (c)).

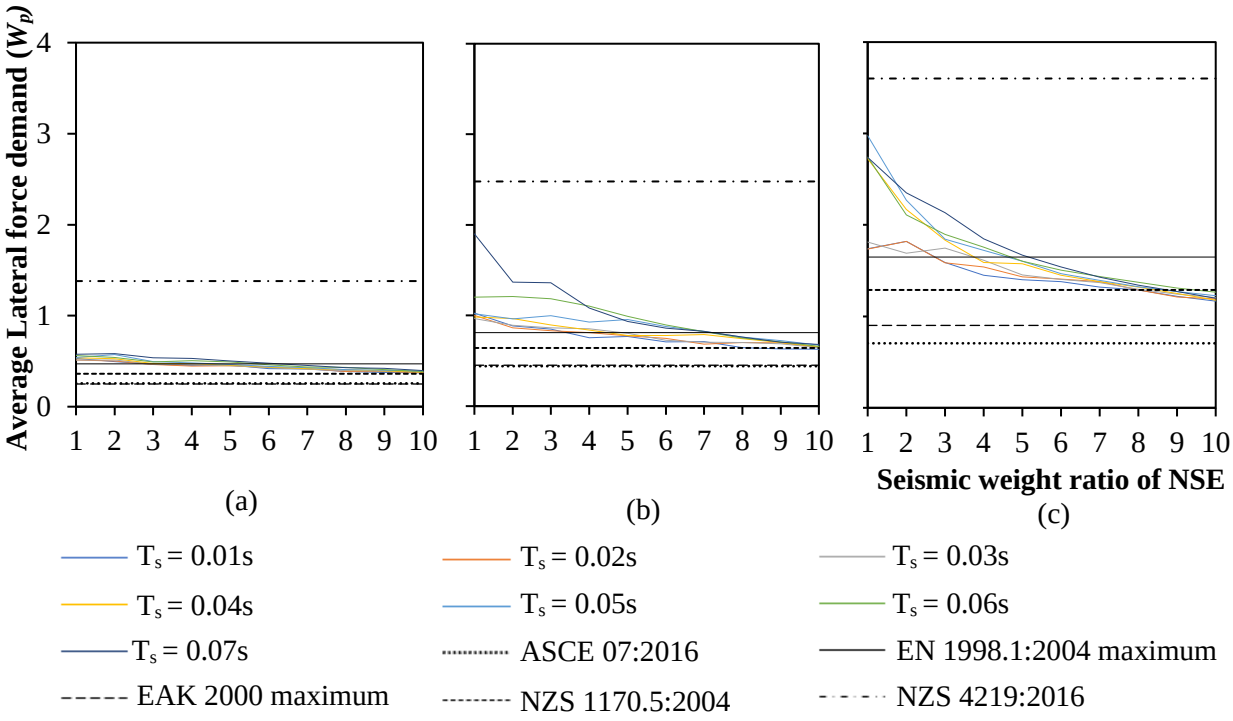


Figure 7: Variation of lateral force demand in buildings designed for PGA (a) 0.2g, (b) 0.36g, and (c) 0.72g

### 4.5 NSE – Building interaction

Providing NSEs with significant weight, stiffness and strength may affect the seismic behaviour of building supporting them or vice-versa. *Complete model* considering both building and NSE is expected to help understand the seismic behaviour interaction between the building and NSE. Linear and nonlinear behaviour of building- NSE interaction from the current work is briefly presented hereunder.

#### *4.5.1. Linear elastic NSE – Building interaction*

Variation of fundamental period of buildings designed for 0.2g, 0.36g and 0.72g are presented in Figure 8. In general, fundamental period of the buildings designed for 0.72g is lower than that of buildings designed for 0.20g. Further, increase in fundamental period of the building is proportional to the increase in seismic weight ratio of NSE, in all buildings. For *e.g.*, the fundamental period of building increased by 10% when seismic weight ratio of NSE was 10%, compared to the same building but without NSE. Further, this behavior is similar for NSEs with similar seismic weight ratio, but different stiffness. Thus, for NSEs with $T_s \leqslant 0.06$s, influence of NSE weight dominates its stiffness, in altering the fundamental linear behaviour of building. Thus, it is crucial to model NSE and building together in the linear elastic analysis to help predict floor demands (acceleration and displacement responses) realistically, for input to NSE.

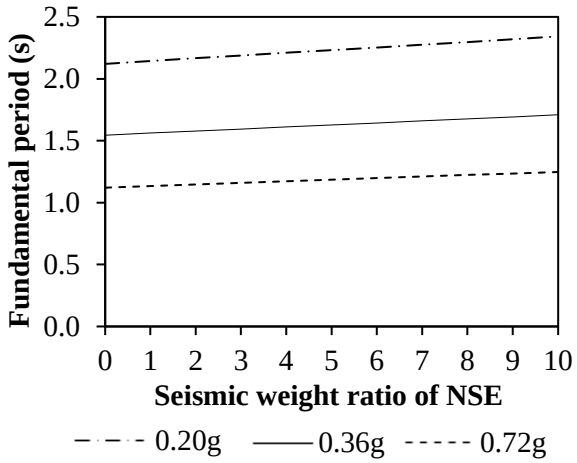


Figure 8: Variation of fundamental period of buildings

### *4.5.2. Nonlinear Building — Linear elastic NSE interaction*

The average CAF decreases with increase in seismic weight ratio of NSE in buildings designed for 0.36g and 0.72g, but insignificant in the building designed for 0.2g (Figure 6). The is because building designed for 0.2g is less stiff compared to buildings designed for 0.36g and 0.72g (Figures 9 (a), (b) and (c)), thereby reducing rate of amplification of component acceleration. In particular, for Sikkim earthquake, PCA is about 6.8 (Figure 9 (c)). But, in the relatively stiffer building designed for 0.72g and 0.36g, an increase in the rate of amplification of component acceleration is observed especially upto 5% seismic weight ratio. Also, in general, it is observed that the amplification of component acceleration increases with increase in fundamental period of the NSE. Similar trend is observed in the lateral force demand in the above buildings (Figure 7). Thus, lateral stiffness of structure also influences the CAF and lateral force demand on NSE.

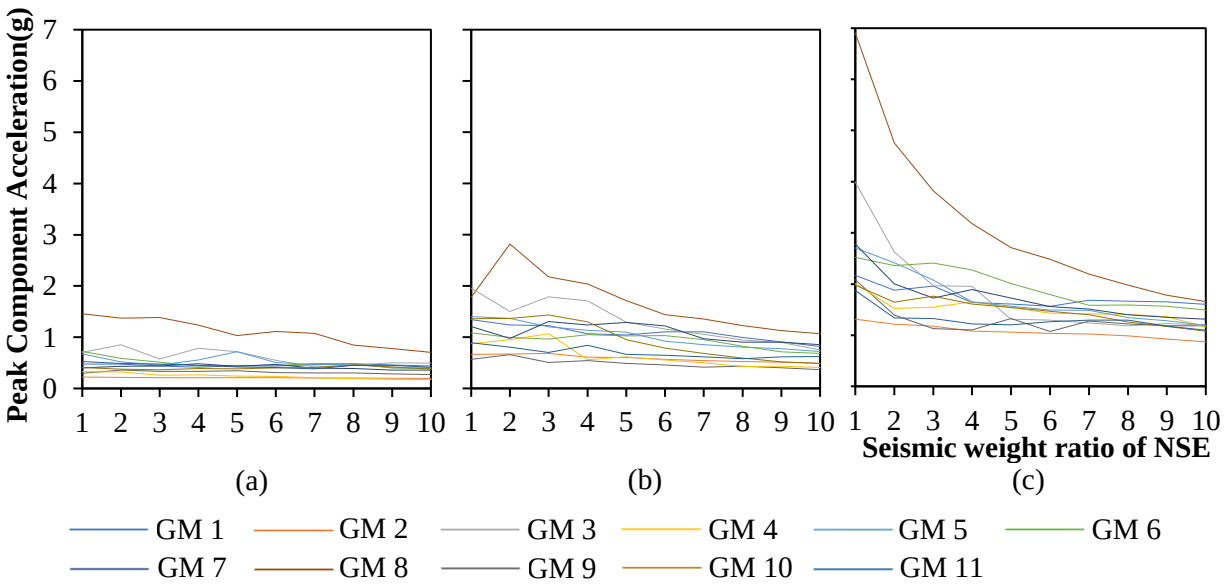


Figure 9: Variation of PCA in buildings designed for PGA (a) 0.2g, (b) 0.36g, and (c) 0.72g , $T_s$ = 0.06s

## 5 SUMMARY AND CONCLUSIONS

In this study, *complete model* method of *NSEs* is adopted to capture the behaviour of *NSEs* more realistically. Numerical seismic behaviour of 3 sets of buildings designed for 3 values of PGAs and 7 sets of NSEs with varying seismic weight ratio are studied to draw inferences. Salient conclusions from the study are:

- FAF, CAF and lateral force demand depends on both characteristics of buildings, NSE and ground motions. In particular, fundamental period of the building and *NSE*, design PGA and lateral stiffness of building and floor response under ground motions influence the NSE demand parameters.
- FAF varies nonlinearly across height of building; it is higher in the lower storeys thereby increasing demands and damage vulnerability of NSEs. Thus, it is recommended that *NSEs* present in lower storeys of buildings should be designed for higher FAF compared to that used for upper storeys.
- CAF varies in the range 1-2, and hence the recommended CAF for rigid NSEs used in important buildings is 2.

However, more nonlinear dynamic numerical investigations on a spectrum of buildings and NSEs commonly used, supplemented by possible experimental validation, are required to complement the results obtained from this study.

## REFERENCES

[1] ASCE 07:2016, Minimum design loads and associated criteria for buildings and other structures. *American Society of Civil Engineers*, Reston, Virginia, 2017.

[2] A. Campiche, S. Shakeel, Effect of architectural non-structural components on lateral behaviour of CFS structures: Shake-table tests and numerical modelling. *Proceedings in 7th ECCOMAS Thematic Conference on Computational Methods in Structural Dynamics and Earthquake Engineering, COMPDYN*, Crete, Greece, 3, 5791-5801, Paper No 7345, June 24-26,2019.

[3] S.I. Pardalopoulos, V.A. Lekidis, Experimental evaluation of a practical methodology for assessing the seismic demand from acceleration-sensitive secondary systems installed in RC buildings. *Earthquake Engineering & Structural Dynamics*, John Wiley and Sons, 50 (15), 3962-3980, 2021.

[4] A.H. Hadjian, On the decoupling of secondary systems for seismic analysis. *6th World Conference on Earthquake Engineering*, New Delhi, India, January 10-14, 1977.

[5] C.V.R. Murty, R. Goswami, A.R. Vijayanarayanan, R. Pradeep Kumar, V.V. Mehta, *Introduction to earthquake protection of non- structural elements in buildings*. Gujarat State Disaster Management Authority, Gandhinagar, India, 2012.

[6] C.E. Kerr, D.G. Proudfoot, C.L. Lee, Investigation of modelling methods for buildings with non-structural elements. *NZSEE Conference*, Wellington, New Zealand, April 27-29, 2017.

[7] M. Fragiadakis, S. Diamantopoulos, Fragility and risk assessment of freestanding building contents. *Earthquake Engineering & Structural Dynamics*, John Wiley and Sons, 49 (10),1028-1048, 2020.

[8] J. Penzien, A.K. Chopra, Earthquake response of appendage on a multi-story building. *Proceedings in 3rd World Conference on Earthquake Engineering*, Auckland, and Wellington, New Zealand, 2, 473-490, January 22-February 1,1965.

[9] J.L. Sackman, J.M. Kelly, Seismic analysis of internal equipment and components in structures. *Engineering Structures*, IPC Business Press, 1 (4), 179-190, 1979.

[10] J. Hur, E. Althoff, H. Sezen, R. Denning, T. Aldemir, Seismic assessment and performance of nonstructural components affected by structural modeling. *Nuclear Engineering and Technology*, Elsevier, 49 (2), 387-94, 2017.

[11] R. Villaverde, N.M. Newmark, Seismic response of light attachments to buildings. Department of Civil Engineering, *University of Illinois*, Structural Research Series No.469, Urbana, Illinois, 1980.

[12] R. Villaverde, Approximate formulas to calculate the seismic response of light attachments to buildings. *Nuclear engineering and design*, Elsevier Science Publishers B.V. (North-Holland), 128 (3), 349-368, 1991.

[13] R. Villaverde, Simplified approach for the seismic analysis of equipment attached to elastoplastic structures. *Nuclear engineering and design*, Elsevier Science Publishers B.V. (North-Holland), 103 (3), 267-279, 1987.

[14] R. Villaverde, Simple method to estimate the seismic nonlinear response of non-structural components in buildings. *Engineering Structures*, Elsevier, 28 (8), 1209-1221, 2006.

[15] D. Segal, W.J. Hall, Experimental seismic investigation of appendages in structures. Department of Civil Engineering, *University of Illinois*, Structural Research Series No.545, Urbana, Illinois, 1989.

[16] C. Adam, P.A. Fotiu, Dynamic analysis of inelastic primary–secondary systems. *Engineering Structures*, Elsevier, 22 (1), 58-71, 2000.

[17] E. Lim, N. Chouw, Review of approaches for analysing secondary structures in earthquakes and evaluation of floor response spectrum approach. *International Journal of Protective Structures*, 6 (2), 237-261, 2015.

[18] M. Oropeza, P. Favez, P. Lestuzzi, Seismic response of non-structural components in case of nonlinear structures based on floor response spectra method. *Bulletin of earthquake engineering*, Springer, 8 (2), 387-400, 2010.

[19] Y. Chen, T.T. Soong, State-of-the-art-review- Seismic response of secondary systems, *Engineering Structures*, 10 (4), Elsevier, 218-228, 1988.

[20] R. Villaverde, Seismic design of secondary structures: state-of-the-art. *Journal of Structural Engineering*, ASCE, 123 (8), 1011-1019, 1997.

[21] C. Karakostas, V. Lekidis, T. Makarios, T. Salonikios, I. Sous, M. Demosthenous, Seismic response of structures and infrastructure facilities during the Lefkada, Greece earthquake of 14/8/2003. *Engineering Structures*, Elsevier, 27 (2), 213-27, 2005.

[22] C.A. Maniatakis, I.N. Psycharis, C.C. Spyrakos, Effect of higher modes on the seismic response and design of moment-resisting RC frame structures. *Engineering Structures*, Elsevier, 56, 417-430, 2013.

[23] S. Cao, Z. Duan, B. Li, Parametric study on seismic demand assessment of acceleration-sensitive non-structural components of RC frames. *Structures*, Elsevier, 47, 1441-1458, 2023.

[24] CSI, Nonlinear analysis and performance assessment for 3D structures, PERFORM-3D. Computers and Structures Inc, Berkeley, U.S.A, 2018.

[25] M. Rashid, R.P. Dhakal, T.J. Sullivan, Seismic design of acceleration-sensitive non-structural elements in New Zealand: State-Of-Practice and Recommended Changes. *Bulletin of the New Zealand Society for Earthquake Engineering*, 54 (4), 243-262, 2021.

[26] Greek Code for Seismic Resistant Structures, EAK 2000, 2000.

[27] Eurocode 8: Design of structures for earthquake resistance–Part 1: General rules, seismic actions and rules for buildings. *European Committee for Standardisation*, Brussels, Belgium, 2004.

[28] NZS1170.5, Structural design actions. Part 5: Earthquake actions-New Zealand. *Standards New Zealand*, Wellington, New Zealand, 2004.

[29] NZS 4219, Seismic performance of engineering systems in buildings. *Standards New Zealand*, Wellington, New Zealand, 2009.

[30] IS 1893 (Part 1), Criteria for earthquake resistant design of structures. *Bureau of Indian Standards*, New Delhi, 2016.

[31] IS 13920, Ductile design and detailing of reinforced concrete structures subjected to seismic forces – Code of Practice. *Bureau of Indian Standards*, New Delhi, 2016.

[32] J.B. Mander, M.J.N. Priestley, R. Park, Theoretical stress-strain model for confined Concrete. *Journal of Structural Engineering*, ASCE, 114(8), 1804-1826, 1988.

[33] E. Kalkan, A. Chopra, Practical guidelines to select and scale earthquake records for nonlinear Response History Analysis of Structures, Open-File Report, EERI and USGS, 2010.

[34] PEER NGA Database, Pacific Earthquake Engineering Research Center, *University of California*, Berkeley, CA, USA, 2010.

[35] COSMOS, Consortium of Organizations for Strong-Motion Observation Systems, Pacific Earthquake Engineering Research Center, *University of California*, Berkeley, CA, USA, 2012.

[36] H. Mittal, A. Kumar, R. Ramhmachhuani, Indian strong motion instrumentation network and its site characterization. *International Journal of Geosciences*, Scientific Research, 3(6), 1151-1167, 2012.

[37] G. Yu, K.N. Khattri, J.G. Anderson, J.N. Brune, Y. Zeng, Strong ground motion from the Uttarkashi, Himalaya, India, earthquake: comparison of observations with synthetics using the composite source model. *Bulletin of the Seismological Society of America*, GeoScienceWorld, 85(1), 31-50, 1995.

[38] J.E. Alarcón, F. Taucer, E. So, The 15 August 2007 Pisco, Peru, earthquake-post-earthquake field survey. *Proceedings in the 14th World Conference on Earthquake Engineering*, October 12-17, Beijing, China,2008.

[39] NIST, Recommendations for Improved Seismic Performance of Nonstructural Components, NIST GCR 18-917-43, *Applied Technology Council*, Redwood City, CA, USA, 2018.

COMPDYN 2023
9th ECCOMAS Thematic Conference on
Computational Methods in Structural Dynamics and Earthquake Engineering
M. Papadrakakis, M. Fragiadakis (eds.)
Athens, Greece, 12-14 June 2023

# INVESTIGATING THE EFFICIENCY AND THE SUFFICIENCY OF IMs FOR THE PROBABILISTIC SEISMIC ASSESSMENT OF THE POUNDING EFFECT BETWEEN ADJACENT RC STRUCTURES

**Maria G. Flenga**[1], **Maria J. Favvata**[2]

[1] University of Patras
Civil Engineering Department
26504 Rio, Greece
e-mail: mariaflenga@upnet.gr

[2] University of Patras
Civil Engineering Department
26504 Rio, Greece
e-mail: mfavvata@upatras.gr

## Abstract

*The objective of this study is to identify appropriate intensity measures (IMs) for use in the probabilistic seismic assessment of the pounding effect between adjacent reinforced concrete (RC) structures. For this purpose, the efficiency and the sufficiency of twenty-three seismic IMs of forty-nine 2-component ground motions, are investigated. The structural pounding between multistory RC structures is examined taking into account three different separation gap distances. 294 nonlinear dynamic analyses are performed in the concept of the Cloud Analysis method to define the seismic demand parameters of an eight-story RC structure due to the pounding effect. Structural demands in terms of a) maximum displacement at the top of the contact point $\delta_{max}$, b) maximum interstory drifts, $IDR_{max}$, and c) maximum curvature ductility demand $\mu_{\varphi,max}$ of the most critical column, are estimated. Thereafter, the efficiency and the sufficiency of each IM are evaluated. The results of this study indicate; (a) the structural dependent IMs are more efficient in predicting the seismic demands of the RC structure, (b) an optimal IM that satisfies simultaneously the criteria of efficiency and sufficiency is difficult to be identified, (c) the efficiency of an IM is usually accompanied with lack of its sufficiency and vice versa, (d) the local demands of the critical column that suffers the pounding effect alter the results of the IMs' sufficiency, and (e) the superiority of the $S_{a,T1}$ compared to the structural independent IMs is justified when the relative sufficiency between IMs and seismic demands is evaluated.*

**Keywords:** structural pounding, ground motion IMs, efficiency property, sufficiency property, nonlinear dynamic analyses, reinforced concrete structure, Eurocodes 2 & 8

# 1 INTRODUCTION

In the last three decades, several research has been undertaken to address the seismic performance of structures through probabilistic procedures. The vulnerability of the structures to seismic damage is assessed as the probability of an engineering demand parameter (EDP) to exceed the capacity for a given intensity measure (IM). For this purpose, nonlinear dynamic analysis methods should be performed to generate samples of EDPs|IMs, where the EDP represents the seismic performance of the structure, and the IM describes the ground motion characteristics [1].

The reliability of the overall probabilistic assessment depends on the IM that has been selected to be used. In order to quantify the suitability of an IM, different criteria such as efficiency [2], sufficiency [3], proficiency, practicality [4], hazard computability [5] have been proposed. Among them the efficiency and sufficiency criteria are the most commonly examined properties of IMs in the earthquake structural engineering. An IM is characterized as an efficient one if it predicts the structural response with small variability. Therefore, the uncertainties of record-to-record variability are reduced, and a small number of records can be used for performing nonlinear dynamic analyses. The sufficiency property indicates that the IM is independent of ground motion characteristics and that the vulnerability assessment is not affected by other parameters such as the magnitude $M_w$, the source-to-site distance $R_{rup}$, and the ground motion parameter epsilon ε.

Scalar and vector IMs are evaluated to improve the prediction of the structural response. Scalar IMs are divided into two categories: the structural independent and the structural dependent IMs. The first category of IMs may capture information on the ground motion such as frequency content, duration, and amplitude [e.g., 6-15], while the structural dependent IMs are related to the structure's dynamic characteristics [6, 16, 17]. On the other hand, the vector IMs incorporate different scalar IMs to improve the predictive capability with respect to the examined EDPs [18]. Also, several IMs that constitute modifications of $S_{a,T1}$ and incorporate spectral values of other periods have been proposed to capture the contribution of the higher modes and the period elongation effects [19, 20]. However, the modified IMs are rarely used due to the lack of attenuation relationship, which is needed to compute seismic hazard in terms of IM that is also required for the probabilistic seismic demand analysis [20]. The most widely used IMs for the probabilistic assessment of the structural seismic performance are the peak ground acceleration (PGA), and the spectral acceleration at the fundamental period of the structure ($S_{a,T1}$).

Literature provides research studies that quantify the efficiency and the sufficiency of an IM and evaluate the correlation between IMs and EDPs [21-25] However, only a few studies have focused on the verification of an appropriate IM when considering the earthquake-induced structural pounding phenomenon. Tubaldi et al [26] examined three different IMs regarding efficiency and sufficiency properties to develop an accurate probabilistic seismic demand model for the pounding risk assessment. The examined IMs arise as a modification of the spectral displacement IM, while the examined structural models were single-degree-of-freedom (SDOF) and multi-degree-of-freedom (MDOF) systems. In 2016, Tubaldi et al [27] examined the sufficiency of three different IMs based on the relative sufficiency measure (RSM) in order to develop different types of regression models. For the probabilistic seismic assessment of the pounding effect between reinforced concrete (RC) structures, Flenga and Favvata [28-31] examined the adequacy of the PGA and the $S_{a,T1}$ measures. Finally, Langlade et al [32] examined the efficiency and the sufficiency of six different IMs in the structural pounding framework between two SDOF systems.

The objective of this study is to identify the appropriate IMs for use in the probabilistic seismic assessment of the pounding effect between adjacent RC structures. For this purpose, the efficiency, and the sufficiency of twenty-three seismic IMs of forty-nine 2-component ground motions, are investigated. The structural pounding between an eight-story RC frame structure and a three-story stiffer structure for three different separation gap distances is examined. Nonlinear dynamic analyses are performed and the seismic demand parameters of the eight-story RC structure due to the pounding effect are estimated. Thereafter, the efficiency and the sufficiency of each IM are evaluated. In this study, Pearson's and Spearman's rank correlation coefficients are also incorporated.

## 2 KEY ASSUMPTIONS

### 2.1 Ground motions and intensity measures

For the needs of this study, both horizontal components of forty-nine strong ground motions extracted from PEER's and ESM's databases are used. All ground motions have magnitude $M_w$ greater than 5.5, source-to-site distance $R_{rup}$ greater than 15km, and they have been recorded on soils with average shear wave velocity in the upper 30 m of soil ($v_{s,30}$) that is up to 813.5 m/s (soil class A in EC8). The main characteristics of the seismic excitations are presented in Table 1. For each seismic record, twenty-three intensity measures (IMs) are considered and numerically estimated. The seismic IMs are either structural independent (PGA, PGV e.tc.) or structural dependent ($S_{a,T1}$, $S_{v,T1}$ e.tc.). The structural independent IMs are calculated directly from the time-history of the examined ground motions and describe characteristics such as amplitude, duration, and frequency in terms of acceleration, velocity or displacement. On the other hand, the structural dependent IMs are evaluated by the response spectra of the ground motions and are classified as spectral, integral, and multi-parameter measures [22]. The examined IMs are presented in Table 2.

### 2.2 Examined case of structural pounding

In this work, the seismic performance of an 8-story RC frame structure against pounding with an adjacent three-story rigid structure, is examined (Fig.1). The story levels of the adjacent structures have the same height so that the collisions may occur between the story diaphragms and consequently between the story masses (floor-to-floor interaction). The separation gap distance ($d_g$) between the adjacent structures is considered equal to $d_g = 0.0$ cm (structures are in contact from the beginning), and $d_g = 2.0$ cm. The seismic performance of the 8-story structure without the pounding effect is also addressed. The 8-story RC frame structure has been designed according to Eurocode 2 and 8, and the computer program Drain-2dx has been used to perform the structural modelling and the nonlinear dynamic analyses [34]. More details about the design and the overall modelling assumptions can be found in Flenga and Favvata [29].

Thereafter, two hundred ninety-four (294) nonlinear time history analyses have been performed in the concept of the Cloud Analysis method [1] to define the samples of the EDPs as a function of the IMs. For the correlation process three different EDPs of the 8-story RC frame are considered: (a) the maximum displacement ($\delta_{max}$) at the top level of the contact point of the adjacent structures (4th floor level), (b) the maximum interstory drift ($IDR_{max}$) of the structure as a function of the story height ($\%h_{st}$), and (c) the maximum curvature ductility demand ($\mu_{\varphi,max}$) of the most critical column.

The generated pairs of EDP|IM depict the seismic performance in the case of free vibration of the 8-story RC frame (without pounding) as well as the corresponding responses in the case

where the separation gap distance between the adjacent structures is equal to: (a) $d_g$ = 0.0 cm and (b) $d_g$ = 2.0 cm.

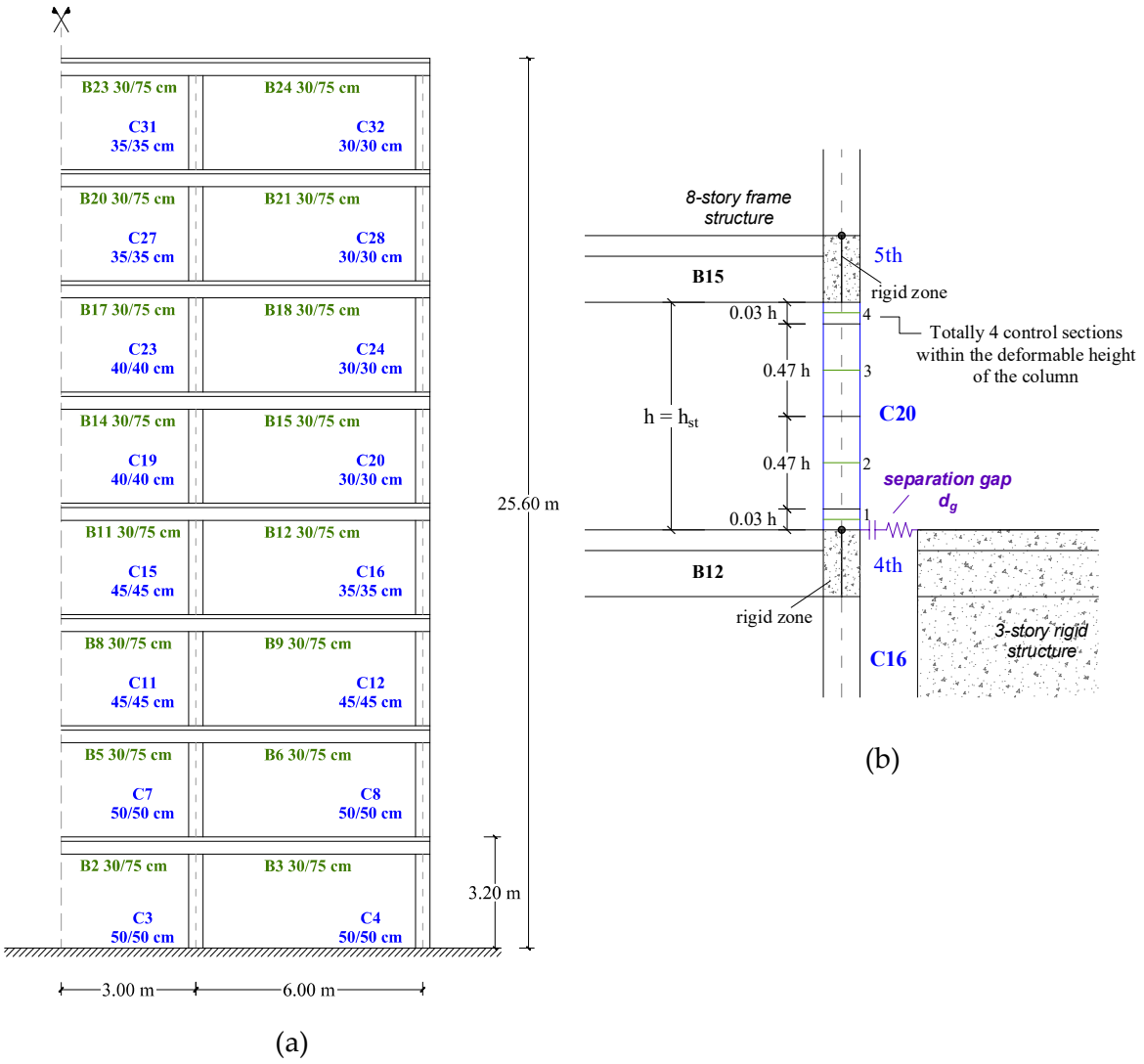


**Figure 1.** (a) Eight-story RC frame structure and (b) idealization of the contact area [29].

## 3 EVALUATION OF THE EXAMINED IMs

The seismic probabilistic assessement of a structure involves the use of an adequate IM that verifies specific criteria of efficiency and sufficiency. An efficient IM denotes small variation in the estimation of the structural demand for a given value of IM, while a sufficient IM indicates that it is independent of ground motion characteristics such as $M_w$, and $R_{rup}$. In the next sections, the adequacy of the examined IMs as indicators of the structural demand against pounding between adjacent structures for three different separation gap distances is addressed and discussesed.

**Table 1:** Ground motions' characteristics

| No | Earthquake ID | Earthquake Name | Station Name | Magnitude ($M_w$) | Closest distance ($R_{rup}$) (km) | Duration (sec) | No. | Earthquake ID | Earthquake Name | Station Name | Magnitude ($M_w$) | Closest distance ($R_{rup}$) (km) | Duration (sec) |
|---|---|---|---|---|---|---|---|---|---|---|---|---|---|
| 1 | RSN 643 | Whittier Narrows-01 | LA - Wonderland Ave | 5.99 | 27.64 | 18.14 | 26 | EMSC-20161030_0000029 | Central Italy | Teramo | 6.50 | 27.87 | 61.38 |
| 2 | RSN 4312 | Umbria-03, Italy | Gubbio | 5.60 | 15.72 | 17.99 | 27 | ME-1979-0003 | Northwestern Balkan Peninsula | Hercegnovi Novi-O.S.D. Pavicic School | 6.90 | 24.00 | 47.96 |
| 3 | IT-2009-0009 | L' Aquila | Montereale | 6.10 | 17.11 | 99.99 | 28 | RSN 5618 | Iwate, Japan | IWT010 | 6.90 | 16.27 | 237.99 |
| 4 | EMSC-20160824_0000006 | Central Italy | Teramo | 6.00 | 22.12 | 78.61 | 29 | RSN 1091 | Northridge-01 | Vasquez Rocks Park | 6.69 | 23.64 | 39.98 |
| 5 | IT-1984-0004 | Lazio Abruzzo | Atina | 5.90 | 16.32 | 30.68 | 30 | RSN 3954 | Tottori, Japan | SMNH10 | 6.61 | 15.59 | 299.99 |
| 6 | RSN 680 | Whittier Narrows-01 | Pasadena - CIT Kresge Lab | 5.99 | 18.12 | 39.99 | 31 | EMSC-20161030_0000029 | Central Italy | Reggiano | 6.50 | 21.27 | 61.38 |
| 7 | GR-1999-0001 | Greece | -(ATH4) | 5.90 | 16.79 | 42.35 | 32 | ME-1979-0003 | Northwestern Balkan Peninsula | Dubrovnik-Pomorska Skola | 6.90 | 64.87 | 33.57 |
| 8 | IT-2009-0009 | L' Aquila | Antrodoco | 6.10 | 23.18 | 120.00 | 33 | RSN 284 | Iprinia, Italy | Auletta | 6.90 | 9.60 | 34.00 |
| 9 | EMSC-20170118_0000034 | Central Italy | Leonessa | 5.50 | 22.40 | 59.90 | 34 | RSN 5006 | Chuetsu-oki, Japan | FKSH07 | 6.80 | 79.54 | 158.99 |
| 10 | IT-1997-0006 | Umbria March | Monte Fiegni | 6.00 | 21.98 | 34.75 | 35 | RSN 5993 | El Mayor-Cucapah | El Monte County Park | 7.20 | 104.9 | 154.84 |
| 11 | RSN 4438 | Molise-02, Italy | Sannicandro | 5.70 | 51.32 | 36.28 | 36 | RSN 3799 | Hector Mine | LA - Griffith Park Observatory | 7.13 | 185.92 | 56.99 |
| 12 | RSN 1649 | Sierra Madre | Vasquez Rocks Park | 5.61 | 39.81 | 39.98 | 37 | RSN 788 | Loma Prieta | Piedmont Jr High School Grounds | 6.93 | 73.00 | 39.99 |
| 13 | IT-2012-0008 | Emilia 1st shock | S Zeno Di Montagna | 6.10 | 77.86 | 200.00 | 38 | RSN 4167 | Niigata, Japan | FKSH07 | 6.63 | 52.3 | 179.99 |
| 14 | EMSC-20161026_0000095 | Central Italy | Monte Murano | 5.90 | 48.95 | 124.81 | 39 | RSN 804 | Loma Prieta | So. San Francisco, Sierra Pt. | 6.90 | 63.10 | 25.00 |
| 15 | RSN 2805 | Chi-Chi Taiwan-04 | KAU003 | 6.20 | 116.20 | 60.00 | 40 | RSN 59 | San Fernando | Cedar Springs, Allen Ranch | 6.60 | 89.70 | 14.00 |
| 16 | ME-1979-0012 | Northwestern Balkan Peninsula | Hercegnovi Novi-O.S.D. Pavicic School | 6.20 | 30.7 | 24.58 | 41 | RSN 283 | Iprinia, Italy | Arienzo | 6.90 | 52.90 | 24.00 |
| 17 | RSN8168 | Parkfield-02, CA | Diablo Canyon Power Plant | 6.00 | 78.32 | 39.67 | 42 | RSN 5363 | Chuetsu-oki, Japan | TCGH17 | 6.80 | 102.41 | 237.99 |
| 18 | GR-1997-0019 | Ionean Sea | Kyparissia | 6.40 | 104.34 | 27.80 | 43 | RSN 6041 | El Mayor-Cucapah | San Diego Road Dept | 7.20 | 110.95 | 163.68 |
| 19 | IT-2012-0008 | Emilia 1st shock | Tregnago | 6.10 | 63.89 | 160.18 | 44 | RSN 5483 | Iwate, Japan | AKTH05 | 6.90 | 39.41 | 177.99 |
| 20 | EMSC-20161026_0000095 | Central Italy | Teramo | 5.90 | 41.70 | 187.49 | 45 | RSN 8167 | San Simeon, CA | Diablo Canyon Power Plant | 6.52 | 37.92 | 29.44 |
| 21 | RSN 3479 | Chi-Chi Taiwan-06 | TCU085 | 6.30 | 83.40 | 42.00 | 46 | RSN 4248 | Niigata, Japan | TCGH17 | 6.63 | 77.50 | 295.99 |
| 22 | RSN 2508 | Chi-Chi Taiwan-03 | CHY102 | 6.20 | 60.36 | 60.99 | 47 | RSN 1245 | Chi-Chi, Taiwan | CHY102 | 7.62 | 37.22 | 89.99 |
| 23 | RSN 80 | San Fernando | Pasadena - Old Seismo Lab | 6.61 | 21.50 | 101.10 | 48 | RSN 1257 | Chi-Chi, Taiwan | HWA003 | 7.62 | 56.14 | 64.99 |
| 24 | RSN 1011 | Northridge-01 | LA - Wonderland Ave | 6.69 | 20.29 | 29.98 | 49 | RSN 2107 | Denali, Alaska | Carlo (temp) | 7.90 | 50.90 | 60.00 |
| 25 | RSN 3925 | Tottori, Japan | OKYH07 | 6.61 | 15.23 | 299.99 | | | | | | | |

**Table 2:** Examined Intensity Measures [6 - 17]

| | IMs | Units | Name | Formula | Ref. |
|---|---|---|---|---|---|
| ***Structural Independent IM*** | | | | | |
| ***Acceleration – based IMs*** | PGA | [m/sec$^2$] | Peak Ground Acceleration | $PGA=\max\|a(t)\|$ | [6] |
| | $RMS_a$ | [m/sec$^2$] | Root-mean-square of acceleration | $RMS_a=\sqrt{\frac{1}{n}\sum_{i=1}^{n}(a(t))^2}$ | [9] |
| | Ia | [m/sec] | Arias Intensity | $I_a=\int_0^{T_d}(a(t))^2 dt$ | [10] |
| | Ic | | Characteristic Intensity | $I_c=a_{rms}{}^{1.5}T_d^{0.5}$ | [11] |
| | CAV | [m/sec] | Cumulative Absolute Velocity | $CAV=\int_0^{t_{tot}}\|a(t)\|\,dt$ | [7] |
| | SMA | [m/sec$^2$] | Sustained Maximum Acceleration | 3$^{rd}$ largest peak in acceleration time history | [8] |
| | EDA | [m/sec$^2$] | Effective Design Acceleration | Peak acceleration value after filtering out time history above 9Hz | [7] |
| | $A_{95}$ | [m/sec$^2$] | $A_{95}$ parameter | The acceleration level below which 95% of the total Arias intensity is contained | [13] |
| ***Velocity – based IMs*** | PGV | [m/sec] | Peak Ground Velocity | $PGV=\max\|v(t)\|$ | [6] |
| | $RMS_v$ | [m/sec] | Root-mean-square of velocity | $RMS_v=\sqrt{\frac{1}{T_d}\int_0^{T_d}(v(t))^2 dt}$ | [9] |
| | SED | [m/sec$^2$] | Specific Energy Density | $SED=\int_0^{T_d}(v(t))^2 dt$ | [6] |
| | SMV | [m/sec] | Sustained Maximum Velocity | 3$^{rd}$ largest peak in velocity time history | [8] |
| | MIV | [m/sec] | Maximum Incremental Velocity | Maximum area under the acceleration curve between two zero crossings of the accelerogram | [12] |
| ***Displacement – based IMs*** | PGD | [m] | Peak Ground Displacement | $PGD=\max\|d(t)\|$ | [6] |
| | $RMS_d$ | [m] | Root-mean-square of displacement | $RMS_d=\sqrt{\frac{1}{T_d}\int_0^{T_d}(d(t))^2 dt}$ | [9] |
| | PGV/PGA | [sec] | Peak velocity and acceleration ratio | $PGV/PGA=\max\|v(t)\|/\max\|a(t)\|$ | [6] |
| ***Structural Dependent IM*** | | | | | |
| ***Spectral IMs*** | $S_{a,T1}$ | [m/sec$^2$] | Spectral Acceleration | Spectral Acceleration at the fundamental period of the structure | [6] |
| | $S_{v,T1}$ | [m/sec] | Spectral Velocity | Spectral velocity at the fundamental period of the structure | [6] |
| | $S_{d,T1}$ | [m] | Spectral Displacement | Spectral displacement at the fundamental period of the structure | [6] |
| ***Integral IMs*** | ASI | [m/sec] | Acceleration Spectrum Intensity | $ASI=\int_{0.1}^{0.5}S_a(0.05,T)\,dT$ | [14] |
| | VSI | [m] | Velocity Spectrum Intensity | $VSI=\int_{0.1}^{2.5}S_v(0.05,T)\,dT$ | [14] |
| | HI | [m] | Housner Intensity | $HI=\int_{0.1}^{2.5}PSV(\xi,T)\,dT$ | [16] |
| ***Multi-Parameter IMs*** | $S_{a,avg}$ | [m/sec$^2$] | Average Spectral Acceleration | $S_{a(T1....TN)}=\left(\prod_{i=1}^{n}S_a(T_i)\right)^{1/n}$ | [17] |

### 3.1 Verification of IMs' Efficiency

The most common method to evaluate the variability of an IM is through the logarithm standard deviation, $\beta_{EDP|IM}$. For this purpose, the EDP|IM pairs are generated through the nonlinear dynamic analyses and linear regression of the EDP|IM pairs in log-log space is performed. Assuming that the structural response demand is following lognormal distribution [2] the logarithm standard deviation $\beta_{EDP|IM}$ is calculated as:

$$\beta_{EDP|IM}=\sqrt{\frac{\sum_{i=1}^{n}\left(\ln EDP_i|IM_i - \ln \widehat{EDP}|IM\right)^2}{n-2}} \tag{1}$$

where, n is the number of the nonlinear dynamic analyses, and $\widehat{EDP}$ is the median structural demand.

Based on Malaioli et al [23] values of dispersion lower than 0.30 indicate ideal efficiency of the seismic intensity measure, however a logarithm standard error in the range of 0.30-0.40 is also acceptable to characterize an IM efficient.

Furthermore, Pearson's and Spearman's rank correlation coefficients could also be used to justify the adequacy of an IM. The Pearson's rank correlation coefficient evaluates the linear relationship between the EDP-IM pairs and can be calculated by the following expression:

$$\rho_{pearson}=\frac{\sum_{i=1}^{n}(X_i-\bar{X})(Y_i-\bar{Y})}{\sqrt{\sum_{i=1}^{n}(X_i-\bar{X})^2\sum_{i=1}^{n}(Y_i-\bar{Y})^2}} \tag{2}$$

where, $X_i$, $Y_i$ are the IM, EDP of the ith pair of data, $\bar{X}_i$, $\bar{Y}_i$ are the mean values of the IMs, EDPs data, and n is the number of the seismic excitations.

On the other hand, the Spearman's rank correlation coefficient evaluates the monotonic relationship of the EDP-IM pairs and can be calculated by the following expression:

$$\rho_{spearman}=1-\frac{6\sum_{i=1}^{n}d_i^2}{n\,(n^2-1)} \tag{3}$$

where, $d_i$ denotes the differences between the ranks of corresponding values of $X_i$, $Y_i$ and n is the number of the seismic excitations.

Values of Pearson's and Spearman's correlation coefficients equal to $\pm 1$ indicate perfect linear relationship between the EDP and the IM. For comparison reasons, absolute values of the correlation between the intensity measures and the demands of the structures are presented. In this study, a value of correlation greater than 0.85 is considered adequate to verify the IMs' efficiency. So, Figure 2 shows values of the logarithm standard deviation $\beta_{EDP|IM}$, the Pearson's rank correlation coefficient, and the Spearman's rank correlation coefficient, when the IMs are evaluated as indicators of the 8-story RC frame demands: (a) maximum displacement demand of at the 4th floor level ($\delta_{max}$), (b) maximum interstory drift ($IDR_{max}$ - $\%h_{st}$), and (c) maximum curvature ductility of the column at the 4th floor level ($\mu_{\varphi,max}$). As it can be observed, with exception the ASI all the other structural dependent IMs are generally more efficient in evaluating the demands in terms of $\delta_{max}$, $IDR_{max}$, and $\mu_{\varphi,max}$ of the RC frame. In general, the values of $\beta_{EDP|IM}$ are lower than 0.40 indicating the superiority of the structural dependent IMs to predict the EDPs with reduced variation. Similarly, Pearson's and Spearman's correlation coefficients are ranged between 0.85-1.00 in the case of structural dependent IMs (blue and green lines in Fig. 2) that indicates an almost linear relationship between IM and EDP.

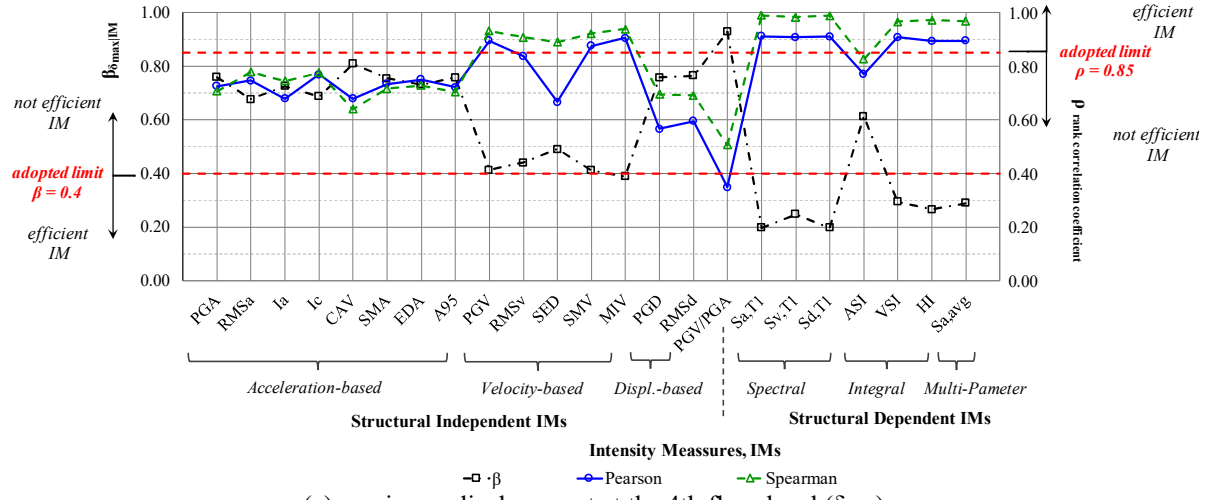


(a) maximum displacement at the 4th floor level ($\delta_{max}$)

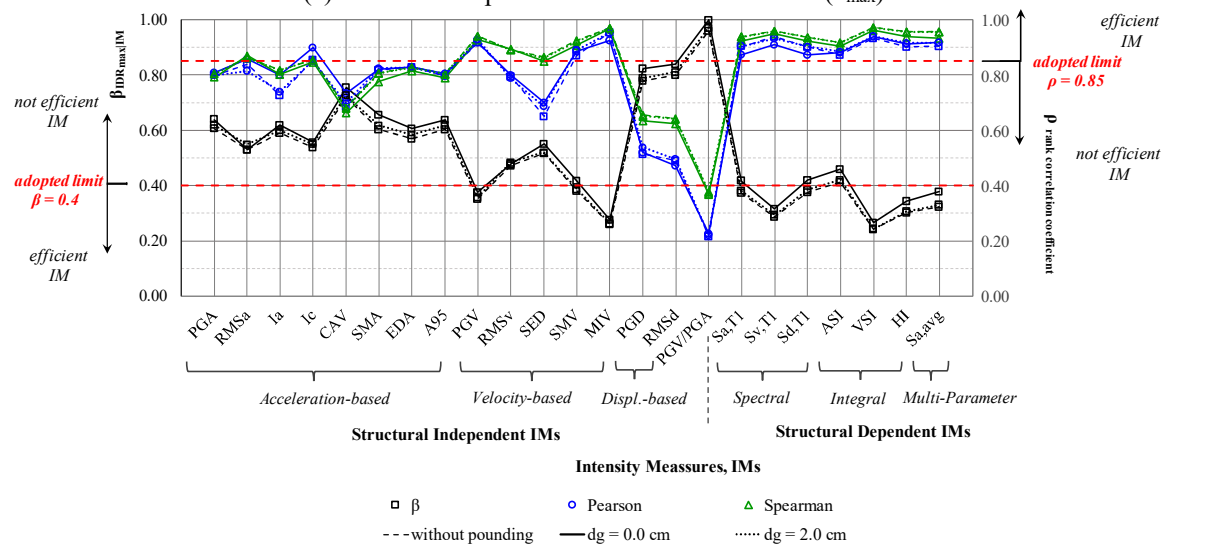


(b) maximum interstory drift ($IDR_{max}$ - $\%h_{st}$)

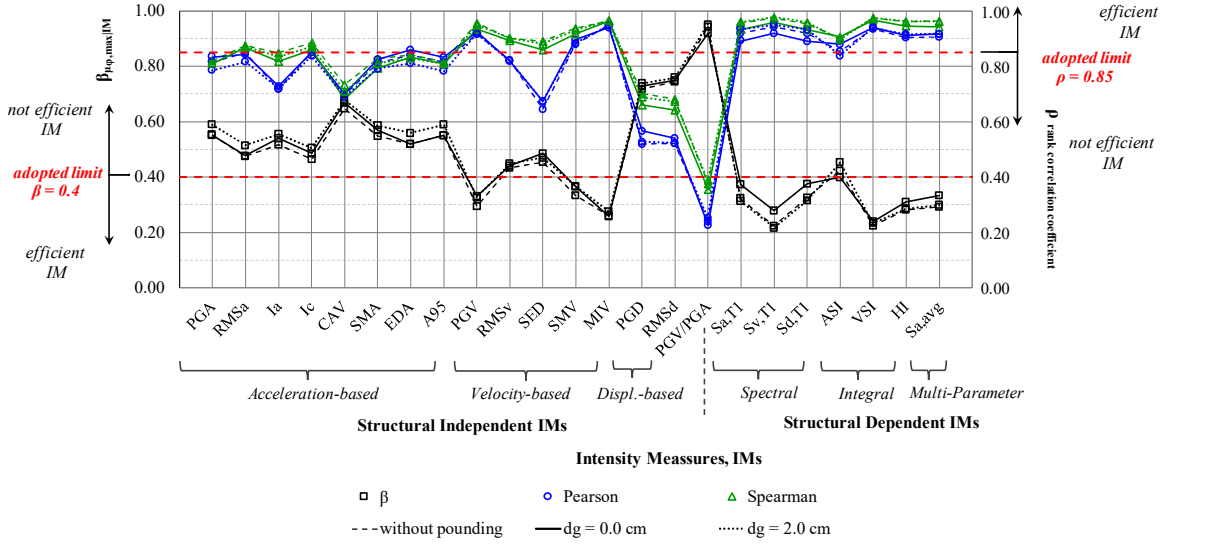


(c) maximum curvature ductility of the column at the 4th floor level ($\mu_{\varphi,max}$)

**Figure 2.** Evaluation of the IMs' efficiency with the EDPs of 8-story RC frame based on the logarithm standard deviation $\beta_{EDP|IM}$, the Pearson's, and the Spearman's rank correlation coefficients.

On the contrary, the structural independent IMs show an increased variation in the prediction of the EDPs. In these cases, the structural independent IMs have values of $\beta_{EDP|IM}$ greater than 0.4, while the values of Pearson's and Spearman's rank correlation coefficients are lower than 0.85. Nevertheless, among all the structural independent IMs, PGV and MIV have shown better predictive capability to EDPs. The least effective structural independent IMs are the acceleration-based and the displacement-based, with the IM of PGV/PGA to be the most invalid indicator to describe the demands of the structure.

The evaluation of the IMs' efficiency seems not to be affected when the structural pounding problem is involved. For example, the estimated values of $\beta_{IDRmax|IM}$ are slightly increased when $d_g$ = 0.0 cm compared to the cases of $d_g$ = 2.0 cm and without pounding. Generally, the dispersion remains within the acceptable range ($\beta_{IDRmax|IM}$ <0.4) for the structural dependent IMs. Also, the estimation of the rank correlation coefficients shows that the interdependence of the IMs with the examined EDPs is slightly changed when structures are in contact from the beginning. The velocity-based IMs remain more efficient for predicting the demands of the 8-story RC frame structure subjected to pounding. The displacement-based IMs indicate no interdependence with EDPs. In Figure 3, indicative results of the relationship between the $IDR_{max}$ and the IMs of PGV, PGD, $S_{a,T1}$, and $S_{v,T1}$ are presented. The results are in log-log space, and the examined case is for separation gap distance $d_g$ = 0.0 cm. As can be observed, the linear regression model is adequate to capture the median $IDR_{max}$ demands of the 8-story RC frame through the IMs of PGV, $S_{v,T1}$ and $S_{a,T1}$, while PGD fails to describe the median structural demands.

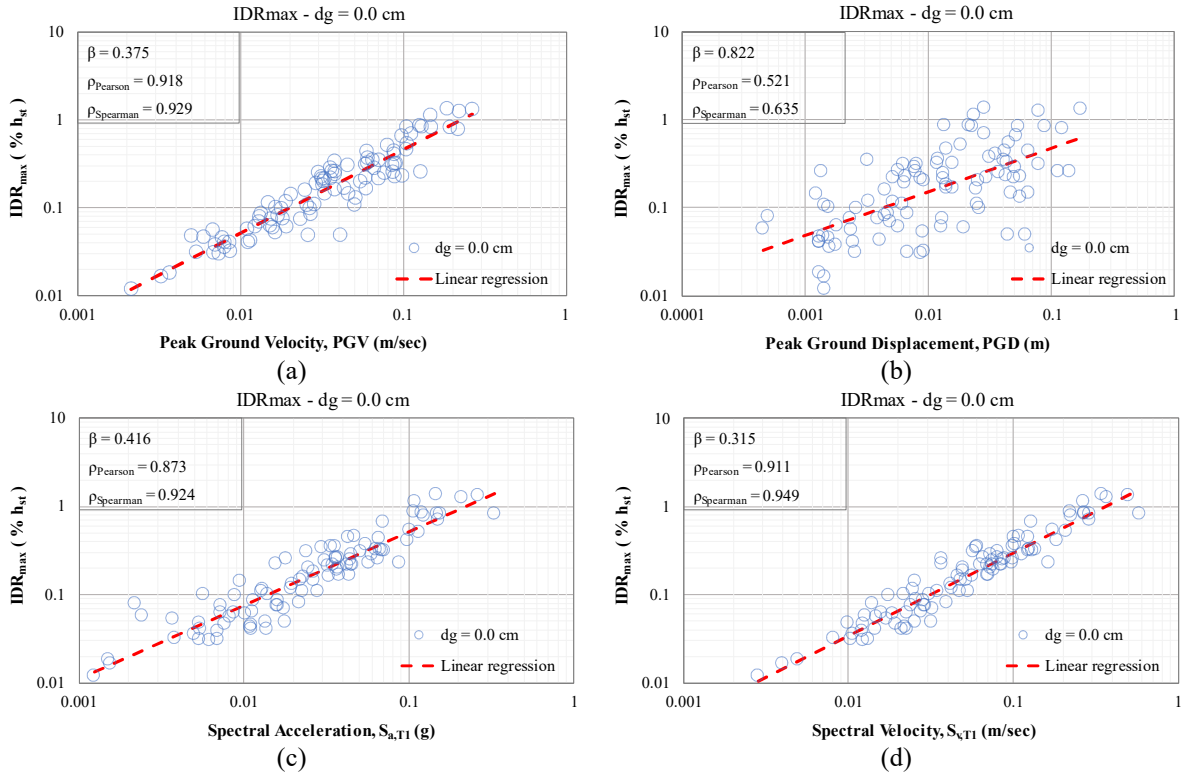


**Figure 3.** Relationship in log-log space between (a) PGV-$IDR_{max}$, (b) PGD-$IDR_{max}$, (c) $S_{a,T1}$-$IDR_{max}$, and (d) $S_{v,T1}$-$IDR_{max}$ . Results for separation gap distance $d_g$ = 0.0 cm.

## 3.2 Verification of IMs' Sufficiency

The criterion of sufficiency is also an important measure for the evaluation of the IM's adequacy. The most common way to evaluate the sufficiency of an IM is through the p-value

between the residuals ε|IM of the regression analysis and the examined characteristic of the ground motion ($M_w$ or $R_{rup}$). In general, p-value represents the probability of rejecting the null hypothesis ($H_o = 0$) which states that the regression coefficient is zero. A small p-value (less than a cut-off value of 0.05 for 95% confidence level) indicates that the regression coefficient is statistically significant, and the IM is insufficient.

The sufficiency of an IM could also be classified based on the Spearman's rank correlation coefficient. In this case, the Spearman method examines the interdependency between residuals ε|IM and the ground motion characteristic ($M_w$ or $R_{rup}$). Coefficient values equal to ±1 indicate the monotonic (linear or nonlinear) relationship between the examined variables and the insufficiency of the IM. For comparison reasons, absolute values of the correlation are presented. De Biaso [35] adopted an arbitrary upper limit of 0.20 as a cut-off value to assess the IM's sufficiency.

The above methodologies evaluate the criterion of sufficiency in an absolute sense. However, it is difficult to satisfy the sufficiency measure of a scalar IM since that requires the independence of all possible values of IM from the examined ground motion characteristics [36]. Jalayer et al [36] introduced the concept of relative sufficiency measure (RSM) to quantify the prediction capability of an IM instead of the reference IM for a certain EDP. The evaluation of RSM is based on relative entropy and measures the similarity of two probability density functions (PDF) (e.g., $p(EDP|IM_i)$, and $p(EDP|IM_j)$) [37]. The RSM can be approximately calculated for a suite of n ground motion by the following expression:

$$I(EDP|IM_2|IM_1) \approx \frac{1}{n}\sum_{i=1}^{n} \log_2 \left( \frac{\beta_{EDP|IM_1}\Phi\left(\frac{\ln EDP_i - \ln \widehat{EDP}|IM_{2,i}}{\beta_{EDP|IM_2}}\right)}{\beta_{EDP|IM_2}\left(\frac{\ln EDP_i - \ln \widehat{EDP}|IM_{1,i}}{\beta_{EDP|IM_1}}\right)} \right) \quad (4)$$

where, $IM_1$ is the reference and $IM_2$ is the candidate IM.

In general, the RSM method quantifies the amount of information gained or lost in the case of using $IM_2$ instead of $IM_1$. Positive values of $I(EDP|IM_2|IM_1)$ indicate that $IM_2$ is more sufficient than $IM_1$, while negative values imply that $IM_2$ is less sufficient of $IM_1$.

So, in this study, the sufficiency of an IM is evaluated based on a) the p-value of the regression analysis, b) the Spearman's rank correlation coefficient and c) the relative sufficiency measure (RSM). In the case of p-value and Spearman's rank correlation coefficient the IMs' sufficiency is evaluated for the examined ground motion characteristic ($M_w$ and $R_{rup}$), while RSM examines the sufficiency property in a relative sense. The IMs' sufficiency is verified for three separation gap distances between the adjacent structures and incorporates EDPs in terms of $\delta_{max}$, $IDR_{max}$, and $\mu_{\varphi,max}$.

Figure 4 shows the evaluation of the IMs' sufficiency in the case of $\delta_{max}$ with respect to $M_w$ and $R_{rup}$. Results indicate that the structural dependent IMs (except ASI) are independent of $M_w$ (blue line) (p-value>0.05). From the acceleration-based IMs only $I_a$, $I_c$, and CAV satisfy the criterion of sufficiency and that may be attributed to the fact that these IMs are characterized by the duration, the amplitude and the frequency of the ground motion. The velocity-based and the displacement-based independent IMs are also independent of $M_w$ except of MIV and SED. Rating the IMs sufficiency with respect to $R_{rup}$, the structural dependent IMs and the acceleration-based IMs are deduced to be independent (Fig. 4 – green line), since p-values are greater than 0.05. The velocity related IMs (except of $RMS_v$ and SED) result to be more sufficient than the displacement-based IMs. Additionally, the structural independent PGV,

SMV, $I_a$ and $I_c$ are simultaneously independent of $M_w$ and $R_{rup}$. Based on Spearman's approach, $I_a$, $I_c$, PGV, SMV, MIV $S_{v,T1}$,VSI, HI, and $S_{a,avg}$ are simultaneously independent of $M_w$ and $R_{rup}$.

In Figure 5, the evaluation of the IMs' sufficiency in terms of $IDR_{max}$ for all the examined structural pounding cases, is presented. As can be observed, the p-values of the structural dependent IMs and the p-values of the velocity-based PGV, $RMS_v$, SED, and SMV are around the limit value of 0.05 both on $M_w$ and $R_{rup}$. However, the acceleration-based IMs of $RMS_a$, $I_a$, and $I_c$, seem to be the most sufficient for predicting $IDR_{max}$ demands of the 8-story structure with respect to the ground motion characteristics. Based on Spearman's rank correlation coefficient approach, the velocity-based PGV, $RMS_v$, SED, and SMV are insufficient IMs to predict the $IDR_{max}$ demands of the 8-story RC structure (Fig. 5). The corresponding evaluation of the structural dependent IMs introduces the $S_{v,T1}$, HI, and $S_{a,avg}$ insufficient on both seismic characteristics $M_w$ and $R_{rup}$ (Fig.5).

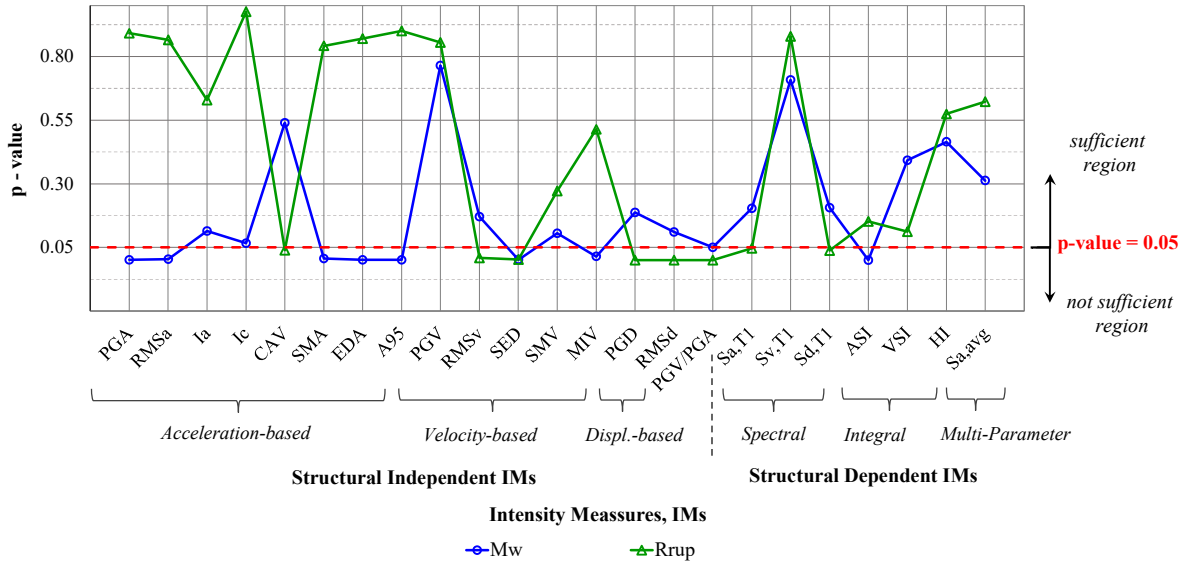


a) p-value

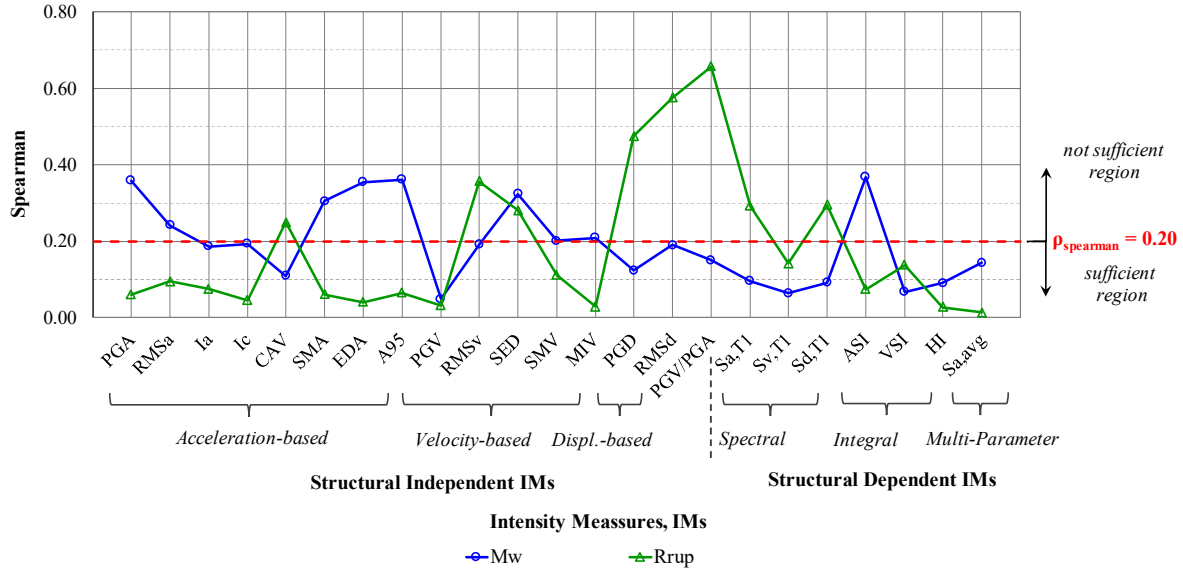


b) Spearman's rank correlation coefficient

**Figure 4.** Evaluation of the IMs' sufficiency with the maximum displacement at the top level of the contact point ($\delta_{max}$) based on a) p-value and b) Spearman's rank correlation coefficient with respect to the magnitude ($M_w$) and to source-to-site distance ($R_{rup}$).

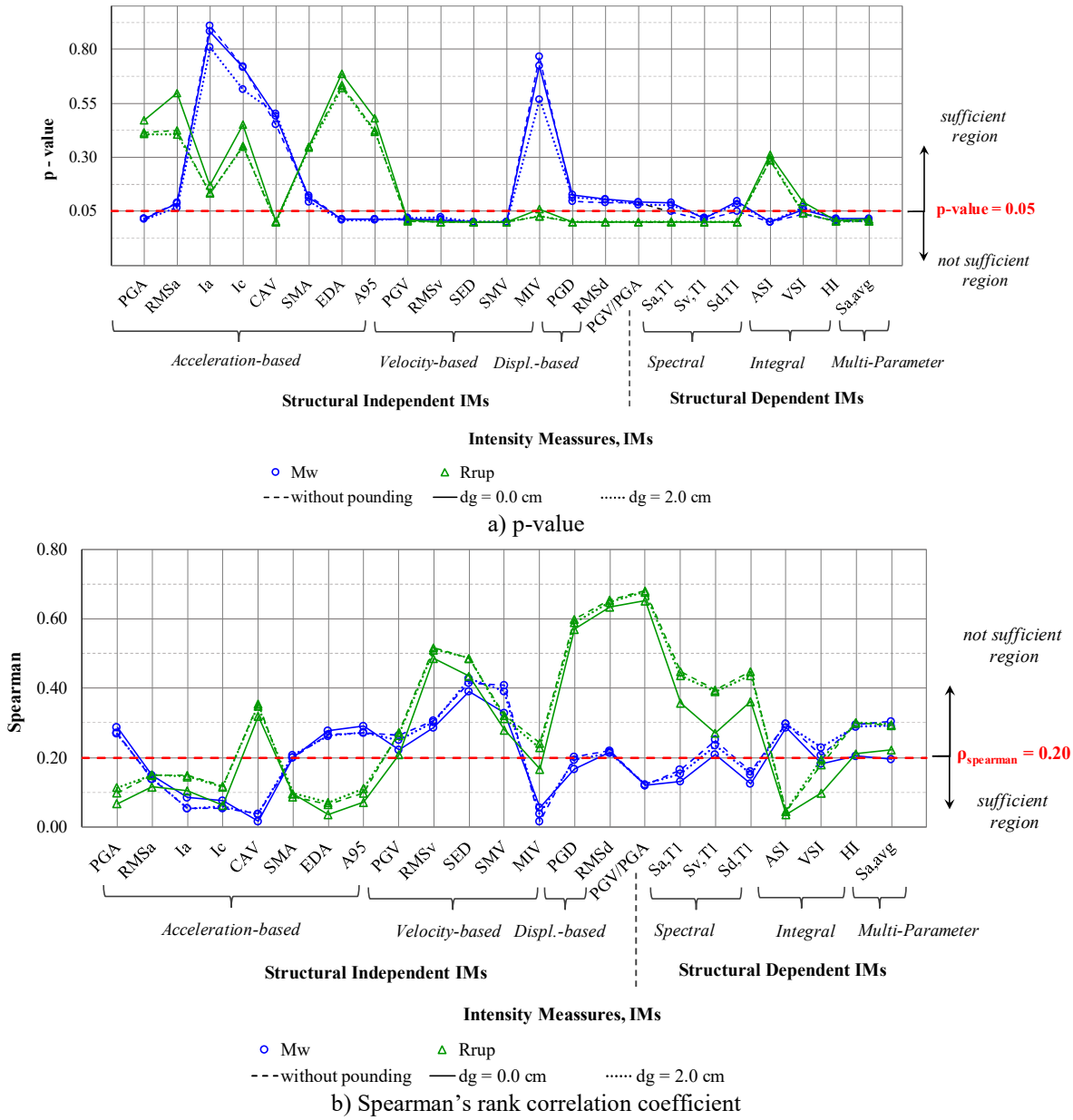


**Figure 5.** Evaluation of the IMs' sufficiency with the maximum interstory drift ($IDR_{max}$-$\%h_{st}$) based on a) p-value and b) Spearman' rank correlation coefficient with respect to the magnitude ($M_w$), and the source-to-site distance ($R_{rup}$).

Furthermore, the results of this study show that the pounding effect does not significantly alter the evaluation of the sufficiency property (Fig. 5). In fact, similar values of p-values and Spearman's correlation coefficients have been estimated either with or without considering the structural pounding effect. Only in the case of separation gap distance $d_g$ = 0.0 cm the p-values with respect to $R_{rup}$, (green lines) are slightly shifted to higher values for some IMs, while the separation gap distance $d_g$ = 2.0 cm slightly reduces the interdependency of $I_a$, $I_c$ and MIV in the case of $M_w$ (blue lines in Fig. 5). However, the verification of the IMs' sufficiency for predicting the local demands of the column is altered due to the pounding effect (Fig. 6).

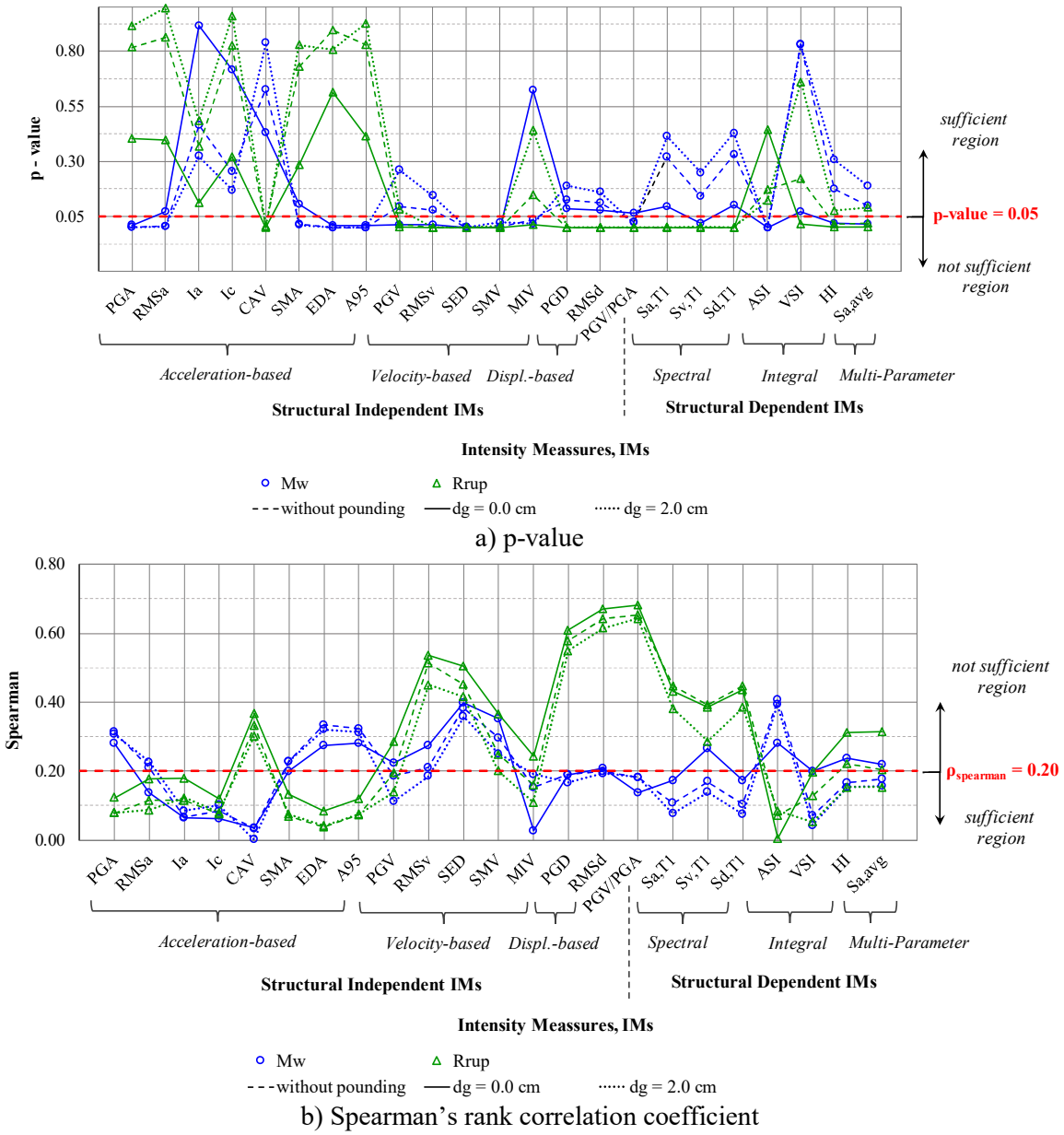


**Figure 6.** Evaluation of the IMs' sufficiency with the maximum curvature ductility $\mu_{\varphi,max}$ of the column C20 based on a) p-value and b) Spearman' rank correlation coefficient with respect to the magnitude ($M_w$), and the source-to-site distance ($R_{rup}$).

For example, as can be observed in Figure 6, the p-values of the structural independent IMs with respect to $R_{rup}$ (green lines) are decreased in the case of $d_g$=0.0 cm compared to the corresponding results without the pounding or $d_g$= 2.0 cm. On the other hand, the p-values of $RMS_a$, $I_a$, $I_c$, and MIV with respect to $M_w$ (blue lines) are increased in the case of $d_g$=0.0 cm. Slight differences in the estimated values of Spearman's correlation coefficients between the examined pounding cases are observed based on the results in Fig. 6b. Based on the p-value and Spearman's method only $I_a$ and $I_c$ are sufficient on $M_w$ and $R_{rup}$ for predicting the $\mu_{\varphi,max}$ of the examined column. The above results (Figs. 2-6) indicate that the satisfaction of IM's sufficiency implies lack of IM's efficiency and vice versa. For instance, the seismic measures $I_a$ and $I_c$ which are independent on $M_w$ and $R_{rup}$ do not pass the efficiency requirements since $\beta_{EDP|IM}$ is greater than the acceptable limit. On the contrary, the more efficient IMs ($\beta_{EDP|IM}$ <0.4)

result to be insufficient for the examined ground motion characteristics. Thereafter, the IMs' sufficiency is evaluated based on the RSM. As reference IM is considered the first-mode spectral acceleration ($S_{a,T1}$) since it is the most commonly IM used in structural engineering.

So, in Figure 7, the verification of the relative sufficiency of the $S_{a,T1}$ with the other IMs, is presented. Demands in terms of $\delta_{max}$, $IDR_{max}$, and $\mu_{\varphi,max}$ are involved for the three examined separation gap distances between the adjacent structures. In the case of $\delta_{max}$, the intensity measure $S_{a,T1}$ provides more information than the other IMs, while is equally sufficient with $S_{d,T1}$. For example, the SMA is insufficient compared to the $S_{a,T1}$ since it provides 1.967 times less information regarding the demand $\delta_{max}$ (Fig. 7a). Evaluating the relative sufficiency in the case of $IDR_{max}$ it can be observed that the structural dependent IMs (except ASI) provide more information than $S_{a,T1}$ (Fig. 7b). Thus, $S_{a,T1}$ is more sufficient in relative sense than the examined independent IMs but it is insufficient with respect to the other structural dependent IMs. Also, it can be observed that considering the pounding effect, the RSM is slightly moved towards higher values for $d_g = 0.0$cm (Fig. 7b). $S_{d,T1}$, HI, $S_{a,avg}$, and MIV are relatively more sufficient than $S_{a,T1}$ for predicting the local demands of the column in terms of $\mu_{\varphi,max}$ (Fig. 7c). On the other hand, $S_{a,T1}$ is equally sufficient with PGV, $S_{v,T1}$, and ASI. Increased values of RSM are observed in the case of $d_g = 0.0$ cm in comparison to the corresponding values without pounding. In the case of $d_g = 2.0$ cm the RSMs are less than the evaluated ones based on the free vibration of the 8-story RC frame structure.

## 4 CONCLUSIONS

In this study, criteria of efficiency and sufficiency are used to identify an adequate IM for the probabilistic assessment of the earthquake-induced pounding between adjacent RC structures. Different methodologies are utilized to estimate the predictive capability of the IMs and their dependence with respect to the ground motion characteristics $M_w$ and $R_{rup}$. Based on the results of this study the following outcomes are noted:

IMs' efficiency

- The structural dependent IMs are more efficient in predicting the examined seismic demands of the 8-story RC frame structure.
- The least effective structural independent IMs are the acceleration-based and the displacement-based, with the PGV/PGA to be the most invalid indicator to describe the demands of the structure.
- IMs' efficiency seems not to be affected when the structural pounding is involved.

IMs' sufficiency

- In the case of $\delta_{max}$ the sufficient IMs (independent of $M_w$ and $R_{rup}$) are; PGV, SMV, $I_a$, $I_c$, $S_{v,T1}$, VSI, HI, and $S_{a,avg}$.
- The acceleration-based $I_a$, $I_c$, and $RMS_a$ seem to be sufficient measures for predicting $IDR_{max}$ demands of the 8-story structure with respect to the ground motion characteristics.
- The acceleration-based $I_a$, and $I_c$ are also sufficient for predicting the $\mu_{\varphi,max}$ of the examined column.
- In all the examined cases, the local demands of the critical column that suffers the pounding effect alter the results of the IMs' sufficiency.

Finally, based on the above notations, it can be concluded that an optimal IM that satisfies simultaneously the criteria of efficiency and sufficiency is difficult to be identified. Usually, the satisfaction of efficiency indicates a lack of sufficiency and vice versa. Nevertheless, the relative sufficiency measure of the IMs indicates the superiority of $S_{a,T1}$ compared to the structural independent IMs.

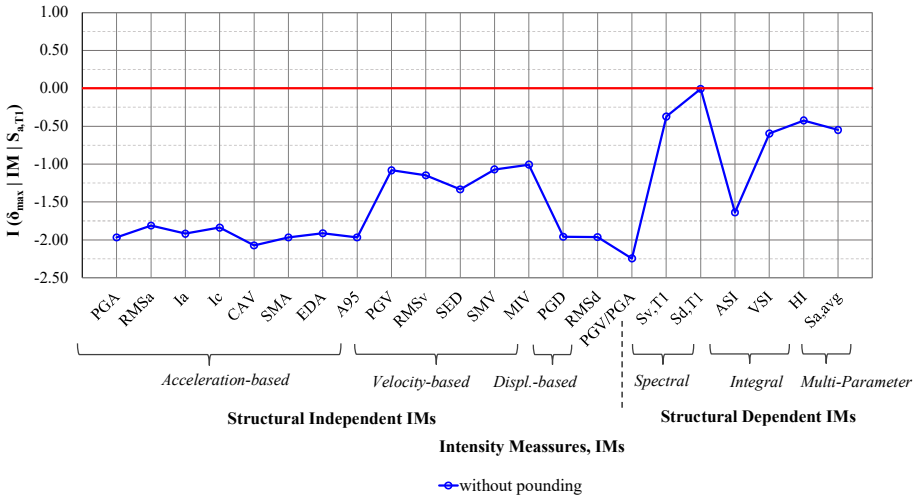


(a)

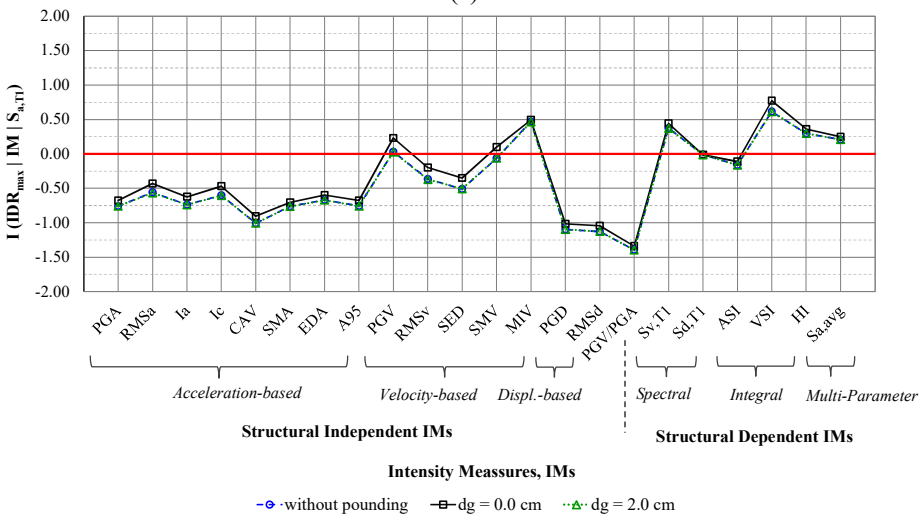


(b)

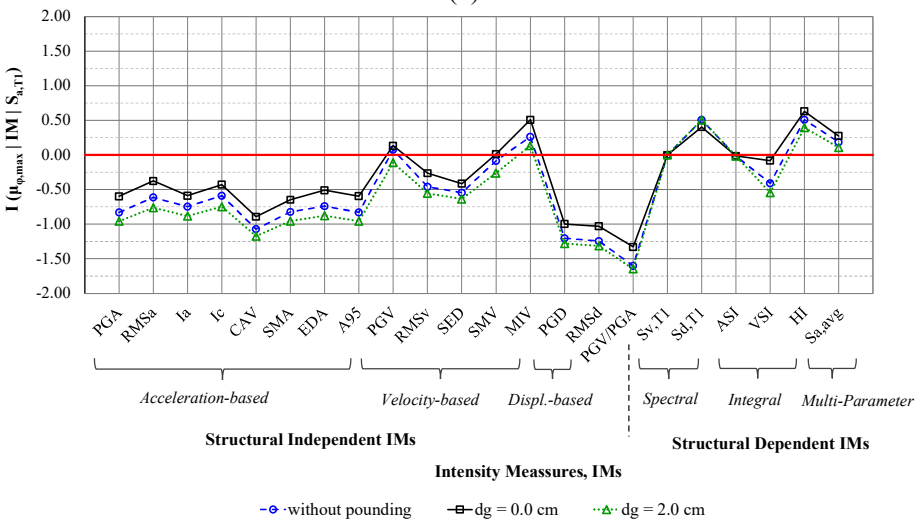


(c)

**Figure 7.** Evaluating the relative sufficiency of the $S_{a,T1}$ in the case of (a) maximum interstory drift ($IDR_{max}$-%$h_{st}$), (b) maximum displacement at the top level of the contact point ($\delta_{max}$), and c) the maximum curvature ductility $\mu_{\varphi,max}$ of the column C20.

## ACKNOWLEDGEMENTS

«This research is co-financed by Greece and the European Union (European Social Fund-ESF) through the Operational Programme «Human Resources Development, Education and Lifelong Learning» in the context of the Act "Enhancing Human Resources Research Potential by undertaking a Doctoral Research" Sub-action 2: IKY Scholarship Programme for PhD candidates in the Greek Universities».

## REFERENCES

[1] C.A. Cornell, F. Jalayer, R.O. Hamburger, D.A. Foutch, Probabilistic Basis for 2000 SAC Federal Emergency Management Agency Steel Moment Frame Guidelines. *Journal of Structural Engineering,* **128**(4), 526–533, 2002.

[2] N. Shome, Probabilistic seismic demand analysis of nonlinear structures. *Report No. RMS-35,* Department of Civil Engineering, Stanford University, 1999.

[3] N. Luco, C.A. Cornell, Structure-specific scalar intensity measures for near-source and ordinary earthquake ground motions. *Earthquake Spectra*, **23**(2), 357–392, 2007.

[4] J.E. Padgett, B.G. Nielson, R. DesRoches, Selection of optimal intensity measures in probabilistic seismic demand models of highway bridge portfolios. *Earthquake Engineering and Structural Dynamics,* **37**(5), 711–725, 2008.

[5] P. Giovenale, C.A. Cornell, L. Esteva, Comparing the adequacy of alternative ground motion intensity measures for the estimation of structural responses. *Earthquake Engineering and Structural Dynamics,* **33**(8), 951–979, 2004.

[6] S.L. Kramer, *Geotechnical Earthquake Engineering 1st Edition,* Prentice Hall, 1996.

[7] J.W. Reed, N. Anderson, N.C. Chokshi, R.P. Kennedy, W.J. Metevia, D.K. Ostrom, J.D. Stevenson, A criterion for determining exceedance of the operating basis earthquake. *EPRI Report NP-5930*, Electric Power Research Institute, Palo Alto, California, **18**(4), 805-810, 1988.

[8] O.W. Nuttli, The relation of sustained maximum ground acceleration and velocity to earthquake intensity and magnitude. *Paper S-71-1, Report 16, U.S. Army Corps of Engineers*, Waterways Experiment Station, Vicksburg, Mississippi, 1979.

[9] G.W. Housner, P.C. Jennings, Generation of Artificial Earthquakes. *ASCE Journal of the Engineering Mechanics,* **90**(1), 113-150, 1964.

[10] A. Arias, A measure of earthquake intensity. *Seismic Design for Nuclear Power Plants*, 438–483, 1970.

[11] Y.J. Park, A.H.S. Ang, Y.K. Wen, Seismic damage analysis of reinforced concrete buildings. *ASCE Journal of Structural Engineering,* **111**(4), 740–757, 1985

[12] J.C. Anderson, V.V. Bertero, Uncertainties in Establishing Design Earthquakes. *ASCE Journal of Structural Engineering,* **113**(8), 1709-1724, 1987.

[13] S.K. Sarma, K.S. Yang, An evaluation of strong motion records and a new parameter A95. *Earthquake Engineering and Structural Dynamics,* **15**, 119-132, 1987.

[14] J.L. Von Thun, L.H. Rochim, G.A. Scott, J.A. Wilson, Earthquake ground motions for design and analysis of dams. *Earthquake Engineering and Soil Dynamics II - Recent Advances in Ground-Motion Evaluation,* **20**, 463-481, 1988.

[15] E. Dimitrakopoulos, A. Kappos, N. Makris, Dimensional analysis of yielding and pounding structures for records without distinct pulses. *Soil Dynamics and Earthquake Engineering* **29**, 1170-1180, 2009.

[16] G.W. Housner, Spectrum intensities of strong motion earthquakes. *Symposium on Earthquake and Blast Effects on Structures*, Los Angeles, California, USA, 1952.

[17] M. Bianchini, P.P. Diotallevi, J.W. Baker, Prediction of Inelastic Structural Response Using an Average of Spectral Accelerations, *10th International Conference on Structural Safety and Reliability* (ICOSSAR09) Osaka, Japan, 2009.

[18] J.W. Baker, C.A. Cornell, Spectral shape, epsilon and record selection. *Earthquake Engineering and Structural Dynamics,* **35**(9), 1077–1095, 2006.

[19] P.P. Cordova, G.G. Deierlein, S.S Mehanny, C.A. Cornell, Development of a two-parameter seismic intensity measure and probabilistic assessment procedure. *2nd US-Japan workshop on Performance-Based Earthquake Engineering Methodology for reinforced concrete building structures*, Sapporo, Japan, 2000.

[20] L. Lin, N. Naumoski, N. Saatcioglu, S. Foo, Improved intensity measures for probabilistic seismic demand analysis. Part 1: development of improved intensity measures. *Canadian Journal of Civil Engineering,* **38**(1), 79–88, 2011.

[21] F. Freddi, A. Dall'Asta, J. Padgett, Bilinear Probabilistic Models of the Seismic Response of a Low Ductility Reinforced Concrete Frame. *15th National Conference ANIDIS*, Padova, Italy, 2013.

[22] H. Ebrahimian, F. Jalayer, A. Lucchini, F. Mollaioli, G. Manfredi, Preliminary ranking of alternative scalar and vector intensity measures of ground shaking. *Bulletin of Earthquake Engineering,* **13**(10), 2805–2840, 2015.

[23] F. Mollaioli, A. Lucchini, Y. Cheng, G. Monti, Intensity measures for the seismic response prediction of base-isolated buildings. *Bulletin of Earthquake Engineering,* **11**(5), 1841–1866, 2013.

[24] K. Kostinakis, A. Athanatopoulou, K. Morfidis, Correlation between ground motion intensity measures and seismic damage of 3D R/C buildings. *Engineering Structures,* **82**, 151-167, 2014.

[25] A. Elenas, K. Meskouris, Correlation study between seismic acceleration parameters and damage indices of structure. *Engineering Structures,* **23**(6), 698–704, 2001.

[26] E. Tubaldi, F. Freddi, M. Barbato, Probabilistic seismic demand and fragility assessment for evaluating the separation distance between adjacent buildings. *11st International Conference on Structural Safety and Reliability (ICOSSAR)*, New York, USA, 2013.

[27] E. Tubaldi, F. Freddi, M. Barbato, Probabilistic seismic demand model for pounding risk assessment. *Earthquake Engineering and Structural Dynamics,* **45**(11), 1743-1758, 2016.

[28] M.G. Flegga, M.J. Favvata, Global and local performance levels on the probabilistic evaluation of the structural pounding effect between adjacent rc structures. *11th International conference on structural dynamics*, EURODYN, Athens, Greece, 2020.

[29] M.G. Flenga, M.J. Favvata, Probabilistic seismic assessment of the pounding risk based on the local demands of a multistory RC frame structure. *Engineering Structures,* **245**(5), 1-17, 2021.

[30] M.G. Flenga, M.J. Favvata, Fragility assessment of the inter-story pounding risk between adjacent reinforced concrete structures based on probabilistic seismic demand models. *13th International Conference on Earthquake Resistant Engineering Structures (ERES)*, Online Conference, 26-28 May, 2021.

[31] M.G. Flenga, M.J. Favvata, Fragility Curves and Probabilistic Seismic Demand Models on the Seismic Assessment of RC Frames Subjected to Structural Pounding. *Applied Sciences*, **11**, 1-24, 2021.

[32] T. Langlade, D. Bertrand, S. Grange, G. Candia, J. Llera, Intensity measures properties and selection for risk analysis on structures subjected to earthquake induced building pounding with a non-smooth contact dynamics method. *8th ECCOMAS Thematic Conference on Computational Methods in Structural Dynamics and Earthquake Engineering (COMPDYN)*, Athens, Greece, 2021.

[33] V. Prakash, G.H. Powell, S. Gampbell, DRAIN-2DX Base Program Description and User's Guide. *UCB/SEMM Report No. 17/93*, University of California, 1993.

[34] M.J. Favvata, Minimum required separation gap for adjacent RC frames with potential inter-story seismic pounding. *Engineering Structures,* **152**, 643–659, 2017.

[35] M. Biasio, Ground motion intensity measures for seismic probabilistic risk analysis. Civil Engineering, Université de Grenoble, 2014.

[36] F. Jalayer, J. Beck, F. Zareian, Analyzing the Sufficiency of Alternative Scalar and Vector Intensity Measures of Ground Shaking Based on Information Theory. *ASCE Journal of Engineering Mechanics,* **138**(3), 307-316, 2012.

[37] S. Theodoridis, *Machine Learning A Bayesian and Optimization Perspective, 2nd Edition*, Academic Press, Elsevier, 2020.

[38] PEER Ground Motion Database; 2011. http://peer.berkeley.edu/peer_ground_motion_database

[39] ESM Database. https://esm-db.eu/#/home

COMPDYN 2023
9th ECCOMAS Thematic Conference on
Computational Methods in Structural Dynamics and Earthquake Engineering
M. Papadrakakis, M. Fragiadakis (eds.)
Athens, Greece, 12-14 June 2023

# INFLUENCE OF BOND-SLIP ON NUMERICAL FRAGILITY CURVES AND STRUCTURAL RELIABILITY OF RC STRUCTURAL INTERNAL BEAM-COLUMN SUB-ASSEMBLY

**L. Audisio[1], M. D'Amato[2] and R. Gigliotti[1]**

[1] DISG, Dept. of Structural and Geotechnics Engineering, Sapienza University of Rome
Via Eudossiana 18, 00184 Rome, Italy
lorenzo.audisio@uniroma1.it, rosario.gigliotti@uniroma1.it

[2] DiCEM, Dept. of European and Mediterranean Cultures: Architecture, Environment and Cultural Heritage, University of Basilicata
Via Lanera, 75100 Matera, Italy
michele.damato@unibas.it

## Abstract

*In this paper results obtained from monotonic nonlinear static analyses performed on Reinforced Concrete (RC) internal beam-column sub-assembly are shown. Bond-slip phenomenon between steel longitudinal bars and surrounding concrete is also taken into account in order to predict the numerical response under lateral actions of the RC internal beam-column sub-assembly investigated.*

*The study is addressed, through parametric models and Monte Carlo simulations, to propose preliminary fragility curves for different damage states of the RC internal beam-column sub-assembly, including materials inherent uncertainties.*

**Keywords:** Bond-Slip, damage states, fragility curves, structural reliability, material uncertainties, Monte Carlo simulations, RC internal beam-column sub-assembly.

## 1 INTRODUCTION

In recent years, structural engineering has increasingly focused on use and development of methodologies for assessing the structural performance based on a probabilistic approach. In this framework, structural or component performance is expressed through a reliability index, related to the failure probability that is the probability that capacity does not satisfy the corresponding demand. To this scope, to date several approaches for calculating structural reliability can be found in the scientific literature, including FORM (First-Order Reliability Methods), SORM (Second-Order Reliability Methods) and numerical methods (Monte-Carlo simulation) [1].

Seismic assessment including economic losses may be carried out following different approaches. For instance, methodologies for seismic risk assessment based on macro-seismic approach have been recently developed, based on an empirical approaches starting from seismic damage observed on several buildings stocks after seismic events ([2]–[4]).

On the contrary, recently the Performance-Based Earthquake Engineering (PBEE) approach has been developed by Pacific Earthquake Engineering Research (PEER) [5], based on a numerical and probabilistic approach for seismic risk assessment of buildings (Fig.1). Also, the Applied Technology Council (ATC), on commission of Federal Emergency Management Agency (FEMA), proposed guidelines containing the PBEE methodology applicable to both new and existing buildings ([6], [7]).

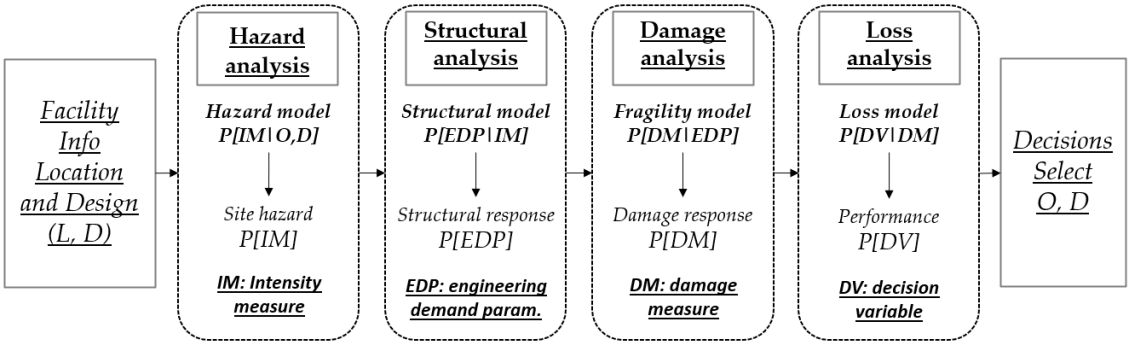


Fig. 1: PBEE schematization [5]

According to the PBEE approach (Fig. 1) Damage Measure – Engineering Demand Parameter (DM-EDP) relationships have a central role in performing the loss analysis. They are often called fragility curves, expressing the exceedance probability of a certain a damage level for a given EDP. The FEMA database P-58 [8] includes a variety of fragility curves of existing reinforced concrete structural and non-structural elements typical of American construction practice. Naturally, the PBEE methodology may be implemented for any type of buildings, requiring in this case specific fragility curves referred to the buildings typologies taken into account. To this scope, to date several studies exist in the literature focusing on the seismic response of existing Reinforced Concrete (RC) buildings designed only for gravity loads with smooth steel bars. As known, under seismic lateral excitations their response is dominated by bond-slips between longitudinal bars and surrounding concrete conspicuously reducing the elements hysteretic capacity ([9], [10], [11]).

In this paper, according to the PBEE methodology, fragility curves of internal beam-column sub-assemblages representative of existing RC buildings built in Italy before '80s with smooth bars are proposed. Monotonic analyses including bond-slips are performed, where uncertainties of material properties (concrete and reinforcing steel) are considered

through Monte Carlo simulations. For this purpose, fragility curves tool is at first extended in order to provide the probability of having a certain section condition (such as yielding in tension or compression, maximum moment) for a given section EDP. Afterwards, fragility curves are derived by varying a given EDP. The results obtained are shown with and without bond-slips and referred to different axial stress ranges.

## 2 NUMERICAL SIMULATIONS

In this study a internal beam-column joint representative of an existing RC building built in Italy before '80s and reinforced with smooth bars is considered (Fig. 1a). The internal joint was tested in [9], where a set of typical internal and external existing RC joints were tested under lateral displacements. More details about this experimental campaign and related results may be found in [9].

Numerical simulations are conducted by means of a Finite Element Model (FEM) of an internal beam-column joint implemented into OpenSees software v. 3.3.0 [12][13] through Python language [14]. ForceBeamColumn fiber elements [15] with a HingeRadau integration method ([16]–[18]) are used, assuming each element elastic in the central region with a fiber length (plastic hinges) only at the element ends (Fig. 1b). Moreover, the nodal panel is considered as a rigid by means of rigid elements. Non-linear stress-strain relationships are considered for materials. In particular, Concrete04 [19] is assigned to concrete fibers, and Steel02 [20] for longitudinal steel in the case of Full-Bond (FB) assumption. Whereas, a multilinear material is assumed when a Model with bond-Slip (MS) is taken into account. The instability of longitudinal bars and the possible interaction between flexural and shear capacity are neglected in this study.

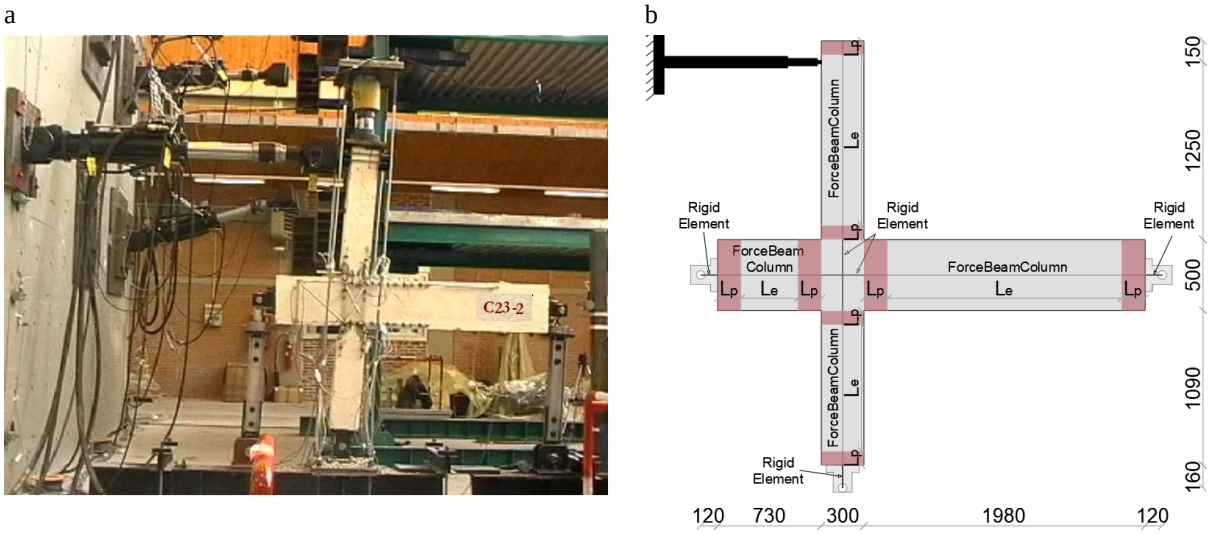


Fig. 2. Internal beam-column sub-assembly: (a) experimental test [9] (b) FEM schematization

Slip phenomenon is considered through a numerical model modifying steel stress-strain relationships of each longitudinal smooth bar for incorporating the Bond-Slips of the longitudinal bars with respect to the surrounding concrete [21]. The model was validated in [22] and subsequently developed to also account for steel hardening [23]. In [24] the model was further extended considering an exponential field for slips, including also a cyclic formulation.

In this study Monte Carlo simulations are performed to consider uncertainties related to material properties. As for bars, AQ50 steel is used usually used in Italy in '50s-'70s [25]. In particular, an average yield stress $f_{ym}$=370,9 MPa with a Coefficient of Variation (CV) of 0,09 are considered. Whereas, for concrete [26] a compressive strength $f_{cm}$=19.53 MPa with a

CV=0.37 are assumed. Finally, the residual bond strength is evaluated according to the formulation proposed in CEB-FIP (2008). Fig. 3 shows in the histograms form for concrete and steel the strength recurrence sampled by means of Monte Carlo simulations. In the same graphs, the Probability Density Function (PDF) considering a normal and log-normal distribution is plotted, too.

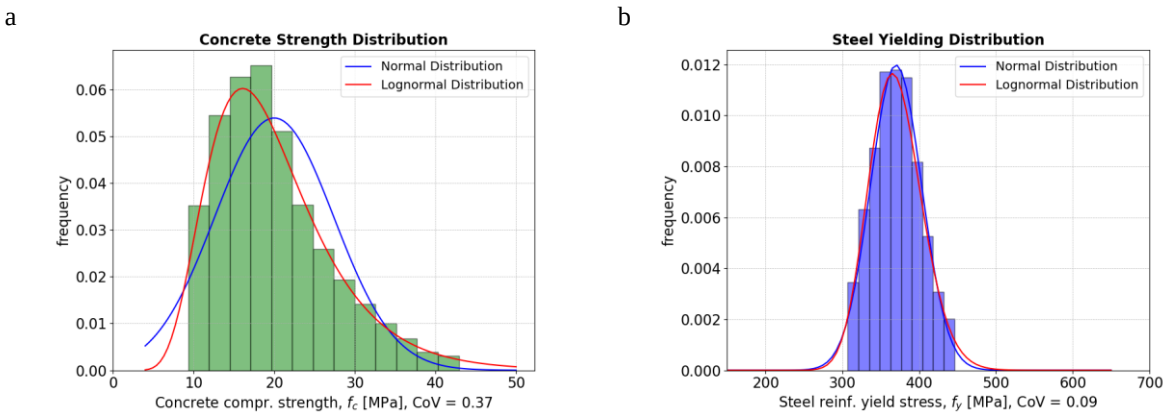


Fig. 3. Material theoretical distribution: (a) Concrete Compressive Strength, (b) Steel Yielding

Table 1 report elements sections details of the internal beam-column joint considered in this study. Numerical investigations are carried out for different axial load ratio ranges ν (10-20%, 20-30%, 30-40%), without considering any P-Δ second-order effect.

| | | Lower column | Upper column | Left beam | | Right beam | |
|---|---|---|---|---|---|---|---|
| Length | L [m] | 1.25 | 1.25 | 0.85 | | 2.1 | |
| Section | B [m] | 0.3 | 0.3 | 0.3 | | 0.3 | |
| | H [m] | 0.3 | 0.3 | 0.5 | | 0.5 | |
| Top reinforcement | φ [mm] | 18 | 18 | 12 | 18 | 12 | 18 |
| | n | 2 | 2 | 2 | 3 | 2 | 3 |
| Bottom reinforcement | φ [mm] | 18 | 18 | 12 | 18 | 12 | 18 |
| | n | 2 | 2 | 2 | 1 | 2 | 1 |
| **Fiber layout** | | 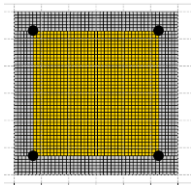 | 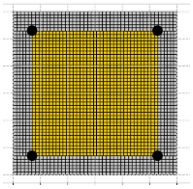 | 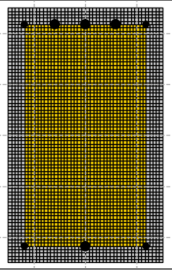 | | 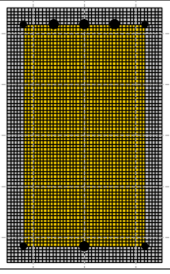 | |

Table 1: Elements Details

## 3 RESULTS

The numerical model adopted for the internal beam-column joint has been firstly validated by comparing it with experimental results. Fig. 4 depicts a comparison in terms of lateral force – displacement at upper column top relationship (F-Δ) between numerical and experimental results [9], [22] are reported. Results are referred to both Full-Bond (FB) and Bond-Slip (BS) of longitudinal bars. Moreover, in the same graph the chord rotation (drift) measured between the lower column base and upper column top is indicated, too. By monitoring

the fibers stress-strain state of the ends sections, it is possible to determine the achievement of several section states (i.e. limit state), such as concrete cracking (when $\varepsilon_{ct}$ is measured at the external deformation of the cover fibers), steel compressive and tensile yield strength (when $\varepsilon_{sy}$ is measured in the reinforcement bars), partial and total failure of the concrete cover (when $\varepsilon_{co}$ and $\varepsilon_{cu}$ is measured at the external or internal deformation of the cover fibers), maximum strength (when the internal beam-column sub-assembly is at maximum force), concrete core failure (when $\varepsilon_{cu}$ is measured within the confined core), steel bar failure (when $\varepsilon_{su}$ is measured in the reinforcement bars). As one may note in Fig. 4, bond-slips effects significantly reduce the lateral stiffness of the internal beam-column joint obtaining a good agreement with the experimental results.

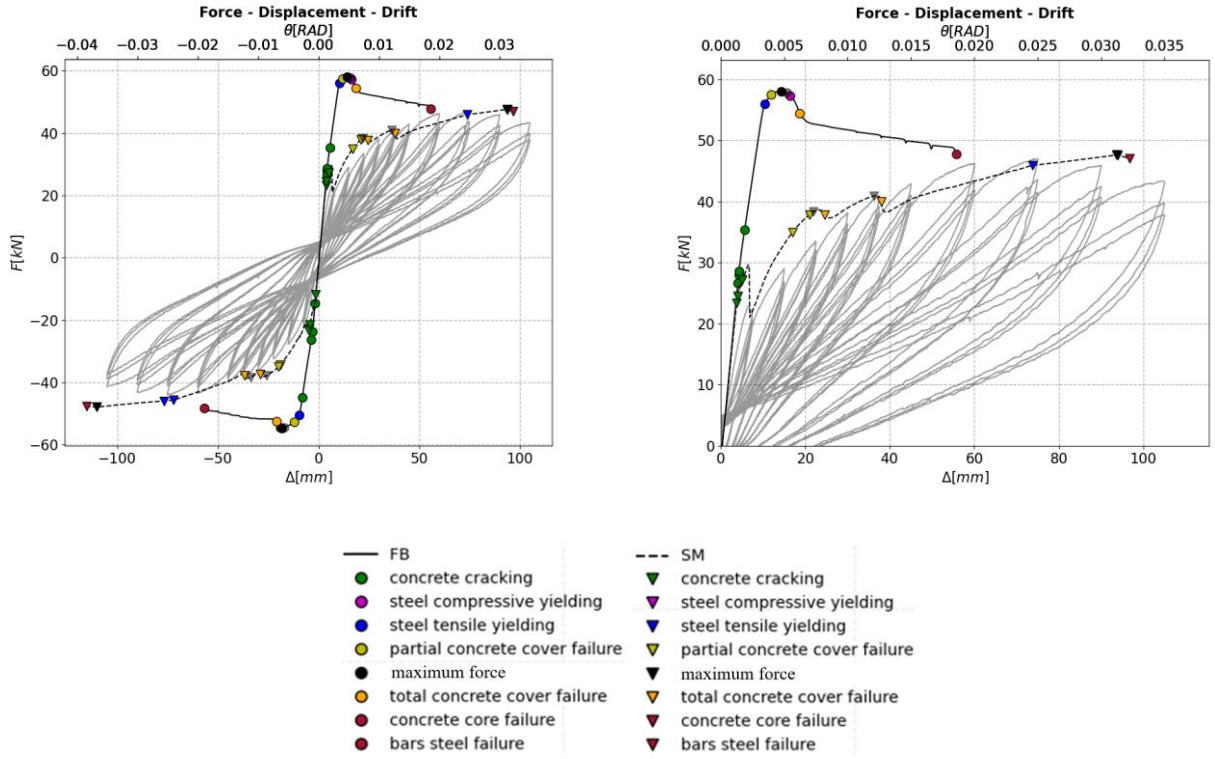


Fig. 4: comparisons with experimental results

From the results obtained, the cumulative probabilistic capacity distribution referring to some particular element conditions can be derived. In Fig.5, for simplicity's sake, the representative element fragility capacity curves refer only to three element conditions, the steel yielding strength in compression ($F_{yc}$) and in tension ($F_{yt}$), and maximum yielding force ($F_{max}$). As one may note that, for a given probability, with the Bond-Slips a force always lower than the one obtained with the Full-Bond assumption is obtained. In this figure three axial load ratio intervals are considered, that are: $\nu$=10-20%, $\nu$=20-30%, $\nu$=30-40%. It is easy to note that when the axial load ratio values increase the tension yielding of longitudinal bars do not occur (Fig.5 b, c).

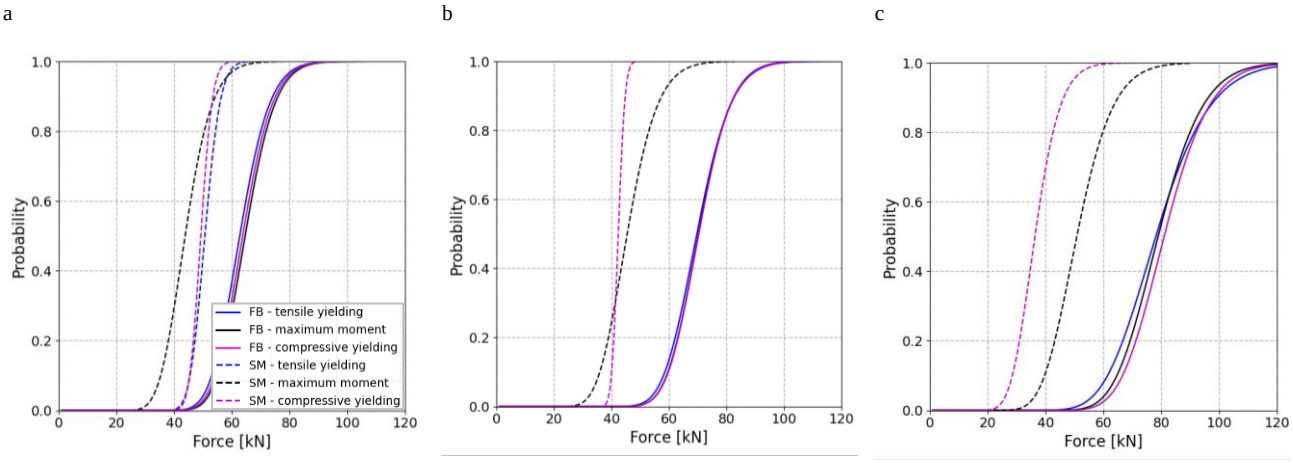


Fig. 5: Probability of having $F_{yt} \leq F^*$, or $F_{yc} \leq F^*$, or $F_{max} \leq F^*$: (a) ν=10-20%, (b) ν=20-30%, (c) ν=30-40%

For completeness a reliability evaluation is also conducted in order to show how bond-slips may affect the reliability index. To this purpose, by assuming an equal demand probability distribution for both the Full-Bond and Bond-Slip models, in Fig.6 the reliability index is calculated with the FORM approach [27]. It is clear to observe that Bond-Slip significantly reduces the reliability of the internal beam-column sub-assembly with respect to the Full-Bond assumption.

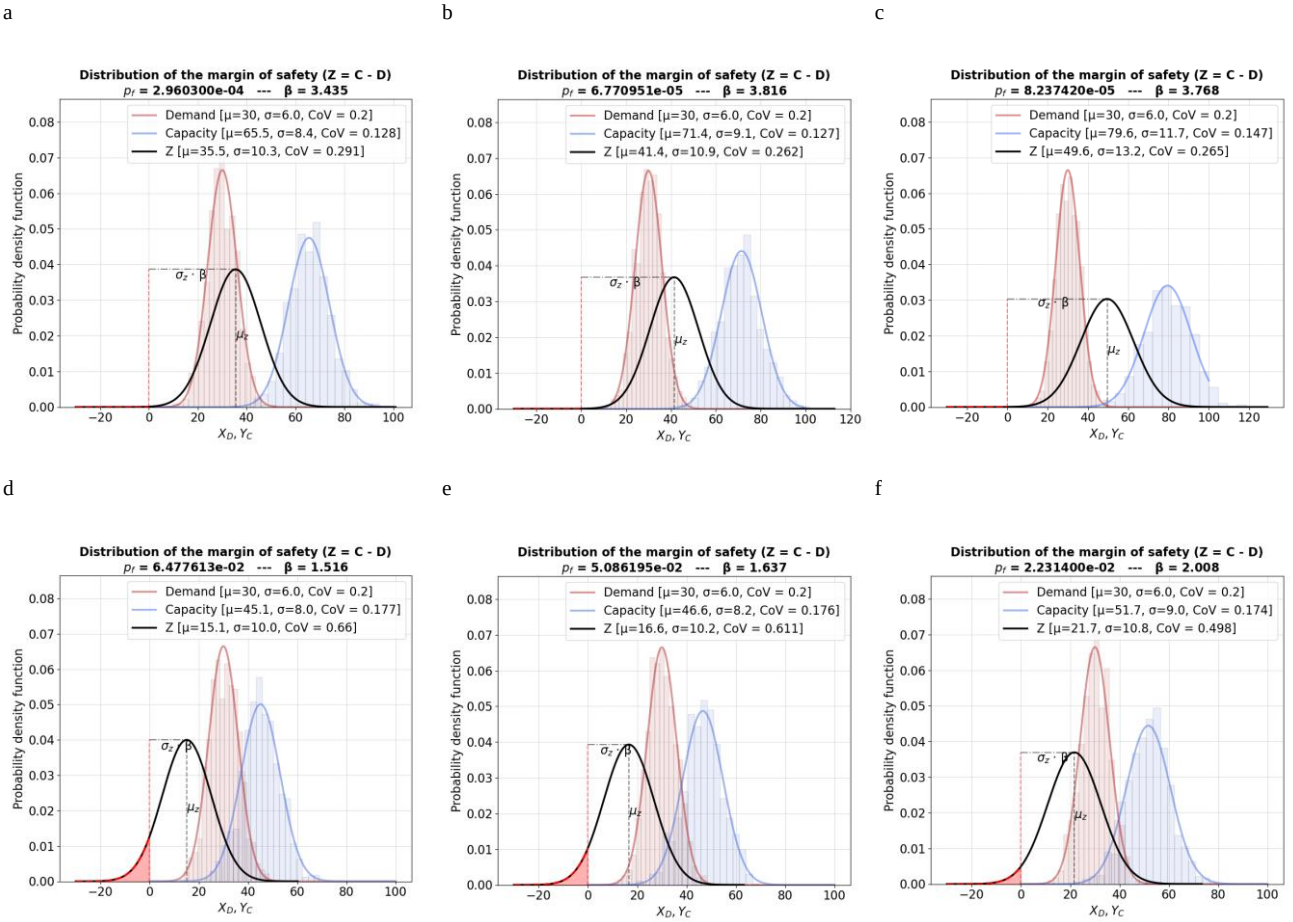


Fig. 6: Reliability index: Full-Bond (a) ν=10-20%, (b) ν=20-30%, (c) ν=30-40%; Bond-Slip (d) ν=10-20%, (e) ν=20-30%, (f) ν=30-40%

The effects of Bond-Slips on the Inter-story Drift Ratio (IDR) are illustrated in Fig. 7. It can be seen that, for a given probability, the IDR corresponding to the three element conditions considered in the Full-Bond case is always lower than that with Bond-Slip. This shows that the Bond-Slip delays the yield point of the steel. Furthermore, in the context of a loss analysis, the curves obtained by considering the Bond-Slip (Fig. 6) would provide a certain advantage, since the probability of obtaining a certain IDR is lower than with the Full-Bond hypothesis. Of course, this conclusion will be better studied in the future, as the definition of damage levels with Bond-Slip should be clearly defined within a seismic risk framework, including a correlation with the required repair cost. These aspects will be further explored in the future.

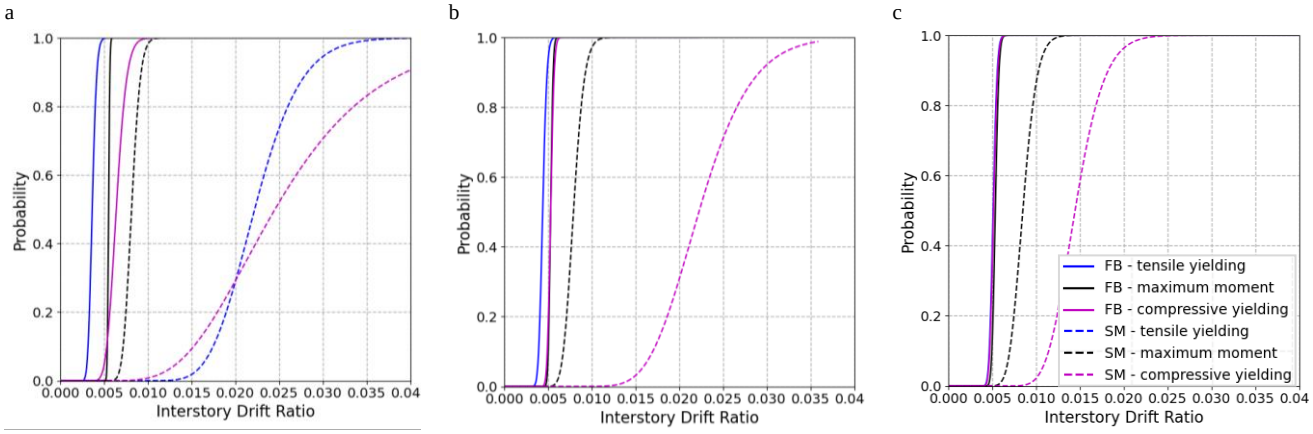


Fig. 7. Probability of having $IDR_{Fyt} \leq IDR^*$, or $IDR_{Fyc} \leq IDR^*$, or $IDR_{Fmax.} \leq IDR^*$: (a) ν=10-20%, (b) ν=20-30%, (c) ν=30-40%

## 4 EVALUATION OF FRAGILITY FUNCTIONS

In order to derive the fragility curves, it is necessary to identify the damage states [28] for elements in which Bond-Slip occurs. In this study, three damage states (DS1, DS2, DS3) are assumed for low-detail elements reinforced with plain bars, which are identified as a function of the damage state of the cover and core.

Numerically, the damage state can be expressed through the deformation state of the section of the elements. In particular, with regard to the damage state of the concrete cover, it is assumed that: DS1 is reached when the external unconfined concrete deformation $\varepsilon_{c0}$ is measured; DS2 corresponds to cover failure (when $\varepsilon_{cu}$ is measured at the external deformation of the cover fibers); and DS3 is assigned when the ultimate deformation of the confined concrete is obtained (when $\varepsilon_{cu}$ is measured within the confined core).

Fragility curves are derived by knowing the parameters θ and β, that may be derived with the maximum likelihood criterion, where the likelihood function is the following [29], [30]:

$$\mathcal{L}(\vartheta,\beta) = \prod_{j=1}^{m} \binom{k_j}{n_j} \Phi\left(\frac{\ln\left(\frac{EDP}{\vartheta}\right)}{\beta}\right)^{k_j} \left[1 - \Phi\left(\left[\frac{\ln\left(\frac{EDP}{\vartheta}\right)}{\beta}\right]\right)\right]^{n_j - k_j} \quad j = 0, \dots, m \tag{1}$$

where the binomial probability distribution is assumed for calculating the probability of observing $k_j$ analysis with a damage equal or greater than a specific value; $n_j$ is the total number of analyses.

Hence, the parameters θ and β for each fragility function are obtained by maximizing the logarithm of the likelihood function, which is expressed with:

$$(\hat{\vartheta},\hat{\beta}) = arg\ max \sum_{j=1}^{m} \left\{ ln\binom{k_j}{n_j} + k_j ln\left[\Phi\left(\frac{\ln\left(\frac{EDP}{\vartheta}\right)}{\beta}\right)\right] + (n_j - k_j) ln\left[\Phi\left(\frac{\ln\left(\frac{EDP}{\vartheta}\right)}{\beta}\right)\right]\right\} \quad j = 0, \dots, m \quad (2)$$

where (θ, β) correspond, respectively, to the median value and the standard deviation of the logarithm of EDP, allowing to have the most likely fragility curve.

Fig. 8 plots the fragility curves obtained for existing RC internal beam-column sub-assembly designed for vertical loads for the concrete damage states, considering both Full-Bond (continuous curves) and the Bond-Slip (dashed curved) and three intervals of axial load ratio. From the results obtained, it can be stated that the Bond-Slip phenomenon induces a rightward shift of the fragility curves, due to greater deformability of internal beam-column sub-assembly.

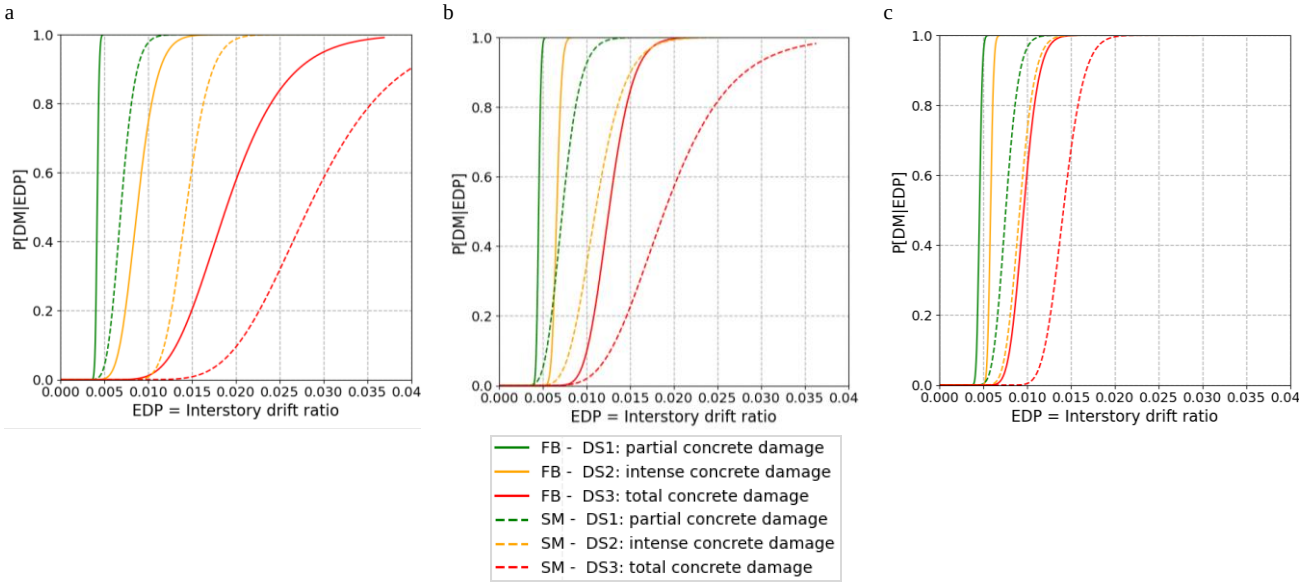


Fig. 8. Fragility functions for the damage level of concrete: (a) ν=10-20%, (b) ν=20-30%, (c) ν=30-40%

## 5 CONCLUSIONS

In this work, monotonic non-linear static analyses have been performed on an existing RC internal beam-column sub-assembly with smooth bars, in order to propose preliminary fragility curves to be implemented within the PBEE framework. The internal beam-column sub-assembly considered is representative of typical existing RC buildings constructed in Italy before the 1980s, and designed for vertical loads with smooth bars. The fragility curves have been derived including the Bond-Slip phenomenon [21], and taking into account the materials uncertainties by means of Monte Carlo simulations.

The results obtained confirm that, according to the PBEE methodology, the Bond-Slip has a relevant impact on the structural analysis, modifying the response of the elements in terms of both strength and deformability. In addition, it has been shown that the phenomenon of slip significantly reduces structural reliability. Furthermore, it is clearly illustrated that, for the element analyzed, Bond-Slips can significantly modify the fragility curves of the concrete damage state compared to those derived with the Full-Bond hypothesis.

The proposed method may be adopted in the future for the development of fragility curves of other structural components to be implemented within the PBEE methodology in order to perform seismic risk analyses.

## REFERENCES


[1] R. E. Melchers and A. T. Beck, *Structural Reliability Analysis and Prediction*. 2018.

[2] M. Tatangelo, L. Audisio, M. D'Amato, and R. Gigliotti, "Seismic risk analysis on masonry buildings damaged by L ' Aquila Seismic risk analysis on masonry buildings damaged by L ' Aquila 2009 and Emilia 2012 earthquakes 2009 and Emilia 2012 earthquakes," *Procedia Struct. Integr.*, vol. 44, no. 2022, pp. 990–997, 2023, doi: 10.1016/j.prostr.2023.01.128.

[3] R. Laguardia, M. D'Amato, M. Coltellacci, G. Di Trocchio, and R. Gigliotti, "Fragility Curves and Economic Loss Assessment of RC Buildings after L'Aquila 2009 Earthquake," *J. Earthq. Eng.*, 2022, doi: 10.1080/13632469.2022.2038726.

[4] M. D'Amato, R. Laguardia, G. Di Trocchio, M. Coltellacci, and R. Gigliotti, "Seismic Risk Assessment for Masonry Buildings Typologies from L'Aquila 2009 Earthquake Damage Data," *J. Earthq. Eng.*, vol. 00, no. 00, pp. 1–35, 2020, doi: 10.1080/13632469.2020.1835750.

[5] J. Moehle and G. G. Deierlein, "A framework methodology for performance-based earthquake engineering," *13Th World Conf. Earthq. Eng.*, no. February, 2004, [Online]. Available: https://www.researchgate.net/publication/228706335.

[6] ATC, "FEMA P-58 Seismic Performance Assessment of Buildings, Vol. 1 - Methodology," *Fed. Emerg. Manag. Agency*, vol. 1, no. December 2018, 2018.

[7] ATC, "FEMA P-58 Seismic Performance Assessment of Buildings, Vol. 2 – Implementation Guide," *Fed. Emerg. Manag. Agency*, vol. 2, no. December 2018, 2018.

[8] P. Assessment and C. Tool, "PACT User Manual," pp. 1–48, 2000.

[9] F. Braga, R. Gigliotti, and M. Laterza, "R/C Existing Structures with Smooth Reinforcing Bars: Experimental Behaviour of Beam-Column Joints Subject to Cyclic Lateral Loads," *Open Constr. Build. Technol. J.*, vol. 3, no. 1, pp. 52–67, 2009, doi: 10.2174/1874836800903010052.

[10] M. Laterza, M. D'Amato, and R. Gigliotti, "Modeling of gravity-designed RC sub-assemblages subjected to lateral loads," *Eng. Struct.*, vol. 130, pp. 242–260, 2017, doi: 10.1016/j.engstruct.2016.10.044.

[11] L. Audisio, M. D'Amato, and R. Gigliotti, "Influence of bond-slip on numerical fragility curves of RC structural Influence of bond-slip on numerical fragility curves of RC structural columns columns," *Procedia Struct. Integr.*, vol. 44, no. 2022, pp. 235–242, 2023, doi: 10.1016/j.prostr.2023.01.031.

[12] F. McKenna, G. L. Fenves, and M. H. Scott, "Open System for Earthquake Engineering Simulation," 2000. http://opensees.berkeley.edu.

[13] S. Mazzoni, F. McKenna, M. H. Scott, and G. L. Fenves, "OpenSees Command Language Manual," *Pacific Earthq. Eng. Res. Center.*, 2006.

[14] M. Zhu, F. McKenna, and M. H. Scott, "OpenSeesPy: Python library for the OpenSees finite element framework," *SoftwareX*, vol. 7, pp. 6–11, 2018, doi: 10.1016/j.softx.2017.10.009.

[15] E. Spacone, F. C. Filippou, and F. F. Taucer, "FIBRE BEAM COLUMN MODEL FOR NON-LINEAR ANALYSIS OF R C FRAMES PART II," *Earthq. Eng. Struct. Dyn.*, vol. 25, pp. 727–742, 1996.

[16] M. H. Scott and G. L. Fenves, "Plastic Hinge Integration Methods for Force-Based Beam–Column Elements," *J. Struct. Eng.*, vol. 132, no. 2, pp. 244–252, 2006, doi: 10.1061/(ASCE)0733-9445(2006)132:2(244).

[17] M. H. Scott, "Numerical Integration Options for the Force-Based Beam-Column Element in OpenSees," *Construction*, pp. 1–7, 2011.

[18] M. H. Scott and K. L. Ryan, "Moment-rotation behavior of force-based plastic hinge elements," *Earthq. Spectra*, vol. 29, no. 2, pp. 597–607, 2013, doi: 10.1193/1.4000136.
[19] J. B. Mander, M. J. N. Priestley, and R. Park, "THEORETICAL STRESS-STRAIN MODEL FOR CONFINED CONCRETE," vol. 114, no. 8, pp. 1804–1826, 1989.
[20] F. C. Filippou, E. P. Popov, and V. V. Bertero, "Effects of bond deteroriation on hysteretic behavior of renforce concrete coint," no. August, p. 212, 1983.
[21] F. Braga, R. Gigliotti, M. Laterza, M. D'Amato, and S. K. Kunnath, "Modified Steel Bar Model Incorporating Bond-Slip for Seismic Assessment of Concrete Structures," *J. Struct. Eng.*, vol. 138, no. November, pp. 1342–1350, 2012, doi: 10.1061/(ASCE)ST.1943-541X.0000587.
[22] M. D'Amato, F. Braga, R. Gigliotti, S. K. Kunnath, F. ASCE, and M. Laterza, "Validation of a modified steel bar model incorporating bond-slip for seismic assessment of concrete structures," *J. Struct. ...*, vol. 138, no. November, pp. 1351–1360, 2012, doi: 10.1061/(ASCE)ST.1943-541X.0000588.
[23] F. Braga, S. Caprili, R. Gigliotti, and W. Salvatore, "Hardening slip model for reinforcing steel bars," *Earthq. Struct.*, vol. 9, no. 3, pp. 503–539, 2015, doi: 10.12989/eas.2015.9.3.503.
[24] S. Caprili, F. Mattei, R. Gigliotti, and W. Salvatore, "Modified cyclic steel law including bond-slip for analysis of RC structures with plain bars," *Earthq. Struct.*, vol. 14, no. 3, pp. 187–201, 2018, doi: 10.12989/eas.2018.14.3.187.
[25] G. M. Verderame, P. Ricci, M. Esposito, and F. C. Sansiviero, "Le Caratteristiche Meccaniche degli Acciai Impiegati nelle Strutture in c.a. realizzate dal 1950 al 1980," *XXVI Convegno Naz. AICAP*, 2011.
[26] A. Masi, A. Digrisolo, and G. Santarsiero, "Concrete strength variability in Italian RC buildings: Analysis of a large database of core tests," *Appl. Mech. Mater.*, vol. 597, no. July, pp. 283–290, 2014, doi: 10.4028/www.scientific.net/AMM.597.283.
[27] C. A. Cornell, "A probability based structural code," *J. Am. Concr. Inst.*, vol. 66, no. 12, 1969, doi: 10.14359/7446.
[28] D. Cardone, "Fragility curves and loss functions for RC structural components with smooth rebars," *Earthq. Struct.*, vol. 10, no. 5, pp. 1181–1212, 2016, doi: 10.12989/eas.2016.10.5.1181.
[29] J. W. Baker, "Efficient analytical fragility function fitting using dynamic structural analysis," *Earthq. Spectra*, vol. 31, no. 1, pp. 579–599, 2015, doi: 10.1193/021113EQS025M.
[30] K. Porter, "A Beginner ' s Guide to Fragility, Vulnerability, and Risk," vol. 16, no. April, 2001.

COMPDYN 2023
9th ECCOMAS Thematic Conference on
Computational Methods in Structural Dynamics and Earthquake Engineering
M. Papadrakakis, M. Fragiadakis (eds.)
Athens, Greece, 12-14 June 2023

# NUMERICAL SEISMIC PERFORMANCE INVESTIGATION OF AAC INFILL WALLS WITH FLAT-TRUSS BED-JOINT REINFORCEMENT

**Omer Faruk Halici**[1,2] **and Alper Ilki**[2]

[1] MEF University, Department of Civil Engineering
e-mail: halicio@mef.edu.tr

[2] Istanbul Technical University, Faculty of Civil Engineering
e-mail: halici@itu.edu.tr
e-mail: ailki@itu.edu.tr

## Abstract

*Autoclaved Aerated Concrete (AAC) is a lightweight, energy-efficient and easy-to-transport material. As a result, AAC walls are becoming increasingly common as an infill solution in earthquake-prone areas such as Turkey, Italy, and Greece. Although infills are considered as secondary components in seismic design, they are extremely vulnerable to damage during earthquakes along both in-plane (IP) and out-of-plane (OOP) directions. Previous post-earthquake site examinations revealed that the failure of infill walls can result in serious injuries and casualties. Furthermore, huge economic losses as well as disruption in the functionality of essential buildings that are supposed to be operational after earthquakes may adversely affect the daily life in the earthquake-affected regions. One of the potential methods for increasing the seismic resilience of infill walls is use of bed-joint reinforcement between infill courses. In this paper, the general approaches in the establishment of the numerical finite element model for infill walls with and without bed-joint reinforcement are presented. The developed model was evaluated according to the previous full-scale experimental test results from strength and damage propagation point of view. The model will be used to investigate the response of infills with various bed-joint reinforcement amounts and height-to-length ratios to generalize the seismic performance improvements obtained by the use of flat-truss reinforcement both in the IP and OOP directions.*

**Keywords:** Infill wall, Autoclaved Aerated Concrete (AAC), bed-joint reinforcement, seismic response

## 1 INTRODUCTION

In typical structural systems like reinforced concrete (RC), steel, masonry, etc., infill walls are generally benefitted as separators and thermal insulators. However, these components are typically made of brittle materials and are not given enough attention in structural design procedures, without adequate safety assessments. Recent earthquakes, such as the 2009 L'Aquila, 2011 Van, and 2020 Izmir earthquakes, have highlighted the potential for infill walls to be subjected to severe damages, resulting in significant injuries and loss of life [1-10]. Additionally, the failure of an infill wall can cause significant damage to non-structural elements and expensive equipment in critical facilities such as hospitals, laboratories, and offices, which can disrupt their functionality in the aftermath of earthquakes.

Autoclaved aerated concrete (AAC) is a construction material that is gaining popularity in seismic regions due to its attractive properties such as being precast, lightweight, fire-resistant and energy-efficient, and is one of the widely used materials in infill walls. AAC is a cementitious material that has visible closed air voids providing its low density, which is an advantageous feature to reduce seismic inertia forces. Material properties of AAC are presented in Table 1.

**Table 1:** Mechanical properties of AAC

| Characteristic | | AAC |
|---|---|---|
| Unit weight | ($kg/m^3$) | 400 to 800 |
| Compressive strength | (MPa) | 2.0 to 7.6 |
| Moisture content after autoclaving | (%) | 30 |
| Moisture content in use | (%) | 5 to 15 |
| Coefficient of thermal expansion | (/°C) | $8.1 \times 10^{-6}$ |
| Coefficient of creep | (/ MPa) | $0.72 \times 10^{-4}$ |

The use of bed-joint reinforcement is one of the most promising solutions to enhance the seismic performance of infill walls. Experimental studies have been conducted to investigate the benefits of using bed-joint reinforcements in infill walls made of clay brick and AAC blocks. Calvi and Bolognini [11] evaluated the in-plane (IP) and out-of-plane (OOP) seismic performance of enhancement of infills made of hollow clay bricks. Penna et.al. [12-13] and Penna and Calvi [14] studies investigated and revealed the benefits of using bed-joint reinforcements to enhance the IP and OOP seismic performance of AAC walls.

This paper presents the numerical study performed to investigate the seismic response of AAC infill walls with and without bed-joint reinforcement that are constructed in RC frames. Previous experimental tests investigating the IP and OOP response of unreinforced and bed-joint reinforced AAC infill walls [15] are benefitted to critically evaluate the model performance from strength and damage propagation point of view. The model adequateness and deficiencies are presented.

## 2 TEST PARAMETERS AND EXPERIMENTAL RESULTS

Full-scale experimental tests were performed at Istanbul Technical University Structural and Earthquake Engineering Laboratory. AAC infill walls in RC frames with and without steel flat-truss reinforcements were tested in IP and OOP directions. The matrix of numerically evaluated specimens is presented in Table 2. All specimens were tested in the OOP direction. One specimen of the unreinforced-type specimen and truss-type reinforced specimens were imposed to an IP drift of 0.005 before tested in the OOP direction. The plan view of

truss-type reinforced infill courses is presented in Figure 1. The specimen geometry, RC reinforcement details and the location of the bed-joint reinforced courses in truss-type reinforced specimens are presented in Figure 2.

**Table 2:** Specimen properties

| Specimen Name | Infill Material | Prior In-plane Drift Ratio | Bed-Joint Reinforcement |
|---|---|---|---|
| W_Ref | AAC | - | Unreinforced |
| W_Ref_PIP_0.005 | AAC | 0.005 | Unreinforced |
| W_ Truss _PIP_0.005 | AAC | 0.005 | Flat-truss |

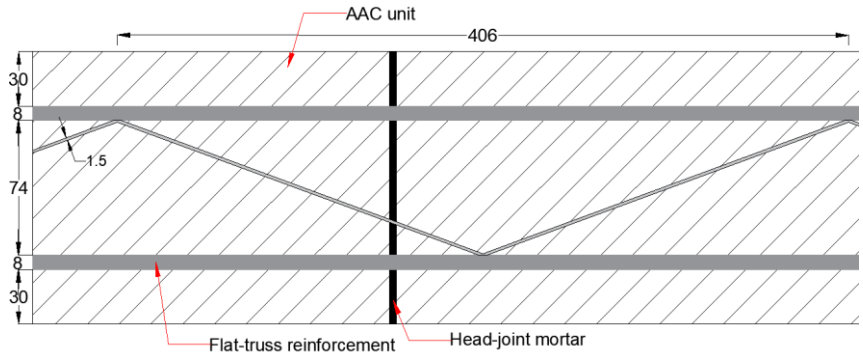


**Figure 1:** Plan view of truss-type reinforced infill course

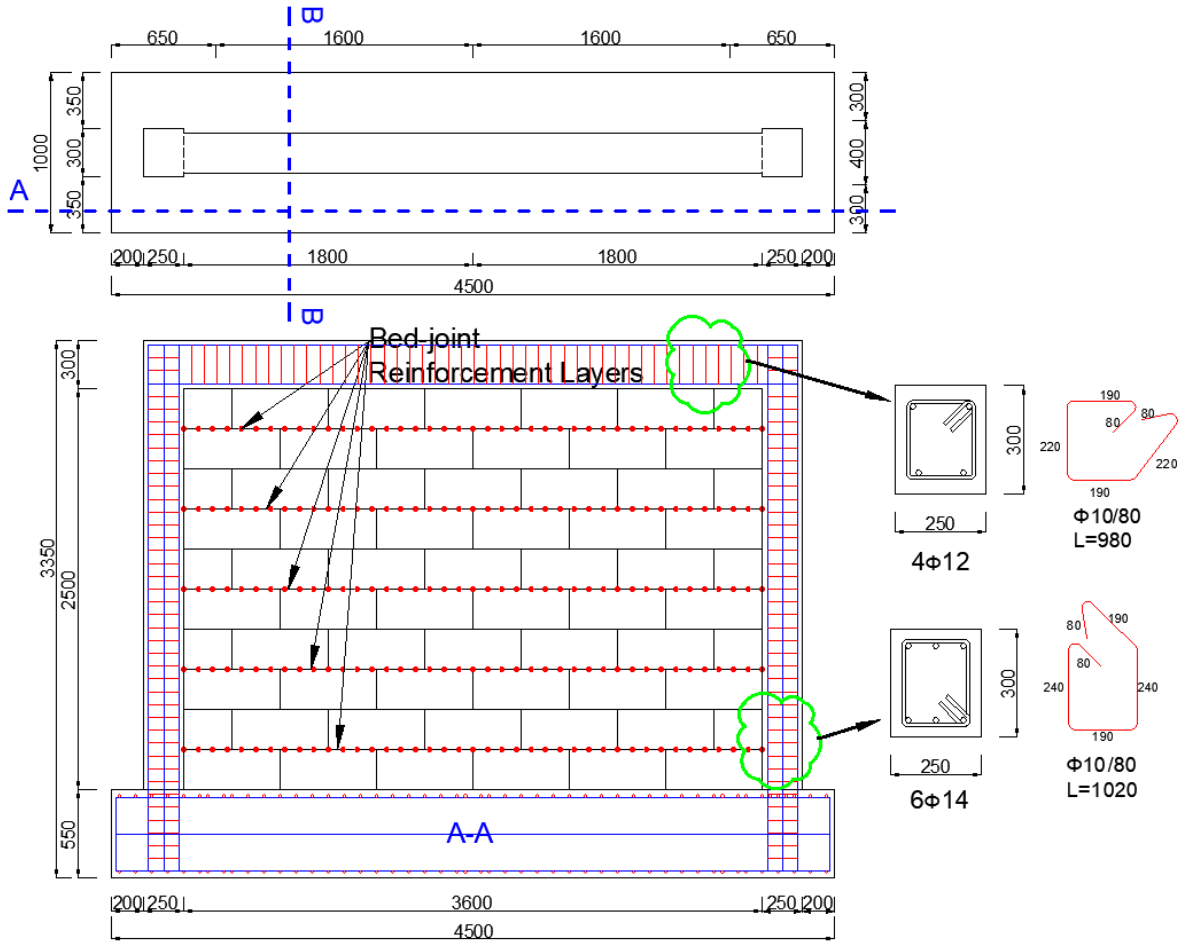


**Figure 2:** Specimen geometry [mm]

All infill walls were constructed with AAC 2.50 strength-class blocks having dimensions of 600×250×150 mm and 300x250x150 mm (length×height×thickness). M10 strength-class thin layer mortar with a thickness of 2 mm was used in the head and bed joints of adjacent AAC blocks in unreinforced specimens. In the reinforced courses of truss-type reinforced specimen, the mortar thickness was 4 mm. In all specimens, there was a 15 mm gap between the top of the AAC infills and the bottom of the RC beams, which was filled with polyurethane spray foam. The loading protocols followed in the IP and OOP tests are presented in Figure 3. The IP tested specimens were imposed to cyclic reversal displacements up to 0.005 drift ratio corresponding to 13.25 mm displacement. The OOP displacements up to 160 mm were applied to the specimens via a 4-point loading apparatus. The OOP displacements were applied at one-third of the length and height of the specimens. The IP and OOP backbone curves of the specimens are presented in Figure 4.

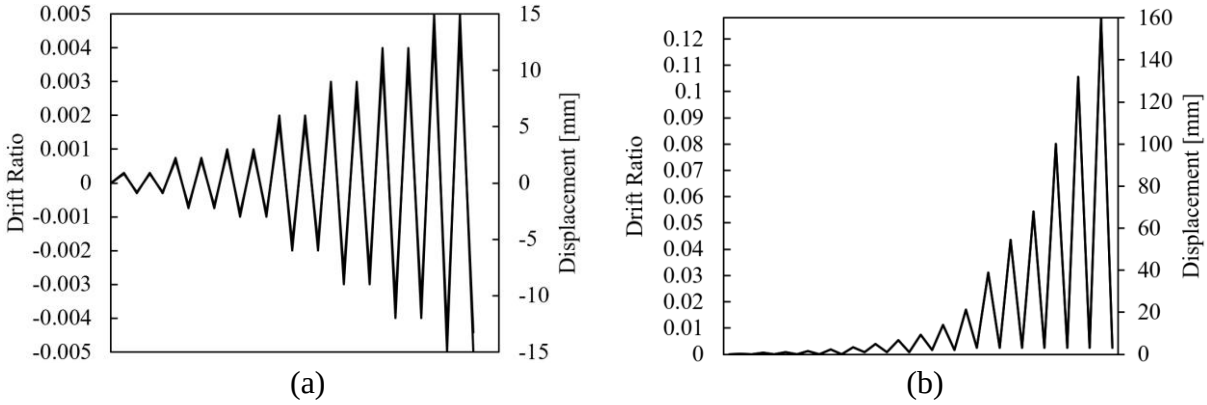


**Figure 3:** Loading protocols: (a) IP cyclic loading protocol; (b) OOP loading protocol

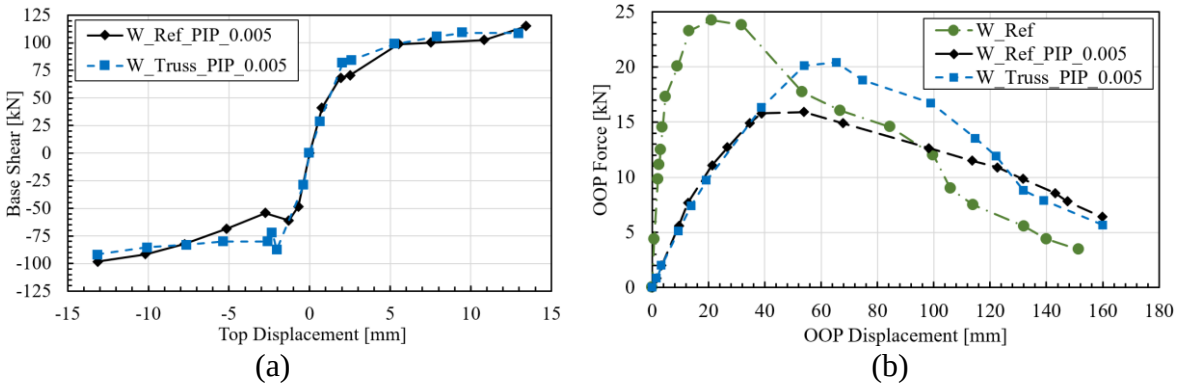


**Figure 4:** Backbone curves: (a) Response in IP direction; (b) Response in OOP direction

## 3 MODELING METHODOLOGY

A numerical 3D Finite Element Model (FEM) was developed in Abaqus 2020 software [16]. Explicit solver was used, and quasi-static dynamic analyses were performed. Simplified micro modeling method was adopted since the mortar thicknesses at the AAC-AAC and AAC-RC Frame interfaces were very thin (1-3 mm) to be modeled as separate elements as in micro modeling approach. Instead, the behavior of joints between the infill units were represented by contact elements. Three-dimensional 8-node hexahedral continuum finite elements with reduced integration (C3D8R) were used in the modeling of RC frame, AAC blocks and the top foam. 2-node linear truss elements (T3D2) were used to model the reinforcements. Elastic-perfectly plastic material models were used for the RC rebars and the bed-joint reinforcements. The reinforcements were embedded to the concrete and AAC elements and bond

slip response was not taken into account. The cyclic IP displacement reversal protocol presented in Figure 3a was defined in the model accordingly. However, the OOP displacements were imposed monotonically.

### 3.1 Material Properties

Concrete Damaged Plasticity (CDP) model was adopted to represent the compressive and tensile response of concrete material. The mean concrete compressive strength used in the RC frame was experimentally determined as 29.4 MPa. The material model is defined accordingly. The typical uniaxial response of concrete under compressive and tensile stresses modeled with CDP are presented in Figure 5 [16]. $E_0$ is the undamaged stiffness of the material and $\varepsilon_c^{\sim pl}$, $\varepsilon_t^{\sim pl}$, $\varepsilon_c^{\sim in}$, $\varepsilon_t^{\sim in}$ are compressive plastic strain, tensile plastic strain, compressive inelastic strain and tensile inelastic strain, respectively. CDP model weakens the unloading stiffness of the material as the material takes inelastic strain. Two damage parameters are used to define the unloading stiffness values: $d_c$ and $d_t$ which are valued between zero and one. Zero represents the undamaged condition of the material, while one represents the total failure. The damage parameters are determined according to the methodology proposed by Alfarah et al. [17] which takes into account the characteristic length ($l_{eq}$) of the mesh elements. The characteristic length is obtained by dividing the element volume by the largest area of mesh faces. Since the RC frame is made of cubic mesh elements with a size of 50 mm, $l_{eq}$ is 50 mm. The compressive and tensile stress-plastic strain relationships are presented in Figure 6. Other CDP parameters are presented in Table 3. $E_0$, $\nu$, $K_c$, $f_{b0}/f_{c0}$ and $\varepsilon$ stand for the undamaged modulus of elasticity, Poisson's ratio, the ratio of second stress invariants on tensile and compressive meridians, the ratio of biaxial compressive strength to uniaxial compressive strength and eccentricity of the plastic potential curve, respectively. The RC frame is modeled as one unified part. The mean tensile strengths of the reinforcement used in the RC frame were experimentally obtained as 476.4 MPa and 523.3 MPa for longitudinal and transversal reinforcements, respectively.

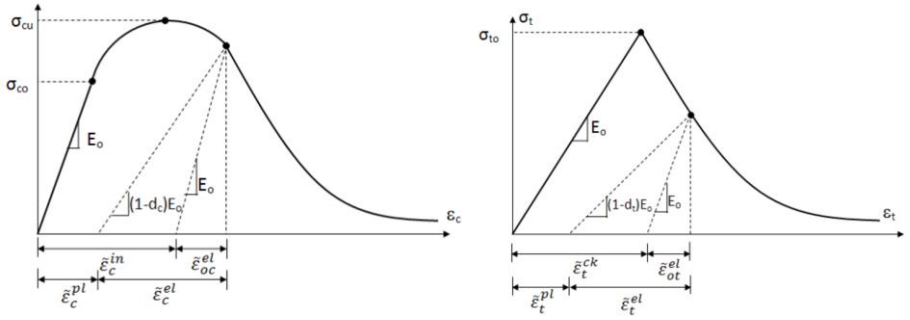


(a) (b)

**Figure 5:** Stress-strain response of concrete under: (a) compression; (b) tension

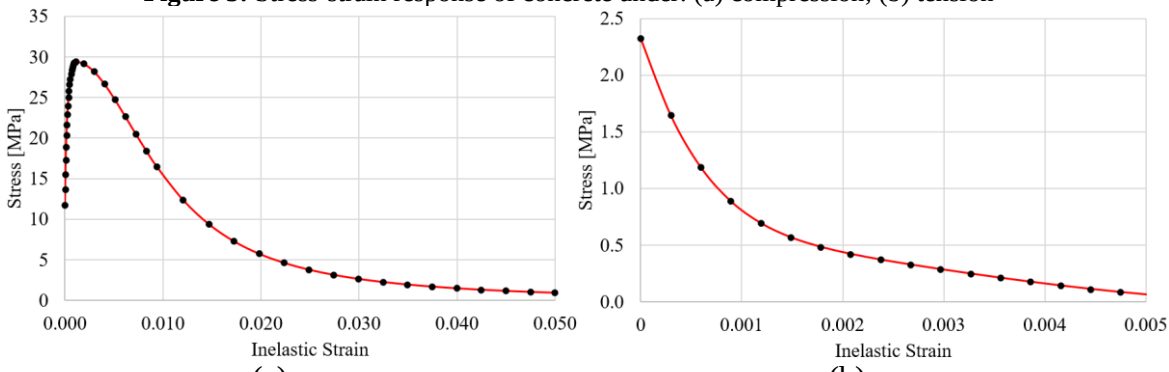


(a) (b)

**Figure 6:** Stress-strain relationships for concrete, $l_{eq}$=50 mm: (a) Compression; (b) Tension

**Table 3:** CDP parameters for concrete

| $E_0$ [MPa] | $v$ | $K_c$ | Dilatancy Angle $\Psi$ [°] | $f_{b0}/f_{c0}$ | $\varepsilon$ |
|---|---|---|---|---|---|
| 30863 | 0.2 | 0.667 | 13 | 1.16 | 0.1 |

The mean compressive strength of AAC infill units was experimentally obtained as 2.54 MPa. Past experimental tests performed by Turkish Autoclaved Aerated Concrete Association (TAACA) indicated that the tensile strength, mean modulus of elasticity and the strain at the peak compression stress for AAC 2.50 were obtained as 0.135 MPa, 990 MPa and 0.0035, respectively. Based on this data and the model developed by Thorenfeldt et.al. [18] the compression and tensile stress-strain relationships for AAC were determined (Figure 7). The damage parameters for AAC were determined according to the methodology suggested by Birtel and Mark [19].

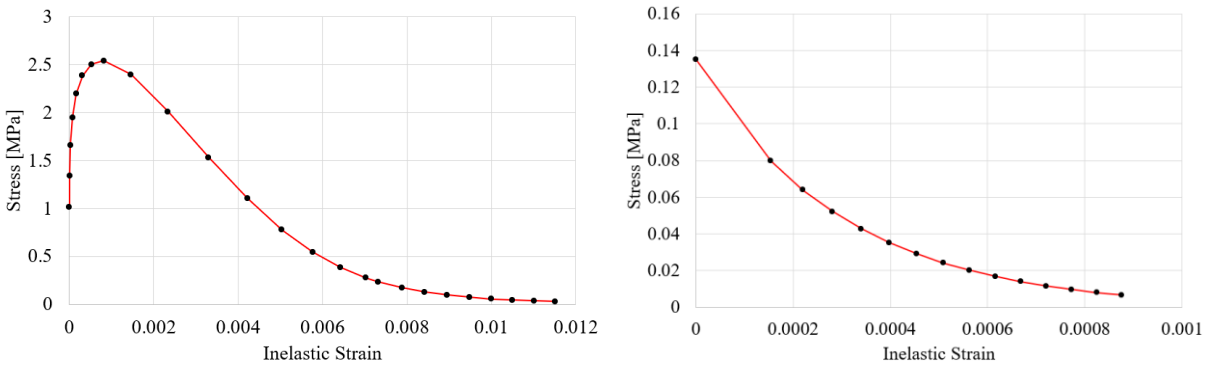


**Figure 7:** Stress-strain relationships for AAC: (a) Compression; (b) Tension

In order to represent the contact conditions between the infill and the RC frame, the polyurethane foam at the uppermost bed-joint of the infill specimens was included in the model. The foam fills the gap between the top of the wall and the RC beam. The density of the foam was 40 kg/m$^3$. During the specimen production, the thickness of the foam was measured as 15 mm. Ogden's model [20] was benefitted to represent the polyurethane foam in the FEM model.

## 3.2 Interaction Properties

A cohesive traction-separation relationship was defined to represent the behavior of bed-joint mortar between AAC infill units and AAC-RC frame interfaces where M10 mortar with an average thickness of 2 mm was used in the construction of the specimens. From the triplet tests performed by TAACA, the average shear stress where slip starts between AAC 2.50 units with M10 mortar was recorded as 0.18 MPa. Also, the friction coefficient measured in these tests was calculated as 0.62. The interface properties used in the model are presented Table 4. The interface between AAC and polyurethane foam, together with RC frame and polyurethane foam was assumed to be perfectly bonded. A tie constraint was assigned to those surfaces. The model assembly and the interactions between the model components were presented in Figure 8.

**Table 4:** Mechanical properties of joint interfaces

| Tensile Strength $f_t$ [MPa] | Shear Strength $f_s$ [MPa] | $\mu$ | $K_{nn}$ [N/mm$^2$/mm] | $K_{ss}$ [N/mm$^2$/mm] | $G_F$ [N/mm] |
|---|---|---|---|---|---|
| 0.30 | 0.18 | 0.62 | 100 | 40 | 0.02 |

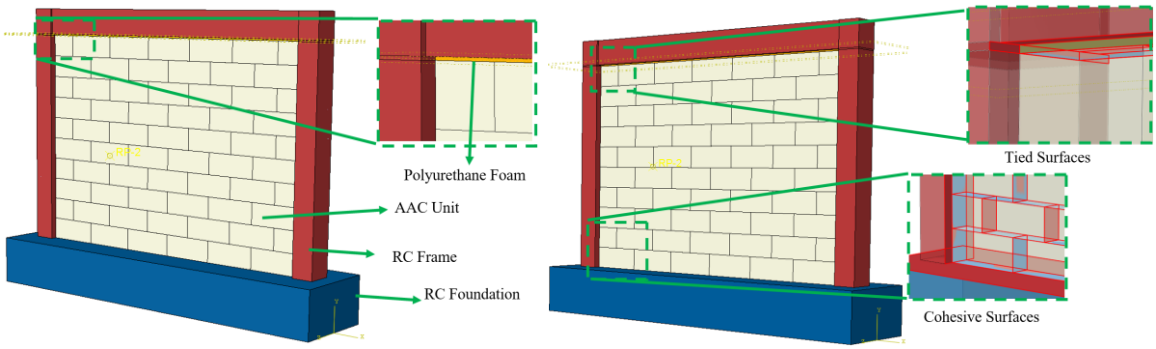


**Figure 8:** (a) model assembly; (b) contact properties in different parts

## 4 MODEL EVALUATION

Numerical analyses were carried out according to the IP and OOP loading protocols applied to the specimens during the experimental tests. The comparison of experimental and numerical damage propagation of W_Ref_PIP_0.005 during the IP loadings is presented for two IP drift levels (i.e., 0.001 and 0.002) in Figure 9. The damage states obtained from the numerical analyses at these imposed drift levels are coherent with the damages observed during the experimental tests.

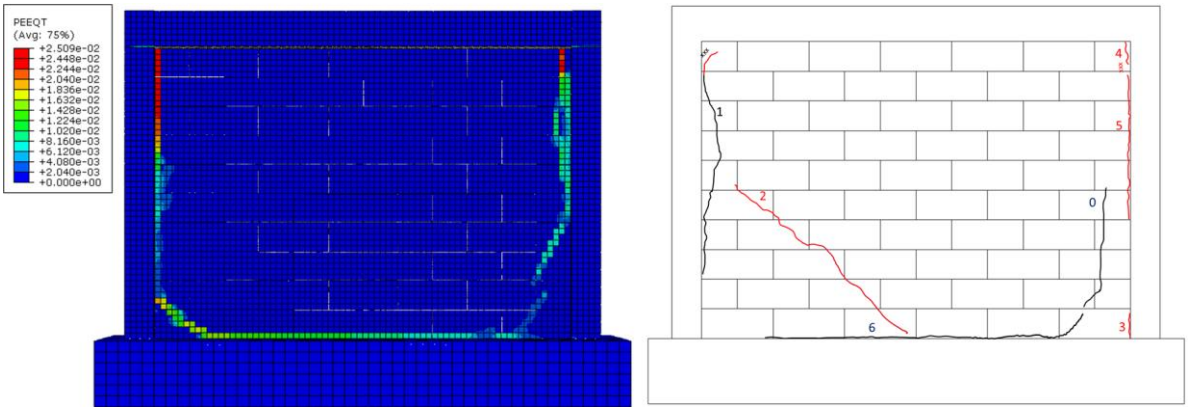


(a)

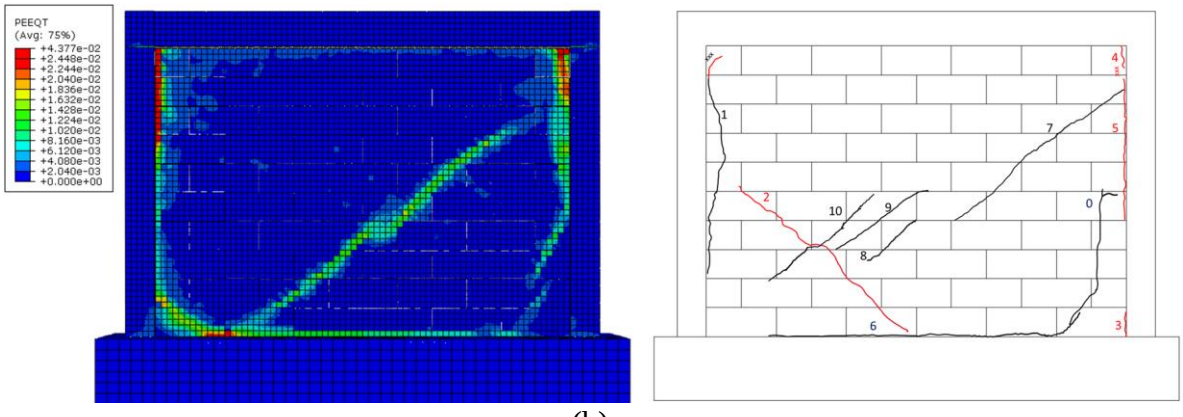


(b)

**Figure 9:** Numerically calculated plastic strains (PEEQT) versus experimentally observed cracks on W_Ref_PIP_0.005: (a) at 0.001 IP drift ratio; (b) at 0.002 IP drift ratio

The obtained OOP force-displacement relationships are presented in Figure 10. The adopted numerical modeling approach reveals the potential to represent the approximate OOP ca-

pacity of the infills with a variation of 10%. Yet, the initial stiffness responses obtained from the numerical analyses for the prior IP damages specimens (i.e., W_Ref_PIP_0.005 and W_Truss_PIP_0.005, shown in Figure 10a,b, respectively) do not seem to be coherent with the experimental response. Further optimization of the numerical modeling approach is needed.

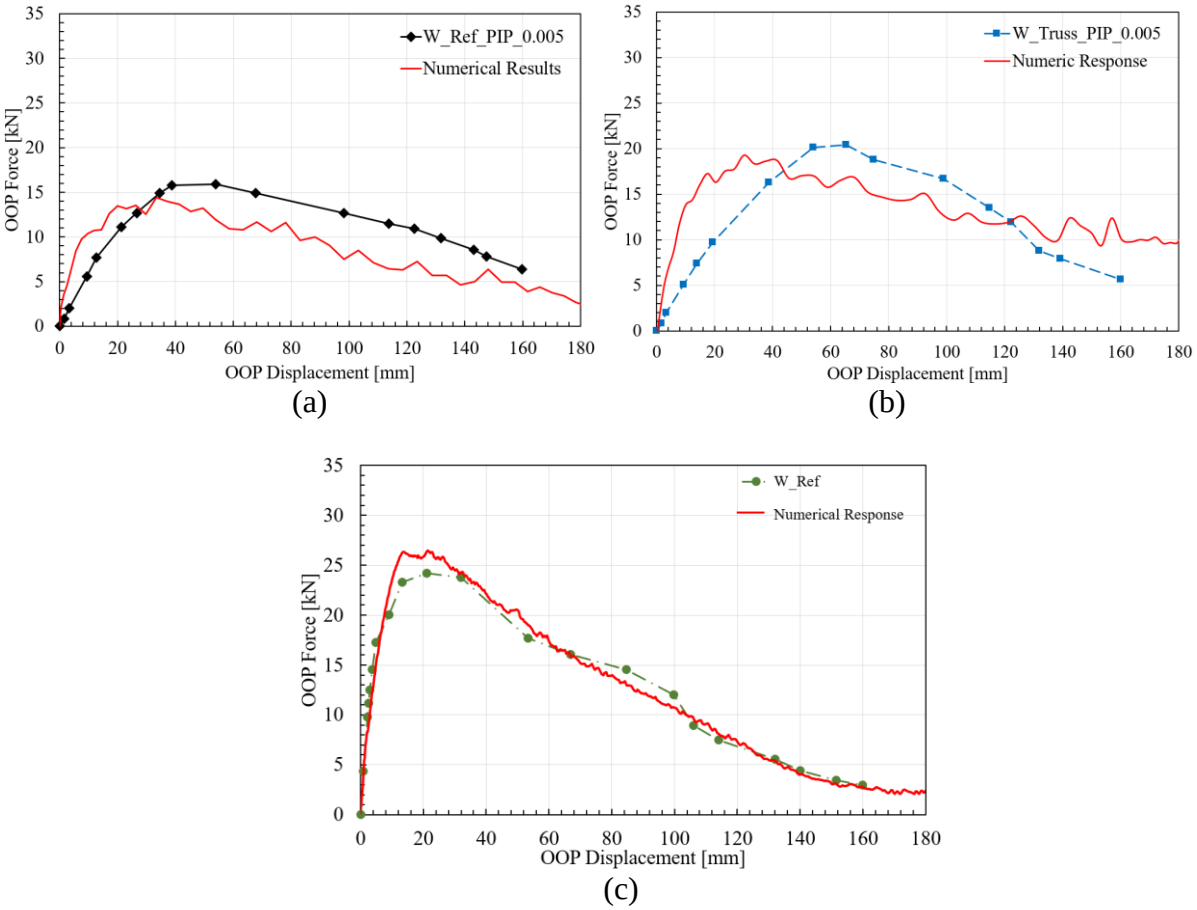


**Figure 10:** Experimental vs numerically obtained OOP force-displacement relationships: (a) W_Ref_PIP_0.005; (b) W_Truss_PIP_0.005; (c) W_Ref

## 5 CONCLUSION

In this paper, the numerical modeling approach with a potential of successfully representing the IP and OOP response of AAC infills is presented. Simplified micro modelling approach was utilized since the mortar layers between AAC units are considerably thin to be modeled as separate elements. The mortar response was represented by a cohesive traction and separation law defined at the AAC interfaces. Concrete damaged plasticity model was used to model the non-linear response of AAC units and RC members, which were modeled with 3D finite elements. The response obtained from this modeling approach indicates a great potential to represent the IP and OOP response of AAC infills together with the OOP response of prior IP damaged infills. Yet, further developments are needed to successfully represent the OOP stiffness of the IP damaged infill walls. Once it is established and validated, the modeling approach will be used to generalize the experimental findings and to investigate the response of various infill configurations including height/length ratio, height/thickness ratio, reinforcement amount and prior IP drift level etc.

## 6 REFERENCES


[1] A. Ceci, A. Contento, L. Fanale, D. Galeota, V. Gattulli, M. Lepidi et al., Structural performance of the historic and modern buildings of the University of L'Aquila during the seismic events of April 2009. *Engineering Structures*. **32**, 1899-924, 2010.

[2] P. Ricci, F. De Luca, G.M. Verderame, 6th April 2009 L'Aquila earthquake, Italy: reinforced concrete building performance. *Bulletin of Earthquake Engineering*. **9**, 285-305, 2011

[3] F. Braga, V. Manfredi, A. Masi, A. Salvatori, M. Vona, Performance of non-structural elements in RC buildings during the L'Aquila, 2009 earthquake. *Bulletin of Earthquake Engineering*. **9**, 307-24, 2011

[4] M. Tapan, M. Comert, C. Demir, Y. Sayan, K. Orakcal, A. Ilki. Failures of structures during the October 23, 2011 Tabanlı (Van) and November 9, 2011 Edremit (Van) earthquakes in Turkey. *Engineering Failure Analysis*. **34**, 606-28, 2013.

[5] M. Di Ludovico, A. Prota, C. Moroni, G. Manfredi, M. Dolce. Reconstruction process of damaged residential buildings outside historical centres after the L'Aquila earthquake: part I—" light damage" reconstruction. *Bulletin of Earthquake Engineering*. **15**, 667-92, 2017.

[6] M. Di Ludovico, A. Prota, C. Moroni, G. Manfredi, M. Dolce. Reconstruction process of damaged residential buildings outside historical centres after the L'Aquila earthquake: part II—"heavy damage" reconstruction. *Bulletin of Earthquake Engineering*. **15**, 693-729, 2017.

[7] B. Yön, O. Onat, M.E. Öncü. Earthquake damage to nonstructural elements of reinforced concrete buildings during 2011 Van seismic sequence. *Journal of Performance of Constructed Facilities*. **33**, 04019075, 2019.

[8] A. Yakut, H. Sucuoğlu, B. Binici, E. Canbay, C. Donmez, A. İlki et al. Performance of structures in İzmir after the Samos island earthquake. *Bulletin of Earthquake Engineering*. 1-26, 2021.

[9] T. Gurbuz, A. Cengiz, S. Kolemenoglu, C. Demir, A. Ilki. Damages and Failures of Structures in İzmir (Turkey) during the October 30, 2020 Aegean Sea Earthquake. Journal of Earthquake Engineering. 1-42, 2022.

[10] H. Varum, A. Furtado, J. Melo. Insights on the Seismic Design of Current RC Buildings: Field Lessons, Codes and Research Needs. *European Conference on Earthquake Engineering and Seismology*, Springer, 2022. p. 311-22.

[11] G. M. Calvi, and D. Bolognini. Seismic response of reinforced concrete frames infilled with weakly reinforced masonry panels. *Journal of Earthquake Engineering*, **5**,153-185, 2001.

[12] A. Penna, G. Magenes, G.M. Calvi, A.A. Costa. Seismic performance of AAC infill and bearing walls with different reinforcement solutions. Proceedings of the 14th International Brick and Block Masonry Conference, 2008. p. 13-20.

[13] A. Penna, M. Mandirola, M. Rota, G. Magenes. Experimental assessment of the in-plane lateral capacity of autoclaved aerated concrete (AAC) masonry walls with flat-truss bed-joint reinforcement. *Construction and Building Materials*. **82**,155-66, 2015.

[14] A. Penna, G. Calvi. Campagna sperimentale su telai in ca con tamponamenti in Gasbeton (AAC) con diverse soluzioni di rinforzo. Experimental report, University of Pavia, Italy (in Italian). 2006.

[15] O.F. Halici, U. Demir, Y. Zabbar, A. Ilki. Out-of-Plane Seismic Performance of Bed-Joint Reinforced Autoclaved Aerated Concrete (AAC) Infill Walls Damaged under Cyclic In-Plane Displacement Reversals. *Engineering Structures,* **286**,116077, 2023.

[16] Simulia. Abaqus FEA. Dassault Systemes Simulia Corporation. 2020.

[17] B. Alfarah, F. López-Almansa, S. Oller. New methodology for calculating damage variables evolution in Plastic Damage Model for RC structures. *Engineering Structures*. **132**, 70-86, 2017.

[18] E. Thorenfeldt, A. Tomaszewicz, J. J. Jensen. Mechanical properties of high-strength concrete and application in design. *Symposium on Utilization of High-Strength Concrete*. Trondheim, Norway. 1987. p. 149-159.

[19] V.A. Birtel, P. Mark. Parameterised finite element modelling of RC beam shear failure. *ABAQUS users' conference.* 2006.

[20] R.W. Ogden. Large deformation isotropic elasticity–on the correlation of theory and experiment for incompressible rubberlike solids. *Proceedings of the Royal Society of London. A. Mathematical and Physical Sciences*, **326(1567)**, 565-584, 1972.

COMPDYN 2023
9th ECCOMAS Thematic Conference on
Computational Methods in Structural Dynamics and Earthquake Engineering
M. Papadrakakis, M. Fragiadakis (eds.)
Athens, Greece, 12-14 June 2023

# DAMPING ASSESSMENT OF BRIDGES FOR PERFORMANCE BASE DESIGN

**Juan M. Mayoral**[1] **and Mauricio Pérez**[1]

[1] Institute of Engineering, Universidad Nacional Autonoma de Mexico, Mexico City, Mexico

e-mail JMayoralV@iingen.unam.mx

## Abstract

*Modern performance bridge design relies on reaching controlled stages of damage and failure modes to ensure both safety and economy. In high seismic zones, the design philosophy should be based on the ability of a bridge to deform inelastically and ductilely, allowing some damage to fused elements to decrease the potential internal forces during earthquakes. This approach, however, requires a careful determination of the potential damping expected to occur on the structure and foundation. In the case of single-span or two-span bridges, the abutments have a significant impact on the bridge's performance, mainly in the longitudinal vibration modes, so the determination of the damping in the abutment is critical. In most reference bridge design manuals, the recommended damping values for abutments usually range from 5% to 10%, which results in a more robust design of the structure due to the limited allowance of energy dissipation.*

*In particular, this paper presents a numerical study of the energy dissipation available in the abutments of common bridge typologies. The observed damage patterns in bridges near the epicentral zone induced by recent subduction earthquakes in Mexico were analyzed using 3D finite difference models. To simulate the development of damping in the abutment, a fully non-linear approach was adopted, where the hysteretic model Sig3 coupled with the Mohr-Coulomb constitutive model was considered for the mechanical and dynamic behaviour. From the results gathered in here, the relationship between damping and abutment displacements was established, and it is clearly demonstrated that the inclusion of large damping values during bridge design can lead to both cost-efficient and safe designs if a good abutment deformation assessment is conducted.*

**Keywords:** Damping assessment, seismic design, bridge abutments, numerical modelling.

# 1 INTRODUCTION

In recent years, it has been proven that the nonlinear stress-strain behaviour of the backfill soil in the abutments has a significant impact on the seismic performance of bridges. When they are skewed with limited spans, the abutments become more important because they absorb a considerable portion of seismic forces, mainly in the longitudinal direction [1-3].

Nevertheless, dynamic equilibrium between inertial forces and, restoring and damping forces is commonly assessed using simplified methods based on beam-spring models, in which the interaction with soil is commonly simulated with linear springs and viscous dashpots. In case of the two last ones, due to soil nonlinearity, such characteristics can vary widely during strong ground motion, modifying the predicted internal forces of the structural elements of the bridge. So, when the abutments have a significant impact on the bridge's performance, it is critical to utilize appropriate stiffness and damping values based on the expected strains or adopt a fully nonlinear approach capable of reproducing the hysteretic behaviour of the soil. For example, when there isn't available data of damping values, the LRFD Seismic Analysis and Design of Bridges Manual [4] suggest a maximum damping ratio of 10% for the longitudinal vibration modes in the case of single-span or two-span bridges with abutments and 5% in the case of longer concrete bridges. However, this approach requires a detailed assessment of the potential damping expected to occur on the structure and foundation, which must be agreed upon with the level of shear strain in the soil because it can experiment yielding during the seismic loads and reach large damping values.

When an extreme event occurs, the performance bridge can be directly assessed by observing and identifying the induced principal damage patterns, and determining whether the design prediction agrees with the observed behaviour. As a result of this evaluation, a back analysis can be made by reproducing the observed performance using appropriate analysis models capable of simulating the structure's conditions. Likewise, it can possible inferred the shear strain levels that the soil reach during the ground shaking as well as the damping developed.

This paper focuses on the assessment of bridge damage caused by the Mw 7.7 September 19, 2022, Michoacán earthquake near the epicentre. In summary, despite the high peak ground acceleration values reached in the visited zone, which nearly reached 1 g according to site seismic stations, good performance was observed [5]. According to the damage observed, abutments were the most affected elements, allowing for quick remedial actions and the avoidance of serviceability loss. This evidence suggests that during the ground shaking, these elements were able to dissipate a large amount of energy, reducing the seismic demand on the bridge's structural elements.

To achieve this, 3D finite difference models were developed with the software FLAC$^{3D}$, where common bridge damaged typologies of the zone were simulated. In summary, two-span and three-span bridges were such with affected abutments, so both of thus were considered in the analysis. The considered input motion, corresponds to the time story recorded by the COMA station, located in rock 40 km away from the studied site, during the mentioned earthquake. With the developed models, the observed damage is reproduced in terms of displacement and plastic zones in the soil backfill, where the hysteretic model Sig3 coupled with the Mohr-Coulomb constitutive model were considered to simulate the mechanical and dynamic behaviour. With the results gathered in here, it was possible to infer the damping values reached during the earthquake, observing that values higher than 10% are available in the abutments.

## 2 OBSERVED DAMAGE FOLLOWING THE 2022 MICHOACAN, MEXICO, EARTHQUAKE

On September 19, 2022, an earthquake with a moment magnitude of M7.7 struck the central region of Michoacan near Coalcoman in Mexico. The massive amount of energy released was caused by a reverse faulting mechanism with a hypocenter 15 kilometers deep at 18.22 north latitude and -103.29 west longitude [6]. This location corresponds with the so-called Middle America Trench, where the Cocos plate is subducting beneath the North American plate. Along this active megathrust plate boundary, there have been numerous M>7 earthquakes in the last 50 years, including the M8.0 Michoacan/Mexico City earthquake of 1985 and the followed large M7.6 aftershock 32 hrs. after (See Figure 1a).

The spatial distribution of the root mean square (RMS) of the horizontal (north-south and east-west components) peak ground accelerations (PGA) obtained from hard-rock recordings is shown in Figure 1b. The map depicts the potential extent of potentially damaging shaking caused by the 2022 earthquake (i.e., light, moderate, and severe). The Coalcoman earthquake produced moderate to high magnitudes in the epicentral region. The highest RMS PGA was recorded at station MMIG, about 8 km from the epicentre, with 902 cm/s², followed by station COMA, about 132 km from the epicentre, with 206 cm/s² [6].

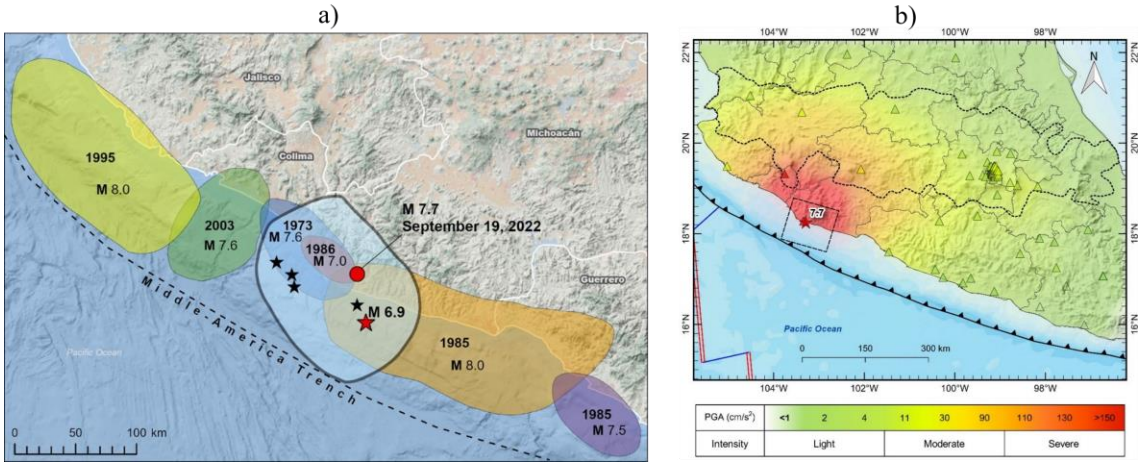


Figure 1: a) Approximate location of subduction zone rupture planes, west-central Mexico, since 1973 [5] b) Map of peak ground acceleration [6].

As can be seen, the seismic event caused significant ground shaking and damage, primarily in the coastal states of Colima and Michoacan, with PGA of up to 1g in the epicentral area. According to the observations made during virtual and visual reconnaissance, the principal affectations along the main and secondary roads of the zone consisted of slides of cutting slopes, lateral and longitudinal cracking of pavement, and damage in the elements of bridges. Regarding the last point, the observed damage was mostly related to the opening of joints in the decks of the bridges (the typical gap of joints was about 6 to 10 cm wide), vertical cracking in abutments, lateral displacements of decks, and cracks in shear keys of pier caps. All the damaged bridges were in operation, and only the bridges located in El Ticuiz, Michoacan, and Colima City, Colima, were undergoing repair work that was initiated after the earthquake [5].




Figure 2: Common bridge damage after the September 19th, 2022, Michoacan Earthquake, in the coastal area of Colima and Michoacan [5].

Figure 2 shows some pictures of the most common damage patterns exhibited by the bridges in the visited zone near the epicentre. As can be seen, the injured elements suffer plastic deformation primarily in the abutments and in the lateral shear keys of the pier caps; on the other hand, the substructure behaved elastically in all cases. Those damage patterns exposed the design philosophy followed in high seismic zones, in which the ability of a bridge to deform inelastically and ductilely is a necessity, due to the inelastic response having both economic and technical bases. In terms of economics, it is rational to allow some damage rather than divert unnecessary resources toward an extreme event with a low probability of occurrence. Technically, it is reasonable to design some elements as fused structures, which limit the internal forces. With this approach it reduces the structure's vulnerability to earthquakes larger than the design event [7].

## 3 REGIONAL GEOLOGY AND $VS_{30}$ ESTIMATION

Following the identification of the damaged bridges, the regional geology in the damaged areas was investigated to determine whether any amplification of the movement was due to site effects. According to the survey areas, almost all the damaged bridges were in the coastal zone, where the topography was moderately flat, implying the presence of unconsolidated materials beneath the most damaged areas.

The following descriptions correspond to the coastal region of Colima, and Michoacan states. Such coastal region is distinguished by the predominance of recent poorly consolidated materials such as polymictic conglomerate and Pleistocene sandstones (QptCgp-Ar), as well as Holocene alluvium, residual soils, and fine sands (Qal). Similarly, there is an alternation between intrusive igneous rocks, primarily granite and granodiorite (KsGr-Gd), and igneous pyroclastic materials such as andesitic tuffs and breccias composed of subangular andesite fragments welded in a sand-clayey matrix (Kapa-A, Kap-BvA, and KapceTa-Ar). Figure 3 depicts the distribution of the dominant geological units in the aforementioned coastal area [5]. The surveyed roads with damaged bridges are also shown, as are the seismic stations where the highest values of PGA were recorded.

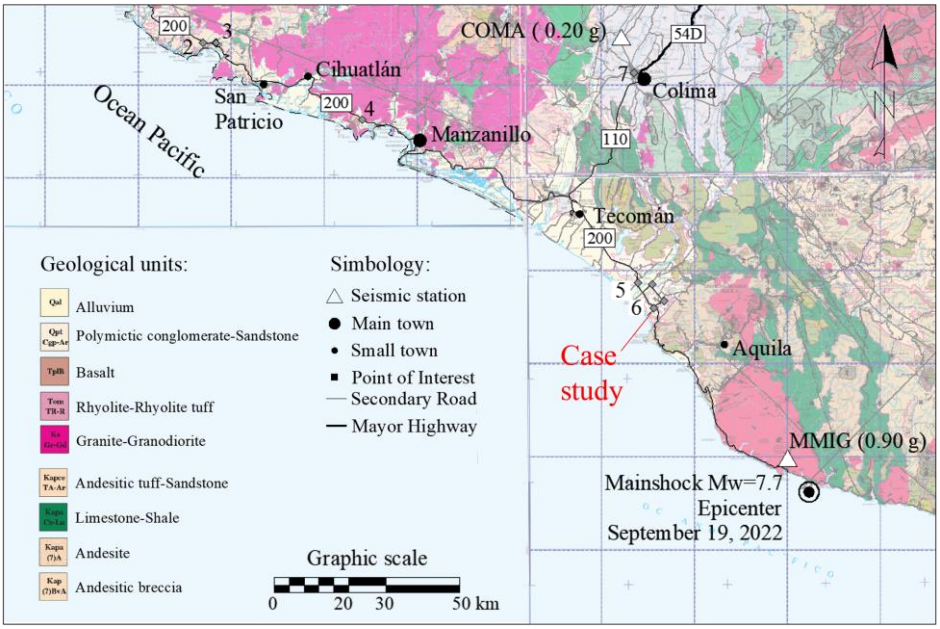


Figure 3: Geological map of the coast areas with bridge damage [5].

Given the lack of Vs data for sites, there were applied proxy models for Vs30 prediction that were developed for California. The procedure involved looking up site surface geology, relating the mapped geology to geologic categories used in California [8], and then assigning the California-based mean $\mu lnV$ and standard deviation $\sigma lnV$ values. The geology used in this process corresponds to the map shown in Figure 3. According to Ahdi et al. [9], using a proxy relationship developed in one region and applied in another without local validation is a reasonable approach as long as the estimation includes epistemic uncertainty.

Figure 4a shows the histogram of the collected Vs30 data in California from downhole, cross hole, and suspension log surveys for young alluvium materials with moderate flat surface slopes. Given a LogNormal distribution, the range of Vs values in the first 30 m is defined as 240 to 365 m/s. In addition, Vs profiles presented by Tonatiuh Dominguez et al. [10] for the region of Manzanillo in similar geological conditions were considered. Figure 4b depicts the Vs profile developed based on the Vs30 estimation, the S1 and S3 profiles corresponding to Manzanillo, and the idealized profile considering all three profiles; as can be seen, the variation was small. This last one, was the Vs profile used to simulate the conditions experienced by bridges damaged during the earthquake.

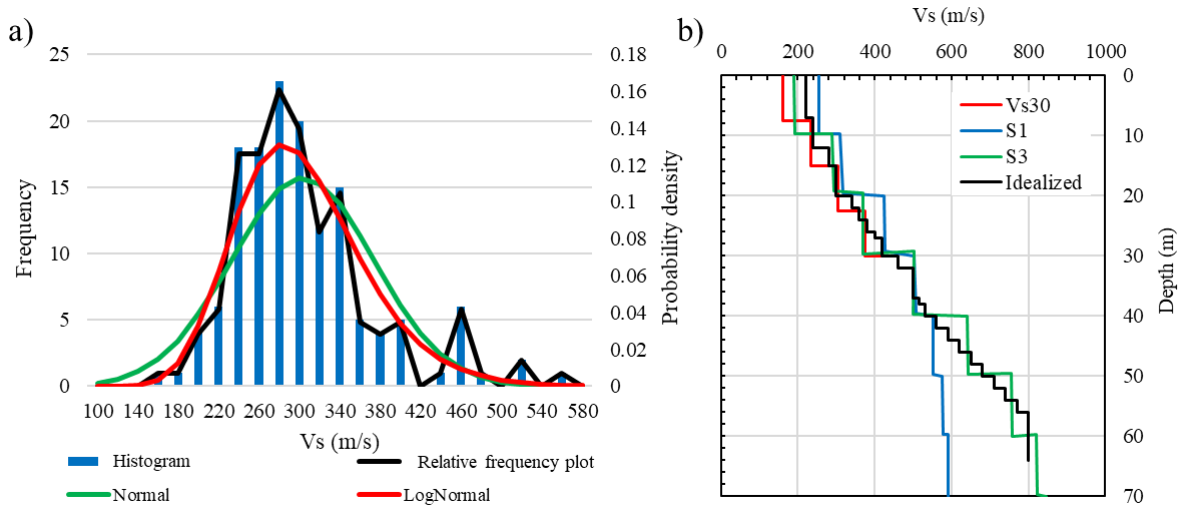


Figure 4: Histogram of Vs30 values obtained in alluvium soil on moderately flat areas from California (modified from [10] b) Estimation of Vs profile for the site under study.

## 4 CASE STUDY

According to the observed common topologies at the visited zone, it was defined a representative three-span bridge as a case of study. Figure 5 describes the structure elements that conform the bridge as well as their dimensions. In summary the superstructure consists of a non-continuous upper deck resting on five support AASHTO I-beams separated every 2.85 m, which are structurally tied. Such beams are simply supported by the pier caps and the abutments. The middle supports are composed by concrete pier caps with shear keys on the sides to restrict the lateral seismic movements, likewise this is supported by four concrete columns of Ø=0.8 m, separated every 4.0 m, which are joined monolithically; regarding to its foundation the same diameter of the columns corresponds to the piles of 8.0 m length which are tied monolithically to the columns with a pile cap of 2.0 m width and 0.8 height. The abutments of the bridge are comprised by a concrete cantilever retaining wall where the support beams lean, at the sides there have wing walls which are used to retain the backfill soil, which were considered as a compacted silty sand. In addition, an earth slope in front of the retaining wall was considered as scour protection.

The location of the bridge was supposed in the coastal area of Michoacan, between the points 5 and 6 in the Figure 3, 70 km away from the epicenter. Corresponding to the mentioned regional geology, it was supposed a homogeneous layer of alluvium soil comprised of fine sand of medium compactness.

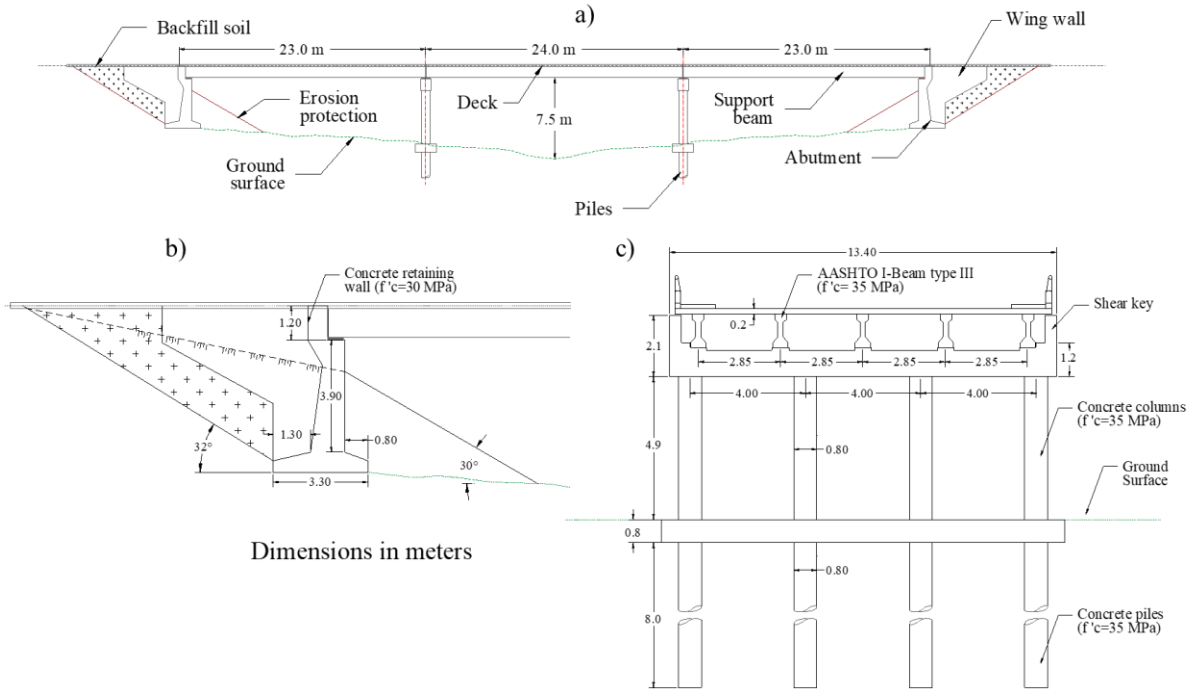


Figure 5: a) Longitudinal view of the bridge under study b) Abutment configuration c) Cross-section of the middle support and foundation.

## 4.1 Input ground motion

The dynamic response of the bridge was computed for the September 19th, 2022, Michoacan Earthquake, taking into account both the soil deposit and the soil-structure system. The strong ground motion recorded at station COMA (located in rock) was used as input time history in the dynamic analyses. Although the study site is located closer to the epicenter, similar seismic intensity was presented in the zone according to Figure 1b, therefore such record was considered reasonable to apply in the analyses. Figure 6 shows the measured accelerations for both orthogonal components, and their corresponding response spectra. Both components of motion were considered in the seismic response analyses.

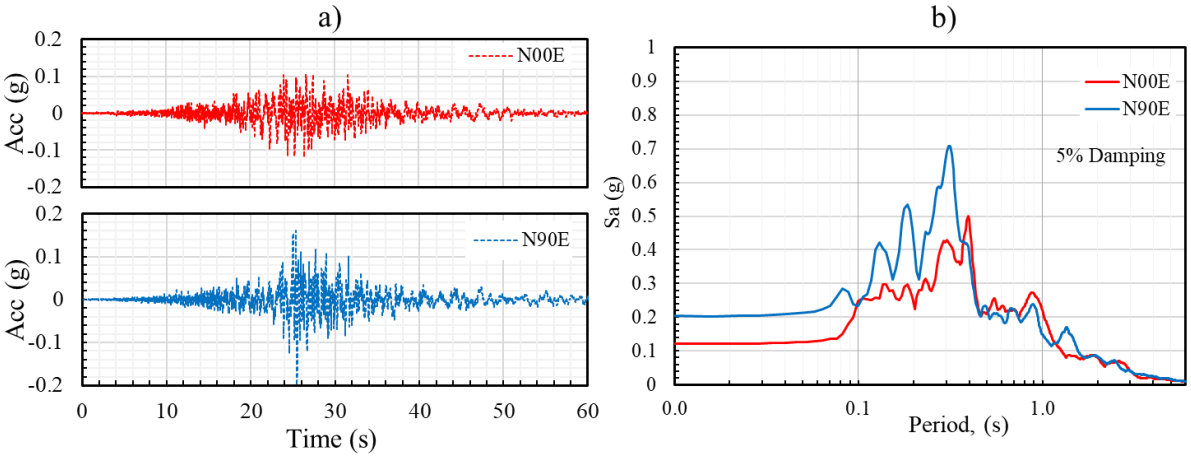


Figure 6: a) Time histories recorded in the COMA station during the September 19th, 2022, Michoacan Earthquake b) Response spectra of the time histories.

## 5 NUMERICAL MODEL

To simulate the strong ground motion caused by the September 19, 2020, Michoacan earthquake, in the studied area, a three-dimensional model was performed with the program FLAC$^{3D}$. Such model, consider the underneath soil, the backfill soil, and the structure elements of the bridge. Figure 7a depicts the global domain of the finite difference mesh, and Figure7b the structural elements of the bridge.

To represent soil behaviour, it was deemed appropriate to consider a Mohr-Coulomb failure criterion, due to the lack of information to define the soil parameters of more complex constitutive models. The geotechnical parameters considered are those shown in Table 1, the distribution of soil foundation was considered homogenous in the whole model and the backfill soil and earth slope protection according to Figure 5.

The model consists of 180960 three-dimensional elements representing the soil mass and the concrete retaining walls of the abutments. Within the domain of the model, further refinement of the mesh was adopted on the zones in contact with the structure. Also, several control points were located in these areas to monitor the interaction effects during the simulation, and at the edges and corners of the model to establish the free field seismic motion. Figure 14 shows the finite difference mesh considered in the simulation and the boundary conditions. To represent the structural elements of the bridge, BEAM elements were used to simulate the support beams, columns and pier caps, PILE elements to simulate the piles, and SHELL elements to simulate the deck of each span. The behaviour of such elements was considered elastic. The structural parameters considered are those shown in Table 2.

Table 1. Mechanical parameters of the solid elements.

| Layer | $\boldsymbol{\gamma}$ (kN/m³) | **c** (kPa) | φ (°) | $\boldsymbol{E_{50}}$ (MPa) | $\boldsymbol{\nu}$ |
|---|---|---|---|---|---|
| Alluvium | 17.0 | 20 | 30 | 80 | 0.35 |
| Backfill | 18.2 | 51.20 | 30 | 140 | 0.28 |
| Scour protection | 17.0 | 15.60 | 27 | 110 | 0.34 |

Where γ is the unit weigh; **c** is the cohesion; $\varphi$ is the friction angle, $\boldsymbol{E_{50}}$ is the secant elasticity modulus, and **ν** is the Poisson's ratio.

Table 2. Mechanical and geometrical parameters of the structural elements.

| Bridge element | $\boldsymbol{\gamma}$ (kN/m³) | H / D (m) | A (m$^2$) | Ix (m$^4$) | Iy (m$^4$) | $f'_c$ (MPa) | $\boldsymbol{E_s}$ (MPa) | **ν** |
|---|---|---|---|---|---|---|---|---|
| Support beam | 24 | 1.15 | 0.35 | 5.2E-2 | 3.5E-3 | 35 | 2.64E+4 | 0.25 |
| Columns and piles | 24 | 0.80 | 0.50 | 2.0E-2 | 2.0E-2 | 35 | 2.64E+4 | 0.25 |
| Pier caps | 24 | 1.20 | 0.96 | 1.2E-1 | 5.1E-2 | 35 | 2.64E+4 | 0.25 |
| Deck | 24 | 0.20 | - | - | - | 30 | 2.52E+4 | 0.25 |

Where H is the height of the element; D is the diameter of the element; A is the cross-sectional area of the element; $I_x$ and $I_y$ are the moments of inertia about the transverse and longitudinal axis of the element, respectively; $f'_c$ is the nominal compression resistance of the concrete; and *Es* is the Young's modulus of the element.

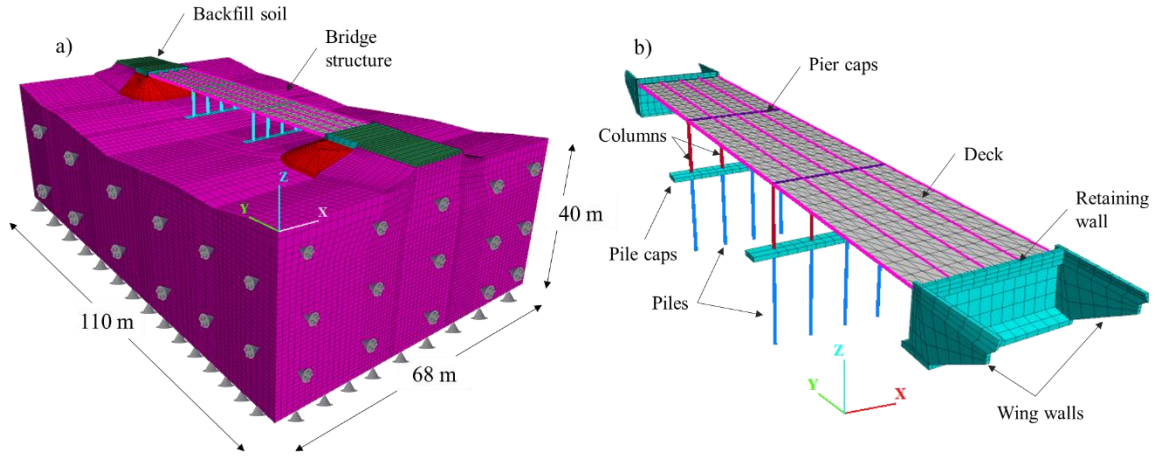


Figure 7: a) 3D numerical model used by the soil-structure interaction analysis b) Structural elements of the simulated bridge.

## 6 THREE-DIMENSIONAL SOIL-STRUCTURE INTERACTION ANALYSIS

Prior to the soil-structure interaction analysis, the input motion to apply at the base of the model was defined by the deconvolution of the surface ground motion with the program SHAKE [11]. To avoid wave reflections during the dynamic simulation and the allowance of radiation damping, quiet boundary conditions were defined at the model's base using Lysmer & Kuhlemeyer [12] formulation. In the case of the lateral faces of the model, Free field boundaries were considered using the formulation available in FLAC$^{3D}$.

Due to the lack of information from undisturbed samples of the site to define the non-linear behaviour of the alluvium soil, the upper and lower bounds proposed by Seed and Idriss [13] for normalized modulus degradation and damping, were deemed appropriate to use in the analysis. The curves proposed by Alhassan and VandenBerge [14] for backfill soil were also implemented. In the case of the concrete structures, a constant value of damping equals to 5% was used in the analyses.

The hysteretic model Sig3, which is available in FLAC$^{3D}$, was used to simulate the stiffness degradation and increase in damping of the soil during ground shaking according to the mentioned curves. Figure 8 depicts the curves defined for each layer, as well as the corresponding expected theoretical curves defined by the type of soil. Therefore, in summary, the aforementioned curves and the Mohr-Coulomb failure criterion characterized the mechanical behaviour of the soil. The bridge construction process was simulated prior to the dynamic analyses in order to establish static equilibrium and the initial conditions of stresses in both the soil and the structural elements.

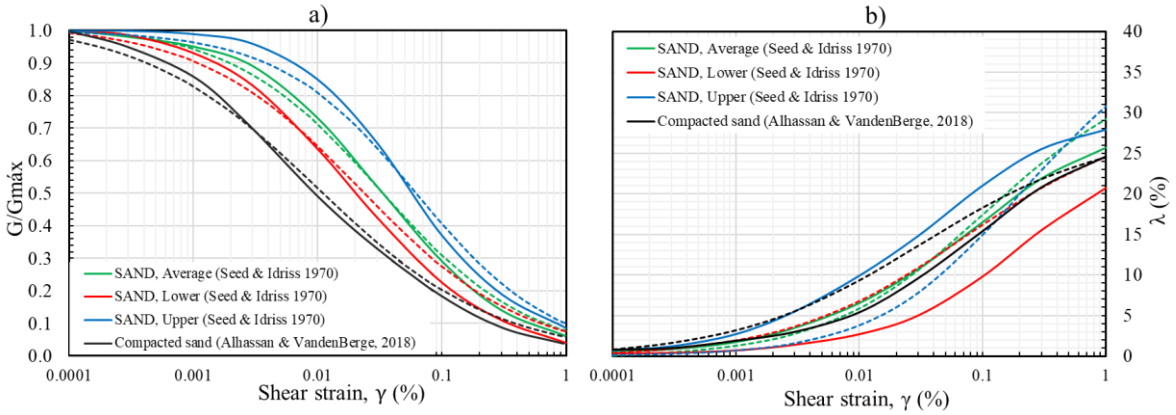


Figure 8: a) Normalized modulus degradation and b) Damping curves.

## 6.1 Results and discussion

The simulation of the strong ground motion caused by the September 19, 2022, Michoacan earthquake, in the coastal area of such state, was performed from the three-dimensional model (Figure 6). In summary the calculated surface and structure response of the simulated bridge, matched quite well with those observed in the visited damaged zones.

First, Figure 8a shows the results gathered from frequency domain and time domain analyses conducted with SHAKE and FLAC$^{3D}$, respectively, assuming one-dimensional SH waves propagating vertically. Also, the response spectrum of the input motion at the base of the model is shown, to observe the amplification caused by the soil column. Good agreement can be shown in the computed response obtained in the analysed case.

To observe the amplification from the foundation to the deck of the bridge, transfer functions were calculated in each direction as the ratio of the Fourier spectra of the deck between the Fourier spectra of the foundation, the obtained results are shown in Figure 8b. In comparison, the amplification is bigger in the transverse direction, reaching values of amplitude up to seven, while in the longitudinal direction the values are smaller than two. These big differences can be associated to the stiffness and damping developed in each direction. In the case of the transverse motion, there are eight columns and a constant damping of 5% due to the influence of the abutments is practically nil, so the stiffness is bigger, and the behaviour is almost linear which results in very little energy dissipation. On the other hand, the longitudinal motion is influenced to greater degree by the presence of the abutments which has nonlinear behaviour, and its stiffness can be degraded, which allows major energy dissipation.

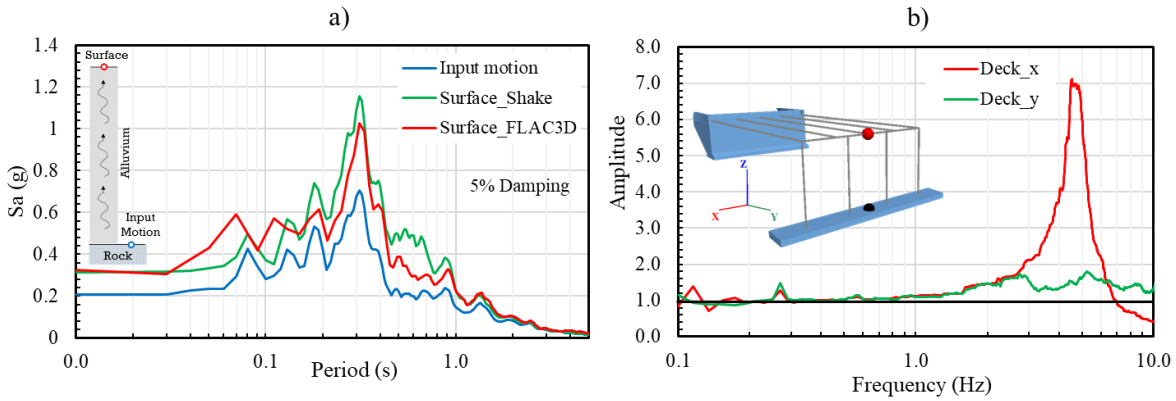


Figure 9: a) Response spectra at model´s surface b) Transfer functions between the foundation and the deck of the bridge.

The stress-strength ratio (SSR) was calculated at the end of the simulation to obtain a more detailed understanding of the abutment backfill soil. The SSR is a local indicator of the stress state's proximity to yield and is defined by the ratio between the deviatoric stress at the failure and the deviatoric stress developed in the simulation, which can be expressed as:

$$SSR = \frac{(\sigma_1 - \sigma_3)f}{(\sigma_1 - \sigma_3)} \quad (1)$$

$$(\sigma_1 - \sigma_3)_f = \frac{2c\cos\varphi + 2\sigma_3 \sin\varphi}{1 - \sin\varphi} \quad (2)$$

where $c$ and $\varphi$ are the cohesion and friction angle values from the Mohr-Coulomb failure criteria; $\sigma_1$ and $\sigma_3$ are the major and minor principal stresses, respectively, and the subindex $f$ denotes failure. Values of $SSR \approx 1.0$ represent that the soil has reached the yielding stage, and the developed deviatoric stresses can induce cracking, instability, or excessive deformations.

Figure 10 depicts the SSR plot contours of one side of the bridge. Taken a simplified approach, the red zones can be associated to some potential mechanism of failure depending on its location. For example, the red zones at the toe of the slope can be interpreted as a sliding movement, and those in the crest of the embankment as settlement, protrusion, or lateral cracking. According to this interpretation, the zones with SSR ≈ 1.0 in the model, match well with the observed damage patterns after the earthquake in some bridges, such as those shown in Figure 3. Regarding to the backfill soil, it can be seen that it reached the yielding condition, so it can anticipate that high damping values were developed by the abutments.

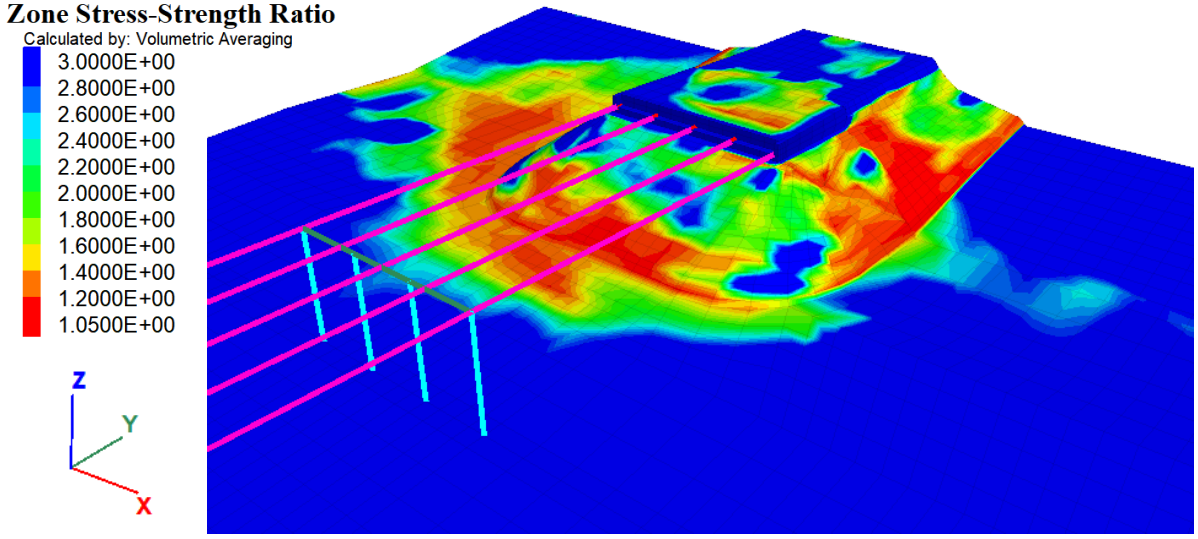


Figure 10: Plot contours of stress-strength ratio from numerical model in at the end the simulation.

To observe the stiffness degradation and the damping variation in the backfill soil, control points were located behind the retaining wall, in which G/Gmax and damping values were stored during the simulation. Figure 11a depicts the location of the control points and Figure 11b shows the obtained stored values by each control point during the simulation. As expected, the abutments developed high damping values up to 25 % in some cases, much more than the recommended value of 10%. However, it is worth defining the conditions experienced by the backfill soil according to the acceleration magnitudes of the time history. When comparing such time history with the values of Figure 11b, it can be noticed that after approximately 25 s (the instant of maximum acceleration), some points continue to grow even as the movement decreases. This phenomenon can be associated to the yielding or the failure of the element which causes the accumulation of plastic strains, allowing more energy dissipation.

So, following these results it is necessary to define that such high damping values are due to the yielding of the backfill soil. Nevertheless, before such instant of break point, it was possible to reach damping values up to 15%, which is still higher than the recommended maximum value.

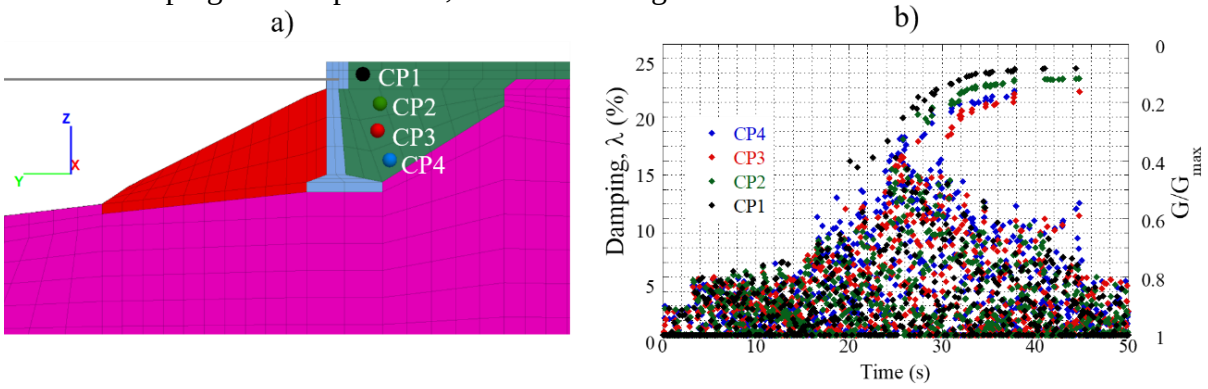


Figure 11: a) Response spectra at model´s surface b) Stored damping and G/Gmax values during simulation.

## 7 CONCLUSIONS

The energy dissipation available in the abutments of common bridge typologies in seismically active areas was assessed. In general, two mechanisms influence energy dissipation during seismic loading: material damping caused by nonlinear hysteretic soil behaviour and radiation, or geometric damping caused by energy dissipation through the half space. According to the developed analyses, it was observed that the abutment can develop damping values up to 15% before yielding and up to 25% after the backfill soil reach the failure, only because of the nonlinear hysteretic behaviour. This energy dissipation it was reflected on the amplification of the seismic motion on the deck of the bridge, particularly in the longitudinal direction where the maximum amplitude of the Transfer function was less than two. On the other hand, the seismic motion in the structure grows up to seven times on the transverse direction due to the influence of the abutment is almost nil, and the energy dissipation was minimal.

According to the results from the 3D numerical model, and the observed damaged patterns after the September 19th, 2022, Michoacan Earthquake, the optimal seismic bridge design is achieved by controlling the damage and failure modes in the bridge elements. This in turn implicates the correct estimation of the yielding point of fused elements, in order to allow some damage on it, giving to the bridge the ability to deform inelastically and ductilely. Likewise, this depends on the correct estimation of the potential damping in the abutments, mainly in the longitudinal vibration modes and in short two to three-span bridges, where its influence is critical.

In conclusion, with the allowance of large damping values during bridge design it is possible to achieve both cost efficiency and safety if a good abutment behaviour assessment is conducted.

## REFERENCES


[1] A. Shamsabadi and M. Kapuskar, 'Nonlinear soil-abutment-foundation- Structure interaction analysis of skewed bridges subjected to near-field ground motions', Transp Res Rec, no. 2202, pp. 192–205, Jan. 2010, doi: 10.3141/2202-23.

[2] A. Shamsabadi and K.M. Rollins, 'Three-dimensional nonlinear continuum seismic soil-structure interaction analysis of skewed bridge abutments', Numerical Methods in Geotechnical Engineering, vol. 1, pp. 933–938, 2014.

[3] Y. Zhang, J. P. Conte, Z. Yang, A. Elgamal, J. Bielak, and G. Acero, 'Two-dimensional nonlinear earthquake response analysis of a bridge-foundation-ground system', Earthquake Spectra, vol. 24, no. 2, pp. 343–386, 2008, doi: 10.1193/1.2923925.

[4] M. L. Marsh, I. G. Buckle, and E. Kavazanjian Jr, 'LRFD seismic analysis and design of bridges: Reference manual', 2014.

[5] K. B. Clahan, D. A. de La Rosa, J. M. Mayoral V, M. D. Perez, and J. P. Stewart, 'GEOLOGICAL AND GEOTECHNICAL ENGINEERING RECONNAISSANCE OF THE SEPTEMBER 19, 2022, MICHOACAN EARTHQUAKE, MEXICO', 2022. doi: 10.18118/G6B95P.

[6] L. Ramírez-Guzmán, M. Jaimes, J. M. Mayoral, J. Aguirre, G. Ayala, M. L. Suárez, M. Contreras, D. de la Rosa, M. Alacaráz, E. F. Salazar, M. A. Macías and M. Ayala, 'The September 19th, 2022, M7.7 Coalcoman Earthquake', II-UNAM, Mexico, City, 2022.

[7] J. M. Mayoral, A. Badillo, and M. Alcaraz, 'Vulnerability and recovery time evaluation of an enhanced urban overpass foundation', Soil Dynamics and Earthquake Engineering, vol. 100, no. May, pp. 1–15, Sep. 2017, doi: 10.1016/j.soildyn.2017.05.023.

[8] C. J. Wills, C. I. Gutierrez, F. G. Perez, and D. M. Branum, 'A next generation Vs30 map for California based on geology and topography', Bulletin of the Seismological Society of America, vol. 105, no. 6, pp. 3083–3091, Dec. 2015, doi: 10.1785/0120150105.

[9] S. K. Ahdi et al., 'Site parameters applied in NGA-Sub database', Earthquake Spectra, vol. 38, no. 1, pp. 494–520, Feb. 2022, doi: 10.1177/87552930211043536.

[10] R. Tonatiuh Dominguez et al., 'Site response in a representative region of Manzanillo, Colima, Mexico, and a comparison between spectra from real records and spectra from normative', Soil Dynamics and Earthquake Engineering, vol. 93, pp. 113–120, Feb. 2017, doi: 10.1016/j.soildyn.2016.11.013.

[11] P. B. Schnabel, J. Lysmer, and H. B. Seed, 'SHAKE: a computer program for earthquake response analysis of horizontally layered sites, software'. 1972.

[12] J. Lysmer and R. L. Kuhlemeyer, 'Finite dynamic model for infinite media', Journal of the engineering mechanics division, vol. 95, no. 4, pp. 859–877, 1969.

[13] H. Bolton Seed and I. M. Idriss, 'Soil moduli and damping factors for dynamic response analyses', Berkeley, California, 1970.

[14] M. M. Alhassan and D. R. VandenBerge, 'Shear modulus and damping relationships for dynamic analysis of compacted backfill soils', Innovative Infrastructure Solutions, vol. 3, no. 1, p. 43, Dec. 2018, doi: 10.1007/s41062-018-0152-5

COMPDYN 2023
9th ECCOMAS Thematic Conference on
Computational Methods in Structural Dynamics and Earthquake Engineering
M. Papadrakakis, M. Fragiadakis (eds.)
Athens, Greece, 12-14 June 2023

# IMPACT OF EARTHQUAKES VS. HEAT WAVES ON THE SOCIO-ECONOMIC LOSSES OF BUILDINGS

**S. Bianchi[1], J. Ciurlanti[2], A. Luna Navarro[1], and E. Brembilla[1]**

[1] Delft University of Technology
Julianalaan 134, Delft 2628 BL, Netherlands
{s.bianchi, a.lunanavarro, e.brembilla}@tudelft.nl

[2] Arup
Naritaweg 118, Amsterdam 1043 CA, Netherlands
jonathan.ciurlanti@arup.com

## Abstract

*Recent earthquakes have confirmed the vulnerability of our built environment, resulting in significant socio-economic losses, market disruptions, and environmental damage. Additionally, climate change is causing more frequent and severe weather-related events such as heat waves, which are impacting the construction sector and the health and well-being of building occupants. This emphasizes the pressing need to increase society's overall resilience by focusing on the various hazards that buildings may encounter throughout their lifespan. Although the need for a multi-risk analysis has been recognized in current performance-based design approaches, existing studies mostly focus on single hazards thereby neglecting the impact assessment of multiple hazards on the building performance.*

*This paper explores the economic and social losses of buildings due to earthquakes and heat waves. The study focuses on a high-rise building consisting of a reinforced concrete structure and masonry/cladding facades, and designed for two different locations in Europe. By means of a numerical model, time-history non-linear analyses are carried out to estimate the probable maximum losses in terms of repair costs and injuries/fatalities. In addition to earthquake scenarios, the study conducts dynamic energy simulations and comfort analyses that consider local climate scenarios and extreme heat events. The energy analysis calculates the economic losses caused by weather-related power consumption while the impact on occupants is assessed in terms of discomfort hours. Results from the seismic and energy simulations are finally compared to quantify and discuss the impact of the two different extreme hazards on the building performance and their potential consequences.*

**Keywords:** Earthquakes, Heat waves, Building performance, Socio-economic losses.

# 1 INTRODUCTION

The vulnerability of our existing building stock to natural disasters such as earthquakes was once again highlighted by recent tragic events, such as the devastating Turkey and Syria earthquake of 2023 (Figure 1a). Such disasters can result in severe direct and indirect economic losses and casualties. Direct losses include damage to buildings, loss of life, and injury, while indirect losses include reduced productivity and loss of income. Climate-related extreme events, such as more severe and frequent heat waves, are also increasingly impacting both the economy and society. In urban areas, buildings and infrastructure are often ill-equipped to cope with high temperatures, leading to significant socio-economic losses. The impact of heat waves on buildings can include increased energy consumption for cooling, reduced indoor air quality, and structural damage. When considering the overall impact of multiple hazards such as geophysical events (including earthquakes) and climatological events like heat waves, the total losses can be substantial, as shown in Figure 1b. According to recent data [1], heat waves have been responsible for the majority of fatalities in the last few decades, accounting for 68% of the total. Meanwhile, earthquakes have caused the greatest economic losses, representing 22% of the total value. Interestingly, despite their devastating impacts, both of these events have resulted in relatively low insurance losses, in contrast to meteorological events such as storms, which account for 62% of total insurance losses.

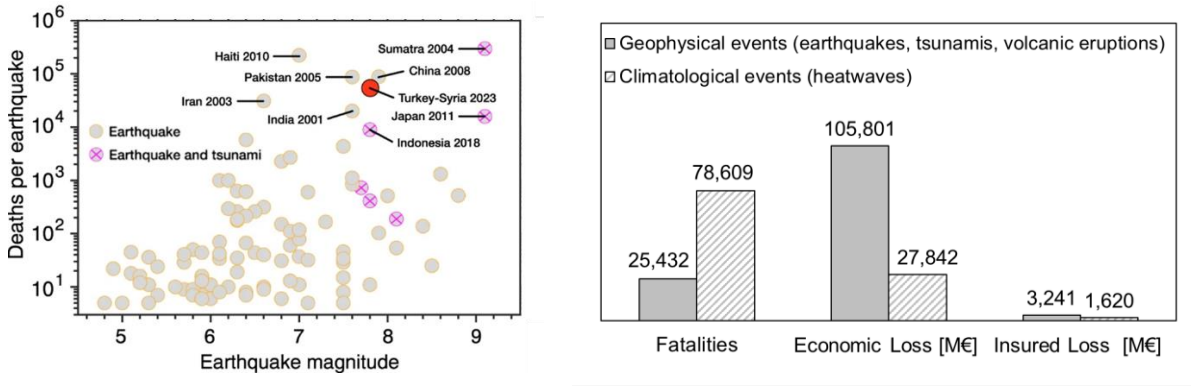


(a) (b)

Figure 1: (a) Impact of Turkey and Syria earthquakes: the fifth worst earthquake since 2000 [2]. (b) Social and economic losses for the period 1980-2017 (data elaborated from the European Environment Agency [1]).

Therefore, it is crucial to consider the potential impact of these hazards throughout the lifespan of buildings and take appropriate measures in design and retrofitting choices to enhance their resilience. This would not only help to minimize socio-economic losses and casualties, but also contribute to creating a safer and more sustainable built environment.

Focusing on earthquakes, different approaches have been developed for vulnerability assessments and loss estimation. In addition to empirical models that estimate damage and losses based on building characteristics such as age, height, and construction type [3, 4], the Performance-Based Earthquake Engineering (PBEE) methodology provides a probabilistic component-based approach to loss modeling [5-7]. PBEE enables the direct evaluation of performance measures such as economic losses, downtime, and casualties that are relevant to stakeholders for managing decisions related to investments and seismic risk mitigation. This comprehensive framework includes the description, definition, and qualification of different variables while considering all inherent uncertainties in earthquake performance assessment. Numerous loss assessment investigations can be found in the literature, focusing on both scenario or intensity-based analyses as well as time-based assessments [e.g. 8-9]. Overall, most of these studies have

focused on assessing the direct and indirect losses resulting from earthquakes on buildings, rather than potential fatalities. The findings emphasize the importance of implementing measures to improve building resilience to earthquakes, and the need for effective policies and strategies to mitigate the impact of earthquakes on buildings, such the adoption of a damage-control philosophy and technologies [10].

When assessing the impacts of heat waves on buildings, energy building performance simulation models [11] and/or empirical data collection through environmental and comfort monitoring [e.g. 12] are typically developed to estimate energy consumption and user response under varying environmental conditions. Several studies have used building performance simulation models to estimate economic losses resulting from increased power consumption [13], as well as the impact on the indoor thermal environment. Conversely, the estimation of potential fatalities caused by high internal temperatures is poorly addressed due to the lack of empirical data available on individual occupant response in buildings during heat waves [14], and this is a barrier to effectively estimate the social losses associated with heat waves depending on building design. Previous research has focused on the relationship between outdoor condition and mortality rate [e.g. 15], while only two studies at the best of our knowledge have studied the relationship between indoor temperature, building characteristics and related mortality rate during heat waves [16].

Although methods are further developing and research efforts are growing on the two separate domains (earthquakes and heat waves), an assessment of the potential losses due to the two hazards is still missing. This paper presents an integrated analysis of the overall impacts resulting from earthquakes and heat waves based on the local scenario. The aim is to compare the direct economic and social losses associated with these events and to highlight the need for integrated assessment to facilitate more effective investment decisions for building projects.

## 2 RESEARCH METHODOLOGY

This paper investigates the direct losses (potential casualties, economic losses) of buildings due to earthquakes compared to heat waves, focusing on a reinforced concrete high-rise new building with precast concrete façade systems as a case study. The selection of this case study is based on the significant impact that high-rise buildings can have on society, urban planning, and the economy of modern cities, especially during extreme events due to the larger number of occupants.

Seismic and energy modelling and simulations are carried out for the high-rise building designed for two different locations. Specifically, non-linear time history analysis and dynamic energy simulations are implemented to assess the seismic and energy performance of the building, respectively. The seismic loss modelling is implemented by following the above-mentioned probabilistic-based PEER procedure, that enables to assess the expected damage due earthquake scenarios to both structural and non-structural components thus assessing the consequent losses. The economic losses due to the heat wave are instead estimated by computing the total energy cost due to higher cooling and ventilation demand during the heat wave. For the social losses, no model can be found in literature that correlate indoor air temperature to mortality rate during heatwaves. Therefore, the cumulative hours of overheating are calculated by considering the indoor operative temperature at the center of the thermal zone and the following comfort thresholds: 26 °C, 28 °C, 30 °C and 32 °C. Temperature above 28 °C are considered to be a hazard for human health, while temperature above 32 °C are considered an extreme hazard for human health.

The simulation results provide a quantification of the impact associated with earthquakes and weather-related extreme events in terms of building performance and potential consequences. An integrated multi-hazard analysis is therefore suggested for informing more

effective decision-making from the early-stage design process, thus targeting an acceptable level of overall resilience.

## 3 APPLICATION TO A CASE STUDY

### 3.1 Description of the case study

The case study is a 18-storey reinforced concrete tower with regularity in plan and elevation. The building scheme derives from a previous study developed by the authors [17]. The tower has plan dimension of 22.05m (spans of 7.35m) in both structural directions and an inter-story height of 3m (Figure 2). The building has open-plan office floors at leach level apart from the last three levels that are residential, while the building roof is not accessible.

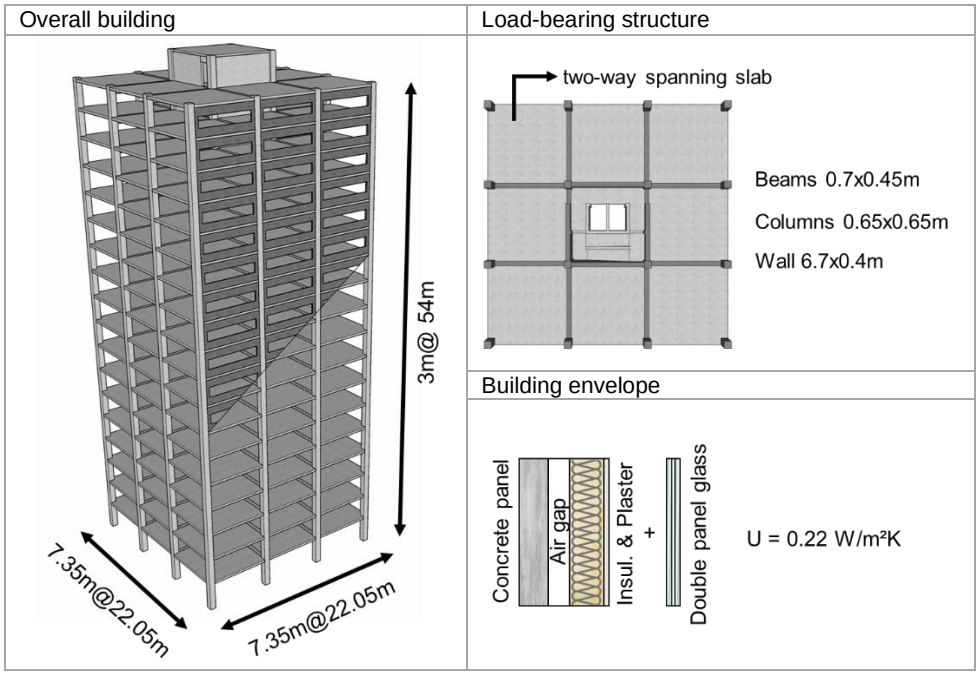


Figure 2: Case-study dimensions and properties.

The lateral loads resisting elements are the two internal frame-wall (dual) systems in each structural direction. A 2-way spanning flat slab 0.25m thick is responsible for ensuring the floor diaphragm, thus is properly connected to transfer the entire floor forces to the seismic-resistant systems. The building seismic mass is 736.0 tons per each floor, while the roof has a mass of 719.8 tons. The building façade is a modular prefabricated steel-stud panel systems with external insulated precast cladding panels and double pane windows, representing a new façade design (thermal transmittance of 0.22 W/m$^2$K, in order to satisfy the national guidelines for energy efficiency of building envelopes). Furthermore, all the other architectural components (drywall gypsum partitions, suspended ceilings), equipment (ideal HVAC systems) and contents (desktops, modular office tables, etc.) are identified and included in the loss modelling.

The study is implemented by considering two different locations in Europe: Messina (IT) and Bucharest (RO) both representing high-seismic prone areas. The cities are instead characterized by different climatic conditions: 1) Messina has a warm temperate Mediterranean climate with dry, warm summers and moderate, wet winters (Köppen-Geiger Climate Classification: "Csa": Mediterranean Climate); 2) Bucharest has a continental climate with cold winters and hot summers (Köppen-Geiger Climate Classification: "Cfa" - Humid Subtropical).

Both locations experienced multiple heatwaves in the past two decades (Figure 3). The most intense heatwave that struck the region of Bucharest took place in 2007 and lasted approximately 11 days, while for the region of Messina the most intense heatwave took place in 2021 and lasted for 60 days, the longest duration ever recorded [18]. The study uses these two periods to represent heat stress conditions. The weather data necessary to create a file in the EPW format, for use in the energy simulation, were sourced from the NOAA[1] and Copernicus online services [19]. Beside these historical data, the study considers the representative climate files (EPW IWEC data) for the two locations when designing the HVAC systems of the case study building.

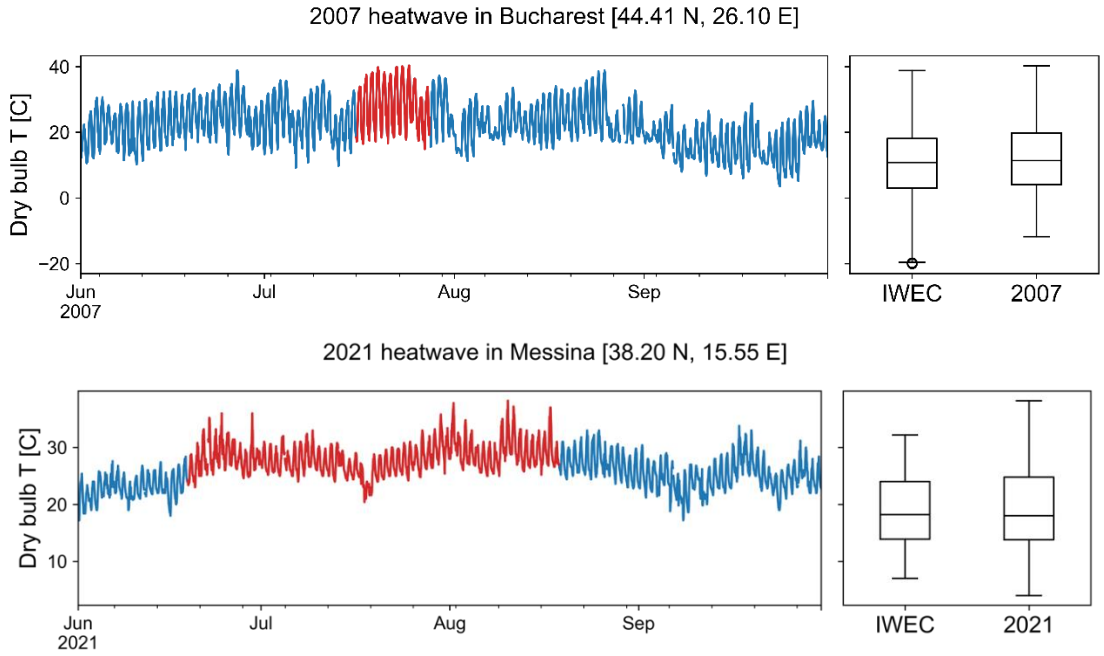


Figure 3: Dry bulb temperatures during the identified heatwaves event (left) and compared with typical temperatures used for building systems design and sizing (right).

### 3.1.1. Structural design

The structural/seismic design of the monolithic cast-in-situ building is implemented by referring to the above-mentioned building scheme, geometry and related vertical loads (self-weight, live loads) and following the principles of the Direct Displacement Based Design (DDBD) [20] adapted for frame-wall systems [21]. The structural/seismic design is carried out targeting a design drift limit ($\theta_d$) that takes into account codes limitations, good practice and/or material strain limits, and assuming 40% as frame overturning-moment ratio ($\beta_F$), which represents the overturning moment contribution of the frame only system vs. the total (frame-wall) system. The design of the reinforced concrete high-rise building is implemented referring to the Maximum Credible Earthquake scenario for both locations, corresponding to an event with 2500 years return period ($T_R$). The corner period ($T_D$) and the peak (plateau) displacement spectral ordinate ($\Delta_D$) are computed using the formula provided by Faccioli *et al.* [22], thus are defined as a function of the Moment Magnitude $M_w$, the fault rapture distance $r$ (Figure 4a) and the local soil factor $C_s$. A firm ground soil is assumed for both locations (meaning a $C_s = 1$) while $M_w$ and $r$ were defined based on the local scenario to define the elastic acceleration and displacement spectra presented in Figure 4b.

[1] NOAA Integrated Surface Database (ISD) was accessed on 06/03/2023 from https://registry.opendata.aws/noaa-isd

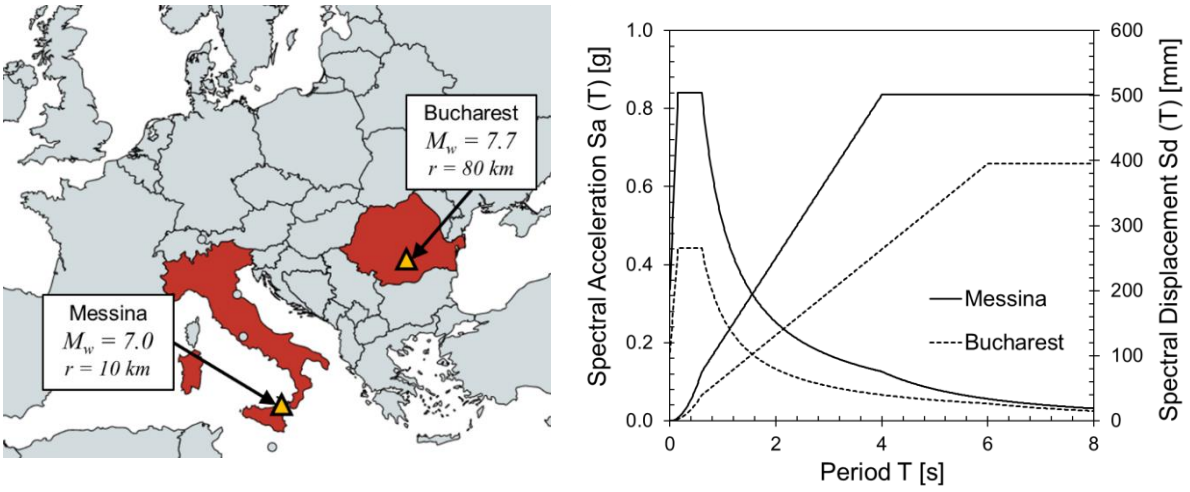


(a) (b)

Figure 4: (a) Building locations and fault properties. (b) Elastic spectra derived from Faccioli et al. [22]

The response spectra are used to develop the DDBD procedure for designing the building in both seismic scenarios. Table 1 summarizes the main design parameters obtained from implementing the displacement-based design. By distributing the base shear from the DDBD throughout the overall structural system, the monolithic cast-in-situ connections are designed, i.e. the steel reinforcement (number and diameter of rebars) of the structural members are identified and, consequently, the local non-linear structural behavior in terms of Moment-Curvature at the end section of beams, columns and at the wall base.

| Parameter | Messina | Bucharest |
|---|---|---|
| Effective Height, $H_e$ [m] | 39.1 | 40.3 |
| Design Displacement, $\Delta_d$ [mm] | 443.2 | 316.2 |
| Effective Mass, $m_e$ [t] | 8879.0 | 8151.6 |
| System Ductility, $\mu_{sys}$ [-] | 2.5 | 1.3 |
| Effective period, $T_e$ [s] | 4.3 | 5.6 |
| Effective stiffness, $K_e$ [kN/m] | 19406.4 | 10119.2 |
| Total Overturning Moment, $OTM_{tot}$ [kNm] | 168280.5 | 64435.1 |
| Total Base Shear, $V_{b,tot}$ [kN] | 4300.8 | 3200.0 |

Table 1: DDBD parameters for the Frame-Wall system.

### 3.2 Seismic modelling and analysis

Numerical modelling of both buildings is implemented in Ruaumoko2D software [23] following a lumped plasticity approach for the simulation of the local regions where the inelastic behavior is expected. The structural elements are therefore modelled as elastic members linked together through springs (simulating the plastic hinge regions), described by moment-rotation relationships and Takeda hysteresis rules. Façade systems are not modelled in this investigation, assuming a poor interaction with the main structure.

The numerical models are initially validated by performing non-linear static analyses: adaptive push-over and cyclic adaptive push-over to better describe the change of structural stiffness. In fact, the load lateral pattern changes every step depending on mass, new effective frequency and displacement shape. The push-over results (Figure 5a) provide useful indications on the

expected capacity of both buildings before developing dynamic analyses, e.g. in terms of strength/stiffness values and sequence of plastic hinges forming during the analysis. For each site seven spectrum-compatible accelerograms are then selected from the European Strong Motion database using REXEL.DISP software [24]. A comparison between the Average Spectra and Design spectra is showed in Figure 5b, where it can be observed a maximum spectral difference of 20% until the corner periods. These records are finally considered for the numerical investigation.

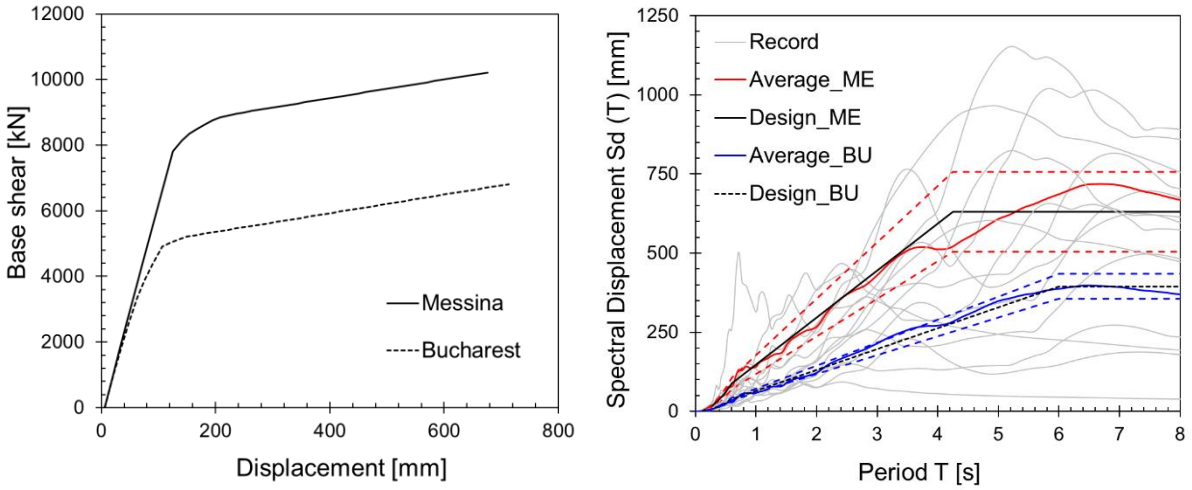


(a) (b)

Figure 5: (a) Capacity curves from adaptive push-over analysis; (b) Selected ground motions with average spectra for both cities of Messina (ME) and Bucharest (BU).

Non-linear time-history analyses are finally carried out to determine the seismic demand in terms of floor accelerations, inter-story drift ratios and residual displacements (Figure 6).

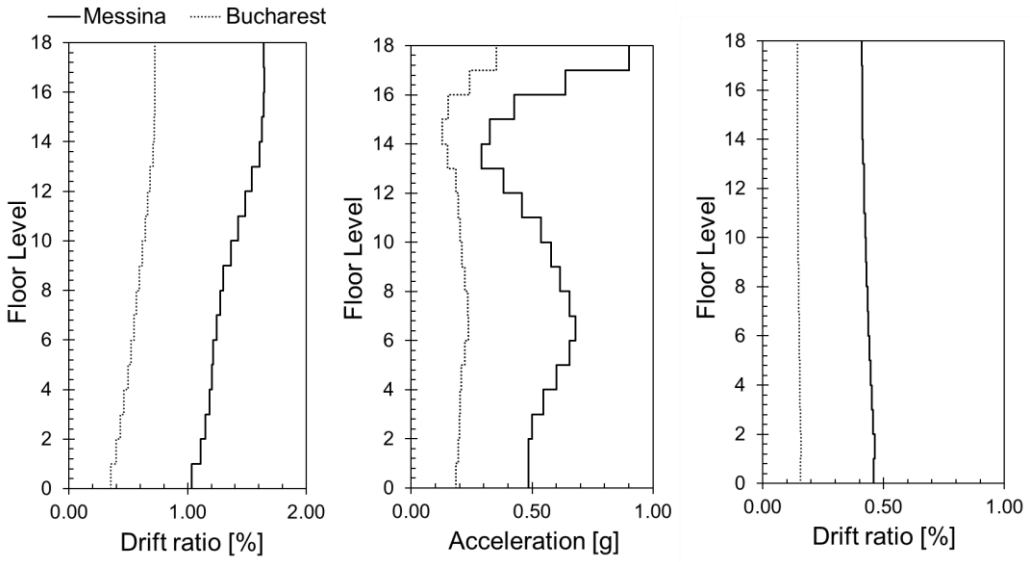


Figure 6: Inter-storey drift ratio, peak floor accelerations and residual drift ratios from time-history analyses.

It can be observed that higher demand parameters are recorded for the case study in Messina, as expected due to the implemented structural design targeting higher design displacement levels and higher earthquake intensities. For both buildings, an increase of floor accelerations is

observed at the upper stories due to higher mode effects. The growing demand for faster acceleration in structures may result in increased damage to acceleration-sensitive components. The post-earthquake residual drift ratios are also recorded (less than 0.5%), being a critical damage indicator that can lead to partial or total loss of structural safety after earthquakes and therefore causing significant losses for a building.

To compute the expected losses, an intensity-based loss analysis is developed following the probabilistic methodology proposed in FEMA P-58 [7]. Input data for the loss assessment are the predicted accelerations and drift ratios as well as the fragility functions, thus the potential damage states, of all structural and non-structural building elements. Fragility and consequence data (as the repair costs) for monolithic cast-in-situ structural members, building facades and other components are defined from the FEMA P-58 fragility database. Moreover, the total building replacement costs are estimated accounting for the specific labor cost and including the quantities of concrete and steel rebars, the cost of formworks, safety, excavation, foundations and geotechnical surveys. Loss assessment results in terms of direct losses are finally elaborated to determine the probable maximum losses. In Figure 7a, the repair costs are shown as a loss curve. The results indicate that Messina and Bucharest experienced repair costs of 0.85% and 0.16%, respectively, as a ratio of the total building replacement cost. Notably, structural components accounted for the majority of the repair costs. As discussed earlier, the higher acceleration demand in Messina resulted in increased damage to acceleration-sensitive components on the upper floors, as depicted in Figure 7b.

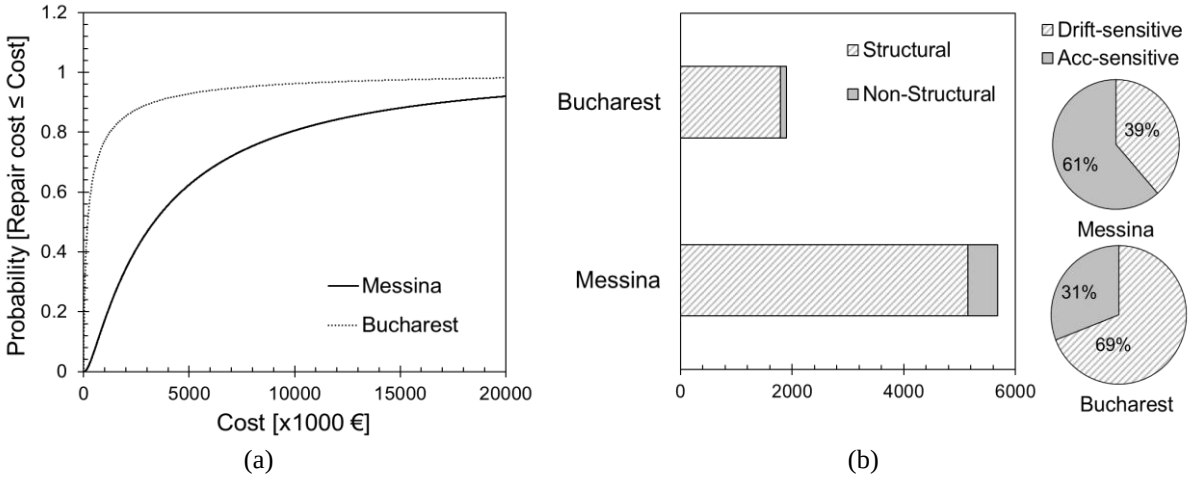


(a) (b)

Figure 7: (a) Loss curves and (b) distribution of losses at building level.

The casualty results reveal a small percentage of injuries and fatalities, considering a building population of 160 people at time the earthquake occurred. Both buildings suffer the same collapse mode, which affect the second story thus resulting in the same number of losses. It is important to note that in this study, collapse modes are assumed to have an equal probability of occurring, and that the collapse of one level do not have a cascading effect on the levels below.

| Expected Losses | Messina | Bucharest |
|---|---|---|
| Repair cost [x1000 €] | 17,075 | 3,310 |
| Injuries | 0.48 | 0.48 |
| Fatalities | 4.35 | 4.35 |

Table 2: Maximum direct losses.

### 3.3 Energy and thermal analysis

The building model for the energy analysis is created in EnergyPlus software v. 9.1.0 [25] by modelling the thermal properties of the building as described in section 3.1. using a combination of geometry, material properties, and system specifications. To accurately represent the building physical and thermal properties, walls (Window-to-Wall ratio of 0.4), roofs, floors, windows (double pane) and doors are properly simulated in the model. Specifically, thermal conductivity, specific heat, density, and emissivity are assigned to each building element. The building model is then divided into thermal zones based on the occupancy and thermal characteristics. The zoning is indeed critical for capturing the dynamic interactions between different building elements and the HVAC system.

Design requirements are set for the internal comfort of building occupants. The cooling set point temperature is 24 °C and the heating set point temperature is 19 °C. For the internal heat gain of either office or residential floors, equipment load is 5 or 10 W/m2 , artificial lighting load is 10 or 5 W/m2 , while the density of occupation is 0.01 or 0.005 persons per square meter. The desired rate of outside air infiltration is 0.0003 m3 /s per square meter of floor. The HVAC is modelled as an Ideal Load System, where therefore inefficiencies of the system are not taken into account. The maximum cooling capacity is determined by first calculating the cooling demand during the design day found in ddy file for each location (Bucharest and Messina). Once the cooling capacity is defined for each zone, the thermal simulation is again run to calculate the indoor operative temperature in each zone. These values are then used to calculate the cumulative number of hours above the comfort thresholds.

The heat wave related social losses are computed by calculating the cumulative number of hours that are above the comfort threshold. In addition, the economic losses are computed by considering the increased in total energy consumption due to the heat wave. Figure 8 shows the total cumulative hours when the operative temperature is above the thresholds of 26 °C, 28 °C, 30 °C and 32 °C. The heatwave in Messina is characterized by higher extreme temperatures and longer times which determine a larger number of hours in extreme discomfort, especially above the threshold of 28 °C. The number of hours in extreme discomfort (above 32 °C), it is instead comparable despite the heatwave in Messina being much longer. The increase in energy consumption due to the heatwave is larger in Messina, which is characterized by more extreme temperatures and larger cooling capacity, while the overall energy consumption is larger in Bucharest since it is driven by the heating season (Figure 9), but proportionally the increase in energy demand is higher for Bucharest than for Messina. This is also a limitation of sizing the cooling capacity based on the design days rather than on actual historical weather.

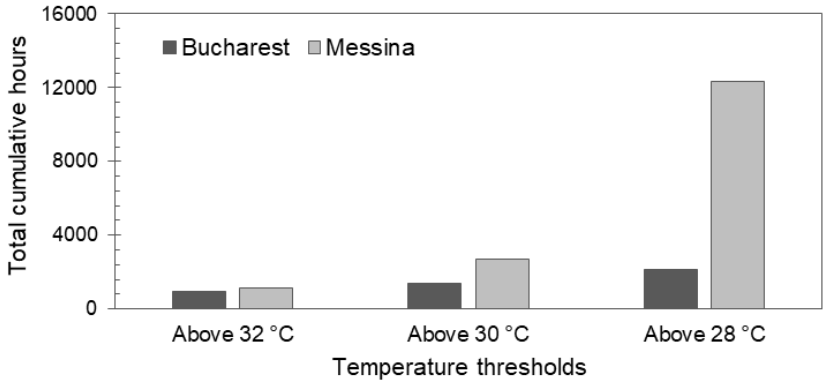


Figure 8: Total cumulative number of hours above 32, 30 and 28 °C.

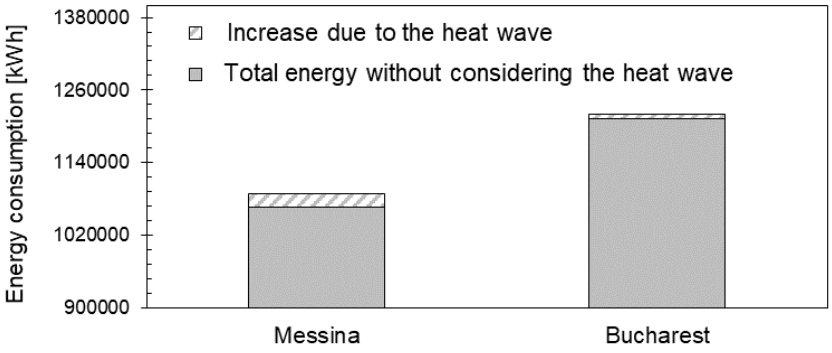


Figure 9: Total energy consumption due to heat wave

Table 3 summarizes the total losses due to heatwave for both Bucharest and Messina, and the related economic losses/cost (considering 0.43 and 0.16 € per kWh of electricity for Messina and Bucharest respectively). Given that in Romania the cost of the energy is lower, the impact of the heatwave is lower than in Italy in terms of energy cost.

| Expected Losses | Messina | Bucharest |
|---|---|---|
| Total cumulative hours of extreme discomfort (T>28 °C) | 2690 | 2143 |
| Total cumulative hours of extreme discomfort (T> 32 °C) | 1138 | 935 |
| Total annual energy consumption [kWh/m$^2$] | 123.58 | 139.73 |
| Total annual energy consumption including the heat wave [kWh/m$^2$] | 125.3 | 141.36 |
| Total energy consumption [kWh] | 1,066,835 | 1,213,376 |
| Total energy consumption including the heat wave [kWh] | 1,088,623 | 1,220,332 |
| Total increase in energy due to the heat wave [kWh] | 21,788 | 6,956 |
| Total increase in energy per m$^2$ [kWh/m$^2$] | 1.72 | 1.63 |
| Total increase in energy cost [€] | 9,370 | 1051 |
| Increased energy cost per m$^2$ [€/m$^2$] | 0.74 | 0.26 |

Table 3: Maximum direct losses due to heat wave hazards.

### 3.4 Earthquakes vs. heat waves impact

Results from the seismic and energy simulations are finally compared to assess the socio-economic impact of the different hazards. The comparison is shown in Figure 10a in terms of overall decision variables including the repair cost and the number of injuries/fatalities for earthquakes, as well as the annual energy cost and the discomfort hours for the heat wave scenario. The graph demonstrates that the Messina case study was more significantly affected by the hazards examined, with the exception of seismic casualties. This is due to the modeling assumptions that resulted in a realization with the same failure mode for both case studies, leading to the same number of casualties in buildings with the same population. The difference between the two case studies is further shown in Figure 10b, where the same scaling in terms of percentage value is adopted for comparing the results. Specifically, the economic losses are expressed as percentage of the total building cost (replacement cost in case of earthquake, thus including the demolition cost). The social impact is instead assessed focusing on the severe danger condition, meaning number of deaths as a percentage of the total building population

for the earthquake vs. the number of discomfort hours (temperature higher than 32 °C) as percentage of the total hours in a year for the heat wave. As expected, the comparison reveals that earthquakes have a significant impact on direct economic losses, whereas heat waves are more likely to cause extreme discomfort, potentially resulting in mortality.

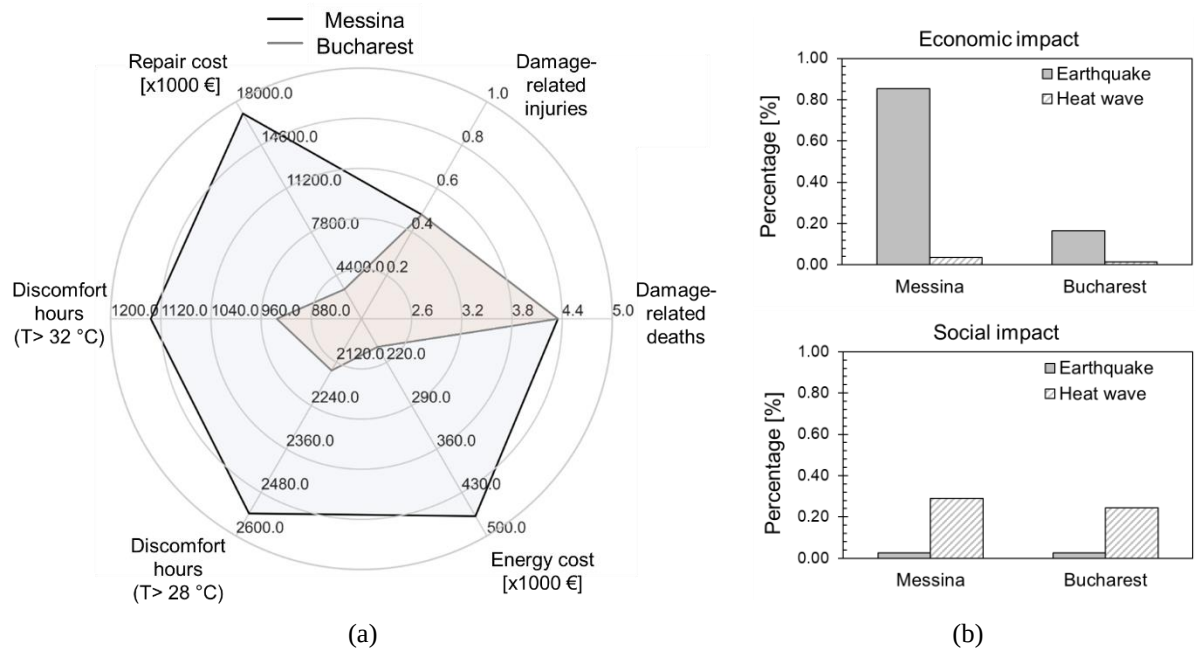


(a) (b)

Figure 10: (a) Comparison in terms of decision variables. (b) Economic and social impact of earthquake vs. heat wave scenarios.

## 4 CONCLUSIONS

The paper discusses the impact of earthquakes and climate change-induced heat waves on buildings in terms of socio-economic impact, thus emphasizing the need for increased resilience and multi-risk analysis. The study is implemented for a high-rise building by means of numerical modelling in order to estimate repair costs, injuries/fatalities in case of earthquake, as well as weather-related power consumption and discomfort hours in case of extreme heat events. The study is implemented for two different locations in Europe (Messina, Bucharest) with high seismicity (but different magnitude and fault distance) and different climatic conditions (warm temperate vs. continental climate). The heat waves scenarios are obtained from historical data considering the most extreme event recorded in the last years. The results of seismic and energy dynamic simulations are finally compared to assess the impact of the two hazards on building performance and potential consequences. It is found that the case study in Messina is affected by higher seismic and energy economic losses, although the energy consumptions are higher in Bucharest where the energy cost has a lower price. The investigation also revealed that Messina experiences a greater number of hours in extreme discomfort, attributable to its higher temperatures and longer duration of high temperatures. Despite this, the implemented seismic loss modelling assumptions yielded the same expected number of casualties for both buildings, due to one probabilistic-based realization experiencing the same collapse mode. Overall, the study highlights the greater economic losses associated with earthquakes, while also underscoring the potential for heat waves to cause fatalities, given their increasing frequency and severity.

However, the study has some limitations that need to be addressed in future research. Firstly, the collapse modes and their cascading consequences at the building level should be properly investigated to quantify the potential damage area and resulting casualties. The sequence of

mechanisms occurring and their correlation at the building level should be taken into consideration and implemented in the study. Furthermore, the study should account for different earthquake scenarios (ranging from low-to-high) with varying return periods. The cooling capacity of a building is a crucial factor in determining its preparedness to withstand heat waves and the associated economic losses. Design days and weather predictions are important considerations that can inform cooling requirements. Metrics used to assess thermal discomfort and the impact of heat waves on human health can affect the overall risk of a building. While the cooling capacity of an existing building is usually known, further work is needed to define the most accurate procedure for evaluating the cooling capacity of new buildings. Additionally, additional research is needed to identify the best metrics to predict the risk of human discomfort and health due to extreme temperatures caused by heat waves.

This investigation underscores the need for further research and the development of methods that can effectively evaluate the cumulative impact of earthquakes and heat waves on buildings and infrastructure. To assess the cumulative losses, an integrated approach should be adopted that considers the probability of both events occurring within a life-cycle framework. This requires the development of new assessment methodologies that take into account the potential interdependence and cascading effects between earthquakes and heat waves. Such methodologies would enable better decision-making by policymakers, building designers, and engineers to develop more resilient buildings and infrastructure that can withstand multiple hazards.

## 5 REFERENCES

[1] EEA, *Economic losses from climate-related extremes in Europe*. European Environmental Agency, Copenhagen, Denmark, 2019.

[2] L. Dal Zilio, J.P. Ampuero, Earthquake doublet in Turkey and Syria. *Communications Earth & Environment*, **4**, 71, 2023.

[3] FEMA, *HAZUS-MH MR3 Technical Manual*. Federal Emergency Management Agency, Washington, USA, 2003.

[4] H. Crowley, J. Dabbeek, V. Despotaki, D. Rodrigues, L. Martins, V. Silva, X. Romão, N. Pereira, G. Weatherill, L. Danciu, *European Seismic Risk Model (ESRM20)*. EFEHR Technical Report 002 V1.0.0, 2021.

[5] J. Moehle, G. Deierlein, A framework methodology for performance-based earthquake engineering. *13th World Conference on Earthquake Engineering (13WCEE)*, Vancouver, B.C., Canada, August 1-6, 2003.

[6] K.A. Porter, An Overview of PEER's Performance-Based Earthquake Engineering Methodology. *9th International Conference on Applications of Statistics and Probability in Civil Engineering (ICASP9)*, San Francisco, California, United States, July 6-9, 2003.

[7] FEMA, *Seismic Performance Assessment of Buildings, Volume 1 – Methodology*. Technical Report FEMA-P-58-1, Federal Emergency Management Agency, Washington, United States, 2012.

[8] D. Cardone, A. Flora, M. De Luca Picione, A. Martoccia, Estimating direct and indirect losses due to earthquake damage in residential RC buildings. *Soil Dynamics and Earthquake Engineering*, **126**, 2019.

[9] F.A. Arifin, T.J. Sullivan, G. MacRae, M. Kurata, T. Takeda, Lessons for loss assessment from the Canterbury earthquakes: a 22-storey building. *Bulletin of Earthquake Engineering*, **19**, 2081–2104, 2021.

[10] S. Bianchi, J. Ciurlanti, S. Pampanin, Comparison of traditional vs. low-damage structural & non-structural building systems through a cost/performance-based evaluation. *Earthquake Spectra*, 1-20.

[11] S. Homaei, M. Hamdy, Thermal resilient buildings: How to be quantified? A novel benchmarking framework and labelling metric. *Building and Environment*, **201**, 2021.

[12] A. Sakka, M. Santamourisa, I. Livadaa, F. Nicolb, M. Wilson, On the thermal performance of low income housing during heat waves. *Energy and Buildings*, **49**, 2012.

[13] S. Bucking, M. Rostami, J. Reinhart, M. St-Jacques, On modelling of resiliency events using building performance simulation: a multi-objective approach. *Journal of Building Performance Simulation*, **15**, 3, 307-322, 2022.

[14] C.Y. Siu, W. O'Brien, M. Touchie, M. Armstrong, A. Laouadi, A. Gaur, Z. Jandaghian, I. Macdonald, Evaluating thermal resilience of building designs using building performance simulation–A review of existing practices. *Building and Environment*, 2023.

[15] S. Tong, X. Wang, W. Yu, D. Chen, X. Wang, The impact of heatwaves on mortality in Australia: A multicity study, *BMJ Open*, **4**, 2, 2014.

[16] M. Alam, J. Sanjayan, P. X. W. Zou, M. G. Stewart, J. Wilson, Modelling the correlation between building energy ratings and heat-related mortality and morbidity. *Sustainable cities and society*, **22**, 29-39, 2022.

[17] J. Ciurlanti, S. Bianchi, S. Pampanin, Feasibility Study of Low-Damage Technology for High-Rise Precast Concrete Buildings. *SECED 2019 Conference*, London, England, 2019.

[18] O. Lhotka, J. Kyselý, The 2021 European Heat Wave in the Context of Past Major Heat Waves. *Earth and Space Science*, **9**, 11, 2022.

[19] M. Schroedter-Homscheidt, F. Azam, J. Betcke, N. Hanrieder, M. Lefèvre, L. Saboret, Y.-M Saint-Drenan. Surface solar irradiation retrieval from MSG/SEVIRI based on APOLLO Next Generation and HELIOSAT-4 methods, *Contrib. Atm. Sci./Meteorol. Z.*, 2022.

[20] M. J. N. Priestley, G. M. Calvi, M. J. Kowalsky, *Direct Displacement-Based Seismic Design of Structures*, IUSS Press, Pavia, Italy, 2007.

[21] A. R. R. Abellán, T. J. Sullivan, S. Pampanin, Adapting DDBD for the design of Frame-Wall Structures with Hybrid-Rocking Joints, *15th World Conference of Earthquake Engineering*, Lisbon, Portugal, 2012.

[22] E. Faccioli, R. Paolucci, J. Rey, Displacement spectra for long periods, *Earthquake Spectra*, **20**, 2, 347-376, 2004.

[23] A.J. Carr, *Ruaumoko Program for Inelastic Dynamic Analysis – User Manual*, University of Canterbury, Christchurch, New Zealand, 2003.

[24] C. Smerzini, C. Galasso, I. Iervolino, R. Paolucci, Ground motion record selection based on broadband spectral compatibility, *Earthquake Spectra*, **30**, 4, 1427–1448, 2013.

US Department of Energy's Building Technologies Office. *EnergyPlus*. DOE-BTO, 2001.

COMPDYN 2023
9th ECCOMAS Thematic Conference on
Computational Methods in Structural Dynamics and Earthquake Engineering
M. Papadrakakis, M. Fragiadakis (eds.)
Athens, Greece, 12-14 June 2023

# PROBABILISTIC SEISMIC DEMAND MODELS FOR THE ASSESSMENT OF UNDERGROUND STRUCTURES

**Grigorios Tsinidis[1], Anna Karatzetzou[2], and Sotiria Stefanidou[2]**

[1] Department of Civil Engineering, University of Thessaly, Greece
Pedion Areos, Volos, 38334
e-mail: gtsinidis@uth.gr

[2] School of Civil Engineering, Aristotle University of Thessaloniki, Greece
Aristotle University of Thessaloniki, 54124,
{akaratze, ssotiria}@civil.auth.gr

## Abstract

*Underground structures (e.g., tunnels, subway stations, underground parking lots, etc.) are increasingly constructed in seismic-prone areas to facilitate the expanding needs of modern societies. The significant downtimes and the accompanying costs associated with seismically induced damage to underground structures led to an increasing interest of the scientific community in the vulnerability assessment of this infrastructure against the seismic hazard. In addition, the performance-based design of new underground structures against seismic hazard has also gained increased attention from practitioners. A critical step in both design and vulnerability assessment of tunnels and underground structures is the development and use of rational Probabilistic Seismic Demand Models (PSDM), which describe the relationship between the amplitude of seismic hazard and the seismic response of the examined structure. Various approaches have been proposed in the literature to develop PSDMs for the assessment of tunnels or underground structures, e.g., subways, against ground seismic shaking and seismically induced ground failures. This paper discusses critical aspects of these approaches, based on a thorough review of the relevant state-of-the-art. Emphasis is placed on the modeling approaches proposed to simulate the seismic response of the structure and the surrounding ground, the determination of the seismic capacity of underground structures, as well as the selection of adequate intensity measures to describe the severity of the seismic hazard. In addition to the review of the existing literature, an effort to propose novel PSDM models for the assessment and design of circular tunnels is presented, based on an ongoing extended numerical study carried out in the frame of research project INFRARES (www.infrares.gr). The discussion highlights acknowledged gaps in the field, and topics calling for further investigation are presented.*

**Keywords:** Tunnels; PSDM; Seismic vulnerability; Seismic Resilience

## 1 INTRODUCTION

Tunnels, subways and large embedded structures, such as underground parking lots, are constructed at an increasing rate in seismic prone areas, to facilitate the expending needs of modern societies. Their importance highlights the need for a rigorous seismic design (i.e., for new structures), as well asadequate assessment of their current condition and their vulnerability against seismic hazard (i.e., for existing structures). Various methodologies have been presented in the recent literature for the seismic analysis, design and vulnerability assessment of tunnels and underground structures [1], [2], with most of these methodologies focusing on the effects of ground seismic shaking. The development of appropriate *Probabilistic Seismic Demand Models (PSDM)*, which correlate the intensity of seismic hazard with the seismic response of the examined structure, constitutes a vital step toward the proposal of an efficient vulnerability assessment method. Moreover, the development of a rational PSDM is a key element for a performance-based seismic analysis method.

This paper initially discusses critical aspects of available methodologies for the derivation of PSDMs for the assessment of tunnels or underground structures based on a literature review. Emphasis is placed on modelling approaches proposed to simulate the structural response and the response of surrounding ground, the determination of the seismic capacity of underground structures, as well as the selection of 'optimal' intensity measures for the description of the intensity of the seismic hazard. Furthermore, a methodology for the development of novel PSDM models for the assessment and design of circular tunnels is proposed, based on an ongoing extended numerical study carried out in the frame of research project INFRARES (www.infrares.gr).

## 2 SEISMIC DEMAND MODELS FOR EMBEDDED STRUCTURES

Most of the available PSDMs for the assessment of embedded structures were developed in the frame of analytical studies aimed at proposing analytical fragility functions to estimate the vulnerability of such structures, when subjected to ground seismic shaking in their transverse direction. *Fragility functions* (i.e., fragility surfaces or fragility curves normally expressed by a lognormal probability distribution) link the probability of exceeding a predefined level of damage due to the examined hazard (e.g., the seismic hazard), with the measure selected to describe the intensity of this hazard. The level of structural damage is commonly expressed by a set of discrete *Limit States* (*LS*) or *Damage States* (*DS*), defined by means of thresholds of a parameter used to describe the structural performance, i.e., the *Engineering Demand Parameter* (*EDP*). The severity of the examined natural hazard is expressed by an Intensity Measure (*IM*) for instance, the Peak Ground Acceleration (*PGA*).

The analytical studies employed 2D numerical models (analysis in plain strain) to perform static or dynamic analyses of the selected ground-structure configurations and compute the structural demand for an increasing level of ground shaking. The analyses were conducted using various *Finite Element (FE)* or *Finite Difference (FD)* codes (e.g., ABAQUS, MIDAS, PLAXIS 2D, FLAC 2D, FLAC 3D etc.).

Most approaches proposed analyses in total stresses and under the assumption of undrained conditions for the ground. Various constitutive models were used to simulate the ground response against seismic shaking, from simplified approximations, such as the equivalent linear approximation to more advanced nonlinear models (e.g., nonlinear models with multi-nested yield surfaces). Figure 1a summarizes the variety of constitutive models used to simulate ground response in studies assessing the vulnerability of various types of embedded structures subjected to ground seismic shaking in the transversal direction.

With reference to the simulation of the lining, most of the studies for mountain tunnels in rock or bored tunnels in alluvial employed a linear elastic model (Figure 1b). The damage index and the damage states thresholds were defined using a separate section analysis for the examined liners, accounting for the effect of axial loading on the capacity of the liners in a simplified manner. Some researchers used concentrated plasticity models to account for the nonlinear seismic response of tunnel liners, i.e., by using inelastic zones/hinges (e.g., [3]). For large rectangular embedded structures (e.g., subways), more advanced nonlinear models were used to simulate the response of concrete liners (e.g., [4]).

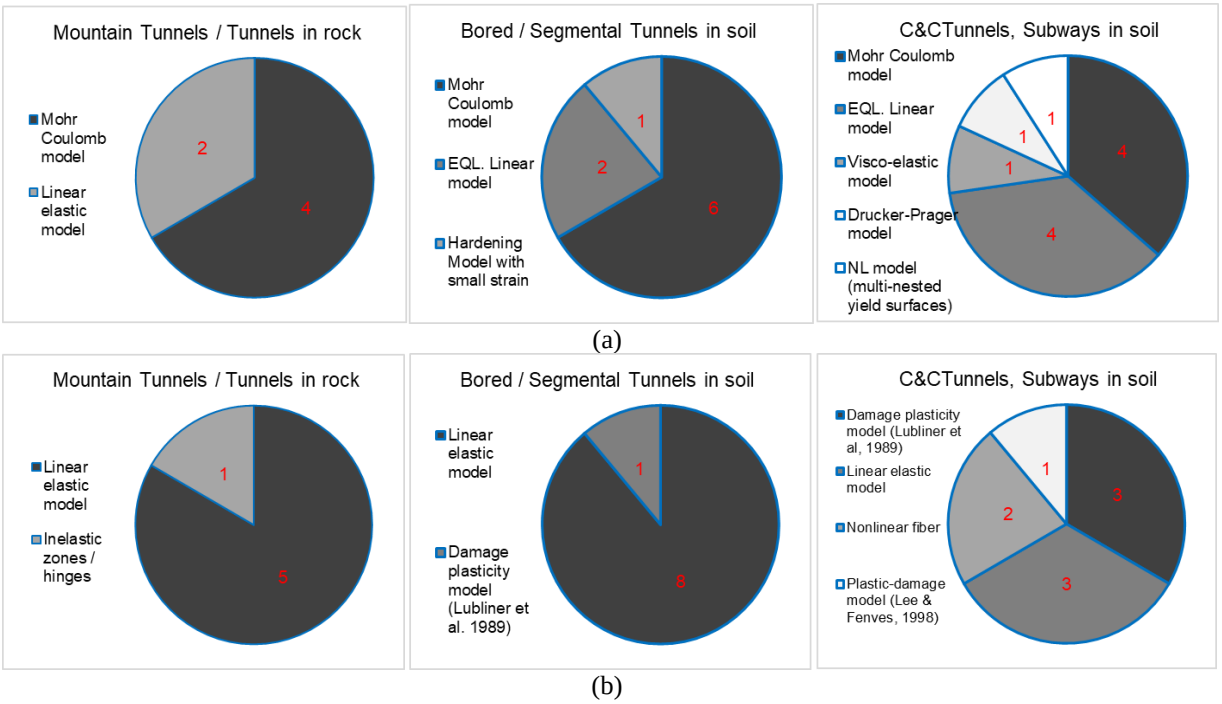


Figure 1: Constitutive models used to simulate the response of (a) ground and (b) the liner in vulnerability assessment studies of various types of embedded structures subjected to ground seismic shaking in the transversal direction.

Peak Ground Acceleration (*PGA*) and Peak Ground Velocity (*PGV*) have been used widely as *IMs* to develop PSDMs and analytical fragility functions for embedded structures subjected to ground seismic shaking in the transversal direction (Figure 2a). Some efforts to identify optimal *IMs* as per definitions of [5], [6] and [7] have recently been presented in the literature for the assessment of embedded structures.

Figure 2b summarizes the *EDPs* used for assessing the performance of various types of embedded structures in relevant vulnerability assessment studies. Argyroudis & Pitilakis [8] proposed the ratio of acting bending moment over the capacity bending moment of the lining (i.e., $M/M_{Rd}$) as an *EDP* for the assessment of bored circular and cut & cover tunnels in soft soil. This metric was then adopted by many researchers. The capacity bending moment was estimated based on section analyses of the examined liners that were carried out separately for various levels of axial loading. Despite the simple and straightforward definition of this *EDP*, the uncoupled approach proposed to compute the lining capacity and, hence, the *EDP*, does not accurately capture the variation of capacity with time during ground shaking, associated with the variation of axial forces acting on the liner during ground shaking. In addition to the metric proposed by Argyroudis & Pitilakis [8], different *EDPs* were used by researchers, with most definitions being based on ratios of acting internal forces over capacity of the liners. Some

studies (referring mainly to the assessment of metro stations) introduced *EDPs* based on the deformation of the embedded structure due to ground shaking.

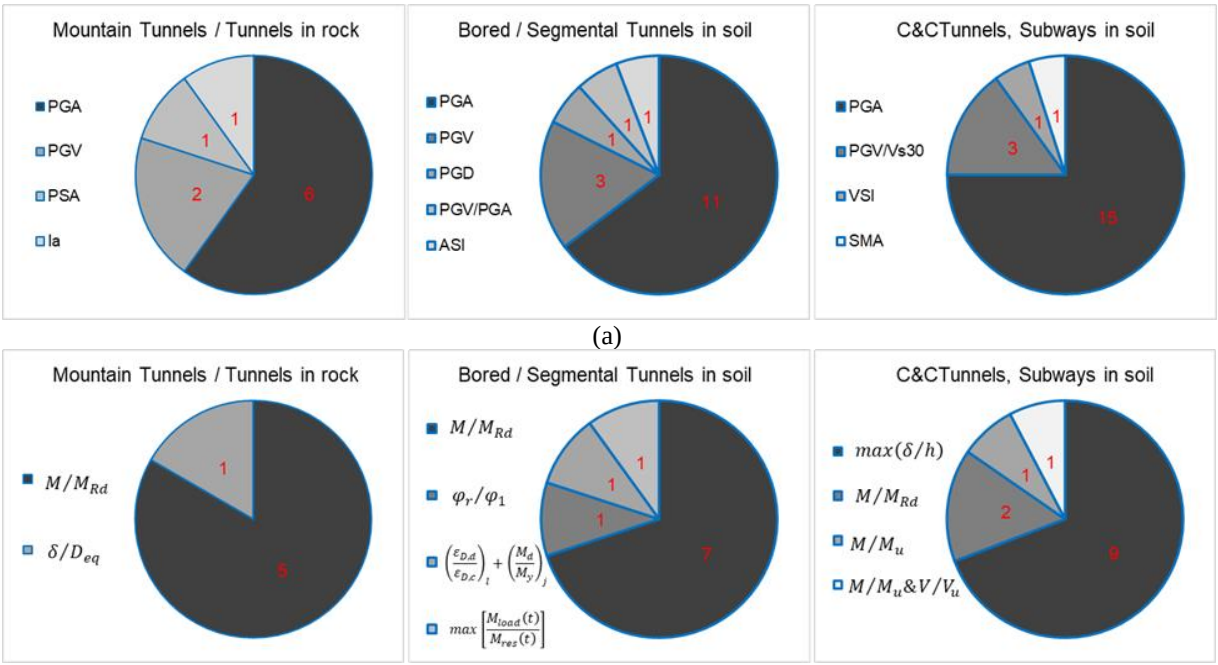


Figure 2: (a) Intensity Measures (*IMs*) and (b) Engineering Demand Parameters (*EDPs*) used in vulnerability assessment studies of various types of embedded structures subjected to ground seismic shaking in the transversal direction.

Regardless of the selected *IM* and *EDP*, most analytical studies proposed least-squares regression analyses on data sets of *EDP-IM*, in the log-log space to establish the PSDM ([9]). This approach is generally associated with a large number of dynamic or static analyses to establish the required data sets of *EDP-IM*, which demand a high computation effort. Artificial Neural Network (ANN) approaches were recently proposed for the development of PSDM (e.g., [10]), reducing the computational effort. The main disadvantage of ANN-based approaches to the moment is the effort required to train properly the ANN model given that available data from field records are generally not available; therefore, the use of output results from numerical analyses is mandatory.

## 3 SEISMIC DEMAND MODELS FOR CIRCULAR TUNNELS

A comprehensive numerical methodology for the derivation of analytical fragility functions for the vulnerability and resilience assessment of tunnels is currently under development in the frame of research project INFRARES. The methodology focuses on the assessment of circular tunnels in soil when subjected to ground seismic shaking in the transverse direction. A critical step of the methodology is the development of new PSDMs for circular tunnels. This section briefly presents the methodology.

After the selection of the ground-tunnel configurations to be examined, as well as the selection of the ground motions to be used in the analyses, the main steps of the methodology refer to: (a) the determination of the capacity of the examined tunnel, and (b) the estimation of the demand, which is related to the expected response of the tunnel for the selected ground motions.

For the determination of the capacity, nonlinear pushover analyses of the ground-tunnel configurations are proposed, whereas for the estimation of demand, nonlinear full dynamic time history analyses are employed. Figure 3 illustrates the proposed numerical models for the two steps. The open-source finite element code OpenSees [11] is used herein to perform the analyses.

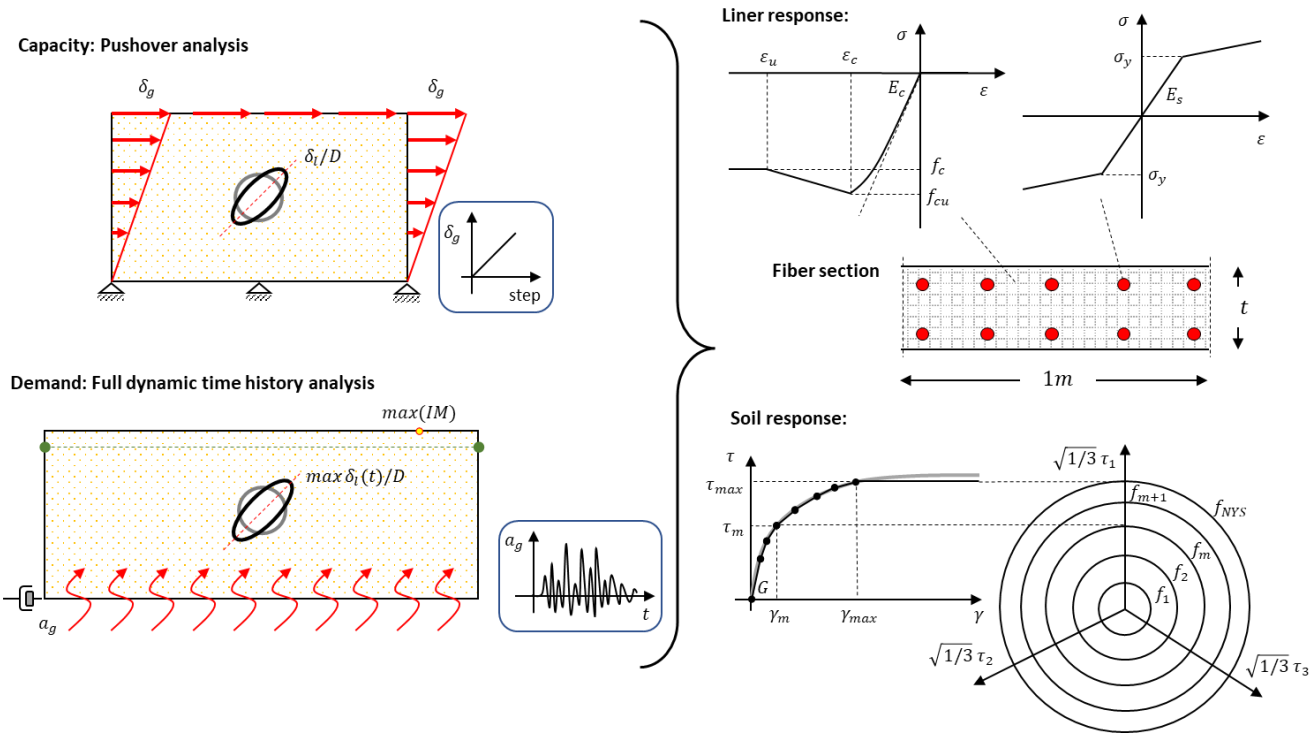


Figure 3: Numerical models used to evaluate the demand and capacity of the examined ground-tunnel configurations against ground seismic shaking in the transverse direction.

### 3.1 Pushover analysis

A two-dimensional (2D) numerical model of the selected ground-tunnel configuration is developed in OpenSees to perform nonlinear pushover analyses. The dimensions of the ground domain are selected based on the actual geometry of the examined tunnel (dimensions, burial depth etc), also accounting for potential boundary effects on the computed liner response. The side boundaries of the model are introduced at a distance from the tunnel, which is tuned accordingly. Plane-strain elements represent the ground, whereas 64 beam elements are used to simulate the liner. The ground response is simulated with a nonlinear multi-yield-surface $J_2$ plasticity constitutive model *('PressureIndependMultiYield Material')*, assuming that its shear behavior is insensitive to the confinement change. The concept of distributed material inelasticity and the fiber model approach is employed to simulate the liner response. Thus, the. *'Concrete01'* material is used to simulate the response of concrete, whereas for the steel reinforcement the *'Steel01'* material is used. Figure 3 illustrates the response of all constitutive models described above for uniaxial loading. The models are calibrated according to the actual mechanical properties of the examined ground-tunnel configurations. A penalty-based frictional contact element that follows the Coulomb frictional behavior is used to simulate the ground-tunnel interface. The *'ZeroLengthContactASDimplex'* element is employed for this purpose, with the coefficient of friction being set equal to 0.5.

Each analysis is conducted in steps as follows: 1. Initially, the geostatic stress field is introduced on the ground. 2. Subsequently, the tunnel cavity is excavated, and the liner is activated.

3. Finally, the ground-tunnel system is subjected to a monotonic simple shear deformation pattern within a pushover analysis step. During the latter step, the numerical model is fixed at the base boundary in both horizontal and vertical directions, while a ground deformation pattern is introduced on both side boundaries of the model (Figure 3), replicating a simple shear deformation field imposed on the examined configuration. The deformation level $\delta_g$ increases gradually, causing an ovaling deformation of the examined tunnel. This ovaling is expressed as the ratio of the diametric deflection of the tunnel $\delta_l$ over the diameter of tunnel *D*, which constitutes the *EDP* for the tunnel. The strain energy $U$ of the liner for each loading step of the pushover analysis is computed as:

$$U = \int \frac{1}{2} \sigma_{ij} \varepsilon_{ij} dv \tag{1}$$

where $\sigma_{ij}$ and $\varepsilon_{ij}$ are the tensors of stress and strain, respectively, and $v$ is the volume of the liner. An 'equivalent force' $F_G$ that is introduced on the liner ring due to the ground deformation may be computed as the derivative of the strain energy $U$ with respect to the selected *EDP*, i.e., $\delta_l/D$ (Figure 4a). The derivative of $F_G$ with respect to $\delta_l/D$ constitutes a measure of an 'equivalent generalized stiffness of the liner', $k_G$, which drops during the gradual increase of ground deformation $\delta_g$ due to the nonlinear response of the liner (Figure 4b). Distinct Limit States ($LS_i$) may be defined by setting the thresholds of $\delta_l/D$ for which the stiffness of ring $k_G$ drops by a certain degree compared to the initial stiffness of the ring $k_{G0}$, e.g., $k_G/k_{G0} = 20\%, 40\%$, for minor and moderate damage states, respectively. The application of the methodology for various parameters that control the seismic response of tunnels may allow the formation of a set pushover curves similar to those presented in Figure 4, which subsequently may allow the quantification of the uncertainty related to both the definition of capacity and definition of limit states.

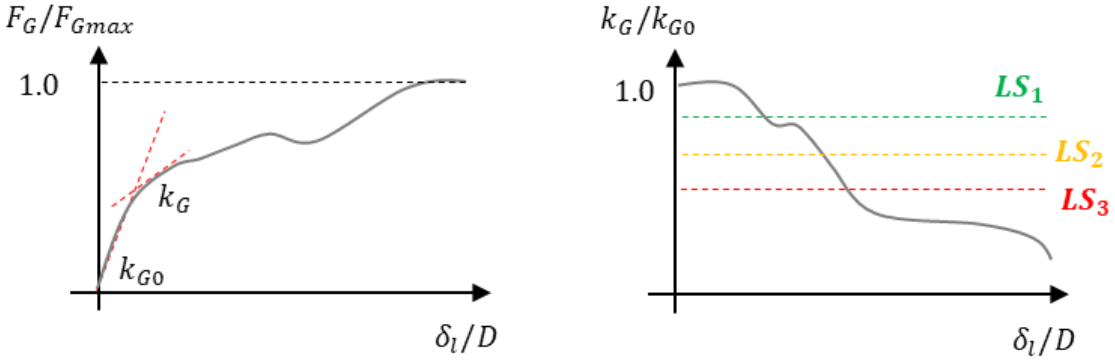


Figure 4: Definition of 'equivalent force' $F_G$ introduced on the liner ring of a circular tunnel due to the ground deformation; definition of equivalent generalized stiffness of the liner ring, $k_G$ to ovalization and definition of Limit States (LS).

### 3.2 Full dynamic time history analysis

A similar simulation strategy is followed to perform dynamic time history analysis of the examined ground-tunnel configuration to determine the demand for of the selected ground motions. The 2D numerical model of the selected ground-tunnel configuration is again developed in OpenSees. This model is more extended in the horizontal direction (compared to the one employed in pushover analysis) to reduce potential boundary effects caused by 'reflections' of seismic waves on the side boundaries. In addition, tie constraints are introduced between the nodes of the side boundaries of the model (Figure 3), imposing the same translational displace-

ments in horizontal and vertical directions), simulating in a simplified way a simple shear response of the ground in 'free-field' conditions. The finite stiffness of the underlying bedrock is simulated via a Lysmer-Kuhlemeyer dashpot that is introduced at the base of the ground domain. The seismic load is introduced at the base of the ground domain through the dashpot as a horizontal force time history, which is proportional to the known velocity time history of the selected ground motion. In addition to the damping induced by the hysteretic behavior of the ground, an additional damping of 2% is introduced in the analysis as Rayleigh damping to simulate energy dissipation at very small shear strain levels of the ground.

Through the analysis, time histories of the diagonal distortions of the tunnel $\delta_l\ (t)$, as well as the acceleration, velocity, and displacement at the ground surface and tunnel depth are computed. The maximum value of the normalized over the diameter of tunnel *D*, diagonal distortion of the tunnel $\delta_l\ (t)$ is used as *EDP*, whereas the *PGA*, *PGV* and *PGD* at the ground surface (computed as the maxima of relevant time histories) are used as *IMs*. New PSDMs are finally proposed based on least-squares regression analyses on data sets of *EDP-IM*, in the log-log space (Figure 5a). Combining these models with the definitions of limit states made via the pushover analyses discussed in *Section 3.1*, analytical fragility functions may be constructed, as per Figure 5b.

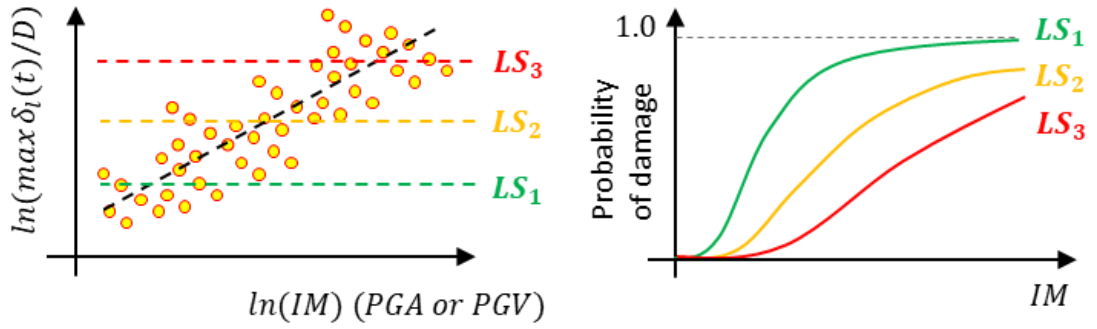


(a) (b)

Figure 5: (a) Development of a PSDM for circular tunnels in soft soil, (b) development of analytical fragility curves.

## 4 CONCLUSIONS

The paper presented critical aspects and assumptions of available methodologies for the development of PSDMs models for the assessment of embedded structures based on a review of the state-of-the-art. In addition, the main steps of an analytical methodology for the development of novel PSDM models for the assessment and design of circular tunnels were presented. The main novel aspects of the proposed analytical method are:

- the proposal of a nonlinear numerical simulation approach of the selected soil-tunnel configurations to define both the capacity of the tunnel, as well as the demand, and
- the definition of an EDP for circular or horse-shoe type tunnel based on a displacement-based metric which accounts for the whole 'stiffness of the ring' and fits better with the physics of the problem in hand.

The methodology is currently applied on various ground-tunnel configurations, covering crucial parameters affecting the seismic response of tunnels to develop PSDMs and analytical fragility functions for such configurations.

## ACKNOLEDGEMENTS

The work reported in this paper was carried out in the framework of the research project *INFRARES "Towards resilient transportation infrastructure in a multi-hazard environment"* (https://www.infrares.gr/), funded by the Hellenic Foundation for Research and Innovation (HFRI) under the *"2nd Call for H.F.R.I. Research Projects to support Post-Doctoral Researchers"* (Project Number: 927).




## REFERENCES

[1] G. Tsinidis, F. De Silva, I. Anastasopoulos, E. Bilotta, A. Bobet, Y.M.A. Hashash, C. He, G. Kampas, J. Knappett, G. Madabhushi, N. Nikitas, K. Pitilakis, F. Silvestri, G. Viggiani, R. Fuentes. Seismic behavior of tunnels: from experiments to analysis. *Tunnelling and Underground Space Technology*, **99**, 103334, 2020.

[2] G. Tsinidis, A. Karatzetzou, S. Stefanidou, O. Markogiannaki. Developments in seismic vulnerability assessment of tunnels and underground structures. *Geotechnics*, **2**, 209-249, 2022.

[3] G. Andreotti, C.G. Lai. Use of fragility curves to assess the seismic vulnerability in the risk analysis of mountain tunnels. *Tunnelling and Underground Space Technology*, **91**, 103008, 2018.

[4] C. Zhang, M. Zhao, Z. Zhong, X. Du. Seismic intensity measures and fragility analysis for subway stations subjected to near-fault ground motions with velocity pulses. *Journal of Earthquake Engineering*, **26** (16), 8724-8750, 2022.

[5] S.A. Argyroudis, K.D. Pitilakis. Seismic fragility curves of shallow tunnels in alluvial deposits. *Soil Dynamics and Earthquake Engineering*, **35**, 1-12, 2012.

[6] J.W. Baker, C.A. Cornell. A Vector-Valued ground motion intensity measure consisting of spectral acceleration and epsilon. *Earthquake Engineering & Structural Dynamics*, **34**, 1193-1217, 2005.

[7] N. Shome, C.A. Cornell, P. Bazzurro, J.E. Carballo. Earthquakes, records, and nonlinear responses. *Earthquake Spectra*, **14**, 469-500, 1998.

[8] N. Luco, C.A. Cornell. Structure-specific scalar intensity measures for near-source and ordinary earthquake ground motions. *Earthquake Spectra*, **23**, 2, 357-392, 2007.

[9] J.W. Baker. Probabilistic Structural Response Assessment Using Vector ‐ Valued Intensity Measures. *Earthquake Engineering and Structural Dynamics*, **36**, 13,1861-1883, 2007.

[10] Z.K. Huang, S. Argyroudis, K. Pitilakis, D. Zhang, G. Tsinidis. Fragility assessment of tunnels in soft soils using artificial neural networks. *Underground Space*, **7**, 2, 242-253, 2022.

[11] S. Mazzoni, F. McKenna, G.L. Fenves. *Open system for earthquake engineering simulation user manual* (Version 1.6.2). Pacific Earthquake Engineering Research Center, University of California, Berkeley, California, 2006.

COMPDYN 2023
9th ECCOMAS Thematic Conference on
Computational Methods in Structural Dynamics and Earthquake Engineering
M. Papadrakakis, M. Fragiadakis (eds.)
Athens, Greece, 12-14 June 2023

# INELASTIC TIME-HISTORY ANALYSES OF FRP-RETROFITTED BRIDGE COLUMNS SUBJECTED TO NEAR-FIELD GROUND MOTIONS

**Konstantinos G. Megalooikonomou**[1]
[1] Hellenic Open University, School of Science and Technology, Parodos Aristotelous 18, 26335 Patras, Greece
e-mail: std153412@ac.eap.gr

## Abstract

*The material model proposed by Megalooikonomou et al. (2012) was added to the source code of OpenSees as a uniaxial material. In order to evaluate the performance of this material model, it was implemented in the simulation of a series of shaking table tests performed by Kumar and Mosalam (2015). The two test specimens, having identical geometry and reinforcement details but different spacing of the transverse bars (one column had closely spaced stirrups satisfying code requirements, and the other had larger spacing, representing a shear-critical column), were subjected to a series of horizontal and vertical excitations on a shaking table and experienced moderate to high damage. The damaged columns were subsequently repaired with unidirectional CFRP and GFRP composite laminates and subjected to the same set of near-field earthquake excitations as the one tested in as-built configuration. Both specimens were simulated using nonlinear beam with hinge elements, in which the FRP-confined concrete was modelled using the aforementioned material model. Comparison between the numerical and experimental time history response of the column is indicative of the effectiveness of the implemented modelling. The numerical model confirmed that the repaired columns were able to resist higher shear and developed fewer peaks of tensile forces due to the vertical component of the ground motion. Therefore, the effect of changes of axial load from compression to tension due to the vertical component which can result in significant decreases in column shear strength, was diminished through the contribution of the FRP jacket. Finally, after performing all time history dynamic analyses, the residual displacements were found to be much lower for both repaired specimens in comparison to their bare counterparts. This is indicative of the effectiveness of the investigated FRP repair technique to produce resilient bridge columns when subjected to earthquake loading with strong vertical component.*

**Keywords:** Bridge Pier, FRP jacket, Vertical Excitation, Nonlinear Dynamic Analysis, OpenSees.

## 1 INTRODUCTION

The library of materials, elements and analysis commands makes OpenSees [1] a powerful tool for numerical simulation of nonlinear structural and geotechnical systems. The OpenSees library of components is ever-growing and at the leading edge of numerical-simulation models. Its interface is based on a command-driven scripting language which enables the user to create more-versatile input files. OpenSees is not a black box, making it a useful educational tool for numerical modeling. Material, element or analysis tools can be incorporated into OpenSees.

Addition of a new uniaxial material module by the developer is achieved by providing a new C++ subclass of the UniaxialMaterial class, along with an interface function which is used to parse the input and create the new material. Unlike the C and Fortran modules, no information about the state of the model is provided as argument to the material routine. Retaining the required information and rejection of the unnecessary one is performed within the material model. This information includes simultaneously (a) parameters, i.e., information needed to define the material, and (b) state variables or history variables, i.e., information needed in order to define its current state and, consequently, compute the applied stress and tangent.

The present work provides information on the implementation of a recently developed material model for Fiber Reinforced Polymer (FRP)- and Steel – confined concrete, proposed by Megalooikonomou et. al. [2], in OpenSees under the name '*FRPConfinedConcrete*'. To date, the model has no tensile strength and uses the degraded linear unloading/reloading stiffness in the case of cyclic loadings based on the work of Karsan and Jirsa [3].

In order to evaluate the performance of this material model, it was implemented in the simulation of a series of shaking table tests performed by Kumar and Mosalam (2015) [4]. The two ¼-scale test specimens, having identical geometry and reinforcement details but different spacing of the transverse bars (one column had closely spaced stirrups satisfying code requirements, and the other had larger spacing, representing a shear-critical column), were subjected to a series of horizontal and vertical excitations on a shaking table and experienced moderate to high damage. The damaged columns were subsequently repaired with unidirectional CFRP and GFRP composite laminates and subjected to the same set of near-field earthquake excitations as the one tested in as-built configuration.

Strong vertical shaking is usually considered in near-field regions and may lead to severe impacts on structures such as buildings and bridges. To be more specific, the Northridge Earthquake (January 17, 1994) whose generated ground motions recorded at Pacioma Dam Station are employed in the current study, was magnitude 6.7 on a previously unidentified thrust fault, creating strong horizontal and vertical ground motion lasting up to 10 seconds. The area of strongest shaking in the earthquake was about 50 km in diameter from Northridge, California, encompassing southern Ventura and northern Los Angeles counties. Earthquake activity was felt as far away as Las Vegas and San Diego. Strong forward directivity was observed also during this seismic event. Directivity is related to the rupture direction. Forward directivity is the case in which the rupture is toward the site while backward directivity is the case in which the rupture is away from the site. For forward directivity, if the slip direction and the rupture direction are aligned, then the SH waves generated between the epicenter and the site will arrive at about the same time at the site and at long periods the SH waves will constructively interfere. For most of the rupture, the SH waves will be primarily on the fault normal component. This leads to a large 2-sided velocity pulse on the fault normal component. Seven major freeway bridges in the above-described area collapsed, and 212 were damaged, disrupting traffic in the Ventura-Los Angeles region for weeks following the earthquake.

Among all the components of a bridge, columns are the most critical from a structural point of view and therefore require precise seismic assessment and retrofit. Confining wraps or jackets to rehabilitate and strengthen existing bridge columns has proven to be an efficient technique for seismic retrofit of structures. However, most of the compressive strength models of confined concrete only consider the increased strength and ductility provided by fiber reinforced polymers (FRPs), neglecting the contribution of the existing steel reinforcement inside the column's section. Even if the existing steel stirrups in a reinforced concrete column are not sufficient to confine the concrete core they must also contribute, along with the FRP jacket, in confining the section. In this context, the Fiber Reinforced Polymer (FRP)-confined concrete model contained in a well-known Bulletin by the International Federation for Structural Concrete (*fib*) [5] has been enhanced to take into account the superposition of the confining effects of the already existing steel reinforcement with that of the FRP jacketing applied when retrofitting reinforced concrete (RC) columns (i.e., '*FRPConfinedConcrete*' implemented in OpenSees).

## 2 FRP-RETROFITTED BRIDGE COLUMNS' MODELING IN OPENSEES

The OpenSees command used in order to construct the uniaxial '*FRPConfinedConcrete*' is provided in the following syntax:

**uniaxialMaterial FRPConfinedConcrete $tag $fpc1 $fpc2 $epsc0 $D $c $Ej $Sj $tj $eju $S $fyl $fyh $dlong $dtrans $Es $vo $k $useBuck**

Each input parameter defined above corresponds to the mechanical and geometrical properties of the FRP&Steel-confined element which affect its overall performance. Their description is provided in Table 1.

Table 1: '*FRPConfinedConcrete*' input parameters.

| | | |
|---|---|---|
| ***1*** | ***tag*** | *Material Tag* |
| ***2*** | ***fpc1*** | *Concrete Core Compressive Strength* |
| ***3*** | ***fpc2*** | *Concrete Cover Compressive Strength* |
| ***4*** | ***epsc0*** | *Strain Corresponding to Unconfined Concrete Strength* |
| ***5*** | ***D*** | *Diameter of the Circular Section* |
| ***6*** | ***c*** | *Dimension of Concrete Cover* |
| ***7*** | ***Ej*** | *Elastic Modulus of the Jacket* |
| ***8*** | ***Sj*** | *Clear Spacing of the FRP Strips - zero if it's continuous* |
| ***9*** | ***tj*** | *Total Thickness of the FRP Jacket* |
| ***10*** | ***eju*** | *Rupture Strain of the Jacket* |
| ***11*** | ***S*** | *Spacing of the Stirrups* |
| ***12*** | ***fyl*** | *Yielding Strength of Longitudinal Steel Bars* |
| ***13*** | ***fyh*** | *Yielding Strength of the Hoops* |
| ***14*** | ***dlong*** | *Diameter of the Longitudinal Bars* |
| ***15*** | ***dtrans*** | *Diameter of the Stirrups* |

| | | |
|---|---|---|
| ***16*** | ***Es*** | *Steel's Elastic Modulus* |
| ***17*** | ***vo*** | *Initial Poisson's Coefficient for Concrete* |
| ***18*** | ***k*** | *Reduction Factor (0.5-0.8) for the Rupture Strain of the FRP Jacket* |
| ***19*** | ***useBuck*** | *FRP Jacket Failure Criterion due to Buckling of Longitudinal Compressive Steel Bars (0 = not include it, 1= to include it)* |

The experimental specimens were SP1 and SP2 and were repaired with continuous unidirectional GFRP and CFRP composite laminates with four layers and with two layers, respectively with both having 1 mm thickness of each layer. The specimens were laterally confined by 6.35 mm deformed hoop bars having a yield strength of 435.3 MPa. The tie reinforcement ratio was 0.545% (50.8 mm spacing) for SP1 and 0.363% (76.2 mm spacing) for SP2. All specimens were reinforced in the longitudinal direction by 16 - 15.875 mm deformed bars having a nominal yield strength of 533.7 MPa. Unconfined concrete compressive strength was 27.6 MPa. Rupture strain of GFRP was 2.3% and of CFRP was 1.2%. Finally, the columns' clear height was 1778 mm and cross section diameter was 508 mm with a clear concrete cover of 25.4 mm. The total load on the top of the column specimens was 380.8 kN, axial load ratio of 6.8%.

Moment curvature analysis was firstly performed in OpenSees of the RC sections of the above two specimens where FRP and Steel confined concrete was modelled with the aforementioned implemented uniaxial material i.e., *FRPConfinedConcrete* and the constitutive model by Menegotto and Pinto (1973) [6] is used to model the longitudinal steel behavior.

A Zero Length element with the fiber discretization of the cross section is used. For the zero-length element, a section discretized by concrete and steel is created to represent the behavior. UniaxialMaterial objects are created which define the fiber stress-strain relationship's. According to *FRPConfinedConcrete* model, the averaged response of the two different regions - concrete core (confined by both the FRP & the existing reinforcement) and concrete cover (confined only with the FRP wrap) - in the cross-section allows the assignment of a unique stress-strain law (*FRPConfinedConcrete*) to all the concrete fibers/layers of the circular section. Reinforcing steel material is modeled with Steel02 [6] -as mentioned before - uniaxial material. The procedure takes as input the tag of the section to be analyzed, the axial load, P, to be applied, the max curvature to be evaluated and the number of iterations to achieve this max curvature. The procedure first creates the model which consists of two nodes, boundary conditions, and a Zero-Length-Section element. After the model has been created, the analysis is performed. A single load step is first performed for the axial load, then the integrator is changed to DisplacementControl to impose nodal displacements, which map directly to section deformations. Figure 1 depicts the results of the above analyses for specimens SP1 and SP2 along with the bilinear idealization of the produced curves to be later employed in the performed time-history analyses and overall modeling.

The experimental specimens consist of a footing, a column and a top block. Steel beams and mass blocks are placed on top of the test specimens and four load cells connect the specimen to the shake table below the footing. These features are expected to affect the dynamic and nonlinear responses of the test columns. Hence, the whole setup above the shake table is

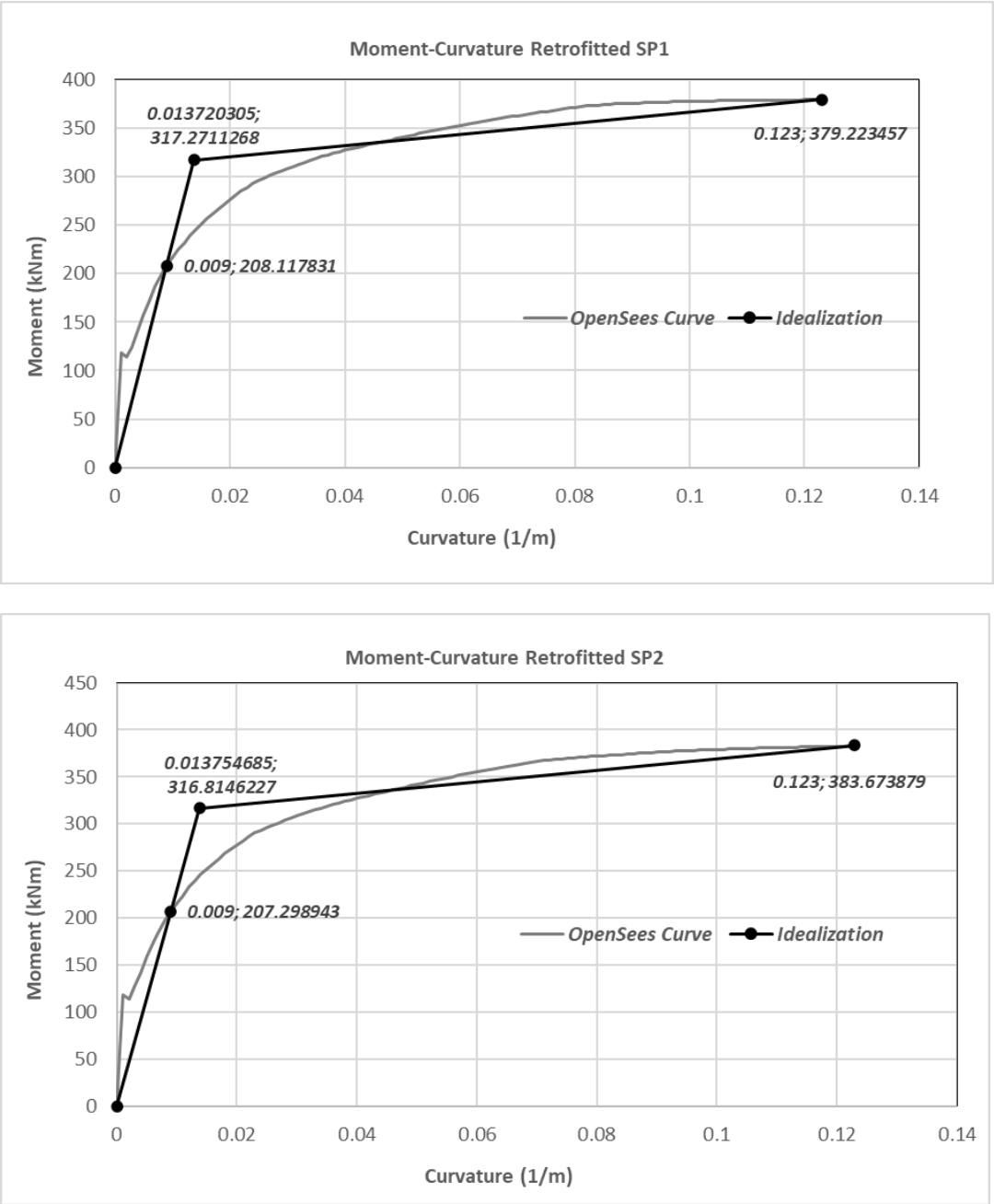


Figure 1: Moment-Curvature Analysis of RC Sections SP1 and SP2 produced in OpenSees along with their bi-linear idealization.

modeled in this computational investigation.

The 'Beam with Hinges' (BWH) element [7] is a commonly used force-based element to examine the nonlinear response of frame structures. It has localized plasticity at the ends i.e., hinges, and the remaining part is kept linear elastic. The length of each hinge is defined by the user. In this study this plastic hinge length is defined according the equations developed by Megalooikonomou et al. (2018) [8], Megalooikonomou (2019) [9]. According to the latter study the definition of plastic hinge length was reassessed through consideration of yield penetration effects. The required confined zone in critical regions of columns and piers undergo-

ing lateral sway during earthquakes is related to the plastic hinge length where inelastic deformation and damage develops. The exact definition of the plastic hinge length stumbles upon several uncertainties, the most critical being that the extent of the inelastic region evolves and spreads with the intensity of lateral displacements. Design codes quantify a reference value for the plastic hinge length, through calibrated empirical relationships that account primarily for the length of the shear span and the diameter of primary reinforcing bars. The latter term reflects the effects of bar yielding penetration in the support of columns. In the aforementioned studies a consistent definition of plastic hinge length was pursued analytically with reference to the actual strain state of the reinforcement.

Figure 2 presents the test specimen model using BWH element to represent the column. Two rigid elements at the top and the base are used for the top block and the footing, respectively. A rotational spring is added below the rigid element at the base, because the specimen was placed on four load cells which were connected to the shaking table and they are not perfectly rigid. A hysteretic material that follows the bilinear moment-curvatures responses of Figure 1 is employed for the section aggregator object in OpenSees which aggregates previously-defined UniaxialMaterial objects into a single section force-deformation model inside the plastic hinge length of the BWH element. Each UniaxialMaterial object represents the section force-deformation response for a particular section degree-of-freedom (*dof*). There is no interaction between responses in different *dof* directions.

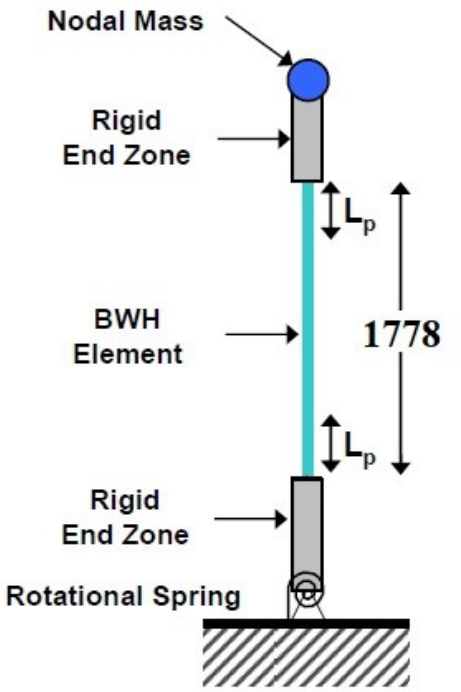


Figure 2: Specimen Modeling

## 3 NONLINEAR TIME - HISTORY BRIDGE PIERS' ANALYSES AND CORRELATION WITH EXPERIMENTAL RESULTS

For the nonlinear dynamic simulation of the two FRP-retrofitted specimens SP1 and SP2 in the horizontal and vertical direction, the same set of horizontal and vertical ground motions were selected as used in testing of as-built specimens. Table 2 gives the details of loading protocol. As it is mentioned before the ground motion recorded at the Pacoima Dam station of

1994 Northridge earthquake was employed for the nonlinear time-history analyses of the specimen model of Figure 2 in OpenSees.

Table 2: Ground motions for shaking table testing

| Test | Earthquake | Station | Scale Factor | Components |
|---|---|---|---|---|
| EQ1 | Northridge | Pacoima Dam | 0.05 | Horizontal and vertical |
| EQ2 | Northridge | Pacoima Dam | 0.125 | Horizontal and vertical |
| EQ3 | Northridge | Pacoima Dam | 0.250 | Horizontal and vertical |
| EQ4 | Northridge | Pacoima Dam | 0.250 | Horizontal only |
| EQ5 | Northridge | Pacoima Dam | 0.500 | Horizontal and vertical |
| EQ6 | Northridge | Pacoima Dam | 0.500 | Horizontal only |
| EQ7 | Northridge | Pacoima Dam | 0.700 | Horizontal and vertical |
| EQ8 | Northridge | Pacoima Dam | 0.950 | Horizontal and vertical |
| EQ9 | Northridge | Pacoima Dam | 1.250 | Horizontal and vertical |
| EQ10 | Northridge | Pacoima Dam | 1.250 | Horizontal only |
| EQ11 | Northridge | Pacoima Dam | 1.250 | Horizontal and vertical |

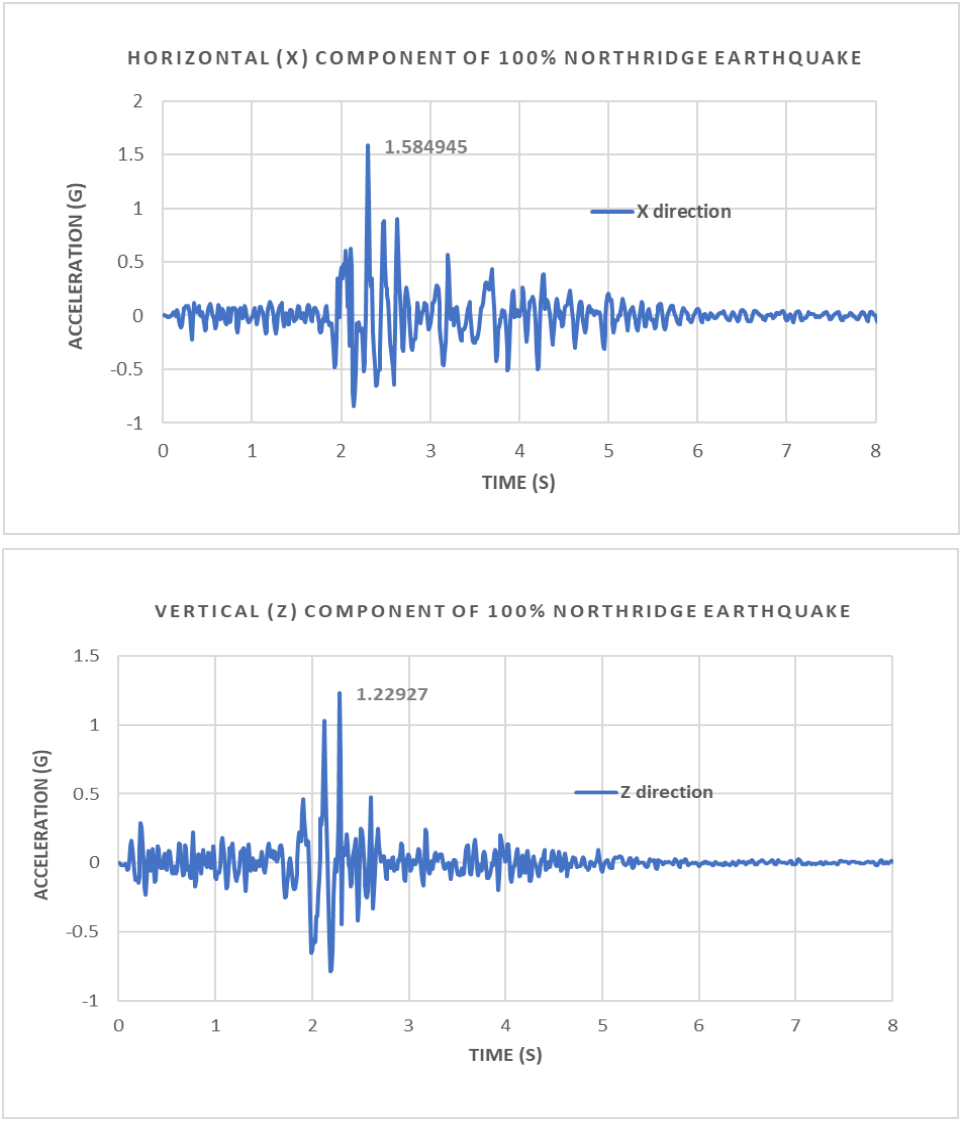


Figure 3: Horizontal (X) and Vertical Components (Z) of 100% Northridge earthquake

Of the two horizontal components, the X component was selected because it produces larger shear strength reduction than the Y component. Since the geometrical scale of the specimen corresponds to the ¼-scale, each component of the ground motion was time-compressed by a factor of 2 as shown in Figure 3. It should be noted that the acceleration history depicted in the latter Figure is 100% unfiltered input ground motion obtained from the PEER NGA database [10].

As it is mentioned already the shaking table is not perfectly rigid. Its flexibility affects the response of the test specimen, especially in the vertical direction. The vertical natural period of the column is much shorter than that of the shaking table and the vertical period of the shaking table is dominant in the whole system (combined test specimen and shaking table as one system). If the shaking table is ignored and the vertical acceleration recorded on the shaking table is directly used as the input to the analytical model (as it is performed in this analytical study), acceleration history with higher frequencies is obtained at the top of the column [11]. However, these high frequencies are not present in the test data because of the dominant shaking table period in the vertical direction. Based on the latter issues, modeling the complex table response with several sources of uncertainties and assumptions is not feasible and should be kept in mind in the correlation with the experimental results as it can be seen below especially for the model in the vertical direction.

### 3.1 Correlation with SP1 shake table test

Figure 4 depicts the results of the inelastic time-history analysis of specimen SP1 for the last ground motion (125% scale) of the ground motions' sequences applied in the already described loading protocol of Table 2. The comparison in Figure 4 is in terms of drift at the top of the column. Overall, the correlation is satisfactory under the view of the complex behavior of the combined test specimen and shaking table system and its complex response. As it can be seen in the response, the residual displacements were found to be much lower for the repaired specimen SP1 in comparison to its bare counterpart [11].

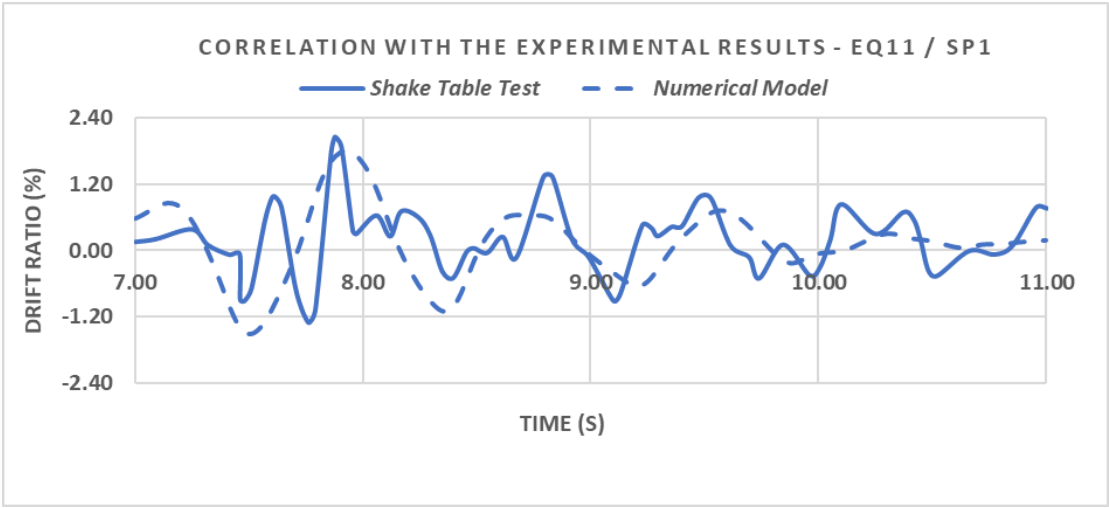


Figure 4: Correlation with experimental test of SP1 specimen in terms of specimen's drift for the last ground motion of the loading protocol

Figure 5, presents the comparison of the recorded axial and shear forces in the analytical bridge column model in OpenSees with the corresponding ones reported in the experimental study of this test specimen. Shear forces are satisfactorily correlated with the experimental results while the axial forces deviate a lot due to the shaking table effect which is not feasible

to be properly modeled in the analytical model of OpenSees. However, it can be stated that the effect of changes of axial load from compression to tension due to the vertical component which can result in significant decreases in column shear strength, was diminished through the contribution of the GFRP jacket.

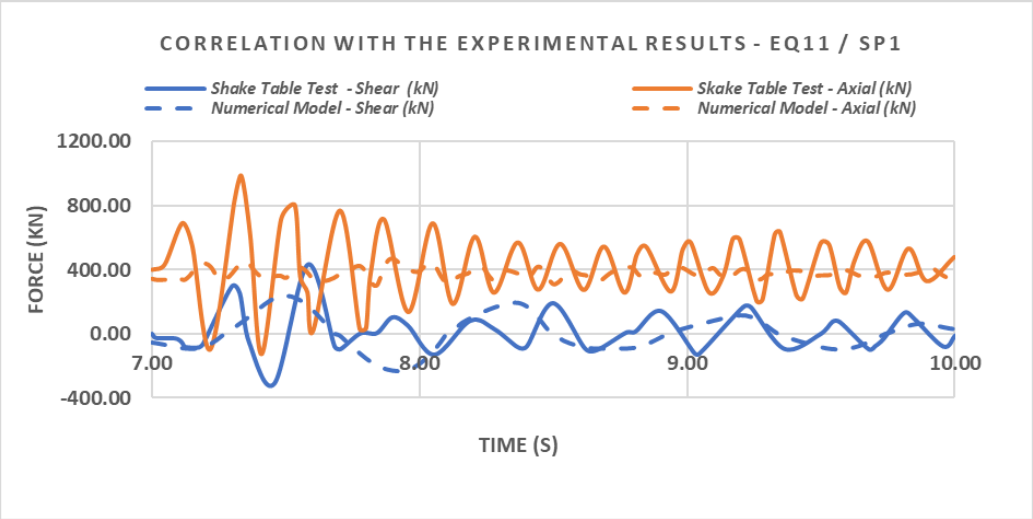


Figure 5: Correlation with experimental test of SP1 specimen in terms of specimen's axial and shear forces for the last ground motion of the loading protocol

## 3.2 Correlation with SP2 shake table test

Figure 6 depicts the corresponding results of the inelastic time-history analysis of specimen SP2 for the last ground motion (125% scale) of the ground motions sequences' applied in the already described loading protocol of Table 2.

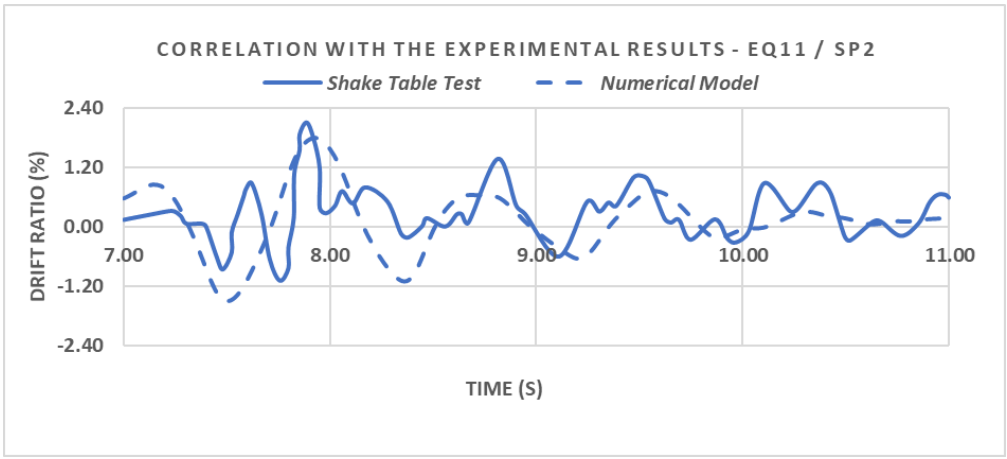


Figure 6: Correlation with experimental test of SP2 specimen in terms of specimen's drift for the last ground motion of the loading protocol

The comparison in Figure 6 is again in terms of drift at the top of the column. Overall, also here the correlation is satisfactory under the view of the complex behavior of the combined test specimen and shaking table system and its complex response. As it can be seen in this response too, the residual displacements were found to be much lower for the repaired specimen SP2 in comparison to its bare counterpart [11].

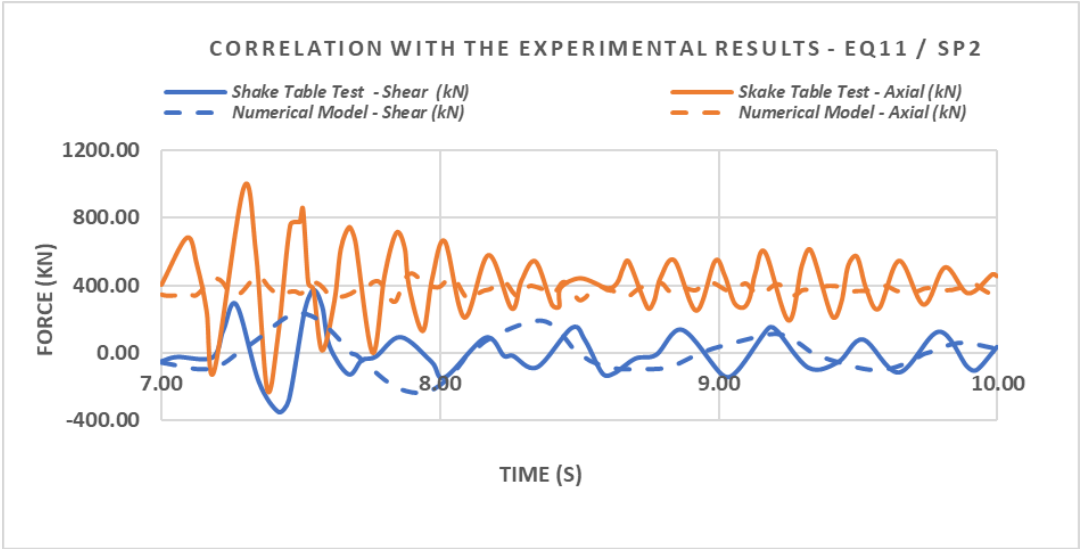


Figure 7: Correlation with experimental test of SP2 specimen in terms of specimen's axial and shear forces for the last ground motion of the loading protocol

Figure 7, presents the comparison again of the recorded axial and shear forces in the analytical bridge column model in OpenSees with the corresponding ones reported in the experimental study of this test specimen. Shear forces are satisfactorily correlated with the experimental results while the axial forces deviate a lot due to the shaking table effect which is not feasible to be properly modeled in the analytical model of OpenSees. However, it can be stated here too that the effect of changes of axial load from compression to tension due to the vertical component which can result in significant decreases in column shear strength, was diminished through the contribution of the CFRP jacket.

One way to overcome the deviation of the analytical results from the experimental ones in the vertical direction is to apply directly to the analytical bridge pier the recorded axial force history (from the load cells installed underneath the test specimen footing and above the shaking table) to the column as an external force excitation in the conducted analyses. Moreover, in this case in order to equate the restoring forces to the external forces, model mass in the vertical direction should be set to zero. However, this data from the shaking table test is not available to the author and therefore the inelastic time-history analyses were performed the way it is described already previously.

## 4 CONCLUSIONS

Based on the analytical study presented in this paper the following useful conclusions can be drawn:

- Comparison between the numerical and experimental time history response of the columns is indicative of the effectiveness of the implemented modelling based on the uniaxial material '*FRPConfinedConcrete*' implemented in OpenSees independently of the type of the FRP jacket applied as a retrofit to the columns.
- The numerical model confirmed that the repaired columns were able to resist higher shear and developed fewer peaks of tensile forces due to the vertical component of the ground motion. Therefore, the effect of changes of axial load from compression to tension due to the vertical component which can result in significant decreases in column shear strength, was diminished through the contribution of the FRP jacket.

- Finally, after performing all time history dynamic analyses, the residual displacements were found to be much lower for both repaired specimens in comparison to their bare counterparts.
- The modeling approach described in this analytical study is indicative of the effectiveness of the investigated FRP repair technique to produce resilient bridge columns when subjected to earthquake loading with strong vertical component.

## REFERENCES

[1] OpenSees (2009) Open System for Earthquake Engineering Simulation, Pacific Earthquake Engineering Research Center, University of California at Berkeley, http://opensees.berkeley.edu.

[2] Megalooikonomou K.G., Monti G., Santini S. (2012) Constitutive Model for Fiber – Reinforced Polymer - and Tie – Confined Concrete, *ACI Structural Journal,* Vol. 109, No. 4, pp. 569-578.

[3] Karsan, I.D., Jirsa, J.O. (1969) Behaviour of concrete under compressive loadings, *Journal of Structural Division ASCE,* Vol. 95, No. 12, pp. 2543-2563.

[4] Kumar P., Mosalam K. M. (2015) Shaking Table Evaluation of Reinforced Concrete Bridge Columns Repaired Using Fiber-Reinforced Polymer Jackets, *Journal of Bridge Engineering, ASCE*, Vol.20; No.12, p. 04015025.

[5] Technical Report (2001) *Externally bonded FRP reinforcement for RC structures*, 14th fib bulletin, The International Federation for Structural Concrete (*fib*), Lausanne, Switzerland

[6] Menegotto M., Pinto, P. (1973) Method of analysis for cyclically loaded reinforced concrete plane frames including changes in geometry and non-elastic behavior of elements under combined normal force and bending, *IABSE Symposium on Resistance and Ultimate Deformability of Structures Acted on by Well Defined Repeated Loads*, Lisbon, Portugal.

[7] Scott, M.H. and G.L. Fenves. (2006) Plastic Hinge Integration Methods for Force-Based Beam-Column Elements, *Journal of Structural Engineering*, *ASCE*, 132(2):244-252.

[8] Megalooikonomou, K.G., Tastani, S. P., Pantazopoulou, S. J. (2018) Effect of Yield Penetration on Column Plastic Hinge Length. *Engineering Structures, Elsevier*, 156:161-174.

[9] Megalooikonomou K.G. (2019) Seismic Assessment and Retrofit of Reinforced Concrete Columns, *Cambridge Scholars Publishing*, 387 p., ISBN (10): 1-5275-2785-9, ISBN (13): 978-1-5275-2785-0.

[10] PEER-NGA Database (2023) Pacific Earthquake Engineering Research Center, University of California, Berkeley, CA, (http://peer.berkeley.edu/nga/).

[11] Lee H, Mosalam K. M. (2014) Effect of Vertical Acceleration on Shear Strength of Reinforced Concrete Columns, *PEER Report 2014/04*, University of California Berkeley.

COMPDYN 2023
9th ECCOMAS Thematic Conference on
Computational Methods in Structural Dynamics and Earthquake Engineering
M. Papadrakakis, M. Fragiadakis (eds.)
Athens, Greece, 12-14 June 2023

# NUMERICAL INVESTIGATION OF RETROFITTING WAFFLE SLABS WITH CARBON FIBRE REINFORCED POLYMER PLATES

**Michael Jung*, and George Markou**

Department of Civil Engineering, University of Pretoria
Republic of South Africa
e-mail: u18127283@up.ac.za*; george.markou@up.ac.za

## Abstract

*As a result of shopping centres closing and being converted into either accommodation or factories, engineers have been needing to come up with new and innovative solutions to help increase the strength and decrease the deflection of already built concrete structures. If the structure's purpose was to change, then the building would need to be redesigned to ensure its structural integrity. The objective of this study is to investigate the effects that retrofitted Carbon Fibre Reinforced Polymer (CRFP) plates have on the strength of healthy and corroded waffle slabs. 3D state-of-the-art finite element modeling software will be used to create accurate models that can be used to perform nonlinear analyses. Within these models, factors such as deteriorated concrete and corroded steel will also be modelled to investigate the effects of using CFRP plates as a strengthening approach to deteriorated Reinforced Concrete (RC) structures, and in this case with waffle slabs.*

**Keywords:** Carbon Fibre Polymer, Waffle Slabs, Corrosion, Retrofit, Reinforced Concrete, Finite Element Method

## 1 INTRODUCTION

The majority of shopping malls in South Africa and around the world make use of the waffle slab system, since it allows one to cover large spans by optimising the use of the RC material. Over time, all RC structures will eventually develop cracks and deteriorate due to environmental hazards that affect the building's material, thus waffle slabs are also affected by this phenomenon. To strengthen existing waffle slabs, CFRP plates can be installed on the tension side of the slab's section. Other advantages such as ductility and shear resistance can also be achieved through this solution. According to Kim et al. [1], CFRPs can increase the stiffness of a beam against impact loading and increase the shear resistance. Soudki et al. [2] concluded in their research that retrofitting a slab with CFRPs increases the punching capacity by 29% as well as the stiffness while lowering deflections. These attributes make CFRP plates a favourable solution when retrofitting RC structures.

This research work's objective is to have an in-depth view into a waffle slab's mechanical response to the retrofitting and the efficiency of implementing CFRP plates as a strengthening method. To make the simulations more realistic, material deterioration is also considered and incorporated within the numerical models.

## 2 METHODOLOGY

The research will be performed through the use of 3D detailed analysis using Finite Element Analysis (FEA) software. It has been shown through numerous numerical investigations by Nicolaides & Markou [3] that Reconan FEA [4] has the ability to capture the realistic behaviour of bare and retrofitted RC structures under monotonic and cyclic limit state loading conditions. A similar approach will be used, and adjustments will be made where needed to model the RC waffle slabs that are bare or retrofitted with CFRP plates. It is important to note here that Reconan FEA was validated through the use of experimental results as presented in [5-8].

The slabs will be modelled and analysed considering different loads as well as different parameters that relate to the material properties and the geometry of the intervention applied herein for the needs of this research work. Parameters such as thickness of plates will be varied to understand the effects of the strengthening approach on the slab's overall mechanical response and ultimate capacity. A RC waffle slab with no CFRP plates will be modelled to form a base line that will be used to compute the overall effect of the retrofitting. Finally, parameters such as corroded rebar and deteriorated concrete will be used to further investigate the effects of CFRP plates when implemented on a structure that has suffered deterioration due to environmental hazards.

### 2.1 Modelling of Waffle Slabs with No Deterioration.

The waffle slab (see Figure 1) that was modelled was discretized using 8-noded hexahedral elements that had an average size of 100x100x100mm. All the reinforcement was discretized and modelled as embedded rod elements except for the longitudinal rebar in the four columns, which were modelled as Natural Beam-Column Force-Based (NBCFB) Elements [9]. A total of 30 916 elements were used to discretize the waffle slab, including the four RC columns. In addition to that, 1 764 hexahedral elements were used to model the slab's CFRP plates for the case of the retrofitted models.

The thicknesses for the CFRP plates on the slab were 1.2, 1.4, 2.4 and 2.8 mm. These thicknesses were acquired from the Sika CarboDur Plates data sheet [10], a product that is used by VSL Construction Solutions (Pty) Ltd, who are specialists in the retrofitting of CFRP plates in South Africa. According to the information found within this sheet [10] the costing

was calculated to assess the cost vs strength benefit for each retrofitting scenario. A total of 196 m of CFRP plates are needed to implement the retrofitting as shown in Figure 1. It is important to note that the most common CFRP plates come in 1.2 mm or 1.4 mm thick strips and cannot be layered in more than 2 layers according to VSL Construction Solutions. Therefore, the 2.4 mm and the 2.8 mm plates were achieved by using a 2-layer implementation of the 1.2 mm and 1.4 mm, respectively.

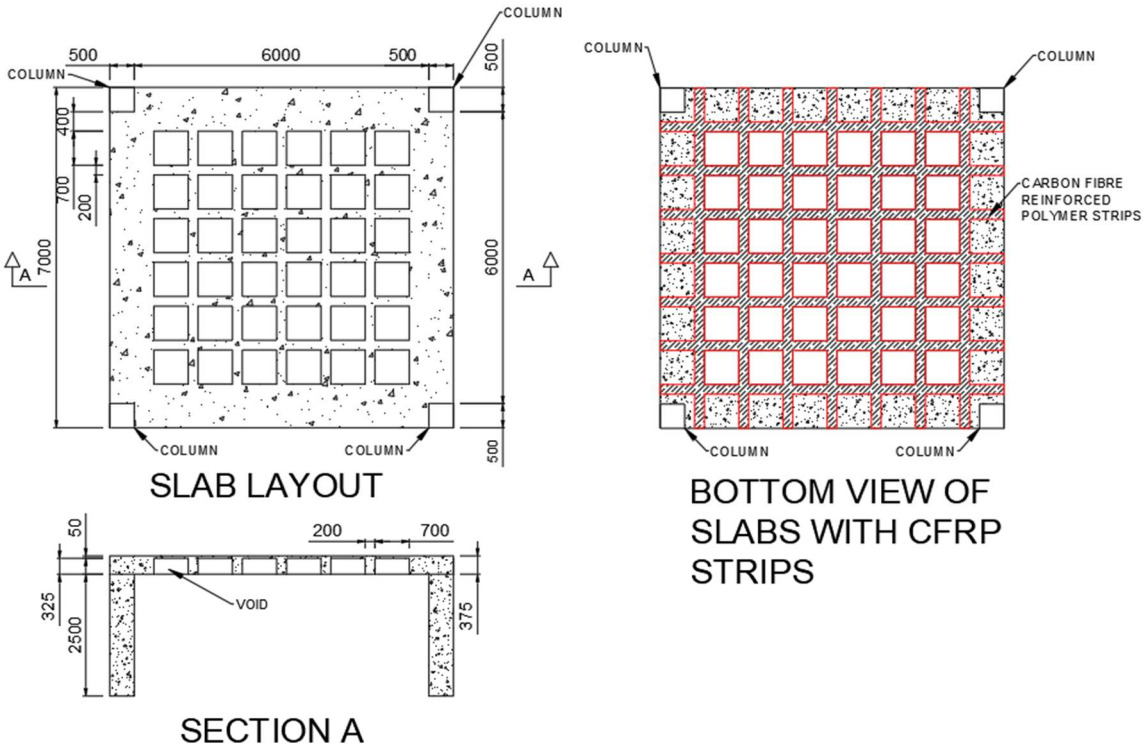


Figure 1: Layout and dimensions of the waffle slab

As it can be seen in Figure 1, the under-study RC waffle slab was 7x7 m, with four 2.5 m in height columns. The full thickness of the slab, web and width of the rib was 375 mm, 50 mm and 200 mm, respectively. In Figure 1, one can see the layout and dimensions of the RC slab that was used to perform the investigation in this research work.

At the base of the columns, a steel plate was modelled to ensure no local failure occurred which would lead to premature analysis instabilities. The reinforcement in the columns consisted of eight Ø20 longitudinal rebars with Ø12 stirrups spaced at 100 mm. In the slab, two Ø12 longitudinal rebar were used in the top and bottom for each rib with Ø8 stirrups spaced at 200 mm. On the outer edges of the slab until the start of the waffle's voids, Ø12 longitudinal rebars spaced at 102.5 mm were used in both directions. In the web of the waffle slab (in between ribs), Ø8 longitudinal steel rebars were used at the top and bottom for in both directions. The concrete cover throughout the slab was assumed to be equal to 50 mm.

Table 1 shows the properties of the materials defined within the numerical models. The 1.2 mm and 1.4 mm CFRP plates had different properties and these different properties were also considered within the models. The CFRP plates were modelled over the ribs and extended to and from the edges of the slab. The CFRP properties were extracted from the Sika CarboDur Plates data sheet [10]. The RC waffle slabs were loaded with a distributed load over the top surface. It is noteworthy to state that the models ran for approximately 12 hours and 10min on a 3.7 GHz PC that had 64 Gb RAM.

| Modelled Properties of the Material | | | | | |
|---|---|---|---|---|---|
| **Concrete** | | **Steel** | | **1.2 mm CFRP Plates (CarboDur S)** | |
| **Young's Modulus** | 30 GPa | **Young's Modulus** | 200 GPa | **Young's Modulus** | 165 GPa |
| **Compressive Strength** | 30 MPa | **Compressive Strength** | 450 MPa | **Tensile Strength** | 3100 MPa |
| **Tensile Strength** | 1.5 MPa | **Poisson Ratio** | 0.3 | **Poisson Ratio** | 0.3 |
| **Poison Ratio** | 0.2 | | | | |
| | | | | **1.4 mm CFRP Plates (CarboDur M)** | |
| | | | | **Young's Modulus** | 210 GPa |
| | | | | **Tensile Strength** | 3200 MPa |
| | | | | **Poisson Ratio** | 0.3 |

Table 1: Properties of the materials used in the numerical model.

| Modelled properties for the corroded and deteriorated materials | | | |
|---|---|---|---|
| **Concrete** | | **Steel** | |
| **Undeteriorated compressive strength** | 30 MPa | **Uncorroded compressive strength** | 450 MPa |
| Percentage decrease from calculations above | 15% | Percentage decrease from calculations above | 20% |
| **Deteriorated compressive strength** | 25.5 MPa | **Corroded compressive strength** | 360 MPa |

Table 2: Modified material properties.

## 2.2 Modelling of the Waffle Slabs with Deterioration of the Concrete or Rebar

For this model, the strength of the rebar and the concrete was decreased to mimic the effects deteriorated concrete and corroded rebar. Franceschini et al. [11], calcualted for certain exposure classes what the strength decrease of the concrete strength and area reduction of the rebar would be at various exposure durations. Based on their assumptions and taking into account the environment of South Africa, it was assumed herein that the lowest exposure class would be applicable. Therefore exposure class XS1 was used, which is described as being exposed to airborne salt, but does not have direct contact with salts. An exposure time of 80 years was implemented and based on Franceschini et al. [11], the calculated percentage decrease of the material strengths was derived and implemented for the needs of this research work.

In regards to steel, the cross-sectional area loss was 18.88% for a 19 mm rebar after 80 years in XS1 exposure class. According to Franceschini et al. [11], it was found that the area loss increased as the original rebar size decreased. It was therefore assumed that a 20% cross-sectional area reduction would be realistic for the RC waffle slab models, considering the rebars used in this research work were 12 mm in diameter. The percentage was applied directly to the strength of the rebar thus the yielding and ultimate stress of the rebars were decreased by 20%. The new corroded rebar strength can be seen in Table 2.

In relation to the concrete material, the compressive strength loss was calculated and was found to be approximately equal to 15% for a 50 MPa concrete after 80 years in XS1 exposure class. In Table 2, one can see the new material properties of concrete, while it is important to

note that it was assumed that this deterioration was uniform throughout the concrete domain. Additionally, the Young modulus for both materials were not modified due to deterioration.

Figures 2 to 6 show the RC waffle slab model that was developed through the use of the pre-processing software FEMAP. These figures show the hexahedral and embedded rebar meshes as they were developed for the needs of this parametric investigation.

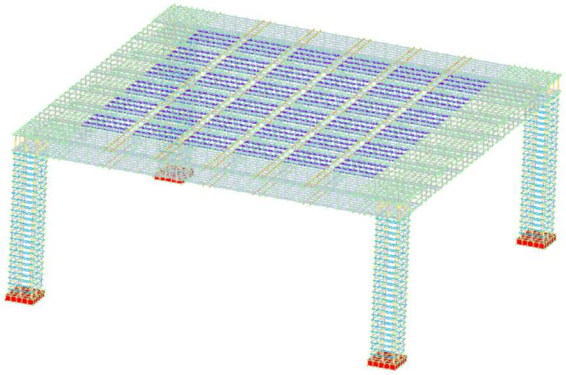

Figure 2: Embedded rebar mesh of the waffle slab.

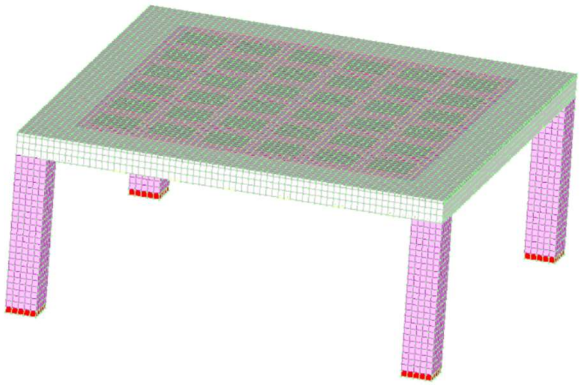

Figure 3: Hexahedral mesh of the waffle slab.

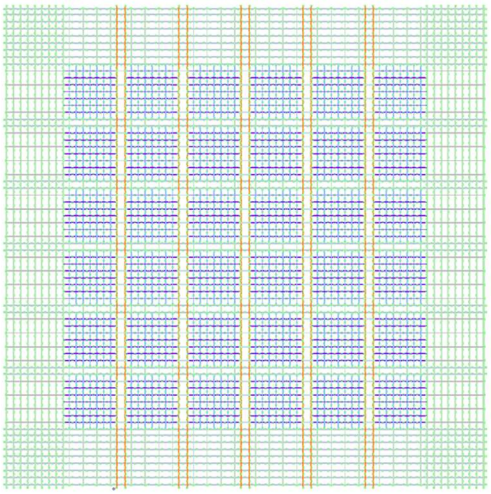

Figure 4: Top view of the embedded rebar mesh of the waffle slab.

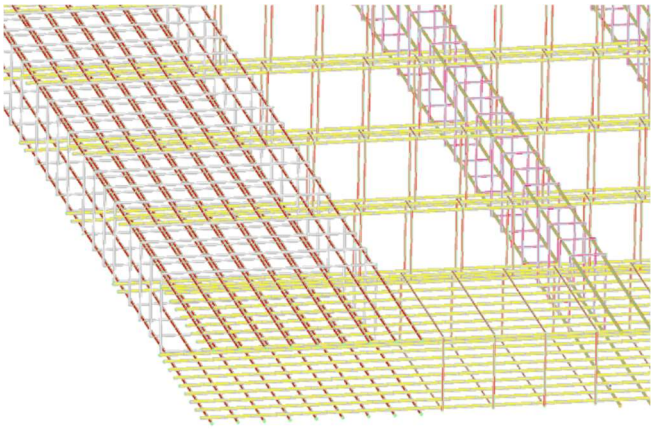

Figure 5: Close up of the embedded rebar mesh of the waffle slab.

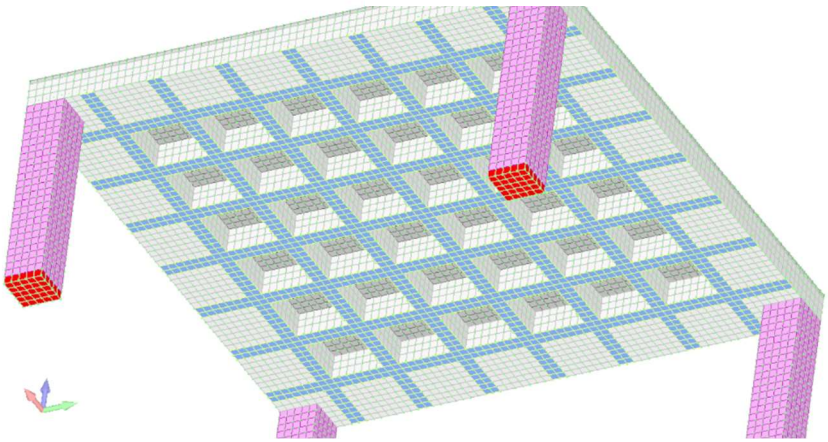

Figure 6: Bottom view of the hexahedral mesh including the CFRP plates on the waffle slab.

## 3 RESULTS AND DISCUSSION FROM THE ANALYSIS WITH NO DETERIORATION.

In Figure 7, one can see the load vs deflection curves of a waffle slab retrofitted with 1.2 mm, 1.4 mm, 2.4 mm and 2.8 mm thicknesses of CFRP plates. The waffle slab without CFRP plates was also added in this graph for comparative reasons. It is easy to observe that the load vs deflection curves numerically obtained from the models indicate that the stiffness, yielding point and overall structural capacity increases as the CFRP plate thickness increases. These results were expected since the addition of thicker CFRP plates made the vertical resistance of the RC waffle slabs higher introducing additional stiffness and strength. In Figure 8 and 9, the deformed shape and the solid von Mises strain contour can be seen prior to failure for different load levels as they resulted from the nonlinear analysis.

Table 3 shows that the implementation of 1.2 mm CFRP plates increased the strength by 123%. On the other hand, by adding a 2.8 mm plate of CFRPs, a 262% increase in strength was observed.

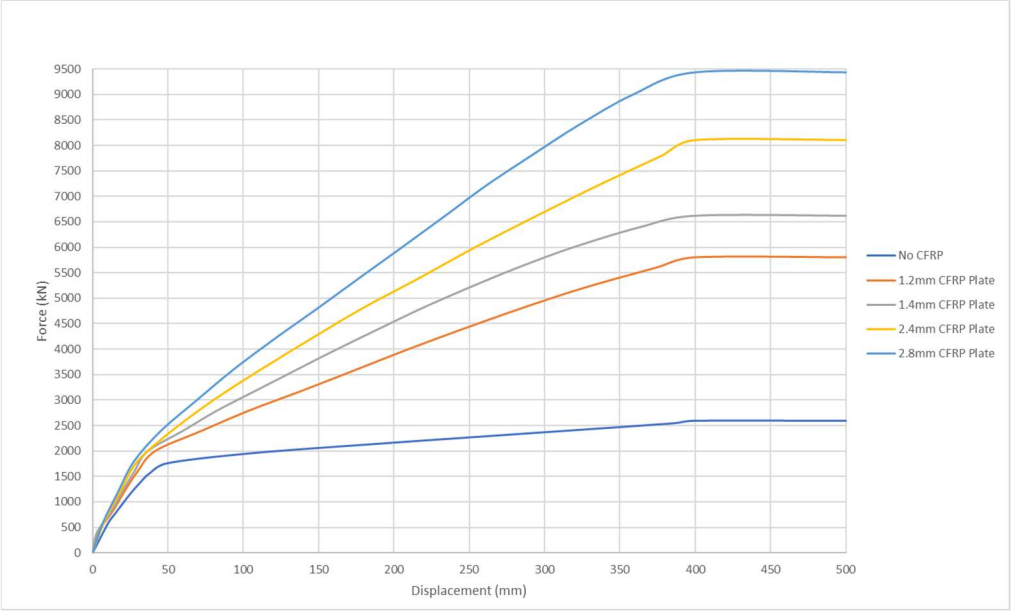


Figure 7: Force vs Displacement for various thicknesses of CFRP plates.

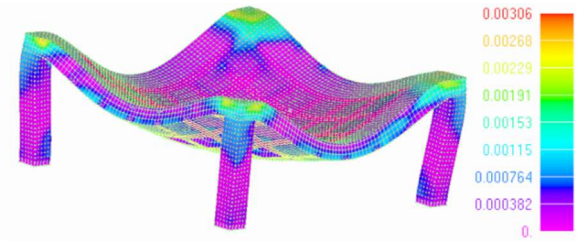


Figure 8: Solid von Mises Strain contour and deformed shape of the waffle slab with 2.4 mm CFRP Plates before the first crack occurred.

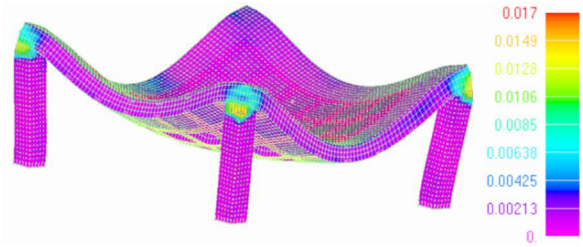


Figure 9: Solid von Mises Strain contour and deformed shape of the waffle slab with 2.4 mm CFRP plates after the first crack occurred.

From Table 3, we can also see the cost of the preparation, supply and installation of each plate thickness used when strengthening the structure. One can see that the installation of the 1.4 mm thick plate is substantially more expensive than the 1.2 mm thick plate. One can see that retrofitting by using two 1.2 mm plates (2.4 mm plate) is more cost effective and provides more strength than when retrofitting with one 1.4 mm plate. In terms of cost vs strength

achieved from the different CFRP plates, the installation of two 1.2 mm thick plates to achieve the thickness of 2.4 mm, would be more economical than the 2.8 mm thick plate (two 1.4mm thick plates), and only provides an extra 50% additional strength. If the price was a large factor in solving the problem, and usually it is in the construction industry, then the 2.4 mm thick plate would be the best option to ensure a substantial increase in strength and be the most cost-effective solution for the problem. In addition to that, Table 3 shows the cost of increasing the strength of the structure by 1%, where once more the most cost-effective strengthening scenario is when the 2.4 mm CFRP plates are used.

| CFRP Plates Thickness | $F_{ND}$ (kN) | Strength Increase due to CFRP | Retrofitting Cost | Cost per 1% of strength increase (R/%) |
|---|---|---|---|---|
| **No CFRP** | 2600 | - | - | |
| **1.2 mm** | 5800 | 123% | =196m x R1015/m =R198 940.00 | 1617 |
| **1.4 mm** | 6620 | 155% | =196m x R1827/m =R358 092.00 | 2310 |
| **2.4 mm** | 8110 | 212% | =196m x R1450/m =R284 200.00 | 1340 |
| **2.8 mm** | 9430 | 262% | =196m x R2610/m =R511 560.00 | 1952 |

Table 3: Summary of the ultimate force for the cases of no deterioration.

As it was stated above, an additional advantage that derives when implementing the CFRP plates is that the slabs' deflection for the same load level decreases as the CFRP plate thickness increases. This can be seen as an advantage since it could be significantly beneficiary in case an owner chose to repurpose an existing structure thus introduce additional loads at the slabs of the building, where the waffle slabs would face a problem in relation to the maximum allowed deflection for the serviceability load combinations.

## 4 RESULTS FROM THE ANALYSIS WITH DETERIORATION.

Figure 10 shows the comparative graph as it derived from the nonlinear numerical analysis by using the assumption that the RC waffle slabs are deteriorated due to the XS1 exposure for 80 years. The results from the deteriorated slab look similar to the curves shown in Figure 7 and therefore it was decided to develop individual graphs for each CFRP plate thickness to further investigate the differences between the deteriorated slabs and the slabs without deterioration. The differences between the two scenarios can be seen in Figures 11, 12, 13, 14 and 15.

Table 4 shows a comparison between the ultimate force obtained from the analysis for the slabs with and without deterioration. As it can be depicted, there was a large difference in the case of the 2 slabs that were not retrofitted. It is evident that a slab without retrofitting will suffer the most when deterioration develops due to environmental hazard exposure. On the other hand, it was found that the thicker the plate for retrofitting, the less the deterioration influenced the numerically derived strength. For the case of the 2.4 and 2.8 mm thick plates, the difference between the deteriorated and healthy slabs were negligible. This phenomenon is attributed to the level of deterioration that was 20% and not larger than 30% that would have significantly affected the overall strength of the structural system.

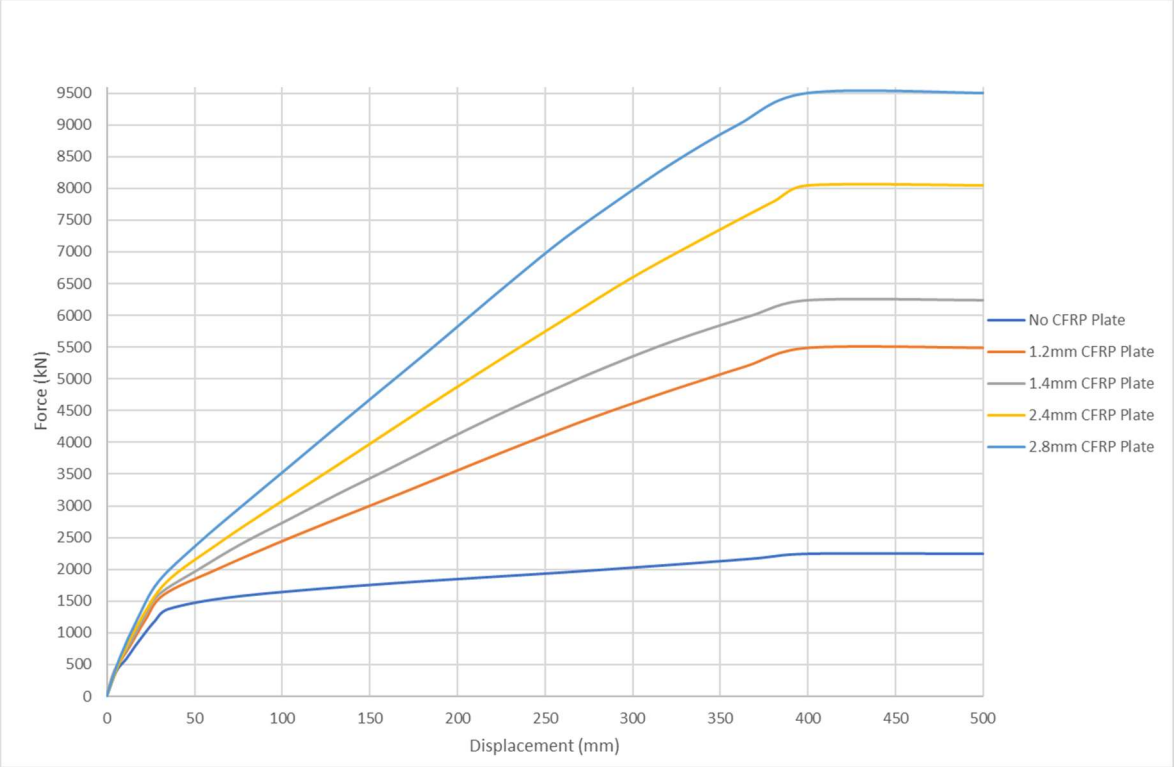


Figure 10: Force vs displacement curves of the deteriorated RC waffle slabs with various thicknesses of CFRP plates.

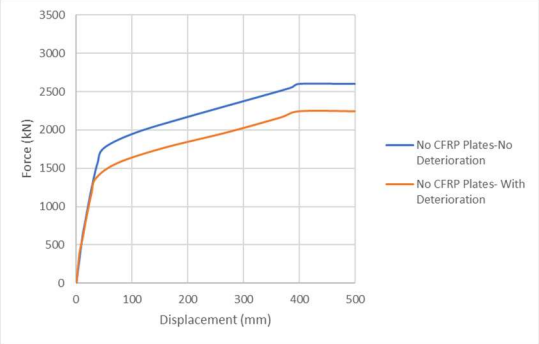


Figure 11: Force vs displacement curve of the deteriorated and undeteriorated waffle slab with no CFRP plates retro fitted.

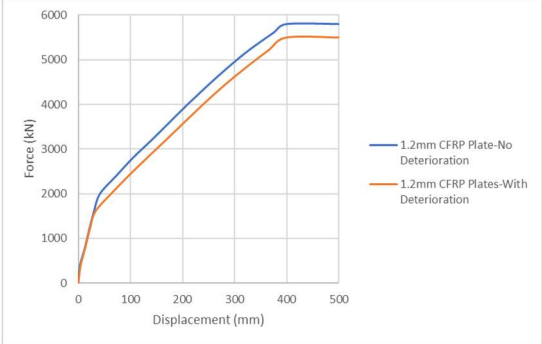


Figure 12: Force vs displacement curve of the deteriorated and undeteriorated waffle slab with 1.2 mm thick CFRP plates retro fitted.

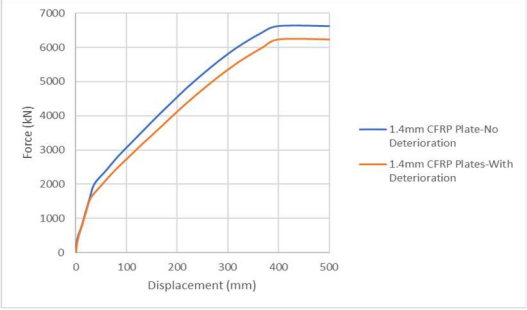


Figure 13: Force vs displacement curve of the deteriorated and undeteriorated waffle slab with 1.4 mm thick CFRP plates retro fitted.

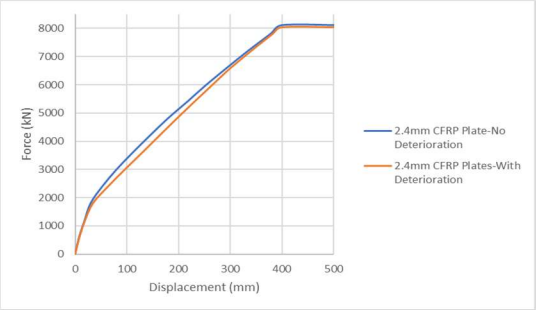


Figure 14: Force vs displacement curve of the deteriorated and undeteriorated waffle slab with 2.4 mm thick CFRP plates retro fitted.

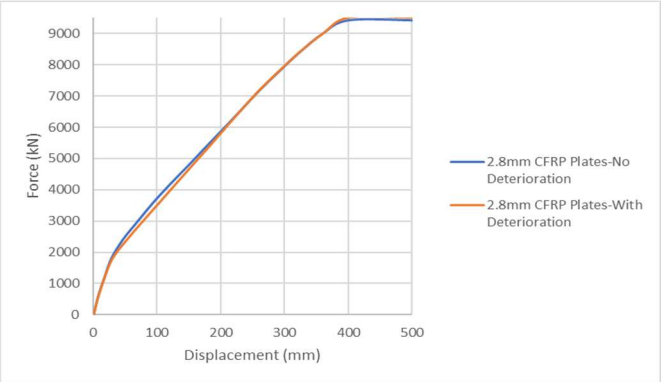


Figure 15: Force vs displacement curve of the deteriorated and undeteriorated waffle slab with 2.8 mm thick CFRP plates retro fitted.

| **CFRP Plates Thickness** | **$F_{ND}$ (kN) No Deterioration** | **$F_D$ (kN) With Deterioration** | **Difference ($F_D$- $F_{ND}$) / $F_{ND}$** | **Strength Increase due to CFRP** |
|---|---|---|---|---|
| **No CFRP** | 2600 | 2240 | -13.8% | - |
| **1.2 mm** | 5800 | 5490 | -5.4% | 145.1% |
| **1.4 mm** | 6620 | 6240 | -5.7% | 178.6% |
| **2.4 mm** | 8110 | 8050 | -0.7% | 259.4% |
| **2.8 mm** | 9430 | 9500 | 0.1% | 324.1% |

Table 4: Table showing the difference between the forces at a deflection of 400 mm between the waffle slab with and without deterioration.

## 5 CONCLUSION AND FUTURE WORK

Within this paper, the effects of CFRP plates on the strength of existing RC waffle slabs was investigated. From the results of the models, it was concluded that CFRP plates can significantly improve the strength of the existing slabs by over 260% and can decrease the deflection of the slab. The cost of the CFRP to be installed made the 2.4 mm thick plate the most economical solution to achieve a high increase in strength vs cost. The CFRP plates also increase the strength of existing RC waffle slabs with deteriorated concrete and corroded rebar. According to the parametric investigation performed in this research work, it was found that the most cost-effective retrofitting solution is the one that foresees the use of the 2.4 mm thick plate.

In future research, it would be beneficial to model the deterioration as an effect that is not uniformly distributed. Due to time and complexity of modelling this approach, it was assumed that the deterioration was uniform throughout the concrete. In addition to this, the development of numerous models should be performed to investigate the ability of developing a formula that would allow professional Civil Engineers to decide the optimum approach and strategy when strengthening or retrofitting RC waffle slabs [12].

## 6 REFERENCES

[1] Kim, M. et al., 2017. The strengthening Effect of CFRP for Reinforced Concrete Beam. *Procedia Engineering,* Volume 210, pp. 141-147.

[2] Soudki, K., K. El-Sayed, A. & Vanzwol, T., 2011. Strengthening of concrete slab-column connections using CFRP strips. *Journal of King Saud University-Engineering Svciences,* Volume 24, pp. 25-33.

[3] Nicolaides, D. and Markou, G., "Modelling the Flexural Behaviour of Fibre Reinforced Concrete Beams with FEM", Engineering Structures, Volume 99, pp. 653–665, 2014.

[4] ReConAn v2.00 Finite Element Analysis Software.User's Manual.[Online]Available at:https://www.researchgate.net/publication/342361609_ReConAn_v200_Finite_Element_Analysis_Software_User%27s_Manual [Accessed 10 08 2021].

[5] Markou, G., Garcia, R., Mourlas, C., Guadagnini, M., Pilakoutas, K. and Papadrakakis, M. (2021), A New Damage Factor for Seismic Assessment of Deficient Bare and FRP-Retrofitted RC Structures, *Engineering Structures*, 248 (2021), 113152.

[6] Markou G. and Roeloffze W. (2021), Finite Element Modelling of Plain and Reinforced Concrete Specimens with the Kotsovos and Pavlovic Material Model, Smeared Crack Approach and Fine Meshes, *International Journal of Damage Mechanics*, 2021;30(6):845-871, https://doi.org/10.1177/1056789520986601.

[7] Mourlas, C., Markou, G. and Papadrakakis, M. (2019), Accurate and Computationally Efficient Nonlinear Static and Dynamic Analysis of Reinforced Concrete Structures Considering Damage Factors, *Engineering Structures*, 178 (2019), pp. 258–285.

[8] Markou, G., Mourlas, C., Bark, H. and Papadrakakis, M. (2018), Simplified HYMOD Non-Linear Simulations of a Full-Scale Multistory Retrofitted RC Structure that Undergoes Multiple Cyclic Excitations – An infill RC Wall Retrofitting Study, *Engineering Structures*, 176 (2018), pp. 892–916.

[9] Markou, G. and Papadrakakis, M., "Accurate and Computationally Efficient 3D Finite Element Modeling of RC Structures", Computers & Concrete, Volume 12 (4), pp. 443-498, 2013

[10] Sika South Africa, 2009. Sika CarboDur Plates Product Data Sheet. 25/02/2009 ed. s.l.:Sika South Africa.

[11] Franceschini, L., Vecchi, F. & Belletti, B., 2021. The PARC_CL 2.1 Crack Model for NLFEA of Reinforced Concrete Elements Subjected to Corrosion Deterioration, Parma, Italy: MDPI.

[12] Markou, G. (2021), A New Method of Seismic Retrofitting Cost Analysis and Effectiveness for Reinforced Concrete Structures, Engineering Structures, 246 (2021), 113083.

COMPDYN 2023
9th ECCOMAS Thematic Conference on
Computational Methods in Structural Dynamics and Earthquake Engineering
M. Papadrakakis, M. Fragiadakis (eds.)
Athens, Greece, 12-14 June 2023

# SEISMIC RESPONSE ASSESSMENT OF AN EXISTING RC STRUCTURE RETROFITTED WITH STEEL EXOSKELETONS

**Francesco Nigro[1], Gaetano Della Corte[2], and Enzo Martinelli[1]**

[1] Department of Civil Engineering, University of Salerno
Via Giovanni Paolo II, 132 - 84084 - Fisciano (SA), Italy
fnigro@unisa.it, e.martinelli@unisa.it

[2] Department of Structures for Engineering and Architecture, University of Naples Federico II
Via Claudio 21 – 80125 – Napoli (NA), Italy
gaetano.dellacorte@unina.it

## Abstract

*Several reinforced concrete (RC) structures built in Europe in the first decades after WWII do not meet the current safety standards, as those older buildings were built without any regard to the seismic actions and the structural details for ductility. Moreover, to reduce land use and environmental impact due to the construction of new buildings, governments are encouraging the upgrading and the reuse of older ones, rather than their demolition. Consequently, nowadays seismic retrofitting of existing structures is a very frequent request that civil engineers must handle. In general, such a challenge could be addressed combining member- and structure-level techniques. In principle, global (or structure-level) techniques may represent a feasible retrofit solution not only for structures characterized by low lateral stiffness, but also for buildings exhibiting a significant number of under-designed members with respect to the design seismic action suggested by modern Codes. Furthermore, these techniques could represent a more cost-effective strategy rather than the upgrading of existing members, especially when the potential disruption of occupancy and the replacement of non-structural elements are considered in the design process. More specifically, this paper aims to show how existing RC buildings can be seismically upgraded through retrofitting by adding external steel bracing systems referred to as "exoskeletons" as they are placed along the outer surface of the building. Although such a technique has a significant impact on the structural dissipation capacity and allows avoiding soft-storey mechanisms, its effectiveness is generally affected by the detailing of the braces and connections against buckling and post-buckling fracture. Consequently, an accurate model of the nonlinear response of the exoskeleton is as essential as representing the existing RC structure response in case of rare or very demanding earthquakes. In this context, this paper describes the modelling and analysis of an existing RC frame structure for which an exoskeleton was designed according to the current Italian code.*

**Keywords: Steel Exoskeletons, Seismic Upgrading, Existing RC structures, Strengthening, SCBF**

## 1 INTRODUCTION

The European Environmental Agency recently stated that Europe has the highest proportion of land use on the globe, with respect to the other continents [1]. However, since land is a finite resource, governments are strongly encouraging the upgrading and the reuse (rather than the demolition) of older structures. Moreover, recent estimates of the Italian society of engineers outlined that huge investments are needed to enhance the safety of many existing Italian buildings, since only 2% of them were built after the year 2000, when technical standards began to impose more restrictive criteria [2].

To address this issue, the effectiveness of the available retrofit intervention techniques has been tested in several occasions during the last decades, resulting into the *fib* bulletin 24, which divides such interventions in two broad classes: on one side, member-level techniques are adopted to enhance both strength and ductility of deficient members , whereas structure-level ones result to be essential to increase the overall structural strength and stiffness [3].

Focusing on the structure-level side, a potential retrofit solution consists in providing some bays of the existing structure with steel braces. The new braces could be either placed inside the existing RC frames ("endoskeletons") or outside them creating completely new steel frames ("exoskeletons"). For instance, in case of endoskeletons steel bracing systems have been proposed exploiting buckling-restraining features of buckling-restrained braces or eccentric bracing ([4],[5],[6],[7]) so that the new braces could be placed close or even inside existing masonry walls.

The steel exoskeleton solution might be feasible when the building is sufficiently distant from other structures and it is particularly feasible to create integrated structural and energy consumption upgrading [8]. When it is feasible, the steel exoskeleton may represent a cost-effective strategy, because it avoids the potential disruption of the building occupancy and the partial demolition/reconstruction of existing non-structural elements.

When a steel exoskeleton is selected as a solution, then the new steel bracing system could be also made of a standard concentrically braced frame (CBF). In such a case, an adequate detailing of the braces and their connections against buckling and post-buckling fracture should be considered, because those phenomena can be detrimental for the global behaviour of the upgraded structure [9]. Despite the fact that several authors have been dealing with the design of such upgrading interventions [10], current seismic design codes do not yet provide specific design rules for a combined RC frame and steel CBF structure.

Therefore, the present paper aims at outlining how different design criteria can influence the effectiveness of the steel exoskeletons, considering some relevant issues that may arise in modelling their non-linear behaviour. After a summary of the models adopted for the braces and their connections (section 2), section 3 illustrates two alternative design procedures and, finally, section 4 reports a numerical application, comparing the outcomes deriving from those design criteria.

## 2 STEEL EXOSKELETON MODEL

The exoskeletons studied in the present work comprise special concentrically braced frames (SCBFs) placed parallel to the facades of the existing building. Due to their strength and stiffness, the added exoskeleton results into a significant modification of the seismic response of the existing building. Consequently, a detailed modelling of the nonlinear behaviour is required to capture accurately their role in withstanding the seismic action. More specifically, a proper model is required to predict the braced frame plastic mechanism and their ultimate failure mode, including the capability of the gusset plate connections to accommodate the inelastic deformations and end rotations due to brace buckling. The following subsections

are devoted to explaining how such aspects have been implemented within the OpenSees framework [11].

## 2.1 Diagonal braces

Since the dissipative elements of a SCBF are represented by its braces, particular attention has been devoted to catching the correct way to represent their buckling and post-buckling behaviour. The braces are modelled adopting force-based elements with a fiber discretization of cross sections ([12]). Moreover, the brace members are discretized into a suitable number of "sub-elements", to apply an equivalent geometrical imperfection with a sinusoidal shape, as reported in Figure 1. The maximum amplitude $e_0$ has been calibrated to obtain a brace buckling load from the numerical model that is close to that evaluated according to the buckling curves of Eurocode 3 [13].

The results from a mesh-sensitivity analysis for the elastic response are summarized in Table 1. The reported results suggest that the adoption of two elements might be enough to model the elastic response of the SCBFs. However, in the present work the braces are modelled using 4 elements to reproduce a sinusoidal shape of the equivalent geometrical imperfections and for a better representation of the nonlinear behavior. This is currently considered a sufficient compromise between accuracy and cost of the numerical analysis for the global system response. However, further study is going to be carried out from this perspective.

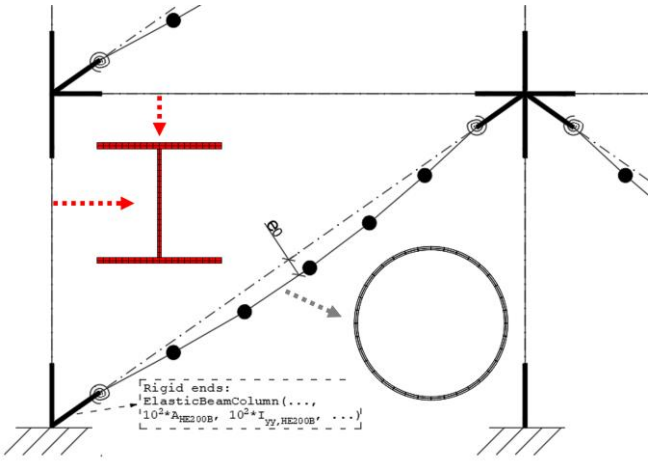


Figure 1 : Brace discretization

| *Number of elements for each brace member* | **Periods [sec]** | | |
|---|---|---|---|
| | **UX** | **UY** | **RZ** |
| *2* | 0.266 | 0.275 | 0.171 |
| *4* | 0.265 | 0.274 | 0.169 |
| *6* | 0.264 | 0.273 | 0.169 |
| *8* | 0.264 | 0.273 | 0.169 |

Table 1: Influence of the number of elements for each brace member on the structural periods

## 2.2 Gusset connections

Although typical modeling approaches for brace members assume that the gusset plate connection is fully restrained or fully pinned, experimental tests have shown that the real restraint condition is intermediate between those two simplified assumptions. Furthermore, an inadequate prediction of the bracing restraint condition can significantly affect the buckling capacity, tensile yielding, distribution of yielding, and post-buckling behavior of the dissipative elements of the frame [14].

Consequently, to enhance the model accuracy, the brace boundary condition were simulated through a nonlinear out-of-plane rotational spring, accounting for the gusset plate stiffness and strength in bending. The remaining part of the connection was assumed to have a rigid behaviour, as reported in Figure 1. Figure 2 shows a brace end connection. A knife plate was adopted in order to accommodate the buckling behavior in the same plane of the exoskeletons.

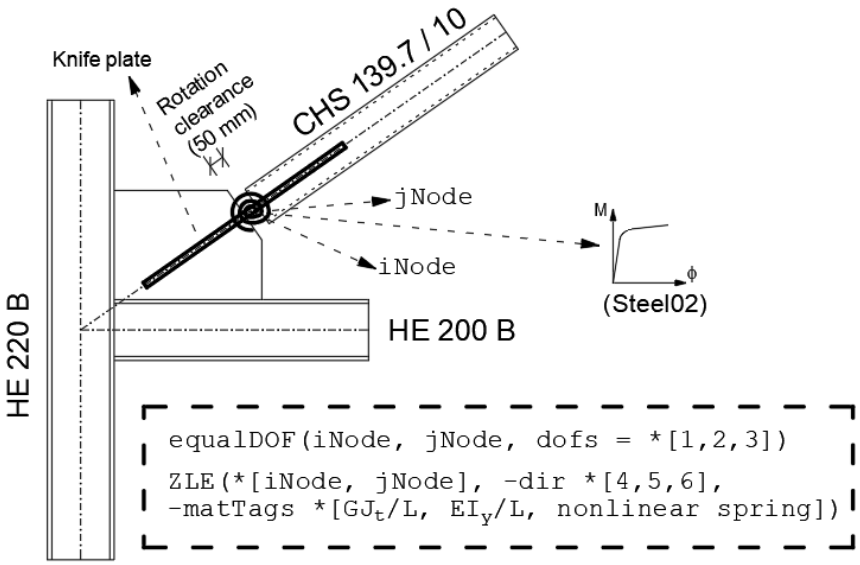


Figure 2 : Gusset to beam-column joint

## 3 DESIGN OF THE UPGRADING INTERVENTIONS

In the present paper two different scenarios are considered with the aim of pointing out how the adoption of a more refined method of designing the exoskeletons can influence the efficiency of the upgrading interventions. For the sake of simplicity, only a height-wise linear distribution of horizontal forces has been considered during the design phase.

### 3.1 Scenario 1: simplified Force-Based Design

Firstly, a simplistic code-compliant design approach is adopted, imagining that the SCBFs are the only structural components devoted to withstanding the seismic actions. This methos is intended to mimic what a practitioner would likely do while solving the design problem. To this aim, the design base shear force applied to the SCBF, is obtained from the design pseudo-acceleration at the "Severe Damage" limit (SDL) state at the SCBF fundamental period of vibration ($T_{1,SCBFs}$). Then, the design spectral ordinate is reduced by means of a q-factor equal to

4, which has been recently demonstrated to be an appropriate assumption [15]. Therefore, the design base shear force is calculated as follows:

$$V_{\text{b, d, Scenario1}} = (\lambda m_{tot}) \cdot \delta \cdot \frac{S_a(T_{1,SCBFs}, PGA_{SD})}{q_{SCBFs}} \tag{1}$$

where $\lambda$ = 0.85 is a correction factor included in the Italian code, $m_{tot}$ is the total mass of the structure for the seismic load combination, $\delta$ = 1.3 is an amplification coefficient representing the effect of accidental torsional effects, $S_a$ is the spectral ordinate, $q_{SCBFs}$ is the behaviour factor.

Secondly, after a simple linear elastic analysis, the dissipative zones (diagonal braces) are designed with respect to this load combination, neglecting the contribution of the braces in compression, while the non-dissipative zones (beams and columns) are subsequently designed according to the resistance hierarchy criteria.

### 3.2 Scenario 2: Design according to a pushover analysis

A more sophisticated design method might be sought and found suitable for a better performance assessment and/or saving the costs of the new structure. To this aim, a nonlinear static (pushover) analysis of the exiting RC structure could be exploited. In fact, the design of a seismic upgrading system is normally preceded by an assessment of the as-built structure. Then, a more rational design strategy can be defined, based on the following hypothesis:

- the overall displacement capacity of the existing structure is not affected by the introduction of the exoskeletons;
- the secant period $T^*$ of the structure equipped with the exoskeleton is still larger than $T_C$, meaning that the so-called "equal displacement rule" can be applied;
- the existing RC structure and the new steel exoskeletons (SCBFs) are described by two independent capacity curves, working in parallel, so that the total yielding strength of the upgraded structure can be expressed as $F_{y,tot} = F_{y,RC} + F_{y,SCBFs}$ .

Consequently, a different design criterion, as depicted in Figure 3, might be defined:

$$V_{\text{b, d, Scenario2}} = \alpha \cdot \Gamma_1 \cdot V_{\text{b, el, SCBFs}} = \alpha \cdot \Gamma_1 \cdot [m^* \cdot S_a(\delta^*_{\text{u, RC}}, PGA_{SD}) - F_{y,RC}] \tag{2}$$

where $\alpha$ represents the fraction of the total elastic base shear ( $\Gamma_1 \cdot V_{\text{b, el, SCBFs}}$ ) that the SCBFs have to withstand, $\Gamma_1$ is the modal participation factor for the 1st mode, $S_a$ is the spectral ordinate corresponding to $\delta^*_{u,RC}$ , that is the displacement capacity of the existing structure, $m^*$ is the mass of an equivalent SDOF system [16] and $F_{y,RC}$ is the yielding strength of the existing structure. It is straightforward that, under the above reported assumptions, a design equation can be expressed in terms of the minimum stiffness required to the equivalent SDOF, $k^*_d$:

$$k^*_{\text{d, Scenario2}} = \left( \frac{2.5 \cdot \eta \cdot S \cdot PGA_{SD} \cdot T_C}{2\pi} \right)^2 \cdot \frac{m^*}{(\delta^*_{\text{u, RC}})^2} \tag{3}$$

where $\eta$ is the damping correction factor, $S$ is the soil factor, $T_C$ is the upper bound of the constant acceleration portion of the design spectrum.

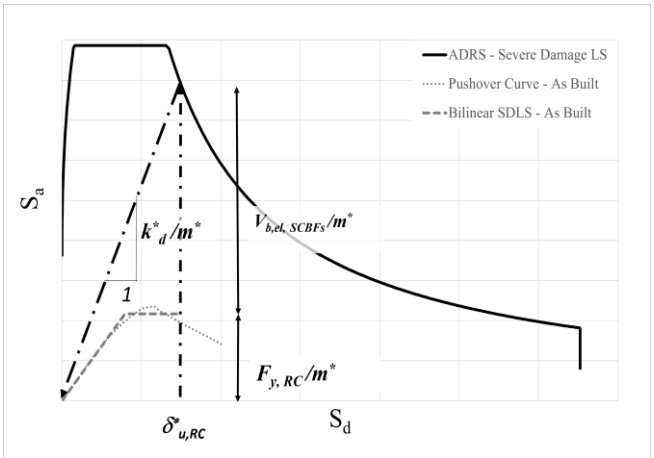


Figure 3 : Graphical representation of the design criterion based on the pushover response of the existing RC structure

# 4 APPLICATION

## 4.1 Structure presentation

The design of an archetype existing 4-storey building has been simulated, using the Codes and practice adopted in Italy during the 1970s. The building is assumed to be in a high seismic hazard region in Italy (Sant'Angelo dei Lombardi, AV, Italy). It has been consequently designed to withstand a minimum value of horizontal forces. The structure is characterized by 4 frames of 5 bays in the longitudinal (X) direction and by 4 frames of 3 bays in the transversal one (Z), having uniform bay width of 5.00 m and uniform interstorey height of 3.50 m. Table 2 summarizes the cross sections of the RC members.

| *Storey* | Columns [cm$^2$] | Beams - X [cm$^2$] | Beams - Y [cm$^2$] |
|---|---|---|---|
| *1st* | 35 x 35 | 30 x 60 | 30 x 60 |
| *2nd* | 30 x 30 | 30 x 60 | 30 x 60 |
| *3rd* | 30 x 30 | 30 x 60 | 30 x 60 |
| *4th* | 30 x 30 | 30 x 60 | 30 x 60 |

Table 2: RC members cross sections

To represent the typical materials utilized in the 1970s, a cylindrical compressive strength $f_{cm}$ = 25 MPa is assumed for concrete, while the average tensile strength of reinforcing bars is assumed equal to $f_{sm}$ = 220 MPa, representative of steel type FeB22k. The construction site is assumed to be Sant'Angelo dei Lombardi (AV, Italy) having a value of $PGA_{SD}$ = 0.266 g for the expected event at SD limit state and $PGA_{DL}$ = 0.082 g for the expected event at "Damage Limitation" (DL) limit state, considering a type "C" soil.

Firstly, a nonlinear static (pushover) analysis was carried out, adopting the N2-Method [16] to assess the performance of the existing RC structure. To this aim, a nonlinear FE model was implemented, utilizing *force-based elements* (distributed plasticity) for all the existing RC members, accounting for both mechanical and geometrical non-linearities. Fiber sections are associated to each member, considering the uniaxial materials *Concrete01* and *Steel02* available in the OpenSees library [11]. The brittle shear failures of RC members and joints were not explicitly included in the FE model, but the corresponding shear resistances were evaluated in the post-processing phase according to the current Italian Seismic Code [17].

## 4.2 Exoskeleton configurations

Figure 4 shows the FE model, highlighting that the connection between the RC and the steel structures was represented by a kinematic constraint (*equalDOF* in OpenSees) applied to the horizontal displacement components of the connected nodes in the two plan directions X and Y. To avoid interactions between the steel frames and the existing structure in bearing the vertical loads, the corresponding nodes are disconnected for the vertical displacement component. An appropriate design of the steel-to-RC connection has to be developed for the applicability if these kinematic constraints, but such a detail is out of the scope of this paper.

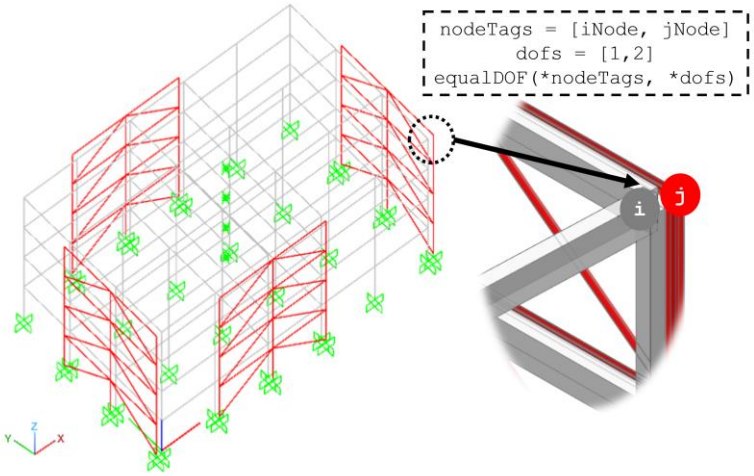


Figure 4 : 3D view of the FE model of the existing structure equipped with the steel exoskeletons

Table 3 summarizes the cross sections adopted for the exoskeletons. It is stressed that the design of the diagonal braces takes into account the design criteria reported in Sections 3.1 and 3.2, as well as code limitations to the brace slenderness $\lambda$ and overstrength ratios $\Omega$ in the frame elevation [18], as expressed by means of the following two equations:

$$\bar{\lambda} = \sqrt{\frac{N_{pl}}{N_{cr}}} = \frac{\lambda}{\pi}\sqrt{\frac{f_y}{E}} \leq 2.0 \tag{4}$$

$$\frac{\Omega_{max} - \Omega_{min}}{\Omega_{min}} \leq 0.25 \tag{5}$$

where $N_{pl}$ is the plastic tension resistance, $N_{cr}$ the Eulerian buckling load and $\Omega$ the ratio between $N_{pl}$ and the corresponding axial force demand deriving from a linear analysis.

| *Storey* | **Brace** cross sections (**CHS type**) | | **Column** cross sections (**HE type**) | | **Beam** cross sections (**HE type**) | |
|---|---|---|---|---|---|---|
| | Scenario 1 | Scenario 2 | Scenario 1 | Scenario 2 | Scenario 1 | Scenario 2 |
| *1st* | 193.7 / 16 | 139.7 / 12.5 | 360 B | 220 B | 300 B | 200 B |
| *2nd* | 193.7 / 12.5 | 139.7 / 12 | 360 B | 220 B | 300 B | 200 B |
| *3rd* | 193.7 / 10 | 139.7 / 10 | 360 B | 220 B | 300 B | 200 B |
| *4th* | 193.7 / 6 | 139.7 / 5 | 360 B | 220 B | 300 B | 200 B |

Table 3: Exoskeleton members cross sections

It is worth mentioning that the ratio between the design base shear forces associated to the two possible upgrading solutions is approximately equal to 1.50, having assumed $\alpha = 0.50$.

### 4.3 Resulting structural response

For the sake of simplicity only a linear (height wise) distribution of horizontal forces has been adopted for the pushover analysis, consistent with the design Eqs. (1) and (2). More specifically, Figure 5 (a-f) outlines the position of the various capacity points on the pushover curves of the existing structure (a-b) and the upgraded ones for Scenario 1 (c-d) and Scenario 2 (e-f). For the sake of brevity, only the results in the X+ and Y+ direction are reported herein.

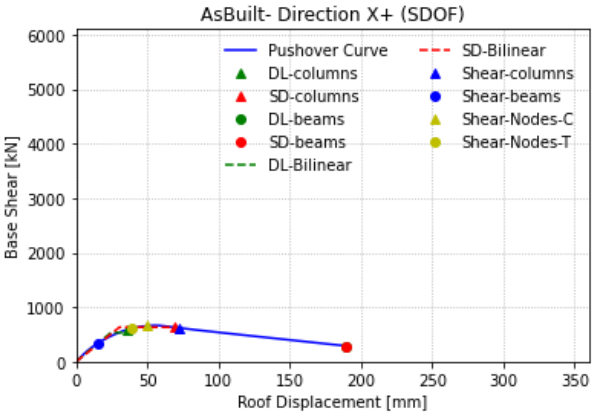


(a)

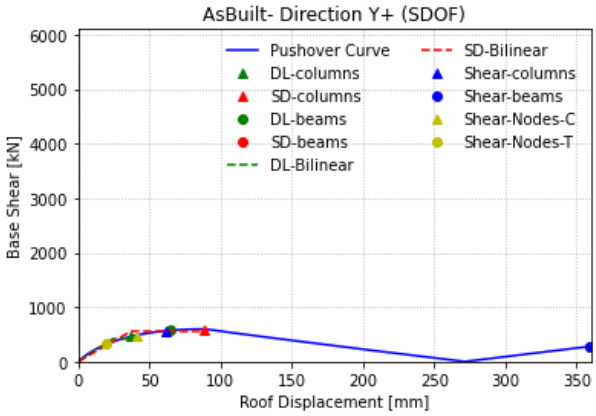


(b)

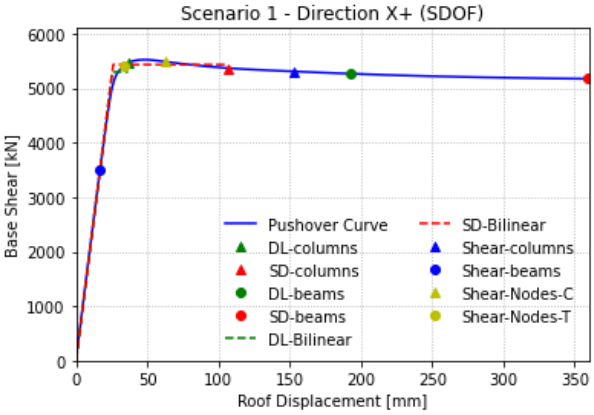


(c)

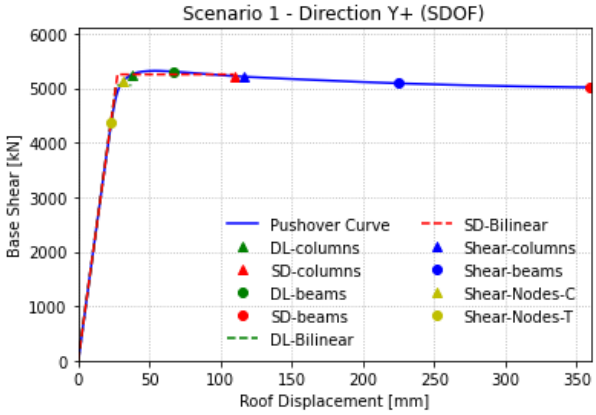


(d)

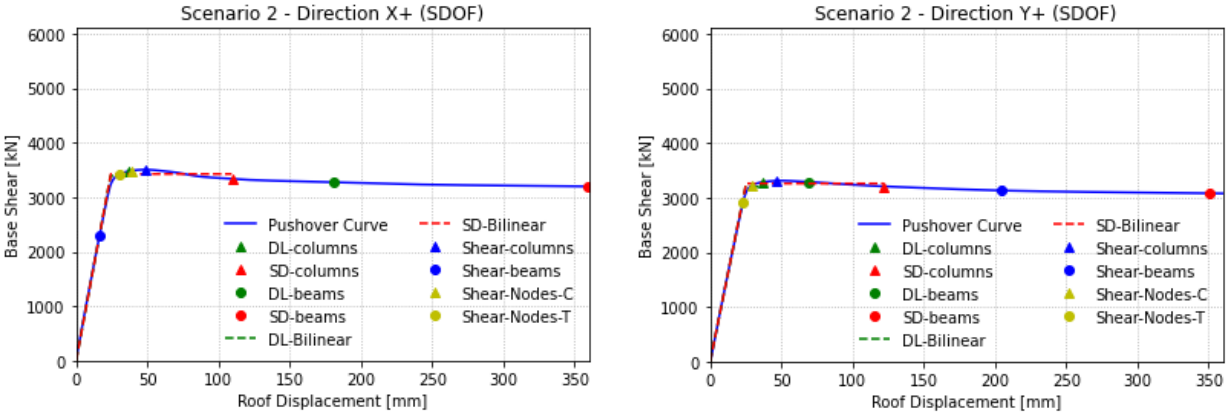


(e) (f)

Figure 5 : Pushover Curves, bilinearizations and Capacity Points of the existing RC structure (a-b) and the upgraded structures for Scenario 1 (c-d) and Scenario 2 (e-f)

Figure 5(a-b) shows that the existing structure is characterized by a global behaviour with a post-peak negative slope in the force-displacement relationship. This response corresponds to a soft-storey collapse mechanism involving the 2nd storey, as shown in Figure 6(a). The introduction of the exoskeletons leads to a more uniform interstorey drift distribution (Figure 6(b-c)), regardless of the adopted design procedure. This benefit derives also from the fulfillment of the braces design criterion expressed in Eq. (5), which tends to provide a uniform brace inelastic deformation along the frame elevation.

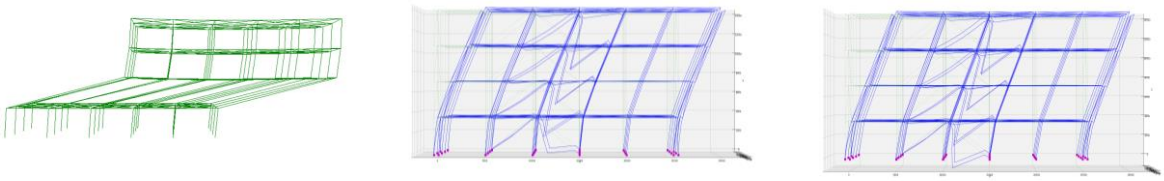

(a) (b) (c)

Figure 6 : Deformed shapes corresponding to the last analysis step for the X+ pushover analysis of the existing RC structure (a) and the upgraded structures for Scenario 1 (b) and Scenario 2 (c)

## 4.4 Capacity evaluation

The safety checks were performed with respect to the current Italian provisions for existing buildings [19]. Two relevant parameters were evaluated: the **safety index $\zeta_E$**, consisting in the capacity-over-demand ratio in terms of PGA, and the **Damage Extension Index (DEI)** accounting for the actual number of under-designed members (or unfavourable mechanisms) for each considered Limit State. More specifically, the elements chord rotation capacity was evaluated as suggested in the Eurocode 8, Part 3, Section A.3.2.2 [20]. Conversely,

the shear resistance of members was evaluated according to the Italian code provisions, considering proportionality to the chord rotation ductility ($\mu_\Delta^{pl}$). In particular, when $\mu_\Delta^{pl} \geq 3$ the expression of the shear cyclic resistance (Eurocode 8, Part 3, Section A.3.3.1) is adopted; when $\mu_\Delta^{pl} \leq 2$ the shear resistance is assumed equal to the maximum between the shear cyclic

resistance and the shear resistance under vertical loads; for intermediate values of $\mu_{\Delta}^{pl}$ an interpolation is performed. Moreover, the following relationships have been utilized for checking shear failures of beam-to-column joints:

$$\sigma_{jc} = \frac{N}{2A_j} + \sqrt{\left(\frac{N}{2A_j}\right)^2 + \left(\frac{V_j}{2A_j}\right)^2} \leq 0.5 f_{cd} \tag{6}$$

$$\sigma_{jt} = \left| \frac{N}{2A_j} - \sqrt{\left(\frac{N}{2A_j}\right)^2 + \left(\frac{V_j}{2A_j}\right)^2} \right| \leq 0.3\sqrt{f_{cd}} \tag{7}$$

where $\sigma_{jc}$ and $\sigma_{jt}$ are the maximum compressive and tensile stress, $f_{cd}$ is the concrete compressive strength assumed for the brittle mechanisms, $A_j$ is the beam-to-column joint area, $N$ is the axial load acting on the column above the joint, $V_j$ is the joint shear demand (depending on the bending moments acting at the joint sides and on the shear force acting on the column above the joint).

Table 4, Figure 7 and Table 5, Figure 8 respectively report the structural capacities in terms of safety index $\zeta_E$ and Damage Extension Index (DEI). To summarize, only the worst values per each analysis direction are reported. For each safety check the minimum safety index and the maximum DEI between the two plan directions are highlighted with a bold character.

| **$\zeta_E$ = $PGA_D$ / $PGA_C$ [-]** | | | | | | |
|---|---|---|---|---|---|---|
| *Limit State*\ **Structure** | **As Built** | | **Scenario 1** | | **Scenario 2** | |
| | **X+ / X-** | **Y+ / Y-** | **X+ / X-** | **Y+ / Y-** | **X+ / X-** | **Y+ / Y-** |
| *DL - Ductile* | 0.91 | **0.83** | 3.30 | 3.15 | 2.29 | 2.32 |
| *SD - Ductile* | **0.51** | 0.56 | 2.86 | 2.72 | 2.43 | 2.16 |
| *SD - Brittle Beams* | **0.12** | 2.30 | **0.50** | 5.34 | **0.37** | 5.66 |
| *SD - Brittle Columns* | 0.54 | **0.39** | 3.57 | 2.88 | 1.01 | **0.93** |
| *SD - Joints Eq. (6)* | 0.81 | **0.27** | 1.34 | **0.93** | 0.79 | **0.59** |
| *SD - Joints Eq. (7)* | 0.30 | **0.14** | 0.96 | **0.70** | 0.60 | **0.48** |

Table 4: Comparison between the upgrading solutions in terms of safety index $\zeta_E$

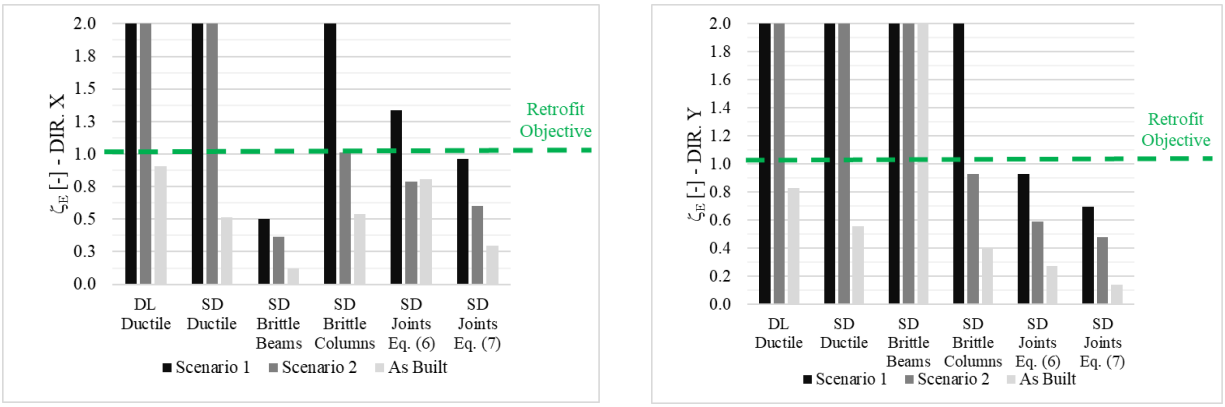


(a) (b)

Figure 7 : Comparison between the upgrading solutions in terms of safety index $\zeta_E$ for X (a) and Y (b) direction

| DEI [%] | | | | | | |
|---|---|---|---|---|---|---|
| *Limit State*\ **Structure** | **As Built** | | **Scenario 1** | | **Scenario 2** | |
| | **X+ / X-** | **Y+ / Y-** | **X+ / X-** | **Y+ / Y-** | **X+ / X-** | **Y+ / Y-** |
| *DL - Ductile* | 25 | **50** | 0 | 0 | 0 | 0 |
| *SD - Ductile* | **25** | **25** | 0 | 0 | 0 | 0 |
| *SD - Brittle Beams* | **16** | 0 | **13** | 0 | **17** | 0 |
| *SD - Brittle Columns* | **25** | **25** | 0 | 0 | 3 | **4** |
| *SD - Joints Eq. (6)* | 2 | **6** | 0 | **3** | **6** | 4 |
| *SD - Joints Eq. (7)* | 21 | **38** | 6 | **31** | 21 | **38** |

Table 5: Comparison between the upgrading solutions in terms of Damage Extension Index

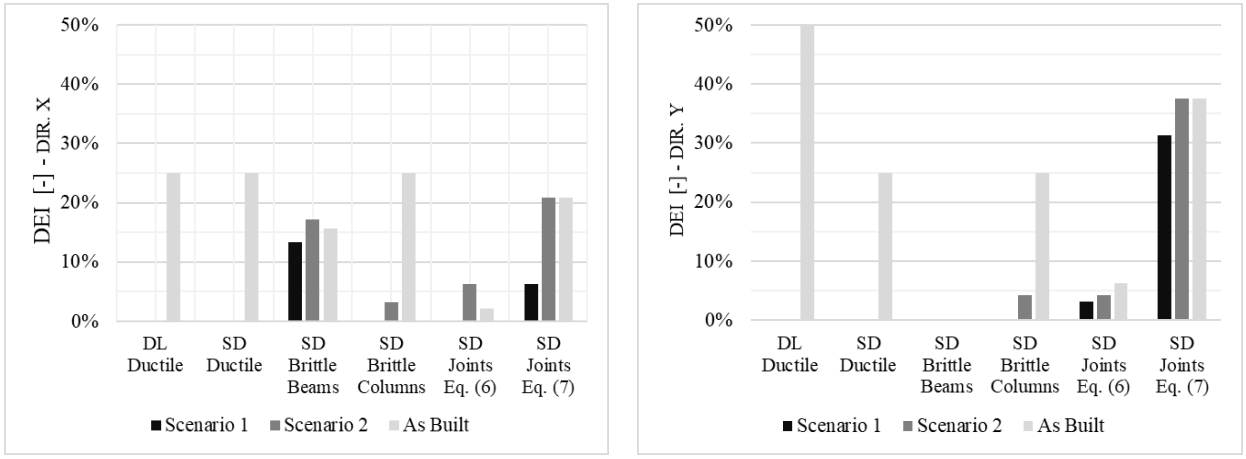


(a) (b)

Figure 8 : Comparison between the upgrading solutions in terms of Damage Extension Index for X (a) and Y (b) direction

Observing the results, it is clear that the advantages of the steel exoskeletons are both in the enhancement of the structural capacity (Figure 7) and the reduction of the number of deficient members (Figure 8), except for the brittle mechanisms involving the beams and the tensile beam-column joint failure.

The exoskeleton modifies the global behaviour (Figure 6), both regularizing the drift distribution and modifying the RC frame internal actions. As a result, not only the number of failing members is generally reduced (Table 5), but also the location of plastic hinges is modified.

Finally, comparing the design criteria, the results show that Scenario 1 is generally characterized by higher values of the safety index and lower values of DEI. However, it is yet not sufficient to fully achieve the retrofit objective. Consequently, it may be advisable to design a less robust exoskeleton (as in Scenario 2) combined with a proper number of member-level techniques. Smaller braces will also limit the costs at the foundation level, which usually have a large impact on the entire cost of the retrofit system.

## 5 CONCLUSIONS

A proper nonlinear model of the steel exoskeleton is required to estimate properly the effectiveness of the examined upgrading technique in enhancing the structural performance of the existing structure under seismic loading. The combined effect of the capacity increase in terms of acceleration and the modification of the collapse mechanism in the existing RC structure will result in a synergistic effect, significantly enhancing the structural performance.

The outcomes deriving from the adoption of two different design criteria have been presented, demonstrating that the adoption of a more rational design criterion based on the assessment of the existing structure can help in avoiding an overestimation of the seismic demand, thus also reducing the cost of the required upgrading at the foundation level.

Nevertheless, it is apparent that the adoption of this structure-level technique alone is not sufficient to fulfill all the retrofit objectives, because of the need to consider those brittle mechanisms representing the main weaknesses of the existing RC structure, i.e. shear failure of beams and shear tensile failure of joints for the considered case study.

Consequently, the results lead to conclude that a complete seismic retrofit of the existing structure requires collaborative efforts, with some member-level interventions in addition to the steel exoskeleton.

Further developments of the present work will be devoted to further explore the effectiveness of a combined intervention, by both refining the design and improving the numerical model.

## REFERENCES

[1] European Environmental Agency, 2020. Land use. Available online at https://www.eea.europa.eu/themes/landuse/intro

[2] CNI, 2012. Elaboration of National Council of Engineers (CNI) Study Center on ISTAT, CRESME, and Civil Protection data

[3] *fib* Bulletin No. 24. “Seismic assessment and retrofit of reinforced concrete buildings”. Federation International du Beton, 2003

[4] G. Della Corte, M. D’Aniello, R. Landolfo. Field testing of all-steel buckling-restrained braces applied to a damaged reinforced concrete building. *Journal of Structural Engineering* **141**, 0733–9445, 2015.

[5] F. Sutcu, A. Bal, K. Fujishita, R. Matsui, O. C. Celik, T. Takeuchi, Experimental and analytical studies of sub-standard RC frames retrofitted with buckling-restrained braces and steel frames. *Bulletin of Earthquake Engineering* **18,** 2389–2410, 2020. https://doi.org/10.1007/s10518-020-00785-4

[6] G. Cantisani, E. Rodontini, G. Della Corte. Numerical modelling and analysis of eccentric bracing with vertical shear links. *Eccomas Proceedia COMPDY, 8th ECCOMAS Thematic Conference on Computational Methods in Structural Dynamics and Earthquake Engineering*, 151-163, Streamed from Athens, Greece, 28 - 30 June 2021. DOI: 10.7712/120121.8470.19269

[7] G. Della Corte, G. Cantisani, FEM Analysis of Steel Eccentric Braces for Seismic Retrofitting. *Procedia Structural Integrity XIX ANIDIS Conference, Seismic Engineering in Italy* **44**, 472–479, 2023. DOI: 10.1016/j.prostr.2023.01.062

[8] G. Scuderi. Building Exoskeletons for the Integrated Retrofit of Social Housing. *Civil Engineering Journal*, **2**, 226-243, 2016. DOI: 10.28991/cej-2016-00000029

[9] D.E. Lehman, C.W. Roeder, D. Herman, S. Johnson, B., Kotulka. Improved Seismic Performance of Gusset Plate Connections, *Journal of Structural Engineering*, **134**(6), 890-901, 2008. DOI: 10.1061/(ASCE)0733-9445(2008)134:6(890)

[10] L. Martelli, L. Restuccia, G.A. Ferro. The exoskeleton: a solution for seismic retrofitting of existing buildings, *Procedia Structural Integrity*, **25**, 294–304, 2020. DOI: 10.1016/j.prostr.2020.04.034

[11] S. Mazzoni, F. McKenna, M.H. Scott, G.L. Fenves, et Al., OpenSEES– Open System for Earthquake Engineering Simulation, *Pacific Earthquake Engineering Research Center*, University of California, Berkeley (USA), 2006.

[12] P.C. Hsiao, D.E. Lehman, C.W. Roeder, Improved analytical model for special concentrically braced frames, *Journal of Constructional Steel Research*, **73**, 80–94, 2012. http://dx.doi.org/10.1016/j.jcsr.2012.01.010

[13] EN 1993-1-1:2005, Eurocode 3, Design of steel structures Part 1-1: General rules and rules for buildings, 2005.

[14] P.C. Hsiao, D.E. Lehman, C.W. Roeder, A model to simulate special concentrically braced frames beyond brace fracture, *Earthquake Engineering & Structural Dynamics*, **42**, 183–200, 2013. http://doi.wiley.com/10.1002/eqe.2202

[15] D. Vamvatsikos, K. Bakalis, S. Pyrza. Q-factor verification of a 6-storey concentrically braced frame via the INNOSEIS risk-based approach. *6th ECCOMAS Thematic Conference on Computational Methods in Structural Dynamics and Earthquake Engineering*, Rhodes Island, Greece, 2017. DOI: 10.7712/120117.5466.18281.

[16] P. Fajfar, Capacity spectrum method based on inelastic demand spectra, *Earthquake Engineering & Structural Dynamics*, **28**, 979-993, 1999.

[17] DM 17/01/2018, Italian Technical Code of Constructions, *Ministerial Decree*, Rome, Italy, 2018.

[18] EN 1998-1:2005, Eurocode 8. Design of structures for earthquake resistance - Part 1: General rules, seismic actions and rules for buildings, *European Committee for Standardization*, Bruxelles. 2005.

[19] C 21/01/2019, Circolare 21 gennaio 2019, n. 7 C.S.LL.PP. Instruction for the application of the DM 17/01/2018, **Chapter 8,** *Ministerial Decree*, Rome, Italy, 2019.

[20] EN 1998-3: 2005, Eurocode 8. Design of structures for earthquake resistance - Part 3: Assessment and retrofitting of building, *European Committee for Standardization*, Bruxelles, 2005.

COMPDYN 2023
9th ECCOMAS Thematic Conference on
Computational Methods in Structural Dynamics and Earthquake Engineering
M. Papadrakakis, M. Fragiadakis (eds.)
Athens, Greece, 12-14 June 2023

# SEISMIC ASSESSMENT AND STRENGTHENING OF THE REMAINING BEIRUT PORT SILOS DAMAGED AFTER THE 2020 AUGUST BLAST- A CASE STUDY

**S. Ismail[1], W. Raphael[2] and F. Kaddah[3]**

[1] Saint Joseph University of Beirut, Beirut 17-5208, Lebanon
sahar.ismail@net.usj.edu.lb

[2] Saint Joseph University of Beirut, Beirut 17-5208, Lebanon
wassim.raphael@usj.edu.lb

[3] Saint Joseph University of Beirut, Beirut 17-5208, Lebanon
fouad.kaddah@usj.edu.lb

## Abstract

*In 2020, the Beirut port silos, located few meters away from the center of August 4 explosion, were severely damaged. The first and second row of Beirut silos/East side were destroyed. However, the third row of silos was damaged and experienced an immediate tilt, except the last two silos in the South block (silos #130 and 137) that were destroyed. As a result, the remaining standing silos, have been monitored since the day of the blast using 3D scan measurements and triaxial inclinometers, experienced severe tilting over time. In July 2022, the rate of silos' inclination increased after a fire broke out in the North block silos due to grains' fermentation. As a result, in August 2022, the last silos of the North block fell after resisting severe tilting for two years with a maximum permanent vertical inclination of 2 m. Consequently, the 8.5 m diameter-42 silos supported by a 2500 pile foundation consisted as of August 2022 of 6 standing South block silos. In this paper, the authors describe the status of these silos and the performed structural health monitoring. A 3D finite element model was built in Abaqus to analyze the behavior of the silos under different seismic loadings. The results are evaluated in terms of horizontal displacements at top of the silos which are used to assess the stability of the structure. The obtained results show that the South block silos will exhibit serious damage and possible failure in case of moderate intensity earthquakes. Therefore, a repair and strengthening method to preserve the remaining standing silos using numerical analysis is proposed.*

**Keywords:** Damage, Collapse, Strengthening method, Blast Loading, Seismic Loading, Numerical Analyses.

## 1 INTRODUCTION

Civil structures deterioration with time is associated with environmental factors such as steel corrosion and concrete carbonation, aging in construction materials and extreme events such as earthquakes, hurricanes, floods, and blast loadings. As such, after these extreme events, Structural Health Monitoring (SHM) is used to provide quantitative and reliable data on the real condition of a structure. SHM is a damage identification technique for damage assessment and performance evaluation for aerospace, civil and mechanical infrastructures. It refers to the observation and analysis of the structure's damage and deterioration level over time using periodically spaced sensing measurements. Moreover, it is associated with life-safety and economic benefits [1 to 3]. Several non-destructive methods are used in SHM such as the wireless sensor networks to sense and collect data [4 to 6]. Recently, SHM has gained important interest in examining the status of health and maintenance of structures such as large-scale bridges [7 and 8].

On the 4$^{th}$ of August 2020, one of the most powerful non-nuclear explosions in history occurred in the port of Beirut, Lebanon [9]. This explosion ripped the city to shreds, caused more than $15 billion in damage, and left more than 200 casualties and 7400 injuries. The August 4, 2020 explosion, was attributed to the detonation of around 1100 to 2750 tons of Ammonium Nitrate [10 to 18, etc.]. It created a crater of 90 m wide X 100 m long X 6 m deep and damaged several significant structures in the area, including the Beirut port silos. As shown in Figure 1, following the explosion, the first and second row of Beirut silos/East side were destroyed. However, the third row of silos was damaged and experienced an immediate tilt, except the last two silos in the South block (silos #130 and 137) that were destroyed (Figure 1 and 2). To assess and monitor the level of damage of Beirut port silos, the structural health monitoring SHM of Beirut port silos following August 4, 2020 explosion was performed by the school of engineering ESIB at Saint Joseph University of Beirut, Lebanon and Amann Engineering using 3D laser scan measurements and four ultraprecise triaxial inclinometers installed in strategic locations on the remaining standing silos (Figure 1 and 2).

The explosion generated an immediate 20 to 30 cm horizontal tilt in the silos, measured East to West. Since that time, the remaining standing silos have been tilting. In fact, the South block silos have been stabled since November 2020 while the North block silos tilt shifted since the blast West to East, towards the explosion crater. In July 2022, fire in the silos, caused by the fermentations of the remaining trapped grains in the silos that could not be removed for several reasons, caused an increase in the rate of silos' inclinations. As a result, silos # 35, 42, 33 and 40 fell on July 31, 2022, silos 49, 56, 47 and 54 fell on August 4, 2022, and silos # 63, 70, 77, 84, 82, 75, 68 and 61 fell on August 23, 2022 (Figures 1 and 2). Note that no injuries were reported following the collapses as the authorities' evacuated parts of the port area in anticipation of them.

Researchers have been studying the failure of real case studies structures including collapsed silos [19 to 23] to prevent future incidents. Since Lebanon is in an active seismic zone and its prone to several seismic events, the behavior of the remaining standing South block silos was simulated in this paper using the Finite Element Software Abaqus following different seismic loadings. The obtained data will serve as guidance of how a damaged structure can behave after a large explosion and partial collapse. Finally, following the decision of the Lebanese authorities to preserve the remaining tilted standing silos to serve as a memorial for August 4, 2020 explosion, a repair and strengthening method of the South block silos using numerical analysis is presented.

a)  b) 

Figure 1: a) The damaged grained Beirut port silos, after August 4, 2020 blast [24] and b) The collapse of the North block silos [25].

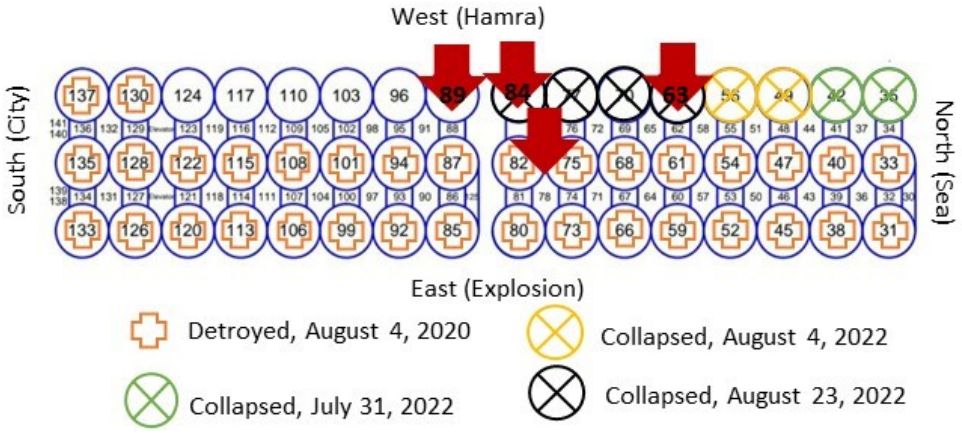


Figure 2: Silos' name tag, status, and tiltmeters' positions Beirut port silos.

## 2 BEIRUT PORT SILOS

The grain storage Beirut port silos were built in 1968 in three phases at a cost of $2.8 million. Beirut port silos, the largest grain facility at the time, was equipped with loading and unloading equipment for ships, railway wagons and cars [26]. As shown in Figure 3, engineers constructed 24 silos formed of 8 columns X 3 rows during phase 1 (in 1968), 18 silos formed of 6 columns X 3 rows during phase 2 (in 1969) and 6 silos formed of 2 columns X 3 rows during phase 3 (in 1997). Thus, the silos, completed and put into operation in 1969, consisted of 14 columns X 3 rows of 48 m high, 8.5 m diameter cylindrical silos with a bearing storage capacity of 105 000 tons of grains. And then in 1997, after the addition of 6 silos, the structures' grain storage capacity was increased by 15 000 tons of grains. Note that from 2000 to 2002, the engineers reinforced the inner walls of the outer silos due to concrete carbonation caused by the deterioration of the cells by the exposure to humidity and seafront. The inner wall of these silos was increased by 12 cm; the silos' original wall thickness was equal to 17 cm.

The concrete silos, constructed with a special water-resistant prescribed type of cement having a mean compressive strength of 30 MPa, were heavily reinforced. On average, the horizontal and vertical reinforcement are formed of 14-mm reinforced steel diameter every 180 cm and 12-mm reinforced steel diameter every 300 cm, respectively. As for the foundation, the Beirut port silos were built on 2500 square (30 X 30 cm) concrete piles driven to embedded lengths between 15 and 17 m in backfill soil consisting of 2 m of miscellaneous backfill

sand material and 15 m of sandy material that presents some levels of gravel and clay. Note that the water table was below the bedrock level.

The grain storage silos situated few meters from the center of the explosion, at about 70 m in front of the silos and 40 m from the side of the silos; based on the data of the Lebanese Army and Forensic Architecture, 2020, in warehouse 12 at the port, absorbed part of the blast energy and shielded some of the Western part of Beirut's structures. The August 4, 2020 explosion destroyed the first and second row of Beirut port silos (the East-face cylinders) while it damaged the third row (the Western-face cylinders) that has been tilting since the timing of the blast (Figures 1 and 2).

Following the explosion, the silos tilted 20 to 30 cm East to West with the highest deformation noted on silos #56 and 63 on the North block [11 to 15]. Even though the silos tilted away from the explosion crater at first (Hamra side), their rotation was shifted as of phase 1: West to East, towards the explosion crater. Note that, the collapse of the North block silos in August 2022, shredded by the massive August 4, 2020 explosion, was inevitable since the structure was beyond repair; severely damaged and unstable.

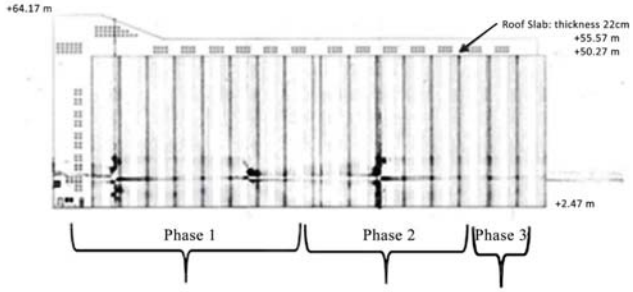


Figure 3: Vertical section and the construction phases of the Beirut port silos.

## 3 FINITE ELEMENT MODEL

The FE software, Abaqus, was applied to analyze the seismic behavior of the remaining standing Beirut port silos using three-dimensional model. The geometric model consisted of the 6, 8.5 m diameter, 48 m height tilted South block silos having a 29 cm wall thickness. The reinforced concrete silos were simulated using 4- node doubly curved shell, reduced integration, hourglass control, finite membrane strains S4R shell elements. Moreover, the silos steel reinforcement was defined as layers of reinforcement as part of the silos' shell elements using the rebars command (rebars' layers option) available in Abaqus.

The nonlinear behavior of the reinforced concrete under the static (the tilting phase) and dynamic loadings were modeled in Abaqus using the concrete damage plasticity model while incorporating strain rate effects (Figure 4). Moreover, the inelastic/plastic behavior of the steel reinforcement was simulated using elastic-perfectly plastic material by defining the steel yield stress. The relevant properties of the reinforced concrete and steel used in the FE model are presented in Table 1 and Figure 4. $\rho$ = density (kg/m$^3$), $E$ = Young modulus (GPa), $\nu$ = Poisson's ratio, $\sigma_y$ = yield stress (MPa), $K$ = the ratio of the second stress invariant on the tensile meridian, *fb0/fc0* = the ratio of initial equibiaxial compressive yield stress to initial uniaxial compressive yield stress, $\psi$ = dilation angle (°), $f'_c$=concrete compressive strength (MPa). Note that the concrete and steel reinforcements in the silos were tied using the tie command in Abaqus and the base of the silos was assumed fixed.

The analysis in Abaqus contained two steps. First, the silos were displaced, based on the 3D scan and tiltmeters' data, to simulate their real movement since the day of the blast. Second, different seismic loads were applied at the base of the tilted silos, as detailed in Figure-

The seismic events were chosen having PGA values between 0.25 and 0.35g based on the seismic hazard for Lebanon study by [27] that shows that Lebanon is in zone 3 having a PGA value of approximately 0.25 g for a 475-year return period and 0.35g for a 950-year return period. Consequently, the structural status of the silos was generated. Note that a 5% damping ratio was considered in the analysis. Unlike the blast loading that resulted from August 4, 2020 explosion and released rapid hot gases, enormous amount of energy as well as high temperature and pressures in only milliseconds and produced a spherical-type wave that went from the superstructure to the foundation; the seismic loading forces the seismic wave to go up from the foundation to the superstructure and affects the system natural frequencies.

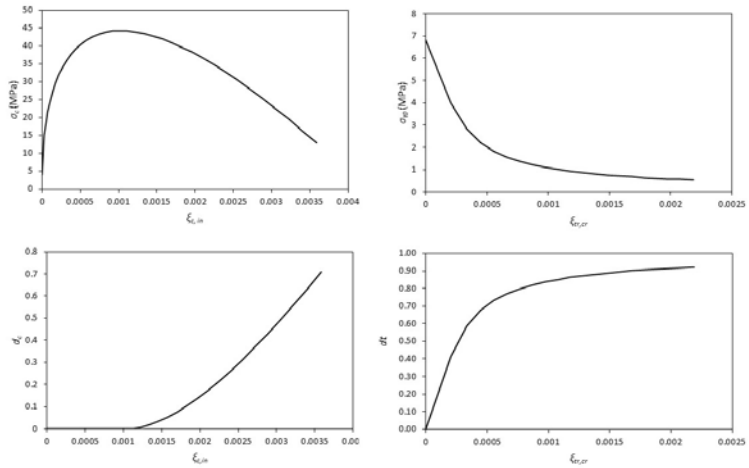

Figure 4: Stress-strain relation of the reinforced concrete in compressive and tensile region-concrete damage plasticity model with high strain rate effect.

| | | | | | |
|---|---|---|---|---|---|
| Concrete | $\rho$ (kg/m$^3$) | 2400 | Steel | $\rho$ (kg/m$^3$) | 7850 |
| | $E$ (GPa) | 43 | | $E$ (GPa) | 206 |
| | $v$ | 0.2 | | $v$ | 0.3 |
| | $\psi$ (°) | 31 | | $\sigma_y$ (MPa) | 448 |
| | Eccentricity | 0.1 | | | |
| | *fb0/fc0* | 1.16 | | | |
| | $K$ | 0.67 | | | |
| | Viscosity parameter | 0 | | | |
| Backfill material | $\rho$ (kg/m$^3$) | 1500 | Sandy Soil with some levels of gravel and clay | $\rho$ (kg/m$^3$) | 1700 |
| | $E$ (GPa) | 40 | | $E$ (GPa) | 25 |
| | $v$ | 0.25 | | $v$ | 0.25 |
| | $c$ (kPA) | 2 | | $c$ (kPA) | 10 |
| | $\Phi$ (°) | 44 | | $\Phi$ (°) | 38 |
| | $\psi$ (°) | 2.5 | | $\psi$ (°) | 10 |

Table 1: Material properties

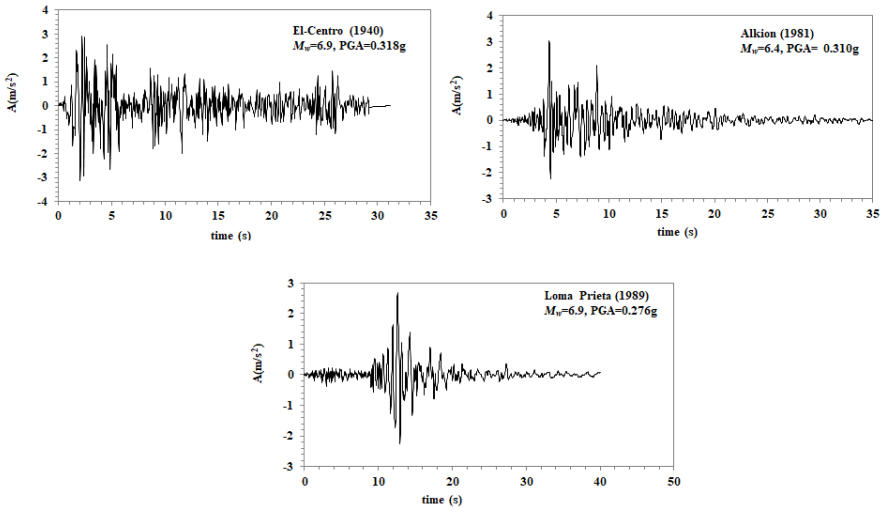


Figure 5: Acceleration with respect to time of El-Centro (1940), Alkion (1981) and Loma Prieta (1989) earthquakes.

## 4 RESULTS AND ANALYSIS

To study the effect of seismic loading, the displacement response of the remaining standing South block silos (Silos #124, 117, 110, 103, 96 and 89, as indicated in Figure 2) was investigated under 3 earthquakes: El-Centro (1940), Alkion (1981) and Loma Prieta (1989). The results, presented in Figure 6, indicate that the simulated seismic cases cause an immediate tilting of the silos towards the Hamra side (away from the explosion crater) under El-Centro (1940) earthquake and towards the explosion crater under Loma Prieta (1989) and Alkion (1981) earthquakes. In fact, the horizontal displacements of the stable South block silos increase from 3 to 30 cm (static condition, in February 2023) up to 73 cm under El-Centro (1940), while they decrease up to -1 cm under Loma Prieta (1989) and Alkion (1981), respectively (Positive displacement is towards the West/Hamra side while Negative displacement is towards the explosion crater). For example, the horizontal displacements at top of silos # 124 and 89 increase from 3 and 20 cm in February 2023 to 59.1 and 69 cm under El-Centro (1940) earthquake, while they decrease to 2 and 13 cm and -0.4 and 7 cm under Loma Prieta (1989) and Alkion (1981) earthquakes, respectively.

To present the state of damage of the simulated cases, the silos' damages in compression and tension were extracted from Abaqus. Figure 7 presents the South block silos' displacement, as well their status in damage and compression when hit by El-Centro (1940) earthquake. The amount of silos' damage, extracted from the FE model, presents the degradation of the silos' elastic stiffness, and is described by the compressive damage variable "$d_c$" (damage in compression) and the tensile damage variable "$d_t$" (damage in tension), where these damage variables range from 0: no damage to 1: destruction. Moreover, to show the state of damage of the silos' elements, the cumulative surface damage rate curves are plotted in Figure 8. The percentage of the damaged surface having undergone the amount of damage indicated is presented on the ordinate and the damage indicator (1 refers to completely damaged elements/surfaces) is presented on the abscissa. As shown in Figures 7 and 8, only 30% of the silos' surface underwent some level of damage. As detailed in Figure 8, only 27% of silos surfaces were 100% damaged under Alkion (1981) while only 18% and 13% of silos surfaces were 100% damaged under El-Centro (1940) and Loma Prieta (1989). The obtained results are in accordance with the North block silos' mode of failure depicted after their collapse. The

tilted silos fell on themselves without marking severe damaged surface first. As a result, any seismic load experienced in Lebanon will cause an important tilting of the remaining standing silos ending in severe silos' displacement, damage and high-risk of collapse.

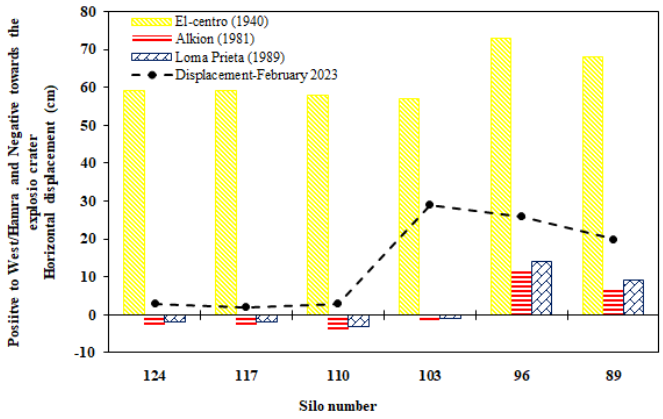


Figure 6: Maximum horizontal displacements at top of the South silos under different seismic loadings.

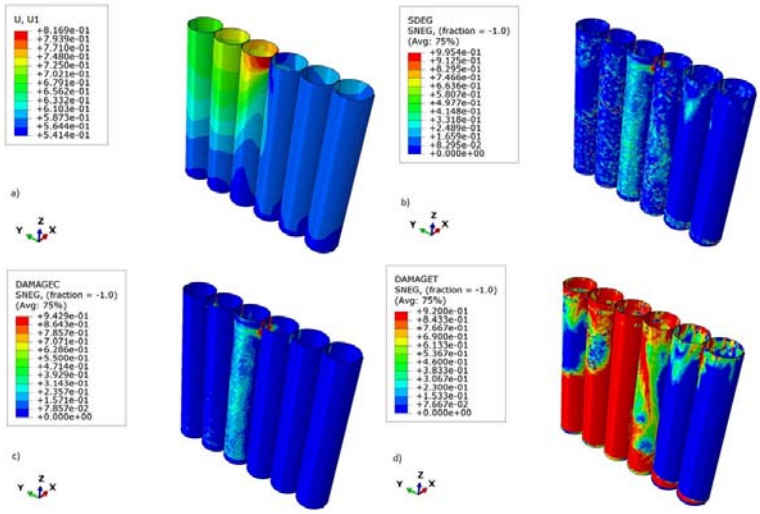


Figure 7: a) Horizontal displacement, b) SDEG output b) Damage in Compression and d) Damage in Tension (Damage variables range from 0 (no damage) to 1 (destruction)) of South Block silos hit by El-Centro (1940) earthquake (fixed-based case).

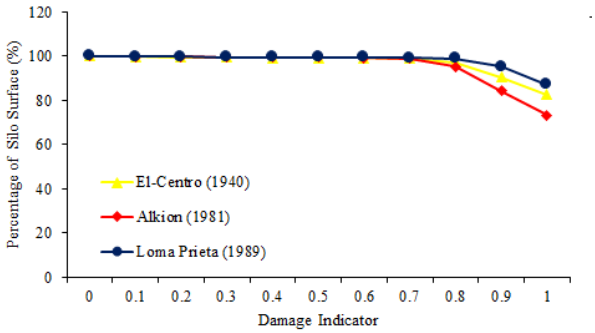


Figure 8: The cumulative surface damage rate curves of the different simulated cases.

## 5 REPAIR AND STRENGTHENING METHOD

As depicted by the 3D scans and tiltmeters' data obtained by [11-15], the high rate of the silos' tilting over the past two and half years was manifested by the appearance of new cracks on the bottom of the silos' walls. These cracks values mean that the damage is not superficial but deep and extends to the pile foundation. In fact, Ismail et al. [12-14] obtained that the pile cap as well as the head of the driven piles displaced on average 35 cm in the direction of the explosion. This value exceeds the allowable limits in all design codes, indicating that the piles' head deformed beyond their elastic limit and thus, the piles are severely damaged.

An explosion on the ground surface produces an air blast pressure as well as a ground shock near the structures that lie close to the detonation point, such as in the case of Beirut port silos. As mentioned previously, Beirut port silos in the late 1960s were built in 2 phases on predominantly sandy fill soil with a silty nature. The percentage of fines varies in the soil beneath the silos. Nevertheless, the highest percentage is located below silos # 126, 128, 130, 133, 135 and 137; i.e. below the destroyed South block silos. The blast exposed but did not widen the 1.2 m concrete gap at the construction joint between the Phase I and Phase II silos [11-15]. Moreover, the office building located next to the South block was destructed by the blast in addition to the first two silos of the South block: silos #137 and 130. Since the 30 X 30 cm, 15 to 17 m length slender piles were not designed to resist a lateral stress such as the one created by the underground component from the blast, then the closer to the explosion epicenter, the more likely the piles got damaged. As observed by the 3D scans and tiltmeters' data [11-15], the rate of silos' inclination increased during the wet season. As a result, the observed cracks at the bottom of the silos caused by the movement of the silos, indicate that the underground concrete piles are heavily damaged, and the structure-foundation-soil platform is getting compacted and sinking into the ground. In other words, the remaining standing silos are rested on damaged pile foundation.

Following the decision of the Lebanese authorities to preserve the remaining tilted standing silos to serve as a memorial for August 4, 2020 explosion, we present hereafter using Abaqus, a repair and strengthening method of the remaining standing South block silos. As such, the strengthen three-dimensional model was formed of the tilted reinforced concrete silos, the pile cap, the pile foundation, and the soil medium. The silos' wall thickness was increased from 29 to 41 cm. Moreover, the pile cap size beneath the remaining South block silos was increased by 3 X 1.12 m from the sides (length X thickness). Finally, 30 X 30 cm, 15 m length square driven piles were inserted below the new pile cap every 1 m. The pile cap and piles were embedded in a 200 X 200 X 17 m soil medium. The first 2 m of the soil profile were defined as miscellaneous backfill sand material while the next 15 m were defined as sandy material that presents some levels of gravel and clay. To account for the absorbed energy from the unbounded soil domain, the far-field soil, in both horizontal directions, was modelled using 8-node linear one-way infinite brick elements CIN3D8 [28]. Finally, to simulate bedrock conditions, the bottom soil boundary was defined as a rigid boundary. Table 1 details the material properties adopted in the numerical model. In Table 1, $c$ is the soil cohesion (kPa) and $\Phi$ and $\psi$ are the friction and dilation angles (°). In this study, the silos, pile cap, piles, and soil were modelled by tying and embedding the different parts together. Note that the strengthened numerical model was only hit in this section by El-Centro (1940) earthquake.

The results, detailed in Figure 9, indicate that adopting this strengthening solution decreases the amount of silos' displacement provoked by the seismic load significantly. In fact, the displacement at top of the silos decreases on average from 62 cm (fixed-based case) to 31 cm (SSI case) and 12 cm (SSI-reinforced case). SSI case refers to the reinforced numerical model while SSI case refers to the tilted silos, rested on the original/unstrengthen pile cap embedded

in the soil domain. For example, the displacement at top of silo#89, increases from 19.93 cm (static condition, displacement in February 2023) to 68 cm and 33.57 cm for the fixed-based and SSI cases while it decreases to 10 cm for the SSI-reinforced case.

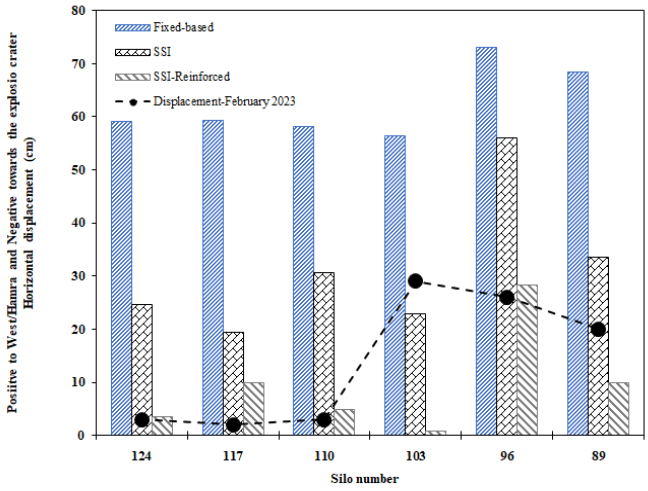


Figure 9: Maximum horizontal displacements at top of the South silos under El-Centro (1940).

## 6 CONCLUSIONS

Beirut port silos' structural health response was monitored since August 4, 2020 using 3D laser scan measurements and triaxial inclinometers installed on strategic locations on the South and North block silos. Since Lebanon is in an active seismic zone, the behavior of the remaining standing South block silos was simulated in this paper using the Finite Element Software Abaqus following different seismic loadings. Moreover, following the decision of the Lebanese authorities to preserve the remaining tilted standing silos to serve as a memorial for August 4, 2020 explosion, a repair and strengthening method of the South block silos is presented. The obtained results showed that:

- The remaining standing South block silos will be highly tilted under any earthquake loading. The horizontal displacements of the stable South block silos increase from 3 to 30 cm (static condition, in February 2023) up to 73 cm under El-Centro (1940), while they decrease up to -1 cm under Loma Prieta (1989) and Alkion (1981), respectively. Moreover, only 30% of the silos' surface undergoes some level of damage.
- Any seismic load experienced in Lebanon will cause an important tilting in the remaining standing silos ending in severe damage and high-risk of collapse.
- The strengthened solution consisting of increasing the silos' wall thickness from 29 to 41 cm, extending the pile cap an additional 3 X 1.12 m from the sides and inserting 15 m length 30 X 30 cm square driven piles every 1 m below the new pile cap improves the behavior of the remaining standing silos under seismic conditions.

## ACKNOWLEDGMENT

The authors would like to acknowledge Eng. Emmanuel Durand (Amann Engineering), M. Christoph Fröhlich, Chris Held from Zoller and Fröhlich GmbH ("Z+F") for their logistics and financial efforts for using the Z+F Imager 5010X scanner (Zoller & Fröhlich) and Move Solutions for using and installing the triaxial inclinometers.

## REFERENCES


[1] S.W. Doebling, C.R Farrar, M.B. Prime, D.W. Shevitz. *Damage identification and health monitoring of structural and mechanical systems from changes in their vibration characteristics: a literature review*. Los Alamos National Laboratory report LA13070-MS, 1996.

[2] H. Sohn, C.R. Farrar, F.M. Hemez, D.D. Shunk, D.W. Stinemates, B.R. Nadler. *A review of structural health monitoring literature: 1996–2001*. Report LA-13976-MS. Los Alamos National Laboratory, 2004.

[3] S. Das, P. Saha, S.K. Patro, Vibration-based damage detection techniques used for health monitoring of structures: a review. *Journal of Civil Structural Health Monitor*ing, **6**, 447–507. 2016. doi: 10.1007/s13349-016-0168-5.

[4] J. P. Lynch, K.J. Loh, A summary review of wireless sensors and sensor networks for structural health monitoring. *Shock Vibration Digest*, **38**, 91–130, 2006. doi: 10.1177/0583102406061499

[5] C.B. Yun, J. Min, Smart sensing, monitoring, and damage detection for civil infrastructures. *KSCE Journal of Civil Engineering*, **15**, 1–14, 2011. doi: 10.1007/s12205-011-0001-y.

[6] Y. Yu, W.H. Kang, C. Zhang, J. Wang, J. Ou, A stochastic analysis framework for a steel frame structure using wireless sensor system measurements. *Measurement*, **69**, 202–209, 2015. doi: 10.1016/j.measurement.2015.03.022.

[7] H.T. Al-Khateeb, H.W. Shenton, M.J. Chajes, C. Aloupis, Structural Health Monitoring of a Cable-Stayed Bridge Using Regularly Conducted Diagnostic Load Tests, *Frontiers in Built Environment*, **5**, 41, 2019. doi: 10.3389/fbuil.2019.00041.

[8] K. Aono, H. Hasni, O. Pochettino, N. Lajnef, S. Chakrabartty, Quasi-Self-Powered Piezo-Floating-Gate Sensing Technology for Continuous Monitoring of Large-Scale Bridges. *Frontiers in Built Environment*, **5**, 29, 2019. doi: 10.3389/fbuil.2019.00029.

[9] How powerful was the Beirut blast Reuters Graphics, https://graphics.reuters.com/LEBANONSECURITY/BLAST/yzdpxnmqbpx/, 2020.

[10] S. Rigby, T. Lodge, S. Alotaibi, A. Barr, S. Clarke, G. Langdon, A. Tyas, Preliminary yield estimation of the 2020 Beirut explosion using video footage from social media, *Shock Waves*, 2020. https://doi.org/10.1007/ s00193-020-00970-z.

[11] J. Diaz, Explosion analysis from images: Trinity and Beirut, *arXiv preprint arXiv*:**2009.05674**, 2020.

[12] S. Ismail, W. Raphael, E. Durand, F. Kaddah, F. Geara, Analysis of the structural response of Beirut port concrete silos under blast loading, *Archives of Civil Engineering*, **67:3**, 619-638, 2021. doi: 10.24425/ace.2021.138074.

[13] S. Ismail, W. Raphael, E. Durand, Monitoring the Beirut port silos structural health response few months after blast loading, *Jordan Journal of Civil Engineering*, **15:3**, 489-505, 2021.

[14] S. Ismail, W. Raphael. E. Durand, Case study of the Beirut port explosion using 3D laser scan and nonlinear finite element model, *Research on Engineering Structures and Materials*, **7:4**, 551-577. doi: 10.17515/resm2021.286st0428.

[15] S. Ismail, W. Raphael, E. Durand, F. Kaddah, Soil structure interaction effect on blast numerical analysis of Beirut port silos, *The Mediterranean Geosciences Union (MedGU2021)*, Istanbul, Turkey, 2021.

[16] C. Stennett, S. Gaulter, J. Akhavan, An estimate of the TNT-equivalent net explosive quantity (NEQ) of the Beirut port explosion using publicly available tools and data, *Journal of Propellants, Explosives and Pyrotechnics*, **45**, 1675-1679, 2020, doi: 10.1002/ prep.202000227.

[17] H. Pasman, C. Fouchier, S. Park, N. Quddus, D. Laboureur, Beirut ammonium nitrate explosion: Are we really not learning anything, *Journal of Process Safety*, **39**, e12203. 2020. doi:10.1002/ prs.12203.

[18] G. Valsamos, M. Larcher, F. Casadei, Beirut explosion 2020: A case study for a large-scale urban blast simulation, *Journal of Safety Science*, **137**, 105190, 2021. doi: 10.1016/j.ssci.2021.105190.

[19] K. Kawashima, Y. Takahashi, H. Ge, Z. Wu, J. Zhang, Reconnaissance report on damage of bridges in 2008 Wenchuan, China, earthquake, *Journal of Earthquake Engineering,* **13**, 956–998, 2009. doi:10.1080/13632460902859169.

[20] H. Daou, W. Abou Salha, W. Raphael, A. Chateauneuf, Explanation of the collapse of Terminal 2E at Roissy–CDG Airport by nonlinear deterministic and reliability analyses, *Case Studies in Construction Materials*, **10** , 2214-5095, 2019. doi: 10.1016/j.cscm.2019.e00222.

[21] Z. Chen. X. Li, Y. Yang, S. Zhao, Z. Fu, Experimental and numerical investigation of the effect of temperature patterns on behaviour of large scale silo, *Engineering Failure Analysis*, **91**, 543–53, 2018. doi: 10.1016/j.engfailanal.2018.04.043.

[22] A. Y. Elghazouli, J. M. Rotter, Long-term performance and assessment of circular reinforced concrete silos, *Construction Building Material*, **10(2)**,117–22, 1996. doi:10.1016/0950-0618(95)00091-7.

[23] F. Giuliani, A. De Falco, S. Landi, M. Giorgio Bevilacqua, L. Santini, S. Pecori, Reusing grain silos from the 1930s in Italy. A multi-criteria decision analysis for the case of Arezzo, *Journal of Culture Heritage*, **29**, 145–59, 2018. doi:10.1016/j. culher.2017.07.009.

[24] AFP, 2020 https://english.alarabiya.net/features/2020/08/11/Beirut-explosion-Six-sources-explain-details-shine-light-on-Hezbollah-link.

[25] S. Sumitro, H. Matsuda, S. Nishimura, Application of smart 3-D laser scanner in structural health monitoring, *Computer Science*, 9693818, 2007. doi: 10.1201/9781439828441.ch290.

[26] K. Kerhart, Spšp pardubice: Construction of a grain silo in Beirut, *Czech Civil Engineering J*ournal, **3**, 1971.

[27] C. Huijer, M. Harajli, S. Sadek, Upgrading the seismic hazard of Lebanon in light of the recent discovery of the offshore thrust fault system, *Lebanese Science Journal*, **12**, 2, 2011.

[28] S. Ismail, F. Kaddah, W. Raphael, Seismic soil structure interaction response of midrise concrete structures on silty sandy soil, *Jordan Journal of Civil Engineering*, **14**, 1, 117-135, 2020.

COMPDYN 2023
9th ECCOMAS Thematic Conference on
Computational Methods in Structural Dynamics and Earthquake Engineering
M. Papadrakakis, M. Fragiadakis (eds.)
Athens, Greece, 12-14 June 2023

# THE CHURCH OF SANTA MARIA DELLE GRAZIE AL CALCINAIO: FROM DIAGNOSTIC STUDIES TO ARCHITECTURAL AND STRUCTURAL REHABILITATION PROJECT.

**Michelangelo Micheloni[1]*, Anna Livia Ciuffreda[2], Gabriela Simoni[3], Federico Salvini[4]**

[1] Studio Micheloni Srl
Via Gramsci 20 - Lastra a Signa (FI) – Italy
michelangelo@micheloni.pro

[2] freelance architect
arch.annaliviaciuffreda@gmail.com

[3] Arno Restauri
gabriela.simoni01@gmail.com

[4] Soprintendenza Archeologia Belle Arti e Paesaggio di Siena, Grosseto e Arezzo
Via di Città 138/140 - 53100 Siena
federico.salvini@cultura.gov.it

## Abstract

*This paper illustrates the results of the cognitive process for the defining structural consolidation interventions, seismic risk reduction and architectural rehabilitation of the church of "Santa Maria delle Grazie al Calcinaio", Cortona (Arezzo, Italy). The church represents a splendid example of Renaissance architecture in which the architect Francesco di Giorgio Martini rigorously applied the architectural principles of proportion and perspective. The use of local stone (sandstone) is evident inside in the frames that decorate the facades.*
*Today the building has several problems. The most important is the advanced state of decay of the external stone cladding. However, over time the structure has highlighted structural instability that have already required interventions in the past and that have given rise to the need for a static analysis and an evaluation of seismic vulnerability. To this end, a cognitive phase was carried out in accordance to the NTC2018 and the Guidelines for the assessment and reduction of the seismic risk of cultural heritage, which included: historical-critical analysis, digital survey, structural and material diagnostic campaign, HBIM modelling, definition of the structural model and dynamic behaviour. All these studies have made it possible to highlight all the criticalities of the building and to plan interventions aimed at reducing structural vulnerabilities and for securing the stone ashlars and strongly protruding cornices in order to minimize the risk of falling fragments and protect the safety of users.*

**Keywords:** Cultural heritage, HBIM, Seismic vulnerability, Calcinaio, Cortona.

## 1 INTRODUCTION

The church of "Santa Maria delle Grazie al Calcinaio" stands on the south-east side of the hill of the city of Cortona (Arezzo, Italy), and with the facade it looks towards the Tuscan Valdichiana (Figure 1).

The building's design is by the architect Francesco di Giorgio Martini and the works began in 1485 and ended in the mid-1500s. The building is located in an area where skins were tanned in vats with quicklime since the 1400s. Its construction is linked to the cult of an icon of the Madonna and Child, painted on the wall of a vat, which began in 1484 to work miracles. The building was entrusted to various ecclesiastical communities and after a period of abandonment and restoration, it was reopened in 1730 and proclaimed a Marian shrine in 1985.

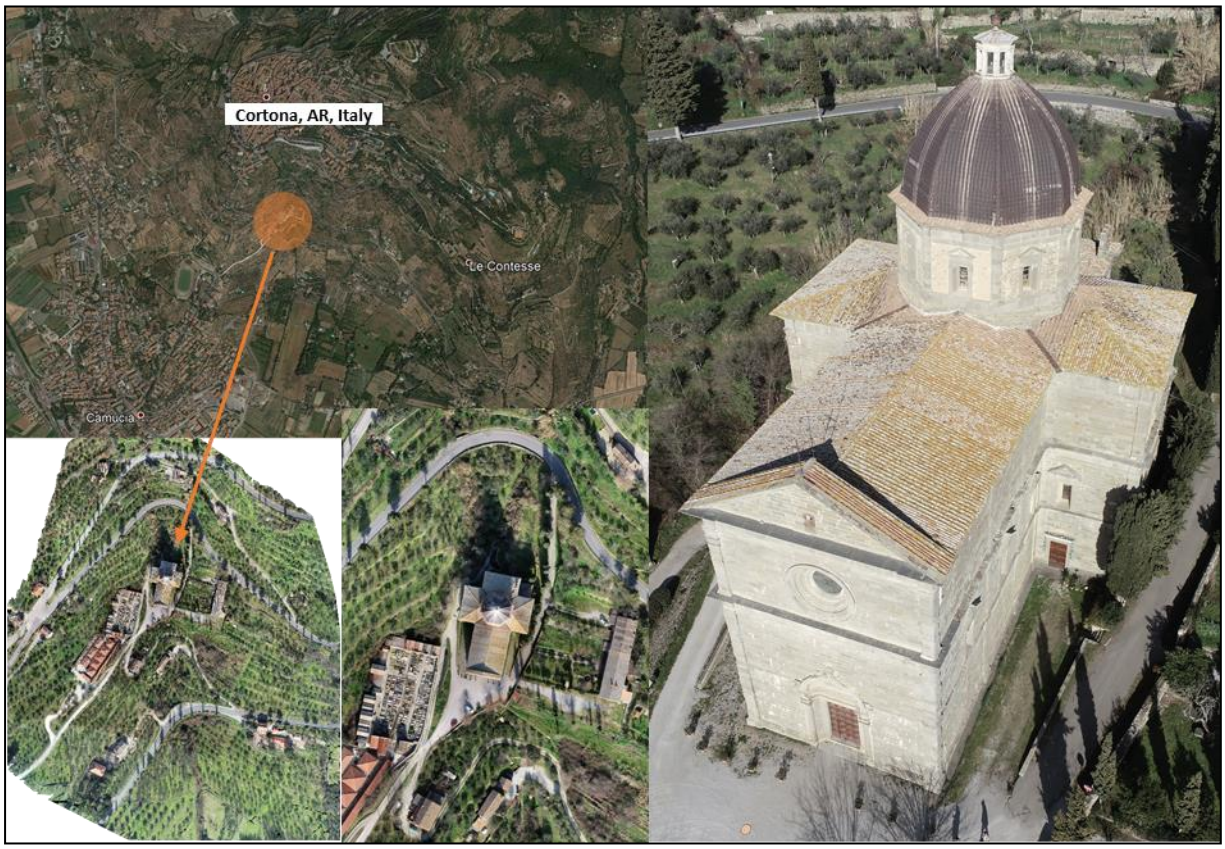


Figure 1: The Church of Santa Maria delle Grazie al Calcinaio, Cortona, (AR)

In 2019-2020, the Soprintendenza Archeologia Belle Arti e Paesaggio di Siena, Grosseto e Arezzo commissioned Studio Micheloni Srl, with a tender, to carry out a study for the knowledge and protection of the complex. This paper presents the result of the studies about the analysis of the vulnerabilities and the state of conservation of the building and the design of specific intervention methodologies. The diagnostic studies start from a detailed geometric survey with advanced laser scanner and photogrammetric technics.

The results of geometric survey and of material analysis merged into an integrated HBIM model, who contained all the data necessary for carrying out the static and seismic vulnerability checks both on the main structures and on the decorative surfaces.

Starting from the cognitive studies and the checks of static stability and seismic vulnerability, have been identified the criticalities that required an intervention in order to guarantee a uniform level of safety.

## 2 THE PROCESS FOR STRUCTURAL AND MATERIAL KNOWLEDGE

An accurate phase of knowledge of a building allows to reach in a conscious way the definition of technical interventions that aim to protect the building in respect of its history, its architectural value and its function, without altering the construction characteristics from the point of view typological, but above all preserving the established structural functioning.

However, to prevent irreparable losses, a campaign of destructive and weakly destructive investigations would be too invasive and incompatible with conservation and protection requirements. The aim was therefore to plan a campaign of non-destructive investigations that would give sufficient certainty of the results, to be calibrated and validated locally by little destructive investigations.

The knowledge path can be traced back to the following activities, in accordance with current legislation (Italian NTC 2018 chap. 8 on existing structures and guidelines for the assessment and reduction of seismic risk for cultural heritage) [1,2] and with the same criteria of the discipline of architectural restoration:

- building identification: first schematic survey and identification of any elements to be safeguarded;
- the geometric survey of the building in its present state, including any cracking and deformation;
- the identification of the historical evolution from the hypothetical original configuration to the current state;
- the identification the elements if the resistant organism, with particular attention paid to the techniques of carrying out the works, the construction details and the connections between the elements;
- the identification of materials, their degradation, their mechanical properties.

The cognitive framework has allowed to increase the level of knowledge of the existing building and to arrive at the definition of a model that describes the structural behaviour to evaluate the intrinsic vulnerabilities and criticalities. Starting from these evaluations, the consolidation measures have been defined to ensure the preservation of the property in full respect of historical and artistic characteristics.

### 2.1 The historical background

The cult building was created to guard and honor an image of the Madonna with child to which miracles were attributed around the mid-fifteenth century. This mural painting was located just outside the walls of Cortona, near a tub where the shoemakers tanned the hides, due to the use of lime in the tanning process the place has been called Calcinaio since then. With the increase in devotion, the Arte de' Calzolai decided to erect a temple where this sacred image could be venerated. Although the initiative was not received with unanimous consent by the population, at the behest of Pope Sixtus IV, the ambitious project was started and in June 1484 Luca Signorelli called Francesco di Giorgio Martini to carry out the project. The following year, in 1485, construction work began on the church which was certainly completed by 1525 [3].

The building stands out on the side of the hill presumably around to the primitive location of the Marian painting, which is found today in the High Altar.

The stream that flowed near the sacred image was regularized and channeled into a winding tunnel that today passes under the building next to the high altar and then runs along the entire length of the nave and flows back to the outside just beyond the facade. The bed of the river follows the natural slope of the hill, the building was built according to the watercourse which has important symbolic meanings for the Christian religion [4].

Construction work began in 1485 based on a project by Francesco di Giorgio Martini multi-faceted personality, like many others of his time, he was an artist, sculptor, architect and engineer. As an architect and military engineer, he built numerous fortresses and castles in many towns of Italy. He worked in many cities of Italy and was a friend of the most renowned artists and intellectuals of the time, one of them was Leonardo Da Vinci [3].

The church of Santa Maria delle Grazie al Calcinaio fits perfectly into the historical period in which it was conceived and built and represents an example of Renaissance architecture of the highest level.

The study and relief from life of ancient buildings and the centrality of man are the cardinal concepts on which the architectural language of the Renaissance is based, which saw the ideas of Humanism bring to maturity where the centrality of man is the point hinge [5].

The building had a troubled conservation history from the first years of its construction; it was built thanks to donations from the people, the municipality and the Guild of Shoemakers but since it was a religious place it was necessary for an ecclesiastical institution to supervise it. The latter gave priority to the construction of a convent near the church before the church itself. Because of this situation there were continuous disagreements and delays in the works as the clerics were more interested in building a convent next door than in completing the construction of the sanctuary [4].

The construction of the dome was completed many years after that of the rest of the factory, the stone decorations inside the building thus remained exposed to the elements for decades causing the degradation of the stone decorations inside the building due to the leaching of the water and wind erosion. The building passed into the management of various religious orders over the centuries, but maintenance and conservation was practically nil.

For some decades the church had been used as a seminary and had been left in a state of complete abandonment; the windows had been walled up and the building had been used partly as a granary and partly as a stable for animals.

After numerous pressures and with the advent of a new Bishop, the church became canonical in 1815; it was immediately evident that numerous restoration works would be necessary to return to office; from 1822 numerous renovations were made.

Important structural consolidation interventions to the dome were made in 1887 through the insertion of tie rods and chains.

Starting from the fifties of the twentieth century, restoration work was carried out on the external face under the direction of the Superintendence; some architectural parts, portions of cornices and tympanums were replaced on the outside while the walls were repainted in white inside.

### 2.2 The integrated digital survey

The knowledge of architectural and structural geometry of the building was achieved through an integrated digital survey. The new methodologies of digital survey allow the acquisition of a large number of data of existing elements by postponing a part of the interpretative-subjective phase to a later time.

The methodology used involves the integration of 3D models realized with LST 3D methodology (Terrestrial Laser Scanner) for the interiors and photogrammetric survey models made by drone for the exteriors. In addition, the combination of aerial and terrestrial photogrammetry allowed the elaboration of high-resolution orthophotos to acquire detailed information about state of conservation of the decorative system of the facades.

The survey operations required two weeks of field work in February 2020 and were planned to define the quantity and location of the scans and the drone's flight area. The laser scanner used is a Trimble TX8 with a "time of flight" measurement principle, a measurement range of

340 m and acquires large quantities of points in a short time (1 million/sec). Scans were performed in all internal areas including the attics and the access staircase to the dome and in the external areas. The scan parameters have been set to have a resolution of 22.6 mm at 30 m indoors and 11.3 mm at 30 m outdoors.

In particular, metal targets have been positioned outside, on the ground, which are useful for recording the cloud from a laser scanner with that from a drone. Similar targets were used to link scans for more complex structures to detect, such as spiral staircases leading to the attic. The instrument is equipped with integrated cameras for acquiring the RGB data which is applied to the point cloud. The survey operations produced a total of 180 scans.

The aero-photogrammetry was carried out using a DJI Phantom 4 RTK drone and a DJI Matrice 300 RTK. The aircraft are equipped in the first case with an integrated camera with a 1" CMOS 20 megapixel sensor with 24mm equivalent lens, in the second case with a DJI P1 camera with a 45 megapixel full-frame sensor and 35mm lens. In the UAV environment, the GPS RTK (Real Time Kinematic) system allows satellite positioning in real time, thanks to GPS, GLONASS and Galileo signals, where a single reference station provides real-time connections with centimeter-level accuracy. Thanks to this system, therefore, the high precision of the survey operation was guaranteed.

An automatic flight performed on two different days and with different atmospheric conditions was planned to evaluate the best possible contrast and lighting conditions. The survey phase ended with the creation of photos in manual mode from a drone and from the ground at close distances from the elevations. This operation was useful for the preparation of detailed orthophotos describing the state of conservation of the stone face. The images were taken with a Sony Alpha 6500 mirrorless camera, with sensor APS-C type Exmor® CMOS sensor (23.5 x 15.6 mm) and 24.2 megapixels.



Figure 2: The point cloud from LST survey and fotogrammetric survey

The photogrammetric survey obtained a GSD (Ground Sample Distance) of less than 3 cm.

The registration procedure of the laser scanner stations was performed using the Trimble Realworks software. Like other registration software, it allows you to rototranslate the scans and connect them automatically by analyzing homologous planes between adjacent scans or manually by identifying common reference points. The resulting cloud is oriented in a local reference system. The images from the drone survey were processed using photogrammetric software producing a point cloud of the surveyed area and the roofs.

The georeferencing of the laser scanner cloud is obtained by roto-translation on the drone point cloud and using the reference targets. The result is a cloud of approximately 700 million points oriented in a WGS 84 / UTM zone 32N geographic reference system and which reported an average residual error of less than 10 mm. The point cloud which, processed using software, has returned all the information regarding geometries and distances of the visible elements of the exterior and interior of the building, which can be navigated in 3D, interrogated and used as a basis for 2D and 3D reconstructions (Figure 2). The elaboration of the orthophotos of the facades required specific elaborations. The same SfM (Structure from motion) algorithms used to process the aerial photogrammetric survey have made it possible to process the photos from the ground and those from the drone together. The combination of the two types of photographic shots made it possible to eliminate occlusions and obtain complete orthoimages. Through various stages of processing (sparse cloud, dense cloud, mesh and texture), five 3D models relating to the facades of the Church were obtained.

High-resolution orthoimages were extracted from these models. In fact, the resolution of the images made it possible to precisely identify the types of deterioration even in areas of the elevation that are not visible from the ground.

### 2.3 The diagnostic campaign

The historical material collected, the surveys and the inspections carried out allowed the achievement of a first level of knowledge of the building. However, this objective is not totally exhaustive for the purposes of defining the structural behavior of the building, therefore in line with the aforementioned regulations, it was necessary to prepare a campaign of diagnostic tests. Documentary knowledge and visual knowledge have made it possible to identify the areas to be investigated by choosing the most significant or most critical points of the structural organism.

The diagnostic operations will focus in particular on the following points:

- The vertical walls, stone masonry
- The vaulted systems and brick and stone arches
- The brick dome
- The wooden structures of the roof.

The in situ investigation techniques are mainly of a little or non-destructive nature:

- Thermographic photos
- Endoscopic investigations on the walls and vaults after drilling;
- PNG tests on mortar;
- Collection of samples of stone material, bricks and mortars for mineralogical, petrographic and mechanical analyses.
- Exploratory tests with removal of plaster to verify the masonry setting of the dome and the connections;
- Visual investigations on the conservation of the wooden elements of the roof.
- Cataloguing of the wooden elements of the roof with the DRESL (Diagnosis of wooden structural elements) method, developed in collaboration with Italian National Research CouncilInstitute of BioEconomy – IBE.

The use of single and double flat jacks on masonry was limited to a couple of trials.

While the geognostic investigations were carried out for the geotechnical characterization of the land and geoelectric investigations to investigate the structure of the subsoil also in relation to the presence of the watercourse and the foundations of the building.

The localization of the investigations was carried out by identifying the critical and most significant elements from a structural point of view, avoiding the execution of investigations in the most valuable areas.

A specific analysis was performed on the wooden elements for the cataloguing and dating based on dendrochronological master chronologies [11]

The complete framework of surveys carried out has made it possible to reach a high level of knowledge which can be identified according to Italian standards as level LC3, with a safety factor FC = 1,0.

## 3 THE BIM METODOLOGY FOR THE DIAGNOSTIC AND SEISMIC VULNERABILITY

With a view to integrating all the information useful for the project phase (architectural, structural, systems engineering, etc.) into a single model, the diagnostic phase and numerical processing for structural verification were managed using the BIM methodology (Building Information Modeling).

In the case of the church of Santa Maria delle Grazie in Calcinaio, a BIM model was created aimed not only at the extraction of the 2D geometric survey drawings, but also to the importation into a software for structural analysis. In this way the "re-modeling" phase of the building within the structural calculation software was eliminated with considerable savings in terms of time and costs to the advantage of the intervention design phase.

The BIM model itself was used as the "first container" of the data collected during the studies and surveys carried out with the possibility of being updated whenever an intervention is carried out on the building about the structures or decorative devices [6,7].

### 3.1 From the real building to the three-dimensional model

The BIM methodology allows, starting from the data coming from the surveys, to convert the information of the point cloud into a 3D model of the built object. In a BIM model each element is a parametric geometric object and the parameters can be of two types:

- **dimensional parameters** that regulate the shape, size and orientation in space of the object, making it capable of adapting to different contexts.
- **informative parameters** already in the survey restitution phase it is possible to proceed with the combination of non-geometric information to each element.

The degree of geometrical and informative development of each object is defined by the LOD (Level of Development) [8].

In the case of the model of the “Calcinaio” church a LOD 300 has been achieved, whereby the quantity, size, shape, position and orientation of the element as designed can be measured directly from the model without referring to information not modeled, and non-graphical information can also be attached to the model element.

The complete point cloud was imported into the modeling environment of the Autodesk Revit software and the architectural and structural modeling phase was prepared. The point cloud maintains its geographic coordinates therefore it follows that the 3D model will acquire its georeference.

The use of system families allowed the modeling of elements such as walls, slabs, roofs and beams.

However, historic buildings have structures with unique and irregular shapes and therefore make the geometric parameterization particularly complex. The use of adaptive families and customized families has allowed the overcoming of geometric difficulties and the creation of families adaptable to various contexts. In this case it concerned particular types of windows, frames, pillars and vaults.

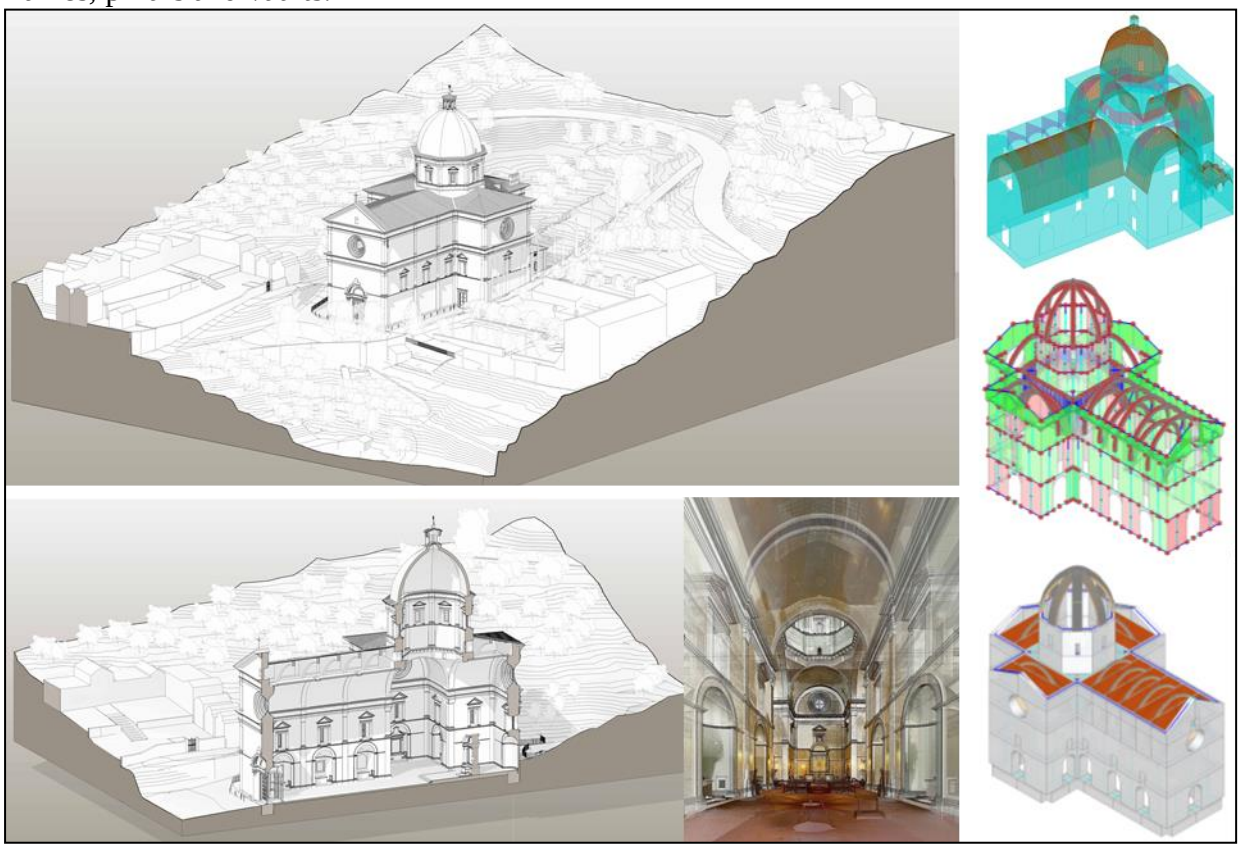

Figure 3: On the left, the complete BIM model; on the right the extracted structural model.

The export of the model without the decorative elements allowed the creation of a model with surface elements and a model with solid elements to be processed with FEM solvers, generating a linear and bidirectional data exchange.

The calculation models were therefore closely interconnected with the geomatic survey models and constituted a real digital-twin of the real building (Figure 3).

### 3.2 The BIM database

The management of a historic building through "informative models" essentially leads to the creation of a database.

The structure of an information model is therefore completely similar to that of any database: each element is associated with a unique code, it can be assigned a name in accordance with a classification system, a position based on georeferencing, as well as pdf files concerning technical specifications, detailed sheets on the state of conservation of the elements or reports relating to diagnostic investigations carried out may be attached.

The types of information inserted in the church model are of two types:

- data relating to the diagnostic campaign;
- data relating to the state of conservation of the stone facing.

The inclusion of surveys in the model was done by creating custom or adaptive parametric families.

The geometry of the objects representing the investigations was studied according to the characteristics of the investigation using symbols that visually refer to the type of investigation. The information entered within specific parameters relates to the date of execution, the description, the tool used and the results, as well as other data relating, for example, to the classification of the masonry (Figure 4).

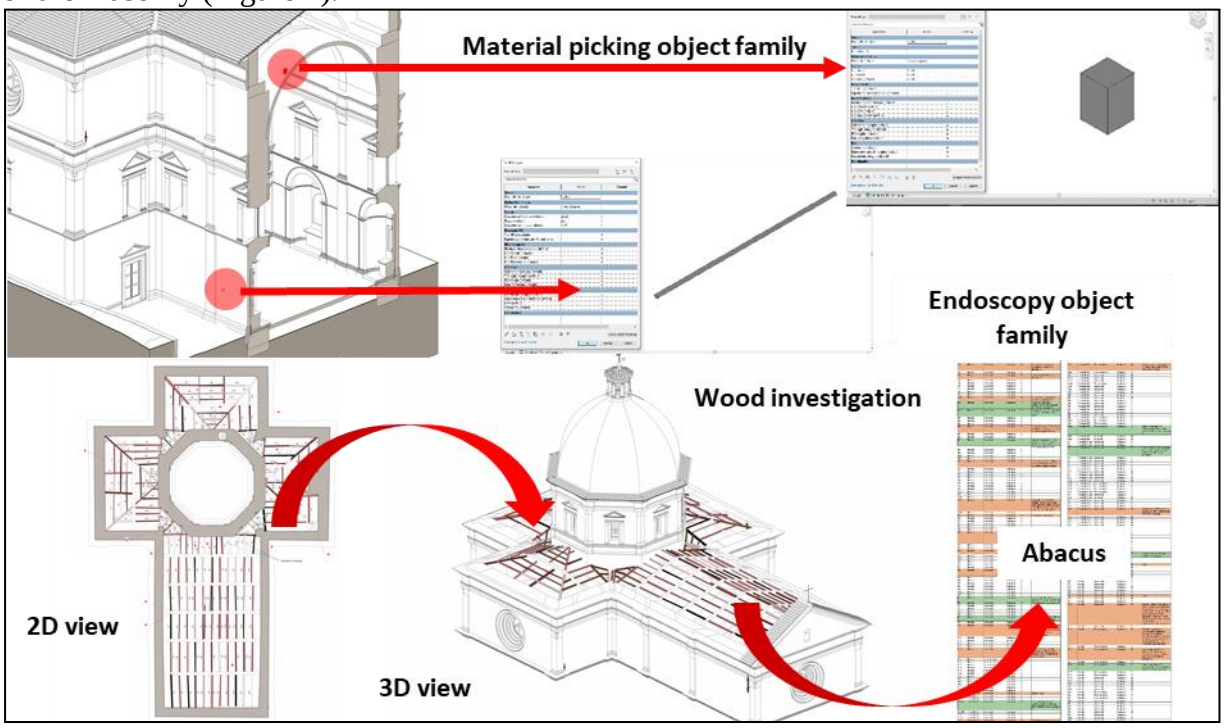


Figure 4: Some examples about implementation of the model with the diagnostic information.

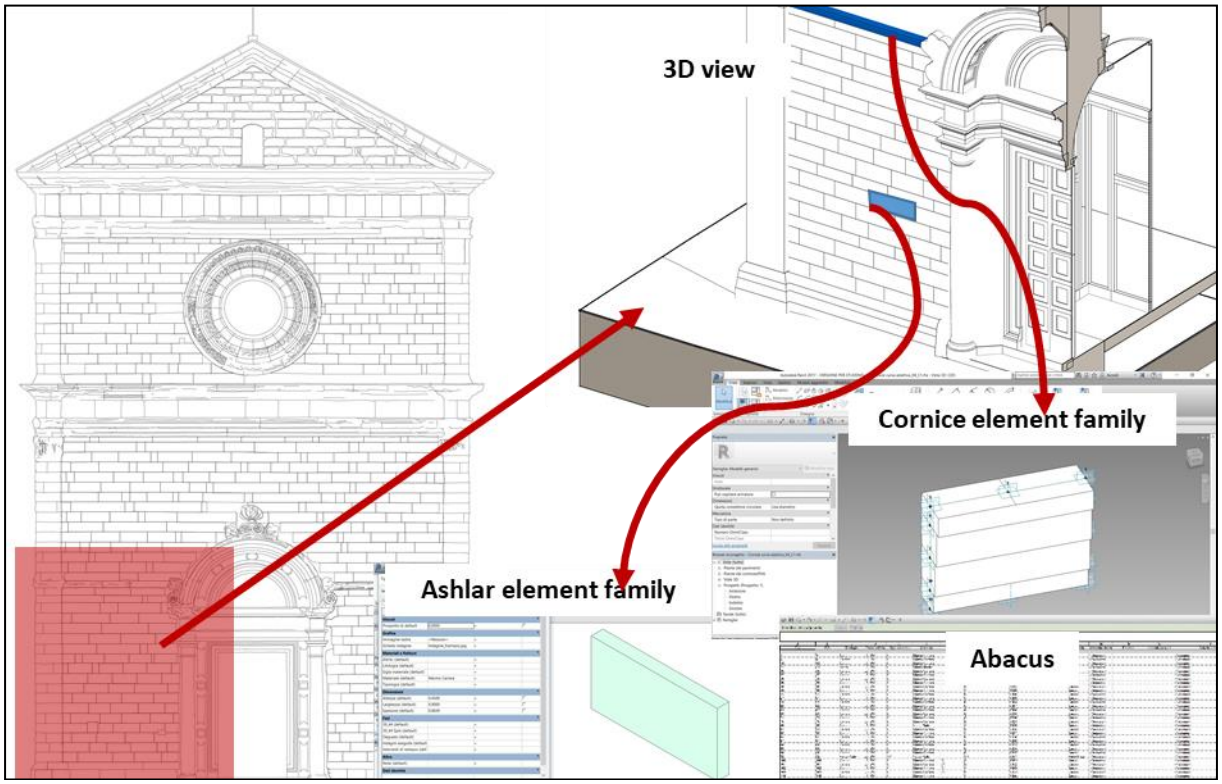


Figure 5: An example about implementation of the model with the stone information.

A particular case is represented by the database of the classification of wooden structures for which the information has been associated directly to the object-beam. The colour filters set in the model views allow you to have a global view of the state of conservation of the beam system (Figure 4).

As regards the decorative elements, a sample of the façade was set up to experiment with an information database relating to the state of conservation of each element. The slab or frame parametric object has been associated with information relating to material, finish, degradation, etc.. (Figure 5).

In general, all the objects of the model, from the wall to the investigations, have been provided with an ID which identifies them and which can be displayed within an abacus which allows the model to be queried.

The one-to-one interaction between 3D views and schedules allows for rapid database management and implementation.

### 3.3 The structural calculation model

From the BIM model was extract the structural model of the whole building and it is imported in the structural calculation software Aedes PCM (Figure 6).

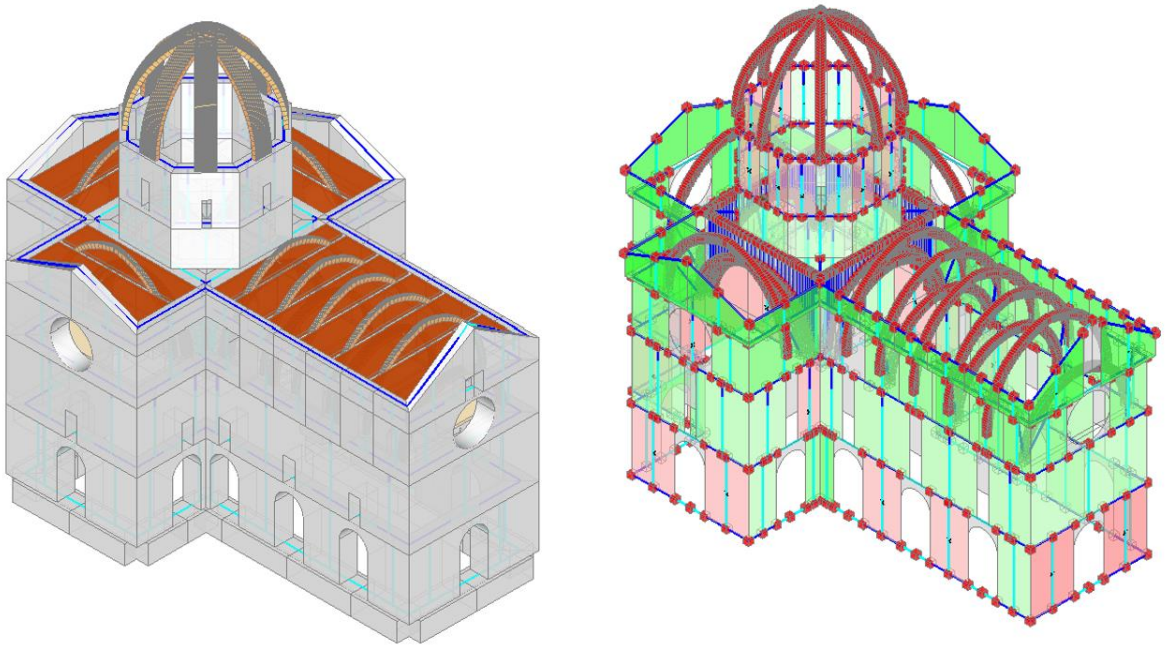

Figure 6: Structural calculation model

Through this structural model, that represent a digital twin of the real building, it was possible to carry out the vulnerability checks of the building.

In detail both the global risk indicators of the building and of the individual local mechanisms of masonry overturning were calculated.

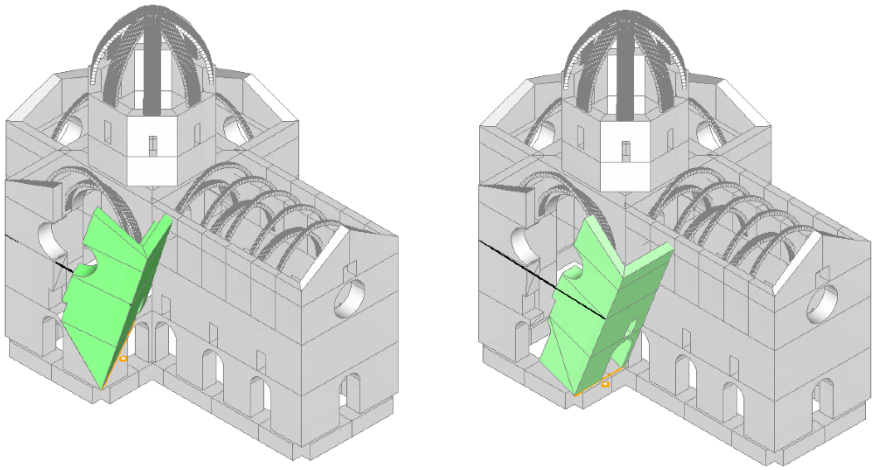

Figure 7: Example of local mechanism of masonry collapse for the transept

A detailed analysis was performed for the dome with three different models:

- The global model of the building with the dome.
- The simplified model of a single arch discretizing a segment of the dome.
- A FEM model with shell element .

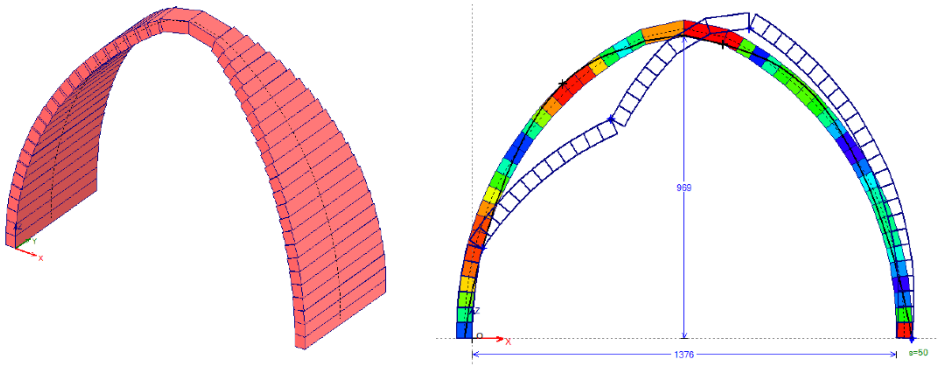

Figure 8: simplified model of a single arch discretizing a segment of the dome with its collapse mechanism

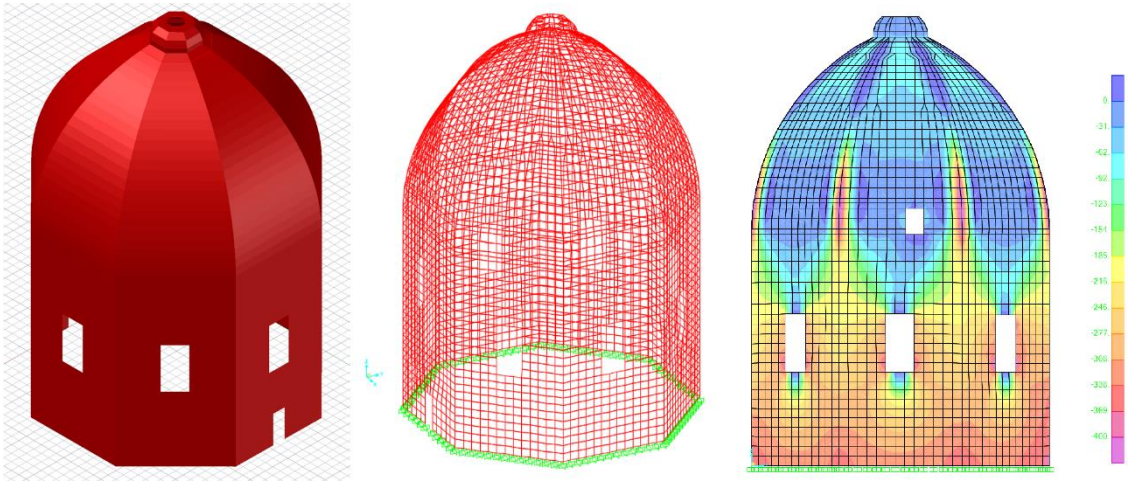

Figure 9: FEM model of the dome with the vertical loads stresses

The checks on the dome therefore is the result of the envelope of the studies carried out with global models and with local models aimed to identify both risk indexes.

# 4 RESULTS ANALYSIS AND PROJECT OF INTERVENTION

From a visual analysis from below and from the analysis of the photoplans obtained by photogrammetry from the ground and from a drone, various degradation phenomena have been identified that are still active today. After an initial analysis it was clear that the state of degradation of the projecting stone parts is very advanced and can represent a risk for people; pending a complete restoration of the entire exterior of the building, however, it was necessary to plan safety operations at the access doors to the church so as to allow the faithful and tourists to access the structure safely. Therefore, surveys and mappings of the deterioration were carried out which acted as a guide for the identification of the operations to be carried out.

The church of Santa Maria delle Grazie al Calcinaio has a stone facing entirely composed of sandstone here the phenomena of exfoliation and detachment [9] are very widespread and in some areas in a very advanced stage of degradation. The surface, in fact, is discontinuous in many points due to the presence of numerous gaps created by the loss of one or more stone layer.

The characteristic deterioration phenomenon of sandstones, exfoliation is mainly caused by water which causes part of the clayey matrix to swell and wash away between the sub-parallel layers that form the stone [10]. The tensions created between the swollen layers are aggravated by the cycles of freezing and thawing and cause the fall of fragments, even of considerable size.

Sometimes there is the total loss of three-dimensional stone elements, such as stone ashlars at the first cornice and the tympanum at one of the access doors to the transept.

Making the stone facing safe is a preventive measure while awaiting the restoration work. Once the scaffolding has been built, it will be possible to carry out in-depth analyzes of the surfaces in order to define the methodological choices for the restoration and integration of the gaps.

Moreover, the results of the static analysis and an evaluation of seismic vulnerability have highlighted a problem on the west transept and on the dome, which require structural interventions. So, an executive project was performed in accordance to the Italian NTC2018 and the Guidelines for the assessment and reduction of the seismic risk of cultural heritage [1,2].

The aim of the project was to implement the necessary consolidations to ensure the structural safety while respecting the historicity of the church.

## 4.1 The structural project

The structural design concerns the resolution of the vulnerabilities identified through cognitive studies and structural checks on the building.

In detail the structural consolidation project involved the following interventions:

- Reinforcement on the dome with carbon fiber textiles confinement
- Reinforcement on the west transept with a steel bar and a shock transmitter system
- Reinforcement of the wooden elements of the roof

For the dome was identified a minimally invasive but at the same time effective intervention to solve problems of seismic vulnerability. Two carbon fiber textiles confinement hopes are designed at the top of the dome and near the lower level of the dome, according with the structural simulations performed.

For the west transept, the existing crack and the local overturning mechanism are reinforced with a steel bar which comes into operation only in case of a seismic event, thanks to a shock transmitter which allows thermal expansion, while it freezes if stressed by a seismic impulsive force.

For the wooden elements reinforcement was identified a consolidation strategy using carbon fibre reinforcements. The aim was to consolidate the existing beams in place without replacing them. In fact, the replacement of the beams would have resulted in the loss of historical elements and difficulties in handling bulky beams in a position that is difficult to access.

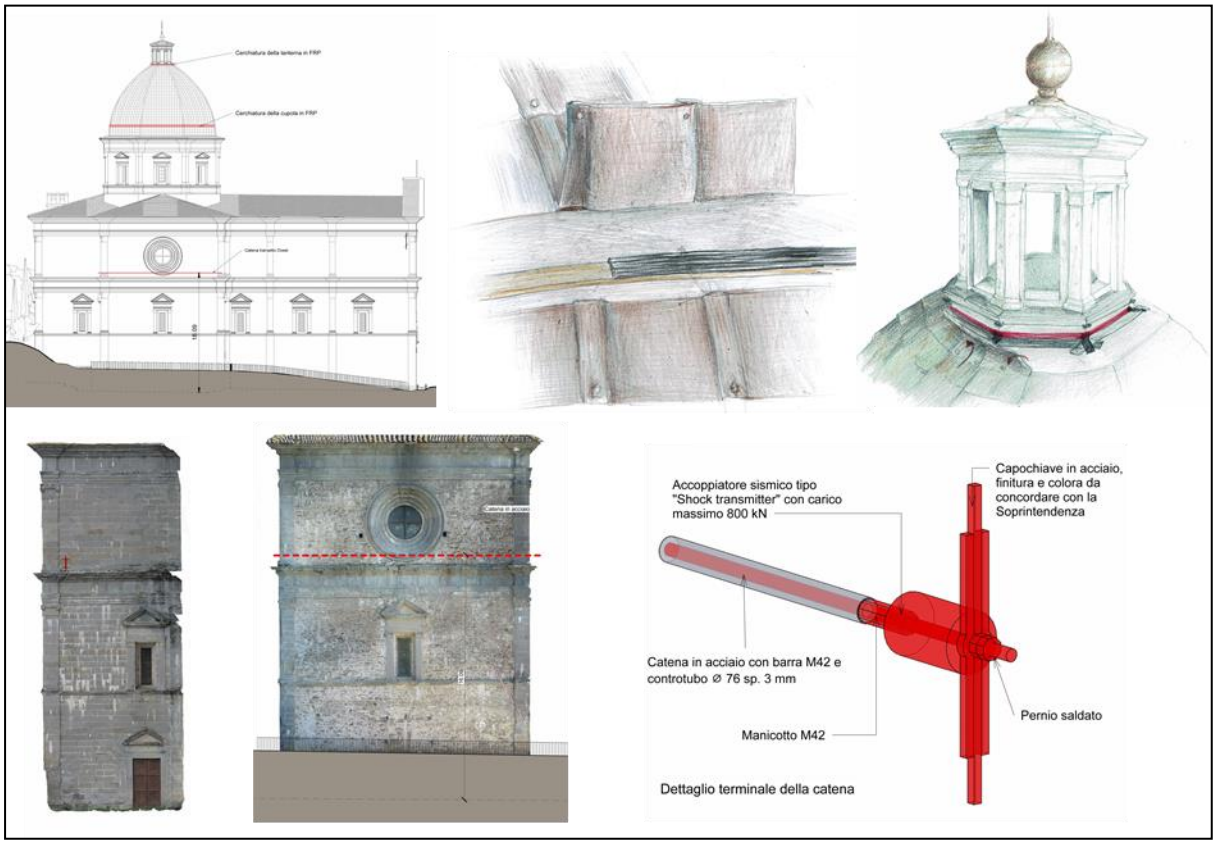


Figure 10: The structural consolidation project:

## 4.2 The project for the securing of stone facing

Given the seriousness of the degradation phenomena and the importance of the work, it is necessary to approach the safety intervention with the technical/scientific and deontological criteria already outlined to avoid losing entire portions of the model which would add serious gaps to those already existing. The removal of unstable portions and elements must be carried out with criteria and method, evaluating the necessary operations on a case-by-case basis.

The safety project involves various processes depending on the type of degradation;

- in areas affected by decohesion phenomena, the surfaces must be pre-consolidated by applying ethyl silicate-based products, a highly recommended and used material because it is chemically compatible with sandstone;
- in the presence of serious cracks and fractures, grouting with hydraulic mortars will be carried out. The phenomena of detachment and exfoliation must be made safe, where it will be possible to do so, through the construction of bridges in epoxy resin and injections with hydraulic mortars;
- we envisaged the application on the horizontal surface of the cornice and along the external slopes of the openings of strips of carbon fibers and epoxy resin, laid so as to form a reticular system according to the morphology of the surface itself. The orthogonal strips in carbon fiber and resin will be anchored to the wall facing by making a break and inserting 10 cm long CFRP connectors;

- at the end of the installation of the fibers above, a shoe grouting must be carried out along the entire area of the upper surface of the stringcourse. From a conservative point of view, this operation is essential as it creates a layer of sacrifice which, by virtue of the slight difference in height, favors the flow of water and protection from the sun's rays, contributing significantly to protecting the original surface and the consolidation system. On an aesthetic level, it camouflages the visual impact of the presence of the carbon fiber mesh;
- the stone elements of the stringcourse which, due to its morphology, cannot be consolidated with the carbon fiber fabric will be anchored by inserting CFRP pins (or connectors) anchored with epoxy resin. These operations must be carried out in correspondence of the elements considered to be at risk of falling.

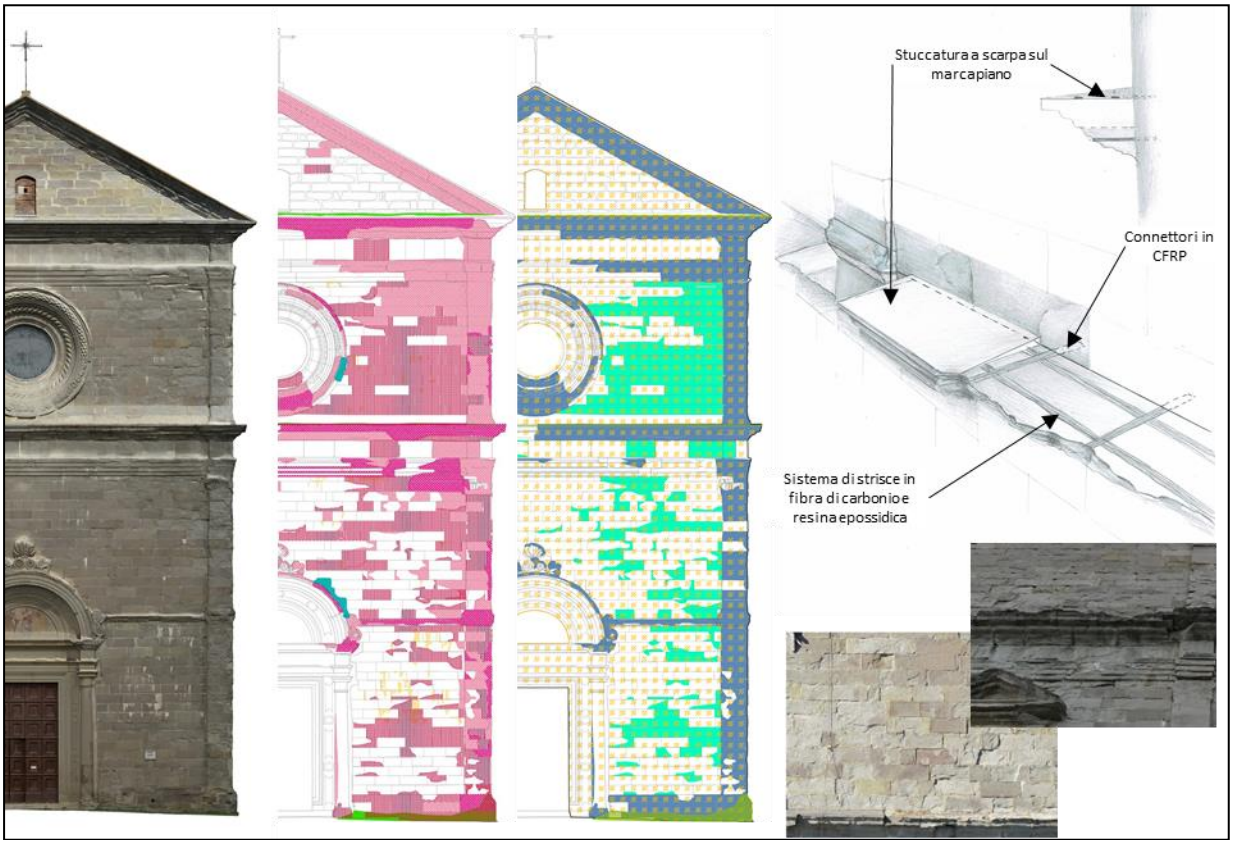


Figure 11: The decay analysis and the project for the securing of stone facing of the main façade.

The structural reinforcement project with composite material in carbon fiber and epoxy resin was preferred because by making a harm/benefit reasoning it emerged that; to put in place protective nets against falling rubble it is necessary to make holes for anchoring, furthermore some more unstable stone portions should be anchored with temporary steel brackets having to create new lodgings on the stone surface. These intervention methods allow, once the restoration site is ready, to be able to remove all the elements but at the same time create damage and gaps in an already very fragile and degraded surface (Figure 11).

The method for the repairing and strengthening of the stone cantilevers involves the stitching of carbon FRP stripes at superior faces of the stones. To perform the design of reinforcements, it was very important to determinate the exact geometry of the stone ledge and the characteristics of the materials. With these information, the structural calculations and the design were performed to determinate the exact layout and the quantity of FRP strips and the level of safety

of the structure. Moreover, the using of FRP strips have many advantages due to the structural resistance and corrosion absence.

The use of these reinforcement techniques on sandstone structures has already been tested in the past on similar churches in Mediterranean areas. [12]

With the aim of making the safety intervention not a source of new damage but a starting point for the future restoration intervention, it is considered appropriate to use a resin composite material (which protects and allows the tensile strength) and carbon fiber fabric.

## 5 CONCLUSIONS

The paper address the main phases relating to the study and planning of the interventions for securing and consolidating the Church "Santa Maria delle Grazie al Calcinaio".

The workflow started from the definition of the cognitive framework which, through modern methodologies, made it possible to identify the critical issues and vulnerabilities of the building.

These methodologies were used for the execution of a very precise geometric and structural survey and through the creation of a BIM model the possibility of digitization and archiving was tested by applying it to a particular case study of cultural heritage.

Therefore, the management of the entire design and knowledge process was performed through the creation of a digital model that describes the current state of the building with a good level of detail and the creation of a BIM model that archives all the information of the project and diagnostic phase in a simple and easily accessible way.

The result of the diagnostic phase took the form of intervention design choices aimed at reducing structural vulnerabilities and securing the decorative apparatus preparatory to the final restoration.

This structural check and the project of the consolidation are driven by a digital twin model derived from the main BIM model of the building.

Moreover, the use of innovative materials and solution permits to guarantee the safety of the heritage building with minimal invasiveness and in compliance with the restoration principles.

In conclusion, a well-structured workflow was outlined, which ensured in-depth knowledge of the building in line with the requirements of current regulations and which made it possible to achieve the expected results.

## REFERENCES

[1] NTC (2018), “Aggiornamento delle «Norme tecniche per le costruzioni». G.U. No. 42 del 20 Febbraio D.M. Ministero Infrastrutture e Trasporti 17 gennaio 2018, Roma (in Italian). NTC (2008) Norme tecniche per le costruzioni. D.M. Ministero Infrastrutture e Trasporti 14 gennaio 2008”, G.U.R.I. 4 febbraio 2008, Rome, (in Italian).

[2] MIBACT (2011), “Linee Guida per la valutazione e riduzione del rischio sismico del patrimonio culturale allineate alle nuove Norme tecniche per le costruzioni (d.m. 14 gennaio 2008)” (in Italian).

[3] G. Mancini, Notizie sulla chiesa del Calcinaio e sui diritti che vi ha il comune di Cortona, Tipografia Bimbi, Cortona.

[4] P. Matracchi, La chiesa di Santa Maria delle Grazie al Calcinaio presso Cortona e l’opera di Francesco di Giorgio, Calosci, Cortona, Gennaio 1992.

[5] F. Di Giorgio Martini edite by C. Salluzzo, Francesco di Giorgio Martini. *Trattato di architettura civile e militare, con dissertazione e note per servire alla storia militare italiana*. Tipografia Chirio e Mina, Torino, 1841.

[6] Coli M., Ciuffreda A. L., Micheloni M. 2019, An informative content 3d model for the hall holding the Resurrection of Christ by Piero della Francesca mural painting at Sansepolcro, Italy. ISPRS - International Archives of the Photogrammetry, Remote Sensing and Spatial Information Sciences, XLII-2/W11, 435-442, 10.5194/isprs-archives-XLII-2-W11-435-2019.

[7] Malinverni, E. S., Mariano, F., Di Stefano, F., Petetta, L., and Onori, F.: Modelling in HBIM to document materials decay by a thematic mapping to manage the cultural heritage: the case of "Chiesa della Pietà" in Fermo, Int. Arch. Photogramm. Remote Sens. Spatial Inf. Sci., XLII-2/W11, 777-784, https://doi.org/10.5194/isprs-archives-XLII-2-W11-777-2019.

[8] The LOD gives the degree of reliability of both the information integrated into the model: level of detail of the geometry and level of information, cfr. Bim Forum, Level Of Development (LOD), Specification Part I & Commentary For Building Information Models and Data, December 2021.

[9] ICOMOS-ISCS : Illustrated glossary on stone deterioration patterns, International Scientific Committee for Stone (ISCS), MONUMENTS AND SITES XV, Electronic Version, 2010

[10] P. Matracchi, C.A. Garzonio, F. Radicioni et all., The Church of Santa Maria della Grazie al Calcinaio by Francesco di Giorgio Martini. New studies on characterization of the facing wall decay in a striking architecture of the Italian renaissance, 1st international and 5th National Conference on Sustainable Architecture and City, Torchia, March 2020.

[11] M. Bernabei, M. Brunetti, N. Macchioni, M. Micheloni, M. Nocetti, Surveying and Dating the Wooden Roof Structure of St Francis of Assisi Church in Valletta, Malta. March 2020. International Journal of Architectural Heritage 15(7):1-9

[12] M. Micheloni, Fiber Reinforced Polymers Textiles for strengthening of historical buildings and the examples for the use in Italian and Maltese heritage. SBE16 Malta, 2016 - Europe and the Mediterranean Towards a Sustainable Built Environment. pp. 149-157 ISBN 978-99957-0-935-8

COMPDYN 2023
9th ECCOMAS Thematic Conference on
Computational Methods in Structural Dynamics and Earthquake Engineering
M. Papadrakakis, M. Fragiadakis (eds.)
Athens, Greece, 12-14 June 2023

# SEISMIC UPGRADING OF TELECOMMUNICATION CENTER IN SKOPJE, NORTH MACEDONIA

**V. Shendova[1], A. Zurovski[1], A Zlateski[1], E. Delova[1], G. Jekic[1], R. Apostolska[1], Z. Bozinovski[2]**

[1] Ss. Cyril and Methodius University in Skopje, Republic of North Macedonia, Institute of Earthquake Engineering and Engineering Seismology, 1000, Skopje
e-mail: {veronika, zurovski, azlate, delova, jekic, beti}@iziis.ukim.edu.mk

[2] Ss. Cyril and Methodius University in Skopje, Republic of North Macedonia, Institute of Earthquake Engineering and Engineering Seismology, 1000, Skopje, retired Professor
e-mail: zivko_bozinovski@yahoo.com

## Abstract

*This paper presents detail analysis of the stability and safety of the existing structural system of the Telecommunication Center facility in Skopje, to define the possibilities and conditions to meet the technical standard Telecommunication Industry Association TIA-942-A, which is requirement for the eventual change of the building function. Considering that it is a building of the high importance in terms of its function, built more than fifty years ago, it was necessary to examine the need for additional structural strengthening and initial cost estimation. The necessity of structural interventions to meet the required technical standards were defined based on (i) input data from limited in situ technical investigations, (ii) assessment of the seismic potential of the site and (iii) analysis of the load-bearing structure for the anticipated imposed loads while simultaneously providing the required structural stability and safety for gravity and earthquake actions according to the existing seismic code in North Macedonia. Findings from the performed analysis enforce the need for both global and local structural strengthening.*

**Keywords:** telecommunication center, nondestructive testing, bearing and deformation capacity, time-history analysis, seismic strengthening.

## 1 INTRODUCTION

The complex of the Telecommunications Center in Skopje, North Macedonia was constructed during the seventies of the last century as a representative of the reinforced concrete buildings typical for the post-earthquake communist period, (fig.1). This creation of the Macedonian architect Janko Konstantinov was exposed at the 2018 New York MoMA exhibition on the topic "Concrete Utopia - Architecture in Yugoslavia 1948-1980", as a representative from North Macedonia. Like other similar buildings from this period, the construction of the building is characterized by bold structural solutions, large spans and storey heights, followed by robust dimensions of the structural elements and the inevitable facade made of popularly called “nature-concrete”.

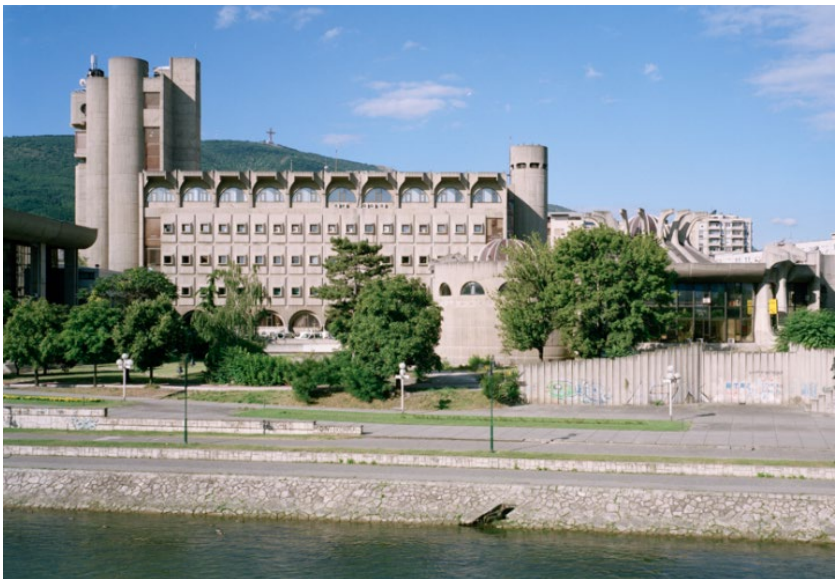

Figure 1: The complex of Telecommunication Center in Skopje, North Macedonia.

To define the possibilities and conditions to meet the technical criteria for level TIER III defined by the standard TIA-942-A [1], which was set as a need for the possible future function of the facility, analysis of the stability and safety of the existing structural system of the Telecommunication Center facility in Skopje was carried out. Considering that it is a building of the high importance in terms of its function, built more than fifty years ago, it was necessary to evaluate its existing stability. Accordingly, the purpose of the analysis is to examine the need for additional strengthening of load-bearing structural elements in order to perform an initial cost estimation. For this purpose, in accordance with the multidisciplinary integrated approach developed in Institute of Earthquake Engineering and Engineering Seismology, IZIIS-Skopje [2], the following activities were carried out:

1. Assessment of the seismic potential of the site
2. On-site building inspection and investigation for providing relevant input structural data for further analysis, which encompasses (i) review of the available technical documentation, (ii) detailed inspection of the building and identification of its main structural system, (iii) definition of quality of built-in materials by non-destructive testing of structural elements and (iv) determination of dynamic characteristics of the structure by experimental in-situ testing using ambient vibration technique
3. Analysis of stability of existing building for gravity and seismic loading, consisting of (i) 3D static and equivalent seismic FE structural analysis for the verified structural

system and built-in materials, (ii) analysis of the bearing and deformation capacity of the existing structural system with identified quality and quantity of built-in materials, and (iii) dynamic response including nonlinear time history analyses of building structure for earthquakes of different intensity and frequency content expected on the considered site.

The knowledge gained through the above investigations and analysis has been used to define preliminary technical solution for strengthening of individual structural elements with a cost estimation for its realization, considering the current conditions of the market and the specifics arising from the method of execution, thus, to define the justification of entering such a process. The actual cost estimation is not subject of this paper and can be find in [3,4].

## 2 ASSESSMENT OF THE SEISMIC SITE POTENTIAL AND IDENTIFICATION OF THE LOAD-BEARING STRUCTURE

### 2.1 Assessment of the seismic site potential

Considering the given limited time framework, the necessary field investigation to define the seismic potential of the particular site have not been done, however, data and results of detailed research for several locations near the existing facility were considered. The seismic potential was assessed based on the results of the investigated location of the Mother Teresa monument, which is the closest to the location of the Telecommunication Center, (fig 2).

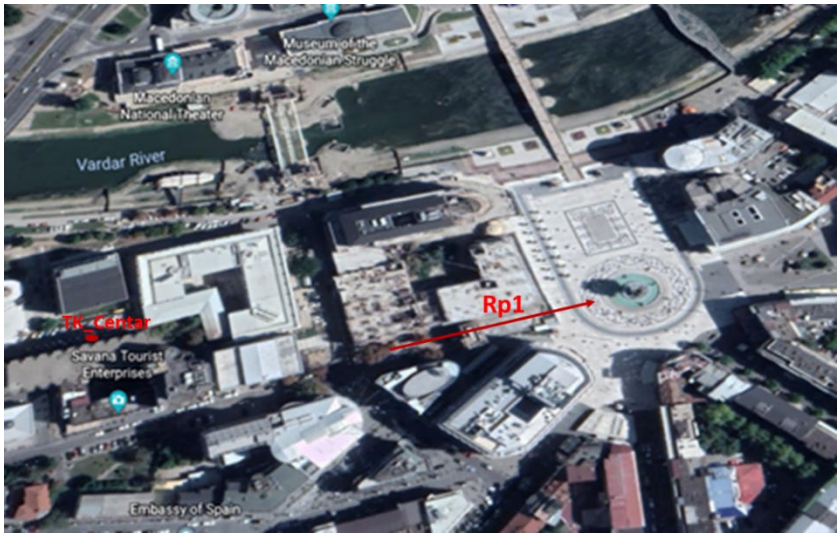


Figure 2: Telecommunication Center in relation to the location of the Mother Teresa monument.

The level of acceptable seismic risk for TK-Center was defined by the standard TIA-942-A. The expected average maximum accelerations at the bedrock for near and far source earthquakes were estimated based on the seismic hazard analysis carried out for the location of the Mother Teresa monument. The upper limit of the average maximum accelerations of the bedrock for a return period of 475 years is 0.29g and at the foundation level is 0.36g, due to the estimated dynamic amplification factor. For time-history analysis of the seismic response of the structure the following set of recorded earthquakes have been selected:

- ACC1: Ulcinj (Albatros) E-W, recorded during the Montenegro earthquake of 15.04.1979 with a magnitude of M=7.0.
- ACC2: El Centro N-S, USA, 1940, with magnitude M=6.7.
- ACC3: Robic N-S, recorded during the Furlania (Italy) earthquake of 15.09.1976 with magnitude M=6.1.

- ACC4: Petrovac (Oliva) N-S, recorded during the Montenegro earthquake of 15.04.1979 with a magnitude of M=7.0
- ACC5: Bar, N-S, recorded during the Montenegro earthquake of 15.04.1979 with a magnitude of M=7.0.

## 2.2 Identification of the load-bearing system

Overview of available technical documentation: The complex of the Telecommunications Center - Macedonian Post Office in Skopje was built in three phases in the period between 1974 and 1982, (Telecommunications Center, Administration and Counter Hall, fig. 3). The subject of analysis is the Telecommunication Center (fig. 3 upper), which together with the tower, from which it is separated by an expansion joint, constitutes the first phase of the construction of this complex.

From the available (uncompleted) technical documentation, the following was observed [3,4]:

- The structural system represents a moment resisting frame consisted of reinforced concrete columns and beams and reinforced concrete floor slabs
- The design calculations are carried out for a live load of 8 kN/m$^2$
- Seismic analysis is provided as for building with high importance (I category) in a zone with seismicity of IX+ degrees according to MCS, corresponding to the first seismic code in the country, (Temporary Technical Provisions for Building in Seismic Regions, Official Gazette SFRJ 39/64), valid for the time when the building was designed
- The proportioning of the load-bearing elements is carried out for concrete quality class of 30MPa (MB30) and plain reinforcement GA 240/360




Figure 3: The Macedonian Telecommunication Complex, Telecommunication center (upper), Administration (lower left), Counter Hall (lower right).

On-site investigations of the structural elements: In order to obtain/confirm the structural system and the existing state of bearing elements, additional technical investigations and control measurements of the geometry of structural elements were performed in-situ. Considering the daily function of the building, non-destructive testing (categorized as an informative method), followed by a minimum number of semi-destructive investigations for identification of the built-in reinforcement in the selected structural elements were carried out. As a result, formwork plans of the individual storeys and characteristic cross-sections of the building have been prepared, (fig. 4).

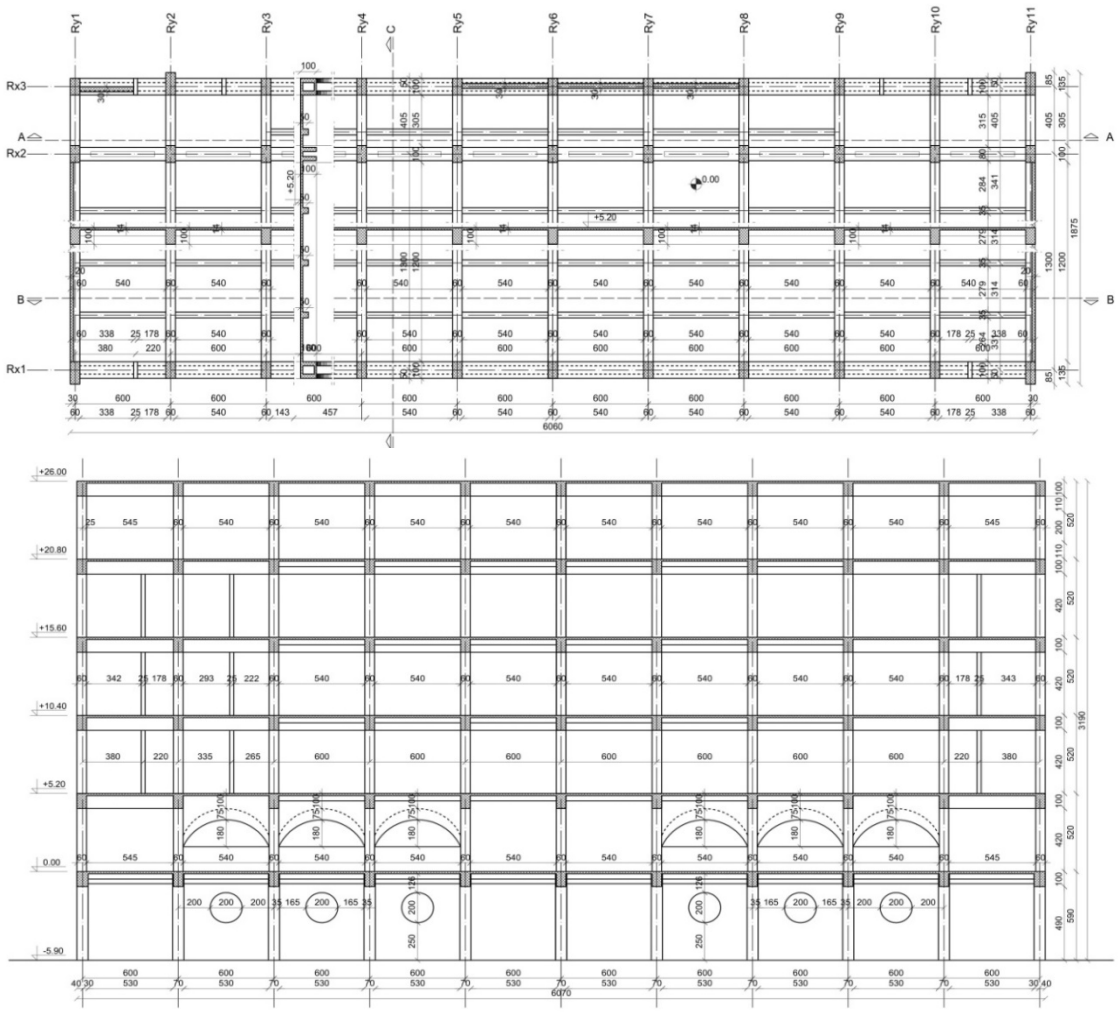


Figure 4: Layout of the ground floor (upper) and longitudinal cross-section (lower) of the building.




Profometer Digi-Schmid Tromino

Figure 5: Nondestructive testing equipment.

The NDT measurements have been done by the following modern equipment for determination of concrete grade and steel rebar disposition in the bearing elements, (fig. 5):

- PROFOMETER 5+ (V2.3.0, 55.60312) (rebar detection system) for identifying the presence of built-in reinforcement, giving information about the cover layer and approximate diameter of the detected metal,
- DIGI-SCHMID 2000, (Modell ND) mechanical device designed to define the compressive strength of a material (primarily concrete),
- TROMINO® - portable ultra-mobile seismometers for definition of structural fundamental dynamic characteristic, (natural frequencies).

Majority of measurements were conducted and recorded in the basement and on the ground floor, while for the upper floors the critical positions were only confirmed. A total of 24 measurements were performed on selected available reinforced concrete elements, (fig. 6).

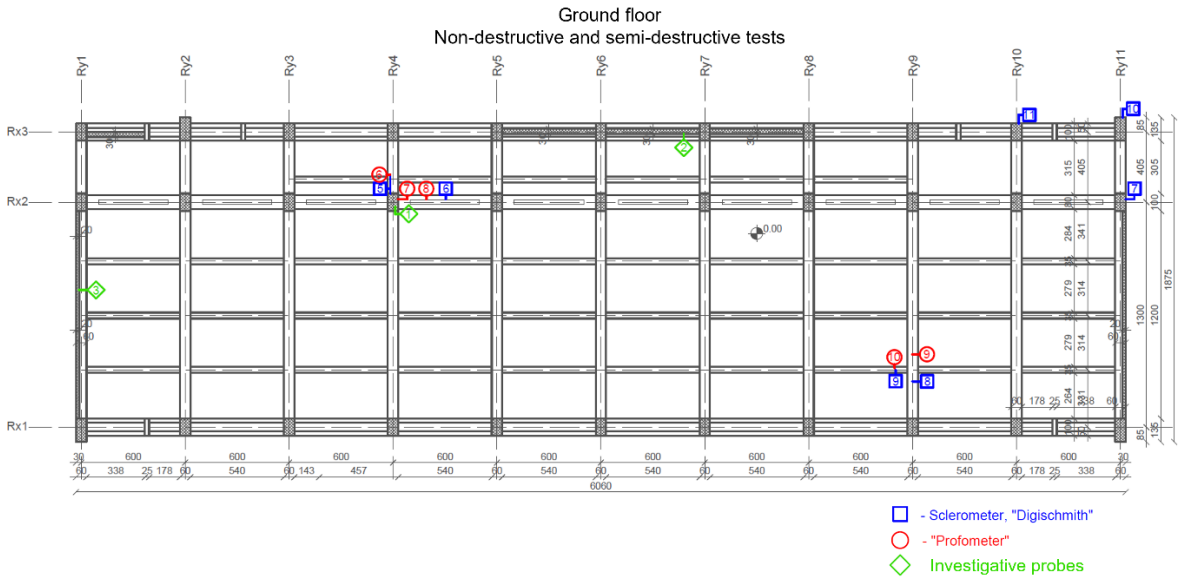


Figure 6: NDT measurement points on ground floor

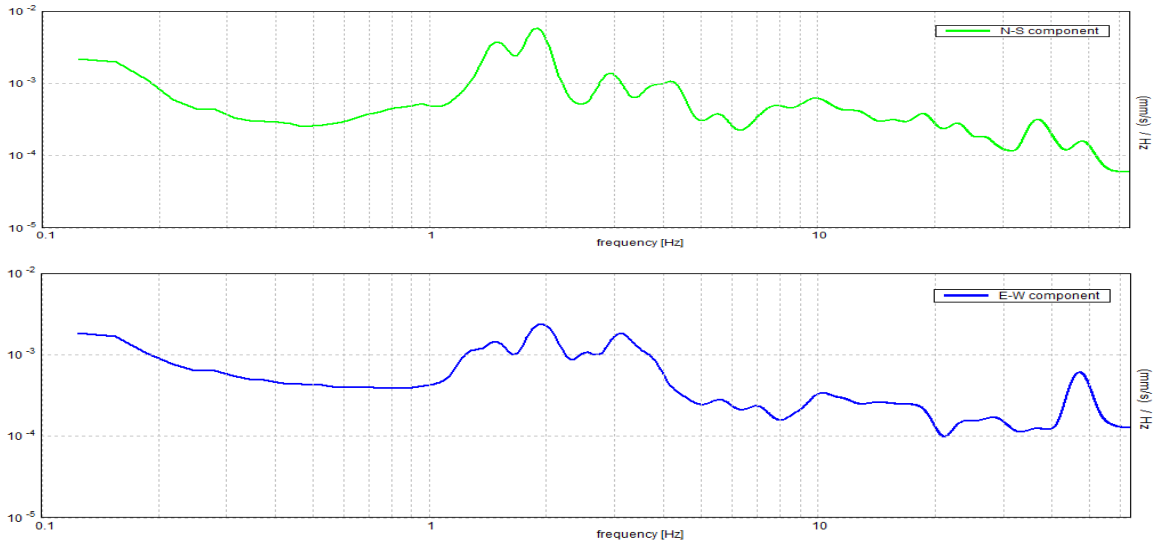


Figure 7: Natural frequency in N-S and E-W direction.

The dynamic characteristics of the sturture were determined using the ambient vibration method, non-destructive "in situ" method based on measurement of structural vibrations caused by ambient forces. The experimentally obtianed dynamic characteristics is of particular importance when calibrating the mathematical models, for a more relevant analysis during the assessment of structural seismic stability, (fig. 7).

To confirm the exact rebar diameter minimum number of destructive investigation probes, were carriod out (fig. 8):



Figure 8: Column rebar diameter measurement (investigation probe 1)

Summary on building structure investigation: The overall site investigations resulted in identification of the main load-bearing structure of the building in its current state, (fig. 4). The principal structural system represents a reinforced concrete frame system. Selected important information are listed below:

- The compressive strength of the built-in concrete in the columns is higher than 40MPa (MB40), while in the shear walls, beams, and floor structure is 30MPa, (MB 30).
- Reinforcement configuration in beams, columns, and floor structures is defined.
- The distance of the shear reinforcement in the columns is 20cm (near the joints) an 40cm at the midspan and in the beams is 15/30cm, accordingly.
- The natural periods of the structure in both directions are $T^{N-S}$=0.55s, $T^{E-W}$=0.52s.
- The columns are reinforced by longitudinal bars with 40 mm diameter and stirrups with 12mm diameter placed on 20-40 cm, (fig. 8).
- Floor plate thickness is d=14cm.

During the visual inspection of the building, no structural damage was found, no settlements or structural distresses, nor damage or repairs due to previous earthquakes were observed. The general conclusion is that the structure has been designed and analysed according to regulations (gravity and seismic codes) at the time of construction on the building, built with exceptional quality and very well maintened.

However, considering that the building was built before the adoption of the current seismic code PIOVS'81 [5], which prescribes additional criteria that the facilitiy should satisfy, it is necessary to perform an analysis of the existing structure for the anticipated imposed gravity and seismic loads.

## 3 ANALYSIS OF EXISTING STRUCTURE ACCORDING TO TIA-942-A STANDARD

To assess the need for structural interventions in order to satisfy the required technical criteria for level TIER III of the TIA-942-A standard, the following structural analyses were performed for gravity and seismic actions: (1) elastic 3D analysis of a mathematical model by application of the finite element method, (2) Analysis of the bearing and deformation capacity, and (3) Nonlinear time-history analysis for the seismic parameters defined in Section 2.1 [3, 4].

### 3.1 Linear-elastic 3D Finite Element Analysis for gravity and seismic actions

For the mathematical model of the defined structural system, (fig. 9), static and lateral force analysis for shear base coefficient equivalent to 15% of the total building weight -design seismic force (according to PIVOS'81) have been performed applying the RadImpex TOWER 7.0 [6]. Gravitational load analysis was carried out taken into consideration the crucial technical requirements for TIA-942-A - TIER III, as follows:

- additional live load of 12 kN/m$^2$ on the third and fourth floor structure
- additional live load of 2.4 kN/m$^2$, suspended on the bottom side of the third and fourth floor slab.

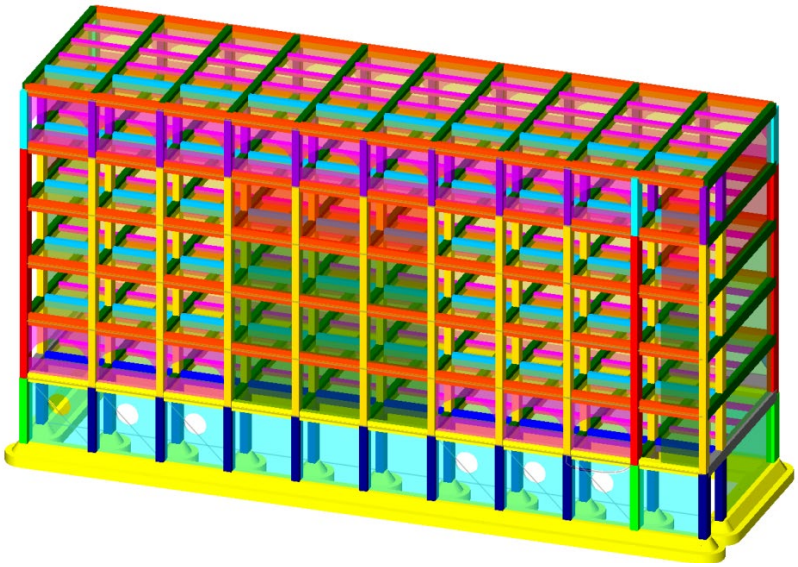

Figure 9: 3D Finite element mathematical model.

The building structure has six storeys (basement, ground floor and four stories), with a total weight of 147759 kN and a total seismic force of 21722 kN. The obtained natural periods were $T^{N-S}$=0.582s, $T^{E-W}$=0.525s, and they are very similar to the experimentally measured ones, (fig.7). The total horizontal displacement of 1.76 cm and 2.01 cm are obtained for transversal and longitudinal direction respectfully, which are less than the maximum allowed (4.33cm), according to the PIOVS'81.

The obtained axial stresses in the columns meet the criteria against brittle failure from vertical loads prescribed in PIOVS'81, ($\sigma_0^{max}$=6.90 MPa < $\sigma_0^{allowed}$=7.175 MPa ). However, certain requirements for reinforcement detailing of load-bearing elements to avoid brittle failure due to seismic actions are not fully met. This especially applies to the distance of shear reinforcement. The distance of the stirrups in the columns is 20cm near the joints and 40cm in the midsection, which is in accordance with the 1964 seismic code, but not completely in accordance with the PIOVS'81 that prescribes 15 cm in the midsection and 7.5 cm near to the joints.

As expected, in most cases the built-in reinforcement in the beams and slabs on the third and fourth storey is less than the required one, which is due to the additional live loading according to the TIA-942-A standard. At the floor levels where there are no such live loads, the built-in reinforcement corresponds to the required one obtained from the analysis.

Consequently, the elastic analysis of the structure carried out according to the current seismic code in the country, shown that the building exposed to the additional loads according to the TIA-942-A - TIER III requirements and seismic actions does not meet the overall safety criteria.

### 3.2 Bearing and Deformation Capacity

Bearing and deformation capacity at element level (Qi-δi relationship) is calculated by inhouse developed software [7]. The cumulative storey Q-δ relationship represents sum of the bearing and deformation capacity of each element, at that story level and considering direction. The storey ductility capacity is defined as ratio between maximum story displacement ($\delta_u$) and displacement at the yield point ($\delta_y$), i.e., $\mu = \delta_u / \delta_y$ .

Bearing capacity of the ground floor, selected as most critical one, is presented on fig.10 and it is larger than the required design seismic force (see 3.1).

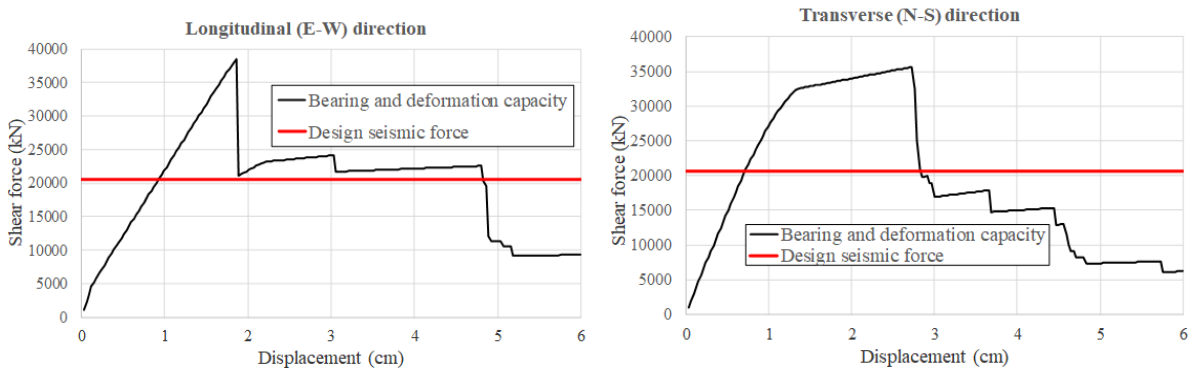


Figure 10: Bearing and deformation capacity for ground floor.

### 3.3 Nonlinear time-history analysis

Nonlinear time-history analysis has been performed by inhouse developed software [7], on the lump-mass structural model that assumes concentration of structural characteristics at story level and using the Q-δ bilinear relationship obtained from the analysis of bearing and deformation capacity, (fig.10).

The results from the dynamic analysis are used for evaluation of the structural performance in nonlinear domain, i.e., verification of the capacity of the structure in respect to the demand for different earthquakes and different levels of input acceleration, as follows: (1) displacement capacity of the structure (δu) in respect to the displacement demand due to an earthquake ($\delta_{RQ}$); (2) displacement ductility capacity of the structure (μ) in respect to the ductility demand ($\mu_{RQ} = \delta_{RQ}/\delta y$).

In accordance with the above:

- if $\delta_{RQ} \leq \delta y$, i.e., $\mu_{RQ} \leq 1$ – the system is in the elastic state,
- if $\delta y \leq \delta_{RQ} \leq \delta u$, i.e., $\mu \geq \mu_{RQ} > 1$ - the system is in the nonlinear range,
- if $\delta_{RQ} > \delta u$, i.e., $\mu_{RQ} > \mu$ - the system experiences deep nonlinearity and possible failure.

A nonlinear time-history analysis has been performed for the structure according to the described procedure and applying selected earthquakes (Section 2.1) with gradual increase of the intensity, (0.24g, 0.27g, 0.30g, 0.33g and 0.36g). Fig.11 illustrates storey displacements required

by the earthquakes with selected intensity of 0.30g (design earthquake) and 0.36g (maximum expected earthquake), compared to the capacity displacement in points "Y" and "U". Ductility capacity of the ground floor level versus ductility demand for each of the earthquakes is presented on fig. 12.

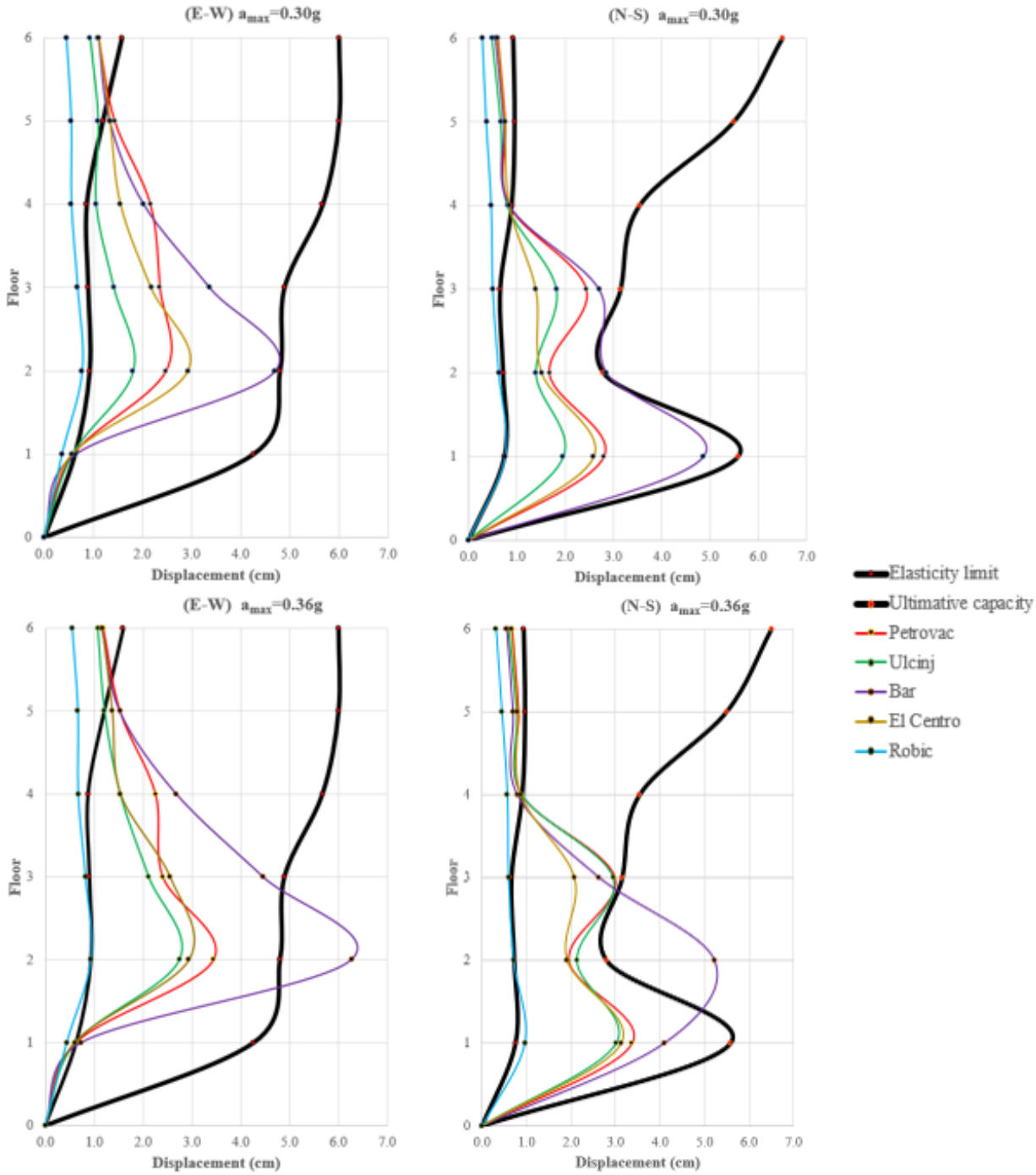


Figure 11: Required displacements versus deformation capacity for longitudinal (E-W) direction (left) and transverse (N-W) direction (right).

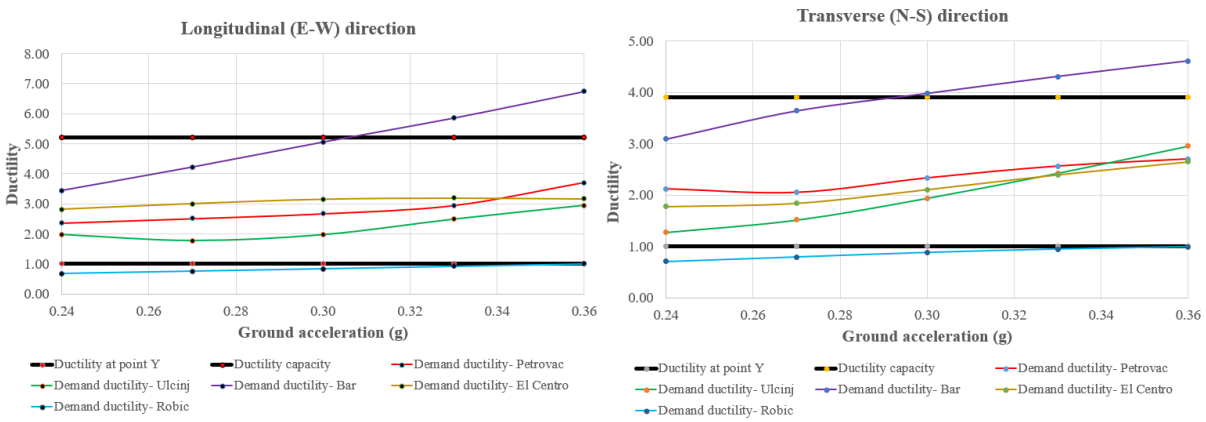


Figure 12: Comparison of demand ductility to ductility capacity for ground floor for longitudinal (E-W) direction (left) and transverse (N-S) direction (right).

### 3.4 Summary on the structural stability and safety

As a result of the overall investigations and analyses shown in the previous Sections, it can be concluded that the structural system was originally designed for gravitational and seismic actions, (according to the seismic code at the time of design) and was built and maintained with high quality.

However, it does not satisfy completely the requirements according to the current seismic code in the country PIOVS'81 and the new requirements according to the standard TIA-942-A - TIER III. This is primarily due to the additional criteria related to the importance class of the building and rules for reinforcing detailing of the load-bearing elements to avoid brittle failure during seismic actions.

The vertical load-bearing elements (columns and shear walls) possess the necessary bearing capacity for seismic actions defined according to PIOVS'81, (fig. 10), however the time-history analysis shows that the ground floor does not have sufficient deformation capacity and ductility for maximum expected earthquake actions (figs. 11 and 12). Also, the horizontal RC elements on 3$^{rd}$ and 4$^{th}$ floor have not enough bearing capacity due to additional exploitation loads according to TIER III.

Finally, according to the structural analysis results, there is a need for global and local strengthening of the building's structure to satisfy completely the current seismic code PIOVS'81 and the specific TIER III criteria.

## 4 PRELIMINARY SOLUTION FOR SEISMIC RETROFITTING OF THE EXISTING STRUCTURE

The proposed solution for seismic retrofitting, based on building's specifics and the conditions for execution, consists of:

1. Strengthening of the reinforced concrete slab on the third and fourth floor due to the additional imposed load, according to TIA-942-A - TIER III standard. It anticipates new secondary steel beams, (fig.13, left). The beam is formed by inserting steel profiles below and above the slab, interconnected one to another and coupled with the existing slab.
2. Strengthening of the longitudinal main reinforced concrete beams on the third and fourth floor due to the additional imposed load, according to the TIA-942-A - TIER III standard. It anticipates inserting steel profiles to reach the required bending moment capacity in the midspan, (fig.13, right).

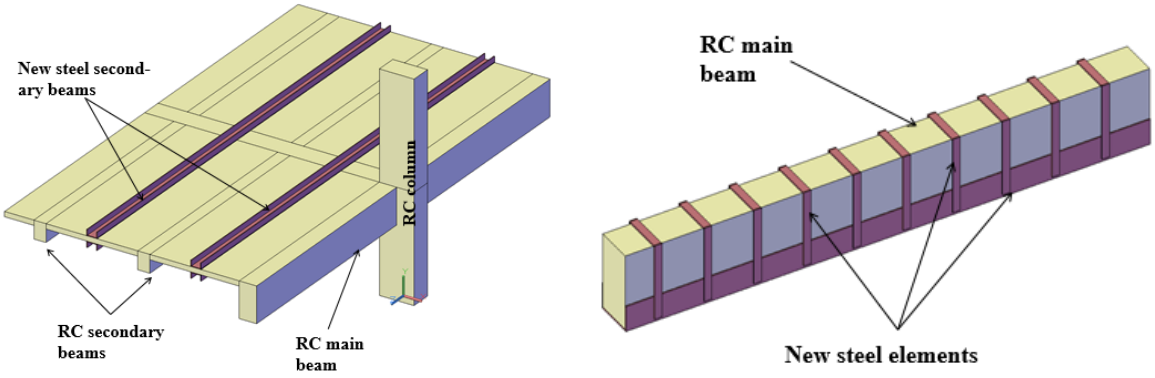


Figure 13: Strengthening of the 3rd and 4th storey: slab (left) and main RC beam (right)

3. Strengthening of reinforced concrete beam-column joints due to seismic action, which anticipates interconnected steel strips, mounted on the top and the bottom edge of the beam (fig. 14).

4. Strengthening of the reinforced concrete columns due to the additional imposed load and seismic action, which anticipates strapping with steel strips which are interconnected and connected to the strips on the strengthened beams, (fig.14).

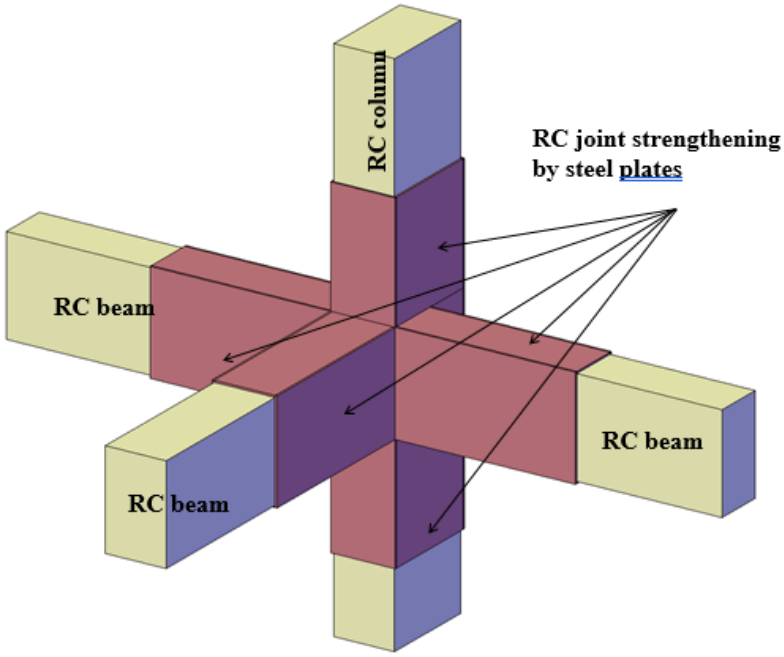


Figure 14: Strengthening of RC columns, beams and joints.

5. Global strengthening of the structure for horizontal seismic action. Introducing additional reinforced concrete shear walls from the basement to the 2nd storey, on their own foundations, at locations where they will not interfere with the equipment and regular functioning of the facility, will reduce structural flexibility, and prevent non-structural damage due to the frequent earthquakes.

## 5 CONCLUSIONS

Telecommunication Center facility in Skopje has existed for more than fifty years. Due to the requirement for eventual change of the building function, detail analysis of the stability and safety of the existing structural system has been carried out according to current seismic code [5] and required technical standard TIA-942-A [1]. The necessity for structural strengthening has been proved and the most appropriate technical solution for strengthening that satisfies the strength and deformability requirements has been proposed.

## REFERENCES

[1] Telecommunications Industry Association, Standards and Technology Department, *Telecommunications Infrastructure Standard for Data Centers, TIA-942-A*, (Revision of TIA-942), August 2012.

[2] R. Apostolska, R., V. Shendova, G. Necevska-Cvetanovska, The need of integrated renovation of the existing buiding stock in North Macedonia, *European Journal of Environmental and Civil Engineering,* doi/full/10.1080/19648189.2020.1798816, 2020.

[3] Z. Bozinovski, V. Shendova, G Jekic, A. Zurovski, E. Delova, Analysis and cost estimation of the retrofitting of the existing structure TK-Center in Skopje, *IZIIS Report 2018-24*, 2018.

[4] Z. Bozinovski, V. Shendova, G. Jekik, A. Zlateski, A. Zurovski, E. Delova, Analysis of the existing structure of the building "Block" and "Tower" of the TK Center in Skopje, *IZIIS Report 2019-64,* 2019.

[5] Rulebook for the construction of buildings in seismic regions" - PIOVS'81, *Official Gazette 31/81 of RM*, 1981.

[6] RadImpex TOWER 7.0, Professional construction software.

[7] G. Necevska-Cvetanovska, R. Apostolska, Methodology for seismic assessment and retrofitting of RC building structures, *Proc. of 15 World Conference on Earthquake Engineering, Lisboa*, (Paper ID 2149), 2012.

COMPDYN 2023
9th ECCOMAS Thematic Conference on
Computational Methods in Structural Dynamics and Earthquake Engineering
M. Papadrakakis, M. Fragiadakis (eds.)
Athens, Greece, 12-14 June 2023

# SYNTHETIC DATA GENERATION FOR THE CREATION OF BRIDGE DIGITAL TWINS WHAT-IF SCENARIOS

**Alejandro Jiménez Rios[1], Vagelis Plevris[2] and Maria Nogal[3]**

[1] Structural Engineering Research Group (SERG), Department of Built Environment (DBE), Faculty of Technology, Art, and Design (TKD), Oslo Metropolitan University (OsloMet)
Rebel Building, Universitetsgata 2, 0164 Oslo, Norway
e-mail: alejand@oslomet.no

[2] Department of Civil and Architectural Engineering, Qatar University
Doha P.O. Box 2713, Qatar
e-mail: vplevris@qu.edu.qa

[2] Materials, Mechanics, Management & Design Department, Delft University of Technology
2628 CN Delft, The Netherlands
e-mail: m.nogal@tudelft.nl

## Abstract

*The Digital Twin (DT) concept, as understood nowadays, appeared in the early 2000s as an attempt to create virtual replicas of physical assets, such as bridges, that can be used to examine, monitor and manage their performance. Up to this day, it has been successfully applied in the fields of aeronautics, manufacturing, medicine, and more recently, in the architecture, engineering, and construction industry. The DT of a bridge requires the creation of a virtual replica of the real-life asset, along with the connection and feedback of information channel between the two of them. This connection is currently achieved through the generation of real-time data by the placement of sensors in the real bridge and the application of structural health monitoring techniques to analyze such data. This connection could result in a complex, time-consuming, and expensive process which would hinder the creation of DT prototypes for development purposes in the bridge engineering field. This paper aims at exploring the currently available synthetic data generation methodologies and tools, which could be used as a faster and a more economically feasible alternative to real monitoring, for the creation and development of DT prototypes of bridges, for both industry and research-oriented purposes. A synthetic data generation framework is proposed that can produce FAIR benchmark databases that are based on Findability, Accessibility, Interoperability, and Reuse, which could be used in the prototyping of bridge DTs. Finally, tentative future improvements in this topic are discussed.*

**Keywords:** Digital Twins, Bridges, Synthetic FAIR Data, Prototyping, Damage Detection.

## 1 INTRODUCTION

Digital twins (DTs) are virtual replicas of physical assets, such as bridges, that can be used to monitor and manage their performance. By creating a digital twin of a built asset, the Architecture, Engineering, and Construction (AEC) professionals can monitor its performance in real-time and identify potential issues before they become serious problems. This can lead to improved safety and reduced maintenance costs, especially for the case of vulnerable cultural heritage structures [1, 2] where there are additional challenges because of the special nature and requirements for these valuable assets [3, 4].

The DT paradigm is nowadays in its early stages of development/adoption within the AEC industry. Nevertheless, and despite all the challenges and constraints that need to be overcome for its full deployment and broad implementation, there seems to be a unified vision and consensus toward the future adoption of DT for bridge design, management, and operation among the scientific community and bridge practitioners [5]. Thus, further research is required before a proper application framework is well established and widely adopted by the industry.

Among the several frameworks proposed for the materialization of DTs for bridges, one that can account also for the cultural heritage of existing bridges was proposed as the integration of fully inter-operable data, geometry, finite element, and data-driven modules within an As-Is [6] Historical Bridge Information Model (AI-HBrIM). The interconnection between the real and digital assets within this AI-HBrIM (and also within other frameworks) is achieved through the continuous real-time collection of multi-metric [7] structural, environmental, and operational data. These data are normally collected by a series of sensors organized within a Bridge Health Monitoring (BHM) system. To optimize the data collection, processing, and storage, such a framework would implement optimized sampling methodologies along with fog and cloud computing services.

The main advantages of implementing a DT paradigm are that the data-driven surrogate models allow real-time damage detection and early warning alerts, whereas the detailed finite element models of the asset are used for damage prognosis purposes and the simulation of what-if scenarios that, in combination with probabilistic and reliability analysis, aid asset managers to take informed decisions about the optimal maintenance, retrofitting and repairing of the physical asset. This new paradigm results in extended life, operation cost reduction, as well as increased resilience and sustainability of the built environment.

Unfortunately, BHM demands a lot of resources, both economic ones and in terms of time. Other than a few well-known benchmark bridges, i.e., Z24 [8], Dona [9], I-40 [10], data are not available for exploitation on open-source databases by researchers working in the field. Moreover, to develop tools capable of damage detection [11], the collection of meaningful data (an actual damage scenario) may not be available within the time frame of most research and development projects (for example, an MSc or Ph.D. thesis, a Postdoctoral research project, etc). Furthermore, the data collected through BHM can be affected by both epistemic and aleatory uncertainties [12] and it is necessary to implement adequate strategies to reduce the estimation error of prediction models using such data [13].

Therefore, the need for a reliable database of benchmark data arises so that new technologies and algorithms can be properly tested and validated within the prototyping stage for bridge DTs. Prototypes are essential means to move from design to production and implementation, thus allowing to overcome the classic gap between ideation and implementation [14]. Furthermore, for the implementation of any new technologies and/or materials [15, 16] on bridges with cultural heritage value, such interventions need to be thoroughly validated before they could be considered adequate in accordance with the guidelines of the ICOMOS Interna-

tional Scientific Committee on the Analysis and Restoration of Structures of Architectural Heritage (ISCARSAH Guidelines) [17].

In this paper, we propose a new synthetic data generation framework within the context of the DT paradigm. The framework will be used to generate a series of benchmark databases containing meaningful data including different damage scenarios which could be used in the development and validation of DT components thus reducing the time and money required for the creation of novel prototypes. Within that context, the synthetically generated data would mock the physical asset components of the DT. This data will be particularly suitable for the prototyping of model-based, data-driven, and/or physics-informed components used for damage detection, localization, description, and prognosis of bridge DT. In Section 2 of this paper, the required data is described. In Section 3 the proposed framework is exposed and discussed. Finally, in Section 4 conclusions are drawn, and further work is proposed.

## 2 REQUIRED DATA

The benchmark data required for prototyping validation depends on the type of anomaly detection algorithm being tested. Anomaly detection algorithms can be classified into four general categories: (i) vibration-based; (ii) strain-based; (iii) visual-based; and (iv) mixed, as shown schematically in Figure 1.

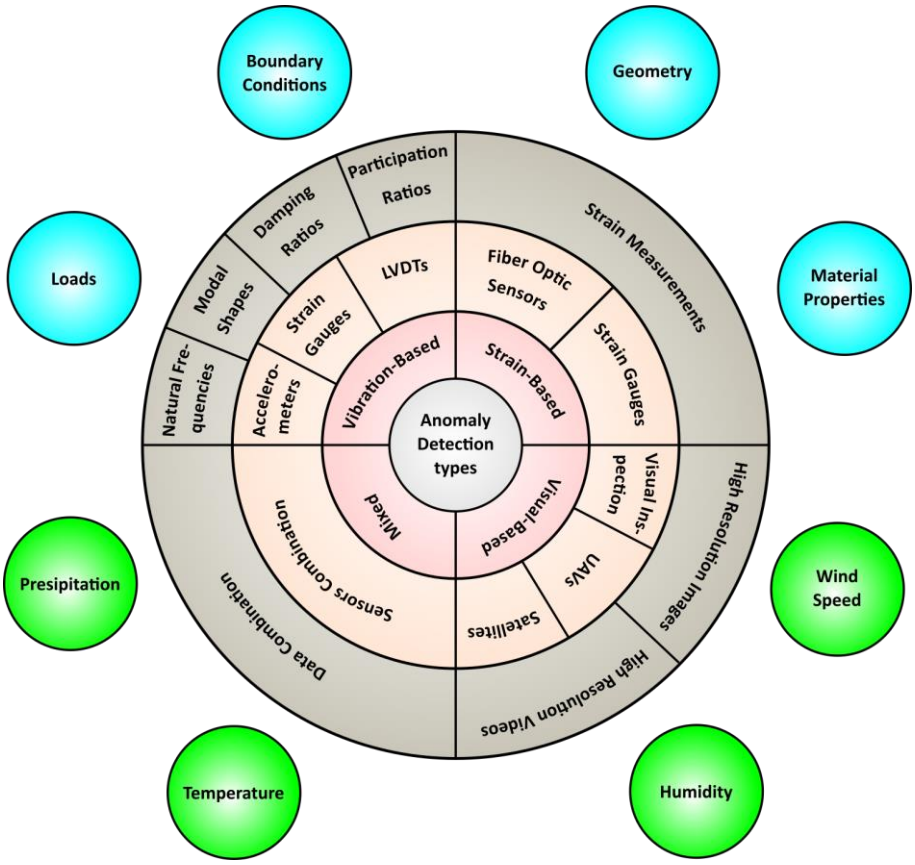


Figure 1. Anomaly detection types are classified based on the data type required, how data is collected, the type of data collected along with environmental and operational conditions.

Vibration-based damage identification on bridges typically requires data on the dynamic response of the bridge [18], which can be obtained through various types of sensors, such as accelerometers, strain gauges, and displacement transducers (Linear Variable Differential

Transformers, LVDTs) [19]. This data is used in Structural Health Monitoring (SHM) to determine the natural frequencies, mode shapes, damping ratios, and modal participation factors of the bridge before and after damage occurs [20].

On the other hand, strain-based damage detection on bridges is based on strain distribution data along the bridge, which can be obtained through strain gauges or fiber optic sensors [21]. The data should include strain measurements at multiple locations on the bridge, both under undamaged and damaged scenarios [22].

Another alternative approach is the so-called visual-based damage detection [23]. The different methodologies implementing this approach, exploit high-resolution images or videos of the bridge surface and its components, which can be obtained through visual inspection, Unmanned Aerial Vehicles (UAVs), or other imaging technologies [24].

Finally, Mixed damage detection on bridges typically involves the combination of multiple types of data to enhance the accuracy and reliability of the damage detection results [25]. The required data can vary depending on the specific combination of techniques used but typically involves a combination of vibration-based, strain-based, and visual-based data [26].

In addition to the collection of the required data for each anomaly detection type, it is also necessary to collect accurate information on the bridge's geometry, material properties, and loading conditions. This can include details such as the bridge span, cross-sectional area, modulus of elasticity, and the types and weights of vehicles that typically cross the bridge. Furthermore, it is important to have data on environmental conditions, such as temperature, wind speed, and precipitation, as these factors can affect the dynamic response of the bridge. Finally, it is essential to have a baseline dataset of the measurements on the undamaged bridge, so that changes in data patterns can be identified and interpreted as damage. Overall, the more comprehensive the data set is and the lower the data uncertainties are, the more accurate and reliable the damage detection results will be.

## 3 PROPOSED FRAMEWORK AND DISCUSSION

The proposed novel framework for the creation of synthetic data that could be used to form benchmark study cases for prototyping and validation of DT components is shown schematically in Figure 2.

The data generated by a BHM system come in the form of time series, i.e., data collected over time at certain intervals, also known as sampling rates. Therefore, the first component of the proposed synthetic data generation framework is the sync main module. This element ensures the correct alignment in time of the different time series data generated, i.e., synthetic monitoring data, environmental data, and operational conditions data. To achieve the synchronization of the different synthetic time series generated within the proposed framework, a Dynamic Time Warping (DTW) function is suggested [27].

The synthetic data artificially generated by the proposed framework, namely, vibration, strain, and visual data, will provide information that can be used in place of real historic data. For such purposes, the generated data will have to be programmable. In other words, the statistical features of the data could be rebalanced, imputed, or have a stricter or looser adherence to the original distributions and correlations [28]. This will allow improving DT bridge model prototyping performance by enabling the simulation of what-if scenarios and the generation of test data with an improved ability to test and validate prototypes. Several Python libraries readily available have the required features to effectively generate programmable data such as PyOD [29], which is a specialized, comprehensive and scalable library for the detection/generation of outlying objects; and ctgan [30], which is a collection of high fidelity synthetic data generators based on deep learning algorithms. Both libraries' capabilities will be integrated and combined within the proposed synthetic data generation framework.

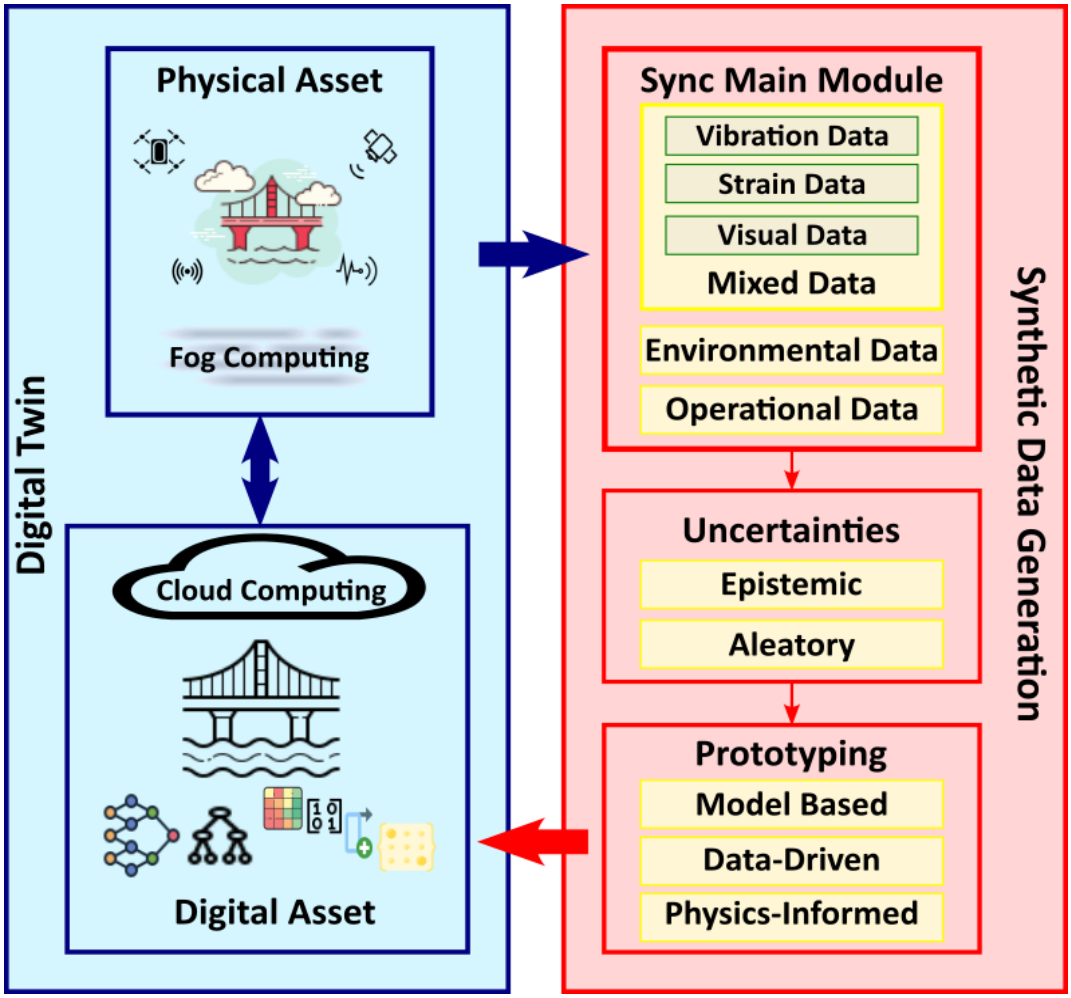


Figure 2. The proposed framework for synthetic data generation, which accounts for uncertainties and could be used in the prototyping of DTs.

The generation of vibration, strain, and visual data will be done within a mixed data component. This sub-module will be developed to generate benchmark databases of multi-metric data which could be used by mixed anomaly detection algorithms prototyping requirements.

The operational conditions data can be used to easily differentiate between damaged and undamaged scenarios, as anomaly conditions often reflect on the properties of the bridge structural components, such as supports, stiffness of members, extraordinary loads leading to permanent deformations, etc. Accounting for environmental data is also of paramount importance within the context of synthetic data generation, as it has been proved by several authors [31, 32] that environmental conditions can modify some properties of the bridge, which does not necessarily mean the asset has suffered some damage.

The framework considers both epistemic and aleatory uncertainties, which are key features to be accounted for in the validation process of any newly developed technology. The uncertainties component of the framework is presented and discussed in more detail in another study of the authors [33].

It is worth mentioning that the data generated by the proposed framework could be used for the prototyping and validation of either model-based or data-driven algorithms as well as by the more complex physics-informed ones. It is important to highlight that the proposed

framework aims to produce realistic data capable of depicting general bridge management and operation scenarios, not to accurately replicate the observable data of a specific bridge study case. Thus, the data produced, should serve as a benchmark, so that novel prototypes can be tested and validated, consequently preparing them for their real-world deployment.

Although the creation of similar synthetic benchmark datasets has been proposed in the past [34], such alternatives are hard to find and even harder to access. Therefore, it is of paramount importance that the data generated comply with the FAIR principles having to do with the "Findability, Accessibility, Interoperability, and Reuse" of digital assets [35], i.e. the data needs to be findable, accessible, interoperable, and usable. To ensure these requirements are fully met, the proposed framework will follow the steps highlighted in the Three-point FAIR-ification Framework [36].

## 4 CONCLUSIONS AND FURTHER WORK

In this article, the shift towards a Digital Twin paradigm by all stakeholders in the engineering, architecture, and construction industry is recognized. As this new approach is currently in its early stages of development and adoption, new proposals to optimize its application need to be explored and developed. Such attempts require the development of prototypes that need to be validated against benchmark data.

Overall, synthetic data used for the creation of "what-if" scenarios for bridge digital twins can provide valuable insights into the bridge's performance under different conditions, allowing AEC professionals to identify potential issues and make informed decisions about maintenance and design challenges.

In this paper, a framework for the creation of a synthetic data generation tool has been proposed. Such framework produces high-quality FAIR data that allows novel developed prototypes to be validated and consequently be implemented in further stages of the Digital Twin creation for real infrastructure assets. The main characteristics of the proposed framework are the following:

- It accounts for the creation of multi-metric data, namely, vibration, strain, visual and mixed synthetic data under both undamaged and damaged scenarios.
- Both environmental and operational conditions can be fine-tuned and included in the data generation.
- A synchronizing module ensures that all data can be correctly tracked over time.
- It considers both epistemic and aleatory uncertainties for the adequate generation of real-world-like scenarios.
- The data generated is suitable for its use in the development and validation of model-based, data-driven, and physics-informed components of a digital asset.

Further work needs to be done, mainly within three directions: (i) operationalization of the proposed framework; (ii) self-validation of the generated synthetic data; and (iii) continuous maintenance/support. The results of these attempts will be presented by the authors in future publications.

## ACKNOWLEDGMENTS

This project has received funding from the European Union's Horizon 2020 research and innovation program under the Marie Sklodowska-Curie grant agreement No. 101066739.

## GLOSSARY

| | |
|---|---|
| AEC | Architecture, Engineering, and Construction |
| AI-HBrIM | As-Is Historical Bridge Information Model |
| BHM | Bridge Health Monitoring |
| DT | Digital Twin |
| DTW | Dynamic Time Warping |
| FAIR | Findability, Accessibility, Interoperability, and Reuse |
| HBrIM | Historical Bridge Information Model |
| ICOMOS | International Council on Monuments and Sites |
| ISCARSAH | International Scientific Committee on the Analysis and Restoration of Structures of Architectural Heritage |
| SHM | Structural Health Monitoring |
| UAV | Unmanned Aerial Vehicle |

## REFERENCES


[1] Kioumarsi, M., V. Plevris, and A. Shabani, *Vulnerability assessment of cultural heritage structures*, in *8th European Congress on Computational Methods in Applied Sciences and Engineering (ECCOMAS 2022)*. 2022: Oslo, Norway. DOI: https://doi.org/10.23967/eccomas.2022.294.

[2] Shabani, A., et al., *Seismic Vulnerability Assessment and Strengthening of Heritage Timber Buildings: A Review.* Buildings, 2021. **11**(12) DOI: https://doi.org/10.3390/buildings11120661.

[3] Shabani, A., et al., *3D simulation models for developing digital twins of heritage structures: challenges and strategies.* Procedia Structural Integrity, 2022. **37**: p. 314-320 DOI: https://doi.org/10.1016/j.prostr.2022.01.090.

[4] Asteris, P. and V. Plevris, eds. *Handbook of Research on Seismic Assessment and Rehabilitation of Historic Structures*. 2015, IGI Global. 1130. DOI: https://doi.org/10.4018/978-1-4666-8286-3.

[5] Jiménez Rios, A., V. Plevris, and M. Nogal, *Bridge management through digital twin-based anomaly detection systems: A systematic review.* Frontiers in Built Environment, 2023. **9**(1176621) DOI: https://doi.org/10.3389/fbuil.2023.1176621.

[6] Hosamo, H.H. and M.H. Hosamo, *Digital Twin Technology for Bridge Maintenance using 3D Laser Scanning: A Review.* Advances in Civil Engineering, 2022. **2022** DOI: https://doi.org/10.1155/2022/2194949.

[7] Lawal, O., et al. *Development and Validation of a Framework for Smart Wireless Strain and Acceleration Sensing*. Sensors, 2022. **22**, DOI: https://doi.org/10.3390/s22051998.

[8] Maeck, J. and G. De Roeck, *Description of Z24 Benchmark.* Mechanical Systems and Signal Processing, 2003. **17**(1): p. 127-131 DOI: https://doi.org/10.1006/mssp.2002.1548.

[9] Dilena, M. and A. Morassi, *Dynamic testing of a damaged bridge.* Mechanical Systems and Signal Processing, 2011. **25**(5): p. 1485-1507 DOI: https://doi.org/10.1016/j.ymssp.2010.12.017.

[10] Farrar, C.R., et al., *Dynamic characterization and damage detection in the I-40 bridge over the Rio Grande.* 1994 DOI: https://doi.org/10.2172/10158042.

[11] Georgioudakis, M. and V. Plevris, *A Combined Modal Correlation Criterion for Structural Damage Identification with Noisy Modal Data.* Advances in Civil Engineering, 2018. **2018**(3183067): p. 20 DOI: https://doi.org/10.1155/2018/3183067.

[12] Peng, T., et al. *Role of Sensors in Error Propagation with the Dynamic Constrained Observability Method*. Sensors, 2021. **21**, DOI: https://doi.org/10.3390/s21092918.
[13] Peng, T., et al., *Planning low-error SHM strategy by constrained observability method.* Automation in Construction, 2021. **127**: p. 103707 DOI: https://doi.org/10.1016/j.autcon.2021.103707.
[14] Deserti, A., et al., *Co-design for society in innovation*, in *Atlas of Social innovation 2nd volume: A world of new practice*. 2019, Oekom. p. 91-96.
[15] Jiménez Rios, A. and D. O'Dwyer. *External Post-tensioning System for the Strengthening of Historical Stone Masonry Bridges*. in *Structural Analysis of Historical Constructions*. 2019. Cham: Springer International Publishing. DOI: https://doi.org/10.1007/978-3-319-99441-3_168.
[16] Jurina, L. and E.O. Radaelli. *"Reinforced Arch Method" as Retrofitting Technique for Masonry Arches. Experimental Tests and Numerical Modelling*. in *Proceedings of ARCH 2019*. 2020. Cham: Springer International Publishing.
[17] Roca, P., L. Pelà, and C. Molins. *The Iscarsah Guidelines on the Analysis, Conservation and Structural Restoration of Architectural Heritage*. in *12th International Conference on Structural Analysis of Historical Constructions (SAHC)*. 2021.
[18] Georgioudakis, M. and V. Plevris, *Investigation of the performance of various modal correlation criteria in structural damage identification*, in *ECCOMAS Congress 2016 - Proceedings of the 7th European Congress on Computational Methods in Applied Sciences and Engineering*, M. Papadrakakis, et al., Editors. 2016: Crete Island, Greece. p. 5626-5645. DOI: https://doi.org/10.7712/100016.2207.11846.
[19] Lu, Q., et al., *Developing a Digital Twin at Building and City Levels: Case Study of West Cambridge Campus.* Journal of Management in Engineering, 2020. **36**(3) DOI: https://doi.org/10.1061/(ASCE)ME.1943-5479.0000763.
[20] Neves, A.C., et al., *Structural health monitoring of bridges: a model-free ANN-based approach to damage detection.* Journal of Civil Structural Health Monitoring, 2017. **7**(5): p. 689-702 DOI: https://doi.org/10.1007/s13349-017-0252-5.
[21] Febrianto, E., et al., *Digital twinning of self-sensing structures using the statistical finite element method.* Data-Centric Engineering, 2022. **3**(3) DOI: https://doi.org/10.1017/dce.2022.28.
[22] Weinstein, J.C., M. Sanayei, and B.R. Brenner, *Bridge Damage Identification Using Artificial Neural Networks.* Journal of Bridge Engineering, 2018. **23**(11) DOI: https://doi.org/10.1061/(ASCE)BE.1943-5592.0001302.
[23] Shim, C.S., et al., *Development of a bridge maintenance system for prestressed concrete bridges using 3D digital twin model.* Structure and Infrastructure Engineering, 2019. **15**(10): p. 1319-1332 DOI: https://doi.org/10.1080/15732479.2019.1620789.
[24] Perry, B.J., et al., *Streamlined bridge inspection system utilizing unmanned aerial vehicles (UAVs) and machine learning.* Measurement: Journal of the International Measurement Confederation, 2020. **164** DOI: https://doi.org/10.1016/j.measurement.2020.108048.
[25] Bao, Y., et al., *Computer vision and deep learning–based data anomaly detection method for structural health monitoring.* Structural Health Monitoring, 2019. **18**(2): p. 401-421 DOI: https://doi.org/10.1177/1475921718757405.
[26] Soman, R., et al., *Numerical evaluation of multi-metric data fusion based structural health monitoring of long span bridge structures.* Structure and Infrastructure

Engineering, 2018. **14**(6): p. 673-684 DOI: https://doi.org/10.1080/15732479.2017.1350984.
[27] Parisi, F., et al., *Automated location of steel truss bridge damage using machine learning and raw strain sensor data.* Automation in Construction, 2022. **138**: p. 104249 DOI: https://doi.org/10.1016/j.autcon.2022.104249.
[28] Mostly AI, *Synthetic Data Generator Documentation*. 2022.
[29] Zhao, Y., Z. Nasrullah, and Z. Li, *PyOD: A Python Toolbox for Scalable Outlier Detection.* Journal of Machine Learning Research, 2019. **20**(96): p. 1-7.
[30] Xu, L., et al. *Modeling Tabular data using Conditional GAN*. in *Advances in Neural Information Processing Systems*. 2019.
[31] Zhu, Y.C., W. Xiong, and X.D. Song, *Structural performance assessment considering both observed and latent environmental and operational conditions: A Gaussian process and probability principal component analysis method.* Structural Health Monitoring, 2022. **21**(6): p. 2531-2546 DOI: https://doi.org/10.1177/14759217211062099.
[32] Filizadeh, R., E. Hernandez, and D. Rosowsky, *Time-Dependent Damage Evolution of Reinforced Concrete Bridge Piers: Implications for Multihazard Analysis.* ASCE-ASME Journal of Risk and Uncertainty in Engineering Systems, Part A: Civil Engineering, 2023. **9**(1) DOI: https://doi.org/10.1061/AJRUA6.RUENG-953.
[33] Jiménez Rios, A., V. Plevris, and M. Nogal, *Uncertainties in the Synthetic Data Generation for the Creation of Bridge Digital Twins,* in *5th International Conference on Uncertainty Quantification in Computational Science and Engineering (UNCECOMP 2023)*. 2023, ECCOMAS: Athens, Greece.
[34] Johnson, E.A., et al., *Phase I IASC-ASCE Structural Health Monitoring Benchmark Problem Using Simulated Data.* Journal of Engineering Mechanics, 2004. **130**(1): p. 3-15 DOI: https://doi.org/10.1061/(ASCE)0733-9399(2004)130:1(3).
[35] Wilkinson, M.D., et al., *The FAIR Guiding Principles for scientific data management and stewardship.* Scientific Data, 2016. **3**(1): p. 160018 DOI: https://doi.org/10.1038/sdata.2016.18.
[36] Schultes, E., *Official GO FAIR Foundation icons for the Three-Point FAIRification Framework.* 2021 DOI: https://doi.org/10.5281/zenodo.4678333.

COMPDYN 2023
9th ECCOMAS Thematic Conference on
Computational Methods in Structural Dynamics and Earthquake Engineering
M. Papadrakakis, M. Fragiadakis (eds.)
Athens, Greece, 12-14 June 2023

# RETROFITTING DAMAGED BUILDINGS UNDER SEISMIC MAINSHOCK-AFTERSHOCK SEQUENCE

**Benyamin Mohebi[1], Farzin Kazemi[2], and Neda Asgarkhani[2]**

[1] Faculty of Engineering and Technology, Imam Khomeini International University, Qazvin, Iran
e-mail: mohebi@eng.ikiu.ac.ir

[2] Faculty of Civil and Environmental Engineering, Gdańsk University of Technology, ul. Narutowicza 11/12, 80-233 Gdansk, Poland
{farzin.kazemi, neda.asgarkhani}@pg.edu.pl

## Abstract

*Mainshock-aftershock sequences are a common occurrence in areas with high seismic activity, and they can significantly increase the damage sustained by a building after the initial seismic event. During severe mainshock earthquake, there is a permanent deformation in the floor levels of the building that increases the risk of further damage and potential collapse in the aftershock earthquake. This research aims to introduce a computational method for retrofitting damaged buildings under seismic mainshock-aftershock sequences using Fluid Viscous Dampers (FVDs) and Buckling-Restrained Braces (BRBs). This retrofitting approach aims to mitigate further damage that may be caused by subsequent aftershocks. The use of computational methods enables engineers to accurately simulate the behavior of damaged structures under various seismic loads, which helps in the design and optimization of retrofitting techniques. Due to ability of FVDs and BRBs, two steel structures having four and six-story floor levels were selected to implement the computational method of retrofitting. The results of analysis confirmed that the mainshock-aftershock sequences can highly affect the performance of damaged buildings, and the proposed method can accurately model the damaged buildings with different pre-defined damage states.*

**Keywords:** Damaged Building, Mainshock-Aftershock Sequence, Computational Methods, Retrofitting Structure, Fluid Viscous Damper.

## 1 INTRODUCTION

Fluid viscous dampers (FVDs) are devices that are used in structural engineering to mitigate the effects of seismic activity. They consist of a piston that moves within a cylinder filled with a viscous fluid, which dissipates energy and reduces the force transmitted to the structure during seismic events [1]. Conventional brace and FVDs have been widely used in retrofitting damaged buildings as they can be installed relatively easily and provide effective seismic performance enhancement [2]. Using FVDs either inside of lateral force-resisting system [3] or between the adjacent colliding structures [4, 5] showed that these passive energy dissipation device can widely implement in purpose of retrofitting.

Buckling-Restrained Braces (BRBs) are another type of device commonly used in the retrofitting of steel structures under seismic Mainshock-Aftershock (MA) sequences. BRBs consist of a steel core surrounded by a steel tube, which acts as a restraint to prevent the core from buckling. BRBs dissipate energy by buckling and yielding in a controlled manner, reducing the force transmitted to the structure and enhancing its seismic performance [6]. Asgarkhani et al. [7] used BRBs in reducing the damage caused by earthquakes in steel structures to ensure their safety and reliability after an earthquake. Yakhchalian et al. [8, 9] numerically modeled BRBs to assess the accuracy of the methods in predicting deflection amplification factor, which plays a key role on their actual behavior and capacity. Kazemi and Jankowski introduced a shape memory-based BRBs to improve the safety and reliability of the steel structures while the residual drift was considerably reduced [10].

Seismic Mainshock-Aftershock (MA) sequences occur when a large earthquake is followed by a series of smaller aftershocks. These aftershocks can cause additional damage to already weakened structures and may lead to local or total collapses [11]. As example of significant MA earthquakes in Turkey, Izmir earthquake struck on October 30, 2020, with a magnitude of 6.9 on the Richter scale, and following the mainshock, a number of significant aftershocks occurred, including a magnitude 5.2 that struck just 30 minutes after the mainshock. The recent earthquake struck on February 6, 2023 with mainshock magnitude of 7.8 on the Richter scale and following with aftershock magnitude of 7.7 on the Richter scale and hundreds of aftershocks. Therefore, MA earthquakes has the sequence time between some minutes till some years and the damaged buildings of mainshock needs to be retrofitted [12, 13].

Since the collapse of structures may occur due to external loads such as impact force of adjacent structures [14-16] or internal loss of strengths due to weakness of structural elements such as connections defects or gusset plates [17-19], there is a need to consider the damaged effects on the retrofitting of structures. The use of FVDs and BRBs in retrofitting damaged buildings under seismic MA sequences is especially important as these devices can absorb energy and reduce the force transmitted to the structure during both the mainshock and aftershocks. Steel structures that use FVDs and BRBs have been shown to have significantly improved seismic performance compared to those without these devices [3, 7]. The use of FVDs and BRBs reduces the stress and deformation on the structural members, preventing damage or collapse during seismic activity. These devices can also be retrofitted to existing structures, making them a cost-effective solution for improving seismic performance [3, 7, 10]. The influence of FVDs and BRBs on the retrofitting of damaged buildings is significant. These devices can increase the strength and ductility of steel structures, improving their ability to withstand seismic activity. The retrofitting process involves a detailed analysis of the existing structure to determine the appropriate placement and design of the devices. The devices are then installed, and the structure is tested to ensure that it meets the desired level of seismic performance [20, 21].

In conclusion, FVDs and BRBs are effective devices for retrofitting damaged buildings under seismic MA sequences. They can significantly improve the seismic performance of steel structures by dissipating energy and reducing the force transmitted to the structure during seismic activity, while the implementing time of devices are lower than other proposed procedures. The cost of implementation and workforce is another important matter that should be considered during the retrofitting process. Retrofitting damaged buildings with FVDs and BRBs involves a detailed analysis of the existing structure and the design and placement of the devices. Overall, the use of FVDs and BRBs in retrofitting damaged buildings is a cost-effective solution for improving the seismic performance of steel structures. In this study, to take the advantages of these devices, a numerical modeling procedure for retrofitting steel damaged buildings is introduced, in which, the damaged building is modeled with its real condition after mainshock earthquake. In addition, it is possible to control the distribution of FVDs or BRBs along the floor levels to reduce the cost of retrofitting.

## 2 MODELS OF STRUCTURES

To properly introduce the proposed modeling approach, two low- to mid-rise steel frames with three-, and five-story floor levels were modeled according to Kazemi et al. [22, 23]. To model the steel frames, it was assumed that the structures had regular plan with five bays in each direction and it was possible to model them as 2D model having the leaning column to consider the p-delta effects (see more detail about modeling process in [24-26]). The frames were located in soil type D with seismic category II having 4 m floor height and 7.5 m bay length. To model frames, OpenSees [27] software was used, in which, the concentrate plastic hinges were assumed for structural members to determine their nonlinear behavior (more details regarding the implementing concentrate plastic hinges can be found in [22-26]). Figure 1 illustrates the structural details of three-, and five-story steel frames.

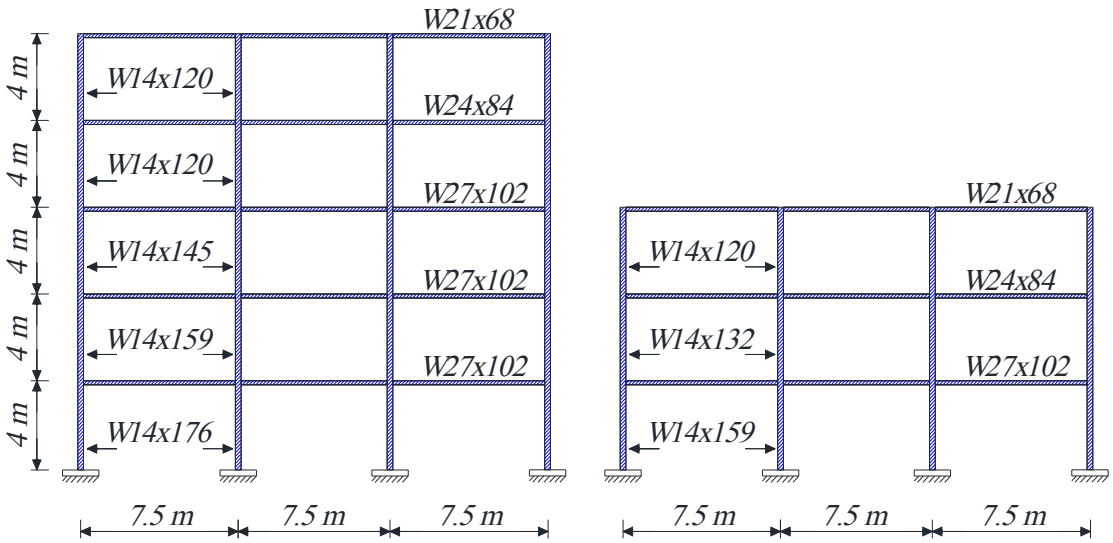


Figure 1: Low- to mid-rise steel frames with three-, and five-story floor levels.

## 3 RETROFITTING PROCEDURE

In this section, the retrofitting procedure is introduced, in which, the modeling of steel structures can be improved with the real condition of damaged structures. Figure 2 illustrates three main conditions of models in the proposed retrofitting procedure for steel damaged buildings under MA sequences. In the first condition, it is assumed that the model of structure

is prepared based on the programming code implemented in OpenSees [27] software, then, mainshock of the assumed MA is applied regarding the selected intensity measure of ground motion. The engineering demand of interstory drift ratio is defined to control the behavior of structure during the analysis. There may be a residual drift after imposing the mainshock. Therefore, the second condition is considered as damaged structural condition, in which, the retrofitting device should be implemented on. Therefore, according to the opinion of the structural designer, the kind of retrofitting device (i.e. FVD or BRB) and the distribution of the devices along floor levels are selected. It is possible to implement device on the all floor levels or specific floor level. In the third condition, the aftershock is applied to the retrofitted damaged structure. It is noteworthy that whole procedure of modeling, applying the MA sequence, and retrofitting are in the one model implemented in OpenSees [27] software; therefore, the real condition of structure after mainshock and its possible structural damages are considered in modeling. In other words, the results of this type of retrofitting procedure is accurate compared to those retrofitted structures that neglects the structural damages in modeling process.

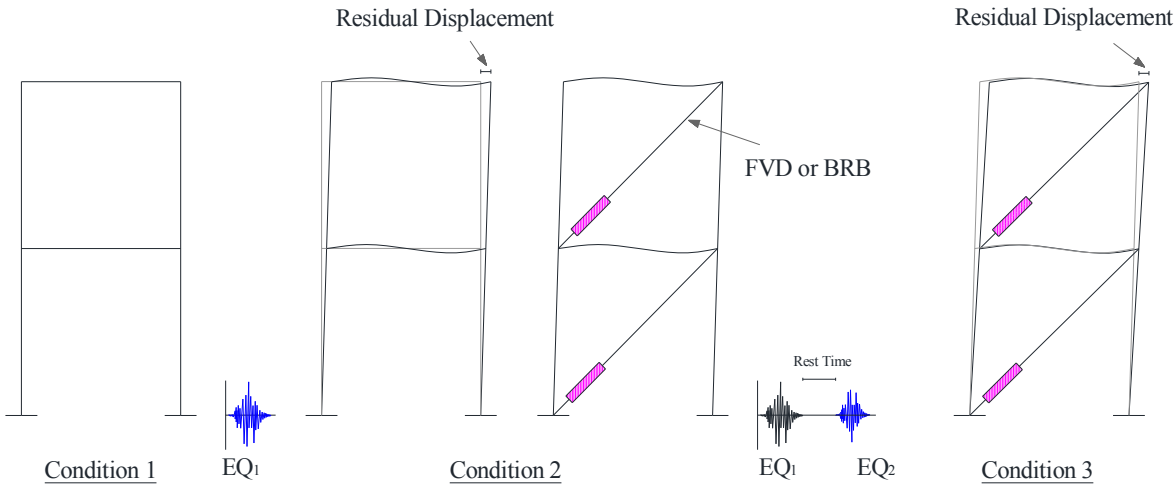


Figure 2: Proposed retrofitting procedure for steel damaged buildings under MA sequences.

## 4 RESULTS

To better compare the results of the proposed retrofitting process, two type of analysis known as nonlinear time-history analysis and Incremental Dynamic Analysis (IDA) [28, 29] were used. The MA sequence of Friuli earthquake (Tolmezzo station, Italy, 5/7/1976) was selected to perform nonlinear time-history analysis on three-, and five-story structures assuming FVDs and BRBs as retrofitting members, which the retrofitting procedure introduced in Figure 2 was applied in modeling. Figures 3 and 4 illustrate the interstory drift ratio-time history curve of the three-, and five-story structures assuming FVDs and BRBs as retrofitting members under MA sequence.

According to Figure 3, after applying mainshock, the three-story structure had a residual drift of 0.39% that is lower than the life safety allowable residual drift [7, 10]. It means that the structure still is able to resist the lateral loads and can be known as damaged structure. According to the procedure introduced in Figure 2, two retrofitting devices were implemented in modeling and then the aftershock is applied. Whole process is in the one model to consider the damages. The results showed that implementing FVDs and BRBs can considerably decrease the second residual drift of the three-story structure by 57.25% (from 1.31% to 0.56%) and 86.25% (from 1.31% to 0.18%), respectively, compared to the not retrofitted structure.

According to Figure 4, after applying mainshock, the five-story structure had a residual drift of 0.016% that is lower than the immediate occupancy allowable residual drift [7, 10]. Therefore, the small residual drift in the structure confirms the lower damages of structure after mainshock earthquake. After implementing FVDs and BRBs, the aftershock is applied and the second residual drift of the five-story structure has been reduced by 78.35% (from 1.94% to 0.42%) and 91.23% (from 1.94% to -0.17%), respectively, compared to the not retrofitted structure. Therefore, the results of analysis confirmed that the retrofitting approach proposed in this research can be effectively reduce the residual drift of structures, while the structural damages of structure after applying mainshock record was considered.

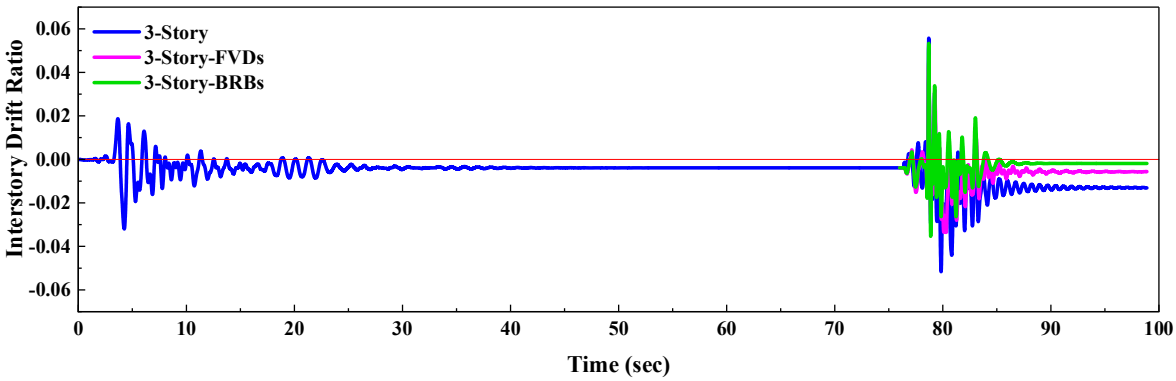


Figure 3: Interstory drift ratio-time history curve of the three-story structure assuming FVDs and BRBs as retrofitting members under MA sequence (Friuli earthquake).

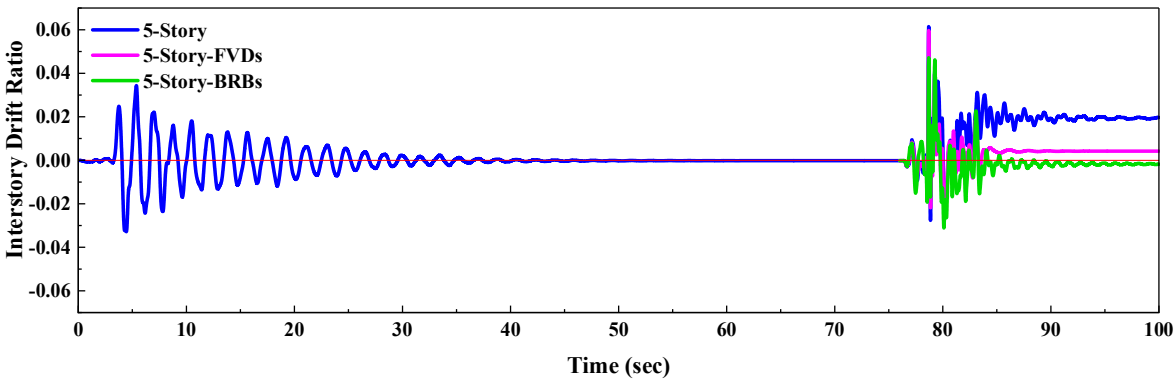


Figure 4: Interstory drift ratio-time history curve of the five-story structure assuming FVDs and BRBs as retrofitting members under MA sequence (Friuli earthquake).

It was assumed that the damaged structures meet the allowable life safety residual drift of 0.5% in the mainshock ground motions. Therefore, the proposed procedure applied for the IDAs of the damaged structures. Figure 5 illustrates the IDA curves of the three-story and five-story structures under ninety mainshock ground motions selected from [11-13]. Figure 6 compares the median of IDAs of the three-story and five-story structures under MA sequences. It can be seen that considered damage state can considerably affect the IDA curves and the median of IDAs, which confirms the importance of the considering the real condition of the structure in the modeling process. The results showed that the median of IDAs were reduced by 9.93% and 14.65% for the three-story and five-story structures under MA sequences considering the damage state of structures.

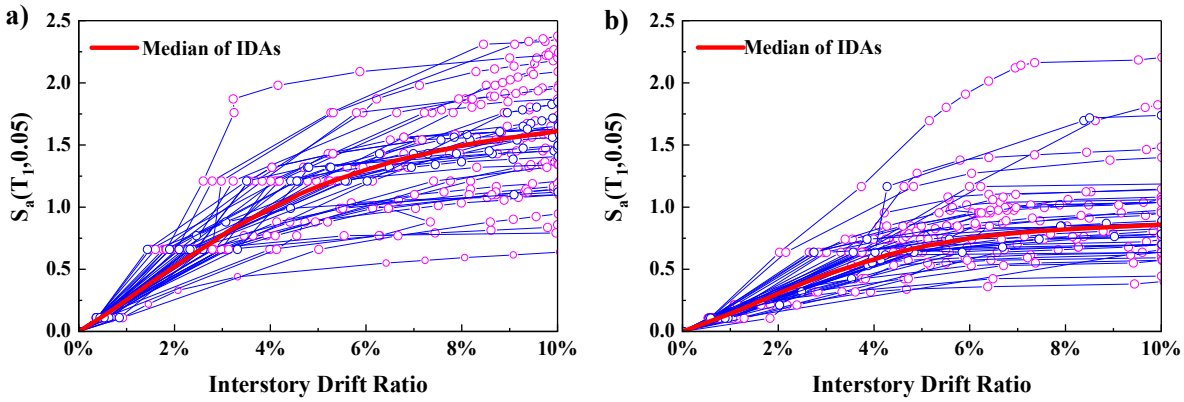


Figure 5: IDA curves of, a) three-story and, b) five-story structures under mainshock.

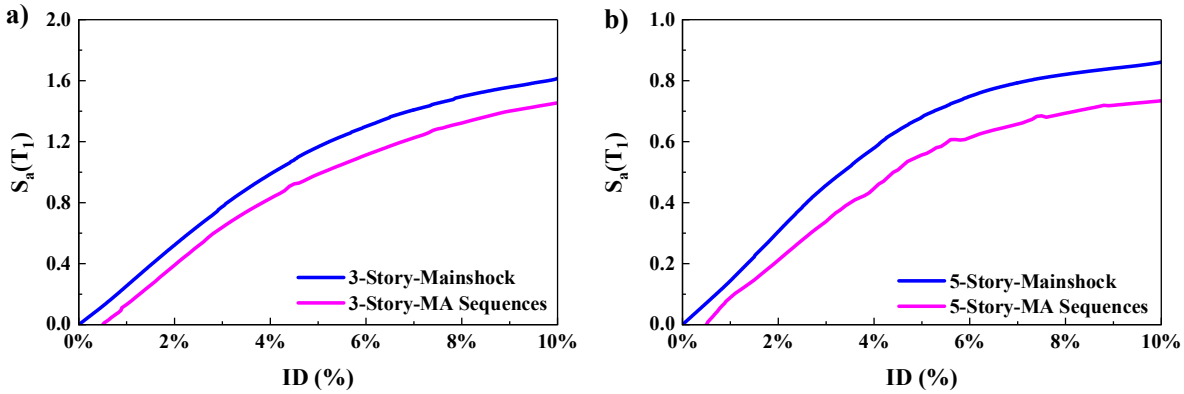


Figure 6: Median of IDAs of, a) three-story and, b) five-story structures under MA sequences.

## 5 CONCLUSIONS

This research proposed a modeling procedure for retrofitting steel damaged buildings with energy dissipation devices such as FVDs and BRBs. The results confirmed the significant effects of the damages on the results of analysis and the assumed retrofitting process can accurately model the damages of structures as it can be observed in real condition. The results showed that the modeling procedure can be applied for retrofitting structures in one model to reduce the time and efforts, while two type of analysis can be employed. In addition, it is possible to define the mainshock damage state in the modeling.

## 6 REFERENCES

[1] Yahyazadeh, A., and M. Yakhchalian. Probabilistic residual drift assessment of SMRFs with linear and nonlinear viscous dampers. Journal of Constructional Steel Research, 148: 409-421, 2018.

[2] Mohebi, B., Kazemi, F., and Yousefi, A. Seismic Response Analysis of Knee-Braced Steel Frames Using Ni-Ti Shape Memory Alloys (SMAs). In Proceedings of the 2022 Eurasian OpenSees Days (pp. 238-247), 2023.

[3] Kazemi, F., Mohebi, B., and Jankowski, R. Predicting the seismic collapse capacity of adjacent SMRFs retrofitted with fluid viscous dampers in pounding conditions. Mechanical Systems and Signal Processing, 161, 107939, 2021.

[4] Asgarkhani, N., Kazemi, F., and Jankowski, R. Optimal retrofit strategy using viscous dampers between adjacent RC and SMRFs prone to earthquake-induced pounding. Archives of Civil and Mechanical Engineering, 23(1), 1-26, 2023.

[5] Kazemi, F., Asgarkhani, N., Manguri, A., and Jankowski, R. Investigating an optimal computational strategy to retrofit buildings with implementing viscous dampers. International Conference on Computational Science (pp. 184-191). Springer, Cham, 2022.

[6] Hosseinzadeh, Sh., and B. Mohebi. Seismic evaluation of all-steel buckling restrained braces using finite element analysis." Journal of Constructional Steel Research 119, 76-84, 2016.

[7] Asgarkhani, N., Yakhchalian, M., and Mohebi, B. Evaluation of approximate methods for estimating residual drift demands in BRBFs. Engineering Structures, 224, 110849. 2020.
[8] Yakhchalian, M., Asgarkhani, N. and Yakhchalian, M. Evaluation of deflection amplification factor for steel buckling restrained braced frames. Journal of Building Engineering, 30, p.101228, 2020.
[9] Yakhchalian, M., Yakhchalian, M. and Asgarkhani, N. An advanced intensity measure for residual drift assessment of steel BRB frames. Bulletin of Earthquake Engineering, 19, pp.1931-1955, 2021.
[10] Kazemi, F., and Jankowski, R. Seismic performance evaluation of steel buckling-restrained braced frames including SMA materials. Journal of Constructional Steel Research, 201, 107750, 2023.
[11] Ruiz-García, J., and Negrete-Manriquez, J.C. Evaluation of drift demands in existing steel frames under as-recorded far-field and near-fault mainshock–aftershock seismic sequences. Engineering Structures, 33(2), pp.621-634, 2011.
[12] Silwal, B., and Ozbulut, O.E. Aftershock fragility assessment of steel moment frames with self-centering dampers. Engineering Structures, 168, pp.12-22, 2018.
[13] Yakhchalian, M., and Yakhchalian M. An advanced intensity measure for aftershock collapse fragility assessment of structures. Structures. Vol. 44, 2022.
[14] Kazemi, F., Mohebi, B., and Yakhchalian, M. Predicting the seismic collapse capacity of adjacent structures prone to pounding. Canadian Journal of Civil Engineering, 47(6), 663-677, 2020.
[15] Mohebi, B., Yazdanpanah, O., Kazemi, F., and Formisano, A. Seismic damage diagnosis in adjacent steel and RC MRFs considering pounding effects through improved wavelet-based damage-sensitive feature. Journal of Building Engineering, 33, 101847, 2021.
[16] Yazdanpanah, O., Mohebi, B., Kazemi, F., Mansouri, I., and Jankowski, R. Development of fragility curves in adjacent steel moment-resisting frames considering pounding effects through improved wavelet-based refined damage-sensitive feature. Mechanical Systems and Signal Processing, 173, 109038, 2022.
[17] Mohebi, B., Asadi, N., and Kazemi, F. Effects of Using Gusset Plate Stiffeners on the Seismic Performance of Concentrically Braced Frame. International Journal of Civil and Environmental Engineering, 13(12), 723-729, 2019.
[18] Kazemi, F., and Jankowski, R. Enhancing seismic performance of rigid and semi-rigid connections equipped with SMA bolts incorporating nonlinear soil-structure interaction. Engineering Structures, 274, 114896, 2023.
[19] Kazemi, F., Asgarkhani, N., and Jankowski, R. Probabilistic assessment of SMRFs with infill masonry walls incorporating nonlinear soil-structure interaction. Bulletin of Earthquake Engineering, 1-32, 2022.
[20] Del Gobbo, G.M., Blakeborough, A., and Williams, M.S. Improving total-building seismic performance using linear fluid viscous dampers. Bulletin of Earthquake Engineering, 16, pp.4249-4272, 2018.
[21] Lu, L. Application of buckling-restrained braces in the seismic control of suspension bridges. Earthquake Engineering and Engineering Vibration, 21(2), pp.543-557, 2022.
[22] Kazemi, F., and Jankowski, R. Machine learning-based prediction of seismic limit-state capacity of steel moment-resisting frames considering soil-structure interaction. Computers & Structures, 274, 106886, 2023.
[23] Kazemi, F., Asgarkhani, N., and Jankowski, R. Predicting seismic response of SMRFs founded on different soil types using machine learning techniques. Engineering Structures, 274, 114953, 2023.
[24] Mohebi, B., Kazemi, F., and Yousefi, A. Enhancing Seismic Performance of Semi-rigid Connection Using Shape Memory Alloy Bolts Considering Nonlinear Soil–Structure Interaction. In Proceedings of the 2022 Eurasian OpenSees Days (pp. 248-256), 2023.
[25] Kazemi, F., Asgarkhani, N. and Jankowski, R. Machine learning-based seismic response and performance assessment of reinforced concrete buildings. Archives of Civil and Mechanical Engineering, 2023.
[26] Kazemi, F., Asgarkhani, N., and Jankowski, R. Machine learning-based seismic fragility and seismic vulnerability assessment of reinforced concrete structures. Soil Dynamics and Earthquake Engineering, 166, 107761, 2023.
[27] McKenna, F., Fenves, G. L., Filippou, F. C., and Scott, M. H. Open system for earthquake engineering simulation (OpenSees). Berkeley: Pacific Earthquake Engineering Research Center, University of California, 2016.
[28] Mohebi B., Kazemi F., Asgarkhani N., Ghasemnezhadsani P., and Mohebi A. Performance of Vector-valued Intensity Measures for Estimating Residual Drift of Steel MRFs with Viscous Dampers, International Journal of Structural and Civil Engineering Research, Vol. 11, No. 4, pp, 2022. 79-83. doi: 10.18178/ijscer.11.4.79-83
[29] Kazemi F., Mohebi B., Asgarkhani N., and Yousefi A. Advanced Scalar-valued Intensity Measures for Residual Drift Prediction of SMRFs with Fluid Viscous Dampers, International Journal of Structural and Civil Engineering Research, Vol. 12, No. 1, pp. 20-25, 2023. doi: 10.18178/ijscer.12.1.20-25

COMPDYN 2023
9th ECCOMAS Thematic Conference on
Computational Methods in Structural Dynamics and Earthquake Engineering
M. Papadrakakis, M. Fragiadakis (eds.)
Athens, Greece, 12-14 June 2023

# VARIANTS OF VIBRO-ISOLATION IN TRAM TRACKS AND EVALUATION OF THEIR EFFECTIVENESS ENGINEERING

**F. Pachla[1], P. Stecz1[2], and T. Tatara[2]**

[1] Cracow University of Technology
31-155 Kraków, ul. Warszawska 24
filip.pachla@pk.edu.pl

[2] Cracow University of Technology
31-155 Kraków, ul. Warszawska 24
{piotr.stecz,Tadeusz.tatara}@pk.edu.pl

## Abstract

*The development of urban agglomerations makes it necessary to build new communication solutions. One of them is the construction of new tram lines or the renovation of degraded tracks. Activities related to the renovation of tracks result from numerous complaints from residents about the negative impact of vibrations generated by trams passing in the vicinity of inhabited buildings. The assessment of the impact of tram vibrations on the surrounding environment is an important aspect of tramway design and construction. The vibrations caused by the movement of trams can affect nearby buildings, structures, people, and the environment. The impact of tram vibrations on the surrounding environment can be evaluated through several methods, including numerical modelling, laboratory testing, and field measurements. The research concerned the vibrations of a selected representative building caused by trams. The building was erected using the traditional method. The building vibration measurements concerned three vibration components (two horizontal and a vertical component) and were performed by the rules specified in the standards. The source of vibrations was the passages of two types of trams with different speeds from 20 to 50 km/h. The analyzes focused on assessing the impact of the speed of trams and their types on building vibrations at two selected levels (ground level and third-floor level). The analysis of the test results shows that the vibration level of the building increases with the increase in the speed of the trams.*

**Keywords:** Buildings, Humans, Vibration Impact, RMS Analysis, Assessment Methods, Polish recommendations for the vibration's impact on structures and humans

## 1 INTRODUCTION

The recent growth in the use of the tram in urban areas highlights the need to investigate and mitigate the harmful effects on structures and humans in buildings. In general, the assessment of the impact of tram vibrations on the surrounding environment is an important aspect of tramway design and construction, as it can help ensure the safety and comfort of the people and the environment.

There are several methods to assess the impact of tram passages' origin vibrations on the surrounding. These vibrations can affect buildings nearby the tram lines and humans staying in buildings.

The numerical method is commonly used involving the use of computer software to simulate the vibrations caused by tram movements.

Another method is laboratory testing, which involves the use of exciters and laboratory equipment to simulate the transportation vibrations. This method can be used to study the behaviour of specific components of the tram and track system and to evaluate the impact of different design options on the vibration levels.

In-situ tests for transportation-induced vibrations refer to the measurement of ground-borne vibrations generated by vehicular traffic, such as trains and trams, in their actual operating environment. In-situ testing is an important step in the assessment of the impact of transportation-induced vibrations on structures and people. The results of these tests identify any potential problems and develop effective mitigation measures to reduce the impact of the vibrations. These tests are typically performed to assess the impact of the vibrations on nearby structures, such as buildings and underground utilities, and to evaluate the effectiveness of various mitigation measures, such as vibration isolation systems and track upgrades. Field measurements can also be used to assess the impact of tram vibrations on the surrounding environment. This involves the use of specific apparatus to measure the vibration levels in the field, such as accelerometers and seismographs. The results of the field measurements can be used to verify the accuracy of the numerical modelling and laboratory testing and to provide valuable data for the design and construction of the tramway. These measures can help to reduce the impact of tram vibrations on buildings and people, ensuring the safety and comfort of the surrounding environment. However, it is important to carefully assess the impact of each measure and to select the most appropriate approach for a given situation, taking into account the specific conditions and constraints of the site. Some of the common methods used for in-situ testing of transportation-induced vibrations include seismic measurements, ambient vibration measurements, field modal testing and structural monitoring [2].

In general, assessing the impact of tram vibrations on the surrounding environment is an important aspect of tramway design and construction, as it can help to ensure the safety and comfort of the people and the environment.

There are many ways to limit the impact of tram vibrations on buildings and people. These include the design of track and vehicle, soil improvement, vibration isolation systems, speed reduction and monitoring and maintenance. Limiting the impact of transportation vibrations on buildings and people can be achieved by base isolation, mass dampers, rubber bearings, air springs, vibration-absorbing pavements and acoustic barriers [3].

These vibration isolation systems can be effective in reducing the impact of transportation vibrations on buildings and people, but the specific type of isolation system required will depend on the specific conditions and constraints of the site [4]. The selection of an appropriate vibration isolation system should be based on a detailed assessment of the vibration levels, the sensitivity of the surrounding environment, and the overall design goals.

Several types of tramway tracks can be used in urban areas. Some of the most common types include grooved rail, flange-less rail, ballasted track, embedded track and concrete track slab [3]. Each type of tramway track has its advantages and disadvantages, and the choice of the track will depend on various factors such as the specific requirements of the project, cost, and local regulations.

In article may provide a comprehensive understanding of the impact of tramway vibrations on buildings and people. The research concerned the vibrations of a selected representative building caused by two types of trams with variable speeds from 20 to 50 km/h. The building vibration measurements concerned three vibration components (two horizontal and a vertical component) and were performed by the rules specified in the standards [5,6].

## 2 MEASUREMENTS

A series of tests were carried out to assess the impact of parameters related to moving trams on the neighbouring buildings. Masonry building was selected for the study. The building was erected with traditional technology.

The selected building is a residential building with four floors above ground, with a basement - see Figure 1. The shape of the building in the plan view is regular. The structure of the building is masonry made of ceramic brick. The distance from the axis of the tram track to the building's front wall is around 9 m.




Figure 1: Building No. 1 (Google Maps).

The research aimed to assess the impact of vibrations from the tram line on the structures of the building and the people inside. For this purpose, controlled runs with different speeds were carried out. Two types of trams were also used in the research: type 105N (compare figure 2) and type 120N (compare figure 3). The trams moved at speeds of 20, 30 and 50 km/h. The tests were performed by the standards [5, 6].




Figure 2: Wagon type 105N (https://tramwar.pl/u1238-85070a.html).




Figure 3: Wagon type 120N (https://tramwar.pl/u1238-85070a.html).

Three components of vibration acceleration were measured: two horizontal x and y components and a vertical z component. The x direction is perpendicular to the road axis, tram and subway tracks (this is the direction of vibration propagation to the building) and the y component is parallel to the road axis.

The x, y, and z symbols next to the sensor numbers correspond to the vibration component measured by the given sensor.

The impact of vibrations on the structure was measured in a rigid node of the structure at the ground level. The impact of vibrations on people was measured on selected floors in the middle of the ceiling span on a 30 kg measuring disc according to standard [6].

The following specialized apparatus was used in the research to measure the accelerations and vibration frequencies of a building:

- 393B12 type accelerometer PCBs,
- the electronic data registration system ESAM Traveler Plus,
- PA16000 EC Electronics signal conditioning system,
- the analyzer (recording and analyzing system) LMS SCADAS Mobile,
- measurement of data analysis software (Matlab 7.3).

## 3 RESULTS OF MEASUREMENTS

Tables 1 and 2 present selected recorded results of vibration acceleration measurements at measurement points for individual vibration components. Table 1 presents the results for the passage of the 105N-type wagon, and Table 2 presents the results for the passage of the 120N-type wagon. Tables 3 and 4 show the average values of accelerations for individual travel speeds, respectively for the 105N and 120N wagons.

| No. | Speed | Ground level measurement | | | 3rd-floor level - ceiling | |
|---|---|---|---|---|---|---|
| | km/h | x | y | z | y | z |
| | | $cm/s^2$ | $cm/s^2$ | $cm/s^2$ | $cm/s^2$ | $cm/s^2$ |
| 1 | 20 | 12.51 | 8.78 | 4.00 | 22.83 | 57.95 |
| 2 | 20 | 6.80 | 5.28 | 3.70 | 13.27 | 32.84 |
| 3 | 20 | 6.45 | 4.50 | 2.66 | 11.33 | 22.63 |
| 4 | 20 | 6.30 | 4.23 | 2.75 | 13.94 | 21.89 |
| 5 | 20 | 7.51 | 6.00 | 2.38 | 10.71 | 23.24 |
| 6 | 30 | 15.62 | 10.88 | 4.77 | 24.32 | 44.77 |
| 7 | 30 | 11.50 | 7.45 | 4.13 | 24.27 | 43.19 |
| 8 | 30 | 12.09 | 9.00 | 4.83 | 15.02 | 34.89 |
| 9 | 48 | 8.35 | 6.91 | 4.17 | 21.81 | 40.58 |
| 10 | 50 | 8.91 | 6.37 | 3.99 | 21.98 | 41.68 |
| 11 | 50 | 9.07 | 7.22 | 3.41 | 15.00 | 38.56 |

Table 1: Vibration measurements – wagon type 105N

| No. | Speed | Ground level measurement | | | 3rd-floor level - ceiling | |
|---|---|---|---|---|---|---|
| | km/h | x | y | z | y | z |
| | | $cm/s^2$ | $cm/s^2$ | $cm/s^2$ | $cm/s^2$ | $cm/s^2$ |
| 1 | 15 | 11.01 | 5.67 | 4.20 | 11.81 | 24.77 |
| 2 | 20 | 11.36 | 8.47 | 5.25 | 12.01 | 32.71 |
| 3 | 20 | 15.13 | 7.67 | 4.94 | 15.31 | 32.88 |
| 4 | 20 | 13.60 | 8.50 | 5.10 | 14.26 | 34.17 |
| 5 | 20 | 14.82 | 8.80 | 4.93 | 17.16 | 29.47 |
| 6 | 30 | 12.14 | 7.73 | 3.53 | 13.51 | 30.06 |
| 7 | 30 | 10.91 | 7.15 | 4.25 | 13.95 | 39.59 |
| 8 | 30 | 11.15 | 8.25 | 3.80 | 15.95 | 46.40 |
| 9 | 50 | 16.78 | 11.69 | 4.76 | 19.17 | 50.71 |
| 10 | 50 | 17.21 | 10.07 | 4.61 | 18.09 | 54.11 |
| 11 | 50 | 16.36 | 10.33 | 4.59 | 18.12 | 52.44 |

Table 2: Vibration measurements – wagon type 120N

| Speed | Ground level measurement - mean acceleration | | | 3rd-floor level - ceiling mean acceleration | |
|---|---|---|---|---|---|
| km/h | x cm/s$^2$ | y cm/s$^2$ | z cm/s$^2$ | y cm/s$^2$ | z cm/s$^2$ |
| 20 | 7.91 | 5.76 | 3.10 | 14.42 | 31.71 |
| 30 | 13.07 | 9.11 | 4.58 | 21.20 | 40.95 |
| 50 | 8.78 | 6.83 | 3.86 | 19.60 | 40.27 |

Table 3: Vibration measurements – mean values– wagon type 105N

| Speed | Ground level measurement - mean acceleration | | | 3rd-floor level - ceiling mean acceleration | |
|---|---|---|---|---|---|
| km/h | x cm/s$^2$ | y cm/s$^2$ | z cm/s$^2$ | y cm/s$^2$ | z cm/s$^2$ |
| 20 | 13.18 | 7.82 | 4.88 | 14.11 | 30.80 |
| 30 | 11.40 | 7.71 | 3.86 | 14.47 | 38.68 |
| 50 | 16.78 | 10.70 | 4.65 | 18.46 | 52.42 |

Table 4: Vibration measurements – mean values– wagon type 120N

Tables 1 - 4 clearly show the difference in the intensity of interactions with two different types of trams. In the case of the 105N tram, vibrations are amplified at a speed of 30 km/h. A slightly different nature of the impact has a tram type 120N, where vibration accelerations are the smallest at 30 km/h.

Figures 4 and 5 show the results of the average values of vibration accelerations on the building structure at the ground level, respectively for the 105N and 120N wagons. The results show the difference in the characteristics of the excitation with different types of trams.

Figures 6 and 7 show the average values of vibration accelerations on the selected floor of the 3rd floor.

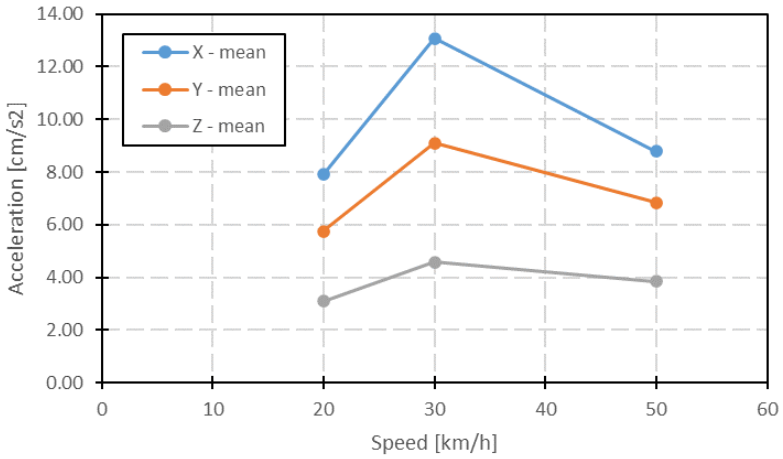


Figure 4: Mean values of accelerations on the ground level - wagon type 105N

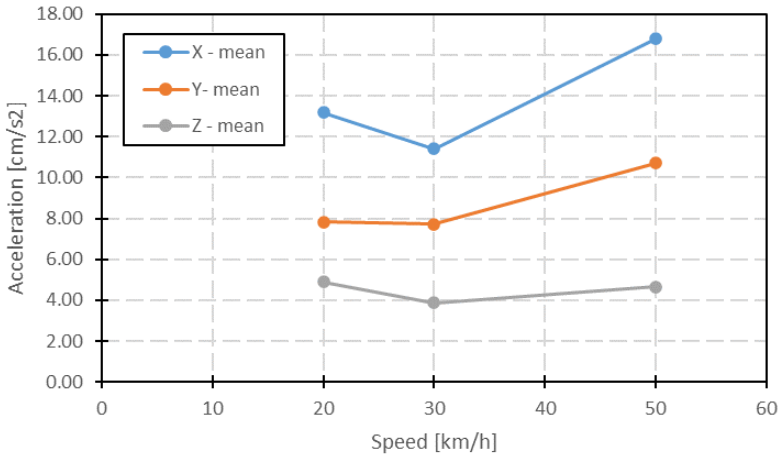


Figure 5: Mean values of accelerations on the ground level - wagon type 120N

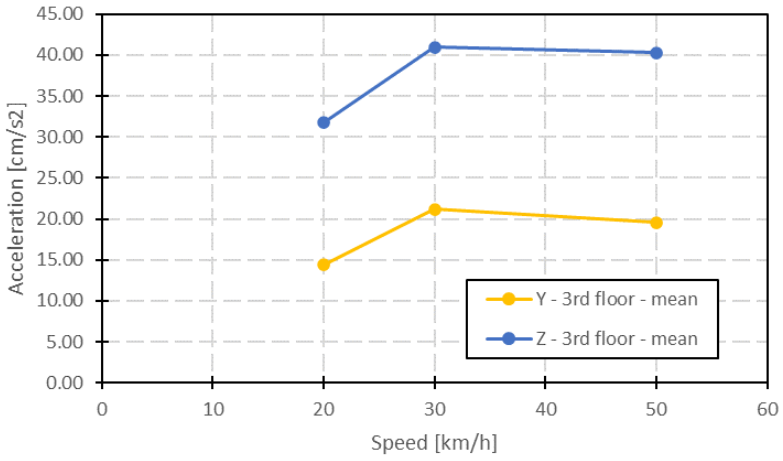


Figure 6: Mean values of accelerations on 3rd-floor level - wagon type 105N

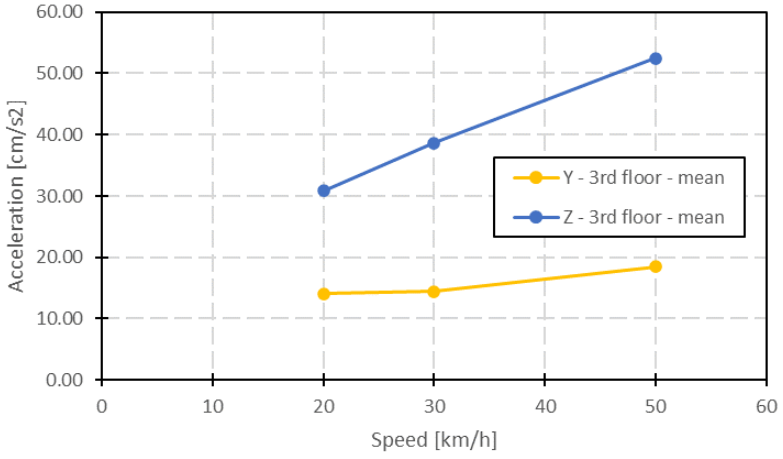


Figure 6: Mean values of accelerations on 3rd-floor level - wagon type 120N

The analysis of the results presented in tables 1 - 4 and figures 6 and 7 allows us to conclude that with the increase in speed, the level of vibration acceleration on people in the building increases. The increase in acceleration is not directly proportional to the speed of the tram. In the case of the 105N tram, a similar level of vibration acceleration was recorded for the speed of 30 and 50 km/h. In the case of the 120N tram, the vibration level increases more significantly with increasing speed.

## 4 CONCLUSIONS

The paper presents selected results of the impact of vibrations on the building structure and people in the building from the nearby tram line. The conclusions were based on field research on a selected building located approximately 9 m from the tram line.

During the tests, vibration accelerations were measured at the ground level and on the selected ceiling of the 3rd floor. The measurements were carried out by the current standards for measuring the impact of vibrations on the structure of buildings [5] and people in buildings [6]. The tests were carried out by an accredited laboratory.

The work analyzes the influence of the speed and type of wagon on the level of generated vibrations. A significant influence of the speed of the tram on the level of generated vibrations was found. Also, the type of wagon has a significant impact on the impact of vibrations on the structure of the building and the people staying in it. The conducted tests can be the basis for the selection of appropriate solutions to minimize vibrations, such as vibroinsulating mats, block supports, and rail pads.

## REFERENCES


[1] J. Real, P. Martínez, L. Montalbán, A. Villanueva, Modelling vibrations caused by tram movement on slab track line. *Mathematical and Computer Modelling*, **54(1-2)**, 280-291, 2011.

[2] P. M. Fernández, I. V. Sanchís, F. B. Rojas, R. I. Franco, Monitoring and analysis of vibration transmission for various track typologies. A case study, *Transportation Research Part D: Transport and Environment*, 24, 98-109, 2013.

[3] J. Real, C. Zamorano, T. Asensio, T. Real, Study of the mitigation of tram-induced vibrations on different track typologies. *Journal of Vibroengineering*, **15(4)**, 2057-2075, 2013.

[4] M. Cik 1, M. Lienhart, P. Lercher, Analysis of Psychoacoustic and Vibration-Related Parameters to Track the Reasons for Health Complaints after the Introduction of New Tramways. *Applied Sciences*, **6**, 2016.

[5] PN-B-02170:2016-12 Assessment of the harmfulness of vibrations transmitted through the ground to buildings.

[6] PN-B-02171:2017-06 Assessment of the impact of vibrations on people in buildings.

COMPDYN 2023
9th ECCOMAS Thematic Conference on
Computational Methods in Structural Dynamics and Earthquake Engineering
M. Papadrakakis, M. Fragiadakis (eds.)
Athens, Greece, 12-14 June 2023

# DEVELOPMENT OF A COMPLIANT MECHANISM TO ISOLATE THE BASE VIBRATIONS AND MINIMIZE THE SHOCK RESPONSE USING AN OPTIMIZED DYNAMIC MATHEMATICAL MODEL

**Kazım Yüksel**[1,2]**, Ata Muğan**[2]

[1] ASELSAN A.Ş.
06830, Ankara, Turkey
kazimyuksel@aselsan.com.tr

[2] Department of Mechanical Engineering, Istanbul Technical University
34467, İstanbul, Turkey
{yukselka20, mugan}@itu.edu.tr

## Abstract

*In high-precision ground-based electo-optical object tracking, physical shock absorption and random vibration isolation devices play a critical role. These systems require three degrees of freedom translational shock absorbers in order to maintain exact orientation with the ground frame to achieve high precision angular position since any angular deviations that are unaccounted for can result in irreparable loss of sight of the object being tracked. Parallel manipulator-based absorption systems that have been currently in use consist of numerous hard to manufacture high precision backlash-free components and external springs that require protection against harsh environmental conditions and periodic maintenance. In this study, we focused on designing and optimizing maintenance-free flexure based compliant shock absorber mechanism with center of percussion optimized linkage that minimizes shock response. Linkage and flexure parameters were optimized in order to achieve minimal acceleration transmission while maintaining the orientation. A single degree of freedom system was designed and optimized. The Lagrangian method was used to derive equations of motion, and simulations were conducted based on these. This study put forth a fundamental framework for compliant translation shock absorber mechanism optimization and demonstrate in right configuration, with appropriately selected masses and optimized link parameters, that highly effective monolithic shock absorber and vibration isolation system can be achieved.*

**Keywords:** Translational Shock Absorber, Vibration Isolator, Compliant Mechanism, Center of Percussion, Optimum Design.

# 1 INTRODUCTION

Environmentally challenging engineering applications require vibration isolation and shock absorption measures in order to protect sensitive equipment. In majority of these engineering applications, commercially available simplistic twisted steel wire rope isolators, metal mesh dampers, rubber viscoelastic dampers or bellow type air springs suffice the need. Wire rope isolators consists of looped twisted cables that dissipates energy by friction of the steel fibers [1]. Viscoelastic dampers, which are generally manufactured using high damping silicone, rubber or neoprene, dissipates energy using internal friction. These systems act as 6 degrees of freedom isolators. Lateral loading of such systems results in pitch and roll motion of the system. If the system is on a vehicle, turning motion results in yaw motion of the system relative to the base frame. Optical tracking devices require 3 degrees of freedom translational isolators in order to maintain exact orientation with ground frame to achieve high precision angular position since in 6 degrees of freedom passive systems, any angular deviations that are unaccounted for may result in irreparable loss of sight of the object being tracked [2]. In rotational stabilization systems, pointing vector of the system relative to ground frame is generally calculated using data from microelectromechanical systems (MEMS) based inertial measurement unit. Tuning fork based MEMS gyroscopes are susceptible to impulsive loading and vibrations which generates unwanted noise in readings [3]. These noises can result in failure of stabilization platform. Unwanted vibrations in MEMS device can be eliminated with isolators but use of 6 degrees of freedom system isolators mentioned above can result in rotation of coordinate system which is critical to the reading of velocities. Translational vibration isolators and shock absorbers can solve the stated problems.

In this study, single degree of freedom linkage system with revolute flexure bearings was designed and optimized. Lagrangian method was used to derive equations of motion of translational manipulator with link mass and inertia effects. Based on the equations of motion, Simulink model was built in order the optimize the shock response of the system. Screw theory based numerical modal analysis method [4] was used to iteratively optimize the link and flexure parameters. Mechanism design and equation of motion derivation of the mechanism are given in Section 2. Simulation results for the initial and optimized structure are given Section 3.

# 2 MECHANISM DESING AND EQUATION OF MOTION

A single degree of freedom shock absorber mechanism with symmetric linkages was designed. The mechanism consists of rigid links and flexure joints acting as revolute joints with torsional springs. A similar mechanism layout without flexures was used by Zeng et al. [5] that investigated the quasi-zeros stiffness effect as a part of vibration isolation method where they neglected the link masses and inertias. Quasi-zero stiffness effects are out of scope of this study where main target is optimization of link masses in order to achieve minimal acceleration transmission in payload mass.

## 2.1 Mechanism design and optimization parameters

Layout of the single degree of freedom mechanism with symmetric linkage and parameters are shown in Figure 1. Here, $m_1$ and $m_2$ are the link masses. $m_p$ is the payload mass. $I_1$and $I_2$ are the link inertias. $L$ is the link length. $L_{cm,1}$ and $L_{cm,2}$ are the center of mass distance from pivot points. $y_b$ is the base excitation and the $y_p$ is the payload displacement. $\theta_0$ is the initial configuration angle of the system and $\theta$ is the deviation from initial angle. Joint torsional stiffness and viscous damping parameters are denoted by $K_\theta$ and $B_\theta$, respectively. The same joint parameters were used for all three joints. Initial angle $\theta_0$ was selected as $45°$.

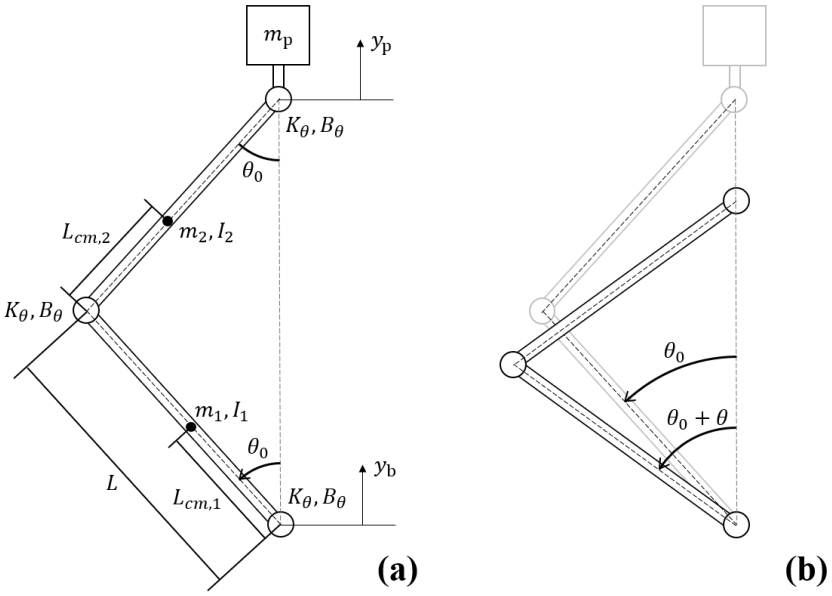


Figure 1: Designed 1 DOF Mechanism: mechanism parameters (a) and angle parameters (b).

The mechanism layout given in the Figure 1 does not constrain the motion of the payload to single degree of freedom in three-dimensional space. The mechanism is capable of motion in three degrees of freedom. In order to fully constraint the mechanism in unwanted motion, axisymmetric mechanism with at least three planar mechanism is required. Initial axisymmetric solid model with three planer linkages prior to optimization is given in Figure 2 below. Revolute joint selection criteria and calculations are given in Section 2.4.

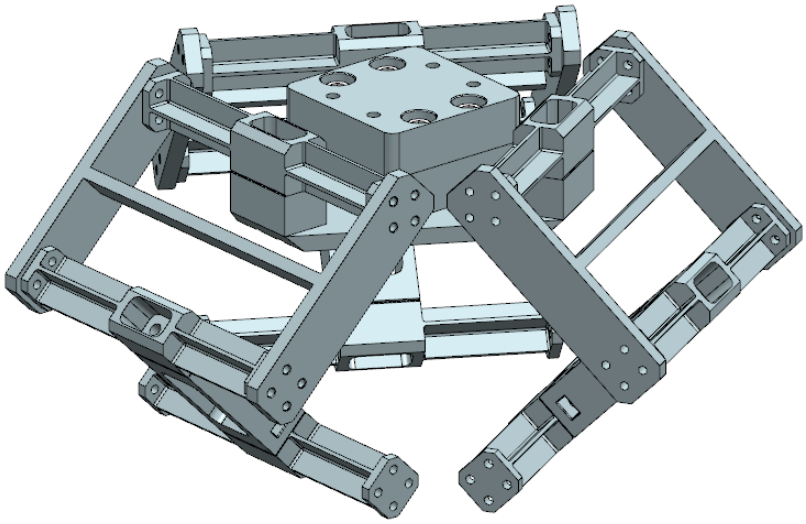

Figure 2: Designed 1 DOF Mechanism: mechanism parameters (a) and angle parameters (b).

## 2.2 System energy and equation of motion

In order to simulate the response of the system with base excitation, equation of motion of the system was required. The mechanism that was outlined in the Section 2.1 is an axisymmetric system. Therefore, modelling of the entire system was not required. One third of the system given in Figure 1 was sufficient to model the system. The parameters that were defined in

Section 2.1 was used in modelling of the system. Equation of motion of the mechanism was derived using Lagrange's energy equation which is expressed as:

$$\frac{d}{dt}\left(\frac{\partial KE}{\partial \dot{q}_i}\right) - \frac{\partial KE}{\partial q_i} + \frac{\partial PE}{\partial q_i} + \frac{\partial DF}{\partial \dot{q}_i} = Q_i \tag{1}$$

where $KE$, $PE$ are respectively kinetic and potential energies, $DF$ is the dissipative function, $q_i$ is the generalized coordinate number $i$ and $Q_i$ is the generalized force acting on the generalized coordinate number $i$. Since it is a single degree of freedom passive system, generalized force can be assumed zero. The energy equations of system are evaluated with $\theta$ as the generalized coordinate.

Kinetic energy of the system is evaluated as:

$$\begin{aligned} KE \;=\; & \left[\frac{m_1}{2} + \frac{m_2}{2} + \frac{m_p}{2}\right]\dot{y}_b{}^2 \\ & + \left[\frac{I_1}{2} + \frac{I_2}{2} + \frac{m_1 {L_{cm,1}}^2}{2} + \frac{m_1\left({L_{cm,1}}^2 + L^2\right)}{2} - m_2 L L_{cm,2}\right. \\ & \left. + \left(2m_2 L L_{cm,2} + 2m_p L^2\right)\sin^2(\theta_0+\theta)\right]\dot{\theta}^2 \\ & + \left[\left(-m_1 L_{cm,1} - m_2\left(L + L_{cm,2}\right) - 2m_p L\right)\sin(\theta_0+\theta)\right]\dot{y}_b\dot{\theta} \end{aligned} \tag{2}$$

Potential energy of the system is evaluated as:

$$PE \;= \frac{1}{2}K_\theta\theta^2 + \frac{1}{2}K_\theta(2\theta)^2 + \frac{1}{2}K_\theta\theta^2 = 3K_\theta\theta^2 \tag{3}$$

Dissipative function of the system is evaluated as:

$$DF \;= \frac{1}{2}B_\theta\dot{\theta}^2 + \frac{1}{2}B_\theta\left(2\dot{\theta}\right)^2 + \frac{1}{2}B_\theta\dot{\theta}^2 = 3B_\theta\dot{\theta}^2 \tag{4}$$

Generalized force is evaluated as:

$$Q_1 \;= -2LF_{\mathrm{y}}\sin(\theta_0+\theta) \tag{5}$$

By using eq. (1), equation of motion of the designed system was evaluated as:

$$\left[I_{\mathrm{eq}}(\theta)\right]\ddot{\theta} + \left[N_{\mathrm{eq}}(\theta)\right]\dot{\theta}^2 + \left[B_{\mathrm{eq}}\right]\dot{\theta} + \left[K_{\mathrm{eq}}\right]\theta = \left[M_{\mathrm{b}}(\theta)\right]\ddot{y}_{\mathrm{b}} \tag{6}$$

where,

$$\begin{gathered} I_{\mathrm{eq}}(\theta) = I_1 + I_2 + m_1{L_{cm,1}}^2 + m_1\left({L_{cm,1}}^2 + L^2\right) - 2m_2 L L_{cm,2} \\ + \left(4m_2 L L_{cm,2} + 4m_p L^2\right)\sin^2(\theta_0+\theta) \\ N_{\mathrm{eq}}(\theta) = \left(4m_2 L L_{cm,2} + 4m_p L^2\right)\sin(\theta_0+\theta)\cos(\theta_0+\theta) \\ B_{\mathrm{eq}} = 6B_\theta \\ K_{\mathrm{eq}} = 6K_\theta \\ M_{\mathrm{b}}(\theta) = \left(m_1 L_{cm,1} + m_2\left(L + L_{cm,2}\right) + 2m_p L\right)\sin(\theta_0+\theta) \end{gathered} \tag{7}$$

Equation (6) gives the relationship between base excitation acceleration and link angle. Payload's position and acceleration was calculated using the trigonometric relationship in the symmetric linkage. Payload position can be calculated as $y_p = y_b + 2L\cos(\theta_0 + \theta)$.

### 2.3 System transfer function and center of percussion

In a single rigid body system with a finite mass and inertia, any impulsive load on the body will result in translation and rotation of the body in global frame, which means the motion of the system can be converted into rotation around an instantaneous rotation center. For rigid body that is connected to a pivot, if the instantaneous rotation center for the applied load coincides with the pivot, point where the impulsive force is applied is called center of percussion. At the instance of impulsive force application, pivot point will experience zero reaction force [6]. Since the instantaneous rotation center depend on center of mass, mass and inertia of the rigid body; center of percussion point can be optimized. This concept of zero reaction force by center of percussion optimization was used by Atik et al.[7] to design an optimal simple pendulum wishbone suspension system with minimal transmissibility to increase ride comfort. But in a compound linkage mechanism, center of percussion optimization of each link on its own does not guarantee the system's optimization. Garoi et al.[8] showed that in a compound link mechanism, system response tends to approach a finite value as frequency increases. This asymptotic value can be calculated using the transfer function of the compound system. In order to calculate the linear system transfer function, equation of motion of the system given in eq. (6) can be linearized by assuming $\dot{\theta}^2$ is negligible. Linear system's payload displacement to unit base excitation transfer function is evaluated as:

$$H(s) = \frac{Y_p(s)}{Y_b(s)} = \frac{\left(I_{\mathrm{eq}}(\theta_0) - A(\theta_0)\right)s^2 + B_{\mathrm{eq}}s + K_{\mathrm{eq}}}{I_{\mathrm{eq}}(\theta_0)s^2 + B_{\mathrm{eq}}s + K_{\mathrm{eq}}} \tag{8}$$

where $A(\theta_0)$ is,

$$A(\theta_0) = \left(2m_1 L L_{cm,1} + 2m_2 L\left(L + L_{cm,2}\right) + 4m_p L^2\right)\sin^2(\theta_0)$$

As it can be seen in the eq. (8), at high frequencies, system response asymptotically approaches to $\left(I_{\mathrm{eq}} - A\right)/I_{\mathrm{eq}}$ term. In order to minimize the response of the system with a decay at high frequencies, order of the numerator has to be reduced. Therefore, center of percussion criteria of the designed system expressed as:

$$I_{\mathrm{eq}}(\theta) - A(\theta) = 0 \tag{9}$$

By applying an initial angle of 45°, the equation is reduced to:

$$\left(I_1 + m_1 L_{cm,1}\left(L_{cm,1} - L\right)\right) + \left(I_2 + m_2 L_{cm,2}\left(L_{cm,2} - L\right)\right) = 0 \tag{10}$$

which is the mechanism's percussion center condition with given initial angle condition. The terms in the equation corresponds to the percussion center condition of a single rigid body. Designed mechanism's center of percussion can be optimized either by optimizing each link on its own or by optimizing entire mechanism. It is important to state that 45° initial angle is a

special case of the mechanism where one can optimize the linkages individually because the links are perpendicular. For any other initial angle, optimizing each link on its own will not result in an optimized mechanism.

### 2.4 Flexure joints and stiffness calculation

Designed link mechanism uses revolute joints with torsional springs. Compliant counterpart of this joint is revolute flexure joints. Wide variety of revolute flexure joints exist in literature [9].Two commonly used joint types in industry are butterfly flexure and cross axis blade flexure joints which are shown in Figure 3. Both flexures are capable of large motion range. Cross axis blade flexure does a rolling motion instead of pure rotation. Therefore, a parasitic displacement is introduced to the mechanism. Off-axis stiffness of the both flexures degrade drastically as the joint rotates. In order for the designed mechanism to perform as single degree of freedom translational system, revolute flexure joint has to have near zero motion at axes other than designed revolute axis.

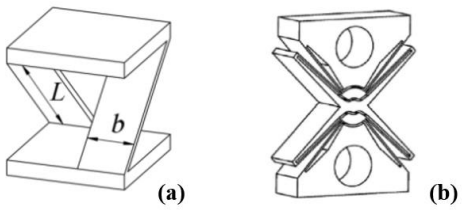


Figure 3: Revolute Flexure Joints. Cross Axis (a) and Butterfly (b).

Trease et al. [10] proposed a compact revolute joint capable of large deflection with cruciform cross section. Due to symmetry of the joint, it has pure rotation capability with zero axis drift in entire motion range while still maintaining large off-axis stiffness. Due to compactness and superior performance as revolute joint, cruciform cross section joint was selected to be used in the system. Layout and dimensional parameters of the joint given in Figure 4 below.

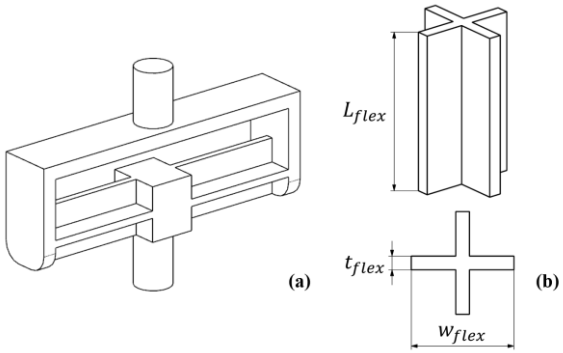


Figure 4: Cruciform Flexure Joint. Layout (a) and dimensional properties (b).

Proposed joint has two symmetric flexure elements with equal torsional stiffness Torsional stiffness of the single flexure joint with unconstrained boundaries is calculated with:

$$K_\theta = \frac{GJ}{L_{flex}} \tag{11}$$

where $G$ is the shear modulus of the material, $L_{flex}$ is the length of the flexure and $J$ is the torsion constant of the cross section instead of polar inertia since the cross section is non-circular. Torsion constant for the cruciform cross-section can be approximated as [11]:

$$J = \left(\frac{w_{flex}}{\mathrm{t}_{flex}} - 0.373\right)\frac{2{t_{\mathrm{flex}}}^4}{3} \tag{12}$$

where $w_{\mathrm{flex}}$ is the width and $t_{\mathrm{flex}}$ is the thickness of the flexure. When the analytical stiffness calculated with eq.(10) and stiffness derived from finite element method (FEM) model compared, analytical model under estimated the stiffness. Since proposed revolute joint has non-circular cross section with fixed-clamped boundary conditions, end planes of the flexure cannot deform freely, restraint warping takes place which increases the stiffness of the flexure. Torsional stiffness of the flexure joint with constrained ends with warping effect is calculated with [12]:

$$K_\theta = \left(\frac{\beta L_{flex}}{\beta L_{flex} - 2\tanh\left(\frac{\beta L_{flex}}{2}\right)}\right)\frac{GJ}{L_{flex}} \tag{13}$$

where $\beta = \sqrt{GJ/EC_w}$. $E$ is the Young's Modulus, $G$ is the shear modulus and $C_w$ is the warping constant of the cross-section. The parameter $\beta$ is both dimensional and material property. For thin-walled closed sections, warping is usually small which is generally neglected [13]. But as the $L_{\mathrm{flex}}/w_{\mathrm{flex}}$ ratio of flexure link decreases, dominance of warping effects increases compared to torsion. Since warping constant of closed sections are generally neglected, analytical formulation of warping constant for cruciform cross-section could not be found in literature survey, therefore 2D finite element method (FEM) is used to calculate section parameters for a wide variety of dimensional parameters. Curve fitting is applied on 2D FEM data. Dimensional constant for the warping modification can be approximated as:

$$\sqrt{\frac{J}{C_w}} = \frac{1}{w_{flex}}\left(36.3\left(\frac{w_{flex}}{\mathrm{t}_{flex}}\right)^{-2.454} + 6.931\right) \tag{14}$$

Aluminum flexure joint was modelled in ANSYS with Young's Modulus of 71GPa and shear modulus of 26.692GPa. Torsional stiffness values of the revolute flexure joint proposed by Trease et al. [10] is compared with warping modified torsional stiffness and FEM results. Comparison of results is given in Table 1. As the $L_{\mathrm{flex}}/w_{\mathrm{flex}}$ ratio of flexure increases, warping effects become negligible. But becomes dominant as the $L_{\mathrm{flex}}/w_{\mathrm{flex}}$ ratio decreases. For compact flexure joints, torsional stiffness formulation alone can result in wrong modal frequencies since stiffness value can be lower.

| L (mm) | w (mm) | t (mm) | FEM (Nm/rad) | Warping Modified Stiffness (Nm/rad) | Conventional Torsional Stiffness (Nm/rad) |
|---|---|---|---|---|---|
| 64 | 32 | 1 | 11.613 | 11.494 | 8.794 |
| 64 | 32 | 2 | 90.982 | 90.737 | 69.519 |
| 64 | 32 | 4 | 686.847 | 703.175 | 542.874 |
| 640 | 32 | 1 | 0.894 | 0.901 | 0.879 |
| 640 | 32 | 2 | 7.022 | 7.118 | 6.952 |
| 640 | 32 | 4 | 53.650 | 55.554 | 54.287 |

Table 1: Torsional stiffness comparison of cruciform cross section for different dimensional parameters.

## 3 ANALYSIS AND OPTIMIZATION

The parametric model of the axisymmetric mechanism given in Figure 2 was built for optimization. For optimization case study, design choices, constants, optimization parameters are given as bullet points below:

- Shock isolator was designed with 2.3kg payload.
- 5Hz natural frequency was set as the optimization target.
- As shock input, 20g 11ms sawtooth profile was applied as base excitation.
- Link length $L$, was bounded between 60mm and 80mm with 1mm increments.
- Flexure length $L_{flex}$, was set as constant at 60mm.
- Flexure width $w_{flex}$ was bounded between 24mm and 40mm with 1mm increments.
- Flexure thickness $t_{flex}$ was bounded between 1.2mm and 3.6mm with 0.4mm increments due to 3D printer's capability of layer height increments.
- 3D print material PETG was selected as flexure material with Young's modulus of 1.6GPa, shear modulus of 579.7MPa and density of 1270 kg/m$^3$.
- 3D print material PLA was selected as link and payload base plate material with density of 1230 kg/m$^3$.
- Linkage was assumed as rigid.
- In order to optimize the percussion center of the mechanism according to eq.(10), only Link #1's center of mass was optimized with counterweights that were added to end points of Link #1.
- Torsional stiffness of the flexures are assumed to be linear.

The mechanism is parametrically designed in MATLAB algorithm that is based on the screw theory based meshless modal analysis method developed by Hopkins et al. for flexure analysis [4]. Payload mass is applied to the system as point mass. Optimization algorithm used analytical model of the mechanism to match the system natural frequency to optimization target using mass and inertia parameters generated by MATLAB algorithm. After frequency optimization, algorithm used brute force calculate counterweight mass to maintain center of percussion criteria given in eq. (9). The addition of counterweight changes the equivalent mass of the system which in return changes the natural frequency of the system. Therefore, frequency matching

and brute force center of percussion optimization steps repeated until parameters converged. Optimized structure with added counterweight is given in Figure 5 below. The parameters of the optimized structure are given in Table 2.

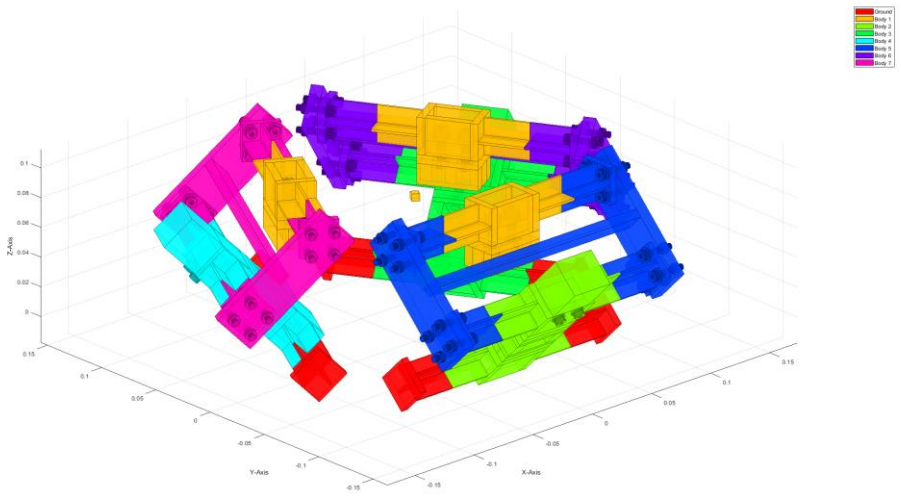

Figure 5: Parametrically designed and optimized 1 DOF mechanism with counterweight added to Link #1.

| Optimization parameter | Parameters after optimization |
|---|---|
| $L$ | 65 $mm$ |
| $L_{cm,1}$ | 44.1 $mm$ |
| $L_{cm,2}$ | 32.5 $mm$ |
| $m_1$ | 173.4 $g$ |
| $m_2$ | 165.9 $g$ |
| $I_1$ | 181.3 $kgmm^2$ |
| $I_2$ | 153.8 $kgmm^2$ |
| $L_{flex}$ | 60 $mm$ |
| $w_{flex}$ | 25 $mm$ |
| $t_{flex}$ | 1.6 $mm$ |
| Natural Frequency | 5.06 Hz |

Table 2: Mechanism parameters after optimization.

In order to compare the response of the system prior to optimization and after, bode plots of the payload displacement to unit base excitation transfer function are given in Figure 6 below, in which initial system, optimized system and system with excessive counterweight which eight times the mass of the optimized counterweight, are compared. As it can be seen in the plots, response of the initial system converges to constant value at high frequencies whereas center of percussion optimized system has decayed.

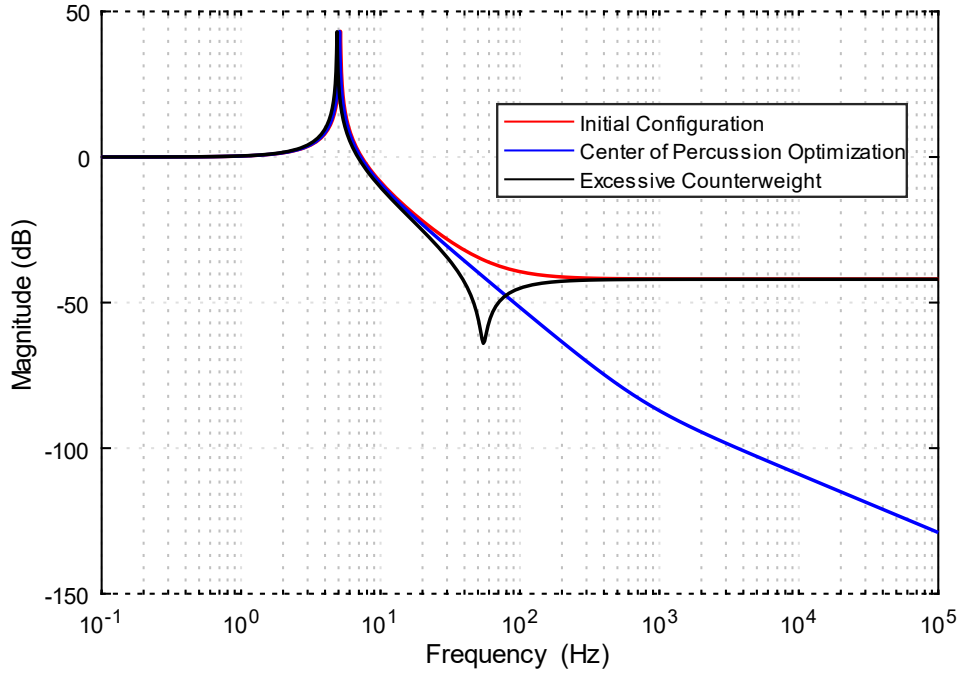


Figure 6: Comparison of the system response for different configurations.

In order to compare the shock response of the systems shown in Figure 6, Simulink model of system was built using the equation of motion. Layout of the Simulink model can be seen in Figure 7.

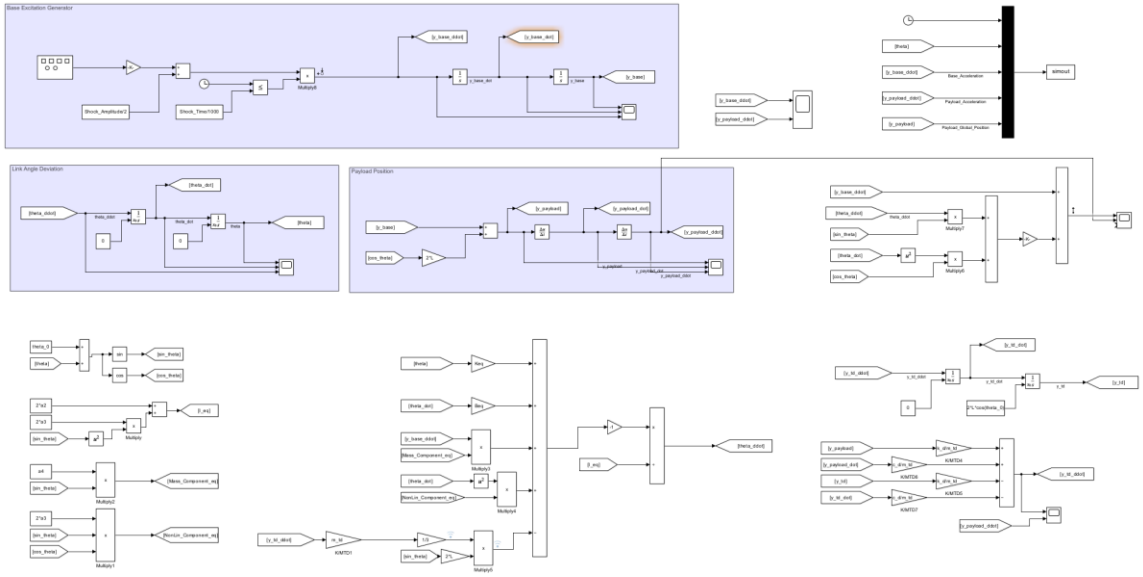

Figure 7: Layout of the Simulink model.

The shock response of the system with different initial condition are given below in Figure 8, Figure 9 and Figure 10. Shock duration comparison with different initial conditions is given in Figure 11.

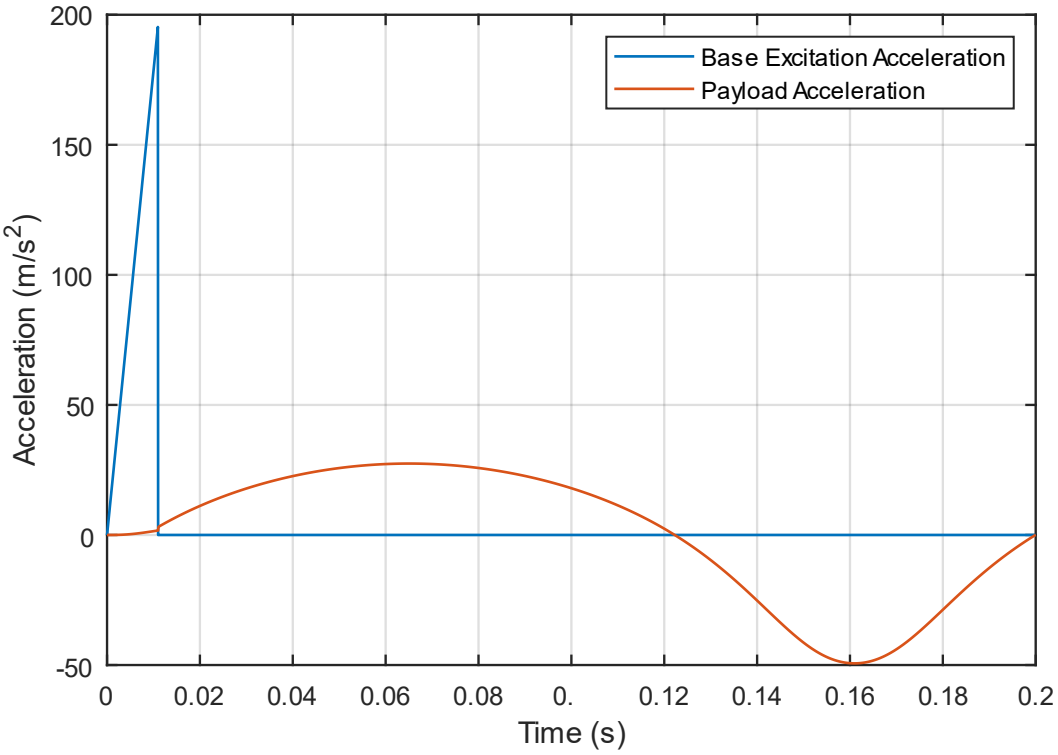


Figure 8: Center of percussion optimized system shock response.

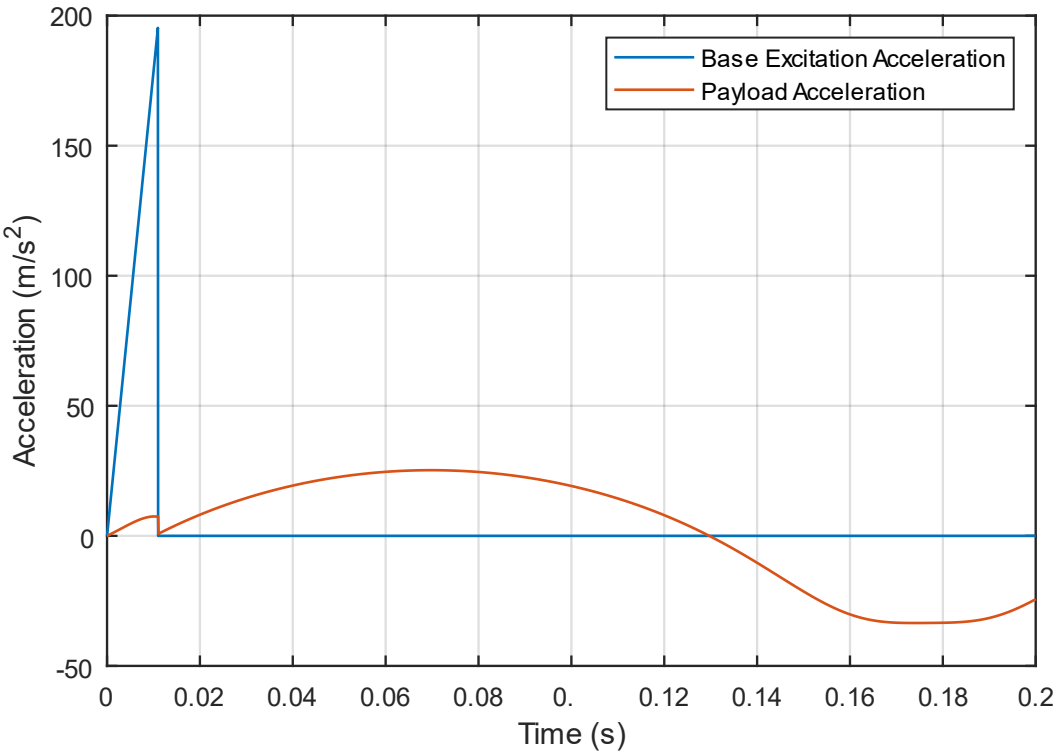


Figure 9: Shock response of the unoptimized system with excessive counterweight.

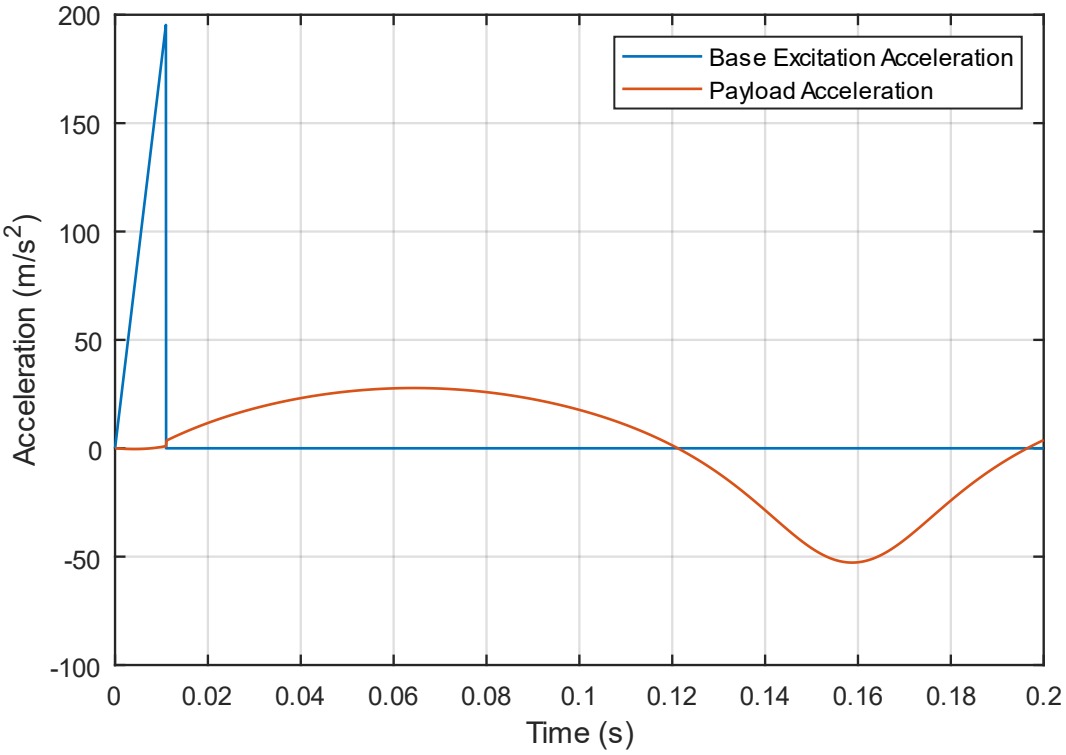


Figure 10: Shock response of the initial system prior to optimization.

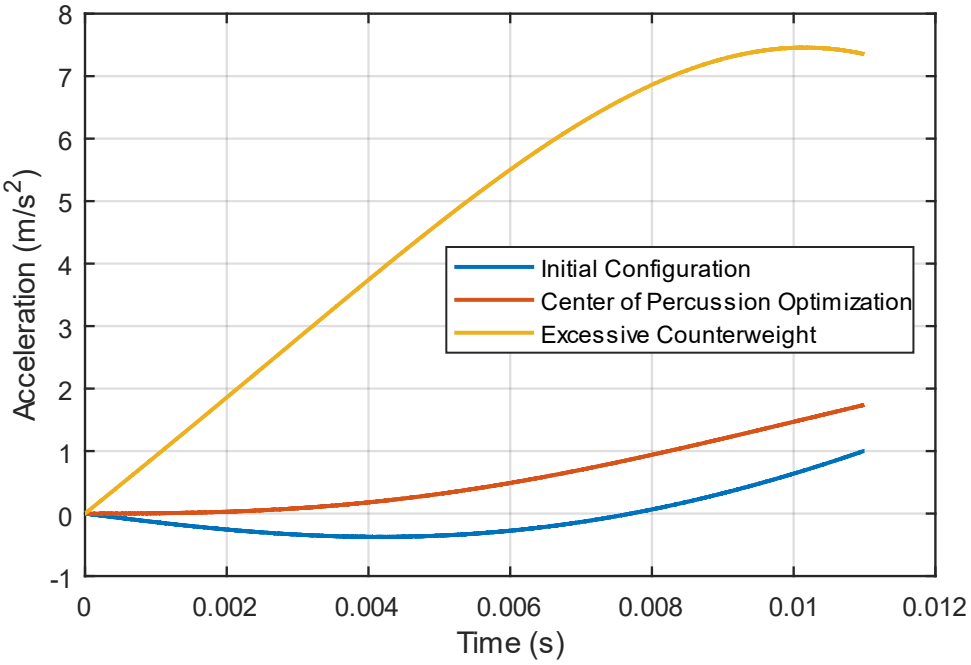


Figure 11: Shock response of all systems at the duration of the shock input.

As it can be seen in Figure 11, center of percussion optimized system has the least jerk, rate of change of acceleration, at the beginning of the shock. Initial system has the least peak acceleration. In the system with excessive counterweight, due to high inertia, links resists to rotation. Therefore, transmitting higher portion the of the shock to the payload.

Since the deformable linkage was out of scope of this study, one can say that initial system without the center of percussion optimization performed better at sawtooth shock response since peak acceleration was lower. But in deformable system with finite step jerk at the instance of shock application will result in high frequency residual vibrations in the payload which may be unwanted due to payload specifications. The responses given in Figure 11 is the result of 20g, 11ms sawtooth shock profile. If the amplitude, duration or the profile is changed, response characteristics change for unoptimized structures. But with center of percussion of the mechanism, minimum jerk condition holds.

## 4 CONCLUSIONS

The present work studied optimization of the compound link mechanism translational shock absorber and outlined a basic iterative optimization frame work for the given mechanism. This study showed that in a mechanism-based isolation structure, response of the structure can be further improved by merely adding a counterweight to the link to shift the link's center of mass to obtain mechanism's center of percussion. Center of percussion optimization of the mechanism at the initial angle will result in instantaneous zero acceleration of the payload but this does not mean the minimum response at entire shock duration. If system's deformed angle is known at the end of the shock duration, the system can be further optimized by maintaining an initial angle but shifting the optimization angle to the mean angle at shock duration. As the angle of the system deviates from the angle that center of percussion was optimized, effect of the optimization degrades. Therefore, by further optimizing the center of percussion angle, system can benefit optimally from the effect at entire shock duration. If the minimum peak acceleration is required, system can be optimized with the mean deformation angle. If the reduction of high frequency component is required, system can be optimized with initial angle.

In our future work, we will further investigate center of percussion effects in a 2 and 3 degrees of freedom system by optimizing structure to have minimal shock response independent of the direction of the applied load. Compliant tuned mass damper will be added to dampen out the residual harmonic oscillation after the shock input. Non-linear torsional stiffness effect caused by local elongation of the flexure will be modelled and used in optimization algorithm.

## 5 ACKNOWLEDGEMENTS

This study was conducted as a part currently ongoing Master's Thesis that is pursued at Istanbul Technical University as a part of Solid Mechanics Graduate Program with the cooperation of ASELSAN Academy. This study was funded by ASELSAN A.Ş.

## REFERENCES

[1] K. Qi, L. Dai, S. Wang, Y. Yang, C. Fang and C. Lin, Design Methodology of a Passive Vibration Isolation System for an Optical System with Sensitive Line-of-Sight, *Photonic Sensors*, **11(4)**, 435-447, 2021.

[2] P. Balaji, M. Rahman, L. Moussa and H. Lau, Wire Rope Isolators for Vibration Isolation of Equipment and Structures - A Review, *IOP Conference Series: Materials Science and Engineering*, **78**, 2015.

[3] W. Y. Sang, L. Sangwoo and N. Khalil, Vibration-Induced Errors in MEMS Tuning Fork Gyroscopes, *Sensors and Actuators A: Physical*, **180**, 32-44, 2012.

[4] J. B. Hopkins, K. J. Lange and C. M. Spadaccini, Designing Microstructural Architectures with Thermally Actuated Properties Using Freedom, Actuation, and Constraint Topologies, *ASME Journal of Mechanical Design*, **135(6)**, 2013.

[5] R. Zeng, G. Wen, J. Zhou and G. Zhao, Limb-Ispired Bionic Quasi-Zero Stiffness Vibration Isolator, *Acta Mechanica Sinica*, **37**, 1152-1167, 2021.

[6] D. T. Greenwood, *Principles of Dynamics*, Prentice Hall, 1987.

[7] E. Atik, M. Karadeniz, A. Muğan, B. Keşli, A. Kanbolat, Optimum Design of Suspension Systems Under Kinematical Constraints, *SAE Technical Paper 2005-013608*, 2005.

[8] F. Garoi, J. Winterflood, L. Ju, J. Jacob and D. G. Blair, Passive Vibration Isolation Using a Roberts Linkage, *Review of Scientific Instruments*, **74**, 3487-3491, 2003.

[9] D. F. Machekposhti, N. Tolou, J L. Herder, A Review on Compliant Joints and Rigid-Body Constant Velocity Universal Joints Toward the Design of Compliant Homokinetic Couplings, *ASME Journal of Mechanical Design*, **137(3)**, 2015.

[10] B. P. Trease, Y. Moon, S. Kota, Design of Large-Displacement Compliant Joints, *ASME Journal of Mechanical Design*, **127(4)**, 788-798, 2015.

[11] S. T. Smith, *Flexures: Elements of Elastic Mechanisms – 1st Edition*, CRC Press, 2000.

[12] W. C. Young, R. G. Budynas, *Roark's Formula for Stress and Strain – 7th Edition*, McGraw-Hill, 2001.

[13] K. Rajagopalan, *Torsion of Thin Walled Structures*, Springer, 2022.

COMPDYN 2023
9th ECCOMAS Thematic Conference on
Computational Methods in Structural Dynamics and Earthquake Engineering
M. Papadrakakis, M. Fragiadakis (eds.)
Athens, Greece, 12-14 June 2023

# NONLINEAR FINITE ELEMENT MODELING OF PRESTRESSED LEAD EXTRUSION DAMPERS

**F. Çalım[1*], A. Güllü[2], C. Soydan[3], and E. Yüksel[1]**

[1] Faculty of Civil Engineering, Istanbul Technical University
Maslak, 34485 Sariyer, Istanbul, Türkiye
calimf@itu.edu.tr, yukselerc@itu.edu.tr

[2] Ingram School of Engineering, Texas State University
San Marcos, TX 78666, USA
ahmetgullu@txstate.edu

[3] Department of Civil Engineering, Tekirdag Namik Kemal University
59030 Suleymanpasa, Tekirdag, Türkiye
csoydan@nku.edu.tr

## Abstract

*In the earthquake-resistant design of the structures, supplemental energy dissipative devices have increasingly been utilized for structural response control. The lead extrusion damper (LED) is one of the prominent versions of metallic dampers, as it dissipates high amounts of seismic energy by the extrusion of lead through the displacement of a bulged shaft. Its geometric properties, i.e., length and diameter of the tube, shaft, bulge, and lead, should be designed based on the target performance level of the host structural system. Thus, determining the LED's force-displacement relationship and seismic energy dissipation characteristics becomes essential for a proper design. In this study, the developed three-dimensional finite element modeling (FEM) strategy for the LED is examined through some literature experiments. The comprehensive three-dimensional model was utilized with the exact material characteristics determined through the coupon tests to increase the accuracy of predicting the LED's behavior. The numerical models were verified using the experimental results of the LEDs with different geometries adapted from the literature. The low relative differences between the numerically and experimentally obtained damper forces, i.e., 4.3% mean error, exhibited that the developed modeling strategy can accurately simulate the LED's hysteretic behavior. The consistency of the modeling strategy with different devices' behavior proved the versatility of the developed FEM. In addition, the effects of the different geometric properties on the LED's cyclic behavior were discussed numerically.*

**Keywords:** Finite Element Analysis, High Force-to-Volume, Lead Extrusion Damper, Passive Energy Dissipater, Seismic Energy Dissipation.

## 1 INTRODUCTION

The seismic energy imparted into the structures converts into kinetic energy ($E_k$), damping energy ($E_d$), and strain energy ($E_s$). The $E_s$ term comprises recoverable elastic and irrecoverable inelastic (hysteretic) energy terms. This energy must be dissipated to prevent life and financial losses during seismic excitations. Based on the conventional earthquake-resistant design practice, it is dissipated through structural members' internal damping and hysteretic behavior. On the other hand, the modern earthquake-resistant design practice promotes using supplementary energy dissipative devices as fuse elements. The purpose is to protect new structures and retrofit the existing ones against nonstructural and structural damage due to strong ground motions [1-4].

A lead extrusion damper (LED) is a metallic damper utilizing a passive control system, and it employs the hysteretic energy dissipation characteristics of lead by an extrusion process. For this process, either a constricted tube or a bulged shaft is utilized [5-6]. The damper has three main components: lead, steel shaft, and steel cylinder.

LED has been a preferable energy dissipative device in recent years for several advantages. Since lead is a very soft metal with a high plastic deformation capacity, it can be employed in energy dissipation even under small displacements. It returns to its original state through recrystallization [7-8]. This phenomenon provides the recentering ability to the device, which results in being free of additional maintenance costs after an earthquake. Also, LED is unaffected by aging effects and environmental factors, and its load-deformation curves remain stable [9]. In addition, the low-cycle fatigue effect is insignificant for the device since lead is the only part going under plastic deformations [10].

Other than the geometric properties of the device, the amount of dissipated energy mainly depends on if the lead inside the tube is prestressed. The prestressing procedure results in less void formation inside the lead, consequently improving the damping properties. Thus, LEDs can be produced as high force-to-volume (HF2V) devices by achieving high damper forces even with smaller device dimensions when the lead is prestressed [11].

Several research groups have produced LEDs with different design approaches and geometric properties [12-17]. Later, the efficiency of LEDs was experimentally and analytically proven for the seismic response control of structures such as beam-to-column connections [18], frames [19], damage-free steel connections [20], interconnected structures [21], precast buildings [22].

This study numerically investigated the effects of the different geometric properties on the energy dissipation characteristics of LEDs. For this purpose, some literature examples, which have experimentally been tested, were adapted for finite element modeling.

## 2 LEAD EXTRUSION DAMPERS

The geometric properties of the LEDs modeled in this study were adapted from the literature study of Vishnupriya et al. [23]. The section view for the devices is illustrated in Figure 1. The LEDs have a bulged shaft, which extrudes the lead from the gap between the bulge and the tube.

The geometric properties, i.e., the diameter of the cylinder ($D_{cyl}$), the diameter of the bulge ($D_{blg}$), the diameter of the shaft ($D_{shaft}$), the length of the cylinder ($L_{cyl}$), the length of the bulge ($L_{blg}$), and the length of the bulge's flat section ($L_{blg_flat}$), are shown in Table 1 for the modeled LEDs. The dampers have a constant shaft diameter of 30 mm, whereas all other geometric properties are varying parameters.

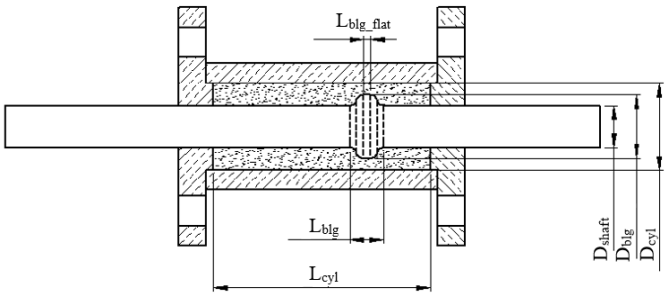


Figure 1: Section view of the modeled LEDs.

Table 1: Geometric properties of the modeled LEDs [23].

| LED # | $D_{cyl}$ (mm) | $D_{blg}$ (mm) | $D_{shaft}$ (mm) | $L_{cyl}$ (mm) | $L_{blg}$ (mm) | $L_{blg_flat}$ (mm) |
|---|---|---|---|---|---|---|
| 1 | 89 | 50 | 30 | 110 | 30 | 5 |
| 2 | 89 | 58 | 30 | 110 | 30 | 5 |
| 3 | 66 | 40 | 30 | 130 | 30 | 6 |
| 4 | 66 | 50 | 30 | 130 | 30 | 5 |
| 5 | 54 | 35 | 30 | 160 | 20 | 3 |
| 6 | 54 | 38 | 30 | 160 | 20 | 3 |

## 3 FINITE ELEMENT MODELING

The three-dimensional modeling strategy adapted by Çalım et al. [24] was utilized in developing the finite element models in Abaqus FEA software [25]. Each component of the LEDs was modeled as three-dimensional deformable parts, and solid, homogenous sections were assigned to each part.

To properly simulate the nonlinear material property of lead, true stress-strain data computed through standard tension tests of Çalım et al. [24] was used. It also accounts for the degrading part of the material's stress-strain curve, unlike the material model used by Vishnupriya et al. [23], Figure 2. Young's modulus and Poisson's ratio were defined as 9 MPa and 0.44, respectively, for the elastic behavior of the lead. On the other hand, a combined isotropic/kinematic hardening model with the "Half Cycle" option was employed to consider ratcheting and cyclic hardening effects in modeling the inelastic behavior.

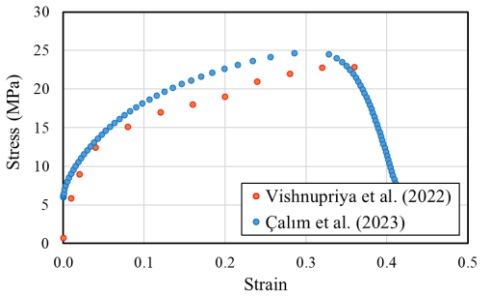


Figure 2: Plastic material data for lead.

The movement of the cylinder was restricted by assigning an "encastre" (fixed) type boundary condition to both ends. Standard surface-to-surface contact interaction was defined between the steel and lead surfaces with a friction coefficient of 0.25. The effects of nonlinearity caused by both material and geometry were considered in the finite element models. In addition, C3D8R-type elements (8-node linear brick, reduced integration with an

hourglass control element) were adapted for the three-dimensional meshing of the finite element models.

Two diverse models were generated for each LED. In the first model, a ramp-type amplitude was applied to the shaft through a displacement/rotation-type boundary condition. This model was used to validate the finite element models since the LEDs were tested under monotonic loading in the experimental study. In the second model, a sinusoidal displacement procedure with an amplitude of 5 mm was applied to the shaft. This model was used for the numerical investigation of the LEDs' cyclic behavior.

## 4 RESULTS AND DISCUSSION

### 4.1 Experimental validation

First, the finite element models were validated through the experimental data. The LEDs studied in this paper have experimentally been tested under a monotonically increasing displacement pattern [23]. Thus, the force-displacement curves of devices under a ramp-type loading were compared with the experimental ones, as illustrated in Figure 3.

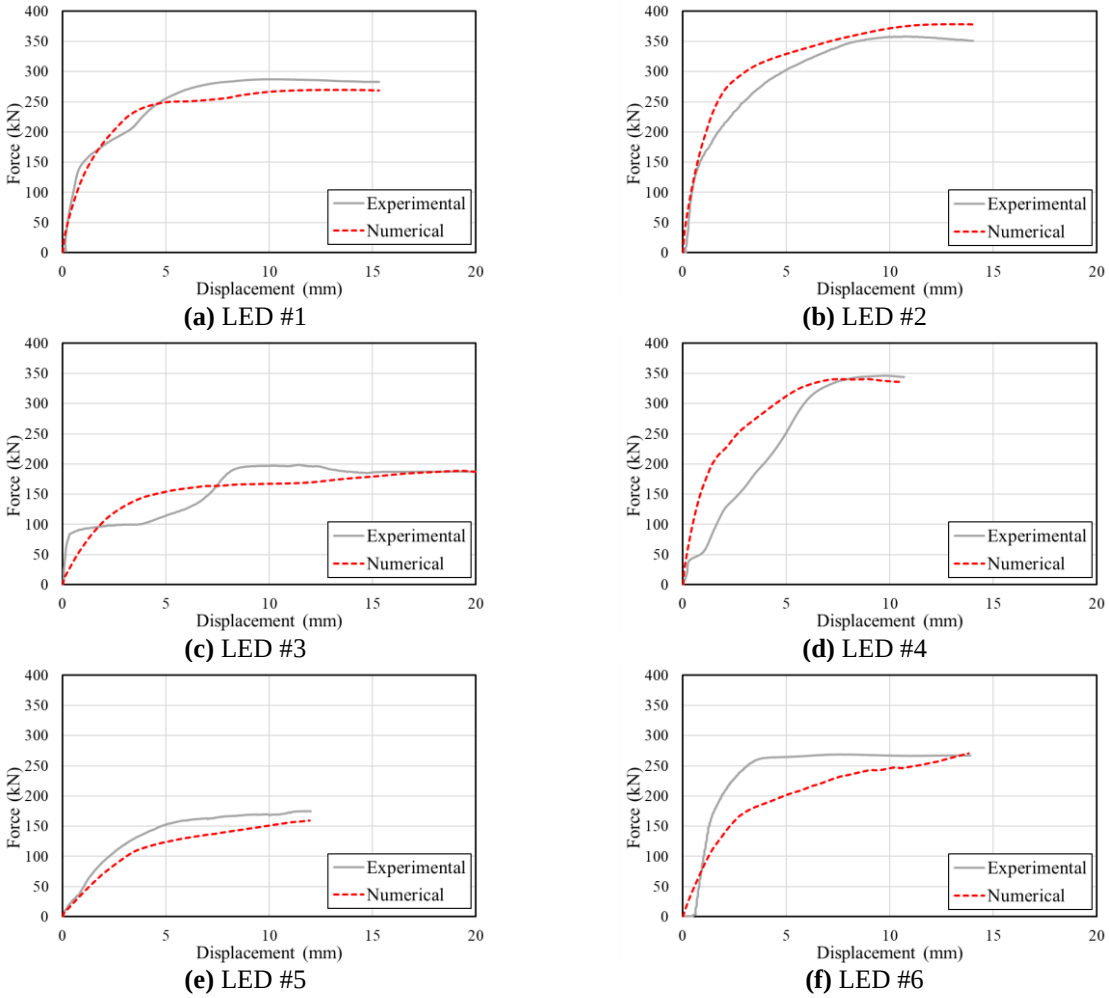


Figure 3: Experimental validation of the finite element models.

Experimentally and numerically computed damper forces are presented in Table 2. The relative differences between them are also displayed in the table, where "+" represents an overestimation and "-" represents an underestimation in the damper force predictions. The

low relative differences in the damper force predictions proved the accuracy of the adapted finite element modeling strategy. While the maximum relative difference in the damper force prediction for six LEDs was 5.9% (LED #1 and #5), the absolute average value was 4.3%.

Table 2: Damper force comparisons.

| LED # | Experimental Damper Force (kN) | Numerical Damper Force (kN) | Relative Difference (%) |
|---|---|---|---|
| 1 | 287 | 270 | -5.9 |
| 2 | 358 | 378 | +5.6 |
| 3 | 199 | 188 | -5.5 |
| 4 | 346 | 340 | -1.7 |
| 5 | 170 | 160 | -5.9 |
| 6 | 268 | 271 | +1.1 |

## 4.2 Analysis of the numerical results

After validating the finite element models using the experimental data, a sinusoidal displacement pattern with an amplitude of 5 mm was applied to the LEDs to compare their cyclic behavior. The achieved hysteresis curves are presented in Figure 4 for each damper.

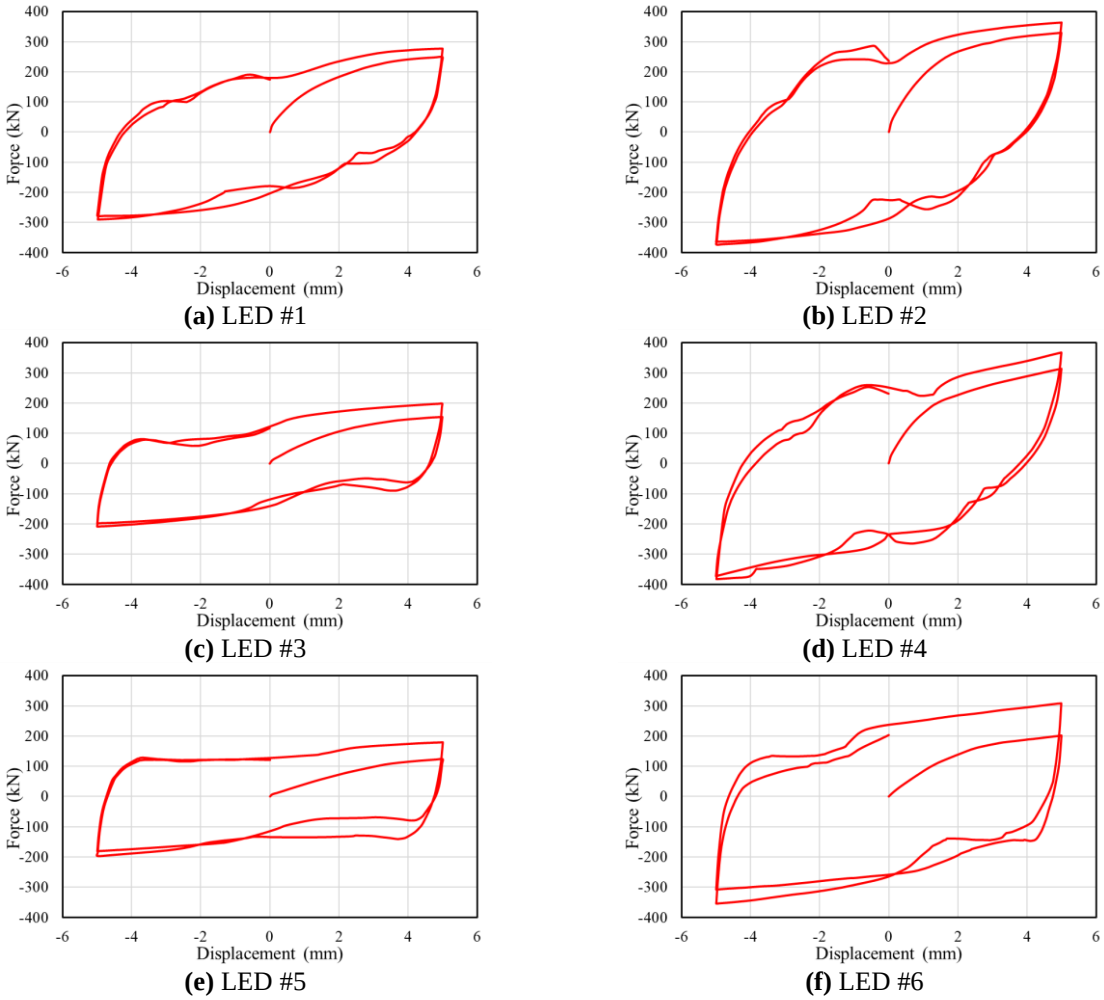


Figure 4: Hysteresis curves of the LEDs.

A loop discretization method was applied to the hysteresis curves to calculate the amounts of dissipated energy in each cycle. As a result, they were computed as 3307.8, 4317.5, 2446.3, 4042.8, 2723.7, and 4226.2 kN·mm, respectively, for each damper.

The relationships between the geometric properties and behavior of the dampers were also investigated. For this purpose, the damper force ($F_d$) and the amount of dissipated energy ($E_D$) were correlated with the bulge diameter ($D_{blg}$), the cross-sectional area of lead ($A_{lead}$), and the ratio of the cross-sectional area of the bulge ($A_{blg}$) to $A_{lead}$, as illustrated in Figure 5. Here, each blue point represents the behavior of a single damper. In addition, the linear trendlines that best fit the data points and their equation are displayed in the figures.

The best fit was achieved for the $F_d$ – $D_{blg}$ (Figure 5a) and $F_d$ – $A_{blg}/A_{lead}$ (Figure 5c) relationships. The R-squared value, which measures the trendline reliability, was around 0.8 for both cases. It can be concluded that the damper force is mainly dependent on the bulge geometry, and it can reliably be estimated through $D_{blg}$ or the ratio of $A_{blg}$ to $A_{lead}$.

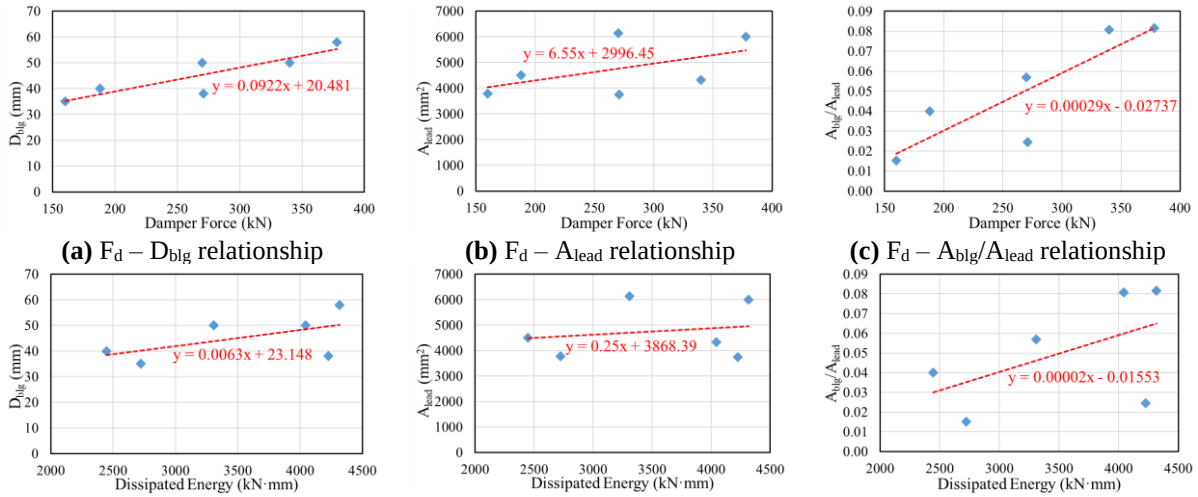


**(a)** $F_d$ – $D_{blg}$ relationship **(b)** $F_d$ – $A_{lead}$ relationship **(c)** $F_d$ – $A_{blg}/A_{lead}$ relationship

**(d)** $E_D$ – $D_{blg}$ relationship **(e)** $E_D$ – $A_{lead}$ relationship **(f)** $E_D$ – $A_{blg}/A_{lead}$ relationship

Figure 5: The relationships between the geometric properties and behavior of the dampers.

## 5 CONCLUSIONS

The nonlinear finite element models of six lead extrusion dampers (LEDs) with varying geometric properties were generated by adapting a three-dimensional modeling strategy. After the models were validated through the experimental data in the literature, cyclic analyses were conducted. As a result, the following conclusions were obtained:

- The adapted finite element modeling strategy yielded accurate results in the damper force predictions. The relative differences between the experimental and numerical damper forces ranged between 1.1% and 5.9%, with an average of 4.3%.
- The hysteresis curves were numerically obtained under a sinusoidal displacement pattern with an amplitude of 5 mm. Very stable and almost rectangular curves were achieved for each damper. For the studied geometries, the energy dissipation in each cycle was computed in the range of 2446.3 to 4317.5 kN·mm.
- The effect of different geometric properties on the damper force and energy dissipation capacities was investigated. The damper force was observed to primarily rely on the bulge's shape. It can be most effectively approximated by using the bulge diameter or the bulge-to-lead area ratio.

## ACKNOWLEDGMENTS

The study was supported by the Scientific and Technological Research Council of Türkiye (TÜBİTAK) research project 121M719. All the support is acknowledged. Additionally, the authors sincerely thank Dr. Vishnupriya and her co-authors for sharing their experimental data.

## REFERENCES

[1] R.D. Hanson, I.D. Aiken, D.K. Nims, P.J Richter, R.E. Batchman, State of the art and state of the practice in seismic engineering dissipation. *Proceedings of ATC-17-1 Seminar on Seismic Isolation, Passive Energy Dissipation and Active Control, Advanced Technology Council*, San Francisco, California, 1993.

[2] I.D. Aiken, Passive energy dissipation-hardware and applications. *Proceedings of the Los Angeles County and SEAOSC Symposium on Passive Energy Dissipation Systems for New and Existing Buildings*, Los Angeles, 1996.

[3] A.H. Barbat, L.M. Bozzo, Seismic analysis of base isolated buildings. *Archives of Computational Methods in Engineering*, **4(2)**, 153-192, 1997. https://doi.org/10.1007/bf03020128

[4] T.T. Soong, B.F. Spencer, Supplemental energy dissipation: State-of-the-art and state-of-the-practice. *Engineering Structures*, **24(3)**, 243–259, 2002. https://doi.org/10.1016/s0141-0296(01)00092-x

[5] W.H. Robinson, L.R. Greenbank, Properties of an extrusion energy absorber. *Bulletin of the New Zealand Society for Earthquake Engineering*, **8(3)**, 187-191, 1975. https://doi.org/10.5459/bnzsee.8.3.187-191

[6] W.H. Robinson, L.R. Greenbank, An extrusion energy absorber suitable for the protection of structures during an earthquake. *Earthquake Engineering and Structural Dynamics*, **4(3)**, 251–259, 1976. https://doi.org/10.1002/eqe.4290040306

[7] J. Wulff, J.F. Taylor, A.J. Shaler, *Metallurgy for engineers*. John Wiley and Sons, New York, 1956.

[8] C.E. Birchenall, *Physical metallurgy*. McGraw Hill, London, 1959.

[9] F. Sadek, B. Mohraz, A.W. Taylor, R.M. Chung, Passive energy dissipating devices for seismic applications. *Report NISTIR 5923. Building and Fire Research Laboratory*. National Institute of Standards and Technology. Gaithersburg, Maryland, 1996. https://doi.org/10.6028/nist.ir.5923

[10] G.W. Rodgers, J.G. Chase, J.B. Mander, Repeatability and high-speed validation of supplemental lead-extrusion energy dissipation devices, *Advances in Civil Engineering*, 1–13, 2019. https://doi.org/10.1155/2019/7935026

[11] G.W. Rodgers, J.G. Chase, J.B. Mander, N.C. Leach, C.S. Denmead, L. Cleeve, D. Heaton, High force-to-volume extrusion dampers and shock absorbers for civil infrastructure, *Progress in Mechanics of Structures and Materials*, 415–420. CRC Press, 2007.

[12] G.W. Rodgers, Next generation structural technologies: Implementing high force-to-volume energy absorber, Ph.D. Dissertation, *University of Canterbury*, Christchurch, New Zealand, 2009.

[13] C. Soydan, A. Güllü, O. Hepbostancı, E. Yüksel, E. İrtem, Design of a special lead extrusion damper. *15th World Conference of Earthquake Engineering*, Portugal, 2012.

[14] C. Soydan, A new beam-to-column connection for the precast concrete structures and evaluation of its performance. Ph.D. Dissertation, *Istanbul Technical University*, Istanbul, Türkiye, 2015.

[15] V. Vishnupriya, G.W. Rodgers, J.B. Mander, J.G. Chase, Precision design modeling of HF2V devices. *Structures*, **14**, 243–250, 2018. https://doi.org/10.1016/j.istruc.2018.03.007

[16] V. Vishnupriya, Modelling force behaviour and contributions of metallic extrusion dampers for seismic energy dissipation, Ph.D. Dissertation, *University of Canterbury*, Christchurch, New Zealand, 2019.

[17] V. Quaglini, C. Pettorruso, E. Bruschi, Design and experimental assessment of a prestressed lead damper with straight shaft for seismic protection of structures. *Geosciences*, **12**, 182, 2022. https://doi.org/10.3390/geosciences12050182

[18] C. Soydan, E. Yuksel, E. İrtem, The behavior of a steel connection equipped with lead extrusion damper. *Advances in Structural Engineering*, **17(1)**, 25-39, 2014. https://doi.org/10.1260/1369-4332.17.1.25

[19] T. Bacht, J.G. Chase, G. MacRae, G.W. Rodgers, T. Rabczuk, R.P. Dhakal, J. Desombre, HF2V dissipator effects on the performance of a 3 story moment frame. *Journal of Constructional Steel Research*, **67**, 1843-1849, 2011. https://doi.org/10.1016/j.jcsr.2011.05.007

[20] J. Desombre, G.W. Rodgers, G.A. MacRae, T. Rabczuk, R.P. Dhakal, J.G. Chase, Experimentally validated FEA models of HF2V damage free steel connections for use in full structural analyses. *Structural Engineering and Mechanics*, **37(4)**, 385–399, 2011.

[21] C.C. Patel, Seismic analysis of parallel structures coupled by lead extrusion dampers, *International Journal of Advanced Structural Engineering*, **9,** 177-190, 2017. https://doi.org/10.1007/s40091-017-0157-x

[22] C. Soydan, E. Yuksel, E. İrtem, Seismic performance improvement of single-story precast reinforced concrete industrial buildings in use. *Soil Dynamics and Earthquake Engineering*, **135**, 106167, 2020. https://doi.org/10.1016/j.soildyn.2020.106167

[23] V. Vishnupriya, G.W. Rodgers, J.G. Chase, Nonlinear finite-element modeling of HF2V lead extrusion damping devices: generic design tool. *Journal of Structural Engineering*, **148(1)**, 04021227, 2022. https://doi.org/10.1061/(ASCE)ST.1943-541X.0003170

[24] F. Çalım, A. Güllü, C. Soydan, E. Yüksel, Development and experimental validation of finite element models for a prestressed lead extrusion damper. *Structures*, **50**, 1114-1125, 2023. http://doi.org/10.1016/j.istruc.2023.02.094

[25] SIMULIA Abaqus/CAE (Vers. 2020) [Computer software]. Vélizy-Villacoublay: Dassault Systems.

COMPDYN 2023
9th ECCOMAS Thematic Conference on
Computational Methods in Structural Dynamics and Earthquake Engineering
M. Papadrakakis, M. Fragiadakis (eds.)
Athens, Greece, 12-14 June 2023

# EFFECTS OF FAR FAULT EARTHQUAKES IN RETROFITTED SEISMICALLY ISOLATED BUILDING

**Antonello Salvatori** [1]

[1] University of L'Aquila
Piazzale E. Pontieri 2, Monteluco di Roio, L'Aquila, Italy
e-mail: antonello.salvatori@univaq.it

## Abstract

*The seismic sequence during years 2016 and 2017 involved a great area In Central Italy, involving four regions and more than 100.000 buildings. Many main shock events occurred, namely Amatrice earthquake (Mw 6.0 on August 24th, 2016), Valnerina earthquakes (Mw 5.9 and 5.4 on October 26th, 2016), Norcia earthquake (Mw 6.5 on October 30th, 2016), and Montereale – Capitignano earthquakes (Mw 5.0, 5.5 on January 18th 2017) About 80.000 buildings were damaged in the seismic events. Some areas were involved also in the 2009 seismic events (L'Aquila earthquake).*
*After L'Aquila earthquake, during reconstruction period, many collapsed buildings, or heavily damaged buildings, were demolished and reconstructed with base isolation (both in foundation and above first elevation columns). Some buildings, which reported less structural damage during 2009 L'Aquila earthquake, were retrofitted with isolation systems. The isolation systems were generally composed by both rubber high damping isolators, and plane friction isolators (sliding devices).*
*Several different dynamic and seismic behaviour were observed in those buildings, depending upon isolation system (noticeable differences have been observed between curved sliding isolators and rubber high damping isolators) and upon soil – structure interaction. Significant displacement has been observed caused by soft soil, and inverse velocity seismic soil profile. Also, frequency response influenced isolated building behaviour.*
*In the work several buildings are examined, analyzing the seismic behaviour both in the 2009 earthquake (with no isolation system) and during 2016 – 2017 seismic events (with isolation system).*

**Keywords:** Seismic isolation, earthquake, structure monitoring.

## 1 INTRODUCTION

Seismic isolation is based on the terrific reduction of the energy that the soil transmits to a structure instead of relying on its resistance, so that the structure itself becomes less vulnerable to earthquakes. This result is obtained by increasing the fundamental period of vibration of a structure. As a result, the superstructure will be subject to very low accelerations under the design earthquake and can support its effects in the elastic range, without any damage to the structure and its content. The displacements, which increase with the period of vibration, are concentrated at the base of the building, i.e., at the isolation devices. These are subject to large relative displacements, while the superstructure vibrates slowly, almost like a rigid body. The historic analysis demonstrated that the concept of decoupling the motion of the structure from that of the soil is not new, even though the device technology developed recently.

According to the available data, more than 20,000 structures in the world have been protected by passive anti-seismic (AS) techniques such as seismic isolation (SI) or energy dissipation (ED) systems, shape memory alloy devices (SMADs), or shock transmitter units (STUs) [1-5]. They are in more than 30 countries (Fig. 1) and concern both new constructions and retrofits of existing structures of all kinds: bridges & viaducts, civil and industrial buildings, cultural heritage and industrial components and installations, including some high risk nuclear and chemical plants and components.

Base isolated structures are designed to satisfy:

- The no-collapse requirement, according to which the structure should withstand the design seismic action without local or global collapse. To address this requirement, the ultimate capacity of the isolating devices, in terms of strength and deformability, is not exceeded, at the ultimate limit state, at which the isolating devices may attain their ultimate capacity, while the superstructure and the substructure remain in the elastic range.
- The damage limitation requirement, according to which the structure should withstand a seismic action having a larger probability of occurrence than the design seismic action, without damage and limitations of use. To address this requirement, the interstorey drifts are limited in the substructure and the superstructure at the damage limitation state.

Following the probabilistic approach, the design earthquake is the event with a certain probability of exceedance in a fixed time length. In the optic of a deterministic approach, it is the maximum credible event at the site.

Values of the isolation system properties to be used in the analysis shall be the most unfavorable ones to be attained during the lifetime of the structure. The check of isolation devices is performed with reference to the maximum displacement, which are obtained by using their minimum stiffness at the time of their production. On the contrary, the check of the superstructure is done using the isolator stiffness after aging, which is higher than the initial one and corresponds to the maximum acceleration value

The use of SI became particularly rapid especially after the Abruzzo earthquake of April 6, 2009, because of the large damage caused by this event to the conventionally founded structures and cultural heritage [8-9]. The use of the traditional High Damping Rubber Isolators (HDRBs), in conjunction with some sliding devices (SDs), is also going on, in both L'Aquila and other Italian sites, for several new constructions and retrofits [6, 7, 10, 11]. The application of new retrofit techniques using SI, has also been applied for both reconstructing L'Aquila and for enhancing the seismic protection in a very earthquake-prone area.

It appears obvious that the seismic response of the isolation system under earthquakes with energy lower than the design one may be quite different than that under the design earthquake, and The stiffness of isolators that corresponds to very low shear strain determines an increase of the isolation vibration frequencies.

## 2 2009 L'AQUILA EARTHQUAKE

L'Aquila city was struck down by a 6.3 Mw and seismic moment M0 = 3.7 x 1018 N m (according to INGV) earthquake in 2009 April 6th. Its historical centre and all the surrounding suburbs were severely damaged, causing 309 casualties, and more than 1500 people injured. L'Aquila has been the first Italian important city directly destroyed by a near fault earthquake since Messina earthquake (1908). Many buildings collapsed completely, both in masonry structure and in reinforced concrete ones. Many buildings suffered heavy structural damages, like shear cracks in the pillars, shear cracks in the concrete walls, nodal ruptures, and even total or partial collapses. Some more recent buildings evidenced noticeable structural damage, mainly due to design errors and constructive inadequacy.

Registered data showed response spectra very different due to the local amplification effects.as shown in Fig. 1. Response spectra evidenced a local strong amplification in correspondence of the high frequencies (0 – 3 Hz) in the suburbs (Mount Pettino west area, in correspondence with an active local fault), where several reinforced concrete buildings were heavily damaged also in structural elements.

The damage can be associated to dynamic resonance in correspondence of the highest values in the response spectra, due to the reinforced concrete building characteristics (main frequency often in the range 2.0 – 10.0 Hz). Some differences, due to soil amplification effect, were found in the center of the city, as shown in fig. 3. The local site effect reveals itself noticeable in relationship with the dynamic behaviour of seismic isolated buildings.

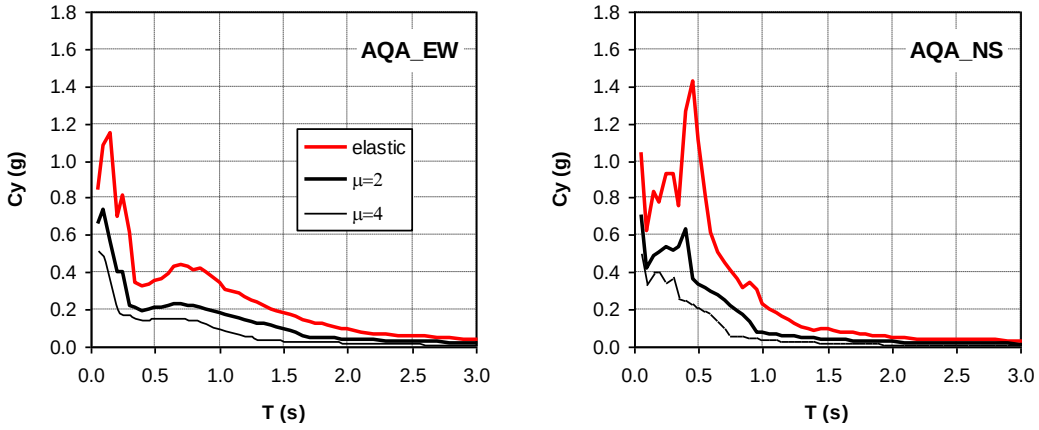


Figure 1. Response spectra in L'Aquila west area (near fault), amplification effect at 10.0 – 2.0 Hz

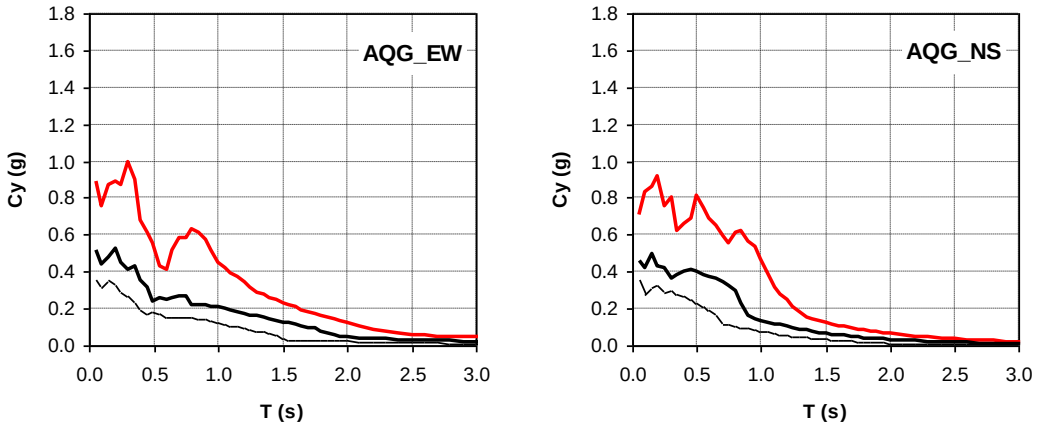


Figure 2. Response spectra in L'Aquila central area, with secondary amplification effect at 0.6 – 0.7 Hz

## 3 POST EARTHQUAKE RECONSTRUCTION AND ISOLATED RETROFITTED BUILDING

After the main seismic event, many buildings were retrofitted by the application of an isolation system.

The base isolation seismic protection is a technique increasingly widespread in Central Italy, which is strategic for repair and strengthening both damaged and retrofitted buildings and new ones. In particular, when in the presence of structures with considerable structural irregularities, both elevations that planimetric, with structural elements with poor energy dissipating capacity of the seismic input energy, and construction details not satisfying due to the seismicity of the area, the base seismic isolation is the only constructive solution to the problem of making these structures seismic-resistant under conditions compatible even with a complex architectural appearance of the buildings themselves.

The use of the anti-seismic systems and devices in the city context already includes not only the strategic structures (civil defence centres, hospitals) and the public ones (schools, churches, commercial centres, hotels), but also, and mainly, residential buildings and even many small and light private houses.

A noticeable number of existing (and also reconstructed) buildings were seismically improved by application of seismic isolators, in particular High Damping Rubber Isolators (HDRB) and Sliding Devices (SD). In the following some of them will be examined in their main features.

### 3.1 Building #1 (near west area)

The first building under examination is located in the west area of the city, were no secondary amplification effect are detected. The building was heavily damaged during L'Aquila earthquake and was retrofitted by an isolation system. The damage concerned mainly brittle fracture in some pillars at low levels, and significant damage to the external infill panels, internal brick masonry panels and secondary non-structural elements. The type of non-structural elements damage is strongly variable but it is mainly related to wrong construction techniques, and, in second order, to wrong design.

In most of these collapses, the presence of non-structural columns would prevent the rotation and failure.

The high deformability of reinforced concrete structures has carried out to high levels of the compression and shear forces. Storey drifts have reached high values, not compatible with the stiffness and relevant flexibility of masonry infills. After 2009 earthquake, which caused the noticeable damage in structural and non-structural elements, the only way to prevent further damage and increased collapse risk probability has been the seismic behaviour enhancement by applying anti seismic devices (isolators) with a retrofitting technique. Furthermore, the high planimetric non regularity of the building (T-shaped) can be regularized only by the application of an isolation system.



Figure 3. a) Building # 1 (seven storeys)



b) Brittle fracture in a pillar

By cutting pillar top edge, after reinforcing foundation and pillar lower part, 32 elastomeric isolators and sliders have been positioned. The HDRBs are 9 FIP SI-S 700/200 and 10 SI-S 800/200, and the sliding devices area 13 FIP VM 250/700/100. In fig. 5 the insertion of an isolator in the top of the pillar is shown.

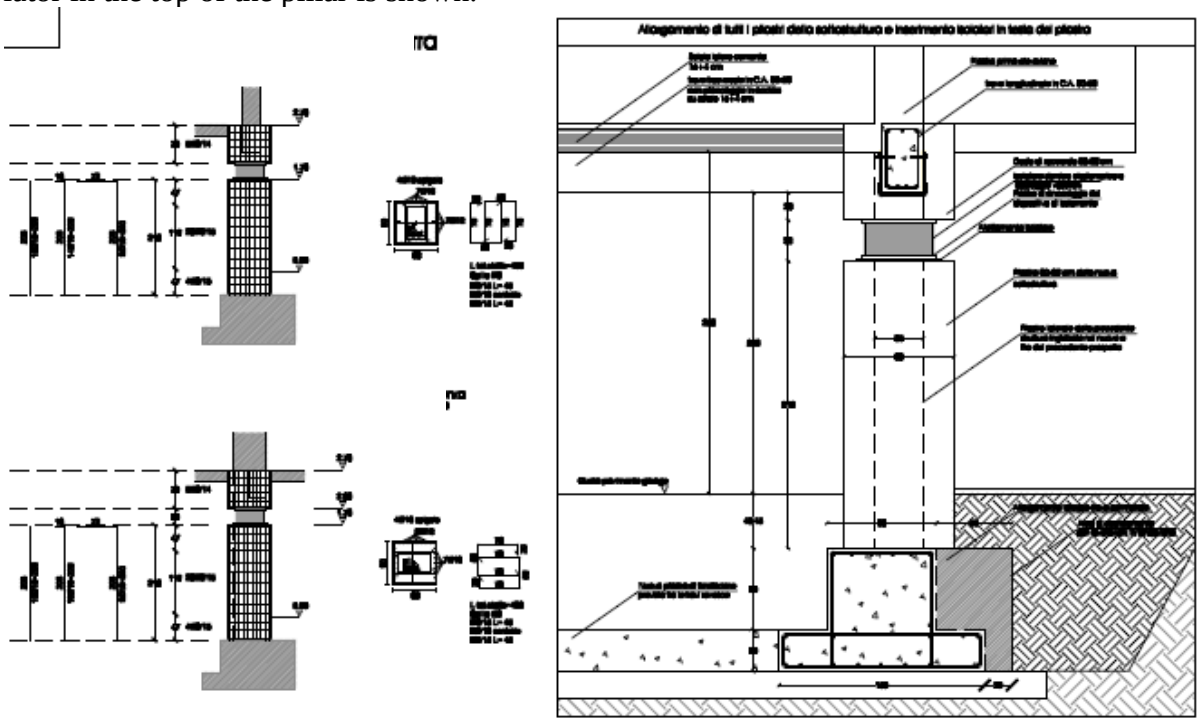

Figure 4. a) Enhancement of the lower part of pillars b) Insertion of a HDRB isolators at the top of the pillar





Figure 5. a) Strengthening of a pillar b) Cutting of a pillar for isolator insertion





Figure 6. a) Strengthening and cutting a pillar b) Control of a pillar cutting





Figure 7. a, b) Level 0 with all isolators at the top of strengthened pillars b)

The retrofitted structure has reached a level of vulnerability, by applying anti-seismic isolation, equal to the 80% of the corresponding new structure, according Italian seismic code. The same level of seismic vulnerability, before the application of the isolation system, was equal to only the 15%, value which is confirmed by the damage in the 2009 earthquake. This building was hit again by nine strong earthquakes almost in the same area (Central Italy, epicentral distance from 30 to 50 km), in 2016 and 2017, (Mw 6.0 on August 24th, 2016), Valnerina 3 earthquakes (Mw 5.9 and 5.4 on October 26th, 2016), Norcia earthquake (Mw 6.5 on October 30th 2016), and Montereale – Capitignano 4 earthquakes (Mw 5.0, 5.5 on January 18th 2017) with no damage at all.

### 3.2 Building #2 (west area)

The second building under examination is located in the west area of the city too, were no secondary amplification soil effect are detected. Also this building was heavily damaged during L'Aquila earthquake, and was retrofitted by an isolation system. The damage concerned mainly brittle fracture in almost all pillars at ground level, and heavy damage to the external infill panels, internal brick masonry panels and secondary non-structural elements. The type of non-structural elements damage has been caused by the low stiffness of the vertical structure, with expulsion of the infills at the first and second storey.

The high deformability of reinforced concrete structures has carried out to high levels of the compression and shear forces. Storey drifts have reached high values, not compatible with the stiffness and relevant flexibility of masonry infills. After 2009 earthquake, which caused the noticeable damage in structural and non-structural elements, the only possibility to prevent further damage and increased collapse risk, also for this building, has been evaluated by enhancing the seismic behaviour with the application of anti-seismic devices (isolators) with a retrofitting technique. Instead of realizing great plinth above the pillars, in this building the uplift of the structure was performed by inserting high strength steel bars, sustaining all the structure weight during isolators insertion in the top of the pillars.

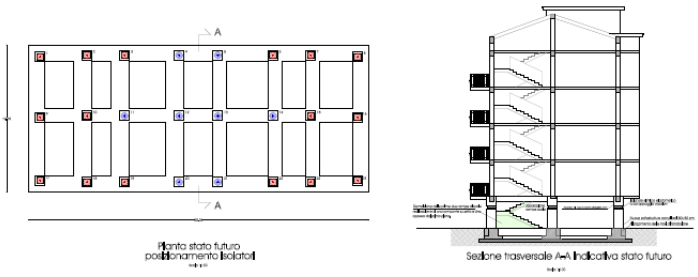

Figure 8. a) Position of isolators: red rubber isolator SI/N 450/126, blue sliders VM 250/250; b) section.





Figure 9. a) Building # 2 (six storeys) b) damage end demolition of the infills

The damage caused by the 2009 earthquake in the building infills determined the need to completely demolish all the infills at the first two levels, and partially at superior levels (Fig. 8).

The particular (and regular) shape in plan ed in elevation permitted to easily insert an isolation system, directly in the zero level, at the top of pillars, without any interference with secondary elements (infills, garage doors, lift) and with no compromission of the utilization of the rooms at that level.

In order to strengthen the structure, an enlarged concrete section with new reinforcement bars were set up in all the pillars (Fig. 10 b).





Figure 10. a) Brittle fracture in the top of a pillar b) Increase of section and reinforcement bar in a pillar

Depending on the structural characteristics (stiffness, residual capacity, deformability and interaction with infills), the isolation system has been designed in order to full satisfy the seismic demand in terms of displacement at the isolation level. It's worth noticing that this building is located near an important fault (which caused destructive earthquake in the pas centuries), were near faults effects have to be taken into account in order to avoid inappropriate dynamical behaviour (vertical and horizontal resonances, soil – isolation system – structure interaction)





Figure 11. a) HDRB and sliding devices at top of pillar b) Sliding device at top of a pillar





Figure 12. a) HDRB rubber isolator SI/N 450/126 b) Sliding device in correspondence of the staircase

The building has been retrofitted with sixteen SI-N 450/126 high damping rubber isolators and eight sliding devices VM 250/250. It's worth noticing the position of sliding devices in correspondence of the staircase, (Fig. 12b) where they have been placed at a different height with respect the isolation level. The area of this retrofitted building is quite different from the preceding one, and is located near an active fault which caused several strong earthquakes in the past. The area has some resonances caused by the fault proximity. Also, this structure has been completely designed according to Italian code for new structures.

### 3.3 Building #3 (central area)

The third building under examination is located in the central area of the city, were an important secondary amplification soil effect is detected. Also this building was heavily damaged during L'Aquila earthquake, and after demolition has been rebuilt with isolation system.

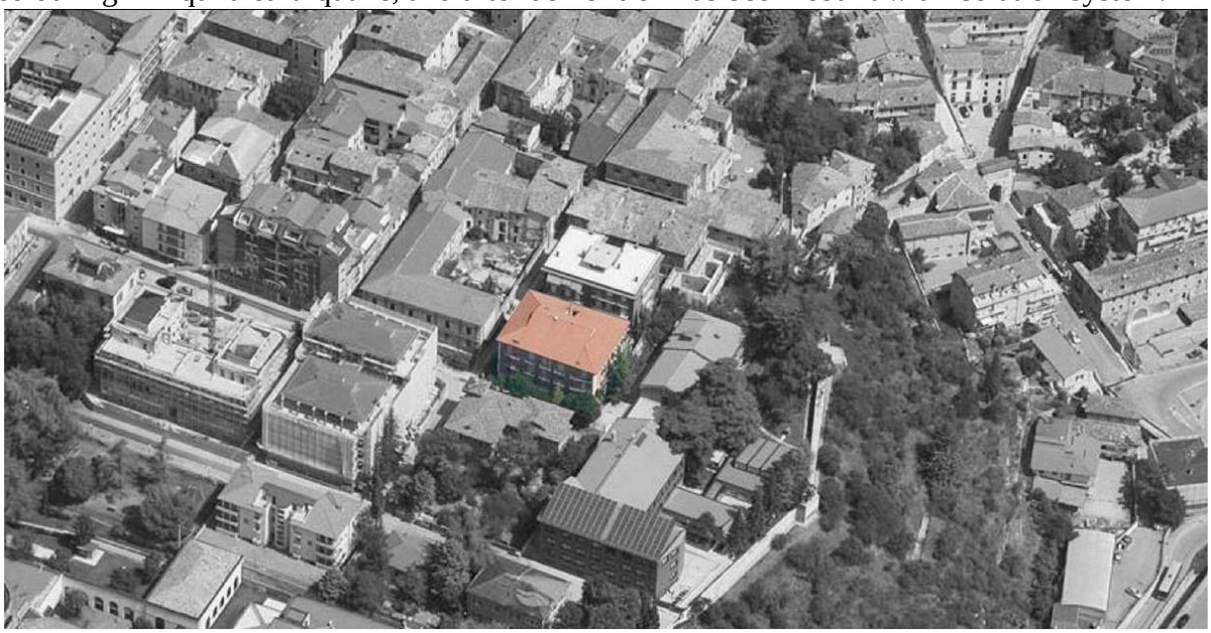

Figure 13. Isolated building in the centre of L'Aquila, with secondary amplification effect at low frequencies.

The maximum seismic performance for this building has been gained by seismic isolation, but, according to the shown amplification effect (fig. 2), an accurately seismic design has been performed to take into account the probable high displacement during earthquakes in this area. Isolators were positioned underground, in correspondence of the new pillars, following the scheme in fig. 13a, with HDRB isolators FIP SI-S 800/160, and sliding devices FIP VM 300/600/600.

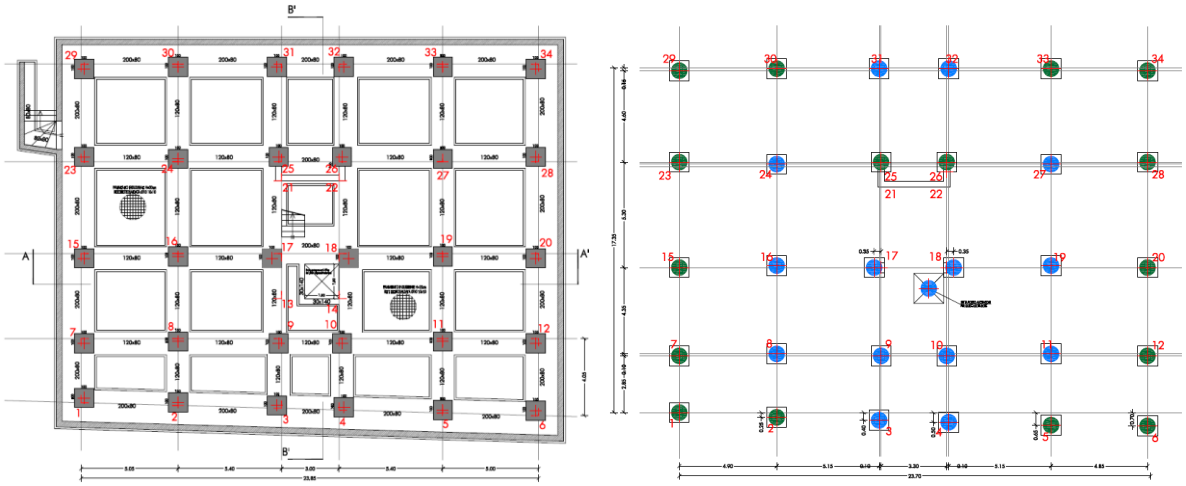

Figure 14. a) Understructure of isolation system b) HDRB isolator SI-S 800/160, sliders VM 300/600/600

The isolation system has been designed in order to take into account not only the structure typology, but also the soil – structure interaction, in particular the secondary resonance at low frequencies which area typical of the centre of the city (Fig. 2). In particular (Figs. 14, 15), seismic movement joints have been designed to permit large displacement of the superstructure.



Figure 15. a) HDRB isolator SI-S 800/160 b) sliding device VM 300/600/600



Figure 15. a) HDRB isolator and external seismic gap b) Horizontal gap understructure - superstructure

### 3.4 Building #4 (Umbria Civil Protection Center In Foligno)

The Operative Centre Building of the Umbria Civil Protection Centre at Foligno is composed by several isolated buildings, among which a hemispherical shape, with four storeys

above the ground level, the first of which contain the isolators, and an underground storey, and more regular buildings.

The superstructure of the dome building is seismically isolated by means of ten high damping rubber bearings, located along the perimeter, which transfer the loads to the foundations. These are composed of reinforced concrete plinths, supported by four piles each and connected to each other by means of reinforced concrete beams. The height of the building from the extrados of the isolators is 17.6 m, the diameter of the first floor is 31.4 m. The characteristics of the isolation devices assumed in the structural design are reported in Tab. 1. As usual, the nominal values of G and $\xi$ are referred to a unitary shear strain.



Fig. 16 – The structure of the Operative Centre of the Civil Protection Department at Foligno during the construction

The superstructure is formed of ten radial arch elements, equally spaced along the perimeter and corresponding to the isolation device locations. They run from the first floor, where they are connected by a perimeter ring beam, to the top of the building, where they are connected to another smaller ring beam. The arches support two other intermediate floors by means of ring beams along their perimeters. All the three floors can be considered rigid in their plane. They have a central hole delimited by an outer concrete cylinder, 16 cm thick, which starts from the first floor and rises up to the top, linking all the floor. Another 16 cm thick cylinder is inside the previous one and contains the elevator and all the facilities. It has a concrete slab at its lower end, is suspended from the top ring beam and ends 3.74 m below the ground level. A helicoidal staircase, with a concrete slab of 12 cm, and the landings at the floors connect the two cylinders. Inside the lift cylinder there is a metal structure that support the infill masonry wall, which has a negligible interaction with the concrete structure.

Both the cylinders were supported at their base during the construction of the building. Then the provisional support structures were removed and the loads acting on the cylinders (self-weight and additional permanent loads) were transferred to the arch elements at their top.

The building was designed according the Italian code for building in seismic area in force at the time of construction (OPCM 3274, 2003). A detailed analysis of the seismic hazard was carried out on purpose and allowed assuming a design value for the peak ground acceleration on rigid soil equal to 0.28g.

| | |
|---|---|
| Diameter $\Phi$ (mm) | 1000 |
| Thickness of the rubber layers $t_i$ (mm) | 10 |
| Total rubber thickness $t_e$ (mm) | 240 |
| Shear modulus of the rubber G (N/mm$^2$) | 0.4 |
| Thickness of the steel laminates $t_s$ (mm) | 4.0 |
| Thickness of the end steel plates $t_{ss}$ (mm) | 30 |
| Equivalent horizontal stiffness $K_e$ (kN/m) | 1310 |
| Equivalent damping ratio $\xi$ (%) | $\geq 10$ |

Table 1 – Geometrical and mechanical characteristics of the HDRBs

The seismic monitoring system is composed of twelve accelerometers, deployed in the building as follows (Fig. 17):

- three accelerometers were at the basement (A01 along x direction, A02 in the vertical direction and and A03 in y direction);
- seven accelerometers were at the first floor, just above the isolation system: three of them in the vertical direction (A04, A05 and A06), two in y direction (A07 and A09) and two in x direction (A08 and A10; A10 is oriented in the opposite direction of A08, therefore the sign of the recorded time histories was changed and indicated as -A10);
- two accelerometers were at the top of the building in the horizontal directions (A11 in y direction, A12 in x direction).

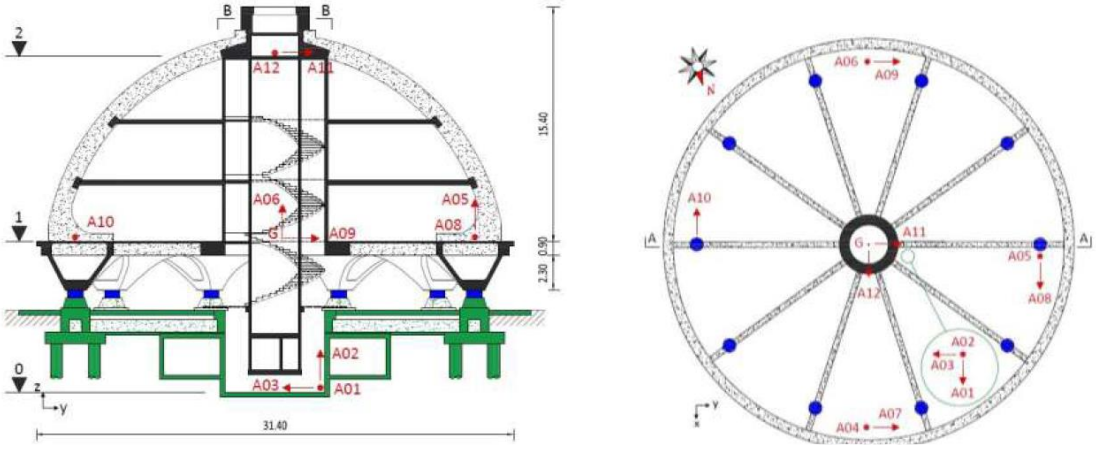


Fig. 17 – Accelerometers network: A01, A02 and A03 are at the basement inside the building; A04 to A10 are at the first floor above the isolation system; A11 and A12 are at the top of the building.

The accelerometer network recorded all the events that struck Central Italy since August 24th, 2016. The epicentres of earthquakes occurred in far field, as the epicentral distance of

2016 – 2017 earthquakes was at about 50 km. A detailed analysis of the behaviour of the seismic isolation system under different energy earthquakes was carried out.

The design fundamental frequency of the isolated building was equal to 0.38 Hz. Actually, different values were found during the earthquakes recorded. A fundamental frequency of about 1.9 Hz was estimated during ambient vibration tests and low energy earthquakes, whiled a first resonance frequency of about 1.0 Hz was found under the strongest event recorded. Anyway, the effectiveness of the seismic isolation system under all the events of the sequence was verified and discussed in a previous paper.

A secondo building in the Civil Protection Center in Foligno is the Forest Ranger Building and the Monitoring System, with an Isolation System

The Forest Ranger building of the Umbria Civil Protection Centre in Foligno is a seismically isolated reinforced concrete building (Figure 18). It has an underground level and two floors above the ground. The maximum dimensions in plan are about 16 x 31 m, in x and y direction, respectively. The inter-floor heights are 3.14, 4.14, and 3.34 m, for the underground, first and second level, respectively.



Figure 18. View of the Forest Ranger building (photo P. Clemente)

The isolation system is composed by (Figure 19):

1. 12 HDRBs of Type 1, located along the perimeter of the main rectangular portion;
2. 4 flat slider devices (SD) with a lubricated steel-PTFE (polytetrafluoroethylene) interface, having a nominal friction factor of 1.0%, located at the internal column of the main rectangular portion;
3. 4 HDRBs of Type 2, located at the columns external to the main portion.

The isolation devices are located at the top of the columns of the underground level. The characteristics of the HDRBs are shown in Table 2. Schematic outlines of the isolators are in Figure 19.

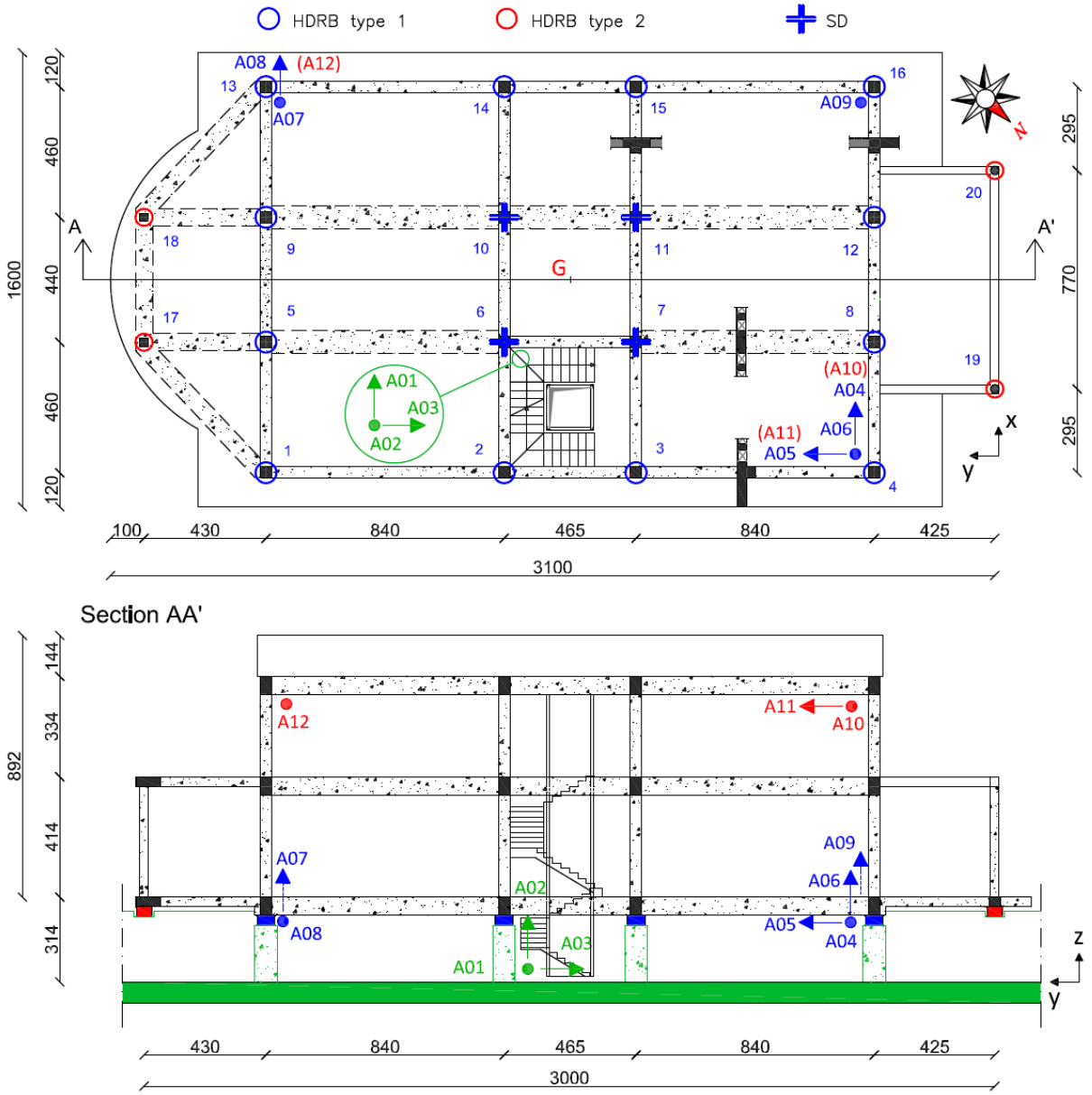


Figure 19. First floor with isolation system and vertical section.

| Characteristic | Type 1 | Type 2 |
|---|---|---|
| Number of devices | 12 | 4 |
| Diameter (mm) | 700 | 550 |
| Total rubber thickness (mm) | 284 | 300 |
| Thickness of a single rubber layer (mm) | 7 | 5 |
| Shear modulus of rubber at $\gamma$ = 1 (N/mm2) | 0.4 | 0.4 |
| Equivalent horizontal stiffness at $\gamma$ = 1 (N/mm) | 541 | 317 |
| Equivalent damping factor at $\gamma$ = 1 (%) | 10 | 10 |
| Maximum displacement (mm) | 379 | 395 |

Table 2. Nominal characteristics of the two types of HDRBs.

The substructure is composed by the foundation beams (120 x 75 cm) and 16 columns (80 x 80 cm), on which the isolators are placed. The superstructure is a frame structure (columns 40 x 40 cm, beams 40 x 64 or 80 x 34 cm). The floors are reinforced concrete and hollow tiles mixed floors, while the external cornices are in reinforced concrete as well as the stairs between the first floor and the second floor. The elevator shaft is a light steel structure linked to the first, second and covering floors and suspended to them. Additionally, the stairs between the underground and the first floor are in steel and hanged to the elevator steel structure.

## 4 THE 2016 – 2017 SEISMIC EVENTS AND THE BEHAVIOUR OF THE ISOLATED BUILDINGS

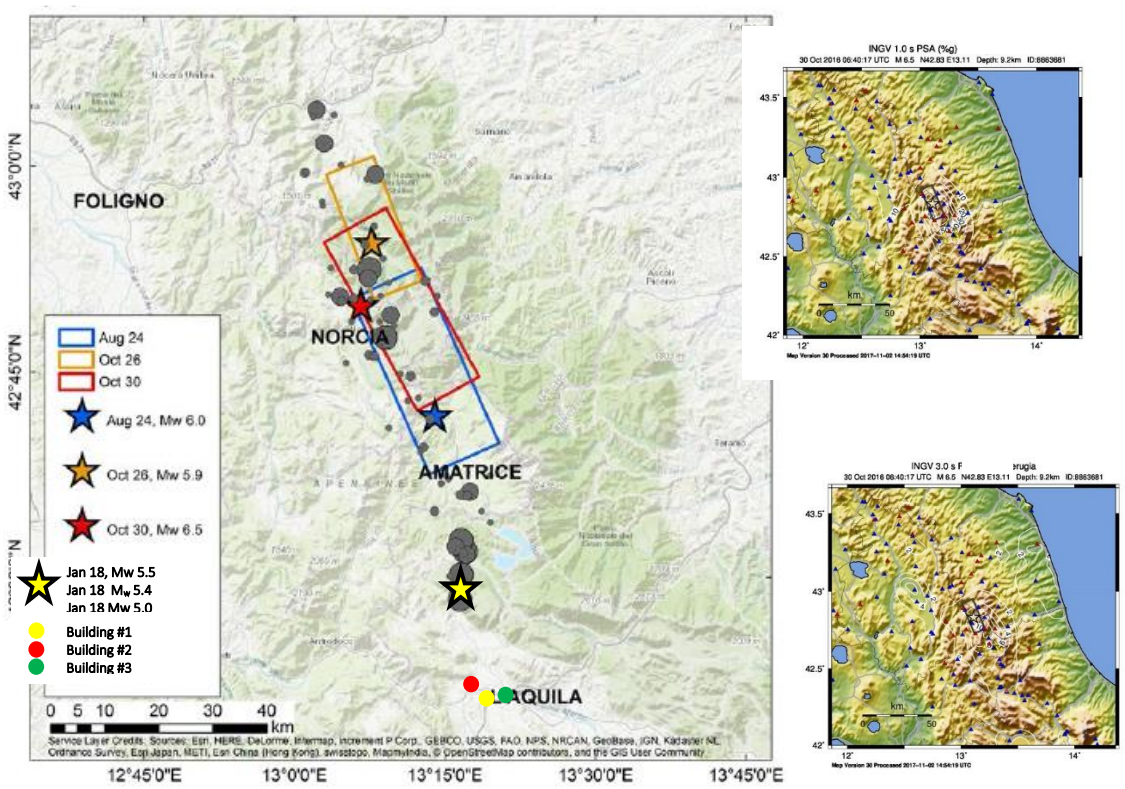


Figure 20 a)– 2016 – 2017 seismic events and position of the isolated buildings b) spectral data (INGV)

The above mentioned earthquakes, with a continued sequence of nine mainshocks, occurred in the same area of L'Aquila and 2009 earthquake. In particular, the buildings under examination have a short distance from the epicentres (about 35 km from Amatrice, 55 km from Norcia, and 20 km from the 2017 sequence). The overall main events are reported in the following table.

| SOURCE Time [Utc] | Latit. | Longit. | Depth [km] | Magnitude | Name Record |
|---|---|---|---|---|---|
| **24/08/2016 01:36:32** | **42,698** | **13,234** | **8.1** | **6.0-Mw** | **TN015** |
| 24/08/2016 01:56:01 | 42,601 | 13,276 | 7.7 | 4.3-Mw | **TN018** |
| 24/08/2016 02:33:29 | 42,792 | 13,151 | 8.0 | 5.4-Mw | **TN032** |
| 24/08/2016 03:40:11 | 42,614 | 13,244 | 10.7 | 4.1-Mw | **TN045** |
| 24/08/2016 04:06:51 | 42,771 | 13,124 | 6.2 | 4.4-Mw | **TN047** |
| 24/08/2016 11:50:31 | 42.82 | 13.16 | 9.8 | 4.5-Mw | **TN066** |
| 24/08/2016 17:46:09 | 42,659 | 13,215 | 10.3 | 4.2-Mw | **TN074** |
| 24/08/2016 23:22:06 | 42,654 | 13.21 | 11.8 | 4.0-Mw | **TN078** |
| 25/08/2016 03:17:17 | 42,745 | 13,193 | 9.0 | 4.3-Mw | **TN080** |

| | | | | | |
|---|---|---|---|---|---|
| 25/08/2016 12:36:05 | 42.6 | 13,282 | 7.5 | 4.4-Mw | **TN083** |
| 26/08/2016 04:28:26 | 42,605 | 13,292 | 8.7 | 4.8-Mw | **TN086** |
| 27/08/2016 02:50:59 | 42,843 | 13,238 | 7.8 | 4.0-Mw | **TN093** |
| 28/08/2016 15:55:35 | 42,823 | 13,232 | 8.7 | 4.2-Mw | **TN102** |
| 03/09/2016 01:34:12 | 42.77 | 13,132 | 8.9 | 4.2-Mw | **TO015** |
| 03/09/2016 10:18:51 | 42,861 | 13,217 | 8.3 | 4.3-Mw | **TO017** |
| 16/10/2016 09:32:35 | 42,748 | 13,176 | 9.2 | 4.0-Mw | **TP016** |
| **26/10/2016 17:10:36** | **42.88** | **13,128** | **8.7** | **5.4-Mw** | **TP021** |
| **26/10/2016 19:18:06** | **42,909** | **13,129** | **7.5** | **5.9-Mw** | **TP026** |
| 26/10/2016 21:42:02 | 42,863 | 13,121 | 9.9 | 4.5-Mw | **TP053** |
| 27/10/2016 03:19:27 | 42,843 | 13,143 | 9.2 | 4.0-Mw | **TP071** |
| 27/10/2016 03:50:24 | 42,984 | 13.12 | 8.7 | 4.1-Mw | **TP073** |
| 27/10/2016 08:21:46 | 42,873 | 13,097 | 9.4 | 4.3-Mw | **TP086** |
| 27/10/2016 17:22:23 | 42,839 | 13,099 | 9.0 | 4.2-Mw | **TP103** |
| 29/10/2016 16:24:33 | 42,811 | 13,095 | 10.9 | 4.1-Mw | **TP144** |
| **30/10/2016 06:40:17** | **42,832** | **13,111** | **9.2** | **6.5-Mw** | **TP151** |
| 30/10/2016 07:34:48 | 42,922 | 13,129 | 9.9 | 4.0--ML | **TP170** |
| 30/10/2016 11:58:17 | 42.84 | 13,056 | 10.2 | 4.0-Mw | **TP235** |
| 30/10/2016 12:07:00 | 42,845 | 13,078 | 9.7 | 4.5-Mw | **TP237** |
| 30/10/2016 13:34:54 | 42,803 | 13,165 | 9.2 | 4.1-Mw | **TP251** |
| 30/10/2016 18:21:09 | 42.79 | 13,152 | 9.6 | 4.0-Mw | **TP275** |
| 31/10/2016 03:27:40 | 42,766 | 13,085 | 10.6 | 4.0-Mw | **TP310** |
| 31/10/2016 07:05:45 | 42,841 | 13,129 | 10.0 | 4.0-Mw | **TP322** |
| 01/11/2016 07:56:40 | 43 | 13,158 | 9.9 | 4.8-Mw | **TP354** |
| 03/11/2016 00:35:01 | 43,029 | 13,049 | 8.4 | 4.7-Mw | **N.R.** |
| 12/11/2016 14:43:34 | 42,723 | 13,209 | 10.1 | 4.1-Mw | **TQ077** |
| 14/11/2016 01:33:44 | 42.86 | 13,158 | 11.0 | 4.0--ML | **TQ092** |
| 29/11/2016 16:14:03 | 42,529 | 13.28 | 11.1 | 4.4-Mw | **TQ171** |

Table 3 – main seismic 2016 events in the area

Many buildings in the area are under monitoring. The examined buildings reported an ideal behaviour in heavy seismic conditions.

Spectral data, recorded at the site of L'Aquila, evidenced some differences between central area and the western area of the city, due to well-known soil resonances in the central area.

The 2016 Norcia earthquake, in particular, caused a damaged building collapse in the central area.

The isolated building had an optimal behaviour during the earthquake. They reported absolute absence of any kind of damage, structural and non-structural. Also, isolators (both HDRB and SD) had no damage and no residual displacement.

The control of the displacement of the isolated structures, in the examined buildings, put into evidence some differences.

In particular, maximum displacement was measured for each superstructure and insolation system in each building, as follows:

Building #1 – maximum displacement 25 mm

Building #2 – maximum displacement 30 mm

Building #3 – maximum displacement 100 mm

Building #4 – maximum displacement 10 mm

Building #5 – maximum displacement 10 mm

The difference of displacement depends on the soil – structure interaction and the relevant differences between the considered areas, and also on the directivity of the earthquake waves.

It's worth noticing that each system has been designed according to the parameters reported in table 2.

| Building # | HDRB | SD | $K_{esi}$ [KN/mm] | x | Isolation Period | Design displacement | Maximum displacement |
|---|---|---|---|---|---|---|---|
| 1 | 9 FIP SI-S | 13 FIP VM | | | | | |

| | | | | | | | |
|---|---|---|---|---|---|---|---|
| | 700/200<br>10 FIP SI-S 800/200 | 250/700/100 | 17.03 | 15% | 2.64 s | 300 mm | 25 mm |
| 2 | 16 FIP SI-N 450/126 | 8 FIP VM 250/250 | 16.16 | 10% | 2.28 s | 250 mm | 30 mm |
| 3 | 16 FIP SI-S 800/160 | 15 FIP VM 300/600/600 | 20.16 | 10% | 2.43 s | 300 mm | 100 mm |
| 4 | 10 SI-S 1000/240 | - | 13.10 | 10% | 2.56 s | 400 mm | 10 mm |
| 5 | 12 SI-N 700/284<br>4 SI-N 550/300 | 4 FIP VM 550/600/600<br>- | 7.76 | 10% | 2.56 s | 400 mm | 9.28 mm |

Table 4 – design parameter and maximum displacement for the buildings

As for the isolated building in Foligno, the effects of the Norcia earthquake of October 30th, 2016, were quite attenuated at Foligno site, due to the distance and the different directivity. It is interesting to evaluate the effects under a strong earthquake. Therefore, the acceleration due to the same event of October 30th, 2016, but recorded at Norcia La Castellina (NOR station), was assumed as input for the dynamic nonlinear analysis of the building. Nor station is very close to the epicentre, at a site with flat surface and subsoil classified as type B.

### 4.1 Behavior under Ambient Vibrations

The structure was first dynamically characterized using ambient vibrations. For this purpose, a temporary network of 12 velocimeter sensors deployed in the same location of the accelerometers of the permanent network, was used. Data were analyzed in the frequency domain evaluating the power spectral densities (PSD) of all the recording and the cross spectral densities (CDS) of all the significant couples of sensors. The following first three resonance frequencies were extracted by means of the peak picking technique:

3.13 Hz, 3.71 Hz and 3.88 Hz. These resonance frequencies are related to the superstructure modes because the isolation system was not excited by ambient vibrations. The analysis of the phase factors of CSDs allowed to state that the first frequency is associated with a torsional mode, while the second and the third ones are associated with translational modes. They will be compared with the frequencies recorded during the seismic events, in order to check the decoupling of the motion between the superstructure and the ground.

The permanent monitoring system is composed by a data acquisition system Kinemetrics K2 and 12 accelerometric sensors Kinemetrics FBA11. The sensors are deployed as follows (Figure 2):

1. Three accelerometers, A01, A02 and A03, are at the basement (level 0, L0) in x, vertical and y direction, respectively;
2. Five accelerometers are on the slab above the isolation interface (level 1, L1), as follows: A04 and A08 in x direction, A05 in y direction, and A06, A07 and A09 in the vertical direction;
3. Three accelerometers are at the top of the building (level 2, L2), as follows: A10 and A12 in x direction and A11 in y direction.

A short term average/long term average (STA/LTA) logic is used to recognize seismic events. The mean value of a signal in a short-time interval of 6 s is compared with the mean value of the same signal in a long-time interval of 60 s.

The permanent monitoring system recorded all the seismic events that struck Central Italy between August 2016 and January 2017. Among these only the most representative earthquakes were chosen to analyze the behavior of the building.

The 30 October 2016 Norcia earthquake was the event with the maximum magnitude in the sequence, but also the event that induced the maximum effects at the site of the building.

In Figure 21 the acceleration time histories recorded in x and y direction, respectively, at the basement L0 (A01 and A03), at the first floor above the isolation interface L1 (A04 and A05) and at the top of the building L2 (A10 and A11) are plotted. The peaks of the acceleration, for the same levels, are PBA = 0.098 g, PIA = 0.054 g and PTA = 0.059 g, respectively.

The absence of amplification from the basement to the top, which characterizes isolated structures, is clearly recognizable. On the contrary, there is a reduction in acceleration between the basement (L0) and the first floor above the isolation system (L1).

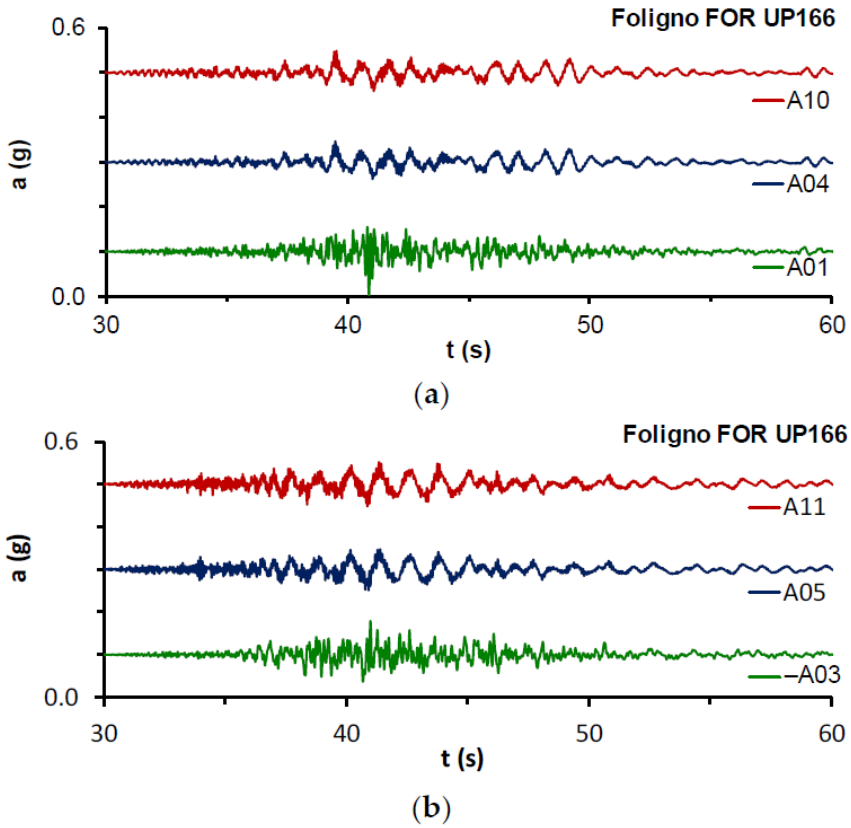


Figure 21. Time histories at the basement (green), at the first floor above the isolation system (blue) and at the top of the building (red) during the 30 October 2016, Norcia earthquake in (a) x direction and (b) y direction (the sign of record at A03 has been changed; therefore, it is named –A03

The Fourier spectra for the horizontal sensors are plotted in Figure 22.

The sensors in the same direction, deployed in the superstructure, show a peak of amplitude for the same frequency, equal to 0.95 Hz in x direction and 0.81 Hz in y direction. These resonance frequencies are much lower than the resonance frequencies recorded under ambient vibrations and related to the superstructure. The spectrum rotates of the recordings obtained at the couples A04–A05 and A10–A11 confirmed the presence of two different frequencies along the two main directions.

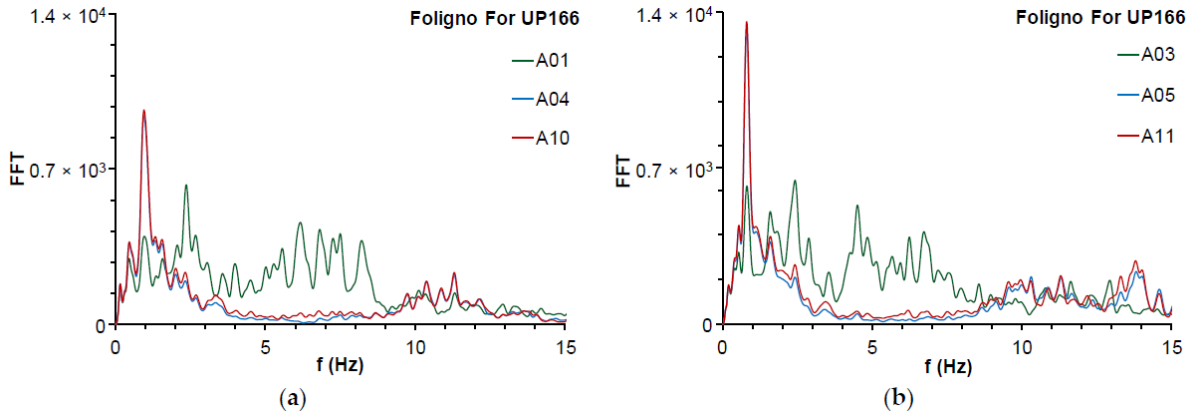


Figure 22 - Fourier spectrum amplitude at different levels obtained during the 30 October 2016 Norcia Earthquake in (a) x direction and (b) y direction

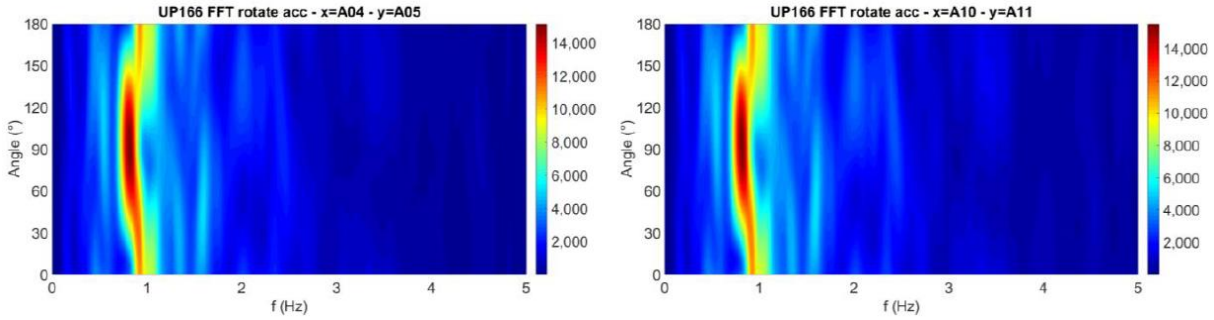


Figure 23. Spectrum rotates of the couples of recordings A04-A05 and A10-A11, obtained during the 30 October 2016 Norcia earthquake

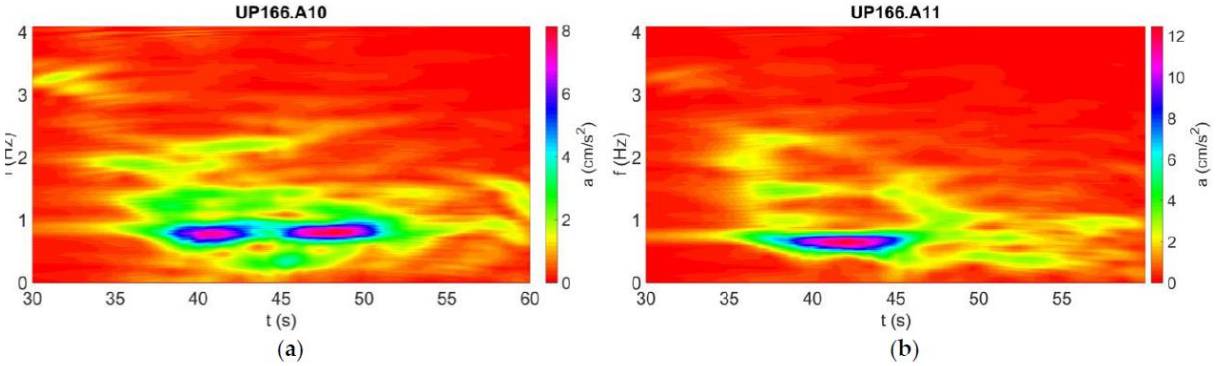


Figure 24. Time-frequency analysis for (a) A10 and (b) A11

The presence of two different resonance frequencies in the two directions could be related to a non-perfect symmetry of the isolation system. The wavelet transform, plotted in Figure 24 for sensors A10 and A11, show that the dominant frequencies vary during the seismic event and the frequencies related to the isolation system are particularly evident only during a small portion of the time histories.

One can deduce that the resonance frequencies changed during the earthquake and that the isolation system did not work for the entire recording.

These occurrences justify the presence of more peaks in the spectra around the resonance frequency. Furthermore, between 46 s and 50 s, vibrations prevail in x direction.

By means of a double integration in the frequency domain, the time histories of the displacements (Figure 25) were obtained from the acceleration time histories. The maximum values of the horizontal displacements of the gravity centers at L0, L1 and L2 were 27.3, 31.8 and 32.0 mm, respectively.

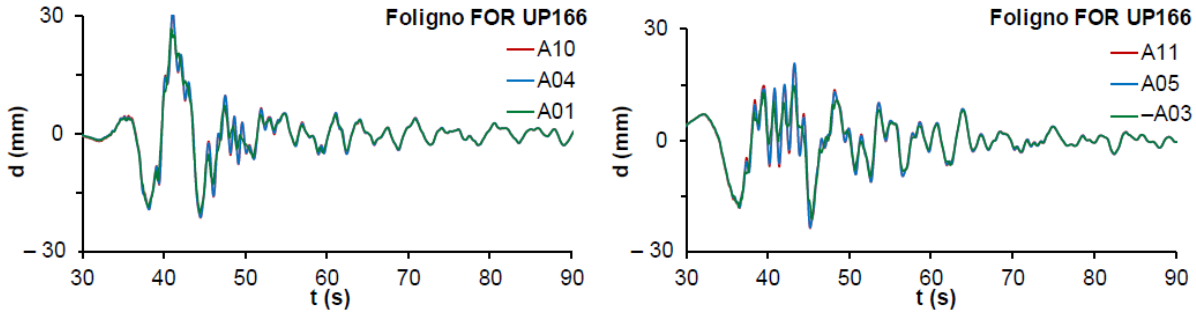


(a) (b)

Figure 25. Time histories of the absolute displacements at different level in (a) x direction (b) y direction (the sign of record at A03 has been changed; therefore, it is named –A03 in the legend).

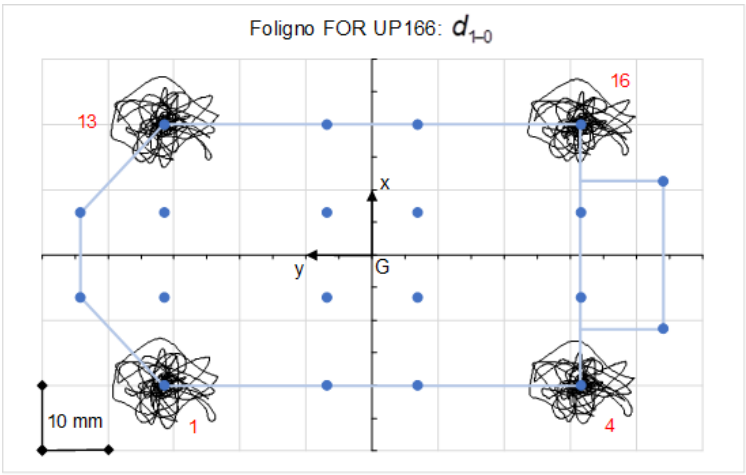


(a)

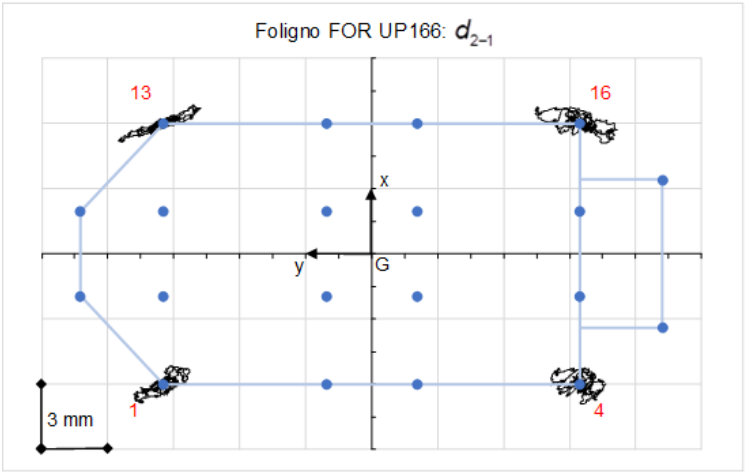


(b)

Figure 26. Relative particle motions at the points corresponding to the position of the corner isolation devices between (a) L1 and L0, and (b) L2 and L1

The relative horizontal displacements between L1 and L0, and between L2 and L1 were obtained for the 4 corner points, which correspond to the position of the isolation devices Is01, Is04, Is13 and Is16. The relative particle motions of these points are plotted in Figure 26, while the maximum values are summarized in Table 3. As one can see, the maximum displacement of the building does not exceed 32 mm.

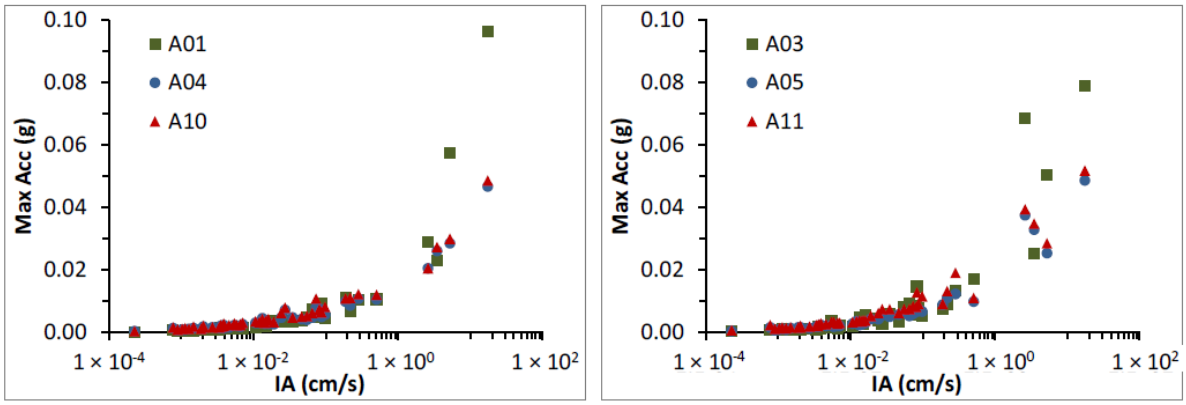


Figure 27. Maximum absolute acceleration at the basement PBA (A01 and A03 in x and y direction, respectively), above the isolation system PIA (A04 and A05), and at the top of the building PTA (A10 and A11), for all the recorded seismic events

The superstructure has a maximum relative displacement of about 2.2 mm between L2 and L1. This value is much lower than the limit value allowed by the Italian technical code at the serviceable limit state for strategic seismic isolated buildings, which is equal to h/450, h being the inter-story height. The displacement is concentrated at the level of the isolation system, where the maximum relative displacement in the isolation devices is about 9.3 mm, corresponding to a shear strain of 0.033.

| | **Event SH0 08** | **TX064** | **TX066** | **UR115** | **TX053** | **UP036** | **UP041** | **TX040** | **UP166** |
|---|---|---|---|---|---|---|---|---|---|
| PBA (g) | 0.0005 | 0.0012 | 0.0054 | 0.0094 | 0.0175 | 0.0706 | 0.0291 | 0.0575 | 0.0975 |
| PIA (g) | 0.0008 | 0.0014 | 0.0043 | 0.0111 | 0.0134 | 0.0379 | 0.0397 | 0.0300 | 0.0539 |
| PTA (g) | 0.0011 | 0.0017 | 0.0053 | 0.0136 | 0.0136 | 0.0411 | 0.0373 | 0.0327 | 0.0589 |
| PBD (mm) | 0.006( | 0.0271 | 0.2439 | 2.2917 | 1.1813 | 3.3642 | 9.7588 | 15.415 | 27.302 |
| PID (mm) | 0.013{ | 0.0378 | 0.2467 | 2.3663 | 1.3072 | 5.5737 | 14.443 | 16.213 | 31.809 |
| PTD (mm) | 0.017: | 0.0417 | 0.2524 | 2.3821 | 1.3349 | 5.8568 | 14.367 | 15.765 | 31.956 |
| $d_{1\text{-}0}$ (mm) | 0.011( | 0.0230 | 0.0728 | 0.2907 | 0.6282 | 5.0766 | 6.7810 | 4.9572 | 8.7882 |
| $d_{2\text{-}1}$ (mm) | 0.004( | 0.0107 | 0.0261 | 0.1503 | 0.1453 | 0.3685 | 0.6432 | 1.1301 | 1.6426 |
| $d_{1\text{-}0}$ Is01 | 0.0116 | 0.0224 | 0.0744 | 0.2869 | 0.6686 | 5.0513 | 6.6656 | 5.2281 | 9.2833 |
| $d_{1\text{-}0}$ Is04 | 0.0142 | 0.0236 | 0.0727 | 0.2847 | 0.6206 | 5.0211 | 6.7040 | 4.7085 | 8.7999 |
| $d_{1\text{-}0}$ Is13 | 0.0114 | 0.0234 | 0.0730 | 0.2968 | 0.6384 | 5.1327 | 6.8636 | 5.2482 | 8.8119 |
| $d_{1\text{-}0}$ Is16 | 0.0149 | 0.0251 | 0.0738 | 0.2947 | 0.5880 | 5.1030 | 6.9015 | 4.7466 | 8.3750 |
| $d_{2\text{-}1}$ Is01 | 0.0045 | 0.0107 | 0.0279 | 0.1439 | 0.1424 | 0.4136 | 0.5993 | 0.9671 | 1.4852 |
| $d_{2\text{-}1}$ Is04 | 0.0046 | 0.0111 | 0.0292 | 0.1385 | 0.1310 | 0.4408 | 0.5747 | 0.9542 | 1.3457 |
| $d_{2\text{-}1}$ Is13 | 0.0047 | 0.0113 | 0.0272 | 0.1735 | 0.1680 | 0.3127 | 0.7596 | 1.5602 | 2.1928 |
| $d_{2\text{-}1}$ Is16 | 0.0049 | 0.0109 | 0.0264 | 0.1631 | 0.1531 | 0.3454 | 0.7973 | 1.5626 | 2.1249 |

Table 5. Maximum accelerations, displacements, relative displacements of the gravity centers and maximum relative displacements at the corner isolators for the selected seismic events

For all the recorded events a frequency domain analysis was performed. In a lower energy range, the resonance frequency is independent of the seismic energy and varies in a small range around the value related to the superstructure. In these cases, the isolation system was not activated probably because of the friction forces of the SDs. For higher values of IA, instead, the seismic isolation system was put in action and the first resonance frequencies, related to the isolation system, decrease almost linearly with Log(IA). For low energy earthquakes the resonance frequencies approach those of the superstructure and there was no decoupling of motion.

The displacement is concentrated at the level of the isolation system, where the maximum relative displacement in the isolation devices is about 9.3 mm, corresponding to a shear strain of 0.033.

The results of the dynamic numerical analysis were compared to the seismic behavior observed during the Norcia earthquake. The good agreement between the acceleration time histories is apparent (Figure 28). Little discrepancies in terms of amplitudes can be attributed to a little lower stiffness of the numerical model with respect to the real structure. For the same reason the numerical displacement peaks are a little higher than those recorded during the earthquake (Figure 29). However, the frequency content of the recordings obtained during the event is well reproduced by the numerical model, as both the acceleration and displacement time histories show.

As already said, some crack patterns were observed on the partition walls of the first floor after the main event of 30 October 2016. In order to investigate this aspect, the relative displacements between the lower and upper beams were analyzed. It can be seen that an excursion greater than 2.0 mm around the value under vertical loads with a high frequency content, which occurred during the quake, can justify the cracks.

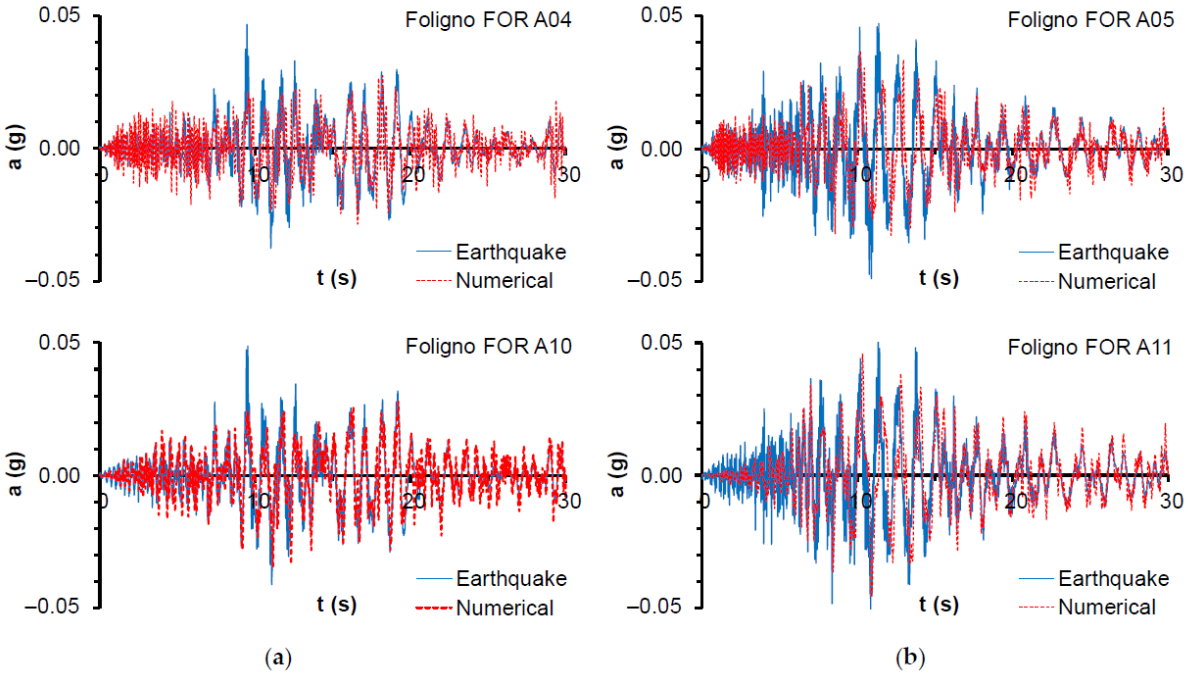


Figure 27. Comparison between the earthquake and numerical accelerations (a) in x direction and (b) in y direction

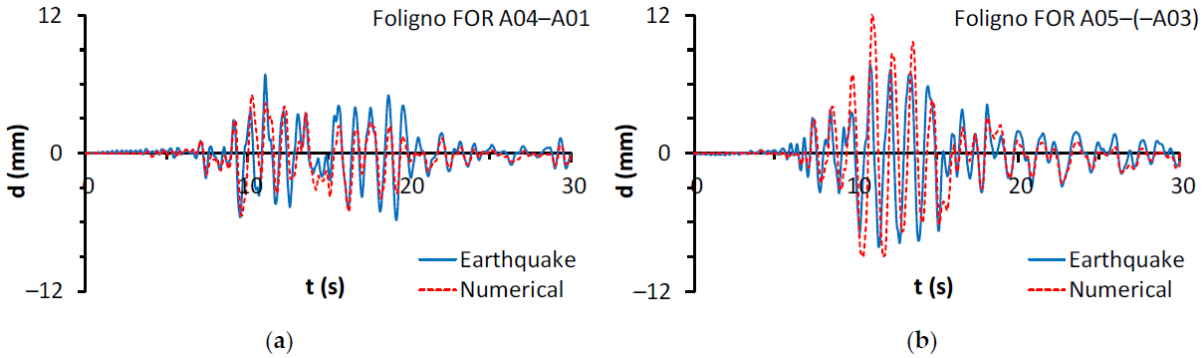


Figure 28. Comparison between the earthquake and numerical relative displacements between L1 and L0, (a) in x direction and (b) in y direction

## 5 CONCLUSION

The behaviour of the isolated buildings retrofitted or rebuilt after L'Aquila earthquake, subjected to new strong earthquakes in the same area, has been clear evidence of the excellent performance obtained by seismic isolation. After the 2009 earthquake, in the city of L'Aquila some hundred buildings have been seismically isolated. None of them reported any damage in consequence of the seismic events of 2016 – 2017, in the neighbourhoods of L'Aquila and in FOligno. In particular, five isolated buildings have been monitored and controlled, and the results show that each building, without damage, had an optimal performance, permitting the use of the buildings itself with no interruption. Also the isolation system didn't reported any damage and any residual displacement and deformation.

Seismically isolating the structure represents the best tool in order to maintains seismic security, resilience, total absence of damage (both structural and non-structural) and immediate usage of buildings and infrastructures even during very strong earthquakes.

A detailed analysis of the recorded behavior during the main event of 30 October 2016 was first shown. Then, the effects of a number of selected events were analyzed and compared. Finally, a suitable finite element model was set up, in which a non-linear model for the elastomeric isolators, based on previous experimental data, and a friction model for the sliders were assumed.

## 6 REFERENCES

[1] Buffarini, G., Clemente, P., De Flaviis, A., Ormando, C., Salvatori, A., (2023), Seismic Retrofit of r.c. Buildings with Base Isolation. In: *Cimellaro, G.P. (eds) Seismic Isolation, Energy Dissipation and Active Vibration Control of Structures. WCSI 2022. Lecture Notes in Civil Engineering*, vol 309, Springer, Cham. https://doi.org/10.1007/978-3-031-21187-4_85 , ISBN 978-3-031-21186-7, Online ISBN 978-3-031-21187-4

[2] Antonello Salvatori, Giovanni Bongiovanni, Paolo Clemente, Chiara Ormando, Fernando Saitta, Federico Scafati. (2022). Observed seismic behavior of a HDRB and SD isolation system under far fault earthquakes. *Infrastructure*, Vol 7 N. 2, 13, DOI: https://doi.org/10.3390/infrastructures7020013

[3] Paolo Clemente, Antonio Di Cicco, Fernando Saitta, Antonello Salvatori. (2021). Seismic behaviour of the base isolated Civil Protection Operative Centre at Foligno, Italy.

*ASCE Journal of Performance of Constructed Facilities*, Vol 35 (4); 04021027, Article ID CFENG-3346R2, pages 04021027-1 – 04021027-12, DOI: 10.1061/(ASCE)CF.1943-5509.0001589, ISSN (print): 0887-3828 | ISSN (online): 1943-5509

[4] Fernando Saitta, Paolo Clemente, Giacomo Buffarini, Giovanni Bongiovanni, Antonello Salvatori and Cristian Grossi. (2018). Base Isolation of Buildings with Curved Surface Sliders: Basic Design Criteria and Critical Issues. *Advances in Civil Engineering*, vol. 2018, Article ID 1569683, 14 pages, ISSN: 1687-8094, DOI 10.1155/7074, https://doi.org/10.1155/2018/1569683

[5] A.Martelli, P. Clemente, A. De Stefano, M.Forni and A.Salvatori. (2014). Recent development and application of seismic isolation and energy dissipation and conditions for their correct use. *In Geotechnical, Geological and Earthquake Engineering*, vol. **34**, pages 449-488, ISSN 1573-6059, ISSN 1872-4671 (electronic), ISBN 978-3-319-07117-6, ISBN 978-3-319-07118-3 (eBook**),** DOI 10.1007/978-3-319-07118-3_14, Kluwer Academic Publisher, Springer Cham Heidelberg New York Dordrecht London, Library of Congress Control Number: 2014946618

[6] Salvatori A., Di Cicco A., Clemente P.. (2021). Monitoring of base isolated building subjected to far fault earthquake. In: *Rainieri C., Fabbrocino G., Caterino N., Ceroni F., Notarangelo M.A. (eds) Civil Structural Health Monitoring. CSHM 2021. Lecture Notes in Civil Engineering*, vol 156. Springer, Cham. DOI https://doi.org/10.1007/978-3-030-74258-4_21 , pages 311 - 338, ISSN 23662557; Print ISBN 978-3-030-74257-7, Online ISBN 978-3-030-74258-4

[7] A. Salvatori, A. Di Cicco e P.Clemente. (2019) Seismic Monitoring Of Buildings With Base Isolation. In ”*7th ECCOMAS Thematic Conference on Computational Methods in Structural Dynamics and Earthquake Engineering”, COMPDYN 19*, M. Papadrakakis, M. Fragiadakis (eds.), ISBN 978-618-82844-5-6, id SCOPUS 2-s2.0-85079091857, DOI: 10.7712/120119, DOI URL: https://doi.org/10.7712/120119.7301.19221 , pagg. 5254 - 5275 , ISSN:2623-3347

[8] Bongiovanni, G., Buffarini, G., Clemente, P., Saitta, F., Salvatori, A., Scafati, F. (2019). Experimental seismic behaviour of base isolation systems in Italy during the 2016-2017 seismic sequence in central Italy., In Proceedings of XVIII Convegno Nazionale ANIDIS L’Ingegneria Sismica in Italia, SS01-125 – SSS01-133, Ascoli Piceno, Italy, ISBN 978-88- 3339-256-1, ISSN 2532-120X

[9] Buffarini, G., Clemente, P., Serafini, S., De Stefan,o A., Olivieri, R, Salvatori, A. (2012). Experimental dynamic analysis and seismic rehabilitation of Palazzo Margherita in L'Aquila. EAI Knowledge, Diagnostics and Preservation of Cultural Heritage, spec. II, ISBN E185775

[10] Clemente, P., Bongiovanni, G., Benzoni, G. (2017). Monitoring of seismic isolated buildings: state of the art and results under high and low energy inputs. Proc. New Zealand Society for Earthquake Annual Conf. and 15th World Conf. on Seismic Isolation, Energy Dissipation and Active Vibration Control of Structures, NZSEE2017 and 15WCSI, Wellington, 27-29).

[11] A. Salvatori. (2018). Seismic base isolation: retrofitting application in structures damaged by earthquake. In ”16th European Conference on Earthquake Engineering”, 18-21/06/2018, Thessaloniki, Greece.

[12] F. Braga, V. Manfredi, A. Masi, A.Salvatori, M. Vona- performance of non-structural elements in RC buildings during the L’Aquila, 2009 earthquake. *Bulletin of Earthquake Engineering*, **2011** , pp. 307-324, E185447 - issn: 1570-761X, doi: 10.1007/s10518-010-9205-7, Kluwer Academic press

COMPDYN 2023
9th ECCOMAS Thematic Conference on
Computational Methods in Structural Dynamics and Earthquake Engineering
M. Papadrakakis, M. Fragiadakis (eds.)
Athens, Greece, 12-14 June 2023

# THE LATERAL CAPACITY OF CONCRETE PILES IN STIFF CLAY TO DENSE SAND

**Mina Mikaeel** [1], **Andrew G. Gouda**[2]

[1] Principal Geotechnical Engineer, P.E., Kiro Engineering, LLC., Hamilton, NJ, USA mina@kiroengineering.com
[2] Assistant Lecturer , Construction & Building Eng. Dept., Arab Academy for Science & Technology and Maritime Transport AASTMT Portsaid, Egypt
andrew.gouda@aast.edu

## Abstract

*Pile foundations, either precast or cast-in-situ, are popular for usage worldwide in many important and costly projects, such as bridges, or jetties in harbor areas, etc. In addition, the stability and safety of such strategic structures count to a great extent on the serviceability of the carrying foundations system. Thus, the integrity of the soil-pile foundation systems governs sharply the service life of the supported structures.*
*Based on such complexity of modeling the problem, it may be beneficial to use field test results such as PDA tests and CAPWAP analysis to give a close estimate of the actual piles' lateral Capacity. Such results can act as proof testing, providing confirmation that the expected capacities assumed in design are in fact, available in the field.*
*Thus, based on accumulative results of PDA-CAPWAP tests in different types of soil for different types of piles and by modeling the soil pile system and asymptotically loading laterally till critical displacements are achieved, a stochastic equation is derived to correlate the piles' lateral capacities to available geotechnical information and PDA-CAPWAP tests. This is based on the assumption that the resistance to penetration can be divided into lateral and vertical components..*

**Keywords:** soil-structure interaction, impact load, Structural Dynamics, Earthquake Engineering, Proceedings.

# 1 INTRODUCTION

Design of foundations subjected to large lateral forces caused by wind, wave action, earthquake and lateral earth pressures is a challenging task especially if found in a soft soil which is usually prevalent in lowland regions of the earth pile Driving Analyzer (PDA) has to be mentioned as early as possible .In addition, structures such as transmission lines towers, bridges and hi-rise buildings, which are usually found on piles, must be designed to support both axial and lateral loads as well as moments. Therefore, the lateral resistance of piles is governed by several factors, the most important of which being the ratio of the structural stiffness of the pile to the soil stiffness. Moreover, the relative stiffness of the foundation element with respect to the soil controls the mode of failure and the manner in which the pile behaves under an applied lateral load. Thus, estimation of the lateral pile load capacity is a key design procedure for structures design, where lateral loads are predominant, such as in bridges, tall buildings, and transmission tower structures.

Furthermore, although the usual application of a pile foundation results primarily in axial loading, there exist numerous situations in which components of load at the pile head produce significant lateral displacements as well as bending moments and shear forces. Unlike axial loads, which only produce displacements parallel to the axis of the pile (a one-dimensional system), lateral loads may produce displacements in any direction. Unless the pile cross section is circular, the laterally loaded pile/soil system represents a three-dimensional problem. Most of the research on the behavior of laterally loaded piles has been performed on piles of circular cross section in order to reduce the three-dimensional problem to two dimensions. Little work has been done to investigate the behavior of noncircular cross-section piles under generalized loading. In many applications, battering of the piles in the foundation produces combined axial and lateral loads.

Piles during their lifetime may in practice be subjected to severe dynamic excitations as earthquakes. Damage resulting from such excessive lateral loading and its location are usually unexpected. This is the case together with knowing that economic and social effects of earthquake disasters can be efficiently reduced through a comprehensive assessment of seismic hazard and the associated risk [1]Thus, protection of piles against excessive loading hazards from earthquakes has become one of the essential goals for structural engineers.

However, the soil profile properties under any structure cannot be thus neglected in such an assessment. This is the case since the soil underneath structures is undoubtedly the medium that transfers the seismic excitation to the foundations of the structure. The process in which the soil response influences the motion of the structure and vice versa is termed as Soil Structure Interaction (SSI).) [2].

## 2 PROBLEM DEFINITION

Designers usually need to identify the lateral Capacity of piles to check for the stability of structures under lateral seismic loads. Pile foundations usually find resistance to lateral loads from (a) passive soil resistance on the face of the cap, (b) shear on the base of the cap, and (c) passive soil resistance against the pile shafts. The latter source is usually the only reliable one. Analysis of the problem yields deflections, rotations, moments, shears, and soil reactions as required for structural design. Beam-on-elastic-foundation theory is adequate for the analysis of the problem [3].

In addition, (PDA, CAPWAP) field tests are used to obtain the vertical Capacity of driven piles. In general, most piles are considered relatively flexible, but only short rigid piles are likely to require consideration of the lower boundary conditions in analysis. Non-dimensional solutions are available for both constant and linearly increasing modulus-depth relationships [3].

However, the majority of the research on lateral load behavior has been restricted to vertical piles subjected to loads that produce displacements perpendicular to the axis of the pile. In the discussions which follow, it is assumed that the pile has a straight centroid vertical axis. If the pile is non-prismatic and has a noncircular cross-section, it is assumed that the principal axes of all cross-sections along the pile fall in two mutually perpendicular planes and that the loads applied to the pile produce displacements in only one of the principal planes.

## 3 LITERATURE REVIEW

Laterally loaded piles may be classified as active piles or passive piles with regard to the loading transferring direction between the piles and the surrounding soils [4]. An active pile is principally loaded at its top, with the lateral load being transferred to the soil, such as piles acting as foundations for transmission towers, advertisement posts, and offshore structures. A passive pile usually sustains lateral thrusts along its shaft arising from horizontal movement of the

surrounding soils, such as piles in a moving slope or landslides. A variety of design and analysis methods have been developed for both active and passive piles. These methods range from relatively simplistic approaches that calculate the ultimate lateral Capacity to relatively sophisticated methods involving advanced numerical analyses that estimate the pile deflections. By reviewing the approaches for analyzing piles, one can distinguish that these approaches are subdivided into five sections: (1) pile flexibility and critical length; (2) failure modes; (3) limiting force or ultimate soil resistance profiles; (4) ultimate lateral Capacity; and (5) load- deflection calculation of laterally loaded piles [5].

## 4 CASE STUDY

Evaluating the lateral load resistance of pile foundations is critically important in the design of structures which may be subjected to earthquakes, high winds, wave action, and ship impacts. However, this is hampered by the high cost and logistical difficulty of conducting lateral load tests on piles. Several case studies are conducted on 16 driven prestressed concrete piles within areas in Route 52 Causeway, New Jersey, United States of America (Fig. 1). As part of the site investigation, cone penetration tests are performed to characterize the subsurface conditions. The pile load testing program consisted of dynamic testing by means of the Pile Driving Analyzer (PDA), CAPWAP, and full-scale static load tests.

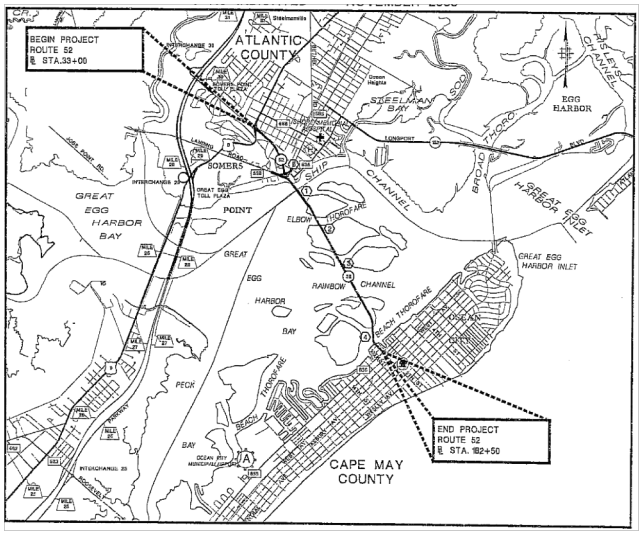


Figure 1. The region of the studied piles

The results of the cone penetration tests, dynamic and static load tests, and pile driving records were analyzed to form a database of high-quality, well-correlated data to inform the models. The results indicate that cone penetration tests can be used to accurately predict Capacity and required embedment lengths for the tapered piles. PDA and CAPWAP testing measures acceleration and strain imparted to a pile during driving. This data are then used in CAPWAP to calculate pile capacity. The CAPWAP program runs a numerical simulation of load testing the pile. The program compares the calculated Capacity to the acquired PDA data, iterating until it converges on the indicated pile capacity.

## 5 DATABASE

Data were collected from 16 PDA tests for the purposes of this study, where driven piles were installed for bridge foundations. Typical records of pile driving (pile penetration rate and hammer stroke) were accompanied with dynamic measurements using a Pile Driving Analyzer (PDA) for both ends of driving and the beginning of restrike conditions. All piles were square prestressed concrete piles driven with an impact hammer, and is presented in Table 1. For the case of the square piles, the equivalent diameter was calculated for simplicity. According to (AASHTO bridge design specifications) [6], the resistance factor for driven piles is 0.65.

## 6 SOIL STRATIFICATION

The subsurface profile was characterized using a variety of methods to provide basic geotechnical data for use in subsequent computer analyses of the test results, as shown in Fig. 2. Based on the results of the field and laboratory testing, and to simplify reading the soil properties of each layer, the soil profile shown in Table 2 was developed. The main studied soil profiles in this paper generally consider the general case of having two main layers. The first layer is stiff soil (e.g. clay), and the second layer is dense soil (e.g. sand).

**Table 1. Dimensions and allowable capacities of the studied piles**

| no. | Dimensions | | Mobilized axial Capacity | allowable axial Capacity |
|---|---|---|---|---|
| | Side. | pile length | | |
| | m | m | KN | KN |
| **1** | 0.76 | 23.16 | 7302.03 | 4746.32 |
| **2** | 0.76 | 21.49 | 7671.35 | 4986.38 |
| **3** | 0.76 | 24.38 | 9744.93 | 6334.21 |
| **4** | 0.76 | 25.76 | 7475.57 | 4859.12 |
| **5** | 0.76 | 25.76 | 8232.02 | 5350.81 |
| **6** | 0.76 | 19.05 | 8543.50 | 5553.28 |
| **7** | 0.76 | 30.94 | 7706.95 | 5009.52 |
| **8** | 0.76 | 18.59 | 8721.49 | 5668.97 |
| **9** | 0.76 | 25.76 | 7653.55 | 4974.81 |
| **10** | 0.76 | 22.92 | 10367.90 | 6739.13 |
| **11** | 0.76 | 21.18 | 8948.43 | 5816.48 |
| **12** | 0.76 | 31.09 | 8410.01 | 5466.51 |
| **13** | 0.76 | 23.93 | 6603.42 | 4292.22 |
| **14** | 0.76 | 23.47 | 6941.60 | 4512.04 |
| **15** | 0.76 | 23.62 | 7965.04 | 5177.27 |
| **16** | 0.76 | 32.61 | 8677.00 | 5640.05 |

**Table 2. The soil profile layers versus depth for one of the studied piles**

| Pile no. | clay | | | sand | | |
|---|---|---|---|---|---|---|
| | Layer thickness | ɣ | c | Layer thickness | ɣ | ϕ |
| | m | kN/m3 | kN/m2 | m | kN/m3 | |
| **1** | 16.00 | 19.76 | 59.99 | 45.72 | 21.57 | 42 |
| **2** | 17.53 | 19.47 | 69.87 | 53.34 | 19.69 | 39 |

| | | | | | | |
|---|---|---|---|---|---|---|
| **3** | 17.68 | 17.68 | 50.00 | 30.48 | 20.63 | 37 |
| **4** | 16.76 | 18.56 | 50.00 | 30.48 | 21.26 | 38 |
| **5** | 15.85 | 18.50 | 49.94 | 30.48 | 20.16 | 36 |
| **6** | 13.72 | 19.10 | 51.03 | 30.48 | 21.73 | 41 |
| **7** | 21.34 | 19.28 | 50.00 | 42.67 | 21.73 | 41 |
| **8** | 13.72 | 19.24 | 52.60 | 30.48 | 21.73 | 41 |
| **9** | 16.76 | 17.19 | 50.00 | 28.96 | 20.79 | 38 |
| **10** | 18.29 | 19.65 | 50.58 | 25.91 | 21.73 | 41 |
| **11** | 11.00 | 19.80 | 50.00 | 45.72 | 20.00 | 39.5 |
| **12** | 21.34 | 19.78 | 59.06 | 42.67 | 21.73 | 41 |
| **13** | 12.80 | 17.48 | 50.75 | 30.48 | 21.73 | 41 |
| **14** | 16.76 | 17.48 | 52.67 | 30.48 | 21.73 | 41 |
| **15** | 9.14 | 18.11 | 50.00 | 30.48 | 21.73 | 40 |
| **16** | 15.24 | 17.48 | 50.02 | 36.58 | 21.57 | 40 |

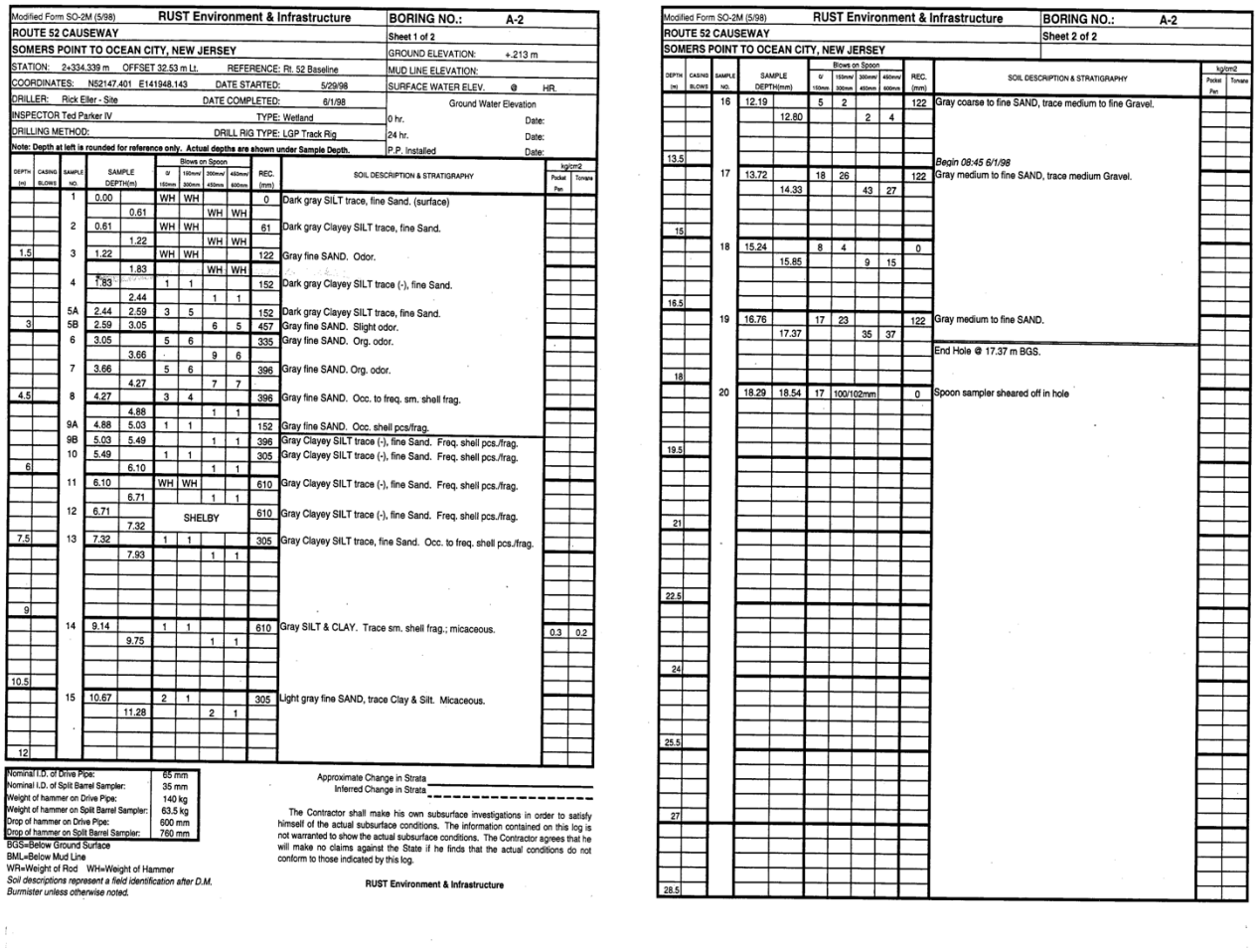


**Figure 2. Borehole sample for one of the studied piles**

## 7 METHODOLOGY

The present study focuses on determining the pile-head deflections. Typically, these values may often govern the design of laterally loaded piles. Therefore, an estimate of these values is of primary importance. In the present study, the LPile program was utilized to determine the pile-head deflections corresponding to the applied lateral load of the pile head at the ground surface (i.e. lateral load applied at an eccentricity from the ground surface). The latter program has the capability to generate and take into account nonlinear values of flexural stiffness (EI). These values are generated internally by the program based on cracked/uncracked concrete behavior and user-specified pile dimensions, and material properties for reinforced concrete sections. The program includes a feature for analyzing prestressed concrete sections as well. LPile software can perform pushover analyses and analyze the pile behavior after a plastic hinge (yielding) develops. The soil-layers data structures can be entered conveniently with default values

provided. Therefore, LPile may be advantageous over other applications for the subject handled in this research. However, future studies would use other techniques, such as finite element analysis for soil modeling in the studied problem for comparison.

The piles were assumed to be embedded in a uniform granular soil deposit. The LPile program was utilized to perform lateral load analyses for various pile types and pile sizes. The pile types included square concrete prestressed piles where the width ranges from 609.6 mm (24 in) to 762 mm (30 in).

By using (Poulos et al., 1980) [7] method, a linear elastic soil response due to lateral pile movements was assumed. A critical length, Lc, exists for a laterally-load pile, over which any increase in pile length has no influence on the ground line deflection δ. The critical pile length Lc is a function of the relative stiffness of the pile and soil nature [8]. Lc can be calculated from the following equations:

$$L_c = 4.44\sqrt[4]{\frac{E_p I_p}{E_s}}$$

Where: EpIp is the bending stiffness of the pile, and Es is Young's modulus of soil.

## 8 FAILURE CRITERIA

There are many methods of analyzing the response of a laterally loaded pile. These methods can be categorized into the subgrade reaction approach and elastic continuum approach. The subgrade reaction approach was initially proposed by Palmer and Thompson [9], and subsequently further developed by Reese and Matlock [9].Further advancements lead to the development of p-y curves which are commonly used to model the nonlinear pile and soil behavior. These have been described by McClelland [10], where nonlinearity often typifies the pile load-deflection behavior.

The p-y curve simply relates the unit soil resistance to pile deflection. Theoretically, it is normally assumed that the soil in the back and front of the pile will remain in contact with reference to the pile during lateral displacement. The slope of the p - y curve at any deflection represents the tangent soil stiffness at that deflection. The ratio p/y at any deflection represents the secant soil stiffness corresponding to that deflection [11].

Matlock and Hudson [12]developed the empirical expression to represent the p - y curve defined by the power function of deflection normalized by pile deflection at 50% of the ultimate soil reaction. Integrated clay criteria [13] proposed three expressions to represent the different segments of the p - y curve. The reference displacement ($y_c$) is taken as the displacement of a pile that will occur at 50% of the ultimate soil resistance. The ultimate soil resistance occurs at a displacement of $y_u$, and beyond, remains constant for ideally plastic clays [14] O'Neill and Gazioglu, Sal M. [13] proposed a p - y curve development procedure that would be applicable to all clays in order to remove the subjective distinction associated with the characterization of cohesive soils as either soft clays or stiff clays. The integrated clay criteria is developed by making a number of reasonable assumptions regarding the influence of factors like pile diameter, pile length, and soil stiffness and by optimizing the several parameters to produce a procedure that provides the best agreement with the available field data. The following equation can be used to calculate the critical deflection

$$y_c = 0.8*\varepsilon_{50}*d^{1/2}*(E_pI_p/E_s)^{1/8} \quad (2)$$

Where:

- $E_pI_p$ = bending stiffness of pile
- $E_s$ = Young's modulus of soil
- $d$= diameter of pile
- $\varepsilon_{50}$= strain at 50% of ultimate strength from a laboratory stress-strain curve from Table 3.

- Table 3. Values of undrained shear strength

| **Undrained Shear strength, $c_u$ [kN/m$^2$]** | **$\varepsilon_{50}$** |
|---|---|
| <12 | 0.02 |
| 12-24 | 0.02 |
| 24-48 | 0.01 |
| 48-96 | 0.006 |
| 96-192 | 0.005 |
| >192 | 0.004 |

## 9 ANALYSIS OF CASE STUDY

Moreover, the soil is modeled as a linear hysteretic material of Young's modulus, E, Poisson's ratio, υ, material damping ratio, ζ, and shear velocity, vs, see Figure 3.. Meanwhile, to calculate the single pile stiffness in the strips embedded in the sandy soil or clay soil, the geotechnical engineering software LPile [15]is used. The software (LPile) directly uses COM624S calculation methods for lateral analysis. The COM624S program solves the nonlinear differential

equations representing the behavior of the pile-soil system to lateral (shear and moment) loading conditions in a finite difference formulation using p-y method of analysis by Reese et [16]For each set of applied boundary loads the program performs an iterative solution which satisfies static equilibrium and achieves an acceptable compatibility between force and deflection (p and y) in every element. For details on COM624, please refer to the FHWA publications. In summary, COM624S uses the four nonlinear differential equations to perform the lateral analysis.

$$EI\frac{d^4Y}{dZ^4} + Q\frac{d^2}{dZ^2} - R - Pq = 0 \tag{3}$$

$$EI\frac{d^3Y}{dZ} + Q\frac{dY}{dZ} = P \tag{4}$$

$$\frac{dY}{dZ} = St \tag{5}$$

$$EI\frac{d^3Y}{dZ} = M \tag{6}$$

where Q is the axial compression load on the pile, y is the lateral deflection of pile at depth z, z is the depth from top of pile, R is the soil reaction per unit length, E is the modulus of elasticity of the pile, I is the moment of inertia of the pile, and Pq is the distributed load along the length of the pile, P is the shear in the pile, St is the slope of the elastic curve defined by the axis of pile, and M is the bending moment on the pile

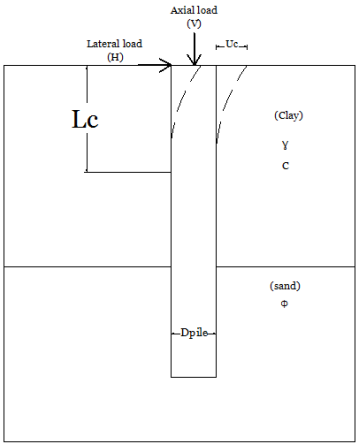


Figure 3. Pile-Soil system model

## 10 RESULTS AND DISCUSSION

For a given pile and a given set of soil conditions, pile-head load versus deflection curves were generated by increasing the lateral load as shown in Figure 4. For the range of pile sizes and soil parameters used in this study, it was determined that the minimum embedment depth

beyond which the pile response remains unaffected after critical length. Most of the piles achieved complete bending with zero deflection at the pile tip.

**Estimation of lateral load capacity of pile using LPile**

LPile is capable to determine the flexural response of pile where the load is increased in a step by step manner. Passive resistance of soil is considered in the model and the program stops whenever the critical deformation is exceeded. This principle has been considered taking into the account the generated P-Y curves. In the present paper, the load acting at pile head and number of increments has been provided to reach the load. In LPile software, an automatic load increment feature is available which is used to estimate the lateral load capacity of pile as shown in Table 4. In the following Table 4, the lateral load capacity of piles have been estimated from the LPile software considering the permissible deflection at critical deflection capacity.

Table 4. The results of critical deflection and lateral Capacity for the studied piles

| Pile no. | yc (critical def.) | (H) lateral Capac-ity |
|---|---|---|
| | cm | KN |
| **1** | 0.478 | 353 |
| **2** | 0.464 | 380 |
| **3** | 0.498 | 307 |
| **4** | 0.498 | 317 |
| **5** | 0.498 | 314 |
| **6** | 0.496 | 318 |
| **7** | 0.498 | 317 |
| **8** | 0.492 | 321 |
| **9** | 0.498 | 314 |
| **10** | 0.497 | 310 |
| **11** | 0.498 | 314 |
| **12** | 0.480 | 345 |
| **13** | 0.496 | 322 |
| **14** | 0.492 | 326 |
| **15** | 0.498 | 314 |
| **16** | 0.503 | 303 |

## ESTIMATION OF LATERAL LOAD CAPACITY OF PILE

From the above observation, the lateral load capacity of the pile has been estimated from the LPile software. The lateral load-carrying Capacity of a single pile depends not only on the horizontal subgrade modulus of the surrounding soil within the critical depth of the pile but also on the structural strength of the pile shaft against bending resulting from the application of the lateral load on the pile. While considering lateral loads on piles, the effect of other co-existent loads, including the axial load on the pile, should be taken into consideration for checking the pile's lateral Capacity.

Therefore, after the analysis of these results, it was tried to find a relation between the lateral load (H) versus the coefficient of cohesion (c), as well as the relation with the unit weight (ɣ) of the soil where the pile-soil system is assumed to deflect along the critical length. A nearly linear relations were found in both cases, as shown Figures 4, 5.

In addition, it was also observed that there isn't a clear relation between the lateral load capacity and axial load, therefore, it was tried to find a relation between the ratio (H/V) versus the axial vertical load (V). It is found that the relationship is nonlinear between H, and (H/V) as shown in Figure 6. Moreover, it is shown from Figure 6 that the lateral to vertical capacities ratio ranges from 5% to 7.5% of the axial Capacity.

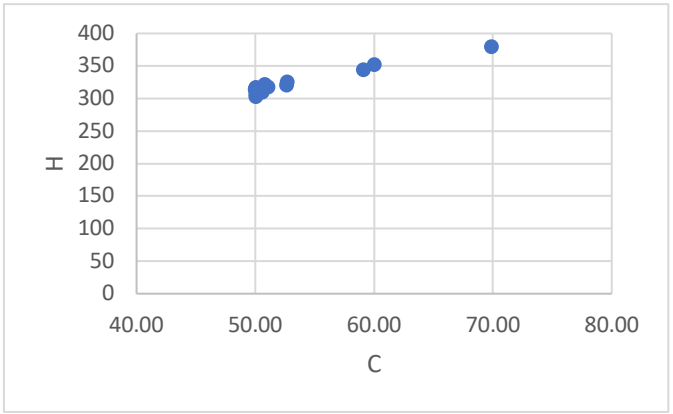


Figure 4. The relation between *H* in *kN* vs. the cohesion coefficient C in $kN/m^2$

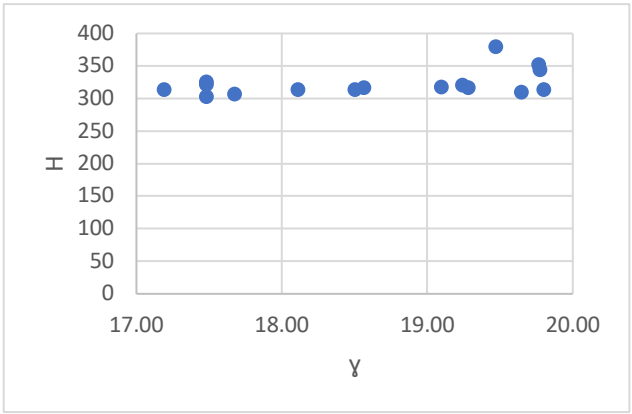


Figure 5. *H* in *kN* vs. the unit weight **ɣ in** $kN/m^3$

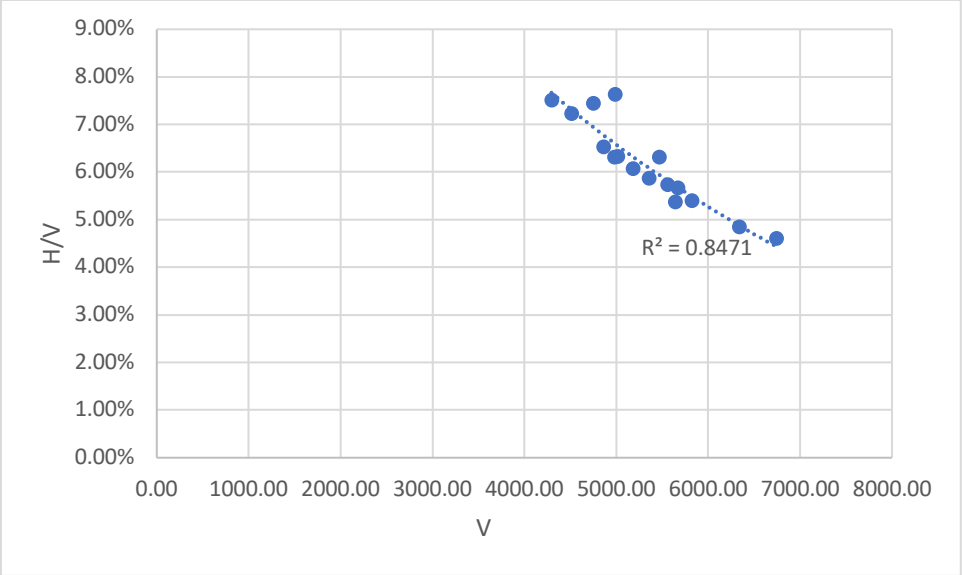


Figure 6. The relation between the ratio (*H/V*) vs. the axial load (*V*)

Based on the observed relations from Figures (4),(5),(6), one can distinguish that there are multiple parameters that affect the estimate of the lateral Capacity, such as the soil cohesion, c, the unit weight, ɣ, and the vertical Capacity, V. Moreover, studying the results as shown in Figure (6), one can realize that there is not one parameter that is solely sufficient to identify the lateral Capacity. Thus, a multiple nonlinear regression analysis using the SPSS program is applied to relate the correlated parameters to the lateral Capacity of piles. The latter analysis between the coefficient of cohesion (c), the soil unit weight (ɣ), and the axial load (V) is used to obtain a four-dimensional relationship between the above-mentioned parameters versus the lateral load capacity.

Moreover, from the defined nonlinear multi-parametric equation, by setting the unit weights to be in the range between 16 to 20 kN/m3, the space schematic shown in Figure (7) is obtained. The latter schematic incorporates the full results from the CAPWAP tests and the available soil profile properties for all piles to allow users to estimate a lateral capacity for any driven prestressed pile.

Furthermore, Figure (8) shows a three-dimensional surface that relates the soil properties and the CAPWAP results for the case of having a unit weight of 17 kN/m3 for the soil layers within the critical depth of the piles. Similarly, other three-dimensional surfaces can be obtained for other unit weights of the soil within the critical depth of the pile along which the

pile deflects. The lateral Capacity for the driven piles can be obtained easily from such relations.

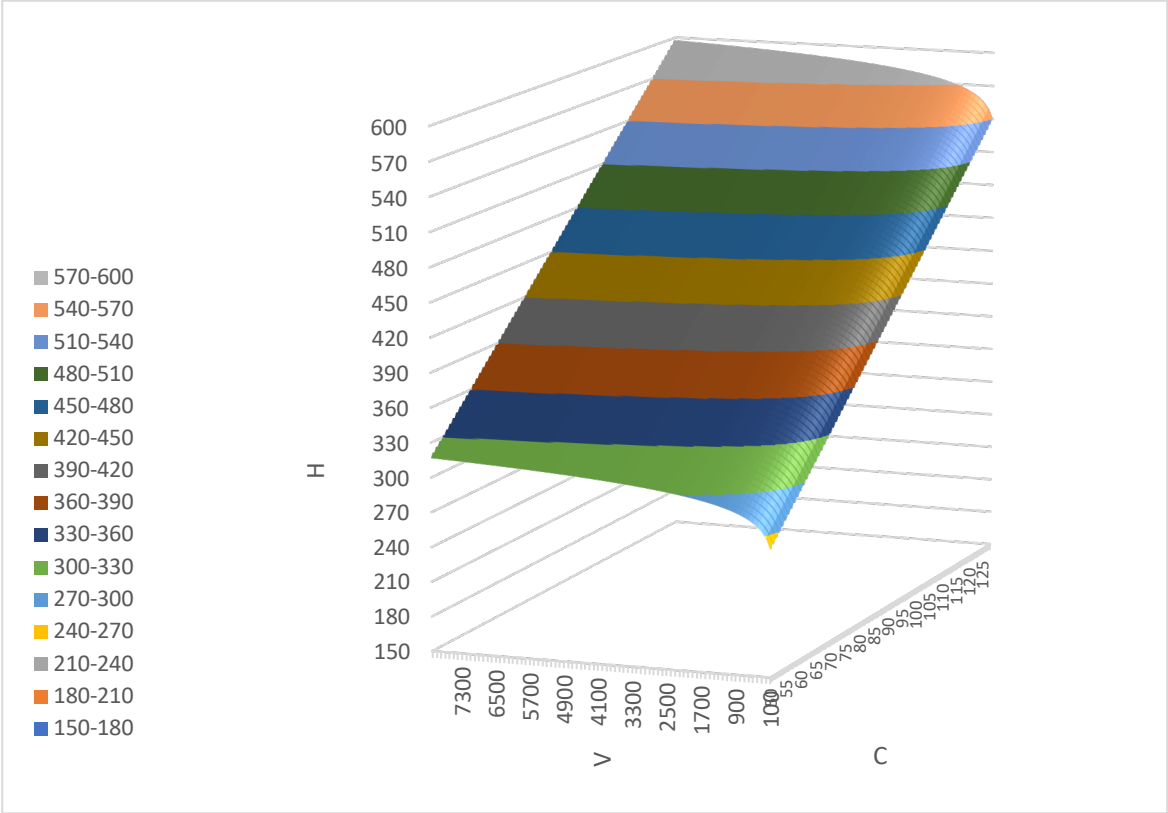


Figure (7) The relation between lateral Capacity (H), vertical Capacity (V) and cohesion coefficient (c ) for a unit weight (ɣ) from 16-20(kN/m3)

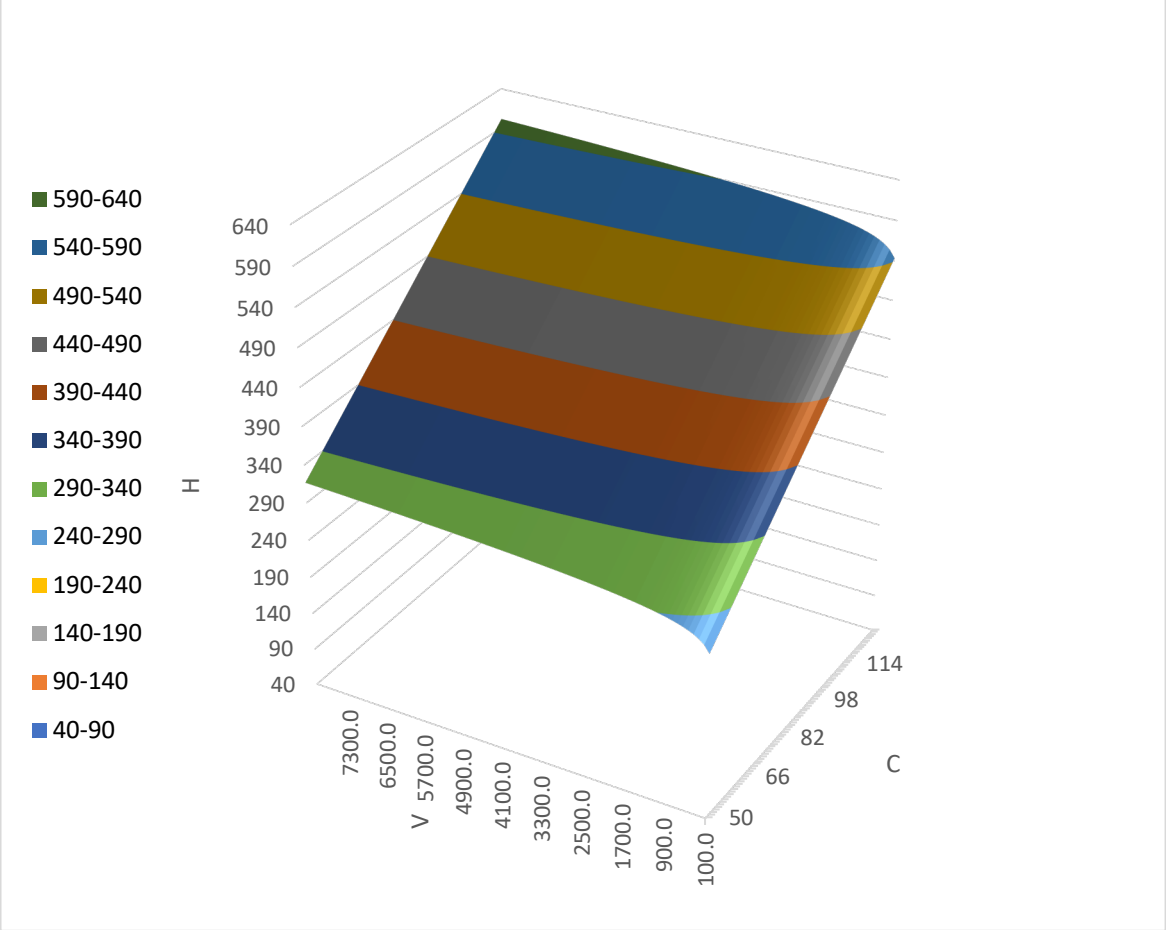


Figure (8) The relation between lateral load (H) & axial load (V) & coefficient of cohesion (c ) at a unit weight (ɣ) =17(kN/m3

## 11 CONCLUSIONS

As Designers usually seek simpler methods for applications in their design and assessments, it would be beneficial to help designers to obtain estimates of the piles' lateral Capacity from available soil properties and axial load. This study focuses on piles behavior in soil profiles that are composed of soft stratum right below the surface, followed by a stiff stratum underneath. In this paper, the lateral Capacity of pile was found to depend mainly on three major parameters. These parameters include the coefficient of cohesion (c), and unit weight (ɣ) for the soil layers within the critical depth of the pile from the surface in which the pile is allowed to deflect, in addition to the vertical axial load capacity of piles (V).

Based on the present study and from the results of analysis, it is observed that the lateral load capacity of pile increases in nearly linear relation to the coefficient of cohesion (c), unit weight (ɣ), and a nonlinear logarithmic attitude is revealed on studying the relation between the vertical axial load capacity (V) and the ratio between the lateral and axial vertical capacities (H/V).

It was also found that the lateral capacity ratio mentioned above for prestressed driven piles ranges from 5% to 7.5% of the axial vertical Capacity. Finally, a multiple nonlinear regression was applied using SPSS software to identify the four-dimensional nonlinear relation between the lateral Capacity (H), the vertical Capacity (V), the soil cohesion (c), and the soil unit weight (ɣ). The resulting space schematic and three-dimensional surface relations can successfully be used to identify the lateral Capacity based on CAPWAP test results that identify the vertical Capacity and the soil properties within the critical depth of the studied piles.

# References

[1] Kumar G., Shruti H.K., (2014). Soil Structure Interaction Effect On 200m Tall Industrial Chimney Under Seismic Load. International Journal of Civil and Structural Engineering Research, 2, pp. 111-118..

[2] Kumar S.S., Krishna A.M., A. Dey (2013), Parameters Influencing Dynamic Soil Properties, A Re-view Treatise. National Conference on Recent Advances in Civil Engineering,..

[3] DAVISSON M. T.,(1970) Lateral Load Capacity of Piles, Department of Civil Engineering, University of Illinois, Urbana.

[4] • DAVISSON M. T. 1970. Lateral Load Capacity of Piles, Department of Civil Engineering, University of Illinois, Urbana..

[5] Qin H. (M. Eng.), (2010). Response of pile foundations due to lateral force and soil movements Griffith School of Engineering Science, Environment, Engineering and Technology Griffith University.

[6] AASHTO LRFD, Bridge Design Specifications [Richard M. Barker, Jay A. Puckett].

[7] Poulos, H. G. and Davis, E. H. (1980). Pile Foundation Analysis and Design. John Wiley and Sons, New York..

[8] Poulos, H. G. and Hull, T. S. (1989). The role of analytical mechanics in foundation engineering. Foundation Engineering, Current Principals and Practices. F.H. Kulhawy ed., Proceedings of the congress sponsored by the Geotech. Engrg. Div.,ASCE, Evanston.

[9] Palmer, L.A. and Thompson, J.B. (1948). The Earth Pressure and Deflection Along the Embedded Lengths of Piles Subjected to Lateral Thrust. Proceedings of the Second International Conference on Soil Mechanics and Foundation Engineering, Rotterdam, vol. 5,.

[10] McClelland, B. and Focht J.A. Jr. (1958), "Soil Modulus of Laterally Loaded Piles,"Transactions, American Society of Civil Engineers, Vol 123, 1958, pp 1049-1063.

[11] Kramer, S. L. 1988. Development of p-y curves fro analysis of laterally loaded piles in western..

[12] Matlock, Hudson,( 1970) "Correlations for Design of Laterally Loaded Piles in Soft Clay," Presented at the Second Annual Offshore Technology Conference, Houston, Texas, 1970, Vol 1, pp 577-588..

[13] O'Neill, M.W., and Gazioglu, Sal M., (1984), An Evaluation of p-y Relationships in Clays, A Report to the American Petroleum Institute, (PRAC 82-41-2), University of Houston- University Park, Department of Civil Engineering, Research Report No. UHCE-84-3,.

[14] Kodikara J., Haque A and Lee H., (2010). Theoretical p-y curves for laterally loaded single piles in undrained clay using bezier curves, Journal of Geotechnical and Geoenvironmental Engineering - ASCE, vol. 136, pp 265-268.

[15] LPile. 2015. for Windows, Data Format 6 (version 2015.8.03) through 2015-6-37..

[16] Reese, L.C., Cox W.R. and Koop F.D. 1975. Field testing and analysis of laterally loaded piles in stiff clay. Proceedings of the VII Annual Offshore Technology Conference, Houston, Texas, 2(OTC 2312): 672 -690.

[17] DAVISSON M. T.,(1970) Lateral Load Capacity of Piles, Department of Civil Engineering, University of Illinois, Urbana.

COMPDYN 2023
9th ECCOMAS Thematic Conference on
Computational Methods in Structural Dynamics and Earthquake Engineering
M. Papadrakakis, M. Fragiadakis (eds.)
Athens, Greece, 12-14 June 2023

# SEISMIC ANALYSIS FOR BUILDING STRUCTURES UNDER DYNAMIC SOIL-PILE INTERACTION USING SIMPLIFIED MODELS

**Jun-Yang Shi**[1]

[1] Department of Civil and Environmental Engineering, National University of Kaohsiung, Taiwan
700, Kaohsiung University Rd., Nanzih District, Kaohsiung 811, Taiwan
e-mail: jyshi@nuk.edu.tw

## Abstract

*This paper presents the application of a new simplified model to simulate dynamic soil-pile interaction undergoing coupled sliding and rocking motions. The developed model's components and parameters are calculated using the theory of equivalent models developed in the previous work. A parametric analysis has been carried out for structural responses using dimensionless parameters considering dynamic soil-pile-structure interaction (SPSI). The analyzed parameters include earthquake frequencies, pile tip conditions, story mass ratios, and story stiffness ratios. The results show that the simplified model accurately estimates the peak response of the SPSI system at low frequencies. The magnification factors analyzed by the simplified model also agree well with the analytical solutions at high frequencies when the pile tip is fixed. Besides, the simplified model slightly overestimates the dynamic responses at high frequencies for the SPSI system when the pile tip is considered simply supported. Hence, the simplified model proposed has a good potential to be applied to the seismic analysis for building structures considering dynamic SPSI.*

**Keywords:** Pile Foundation, Soil-Pile Interaction, Discrete-Element Model.

## 1 INTRODUCTION

In recent years, the development of high-rise urban buildings has been increasing with the rapid urban population growth. Since high-rise buildings are heavy structures, if they are located on soft shallow soil, it is often necessary to use pile foundations to support the various loads transmitted from the building. A pile foundation is usually composed of pile caps, which are connected to the superstructure. The load of the superstructure determines the distance and number of piles. The static analysis method is used in most of its designs. However, for essential high-rise structures, it is necessary to consider the dynamic effects caused by earthquakes and shock loads. The research on soil-pile interactions mainly started from Mindlin [1], who deduced the basic elastic solution for static analysis of soil-pile interaction. Later, many studies applied this elastic solution to explore the static behavior of pile groups. Currently, studies on soil-pile interactions considering dynamic effects can be mainly divided into three categories, including the Winkler-beam model [2,3], the continuous method [4,5], and the finite element method [6,7]. However, all the above methods may have their limitations. The Winkler-beam mode needs the inputs of soil spring to simulate the soil stiffness. In addition, the continuous method requires special Green functions, and the finite-element method requires appropriate viscous boundaries to simulate the semi-infinite soil medium.

Due to the complexity of dynamic soil-structure interaction (SSI), numerous simplified models have been developed to simulate the SSI efficiently. The simplified model for simulating soil dynamic behavior mainly began with Lysmer and Richart [8] using a single-degree-of-freedom system to simulate the dynamic characteristics of semi-infinite half-space. Subsequently, similar concepts have been further extended. Meek and Veletsos [9] added an additional degree of freedom (DOF) into the simplified model, which became a 2-DOF system to simulate the dynamic response of the foundation under horizontal and rocking vibration. Wolf and Somaini [10] and de Barros and Luco [11] also used the 2-DOF system to simplify the dynamic behavior of embedded foundations. Jean, Lin, and Penzien [12] used a simple model with three DOFs and ten parameters to simulate the vertical, horizontal, rocking, and torsional vibration of a rigid foundation. Wolf and Paronesso [13] also simulated the dynamic interaction between rigid foundations and soil using a simplified model using multiple DOFs. The consistent model developed by Wolf [14,15] and the nested model constructed by Wu and Lee [16] attempt to construct a multi-degree-of-freedom system systematically to simulate the interaction between soil and foundation. However, previous studies [14-16] also ignore the coupling behavior of the foundation subjected to horizontal and rocking vibration.

The previous work [17-19] recently proposed systematic, simplified models with adapted accuracies to simulate the dynamic interactions between embedded foundations and layered soils subjected to vertical, horizontal, and rocking vibrations. The developed model could simulate the coupling behavior between horizontal and rotational motion. This paper aims to present the application of the newly developed model to simulate dynamic soil-pile interaction subjected to coupled horizontal and rocking excitations. This study also performs a parametric analysis for structural responses using dimensionless parameters considering dynamic soil-pile-structure interaction (SPSI) in the frequency domain. The analyzed result will show the potential application of the newly developed model in dynamic SPSI analysis.

## 2 METHOD

The previous work [17-19] developed the theory of equivalent model to construct a simplified model simulating unbounded soil. The concept is first to calculate the parameters of the simplified model conforming to the equivalent condition for a single frequency point, which includes equivalent static displacement, equivalent dynamic amplification factor, and equiva-

lent dynamic dissipation energy. Subsequently, the corresponding equivalent models was solved for $N$ frequency points, and an error function was used to select the optimal model for simulating dynamic soil behavior from the $N$ equivalent models. This paper uses the theory of equivalent model to establish the simplified model for simulating the soil-pile system subjected to horizontal and rotational motions, as shown in Figure 1(a). In addition, Figure 1(b) shows the simplified model, which uses the modulized units developed in the previous work [19], as shown in Figure 2. The equivalent parameters of the simplified model are determined by the governing equations based on the three equivalent criteria considering horizontal and rotational responses. The optimal model parameters are then found by using an error function regarding the magnification factors in the horizontal and rotational directions.

This study analyzes the dynamic response of building structures with pile foundations induced by seismic excitations. This study also performs dimensionless parametric analysis for the transfer function of structural displacements considering the influence of inertial interactions. A lumped-mass model is used to simulate the superstructure, as shown in Figure 3. When the building system is subjected to seismic excitations, the dynamic equilibrium equation for each floor at the superstructure can be constructed as follows.

$$\mathbf{M}\ddot{\mathbf{U}} + \mathbf{C}\dot{\mathbf{U}}_{\mathbf{r}} + \mathbf{K}\mathbf{U}_{\mathbf{r}} = \mathbf{0} \tag{1}$$

where $\mathbf{M}$, $\mathbf{C}$, $\mathbf{K}$ are the mass matrix, damping matrix, and stiffness matrix of the superstructure, respectively; $\mathbf{U}$ and $\mathbf{U_r}$ are the vectors collecting the total displacement, $U_j$, and the relative displacement, $U_{rj}$, at each floor in the horizontal direction. The total horizontal displacement at the $j$-th floor is defined as

$$U_j = U_{rj} + U_b + h_j \Phi_b \tag{2}$$

where $U_b$ is the horizontal displacement at the foundation top and $\Phi_b$ is the rotation angle of the foundation. Further details could be found in the previous work [20]. As the building system is undergoing harmonic horizontal excitations, the transfer function for the horizontal response can be derived from the structural dynamics, as given below.

$$\frac{u_j}{u_g} = \frac{u_{rj}}{u_g} + \frac{u_b}{u_g} + \frac{h_j \phi_b}{u_g} \tag{3}$$

where $u_g$ is the displacement amplitude of input motion; $u_j$ is the total displacement amplitude at the $j$-th floor; ; $u_{rj}$ is the relative displacement amplitude at the $j$-th floor; $u_b$ is the displacement amplitude at the foundation top; $\phi_b$ is the rotational amplitude of the foundation; and $h_j$ is the height measured from the $j$-th floor to the foundation top. Note that the transfer function defined in Eq. (3) depends on a dimensionless frequency ratio, $a_0 = \omega R/V_s$, with the exciting frequency $\omega$, the soil density $\rho$, and the characteristic length of the foundation $R$. In this study, the superstructure is supposed to have identical lumped mass and lateral stiffness at each story. By doing so, two dimensionless parameters are defined below, which significantly affect the dynamic response of the building system.

$$b_s = M_b / \rho R^3; \qquad r_{sx} = K_b / K_{sx} \tag{4}$$

where $b_s$ is the story mass ratio; $r_{sx}$ is the story stiffness ratio; $M_b$ is the story mass; $K_b$ is the lateral story stiffness; $K_{sx}$ is the static foundation stiffness in the horizontal direction. This study uses Eq. (3) to analyze the transfer function of the building system with pile foundations subjected to horizontal excitations. The theoretical impedance function is used to calculate the actual system response. The approximate impedance function of the simplified model is also

applied to calculate the system response for further comparisons. The results will demonstrate the effectiveness of the simplified model applied in the dynamic SPSI analysis.

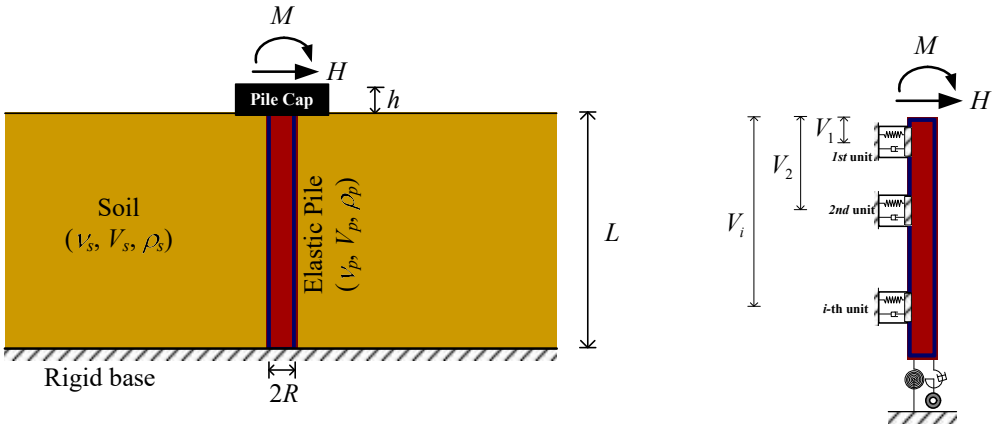


(a) soil-pile system (b) simplified model

Figure 1:Dynamic soil-pile interaction models.

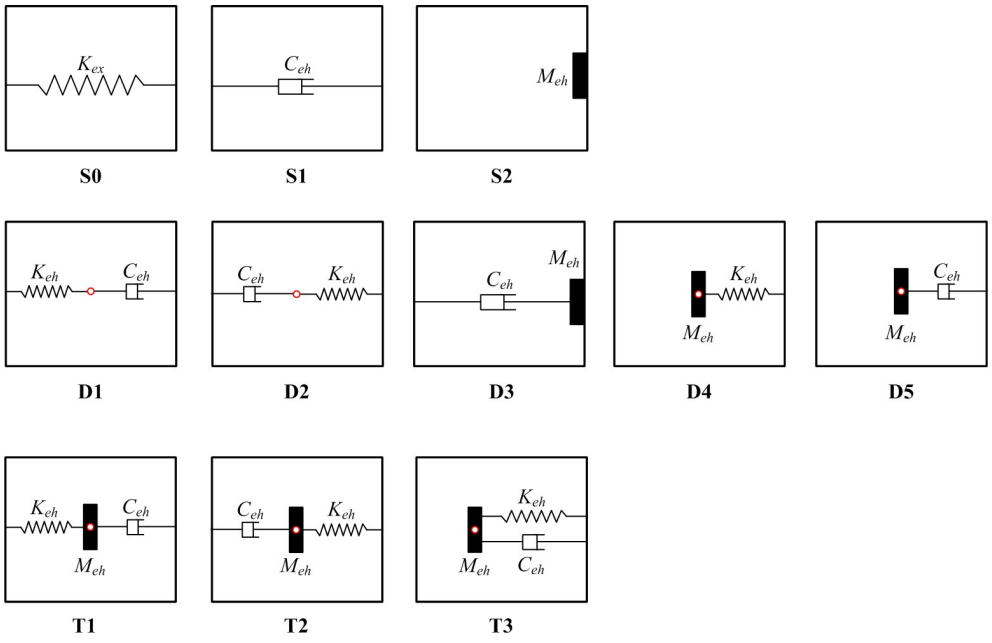


(a) horizontal units

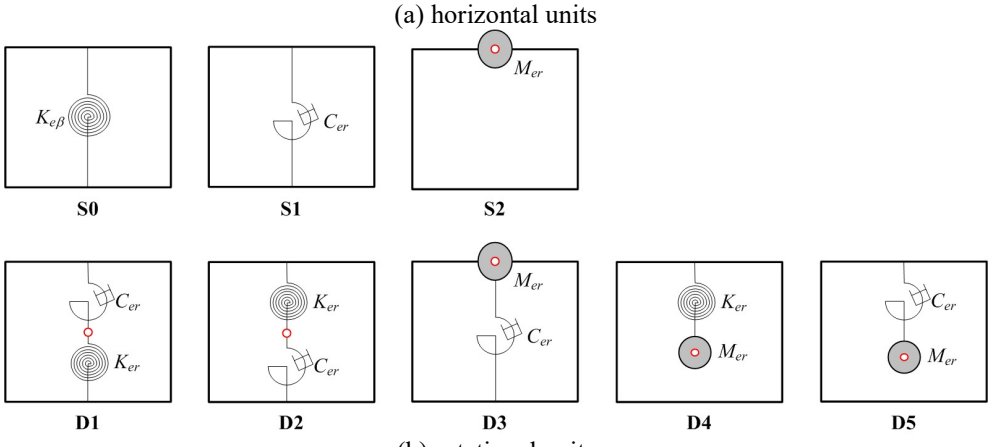


(b) rotational units

Figure 2: Modulized unit for simplified models (adapted from Ref. [19]).

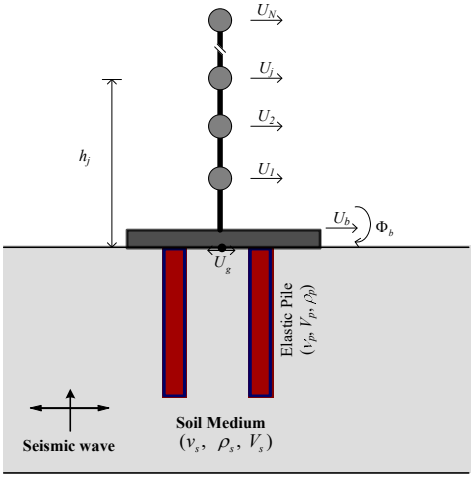


Figure 3: Building system with dynamic SPSI.

## 3 RESULTS

The study considers dynamic interactions between piles and soils to establish the simplified model for dynamic SPSI analysis through the systematic method described in Section 2. This section uses the simplified model to calculate the dynamic response of the building structure with pile foundations subjected to horizontal excitations. In the complete SPSI system, suppose an elastic pile has a radius $R$, a length $H$ = 15R, and a pile cap with a height $h = 2R$, buried in the homogeneous soil layer. The other parameters for the soil-pile system investigated include a Poission's ratio of soil $\nu = 0.5$, a material damping ratio of soil $\xi_s = 0.02$, a ratio of the density of the pile to that of soil $\rho_p/\rho_s = 0.6$, a ratio of the shear-wave velocity of soil to the compression-wave velocity of the pile $V_s/V_p = 0.01$. In addition, the pile tip is simulated as a fixed end and a simply-supported end, respectively, to analyze the influence of boundary conditions on the dynamic response of the SPSI system. For the superstructure structure, the contribution of lateral story stiffness, story mass, and story damping to the dynamic response of the SPSI system is analyzed by using a lumped-parameter model. In this section, the pile impedance function developed by Novak and Nogami [21] is used to calculate the optimal simplified model for simulating the dynamic soil behavior. Eq. (3) is used to calculate the dynamic magnification factor, defined as a norm of the transfer function, at the floors for the SPSI system under horizontal excitations. Note that the theoretical frequency-dependent impedances are used to compute the response of a complete SPSI system, and the approximate impedances of the simplified model with frequency-independent parameters are applied to calculate the response of a simplified SPSI system. Further comparisons are performed for the analyzed results.

The horizontal magnification factor at the top floor in a ten-story building structure is shown in Figures 4-6. In Figure 4, the story mass ratio, $b_s$ = 0.5, and story stiffness ratio, $r_{sx}$ =0.5, are typical parametric values. In addition, Figure 5 shows the analyzed results regarding two times the typical parametric values. Figure 6 analyzes a specific condition when the story mass ratio and the story stiffness ratio are four times the typical parametric values. The results show that the dynamic magnification factor by the simplified model agrees well with the analytical solution. This agreement is also observed at the peak response of the SPSI system in the low-frequency region. However, the dynamic magnification factor by the simplified model is slightly higher than the analytical solution in the high-frequency region. The observed discrepancy shows that the simplified model may underestimate the soil damping in the high-frequency region. However, the discrepancy at the high frequencies does not magnify signifi-

cantly with the increase of story mass ratios and story stiffness ratios. In addition, when the pile tip is simply supported, and the story mass ratio and the story stiffness ratio are two times the typical parametric values, the dynamic magnification factor at the high frequencies changes gently with the exciting frequency. These results indicate that the high-frequency excitations will significantly affect the ten-story building system under this condition. However, when the story mass ratio and the story stiffness ratio are four times the typical parametric values, the response at the top floor in the high-frequency region will decrease with the increase of the exciting frequency. These results show that soil radiation damping can effectively reduce the system response in this case.

In brief, the analyzed results prove that the newly-developed simplified model may effectively simulate the dynamic soil-pile interaction and accurately simulate the peak response of the SPSI system in the low-frequency region. If the pile tip is fixed, the simplified model may accurately provide the magnification factors within the analyzed frequency range. If the pile tip is simply supported, the simplified model will slightly overestimate the system response at high frequencies because the simplified model may underestimate the contribution of soil radiation damping in such a case. The overestimation of the system response will not be aggravated if the story mass ratio and story stiffness ratio are increased.

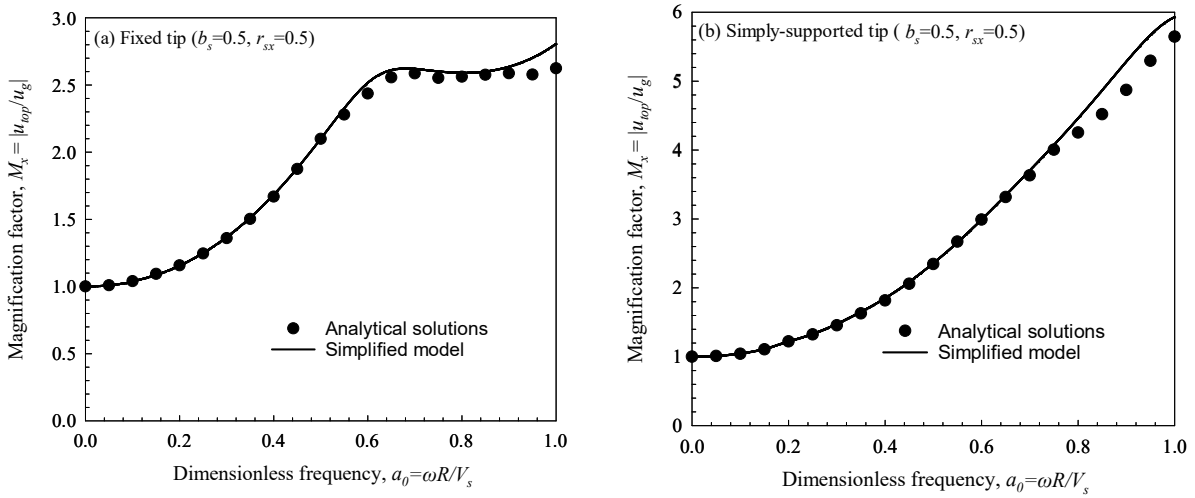


Figure 4: Magnifcaitor factors at the top floor in the SPSI system with typical parametric values.

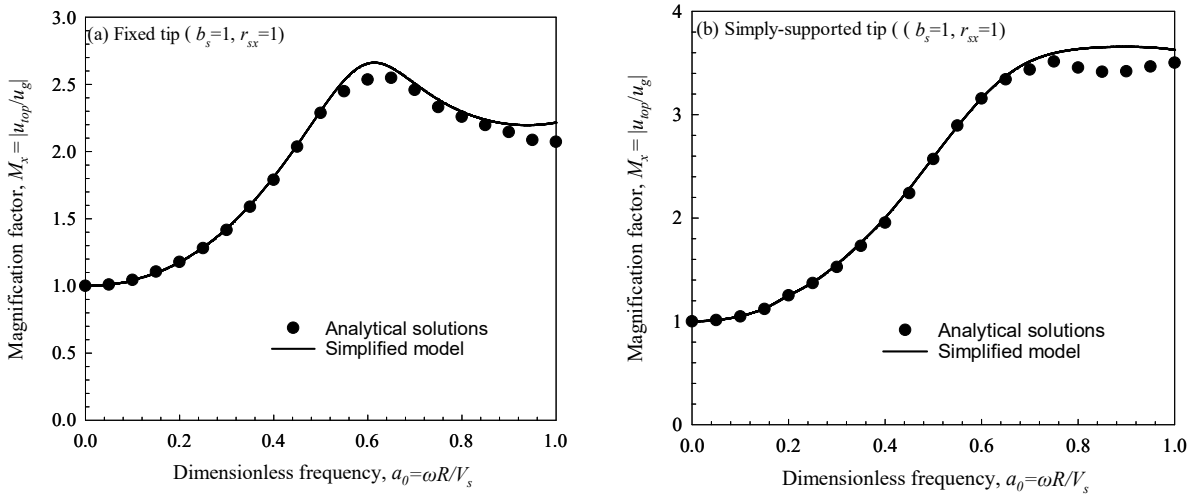


Figure 5: Magnifcaitor factors at the top floor in the SPSI system with two times typical parametric values.

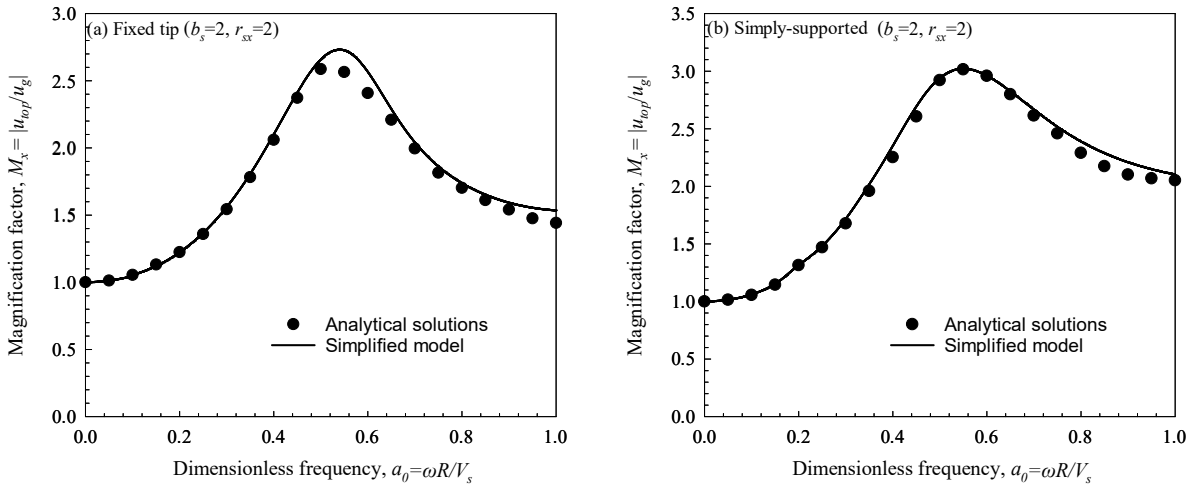


Figure 6: Magnifcaitor factors at the top floor in the SPSI system with four times typical parametric values.

## 4 CONCLUSIONS

- This study shows the newly-developed simplified model may effectively simulate the dynamic soil-pile interaction for building structures subjected to horizontal excitations.
- The simplified model is found to accurately simulate the peak response of the SPSI system in the low-frequency region when the pile tip is fixed or simply supported.
- The simplified model will slightly overestimate the system response at high frequencies when the pile tip is simply supported on the rigid base.
- The overestimation of the system response caused by the simplified model is not found to be aggravated when the story mass ratio and story stiffness ratio increase.

## 5 ACKNOWLEDGMENTS

The author is grateful for the financial support from the National Science and Technology Council in Taiwan under Grant No. MOST 111-2221-E-390-019. The author also appreciates valuable comments from Prof. Ke-Hung Liao and Prof. Shi-Shuenn Chen.

## REFERENCES

[1] R.D. Midlin, Forced at a point in the interior of a semi-infinite solid, *Physics*, **7**, 195-202, 1936.

[2] M. Novak, Vertical vibrations of floating piles, *Journal of the Engineering Mechanics Division*, **103**, 153-168, 1977.

[3] R. Flores-Berrones, R. Whitman, Seismic response of end-bearing piles, *Journal of the Geotechnical Engineering Division*, **108**, 554-569, 1982.

[4] M. Novak, F. Howell, Dynamic response of pile foundations, *Journal of Geotechnical Engineering Division*, **104**, 535-552, 1978.

[5] M. Novak, F. Aboul-Ella, Impedance functions of piles in layered media, *Journal of Engineering Mechanics Division*, **104**, 643-661, 1978.

[6] G.W. Blaney, E. Kausel, J.M. Roesset, Dynamic stiffness of piles, *2nd International Conference on Numerical Methods in Geomechanics*, 1001-1012, 1976.

[7] R. Dobry, E. Vicenti, M.J. O'Rourke, J.M. Roesset, Horizontal stiffness and damping of single piles, *Journal of the Geotechnical Division*, **108**, 439-459, 1982.

[8] J. Lysmer, F.E. Richart, Dynamic response of footings to vertical loading, *Journal of the Soil Mechanics and Foundations Division*, **92**, 65-91, 1966.

[9] J.W. Meek, A.S. Veletsos, Simple models for foundations in lateral and rocking motion, *Proc. 5th World Conference on Earthquake Engineering*, Rome, Italy, 1974.

[10] J.P. Wolf, D.R. Somaini, Approximate dynamic model of embedded foundation in time domain, *Earthquake Engineering & Structural Dynamics*, **14**, 683-703, 1986.

[11] F.C.P. De Barros, J.E. Luco, Discrete models for vertical vibrations of surface and embedded foundation, *Earthquake Engineering & Structural Dynamics*, **19**, 289-303, 1990.

[12] W.Y. Jean, T.W. Lin, J. Penzien, System parameters of soil foundation for time domain dynamic analysis, *Earthquake Engineering & Structural Dynamics*, **19**, 541-553, 1990.

[13] J.P. Wolf, A. Paronesso, Lumped-parameter model for foundation on layrer, *Proc. 10th European Conference on Soil Mechanics Engineering*, 1, 287-290, 1991.

[14] J.P. Wolf, Consistent lumped-parameter models for unbounded soil: physical representation, *Earthquake Engineering & Structural Dynamics*, **20**, 11-32, 1991.

[15] J.P. Wolf, Consistent lumped-parameter models for unbounded soil: frequency-independent stiffness, damping and mass matrices, *Earthquake Engineering & Structural Dynamics*, **20**, 33-41, 1991.

[16] W.H. Wu, W.H. Lee, Nested lumped-parameter models for foundation vibrations, *Earthquake Engineering & Structural Dynamics*, **33**, 1051-1058, 2004.

[17] J.Y. Shi, S.S. Chen, C.J. Kao, K.Y. Chen, An adaptive finite-unit method for simulating frequency-dependent responses of shallow foundations in layered soil under vertical dynamic loads, *International Journal for Numerical and Analytical Methods in Geomechanics*, **45**, 2756-2779, 2021.

[18] J.Y. Shi, S.S. Chen, K.Y. Chen, A simplified model of layered soil for analyzing vertical vibration of loaded foundations, *Journal of Structure and Infrastructure Engineering*, **19**, 21-38, 2023.

[19] J.Y. Shi, A systematic modeling approach for layered soil considering horizontal and rotational foundation vibrations, *Computers & Structures*, **239**, 1-20, 106336, 2020.

[20] S.S. Chen, J.Y. Shi, Simplified soil–structure interaction analysis for high-tech industrial buildings subjected to forced vibrations. *International Journal of Structural Stability and Dynamics*, **15**, 1-22, 2015.

[21] M. Novak, T. Nogami, Soil-pile interaction in horizontal vibration. *Earthquake Engineering & Structural Dynamics*, **5**, 263-281, 1977.

COMPDYN 2023
9th ECCOMAS Thematic Conference on
Computational Methods in Structural Dynamics and Earthquake Engineering
M. Papadrakakis, M. Fragiadakis (eds.)
Athens, Greece, 12-–14 June 2023

# COUPLING OF THE ANALYTICAL SOLUTION FOR THE TIMOSHENKO BEAM WITH A FULLY SATURATED HALFSPACE BY APPLICATION OF THE WAVE BASED METHOD

**M. Lainer and G. Müller**

Chair of Structural Mechanics, Technical University of Munich
Arcisstrasse 21, 80333 Munich
e-mail: mirjam.lainer@tum.de, gerhard.mueller@tum.de

**Abstract.** *To model the field response of a fully saturated halfspace coupled with an elastodynamic trench, the Wave Based Method (WBM) is applied. This numerical method represents an indirect Trefftz approach and is based on weighted wave functions to describe field responses. The wave functions are derived from the analytical solutions for the underlying differential equations. This method has firstly been introduced for vibroacoustic problems in the mid-frequency range. Amongst others, the performance of the WBM strongly depends on the relation between the applied excitation frequency and the dimensions of the observed problem. This relation lies about in the same range for a vibroacoustic structure as for a soil halfspace, which permits to use similar wave function sets. Considering a fully saturated poroelastic halfspace, a second irrotational potential is introduced according to Biot's theory. This so-called second P-wave is approximated by an additional set of wave functions, which increases the number of unknowns for the numerical model. To reduce the total number of wave functions, the coupled trench is modeled by a Timoshenko beam. This permits to replace the wave function sets of the original elastodynamic trench by the analytical solution for the Timoshenko beam. Simulation results are used to assess the accuracy and the mitigation efficiency of the wave barrier.*

**Keywords:** Wave Based Method, Biot's theory, Soil structure interaction, Timoshenko beam.

## 1 INTRODUCTION

Open or infilled trenches [1, 2, 3] are often installed to reduce vibrations induced for example by traffic or machinery, which are acting on constructions. Even though pure open trenches are highly effective as wave barriers against incoming Rayleigh waves, their excavation often needs to be stabilized to reach an effective depth. This is especially the case, when the trench is inclined or the surrounding ground is water saturated. To stabilize such an excavation, it is possible to create i.a. a simple wall, an infilled trench with concrete or an open trench with sheet walls. To consider the interaction between such a wave barrier and a water saturated halfspace, different numerical methods have been introduced. One often used approach is to model the wave barrier and the halfspace by the finite element method (FEM) [4, 5]. This usually requires a large amount of degrees of freedom, to model the far field of of the poroelastic halfspace adequately. An alternative presents for example the coupling of the FEM mesh for the wave barrier to a boundary element model (BEM) for the poroelastic halfspace [6].

In this paper, the Wave Based Method (WBM) is extended to model a simple wall as a wave barrier, which is coupled to a poroelastic halfspace. This approach is chosen as the WBM needs less degrees of freedom than a FEM approach. Moreover, the WBM permits to extend such a model by additional inclined soil layers, by introducing compatibility and equilibrium equations between the different soil layers. However, the investigation of different soil layers with the WBM is not analyzed in this paper and is part of future work. The WBM is originally developed by [7] to describe vibro-acoustic problems in the mid-frequency range. It is based on weighted wave functions to approximate the underlying potentials of a boundary value problem. As shown by [7] for an acoustic problem and by [8] for an elastodynamic problem, these wave functions are derived from the underlying analytical solution of a boundary value problem. In further publications, the WBM is extended to model coupled FEM and WBM domains [9, 10] and to treat poroelastic materials according to Biot's theory for higher frequencies [11]. These publications revealed that the WBM shows a high convergence rate and requires significantly less degrees of freedom than a FEM approach. Moreover, [11] gives an example to model coupled poroelastic domains with different material properties by introducing compatibility and equilibrium equations.

These findings motivated to extend the WBM by Biot's theory for low frequencies [12, 13] to model a poroelastic halfspace, coupled to a simple wall. To approximate the Sommerfeld radiation condition, the WBM is extended by an absorbing boundary condition [14], which transmits normally incident wave fronts. The trench wall is modeled by the analytical solution for a Timoshenko beam [15, 16, 17], to consider influences from its shearing behaviour. To couple the deformation field of the Timoshenko beam to a poroelastic halfspace, compatibility and equilibrium conditions are set up and boundary conditions are formulated for the beam. These compatibility and equilibrium equations are involved into a weighted residual Galerkin approach, to derive the final system of linear equations. The defined boundary conditions for the beam are then added to the final system of linear equations, which is solved to derive the unknown weighting values for the wave functions of the WBM domains and the homogeneous solution of the beam. A similar approach is also presented by [7] to couple a Kirchhoff plate to an acoustic cavity.

The paper is organized as follows. In Section 2, Biot's theory for low frequencies is introduced and it is described, how the defined displacement fields for a poroelastic halfspace are approximated by the WBM. Moreover, the analytical solution for the longitudinal and vertical displacement field of a Timoshenko beam are presented and it is shown how these are coupled

to the attached WBM domains. In Section 3, a numerical example is presented to check the convergence of the WBM and to compare the results with data from the publication [6].

## 2 GOVERNING EQUATIONS AND NUMERICAL MODEL

### 2.1 Biot's theory for a fully saturated halfspace

The displacement field for a fully saturated halfspace is divided into the solid phase displacements $\mathbf{u}^s = [u_x, u_y]^T$ and the fluid seepage field $\mathbf{U} = [U_x, U_y]^T$. The fluid seepage field describes the relative displacements between the enclosed fluid and the solid skeleton, which is weighted by the porosity $n^f$: $\mathbf{U} = n^f(\mathbf{u}^f - \mathbf{u}^s)$. These displacement fields are described by a superposition of the gradients of two irrotational potentials $\Phi_{p_{1/2}}$ and the curl of one solenoidal potential $\Psi_s$, based on Biot's theory [12, 13]. The approximation of these potentials with the Wave Base Method (WBM) is shown in the next subsection.

$$\mathbf{u}^s = \boldsymbol{\nabla}\Phi_{p_1} + \boldsymbol{\nabla}\Phi_{p_2} + \widetilde{\boldsymbol{\nabla}}\Psi_s \tag{1}$$

$$\mathbf{U} = \gamma_{p_1}\boldsymbol{\nabla}\Phi_{p_1} + \gamma_{p_2}\boldsymbol{\nabla}\Phi_{p_2} + \gamma_s\widetilde{\boldsymbol{\nabla}}\Psi_s \tag{2}$$

The values $\gamma_{p_{1/2}}$ and $\gamma_s$ in equation (2) describe eigenvalues of the two dynamic equations according to Biot's theory for low frequencies [12], when these are solved either for $\boldsymbol{\nabla}\Phi_{p_{1/2}}$ or $\widetilde{\boldsymbol{\nabla}}\Psi_s$. Moreover, these potentials correspond to the so-called first and second P-wave and the S-wave, which are characterized by their wave numbers $k_{p_{1/2}}$ and $k_s$. These wave numbers are described by the following equation and depend on the radial excitation frequency $\omega = 2\pi f$ as well as on the material parameters summarized in Table 1. Moreover, the wave numbers for the first and second P-wave depend on the parameter $\rho_{f2}$, which indicates the coupling between fluid phase and solid skeleton. Its imaginary part depends on the dissipation parameter $\xi$.

$$k_{p_{1/2}} = \sqrt{\frac{\rho_f + \gamma_{p_{1/2}}\rho_{f2}}{(\alpha + \gamma_{p_{1/2}})M}} \cdot \omega, \quad k_s = \sqrt{\left(1 + \gamma_s\frac{\rho_f}{\rho}\right)\frac{\rho}{\mu}} \cdot \omega \tag{3}$$

$$\text{with } \rho_{f2} = \frac{\rho_f a}{n^f} - \frac{\mathrm{i}\xi}{\omega(n^f)^2}, \quad \xi = \frac{\rho_f \cdot (n^f)^2}{k_c} \cdot 9.81\mathrm{m/s^2}, \quad k_c = \frac{\kappa \cdot \rho_f}{\eta_f} \cdot 9.81\mathrm{m/s^2}$$

Based on the description of the displacement fields, given by the equations (1) and (2), the following compatibility equations are defined for a poroelastic halfspace. Here, the value $\zeta$ describes the divergence of the fluid seepage field, or respectively the amount of fluid leaving the pores.

$$\begin{pmatrix} \varepsilon_{xx} \\ \varepsilon_{yy} \\ \gamma_{xy} \\ \zeta \end{pmatrix} = \begin{bmatrix} \frac{\partial}{\partial x} & 0 & 0 & 0 \\ 0 & \frac{\partial}{\partial y} & 0 & 0 \\ \frac{\partial}{\partial y} & \frac{\partial}{\partial x} & 0 & 0 \\ 0 & 0 & \frac{\partial}{\partial x} & \frac{\partial}{\partial y} \end{bmatrix} \begin{pmatrix} u_x \\ u_y \\ U_x \\ U_y \end{pmatrix} \tag{4}$$

These expressions permit to evaluate the total stresses within a poroelastic halfspace. The following constitutive equations consider the two Lamé coefficients $\lambda$ and $\mu$ and the two Biot coefficients $M$ and $\alpha$. The value $\sigma_f$ describes the total fluid stresses.

$$\begin{pmatrix} \sigma_{xx} \\ \sigma_{yy} \\ \tau_{xy} \\ \sigma_f \end{pmatrix} = \begin{bmatrix} \lambda + 2\mu + \alpha^2 M & \lambda + \alpha^2 M & 0 & \alpha M \\ \lambda + \alpha^2 M & \lambda + 2\mu + \alpha^2 M & 0 & \alpha M \\ 0 & 0 & \mu & 0 \\ \alpha M & \alpha M & 0 & M \end{bmatrix} \begin{pmatrix} \varepsilon_{xx} \\ \varepsilon_{yy} \\ \gamma_{xy} \\ \zeta \end{pmatrix} \tag{5}$$

| Symbol | Value | Definition |
|---|---|---|
| $\rho_s$ | $2650\ \mathrm{kg/m^3}$ | density, solid matrix |
| $\rho_f$ | $1000\ \mathrm{kg/m^3}$ | density, water |
| $n^f$ | $0.20$ | porosity |
| $\rho$ | $2320\ \mathrm{kg/m^3}$ | density, mixture |
| $\eta$ | $0.00$ | loss factor, drained rock |
| $E$ | $19.333 \cdot 10^9\ \mathrm{N/m^2}$ | E-modulus, drained rock |
| $\nu$ | $0.30$ | Poisson's ratio |
| $K$ | $18.891 \cdot 10^9\ \mathrm{N/m^2}$ | bulk modulus, mixture |
| $\alpha$ | $0.55$ | first Biot coefficient |
| $M$ | $9.11 \cdot 10^9\ \mathrm{N/m^2}$ | second Biot coefficient |
| $k_c$ | $[10^{-6}; 10^{-2}]\ \mathrm{m/s}$ | hydraulic conductivity |
| $a_t$ | $1.0$ | tortuosity |

Table 1: Material parameters for water saturated sandstone [6, 18]

### 2.2 Description of a poroelastic halfspace with the Wave Based Method

The Wave Based Method (WBM) permits to approximate the displacement fields for the solid skeleton $\mathbf{u}^s$ and the fluid seepage field $\mathbf{U}$ by a sum of weighted wave functions. The following equations refer to displacement fields, which are described by their homogeneous solution. For this, the equations (1) and (2) are approximated by the following WBM approaches $\widehat{\mathbf{u}}_h^s$ and $\widehat{\mathbf{U}}_h$.

$$\mathbf{u}^s \cong \widehat{\mathbf{u}}_h^s = \sum_{i=1}^{n_{p1}} c_{p_1,i} \boldsymbol{\nabla} \Phi_{p_1,i} + \sum_{j=1}^{n_{p2}} c_{p_2,j} \boldsymbol{\nabla} \Phi_{p_2,j} + \sum_{k=1}^{n_s} c_{s,k} \widetilde{\boldsymbol{\nabla}} \Psi_{s,k} \tag{6}$$

$$\mathbf{U} \cong \widehat{\mathbf{U}}_h = \sum_{i=1}^{n_{p1}} \gamma_{p_1} c_{p_1,i} \boldsymbol{\nabla} \Phi_{p_1,i} + \sum_{j=1}^{n_{p2}} \gamma_{p_2} c_{p_2,j} \boldsymbol{\nabla} \Phi_{p_2,j} + \sum_{k=1}^{n_s} \gamma_s c_{s,k} \widetilde{\boldsymbol{\nabla}} \Psi_{s,k} \tag{7}$$

The wave functions $\Phi_{p_1,i}, \Phi_{p_2,j}$ and $\Psi_{s,k}$ are chosen according to [11] and are derived from the underlying analytical solution for an elastodynamic problem, as shown by [8]. These permit to describe the displacement fields of convex domains, by approximating each body wave (P- and S-waves) with a finite number of wave functions. The minimum number of wave functions $(n_{p_1}, n_{p_2}, n_s)$ is derived from the maximum wave number, respectively the highest oscillating wave, used in a WBM approach, which must be larger than the truncated physical wave number of the approximated body wave [7]. This relation is given by the following equation, in which the parameter $T$ denotes a truncation factor chosen by the user. For the simulation results presented in this paper, the value is set to $T = 2$, based on the publications by [8, 11].

$$k^{\max} \geq T \cdot k, \qquad T \in [1; 6] \tag{8}$$

In the equations (6) and (7), the unknowns $c_{p_1,i}, c_{p_2,j}$ and $c_{s,k}$ represent the weighting values of the wave functions for a boundary value problem and are derived within a weighted residual Galerkin approach. Figure 1 shows an exemplary boundary value problem, which is divided into two convex subdomains, whose edges are described by different boundary conditions. These consist of Neumann ($\Gamma_\sigma$), coupling ($\Gamma_{(\alpha,\beta)}$), mixed ($\Gamma_{SE}$) and absorbing ($\Gamma_Z$) boundary conditions, defined according to the publications [14, 19, 20].

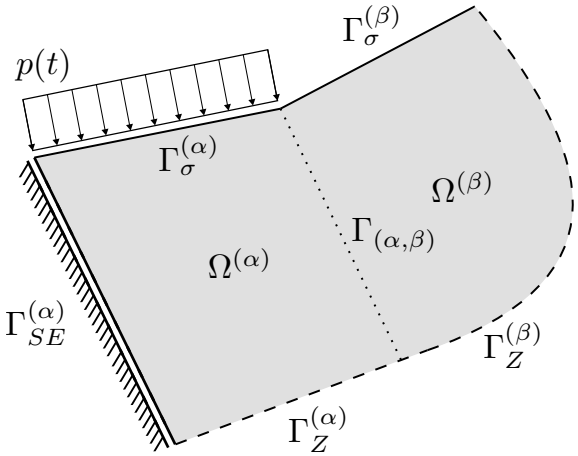


Figure 1: Example for the definition of boundaries

### 2.3 Description of the displacement fields of a Timoshenko beam

In the following, the displacement field of a beam is divided into its longitudinal $u(s)$ and vertical displacements $y(s)$, which are described separately from each other. The longitudinal and vertical displacements of the beam consist of a homogeneous solution ($u_h(s), y_h(s)$) and a particular solution ($u_p(s), y_p(s)$). The derivation of the longitudinal and vertical displacement fields is for example shown in [21, 22] and applied in [16, 17].

$$u(s) \cong \underbrace{\sum_{r=1}^{2} c_r^{(u)} \Theta_r^{(u)}}_{u_h(s)} + \underbrace{\sum_{m=1}^{n_{(\alpha)}} c_m u_m^{(\alpha)} + \sum_{q=1}^{n_{(\beta)}} c_p u_q^{(\beta)}}_{u_p(s)} \tag{9}$$

$$y(s) \cong \underbrace{\sum_{l=1}^{4} c_l^{(y)} \Theta_l^{(y)}}_{y_h(s)} + \underbrace{\sum_{m=1}^{n_{(\alpha)}} c_m y_m^{(\alpha)} + \sum_{q=1}^{n_{(\beta)}} c_p y_q^{(\beta)}}_{y_p(s)} \tag{10}$$

The homogeneous solution $u_h(s)$ consists of two wave functions $[\Theta^{(u)}]$, whereas $y_h(s)$ is presented by four wave functions $[\Theta^{(y)}]$. These are derived analytically by assessing the underlying dynamic equations for the unloaded case of a longitudinal rod and a Timoshenko beam [15]. The homogeneous solutions depend either on the wave number $k_{(u)}$ (longitudinal rod) or on the two wave numbers $k_{(y,1)}$ and $k_{(y,2)}$ (Timoshenko beam). The values, which are necessary to evaluate these wave numbers, are summarized in Table 2.

$$[\Theta^{(u)}] = [\mathrm{e}^{\mathrm{i}k_{(u)}s}, \mathrm{e}^{-\mathrm{i}k_{(u)}s}], \qquad k_{(u)} = \sqrt{\omega^2 \cdot \rho / E} \tag{11}$$

$$[\Theta^{(y)}] = [\mathrm{e}^{\mathrm{i}k_{(y,1)}s}, \mathrm{e}^{-\mathrm{i}k_{(y,1)}s}, \mathrm{e}^{\mathrm{i}k_{(y,2)}s}, \mathrm{e}^{-\mathrm{i}k_{(y,2)}s}] \tag{12}$$

$$k_{(y,1)} = \pm\sqrt{\left(-\chi + \sqrt{\chi^2 + 4\varsigma}\right)/2}, \qquad k_{(y,2)} = \pm\sqrt{\left(-\chi - \sqrt{\chi^2 + 4\varsigma}\right)/2}$$

| Symbol | Value | Definition |
|---|---|---|
| $E$ | $210 \cdot 10^9\ \mathrm{N/m^2}$ | Young's E-modulus |
| $\eta$ | $0.10$ | loss factor |
| $\nu$ | $0.30$ | Poisson's ratio |
| $\rho$ | $7850\ \mathrm{kg/m^3}$ | density |
| $T$ | $[0.5; 1.5] \cdot \lambda_r$ | length |
| $B$ | $\{0.10; 0.05\} \cdot T$ | width |
| $G$ | $E/(2 \cdot (1+\nu))$ | shear modulus |
| $A$ | $1\ \mathrm{m} \cdot B$ | cross section |
| $I$ | $1\ \mathrm{m} \cdot B^3/12$ | second moment of inertia |
| $\kappa$ | $10 \cdot (1+\nu)/(12+11 \cdot \nu)$ | shear correction factor |
| $\chi$ | $-\frac{\rho\omega^2}{G\kappa} - \frac{\rho\omega^2}{E}$ | – |
| $\varsigma$ | $-\frac{\rho^2\omega^4}{EG\kappa} + \frac{\rho A\omega^2}{EI}$ | – |
| $\widetilde{A}$ | $\frac{1}{EI} - \frac{\rho\omega^2}{EGA\kappa}$ | – |
| $\widetilde{B}$ | $\frac{1}{GA\kappa}$ | – |

Table 2: Parameters for the Timoshenko beam with respect to the Rayleigh wave length $\lambda_r$ [6]

For the particular solution of the longitudinal and vertical displacement field, it is necessary to evaluate the tangential and normal stresses of the attached WBM domains, as indicated in Figure 2. The difference between the tangential stresses $\sigma_t^{(\alpha)}$ and $\sigma_t^{(\beta)}$ then corresponds to the longitudinal loading $q_t$, generating longitudinal displacements along the beam. In contrast to this, the normal stresses $\sigma_{n/f}^{(\alpha)}$ and $\sigma_{n/f}^{(\beta)}$ contribute to the normal loading $q_n$, which causes vertical displacements along the beam. The following particular solutions describe the displacements $[u^{(\diamond)}(s)]$ and $[y^{(\diamond)}(s)]$, with $\diamond \in [\alpha, \beta]$. The stresses $[\sigma_t^{(\diamond)}]$ and $[\sigma_{n/f}^{(\diamond)}]$ depend on the wave functions of the respective domain $\Omega^{(\diamond)}$. The function $\mathrm{H}(s)$ corresponds to the Heaviside step function.

$$[u^{(\diamond)}(s)] = \frac{\mathrm{i}}{2EAk_{(u)}} \cdot \int_0^L [\sigma_t^{(\diamond)}(\xi)] \cdot \mathrm{H}(s-\xi) \cdot \left(\mathrm{e}^{\mathrm{i}k_{(u)}(s-\xi)} - \mathrm{e}^{-\mathrm{i}k_{(u)}(s-\xi)}\right) \mathrm{d}\xi \tag{13}$$

$$[y^{(\diamond)}(s)] = \frac{\mathrm{i}}{2(k_{(y,1)}^2 - k_{(y,2)}^2)} \cdot \int_0^L \frac{\widetilde{A} + k_{(y,1)}^2\widetilde{B}}{k_{(y,1)}} \cdot [\sigma_{n/f}^{(\diamond)}(\xi)] \cdot \mathrm{H}(s-\xi) \cdot \left(\mathrm{e}^{\mathrm{i}k_{(y,1)}(s-\xi)} - \mathrm{e}^{-\mathrm{i}k_{(y,1)}(s-\xi)}\right) \ldots$$
$$\ldots - \frac{\widetilde{A} + k_{(y,2)}^2\widetilde{B}}{k_{(y,2)}} \cdot [\sigma_{n/f}^{(\diamond)}(\xi)] \cdot \mathrm{H}(s-\xi) \cdot \left(\mathrm{e}^{\mathrm{i}k_{(y,2)}(s-\xi)} - \mathrm{e}^{-\mathrm{i}k_{(y,2)}(s-\xi)}\right) \mathrm{d}\xi \tag{14}$$

For the evaluation of the internal forces of a Timoshenko beam, it is necessary to compute the angular rotation $\varphi(s)$. The homogeneous and particular solution for $\varphi(s)$ are derived from the underlying dynamic equations [15], which is similar to the derivation procedure for $y(s)$. The angle of shear is then defined as follows.

$$\gamma = y' - \varphi \tag{15}$$

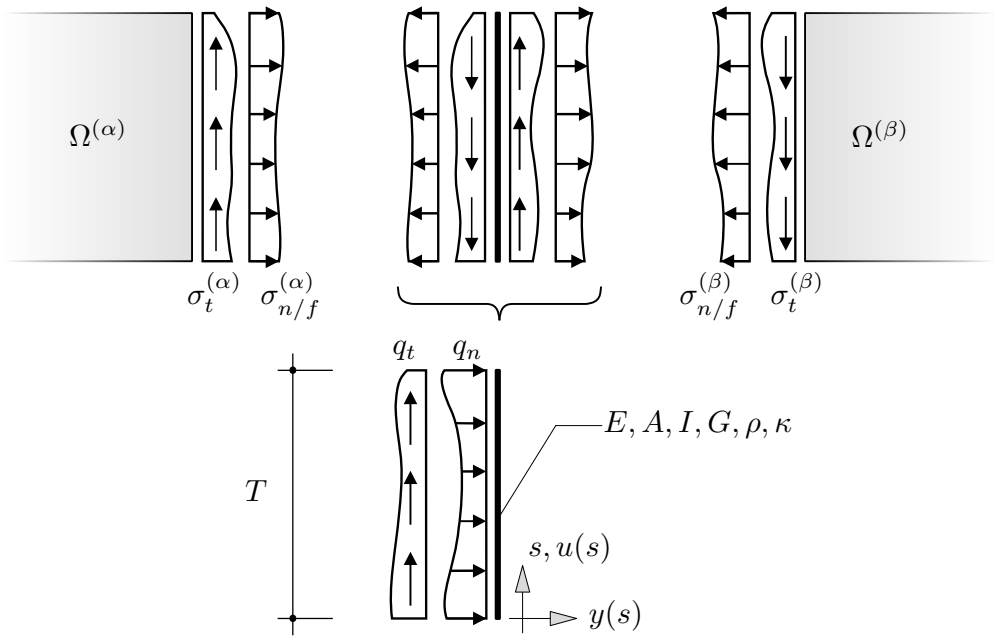


Figure 2: Stresses from coupled WBM domains acting on a beam

## 2.4 Coupling of the displacement field of a Timoshenko beam to a poroelastic halfspace

The following coupling approach describes the connection of the displacement field of a Timoshenko beam to a poroelastic halfspace, and is based on the coupling procedure between a Kirchhoff plate and an acoustic cavity according to [7]. Therefore, it is necessary to set up compatibility conditions between the normal and tangential displacements of a WBM domain $\Omega^{(\diamond)}$, with $\diamond \in \{\alpha, \beta\}$, and the beam. In the case of a water saturated halfspace, the beam is assumed to be impermeable, so that the fluid flux along the coupled edge of a WBM domain is set to $U_n^{(\diamond)} = 0$. These compatibility conditions are defined for each coupled WBM domain.

$$R^{(\alpha,\text{beam})}(\mathbf{r}) = \begin{cases} R_{u_n}^{(\alpha,\text{beam})}(\mathbf{r}) & = u_n^{(\alpha)} - y = 0 \\ R_{u_t}^{(\alpha,\text{beam})}(\mathbf{r}) & = u_t^{(\alpha)} - u = 0 \\ R_{U_n}^{(\alpha,\text{beam})}(\mathbf{r}) & = U_n^{(\alpha)} = 0 \end{cases} \tag{16}$$

$$R^{(\beta,\text{beam})}(\mathbf{r}) = \begin{cases} R_{u_n}^{(\beta,\text{beam})}(\mathbf{r}) & = u_n^{(\beta)} + y = 0 \\ R_{u_t}^{(\beta,\text{beam})}(\mathbf{r}) & = u_t^{(\beta)} + u = 0 \\ R_{U_n}^{(\beta,\text{beam})}(\mathbf{r}) & = U_n^{(\beta)} = 0 \end{cases} \tag{17}$$

In the next step, these compatibility conditions go through a weighted residual Galerkin approach, to set up their contributions to the final system of linear equations. Its unknowns

represent the weighting values for the wave functions of the WBM domains and the weighting values for the homogeneous solution of the longitudinal and vertical displacement field of the beam. The last contributions to the final system of linear equations represent the boundary conditions of the coupled beam in the model. The two ends of the beam are supposed to be free, so that the normal force, the shear force and the moment have to be zero at these points.

$$R^{(\text{beam},\alpha/\beta)}(\mathbf{r}) = \begin{cases} \mathrm{N}(0) & = EA \cdot u'(0) = 0 \\ \mathrm{N}(L) & = EA \cdot u'(L) = 0 \\ \mathrm{Q}(0) & = GA\kappa \cdot \gamma(0) = 0 \\ \mathrm{Q}(L) & = GA\kappa \cdot \gamma(L) = 0 \\ \mathrm{M}(0) & = -EI \cdot \varphi'(0) = 0 \\ \mathrm{M}(L) & = -EI \cdot \varphi'(L) = 0 \end{cases} \tag{18}$$

## 3 NUMERICAL EXAMPLE

### 3.1 Model description

Figure 3 depicts a water saturated halfspace, which is excited by a harmonic line loading $p(t) = p_0 \cdot \mathrm{e}^{\mathrm{i}\Omega t}$ with the amplitude $p_0 = 100\ \mathrm{N/m}$ and the excitation frequency $f = 350\ \mathrm{Hz}$ ($\Omega = 2\pi f$). This loading results in a Rayleigh wave length of approximately $5\ \mathrm{m}$, which is evaluated according to the derivations of [6]. The material data for the poroelastic halfspace and the coupled beam are given in Table 1 and Table 2, referring to [6, 18]. The dissipation coefficient $\xi$ is described as a dimensionless value $\xi^* = \xi \cdot T/\sqrt{\mu\rho}$, which is chosen to be $\xi^* = 0.2$ for the following evaluations in order to compare them with the results given by [6]. The dimensionless dissipation coefficient $\xi^*$ and the trench length $T$ become then decisive for the computation of the hydraulic conductivity, which is described within the equation 3.

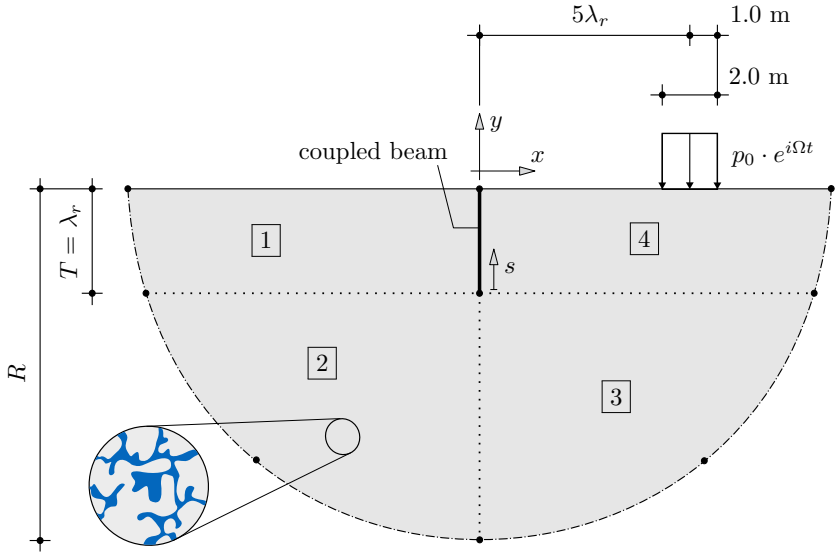


Figure 3: Model description of a beam coupled to a water saturated halfspace

The poroelastic halfspace in Figure 3 is divided into four domains 1 - 4, of which each is defined by four nodes. The surface of the halfspace is modeled with Neumann boundary conditions and the circular edges correspond to absorbing boundaries, which transmit incident

wave fronts [14]. The domains $\boxed{1}$ and $\boxed{4}$ are coupled to a beam with the length $T$ and the local $s$-coordinate system. Dotted lines indicate that two domains are coupled by compatibility and equilibrium equations [20].

Figure 4 illustrates the absolute value for the displacement $|u_y|$ in vertical direction in the vicinity of the coupled beam for $T = \lambda_r$ and $T/B = 10$ ($\lambda_r = 5$ m). The peaks and valleys in front of the barrier indicate that the incoming Rayleigh wave is reflected, as especially the distance between two valleys corresponds to about $\lambda_r/2$. In front of the beam, the absolute value of the vertical displacement goes up to $|u_y| = 3.3 \cdot 10^{-9}$ m along the surface. Behind the trench in its shadow zone, these values decrease and are between $1.0 \cdot 10^{-9}$ m and $1.3 \cdot 10^{-9}$ m. In order to show exemplarily that the defined boundary conditions from equation (18) are fulfilled, Figure 5 depicts the real part of the moment $M(s)$ for the Timoshenko beam. It can be seen, that the moment vanishes at both ends, which fulfills the predefined boundary conditions adequately.

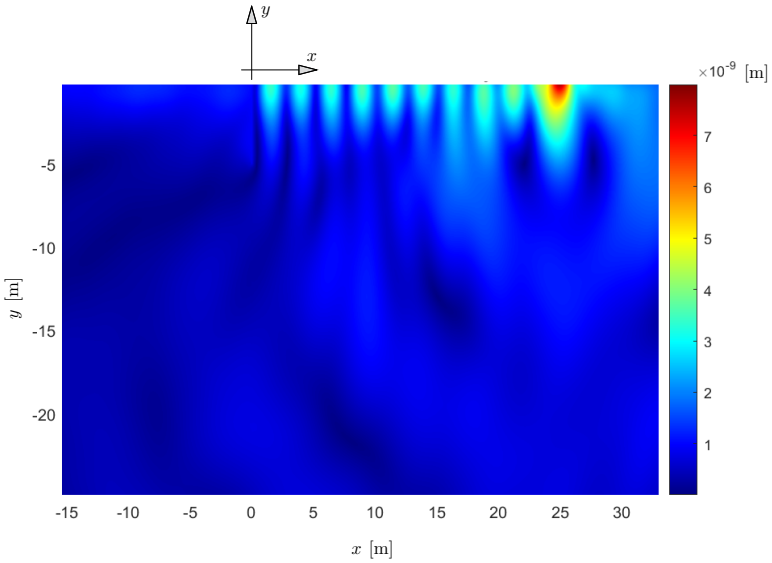


Figure 4: Absolute value of the vertical displacement amplitude $|u_y|$ for the water saturated halfspace coupled to a Timoshenko beam

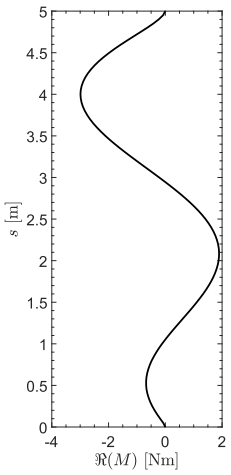


Figure 5: Real part of the moment for the Timoshenko beam

### 3.2 Convergence of the WBM model

For the presented example, the sum of the square of the residuals for the compatibility conditions between the WBM domains $(\Omega^{(\alpha)}, \Omega^{(\beta)})$ and the coupled beam is evaluated. Two integral expressions are set up, to compute the square of the residuals for the longitudinal and vertical displacements along the beam length $T$. These residuals are given by the equations (16) and (17). The expression $\widehat{\diamond}$ denotes here a complex conjugate field variable.

$$\|R_u\|_2 = \int_0^T (u_t^{(\diamond)}(s) - u(s)) \cdot (\widehat{u}_t^{(\diamond)}(s) - \widehat{u}(s)) \, \mathrm{d}s, \quad \text{with } \diamond \in \{\alpha, \beta\} \tag{19}$$

$$\|R_y\|_2 = \int_0^T (u_n^{(\diamond)}(s) - y(s)) \cdot (\widehat{u}_n^{(\diamond)}(s) - \widehat{y}(s)) \, \mathrm{d}s, \quad \text{with } \diamond \in \{\alpha, \beta\} \tag{20}$$

These residuals are normalized by the square of the maximum amplitude of the longitudinal displacement ($|u_{\max}|^2$), or respectively the maximum vertical displacement ($|y_{\max}|^2$), of the beam. These values are computed for several sets of wave functions and plotted in Figure 6 and Figure 7. In these figures, the value $n_{\mathrm{DOF}}$ denotes the total number of unknowns, respectively the number of degrees of freedom (DOF). Both figures indicate, that the sum of the squared residuals decreases steadily for a higher number of wave functions. However, for $4000 < n_{\mathrm{DOF}} < 6000$, this value remains between $10^{-5}$ and $10^{-4}$ without changing significantly. For $1000 < n_{\mathrm{DOF}} < 2000$, a substantial drop is observed in both figures. This indicates, that the generated wave numbers for the wave functions of the WBM domains are lower than the physical wave numbers for the body waves of the poroelastic halfspace and the Timoshenko beam. This violates the condition defined in equation (8), revealing a strong mismatch between the coupled displacement fields of the beam and the attached domains.

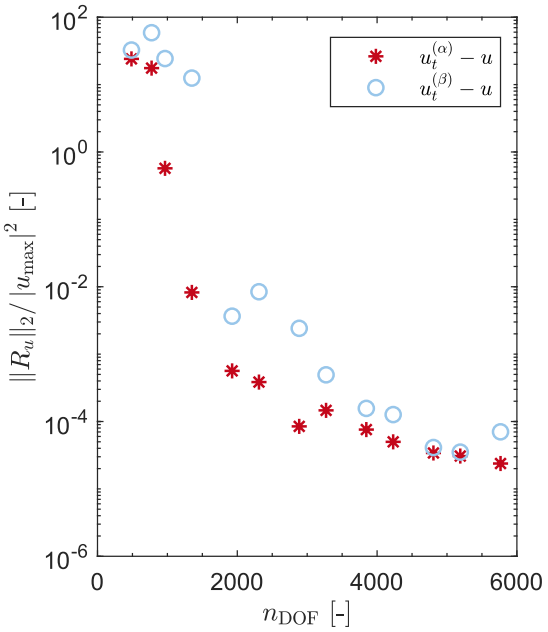


Figure 6: $\|R\|_2$ for the longitudinal displacements along the coupled beam

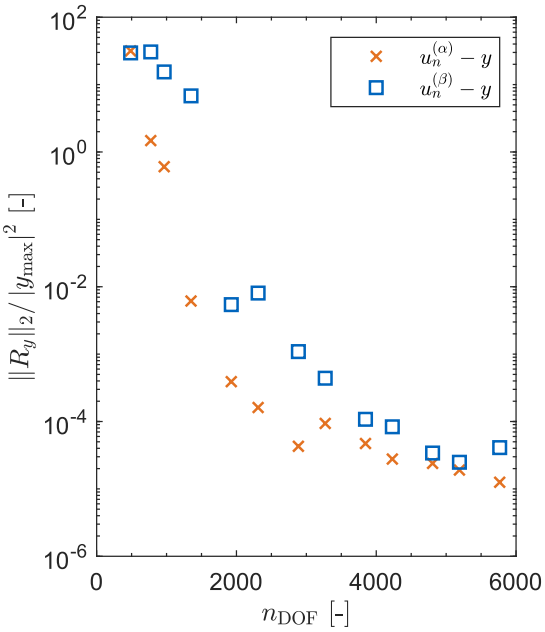


Figure 7: $\|R\|_2$ for the vertical displacements along the coupled beam

### 3.3 Comparison with reference data

To compare the introduced example in Figure 3 with data from literature [6], the average vertical displacement amplitude reduction ratio $\overline{A}_y$ is calculated.

$$\overline{A}_y = \frac{1}{10\lambda_r} \int_0^{-10\lambda_r} \frac{|u_{y,\mathrm{beam}}(x, y=0)|}{|u_{y,\mathrm{ref}}(x, y=0)|} \, \mathrm{d}x \tag{21}$$

$\overline{A}_y$ corresponds to the mean value of the ratio between the absolute displacement amplitudes $|u_{y,\mathrm{beam}}|$ and $|u_{y,\mathrm{ref}}|$. The value $|u_{y,\mathrm{beam}}|$ stands for displacements with an installed beam, whereas $|u_{y,\mathrm{ref}}|$ refers to the displacement field without a wave barrier. In the following, $\overline{A}_y$ is evaluated along the surface of the halfspace in the shadow zone of the beam, respectively for $x \in [0; -10\lambda_r]$ and $y = 0$.

Figure 8 depicts results for $\overline{A}_y$ in dependency of the trench length $T/\lambda_r \in [0.5; 1.5]$ and the trench widths $B$, which is chosen as $T/B \in \{10; 20\}$. For $T/\lambda_r \leq 1.3$, the average reduction ratio $\overline{A}_y$ with the WBM model lies under the results by [6], in which a BEM-FEM approach is used. The maximum difference is $0.051$ for $T/B = 10$ and $0.029$ for $T/B = 20$. The best compliance is reached for $T/\lambda_r > 1.3$ with differences of $0.008$ ($T/B = 10$) and $0.004$ ($T/B = 20$). The presented data indicates that the WBM model predicts mostly lower values for $\overline{A}_y$ than the BEM-FEM approach. This corresponds to a slightly higher mitigation efficiency of the beam according to the WBM model. However, these differences are still in an acceptable range.

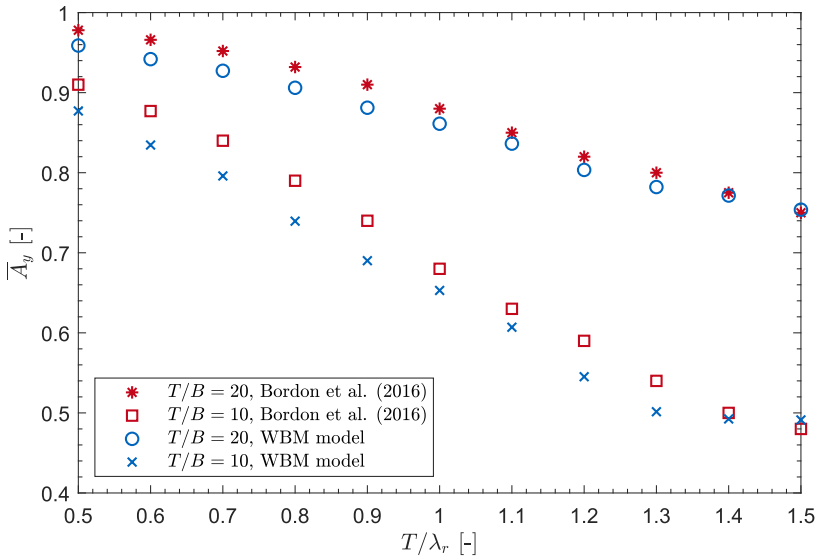


Figure 8: Comparison of $\overline{A}_y$ in dependency of the trench length $L$ and the width $B$, computed with the WBM model and a BEM-FEM approach [6]

## 3.4 CONCLUSION

In this paper, the Wave Based Method (WBM) is extended by Biot's theory for low frequencies [12, 13] and coupled to the analytical solution of the Timoshenko beam [15, 16]. This coupling approach is based on [7], in which a Kirchhoff plate is connected to an acoustic cavity. The presented coupling approach permits to model a water saturated halfspace with a simple wall, which is installed as a wave barrier against an incoming Rayleigh wave. It is shown that the residuals of the compatibility conditions between the beam and the attached halfspace reduce significantly and also converge for an increasing number of wave functions. For a total number of unknowns between $1000$ and $2000$ considerable drops are observed for the squared residuals of the coupled displacement fields. The reason for this is, that the wave numbers of the wave function sets of the WBM domains become lower than the wave numbers of the approximated body waves within the halfspace. Moreover, the average vertical displacement amplitude reduction ratio is evaluated for different trench dimensions and compared with results from the BEM-FEM model presented in [6]. The simulation results with the WBM approach reveal an adequate accordance with the data from the BEM-FEM model.

## REFERENCES


[1] W. Haupt, Isolation of vibrations by concrete core walls. *Proceedings of the 9th International Conference on Soil Mechanics and Foundation Engineering*, Tokyo, Japan, 1977.

[2] D. Beskos, B. Dasgupta, I. Vardoulakis, Vibration isolation using open or filled trenches. *Computational Mechanics*, **1**(1), 43-63, 1986.

[3] J. Freisinger, G. Müller, Coupled ITM-FEM approach for the assessment of the mitigation efficiency of finite and infinite open trenches and infilled barriers. *XI International Conference on Structural Dynamics (EURODYN 2020)*, Athens, Greece, November 23-26, 2020.

[4] A.E. Moghadam, R. Rafiee-Dehkharghani, Ground-borne vibration screening in layered dry and saturated grounds using optimal inclined wave barriers. *Soil Dynamics and Earthquake Engineering*, **162**, 2022.

[5] J.P. Li, X.L. Zhang, S.J. Feng, Z.L. Chen, Y.C. Li, Numerical Investigation of ground-borne vibration mitigation by infilled trenches in a poroelastic half-space considering the moving water table. *International Journal of Geomechanisc*, **21**(10), 2021.

[6] J.D.R. Bordón, J.J. Aznárez, O. Maeso, Two-dimensional numerical approach for the vibration isolation analysis of thin walled wave barriers in poroelastic soils. *Computers and Geotechnics*, **71**, 168-179, 2016.

[7] W. Desmet, *A wave based prediction technique for coupled vibro-acoustic analysis, PhD. thesis 98D12*. Faculteit Toegepaste Wetenschappen, Katholieke Universiteit Leuven, 1998.

[8] C. Vanmaele, *Development of a wave based prediction technique for the efficient analysis of low- and mid-frequency structural vibrations, PhD. thesis 2007D11*. Faculty of Engineering, Katholieke Universiteit Leuven, 2007.

[9] B. Van Hal, *Automation and performance optimization of the wave based method for interior structural-acoustic problems, PhD Thesis*. Faculteit Toegepaste Wetenschappen, Katholieke Universiteit Leuven, 2004.

[10] B. Pluymers, *Wave based modelling methods for steady-state vibroacoustics, PhD thesis 2006D04*. Faculty of Engineering, Katholieke Universiteit Leuven, 2006.

[11] E. Deckers, *A wave based approach for steady-state Biot models of poroelastic materials, PhD. thesis 2012D12*. Faculty of Engineering, Katholieke Universiteit Leuven, 2012.

[12] M.A. Biot, Theory of propagation of elastic waves in a fluid-saturated porous solid. I. Low-frequency range. *Journal of the Acoustical Society of America*, **28**(2), 168-78, 1956.

[13] M.A. Biot, Mechanics of deformation and acoustic propagation in porous media. *Journal of Applied Physics*, **33**(4), 1482-98, 1962.

[14] G. Degrande, *A spectral and finite element method for wave propagation in dry and saturated poroelastic media, PhD Thesis*. Katholieke Universiteit Leuven, 1992.

[15] S.P. Timoshenko, LXVI. On the correction for shear of the differential equation for transverse vibrations of prismatic bars. *The London, Edinburgh, and Dublin Philosophical Magazine and Journal of Science*, **41**, 744-746, 1921.

[16] G.G.G. Lueschen, L.A. Bergman, Green's function for uniform Timoshenko beams. *Journal of Sound and Vibration*, **194**(1), 93-102, 1996.

[17] C.M. Wang, K.Y. Lam, X.Q. He, Exact solutions for Timoshenko beams on elastic foundations using Green's functions. *Mechanics of Structures and Machines*, **26**(1), 101-113, 1998.

[18] C.H. Lin, V.W. Lee, M.D. Trifunac, The reflection of plane waves in a poroelastic halfspace saturated with inviscid fluid. *Soil Dynamics and Earthquake Engineering*, **25**(3), 205-223, 2005.

[19] P. Debergue, R. Panneton, N. Atalla, Boundary conditions for the weak formulation of the mixed (u,p) poroelasticity problem. *Journal of the Acoustical Society of America*, **106**(5), 2383–2390, 1999.

[20] J.F. Allard, N. Atalla, *Propagation of sound in porous media: modelling sound absorbing materials*. JohnWiley & Sons, 2009.

[21] J.F. Doyle, *Wave propagation in structures, 2nd Edition*. Springer-Verlag New York, 1997.

[22] M.C. Junger, D. Feit, *Sound, structures and their interaction, 2nd Edition*. The MIT Press, 1986.

COMPDYN 2023
9th ECCOMAS Thematic Conference on
Computational Methods in Structural Dynamics and Earthquake Engineering
M. Papadrakakis, M. Fragiadakis (eds.)
Athens, Greece, 12-–14 June 2023

# A 2D MACRO-ELEMENT FOR EFFICIENT NONLINEAR ANALYSIS OF PILE FOUNDATIONS UNDER SEISMIC LOADING

**Thomas Lhermitte[1,2], Florent Prunier[1], David Bertrand[1], Stéphane Grange[1], Pierre Wyniecki[2], Evan Monroig[2], and Thomas Jochyms[3]**

[1]Univ Lyon, INSA Lyon, GEOMAS, EA7495
69621 Villeurbanne, France
e-mail: {thomas.lhermitte, florent.prunier, david.bertrand, stephane.grange}@insa-lyon.fr

[2] STABILIS
01210 Ferney-Voltaire, France
e-mail: {pierre.wyniecki,evan.monroig}@stabilis.fr

[3] VINCI Construction Grands Projets
92000 Nanterre, France
e-mail: thomas.jochyms@vinci-construction.fr

**Abstract.** *The nonlinear behaviour of pile group foundations subjected to earthquake loading involves several varied phenomena such as soil-pile interaction, pile-raft interaction, soil nonlinearities and pile damaging. To accurately account for these phenomena, a significant number of degrees of freedom are required, especially close to the contact zone between the pile and the soil. This research proposes a novel two-phase model formulated within the framework of a macroelement to take into account the soil-pile interaction. The proposed macro-element uses a multi-scale substructuring approach based on FEM. Each macro-element represents a single-pile and its immediately surrounding soil. The macro-element is an assembly of two-phase elements based on two independent meshes for the pile and for the soil. Interface forces between the pile and the soil are integrated continuously on the interface length with an ad hoc interface constitutive model. The focus of the paper is the presentation of 1D and 2D two-phase elements. Test cases with both linear and nonlinear interface laws are shown to validate the elements.*

**Keywords:** Macro-element, Pile foundation, Earthquake Engineering, Two-phase model, Interface law.

# 1 INTRODUCTION

Use of pile foundations for the construction of large-scale projects on medium quality soils is inevitable. Their earthquake design involves different scales and relates to both structural and geotechnical engineering. Moreover, pile foundations induce a strong coupling of superstructure and foundation behaviour. Both the multi-scale aspect, and the coupling between superstructure and foundation behaviour, make global models difficult to implement, and very time consuming. Thus, the use of macro-element tools appears strongly appealing for modelling soil-structure interaction, in particular for earthquake applications.

The idea of the finite macro-element is to condense the whole {near-field soil + pile + foundation} system response at the foundation center ; the system response is thus formulated as a constitutive force-displacement law in generalized variables.

A number of macro-elements for pile foundations have been developed over the last decade. Among these, an elasto-plastic macro-element was introduced by Correia [1] for bridge monopiles. It takes into account soil plastification and slip between soil and pile. Li and co-workers introduced the first hypo-plastic macro-element for pile foundations [2]. It models in particular the degradation of soil properties with cyclic loading. It was extended by Pérez-Herreros [3] to dynamic pile-group effects.

The present work falls within the framework of the development of a macro-element (2D for the time being) for pile foundations under seismic loading. The macro-element is different from regular macro-elements because it uses a multi-scale substructuring approach based on finite element modelling. It can be considered as an alternate modeling technique at the crossroads between regular macro-element modeling and direct FEM approach. The macro-element represents a single-pile and its immediately surrounding soil. An internal Newton-Raphson procedure solves the nonlinear equations governing the macro-element equilibrium. The computed forces are dynamically condensed [4] on the external nodes of each macro-element for the computation of the global {soil + foundation + structure} response.

This paper focuses on one of the constituents of the macro-element, namely the modelling of the interaction between the pile and its surrounding soil. The nonlinear behaviour of the interaction is described at the interface scale through an ad hoc phenomenological law.

Firstly, new finite elements, taking into account interface forces between soil and pile, are introduced. Secondly, test cases for the validation of these elements are presented and discussed.

# 2 METHODS

## 2.1 Two-phase element-modelling

This section adresses the modelling of the nonlinear soil-pile interface. A two-phase modelling concept is assumed : the pile and the soil are represented by two distinct phases, supported by their own distinct finite element mesh. The interaction between the pile phase and the soil phase is computed by continuous integration over the interface of a phenomenological law describing the interface force density in function of the relative displacement between phases. In the general case, the interface law governs the coupled vertical and horizontal responses of the interface.

The following paragraph introduces a new two-dimensional two-phase element that includes the continuous integration over the interface length. The two-dimensional two-phase element is supported by two finite elements types, namely a nine-node quadrilateral (QUA9) for the soil phase of the element, and two two-node Euler-Bernoulli beams for the pile phase (see figure 1). The elements account for the behaviour of the soil, the pile and the soil-pile interface. The shape

functions of the supporting elements are used to interpolate the relative displacement between phases.

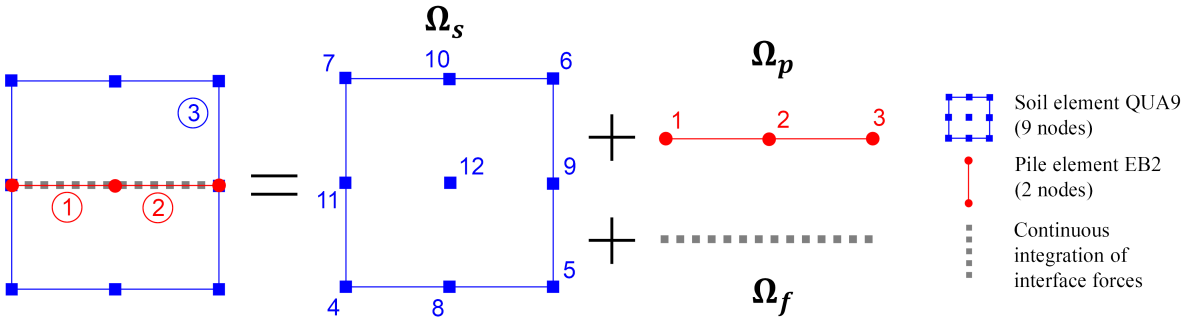


Figure 1: Two-dimensional two-phase element decomposition

Let the Principle of virtual work be applied on an element :

$$\underbrace{\int_{\Omega_{el}} {}^t\boldsymbol{u}^* \rho \ddot{\boldsymbol{u}}\, d\Omega + \int_{\Omega_{el}} {}^t\boldsymbol{\epsilon}^* \boldsymbol{\sigma}\, d\Omega}_{W^*_{int}} = W^*_{ext} \tag{1}$$

where $\boldsymbol{u}$ are the displacements anywhere on the element defined by the domain $\Omega_{el}$ and $\boldsymbol{\epsilon}$ and $\boldsymbol{\sigma}$ are respectively the strain and stress tensors rearranged in vectorial form.$\rho$ is the volumic mass. The domain $\Omega_{el}$ comprises the pile phase $\Omega_p$ and the soil phase $\Omega_s$. The interface is defined as the intersection of both $\Omega_f = \Omega_p \cap \Omega_s$.

The contributions of each of the subdomains to the internal work of the element subjected to the virtual displacement field $\boldsymbol{u}^*$ can be distinguished as follows : a pile contribution $W^*_p = W^*_{pp} + W^*_{pf}$, where $W^*_{pf}$ is the contribution of the soil on the pile at the interface, and a soil contribution $W^*_s = W^*_{ss} + W^*_{sf}$, where $W^*_{sf}$ the contribution of the pile on the soil at the interface.

The contributions $W^*_{pp}$ et $W^*_{ss}$ come from the assembly of the linear mass and stiffness matrices of the two beams and of the quadrilateral of the two-phase element. The contribution of the interface work $W^*_f = W^*_{pf} + W^*_{sf}$ is detailed in the following :

$$\begin{cases} W^*_{pp} = \displaystyle\int_{\Omega_p} {}^t\boldsymbol{u}_p{}^* \rho_p \ddot{\boldsymbol{u}}_p\, d\Omega + \int_{\Omega_p} {}^t\boldsymbol{\epsilon}^*_p \boldsymbol{\sigma}_p\, d\Omega & (2) \\ W^*_{ss} = \displaystyle\int_{\Omega_s} {}^t\boldsymbol{u}_s{}^* \rho_s \ddot{\boldsymbol{u}}_s\, d\Omega + \int_{\Omega_s} {}^t\boldsymbol{\epsilon}^*_s \boldsymbol{\sigma}_s\, d\Omega & (3) \\ W^*_f = \displaystyle\int_{\Omega_f} \left[ -{}^t\boldsymbol{u}_{sf}{}^* \boldsymbol{\tau}_s - {}^t\boldsymbol{u}_{pf}{}^* \boldsymbol{\tau}_p \right] d\Omega = \int_{\Omega_f} {}^t\boldsymbol{u}_r{}^* \boldsymbol{\tau}_s \left(\boldsymbol{u}_r\right) d\Omega & (4) \end{cases}$$

where $\boldsymbol{u}_p$ and $\boldsymbol{u}_s$ are the displacements of the pile and the soil in the element, ${}^t\boldsymbol{u}_{sf}$ and ${}^t\boldsymbol{u}_{pf}$ are the displacements evaluated at the interface from $\boldsymbol{u}_p$ and $\boldsymbol{u}_s$. $\boldsymbol{\tau}_p = -\boldsymbol{\tau}_s = -\boldsymbol{\tau}$ is the interface force density which is a function of the relative displacement $\boldsymbol{u}_r = \boldsymbol{u}_{pf} - \boldsymbol{u}_{sf}$ between phases : $\boldsymbol{\tau} = \boldsymbol{\tau}\left(\boldsymbol{u}_r\right)$.

Remark : The Euler-Bernoulli beam assumes plane stresses and the soil quadrilateral plane strains.

Assuming small displacements and strains, and assuming linear behaviour for pile and soil, the contributions $W^*_{pp}$ et $W^*_{ss}$ are expressed classically as :

$$W^*_{ii} = {}^t\boldsymbol{U}_i^{el^*} \left[\int_{\Omega_i} \rho {}^t\mathbb{N}_i\mathbb{N}_i \, d\Omega\right] \ddot{\boldsymbol{U}}_i^{el} + {}^t\boldsymbol{U}_i^{el^*} \left[\int_{\Omega_i} {}^t\mathbb{B}_i\mathbb{C}\mathbb{B}_i \, d\Omega\right] \boldsymbol{U}_i^{el} \ , \quad i \in [p, s] \tag{5}$$

where ${}^t\boldsymbol{U}^{el} = {}^t[\boldsymbol{U}_p^{el}, \boldsymbol{U}_s^{el}]$ are the node displacements of the element and $\boldsymbol{U}_p^{el}$ respectively the pile and $\boldsymbol{U}_s^{el}$ the soil node displacements of the element. $\mathbb{N}_p$ and $\mathbb{N}_s$ are the interpolation functions of the soil and pile elements and $\mathbb{B}_p$ and $\mathbb{B}_s$ their derivatives : $\boldsymbol{u}_p = \mathbb{N}_p\boldsymbol{U}_p^{el}$, $\boldsymbol{u}_s = \mathbb{N}_s\boldsymbol{U}_s^{el}$. Matrix $\mathbb{C}$ contains the material properties, and additionally the cross-section properties in the case of beams.

The interface work $W^*_f$ is integrated over the interface $\Omega_f$. The node displacements at the interface can be written as

$$\boldsymbol{u}_{pf} = \mathbb{N}_{pf}\boldsymbol{U}_p^{el} \tag{6}$$

$$\boldsymbol{u}_{sf} = \mathbb{N}_{sf}\boldsymbol{U}_s^{el} \tag{7}$$

where $\mathbb{N}_{pf}$ and $\mathbb{N}_{sf}$ are the projections of the interpolation functions of the pile and of the soil on the interface (defined by a segment).

Then the virtual relative displacement at the interface can be rewritten as

$${}^t\boldsymbol{u}_r{}^* = {}^t\boldsymbol{u}_{sf}{}^* - {}^t\boldsymbol{u}_{pf}{}^* = \begin{bmatrix} {}^t\boldsymbol{U}_p^{el^*} & {}^t\boldsymbol{U}_s^{el^*} \end{bmatrix} \begin{bmatrix} -{}^t\mathbb{N}_{pf} \\ {}^t\mathbb{N}_{sf} \end{bmatrix} \tag{8}$$

Thus, the interface work can be rewritten as

$$W^*_f = \int_{\Omega_f} \begin{bmatrix} {}^t\boldsymbol{U}_p^{el^*} & {}^t\boldsymbol{U}_s^{el^*} \end{bmatrix} \begin{bmatrix} -{}^t\mathbb{N}_{pf} \\ {}^t\mathbb{N}_{sf} \end{bmatrix} \boldsymbol{\tau} \, d\Omega \tag{9}$$

Interface forces are coupled in vertical and horizontal directions. Simplification of the previous equation by the virtual displacement leads to the elementary effort originating from the interface on the two subdomains of the element.

$$\boldsymbol{p}_f = \begin{bmatrix} \boldsymbol{p}_{pf} \\ \boldsymbol{p}_{sf} \end{bmatrix} = \int_{\Omega_f} \begin{bmatrix} -{}^t\mathbb{N}_{pf} \\ {}^t\mathbb{N}_{sf} \end{bmatrix} \boldsymbol{\tau} \, d\Omega \tag{10}$$

The tangent operator associated to the interface is derived from the latter.

$$\frac{\partial \boldsymbol{p}_f}{\partial \boldsymbol{U}^{el}} = \int_{\Omega_f} \begin{bmatrix} -{}^t\mathbb{N}_{pf} \\ {}^t\mathbb{N}_{sf} \end{bmatrix} \frac{\partial \boldsymbol{\tau}}{\partial \boldsymbol{U}^{el}} \, d\Omega = \int_{\Omega_f} \begin{bmatrix} -{}^t\mathbb{N}_{pf} \\ {}^t\mathbb{N}_{sf} \end{bmatrix} \frac{\partial \boldsymbol{\tau}}{\partial \boldsymbol{u}_r} \begin{bmatrix} -\mathbb{N}_{pf} & \mathbb{N}_{sf} \end{bmatrix} \, d\Omega \tag{11}$$

because

$$\frac{\partial \boldsymbol{\tau}}{\partial \boldsymbol{U}^{el}} = \frac{\partial \boldsymbol{\tau}}{\partial \boldsymbol{u}_r} \frac{\partial \boldsymbol{u}_r}{\partial \boldsymbol{U}^{el}} \tag{12}$$

where $\frac{\partial \boldsymbol{\tau}}{\partial \boldsymbol{u}_r}$ is the tangent operator returned by the interface law.

From a numerical point of view, two integration points are used on each of the beams in the two-phase element, thus amounting to a total of four integration points.

The same strategy can be used to develop other two-phase elements, be they one or three-dimensional. The test case below shows a one-dimensional two-phase element supported by quadratic three-node bars.

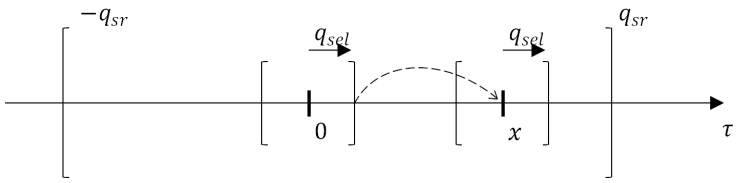


Figure 2: One-dimensional interface law with kinematic hardening

## 2.2 Interface laws

The interface law expresses the linear density of interface forces as a function of the relative displacement between phases. The law is uncoupled in horizontal and vertical directions for the validation test cases below, but the developed formulation does not preclude the use of a coupled law in the element in a more general case. The same interface law is assumed for horizontal and vertical relative displacements. Two different one-dimensional interface laws are used in the test cases and presented hereafter. The first one is linear elastic :

$$\tau = \pi D k_\tau u_r. \tag{13}$$

where $D$ is the pile diameter, $u_r$ the relative displacement, and $k_\tau$ the interface stiffness. This law is used for validation purposes only.

The second law is written within the elastoplastic framework where $du = du^e + du^p$, with $du^e$ and $du^p$ the elastic and plastic relative displacement increments. The law accounts for kinematic hardening. The yield surface $f$ and the hardening rule of the surface are given in the following, distinguishing between a positive and negative trial interface force increment $d\tau_{trial}$:

$$\begin{cases} \text{if } d\tau_{trial} \geq 0 & \\ \qquad f = \tau - (x + q_{sel}) & (14) \\ \qquad x\left(u^p\right) = x_0 + \dfrac{q_{sr} - (q_{sel} + x_0)}{B_p + (u^p - u^{p0})}\left(u^p - u^{p0}\right) & (15) \\ \text{if } d\tau_{trial} < 0 & \\ \qquad f = -\tau + (x + q_{sel}) & (16) \\ \qquad x\left(u^p\right) = x_0 - \dfrac{q_{sr} - (q_{sel} + x_0)}{B_p + (u^p - u^{p0})}\left(u^p - u^{p0}\right) & (17) \end{cases}$$

where $x$ is the moving center of the elastic forces interval, $q_{sel}$ the elastic threshold and as such representing the half-size of the elastic forces interval, $q_{sr}$ the interface force plateau value, $x_0$ and $u^{p0}$ the values of $x$ and $u^p$ at cycle change (figure 2). $B_p$ is the fitting parameter of the hyperbolic law ; it represents the plastic displacement $u^p$ at $\tau = \frac{q_{sr}}{2} - q_{sel}$ in monotonic loading. If $q_{sel} << q_{sr}$ is assumed, then $B_p$ can be calculated simply from the secant modulus $G_{50}$ at $\frac{q_{sr}}{2}$ following the expression

$$B_p \approx \frac{q_{sr}}{2G_{50}} \tag{18}$$

The flow rule is given by :

$$du^p = d\lambda \frac{\partial f}{\partial \tau} \tag{19}$$

where $d\lambda$ represents the plastic increment.

| material | $i$ | $n_i[-]$ | $H_i[m]$ | $v_i[m.s^{-1}]$ | $S_i[m^2]$ | $\rho_i[kg.m^{-3}]$ | $\eta_i[kg.m.s^{-1}]$ | $Z_i[kg.m^{-2}.s^{-1}]$ |
|---|---|---|---|---|---|---|---|---|
| Air | $a$ | 10 | 200 | 300 | 0.04 | $1.10^{-6}$ | 0 | $3.10^{-4}$ |
| Soft soil | $s$ | 20 | 400 | 100 | 0.02 | 1900 | $5.10^6$ | $1,9.10^5$ |
| Pile | $p$ | 20 | 400 | 582 | 0.02 | 2100 | $2.10^6$ | $12,2.10^5$ |
| Rock | $r$ | 20 | 1000 | 500 | 0.04 | 1900 | 0 | $9,5.10^5$ |

Table 1: Properties of soil layers and pile

The elastic displacement increment is calculated as

$$du^e = G^t_{ini} d\tau \tag{20}$$

where $G^t_{ini}$ the initial tangent pseudo-module.

Finally, the tangent modulus of the law is given by

$$G^t = \frac{\frac{\partial f}{\partial x}\frac{\partial x}{\partial u^p} G^t_{ini}}{\frac{\partial f}{\partial x}\frac{\partial x}{\partial u^p} - G^t_{ini}} \tag{21}$$

Only three parameters are involved in this law, namely the elastic threshold $q_{sel}$, the interface force plateau value $q_{sr}$, and the secant modulus $G_{50}$ at $\tau = \frac{q_{sr}}{2}$ in monotonic loading.

## 3 NUMERICAL RESULTS AND DISCUSSION

This section presents two validation test cases. The first one validates a 1D two-phase model composed of two three-node bars under dynamic forces. The second one validates the previously presented 2D two-phase element based on Euler Bernoulli beams and nine-node quadrilateral (QUA9) under static cyclic forces. The main idea in these validation cases is to vary the interface stiffness and compare it to a case where an infinite interface stiffness is defined. The interface behaviour is also tested in a nonlinear case.

### 3.1 Test case for 1D two-phase element : dynamic loading

A three-layered soil under compression waves is considered. A pile is embedded in the intermediate soil layer. The whole system is modeled by 1D two-phase elements composed of two three-node bars (figure 3). Interface stiffness is only added in the intermediate soil layer. Each bar is defined by its cross-section area $S_i$, volumic mass $\rho_i$, Young's modulus $E_i$ calculated from the wave propagation velocity $v_i$, and internal damping coefficient $\eta_i$. All soil layer properties are given in table 1 below, including the impedances $Z_i = \rho_i v_i$, the heights $H_i$, and the number of bar elements per layer $n_i$.

Viscous dampers are added at the top and bottom of the model to simulate no-reflection boundaries. Their damping parameter $c$ is chosen so as to cancel out the incoming stress, according to Lysmer and Kuhlemeyer with $a = 1$. The above mentioned linear elastic interface law is used (eq 13). Different interface stiffnesses are tested : $k_\tau = 0$, $2.10^2$, $3.10^3$, $1.10^4$, $1.10^5$ and $1.10^8$ $Pa/m$. When the interface stiffness is high, the system is supposed to behave as if the soil and pile phases acted as one layer of equivalent {soil+pile} properties. When the interface stiffness is null, phases should behave independently. The transfer functions between bottom and top of the intermediate layer are calculated analytically on both phases to serve as reference. Assuming an equivalent intermediate soil layer indexed $ps$, and considering that impedances $Z_{ps} << Z_a$, the transfer function can be expressed as :

$$F(\omega) = \left| \frac{2}{e^{ik^*_{ps}h_{ps}} + e^{-ik^*_{ps}h_{ps}}} \right| \tag{22}$$

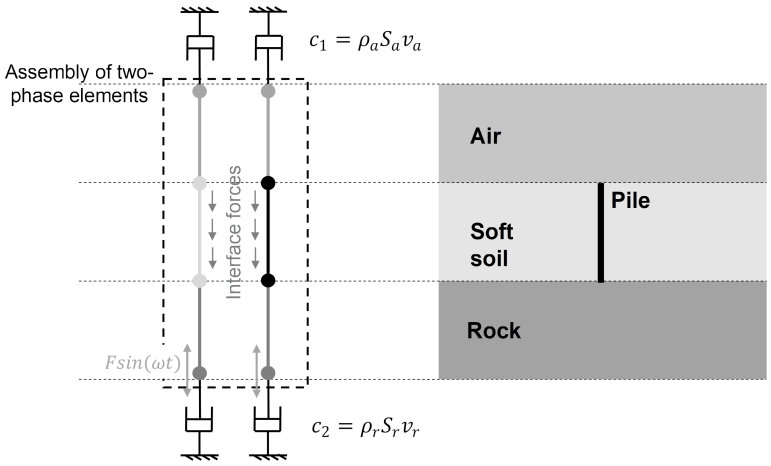


Figure 3: Interface stiffness and boundary conditions of the one-dimensional test case model

where $k^* = \frac{k}{\sqrt{1+\frac{\eta_{ps} i\omega}{\rho_{ps} v_{ps}^2}}}$ and $k = \frac{\omega}{v_{ps}}$ the wave number.

Assuming $\alpha$ and $\beta$ such that $S_p = \alpha S_{eq}$ and $S_s = \beta S_{eq}$ (here $\alpha = \frac{1}{2}$ and $\beta = \frac{1}{2}$), equivalent properties can be expressed as

$$\begin{cases} \rho_{eq} = \alpha\rho_p + \beta\rho_s & (23) \\ v_{eq} = \sqrt{\dfrac{\alpha\rho_p v_p^2 + \beta\rho_s v_s^2}{\rho_{eq}}} & (24) \\ \eta_{eq} = \alpha\eta_p + \beta\eta_s & (25) \end{cases}$$

Remark : The analytical equilibrium is written with stresses, which explains that the cross-section area needs to be constant between layers. In the intermediate layer, the area is therefore shared between the pile and the soil.

Transfer functions, both analytical and numerical, are presented hereafter firstly for limit interface stiffness values (figure 4) and secondly for intermediate ones (figure 5). Figure 4, shows that the two-phase model matches the reference on the limit cases. When the interface stiffness is very high, the intermediate layer behaves as if phases were glued. As can be observed on figure 5, when the interface stiffness is slightly different from the limit cases, transfer functions also slightly vary from the reference functions. When the interface stiffness varies, resonance frequencies change.

### 3.2 Test case for 2D two-phase element

#### 3.2.1 Static monotonic loading

The two-dimensional model represents a pile embedded in homogeneous soil. The pile properties are as follows : length $L_p = 13\ m$, cross-section $S_p = 0.5\ m^2$, inertia $I_p = 0.01\ m^4$, circumference $p_p = 2\sqrt{\pi S_p}\ m$ and Young's modulus $E_p = 210.10^9\ Pa$. The soil properties are given hereafter : length $L = 15\ m$, width $H = 10\ m$, Young's modulus $\frac{E_p}{E_s} = 10^2$ (case B) or $10^4$ (case A), Poisson's ratio $\nu_s = 0.2$.

Displacements are zero on three boundaries as shown on figure 6a. Static Horizontal unitary displacement is imposed on the pile head. Two models are considered. The reference model

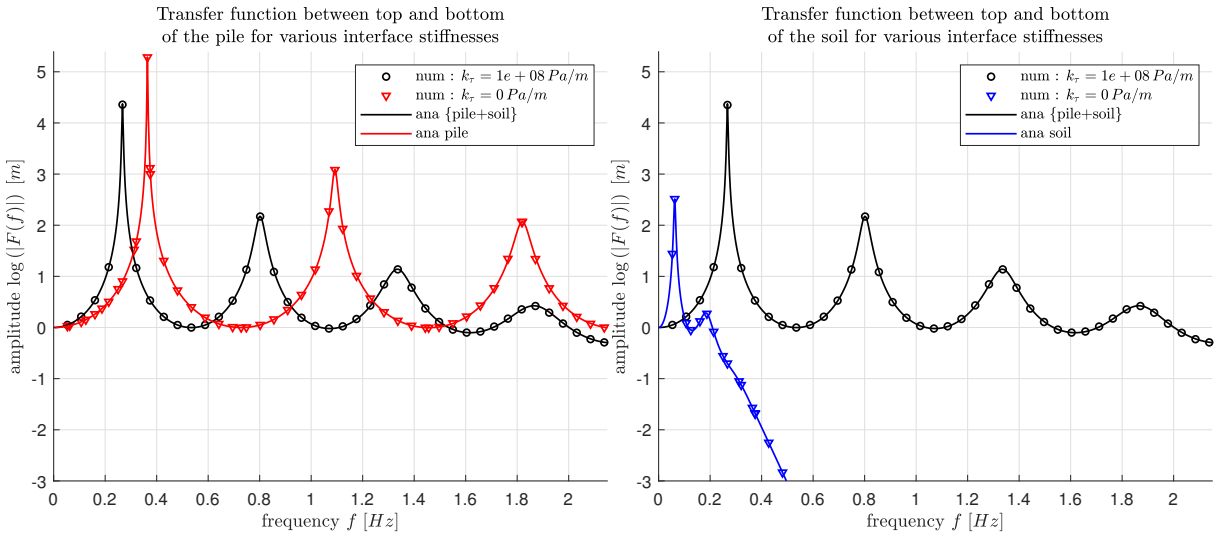


(a) pile (b) soil

Figure 4: Comparison of analytical and numerical transfer functions on the pile (a) and the soil (b) for interface stiffnesses $k_\tau = 0\,Pa/m$ and $k_\tau = 1.10^8\,Pa/m$

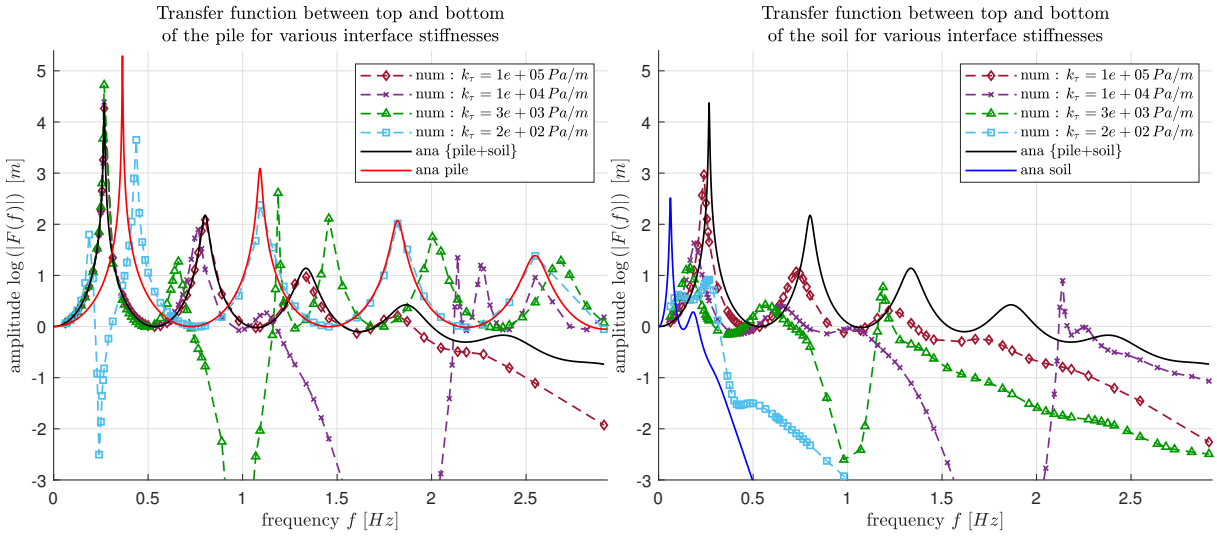


(a) pile (b) soil

Figure 5: Numerical transfer functions for different interface stiffnesses on pile (a) and soil (b)

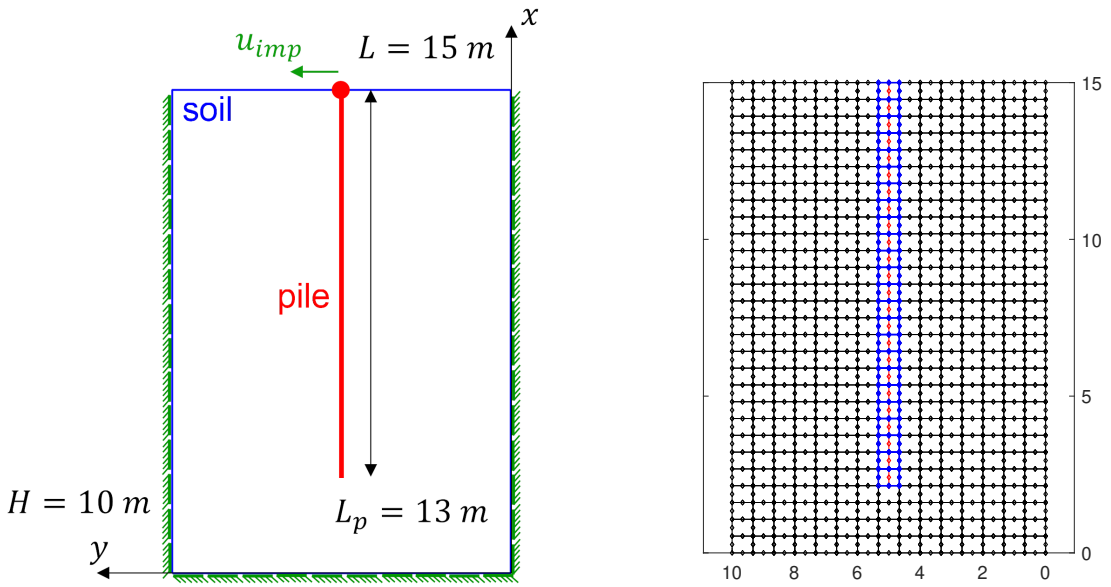


(a) Boundary conditions for the soil box (b) Finite element mesh

Figure 6: Illustration of 2D test case : pile in soil box

| $case$ | $\frac{E_p}{E_s}$ | $k_\tau$ |
|---|---|---|
| $A1$ | 10000 | $1.00E+08$ |
| $A4$ | 10000 | $1.00E+11$ |
| $B1$ | 100 | $1.00E+10$ |
| $B4$ | 100 | $1.00E+13$ |

Table 2: Model properties for 2D test case in monotonic loading

does not use two-phase elements. Its pile nodes are merged with those of the soil. The two-phase model uses the linear elastic law presented above. Multiple stiffness values are tested to verify that the two-phase model behaviour tends to the reference model's behaviour with increasing interface stiffness.

The following table 3 shows the horizontal displacement at pile foot $U_{p,foot}$ and the horizontal reaction force at pile head $P_{p,head}$ and their relative difference to the reference model (indexed $R$). Table 3 shows very low relative deviation on target displacement and reaction force between the reference and the two-phase model with high stiffness (cases A4 and B4). A mesh refining study (not presented here) has shown that the elements do converge.

### 3.2.2 Static cyclic loading

The same model as before is used, except for the interface law and for the loading. Instead of a unitary static displacement, a static cyclic displacement ranging from $0$ to $1.5\,m$ is imposed. The cyclic interface law parameters are uniform with pile depth : $q_{sr} = 2.10^9 \frac{Es}{Ep}\,Pa$, $q_{sel} = 10^4 \frac{Es}{Ep}\,Pa$ and $G_{50} = 4.10^{10} \frac{Es}{Ep}\,Pa$. Parameters are the same for vertical and horizontal relative displacements, though the horizontal interface only very slightly reacts since its relative displacement is only due to Poisson effect.

The force-displacement curves for both test cases A and B are given in figure 8. They serve

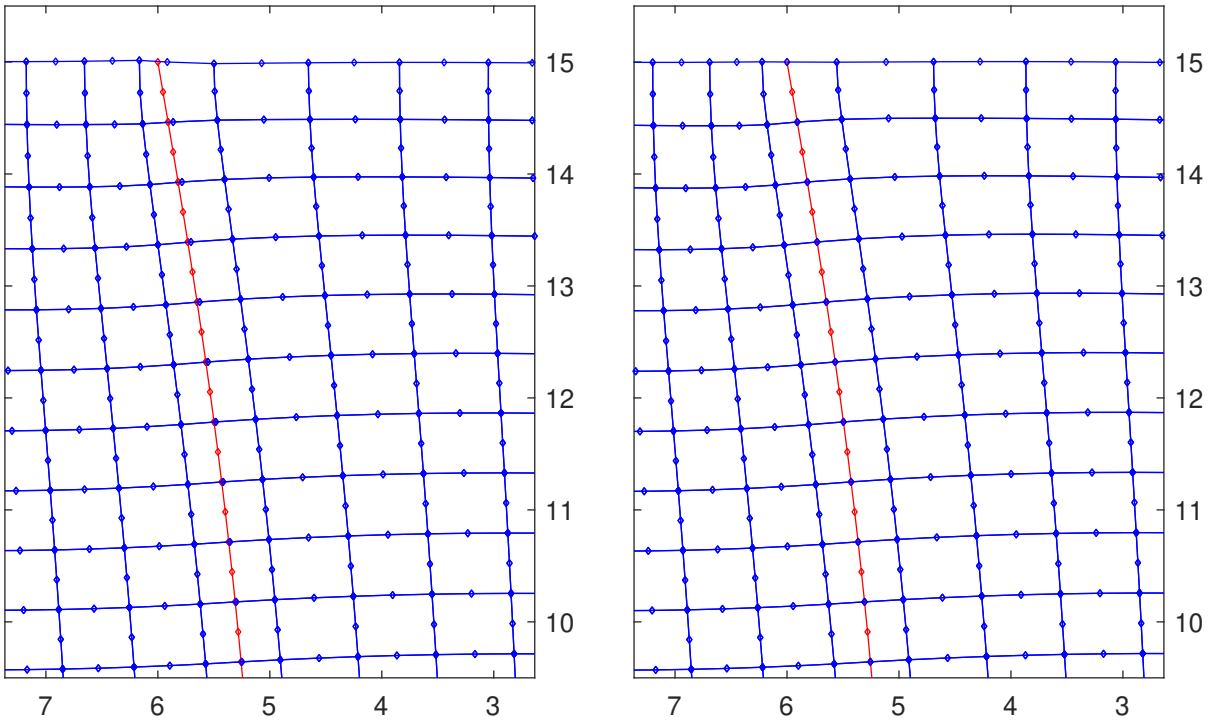


(a) case A1




(b) case A4

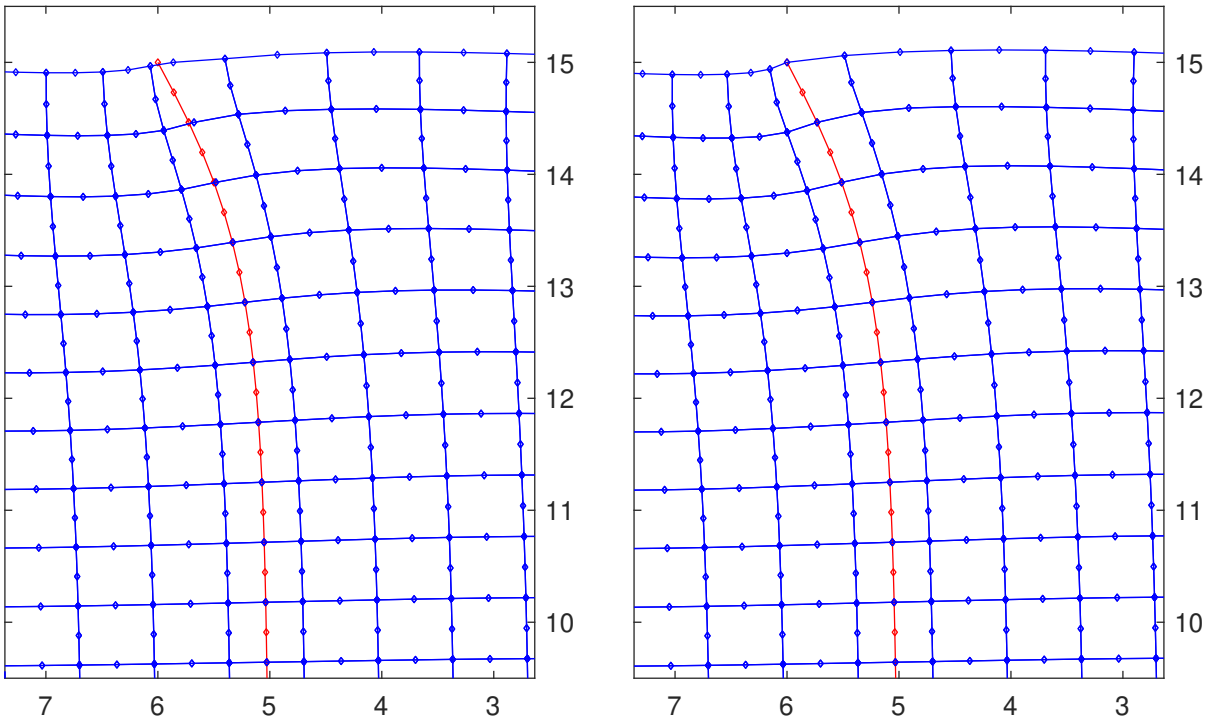


(c) case B1




(d) case B4

Figure 7: Comparison of deformed shape at pile head for 2D two-phase model between cases A1, A4, B1 and B4

| $case$ | $U_{p,foot}\,[m]$ | $P_{p,head}\,[N]$ | $\frac{\Delta U_{p,foot}}{U^*_{p,foot}}\,[\%]$ | $\frac{\Delta P_{p,head}}{P^*_{p,head}}\,[\%]$ |
|---|---|---|---|---|
| $AR$ | $-0.1211$ | $2.954E+07$ | | |
| $A1$ | $-0.1387$ | $2.826E+07$ | $14.59$ | $4.32$ |
| $A4$ | $-0.1211$ | $2.954E+07$ | $0.03$ | $0.00$ |
| $BR$ | $-3.502E-04$ | $1.537E+09$ | | |
| $B1$ | $-3.779E-04$ | $1.407E+09$ | $7.91$ | $8.44$ |
| $B4$ | $-3.499E-04$ | $1.537E+09$ | $0.08$ | $0.04$ |

Table 3: Comparison of two-phase element model with reference model (merged nodes) (R) for low stiffness value case A and high stiffness value case B

illustrative purposes, showing nonlinear capabilities of the interface modeling.

## 4 CONCLUSION

New pile-soil interface finite element modelling has been introduced based on a two-phase approach. Its static and dynamic behaviour has been validated for one- and two-dimensional finite elements. A simple one-dimensional interface law has been introduced for illustrative purposes. Future developments will focus on improving pile-soil interface law in 3D with coupled axial and transverse directions. These improvements are to be included in a 3D macro-element for pile group foundations, which is intended to further model the nonlinear pile-head connection and nonlinear behaviour of reinforced concrete piles. The advantages of such macro-element modelling are the improved ergonomy and numerical convergence properties through a substructuring approach, especially in the case of numerous nonlinearities.

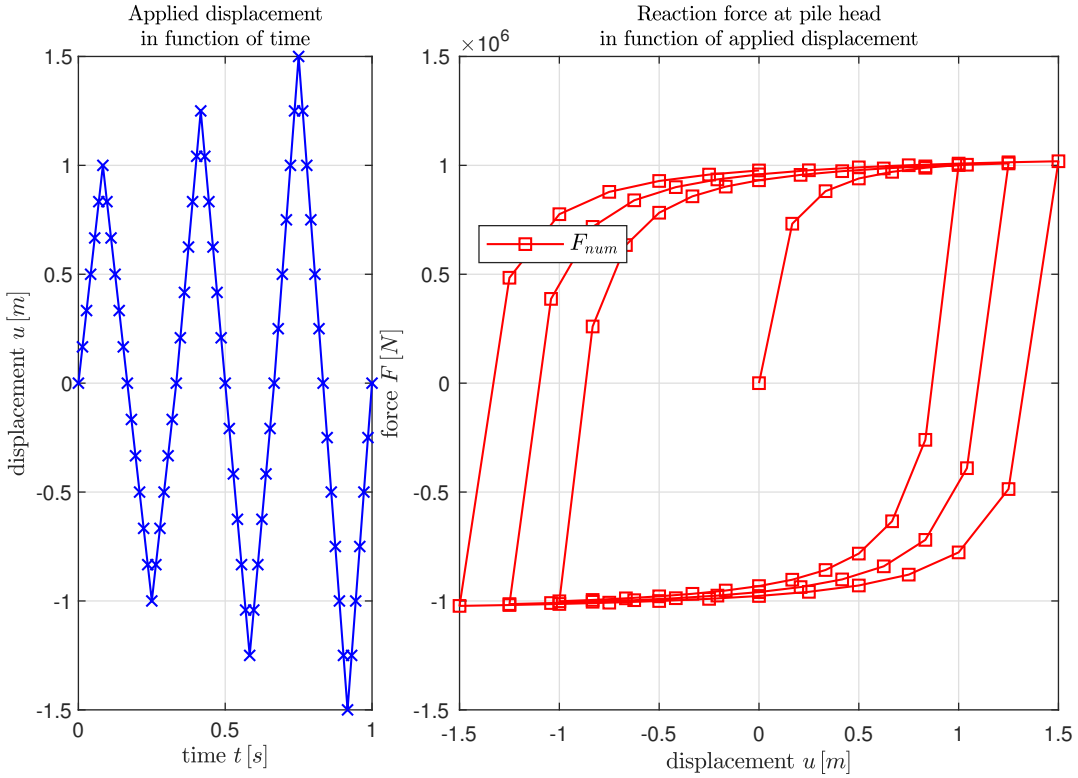


(a) case A

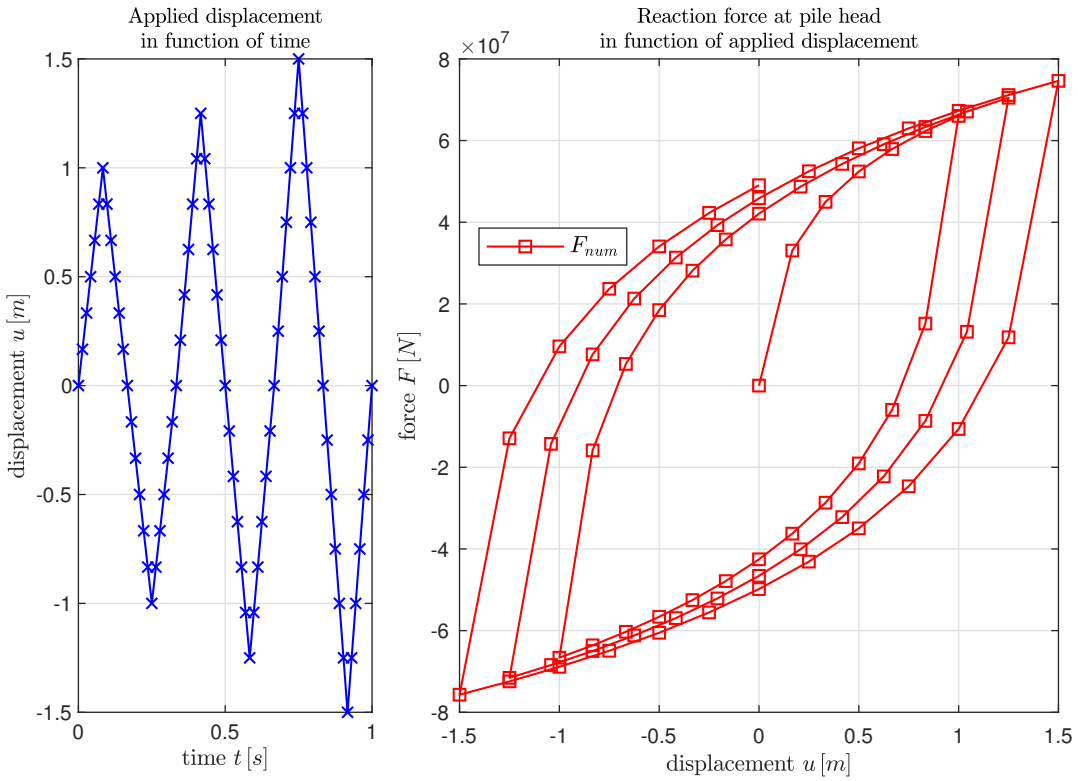


(b) case B

Figure 8: Force-displacement curves at pile head for cyclic loading on cases A and B

## REFERENCES

[1] A. A. Correia. *A pile-head macro-element approach to seismic design of monoshaft-supported bridges*. PhD Thesis, Università degli Studi di Pavia, 2011.

[2] Z. Li. *Experimental and numerical study of deep foundations under seismic loading: vertical piles and inclined piles*. PhD Thesis, École centrale de Nantes, January 2014.

[3] J. Pérez-Herreros. *Dynamic soil-structure interaction of pile foundations : experimental and numerical study*. PhD Thesis, École centrale de Nantes, February 2020.

[4] S. Grange and D. Bertrand. Implicit coupling of heterogeneous and asynchronous time-schemes using a primal approach based on velocity continuity at the subdomain interface. *Finite Elements in Analysis and Design*, 196:103604, November 2021.

COMPDYN 2023
9th ECCOMAS Thematic Conference on
Computational Methods in Structural Dynamics and Earthquake Engineering
M. Papadrakakis, M. Fragiadakis (eds.)
Athens, Greece, 12-14 June 2023

# CROSS INTERACTION FOR A SMALL GROUP OF SHALLOW FOUNDATIONS

**E. Zeolla[1], F. de Silva[2], S. Sica[1]**

[1] Department of Engineering, University of Sannio
Benevento, Italy
{ezeolla, stefsica}@unisannio.it

[2] Department of Civil, Architectural and Environmental Engineering, University of Federico II
Naples, Italy
filomena.desilva@unina.it

## Abstract

*A few literature studies have highlighted the dynamic interaction that occurs through the underlying soil among closely spaced structures (SSSI). This interaction, although neglected in most technical codes, could affect the seismic response of structures located in densely urbanized areas. Extensive studies on this topic are still limited and more refined approaches accounting for soil continuity are needed. In this context, the work illustrates a three-dimensional numerical study aimed at quantifying the effect of SSSI on the dynamic impedance of a shallow rectangular rigid foundation in the presence of two lateral neighbors. The key factors accounted in the parametric study are: (i) the relative distance between three nearby foundations, (ii) the position of the foundation in the group and (iii) the input frequency of the harmonic loads exciting the three foundations. At this stage of the work, a viscoelastic linear behavior was assumed for the soil. Due to SSSI, a decrease of the static stiffnesses of the reference foundation in the group was computed. This reduction depends on the distance among the foundations and its position in the group (central or lateral). Lateral foundations are less affected by the mutual interaction.*

**Keywords:** SSSI, Impedance function, Shallow foundations, 3D numerical modelling.

## 1 INTRODUCTION

Even though in current design buildings are analyzed as isolated structures (i. e. without other structures nearby), the seismic response of a structure located among others can be different from that of the same structure alone. This is the case, for example, of large metropolises or the historic quarters of small villages, where buildings are very close to each other and, hence, may interact through the underlying soil. In literature, this phenomenon is referred to as Structure-Soil-Structure Interaction (SSSI). From the first studies dating back to the 70s [1-3] to the most recent ones, it emerged that in some cases the effects of through-soil interaction are not negligible and depend on various factors, such as the distance between the foundations, their plan layout, the dynamic features of the structures, the frequencies of the input motion and the subsoil characteristics.

An oscillating foundation generates surface and body waves that spread through the soil, reaching the neighboring passive foundations. These latter ones may experience additional displacement and stress fields, which in some cases may be comparable to that of the active foundation. For a given structure [4], this additional cross coupling could affect soil compliance with the consequent modification of the fundamental period of the overall soil-structure system [5].

If SSSI occurs, in addition to the soil reactions in the direction of the applied load, further stresses perpendicular to it are generated at the soil-foundation contact [6-9]. The displacement (or rotation) components of two or more nearby foundations can be mutually in phase or out of phase with respect to each other but also to the ground as evidenced by Betti for different types of incident waves [10]. Interaction phenomena generally produce higher effects when the number of foundations increases and their clear spacing decreases [11-13]. The SSSI effects may be emphasized or not depending on the specific soil properties [14-17], the plan layout of the building stock and the dynamic features of the buildings (fundamental period, etc.) [18-21].

Despite the knowledge gained so far, it is still not easy to predict when through-soil interaction effects may affect the dynamic response of a structure, in consideration of several factors involved. For this reason, to date there is a gap in design code or guidelines on SSSI; hence, to improve current standards more extensive numerical and experimental investigations are needed. In this vein, the paper aims to find a simple but practical procedure to account for SSSI in the design (or verification) of buildings in highly urbanized context. Since the well-known substructure (impedance) approach is still the fastest and most manageable analysis method to handle classical soil-structure interaction (SSI) problems, this approach with all related advantages will be proposed to solve even the more complex problem of structure-soil-structure interaction (SSSI). In short, the idea is to include the presence of other neighboring foundations in the impedance function of the target foundation (and structure).

Using a continuous 3D finite difference approach, a simple scheme of three shallow rigid foundations on a homogeneous linear elastic halfspace under harmonic excitation was analyzed. In the parametric study, the distance between the foundations and the input frequency were varied and the different components of the soil-foundation impedance matrix were rigorously calculated. In a previous works of the same authors [22], the impedance functions for two closely-spaced foundations have already been obtained, and suitable interaction coefficients proposed. These interaction coefficients allow the static stiffness of the single foundation to be modified in order to take into account for the presence of its neighbor. In this way, the target foundation can still be modelled as “isolated” but equipped at its base with modified stiffnesses accounting for the presence of the close foundation.

In this study, the same procedure already validated for the couple of footings, will be extended to the case of three independent foundations. These could represent, for example, the

foundations of ancient masonry buildings without a proper connection in the transversal direction.

## 2 FEATURES OF THE NUMERICAL MODEL

The reference scheme considered in this numerical study is illustrated in Figure 1. It consists of three infinitely rigid and equally-spaced foundations with their length parallel to the horizontal global axis x and placed on the surface of a linear, isotropic, elastic half-space (Figure 1a). The geometric features of the foundations are shown in Figure 1b: the three foundations are assumed to be rectangular, with length, 2L, and width, 2B. The free distance between the foundation edges, S, is varied between 0.5B and 4B and the properties assigned to the soil, assumed linear elastic, are listed in Table 1. It is worth emphasizing that at this stage of the work a very low Vs value was intentionally assigned to the soil to maximize the interaction effects among the neighboring foundations.

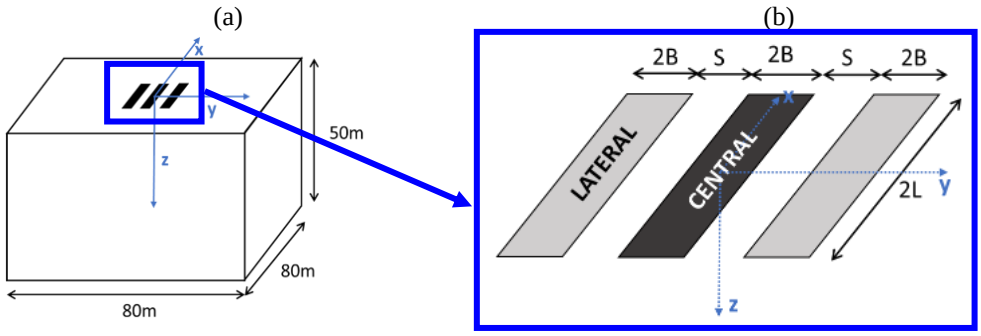


Figure 1. Analysis domain (a) and layout (b) of the three foundations considered in this study

Since it is needed to model the soil as a continuum to properly analyze the cross interaction between adjacent foundations, the 3D soil domain shown in Figure 1a was implemented in FLAC3D [30] and discretized through the finite difference technique (Itasca, 2004). A grid spacing, $\Delta$, respecting the rule of Kuhlemeyer and Lysmer (1973) ($\Delta<V_s/8f_{max}$) was chosen, so that input frequencies up to a maximum value $f_{max}$= 25 Hz can reliably be propagated in the soil with shear wave velocity, $V_s$.

| | $\gamma$ [kN/m$^3$] | K [MPa] | G [MPa] | $V_S$ [m/s] |
|---|---|---|---|---|
| Halfspace | 19 | 12.2 | 5.6 | 54 |

Table 1. Soil parameters

The three foundations were simultaneously loaded through a harmonic displacement associated with the stiffness component to be calculated. The frequency of the applied harmonic oscillation ($f=\omega/2\pi$) was alternately set equal to the odd frequencies in the range 1-13 Hz to cover a probable frequency band of interest in the engineering field. A further case, corresponding to a zero-excitation frequency, was simulated to obtain the static stiffness that appears in the real part of

the impedance function in Equation 2. Addinational features of the model and its validation may be found in [23].

## 3 NUMERICAL RESULTS

In Figure 2, the static stiffnesses associated to the translational and rotational modes of the single foundation were compared with those of the same foundation in the presence of its twins, loaded equally and simultaneously. The translational stiffnesses ($K_{zz}$, $K_{yy}$ and $K_{xx}$) were normalized with respect to the soil shear modulus, G, and the half-width of the foundation, B, while the rotational stiffnesses ($K_{rx}$ and $K_{ry}$) were divided by G and B cubed. The clear horizontal (edge-to-edge) distance S between the three foundations was also normalized to the foundation half-width, B.

It emerged that when the target foundation is adjacent to the other two (clones), its static stiffnesses decrease compared to the values corresponding to the same foundation isolated and the reduction in stiffness decreases as the distance between them increases. On the other hand, for S/B=4, the cross interaction between the two foundations is still found to be non-negligible. Moreover, the reduction also depends on the position of the target foundation in the group. As expected, the reduction is greater if the foundation is central. When the distance is short (e.g. S=0.5B), a percentage difference with respect to the value of the individual foundation more than 50% for the central foundation and more than 30% for the lateral ones is achieved. For larger distances (e.g. S=4B), the above differences decrease, being around 40% for the central foundation and more than 20% for the lateral ones.

For the oscillation around the x-axis (Figure 1), the neighboring foundations exert a kind of mutual constraint on the central one, which causes an increase in its rotational stiffness. Regardless of the position of the foundation (central or lateral), the interaction effect on the rocking motion is more sensitive to the distance. For small values of the foundation-foundation spacing, the difference is still around 50% and 30%, while it decreases to 2% and 10% for S/B=4

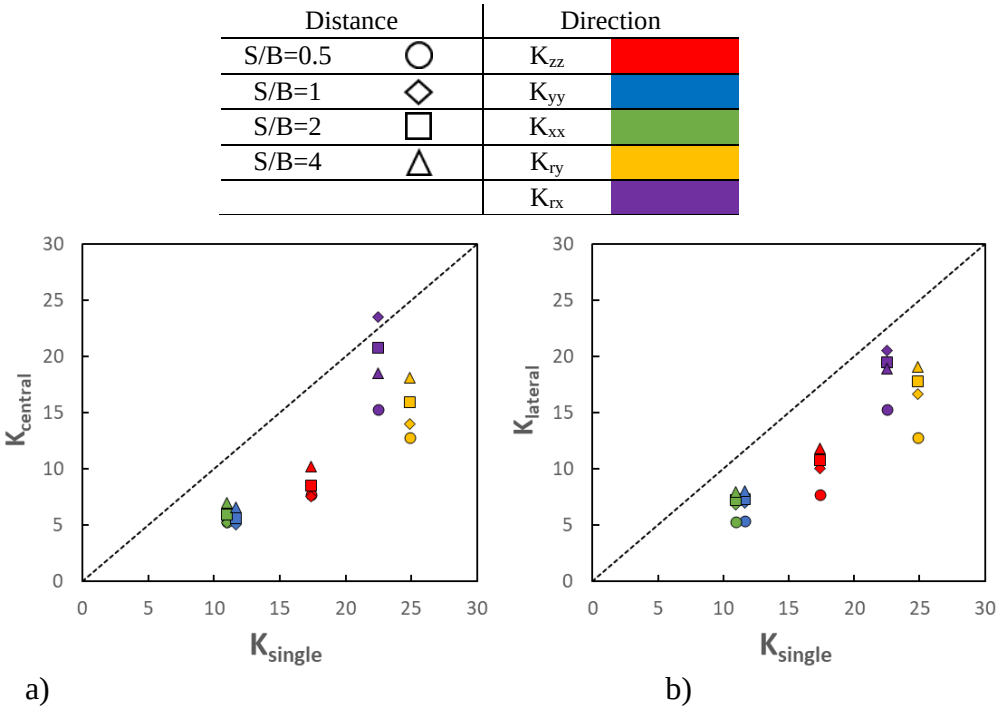


Figure 2. Dimensionless static stiffness of the central (a) or lateral (b) foundation of the group vs the static stiffness of the single footing.

## 4 COMPARISON WITH ANALYTICAL SOLUTIONS

For the couple of foundations, the authors defined interaction coefficients that allow the static stiffnesses of the single foundation to be modified in presence of its twin foundation:

$$\alpha_{ij} = (K_{ij,single} - K_{ij,group})/K_{ij,single} \quad (2)$$

where $K_{ii,single}$ and $K_{ii,group}$ are the stiffnesses of the target foundation in case it is alone or in couple. The cross-interaction modifiers $\alpha_{ij}$ are provided in an exponential law:

$$\alpha_{ij} = a_{ij}\exp\left[b_{ij}\,(S/B)\right] \qquad \text{with S/B} \in [0.5;\infty[ \quad (3)$$

where $a_{ij}$ and $b_{ij}$ are the coefficients for each foundation oscillation mode, given in Table 2 in the case of an elastic halfspace. Other subsoil configurations can be found in [23].

Assuming that the stiffness component linking the forces below the master footing to its displacement is the same if the foundation is in a couple or in a triplet, the analytical stiffness of the lateral foundation was computed by:

$$K_{ij,lateral} = K_{ij,single}(1 - \alpha_{ij}) \quad (4)$$

For the central foundation, the presence of the two equally-spaced lateral neighbors was expressed by:

$$K_{ij,central} = K_{ij,single}(1 - 2\alpha_{ij}) \quad (5)$$

| $\mathbf{a_{zz}}$ | $\mathbf{a_{yy}}$ | $\mathbf{a_{xx}}$ | $\mathbf{a_{ry}}$ | $\mathbf{a_{rx}}$ |
|---|---|---|---|---|
| 0.30 | 0.30 | 0.30 | 0.30 | -0.48 |
| $\mathbf{b_{zz}}$ | $\mathbf{b_{yy}}$ | $\mathbf{b_{xx}}$ | $\mathbf{b_{ry}}$ | $\mathbf{b_{rx}}$ |
| -0.18 | -0.07 | -0.13 | -0.62 | -0.32 |

Table 2. Coefficients of the exponential law in Eq.3 for the case of two interacting foundations on halfspace

Figure 4 shows the ratio between the numerically and analytically-computed stiffnesses versus the dimensionless spacing, S/B, for both the central and the lateral foundation of the trio. From Figure 4-a it could be observed that for the swaying and rocking modes of the central foundation the ratio is always greater than one for the S/B considered and tends to one for larger spacing (greater than 4B). This means that when the foundations are very close together and placed in the centre, the stiffness predicted by Eq. 5 underestimates the numerical value. This is due to the fact that the analytical approach neglects the stiffening effect provided by the lateral foundations on the central one. As the clear distance increases, the mismatch decreases and the analytical predictions are in good agreement with the numerical ones provided by the rigorous 3D analyses with FLAC3D. Conversely, for the lateral foundations of the trio (Figure 4-b), the mismatch between numerically and analytically predicted static stiffnesses does not exceed 5-10%.

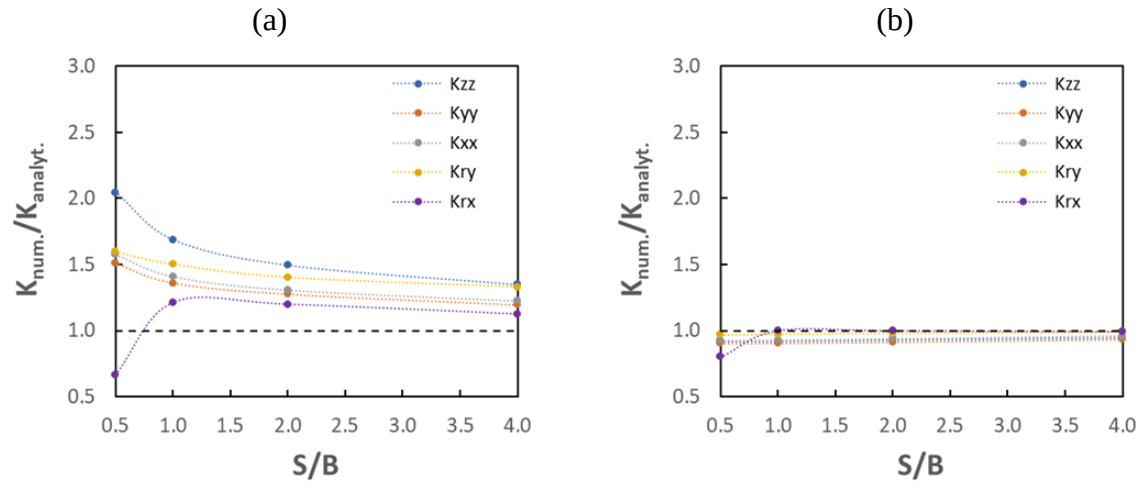


Figure 4. Ratio between numerical and analytical stiffnesses for the central (a) and lateral (b) foundation of the trio.

## 5 CONCLUSIONS

The static interaction among three closely-spaced shallow foundations through the underlying soil was investigated by means of a 3D continuum approach. In the performed study, a simple scheme of three shallow foundations placed on an ideal halfspace was considered and a parametric study was carried out considering different values of the foundation-foundation spacing.

Due to soil continuity, the phenomenon of cross interaction among multiple footings produces a reduction of the low-frequency (static) stiffness terms of the impedance matrix for all degrees of freedom of the foundation. For smaller values of the foundation-foundation spacing, the cross-interaction revealed to be not negligible, either for the central foundation of the group or for the lateral one.

Suitable coefficients, which reduce the static stiffnesses of the reference foundation in presence of its neighbors, were formerly derived by the authors for a group of two foundations [23]. In this work, the same modifiers have been adopted to estimate the static stiffnesses of the foundation placed in a small group of three footings. The closed-form solutions found for the foundation couple also proved reliable for the foundation trio in the case of a lateral foundation. For a central foundation, the same solutions are applicable for clear distances among the foundations greater than 4 times the half-width of the foundation. For shorter distances, an underestimation of the stiffness modifiers occurs.

## 6 ACKNOWLEDGEMENTS

The work has been developed in the framework of the 2022–2024 ReLUIS-DPC research programme funded by the Italian Civil Protection Department, as a contribution to the geotechnical Work Package ‘Soil-Foundation-Structure Interaction’ (Task 16.3) by the UniSannio-Sica Research Unit.

## REFERENCES

[1] G. B. Warburton, J. D. Richardson, & J. J. Webster. Forced vibrations of two masses on an elastic half space. 1971.

[2] C. Liang, Dynamic response of structures in layered soils. *Doctoral dissertation, Massachusetts Institute of Technology*. 1974.

[3] J. J. Gonzalez, & J. M. Roesset, Dynamic interaction between adjacent structures. *Research report, 1976--1977 (No. PB-287079)*. Massachusetts Inst. of Tech., Cambridge (USA). Constructed Facilities Div. 1977.

[4] H. T. Lin, J. M. Roesset, & J. L Tassoulas. Dynamic interaction between adjacent foundations. *Earthquake engineering & structural dynamics*, 15(3), 323-343. 1987.

[5] E. Zeolla, S. Sica, & F. De Silva, Dynamic impedance functions for neighbouring shallow footings. In Geotechnical Engineering for the Preservation of Monuments and Historic Sites III (pp. 883-892). CRC Press. 2022.

[6] T. Triantafyllidis, & B. Prange. Dynamic subsoil-coupling between rigid rectangular foundations. *Soil Dynamics and Earthquake Engineering*, 6(3), 164-179. 1987.

[7] T. Triantafyllidis, & B. Prange.. Dynamic subsoil-coupling between rigid, circular foundations on the halfspace. *Soil Dynamics and Earthquake Engineering, 8(1), 9-21*. 1989.

[8] T. Triantafyllidis, & T. Neidhart. Diffraction effects between foundations due to incident Rayleigh waves. *Earthquake engineering & structural dynamics*, 18(6), 815-835. 1989.

[9] J. S. Mulliken, & D. L. Karabalis. Discrete model for dynamic through the soil coupling of 3D foundations and structures. Earthquake Engineering & Structural Dynamics, 27(7), 687-710. 1998.

[10] R. Betti. Effects of the dynamic cross‐interaction in the seismic analysis of multiple embedded foundations. *Earthquake engineering & structural dynamics*, 26(10), 1005-1019. 1997.

[11] J. Qian, & D. E. Beskos, Dynamic interaction between 3D rigid surface foundations and comparison with the ATC3 provisions. *Earthquake engineering & structural dynamics*, 24(3), 419-437. 1995.

[12] J. Qian, & D. E. Beskos. Harmonic wave response of two 3-D rigid surface foundations. Soil Dynamics and Earthquake Engineering, 15(2), 95-110. 1996.

[13] J. Qian, L. G. Tham, & Y. K. Cheung, Dynamic cross interaction between flexible surface footings by combined bem and fem. *Earthquake engineering & structural dynamics*, 25(5), 509-526. 1996.

[14] D. L. Karabalis, & M. Mohammadi, 3D dynamic foundation-soil-foundation interaction on layered soil. *Soil Dynamics and Earthquake Engineering*, 17(3), 139-152. 1998.

[15] B. Sbartai, Dynamic interaction of two adjacent foundations embedded in a viscoelastic soil. *International Journal of Structural Stability and Dynamics*, 16(03), 1450110. 2016.

[16] M. Bybordiani, & Y. Arici, Structure‐soil‐structure interaction of adjacent buildings subjected to seismic loading. *Earthquake Engineering & Structural Dynamics*, 48(7), 731-748. 2019.

[17] J. Wang, T. Guo, Y. Xie, & Z. Du, Parametric analyses of dynamic interaction between three-dimensional soil and frame structure group under earthquake loadings. *Bulletin of Earthquake Engineering*, 20(15), 8305-8324. 2022.

[18] L. A. Padron, J. J. Aznarez, & O. Maeso, Dynamic structure–soil–structure interaction between nearby piled buildings under seismic excitation by BEM–FEM model. *Soil dynamics and earthquake engineering*, 29(6), 1084-1096. 2009.

[19] N. A. Alexander, E. Ibraim, & H. Aldaikh, A simple discrete model for interaction of adjacent buildings during earthquakes. *Computers & Structures*, 124, 1-10. 2013.

[20] J. A Knappett, P. Madden, , & K. Caucis,. Seismic structure–soil–structure interaction between pairs of adjacent building structures. *Geotechnique*, 65(5), 429-441. 2015.

[21] F. Vicencio, & N. A. Alexander, Method to evaluate the dynamic structure-soil-structure interaction of 3-D buildings arrangement due to seismic excitation. *Soil Dynamics and Earthquake Engineering*, 141, 106494. 2021.

[22] E. Zeolla, S. Sica, & F. De Silva, Dynamic Interaction Between Adjacent Shallow Footings in Homogeneous or Layered Soils. In *Proceedings of the 4th International Conference on Performance Based Design in Earthquake Geotechnical Engineering* (Beijing 2022) (pp. 1257-1264). Cham: Springer International Publishing. 2022.

[23] E. Zeolla, S. Sica, & F. De Silva. *A simplified approach to account for through-soil interaction between two adjacent shallow foundations*. Bulletin of Earthquake Engineering. https://doi.org/10.1007/s10518-023-01621-1. 2023.

[24] G. Gazetas, Formulas and charts for impedances of surface and embedded foundations. *Journal of geotechnical engineering*, 117(9), 1363-1381. 1991.

[25] A. Pais, & E. Kausel, Approximate formulas for dynamic stiffnesses of rigid foundations. *Soil dynamics and earthquake engineering*, 7(4), 213-227. 1988.

[26] G. Mylonakis, S. Nikolaou, G. & Gazetas, Footings under seismic loading: Analysis and design issues with emphasis on bridge foundations. Soil Dynamics and Earthquake Engineering, 26(9), 824-853. 2006.

[27] C. Vrettos, Vertical and rocking impedances for rigid rectangular foundations on soils with bounded non homogeneity. *Earthquake engineering & structural dynamics*, 28(12), 1525-1540. 1999.

[28] R. J. Apsel, J. E. & Luco, Impedance functions for foundations embedded in a layered medium: an integral equation approach. *Earthquake Engineering & Structural Dynamics*, 15(2), 213-231. 1987.

[29] M. Iguchi, J. E. & Luco, Vibration of flexible plate on viscoelastic medium. *Journal of the Engineering Mechanics Division*, 108(6), 1103-1120. 1982.

[30] FLAC3D User Manual: Version 5.0. USA. Itasca Consulting Group, Inc. 2004.

COMPDYN 2023
9th ECCOMAS Thematic Conference on
Computational Methods in Structural Dynamics and Earthquake Engineering
M. Papadrakakis, M. Fragiadakis (eds.)
Athens, Greece, 12-14 June 2023

# APPLICABILITY OF GYRO-LUMPED PARAMETER MODEL IN IDENTIFYING HORIZONTAL IMPEDANCE FUNCTIONS OF PILE GROUPS

**Masato Saitoh**[1]

[1] Graduate School of Science and Engineering, Saitama University
255 Shimo-Okubo, Sakura-ku, Saitama, Japan
e-mail: saity@mail.saitama-u.ac.jp

## Abstract

*In recent years, the effects of frequency dependency of impedance functions (IFs) of various soil-foundation systems upon nonlinear structural systems have been revealed. So-called "Gyro-Lumped Parameter Models (GLPMs)" have been playing a vital role on numerical computations for estimating the dynamic response of nonlinear structural systems with frequency dependent IFs. GLPMs consist of frequency independent mechanical elements such as springs, dampers, and gyromasses, which generate a reaction force that is proportional to the relative acceleration of two nodes where the element is placed. These models can help predict the seismic response of structures interacting with soil-foundation systems, mostly for design purpose. When it comes to real existing structures, however, there have never been a technology proposed to identify the frequency dependent IFs. A proper identification of IFs is indispensable in predicting damage to structures in enhancing their resilience against earthquakes. Current work proposes a new method for identifying the frequency dependent IFs using GLPMs based on transfer functions processed from recorded small-amplitude earthquake waves measured on and near the target structures. In this paper, a simple two degrees of freedom system consisting of superstructure and footing supported by a 2×4 pile group is targeted. In the identification procedure, the trust region method (TRM) is applied to fit the transfer functions of the system with variables of the system including the mechanical elements of GLPMs. In the TRM, various objective functions are dealt with and hypothetical unknown quantities such as the static stiffness of the soil-pile system, the damping of the superstructure, and the masses of the structural system are assumed to verify the performance of the identification. The results indicate that accurate mass identification is prerequisite to accomplish an appropriate identification of the frequency dependent IFs.*

**Keywords:** Impedance Functions, System Identification, Gyro-Lumped Parameter Models, Trust Region Method, Pile Foundations, Frequency Dependency

## 1 INTRODUCTION

For decades, researchers struggled for finding a way to incorporate the frequency dependent characteristics of soil-foundation systems into ordinary time-stepping methods for estimating the dynamic response of structures. These days, several lumped parameter models (LPMs) have been contrived for representing a variety of frequency dependencies [e.g.,1-7], and they have been used for computing the dynamic response of structures even beyond the elastic region of structural members. The so-called "Gyro-Lumped Parameter Models (GLPMs)" have been recognized as a vital tool to compute the structural response when subjected to earthquake ground motions due to use of gyromass instead of using the ordinary mass in LPMs [e.g.,8-13]. Gyromass generates a reaction force that is proportional to the relative acceleration of two nodes where the element is placed. The advantage of the gyromass is that any inertia force due to the acceleration of ground motions never appears in it at all whereas inertia force occurs when the ordinary mass is used, which distorts the original frequency dependent characteristics of IFs. In addition, a smaller number of mechanical elements can emulate intricated fluctuations of IFs by using GLPMs than other LPMs.

GLPMs can help predict the seismic response of structures interacting with soil-foundation systems, mostly for design purpose. When it comes to real existing structures, although the frequency dependent IFs should be considered in predicting the response for achieving high accuracy, there have never been a technology proposed to identify the frequency dependent IFs. A proper identification of IFs is indispensable in predicting damage to structures in enhancing their resilience against earthquakes.

Current work proposes a new method for identifying the frequency dependent IFs using GLPMs based on transfer functions (TFs) processed from recorded small-amplitude earthquake waves measured on and near the target structures. In this paper, a simple two degrees of freedom system consisting of superstructure and footing supported by a 2×4 pile group is targeted. In the identification procedure, the trust region method (TRM) is applied to fit the TFs of the system with variables of the system including the mechanical elements of GLPMs. In the TRM, various objective functions are dealt with and hypothetical unknown quantities such as the static stiffness of the soil-pile system, the damping ratio of the superstructure, and the masses of the structural system are assumed to verify the performance of the identification.

## 2 METHODOLOGIES

In this study, a soil-pile-structure system is targeted to verify the performance of the proposed IF identification method. A superstructure is represented by a single degree of freedom system while a footing by a mass, where they are allowed to move only in the horizontal direction. The footing is supported by the published IFs of a 2×4 pile group embedded in a layered soil [9]. Properties of the considered system are as follows: the masses of the superstructure $m_s$ and footing $m_f$ are 450t and 350t, respectively; the stiffness $k_s$ and damping ratio $\zeta$ of the superstructure are $7.1\times10^4$ kN/m and 0.05, respectively; and the static stiffness of the soil-pile system $K$ is $2.4\times10^5$ kN/m.

In this study, the target TFs of the superstructure and the footing with respect to input ground motions is estimated. In practice, this procedure is equivalent to the data process to obtain the TFs from recorded small-amplitude earthquake waves measured on the target structures, and on the ground surface near the structures as the input motion.

In the identification procedure, the frequency dependent IFs of the superstructure and footing model are replaced by a so-called Type-III GLPM [9] as shown in Figure 1. The GLPM consists of three core systems (a total of 15 mechanical elements). The properties of the elements are determined by applying the TRM to reproduce the TFs. The TRM is a well-known

method applicable to nonlinear least squares problems. This study uses the following three types of objective functions to dealt with in the TRM.

$$f = \delta^2_{super-R} + \delta^2_{super-I} + \delta^2_{foot-R} + \delta^2_{foot-I} \tag{1}$$

$$f = \delta^2_{super-R} + \delta^2_{super-I} \tag{2}$$

$$f = \delta^2_{foot-R} + \delta^2_{foot-I} \tag{3}$$

where $\delta$ denotes the difference in the TFs estimated by the TRM from the target TFs. Here, subscripts "super" and "foot" indicate the TFs of the superstructure and the footing, respectively. In addition, "R" denotes the real part while "I" the imaginary part.

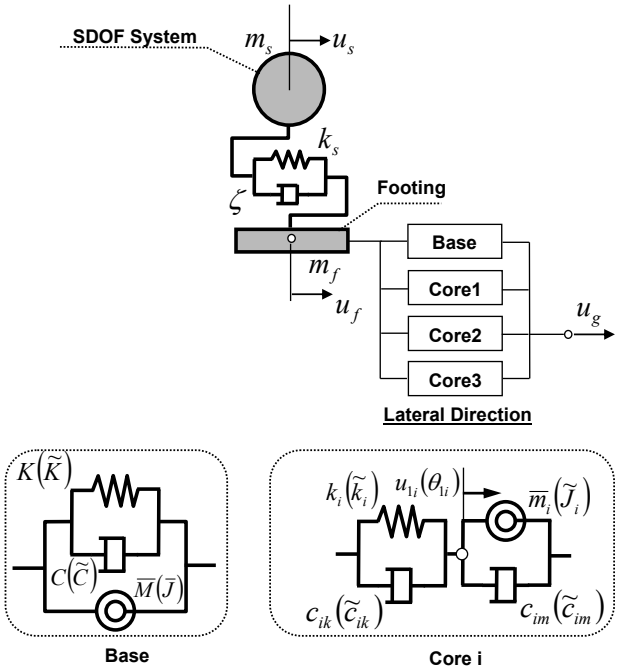


Figure 1: Structural system with Type-III GLPM

The objective functions are minimized by adjusting the properties of the elements through the algorithm of the TRM. The TRM needs the initial values of the variables, and this study assumes 0.01 for each value. The IFs expressed by the GLPM having the converged properties through the TRM are considered as the identified frequency dependent IFs.

## 3 VERIFICATION OF IF IDENTIFICATION METHOD

In this section, at first, the influence of the objective functions is investigated. Then the influence of parameters such as the static stiffness of the soil-pile system, the damping ratio of the superstructure, and the masses of the structural system, which may be unknown or vague in practice without detailed inspections, on the accuracy of the IF identification is studied.

### 3.1 Objective functions

Figures 2-4 show the resultant TFs and the identified IFs with different objective functions. In case of using Eq.1, although the fitted TFs of both the superstructure and the footing show a good match with the target TFs, the identified IFs show a discrepancy above 2Hz, especially around the local maxima of both the real and imaginary parts. In case of using Eq.2, a larger

discrepancy appears in the IFs than those in case of Eq.1. On the other hand, a good match can be achieved in case of using Eq.3. These results imply that the targeting TFs of footing is effective to achieve the IF identification with appreciable accuracy. Applying the TFs of the superstructure to the objective function may dilute the characteristics of IFs due to its large amplitude of TFs associated with the resonance of the superstructure. In the following parts, therefore, Eq.3 is applied to the TRM.

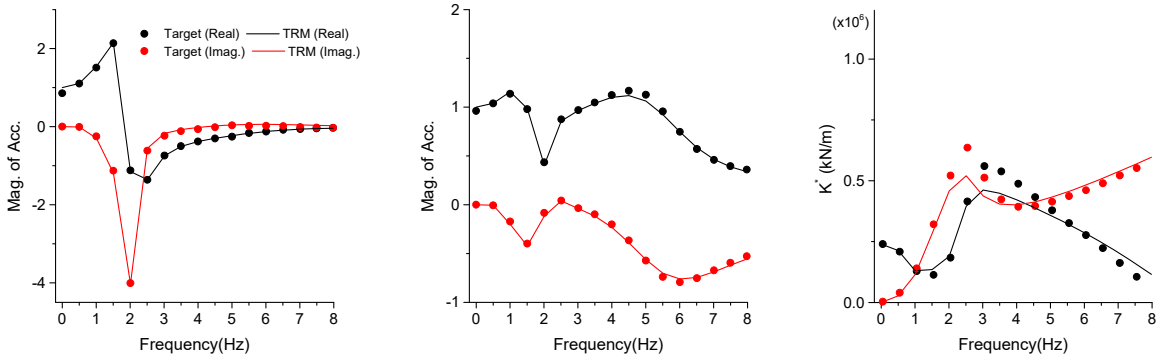


Figure 2: Transfer functions (left: superstructure, center: footing) and impedance functions (right) obtained from TRM: Equation 1 is used for objective function

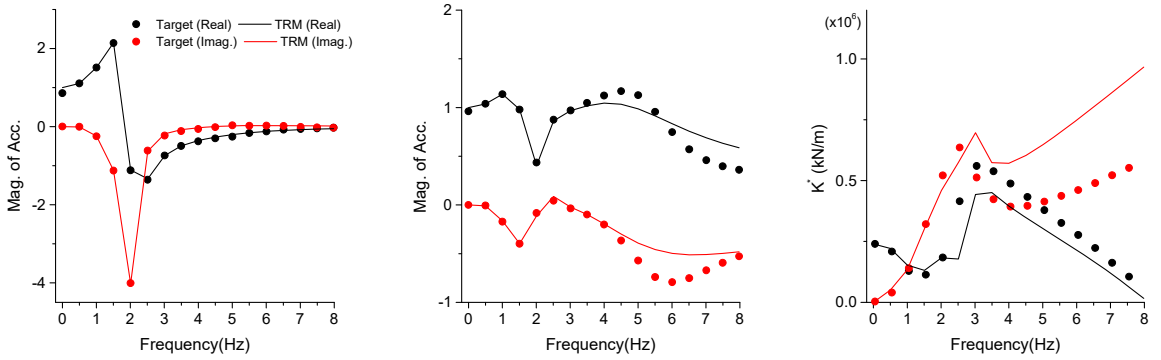


Figure 3: Transfer functions and impedance functions obtained from TRM: Equation 2

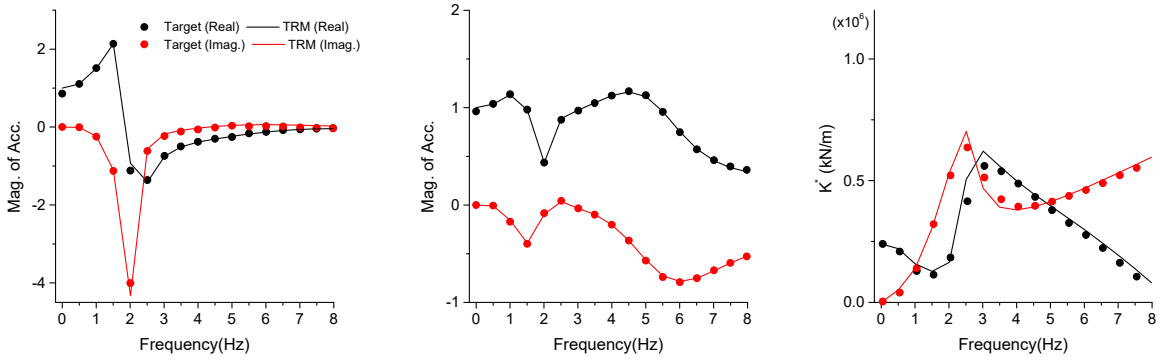


Figure 4: Transfer functions and impedance functions obtained from TRM: Equation 3

### 3.2 Static stiffness of soil-pile system

The static stiffness of the soil-pile system is the property of one of the mechanical elements in the GLPM. In practice, a couple of non-destructive technologies have been proposed to identify the static stiffness whereas the accuracy of them is still insufficient. Therefore, it is interesting to see how the proposed method applies to identify the static stiffness.

Figure 5 shows the results when the static stiffness is provided as a variable of the TRM. The TFs show a large discrepancy while the identification of the IFs is failed. Instead of setting the initial stiffness as a variable, the initial stiffness is set as a fixed value with a certain discrepancy by multiplying by 0.6. Figure 6 shows that an appropriate match with the target TFs is attained while the identified IFs are quite well reproduced. In details of the IFs, a discrepancy in lower frequency range, whose amounts are almost proportional to $\alpha$, tends to appear. Therefore, it is presumed that not the exact but an approximate value (at least the same order) could be acceptable to identify the IFs with appreciable accuracy in the middle and high frequency range whereas the IFs in lower frequency range may show a certain discrepancy.

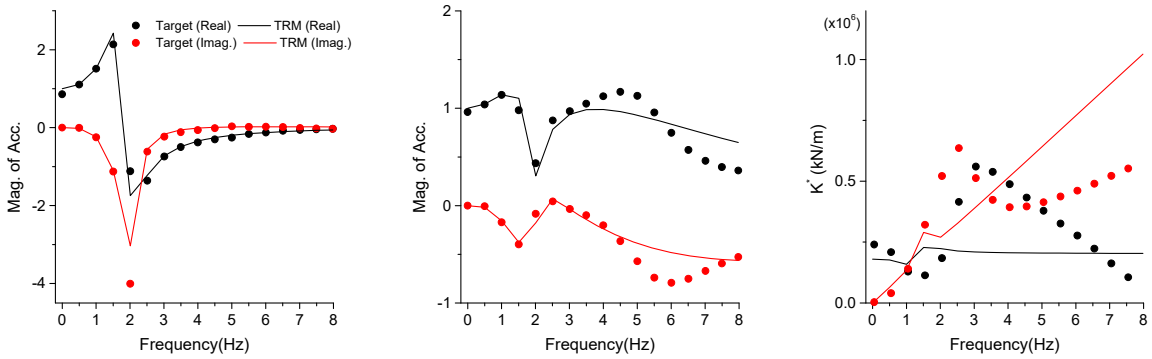


Figure 5: Transfer functions and impedance functions obtained from TRM: Static stiffness of soil-pile system as variable in TRM

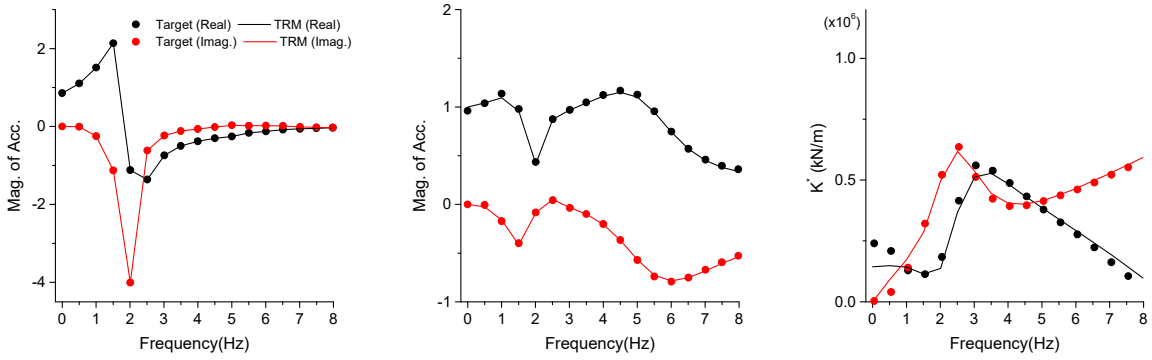


Figure 6: Transfer functions and impedance functions obtained from TRM: Static stiffness of soil-pile system containing discrepancy (multiplying by 0.6) treated as constant in TRM

### 3.3 Damping ratio of superstructure

In practice, the damping ratio of superstructures can be estimated from the TFs obtained from recorded data measured on the system. Generally, the estimated damping ratio has certain errors. Therefore, the influence of errors on the identified IFs is proved by multiplying the

exact damping ratio by 0.6. In the following identification, this damping ratio is applied to the TRM as an initial value. Therefore, the damping ratio is treated as a variable in the TRM.

Figure 7 shows that the imaginary part of the TFs of the superstructure at the first predominant frequency (around 2Hz) increases. It is found that the identified value of the damping ratio is almost the same as the initial value. Therefore, the decrease in the damping ratio attributes to the increase in the TFs. On the other hand, the TFs of the footing show a good match with the target TFs as Eq.3 is used for the objective function of the TRM, which minimizes the discrepancy in the TFs of the footing. The IFs are identified in a fairly good manner. In details, the imaginary part of the identified IFs tends to increase rapidly at the predominant frequency. This is because the imaginary part deals with the damping effect, which compensates the decrease in the damping ratio of the superstructure to attain the accurate fitting of the TFs of the footing. Therefore, errors in the damping ratio of superstructures tend to distort the IFs locally around the predominant frequency of superstructures.

A possible alternate option is that the damping ratio with an error (multiplying by 0.6) is applied as the initial value to the TRM whereas Eq. 1 is selected as the objective function to adjust the damping ratio appropriately by considering both the differences in the TFs of the superstructure and the footing.

Figure 8 shows that, although a good match in the TFs of the superstructure is attained, the TFs of the footing cannot sufficiently reproduce the target TFs, indicating inadequacy of identified IFs.

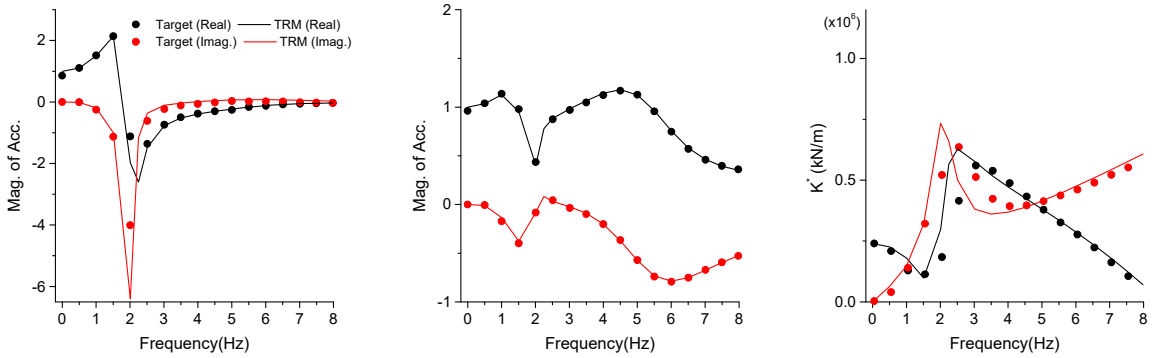


Figure 7: Transfer functions and impedance functions obtained from TRM: Damping ratio of superstructure containing discrepancy (multiplying by 0.6) treated as initial value in TRM

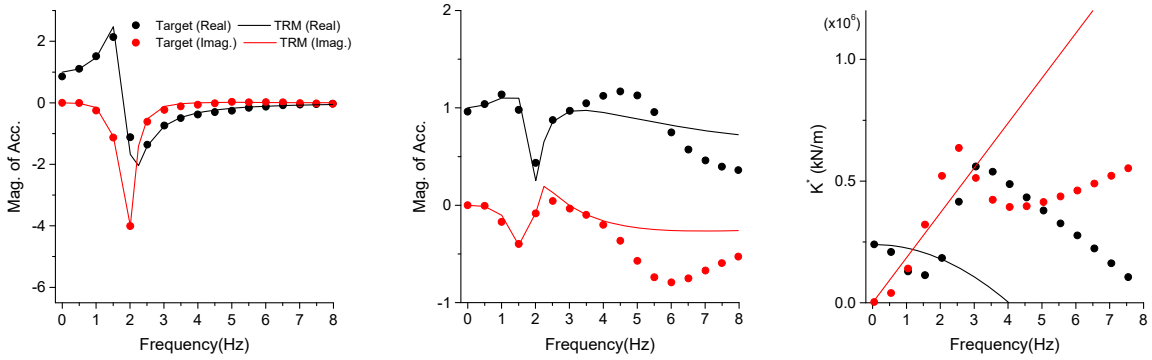


Figure 8: Transfer functions and impedance functions obtained from TRM: Damping ratio of superstructure containing discrepancy (multiplying by 0.6) treated as initial value in TRM using Equation 1

### 3.4 Masses of superstructure and footing

In practice, the estimation of the masses of structural systems is quite approximate. Non-structural elements may change the weight of each floor, which may affect the accuracy of the identification of IFs. In this part, the masses of the superstructure and the footing are assumed as the variables of the TRM. Here, a certain discrepancy is provided to them, and they are applied as their initial values in the TRM. In the following identification, the initial value of the mass of the footing is given as the product of $m_f$ by $\alpha_f$; the ratio of the mass of the superstructure to the footing is expressed as $\beta$ multiplied by $\gamma$.

Figure 9 shows the resultant TFs and IFs in case of $\alpha_f$=1 and $\gamma$=1. The converged values of $\alpha_f$ and $\gamma$ through the TRM are 1.01 and 1.19, respectively. The figure indicates a good performance of the identification. Figure 10 shows the results in case of $\alpha_f$=0.9 and $\gamma$=1. In contrast, although the resultant TFs shows a good match with the target TFs, a significant difference appears in the identified IFs. The converged values of $\alpha_f$ and $\gamma$ are 1.88 and 1.16, respectively. This is an important issue when the identification of the IFs is performed for structural systems whose masses are unknown. Figure 9 implies that the masses should not be a variable in the TRM as even a small difference in the initial value of the masses will converge to far different IFs. The reason for the marked difference in the identification can be simply explained from the following simultaneous equations of motion for the system.

$$\begin{bmatrix} 1 & 0 \\ 0 & 1/\beta \end{bmatrix} \begin{Bmatrix} \ddot{u}_s \\ \ddot{u}_f \end{Bmatrix} + \begin{bmatrix} 2\zeta\omega_s & -2\zeta\omega_s \\ -2\zeta\omega_s & 2\zeta\omega_s \end{bmatrix} \begin{Bmatrix} \dot{u}_s \\ \dot{u}_f \end{Bmatrix} + \begin{bmatrix} \omega_s^2 & -\omega_s^2 \\ -\omega_s^2 & \omega_s^2 + g(p_i)\omega_f^2 \end{bmatrix} \begin{Bmatrix} u_s \\ u_f \end{Bmatrix} = -\begin{bmatrix} 1 & 0 \\ 0 & 1/\beta \end{bmatrix} \begin{Bmatrix} \ddot{u}_g \\ \ddot{u}_g \end{Bmatrix} \quad (4)$$

where $u_s$ and $u_f$ are the response displacements of the superstructure and the footing, respectively; $u_g$ is the input motion; $\omega_s = \sqrt{k_s/m_s}$; $\omega_f = \sqrt{K/m_f}$; and $g(p_i)$ is the frequency dependent impedance function normalized by the static stiffness, consisting of GLPM parameters $p_i$.

Equation 4 indicates that $g(p_i)\omega_f^2$ is the product of the two terms: and the same response occurs in different structural systems when the product is consistent with each other. There are infinite numbers of combinations of $g(p_i)$ and $\omega_f^2$ to achieve a consistent value of $g(p_i)\omega_f^2$. Accordingly, the masses of the system should not be the variables of the TRM.

Figure 11 shows the influence of discrepancy in the mass of the footing where $\alpha_f$=0.8 is assumed. Herein, the masses are assumed to be constants in the TRM. The TFs show a good agreement with the target TFs whereas the identified IFs tend to deviate from the target IFs.

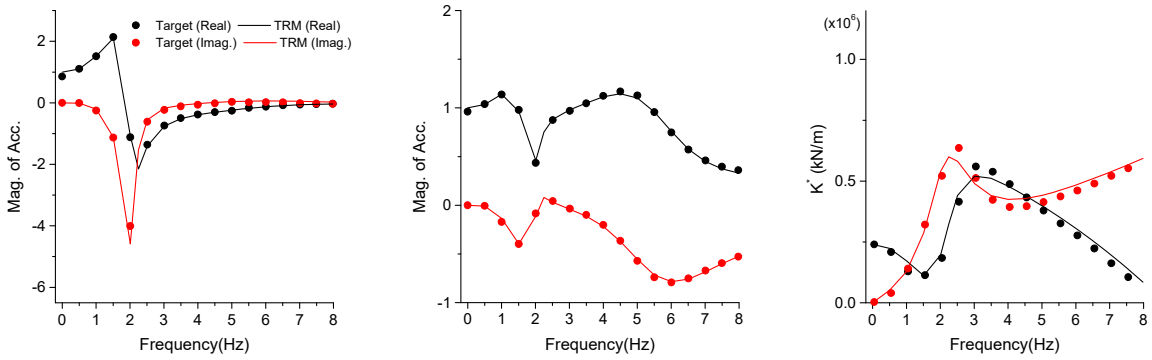


Figure 9: Transfer functions and impedance functions obtained from TRM: Masses of superstructure and footing treated as variables in TRM ($\alpha_f$=1 and $\gamma$=1)

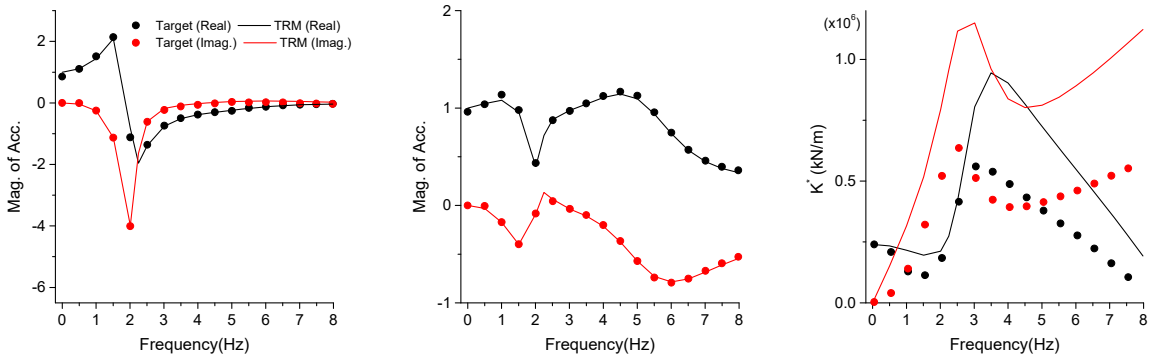


Figure 10: Transfer functions and impedance functions obtained from TRM: Masses of superstructure and footing treated as variables in TRM ($\alpha_f$=0.9 and $\gamma$=1)

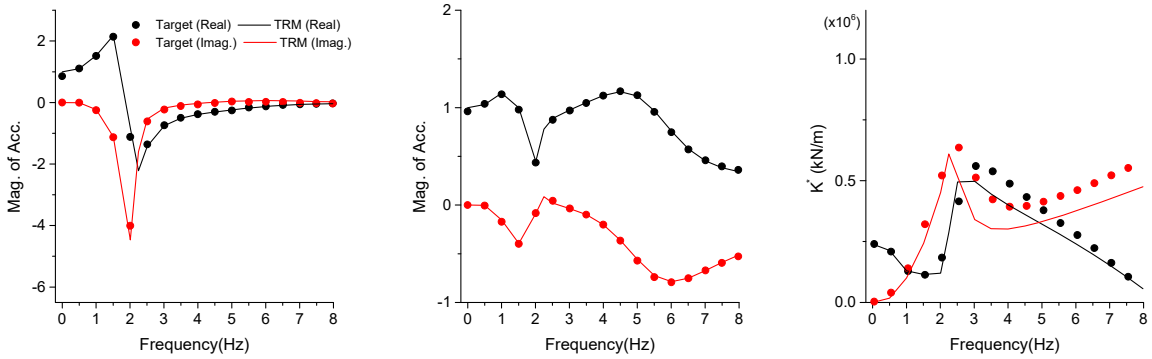


Figure 11: Transfer functions and impedance functions obtained from TRM: Masses of superstructure and footing containing discrepancy (multiplying by 0.8) treated as constants in TRM

## 4 CONCLUSIONS

- This study proposes an identification method for frequency dependent impedance functions (IFs) of soil-foundation-structure systems. In this method, so-called "Gyro-Lumped Parameter Models (GLPMs)" are utilized to represent the IFs. The trust region method (TRM) is applied for finding variables comprising the mechanical elements of GLPMs where objective functions regarding the transfer functions (TFs) are minimized through the TRM procedure. In this paper, a simple two degrees of freedom system consisting of a superstructure and a footing supported by a 2×4 pile group is targeted.
- In the TRM, objective functions in terms of the TFs of the footing is found to be effective to achieve the IF identification with appreciable accuracy. Applying the TFs of the superstructure to the objective function may dilute the characteristics of IFs, thus leading to undermining the accuracy of the IF identification.
- The static stiffness of soil-foundation systems should not be set as a variable in the TRM. The TFs show a large discrepancy while the identification of the IFs is inadequate. A certain discrepancy in the static stiffness may show a difference in lower frequency range. In practice, an approximate value of the static stiffness having the same order with the exact value could be acceptable to identify the IFs with appreciable accuracy in the middle and high frequency range.

- The damping ratio of superstructures tend to distort the IFs locally around the predominant frequency of superstructures.
- When the masses of superstructure and footing are unknown, and they are dealt with as variables in the TRM, the resultant TFs shows a good match with the target TFs whereas a significant difference may appear in the identified IFs. In addition, the masses are assumed to be constants with some discrepancies from the exact values in the TRM, although the TFs show a good agreement with the target TFs, the identified IFs tend to deviate from the target IFs.

## REFERENCES


[1] J.W. Meek, A.S. Veletsos, Simple models for foundations in lateral and rocking motion, *Proc., 5th World Conf. on Earthquake Engrg.,* **2**, Rome, Italy, pp.2610-2613, 1974.

[2] J.P. Wolf, D.R. Somaini, Approximate dynamic model of embedded foundation in time domain, *Earthquake Engineering and Structural Dynamics*, **14**, pp. 683-703, 1986.

[3] T. Nogami, K. Konagai, Time domain axial response of dynamically loaded single piles, *J. Engrg. Mech., ASCE*, **112**(11), pp. 1241-1252, 1986.

[4] F.C.P. de Barros, J.E. Luco, Discrete models for vertical vibrations of surface and embedded foundations, *Earthquake Engineering and Structural Dynamics*, **19**, pp. 289–303, 1990.

[5] W.Y. Jean, T.W. Lin, J. Penzien, System parameters of soil foundations for time domain dynamic analysis, *Earthquake Engineering and Structural Dynamics*, **19**, pp.541-553, 1990.

[6] W.H. Wu, C.Y. Chen, Simple lumped-parameter models of foundation using mass-spring-dashpot oscillators, *J Chin Inst Eng,* **24**(6), pp. 681-97, 2001.

[7] R. Taherzadef, D. Clouteau, R. Cottereau, Simple formulas for the dynamic stiffness of pile groups, *Earthquake Engineering and Structural Dynamics*, **38**(15), pp.1665-1685, 2009.

[8] M. Saitoh, Simple model of frequency-dependent impedance functions in soil-structure interaction using frequency-independent elements. *J. Eng. Mech.*, **133** (10), 1101–1114, 2007.

[9] M. Saitoh, On the performance of lumped parameter models with gyro-mass elements for the impedance function of a pile-group supporting a single-degree-of-freedom system, *Earthquake Eng. Struct. Dyn.,* **41**, 623–641, 2012.

[10] N. Lesgidis, O.-S. Kwon, A. Sextos, A time-domain seismic SSI analysis method for inelastic bridge structures through the use of a frequency-dependent lumped parameter model, *Earthquake Engng. Struct. Dyn.,* **44** (13), 2137–2156, 2015.

[11] S.M. Papathanasiou, T. Panos, E. Prapa, A. Ucak, Influence of soil-structure interaction modeling on the response of seismically isolated bridges. *Int. J. Bridge Eng. Special Issue*, 39–70, 2016.

[12] N. Lesgidis, A. Sextos, O.-S. Kwon, Influence of frequency dependent soil–structure interaction on the fragility of R/C bridges. *Earthquake Engng. Struct. Dyn.,* **46**, 139–158, 2017.

[13] M. Saitoh, On the modeling of frequency- and intensity-dependent impedance functions at the head of horizontally loaded single piles, *Soils and Foundations,* **62**(2):101107, 2022.

## ACKNOWLEDGEMENTS

This work was supported by KAKENHI Grant-in-Aid for Scientific Research (B) JP 21H01414 from the Japan Society for the Promotion of Science.

COMPDYN 2023
9th ECCOMAS Thematic Conference on
Computational Methods in Structural Dynamics and Earthquake Engineering
M. Papadrakakis, M. Fragiadakis (eds.)
Athens, Greece, 12-–14 June 2023

# SCALING AND MODELING OF AN IMPACT PILE DRIVING 1G LABORATORY SCALE TEST

**Tamara Wehbe[1,3], George Anoyatis[2], Hadrien Rattez[3] and Stijn François[1]**

[1]KU Leuven, Department of Civil Engineering, Structural Mechanics Section
Kaastelpark Arenberg, 40 Box 2448, 3001 Leuven, Belgium
tamara.wehbe,stijn.francois@kuleuven.be

[2] KU Leuven, Department of Civil Engineering, Hydraulics and Geotechnics Section
Campus Bruges, 8200 Bruges, Belgium
george.anoyatis@kuleuven.be

[3] UC Louvain, Institute of Mechanics, Materials and Civil Engineering
GCE, Place du Levant, 1348 Louvain-la-Nauve, Belgium
hadrien.rattez@uclouvain.be

**Abstract.** *The widespread deployment of offshore wind turbines requires the use of fast, low-cost and reliable foundation installation methods. Despite the fact that vibratory driving provides an adequate alternative to the predominantly used impact driving technique, lack of data concerning the effects of impact driving on the lateral behavior of foundations in the short and long term indicates a need for a detailed study to understand the parameters influencing the procedure and how it could be improved. For this purpose, a small-scale well-controlled impact pile driving in a sand filled container experiment has been developed and numerically simulated. Numerical models are employed to study to dynamic behavior of the 1g laboratory scale test which allows for better understanding of the test setup. The numerical model includes a multi-body dynamic model to compute the force response on the pile head. Furthermore, scaling laws are derived to provide the best correspondence with a full-scale numerical model from the laboratory scale model. These include scaling the pile dimensions as well as the quantities that alter the force applied on the pile head. Results obtained allow us to optimize the current laboratory setup.*

**Keywords:** Offshore Wind Turbines, Scaling laws, Impact Pile Driving, Numerical Modeling

# 1 INTRODUCTION

Offshore wind power is a rapidly growing industry and a key component in the transition towards a more sustainable energy future. Monopiles are the most popular foundation type for offshore wind turbines due to their simple design, cost-effectiveness, and ease of installation. The installation of monopiles typically involves several stages and methods, which can vary depending on the site-specific conditions, such as water depth, soil conditions, and wind conditions. The most common method for installing monopiles for offshore wind turbines into seabed is impact hammering. A large hydraulic hammer is used to drive the monopile into the seabed until it reaches a specified depth. The hammering process though creates vibrations that can cause noise and potentially harm marine life. Mitigation measures are often taken to reduce the impact. Vibratory driving is an appealing alternative which is recently gaining more ground in offshore applications. It involves using a vibrating pile driver to embed the monopile into the seabed. This method present many advantages such as faster installation, reduced noise and vibration than hammering. However, it may not be suitable for all soil types, although recent developments have resulted in powerful vibratory hammers.

This study focuses on the analysis of the drivability mechanisms during impact driving, and is part of a broader research effort of the authors which aims to assess both installation methods for offshore applications to monopiles, by means of theoretical developments and laboratory tests. To analyze pile drivability under impact driving, an analytical solution was originally developed by Deeks & Randolph [1], This model has been successfully applied to dynamic large diameter pile driving numerical models [6], experimental models of impact driving [4] and numerical modeling of ground borne vibrations [8] and provides an adequate estimate for pile driving characteristics. In this work, the Deeks & Randolph model is solved numerically. In this regard, a numerical model is implemented in Matlab, using the toolbox Stabil [2]. At first, comparisons with the analytical model in terms of force-time response due to hammer impact validate the proposed formulation. Then the model is used to design a 1G laboratory test, presented in Figure 1. A discussion on scaling laws is provided. The prototype impact pile driving system presented in Deeks & Randolph is herein down-scaled to a laboratory pile driving set up. Results obtained from the numerical model are shown for both the prototype and the scaled model for the time history of the force applied at the pile head due to the hammer impact. Finally, a discussion on the envisioned laboratory test is provided. Such physical modelling is a first approach to gain further understanding in the phenomenon of impact pile driving for offshore applications, which in a second phase will be extended to account for saturated soil conditions and vibratory hammers.

# 2 THEORETICAL INVESTIGATION

## 2.1 Proposed numerical model and validation

The force at the head is computed by means of the model originally developed by Deeks & Randolph [1]. The model is based on lumped ram and anvil masses separated by a cushion with internal damping, and connected to the pile which is modelled as a dashpot. The main components of the system are the ram, the cushion, and the anvil as shown in Figure 2. The solution models the pile as a dashpot of impedance $Z$:

$$Z = \frac{A_{\mathrm{p}} E_{\mathrm{p}}}{C_{\mathrm{p}}} \tag{1}$$

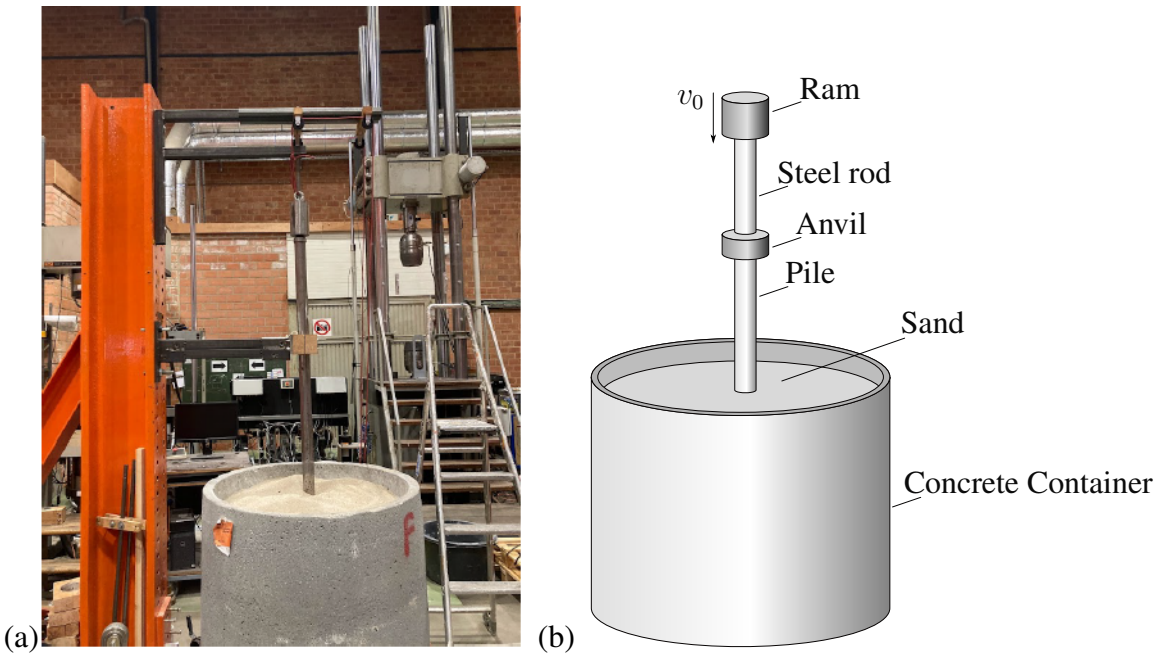


Figure 1: Laboratory setup: a) Physical model at the laboratory in UC Louvain and b) Schematic representation of the main components of the test.

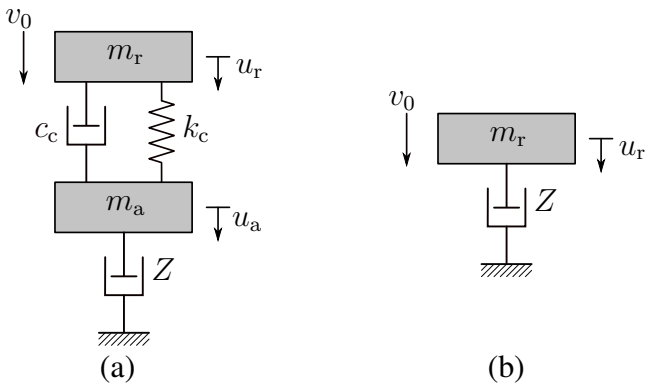


Figure 2: Deeks and Randolph model (a) for a ram with a cushion and anvil and (b) without cushion and anvil.

where $A_\mathrm{p}E_\mathrm{p}$ is the pile's cross-sectional rigidity, and $C_p$ is the (one-dimensional) wave speed in the pile. To account for the fact that in practice the cushion deforms non-linearly, and absorbs energy, Deeks & Randolph used a combined linear spring in parallel with dashpot for the cushion (Fig. 2). The equations of motion of the system are written as

$$m_\mathrm{r}\ddot{u}_\mathrm{r} + c_c(\dot{u}_\mathrm{r} - \dot{u}_\mathrm{a}) + k_c(u_\mathrm{r} - u_\mathrm{a}) = 0 \tag{2}$$

and

$$m_\mathrm{a}\ddot{u}_\mathrm{a} + Z\dot{u}_\mathrm{a} + c_c(\dot{u}_\mathrm{a} - \dot{u}_\mathrm{r}) + k_c(u_\mathrm{a} - u_\mathrm{r}) = 0 \tag{3}$$

where $m_a$ is the mass of the anvil and $u_a$ its displacement (pile head displacement), cushion stiffness $k_c$ and internal damping $c_c$. The initial conditions of the system are $\dot{u}_r = v_0$ and $u_r = 0$. The force exerted on the pile $F_p$ is obtained by multiplying the pile impedance by the ram velocity, as shown below

$$F_\mathrm{p} = Z\dot{u}_\mathrm{r}^* \tag{4}$$

The system of equations can be alternatively written in matrix form as follows:

$$\underbrace{\begin{bmatrix} m_{\mathrm{r}} & 0 \\ 0 & m_{\mathrm{a}} \end{bmatrix}}_{\mathbf{M}} \underbrace{\begin{bmatrix} \ddot{u}_{\mathrm{r}} \\ \ddot{u}_{\mathrm{a}} \end{bmatrix}}_{\ddot{\mathrm{u}}} + \underbrace{\begin{bmatrix} c_{\mathrm{c}} & -c_{\mathrm{c}} \\ -c_{\mathrm{c}} & Z + c_{\mathrm{c}} \end{bmatrix}}_{\mathbf{C}} \underbrace{\begin{bmatrix} \dot{u}_{\mathrm{r}} \\ \dot{u}_{\mathrm{a}} \end{bmatrix}}_{\dot{\mathrm{u}}} + \underbrace{\begin{bmatrix} k_{\mathrm{c}} & -k_{\mathrm{c}} \\ -k_{\mathrm{c}} & k_{\mathrm{c}} \end{bmatrix}}_{\mathbf{K}} \underbrace{\begin{bmatrix} u_{\mathrm{r}} \\ u_{\mathrm{a}} \end{bmatrix}}_{\mathrm{u}} = \begin{bmatrix} m_r v_o \\ 0 \end{bmatrix} \tag{5}$$

The solution is obtained numerically using the direct time integration method. In this regard, the Wilson-theta method is implemented in the Matlab toolbox Stabil [2]). The analysis yields results for the nodal displacements $u$, the velocities $\dot{u}$ and accelerations $\ddot{u}$ of a dynamic system with mass **M**, damping **C** and stiffness **K** matrices, subjected to external excitation **P**. At time $t = 0$, the ram hits the pile head with a velocity $v_{drop} = v_0$. To ensure numerical stability, the parameters $\alpha$, $\delta$ and $\theta$ in the Wilson-theta method are set equal to 0.25, 0.5 and 1, respectively. The time window $t$ is equal to 0.1 s and the time step $\Delta$t is set equal to 0.0001 s, which is small enough to ensure the stability and the precision of the integration scheme.

The performance of the numerical model is validated through comparisons with results obtained from the model of Deeks & Randolph. Figure 3 shows results in terms of force time history. In their original work, a BSP 357 hammer was used to drive a 762 mm diameter pile of 18.5 mm wall thickness, and an equivalent impedance of 1750 kNs/m. The cushion was steel with a stiffness of $1.6 \times 10^6$ kN/m, whereas the cushion damping is neglected. The ram and anvil masses for this hammer were 6860 kg and 850 kg, respectively. The results for the variation of the pile head force with time are in perfect agreement.

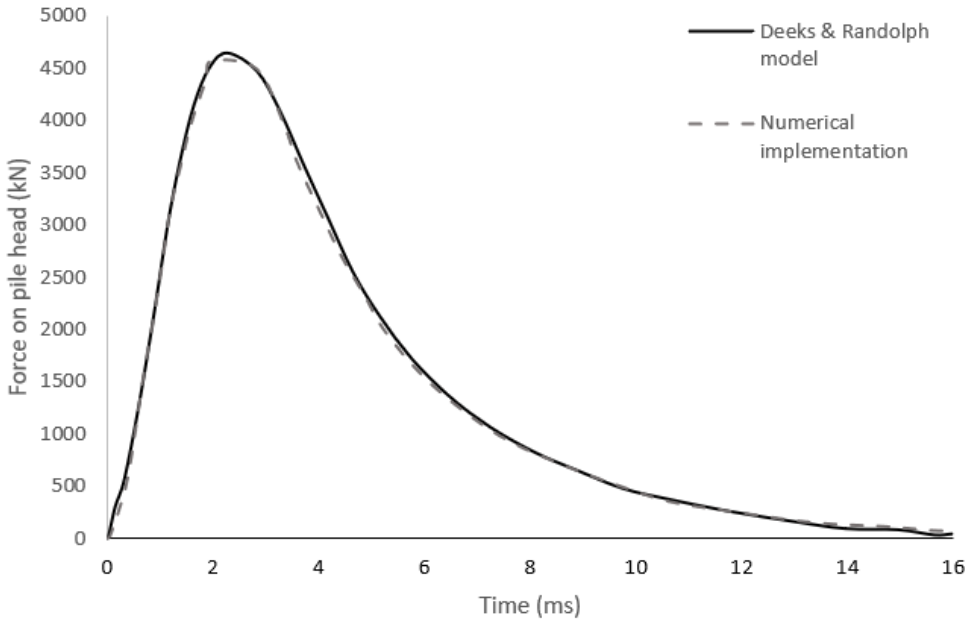


Figure 3: Variation of pile head force-time response with time; dashed line: Deeks & Randolph model [1], solid line: proposed numerical model.

**Impact hammering without cushion** As a first step in the envisioned laboratory setup, no anvil is installed. In this case, the system reduces to a single degree of freedom (SDOF) system, as shown in Figure 2 (which is also due to the same stiffness of the ram and the anvil). Thus the

equation of motion of the system dully reduces to:

$$m_r\,\ddot{u}_r + Z\,\dot{u}_r = 0 \tag{6}$$

### 2.2 Scaling laws and experimental test design

Scaling laws are mathematical relationships that describe how the physical properties of an object or system change as its size or scale changes [7]. In the hammer-pile impact system adopted in this study, three quantities should be scaled: the mass of the ram, the pile impedance and the falling velocity of the ram. The self-weight of the hammer, which is represented by the ram in the 1G scale test should be scaled by a factor of $1/N^3$ . This is achieved by scaling down all pile dimensions by a factor $N$, using the same pile material as in the prototype. As a result of the pile diameter being reduced by $1/N$, the cross sectional area of the pile is reduced by $1/N^2$. The pile impedance is thus reduced by $1/N^2$. The mass drop velocity is scaled by a factor of $1/\sqrt{N}$. This is achieved by scaling the length of the free fall by $1/N$, and thus the duration of free fall by $1/\sqrt{N}$. The scaling of the duration of impact, scaled by $1/N$ is in accordance with the scaling of the length of the pile, which is also scaled by $1/N$. Consequently, the scaling of the force on the pile head, which is the product of multiplying the pile impedance by the velocity at which the ram hits the pile head is concluded to be $1/N^{2.5}$. This complies with Newton's second law and assuming no energy loss in the ram-anvil-pile system. Table 1 provides a summary of the scaled quantities. Herein the prototype model presented in Deeks

| Impact-driving parameters | Units | Scale factor |
|---|---|---|
| Pile diameter, $D_{\text{pile}}$ | m | $\frac{1}{N}$ |
| Pile impedance, $Z$ | Ns/m | $\frac{1}{N^2}$ |
| Impact hammer mass, $m_{\text{r}}$ | kg | $\frac{1}{N^3}$ |
| Mass drop velocity, $v_{\text{drop}}$ | m/s | $\frac{1}{\sqrt{N}}$ |
| Force on pile head, $F_{\text{p}}$ | N | $\frac{1}{N^{2.5}}$ |

Table 1: Scaled quantities for 1G laboratory test

& Randolph is scaled down to a laboratory set up, using the scaling laws discussed above. The geometry and parameters of the laboratory test are shown in Table 2.

| Parameter | Unit | Prototype | Scale model |
|---|---|---|---|
| Pile diameter, $D$ | m | 0.762 | 0.019 |
| Pile impedance, $Z$ | Ns/m | $1750 \times 10^3$ | 1093 |
| Impact hammer mass, $m_{\text{r}}$ | kg | 6860 | 0.107 |
| Mass drop velocity, $v_{\text{drop}}$ | m/s | 3.27 | 0.517 |

Table 2: Parameters used in the numerical application for the prototype and the scaled model

Figures 4(a) and 4(b) present the force-time history and the corresponding frequency content of the force, computed at the pile head of the scaled model. Figure 4(a) show that the force at pile head of scaled model is 0.565 kN for a duration of impact of 0.5 ms. The latter value is equal to the scaled force factor $1/N^{2.5}$, and the scaled impact time factor of $1/N$, considering a scaling factor of 40. These correspond at the full-scale to a force of 5722.5 kN during an impact time of 20 ms. Moreover, Figure 4(b) show that the frequency content of the force is more than 5000 Hz which provides us insight on the sampling frequencies to be used in the envisioned in laboratory setup and how are these scaled, and hence a better understanding of the dynamic response of the pile-hammering system.

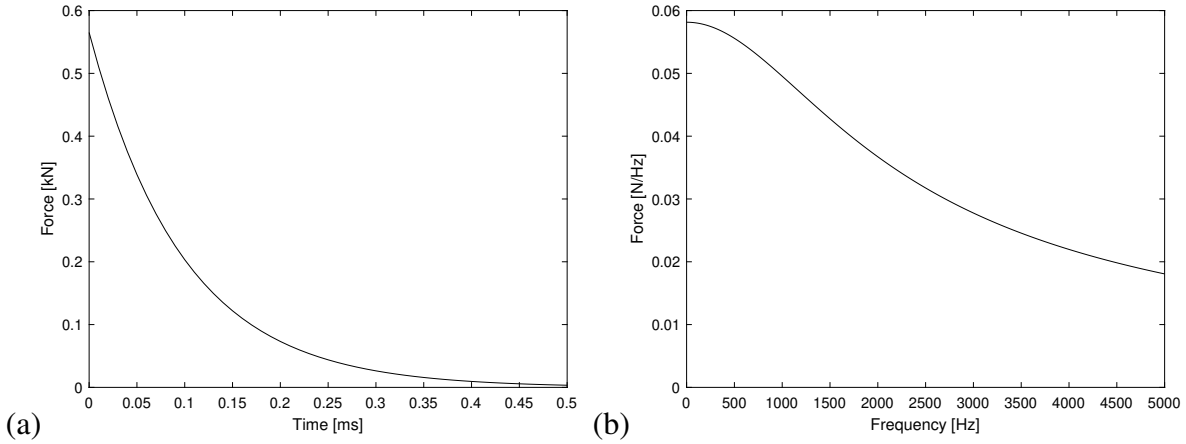


Figure 4: Variation of pile head response with (a) time and (b) frequency for the scaled impact hammering system.

## 3 EXPERIMENTAL INVESTIGATION

The envisioned laboratory setup is shown in Figure 1. It is based on the system initially developed by Holeyman [3], and has been used to drive tubular steel piles into rock masses [5]. The current set up consists of 10 kg drop weight (ram), which is attached to a rope and a pulley system, and a 0.6 kg anvil. A centering rod is fixed at the top of the hammer frame and ends inside the pile. Lateral supports to keep the pile vertical during the driving process are attached to the frame. The existing pile is a hollow steel cylinder of external diameter $D = 6\,\mathrm{cm}$, length $L = 50\,\mathrm{cm}$ and wall thickness $t = 6\,\mathrm{mm}$. A $1000\,g$ accelerometer is attached at a distance of $50\,\mathrm{mm}$ from the pile head. The pile is driven in a dry homogeneous sand of dry unit weight $\gamma_{\mathrm{dry}} = 1800\,\mathrm{kg/m^3}$, and relative density $D_r = 80\%$ that is representative of the soil conditions met in the North sea. The sand is placed in a concrete container of inner diameter $D_{\mathrm{box}} = 1\,\mathrm{m}$, inner height $H_{\mathrm{box}} = 1\,\mathrm{m}$ and thickness $t_{\mathrm{box}} = 5\,\mathrm{cm}$.

The relative density of sand was controlled using a sand pluviation system which is shown in Figure 5(a). This allows relatively homogeneous sand samples to be generated. The system is made up of three plates with holes with different diameters, namely 13 mm, 8 mm and 6 mm. Figure 5(b) shows the frame constructed which ensures the correct positioning of the pile during the installation process. Figure 6 shows a close up view of the location of the accelerometer, in preparation of a test.

(a)  (b) 

Figure 5: (a) Sand pluviation system (b) Positioning of the pile (hammered) to required depth.



Figure 6: Accelerometer positioned at 50 mm from pile head

## 4 CONCLUSIONS

This work presents a theoretical and an experimental attempt to study pile driving by impact hammering. For this purpose a numerical model has been developed, based on the seminal analytical work of Deeks and Randolph, as well as a small-scale well-controlled experimental set up for impact pile driving in a sand filled container. The numerical model includes a multi-body dynamic model to compute the force response on the pile head. Comparisons against the aforementioned analytical model validate the performance of the proposed approach. The numerical model can be then used to optimize the current laboratory setup by adding a cushion to the system and an absorbing membrane at the sides of the sand container to minimize wave reflections during the pile driving. In light of laboratory tests, scaling laws are discussed herein to help realistically scale down a prototype pile impact hammering system to a 1G laboratory

model. Comparisons obtained in this study in terms of force-time response, between a prototype from the literature and a proposed scaled model, demonstrate the applicability of the scaling laws

## Acknowledgements

Results presented in this paper were obtained within the frame of the project 3E220488 "Novel Installation and Extraction methods for Foundations of Offshore Wind Turbines" funded by the Global PhD partnerships (between KU Leuven and UCLouvain). The financial support is gratefully acknowledged. Furthermore, the authors highly appreciate the technical input and assistance provided by Eli Hamels and Pierre Mertens de Wilmars from the civil engineering laboratory at KU Leuven and UC Louvain, respectively..

## References

[1] A. J. Deeks and M. F. Randolph. Analytical modelling of hammer impact for pile driving. *International Journal for Numerical and Analytical Methods in Geomechanics*, 17(5):279–302, 1993.

[2] S. François, M. Schevenels, D. Dooms, M. Jansen, J. Wambacq, G. Lombaert, G. Degrande, and G. De Roeck. Stabil: An educational matlab toolbox for static and dynamic structural analysis. *Computer Applications in Engineering Education*, 29(5):1372–1389.

[3] A. Holeyman. Battage de pieux métalliques dans la roche. *Revue Française de Géotechnique*, pages 1–21, 12 2017.

[4] L. Hu, Q. Li, X. Li, and L. Huang. Experimental study and theoretical analysis on impact characteristics of single pile. *E3S Web of Conferences*, 272:2–9, 01 2021.

[5] M. Jafari. *Numerical and experimental investigation of monopile driving resistance in carbonate rocks*. PhD thesis, 2020.

[6] A. M. Kaynia, J. Hebig, T. Pein, and Y. Shin. Numerical model for dynamic installation of large diameter monopiles. *Soil Dynamics and Earthquake Engineering*, 161:107393, 2022.

[7] D. Muir Wood. *Geotechnical Modelling*. 12 2017.

[8] T. Sofiste, L. Godinho, D. Soares Jr, and P. Alves Costa. Numerical modeling of ground-borne vibrations induced by pile driving with a simple and direct material damping approach. 08 2021.

COMPDYN 2023
9th ECCOMAS Thematic Conference on
Computational Methods in Structural Dynamics and Earthquake Engineering
M. Papadrakakis, M. Fragiadakis (eds.)
Athens, Greece, 12-14 June 2023

# OPERATIONAL MODAL ANALYSIS OF NON-REDUNDANT WOOD FRAME BUILDING

**Dipendra Gautam, Simon Olafsson, and Rajesh Rupakhety**

Earthquake Engineering Research Center, Faculty of Civil and Environmental Engineering, University of Iceland, Austurvegur 2a, 800 Selfoss, Iceland
{dig17, simon, rajesh}@hi.is

## Abstract

*For the design and assessment of structures, precise dynamic characteristics are a must. A vast array of literature regarding dynamic characteristics of RC and steel structures estimated using experimental and numerical analyses can be found in either published research as well as codal provisions. On the other hand, similar studies for structures constructed using uncommon materials are limited. This adds uncertainties in the design and assessment of structures as experimental studies prior to construction or assessment are rather unpragmatic. We address a unique issue that sheds light on the identification of dynamic characteristics of a 12.8 m tall non redundant wood frame building. The building has two bays along the longer direction and one bay along the shorter direction. The columns in the buildings are made up of Sal timber (hardwood). We conducted ambient vibration measurements in the building near the geometrical center and performed system identification using the numerical algorithm for subspace state space system identification (N4SID) approach. Using operational modal analysis, the first mode frequencies and damping ratios of the building are estimated for the shorter (X) as well as the longer (Y) directions. The fundamental vibration frequency of the building along the X direction is found to be 1.16 Hz with a damping ratio of 3.02%. Along the Y direction, the fundamental vibration frequency was obtained as 1.26 Hz with a damping ratio of 2.84%. We have compared the results from system identification with several codal formulas used to estimate fundamental period/frequency to provide a rational basis for the selection of period-height or frequency-height relations. The results could serve as a notable reference in the formulation of guidelines that are likely to be developed in the future.*

**Keywords:** Operational modal analysis, System identification, Ambient vibration, N4SID, Wood frame building.

# 1 INTRODUCTION

Wood frame construction system comprises the second largest building population in Nepal after stone masonry [1]. Until a few decades ago, the abundance of lumber in the vicinity attracted people to construct wood frame buildings when reinforced concrete (RC) construction system had not gained enough momentum. Until 2011, wood frame buildings were nearly 2.5 times more than RC buildings in Nepal. Wood frame buildings are mostly found in the southern plains and Siwalik regions of Nepal. A wide variation in terms of timber species exists in Nepal and so does the wood frame construction system because such buildings are constructed using locally available timber with little to no processing. Although wood frames are one of the most dominant construction systems, studies incorporating dynamic identification, seismic and other natural hazard related vulnerabilities, and mechanical characterization are not common yet. Neither do exist any specific codal provisions for wood frame buildings so far. The building codes so far designate wood frame constructions as 'other structures', which incorporate all building forms except for RC and steel frame constructions. This ambiguity is particularly posing a challenge in the design and assessment of several types of construction systems including wood frame buildings. Thus, there lies a scope for the identification of dynamic characteristics to quantify the behavior of wood frame construction under dynamic actions such as earthquakes, wind, floods, etc. Also, the design of such structures can be more precise if dynamic characteristics are estimated with adequate confidence so as to use equivalent static methods.

Wood frame buildings and several sub-forms of wood frame buildings have been studied for quite some time worldwide. Some studies used ambient vibration and other dynamic measurement techniques to estimate dynamic characteristics such as frequency and damping ratio [2–5]. Some other studies performed numerical and experimental analyses to quantify the behavior of various forms of wood frame buildings (e. g. [6]). A realistic depiction of dynamic characteristics of any construction system will be the first step regarding design and assessment or even to assess health in the long run. Ambient vibration testing is one of the efficient and economic techniques to acquire the time domain response of the structure. The use of ambient vibration-based system identification covers dynamic characterization under ambient as well as excited conditions (e. g. [7–12]). In this paper, we assess the time series data collected from a wood frame building to estimate dynamic characteristics using operational modal analysis. Based on the system identification results, we also compare codal provisions and recommend a reliable fundamental period estimation formula for future use.

# 2 MATERIALS AND METHODS

## 2.1 Wood frame buildings

Wood frame buildings comprise 24.9% of the total building stock (~5.5 million) in Nepal and more than 90% of such constructions are in the southern plains and Siwalik regions. Virtually all such buildings are constructed using lumber directly providing connections at the floor level to establish floor diaphragm. A vast majority of such constructions use Sal timber (*Shorea robusta*) hardwood, meanwhile, newer constructions also use other timber species as Sal timber is not adequately available these days. Wood frame buildings are mostly two storied constructions with an open ground story, which is mostly used for non-residential purposes. The infills range from *ikra* (overlapped folded bamboo sheets) to wooden planks, whereas the flooring system comprises wooden joists and planks. The long wall direction will have a major wooden joist, which is sometimes supported by wooden pillars. The joists along the short wall direction are either throughout or sometimes slightly more than the half length

of the short wall direction and thus two joists are required along the short wall direction. In the case of the unavailability of throughout lumber for the joist along the long wall direction, lumber is joined, and post support is provided underneath.

Ambient vibration measurement was taken in a four-story wood frame building as shown in Fig. 1. Corrugated galvanized iron (CGI) sheets are used for roofing. and the rest of the components are wood elements except for nails. In this type of construction, holes are dug first, and wooden pillars are erected. Meanwhile, the ground floor is sometimes plastered later. The case study building is a non-redundant wood frame building along the shorter direction that corresponds to the X direction of the instrument.

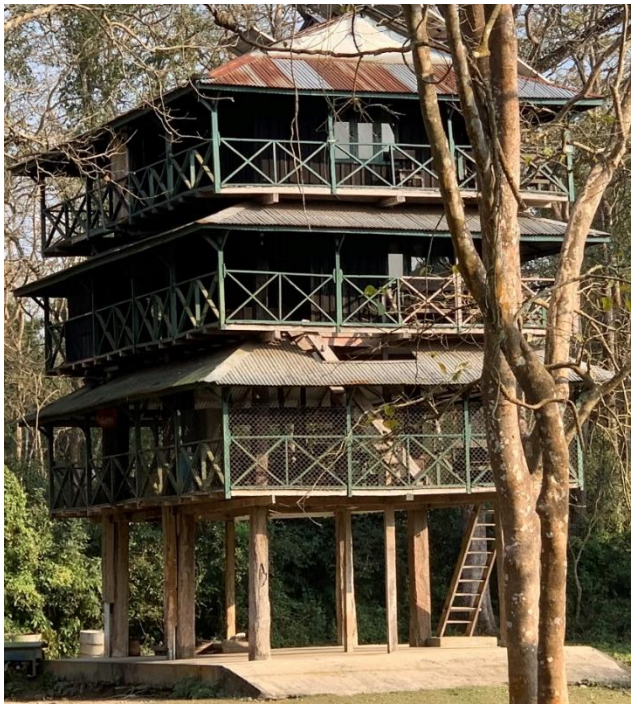

Figure 2: Case study building (Image by: Prasanna Poudel, with permission).

## 2.2 Ambient vibration measurement

We took ambient vibration records in the case study building using three ETNA-2 triaxial accelerometers manufactured by Kinemetric Inc. One accelerometer was set on each story. The instruments were aligned vertically placing all of them at the tentative geometrical center of the building (Fig. 2). Several sets of 30-minute vibration records were taken at 100 Hz sampling frequency. Three GPS devices were also connected to the accelerometers to synchronize time series data. Vibration measurements were taken in the operational state of the building with the occupants and regular activities continued. However, no other excitation existed during the recording.



Figure 2: Accelerometer set up for ambient vibration recording.

## 2.3 Operational modal analysis

Operational modal analysis (OMA) comprises the development of mathematical models using input-output measurements of a structure, which is based on parametric identification of dynamic characteristics using autoregressive (AR), moving average (MA), autoregressive moving average (ARMA), autoregressive with extra input (ARX), among other models [13]. These models are developed using time domain modeling of the recorded response data [14]. We adopted an output-only modal identification technique to determine dynamic characteristics of the building using ambient vibration records that do not require input information. Two orthogonal components referred to as X and Y direction hereafter, of the ambient vibration records, were selected for system identification. Transients were corrected manually, and the signals were filtered using a fourth-order Butterworth filter of 20 Hz corner frequency. Then, the signal was tapered using Tukey window and finally, the preprocessed signals were processed using the Numerical Algorithm for Subspace State Space System Identification (N4SID) [15]. The algorithm constructs state matrices so that system identification to estimate frequency, damping ratio, and mode shape can be conducted [15, 16]. State space models

were developed for each direction and oblique projection of subspaces from the block Hankel matrices were estimated for the output response using N4SID. When considering $q$ input measurements ($u_k \in \mathbb{R}^m$) and output $y_k \in \mathbb{R}^l$ from the unknown deterministic system of order $n$, the discrete system equations can be written as:

$$x_{k+1} = Ax_k + Bu_k \tag{1}$$

$$y_k = Cx_k + Du_k \tag{2}$$

Here, the aim is to determine $n$ and realization of $A$, $B$, $C$, and $D$ for the similarity transformation $A \in \mathbb{R}^{n\times n}$, $B \in \mathbb{R}^{n\times m}$, $C \in \mathbb{R}^{l\times n}$, and $D \in \mathbb{R}^{l\times m}$. Using Hankel block, the following matrix equations can be derived from Eq. (1) and Eq. (2):

$$X_f = A^i X_p + \Delta_i U_p \tag{3}$$

$$Y_p = \Gamma_i X_p + H_i U_p \tag{4}$$

$$Y_f = \Gamma_i X_f + H_i U_f \tag{5}$$

Considering the input of order $2i$, intersection occurs between the row space of matrix $U_f$ and one of matrix $X_p$, and the weighting matrix $W_1 \in \mathbb{R}^{li\times li}$ is of full rank and $W_2 \in \mathbb{R}^{j\times j}$ holds true for:

$$rank(Z_p) = rank(Z_p W_2) \tag{6}$$

If the oblique projection be $O_i$,

$$O_i = Y_{f/U_f} Z_p \tag{7}$$

$$W_1 O_i W_2 = [U_1 \quad U_2] \begin{bmatrix} S_1 & 0 \\ 0 & 0 \end{bmatrix} \begin{bmatrix} V_1^T \\ V_2^T \end{bmatrix} \tag{8}$$

$$W_1 O_i W_2 = U_1 S_1 V_1^T \tag{9}$$

$$O_i = \Gamma_i X_f \tag{10}$$

$W_1$ and $W_2$ are the weighting matrices that rectify the $\Gamma_i X_f$ estimate. The number of singular values except for zero denote the order of the model, which is given by the matrix $S_1$. The extended observability matrix $\Gamma_i$ becomes:

$$\Gamma_i = W_1^{-1} U_1 S_1^{1/2} T \tag{11}$$

$$X_f W_2 = T^{-1} S_1^{1/2} V_1^T \tag{12}$$

$$X_f = \Gamma_i^{\dagger} O_i \tag{13}$$

Where non-singular similarity transformation matrix can be written as $T \in \mathbb{R}^{n \times n}$. The matrix $Z_p = (Y_p,\ U_f)^T$ is formulated from the Hankel matrices $(Y_p,\ Y_f)^T$ and $(U_p,\ U_f)^T$ using Eq. (7) and Eq. (9). Thereafter, the singular value decomposition of $W_1 O_i W_2$ is performed. The order is determined as $n$ when $S_1$ is identified as the diagonal matrix composed of $n$ singular values. $A$ and $C$ can be estimated once $\Gamma_i = (C\ \ CA\ \ \ldots CA^{i-1})^T$ is evaluated. $C$ is obtained from the first $l$ rows of $\Gamma_i$ and $A$ is obtained from the shift structure of $\Gamma_i$ as follows:

$$\underline{\Gamma_i} A = \overline{\Gamma_i} \tag{14}$$

$\underline{\Gamma_i}$ denotes that the matrix $\Gamma_i$ that does not include the last $l$ rows:

$$\underline{\Gamma_i} = \left(C\ \ CA\ \ \ldots CA^{i-2}\right) \tag{15}$$

Similarly, $\overline{\Gamma_i}$ denotes that the matrix $\Gamma_i$ that does not include the first $l$ rows:

$$\overline{\Gamma_i} = \left(CA\ \ CA^2\ \ \ldots CA^{i-1}\right) \tag{16}$$

Thus, $A$ is given as:

$$A = \underline{\Gamma_i}^{\dagger} \overline{\Gamma_i} \tag{17}$$

Pre-multiplying Eq. (5) by $\Gamma_i^{\perp}\, \mathrm{U}_f^{\dagger}$, it yields:

$$\Gamma_i^{\perp} Y_f \mathrm{U}_f^{\dagger} = \Gamma_i^{\perp} \Gamma_i X_f \mathrm{U}_f^{\dagger} + \Gamma_i^{\perp} H_i U_f \mathrm{U}_f^{\dagger} \tag{18}$$

Since $\Gamma_i^{\perp} \Gamma_i = 0$, Eq. (18) deduces to:

$$\Gamma_i^{\perp} Y_f \mathrm{U}_f^{\dagger} = \Gamma_i^{\perp} H_i \tag{19}$$

Denoting $\Gamma_i^{\perp}$ by $L$ and $\Gamma_i^{\perp} Y_f \mathrm{U}_f^{\dagger}$ by $M$, Eq. (19) becomes:

$$M = L H_i \tag{20}$$

$L = (L_1\ \ L_1\ \ \ldots\ L_i)$ and $M = (M_1\ \ M_1\ \ \ldots\ M_i)$. Thereafter, $B$ and $D$ are estimated using linear regression. We executed the algorithm in MATLAB R2022b [17].

## 3 RESULTS AND DISCUSSIONS

We first assessed signal health by visually selecting and removing the transients. Fig. 3 shows the signal after removing transients manually. Both trend and seasonality affect the

characteristics of the system at various times, thus the major tasks of system identification are detrending and stationarity check. We confirmed the stationarity of the time series records plotting the cumulative power build-up of the signal. A uniform slope of the power spectral density function (Fig. 4) indicates considerable stationarity.

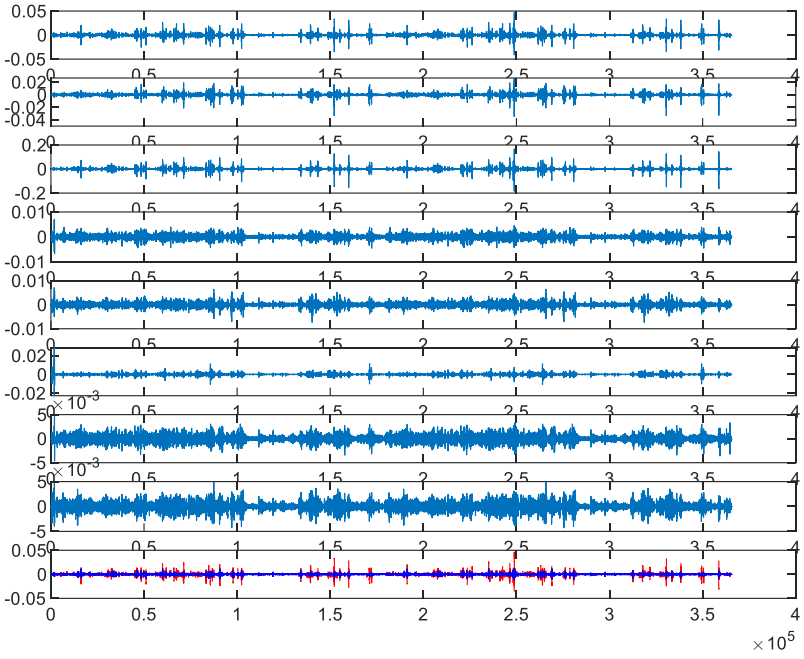

Figure 3: Synchronized time series record after removing transients.

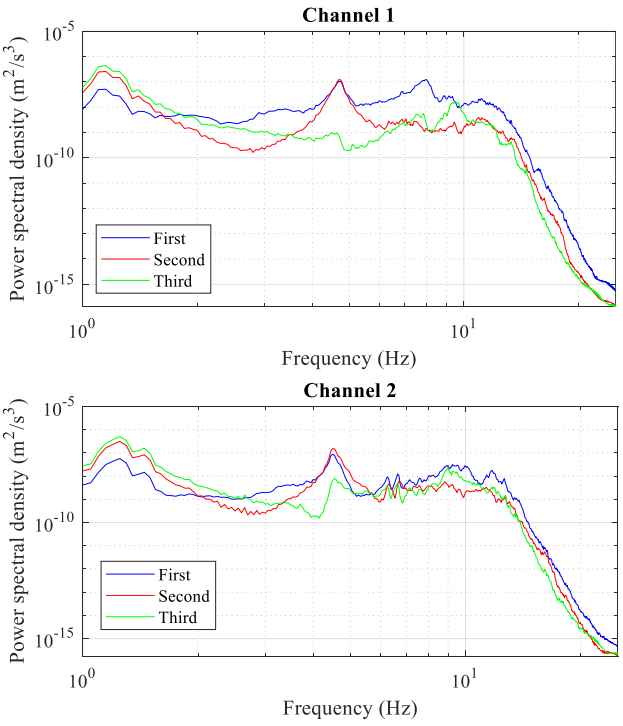

Figure 4: Power spectral density plots for two orthogonal directions X and Y.

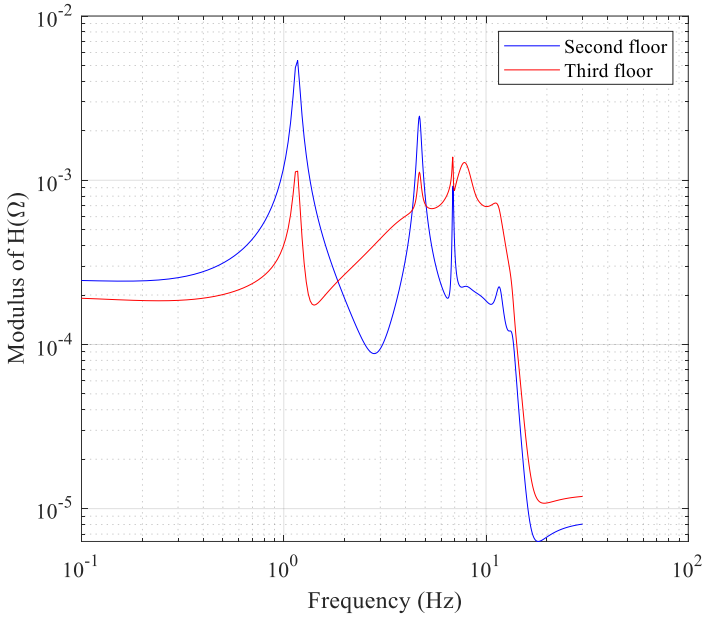


Figure 5: Frequency response function plot for second and third story.

The frequency response function, which indicates the Fourier transform of the ratio of time domain response to input that reflects dynamic flexibility, is shown in Fig. 5. We constructed two state space models for X and Y directions independently. For the unknown input excitation, the response was considered for the second and the third story. At least three translational modes are identified with confidence as shown in Fig. 5. The summary of the identified dynamic characteristics of the building is presented in Table 1. As shown in Table 1, the first translational mode of the building is in the X direction. For the first translational mode of vibration, frequencies along the X and Y directions are identified as 1.16 Hz and 1.26 Hz, respectively. Similarly, damping ratios are determined as 3.02% and 2.84%, respectively along the X and Y directions. Similarly, for the second translational mode, frequencies are identified as 4.68 Hz and 4.29 Hz, respectively for the X and Y directions. For the second mode, damping ratios are estimated as 2.27% and 5.24%, respectively along the X and Y directions.

| Mode | Frequency (Hz) | | Damping ratio (%) | |
|---|---|---|---|---|
| | X | Y | X | Y |
| 1 | 1.16 | 1.26 | 3.02 | 2.84 |
| 2 | 4.68 | 4.29 | 2.27 | 5.24 |
| 3 | 6.86 | 4.49 | 0.66 | 0.69 |

Table 1: Summary of dynamic characteristics of the building.

The past and current building codes in Nepal do not incorporate any provisions regarding the design of wood frame buildings; however, any building form except for reinforced concrete and steel frame buildings are classified under the same category. For other structures category, the fundamental period of vibration (T) recommended by the Nepal Building Code-1994 (NBC 1994) [18] is as follows:

$$T = \frac{0.09H}{\sqrt{D'}} \qquad (21)$$

Where $H$ is the height of the building and $D'$ is the overall length of the building at the base in the direction under consideration. The recently formulated building code in Nepal (NBC 2020) [19] recommends a more conservative fundamental period of vibration formula that does not account for the length of the building as:

$$T = 0.05H^{3/4} \qquad (22)$$

As neither of these regulations considers wood frame buildings, we assessed codal formulas from several building codes to demarcate the most representative empirical formula that could be used for wood frame buildings in Nepal. Based on the comparison between NBC (1994) [18], NBC (2020) [19], Indian Standard (IS) Code-1893 (2002) [20], Indian Standard (IS) Code-1893 (2016) [21], National Building Code of Canada (NBCC 2015) [22], Uniform Building Code (UBC 1997) [23], Camelo (2003) [5], and Eurocode 1-4 (2010) [24] as shown in Fig. 6, we conclude that the frequency estimate of similar wood frame buildings would be best represented by the NBCC (2015). Similarly, the earlier version of the Nepali building code (NBC-1994) is more representative than the recent NBC-2020 for wood frame buildings as shown in Fig. 6. Thus, the NBCC (2015) can be used to design or assess similar wood frame buildings in Nepal.

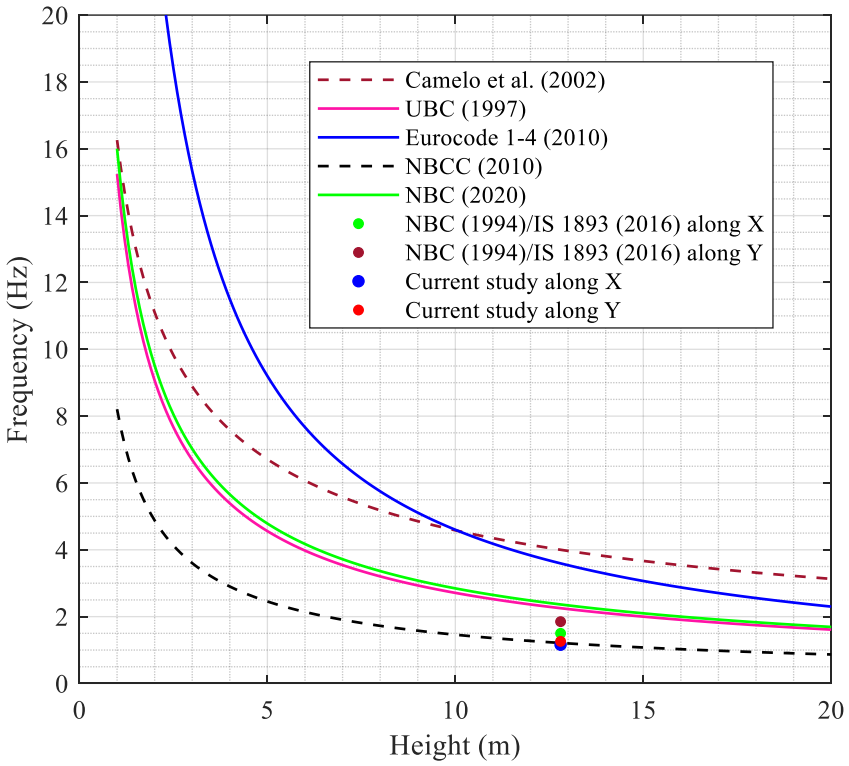


Figure 6: Frequency-height plots based on various building regulations together with the experimentally identified frequency characteristics of the case study building.

## 4 CONCLUSIONS

Using operational modal analysis, we estimated vibration frequencies and damping ratios for some translational modes of vibration of a four-story wood frame building. We used N4SID algorithm to estimate the dynamic characteristics based on ambient vibration records on the first, second, and third stories of the building. The fundamental period of vibration, which is one of the major design/assessment parameters, is estimated as 0.86 sec. The estimated fundamental period of vibration depicts that wood frame buildings possess a higher vibration period than other construction systems such as reinforced concrete and masonry buildings of the same height. In one of the first attempts to characterize wood frame constructions in Nepal, we conclude that the damping ratio of wood frame buildings is around 3%. In comparison with the current and past building regulations, we conclude that the recently updated building code recommendation strays more than the preceding one. Thus, we recommend using the past building code, NBC-1994, to estimate the fundamental period of vibration for wood frame buildings when required. We also compared several building code recommendations and found that the NBCC (2015) recommendation would be the most representative to be used in the estimation of the fundamental period of vibration for similar buildings. This study uses single building measurement, future studies can conduct ambient vibration measurement in many sample buildings of the same class and develop frequency-height relation, which could be more representative to be used instead of using the formula recommended for undefined building category. We are also testing other wood frame buildings and we plan to develop a refined finite element model for wood frame construction to assess seismic performance.

## ACKNOWLEDGMENTS

We acknowledge support from Subash Joshan, Shiva Chapagain, Upendra Subedi, Madan Khakurel, Pradip Shrestha, Gunjan Sharma Gautam, and Prasanna Poudel.

## REFERENCES

[1] Central Bureau of Statistics, “National Population and Housing Census 2011,” Kathmandu, 2011.

[2] T. Reynolds, R. Harris, W. S. Chang, J. Bregulla, and J. Bawcombe, “Ambient vibration tests of a cross-laminated timber building,” *Proceedings of Institution of Civil Engineers: Construction Materials*, vol. 168, no. 3, 2015, doi: 10.1680/coma.14.00047.

[3] G. Hafeez, G. Doudak, and G. McClure, “Establishing the fundamental period of light-frame wood buildings on the basis of ambient vibration tests,” *Canadian Journal of Civil Engineering*, vol. 45, no. 9, 2018, doi: 10.1139/cjce-2017-0348.

[4] A. Feldmann *et al.*, “Dynamic properties of tall timber structures under wind-induced vibration,” in *WCTE 2016 - World Conference on Timber Engineering*, 2016.

[5] V. Camelo, “Dynamic characteristics of wood frame buildings,” California Institute of Technology, California, 2003.

[6] A. S. Cao and H. Stamatopoulos, "A theoretical study of the dynamic response of planar timber frames with semi-rigid moment-resisting connections subjected to wind loads," *Eng Struct*, vol. 240, 2021, doi: 10.1016/j.engstruct.2021.112367.

[7] Y. Sawaki, R. Rupakhety, S. Ólafsson, and D. Gautam, *System identification of a residential building in Kathmandu using aftershocks of 2015 Gorkha earthquake and triggered noise data*, vol. 47. 2019. doi: 10.1007/978-3-319-78187-7_18.

[8] R. Dhakal, R. Rupakhety, and D. Gautam, "System Identification and Seismic Performance Assessment of Representative RC Buildings in Kathmandu Valley," *Front Built Environ*, vol. 6, 2020, doi: 10.3389/fbuil.2020.601116.

[9] R. Rupakhety, D. Gautam, R. Adhikari, P. Jha, L. Bhatt, and R. Baruwal, "System Identification and Finite Element Modelling of Damaged Bal Mandir Monument in Kathmandu After the 2015 Gorkha Earthquake," 2022, pp. 222–231. doi: 10.1007/978-3-030-90788-4_21.

[10] H. Varum, A. Furtado, H. Rodrigues, J. Dias-Oliveira, N. Vila-Pouca, and A. Arêde, "Seismic performance of the infill masonry walls and ambient vibration tests after the Ghorka 2015, Nepal earthquake," *Bulletin of Earthquake Engineering*, vol. 15, no. 3, 2017, doi: 10.1007/s10518-016-9999-z.

[11] A. Niraula, D. Gautam, and R. Rupakhety, "System identification of a tall office building in Kathmandu, Nepal, using ambient vibration measurements," in *3rd European conference on earthquake engineering and seismology*, Sep. 2022, pp. 1317–1325.

[12] D. Gautam, R. Rupakhety, R. Adhikari, R. Baruwal, S. Pokhrel, and S. Aryal, "System identification of a typical pre-code highway bridge in operation using heavy vehicle excitations," in *17th World Conference on Earthquake Engineering*, Sep. 2020.

[13] W. F. Freiberger, G. M. Jenkins, and D. G. Watts, "Spectral Analysis and its Applications.," *J Am Stat Assoc*, vol. 64, no. 328, 1969, doi: 10.2307/2286100.

[14] L. Ljung, "System identification," in *The Control Systems Handbook: Control System Advanced Methods, Second Edition*, 2010. doi: 10.1201/b10384.

[15] P. van Overschee and B. de Moor, "N4SID: Subspace algorithms for the identification of combined deterministic-stochastic systems," *Automatica*, vol. 30, no. 1, 1994, doi: 10.1016/0005-1098(94)90230-5.

[16] S. Hachicha, M. Kharrat, and A. Chaari, "N4SID and MOESP algorithms to highlight the ill-conditioning into subspace identification," *International Journal of Automation and Computing*, vol. 11, no. 1, 2014, doi: 10.1007/s11633-014-0763-z.

[17] MathWorks Inc., "MATLAB." MathWorks Inc., California, 2022.

[18] NBC-105, *Seismic Design of Buildings in Nepal, Department of Urban Development and Buildings Construction, Ministry of Physical Planning and Works, Government of Nepal*. Nepal, 1994.

[19] Department of Urban Development and Building Construction, *NBC-105:2020 Nepal National Building Code for Seismic Design of Buildings in Nepal*. Nepal, 2020.

[20] IS 1893 (part 1), *Indian Standard Criteria for Earthquake Resistant Design of Structures, 5th Revision, Bureau of Indian Standards, Manak Bhavan, Bahadur Shah Zafar Marg, New Delhi*. India, 2002.

[21] Bureau of Indian Standards, *IS 1893 (Part1):2016 Indian Standard Criteria for Earthquake Resistant Design of Structures*. India, 2016.

[22] National Research Council of Canada, *National Building Code of Canada (NBCC 2015)*. Canada, 2015.

[23] Uniform Building Code (UBC-1997), *Structural engineering design provisions*. 1997.

[24] European Committee for Standardization, *Eurocode 1: Actions on structures - Part 1-4: General actions - Wind actions*. Belgium, 2010.

COMPDYN 2023
9th ECCOMAS Thematic Conference on
Computational Methods in Structural Dynamics and Earthquake Engineering
M. Papadrakakis, M. Fragiadakis (eds.)
Athens, Greece, 12-–14 June 2023

# MODULAR DEPLOYMENT OF MICROPROCESSOR-CONTROLLED DATA ACQUISITION AND CONTROL WITHIN A DIGITAL TWIN

**Matthew Bonney[1], Matthew Tipuric[1], David Wagg[1], Ian Stothers[2]**

[1] Dynamics Research Group
The University of Sheffield, UK
e-mail: {m.bonney,m.tipuric,david.wagg}@sheffield.ac.uk

[2] St Others Ltd. UK
e-mail: st.others.ltd@gmail.com

**Abstract.** *One major component of building management is the understanding of the current state of the system, typically using sensor measurements. To achieve this, many building managers are interested in the deployment of a digital twin for each building that allows for remote inquiries. However, many commercial data acquisition systems use proprietary connections or data formats putting a large barrier for interoperability between sensors and digital twins. To remove this barrier, this work develops a transparent data acquisition system using microprocessors and the remote connection to this system through a python-based remote digital twin operational platform. The use of microprocessors allows for nearly complete control of the data processing from the analogue to digital converter, data sampling, and data recording. There are many possibilities to process this data, so this paper focuses on identifying the various possibilities and demystifying this computer science topics for engineers. To access this data, a remote connection allows for multiple users to simultaneously access the current operational data. Using an interface, such as the digital twin operational platform, reduces the required knowledge to promote a multi-disciplinary culture through shared data within the digital twin.*

**Keywords:** Digital Twins, Internet of Things, Open-Source, Microprocessor

## 1 Introduction

Recently, the concept of a Digital Twin (DT) has been introduced to a wide variety of industries and applications. Through this introduction, there have been many interpretations on what a DT is and what it does [1]. As of late 2020, there has been more than 30 definitions for what a DT is [2], and it is expected that there are many more since that specific literature review due to the rapid increase in popularity in both research and industry for DTs. Among the myriad of definitions, one of the most common concepts is the connectivity between the physical and digital twins. There are multiple methodologies that have been applied to establish this connectivity, as well as the meaning of "connected". The two main methodologies are: 1) connection via access to embedded sensors and industrial Internet of Things (IoT) [3, 4] or, 2) connection via a collection of data-sets obtained during regular intervals. Selection of the connectivity methodology is highly related to the application, security, industry, and systems.

An important component of the twinning concept is the multi-disciplinary nature of systems. Particularly when using IoT to establish connectivity, the incorporation of hardware, software, human factors, and decision making promotes highly collaborative and multi-disciplinary understanding of a system [5]. IoT refers to a network of sensors and computing to provide useful data to better understand the connected physical system(s). This connectivity is done typically through networking (such as Ethernet or WiFi) due to the difficulties associated with mechanical safety, physical distance between sensors/systems and users, and user ease-of-use.

Due to the complexity of this connectivity, IoT platforms tend to be closed-source and/or proprietary in nature. Some common commercial products include cloud data-services (e.g. Google Cloud, AWS, and Microsoft Azure) or low-code solutions (e.g. Blynk IoT, Particle, and ThingWorx). Due to this obfuscation of information, it is difficult to fully understand the processes being used, thus declining the level of trust in the results presented. In order to increase the trust in both the IoT platform and the DT, an open-source methodology is proposed. To demonstrate this methodology, this work discusses some of the various options for developing an IoT platform including both the software and hardware components of the setup.

## 2 Software Setup

The development of an IoT platform (specifically within a DT) is comprised of both software and hardware components. This section discusses several of the software components including:

- Network connectivity options
- Data access options
- User access options

While some of these components seem similar, there are some slight differences between these topics that require some specific discussions. The network connectivity options refer to protocols that the sensors are connected to the sensor network, the data access options refers to how the data is managed along the network, and the user access options refer to how the user accesses this network of information through the DT.

### 2.1 Network Connectivity Options

The methods of communication between devices (sensors primarily in this case) is dedicated into two main categories, TCP/IP and UDP. For the majority of uses, it is common to use

Transmission Control Protocol and Internet Protocol (TCP/IP). TCP is used for general internet access and is the most commonly used protocol for secure networking. The other major alternative is User Datagram Protocol (UDP), commonly used for fast networking. While the discussion here is based on the author's experience, the reader is referred to [6] and similar papers for a quantitative comparison between the protocols.

Although the same data can be transferred through either protocol, there are some significant differences between the protocols. A summarized list is shown in Table 1, but there are some specific differences to highlight. The first difference is the reliability of the transfer of data. For TCP, there is a "handshake" (a communication between devices for verification) to ensure that the requested data is sent and received. Once the requester has received the data, a signal is sent back to the source to verify the transfer. However for UDP, there is no handshake, so once the requester has established a connection, it purely receives the data. If there is a disconnection, the UDP protocol purely loses the data that was sent during the disconnect while TCP will ensure that all the data is received. Because of this handshake, there is extra latency when using the TCP protocol causing it to be a slower transfer speed. For most general internet usage, this latency is not perceivable, but can be noticed for real-time applications as jitter or lag.

Table 1: Main differences between TCP and UDP protocols

| **TCP** | **UDP** |
|---|---|
| Secure | Unsecured |
| Slow | Fast |
| Guaranteed Transmission | No Guarantee |
| Critical Applications | Real-Time Applications |
| Packet Reorder Mechanism | No Reorder Mechanism |
| Advanced Error Checking | Basic Error Checking |
| 20 Byte Header | 8 Byte Header |
| Three-Way Handshake | No Handshake |

The majority of the differences derive from the inclusion of a handshake protocol in the TCP protocol. This handshake makes the TCP protocol a three part transfer (request - send - receipt), while the UDP protocol is only a two part transfer (request - send). In addition to the handshake, TCP also introduces a larger header file attached to the transferred data. This means that for a singular piece of data, the packet for TCP, which paired with the handshake, is larger and slower than a comparable UDP packet for the same piece of data.

### 2.2 Data Access Options

The data access options commonly refer to the communication between machines. This communication can occur from sensor to sensor or from sensor to a centralised "broker" (also commonly called a server) such as a digital twin. Often, this communication is also referred to as messaging protocols [7]. While this section will give a general overview, it is not an extensive review of every messaging protocol developed.

One of the basic forms of messaging is the Constrained Application Protocol (CoAP). This messaging establishes a synchronous request/response direct connection between machines. Originally, this was established for tiny devices with low power to utilise REpresentational State Transfer (REST) operations. CoAP is a binary protocol that runs over UDP thus providing a direct connection with the least amount of lag possible. While this connection is quick, since

it uses UDP, there is an issue with scalability. Since there is a direct UDP connection, the user must establish a connection to each machine, which has a limit for the number of sensors it can access.

One methodology to increase the scalability is to implement Message Queue Telemetry Transport (MQTT) protocol. This establishes an asynchronous publish/subscribe protocol that runs using the TCP[1] stack to the user. MQTT establishes a broker to facilitate connections between users and sensors. Since the user only have to interact with the broker, there is only one permanent connection, while there can be any number of connections between the broker and the sensors. Due to the broker setup, there is the ability to establish multiple queues and human-readable organisation of sensor information. One example would be to establish queues for similar sensors (accelerometer, temperature probes, etc.) or sensors that a physically nearby (a singular floor, specific cluster, etc.). MQTT excels on the ability for expansion, it's light-weight requirements, and its human-readable interactions/queues.

MQTT works well for establishing connections on dependable networks. However, as commonly implemented, if the network is disconnected the data that would be sent during this down-time would normally be lost. To address this issue, the Advanced Message Queuing Protocol (AMQP) has been developed, mainly by the financial industry [7]. The main advantage that this protocol introduces is a "store-and-forward" feature to account for network disruptions. While this feature provides robustness for network disruptions, it also introduces a much heaver load on the broker system compared to MQTT. This is similar to establishing a database buffer between the sensors and the broker. To summarise these various options, Table 2 provides a simple comparison between options.

Table 2: Summary of basic data access options

| CoAP | MQTT | AMQP |
|---|---|---|
| Direct Connect | Broker | Broker |
| UDP | TCP or UDP | TCP |
| Header-less | Header | Store-and-forward |
| Fastest | Fast | Stored history |

### 2.3 User Access Options

The last component for consideration is the platform for which the user access the data from the sensors. In general there are 3 main types of accessibility: high-code, low-code, and no-code. Each type requires a varying level of expertise from the user in order to operate. To summarise these options, Figure 1 gives a better understanding of the options.

High-code represents the modifying of the source code in order to communicate. This is typically the starting point of any program or setup and requires a high level of expertise is order to operate. Due to this required expertise, it is expected that the user will be the same (or similar) developer. Using a high-code option provides a high level of granular control, but greatly reduces productivity since the developer will have to search for specific lines of code in order to make any modifications.

To expand the desired user-base, the low-code option increases the ease-of-use for users. This is targeted towards tech user, or users with application expertise and light programming

[1]Some lightweight implementations of MQTT do use UDP, such as MQTT/UDP and MQTT-SN. These implementations are not particularly commonly used.

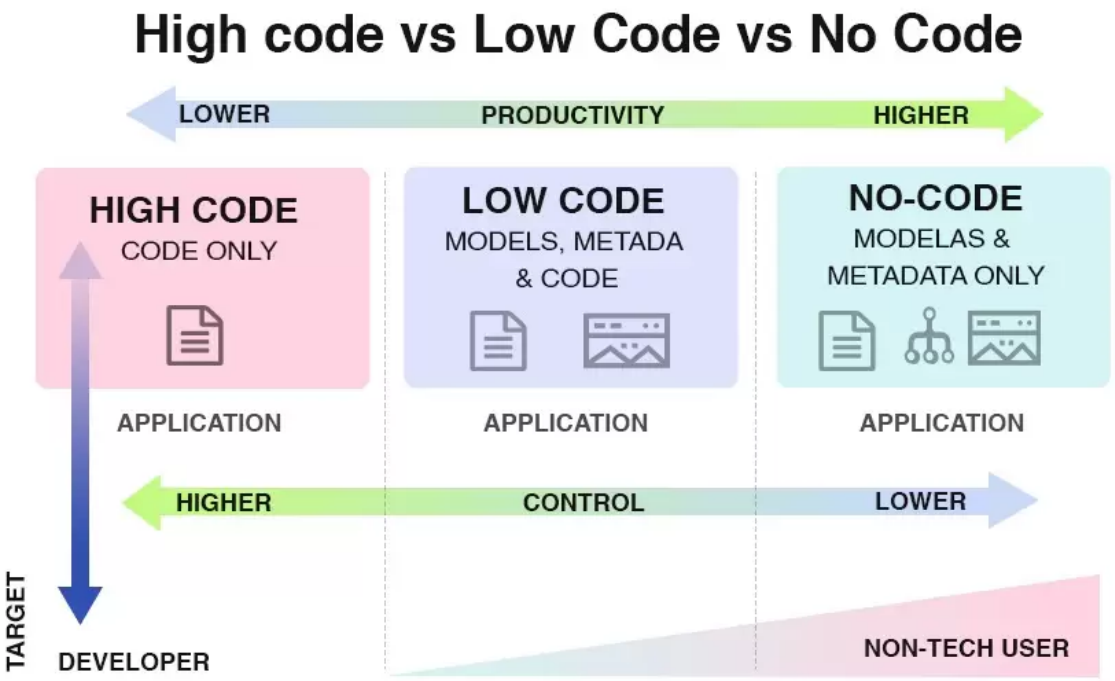


Figure 1: Summary of user access options. Taken from [8]

knowledge. For example, if the IoT sensors are attached to a manufacturing robot, the expected user for the low-code option would be the mechanical engineers or technicians. This accessibility option uses specifically made techniques/functions/classes to allow users to have access to functions/techniques without the need to modify source code. In addition to this ease-of-use, this option is also very helpful for other aspects such as collaborative working and version controlling. If there is a change in the algorithm implementation (typically for reduced computational effort), the end-user's code does not need any modifications, just a simple update of the package. For many engineering applications, this is the furthest that most platforms will obtain since the expected users will almost always be technical experts.

While low-code is typically the end-point for most engineering applications, the barrier for entry is till too high for many users and decision makers, making it difficult to market to a general audience. For these users, a no-code option is required. This reduces the required expertise of the user to a general, possibly trained, person. The wide-spread nature of the user-base, with limited access to source code, greatly benefits commercial interests in the development of software and platforms. This commonly reduces the user's experience to simple drag-down menus, button selects, and graphs.

One example of a no-code solution that also is open-source is the Digital Twin Operational Platform (DTOP) Cristallo [9] and other DTOPs created by the authors [10, 11]. This uses a python back-end and HTML front-end to reduce the knowledge burden on users to operate the digital twin. A demonstration of how this DTOP system can be used in a IoT context can be found in [12] where the DTOP system was used to activate and collect sensor readings though a direct connection. The user-interface for this access is shown in Figure 2. This interface allows the user to input the simple parameters such as sample rate and the measurement time. The user simply has to input these values into a HTML page and click "start". The DT will then activate the data acquisition system to collect the data and display it to the user. Additionally, the user

can download this data for further analysis.

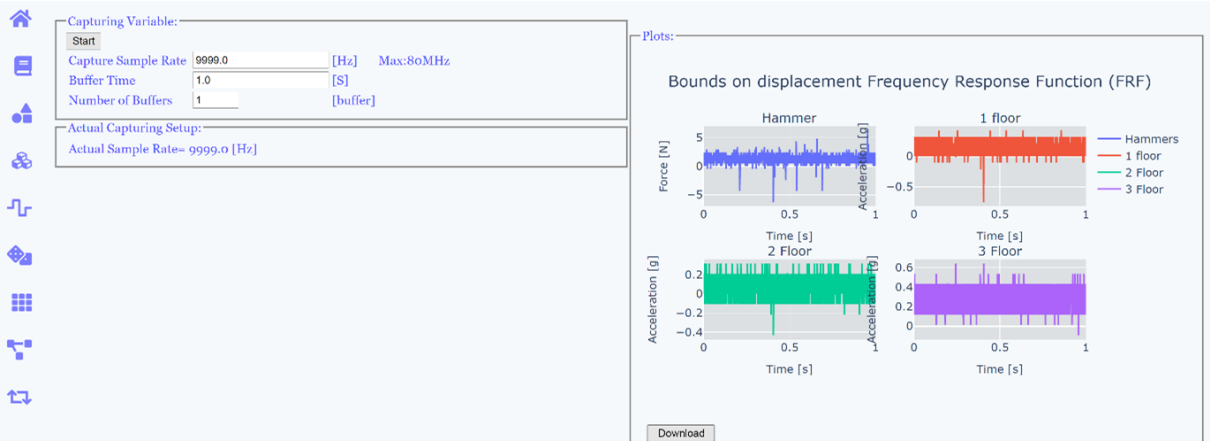


Figure 2: DTOP user interface for demonstration IoT interaction. Taken from [12]

## 3 Hardware Setup

The other major component of an IoT platform is the hardware physically connected to the system. This connection is done through various sensors such as accelerometers, temperature probes, pitot tubes, strain gauges, and a multitude of other sensors. The output of these sensors can vary, but generally fall into two main categories: voltage or current output. Using a voltage reading is common for non-intrusive electronics or systems that are sensitive to electronic coupling. For mechanical systems, sensors like accelerometers commonly use voltage outputs via piezoelectric components that create an electrical voltage when under mechanical strain. One common issue with voltage-based sensors is the voltage loss when the signal is being transported on long wires. In contrast, current-based sensors have a variable resistance across a constant voltage to relate to the output. Commonly, these sensors are limited to the current range of $4-20$mA where an output of $4$mA refers to the zero point of calibration and $20$mA corresponds to the maximum value recordable.

The selection of sensors is highly dependent on the system, quantity of interest, accessibility, and cost. With the selection of the sensors, the Data AcQuisition (DAQ) system must also be designed. There are many commercial options for these DAQ systems, but tend to require proprietary software packages in order to operate these systems commonly with low- or no-code interfaces. However, some provide drivers for high-code incorporation into other frameworks. The demonstration in Figure 2 is one example of this type of setup. This work aims to implement a microprocessor-controlled network of DAQ systems to connect the physical and digital twins together in an open-source and modular framework. This modularity is especially important when considering the multi-disciplinary nature of complex engineering systems and the variety of sensors required to measure these quantities.

### 3.1 Microprocessor Controllers

In contrast to the proprietary nature of commercial DAQ systems, one alternative (both technically and financially) is the utilisation of microprocessors to interface between raw sensor readings (mV or mA) and human-readable data (in units such as g, C, etc.). The inclusion of microprocessors allow for the embedding of meta-data into the data and supplying any power or

signal requirements. While the actions performed is not limited to microprocessors, these provide a flexibility not available for commercial solutions. While there are many different types of microcontroller available (Singh et al. [13] provide a comparison of some of the boards available in 2020), two makes will be discussed here for comparison. These are STMicroelectronics (STM) and Raspberry

STMicroelectronics is a global leader is semiconductor manufacturing. They produce a while variety of processors and associated circuitry for various uses in systems. These processors run using either C or C++ programming for hardware-level programming. This provides the quickest operation of programming available. Some of the most commonly used STM development boards are the black-pill (STM32F411) and the more expensive Nucleo range. These boards excel for high speeds at low cost, but do require a higher degree of technical knowledge than some competitors.

As an alternative, Raspberry is a UK-based company focusing on ease-of-use and accessibility. Commonly, these are used to teach programming at schools; this shows one of the advantages the Raspberry has compared to STM, ease-of-use. This focus on ease-of-use and teaching means that there are a large amount of resources available for new designers and open-source low-code packages already developed. Raspberry Pis (processors created by Raspberry) run using a lightweight build of python call micro-python or C. The default inclusion of python provides easier to read programming such that non-experts can understand the process flow and grow the inherent trust in the processing. Another advantage is the capability for many of the processors to have an operating system installed with a graphical user interface. This is an adaptation of Linux and several processors have the capability of running Linux directly. Some of the common controllers include Raspberry Pi 4 (with operating system) and Raspberry Pi Pico (without operating system and is similar to STM black-pill).

## 4 Example Implementation Demonstration

This section discusses one possible implementation for a Building Information Management Digital Twin (BIM-DT) and an example messaging system on hardware. This is selected as an example due to the large scale nature of buildings and the variety of sensors needed to create a DT (to measure aspects such as earthquake vibrations, room conditions such as temperature, and energy usage for efficiency and certification). This section contains two subsections, Section 4.1 gives a possible architecture design from sensors to digital twin to user and Section 4.2 shows a demonstrative example messaging system using CoAP.

### 4.1 Example Architecture

The example architecture for this setup is shown on a scaled 3-storey structure (used in DTOP-Cristallo) in Figure 3. This contains the entire design from sensors, to server, to user.

In Figure 3, the teal squares represents the microprocessors proposed for this setup. These are Raspberry Pi Pico W that cost less than £10 each and has both wired and wireless connectivity options. These Picos are attached by wires to three different types of sensors via the general purpose input/output pins. The black sensors are accelerometers to measure seismic activity and wind induced vibrations; the red sensors are temperature sensors that tie into the climate control system, and the green sensors are occupancy/motion sensors to identify if someone is using the space and adjust the lights accordingly. Since this system has multiple controllers, a MQTT broker is setup on a Raspberry Pi3 with wireless connections to each controller. The W variant of the Pico has the WiFi connectivity that reduces the amount of wires needed to be sent

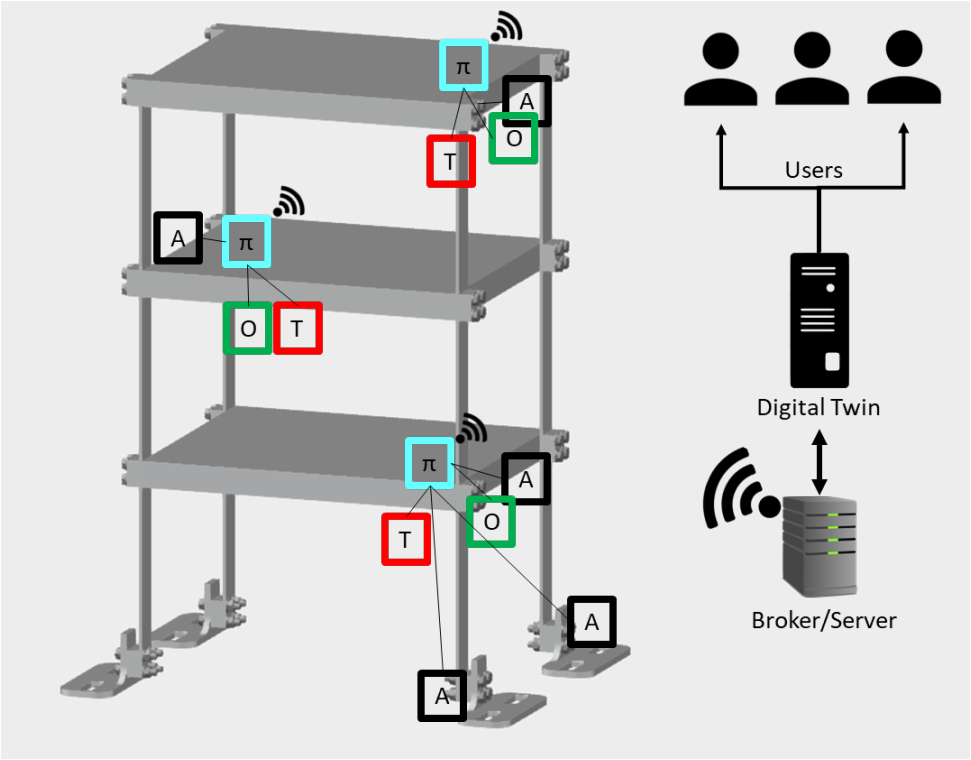


Figure 3: Example sensor layout for building management. Teal are microprocessors, black are accelerometers, red are temperature sensors, and green are occupancy/motion sensors.

throughout the building and reducing the voltage loss due to long cabling. This also allows for more flexibility when deploying new sensors or redesigning each floor (for example changing the amount of rooms on a floor).

With a centralised server using MQTT, the DT can access this directly and gain access to each and every sensor of interest. This can be used to directly control aspects of the building operation such as lighting and climate control in "real-enough" time (lights operate in less than a half second and climate control on the scale of seconds). This control can be done automatically through algorithms or manual through the user interaction with the DT. For more time critical control, such as for emergency systems, local control could be achieved on the relevant Picos. The Raspberry Pi Pico can run the control logic on the inbuilt microprocessor to reduce overall processing time, while still providing override or monitoring information to the DT. This use of local control algorithm would be required for any active seismic control mechanisms implemented within the building due to the need to respond quickly to sudden earthquakes, for example.

### 4.2 Octave-based CoAP

To show an example implementation of a messaging system on hardware, this section discusses a CoAP messaging protocol with a UDP connection to a STM microprocessor (black-pill). There are 5 sensors used and are piezoelectric sensors placed along the length of a long slender beam, similar to the support pillar from the scaled 3-storey structure in Figure 3. This setup is seen in Figure 4 with the circles on the beam being the piezoelectric sensors, attached to the STM black-pill (outlined in red) with an external Ethernet port (outlined in black) that is connected to the user's computer.

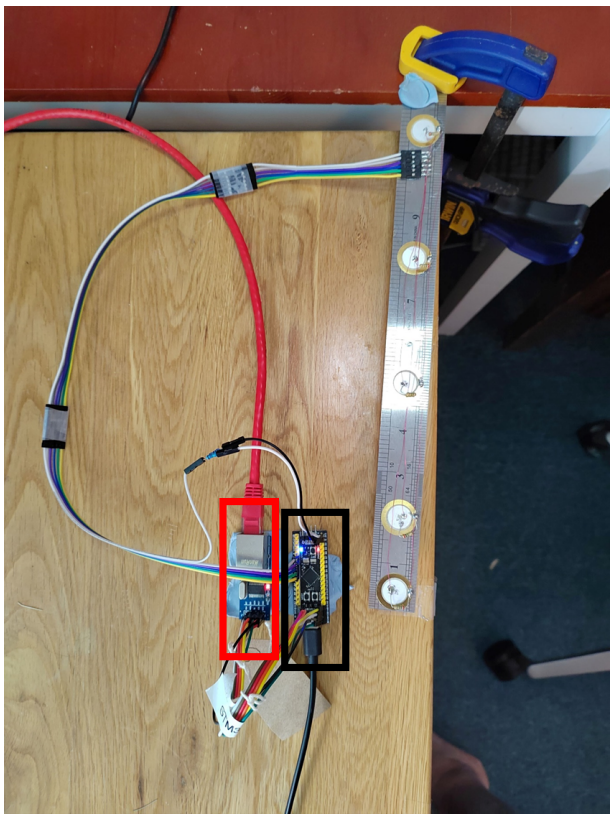

Figure 4: Physical setup for STM-based CoAP connectivity, with the STM black-pill outlined in black and the external ethernet port outlined in red

The piezoelectric sensors take the mechanical deformation to produce a voltage that is read by the STM black-pill. These sensors are common in building health monitoring due to the physically lightweight materials and relative inexpensive cost (under £1 each). Overall, this entire hardware system costs less than £20.

In order for the user to access this data, a CoAP messaging protocol is implemented using a mixture of C for the hardware processing and Octave (similar to Matlab) for the software processing. For the hardware, the board is programmed to take the appropriate signals to generate digital signals and establish the scheduler to facility the CoAP messaging. The processing and visualisation is performed via software on the user's computer via purely Octave programming. As a demonstration of a seismic shock, the base is excited through an impact of the table that the base is attached to and the Octave results in shown in Figure 5.

This implementation CoAP involves two main portions, the gathering and the visualisation of the data packet. In Figure 5a, the bottom window is active collection of data and storing it locally via a binary file. This collection is continuous until the user clicks "END ACQUIRE" that terminates this connection. One interesting aspect of this implementation is the use of a scheduler that allows for multiple users to create UDP stack connections for retrieving the data. In this example, the computer is connected directly to the microprocessor (see Figure 4) so only one user can connect at a time. However, if this microprocessor was connected to a router, then multiple people would be able to connect and access this data simultaneously.

The second window in Figure 5a (the top) shows a graphical representation of the sensor data. This shows a selected time section from the streaming binary file being written to in the first window. One advantage of this binary file is the ability to do quick (non-sequential) search-

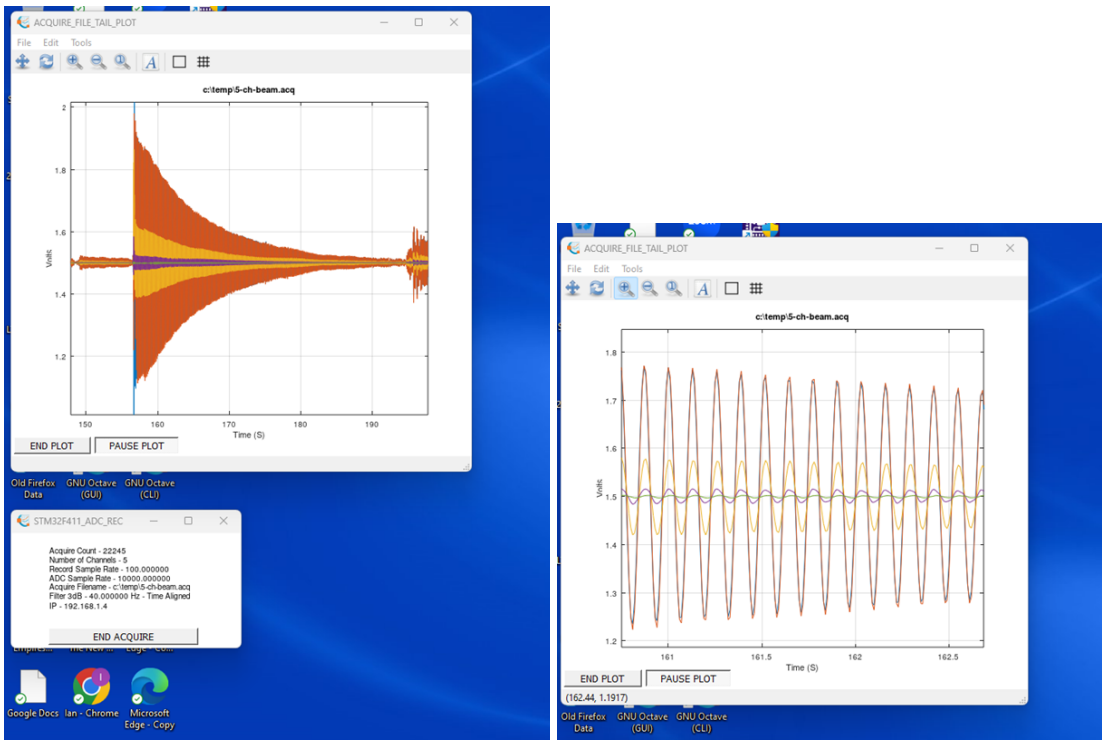


(a) Ring down data for all sensors

(b) Zoomed in graph to visualize sensor differences

Figure 5: Octave output of CoAP messaging

ing with limited loading that is not available in ASCII files such as CSV format. Because this visualisation is purely reading a local binary file, the user can select what time limits and channels to investigate. Figure 5b shows a more detailed view of the response of the sensors. This also shows the various sensors and the relative amplitudes of vibration caused by the geometric location of the sensors. While these plots only shows the data in voltage, the microprocessor can also inject meta-data into the signal to denote the units of measurement, physical location, calibration information, and other pieces of data such that the data received by the user is self-describing.

## 5 Remarks

During the course of this work, there was a multitude of knowledge gained through the investigation of multi-disciplinary aspects of IoT-based digital twins. It was found that there any many solutions to the same problem, for example the hardware selection between STM and Raspberry. This variety of solutions made the collection of information difficult, thus this paper has focused on the distillation of information gathered for a mechanical/industrial engineering audience. The first example shows a planned designed system from sensor, to server, to digital twin, to user, while the second example shows an implemented CoAP connection from a STM microprocessor to a low-code environment within Octave.

Future work by the authors will include a physical demonstration of the architecture proposed in Section 4.1. This will include the use of various sensors, multiple controllers, a centralised MQTT server, and a DTOP for user interactivity with the various sensors and data. To aid in the open-source dissemination and demystification of these platforms, the software component

will be publicly available via GitHub when the finalised journal paper is published.

**Acknowledgement**

The authors would like to acknowledge the support of EPSRC via the DigiTwin project (grant number EP/R006768/1). The authors would also like to specially thank the coauthor Ian Stothers for the open-source, commercial demonstration free-of-charge for Section 4.2.

## REFERENCES

[1] D. J. Wagg, K. Worden, R. J. Barthorpe, and P. Gardner. Digital Twins: State-of-the-Art and Future Directions for Modeling and Simulation in Engineering Dynamics Applications. *ASCE-ASME J Risk and Uncert in Engrg Sys Part B Mech Engrg*, 6(3), 05 2020. 030901.

[2] C. Semeraro, M. Lezoche, H. Panetto, and M. Dassisti. Digital twin paradigm: A systematic literature review. *Computers in Industry*, 130:103469, 2021.

[3] J. Lee, E. Lapira, B. Bagheri, and H. Kao. Recent advances and trends in predictive manufacturing systems in big data environment. *Manufacturing Letters*, 1(1):38 – 41, 2013.

[4] T. H.-J. Uhlemann, C. Schock, C. Lehmann, S. Freiberger, and R. Steinhilper. The digital twin: Demonstrating the potential of real time data acquisition in production systems. *Procedia Manufacturing*, 9:113 – 120, 2017. 7th Conference on Learning Factories, CLF 2017.

[5] M. S. Bonney, M. de Angelis, M. Dal Borgo, and D. J. Wagg. Contextualisation of information in digital twin processes. *Mechanical Systems and Signal Processing*, 184:109657, 2023.

[6] F. T. AL-Dhief, N. Sabri, N. M. A. Latiff, N. N. N. A Malik, M. A. A. Albader, M. A. Mohammed, R. N. AL-Haddad, Y. D. Salman, M. K. A. Ghani, and O. I. Obaid. Performance comparison between TCP and UDP protocols in different simulation scenarios. *International Journal of Engineering & Technology*, 7(4.36):172–176, 2018.

[7] T. M. Tukade and R. Banakar. Data transfer protocols in IoT-an overview. *International Journal of Pure and Applied Mathematics*, 118:121–138, 01 2018.

[8] iTech India. Will low code/no-code solutions overtake custom software?, March 2022.

[9] M. S. Bonney, M. de Angelis, M. Dal Borgo, L. Andrade, S. Beregi, N. Jamia, and D. J. Wagg. Development of a digital twin operational platform using python flask. *Data-Centric Engineering*, 3:e1, 2022.

[10] M. S. Bonney, P. Gardner, D. Wagg, and R. Mills. Case study of connectivity of digital twins and experimental systems. In *Proceedings of the 8th International Conference on Computational Methods in Structural Dynamics and Earthquake Engineering*, pages 1416–1425, Streamed from Athens, Greece, June 2021.

[11] M. S. Bonney, M. de Angelis, M. Dal Borgo, and D. Wagg. Digital twin operational platform for connectivity and accessibility using Flask Python. In *Proceedings of the 24th International Conference on Model-Driven Engineering Languages and Systems*, 2021.

[12] R. Wang and M. S. Bonney. Novel data acquisition utilising a flask python digital twin operational platform. In Matt Allen, Sheyda Davaria, and R. Benjamin Davis, editors, *Special Topics in Structural Dynamics & Experimental Techniques, Volume 5*, pages 7–13, Cham, 2023. Springer International Publishing.

[13] D. Singh, A. Sandhu, A. Thakur, and N. Priyank. An overview of iot hardware development platforms. *International Journal of Emerging Technolgy*, 11:155–163, 2020.

COMPDYN 2023
9th ECCOMAS Thematic Conference on
Computational Methods in Structural Dynamics and Earthquake Engineering
M. Papadrakakis, M. Fragiadakis (eds.)
Athens, Greece, 12-14 June 2023

# THE DYNAMIC PROBLEM OF AN ELASTICALLY SUPPORTED BEAM ANALYSIS USING NEURAL ARCHITECTURE SEARCH WITH AUTOMATIC DIFFERENTIATION

**Konstantinos S. Demertzis[1], Konstantinos E. Morfidis[2], Konstantinos G. Kostinakis[3], Lazaros S. Iliadis[4]**

[1] School of Science & Technology, Informatics Studies, Hellenic Open University, Greece
e-mail: demertzis.konstantinos@ac.eap.gr

[2] Earthquake Planning and Protection Organization (EPPO-ITSAK), Terma Dasylliou, 55535, Thessaloniki, Greece
e-mail: konmorf@gmail.com

[3] Department of Civil Engineering, Aristotle University of Thessaloniki, Aristotle University Campus, 54124, Thessaloniki, Greece
e-mail: kkostina@civil.auth.gr

[4] School of Engineering, Department of Civil Engineering, Faculty of Mathematics Programming and General Courses, Democritus University of Thrace, Kimmeria, Xanthi, Greece
e-mail: liliadis@civil.duth.gr

## Abstract

*The equations of motion for linear structures considered as continuous systems are generally non-homogeneous linear partial differential equations. Their solution is functions of time and spatial variables. The traditional analysis approach involves solving the eigenvalue problem. This yields the eigenvalues and eigenvectors, which can be used to construct the general solution of the differential equations. This approach has been widely used in mechanics and has proven effective in solving many engineering problems. In recent years, machine learning methods, particularly neural networks, have also been used to solve differential equations. These methods can learn the equation's solution directly from data without the need for explicit analytical expressions. This makes them particularly useful for complex problems that may need analytical solutions or for problems where obtaining analytical solutions takes time and effort. This paper compares the performance of these two approaches for a specific problem of the vibration of the Euler-Bernoulli beam on a Winkler-type elastic foundation subjected to a moving load. The machine learning approach learns the solution directly from data generated by solving the differential equation using a Neural Architecture Search (NAS) with Automatic Differentiation (AD) method (NASAD). The paper provides insights into the relative strengths and weaknesses of each method and highlights the potential of machine learning to solve complex problems with high accuracy and low computational sources.*

**Keywords:** Neural Architecture Search; Automatic differentiation; Dynamic response; Beams on elastic foundation; Eigenvalue problem; Forced vibrations

## 1 INTRODUCTION

The solution of the equation of motion of structures is one of the most important issues in earthquake engineering as it is directly related to the determination of their seismic response [1]. The equations governing the motion are generally non-homogeneous linear partial differential equations with respect to time and spatial variables. This is due to the fact that structures are in effect "continuous systems" with infinite degrees of freedom [2]. Solving equations of this type is particularly difficult or even impossible as structures consist of many more than one structural element. Thus, for the solution of the equations of dynamic equilibrium the consideration of structures as discrete systems has prevailed [1]. In this case the structures are transformed into systems with a finite number of degrees of freedom by means of inertial and elastic discretization ("discrete systems"). Thus, in combination with the application of the finite element method, the solution of the dynamic problem is achieved by solving systems of second-order linear differential equations for which there is a large number of implementations available in computer code (see e.g. [3]). Despite the fact that nowadays the Finite Element Method is almost exclusively used for solving dynamic problems of structures (see e.g. [4,5,6]), the study of the solution in terms of "continuous systems" remains particularly useful for applications to simple structural systems such as elastically supported beams which can also be used for example to model pile foundation systems (see e.g. [7,8,9]).

The difficulty of solving the dynamic problem by considering structures as "continuous systems" (as described above) leads to the consideration of the possible feasibility of solving it using methods that fall within the scientific field of machine learning. This paper proposes a method to learn the solution directly from data generated by solving the differential equation using a neural architecture search with automatic differentiation. Automatic Differentiation (AD) [10] is a technique used to compute the derivatives of a function concerning its inputs and is a crucial component of modern neural network training algorithms [11]**.** On the other hand, the Neural Architecture Search (NAS) [12] is a technique used in machine learning to design and optimize neural network architectures automatically [13]. In traditional machine learning approaches, the architecture of a neural network is often manually designed by a human expert, which can be a time-consuming and challenging process. NAS automates this process to search for the optimal neural network architecture based on predefined constraints or objectives. The process involves exploring a large search space of possible network architectures and evaluating their performance on a given task. To apply the Neural Architecture Search with Automatic Differentiation (NASAD) method as a technique for the solution of differential equations, we formulate the problem as an optimization problem, where the goal is to minimize the error between the predicted and actual solution of the differential equation. The neural network architecture is designed to take the initial conditions and any relevant differential equation parameters as inputs and output the solution at a given time. The optimization problem is solved using gradient descent, where the error gradient with respect to the network weights is computed using automatic differentiation [14]. This allows the network weights to be updated to minimize the error between the predicted and actual solution of the differential equation.

The proposed method is a pilot application to optimal solution of dynamic problems of structures considered as continuous systems. To this end, the solution of the dynamic problem of the Euler-Bernoulli beam supported on a Winkler-type elastic foundation, which has been studied in a large number of published research papers using various classical methods of structural dynamics (see e.g. [15,16,17,18]), has been chosen at this stage of the investigation. More specifically, in this paper the problem of vibration of elastically supported Euler-Bernoulli beams due to a moving concentrated force (see e.g. [19,20,21]) is studied. The problem is solved both by the classical method of separation of variables and application of the eigenproblem solution

[1,2,22] and by NASAD method. The results of the solutions by both methods prove that the NASAD method can approach the results obtained by the classical solution method to an extremely high degree. This conclusion sets the stage for further investigation of the application of machine learning methods to the solution of dynamic equilibrium problems of more complex structures.

## 2 THE SOLUTION OF THE EQUATION OF MOTION FOR EULER-BERNOULLI BEAMS ON WINKLER TYPE ELASTIC FOUNDATION

### 2.1. The solution procedure based on the eigenvalue analysis approach

The governing equation of motion for Euler-Bernoulli beams on a Winkler type elastic foundation (ignoring the damping) in the framework of the first order theory is [23]:

$$EI\cdot\frac{\partial^4 w}{\partial x^4}+\rho A\cdot\frac{\partial^2 w}{\partial t^2}+k\cdot w=p(x,t) \tag{1}$$

Where:
w(x,t) is the lateral deflection of cross-sectional centroid axis (m),
EI is the flexural stiffness of beam ($kNm^2$),
ρ is the mass density (mass per unit of area, ($kg/m^2$)),
A is the cross-sectional area in ($m^2$),
k is the modulus the of sub-grade reaction ($kN/m^2$),
p(x,t) is the external dynamic load (kN/m)

If the external dynamic load p(x,t) is equal to zero then the equation (1) governs the free vibration of a beam without damping. In this case the vibration is due to the initial conditions which regard the imposed displacements and velocities at t=0.

A conventional procedure for the solution of (1) (with or without external dynamic load) is the mode superposition method [1,2]. In the framework of this method the eigenmodes of the vibrating structural system must be calculated at first. To this end, the eigenvalue problem must be solved. This problem is governed by Eq. (1) ignoring the external load (i.e. p(x,t)=0). The solution is based on the hypothesis that the unknown function of lateral deflection w(x,t) can be expressed as a product of an unknown function X(x) of the spatial variable x and an also unknown function f(t) of time t (method of separation of variables or Fourier method). Thus:

$$w(x,t)=X(x)\cdot f(t) \tag{2}$$

Substituting the Eq. (2) in Eq. (1) and after the appropriate transformations the two following differential equations are extracted:

$$EI\cdot\frac{d^4X}{dx^4}+(k-\omega^2\cdot\rho A)\cdot X(x)=0 \;\Rightarrow\; \frac{d^4X}{dx^4}-\frac{(\omega^2\cdot\rho A-k)}{EI}\cdot X(x)=0 \tag{3a}$$

$$\frac{d^2f}{dt^2}+\omega^2\cdot f(t)=0 \tag{3b}$$

Where X(x) and ω are an eigenvector and its corresponding eigenfrequency.

The Eq. (3a) is a linear homogeneous differential equation with constant coefficients which can be solved using four boundary conditions that are depended on the types of the supports of the beam (for a simply supported beam: Fig. 1). The general form of the solution of (3a) is:

$$X(x)=C_1\cdot e^{PL}+C_2\cdot e^{-PL}+C_3\cdot\cos(PL)+C_4\cdot\sin(PL) \quad \text{where} \quad P=P(\omega)=\sqrt[4]{\frac{\omega^2\cdot\rho A-k}{EI}} \tag{4}$$

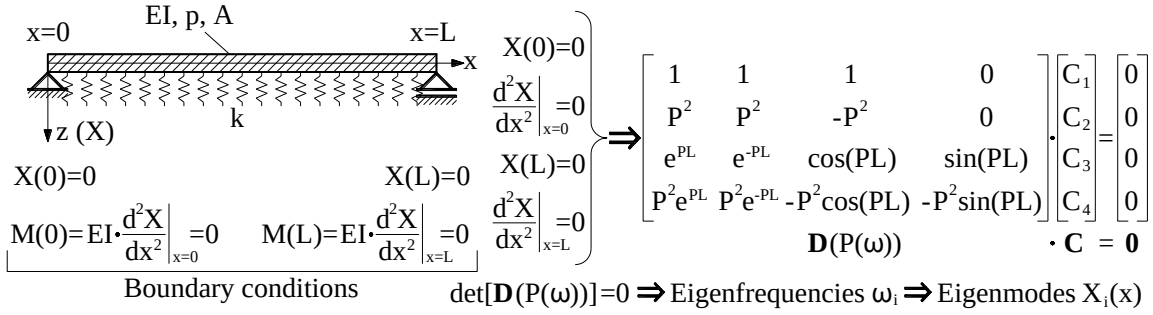


Figure 1: Definition and solution of the eigenvalue problem of a simply supported Euler beam on elastic foundation

The calculation of the constants of integration $C_1$-$C_4$ can be achieved using the four boundary conditions which form a homogeneous system with four equations. The non-trivial solution of this system arises when the determinant of the matrix **D** of the coefficients $C_1$-$C_4$ (Fig. 1) is set to zero:

$$\det\left[D(P(\omega))\right]=0 \tag{5}$$

The Eq. (5) is the characteristic equation of the eigenvalue problem. It can be proved that for the simply supported beam of Fig. 1 the characteristic equation is:

$$\det\left[D(P(\omega))\right]=0 \Rightarrow \sin\left[\left(\sqrt[4]{\frac{\omega^2\cdot\rho A-k}{EI}}\right)\cdot L\right]=0 \Rightarrow \omega_i=\sqrt{\frac{1}{\rho A}\cdot\left[\frac{i^4\cdot\pi^4\cdot EI}{L^4}+k\right]} \quad (i=1,2,...) \tag{6}$$

This trigonometric equation has infinite solutions which are the eigenvalues $\omega_i$ of the vibrating system. For each one of the eigenvalues $\omega_i$ the Eq. (4) leads to an eigenfunction $X_i(x)$. For the simply supported beam of Fig. 1 the form of the eigenfunctions is:

$$X_i(x)=\sin(P_i x) \quad \text{with} \quad P_i=P(\omega_i)=\sqrt[4]{\frac{\omega_i^2\cdot\rho A-k}{EI}} \tag{7}$$

Once the eigenfrequencies and the corresponding eigenfunctions are known, the solution of (1) for the undamped free vibration (p(x,t)=0) can be expressed in a infinite series of terms:

$$w(x,t)=\sum_{i=1}^{\infty}X_i(x)\cdot q_i(t) \tag{8}$$

Thus, the solution of Eq. (1) (for p(x,t)=0) is based on the complete set of the eigenmodes of the studied beam and on the "main coordinates" $q_i(t)$. In other words, the solution (8) i.e. the unknown function of the lateral deflection w(x,t) is expressed by means of the eigenvectors. The participation of each one of the eigenvectors to the solution is represented by the functions $q_i(t)$ as it is shown in Fig. 2.

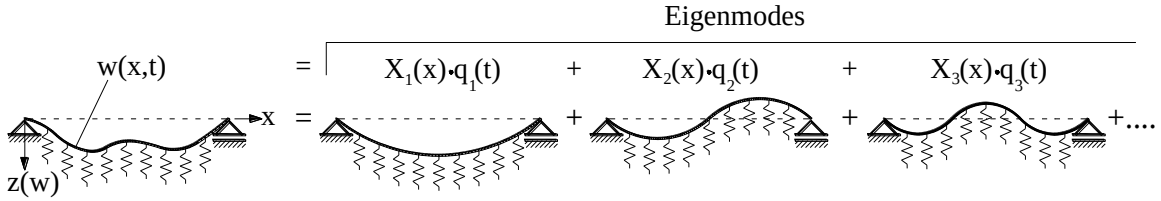


Figure 2: The rationale of the modal superposition method

In many cases an acceptable solution (as regards the precision) is reachable considering only a finite number of terms in (8).

Let's now consider the case of the vibration of a simply supported beam on a Winkler-type elastic foundation due to a moving transverse load $P_e$ which is moved on the beam with velocity equal to c (Fig. 3).

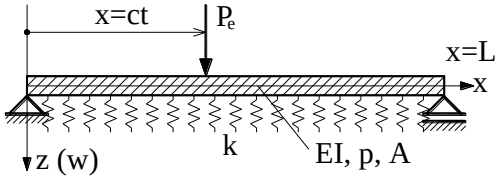


Figure 3: The vibration of a simply supported beam on a Winkler-type elastic foundation due to a moving transverse load

For this case the external dynamic load p(x,t) in the Eq. 1 is expressed as follows:

$$p(x,t)=P_e\cdot\delta(x-c\cdot t) \tag{9}$$

Where δ is the Dirac function, whereas c is the velocity (m/sec) of the external load $P_e$.

The substitution of Eq. (8) to Eq. (1) leads to the following Equation:

$$\sum_{i=1}^{\infty}\left[q_i(t)\cdot EI\cdot\frac{d^4X_i(x)}{dx^4}\right]+\sum_{i=1}^{\infty}\left[\rho A\cdot\frac{d^2q_i(t)}{dt^2}\cdot X_i(x)\right]+k\cdot\sum_{i=1}^{\infty}\left[q_i(t)\cdot X_i(x)\right]=P_e\cdot\delta(x-c\cdot t) \tag{10}$$

Then, an infinite sequence of differential equations is created by means of manipulation of (10) with each one of the infinite eigenmodes $X_k(x)$ and the integration along the length L of the beam.

$$\sum_{i=1}^{\infty}\left[q_i\cdot\int_0^L EI\cdot\frac{d^4X_i}{dx^4}\cdot X_k\cdot dx\right]+\sum_{i=1}^{\infty}\left[\frac{d^2q_i}{dt^2}\cdot\int_0^L\rho A\cdot X_i\cdot X_k\cdot dx\right]+k\cdot\sum_{i=1}^{\infty}\left[q_i\int_0^L X_i\cdot X_k\cdot dx\right]=\int_0^L X_k\cdot P_e\cdot\delta(x-c\cdot t)\cdot dx \tag{11}$$

Using the orthogonality conditions:

$$\int_0^L EI\cdot\frac{d^4X_i}{dx^4}\cdot X_k\cdot dx=\omega_i^2\cdot\rho A\cdot N_i\cdot\delta_{ik}\quad\text{and}\quad\int_0^L\rho A\cdot X_i\cdot X_k\cdot dx=\rho A\cdot N_i\cdot\delta_{ik}$$
$$\text{where:}\quad N_i=\int_0^L X_i^2\cdot dx=\frac{L}{2}-\frac{\sin(2\cdot P_i\cdot L)}{4\cdot P_i}\quad\text{and}\quad\delta_{ik}=\text{Kronecker delta} \tag{12}$$

the infinite number of equations take the following general form:

$$\frac{d^2q_i(t)}{dt^2}+\left(\frac{\omega_i^2\cdot M_i+k\cdot N_i}{M_i}\right)\cdot q_i(t)=\left(\frac{P_e}{M_i}\right)\cdot\sin(P_i\cdot c\cdot t)\quad\text{where}\quad M_i=\rho A\cdot N_i \tag{13}$$

Using as initial conditions for the above equation:

$$q_i(t)=0 \quad \text{and} \quad \frac{dq_i(t)}{dt}=0 \tag{14}$$

the solution of (13) is:

$$q_i(t)=\frac{2\cdot P_e}{L\cdot\left[k+\rho A\cdot\left(\omega_i^2-c^2\cdot P_i^2\right)\right]}\cdot\left[\sin\left(P_i\cdot c\cdot t\right)-\frac{P_i\cdot c}{\sqrt{\omega_i^2+\left(k/\rho A\right)}}\cdot\sin\left(\sqrt{\frac{\omega_i^2\cdot\rho A+k}{\rho A}}\cdot t\right)\right] \tag{15}$$

Combining the Eqs. (8), (15) and considering the Eq. (9) the form of the solution of Eq. (1) is:

$$w(x,t)=\sum_{i=1}^{\infty}X_i(x)\cdot\frac{2\cdot P_e}{L\cdot\left[k+\rho A\cdot\left(\omega_i^2-c^2\cdot P_i^2\right)\right]}\cdot\left[\sin\left(P_i\cdot c\cdot t\right)-\frac{P_i\cdot c}{\sqrt{\omega_i^2+\left(k/\rho A\right)}}\cdot\sin\left(\sqrt{\frac{\omega_i^2\cdot\rho A+k}{\rho A}}\cdot t\right)\right] \tag{16}$$

## 2.2. The solution procedure based on the NASAD approach

In this paper, based on the meta-learning logic [24], we build a system for identifying the optimal hyperparameters of a neural network model using the NAS technique [25]. It is a technique to automate the design of artificial neural networks by searching for optimal hyperparameters, minimizing the number of operations required while providing an explicit methodology for knowledge discovery in unknown environments. Typical hyperparameters the technique in question can optimize include the optimization algorithms (SGD, Adam, etc.), learning rate, regularization, etc. Essentially, it enables the creation of optimal learning techniques for high-performance success with minimal up-front effort and minimal expertise.

In particular, and given a neural architecture search space $F$, where the input data $D$ is divided into $D_{train}$ and $D_{val}$ and the cost function $Cost(\cdot)$ (e.g., accuracy, mean squared error, etc.), the goal is to find an optimal neural network $f^* \in F$ that can achieve the lowest cost on the dataset $D$. Finding the optimal neural network $f^*$ is equivalent to [12,24,26]:

$$f^*=\text{argmin}_{f\in F}Cost\left(f\left(\theta^*\right),D_{val}\right) \tag{17}$$

$$\theta^*=\text{argmin}_{\theta}L\left(f\left(\theta\right),D_{train}\right) \tag{18}$$

Where $\theta^*$ is the learning parameter of the network.

The mode of operation of the proposed NAS strategy is enhanced by techniques based on how nature works and, in particular, finding analogies between techniques where instinct as a genetic trait overrides training. For example, some species in biology possess predatory behaviors from birth, allowing them to perform complex motor and sensory tasks without learning, which in most cases are fully sufficient for the species' survival. In contrast, in training artificial neurons it is usually chosen to perform a task, an architecture that is considered suitable for modeling the task; the search mainly focuses on finding the weight parameters using a learning algorithm. Inspired by social behaviors evolved in nature, neural networks can be developed with architectures that can perform a given task even when the weight parameters are randomized. Hence, they can perform well without training, and their performance can be further maximized through training.

Thus, the proposed architecture is characterized by a stacked hierarchy of layers, where at each time step t, the first recurrent layer is fed by the external input u(t). In contrast, each successive layer is fed by the output of the previous one in the stack. Although their architectural organization allows for general flexibility in the size of each layer, to avoid complexity, we consider a hierarchical setup with recurrent layers $N_L$, each containing the same number of units

$N_R$. Moreover, we use $x^{(l)}(t) \in R^{N_R}$ to denote the state of layer $l$ at time $t$. Omitting bias terms, the state transition function of the first layer is defined as follows [27,28]:

$$x^{(1)}(t)=\left(1-\alpha^{(1)}\right)\cdot x^{(1)}(t-1)+\alpha^{(1)}\cdot\tanh\left(W_{in}\cdot u(t)+\hat{W}^{(1)}\cdot x^{(1)}(t-1)\right) \tag{19}$$

For each layer $l$>1:

$$x^{(l)}(t)=\left(1-\alpha^{(l)}\right)\cdot x^{(l)}(t-1)+\alpha^{(l)}\cdot\tanh\left(W^{(l)}\cdot u^{(l-1)}(t)+\hat{W}^{(l)}\cdot x^{(l)}(t-1)\right) \tag{20}$$

where $W_{in} \in R^{N_R \times N_U}$ is the input weight matrix, $\widehat{W}^{(l)} \in R^{N_R \times N_R}$ is the recurrence weight matrix for level $l$, $W^{(l)} \in R^{N_R \times N_R}$ is the matrix concerning the connection weights between levels from level $l$-1 to level $l$, $a^{(l)}$ is the leaky parameter at level $l$. Finally, tanh represents the elementary application of the hyperbolic tangent.

Random weights improve the generalization properties of the solution of an original linear system because they produce nearly orthogonal (weakly correlated) features. Given that the output of the linear system is always correlated with the input data if the range of solution weights is limited, orthogonal inputs provide a wider range of solutions than those supported by weights. Also, small variations in weights allow the system to become more stable and noise tolerant, as input errors will not be amplified at the output of a linear system with little correlation between input and output weights. Thus, the random ranking of weights, which produces weakly correlated features in the hidden layer, allows us a satisfactory solution and good generalization performance. In general, it is an evolutionary neural network development strategy that can perform a specialized task independently of the connection weights, equivalent to the absence of training. The logic of not using training involves a basic exploration in the search for neural network architectures with specific biases that can potentially perform categorization on the given problem, even when using random weights. By exploring such architectures, it is possible to explore agents that can perform well in their interaction environment without the need to be trained. An engineering system can create robust self-determining systems capable of coping with complex situations.

To evaluate and validate the final model capability resulting from applying the proposed methodology, we use the [29,30,31] constant, which allows us to study the behavior of the scattering transformation when a set of similar inputs is introduced as input. This transformation can approximate the operation of a simple neural network architecture by allowing the study of how neural networks succeed in solving difficult problems in which multiscale feature extraction is required. At the same time, the properties of the transformation in question explain how a neural network can achieve invariance to input displacement and small input deformations, such as in cases of elastic deformation. In particular, new inputs are generated when a very small variation $p$ is added to the input $h$, so that we obtain the new input $h + p$, which, with an appropriately chosen input function $p$, is ordered differently from the original input such that [32,33]:

$$\left\|S[m](h+p)-S[m](h)\right\| \le \|p\| \tag{21}$$

Thus, it follows that the output for a new variable input does not differ from the original input by more than $\|p\|$. So, if the transformation follows the constraints of the scattering transformation:

$$\sum_{i=1}^{N}\left|\hat{\psi}_{(i,j)(\omega)}\right|^2 \le \frac{C^2}{N}, \quad \left|\hat{\varphi}_{(\omega)}\right|^2 \le C^2 \tag{22}$$

For $C \in R$:

$$\|S[m](h+p)-S[m](h)\| \le C^{m+1}\|p\| \tag{23}$$

This means that the constant *C* determines how vulnerable the transformation is to changes in the input by *p*. Therefore, as the Lipschitz constant determines the ability of the classifier to cope with new inputs, in the considered research, we propose to use it to detect how this constant evolves when searching for hyperparameters of a neural network. In particular, suppose that the input of a convolutional neural network is in the form of a vector, with $f(x_{in}, c)$ the network output for the category $c$ with the vector $x_{in}$ as input. Suppose two different input vectors $y_{in}, h_{in}$ and the corresponding outputs $f(y_{in}, c)$, $f(h_{in}, c)$ so as $y_{ik}, h_{ik}$ the $k$-th level outputs in the channel *i* for each of the two inputs. The convolutional neural network consists of convolution layers, pooling layers, and ReLU activation functions. So, for each of the three kinds of layers, we have:

1) Let layer $k$ is a convolution layer. As we express the inputs as one-dimensional vectors, the convolution with a two-dimensional kernel $\psi_{ijk}$, which connects the *i* channel of the output to the *j* channel of the input, is implemented by multiplying the input vector by a matrix $A_{ijk}$ generated by the original kernel, such that [30,34]:

$$x_{ik} = \sum_{j=1}^{N_k} A_{ijk} \cdot x_{j(k-1)} \quad i=1,2,....,M_k \tag{24}$$

where $N_k$ is the number of channels of the input and $M_k$ is the number of channels of the output of the convolutional level $k$. Thus:

$$\begin{aligned} \|y_{ik}-h_{ik}\|_2 &= \left\| \sum_{j=1}^{N_k} A_{ijk} \cdot y_{j(k-1)} - \sum_{j=1}^{N_k} A_{ijk} \cdot h_{j(k-1)} \right\|_2 = \left\| \sum_{j=1}^{N_k} A_{ijk} \cdot \left( y_{j(k-1)} - h_{j(k-1)} \right) \right\|_2 \\ &\le \sum_{j=1}^{N_k} \left\| A_{ijk} \cdot \left( y_{j(k-1)} - h_{j(k-1)} \right) \right\|_2 \le \sum_{j=1}^{N_k} \|A_{ijk}\| \cdot \left\| y_{j(k-1)} - h_{j(k-1)} \right\|_2 \\ \Rightarrow \|y_{ik}-h_{ik}\|_2 &\le \sum_{j=1}^{N_k} \|A_{ijk}\| \cdot \left\| y_{j(k-1)} - h_{j(k-1)} \right\|_2 \end{aligned} \tag{25}$$

Suppose that $k$ is a Pooling plane in which no overlapping regions exist, then:

$$\|y_{ik}-h_{ik}\|_2 \le \left\| y_{j(k-1)} - h_{j(k-1)} \right\|_2 \tag{26}$$

2) Assuming that k is ReLU, then the output vector has the form:

$$x_{ik} = \left[ x_{ik}(1) \quad x_{ik}(2) \quad .... \quad x_{ik}(m) \right]^T \tag{27}$$

The output $x_{ik}(t)$ defined as:

$$x_{ik}(t) = max\left(0, x_{i(k-1)}(t)\right) \tag{28}$$

Thus

$$\begin{aligned} \|y_{ik}-h_{ik}\|_2^2 &= \sum_{t=1}^{m} \left| max\left(0, y_{i(k-1)}(t)\right) - max\left(0, h_{i(k-1)}(t)\right) \right|^2 \\ &\le \sum_{t=1}^{m} \left| y_{j(k-1)}(t) - h_{j(k-1)}(t) \right|^2 = \left\| y_{j(k-1)} - h_{j(k-1)} \right\|_2^2 \Rightarrow \|y_{jk}-h_{jk}\|_2 \\ &\le \left\| y_{j(k-1)} - h_{j(k-1)} \right\|_2 \end{aligned} \tag{29}$$

where $|\max(0,\alpha) - \max(0,\beta)| \leq |\alpha - \beta|$.

Using the above equations, a constant $L_{ik}$ can be calculated for which it holds that:

$$\left\|y_{jk} - h_{jk}\right\|_2 \leq L_{ik} \cdot \left\|y_{10} - h_{10}\right\|_2 \tag{30}$$

We define the constant recursively as $L_{ik}$ = 1, so that for each type of level it holds:

- Convolution layer: $L_{ik} = \sum_{j=1}^{N_k} \left\|A_{ijk}\right\|_2 \cdot L_{j(k-1)}$
- Pooling layer: $L_{ik} = L_{i(k-1)}$
- ReLU function: $L_{ik} = L_{i(k-1)}$

Therefore, if the network has $p$ levels we can find the Lipschitz constant that satisfies the relation:

$$\left\|f\left(y_{in},c\right) - f\left(h_{in},c\right)\right\|_2 \leq L_{cp} \cdot \left\|y_{in} - h_{in}\right\|_2 \tag{31}$$

Having developed the method for finding a Lipschitz constant for the network, we study how it evolves when finding the appropriate hyperparameters of a neural network in solving the given problem.

AD is a technique used to compute derivatives of functions. It is commonly used in machine learning, optimization, and scientific computing. The basic idea of AD is to decompose a function into a sequence of elementary operations, such as addition, multiplication, and exponentiation, and then compute the function's derivative by applying the chain rule of calculus to each operation. This process can be done efficiently using computer algorithms without explicitly computing the function's derivative.

There are two main approaches to AD: forward mode and reverse mode. In forward mode, the derivatives of all intermediate variables are computed simultaneously as the function is evaluated. Specifically, forward accumulation computes the recursive relation [10,14]:

$$\frac{\partial w_i}{\partial x} = \frac{\partial w_i}{\partial w_{i-1}} \cdot \frac{\partial w_{i-1}}{\partial x} \quad with \quad w = y \tag{32}$$

In contrast, in reverse mode, the derivatives of the output variable are computed first and then propagated backward through the sequence of operations. Specifically, reverse accumulation computes the recursive relation:

$$\frac{\partial y}{\partial w_i} = \frac{\partial y}{\partial w_{i+1}} \cdot \frac{\partial w_{i+1}}{\partial w_i} \quad with \quad w = x \tag{33}$$

AD has several advantages over traditional methods of computing derivatives, such as finite differences and symbolic differentiation. It is more accurate and efficient, particularly for functions with a large number of variables or complex compositions of functions. It can also handle functions with discontinuities, such as piecewise-defined functions, more easily than other methods.

In this study, differential equations are solved using a neural search architecture with automatic differentiation that is trained to understand the behavior of the differential equation. The loss function for the network's training is the differential equation itself, which is then automatically differentiated to minimize. Below is a summary of the architecture at a high level:

1. The beginning and boundary conditions, as well as the differential equation to be solved, were defined.
2. A collection of input-output pairs was created from the differential equation, where the inputs represent the independent variables and the outputs represent the dependent variables.
3. A neural network was trained to forecast the values of the output given the values of the input.
4. The gradients of the loss function were computed with respect to the network parameters using automatic differentiation.
5. An optimizer was used to make network parameter updates that would reduce loss.

By minimizing the error between the predicted and actual solutions of the differential equation, the neural network can learn the system's underlying behavior and provide accurate solutions for different inputs. This approach can be particularly useful for problems where analytical solutions are not readily available or where the analytical solution is too complex to be obtained or is computationally expensive.

## 3 NUMERICAL EXAMPLE

This section presents the results of the comparative solution of the two methods presented in the previous section using the numerical example depicted in the Fig. 4.

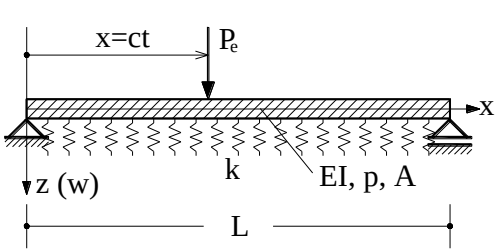


$E=29000000kN/m^2$
$I=0.00423m^4$
$A=0.69m^2$
$p=27395.51kg/m^2$
$k=1500kN/m^2$
$P_e=500kN$
$c=1.00m/sec$
$L=4.00m$

Figure 4: The values of the parameters of the studied numerical example

As far as the solution by the classical method of solving the differential equation of the problem (Eq. (1)) is concerned, it should be noted that only the first term in the equation (Eq. (16)) was used as the other terms turned out to have negligible influence. Thus, the solution of the problem by the classical method is obtained for the numerical example by the Eq. (34):

$$w(x,t)=X_1(x)\cdot\frac{2\cdot P_e}{L\cdot\left[k+\rho A\cdot\left(\omega_1^2-c^2\cdot P_1^2\right)\right]}\cdot\left[\sin(P_1\cdot c\cdot t)-\frac{P_1\cdot c}{\sqrt{\omega_1^2+(k/\rho A)}}\cdot\sin\left(\sqrt{\frac{\omega_1^2\cdot\rho A+k}{\rho A}}\cdot t\right)\right] \quad (34)$$

The solution of the eigenproblem resulted in:

$$\omega_1=1.5964rad/sec \;\rightarrow\; P_1=0.7854 \;\rightarrow\; X_1(x)=\sin(0.7854\cdot x) \quad (35)$$

As a parameter for comparing the results, the variation of the lateral deflection in the middle of the beam w(L/2) as a function of time (t) was used. This variation is depicted in Fig. 5. It should be stressed that the solution resulting from Eq. (34) is valid for the time interval from t=0 sec to t=L/c=4.00/1.00=4 sec. For t>4.00 sec the moving load is outside the beam and the vibration becomes free. For this reason, the diagram in Fig. 5 has a time range of [0.00sec, 4.00sec].

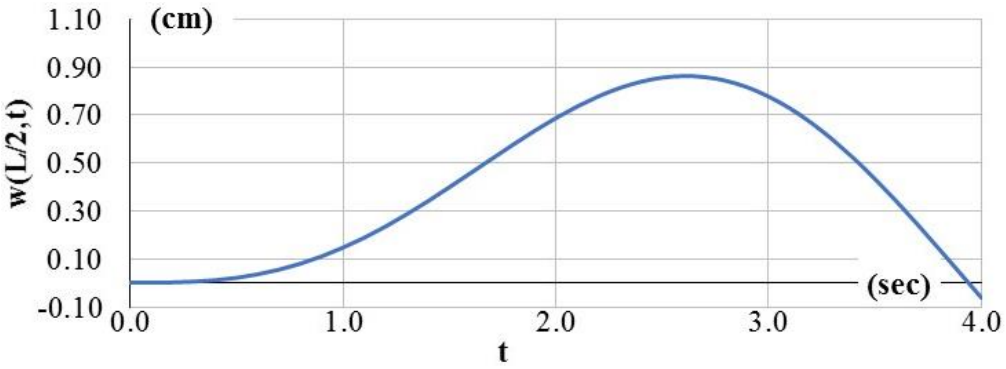


Figure 5: Time variation of the lateral deflection in the middle of the beam

Table 1 shows the results of the NASAD approach for predicting the displacement of the Euler-Bernoulli beam on an elastic foundation subjected to a moving load for 14 different time inputs. The table includes the time, the displacement calculated using the classical method and the displacement predicted by the NASAD approach.

| ID | Time (sec) | Displacement (cm) – Classical method | Displacement (cm) - Predicted |
|---|---|---|---|
| 1 | 0.3 | 0.004605411 | 0.004461994 |
| 2 | 0.63 | 0.040570695 | 0.039418149 |
| 3 | 0.65 | 0.044371532 | 0.042154818 |
| 4 | 0.66 | 0.046351195 | 0.0485189 |
| 5 | 0.67 | 0.048384207 | 0.051071586 |
| 6 | 2.15 | 0.760442817 | 0.758433355 |
| 7 | 2.44 | 0.85035003 | 0.849373095 |
| 8 | 2.6 | 0.865912826 | 0.865749313 |
| 9 | 2.86 | 0.830896232 | 0.832665859 |
| 10 | 3.27 | 0.621689162 | 0.624985816 |
| 11 | 3.46 | 0.469491684 | 0.474114383 |
| 12 | 3.6 | 0.340983069 | 0.350375689 |
| 13 | 3.77 | 0.172549928 | 0.177670435 |
| 14 | 3.95 | -0.012383849 | -0.008466525 |

Table 1: Comparative results extracted from the classical method and from the NASAD approach

The NASAD approach provides accurate displacement predictions for different time inputs, with small differences between the predicted and the classically calculated values.

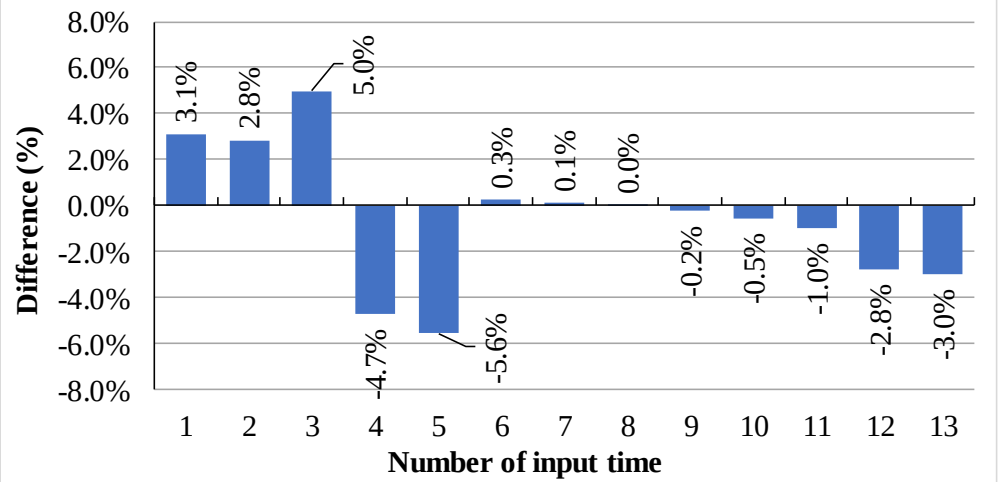


Figure 6: Differences (%) of classically calculated and predicted values (NASAD) for the input times of Table 1

Figure 6 depicts the comparison of the analytically calculated vs predicted displacements in terms of Difference (%). This comparison provides a visual representation of the accuracy of the NASAD approach in predicting the displacement of the Euler-Bernoulli beam on an elastic foundation subjected to a moving load. The predicted displacement is very close to the analytically calculated one, and the differences between the two methods are negligible, indicating the good performance of the NASAD approach. By comparing the analytically calculated and predicted displacement on the graph, the reader can understand the accuracy of the NASAD approach in predicting the displacement for different time inputs.

| | |
|---|---|
| Training Set Mean Squared Error: | 1.175e-06 |
| Test Set Mean Squared Error: | 8.422e-06 |
| Mean Absolute Error: | 0.00217 |
| Root Mean Squared Error: | 0.0029 |
| Coefficient of Determination ($R^2$): | 0.999965 |

Table 2: NASAD Performance Metrics

Table 2 provides the performance metrics for the NASAD approach used in this study to solve the differential equation. The metrics [35] include the Mean Squared Error (MSE) for the training and test sets, the Mean Absolute Error (MAE), the Root Mean Squared Error (RMSE), and the Coefficient of Determination ($R^2$). The training set MSE is 1.175e-06, indicating that the predicted values are very close to the actual values in the training set. The test set MSE is 8.422e-06, which is slightly higher than the training set MSE, but still a relatively small value, indicating the model's good performance on unseen data. The MAE is 0.00217, which measures the average magnitude of the errors in the predictions. The RMSE is 0.0029, which measures the average magnitude of the errors in the predictions, with higher weight given to larger errors. These values suggest that the NASAD approach has low errors and provides accurate predictions. Finally, the $R^2$ value is 0.999965, which measures the model's goodness of fit. This value is very close to 1, indicating that the NASAD approach provides an excellent fit to the data, with only a small amount of unexplained variance. Overall, these performance metrics suggest that the NASAD approach effectively solves the differential equation and provides accurate predictions of the displacement of the Euler-Bernoulli beam on an elastic foundation subjected to a moving load.

## 4 CONCLUSIONS

The solution of dynamic problems of structures is a significant field of research in the context of earthquake engineering. The solution of these problems by considering structures as "continuous systems" is very difficult or even impossible, except for very simple problems of structural systems consisting of a single structural member. Thus, for the easy and sufficiently accurate solution of the dynamic problems of structures, extensive use is made of discrete systems obtained by elastic and inertial discretization. The discrete systems lead to reliable results using the finite element method.

The present paper proposes a different approach to solving the dynamic problem of continuous systems by applying machine learning methods and, more specifically, the NASAD method based on artificial neural networks and automatic differentiation. The paper aims to document that these methods lead accurately to the solution of the differential equations governing the dynamic equilibrium of continuous systems. To this end, both a classical solution method (method of separation of variables and the solution of the eigenproblem) and the NASAD method have been used to study the vibration of an Euler-Bernoulli beam resting on

an elastic Winkler-type foundation subjected to a moving concentrated load. The traditional modal analysis approach is a well-documented method in mechanics for solving differential equations, but it is computationally intensive, especially for large and complex structures. On the other hand, the proposed machine learning method offers an alternative high-accurate approach that learns the solution directly from the data, which can be particularly useful for problems where obtaining analytical solutions requires time and effort. The comparative results of the two approaches showed that the considered NASAD method can lead to almost identical results with the classical solution method. In the future, the research will focus on how the proposed machine learning approach solves more complex structural systems.

Overall, this paper highlights the potential of machine learning methods in solving complex problems in engineering and mechanics and how they can complement traditional analytical methods. It's exciting to see how machine learning can advance our understanding and ability to solve complex problems in various fields.

## REFERENCES

[1] A.K. Chopra, *Dynamics of Structures, Theory and Applications to Earthquake Engineering, 5th Edition*, NJ, USA, Prentice Hall, 2016.

[2] S.S. Rao, *Vibration of Continuous Systems*, Wiley, New York, 2007.

[3] P. Bhatt, *Programming the Dynamic Analysis of Structures*, Spon Press, New York, 2002.

[4] T.J.R. Hughes, *The Finite Element Method: Linear Static and Dynamic Finite Element Analysis*, Prentice-Hall International Editions, Inc., 1987.

[5] K-J Bathe, *Finite Element procedures*, Prentice-Hall, Boston, 2006.

[6] W. Weaver, P.R. Jonhston, Structural Dynamics by Finite Elements, *1st Edition*, Prentice-Hall, Englewood Cliffs, NJ, 1987.

[7] A.J. Valsangkar, R.B. Pradhanang, Free Vibration of Partially Supported Piles, *Journal of Engineering Mechanics*, **113(8)**, 1244-1247, 1987.

[8] B.K. Lee, J.S. Jeong, L.G. Fan, T.K. Jin, Free Vibrations of Tapered Piles Embedded Partially in Winkler Type Foundations, *KSCE Journal of Civil Engineering*, **3(2)**, 195-203, 1999.

[9] H.H. Catal, Free vibration of partially supported piles with the effects of bending moment, axial and shear force, *Engineering Structures*, **24**, 1615-1622, 2002.

[10] A. G. Baydin, B. A. Pearlmutter, A. A. Radul, and J. M. Siskind, "Automatic differentiation in machine learning: a survey." arXiv, Feb. 05, 2018. doi: 10.48550/arXiv.1502.05767.

[11] J. Bolte and E. Pauwels, "A mathematical model for automatic differentiation in machine learning." arXiv, Oct. 29, 2020. doi: 10.48550/arXiv.2006.02080.

[12] T. Elsken, J. H. Metzen, and F. Hutter, "Neural Architecture Search: A Survey." arXiv, Apr. 26, 2019. doi: 10.48550/arXiv.1808.05377.

[13] G. Franchini *et al.*, "Neural architecture search via standard machine learning methodologies," *Math. Eng.*, vol. 5, no. 1, Art. no. mine-05-01-012, 2023, doi: 10.3934/mine.2023012.

[14] W. Morningstar, S. Vikram, C. Ham, A. Gallagher, and J. Dillon, "Automatic Differentiation Variational Inference with Mixtures," in Proceedings of The 24th International Conference on Artificial Intelligence and Statistics, Mar. 2021, pp. 3250–3258. Accessed: Mar. 18, 2023. [Online]. Available: https://proceedings.mlr.press/v130/morningstar21b.html

[15] M. Eisemberger, D.Z. Yankelevski, M.A. Adin, Vibration of beams fully or partially supported on elastic foundation, *Earthquake Engineering and Structural Dynamics*, **13**, 651 – 660, 1985.

[16] F.W. Williams, D. Kennedy, Exact dynamic member stiffnesses for a beam on an elastic foundation, *Earthquake Engineering and Structural Dynamics*, **15**, 133-136, 1987.

[17] Y.C. Lai, B.Y. Ting, W-S Lee, B.R. Becker, Dynamic Response of Beams on Elastic Foundation, *Journal of Structural Engineering*, **118(3)**, 853-858, 1992.

[18] C-N. Chen, Vibration of Prismatic beam on an Elastic Foundation by differential quadrature element method, *Computers and Structures*, **77(1)**, 1-9, 2000.

[19] L. Fryba, *Vibration of Solids and Structures under Moving Loads, 3rd Edition,* Thomas Telford, 1999.

[20] O.R. Jaiswal, R.N. Iyengar, Dynamic response of a beam on elastic foundation of finite depth under a moving force, *Acta Mechanica*, **96**, 67-83, 1993.

[21] W. Abbas, O.K. bakr, M.M. Nassar, M.A.M. Abdeen, M. Shabrawy, Analysis of Tapered Timoshenko and Euler-Bernoulli Beams on an Elastic Foundation with Moving Loads, *Journal of Mathematics*, Volume 2021, Article ID 6616707

[22] R.W. Clough, J. Penzien, *Dynamics of Structures, 3rd edition*, Computers and Structures, Inc., 2003.

[23] M. Rades, Steady-State Response of a finite beam on a Pasternak-Type Foundation, *International Journal of Solids and Structures*, **6**, 739 – 756, 1970.

[24] M. Feurer, K. Eggensperger, S. Falkner, M. Lindauer, and F. Hutter, "Auto-Sklearn 2.0: Hands-free AutoML via Meta-Learning," arXiv, arXiv:2007.04074, Sep. 2021. doi: 10.48550/arXiv.2007.04074.

[25] M. Lindauer and F. Hutter, "Best Practices for Scientific Research on Neural Architecture Search." arXiv, Nov. 03, 2020. doi: 10.48550/arXiv.1909.02453.

[26] J. Casebeer, N. J. Bryan, and P. Smaragdis, "Meta-AF: Meta-Learning for Adaptive Filters." arXiv, Nov. 21, 2022. doi: 10.48550/arXiv.2204.11942.

[27] J.-S. Kang, J. Kang, J.-J. Kim, K.-W. Jeon, H.-J. Chung, and B.-H. Park, "Neural Architecture Search Survey: A Computer Vision Perspective," *Sensors*, vol. 23, no. 3, Art. no. 3, Jan. 2023, doi: 10.3390/s23031713.

[28] D. T. Speckhard, K. Misiunas, S. Perel, T. Zhu, S. Carlile, and M. Slaney, "Neural architecture search for energy-efficient always-on audio machine learning," *Neural Comput. Appl.*, Feb. 2023, doi: 10.1007/s00521-023-08345-y.

[29] G. Alessandrini, M. V. de Hoop, R. Gaburro, and E. Sincich, "Lipschitz stability for a piecewise linear Schrödinger potential from local Cauchy data," *Asymptot. Anal.*, vol. 108, no. 3, pp. 115–149, Jan. 2018, doi: 10.3233/ASY-171457.

[30] K. Demertzis, L. Iliadis, and P. Kikiras, "A Lipschitz - Shapley Explainable Defense Methodology Against Adversarial Attacks," in *Artificial Intelligence Applications and Innovations. AIAI 2021 IFIP WG 12.5 International Workshops*, Cham, 2021, pp. 211–227. doi: 10.1007/978-3-030-79157-5_18.

[31] C. Freer, B. rn Kjos-Hanssen, A. Nies, and F. Stephan, "Algorithmic Aspects of Lipschitz Functions," *Computability*, vol. 3, no. 1, pp. 45–61, Jan. 2014, doi: 10.3233/COM-14025.

[32] Y. Gao and L. Jia, "Stability in measure for uncertain delay differential equations based on new Lipschitz conditions," *J. Intell. Fuzzy Syst.*, vol. 41, no. 2, pp. 2997–3009, Jan. 2021, doi: 10.3233/JIFS-210089.

[33] K. Demertzis, L. Iliadis, P. Kikiras, and E. Pimenidis, "An explainable semi-personalized federated learning model," *Integr. Comput.-Aided Eng.*, vol. Preprint, no. Preprint, pp. 1–16, Jan. 2022, doi: 10.3233/ICA-220683.

[34] Y. Wang and M. Sui, "Finite lattice approximation of infinite lattice systems with delays and non-Lipschitz nonlinearities," *Asymptot. Anal.*, vol. 106, no. 3–4, pp. 169–203, Jan. 2018, doi: 10.3233/ASY-171444.

[35] A. Botchkarev, "Performance Metrics (Error Measures) in Machine Learning Regression, Forecasting and Prognostics: Properties and Typology," *Interdiscip. J. Inf. Knowl. Manag.*, vol. 14, pp. 045–076, 2019, doi: 10.28945/4184.

COMPDYN 2023
9th ECCOMAS Thematic Conference on
Computational Methods in Structural Dynamics and Earthquake Engineering
M. Papadrakakis, M. Fragiadakis (eds.)
Athens, Greece, 12-14 June 2023

# MATRIX EQUATIONS MODELS FOR SOLVING THE DYNAMIC RESPONSE OF INELASTIC CANTILEVER STRUCTURES

**Shmerling A.**[1]

[1] Department of Civil and Environmental Engineering, Ben-Gurion University of the Negev
POB 653, Beer-Sheva, 84105, ISRAEL
e-mail: assafs@bgu.ac.il

## Abstract

*This work presents a matrix equations model approach for analyzing the dynamic response of cantilever structures. The method can be used for assessing the linear-elastic or inelastic response of buildings with a symmetric or anti-symmetric floorplan. The proposed model constitutes an alternative to finite-element analysis and a valuable tool for introducing two-dimensional and three-dimensional cantilever structures to control the theory's state-space representation and structural dynamics' equation of motion. The model regards the stiffness and mass matrices. The proposed displacement-related stiffness matrix of cantilever elements satisfies the elemental boundary conditions while deriving a symmetric stiffness matrix. The linear-elastic response analysis is performed in displacement coordinates. But, the inelastic response analysis is conducted in bending curvature coordinates to coop with smooth hysteretic models that refer to the relation between the bending moment and the bending curvature through the bending stiffness. The transformation from displacement coordinates to bending curvature coordinates is explained. In the case of buildings with an anti-symmetric floorplan, the Direct Stiffness Method (DSM) is employed to transfer the cantilever elements from their local coordinates into the global degree-of-freedom (DOF) system. The numerical accuracy of the matrix equations model is examined and showcases its reliability.*

**Keywords:** Numerical Analysis, Cantilever Structure, Structural Dynamics, Deteriorating Inelastic Structures, Nonlinear Dynamics.

## 1 INTRODUCTION

Numerical analysis is a powerful mathematical tool used to approximate and solve complex engineering problems that are difficult to solve using analytical methods. In the case of determining the dynamic response of cantilever structures, numerical analysis techniques can be used to approximate the structural behavior of the system under dynamic loading. Typically, the cantilever structure is modeled as a finite element model, dividing the structure into a finite number of interconnected more minor elements. Each element is then analyzed separately, and the results are combined to determine the overall behavior of the structure. Several numerical analysis methods can be used for determining the dynamic response of cantilever structures, including the finite element method (FEM), the boundary element method (BEM), and the spectral element method (SEM) ([1];[2]). These methods can provide accurate predictions of the structure's dynamic behavior, such as the natural frequencies, mode shapes, and dynamic response to external loads.

One of the main downsides of FEM is the approximation error, which arises due to the discretization of the problem domain into finite elements. The accuracy of the FEM solution depends on the quality of the finite element mesh used, and a poorly designed or inaccurate mesh can lead to significant errors in the computed solutions. This issue is discussed in more detail in [3] and [4]. Another downside of FEM is the computational complexity, which arises due to the solution of an extensive system of equations. The size of the system of equations overgrows as the number of elements and degrees of freedom increases, making FEM computationally expensive and time-consuming for large-scale problems. This issue is discussed in more detail in [5] and [6]. Also, FEM may not be effective for highly nonlinear problems, as it may not accurately capture the system's complex behavior. This issue is discussed in more detail in [7] and [8]. FEM also relies on modeling assumptions, which may not accurately reflect the real-world behavior of the system. This issue is discussed in more detail in [9] and [10]. Finally, FEM can be numerically unstable for specific problems, leading to unpredictable results. This issue is discussed in more detail in [11].

One of the main disadvantages of BEM is that it is limited to problems with homogeneous boundary conditions, which restricts its applicability in certain fields such as fluid-structure interaction and acoustics. In contrast, FEM can handle problems with more general boundary conditions [12]. Another challenge of BEM is its sensitivity to the choice of fundamental solution used to represent the solution of the problem. Specifically, singularities (or nearly singularities) in the solution can result in a loss of accuracy or convergence. Additionally, BEM can be computationally expensive in certain situations, such as problems with complex geometries or nonlinear materials. This results in large matrices to solve and slow convergence of the iterative solvers [13].

One potential disadvantage of SEM is its computational cost. The method requires significant computational resources to carry out simulations accurately. This is because SEM involves using high-order polynomials to represent the solution in each element, which can lead to many degrees of freedom. As a result, SEM simulations can be more computationally expensive than other numerical methods, such as finite element methods (FEM) and finite difference methods (FDM) [14]. Another potential disadvantage of the SEM is its difficulty in handling irregular geometries. The SEM is designed to work with regular geometries, such as rectangles and cubes, which can be subdivided into elements of equal size and shape. However, irregular geometries may require more complex element shapes, leading to difficulties in the SEM. Another issue is that the SEM can suffer from "spectral pollution," leading to inaccurate solutions. Spectral pollution occurs when the high-order polynomials used in the SEM fail to represent sharp

discontinuities in the solution accurately. This can result in a loss of accuracy and convergence, particularly for problems with strong gradients or shocks ([15]).

This paper goes in a different direction and presents a matrix equations model approach for analyzing the dynamic response of cantilever structures. The method can be used for assessing the linear-elastic or inelastic response of buildings with symmetric or anti-symmetric floorplan. Accordingly, it constitutes an alternative to FEM, BEM, and SEM in case they are less feasible.

## 2 ANALYTICAL METHOD

### 2.1 Differential equation

The PDE defining the dynamic stability of a uniform cantilever element is determined. Fig 1 depicts the elevation of the element. At $z$=0, the horizontal displacement and slope are zero. At $z$=$H$, the distributed shear force and bending moment are zero. Hence, the lateral force equilibrium at time $t$ at coordinate $z$ is described by:

$$\begin{aligned} &\mathrm{m(z)\ddot{u}^{w}(z,t) + f^{R}(z,t) = p(z,t)} \\ &\mathrm{s.t.} \\ &\mathrm{0 \le z \le H} \\ &\mathrm{V^{R}(H,t) = 0} \\ &\mathrm{M^{R}(H,t) = 0} \\ &\mathrm{u^{w\prime}(0,t) = 0} \\ &\mathrm{u^{w}(0,t) = 0} \end{aligned} \tag{1}$$

Where $m(z)$ is the element characterized by distributed mass per unit length, $EI(z)$ is the distributed elasticity, $p(z,t)$ is the applied lateral load, $f^R(z,t)$ is the elemental resisting force, $u^w(z,t)$ is the lateral displacement, $\ddot{u}^w(z,t)$ is the horizontal acceleration, $M^R(z,t)$ is the distributed bending moment, and $V^R(z,t)$ is the distributed shear force.

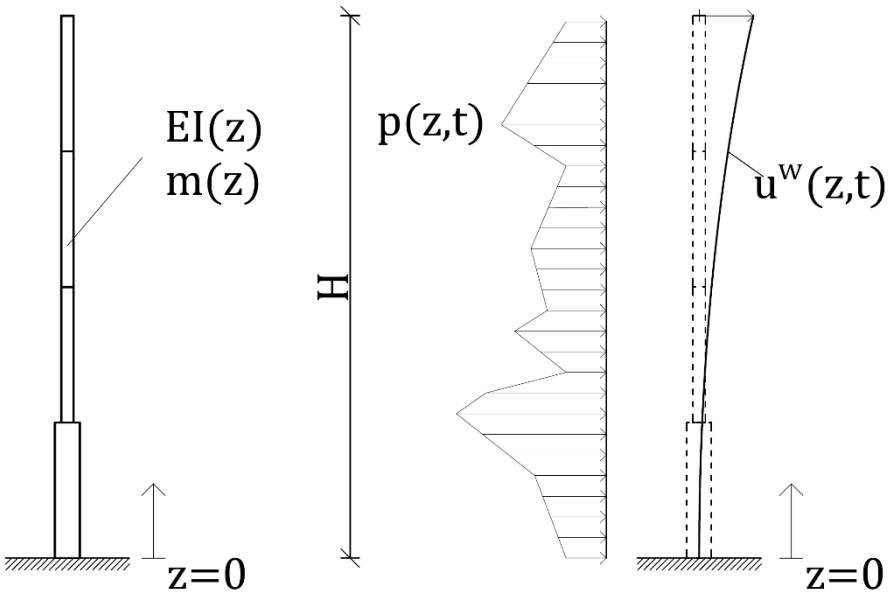


Figure 1: Cantilever element scheme

The bending moment corresponds to the distributed shear force and resisting force through the following terms:

$$V^R(z,t) = \partial M^R(z,t)/\partial z \tag{2}$$

$$f^R(z,t) = \partial^2 M^R(z,t)/\partial z^2 \tag{3}$$

Also, neglecting the shear stain in the axial stress-strain relationship provides:

$$M^R(z,t) = EI(z)u^{w\prime\prime}(z,t) \tag{4}$$

Hence, Eqs. (3) and (4) provide:

$$f^R(z,t) = \partial\big(EI(z)\varphi(z,t)\big)/\partial z^2 \tag{5}$$

Substituting Eq. (5) into Eq. (1) while using linear system modal analysis composition of the form:

$$u^w(z,t) = \sum_{v=1}^{\infty} \phi_v(z) q_v(t) \tag{6}$$

Yields the differential equation that governs the lateral motion of the cantilever element::

$$\left.\begin{array}{l} m(z)\sum_{v=1}^{\infty}\phi_v(z)\ddot{q}_v(t) + \sum_{v=1}^{\infty} F_v(z) q_v(t) = p(z,t) \\ s.t. \\ 0 \le z \le H \\ F_V(z) = \partial\big(EI(z)\phi_v''(z)\big)/\partial z^2 \\ EI(H)\phi_v{}^{(3)}(H) = 0 \\ EI(H)\phi_v{}''(H) = 0 \\ \phi_v{}'(0) = 0 \\ \phi_v(0) = 0 \end{array}\right\} \quad \forall \quad v = 1, \dots, \infty \tag{7}$$

Where $F_V(z)$ is the v$^{th}$ modal resisting spatial force function, $q_v(t)$ governs the v$^{th}$ modal system's dynamic response, and $\phi_v(z)$ is the v$^{th}$ modal spatial function.

## 2.2 Modal analysis using structural matrices

Eq. (7) is addressed and analyzed using the matrix model developed by this paper instead of assuming a general solution function. Define the relationship between $\phi_v(z)$ and $F_V(z)$ through the function $k^{-1}(z)$, which resembles the elemental flexibility distribution. That is:

$$\phi_v(z) = k^{-1}(z)\, F_v(z) \quad \forall \quad v = 1, \dots, \infty \tag{8}$$

In essence, such a function is a quad integration operator of the form:

$$k^{-1}(z) \equiv \iint \frac{1}{EI(z)} \iint dz dz dz dz \tag{9}$$

However, it should count for the boundary conditions of Eq. (7). In the case of the cantilever element, since the homogenous set of boundary condition equations relates to four different derivative orders, the conditions can all be satisfied by calculating the following integration limitations:

$$\begin{aligned}
&\int_H^z \mathrm{F_v}(z)dz = \mathrm{EI(z)}\phi_\mathrm{v}{}^{(3)}(\mathrm{z}) && \leftrightarrow \quad \mathrm{EI(H)}\phi_\mathrm{v}{}^{(3)}(\mathrm{H}) = 0\\
&\int_H^z \int_H^z \mathrm{F_v}(z)dz\,dz = \mathrm{EI(z)}\phi_\mathrm{v}{}''(\mathrm{z}) && \leftrightarrow \quad \mathrm{EI(H)}\phi_\mathrm{v}{}''(\mathrm{H}) = 0\\
&\int_0^z \frac{1}{EI(z)} \int_H^z \int_H^z \mathrm{F_V}(z)dz\,dz\,dz = \phi_\mathrm{v}{}'(\mathrm{z}) && \leftrightarrow \quad \phi_\mathrm{v}{}'(0) = 0\\
&\int_0^z \int_0^z \frac{1}{EI(z)} \int_H^z \int_H^z \mathrm{F_V}(z)dz\,dz\,dz\,dz = \phi_\mathrm{v}(\mathrm{z}) && \leftrightarrow \quad \phi_\mathrm{v}(0) = 0
\end{aligned} \tag{10}$$

That is:

$$\mathrm{k^{-1}(z)} = \int_0^\mathrm{z} \int_0^\mathrm{z} \frac{1}{\mathrm{EI}(z)} \int_\mathrm{H}^\mathrm{z} \int_\mathrm{H}^\mathrm{z} \mathrm{F_v}(z)\mathrm{d}z\,\mathrm{d}z\,\mathrm{d}z\,\mathrm{d}z \quad \forall \quad \mathrm{v} = 1,2,\dots,\infty \tag{11}$$

Numerical integration is now utilized to define the matrix representation of $k^{-1}(z)$ (i.e., the flexural matrix) while accounting for its symmetricity. The matrix corresponds to a mesh size of $\Delta z$ and is denoted as:

$$\mathbf{k}_{\Delta\mathrm{z}}{}^{-1} = \mathbf{T}_{z\in[0\to\mathrm{z}]}^{\int \mathrm{d}z}\, \mathbf{T}_{z\in[0\to\mathrm{z}]}^{\int \mathrm{d}z}\, (\mathbf{EI}_{\Delta\mathrm{z}})^{-1}\, \mathbf{T}_{z\in[\mathrm{H}\to\mathrm{z}]}^{\int \mathrm{d}z}\, \mathbf{T}_{z\in[\mathrm{H}\to\mathrm{z}]}^{\int \mathrm{d}z} \tag{12}$$

Given that the mesh size yields an $N=H/\Delta z$ grid, the matrix $\mathbf{EI}_{\Delta\mathrm{z}}$ is diagonal and defined as:

$$\mathbf{EI}_{\Delta\mathrm{z}} = \Delta\mathrm{z}\ \mathrm{diag}\{\mathrm{EI}(0) \quad \cdots \quad \mathrm{EI}(\mathrm{n}\,\Delta\mathrm{z}) \quad \cdots \quad \mathrm{EI}(\mathrm{N}\,\Delta\mathrm{z})\} \tag{13}$$

The symmetricity of $\mathbf{k}_{\Delta\mathrm{z}}{}^{-1}$ is provided by employing the Riemann Left Sum (RLS) scheme, which corresponds to the following transformation matrices:

$$\mathbf{T}_{z\in[0\to\mathrm{z}]}^{\int \mathrm{d}z} = \Delta\mathrm{z}\begin{bmatrix} 0 & 0 & 0 & \cdots & 0 & 0 & 0\\ 1 & 0 & 0 & \cdots & 0 & 0 & 0\\ 1 & 1 & 0 & \cdots & 0 & 0 & 0\\ \vdots & \vdots & \vdots & \ddots & \vdots & \vdots & \vdots\\ 1 & 1 & 1 & \cdots & 0 & 0 & 0\\ 1 & 1 & 1 & \cdots & 1 & 0 & 0\\ 1 & 1 & 1 & \cdots & 1 & 1 & 0 \end{bmatrix}_{\mathrm{N+1\times N+1}} \cong \int_0^\mathrm{z} \mathrm{d}z \tag{14}$$

$$\mathbf{T}_{z\in[\mathrm{H}\to\mathrm{z}]}^{\int \mathrm{d}z} = -\Delta\mathrm{z}\begin{bmatrix} 0 & 1 & 1 & \cdots & 1 & 1 & 1\\ 0 & 0 & 1 & \cdots & 1 & 1 & 1\\ 0 & 0 & 0 & \cdots & 1 & 1 & 1\\ \vdots & \vdots & \vdots & \ddots & \vdots & \vdots & \vdots\\ 0 & 0 & 0 & \cdots & 0 & 1 & 1\\ 0 & 0 & 0 & \cdots & 0 & 0 & 1\\ 0 & 0 & 0 & \cdots & 0 & 0 & 0 \end{bmatrix}_{\mathrm{N+1\times N+1}} \cong -\int_\mathrm{H}^\mathrm{z} \mathrm{d}z \tag{15}$$

Accordingly, the general form of the derived $\mathbf{k}_{\Delta\mathrm{z}}{}^{-1}$ is:

$$\mathbf{k}_{\Delta\mathrm{z}}{}^{-1} = \begin{bmatrix} \mathbb{Z}_{2\times 2} & \mathbf{0}_{2\times N-1} \\ \mathbf{0}_{N-1\times 2} & \boldsymbol{\mathcal{F}}_{\Delta\mathrm{z}} \end{bmatrix} \tag{16}$$

In Eq. (16), $\mathbb{Z}$ is a 2×2 diagonal matrix whose components are close to zero.

The inverse of $\mathbf{k}_{\Delta\mathrm{z}}{}^{-1}$ resembles the stiffness matrix of the cantilever element and is defined by the expression:

$$\mathbf{k}_{\Delta\mathrm{z}} = \begin{bmatrix} \boldsymbol{\Lambda} & \mathbf{0}_{2\times N-1} \\ \mathbf{0}_{N-1\times 2} & (\boldsymbol{\mathcal{F}}_{\Delta\mathrm{z}})^{-1} \end{bmatrix} \quad \leftrightarrow \quad \boldsymbol{\Lambda} = \begin{bmatrix} \Lambda_1 & 0 \\ 0 & \Lambda_2 \end{bmatrix} \equiv \begin{bmatrix} \infty & 0 \\ 0 & \infty \end{bmatrix} \tag{17}$$

So that $\boldsymbol{\Lambda}$ a 2×2 diagonal matrix whose components are of a large magnitude that simulates infinity. Also, the mass matrix of the cantilever element may be defined as:

$$\mathbf{m}_{\Delta z} = \Delta z \, \mathrm{diag}\left\{\frac{m(0)}{2} \quad m(\Delta z) \quad \cdots \quad m(n\,\Delta z) \quad \cdots \quad m\big((N-1)\,\Delta z\big) \quad \frac{m(N\,\Delta z)}{2}\right\} \tag{18}$$

Having defined the stiffness and mass matrix, the modal frequencies and modal shape vectors stem from the eigenvalue problem:

$$\det\left|\mathbf{m}_{\Delta z}{}^{-1}\mathbf{k}_{\Delta z} - \omega_{\Delta z,v}{}^{2}\mathbf{I}\right| = 0 \quad \leftrightarrow \quad \omega_{\Delta z,1} < \omega_{\Delta z,2} < \cdots \omega_{\Delta z,N+1} \tag{19}$$

$$\left(\mathbf{m}_{\Delta z}{}^{-1}\mathbf{k}_{\Delta z} - \omega_{\Delta z,v}{}^{2}\mathbf{I}\right)\boldsymbol{\phi}_{\Delta z,v} = \mathbf{0} \quad \forall \quad v = 1,2,\ldots,\infty \tag{20}$$

### 2.3 Numerical accuracy

The numerical accuracy of the matrix equations model is exemplified by referring to the modal frequencies of a cantilever element of uniform mass per unit length $m(z)=m$ and constant elasticity function $EI(z)=EI$. Using the analytical solution provided in chapter 17 in [16], we have the following exact terms for $\omega_v$ and $\phi_v(z)$:

$$\omega_v = \frac{(\varepsilon_v H)^2}{H^2}\sqrt{\frac{EI}{m}} \quad \forall \quad v = 1,2,\ldots,\infty \tag{21}$$

$$\phi_v(z) = C_v\left[\cosh(\varepsilon_v z) + \cos(\varepsilon_v z) + \frac{\cosh(\varepsilon_v H)-\cos(\varepsilon_v H)}{\sinh(\varepsilon_v H)-\sin(\varepsilon_v H)}\left(\sinh(\varepsilon_v z) - \sin(\varepsilon_v z)\right)\right] \tag{22}$$

So that $\varepsilon_v H$ stems from:

$$1 + \cos(\varepsilon_v H)\cosh(\varepsilon_v H) = 0 \quad \leftrightarrow \quad 0 < \varepsilon_1 H < \varepsilon_2 H < \cdots < \varepsilon_v H < \cdots \tag{23}$$

The examination herein observes the first six modal systems and employs eight mesh-size cases of $\Delta z$={H/8000; H/4000; $H$/2000; $H$/1000; $H$/500; $H$/200; $H$/100; $H$/50; $H$/20; $H$/10} so that the corresponding number of lateral DOFs is $N$+1={8001; 4001; 2001; 1001; 501; 201; 101; 51; 21; 11}. The results for err($\omega_{\Delta z,v}$) and err($\phi_{\Delta z,v}(H)$) versus $\Delta z/H$ are depicted in Figures 2 and 3, respectively. Figure 2 shows that for $\Delta z/H$<0.01, the relative error decreases linearly with $\Delta z/H$, while Figure 3 shows the same for $\Delta z/H$<0.002. It can also be concluded that for err( )<0.01, a mesh size of $\Delta z/H$<0.01 is recommended. Lastly, the figures exemplify that the numerical accuracy is deterred for $\Delta z/H$<0.0005

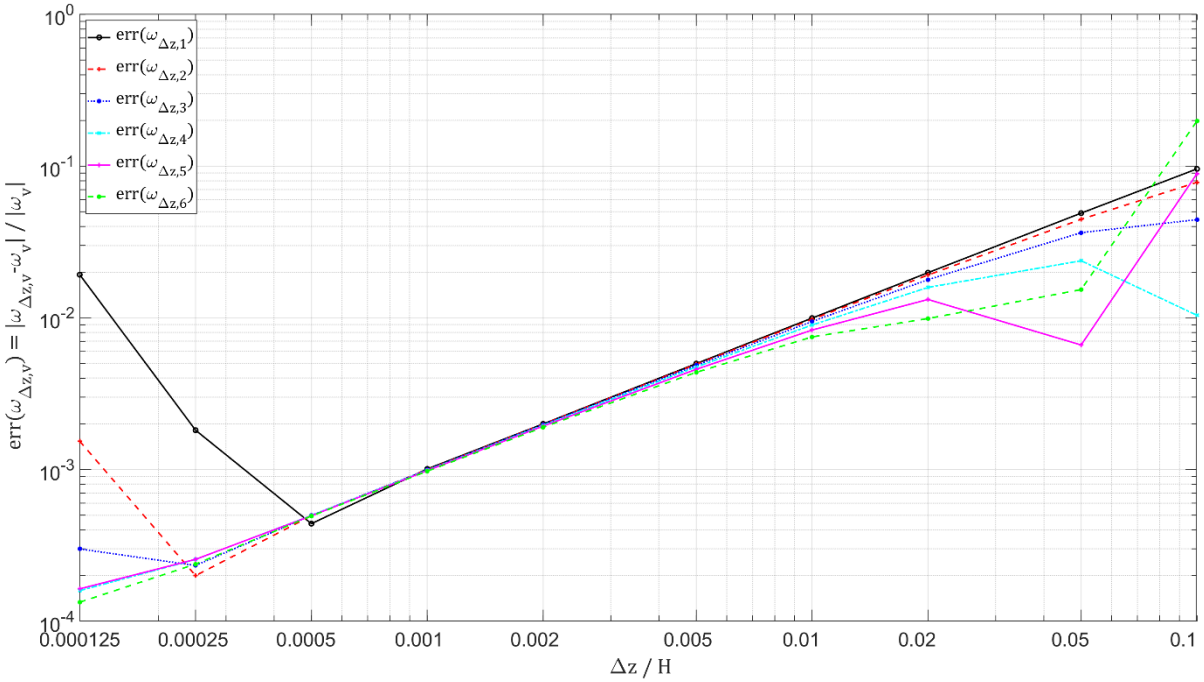


Figure 2: Modal frequency error

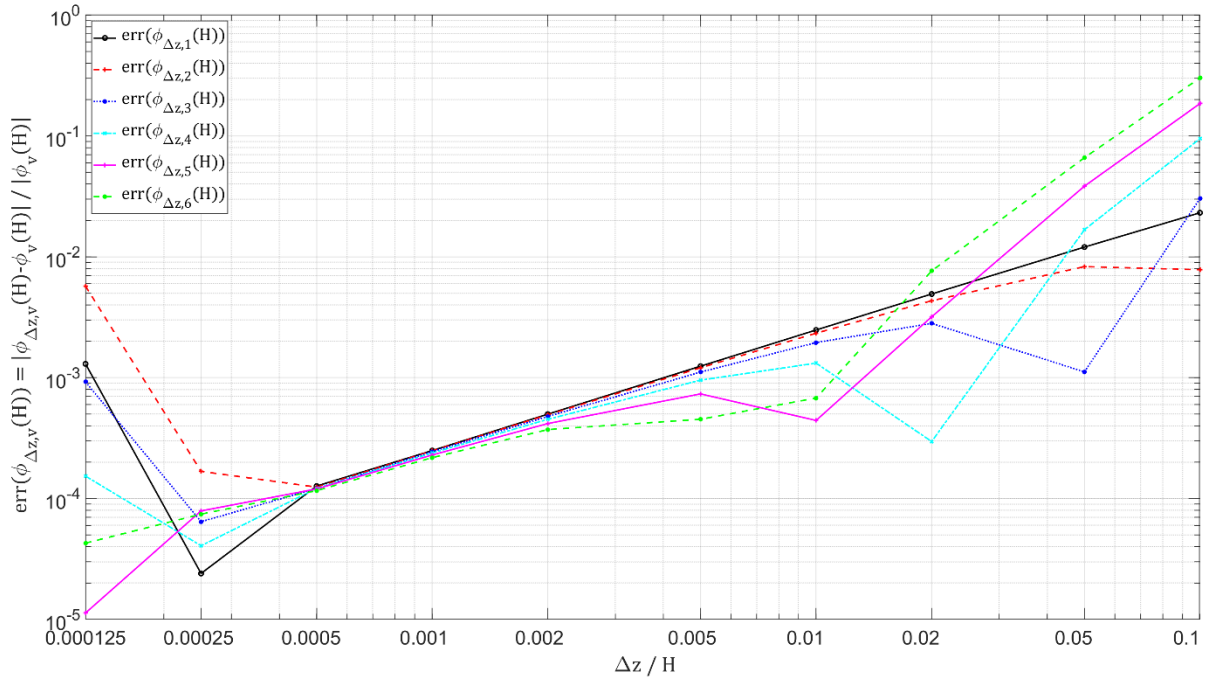


Figure 3: Modal spatial function error

## 3 INELASTIC ANALYSIS

The inelasticity of the cantilever structure can be introduced to the stiffness matrix using smooth hysteretic models, for example, the model presented by [17]. The model implementation approach is detailed in [18]. Most hysteretic models refer to the behavior of the bending moment instead of the lateral force equilibrium. Consequently, the cantilever element is analyzed in bending-curvature coordinates.

When working in bending coordinates, the stiffness matrix becomes:

$$\mathbf{k}^*_{\Delta z} = \Delta z \, \mathrm{diag}\left\{\frac{EI(0)}{2} \quad EI(\Delta z) \quad \cdots \quad EI(n\,\Delta z) \quad \cdots \quad EI\big((N-1)\,\Delta z\big) \quad \frac{EI(N\,\Delta z)}{2}\right\} \tag{24}$$

And the mass matrix becomes:

$$\mathbf{m}^*_{\Delta z} = \mathbf{T}^{\int dz}_{z\in[H\to 0]}\mathbf{T}^{\int dz}_{z\in[H\to 0]}\mathbf{m}_{\Delta z}\mathbf{T}^{\int dz}_{z\in[0\to H]}\mathbf{T}^{\int dz}_{z\in[0\to H]} \tag{25}$$

The elemental inelasticity is applied to the components of $\mathbf{k}^*_{\Delta z}$.

## 4 THREE-DIMENSIONAL STRUCTURES

The structural matrices representing the cantilever element's mass and stiffness can be used to analyze buildings with anti-symmetric floorplan (i.e., three-dimensional structures). The Direct Stiffness Method (DSM) adds elements to the global matrices, and the building is addressed as a whole. Such implementation is exemplified in [18]. The three-dimensional model refers to the Euler-Bernoulli assumption, so the ceilings are considered rigid diaphragms of zero mutuality between the horizontal *x* and *y* directions. The elements have no movement in the z-direction.

The DSM transformation matrices, from local coordinates into the building's global coordinates, are:

$$\mathbf{a}_{k,x} = \begin{bmatrix} 1 & & \rho_{xy,0} & & & -\Delta y_0 & & \\ & \ddots & & \ddots & & & \ddots & \\ & & 1 & & \rho_{xy,N} & & & -\Delta y_N \end{bmatrix}^T \tag{26}$$

$$\mathbf{a}_{k,y} = \begin{bmatrix} \rho_{yx,0} & & & 1 & & \Delta x_0 & & \\ & \ddots & & & \ddots & & \ddots & \\ & & \rho_{yx,N} & & & 1 & & \Delta x_N \end{bmatrix}^T \tag{27}$$

So that $\Delta y_n$ is the distance between the center of the cantilever element and the DOFs origin in the *y*-direction, $\Delta x_n$ is the distance between the center of the cantilever element and the DOFs origin in the $\underline{x}$-direction, $\rho_{xy,n}$ is the stiffness mutuality from the x-direction to the y-direction at the $n^{th}$ DOF level, and $\rho_{yx,n}$ is stiffness mutuality from the y-direction to the x-direction at the $n^{th}$ DOF level. Accordingly, the global stiffness matrix is defined by:

$$\mathbf{K}_{\Delta z} = \sum \mathbf{a}_{k,x}\mathbf{k}_{\Delta z,x}\mathbf{a}_{k,x} + \sum \mathbf{a}_{k,y}\mathbf{k}_{\Delta z,y}\mathbf{a}_{k,y} \tag{28}$$

Here, $\mathbf{k}_{\Delta z,x}$ denotes the elemental stiffness in the x-direction, and $\mathbf{k}_{\Delta z,y}$ represents the stiffness in the *y*-direction.

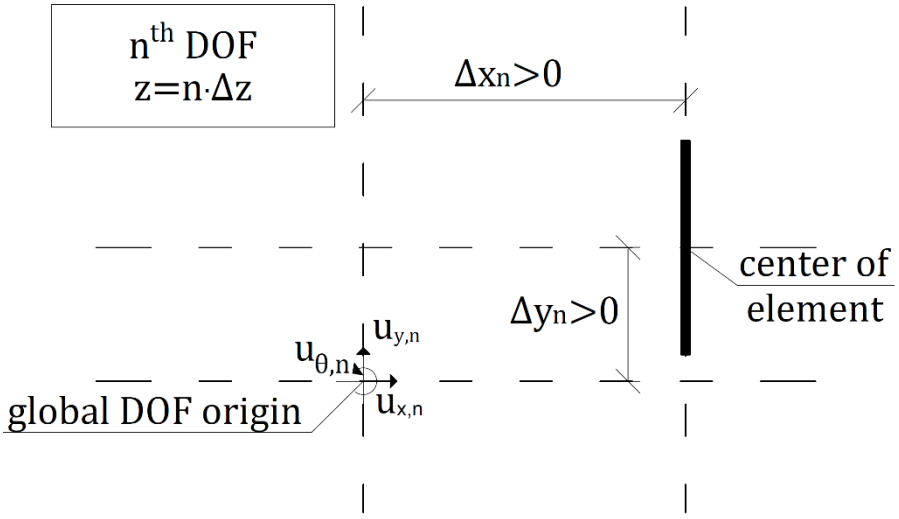


Figure 4: Distance depiction and sign

## 5 CONCLUSIONS

The paper presents an alternative approach to the dynamic analysis of inelastic structures with cantilever load-carrying elements. The partial differential equation governing the lateral motion and the boundary conditions of a cantilever element is described and added with modal superposition. Then, the relationship between the modal resisting force and the modal spatial function is defined and addressed through the flexibility function.

The flexibility function is, in essence, a quad integration operator that counts for the boundary condition. Since the homogenous set of boundary condition equations of a cantilever element refers to four different derivative orders of the lateral displacement function, numerical integration is applied to satisfy all conditions uniquely. Also, The LRS method is employed to yield a symmetric flexibility matrix. The flexibility matrix is then inverted into the stiffness matrix representing the elemental resistance to lateral dynamic load. The stiffness and mass matrices are employed in the three-dimensional analysis using the DSM and inelastic response analysis using continuous hysteretic models.

The numerical accuracy of the proposed approach is examined and presented in terms of modal frequencies and spatial functions. For $\Delta z/H<0.01$, the relative error decreases linearly with $\Delta z/H$, and the numerical accuracy is reduced for $\Delta z/H<0.0005$. These results indicate that the matrix equations model offers a solid and reliable method for analyzing buildings with cantilever elements using matrix equations.

## REFERENCES

[1] T. Chandrupatla, A. Belegundu, *Introduction to Finite Elements in Engineering.* Pearson Education, 2021.

[2] T.J.R. Hughes, *The finite element method: linear static and dynamic finite element analysis.* Courier Corporation, 2012.

[3] O.C. Zienkiewicz, R.L. Taylor, *The finite element method for solid and structural mechanics.* Elsevier, 2005.

[4] K.J. Bathe, *Finite element procedures.* Prentice-hall New Jersey, 1996.

[5] T.J.R. Hughes, *The finite element method: linear static and dynamic finite element analysis.* Courier Corporation, 2012.

[6] J.N. Reddy, *An Introduction to the Finite Element Method,* McGraw-Hill. Inc., New York, 1993.

[7] P. Wriggers, *Nonlinear finite element methods.* Springer Science & Business Media, 2008.

[8] T. Belytschko, W.K. Liu, B. Moran, K. Elkhodary, *Nonlinear finite elements for continua and structures.* John Wiley & sons, 2014.

[9] X. Chen, Y. Liu, *Finite element modeling and simulation with ANSYS Workbench.* CRC press, 2018.

[10] J.S. Przemieniecki, *Theory of matrix structural analysis.* Courier Corporation, 1985.

[11] J. Donea, A. Huerta, *Finite element methods for flow problems.* John Wiley & Sons, 2003.

[12] J.T. Katsikadelis, *The boundary element method for engineers and scientists: theory and applications.* Academic Press, 2016.

[13] F. Paris, J. Canas, *Boundary element method: fundamentals and applications.* Oxford University Press, USA, 1997.

[14] G.E. Karniadakis, G. Karniadakis, S. Sherwin, *Spectral/hp element methods for computational fluid dynamics.* Oxford University Press on Demand, 2005.

[15] A.T. Patera, A spectral element method for fluid dynamics: laminar flow in a channel expansion. *J. Comput. Phys*. **54**, 468–488, 1984.

[16] A.K. Chopra, Dynamics of Structures 5th Edition, *Prentice-hall International Series*, 2016.

[17] M. V. Sivaselvan, A. M. Reinhorn, Hysteretic models for deteriorating inelastic structures. *J. Eng. Mech*. **126**, 633–640, 2000.

[18] A. Shmerling, Matrix equations models for nonlinear dynamic analysis of two-dimensional and three-dimensional RC structures with lateral load resisting cantilever elements. *Nonlinear Dyn.* **111**, 493–528 (2023).

COMPDYN 2023
9th ECCOMAS Thematic Conference on
Computational Methods in Structural Dynamics and Earthquake Engineering
M. Papadrakakis, M. Fragiadakis (eds.)
Athens, Greece, 12-14 June 2023

# ACTIVE NOISE CONTROL OF AIR CONDITIONING SYSTEM NOISE

**Orhun Okcu[1], Kanghyun An[2], and Sang-kwon Lee[3]**

[1]Inha University
100 Inha-ro, Michuhol-gu, Incheon 22212 Korea
e-mail:orhun.okcu,@inha.edu

[2] Inha University
100 Inha-ro, Michuhol-gu, Incheon 22212 Korea
ankh4059@naver.com

[3] Inha University
100 Inha-ro, Michuhol-gu, Incheon 22212 Korea
sangkwon@inha.ac.kr

## Abstract

*A HVAC (Heat Ventilation Air Condition) system of passenger seat in autonomous bus is used for heating and cooling of the seat. The compressor of the HVAC system generates the operating noise, and the noise makes passengers annoyance. Frequency spectrum of the compressor noise composes of operating frequency and its harmonics components. Frequency band of operating frequency is low, and that of harmonic frequencies is high. Active noise control (ANC) has been used for reduction of low frequency noise while a passive method using absorption material has been used for attenuation of high frequency harmonic noise. However, some part of harmonic components at low frequency band among harmonic components is not able to reduce by using absorption materials. In this paper, a new ANC method is proposed for the reduction of noise level of low frequency harmonic components based on harmonic flited x-LMS (HFX-LMS) algorithm. The novel method is successfully applied to the noise control of compressor of HVAC system of passenger seat in autonomous bus.*

**Keywords:** FXLMS algorithm, Active Noise Control.

## 1 INTRODUCTION

FXLMS algorithm, today, is widely used in ANC systems. Since the air conditioning system generates low-frequency noise dominantly, the ANC technique can be applied to this system successfully. Therefore, much work has been done recently to suppress this type of noise that is generated by refrigerators because our system mostly resembles the air conditioning system of the refrigerator. However, there is not enough room for a large loudspeaker which can produce low-frequency noise. In this case, to increase the ANC technique's performance, the filter coefficient's low-frequency component can be filtered out [1]. Moreover, the POCS technique has been implemented to increase the performance of the ANC system [2]. In addition, the hybrid techniques, a combination of passive and active techniques, can be used to obtain a reduction in the overall frequency range by designing the air conditioning room in a way that the natural frequency of the air conditioning room is attenuated by the ANC system [3]. Generally, the compressor is dominant in the air conditioning noise. If the natural frequency of the compressor shell is relatively high, the rubber vibration absorber provides sufficient noise reduction for the compressor noise [4].

## 2 NOISE MEASUREMENTS

Most of the work that has been done before about air conditioning noise has focused on reducing the most dominant noise source, the compressor. In this study, the noise generated from the whole component of the air conditioning noise has been targeted. The sound pressure level measurement has been carried out to identify the frequency content of the noise and the directional properties of the noise. Five microphones have been replaced on the front, back, right, left, and top of the air conditioning system within a 1-meter distance. The experiment setup is shown in Figure 1.

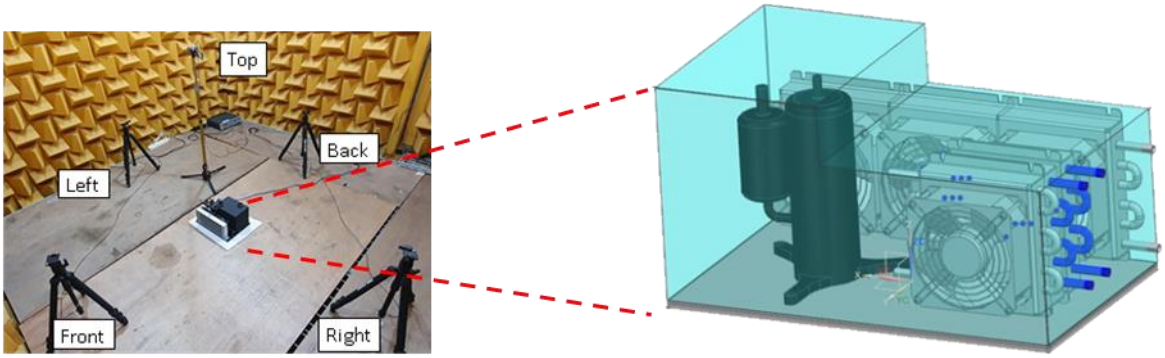


Figure 1: Sound pressure level measurement setup.

The compressor as shown in Figure 1 starts to operate a while after the air conditioning system operates. Therefore, the order of the compressor noise can be determined. The result of the measurement of vibration of the compressor shell is also supported that these frequencies are generated from the compressor. Consequently, the A-weighted sound pressure level (SPL) in the overall frequency range (0-5000 Hz) is presented in Table 1.

| Microphones | Front | Back | Right | Left | Top |
|---|---|---|---|---|---|
| Average SPL | 46.66 dB | 48.46 dB | 42.65 dB | 46.56 dB | 43.25 dB |

Table 1: A-weighted sound pressure level of all microphones.

The SPL of the front microphone is the greatest among all microphones because the front microphone picks up both fan and compressor noise.

## 3 ACTIVE NOISE CONNTROL

The target of the LMS algorithm is to compute optimum filter coefficients that minimize the mean square error. Thus, the iterative steepest descent method is used to determine these filter coefficients. Each iteration is carried out in the direction of the gradient of the error surface [5].

$$W_{n+1} = W_n + \mu(-\nabla_n) \tag{1}$$

The error signal can be expressed as

$$e(n) = d(n) - x(n)W_n \tag{2}$$

Consequently, the gradient of squared error becomes

$$\nabla e^2(n) = -2e(n)x(n) \tag{3}$$

If Equation 4 is substituted in Equation 2, the final LMS algorithm becomes as follows

$$W_{n+1} = W_n + \mu e(n)x(n) \tag{4}$$

where $\mu$ is a convergence factor (step size) that controls stability. To avoid divergence which occurs from insufficient spectral excitation, the leaking mechanism is used during the weight update calculation. The leaky LMS algorithm can be written as

$$W(n+1) = \nu W(n) + \mu x(n)e(n) \tag{5}$$

where $\nu$ is the leakage factor with $0 < \nu \leq 1$.

There is a trade-off between robustness and the loss of performance while adjusting the leakage factor [5,6].

There are many electronic components such as microphones, filters, and amplifiers between the error microphone and the loudspeaker. This signal path is called the secondary path. Since these components degrade the performance of the ANC system, compensation of the secondary effect is proposed [3]. The system performance can be increased by filtering the reference signal with an identical secondary path filter. Consequently, the widely used FXLMS algorithm is invented. The error signal can be expressed as follows.

$$\begin{aligned} e(n) &= d(n) - \hat{y}(n) \\ &= d(n) - s(n) * y(n) \\ &= d(n) - s(n) * y(n)[w^T(n)x(n)] \end{aligned} \tag{6}$$

where $s(n)$ is the impulse response of secondary path, $*$ denotes linear convolution. The gradient of squared error can be rewritten as

$$\nabla e(n) = -2\hat{x}(n)e(n). \tag{7}$$

Finally, the optimum filter weights are computed by the FXLMS algorithm as follows.

$$W(n+1) = W(n) + \mu\hat{x}(n)e(n) \tag{8}$$

Since $S(z)$ is unknown, it can be estimated by an additional filter that is obtained by the separate LMS algorithm. The block diagram of the FXLMS algorithm is shown in Figure 2.

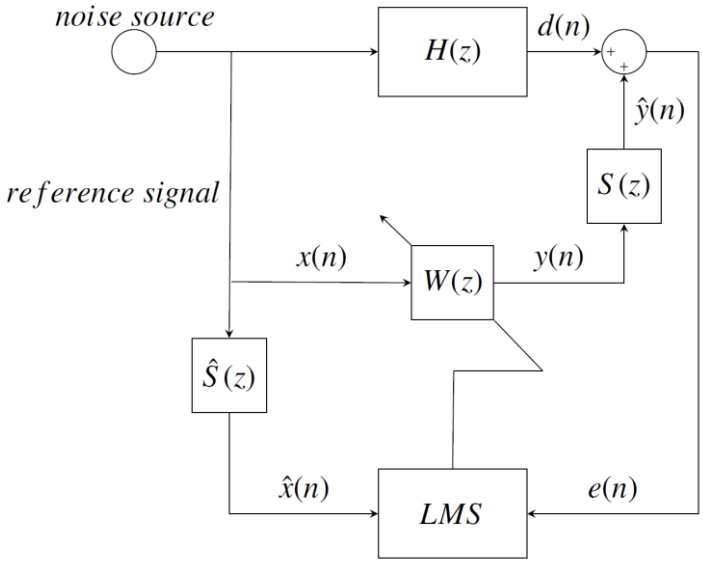


Figure 2: Block diagram of ANC system using the FXLMS algorithm.

## 4 APPLICATION OF ACTIVE NOISE CONTROLING

The compressor noise is the dominant noise source in the low-frequency region. Therefore, low-frequency drivers and data captured from the accelerometer that is stuck on the compressor shell have used this system. In addition, since the drivers are not directional, a far-field application is suitable for this application. The 44, 51, and 88 Hz which are the order of the compressor noise were controlled by the reference signal from the accelerometer stuck on the compressor shell. Noise at 132 Hz was reduced by using a sine wave generator as a reference signal. Noise reduction ranging from 12 dB to 27 dB has been accomplished for these frequencies at both error microphones. The frequency responses of both error microphones are shown in Figure 6.

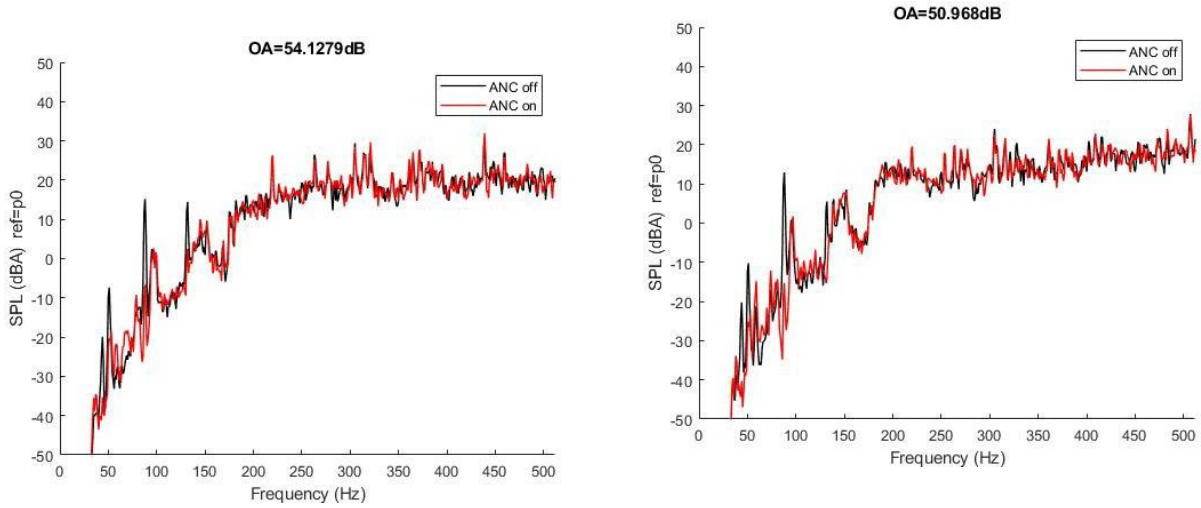


(a) Frequency response of front microphone microphone

(b) Frequency response of right

Figure 6: Frequency response of error microphones

## 5 FINAL COMMENTS AND CONCLUSIONS

In this study, the noise characteristic of the air conditioning system has been investigated via sound pressure level and intensity measurements. The FXLMS algorithm has been implemented in the ANC system to attenuate the noise. In the ANC application, the low-frequency noises that are the order of the compressor noise have been controlled by low-frequency drivers. The orders of the compressor noise have been decreased by 12 to 27 dB.

## ACKNOWLEDGEMENTS

This work was supported by the grant funded by the Korea evaluation institute of industrial technology (KEIT)(No. 20018706). This work was supported by the National Research Foundation of Korea (NRF) grant funded by the Korea government (MSIT) (No. 2022R1F1A1062889).

## REFERENCES

1. JM Ku, WB Jeong, and C Hong. Active control of compressor noise in the machinery room of refrigerators. Noise Control Engineering Journal, 67(5):350–362, 2019.

2. Jeong-Mo Ku, Weui-Bong Jeong, and Chinsuk Hong. Controller design for active noise controlof compressor by using the time window pocs technique. Journal of Mechanical Science and Technology, 34(7):2693–2700, 2020.

3. DG Smith, MF Arnold, EW Ziegler, Kh Eghtesadi, and M Brown. A systems approach to
4. appliance compressor quieting using active noise control techniques. 1992.

5. Wongul Hwang, Ilkwon Oh, Byounggu Kim, Sungwoo Park, and Kio Ryu. A study on noise
6. radiation from compressor shell. 2006.

7. Sen M Kuo and Dennis R Morgan. Active noise control systems, volume 4. Wiley, New York, 1996.

8. Sang-Kwon Lee, Seungmin Lee, Jiseon Back and Taejin Shin, A New Method for Active Cancellation of Engine Order Noise in a Passenger Car, Appl. Sci. 2018, 8(8), 1394; https://doi.org/10.3390/app8081394

COMPDYN 2023
9th ECCOMAS Thematic Conference on
Computational Methods in Structural Dynamics and Earthquake Engineering
M. Papadrakakis, M. Fragiadakis (eds.)
Athens, Greece, 12-14 June 2023

# EFFECT OF DEEP FOUNDATION ELEMENTS ON TRANSFER MOBILITIES FOR GROUND-BORNE VIBRATIONS IN URBAN RAILWAY TUNNELS

**Theodora Makrypidi[1], Charisis Chatzigogos[1], Stefania Gobbi[1], and Pierre-Alain Nazé[1]**

[1] Géodynamique & Structure
106 Avenue Marx Dormoy, 92120 Montrouge, France
e-mails : {theodora.makrypidi, charisis.chatzigogos, stefania.gobbi, pierre-alain.naze}@geodyna-mique.com

## Abstract

*The continuous development of underground tunnel networks in large urban agglomerations requires for a systematic study of ground-borne vibrations induced by the construction and/or the operation of such tunnels for estimating their impact on population and the built environment. Existing deep foundations may be damaged by nearby tunneling activities or function as wave guides that could amplify the tunneling-induced ground-borne vibration that reaches ground surface. In this context, this paper presents the results of a parametric study aiming at quantifying the effects of the presence of deep foundation elements on the calculation of transfer mobilities in ground-borne vibration assessment studies of metro railway tunnels. The transfer mobilities are calculated using a FEM-BEM model incorporating the tunnel, the surrounding soil and the eventual presence of deep foundation elements. The present work is performed as a part of a wider parametric study that will study several aspects of the problem, such as: the rigidity contrasts in the soil layers down to the tunnel depth, the relative location of foundation elements with respect to tunnel axis, the distance between the pile toe and the tunnel lining, the effect of pile group, the type of vibratory source (train passage in tunnel operation or TBM advancement in tunnel construction). This study: a) allows identifying the configurations that lead to the most pronounced vibration amplifications and may thus be harmful for the structural integrity of the piles and b) leads to the definition of a set of dimensionless factors that can be used to "correct" the free-field transfer mobility to take into account the presence of deep foundation elements.*

**Keywords:** deep foundations, ground-borne vibration, transfer mobility, FEM-BEM modeling, urban tunneling

## 1 INTRODUCTION

The continuous development of underground tunnel networks in large urban agglomerations requires for a systematic study of ground-borne vibrations induced by the construction and/or operation of such tunnels to estimate their impact on population and the built environment. The impact that these vibrations can create is multiple and one can name: a) the risk of structural damage to foundation elements and buildings, b) the annoyance to occupants because of tactile perception of ground-borne vibration (typically, in the frequency range from 1Hz to 80Hz), c) the annoyance because of ground-borne noise (in the frequencies from 16Hz to 250Hz) and d) the disturbance on equipment and tasks that are very sensitive to vibration and/or noise (*e.g.* concert halls, recording studios, research laboratories, hospitals *etc*.)

The objectives of vibration studies in a tunneling project are thus three-fold:

a) to define the acceptable vibration and ground-borne noise limits for the structures encountered along the tunnel alignment,

b) for the phase of construction, to ensure that the tunnel excavation techniques will produce vibration levels that respect the adopted limits and most importantly that they will not induce structural damage to nearby foundations and structures,

c) for the phase of operation, to propose a design of the track system in the tunnel that will provide the necessary attenuation (insertion loss function) for keeping vibration and ground-borne noise at acceptable levels all along the tunnel length while respecting the maximum vehicle speeds.

In this context, the presence of existing deep foundations at a small distance from the tunnel requires special attention. Such elements may be damaged by nearby tunneling activities or function as wave guides that could amplify the tunneling-induced ground-borne vibration that reaches ground surface.

This paper presents the calculation methodology and some preliminary results of a parametric study aiming at quantifying the effects of the presence of deep foundation elements on the calculation of transfer mobilities in ground-borne vibration assessment studies of metro railway tunnels. The transfer mobilities are calculated using a FEM-BEM model incorporating the tunnel, the surrounding soil and the eventual presence of deep foundation elements.

Several aspects of the problem will be considered in the wide parametric study, such as: the rigidity contrasts in the soil layers down to the tunnel depth, the relative location of foundation elements with respect to tunnel axis, the distance between the pile toe and the tunnel lining, the effect of pile group, the type of vibratory source (train passage in tunnel operation or TBM advancement in tunnel construction). The study: a) allows identifying the configurations that lead to the most pronounced vibration amplifications and may thus be harmful for the structural integrity of the piles and b) leads to the definition of a set of dimensionless factors that can be used to "correct" the free-field transfer mobility to take into account the presence of deep foundation elements.

## 2 GENERAL METHODOLOGY FOR GROUND-BORNE VIBRATION

The general methodology for the estimation of ground-borne vibration and noise levels from the operation of urban railway tunnels follows the principles set out in norm ISO14837-1 [3]. According to this methodology, it can be admitted that the generation of ground-borne vibration can be decomposed into three distinct and interdependent phases: emission, transmission and immission (*cf.* Figure 1).

Each of these three phases can be modeled with a separate and dedicated model and the final result can be obtained as the superposition of these three models.

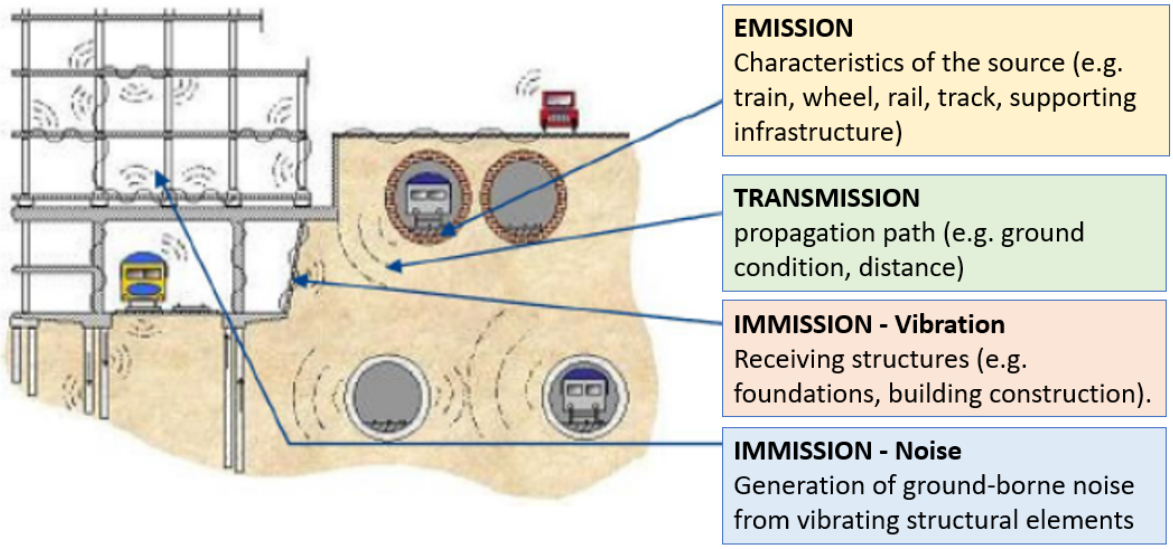


Figure 1: General method for assessment of ground-borne vibration

- *Emission phase* concerns the simulation of the excitation force, which is the source of ground-borne vibration. For the operation of railway tunnels, the vibratory source is the force regime that is developed along the tracks during the passage of the vehicles. In the case of tunnel construction, the vibratory source is the force regime that is exerted by the tunnel boring machine at the tunnel face during excavation.
- *Transmission phase* concerns the simulation of the dynamic interaction between the tunnel and the surrounding soil together with the propagation of vibratory waves within the soil domain: these waves emanate from the vibratory source and reach an observation point which can be within the soil or on the soil surface or on a foundation element.
- *Immission phase* concerns the simulation and transmission of vibrations between a point in the soil close to a structure and a point which is located on a floor at the interior of the structure. Immission phase also includes the simulation of ground-borne noise within a structure: this noise results from the vibration of structural elements, especially slabs.

In the following, we will only focus on ground-borne vibration, which will be studied in the frequency range [1Hz, 80Hz]. The generic equation for obtaining the vibration levels $L_V$ that result from the passage of a vehicle within a railway tunnel in a given slab at the interior of a critical structure is written as follows:

$$L_V = LF + C_{eq} + C_{crv} + TM + C_{SSI} + C_{fl} + C_{str} \quad (1)$$

All the quantities that appear in eq. (1) are expressed in decibels [dB], *i.e.*, via the logarithm of the physical quantity of interest divided by a reference quantity. Because of this (the use of logarithms transforms the product of several terms to a sum), the vibration level $L_V$ is obtained as the sum of several factors that pertain to the three aforementioned phases (emission, transmission, immission). Additionally, all of these quantities are defined as functions of frequency and are typically provided as spectra defined in one-third octave bands that go up to 80Hz for estimating vibration levels and up to 250Hz for estimating ground-borne noise.

The quantities that appear in equation (1) are defined as follows:

- $L_V$: velocity developed at a slab of interest within the studied structure [dB ref. $5\times10^{-8}$m/s]

- $LF$: force spectrum [dB ref. 1N] describing the excitation force at the tunnel slab for the passage of a vehicle at a given speed. This quantity depends on the design of vibration attenuation systems that can be introduced in the tracks. Quantity $LF$ can be either defined as a force spectrum or as force density spectrum: in the latter case, it will be denoted as $LF_d$ and will be defined in units [dB ref. 1N/m$^{0.5}$].
- $C_{eq}$: factor describing the possible amplification in the excitation force because of the presence of track equipment such as crossovers, junctions, switches *etc*. This factor is dimensionless [dB ref. -].
- $C_{crv}$ : factor describing the additional amplification in the excitation force because of the curvature of the track. This factor is typically taken into account when the curvature radius of the track is smaller than 400m. This factor is dimensionless [dB ref. -].
- $TM$: transfer mobility between the tunnel tracks and a specific point in the free-field close to the foundation of a structure of interest. If the excitation is defined via a force spectrum $LF$, the corresponding transfer mobility $TM$ is defined in units [dB ref. 5×10-8m/s/N]. If the excitation is expressed via a force density spectrum $LF_d$, we then need to define a linear transfer mobility $TM_L$ in units [dB ref. 5×10-8m/s/(N/m$^{0.5}$)] so that the addition of $LF$ and $TM$ (respectively $LF_d$ and $TM_L$) will provide the quantity $L_V$ in units of velocity.
- $C_{SSI}$: this is a dimensionless factor [dB ref. -] which expresses the difference of vibration levels between the point in the ground and a characteristic point in the foundation of the structure. This factor thus quantifies the effect of Soil-Structure Interaction (SSI) in the vibration transmission within the structure.
- $C_{fl}$: this is a dimensionless factor [dB ref. -] which expresses the attenuation as the vibration propagates through the higher floors of a building.
- $C_{str}$: finally, this is a dimensionless factor [dB ref. -] that expresses the amplification in vibration because of the dynamic response of the impacted structural elements, in particular horizontal slabs.

With the above definitions at hand, it follows that the emission phase is described by quantities $LF$, $C_{eq}$ and $C_{crv}$. The transmission phase is described by the notion of transfer mobility $TM$ (or $TM_L$). Finally, the immission phase is described by factors $C_{SSI}$, $C_{fl}$ and $C_{str}$.

## 3 EFFECT OF DEEP FOUNDATION ELEMENTS

Among the definitions provided above, our interest will be focused on terms $TM$ and $C_{SSI}$. We will search to quantify factor $C_{SSI}$ for the case of an isolated pile. A similar study has been presented very recently in [1] using an iterative PiP-BEM approach. The analyses in [1] highlighted the counteracting mechanisms that can affect the vibratory response at the pile head. On one hand, since the pile is stiffer it tends to constrain the motion of the surrounding soil and thus to reduce the pile head response with respect to the free-field response. On the other hand, the pile may act as a wave guide, providing a more efficient transmission path than the soil for the waves propagating from the tunnel to ground surface and this tends to increase the response.

It has been noted in [1] that the wave guide mechanism is mainly limited for the cases where the pile tip is very close to the tunnel while for the majority of cases, the prevalent mechanism is the one in which the pile constrains soil motion.

The analyses presented in [1] have considered a homogeneous soil profile and a vibratory source corresponding to a realistic vehicle that moves along the tunnel. In the present work, we

focus on layered soil profiles with different rigidity contrasts. The analyses are performed with a FEM-BEM approach using software SASSI2015 [5]. The tunnel and the pile are modeled with finite elements. The stratified soil domain is modeled with a special BEM formulation. The vibratory source will be a concentrated unitary harmonic vertical force acting at the tunnel slab (this source corresponds to the definition of transfer mobility $TM$ which should then be added logarithmically to a given force spectrum $LF$ for obtaining the sought vibration levels). The transfer mobilities are calculated in the free field ($TM_{ff}$) and at the pile head ($TM_{ph}$) and factor $C_{SSI}$ is obtained as the difference of these two quantities:

$$C_{SSI} = TM_{ph} - TM_{ff} \tag{2}$$

## 4 PARAMETRIC STUDY

### 4.1 Description of studied cases

A comprehensive parametric study of a stratified soil profile with or without the presence of piles, simple enough to facilitate extrapolation of conclusions, has been held in order to identify the configurations that lead to the most pronounced vibration amplifications and to define a dimensionless factor that can be used to "correct" the free-field transfer mobility to take into account the presence of deep foundation elements.

The base configuration is composed of a stratified soil profile where the tunnel is located in a rather soft layer at the depth of 35m below surface, surmounted by a stiff layer so that the "screen effect" of the wave propagation occurs (*cf.* Figure 2). The considered model integrates the structural elements of the tunnel, such as tunnel lining segments and its invert, but not the buildings located in the vicinity. Thus, the transfer mobility can be calculated at a "free field" ground point located at different depths into the ground.

This configuration is parametrized on the basis of two aspects: i) consideration of embedded piles founded at a depth of 15m and ii) rigidity contrast between soil layers. The total number of examined configurations is 6.

The vibratory source is introduced as a concentrated unitary harmonic vertical force acting at the tunnel slab. For convenience purposes and as tunnel structure presents two symmetry planes, calculations are performed with a quarter of model.

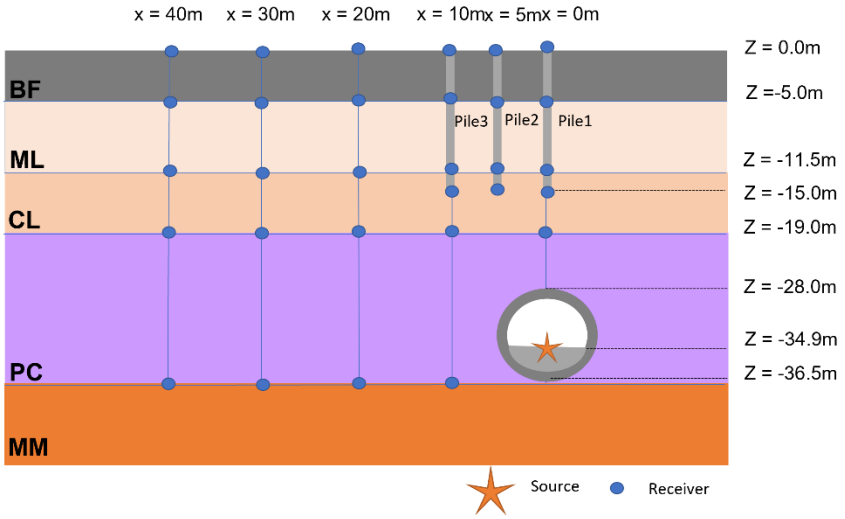


Figure 2 - Base configuration of the parametric study

### 4.2 Geometric and mechanical parameters

In the current study, the parameters used to characterize the tunnel and the pile are fixed at typical values, with the focus being on how the wave propagation and thus the vibration depends on the properties and the contrast of the layered soil profile.

The geometrical and mechanical characteristics of the tunnel lining and invert taken into account in the numerical simulations undertaken for the vibratory studies are summarized in Table 1. This is broadly representative of a modern underground railway tunnel.

| Component | Symbol | Value |
|---|---|---|
| Inner diameter of the tunnel | $D_{tin}$ | 8.50m |
| Thickness of the tunnel | $e_t$ | 0.40m |
| Height of the tunnel's invert | $h_{inv}$ | 1.60m |
| Tunnel Young's modulus | $E_t$ | 35.2GPa |
| Tunnel Poisson's ratio | $\nu_t$ | 0.20 |
| Tunnel mass density | $\rho_t$ | 2500kg/m$^3$ |
| Invert Young's modulus | $E_i$ | 25GPa |
| Invert Poisson's ratio | $\nu_i$ | 0.20 |
| Invert mass density | $\rho_i$ | 2200kg/m$^3$ |

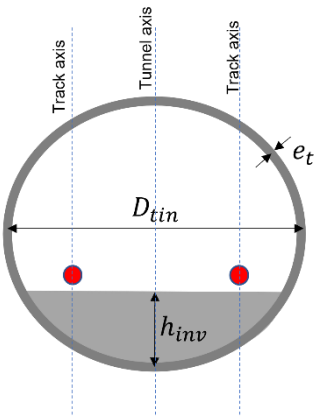


Table 1 : Tunnel's geometric and mechanical input parameters

The damping loss factor of the tunnel structure and the refill concrete is taken equal to $\eta_t$=1%. This parameter is used in the vibration analyses but its identification (by measurement or experimental test) remains difficult. However, the variation of the value of this parameter according to the classes of concrete can be considered negligible.

The pile is assumed to be made of concrete, with diameter fixed at $d_p$=1.2m, Young's modulus $E_p$=30GPa, Poisson's ratio $\nu_p$=0.2 and density $\rho_p$=2500kg/m$^3$. These parameters are representative of typical piles, stiff enough in order to reflect their impact on the vibration response. Material damping is governed by a hysteretic loss factor $\eta_p$=1%.

The mechanical characteristics of the geological layers used to model the propagation of vibration waves through the soil to the surface are the shear wave velocity $V_S$, the compression wave velocity $V_P$, and the density $\rho_s$ of the different soil layers. The material damping selected for the soil is on the order of 1-2%, due to the small distortions that are similar to the studied phenomena. Table 2 summarizes the mechanical characteristics of the geological layers considered for the base configuration.

| Soil | Thickness [m] | $V_S$ [m/s] | $V_P$ [m/s] | $\rho_s$ [kg/m$^3$] |
|---|---|---|---|---|
| Backfill (BF) | 5.00 | 400 | 1250 | 1900 |
| Marly Limestone (ML) | 6.50 | 450 | 1550 | 2000 |
| Coarse Limestone (CL) | 7.50 | 600 | 1750 | 2250 |
| Plastic Clay (PC) | 17.50 | 250 | 1400 | 1900 |
| Bedrock Marl (MM) | - | 1050 | 2300 | 2200 |

Table 2 : Soil parameters for base configuration

In the parametric study, soil variables are parametrized on the basis of the shear wave velocity $V_S$ in order to create a stiffer as well as a softer soil profile than this considered for the base configuration. Table 3 and Table 4 present the soil parameters for the two additional configurations considered in this study.

| Soil | Thickness [m] | $V_S$ [m/s] | $V_P$ [m/s] | $\rho_s$ [kg/m$^3$] |
|---|---|---|---|---|
| Backfill (BF) | 5.0 | 400 | 1230 | 1900 |
| Marly Limestone (ML) | 6.5 | 450 | 1535 | 2000 |
| Coarse Limestone (CL) | 25 | 600 | 1760 | 2250 |
| Bedrock Marl (MM) | - | 1050 | 2310 | 2200 |

Table 3 : Soil parameters for “soft” soil profile

| Soil | Thickness [m] | $V_S$ [m/s] | $V_P$ [m/s] | $\rho_s$ [kg/m$^3$] |
|---|---|---|---|---|
| Backfill (BF) | 5.0 | 200 | 735 | 1900 |
| Silt Clay (SC) | 6.5 | 225 | 945 | 2000 |
| Plastic Clay (PC) | 25 | 250 | 1420 | 1900 |
| Bedrock Marl (MM) | - | 1050 | 2310 | 2200 |

Table 4 : Soil parameters for “stiff” soil profile

The variation of shear wave velocity profiles for the three considered configurations is presented in Figure 3.

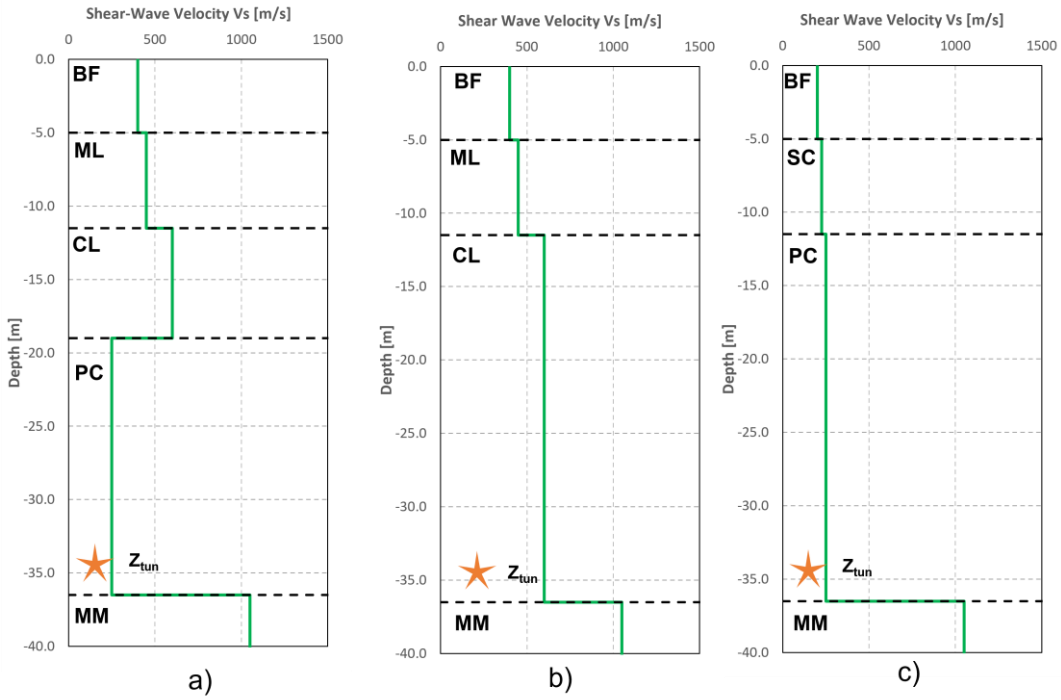


Figure 3 : Variation of shear wave velocity profiles for a) Base configuration, b) Stiff soil profile and c) Soft soil profile

### 4.3 Solution strategy

The analyses are performed with a 3D FEM-BEM coupling approach using software SASSI2015 [5]. SASSI2015 is a code specially dedicated to dynamic soil-structure interaction problems.

Soil is represented as an idealized horizontal stratigraphy, consisting of infinite viscoelastic layers. A variant of the boundary element method, called "Thin Layer Method" (TLM) is implemented to model the soil domain. Each layer is represented by its thickness, mass density, elastic parameters (propagation velocities $V_P$ and $V_S$) and material damping characteristics

(damping ratios $\beta_P$ and $\beta_S$). The modeling of radiation damping is integrated into the TLM formalism by ensuring that the Sommerfeld radiation condition is respected at infinity.

The finite element formulation (FEM) is adopted for modelling the structural elements (tunnel, invert, pile foundation). The finite element model is connected with the soil model via "interaction" nodes, which provide the coupling between the FEM (structural) model and the soil stratigraphy.

The mesh used for the FEM and BEM models must be compatible with the range of frequencies sought in the analysis and the following criterion is adopted:

$$e \leq \frac{V_S}{5 f_{\max}}$$

Where:

- $e$ : maximum layer thickness or mesh size,
- $V_S$ : shear wave propagation velocity in a given layer,
- $f_{\max}$ : the highest frequency used in the analysis (set equal to 80Hz for the present study).

In the models established for the transfer mobility calculations, the concrete structures of the tunnel and the invert are modeled using surface and volume finite elements. Referring to Figure 4 ($X$: transverse axis of the tunnel, $Y$: longitudinal axis of the tunnel, $Z$: vertical axis; the origin is placed at the center of the invert), the tunnel structure has two planes of symmetry ($XY$ and $YZ$ planes).

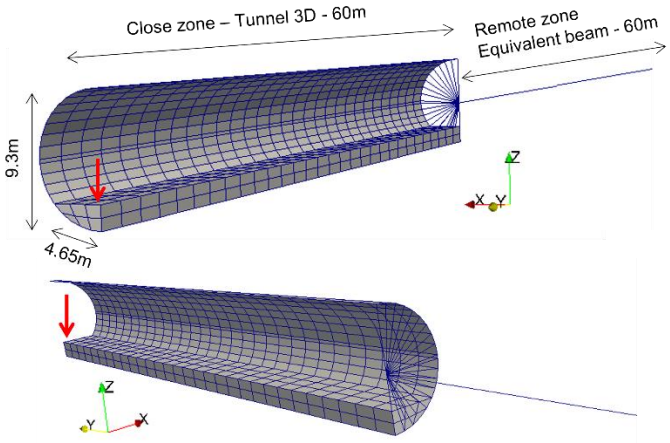


Figure 4 : Typical mesh of the tunnel and the invert for the calculations

For the zone close to the excitation source (unitary harmonic vertical force) the tunnel is represented by a detailed 3D model, 60m long. Beyond this close zone, the tunnel is modeled by an equivalent beam of 60m length with the mass and stiffness characteristics of the tunnel section (lining segments + invert). Close and remote zones are rigidly connected with very stiff weightless beams (nodes belonging to the tunnel with the extreme node of the equivalent beam). Figure 4 shows a schematic view of the mesh developed for the tunnel and invert.

It is noted that Young's modulus for the equivalent beam is the one used for the tunnel. The geometrical characteristics of the equivalent beam are calculated as follows:

$$A = \frac{E_t A_t + E_i A_i}{E}$$

$$I_x = \frac{E_t I_{xt} + E_i I_{xi}}{E};\ I_z = \frac{E_t I_{zt} + E_i I_{zi}}{E};\ I_y = I_x + I_z$$

Where:

- $E, A, I_x, I_y, I_z$ : Young's modulus, area, moment of area of the equivalent beam
- $E_t, A_t, I_{xt}, I_{yt}, I_{zt}$ : Young's modulus, area, moment of area of the tunnel
- $E_i, A_i, I_{xi}, I_{yi}, I_{zi}$ : Young's modulus, area, moment of area of the invert

The piles are modelled with Timoshenko beam elements (bending + shear). On the symmetry and anti-symmetry planes, the pile geometric characteristics are divided by 2. For the central pile (located exactly above the tunnel axis), the geometric characteristics are divided by 4. The nodes of each pile element are situated at the same depths as the nodes of the foundation soil elements

The vibratory source is introduced as a concentrated harmonic vertical force equal to one quarter of unity, of frequency $f = \omega/2\pi$ applied to the middle of the invert (point modeling the rail location).

It is noteworthy that a pile located directly above the tunnel (a centered pile) will only produce a vertical response, due to problem's symmetry. On the contrary, response of an off-centered pile (piles 2 and 3 as illustrated in Figure 2) will involve both vertical and horizontal directions. Although modelling employed in our analyses allows for the consideration of all three orthogonal directions, only the vertical direction is considered in this study.

## 5 RESULTS

The results of this work have been focused on highlighting two principal phenomena: a) identification of configurations that lead to amplification or attenuation of the vibration response and b) definition of a dimensionless factor $C_{SSI}$ for the case of an isolated pile.

All the results presented here focus on excitation frequencies between 0.1 and 89Hz (which allows obtaining one third octave bands up to 80Hz), which is the range most associated with the tactile perception of ground-borne vibration.

### 5.1 Presentation for calculated frequencies

Figure 5 presents the deformed shapes of the model for the Configuration 1 and for some selected frequencies {$f$=0.1Hz | $f$=20Hz | $f$=40Hz | $f$=89Hz}. It allows visualizing the harmonic response of the tunnel for the vibratory source introduced in the lower right corner of the slab.

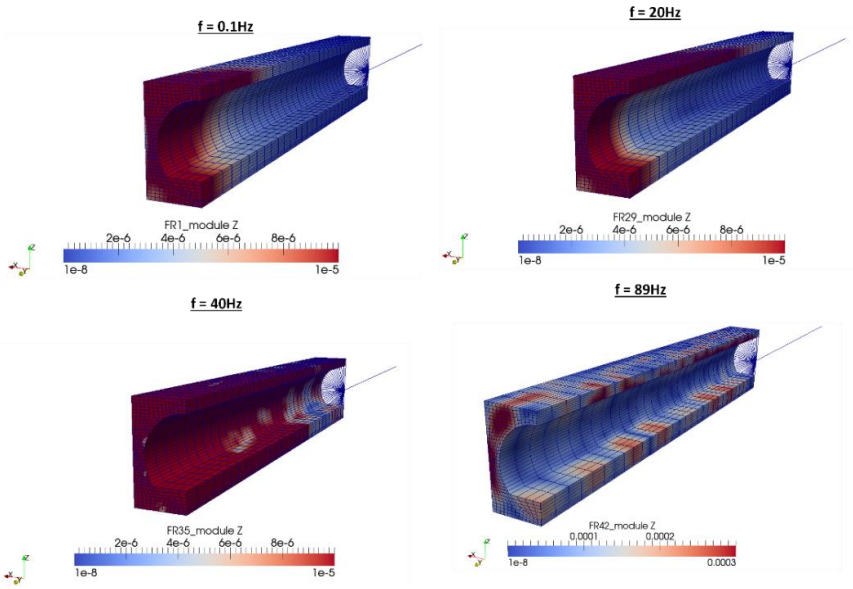


Figure 5 : Deformed shapes of Configuration 1 for different frequencies

The consideration of three isolated piles (one centered-pile and two off-centered piles located at a distance of 5m) does not impact the response in the tunnel's level as Figure 6 illustrates. This is due to the fact that the pile tips are not close enough to the tunnel embedment so as to modify the vibratory response.

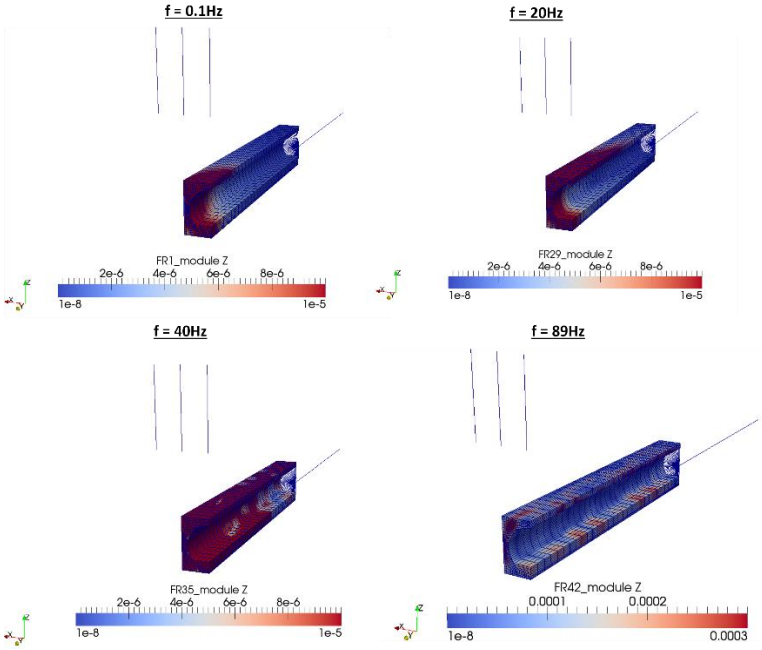


Figure 6 : Deformed shapes of Configuration 1 with piles for different frequencies

On the contrary, the impact of the presence of piles is more obvious in Figure 7 that presents the transfer mobilities for a series of points located at different depths above the tunnel axis. One can observe an attenuation of the transfer mobility for depths over 15m (pile's embedment equal to 15m). Similar results are also obtained for the two additional soil configurations.

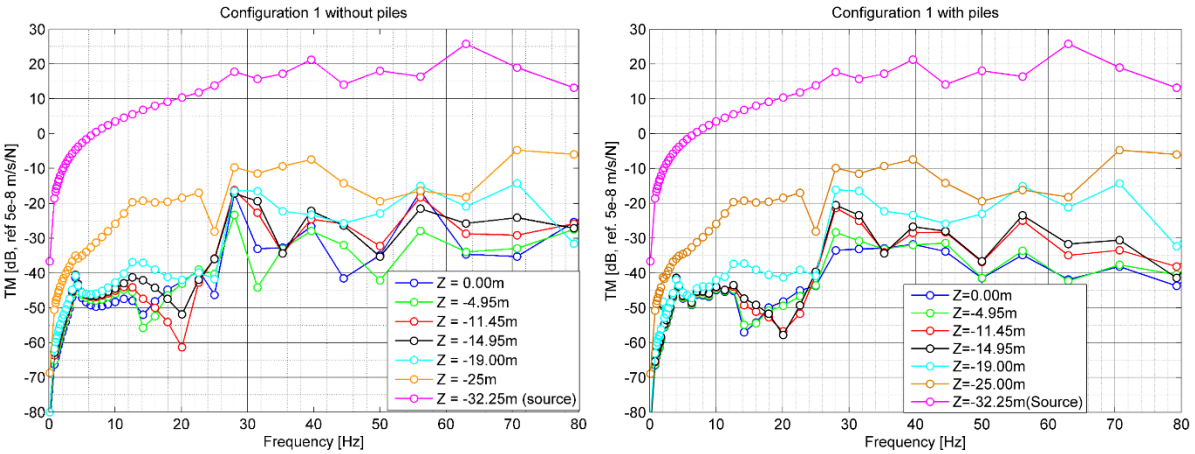


Figure 7 : Raw transfer mobilities for Configuration 1

## 5.2 Presentation in one-third octave bands

All of the above-mentioned quantities are defined as functions of frequency and are typically provided as spectra defined in one-third octave bands that go up to 80Hz for estimating vibration levels. Figure 8 provides the same results as Figure 7 but they are determined by means of a filter cutting off frequencies outside a band, where the maximum frequency in each band is equal to the minimum frequency multiplied by 2.

This representation leads to smoothed spectra that facilitate the interpretation. Actually, added-pile impact gets even more obvious in Figure 9, where free-field curves reflect the results obtained by analyses of Configuration 1 without any pile consideration, whilst pile curves refer to the centered-pile response.

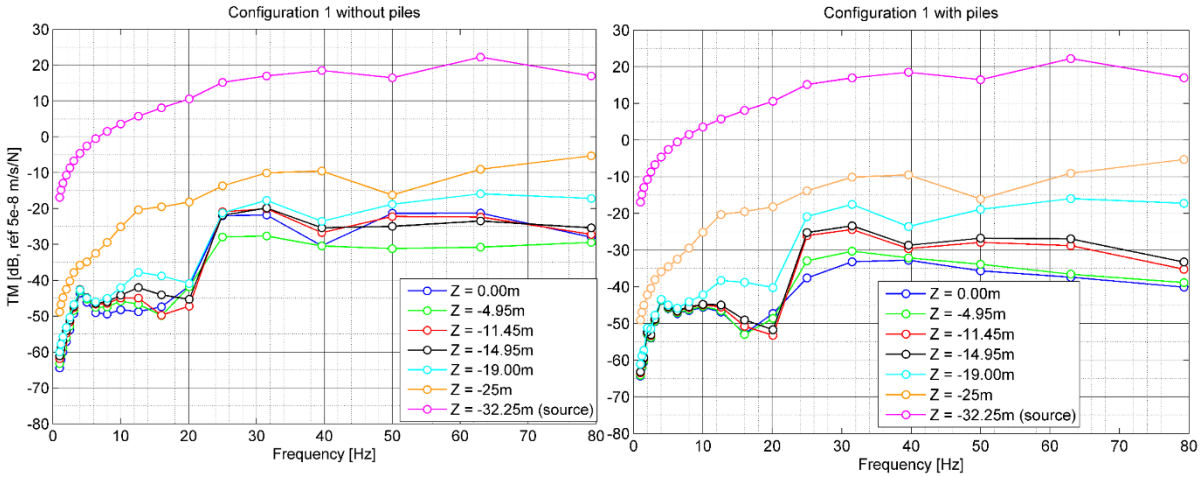


Figure 8 : One-third octave band transfer mobilities for Configuration 1

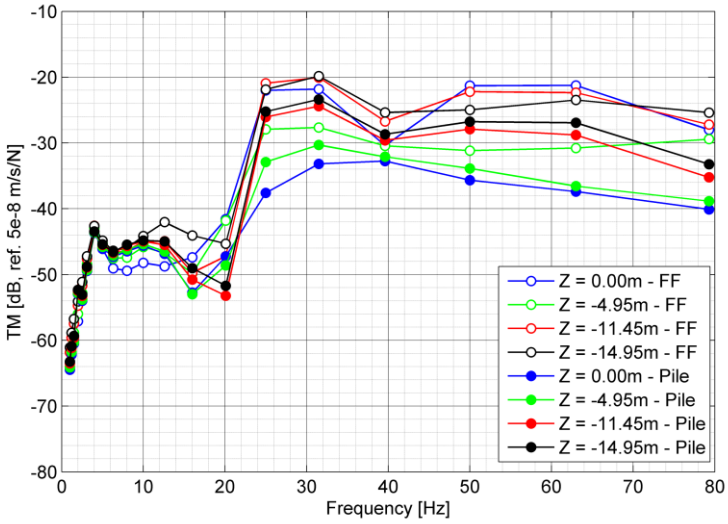


Figure 9 : Comparison of transfer mobility for Configuration 1

In regards to the transfer mobility obtained for the three different piles (see Figure 10), we can conclude that the response is very close for the entire frequency range ( difference less than 2dB between Pile 1 and 2 and 4dB between Pile 1 and 3). Furthermore, for all the three piles the response remains constant at different depths for frequencies up to 20Hz. This can be attributed to the fact that pile is stiff enough to propagate the wave up to the surface with the same amplitude. Some slight differences can be noticed for high frequencies, but they stay limited (less than 2-3dB).

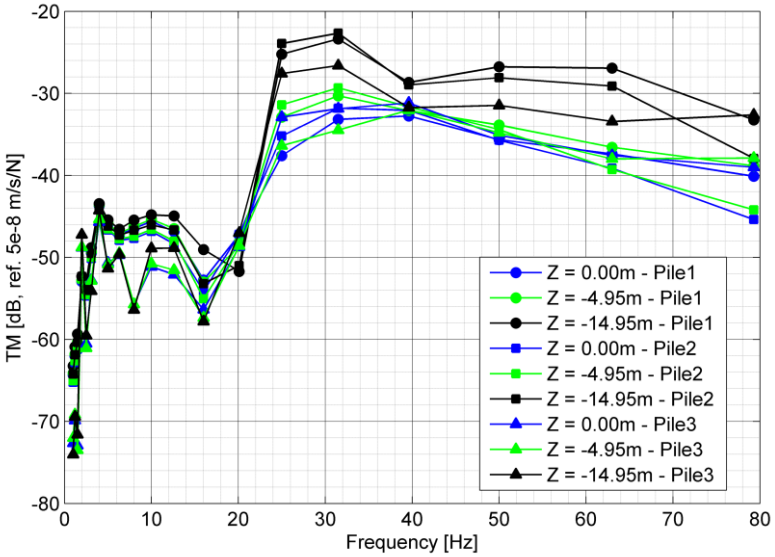


Figure 10 : Comparison of transfer mobility among pies of Configuration 1

Another important point is that if the tunnel is located in a rather soft layer, surmounted by a stiff layer as in Configuration 1, the upper layer "screens" the wave propagation (*cf.* Figure 11, *e.g.* Config1 vs Config3 – soft layers- for the depths of Z=0.00m and Z=14.95m). Furthermore, relatively soft geological layers lead to high attenuations. However, soft layers vibration is very important. This means that for the same excitation level, the vibratory response of this layer will be greater than this developed in the case of a stiff soil layer (*e.*g. Config2 vs Config3).

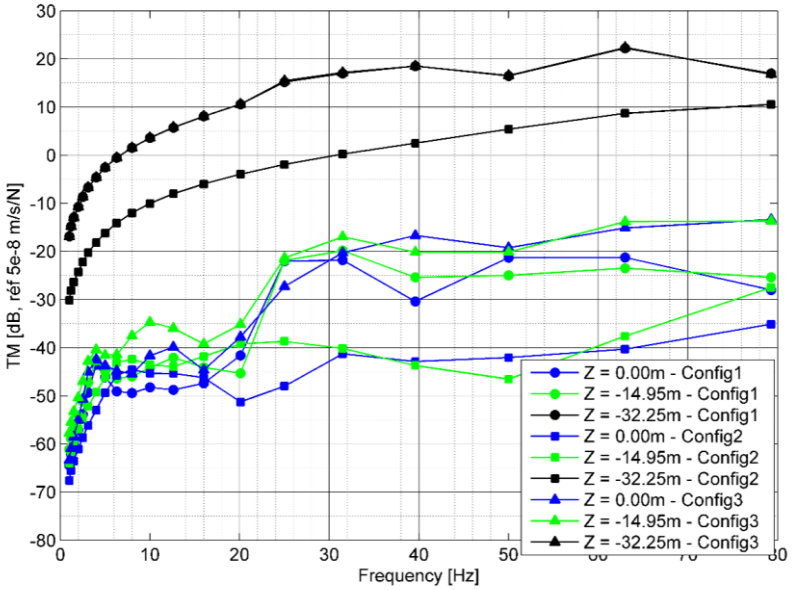


Figure 11 : Comparison of the transfer mobility among the considered soil configurations (without piles)

### 5.3 Calculation of $C_{SSI}$ for single pile

The transfer mobilities are calculated in the free field ($TM_{ff}$) and at the pile head ($TM_{ph}$) and factor $C_{SSI}$ is obtained as the difference of these two quantities (*cf.* Equation2).

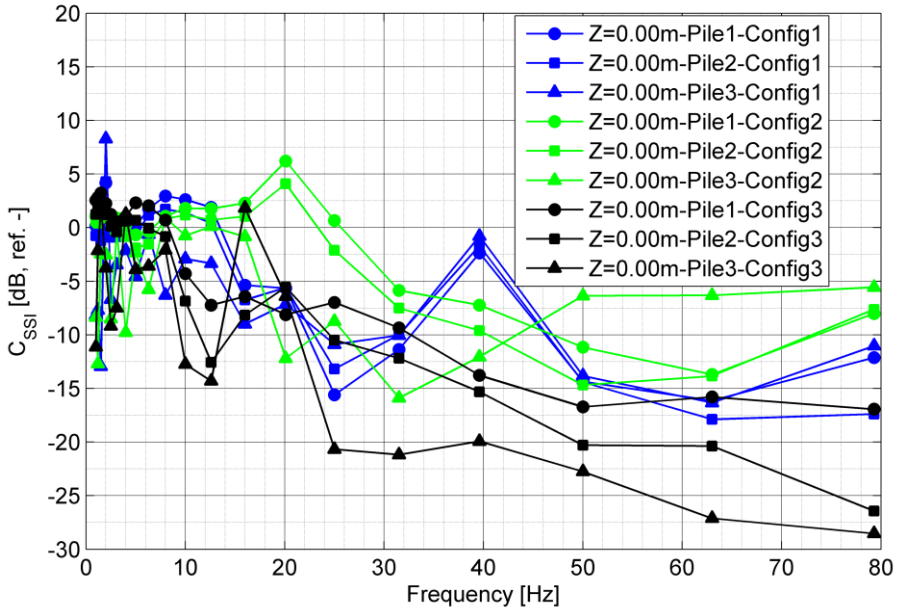


Figure 12 : $C_{SSI}$ factor for the three considered soil configurations

Figure 12 illustrates the impact of the three piles for different soil profile stiffness. It is noteworthy that for low frequencies, this factor is close to 0dB or positive but a significant attenuation can be observed for high frequencies. This attenuation can be up to 15dB. Positive values or peaks observed for some frequencies should probably not be considered as true amplification of the vibratory response. A single pile which is located away from the tunnel is less likely to lead to a dynamic coupling highlighting a resonance phenomenon of the system.

Another important point is that $C_{SSI}$ factor for the Configuration 1 ("screen effect" profile) stays similar for the three considered piles. On the contrary, Configurations 2 and 3 reveal a more important $C_{SSI}$ factor for Pile 3 (the most distant from the tunnel) than the other two piles.

## 6 CONCLUSIONS AND PERSPECTIVES

The present work constitutes a part of a wider parametric study and aims at presenting the calculation methodology and the type of obtained results with some preliminary conclusions. The transfer mobilities are calculated using a FEM-BEM model incorporating the tunnel, the surrounding soil and the eventual presence of deep foundation elements.

The obtained results allow to highlight the configurations that lead to the most pronounced vibration amplifications and may thus be harmful for the structural integrity of the piles. Furthermore, a set of dimensionless factors that can be used to "correct" the free-field transfer mobility to take into account the presence of deep foundation elements has been defined.

Notwithstanding the elements provided in the present paper, further calculations considering the several aspects of the problem are in progress and their results are expected to be integrated in future work. The principal aspects that are targeted are: the tunnel depth, the relative location of foundation elements with respect to tunnel axis, the distance between the pile toe and the

tunnel lining, the effect of pile group, the type of vibratory source (train passage in tunnel operation or TBM advancement in tunnel construction) and the consideration of the whole superstructure located at the vicinity of the tunnel.

Finally, the ultimate perspective of the work consists in formulating sets of dimensionless factors for characterizing the transmission and the immission phases of the problem.

## REFERENCES

[1] Edirishinghe TL, Talbot JP, A Parametric study of the train-induced vibration of a single pile near underground railway tunnel. *Soil Dynamics and Earthquake Engineering*, **158**, 107274, 2022.

[2] Federal Transit Administration, *Transit Noise and Vibration Impact Assessment Manual*, FTA Report N°0123, September 2018.

[3] ISO 14837-1:2005, *Mechanical vibration - Ground-borne noise and vibration arising from rail systems - Part 1: General guidance*

[4] Ntotsios E, Thompson D, *MOTIV (Modelling of Train-Induced Vibrations): A semi-analytical tool for prediction of ground vibration by surface and underground trains*, Institute of Sound and Vibration Research, University of Southampton, UK, June 2019

[5] Ostadan F, Deng N, *SASSI 2015: A system for the analysis of soil-structure interaction*. Civil Engineering Department, University of California at Berkeley, 2019.

[6] RIVAS Collaborative Project, *Review of existing standards, regulations and guidelines, laboratory and field studies concerning human exposure to vibration*, Deliverable D1.4, 2011

[7] Thompson DJ, Kouroussis G, Ntotsios E, Modelling, simulation and evaluation of ground vibration caused by rail vehicles. *Vehicle System Dynamics*, **57**, 936-983, 2019

COMPDYN 2023
9th ECCOMAS Thematic Conference on
Computational Methods in Structural Dynamics and Earthquake Engineering
M. Papadrakakis, M. Fragiadakis (eds.)
Athens, Greece, 12-14 June 2023

# CASE STUDY APPLICATIONS OF PERFECTLY MATCHED LAYERS IMPLEMENTED IN THE ANALYSIS OF VIBRATIONS INDUCED BY TRAIN PASSING

**A. Zhelyazkov[1], H. Töll[2], and D. Pichler[2]**

[1] Vienna Consulting Engineers ZT GmbH
Untere Viaduktgasse 2, Vienna
e-mail: e-mail: zhelyazkov@vce.at

[2] Vienna Consulting Engineers ZT GmbH
Untere Viaduktgasse 2, Vienna
{toell,pichler}@ vce.at

## Abstract

*Two case study applications of perfectly matched layers (PML) combined with finite elements are demonstrated. The first case concerns a vibration analysis of an office building to be constructed in close vicinity to rail tracks. A rigorous finite element model, including solid elements for representation of the soil, was built and used for estimating vibrations transferred to the building from a passing train. The size of modelled soil domain was kept within reasonable limits thanks to the wave absorbing properties of the PML's. The second case is a part of a train-bridge interaction analysis related to the train's transition from an embankment to a bridge. Due to the unusually high maximum operational velocity foreseen (360 km/h), vibrations in the train's body and displacements in the transition zone required special attention. Modelling of the soil within the transition zone was again achieved with the above described approach. A finite element model combining both the bridge and transition was built. This allowed the estimation of response quantities, which otherwise cannot be obtained with a more simplified modelling approach.*

**Keywords:** Vibration control, Train-track interaction, Wave propagation, Non-reflecting boundaries.

## 1 INTRODUCTION

In civil engineering practice, the challenge of modeling vibration propagation through an infinite soil domain is a recurring issue. Typically, numerical modeling is used to investigate the interaction between engineered structures and infinite soil domains, with a particular focus on soil-structure interaction during seismic events. As a result, there are numerous standards and research studies dedicated to this problem. In contrast, modeling traffic-induced vibrations is not as commonly encountered, leading to a smaller number of standards and recommendations and a less well-established procedure for numerical modeling.

This paper aims to shed more light on the issue by presenting two case studies that involve numerical modeling of traffic-induced vibrations in engineered structures. The first case study involves modeling the vibrations induced by a passing train on a currently designed office building. Vibrations are generated at the wheel-rail interface and transmitted via the track structure into the adjacent soil and nearby office building. The ultimate goal of the vibration assessment is to identify if the potential impacts on sensitive receivers exceed the acceptance criteria and consequently recommend mitigation measures. The second case-study deals with the dynamic analysis of a high-speed train going over a transition from earthworks to a bridge structure. Such transitions along a rail track are usually accompanied by a change in the track stiffness. Special measures have to be undertaken both in the design and construction phases in order to avoid a sharp change in the track stiffness. A sharp increase or a decrease in the stiffness might lead to passenger discomfort and increased dynamic loading on the track.
In both of the above described analyses a finite element model is built combining the civil structure of interest and the surrounding soil domain. For the modelling of the structures beam and shell elements are implemented, whilst the soil is represented entirely by solid elements. More details on the modelling approach are provided in Sections 3 and 4, but here it is important to mention that perfectly matched layers (PML) are used for the efficient representation of unbounded soil domains as bounded ones. With the introduction of PML's at the boundaries of the finite element soil models the incident waves are absorbed effectively simulating an unbounded domain at a relatively low computational cost. Further details can be found in Section 2.

The paper has the following structure:

(ii) Introduction to the theory behind perfectly matched layers
(iii) Case-study 1 - Vibration assessment in an office building near train tracks
(iv) Case-study 2 - Dynamic analysis of a high-speed train transitioning from earthworks to a bridge
(v) Conclusions

All analyses presented herein are performed with the finite element software LS-DYNA. Therefore the theoretical background and model definitions will be described with reference to the functionalities of LS-DYNA.

# 2 PERFECTLY MATCHED LAYERS

## 2.1 Backround

PMLs are a numerical method used to simulate wave behavior in unbounded domains. The technique involves adding a layer of material around the domain of interest that can absorb waves attempting to pass through it, creating a boundary condition that mimics an infinite domain. The key to PMLs is ensuring that the absorbing layer matches the wave impedance of the surrounding medium, which facilitates a smooth transition between the PML and the domain of interest. This is crucial because any mismatch in the impedance could result in wave energy being reflected back into the domain of interest, leading to unrealistic estimations of the response. The absorbing layer is typically implemented as a complex-valued material with a variable elastic modulus that gradually increases towards the boundary of the domain. The complex nature of the material allows it to absorb waves with different frequencies, while the variable elastic modulus ensures that the absorption is gradual and doesn't cause any unwanted wave reflections.

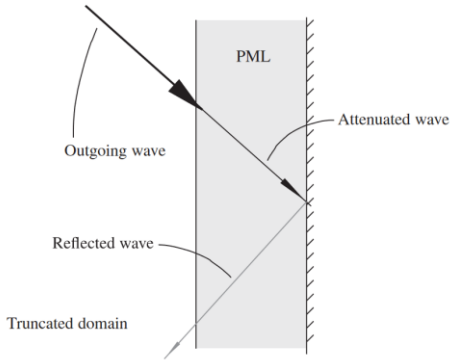


Figure 1: A PML adjacent to a truncated domain attenuates and reflects back an outgoing wave [5]

PML was initially developed for electromagnetic waves in seminal works by Bérenger and Chew [7]. Since then, extensive research has been conducted on electromagnetic PMLs by numerous researchers, with extensions to other fields such as elastic waves for seismic applications. However, most of the formulations and implementations used finite-difference split-field methods to implement the PML, which had two disadvantages. Firstly, the finite-difference methods could not be easily used with finite-element models for structures, and secondly, the split-field formulation often led to long-time instability. To overcome these shortcomings, Başu and Chopra [5] developed a displacement-based finite-element implementation for elastic PMLs. This allowed for explicit analysis, enabling realistic analysis of three-dimensional soil-structure systems. Exactly this numerical procedure is applied in the current paper. A brief theoretical explanation of the main concept behind the implemented numerical solution is provided hereafter.

## 2.2 Basics

Consider a simple model of a semi-infinite rod unbounded on the right side (Figure 2). The equations describing the elastic medium of the rod can be transformed into equations for a perfectly matched layer (PML). The PML is designed mathematically to dampen waves by utilizing a damping function *f(x)* that increases in the unbounded direction. The PLM is placed next to the bounded rod and absorbs all incident waves in the direction of the unbounded medium.

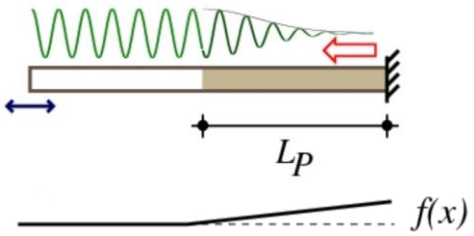


Figure 2: PML concept [6]

The PLM is truncated once the outgoing waves are sufficiently damped. A partial reflection of the wave will occur with the amplitude of the reflected wave given by:

$$|R| = \exp\left[-2F(L_P)\right], \quad F = \int f \, \mathrm{d}x \tag{1}$$

The amplitude is controlled by $f$ and $L_p$ and can be made as small as desired. The attenuation function is according to the equation:

$$f(x) = f_0 \left(\frac{x}{L_P}\right)^m \tag{2}$$

$m = 2$ works best for finite element analysis and f0 is chosen from a simplified discrete analysis. An automatic estimation of f0 is performed in LS-DYNA according to the depth of the layer. The depth Lp of the layer may be chose so that the layer is about 5-8 elements deep, with the mesh density of the PML similar to that of the bounded medium. The PML material is forms a parallelepiped around the bounded domain, which is aligned to the coordinate axes. The outer boundary of the PML is fixed.

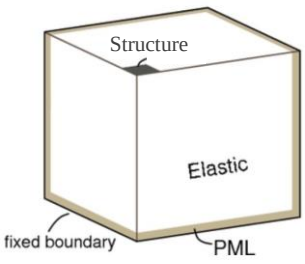


Figure 3: Unbounded domain representation [6]

# 3 CASE-STUDY 1 - VIBRATION ASSESSMENT IN AN OFFICE BUILDING NEAR TRAIN TRACKS

## 3.1 General

Noise & Vibration (N&V) are an important aspect to be assessed when building in near proximity to rail tracks. N&V are generated at the wheel-rail interface and are transferred via the track to the soil and the adjacent buildings. Inside those buildings vibrations could be perceptible to the inhabitants and cause discomfort and/or induce structure borne noise radiated by surrounding walls and ceilings. The acceptance criteria for N&V are defined according to the local regulations. A detailed analysis for vibrations and ground borne noise generally uses all available tools to accurately predict the vibration impact on specific sites. The procedure includes defining the forces generated by the vibration source and defining how the local geology affects vibration propagation. Furthermore, details of structural dynamics of the affected buildings need to be assessed to predict the impact on objects inside the building. In this case study the analysis of an office building to be built in Köln, Germany nearby existing rail tracks is presented. The main objective of the numerical analysis was to conclude if mitigation measures related to N&V are required. Project restraints allowed only for mitigation measures applied on the building. After a close cooperation with the designer of the building it was concluded that the only feasible mitigation measure for the specific project is a trench along the perimeter of the building facing the tracks. It was decided to perform the analysis first with no trench included and then with the trench. Although, as concluded later, no mitigation measures were required the analysis with a trench was performed as a helpful reference for future projects.

## 3.2 Validation of the numerical model and determination of the train loading function

Since the dynamic loads induced in the track by the train are unknown, the following approach is applied:

1) Estimation of the transfer function between the load application points (Figure 8) and a node corresponding to a channel *X* (*X* is an example value) from the model. The transfer function describes the behavior of the system in the frequency domain:

$$UF_X(f) \tag{3}$$

The transfer function is calculated by applying an impulse load, solving the response with explicit time-integration and then transferring the obtained response in the frequency domain.

2) The in-situ measured response for channel *X* ($A_{X,in-situ}$) is divided by the transfer function (*UF*) to give an estimate of the load function (L) in the frequency domain:

$$L(f) = \frac{A_{in-situ}}{UF_X} \tag{4}$$

3) For the validation of the model, the transfer function $UF_Y$ is calculated between the load application points on the track and a node, which in turn corresponds to a channel in

the model. The load function ($L$) is multiplied by $UF_Y$ and compared to the in-situ measured response $A_{Y,in-situ}$.

If the multiplication approximates well the in-situ measured response ($L * UF_Y \approx A_{Y,in-situ}$), it can be assumed that the numerical model is validated. If $A_{Y,in-situ}$ deviates from the numerical estimation a calibration of the model has to be performed.

4) The dynamic response of the building is obtained by multiplying $A_{Z,Neubau} = L * UF_Z$. $UF_Z$ is the transfer function between the load application points on the track and the newly constructed building.

The above described procedure was implemented for model validation using several field measurements as references. Results for point MP6 (see Figure 4) are shown on Figure 5.The load *L(f)* is applied according to Figure 6 as an area load (force) in the vertical direction.

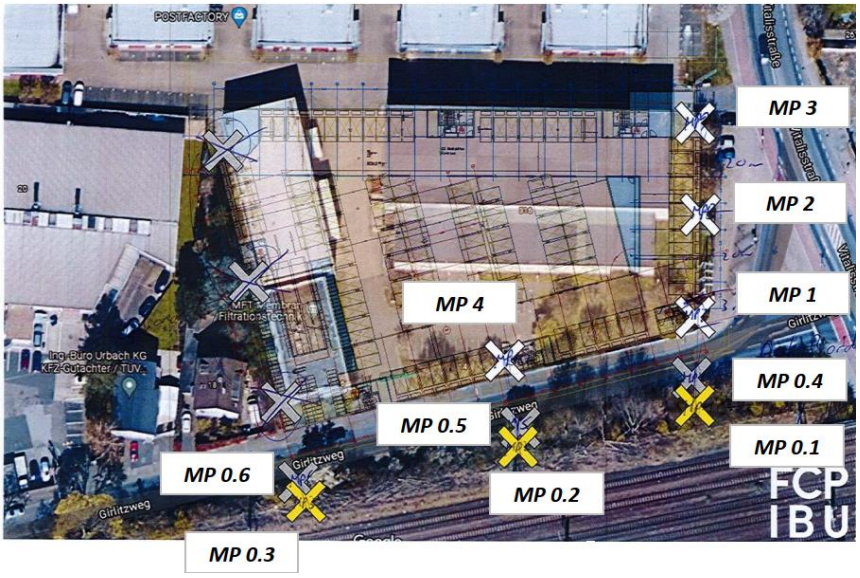


Figure 4: Measurement points on the free filed before construction of the building

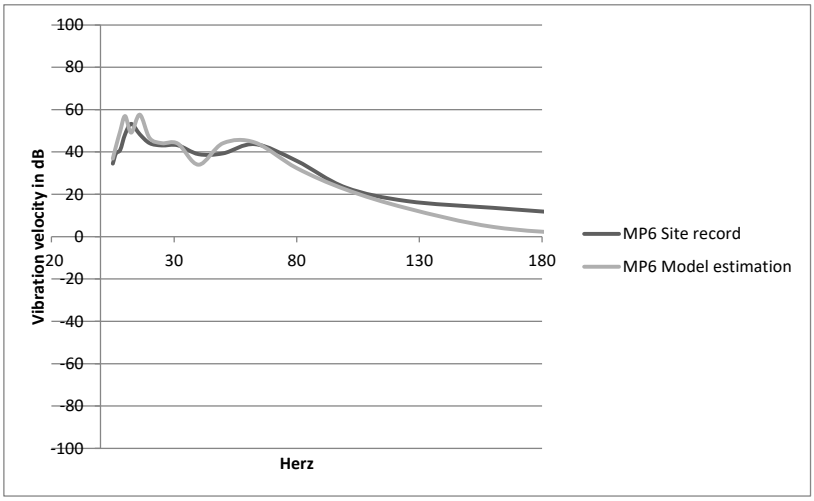


Figure 5: Comparison between estimated and measured vertical vibration velocity at the free field near the rail tracks

### 3.3 Estimating the vibrations in the building

By applying the already deduced in Section 3.2 train loading function L(f) along the length of the track (see load application on Figure 6) the vibration velocity spectra in the building are predicted.

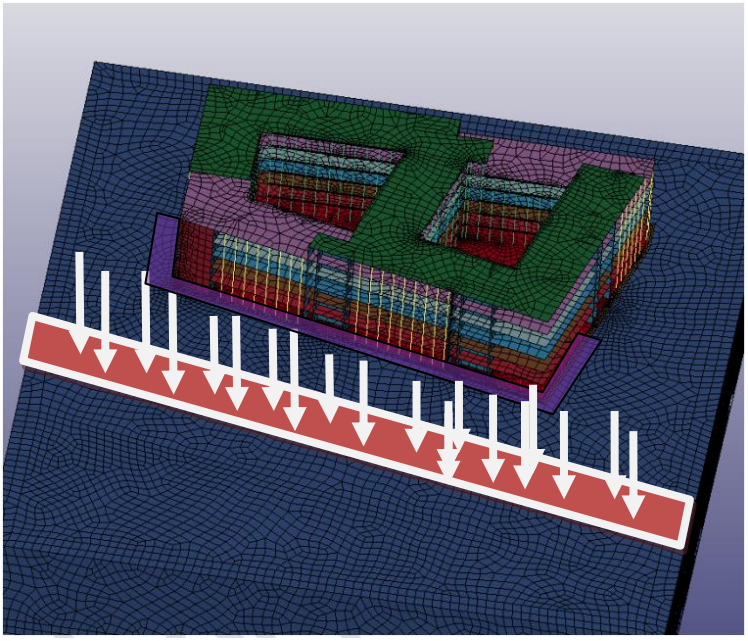

Figure 6: Finite element model of the analyzed building

**Figure 7** presents the results **with** and **without** the presence of a trench for the second floor of the building.

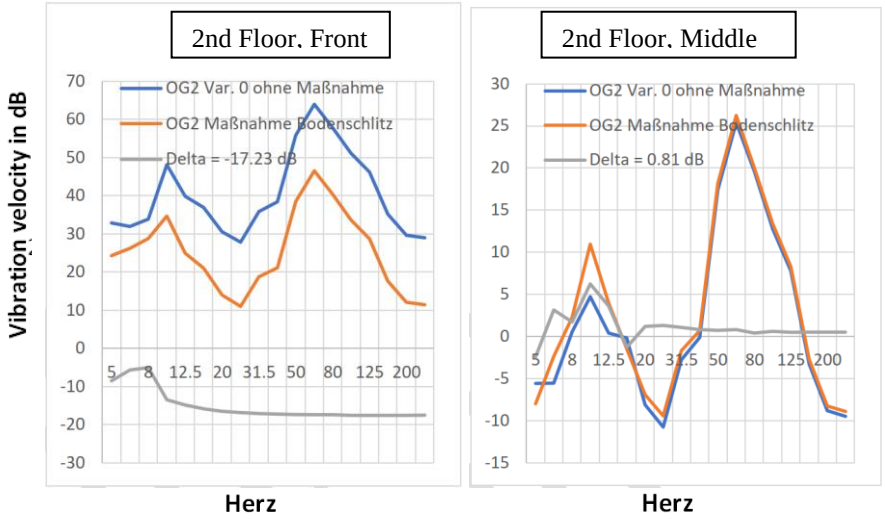


Figure 7: Vibration velocity spectra

From the above figure it can be concluded that the trench has a significant effect along the perimeter of the building facing the track and less so towards the middle of the building. This is mainly because in the middle of the building a very small part of the vibrations is transmit-

ted. The vibration is also reduced at the higher floors, which is expected due to wave distance attenuation.
Once the vibration velocity within the building is obtained an estimation of vibration and structure borne noise as perceived by the inhabitants has to be performed. The procedure is according to DIN4150 [2]. This part of the analysis is not included, as the focus of the paper is on the practical application of the PML's.

## 4 CASE STUDY 2 - DYNAMIC ANALYSIS OF A HIGH-SPEED TRAIN TRANSITIONING FROM EARTHWORKS TO A BRIDGE

### 4.1 General

As already elaborated on the transition zones between parts of a rail way track with pronounced changes in the vertical stiffness are usually problematic zones and require special attention. If the change in stiffness is too sharp this would lead to an increase of the dynamic contact forces acting at the wheel-rail interface. As a result passenger comfort might be compromised accompanied with an increased maintenance demands on the track. To avoid these undesired scenarios a smooth transition in the track stiffness has to be assured.

In this case-study the transition of a high-speed train between a slab track system placed on earthworks and a slab track system placed on a bridge is analyzed. Due to the exceptionally high foreseen operational velocity between 360 and 400 kph a detailed finite element analysis was deemed necessary.

The analysis is dynamic and performed in the time-domain. It includes in an explicit manner the stiffness, mass and damping of earthworks train and bridge. For the modelling of the earthworks part at the transition a solid element model is built. As the earthworks, or soil domain is again infinite PML had to be implemented. The application of the PMLs is according to the above described approach and shown on Figure 11 The bridge is modelled using beams, spring, dampers and constraints according to the description in Section 4.2. The train is modelled according to the multi-body dynamics approach with a detailed description in Section 4.4.

The main purpose of the analysis is to include a more detailed representation of the track component and potentially capture resonant effects, which cannot be captured by conventional modelling techniques. Such effects could be resonance due to the gap at the track slab and base layer, or exceptionally high dynamic amplifications at the transition between embankment and bridge. Further, the track slabs are supported on a polymer elastic layer used for noise mitigation. Analyzing the dynamic behavior with the elastic layer included for an operational velocity of 400 kph was also deemed as useful.

### 4.2 Bridge model

As previously described the bridge model consists entirely of beam elements, springs, dampers, masses and rigid constraints.

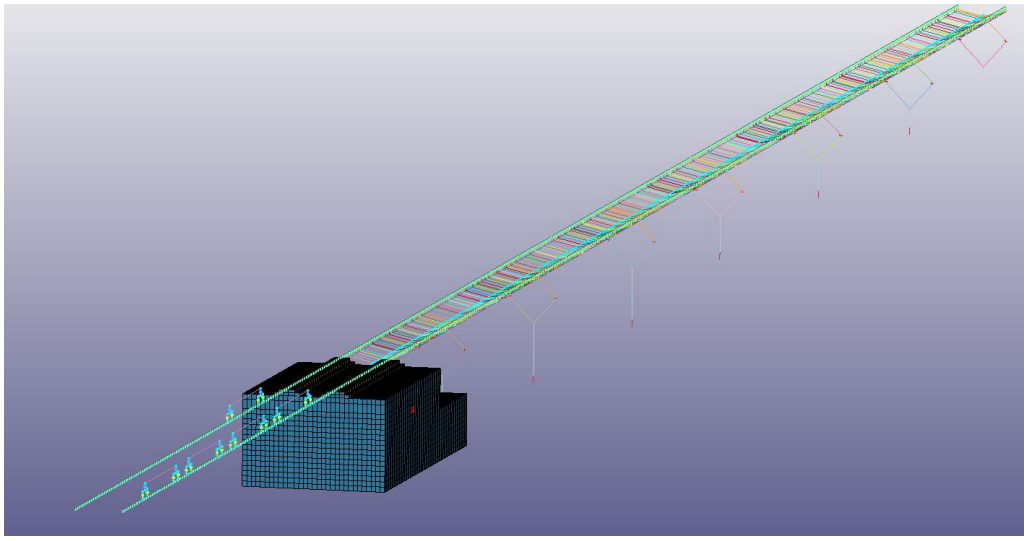

Figure 8: Finite Element Model define in LS-DYNA

A schematic view of the model definition is shown below:

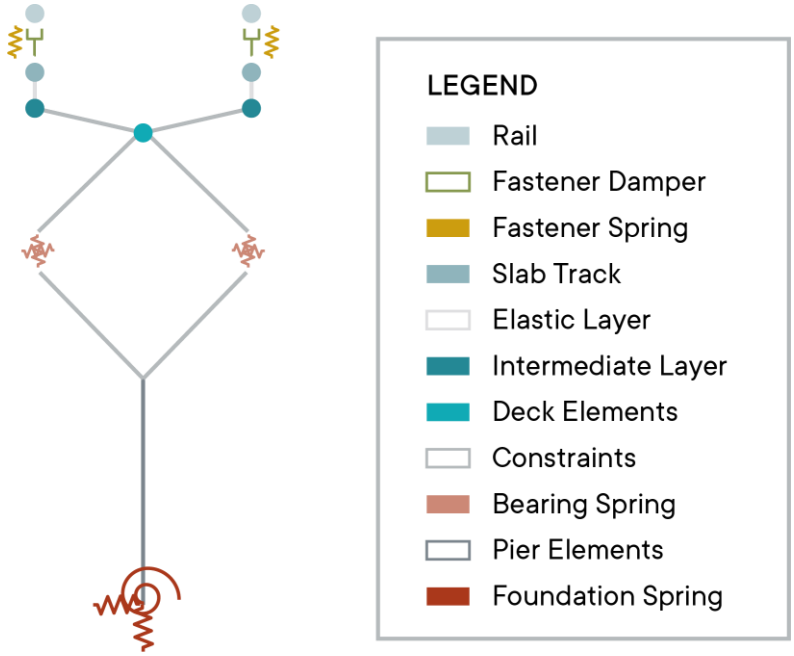


Figure 9: Schematic view of the FE model used for representing the bridge

All properties used for the analysis were provided to Vienna Consulting Engineers ZT GmbH for the purpose of performing the dynamic analysis. It is worth noting that the impedance function of the foundation spring stiffness was not available. For this reason the analysis was performed only with the static stiffness accompanied by a sensitivity analysis

### 4.3 Modelling of earthworks (embankment)

A dense mesh of solid elements is used to model the transition zone (see Figure 11). PML's are used along the surrounding surface of the transition zone with the function of absorbing the waves being generated by the vehicle passing, and therefore, simulating an infinite elastic half-space. The mesh size is selected, such that a response of up to 30 Hz is captured.

Response in the higher frequencies is not considered necessary, since the first 5 dominant modes of the bridge are below 30 Hz (see criterion defined per Eurocode 1990).

A sketch of the transition zone containing geometric and physical properties is presented below.

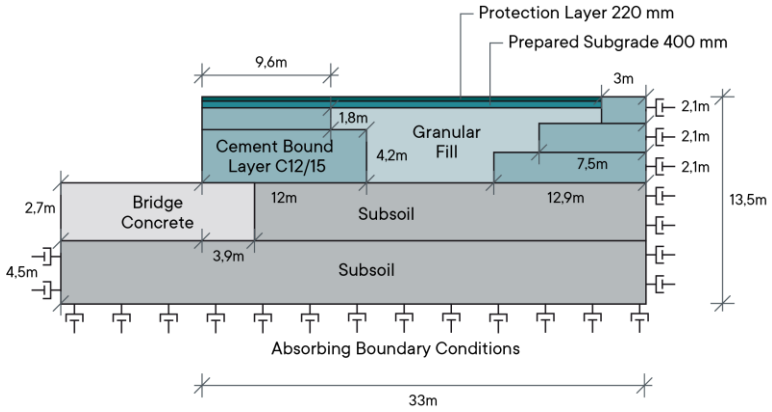


| | E [MPa] | γ | ρ [kg/m³] |
|---|---|---|---|
| Subsoil | 200 | 0.3 | 1700 |
| Embankment | 300 | 0.3 | 1750 |
| Granular Fill | 300 | 0.3 | 1750 |
| Prepared Subgrade 400 mm | 350 | 0.25 | 1800 |
| Protection Layer 220 mm | 400 | 0.25 | 1900 |

Figure 10: Assumed geometric and material properties for the transition zone

The following figure shows the finite element model of the transition zone. The solid elements along the outer edge of the transition zone are the non-reflecting boundaries marked as dashpot damper on Figure 10.

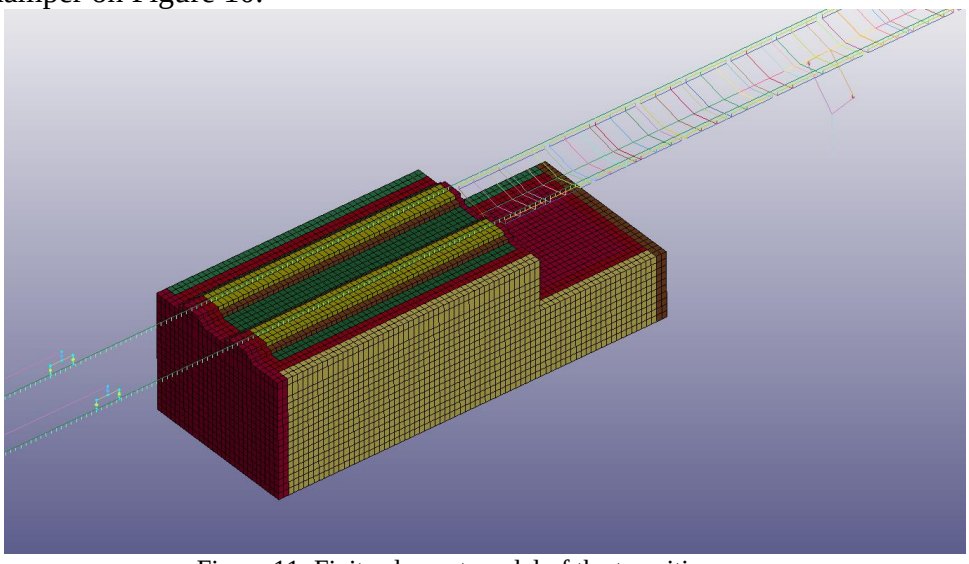

Figure 11: Finite element model of the transition zone

## 4.4 Model of the train

The train is modelled according to the multibody approach. This approach consists of representing the vehicle by a set of masses, springs, dampers, and constraints. This approach is widely accepted in research and professional engineering because of the good balance between accuracy and computational expenses.

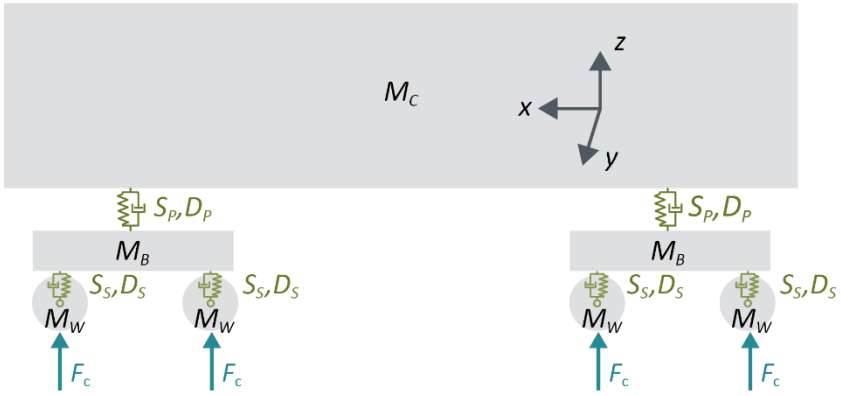


**Figure 12 Multi-body representation of the train**

The following variables are used:
$M_C$ – mass of the car;
$M_{CI}$ – inertia of the car at axis *y*
$M_B$ – mass of a bogie;
$M_{BI}$ - inertia of the bogie at axis *y*
$M_W$ – mass of a wheel;
$S_P$ – primary spring stiffness;
$D_P$ – primary damper property;
$S_S$ – secondary spring stiffness;
$D_S$ – secondary damper property;
$F_C$ – axle load;
*Note: Only data relevant for the performed planar analyses is used. The moments of inertia at axes x and z are not of relevance since the performed analyses are two dimensional. The moments of inertia of the wheels have no effect on the results and therefore are not considered.*

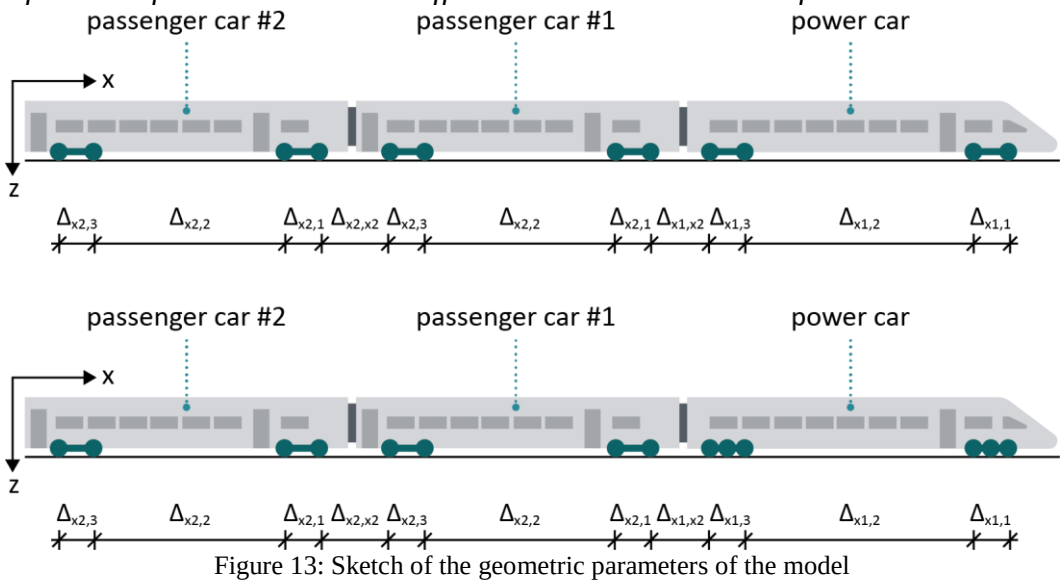


Figure 13: Sketch of the geometric parameters of the model

A total of one power car and three wagons are moving together over the bridge in the model:

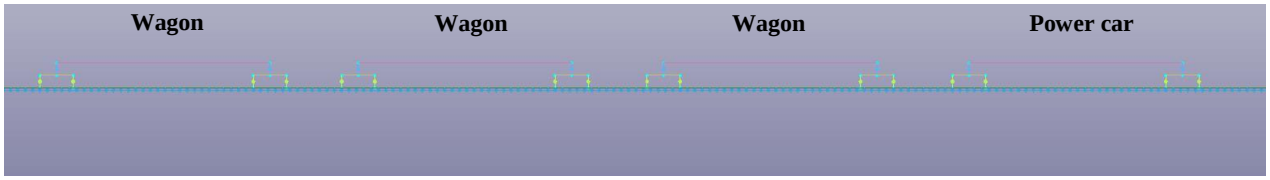


Figure 14: Multibody vehicle definition in LS-DYNA

The damping is defined according to Rayleigh model with coefficients corresponding to a damping ratio of 3% between for 1 and 50Hz.

## 4.5 Definition of rail irregularity

An irregularity profile generated from a power spectrum corresponding to a high-quality track is applied at the wheel rail contact. The power spectrum generation is according to [3]. Figure 14 depicts a single generation of a rail irregularity profile evaluated in the longitudinal direction of the rail. The ordinate shows the vertical deviation of the rail from the perfect rail geometry.

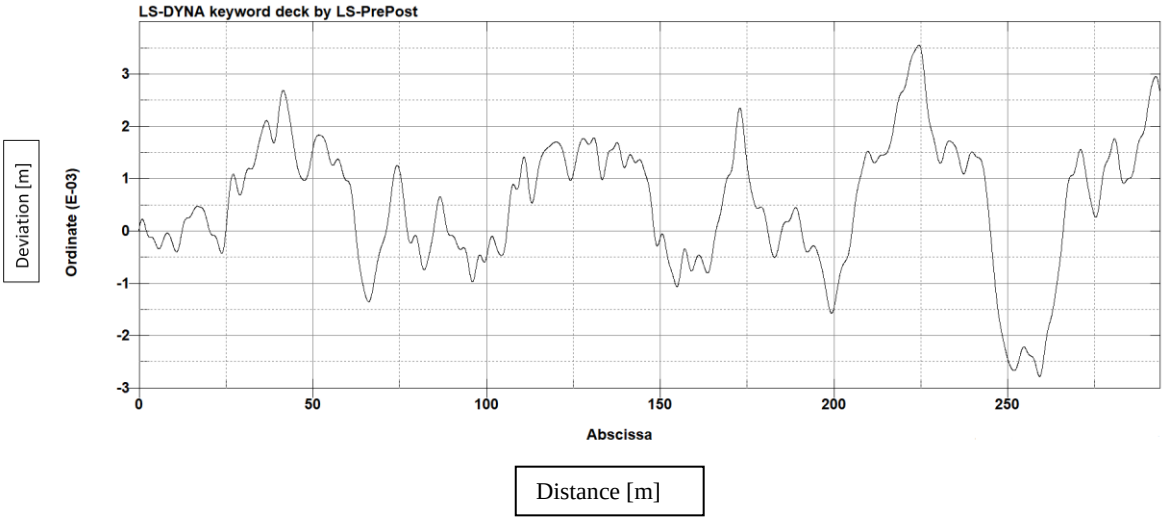


Figure 15: Single realization of a rail irregularity profile

### 4.6 Contact between wheel and rail

A penalty based contact is used to constrain the wheel loads to moving along the rails. For every time step a search for penetration between rail and wheel is performed. When a penetration is found a force proportional (VERTSTF) to the penetration depth (D) is applied to reverse the penetration.

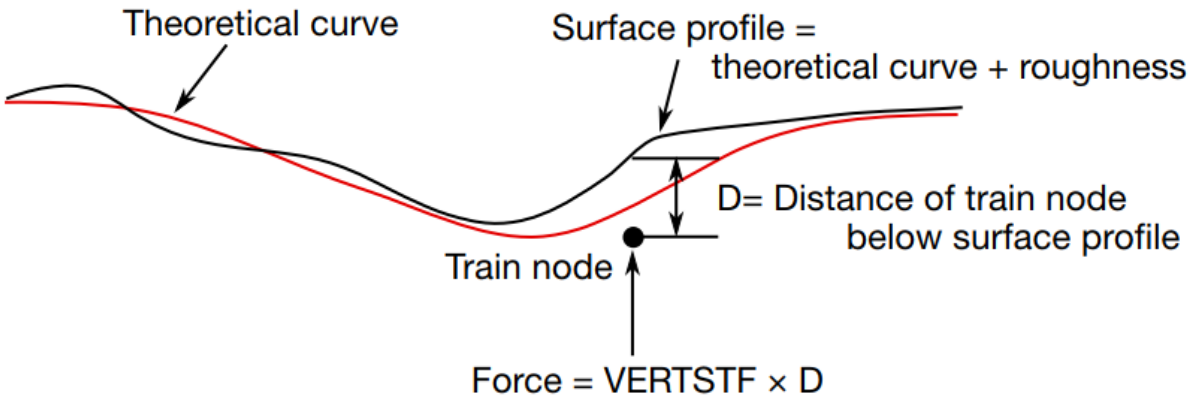


Figure 16: Contact definition according to the penalty method (extracted from LS-DYNA reference manual [4])

### 4.7 Results

The response is extracted for velocities between 50 km/h and 360 km/h. The dynamic amplification for a velocity of 50 km/h is negligible. Additionally no rail irregularities are introduced for the analysis with 50 km/h. Therefore, it can be assumed that the analysis with a velocity of 50 km/h has no meaningful dynamic amplification and can be used as a basis for calculating the amplification at 360 km/h and 400 km/h (in other words the dynamic response at 50 km/h is a good approximation of the static response). The following figures present the results for velocities of 50 km/h, 360 km/h and 400 km/h. Results at 360 km/h and 400 km/h are extracted for 3 different irregularity profiles for the purpose of estimating the sensitivity of the response to rail irregularity.

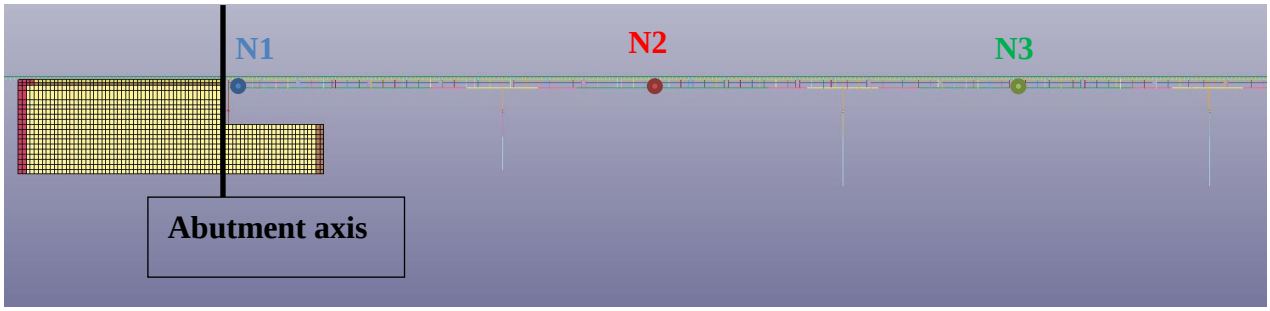


Figure 17: Result extraction points

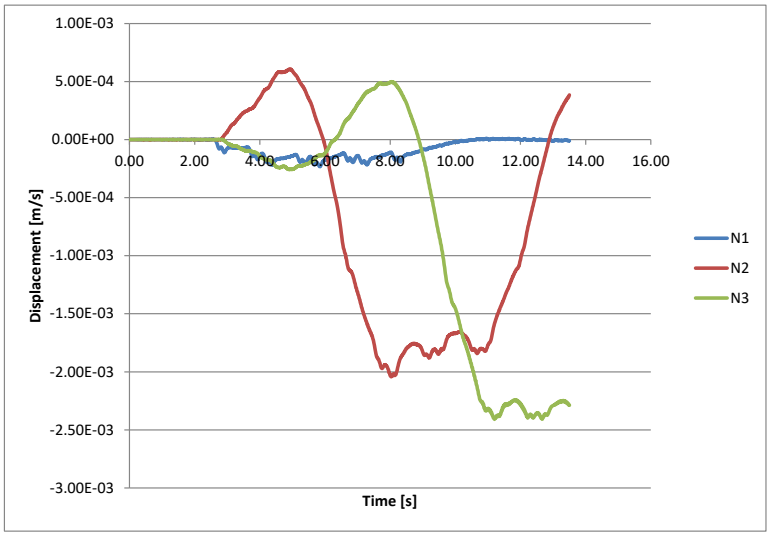


Figure 18: Vertical displacement at 50 km/h

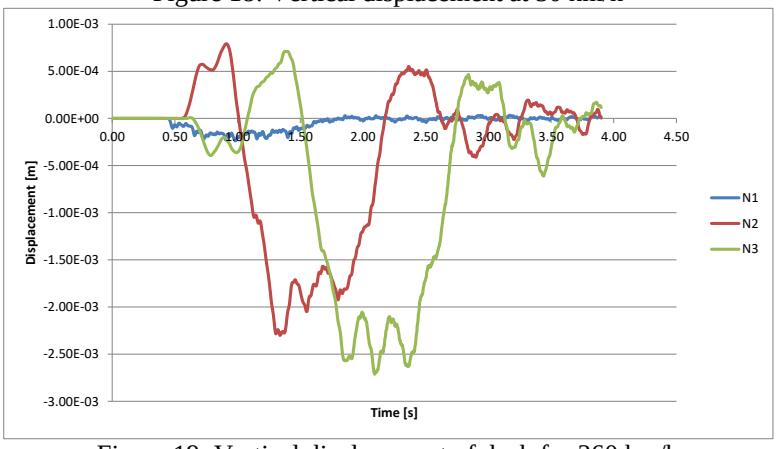


Figure 19: Vertical displacement of deck for 360 km/h

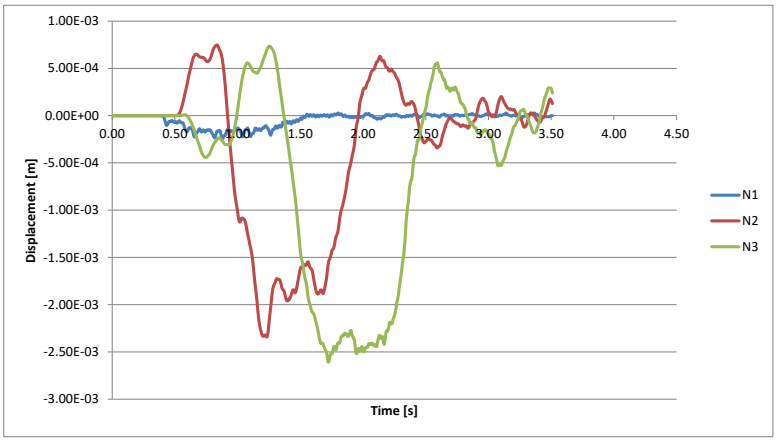


Figure 20: Vertical displacement of deck for 400 km/h

The dynamic amplification factor at the *i*-th Node $\alpha_i$ is the ratio of the peak vertical displacement from dynamic analysis $max(|u_{D,i}(t)|)$ and the peak vertical displacement from static analysis $max(|u_{S,i}(t)|)$:

$$\alpha_i = \frac{max(|u_{D,i}(t)|)}{max(|u_{S,i}(t)|)} \quad (5)$$

The following table presents the results for a set of velocities. It is observed that a plateau in the amplification occurs between the velocities 250 -360 km/h followed by a drop at 400 km/h and then a sharp increase. Performing the analyses with 450 and 500 km/h was necessary only for the purpose of identifying the general relationship between the amplification factor and velocity. In this way the expected general trend of increase in the amplification factor with the increase in the velocity was confirmed. This behaviour is not strict and depends on the relationship between the excitation frequency of the external loading for a given train speed and the natural frequencies of the bridge.

| Velocity [km/h] | Displacement [mm] | Amplification factor |
|---|---|---|
| 200 | 2.6 | 1.08 |
| 250 | 2.73 | 1.12 |
| 300 | 2.75 | 1.13 |
| 360 | 2.76 | 1.13 |
| 400 | 2.64 | 1.10 |
| 450 | 2.78 | 1.16 |
| 500 | 2.90 | 1.21 |

Table 1: Velocity vs. deck displacement and amplification facto.

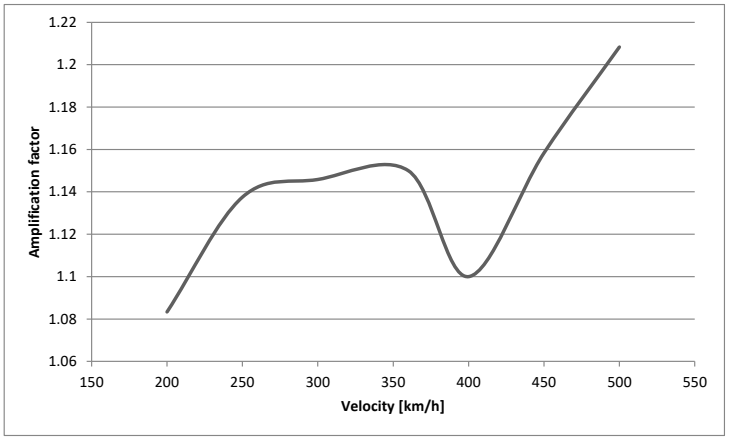


Figure 21 :Amplification factor vs. velocity

The maximum permitted peak design values of bridge deck acceleration calculated along the line of a track shall not exceed the recommended values given in A2 of EN 1990 (5 m/s$^2$). As can be concluded from Figure 22 this limit is kept.

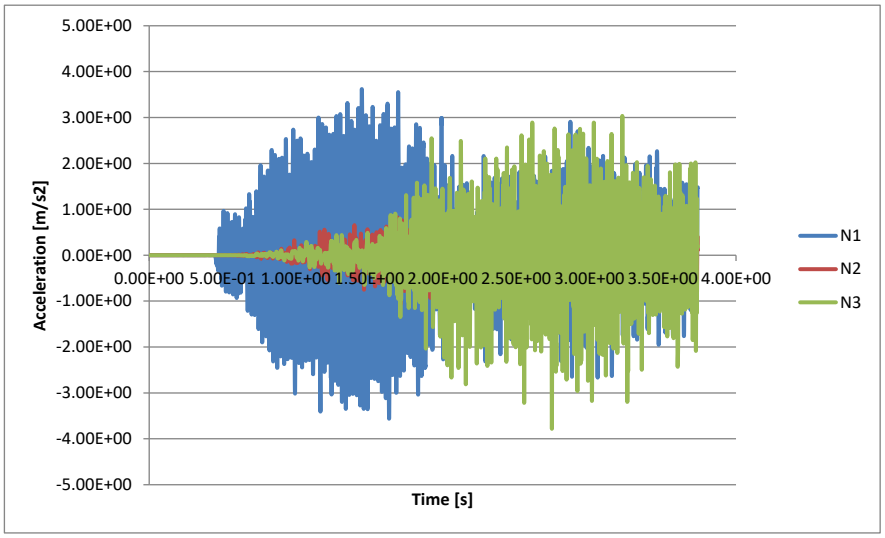


Figure 22: Peak accelerations at top of slab track obtained from the multi-body FEM analysis

From the above presented results it was concluded that no unusual, or unexpected dynamic responses should occur. The response parameters at the transition are within limits, indicating that the life-time expectation of the track will be satisfied. Finally the passenger comfort criterium according to [1] is also satisfied even for an operational velocity of 400 kph. No local resonant effects of the track slabs occur, which was considered a possibility due to the elastic polymer layer on which they are supported.

## 5 CONCLUSIONS

The above presented case-studies demonstrate the applicability of the PML method for problems usual for the civil engineering practice. With the highly efficient explicit time-integration in LS-DYNA the large numerical models described in the paper are solved with a relatively low computational cost. One present challenge is that the applied PLM procedure does not allow for a static analysis, which presents a limitation. To overcome this limitation the problem has to be decoupled into a static and dynamic part presenting additional challenges to the engineer when aiming to use a single model for the entire design. Nevertheless, in the experience of the authors, the PLM procedure as implemented in LS-DYNA can easily address most engineering problems related to the simulations of unbounded domains.

## REFERENCES

[1] EN 1990 A1, Basis of structural design, Amendment application for bridges.

[2] DIN 4150, Erschütterungen im Bauwesen (Vibrations in Structures, in German).

[3] Claus, H., & Schiehlen, W. (1998). Modeling and simulation of railway bogie structural vibrations. *Vehicle System Dynamics*, *29*(S1), 538-552.

[4] LS-DYNA_Manual_Volume_I_R9.0, LS-DYNA Keywords manual Volume I.

[5] Basu, U., & Chopra, A. K. (2003). Perfectly matched layers for time-harmonic elastodynamics of unbounded domains: theory and finite-element implementation. *Computer methods in applied mechanics and engineering*, *192*(11-12), 1337-1375.

[6] LS-DYNA Overview of PML, https://lsdyna.ansys.com/pml-results/

[7] Chew, W. C., & Weedon, W. H. (1994). A 3D perfectly matched medium from modified Maxwell's equations with stretched coordinates. *Microwave and optical technology letters*, *7*(13), 599-604.

COMPDYN 2023
9th ECCOMAS Thematic Conference on
Computational Methods in Structural Dynamics and Earthquake Engineering
M. Papadrakakis, M. Fragiadakis (eds.)
Athens, Greece, 12-14 June 2023

# MODAL CHARACTERIZATION AND ROAD ROUGHNESS RECONSTRUCTION USING DYNAMIC VEHICLE ACCELERATIONS AND ANNS

**Kais Douier[1], Mohammed F. M. Hussein[2], and Jamil Renno[3]**

[1 2] Department of Civil and Architectural Engineering
Qatar University, Doha Qatar
e-mail: kd1204127@student.qu.edu.qa, mhussein@qu.edu.qa

[3] Department of Mechanical and Industrial Engineering
Qatar University, Doha Qatar
e-mail: jamil.renno@qu.edu.qa

## Abstract

*Road networks are considered huge and critical infrastructures that support the development and growth of societies. These infrastructures deteriorate over time due to regular usage and/or external environmental factors. Deteriorating road networks eventually cause ride discomfort for their users and the production of ground-borne noise and vibrations. Thus, maintaining these infrastructures is essential, and monitoring the condition of the roads is one of the most important steps in maintaining these road networks. Road roughness could be considered as one of the main indicators of the road's overall health. The International Roughness Index (IRI) is used to describe the road roughness profile numerically in a single value. Traditionally the IRI is obtained through manual or automated profilometers, profilographs, or dipstick profilers, which could be time/money consuming. Therefore, this study investigates the ability of Artificial Neural Networks (ANNs) in reconstructing road roughness profiles from dynamic vehicle accelerations. This study also investigates the ANNs ability to predict the model characteristics of a 7-DOF Full Car (FC) model, which is constructed to extract the dynamic vehicle accelerations of a vehicle moving on various roughness profiles. First, the FC model will be moving over a certain obstacle so that the developed ANN could take the dynamic vehicle accelerations as inputs and predict the FC model characteristics. Once the model characteristics are obtained, another ANN will be trained using the dynamic vehicle acceleration of an FC model with the same characteristics to reconstruct the road roughness profile.*

**Keywords:** Artificial Neural Networks, Dynamic Vibrations, Modal Characterization, Road Roughness.

## 1 INTRODUCTION

The continuous measurement of road roughness levels is essential for maintaining the overall health and functionality of the road network. These levels provide a reliable indication of the road's ability to serve the public safely and efficiently. The ISO 8608 guidelines classify road roughness into eight categories, ranging from class A to class H, which describe the overall condition of a road section [1]. These roughness classes can also be assigned to road sections based on the International Roughness Index (IRI), which summarizes the road section's roughness profile into a single value [2]. Usually, the IRI is computed by utilizing a quarter-car model that travels on a road with a particular roughness level. Conventional manual and automated techniques, such as dipstick profilometer, profilograph, or automated road meters, are capable of determining the IRI of a road section[3]–[6]. Nonetheless, implementing these methods across an entire road network can be both expensive and time intensive.

Highway agencies and researchers have sought to find a more efficient method of monitoring road profiles by using specially designed trucks equipped with high-resolution cameras and lasers [7]–[11]. However, mounting such equipment on trucks requires significant capital and operational expenses, making it expensive compared to manual monitoring. Researchers have also explored using unmanned air vehicles (UAVs) to train artificial neural networks (ANNs) and convolutional neural networks (CNNs) to detect surface defects [12], [13]. Although these methods have the potential to be time and cost-effective, they lack the necessary accuracy to be integrated into highway management systems.

Boyu et al. [14] proposed a new technique for estimating road profiles using only a smartphone to measure the responses of an ordinary vehicle. They proposed a new algorithm that involves two main stages. Initially, the ordinary vehicle is modeled as a half car (HC), and a genetic algorithm (GA) is employed to identify its parameters by analyzing the vehicle's responses when it passes over a well-defined speed bump. Using the vehicle model that was estimated, a Kalman filter that incorporates the road profile as a part of the state vector is employed to estimate the road profile.

This research proposes the use of dynamic vehicle responses along with artificial neural networks (ANNs) to estimate road roughness profiles. A full car (FC) model will be developed for exporting the dynamic vehicle response of a normal car passing over randomly generated roughness profiles. The FC model will be also subjected to a road profile with a predefined speed bump to calibrate the model for road roughness estimations.

## 2 METHODOLOGY

This study aims towards reconstructing road roughness profiles using ANNs and dynamic vehicle responses. A numerical FC model will be used throughout this research. The FC model will be used to extract the vehicle dynamic responses to be later used for training the ANNs. Initially, the FC model with randomly varied parameters will be subjected to a predefined speed bump, from which the dynamic vehicle response will be used with ANN to calibrate the developed FC model. Then the calibrated FC model will be used with randomly generated roughness profiles to train another ANN in estimating the road roughness profile.

### 2.1 Full car (FC) model

This study utilizes a 7-degree-of-freedom (7-DOF) FC model that includes four unsprung masses on behalf of the vehicle's wheels and a single sprung mass representing the vehicle's body. The model also takes into account the pitch and roll of the vehicle's body as shown in Figure 1. Equations (1-15) [15], [16] provide a summary of the governing equations for the FC model.

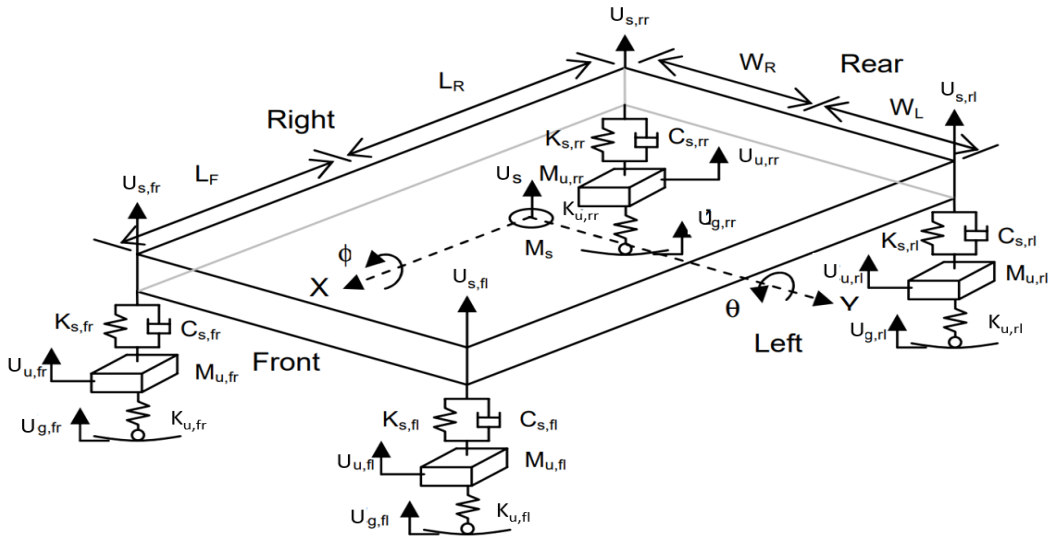


Figure 1: Full car model demonstration [14].

$$I_{yy}\ddot{\theta} = L_r\left(F_{s,rr} + F_{s,rl}\right) - L_f\left(F_{s,fr} + F_{s,fl}\right) \quad (1)$$

$$I_{xx}\ddot{\Phi} = W_l\left(F_{s,fl} + F_{s,rl}\right) - W_r\left(F_{s,fr} + F_{s,rr}\right) \quad (2)$$

$$F_{s,fr} = K_{s,fr}\left(U_{u,fr} - U_{s,fr}\right) + C_{s,fr}\left(\dot{U}_{u,fr} - \dot{U}_{s,fr}\right) \quad (3)$$

$$F_{s,fl} = K_{s,fl}\left(U_{u,fl} - U_{s,fl}\right) + C_{s,fl}\left(\dot{U}_{u,fl} - \dot{U}_{s,fl}\right. \quad (4)$$

$$F_{s,rr} = K_{s,rr}\left(U_{u,rr} - U_{s,rr}\right) + C_{s,fl}\left(\dot{U}_{u,rr} - \dot{U}_{s,rr}\right) \quad (5)$$

$$F_{s,rl} = K_{s,rl}\left(U_{u,rl} - U_{s,rl}\right) + C_{s,rl}\left(\dot{U}_{u,rl} - \dot{U}_{s,rl}\right) \quad (6)$$

$$M_S\ddot{U}_S = F_{s,fr} + F_{s,fl} + F_{s,rr} + F_{s,rl} \quad (7)$$

$$M_{u,fr}\ddot{U}_{u,fr} = F_{u,fr} - F_{s,fr} \quad (8)$$

$$M_{u,fl}\ddot{U}_{u,fl} = F_{u,fl} - F_{s,fl} \quad (9)$$

$$M_{u,rr}\ddot{U}_{u,rr} = F_{u,rr} - F_{s,rr} \quad (10)$$

$$M_{u,rl}\ddot{U}_{u,rl} = F_{u,rl} - F_{s,rl} \quad (11)$$

where:

$$U_{s,fr} = U_s - L_f\theta - W_r\Phi \quad (12)$$

$$U_{s,fl} = U_s - L_f\theta + W_l\Phi \quad (13)$$

$$U_{s,rr} = U_s + L_r\theta - W_r\Phi \quad (14)$$

$$U_{s,rl} = U_s + L_r\theta + W_l\Phi \quad (15)$$

The equations listed above involve variables such as pitch angle (θ) and roll angle (Φ) that refer to the body of the vehicle and its corresponding mass moment of inertia Iyy and Ixx about the respective axes. The subscripts s, u, fr, fl, rr, and rl denote the sprung, unsprung,

front right, front left, rear right, and rear left parts of the vehicle. Additionally, the terms $L_f$, Lr, Wr, and $W_l$ refer to specific distances shown in Figure 1.

## 2.2 Levenberg-Marquardt ANNs

In this research, Levenberg-Marquardt ANNs are used to estimate the developed FC parameters and road roughness profiles. Compared to other techniques that require solving the Hessian matrix, the Levenberg-Marquardt method approximates it, which usually results in faster training of artificial neural networks.

The FC model parameter estimation ANN consisted of 387 input neurons containing the sprung mass accelerations, and the vehicle pitch and roll response. It also had 15 hidden tan sigmoidal neurons, with 6 linear output neurons corresponding to the roll and pitch moment of inertia, front and rear axles suspension stiffness, and front and rear axles suspension damping as shown in Figure 2 (a).

The road roughness estimation ANN consisted of 225 input neurons containing the sprung and unsprung masses' accelerations. It also had 20 hidden tan sigmoidal neurons, and 50 linear output neurons corresponding to the road profile in Figure 2 (b).

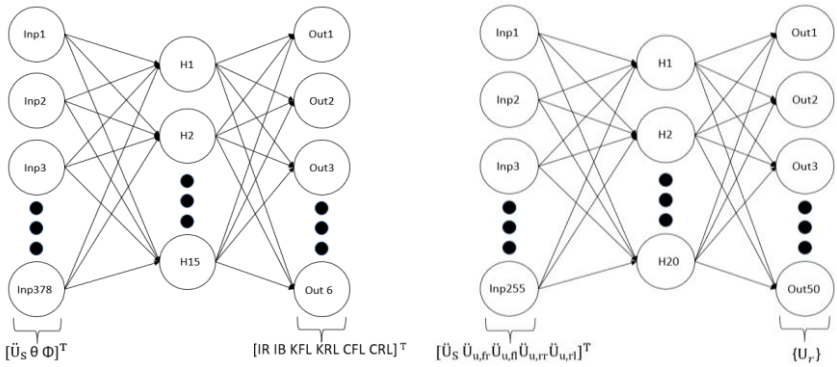


(a) (b)

Figure 2: ANN architecture.

## 2.3 Training Data Sets

The FC model parameter estimation ANN was trained by dynamic vehicle responses which were exported from the FC model moving over a predefined speed bump with a length of 1 m, and a height of 0.5 m. Figure 3 shows the front and rear left-wheel road profiles.

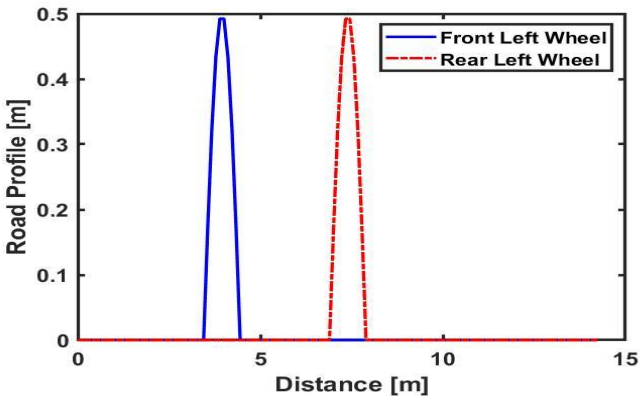


Figure 3: speed bump road profile.

A total of 3000 varied FC models were simulated moving over the above-mentioned speed bump. Each of the Varied FC models had a randomly assigned roll and pitch moment of inertia, front and rear axles suspension stiffness, and front and rear axles suspension damping. The ANN was later trained using the exported sprung mass accelerations, and the vehicle pitch and roll response as inputs, and the randomly assigned parameters as outputs. The vehicle sprung mass and the rear and front axle masses were fixed at 1500 and 60 kg, respectively. Also, the wheel stiffness for all four wheels was fixed at 190000 kN/m.

The road roughness estimation ANN was trained by the dynamic vehicle masses' accelerations which were exported from the calibrated FC model moving over various randomly generated roughness profiles. A total of 3000 randomly generated road roughness class C profiles were generated. The sprung and unsrpung mass accelerations were considered as inputs, while the randomly generated road roughness profiles were considered as outputs.

## 3 RESULTS AND DISCUSSION

Two separate ANNs were developed and tested in this research. The first ANN was used to calibrate the developed FC model, and the second ANN was used to estimate the road roughness profile. The randomly generated model parameters and the estimated model parameters with their error percentage are summarized in Table **1**. Also, the sprung mass acceleration of the true and estimated model parameters of an FC model passing over a speed bump is shown in Figure 4.

| Parameters | True Values | Estimated Values | Percentage error (%) |
|---|---|---|---|
| Roll moment of Inertia (kg.m$^2$) | 961.3 | 947.7 | 1.41 |
| Pitch moment of Inertia (kg.m$^2$) | 1970 | 1986.9 | 0.86 |
| Front axle suspension stiffness (kN/m) | 23000 | 22960 | 0.17 |
| Rear axle suspension stiffness (kN/m) | 19210 | 19242.3 | 0.17 |
| Front axle suspension damping (kN s/m) | 226.9 | 225 | 0.85 |
| Rear axle suspension damping (kN s/m) | 923.5 | 932.7 | 1.00 |

Table 1: True and estimated FC model parameters and their error percentages

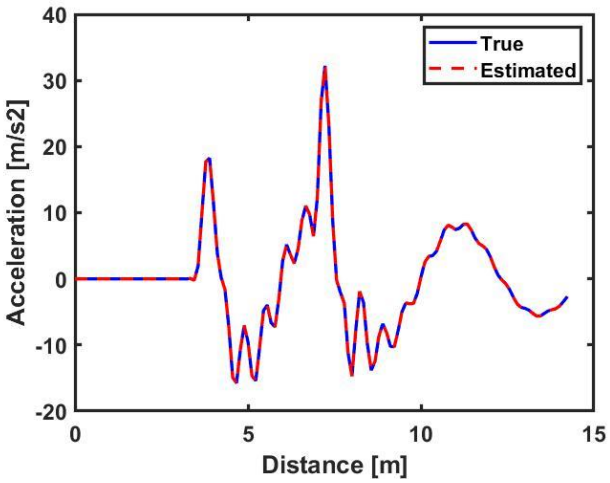


Figure 4: sprung mass acceleration of the true (solid blue) and estimated (dashed red) FC model.

Various runs were tried with randomly varying modal parameters. However, the model parameters were consistently estimated with less than 10% error. The resulting sprung mass acceleration of the estimated FC model showed great agreement with the true FC model, as shown in Figure 4.

The calibrated FC model was then used to train a different ANN to reconstruct the road roughness profile. The testing profile was comprised of 1000 data points that were randomly generated. Consequently, the reconstruction process of the roughness profile involved splitting it into 20 sections and utilizing the same ANN on each of the sections. Figure 5 (a) summarizes the true and estimated testing profile, while Figure (b) shows the regression between the two profiles. The road profile estimation ANN was able to reconstruct the road roughness profile with a regression of 0.94869 and a total root mean square error of 0.0064.

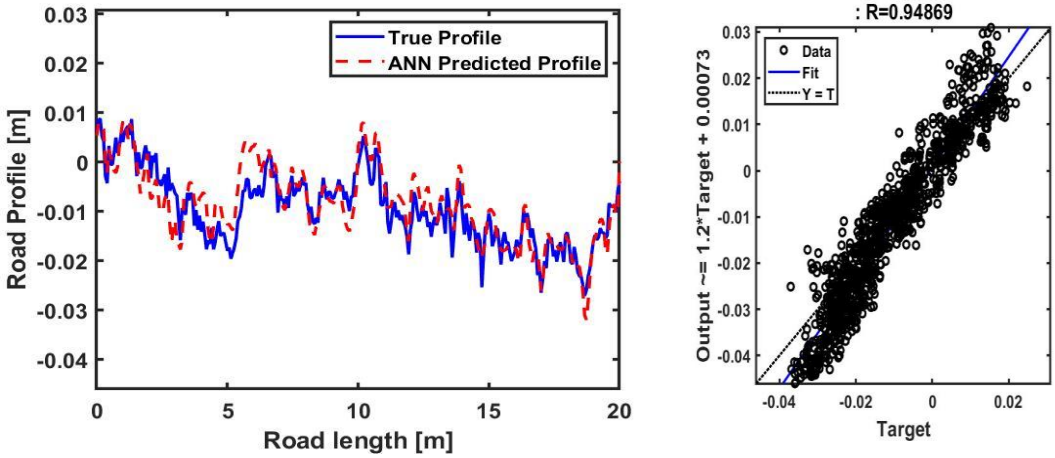


Figure 5: a) reconstructed (dashed red) and true (solid blue) road roughness profile, b) regression between the reconstructed and true roughness profiles.

## 4 CONCLUSION

The ability of ANNs to estimate the road roughness profile and FC model parameters was tested in this study. An FC model was subjected to a predefine speed bump, from which the sprung mass acceleration and the pitch and roll of the vehicle's body were used by a trained ANN to estimate the FC model's parameters. After this, the calibrated FC model was used to train a different ANN by subjecting the FC model to various randomly generated road profiles. The sprung and unsprung masses accelerations were exported from the FC model and utilized by the ANN to estimate the road roughness profile. Overall, both ANNs showed great potential in their ability to estimate unknown parameters such as the varied FC model parameters and randomly generated road roughness profiles.

## 5 ACKNOWLEDGMENT

The authors would like to acknowledge funding from Qatar University through a Graduate Assistantship. The authors would also like to acknowledge funding from Qatar Rail through grant number QUEX-CENG-QR-21/22-1.

## REFERENCES


[1] I. 8608:2016(E), "INTERNATIONAL STANDARD ISO Mechanical vibration — Road surface profiles — Reporting of measured data," 2016.

[2] D. K. Singh and P. P. J. Gundaliya, "FLEXIBLE PAVEMENT," pp. 1024–1028, 2018.

[3] M. W. Sayers and S. M. Karamihas, "The little book of profiling," *Basic Inf. about Meas. Interpret. Road Profiles*, no. September, p. 100, 1998.

[4] A. Shtayat, S. Moridpour, B. Best, A. Shroff, and D. Raol, "A review of monitoring systems of pavement condition in paved and unpaved roads," *J. Traffic Transp. Eng. (English Ed.*, vol. 7, no. 5, pp. 629–638, 2020, doi: 10.1016/j.jtte.2020.03.004.

[5] M. J. Markow, "Highway Management Systems: State of the Art," *J. Infrastruct. Syst.*, vol. 1, no. 3, pp. 186–191, 1995.

[6] K. R. Benson, G. E. Elkins, W. Uddin, and W. R. Hudson, "Comparison of Methods and Equipment to Conduct Pavement Distress Surveys," 1999.

[7] L. Amador-Jimenez and N. Matout, "A low cost solution to assess road's roughness surface condition for Pavement Management," 2014.

[8] B. Becerik-Gerber, S. F. Masri, and M. R. Jahanshahi, "An Inexpensive Vision-Based Approach for the Autonomous Detection, Localization, and Quantification of Pavement Defects," *Innov. Deserving Explor. Anal.*, vol. 169, no. August, 2015.

[9] S. Sreedhar and E. Coleri, "The effect of long-term aging on fatigue cracking resistance of asphalt mixtures," *Int. J. Pavement Eng.*, vol. 0, no. 0, pp. 1–13, 2020, doi: 10.1080/10298436.2020.1745206.

[10] J. S. Miller and W. Y. Bellinger, "FHWA, Distress Identification manual for the Long-Term Pavement Performance Program. Report FHWA-HRT-13-092," 2014.

[11] H. E. M. Hunt and M. F. M. Hussein, "Ground-Borne Vibration Transmission from Road and Rail Systems: Prediction and Control," in *Handbook of Noise and Vibration Control*, M. J. Crocker, Ed. New York: John Wiley and Sons, 2007, pp. 1458–1469.

[12] C. Zhang and A. Elaksher, "An Unmanned Aerial Vehicle-Based Imaging System for 3D Measurement of Unpaved Road Surface Distresses," *Comput. Aided Civ. Infrastruct. Eng.*, vol. 27, pp. 118–129, 2012.

[13] M. Khoudeir, J. Brochard, V. Legeay, and M.-T. Do, "Roughness Characterization through 3D Textured Image Analysis: Contribution to the Study of Road Wear Level," *Comput. Civ. Infrastruct. Eng.*, vol. 19, no. 2, pp. 93–104, 2004, doi: https://doi.org/10.1111/j.1467-8667.2004.00340.x.

[14] B. Zhao, T. Nagayama, and K. Xue, "Road profile estimation, and its numerical and experimental validation, by smartphone measurement of the dynamic responses of an ordinary vehicle," *J. Sound Vib.*, vol. 457, pp. 92–117, 2019, doi: 10.1016/j.jsv.2019.05.015.

[15] K. M. Mahala, P. Gadkari, and A. Deb, "Mathematical Models for Designing Vehicles for Ride Comfort," *ICORD 09 Proc. 2nd Int. Conf. Res. into Des. Bangalore, India 07.-09.01.2009*, no. i, pp. 168–175, 2009.

[16] M. Saifuddin and M. Yusof, "Parametric Studies on Tramcar Suspension System," *1st Int. Conf. Nat. Resour. Eng. Technol.*, 2006.

COMPDYN 2023
9th ECCOMAS Thematic Conference on
Computational Methods in Structural Dynamics and Earthquake Engineering
M. Papadrakakis, M. Fragiadakis (eds.)
Athens, Greece, 12-–14 June 2023

# MECHANICAL-BASED SEISMIC VULNERABILITY ANALYSIS OF INDUSTRIAL STEEL STRUCTURES WITH MASONRY INFILLS

**Francesco S. Liguori**[1], **Antonio Madeo**[1], **and Antonio Formisano**[1]

[1]DIMES, University of Calabria
Ponte P. Bucci, 87036 Rende (Cosenza), Italy
e-mail: {francesco.liguori, antonio.madeo81}@unical.it

[2] Department of Structures for Engineering and Architecture, University of Naples Federico II
Piazzale Tecchio 80, 80125 Naples, Italy
e-mail: antoform@unina.it

**Abstract.** *This work presents a numerical procedure for constructing mechanical-based fragility curves for industrial steel structures. In particular, the structures under considerations are characterised by the absence of anti-seismic details and by the presence of masonry infills. This structural typology has been identified in southern Italy and represents a widespread construction technology. The exposure information are obtained by an in-situ survey of the industrial area in the municipality of Spezzano Albanese (Italy) using the CARTIS-GL form. Fragility curves are constructed using Monte Carlo simulations and the industrial structures are modelled using mixed frame finite elements accounting for geometrical and material non-linearities.*

**Keywords:** seismic vulnerability, steel structures, industrial structures, masonry infills.

## 1 INTRODUCTION

As demonstrated by the recent earthquakes occurred in different areas of the Italian territory, industrial structures represent a structural typology at high seismic risk [1]. In particular, steel structures usually exhibit a better response to seismic action than precast concrete ones [2], as damages produced by Emilia earthquake in 2012 have highlighted [3]. However, if designed without any seismic criteria, even steel structures can undergo severe damages and collapses under seismic actions [4]. For this reason, recent works are focusing on developing strategies for estimating the seismic vulnerability of steel structures in residential [5, 6, 7] and industrial areas [8, 9]. This interest is further remarked by the long-span (GL) CARTIS database, developed by Italian Civil Protection and many Italian universities [10], which collects data on industrial structures in the Italian territory with the final purpose of providing a reliable seismic risk assessment.

Within the framework of urban scale seismic vulnerability estimate, empirical methods, based on observed damages due to earthquakes, are usually adopted [11]. However, the low number of post-earthquake damage data and the high variability of the typological features of industrial steel structures prevent empirical methods to be used and mechanical-based methods [12, 13] should be adopted.

This work focuses on the seismic vulnerability of industrial steel structures using a mechanical-based approach. In particular, we focus on structures designed without any seismic criteria and characterised by the total absence of bracings, but with masonry infills that provide a certain resistance to horizontal actions [14]. In fact, secondary elements, as masonry infills, can play a significant role on the fragility of civil [15] and industrial buildings [16].

This typology has been recognised in many Italian areas, such as that of Spezzano Albanese, in southern Italy. The starting point is the exposure analysis conducted by using CARTIS-GL form [9]. Then, Finite Element (FE) models are constructed, considering both geometrical and material nonlinearities. Sensitivities analysis are conducted to recognise the influence of geometrical and mechanical features on the seismic behaviour. Finally, mechanical-based fragility curves are constructed and the role played by masonry infills is highlighted. Fragility curves are evaluated using a full-blown Monte Carlo method, considering the variability of the structural features observed in the studied area [17].

The work is organised as follows. The description of the industrial area os Spezzano Albanese is given in Section 2. The FE model of nonlinear steel structures is presented in Section 3. Sensitivity analyses and the construction of the mechanical-based fragility curves is shown in Section 4. Finally, conclusions are drawn in Section 5

## 2 EXPOSURE ANALYSIS

The area under consideration, indicated in Fig. 1, is located in the municipality of Spezzano Albanese, in Calabria region, southern Italy. It is an industrial area built before 1980 and mainly devoted to agricultural purpose which is the principal economic activity of the zone. The total number of industrial buildings is 48, of which 14 made of steel. The structural data for 11 structures is collected using CARTIS-GL form.

The structures are composed by a sequence of parallel frames, realised by steel columns and a truss arch. A typical plan view of the industrial structure is shown in Fig. 2. Figure 3 shows some pictures of the industrial steel structures. It is possible to observe how masonry walls are present along the perimeter. In particular, three configurations are recognised, depending on the walls height, as shown in Figure 4.

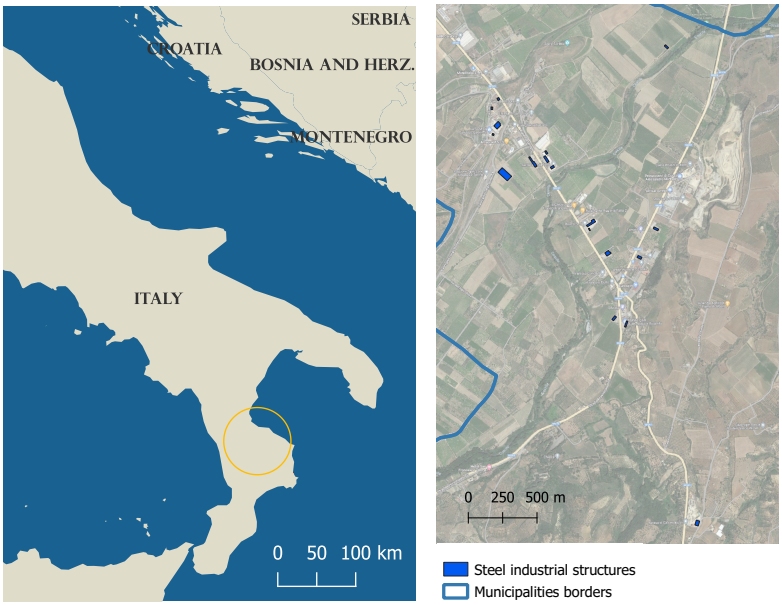


Figure 1: Localisation of the studied area.

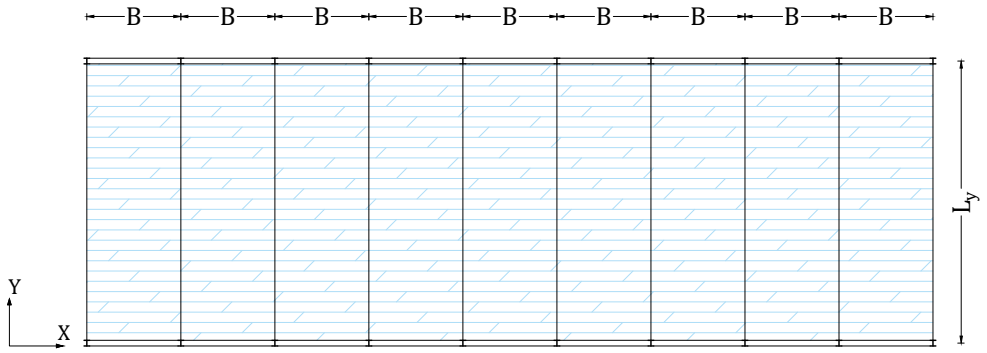


Figure 2: Plan of an industrial steel structure under consideration.

Each surveyed structure is characterised by the group of data listed in Table 1 in which their ranges of variations are also given.

The masonry infills are made of concrete blocks.

## 3 NUMERICAL MODEL

### 3.1 Finite Element

The structure is modelled using plane beam FE. In particular, we make use of a shear deformable mixed assumed stress FE [18] in which displacements and generalised stresses are considered as primary variables. The assumed stress interpolation satisfies equilibrium equations for zero bulk loads [19]. An elastic-perfectly plastic behaviour is assumed for steel members and the yield surface is represented by an ellipsoid to efficiently consider axial-flexural interaction. The accuracy of the representation of the yield surface can be readily improved by adopting techniques based on the Minkowsky sum of ellipsoids [20]. Plasticity is checked at 3 Gauss-Lobatto points on each FE and the integration of the constitutive equation is performed at the element level in order to preserve the assumed stress interpolation [21, 22].



(a) (b) (c)

(d) (e) (f)

Figure 3: Some pictures of the industrial structures in the area under consideration.

Table 1: Variability of geometrical and mechanical parameters of the recognised industrial buildings

| parameter | description | minimum value | maximum value |
|---|---|---|---|
| $L_y$ | Length | 11 m | 15 m |
| $H$ | Column height | 4.5 m | 7.3 m |
| $H_m$ | Arc height | 0.4 m | 2.8 m |
| $H_w$ | Windows height | 0.7 m | 2.0 m |
| $n_t$ | Number of frames | 4 | 16 |
| $B$ | Frame distance | 5 m | 5 m |
| $C_s$ | Column section | IPE270 | HE300A |
| $B_s$ | Beam section | IPE 140 | IPE 240 |

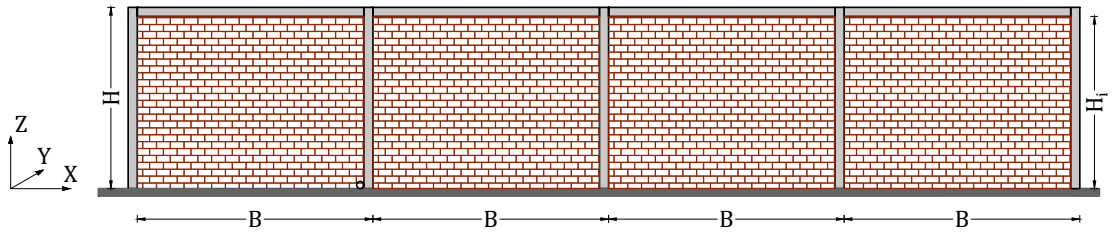


(a) Type A: full height

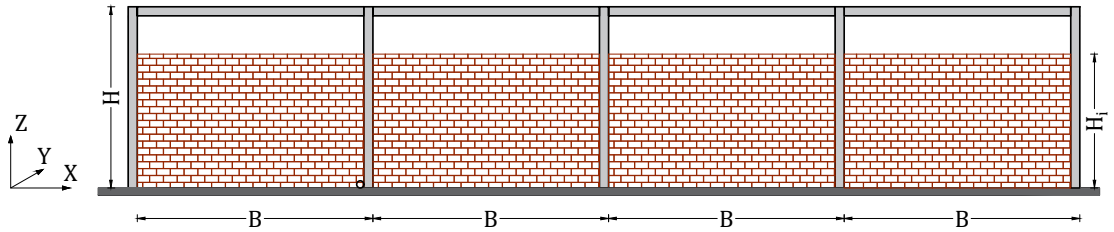


(b) Type B: windows

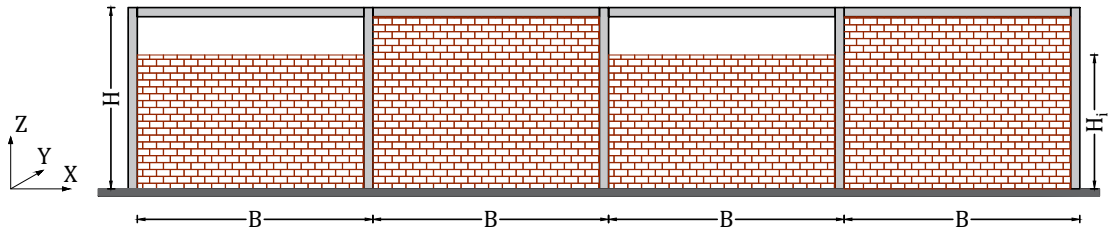


(c) Type C: alternated

Figure 4: Configurations of infilled frames along $x$ direction.

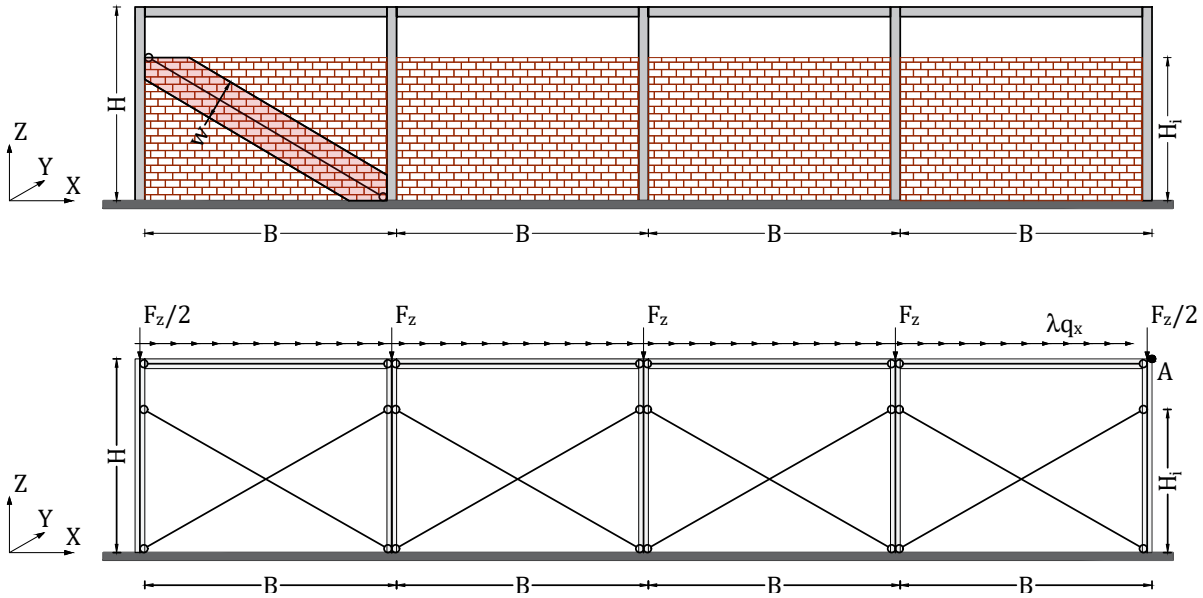


Figure 5: Model of an infilled frame along $x$ direction.

Masonry infills are modelled by adopting a simple single equivalent strut description (see Fig. 5), even if more complex model can be used to improve accuracy [23, 24]. A backbone uniaxial response is adopted [25, 26].

Columns are supposed to be fully clamped on foundations.

The model has been validated by comparing the results with those obtained using the commercial FE software SAP 2000 [27] and Abaqus [28].

### 3.2 Capacity curve

Nonlinear static analyses are performed on the FE model to simulate the seismic response. An arc-length algorithm is employed to trace the equilibrium path [22].

Figure 6 shows the capacity curves obtained both for the infilled structure and the bare one. It is possible to observe that the presence of the masonry infill increases the initial stiffness and the peak shear force ($T$). After peak, a strong degradation is observed and the infills contribution vanishes, so that the structural behaviour coincides with that of the bare frame [29].

Three damage levels are considered, namely immediate occupancy (IO), Life Safety (LS) and Near Collapse (NC) [30, 4, 9]. The damage state is defined in terms of inter-storey drift, on the basis of the FEMA [30] legislative provisions, which refers to the following limits: 0.0075 for IO, 0.025 for LS and 0.05 for NC.

### 3.3 Inelastic spectra

The seismic action is represented by the idealised spectra of Newmark–Hall type defined by Italian seismic code [31] for the municipality of Spezzano Albanese, considering a soil of class C and a topography type T1. In order to obtain the displacement demand, we make use of the inelastic spectra method. In particular, we adopt the modified N2 method [32, 33, 34], specifically devised to be used in presence of masonry infills.

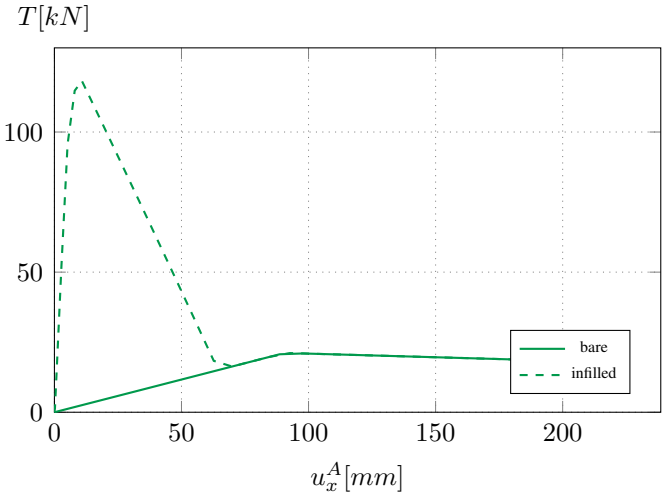


Figure 6: Capacity curves for bare and infilled frames.

Table 2: Variability of additional parameters

| parameter | description | minimum value | maximum value |
|---|---|---|---|
| $\sigma_y$ | Steel yield stress | 200 MPa | 350 MPa |
| $f_{vt}$ | Infill shear resistance | 0.1 MPa | 0.3 MPa |
| $q$ | Permanent roof load | 0.3 kN/$m^2$ | 2 kN/$m^2$ |

## 4 FRAGILITY CURVES

In this work we focus on the structural behaviour along $x$ direction only (See Fig. 5). First, a sensitivity analysis is presented. Then, the fragility curves are obtained using Monte Carlo simulations.

### 4.1 Sensitivity analyses

In this Section, a sensitivity analysis is presented, with the aim of identifying the influence that each structural parameter has on the seismic capacity. We consider the variation ranges obtained by in-situ survey presented in Table 1, plus the variations of other parameters given in Table 2.

A reference structure is considered, characterised by the parameter values given in Table 3, and, on its basis, sensitivity curves are constructed by varying each parameter and obtaining the seismic peak ground acceleration $a_g$ which produces the damage levels. For columns and beams, the section and the related index are given in Tables 4 and 5.

Figure 7 shows the sensitivity curves for the case of bare frames. It is possible to observe that high significance is given by the column type, which influence both the elastic and plastic response. Additionally, the permanent load has a high relevance, especially on the damage levels LS and NC, since it influence the total mass of the dynamic system.

Figures 8, 9 and 10 show the sensitivity curves for the infilled frames for the infill types A, B and C, respectively. In general, one can observe how the $a_g$ values that produce each damage level significantly increase with respect to the bare frame case.

Table 3: Parameters of the reference structure

| parameter | $L_y$ | $H$ | $H_w$ | $n_t$ | $B$ | $C_s$ | $B_s$ | $\sigma_y$ | $f_{vt}$ | $q$ |
|---|---|---|---|---|---|---|---|---|---|---|
| value | 15 m | 4 m | 1.5 m | 6 | 5 m | HE240A | IPE200 | 275 MPa | 0.2 MPa | 1.5 kN/$m^2$ |

Table 4: Section types used for columns in the sensitivity analysis.

| index | 1 | 2 |
|---|---|---|
| section - IPE | 270 | 300 |

| index | 3 | 4 | 5 | 6 | 7 | 8 | 9 | 10 | 11 | 12 | 13 |
|---|---|---|---|---|---|---|---|---|---|---|---|
| section - HE | 200A | 220A | 200B | 240A | 220B | 260A | 240B | 280A | 260B | 300A | 280B |

## 4.2 Fragility curves

Fragility curves are constructed for the structural typology under consideration. As usual [13, 17, 9], fragility curves are expressed by means of cumulative lognormal probability functions, as

$$p(d \geq d_i) = \Phi\left(\frac{log\left(\frac{\lambda_i}{a_g}\right)}{\beta_i}\right), \quad i = 1, \ldots, 3, \tag{1}$$

where $d$ is the structural damage (IO, LS, NC), $\Phi$ is a normal cumulative probability function, while $\lambda_i$ and $\beta_i$ are the mean value and the logarithmic standard deviation of the $a_g$ values that cause the $d_i$ damage grade, respectively. For each damage grade $d_i$, the definition of a fragility curve requires the evaluation of the two parameters $\lambda_i$ and $\beta_i$. To this end, it is necessary to obtain a population of buildings reflecting the in-situ variation of the significant features of the masonry buildings under consideration and to model the uncertainties involved in the seismic vulnerability.

This population is built using Monte Carlo simulation, based on a random generation considering the variability ranges in Tables 1 and 2. For each parameter, a uniform distribution is assumed.

Fragility curves are given in Fig 11 for the bare and type A infilled frames. It is possible to observe how the bare frame shows significantly higher vulnerability than the infilled structure. This aspects highlights the fact that for this type of structure modelling the infill is of crucial importance and suggests that it does not play a secondary structural role, but represents the main seismic-resistant component.

Table 5: Section types used for beams in the sensitivity analysis.

| index | 1 | 2 | 3 | 4 | 5 | 6 | 7 | 8 | 9 | 10 | 11 |
|---|---|---|---|---|---|---|---|---|---|---|---|
| section - IPE | 140 | 160 A | 160 | 180 A | 180 | 200 A | 200 | 220 A | 220 | 240 A | 240 |

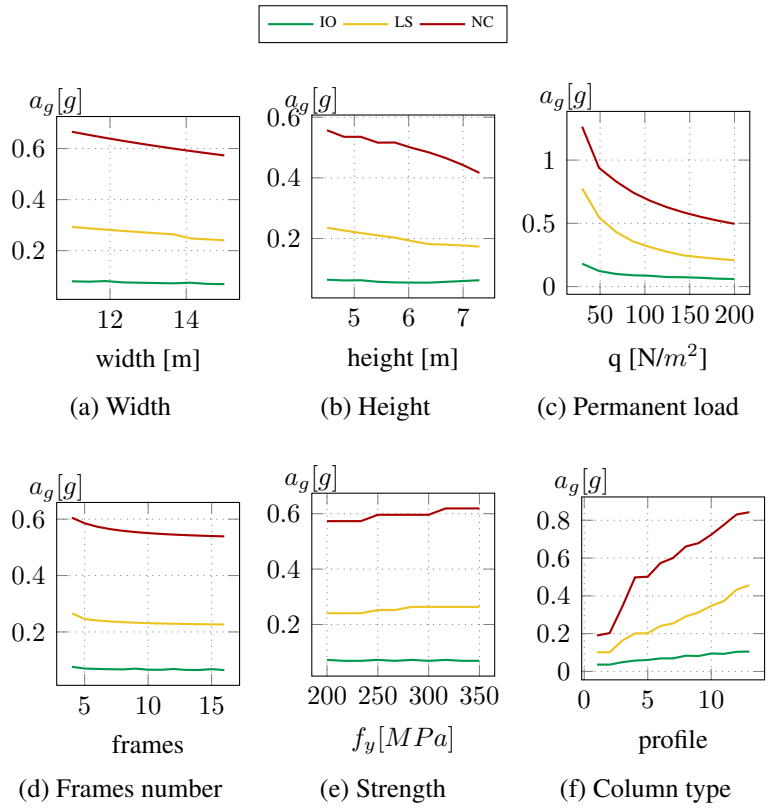


(a) Width (b) Height (c) Permanent load

(d) Frames number (e) Strength (f) Column type

Figure 7: Sensitivity analysis for some geometrical and mechanical attributes, bare frame.

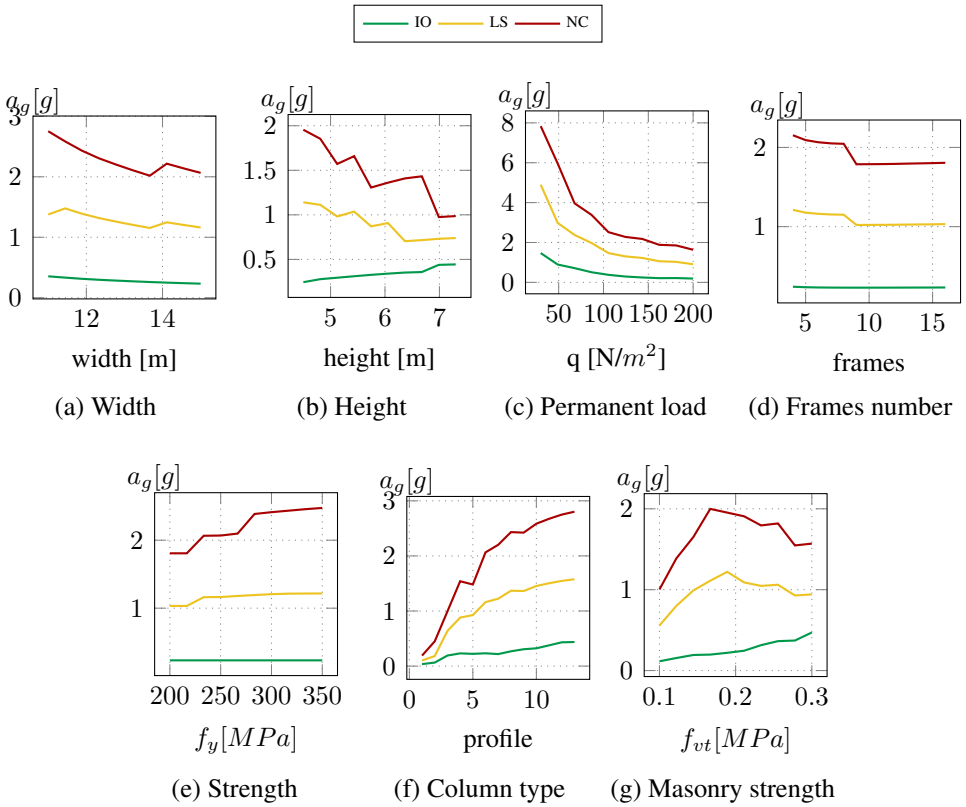


(a) Width (b) Height (c) Permanent load (d) Frames number

(e) Strength (f) Column type (g) Masonry strength

Figure 8: Sensitivity analysis for some geometrical and mechanical attributes, type A infills, X direction.

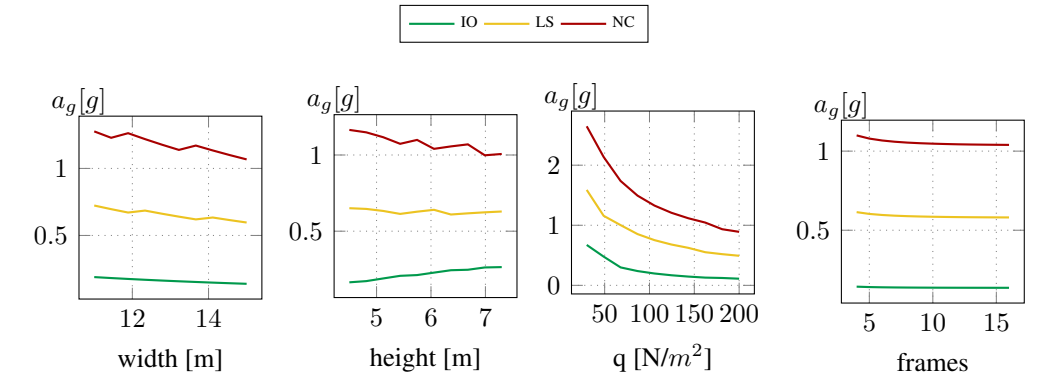


(a) Width (b) Height (c) Permanent load (d) Frames number

(e) Strength (f) Column type (g) Masonry strength (h) Windows height

Figure 9: Sensitivity analysis for some geometrical and mechanical attributes, type B infills, X direction.

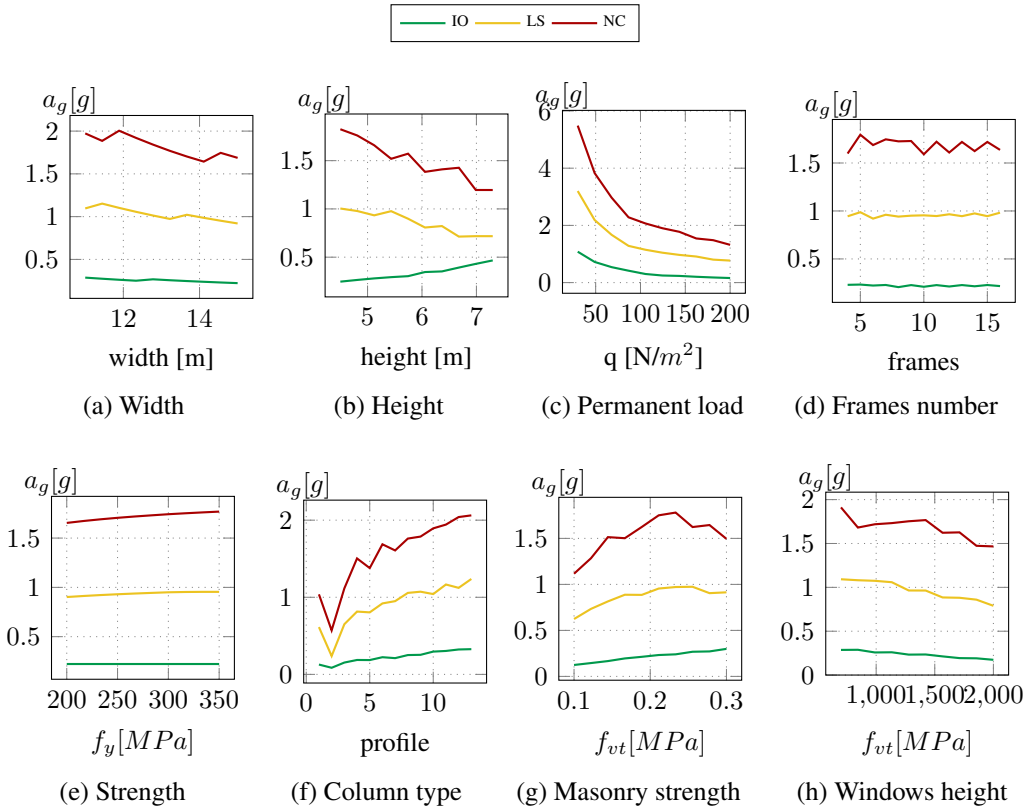


(a) Width (b) Height (c) Permanent load (d) Frames number

(e) Strength (f) Column type (g) Masonry strength (h) Windows height

Figure 10: Sensitivity analysis for some geometrical and mechanical attributes, type C infills, X direction.

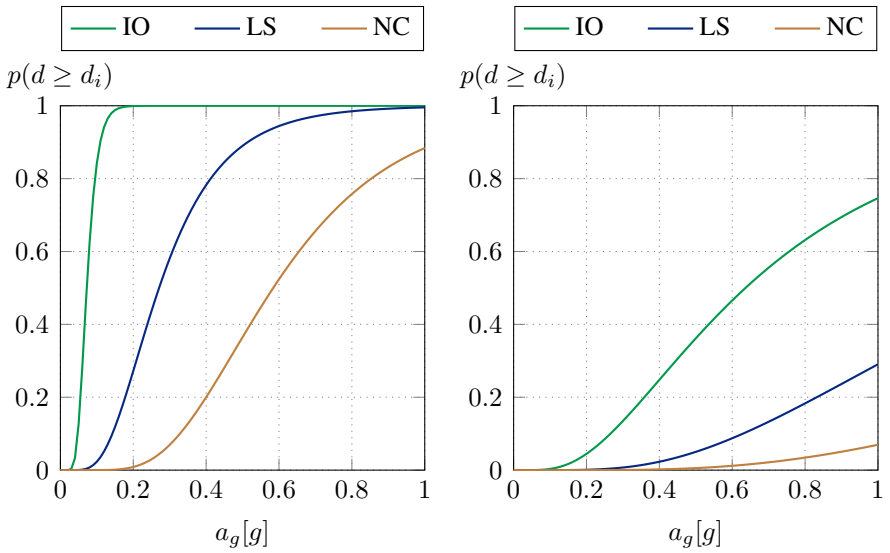


(a) Bare frame (b) Infilled type A

Figure 11: Fragility curves.

## 5 CONCLUSIONS

In this work, the problem of the seismic vulnerability of steel industrial structures designed without anti-seismic criteria and with masonry infills has been addressed. An exposure analysis of an industrial area in the municipality of Spezzano Albanese (Italy) has been conducted using CARTIS-GL form. A numerical model, based on beam FE having geometrical and mechanical nonlinearities has been constructed to analyse the industrial structures. On the basis of the surveyed data, sensitivity analysis has been conducted to identify the most relevant parameters. Results have shown that the mass of the construction has a remarkable influence on the seismic vulnerability, thereby suggesting to reduce the weight of the roof to alleviate the seismic risk. By comparing fragility curves for bare and infilled frames, it has been shown that the presence of masonry infills has a positive influence on the seismic vulnerability.

### Funding

This work was supported by the Civil Protection Department in the framework of the WP2 line CARTIS of the DPC-ReLUIS research project.

## REFERENCES

[1] N. Buratti, F. Minghini, E. Ongaretto, M. Savoia, and N. Tullini, "Empirical seismic fragility for the precast rc industrial buildings damaged by the 2012 emilia (italy) earthquakes," *Earthquake Engineering & Structural Dynamics*, vol. 46, no. 14, pp. 2317–2335, 2017.

[2] A. Formisano, R. Landolfo, and F. Mazzolani, "Robustness assessment approaches for steel framed structures under catastrophic events," *Computers & Structures*, vol. 147, pp. 216–228, 2015. CIVIL-COMP.

[3] M. Savoia, N. Buratti, and L. Vincenzi, "Damage and collapses in industrial precast buildings after the 2012 emilia earthquake," *Engineering Structures*, vol. 137, pp. 162–180, 2017.

[4] A. Formisano, G. Di Lorenzo, I. Iannuzzi, and R. Landolfo, "Seismic vulnerability and fragility of existing italian industrial steel buildings," *The Open Civil Engineering Journal*, vol. 11, pp. 1122–1137, 2017.

[5] C. D. Annan, M. A. Youssef, and M. H. E. Naggar, "Seismic vulnerability assessment of modular steel buildings," *Journal of Earthquake Engineering*, vol. 13, no. 8, pp. 1065–1088, 2009.

[6] A. Silva, L. Macedo, R. Monteiro, and J. Castro, "Earthquake-induced loss assessment of steel buildings designed to eurocode 8," *Engineering Structures*, vol. 208, p. 110244, 2020.

[7] F. M. Nazri, C. G. Tan, and S. N. A. Saruddin, "Fragility curves of regular and irregular moment-resisting concrete and steel frames," *International Journal of Civil Engineering*, vol. 16, pp. 317–927, 2017.

[8] A. Formisano, G. Di Lorenzo, and R. Landolfo, "Non-linear analyses and fragility curves of european existing single-story steel buildings," *AIP Conference Proceedings*, vol. 2116, no. 1, p. 260020, 2019.

[9] A. Formisano, E. Meglio, G. Di Lorenzo, and R. Landolfo, "Vulnerability curves of existing italian industrial steel buildings designed without seismic criteria," in *Proceedings of the 10th International Conference on Behaviour of Steel Structures in Seismic Areas* (F. M. Mazzolani, D. Dubina, and A. Stratan, eds.), (Cham), pp. 872–880, Springer International Publishing, 2022.

[10] G. Zuccaro, M. Dolce, D. De Gregorio, E. Speranza, and C. Moroni, "La scheda cartis per la caratterizzazione tipologico-strutturale dei comparti urbani costituiti da edifici ordinari. valutazione dell'esposizione in analisi di rischio sismico.," *34° Convegno Nazionale GNGTS*, 2015.

[11] G. Zuccaro, F. L. Perelli, D. D. Gregorio, and F. Cacace, "Empirical vulnerability curves for italian mansory buildings: evolution of vulnerability model from the dpm to curves as a function of acceleration," *Bulletin of Earthquake Engineering*, pp. 1573–1456, 2020.

[12] M. Polese, G. M. Verderame, C. Mariniello, I. Iervolino, and G. Manfredi, "Vulnerability analysis for gravity load designed rc buildings in naples – italy," *Journal of Earthquake Engineering*, vol. 12, no. sup2, pp. 234–245, 2008.

[13] M. Rota, A. Penna, and G. Magenes, "A methodology for deriving analytical fragility curves for masonry buildings based on stochastic nonlinear analyses," *Engineering Structures*, vol. 32, no. 5, pp. 1312–1323, 2010.

[14] L. Di Sarno, F. Freddi, M. D'Aniello, O.-S. Kwon, J.-R. Wu, F. Gutiérrez-Urzúa, R. Landolfo, J. Park, X. Palios, and E. Strepelias, "Assessment of existing steel frames: Numerical study, pseudo-dynamic testing and influence of masonry infills," *Journal of Constructional Steel Research*, vol. 185, p. 106873, 2021.

[15] G. Uva, F. Porco, and A. Fiore, "Appraisal of masonry infill walls effect in the seismic response of rc framed buildings: A case study," *Engineering Structures*, vol. 34, pp. 514–526, 2012.

[16] A. Babič and M. Dolšek, "Seismic fragility functions of industrial precast building classes," *Engineering Structures*, vol. 118, pp. 357–370, 2016.

[17] F. S. Liguori, S. Fiore, F. Perelli, D. De Gregorio, G. Zuccaro, and A. Madeo, "Seismic vulnerability of masonry structures through a mechanical-based approach," *ECCOMAS Congress 2022 - 8th European Congress on Computational Methods in Applied Sciences and Engineering*, 2022.

[18] G. Garcea, A. Madeo, and R. Casciaro, "The implicit corotational method and its use in the derivation of nonlinear structural models for beams and plates," *Journal of Mechanics of Materials and Structures*, vol. 7, no. 6, pp. 509–538, 2012.

[19] F. S. Liguori and A. Madeo, "A corotational mixed flat shell finite element for the efficient geometrically nonlinear analysis of laminated composite structures," *International Journal for Numerical Methods in Engineering*, vol. 122, no. 17, pp. 4575–4608, 2021.

[20] D. Magisano, F. Liguori, L. Leonetti, and G. Garcea, "Minkowski plasticity in 3d frames: Decoupled construction of the cross-section yield surface and efficient stress update strategy," *International Journal for Numerical Methods in Engineering*, vol. 116, no. 7, pp. 435–464, 2018.

[21] D. Magisano and G. Garcea, "Fiber-based shakedown analysis of three-dimensional frames under multiple load combinations: Mixed finite elements and incremental-iterative solution," *International Journal for Numerical Methods in Engineering*, vol. 121, no. 17, pp. 3743–3767, 2020.

[22] F. S. Liguori, A. Madeo, and G. Garcea, "A dual decomposition of the closest point projection in incremental elasto-plasticity using a mixed shell finite element," *International Journal for Numerical Methods in Engineering*, vol. 123, no. 24, pp. 6243–6266, 2022.

[23] M. Yekrangnia and M. Mohammadi, "A new strut model for solid masonry infills in steel frames," *Engineering Structures*, vol. 135, pp. 222–235, 2017.

[24] R. Gentile, S. Pampanin, D. Raffaele, and G. Uva, "Non-linear analysis of rc masonry-infilled frames using the slama method: part 1—mechanical interpretation of the infill/frame interaction and formulation of the procedure," *Bulletin of Earthquake Engineering*, vol. 17, pp. 3283–3304, Jun 2019.

[25] L. Cavaleri, M. Papia, G. Macaluso, F. Di Trapani, and P. Colajanni, "Definition of diagonal poisson's ratio and elastic modulus for infill masonry walls," *Materials and Structures*, vol. 47, pp. 239–262, Jan 2014.

[26] L. Cavaleri and F. Di Trapani, "Cyclic response of masonry infilled rc frames: Experimental results and simplified modeling," *Soil Dynamics and Earthquake Engineering*, vol. 65, pp. 224–242, 2014.

[27] "SAP2000. Advanced 14.2.2 Structural Analysis Program – Manual," *Computer and Structures, Inc.*, 2010.

[28] K. Hibbit and P. Sorenson, "Abaqus analysis user's manual version 6.7," 2007.

[29] F. De Luca, D. Vamvatsikos, and I. Iervolino, "Near-optimal piecewise linear fits of static pushover capacity curves for equivalent sdof analysis," *Earthquake Engineering & Structural Dynamics*, vol. 42, no. 4, pp. 523–543, 2013.

[30] F. Agency, *Prestandard and Commentary for the Seismic Rehabilitation of Buildings (FEMA 356)*. CreateSpace Independent Publishing Platform, 2013.

[31] M. Decree, "Technical codes for constructions (NTC 2018," *Official Gazette of the Italian Republic*, pp. 1–434, 2008.

[32] M. Dolšek and P. Fajfar, "Inelastic spectra for infilled reinforced concrete frames," *Earthquake Engineering & Structural Dynamics*, vol. 33, no. 15, pp. 1395–1416, 2004.

[33] M. Dolšek and P. Fajfar, "Simplified non-linear seismic analysis of infilled reinforced concrete frames," *Earthquake Engineering & Structural Dynamics*, vol. 34, no. 1, pp. 49–66, 2005.

[34] M. Dolšek and P. Fajfar, "The effect of masonry infills on the seismic response of a four-storey reinforced concrete frame — a deterministic assessment," *Engineering Structures*, vol. 30, no. 7, pp. 1991–2001, 2008.

COMPDYN 2023
9th ECCOMAS Thematic Conference on
Computational Methods in Structural Dynamics and Earthquake Engineering
M. Papadrakakis, M. Fragiadakis (eds.)
Athens, Greece, 12-14 June 2023

# NUMERICAL ANALYSIS ON A REVERSIBLE CONNECTION FOR STEEL MODULAR BUILDINGS

**A. Palmiotta[1], M. D'Amato[2] and R. Gigliotti[1]**

[1] DISG, Dept. Of Structural and Geotechnics Engineering, Sapienza University of Rome,
Via Eudossiana 18, 00184 Rome.
e-mail: {annarita.palmiotta,rosario.gigliotti}@uniroma1.it

[2] DiCEM, Dept. of European and Mediterranean Cultures: Architecture, Environment and Cultural Heritage, University of Basilicata,
Via Lanera, 75100 Matera, Italy.
e-mail: michele.damato@unibas.it

## Abstract

*Modular buildings are a new type of structural system composed by prefabricated modular units and assembled on site through inter-modular connections. These structures can form complete building blocks with suspended ceilings and installations, including electrical and water systems. These modular solutions can be adapted to any use like hospitals, housing schools, etc.*
*This work focuses on the analysis of structural behavior on a reversible steel connection modelling with finite element approach.*
*To this scope, in the paper an ideal case study is considered, characterized by steel elements. The modules are assembled by inter-module connections that allow for rapid assembly on-site, without any need of skilled workmanship reducing the welding and the use of bolts. Therefore, Midas Fea NX is used to define the contact between steel elements in detail.*

**Keywords:** Green design, modular constructions, reversible connection, seismic analysis, steel connections.

## 1 INTRODUCTION

The use of the term "modular construction" refers to a method of building structural elements according to which they are manufactured by industrial processes and assembled on site. Use of modular structures dates to the end of the 1990s and has evolved significantly to play an important role in the construction industry worldwide. Major applications have occurred in the construction of hotels, residential apartments, school buildings, temporary post-catastrophe housing, and military operations. This development is mainly due to the main benefits such solutions have. In particular, the cost of designing and building a structure using modules is generally lower than the conventional method; design, construction and installation of the various modules are much quicker than the equivalent cast-in-place solution and therefore there is a saving in terms of time as well; there is a saving in terms of waste produced since building the individual modules in-house results in waste production that is significantly inferior to conventional construction techniques.

Modular steel buildings can be divided, depending on the structural system, into different types, including entirely modular structures and hybrid structures. The first concerns individual modular units linked together and made integral through connections. The second combines modules assembled with a primary structure made of steel or reinforced concrete, so as to improve resistance for gravitational loads.

This paper will discuss the first type mentioned earlier and referred to as a Modular Functional Unit (MFU). The structure of which the individual modules are composed is called Modular Structural Units (MSU), and the individual structural components are called Elementary Structural Units (ESU), Figure 1.

The ESUs, that are part of the steel structure, are held together through steel connections, which is also an important structural element for the purpose of absorbing seismic action. In modular buildings, connections can be regrouped into inter-modular, intra-modular and module-foundation buildings.

The work presented is part of an on-going research project [1] aimed at proposing reference for modules, suitable for seismic zones and characterized by low seismic damage. In particular, the focus is on inter-modular connections.

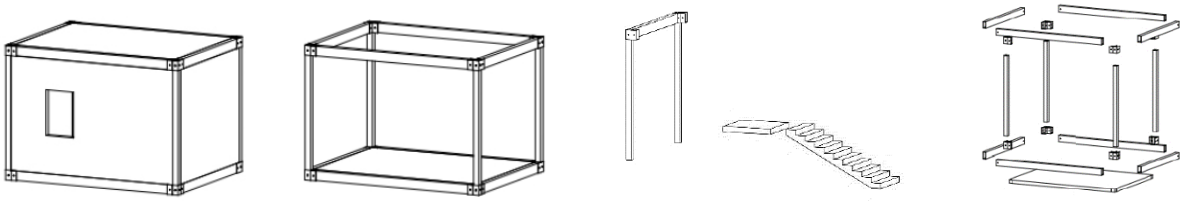

a) b) c) d)

Figure 1: a) Modular Functional Unit (MFU); b) Modular Structural Units (MSU); c) Elementary Structural Unit (ESU); c) Elementary Structural Component (ESC).

## 2 STATE OF ART

The work focuses on inter-modular connections. This type of connection must be able to assure horizontal connection between adjacent modules and vertical connection between piled modules. The need to connect modules vertically often finds difficulties because it is necessary to provide a gap between the floor and ceiling beams that allows access to the connections from the outside and the passage of services between the beams. Different solutions can be found in the literature, and a few are shown thereafter.

The first example of connection considered is analyzed by T. Gunawardena [2]. This connection is designed to connect the modules both horizontally and vertically and transfer their actions in both directions. The connection consists of four different plates, each welded to the hollow columns Figure 2a. Only two of these horizontally cover the entire connection. The plates are connected through bolts, with the center bolts spanning three shear zones and the bolts placed in the two lateral zones (Figure 2b). The horizontal plates cause creep failure in the presence of horizontal forces, such as those that can occur in earthquakes.

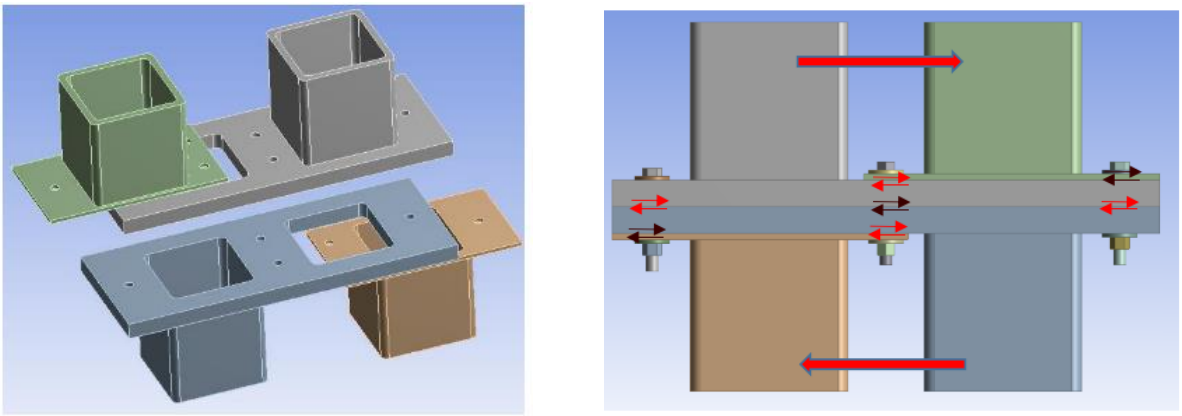

a) b)

Figure 2: Modular connection: a) components; b) existing shear planes in the connection when column is axially loaded (T. Gunawardena [2])

Another example is presented by Z. Chen et al. [3] in two different versions shown in Figure 3. Both versions have a plug-in device to transfer horizontal loads and a beam-to-beam bolt as the vertical connection. The difference between the two solutions is the presence of a stiffener in the weld zone between the column and the beam (element 9 on the right of Figure 3). Of these two proposals, in addition to analysis through Finite Element software, experimental tests have been carried out. The experimental results show that the connections, subjected to static loading failed with fracture in the unit joint welds. The diagonal stiffeners effectively strengthen the connection in the unitary joint.

However, the connection in reference possesses significant post-serving deformation capacity and ductility.

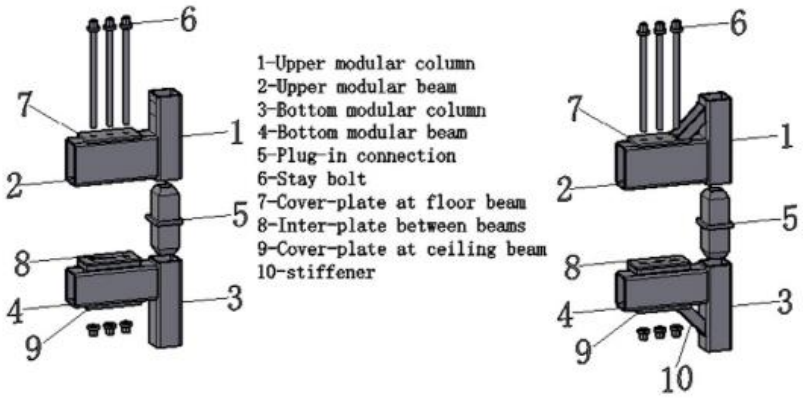


Figure 3: Z. Modular Connections (Chen et al. [3])

## 3 INTER-MODULE CONNECTION PROPOSED

Starting from the state of the art and analyzing some of the connections, the following study presents a first part of the design of an inter-modular connection that can minimize the use of bolts and avoid sliding between its components. The connection consists of tubular columns joined through a connection plug-in. A u-shaped profile is welded to the columns, on which the beam is placed. The two elements are fixed through a single pin (Figure 4a). This connection can also be used to connect 4 or 8 modules (Figure 4c). For this study, the simplest case is considered: two columns and one beam that are part of a MFU (Figure 5) consisting of structural elements described in Table 1.

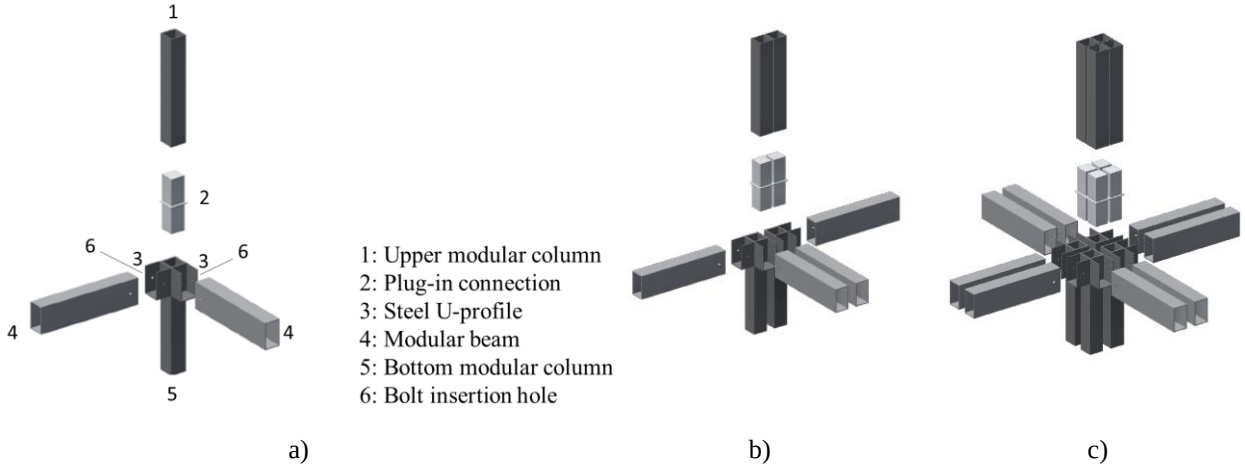


a) b) c)

Figure 4: Proposal inter-module connection

| Element | Width (mm) | Height (mm) | Thickness (mm) | Length (mm) |
|---|---|---|---|---|
| Beam | 150 | 250 | 8 | 1000 |
| Column (Upper and Bottom) | 150 | 150 | 8 | 1000 |
| Plug-in (Upper and bottom) | 134 | 134 | 8 | 250 |
| Plate | 166 | 166 | 8 | - |

Table 1: Characteristics of structural element

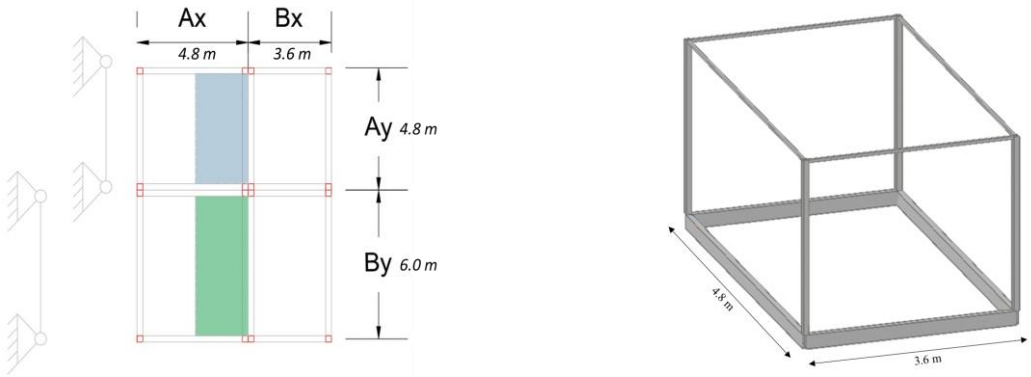


a) b)

Figure 5: MFU dimensions.

### 3.1 Numerical modelling

Modeling of the connection is conducted through Midas FEA NX 2023 v.1.1 using solid elements. During this type of modeling, it is important to define the contact between the individual elements that make up the connection. In fact, contact conditions are applied to the meshes of the solid elements (visible in exploded view in Figure 6a) according to their real condition (Figure 6b). The software presents 4 contact types described in detail in Table 1 [4] [5]. For the present study, three contacts are mainly used, welded contact and rough contact. The first one is used between the welded surfaces and that therefore the load distribution does not vary as the mesh changes because the faces are completely joined; the second considers the impact between the solids preventing penetration; the third considers the sliding between two surfaces.

All elements are in steel and they are defined through a bilinear isotropic bond considering Von Mises plasticity. The material considered is Fe510 steel with a modulus of elasticity of 206 GPa and Poisson's ratio 0.3, according to EN 10025-2:2019 [7]).

The maximum horizontal displacement is equal to 20 mm (corresponding to drift 1%) in Y-direction, and it is applied at the top of the upper column. The sub-assemblage considered in this studied reproduces a beam-column joint between two consecutive steel modules. Therefore, in order to better investigate the joint behavior under static lateral loads the numerical model has a hinge at the base of the lower column and at the end of the horizontal beam. In order to permit horizontal displacement of the beam the hinged end has the possibility as well of moving horizontally. Pushover nonlinear analyses have been performed. For simplicity in this study no axial load has been applied at the top of the column.

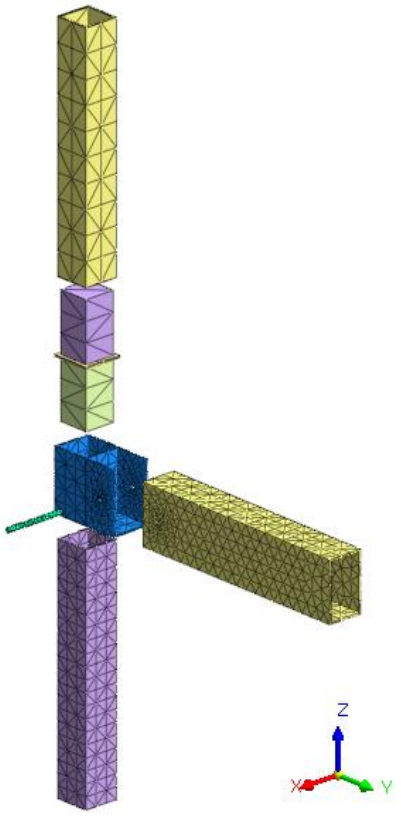


a)

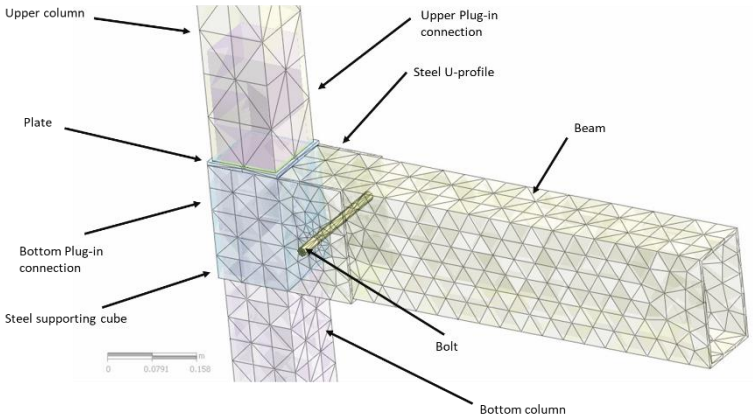


| Element | Contact Type |
|---|---|
| Upper column – upper plug-in connection | IV |
| Upper plug-in connection - plate | I |
| Plate – bottom plug-in connection | I |
| Bottom plug-in connection – bottom column | IV |
| Steel u-profile – steel supporting cube | I |
| Steel supporting cube – bottom column | I |
| Beam – steel u-profile | II |
| Beam – steel supporting cube | IV |
| Bolt – steel u-profile | IV |

b)

Figure 6: a) exploded view of beam, columns and their connections; b) contact types used in the study.

| Type | Typology | Description | Graphic description |
|---|---|---|---|
| Type I | Linear | Welded contact: This is a type of contact who considers at the start of the analysis the welded between two objects. | 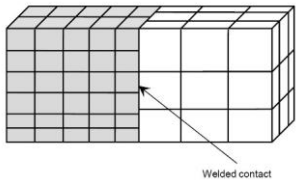 |
| Type II | Linear | Bi-directional sliding contact: it considers only the slidings. | 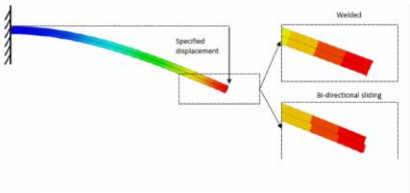 |
| Type III | Non Linear | General contact: this contact considers the impact and friction between two objects not in contact at the start of the analysis. | 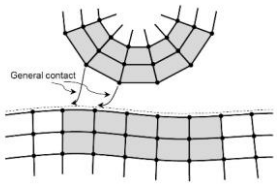 |
| Type IV | Non Linear | Rough contact: This type of contact considers only the impact. It does not consider sliding between two faces. | 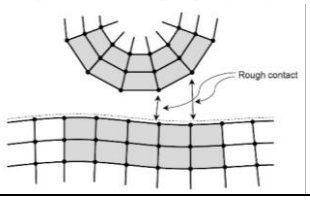 |

Table 2: Different type of contact in Midas Fea NX [4], [5].

## 4. RESULTS

The maximum force applied at the head node of the upper column can be read in the force-displacement graph shown in Figure 7.

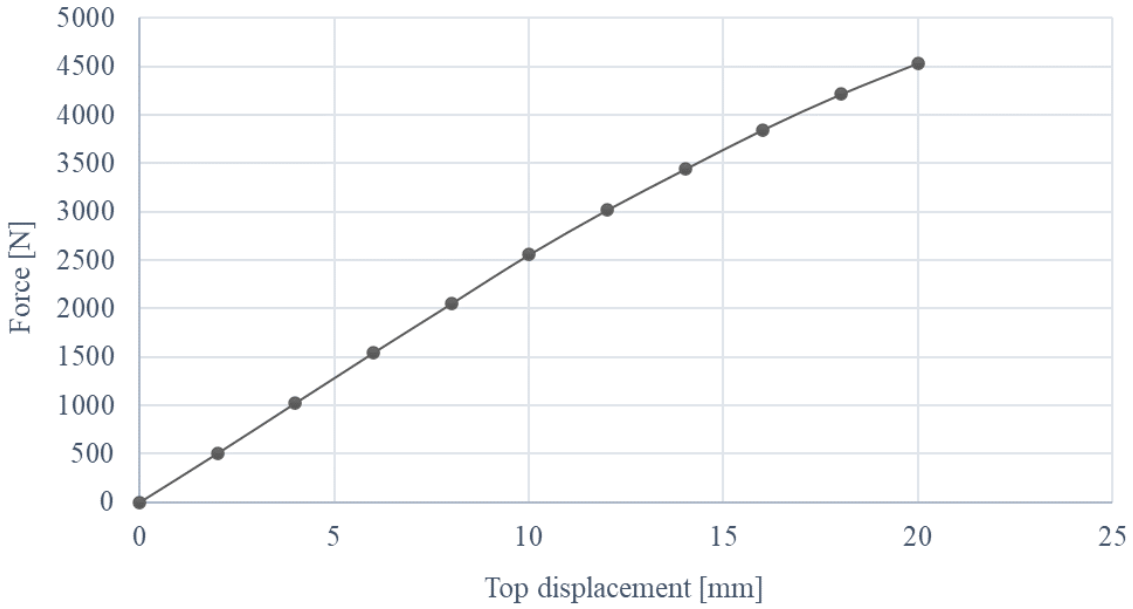


Figure 7: Force-displacement graph.

The Figure 8a shows the Von Mises stress results accounting for all possible combinations of stresses present in the analysis model. The Figure 8b shows the stress distribution in Y-direction where, areas subjected to compression are visible in blue while areas subject to tension are in red.

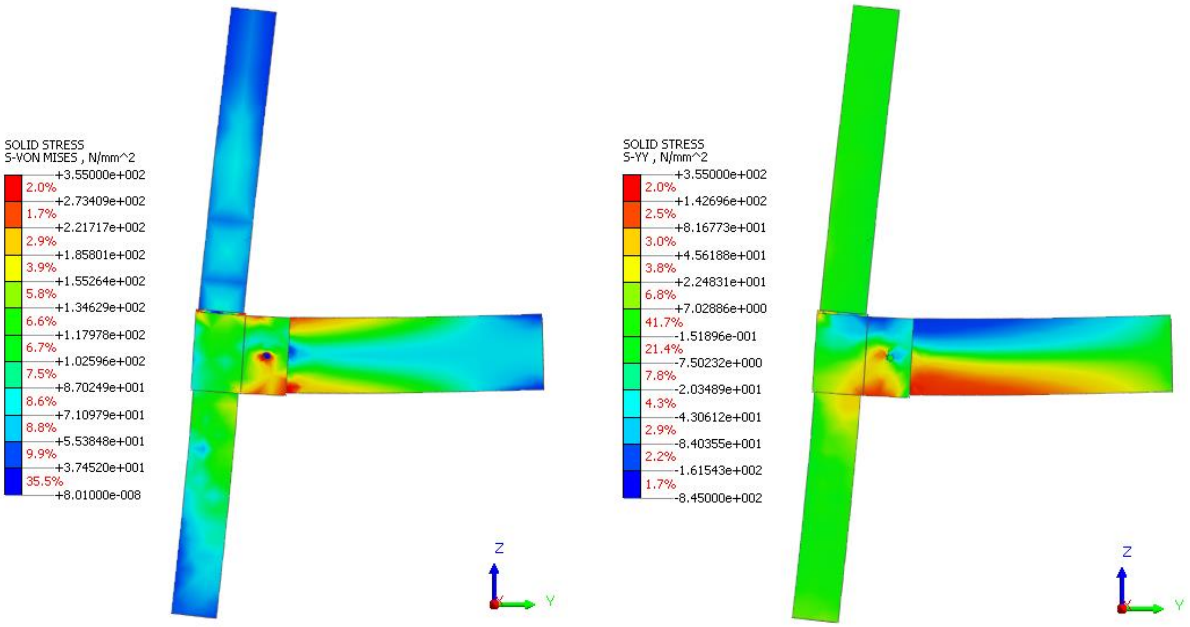


a) b)

Figure 8: a) Von Mises stress distribution; b) Y- direction stress distribution.

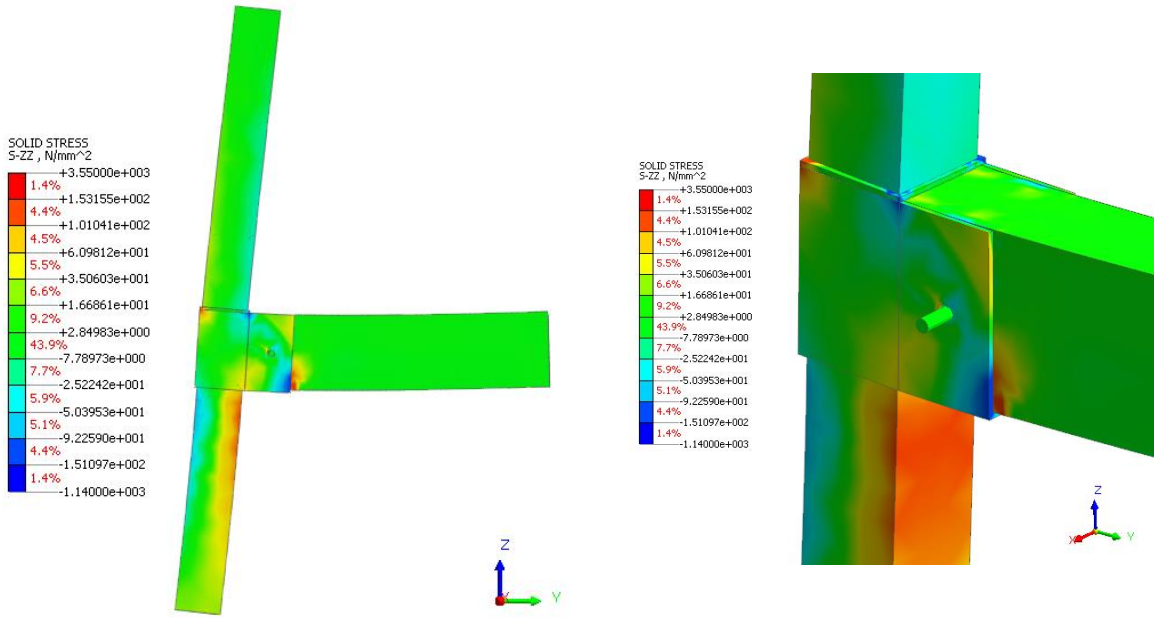


Figure 9: Z – direction stress distribution.

The stress state in the Z-direction shows that higher stress states occur near the welding, as visible in Figure 9 and in Figure 10.

In Figure 11 the plastic state of the elements is observed. Specifically, Figure 11a shows the state of plasticization at the first steps of analysis, and Figure 11b shows the final plastic state. The areas principally affected by material plasticization are the u-profile, the connection (plug-ins and connection plate), and the connection cube.

The graph in Figure 12 shows the maximum yield stress for element as the drift increases. The plate is the first to start the plastic status (0.3% drift), while the u-profile and the bottom plug-in are the last (0.6% drift). The plate achieves maximum yield stress at 1% drift.

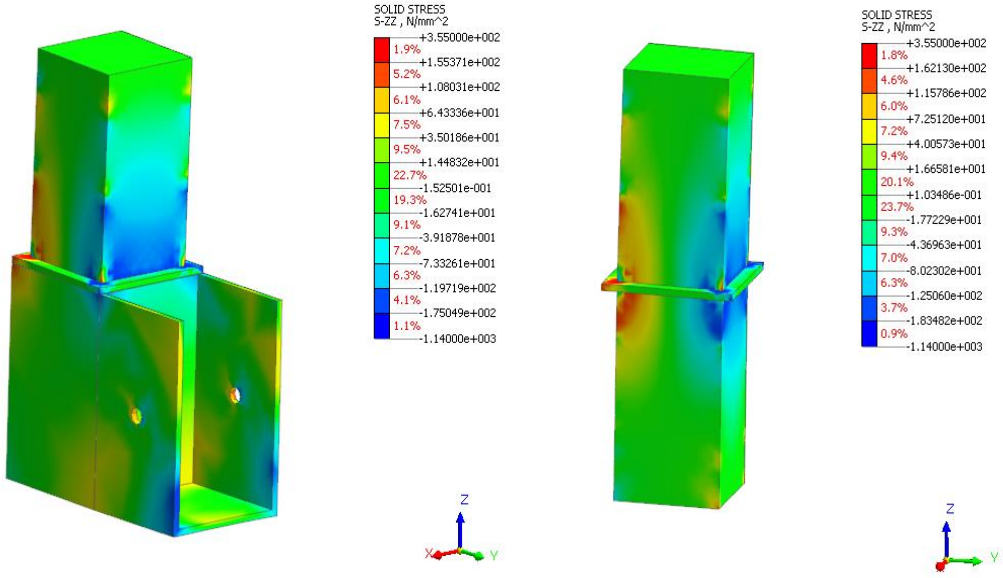


a) b)

Figure 10: a) Steel u-Profile stress distribution; b) Plate, upper and bottom plug-ins stress distribution.

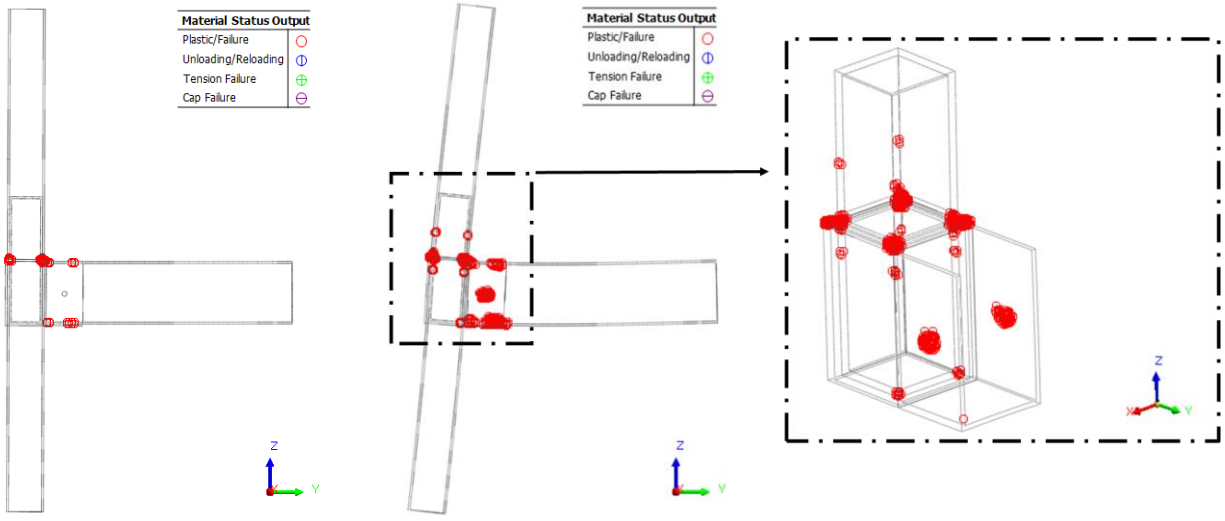


a) b)

Figure 11: a) Starting of plastic status; b) Final plastic status.

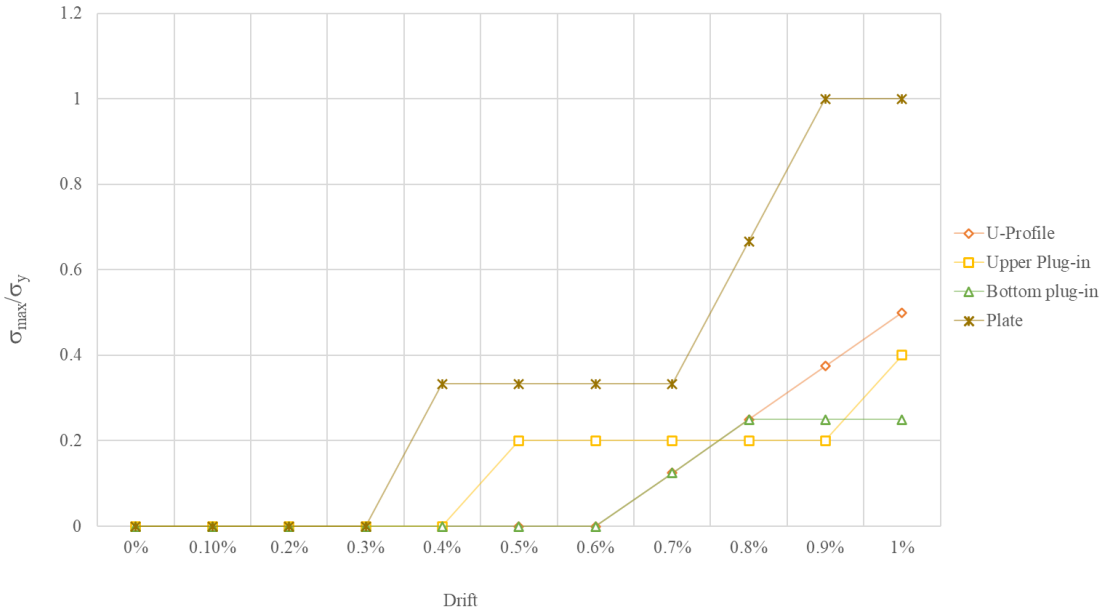


Figure 12: Individual steel element stress status as drift increasing.

## 4 CONCLUSIONS

This study focused on numerical analysis on a reversible connection for steel modular buildings designed by combining existing connection types from the literature. The modeling has been performed using Midas Fea NX and using the Von Mises material model. This work has focused mainly on the study and proper use of the contact types present within the software. These contact types, moreover, influenced the type of analysis to be performed.

Three types of contact are used for this preliminary study, two of the liner type (Welded contact and Bi-directional sliding contact) and one of the nonlinear type (Rough contact). Welded contact is used for surfaces in contact from the beginning of the analysis, bi-directional sliding contact to consider sliding between the beam and the u-profile, and rough contact for all other surfaces.

By applying a displacement at the upper column, the behavior of the internal connection formed by two plug-ins welded to a plate has been evaluated. The results of the analysis show that the horizontal plate reaches yield stress before the other elements.

The study presented in this paper represents a preliminary investigation on the structural behavior of the connection of the beam-column joint considered. In the future, numerical investigations will be validated with experimental tests, conducted either with static or dynamics lateral loads. The comparisons between numerical and experimental investigations will permit of highlighting how the connection investigating may be improved in order to obtain a better structural performance. Moreover, additional investigations will be conducted in order to take into account different levels of axial load on the preliminary connection considered in this study.

## REFERENCES

[1] A. Palmiotta, S. Garbellini, L. Audisio, R. Sulla, M. D'Amato, R. Gigliotti, Seismic behaviour of steel modular buildings: numerical analysis and comparisons between different design solutions. Procedia Structural Integrity, 2023. https://doi.org/10.1016/j.prostr.2023.01.149

[2] T. Gunawardena, Behaviour of Prefabricated Modular Buildings Subjected to Lateral Loads, The University of Melbourne, 2016.

[3] Z. Chen, J. Liu, Y. Yu, C. Zhou, R. Yan, Experimental study of an innovative modular steel building connection. *J. Constr. Steel Res.*, **139**, pp. 69 – 82, 2017. doi:10.1016/j.jcsr.2017.09.008

[4] MIDAS Information Technology Co., Midas GTS NX 2023 v1.1 Analysis Reference, Chapter 5: Analysis Method, pp. 361-363, 2023.

[5] MIDAS Information Technology Co., Midas GTS NX 2023 v1.1 Tutorials, Contact Analysis, pp.29, 2023.

[6] F. J. Luo, C. Ding, A. Styles and Y. Bai, End Plate-Stiffener Connection for SHS Column and RHS Beam in Steel-Framed Building Modules, *International Journal of Steel Structures*, 2019. https://doi.org/10.1007/s13296-019-00214-6

[7] EN 10025-2:2019, Hot rolled products of structural steels - Part 2: Technical delivery conditions for non-alloy structural steels.

COMPDYN 2023
9th ECCOMAS Thematic Conference on
Computational Methods in Structural Dynamics and Earthquake Engineering
M. Papadrakakis, M. Fragiadakis (eds.)
Athens, Greece, 12-14 June 2023

# SEISMIC EFFECT ON THE MICADO STRUCTURAL SOLUTION. A NUMERICAL ANALYSIS.

**A. Dalalbashi[1], J. Pinto[2], C. Reis[3], F. Pimenta[4], N. Oliveira Ferreira[4], N. Bento Pereira[5]**

[1] Postdoctoral researcher
Engineering Department, University of Trás-os-Montes and Alto Douro, Vila Real, Portugal
e-mail: alidalalbashi@gmail.com

[2] Assistance Professor
Engineering Department, University of Trás-os-Montes and Alto Douro, Vila Real, CMADE, Portugal
tiago@utad.pt

Engineering Department, University of Trás-os-Montes and Alto Douro, Vila Real, Construct, Portugal
crisreis@utad.pt

[3] Researcher
CICon – Center for Innovation in Construction, Vila Pouca de Aguiar, Portugal
fernando@cicon.pt, nuno@cicon.pt

[4] Chief scientist
Graniparalelo Construction, Vila Pouca de Aguiar, Portugal
research@graniparalelo.com

## Abstract

*MICADO is a modular construction system for dwellings, proposed and developed by a Portuguese construction startup. In brief, it consists of building the dwelling envelope using prefabricated panels. The panels come pre-finished and include adequate thermal insulation. They have a width range between 300 mm to 1200 mm. Each panel is vertically perforated to assist with its on-site assemblage, and accommodate the structural components. The solution allows a wide range of architectural solutions, as well as multiple size openings (e.g., doors and windows). The present paper aims to propose a structural solution for the MICADO construction system. Considering the modular building requirement and using prefabricated panels, assembling a particular type of column-to-beam connections and structural behavior under gravity and seismic loads should be investigated. The structural solution is formed by steel pipe, box, and L-shaped prefabricated profile columns, steel H-shaped pro-file beams, and a steel-deck composite floor. The panels are assembled in the steel profile columns. For this purpose, a two-floor MICADO dwelling is analyzed and designed using numerical modeling, and the structural performance is evaluated. The results show valuable insights into the design and construction of the MICADO method as a steel-based modular structure.*

**Keywords:** Modular construction, Seismic load, Connection, Steel structures, Industrialized construction.

## 1 INTRODUCTION

Modular structure or construction is an innovative approach that has recently gained popularity. This method involves the use of prefabricated building components or modules that are manufactured off-site and then assembled on-site to create larger structures. This approach offers a range of benefits over traditional construction methods, including faster construction times, improved quality control, and increased sustainability [1–3]. Modular construction has been applied to various building types, including residential homes, commercial buildings, and schools [4]. As the demand for faster, more efficient construction methods continues to grow, modular construction is likely to become an increasingly important technique for meeting the needs of the building industry.

There are varied types of modular construction, such as steel-, concrete-, and wood-based materials [5–7]. However, research has focused more on case studies and aimed at developing and solving the challenges in these types of structures. Steel-based modular structures have received considerable attention due to their speed, quality control, and reduced waste. Recently, a particular focus has been on the connection of steel modular structures, seismic response, and construction planning [4,8].

This study examines the parametric development of the MICADO method for use in modular structures. MICADO is a structural method composed of modular systems and prefabricated panels. For this purpose, a case study is selected, and possible challenges and limitations of this method (such as assembling, structural elements, and structural behavior) are examined. A case study includes a modular steel structure analyzed and designed using numerical modeling.

## 2 MICADO SOLUTIONS

The MICADO method is designed to address the main problems faced by the small building industry, allowing its evolution and application to that of manufacturing. MICADO consists of developing a new advanced building production system, including components produced in autonomous production lines and assembled on-site. This method includes prefabricated thermal insulation panels and structural steel, concrete, or wood-based elements.

### 2.1 Panels

MICADO elements consist of panels with drilling, rectangular, and L-shaped sections (Figure 1) and with 650mm and 2500 mm high. The panels are clad inside with gypsum plasterboard, and the outside cladding is made of cementitious panels. Panels with drilling sections are used for constructing the facade of the structure. Rectangular and L-shaped panels are used next to the opening and at the corner of the structure, respectively. From center to center, the minimum and maximum distances between the two circular sections are 225 mm and 450 mm, respectively.

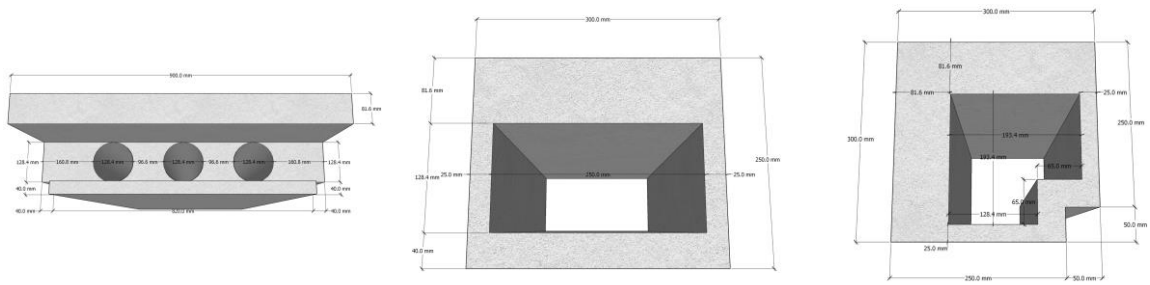

(a) (b) (c)

Figure 1. MICADO Elements: (a) Drilling section; (b) Rectangular section; (c) L-shaped section.

### 2.2 Structure and assembling

Steel profiles were selected for constructing MICADO structures based on the panel's shapes. Figure 2 shows the steps for assembling these types of structures. In the first step, the base plates were executed simultaneously with the construction of the foundation. Then the columns and panels were placed. Next, the main beams placed around the structure were implemented. Then, the columns of the second floor were placed. In the end, the secondary beams were executed to construct the floor and roof.

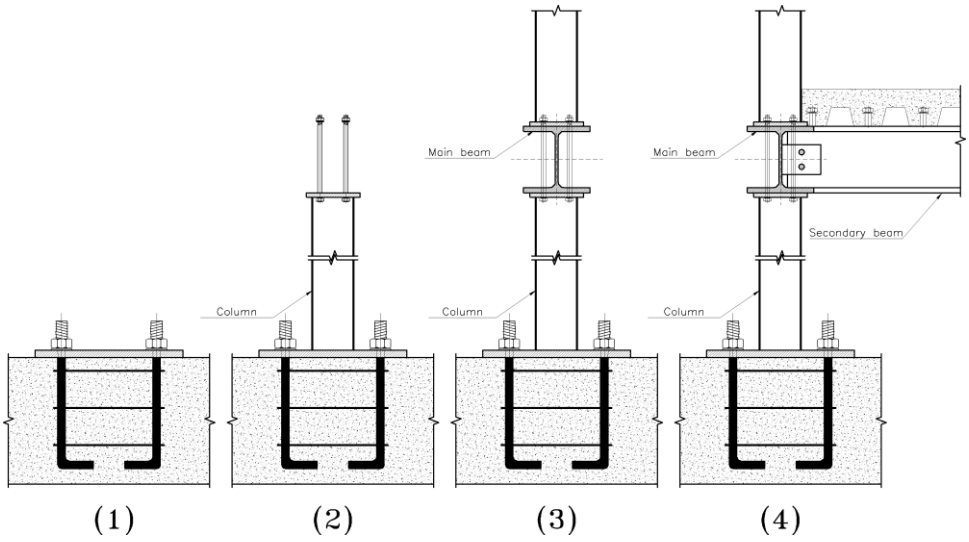


Figure 2. Assembling of steel-based MICADO structures.

## 3 NUMERICAL MODELING

Linear static analysis was carried out in commercial software, and the elements of the steel-based modular structure were analyzed and designed based on Eurocodes 3 and 8 [9,10]. Figure 3 shows a 3D view of the numerical model. The general case study was rectangular, with 12 m in 7 m and a story high of 3.15 m. The model had four openings with a 3.15 m width at each structure corner. The column distance was determined as 450 mm to consider the critical situation in MICADO structures.

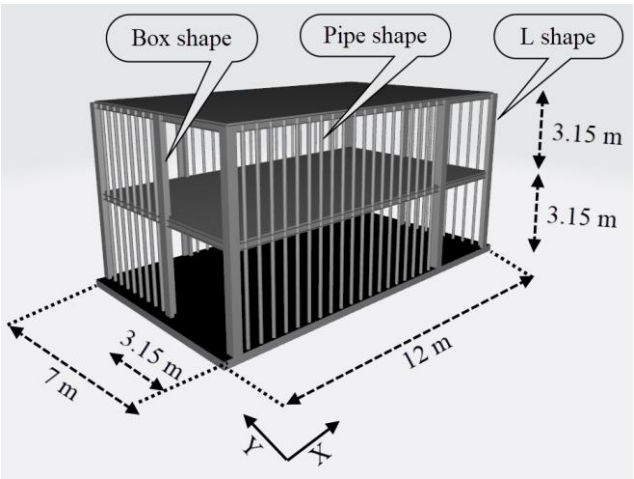


Figure 3. 3D view of the numerical model.

Frame element was used to model beams and columns, including the effects of biaxial bending, axial force, shear force, and deformation of elements. The connection of the secondary beam to the main beam was determined as a hinge joint. The moment-resisting connection was determined for beam-to-column joints. Furthermore, connections between columns and foundations were restrained in all three directions, including translation and rotation.

### 3.1 Elements

Steel profiles were used for modeling the structure with 240 MPa tensile strength and 200 GPa elastic modulus. Columns profiles were pipe, box, and L-shaped prefabricated profiles, as shown in Figure 4. Furthermore, for both the main and secondary beams H-shaped section was used. The gravity loads were also borne using a steel-deck composite, which includes secondary steel beams and a one-way concrete slab with 110 mm thickness.

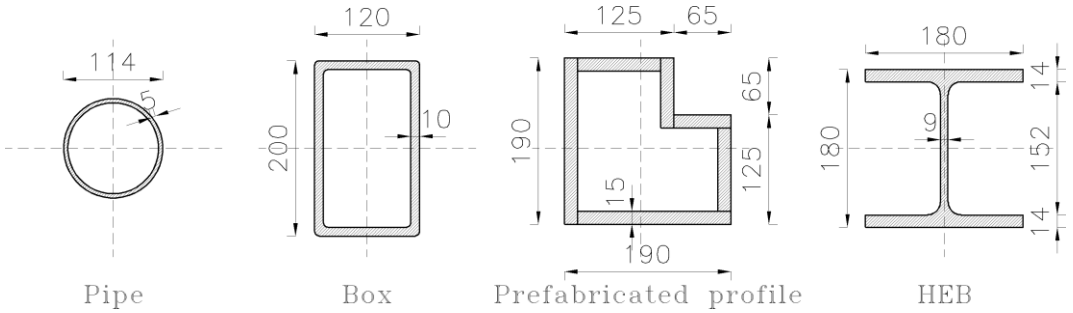


Figure 4. Cross-section of the elements used for the numerical modeling (mm).

### 3.2 Loading

Gravity load included dead load (DL) equal to 3.5 kN/m$^2$ and 5 kN/m$^2$ of floor and roof, respectively. The live load (LL) of the floor and roof was considered to be 2 kN/m$^2$ and 0.4 kN/m$^2$, according to [11]. Table 1 reports seismic parameters for a structure in southern Portugal based on Eurocode 8 [9]. In this table, S is the soil factor; $T_B$, $T_C$, and $T_D$ are the period of the elastic response spectra; β is the lower bound factor for the horizontal design spectrum; q and $\gamma_1$ are the behavior and important factor. Structure mass, including dead and live load, and weight of structural elements that must be included in earthquake analysis were equal to DL +0.8 (0.3 LL), based on [9]. Furthermore, the maximum story drift under seismic load should be less than 0.005 of the height of each story [9].

| Spectrum type | Ground Acceleration | Ground type | S | $T_B$ | $T_C$ | $T_D$ | β | q | $\gamma_1$ |
|---|---|---|---|---|---|---|---|---|---|
| 1 | 2.5 | C | 1.15 | 0.2 | 0.6 | 2 | 0.2 | 2 | 1 |
| 2 | 2.5 | C | 1.5 | 0.1 | 0.25 | 1.2 | 0.2 | 2 | 1 |

Table 1. Seismic parameters of MICADO structures for the south of Portugal.

## 4 RESULTS AND DISCUSSIONS

### 4.1 Strength check

The design of secondary beams is based on bearing gravity loads (dead and live loads) and beam deflection under service loads (DL +0.3 LL). The strength of the structural elements is checked based on the load combinations provided in Eurocode [12]. Eurocode 3 suggested that

the maximum deflection of the secondary beam should be limited by L/250 (L is a span length equal to 7000 mm). Therefore, the cross-section required for these elements is HEB 180, as reported in Table 2.

| Story | Section | Tributary area [m] | DL [kN/m$^2$] | LL [kN/m$^2$] | Deflection [mm] | Flexural capacity |
|---|---|---|---|---|---|---|
| 1 | HEB 180 | 1.80 | 3.5 | 2.0 | 29 | 0.74 |
| 2 | HEB 180 | 1.35 | 5.0 | 0.4 | 29 | 0.55 |

Table 2. Summary of the secondary beam design.

The critical load combination in longitudinal beams includes dead, live, and earthquake loads, while for transverse beams, it combines dead and earthquake loads. Figure 5 shows the bending strength of the main beams, and Figure 6 shows the axial-bending strength of the columns. The moment stress ratio in beams compared to their permissible moment capacity is lower than one, which indicates the section could bear the imposed loads.

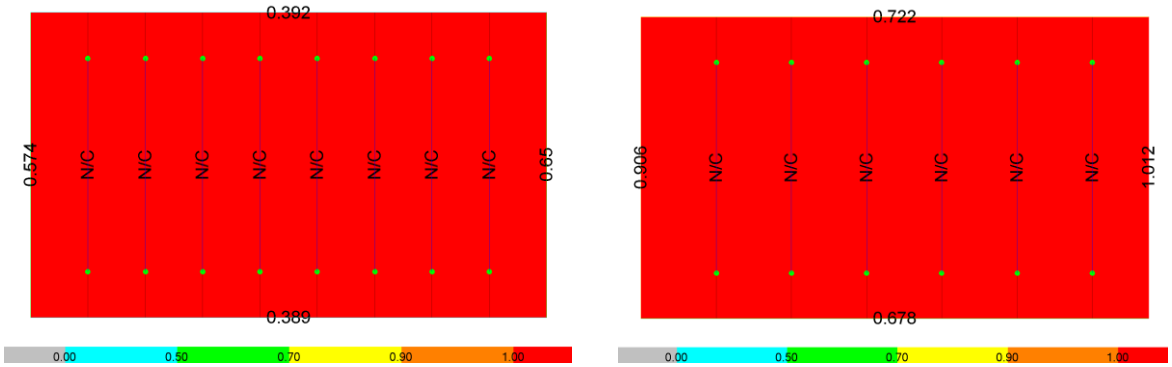


Figure 5. Maximum stress ratio of beams: (a) first story; (b) second story.

The resistance of the regular columns (pipe shape) and columns next to openings (box shape) are also suitable against the incoming loads. However, the first story's corner columns (L-shaped prefabricate) show over stress ratio (of 1.402 and 1.307). Dead, live, and earthquake loads are combinations of critical loads in these columns. When using a plate with a tensile strength of 355 MPa, the maximum stress ratio in these columns is reduced to 0.95.

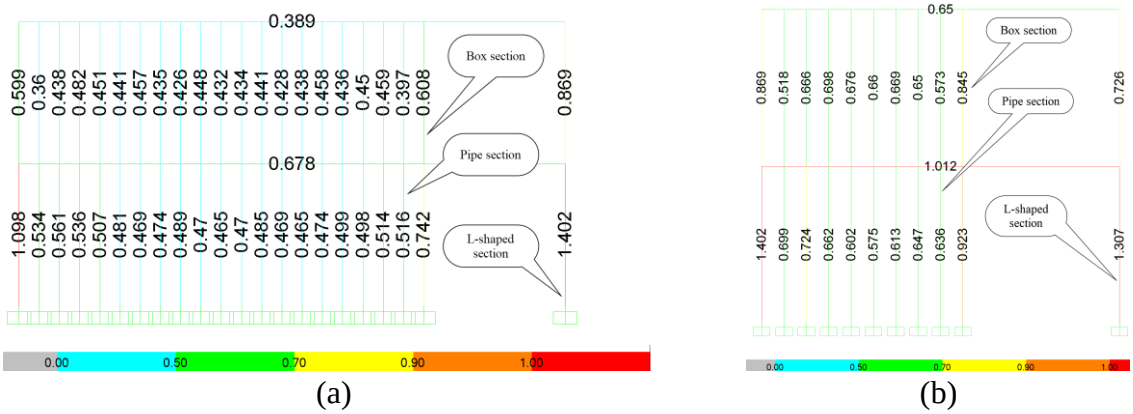


Figure 6. Maximum stress ratio of columns: (a) longitudinal direction; (b) transverse direction.

### 4.2 Stability check

The lateral displacement or drift of the MICADO structure is determined based on Eurocode 8 [9], which is equal to 15.75 mm. Table 3 presents a summary of the story drift of structure (first row), showing that the stories drift in both X (longitudinal) and Y (transverse) directions is more than the maximum value set by the code. While the considered profiles have adequate strength to incoming loads, the system's displacement under an earthquake load can damage nonstructural elements or create a sense of insecurity for residents.

| Model | Column distance [mm] | Span [m] | Roof DL [kN/m$^2$] | $D_X$- 1$^{st}$ [mm] | $D_X$- 2$^{nd}$ [mm] | $D_Y$- 1$^{st}$ [mm] | $D_Y$- 2$^{nd}$ [mm] |
|---|---|---|---|---|---|---|---|
| 1 | 450 | 7 | 5.0 | 17.8 | 17.4 | 21.8 | 24.9 |
| 2 | 300 | 7 | 5.0 | 15.1 | 14.5 | 19.2 | 22.3 |
| 3 | 450 | 7 | 3.5 | 15.1 | 13.8 | 18.3 | 19.9 |
| 4 | 450 | 6 | 5.0 | 15.7 | 15.3 | 20.2 | 23.6 |
| 5 | 450 | 7 | 5.0 | 12.3 | 12.6 | 15.0 | 18.0 |

Table 3. Story drift of the modular structure based on different scenarios.

A parametric study is performed to investigate the effect of different parameters (e.g., column distance, roof DL, span, and sections) on the story drift of the structure, as reported in Table 3. By decreasing the column distance to 300 mm (model 2), the story drift in X and Y directions decreases by 15% and 12%, respectively, compared with model 1. The dead load effect on the drift of the second story is considerable (model 3), so the drift in X and Y directions decreases by 21% and 20%. A decrease in width from 7 m to 6 m significantly affects X direction story drift, but a slight reduction in Y direction story drift (model 4). It means drift in X and Y directions decreases by 12% and 7%, compared with model 1.

If larger sections are used in model 1, the drift of the structure can be controlled to a great extent. However, this increase in cross-section is limited to the dimensions of the MICADO elements (Figure 1). For example, If the pipe and box profiles with 114.3×8 and 245×125×20 sections and the L-shaped profile with a 20 mm plate are used, the drift values of the structure in the X direction for both stories will be less than 15.75 mm. In the opposite direction, it is only valid for the first story. Although in the second story, the drift value is 14% more than the value suggested by the code [9].

## 5 CONCLUSIONS

In conclusion, the research conducted on the MICADO structure has shown promising results regarding its feasibility and effectiveness as a construction method. The proposed assembly techniques, numerical modeling, and investigations into structural behavior have provided valuable insights into the design and construction of modular steel structures. The research has also explored different scenarios and parameters such as column distance, roof dead load, various spans, and sections to control story drift and ensure the structural integrity of the building.

Furthermore, the research demonstrated the potential of this construction method to revolutionize the building industry. With ongoing advancements in technology and construction techniques, modular steel structures will likely become an increasingly popular choice for a wide range of building types in the future. The insights from this research will be valuable for engineers, architects, and construction professionals looking to adopt this innovative construction method in their projects.

## ACKNOWLEDGEMENTS

This research work was financed by the MICADO Project - Modular Insulated Concrete core- ADvanced and Optimized panelized production system, operation n.º NORTE-01-0247-FEDER-113482, co-financed by the European Regional Development Fund (ERDF) through NORTE2020 - the Northern Regional Operational Programme 2014/2020.

## REFERENCES

[1] Y.H. Ahn, K.T. Kim, Sustainability in modular design and construction: a case study of 'The Stack,' Int. J. Sustain. Build. Technol. Urban Dev. 5 (2014) 250–259. https://doi.org/10.1080/2093761X.2014.985758.

[2] S. Aghasizadeh, A. Tabadkani, A. Hajirasouli, S. Banihashemi, Environmental and economic performance of prefabricated construction: A review, Environ. Impact Assess. Rev. 97 (2022) 106897. https://doi.org/10.1016/j.eiar.2022.106897.

[3] P.F. Rocha, N.O. Ferreira, F. Pimenta, N.B. Pereira, Impacts of Prefabrication in the Building Construction Industry, Encyclopedia. 3 (2022) 28–45. https://doi.org/10.3390/encyclopedia3010003.

[4] Y.W. Lim, P.C.H. Ling, C.S. Tan, H.Y. Chong, A. Thurairajah, Planning and coordination of modular construction, Autom. Constr. 141 (2022) 104455. https://doi.org/10.1016/j.autcon.2022.104455.

[5] S. Navaratnam, D. Widdowfield Small, P. Gatheeshgar, K. Poologanathan, J. Thamboo, C. Higgins, P. Mendis, Development of cross laminated timber-cold-formed steel composite beam for floor system to sustainable modular building construction, Structures. 32 (2021) 681–690. https://doi.org/10.1016/j.istruc.2021.03.051.

[6] A.M. Philip, M.R. Kannan, Constructability assessment of cast in-situ, precast and modular reinforced concrete structures, Mater. Today Proc. 45 (2020) 6011–6015. https://doi.org/10.1016/j.matpr.2020.09.528.

[7] C.D. Aquino, J.M. Branco, Experimental evaluation of a modular timber unit filled with insulated corkboard, J. Build. Eng. 32 (2020) 101725. https://doi.org/10.1016/j.jobe.2020.101725.

[8] E. Bazarchi, A. Davaran, C.P. Lamarche, N. Roy, S. Parent, Experimental and numerical investigation of a novel vertically unconstrained steel inter-modular connection, Thin-Walled Struct. 183 (2023) 110364. https://doi.org/10.1016/j.tws.2022.110364.

[9] E.C. for Standardization, EN 1998-1: Eurocode 8- Design of structures for earthquake resistance- Part 1: General rules, seismic actions and rules for buildings, 2004.

[10] E.C. for Standardization, EN 1993-1-1: Eurocode 3- Design of steel structures- Part 1-1: General rules and rules for buildings, 2005.

[11] E.C. for Standardization, EN 1991-1-1: Eurocode 1- Actions on structures- Part 1-1: General actions- Densities, self-weight, imposed loads for buildings, 2001.

[12] E.C. for Standardization, EN 1990: Eurocode- Basis of structural design, 2002.

COMPDYN 2023
9th ECCOMAS Thematic Conference on
Computational Methods in Structural Dynamics and Earthquake Engineering
M. Papadrakakis, M. Fragiadakis (eds.)
Athens, Greece, 12-14 June 2023

# SEISMIC PERFORMANCE OF SPECIAL STEEL MOMENT FRAMES USING DETAILED VS SIMPLE HYSTERIC CURVES

**E. Clavijo[1], J. Molina[1], N. Coello[1], X. Vintimilla[1], F. Flores [1] and P. Quinde[1]**

[1] Department of Civil Engineering, University of Azuay
Cuenca 010204, Ecuador
{emiclavijoc, mpjorgel}@es.uazuay.edu.ec
{nicolas.coello99, xavier.vintimillas30}@ucuenca.edu.ec
{fflores, pabloquinde}@uazuay.edu.ec

## Abstract

*It is a common belief that modeling structures using bilinear materials with no strength or stiffness degradation perform better than modeling structures with more detailed materials that include degradation. This investigation focuses on the effects of modeling in two different ways the hysteretic curves of beams and columns in special steel moment resisting frames. The analyzed structure is an 8-Story Special Steel Moment Frame where its performance is measured by means of static and dynamic analyses. Inter-story drifts and energies are quantified at different intensity levels and using multiple ground motions to establish the difference of using a simple vs a detailed hysteretic curve. It was found that unlike what is commonly believed, structures modeled with a simple hysteretic behavior do not capture properly the seismic response of a structure. It was demonstrated that hysteretic energy dissipation is not an indicator of seismic performance.*

**Keywords:** Energy Dissipation, OpenSees, Special Steel Moment Frames, FEMA P695.

# 1 INTRODUCTION

The study of the response of a structure subjected to earthquake-induced motion depends primarily on the quality of the mathematical model. Structures idealized with concentrated inelasticity elements can be modeled with a wide range of materials that represent their behavior under a cyclic load. It is commonly believed that the incorporation of a simple bilinear model will dissipate more energy due to the lack of strength degradation leading to a better seismic performance. As established by Kazantzi & Vamvatsikos [1] "It is no wonder then that higher energy dissipation seems to be equivalent to higher damping, ergo better performance". The purpose of this investigation is to evaluate the adequacy of using two different hysteretic curves with and without strength degradation in terms of energy dissipation, drift limits and collapse evaluation. This study tries to fill the void of previous investigations that focuses mainly on the effect of the hysteresis type on the global collapse drift limit [2]. Also, to verify the correlation between energy dissipation and the behavior of a structure subjected to different intensity level earthquakes.

Analyzing energy dissipation of a building during seismic loads helps to evaluate the ability of a structure to absorb and dissipate energy considering that each structural member contributes to energy dissipation. Damping energy is the energy that is diminished by different mechanisms as inherent and hysteretic when cycling forces or deformations occur. "Dynamic loading conditions differ as energy input and energy dissipation are intimately related with the details of the system's hysteresis" [1]. Hysteretic energy dissipation is often understood as a synonym of seismic performance as seen in many seismic codes. Recent studies question the truthfulness of this belief due to the limited evidence on it. Kazantzi & Vamvatsikos [3] demonstrated that energy dissipation is not an index of seismic performance. Therefore, there is an unconscious use the concept of energy dissipation.

The building used to perform the proposed analyses is found at NIST GCR 10-917-8 [4] report as the 4RSA 8-story Special Steel Moment Frame Archetype. The plastic hinges were defined in two different models, the first one using a simple bilinear hysteretic curve with strain hardening (Steel01) and the second one with a hysteretic curve that includes strength degradation (Bilin). Analyses were made to compare their performance using inter-story drifts and energy dissipation when multiple ground motions are applied. Far-Field ground motion record set (22 component pairs) provided by the FEMA P-695 [5] methodology was considered under different seismic intensities.

Furthermore, the collapse margin ratio (CMR) was computed according to the FEMA P-695 as the ratio of the median value of collapse level earthquake spectral acceleration, to the MCE spectral response acceleration at the fundamental period of the building. The median collapse intensity was obtained as the incremental dynamic factor for the structure to collapse with 22 out of 44 ground motions. According to Vamvatsikos & Cornell [6], a collapse occurs when the local tangent of an incremental dynamic analysis (IDA) curve reaches 20% of the elastic slope (first slope in the IDA curve), or when a story reaches a 10% drift, because it is unlikely that the structure will recover.

# 2 BUILDING OVERVIEW

## 2.1 Geometry

The building used for this investigation was taken from the NIST GCR 10-917-8 [4].The 8-story SMF designed with the modal response spectrum (RSA) was studied. The structure's design was followed according to the ASCE 7-05 [7]. The plan view layout of the structure is presented in Figure 1. The SMF consist of a 3-bay perimeter frame on each side with

prequalified reduced beam sections (RBS) connections. The bay width (centerline dimensions) is 6.1 m (20 ft). The height of the first story is 4.6 m (15 ft) and the height of all other stories is 4 m (13 ft). The member sizes were assigned according to the NIST [4] archetype data. Axial reduction of the columns was contemplated as required by the FEMA P-695 [5] methodology.

## 2.2 Design Loads

According to the NIST [4] the dead load (*D*) was 4.31 kN/m$^2$ (90 psf) uniformly distributed over each floor and a cladding load was applied as a perimeter load of 1.2 kN/m$^2$ (25 psf). The design life load (*L*) was 2.4 kN/m$^2$ (50 psf) on all floors and 0.96 kN/m$^2$ (20 psf) on the roof. Loads were distributed on the tributary areas as shown in Figure 1.

The recommended load combination considered to obtain the acting loads and the corresponding story masses is 1.05*D*+0.25*L*.

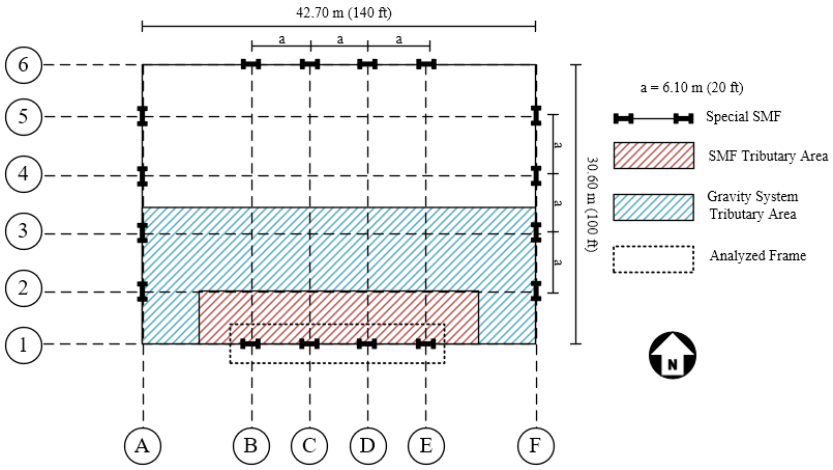


Figure 1: Building plan view layout.

# 3 NONLINEAR MODEL

## 3.1 Hysteresis Type

The models and analyses were carried out via OpenseesPy [8] as it allows the utilization of an extended number of materials that can be studied for the objective of this investigation. The selected materials as presented in Figure 2 were Steel01 as the simple material and the Modified Ibarra-Medina-Krawinkler Deterioration Model with Bilinear Hysteretic Response (Bilin Material) as the detailed one. Beams and columns were incorporated by using elastic elements with plastic hinges (zero-length elements) at the ends of the elements. The hysteretic behavior of beams and columns considers one model with stiffness and strength degradation and other with a simplified model with no deterioration.

The modeling of the Bilin and Steel01 materials were made according to Dimitrios Lignos' investigation [9]. The calibration parameters of plastic hinges were considered according to the w-section properties.

Hysteretic curves presented below were obtained to verify the correct behavior of the materials incorporated in the models. Figure 2 corresponds to a plastic hinge of the 1$^{st}$ story beam W30x108.

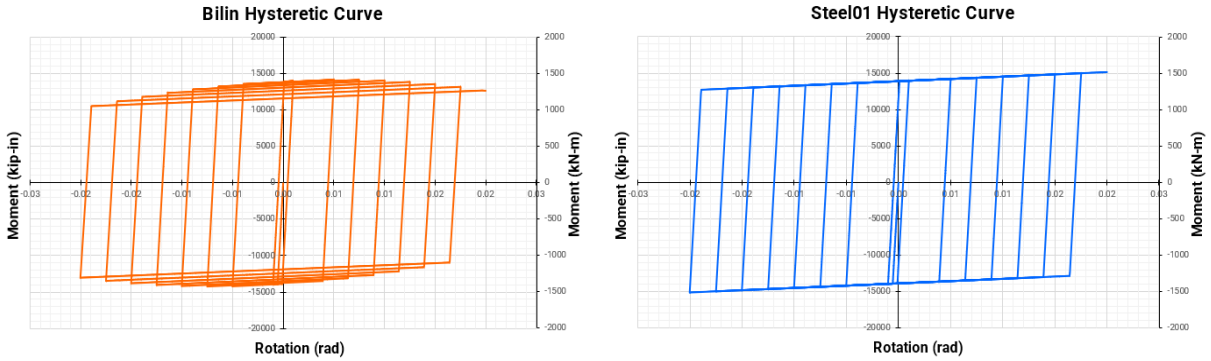


Figure 2: Beam W30x108 hysteretic behavior.

Panel zones were modeled using a rectangular region composed with eight rigid elements and a nonlinear rotational spring on the right top corner defined by a hysteretic material [10]. Connections at the base of the columns are fixed and compounded by very stiff plastic hinges.

## 3.2 P-Delta considerations

Geometric nonlinearities were incorporated using a leaning column with no flexural stiffness to consider P-Delta effects of the seismic mass that is not tributary to the frame (one-half the load of the gravity system) [5]. It consists of elements with end-to-end releases that are joined to the structure by truss-like elements. Moment transmission is not permitted and the stiffness of the seismic-force-resisting system is not compromised. The resulting model is shown in Figure 3, which provides a visual representation of the structure used in the analyses.

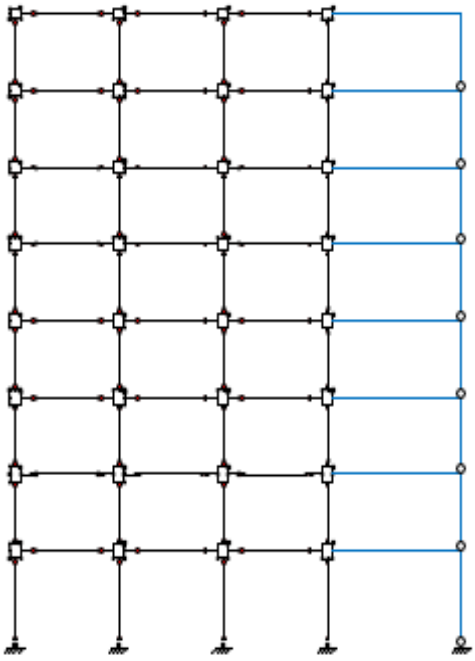

Figure 3: Mathematical model of the 4RSA 8-story building.

## 4 GROUND MOTIONS SCALING METHOD

As mentioned previously, the 22 horizontal component pairs of Far-Field records with similar characteristics provided by the FEMA P-695 [5] were used to perform the analyses in this investigation. Scaling process as shown in Figure 4 was necessary to perform nonlinear dynamic analysis.

The FEMA P-695 was also followed to scale the ground motions. This two-step process involves first normalizing the individual ground motions by their respective PGVs, and second, scaling the records to the MCE intensity at the fundamental period of the analyzed archetype.

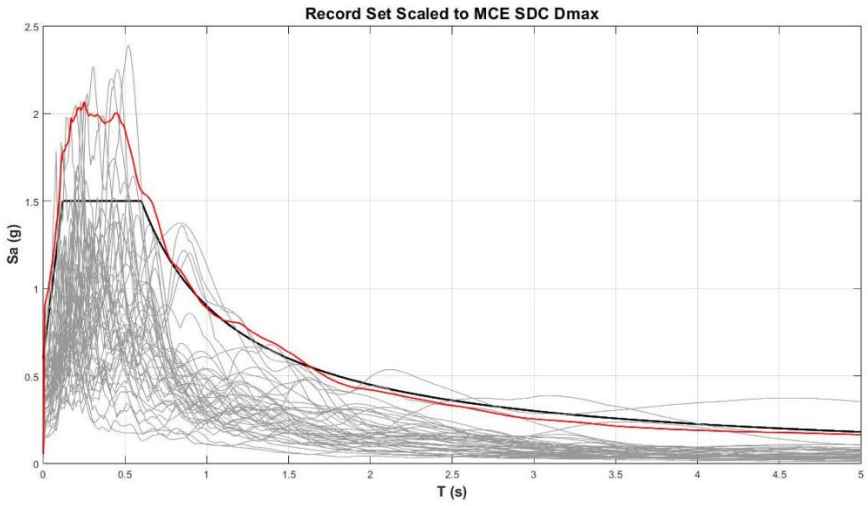


Figure 4: Median spectrum of the Far-Field record set anchored to the MCE.

## 5 MODEL BEHAVIOR CHECKS

It is required to make some model behavior checks to verify that the characteristics of the modeled building matches the archetype data proposed by the NIST report. These procedures assure somehow the reliability of the mathematical model when evaluating seismic performance and the results to be precise. It is important to conduct linear checks such as Modal Analysis, Free Vibration and to perform nonlinear analysis such as Pushover Analysis and its Sequence of Yielding.

### 5.1 Modal Analysis

Firstly, the modes and mass participation factors of the structure were analyzed in order to compare with the ones reported by the NIST. The corresponding value of the natural frequency of the selected system is *T=2.29s* as shown in Table 6-4 of the NIST [4]. Accordingly, the results obtained in both Steel01 and Bilin models were computed as 2.28s as shown in Figure 5 that displays the concordance with the archetype.

All the modes obtained by the modal analysis and their respective participation mass factors are summarized in Table 1.

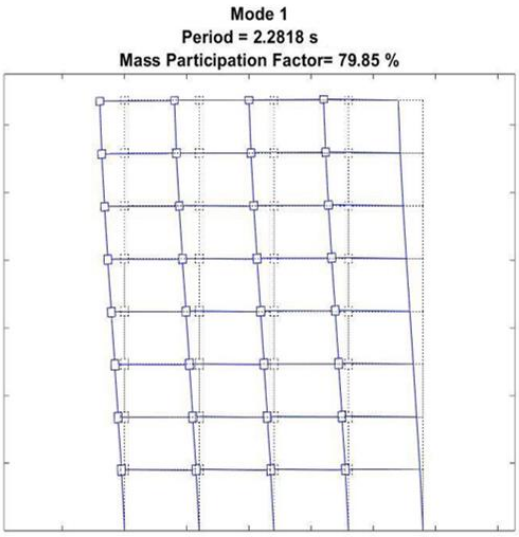


Figure 5: Fundamental Mode of Vibration of the systems.

| Mode | Period (s) | MPF (%) |
|---|---|---|
| 1 | 2.2818 | 79.85 |
| 2 | 0.7936 | 12.75 |
| 3 | 0.4349 | 3.8 |
| 4 | 0.2791 | 1.83 |
| 5 | 0.1981 | 0.98 |
| 6 | 0.1467 | 0.47 |
| 7 | 0.1141 | 0.23 |
| 8 | 0.0919 | 0.09 |

Table 1: Summary of Modal Analysis.

## 5.2 Free Vibration

As the rate at which the motion decays is controlled by the damping ratio, it is correct to use a free vibration analysis to prevent wrong damping assumptions. In this way, the actual damping presented by the model is ensured to avoid high damping forces that are hard to identify in areas of concentrated inelasticity, which can lead to an invalid analysis [11]. The obtained damping ratio was 2.43% compared to the Rayleigh's damping ratio of 2.5% assigned to the first and third modes, as shown in Figure 6.

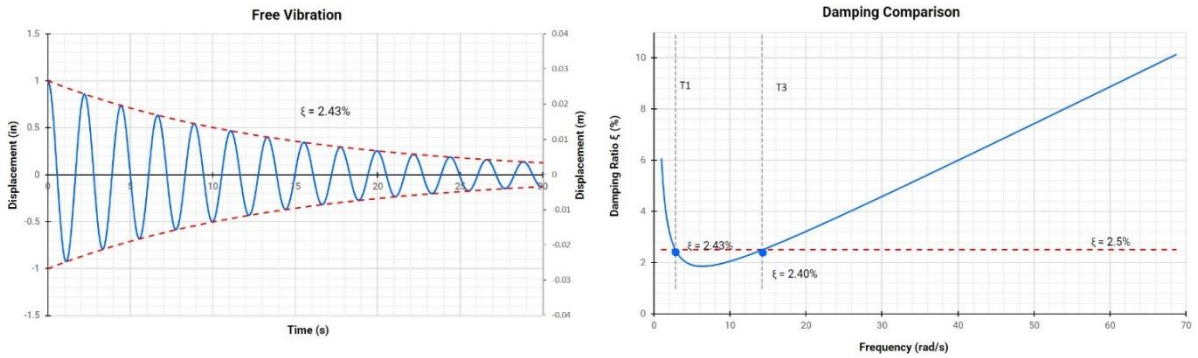


Figure 6: Rayleigh's damping obtained by logarithmic decay of Free vibration.

It is important to check the assumed damping assigned to each mode. It is very easy to lose the sense of the effective damping that the mathematical model has if this step is omitted. Table 2 shows the computed Rayleigh's damping value of each mode compared to the one assigned by OpenSees.

| Mode | Real Damping (%) | Theoretical Damping (%) |
|---|---|---|
| 1 | 2.43 | 2.5 |
| 2 | 1.87 | 1.91 |
| 3 | 2.4 | 2.5 |
| 4 | 3.48 | 3.59 |
| 5 | 4.84 | 4.86 |
| 6 | 6.32 | 6.44 |
| 7 | 7.98 | 8.2 |
| 8 | 10.05 | 10.13 |

Table 2: Real damping of the structure and Rayleigh's theoretical damping.

### 5.3 Pushover checks

Pushover analysis was performed to evaluate different parameters such as overstrength, ductility and secondary stiffness. According to Table 6-9 of the NIST [4], the archetype was presented with an overstrength of $\Omega$=3.27 and a ductility value of $\mu$=2.74. Figure 7 shows that both models have near values of overstrength and ductility that can be accepted to represent the NIST model. Ductility and post yield negative stiffness depend on the complexity of the hysteretic model.

The procedures presented in this section help to both validate the model and verify the values presented by the NIST report, also provide insight of the hysteretic behavior effects. These checks are important to ensure that the upcoming analyses present the correct results.

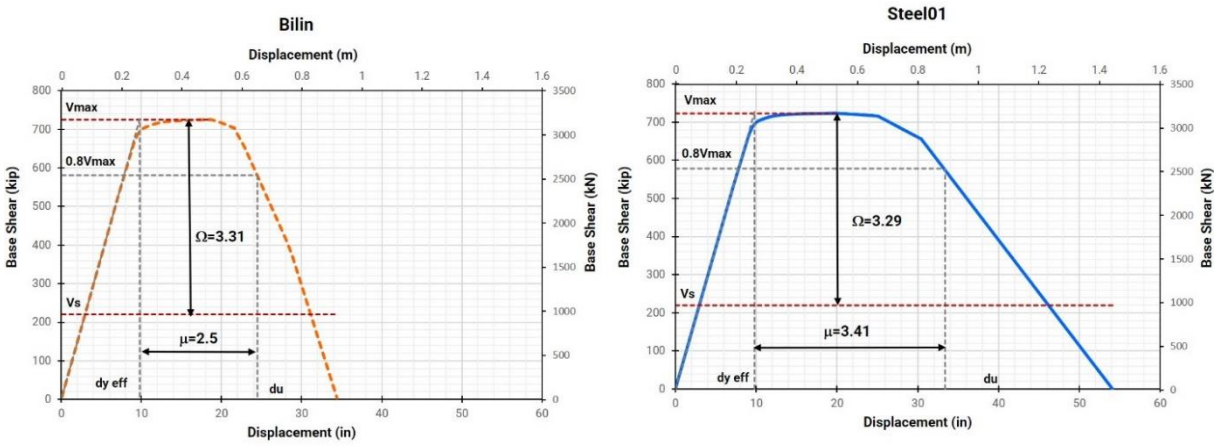


Figure 7: Pushover results of ductility and overstrength of the models.

Nonlinear incremental static analysis was performed by assigning a lateral load according to the shape of the first vibration mode to obtain the capacity curve of the models. Plastic hinges develop stiffness changes that can be visualized on the sequence of yielding of the structure. As shown in Figure 8 the mathematical model displays a correct damage behavior in both models. The plastic hinges at the bases of the structure yield first, followed by the beams and finally the columns of the 1st and 2nd stories.

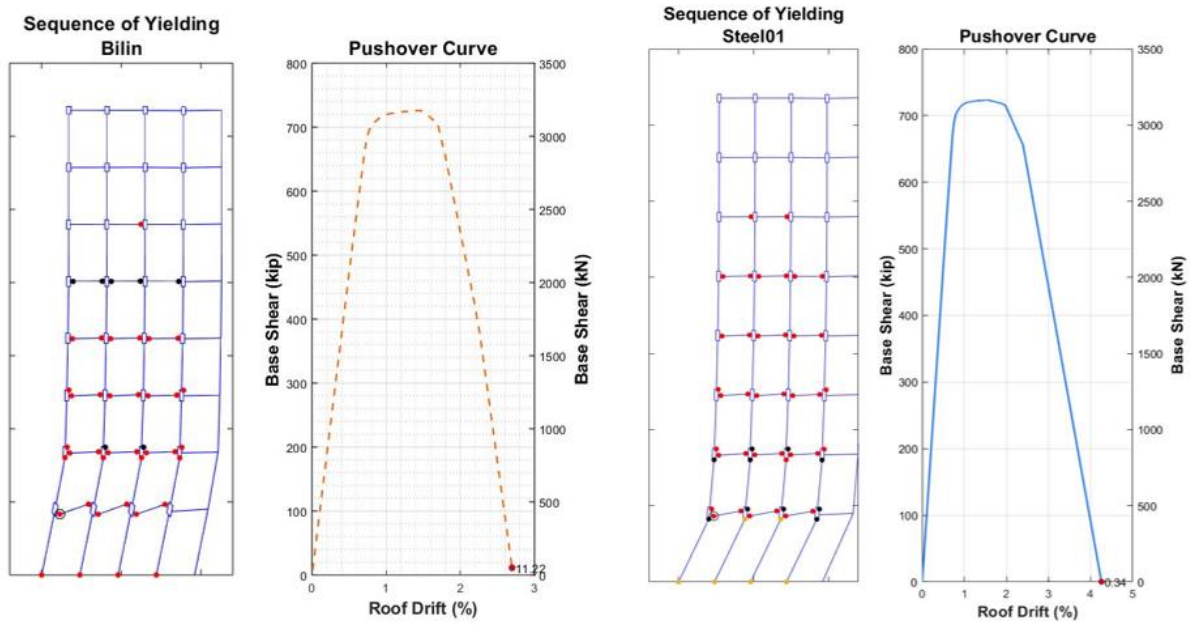


Figure 8: Sequence of yielding of the models.

## 6 RESULTS

Based on the work presented herein, results of a comparison between the simple and detailed models are provided. The analyses performed include nonlinear time history (NTH) analysis, energy dissipation, and collapse margin evaluation.

The comparison of the results provides a comprehensive view of the seismic behavior and performance of both models.

### 6.1 Nonlinear Static Pushover Analysis

In this approach, base shear vs roof displacement curves were considered with and without P-Delta effects. It can be seen that P-Delta effects are significant for buildings with a considerable number of stories as shown in Figure 9. Negative stiffness occurs due to two main reasons: material degradation and P-Delta effects. For these structures, P-Delta effects might be the factor that contributes the most to the seismic performance of the structure, thus causing the amplification of story drifts. When the roof drift reaches 1.35%, the corresponding 1$^{st}$ story drift is 2.29%. At this point it can be seen that both models start to show differences and the Steel01 model largely surpasses the Bilin's capacity. The capacity of the Bilin material is compromised due to the material degradation that can be seen on the secondary stiffness of its pushover curve.

Inter-story drifts in lower stories must be checked since SSMFs tend to concentrate story drifts in lower levels [12].

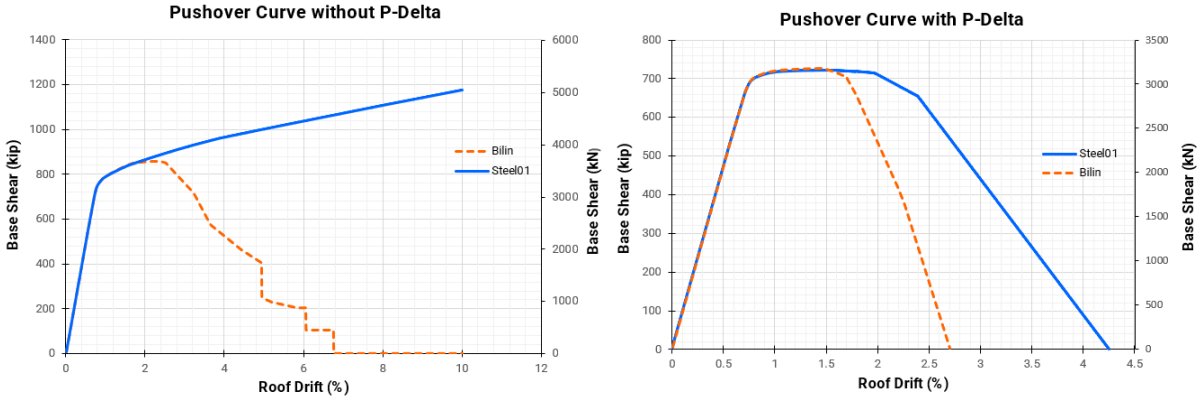


Figure 9: Pushover curves with and without P-Delta effects.

## 6.2 Nonlinear Time History Analysis

NTH analyses were performed following the FEMA P-695 methodology [5]. Two intensities such as the MCE and higher intensities determined by IDAs were selected. The analyses were conducted with and without P-Delta effects to compare their influence on the seismic behavior of an 8-story SMF building. Second-order effects are essential on predicting the earthquake response of buildings that have significant deformations into their inelastic range [13].

Figure 10 shows the first-story drifts at the MCE intensity, including P-Delta effects for two different ground motions. It can be observed that the MCE intensity is not high enough to show a difference between the models' drifts. This occurs because there is not enough damage induced at the hinges, as follows both hysteretic curves will have the same results. The analyses were computed for every Far-Field ground motion record, but only two were selected to be presented.

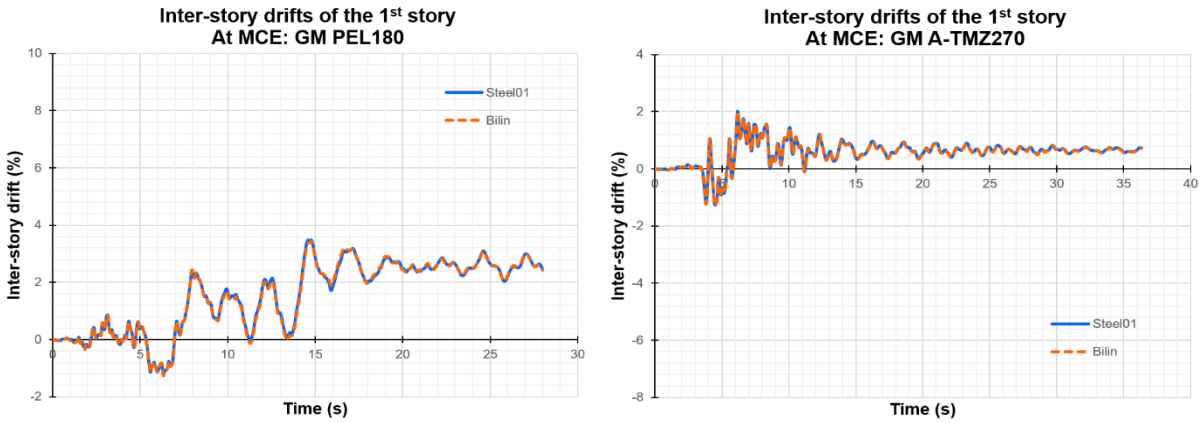


Figure 10: First story drifts at the MCE intensity with P-Delta effects.

The same ground motions, at higher intensities are shown in Figure 11. The Bilin model clearly shows larger drifts, which means it will collapse before than the Steel01. In addition to the significant influence of P-Delta effects at higher intensities, it is important to consider the strength degradation of the material. As stated by Ibarra et al. [14], "results from the seismic evaluation of various systems demonstrate that strength deterioration becomes a dominant factor when the response of a structure approaches the limit state of collapse". The Bilin behavior presented below shows the influence of both factors. On the contrary, Steel01 is not conditioned by the deterioration phase, this is the reason why P-Delta effects are better received

by this material. It can be clearly seen that Steel01 does not capture large displacements in the same way that the Bilin model does.

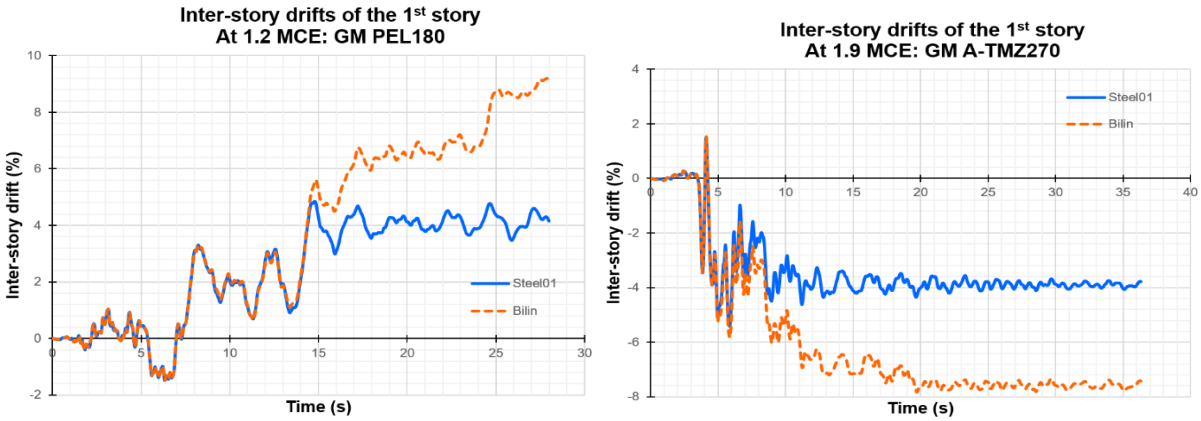


Figure 11: First story drifts at higher intensities with P-Delta effects.

When P-Delta effects are not considered, both models show similar first-story drifts throughout the entire motion as shown in Figure 12. It can be seen that grey lines represent P-Delta effects that are considerably increasing inter-story drifts compared to the results without P-Delta. These results demonstrate that P-Delta effects are more significant than strength degradation in this building model.

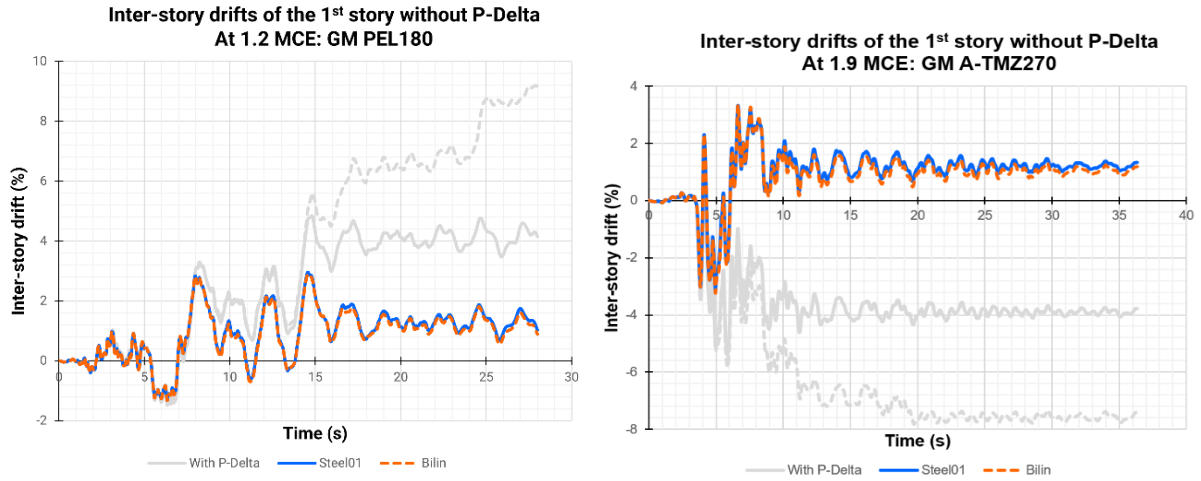


Figure 12: First story drifts at higher intensities without P-Delta effects.

## 6.3 Energy Dissipation

Input, kinetic, inherent damping, hysteretic damping, potential and total energy were considered to obtain the energy balance of the structure considering P-Delta effects.

At the MCE intensity, both models have approximately the same energy dissipation as shown in Figure 13 for two different ground motions. Therefore, their displacements are almost the same (Figure 10). The Bilin material has not been subjected to enough stress to develop the strength degradation phase so it behaves similarly to Steel01.

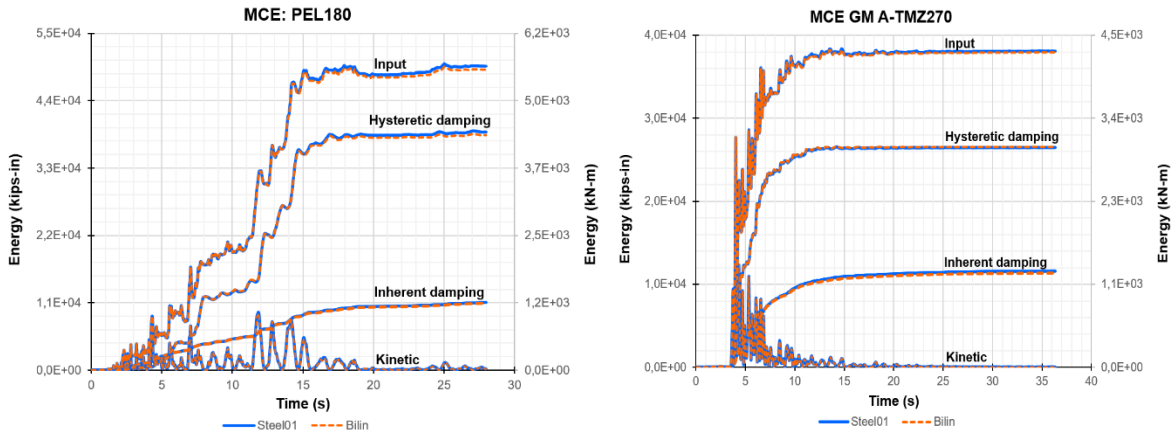


Figure 13: Energy balance at the MCE intensity.

At higher intensities, hysteretic energy has the largest differences because it is related to the moment-rotation curve which depends directly on the material behavior.

There are two possible cases that can occur, considering that the detailed model always develops the largest drifts as shown in Figure 11. First, the Steel01 model dissipates more energy as shown in Figure 14. It can be noticed that the Steel01 model has a higher hysteretic energy and a better behavior in this case.

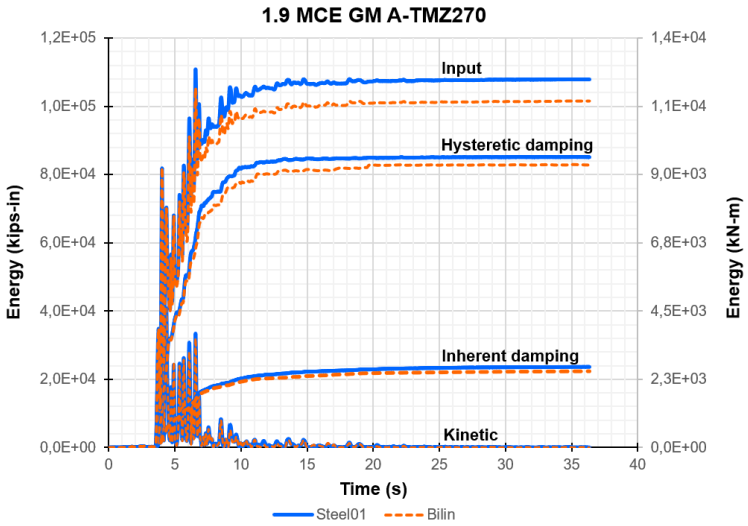


Figure 14: Energy balance of A-TMZ270 at higher intensities.

Second, contrary to what is believed there are several cases where the Bilin model dissipates more energy as shown in Figure 15 and has a worse performance as it reaches higher drifts.

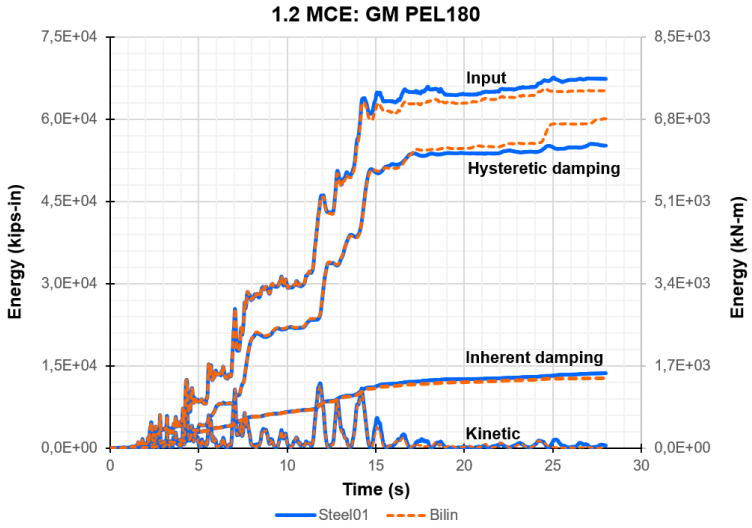


Figure 15: Energy balance of PEL180 at higher intensities.

As found in the analyses, it is not possible to determine which model has a better seismic performance by analyzing energies only. These results do not provide the accurate information about the damage that this structure can develop. Although in some cases the Steel01 model can reach higher energy dissipation, the Bilin model for this study always had larger drifts. These energies results cannot determine the seismic performance evaluation of the structure.

## 6.4 Collapse Evaluation

Using the OpenSees software, IDAs considering P-Delta effects were conducted until any inter-story drift reached 10%. In order to calculate the median with two-decimal precision, the stepping method proposed by Hardyniec & Charney [15] was applied. The summary of the computed results is shown in Figure 16 as IDA curves. A flattening can be seen at the end of the curves, indicating that a collapse was reached.

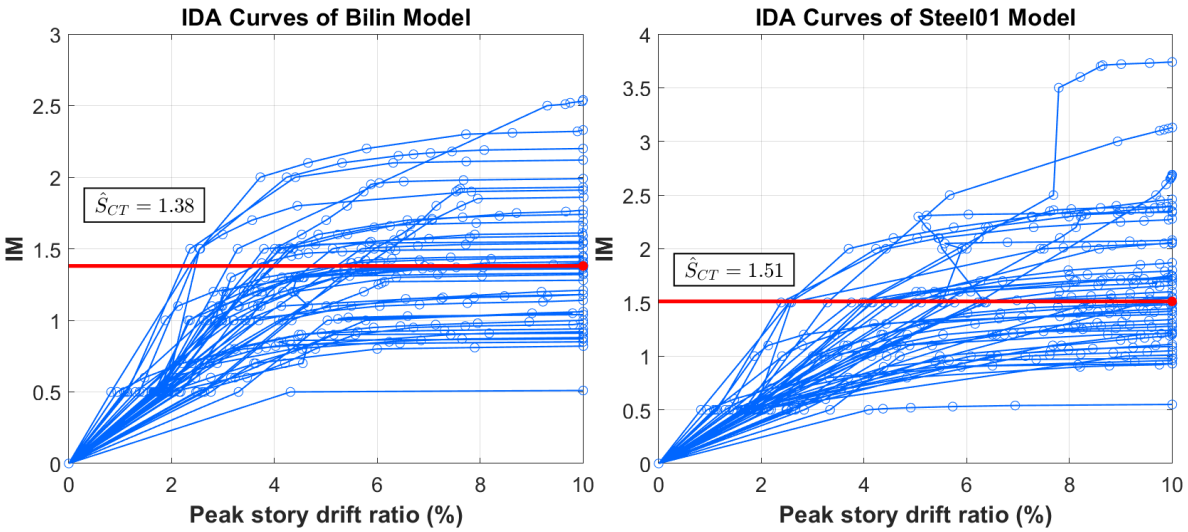


Figure 16: Incremental Dynamic Analyses Curves of the models.

There is a specific factor for each ground motion that causes the structure to collapse, these factors were plotted against the probability of collapse. The fragility curve was fitted following the explanation of Porter et al. [16], which estimates the logarithmic standard deviation through

an equation. In addition, the previously obtained median collapse intensity was used in the fitting. Figure 17 presents the fragility curves with the corresponding CMR of both models. It can be seen that Bilin has a lower CMR and it closely matches the value reported by NIST of a *CMR=1.42*, as shown in Table 3.

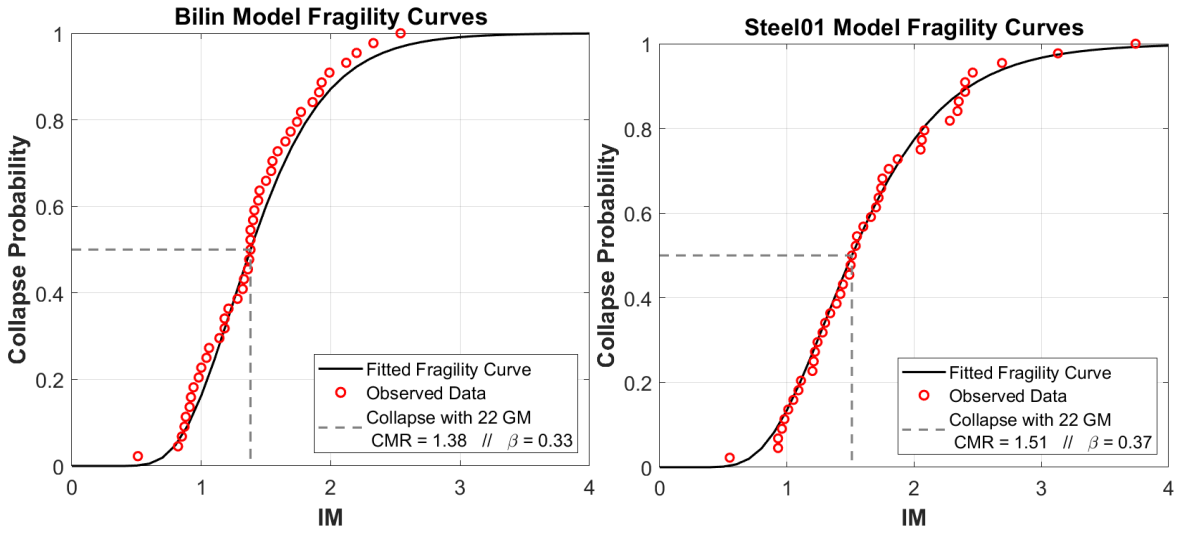


Figure 17: Fragility curve and CMR computation of the models.

| Model | CMR |
|---|---|
| NIST | 1.42 |
| Steel01 | 1.51 |
| Bilin | 1.38 |

Table 3: CMR comparison of the NIST and the models analized.

## 7 CONCLUSIONS

In this paper, it was presented a seismic performance evaluation when modeling an 8-story SMRF with the Bilin material that represents a hysteretic model with strength degradation and the Steel01 material that represents a simple bilinear model with no degradation.

The purpose of the study was to determine the level of detail that the hysteretic model should have to obtain the most accurate mathematical model. The effect of the hysteresis type based on the results described previously lead to the following conclusions:

1) Energy dissipation cannot provide enough information to determine which material will have a better seismic performance on a structure. The simplified model that has no strength degradation (Steel01) does not properly capture large displacements that the structure can reach. There are parameters such as ductility, secondary stiffness or the post yield slope that are better indicators of seismic performance.
2) According to the NTH analyses results, it can be concluded that the material with strength degradation (Bilin) is always the first one collapsing. Therefore, strength and stiffness degradation are necessary to capture large displacements.
3) The post yield capacity of a structure is mainly conditioned by two parameters: secondary order effects and material degradation. In this study P-Delta effects controlled over degradation due to the height of the structure. Further investigation needs to be done in shorter buildings to explore the influence of strength degradation and P-Delta effects.

4) Inherent damping energy of approximately 20% of the input energy was reached by incorporating a damping ratio of 2.5%. Additional investigation can be done to analyze the influence of higher damping ratio on the contribution of inherent damping in the energy dissipation and the structure's collapse evaluation.
5) Hysteresis type becomes significant when the structure approaches to a collapse state. The structural response is impacted by the level of detail of the hysteretic and capacity curves in ways that cannot be described by energy dissipation. The simple hysteretic behavior can be incorporated when drifts are limited to short displacements.

## 8 ACKNOWLEDGEMENTS

The work presented herein was possible through the financial support of the University of Azuay in Cuenca-Ecuador.

## REFERENCES

[1] A. K. Kazantzi and D. Vamvatsikos, "A study on the correlation between dissipated hysteretic energy and seismic performance," 2012.
[2] Z. Huang and D. A. Foutch, "Effect of hysteresis type on drift limit for global collapse of moment frame structures under seismic loads," *Journal of Earthquake Engineering*, vol. 13, no. 7, pp. 939–964, Sep. 2009, doi: 10.1080/13632460902859144.
[3] A. K. Kazantzi and D. Vamvatsikos, "The hysteretic energy as a performance measure in analytical studies," *Earthquake Spectra*, vol. 34, no. 2, pp. 719–739, May 2018, doi: 10.1193/112816EQS207M.
[4] NIST, "Evaluation of the FEMA P-695 Methodology for Quantification of Building Seismic Performance Factors NEHRP Consultants Joint Venture A partnership of the Applied Technology Council and the Consortium of Universities for Research in Earthquake Engineering," 2010.
[5] Fema, *Quantification of Building Seismic Performance Factors*. 2009. [Online]. Available: www.ATCouncil.org
[6] D. Vamvatsikos and C. A. Cornell, "Applied incremental dynamic analysis," *Earthquake Spectra*, vol. 20, no. 2, pp. 523–553, 2004, doi: 10.1193/1.1737737.
[7] ASCE, "SEISMIC DESIGN REQUIREMENTS FOR BUILDING STRUCTURES 12.1 STRUCTURAL DESIGN BASIS 12.1.1 Basic Requirements," 2005.
[8] F. McKenna and F. Gregorie, "OpenSees." 2000.
[9] D. Lignos and H. Krawinkler, "SIDESWAY COLLAPSE OF DETERIORATING STRUCTURAL SYSTEMS UNDER SEISMIC EXCITATIONS," 2012. [Online]. Available: http://blume.stanford.edu
[10] A. Gupta and H. Krawinkler, "SEISMIC DEMANDS FOR PERFORMANCE EVALUATION OF STEEL MOMENT RESISTING FRAME STRUCTURES," 1999. [Online]. Available: http://blume.stanford.edu
[11] F. A. Charney and F. Asce, "Unintended Consequences of Modeling Damping in Structures," pp. 1–12, 2008, doi: 10.1061/ASCE0733-94452008134:4581.
[12] F. X. Flores, B. X. Astudillo, and S. Pozo, "Effective Modeling of Special Steel Moment Frames for the Evaluation of Seismically Induced Floor Accelerations," *Journal of Structural Engineering*, vol. 147, no. 1, Jan. 2021, doi: 10.1061/(asce)st.1943-541x.0002851.

[13] A. K. Chopra, "DYNAMICS OF STRUCTURES Theory and Applications to Earthquake Engineering Fifth Edition in SI Units," 2020.
[14] L. F. Ibarra, R. A. Medina, and H. Krawinkler, "Hysteretic models that incorporate strength and stiffness deterioration," *Earthq Eng Struct Dyn*, vol. 34, no. 12, pp. 1489–1511, 2005, doi: 10.1002/eqe.495.
[15] A. Hardyniec and F. Charney, "A new efficient method for determining the collapse margin ratio using parallel computing," *Comput Struct*, vol. 148, pp. 14–25, 2015, doi: 10.1016/j.compstruc.2014.11.003.
[16] K. Porter, R. Kennedy, and R. Bachman, "Creating fragility functions for performance-based earthquake engineering," *Earthquake Spectra*, vol. 23, no. 2, pp. 471–489, 2007, doi: 10.1193/1.2720892.

COMPDYN 2023
9th ECCOMAS Thematic Conference on
Computational Methods in Structural Dynamics and Earthquake Engineering
M. Papadrakakis, M. Fragiadakis (eds.)
Athens, Greece, 12-14 June 2023

# INELASTIC TORSIONAL BUCKLING OF A SYMMETRIC THREE-DIMENSIONAL MOMENT-RESISTING FRAME SUBJECTED TO HORIZONTAL FORCE IN THE DIAGONAL DIRECTION

**Iori Fukuda[1], Kohju Ikago[1], Takahito Maeda[2], Atsushi Nishimoto[3], and Yoshikazu Araki[2]**

[1] Tohoku University
468-1-E402(IRIDeS), Aoba Aramaki, Aoba-ku, Sendai, 980-8572, Japan
iori.fukuda.q3@dc.tohoku.ac.jp, ikago@irides.tohoku.ac.jp

[2] Nagoya University
ES538, Chikusa, Nagoya, 464-8603, Japan
yoshikazu.araki@nagoya-u.jp, maeda.takahito.1019@gmail.com

[3] NIKKEN SEKKEI LTD
4-15-32, Sakae, Naka-ku, Nagoya, 460-0008, Japan
nishimoto.atsushi@nikken.jp

## Abstract

*In this study, numerical analyses demonstrate that a simple symmetrical 3D steel moment resisting frame with slight eccentricity can exhibit torsional behaviour despite a diagonal load being applied in a perfectly symmetrical manner. The torsion may be caused by inelastic bifurcation buckling, where the combined effect of the material and geometrical nonlinearity plays an important role. The similarities between this phenomenon and the inelastic buckling theories found in the literature are discussed.*

**Keywords:** Inelastic Buckling, Geometrical Nonlinearity, Torsion, Moment Resisting Frame, 3D, Numerical Analysis

# 1 INTRODUCTION

Although sophisticated analytical software allows the analysis of complicated large-scale structural models, epistemic uncertainties remain in the numerical analysis technique for tracing the inelastic torsional behaviour of three-dimensional (3D) frames. Researchers have reported that various uncertainties and irregularities in the stiffness and mass distribution leading to eccentricity as well as combined nonlinearity cause torsion. For example, Kohiyama and Yokohama [1] highlighted the existence of a geometrical nonlinearity referred to as the Q-Delta effect and evaluated its influence on the elastic torsional response. Flores *et al*. [2] conducted numerical analyses of frames considering the material and geometrical nonlinearities and demonstrated the importance of geometrical nonlinearities, namely, the P-Theta effect [3] and the P-Delta effect. Additionally, studies regarding the torsional behaviour of a perfectly symmetrical frame with no irregularities subjected to a symmetrical load are limited, while accidental torsion has been well-studied and considered in the structural design in practice.

In this study, quasi-static and dynamic analyses demonstrate that a simple symmetrical 3D steel moment resisting frame (SMRF) with slight eccentricity can undergo drastic torsional behaviour, despite a diagonal load being applied in a symmetric and deterministic manner. Namely, torsional behaviour in a structure can occur without irregularities in loading as well as in mass and stiffness distributions. Moreover, analysis demonstrates that the torsion is caused by inelastic bifurcation buckling, which is proven by the similarity between the results of the quasi-static analysis and inelastic column theory by Shanley [4], as well as the agreement between the results and the predicted behaviour presented in studies by Fukuda and Ikago [5, 6], who theoretically considered the torsion of an SMRF owing to inelastic bifurcation buckling. OpenSees [7] is used as the analysis framework, in which the combined effect of the material and geometrical nonlinearity is considered.

# 2 MODEL AND ANALYSIS CONDITIONS

## 2.1 Overview of the model

Consider a one-bay, one-storey, and perfectly symmetric SMRF, as shown in Figure 1, where pins support the bottom of the columns. The span and storey height are both 4 m. Here, (1), (2), (3), and (4) shown in Figure 1 indicate the number of the frames; the red arrows indicate the global axis of the coordinates. Regarding the beams in this model, only the in-plane bending stiffness is considered, while the torsional and out-of-plane bending stiffness are neglected. Euler-Bernoulli beam-column elements are used; the beams are connected to the nodes via bi-linear rotational spring elements. The yielding stress of the beams in frames (1) and (2) is reduced by 1% relative to that of frames (3) and (4), introducing an initial imperfection. The tops of the columns are connected to a rigid floor diaphragm, and its central node is referred to as the ‘master node’ hereafter. The in-plane rotation angle of the rigid diaphragm around the vertical axis is represented by $\theta$, as shown in Figure 1. The master node and the ground are connected by elastic horizontal shear springs to ensure the stability of the model after yielding of the beam-end rotational spring elements. Note, these shear springs are not arranged in the global $X$ and $Y$ directions, but in the direction parallel to frames (1) and (4). Finally, the lumped mass and mass moment of inertia are placed at the master node.

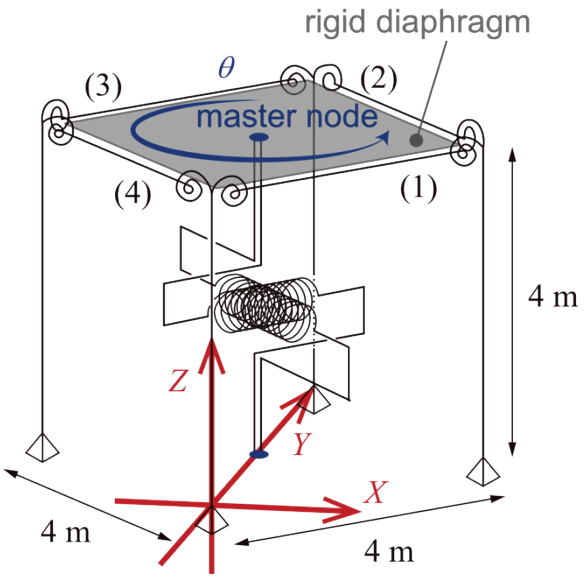


Figure 1: SMRF model

## 2.2 Member specifications, constitutive law of materials, and mass (moment of inertia)

The columns and beams are steel members (Young's modulus $E = 2.05 \times 10^8$ kN/m$^2$), which have box- (Figure 2(a)) or wide-flange shaped (Figure 2(b)) cross sections, respectively. The dimensions and specifications of the columns and beams are given in Table 1. Here, the local axes of the members are shown in Figure 2(a, b); the local $z$-axis direction of the beam shown in Figure 2(b) coincides with the global $Z$-axis direction shown in Figure 1. An infinitesimal value ($10^{-15}$) was assigned for the neglected stiffness, which can be regarded as zero in the numerical analysis.

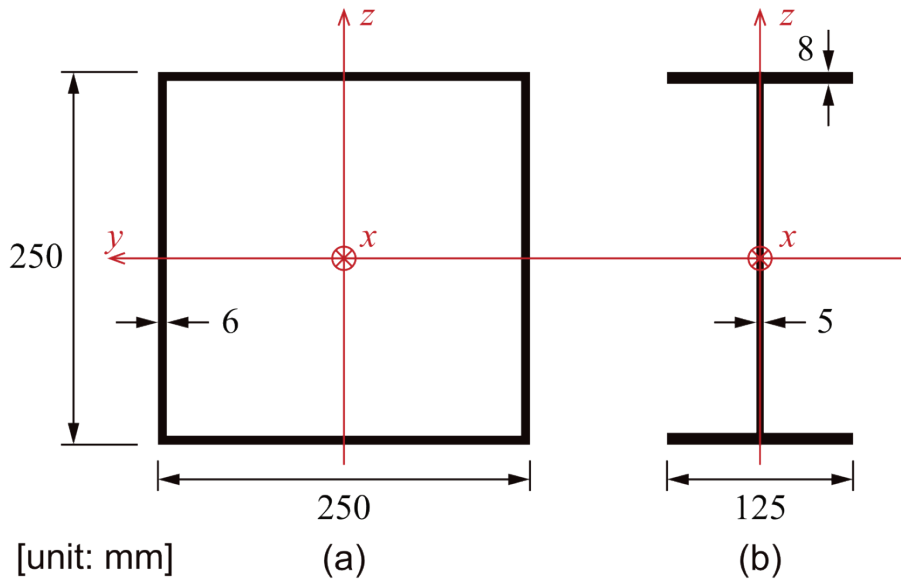


Figure 2: Cross section of the (a) columns and (b) beams

Considering the bilinear hysteresis of the beams, the initial stiffness $k_{Ry} = 6EI_y/l$ corresponds to the bending stiffness of the Euler-Bernoulli element subjected to an asymmetrical bending moment (Figure 3). The ratio of the initial and post-yielding stiffnesses is $\alpha = 0.01$. The yielding bending moment of the beams of frames (3) and (4) is $M_{\text{yield}} = 32$ kN, and that of

frames (1) and (2) is 31.68 kN (= $M_{yield} \times 0.99$). The stiffness of the elastic horizontal shear springs between the master node and the ground is 40 kN/m in both directions.

| | Columns | Beams |
|---|---|---|
| Dimension | 250 × 250 × 6 mm | 250 × 125 × 5 × 8 mm |
| Length: $l$ | 4 m | |
| Cross sectional area: $A$ | $5.763 \times 10^{-3}$ m$^2$ | $3.199 \times 10^{-3}$ m$^2$ |
| Second moment of area about the local $y$-axis: $I_y$ | $5.67 \times 10^{-5}$ m$^4$ | $3.45 \times 10^{-5}$ m$^4$ |
| Second moment of area about the local $z$-axis: $I_z$ | | $10^{-15}$ m$^4 \approx 0$ (ignored) |
| St. Venant torsional constant of the cross section: $J_x$ | $10^{-15}$ kNm/rad $\approx 0$ (bottoms are pin-supported) | $10^{-15}$ kNm/rad $\approx 0$ (ignored) |

Table 1: Specifications of members

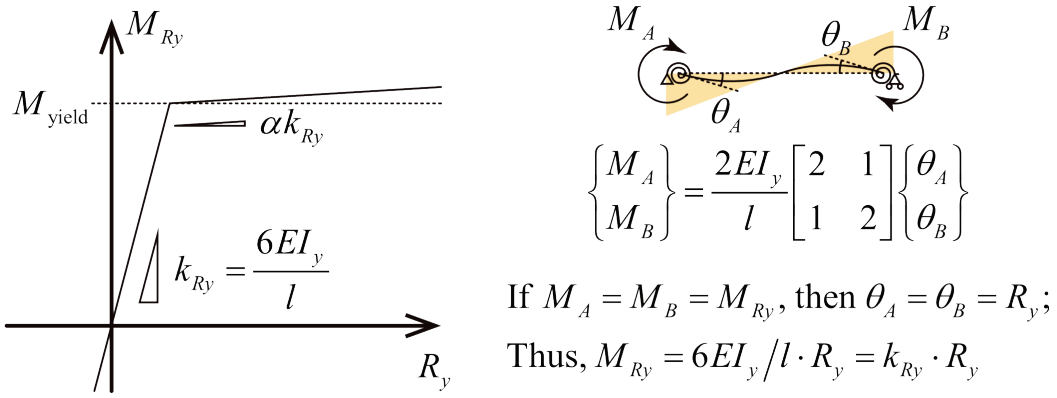


Figure 3: Nonlinear constitutive law of beam-ends

The mass in the global $X$ and $Y$ directions, represented by $m_X$ and $m_Y$, respectively, are placed at the master node, while that for the global $Z$ direction, $m_Z$, is neglected. Furthermore, only the mass moment of inertia around the $Z$-axis, ${}_Z I_m$, is considered and placed at the master node, while the mass moment of inertia around the $X$- and $Y$-axis, represented by ${}_X I_m$ and ${}_Y I_m$, respectively, are neglected. Note, an infinitesimal value ($10^{-15}$) was assigned for the neglected mass or mass moment of inertia. The mass is calculated provided that the mass per unit area at the top floor is 0.8 ton/m$^2$, and its distribution is uniform (0.8 ton/m$^2$ × 4 m × 4 m = 12.8 ton). ${}_Z I_m$ is calculated using Equation (1), assuming that the lumped masses of 1/4 of the total mass, that is, 3.2 ton, were located at the centre of each quarter block shown in Figure 4(a).

$$ {}_Z I_m = \sum_i^n r_i^2 \cdot m_i \tag{1} $$

Here, $n$ is the total number of lumped masses ($n = 4$), $r_i$ ($i = 1, 2, \ldots, n$) is the distance from the master node to each lumped mass (uniformly $r_i = \sqrt{2}$ m), and $m_i$ ($i = 1, 2, \ldots, n$) represents the lumped mass ($m_i = 3.2$ ton for each $i$); therefore, ${}_Z I_m$ is 25.6 ton·m$^2$. In this study, two comparison models were also employed, whose $r_i$ values were 1 and $1/\sqrt{2}$ m, respectively (Figure 4(b)). Their ${}_Z I_m$ values were also calculated by the same procedure; ${}_Z I_m$ = 12.8 ton·m$^2$ and ${}_Z I_m$ = 6.4 ton·m$^2$ for $r_i = 1$ and $r_i = 1/\sqrt{2}$, respectively.

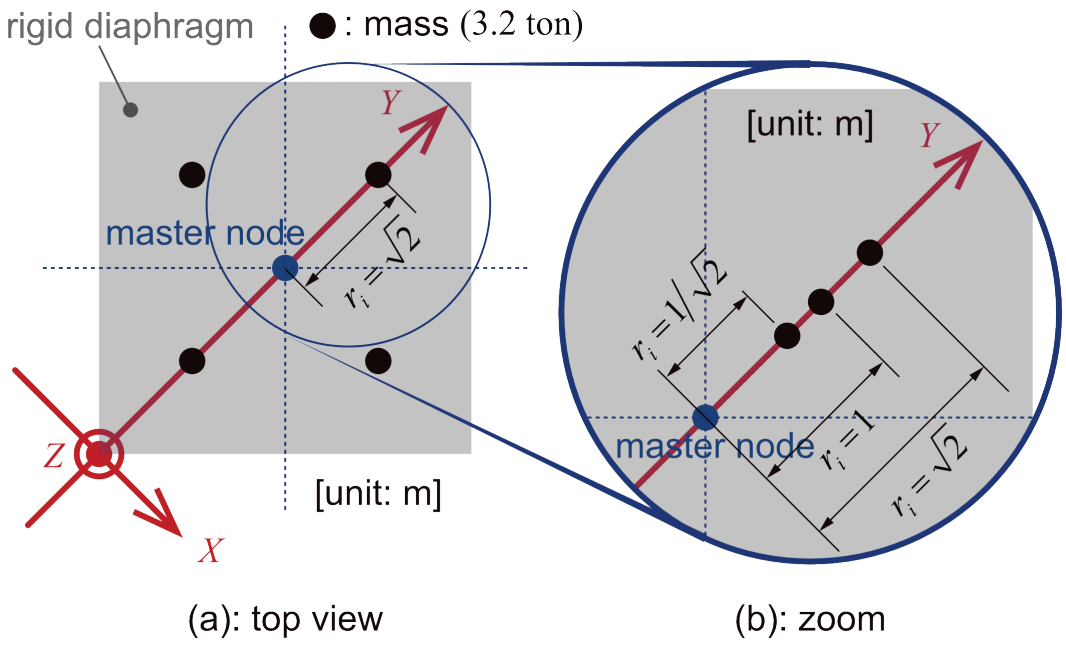


Figure 4: Calculation of the moment of inertia

Table 2 presents the 1st to 3rd natural periods of these models. The 1st and 2nd natural periods of all the models are identical. Figure 5(a–c) depicts the 1st to 3rd eigenmodes of the model whose $r_i = \sqrt{2}$. The 1st eigenmode exhibits a drift in the loading direction, as shown in Fig. 5(a), the 2nd eigenmode exhibits a drift in the orthogonal direction of loading, as shown in Fig. 5(b), and the 3rd eigenmode is a torsional mode, as shown in Fig. 5(c).

| | $r_i = \sqrt{2}$ m | $r_i = 1$ m | $r_i = 1/\sqrt{2}$ m |
|---|---|---|---|
| 1st natural period | 0.690 s | | |
| 2nd natural period | 0.509 s | | |
| 3rd natural period | 0.307 s | 0.217 s | 0.153 s |

Table 2: 1st to 3rd natural periods of the models

## 2.3 Analysis cases

For all the analysis cases, a vertical load of 31.36 kN that was divided into 10 000 steps was incrementally applied on the top of the columns. This vertical load was also calculated based on the assumption that the mass per unit area, 0.8 ton/m$^2$, was uniformly distributed.

Two types of horizontal loading analyses were performed, namely quasi-static and dynamic. In both cases, the degree of freedom in the $X$-axis was not fixed. In the quasi-static analysis, a load of 55 kN that was divided into 100 000 steps was incrementally applied to the master node from the global $Y$-axis direction. In the dynamic analysis, a 1940 El Centro NS wave whose peak ground velocity (PGV) was scaled to 100 cm/s was input in the global $Y$-axis direction for each model. The duration of the analysis was set to 80 s to examine the free vibration after the seismic input ended. A time interval of 0.001 s was used for the numerical integration. We assume an initial stiffness-proportional damping, where the damping ratio for the 1st mode $h_1$ was 2% to the critical damping coefficient.

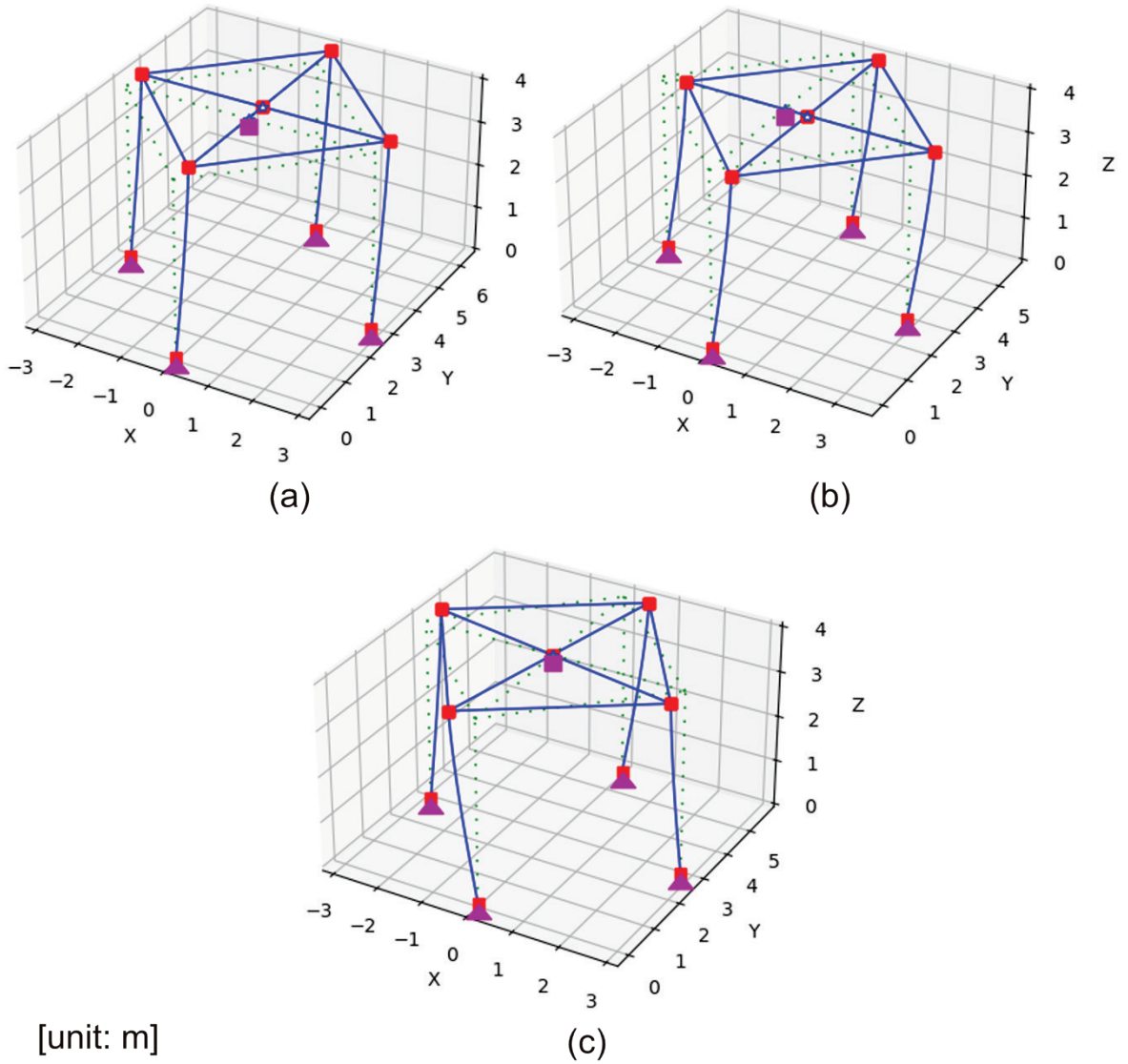


Figure 5: The (a) 1st, (b) 2nd, and (c) 3rd mode shapes of the $r_i = \sqrt{2}$ model

## 2.4 Modeling in OpenSees

The elasticBeamColumn elements were used for the Euler-Bernoulli elements. The bilinear rotational springs at the beam ends are implemented by zeroLength elements. Double nodes are created at each beam-end to insert the zeroLength elements. The elastic horizontal shear springs are represented by an equivalent zeroLength element, and a double node at the location of the master node is created to insert the zeroLength element. Steel01 and Elastic uniaxialMaterial are used to represent the hysteresis of the elastoplastic hinges and the elastic horizontal shear springs, respectively. The rigid floor diaphragm is implemented using elasticBeamColumn elements, where sufficiently large or small values ($10^{10}$ and $10^{-15}$, respectively) that numerically represent the rigid or pin connection are assigned to the cross-sectional area and bending stiffness. The PDelta option of the geomTransf command is specified to account for the geometrical nonlinearity of the columns. The PDelta option assumes finite deformations, that is, the rotational deformation of the columns, $\varphi$, is small, and the approximations of $\sin\varphi \approx \varphi$ and $\cos\varphi \approx 1$ are valid. The geometrical stiffness matrix is calcu-

lated with this 1st order approximation and subtracted from the tangent stiffness matrix [8]. The other options are summarised in Table 3.

| | Gravity Loading | Horizontal Loading | |
|---|---|---|---|
| | | Quasi-static | Dynamic |
| constraints | Penalty 1.0e+15 1.0e+15 | Pentalty 1.0e+18 1.0e+18 | |
| numberer | RCM | RCM | |
| system | SparseGEN (SuperLU) | FullGeneral | |
| test | NormDispIncr 1.0e-8 100 | NormDispIncr 1.0e-2 1000 | |
| algorithm | NewtonLineSearch -maxIter 10000 | Broyden -count 50 | |
| integrator | LoadControl | LoadControl | Newmark 0.5 0.25 |
| analysis | Static | Static | Transient |

Table 3: Options of OpenSees

## 3 RESULTS OF NUMERICAL ANALYSIS

This section first presents the quasi-static analysis results and demonstrates that torsion can occur even in a symmetrical SMRF with an infinitesimal stiffness eccentricity, whose effect is generally considered to be negligible. Second, the fact that the torsion was apparently caused by inelastic bifurcation buckling is presented, followed by the discussion regarding the similarity between the analytical results and the inelastic column buckling theory proposed by Shanley [4]. Finally, the dynamic analysis results reveal that torsional deformation occurred in the seismic response of these models, and the extent of torsion was influenced by the mass moment of inertia associated with the torsional resistance of the model.

### 3.1 Quasi-Static Analysis

Figure 6 depicts the step histories of the master node in the $X$-, $Y$-, and $\theta$-directions, demonstrating that the torsional deformation $\theta$ occurs near step 82 000; thereafter, displacements in the $\theta$- and $Y$-directions significantly increase. Namely, a torsion can occur even in a symmetrical SMRF with an infinitesimal stiffness eccentricity. Note, displacement also occurs in the orthogonal $X$-direction to loading, but its overall effect is small because the increasing rate of the $X$-displacement is smaller than that in the $Y$- and $\theta$-directions. Figure 7 depicts the overall deformation at the end of loading without any scale factor, confirming that the contribution of the $X$-displacement to the overall deformation is insignificant.

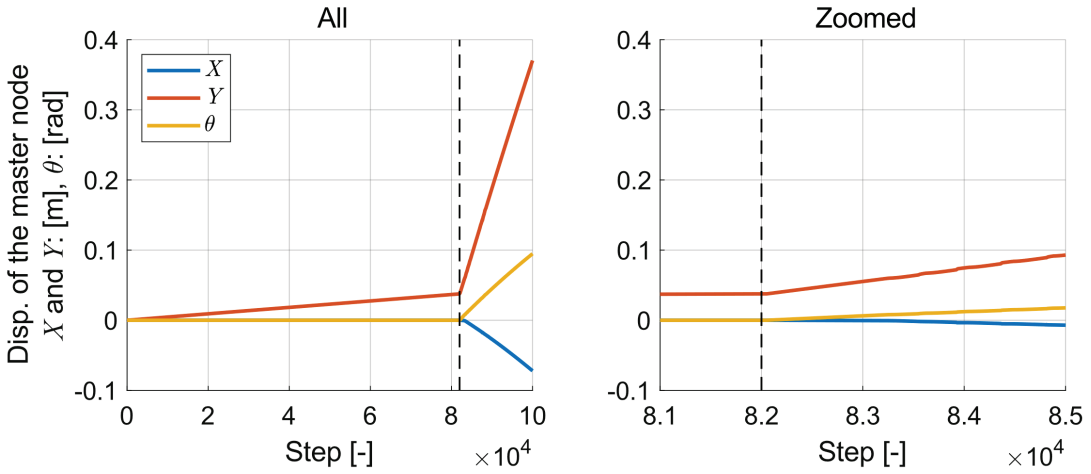


Figure 6: Step history of the master node displacement

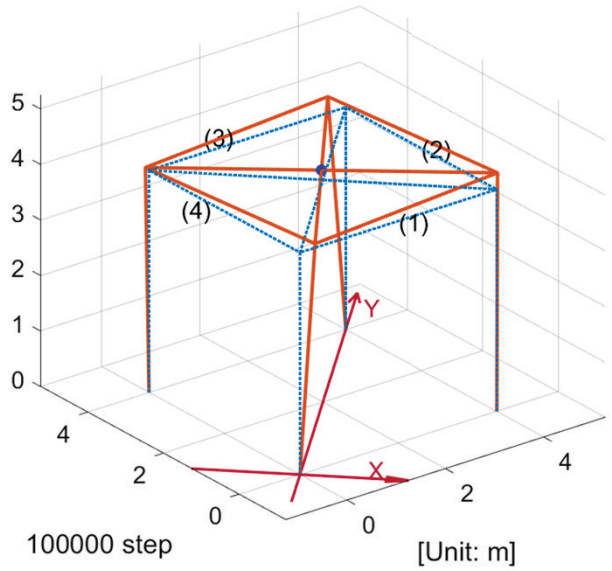


Figure 7: Global deformation of the SMRF model at 100 000 steps

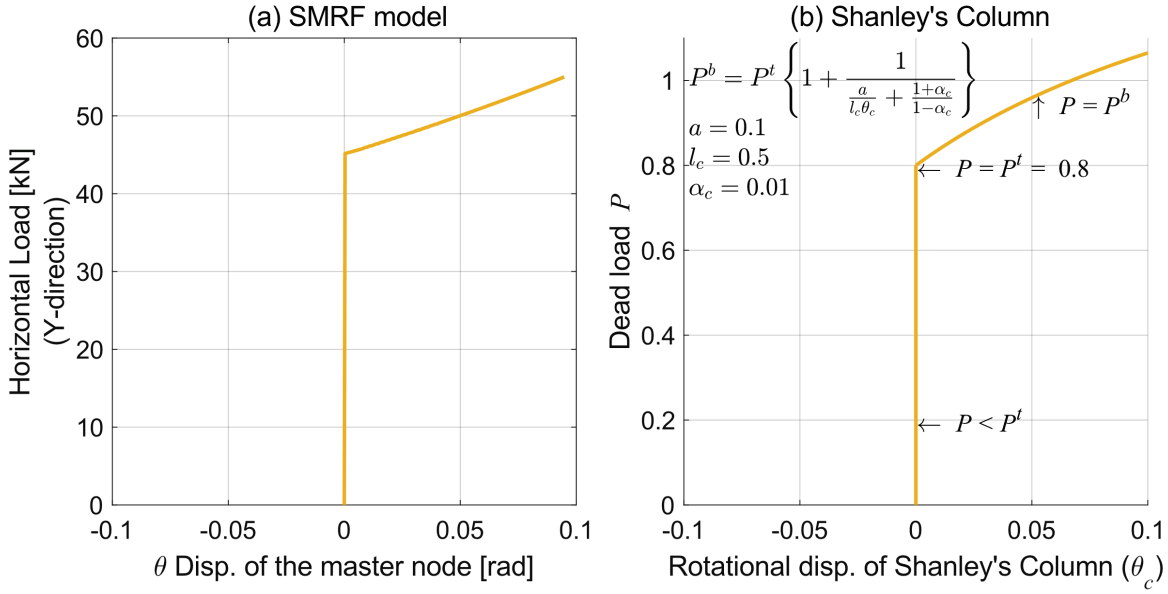


Figure 8: (a) Relationship of the horizontal load–master node $\theta$ of the SMRF model, and (b) P–$\theta_c$ relationship of the Shanley Column

The horizontal load–$\theta$ relationship in this SMRF model, Figure 8(a), is one source of evidence that suggests that this torsion is inelastic bifurcation buckling. This is because a similar relationship (Figure 8(b)) can be found in an inelastic buckling problem of a centre-compressed short column discussed by Shanley [4] (Figure 9, designated Shanley's Column here). If a bifurcation occurs at the tangent modulus load $P^t$ in a Shanley's Column with elastoplastic springs whose hysteresis is bilinear, the load after the bifurcation $P^b$ and the buckling deformation $\theta_c$ satisfy the following relationship.

$$P^b = P^t \left\{ 1 + \frac{1}{a/l_c\theta_c + (1+\alpha_c)/(1-\alpha_c)} \right\} \tag{2}$$

where $a$ and $l_c$ are the parameters related to the dimensions of the Shanley's Column, and $\alpha_c$ is the tangent stiffness ratio of the elastoplastic springs. Figure 8(b) is based on the following conditions: $P^t = 0.8$, $a = 0.1$, $l_c = 0.5$, and $\alpha_c = 0.01$. Based on this similarity, a load-controlled inelastic torsional bifurcation theory should be developed for the SMRF used in this study, and a relationship of the horizontal load–master node $\theta$ similar to Equation (2) can also be derived.

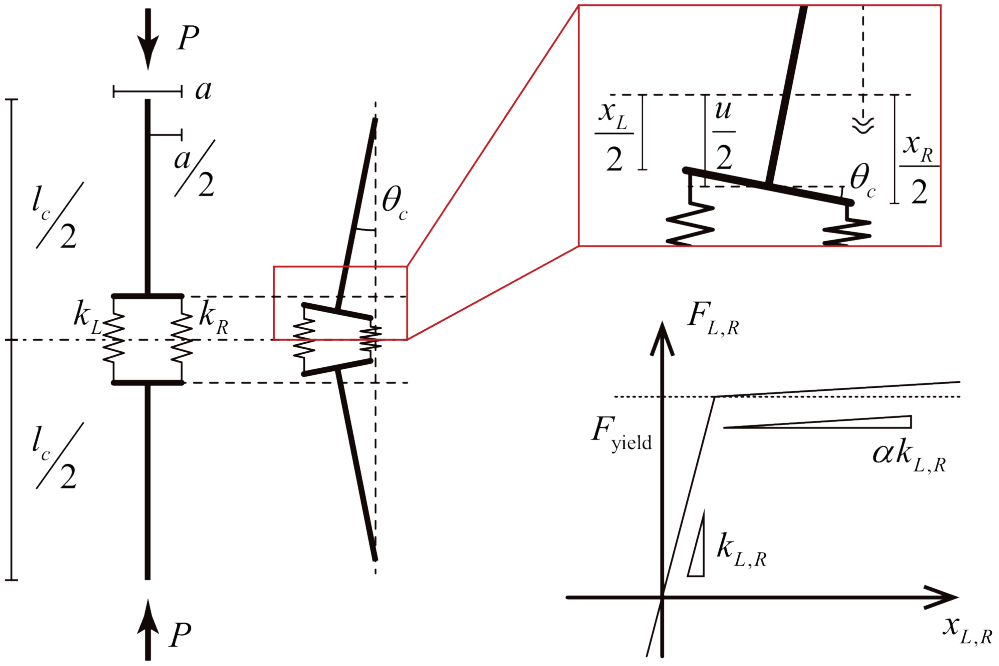


Figure 9: Shanley's Column model

Another source of evidence that suggests that this torsion is an inelastic bifurcation is shown in Figure 10, which depicts the displacements of the rigid diaphragm and the yielding status of the beam-ends at every 1000 steps from steps 82 000 to 85 000. This verifies the results discussed in the study by Fukuda and Ikago [5, 6], who theoretically investigated the inelastic torsional bifurcation of a simple SMRF under limited conditions. According to Fukuda and Ikago [5, 6], if the SMRF used in this study is subjected to a controlled load or controlled displacement resulting in torsion, it is expected that the beam-ends of frames (1) and (2) will be in a post-yielding or designated loading state, while that of frames (3) and (4) will be in an elastic or unloading state after the bifurcation. The results shown in Figure 10 are consistent with this prediction, except for step 85 000. Note, this prediction is inspired by the bifurcation process of Shanley's Column revealed in the inelastic column theory as follows [4]: i) When a bifurcation occurs in a Shanley column, one of the two inelastic springs at the centre of the column is in a loading state, and the other spring is in a neutral state, which is neither in a loading nor unloading state, ii) the spring in the neutral state is continuously unloaded immediately after the bifurcation displacement occurs, and iii) subsequently, the states of these springs are fixed in a combination such that one is in a loading state, and the other in an unloading state. A similar process applies to a simple SMRF model in this study as follows: i) When a torsion occurs in this SMRF, a couple of frames orthogonal to one another,

that is, either frames (1) and (2) or frames (3) and (4) are in a state where their beam-ends are in loading, while the other couple are in a state in which their beam-ends are in a neutral state, which is neither in a loading nor unloading state, ii) immediately after the torsion occurs, the beam-ends in the neutral state are unloaded, and iii) subsequently, the state of the couples of frames and their beam-ends are fixed in a combination such that the beam-ends of one couple of frames are in a loading state and those of the other couple of frames are in an unloading state. Because the initial imperfection is intentionally introduced in this study, the frame couple of frames (1) and (2) is the former, and the remaining frames are the latter in this case.

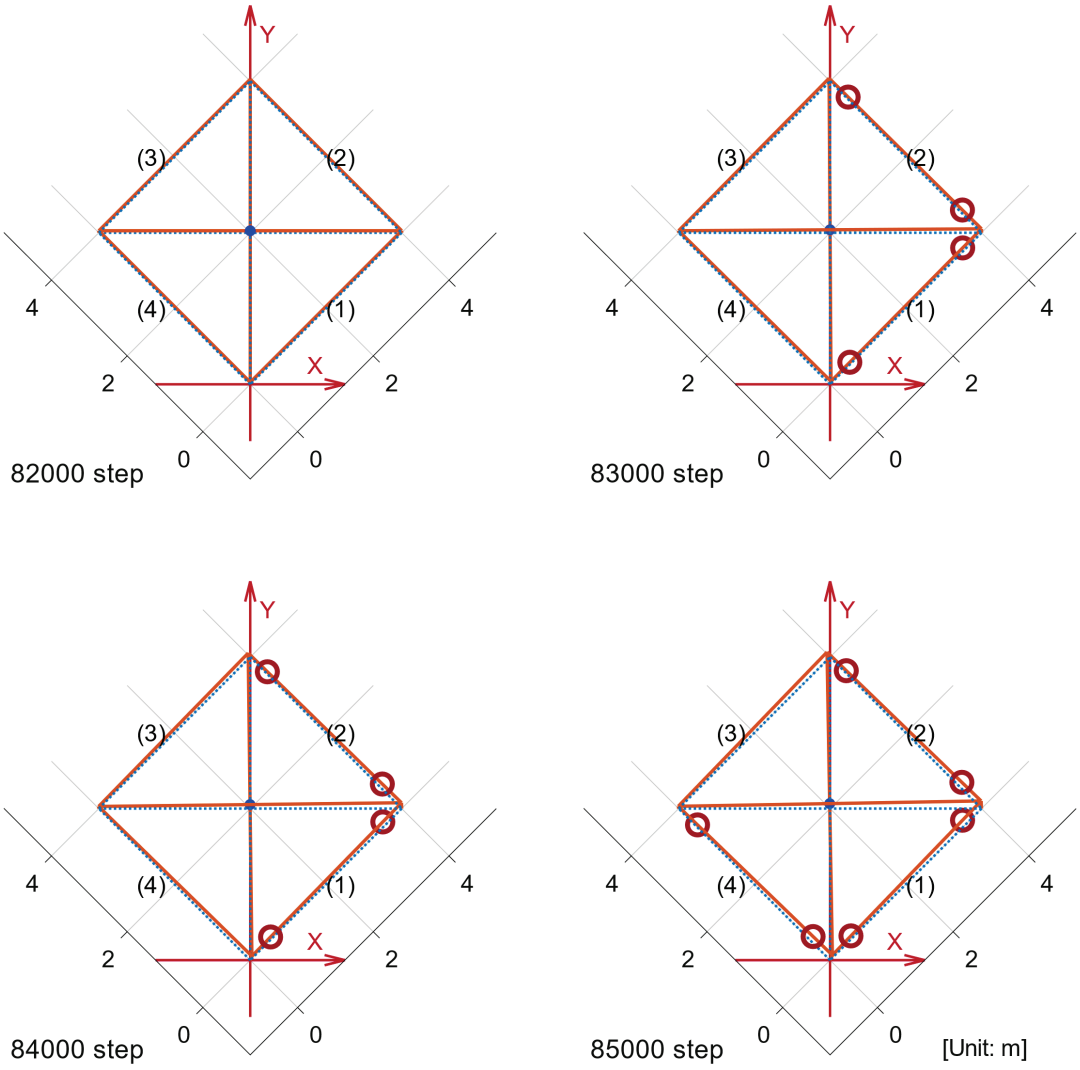


Figure 10: Displacements of the rigid diaphragm and the yielding status of the beam-ends

The yielding state of step 85 000 shown in Figure 10 violates this prediction, which may be related to the $X$-displacement. According to Fukuda and Ikago [6], bifurcation in the orthogonal direction of a controlled displacement can occur in a similar model if the problem considered is displacement-controlled. In these cases, couples of frames change to frames (2) and (4), and frames (1) and (3). A superposition of bifurcation may occur in the torsional and perpendicular directions after step 85 000. As a result, in addition to frames (1) and (2), frame (4)

may also proceed into a yielding state at that time. Note, a load-controlled numerical analysis is conducted in this study, for which the details differ from the theoretical analysis presented by Fukuda and Ikago [6]; therefore, further investigation is required to clarify this behaviour.

### 3.2 Dynamic Analysis

Figure 11(a–c) presents the time history of the master node displacement for each model and demonstrates that torsion can occur even in a model with infinitesimal eccentricity during the dynamic response. Torsion occurs and increases in the $r_i = 1/\sqrt{2}$ m and $r_i = 1$ m models, whereas almost no torsion can be observed in the $r_i = \sqrt{2}$ m model. Overall, a larger mass moment of inertia results in a smaller torsional deformation.

The main cause of the torsion in this model is unclear at this stage because the damping, instantaneous eccentricity owing to plasticisation, fluctuations in the eigenvalues, Q-Delta effect, as well as inelastic bifurcation buckling, affect the response in a dynamic problem, and the contribution of each factor is complicatedly related to one another. For a clear understanding of this phenomenon, further investigations from various point of views are needed to clarify the contribution of each factor. Therefore, other interesting points relevant to understanding the phenomenon are reserved herein. First, when comparing two models in which torsional deformation occurs (the $r_i = 1/\sqrt{2}$ m and $r_i = 1$ m models), the torsional deformation converges to a constant value in the model with $r_i = 1$ m, whereas the model with $r_i = 1/\sqrt{2}$ m demonstrates a diverging behaviour. However, note that a finite deformation is assumed in this analysis despite the deformation being relatively large. Therefore, the result can be meaningful for tracing the occurrence of a torsion but may underestimate the maximum response compared to the actual behaviour. Second, when comparing the results considering whether torsional deformation occurs, the *X*-axis deformation is apparently related to the torsional deformation. In addition, the $r_i = \sqrt{2}$ m model, which presents a small torsional deformation, demonstrates a free vibration with damping in the *Y*-direction after the seismic excitation ends, whereas the $r_i = 1$ m model, which exhibits converged torsional deformation, exhibits free-vibration behaviour without damping in the *X*- and *Y*-directions.

## 4 CONCLUSION

In this study, a symmetric SMRF with infinitesimal eccentricity subjected to quasi-static and dynamic horizontal loading in a diagonal direction is examined by a numerical analysis. The results of quasi-static loading indicate that torsion can occur in an SMRF with infinitesimal eccentricity, suggesting that this torsion is caused by inelastic bifurcation buckling. This is demonstrated by the discussion regarding the similarities between the results of the analysis and Shanley's inelastic column theory. One of these similarities is the load–bifurcation displacement relationship, and another similarity is the yielding status of the elastoplastic elements at the beginning of bifurcation. This result partially supports the theoretical predictions by Fukuda and Ikago. In addition, the torsional response in the SMRF also occurs when subjected to dynamic excitation. The degree of torsion depends on the mass moment of inertia that is related to the torsional resistance. Further challenges are identified to determine the contribution of inelastic bifurcation buckling and other factors in the dynamic response.

## ACKNOWLEDGEMENTS

This study was supported by the JSPS Grant-in-Aid for the JSPS Research Fellow (Grant Number: JP22J13566).

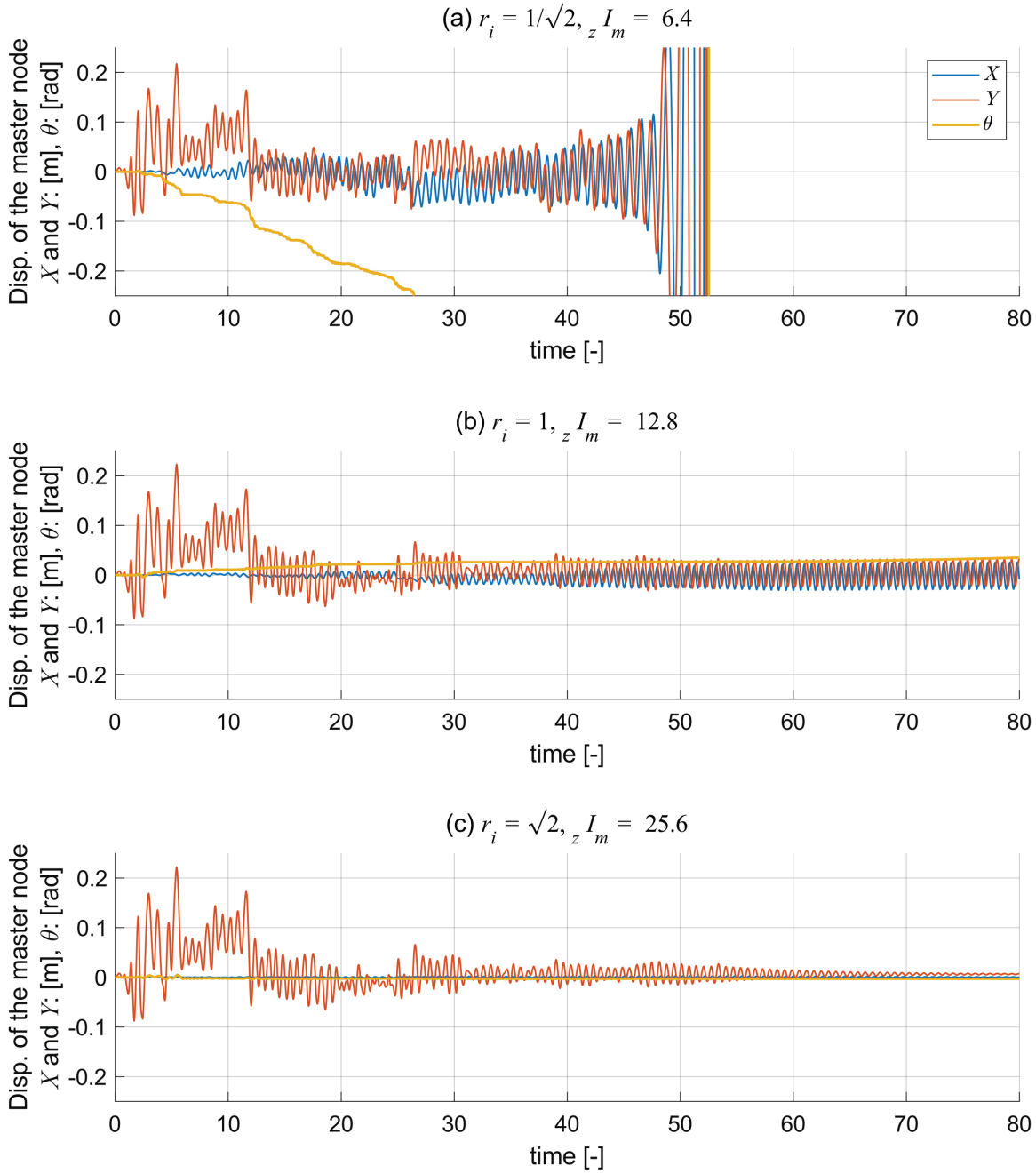


Figure 11: Time history of the master node displacement for each model

## REFERENCES

[1] M. Kohiyama, H. Yokoyama, Torsional Response Induced by Lateral Displacement and Inertial Force, *Frontiers in Built Environment*, **4**, 38, 2018.

[2] F. Flores, F.A. Charney, D. Lopez-Garcia, The Influence of Accidental Torsion on the Inelastic Dynamic Response of Buildings during Earthquakes, *Earthquake Spectra*, **34**(1), 21–53, 2018.

[3] E.L. Wilson, A. Habibullah, Static and Dynamic Analysis of Multi-Story Buildings, Including P-Delta Effects, *Earthquake Spectra,* **3**(2), 289–298, 1987.

[4] F.R. Shanley, Inelastic Column Theory, *Journal of the Aeronautical Sciences,* **14**(5), 261–268, 1947.

[5] I. Fukuda, K. Ikago, Global Buckling Analysis of High-Rise Steel Moment-Resisting Frames Involving Inelastic Torsional Deformation Concentration, *12th Pacific Structural Steel Conference*, Tokyo, Japan, November 9–11 2019.

[6] I. Fukuda, K. Ikago, Inelastic Torsional Buckling Analysis of a Single-Story Cubic Frame, *17th World Conference on Earthquake Engineering*, Sendai, Japan, September 27–October 2, 2021. (Postponed from September 13–18, 2020)

[7] https://opensees.berkeley.edu/

[8] M.D. Denavit and J.F. Hajjar, Description of Geometric Nonlinearity for Beam-Column Analysis in OpenSEES, *Department of Civil and Environmental Engineering Reports*, Report No. NEU-CEE-2013-02, Department of Civil and Environmental Engineering, Northeastern University, Boston, Massachusetts, 2013.

COMPDYN 2023
9th ECCOMAS Thematic Conference on
Computational Methods in Structural Dynamics and Earthquake Engineering
M. Papadrakakis, M. Fragiadakis (eds.)
Athens, Greece, 12-14 June 2023

# ADVANCED OPTIMIZATION PROCESSES FOR THE DESIGN OF 3D-PRINTED METAL DAMPERS

**Francesca Romana Andreacola**[1] **and Giuseppe Brando**[1]

[1] Department of Engineering and Geology, University "G. d'Annunzio" of Chieti-Pescara
Viale Pindaro, 42, 65127 Pescara, Italy
e-mail: giuseppe.brando@unich.it, francesca.andreacola@unich.it

## Abstract

*Over the past years, the research field concerning the passive seismic protection of buildings gained relevance more and more, due to the severe earthquakes affecting several parts of the world, often hitting very populous areas. Meanwhile, recent additive manufacturing technologies allowed the implementation of innovative metal passive protection devices (dampers), that are ground-breaking both in terms of final geometry and design approaches.*
*This paper describes an innovative damper typology obtained through the application of additive manufacturing processes and by exploiting advanced topological and geometric optimization algorithms, which are developed within the Abaqus virtual environment. The damper is conceived starting from common geometric shapes, and then designed, through optimization processes, to obtain unconventional shapes, which can be easily obtained through 3D printing processes only, which allow to comply with objective performance in terms of strength, stiffness and dissipative capacity. Moreover, the consequent elimination of parts enables the pursuit of relevant targets, such as material savings, weight and cost reductions. The model threated in this paper, which was obtained by optimizing a spherical shape, was designed to withstand axial stress, simulating the load being transmitted across a diagonal brace of a concentrically braced frame in the event of an earthquake. The performance of the damper proves how the optimization process actually allowed to obtained pre-established and convenient decoupled levels of strength and stiffness.*

**Keywords:** Additive manufacturing, Metal 3D printing, Selective Laser Melting, Seismic dissipation devices, Optimization process, Damper.

# 1 INTRODUCTION

In recent years, seismic risk mitigation has become a topic of great interest for both researchers and experts operating in the field of building engineering. For this reason, nowadays, earthquake engineering plays an increasingly central role in structural design.
Seismic design processes target to achieve a sufficient level of safety, in order to avoid sudden catastrophic collapse of the structure and subsequent loss of life under severe events. A correctly designed building, therefore, must provide for the possibility of evacuation following rare seismic event, reaching an admissible state of damage, but not involving the collapse of structural components [1], [2]. This can be achieved, for example, by introducing additional dissipative elements into the structure, which attract most of the input energy, thus preserving the primary structural members [3], [4]. Several types of supplementary energy dissipation devices have been introduced in literature. These can be classified with respect to the type of mechanism required for activation [5]. In fact, depending on the way they react to earthquake-induced excitation, additional energy dissipation systems can be classified into active and semi-active systems (e.g. Active Bracing Systems, Active Mass Dampers, Variable Stiffness or Damping Systems, Smart Materials) and passive systems (Metallic Dampers, Friction Dampers, Viscoelastic Dampers, Viscous Fluid Dampers, Tuned Mass Dampers, Tuned Liquid Dampers) [3], [6]–[9]. These devices are conceived according to different approaches, depending on how they reduce the effects of earthquakes on structures [2], [4], [10], [11].
In this research area, this paper presents a new type of damper whose shape is achieved by applying advanced optimisation algorithms to a simple geometric starting shapes, namely a sphere. The implementation of optimisation processes allows particularly challenging shapes, to be created through the rationalisation of the simpler geometry by removing portions of material, which allow to achieve pre-established levels of reduced strength, but not modifying the stiffness significantly. This means that the obtained new damper is able to attract, when installed in a frame. the same aliquot of seismic energy but anticipating its dissipative function to low earthquake demands.
3D printing is proposed for production, due to the fact that additive manufacturing allows the production of complex components that would be hard to produce with conventional techniques. Selective Laser Melting, one of the most widely used methods in metal 3D printing, is proposed to this purpose. Through this design process, the desired performance is achieved by decoupling stiffness and strength, so to control them, as target parameters of the optimization process, separately. The aim is therefore to obtain a device that can more efficiently meet the requirements of a structural protection system. The results in terms of force-displacement diagram of the optimisation carried out in the Abaqus environment of a sphere designed to absorb the axial load transmitted by a brace during a seismic action, and the comparison with the starting models are reported.

# 2 THE PROPOSED MODEL

## 2.1 The starting shapes

The idea behind the design of the damper was to start with an optimal geometric model withstanding specific design demands in terms of stiffness, also depending on its positioning in the structure. In the current case, a spherical geometry was selected as it is the shape with the ideal best cyclic response, because of its compactness, which is unaffected by buckling phenomena and therefore able to provide ideal dissipative mechanisms. The spherical model was designed to be placed on steel concentrically braced frames (CBF).

The model and the analysis of the damper were implemented within the Finite Element Model software Abaqus. The starting model, shown in Figure 1a, consisted of a spherical geometry with a diameter of 100 mm.
On the end of the sphere two truncated cones constituting the elements that allow the connection, through metallic plates, of the device to the bracing, have been modeled. As for the constraint conditions, an encastre has been applied to the surface of one of the two truncated cones. An axial displacement towards the core of the sphere of 50 mm has been applied, instead, to the opposite end. This displacement was determined by assuming that the damper is installed on the bracing of a single-story frame with dimensions 6000 mm (W) x 3500 mm (H). In order to identify the deformation that the damper have to withstand, the maximum elongation of the entire bracing system (brace + sphere), when the life-safety limit state is reached, was assessed. In the case of CBF, the FEMA Standard recommends calculating the maximum strain of the bracing starting from a limit story drift corresponding to 1.5% of the frame height [12].
This starting model, henceforward referred to as the "full-shape model" (see Figure 1a) was realized with C3D8R elements (8-node general purpose linear brick elements, with reduced integration) with radial mesh distribution from the center of the sphere outwards. To improve the mesh distribution, three partitions were created in the model. One partition is orthogonal to the longitudinal axis of the sphere, while two partitions are parallel to the longitudinal axis of the sphere and mutually perpendicular.
In order to obtain a different material distribution, a second model (Figure 1b), subsequently defined as the "holed model", was developed by subtracting an ellipsoid with dimensions 95 mm ($r_1$) x 30 mm ($r_2$) from the starting solid sphere. As can be seen from Figure 1b, it has the same geometric dimensions and modelling features as the full-shape model. However, additional partitions were added.

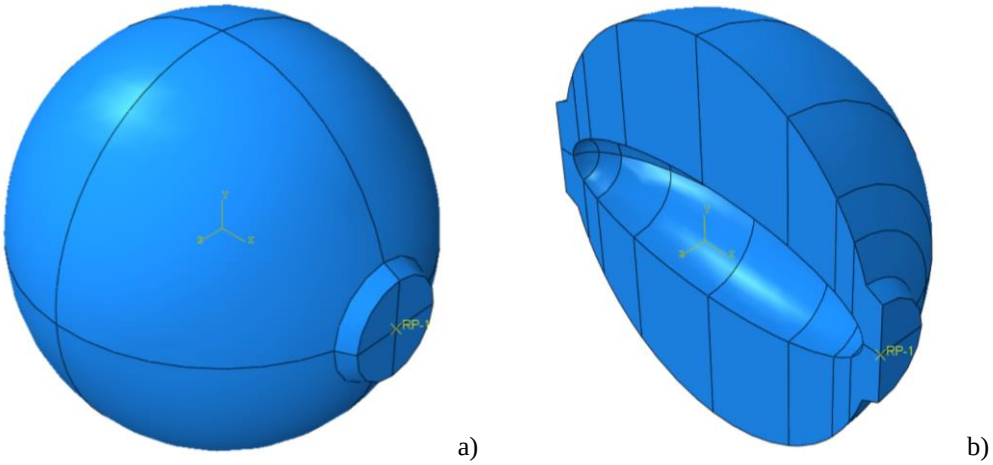


a) b)

Figure 1: The starting models: a) The full-shape model; b) The holed model.

The material adopted for both models was 17-4 Precipitation Hardening stainless steel (AISI 630). The mechanical parameters were derived from the technical data sheet of the powder material the additively manufactured dampers will be made of, provided by the manufacturer [13]. The constitutive model of the material, implemented in the FEM software, was a trilinear true stress-strain relationship with softening.
Cyclic analyses were conducted on the models. The analyses were performed considering a cyclic loading history with constant amplitude, applying a maximum displacement of 50 mm,

in accordance with the ECCS loading protocol. The analysis in the cyclic field was carried out by applying a quasi-static force with displacement control.
The cyclic loading protocol adopted was selected according to the ECCS standards for structural steel components ("Recommended Testing Procedure for Assessing the Behaviour of Structural Steel Elements under Cyclic Loads", Publication 045 – 1986) [14], in which the key parameter for defining the cyclic loading is the yield displacement $d_y$, obtained from monotonic tests.

## 2.2 Optimization processes

Starting with the two preliminary models, various optimization processes were carried out by implementing the Abaqus software optimization module ATOM (Abaqus Topology Optimization Module). The aim of the performed optimization process is to design a structural element with a low pre-established strength but with a stiffness as close as possible to the one of the original shape, so to ensure that the seismic forces are attracted appropriately and significantly by the device.
The process starts with a conventional geometric shape, a solid sphere. The shape of the initial element was selected according to its position within the structure, i.e. on the bracing, and consequently the stress it will be exposed to. The initial stiffness, which can be easily determined by modifying the diameter of the starting geometry, can be established beforehand in accordance with the targets imposed by the service limit states or the rate of seismic force that the damper must attract in the elastic field.
The subsequent step, from a theoretical point of view, is the topological and geometrical optimization of the solids. This process, through the removal of material in excess of the actual structural purposes, ensures that the optimized model provides:
- stiffness similar to the starting solid;
- strength properly reduced to ensure compliance with the targeted activation of the damper dissipative function;
- ductility capacity for accommodating the request of inelastic deformation.

The activation of the dissipative capacity of the damper is managed by reducing the strength of the device to the pre-established design levels, without significantly reducing the original stiffness. The decoupling of strength and stiffness is possible thanks to the shape effect obtained downstream the application of the optimization method, which allows the two parameters to be controlled independently. Figure 2 conceptually shows how the optimization process should bring from the curve of the original shape (the grey curve) to the curve (bolded black) of the optimized damper. This transformation can be carried out by controlling a series of parameters: the objective functions, the constraints and eventual geometric restrictions.
The shapes resulting from the optimization processes will have unconventional and extremely challenging geometries that are not easily realized by conventional manufacturing processes. As a result, additive manufacturing can be considered as an alternative approach that works with design and geometry rather than material.

## 2.3 The optimized model

From the results of several preliminary optimization attempts, one model was considered particularly successful. This model was obtained by considering as initial model the hollow sphere and by imposing, as main objective functions, the halving of the strength and the maximization of the strain energy, so to maximize the stiffness of the damper. Moreover, some constraints concerning the parts of the initial model to be preserved in the optimization process, defined as frozen areas, have been imposed.

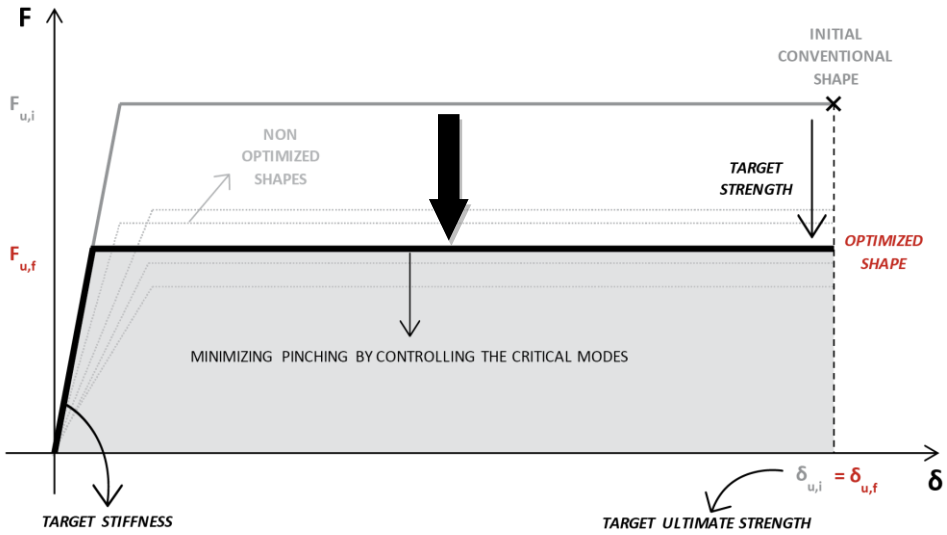


Figure 2: The result of the optimization process.

In particular, 12 outer sectors on the external surface have been constrained to remain after the optimization process, so to assure that the optimized damper has some external parts that undergo plastic mechanisms in bending for very low displacement demands.
In order to better distribute the meshes, the initial model addressed for optimization has been subjected to radial partitions with a relative angle of 15°, this enabling greater manageability of the regions to be frozen. The sphere was therefore divided into 24 sectors. An additional partition orthogonal to the longitudinal axis of the sphere allowed the frozen areas to be thickened.
The geometry of the optimized damper, which was subjected to a subsequent revision, is shown in Figure 3. The revision process consisted in adding to the central core three transverse ribs and eight longitudinal ribs to strengthen the most stressed central section with respect to possible buckling phenomena, which have been controlled through several preliminary buckling analyses that allowed to achieve the final solution. Also, support elements at the two ends of the internal hollow core have been added to avoid manufacturing problems caused by excessive overhang angles.
The same constraint conditions of the two starting models were also maintained on this model, i.e. an encastre on one of the two ends and the same displacement history (maximum amplitude of 50 mm) on the opposite end.

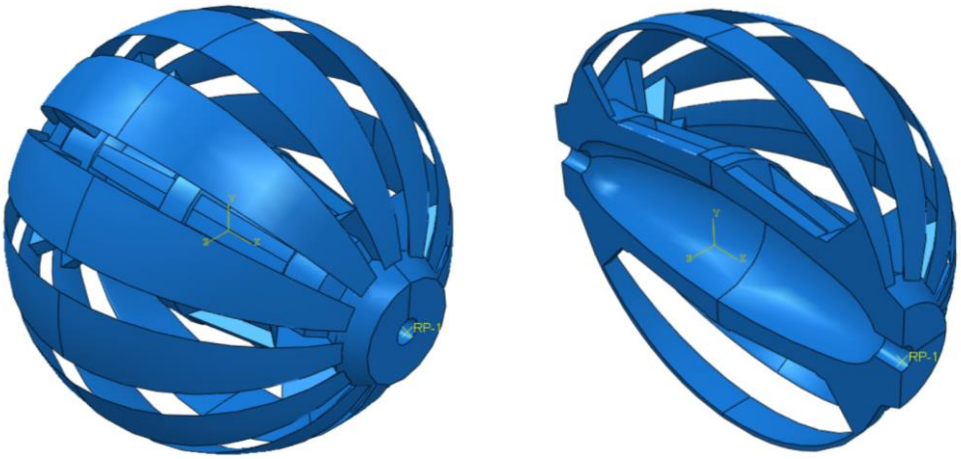

Figure 3: The optimized model and a section of the model.

The numerical model consisted of 10-node tetrahedral configuration 3D elements, defined in Abaqus software as C3D10 elements (general purpose tetrahedral element with 4 integration points).

## 3 RESULTS AND REMARKS

The results of the numerical tests performed on the three models are shown in Figure 4, in terms of force-displacement cyclic curves. As it is possible to observe, the objective of the optimization process was successfully achieved. In fact, the optimized damper present a strength of about 360 kN versus the strength of about 720 kN provided by the hollow sphere considered as initial shape. Also, the optimized damper presents the same stiffness of both the holed model and the full shape, as it is possible to observe by comparing the unloading branches of the cycles. Finally, it must be pointed out that the optimized damper features full cycles that are not affected by pinching phenomena, this meaning that the addition of ribs in the inner core allowed to avoid buckling phenomena which would have provoked undesired detrimental effects.

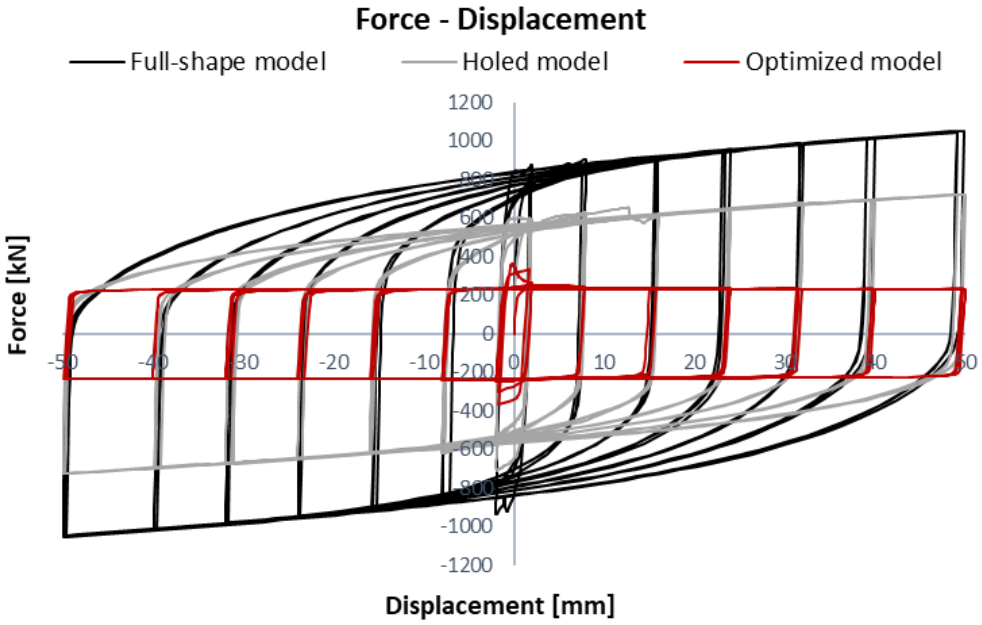


Figure 4: Results of the numerical tests.

The optimized damper features a weight of 6.13 kg versus 41.4 kg (saving of material equal to 85%) and 37.9 kg (saving of material equal to 77%) of the full and the hollow shapes respectively.

## 4 CONCLUSIONS

In this paper a new metallic damper has been presented. It has been conceived by exploiting the potentialities of some optimization algorithms that allowed to transform a conventional shape, a sphere, so to decouple the strength and the stiffness once that it is subjected to axial force. Both the optimization process and the cyclic non linear analyses have been developed through the FEM software Abaqus.
Based on the cyclic tests performed on the starting models and the final optimized damper, the following conclusions can be given:

- The optimized damper presents a good dissipative behavior, with full cycles, that are not affected by pinching phenomena, and a high ductility.
- The objective of the optimization process concerning the halving of strength with respect to the original shape have been successfully achieved.
- Also, the optimized damper guaranteed a stiffness that is very close to the one provided by the original shape and this is a not trivial achievement, considering the reduction of strength, that is completely due to the new shape obtained downstream the application of the optimization process.
- The new shape featured a weight that allowed the 85% of saving of material.

The new damper, perfectly match one of the main targets of the design processes to be implemented for the passive protection of buildings through special devices: providing supplemental damping through dampers characterized by a low strength, so to activate their dissipative function already for low demands, but characterized by a high stiffness, which allows to attract toward the dampers themselves the seismic actions, so to preserve from damage the other primary elements of the structure. In the case being, the stiffness of the optimized damper is very closed to the one of the original shape that, moreover, represents a design parameter that can be easily managed.
The new shape of the optimized damper is for sure one of the challenging issues to be e faced, but as it was widely discussed in the paper, it can be easily threated by recurring to the modern additive manufacturing process.

## ACKNOWLEDGEMENTS

This research was developed during the Italian Research Project “3D-DAMPER -Processi di ottimizzazione di dampers metallici innovativi stampati in 3D”, framed in the PON action “Fabbrica Intelligente, Agrifood e Scienza della Vita”, funded by the Italian Ministry for the Economic Development.

## REFERENCES

[1] D. De Domenico, E. Tubaldi, I. Takewaki, T. Karavasilis, A. Dall’Asta, and O. Lavan, “Editorial: Recent Advances and Applications of Seismic Isolation and Energy Dissipation Devices,” *Front. Built Environ.*, vol. 6, no. August, pp. 1–5, 2020, doi: 10.3389/fbuil.2020.00126.

[2] T. E. Saaed, G. Nikolakopoulos, J. E. Jonasson, and H. Hedlund, “A state-of-the-art review of structural control systems,” *JVC/Journal Vib. Control*, vol. 21, no. 5, pp. 919–937, 2015, doi: 10.1177/1077546313478294.

[3] W. Pu and C. He, “Seismic design framework for steel structures with hysteretic and viscous dampers,” *J. Constr. Steel Res.*, vol. 194, no. April, p. 107330, 2022, doi: 10.1016/j.jcsr.2022.107330.

[4] G. Brando, F. D’Agostino, and G. De Matteis, “Seismic performance of MR frames protected by viscous or hysteretic dampers,” *Struct. Des. Tall Spec. Build.*, vol. 24, no. 9, pp. 653–671, 2015, doi: 10.1002/tal.1204.

[5] M. D. Symans *et al.*, “Energy Dissipation Systems for Seismic Applications: Current Practice and Recent Developments,” *J. Struct. Eng.*, vol. 134, no. 1, pp. 3–21, 2008,

doi: 10.1061/(asce)0733-9445(2008)134:1(3).

[6] P. C. Talley, A. Javidialesaadi, N. E. Wierschem, and M. D. Denavit, "Evaluation of steel building structures with inerter-based dampers under seismic loading," *Eng. Struct.*, vol. 242, no. May, p. 112488, 2021, doi: 10.1016/j.engstruct.2021.112488.

[7] A. Farsi, H. R. Amiri, and S. H. Dehghan Manshadi, "An innovative C-shaped yielding metallic dampers for steel structures," *Structures*, vol. 34, no. January, pp. 4254–4268, 2021, doi: 10.1016/j.istruc.2021.08.069.

[8] G. De Matteis, G. Brando, F. Caldoso, and F. D'Agostino, "Seismic performance of dual steel frames with dissipative metal shear panels," *Ing. Sismica*, vol. 35, no. 2, pp. 124–141, 2018.

[9] G. De Matteis and G. Brando, "Metal shear panels for seismic protection of buildings: Recent findings and perspectives," *Ing. Sismica*, vol. 33, no. 3, pp. 5–27, 2016.

[10] J. Yang, H. Jing, and P. Li, "Shaking table test and simulation of 12-story buildings with metallic dampers located on soft soil," *J. Build. Eng.*, vol. 46, no. July 2021, p. 103585, 2022, doi: 10.1016/j.jobe.2021.103585.

[11] G. W. Housner *et al.*, "Structural Control: Past, Present, and Future," *J. Eng. Mech.*, vol. 123, no. 9, pp. 897–971, 1997, doi: 10.1061/(asce)0733-9399(1997)123:9(897).

[12] Fema, *2009 NEHRP Recommended Seismic Provisions: Design Examples*. 2012.

[13] SLM Solutions, "Material Data Sheet Stainless Steel 17-4PH/1.4542/A564." SLM Solutions Group AG, Lubeck (DE), 2022.

[14] ECCS, "EUROPEAN CONVENTION FOR CONSTRUCTIONAL STEELWORK. (1986). Recommended testing procedure for assessing the behaviour of structural steel elements under cyclic loads. Brussels, Belgium, ECCS General Secretariat.," *Technical Committee 1, TWG 1.3 — Seismic Design*. p. N.45/86, 1986.

COMPDYN 2023
9th ECCOMAS Thematic Conference on
Computational Methods in Structural Dynamics and Earthquake Engineering
M. Papadrakakis, M. Fragiadakis (eds.)
Athens, Greece, 12-14 June 2023

# IMPROVING THE PERFORMANCE OF I-SHAPED DAMPERS USING STIFFENERS

**Ahmad Jabbar Hussain Alshimmeri**[1], **Denise-Penelope N. Kontoni**[2,3,*], **and Ali Ghamari**[4,*]

[1] Department of Civil Engineering, College of Engineering, University of Baghdad, Baghdad, Iraq
e-mail: dr.ahmadalshimmeri@coeng.uobaghdad.edu.iq

[2] Department of Civil Engineering, School of Engineering, University of the Peloponnese, GR-26334 Patras, Greece
e-mail: kontoni@uop.gr (* *corresponding author*)

[3] School of Science and Technology, Hellenic Open University, GR-26335 Patras, Greece
e-mail: kontoni.denise@ac.eap.gr

[4] Department of Civil Engineering, Ilam Branch, Islamic Azad University, Ilam, Iran
e-mail: aghamari@alumni.iust.ac.ir (* *corresponding author*)

## Abstract

*Research reports on the behavior of metallic dampers have confirmed that the I-shaped link, while designed under a shear mechanism, acts as a ductile fuse. The main weakness of these links is the reduction of stiffness of the system when they are connected directly to the diagonal member of the concentrically braced frame. To increase the stiffness and ultimate strength of the I-shaped links, increasing the thickness of the web plate has been proposed by researchers, which causes an increase in the imposed load on the members of the braces. An innovative idea to overcome this problem is adding diagonal stiffeners to the dampers. In this paper, the stiffening of the I-shaped links is examined numerically and parametrically using the finite element method (FEM). Numerical results reveal that the stiffeners not only prevent the buckling of the web plate (which causes improvement in its performance), but they also share the imposed loading. By adding the stiffeners, a thinner web plate can be used instead of increasing the thickness of the web plate to achieve larger ultimate strength and stiffness. The parametrical study indicated that the thickness of the stiffeners is much more important than the properties of the flange and web plate in case of the damper performance.*

**Keywords:** Damper; Stiffness; Strength; Seismic; Ductility; Stiffener; FEM.

## 1 INTRODUCTION

Since the undesirable buckling of the Concentrically Braced Frame (CBF) has been acknowledged by engineers, many researchers have tried to overcome this defect. In this regard, the use of passive energy devices as dampers has been introduced as a successful, economic, and practical solution. Several dampers have emerged to improve the behavior of CBFs up to now. The shear damper, I-shaped, directly connected to the CBFs was introduced first by Ghamari et al. [1] as a simple and practical device with desirable behavior in comparison with the other dampers. To build the mentioned damper, shear plates were surrounded by a cylinder. Ghamari et al. [1] confirmed that the bucking was prevented and the ductility and dissipating energy of CBF were enhanced.

Although this I-shaped damper was cheaper and easier to build compared to other shear dampers such as ADAS [2], TADAS [3], Shear panel [4], Slit dampers [5], and edge, longitudinal and internal stiffeners [6], it faced a problem concerning stiffness reduction. To overcome this problem, surrounding the shear plates with an octagonal-shaped instead of a cylinder-shaped was proposed by Ghamari et al. [7,8]. They accomplished several experimental tests to achieve the optimum dimension of that damper. Also, its behavior with the imposing of the shear or flexural or shear-flexural mechanism was examined. Although changing the cylinder cover into an octagon cover made it simpler to produce, the damper's weight was increased, which affected the manufacturer and installer during installation. Consequently, inspired by the suitable performance of the shear link with the shear mechanism in Eccentrically Braced Frame (EBFs) [9,10], some researchers proposed the use of an I-shaped shear link attached to CBFs. Experimental studies [11-13] approved that using the I-shaped dampers prevents CBF's buckling and improves the dissipating energy. Also, it pertains to simple manufacturing and installation than other ones.

In spite of the significant benefits of the damper, as all dampers are attached to the CBFs, it caused to reduce the stiffness and ultimate strength [14,15]. To overcome this shortcoming, two general ways can be used, which include: a) using an I-shaped section with a greater thickness, or b) adding the number of dampers (and braces) in the structure. Although increasing the thickness of the damper can increase the capacity, it does not have much effect on the stiffness. In addition, increasing the capacity increases the stresses created in elements outside the damper mainly in the brace's elements, which may cause it to buckle. In such a situation, the damper not only does not perform suitably but in addition to reducing the stiffness and strength of the system, it will also have a brittle behavior. Moreover, increasing the number of dampers to compensate for the stiffness, brings construction costs and architectural limitations. Therefore, the use of stiffeners can be a worthy solution to compensate for the weakness of stiffness and ultimate strength. Due to the number of stiffeners materials used in the damper being low and also its implementation being simple, Figure 1, accordingly can be introduced as a successful solution.

## 2 I-SHAPED DAMPER WITH STIFFENERS

Referring the Figure 1, the damper is attached to an end of CBFs. It is obvious to confirm the simplicity of manufacturing and installation. Also, it can be replaced after a severe earthquake. to assure the damper yield before other elements, elements outside the damper must be designed for forces larger than the capacity of the damper. It is recommended to design the mentioned element for $F_{design}$ that is determined as:

$$F_{design} = \Omega V_{n,damper} \tag{1}$$

In this equation, the Ω is the overstrength that is investigated in the present paper and $V_{n,damper}$ is the nominal strength of the damper. The overstrength for each structure and element is defined as the nominal strength, $V_n$, divided by the strength corresponding to the first hinge formation, $V_s$.

$$\Omega = \frac{V_n}{V_s} \tag{2}$$

The AISC 341-16 [16] for shear links with I-shaped forms, is recommended to calculate the strength as $Vp = 0.6F_{yw}bt_p$ where $F_{yw}$, b, and $t_p$ are yielding stress of the web plate. In this code, the shear mechanism is defined as ρ < 1.6 where the ρ is equal to $\frac{link\ length}{\frac{M_p}{V_p}}$.

For the damper with X-stiffeners, the nominal strength is determined as:

$$V_n = n(V_p + V_f + V_{st}) \tag{3}$$

where n is the number of the web plates. The $V_f$ and $V_{st}$ represent the shear strength of the flange plate and X-stiffeners, respectively. Researchers have confirmed that the flange plate contributes to load-resisting [17]. Using the plastic theory, the ultimate strength of the flange plate is given when the flexural hinges are formed at the two ends of the flange plates. Hence, $V_f$ is calculated as $V_f = \frac{4M_{pf}}{h'}$ where $M_{pf}$ is the plastic moment of the flange plate, and $M_{pf} = \frac{b_f t_f^2}{4} F_{yf}$.

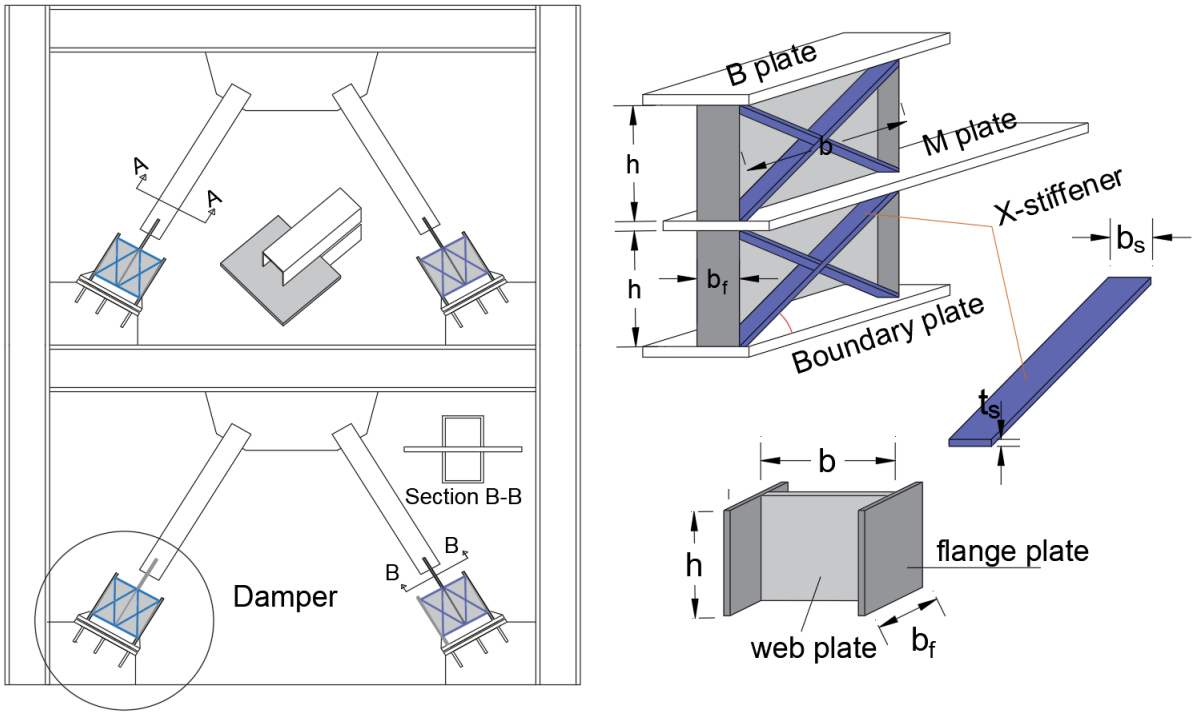


Figure 1: Strengthening of I-shaped damper with stiffeners.

Because at the beginning of the hinge formation, all components are involved, $V_s$ is calculated as:

$$V_s = V_p + \Delta_p K_f + \Delta_p K_s \tag{4}$$

By taking $\Delta_p = \frac{V_p}{K_p}$, Equation (4) can be written as $V_s = V_p(1 + \frac{K_f + K_s}{K_p})$. Consequently, the Ω is obtained as:

$$\Omega = \frac{1 + \frac{V_s}{V_p} + \frac{V_f}{V_p}}{1 + \frac{K_f + K_s}{K_p}} \tag{5}$$

## 3 NUMERICAL STUDY

### 3.1 Numerical models

In the present paper, numerical models were simulated using ANSYS [18] software. To do so, the damper's component was modeled with the SHELL181 element. This element can account for the large displacement and buckling. All Finite Element (FE) models include h=140 mm, $t_p$=6 mm, $b_s$==160 mm, and $b_f$=160 mm. the variable investigated in this paper includes the $t_p$, $t_s$ that they ended up with different $V_p$ and ρ.

### 3.2 Verification of FE results

An experimental specimen, a shear link, reported by Tanaka and Sasaki [19] was selected for verification of FE modeling. Since the damper investigated in the paper and the test is under pure shear, their performance is the same. Accordingly, the main feature of both studies is the shear deformation. Figure 2 reveals a good agreement between the experimental test results [19] and the FE results.

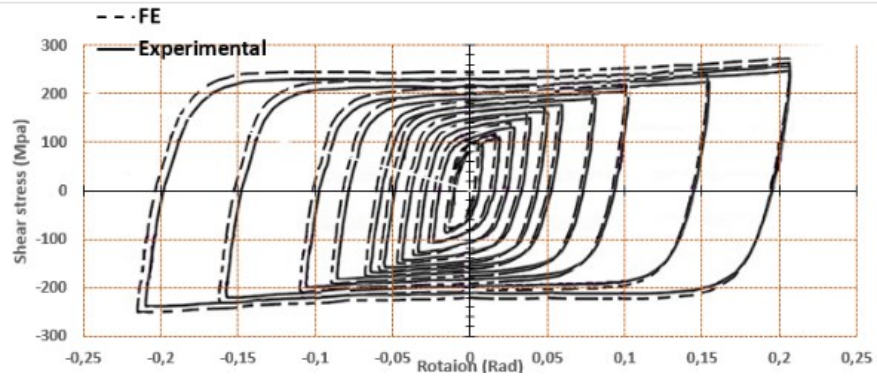


Figure 2: Comparison of the experimental test results [19] and the FE results.

## 4 DISCUSSION

### 4.1 Comparing the curves of stiffened/unstiffened dampers

Figure 3 illustrates the load-rotation of the dampers for different ρ. As shown in this figure, adding stiffeners to the damper caused it to move up the curve which ended up increasing the elastic stiffness, ultimate strength, and energy dissipation. The noticeable finding is that all damper's stiffness is coincide around the rotation of 0.005; it means, although reinforcing the I-shaped damper with stiffeners increases the elastic stiffness, it does not cause a considerable effect on the stiffness in the nonlinear zone.

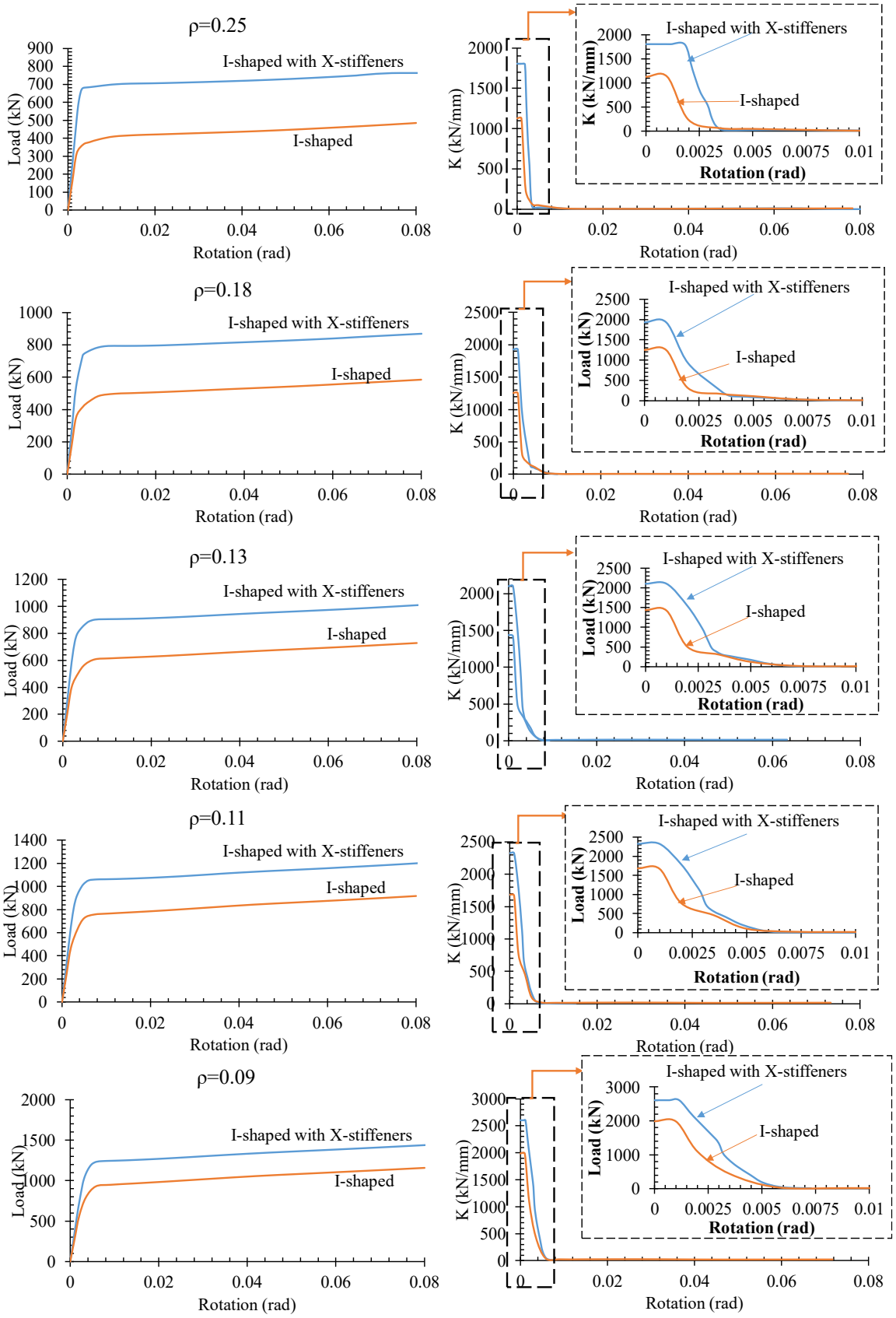


Figure 3: Comparison of the curves of the unstiffened I-shaped dampers and the I-shaped dampers reinforced with X-stiffeners.

## 4.2 Overstrength

Because the element outside the damper must be designed for amplitude force by Ω, the Ω of the dampers are listed in Table 1. The average amount of the Ω is 1.97 which is greater than proposed by AISC=1.5. Therefore, it is recommended to use Ω=2.0 for the damper.

In the sixth column of the table, the Ω of dampers with different flange plates are divided by the dampers with $t_f$=10mm. results indicated that increasing the flange plate cause to increase in the Ω. Also, in the seventh column of the table, the Ω of stiffened dampers are divided by the dampers I-shaped dampers with the same $t_f$. Except for the damper with ρ=0.25, the stiffeners increase the Ω between 2% to19%.

| Dampers | | $t_f$ (mm) | $t_s$ (mm) | Ω | $\frac{damper\ with\ t_f=i}{damper\ with\ t_f=10mm}$ | $\frac{I-shaped\ damper}{Stiffened\ damper}$ |
|---|---|---|---|---|---|---|
| I-shaped | ρ=0.25 | 10 | | 1.54 | | |
| | ρ=0.18 | 15 | | 1.67 | 1.08 | |
| | ρ=0.13 | 20 | | 1.82 | 1.18 | |
| | ρ=0.11 | 25 | | 1.95 | 1.27 | |
| | ρ=0.09 | 30 | | 2.08 | 1.35 | |
| I-shaped with stiffeners | ρ=0.25 | 10 | 2.5 | 1.36 | | 0.89 |
| | | 10 | 5 | 1.63 | 1.20 | |
| | | 10 | 10 | 2.04 | 1.50 | |
| | | 10 | 20 | 2.38 | 1.75 | |
| | | 15 | 2.5 | 1.51 | 1.11 | |
| I-shaped with stiffeners | ρ=0.18 | 15 | 5 | 1.70 | | 1.02 |
| | | 15 | 10 | 2.11 | 1.24 | |
| | | 15 | 20 | 2.42 | 1.42 | |
| | | 20 | 2.5 | 1.64 | 0.96 | |
| | | 20 | 5 | 1.82 | 1.07 | |
| I-shaped with stiffeners | ρ=0.13 | 20 | 10 | 2.16 | | 1.10 |
| | | 20 | 20 | 2.44 | 1.13 | |
| | | 25 | 2.5 | 1.75 | 0.81 | |
| | | 25 | 5 | 1.93 | 0.90 | |
| | | 25 | 10 | 2.23 | 1.03 | |
| I-shaped with stiffeners | ρ=0.09 | 25 | 20 | 2.47 | | 1.19 |
| | | 30 | 2.5 | 1.90 | 0.77 | |
| | | 30 | 5 | 2.06 | 0.83 | |
| | | 30 | 10 | 2.31 | 0.94 | |
| | | 30 | 20 | 2.51 | 1.02 | |

Table 1: The overstrength of the dampers.

To have a better consideration of the effect of the variable on the overstrength, in Figure 4, the overstrength versus different variables is plotted. As shown in this figure, by increasing the ratio of $t_s/t_p$ and $t_s/t_f$, the Ω is increased but this increase follows a nonlinear function. Also, by increasing the slenderness of the stiffeners, the ratio of $b_s/t_s$ and $L_s/t_s$, reduce Ω. Therefore, the limitation of $b_s/t_s$=35 and $L_s/t_s$=50 is proposed to prevent the high reduction of Ω.

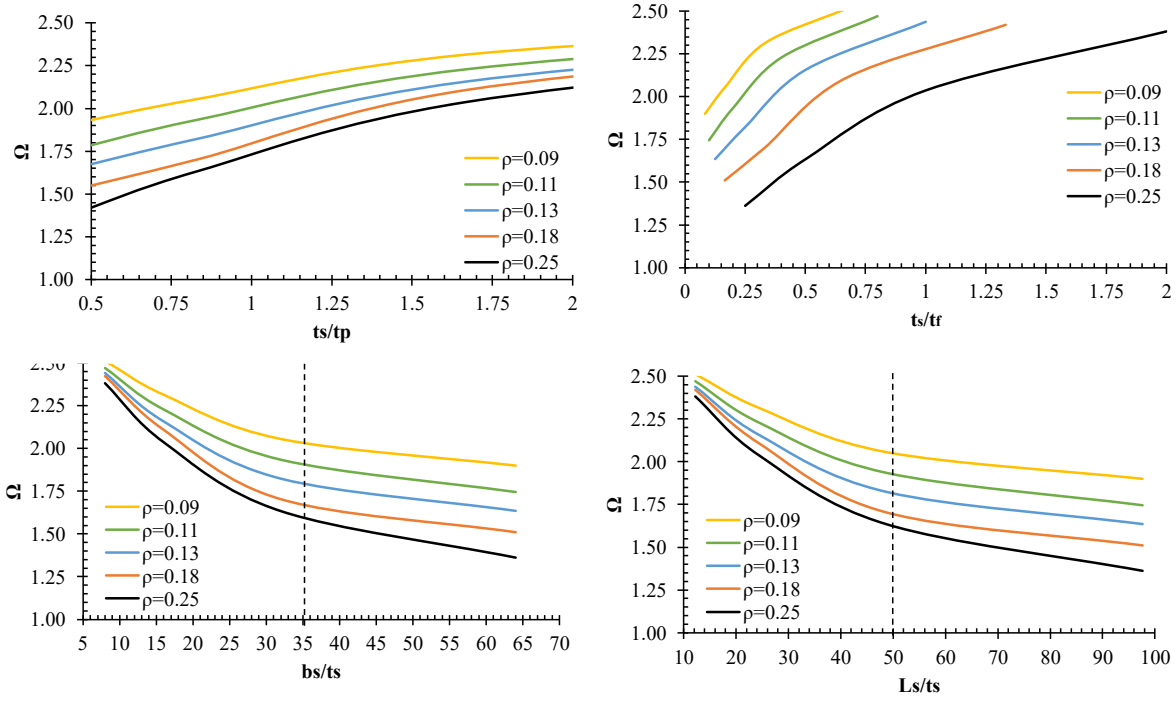


Figure 4: The overstrength.

## 4.3 Limitation of stiffeners' slenderness

To consider the accuracy of the limitation of $b_s/t_s$=35 and $L_s/t_s$=50, the ultimate strength and stiffness are plotted versus the variables in Figure 5. Like with the overstrength, the ultimate strength, and stiffness are reduced by increasing the slenderness. At the $b_s/t_s$=35 or $L_s/t_s$=50 the rate of reduction of the mentioned stiffness and strength tend to smooth. Subsequently, the mentioned limitation can be accounted as a suitable and capable suggestion.

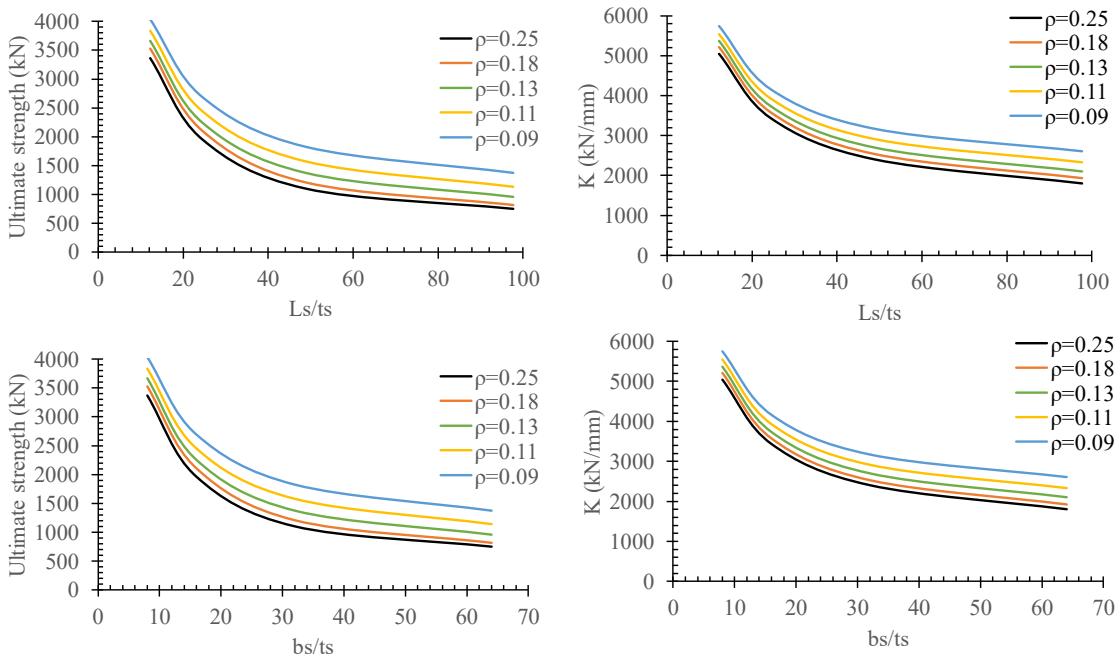


Figure 5: The ultimate strength and stiffness versus slenderness.

### 4.4 Yielding state of the damper

In Figure 6, the hinge formation of the damper component is shown. In this figure, only a damper with $t_s = 2.5$, 20 mm and $t_f = 10$, 30 mm as a thicker and thinner damper has been shown. Referring to Figure 6, the web plate of all the damper is yielded completely. Also, at two ends of the flange plates, hinge formation is accomplished. Moreover, in the middle of X-stiffeners, hinges are formed. This hinge formation confirms that all components of the damper contribute to the energy dissipation. The considerable notice is that thin stiffeners are subjected to buckle.

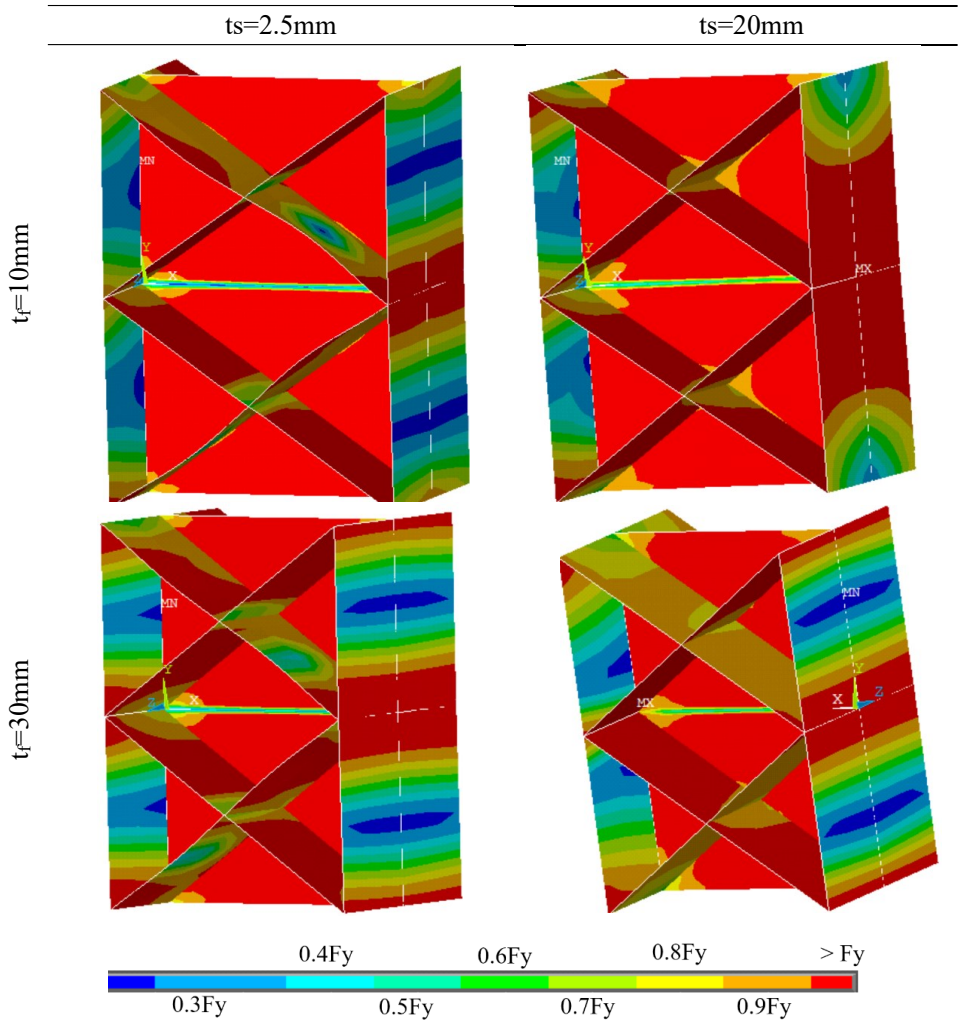


Figure 6: The yielding state of the damper for various configurations.

## 5 CONCLUSIONS

In this paper, the behavior of an I-shaped damper reinforced with stiffeners was investigated. The findings are summarized in the following:

- Adding stiffeners to the I-shaped damper cause to enhance the elastic stiffness, ultimate strength, and energy dissipation but it does not have a considerable effect on the stiffness in the nonlinear zone.
- The average overstrength, Ω, of the I-shaped damper with and without stiffeners was obtained equal to 1.97 which is greater than proposed by AISC=1.5. Therefore, it is recommended to use Ω=2.0 for the damper.

- The properties of flange and stiffeners affect the Ω. Increasing the flange plate increases the Ω. Also, except damper with $\rho$=0.25, the stiffeners increase the Ω between 2% to19%.
- Also, increasing the slenderness ($b_s/t_s$ and $L_s/t_s$) of the stiffeners reduce Ω. Therefore, the limitation of $b_s/t_s$=35 and $L_s/t_s$=50 is proposed to prevent the high reduction of Ω.
- At the $b_s/t_s$=35 or $L_s/t_s$=50 the rate of reduction of the mentioned stiffness and strength tend to smooth. Subsequently, the mentioned limitation can be considered as a suitable and capable suggestion.

## REFERENCES


[1] A. Ghamari, H. Haeri, A. Khaloo, Z. Zhu, Improving the hysteretic behavior of Concentrically Braced Frame (CBF) by a proposed shear damper. *Steel and Composite Structures*, **30**(4), 383-392, 2019. https://doi.org/10.12989/scs.2019.30.4.383.

[2] M. Khazaei, Investigation on Dynamics Nonlinear Analysis of Steel Frames with Steel Dampers. *Procedia Engineering*, **54**, 401-412, 2013. https://doi.org/10.1016/j.proeng.2013.03.036.

[3] R.K. Mohammadi, A. Nasri, A. Ghaffary, TADAS dampers in very large deformations. *International Journal of Steel Structures*, **17**, 515-524, 2017. https://doi.org/10.1007/s13296-017-6011-y.

[4] R.W.K. Chan, F. Albermani, M.S. Williams, Evaluation of yielding shear panel device for passive energy dissipation. *Journal of Constructional Steel Research*, **65**(2), 260-268, 2009. https://doi.org/10.1016/j.jcsr.2008.03.017.

[5] V. Saberi, H. Saberi, N. Amirikia, F. Jadali, A. Sadeghi, Cyclic Performance Evaluation of Steel Structures Retrofitted by Slit Dampers. *Advance Researches in Civil Engineering*, **3**(3), 42-60, 2021. https://doi.org/10.30469/arce.2021.139738.

[6] M. Ebadi-Jamkhaneh, D.-P.N. Kontoni, M. Ahmadi, Evaluation of the Behavior of Gusset Plates in Concentrically Braced Steel Frames Under Cyclic Loading. A. Sil, D.-P.N. Kontoni, R.K. Pancharathi (eds), *Recent Trends in Civil Engineering. Lecture Notes in Civil Engineering,* vol. 274, Springer, Singapore, pp. 371-387, 2023. https://doi.org/10.1007/978-981-19-4055-2_30.

[7] A. Ghamari, B. Almasi, C.-h. Kim, S.-H. Jeong, K.-J. Hong, An Innovative Steel Damper with a Flexural and Shear–Flexural Mechanism to Enhance the CBF System Behavior: An Experimental and Numerical Study. *Applied Sciences*, **11**(23), 11454, 2021. https://doi.org/10.3390/app112311454.

[8] A. Ghamari, C. Kim, S.H. Jeong, Development of an innovative metallic damper for concentrically braced frame systems based on experimental and analytical studies. *The Structural Design of Tall and Special Buildings*, **31**(8), e1927, 2022. https://doi.org/10.1002/tal.1927.

[9] A. Ghamari, Y.-J. Kim, J. Bae, Utilizing an I-shaped shear link as a damper to improve the behavior of a concentrically braced frame. *Journal of Constructional Steel Research*, **186**, 106915, 2021. https://doi.org/10.1016/j.jcsr.2021.106915.

[10] A. Ghamari, Y.-J. Kim, J. Bae, An Innovative shear link as damper: an experimental and numerical study. *Steel and Composite Structures*, **42**(4), 539-552. 2022. https://doi.org/10.12989/scs.2022.42.4.539.

[11] M. Lian, M. Su, Seismic performance of high-strength steel fabricated eccentrically braced frame with the vertical shear link. *Journal of Constructional Steel Research*, **137**, 262-285, 2017. https://doi.org/10.1016/j.jcsr.2017.06.022.

[12] J.-Z. Zhao, M.-X. Tao, Z.-H. Wu, L.-D. Zhuang, Experimental and numerical study on bent shear panel damper made of BLY160 steel. *Engineering Structures*, **260**, 114229, 2022, https://doi.org/10.1016/j.engstruct.2022.114229.

[13] C. Thongchom, N.M. Mirzai, B. Chang, A. Ghamari, Improving the CBF brace's behavior using I-shaped dampers, numerical and experimental study. *Journal of Constructional Steel Research*, **197**, 107482, 2022. https://doi.org/10.1016/j.jcsr.2022.107482.

[14] C. Thongchom, A. Ghamari, R. Putra Jaya, O. Benjeddoud, Experimental and Numerical Study on an Innovative Trapezoidal-Shaped Damper to Improve the Behavior of CBF Braces. *Buildings*, **13**(1), 140, 2023. https://doi.org/10.3390/buildings13010140.

[15] C. Thongchom, A. Bahrami, A. Ghamari, O. Benjeddou, Performance Improvement of Innovative Shear Damper Using Diagonal Stiffeners for Concentrically Braced Frame Systems. *Buildings*, **12**(11), 1794, 2022. https://doi.org/10.3390/buildings12111794.

[16] ANSI/AISC 341-16, *Seismic Provisions for Structural Steel Buildings*, American Institute of Steel Construction (AISC), Chicago, Illinois, USA, 2016.

[17] A. Ghadami, G. Pourmoosavi, A. Ghamari, Seismic design of elements outside of the short low-yield-point steel shear links, *Journal of Constructional Steel Research*, **178**, 106489, 2021. https://doi.org/10.1016/j.jcsr.2020.106489.

[18] Ansys® Academic Research Mechanical, Release 2021R2, ANSYS, Inc., 2021. https://www.ansys.com.

[19] K. Tanaka, Y. Sasaki, Hysteretic Performance of Shear Panel Damper Ultra Low Yield Strength Steel for Seismic Response Control of Buildings, *12th World Conference on Earthquake Engineering-12WCEE 2000,* Auckland, New Zealand, January 30 - February 4, 2000.

COMPDYN 2023
9th ECCOMAS Thematic Conference on
Computational Methods in Structural Dynamics and Earthquake Engineering
M. Papadrakakis, M. Fragiadakis (eds.)
Athens, Greece, 12-14 June 2023

# DEVELOPMENT OF A SIMPLIFIED BEAM MODEL FOR TUBULAR JOINTS IN JACKET STRUCTURES

**A. Sindoni[1], A. Sadeqi[1], J. H. Nielsen[1] and E. Katsanos[1]**

[1] Technical University of Denmark DTU
Department of Civil and Mechanical Engineering
Brovej B118, Kongens Lyngby 2800, Denmark
e-mail: antoniosindoni7@gmail.com , amisa@dtu.dk , jhni@dtu.dk , vakat@dtu.dk

## Abstract

*Jacket structures are extensively used to support heavy-weight offshore infrastructure systems. Hence, reliable simulations and designs are vital to facilitate the safe extraction of offshore energy sources, accommodating the gradual transition to green energies. The tubular members of a typical jacket structure, i.e., braces and chords, are usually simulated by either shell or beam elements. However, the latter typically disregard local flexibility contributions at the point of connection that may lead to an overestimated stiffness of the joint. As reported in the literature, the local deformations in the beam models are not negligible, influencing both the static and dynamic performance of the joint and thereby the entire jacket structure. The present paper introduces a simplified method applying a standard beam element in order to account for the joint flexibility providing a low-dimensional finite element model for jacket structures. To this end, a differential evolution optimization algorithm is applied, considering modal parameters as the objective function. The procedure results in obtaining the geometrical and mechanical properties of the simplified beam element introduced herein to model the tubular joints. The investigation of several case studies with different joint types verifies the effectiveness and the application range of the introduced element in modal and static analyses.*

**Keywords:** Tubular joint, Finite Element Model, Optimization, Joint Flexibility, Jacket Structures, Differential Evolution.

## 1 INTRODUCTION

Tubular joints refer to the members' connection points of circular hollow sections, extensively used in steel jacket structures and offshore platforms. The behavior of tubular joints must be studied to ensure such systems' safe and reliable design and construction. Using beam tubular (pipe) elements for modeling jacket structures' tubular members (i.e., braces and chords), they are rigidly connected at the nodal points. However, Local Joint Flexibility (LJF) is an intrinsic feature of tubular joints that affects jacket structures' global static and dynamic responses. One of the critical effects concerning LJF is the ovalization as the local deformation of the chord cross section due to large flexibility in the radial direction. The LJF may increase the deflections, redistribute the nominal stresses, reduce the buckling loads, and change the structure's natural frequencies. The analysis of a jacket platform considering LJF results in lower natural frequencies than the model with rigid joints. However, the LJF effects vary with different brace and chord geometry for a given joint shape [1], [2].

Several studies have been dedicated to developing appropriate formulation and parametric equations for LJF with different brace-chord connection shapes based on finite element (FE) analysis and experimental testing. The early works reported parametric equations for tubular T-joints [3] and T-, Y- and K-joints [4], where the braces were subjected only to bending loads. Considering the axial loads, the TY joints were also parameterized compared with experimental results and extended to additional joint types and geometric parameters affecting the LJF [5]. The interaction between braces and the effect of gap length on LJF have been investigated [6]. Despite the advancements found in existing studies, the proposed relationships regarding the LJF highly depend on the joint shape and geometry, loading conditions, structure geometry, and global dynamics [7].

The present study aims to develop a simplified FE submodel based on tubular beam elements with LJF features in the peer shell model. The procedure consists of two FE simulation steps in Abaqus for a given shell model (brace-chord) and a desired beam model connected to a Differential Evolution (DE) optimization step that results in optimal geometry and material properties for the beam. The procedure is straightforward and applicable to different tubular joint shapes, geometry, and loading. Investigating several case studies with various joint forms verifies the introduced element's effectiveness and application range in modal and static analyses.

## 2 METHODOLOGY

The present work develops a special beam element with LJF features via a combined simulation-optimization process determining geometric and material properties. The steps are demonstrated in Figure 1 and listed in the following.

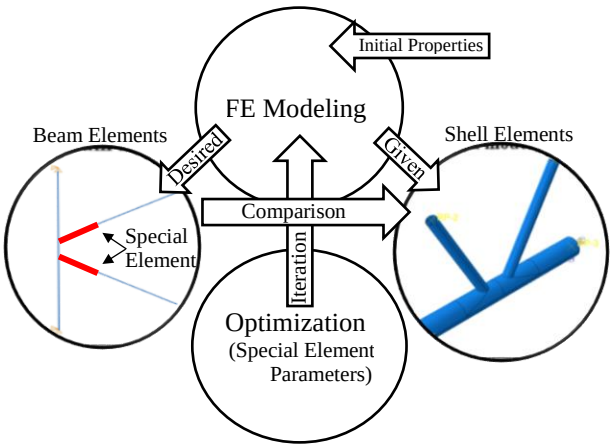


Figure 1: Proposed procedure for developing special beam element with joint flexibility features.

**Input**: Initial geometric and material properties of the chord-brace
**Output**: Optimal values for the special beam element's properties (joint) including length, Young's modulus, diameter, thickness (L, E, D, t)
**Steps**:

1. Simulation of the reference FE model with shell elements, extracting modal parameters.
2. Simulation of the beam FE model within a loop with initial values of the shell model for both brace-chord and special beam elements at the joint locations, extracting modal parameters.
3. Defining the objective function for DE optimization, in terms of natural frequencies and mode shapes with uniform weights for each mode, calculated within the loop in Step 2.
4. Defining the constraint for parameters L, E, D, and t and initial population for DE within the loop in Step 2.
5. Performing initial optimization (few iterations) to modify the weights in Step 3 with respect to the difference between beam and shell models' modal parameters.
6. Running Step 2 in the loop until the convergence of DE with optimal L, E, D, t.

## 2.1 Special Beam Element Properties

The procedure graphically depicted in Figure 1 starts with creating the FE model of a typical brace-chord assembly with shell elements. In contrast, the peer FE beam model (i.e., rigid joint) does not account for any flexibility at the connection point called LJF. In order to add LJF features to the beam model, the geometry and material properties of a special beam element at the connection point are updated iteratively within a DE optimization process. Figure 2 illustrates some special beam elements for different brace-chord assemblies. Notably, the dimensions of the brace-chord assembly must be appropriate beforehand, so the analysis based on the two FE models (i.e., the shell and the beam with a rigid joint) are remarkably different, and the LJF is considerable. To this end, a comparison is made based on the following ratios:

$$r_k = \frac{K_{Beam}}{K_{Shell}} \tag{1}$$

$$r_\omega = \frac{\omega_{Beam}}{\omega_{Shell}} \tag{2}$$

where $K$ is the lateral stiffness (i.e., force/displacement) and $\omega$ is the eigen frequency. Hence, having $r_k$ and $r_\omega$ close to 1, it refers to a better match between shell and beam models in terms of static and dynamic behavior, respectively. While the values deviating from unity refer to better case studies (initial geometry and material properties of the brace-chord assembly) for the optimization step. However, after selecting appropriate initial geometry and material properties, in the optimization step in this study, only the eigen frequencies (and mode shapes are) used to assess the fitness since, in contrast to the lateral stiffness, they are not load-dependent.

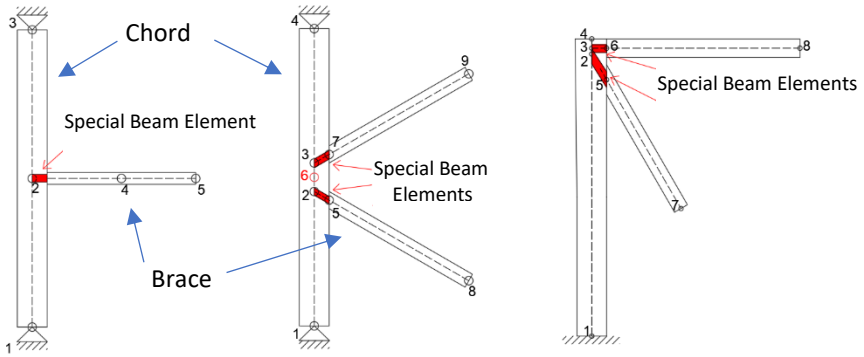


Figure 2: Schematic of special beam elements with joint flexibility for various tubular joints

The parameters to be optimized to define the special joint element are the length (L), Young's modulus of Elasticity (E), the diameter (D), and the thickness (t). These four parameters are referred to each joint element, so for the TY joints eight parameters in total need to be optimized. The number of parameters for the K joint reduces to four due to the symmetric geometry. The initial values for L, E, D, and t are chosen the same for the brace. Then they are constrained by reasonable upper and lower bounds to make the optimization process more efficient.

## 2.2 Optimization

The implemented DE optimization algorithm finds the global minimum of a multivariate function. The DE algorithm can be considered as a sequence of steps: initialization of the population, evaluation, mutation and recombination, replacement and final evaluation. The difficulty of finding the optimal solution for high dimensional variables can be solved by increasing the population size or increasing the number of iterations [8]. Using the DE algorithm, the parameters L, E, D, and t for each special joint element are found by minimizing two objective functions. One based on the eigenfrequencies:

$$f_{\omega}(\Delta\omega_1, \Delta\omega_2, \ldots, \Delta\omega_n) \tag{3}$$

where $\Delta\omega_j$ is the difference between the two models eigenfrequency as:

$$\Delta\omega_j = \left|\omega_{j,Shell} - \omega_{j,Beam}\right| \tag{4}$$

The other objective function is based on the mode shapes:

$$f_{\phi}(e_1, e_2, \ldots, e_n) \tag{5}$$

and

$$e_j = 1 - MAC(\phi_{j,Shell}, \phi_{j,Beam}) \tag{6}$$

Where *MAC* is the Modal Assurance Criterion between two mode shape vectors defined as

$$MAC(\phi_i, \phi_j) = \frac{\left|\phi_i^T . \phi_j\right|^2}{\left|\phi_j\right|^2 . \left|\phi_j\right|^2} \tag{7}$$

The *MAC* values vary from zero to one, indicating the two mode vectors' complete difference and similarity, respectively. Considering the first *n* modes in the process with weighting coefficients, the total values for Eqs. (4) and (6) to minimize become

$$\Delta\omega_{Total} = \sum_{j=1}^{n} W_j \Delta\omega_j \tag{8}$$

$$e_{Total} = \sum_{j=1}^{n} W_j \Delta e_j \tag{9}$$

where $W_j$ is the weighting coefficient that must be chosen according to each mode's contribution so that $\sum_{j=1}^{n} W_j = 1$. However, the difference between the mode shapes of the beam and shell models is not as much as the frequencies and, hence, Eq. (8) becomes dominant in the optimization.

## 3 FINITE ELEMENT SIMULATION

The beam FE model is built based on the 2D Bernoulli-Euler beam theory in Abaqus using two-node elements with three DOFs (two translations and one rotation) at each node. The reference shell model is a thin shell element with six DOFs (three translations and three rotations) at each node, considering both in-plane and out-plane deformations. The steel material properties are chosen for the models with Young's modulus of Elasticity equal to 200 GPa and mass density of 7770 kg/m3. Figure 3 exhibits the beam and shell FE models developed in Abaqus for tubular T, K, and TY brace-chord assemblies (or briefly T, K, and TY joints). The two ends of the chord are pinned for T and K joints, and the bottom end of the TY joint is fixed. The chord cross-section and generated meshes for T joint are displayed in Figure 4.

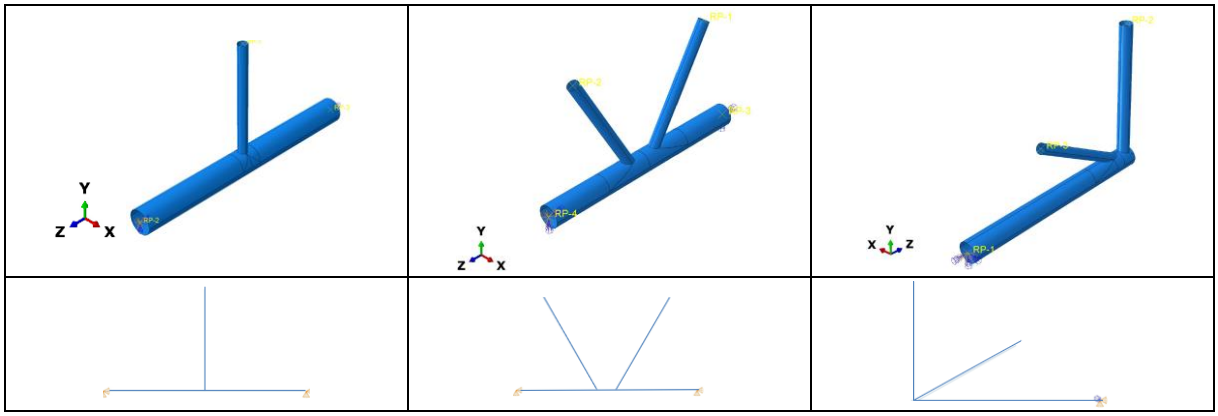

Figure 3: Beam and shell FE model for tubular T-, K- and TY joints

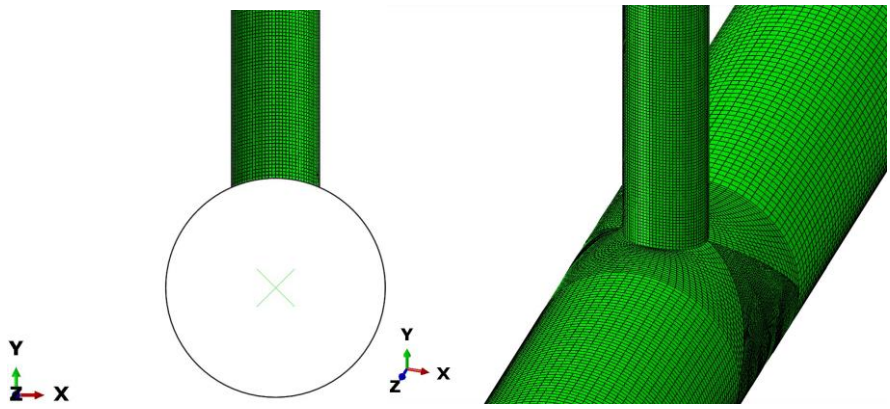

Figure 4: FE model of the T joint in Abaqus shell model with quadratic meshes

In order to find appropriate geometry range for the brace-chord assembly with considerable LJF, several beam and shell models with different geometries have been developed. At this step, the lowest $r_k$ and $r_\omega$ introduced in Eqs. (1)-(2) are investigated, indicating the significant difference between the shell and the beam models, and the effectiveness of the optimization process. Figure 5 depicts three types of brace-chord assembly (T, K and TY joints) subjected to two load cases to investigate $r_k$ through the static analysis. The selected dimensions for the brace-chord assembly are presented in Table 1.

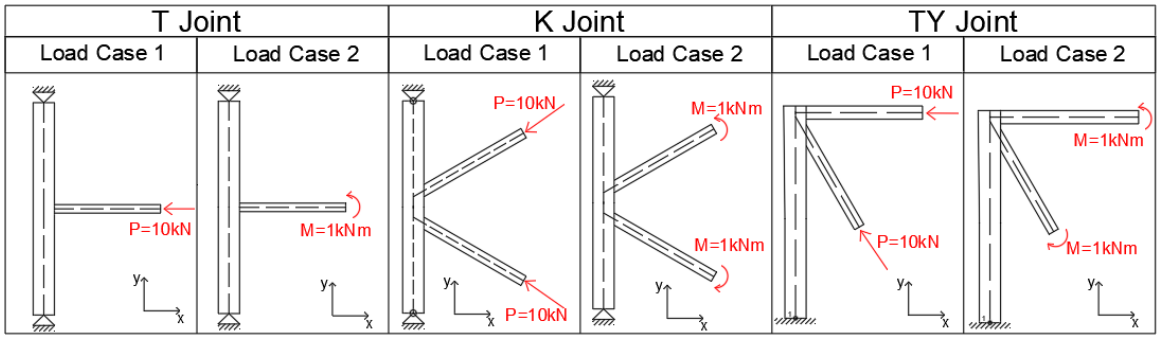


Figure 5: Applied loads to various joints in static analysis

| Joint Type | T | | K | | TY | | |
|---|---|---|---|---|---|---|---|
| Component | Chord | Brace | Chord | Brace | Chord | Brace (Horizontal) | Brace (Skewed) |
| Length | 2.0 | 1.3 | 2.0 | 1.0 | 2.0 | 1.3 | 1.0 |
| Diameter | 0.2 | 0.125 | 0.2 | 0.1 | 0.2 | 0.125 | 0.1 |
| Thickness | 0.005 | 0.0045 | 0.007 | 0.005 | 0.005 | 0.0045 | 0.0045 |

Table 1: Dimension of the brace-chord assemblies utilized in the FE simulation (m)

## 4 RESULTS

### 4.1 Special beam element for joint modeling

The DE optimization has been performed to find special beam element parameters (E, L, D, t) concerning the red elements highlighted in Figure 2. The special beam element considers the LJF in the shell model of brace-chord assembly with T, K and TY shapes. The first four eigenfrequencies and mode shapes are considered as the objective function, and the parameters are constrained as $1.8 \times 10^{11} < E < 2.2 \times 10^{11}$ Pa, $0.1 < L < 0.5$ m, $0.07 < D < 0.13$ m, $0.002 < t < 0.005$ m. The initial guess for them in the optimization process is selected to be identical with the full assembly according to Table 1. Table 2 represents the effectiveness of the optimization process for developing special beam element in the T joint, where $W$ indicates the weighting percentage of each mode in four different optimization cases. Additionally, $e_{rgd}$ is the relative error between the shell and rigid beam models' eigenfrequency while $e_{opt}$ is the relative error between the shell and optimized (special beam) models' eigenfrequency.

| Optimization Case | 1 | | | 2 | | | 3 | | | 4 | | |
|---|---|---|---|---|---|---|---|---|---|---|---|---|
| Mode | $W$ | $e_{rgd}$ | $e_{opt}$ | $W$ | $e_{rgd}$ | $e_{opt}$ | $W$ | $e_{rgd}$ | $e_{opt}$ | $W$ | $e_{rgd}$ | $e_{opt}$ |
| 1st | 25 | 43.10 | 3.70 | 40 | 43.10 | 0.09 | 30 | 43.10 | 0.13 | 10 | 43.10 | 3.08 |
| 2nd | 25 | 3.17 | 6.59 | 40 | 3.17 | 4.04 | 60 | 3.17 | 3.80 | 90 | 3.17 | 3.79 |
| 3rd | 25 | 15.41 | 0.12 | 10 | 15.41 | 1.98 | 5 | 15.41 | 1.93 | 5 | 15.41 | 1.37 |
| 4th | 25 | 15.60 | 11.0 | 10 | 15.60 | 11.13 | 5 | 15.60 | 11.12 | 5 | 15.60 | 10.96 |
| Total | 100 | 77.3 | 21.4 | 100 | 77.3 | 17.2 | 100 | 77.3 | 17.0 | 100 | 77.3 | 19.2 |

Table 2: Percentages of weighting coefficients and eigenfrequency errors for T joints

As seen in Table 2, without special beam element optimization (namely, the rigid joint modelling choice), the error for the 1st fundamental mode is more than 43% and in total becomes more than 77%. Hence, the deviation of the beam model only by disregarding LJF is significant. On the other hand, the use of weights in optimization cases 2 and 3 significantly reduces the error for the 1st and 3rd modes and in total results in 60% percent error reduction. Notably, the 2nd mode error is already low and is not improved by the optimization. As such, the effectiveness of the special beam element in the K and TY shape joints can be seen in Table 3, indicating almost 40% and 80% total error reduction after using the optimized special beam element with LJF.

| Type | | K | | | TY | |
|---|---|---|---|---|---|---|
| Mode | $W$ | $e_{rgd}$ | $e_{opt}$ | $W$ | $e_{rgd}$ | $e_{opt}$ |
| 1st | 50 | 15.90 | 0.10 | 43 | 9.30 | 3.31 |
| 2nd | 40 | 18.80 | 1.84 | 42 | 44.30 | 0.02 |
| 3rd | 0 | 1.91 | 1.91 | 7.5 | 13.42 | 0.01 |
| 4th | 10 | 9.91 | 0.01 | 7.5 | 15.94 | 1.32 |
| Total | 100 | 44.5 | 1.9 | 100 | 83.0 | 4.7 |

Table 3: Percentages of weighting coefficients and eigenfrequency errors for K and TY joints

Table 4 represents the optimized parameters of the special beam element with LJF features based on the weights discussed in Table 2 (optimization case 3) and Table 3. The K-joint parameters' variation and convergence are typically plotted versus the optimization iterations in Figure 6. As one can see, D and E are dominant and converge faster than t and L. Hence, the optimization is more sensitive to the length and thickness of the developed joint element and requires the upper-lower bounds for the population generation (i.e., 0.1 m < L < 0.5 m) to be initially adjusted.

| Type | T | K | TY | |
|---|---|---|---|---|
| Component | Horizontal | Two Skewed | Horizontal | Skewed |
| E (× $10^{11}$ Pa) | 1.84 | 2.03 | 2.14 | 1.84 |
| L (m) | 0.103 | 0.453 | 0.478 | 0.252 |
| D (m) | 0.075 | 0.081 | 0.062 | 0.104 |
| t (m) | 0.0047 | 0.0078 | 0.0078 | 0.0046 |

Table 4: Optimized parameters for the special joint elements

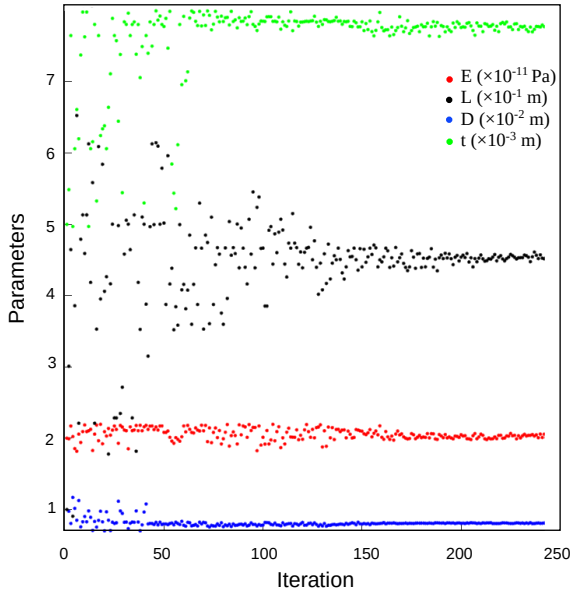


Figure 6: The K-joint parameters' optimization convergence versus the number of iterations

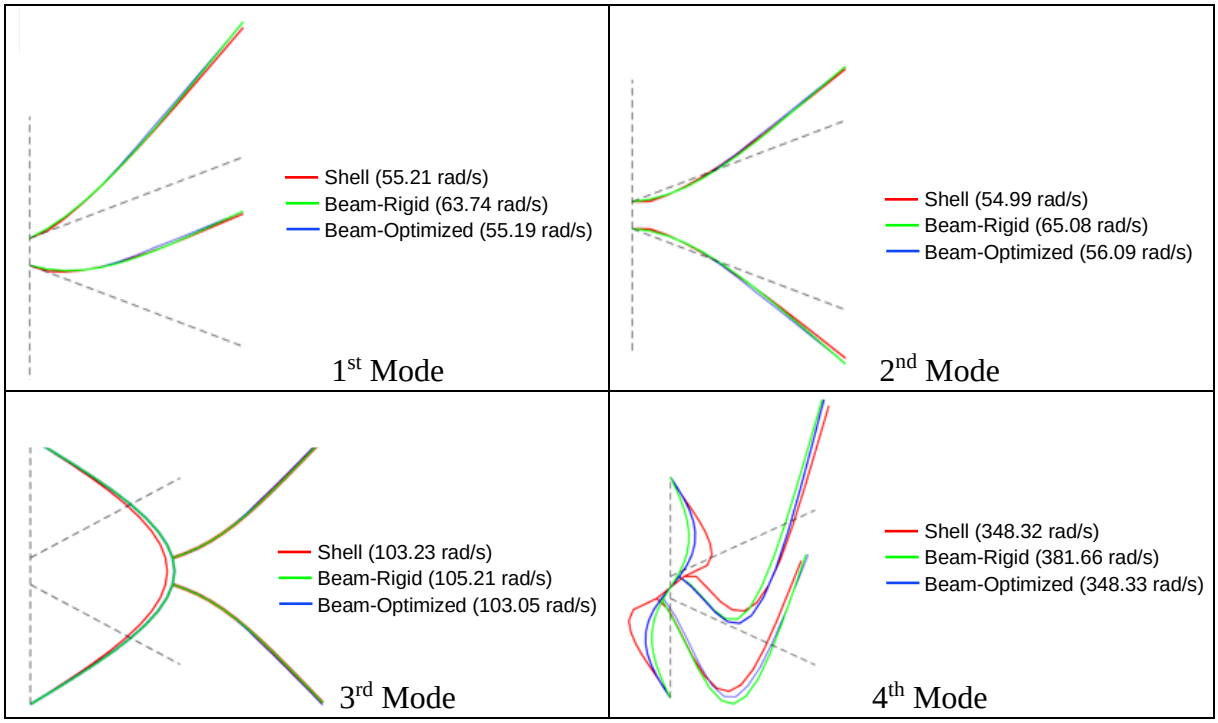


Figure 7: The first four eigenfrequencies and mode shapes of the K-joint FE models

The eigenfrequencies and mode shapes corresponding to the FE beam model with optimized parameters of the special beam element are shown in Figure 7 for the K-joint. The eigenfrequencies are significantly improved in the model with the special joints. In contrast, the mode shapes are not highly different from to model with rigid joints (no special element), except in the 4$^{th}$ mode. Therefore, as mentioned after Eq. (9), the weight of the mode shapes is negligible in the optimization.

The static analysis is also performed with the conditions shown in Figure 5 for two load cases. Table 5 indicates the lateral stiffness $r_k$ (Eqs. (1)) for the rigid model and the optimized model (i.e., with special joint element). The improvement in the T and K joints, especially for Load Case 2, is remarkable. Hence, the special element developed based on the modal parameters as the objective function in the DE optimization, is applicable herein also for the static analysis. It is to be reminded, the deviation of values of $r_k$ from 1, indicates the difference between the shell model and the beam model due to ignoring LJF and ovalization effects in the latter. Figure 8 illustrates the ovalization of the T assembly in the shell model for Load Case 1.

| Type | T | | K | | TY | |
|---|---|---|---|---|---|---|
| | Rigid | Optimized | Rigid | Optimized | Rigid | Optimized |
| Load Case 1 | 1.17 | 1.16 | 1.31 | 0.88 | 1.09 | 1.06 |
| Load Case 2 | 1.28 | 0.98 | 1.09 | 0.93 | 1.50 | 0.81 |

Table 5: Lateral stiffness ratio $r_k$ for rigid and special joint elements

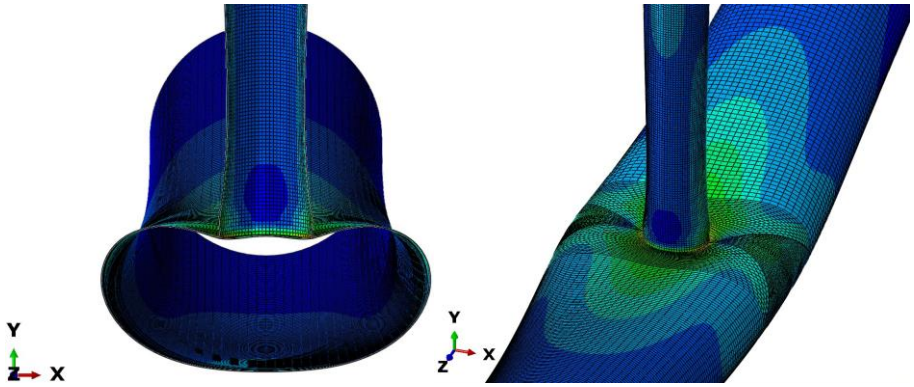


Figure 8: Ovalization of the T-shape shell model subjected to Load Case 1

## 4.2 Full structure application

The developed special joint elements in specific T, K and TY assemblies, are integrated and applied to a frame structure. Figure 9 displays the geometry of the frame, and the corresponding FE models in Abaqus using beam and shell elements. The thickness of the vertical links (chord) is 0.005m, and the thickness of the horizontal and skewed links is (brace) is 0.0045m.

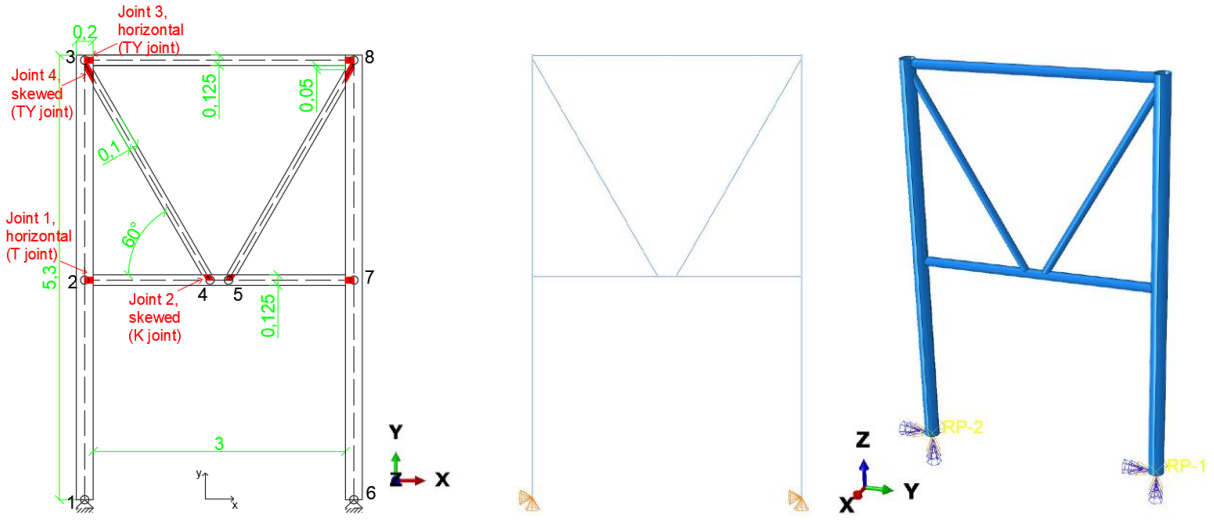


Figure 9: Geometry of the frame with combined joints, and corresponding beam and shell models in Abaqus

The optimization is performed for each joint separately and the obtained parameters (E, L, D, and t) of special joint elements are directly transferred and adopted by the frame structure model. An alternative approach is to perform the optimization considering the full frame beam and simultaneously obtaining parameters for all joints. The results were found to be nearly identical. However, the approach of optimizing the entire structure requires higher computational burden while loses the generality that is associated with the ad-hoc optimization in joint-level and the consequent use of the optiomized joint element to a bigger structure. Table 6 represents the error of the frame's eigenfrequencies modeled by beam elements with rigid joints ($e_{rgd}$) and optimized beam element with LJF ($e_{opt}$) compared to the reference shell model.

| Mode Number | 1st | 2nd | 3rd | 4th | Total |
|---|---|---|---|---|---|
| $e_{rgd}$ | 5.5 | 15.1 | 4.9 | 11.4 | 36.9 |
| $e_{opt}$ | 1.1 | 0.3 | 1.6 | 0.6 | 3.7 |

Table 6: Relative error percentage of frame's eigenfrequencies

As seen in Table 6, the error reduction in the frame's 2nd and 4th frequencies, due to the use of the developed special element with LJF is considerable and, in total, results in more than 30 percent error reduction. The static performance of the model is also evaluated by applying a 1 kN horizontal load to the frame's head at node 3.

| Frame FE Model | $x_2 \times 10^{-3}$ | $x_3 \times 10^{-3}$ | $r_k$ |
|---|---|---|---|
| Shell (reference) | 1.94 | 2.05 | - |
| Beam with Rigid Joint | 1.80 | 1.90 | 1.08 |
| Beam with special Joint | 1.92 | 2.01 | 1.02 |

Table 7: Frame's displacement along x axis at nodes 2 and 3 and stiffness ratio $r_k$

Table 7 displays the displacement of typical nodes 2 and 3 of the frame and the concerning lateral stiffness ratio $r_k$. Despite the insignificant difference between the rigid joint and shell model under the given static load, 7% improvement is seen for using the special beam with LJF.

## 5 CONCLUSIONS

The study aims to develop a simplified submodel that considers the tubular local joint flexibility. The latter can be captured by a shell model of a jacket structure but commonly waived by a simplified beam model with a rigid connections. To reach the goal of this study, a simplified beam is introduced by optimizing a special beam element' geometric and material properties within a differential evolution algorithm. The main conclusions of this research work are summarized below:

- Implementing the procedure for various tubular joint assemblies results in acceptable accuracy and effectiveness of the developed beam element to capture the joint flexibility. However, higher accuracy requires considering other element parameters and extending the search bounds in the optimization process.
- The joint's eigenfrequencies and mode shapes were selected as the objective function since they are independent from the loading conditions. However, the evaluation of the refined submodels subjected to static loads indicates improvements in the response and lateral stiffness.
- The main difference between the mode shapes of the beam and shell model is due to the fact that the shell model's local effects do not appear in the beam model's lower modes. Therefore, the contribution and weight of the mode shapes in the optimization was found to be lower than the eigenfrequencies.
- Substituting simplified beam elements of different joint types in a frame structure indicates both static and dynamic improvements. The latter highlights the capability of such an element to be locally and separately developed and later assembled within large-scale jacket structures with multiple joints.
- The study needs more in-depth investigation to generalize the idea of developing 3D beam joint elements by geometric parametrization, considering nonlinear features, a wider variety of joints, and additional loading conditions.

## ACKNOWLEDGEMENTS

The authors would like to acknowledge the Innovation Foundation of Denmark (IFD), which has funded this study via the financial support of the Grand Solutions Project titled "Innovative Structural Health Monitoring and Risk Informed Structural Integrity Management (InnoSHM) (0175-00028B).

## REFERENCES

[1] H. Ahmadi and A. Ziaei Nejad, "A study on the Local Joint Flexibility (LJF) of two-planar tubular DK-joints in jacket structures under in-plane bending loads," *Applied Ocean Research*, vol. 64, 2017.

[2] P. Alanjari, B. Asgarian, and N. Salari, "Elastic tubular joint element for modelling of multi-brace, uni-planar tubular connections," *Ships and Offshore Structures*, vol. 10, no. 4, 2015.

[3] "DNV, Rules for the Design, Construction and Inspection of Offshore Structures. ," *Det Norske Veritas*, 1977.

[4] M. Efthymiou, "Local rotational stiffness of unstiffened tubular joints," *KSEPL Report RKER*, vol. 85, 1985.

[5] H. Fessler, P. B. Mockford, and J. J. Webster, "Parametric equations for the flexibility matrices of single brace tubular joints in offshore structures.," *Proceedings of the Institution of Civil Engineers (London)*, vol. 81, no. pt 2, 1986.

[6] B. Asgarian, V. Mokarram, and P. Alanjari, "Local joint flexibility equations for Y-T and K-type tubular joints," *Ocean Systems Engineering*, vol. 4, no. 2, 2014.

[7] R. Khan, "Structural integrity management and improved joint flexibility equations for uniplanar K-type tubular joints of fixed offshore structures," *Diss. London South Bank University*, 2016.

[8] K. Deb, "Multi-Objective Optimization Using Evolutionary Algorithms: An Introduction Multi-Objective Optimization Using Evolutionary Algorithms: An Introduction," *Wiley-Interscience Series in Systems and Optimization*, no. June, 2001.

COMPDYN 2023
9th ECCOMAS Thematic Conference on
Computational Methods in Structural Dynamics and Earthquake Engineering
M. Papadrakakis, M. Fragiadakis (eds.)
Athens, Greece, 12-14 June 2023

# ESTIMATION OF THE DYNAMIC RESPONSE OF BUILDINGS THROUGH TRANSFER FUNCTIONS. A PROBABILISTIC APPROACH

**Rodolfo J. Tirado-Gutierrez[1], Yeudy F. Vargas-Alzate[2], Ramon Gonzalez-Drigo,[3] Ana M. Zapata- Franco[4]**

[1,2,4] Department of Civil and Environmental Engineering. Polytechnic University of Catalonia (UPC), Jordi Girona, 1-3, 08034, Barcelona (Spain)
rodolfo.javier.tirado@upc.edu; yeudy.felipe.vargas@upc.edu; ana.maria.zapata@upc.edu

[3] Department of Structural Engineering. Polytechnic University of Catalonia (UPC), Jordi Girona, 1-3, 08034, Barcelona (Spain)
jose.ramon.gonzalez@upc.edu

## Abstract

*The significant number of seismic ground motion records to be considered when designing or assessing civil structures is a common restriction. This is because the large computational time involved in the calculation of the nonlinear dynamic response of complex multi-degree-of-freedom system. There are several strategies to overcome this limitation; however, the reliability estimation of the analyzed systems can be compromised. This research is focused on developing a simplified methodology to obtain a probabilistic and reliable estimate of the seismic response of buildings. To do so, a set of transfer functions associated to the dynamic response of a building model are obtained. Then, an optimal transfer function is identified as the one maximizing the prediction of engineering demand parameters (EDPs) when the structure is subjected to a large set of ground motions records. Results show that using a reduced number of records allows developing an enhanced strategy to obtain reliable results in terms of the main statistical moments of the EDPs. This increased capacity to analyze complex systems in an affordable time has important consequences in the identification of optimal designs in terms of material-performance relationship, as well as in the estimation of the expected risk.*

**Keywords:** *Transfer function, dynamic non-linear analysis, spectral analysis, fragility curves, reliability.*

# 1 INTRODUCTION

During the last decades, a great variety of investigations has been carried out focused on the estimation of the dynamic response of civil structures in a non-linear regime. This is because in several regions of the planet the seismic risk is still very high. In fact, it cannot be affirmed that there is an area with zero seismic risk. For this reason, the design of earthquake resistant structures has been, and continues to be, one of the main challenges of structural engineering. However, epistemic and random uncertainties appear in all current methodological developments that seek to estimate the seismic effect on the structures.

Depending on the level of sophistication in modelling, the uncertainty varies. It means, the more sophisticated the type of analysis, the lower the level of uncertainty associated with the modelling. In this respect, there are several ways to assess the seismic behavior of a structure, ranging from the Equivalent Horizontal Force method (EHF), through the Response Spectrum Method (RSM), nonlinear static analysis (pushover analysis), to the nonlinear dynamic analysis (NLDA) [1]. The latter is considered the most reliable numerical procedure to estimate the response of a structure subjected to seismic actions. It should be noted that current seismic design practice admits a certain degree of damage, for which the use of the NLDA is essential to properly capture the statistical variability of a structure in a non-linear regime[2].

From the NLDA, it is possible to calculate, over time, the evolution of stresses, deformations and dissipated energy, among other variables, in any element that is part of the resistant structure [3]. This type of analysis allows incorporating characteristics of the nonlinear dynamic response of structural elements such as plasticization, strength degradation and loss of stiffness, among many others. The results obtained through the NLDA are considered as a reference for any simplified analysis and evaluation method used to obtain the seismic response of a structure [4]. However, the computational cost involved has been one of its main drawbacks. Hence, this article focuses on developing a method that allows estimating, in a fraction of time, engineering demand parameters (EDP) considering uncertainties in the seismic action. EDPs of special interest are the story drift, base shear, roof displacement, accelerations, velocities and story displacements, among others. As a case study, a building previously designed through the NLDA is analyzed. The proposed building follows the requirements of the Colombian seismic-resistant design regulations, NSR-10 [5] and the specifications of the American Concrete Institute, ACI-318 [6].

The proposed method will be identified hereinafter as ROM (Reduced Order Methodology) and it is mainly based on the development of transfer functions. Its main basis is the spectral analysis using the Fourier spectrum of signals that represent both seismic action and structural response. [7]. This approach allows complex systems to be analyzed in a short time. It is also expected that the method proposed here will serve to improve the efficiency of seismic risk estimates, thus increasing the protection of urban environments.

# 2 CASE OF STUDY

## 2.1 Building description

The building under study is located in the city of Pereira, Colombia. Its approximate height is 73.10 meters (23 stories), measured from the base to the roof. The structural system (combined) is composed by connected walls, columns and reinforced concrete beams. These elements transmit the loads of the building to the supports, guaranteeing balance, stability, as well as the compatibility of deformations with each other. The building has been designed based on the NLDA, considering the seismic hazard of the region according to the NSR-10 (AIS,

2010). Note that NLDA demands that the seismic hazard is represented by means of a group of compatible accelerograms with the design spectrum. That is, the seismic hazard is considered using accelerograms whose response spectra are compatible with the design spectrum.

In order to estimate the dynamic response of the structure, a three-dimensional model has been developed using Frame and Shell type elements. Frame elements are used to model beams and columns; membranes to model floors; and for the structural walls shell elements have been used. For the purposes of the model, and according to the type of foundation and the stiffness and capacity of the soils that serve as support, the building was considered to be embedded in the foundation. Figure 1, Figure 2 and Figure 3 show the 3D model, the elevation of two of the main frames, and the most typical floor plan of the building, respectively. Additionally, Table 1 presents some of the most relevant geometric and material characteristics of the structural system.



**Figure 1. 3D-model, front and back view of the building.**

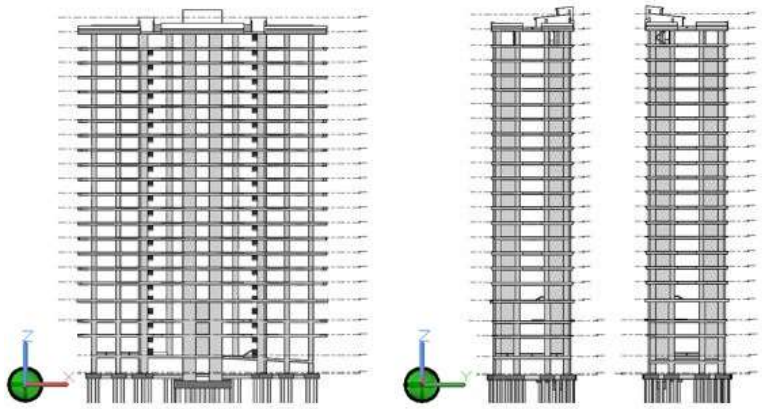

**Figure 2. Front and side frames elevations**

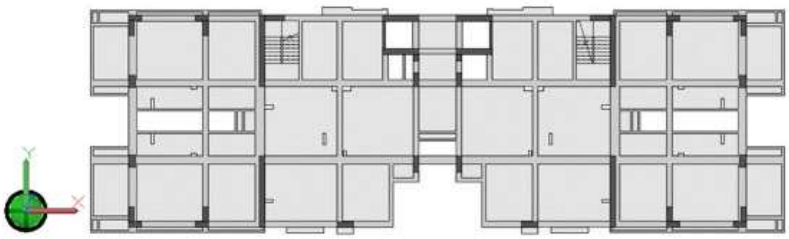

**Figure 3. Structural floor plan of the representative building floor**

**Table 1. Geometric and material characteristics of the structural system**

| | | | Beams | | | Columns | | | Walls | | |
|---|---|---|---|---|---|---|---|---|---|---|---|
| **Level** | **$f_c$ (MPa)** | **H (m)** | **b (cm)** | **h (cm)** | **ρ** | **b (cm)** | **h (cm)** | **ρ** | **b (cm)** | **h (cm)** | **ρ** |
| 0-10 | 35 | 3.45 | 40-60 | 55 | >0.33% | 40-50 | Variable | 1–3 % | 40 | Variable | 1-2 % |
| 11-17 | 28-35 | 3.00 | 40-60 | 50 | >0.33% | 40-50 | Variable | 1-3 % | 40 | Variable | 1-2 % |
| 18-23 | 28 | 2.95 | 40-60 | 45 | >0.33% | 40-50 | Variable | 1-2 % | 40 | Variable | 1-2 % |

In this table, $f_c$ represents the compressive concrete strength; *H* is the story height; *b and h are the* width and height of the cross sections; ρ is the steel percentage

## 2.2 Modelling considerations

The hysteretic properties of the material used, in this case reinforced concrete, are defined from the pivot hysteresis model [8]. This model adequately represents the nonlinear response of reinforced concrete elements, since it includes cyclical axial load effects, asymmetric sections and biaxial bending, among others features. The main advantage of this model is the ability to capture the dominant nonlinear characteristics of the seismic response by means of three simple geometry-based rules. Despite its simplicity, the obtained results fit in an adequate and rational way when compared with the results obtained by applying more advanced models such as fiber models [9]. Regarding the damping model, the Rayleigh proportional damping has been used in this research [10].

The performance of a structure exposed to a seismic event can be described by the maximum state of damage allowed, (represented by the deformation of the hinges). This performance can be defined based on three specific levels (Immediate Occupancy, IO, Life Safety, LS, and Collapse Prevention, CP) proposed in FEMA 356 [11]. Figure 4 depicts these performance levels. Finally, in this research, the yielding surfaces are defined by means of the flexo-compression diagram for columns and moment-rotation diagram for beams, according to the requirements established in ASCE 7-16 [12]. The spectral modal analyses and the nonlinear dynamic analyses have been developed by using the specialized software code for structural analysis, Etabs [13].

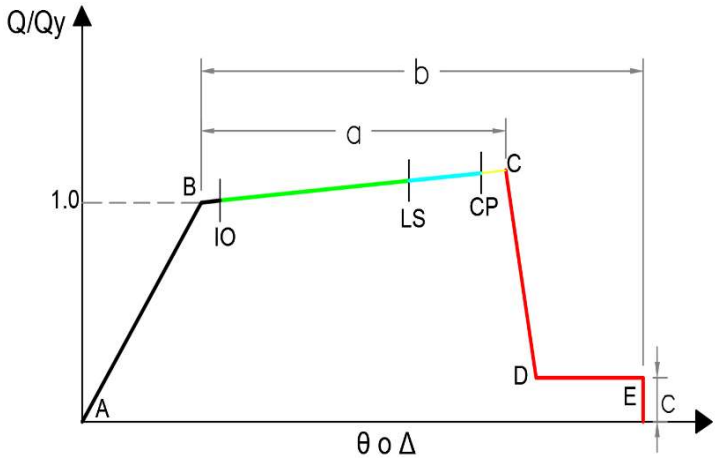


**Figure 4. Generalized force-deformation relations for concrete elements or components and levels of structural performance. Source: American Society of Civil Engineers, ASCE 7-16 (2017) and Federal Emergency Management Agency, FEMA 356 (2000)**

## 3 SEISMIC HAZARD

There are several ways to characterize seismic hazard, three of them are used in this work. The first is based on the design elastic spectrum and it is used in the RSM method. This spectrum is obtained from the smoothed curves given by the Colombian seismic-resistant design regulations (AIS, 2010). This spectrum is used to perform a first approximation of the structural configuration. The second way is by using hybrid accelerograms (generally to check performance levels in the design phase). In brief, they are generated from real accelerograms, which undergo a mathematical treatment so that their response spectra fit a target spectrum in a given range of periods. It is worth mentioning that, when employing NLDA in design, the Colombian code NSR-10 prescribes a set of minimum 7 seismic records. Note that the original signals used to develop these records should meet a series of characteristics typical of the region, such as similar acceleration in a range of frequencies, magnitudes, and hypocentral distances to the fault [14]. These features must be as representative as possible of the expected seismic event in the area. Figure 5 shows both the design elastic spectrum for the building location site, as well as the response spectra of ten selected and fitted signals.

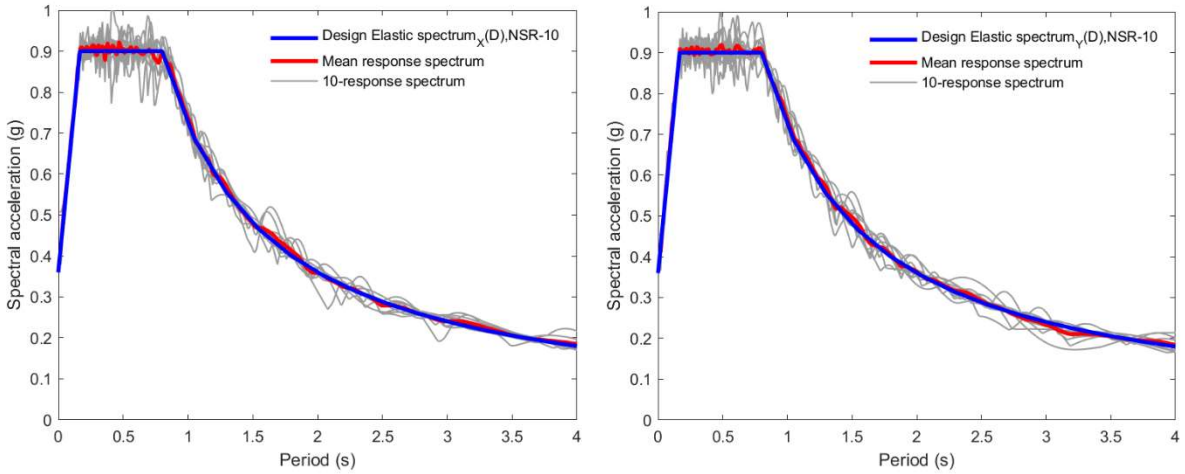


**Figure 5. Blue: Design elastic spectrum; red: mean of the response spectra of the 10 fitted ground motion records; grey: response spectrum of the 10 fitted ground motion records**

The third way used in this research to characterize seismic hazard consists of selecting real ground motion records (one-hundred in this case) incrementally scaled with respect to an intensity measure (IM) (see Figure 6). Based on these records, fragility functions based on the cloud analysis have been generated (Jalayer et al., 2015). These curves have been used to validate the simplified methodology proposed in this article.

The goal of scaling records for deriving fragility functions is that the structure reaches different performance levels. For the purpose of this study, it should be avoided to scale the same record to different intensity levels since this introduce a false correlation between IMs and EDPs. In summary, the following procedure has been used to select and scale the set of one-hundred ground motion records:

1. Identify the IM to scale. In this case, the average spectral acceleration (AvSa) is used (Vargas-Alzate & Hurtado, 2021).
2. Define the maximum value of the IM in order to define the scaling bands (ten in this case). This value depends on the level of intensity used for the building design.
3. Select one-hundred ground motion records from a database, which have been previously sorted with respect to AvSa.

4. The ground motion record with the highest IM is scaled so that its new IM value belongs to the highest scaling interval. If the IM naturally fulfils the interval condition, no scale factor is considered. This step is repeated with the subsequent records, according to the sorted list, until the desirable number of records belonging to the highest interval (ten) is obtained.
5. The previous step is repeated for all intervals. The scale factor in step 4 is calculated having in mind that the IM values are uniformly distributed within each interval.

Figure 6 shows the geometric mean spectra of the horizontal components of the records selected according to the steps described above.

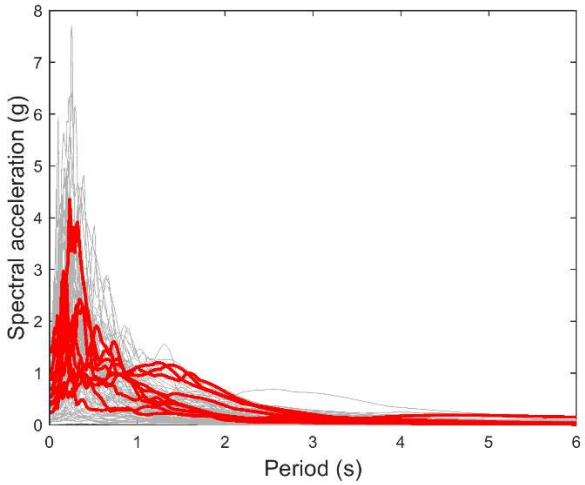


**Figure 6. Geometric mean spectra of the 100 selected records (grey) and the selected records, one for each scaled band (red).**

Once the building has been designed (Based on the records whose spectra are shown in Figure 5) and the seismic action characterized (Figure 6), the next step is to perform one-hundred time-history analyses, where the evolution of stiffness degradation and damping dissipation of the different elements that make up the structure will be stored and post-processed. Based on these results, the next section is dedicated to explain the reduced order methodology.

## 4 REDUCED ORDER METHODOLOGY

It is common to find a multitude of physical problems that require a dynamic study. In the field of civil engineering, the dynamic behavior of buildings is one of the most demanded. In this case, the dynamic equilibrium equation allows estimating the temporal evolution of multiple variables of interest to engineering. Note that finding an analytical solution of this equation is only possible for simple cases. For complex systems (MDoFs), the use of advanced numerical methods is required. However, the great variety of dynamic situations to which a structure may be exposed, combined with the need to estimate its behavior in a 'precise' way, highlights the importance of making a good choice about the numerical procedure to be used.

There are several numerical methods to solve the dynamic equilibrium equation (Newmark, Hilber-Hughes-Taylor and Wilson, among others) [16]. However, as commented above, solving this differential equation is computationally expensive if all the variables involved are exhaustively evaluated, especially if the structures fall into the nonlinear range. For instance, the time taken to achieve the one-hundred NLDA results was 4 months. For this reason, a simplified method is proposed herein that allows estimate the dynamic response of the structure in a quick and efficient manner.

In brief, this method characterizes the dynamic response of a structure from a transfer function, *TF*. This function is obtained by considering the Fast Fourier transform (FFT) of the analyzed response (for instance the Maximum Inter-Storey Drift Ratio, MIDR, obtained by means of NLDA) and the Fast Fourier transform of the seismic action used as input [17]. Eq.2 shows the mathematical form that characterizes a *TF*:

$$TF_{i,j} = \frac{f_{i,j}(\omega)}{g_j(\omega)} \tag{2}$$

where $f_{i,j}(\omega)$ represents the Fourier amplitude spectrum of the response variable of the structure; $g_j(\omega)$ is the Fourier amplitude spectrum of the accelerogram; subscripts *i* and *j* stand for a specific response of the structure (for instance MIDR of the storey *i*) and for a specific ground motion record, respectively.

The main hypothesis is that given the response of a structure to a specific ground motion record, the *TF* obtained through equation 2 can be used to evaluate the response of the system to another record, without having to resort to the use of the NLDA. However, it has been found that the precision of the *TF*s to predict EDPs is variable. Hence, it has been proposed to analyze a subset of the one-hundred records selected in section 3 in order to identify an optimal *TF*. Specifically, ten records are selected, one for each scaled band, with the purpose of performing ten NLDAs that allow obtaining an optimal transfer function. This function has been identified considering the predictive capacity of the *TF*s. Figure 6 shows the geometric mean spectra of the selected records in red line.

Six fundamental steps have been described for the identification of an optimal TF starting from a subset of ten ground motion records:

- Step 1: Perform ten NLDAs using the preselected signals. In this way, the response parameters can be obtained in terms of acceleration, velocity and displacement of the structure (Figure 7, left).
- Step 2: Calculate the EDP of interest (MIDR)
- Step 3: Calculate the *TF*s based on the MIDR. Note that, for each NLDA, it is necessary to calculate a *TF* for the inter-storey associated to each storey ($IDR_{i,j}(t)$) in order to capture the evolution of the MIDR in the entire structure (Figure 7, right).

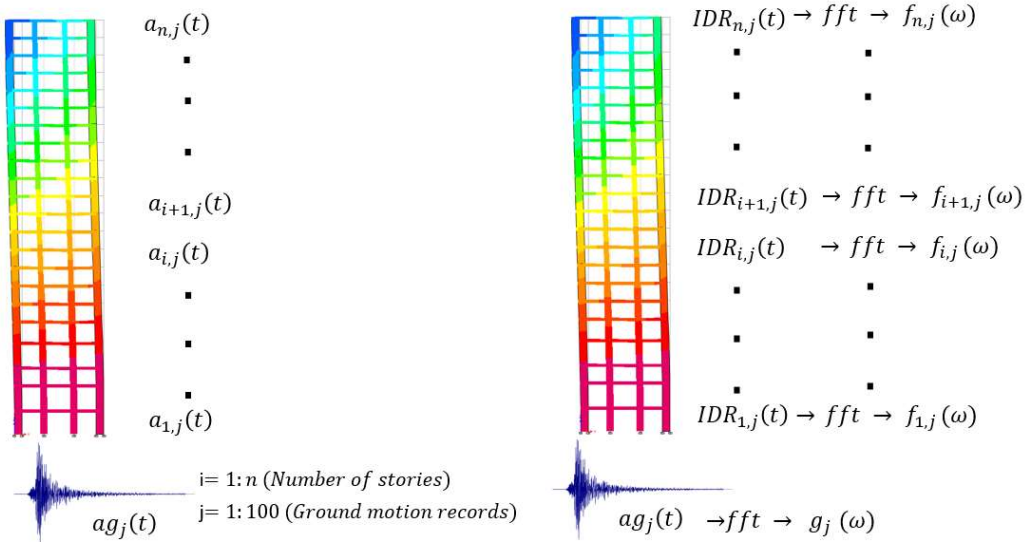


**Figure 7. Left: Calculation of the different EDPs for each floor; right: Calculation of the different TFs for each floor**

- Step 4: Estimation of the structural response (MIDR) through each one of the ten *TF*s, for the total number of preselected signals.
- Step 5: Selection of the optimal *TF* as the one minimizing the mean square error between the response obtained through the NLDA and ROM.
- Step 6: Finally, using the optimal *TF*, predict the response of the remaining set of ninety ground motion records.

## 5 ANALYSIS OF RESULTS

In this research work, the results of the MIDR obtained from NLDA are compared with those derived through ROM, for each of the main direction of the analyzed structure (see Figure 8). The ordinates show the MIDR data obtained through ROM whilst the abscissas show those calculated using the NLDA.

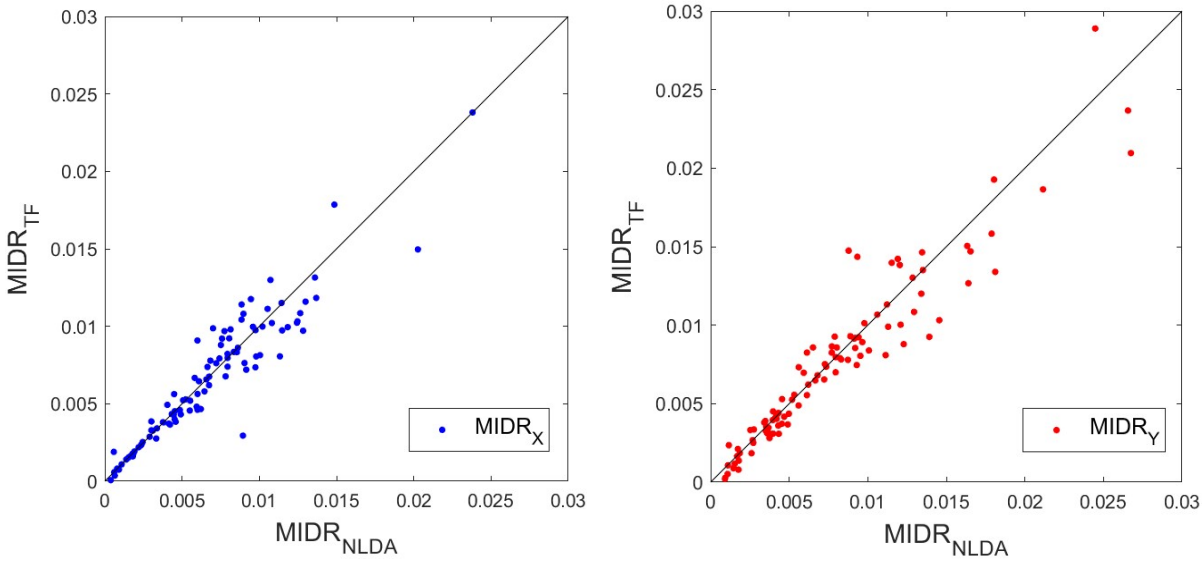


**Figure 8. Maximum inter-story drift: $MIDR_{NLDA}$ Vs $MIDR_{TF}$**

The vulnerability of a building is related to its fragility. This property can be quantified by means of fragility curves. These functions represent the cumulative distribution of the probability of reaching or exceeding a specific damage state, given a determined seismic action [18]. Damage states are usually expressed by parameters associated with strength, stiffness, ductility, or lateral displacements. The description of such damage states depends on the type of structure. For example, the damage state related to 'service' in reinforced concrete structures is described as the beginning of cracking due to flexo-compression and shear, among others, both in beams, columns or walls that are part of the seismic resistant system. For the extensive damage state, the non-structural elements present severe damage whilst the damage to the main structural elements can be significant although the entire structure must be able to continue supporting its own weight [19].

It should be noted that regression analysis plays a central role in the development of fragility functions, since it can be used to identify, describe or predict the response of systems from predictor variables, as well as to derive an optimal mathematical function that models this relationship. It is important to mention that, in cloud statistics, the dispersion and the mean of the bivariate distribution (IM-EDP) play a central role [20]. Thus, using the data shown in Figure 8, fragility curves are derived for NLDA and ROM results. Figure 9 shows the fragility curves related to the service damage state (MIDR=1.00%) using both approaches. $QR_x$ and $QR_y$

stand for Quadratic Regression. It means, when deriving fragility functions based on the cloud analysis, a quadratic regression model has been used.

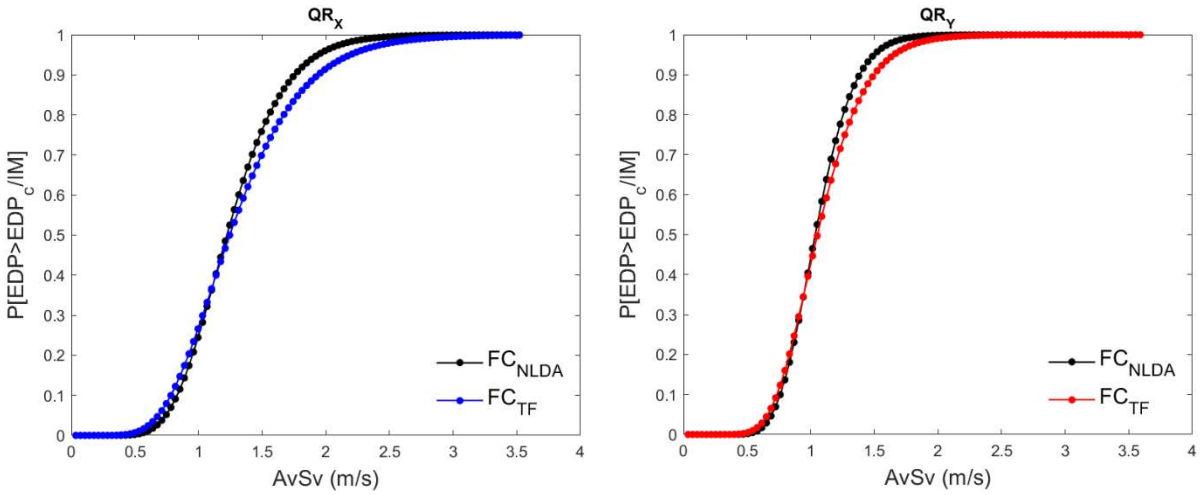


**Figure 9. Fragility curves for the same state of damage (service) for the X and Y direction of the building, black curve: NLDA_X_Y, blue curve: ROM_X, red curve: ROM_Y**

Figure 10 shows the fragility curves related to the extensive damage state (MIDR=2.50%) using both approaches. These curves (Figure 9 and Figure 10) were calculated using the most efficient IM to predict the MIDR. In this sense, current studies show that the most efficient and stable IM is the average spectral velocity given in a range of periods (AvSv, Vargas-Alzate et al., 2022). This IM has also been the most efficient one when compared in this research.

For both damage states, fragility functions show how the approximation made by ROM (blue and red curves) exhibits a good fit to the curve obtained by the target method (NLDA).

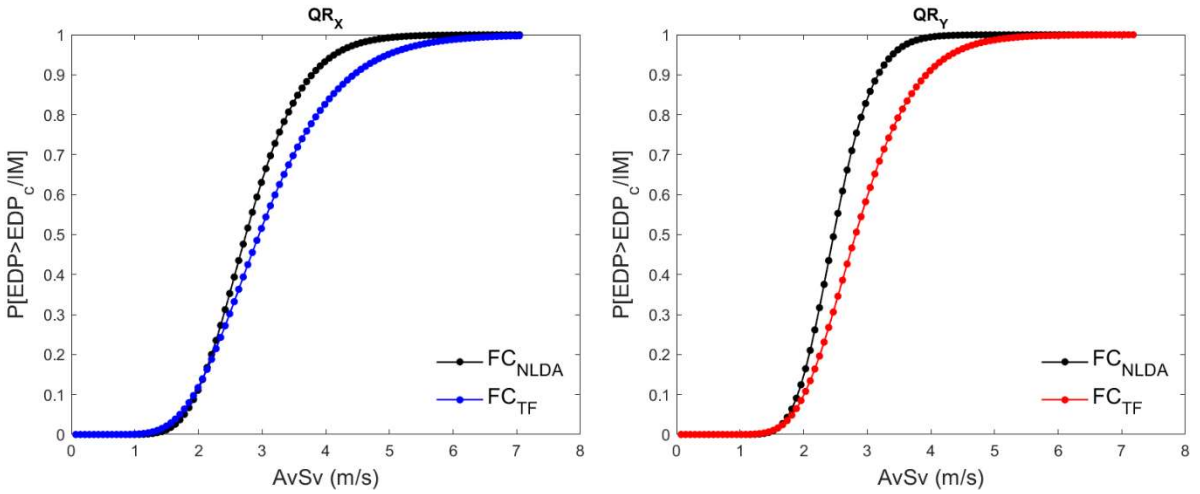


**Figure 10. Fragility curves for the same state of damage (extensive) for the X and Y direction of the building, black curve: NLDA_X_Y, blue curve: ROM_X, red curve: ROM_Y**

## 6 CONCLUSIONS

This work has been motivated by the need to calculate the probabilistic nonlinear structural response of complex systems in an affordable time. The developed method exhibits similar statistical distribution as those obtained with NLDA, which allows evaluating the seismic vulnerability of complex systems in a reliable and efficient manner. This improved ability to

analyze this type of system may derive in a significant contribution for methodologies related to seismic risk estimates, increasing the protection of our urban environments.

It is noteworthy that, in a vulnerability and seismic risk assessment, regardless of the methodology to be used, it is essential to follow an approach that takes into account the non-linear behavior of the structure, as well as the uncertainty associated with the seismic action. Note that the most important source of uncertainty in the dynamic response of a structure comes from this variable. This is due to the complex interaction of the mechanisms involved in the release of energy and the propagation of waves. For this reason, it is important to have a significant number of seismic records that allow characterizing the seismic hazard adequately.

In this respect, nowadays exists adequate methodologies, tools and technology to design and evaluate a structure potentially exposed to the most restrictive and demanding performance requirements. Hence, current computational capacity, combined with advanced statistical approaches, allow the development of probabilistic frameworks to estimate the nonlinear response of civil structures exposed to seismic actions. However, reducing the computational cost without unduly sacrificing precision would help to generalize the use of more exhaustive theories. To do so, it is necessary to develop tools that allow the analysis of complex systems in an affordable time, such as the one proposed herein. However, in order to properly calibrate the proposed method, a higher number of calculations must be made, where structures with different natural periods and configurations, both in plan and in elevation, are included.

It is important to mention that the maximum inter story drift is one of the most complex EDPs to evaluate. This is due to its relative character, which can be affected by the phases in the Fourier transformation. However, a good approximation of the fragility curves has been observed, even for the extensive damage state.

Finally, it can be concluded that the proposed simplified method presents a high potential for future research, since it will allow calculating seismic risk scenarios under robust statistics. It should be noted that this method can be improved in terms of efficiency if, for example, transfer functions are developed through signals that excite the structure in a wider range of periods, for instance, using white noise signals.

**Acknowledgment and Funding:**

We thank the company "Constructora Triple A", as well as the architects Augusto Acuña and Carlos García, since they have allowed the use of the results of the studied building, whose name is "Ittos-19". This research has been partially funded by the Spanish Research Agency (AEI) of the Spanish Ministry of Science and Innovation (MICIN) through project with reference: PID2020-117374RB-I00/AEI/10.13039/501100011033.

## 7 REFERENCES

[1] P. Fajfar, “Analysis in seismic provisions for buildings: Past, present and future,” in *Geotechnical, Geological and Earthquake Engineering*, vol. 46, 2018. doi: 10.1007/978-3-319-75741-4_1.

[2] Y. F. Vargas-Alzate, N. Lantada, R. González-Drigo, and L. G. Pujades, “Seismic risk assessment using stochastic nonlinear models,” *Sustain.*, vol. 12, no. 4, 2020, doi: 10.3390/su12041308.

[3] J. Moehle, Y. Bozorgnia, and T. Y. Yang, “The Tall Buildings Initiative,” *Struct. Eng. Assoc. Calif.*, 2007.

[4] Y. Vargas, "Análisis estructural estático y dinámico probabilista de edificios de hormigón armado. Aspectos metodológicos y aplicaciones a la evalua- ción del daño.," p. Spanish, 2013.

[5] A. colombiana de ingeniería sismica- AIS, "Reglamento Colombiano de Construcción Sismo Resitente NSR-10," *Scielo*, p. Spanish, 2010.

[6] ACI 318, *Building Code Requeriments for Reinforced Concrete, American Concrete Institute, Detroit, Michiga*. 2019.

[7] J. W. Cooley, P. A. W. Lewis, and P. D. Welch, "Application of the Fast Fourier Transform to Computation of Fourier Integrals, Fourier Series, and Convolution Integrals," *IEEE Trans. Audio Electroacoust.*, vol. 15, no. 2, 1967, doi: 10.1109/TAU.1967.1161904.

[8] R. K. Dowell, F. Seible, and E. L. Wilson, "Pivot Hysteresis Model -Dowell, Seible & Wilson ACI 1998," *ACI structural journal*, vol. 95. pp. 607–617, 1988.

[9] Y. Ling, "Parameter optimization for Pivot hysteresis model for reinforced concrete columns with different failure modes," no. April, pp. 2167–2187, 2022, doi: 10.1002/eqe.3658.

[10] A. Carr, *Ruaumoko-Inelastic Dynamic Analysis Program; Department of Civil Engineering, University of Canterbury: Christchurch, New Zealand*. New Zealand, 2000. doi: 10.13140/RG.2.1.4755.8567.

[11] FEMA, "Prestandard and Commentary for the Seismic Rehabilitation of Buildings," *Rehabil. Requir.*, no. 1, pp. 1–518, 2000.

[12] ASCE 7-16, *Minimum Design Loads and Associated Criteria for Buildings and Other Structures*. Reston, VA: American Society of Civil Engineers, 2017. doi: 10.1061/9780784414248.

[13] CSI, "Computers & Structural, INC," *Struct. Earthq. Eng. Software, www.csiamerica.com*, 2017.

[14] C. B. Haselton, A. S. Whittaker, A. Hortascu, J. W. Baker, J. Bray, and D. N. Grant, "Selecting and scaling ground motions for performing response-history analyses," in *15th World Conference on Earthquake Engineering*, 2012.

[15] Y. Vargas-Alzate and J. Hurtado, "Efficiency of Intensity Measures Considering Near- and Far-Fault Ground Motion Records," *Geosciences*, vol. 11, no. 6, p. 234, May 2021, doi: 10.3390/geosciences11060234.

[16] T. C. Fung, "Numerical dissipation in time-step integration algorithms for structural dynamic analysis," *Prog. Struct. Eng. Mater.*, vol. 5, no. 3, 2003, doi: 10.1002/pse.149.

[17] J. Bobadilla, "La transformada de Fourier. Una visión pedagógica," *Estud. fonética Exp.*, vol. 10, p. Spanish, 1999.

[18] R. L. Bonett Díaz, "Vulnerabilidad y riesgo sísmico de edificios. Aplicación a entornos urbanos en zonas de amenaza alta y moderada.," dissertation, Universitat Politècnica de Catalunya, 2003.

[19] J. Vielma, "Damage Trhesholds for Limit States of Reinforced Concrete Framed Buildings Designed According To Aci- 318/Ibc-2006," *Rev. Int. Desastr. Nat. Accid. e Infraestruct. Civ.*, vol. 8, no. 2, p. Spanish, 2008.

[20] F. Jalayer, R. De Risi, and G. Manfredi, "Bayesian Cloud Analysis: Efficient structural fragility assessment using linear regression," *Bull. Earthq. Eng.*, vol. 13, no. 4, pp. 1183–1203, 2015, doi: 10.1007/s10518-014-9692-z.

[21] Y. F. Vargas-Alzate, J. E. Hurtado, and L. G. Pujades, *New insights into the relationship between seismic intensity measures and nonlinear structural response*, vol. 20, no. 5. Springer Netherlands, 2022. doi: 10.1007/s10518-021-01283-x.

COMPDYN 2023
9th ECCOMAS Thematic Conference on
Computational Methods in Structural Dynamics and Earthquake Engineering
M. Papadrakakis, M. Fragiadakis (eds.)
Athens, Greece, 12-–14 June 2023

# STOCHASTIC GENERATION OF ARTIFICIAL ACCELEROGRAMS USING THE CONTINUOUS WAVELET TRANSFORM METHOD

**Hera Yanni[1], Michalis Fragiadakis[1], and Ioannis P. Mitseas[1,2]**

[1]National Technical University of Athens, Athens, Greece
Iroon Politechniou 9, 15780, Athens, Greece
e-mail: heragian@mail.ntua.gr; mfrag@mail.ntua.gr; Imitseas@mail.ntua.gr

[2] University of Leeds, Leeds, United Kingdom
LS2 9JT, Leeds, UK
e-mail: I.Mitseas@leeds.ac.uk

**Keywords:** artificial accelerogram, stochastic model, temporal and spectral non-stationarity, continuous wavelet transform, wavelets, spectrum-compatible.

**Abstract.** *A new stochastic methodology for the generation of artificial, fully non-stationary, spectrum-compatible accelerograms is proposed. Time-history analysis requires the use of suites of accelerograms that can be either recorded, or artificially generated. Hazard consistency can be achieved if their mean spectrum is matched to a target design spectrum. Artificial earthquake ground motions can be easily generated at frequency bands of interest and have features compatible with desired target characteristics. The proposed model operates in the time-frequency (TF) domain using the continuous wavelet transform (CWT). The methodology follows the rationale of the techniques that use an evolutionary power spectral density function, where the temporal and spectral non-stationarity is modeled by a TF envelope function. More specifically, a zero mean stationary Gaussian stochastic process is generated using the spectral representation method and defines: the target peak ground acceleration, the frequency range, and the phase distribution. Additionally, it ensures the spectrum compatibility through the power spectral density function. A recorded accelerogram is consistent with the characteristics of the site of interest and models the temporal and spectral modulation. Both generated and recorded signals are analyzed in the TF domain using the CWT and their wavelet coefficients are obtained respectively. The time-frequency envelope is then extracted from the modulus of the CWT coefficients of the recorded accelerogram and modifies accordingly the stationary stochastic process in the TF domain. Energy distribution compatibility is also imposed at each frequency, and new wavelet coefficients are produced. The simulated signal is then transformed in the time domain using the inverse CWT. The proposed methodology provides an arbitrary number of seismic accelerograms whose temporal and spectral modulation is modeled by a recorded ground motion.*

## 1 INTRODUCTION

The most realistic method for the assessment of the seismic response of structures is the time-history analysis. A critical stage in the process of performing this analysis is the definition of appropriate suites of acceleration time histories that represent the input ground motion. These accelerograms can be either recorded, or artificially generated. In both cases, the seismic motions must be compatible with a target design spectrum. Furthermore, they should exhibit frequency and energy characteristics that are consistent with the site of interest.

In this framework, engineers typically choose to select appropriate recorded ground motions from databases. Different approaches for selecting records without biasing the response estimates have been proposed in the literature (e.g. [1]). Historical accelerograms, however, correspond to different hazard scenarios and soil conditions as they are obtained from different sites from the site of interest. Furthermore, the lack of recorded ground motions of earthquakes with large magnitudes at small epicentral distances confines the analysis of large limit states, like the collapse limit state. To overcome these limitations, simulated artificial accelerograms are finding increased use.

Artificial earthquake ground motions can be easily generated at frequency bands of interest and have features that match desired target characteristics. Moreover, seismic codes (e.g. Eurocode 8 -EC8- [2]) establish the use of artificial or synthetic ground motions, without proposing any specific method for their simulation. Due to the random nature of seismic actions, artificial ground motion time-histories can be generated as stochastic processes. Various methods have been proposed in the literature, like methods that depend on seismological parameters (e.g. [3]), and methods that model the ground motion for a specific site by using a target recorded accelerogram, or a target spectrum (spectrum-compatible).

The latter stochastic models are more simple, thus they are the most adopted in practice. The most popular of these approaches is the spectral representation method (SRM) proposed by Shinozuka and Deodatis [4]. In this case, the ground motion time-histories are simulated mathematically as a superposition of harmonic components with random phase angles, directly related to the power spectral density (PSD) function of the process. Moreover, the relationship between the values of the PSD function and the response spectral values for a given spectral damping ratio is the basis for the generation of target spectrum compatible accelerograms [5].

The seismic time-histories simulated using the PSD function can be stationary, quasi-stationary and fully non-stationary. Natural earthquake ground motions inherently exhibit both temporal and spectral non-stationarity or in other words, they are fully non-stationary. Thus, several approaches have been proposed in order to generate fully non-stationary accelerograms using the SRM. The most popular is the use of an evolutionary power spectral density (EPSD) function, i.e. a PSD function that varies in time [6]. This may be achieved by introducing a time-frequency (TF) envelope function that modifies a stationary accelerogram both in time and in frequency in order to simulate the characteristic behavior of natural accelerograms (e.g. [7]). Another approach is the one proposed by Cacciola [8], where fully non-stationary accelerograms are produced as the superposition of a fully non-stationary counter-part modeled by a real accelerogram and a stationary process modeled with the SRM.

More recent methodologies for the generation of artificial accelerograms are based on signal processing operations (e.g. [9], [10]). This is due to their ability to analyze and synthesize the signals simultaneously in both time and frequency, thus allowing to directly model the accelerograms' evolutionary frequency content (i.e. non-stationary characteristics). The wavelet transform is a tool that allows to obtain a joint-time frequency representation of non-stationary

signals. More specifically, it employs localised wave-like functions (wavelets) instead of continual harmonics as a base to decompose a signal. Different wavelet-based approaches have been proposed in the literature for generating artificial non-stationary accelerograms (e.g. [11], [12], [13]).

In this paper the first steps for a new stochastic methodology for the generation of artificial, fully non-stationary, spectrum-compatible accelerograms are presented. The proposed approach uses the CWT method in order to operate in the TF domain. More specifically, the SRM is combined with the CWT in order to simulate accelerograms that are consistent with both the temporal and the frequency characteristics of seismic ground motions from the site of interest. The methodology follows the rationale of the techniques that use an EPSD function, where the temporal and spectral non-stationarity is modeled by a TF envelope function. Additionally, a new approach is proposed for the modeling of the envelope function, based on the site's historical records. That is, a recorded accelerogram is analyzed in the TF domain using the CWT, and the TF envelope is extracted from the modulus. Therefore, the proposed methodology provides an arbitrary number of seismic accelerograms whose temporal and spectral modulation is modeled by a recorded ground motion.

## 2 PRELIMINARY CONCEPTS

### 2.1 The Continuous Wavelet Transform (CWT)

The Continuous Wavelet Transform (CWT) method is based on a set of basis functions (wavelet family) formed by dilation and translation of a prototype mother function (wavelet) $\psi(t)$ and is used to decompose a function (signal) $u(t)$ into the time-frequency domain. Definitions in the literature vary slightly and depend on the choice of normalization of the wavelets. In this study, the $L^2(\mathbb{R})$ normalization was employed [14].

Let $\psi(t)$ be a window function that fulfills the admissibility conditions. This function is called the mother (analyzing) wavelet, and the corresponding family of wavelets is the group of shifted and scaled (dilated) copies of $\psi$, defined as:

$$\psi_{b,a}(t) = \frac{1}{\sqrt{a}}\psi\left(\frac{t-b}{a}\right) \quad , \quad t \in \mathbb{R} \tag{1}$$

where $a > 0$ is a scaling parameter that defines the dilation of the mother wavelet $\psi(t)$ and $b$ is the translation parameter related to time. Scale factor $a > 1$ corresponds to dilation and $0 < a < 1$ corresponds to compression. The mother wavelet is the member of the family where $b = 0$ and $a = 1$, and it can be either real or complex. The choice of the mother wavelet is dictated by the characteristics of the signal and the application. A complex wavelet function will return information about both amplitude and phase and is better adapted for capturing oscillatory behavior.

Let $u(t)$ be a signal that is of finite energy and a piece-wise continuous function of $t$. Given a mother wavelet $\psi(t)$, the continuous wavelet transform of this signal is given by the integral:

$$T_\psi[u](b,a) = \frac{1}{\sqrt{a}}\int_{-\infty}^{+\infty} u(t)\overline{\psi}\left(\frac{t-b}{a}\right)dt \tag{2}$$

where $a > 0$ is a scaling parameter that defines the dilation of the mother wavelet $\psi(t)$ and $b$ is the translation parameter related to time. The symbol $\overline{\psi}$ denotes the complex conjugate. As it is observed by Eq.2, CWT transforms a one-dimensional (time domain) signal $u(t)$ to a two-dimensional representation: the time-scale plane. When the admissibility condition is fulfilled,

the original signal $u(t)$ can be reconstructed as:

$$u(t) = \frac{1}{C_\psi} \int_{-\infty}^{+\infty} \int_{0}^{+\infty} T_\psi[u](b,a)\psi\left(\frac{t-b}{a}\right)\frac{da}{a^2}db \tag{3}$$

where $C_\psi$ is a finite constant given by the integral:

$$0 < C_\psi = \int_{-\infty}^{+\infty} \frac{|\widehat{\psi}(\omega)|^2}{|\omega|}d\omega < +\infty \tag{4}$$

As shown in the previous, the CWT is defined with scales. Scales are directly linked with frequencies: a scale $a$ corresponds to a scaled version of the mother wavelet with center frequency $\omega_\psi/a$, thus bringing the CWT on the time-frequency plane. Therefore, in the rest of the paper, the CWT will be used in terms of time and angular frequency, $T_\psi[u](\omega, b)$.

### 2.2 Generation of stationary, spectrum compatible artificial accelerograms

Stationary and target spectrum-compatible accelerograms are simulated following the spectral representation method (SRM) proposed by Shinozuka and Deodatis [4]. The signal is modeled as a zero mean stationary Gaussian stochastic process $a_s(t)$ of finite duration $T_s$ and is generated as the superposition of harmonic functions with random phase angles:

$$a_s(t) = \sum_{i=1}^{N} \sqrt{2G_s(\omega_i)\Delta\omega}\cos\left(\omega_i t + \theta_i\right) \tag{5}$$

where $N$ is the number of harmonics to be superimposed, $\omega_i$ is the angular frequency of the $i^{th}$ harmonic, $\Delta\omega$ is the constant integration step, and $\theta_i$ are random phase angles uniformly distributed over the interval $[0, 2\pi]$. Furthermore, the amplitude of each component is related to the one-sided PSD function $G_s(\omega_i)$ of the stochastic process. Compatibility with a target spectrum is achieved by the evaluation of $G_s(\omega_i)$ based on the random vibration analysis approach proposed by Cacciola et al. [15]:

$$G_s(\omega_i) = \begin{cases} \dfrac{4\zeta}{\omega_i\pi - 4\zeta\omega_{i-1}}\left(\dfrac{{S_a}^2(\omega_i,\zeta)}{\eta_{X_i}^2} - \Delta\omega\displaystyle\sum_{k=1}^{i-1} G_s(\omega_k)\right), & \omega_i > \omega_0 \\ 0, & \omega_i \leq \omega_0 \end{cases} \tag{6}$$

where $S_a(\omega_i, \zeta)$ is the target spectral acceleration at frequency $\omega_i$, $\zeta$ is the target spectrum's damping ratio, and $\eta_{X_i}$ is the peak factor. According to the hypothesis of a barrier outcrossing in clumps [16], the peak factor is evaluated as:

$$\eta_{X_i}(T_s, p) = \sqrt{2\ln\left\{2N_{X_i}\left[1 - \exp\left(-\delta_{X_i}^{1.2}\sqrt{\pi\ln\left(2N_{X_i}\right)}\right)\right]\right\}} \tag{7}$$

where $N_{X_i}$ is the mean zero crossing rate and $\delta_{X_i}$ is the spread factor of the stochastic response process $X_i(t)$, evaluated approximately with reference to a white-noise input [15] as:

$$N_{X_i} = \frac{T_s}{2\pi}\omega_i(-\ln p)^{-1} \tag{8a}$$

$$\delta_{X_i} = \sqrt{1 - \frac{1}{1-\zeta^2}\left(1 - \frac{2}{\pi}\arctan\frac{\zeta}{\sqrt{1-\zeta^2}}\right)^2} \tag{8b}$$

The range of $\omega_i$ is defined in the interval $[\omega_0, \omega_u]$, where $\omega_u$ is an upper cut-off frequency beyond which the PSD function $G_s(\omega_i)$ is assumed to be zero for either mathematical or physical reasons and $\omega_0$ is the lowest frequency bound of the existence domain of Eq.7. For Eq.8 in particular, $\omega_0 = 0.36$ rad/s. It should be noted that, for $i = 1$, $G_s(\omega_1) = 0$. The accelerograms generated combining Eqs.5 and 6 have all the same duration $T_s$ and are stationary, i.e. amplitude and PSD function are not a function of time.

## 3 THE PROPOSED METHODOLOGY

The proposed methodology generates artificial, fully non-stationary, and spectrum-compatible accelerograms. Furthermore, the model produces accelerograms that reflect the temporal and frequency characteristics of seismic ground motions from the site of interest by combining spectral representation techniques with signal processing operations. The proposed model employs the CWT in order to operate in the time-frequency (TF) domain.

First, the desired target spectrum and frequency range $[\omega_0, \omega_u]$ are defined. The temporal and spectral modulation (i.e. the non-stationarity) is modeled by a TF envelope function that is extracted from a historical ground motion. Therefore, a recorded accelerogram from the site of interest is selected and analyzed in the time-frequency domain using the CWT. The TF envelope function is then obtained from the normalized modulus of the obtained CWT coefficients, leading to realistic modeling of the time-varying spectral energy distribution.

A zero mean stationary Gaussian stochastic process is then generated using the SRM and defines the target peak ground acceleration, the frequency range, and the phase distribution. In this step, spectrum compatibility is also ensured by proper computation of the power spectral density function (PSD). The generated signal is then analyzed in the TF domain using the CWT.

The TF envelope then modifies accordingly the stationary stochastic process in the time-frequency domain, and new wavelet coefficients are obtained. The simulated signal is transformed in the time domain using the inverse CWT and the desired new artificial accelerogram is obtained. Corrective iterations in the frequency domain may also be required in order to achieve enhanced spectrum matching. The proposed methodology provides seismic accelerograms whose temporal and spectral modulation is modeled by a historical ground motion.

### 3.1 Time-Frequency envelope extraction

Once the desired target spectrum and frequency range $[\omega_0, \omega_u]$ are defined, a recorded accelerogram $\ddot{u}(t)$ is selected from the site of interest, and its total duration $t_f$ and peak ground acceleration $pga_{\ddot{u}}$ are obtained. Then the signal is analyzed with the CWT at frequency range $[\omega_0, \omega_u]$, with fine frequency resolution, and the wavelet coefficients $T_\psi[\ddot{u}](\omega, b)$ are calculated using Eq.2. The complex Morlet wavelet (see Fig.1) is chosen as a mother wavelet, as it also has a a wave-like shape with an increased number of oscillations. Next, the time-frequency envelope $\Phi(\omega, t)$ is defined as the normalized modulus of the CWT coefficients $T_\psi[\ddot{u}](\omega, b)$, so that the peak of the envelope to be equal to one:

$$\Phi(\omega, t) = \frac{|T_\psi[\ddot{u}](\omega, b)|}{\max\left(|T_\psi[\ddot{u}](\omega, b)|\right)} \tag{9}$$

### 3.2 Generation of the non-stationary accelerograms with the CWT method

Having the desired target spectrum, the same frequency range $[\omega_0, \omega_u]$, and the same total duration $t_f$, a stationary, spectrum-compatible, artificial accelerogram $a_s(t)$ is generated following Eqs.5-8, by setting $T_s$=$t_f$. Then its peak acceleration value $pga_s$ is obtained and the

following coefficient is calculated:

$$a_{sc} = \frac{pga_s}{pga_{\ddot{u}}} \tag{10}$$

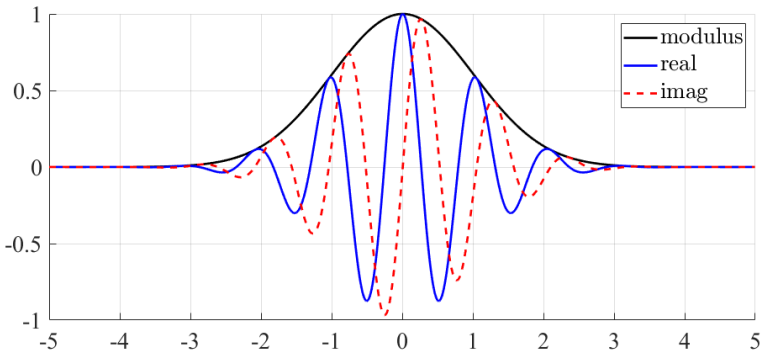


Figure 1: The Complex Morlet Wavelet.

The generated signal $a_s(t)$ is analyzed with the CWT, following Eq.2 with the same filterbank as the recorded accelerogram, and the wavelet coefficients $T_\psi[a_s](\omega, b)$ are obtained. Ensuring spectral energy distribution compatibility, for every frequency, from $\omega_0$ to $\omega_u$:

$$A_s(\omega) = \int_0^{t_f} |T_\psi[a_s](\omega, b)|dt \tag{11}$$

$$A_{\ddot{u}}(\omega) = \int_0^{t_f} |T_\psi[\ddot{u}](\omega, b)|dt \tag{12}$$

Finally, new wavelet coefficients are produced, that correspond to the artificially generated accelerogram:

$$T_\psi[a(t)](\omega, b) = T_\psi[a_s](\omega, b)\Phi(\omega, t)\frac{A_s(\omega)}{a_{sc}A_{\ddot{u}}(\omega)} \tag{13}$$

Finally, the generated accelerogram $a(t)$ is obtained by applying the inverse CWT on $T_\psi[a(t)](\omega, b)$, by following Eqs.3-4.

### 3.3 Post processing

If further spectrum compatibility is desired, corrective iterations are carried out in the frequency domain, by using the Fourier Transform. Then, the new signal is transformed back in the time domain by using the inverse Fourier Transform [17].

Moreover, in order to obtain realistic velocity and displacement time-histories through numerical integration of the acceleration signals, baseline correction is applied. A simple quadratic curve for polynomial fitting is employed.

## 4 NUMERICAL APPLICATION

The efficiency of the proposed methodology is demonstrated through a numerical application. The site of interest is a region in central Greece, with soil conditions that correspond to type C soil according to EC8 [2] ($V_{S30} \approx 360$ m/s). Moreover, the target spectrum is the elastic EC8 spectrum, for peak ground acceleration (PGA) equal to 0.24g and damping ratio $\zeta = 5\%$. The target frequency range is $[\omega_0, \omega_u] = [1, 150]$ rad/s.

The first step is to select a recorded accelerogram $\ddot{u}(t)$ from the site of interest. The Corinth earthquake (Corinth, Greece, 2/24/1981, Corinth, T, see Fig.2) is chosen from the PEER NGA-West 2 database [18], with $V_{S30} = 361$ m/s. The total duration of the accelerogram is $t_f = 40.93$ s and $pga_{\ddot{u}} = 0.30$ g. Next, the recorded ground motion $\ddot{u}(t)$ is analyzed in the TF domain using the CWT method (see section 2.1), and the modulus of the CWT coefficients are obtained (see Fig.3). Following Eq.9, the TF envelope is extracted from the modulus (see Fig.4). As it is observed, the time and frequency locations of the dominant energetic features of the recorded accelerogram are preserved within the envelope.

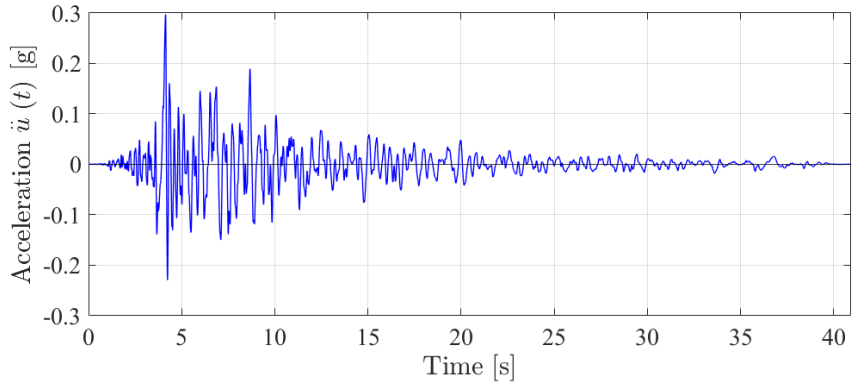


Figure 2: The selected recorded accelerogram: Corinth, Greece, 2/24/1981, Corinth, T.

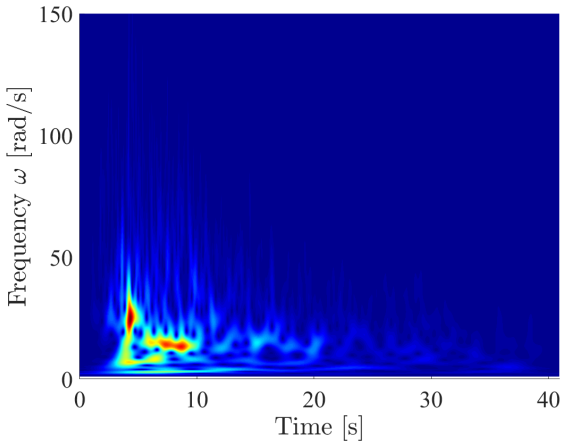


Figure 3: CWT modulus Scalogram of the recorded ground motion.

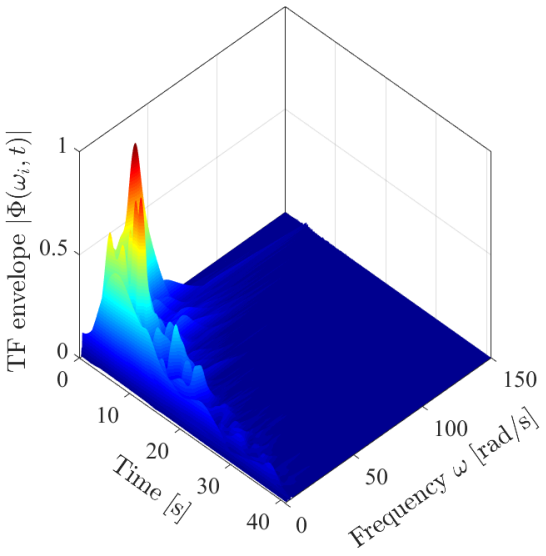


Figure 4: The respective extracted and normalized time-frequency envelope.

It should be noted that for the implementation of the CWT, the MATLAB Wavelet Toolbox of the MATLAB R2018b version [19] was used. The MATLAB Wavelet Toolbox has its own built in "cwt" command, which employs a discretized version of the CWT and computes the coefficients as a convolution product. In this paper, the new "cwt" command was used, with several modifications in order to adopt the $L^2(\mathbb{R})$ normalization.

For the next step, a stationary, target spectrum-compatible accelerogram $a_s(t)$ is generated following the procedure presented in section 2.2, for frequency range $[\omega_0, \omega_u] = [1, 150]$ rad/s, total duration $T_s = t_f = 40.93$ s. The generated accelerogram is shown in Fig.5. This component ensures the compatibility of the final accelerogram with the target spectrum, as its response spectral values match the target ones. To highlight this, Fig.6 shows the target EC8 elastic spectrum and the response spectrum of the generated stationary accelerogram.

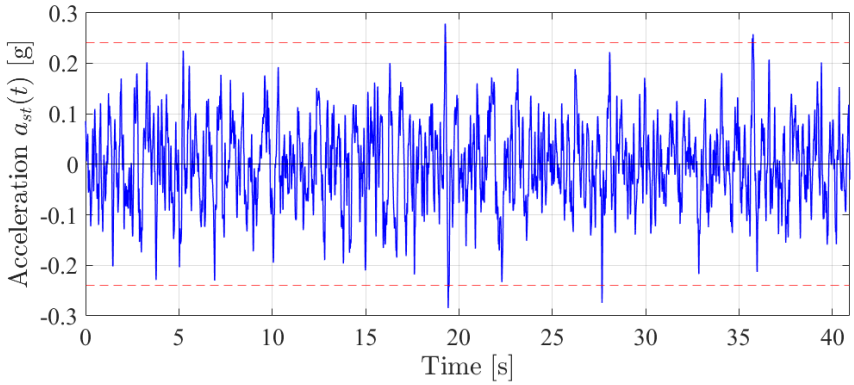


Figure 5: The generated with the SRM stationary accelerogram.

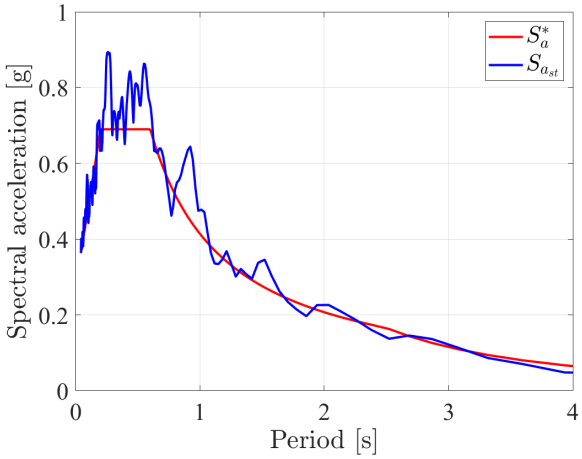


Figure 6: Comparison of the matching between the target EC8 elastic response spectrum $S_a^*$ with the generated stationary accelerogram's response spectrum $S_{a_{st}}$.

The generated stationary accelerogram is then analyzed in the TF domain by applying the CWT method presented in section 2.1, with the same filterbank used for the CWT analysis of the recorded accelerogram. Fig.7 shows the one-sided PSD function of the stationary accelerogram, with its dominant frequency highlighted. Fig.8 shows the modulus of the CWT coefficients of the same signal. As it is observed, the dominant frequency is evident through the energy concentration region of the Scalogram. This is a direct result of the $L^2(\mathbb{R})$ normalization that was applied in the CWT definition.

Next, the PGA value of the stationary accelerogram is obtained, equal to $pga_s = 0.28$g and the coefficient $a_{sc} = 0.96$ is calculated, according to Eq.10. Moreover, the areas $A_s(\omega)$ and $A_{\ddot{u}}(\omega)$ are computed, following Eqs.11 and 12 respectively.

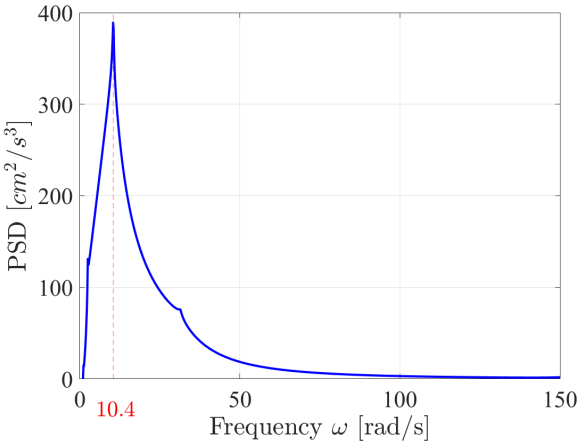


Figure 7: The one-sided PSD function $G(\omega)$ of the stationary accelerogram and its dominant frequency.

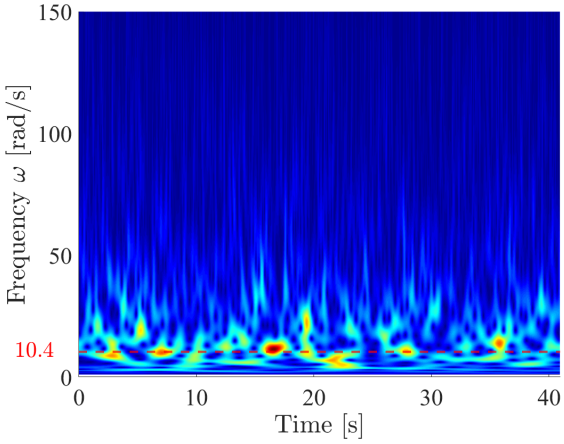


Figure 8: CWT modulus Scalogram of the stationary accelerogram. The dominant frequency of the one-sided PSD function $G(\omega)$ is clearly distinguishable.

Finally, Eq.13 is applied and the new wavelet coefficients are obtained. The new accelerogram $a(t)$ is simulated by applying the inverse CWT on $T_\psi[a(t)](\omega, b)$, by following Eqs.3-4. One corrective iteration is applied for greater spectrum matching, and the new accelerogram is obtained, shown in Fig.9. As it is observed, the PGA values correspond to the target. The produced accelerogram is spectrum-compatible as it is seen in Fig.10, where its response spectral values are compared to the target EC8 elastic spectrum.

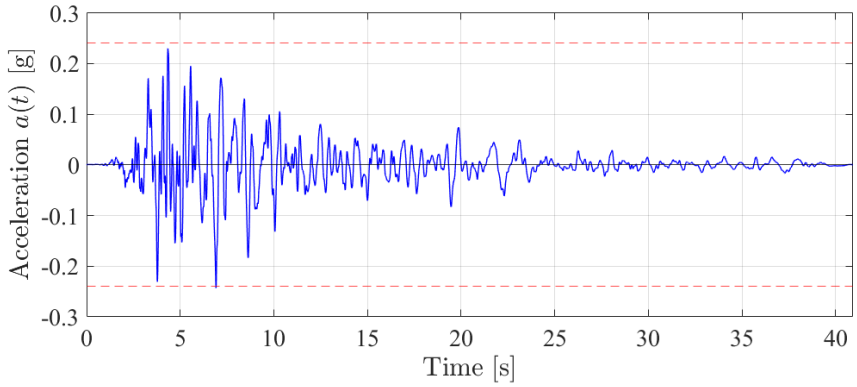


Figure 9: The new accelerogram, generated with the proposed method.

The produced accelerogram is fully non-stationary. This is observed in Fig.11, where the signal is analyzed in the TF domain with the CWT. Both temporal and frequency modulation are evident. Also, in comparison with Fig.3, it is obvious that the energy distribution is modeled after the recorded accelerogram. As it is seen, the frequency range of the generated accelerogram matches target. Furthermore, the influence of the recorded accelerogram to the temporal non-stationarity is observed in Fig.12, where the Husid function plot of both of the signals are shown. This is also seen by defining and calculating the significant duration as the interval between $5\%$ and $95\%$ of the total energy. The recorded accelerogram has a strong motion duration of 13.94 s, whereas for the produced accelerogram it is equal to 16.62 s. These two values are

very close, and the Husid plots are in good agreement.

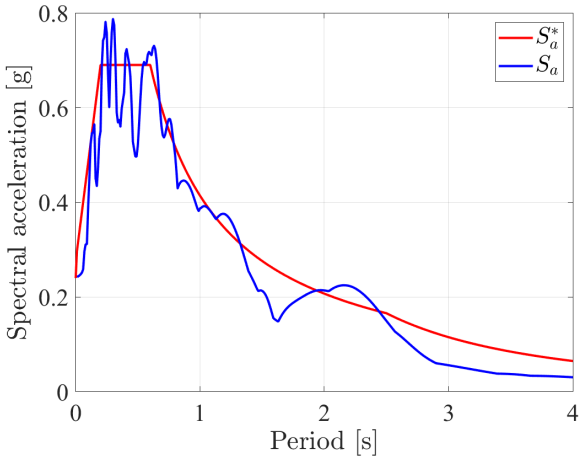


Figure 10: Comparison of the matching between the target EC8 elastic response spectrum $S_a^*$ with the produced accelerogram's response spectrum $S_a$.

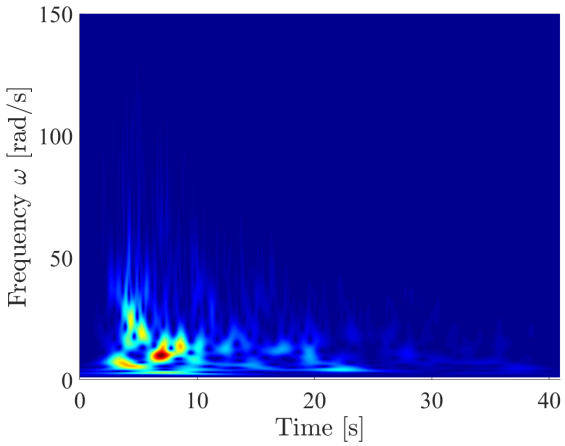


Figure 11: CWT modulus Scalogram of the new generated accelerogram.

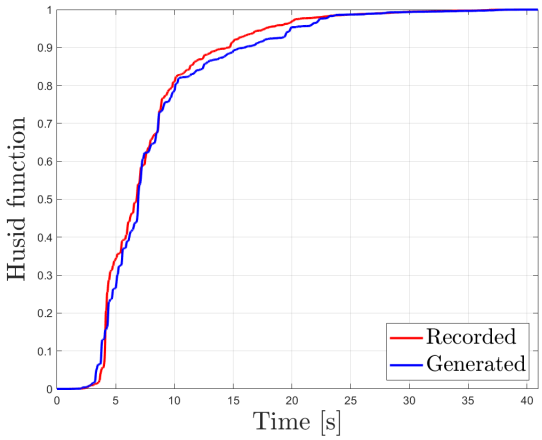


Figure 12: Comparison of the Husid function plot of the recorded ground motion with the generated accelerogram.

## 5 CONCLUSIONS

A novel stochastic methodology for the generation of artificial accelerograms by combining the Spectral Representation Method with the Continuous Wavelet Transform method is proposed. The temporal and frequency non-stationarity is modeled after a recorded accelerogram from the site of interest. The methodology produces good results by generating accelerograms that are fully non-stationary and spectrum-compatible. However, the model is in the early stages of development, thus issues concerning better energy preservation for modeling the temporal non-stationarity and a probabilistic treatment using more historical records will be addressed in future work.

## 6 ACKNOWLEDGEMENTS

The research project was supported by the Hellenic Foundation for Research and Innovation (H.F.R.I) under the "2nd Call for H.F.R.I. Research Projects to support Post-Doctoral Researchers" (Project Number: 1261). This support is gratefully acknowledged.

## REFERENCES

[1] M. Georgioudakis, M. Fragiadakis, Selection and scaling of ground motions using multi-criteria optimization. *Journal of Structural Engineering*, **146**(11):04020241, 2020.

[2] CEN (European Committee for Standardization), *EN1998-1: Design of structures for earthquake resistance. Part I: General rules, seismic actions and rules for buildings*. Brussels, Belgium, 2004.

[3] D. M. Boore, Simulation of ground motion using the stochastic method. *Pure applied geophysics*, **160**, 635—676, 2003.

[4] M. Shinozuka, G. Deodatis, Simulation of stochastic processes by spectral representation. *Applied Mechanics Reviews (ASME)*, **44**(4), 191–204, 1991.

[5] E. H. Vanmarcke, *Developments in Geotechnical Engineering, volume 15, Chapter 8: Structural Response to Earthquakes*, Elsevier, 1976.

[6] P.D. Spanos, L.M. Vargas Loli, A statistical approach to generation of design spectrum compatible earthquake time histories. *International Journal of Soil Dynamics and Earthquake Engineering*, **4**(1), 2–8, 1985.

[7] A. Preumont, The generation of non-separable artificial earthquake accelerograms for the design of nuclear power plants. *Nuclear Engineering and Design*, **88**(1) 59–67, 1985.

[8] P. Cacciola, A stochastic approach for generating spectrum compatible fully nonstationary earthquakes. *Computers and Structures*, **88**, 889–901, 2010.

[9] J. Liang, S. R. Chaudhuri, M. Shinozuka, Simulation of nonstationary stochastic processes by spectral representation. *Journal of Engineering Mechanics*, **133**(6), 616–627, 2007.

[10] T. Huang, M. Lou, H. Chen, N. Wang, An orthogonal Hilbert-Huang transform and its application in the spectral representation of earthquake accelerograms. *Soil Dynamics and Earthquake Engineering*, **104**, 378–389, 2018.

[11] P.D. Spanos, G. Failla, Evolutionary spectra estimation using wavelets. *Journal of Engineering Mechanics*, **130**(8), 952–960, 2004.

[12] L.E. Suárez, L. A. Montejo, Generation of artificial earthquakes via the wavelet transform. *International Journal of Solids and Structures*, **42**(21–22), 5905-5919, 2005.

[13] D. Wang, F. Yu, F. Kong, J. Xu, Simulation of fully nonstationary random processes using generalized harmonic wavelets. *Mechanical Systems and Signal Processing*, **181**, 109468, 2022.

[14] C.K. Chui, R.C. Taylor, *An Introduction to Wavelets, Vol. I*. Academic Press, 1992.

[15] P. Cacciola, P. Colajanni, G. Muscolino, Combination of Modal Responses Consistent with Seismic Input Representation. *Journal of Structural Engineering*, **130**(1), 47–55, 2004.

[16] E. H. Vanmarcke, Properties of Spectral Moments with Applications to Random Vibration. *Journal of the Engineering Mechanics Division*, **98**(2), 425–446, 1972.

[17] H. Yanni, M. Fragiadakis, I. P. Mitseas, A novel method for the stochastic generation of artificial accelerograms. *5$^{th}$ Panhellenic Conference on Earthquake Engineering and Engineering Seismology*, Athens, Greece, 2022.

[18] PEER (Pacific Earthquake Engineering Research Center). "Shallow crustal earthquakes in active tectonic regimes." Accessed December 14, 2022. http://ngawest2.berkeley.edu.

[19] MathWorks, MATLAB version 2018b [Computer Program].

COMPDYN 2023
9th ECCOMAS Thematic Conference on
Computational Methods in Structural Dynamics and Earthquake Engineering
M. Papadrakakis, M. Fragiadakis (eds.)
Athens, Greece, 12-14 June 2023

# EFFECT OF DEBONDING ON GUIDED WAVE PROPAGATION IN STIFFENED COMPOSITE PLATE UNDER OPERATIONAL LOADING AND HYGROTHERMAL ENVIRONMENT

**Akshay Prakash Kalgutkar[1], and Sauvik Banerjee[2]**

[1] Research scholar, Department of Civil Engineering,
Indian Institute of Technology Bombay, Mumbai, 400 076, India
e-mail: akshay_kalgutkar@iitb.ac.in

[2] Professor, Department of Civil Engineering,
Indian Institute of Technology Bombay, Mumbai, 400 076, India
e-mail: sauvik@civil.iitb.ac.in

## Abstract

*Composite stiffened panels are extensively used in a wide range of engineering structures. However, these structures are subjected to external environmental and operational loading conditions, which may cause damage such as interlayer delamination or skin-stiffener interfacial debonding due to the development of enormous stresses. As a result, monitoring the induced hidden flaws and discontinuities in these structures becomes critical. Ultrasonic-guided wave techniques exhibit an efficient and accurate approach for monitoring discontinuities or damages in composite structures. The current study proposes a multiphysics numerical simulation using commercially available finite element software COMSOL Multiphysics to study guided wave propagation in a stiffened composite plate debonded at the plate-stiffener interface with a piezoelectric transducer subjected to in-plane mechanical load and hygrothermal environment. The plate and PZT patch are modelled using the brick element, and the debond is simulated using a through-width groove of 0.1 mm depth in the attached stiffener. A detailed parametric investigation considers the variations in debonding size, in-plane load and hygrothermal load intensity. The results show that the magnitude of the A0 mode is high in the bonded panel, whereas the S0 mode amplitude is low. In contrary, the scattered wave shows high S0 mode amplitude and a relatively low A0 mode amplitude in the debonded panel. Furthermore, as the magnitude of the compressive edge load increases, the group velocity of the A0 mode decreases, whereas, the group velocity of the S0 mode doesn't change significantly. Also, the size of time interval of the A0 mode packet and its amplitude reduce with the rise in the moisture concentration.*

**Keywords:** Debonded stiffened composite panel, guided wave, in-plane edge load, hygrothermal load, COMSOL Multiphysics, piezoelectric patches.

## 1 INTRODUCTION

Thin-walled structures are usually supported on the stiffener to enhance the structural strength without significantly increasing to overall weight. However, the stiffened plate is vulnerable to damage such as fibre breakage, interlayer delamination or skin-stiffener debonding caused by the external in-plane load or extreme environmental conditions. Sometimes, these damages are not always detectable through visual inspection. These discontinuities may advance progressively, leading to catastrophic failure if not inspected and repaired in the early stage. It is observed that damage detection in the composite structure is more intricate when compared to the metallic forms due to its anisotropic [1, 2] and diverseness in the arrangement of plies. Therefore, it is imperative to evaluate the health of the composite material. Today, many nondestructive testing (NDT) methods are available that can easily detect and feature the surface and internal structural discontinuities without causing any damage. Some of them are ultrasonic C-scan [3], ultrasound wave distortion indicator [4], and laser ultrasonic [5], to name a few. These techniques are costly and time-consuming to use for inspecting large structures. On the other hand, monitoring damages or discontinuities in composite structures can be done efficiently and accurately using ultrasonic-guided wave (GW) methods. To develop infallible damage monitoring systems, it is necessary to have a thorough understanding of the quantitative characteristics of ultrasonic-guided waves that travel through composite laminates.

Lamb wave-based damage detection methods have been widely used to inspect thin structures [6]. The detection of debond [7-9] or low-velocity impact damage in stiffened composite panels [10] has been the subject of numerous numerical simulations and experiments using an actuator-sensor network. However, these techniques have difficulty dealing with general stiffened composite panels. Because of the multi-mode characteristics, dispersion, and direction dependence of the wave velocity, lamb wave propagation in composite plates is complicated [11]. Analyses can become more complex as a result of the addition of stiffeners. Finite element analysis and experiment were used by Guo and Cawley [12] to study the interaction of the S0 Lamb mode with delamination. The transmission and mode conversion of Lamb waves across adhesively bonded lap joints were investigated by Lowe et al. [13] employing finite element method (FEM).

Despite some progress, the knowledge of Lamb wave propagation in stiffened panels is still largely restricted to homogeneous and isotropic plates. To eliminate the direction dependence of the Lamb wave velocity, most researchers have concentrated on quasi-isotropic composite panels. Through FE simulations and experiments, Ramadas et al. [14] investigated the incident A0 mode interaction with a T-joint structural discontinuity in a composite structure. The authors noticed that a converted S0 mode is generated with the interaction of A0 mode with the junction. Han et al. [15] conducted a thorough investigation of the interaction between GW signals and structural discontinuity. The study demonstrated that when a signal propagates through a T- stiffener, a variety of modes are generated.

Chen and Wilcox [16] examine the effects of axial load on the guided wave characteristics. They showed that at low frequency-thickness values, the change in phase velocity caused by applied strain is nonlinear. Further, Lee et al. [17] demonstrated that a change in applied load primarily affects the time or phase of the scattered Lamb wave signals. In another study, Michaels et al. [18] looked into the effects of uniaxial loading on signals. The scatter signal's amplitudes were seen to rise monotonically as the load increases, but their shapes did not significantly alter. In order to account for changes in phase shifts and signal amplitude, Roy et al. [19] developed a load compensation model for ultrasonic-guided waves based structural

health monitoring (SHM). The literature shows that no study investigates the scattered wave response in the plate with debonding subjected to the external loading condition.

On the other hand, many researchers have examined the effects of temperature variations on Lamb wave propagation through experimentation. Generally, Lamb wave amplitude and arrival time are typically impacted by temperature variations [20]. In an experimental study, Boon et al. [21] showed that rising temperature reduces the group velocity of the wave. Later, to investigate the effects of changes in plate material properties on Lamb wave propagation due to temperature variations, Roy et al. [22] conducted the parametric studies using numerical wave propagation simulations. To understand the behaviour of Lamb modes due to change in ambient temperature, Sikdar et al. [23] performed a combined theoretical analysis, time-domain spectral element simulation and experimental analysis of elastic wave propagation in a carbon-fibre reinforced adhesively-bonded composite structure. Dan et al. [24] introduced the Equivalent Wave method (EWM) for developing new Rayleigh-Lamb equations with temperature-dependent variables. Without prior knowledge of the temperature dependencies of the material properties, EWM facilitates the prediction of the Lamb wave behaviour with temperature. Few studies have been done to investigate the impact of moisture concentration on the scattered wave response, aside from the analysis of the wave response under the influence of temperature. The effect of moisture absorption on the propagation of Lamb waves in viscoelastic composite materials was studied by Schubert and Herrmann [25]. They have demonstrated that moisture absorption results in a significant decrease in the sensor response's amplitude, which is linked to both changes in the material's and the adhesive layer's properties, and a relatively minor decrease in Lamb wave velocity in composite materials.

From the review, only few numerical techniques have been developed to simulate the hygral effect on the scattered wave response. Recently, a good amount of research has been carried out on the guided wave response in the panel under in-plane edge or operational loading conditions. However, as evidenced by the preceding literature, only a few works have considered GW response study in the panel debonding between the skin and stiffener interface. It becomes practically essential to consider the effect of the environmental condition and external loading on analysing the wave response in the plate with plate-stiffener interfacial debonding, which remains unexplored and inadequately represented.

The current investigation deals with the influence of environmental effect and loading effect on the GW response of the interfacial debonded stiffened panel while taking into account the residual stress generated due to hygrothermal load and in-plane load. A numerical study is conducted using FE simulation software "COMSOL Multiphysics". The current model considers two critical mechanisms coupled to each other to investigate the influence of in-plane edge load and hygrothermal load on GW propagation. A through-width groove of 0.1 mm depth is added to the lower surface of the stiffener to simulate debonding in the model. Furthermore, a preliminary non-linear numerical analysis is carried out to consider the impact of loading. The investigation is carried out in two stages. To start, a static analysis is performed to determine the stress that is induced due to mechanical and hygrothermal loading. The stress developed in the static study is employed as the initial condition to carry out guided wave investigation, which is a time-dependent investigation that employs an implicit time-step analysis. A detailed parametric investigation is carried out by considering the variations in debonding size, in-plane load and hygrothermal load intensity on the behaviour of the guided wave using different wave features.

## 2 MODELLING APPROACH IN THE COMSOL MULTIPHYSICS

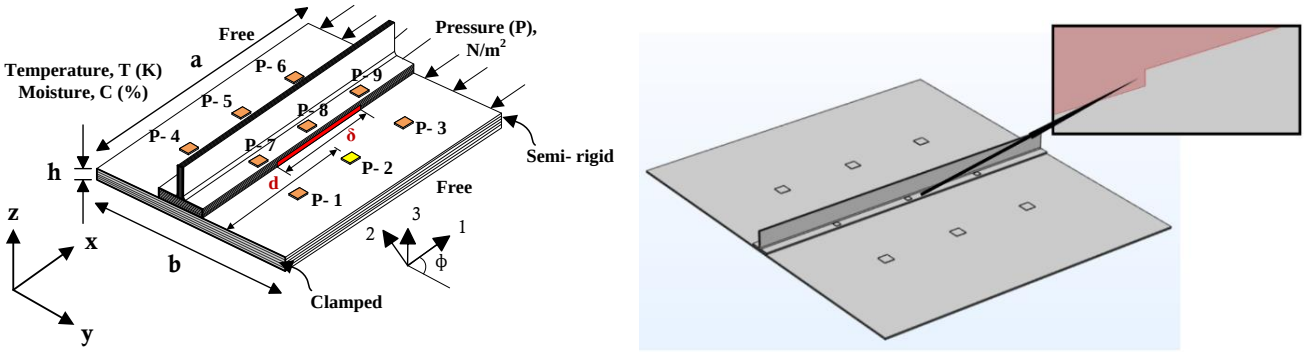


(a) (b)

Figure 1: (a) Model of stiffened panel attached with the piezoelectric patches, (b) Debonded stiffened panel modelling in COMSOL.

This study aims to investigate the wave propagation behaviour in a T-stiffened composite plate with interfacial debonding attached with PZT patches using finite element modelling. The finite element analysis (FEA) is completed with the software package COMSOL Multiphysics version 5.5. The current study is conducted on the T-stiffened panel that is debonded at the plate-stiffener interface and exposed to external environmental and in-plane loading. The panel has a dimension of a, b, and h in the x, y, and directions, respectively. The T stiffener is attached on the top surface of the panel, which has a flange of $b_f \times t_f$ and a web of $t_w \times d_w$. The panel is exposed to the non-mechanical load of temperature 'T' and moisture 'C', as shown in Fig. 1 (a). This section overviews the settings and initial setup of COMSOL employed for this research. The current study considers the solid mechanics and electrostatics modules coupled with piezoelectric effect multiphysics. Finally, the two steps studies are carried out with an initial stationary study to carry out the stress analysis due to in-plane load or hygrothermal load, followed by the time-dependent study to simulate the wave propagation study in the stressed plate.

### 2.1 Physics of simulation

The physics of simulating GW in the stiffened composite panel under load conditions or hygrothermal environment is simplified and shown in Fig. 1 (a). A stiffened plate is loaded at one end and fixed on the other end. Nine piezoelectric sensors (PZT 1 to PZT 9) are mounted on the plate and stiffened flange surface, as shown in Fig. 1(a). The current study ignores the adhesive layer because the load introduce has little influence on it [26]. As a result, one simulation model should integrate the acoustoelastic effect, piezoelectric effect, and loading influence on piezoelectric sensors. In addition, the static load is considered. Thus, the GW excitation and response process must be simulated under static load conditions. Considering the above-discussed physics, the multiphysics module called the Piezoelectric effect is adopted, as shown in Fig. 2. The mechanics features of the stiffened composite plate and the piezoelectric sensors are simulated using solid mechanics physics, while the electric features of the piezoelectric sensors are simulated using electrostatics physics. However, these two physics are coupled by the Multiphysics-Piezoelectric Effect. The details of the steps carried out in each physics of the simulation are explained elaborately as follows:

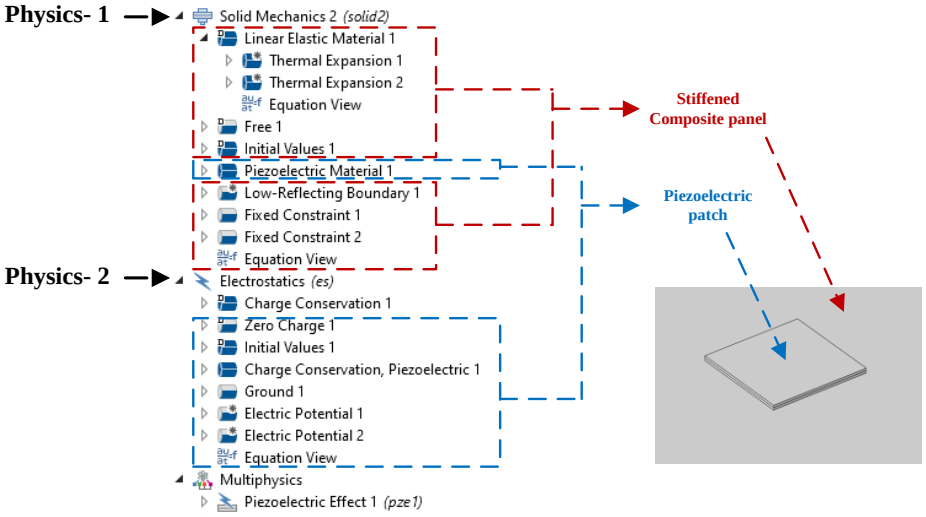


Figure 2: The simulation physics in COMSOL of GW propagation under thermal condition

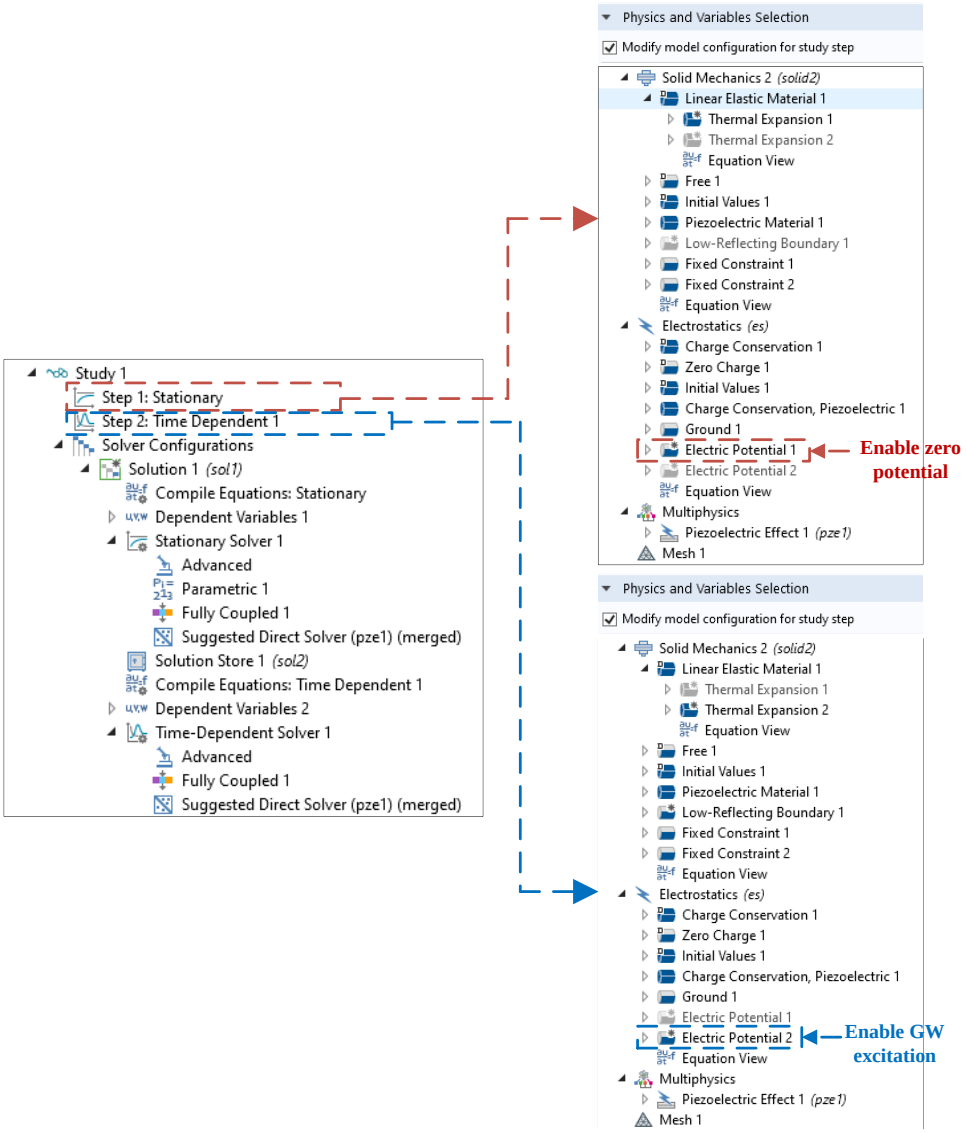


Figure 3: The solver settings of the Multiphysics simulation model.

**Solid Mechanics:**

- Initially, the material behaviour with the properties for the stiffened panel and the piezoelectric patches are assigned using the linear elastic material and piezoelectric material options, respectively.
- The Fixed Constraints and Prescribed Displacement options are used to simulate boundary conditions, while the Boundary Load option is used to apply an external in-plane load to the plate.
- Similarly, the hygrothermal load is applied as the lumped mass using the thermal expansion and hygroscopic swelling option under the linear elastic material model.
- Furthermore, the opposite edges of the stiffened plate are constraints such that in-plane is not allowed. As the current investigation is carried out using two studies, the load, regardless of the external in-plane load or hygrothermal load, is applied as the two loading options. In the static study, the load is applied incrementally to converge the results well. Further, the load is directly applied in one step so that the applied load is maintained constant during the time-dependent step.
- Low-Reflecting Boundary is employed to reduce the boundary edge reflection of GW. The damping type is set to be "User defined", with the mechanical impendence set to density times the average of P and S waves velocities.
- Piezoelectric material combined with Electrostatics is employed to simulate the piezoelectric sensors.

**Electrostatics:**

- This physics, along with the piezoelectric material option, is employed to the geometry that is used as the piezoelectric sensors.
- The lower surface of all the piezoelectric sensors are grounded to zero electric potential using the Ground option.
- Similar to the loading, electric potential is applied in two devises, Electric Potential 1 and Electric Potential 2, which are set to zero potential and a voltage waveform of the GW excitation, respectively. They are applied on the upper surface of the piezoelectric patch that is used as an exciter. However, there are mutually exclusive in the subsequent studies, which will be explained in section 2.2.

Further, the elastic properties of the piezoelectric patches are coupled with the electrical properties with the use of the Piezoelectric Effect option in the Multiphysics module.

## 2.2 Study solver of simulation

The current study considers two study steps for solving the considered multiphysics model, as shown in Fig. 3. The first step is carrying out the stress analysis using the stationary study. The load is employed incrementally to improve the convergence of the result. Further, the results of the stationary study are used as the initial value of the time-dependent study, which simulates the process of GW excitation-propagation-response under the loading condition.

Fig. 3 presents the physics setting for each study step. In the stationary study, zero voltage is applied on the surface of the actuator patches. This directly shows that Electric Potential 1 of zero potential is enabled, but Electric Potential 2 of GW excitation is disabled. This is carried out to avoid the generation of the DC bias voltage, which would introduce the stress caused due to the load. However, if the DC bias voltage is induced, it would be a step excitation in the time-dependent study initiating a wideband GW propagating on the stiffened plate leading to a false GW response signal output from receiver PZTs [27]. Further, it is observed that

when the stress induced in the plate is high, the receiver PZT produces a false output signal due to improper convergence of the result of Step 1. Further, load ramping is performed using an auxiliary sweep technique, in which the load is applied incrementally to improve convergence. In the time-dependent step, Electric Potential 1 is disabled, and Electric Potential 2 is enabled for GW excitation. Thus, the GW signals for different parametric conditions can be obtained. Guided wave simulation is carried out by employing a generalised alpha method time stepping method with a constant time step of $5\times10^{-8}$ s.

## 3 PROBLEM DESCRIPTION AND SIGNAL PROCESSING TECHNIQUES

### 3.1 Problem definition

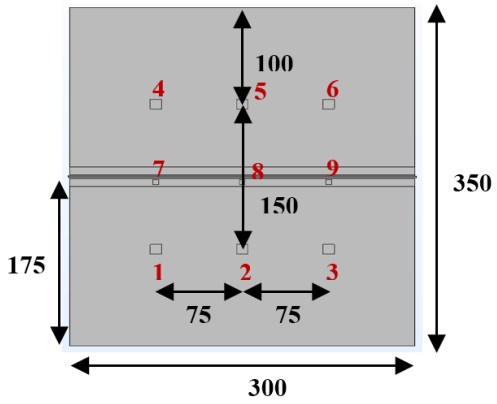


Figure 4: Arrangement of PZT patches on the surface of stiffened composite panel.

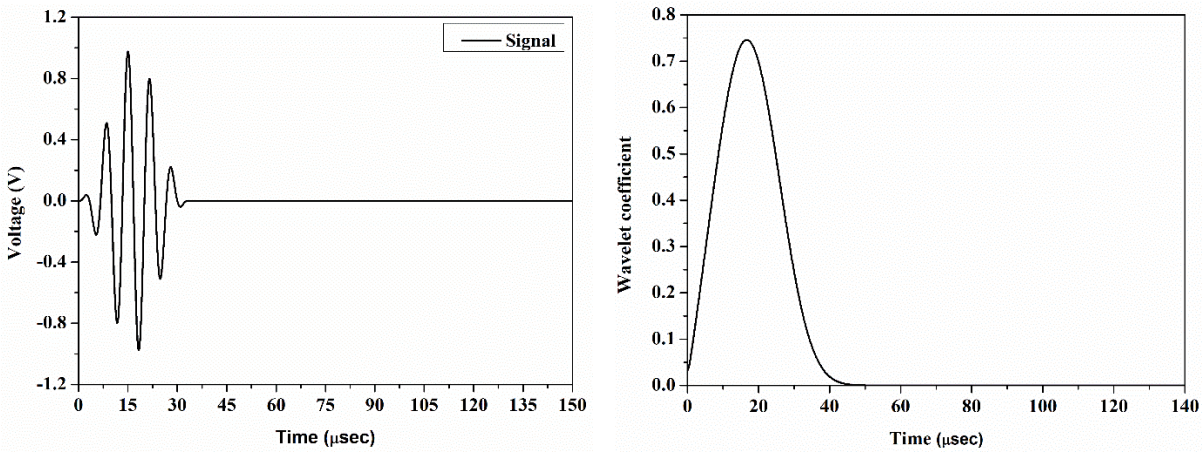


(a) (b)

Figure 5: 5-cycle Hanning window response excited at 150 kHz and (b) Wavelet of the response at 150 kHz frequency.

The investigation is conducted on the stiffened composite panel with the $0^o$ ply orientation, i.e., fibres along the length of the attached stiffener. The plate with length, a= 300 mm, breadth, b= 350 mm and thickness, h= 2 mm, is considered, which is exposed to the non-mechanical load with a reference temperature of 300 K and reference moisture of 0.0 %. In this investigation, the centrally placed T-stiffener is considered with the width of the flange $b_f$ of 20 mm, and thickness $t_f$ is considered to be 2 mm, whereas the depth $d_s$ and width $b_s$ of the web are 18 mm and 2 mm, respectively. The debond of length 'δ' is introduced at the inter-

face of the stiffener and plate at the distance of 'd' from the clamped edge. The investigation considers nine piezoelectric patches from P-1 to P-9, with the centre to centre distance of 75 mm along the length and 150 mm along the plate's width between P1 to P-9 PZT, as shown in Fig. 4. Piezoelectric patches of P-7 to P-9 are attached to the surface of the stiffener flange, having a size of 5 mm x 5 mm with a thickness of 0.4 mm. The size of PZT P1 to P6, which are attached to the plate, has dimensions of 10 mm x 10 mm and a thickness of 0.4 mm. In the current study, the PZT- 2 is used as the actuator through which the 5-cycle sine pulse modulated with Hanning window, shown in Fig. 5, is employed as the input pulse, with all of the other PZTs acting as receivers to obtain the scattered wave in the structure. Hanning pulse is defined as:

$$F(t)= 0.5\times (1-\cos(2\times\pi\times f\times t/N)) \times\sin(2\times\pi\times f\times t) \quad (1)$$

The panel under consideration is clamped at one end and semi-rigid conditions on the other. In the case of the semi-rigid condition, the edge (i.e., x= a) is restrained in all the transverse and rotational directions but free to move in the in-plane loading direction. Furthermore, the panel is maintained free on the edge parallel to the stiffener position (i.e., y= 0 and y=b), as shown in Fig. 1(a). To reduce the boundary edge reflection of the scattered wave, Low-Reflecting Boundary is employed with damping set to "User defined", with the mechanical impendence set to density times the average of P and S waves velocities.

### 3.2 Structural meshing

The current study employs a physics-controlled Tetrahedral mesh, with the mesh size determined by the wavelength of GW. Based on the literature [8], the Courant-Friedrichs-Lewy (CFL) convergence conditions suggest that the widest mesh be less than 1/6 of the wavelength of the wave modes. For instance, when the Hanning pulse is excited with 150 kHz in a 2 mm thick composite plate, the wavelength of S0 mode is nearly 14.9 mm, and the wavelength of A0 mode is found to be 6.78 mm from the dispersion curve for $0^o$ laminated plate shown in Fig. 7. Further from the Courant-Friedrichs-Lewy criteria, the mesh size should be less than 1.13 mm, leading to high computational cost. For the piezoelectric sensors, the smallest mesh size is set to be 1 mm. The complete mesh consists of 1420637 domain elements, 653315 boundary elements, and 10833 edge elements with 3353355 degrees of freedom.

**Courant–Friedrichs–Lewy condition**

**Mesh and time step Criteria:**

The CFL condition becomes

$$C = \frac{u_x \Delta t}{\Delta x} + \frac{u_y \Delta t}{\Delta y} \leq 1 \quad \text{and} \quad \Delta x \leq \frac{u_x}{6f}, \quad \Delta y \leq \frac{u_y}{6f} \quad (2)$$

where the dimensionless number C is called the Courant number,

- $u_x$ and $u_y$ is the magnitude of the velocity in the x and y-axis. (whose dimension is length/time)
- $\Delta t$ is the time step (whose dimension is time)
- $\Delta x$ and $\Delta y$ is the length interval (whose dimension is length).

### 3.3 Material properties

Table 1: Elastic moduli of carbon/epoxy at various temperatures; $G_{13} = G_{12}$, $G_{23} = 0.4G_{12}$, $\upsilon_{12} = 0.3$, $\alpha_1 = -0.3\times10^{-6}$/K and $\alpha_2 = 28.1\times10^{-6}$/K. C= 0.0 %

| **Elastic Moduli** | **Temperature T (K)** | | | | | |
|---|---|---|---|---|---|---|
| **(GPa)** | 300 | 325 | 350 | 375 | 400 | 425 |
| $E_1$ | 172.5 | 172.5 | 172.5 | 172.5 | 172.5 | 172.5 |
| $E_2$ | 6.9 | 6.17 | 5.81 | 5.45 | 5.08 | 4.9 |
| $G_{12}$ | 3.45 | 3.45 | 3.16 | 2.88 | 2.73 | 2.59 |

The present investigation mainly focuses on the wave propagation response of a debonded stiffened composite panel under the influence of in-plane edge load and hygrothermal conditions. The material properties of the composite laminated panel and stiffener cases considered in this study are presented in Tables 1 and 2 for different temperatures and moisture concentrations. These properties have been referred from Parhi et al. [28] work.

Table 2: Elastic moduli of carbon/epoxy at various moisture concentrations; $G_{13} = G_{12}$, $G_{23} = 0.4G_{12}$, $\upsilon_{12} = 0.3$, $\beta_1 = 0$ and $\beta_2 = 0.44$. T= 300 K

| **Elastic Moduli** | **Moisture Concentration, C%** | | | | | |
|---|---|---|---|---|---|---|
| **(GPa)** | 0.25 | 0.50 | 0.75 | 1.00 | 1.25 | 1.50 |
| $E_1$ | 172.5 | 172.5 | 172.5 | 172.5 | 172.5 | 172.5 |
| $E_2$ | 6.72 | 6.54 | 6.36 | 6.17 | 6.17 | 6.17 |
| $G_{12}$ | 3.45 | 3.45 | 3.45 | 3.45 | 3.45 | 3.45 |

Table 3: Material property of piezoelectric sensor (PZT-5A) under loading condition.

| **Parameter** | | **Values** |
|---|---|---|
| **Relative permittivity** | $\varepsilon_{11}$ | 1730 |
| | $\varepsilon_{33}$ | 1700 |
| **Piezoelectric constant ($\times10^{-10}$ C/N)** | $d_{31}= d_{32}$ | $-1.71-1.71\times (0.1328.e^{0.0022.\sigma} - 0.1328.e^{-0.0476.\sigma})$ |
| | $d_{33}$ | 3.74 |
| | $d_{15}$ | 5.84 |
| **Compliance coefficient ($\times10^{-12}$ m$^2$/N)** | $sE_{11}$ | 16.4 |
| | $sE_{12}$ | -5.74 |
| | $sE_{13}$ | -7.22 |
| | $sE_{33}$ | 18.8 |
| | $sE_{55}$ | 4.75 |
| | $sE_{66}$ | 4.43 |
| **Density (kg/m3)** | $\rho$ | 7750 |
| **Elastic properties (GPa)** | $E_{11}= E_{22}$ | 60.97 |
| | $E_{33}$ | 53.19 |
| **Poison ratio** | $\nu_{13}= \nu_{23}$ | 0.4402 |
| | $\nu_{12}$ | 0.35 |

Similar to the degradation of the elastic properties of the composite material, the external load change the piezoelectric material's electrical properties. Table 3 shows the material properties of the piezoelectric sensors PZT-5A as a function of loading. It is observed that only the $d_{31}$ parameter is varied when the plate is under the action of external load, and an em-

pirical relation referred from the work of Qiu et al. [27] is employed in which σ is the applied pressure in MPa.

Table 4: Material property of piezoelectric sensor (PZT-5A) under elevated temperature.

| Parameter | | At T= 300 K | Elevated temperature (ΔT= T-273), K |
|---|---|---|---|
| **Density (kg/m$^3$)** | ρ | 7750 | $7751.80 - 7.26e^{-02}\Delta T$ |
| **Elastic properties** | $E_{11}= E_{22}$ | 60.97 | $60.45 + 2.09e^{-02}\Delta T$ |
| **(GPa)** | E33 | 53.19 | $52.95 + 9.8e^{-03}\Delta T$ |
| | $\nu_{13}= \nu_{23}$ | 0.4402 | $0.43 + 3e^{-04}\Delta T - 3e^{-06}(\Delta T)^2 – 1e^{-09}(\Delta T)^3$ |
| **Poison ratio** | $\nu_{12}$ | 0.35 | $0.35 + 2e^{-04}\Delta T - 8e^{-07}(\Delta T)^2 + 2e^{-09}(\Delta T)^3$ |
| | $d_{31}= d_{32}$ | -171 | $170.78 – 7.1e^{-03}\Delta T+6e^{-04}(\Delta T)^2 + 2e^{-16}(\Delta T)^3$ |
| **Piezoelectric constant** | $d_{33}$ | 374 | $369.12 +1.49e^{-01}\Delta T+1.9e^{-03}(\Delta T)^2$-4e-$^{09}$ $(\Delta T)^3$ |
| **(×10$^{-12}$ C/N)** | $d_{15}$ | 584 | 584 |

Further, thermal load has an impact on both the piezoelectric material's electrical and elastic properties and are shown in Table 4. The density, elastic properties and piezoelectric parameters are varied for different intensities of temperature. Further, for obtaining the value of the different material constant, an empirical relation referred from the work of Roy et al. [22] is employed, where ΔT is the elevated temperature from 273 K temperature. However, no existing literature on the influence of moisture on piezoelectric properties is available. Hence, the piezoelectric constant at the reference temperature of 300 K is used for the elevated moisture concentration, and only the elastic properties of the composite material are varied, as presented in Table 2.

### 3.4 Signal processing techniques

The characteristics of guided waves have been thoroughly investigated using conventional non-destructive evaluation, making them an intriguing technique for inspecting intricate structures. Inspection of complex structures is difficult due to the generation of new modes or the reflections from overlapping features. Therefore, determining the number and amplitude of the wave packets present in ultrasonic time traces is essential for creating a robust guided wave inspection system that can identify changes in the measured signal over time caused on by particular parameters. To resolve closely spaced events and distinguish the parametric changes caused by structural features, an appropriate and reliable signal processing tool for structural health monitoring is therefore required. Hence, in the current investigation, the peak of the wave modes and Continous wavelet coefficient (CWT) along with the correlation coefficient of the response are used as a tool for measuring the wave features.
The continuous wavelet transform is defined as follows

$$CWT_x^{\psi}(\tau,s) = \Psi_x^{\psi}(\tau,s) = \frac{1}{\sqrt{|s|}}\int x(t)\ \psi^*\left(\frac{t-\tau}{s}\right)dt \tag{3}$$

where s and τ is the scaling and the translation parameters, respectively. ψ(t) is the transforming function, and it is called the mother wavelet.

Further, the Correlation Coefficient is used to compare the signal from the various parameters with a signal of the bonded plate subjected to no loading conditions. The correlation coefficient of two random variables is defined as

$$\rho(A,B) = \frac{1}{N-1}\sum_{i=1}^{N}\left(\frac{A_i - \mu_A}{\sigma_A}\right)\left(\frac{B_i - \mu_B}{\sigma_B}\right) \tag{4}$$

where $\mu_A$ and $\sigma_A$ are the mean and standard deviation of signal A, respectively, and $\mu_B$ and $\sigma_B$ are the mean and standard deviation of response B.

## 4 RESULTS AND DISCUSSION

This section discusses the theoretical investigation of the scattered guided wave response characteristics in debonded stiffened panels subjected to in-plane edge loading and hygrothermal environment using COMSOL Multiphysics. In order to comprehend the effects of in-plane loading and hygrothermal conditions on the structure, the scattered wave response in the stiffened plate is investigated in this work. Various signal processing techniques are used to investigate the signal's features.

### 4.1 Validation study of the wave response

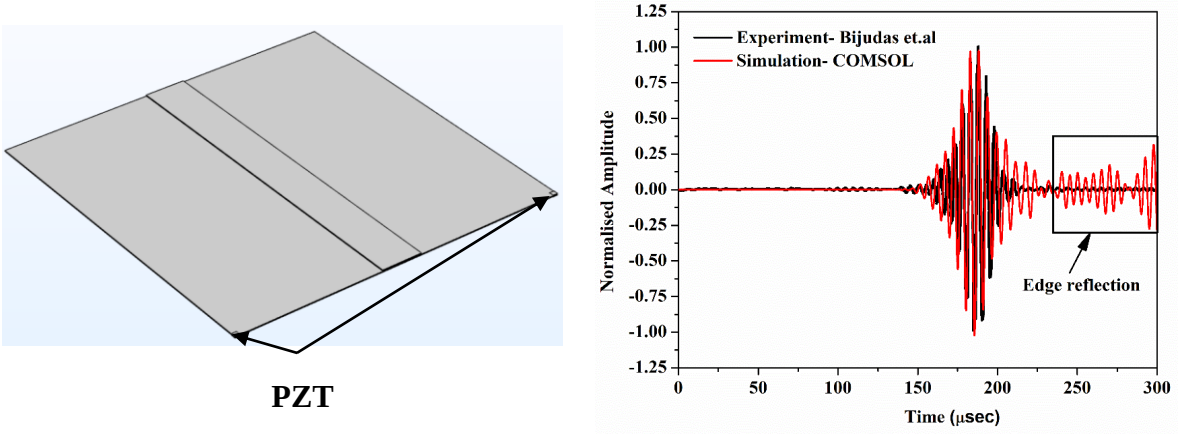


(a) (b)

Figure 6: (a) current COMSOL Multiphysics model, (b) Validation study of the wave response in the stiffened aluminum panel.

To carry out any numerical simulation, it is necessary to validate the outcomes of the developed model against the response of the existing available literature. In the current work, the guided wave response of the spread-stiffened panel obtained from the current simulation is compared with the experimental results of Bijudas et al. [29]. The experiment is carried out on an aluminum-stiffened panel with a spread stiffener attached across its width at the centre of the panel. The PZT patches are attached to the top and bottom surfaces of the panel in order to generate a specific wave mode by adjusting the polarity of the actuating signal. A square piezoelectric patch is attached at the one corner of the panel, and the response is captured using top and bottom bonded PZT on the other end corner. The study is conducted by exciting the 8-cycle Hanning window at 200 kHz. The current study response is plotted against the exist-

ing work response in Fig. 6 (b). To compare the two signals, the response is normalised using the min-max normalisation method. The results show that the first wave packet from 150 μsec to 220 μsec closely matches each other. However, a wave packet due to edge reflection is observed after 225 μsec. This is due to the attachment of receiver PZT at other edges of the simulated panel, which is not the case in the experiment setup, as the PZT is attached far from the edge to avoid reflection. As a result, the current model can be used to carry out parametric investigations considering the effect of in-plane edge and hygrothermal conditions.

## 4.2 Effect of excitation frequency on the amplitude of the scattered wave

Prior to conducting the parametric study with guided wave, it is essential to identify the various wave modes generated in the structure. To understand the behaviour of the various modes, a slowness curve is initially plotted using the semi-analytical finite element (SAFE) method [30] at 150 kHz frequency, as presented in Fig. 7 (a) to understand the variation of velocity of wave modes in different propagating direction. This study is required due to the anisotropic behaviour of the composite material. The plot shows that the wave propagates with maximum velocity along the fibre direction and gradually drops when the wave travels normal to the fibre direction. Further, the dispersion curve is plotted as shown in Fig. 7 (b) by considering the wave propagating normal to the fibre length to identify the wave modes based on the group velocity for different excitation frequencies.

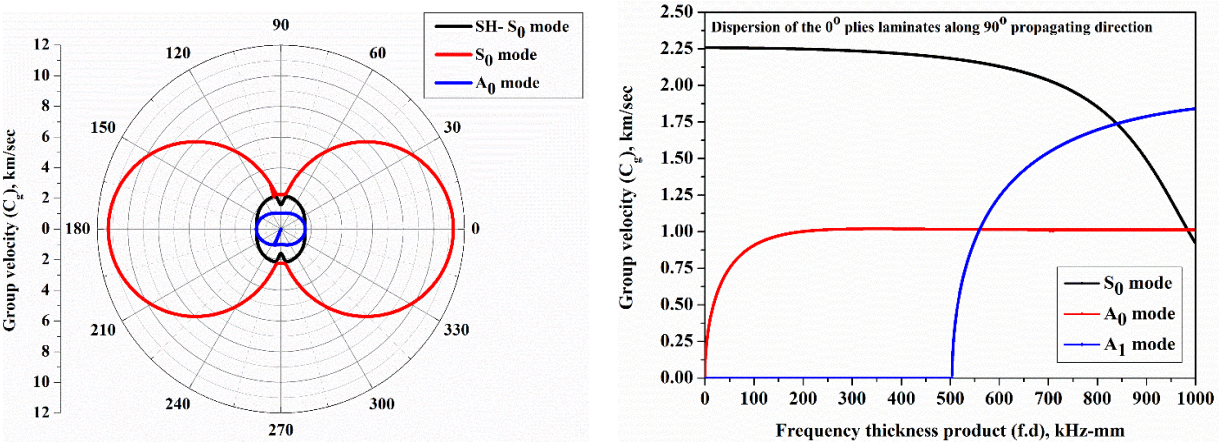


(a) (b)

Figure 7: (a) Slowness curve of the 2 mm panel at 150 kHz excitation frequency (b) Dispersion curve of the 0° laminated panel along 90° propagating direction.

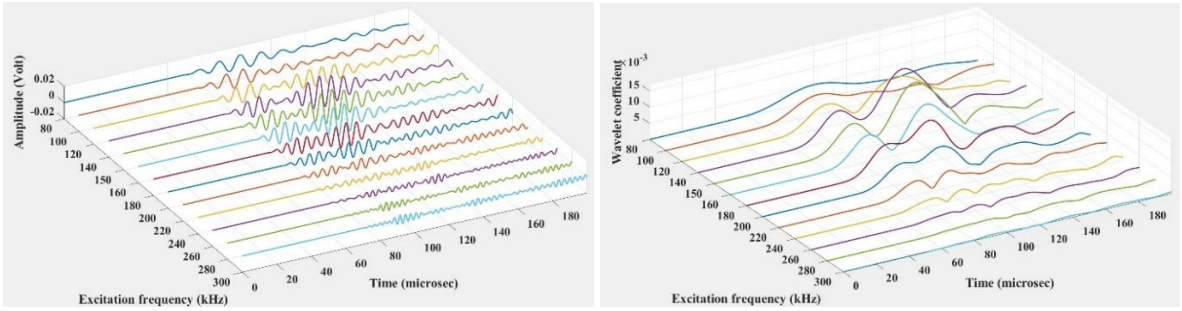


(a) (b)

Figure 8: Wave response and the wavelet plot for different excitation frequencies.

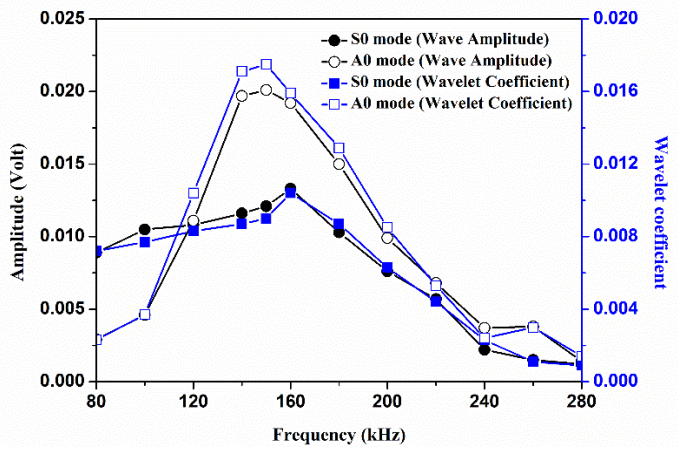


Figure 9: Frequency modulation curve of the 0° T-stiffened composite panel.

Subsequently, in this section, the frequency-amplitude modulation curve is plotted to understand the effect of excitation frequency on the amplitude of S0 and A0 modes. The current investigation is conducted on the bonded rectangular composite stiffened panel with 0° orientated laminates. The 5-cycle Hanning window is used in the study, with the excitation frequency varied from 80 kHz to 280 kHz, and the corresponding peak amplitude and wavelet coefficient of the two fundamental modes (A0 and S0) are recorded. The wave is excited in the panel using the P2 patch, and the response is captured at the P5 patch, such that the exciter and the receiver PZTs are positioned collinearly. Fig. 8 depicts the wave response and the wavelet plot at the corresponding excitation frequency. The frequency modulation curve of the current study is presented in Fig. 9. The obtained response shows that with the rise in the excitation frequency upto 150 kHz, the peak amplitude and wavelet coefficient of A0 mode initially increases, and a further increase in the excitation frequency reduces the signal's amplitude. However, the amplitude and wavelet coefficient of the S0 mode increases upto 160 kHz, and then a drop is noticed with the rise in the signal excitation frequency. Hence, this shows that both the modes have a significant effect when excited at the frequency close to 150 kHz and in the further parametric study, the plate is excited with a 5-cycles Hanning pulse at the 150 kHz frequency using PZT patch P2 unless otherwise specified.

### 4.3 Parametric investigation to understand the effect on the guided wave response

This section investigates the influence of different parameters like debond size, inplane edge load intensity and hygrothermal condition on the scattered wave response in the panel. The study is conducted on the rectangular panel provided with the T-stiffened at the centre. In the current study, the edges at which the stiffened is connected are rigidly held, and the other two edges are freely supported unless the in-plane load is applied. In the case of in-plane load, the non-loaded edge is rigidly connected, while the other edge is made semi-rigid, allowing the plate to move in the loading direction. The current investigation uses 8 PZTs to capture the structure's wave response, with P2 acting as the actuator. In the study, a 5-cycles Hanning window is excited at a frequency of 150 kHz as it significantly influences the wave modes amplitude, as noticed in the previous study. Furthermore, various signal processing techniques, such as CWT peak and correlation coefficient, are used to understand the wave's features under different parametric variations.

### 4.3.1 Effect of debonding size on the scattered GW response

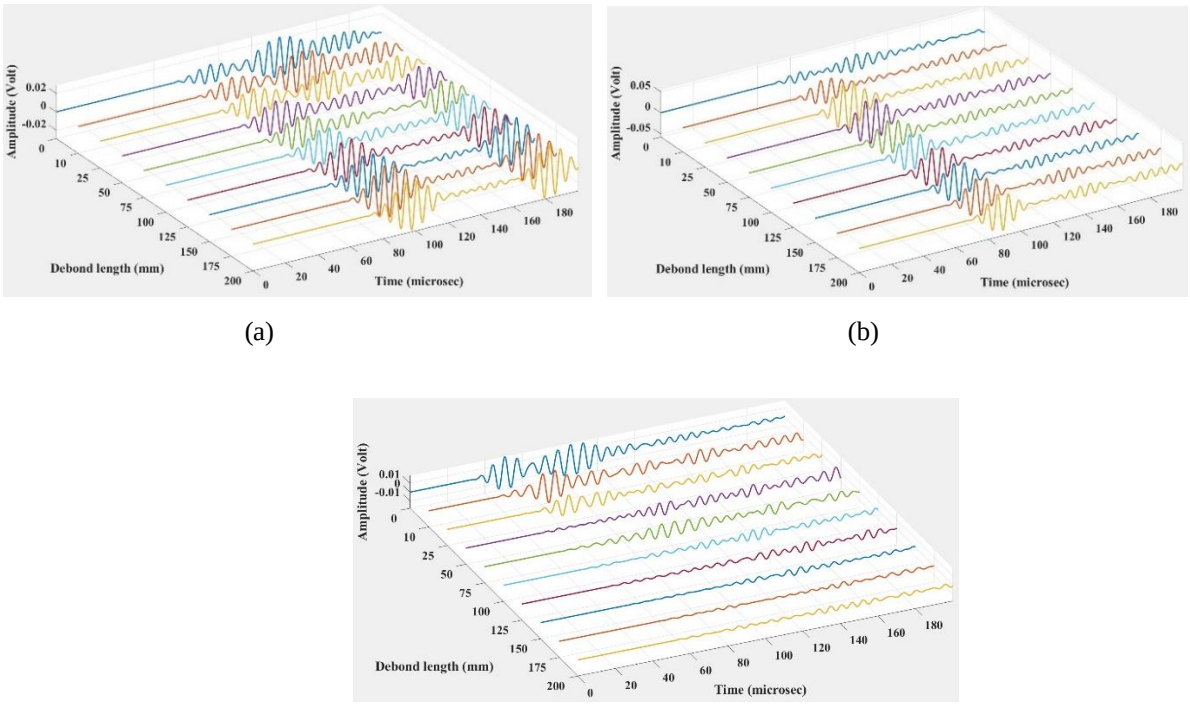


Figure 10: Variation of response for different debonding lengths captured at (a) P4, (b) P5 and (c) P8.

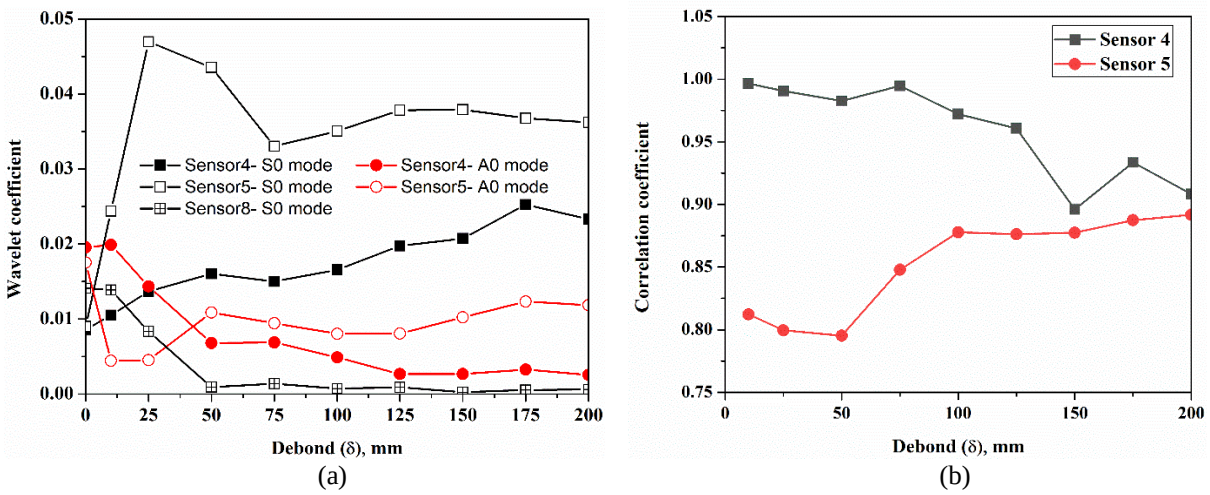


Figure 11: Variation of the (a) wavelet coefficient and (b) correlation coefficient of the wave response for different debonding sizes.

This section provides insight into debonding size impact on the scattered wave response. The current study uses the rectangular stiffened panel to understand the wave response. The investigation is carried out by introducing the debond between the plate and the stiffener in the central region of the panel. The debond is introduced by creating a grove of 0.1 mm depth over a stiffener flange surface so that the plate and stiffener do not come into contact. Also, this will avoid the contact non-linearity developed during the loading time, which increases the computational cost. However, with this type of modelling, the boundary reflection may be captured in the response from the edge of the groove. Fig. 10 shows the wave response in the

panel due to different debonding sizes captured at various PZTs. Fig. 11 (a) shows the wave response that is captured at P4, P5 and P8, and it is observed that the amplitude of the S0 mode of the signal captured through P4 enhances tremendously as the size of debonding increases. However, as the size of the debonding increases, the amplitude of the A0 mode decreases. Similar behaviour is observed in the response captured at the P5 patch, where the peak of the A0 mode wavelet coefficient drops initially with the introduction of debond and then increases marginally with the enhancement in the debond size. On the other hand, the signal captured by the patch P8 attached to the surface of the stiffener shows a reduction in the S0 mode wave amplitude due to debonding. The behaviour of this mode is due to the increase in the signal travel path caused by an increase in the debond size, as the stiffener is not in contact with the panel.

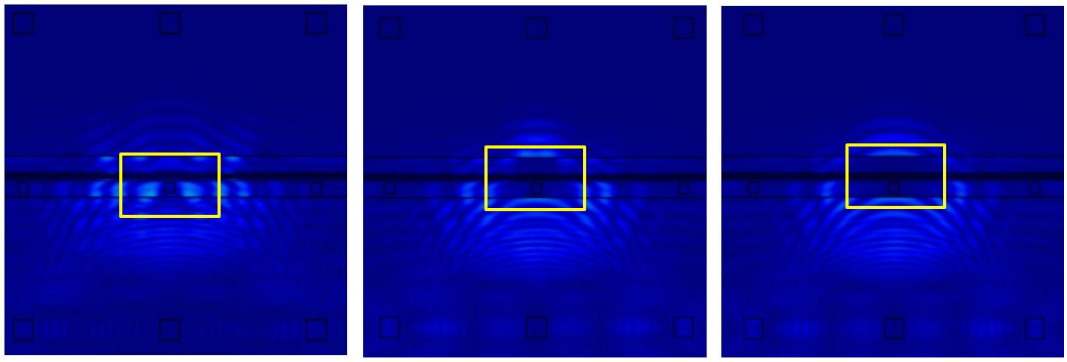

(a) (b) (c)

Figure 12: Top view of the displacement profile of the response around the attached stiffener in the panel provided with (a) δ= 0mm (b) δ= 25mm (c) δ= 50mm.

Further, to have a sight on the propagation of the wave across the debonded region in the stiffener, a displacement plot of the panel with centrally positioned debond of various length is shown in Fig. 12. It can be observed that in the case of the bonded plate, the wave propagates through the stiffener, which is shown by the wavy colour in the highlighted portion. This shows a greater amplitude of the first wave packet in Fig. 10 (c). However, as the debonding length increases, the wave propagates only through the plate in the debonded region, which is shown by a constant colour around the highlighted portion in the displacement plot. This demonstrates the reduction in the amplitude along with the delay in the propagating packet of the response captured by the P8 sensor, as shown in Fig. 10 (c).

The correlation coefficient of the S0 mode of the wave is established to understand the change in the wave response due to debonding, as presented in Fig. 11 (b). In the case of the P4 patch response, the similarity of the debonded condition signal to the bonded condition response decreases as the debonding length increases. However, in the case of the P5 patch response, the correlation coefficient reduces marginally with the initiation of debonding and then increases with the debonding size.

### 4.3.2 Effect of in-plane load on the scattered GW response for different debonding length

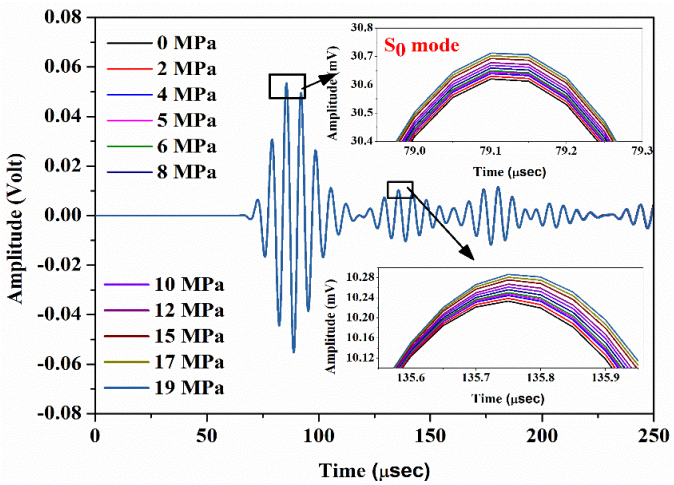


Figure 13: Wave response obtained at P5 sensor for δ= 25 mm.

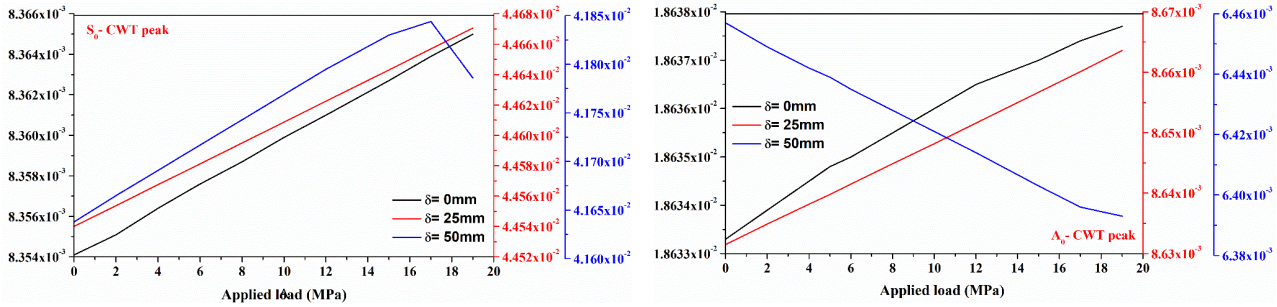


(a) (b)

Figure 14: Variation of the CWT peak of (a) S0 mode and (b) A0 mode obtained at P5 for different debond sizes.

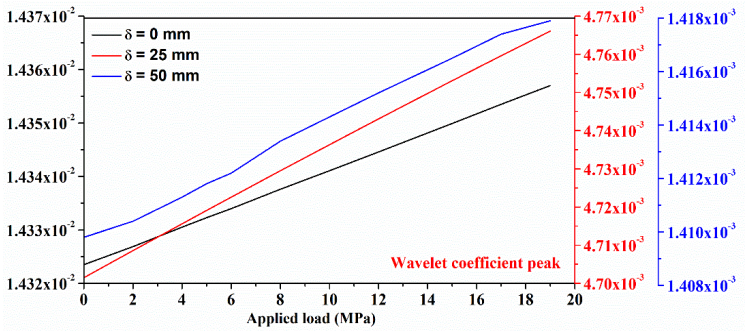


Figure 15: Influence of in-plane load on the CWT peak of the signal obtained at P8 for different debond length

The impact of the in-plane edge on the scattered guided wave response in an interfacial debonded stiffened composite plate is investigated in this section. The current investigation considers three contact conditions: no debond condition and centrally positioned debond of 25 mm and 50 mm centrally induced debond. The investigation is conducted by exciting a 5-cycles Hanning window through the P2 patch, and response is captured at the other eight piezoelectric patches. Compressive loading is applied in terms of pressure at the semi-rigid edge, while the opposite edge is rigidly held. According to the stability study, it is observed that the panel buckles at a pressure of 19.538 MPa, 19.523 MPa and 19.484 MPa for the bonded pan-

el, 25 mm debond panel, and 50 mm debond panel, respectively. Hence, in the current study, the load is applied from 0 to 19 MPa.

Fig. 13 shows the scattered wave response obtained at P5 for the case of the bonded stiffened panel. According to the study, the applied load has minimal effect on the wave response. Furthermore, as the intensity of the pressure increases, the wave amplitude increases marginally for both wave modes. Aside from the reduction in A0 mode amplitude, a slight delay in group velocity is observed. Fig. 14 (a) shows the CWT peak of the S0 mode for various debonding sizes. It demonstrates that the amplitude of the CWT peak rises as the intensity of the applied pressure increases. However, in the case of the 50 mm debonded panel, the peak of S0 mode CWT enhances, and then it starts to drop as the load approaches the buckling load. It can also be observed that the magnitude of the wavelet coefficient peak increases abruptly with the introduction of debonding and further drops, with an increase in the debonding size. However, in the case of the A0 mode wavelet peak, the rise in the magnitude of the peak is observed for the bonded panel and debond of 25 mm, as shown in Fig. 14 (b). Contrary, in the case of a 50 mm debond panel, the magnitude of the wavelet peak drops with the rise in the pressure intensity. Apart from this, the magnitude of the A0 mode CWT peak reduces with the enhancement in the debonding size.

Further, the P8 sensor response is studied using the CWT peak feature of the S0 mode (first packet) of the response for different debonding sizes. From Fig. 15, it is observed that the peak magnitude of the CWT increases with the enhancement in the applied load. However, the magnitude of CWT reduces as the size of debonding increases. This is due to the gap created in the stiffener representing the debond, which will increase the wave's travel path by damping the signal amplitude.

### 4.3.3 Effect of temperature on the scattered GW response for different debonding length

This section investigates the influence of temperature on the scattered wave response for various debonding sizes by maintaining the structure at a uniform temperature throughout the study. As discussed earlier, the temperature will degrade the composite material's elastic properties and the piezoelectric patch's elastic and electrical properties. As a result, temperature-dependent material properties are used in the study. Also, the stability study showed that the panel buckles at the temperature of 524.65 K, 524.42 K and 524.08 K for the bonded panel, 25 mm and 50 mm debonded panel, respectively. Therefore, the current investigation is carried out for the temperature ranging from 300 K to 425 K at an interval of 25 K. Fig. 16 shows the response of the wave captured through the P5 sensor for various temperature intensities and for different debonding lengths by considering a through-width debond of 20 mm. From the plot, it is noticed that in the case of a bonded panel, the amplitude of the A0 mode reduces significantly with the introduction of temperature. On the other hand, the amplitude of the S0 mode increases substantially with debonding, whereas the A0 mode will propagate with a much-diminished amplitude. Fig. 17 presents the CWT plot obtained at 150 kHz for the P5 patch response in a 25 mm debonded stiffened panel. The amplitude of the wavelet decreases initially and further increases with the rise in temperature. Along with this, there is a drop in the wave's group velocity as the intensity of temperature increases, evidenced by the shift in the wavelet peak towards the higher time.

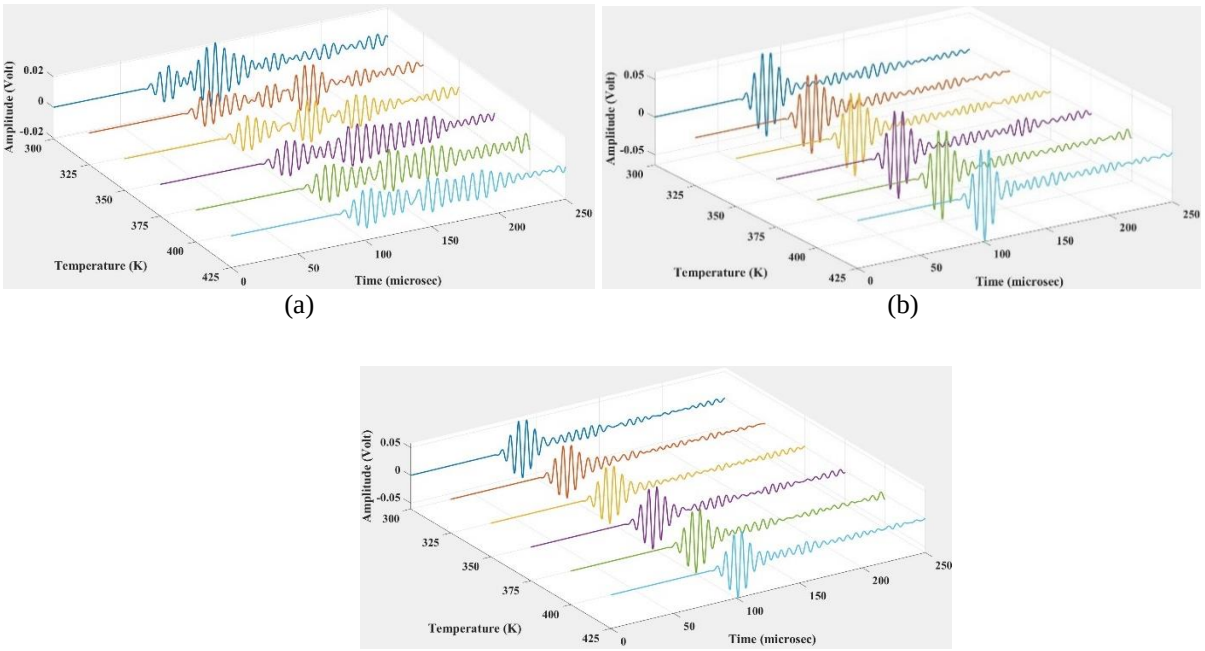


Figure 16: Response obtained at P5 for different intensities of temperature exposure in the panel with debond size of (a) δ= 0 mm, (b) δ= 25 mm and (c) δ= 50 mm.

Furthermore, the investigation is being carried out to examine the variation of the CWT peak and group velocity of the S0 mode of the wave under the influence of temperature for different debonding lengths. Fig. 18 (a) depicts a gradual enhancement in the magnitude of the CWT peak of S0 mode with the temperature rise. However, the magnitude of the CWT peak increases significantly in the presence of debonding. On the other hand, the magnitude of the wavelet peak of A0 mode drops initially with a slight rise in the temperature and further enhances with the increase in temperature. Further, at a higher temperature intensity, the CWT peak drops in the bonded panel. Apart from this, the group velocity of the S0 mode reduces gradually as the temperature is increased, regardless of the debonded length. However, at the reference temperature, a quite noticeable drop is noticed in the velocity with debonding. At the higher temperature, the group velocity of the S0 mode in the debonded panel is slightly higher than the bonded panel S0 mode group velocity, as observed in Fig. 18 (b).

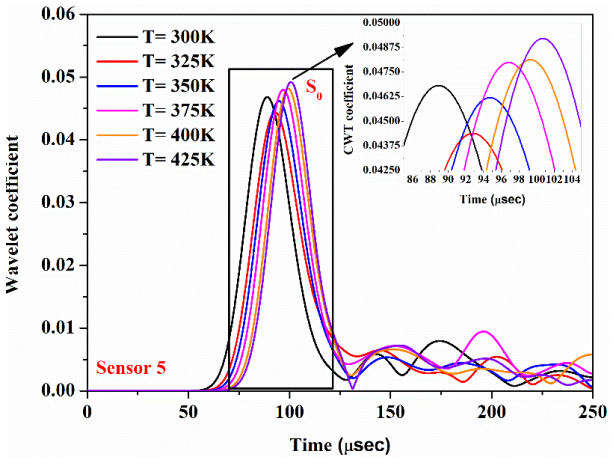


Figure 17: CWT of the P5 sensor signal obtained at 150 kHz for the panel with δ= 25 mm.

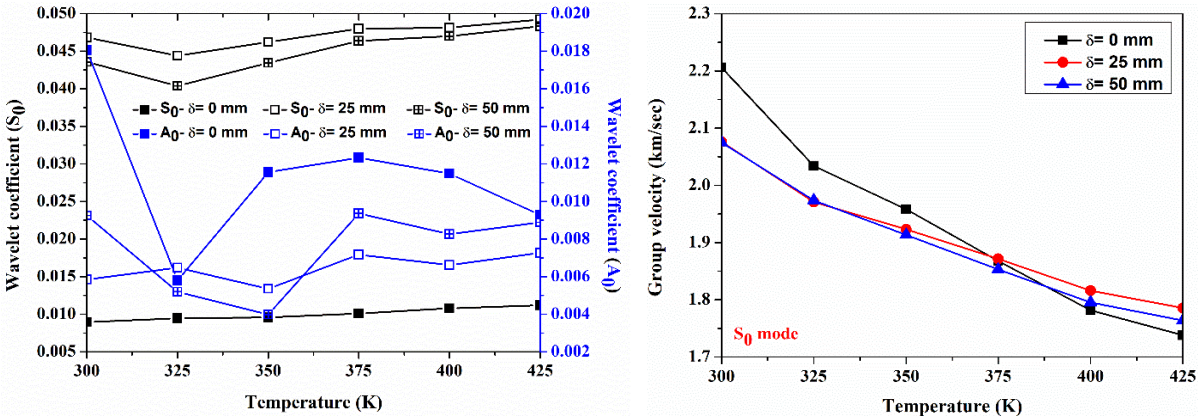


Figure 18: Influence of the thermal variation on the (a) CWT of the response (b) group velocity of the S0 mode of the wave obtained at P5.

### 4.3.4 Influence of moisture concentration on the scattered GW response for different debonding length

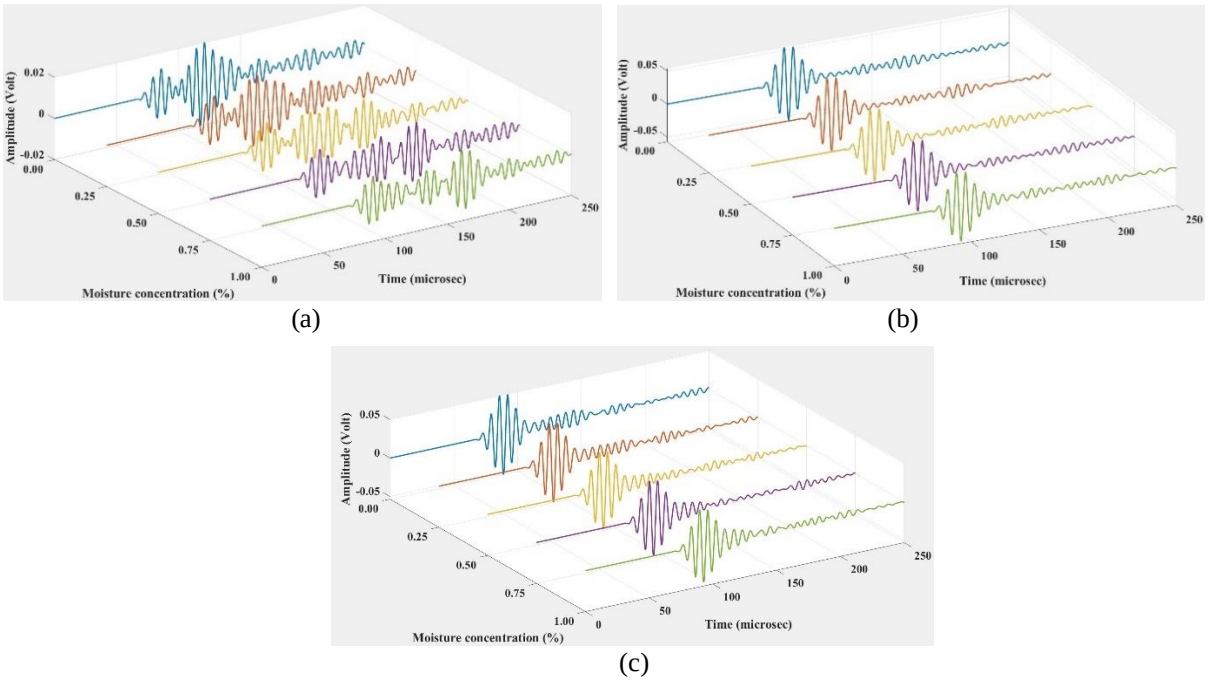


Figure 19: Response obtained at P5 for different moisture concentrations in the panel with debond size of (a) δ= 0 mm, (b) δ= 25 mm and (c) δ= 50 mm.

This section discusses the study conducted to comprehend the influence of moisture concentration on the scattered guided wave's response for different debonding lengths. Similar to the thermal variation, uniform moisture is exposed on the panel. Apart from this moisture dependent material properties are used for the composite structure. As no works of literature are available on the variation of moisture concentration on the piezoelectric material properties, therefore, the piezo properties are maintained constant throughout the study. The stability study showed that the panel buckles at a moisture concentration of 1.1427%, 1.1422% and 1.1401% for a bonded panel, 25 mm debonded panel, and 50 mm debonded panel. Hence, the current study is conducted by varying the moisture from 0.0% to 1.0% at an interval of 0.25%. The response of the wave obtained at P5 is shown in Fig. 19 for various lengths of

debonding. The plot shows that the time range of the S0 mode packet slightly broadens as the moisture concentration rises for a larger debond length. However, with debonding, the amplitude of the S0 mode response increases significantly. On the other hand, contrary behaviour is noticed in the case of A0 mode. The amplitude of the mode reduces tremendously and narrows down the A0 wave packet propagating length with the enhancement in the moisture concentration. It is interesting to notice that with debonding, the S0 mode travels with a higher amplitude, whereas the A0 mode amplitude reduces.

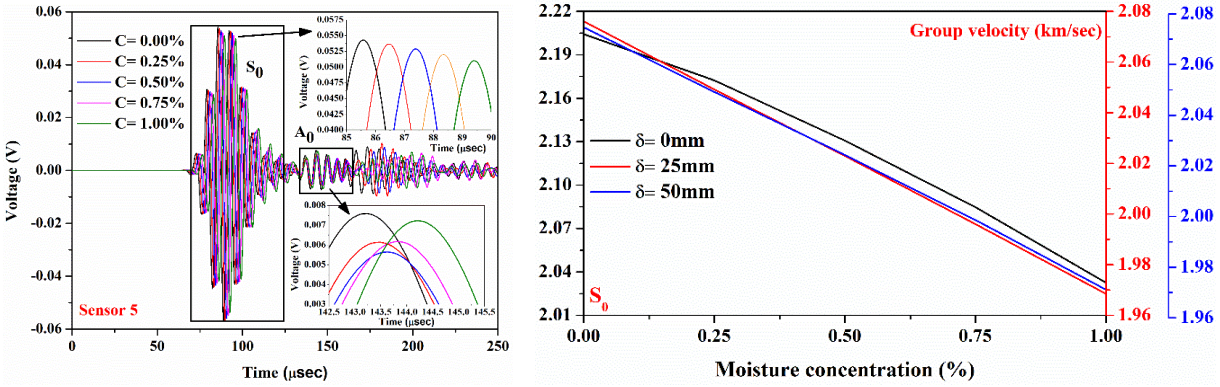


(a) (b)

Figure 20: (a) Response obtained at the P5 sensor signal in the panel with δ= 25 mm, (b) Influence of moisture concentration on the group velocity of the S0 mode for different debonding sizes.

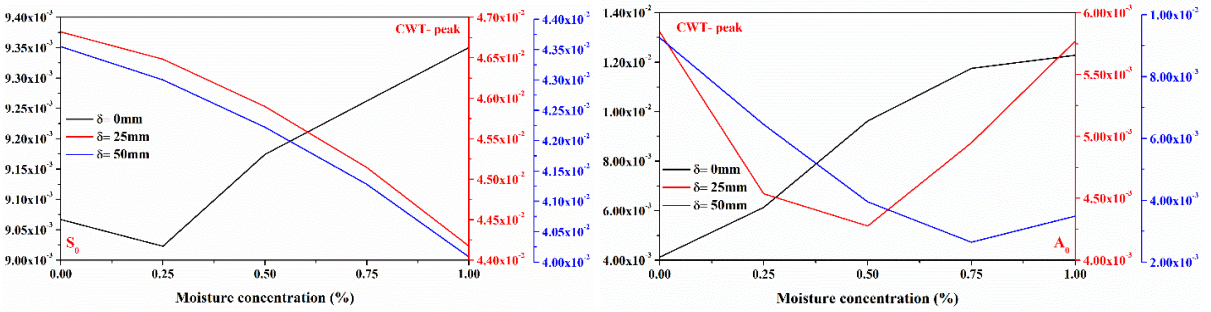


(a) (b)

Figure 21: Variations of the magnitude of the CWT peak for (a) S0 mode and (b) A0 mode for different sizes of debonding.

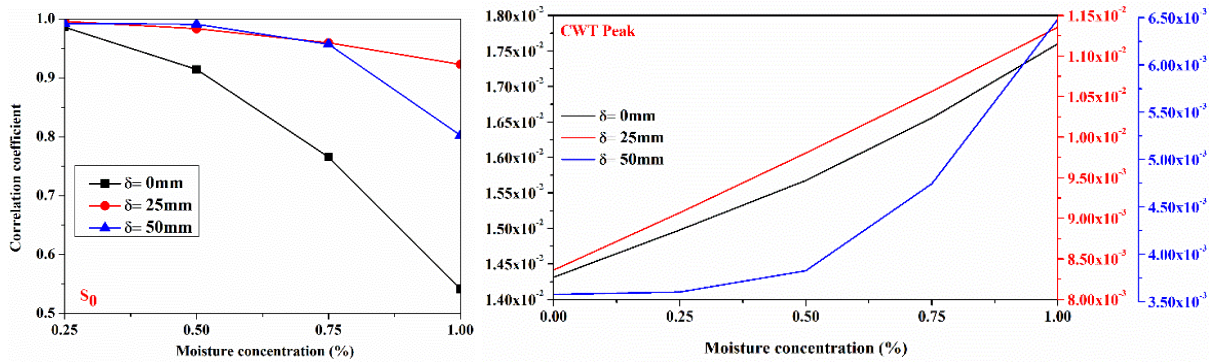


(a) (b)

Figure 22: Influence of moisture concentration on (a) correlation coefficient of the response obtained at P5 and (b) magnitude of the CWT peak of the S0 mode response captured at P8 for different debonding lengths.

Fig. 20 (a) shows the 25 mm debonded panel response obtained at P5 for different moisture concentration exposure. It is observed that similar to the loading influence, the moisture mar-

ginally influences the wave response of the panel. The amplitude of the S0 mode reduces gradually with some delay in the arrival of the mode. This shows the reduction in the group velocity of the wave mode with the rise in the moisture concentration. On the other hand, the amplitude of the A0 mode decreases with the initial exposure to low moisture concentration, and at higher moisture concentration, the amplitude enhances with the rise in the moisture concentration along with the delay in the arrival of the packet, indicating the reduction in the group velocity. Fig. 20 (b) depicts the variation in S0 mode group velocity in the transverse direction of the plies for various debonding lengths. Here, it is observed that moisture noticeably reduces the wave's group velocity with the increase in the moisture concentration, irrespective of the debonding size. However, a sudden drop in the wave's group velocity occurs with the introduction of debonding. Further increase in the debond marginally reduces the group velocity.

The influence of the moisture concentration on the magnitude of the CWT peak of the S0 and A0 wave modes for different debonding sizes is presented in Fig. 21. The plot shows that the magnitude of the CWT peak of the S0 mode in the bonded panel response initially reduces with the introduction of moisture, and then it increases with the moisture concentration. However, as the debonding size increases, the peak's magnitude decreases with moisture concentration. On the other hand, the magnitude of the CWT peak of the A0 mode in the bonded panel increases as the moisture concentration increases. The CWT peak of the A0 mode in the debonded panel initially drops and then increases with increasing moisture concentration. As the debonding increase, the peak drops for higher moisture concentration.

From Fig. 22 (a), it is noted that the correlation coefficient of the scattered wave reduces with the increases in the moisture concentration. However, the debonded panel signal features change slightly as the moisture concentration increases in comparison to the signal in the panel subjected to 0% moisture. This demonstrates that the wave features in a bonded panel change more abruptly as a result of moisture exposure than the wave features in a debonded panel.

Fig. 22 (b) highlights the variation of the CWT peak of the first packet in the response obtained at the P8 sensor, which is attached to the top surface of the stiffener flange right above the debond. According to the findings, the CWT peak increases linearly with the rise in the moisture concentration in the bonded panel. However, as the debonding size increases, the CWT peak enhancement exhibits a parabolic variation. Aside from that, the magnitude of the CWT peak decreases with debonding propagation.

## 5 CONCLUDING REMARKS

The current research investigates the impact of environmental and loading factors on the GW response of an interfacial debonded stiffened panel while accounting for residual stress developed by hygrothermal load and in-plane load. Numerical modelling with multiphysics coupling has been developed using finite element simulation software "COMSOL Multiphysics". Apart from numerical modelling, the scattered signals are processed to understand the variation of different wave features under the influence of hygrothermal and external loading conditions. Detailed numerical investigations of the scattered response obtained from the simulation are performed to investigate the external loading and environmental effect. Based on the results obtained from this investigation, the following conclusion can be reached:

i. Based on the frequency modulation study, the 5-cycle Hanning window excited with 150 kHz frequency has better A0 and S0 mode scattered response and is used as excitation frequency for the other parametric studies.

ii. In the case of the bonded panel, the response signal has a high A0 mode amplitude and a smaller S0 mode amplitude. However, a contrary behaviour is noticed in the debonded panel, as the scattered wave will have a high S0 mode amplitude and a smaller A0 mode amplitude.
iii. The amplitude of the A0 mode of the scattered GW response reduces as the debonding size increases, which contradicts the behaviour of the S0 mode.
iv. The amplitude of the scattered S0 mode GW response captured by the attached PZT enhances as the debonding length increases. However, the amplitude of the S0 mode obtained using PZT bonded on the stiffener flange reduces as the debonding length increases.
v. Inplane load marginally affects the response of the scattered wave. However, the peak of the S0 and A0 modes reduces with the increase in the magnitude of the compressive edge loading.
vi. The group velocity of the A0 mode drops with the enhancement in the intensity of compressive edge load, but it is insignificant in the case of the S0 mode.
vii. The CWT peak of the S0 and A0 modes increases as the applied in-plane pressure enhances. However, a slight drop in the peak is observed in the case of a 50 mm debonded panel response.
viii. Similar to the external in-plane load, the temperature reduces the group velocity of the S0 mode.
ix. The amplitude of the S0 mode initially reduces with the rise in the moisture concentration for the bonded panel. In the case of a debonded panel, the wave amplitude reduces parabolically with the moisture concentration.
x. The time drift of the S0 mode packet of the response in the bonded panel reduces significantly. However, it widens as the debonded length increases.
xi. The time length of the A0 mode of the response reduces with the increase in the moisture concentration in the panel. However, the amplitude analogously reduces, as observed in the other loading case.

The above findings show that the hygrothermal loading significantly influences the scattered wave response more than the applied in-plane pressure. Therefore, this study can be used as a reference investigation to apprehend the influence of the complex loading conditions on the guided wave response.

## REFERENCES

[1] J. Guo, X. Gao, E. Toma, U. Netzelmann, Anisotropy in carbon fiber reinforced polymer (CFRP) and its effect on induction thermography, *NDT & E International.* **91** 1-8, 2017.
[2] M.F. Haider, M.M. Haider, F. Yasmeen, Micromechanics model for predicting anisotropic electrical conductivity of carbon fiber composite materials, *AIP Conference Proceedings.* **1754 (1),** 030011, 2016.
[3] C. Meola, S. Boccardi, G.M. Carlomagno, Composite material overview and its testing for aerospace components, in: M. Jawaid, M. Thariq (Eds.) Sustainable Composites for Aerospace Applications, Woodhead Publishing, 2018, pp. 69-108.
[4] X. Zhang, X. Wu, Y. He, S. Yang, S. Chen, S. Zhang, D. Zhou, CFRP barely visible impact damage inspection based on an ultrasound wave distortion indicator, *Composites Part B: Engineering.* **168** 152-158, 2019.

[5] B. Park, Y.-K. An, H. Sohn, Visualization of hidden delamination and debonding in composites through noncontact laser ultrasonic scanning, *Composites Science and Technology.* **100** 10-18, 2014.
[6] L. Ye, Z. Su, Identification of damage using Lamb waves, *J Lecture notes in applied computational mechanics.* **48** 4-5, 2009.
[7] J.-R. Lee, J. Takatsubo, N. Toyama, Disbond monitoring at wing stringer tip based on built-in ultrasonic transducers and a pulsed laser, *Smart Materials and Structures.* **16 (4),** 1025-1035, 2007.
[8] G.A.O. Davies, D. Hitchings, J. Ankersen, Predicting delamination and debonding in modern aerospace composite structures, *Composites Science and Technology.* **66 (6),** 846-854, 2006.
[9] H. Sohn, D. Dutta, J.Y. Yang, M. DeSimio, S. Olson, E. Swenson, Automated detection of delamination and disbond from wavefield images obtained using a scanning laser vibrometer, *Smart Materials and Structures.* **20 (4),** 045017, 2011.
[10] R. Seydel, F.-K. Chang, Impact identification of stiffened composite panels: I. System development, *Smart Materials and Structures.* **10 (2),** 354-369, 2001.
[11] J.L. Rose, Ultrasonic waves in solid media, in, Acoustical Society of America, 2000.
[12] N. Guo, P. Cawley, The interaction of Lamb waves with delaminations in composite laminates, *The Journal of the Acoustical Society of America.* **94 (4),** 2240-2246, 1993.
[13] M.J.S. Lowe, R.E. Challis, C.W. Chan, The transmission of Lamb waves across adhesively bonded lap joints, *The Journal of the Acoustical Society of America.* **107 (3),** 1333-1345, 2000.
[14] C. Ramadas, K. Balasubramaniam, M. Joshi, C.V. Krishnamurthy, Interaction of Lamb mode (Ao) with structural discontinuity and generation of "Turning modes" in a T-joint, *Ultrasonics.* **51 (5),** 586-595, 2011.
[15] C. Han, G. Yang, J. Wang, X. Guo, The research on propagation characteristics of acoustic emission signals in stiffened plates based on the multipath propagation model, *Ultrasonics.* **108** 106177, 2020.
[16] F. Chen, P.D. Wilcox, The effect of load on guided wave propagation, *Ultrasonics.* **47 (1),** 111-122, 2007.
[17] S.J. Lee, N. Gandhi, J.E. Michaels, T.E. Michaels, Comparison of the effects of applied loads and temperature variations on guided wave propagation, in: AIP Conference Proceedings, American Institute of Physics, 2011, pp. 175-182.
[18] J.E. Michaels, S.J. Lee, T.E. Michaels, Impact of applied loads on guided wave structural health monitoring, in: AIP Conference Proceedings, American Institute of Physics, 2011, pp. 1515-1522.
[19] S. Roy, P. Ladpli, F.-K. Chang, Load monitoring and compensation strategies for guided-waves based structural health monitoring using piezoelectric transducers, *Journal of Sound and Vibration.* **351** 206-220, 2015.
[20] R. Radecki, W.J. Staszewski, T. Uhl, Impact of Changing Temperature on Lamb Wave Propagation for Damage Detection, *Key Engineering Materials.* **588** 140-148, 2014.
[21] M.J. Boon, D. Zarouchas, M. Martinez, D. Gagar, B. Rinze, P. Foote, Temperature and load effects on acoustic emission signals for structural health monitoring applications, in: EWSHM-7th European Workshop on Structural Health Monitoring, 2014.
[22] S. Roy, K. Lonkar, V. Janapati, F.-K. Chang, A novel physics-based temperature compensation model for structural health monitoring using ultrasonic guided waves, *J Structural Health Monitoring.* **13 (3),** 321-342, 2014.

[23] S. Sikdar, P. Fiborek, P. Kudela, S. Banerjee, W. Ostachowicz, Effects of debonding on Lamb wave propagation in a bonded composite structure under variable temperature conditions, *Smart Materials and Structures.* **28 (1),** 015021, 2018.
[24] C.A. Dan, P. Kudela, M. Radzienski, W. Ostachowicz, Temperature effects compensation strategy for guided wave based structural health monitoring, in: 6th International Symposium on NDT in Aerospace, Madrid, Spain, 2014.
[25] K.J. Schubert, A.S. Herrmann, On the influence of moisture absorption on Lamb wave propagation and measurements in viscoelastic CFRP using surface applied piezoelectric sensors, *Composite Structures.* **94 (12),** 3635-3643, 2012.
[26] K. Lonkar, Modeling of piezo-induced ultrasonic wave propagation for structural health monitoring Stanford, in, PhD Thesis, 2013.
[27] L. Qiu, R.S. Venkat, C. Boller, S. Yuan, Multiphysics Simulation of Guided Wave Propagation under Load Condition, in: 8th Internat. Symp. on NDT in Aerospace, 2016.
[28] P.K. Parhi, S.K. Bhattacharyya, P.K. Sinha, Hygrothermal effects on the dynamic behavior of multiple delaminated composite plates and shells, *Journal of Sound and Vibration.* **248 (2),** 195-214, 2001.
[29] C. Bijudas, M. Mitra, P. Mujumdar, Time reversed Lamb wave for damage detection in a stiffened aluminum plate, *J Smart materials structures.* **22 (10),** 105026, 2013.
[30] A.P. Kalgutkar, S. Banerjee, Semi-Analytical Finite Element Method for the Analysis of Guided Wave Dispersion in the Pre-stressed Composite Plates, *ASPS Conference Proceedings.* **1 (5),** 1413-1421, 2022.

COMPDYN 2023
9th ECCOMAS Thematic Conference on
Computational Methods in Structural Dynamics and Earthquake Engineering
M. Papadrakakis, M. Fragiadakis (eds.)
Athens, Greece, 12-14 June 2023

# A MODEL FOR THE STRUCTURAL AND SEISMIC ASSESSMENT OF THE MOSQUE-CATHEDRAL OF CORDOBA

**M.V. Requena-Garcia-Cruz[1], E. Romero-Sánchez[2], A. Morales-Esteban[13] and N. Fernández-Pérez[2]**

[1] Department of Mechanical Engineering and Industrial Design. University of Cadiz. Spain
mariavictoria.requena@uca.es

[2] Department of Building Structures and Geotechnical Engineering. University of Seville. Spain
{eromero13, ame}@us.es; natalia.fdez@msn.com

[3] Instituto Universitario de Ciencias de la Construcción. University of Seville. Spain

## Abstract

*Monumental heritage buildings were typically built without considering the seismic action. Therefore, they are potentially susceptible to seismic damage. The structural assessment and the vulnerability analysis of historical buildings is a complicated task. It requires a complex study and specialised technical skills. In order to gain some insight and to provide refined results, a model for the structural and the seismic performance of the Abd ´al-Rahman I sector of the Mosque-Cathedral of Cordoba (Spain) has been presented. The Mosque-Cathedral of Cordoba, its monumental core and its surroundings were included in the World Heritage List in 1984. Its structural system is based on parallel arcades and naves. It was started to be built in the 8th century and it has been enlarged several times. This monumental building is located in a seismic area of the southern Iberian Peninsula, characterised by large/very large earthquakes of long-return periods. In this work, a novel 3D model has been developed based on the finite element (FE) method in the OpenSees framework. The model has been elaborated through the analysis of historical data and in situ verifications. An experimental campaign has been carried out to calibrate the numerical model. Gravitational and horizontal nonlinear static analyses have been performed to determine the structural and the seismic capacity of the structure. The results have shown that the building presents the worst seismic behaviour in the direction perpendicular to the arcades. This study represents a pioneer experiment concerning the structural and seismic analysis of this building.*

**Keywords:** Seismic Performance, Cultural Heritage, Existing Buildings, Finite Element Method, Masonry, Nonlinear Static Analyses.

## 1 INTRODUCTION

Monumental heritage buildings represent the cultural identity and the history of regions [1]. Moreover, they are valuable assets for the economy of cities and countries. From a structural point of view, they were typically built only considering the gravitational loads and omitting the horizontal loading, such as the seismic action. Furthermore, most heritage buildings were constructed with unreinforced masonry (URM) walls. This is one of the structural configurations most vulnerable to earthquakes [2] due to: i) their aseismic design, mainly given by their poor horizontal connections between walls and diaphragms; ii) their low tensile strength; and iii) the difficulty in predicting their behaviour due to their heterogeneity and constructive procedure [3]. Hence, heritage buildings are potentially susceptible to seismic damage, which might result in catastrophic consequences from a social, cultural and economic point of view. In fact, this type of buildings suffered from considerable seismic damage during the recent earthquakes of 2011 in Lorca (Spain) ($M_w$=4.6) [4], 2009 in L'Aquila (Italy) ($M_w$=5.8) [5] and 2012 in Emilia (Italy) ($M_w$=6.1) [6].

In recent years, a strong will to conserve and to protect such buildings against seismic events has increased in all European countries [7]. However, the structural assessment and the vulnerability analysis of historical buildings are complicated tasks. This is mainly due to the transformations that the buildings have undergone over the years and the difficulty in obtaining the *as built* information [8]. Furthermore, this type of analysis requires a complex study and specialised technical skills.

The diagnosis and the safety assessment of historical buildings enables characterising their current state for a better understanding of their structural features and safety [9]. For this purpose and to provide reliable safety assessment, it is necessary to obtain validated and calibrated numerical models [10]. This type of careful analyses of case studies or sectors can provide useful information [11], which can be used later in global analyses. For the seismic assessment of historical buildings, nonlinear static analysis (NLSA) is usually carried out [12]. Despite its simplifications, it has been proved to be a suitable approach for a preliminary assessment of historical buildings, as suggested in [8,13].

Owing to the impossibility of performing destructive campaigns, non-destructive tests (NDT) are usually carried out for the structural analysis of URM heritage buildings. Operational modal analysis (OMA) is one of the most used NDT to calibrate numerical models, as suggested in [8]. This enables obtaining the dynamic properties of the buildings. The numerical modelling of URM heritage buildings is usually carried out in 3D through the finite element (FE) method. In spite of the computational burden, FE modelling enables modelling the geometry and simulating the behaviour of the structure in a more realistic way compared to other modelling strategies. Such is the case of the equivalent frame method that leads to several assumptions and limitations as concluded in [14].

The Mosque-Cathedral of Cordoba (Spain) is one of the most visited monuments in Spain. It constitutes a unique artistic achievement due to its building techniques, the wideness of the space created and its relevance in later Muslim architecture. Owing to these features, its monumental core and its surroundings were included in the UNESCO World Heritage List in 1984 [15]. The complex is composed of parallel naves of arches and vaults built with stone columns and URM walls. The structural and the seismic performance of the complex has not been performed to date. Nevertheless, several works can be found on its acoustic and geometric features [16–18]. The building is located in a moderate seismic activity region, in southern Spain. This is due to the convergence between the Eurasian and the African tectonic plates [19]. The area is characterised by intraplate seismicity of moderate magnitude and offshore far away earthquakes of large/very large magnitude with long return periods [20,21].

The area had to endure the well-known 1755 Lisbon earthquake ($M_w$=8.5), which resulted in several parts of the asset being damaged.

Given the cultural relevance and the potential seismic risk of the asset, this work presents the preliminary structural and seismic performance of one of the sectors of the Mosque-Cathedral of Cordoba, the Abd ´al-Rahman I sector. This dates from the 8th century, being the oldest part, which was mainly constructed with reused materials. In this work, a novel 3D model has been developed based on the FE method in OpenSees framework. The model has been elaborated analysing historic data and performing in situ verifications. Gravitational and horizontal NLSA have been performed to obtain the structural and the seismic capacity of the structure.

## 2 THE MOSQUE-CATHEDRAL OF CORDOBA

The Mosque-Cathedral of Cordoba is among the most visited monuments in Spain [22]. The asset is one of the most significant buildings in the history of the Mediterranean Muslim world. Its construction started in the 8th century and it was finished in the 15th, after being expanded in several occasions. The asset is composed of a courtyard with a minaret and a rectangular hypostyle hall, following the typical mosque configuration (Figure 1(a)). The relevance of the monument relies on the use of elements hitherto unheard-of in Islamic architecture, such as the double arches in the form of horseshoes to create the parallel naves or the 'honeycomb' capitals [15] (Figure 1(b)). This configuration allows creating a diaphanous structure based on parallel arcades and naves that went through various extensions, such as transitioning from Islamic to Christian worship. The arcades were constructed with masonry walls and arches, stone columns and timber roofing. The perimeter walls are composed of limestone masonry. Further information on the historical and architectural features of the asset can be found in [23].

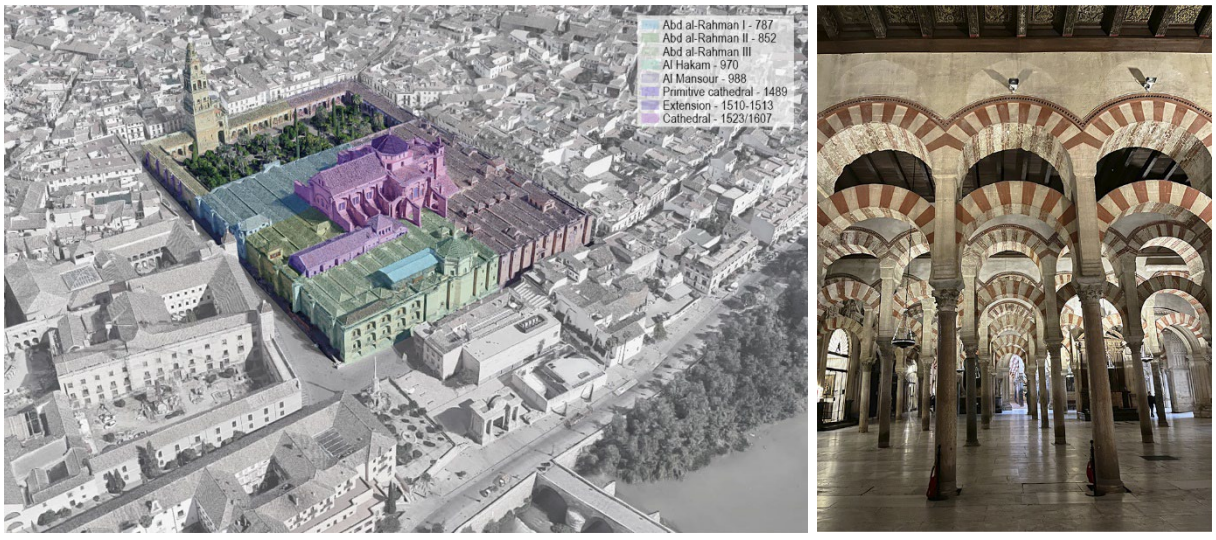


(a) (b)

Figure 1: (a) View of the Mosque-Cathedral of Cordoba highlighting the extensions. (b) Interior view of the Abd 'al-Rahman I sector, with the coffered ceiling and the double horseshoe arches (photograph taken by the authors).

### 2.1 Geometrical and structural features

Due to the complexity of the monument, this work has focused on the development of a 3D FE model for the structural and seismic assessment of the Abd 'al-Rahman I sector (Figure

1(a)). The dimensions of the sector are 90 m wide and 20 m long and it is composed of 11 longitudinal naves (Figure 2). The arches are made up of stone columns with bases, shafts, capitals and cymatiums that date from the Roman period. The arches follow an aqueduct-like composition to evacuate the rainwater and to support the timber roofing. They also sustain the coffered ceiling. In some naves, the timber trusses were changed for steel ones in the 20th century (Figure 3).

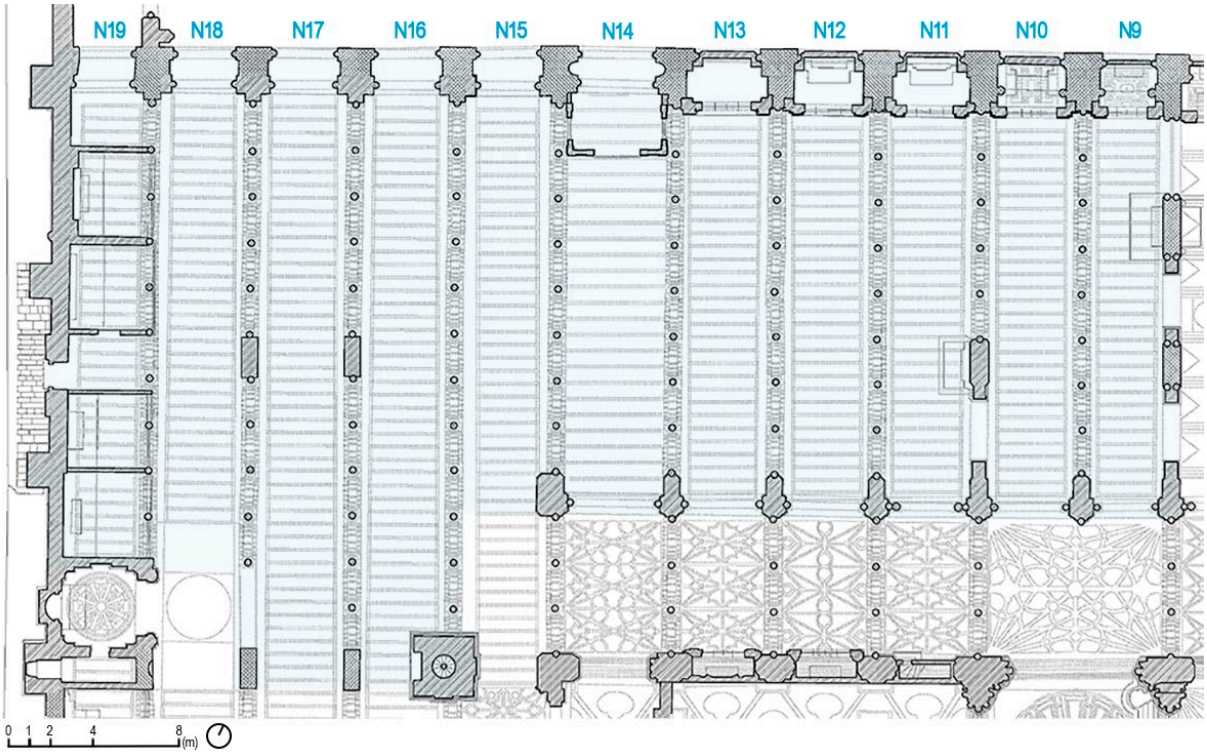


Figure 2: Plan view of the Abd 'al-Rahman I sector (naming the naves in light blue, $N_i$).

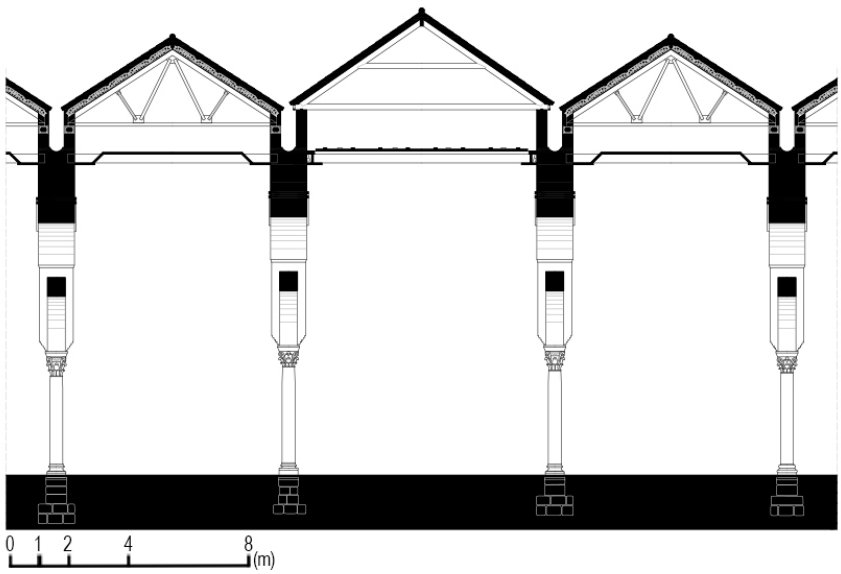


Figure 3: Type of roofing found in the Abd 'al-Rahman I sector. Drawings adapted by the authors from [24], including the foundation.

## 2.2 Mechanical parameters

The NDT campaign has been based on performing Schmidt Hammer (SH) tests to obtain the compressive strength of the structural materials and an OMA to identify the overall dynamic behaviour of the building. For each structural element tested, nine different SH tests were performed. It was observed that columns were mainly composed of marble (69%), granite (26%) and limestone (5%). The maximum, the minimum and the average compressive strength ($f_c$) obtained for each structural material is listed in (Table 1).

| Material | $f_{c,max}$ (MPa) | $f_{c,min}$ (MPa) | $f_{c,aver}$ (MPa) | $\sigma$ |
|---|---|---|---|---|
| Marble | 84 | 35 | 67 | ± 7.90 |
| Granite | 89 | 35 | 63 | ± 8.16 |
| Limestone | 89 | 59 | 75.5 | ± 4.16 |
| URM brick walls | 28.5 | 25 | 27 | ± 1.10 |
| URM limestone walls | 46 | 22 | 30.20 | ± 4.70 |

Table 1: Maximum ($_{max}$), minimum ($_{min}$) and average ($_{aver}$) compressive strength ($f_c$) obtained from the SH tests, including the standard deviation ($\sigma$).

The OMA has been performed to obtain a more reliable modelling of the building. To do so, force-balance triaxial accelerometers were used and placed on the arcades (Figure 4). The ARTeMIS Modal software [25] has been employed to calculate the modes of vibration and the frequencies of the sector under study. The Enhanced Frequency Domain Decomposition (EFDD) method has been followed, similarly to [26,27]. According to the results obtained, the complexity of the modes has been lower than 10%. After performing the calibration, a relative error between the experimental and numerical frequencies lower than ±3% has been obtained. It has been found that the Mode 1 and 3 are translational in the Y direction (east-west). By contrast, Mode 2 is rotational.



Figure 4: Location of the accelerometers in the arcades for the OMA.

The mechanical parameters have been defined according to the NDT campaign and the calibration of the model: the compressive strength ($f_c$), the elastic modulus ($E$) and the density ($\rho$). The rest of the mechanical parameters needed for the NLSA have been defined according

to the reference values proposed in [28], being, in this case, the shear modulus ($G$), the tensile strength ($f_t$) and the Poisson ratio ($v$). They have been selected according to the values obtained in the NDT campaign.

| Material | $\rho$ (T/m3) | $E$ (GPa) | $G$ (GPa) | $v$ | $f_c$ (MPa) | $f_t$ (MPa) |
|---|---|---|---|---|---|---|
| Clay bricks and lime mortar masonry | 1.8 | 2.0 | 0.55 | 0.2 | 3.57 | 0.21 |
| Limestone and lime mortar masonry | 1.8 | 1.8 | 0.42 | 0.3 | 2.78 | 0.10 |
| Marble | 2.8 | 16 | 6 | 0.25 | 67 | 3.50 |
| Granite | 2.8 | 42 | 14 | 0.25 | 63 | 3.45 |
| Limestone | 2.7 | 10 | 2 | 0.25 | 75.5 | 3.80 |
| Timber (old roof) | 0.45 | 11 | 4 | 0.4 | 40 | 10 |
| Steel (new roof) | 78 | 210 | 81 | 0.3 | 410 | 275 |

Table 2: Mechanical properties of the materials used for the NLSA.

## 3 NUMERICAL MODELLING

The 3D numerical model has been developed in the OpenSees framework [29], based on the macro-mechanical approach and using solid elements (Figure 5). These elements enable obtaining a comprehensive stress-strain behaviour of the elements and the materials needed for a thorough analysis of historical buildings [9]. The FE meshing has been developed in a pre- and post-processor for OpenSees, the STKO software [30]. The FE mesh has been developed to preserve, as much as possible, the real configuration of the building. As followed in [13,31,32], the mesh size has been defined to obtain a fair compromise between the computational burden, the accuracy and the robustness of the modelling. Hence, a mesh size of 0.3 m and 0.2 m has been defined for the external walls and the inner parts, respectively. Tetrahedron elements have been needed to fit the irregular parts. In total, the FE mesh is composed of 306,386 nodes and 1,124,353 solid elements. The model has been fixed at the base. The presence of the adjacent structure has been considered through zero-length 3D elements and the materials have been calibrated with the OMA.

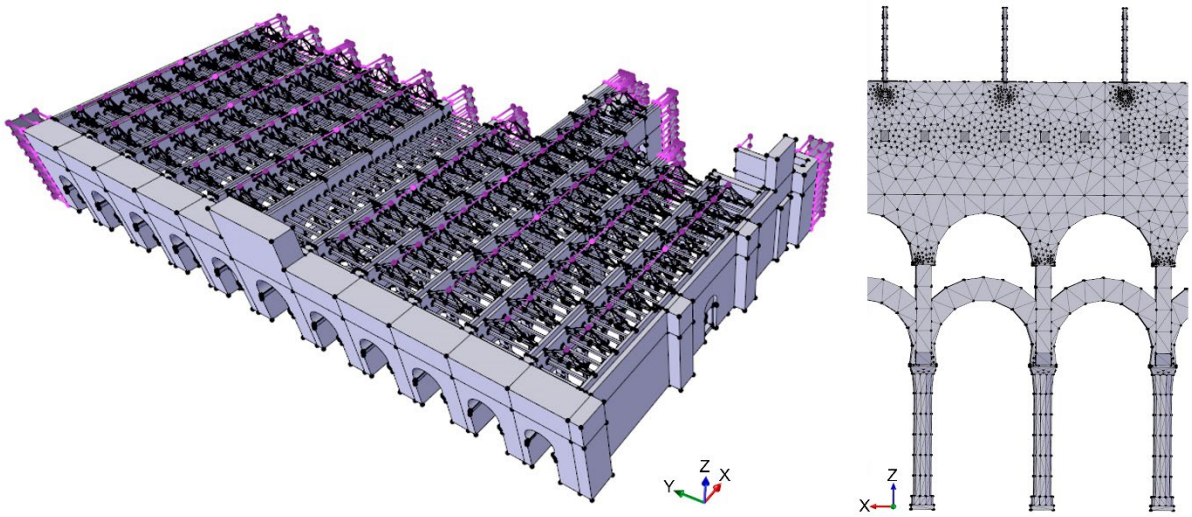


Figure 5: 3D model developed for the Abd 'al-Rahman I sector and detail of the FE meshing.

In order to simulate the nonlinear behaviour of the structural elements, a damage-plasticity material has been implemented [33]. This is typically used to simulate the nonlinear

behaviour of quasi-brittle materials such as masonry. This material is based on two independent tensile and compressive constitutive laws (Figure 6). The parameters needed for the definition of the material have been defined according to [34]: the peak ($f_{cp}$), the elastic ($f_{c0}$) and the residual ($f_{cr}$) compressive strengths and the strain ($\varepsilon_{cp}$) at peak compressive strength. The compressive ($G_c$) and the tensile ($G_t$) fracture energies have been computed according to the equations proposed in [35]. In this case, the input fracture energies have been divided by the characteristic element length ($l_{ch}$) to obtain a response that is mesh-size independent.

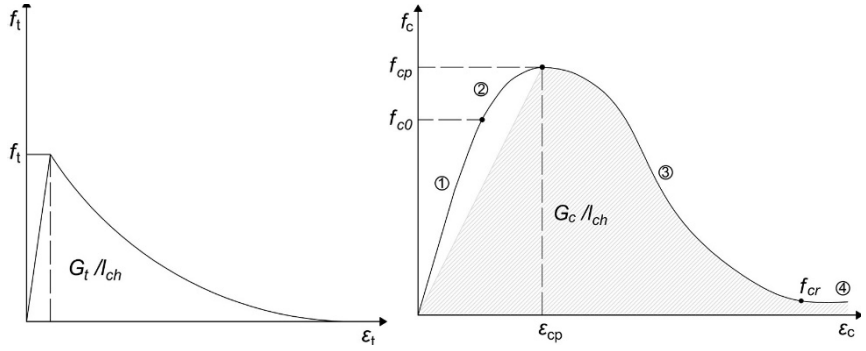


Figure 6: Tensile and compressive constitutive laws, adapted from [33].

## 4 RESULTS

First, a gravitational NLSA has been performed. To do so, the gravitational loads have been applied as volume forces according to the density of the materials. A load-control integrator has been used to perform this analysis. In Figure 7, the damage pattern in compression ($d^-$) and in tension ($d^+$) are presented after applying the gravitational loads. Damage is expressed as a range between 0, non-damaged, to 1, totally damaged. As can be observed, the structural elements do not present damage after the application of the gravitational loads. This is in good agreement with the real situation of the building. However, it has been obtained that the cymatiums present damage that reaches values close to 0.7 and 0.9 in $d^-$ and $d^+$, respectively. This is mainly because they are the most demanded structural elements as they receive the total gravitational loads from the upper body.

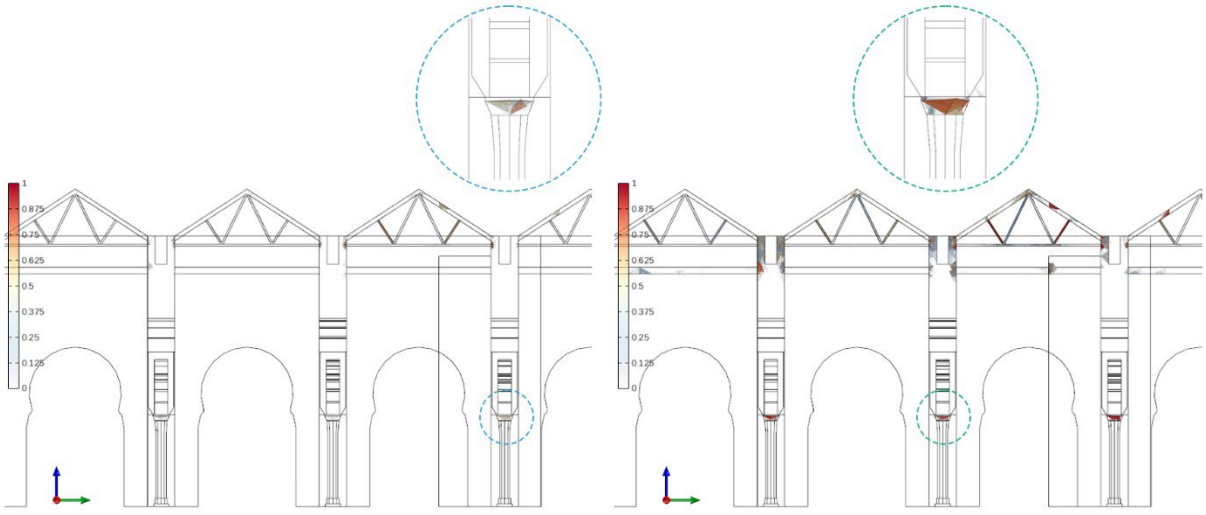

(a) (b)

Figure 7: Damage in compression ($d^-$) (a) and in tension ($d^+$) (b) after the performance of the gravitational loads.

Later, horizontal NLSA has been carried out, considering a uniform load pattern, which is generally accepted for the seismic analysis of historical buildings [8,13]. The loads have been applied in the two main directions of the building, the X (north-south) and Y (east-west), for both the positive and negative orientations. The ultimate displacement has been obtained by considering a 20% decay of the pushover curve, as suggested in [31] and in the Eurocode-8. In Figure 8, the pushover curves obtained are plotted. They have been normalised by a load factor (total base shear ($V_b$) divided by the weight ($W$) of the structure) and considering the displacement of the control node at the top ($d_{top}$). The control node is located at the centre of the masses. The pushover curves are expressed for a single-degree-of-freedom (SDOF) system. As observed, the initial stiffness of the curves is similar. However, the system presents a higher resistance in the X (N-S) direction compared to the Y direction (E-W). This might be due to the bracing effect generated by the arcades in the X direction.

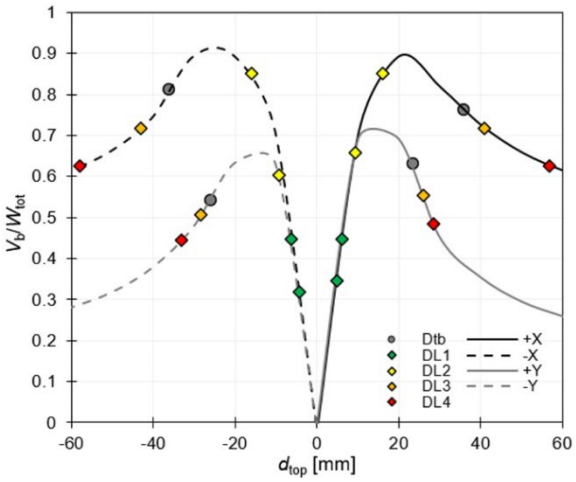


Figure 8: SDOF capacity curves obtained in the NLSA.

After the NLSA, the performance assessment has been carried out. In this work, the guidelines proposed in [8] for the global scale approach have been followed. In total, four performance levels have been defined, which are correlated to the different damage limits (DL): DL1, no damage; DL2, damage limitation; DL3, significant but repairable damage; and DL4, near collapse. Each DL has been computed as follows: DL1≥0.5$V_b$; DL2=0.95$V_b$; DL3=0.8$V_b$; and DL4=0.7$V_b$. The seismic demand has been computed according to the N2-method [36]. The response spectrum has been defined according to the Eurocode-8 part 1 provisions. A peak ground acceleration (PGA) of 0.09g has been defined for Cordoba considering the updated values of the Spanish seismic code proposed in [37]. This PGA is expressed for a probability of exceedance of 10%, which represents a return period of 475 years. This probability of exceedance corresponds to the severe damage limit state, DL3.

As can be seen in Figure 8, for the seismic demand displacement ($d_{tb}$) expected, in both directions, the damage ranges between DL2-DL3. As defined in [8], this represents the light damage state, which leads to some parts of the building being slightly damaged. It can also be seen that the damage in the Y direction (N-S) is expected to be higher than in the X direction (E-W).

Detailed 3D models with damage concentration have been obtained for each of the two principal directions of the building and for the attainment of the $d_{tb}$. Only the damage patter in tension is presented as no excessive damage in compression has been obtained. As observed in Figure 9(a), for the +X direction, the tension is mainly concentrated in: the low part of the north wall of the building, its contact with the arcades and in the first row of the arches. As

for the +Y direction, in Figure 9(b), it can be observed that the western wall might be significantly damaged, mainly in the lower parts. Also, the north wall would be notably damaged in its contact with the transversal arcades.

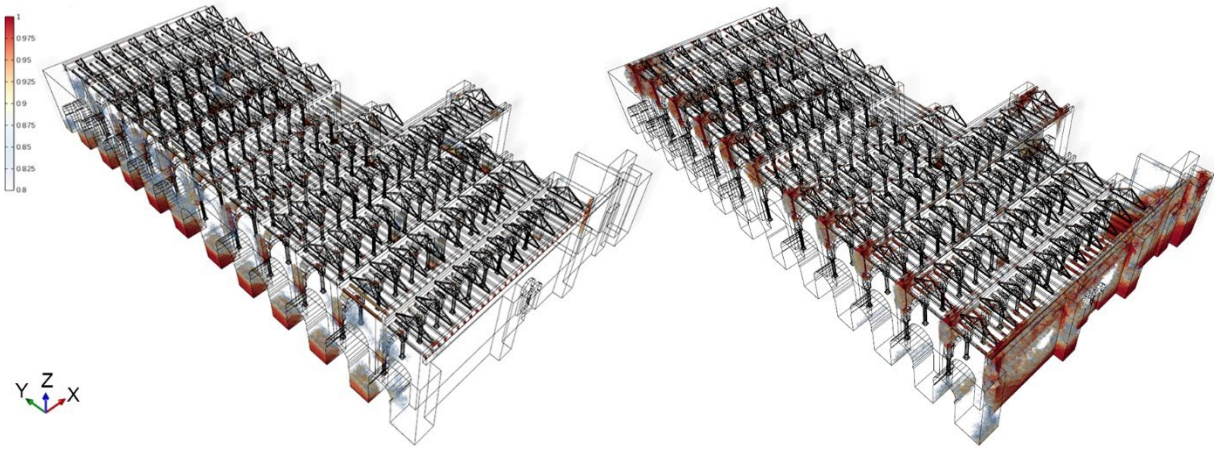


(a) (b)

Figure 9: Damage pattern in tension for the +X (a) and +Y (b) directions.

## 5 CONCLUSIONS

This paper has presented the preliminary structural and seismic performance of one of the sectors of the Mosque-Cathedral of Cordoba, the Abd `al-Rahman I sector, which dates from the 8$^{th}$ century. The building is located in a seismic-prone region and it was declared as a UNESCO World Heritage Site. Despite the cultural value of the complex and the seismic hazard of the region, the analysis of its structural features and its seismic behaviour has not been performed to date. In this paper, an advanced FE-based model has been developed and calibrated through NDT and OMA. The compressive strength of the materials and the dynamic properties of the building have been obtained. It has been found that the columns are mainly composed of marble (69%) and, to a lesser extent, of granite (26%) and limestone (5%).

The results of the gravitational NLSA are in a good agreement with the real situation of the monument. It has been concluded that particular attention should be paid to the cymatiums, as the damage expected reaches values close to 0.7 in compression and 0.9 in tension. The horizontal NLSA has resulted in different capacity curves for each of the main directions of the building. In this case, the higher capacity has been obtained for the +X direction (N-S), which can be due to the bracing effects of the arcades. According to the damage assessment, for the seismic demand of Cordoba, the damage is expected to range between DL2 andDL3. This represents a light damage that could be easily restored. As previously indicated, in the Y direction (E-W), the building presents a lower capacity and, therefore, the damage expected is higher.

This work represents the first attempt carried out by the authors to study the structural and the seismic performance of the Mosque-Cathedral of Cordoba. The goal is to obtain some preliminary results and conclusions on the structural and seismic features of the monument. Despite its advantages, horizontal NLSA leads to certain simplifications and limitations. Therefore, for complex buildings such as the Mosque-Cathedral of Cordoba, it might not be enough to obtain a detailed seismic assessment. Hence, as a future development of this work, special interest is taken in the study of the dynamic behaviour of the building and in considering the effects of the soil-structure interaction [38,39].

## ACKNOWLEDGEMENTS

This work has been supported by the "Fondo Europeo de Desarrollo Regional", FEDER_US-1380730 project. The authors would like to thank the Cabildo Catedralicio of Cordoba for their support. Especially, the authors want to thank the architect Gabriel Rebollo Puig for his outstanding to help. The funding provided by the *Instituto Universitario de Arquitectura y Ciencias de la Construcción* is also acknowledged.

## REFERENCES

[1] Valente M, Milani G. Seismic assessment of historical masonry towers by means of simplified approaches and standard FEM. Constr Build Mater 2016;108:74–104. https://doi.org/10.1016/j.conbuildmat.2016.01.025.

[2] Kaya A, Adanur S, Bello RA, Genç AF, Okur FY, Sunca F, et al. Post-earthquake damage assessments of unreinforced masonry (URM) buildings by shake table test and numerical visualization. Eng Fail Anal 2023;143:106858. https://doi.org/10.1016/j.engfailanal.2022.106858.

[3] Segovia-Verjel ML, Requena-García-Cruz MV, De-Justo-Moscardó E, Morales-Esteban A. Optimal seismic retrofitting techniques for URM school buildings located in the southwestern Iberian peninsula. PLoS One 2019;14:1–18. https://doi.org/10.1371/journal.pone.0223491.

[4] M. Feriche, F. Vidal, G. Alguacil, C. Aranda, J. Pérez-Muelas, M. Navarro, et al. Performance of cultural heritage of Lorca (Spain) during the two small earthquakes of May 11th, 2011 . 11th World Conference on Earthquake Engineering, Lisbon: 2021.

[5] Lagomarsino S. Damage assessment of churches after L'Aquila earthquake (2009). Bulletin of Earthquake Engineering 2012;10:73–92. https://doi.org/10.1007/s10518-011-9307-x.

[6] Cattari S, Degli Abbati S, Ferretti D, Lagomarsino S, Ottonelli D, Tralli A. Damage assessment of fortresses after the 2012 Emilia earthquake (Italy). Bulletin of Earthquake Engineering 2014;12:2333–65. https://doi.org/10.1007/s10518-013-9520-x.

[7] Lagomarsino S. On the vulnerability assessment of monumental buildings. Bulletin of Earthquake Engineering 2006;4:445–63. https://doi.org/10.1007/s10518-006-9025-y.

[8] Lagomarsino S, Cattari S. PERPETUATE guidelines for seismic performance-based assessment of cultural heritage masonry structures. Bulletin of Earthquake Engineering 2015;13:13–47. https://doi.org/10.1007/s10518-014-9674-1.

[9] Dinani AT, Bisol GD, Ortega J, Lourenço PB. Structural Performance of the Esfahan Shah Mosque. Journal of Structural Engineering 2021;147:05021006. https://doi.org/10.1061/(ASCE)ST.1943-541X.0003108.

[10] Haddad J, Cattari S, Lagomarsino S. Sensitivity and Preliminary Analyses for the Seismic Assessment of Ardinghelli Palace. RILEM Bookseries 2019;18:2412–21. https://doi.org/10.1007/978-3-319-99441-3_259/TABLES/3.

[11] Bento R. Analysis Case Studies in Evaluation, Rehabilitation and Reconstruction of the Built Heritage. European Conference on Earthquake Engineering and Seismology, Springer; 2022, p. 245–60. https://doi.org/10.1007/978-3-031-15104-0_15.

[12] de-Miguel-Rodríguez J, Morales-Esteban A, Requena-García-Cruz M-V, Zapico-Blanco B, Segovia-Verjel M-L, Romero-Sánchez E, et al. Fast Seismic Assessment of Built Urban Areas with the Accuracy of Mechanical Methods Using a Feedforward Neural Network. Sustainability 2022;14:5274. https://doi.org/10.3390/su14095274.

[13] Vuoto A, Ortega J, Lourenço PB, Javier Suárez F, Claudia Núñez A. Safety assessment of the Torre de la Vela in la Alhambra, Granada, Spain: The role of on site works. Eng Struct 2022;264. https://doi.org/10.1016/J.ENGSTRUCT.2022.114443.
[14] Requena-García-Cruz MV, Cattari S, Bento R, Morales-Esteban A. Comparative study of alternative equivalent frame approaches for the seismic assessment of masonry buildings in OpenSees. Journal of Building Engineering 2023;105877. https://doi.org/10.1016/j.jobe.2023.105877.
[15] Word Heritage Committee. United Nations Educational. Inscription: The Mosque of Cordoba (Spain) (08COM IXA). Convention concerning the protection of the world cultural and natural heritage, 1984.
[16] Cantizani-Oliva J, Reinoso-Gordo J-F, Gámiz-Gordo A. Proportions and Deformations in the Mosque-Cathedral of Cordoba. Nexus Network Journal 2022 2022:1–21. https://doi.org/10.1007/S00004-022-00622-Y.
[17] Hidalgo Fernández RE, Ortiz-Cordero R. The Mosque-Cathedral of Córdoba: Evidence of column organization during their first construction s. VIII A.D. J Cult Herit 2020;45:215–20. https://doi.org/10.1016/j.culher.2020.05.011.
[18] Suárez R, Alonso A, Sendra JJ. Virtual acoustic environment reconstruction of the hypostyle mosque of Cordoba. Applied Acoustics 2018;140:214–24. https://doi.org/10.1016/J.APACOUST.2018.06.006.
[19] Fazendeiro Sá L, Morales-Esteban A, Durand P. A Seismic Risk Simulator for Iberia. Bulletin of the Seismological Society of America 2016;106:1198–209. https://doi.org/10.1785/0120150195.
[20] Amaro-Mellado JL, Morales-Esteban A, Asencio-Cortés G, Martínez-Álvarez F. Comparing seismic parameters for different source zone models in the Iberian Peninsula. Tectonophysics 2017;717:449–72. https://doi.org/10.1016/J.TECTO.2017.08.032.
[21] Amaro-Mellado JL, Morales-Esteban A, Martínez-Álvarez F. Mapping of seismic parameters of the Iberian Peninsula by means of a geographic information system. Cent Eur J Oper Res 2017. https://doi.org/10.1007/s10100-017-0506-7.
[22] Consejería de Turismo y Deporte de la Junta de Andalucía. Balance del Año Turístico en Andalucía. 2016. https://doi.org/10.1080/02103702.1980.10821816.
[23] Requena-Garcia-Cruz M, Romero-Sanchez E, Lopez-Piña P, Morales-Esteban A. Preliminary structural and seismic performance assessment of the Mosque-Cathedral of Cordoba: the Abd al-Rahman I sector. Engineering Structures (Under Review) 2023.
[24] Almagro Gorbea A. Arquitectura Al-Andalus. Catálogo digital de arquitectura RABASF, 2022.
[25] ARTeMIS Modal - Structural Vibration Solutions n.d. https://svibs.com/ (accessed November 10, 2022).
[26] A. Hasan MD, Ahmad ZAB, Salman Leong M, Hee LM. Enhanced frequency domain decomposition algorithm: a review of a recent development for unbiased damping ratio estimates. Journal of Vibroengineering 2018;20:1919–36. https://doi.org/10.21595/jve.2018.19058.
[27] GeoSIG Software - GeoDAS n.d. https://www.geosig.com/GeoDAS-id12565.aspx (accessed November 10, 2022).
[28] Kržan M, Gostič S, Cattari S, Bosiljkov V. Acquiring reference parameters of masonry for the structural performance analysis of historical buildings. Bulletin of Earthquake Engineering 2015;13:203–36. https://doi.org/10.1007/s10518-014-9686-x.

[29] McKenna F, Fenves GL, Scott MH. OpenSees: Open system for earthquake engineering simulation. Pacific Earthquake Engineering Research Center. Berkeley, CA: University of California; 2000.
[30] Petracca M, Candeloro F, Camata G. "STKO user manual". ASDEA Software Technology. Pescara, Italy: 2017.
[31] Malcata M, Ponte M, Tiberti S, Bento R, Milani G. Failure analysis of a Portuguese cultural heritage masterpiece: Bonet building in Sintra. Eng Fail Anal 2020;115. https://doi.org/10.1016/J.ENGFAILANAL.2020.104636.
[32] Romero Sanchez E, Bento R, Morales Esteban A, Navarro Casas J. Numerical modelling for the seismic assessment of complex masonry heritage buildings: the case study of the Giralda tower. Bulletin of Earthquake Engineering 2023;(Under review).
[33] Petracca M, Pelà L, Rossi R, Zaghi S, Camata G, Spacone E. Micro-scale continuous and discrete numerical models for nonlinear analysis of masonry shear walls. Constr Build Mater 2017;149:296–314. https://doi.org/10.1016/j.conbuildmat.2017.05.130.
[34] Cattari S, Camilletti D, D'Altri AM, Lagomarsino S. On the use of continuum Finite Element and Equivalent Frame models for the seismic assessment of masonry walls. Journal of Building Engineering 2021;43:102519. https://doi.org/10.1016/j.jobe.2021.102519.
[35] Petracca M, Pelà L, Rossi R, Oller S, Camata G, Spacone E. Multiscale computational first order homogenization of thick shells for the analysis of out-of-plane loaded masonry walls. Comput Methods Appl Mech Eng 2017;315:273–301. https://doi.org/10.1016/j.cma.2016.10.046.
[36] Fajfar P. A nonlinear analysis method for performance-based seismic design. Earthquake Spectra 2000;16:573–92. https://doi.org/https://doi.org/10.1193/1.1586128.
[37] Spanish Ministry of Public Works [Ministerio de Fomento de España]. Update of the seismic hazard maps [Actualización de mapas de peligrosidad sísmica de España]. Spain, Spain: 2012.
[38] Requena-Garcia-Cruz MV, Romero-Sánchez E, Morales-Esteban A. Numerical investigation of the contribution of the soil-structure interaction effects to the seismic performance and the losses of RC buildings. Developments in the Built Environment 2022;12:100096. https://doi.org/10.1016/j.dibe.2022.100096.
[39] Requena-Garcia-Cruz MV, Bento R, Durand-Neyra P, Morales-Esteban A. Analysis of the soil structure-interaction effects on the seismic vulnerability of mid-rise RC buildings in Lisbon. Structures 2022;38:599–617. https://doi.org/10.1016/j.istruc.2022.02.024.

COMPDYN 2023
9th ECCOMAS Thematic Conference on
Computational Methods in Structural Dynamics and Earthquake Engineering
M. Papadrakakis, M. Fragiadakis (eds.)
Athens, Greece, 12-14 June 2023

# SEISMIC ASSESSMENT OF HISTORIC COMPLEX TOWERS. THE CASE STUDY OF THE GIRALDA TOWER

**E. Romero-Sánchez[1], M.V. Requena-Garcia-Cruz[2], and A. Morales-Esteban[13]**

[1] Department of Building Structures and Geotechnical Engineering. University of Seville. Spain
e-mail: eromero13@us.es

[2] Department of Mechanical Engineering and Industrial Design. University of Cadiz Spain
mariavictoria.requena@uca.es

[3] Instituto Universitario de Ciencias de la Construcción. University of Seville. Spain
ame@us.es

## Abstract

*The Giralda tower of Seville is an ancient complex tower. It is composed of an inner and an outer wall connected by an ascending ramp that varies with its height. The ascending ramp makes every façade be different in height and composition. Also, the unreinforced masonry varies and it has some parts made of stone. Moreover, the western façade partly connects with the cathedral and the southern area. It reaches a total height of 95 m and it is one of the most ancient buildings in Seville. It was listed as a World Heritage Site by the UNESCO in 1987 with the maximum level of protection: Outstanding Universal Value. The tower is located in a seismically-prone area and it is known to have been severely damaged during past historic earthquakes. Therefore, a complete and adequate seismic analysis of its seismic behaviour is mandatory. This work has focused on a refined analysis of its seismic performance to provide reliable results. A detailed 3D architectural model of the monument has been created in the Rhinoceros software. The seismic assessment has been carried out following the Finite Element Method (FEM) with the OpenSees software. This approach is based on a numerical procedure grounded on the use of nonlinear static analysis. Equivalent boundary conditions have been introduced to assess the interaction among the different parts of the tower with the cathedral. To minimise the uncertainties in complex masonry buildings and to calibrate the numerical model in situ experimental tests have been carried out. Finally, different horizontal load patterns have been considered in the analyses to assess its seismic behaviour.*

**Keywords:** seismic performance, cultural heritage, existing buildings, finite element method, masonry, nonlinear static analyses.

## 1 INTRODUCTION

Built cultural heritage has a big impact on the European Union (EU). Its conservation is a current and difficult issue. In this regard, the EU countries have committed themselves, through policies and programmes, to preserving and to improving their cultural heritage.

Seville is a Spanish city located in the southwestern Iberian Peninsula (IP). The IP seismic activity is moderate. However, the southern area is characterized by the occurrence of large earthquakes ($M_w$>7) with long-return periods [1]. This is due to the contact area between the Eurasian and African tectonic plates. According to the earthquake record, the south of the IP is the most seismic area. Seville has a moderate seismic risk, but its soft alluvial strata are known to increase the effects of earthquakes [2–4].

The city has a great cultural heritage which depicts its historic and social identity. Furthermore, it is one of the bases for the social and economic development of the city. In this context, the Giralda tower is the most representative building of the cultural identity and economic base of Seville. Due to its cultural relevance, it was declared as a Word Heritage Site of Outstanding Universal Value by the UNESCO. Originally, it was built as a minaret for the major Islamic mosque of the city in 1198. However, the tower has undergone different construction phases and significant modifications over time. Furthermore, it has been damaged by several historic earthquakes [5].

The seismic assessment of heritage buildings is an important issue, which has been studied in depth due to their complexity [6–9]. This is a complicated task mainly due to the difficulty in characterising the constructive materials (they are heterogeneous), the different construction phases and the rehabilitation interventions. In these buildings, their original appearance cannot be altered with *in situ* characterisation surveys. In that sense, non-destructive testing (NDT) has been discussed and illustrated in the literature [10,11] as a procedure to typify and calibrate the numerical models for the analytical analysis [12].

The main objective of this work is to numerically model the Giralda tower using the 3D Finite Element Model (FEM) method to assess its seismic behaviour. For this aim, the OpenSees [13] and the STKO softwares [14] have been employed. A modal and a nonlinear static analysis (Pushover) have been carried out to obtain a first approximation of the seismic behaviour of the tower. This analysis is important because of the great amount of historic architectural heritage that was constructed with masonry structures (buildings, towers, castles, churches, etc.) [15] .

The rest of the manuscript is organised as follows. In Section 2, the case study is described. In Section 3, the methodology followed in this work is shown and the numerical modelling of the tower is described. In Section 4, the results are presented and discussed. Finally, in Section 5, the conclusions of the work are drawn.

## 2 CASE STUDY: THE GIRALDA TOWER

The Giralda is the most representative building of Seville. It is an excellent example of the different cultures that have lived in the city. The tower has undergone several construction phases and modifications over time. Furthermore, it had to endure several historic earthquakes, such as the 1755 Lisbon earthquake ($M_w$=8.9), that led to the tower being severely damaged [16].

Originally, the tower was built between 1184 and 1198, as a minaret for the main Islamic Mosque of the city. It was crowned by four golden spheres, which fell during the 1356 earthquake. The most relevant intervention was the addition of the Renaissance bell tower de-

signed by the architect Hernán Ruiz in 1568 [17]. The building acquired a similar appearance to its current one (Figure 1).

The tower was built with ceramic brick and stone masonry. The structural system is made up of two parallel brick masonry walls. The floor has a quadratic dimension of 13.60x13.60 m and the height reaches around 95 m (Figure 1). The thickness of the outer masonry wall ranges between 2.00 and 2.30 m. The inner body is of 6x6 m composed of brick masonry walls of around 1.30 m thickness. It is important to note that both walls are connected by the ascent ramp that reaches the belfry level. These ramps are composed of brick masonry vaults and compact limestone with different thicknesses to build the slope. Furthermore, several brick masonry vaults limit seven inner rooms in the core of the tower.

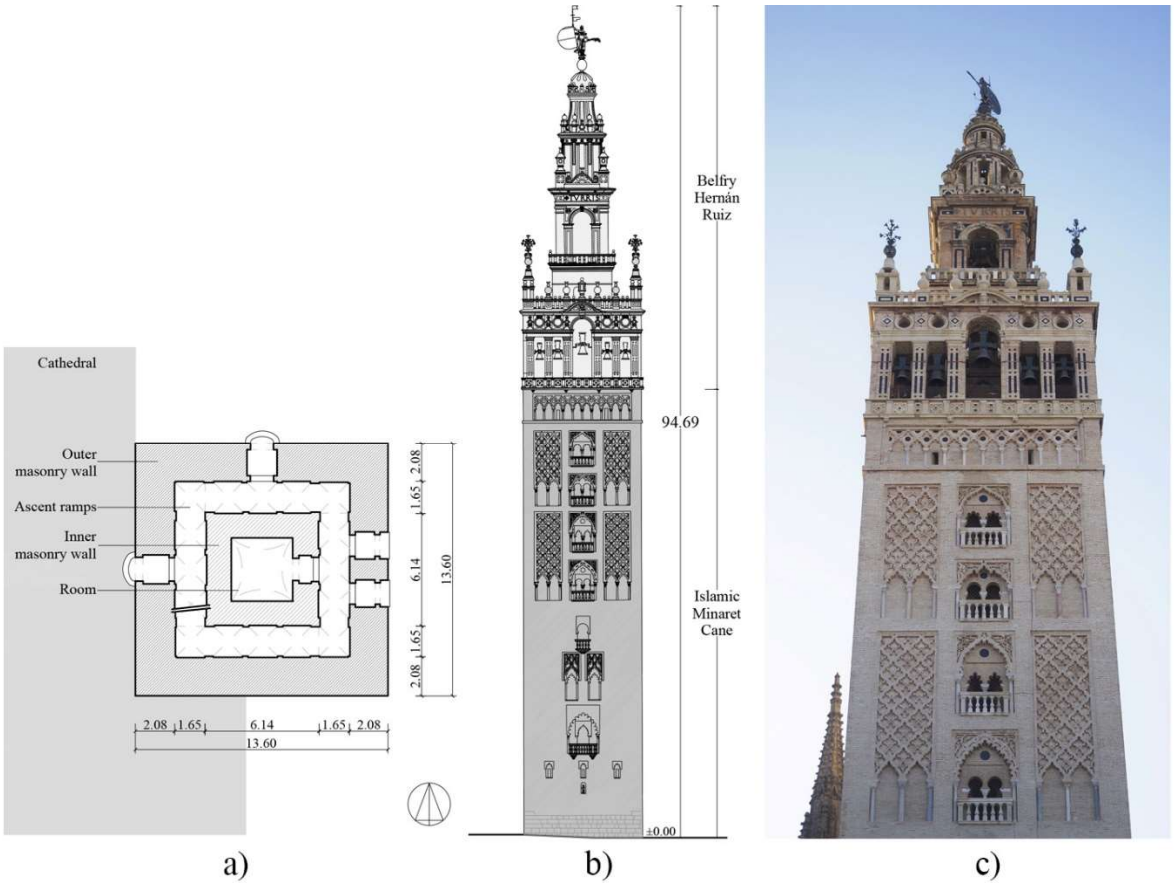


Figure 1: Schematic configuration of the Giralda tower. a) plan; b) west façade and c) current appearance.

## 3 METHOD

In this section, the methodology used to develop the work is shown. The steps followed have been plotted in Figure 2.

First, a historic analysis of the tower and its surroundings has been performed. For this purpose, the available information of the building has been collected. During this phase, different research works and previous projects [17–19] have been consulted and evaluated. This is a significant phase to know the historic evolution of the building, identifying its historic construction phases and its rehabilitation projects.

Second, an accurate geometry of the building has been developed. By doing this, the available tower blueprints [20] have been compared and completed with several *in situ* surveys. This *in situ* campaign has consisted of a visual inspection, digital images analysis and laser

measurements. An *in situ* ambient vibration test has been carried out to obtain the dynamic characteristic of the tower.

Next, a simplified 3D CAD model has been developed based on the precise geometry obtained in the previous phase. For this, the Rhinoceros software v7 [21] has been employed. Later, this 3D CAD model has been exported to the STKO software to develop the FEM. The different parameters of the numerical model (solid mesh, boundary condition and materials properties) have been defined in this software.

Finally, a modal analysis and a nonlinear static analysis (NLSA) have been performed using the OpenSees open-source software [13]. The modal analysis has been done to calibrate the numerical model, comparing the values of the periods and the frequencies with the *in situ* measurements obtained with the Operational Modal Analysis (OMA). This is important in order to obtain a reliable and robust FEM [7]. Then, a gravitational and horizontal NLSA have been carried out in both directions to obtain the capacity curves of the building, applying several load patterns.

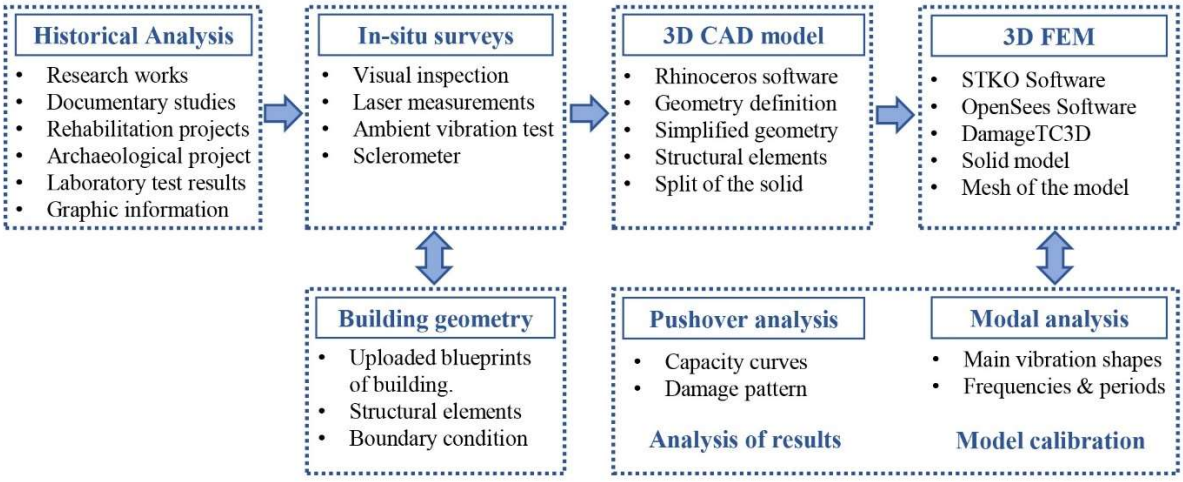


Figure 2: Schematic diagram of the method.

## 4 NUMERICAL MODEL

In this section the process to obtain the numerical model of the tower has been presented.

### 4.1 3D CAD MODEL

The 3D CAD model of the building geometry has been developed according to available information and to the *in situ* surveys (Figure 3). This model has been carried out in the Rhinoceros v7 software [21] which is a NURB-based 3D modelling tool.

Several factors have been considered in order to develop the geometry model. In that respect, the inner body has been modelled considering the different levels and openings up to the upper level (94.69 m height). The ramps have been modelled as different horizontal planes, reaching the level of the belfry. The outer wall has been modelled considering the different openings and the bell tower on the top. Different wall thicknesses have been borne in mind for the numerical model. In addition, the boundary condition of the nearby Cathedral has been considered. Accordingly, two equivalent masonry walls, that belong to the cathedral, have been modelled on the western and southern façades (Fig. 3).

Finally, it is important to highlight that the model has been split into different parts according to the different inner levels. This division has been made with the aim of improving the exportation to the STKO software.

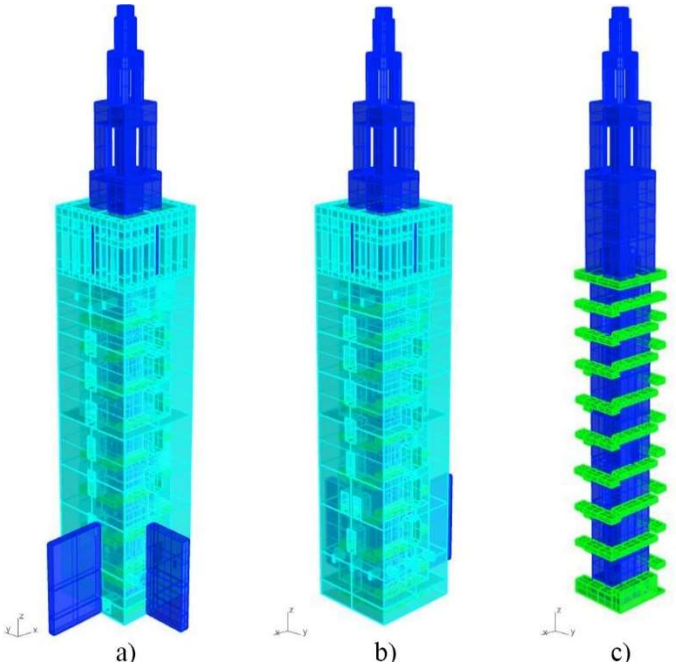


Figure 3: 3D CAD model. a) and b) outer wall and upper body; c) inner body and ramps.

## 4.2 3D FINITE ELEMENT MODEL

The definition of the 3D FEM model (Figure 4) has been carried out using the pre- and the post- STKO processor for OpenSees. The 3D CAD has been exported to obtain the base of the building geometry. Due to the complexity and to the size of the tower, the 3D FEM model has been developed as a solid model, following the macro-mechanical approach [22]. It has been meshed as non-structured tetra mesh, applying a four-node tetrahedron element (Figure 4). Furthermore, a 40 cm mesh size has been adopted due to its balance between accuracy and computational effort.

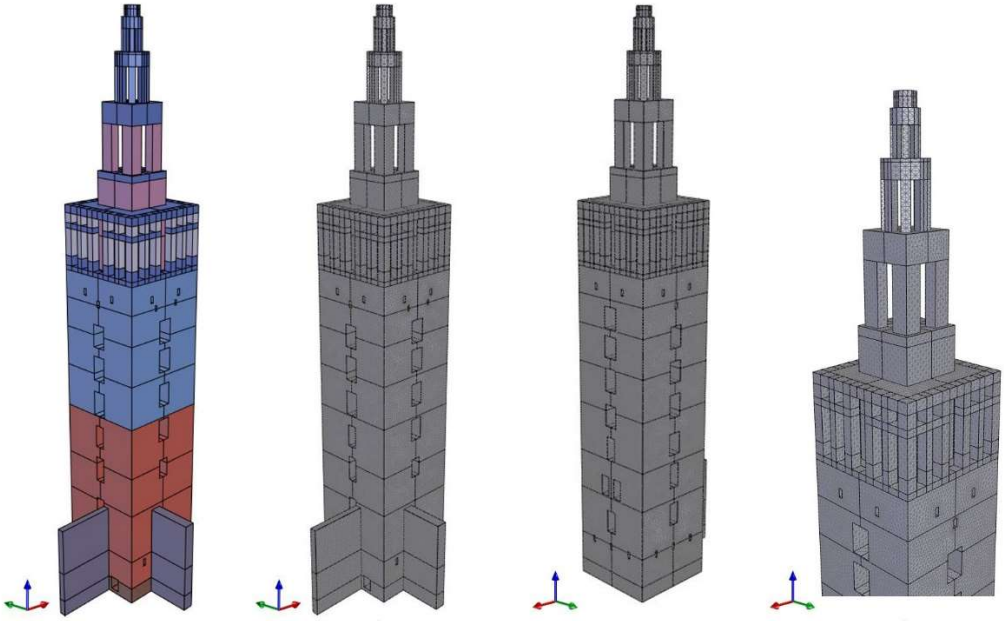


Figure 4: 3D FEM model. a) material properties; b) and c) mesh; d) belfry level.

A 3D Tension-Compression damage material has been applied to define the nonlinearity behaviour of the masonry material. This material model is implemented in the OpenSees software. It is expressed as two independent failure criteria for the tensile and for the compressive range, respectively. Different materials have been defined: brick and stone masonry for the walls and another one for the ramp. The mechanical properties of the materials have been listed in Table 1. These have been obtained from previous laboratory tests [23], building codes [24–26] and research works [27]. Furthermore, these parameters have been calibrated according to the OMA results.

| Mechanical parameters | Brick masonry | | | Stone Masonry | Stone masonry base | Lime concrete ramp | Units |
|---|---|---|---|---|---|---|---|
| | Bottom | Middle | Upper | | | | |
| **Mass** | | | | | | | |
| Density *(ρ)* | 1,800 | 1,800 | 1,800 | 2,200 | 2,500 | 2,500 | kg/m$^3$ |
| **Elasticity** | | | | | | | |
| *Young's modulus (E)* | 2.90 | 2.27 | 1.81 | 2.50 | 2.50 | 3.00 | GPa |
| *Poissons's ratio (v)* | 0.2 | 0.2 | 0.2 | 0.25 | 0.25 | 0.2 | |
| **Tension** | | | | | | | |
| *Tensile strength ($f_t$)* | 218 | 170.4 | 134 | 143.8 | 130.2 | 312 | kN/m$^2$ |
| **Compression** | | | | | | | |
| *Comp. elastic limit ($f_{c0}$)* | 2,441 | 1,988 | 1,582 | 1,677 | 1,519 | 2,600 | kN/m$^2$ |
| *Comp. peak strength ($f_{cp}$)* | 3,630 | 2,840 | 2,260 | 2,396 | 2,170 | 5,200 | kN/m$^2$ |
| *Comp. residual strength ($f_{cr}$)* | 363 | 284 | 226 | 239 | 217 | 520 | kN/m$^2$ |

Table 1: Mechanical properties used in the 3D FEM.

Finally, two horizontal load patterns have been applied: proportional to the mass and to the height of the interior levels (pseudo-triangular) and proportional to the mass (uniform). The control node has been placed in the centre of the masses at the top level of the building. The model has been calculated with the parallel option in OpenSees, using multiprocessors. Due to the characteristics of the computer, the model has been divided into 24 parts.

# 5 RESULT AND DISCUSSION

In this section, the results obtained from the modal analysis and the NLSA have been analysed and discussed. Furthermore, the damage analysis of the tower has been shown by means of the damage patterns.

## 5.1 Modal analysis

The modal analysis has been carried out in order to obtain de main vibration shapes and the periods of the tower. In this regard, the results have been compared with the *in situ* measurements used to calibrate the numerical model. Mode of vibration 1 and 2 are translational in the X and the Y direction, respectively. Mode 3 is torsional. It is important to note that the translational modal shapes deform diagonally. The experimental dynamic parameters of the tower have been extracted from the OMA. For this, the ARTeMis Modal Pro software [28] has been used. The values of the periods and the frequencies obtained are very close to the *in situ* measurements results (OMA). The period values obtained with the FEM are 1.51 s and 1.46 s for Mode 1 and Mode 2, respectively, and 0.43 s in the torsional mode (Table 2).

| Modes | FEM Frequencies (Hz) | OMA Frequencies (Hz) | FEM Periods (s) | OMA Periods (s) | Difference (%) |
|---|---|---|---|---|---|
| 1 | 0.66 | 0.66 | 1.51 | 1.51 | 0.0 |
| 2 | 0.68 | 0.70 | 1.46 | 1.42 | -2.9 |
| 3 | 2.28 | 2.01 | 0.43 | 0.49 | 11.9 |

Table 2: Results of modal analysis. Experimental and numerical results of three vibration modes.

## 5.2 Non-linear static analysis

The global seismic behaviour of the tower has been assessed through NLSA. This method has been widely used for this purpose [29] and suggested in the Eurocode 8 [30]. Due to the unsymmetric configurations caused by the irregular distribution of the ramps and the openings, the NLSA has been conducted in both directions (X and Y). It has also been applied in the negative and the positive orientations. Furthermore, two load patterns (triangular and uniform) have been employed to compare the results (Figure 5). The analysis has been performed until the base shear dropped by 20%, usually indicating the collapse state of the structure.

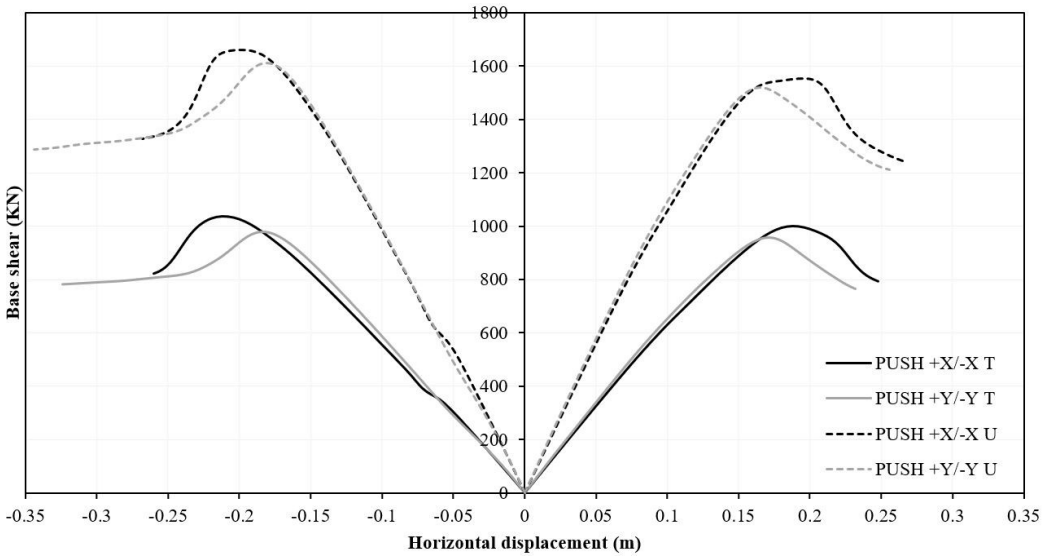


Figure 5: Capacity curves of the NLSA. Triangular (T) and Uniform (U) load patterns.

As Figure 5 shows, the models calculated with the uniform load pattern have a higher capacity than those calculated with the triangular one. This may be explained by the application of the horizontal load, which is added throughout the cane. This is more massive than the upper bodies. In general, the capacity in the X direction is higher than in the Y direction.

### 5.3 Damage pattern

The global damage distribution has been analysed using the different damage patterns from the NLSA in the X and Y direction (Figure 6 and 7). In this regard, the tensile damage models have been plotted because they are more severe than the compressive damage. Furthermore, these models have been plotted for the ultimate displacement. The main objective is to identify the areas of damage concentration in the tower.

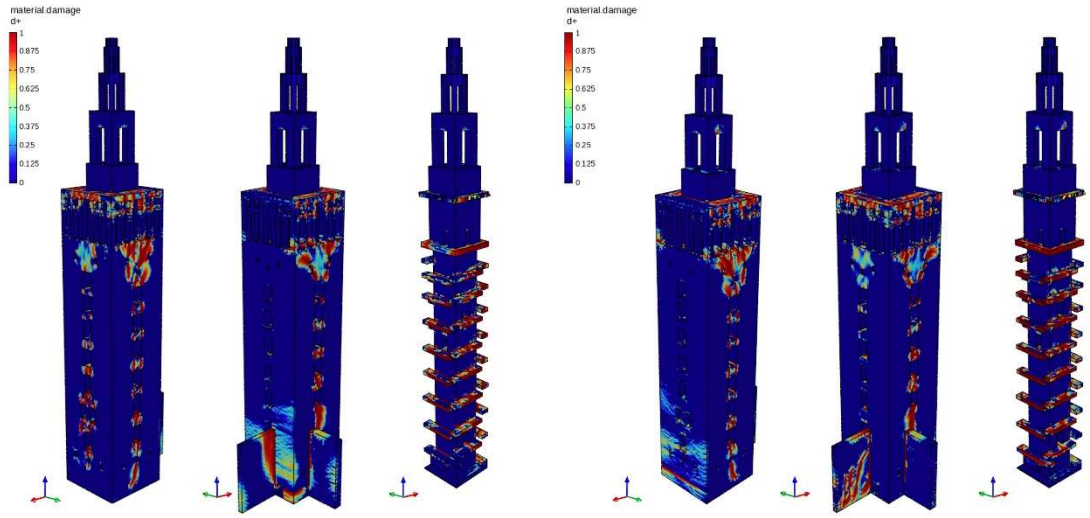


Figure 6: NLSA damage patterns X direction. a) +X direction and b) -X direction.

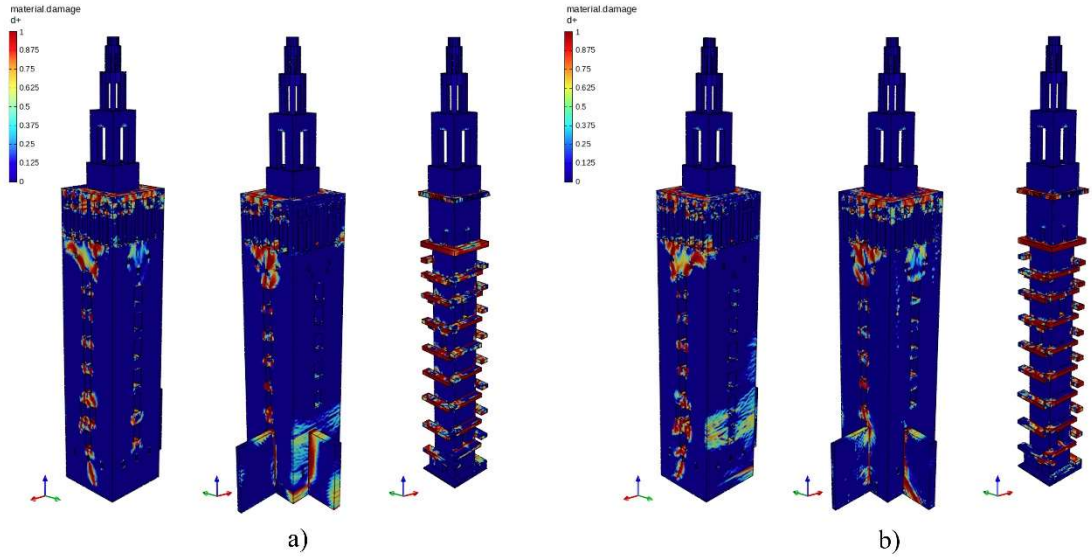


Figure 7: NLSA damage patterns Y direction: a) +Y direction and b) -Y direction.

In the cane of the tower, the greatest damage is concentrated near the openings since it is a very weak area: the hollows are irregularly located in the middle of each façade. Overall, the highest damage is concentrated near the belfry level. Figures 6 and 7 show that the ramp elements would be seriously damaged. Damage is also concentrated in the contact between the tower and the equivalent wall of the Cathedral. Furthermore, these walls produce a significant irregularity in the deformation of the numerical model. This is due to the fact that these walls are not symmetrical, being only in two façades. Finally, the upper body is not expected to suffer from significant damage.

## 6 CONCLUSIONS

This work has presented a preliminary seismic assessment of the historical Giralda tower. To do so, an advanced 3D FEM model has been developed, considering the available information of the building and *in situ* surveys. The results of the numerical modal analysis and the ambient vibration test (OMA) have been used to calibrate the 3D FEM. Finally, the global seismic behaviour of the tower has been assessed through NLSA. The following conclusions are derived from this work:

- These types of work provide useful information and knowledge about the seismic safety of complex heritage buildings. The results obtained can be used in future restoration projects of heritage buildings. Furthermore, the method developed in this work can be also applied for the assessment of other masonry towers.
- The field surveys conducted in this study have been important to identify the mechanical characteristics of the materials and the geometrical issues for the development of the numerical model. In this regard, the ambient vibration test is fundamental in the calibration of the FEM of complex ancient buildings.
- This work has revealed that it is important to apply at least two different load patterns in the NLSA, as recommended by Eurocode 8. Furthermore, it is highly important to consider the boundary conditions since they might introduce some irregularities in the behaviour of heritage buildings.
- The highest damage is concentrated near the belfry level because it is a weaker part compared to the cane of the tower. Furthermore, the interior ramps might be completely damaged. These are very weak structural element between two rigid bodies. Note that these structural elements were the most damaged ones in past earthquakes, according to the testimonies.
- In this study, NLSA has been applied to assess the global seismic behaviour of the tower. In future studies, nonlinear dynamic analyses are expected to be carried out.

## ACKNOWLEDGEMENTS

Romero-Sánchez, E. (author) gratefully acknowledges the FPU Programme of Spain´s Ministry of Universities (FPU19/03597) for the financial support provided. This work has been supported by the FEDER_US-1380730 research project entitled “Proyecto para un patrimonio cultural resiliente a los terremotos. Casos de estudio: La Mezquita de Córdoba y la Giralda de Sevilla”.

## REFERENCES


[1] J.L. Amaro-Mellado, A. Morales-Esteban, G. Asencio-Cortés, F. Martínez-Álvarez, Comparing seismic parameters for different source zone models in the Iberian Peninsula, Tectonophysics. (2017). https://doi.org/10.1016/j.tecto.2017.08.032.

[2] M.V. Requena-Garcia-Cruz, S. Cattari, R. Bento, A. Morales-Esteban, Comparative study of alternative equivalent frame approaches for the seismic assessment of masonry buildings in OpenSees, Journal of Building Engineering. 66 (2023) 105877. https://doi.org/10.1016/j.jobe.2023.105877.

[3] M. V. Requena-Garcia-Cruz, A. Morales-Esteban, P. Durand-Neyra, Assessment of specific structural and ground-improvement seismic retrofitting techniques for a case study RC building by means of a multi-criteria evaluation, Structures. 38 (2022) 265–278. https://doi.org/10.1016/j.istruc.2022.02.015.

[4] M. V. Requena-Garcia-Cruz, E. Romero-Sánchez, A. Morales-Esteban, Numerical investigation of the contribution of the soil-structure interaction effects to the seismic performance and the losses of RC buildings, Developments in the Built Environment. 12 (2022). https://doi.org/10.1016/j.dibe.2022.100096.

[5] E. Romero Sánchez, A. Morales Esteban, J. Navarro Casas, Analysis of the Historical Settlements of the Giralda, International Journal of Architectural Heritage. 00 (2022) 1–19. https://doi.org/10.1080/15583058.2022.2034070.

[6] S. Degli Abbati, A.M. D'Altri, D. Ottonelli, G. Castellazzi, S. Cattari, S. de Miranda, S. Lagomarsino, Seismic assessment of interacting structural units in complex historic masonry constructions by nonlinear static analyses, Comput Struct. 213 (2019) 51–71. https://doi.org/10.1016/j.compstruc.2018.12.001.

[7] M. Malcata, M. Ponte, S. Tiberti, R. Bento, G. Milani, Failure analysis of a Portuguese cultural heritage masterpiece: Bonet building in Sintra, Eng Fail Anal. 115 (2020). https://doi.org/10.1016/j.engfailanal.2020.104636.

[8] A. Vuoto, J. Ortega, P.B. Lourenço, F. Javier Suárez, A. Claudia Núñez, Safety assessment of the Torre de la Vela in la Alhambra, Granada, Spain: The role of on site works, Eng Struct. 264 (2022). https://doi.org/10.1016/j.engstruct.2022.114443.

[9] M. V. Requena-Garcia-Cruz, E. Romero-Sánchez, M.P. López-Piña, A. Morales-Esteban, Preliminary structural and seismic performance assessment of the Mosque-Cathedral of Cordoba: the Abd al-Rahman I sector, Eng Struct. Under Review (2023).

[10] D.M. McCann, M.C. Forde, Review of NDT methods in the assessment of concrete and masonry structures, NDT and E International. 34 (2001) 71–84. https://doi.org/10.1016/S0963-8695(00)00032-3.

[11] S. Boschi, L. Galano, A. Vignoli, Mechanical characterisation of Tuscany masonry typologies by in situ tests, Bulletin of Earthquake Engineering. 17 (2019) 413–438. https://doi.org/10.1007/s10518-018-0451-4.

[12] M. Ponte, R. Bento, S.D. Vaz, A Multi-Disciplinary Approach to the Seismic Assessment of the National Palace of Sintra, International Journal of Architectural Heritage. 15 (2021) 757–778. https://doi.org/10.1080/15583058.2019.1648587.

[13] F. McKenna, G.L. Fenves, M.H. Scott, OpenSees: Open system for earthquake engineering simulation, (2000).

[14] M. Petracca, F. Candeloro, G. Camata, STKO User manual. Astea software Technology, (2017) 1–228. http://www.asdeasoft.net/stko?stko-academy.

[15] F. Peña, P.B. Lourenço, N. Mendes, D. V. Oliveira, Numerical models for the seismic assessment of an old masonry tower, Eng Struct. 32 (2010) 1466–1478. https://doi.org/10.1016/j.engstruct.2010.01.027.

[16] P. Gentil, EL riesgo sísmico de Sevilla, Publicaciones de la Universidad de Sevilla, Sevilla, 1989.
[17] A. Jiménez Martín, Notas sobre el Alminar de la Aljama de Isbiltya, in: VIII Centenario de La Giralda (1198-1998), 1998: pp. 31–43.
[18] Á. Barrios Padura, J. Barrios Sevilla, J. García Navarro, Settlement predictions, bearing capacity and safety factor of subsoil of Seville's Giralda, International Journal of Architectural Heritage. 6 (2012) 626–647. https://doi.org/10.1080/15583058.2011.594933.
[19] A. Jiménez Martín, J.M. Cabeza Méndez, Turris Fortissima: documentos sobre la construcción, acrecentamiento y restauración de la Giralda., 1988.
[20] A. Almagro, J.I. Zúñiga, Atlas arquitectónico de la Catedral de Sevilla, Escuela de, Cabildo de la Santa, Metropolitana y Patriarcal Iglesia Catedral de Sevilla, Sevilla - Granada, 2007.
[21] R. McNeer, Rhinoceros v7, (2021).
[22] A.M. D'Altri, V. Sarhosis, G. Milani, J. Rots, S. Cattari, S. Lagomarsino, E. Sacco, A. Tralli, G. Castellazzi, S. de Miranda, Modeling Strategies for the Computational Analysis of Unreinforced Masonry Structures: Review and Classification, Archives of Computational Methods in Engineering. 27 (2020) 1153–1185. https://doi.org/10.1007/s11831-019-09351-x.
[23] S.A. Laboratorio Análisis Industriales Vorsevi, DETERMINACIONES REALIZADAS A UNAS MUESTRAS GIRALDA, (1985).
[24] European Union, Eurocode-6: Design of masonry structures. Part 1-1: General rules for reinforced and unreinforced masonry structures, Brussels, 2005.
[25] Ministerio delle Infrastrutture e dei Trasporti, Aggiornamento delle 'Norme tecniche per le costruzioni'» di cui al decreto ministeriale 17 gennaio 2018. (Italian Guideline), 2018.
[26] Ministerio de Fomento, CTE DB SE-F Basic Document. Structural Security. Spanish Technical Building Code, 2019.
[27] M. Kržan, S. Gostič, S. Cattari, V. Bosiljkov, Acquiring reference parameters of masonry for the structural performance analysis of historical buildings, Bulletin of Earthquake Engineering. 13 (2015) 203–236. https://doi.org/10.1007/s10518-014-9686-x.
[28] Structural Vibration Solutions A/S, ARTeMIS Modal Pro, (2019).
[29] S. Lagomarsino, S. Cattari, PERPETUATE guidelines for seismic performance-based assessment of cultural heritage masonry structures, Bulletin of Earthquake Engineering. 13 (2015) 13–47. https://doi.org/10.1007/s10518-014-9674-1.
[30] European Union, Eurocode-8: Design of structures for earthquake resistance. Part 3: Assessment and retrofitting of buildings, Brussels, 2005. http://www.phd.eng.br/wp-content/uploads/2014/07/en.1998.3.2005.pdf.

COMPDYN 2023
9th ECCOMAS Thematic Conference on
Computational Methods in Structural Dynamics and Earthquake Engineering
S. Banerjee, D. Singh, S. Shiradhonkar
Athens, Greece, 12-14 June 2023

# ESTIMATION OF SEISMIC DESIGN FACTORS FOR RC-SMRF BUILDINGS IN SEISMIC RISK FRAMEWORK

**Suman Banerjee**[1], **Devendra Singh**[2], **and Saurabh Shiradhonkar**[3]

[1] Ph.D. Student, Dept. of Earthquake Engineering
Indian Institute of Technology, Roorkee
e-mail: s_banerjee@eq.iitr.ac.in

[2] Ph.D. Student, Dept. of Earthquake Engineering
Indian Institute of Technology, Roorkee
e-mail: devendra_s@eq.iitr.ac.in

[3] Assistant Professor, Dept. of Earthquake Engineering
Indian Institute of Technology, Roorkee
e-mail: saurabh.shiradhonkar@eq.iitr.ac.in

## Abstract

*In seismic design, buildings are usually designed for a seismic demand lower than the actual expected during ground shaking. The seismic demand is scaled using Response Reduction factor (R-factor) and Importance factor (I-factor). R-factor considers the capacity of RC members in post-yield response, over-strength, and indeterminacy. I-factor represents the occupancy of the building. Indian seismic design code, IS 1893: 2016 [1], prescribed R-factor for various ductility classes and I-factor for different occupancy classes to determine design force for Reinforced Concrete-Moment Resisting (RC-MR) frame buildings. The rationality of R-factor and I-factor in the seismic design code has not been evaluated adequately in available literature. This study evaluates R-factors and I-factors in seismic design code in seismic risk framework. Seismic risk characterizes the performance of a building under uncertain seismic hazard and seismic capacity. The collapse seismic risk of the building is determined as the integration of the collapse fragility and seismic hazard curve. The collapse fragilities of building archetypes are estimated using Incremental Dynamic Analyses (IDA) [2] for 22 pairs of ground motion given in FEMA P695 (2009) [3]. The seismic performances of a set of RC-SMRF buildings, designed for different seismic hazard and importance levels of IS 1893: 2016 [1], are estimated in terms of conditional collapse risk and mean annual collapse risk. Seismic design parameters viz. available Response Reduction factor ($R_{avl}$) and Overstrength factor ($\Omega$) of the buildings designed as per prevalent Indian Standards are determined for acceptable risk levels.*

**Keywords:** RC-SMRF, Occupancy Class, R-factor, Importance Factor, Seismic Risk, IDA.

# 1 INTRODUCTION

The principle objective of seismic design is to prevent collapse of buildings under rare major earthquakes and also to ensure life safety of occupants under frequent earthquakes [1, 4]. National seismic design codes follow force-based method for seismic design of buildings. The buildings are designed for lower lateral forces than expected during rare major earthquake. It is expected that buildings utilize inherent ductility, indeterminacy and overstrength to avoid collapse [1] under strong ground shaking. The inherent ductility in a building structure is implicitly accounted for in seismic design by scaling down the base shear force by R-factor. IS 1893: 2016 [1] prescribes value of 3 and 5 for R-factor in seismic design of RC ordinary moment resisting frame (RC-OMRF) and RC special moment resisting frame (RC-SMRF) buildings respectively.

Design seismic force is scaled by another parameter known as Importance factor (I-factor). This factor is related to life risk to occupants posed by building damage. Buildings are expected to have damage during earthquake and thus, buildings with higher occupancy will have larger risk to life during major earthquakes. Therefore, buildings with higher occupancy are designed to resist higher lateral force than the building with lower occupancy. Buildings with different occupancy classes are designed to resist different lateral force. Occupancy classes are categorised based on the number of lives in the building and the socio-economic importance of the building. IS 1893: 2016 [1] categorises buildings in three classes – i, ii, and iii, and provides I-factor values of 1.5, 1.2, and 1 for these occupancy classes respectively. Importance factor 1 and 1.2 of IS 1893: 2016 [1] are based on number of occupants. Importance factor 1.5, on the other hand, is defined based on of occupancy class i.e. important buildings such as school, government offices, hospital etc.

Response Reduction factors (R) and Importance Factors (I) in IS 1893 [1] are established based on of engineering judgment and expert's opinion [5]. Seismic Performance assessment of buildings, designed for different Response Reduction factors and occupancy classes, is required to ensure viability of the factors used in seismic design. Main objective of the study is to evaluate seismic performance of building, designed for different ductility and occupancy classes as per IS 1893: 2016 [1] in a probabilistic framework. Seismic performance of buildings is determined in terms of conditional collapse risk and mean annual collapse risk.

# 2 SEISMIC RISK FRAMWORK, METHODOLOGY, AND ACCEPTABLE LIMITS

## 2.1 Seismic Risk Framework

Performance of the building structures is assessed in the seismic risk framework, proposed by Cornel and Krawinkler [6]. Seismic risk is estimated from integration of fragility function of exceeding a damage state with seismic hazard curve. Mean annual rate of collapse, λ, is estimated as,

$$\lambda = \int_{s=0}^{\infty} -F(s)\frac{dG(s)}{ds}ds \tag{1}$$

where, F(s) is collapse fragility function, G(s) is the hazard curve, and 's' is the intensity measure. Seismic fragility function gives the probability of exceeding a damage state as a function of intensity measure. Seismic hazard curve is a plot of probability of exceedance against ground motion intensity measure. The annual probability of exceedance of collapse of the building ($P_f$) is estimated from Poisson's distribution as,

$$P_f = 1 - \exp^{-\lambda \cdot t} \tag{2}$$

## 2.2 Methodology

The methodology adopted in the study is shown in Figure 1. The building archetype are designed as per IS 1893: 2016 [1]. Design base shear force is calculated from product of seismic weight and base shear coefficient $A_h$. Base shear coefficient, $A_h$ is estimated as,

$$A_h = 1.5 \times \frac{Z}{2} \times \frac{I}{R} \times \frac{Sa}{g} \tag{3}$$

where, Z is the seismic zone factor; I, and R are importance and response reduction factors respectively. Sa/g is design spectral acceleration at the code-prescribed fundamental time period ($T_a$) of the building. A factor of 1.5 is multiplied to take into account the load factors used in load combinations in seismic design.

OpenSees [7] environment is used for analytical modelling of building frames. Overstrength factors are calculated from nonlinear static pushover analysis. Overstrength factor is determined as the ratio of maximum base shear force resisted by the frame in pushover analysis ($V_{max}$) to the design base shear force ($V_d$). The definition of overstrength factor is shown in Figure 2. The static pushover analyses are carried using analytical model of archetype building frames. Story shear distribution along height of the building is taken as triangular for static pushover analysis.

Collapse fragility function is estimated from Incremental Dynamic Analyses (IDA) [2]. Available response reduction factor ($R_{avl}$) is estimated from the method given by Badal and Sinha [8]. The response reduction factor is estimated from relationship between collapse margin ratio (CMR) [3] and design base shear force of a building ($C_s$). Estimation of available response reduction factor ($R_{avl}$) is explained in Figure 3. Available response reduction factor is formulated as

$$R_{avl} = \frac{I}{2} \frac{\mu_{Sa,CP}}{C_s} \exp\left(\beta_{TOT} \cdot \Phi^{-1}(p_{collapse|MCE})\right) \tag{4}$$

where, $\mu_{Sa,CP}$ is the median collapse intensity, $\beta_{TOT}$ is the total uncertainty, and $p_{collapse|MCE}$ is allowable conditional probability of collapse at MCE.

Seismic hazard is defined in terms of zone factor in IS 1893: 2016 [1]. As probabilistic assessment of seismic hazard is not robustly available for India, the seismic hazard curve is approximated using power law [9] to determine seismic risk. The hazard curve is formulated as,

$$H(S_a) = k_o \cdot im^{-k} \tag{5}$$

where, $H(S_a)$ is the probability of exceedance of intensity measure, 'im'. The constants 'k' and '$k_o$' are estimated from IS 1893: 2016 [1] seismic demand, where MCE level has a 2% probability of exceedance and DBE level has 10% probability of exceedance. The values of zone factors considered in this study and constants 'k' and '$k_o$' are summarized in Table 1.

| Seismic Zone | Zone Factor (Z) | k | $k_o$ |
|---|---|---|---|
| III | 0.16 | 2.32 | 0.002 |
| IV | 0.24 | 2.32 | 0.004 |
| V | 0.36 | 2.32 | 0.1 |

Table 1: Details of seismic hazard estimation

## 2.3 Acceptable Limits

IS 1893: 2016 [1] remains silent on acceptable seismic performance of the buildings. ASCE-7: 2016 [4] has provided limiting values of Probability of collapse for buildings with different occupancy classes. The limiting values for acceptable seismic risk of buildings are given in Table 2. The study also evaluates available ductility ($R_{avl}$), and overstrength factor ($\Omega$) of the buildings designed as per IS 1893: 2016 [1] in a probabilistic framework.

| Risk Category (ASCE-7, 2016) | P[CP\|MCE] | Annual Probability of Collapse ($\lambda$) |
|---|---|---|
| I & II | 10% | 0.02% |
| III | 5% | 0.02% |
| IV | 2.5% | 0.02% |

Table 2: Acceptable Seismic performance of RC-MR frames as per ASCE 7: 2016

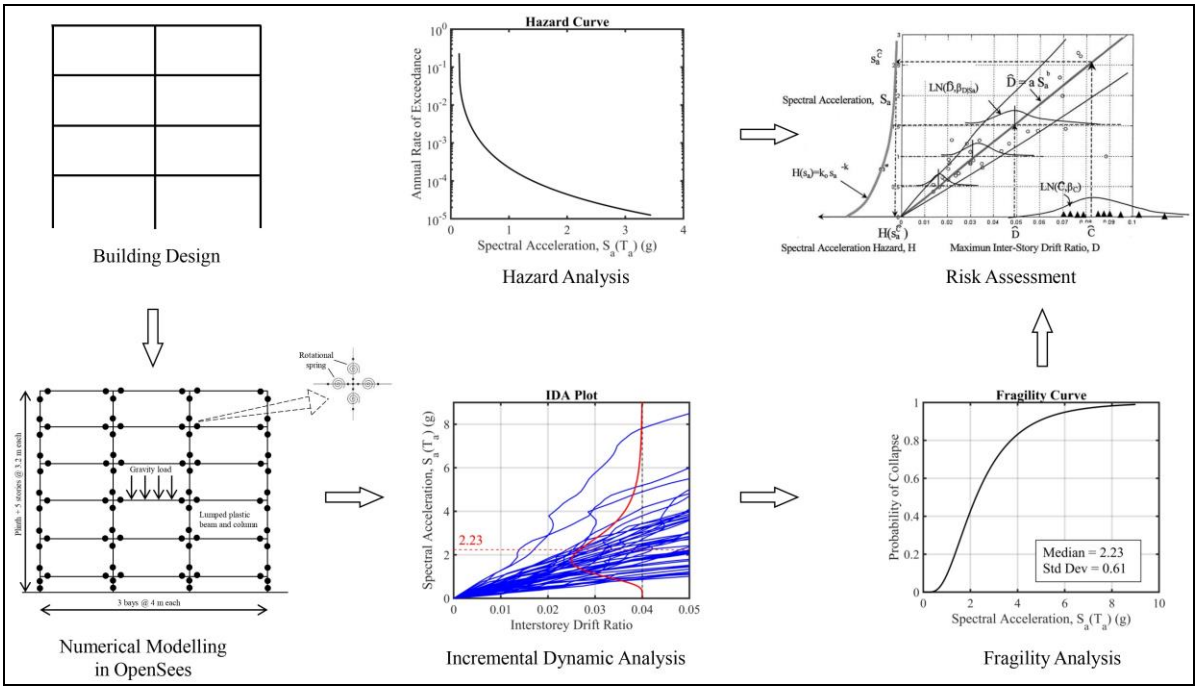


Figure 2: Meta-flowchart of the methodology followed for seismic risk estimation of RC-SMRFs

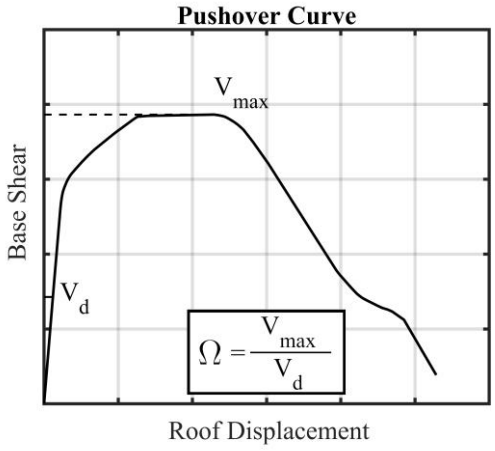


Figure 2: Definition of overstrength factor

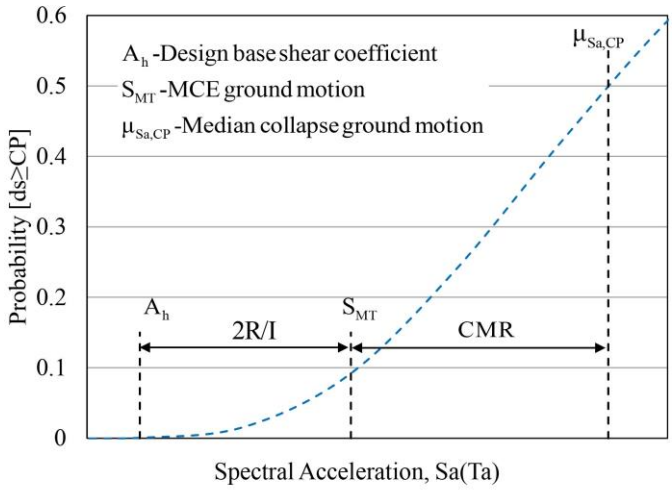


Figure 3: Estimation of Response reduction factor ($R_{avl}$) from collapse fragility and allowable conditional probability of collapse at MCE (Badal and Sinha [8])

Acceptable limits of Risk category I is similar to buildings designed with importance factors 1 and 1.2 of IS 1893: 2016 [1]. There is no direct relationship between building occupancy class corresponding to importance factor 1.5 of IS 1893: 2016 [1] and Risk categories summarized in Table 1. The acceptable limits of risk categories II and III from ASCE-7: 2016 [4] are similar to building occupancy class corresponding to importance factor 1.5 of IS 1893: 2016 [1]. In the present study, response reduction factor is estimated for 10 % conditional probability of collapse at MCE (i.e. $p_{collapse|MCE} = 0.1$).

## 3 SELECTION OF BUILDING ARCHETYPES

Building archetypes are selected based on building configurations in India. The selected RC building configuration has 9 bays in one direction and 3 bays in the other direction. Figure 4 shows the plan and elevation of the selected buildings. A total of 36 regular RC-SMRFs are adopted in the study. Plan is identical for all the buildings. Building height is varied to study the effect of building height on seismic performance. Plinth height is 1.2 m for all the buildings.

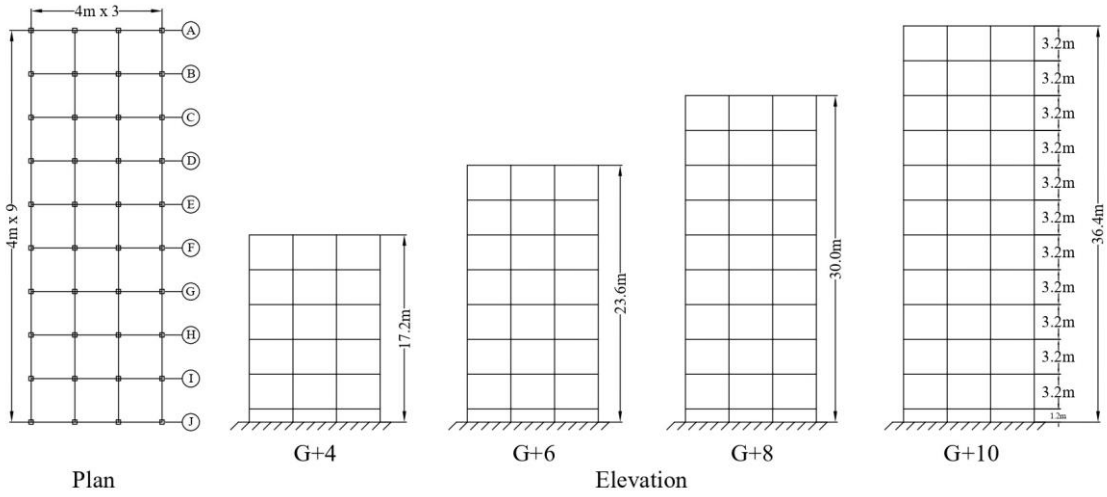


Figure 4: Plan and elevation of the buildings considered in the study

| Building ID | Zone | I-factor | # Storey | Height | $T_a$ (sec)[1] | $T_1$ (sec)[2] | $A_h$ (%) |
|---|---|---|---|---|---|---|---|
| C14310 | III | 1.0 | 5 | 17.2 m | 0.633 | 1.48 | 3.44% |
| C14312 | III | 1.2 | 5 | 17.2 m | 0.633 | 1.32 | 4.13% |
| C14315 | III | 1.5 | 5 | 17.2 m | 0.633 | 1.33 | 5.16% |
| C14410 | IV | 1.0 | 5 | 17.2 m | 0.633 | 1.32 | 5.16% |
| C14412 | IV | 1.2 | 5 | 17.2 m | 0.633 | 1.29 | 6.19% |
| C14415 | IV | 1.5 | 5 | 17.2 m | 0.633 | 1.22 | 7.73% |
| C14510 | V | 1.0 | 5 | 17.2 m | 0.633 | 1.21 | 7.73% |
| C14512 | V | 1.2 | 5 | 17.2 m | 0.633 | 1.21 | 9.28% |
| C14515 | V | 1.5 | 5 | 17.2 m | 0.633 | 1.20 | 11.60% |
| C16310 | III | 1.0 | 7 | 23.6 m | 0.803 | 1.90 | 2.71% |
| C16312 | III | 1.2 | 7 | 23.6 m | 0.803 | 1.85 | 3.25% |
| C16315 | III | 1.5 | 7 | 23.6 m | 0.803 | 1.65 | 4.06% |
| C16410 | IV | 1.0 | 7 | 23.6 m | 0.803 | 1.73 | 4.06% |
| C16412 | IV | 1.2 | 7 | 23.6 m | 0.803 | 1.69 | 4.88% |
| C16415 | IV | 1.5 | 7 | 23.6 m | 0.803 | 1.55 | 6.10% |
| C16510 | V | 1.0 | 7 | 23.6 m | 0.803 | 1.60 | 6.10% |
| C16512 | V | 1.2 | 7 | 23.6 m | 0.803 | 1.41 | 7.32% |
| C16515 | V | 1.5 | 7 | 23.6 m | 0.803 | 1.36 | 9.15% |
| C18310 | III | 1.0 | 9 | 30.0 m | 0.961 | 2.10 | 2.26% |
| C18312 | III | 1.2 | 9 | 30.0 m | 0.961 | 2.09 | 2.82% |
| C18315 | III | 1.5 | 9 | 30.0 m | 0.961 | 2.09 | 3.40% |
| C18410 | IV | 1.0 | 9 | 30.0 m | 0.961 | 2.02 | 3.40% |
| C18412 | IV | 1.2 | 9 | 30.0 m | 0.961 | 1.95 | 4.08% |
| C18415 | IV | 1.5 | 9 | 30.0 m | 0.961 | 1.92 | 5.09% |
| C18510 | V | 1.0 | 9 | 30.0 m | 0.961 | 1.89 | 5.09% |
| C18512 | V | 1.2 | 9 | 30.0 m | 0.961 | 1.85 | 6.11% |
| C18515 | V | 1.5 | 9 | 30.0 m | 0.961 | 1.65 | 7.64% |
| C110310 | III | 1.0 | 11 | 36.4 m | 1.11 | 2.58 | 1.96% |
| C110312 | III | 1.2 | 11 | 36.4 m | 1.11 | 2.57 | 2.35% |
| C110315 | III | 1.5 | 11 | 36.4 m | 1.11 | 2.53 | 2.94% |
| C110410 | IV | 1.0 | 11 | 36.4 m | 1.11 | 2.50 | 2.94% |
| C110412 | IV | 1.2 | 11 | 36.4 m | 1.11 | 2.43 | 3.53% |
| C110415 | IV | 1.5 | 11 | 36.4 m | 1.11 | 2.19 | 4.41% |
| C110510 | V | 1.0 | 11 | 36.4 m | 1.11 | 2.22 | 4.41% |
| C110512 | V | 1.2 | 11 | 36.4 m | 1.11 | 2.02 | 5.29% |
| C110515 | V | 1.5 | 11 | 36.4 m | 1.11 | 1.82 | 6.62% |

[1] Fundamental time period of building as per IS 1893: 2016 [1]
[2] Fundamental time period of building from modal analysis

Table 3: Details of archetypical buildings adopted in the study

Archetype building structures are designed for different seismic demands i.e. zone III, IV, V, and for importance factors 1.0, 1.2, and 1.5. The details of the selected building structures are summarised in Table 3. The buildings are designed and detailed as per IS 1893: 2016 [1], IS 13920: 2016 [10] and IS 456: 2002 [11]. The details of the design of the buildings are mentioned in Table 4. Design details of beam and column elements of example building ID C16512 are shown in Table 5.

| Particulars | Description |
|---|---|
| Frame type | Special moment resisting bare space frame |
| Seismic design lateral force | Response spectrum method |
| Loading | Slab thickness: 150 mm<br>Superimposed load: Floor finish 1.8 kN/m$^2$ (IS 875, 1987)<br>Live load: 2 kN/m$^2$ (for I 1.0, 1.2); 3kN/m$^2$ (for I 1.5),<br>Roof live load: 1.5 kN/m$^2$ (IS 875 (Part 2), 1987) |
| Limit state load combinations | [1.5 DL + 1.5 LL]<br>[1.5 DL + 1.5 EQL]<br>[1.2 DL + 1.2 LL + 1.2 EQL] |
| General ductile detailing | 135◦ hooks for stirrups with 10 × diameter of extension<br>Shear capacity > Shear force corresponding to 1.4 times unfactored moment capacity |
| SCWB ratio | 1.4 |
| Max interstorey drift | 0.4% |

Table 4: Loading, design, and detailing of building structures

| Storey | Member | Length (mm) | Section (mm × mm) | Concrete Grade (MPa) | Long. r/f | | Trans. r/f |
|---|---|---|---|---|---|---|---|
| | | | | | Top | Bottom | |
| 7 | Beam | 4000 | 300 × 350 | M40 | 0.42% | 0.26% | 0.45% |
| 6 | Beam | 4000 | 300 × 350 | M40 | 0.62% | 0.31% | 0.45% |
| 5 | Beam | 4000 | 300 × 400 | M40 | 0.62% | 0.35% | 0.45% |
| 4 | Beam | 4000 | 300 × 400 | M40 | 0.71% | 0.47% | 0.45% |
| 3 | Beam | 4000 | 300 × 400 | M40 | 0.79% | 0.54% | 0.45% |
| 2 | Beam | 4000 | 300 × 400 | M40 | 0.84% | 0.59% | 0.45% |
| 1 | Beam | 4000 | 300 × 400 | M40 | 0.81% | 0.55% | 0.45% |
| Plinth | Beam | 4000 | 300 × 350 | M40 | 0.32% | 0.29% | 0.45% |
| 7 | Column | 3200 | 300 × 350 | M40 | 3.06% | | 0.67% |
| 6 | Column | 3200 | 300 × 350 | M40 | 3.06% | | 0.67% |
| 5 | Column | 3200 | 300 × 350 | M40 | 3.06% | | 0.67% |
| 4 | Column | 3200 | 400 × 450 | M40 | 1.79% | | 0.50% |
| 3 | Column | 3200 | 400 × 450 | M40 | 1.79% | | 0.50% |
| 2 | Column | 3200 | 400 × 450 | M40 | 1.79% | | 0.50% |
| 1 | Column | 3200 | 400 × 450 | M40 | 2.68% | | 0.50% |
| Plinth | Column | 1200 | 400 × 450 | M40 | 2.68% | | 0.50% |

Table 5: Design detail of structural members for building ID C16512

## 4 NONLINEAR MODELLING OF BUILDING STRUCTURES

### 4.1 Line Elements with Concentrated Plasticity

2D nonlinear analytical model of each building frame is developed in OpenSees [7]. The frame elements are modelled as linear elastic elements, and zero-length rotational plastic hinges at the end. The Rotational hinges model nonlinear flexural response of the RC member. Stiffnesses of the elastic line elements are taken as 35% and 70% of $EI_{gross}$ for beams and columns respectively. Beam-column joints are modeled with rigid offsets. Capacity design prin-

ciple is followed in the design of buildings. The shear capacity of structural members (both beams and columns) is ensured larger than the flexural capacity. This eliminates possibility of shear failure before flexural collapse of RC member, Thus, shear hinges are not explicitly modeled in the present study. Figure 5 presents a schematic diagram of the node and element assignments in the current modelling scheme.

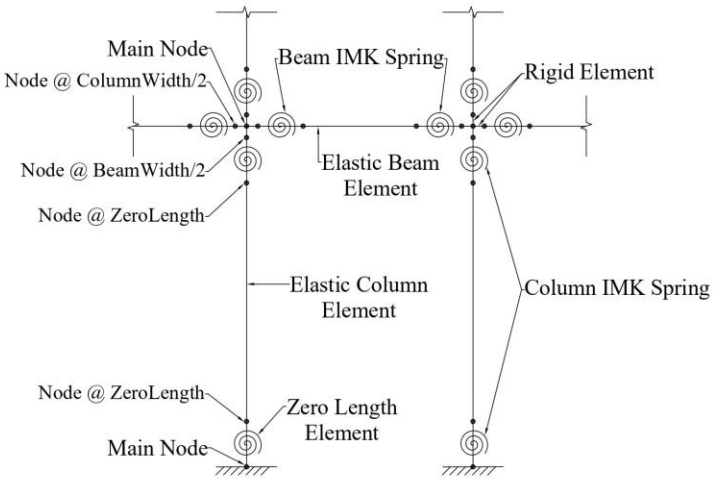


Figure 5: Numerical modelling scheme for building frames

### 4.2 Modeling Inelastic Behaviour of RC Member

The inelastic flexural response is modeled using concentrated plastic hinge. The inelastic flexure behavior of RC members is represented by the moment-rotation relationship. Hysteretic characteristics of RC members viz. strength degradation, stiffness degradation, and pinching under cyclic loading, are modeled as per Ibarra-Medina-Krawinkler model [12]. The definitions of backbone curve and parameters for the representation of hysteretic behavior are shown in Figure 6. The key components of the IMK model are flexural stiffness ($K_e$), yield moment capacity ($M_y$), capping to yield moment ratio ($M_c/M_y$), capping rotation ($\theta_p$), post-capping rotation ($\theta_{pc}$), ultimate rotation ($\theta_u$), residual strength, and the strength and stiffness degradation parameters ($\lambda$). Yield moment capacity ($M_y$) is calculated from section analysis of designed RC sections. The initial flexural stiffness of a member is taken as the secant value of the effective stiffness at 40% of the yield force of the component (i.e. $K_{stf_40}$ or $EI_{stf_40}$) [13]. The parameters defining hysteretic behavior are determined using expressions proposed by Haselton [13].

## 5 ESTIMATION OF COLLAPSE SEISMIC RISK OF BUILDINGS

The two components of seismic risk calculation are seismic hazard curve and seismic fragility function. The collapse fragility function is calculated using IDA in this study.

### 5.1 Incremental Dynamic Analysis and Estimation of Collapse Fragility Function

Vamvatsikos and Cornell [2] proposed incremental dynamic analysis (IDA) to estimate fragility function of a structure. Nonlinear time-history analyses of the analytical model of the building is carried out using ground motions with increasing intensities. The incremental analyses are carried out until the target (collapse) damage state is reached. Figure 7(a) shows output from IDA. Collapse damage state of building is defined at 4% maximum IDR in the

building. Fragility function is assumed to be lognormally distributed [14]. The parameters of lognormal distribution are determined statistically from collapse intensities ($S_a(T_a)$). Collapse fragility curve is plotted by fitting a lognormal distribution through the collapse data points from IDA. Figure 7(b) shows example of collapse fragility.

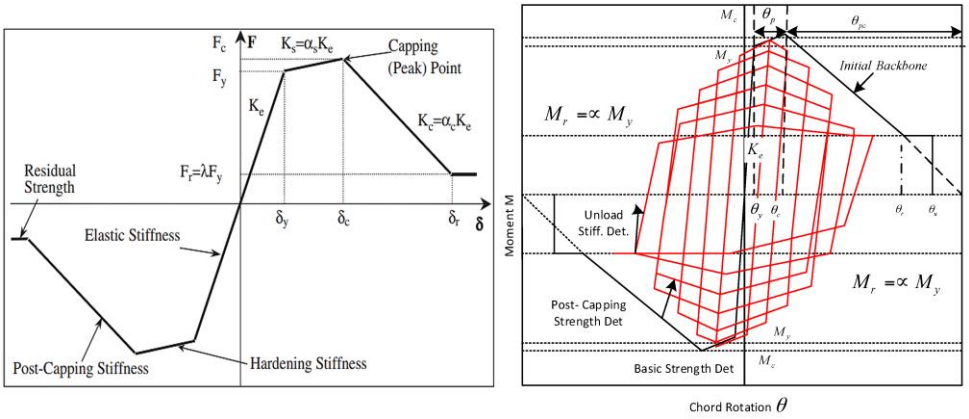


(a) Backbone curve for m-θ relationship (b) Hysteretic model for cyclic deterioration

Figure 6: Ibarra-Medina-Krawinkler model for inelastic response of RC member

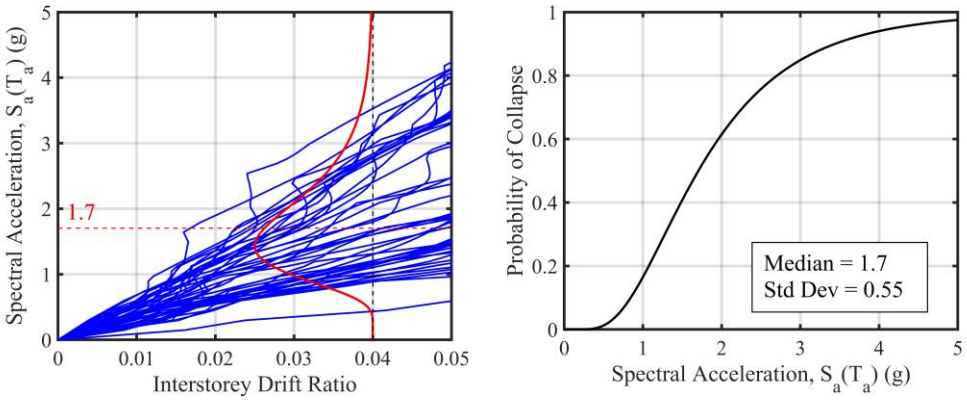


(a) IDA Plot (b) Fragility function

Figure 7: Estimation of Collapse Fragility function from IDA

## 5.2 Selection of Ground Motions

In the present study, 22 × 2 far-field ground motion records, mentioned in FEMA P695 [3], are adopted for IDA. A key requirement in the choice of ground motions is that the set of ground motions should sufficiently represents the mean and variance in design response spectrum [15]. Figure 8 shows the response spectrum of the selected ground motions along with their median and the IS 1893: 2016 [1] design response spectrum. The design response spectrum is scaled to show match of shape in the range of time periods of interest. The fundamental time periods of the archetype buildings ranges from 1.20 second to 2.58 second. A good match in spectral shape can be observed for design response spectrum and median of response spectrum of the selected ground motions in this period range.

IDA of analytical models of archetype building frames is carried out using 44 (22 x 2) set of ground motions. The collapse fragility functions of archetype building frames are determined from the statistics of ground motion intensities collected from IDAs. The collapse fra-

gility functions and seismic hazard curves are used to determine conditional probability of collapse at MCE, annual rate of collapse, and available response reduction factor for all archetype building frames.

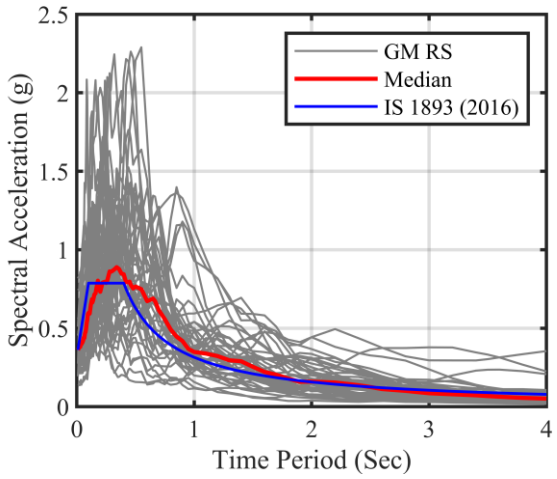


Figure 8: Spectral shape match between design response spectrum and median of response spectrum of the selected ground motions. Blue line represents IS 1893: 2016 [1] design spectrum scaled at 2.0 sec and Red line represents median of the selected ground motion response spectra

## 6 RESULTS AND OBSERVATIONS

Pushover analyses of analytical models of the archetype buildings are carried out and overstrength factors are determined on the basis of Figure 2. The over strength factors from pushover analyses are presented in Table 6. The overstrength factor (Ω) ranges from 1.37 to 2.63. From Table 6 it is observed that the overstrength factors reduces with increase in building height in all seismic zones and irrespective of I-factor. The over strength factor marginally reduces with increase in design base shear for G+4, G+6, and G+8 buildings. However, the over strength increases with increase in design base shear for G+10 building for all three importance factors. The lowest value of over strength factor, 1.37, is found to be lower than the factor of 2.5, used in the design of soft-storey floors and connection in IS 1893: 2002 [16].

Variation of conditional probability of collapse at MCE and annual rate of collapse (λ) against importance factors for seismic zones III, IV, and V are shown in Figures 9 and 10, respectively. For each building height, both conditional probability of collapse at MCE and annual rate of collapse remain nearly constant with increase in importance factor and seismic demand in each zone. Thus, the conditional probability of collapse does not reduce significantly with increase in design forces. The conditional probability of collapse at MCE remains below allowable probability of 10% for G+6, G+8, and G+10 designed for seismic demands as per zone III, IV, and V and important factors 1, 1.2, and 1.5. The conditional probability of collapse at MCE for G+4 building designed for zone V seismic demand is higher than allowable limit for all three values of importance factors. The annual rate of collapse (λ) remains below allowable limit of 0.02% for G+6, G+8, and G+10 designed for seismic demands as per zone III, IV, and V and important factors 1, 1.2, and 1.5. The annual rate of collapse (λ) for G+4 building designed for zone V seismic demand with the importance factor of 1 is found to be largest (0.02%) among all the values. However, this rate does not exceed the allowable limit of 0.02%.

| | G+4 | | | G+6 | | | G+8 | | | G+10 | | |
|---|---|---|---|---|---|---|---|---|---|---|---|---|
| Zone | I=1.0 | I=1.2 | I=1.5 | I=1.0 | I=1.2 | I=1.5 | I=1.0 | I=1.2 | I=1.5 | I=1.0 | I=1.2 | I=1.5 |
| Zone III | 2.29 | 2.21 | 1.93 | 2.11 | 1.96 | 2.63 | 1.90 | 1.73 | 1.55 | 1.55 | 1.45 | 1.37 |
| Zone IV | 2.00 | 1.83 | 1.83 | 1.86 | 1.81 | 2.21 | 1.59 | 1.56 | 1.56 | 1.39 | 1.44 | 1.47 |
| Zone V | 1.84 | 1.80 | 1.67 | 1.81 | 1.68 | 2.19 | 1.50 | 1.58 | 1.56 | 1.45 | 1.48 | 1.51 |

Table 6: Overstrength factor (Ω) observed in the building structures

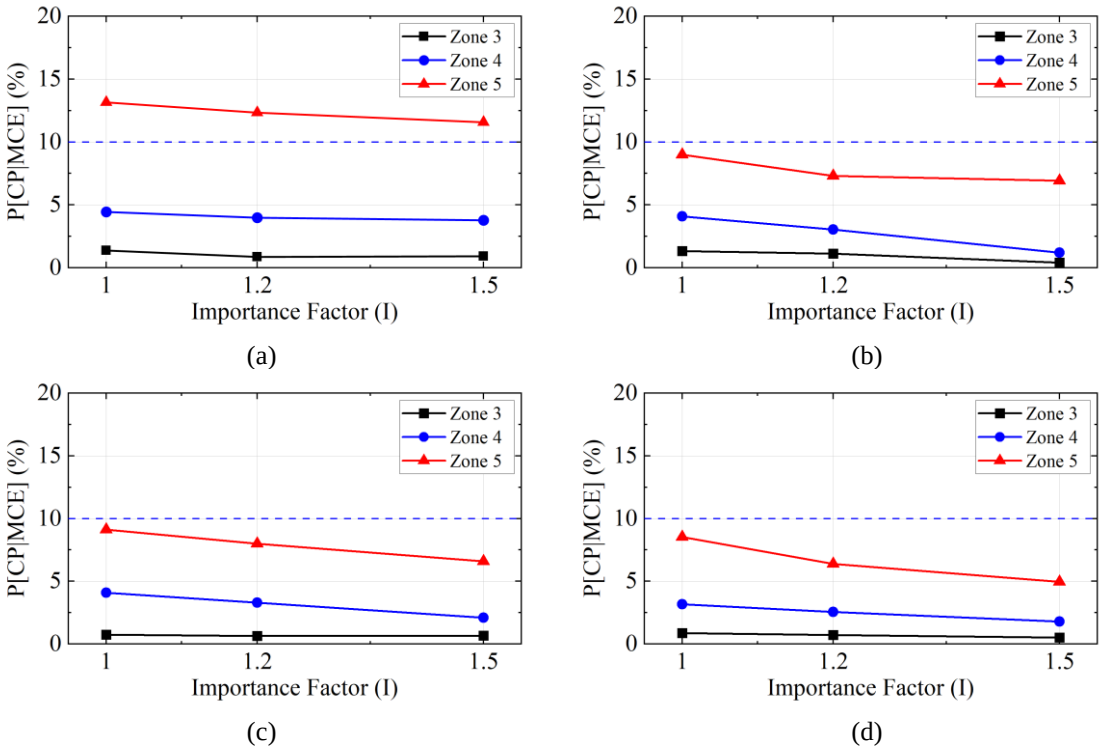


Figure 9: Observed conditional probability of collapse in buildings with different I-factors for: (a) G+4; (b) G+6; (c) G+8; (d) G+10 (Values lying below blue dashed line are within acceptable limits)

To study the effect of building height on conditional probability of collapse at MCE and annual rate of collapse, the variation of these quantities against number of stories are shown in Figures 11 and 12, respectively. Subfigure in figures 11 and 12 represent variation of conditional probability and rate of collapse for various importance factors. Each subplot show variation for seismic zones III, IV, and V. From Figure 11 it can be seen that the conditional probability of collapse at MCE increases with increase in seismic zone in buildings of all heights and importance factors. The conditional probability of collapse decreases with increase in number of stories (building height). The conditional probability of collapse of buildings with different height in all seismic zones of IS 1893: 2016, with the exception of G+4 building in zone V, are found to be below acceptable limits. The conditional probability of collapse of G+4 building is found to be above allowable limit in seismic zone V.

Similar trends are observed in the comparison of annual rate of collapse with number of stories. The annual rate of collapse of buildings with different height in all seismic zones of IS 1893: 2016 are found to be below acceptable limits. The annual rate of collapse of G+4 story building in high seismic zone (zone V) is found to be the highest. Thus, the seismic risk of low-rise building is found to be larger than that of mid-rise buildings particularly when the building is located in higher seismic zones.

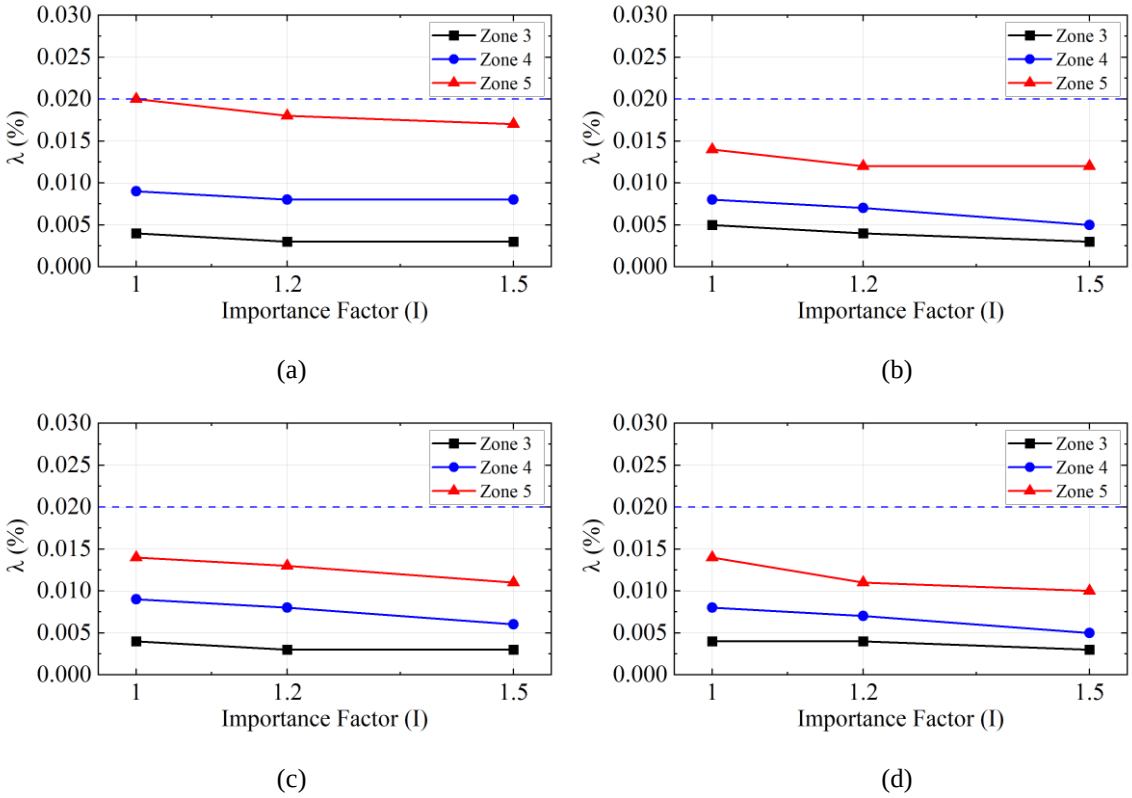


Figure 10: Observed mean annual collapse rate in buildings with different I-factors for: (a) G+4; (b) G+6; (c) G+8; (d) G+10 (Values lying below blue dashed line are within acceptable limits)

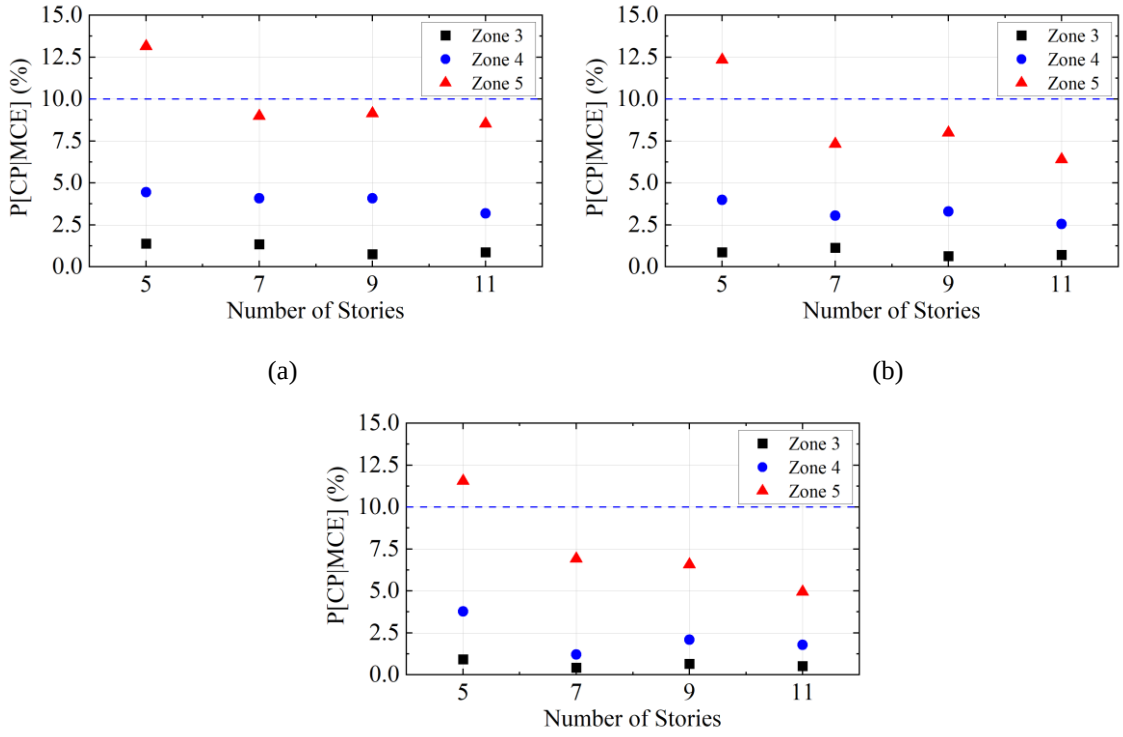


Figure 11: Observed conditional probability of collapse in buildings with different number of stories for: (a) I = 1.0; (b) I = 1.2; (c) I = 1.5. (Values lying below blue dashed line are within acceptable limits)

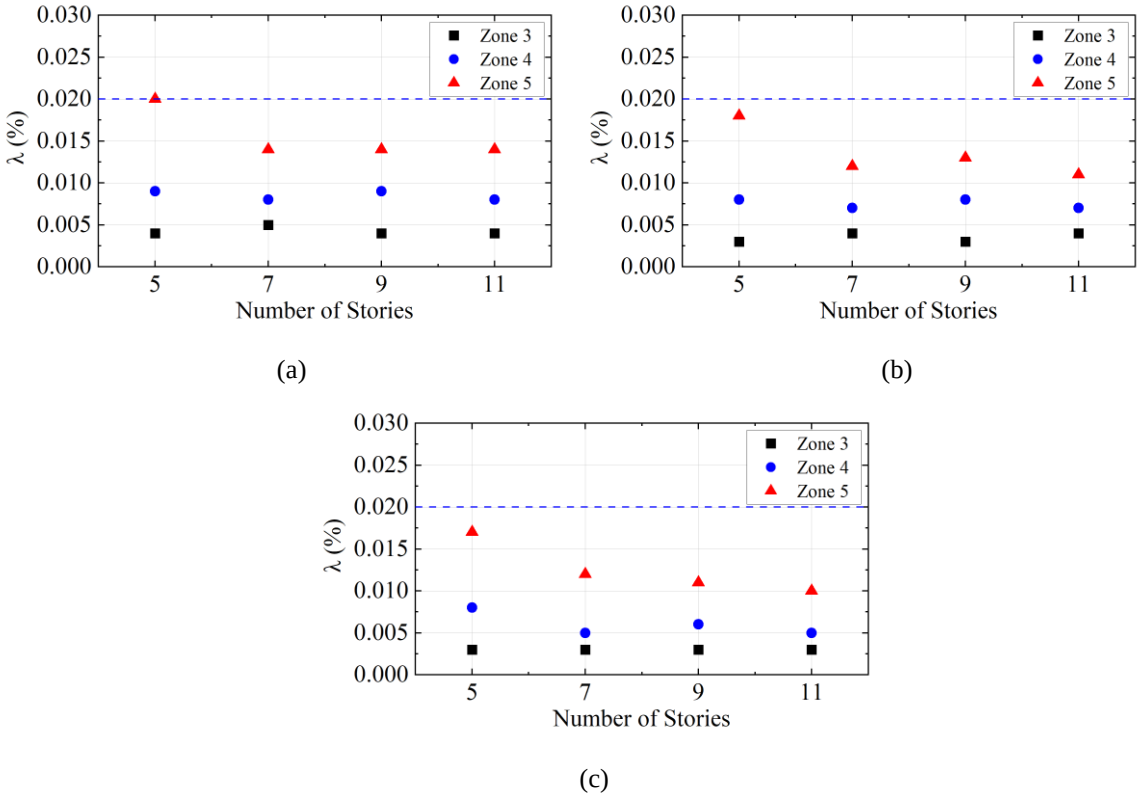


Figure 12: Observed mean annual collapse rate in buildings with different number of stories for: (a) I = 1.0; (b) I = 1.2; (c) I = 1.5. (Values lying below blue dashed line are within acceptable limits)

Figures 13 and 14 show variation of available response reduction factor against importance factors and number of stories, respectively. The variations are shown for each zone factor. From Figure 13 it is observed that the available response reduction factor remains nearly constant even with increase in importance factor. This trend is observed for buildings of different stories in all seismic zones. From Figure 14, it is observed that the available response reduction factor increases with increase in number of stories. The available response reduction factor increases with seismic zone considered in the design. The increase in available response reduction factor from code specified value is larger for seismic zone III and importance factor 1. The increases are relatively smaller or negligible for higher seismic zones (IV and V) and larger importance factors (1.2 and 1.5). Available response reduction factors for all the buildings, except G+4 in seismic zone V, are found to be larger than R value used in the design. Available response reduction factor for low rise building (G+4) in higher seismic zone is found to be slightly lower than R value used in the design. Available response reduction factors of buildings in lower seismic zone is found to be nearly 50% larger than buildings in higher seismic zones for all importance factors. This can be due to minimum member size provisions and capacity based design ensuring strong column-weak beam principle of ductile detailing code, IS 13920: 2016 [1].

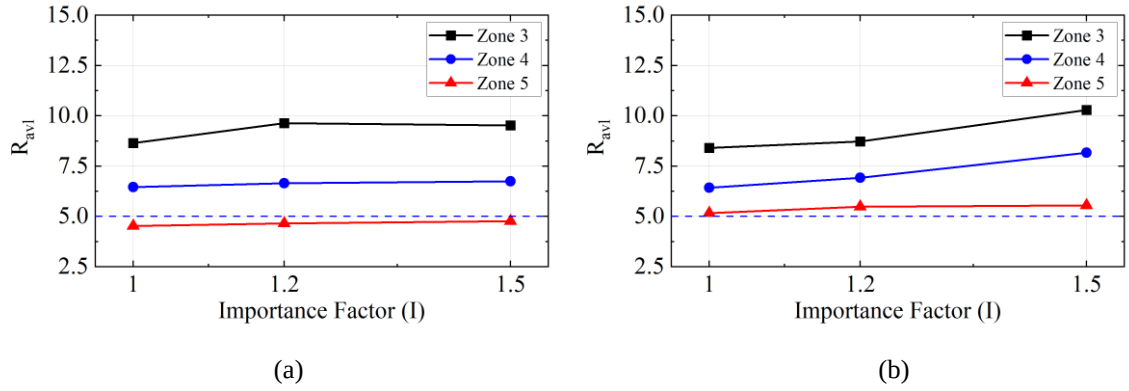


(a)




(b)

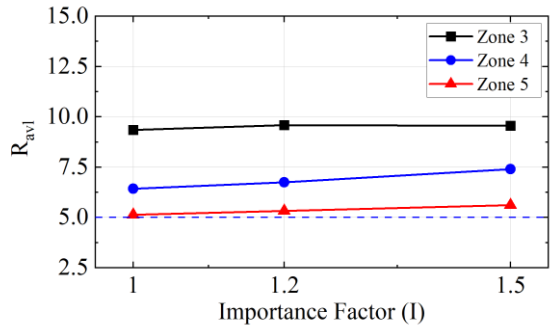


(c)

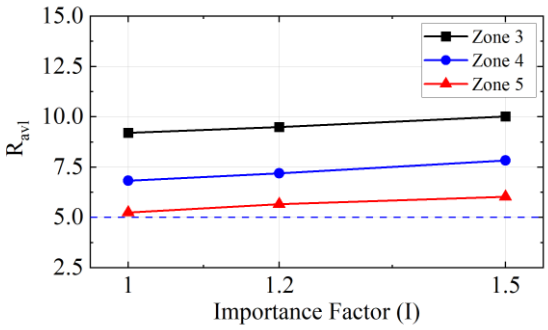


(d)

Figure 13: Observed $R_{avl}$ in buildings with different I-factors for: (a) G+4; (b) G+6; (c) G+8; (d) G+10 (Values lying above blue dashed line are within acceptable limits)

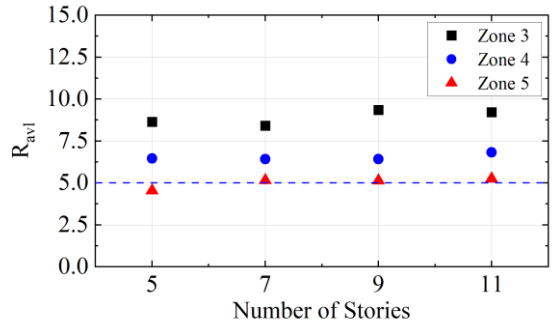


(a)

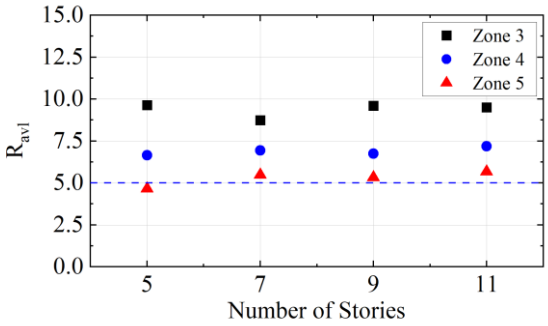


(b)

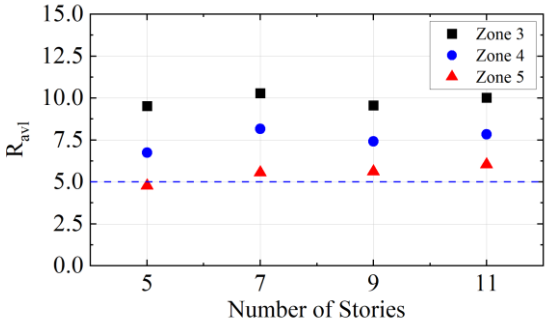


(c)

Figure 14: Observed $R_{avl}$ in buildings with different number of stories for: (a) I = 1.0; (b) I = 1.2; (c) I = 1.5. (Values lying above blue dashed line are within acceptable limits)

## 7 SUMMARY AND CONCLUSIONS

This study assesses performance of RC-SMRFs, designed as per Indian design standards, in seismic risk framework to study the viability of the seismic design factors (R-factor and I-factor). A series of RC SMRF buildings, designed for different seismic zones and different I-factors as per IS 1893: 2016, are numerically modeled in OpenSees environment as 2D non-linear models. The models are subjected to static pushover analyses and IDA using 22 x 2 set of ground motions from FEMA P695 [3]. Collapse fragility function is estimated from IDA results. Seismic hazard is estimated from IS 1893: 2016 [1]. The seismic risk is calculated by integration of fragility function with seismic hazard curve. The following conclusions can be drawn from the present study:

1. There is no significant reduction in annual rate of collapse of RC-SMRF buildings designed for the higher importance factor.
2. No direct relationship exists between importance factor, used in Indian seismic design code, and conditional probability of collapse or annual rate of collapse of RC-SMRF building frames.
3. The available response reduction factor increases with increase in number of stories.
4. Seismic risk of low-rise RC-MR building located in high seismic zone is found to be larger compared to mid-rise RC-MR building.
5. The response reduction factor provided in IS 1893: 2016 for RC-SMRF is found to be conservative for low-rise and mid-rise buildings.

## References

[1] IS 1893 (Part 1). *Criteria for Earthquake Resistant Design of Structures, Part 1: General Provisions and Buildings*. New Delhi: Bureau of Indian Standards, 2016.

[2] D. Vamvatsikos and C. A. Cornell, "Incremental dynamic analysis," *Earthquake engineering & structural dynamics*, vol. 31, no. 3, pp. 491–514, 2002.

[3] FEMA P695. *Quantification of building seismic performance factors*. Redwood City, California: Applied Technology Council, 2009.

[4] ASCE 7, *Minimum design loads for buildings and other structures (ASCE/SEI 7-10)*. Reston, Virginia: American Society of Civil Engineers, 2016.

[5] P. K. Dhir, N. P. Zade, A. Basu, R. Davis, and P. Sarkar, "Implications of importance factor on seismic design from 2000 SAC-FEMA perspective," *ASCE-ASME Journal of Risk and Uncertainty in Engineering Systems, Part A: Civil Engineering*, vol. 6, no. 2, p. 04020016, 2020.

[6] C. A. Cornel and H. Krawinkler, "Progress and challenges in seismic performance assessment," *PEER Centre News*, 3, 1-3, 2000.

[7] S. Mazzoni, F. McKenna, M. H. Scott, G. L. Fenves, et al., "Open system for earthquake engineering simulation, user command-language manual, pacific earthquake engineering research center," *University of California, Berkeley, OpenSees version*, vol. 2, no. 0, 2009.

[8] P. S. Badal and R. Sinha, "A framework to incorporate probabilistic performance in force-based seismic design of RC buildings as per Indian standards," *Journal of Earthquake Engineering*, vol. 26, no. 3, pp. 1253–1280, 2020.

[9] C. A. Cornell, F. Jalayer, R. O. Hamburger, and D. A. Foutch, "Probabilistic basis for 2000 sac federal emergency management agency steel moment frame guidelines," *Journal of structural engineering*, vol. 128, no. 4, pp. 526–533, 2002.

[10] IS 13920. *Ductile design and detailing of reinforced concrete structures subjected to seismic forces - code of practice*. New Delhi: Bureau of Indian Standards, 2016.

[11] IS 456. *Plain and reinforced concrete - code of practice*, Bureau of Indian Standards, New Delhi. New Delhi: Bureau of Indian Standards, 2002

[12] L. F. Ibarra, R. A. Medina, and H. Krawinkler, "Hysteretic models that incorporate strength and stiffness deterioration," *Earthquake engineering & structural dynamics*, vol. 34, no. 12, pp. 1489–1511, 2005.

[13] C. B. Haselton, *Assessing seismic collapse safety of modern reinforced concrete moment frame buildings*. PhD thesis, Stanford University, 2006

[14] A. Singhal and A. S. Kiremidjian, "Method for probabilistic evaluation of seismic structural damage," *Journal of structural Engineering*, vol. 122, no. 12, pp. 1459–1467, 1996.

[15] E. I. Katsanos, A. G. Sextos, and G. D. Manolis, "Selection of earthquake ground motion records: A state-of-the-art review from a structural engineering perspective," *Soil dynam-ics and earthquake engineering*, vol. 30, no. 4, pp. 157–169, 2010.

[16] IS 1893 (Part 1). *Criteria for earthquake resistant design of structures*. New Delhi: Bureau of Indian Standards, 2002

COMPDYN 2023
9th ECCOMAS Thematic Conference on
Computational Methods in Structural Dynamics and Earthquake Engineering
M. Papadrakakis, M. Fragiadakis (eds.)
Athens, Greece, 12-–14 June 2023

# SEISMIC VULNERABILITY ASSESSMENT OF CONCRETE BLOCK CONFIGURATIONS FOR RADIATION SHIELDING

**Luca Sironi[1], Marco Andreini[1], Ziran Zhou[2], José Andrade[2], Pierino Lestuzzi[3], Edward Andò[3], Frédéric Dubois[4], Filippo Dacarro[5], Davide Bolognini[5]**

[1]CERN
European Organization for Nuclear Research
Esplanade des Particules 1 - 1217 Meyrin (Switzerland)
e-mail: {luca.sironi, marco.andreini}@cern.ch

[2]Caltech
California Institute of Technology
1200 E. California Blvd., MC 104-44 Pasadena, CA 91125 (USA)
e-mail: {zzhou2, jandrade}@caltech.edu

[3]EPFL ENAC IIC EESD
Swiss Federal Institute of Technology Lausanne
GC B2 485 (Bâtiment GC) - Station 18 - CH-1015 Lausanne (Switzerland)
e-mail: {pierino.lestuzzi, edward.ando}@epfl.ch

[4]LMGC, Univ. Montpellier, CNRS, Montpellier
cc048, 163 rue Auguste Broussonnet, 34090 Montpellier (France)
e-mail: frederic.dubois@umontpellier.fr

[5]EUCENTRE
European Centre for Training and Research in Earthquake Engineering
Via Adolfo Ferrata,1 – 27100 Pavia (Italy)
e-mail: {filippo.dacarro, davide.bolognini}@eucentre.it

**Abstract.** *This paper describes the methodology, related steps and results of a research project on the seismic vulnerability assessment for configurations of radiation shielding blocks. The project was mainly carried out in the decade 2012-2022, with the collaboration of several research institutions (i.e., LMGC, EPFL, EUCENTRE and Caltech). First, the research was oriented to calibrate discrete element software for the dynamic behaviour simulations of blocks' configurations by means of full-scale experimental tests. In a second stage, a methodology based on the Incremental Dynamic Analysis (IDA) for the seismic risk assessment was developed. The paper presents also the results of the application of such a methodology to a real case study at CERN.*

**Keywords:** Concrete Blocks, Discrete Element Models, Incremental Dynamic Analysis, Radiation Shielding, Seismic Vulnerability.

## 1 INTRODUCTION

Particle physics research laboratories like the European Organisation for Nuclear Research (CERN) have a duty to protect and shield personnel, equipment and high-technology devices from radiation produced during daily operations, such as those of particle accelerators. The most widespread approach used to achieve the required level of shielding implies the use of concrete blocks with a significant mass [1]. Among similar research centres around the world (i.e., Fermilab and KEK), CERN appears as one of the few that uses these blocks without any joint-connection or any additional metallic bracing system resistant to lateral forces (Figure 1). In this context, if on one hand there are radiation protection safety requirements to be met, on the other hand there is the need to guarantee an adequate level of structural safety of stacked block assemblies under static and dynamic loads, i.e., seismic actions. Although simple block piles might be analysed by means of analytical procedures, more complex block configurations require advanced numerical Discrete Element Models (DEMs) [2] to be assessed. These DEMs shall account for the non-smoothness tied to the frictional contacts between the blocks and the energy dissipation due to friction and eventual shocks, which can occur in case of earthquakes of a certain magnitude. A validation of these models against the results of experimental tests is needed.

This paper deals firstly with the calibration procedure that has been adopted to define the variables of two DEM software applications: the "*Logiciel de Mécanique Gérant le Contact 90*" (LMGC90) [3, 4] and the Level Set Discrete Element Method (LS-DEM) [5], developed respectively at the University of Montpellier and at California Institute of Technology (Caltech). This calibration is based on the results of an experimental campaign carried out on full-scale samples at the European Centre for Training and Research in Earthquake Engineering (EUCENTRE) [6, 7]. In addition, the paper shows the developed methodology for the seismic assessment of complex block configurations based on Incremental Dynamic Analyses [8]. The application of such a methodology to a case-study in a CERN experimental area is finally presented.

## 2 RESEARCH PROJECT ON THE SEISMIC BEHAVIOUR OF CONFIGURATIONS OF RADIATION SHIELDING BLOCKS

### 2.1 Standard CERN shielding blocks

The blocks used in the shielding configurations at CERN are made of concrete, steel, or lead. The most used ones are made of precast concrete, having a weight of 77 kN and a standardized parallelepipedal shape of these dimensions: 2.40 x 1.60 x 0.80 m. Several multiples or sub-multiples of this standard shape are used for specific installations on CERN sites. These blocks have been designed according to the norms EN 206-1 [9] and Eurocode 2 [10]. Referring to the nomenclature adopted by such norms, the main characteristics are: concrete quality C40/50, exposure class XC4-XD3-XF3, maximum diameter of the aggregate equal to 32mm, chloride content equal to 0.20, metallic formwork type IV, edge chamfers of 2 cm, and reinforcement steel grade B500B.

### 2.2 The experimental test campaign at EUCENTRE

The dynamic response of four different configurations of full-scale stacked concrete blocks has been investigated conducting an experimental campaign consisting of shaking table tests. Four different configurations of blocks, whose height varied from 4.8 m to 7.6 m have been assembled in EUCENTRE laboratory and tested (Figure 2). The first and the second configura-




Figure 1: Examples of concrete block configurations at CERN: 1) Beam line shielding in the Neutrino Platform Trenches, 2) Experimental Hall North 1 (EHN1), 3) Bunker of the Gravitational Behaviour of Antimatter at Rest (GBAR) experiment and 4) Proton Synchrotron East Area Facility.

tions consisted of simple piles of respectively three and four stacked blocks. The third and the fourth ones consisted of two piles of four stacked blocks, with a block on the top. The latter was supported by four steel profiles in the fourth configuration.
All configuration specimens were assembled on a base concrete slab, fixed to the platform of the testing shaking table. Two acceleration time-histories, called Alkion and Basso Tirreno, typical of the Mediterranean region, have been applied at the base of the configuration specimens with increasing amplitude levels. The full description of this experimental test campaign is available in [6].

## 2.3 Calibration of numerical model variables

### 2.3.1 Brief introduction to LMGC90 and LS-DEM

LMGC90 is an open-source software, developed by the Mechanical and Civil Engineering Laboratory (LMGC) of the University of Montpellier and of the French "*Centre National de la Recherche Scientifique*" (CNRS). The software implements the Non-Smooth Contact Dynamic Discrete Element Method.
"*The LMGC90 software is dedicated to the modelling of large object collections in interaction. It enables to simulate complex systems thanks to sophisticated and very detailed models. Each object modelled is defined throughout its own geometry and a proper behaviour is associated to each body. A wide range of models (rigid, elastic, viscoelastic, etc.) may be used to model objects behaviours. Moreover, behaviours between objects are modelled by using many contacts*

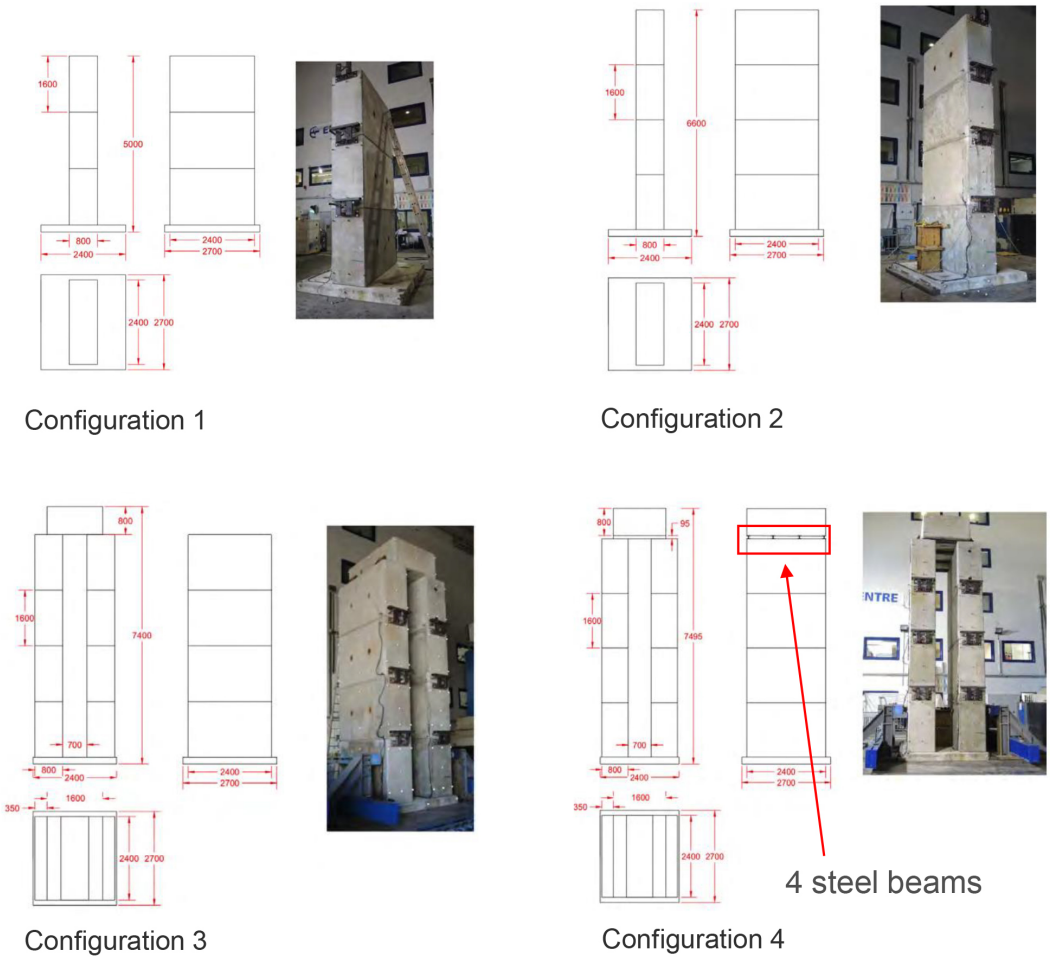


Figure 2: The four blocks' configurations tested at EUCENTRE, Pavia-Italy in 2019

*laws*"[3, 4].
LS-DEM is a software developed by the Cosymo Laboratory of Caltech.
"*LS-DEM is a discrete element method variant able to simulate systems of particles with arbitrary shape using level set functions as a geometric basis. LS-DEM is similar to the classic discrete element method (DEM) in that it simulates the kinematics and mechanics of a system of discrete particles, with the only difference being its ability to capture arbitrary shape as opposed to only spheres as in DEM*" [5].

### 2.3.2 Calibration procedure

A semi-probabilistic approach was adopted to calibrate the input variables of numerical models developed with LMGC90 and LS-DEM. Models of the tested configuration specimens have been generated with both software applications. The geometrical variables have been treated as deterministic while the main mechanical ones (e.g., friction coefficients, material densities, moduli of elasticity, etc.) have been considered as random and, therefore, described by distribution models. This approach was chosen mainly because of the large variation of the friction coefficients of concrete-concrete and steel-concrete presented in the technical literature. A Correlation Controlled Latin Hypercube Sampling methodology [11] was used to sample values from the mechanical variables' distributions. Such a methodology was chosen because it's effi-

cient and accurate for small sample sizes. Indeed, in the preliminary analyses, it was observed that 20 samples would have been reasonably acceptable in terms of achieving an appropriate level of accuracy. The calibration procedure consisted in tuning the mechanical variables' distribution parameters (i.e., the mean, the standard deviation (SD) and, consequently, the coefficient of variation (C.o.V.)) and checking whether the numerical models' analyses results, in terms of maximum and minimum block displacements, were compatible with those observed experimentally for the four tested configurations.
The final set of variable distribution parameters that provided the most satisfactory results are shown in Table 1.

| Variable | Distribution Model | Mean | SD | C.o.V. |
|---|---|---|---|---|
| Friction Concrete/Concrete [-] | Log-normal | 0.75 | 0.075 | 0.1 |
| Friction Concrete/Foundation [-] | Log-normal | 0.75 | 0.075 | 0.1 |
| Friction Steel/Concrete [-] | Log-normal | 0.3 | 0.03 | 0.1 |
| Concrete Density [kg/m$^3$] | Log-normal | 2400 | 96 | 0.04 |
| Concrete Young's Modulus [Pa] | Log-normal | 3.45E+10 | 5.175E+09 | 0.15 |
| Concrete Viscous Modulus [Pa] | Log-normal | 1.5E+08 | 2.25E+07 | 0.15 |
| Steel Density [kg/m$^3$] | Log-normal | 7700 | 77 | 0.01 |
| Steel Young's Modulus [Pa] | Log-normal | 0.21E+12 | 6.3E+09 | 0.03 |
| Steel Viscous Modulus [Pa] | Log-normal | 0.21E+10 | 6.3E+07 | 0.03 |

Table 1: Model variables' distributions and related parameters obtained after the calibration process [7].

## 3 SEISMIC VULNERABILITY ASSESSMENT OF BLOCK CONFIGURATIONS

### 3.1 Introduciton to Seismic hazard and design requirements for CERN

#### 3.1.1 Seismic hazard models for CERN territory

Seismic hazard identification is the subject of continuous updates. Considering the scope of this paper, we define a limit by referring to the web-platform developed by the European Facilities for Earthquake Hazard and Risk (EFEHR), which is accessible at `http://hazard.efehr.org/en/home/`. Such a platform provides access to interactive tools such as seismic hazard models, products and information. Distributed data, models, products and information are based on research projects carried out by academic and public organisations. For instance, Figure 3a shows the map of the CERN region indicating the spectral horizontal acceleration at 5 Hz as per the European Seismic Hazard Model 2020 (ESHM2020)[12], for a seismic event having a Probability of Exceedance (POE) of 10% in 50 years (POE 10%50years). Figure 3b shows the seismic hazard curve for the CERN Globe of Science according to ESHM2020.

#### 3.1.2 Seismic Design and Assessment Requirements

According to the French "*Décret n°2000-892 du 13 septembre 2000*" [13], new constructions or constructions submitted to important modifications in seismic regions shall comply with the applicable seismic design requirements. CERN does not have a specific internal seismic safety rule in force at present and, consequently, regulations of Host States (France and Switzerland) are considered as applicable. In particular, the French "*Décret no 2010-1254 du 22 octobre 2010*" [14] foresees that buildings, equipment and installations "à risque normal" are those for

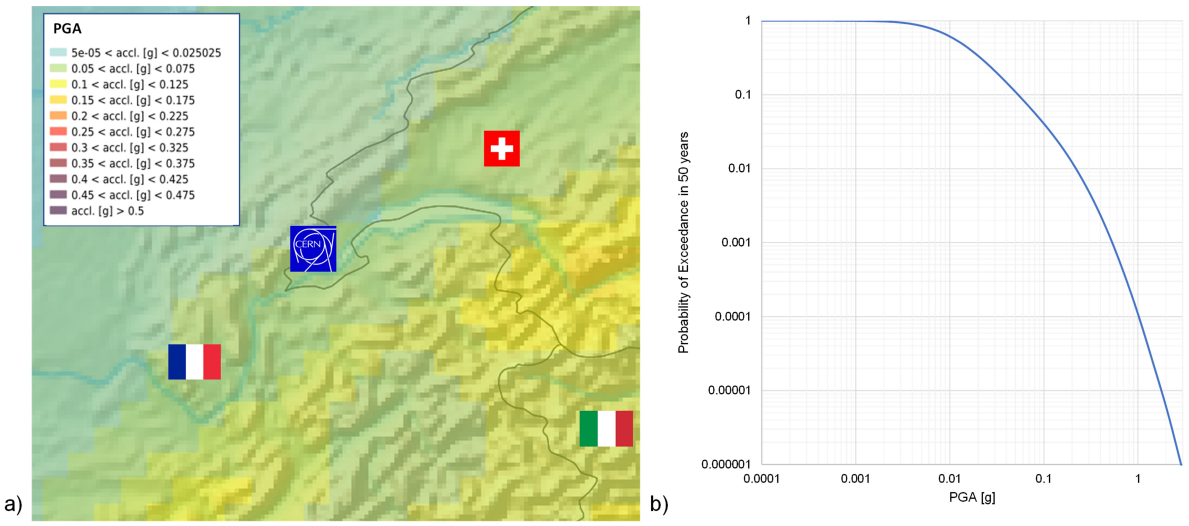


Figure 3: a) Seismic Hazard Map for CERN region: spectral horizontal acceleration at 5 Hz as per ESHM2020, for a seismic event having a POE 10%50years. b) Seismic Hazard Curve for the CERN Globe of Science and Innovation: Peak Ground Acceleration (PGA) versus O in 50 years as per ESHM2020.

which the consequences in the event of an earthquake are limited to an area within the vicinity. Buildings, equipment and installations for which the consequences in case of an earthquake may have an impact outside the vicinity, due to explosions, pollution or fire, are classified as being "*à risque special*". According to [14], French territory is divided in five seismic zones from very low seismicity (seismic zone 1) to strong seismicity (seismic zone 5). CERN is included in seismic zone 3 ("*sismicité modérée*"), according to the French "*Arrêté du 22 octobre 2010*" [15]. For such a zone, Peak Ground Acceleration (PGA) values to be used in the structural design and assessment at the Ultimate Limit State (ULS) are given. For the sake of example, the PGA for buildings belonging to the Importance Class II (e.g. residential buildings, office and commercial purpose buildings, etc.), realised on type-A ground soil, is equal to 1.10 m/s$^2$. Such a value corresponds to a seismic event having a POE 10%50years and represents the life-safety requirement foreseen for this kind of buildings.

In case of buildings or infrastructures having more (or less) severe consequences in case of failure, the mentioned value of the PGA shall be magnified (or reduced) by a so-called Importance Factor $\gamma_I$, which allows to account for POE and reference periods different to those mentioned above. The role played by the different ground soils is also accounted for, applying a PGA multiplication factor *S*. To account for the different vibration frequencies/modes, it is prescribed to use the shapes of the elastic response spectra of the horizontal and vertical accelerations as defined in the norm Eurocode 8 [16]. As the Eurocode 8 (together with the related National Determined Parameters [17]) is also applicable in the Swiss territory of CERN and for the sake of brevity, the description of the Swiss regulation seismic assessment approach is omitted in this paper. The reader is invited to refer to the SIA 260 and 261 [18, 19] for all the related information.

### 3.2 Seismic Vulnerability Assessment of Block Configurations by IDA

IDA is a computational analysis method of earthquake engineering to achieve an assessment of the dynamic behaviour of structures, with respect to a time-history input [8]. IDA methodology requires to perform multiple nonlinear dynamic analyses of a structural model, under a series of ground motion records, each of them scaled to several levels of seismic intensity. The

scaling levels are selected to force the structure through the entire range of behaviour, from rigid to dynamic instability and collapse. The seismic risk assessment procedure for shielding block configurations consists essentially in selecting the basic accelerograms, generating the mechanical models, running the IDA, post-processing the obtained results and comparing with the acceptance thresholds. These phases are described in the following sub-sections.

With the intention to be as compliant as possible with the French "*Arrêté du 22 octobre 2010*" [15], we refer to the shapes of the Type-I elastic response spectra of the acceleration indicated in the Eurocode 8 [16]. We retrieve from the European Strong Motion (ESM) database (`https://esm-db.eu/#/rexel`) [20] 7 sets of 3-component accelerograms (2 horizontal and 1 vertical) compatible with such spectra.

It is worth mentioning that, with regards to section 2.3.2 of this paper, the mechanical variable distributions and the 20 related samples have to be considered to create the same number of models with LMGC90 or LS-DEM.

The process to run IDA on block configuration models involves the following stages:

1. Identify the blocks to be monitored, representative of the most probable failure mechanism.
2. Select a 3-component accelerogram among the 7 compatible with the elastic response spectra foreseen for the location of interest.
3. Normalize such an accelerogram to the PGA of the main horizontal component .
4. Create a range of Scale Factors (SCFs), e.g. [0.02, 0.04, ..., 1], and generate as many sets of scaled 3-component accelerograms as the number of the considered SCFs.
5. Run a non-linear dynamic analysis for each model (generated for every sample – see section 2.3.2) subjected to every scaled 3-component accelerogram (point 4).
6. Collect the results in terms of Damage Measure (DM) (i.e., maximum relative and residual displacement vector) for every generated model and each monitored block.
7. Display on the same graph the DM results in function of the earthquake Intensity Measure (IM) (e.g., PGA) corresponding to the related SCF for each model (IDA curves).
8. Calculate the DM median and relevant percentiles for any considered IM value.
9. Repeat the procedure from point 2 for each of the other 6 accelerograms.

Referring to section 3.1, the overall seismic risk assessment of a block configuration can be carried out comparing the IDA curves for the monitored blocks with the hazard curve, expressed in terms of the same IM for the related reference period (e.g., the lifetime of the experiment/equipment to be shielded) and location. This way one can link the respective DM value to a frequency of occurrence or a POE and see whether this is acceptable or not. In case one or more couples DM – POE/frequency are unacceptable, one can either decide to modify the block configuration or reduce the lifetime of the concerned experiment/equipment.

## 4 CASE STUDY: BUNKER AT THE EXPERIMENTAL HALL NORTH 2 (EHN2) OF CERN

EHN2 hosts the Apparatus for Meson and Baryon Experimental Research (AMBER). In particular, the measurements of the so called Drell-Yan processes requires an experimental setup that concerns the use of a significant radiation shielding mass. A bunker concerning 155 blocks in concrete and steel is foreseen to be realised. Its dimensions in plan are 7.1m x 6.4m, the maximum height is 7.2m and the total mass is 727.7 tons (see Figure 4).

EHN2 appears as an ordinary industrial building. As foundation, EHN2 has a shallow concrete slab laying on a type-E soil, according to the Eurocode 8 [16], for which an amplification

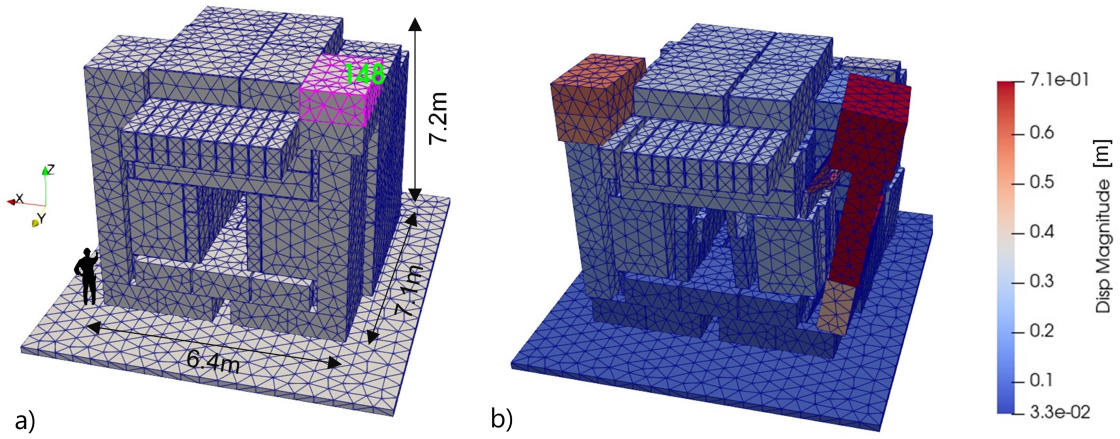


Figure 4: The EHN2 Bunker: a) The LMGC90 rigid block mechanical model, indicating dimensions and the monitored Block #148; b) Block configuration kinematisms expected for one of the earthquake among the 7 considered scaled up to a PGA = 1g, using the median value of the mechanical properties indicated in the Table 1.

factor $S$=1.8 is adopted. Keeping this normative reference, we considered earthquakes having a POE 10%50years, which corresponds to the ULS requirement for buildings of Importance Class II, as per French "*Arrêté du 22 octobre 2010*" [15]; this is linked to an Importance Factor $\gamma_I$=1 [16]. Figure 5 shows the resulting elastic response spectrum of the horizontal acceleration and those of the natural acceloragrams obtained by the ESM [20], related to the 7 earthquakes (sets of 3 accelerograms) considered in this seismic assessment.

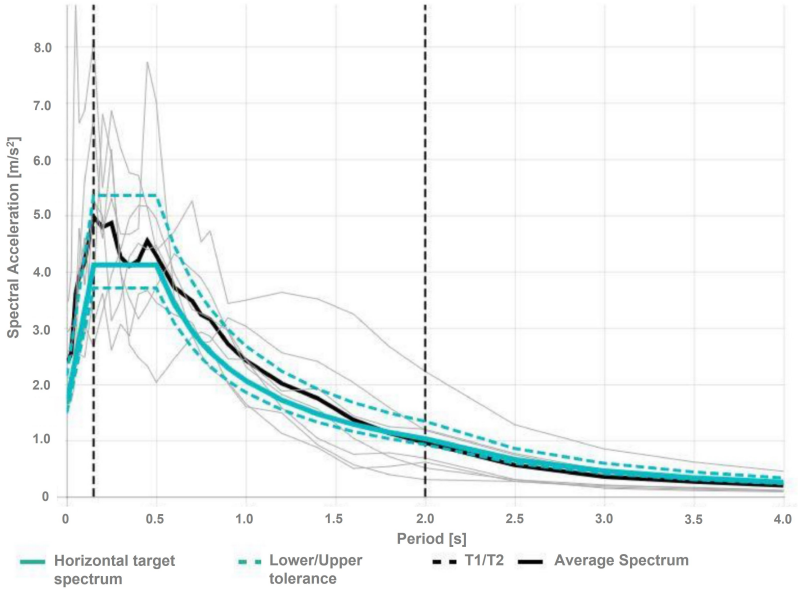


Figure 5: Response spectra of the horizontal acceleration conisdered in the EHN2 bunker assessment: Aqua-color continous line represents the shape of the elastic spectrum given by Eurocode 8 considering a PGA = 1.98 m/s$^2$, value obtained by amplifying the PGA(POE 10%50years for type-A soil) 1.1 m/s$^2$ by the factor $S$(type-E soil) = 1.8. Gray lines are the compatible spectra of the 7 earthquakes obtained by ESM [20] and considered in the assessment.

The IDA curves for the first set of 3 accelerograms are shown in Figure 6, where the horizontal axis shows the DM expressed in terms of maximum relative displacement of a monitored block along a certain direction; the vertical axis shows the IM in terms of PGA; the 20 IDA

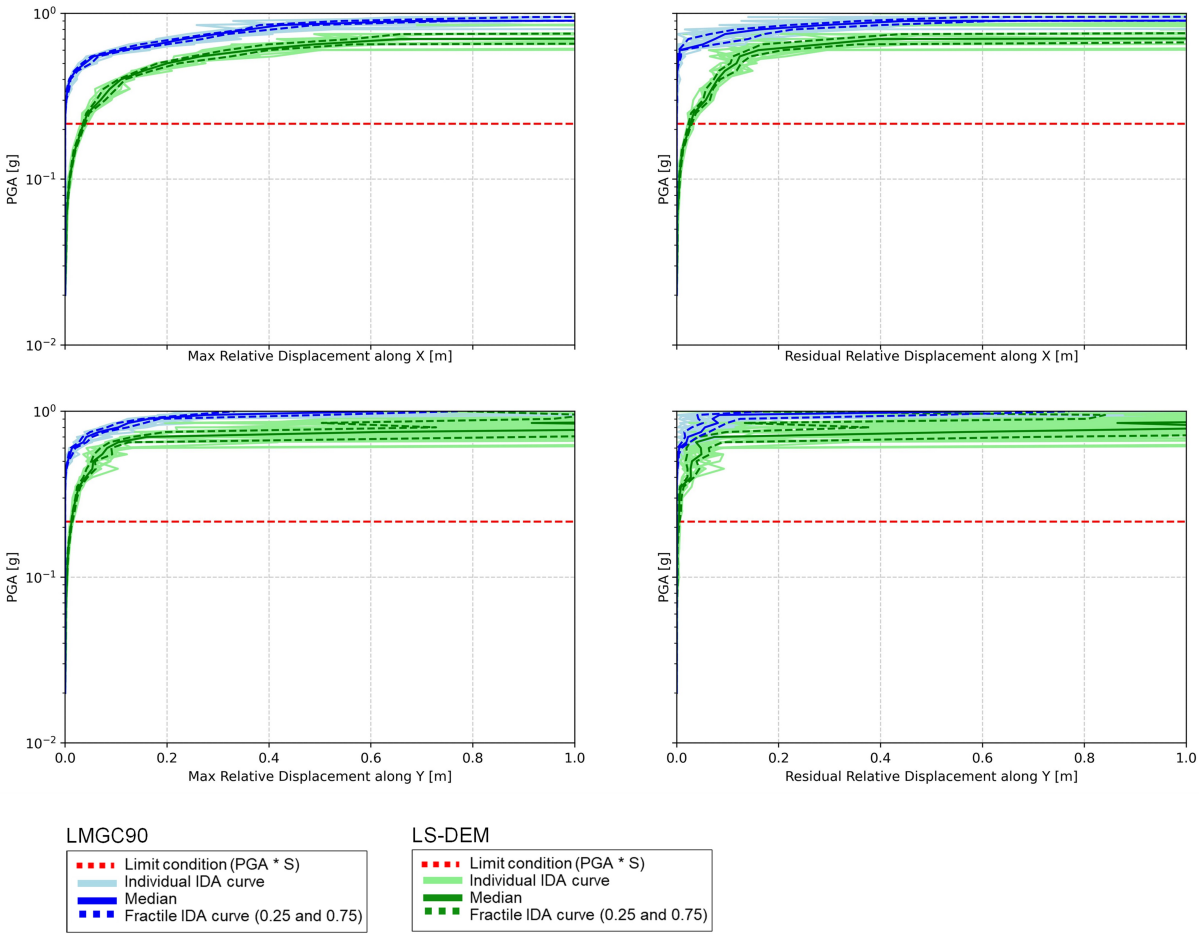


Figure 6: IDA curves for the Block #148 of the EHN2 bunker, subjected to the first set of scaled accelerograms among the 7 considered.

curves for each analysed model with the related variable sample are respectively in light blue for LMGC90 and green for LS-DEM. The darker continuous lines are the median value while the dashed-lines correspond to the 25th and 75th percentiles; the horizontal red dashed-line is the reference PGA (POE 10%50years).

From the comparison plot of IDA curves between LMGC90 and LS-DEM, it can be seen that LS-DEM model yields the same relative displacement at a lower PGA value. Given the different nature of the two simulation methods, differences between results can be expected. Compared to tested configurations with a maximum of 9 blocks in [7], the system simulated here has over 100 blocks, which significantly increases the modeling complexity and hence results in greater deviations between the two simulation methods. Furthermore, LMGC90 implements non-smooth contact. Shear force is zero in the static friction regime and jumps instantly to some value upon sliding. In the contrary, in LS-DEM, shear force increases linearly until sliding starts, resulting in non-zero shear force even in the static friction regime. Consequently, a small distance in shear direction could be present even at low PGA.

## 5 CONCLUSIONS

This research project aimed to define a seismic risk assessment methodology for configurations of radiation shielding blocks carried out during 2012-2022, with the collaboration of

several institutions (i.e., Université de Montpellier, EPFL, EUCENTRE and Caltech). Starting from the seismic hazard defined for CERN territory, the variables of advanced numerical models for the seismic analyses were calibrated by experimental tests. A seismic risk assessment procedure based on IDA was developed. The case study of the AMBER bunker in the Experimental Hall North 2 (EHN2) of CERN has been finally presented, highlighting the difference in results obtained by using LMGC90 and LS-DEM.

## REFERENCES


[1] M.F. Kaplan, *Concrete Radiation Shielding: Nuclear Physics, Concrete Properties, Design and Construction*. John Wiley Sons, 1989.

[2] P.A. Cundall, Formulation of a three-dimensional distinct element model—Part I. A scheme to detect and represent contacts in a system composed of many polyhedral blocks. *International Journal of Rock Mechanics and Mining Sciences & Geomechanics Abstracts*, **25(3)**, 107–116, 1988.

[3] M. Jean, The non-smooth contact dynamics method. *Computer Methods in Applied Mechanics and Engineering*, **177(3)**, 235–257, 1999.

[4] F. Dubois, V. Acary, M. Jean, The Contact Dynamics method: A nonsmooth story. *Comptes Rendus Mécanique*, **346(3)**, 247–262, 2018.

[5] R. Kawamoto, E. Andò, G. Viggiani, J.E. Andrade, Level set discrete element method for three-dimensional computations with triaxial case study. *Journal of the Mechanics and Physics of Solids*, **91**, 1–13, 2016.

[6] L. Sironi, M. Andreini, C. Colloca, M. Poehler, D. Bolognini, F. Dacarro, P. Lestuzzi, F. Dubois, Z. Zhou, J.E. Andrade. Shaking table tests for seismic stability of stacked concrete blocks used for radiation shielding. *Paper currently under review*.

[7] Z. Zhou, M. Andreini, L. Sironi, P. Lestuzzi, E. Andò, F. Dubois, D. Bolognini, F. Dacarro, J.E. Andrade. Discrete Structural Systems Modeling: Benchmarking of LS-DEM and LMGC90 with Seismic Experiments. *Paper currently under review*.

[8] D. Vamvatsikos , C.A. Cornell, Incremental Dynamic Analysis. *Earthquake Engineering and Structural Dynamics*, **31(3)**, 491–517, 2002.

[9] European Committee for Standardization (CEN). EN 206-1:2000 - Concrete - Part 1: Specification, performance, production and conformity.

[10] European Committee for Standardization (CEN). EN 1992-1-1:2004 - Eurocode 2 - Design of concrete structures - Part 1-1: General rules and rules for buildings.

[11] M. Vořechovský, D. Novák, Correlation control in small-sample Monte Carlo type simulations I: A simulated annealing approach. *Probabilistic Engineering Mechanics*, **24(3)**, 452–462, 2009.

[12] L. Danciu, S. Nandan, C. Reyes, R. Basili, G. Weatherill, C. Beauval, A. Rovida, S. Vilanova, K. Sesetyan, P-Y. Bard, F. Cotton, S. Wiemer, D. Giardini, The 2020 update of the European Seismic Hazard Model: Model Overview. *EFEHR Technical Report 001, v1.0.0*, 2021.

[13] *Décret n° 2000-892 du 13 septembre 2000 portant modification du code de la construction et de l'habitation et du décret n° 91-461 du 14 mai 1991 relatif à la prévention du risque sismique* (in French).

[14] *Décret n° 2010-1254 du 22 octobre 2010 relatif à la prevention du risque sismique* (in French).

[15] *Arrêté du 22 octobre 2010 relatif à la classification et aux règles de construction parasismique applicables aux bâtiments de la classe dite à risque normal* (in French).

[16] European Committee for Standardization (CEN). EN 1998-1:2004 - Eurocode 8 - Design of structures for earthquake resistance - Part 1 : General rules, seismic actions and rules for buildings.

[17] Swiss Society of Engineers and Architects. SN EN 1998-1:2019 - Eurocode 8 - Design of structures for earthquake resistance - Part 1 : General rules, seismic actions and rules for buildings - National Annex to SN EN 1998-1:2004.

[18] Swiss Society of Engineers and Architects. SIA 260. Basis of Structural Design. 2013.

[19] Swiss Society of Engineers and Architects. SIA 261. Actions on Structures. 2020.

[20] S. Sgobba, R. Puglia, F. Pacor, L. Luzi, E. Russo, C. Felicetta, G. Lanzano, M. D'Amico, R. Baraschino, G. Baltzopoulos, I. Iervolino. REXELweb: a tool for selection of ground-motion records from the Engineering Strong Motion database (ESM). *$7^{th}$ International Conference on Earthquake Geotechnical Engineering (ICEGE)* 17 - 20 June 2019, Roma, Italy.

COMPDYN 2023
9th ECCOMAS Thematic Conference on
Computational Methods in Structural Dynamics and Earthquake Engineering
M. Papadrakakis, M. Fragiadakis (eds.)
Athens, Greece, 12-14 June 2023

# SEISMIC FRAGILITY AND EXPECTED DAMAGE OF MASONRY SCHOOL BUILDINGS IN ITALY

**Elisa Saler**[1] **and Francesca da Porto**[1]

[1] Department of Geosciences, University of Padova
Via Gradenigo 6, 35131 Padova, Italy
e-mail: {elisa.saler, francesca.daporto}@unipd.it

## Abstract

*The relevance of school buildings in the response of a community to a seismic event is well-known, and it was observed in the aftermath of recent seismic events. The consequences of school collapses are huge, and their unusability after an earthquake may impact on community disaggregation due to the lack of an essential service for children and youth. In addition, school buildings may be crucial elements in the post-event planning, offering shelters for dislocated people in the first emergency phases. Therefore, seismic risk and scenario estimates for school buildings are fundamental to plan realistic post-event operations, as well as to devise mitigation strategies.*
*With this purpose, in this contribution, mechanics-based fragility sets were derived for 265 macro-classes of masonry school buildings, representative of the taxonomy of Italian school building, based on the national school building registry. This fragility sets were then used to derive maps of expected damage through the web-tool IRMA schools, developed by Eucentre. Damage estimates were computed for a specific return period (conditional damage) and for a time window (unconditional damage). In addition, damage scenarios were calculated by implementing shake maps of recent earthquake occurred in Central Italy.*

**Keywords**: masonry buildings; school buildings; seismic maps; seismic scenario; seismic vulnerability; mechanical method.

## 1 INTRODUCTION

School buildings represents a fundamental asset to be evaluated towards natural disasters, for civil protection purposes, emergency preparedness and mitigation planning. Not only are school relevant due to the consequences associated to their collapse [1,2], they also represent one of the largest stock of public buildings, and they can provide shelter to displaced people during a post-event emergency.

Within the Italian framework, the seismic vulnerability of school buildings was largely investigated, often in the aftermath of a seismic event [3–7].

However, risk analyses require the seismic vulnerability to be expressed in probabilistic terms. Fr this purpose, fragility curves were generally used. Despite the importance of school buildings, there remains a paucity of studies on this specific asset, and much of these were derived with reference to national context other than Italy [8–11].

Vulnerability of specific assets, such as schools, has yet to be included in the Global Earthquake Model (GEM) [12].

In the Italian framework, a cooperative national project has been funded by the Department of Civil Protection (DPC), involving two Centres of Competence of the DPC: EUCENTRE (*European Centre for Training and Research in Earthquake engineering*) and ReLUIS (*Network of university laboratories for seismic engineering*). Seismic risk was primarily investigated for ordinary buildings [13,14], providing novel fragility models for masonry [15–18] and r.c. [19,20] structures. Then, vulnerability assessment was extended to specific assets [21], such as schools and churches [22].

In this framework, a web platform (named IRMA) [23] was developed by EUCENTRE to compute seismic damage and risk of the investigated assets.

In this work, maps of expected damage for unreinforced masonry (URM) school buildings in Italy were derived thanks to the IRMA platform. Damage maps depends on all risk components: *i*) the hazard model, directly implemented in the platform [24]; *ii*) the exposure model, referring to the national registry of the Italian Ministry of Education [25], presented in the next section; and *iii*) on the vulnerability model which was derived by the authors through a mechanics-based fragility assessment procedure [26], briefly presented in section 3.

In addition, simulated scenarios were developed based on the shake maps of two recent seismic events which hit Italy (the 2009 L'Aquila earthquake and the 2016 Norcia earthquake).

## 2 EXPOSURE: ITALIAN SCHOOL BUILDING REGISTRY

Risk assessment at a large scale for a specific asset requires a dataset of exposure to be collected and georeffered, throughout the investigated area. Collected typological data (and structural information when available) contribute to defining the building taxonomy which should be consistent with building types adopted in the vulnerability model.

In this contribution, the reference dataset for exposure model was adopted according to the Italian school building registry (ISBR) [25], by the Ministry of Education, of 2005.

Data from the registry were processed and made available within the IRMA platform by *Eucentre* [27,28]. By querying the IRMA platform, data distributions presented in this section were obtained.

The registry counts 49351 school buildings, for which a limited number of parameters was collected:

- Structural type and construction material; masonry, r.c. precast, steel, and mixed structures are the proposed types.
- Construction ages (Before XIX century, XIX century, 1900-1920, 1921-1945, 1946-1960, 1961-1976, and after 1976).

- Number of storeys, grouping together buildings with four or more storeys.
- Covered plan area (less than 500 m2, 500-1000 m2, 1000-2000 m2, 2000-5000 m2, and more than 5000 m2).
- Type of floors; r.c. with clay elements, steel beams with clay elements, timber, vaults, and mixed are the proposed types, with also "other" as possible choice.

The three most ancient construction ages (i.e., "Before XIX century", "XIX century", and "Before 1920") were grouped together hereinafter, assuming homogeneous seismic behaviour.

This dataset was not collected homogeneously throughout the country. It was affected by lack of data, in particular concentrated in some Italian regions, as showed in Figure 1.

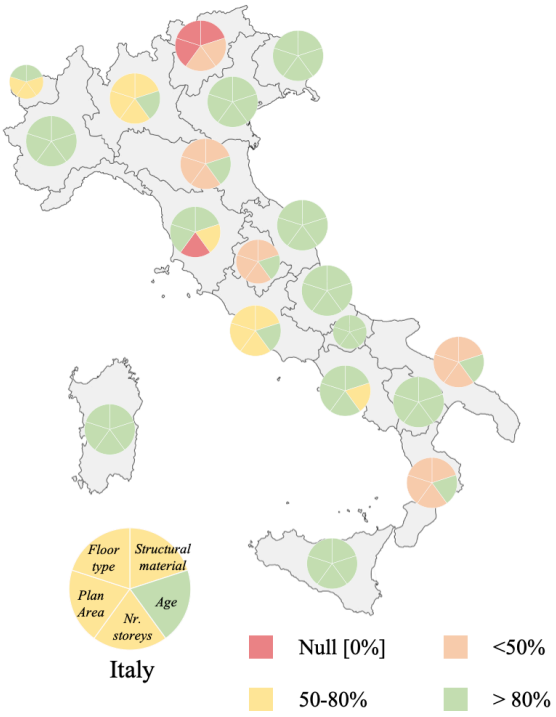


Figure 1. Completeness of data for Italian regions and overall country.

Figure 2 shows the frequencies of structural types (i.e., material of vertical structures). Reinforced concrete (r.c.) and masonry were the most frequent types. However, structural type data was not available for more than 30% of registered buildings.

Masonry schools represented almost a fifth (21%) of the ISBR of 2005, corresponding to 10352 buildings. Figure 3 shows the frequency distribution of typological (a, b, c, d) and structural (e, f) parameters of URM school buildings in the reference inventory. Masonry schools were built with similar frequencies in ages up to 1975, while the rate of new URM schools after 1976 almost halved. They are mainly low-rise buildings, with a significant peak (48%) of two-storey structures. According to plan area, small to medium schools prevail, while the frequency of very large URM structures is rather low. As illustrated in Figure 3d, most schools built before 1960 had two storeys, while the frequency of single-storey buildings has grown over time, becoming prevalent in the most recent period. This fact could be due to increasing request of pre-school facilities which led to enhancing of early childhood services, typically located in single-storey buildings. Furthermore, in 1975 technical provisions for school buildings were issued [29], setting a maximum number of storeys on which didactic

activities can take place, depending on the level of education. One storey was set as maximum for pre-school, two storeys for primary and lower secondary schools, and three storeys for higher secondary schools. The ISBR also collected data on types of floors. Most schools (64%) have rigid r.c. floors, while the frequencies of other types are significantly lower. Lastly, Figure 3f shows frequencies of types of masonry in the national registry. For most schools (81.5%) the pattern of masonry (either regular or irregular) was unspecified; thus, this data was insufficient to define percentage of masonry quality throughout the country.

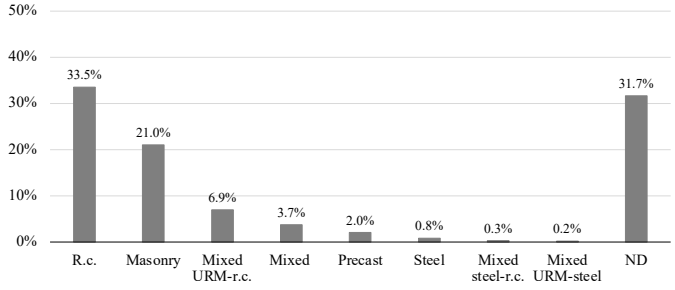


Figure 2. Frequency distribution of structural types in ISBR.

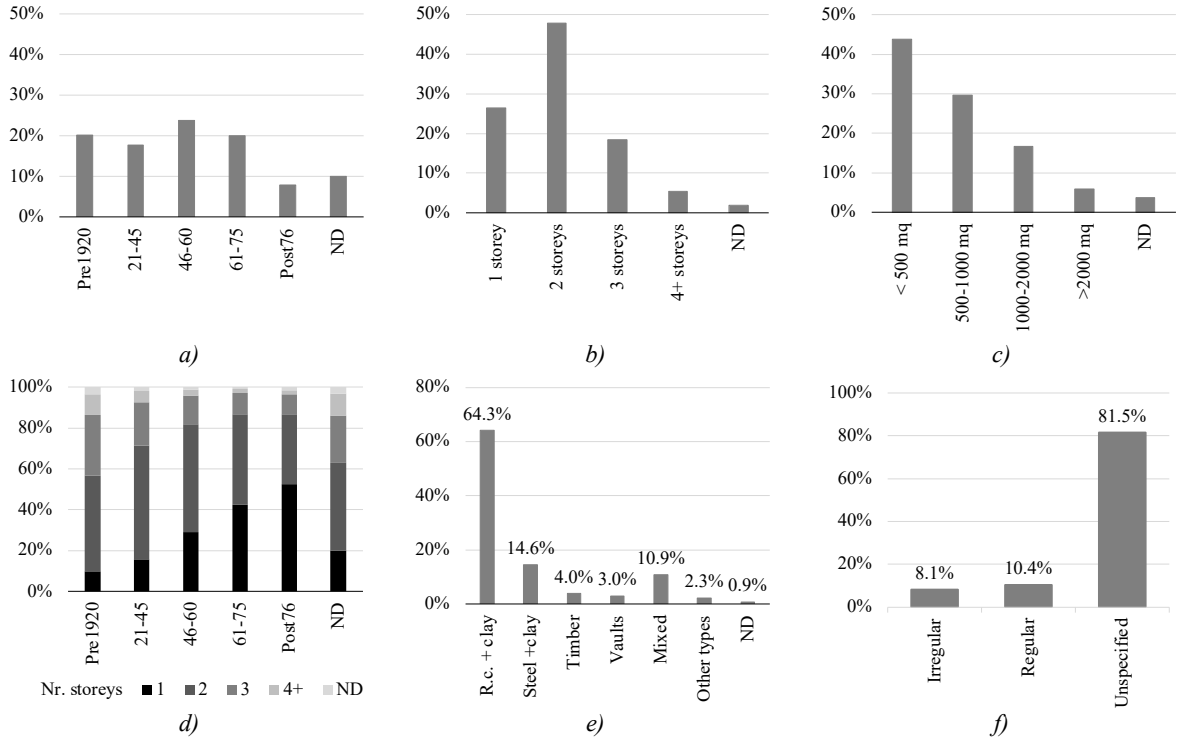


Figure 3. Frequency distribution of typological and structural parameters in ISBR.

## 3 VULNERABILITY: MECHANICS-BASED FRAGILITY MODEL

The vulnerability of unreinforced masonry (URM) was quantified through a fragility model derived through a mechanics-heuristic method [17,26]. Fragility curves were derived for analyses at national scale, by defining a taxonomy of buildings consistent with ISBR [25], thus defined by a limited number of parameters (i.e., construction age, number of storeys, plan area).

The procedure for fragility assessment combined a mechanics-based approach (*Vulnus*) [30–32], developed at the University of Padova, and a macroseismic heuristic model from the

literature [33]. The following steps were performed to estimate fragility of URM schools in Italy:

1. Definition of a dataset of more than 7500 prototype school buildings, based on the architectural configuration of 14 existing buildings [34–36].
2. Analysis of each prototype with Vulnus to derive fragility curves for a damage state intermediate between DS2 and DS3 (thus, DS2.5 hereinafter), according to the definition by EMS98 [37].
3. Linear combination of prototype fragilities according to exposure matrix, to obtain fragility model of the considered taxonomy (for DS2.5).
4. Calibration of the reference macroseismic-heuristic model [33] to derive fragility sets from DS1 to DS5 (i.e., from slight damage to collapse). Optimal coefficient of combination were calculated through NSGA-II algorithm (i.e., nondominated sorting genetic algorithm) [38].
5. Combination (named LUW) of fragility sets (average, lower- and upper-bounds) to include uncertainties and increase dispersion.

The steps of the procedure are showed in Figure 4. For further details on the fragility assessment, please refer to Saler et al. [26]. Log-normal fragility curves were thereby derived for 265 macro-classes of URM school buildings in Italy. Peak ground acceleration (PGA) was adopted as intensity measure. The parameters – median value (μ) and logarithmic standard deviation (β) – of more generalised macro-classes (based on construction age and number of storeys only) are summarised in Table 1.

Figure 5 summarises the main findings, in terms of trends of median values, of the proposed fragility model. Figure 5a and b refers to the representative macro-class of schools with two-storey, and they show median values as the ages and plan areas vary, respectively. The school vulnerability tends to decrease during ages, and small buildings appeared less vulnerable than medium to large schools. This latter result can be linked to a common greater complexity of larger buildings.

Figure 5c and d show trends of median values as number of storeys changes. The former refers to the period 1921-1945, and it is representative also of other epochs, excluding the most recent (Post 1976), thus displayed in the latter figure. For most macro-classes, the seismic vulnerability tended to increase with the number of storeys. A modest inversion was instead observed for schools built after 1976, for which two-storey schools appeared less vulnerable than single-storey buildings. This result may be explained by the decreased susceptibility of modern buildings to local mechanisms, and thereby a prevalence of in-plane shear failures. The resistance towards these latter mechanisms can be increased by vertical loads due to the second storey, compared to single-storey buildings.

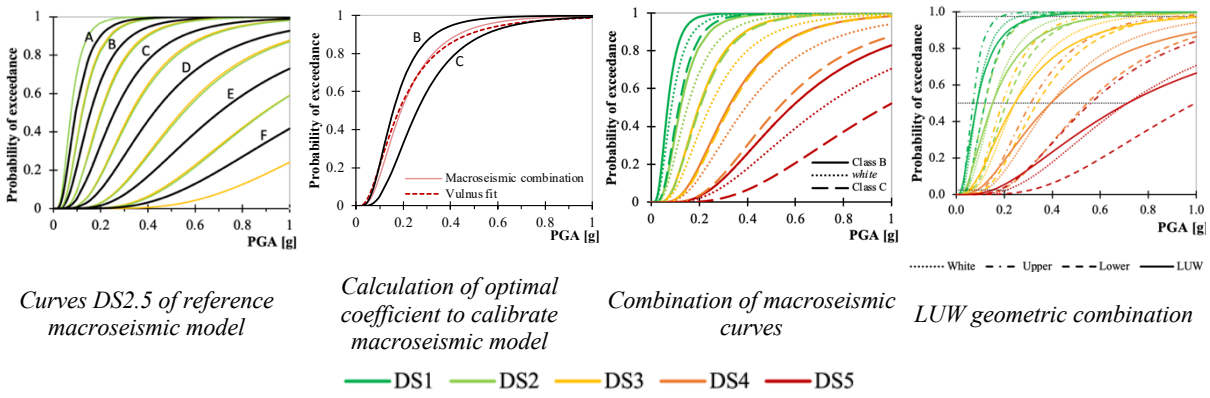


Figure 4. Steps of mechanics-based fragility assessment.

| | | DS1 | | DS2 | | DS3 | | DS4 | | DS5 | |
|---|---|---|---|---|---|---|---|---|---|---|---|
| *Age* | *Storeys* | *μ (g)* | *β (-)* | *μ (g)* | *β (-)* | *μ (g)* | *β (-)* | *μ (g)* | *β (-)* | *μ (g)* | *β (-)* |
| Pre 1920 | 1 | 0.105 | 0.790 | 0.187 | 0.798 | 0.302 | 0.797 | 0.488 | 0.811 | 0.894 | 0.825 |
| Pre 1920 | 2 | 0.085 | 0.740 | 0.151 | 0.753 | 0.244 | 0.747 | 0.394 | 0.762 | 0.713 | 0.795 |
| Pre 1920 | 3 | 0.073 | 0.772 | 0.130 | 0.802 | 0.209 | 0.804 | 0.338 | 0.825 | 0.613 | 0.860 |
| Pre 1920 | 4 | 0.064 | 0.767 | 0.114 | 0.794 | 0.184 | 0.787 | 0.297 | 0.805 | 0.535 | 0.834 |
| 1921-1945 | 1 | 0.118 | 0.738 | 0.209 | 0.757 | 0.337 | 0.761 | 0.546 | 0.768 | 0.997 | 0.780 |
| 1921-1945 | 2 | 0.105 | 0.761 | 0.186 | 0.779 | 0.300 | 0.777 | 0.485 | 0.786 | 0.888 | 0.791 |
| 1921-1945 | 3 | 0.092 | 0.745 | 0.163 | 0.763 | 0.263 | 0.759 | 0.426 | 0.778 | 0.774 | 0.811 |
| 1921-1945 | 4 | 0.084 | 0.704 | 0.148 | 0.729 | 0.239 | 0.725 | 0.387 | 0.740 | 0.701 | 0.781 |
| 1946-1960 | 1 | 0.142 | 0.668 | 0.253 | 0.688 | 0.408 | 0.690 | 0.659 | 0.703 | 1.197 | 0.745 |
| 1946-1960 | 2 | 0.114 | 0.656 | 0.203 | 0.677 | 0.328 | 0.677 | 0.530 | 0.683 | 0.970 | 0.737 |
| 1946-1960 | 3 | 0.102 | 0.649 | 0.181 | 0.674 | 0.292 | 0.670 | 0.473 | 0.682 | 0.864 | 0.740 |
| 1946-1960 | 4 | 0.088 | 0.682 | 0.157 | 0.700 | 0.253 | 0.693 | 0.409 | 0.711 | 0.743 | 0.763 |
| 1960-1975 | 1 | 0.172 | 0.792 | 0.305 | 0.818 | 0.493 | 0.814 | 0.800 | 0.802 | 1.463 | 0.859 |
| 1960-1975 | 2 | 0.143 | 0.771 | 0.254 | 0.789 | 0.410 | 0.792 | 0.662 | 0.795 | 1.202 | 0.838 |
| 1960-1975 | 3 | 0.129 | 0.761 | 0.229 | 0.783 | 0.370 | 0.791 | 0.597 | 0.813 | 1.086 | 0.870 |
| 1960-1975 | 4 | 0.107 | 0.806 | 0.190 | 0.815 | 0.306 | 0.821 | 0.496 | 0.838 | 0.909 | 0.846 |
| Post 1976 | 1 | 0.200 | 0.832 | 0.356 | 0.870 | 0.574 | 0.884 | 0.923 | 0.858 | 1.650 | 0.867 |
| Post 1976 | 2 | 0.211 | 0.835 | 0.375 | 0.872 | 0.605 | 0.880 | 0.970 | 0.873 | 1.727 | 0.872 |
| Post 1976 | 3 | 0.182 | 0.854 | 0.322 | 0.890 | 0.521 | 0.904 | 0.844 | 0.864 | 1.538 | 0.890 |
| Post 1976 | 4 | 0.160 | 0.864 | 0.284 | 0.890 | 0.458 | 0.906 | 0.742 | 0.874 | 1.352 | 0.901 |

Table 1. Fragility curves for generalised macro-classes of URM schools in Italy.

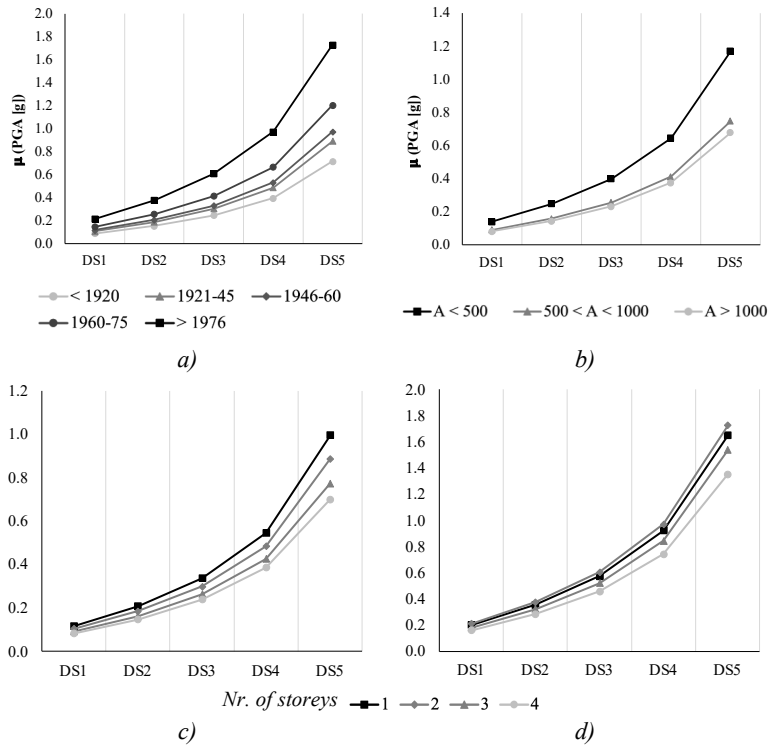


Figure 5. Trend of median values varying a) construction ages and b) plan area (for two-storeys schools); and number of storeys for construction periods c) 1921-1945 and d) post 1976.

## 4 SEISMIC MAPS OF THE ITALIAN URM SCHOOL ASSET

Maps of expected damage at national scale were derived for URM schools in Italy, based on the proposed mechanics-based fragility model.

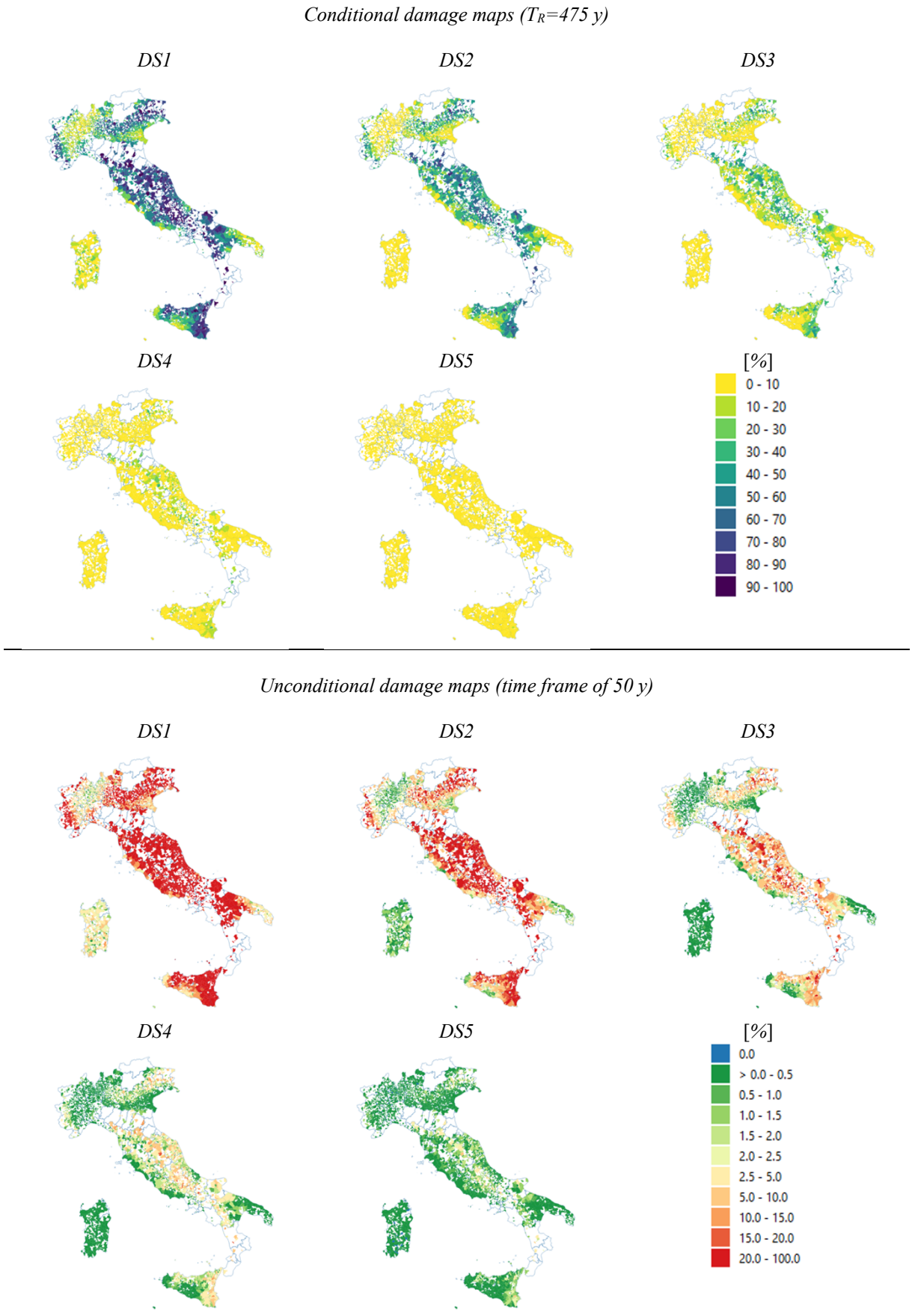


Figure 6. Conditional and unconditional damage maps: rate of URM schools for each DS.

These maps were developed within the IRMA (i.e., Italian Risk Maps) web platform, developed by EUCENTRE (*European Centre for Training and Research in Earthquake engineering*) [27,28]. The web platform was developed in the framework of the cooperative national project *ReLUIS-DPC 2019-2021* [21] for residential buildings and for specific assets (e.g., schools, churches).

IRMA implemented OpenQuake engine [39] to compute seismic risk. Hazard was based on national maps by Stucchi et al. (namely, MPS04) [24], while exposure referred to the above-mentioned Italian School building Registry of 2005 [25]. Vulnerability models should be uploaded by researchers taking parts in the national project. In this work, the proposed fragility model presented in the previous section was implemented.

Conditional and unconditional damage/risk computation were included in the web platform, which respectively refers to a specific return period and to an observation time frame. Note that the design return period (Life Safety limit state) for relevant structures with design working life of 50 years (712 years), such as schools [40], was not included. Unconditional damage/risk can be computed for the following time frames: 1, 10, and 50 years.

Maps for both conditional and unconditional damage were derived for the five damage states (DS) of the European Macroseismic Scale [37] described in the vulnerability model. In this case, maps represented the expected frequencies of each DS (Figure 6). Another possible representation of both conditional and unconditional damage is the expected mean damage, ranging from 0 to 5 (Figure 7).

In the derived maps, presented as follows, some regions (such as Emilia-Romagna and Calabria) resulted mainly blank, despite being characterised by moderate or high seismic risk. This stems from the lack of data in these regions (Figure 1). Indeed, structural type was available for none of schools in the Trentino-Alto Adige region, and only for 10% of schools in the Emilia-Romagna region, and 28% in the Calabria region. Thus, a set of 9233 out of 10352 URM schools were included in the computation of risk. About 10% of the total amount of URM school buildings in the registry [25] were indeed not processed due to lack of typological data that were needed to assign them to building macro-classes, associable to fragility curves.

Maps of expected damage appeared to be primarily dependent on hazard, and then on the distribution over the country of macro-classes (and then exposure and vulnerability), which make the colouring gradient irregular between contiguous municipalities.

Maps of damage were also derived for URM school buildings for two scenarios: the mainshock of the L'Aquila earthquake (6$^{th}$ April 2009), in Figure 8; and the Norcia earthquake (30$^{th}$ October 2016), in Figure 9. The shake maps [41] of these events (in terms of peak ground acceleration) were available in the web platform.

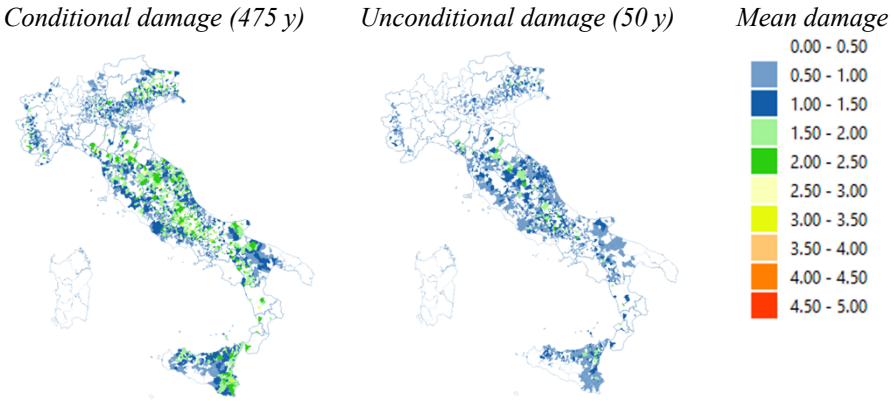


Figure 7. Conditional and unconditional damage maps: mean expected damage.

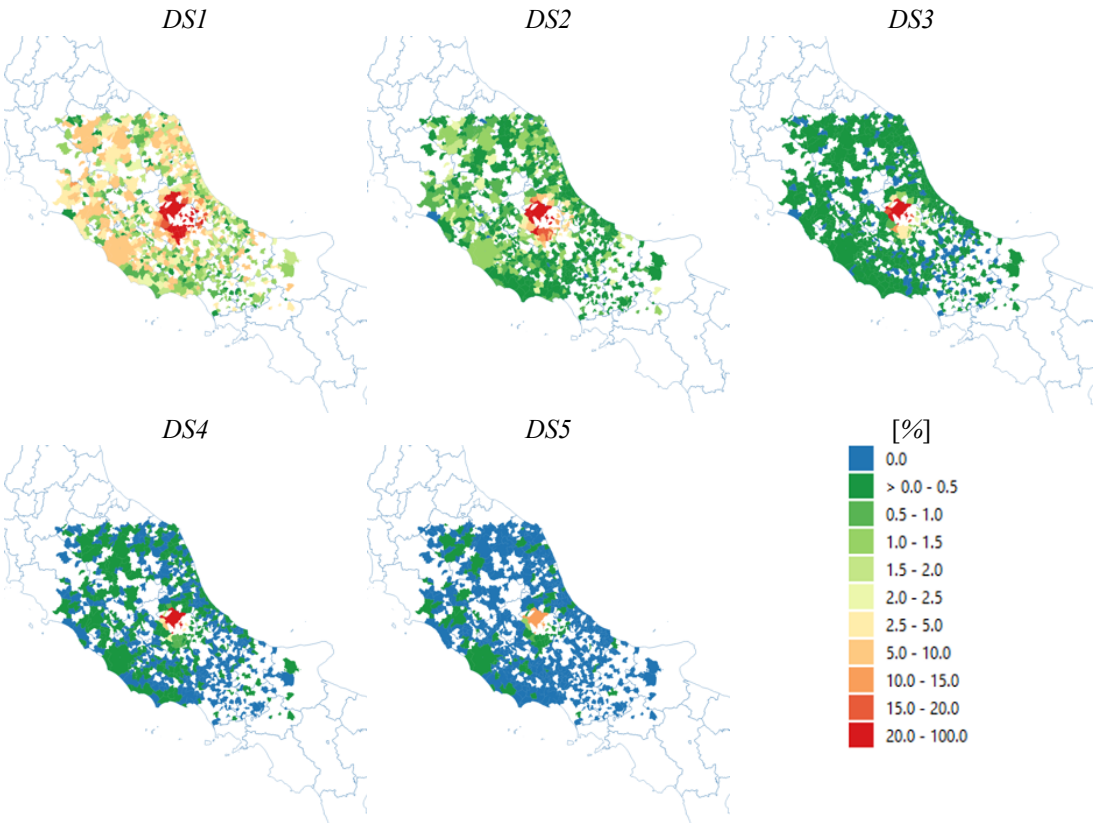


Figure 8. Damage scenario for the L'Aquila mainshock (6th April 2009).

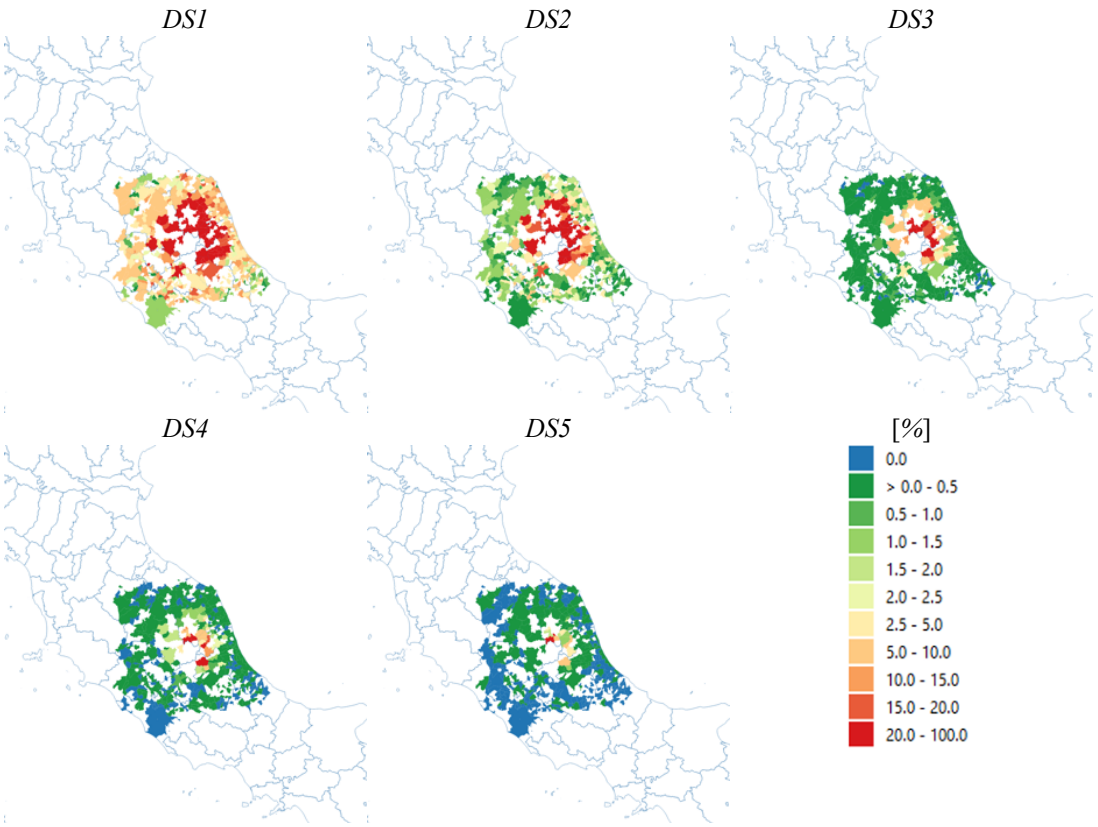


Figure 9. Damage scenario for the Norcia earthquake (30th October 2016).

## 5 CONCLUSIONS

- In this paper, a novel proposed fragility model for masonry school buildings was applied to develop maps of expected damage at national scale. The proposed fragility model was derived through a mechanical-heuristic approach, and it described the probability of exceeding five damage states (EMS98 [37]) conditional to peak ground acceleration, as intensity measure.
- The adopted macro-typology was based on a limited number of parameters available in the Italian school building registry, collected at national scale. These parameters were construction ages, number of storeys, and plan area. Typological parameters, such as number of storeys, construction ages and plan area appeared to consistently influence the seismic response of the investigated asset.
- Maps of expected damage were derived for Italy, for a time frame (i.e., unconditional damage) and for a return period (i.e., conditional damage). These maps appeared primarily influenced by the local seismicity, but also by the distribution of macro-classes.
- Further research should focus on determining consequence functions specific for school buildings, required to properly evaluating seismic risk associated to this relevant asset.

## ACKNOWLEDGEMENTS

Special thanks are due to ReLUIS and the Italian Department of Civil Protection, as the research was carried out in the framework of the *ReLUIS-DPC Project 2022-2024 – Work Package 4 – Task 4: Schools and hospitals*.

## REFERENCES

[1] M. di Ludovico, A. Digrisolo, C. Moroni, F. Graziotti, V. Manfredi, A. Prota, M. Dolce, G. Manfredi, Remarks on damage and response of school buildings after the Central Italy earthquake sequence, Bulletin of Earthquake Engineering. 17 (2019) 5679–5700. https://doi.org/10.1007/s10518-018-0332-x.

[2] D. Alexander, S. Bhatia, D. Benouar, J. Kumar, O. Cardona, School Seismic Safety: Case Studies, Encyclopedia of Earthquake Engineering. (2015) 1–16. https://doi.org/10.1007/978-3-642-36197-5_406-1.

[3] M. Dolce, A. Masi, C. Moroni, D. Liberatore, et al. Valutazione della vulnerabilità sismica di edifici scolastici della Provincia di Potenza, L'ingegneria Sismica in Italia. 1980 (2004).

[4] S. Cattari, S. Frumento, S. Lagomarsino, S. Parodi, S. Resemini, Multi-Level Procedure for the Seismic Vulnerability Assessment of Masonry Buildings: the Case of Sanremo ( North-Western Italy ), (2006) 3–8.

[5] F. Clementi, E. Quagliarini, G. Maracchini, S. Lenci, Post-World War II Italian school buildings: Typical and specific seismic vulnerabilities, Journal of Building Engineering. 4 (2015) 152–166. https://doi.org/10.1016/j.jobe.2015.09.008.

[6] N. Augenti, E. Cosenza, M. Dolce, G. Manfredi, A. Masi, L. Samela, Performance of school buildings during the 2002 Molise, Italy, earthquake, Earthquake Spectra. 20 (2004). https://doi.org/10.1193/1.1769374.

[7] F. Ceroni, N. Caterino, A. Vuoto, Simplified seismic vulnerability assessment methods: A comparative analysis with reference to regional school building stock in Italy, Applied Sciences (Switzerland). 10 (2020) 1–37. https://doi.org/10.3390/app10196771.

[8] P. Hannewald, C. Michel, P. Lestuzzi, H. Crowley, J. Pinguet, D. Fäh, Development and validation of simplified mechanics-based capacity curves for scenario-based risk assessment of school buildings in Basel, Eng Struct. 209 (2020) 110290. https://doi.org/10.1016/j.engstruct.2020.110290.

[9] D. D'Ayala, C. Galasso, A. Nassirpour, R.K. Adhikari, L. Yamin, R. Fernandez, D. Lo, L. Garciano, A. Oreta, Resilient communities through safer schools, International Journal of Disaster Risk Reduction. 45 (2020) 101446. https://doi.org/10.1016/j.ijdrr.2019.101446.

[10] R. Gentile, C. Galasso, Y. Idris, I. Rusydy, E. Meilianda, From rapid visual survey to multi-hazard risk prioritisation and numerical fragility of school buildings, Natural Hazards and Earth System Sciences. 19 (2019) 1365–1386. https://doi.org/10.5194/nhess-19-1365-2019.

[11] N. Giordano, F. De Luca, A. Sextos, F. Ramirez Cortes, C. Fonseca Ferreira, J. Wu, Empirical seismic fragility models for Nepalese school buildings, Natural Hazards. (2020). https://doi.org/10.1007/s11069-020-04312-1.

[12] V. Silva, D. Amo-Oduro, A. Calderon, C. Costa, J. Dabbeek, V. Despotaki, L. Martins, M. Pagani, A. Rao, M. Simionato, D. Viganò, C. Yepes-Estrada, A. Acevedo, H. Crowley, N. Horspool, K. Jaiswal, M. Journeay, M. Pittore, Development of a global seismic risk model, Earthquake Spectra. 36 (2020) 372–394. https://doi.org/10.1177/8755293019899953.

[13] M. Dolce, A. Prota, B. Borzi, F. da Porto, S. Lagomarsino, G. Magenes, C. Moroni, A. Penna, M. Polese, E. Speranza, G.M. Verderame, G. Zuccaro, Seismic risk assessment of residential buildings in Italy, Bulletin of Earthquake Engineering. (2020). https://doi.org/10.1007/s10518-020-01009-5.

[14] F. da Porto, M. Donà, A. Rosti, M. Rota, S. Lagomarsino, S. Cattari, B. Borzi, M. Onida, D. De Gregorio, F.L. Perelli, C. Del Gaudio, P. Ricci, E. Speranza, Comparative analysis of the fragility curves for Italian residential masonry and RC buildings, Bulletin of Earthquake Engineering. 19 (2021) 3209–3252. https://doi.org/10.1007/s10518-021-01120-1.

[15] G. Zuccaro, F.L. Perelli, D. De Gregorio, F. Cacace, Empirical vulnerability curves for Italian mansory buildings: evolution of vulnerability model from the DPM to curves as a function of accelertion, Bulletin of Earthquake Engineering. (2020). https://doi.org/10.1007/s10518-020-00954-5.

[16] S. Lagomarsino, S. Cattari, D. Ottonelli, The heuristic vulnerability model: fragility curves for masonry buildings, Bulletin of Earthquake Engineering. 19 (2021) 3129–3163. https://doi.org/10.1007/s10518-021-01063-7.

[17] M. Donà, P. Carpanese, V. Follador, L. Sbrogiò, F. da Porto, Mechanics-based fragility curves for Italian residential URM buildings, Bulletin of Earthquake Engineering. (2021) 1–34. https://doi.org/10.1007/s10518-020-00928-7.

[18] A. Rosti, M. Rota, A. Penna, Empirical fragility curves for Italian URM buildings, Bulletin of Earthquake Engineering. (2020). https://doi.org/10.1007/s10518-020-00845-9.

[19] A. Rosti, C. Del Gaudio, M. Rota, P. Ricci, M. Di Ludovico, A. Penna, G.M. Verderame, Empirical fragility curves for Italian residential RC buildings, Bulletin of Earthquake Engineering. 19 (2021) 3165–3183. https://doi.org/10.1007/s10518-020-00971-4.

[20] B. Borzi, M. Faravelli, A. Di Meo, Application of the SP-BELA methodology to RC residential buildings in Italy to produce seismic risk maps for the national risk assessment, Bulletin of Earthquake Engineering. 19 (2021) 3185–3208. https://doi.org/10.1007/s10518-020-00953-6.

[21] A. Masi, S. Lagomarsino, M. Dolce, V. Manfredi, D. Ottonelli, Towards the updated Italian seismic risk assessment: exposure and vulnerability modelling, Springer Netherlands, 2021. https://doi.org/10.1007/s10518-021-01065-5.

[22] F. Ceroni, C. Casapulla, E. Cescatti, V. Follador, A. Prota, F. da Porto, Damage assessment in single-nave churches and analysis of the most recurring mechanisms after the 2016–2017 central Italy earthquakes, Bulletin of Earthquake Engineering. 20 (2022) 8031–8059. https://doi.org/10.1007/s10518-022-01507-8.

[23] Eucentre, Italian Risk Maps (IRMA) platoform, (2018).

[24] M. Stucchi, C. Meletti, V. Montaldo, A. Akinci, E. Faccioli, P. Gasperini, L. Malagnini, G. Valensise, (2004). Pericolosità sismica di riferimento per il territorio nazionale MPS04 [Data set]. Istituto Nazionale di Geofisica e Vulcanologia (INGV)., (2004). https://doi.org/10.13127/sh/mps04/ag.

[25] L. 23/1996, Regulation for School Buildings, Official Gazzette of Italian Republic N°15 of 19th January 1996. Rome, Italy. (1996) (in Italian).

[26] E. Saler, V. Follador, P. Carpanese, M. Donà, F. da Porto, Development of mechanics-based fragility curves for the Italian masonry school asset, Submitted to the Bulletin of Earthquake Engineering. (n.d.).

[27] B. Borzi, M. Onida, M. Faravelli, D. Polli, M. Pagano, D. Quaroni, A. Cantoni, E. Speranza, C. Moroni, IRMA platform for the calculation of damages and risks of Italian residential buildings, Bulletin of Earthquake Engineering. 19 (2021) 3033–3055. https://doi.org/10.1007/s10518-020-00924-x.

[28] M. Faravelli, B. Borzi, M. Onida, S. Cattari, S. Alfano, A. Masi, V. Manfredi, S. Lagomarsino, An Italian platform for the seismic risk assessment of school buildings, Procedia Structural Integrity. 44 (2023) 107–114. https://doi.org/10.1016/j.prostr.2023.01.015.

[29] DM 18/12/1975, Norme tecniche aggiornate relative all'edilizia scolastica, ivi comprei gli indici minimi di funzionalità didattica, edilizia ed urbanistica, da osservarsi nella esecuzione di opere di edilizia scolastica (in Italian)., (n.d.).

[30] A. Bernardini, R. Gori, C. Modena, A structural model for continuous masonry building systems in historical centres, in: Structural Conservation of Stone Masonry. International Technical Conference. Athens, 31. X.-3. XI. 1989. Conservation Structurelle de La Maçonnerie En Pierre. Conférence Internationale Technique. Athènes, 31. X.-3. XI. 1989, Athens, Greece, 1989: pp. 29–36.

[31] A. Bernardini, R. Gori, C. Modena, M.R. Valluzzi, Vulnus 4.0 - Automatic procedure for the seismic vulnerability analysis of masonry buildings (in Italian), (2009).

[32] A. Bernardini, R. Gori, C. Modena, Application of Coupled Analytical Models adn Experientail Knowledge to Seismic Vulnerability Analyses of Masonry Buildings, in: A. Koridze (Ed.), Earthquake Damage Evaluation and Vulnerability Analysis of Building Structures, Omega Scientific, Wallingford, United Kingdom, 1990.

[33] S. Lagomarsino, S. Giovinazzi, Macroseismic and mechanical models for the vulnerability and damage assessment of current buildings, Bulletin of Earthquake Engineering. 4 (2006) 415–443. https://doi.org/10.1007/s10518-006-9024-z.

[34] E. Saler, P. Carpanese, V. Pernechele, Priority-ranking procedure to assess seismic vulnerability of school buildings at territorial scale, in: XVIII CONVEGNO ANIDIS - L'ingegneria Sismica in Italia, Ascoli Piceno, Italy, 2019.

[35] N. Gattesco, I. Boem, Classification of Friuli-Venezia Giulia masonry school buildings for seismic risk models purposes, in: XVIII CONVEGNO ANIDIS - L'ingegneria Sismica in Italia, Ascoli Piceno, 15-19 September 2019, 2019: pp. 79–86.

[36] D. Ottonelli, S. Alfano, S. Cattari, M. Di Ludovico, A. Prota, Structural and damage data analysis of a stock of URM schools struck by the 2016/2017 Central Italy earthquake, in: XVIII CONVEGNO ANIDIS - L'ingegneria Sismica in Italia, Pisa University Press, Ascoli Piceno, 15-19 September 2019, 2019: pp. 43–53.

[37] G. Grünthal, EMS98 - European Macroseismic Scale 1998, Conseil de l'Europe - Cahiers du Centre Européen de Géodynamique et de Séismologie, Luxemburg, 1998.

[38] K. Deb, A. Pratap, S. Agarwal, T. Meyarivan, A fast and elitist multiobjective genetic algorithm: NSGA-II, IEEE Transactions on Evolutionary Computation. 6 (2002). https://doi.org/10.1109/4235.996017.

[39] M. Pagani, D. Monelli, G. Weatherill, L. Danciu, H. Crowley, V. Silva, P. Henshaw, L. Butler, M. Nastasi, L. Panzeri, M. Simionato, D. Vigano, Openquake engine: An open hazard (and risk) software for the global earthquake model, Seismological Research Letters. 85 (2014) 692–702. https://doi.org/10.1785/0220130087.

[40] NTC2018 - D.M. 17/01/2018, Aggiornamento delle "Norme tecniche per le costruzioni" (in Italian), Official Gazzette of Italian Republic N°42 of 20th February 2018. (2018).

[41] INGV (Istituto Nazionale di Geofisica e Vulcanologia), ShakeMap v4, (n.d.). http://shakemap.ingv.it/shake4/ (accessed February 20, 2022).

COMPDYN 2023
9th ECCOMAS Thematic Conference on
Computational Methods in Structural Dynamics and Earthquake Engineering
M. Papadrakakis, M. Fragiadakis (eds.)
Athens, Greece, 12-14 June 2023

# TYPOLOGICAL FRAGILITY ASSESSMENT OF PRESTRESSED CONCRETE GIRDER BRIDGES SUBJECTED TO TRAFFIC LOADS AFFECTED BY CORROSION

**Alessandro Nettis[1], Andrea Nettis[1], Sergio Ruggieri[1] and Giuseppina Uva[1]**

[1] Department of Civil, Environmental, Land, Building Engineering and Chemistry,
Polytechnic University of Bari, via E. Orabona 4, 70125, Bari, Italy
e-mail: {alessandro.nettis, andrea.nettis, sergio.ruggieri, giuseppina.uva}@poliba.it

## Abstract

*Most of the Italian roadway bridges, built from 60s to 80s, are simply supported, girder-type, prestressed concrete bridges. After at least 50 years of service life, material degradation and functional obsolescence problems are coming out leading to the need for evaluating bridge vulnerability to natural and anthropic hazards. Particularly, this study aims at investigating the structural response to traffic loads of different typologies belonging to this bridge class. In this study, geometric and material random variables are assumed to simulate inter-class property variability and statistical sampling techniques are used to randomly generate bridge realisation for each investigated bridge typology. A simplified traffic load analysis is performed, subjecting each bridge realisation to various traffic load models (TLMs) proposed by the current Italian building code. Particularly, different post-tensioned tendon corrosion scenarios are assumed, evaluating the variation in response. Fragility curves are built for each bridge typology for each corrosion scenario and results are discussed with a view to prioritisation in the large-scale assessment of existing prestressed concrete bridge class.*

**Keywords:** Prestressed bridges, traffic loads, post-tensioning, fragility assessment, corrosion.

# 1 INTRODUCTION

The structural performance of bridges under traffic loads and natural hazards affects the serviceability and safety of transportation networks. Recent bridge collapses [1, 2] proved that these tragic events can lead to huge direct losses, mainly related to casualties, together with economic losses, involving significant transport disruptions affecting large urban and industrial contexts, reparation or replacement costs. The structural safety of bridges can be threatened by ageing, material deterioration and human-related and natural hazards. Currently, extensive bridge assessments are required by transportation managers to evaluate the performance of these structures under actions induced by natural hazards, which, generally, were not included in past design codes. Particularly, several research studies address refined and simplified methodologies to calculate fragility and risk (e.g. direct and indirect losses) considering seismic actions [3, 4] and floods [5]. Another source of fragility for existing bridges is related to service traffic loads [6–8], which are more severe in terms of number and mass of vehicles with respect to the past. Indeed, most of the existing bridges were designed considering old design traffic load schemes which may be inadequate compared to the current traffic demand. In recent literature studies, Fiorillo et al. [6] use real field truck data to perform fragility analysis of existing bridges considering overweight traffic loads. Miluccio et al. [7] characterise statistical distributions of significant geometric and structural variables for the general class of existing prestressed concrete girder superstructures and perform fragility analysis considering traffic loads.

In European countries, many existing bridges built in the post-war period exhibit severe degradation conditions caused by aggressive environmental agents together with inadequate durability requirements of materials and structural details. Material deterioration should be accounted for during on-site visual inspections for condition rating [9] and for defining targeted network-scale prioritisation of retrofit interventions [10]. Corrosion of prestressing steel strands or wires is considered one of the main causes of capacity degradation of prestressed concrete girder bridges with pre-tensioned and post-tensioned tendons. Particularly, in girders characterised by post-tensioned tendons, corrosion of strands may be triggered by corrosive agents penetrating anchorages and enhanced by construction errors such as incomplete grouting causing voids in the ducts. As evidenced by recent collapses of bridges in Italy [11, 12], corroded tendons may involve significant loss of structural capacity under gravity loads and cause structural failure. Corrosion effects on internal tendons and presence of voids inside the ducts cannot be detected by bridge inspectors via simple visual inspections. Indeed, according to guidelines developed in Italy [13] and United States [14], the condition rating of prestressed girders characterised by post-tensioned tendons requires special inspections in which non-destructive and destructive non-invasive tests are used to detect voids and identify corroded tendons inside the ducts.

Transport network managers are in charge of performing extensive surveys and assessments considering the large amount of prestressed concrete girder bridges equipped with post-tensioned internal tendons built in past decades. In this context, transport authorities' operators require efficient procedures for evaluating the corrosion-induced potential loss of structural capacity for existing bridges. These procedures should accurately and efficiently account for the relevant significance of the epistemic uncertainty commonly affecting the safety assessment, intending to prioritise critical structures to be subjected to refined diagnostic campaigns, assessment and retrofit.

This study investigates the fragility of prestressed concrete girder bridges subjected to traffic loads considering tendon corrosion. A probabilistic assessment methodology is used to evaluate the failure probability under traffic loads. The propagation of epistemic uncertainty

affecting geometric and structural parameters in results is considered through statistical sampling techniques. In this study, the methodology is used to investigate the structural safety of nine different bridge superstructure typologies. Results can be adopted to guide operators for cases within the investigated typologies. However, the same methodology can be similarly applied to investigate other case-study bridges in practice.

## 2 METHODOLOGY FOR FRAGILITY ANALYSIS

In this section, the adopted methodology for fragility analysis considering the involved uncertain parameters is described (Figure 1). It is worth specifying that a set of different prestressed concrete girder bridge typologies are considered in the study, whose characteristics are specified in section 3.1. In the following, the statistical sampling technique, the simplified modelling and analysis to calculate failure datasets and the algorithm to achieve fragility curves are presented.

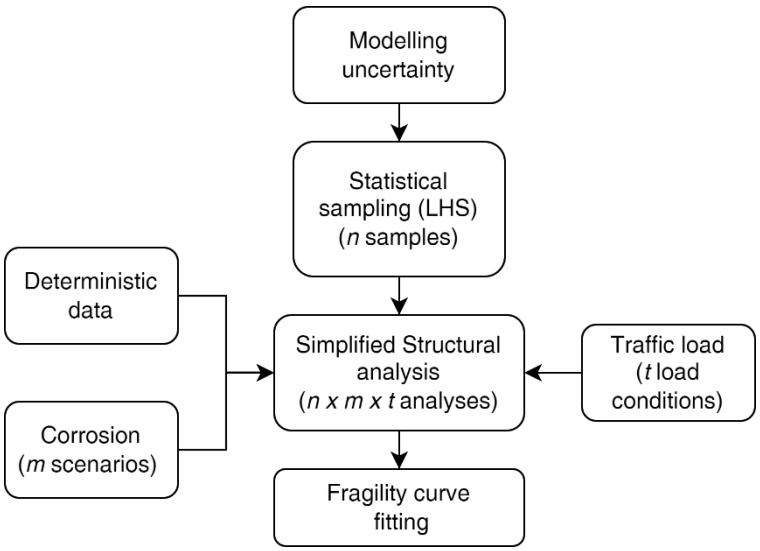


Figure 1: Flowchart for fragility analysis

### 2.1 Modelling uncertainties

Geometric and mechanical parameters affecting the structural safety assessment of the investigated bridge typologies are required as input for the proposed approach. In practical application, only few geometric parameters are deterministically modelled since these have poor influence in response computation or have low variability within the considered bridge typologies. They can be accurately deduced by design blueprints or by using on-site measurements [15]. Conversely, the determination of accurate values for other geometric structural variables and mechanical parameters of materials would require running an appropriate diagnostic campaign based on non-destructive and destructive tests, involving inevitably additional effort in the assessment process. In this methodology, such variables are assumed as epistemic uncertainties (i.e., deriving from an imperfect initial knowledge [16]) and two kinds of variables, a set of independent variables and few dependent variables through regression models, are considered. Independent variables are represented by random variables following appropriate statistical distributions. Several studies provide statistical distributions and regression models derived from statistical analysis for parameters affecting the probabilistic structural assessment of existing bridges [7, 17, 18].

After the definition of deterministic and probabilistic independent and dependent variables, the Latin Hypercube Sampling (LHS) [19] is used as a statistical sampling technique for the random generation of a population of bridge model realisations. Particularly LHS generation is applied to get random samples of independent variables. Once these are available, dependent variables are inferred through regression models. The model realisations exhibit the same deterministic parameters, but different uncertain parameters depending on the associated statistical distributions and regression models. The LHS is widely used in literature for the probabilistic seismic analysis of both single or portfolios of bridges (e.g. [20, 21]) and is usually preferred over the standard Monte Carlo technique since it requires less computational effort and ensures more accurate sampling from a random variable population. In the LHS framework, the cumulative distributions of the $m$ random variables $X_j$ $(j = 1,2,\dots,m)$ are divided into $N$ equal probability intervals (stratification of the input), where $N$ is the target number of realisations. For the characterisation of each realisation, a single value is randomly extracted from each interval. The output samples are $N$ vectors of size $m$ (i.e., $N$ bridge realisations), in turn, composed of values randomly paired under the assumption that these belong to different intervals. At the end of the sampling process, convergence in statistics should be checked to reach a number of model realisations representative of the real distribution and convenient in terms of computational effort. To do it, a sensitivity analysis [22] is carried out, setting the results obtained from a large set of realisations as a benchmark, and getting different analysis results obtained from smaller sets of bridge realisations. For each number of model realisations, the relative error compared to benchmark results is computed. The desired number of realisations is derived, considering a sample size which ensures that the relative error remains below an imposed threshold. At the end of the process, each realisation is deterministically analysed by using a practical structural analysis approach.

### 2.2 Simplified structural analysis

The simplified modelling and analysis strategy adopted in this study is suitable for the structural assessment of a simply supported superstructure. Particularly, the so-called Courbon-Albenga method [23] is used for calculating maximum flexure and shear demands for the girders of a given bridge grillage superstructure. According to this method, an infinite flexural stiffness of the transverse diaphragms and a negligible torsional stiffness of the girders is assumed. Under these assumptions and regardless of the position of the diaphragms, the transverse distribution of a given load on the deck among the different girders can be simulated by using distribution coefficients depending only on the number and position of the girders.

Gravity loads in terms of self-weight of the bridge elements and non-structural components are simulated by using uniformly distributed loads. Traffic loads are modelled by adopting the load schemes (tandem plus distributed loads) provided by Eurocode 1-Part 2 [24]. For each model realisation, the demand parameters extracted from the analysis are the maximum bending moment, registered at mid-span, and the maximum shear demand, registered at the support, for the edge girder. The number and arrangement of loaded traffic lanes to be considered in the analysis are defined in such a way as to maximise the flexural and shear demand for the edge girder.

For each model realisation, the demand parameter for flexure and shear, calculated as above, is compared with the corresponding capacity.

## 2.3 Capacity modelling

As far as capacity is concerned, flexure and shear behaviours are modelled as follows. Mild and prestressing steel areas are modelled as lumped in their centroids within the considered cross-section. For the assessment of the girder capacity, an effective width of the slab equal to the width of the top flange of the beam is assumed.

The computation of the ultimate bending moment strength $M_R$ is based on the following assumptions suggested by the codes [25, 26]: 1) plane cross-sections and perfect steel-concrete bonding after flexural deformation; 2) stress-block model for concrete constitutive law in compression and ultimate concrete compressive strain equal to 0.35%; 3) elastic-perfectly plastic behaviour for mild and prestressing steel.

Generally, the flexure capacity calculation requires the computation of prestressing tendon area in balanced rupture hypothesis, i.e., failure due to simultaneous attainment of ultimate compression strain for upper concrete fibre and yielding tensile strain for mild and prestressing steel. This is necessary for distinguishing between fragile and ductile flexural failures of the analysed transverse section, leading to different ways of ultimate capacity calculation.

For the sake of brevity, it is worth specifying that, for appropriate design of prestressed girders, a ductile failure can be considered. In this case, the computation of ultimate bending is performed through the following equation:

$$M_R = \left(A_{sp} f_{p,01} + A_s f_y\right) z \tag{1}$$

where $z$ is the internal lever arm, depending on the neutral axis position. Concerning shear capacity, the following equation is considered:

$$V_R = 0.7 b_w d \sqrt{f_{ct}^2 + \sigma_{cp} f_{ct}} \tag{2}$$

where $b_w$ is the girder web width; $d$ is the distance of the reinforcing steel from the top compression side (equal to girder height minus concrete cover); $f_{ct}$ is the concrete tensile strength; $\sigma_{cp}$ is the average compressive concrete stress due to residual prestressing action $\sigma_{sp}$. This formulation is derived from Eurocode 2 [26] and retains for prestressed concrete beam members in uncracked configuration.

The influence of tendon corrosion in the abovementioned capacity models is modelled through a percentage reduction of prestressing area proportional to a given corrosion degree defined according to Yu et al. [27]. The influence of corrosion degree on significant tendon mechanical properties is, additionally, modelled according to the study by Yu et al. [27].

## 2.4 Fragility analysis

In this study, fragility curves express the probability of failure for a given intensity of traffic loads. The failure is achieved for either flexure or shear demand exceeding the corresponding capacity. This sub-section describes the approach for calculating fragility curves, which is developed based on the multi-stripe seismic fragility analysis approach according to Baker [28] and, subsequently, applied by Miluccio et al. [7] for traffic loads.

First, each bridge model realisation is analysed considering increasing value of the traffic load. For this purpose, each realisation is analysed for a set of traffic load scenarios in which the traffic load scheme is multiplied by a factor $\alpha$ ranging from 0 to 2.8 considering an increasing load by steps equal to 0.005. In this case, the $\alpha$ parameter is used as load intensity

measure (IM) for the fragility analysis. Particularly, such a range is considered to get both flexural and shear failures for most of the generated model realisations, as explained in Section 4. For each load step, the demand-to-capacity ratio is derived, considering both flexure and shear demand ($DCR_f$ and $DCR_s$, respectively). Failure is achieved when:

$$DCR_t = max\left(DCR_f, DCR_s\right) \geq 1 \tag{3}$$

This process is repeated for all the $N$ model realisations included within the whole model population generated via LHS.

The output of this analysis consists of $N$ values of demand-to-capacity ratio collected for each load multiplier of the traffic load scheme described in sub-section 2.2. For each load scenario, the probability of failure conditioned to a load multiplier $P[failure|\alpha]$ is calculated as the ratio between the number of realisations associated with failure $N_{fail}$ ($DCR_t \geq 1$) and the total size $N$ of the model population (Equation (4)).

$$P[failure|\alpha] = P[DCR_t \geq 1|IM = im] = N_{fail}/N \tag{4}$$

Finally, the final fragility function is derived by fitting a lognormal cumulative distribution to the dataset of $P[failure|\alpha]$ related to the considered load scenarios by using the maximum likelihood method [28].

To investigate the influence of tendon corrosion on the fragility of a single bridge typology, fragility functions are calculated for several corrosion scenarios. A comparison between the achieved dataset of fragility curves allows for quantifying the variation in probability of failure for the variation in the intensity of tendon corrosion.

The entire process is then repeated for different bridge typologies, with different values of span length and beam number of the deck.

## 3 DESCRIPTION OF CASE-STUDY BRIDGE SUPERSTRUCTURES

### 3.1 Case studies

Different prestressed girder highway bridge typologies, assumed typical of bridges built between 1965 and 1970, are analysed in this study as case studies.

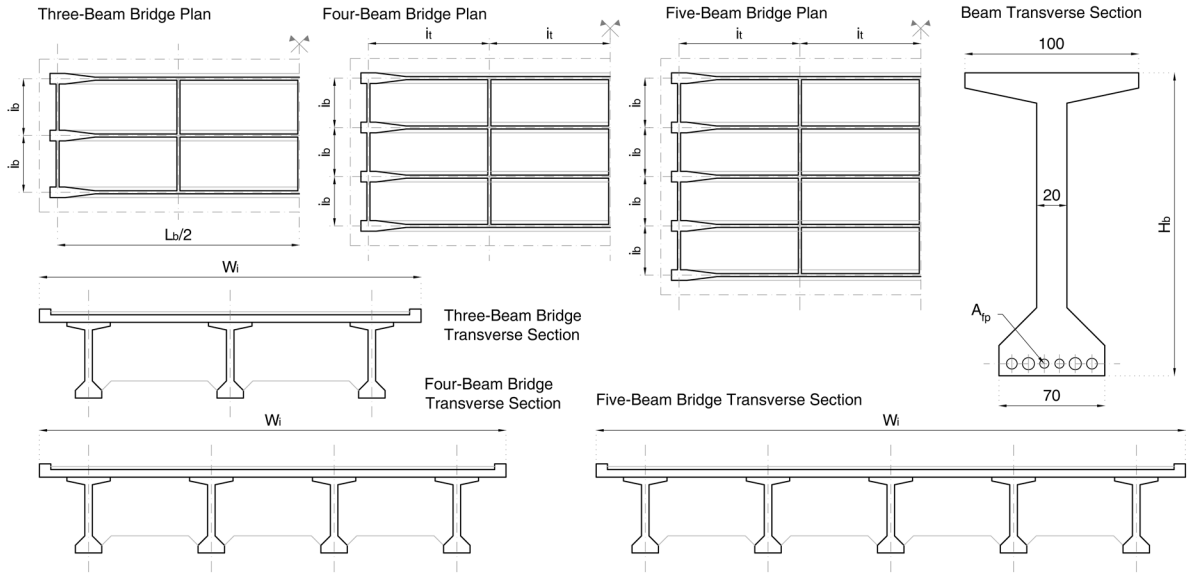


Figure 2: Case-study characteristics

Particularly, nine typologies are obtained, considering: 1) three different values of beam number of the deck (from three to five) and 2) three different values of span length (a short-span typology equal to 15 m, a medium-span typology equal to 35 m and a long-span typology equal to 55 m). These exhibit structural and constructive characteristics representative of the widespread class of simply supported post-tensioned girder bridges in Italy designed in ’60 and ’70 decades (Figure 2). Bridges exhibit multiple simply supported grillage superstructures having repetitive characteristics. The superstructure of each typology is composed of a varying number of girders with a reinforced concrete deck having a total width dependent on the spacing between the girders, which in turn depends on the beam height and the span length. For each case, the girder height varies with the span length and prestressed diaphragms guarantee the transverse load distribution among the girders of the same superstructure. Those components ensure the validity of the assumption of infinite bending stiffness of diaphragms compared to the torsional stiffness of the individual girders, for each typology. The girders of the superstructure present a variable number of tendons collected in specific ducts filled with cementitious grouts. The value of prestressing steel area is related to the span length and is computed through the prestressing steel ratio, i.e., the ratio between the prestressing steel area and the tension area of the concrete cross-section, as stated in section 3.2.

Other geometric data and constructive details of the case-study bridge typologies, which are considered deterministic in the following calculations, are shown in Figure 2. Bridge typologies are assumed designed according to the old Italian regulation *Circolare n.384 del 14.02.1962, Norme relative ai carichi per il calcolo dei ponti stradali* [29]. The carriageways of bridges host different values of real traffic lanes, depending on the deck width, subtracted of the total kerb length.

### 3.2 Uncertainties and corrosion scenarios

In addition to the deterministic input data, according to the methodology described in Section 2, the epistemic uncertainty related to the lack of deterministic knowledge for other parameters essential for the structural analysis, is modelled through statistical distributions

and regression models. In this case, statistical distributions and regression models useful for the purpose of this study are retrieved from the study by Miluccio et al. [7], who collected data on bridges in South Italy and perform statistical analysis to produce statistical distributions for significant structural and constructive parameters. Such distributions and models are listed in Table 1-2. As shown in the tables, two different kinds of variables are considered in this study, a set of independent variables and few dependent ones, derived via statistical distribution or regression models from other variables assumed as predictors.

For parameters whose statistical distributions are not available, the maximum uncertainty is assumed using a continuous uniform distribution. It is worth mentioning that the use of statistical distributions representative of the considered structural typology and geographical contexts is desirable to achieve a reliable simulation of epistemic uncertainty for the analysed case. A general lack of statistical distributions useful for the investigated purpose is registered in Italy. Although statistical distributions from different contexts are used in this study, it is expected that more statistical data about Italian highway bridges will be available in future, improving the reliability of such an approach.

To investigate the influence of the degree of tendon corrosion on structural response, different corrosion scenarios are considered. Each corrosion scenario is associated with a corrosion degree quantified as the (percentage) ratio $\xi$ of the tendon mass considered affected by corrosion and the initial total one. In the adopted methodology, no variation in the distribution of corrosion among the different tendons for a given girder cross-section is considered. This is because the adopted algorithm for section strength calculation considers the entire set of tendons as a single equivalent one with a mass equal to the sum of the tendon mass, (lumped in the tendon system centroid), neglecting their real distribution within the cross-section. Additionally, the variation in corrosion distribution along the girder longitudinal axis is neglected since only significant cross-sections are considered in the following analyses (sub-section 2.2). For each corrosion scenario, the tendon mass loss is associated with the girder cross-sections considered to calculate the DCR (i.e., mid-span for flexure and at the supports for shear), in which the corrosion degree $\xi$ is equal to [0-20-40] % of the initial tendon mass. Thus, an effective percentage of tendon area $\eta$ respectively equal to [100-80-60] % is considered in section strength computation.

| Parameter | Distribution | Parameters | |
|---|---|---|---|
| Mean concrete compressive strength ($f_{cm}$) [7] | Lognormal | μ = 38.5; COV = 11.4% | MPa |
| Mean steel tensile strength ($f_{ym}$) [7] | Lognormal | μ = 451; COV = 7.2% | MPa |
| Conventional yield strength of prestressing steel ($f_{p,01}$) [7] | Lognormal | μ = 1665; COV = 7.5% | MPa |
| Slab thickness ($s$) | Uniform | μ = 0.25; COV = 12.0% | m |
| Road pavements thickness ($h_{bit}$) | Uniform | μ = 0.14; COV = 24.7% | m |
| Residual stress level of prestressing steel ($\sigma_{sp}$) | Uniform | μ = 600; COV = 11.5% | MPa |

Table 1: Statistical distributions for independent variables

| Parameter | Predictors | Distribution/Regression model | Bounds | |
|---|---|---|---|---|
| Beam height ($H_b$) | $L_b$ | Uniform | $[{L_b}/{20}; {L_b}/{15}]$ | m |
| Beam spacing ($i_b$) [7] | $L_b, H_b$ | $H_b = 0.28 i_b + 0.03 L_b$ | - | m |
| Prestressing steel ratio ($\rho_{sp}$) [7] | $L_b$ | $\rho_{sp} d_{sp} = 8.16 \cdot 10^{-5} L_b + 1.85 \cdot 10^{-5} L_b^2$ | - | - |

Table 2: Statistical distributions and regression models for dependent variables

### 3.3 Sensitivity analysis

When using a random sampling technique as LHS to randomly generate portfolios of bridges, it is important to ensure that convergence in results is achieved. In this study, for reasons related to computational effort and analysis velocity, it is necessary to set the proper sample size to be generated, to guarantee that additional specimens would not alter the statistics of the sample, within a certain tolerance. The level of variability in the capacity of the randomly generated bridge realisations is obviously connected to the variability of material and geometric properties used in the sampling process.

In the present study, a set of $10^5$ bridge realisations of the three-beam medium-span typology, i.e., 35 m-span bridge, for three different corrosion degrees, is used as a reference to estimate the mean fragility curve. Because of the very large size of the sample, this fragility curve is assumed to provide the exact solution for the problem.

Subsequently, a number of samples with increasing sizes, from 5 to 500, are produced and their fragility curves are compared with the result obtained with the reference sample size. The comparison is performed in terms of relative error between the medians of the fragility curves, i.e., the relative difference between the fragility curve median of each sample size and the reference one.

This process is repeated several times for different randomly generated samples and for the three different corrosion scenarios. In Figure 3 the results are shown for ten repetitions of sample generation, for two different values of corrosion degree, equal to 40% and 20%. A relative error threshold of 2% is set and a sample size of 250 model realisations turns out to be the best choice. Beyond this sample size, no significant changes are observed in the results within a 2% tolerance. Thus, throughout this study, a sample size of 250 bridge model realisations is used to perform the analyses.

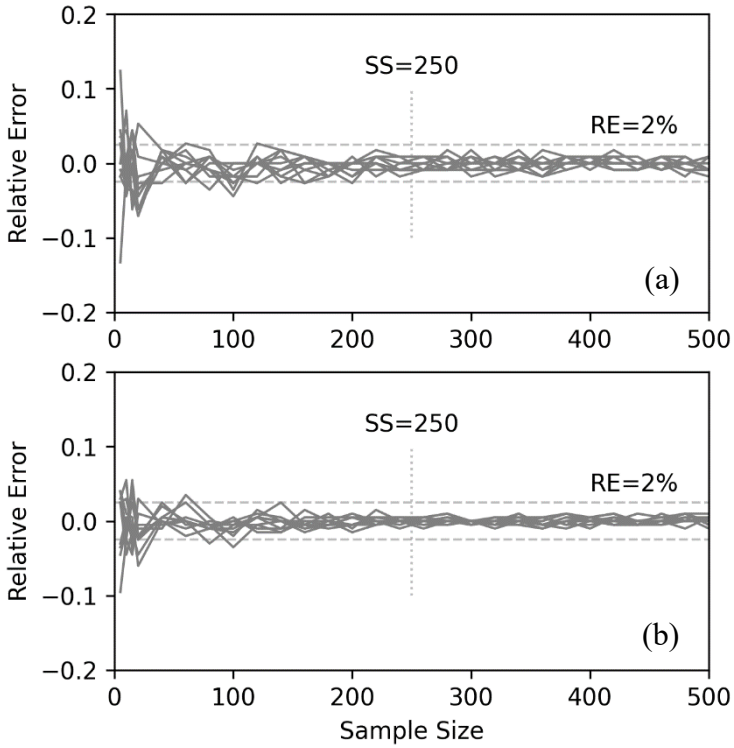


Figure 3: Relative errors as a function of sample size for ten repetitions, (a) 40% of corrosion degree and (b) 20% of corrosion degree

## 4 DISCUSSION OF RESULTS

In this section, the results and the obtained fragility curves are discussed, mainly focusing on the influence of different corrosion scenarios on bridge response to traffic loads.

Part of the results of the analyses are shown in Tables 3-5; results are given for corrosion degree values of 40, 20 and 0%, and span values of 15, 35 and 55 m, i.e., short-, medium- and long-span typologies.

| Bridge type | ξ [%] | Median | Dispersion |
|---|---|---|---|
| Three-beam | 40 | 0.305 | 0.060 |
| Three-beam | 20 | 0.540 | 0.076 |
| Three-beam | 0 | 0.765 | 0.091 |
| Four-beam | 40 | 0.350 | 0.069 |
| Four-beam | 20 | 0.595 | 0.085 |
| Four-beam | 0 | 0.840 | 0.101 |
| Five-beam | 40 | 0.375 | 0.079 |
| Five-beam | 20 | 0.630 | 0.101 |
| Five-beam | 0 | 0.880 | 0.120 |

Table 3: Fragility parameter corresponding to 15 m-span bridge

| Bridge type | ξ [%] | Median | Dispersion |
|---|---|---|---|
| Three-beam | 40 | 0.560 | 0.135 |
| Three-beam | 20 | 0.990 | 0.135 |
| Three-beam | 0 | 1.300 | 0.164 |
| Four-beam | 40 | 0.570 | 0.151 |
| Four-beam | 20 | 1.010 | 0.153 |
| Four-beam | 0 | 1.335 | 0.172 |
| Five-beam | 40 | 0.595 | 0.160 |
| Five-beam | 20 | 1.060 | 0.159 |
| Five-beam | 0 | 1.400 | 0.182 |

Table 4: Fragility parameters corresponding to 35 m-span bridge

| Bridge type | ξ [%] | Median | Dispersion |
|---|---|---|---|
| Three-beam | 40 | 0.705 | 0.168 |
| Three-beam | 20 | 1.015 | 0.218 |
| Three-beam | 0 | 1.215 | 0.237 |
| Four-beam | 40 | 0.695 | 0.192 |
| Four-beam | 20 | 1.030 | 0.241 |
| Four-beam | 0 | 1.235 | 0.261 |
| Five-beam | 40 | 0.710 | 0.211 |
| Five-beam | 20 | 1.070 | 0.272 |
| Five-beam | 0 | 1.295 | 0.287 |

Table 5: Fragility parameters corresponding to 55 m-span bridge

In general, results show low values of dispersion in fragility curves in most of the cases (Figures 4-6), except for the long-span typology, pointing out a low influence of the considered variables, on average, in the response. Fragility curves highlight that medium- and long-span typologies are adequate for the code-based traffic load up to a 20% of corrosion rate. The short-span typology, on the other hand, seems not adequate for Italian regulation, even with a zero-corrosion value. Therefore, from this study appears that this latter is the typology to be given the most attention in a large-scale analysis. The reasons for this result might lie in the choice of beam height and post-tensioning reinforcement modelling. These

are influenced by the span length value and are lower in case of shorter spans. Thus, future developments need to investigate the problem more in detail, refining the analysis by implementing a simulated design procedure according to the old design code, to further validate the obtained results.

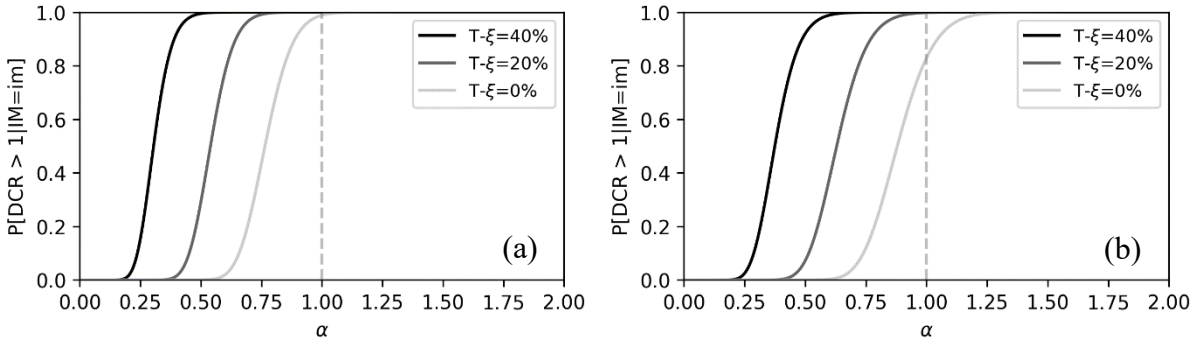


Figure 4: Fragility curves for (a) three- and (b) five-beams, 15 m-span bridge

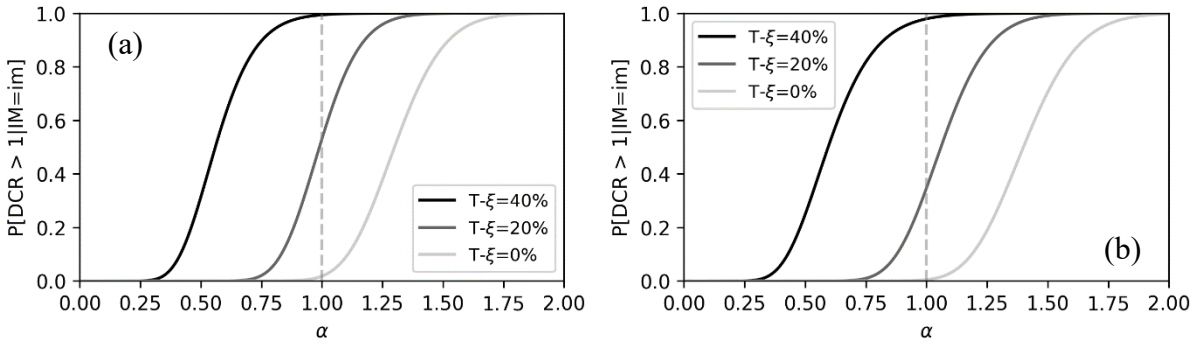


Figure 5: Fragility curves for (a) three- and (b) five-beams, 35 m-span bridge

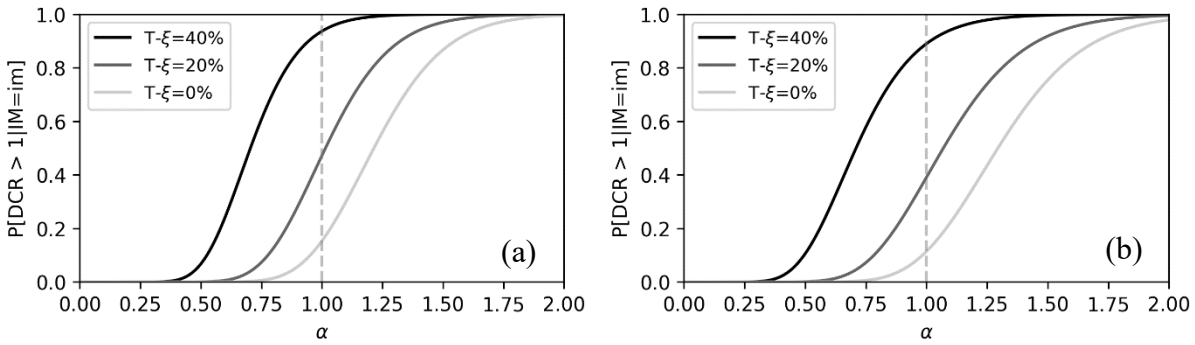


Figure 6: Fragility curves for (a) three- and (b) five-beams, 55 m-span bridge

Span length variation has a strong influence on the structure response to traffic loads. As the span decreases, the structure tends to bear lower loads, for the abovementioned reasons. There is an almost constant response for medium- and long-span typologies. The difference becomes significant when comparing to the short-span ones, which show a decrease in the maximum load-bearing capacity of approximately 40% on average compared to the medium- and long-span, up to a maximum value of 56%, between the long- and short-span, for a three-beam deck typology.

In contrast, the variation in the beam number has a much smaller influence on bridge fragility. There is a slight increase in the load-bearing capacity as the number of beams increases, for the small-span typology the maximum variation in the fragility curve median is obtained for a zero-corrosion value and is equal to 19%, while for the medium- and large-span ones the maximum variation is approximately constant and equal to 7%.

As for the influence of corrosion for the same span value, the response of the bridge is increasingly weaker as the corrosion level increases. By comparing the fragility variation magnitude as the bridge span varies, it can be seen that there is no great difference in terms of fragility curve median variation, which remains approximately constant as span length varies. Indeed, the median variation is about 60% in case of short- and medium-span length, and it drops to around 45% for the longest span. Therefore, there is no evidence of different influence of corrosion among different span typologies, corrosion induces a similar increase in fragility regardless of the span length. It is worth noting that tendon corrosion may determine a significant increase in the bridge fragility, until a 60% of decrease in the fragility curve median value for a corrosion degree increasing from 0 to 40%.

Another consideration concerns the influence of corrosion on bridge response considering the variation of beam number of the deck. In this case, it is clear that there is no evidence of a greater influence of corrosion degree for different values of beam number. Indeed, the variation of the fragility due to varying corrosion levels is nearly constant as the beam number varies and is equal to the abovementioned values, i.e., about a 7% of decrease in fragility curve median values on average for a decreasing beam number.

As far as the dispersion of the fragility curves is concerned, it can be seen that the alteration of corrosion level does not lead to a significant change. The dispersion appears to be roughly constant as the corrosion degree varies, for the same span value and the same number of beams. Conversely, a slight increase in the dispersion is noted as the number of beams increases and it is more pronounced as the span value increases. The latter may be related to the greater variability of the beam height adopted in dependent variable modelling, as this characteristic is related to span value. The greater the span value, the greater the variation of beam height between the two extremes considered. The same applies to the deck width, in turn related to span length and beam height. As these two parameters vary more for greater span values, they result in a greater dispersion in the relative fragility curves.

| Failure mode | $\xi$ [%] | Median | Dispersion |
|---|---|---|---|
| Flexural | 40 | 0.375 | 0.079 |
| Flexural | 20 | 0.630 | 0.101 |
| Flexural | 0 | 0.880 | 0.120 |
| Shear | 40 | 1.360 | 0.079 |
| Shear | 20 | 1.480 | 0.166 |
| Shear | 0 | 1.585 | 0.176 |

Table 6: Flexural and shear fragility parameters for a five-beam 15 m-span bridge

| Failure mode | $\xi$ [%] | Median | Dispersion |
|---|---|---|---|
| Flexural | 40 | 0.595 | 0.160 |
| Flexural | 20 | 1.085 | 0.174 |
| Flexural | 0 | 1.575 | 0.199 |
| Shear | 40 | 1.065 | 0.164 |
| Shear | 20 | 1.250 | 0.183 |
| Shear | 0 | 1.425 | 0.197 |

Table 7: Flexural and shear fragility parameters for a five-beam 35 m-span bridge

| Failure mode | ξ [%] | Median | Dispersion |
|---|---|---|---|
| Flexural | 40 | 0.820 | 0.259 |
| Flexural | 20 | 1.455 | 0.258 |
| Flexural | 0 | 1.885 | 0.237 |
| Shear | 40 | 0.815 | 0.273 |
| Shear | 20 | 1.070 | 0.293 |
| Shear | 0 | 1.295 | 0.289 |

Table 8: Flexural and shear fragility parameters for a five-beam 55 m-span bridge

The fragility analysis for the two different flexural and shear failure modes in Tables 6-8 and in Figure 7 shows that there is no clear dominant failure type for the medium- and long-span typologies. On the contrary, it can be stated that the dominant failure type for short-span decks is related to flexure. As the span increases, the shear failure type becomes increasingly dominant and this is due to the tendon area modelling methods already mentioned. It can also be seen, on the medium- and long-span typologies, that as corrosion increases, flexural failure tends to overwhelm shear failure. This is related to the decrease in the reinforcement considered in the calculation algorithm for flexural strength, a variation which, on the other hand, has a lower influence on shear strength, contributing only to the compression state of the beam cross-section.

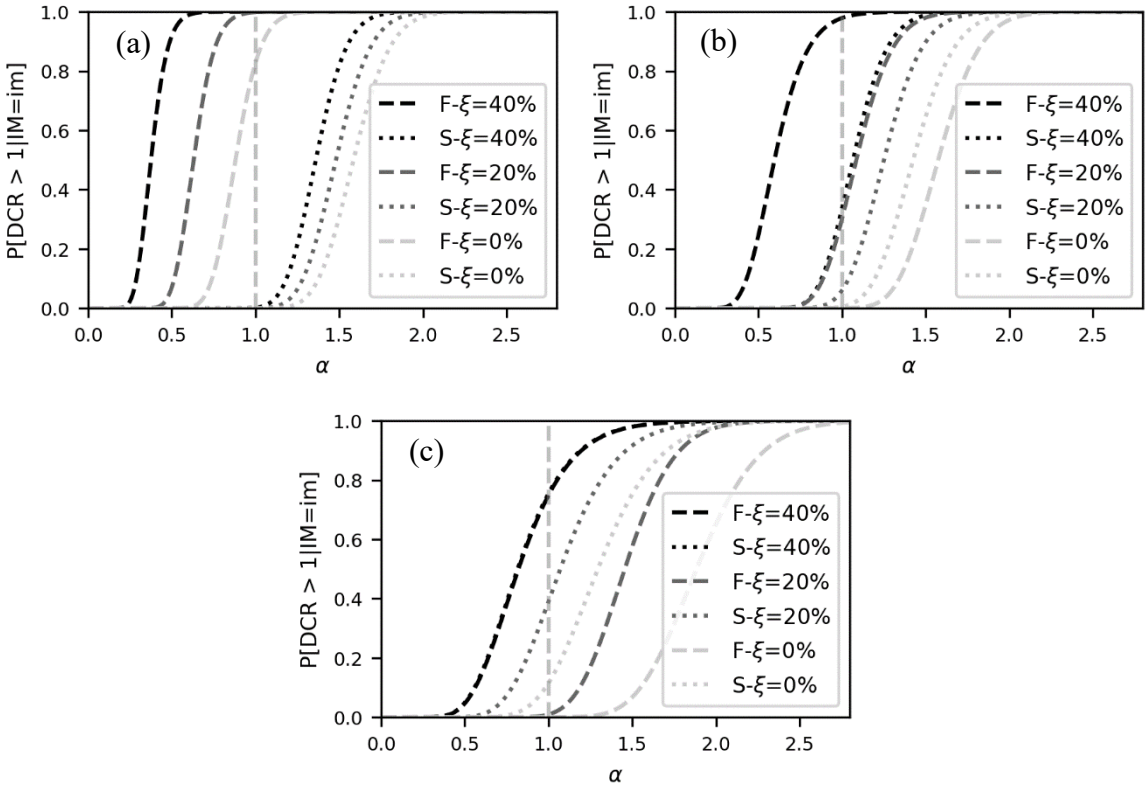


Figure 7: Flexural and shear fragility curves for five-beam bridge type, (a) 15 m-, (b) 35 m- and (c) 55 m-span. F: flexure; S: shear

In general, one can state that the variation of the geometric and mechanical characteristics analysed in this study does not strongly influence the response of the structure as fragility curves show low values of dispersion in most of the cases, while the state of prestressing tendon corrosion is much more decisive. This suggests, with a view to prioritisation during

bridge inspections, to focus attention and available resources on the state of prestressing tendons, which is fundamental for the response, while an investigation of the remaining characteristics could only be considered at a later stage. In addition, the study shows a greater vulnerability for short-span bridge typology, a consideration, however, to be validated with further investigation in future.

## 5 CONCLUSIONS

The fragility of prestressed concrete girder bridges subjected to traffic loads considering tendon corrosion is investigated in this study. A probabilistic assessment methodology is presented to evaluate the failure probability under traffic loads. The probabilistic assessment considers the influence of epistemic uncertainty on selected geometric and structural parameters which are unknown to operators during preliminary bridge assessment. The propagation of uncertainty is considered through statistical sampling techniques. In this study, the methodology is used to investigate the failure probability of nine prestressed concrete bridge superstructure typologies. Results show that particular attention should be given to the short-span typology which, according to the variable modelling choices adopted in this study, exhibits the weakest resistance to traffic loads, modelled as Italian code [25]. Variation of span length tends to considerably alter bridge fragility, particularly for short-span typology, leading up to a maximum of 56% of decrease in load-bearing capacity compared to the long-span one. The same cannot be stated for the beam number of the deck, which appears not to significantly affect the results, with a 10% of increase in the fragility curve median on average as the beam number increases, and a maximum value of 19% only in case of a short-span typology. Investigation on the influence of corrosion level for diverse span lengths and beam numbers leads to the conclusion that there is no need for particular attention to corrosion level for a specific bridge typology. Corrosion level is equally important for every investigated bridge typology and significantly affects the fragility, up to a decrease of 60% in load-bearing capacity for increasing corrosion level from 0 to 40%. Besides, for the long-span typology, results show a greater dispersion in fragility curves. This might be related to a larger variability of beam height and deck width for this particular bridge typology. To reduce this uncertainty in the fragility, as for validating the results obtained for the short-span typology, implementing simulated design in the procedure should be helpful. Finally, results prove that the flexural response governs the failure of the short-span bridge typology, compared to shear behaviour. The same applies to all the bridge typologies in presence of severe corrosion degree, thus leading to a ductile mechanism. On the other hand, this cannot be stated for low corrosion values for medium- and long-span bridge typologies, as brittle shear failure tends to be the most likely mechanism. The tendon corrosion involves a considerable loss of bridge flexural capacity. The achieved preliminary results can be adopted to guide operators for cases within the investigated bridge typologies. However, the same methodology can be similarly applied for investigating other case-study bridges in practice. Additional studies are needed, to evaluate the approximations related to the initial simplification assumptions on the adopted methodology for structural analysis. Finally, further developments should be aimed to analyse the probability of failure of other case-study bridges representative of existing typologies to be used by transport authority's operators for risk-based prioritisation purposes.

## ACKNOWLEDGEMENTS

The third author acknowledges funding by Italian Ministry of University and Research, within the project 'PON-Ricerca e Innovazione-2014–2020, CUP Code (D.M. 10/08/2021, n. 1062): D95F21002140006. The last author acknowledges funding by Centro Nazionale

Sustainable Mobility Center, within the framework of MOST project, CUP code: D93C22000410001.

## REFERENCES

[1] G. M. Calvi *et al.*, 'Once upon a Time in Italy: The Tale of the Morandi Bridge', *Structural Engineering International*, vol. 29, no. 2, pp. 198–217, Apr. 2019, doi: 10.1080/10168664.2018.1558033.

[2] F. Bazzucchi, L. Restuccia, and G. A. Ferro, 'Considerations over the Italian road bridge infrastructure safety after the polcevera viaduct collapse: Past errors and future perspectives', *Frattura ed Integrita Strutturale*, vol. 12, no. 46, pp. 400–421, Oct. 2018, doi: 10.3221/IGF-ESIS.46.37.

[3] A. Nettis, P. Iacovazzo, D. Raffaele, G. Uva, and J. M. Adam, 'Displacement-based seismic performance assessment of multi-span steel truss bridges', *Eng Struct*, vol. 254, Mar. 2022, doi: 10.1016/j.engstruct.2021.113832.

[4] S. P. Stefanidou and A. J. Kappos, 'Methodology for the development of bridge-specific fragility curves', *Earthq Eng Struct Dyn*, vol. 46, no. 1, pp. 73–93, Jan. 2017, doi: 10.1002/eqe.2774.

[5] A. Anisha, A. Jacob, R. Davis, and S. Mangalathu, 'Fragility functions for highway RC bridge under various flood scenarios', *Eng Struct*, vol. 260, Jun. 2022, doi: 10.1016/j.engstruct.2022.114244.

[6] G. Fiorillo and M. Ghosn, 'Fragility analysis of bridges due to overweight traffic load', *Structure and Infrastructure Engineering*, vol. 14, no. 5, pp. 619–633, May 2018, doi: 10.1080/15732479.2017.1380675.

[7] G. Miluccio, D. Losanno, F. Parisi, and E. Cosenza, 'Traffic-load fragility models for prestressed concrete girder decks of existing Italian highway bridges', *Eng Struct*, vol. 249, Dec. 2021, doi: 10.1016/j.engstruct.2021.113367.

[8] V. Sangiorgio, A. Nettis, G. Uva, F. Pellegrino, H. Varum, and J. M. Adam, 'Analytical fault tree and diagnostic aids for the preservation of historical steel truss bridges', *Eng Fail Anal*, vol. 133, Mar. 2022, doi: 10.1016/j.engfailanal.2021.105996.

[9] A. M. Abdallah, R. A. Atadero, and M. E. Ozbek, 'A State-of-the-Art Review of Bridge Inspection Planning: Current Situation and Future Needs', *Journal of Bridge Engineering*, vol. 27, no. 2, Feb. 2022, doi: 10.1061/(ASCE)BE.1943-5592.0001812.

[10] D. Y. Yang and D. M. Frangopol, 'Life-cycle management of deteriorating bridge networks with network-level risk bounds and system reliability analysis', *Structural Safety*, vol. 83, Mar. 2020, doi: 10.1016/j.strusafe.2019.101911.

[11] G. A. Ferro, L. Restuccia, D. Falliano, A. Devitofranceschi, and A. Gemelli, 'Collapse of Existing Bridges: From the Lesson of La Reale Viaduct to the Definition of a Partial Safety Coefficient of Variable Traffic Loads', *Journal of Structural Engineering*, vol. 148, no. 11, Nov. 2022, doi: 10.1061/(ASCE)ST.1943-541X.0003458.

[12] L. Anania, A. Badalà, and G. D'Agata, 'Damage and collapse mode of existing post tensioned precast concrete bridge: The case of Petrulla viaduct', *Eng Struct*, vol. 162, pp. 226–244, May 2018, doi: 10.1016/j.engstruct.2018.02.039.

[13] Ministero delle Infrastrutture e dei Trasporti, 'Linee guida per la classificazione e gestione del rischio, la valutazione della sicurezza ed il monitoraggio dei ponti esistenti.' 2020.

[14] FHWA - Office of Research Development and Technology, 'Guidelines for Sampling, Assessing, and Restoring Defective Grout in Prestressed Concrete Bridge Post-Tensioning Ducts.', 2013.
[15] A. Nettis, M. Saponaro, and M. Nanna, 'RPAS-based framework for simplified seismic risk assessment of Italian RC-bridges', *Buildings*, vol. 10, no. 9, Sep. 2020, doi: 10.3390/BUILDINGS10090150.
[16] B. A. Bradley, 'Epistemic uncertainties in component fragility functions', *Earthquake Spectra*, vol. 26, no. 1, pp. 41–62, 2010, doi: 10.1193/1.3281681.
[17] C. Zelaschi, R. Monteiro, and R. Pinho, 'Parametric Characterization of RC Bridges for Seismic Assessment Purposes', *Structures*, vol. 7, pp. 14–24, Aug. 2016, doi: 10.1016/j.istruc.2016.04.003.
[18] L. Jacinto, M. Pipa, L. A. C. Neves, and L. O. Santos, 'Probabilistic models for mechanical properties of prestressing strands', *Constr Build Mater*, vol. 36, pp. 84–89, Nov. 2012, doi: 10.1016/j.conbuildmat.2012.04.121.
[19] R. L. Iman and W. J. Conover, 'A Distribution-Free Approach to Inducing Rank Correlation Among Input Variables', *Commun Stat Simul Comput*, vol. 11, no. 3, pp. 311–334, Jan. 1982, doi: 10.1080/03610918208812265.
[20] D. H. Tavares, J. E. Padgett, and P. Paultre, 'Fragility curves of typical as-built highway bridges in eastern Canada', *Eng Struct*, vol. 40, pp. 107–118, Jul. 2012, doi: 10.1016/j.engstruct.2012.02.019.
[21] R. Monteiro, 'Sampling based numerical seismic assessment of continuous span RC bridges', *Eng Struct*, vol. 118, pp. 407–420, Jul. 2016, doi: 10.1016/j.engstruct.2016.03.068.
[22] V. Silva, H. Crowley, H. Varum, R. Pinho, and R. Sousa, 'Evaluation of analytical methodologies used to derive vulnerability functions', *Earthq Eng Struct Dyn*, vol. 43, no. 2, pp. 181–204, 2014, doi: 10.1002/eqe.2337.
[23] G. Albenga, *Lezioni di ponti*. Torino: U.T.E.T., 1930.
[24] CEN, 'Eurocode 1: Actions on structures - Part 2: Traffic loads on bridges', vol. EN 1991-2. Brussels, Belgium, 2003.
[25] Ministero delle Infrastrutture e dei Trasporti, 'Decreto Ministeriale 17 Gennaio 2018. Aggiornamento delle norme tecniche per le costruzioni. Gazzetta ufficiale n.42 del 20 febbraio 2018.' 2018.
[26] CEN, 'Eurocode 2: Design of concrete structures - Part 1-1 : General rules and rules for buildings.', vol. EN 1992-1-1. Brussels, Belgium, 2004.
[27] Q. Q. Yu, X. L. Gu, Y. H. Zeng, and W. P. Zhang, 'Flexural behavior of Corrosion-Damaged prestressed concrete beams', *Eng Struct*, vol. 272, Dec. 2022, doi: 10.1016/j.engstruct.2022.114985.
[28] J. W. Baker, 'Efficient analytical fragility function fitting using dynamic structural analysis', *Earthquake Spectra*, vol. 31, no. 1, pp. 579–599, Feb. 2015, doi: 10.1193/021113EQS025M.
[29] Ministero delle Infrastrutture e dei Trasporti, 'Circolare n.384 del 14.02.1962, Norme relative ai carichi per il calcolo dei ponti stradali.' 1962.

COMPDYN 2023
9th ECCOMAS Thematic Conference on
Computational Methods in Structural Dynamics and Earthquake Engineering
M. Papadrakakis, M. Fragiadakis (eds.)
Athens, Greece, 12-14 June 2023

# REDUCED ORDER MODELS TO ESTIMATE SEISMIC RISK OF UNREINFORCED MASONRY DWELLINGS

**Ana M. Zapata-Franco[1], Yeudy F. Vargas-Alzate [2], José R. Gonzalez-Drigo [3] and Rodolfo J. Tirado-Gutiérrez [4]**

[1,2,4] Department of Civil and Environmental Engineering. Universitat Politècnica De Catalunya
Jordi Girona, 1-3, 08034, Barcelona, Spain
{ana.maria.zapata, yeudy.felipe.vargas, rodolfo.javier.tirado}@upc.edu

[3] Department of Structural Engineering. Universitat Politècnica De Catalunya
Jordi Girona, 1-3, 08034, Barcelona, Spain
jose.ramon.gonzalez@upc.edu

## Abstract

*In order to estimate seismic risk at an urban level it is necessary to consider several sources of uncertainty. However, the higher the uncertainties related to both structural modelling and seismic hazard, the higher the computational time to extract reliable information to assess seismic risk. Thus, simplifying the structural model significantly diminishes the computational effort, allowing analyzing several building models in a fraction of time. In this sense, one of the most simplified representations to approximate the horizontal dynamic response of a structure is the Single Degree of Freedom system (SDoF). It allows calculating time-history responses in an easy way, given a determined fundamental period and damping. Though, the response of an SDoF does not consider neither the stiffness' loss because of plastic damage nor the participation of higher modes. Advanced intensity measures (IMs) look for addressing these shortcomings by averaging spectral quantities around the fundamental period ($T_1$) of the analyzed building. Analogous to this approach, it is proposed to estimate the dynamic response of a building by averaging the time history response of a set of SDoF systems with periods in the interval ($0.1T_1$, $1.8T_1$). The dynamic response associated with each of them has been estimated by means of the dynamic equilibrium equation for SDoF systems. In order to verify the efficiency of the proposed approach, it has been analyzed the dynamic behavior of unconfined masonry. This structural type is very prone to damage during an earthquake, as it has poor seismic performance. Observed damage and consequences of a catastrophic event occurred in Colombia (1999) have been used to verify the methodological approach.*

**Keywords:** Single degree of freedom, unconfined masonry, seismic risk, Monte Carlo simulations.

## 1 INTRODUCTION

Seismic risk mainly depends on the capacity of civil infrastructure to withstand ground motions produced by earthquakes. Current strategies to mitigate this inherent risk to society are oriented to improve design methodologies for new structures and to quantify the expected performance of existing ones. In turn, innovative technologies are implemented day by day to improve this performance.

This research aims to characterize the vulnerability and fragility of Unreinforced Masonry Structures, URMM, by creating a simplified model that allows numerous calculations to be performed in a short time. To this end, it has been decided to use the combined response of a set of single-degree-of-freedom (SDoF) systems. This type of model allows the time-history response of a structure to be approximated with less computational effort. Specifically, to account for plastic damage and the involvement of higher modes, the dynamic response was approximated by averaging the response of a set of SDoFs around the fundamental period of the simulated structures [1]. This period has been obtained through classical relationships in terms of power functions, which depend on the height of the structure (see for instance Martins & Silva, 2021 [2]).

Once the structural models were obtained, the next step was to calculate engineering demand parameters (EDPs), which can be used to obtain fragility curves. These EDPs were estimated by assuming that the fundamental period of the structures varies randomly. Then, clouds of IM-EDP points in log-log space were used to identify the most efficient IMs. Based on these, fragility functions have been derived for the URMM structure typology [3]; cloud analysis has been used to this end [4]. In short, a regression line is obtained from the IM-EDP relationship that is used to calculate the mean of a parametric statistical distribution given an IM. The variation of this distribution is estimated from the standard deviation of the bivariate distribution (IM-EDP) set with respect to the fitted curve, allowing estimating the probability of exceeding a given damage threshold.

To validate the fragility curves obtained, two scenarios are proposed to estimate the number of people that could be affected after a strong ground motion event. In the first case, the simulation of the different structures is carried out with a participation factor ($PF_1$) variable according to the height of the floor, and in the second case, the $PF_1$ is kept constant for all floors, as specified in Martins & Silva, 2021 [5]. After obtaining these fragility curves, the number of people affected is estimated and compared with the data observed after a real catastrophic event, such as the 1999 Armenia earthquake in the coffee region of Colombia [6]. Based on these results, it has been analyzed which of the two simulated scenarios presents a better fit with reality.

## 2 STRUCTURAL MODELLING

URMM typology has been and continues to be a dangerous solution to meet the need for affordable housing in developing countries, especially in areas with moderate to high seismic risk. In the specific case of Colombia, this type of housing is typical in urban and rural areas and represents approximately 60% of the existing housing in the country. In there, one can find URMM structures whose number of stories varies from 1 to 5; the typical height is 2.4 m. This type of construction is very susceptible to damage during an earthquake since it has a low seismic performance. It is worth mentioning that sometimes residents unintentionally increase this vulnerability by making inappropriate modifications to their homes. These modifications are usually made to increase the size of the dwelling. Historically, the inhabitants of other countries in the world have also used this typology, with the consequent increase in seismic risk [7]. In earthquake-prone areas,

there are many regulations for new construction. In these areas, URMM dwellings are generally forbidden due to its high vulnerability. Nevertheless, this type of construction is cheap and is used by a significant number of families with limited resources. This exacerbates the overall picture of seismic risk in Colombia [3].

### 2.1 Surrogate model based on the combined response of single degree of freedom systems.

In order to analyze the expected damage of URMM buildings, it is necessary to consider several sources of uncertainty [5,8]. However, the more complex the structural model, the more computation time is required to extract reliable information from it. Therefore, simplifying the structural model significantly reduces the computational effort, allowing multiple building models to be analyzed in a fraction of the time.

In this sense, one of the most simplified representations of a building is an SDoF system. This model has been extensively used to estimate the dynamic response of civil structures [5]. It allows calculating time-history responses in an easy way, given a determined fundamental period and damping. However, the response of a single SDoF does not consider the loss of stiffness due to plastic damage, nor the participation of higher modes.

In the development of advanced proxies based on seismic intensity measures (IMs) for estimating engineering demand parameters, EDPs, these shortcomings have been addressed by averaging spectral quantities around the fundamental period of the building model. Analogous to this approach, it is proposed to approximate the dynamic response of a URMM building, in each principal direction, by averaging the time-history response of a set of SDoF systems in the interval $(0.1T_n,\ 1.8T_n)$; where $T_n$ represents the fundamental period of the analyzed building.

Thus, the dynamic response associated with each oscillator has been estimated by means of the dynamic equilibrium equation for SDoF systems:

$$m\ddot{u}_n(t) + c\dot{u}_n(t) + ku_n(t) = -m\ddot{u}_{g,n}(t) \tag{1}$$

where $\ddot{u}_n(t)$, $\dot{u}_n(t)$, and $u_n(t)$ are the spectral acceleration, velocity and displacement time history responses of the SDoF in the n direction, respectively; $\ddot{u}_{g,n}(t)$ is the acceleration ground motion; m, c, and k represent the mass, damping, and stiffness of the system, respectively. Thus, the spectral time history response of a building in the n direction (x or y) can be estimated as follows:

$$\ddot{u}_n(t) = \frac{1}{p}\sum_{i=1}^{p} \ddot{u}(t, T_i) \tag{2}$$

$$\dot{u}_n(t) = \frac{1}{p}\sum_{i=1}^{p} \dot{u}(t, T_i) \tag{3}$$

$$u_n(t) = \frac{1}{p}\sum_{i=1}^{p} u(t, T_i) \tag{4}$$

where $T_i$ are the components of a vector of ten periods equally spaced within the interval (0.1Tx, 1.8Tx) for the x and (0.1Ty, 1.8Ty) for the y directions. In this way, the 3D spectral time history response in terms of acceleration, velocity and displacement of the simulated system has been estimated as follows:

$$\ddot{u}_{(x,y)} = \sqrt{\ddot{u}_x^2 + \ddot{u}_y^2} \tag{5}$$

$$\dot{u}_{(x,y)} = \sqrt{\dot{u}_x^2 + \dot{u}_y^2} \tag{6}$$

$$u_{(x,y)} = \sqrt{u_x^2 + u_y^2} \tag{7}$$

For the sake of simplicity, it has been omitted to write explicitly the dependence of the response variables on time in these equations.

### 2.2 Maximum global drift ratio as EDP

Several EDPs can be extracted from the averaged time-history responses described in the previous section. For example, the maximum global drift ratio of a structure, MGDR, which is an EDP that is widely used in seismic risk estimation using the capacity spectrum method [9], can be estimated according to the following equation:

$$MGDR = PF_1 \frac{max\,(u_{(x,y)})}{\mathrm{H}} \tag{8}$$

where $PF_1$ is the load participation factor [10]; H is the height of the building. Regarding $PF_1$, it has been assumed that this variable is a function of the number of stories as depicted in Figure 1. In summary, $PF_1 = (\frac{N_{st}}{10} + 0.9)$, where $N_{st}$ represents the number of stories.

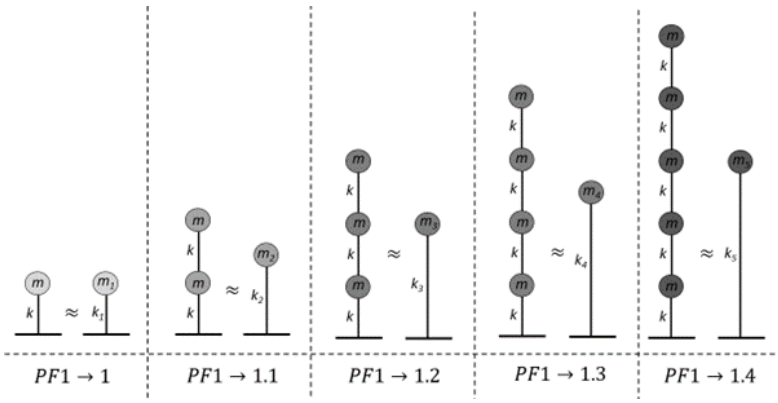


Figure 1: Variation of $\boldsymbol{PF_1}$ depending on the higher of stories.

## 3 SEISMIC HAZARD CHARACTERIZATION

### 3.1 Database of ground motion records

Figure 2 shows the classification of the Colombian territory into three levels of seismic hazard: high in red, medium in yellow, and low in green. These were determined based on historical and instrumental seismic information provided by the National Seismological Network.

In this research, a compilation has been made of the ground motions recorded between 1993 and 2017, with a magnitude greater than 4.0 Mw within Colombia. These records have been extracted from the SGC [11]. A total of 1992 records have been obtained, which have been used to make better statistics, reduce the uncertainty of the data, and provide a better adaptation to the seismogenic conditions of the Colombian territory.

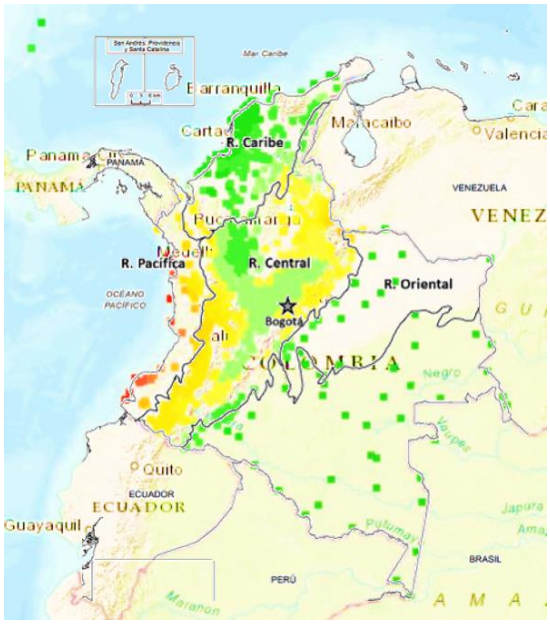


Figure 2: Colombian Seismic Hazard map for PGAs (Image taken from SGC) [11]

The ground motion records were divided into two groups according to the ground conditions in which they were acquired. The first corresponds to signals recorded on bedrock, from which a total of 1236 records were identified. The second group are signals recorded on less rigid ground, with a total of 756 records. For both types of records, environmental noise and other disturbances that could affect the quality of the signal were identified and corrected. A MATLAB code was developed for this purpose. Figure 3 shows the geometric mean of the horizontal spectra of the resulting ground motion records.

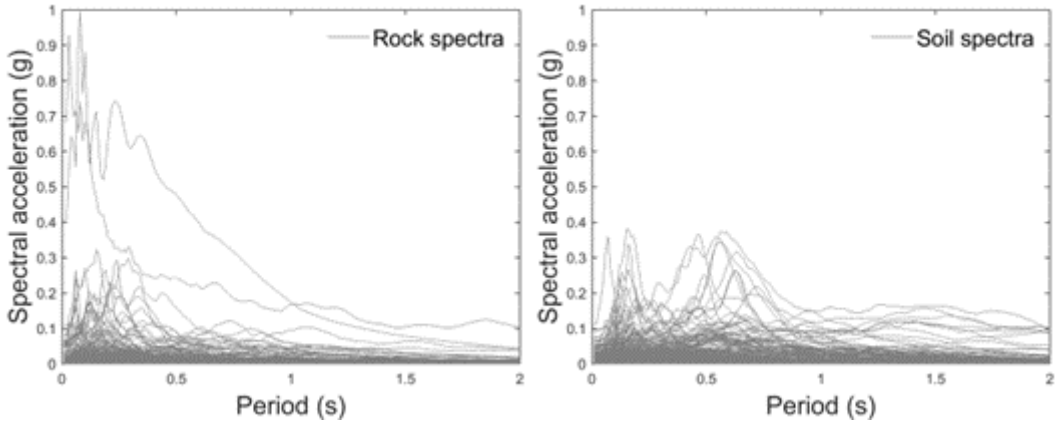


Figure 3: Spectra of the selected records. Above: Geometric Mean Spectra of the horizontal components (Left: Rock Right: Soil). Bottom: Median (Left) and percentile 95 (Right) of the entire set of spectra

### 3.2 Scaling ground motion records

In this article, seismic risk has been quantified in a probabilistic manner. Therefore, fragility functions based on the cloud analysis have been derived [4]. This methodology requires obtaining pairs of points that represent the seismic hazard (in terms of IMs) and the structural response (EDPs). These points have been obtained through time-history analysis by considering uncertainties in the structural modelling. Consequently, the

seismic hazard has been characterized by using a probabilistic set of ground motion records.

There are several methodologies to scale ground motions from a database [12]. Typically, the goal is to find a significant set of records leading the structure to multiple performance levels. However, as indicated by the well-known Richter's law, the number of high-intensity ground motion records is much smaller than the number of low-intensity ones [13]. To mitigate these issues when employing cloud analysis, the procedure employed in Vargas-Alzate et al., 2022 [14] has been used for selecting and scaling (where necessary) ground motion records. In short, this procedure attempts to scale a set of data sets uniformly across a series of intervals of increasing intensity with the goal of minimizing the scale factor. To do so, an IM identified as AvSa is considered herein to perform the selection and scaling of the records. Note that AvSa is calculated as the arithmetic mean of spectral acceleration values around the fundamental period of the analyzed system. Moreover, because of the 3D approach in modelling, AvSa is calculated from the geometric mean of the horizontal spectra.

The period range for averaging the spectral ordinates of the IM should be established from the dynamic properties of the entire population of buildings [1]. Accordingly, this range has been set at (0.1-0.71) sec. This period range will be justified in the next section. The intensity levels defining the upper and lower limits of each band range from 0.2 to 2.0 g at intervals of 0.2 g (i.e., 10 bands have been defined).

Thus, the horizontal components of 1000 ground motion records acquired at the bedrock (100 per band) have been obtained from the seismic database whilst 700 (70 per band) for those recorded at soil. Figure 4 shows the geometric mean spectra of the scaled records.

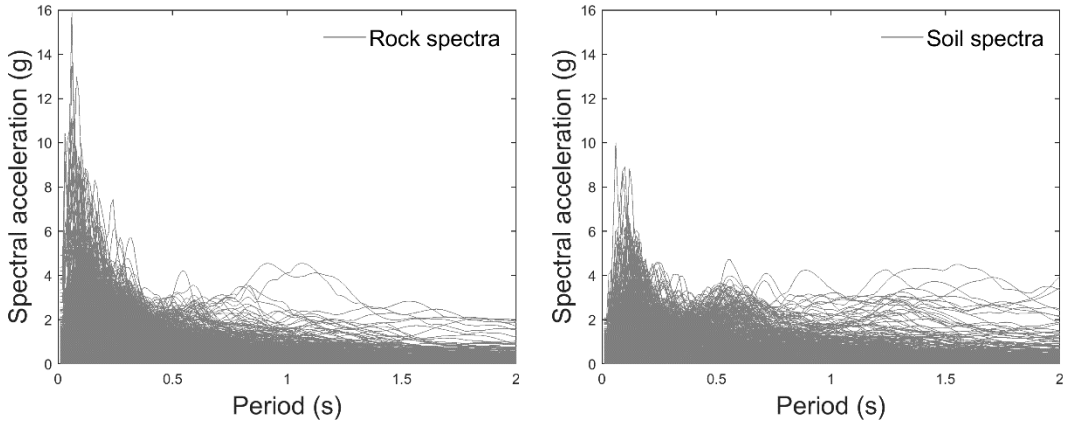


Figure 4: Scaled ground motion records (Left: Rock; Right: Soil)

## 4 FRAGILITY ASSESSMENT

Characterization of fragility is an important step in the probabilistic assessment of seismic risk. This section describes the development of fragility functions for the URMM housing typology. As mentioned above, these functions are derived from the dynamic response of SDoFs subjected to a large number of ground motion records from Colombia. The resulting fragility functions were compared with those proposed for this typology in previous research [5]. The derived set of functions has been used to assess the number of injuries due to earthquakes.

### 4.1 Intensity measures

IMs are parameters extracted from ground motion records. The most important property expected from IMs is their effectiveness in predicting EDPs. Ideally, an IM should contain enough information about the ground motion so that the structural response can be predicted with confidence. An IM that exhibits efficiency could potentially reduce the number of structural calculations in urban earthquake risk assessments. Several of the IMs used in this work are taken from those used in [15]. They have been used to predict the MGDR described in section 2.2.

### 4.2 Random characterization of the fundamental period of the analysed models ($T_1$)

Due to the probabilistic approach followed in this article, it is of paramount importance to generate a set of fundamental periods representing the analyzed typology. To do this, one can take advantage of classical relationships between the evolution of the fundamental period of the analyzed systems and a physical variable representing the height of the structure [2]. For the case of study, it has been considered the following formula to relate the fundamental period vs the height of the structure [8]:

$$T_1 = C_h * H^{0.75} \tag{9}$$

For the orthogonal direction ($T_2$), it has been assumed that the period value is obtained as a random fraction of $T_1$, which varies uniformly in the interval 0.75-1. To consider possible uncertainties in the characterization of $T_1$, it has been considered that $C_h$ in equation (9) is a random term that depends on the type of structure. In the case of URMM typologies its average value is 0.09 and it has been assumed a coefficient of variation equal to 0.12. Figure 5 shows ten thousand realizations of $T_1$ according to the procedure described above. It can be seen the good agreement between the expected value of the generated models and equation (9).

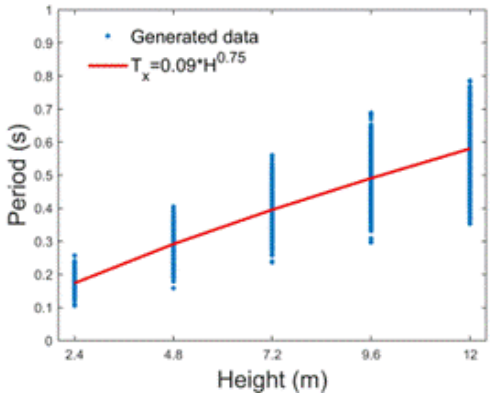


Figure 5: Relationship between $T_x$ and H

Once both set of periods ($T_1$ and $T_2$) have been derived, the procedure described in section 2.2 has been applied to estimate MGDR as a random variable. Note that this calculation was performed for both types of ground motion records (recorded rock and soil locations). Since the number of generated models (ten thousand) significantly exceeds the number of ground motion records (one thousand and seven hundred for rock and soil, respectively), a random pairing between records and realizations of $T_1$ has been performed. In this way, the same ground motion record can be paired several times with realizations of $T_1$. Thus, the MGDR obtained for both type of records has been correlated

with the IMs described in [15]. Figure 6 and Figure 7 show these relationships in the log-log space for ground motions recorded on Rock and Soil, respectively.

### 4.3 Efficiency

In this study, IM-EDP relationships have been characterized by means of nonlinear regression analyses in the log-log space. In this sense, the following general linear least-square model allows several types of regression:

$$y = \sum_{i=1}^{m+1} \alpha_{i-1} z_{i-1} + \varepsilon \tag{10}$$

where $\alpha_0, \alpha_1, \ldots \alpha_m$ are the coefficients providing the best fit between model and data; $z_0$, $z_1$, $\ldots z_m$ are basic functions; $\varepsilon$ represents the residuals. It can easily be seen how polynomial regression falls within this model. That is, $z_0 = 1$, $z_1 = x$, $\ldots z_m = x^m$ [16]. Note that other nonlinear relationship can be used as $z$. Substituting in equation (10) $y = \ln EDP$ and $z_{i-1} = (\ln IM)^{i-1}$, the linear least-square model using polynomial functions can be used to extract statistical information from IM-EDP pairs according to the following equation (11):

$$\ln EDP = \sum_{i=1}^{m+1} \alpha_{i-1} (\ln IM)^{i-1} + \varepsilon \tag{11}$$

For $m=2$, equation (11) adopts the following quadratic form:

$$\ln EDP = \alpha_0 + \alpha_1 \ln(IM) + \alpha_2 \ln(IM)^2 + \varepsilon \tag{12}$$

where $\alpha_0$, $\alpha_1$ and $\alpha_2$ are scalars maximizing the coefficient of determination, $R^2$, between IM-EDP pairs. This variable is generally used to quantify efficiency when analyzing IM-EDP pairs (see for instance Ebrahimian et al. 2015 [17]). For a perfect fit, $R^2$=1, signifying that the quadratic function explains 100% of the data variability. $R^2$ is used herein to provide an estimation of the variability when analyzing relationships involving IM-EDP pairs. That is, the higher $R^2$ the lower the variability when predicting some EDP given an IM. Consequently, the IM providing the highest $R^2$ will be the most efficient one, in the sense that it allows reducing the variability in seismic risk estimations.

### 4.4 Derivation of fragility functions

From a set of IM-EDP pairs, one can derive fragility functions according to the so-called 'cloud analyses approach [4]. This methodology requires calculating the best fit curve between a set of IM and EDP realizations in the log-log space. The resulting curve is used to estimate the mean value of a parametric statistical distribution, given an IM value. The variability of this parametric distribution ($S_{y/x}$) is estimated as the standard deviation of the IM-EDP residuals with respect to the fitted curve. In this way, the probability of exceeding a certain damage threshold can be calculated. These thresholds are realizations of the engineering demand parameter under consideration, $EDP_C$.

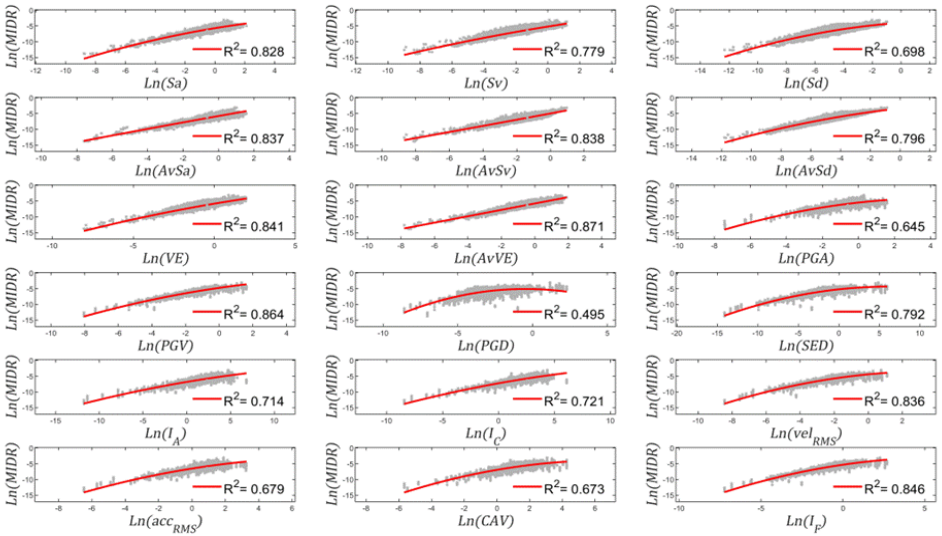


Figure 6: Ten-thousand IM-EDP pairs from URMM building models of one- to five-stories using ground motions recorded on Rock.

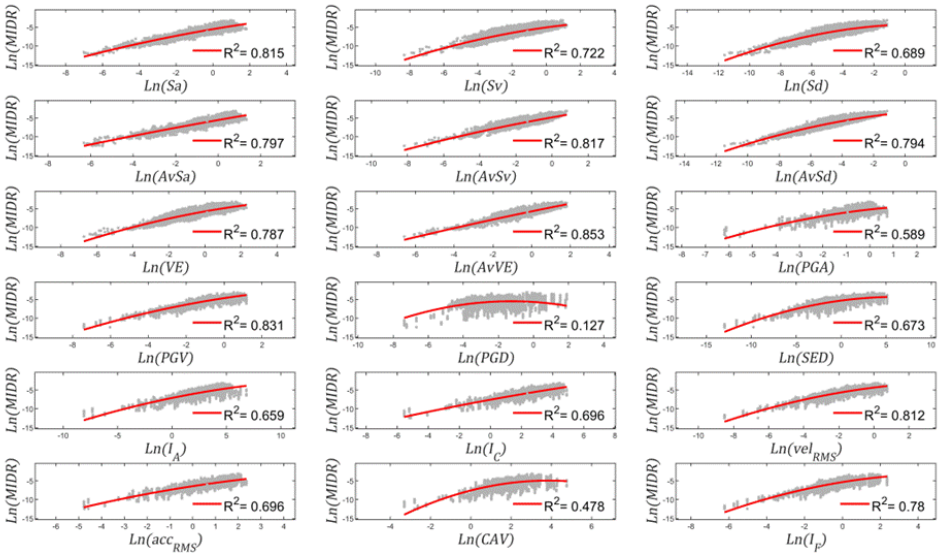


Figure 7: Ten-thousand IM-EDP pairs from URMM building models of one- to five-stories using ground motions recorded on Soil.

In this study, four damage states are considered, ranging from slight to complete damage; they are calculated by means of equation (13) to (16):

$$DS1 = 0.75\ \mathrm{Sd}_y \tag{13}$$

$$DS2 = 0.50\ \mathrm{Sd}_y + 0.33\ \mathrm{Sd}_u \tag{14}$$

$$DS3 = 0.25\ \mathrm{Sd}_y + 0.67\ \mathrm{Sd}_u \tag{15}$$

$$DS4 = \mathrm{Sd}_u \tag{16}$$

In these equations, $\mathrm{Sd}_y$=0.12% (yielding displacement) and $\mathrm{Sd}_u$ =0.55% (ultimate displacement); these limits are obtained from [8,18–20]. Table 1 shows the calculated values according to equation (13) to (16).

| | Slight (DS1) | Moderate (DS2) | Severe (DS3) | Complete (DS4) |
|---|---|---|---|---|
| Damage threshold | 0.0009 | 0.0018 | 0.0039 | 0.0055 |

Table 1: Damage thresholds for URMM [5]

In this manner, fragility functions presented in Figure 8 have been derived by considering the damage thresholds shown in Table 1. It can be seen in these figures that fragility functions derived from records acquired on Soil tend to provide higher probabilities of damage. AvSv has been selected to derive these curves based on the average efficiency to predict the MGDR (see Figure 6 and Figure 7). In fact, this IM has been used not only to develop fragility functions for several damage thresholds but also to estimate the number of affected people according to Hazus 99 [21].

### 4.5 Validation of the fragility function

In order to validate the proposed methodology, a comparison has been made with fragility curves obtained in previous research for a similar structural typology [5]. Specifically, fragility curves derived for one-story URMM building have been extracted from this research. However, such curves have been obtained with respect to the spectral acceleration in a fundamental period equal to 0.3 seconds. In addition, it is worth mentioning that these curves consider that $PF_1$ is equal to 1.4. This differs from the hypothesis presented in this research regarding the evolution of $PF_1$ (see Figure 1). In spite of these differences, fragility functions based on Sa($T_1$) have been calculated obtained considering the one-story simulated models.

From these data, two set of fragility functions are established to calculate damage probabilities. In the first case, it is assumed that the $PF_1$ is variable as a function of story height, as shown in section 2.2. In the second scenario, it is assumed that $PF_1 = 1.4$ and is constant for all the buildings. Figure 9 shows the curves obtained with the current model and the curves referred in Martins & Silva, 2021 [5]. It can be observed that, for the case 1 (left), the curves obtained with the current model exhibit a good fit with the reference ones for the slight and moderate damage states. For the severe and complete damage, the presented model provides lower probabilities of exceedance.

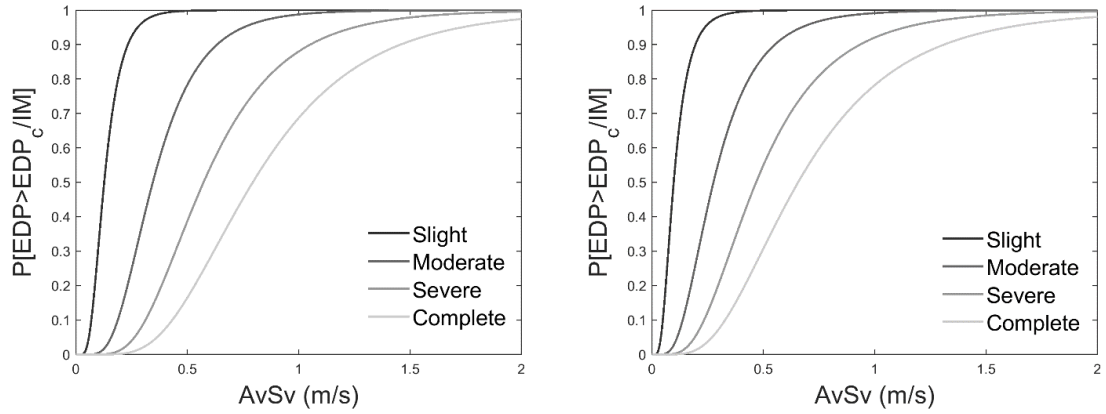


Figure 8: Fragility functions for URMM buildings. Left: Recorded on Rock. Right: recorded on Soil

For the second case (right), it can be observed that the modelled curves for the slight and moderate damage states show a tendency towards higher probability values whilst for severe and complete a good fit is observed.

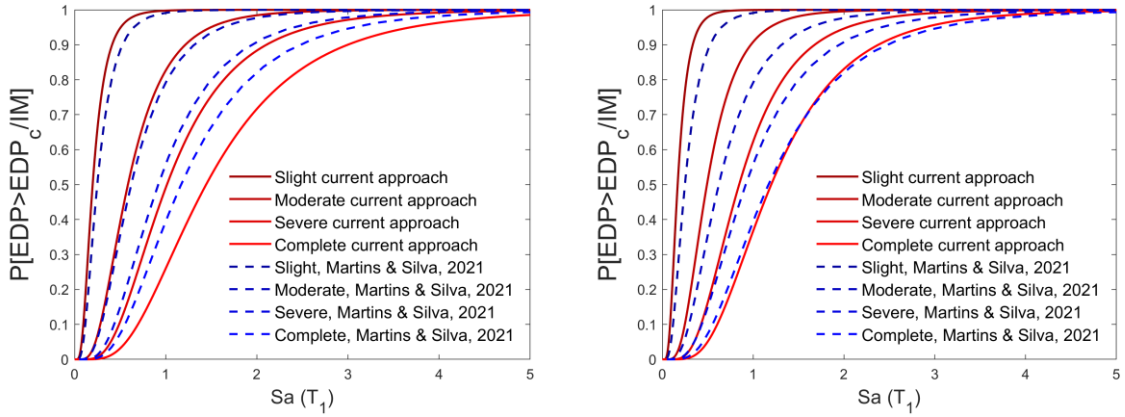


Figure 9: Capacity curves for current approach models (Red lines) and GEM models (Blue dashed lines). Left (Scenario 1): assumed that $PF_1$ is variable as a function of height. Right (Scenario 2): assumed that $PF_1 = 1.4$ is constant for all heights

To verify the performance of the fragility curves obtained, a comparison is made with a real disaster scenario such as the 1999 Armenian earthquake in Colombia [6]. Therefore, an evaluation is made between the real number of victims observed in the Armenia disaster and the number of victims simulated from the two hypotheses regarding $PF_1$ presented above. This allows to determine whether the developed model adapts to the real conditions of the affected area. Because of the soil conditions of the affected area, fragility functions derived for soil conditions have been employed. It is worth mentioning that the number of men reported suffering injury level 4 was equal 573, whilst on the women's site, this number was 731. In addition, the most affected structural typology during this catastrophe was URMM.

The most representative ground motion record of this earthquake was acquired at the Cordoba station. This record has been used as reference to estimate the expected intensities in terms of AvSv and the geometric mean spectrum. From this spectrum, AvSv= 0.617 m/s (the period intervals between 0.04 and 0.7 sec have been used to estimate this IM). The data

on the population affected by this earthquake are taken from the DANE report [6], which states that during the state of emergency a total of 1304 deaths and disappearances were reported for the city of Armenia.

To estimate the number of people having injury level 4 by using the numerical approach of this research, the AvSv value (i.e. AvSv=0.617 m/s) is used to estimate damage probabilities. Based on this, the probability of occurrence of each damage state is estimated from the fragility functions presented in Figure 8, for records on soil (see Table 2).

| | Slight | Moderate | Severe | Complete |
|---|---|---|---|---|
| Probability of occurrence | 0.068 | 0.2357 | 0.2416 | 0.4543 |

Table 2: Probability of occurrence of each damage state given that AvSv=0.6 m/s

Based on these probabilities, and by considering that 214388 were the number of inhabitants in the city of Armenia for that time, Figure 10 shows a summary of the number of affected people discretized by gender and injury level. Also, this figure shows the results obtained for the two cases considered for validation. For the first case (Left), the number of affected people with injury level 4 is 1135.8. For the second case (Right), a total of 1394.6 suffered injury level 4.

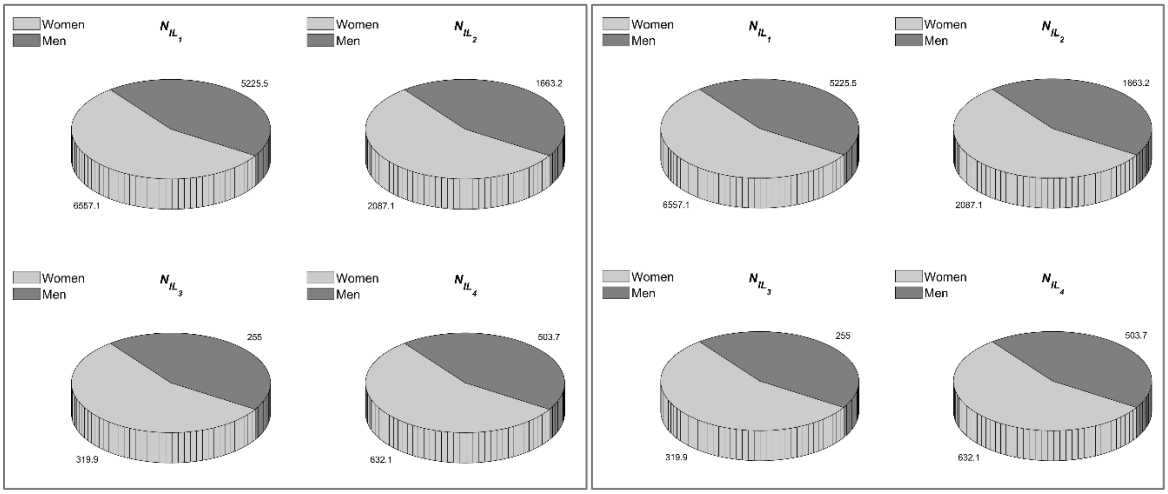


Figure 10: Simulation of the number of affected people in the Armenia's catastrophe. Left (Scenario 1): assumed that $PF_1$ is variable as a function of height. Right (Scenario 2): assumed that $PF_1 = 1.4$ is constant for all heights.

If the total number of casualties, calculated from the simulations (Case 1: 1135.8 people; Case 2: 1394.6 people), is compared with those presented in the DANE's report (1304 people) [6], it can be seen that the second case provides values more similar to those reported for the disaster zone. However, it must be considered that the generated data are based on URMM typology, and they do not reflect other factors that trigger variations, for example, other typologies that are less frequent but more prone to damage can modify this estimate. In this case, data on the number of inhabitants living in different types of family housing should be included in the analysis. In the DANE's report [6], it can be seen that this typology (URMM) was not the only one that collapsed, so it would not be appropriate to attribute all

the risk to this typology. In line with the above, it is decided to opt for the first hypothesis, as it presents more conservative values that are more in line with this scenario. Anyhow, both hypothesis (Case 1 and Case 2) provides very satisfactory results.

## 5 CONCLUSIONS

For this study, a highly vulnerable structural typology (URMM) has been studied. Note that despite the high vulnerability of this typology, it is present in most countries of the world. In fact, several global earthquake-related catastrophes may be associated with the use of this type of vulnerable housing [3].

A fragility model based on the contribution of several SDoF systems, whose vibration periods are around the fundamental one for this typology, has been developed in this research. To do so, a set of ground motions recorded in Colombia has been used to represent seismic hazard. The cloud analysis has been employed to derive the fragility functions [4]. Based on these curves, the expected risk in terms of injuries has been estimated for two cases, one for a $PF_1$ variable as a function of the number of stories and another one assuming that $PF_1$ remains constant. Then, the Hazus methodology has been applied to assess the expected risk in terms of number and severity of injured [21]. The results were compared with the data obtained after the Armenia disaster [6] and it was found that although the two cases produced congruent and fairly accurate data, Case 1 presents the most conservative data. The variation can easily be attributed to various external factors such as other types of structures that could potentially fail and have not been considered.

It was also possible to estimate the influence of soil conditions on the quantification of expected risk. It has been observed that the expected risk increases when records obtained from soil sites are used in the calculation. This can be explained by considering the results shown in Figure 3. That is, the spectral ordinates are higher in soil than in rock records when comparing the same percentiles of the analyzed data. This difference becomes more evident as the percentile increases.

In terms of future research activities, it will be interesting to recalculate the fragility functions by disaggregating the results based on the number of stories. It is expected that results based on this classification will be more reliable. In addition, it has been observed that IMs based on energy are more efficient than those based on acceleration (at least when the entire set of models is considered simultaneously). Regarding the structural typology analyzed, it has been confirmed its low performance in front of ground motion records induced by earthquakes. Further research should be oriented to provide a rapid and economic solution to diminish the vulnerability of this type of structures.

This research should not stop here. Note that the proposed model easily allows the implementation of new structural typologies if relationships between the fundamental period and the height of the structure are available. In this sense, most of the existing typologies have this information [2].

## 6 ACKNOWLEDGMENT AND FUNDING

This research has been partially funded by the Spanish Research Agency (AEI) of the Spanish Ministry of Science and Innovation (MICIN) through project with reference: PID2020-117374RB-I00/AEI/10.13039/501100011033.

## 7 REFERENCES


[1] Y.F. Vargas-Alzate, L.G. Pujades, J.R. González-Drigo, R.E. Alva, L.A. Pinzón, On the equal displacement aproximation for mid-rise reinforced concrete buildings, in: Proceedings of the 7th International Conference on Computational Methods in Structural Dynamics and Earthquake Engineering (COMPDYN 2015), Institute of Structural Analysis and Antiseismic Research School of Civil Engineering National Technical University of Athens (NTUA) Greece, Athens, 2019: pp. 5490–5502. https://doi.org/10.7712/120119.7321.19849.

[2] R.K. Goel, A.K. Chopra, Period Formulas for Moment-Resisting Frame Buildings, Journal of Structural Engineering. 123 (1997) 1454–1461. https://doi.org/10.1061/(ASCE)0733-9445(1997)123:11(1454).

[3] S. Brzev, M. Tomaževič, M. Lutman, M. Bostenaru Dan, D. D'Ayala, M. Greene, The World Housing Encyclopedia: An Online Resource on Housing Construction in High Seismic Risk Areas of the World., (2003). http://db.world-housing.net/building/10/

[4] F. Jalayer, R. De Risi, G. Manfredi, Bayesian Cloud Analysis: Efficient structural fragility assessment using linear regression, Bulletin of Earthquake Engineering. 13 (2015) 1183–1203. https://doi.org/10.1007/S10518-014-9692-Z.

[5] L. Martins, V. Silva, Development of a fragility and vulnerability model for global seismic risk analyses, Bulletin of Earthquake Engineering. 19 (2021) 6719–6745. https://doi.org/10.1007/s10518-020-00885-1.

[6] DANE, Dimensión social y económica de los efectos del terremoto del eje cafetero. Diagnóstico para la reconstrucción, Santafé de Bogotá, 1999.

[7] E. Alarcón, Benito-Oterino M.B., Mucciarelli M., Liberatore D., Bulletin of Earthquake Engineering - v. 12, n. 5, Structurae. (2013) 1871–2298. https://structurae.net/en/literature/periodicals/bulletin-of-earthquake-engineering/20473-12-5

[8] N. Tarque, H. Crowley, R. Pinho, H. Varum, Displacement-Based Fragility Curves for Seismic Assessment of Adobe Buildings in Cusco, Peru, Earthquake Spectra. 28 (2012) 759–794. https://doi.org/10.1193/1.4000001.

[9] Freeman, Development and Use of Capacity Spectrum Method. Proceedings of the 6th U.S. National Conference on Earthquake Engineering, Seattle, Oakland, USA., in: Scientific Research Publishing, 1998. https://www.scirp.org/(S(351jmbntvnsjt1aadkposzje))/reference/ReferencesPapers.aspx?ReferenceID=1773086

[10] Applied Technology Council, ATC-40 Seismic evaluation and retrofit of concrete buildings, Applied Technology Council, Redwood City, California , 1996.

[11] SGC, Sistema de Consulta de la Amenaza Sísmica de Colombia, Colombian Geological Survey. (2020). https://amenazasismica.sgc.gov.co/.

[12] W.A.S., H.A., B.J.W., B.J. and G.D.N. Haselton C.B., Selecting and Scaling Earthquake Ground Motions for Performing Response-History Analyses , 15th World Conference on Earthquake Engineering, Lisboa, Portugal. (2012).

[13] N. Luco, P. Bazzurro, Does amplitude scaling of ground motion records result in biased nonlinear structural drift responses?, Earthq Eng Struct Dyn. 36 (2007) 1813–1835. https://doi.org/10.1002/EQE.695.

[14] Y.F. Vargas-Alzate, R. Gonzalez-Drigo, J.A. Avila-Haro, Multi-Regression Analysis to Enhance the Predictability of the Seismic Response of Buildings, Infrastructures (Basel). 7 (2022) 51. https://doi.org/10.3390/infrastructures7040051.

[15] Y.F. Vargas-Alzate, J. Hurtado, Efficiency of Intensity Measures Considering Near- and Far-Fault Ground Motion Records, Geosciences (Basel). 11 (2021) 234. https://doi.org/10.3390/geosciences11060234.

[16] S.C. Chapra, Applied numerical methods with MATLAB® for engineers and scientists, Fourth, New York, NY : McGraw-Hill Education, 2018.

[17] H. Ebrahimian, F. Jalayer, A. Lucchini, F. Mollaioli, G. Manfredi, Preliminary ranking of alternative scalar and vector intensity measures of ground shaking, Bulletin of Earthquake Engineering. 13 (2015) 2805–2840. https://doi.org/10.1007/s10518-015-9755-9.

[18] N. Tarque, H. Crowley, R. Pinho, H. Varum, Seismic risk assessment of adobe dwellings in Cusco, Peru, based on mechanical procedures | Semantic Scholar, 14th European Conference on Earthquake Engineering Ohrid, North Macedonia. (2010).

[19] F. De Luca, G.M. Verderame, Seismic Vulnerability Assessment: Reinforced Concrete Structures, in: Encyclopedia of Earthquake Engineering, Springer Berlin Heidelberg, Berlin, Heidelberg, 2015: pp. 3182–3210. https://doi.org/10.1007/978-3-642-35344-4_252.

[20] G. Karanikoloudis, P.B. Lourenço, Structural assessment and seismic vulnerability of earthen historic structures. Application of sophisticated numerical and simple analytical models, Eng Struct. 160 (2018) 488–509. https://doi.org/10.1016/j.engstruct.2017.12.023.

[21] FEMA, HAZUS Earthquake Loss Estimation Methodology. Technical Manual, Prepared by the National Ins- titute of Building Sciences for the Federal Emergency Management Agency, Washington D.C., 1999.

COMPDYN 2023
9th ECCOMAS Thematic Conference on
Computational Methods in Structural Dynamics and Earthquake Engineering
M. Papadrakakis, M. Fragiadakis (eds.)
Athens, Greece, 12-14 June 2023

# THE CHALLENGES AND ADVANTAGES OF MACRO MODELING IN ANSYS SOFTWARE FOR SEISMIC VULNERABILITY ASSESSMENT OF HISTORIC MASONRY STRUCTURES

**Hatice Ayşegül Demir**[1], **Kutay Yücetürk**[2], **Engin Aktaş**[2], **Mine Hamamcıoğlu-Turan**[1]

[1] Department of Conservation and Restoration of Cultural Heritage, İzmir Institute of Technology, İzmir, Turkey
e-mail: haticedemir@iyte.edu.tr, mineturan@iyte.edu.tr

[2] Department of Civil Engineering, İzmir Institute of Technology, İzmir, Turkey
e-mail: kutayyuceturk@iyte.edu.tr, enginaktas@iyte.edu.tr

## Abstract

*This study aims at creating an advancement guideline for a software which can be used for seismic vulnerability assessment of historic masonry structures by revealing the results of an experience related to the macro modeling of a historic masonry building. The case study structure is Bergama Bedesten (15th-16th centuries) located in Bergama, İzmir, Turkey. ANSYS software is used for the Finite Element Modeling of the structure. The seismicity at its location is determined and the structural response under lateral loads is obtained together with the dynamic characteristics. Mesh design, component creation according to the used material change in structural elements, contact surface identification, the arrangement of the stress scales, and result interpretation are realized. For these stages, the challenges are discussed with the solutions. The advantageous aspects of the software are explained. For the challenges, in mesh design, the ineffectiveness of cartesian method for some elements was detected and tetrahedrons method was chosen. In contact surface identification, the overlapping portions of structural components could not be detected by the software exactly, so the manual surface separation was realized. In the stress level interpretation, the lack of assignment for material limit strength values to the analysis scale was experienced and the addition of limit values was carried out. The scale also needs manual arrangement for the increase of interval numbers of stress values to emphasize vulnerable zones. This flexibility of scale to be arranged can be seen as an advantage, as well. The 3d section and axonometric view creation provide the presentation of stress changes at inner and outer surfaces of the structure which is another positive side.*

**Keywords:** Macro modeling, masonry structures, modeling strategies, seismic vulnerability.

## 1 INTRODUCTION

The historic masonry structures are vulnerable to seismic loading and their seismic vulnerability assessment varies from simplified to advanced methods such as risk index classification by visual observation [1][2] to numerical modeling for detailed structural behavior determination [3][4]. The combination of these two approaches [5] can be preferred, as well. Modeling of the masonry structural systems is a demanding task and there are different methods chosen according to the structural characteristics of the buildings. For example, historic masonry buildings with a box behavior (e.g. palaces, caravanserais etc.) buildings analyzable by independent macro elements (e.g. churches, mosques etc.) buildings characterized by monodimensional masonry elements (e.g. towers, minarets etc.) and massive structures prevailing local failure of masonry (e.g. fortresses, city walls etc.) may require different approaches such as macro block modeling, discrete element modeling, structural elements modeling and continuous constitutive law modeling for in detail seismic vulnerability assessment investigation [6]. However, the most inclusive choice for differently characterized masonry structures is Finite Element Modeling. It presents micro, simplified-micro, and macro modeling choices changing the detail level in the model. Macro modeling provides the opportunity to assess global structural behavior of monumental scale buildings under seismic loading. In this approach, brick, stone etc. materials put together with mortar are admitted as composite media, so the structural components can be modeled as total elements decreasing the detail and burden during analysis phase [7].

Different analysis softwares are used for seismic vulnerability assessment of historic masonry structures. Each presents a variety of tools for macro modeling and analysis phases. Zucca et al. tried to assess the seismic vulnerability of Santa Maria Novella Basilica in Florence by the macro modeling of the structure in Midas Gen and performing response spectrum analysis defining stress fields in structural components [8]. The study carried out by Ravichandran et al. compared five alternative modeling approaches four produced in ANSYS and one generated in SAP2000. The case study is a small-scale masonry house. The focus is on the suggestion of a FE macro modeling approach to reduce computational effort [9]. Hovaidae et al. generated the macro model of Arge-Tabriz monument in ABAQUS software. By the use of region-specified simulated ground motion records, the probable failures that will be caused by possible earthquakes were determined in the structure [10]. Tomar et al. investigated the seismic vulnerability of a historical brick masonry structure by macro modeling approach benefiting from ANSYS software. As a result, some structural elements were found overly stressed caused by out-of-plane movement and in-plane shear. Retrofitting strategies were suggested for the necessary portions of the structure [11]. Uzdil et al. benefited from linear, nonlinear, and kinematic limit analysis approaches to analyze both the global structural behavior under seismic loading and to assess out of plane behavior of masonry facade walls as local failure caused by earthquakes. The overall seismic vulnerability of the structure was determined considering the limit values stated in building codes by the use of macro model generated in Midas Gen while overturning, vertical and lateral bending mechanisms were detected by the local analysis [12].

The most time-efficient approach decreasing modeling and result interpretation time can be designed by the development of these softwares. However, the presented studies in the literature do not mention about the modeling and analysis process with the experienced challenges and benefited advantages. Instead of this, the selected parameters in macro modeling process and the results of the carried out seismic vulnerability assessment work are

stated only. So, this study aims at explaining the process of macro modeling and analysis stages for seismic vulnerability assessment of a historic masonry structure with their challenging and advantageous sides to emphasize the required advances in the used ANSYS software for a more efficient working environment.

## 2 METHODOLOGY

Within the study, a historic masonry monumental building Bergama *Bedesten* was modeled in ANSYS software by macro modeling approach and Finite Element Method to assess its seismic vulnerability. It is a 15$^{th}$-16$^{th}$ century structure located in Bergama, İzmir Turkey (Figure 1).



Figure 1. Exterior view of Bergama *Bedesten*

During the modeling phase, firstly the structural components and their material usage were considered. The main structural components are constituted by domes, drums, plane triangles, arches, pillars and load-bearing walls. Domes and arches are fully out of brick, while in drums and walls the alternating use of rough-cut stone and brick is visible. However, in the walls, the ratio of stone is higher than brick. So, rough-cut stone masonry parameters were chosen for these components. In the drums, the brick ratio is higher. So, brick masonry assignment was realized for these ones. The pillars are totally rough-cut stone masonry. At the door and window openings, brick arches; and at the two door openings, rough-cut stone masonry arches can be observed (Figure 2).

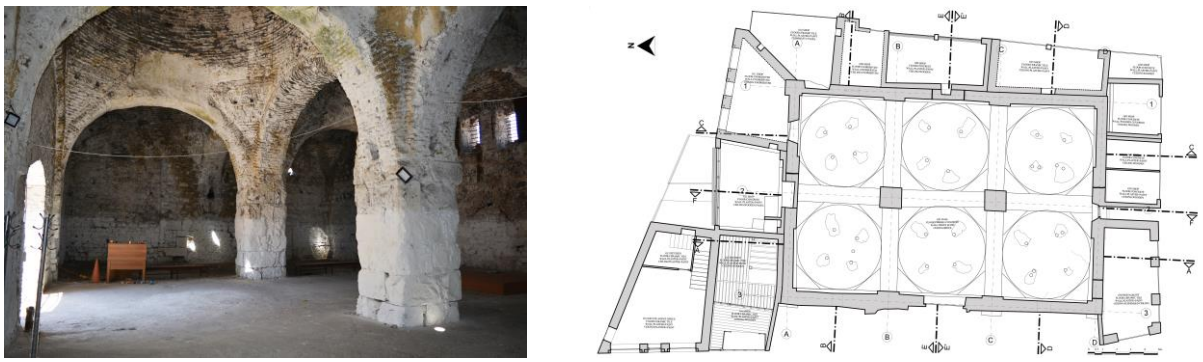

(a) (b)

Figure 2. Inside view of Bergama *Bedesten* showing main structural components and material usage (a), reflected ceiling plan view (b)

In the following Figure 3, the structural components that brick masonry or rough-cut stone masonry assigned can be seen in the macro model of the structure with the parameter values. Material parameters were taken from the guideline ‘’Management of Earthquake Risks for Historical Buildings’’ [13].

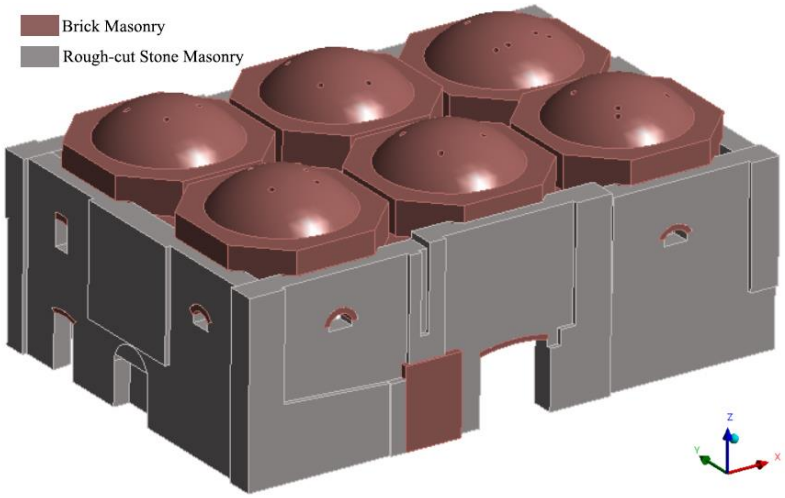


| Parameters \ Masonry Type | Brick Masonry | Rough-cut Stone Masonry |
|---|---|---|
| Compressive Strength $f_m$ (MPa) | 1.8 | 1.1 |
| Shear Strength $T_0$ (kPa) | 60 | 35 |
| Modulus of Elasticity E (MPa) | 1800 | 1020 |
| Shear Modulus G (MPa) | 300 | 170 |
| Unit Weight w (kN/m$^3$) | 18 | 20 |

Figure 3. Assigned materials to the structural components of Bergama *Bedesten* with their parameter values

The control of contact surfaces between different components was carried out and required corrections were made for the overlapping areas. A typical example is shown in Figure 4.

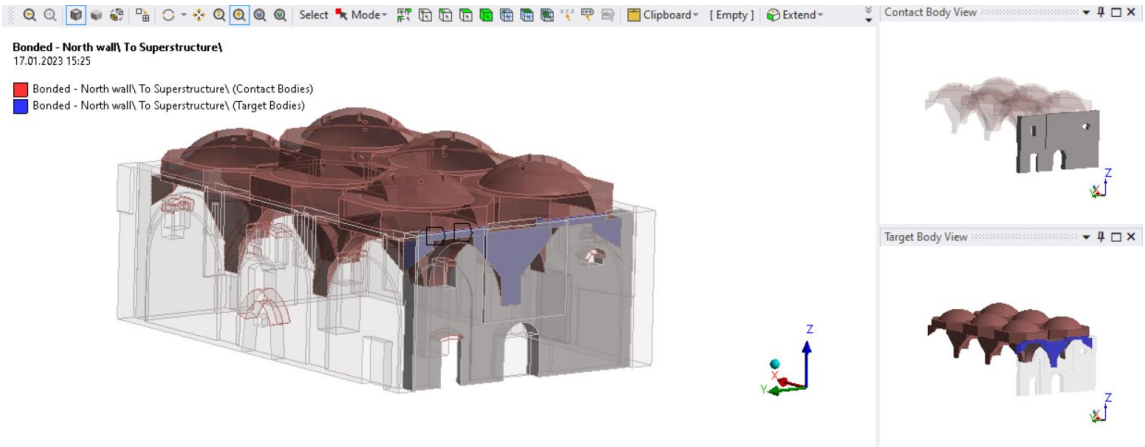


Figure 4. A contact surface example between the north wall and superstructure components

After the completion of component modeling considering material differences and contact surface identification, the finite element mesh design phase was realized. ANSYS presents different meshing styles like tetrahedrons, hex dominant, sweep, multizone, cartesian and layered tetrahedrons (Figure 5a). For the varying structural components, the most suitable mesh pattern was determined as the tetrahedrons and by the use of 0.4 m. average sizing, the meshing application was carried out as can be seen in Figure 5b. At the locations that the geometry changes within small distance, use of lower sizing was considered.

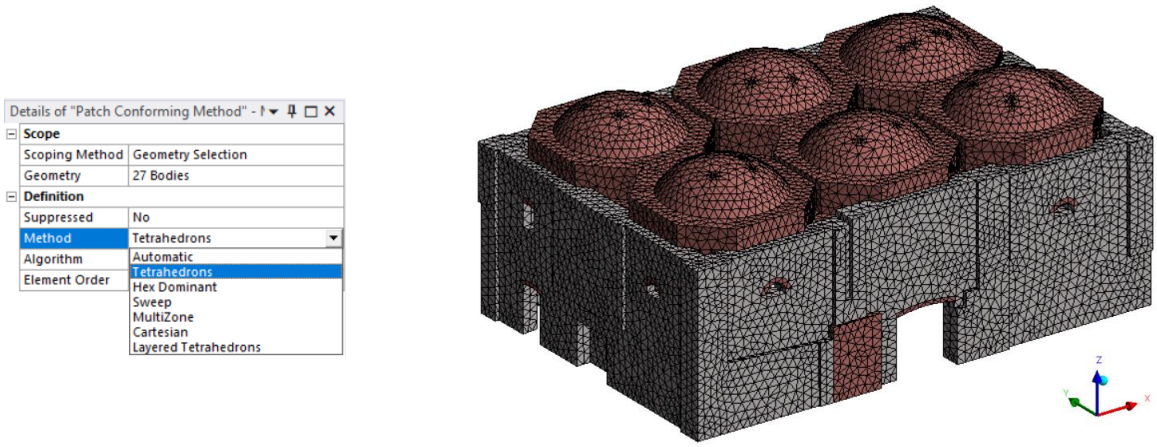


(a) (b)

Figure 5. Mesh types in ANSYS (a), tetrahedrons mesh design in Bergama *Bedesten* (b)

The modal analysis was performed on the structure to determine the natural mode frequencies in x and y-directions to be used in seismic analyses. The seismic vulnerability of the structure was determined by single-mode equivalent earthquake load analysis. It could be possible since the mass participation ratio was high at the first translational modes in both directions. The horizontal elastic acceleration design spectrum at the location of Bergama *Bedesten* is used. The acceleration is obtained from the interactive seismic hazard maps web application of Turkey Disaster and Emergency Management Authority [14]. The derived horizontal acceleration using the first two mode frequencies and horizontal elastic design spectrum knowledge [15] was applied on the structure for x and y-directions as seismic loading, one by one. The gained maximum principal stress values as a result of the analysis showed the seismically vulnerable parts of the structure. The zones exceeding limit tensile strength values for each material type were assessed as vulnerable locations. These locations were compared with the parts of the structure that have failure, deterioration or alteration to detect whether they overlap or not (Figure 6). This step revealed intervention priority for the locations that have failure, deterioration or alteration and seismically vulnerable.

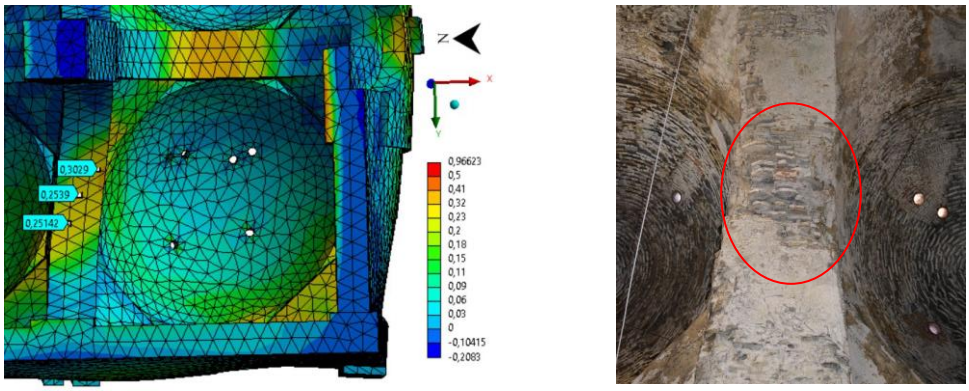


Figure 6. Comparison of maximum principal stress results with the current failures, deteriorations or alterations; a detected vulnerable arch example with section diminishment

The criticism of the carried out work is made for different stages of the study with the challenging and advantageous aspects of the software. In accordance with this, some recommendations for macro modeling in ANSYS and for the development of the software are stated.

## 3 CHALLENGES OF THE SOFTWARE

In this part, the results of the macro modeling process and seismic vulnerability assessment analysis phase are expressed with the encountered errors and they are discussed with the possible solutions.

For the challenges, in mesh design, the ineffectiveness of the cartesian method for thin and curvilinear elements was detected and the tetrahedrons method which has more potential to create curvilinear volumes was chosen. The dome surfaces and arches with thinner sections and curvilinear form have failed parts with cartesian method and 0.2 m. size meshing while the masonry orthogonal walls are well generated with this method (Figure 7).

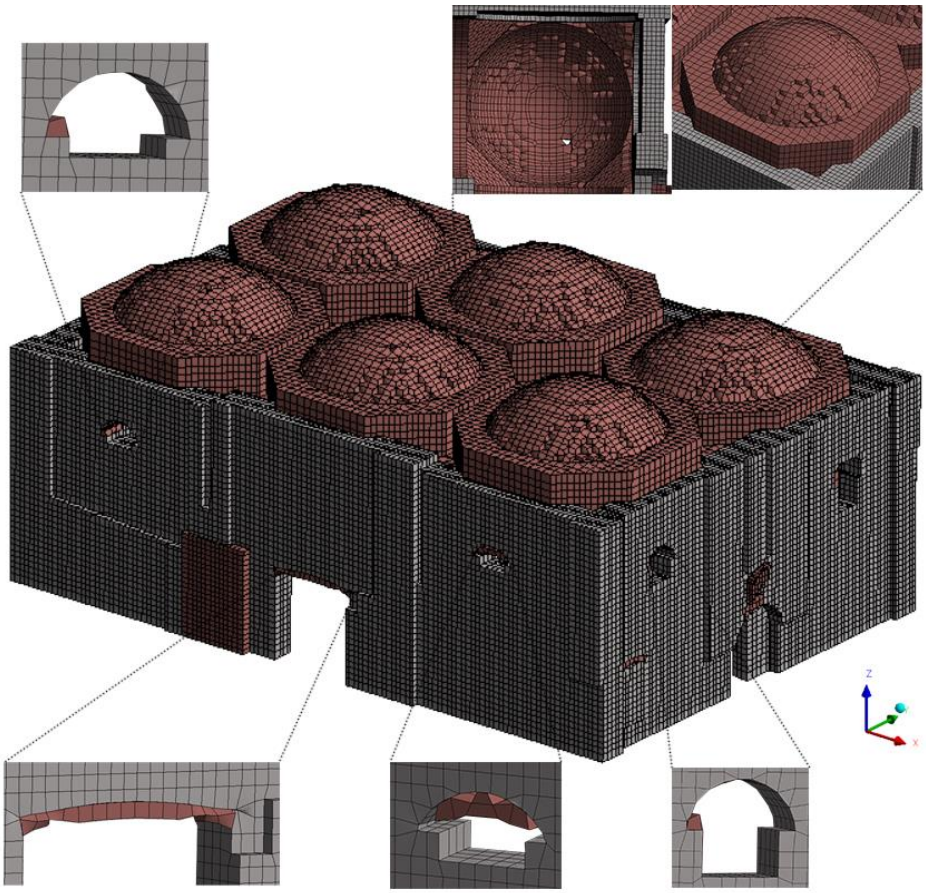

Figure 7. Cartesian meshing in Bergama *Bedesten* and failed components

Although the cartesian mesh is workable in generating orthogonal geometries with 0.2 m. mesh sizing, it is dense and overdetailed mesh unit for the desired numerical analysis of this monumental structure to assess its overall structural behavior. Besides, errors occur during the analysis phase. The deficiencies are seen for the wall details at higher mesh sizes (0.4 m.) for cartesian method, so it is not a suitable mesh type for walls with different projections as seen at the thickened portions of the walls corresponding to load-bearing arches inside. However, tetrahedrons method with 0.4 m. sizing generates the correct geometry of the perpendicular projections from the wall (Figure 8).

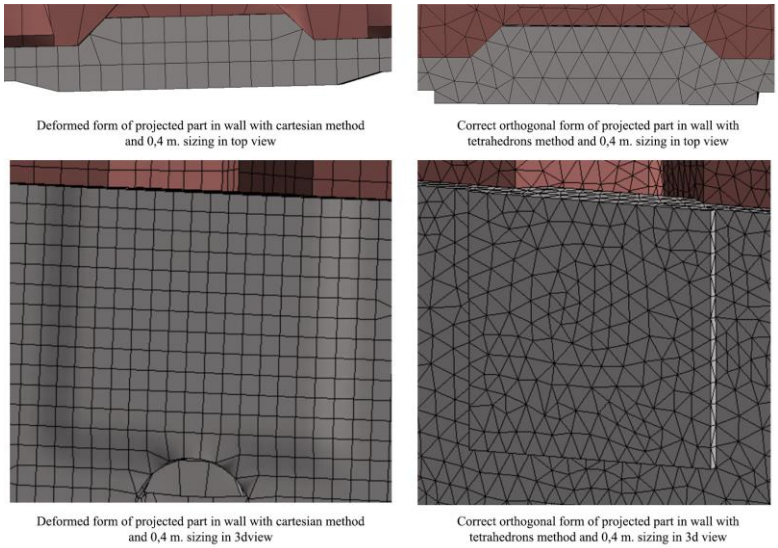


Figure 8. Deformed and correct forms of projected parts in walls with cartesian and tetrahedrons methods

As a result, the ineffectiveness of the cartesian method was detected because of section thickness and curvilinear geometry properties of the components. The tetrahedrons method with 0.4 m. sizing provided the desired geometry generations, so it is preferred for the meshing of the overall structure. In modal analysis phase, the mesh size lower than 0.4 m. did not work which is another reason to choose the assigned mesh size and type and it proves the invalid situation for smaller mesh sizes than 0.4 m. at this scale monumental structures (Figure 9).

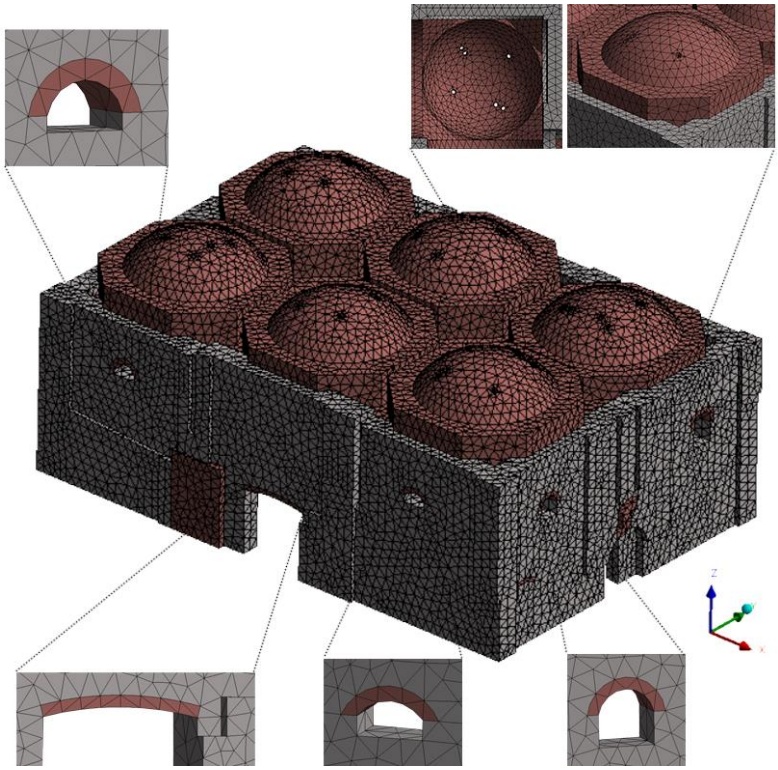

Figure 9. Tetrahedrons meshing in Bergama *Bedesten*

For contact surface identification stage, the overlapping portions of different structural components could not be detected by the software directly, so the manual surface separation by the use of line tool was realized. The overlapping surfaces of superstructure and walls, the overlapped parts of the walls with each other, and contact surfaces between brick arches of windows, doors and rough-cut stone masonry walls were defined (Figure 10).

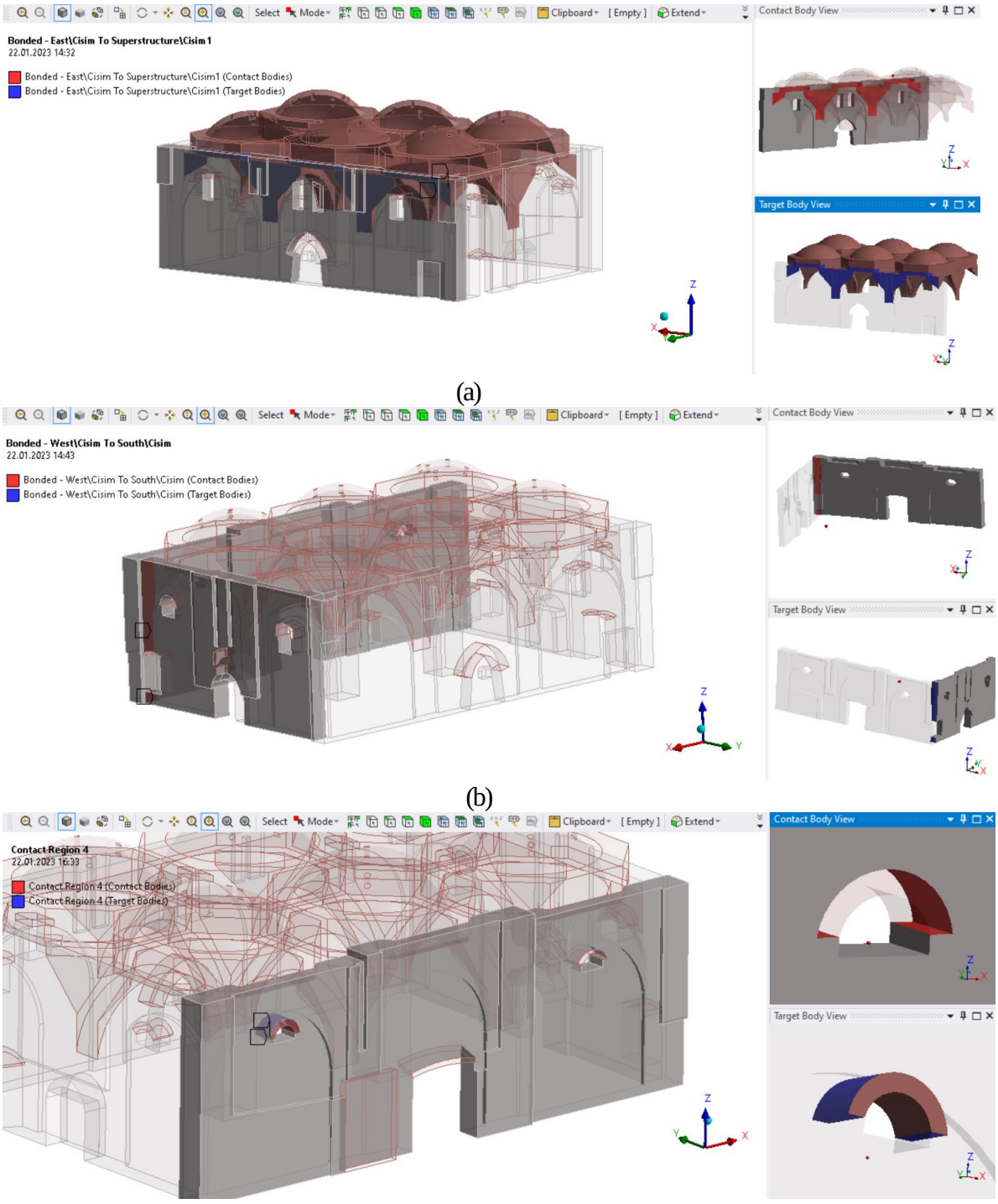


Figure 10. Different overlapping surface types; (a) between wall and superstructure, (b) between two walls, (c) between window/door arch and wall

As an example for the manual surface separation requirement in the software, the east wall and superstructure components can be shown. In the Figure 11, the situation of contact surfaces in both east wall and superstructure defined automatically by the software is seen. These contact areas are more than the overlapping portions and they are nearly the whole surface of each component although they do not touch to each other.

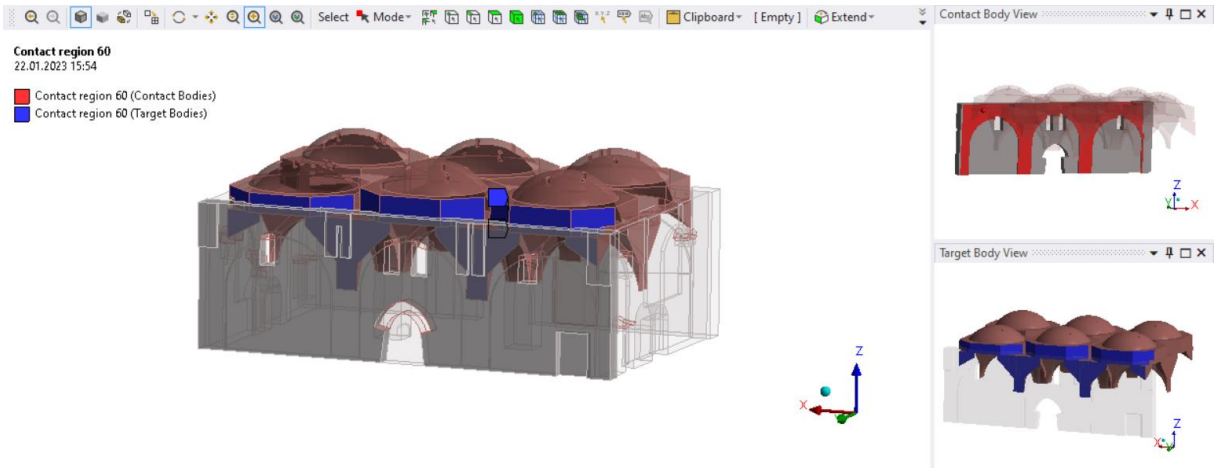


Figure 11. Wrong detection of contact areas in software for east wall and superstructure

Because the software could not detect the overlapping portions automatically, manual surface separation was realized by drawing the overlapping part borders with line tool at the related surfaces, and correct contact areas were generated (Figure 12).

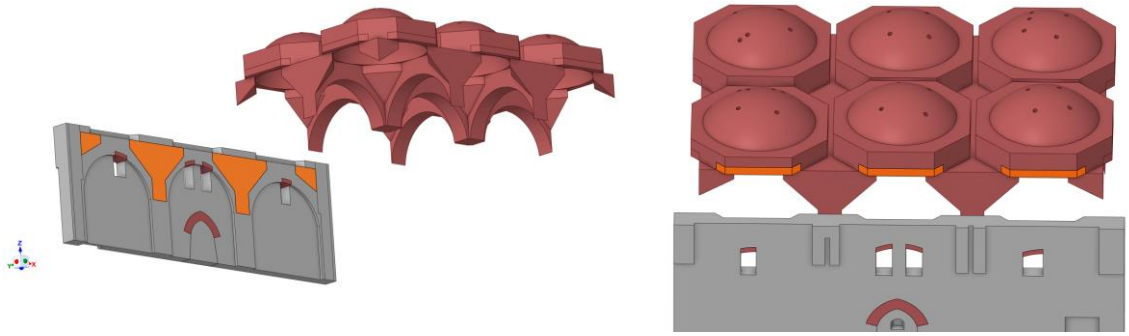

(a) (b)

Figure 12. Manual identification of contact areas by drawing the borders of overlapping areas in each component, as example; for east wall (a) and superstructure (b)

For the detection of the parts in the structure that have seismic vulnerability risk, the maximum principal stress values as the result of single-mode equivalent earthquake load analysis applying the horizontal acceleration on x and y- directions to the structure were examined for whether they exceed the limit tensile strength values for materials or not. However, in the scale automatically created by the software, the limit tensile strength values for materials are not included. So, manual addition of these values to the analysis scale was realized as 0.11 MPa for rough-cut stone masonry and 0.18 MPa for brick masonry (Figure 13).

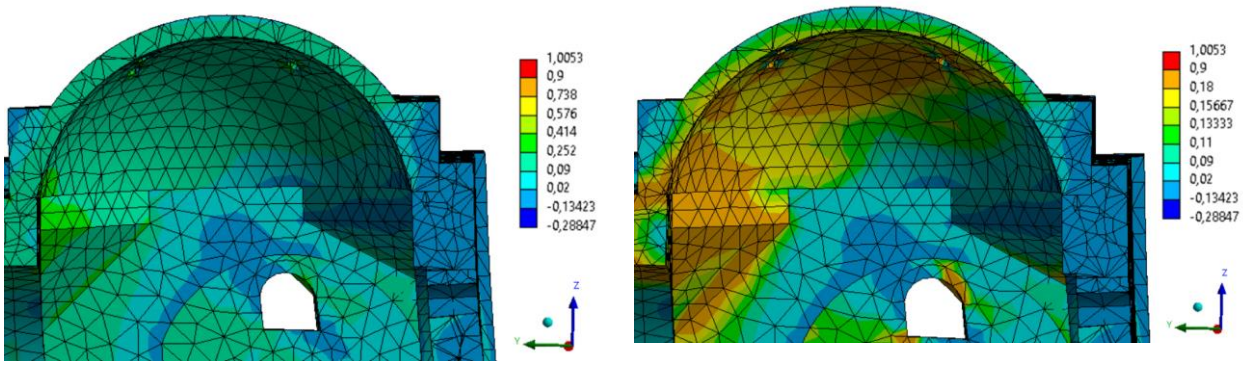


Figure 13. Addition of 0.11 MPa and 0.18 MPa values to the scale, example; maximum principal stress scale under y-direction earthquake loading in the southwestern dome

In addition, at the locations where the stress concentration spread, the exact risky areas could not be deciphered through only addition of the limit strength values. So, by the decrease of stress level intervals and the increase of contour numbers, the vulnerable zones became more identifiable and distinguishable from the remaining (Figure 14).

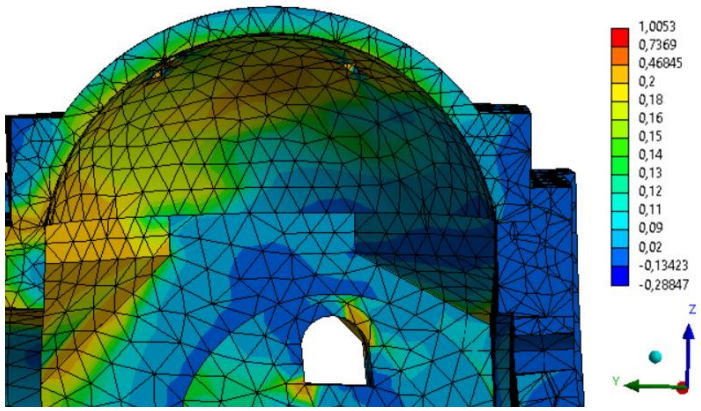


Figure 14. Increased contour numbers emphasizing exactly vulnerable zones in a more sensitive way in southwestern dome for maximum principal stress under y-direction earthquake loading

## 4 ADVANTAGES OF THE SOFTWARE

In this part, the advantageous sides of the software for interpretation of seismic vulnerability assessment results are discussed with the benefited qualities of ANSYS to be directive for further similar structural analysis studies.

As expressed in the previous section, by the control of limit tensile strength values of the materials, the vulnerable zones were tried to be determined. As a further step, whether the portions of the structure that have structural damage or alteration are in vulnerable zones or not was also investigated. At this stage, the increased interval numbers in the scale became effective to detect the overlapping zones. By the addition of stress labels on these zones, the stress levels at the crack traces, at overturned part of the west wall and at other structurally damaged parts, the exact stress levels were made visible numerically on the visuals (Figure 15).

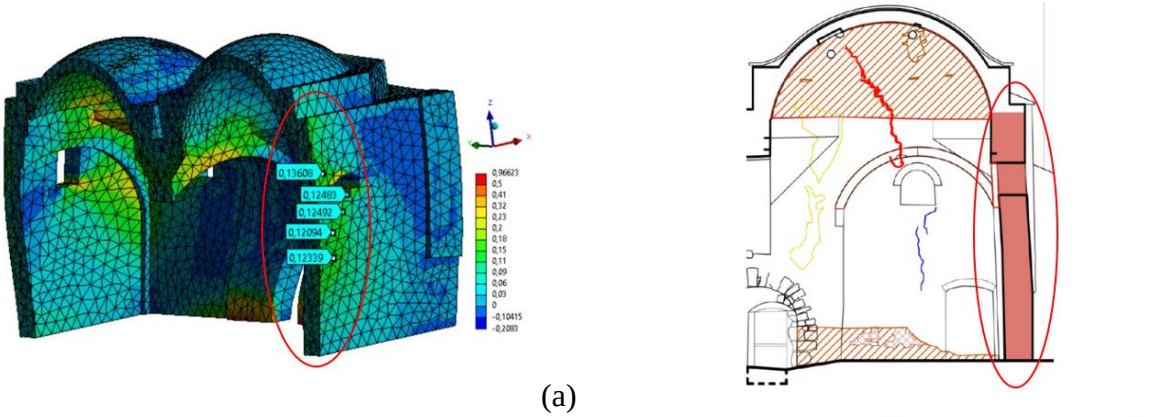


(a)

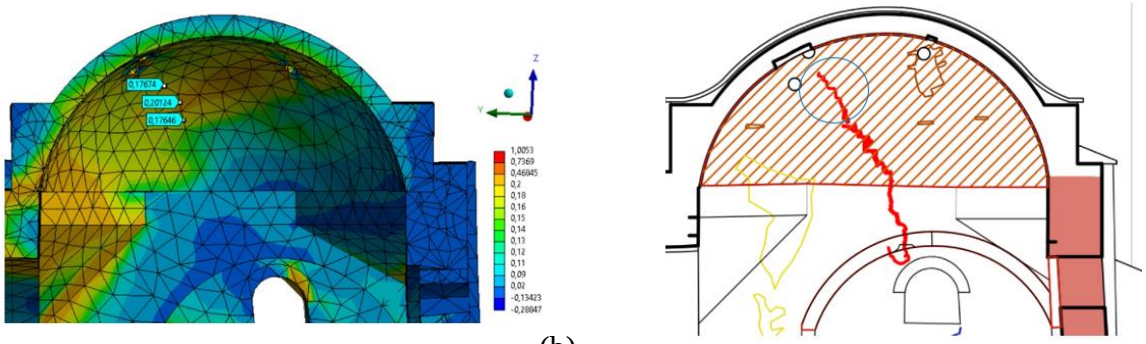


(b)

Figure 15. Detection of overlapped parts for vulnerable zones and structurally damaged areas at overturned west wall (a) and crack in southwestern dome (b) by increase of contour numbers and label tool

This is the advantageous aspect of the software to make the user able to emphasize the vulnerable portions by the production of desired number of contours and label tool providing also the sensitive detection of completely overlapping portions for vulnerable zones and structural damage areas. The same quality is effective for the altered portions to see which part of the structural element is vulnerable by what level of maximum principal stress. In the Figure 16, the alteration of west main entrance door arch profile and its vulnerable zone can be seen for comparison.

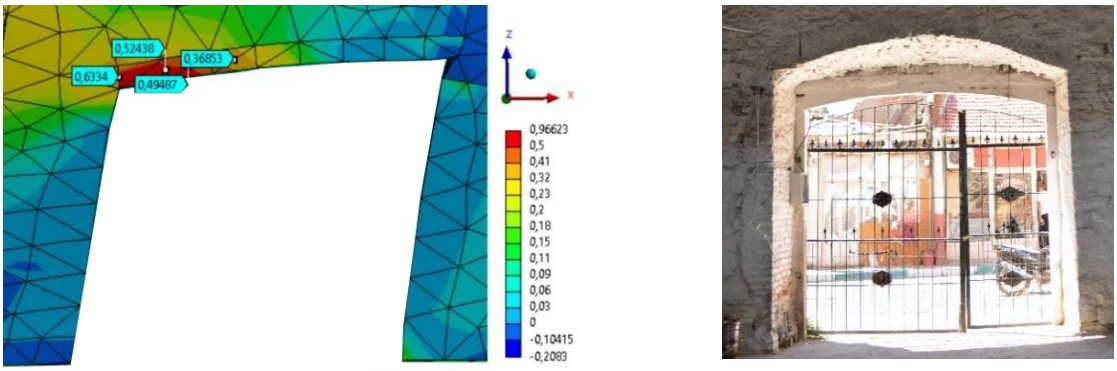


Figure 16. Maximum principal stress levels indicating vulnerable zone in altered west entrance door arch

In the study, all analysis results are shown in roof plan, ceiling plan, 3d section and axonometric views from different angles. This different view creation application allowed to show all the vulnerable zones of the structure located at different parts and the stress changes at inner and outer surfaces of the components were revealed (Figure 17).

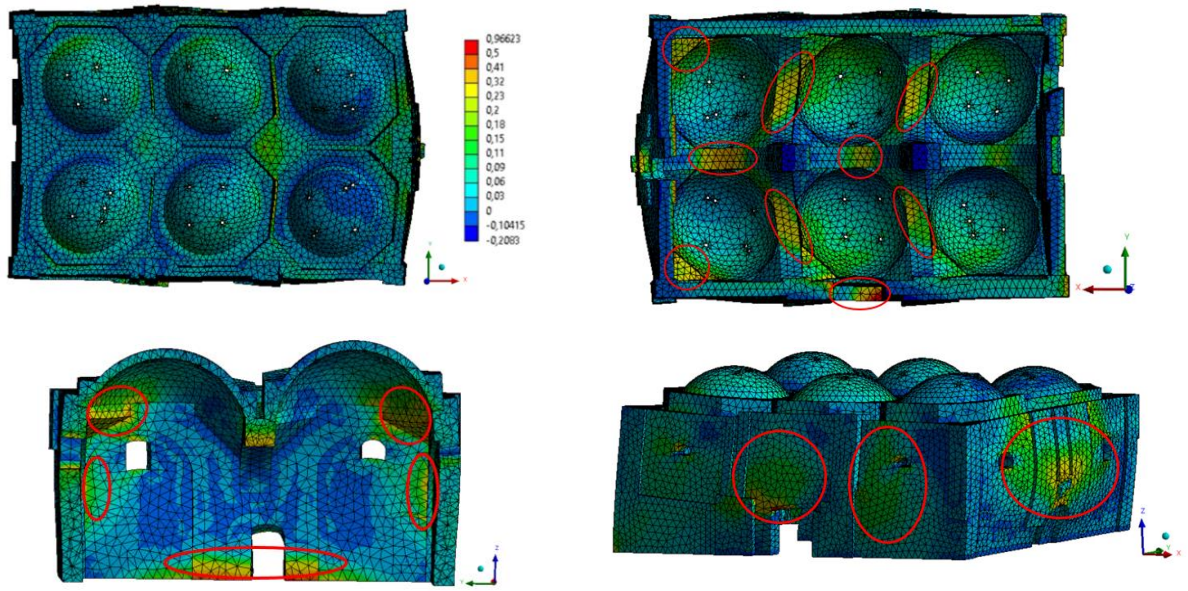


Figure 17. Maximum principal stress level changes and marked vulnerable zones by the application of x-direction earthquake loading shown in different view examples

Through the animations, the stress increase scene-by-scene creates a more perceivable presentation of stress-densified areas in the structure. This is helpful to emphasize the vulnerable zones in a more realistic way (Figure 18).

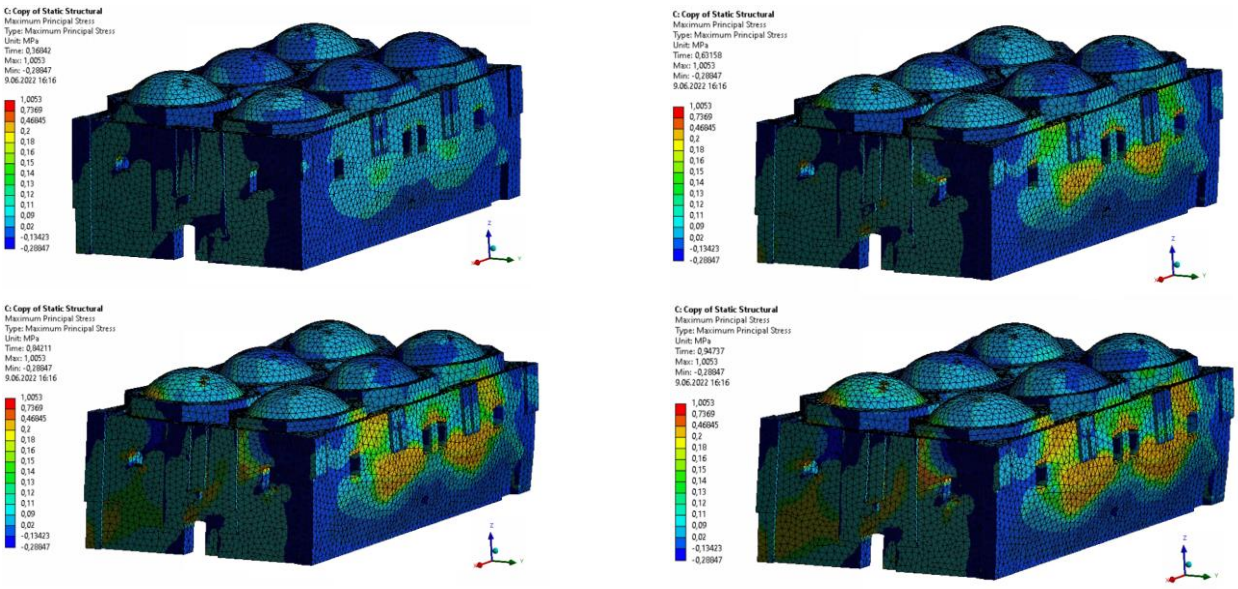

Figure 18. Maximum principal stress level changes by the application of y-direction earthquake loading shown in a 3d view scene by scene

Through 3d section animations, the stress changes presented in interior structural components such as arches, transition zone and domes create a powerful representation of the load-pattern change because of the applied seismic loading, too (Figure 19).

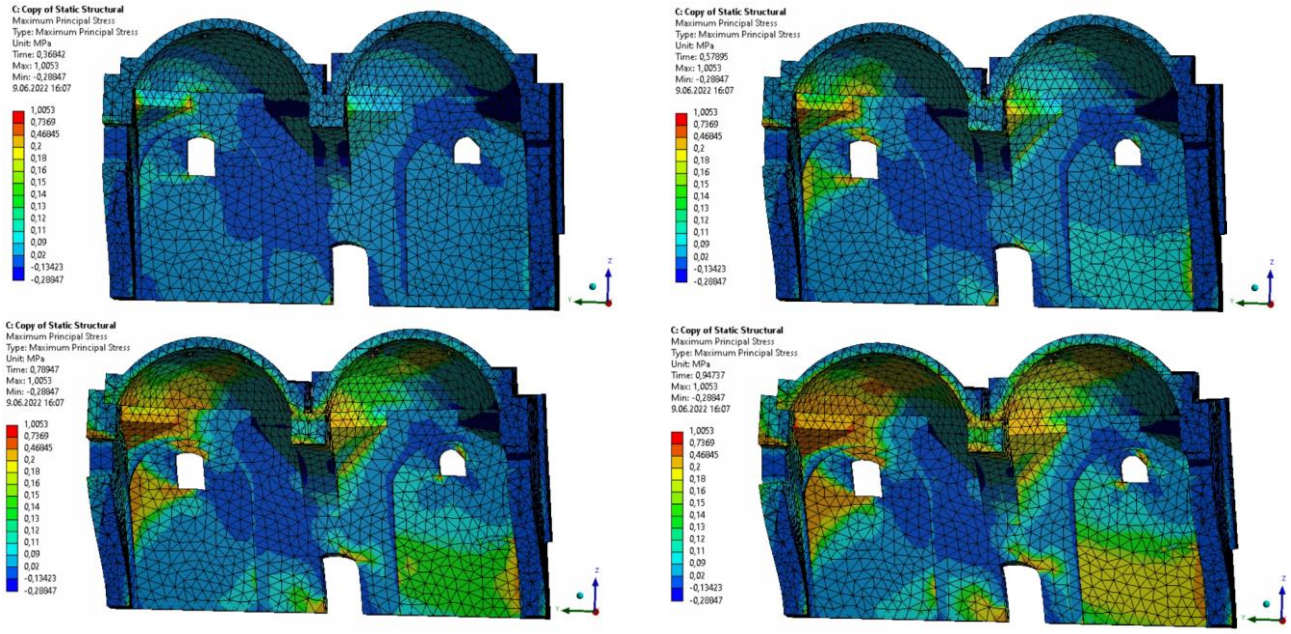


Figure 19. Maximum principal stress level changes by the application of y-direction earthquake loading shown in a 3d section view scene by scene

## 5 CONCLUSIONS AND RECOMMENDATIONS

The macro modeling of historic masonry structures by finite element method requires the combination of different work phases in ANSYS software such as component creation according to material usage change, meshing and contact surface identification. After these phases are realized, the analysis stage is carried out covering modal analysis and single-mode equivalent earthquake load analysis in this study. The macro modeling of Bergama *Bedesten* became the example case study to experience and reveal the challenging and advantageous aspects of the ANSYS software for macro modeling and seismic vulnerability assessment of historic masonry structures.

As a result, the following recommendations can be made for macro modeling in ANSYS and for the development of the software:

1- In mesh design, the tetrahedrons method has more potential to generate thin and curvilinear geometries compared to cartesian method with an efficient mesh size for the global structural behavior assessment of monumental masonry buildings. Therefore, either the use of this method in the overall structure can be preferred for the buildings accommodating this kind of curvilinear geometries with thin section, or the use of different mesh styles can be considered for differently characterized geometries. However, the second choice can lead to the requirement of further adjustments for the compatibility of different mesh types.

2- The contact surface identification between different components may not be created by the software automatically. The manual identification of these areas is time consuming. So, the improvement of the software for this stage can be beneficial decreasing the work time for macro modeling.

3- The automatic assignment of the material limit tensile strengths to the analysis scale was not carried out by the software. After the manual addition of the limit values, the scale still

needs adjustments for the contour intervals and increase of their numbers is required to emphasize the exact locations of the vulnerable parts. These automatic inclusion of limit values for materials to the analysis scale and increase of contour numbers with lower intervals between them around limit value levels can be realized by the software automatically. It leads to the decrease in analysis result deciphering time and creation of effective visuals representing the vulnerable zones.

As the aspects of the software that should be conserved and maybe improved more can be listed as followed:

1- The label tool allowing the numerical representation of stress values on the visuals which provides the comparison between structural damage areas and vulnerable zone stress levels exceeding the limit tensile strength values by maximum principal stress analysis results is a useful quality for the software. This tool is also effective to determine the vulnerable zones at the altered structural components increasing intervention priority for the related parts.

2- The different view generation as roof plan, ceiling plan, 3d section or axonometric views creates the opportunity to represent all vulnerable zones at inner and outer surfaces of the structure which is valuable for interpretation and presentation stages.

3- Thanks to the animations, scene-by-scene stress level changes can be visible to the user showing the effect of seismic loading on the structure and vulnerability increase in the different components. Because in different views like 3d sections, this quality is active, too, it is possible to see the horizontal acceleration effect on internal structural components like arches, domes etc. in a dynamic representation environment. This quality creates an impressive presentation tool for the analysis results.

4- The software allows solid modeling and the introduction of detailed material models. The solid elements allow better representation of geometrically irregular masonry components. It would not be that successful with shell or frame elements.

In conclusion, ANSYS software provides a useful computer environment for seismic vulnerability assessment of historic masonry structures with beneficial sides in analysis result interpretation and presentation stages. It can be further improved by the expressed recommendations for a more time-efficient use in macro modeling and in generation of analysis visuals showing vulnerable zones.

## REFERENCES

[1] N. Chieffo, A. Formisano, and P. B. Lourenço, Seismic Vulnerability Procedures for Historical Masonry Structural Aggregates: Analysis of the Historical Centre of Castelpoto (South Italy). *Structures* 48 (June 2022). Elsevier Ltd: 852–66, 2023.

[2] A. Formasino and N. Chieffo, Seismic Damage Scenarios Induced by Site Effects on Masonry Clustered Buildings: A Case Study in South Italy. *International Journal of Architectural Heritage*, 262-283, 2022.

[3] P. Aghabeigi, and S. Farahmand-Tabar, Seismic Vulnerability Assessment and Retrofitting of Historic Masonry Building of Malek Timche in Tabriz Grand Bazaar. *Engineering Structures.* 240 (June 2020): 112418, 2021.

[4] M. Orlando, M. Betti and P. Spinelli, Assessment of Structural Behaviour and Seismic Retrofitting for an Italian Monumental Masonry Building. *Journal of Building Engineering* 29 (July 2019): 101–15, 2020.

[5] R. Maio, R. Vicente, A. Formisano, and H. Varum, Seismic Vulnerability of Building Aggregates through Hybrid and Indirect Assessment Techniques. *Bulletin of Earthquake Engineering* 13 (10). Springer Netherlands: 2995–3014, 2015.

[6] S. Lagomarsino and S. Cattari, PERPETUATE Guidelines for Seismic Performance-Based Assessment of Cultural Heritage Masonry Structures. *Bulletin of Earthquake Engineering* 13 (1): 13–47, 2015.

[7] P. B. Lourenço, Computational Strategies for Masonry Structures. PhD diss. Delft University of Technology, 1996.

[8] M. Zucca, P. Crespi, and E Perrella, Seismic Vulnerability of Santa Maria Novella Basilica in Florence. *XVII. International Forum of World Heritage and Legacy*, no. June: 1–8, 2019.

[9] N. Ravichandran, D. Losanno, and F. Parisi, Comparative Assessment of Finite Element Macro-Modelling Approaches for Seismic Analysis of Non-Engineered Masonry Constructions. *Bulletin of Earthquake Engineering*. Vol. 19. Springer Netherlands, 5565-5607, 2021.

[10] N. Hoveidae, A. Fathi, and S. Karimzadeh, Seismic Damage Assessment of a Historic Masonry Building under Simulated Scenario Earthquakes: A Case Study for Arge-Tabriz. *Soil Dynamics and Earthquake Engineering* 147 (December 2020). Elsevier Ltd: 106732, 2021.

[11] A.Tomar, P. Agarwal, G. Singh, V.S. Kanwar, Seismic Damage Assessment of a Heritage Brick Masonry Structure. *AIP Conference Proceedings* 2451 (October), 2022.

[12] O. Uzdil, T. Coşgun, B. Sayın and C. Akçay, Seismic Vulnerability Assessment through Global and Local-Scale Analyses for a Historic Masonry Building Constructed in 1896. *Structures*, Vol. 49, 163-182, 2023.

[13] Republic of Turkey General Directorate of Foundations (VGM), Guideline for Management of Earthquake Risks for Historical Buildings. 125–144, https://cdn.vgm.gov.tr/organizasyon/organizasyon12_030619/kilavuz.pdf, 2017.

[14] Republic of Turkey Ministry of Interior Disaster and Emergency Management Authority (AFAD), The Seismic Hazard Maps of Turkey Interactive Web Application Report for Bergama *Bedesten*. https://tdth.afad.gov.tr/TDTH/ozetRapor.xhtml, 2022.

[15] Republic of Turkey Ministry of Interior Disaster and Emergency Management Authority (AFAD), Turkey Building Earthquake Code. http://www.resmigazete.gov.tr/eskiler/2018/03/20180318M1.pdf, 2018.

COMPDYN 2023
9th ECCOMAS Thematic Conference on
Computational Methods in Structural Dynamics and Earthquake Engineering
M. Papadrakakis, M. Fragiadakis (eds.)
Athens, Greece, 12-14 June 2023

# PERFORMANCE EVALUATION OF A MASONRY ARCH BRIDGE UNDER COMBINED SCOUR AND TRAFFIC LOADING

**Prateek K. Dhir[1*], Daniele Losanno[2], Fabrizio Scozzese[3], Enrico Tubaldi[4], and Fulvio Parisi[5]**

[1*] Department of Structures for Engineering and Architecture, University of Naples Federico II, Italy.
e-mail: prateek.dhir@strath.ac.uk

[2] Department of Structures for Engineering and Architecture, University of Naples Federico II, Italy.
e-mail: daniele.losanno@unina.it

[3] School of Architecture and Design, University of Camerino, Italy.
e-mail: fabrizio.scozzese@unicam.it

[4] Department of Civil and Environmental Engineering, University of Strathclyde, Glasgow, UK.
e-mail: enrico.tubaldi@strath.ac.uk

[5] Department of Structures for Engineering and Architecture, University of Naples Federico II, Italy.
e-mail: fulvio.parisi@unina.it

## Abstract

*Masonry arch bridges are highly vulnerable to floods - particularly to scour - due to their stiff and relatively fragile behavior, combined with the fact that they are often built on shallow foundations. In multi-span masonry arch bridges interaction of structural members give rise to a complex response when subjected to scour action combined with traffic loading.*
*The present work evaluates the behavior of a case study scoured masonry bridge under traffic loading with a three-dimensional finite element model developed in Abaqus using a macro-modelling approach. Traffic load model is selected in accordance with a recent guideline for safety assessment of existing bridges in Italy. The scouring process is then imposed through the progressive removal of elements from the model at the foundation. Displacement and internal stress distribution is analyzed under combined action due to increasing traffic load and scour depth.*
*The outcomes of the research lay the basis for an accurate risk assessment and management of masonry arch bridges subjected to multiple hazards. The proposed study can also provide useful information in terms of thresholds levels for bridge monitoring and maintenance.*

**Keywords:** Flood risk assessment, Masonry arch bridges, Floods, Scour, Traffic loading, multi-hazard, Macro-model.

# 1 INTRODUCTION

Masonry bridges are always vulnerable to scour and scour-induced settlements, due to their existing shallow footings. Due to the high population of existing masonry-arch bridges in Europe and worldwide [1] and their socio-economic, cultural, and historical value, the accurate assessment of their capacity against scour is of primary concern.

Only few numerical studies have addressed this issue by considering complex soil-foundation-structure interaction models [2,3]. These studies have investigated the significance of accurately accounting for the geometry of the scour hole when determining the bridge's capability against scour and the mechanism of collapse. Due to the differences in both the geometry and the pattern of the loading, it is not possible to precisely characterise the complicated behavior of these structural systems without using numerical three-dimensional (3D) models. Aiming at describing the progression of the cracking mechanism in the masonry components, improved models have been suggested in recent years (see e.g., [2, 4, 5]).

The performance of scoured masonry bridges under combined traffic loading moving from the case of the Rubbianello bridge is investigated in this study. In this regard, a 3D finite element model is developed in Abaqus software with a macro-modelling approach. While explicitly neglecting soil-foundation interaction, the scouring process is described by the progressive removal of constraints at the foundation level of the model. The outcome of the study facilitates the evaluation of residual capacity to traffic loads while increasing scour depth at the base and provide useful information for future bridge monitoring and maintenance.

# 2 CASE STUDY

The 1906-built stone arch bridge spans over the Aso river in the Central Italian town of Rubbianello. However, a very severe flood in 2013 was responsible for the collapse of two of the seven spans due to the flood induced scour. Again, earthquakes in 2016 as well as the severe rains and flooding until 2017 led to the present condition of the bridge (3 piers and 3 bays) (Figure 1). In this study the remaining bridge portion are modelled by introducing a new artificial abutment on the right side (in place of the existing pier) to obtain a symmetric configuration of the sample bridge.




**Figure 1**: Rubbianello bridge at its present condition [6]: (a) top-view and (b) lateral view.

## 2.1 Bridge geometric details

The original 7-span bridge has a span length of 16 m. Piers are identical and each of size 9.5 m × 3.2 m. Arches were 0.95m thick with a radius of 11.58 m. Spandrel walls of 0.65 m thickness were built. The foundations under the piers were rectangular in plan (11.00 m × 3.90 m) with a depth of 4.15 m. Figure 2 shows more information on the bridge geometry showing the original length (Figure 2a) and transverse (Figure 2b) and longitudinal (Figure 2c) section of the bridge.

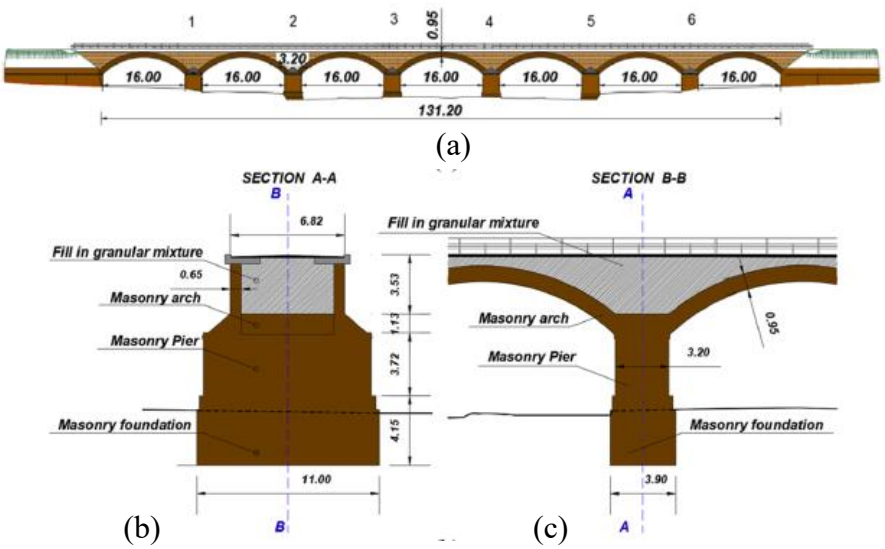


**Figure 2**: Geometrical details showing; (a) original length, (b) transversal, and (c) longitudinal. (Units are in meters) [6].

## 2.2 Materials

The selected material mechanical properties for the present analysis are taken from Scozzese et al. [6]. The material properties assigned to the abutment and the backfill were selected from the literature [2, 4, 5]. The summary of the major mechanical strength parameters presented in Table 1, i.e. density ($\rho$), Young's modulus ($E$), peak compressive strength ($f_{y,c}$), and peak tensile strength ($f_{y,t}$).

| Material | $\rho$ [t/m$^3$] | $E$ [kN/m$^2$] | $f_{y,c}$ [kN/m$^2$] | $f_{y,t}$ [kN/m$^2$] |
|---|---|---|---|---|
| Masonry (Arches & Spandrels) | 1.80 | 3,100,000 | 2,000 | 150 |
| Masonry (Piers) | 1.75 | 2,900,000 | 2,000 | 150 |
| Backfill | 1.70 | 250,000 | 10 | 0 |
| Abutment | 1.90 | 300,000 | - | - |

**Table 1:** Main mechanical properties [6].

## 3 NUMERICAL MODEL

A finite element 3D model was developed using Abaqus 2018 [7] platform, considering both geometrical and mechanical nonlinearities. Continuum (solid) elements are used with C3D8R (8-node linear, reduced integration, hourglass control). To obtain a balance between the computational cost and accuracy, the mesh dimensions are kept in the range between 0.35 m and 0.75 m as per [5, 6]. The material nonlinearity is described by concrete damage plasticity (CDP) model already available in Abaqus [7]. The material flow parameters for the CDP model presented in Table 2 are obtained from [6]. A linear elastic model is employed with a Mohr-Coulomb failure criterion (55° friction angle and 10 kN/m$^2$ cohesion) for the backfill material.

Nonlinear frictional/cohesive interfaces [2, 3] are used to simulate the interactions between the two components (arch-to-pier, spandrel-to-pier, spandrel-to-arch, and masonry-mortar interfaces) of the bridge. These zero thickness interfaces represent the mortar joints present at the

interaction between the parts. A damage criterion is introduced for masonry-mortar interfaces (see Table 3) whose properties are taken from [2, 5].

| dilation angle | flow potential eccentricity | $\frac{f_{b0}}{f_{c0}}$ | $K$ | Viscosity parameter |
|---|---|---|---|---|
| $31^0$ | 0.1 | 1.16 | 0.67 | 0.001 |

Table 2: flow parameters governing the CDP model.

| Interaction Properties | Backfill-masonry | mortar |
|---|---|---|
| Coefficient of friction, $\mu$ (-) | 0.6 | 1.0 |
| $K_n$ per unit area (N/mm$^3$) | 500000 | 500000 |
| $K_t$, $K_s$ per unit area (N/mm$^3$) | 500000 | 500000 |
| $\sigma_t$ (kN/m$^2$) | - | 150 |
| Cohesion, $c$ (kN/m$^2$) | - | 210 |
| Normal fracture energy per unit area, $G_f^I$ (kN/m) | - | 0.05 |
| Shear fracture energy per unit area, $G_f^{II}$ (kN/m) | - | 0.1 |

Table 3: Properties of the contact interfaces.

## 4 TRAFFIC LOAD ANALYSIS

Traffic load is a random variable to be modelled in safety assessment of roadway bridges. To model realistic traffic actions applied to existing bridges, recently developed traffic-load models (TLMs) proposed in [8] are considered in this study. Three load vehicles were considered in terms of spacing and single axles distribution to be representative of heavy (5-axles), medium (3-axles) and light (2-axles) real traffic, respectively (Figure 3). In addition to concentrated loads, uniform load was applied outside the silhouette of the single vehicle for the whole length of the bridge.

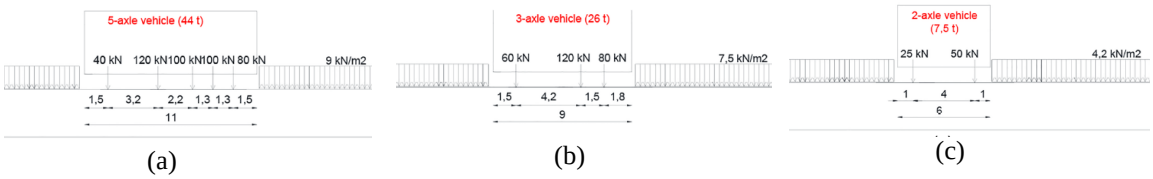


(a) (b) (c)

**Figure 3**: New traffic load models (distance in m): (a) heavy (5-axles), (b) medium (3-axles), (c) light (2-axles) vehicle [8].

A parametric study was conducted to examine stresses and displacements developed at various sections of the bridge with varying TLMs imposed on a single lane on the downstream side. Figure 4 identifies the critical sections under consideration where $F_{1,2}$ refers to the foundations, $P_{1,2}$ refers the piers, $A_{1,2}$ and $B_{1,2}$ refers to the arches and the backfills connecting $P_1$, respectively.

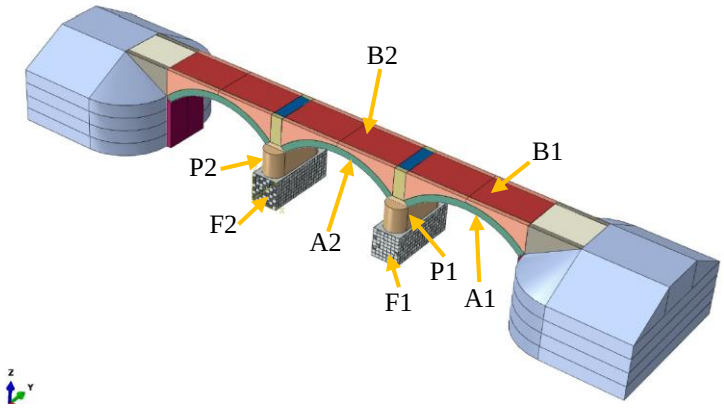


**Figure 4**: Numerical model showing the sections under considerations for stress analysis.

Figure 5a shows a comparison of displacements recorded at the bottom of the pier (P1) for the selected TLMs. After imposing gravity loads (i.e., Step-0), traffic loads were assigned (i.e., Step-1). Figure 5b and Figure 5c shows peak compressive stress and peak tensile stress, attained at selected sections of the bridge. As expected, the highest stresses and displacements are seen for 5-axle followed by 3-axle and 2-axle TLM. The highest stresses are observed in the arches and the lowest in the backfills.

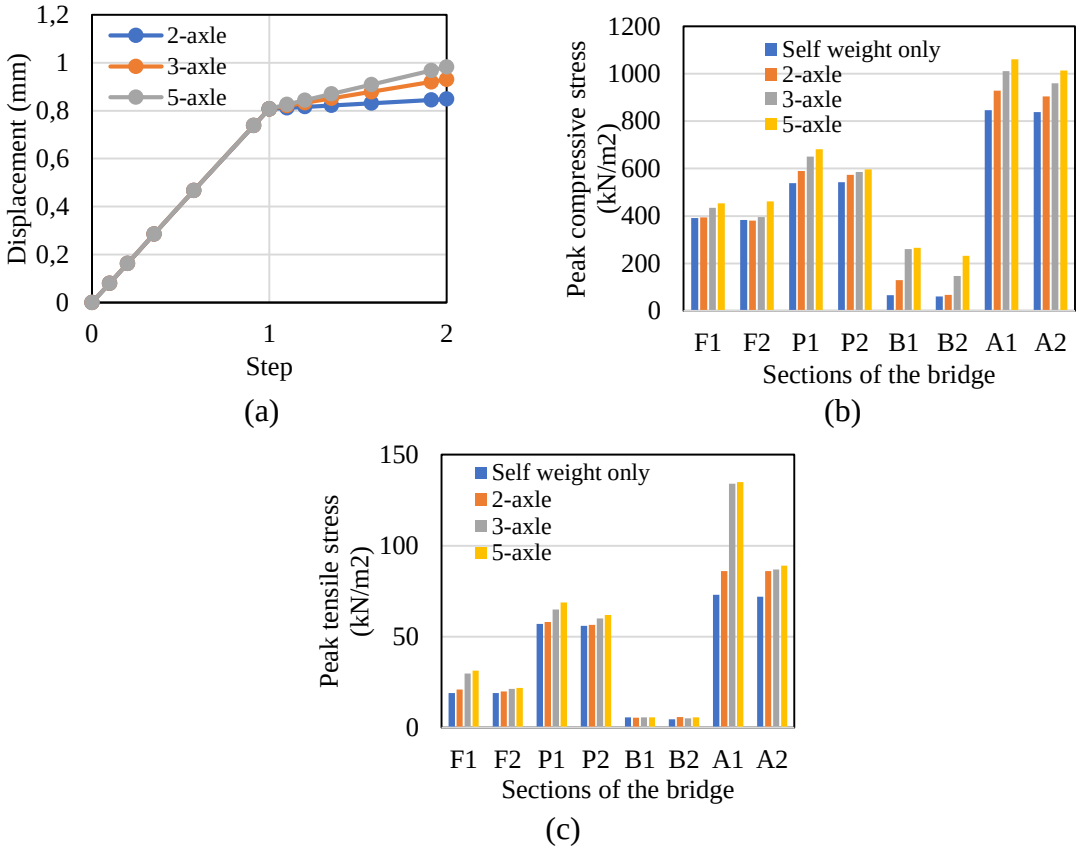


**Figure 5**: (a) Comparisons of displacements recorded at P1 (b) peak compressive stress (c) peak tensile stress under varying heavy TLM.

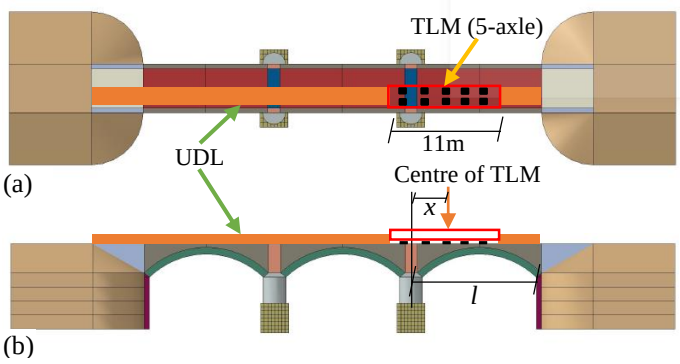


**Figure 6**: (a) top view and (b) side view of the bridge showing the loading schemes of heavy TLM.

A simplified influence line study was also conducted to assess the influence of moving traffic load axles along the span length, *l* of the bridge. Four models are developed for heavy TLM (5-axles). In the first case, the heavy TLM is applied being the centre of the TLM lying on the top of the P1 (i.e., $x$=0). Similarly, in the other three models, the TLM is applied at a length of $x=l/4$, $x=l/2$, and $x=3l/4$ from the center of P1. Figure 6 presents a schematic diagram showing top and side view of the bridge with TLM scheme.

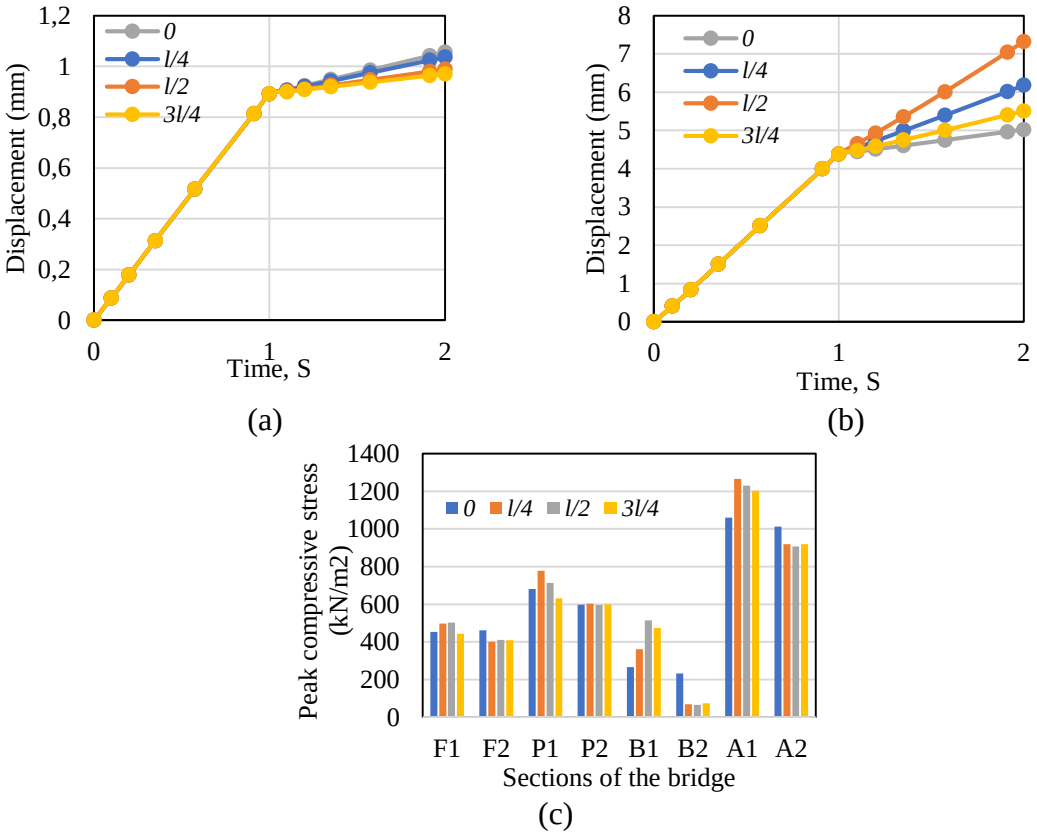


**Figure 7**: Comparisons of displacements recorded at (a) P1 (b) A1, and (c) stresses of 5-axle of traffic loading under varying positions.

Figure 7a shows a comparison of the displacements recorded at the pier top under gravity and traffic loading. The highest displacement is recorded at P1 when the TLM is acting at a distance $x$=0. As we move the TLM towards the crown the displacement recorded at P1 reduces and the least displacement at the pier top (P1) is observed when the traffic load is

at $x=3l/4$. Similarly, the highest displacement in the crown at A1 is observed (Figure 7b) when the center of TLM is close to the crown of A1 (i.e., $x=l/2$), and the least is when the $x=0$. Figure 7c shows the peak compressive stresses developed at the various sections of the bridge for the examined positions.

## 5 COMBINED SCOUR AND TRAFFIC LOAD ANALYSIS

Scour is a natural phenomenon caused by the erosion or removal of streambed or bank material from bridge foundations due to flowing water [2, 8-10]. The progression of scour is numerically simulated by removing support conditions (i.e., releasing joints at the base) under the foundation. A total of 8 scour scenarios were modelled aiming to represent different levels of maximum scour depth (Figure 8). Step 1 corresponds to the starting condition with gravity and traffic loads only acting on the bridge, i.e., no scour. From Step 2 to Step 9, the scour development is simulated by considering increments of scouring depth, for a total maximum scour depth of 5.54m (50% of the total foundation length) attained at Step 9. A dimensionless parameter is introduced in terms of scour portion *b* over total foundation length *B*, i.e., *b/B*, varying from 0 to 0.5.

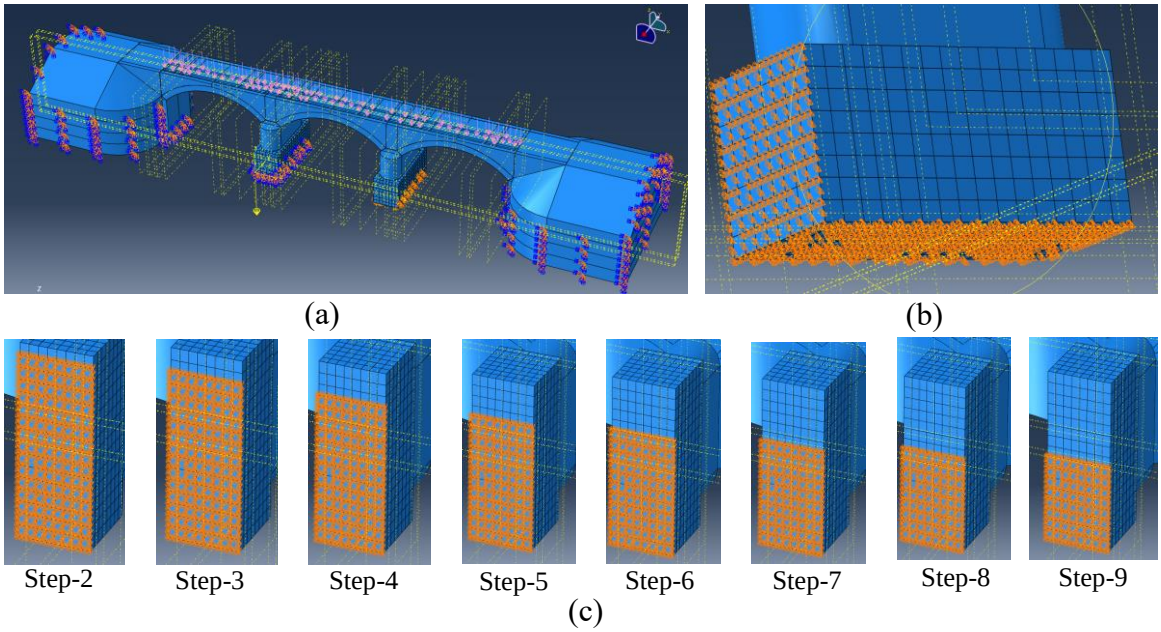


**Figure 8**: (a) Numerical model developed in Abaqus (a) foundation boundary conditions (c) progress of removal of supports representing settlements ($0 < b/B < 0.5$).

Figure 9 show the peak compressive stress distribution in the foundation (F1) subjected to scour under traffic loading at different steps. With gravity load only the stress distribution contours are symmetric with all axes (Step-0). With the addition of traffic loading at one of the two lanes of the road, unsymmetric stresses are developed and higher stresses are seen on the side of the foundation on which the loading is present (Step-1). To impose the most adverse condition, scouring action is simulated (from Step 2 to 9) downstream, i.e., under the same lane traffic has been applied. With the increment of scouring levels, the location of the highest stress point shifts from the edge of the foundation to its center.

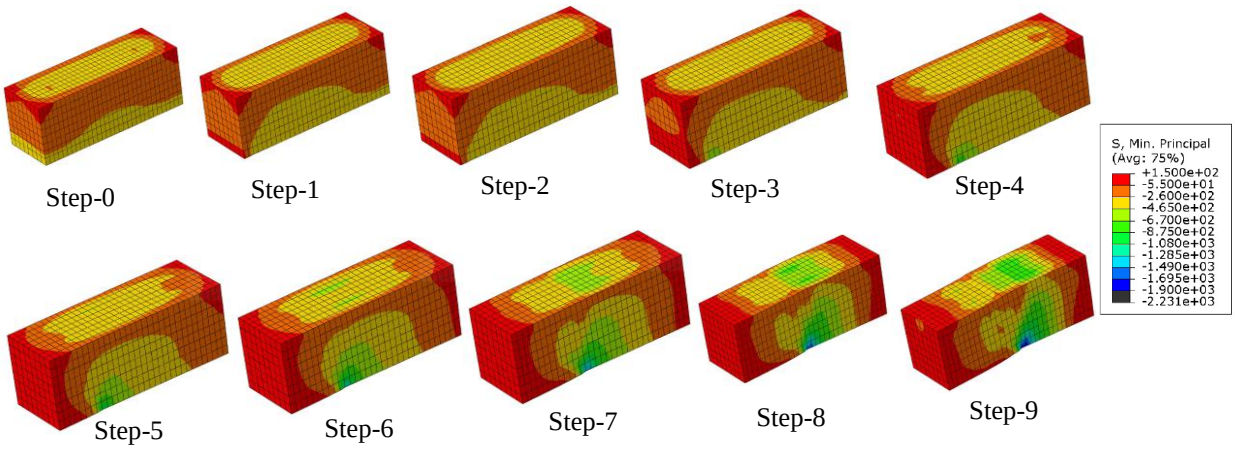


**Figure 9**: Foundation compressive stress distribution subjected to scour under traffic loading.

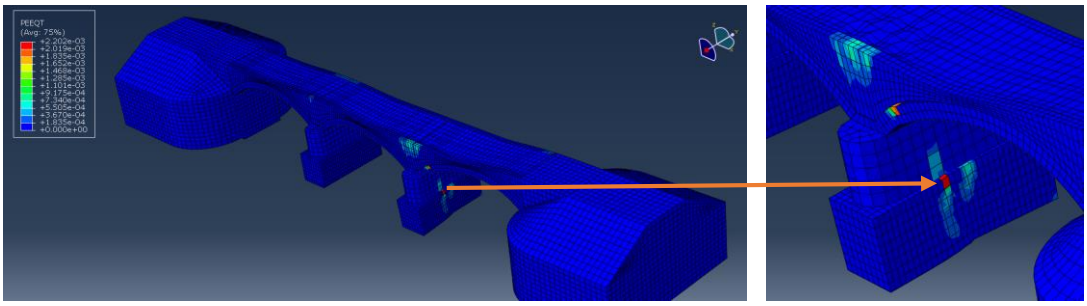

**Figure 10:** Equivalent plastic strain (PEEQT) distribution subjected to scour under traffic loading.

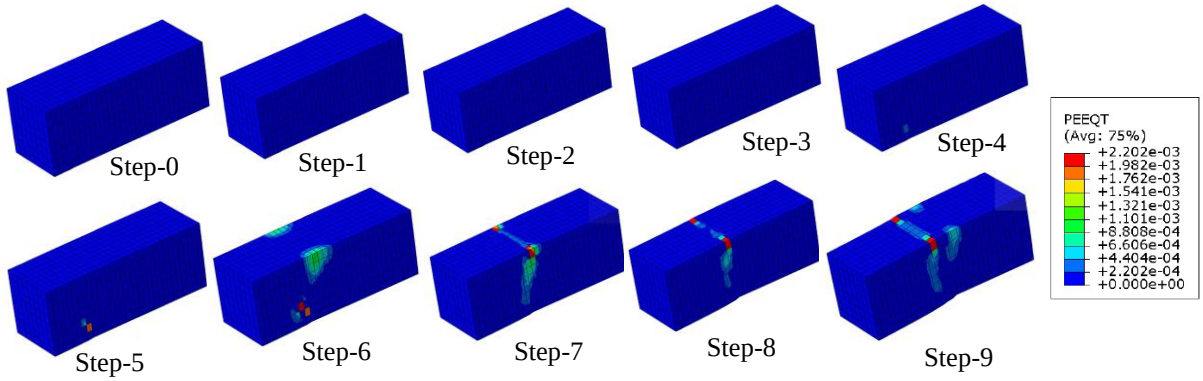


**Figure 11**: Equivalent plastic strain (PEEQT) distribution of the foundation subjected to scour under traffic loading.

Figure 10 shows the plastic strain distribution of the whole model at Step-9 scouring level and the progress of plastic strain in F1 for each step are presented in Figure 11. Up to Step-3 no visible strain is identified whereas from the Step-4 onwards (i.e., $b/B > 0.19$) plastic strains are developed, and stresses start concentrating at F1, which also begins rotating. Figure 12a illustrates the comparisons of the pier's vertical settlement at P1 against $b/B$ with reference to the case where no traffic load is considered. For an increasing heavy TLM intensity by a load multiplier (LM) of 2.5 and 5, the comparisons are shown in Figure 12b, c and finally all the cases are compared in Figure 12d. The vertical settlement notably increases for increasing value of

*b/B*. When the *b/B* reaches 0.3, further small increments induce a very high increase in stresses causing damage to the structure.

Figures 13a shows the peak compressive stress distribution for all critical sections of the bridge subjected to scour only where no traffic load is imposed. Figure 13b shows the condition where a 5-axle TLM is applied and propagated up to 8$^{th}$ scouring level (step-9). In Figure 13c and 12d, traffic load multipliers of 2.5 and 5 were applied and the responses are compared with respect to the condition where scouring occurs without any application of traffic loading. Similarly, Figure 14 shows the peak tensile stresses developed with increasing traffic load factors.

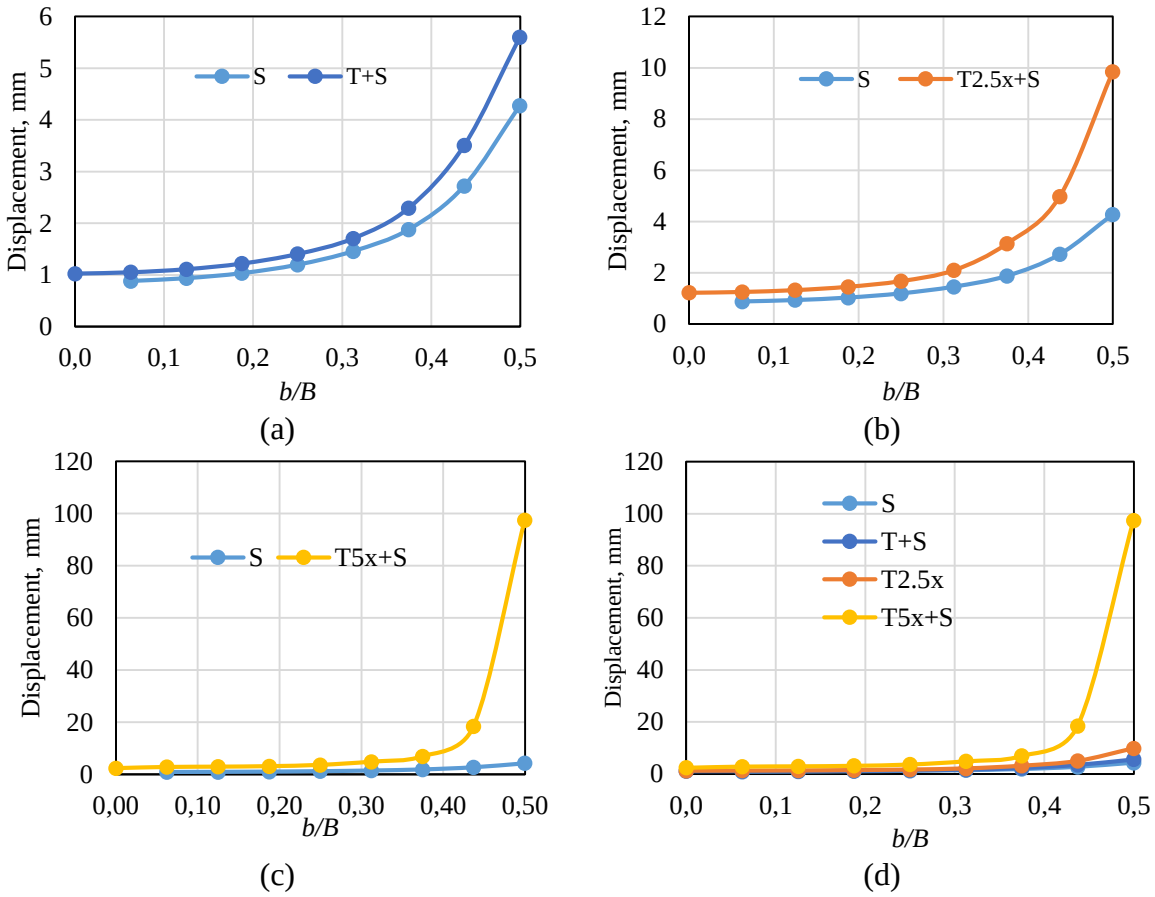


**Figure 12**: Displacement at foundation subjected to scour under heavy TLM: (a) T+S (b)2.5T+S, (c) (5T+S) and (d) all cases.

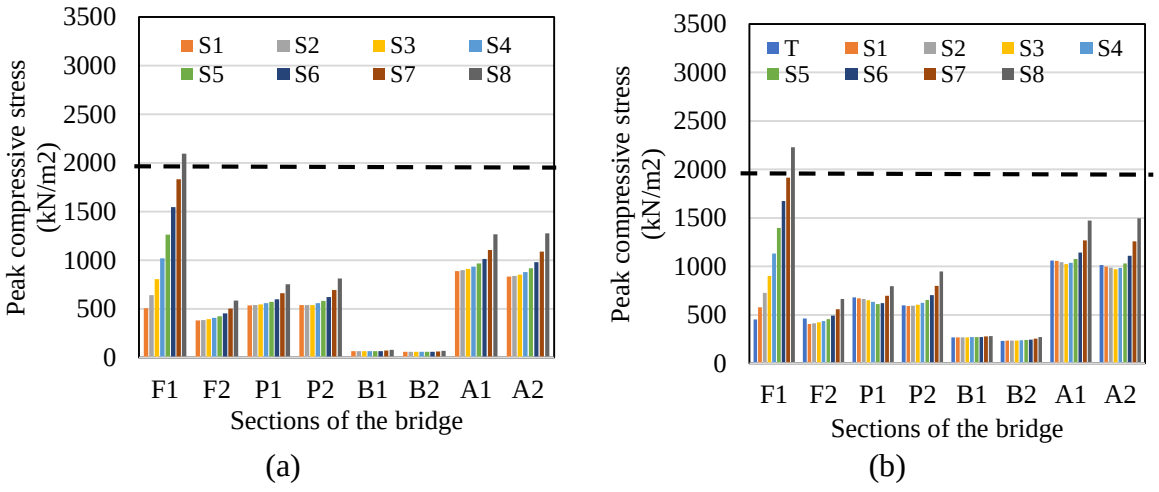

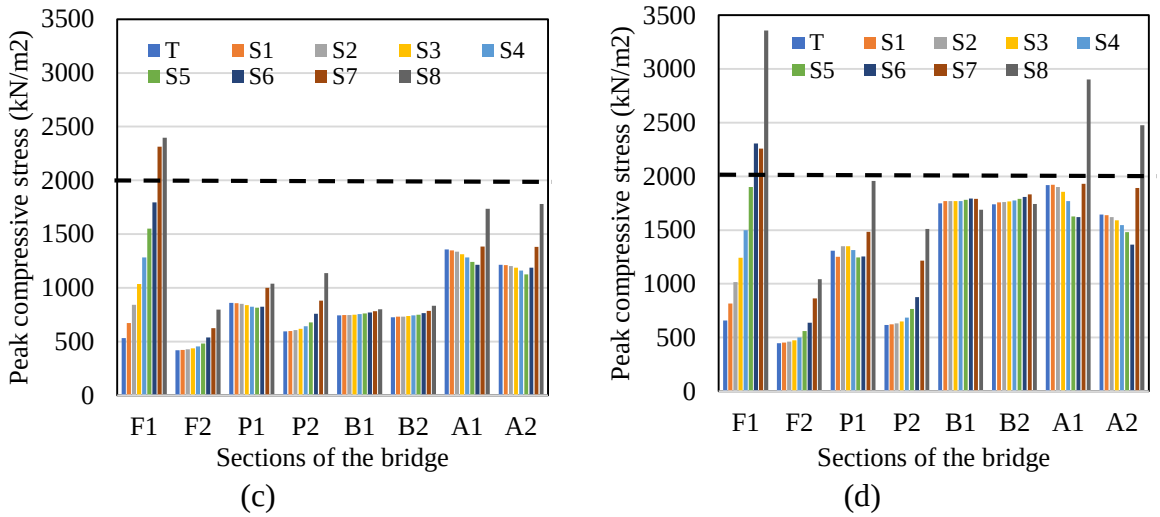


**Figure 13**: Peak compressive stress under combined heavy TLM and scour: (a) T+S (b)2.5T+S, (c) (5T+S) and (d) all cases.

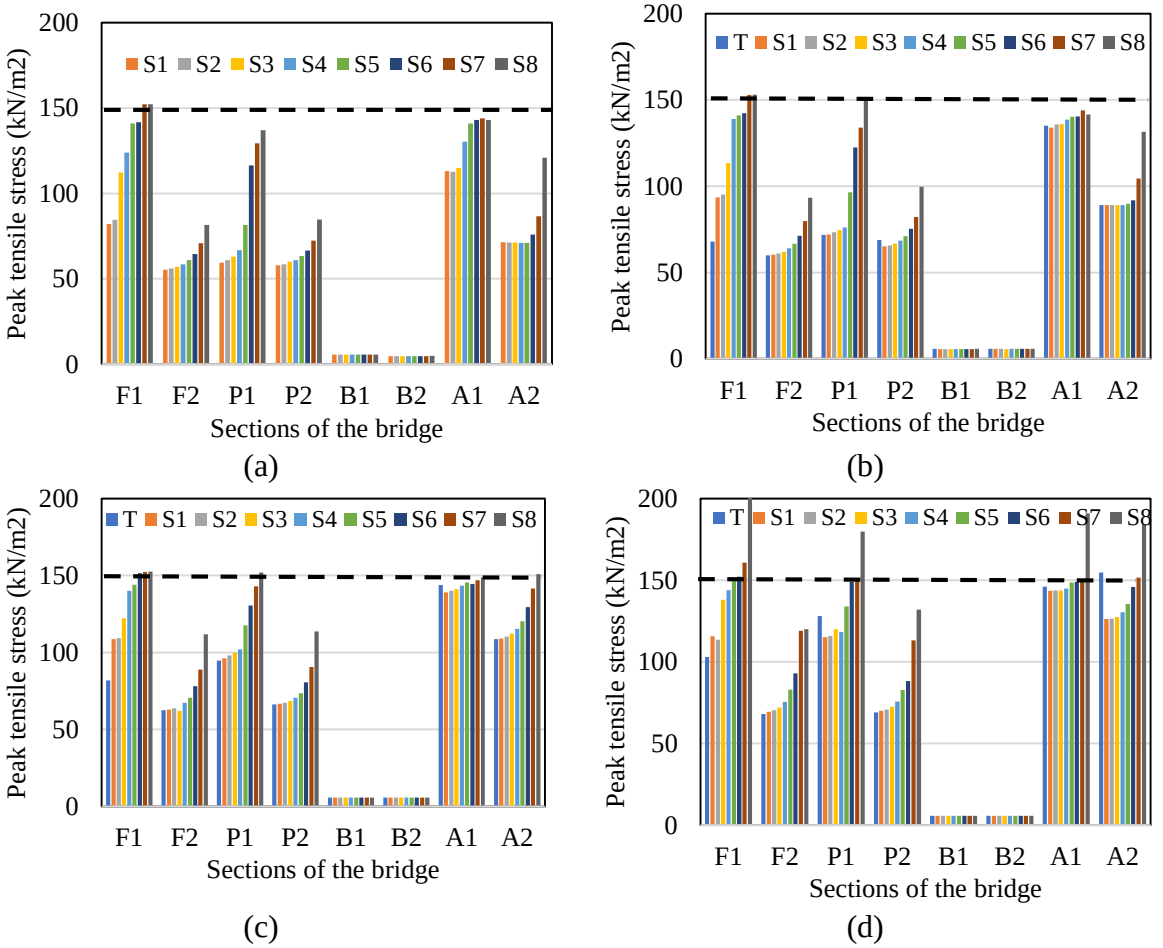


**Figure 14**: Peak tensile stress under combined TLM and scour: (a) T+S (b)2.5T+S, (c) (5T+S) and (d) all cases.

Figure 15a shows the comparison of stresses developed at F1 for all selected steps (Step 1-9) with an increasing TLM factor of 1, 2.5 and 5. Higher compressive stresses are developed with the progress of scouring level which is consistent with increasing traffic load factors. Figure 15b shows a comparison of compressive stress Demand to Capacity ratios (DCR) of the

section F1 against *b/B*. Once the *b/B* reaches 0.3 the DCR rises sharply leading to the failure confirming previous outcomes in terms of plastic strain and vertical displacement.

Similarly, the development of tensile stress recorded for F1 is shown in Figure 15c with an increasing level of traffic load factors. The tensile stress approaches the capacity limit (150 kN/m$^2$) once it completes the Step-3. It increases further with the increase in the scouring levels and Step-5 onward it attains the maximum limit leading to the failure. Figure 15d shows a comparison of tensile DCRs for the section F1 where DCR reaches to 1 at *b/B*>0.3. DCRs provide a useful representation in terms of interaction domain between traffic loads and scour depth accounting for reduced bridge residual safety due to mutual action.

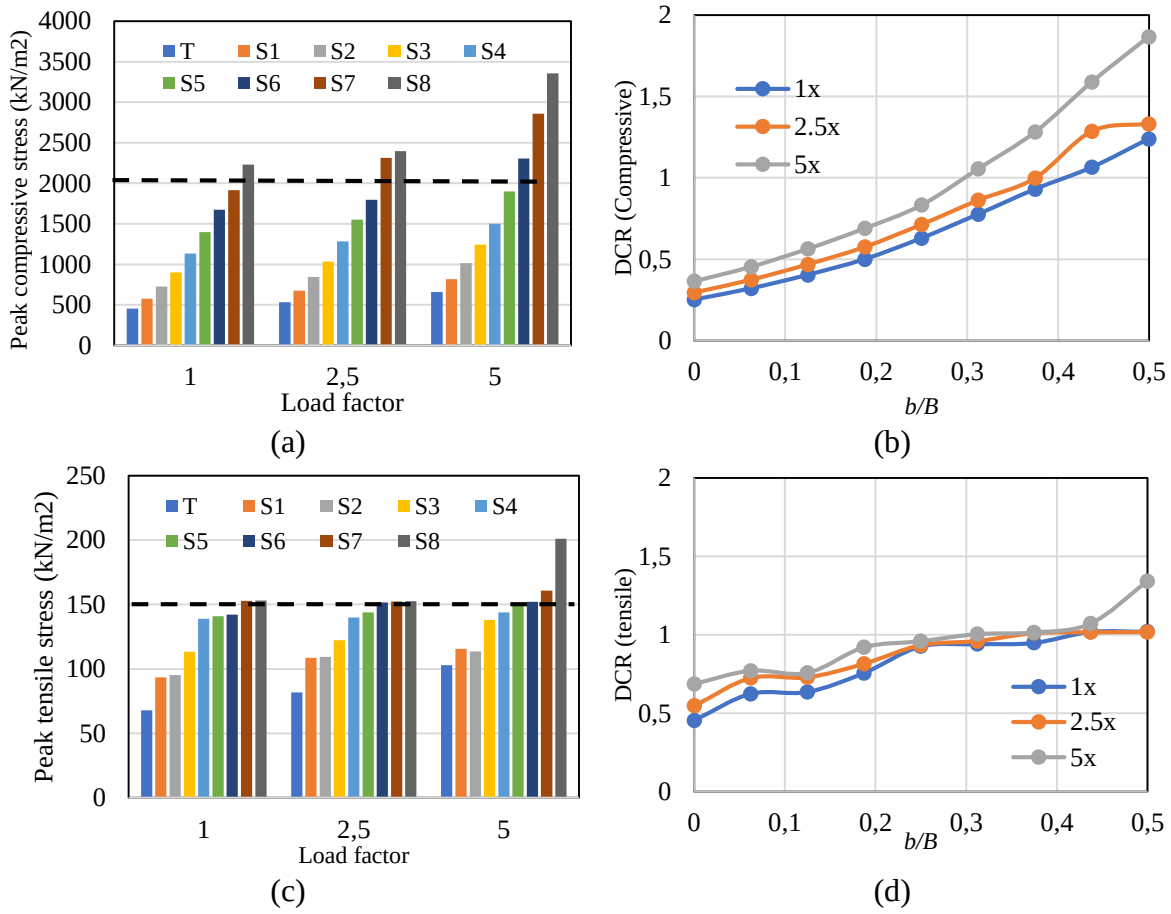


**Figure 15:** (a) Peak compressive stresses (b) compressive DCR (c) Peak tensile stresses (d) tensile DCR

## 6 CONCLUSIONS

This study performs a performance evaluation of scoured masonry bridges under traffic loading. In the initial stage of the study, the solo influence of the traffic loading without scour as well as the scouring without any imposed traffic loading was investigated. Parametric studies were conducted considering loading types and the traffic loading locations. Later, the model was analysed for increasing levels of scour subjected to traffic loading. An increasing level of load factors for the traffic loading was also considered to combine different intensity levels of the actions.

Once the *b/B* reaches 0.3, the DCR rises sharply leading to failure. Both the compressive and the tensile stresses reach close to the capacity limit once *b/B*=0.3. DCR reaches 1 at *b/B*>0.3 as it increases further with the increase in the scouring levels leading to the failure. As far as

the scour depth increases, the safety factor against traffic loads reduces. Once the scouring length of the foundation reaches 30% of its original dimension, any contribution in terms of traffic loading may cause complete failure of the structure.

The outcome of the research facilitates the accurate risk assessment and management of masonry arch bridges subjected to combined scour and traffic action, laying the basis for future studies on multi-hazard scenario and safety assessment of existing bridges.

## ACKNOWLEDGEMENT

This study was carried out in the framework of RESIST project "RobustnEss aSsessment and retrofItting of bridgeS to prevenT progressive collapse under multiple hazards", which is funded by University of Naples Federico II and Compagnia di San Paolo through STAR Plus Programme 2020. The support by ReLUIS through the CS.LL.PP.–ReLUIS programme is also gratefully acknowledged.

## REFERENCES

[1] J. Page, Masonry Arch Bridges: State-of-the-art Review. *HM Stationery Office*, 1993.

[2] E. Tubaldi, L. Macorini, B. A. Izzuddin, Three-dimensional mesoscale modelling of multi-span masonry arch bridges subjected to scour." *Engineering Structures*, **165**, 486-500, 2018.

[3] P. Zampieri, M. A. Zanini, F. Faleschini, L. Hofer, C. Pellegrino, Failure analysis of masonry arch bridges subject to local pier scour. *Engineering Failure Analysis*, **79**, 371-384, 2017.

[4] Y. Zhang, E. Tubaldi, L. Macorini, B.A. Izzuddin, Mesoscale partitioned modelling of masonry bridges allowing for arch-backfill interaction. *Construction and Building Materials*, **173**, 820-842, 2018.

[5] G. Milani, P. B. Lourenço, 3D non-linear behavior of masonry arch bridges. *Computers & Structures*, **110**, 133-150, 2012.

[6] F. Scozzese, L. Ragni, E. Tubaldi, F. Gara, Modal properties variation and collapse assessment of masonry arch bridges under scour action. *Engineering Structures*, **199**,109665, 2019.

[7] S. Dassault. SIMULIA User Assistance 2018: Abaqus Verification Guide. *Dassault Systèmes Simulia Corp*, 2018.

[8] E. Cosenza, D. Losanno, Assessment of existing reinforced ‐ concrete bridges under road ‐ traffic loads according to the new Italian guidelines. *Structural Concrete*, **22 (5)**, 2868-2881, 2021.

[9] G. Hoffmans, *JCM. Scour manual*. Routledge, 2017.

[10] B. W. Melville, S. E. Coleman, Bridge scour. *Water Resources Publication*, 2000.

[11] E. Tubaldi, L. Macorini, B. A. Izzuddin, C. Manes, F. Laio, A framework for probabilistic assessment of clear-water scour around bridge piers. *Structural safety*, **69**, 11-22, 2017.

COMPDYN 2023
9th ECCOMAS Thematic Conference on
Computational Methods in Structural Dynamics and Earthquake Engineering
M. Papadrakakis, M. Fragiadakis (eds.)
Athens, Greece, 12-14 June 2023

# EARTHQUAKE NATECH RISK: NUMERICAL ANALYSIS OF FLOATING ROOF AND SEALING SYSTEM IN CYLINDRICAL STORAGE TANKS

**Michela Salimbeni**[1], **Maurizio De Angelis**[1], **and Mariano Ciucci**[2]

[1] La Sapienza University of Rome
e-mail: {michela.salimbeni,maurizio.deangelis}@uniroma1.it

[2] INAIL (Italian National Institute for Insurance against Accidents at Work), DIT
m.ciucci@inail.it

## Abstract

*Earthquake is one of the natural event that are part of NaTech events (Natural Hazard Triggering Technological Disasters). Cylindrical liquid storage tanks with floating roof are common equipment in industrial plants, and they are vulnerable to earthquakes. In fact, seismic damage to tanks with floating roof can lead to major accidents involving hazardous substances, mainly due to convective fluid movement and to the interactions between the tank wall, the fluid, the floating roof, the sealing system, and the bumper bars. In rim seal fires, which occur when the sealing system is damaged and an impact occurs between the bumper bars and the tank wall, the horizontal dynamics of the floating roof is involved. The horizontal dynamics depends mainly on the mechanical characteristics of the sealing system and the type of impact.*
*The objective is to predict the horizontal vibration response of the floating roof of a tank subjected to seismic excitation, taking into account different boundary conditions. For this purpose, a simplified and reduced model is developed assuming a decoupling hypothesis between the horizontal and the vertical motion of the roof. Different types of sealing systems (i.e., different mechanical properties) are investigated, considering the possibility of impact between the bumper bars and the tank wall. This impact is usually rigid. Later, as a proposal for the prevention of major accidents, deformable bumpers are introduced to reduce the maximum contact force and avoid the impact between two metallic parts.*

**Keywords:** Earthquake NaTech risk, major-hazard industrial plants, storage tanks, floating roof, sealing system, bumper, Finite Element Model, hard impact, soft impact.

## 1 INTRODUCTION

Seismic events in the past have shown that industrial plants are vulnerable to the earthquake. Their vulnerability results from the complexity of the layout: they are characterized by many connections, equipment and components which, combined with the complexity of their operations, make them highly susceptible to seismic excitation. This implies the possibility of accidental chains forming, with a possible domino effect, which can cause explosions, fires and releases of dangerous substances treated by the industrial processes. In cases where natural disasters interact with industrial risk, this is referred to as NaTech events (Natural Hazard Triggering Technological Disasters). Among the NaTech events, the earthquake is one of the most significant, it simultaneously affects the entire plant, and it can cause simultaneous damages to equipment [1,3]. In terms of safety, in Italy industrial plants that operate with hazardous substances are called "major hazard industrial plants" and are subject to Italian standard D.Lgs. 105/2015, transposition of Directive 2012/18/EC – Seveso III.

One of the typical equipment in major hazard industrial plants is the cylindrical liquid storage tanks with floating roof [4]. Seismic damages to the floating roof and non-structural elements can cause hazardous substance releases, fires and explosions.

The floating roof is a circular steel structure equipped with floating caissons that allow it to float above the product stored. A space between the outer edge of the roof and the inside of the tank shell, 200 mm in size, is closed by means of a flexible sealing system. Also, there are limiting bumper bars to guarantee the protection of the sealing system in case of large displacement.

As a part of major accidents, rim seal fire is the most common type of fire in a tank with floating roof. This occurs when the sealing system is damaged, loses its integrity and allows the leakage of vapors that can be ignited [5]. These vapors can be ignited by sparks from impact between bumper bars and the tank wall, two metallic parts. In this framework, the horizontal dynamics of the roof with the sealing system and with the bumper bars is of particular interest for the earthquake NaTech risk assessment of atmospheric tanks with floating roofs.

In Literature, before the 1950s, the floating roof was regarded as a non-structural element and its contribution to the response was limited to an increase in damping; all design was based on theories proposed by Jacobsen [6], Senda [7] and Nakagawa [8] for cylindrical tanks. In Nakagawa [8] the roof was modelled as a rigid plate whit mass, and linear potential theory was applied to solve the fluid-roof interaction problem. Subsequently, in Sakai et al [9] the roof was modelled with an elastic plate with mass, still remaining within the framework of the elastic potential theory. Other authors then dealt with the non-linear aspects of the problem [10,11]. In [12], Matsui presented an analytical solution to predict the sloshing response of a cylindrical liquid storage tank with floating roof under seismic excitation. The author assumed the liquid as inviscid, incompressible, and irrotational, while the floating roof was modeled as an isotropic elastic plate with uniform stiffness and mass. The dynamic interaction between the liquid and the floating roof was considered exactly within the framework of linear potential theory. In [13], Matsui derived an analytical solution for sloshing in a cylindrical liquid storage tank with a single-pontoon floating roof under seismic excitation. Under the same hypothesis and in the same linear framework, the author considered the floating roof composed of an inner deck, which may be idealized as an isotropic elastic plate with uniform thickness and mass, and connected to an outer pontoon, which is modeled as anelastic curved beam. In [12,13], Matsui imposed the free-boundary conditions along the roof edge. Shabani and Golzar [14] investigated the sloshing response of the floating roofs for different ground motion records taking into account the nonlinearity due to large deflection of the deck plate. Free-boundary conditions were required on the roof edge. Hosseini et al [15] proposed a simplified numerical method for

modeling the interaction between the floating roof and the tank wall. The authors assumed that sloshing was suppressed by the presence of the roof, and they modeled the sealing system through pre-compressed only-compression radial springs all around the roof. For the case study, the deformation of the tank wall is comparable with the nominal gap covered by the sealing system. A finite element model was presented in [16], that validated the analytical model presented in [15]. Caprinozzi et al. in [16] were interested to predict the maximum vertical displacement of the roof in order to carry on a seismic fragility analysis for the liquid overtopping. The interaction between the edge of floating roof and the tank wall was frictionless in tangential direction and 'hard contact' type in radial direction. Ahmadi et al [17] modeled a cylindrical tank with floating roof with two different type of sealing system. The authors investigated the effect of friction and damping of the sealing system on the vertical seismic response of the floating roof.

Thus, the vertical response of the floating roof over time has been extensively studied, in some cases taking into account also the presence of the sealing system. On the contrary, the horizontal response of the floating roof has not been discussed yet.

Prediction of the horizontal dynamic response of the floating roof of a tank subject to seismic excitation at the base allows the assessment, the monitoring and the mitigation of the seismic risk. Indeed, some proposals for monitoring have already been made in [18], so models that describe the horizontal dynamics of the roof would be used to estimate some risk thresholds for the activation of early warning systems. In addition, some efforts have already been made in the field of passive seismic protection of industrial components [19], and in particular of the floating roof by Zahedin Labaf et al. in [20], in which a hybrid control system is proposed, where a base isolation system is equipped with a tuned mass damper inerter. This system was experimentally tested in [21].

In this study, the horizontal dynamics of the floating roof with sealing system and bumper bars is the subject of interest. In particular, in the field of impact dynamics, in [22] and [23] the use of collision buffers is proposed for the attenuation of structural pounding in case of earthquakes.

The first purpose is the realization of a simplified and reduced model in order to carry out effortless analyses, without having to rely on a comprehensive model of the type that already exists in the Literature. By the assumption of decoupling between the vertical and horizontal motion of the roof, the geometric and mechanical properties of the tank that characterize the horizontal dynamics are highlighted.

The second purpose concerns the influence of some parameters on the horizontal dynamic response of the roof. As a preliminary study, a parametric analysis is presented, considering the impact between the bumpers and the tank wall. In a first step, the impact is considered as rigid elastic. Then, the hypothesis of partially deformable bumper bars is introduced, which leads to soft elastic impact.

The paper is organized as follows. Section 2 describes the main characteristics of the elements that constitute the tanks with floating roof. Section 3 explains the assumptions underlying the parametric analyses and the simplified model. Section 4 presents a detailed description of the finite element model. Sections 5 and 6 contain the parametric analyses and the results obtained considering, respectively, the elastic hard impact and the elastic soft impact.

# 2 CYLINDRICAL LIQUID STORAGE TANKS WITH FLOATING ROOF

## 2.1. Floating roof

Tanks with floating roof are used for the storage of volatile products. The roof is located on the surface of the product and, by sliding vertically along the shell for product inlet / outlet, ensures that most of the vapor remains contained under the roof.

The roof is a circular steel structure with floating caissons that allow it to float above the product stored. Generally, the diameter of the floating roof is about 400 mm smaller than the inside diameter of the tank. The space between the outer edge of the roof and the inside of the tank shell is closed by a flexible sealing system, which also allows the position of the roof in the tank to be centralized. There are two main types of floating roof, single pontoon and double pontoon. The single pontoon roof owns its inherent buoyancy to an outer annular pontoon, while the central part is formed by a membrane of steel plates welded together and connected to the inner edge of the caissons. The double pontoon roof consists of an upper and lower steel membrane separated by a series of radially divided circumferential stiffeners.

Also, some elements are required for the functionality of the tank, such as flexible piping systems, edge vents, rain drainage system, roof supports, guide pipe, stilling pipe and floating roof sealing system.

## 2.2. Sealing systems

The rim seal must be sufficiently flexible for different reasons:

- to adapt to possible construction irregularities, given by the large size of the elements between which it is inserted;
- to limit the possibility of impact between steel parts;
- to recenter the roof during the operation phases.

In addition, it shall allow the roof to move vertically during the normal operation of the tank.

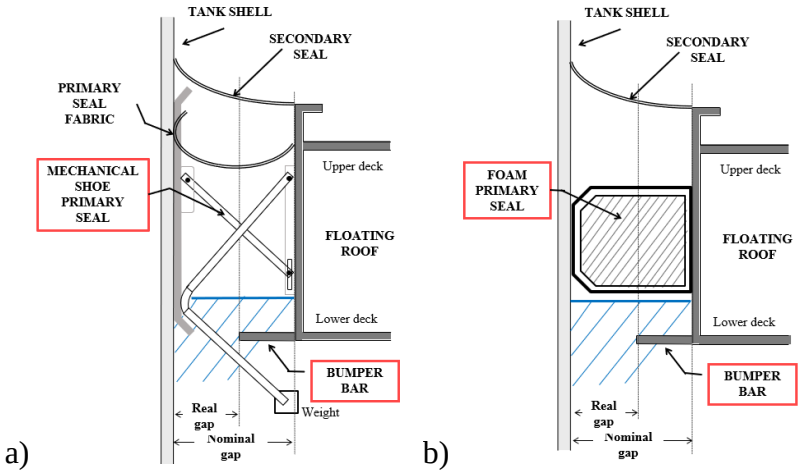


Figure 1: a) Mechanical sealing system, b) Fabric with foam sealing system.

The floating roofs are equipped with the primary and secondary seal: the secondary one is mounted above the primary seal with the aim of minimizing vapor and odor losses. In practical use, different types of sealing rim are currently employed. For primary seal, several solutions are available, including metal shoes (Fig. 1a), non-metallic tubular or fabric seals (Fig. 1b). The working range of sealing systems, as stated by the manufacturers, is usually 205±100 mm. The sealing systems are also installed with initial compression. The initial compression ensures

adherence to the tank wall to prevent the seal from being stretched. Horizontal displacements of the floating roof greater than 205+100 mm will result in excessive compression on one side of the seal and possible separation from the other side of the seal.

### 2.3. Limiting bumper bars

The seal allows variations of 100 mm in the rim space: excessive deformation of the seal is prevented by limiting bumper bars mounted on the lower edge of the outer rim of the roof. The bars are made of steel.

## 3 BASIC ASSUMPTIONS

The constituent elements of a tank with floating roof are as follows: the walls and bottom of the tank, the fluid, the floating roof, the sealing system, the bumper bars. A comprehensive model for assessing the seismic response of tank with floating roof should include all the elements listed above. In order to study the only horizontal dynamics of the floating roof, the vertical motion of the roof can be decoupled from the horizontal one. This hypothesis is based on the following assumptions:

- the hypothesis of small vertical displacements of the roof is true;
- there is no tangential action of the fluid transmitted to the floating roof.

By introducing the decoupling hypothesis, it's possible to move from the comprehensive model to a simplified model where only the horizontal dynamics is relevant.

Furthermore, since the stiffness in the roof plane is much greater than the radial stiffness of the sealing system, the roof can be considered as a rigid body. The simplified model is also reduced in the number of the degrees of freedom.

The proposed model is simplified and reduced. In particular, it considers only 1 degree of freedom of the floating roof- the horizontal displacement in the direction of application of the seismic action- and the degrees of freedom of the bumpers, related to their deformation at the impact.

The dynamic parameters that characterize the horizontal response of the roof are as follows:

- $m$, the mass of the roof,
- $k_S$ and $c_S$, stiffness and damping coefficient of the sealing system (or damping factor $\xi_S$),
- $k_B$ and $c_B$, stiffness and damping coefficient of the bumper bars,
- $G_0$ the initial gap.

Different scenarios are evaluated by varying $k_S$, keeping $m$ constant. The damping associated with the sealing system generally depends on the type of sealing system adopted. In this study, the damping of the sealing system is fixed.

The bumper bars are initially considered rigid. The bumpers, which certainly limit the horizontal displacements of the roof and prevent damage to the stop system, can also cause some issues. The punctual and repeated impact of the bars against the tank wall can generate high contact forces. In addition to producing sparks due to the contact between two metallic materials, the impact can also cause damage to the tank. Evaluation of the contact force is therefore useful for local checks of the tank section.

In the second part of the study, the possibility of using partially deformable bumper bars is investigated. By using deformable bumper bars, it is possible to limit the contact forces generated by the impact, both in forced vibrations and in free vibrations. A parametric analysis is performed by varying the stiffness of the bumper $k_B$, for each scenario of the first part.

The damping of the bumper $c_B$, also a fundamental parameter in the dynamics of the impact, is assumed to be zero in order to study the contribution of the stiffness of the bumper only. Thus, the impact is considered elastic.

In all analyses, the value of the initial real gap is fixed.

## 4 FINITE ELEMENT MODEL

Using the finite element software Abaqus/Explicit, a simplified and reduced model of the tank with floating roof shown in the Fig. 2 is developed. The material properties and dimensions of the tank are reported in Tab. 1. The case study is taken from the tank in [19].

The tank is treated as a rigid body (Discrete Rigid Surface); therefore, it has not been assigned any type of material. The roof is a double pontoon type, like that of Matsui in [12], and it is modeled as an equivalent shell, with distributed mass and stiffness. The sealing system is modelled as an annular shell part: the seal is tied to the outer rim of the roof and the to the inner wall tank. The sealing system is discretized using membrane elements with significantly lower in-plane stiffness than the radial stiffness of the roof. The roof can therefore be considered as a rigid body. Different stiffness values $k_S$ are assigned to the sealing system, in terms of the Young's modulus of the material $E_S$, in order to achieve periods of vibration in a range 3.0-0.5 s. The damping of the sealing system is fixed at 1% in terms of damping factor $\xi_S$.

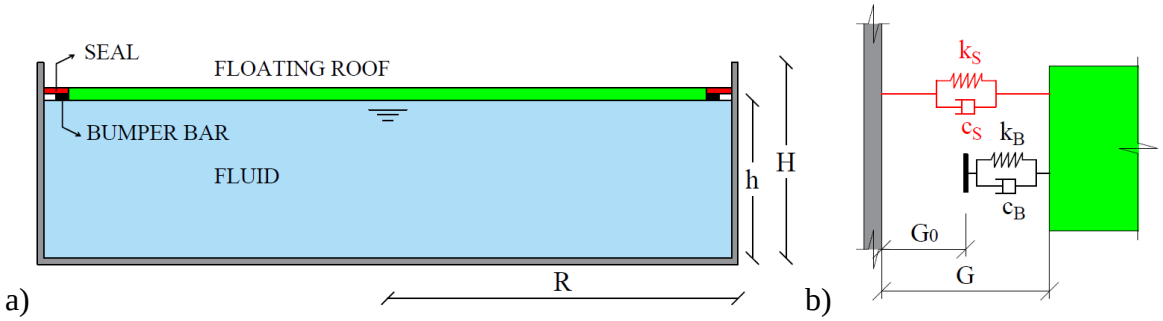


Figure 2: Tank with floating roof: a) a complete model, b) a detail of the simplified and reduced model

| | |
|---|---|
| Tank's radius $R$ [m] | 27.43 |
| Tank's height $H$ [m] | 15.60 |
| Fluid's height $h$ [m] | 13.60 |
| Density of the roof $\gamma$ [kg/m$^3$] | 380.00 |
| Thickness of the roof $t$ [m] | 0.25 |
| Young's modulus of the roof material $E_r$ [Pa] | $2.10\times10^{11}$ |
| Poisson's coefficient of the roof material $\nu$ [-] | 0.3 |
| Young's modulus of the seal material $E_S$ [Pa] | various |
| Damping factor of the seal $\xi_S$ [-] | 0.01 |
| Nominal gap $G$ [m] | 0.20 |
| Real gap $G_0$ [m] | various |
| Linear stiffness of the bumper $k_B$ [N/m] | various |
| Damping coefficient of the bumper $c_B$ [Ns/m] | 0.00 |

Table 1: Geometrical and mechanical properties of the case study.

The limiting bumper bars are continuously modeled by assigning a contact interaction between the outer edge of the roof and the inner wall of the tank. A thickness property is assigned to the contact, reducing the nominal gap. At first, the bumper bars realize a rigid stop by assigning a frictionless tangential behavior and a "hard contact" normal behavior. Later, the contact behavior in the normal direction is assigned as a bilinear pressure-overclosure relationship.

The value of the initial real gap is always fixed.

The fluid is not modeled, due to the decoupling hypothesis.

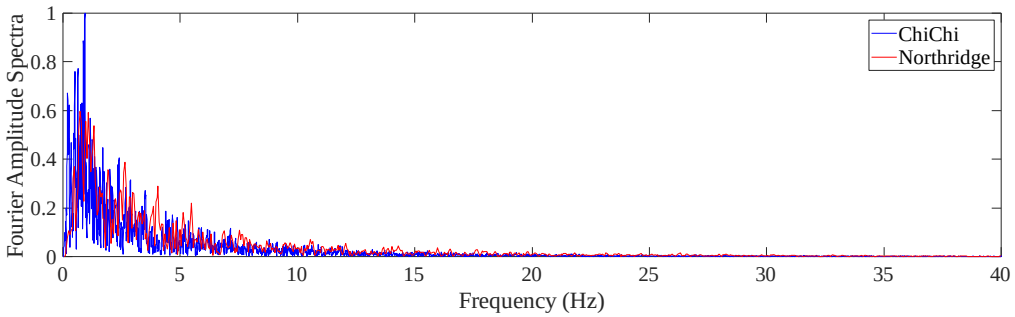


Figure 3: Fourier amplitude spectra of the Northridge and Chi-Chi earthquake.

Two recordings of natural seismic events (Fig. 3) are used to perform the analysis, the Northridge earthquake (1994) and the Chi-Chi earthquake (1999). The seismic excitation is applied in X direction.

## 5 ELASTIC HARD IMPACT ANALYSIS

### 5.1. Parametric analysis

A hard impact is a contact that occurs in an infinitely small time between non-deformable collision bodies. Any loss of energy during the impact is represented by a constant value of the coefficient of restitution $s$, defined as the ratio between the post- ($v_f$) and pre-impact speeds ($v_i$):

$$s = v_f / v_i \tag{1}$$

The coefficient of restitution assumes values between 0 (fully plastic contact) and 1 (fully elastic contact).

Without considering any source of energy loss (no damping) and assuming that the collision bodies are rigid, the impact is elastic hard.

The value of the initial gap is set at 100 mm.

Five Young's modulus values have been assigned to the sealing system material, which are reported in Tab. 2.

A representation of the constitutive relation of the reduced model is shown in Fig. 4.

A total of ten analyses are conducted.

| | | | | | |
|---|---|---|---|---|---|
| $E_S$ [Pa] | 1.00E+4 | 1.85E+4 | 4.00E+4 | 1.40E+5 | 5.00E+5 |
| $T_n$ [s] | 3.00 | 2.25 | 1.50 | 0.75 | 0.50 |

Table 2: Young's modulus values selected for the seal system for parametric analysis.

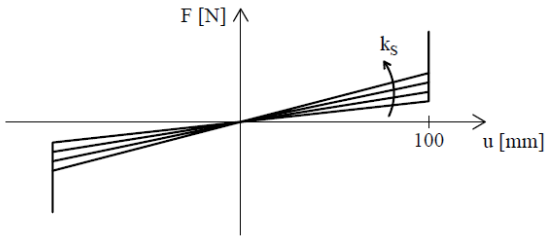


Figure 4: Bilinear force-displacement relationship of the sealing system with rigid bumper bars.

## 5.2. Results and discussion

The seismic response is reported in terms of horizontal displacements of the floating roof relative to the tank, and of the contact forces that occurs as a result of the impact.

The relative horizontal displacements of the roof $u_r(t)$ can be considered, on the other side, as the deformation of the sealing system $\varepsilon(t)$

$$\varepsilon(t) = \frac{[G - u_r(t)]}{G} \tag{2}$$

where which must not be less than 0.5.

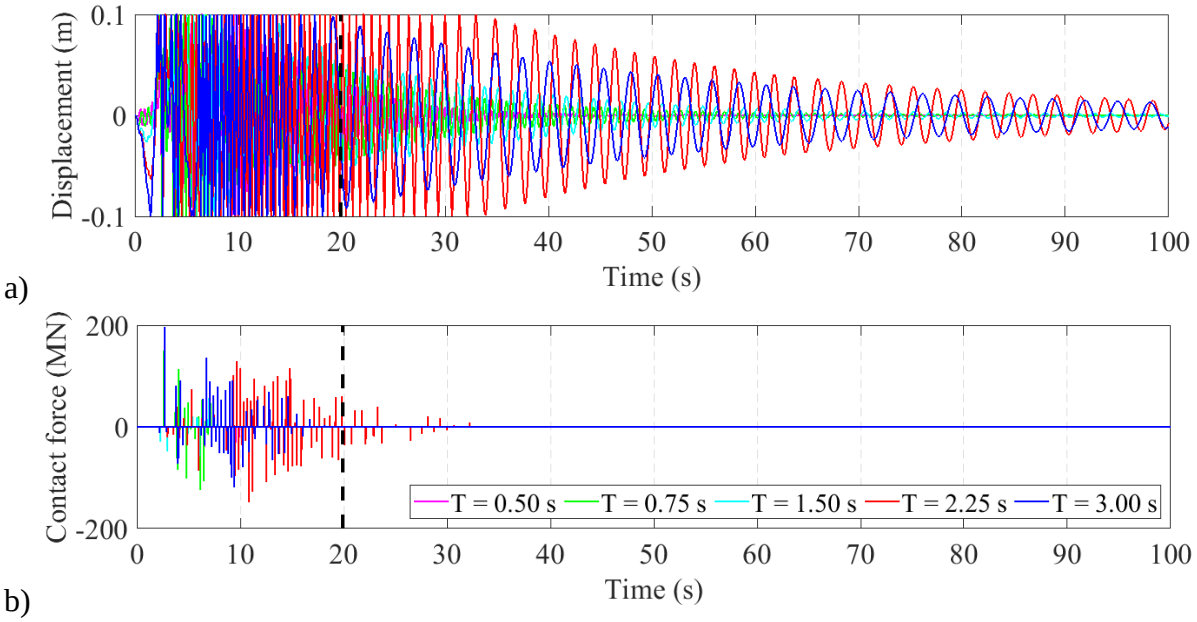


Figure 5: Seismic response for Northridge earthquake for different stiffness of the seal: a) relative displacement of the roof; b) total contact force.

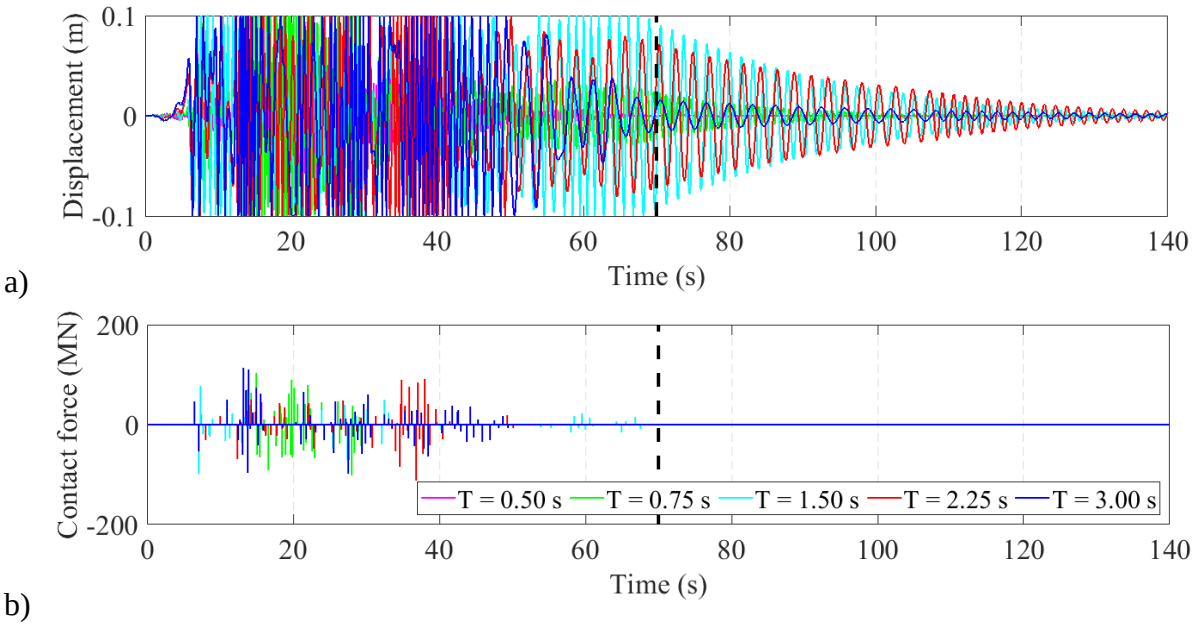


Figure 6: Seismic response for Chi-Chi earthquake for different stiffness of the seal: a) relative displacement of the roof; b) total contact force.

The total contact force it's the integral of the contact pressure on the contact area. The contact force is considered positive when the impact occurs in the +x direction and negative when the impact occurs in the -x direction.

The seismic response is obtained both during forced oscillations and during free oscillations. A black dotted vertical line separates the two phases.

The Northridge earthquake response (Fig. 5) shows that the greatest number of impacts occur during the forced oscillations phase, especially for cases where the sealing system is more deformable. In particular, for $T_n$ = 3.00 seconds, there are also impacts after the end of the earthquake. The number of impacts $n_I$ is variable with the stiffness of the sealing system, while the contact forces remain in the range of 149-197 MN values for all the stiffness values studied, except for the most rigid case, for which only 5 impacts with a contact force value of 53 NM are recorded.

In addition, the free oscillations of the cases where the sealing system is more deformable show a higher roof recentering time, which is more than 80 s for the cases where $T_n$ is equal to 3.00 s, 2.25 s and 1.50 s.

The Chi-Chi earthquake response (Fig. 6) shows that the impact occurs only in the forced oscillation phase. The number of impacts decreases significantly as the stiffness of the sealing system increases, up to the stiffest case with $T_n$ = 0.50 s, where the displacements are always less than the initial gap. Again, for cases where the sealing system is more deformable, there is a longer recentering time of the roof.

From the seismic response to both earthquakes, it is evident that varying the stiffness of the sealing system produces a variation in the number of impacts, the contact force, and the recentering time.

Further studies should be developed to investigate the effect of damping of the sealing system.

| EARTHQUAKE | $T_n$ [s] | $n_I$ [-] | $F_{C,\max}$ [MN] |
|---|---|---|---|
| Northridge | 3.00 | 46 | 197.2 |
| | 2.25 | 75 | 149.0 |
| | 1.50 | 10 | 151.3 |
| | 0.75 | 18.0 | 149.8 |
| | 0.50 | 5.0 | 53.4 |
| Chi-Chi | 3.00 | 73 | 114.3 |
| | 2.25 | 55 | 112.5 |
| | 1.50 | 48 | 97.8 |
| | 0.75 | 38 | 102.0 |
| | 0.50 | 0 | 0.0 |

Table 3: Number of impacts and maximum contact force as a function of the different stiffnesses of the sealing system for the two earthquakes.

## 6 ELASTIC SOFT IMPACT ANALYSIS

### 6.1. Parametric analysis

In soft impact the deformation of collision bodies is considered. The phenomenon of contact can be simulated by different laws of force overclosure. The simplest model is represented by the linear spring element, which assumes a linear relationship between the contact force and the overclosure, without taking into account the energy loss during the impact. In this case, the impact is elastic soft.

In the case of partially deformable bumper bars, where the deformable part will be made of non-metallic material, it must be considered that the working range of the sealing systems is 200±100 mm. Therefore, the deformation of the bumpers must be such as to ensure that the displacements of the roof are always within this range.

For this reason, the bumper bars are such that the initial gap $G_0$ is less than 100 mm, which is equal to 70 mm. The 30 mm difference from the real gap takes into account the partially deformation of the bumper bar. Considering a smaller initial gap will increase the number of impacts while reducing the contact force.

Defining

$$\lambda = \frac{k_B}{k_S} \tag{3}$$

the ratio between the stiffness of the seal and the stiffness of the bumpers, three different values for $\lambda$ are investigated, for each value of $k_S$, except for the highest value of $k_S$, because it's the case where the lower number of impacts are highlighted together with the lower value of maximum contact force. The values for $\lambda$ are shown in Tab. 4. A total of forty analyses are conducted, keeping $\xi_S$ = 0.01.

A representation of the constitutive relation of the reduced model is shown in Fig. 7.

| $T_n$ [s] | $k_S$ [N/m] | $k_B$ [N/m] | | | | |
|---|---|---|---|---|---|---|
| | | λ=10 | λ=100 | λ=300 | λ=600 | λ=1000 |
| 3.00 | 9.71e+5 | 9.71e+6 | 9.71e+7 | 2.91e+8 | 5.82e+8 | 9.71e+8 |
| 2.25 | 1.73e+6 | 1.73e+7 | 1.73e+8 | 5.18e+8 | 1.04e+9 | 1.73e+9 |
| 1.50 | 3.88e+6 | 3.88e+7 | 3.88e+8 | 1.16e+9 | 2.33e+9 | 3.88e+9 |
| 0.75 | 1.55e+7 | 1.55e+8 | 1.55e+9 | 4.66e+9 | 9.32e+9 | 1.55e+10 |

Table 4: $\lambda$ values selected for parametric analysis.

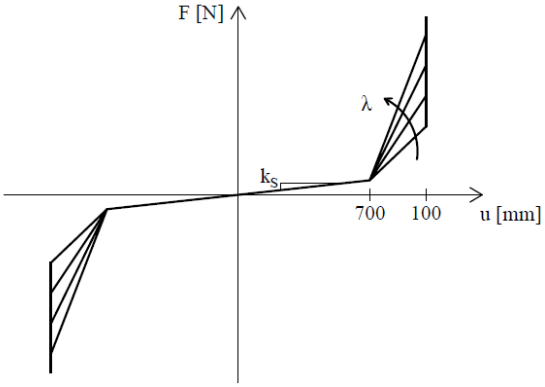


Figure 7: Trilinear force-displacement relationship of the sealing system with deformable bumper bars.

## 6.2. Results and discussion

Fig. 8 shows the maximum contact force $F_{C,\max}$ for the different values of $k_S$ investigated and for the different $\lambda$. These results are compared with the two limit cases of hard impact with $G_0$ = 100 mm (first group of bars on the left) and $G_0$ = 70 mm (last group of bars on the right). In fact, the case of $\lambda = 1000$ tends to the hard impact with $G_0 = 70$ mm. On the contrary, at $\lambda = 10$ the stop is sufficiently deformable that, at the limit, it is as if there were no deforming space for the bumper, as if it were a hard impact with $G_0 = 100$ mm.

The trend of the $F_{C,max}$ for the different $\lambda$ values shows that for $\lambda$ between 10 and 100, the minimum of $F_{C,max}$ are recorded for almost all $k_S$. In particular, for more deformable sealing systems, i.e. those associated with higher vibration periods ($T_n$ = 3.00 s, $T_n$ = 2.25 s), the minimum value of $F_{C,max}$ is recorded for values around $\lambda = 100$. On the other hand, for more rigid systems, the minimum contact force can also be obtained for $\lambda = 10$.

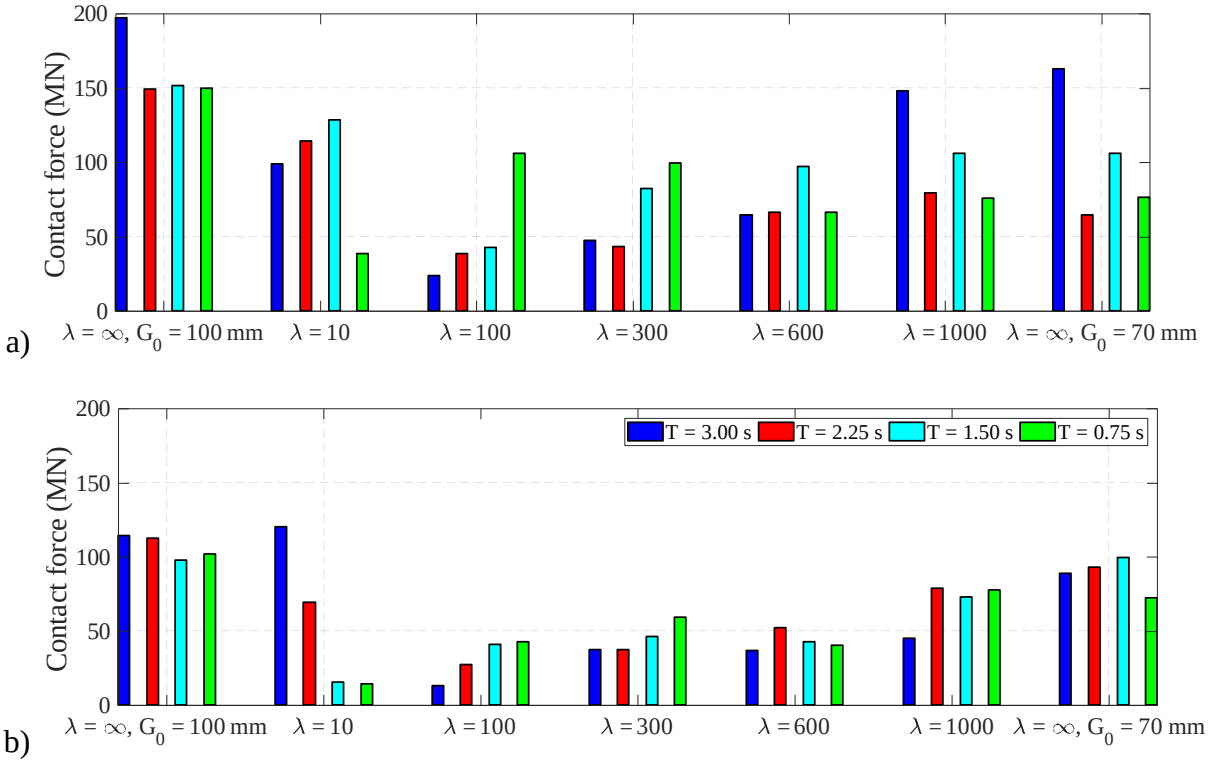


Figure 8: Bar graph of maximum contact force as a function of the different stiffnesses of the sealing system and λ values for the two earthquakes, a) Northridge, b) Chi-Chi.

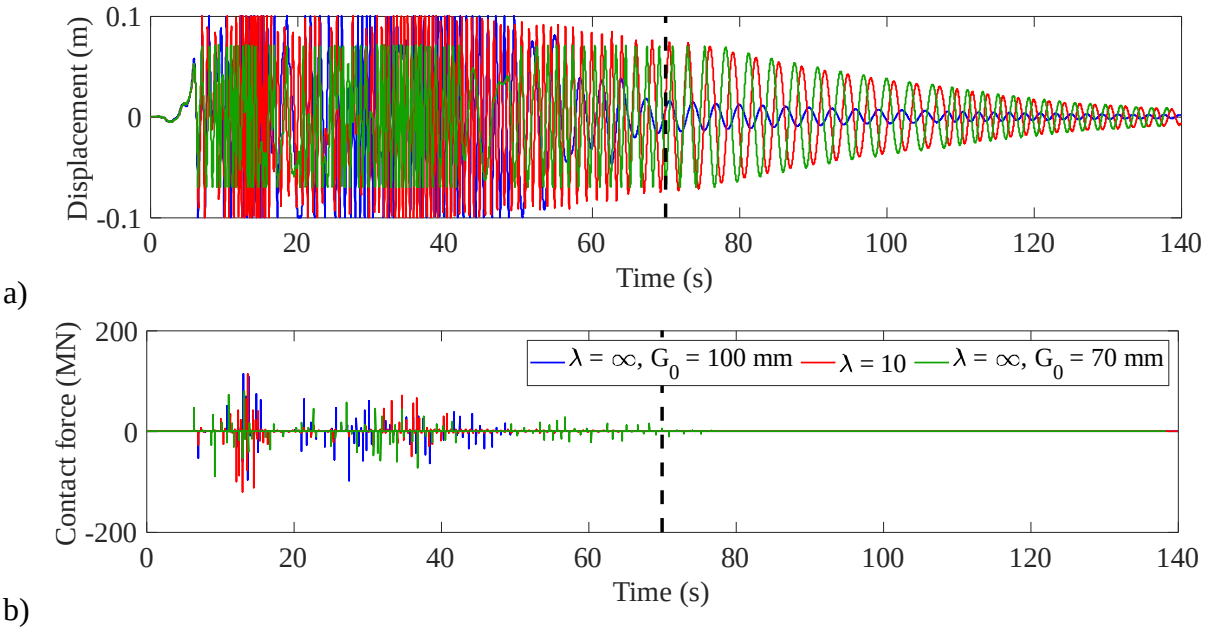


Figure 9: Seismic response for Chi-Chi earthquake for $T_n$ = 3.00 s varying the type of impact, a) relative displacement of the roof; b) total contact force.

There are cases where, for some values of $\lambda$ and $k_S$, higher contact forces than the hard impact are obtained. These are the cases where the deformation space of the bumper is completely saturated. An example is shown in Fig. 9, where the time histories of the relative displacements of the roof and contact force are shown for the cases of soft impact with $\lambda = 10$ and $T_n$ = 3.00 s, hard impact with $G_0 = 100$ mm, and hard impact with $G_0 = 70$ mm for the Chi-Chi earthquake.

Implicitly there is also a comparison between hard impact obtained with different gaps. In all cases, reducing the gap leads to a decrease in the $F_{C,\max}$, while increases the number of impacts $n_I$. Therefore, in order to reduce the maximum contact forces, it may not be sufficient to vary the gap only, since the values of $F_{C,\max}$ in the two limit cases are comparable. In general, the maximum contact forces are recorded for the case of 100 mm gap and rigid stop.

| EARTHQUAKE | | Chi-Chi | | | | Northridge | | | |
|---|---|---|---|---|---|---|---|---|---|
| | $T_n$ [s] | 3.00 | 2.25 | 1.50 | 0.75 | 3.00 | 2.25 | 1.50 | 0.75 |
| $\lambda$ =10 | $n_I$ | 161 | 113 | 105 | 60 | 101 | 64 | 116 | 51 |
| | $F_{C,max}$ [MN] | 120.2 | 69.5 | 15.1 | 14.1 | 98.8 | 114.2 | 128.7 | 38.2 |
| $\lambda$=100 | $n_I$ | 153 | 160 | 125 | 71 | 48 | 40 | 95 | 54 |
| | $F_{C,max}$ [MN] | 12.9 | 27.1 | 40.6 | 42.8 | 23.4 | 38.2 | 42.5 | 106.0 |
| $\lambda$ =300 | $n_I$ | 213 | 182 | 147 | 77 | 139 | 90 | 80 | 75 |
| | $F_{C,max}$ [MN] | 30.5 | 37.5 | 46.4 | 59.1 | 47.3 | 43.1 | 82.4 | 99.5 |
| $\lambda$ =600 | $n_I$ | 201 | 164 | 97 | 73 | 199 | 65 | 71 | 48 |
| | $F_{C,max}$ [MN] | 36.7 | 52.3 | 42.4 | 40.3 | 64.3 | 66.6 | 97.1 | 66.2 |
| $\lambda$ =1000 | $n_I$ | 134 | 200 | 163 | 37 | 48 | 29 | 47 | 28 |
| | $F_{C,max}$ [MN] | 45.2 | 78.8 | 72.9 | 77.7 | 147.9 | 79.2 | 105.9 | 75.7 |
| $\lambda$ =$\infty$ | $n_I$ | 89 | 82 | 89 | 37 | 62 | 24 | 54 | 25 |
| | $F_{C,max}$ [MN] | 88.7 | 92.7 | 99.57 | 72.3 | 162.8 | 64.3 | 106.0 | 76.1 |

Table 5: Number of impacts and maximum contact force as a function of the different stiffnesses of the sealing system and $\lambda$ values for the two earthquakes.

However, it is shown that the use of deformable elements, i.e. acting on the stiffness of the bumpers, not only avoids the impact between two metal parts, but also reduces the maximum contact force by an order of magnitude.

## 7 CONCLUSIONS

In this paper, a preliminary study of the horizontal dynamics of the floating roof of tanks subjected to seismic action at the base is shown.

The tank parameters that affect the horizontal dynamics of the floating roof are the roof mass, the stiffness and damping of the sealing system, the stiffness and damping of the bumper bars, and the initial gap. A simplified and reduced finite element model was developed, based on the hypothesis of decoupling between horizontal and vertical motion of the roof.

Parametric analyses were performed for two earthquakes by varying the stiffness of the sealing system, the stiffness of the bumpers, and the initial gap, keeping the damping constant.

First, the impact was made elastic hard. With fixed damping and the real initial gap, the seismic responses showed that the more deformable the sealing system, the greater the contact forces and the recentering time of the floating roof. Therefore, acting on the stiffness of the sealing system only, can prevent the impact and limit the magnitude of the contact forces.

Next, the bumper bars were considered partially deformable to obtain an elastic soft impact. The parametric analyses were conducted by varying $\lambda$, the ratio between the stiffness of the bumper and that of the sealing system, for the different stiffness values of the sealing system,

keeping the damping of the sealing system fixed and that of the bumper zero. Here, the initial gap was assumed to be smaller than the real gap. In most cases, lambda λ between 10 and 100 provided a reduction of the maximum contact force. There are also cases where the deformation space of the bumper is completely saturated, even for the same λ values.
The maximum contact force is also reduced while the number of impacts is increased by reducing the initial gap in elastic hard impacts.
The variability of these results demonstrates the need for extensive investigations on many more earthquakes. It would also be desirable to further investigate the role of damping, both of the sealing system and of the bumper bars. In particular, damping can be a key aspect in the prevention and mitigation of major accidents, as well as during operation. Optimal design of the parameters characterizing the horizontal dynamics of the roof may result in a reduction of the maximum contact force, the number of impacts, and the recentering time of the floating roof.

## ACKNOWLEDGEMENT

INAIL (Italian National Institute for Insurance against Accidents at Work) is funding PhD scholarship for author Michela Salimbeni.

## REFERENCES

[1] A.S. Kiremidjian, K. Ortiz, R. Nielsen, and B. Safavi, Seismic risk to major industrial facilities. Report - Stanford University, John A. Blume Earthquake Engineering Center, **72**, 1985.

[2] E. Krausmann, V. Cozzani, E. Salzano, and E. Renni, Industrial accidents triggered by natural hazards: An emerging risk issue. *Natural Hazards and Earth System Science*, **11**, 921–929, 2011.

[3] S. Young, L. Balluz, and J. Malilay, Natural and technologic hazardous material releases during and after natural disasters: A review. *Science of the Total Environment*, **322**, 3–20, 2004.

[4] F. Paolacci, R. Giannini, M. de Angelis, and M. Ciucci. Seismic vulnerability of major-hazard industrial plants and applicability of innovative seismic protection systems for its reduction. *11th World Conference on Seismic Isolation, Energy Dissipation and Active Vibration Control of Structures*, Guangzhou, China, Nov. 17-21, 2009.

[5] P. Moshashaei, S.S. Alizadeh, L. Khazini, and M. Asghari-Jafarabadi, Investigate the Causes of Fires and Explosions at External Floating Roof Tanks: A Comprehensive Literature Review. *Journal of Failure Analysis and Prevention*, **17**, 1044–1052, 2017.

[6] B.L.S. Jacobsen, Impulsive hydrodynamics of fluid inside a cylindrical tank and of fluid surrounding a cylindrical pier. *Bulletin of the Seismological Society of America*, **39**, 189–204, 1949.

[7] K. Senda, On the Vibration of an Elevated Water-Tank I. *Technical Reports of Osaka University*, **117**, 247–264, 1954.

[8] K. Nakagawa, On the vibration of an elevated water tank II. *Technical Reports of Osaka University*, **5**, 1955.

[9] F. Sakai, M. Nishimura, and H. Ogawa, Sloshing behavior of floating-roof oil storage tanks. *Computers & Structures*, **19**, 183–192, 1984.

[10] Y. Yamauchi, A. Kamei, S. Zama, and Y. Uchida, Seismic design of floating roof of oil storage tanks under liquid sloshing. *Proceedings of ASME 2006 Pressure Vessels and Piping Division Conference*, 2006.

[11] M.A. Goudarzi, Seismic behavior of a single deck floating roof due to second sloshing mode. *Journal of Pressure Vessel Technology, Transactions of the ASME*, **135**, 1–6, 2013.

[12] T. Matsui, Sloshing in a cylindrical liquid storage tank with a floating roof under seismic excitation. *Journal of Pressure Vessel Technology, Transactions of the ASME*, **129**, 557–566, 2007.

[13] T. Matsui, Sloshing in a cylindrical liquid storage tank with a single-deck type floating roof under seismic excitation. *Journal of Pressure Vessel Technology, Transactions of the ASME*, **131**, 2009.

[14] R. Shabani and F.G. Golzar, Large deflection analysis of floating roofs subjected to earthquake ground motions. *Nonlinear Analysis: Real World Applications*, **13**, 2034–2048, 2012.

[15] M. Hosseini, A. Soroor, A. Sardar, and F. Jafarieh, A simplified method for seismic analysis of tanks with floating roof by using finite element method: Case study of Kharg (Southern Iran) island tanks. *Procedia Engineering*, **14**, 2884–2890, 2011.

[16] S. Caprinozzi, F. Paolacci, and M. Dolšek, Seismic risk assessment of liquid overtopping in a steel storage tank equipped with a single deck floating roof. *Journal of Loss Prevention in the Process Industries*, **67**, 2020.

[17] H. Ahmadi and M.H. Kadivar, Vibration Analysis of Double Deck Floating Roof of Storage Tank in Cases of Tube, Ordinary and Thickened Foam Seals. *International Journal of Engineering, Transactions A: Basics*, **35**, 1398–1415, 2022.

[18] A. Marino, M. Ciucci, and F. Paolacci, Smart technologies for integrated natural risk management: Innovative methodologies and remote sensing. *Proceedings of ASME 2017 Pressure Vessels and Piping Division Conference*, 2017.

[19] F. Paolacci, R. Giannini, M. De Angelis, and M. Ciucci, Experimental investigation on the seismic behaviour of base-isolated steel storage tank. *11th World Conference on Seismic Isolation, Energy Dissipation and Active Vibration Control of Structures*, Guangzhou, China, Nov. 17-21, 2009.

[20] D. Zahedin Labaf, M. De Angelis, and M. Basili. Multi-objective optimal design and seismic assessment of an inerter-based hybrid control system for storage tanks. *Bulletin of Earthquake Engineering*, **21**, 1481–1507, 2023.

[21] D. Pietrosanti, M. De Angelis, and A. Giaralis. Experimental seismic performance assessment and numerical modelling of nonlinear inerter vibration absorber (IVA)-equipped base isolated structures tested on shaking table. *Earthquake Engineering & Structural Dynamics*, **50**, 2732–2753, 2021.

[22] U. Andreaus, P. Baragatti, M. De Angelis, and S. Perno,. Shaking table tests and numerical investigation of two-sided damping constraint for end-stop impact protection. *Nonlinear Dynamics*, **90**, 2387–2421, 2017.

[23] U. Andreaus, P. Baragatti, M. De Angelis, and S. Perno. A Preliminary Experimental Study about Two-Sided Impacting SDOF Oscillator under Harmonic Excitation. *Journal of Computational and Nonlinear Dynamics*, **12**, 2017.

COMPDYN 2023
9th ECCOMAS Thematic Conference on
Computational Methods in Structural Dynamics and Earthquake Engineering
M. Papadrakakis, M. Fragiadakis (eds.)
Athens, Greece, 12-14 June 2023

# ANALYTICAL ASSESSMENT OF SEISMIC DAMAGE AND USABILITY OF RC RESIDENTIAL BUILDINGS BY PERIOD ELONGATION

**Mariano Di Domenico**[1], **Paolo Ricci**[1], **and Gerardo M. Verderame**[1]

[1] Department of Structures for Engineering and Architecture, University of Naples Federico II
Via Claudio 21, 80125, Naples, Italy
e-mail: {mariano.didomenico,paolo.ricci,verderam}@unina.it

## Abstract

*During an earthquake, the progressive damage of structural and nonstructural components of a structure yields to the degradation of their stiffness, thus resulting in a progressive increase of the vibration period of the structure as a whole.*
*Also, the damage amount on structural and nonstructural elements, also known as Damage State (DS), can be determined by visual inspection or predicted, for a given earthquake scenario, by means of numerical analyses by relating the exceedance of a certain Engineering Demand Parameter (EDP) threshold to the attainment of a certain DS. Also, upon an earthquake, the observation of a certain DS in a building is the basis for the decision regarding its usability.*
*In this work, numerical incremental time-history analyses are performed on case-study reinforced concrete residential buildings. The analyses results are used to establish the expected DS attained by structural and nonstructural components and, so, by the considered building: this is also related to a certain usability judgment, as already mentioned. In tune, the analyses results are also used to evaluate the period elongation of the building at increasing intensity of the seismic demand.*
*The objective of the study is establishing a preliminary relationship between a) the DS attained by a certain building due to the occurrence of an earthquake with a certain intensity, and, so, the consequent usability judgment, with b) its period elongation. This is done in order to establish whether the vibration period elongation – which can be practically evaluated by means of ambient vibration tests – can be used for the assessment of structural usability after an earthquake as a tool for decision supporting in the aftermaths of a destructive event.*

**Keywords:** Reinforced concrete, structure, vibration period, damage state, usability.

## 1 INTRODUCTION

The vibration period of a building basically depends on its mass and on its lateral stiffness. The lateral stiffness of a building depends on the structural scheme and on the stiffness of the single members that, in turn, depend on the geometry of the member and on the elastic properties of the materials. This is true when a building is in its initial elastic condition. However, during the seismic event, damage spreads on building members, thus inducing a degradation of their stiffness. For example, in a reinforced concrete (RC) building, the seismic input may yield to cracking of members. As it is well known, a cracked RC members will undergo potential reloading with reduced stiffness with respect to an uncracked/undamaged one; hence, a cracked RC structure has a lower lateral stiffness and, so, a higher vibration period. In general, the heavier the seismic damage, the higher the increase of the period with respect to the initial/elastic/undamaged one: this phenomenon is referred to as "period elongation". The vibration period of the damaged building is also named "inelastic period", $T_{in}$, to highlight its difference from the "elastic period", $T_{el}$, of the structure at its initial, elastic, undamaged state.

Based on the above discussion, it can be simply concluded that, in general, the measure of the period elongation can be assumed as a measure of the damage state of the building: the more the elongation, i.e., the higher the $T_{in}/T_{el}$ ratio, the higher the damage state attained by the building. Despite many studies have been carried out on this topic ([1-12] among others), an explicit relation between the Damage State (DS) of 3D RC buildings modelled and analyzed as nonlinear multi-degree-of-freedom system and in presence of infill walls and their period elongation has never been derived. Note that this kind of relations may be also useful to assess, by means of ambient vibration tests, the usability of buildings for which the usability judgment after earthquake may be uncertain only based on visual inspection.

In this work, numerical incremental time-history analyses are performed on infilled case-study reinforced concrete residential buildings. The analyses results are used to establish the expected DS attained by structural and nonstructural components and, so, by the considered building, due to the occurrence of an earthquake characterized by a certain intensity measure: this is also related to a certain usability judgment, as already mentioned. In tune, the analyses results are also used to evaluate the period elongation of the building at increasing intensity of the seismic demand. This is done with the aim of establishing a preliminary relationship between a) the DS attained by a certain building due to the occurrence of an earthquake with a certain intensity, and, so, the consequent usability judgment, with b) its period elongation.

## 2 CASE-STUDY BUILDINGS

Two example buildings are considered for this study: a code-conforming new RC moment-resisting frame (labeled as "NEW" in the following) and an existing RC moment-resisting frame (labeled as "EX" in the following) designed only to gravity loads. The two buildings share the same site, Avellino, in southern Italy, and overall geometric features. More specifically, they have the same number of storeys, equal to four, the same interstorey height, equal to 3.50 m for the first storey and 3 m for the other storeys, the same number and dimensions of bays in both the planar directions (X and Y). Both buildings are regular in plan and in elevation according to the current Italian building code NTC2018 [13].

The NEW building is framed in both X and Y directions and is designed according to the current Italian building code NTC2018 [13] for the design seismic demand at Life Safety limit state (LS) for the site of Avellino, on a type B horizontal soil according to NTC2018 classification (PGA=0.23 g). It has been designed by adopting class C28/35 concrete ($f_{cm}$ = 36 N/mm$^2$) and grade B450C deformed steel reinforcement ($f_{ym}$ = 517.5 N/mm$^2$). The EX building is framed only in Y direction and is designed to gravity loads according to the old non-

seismic Italian building code Regio Decreto 1939 [14]. It is assumed as realized by adopting concrete with $f_{cm}$ = 16 N/mm$^2$ and grade AQ50 plain steel reinforcement ($f_{ym}$ = 370 N/mm$^2$). Schematic pictures of the case-study structures are shown in Fig. 1.

Note that both buildings have been analyzed as uniformly-infilled (IF) frames. More specifically, NEW-IF building is provided, as typical of current construction practice of 30 cm-thick one-layer infill walls made with clay hollow bricks with vertical holes and good mechanical properties. On the other hand, EX-IF building is provided, as typical of old construction practice [15] of 12+8 cm-thin two-layer infill walls made with clay hollow brick with horizontal holes and poor mechanical properties.

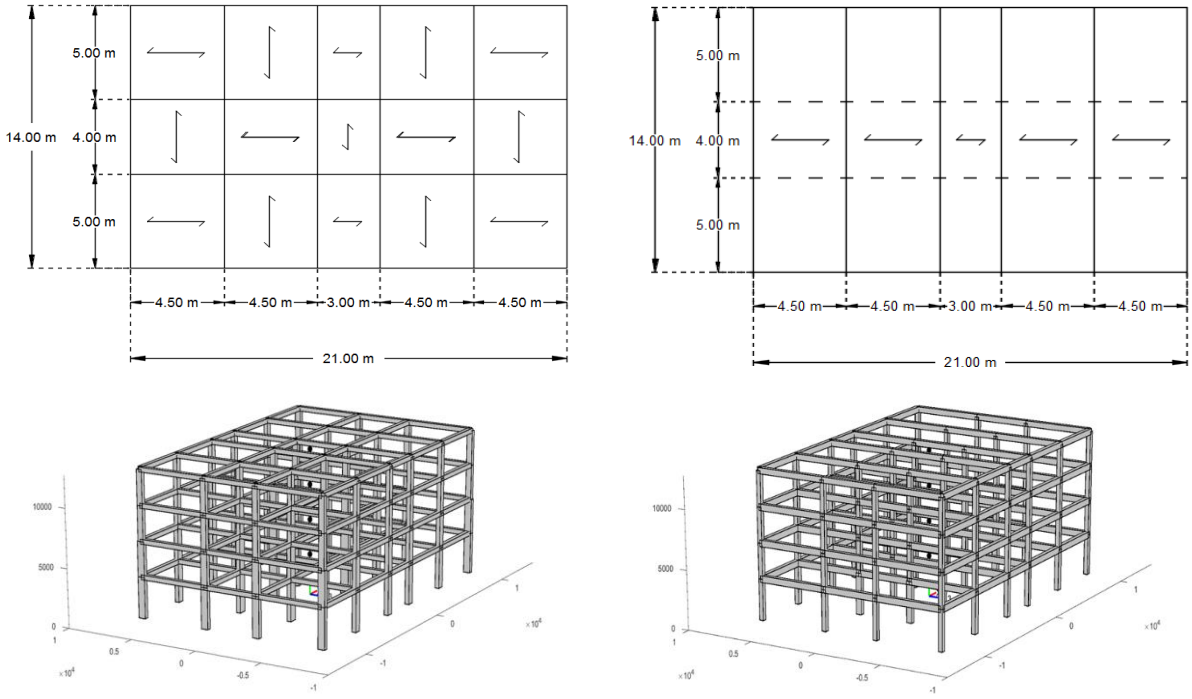


NEW case-study building EX case-study building

Figure 1: Geometry of the case-study buildings. For the sake of clarity, infill walls are not represented.

## 3 MODELING AND ANALYSIS PROCEDURE

The The potential non-linear response of both buildings is modelled in OpenSees software [16] by adopting a lumped-plasticity approach.

All structural members are classified as ductile as their plastic shear is lower than the minimum shear resistance according to NTC2018. So, they are modelled by assigning at both their ends plastic hinges with pre-determined moment-chord rotation response at fixed axial load (the one produced by gravity loads) and shear span length (assumed equal to one-half the member length). The assumed moment-chord rotation responses are multilinear and defined by the following characteristic points: first cracking, yielding, peak, conventional ultimate at 20% strength degradation with respect to peak load, collapse at zero moment resistance. Chord rotation values corresponding to these points are calculated according to [17] for the members with deformed bars of NEW building, according to [18] for the members with plain bars of EX buildings. Both studies also provide hysteretic rules to account for cyclic degradation phenomena.

Infill walls are modelled by adopting the equivalent strut approach with two equivalent no-tension struts whose axial load – deformation response is determined according to [19]. The

material model adopted for numerical model is Concrete01 Uniaxial Material model in OpenSees. As shown in [20], the basic hysteretic rules included in this material model allow a quite satisfying reproduction of the cyclic degradation of reloading stiffness in infill walls under in-plane action, based on experimental data.

Beam-column joints nonlinear response, the out-of-plane response of infill walls and the potential frame-infill local shear interaction were not modelled.

Modal and pushover analyses were performed on the case-study buildings. Modal analyses allowed the assessment of the first vibration mode shape, participation factor, and period; pushover analyses under a first-mode force distribution and with bilinearization of the equivalent single-degree-of-freedom system according to NTC2018 allowed the assessment of the first effective period of the building. The pushover curves in the direction of the first vibration mode are shown in Fig. 2, together with the lines representative of the effective stiffness of the buildings. The elastic and effective first vibration period of the buildings are 0.37 s and 0.48 s for NEW-IF building, respectively, and 0.37 s and 0.54 s for EX-IF building, respectively.

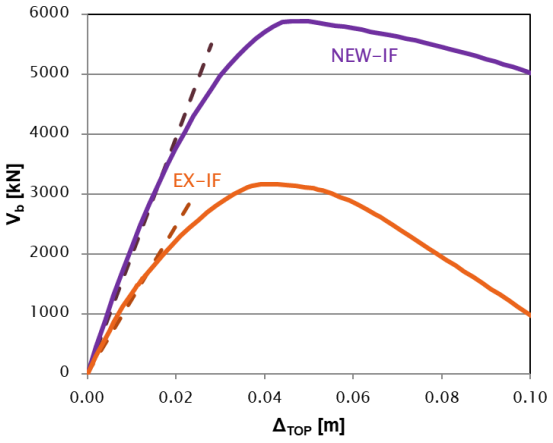


Figure 2: Pushover curves of the case-study buildings..

To perform Incremental Dynamic Analyses (IDAs) [21], seven bidirectional records were selected according to the indications provided by NTC2018 and by using the software Rexel [22]. The target spectrum adopted was the design spectrum at LS for Avellino city, horizontal soil type B. The spectra of the selected records are shown in Fig. 3a. A unique selection was performed for the two case-study buildings. However, the selected seven records were subjected to (limited) scaling for each case-study building, in order to have that for each selected and scaled record, Sa(Teff) was equal to Sa(Teff) of the target spectrum at LS, as shown for example purposes in Fig. 3b.

Once a set of seven records with the same Sa(Teff) at LS, i.e., at return period equal to 475 years, was determined for each case-study building, each set of records was furtherly scaled in order to perform IDAs. More specifically, given a certain case-study building, 15 different scale factors were applied in order to have Sa(Teff) equal to the Sa(Teff) value associated with the design response spectra defined by the code for return period equal to 30 (scale factor equal to 0.22), 50, 72, 101, 140 201, 475 (scale factor equal to 1), 975, and 2475 (scale factor equal to 1.73) years, plus 6 other scale factors (2, 2.25, …, up to 3) determined to investigate the incremental response of the buildings at very high seismic intensity measure (IM).

In other words, for each case-study building, the seismic performance is determined for 15 levels of the seismic intensity measure. For each level of seismic intensity measure, a total of

49 time-history analyses is performed: in fact, each of the seven scaled record is combined with the other six scaled record and with itself to generate a fictitious first-second event sequence with second event characterized by the same seismic intensity of the first event. For time history analyses, the accelerogram of the first event of the sequence is followed by ten seconds of null acceleration input (cf. [5]) and then by the accelerogram of the second event, as shown in Fig. 4. This has been done for reasons that will be cleared in the next section.

## 4 METHODOLOGY FOR THE ASSESSMENT OF DS, USABILITY, AND PERIOD ELONGATION

First, for the definition of DSs an approach based on the European Macroseismic Scale EMS98 [23] is adopted. Four DSs are defined: DS1 corresponding to light damage, DS2 corresponding to moderate damage, DS3 corresponding to severe damage, DS4 corresponding to collapse. The DS attained at increasing seismic demand by the case-study buildings has been determined at the end of each time-history analysis by comparing the maximum Interstorey Drift Ratio (IDR) demand with drift limits defined for both structural (STR) and nonstructural (NSTR) elements.

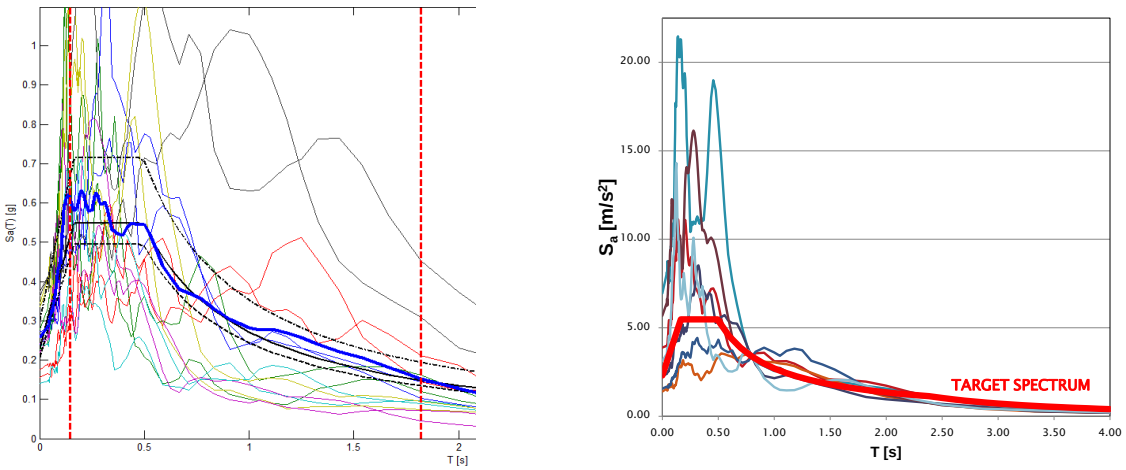


(a) (b)

Figure 3: Response spectra of the selected records (a) and preliminary scaling (b).

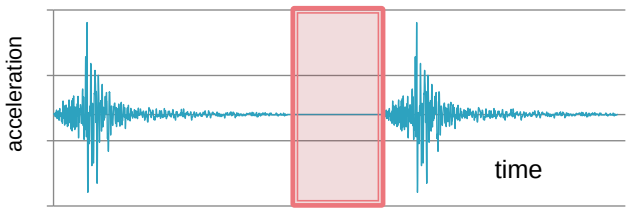


Figure 4: Example input for time-history analyses at given IM level. The red box highlights the presence of zero acceleration input between the first and the second event.

For STR, DS1 is attained at first cracking, i.e., when IDR demand makes at least one column attain a chord rotation demand equal to the chord rotation at cracking; DS2 is attained when at least one column yields; DS3 is attained when at least one column attains the peak moment point; DS4 is attained when at least one column attains the chord rotation at collapse (i.e., at zero moment capacity). This approach is based on [24].

Regarding NSTR, two sets of threshold IDR values are adopted. For NEW-IF building, the thresholds suggested in [25] for thick and strong infill walls are adopted: IDR=0.30% at the attainment of DS1; IDR=0.50% at the attainment of DS2; IDR=1.75% at the attainment of DS3. For EX-IF building, the thresholds suggested by [26] for thin and weak infill walls are adopted: IDR=0.05% at the attainment of DS1; IDR=0.30% at the attainment of DS2; IDR=0.73% at the attainment of DS3. DS4 is not defined for infill walls according to EMS98, which assumes that a building can attain DS4 (collapse) only due to structural damage.

So, for each time-history analysis, at the end of the first event, the attained STR and NSTR DSs are determined; for each level of the intensity measure, the median DSs are calculated based on the results of all the time-history analyses performed. In this way, an incremental curve showing the increase of the median DSs attained at increasing seismic intensity is obtained for both STR and NSTR. The final DS for the building is assigned considering both STR and NSTR, whichever occurs first.

After the first event, the free vibration of the building during the ten seconds of null acceleration input is investigated. More specifically, the acceleration response of the roof during this part of the record is considered and Fast Fourier Transform (FFT) is applied in order to evaluate the inelastic period of the structure after the first event. This allows the assessment, in median terms of each IM level, of the period elongation due to the damage achieved by the structure during the first event. This is done in terms of $T_{in}/T_{el}$ ratio.

For the assessment of usability, two important statements must be considered. First, according to AeDES forms by Italian Department of Civil Protection [27], a building is usable after an earthquake (judgment "A") if it has attained, at maximum, DS1; it is temporarily unusable, i.e., usable only provided that fast and non-invasive interventions are enforced (judgment "B") if it has attained, at maximum, DS2; it is unusable if it has attained DS3 (judgment "E"). However, in addition, the AeDES handbook by the Italian Department of Civil Protection [27] states that, after an earthquake, a building can be deemed usable only if, after a potential second event with lower or equal intensity with respect to the first one, there is no significant increment of the DS.

Given both statements, to assess usability based on time-history analyses, both the response of each building during the first and the second event of the sequence are considered. The DS attained during the first event has already been considered. In addition, the response of the building is considered during the second event: this is done to potentially update the assessment of the attained STR and NSTR DSs during a second event with IM equal to that of the first event according to AeDES handbook.

In summary, if DS1 (or lower) is attained during the first or the second event of each sequence, judgment A (usability) is assigned to that time-history analysis; if DS2 is attained during the first or the second event of each sequence, judgment B (temporary unusability) is assigned to that time-history analysis; if DS3 is attained during the first or the second event of each sequence, judgment E (unusability) is assigned to that time-history analysis. The usability judgment associated with each IM level is assessed as the median usability judgment registered among the 49 time-history analyses performed for each IM level.

In this way, for each case-study building and for each IM level, three important results are obtained: the maximum DS induced by a single event; the period elongation after the first event; the usability judgment at the end of the first event also considering the effects of a potential second event with equal IM. In other words, the period elongation at given IM level is associated with the expected maximum DS and with the usability judgment of the building.

## 5 RESULTS AND DISCUSSION

The results in terms of median maximum DS and period elongation evolution at increasing IM, with special reference to the IM levels set by NTC2018 for the "seismic" serviceability and ultimate limit states, are shown in Fig. 5. At IM corresponding to Immediate Occupancy limit state (IO), both buildings have attained DS1 and are judged usable. This is interesting, since EX-IF building is not designed to lateral actions, while NEW-IF building is explicitly designed to withstand Damage Limitation limit state (DL), while safety against IO is only implicitly assumed if DL is considered during design. Period elongation is already significant, roughly equal to 50% for NEW-IF and to 100% for EX-IF, due to members' and infills' cracking.

At IM corresponding to DL, both buildings are still usable, but EX-IF building is approaching DS2, corresponding to temporary unusability. Period elongation is stable with respect to the IM corresponding to IO.

At IM corresponding to LS, NEW-IF building attains DS2 due to both STR and NSTR and is temporarily unusable, with period elongation roughly equal to 100%; EX-IF building attains DS3 and should be deemed unusable, with period elongation roughly equal to 150%. It should be noted, however, that EX-IF building already attained that period elongation and DS3/unusability for IM equal to 0.67 times the IM corresponding to LS due to NSTR.

NEW-IF building attains DS3/unusability for IM equal to 1.50 times the IM at LS, which is higher than the IM corresponding to Collapse Prevention limit state (CP), due to NSTR, with period elongation roughly equal to 100%; DS4 is attained only for IM equal to 3 times the IM at LS. EX-IF building attains DS4 at IM corresponding to CP, with period elongation roughly equal to 250%.

In summary, based on the above results, a code-compliant infilled building attains temporarily unusability judgement (judgment "B") for IM corresponding to LS with period elongation roughly equal to 100% (i.e., with period doubled with respect to the initial elastic one), while it attains unusability judgment (judgment "E") for IM corresponding to 1.50 times the IM at LS with period elongation roughly equal to 100%. An existing infilled building designed only to gravity loads attains temporarily unusability judgment for IM equal to 0.67 times the IM at LS with period elongation roughly equal to 100%, while it attains unusability judgement for the IM corresponding to LS with period elongation roughly equal to 150%.

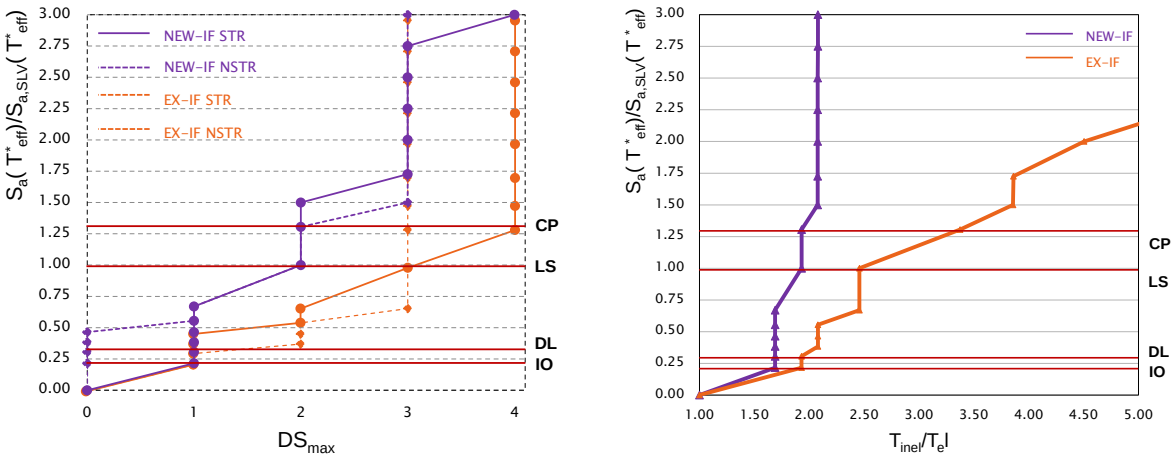


Figure 5: Median maximum DS (a) and median period elongation (b) at increasing IM for the two case-study buildings.

## 6 CONCLUSIONS

In this paper, a methodology for correlating period elongation, damage state and usability judgment has been proposed. The methodology has been applied to two four-storey case-study RC buildings with infill walls, a code-conforming and an existing one. To apply the proposed methodology, nonlinear incremental time-history analyses have been performed on nonlinear models of the case-study buildings.

In summary, based on the above results, a code-compliant infilled building attains temporarily unusability judgement at IM corresponding to LS with period elongation roughly equal to 100%, while it attains unusability judgment for IM corresponding to 1.50 times the IM at LS with period elongation roughly equal to 100%. An existing infilled building designed only to gravity loads attains temporarily unusability judgment for IM equal to 0.67 times the IM at LS with period elongation roughly equal to 100%, while it attains unusability judgement for the IM corresponding to LS with period elongation roughly equal to 150%.

In other words, if the vibration period of an existing RC building has doubled after an earthquake, it should be considered, at least, temporarily unusable; if it has more than doubled, unusability judgment should be considered. If the vibration period of a code-compliant RC building has doubled after an earthquake, it should be considered, at least, temporarily unusable; unusability judgment should be considered only if the registered IM significantly overcame the design IM at LS and/or for higher period elongation.

Of course, these are only preliminary results. Future studies will consolidate/update them based on a larger number of numerical analyses on a larger number of case-study buildings and, potentially, with validation based on field evidence.

## ACKNOWLEDGMENTS

This work was developed under the financial support of ReLUIS 2022-2023 research project, funded by the Italian Department of Civil Protection.

## REFERENCES

[1] Trifunac, M.D., Ivanovic, S.S., Todorovska, M.I., 2001. Apparent periods of a building. Part II: Time-frequency analysis. Journal of Structural Engineering, 127.5, 527-537.

[2] Mucciarelli, M., Masi, A., Gallipoli, M.R., Harabaglia, P., Vona, M., Ponzo, F., Dolce, M., 2004. Analysis of RC building dynamic response and soil-building resonance based on data recorded during a damaging earthquake (Molise, Italy, 2002). Bulletin of the Seismological Society of America, 94.5, 1943-1953.

[3] Zembaty, Z., Kowalski, M., Pospisil, S., 2006. Dynamic identification of a reinforced concrete frame in progressive states of damage. Engineering Structures 28, 668-681.

[4] Calvi, G.M., Pinho, R., Crowley, H., 2006. State-of-the-knowledge on the period elongation of RC buildings during strong ground shaking, 1st European conference on earthquake engineering and seismology. Geneva, Switzerland, paper #1535.

[5] Lin, L., Naumoski, N., Foo, S., Saatcioglu, M., 2008. Elongation of the fundamental periofs of reinforced concrete frame buildings during nonlinear seismic response, 14th World conference on earthquake engineering. Beijing, China.

[6] Masi, A., and Vona, M., 2010. Experimental and numerical evaluation of the fundamental period of undamaged and damaged RC framed buildings. Bulletin of Earthquake Engineering, 8, 643-656.

[7] Di Sarno, L., 2013. Effects of multiple earthquakes on inelastic structural response. Engineering Structures, 56, 673-681.

[8] Ditommaso, R., Vona, M., Gallipoli, M.R., Mucciarelli, M., 2013. Evaluation and considerations about fundamental periods of damaged reinforced concrete buildings. Natural Hazards and Earth System Sciences, 13, 1903-1912.

[9] Katsanos, E.I., Sextos, A.G., Elnashai, A.S., 2014. Prediction of inelastic response periods of buildings based on intensity measures and analytical model parameters. Engineering Structures, 71, 161-177.

[10] Gallipoli, M.R., Stabile, T.A., Guéguen, P., Mucciarelli, M., Comelli, P., Bertoni M., 2016. Fundamental period elongation of a RC building during the Pollino seismic swarm sequence. Case Studies in Structural Engineering 2016, 45-52.

[11] Di Sarno, L., and Amiri, S., 2019. Period elongation of deteriorating structures under mainshock-aftershock sequences. Engineering Structures 196.

[12] Arezzo, D., Nicoletti, V., Carbonari, S., Gara, F., 2021. The tracking of modal parameters for a reinforced concrete building during low-medium intensity earthquakes, 8th ECCOMAS thematic conference on computational methods in structural dynamics and earthquake engineering. Athens, Greece.

[13] MIT - Ministero delle Infrastrutture e dei Trasporti, 2018. Norme Tecniche per le Costruzioni. Decreto Ministeriale 17 gennaio 2018. Supplemento ordinario n. 8 della Gazzetta Ufficiale della Repubblica Italiana del 20 febbraio 2018, n.42. Rome, Italy. (in Italian).

[14] Regio Decreto 1939. Norme per la esecuzione delle opere in conglomerato cementizio semplice od armato. Regio Decreto 16 novembre 1939 n. 2229 pubblicato nel supplemento ordinario alla Gazzetta Ufficiale del Regno d'Italia n. 92 del 18 aprile 1940. Rome, Italy. (in Italian).

[15] Di Domenico, M., De Risi, M.T., Manfredi, V., Terrenzi, M., Camata, G., Mollaioli, F., Noto, F., Ricci, P., Franchin, P., Masi, M., Spacone, E., Verderame, G.M., 2022. Modelling and seismic response analysis of pre-code and low-code reinforced concrete buildings in Italy. Part II: infilled frames. Journal of Earthquake Engineering, in press.

[16] McKenna, F., Fenves, G.L., Scott, M.H., 2004. OpenSees: Open System for Earthquake Engineering Simulation. Pacific Earthquake Engineering Research Center. University of California, Berkeley, CA, USA.

[17] Haselton, C.B., Liel, A.B., Taylor-Lange, S., Deierlein, G.G., 2008. Beam-column element model calibrated for predicting flexural response leading to global collapse of RC frame buildings. PEER Report No. 2007/03. Pacific Earthquake Engineering Research Center, University of California, Berkeley, CA, USA.

[18] Di Domenico, M., Ricci, P., Verderame, G.M., 2021. Empirical calibration of hysteretic parameters for modeling the seismic response of reinforced concrete columns with plain bars. Engineering Structures, 237.

[19] Decanini, L., and Fantin, G.E., 1986. Modelos simplificados de la mampostería incluidas en porticos. Características de rigidez y resistencia lateral en estado límite. Actas de las VI Jornadas Argentinas de Ingenieria Estructural, Buenos Aires, Argentina, October 1–3, 1986. (in Spanish).

[20] Noh, N.M., Liberatore, L., Mollaioli, F., Tesfamariam, S., 2017. Modelling of masonry infilled RC frames subjected to cyclic loads: State of the art review and modelling with OpenSees. Engineering Structures, 150, 599–621.

[21] Vamvatsikos, D., and Cornell, C.A., 2002. Incremental dynamic analysis. Earthquake Engineering and Structural Dynamics, 31, 491-514.

[22] Iervolino, I., Galasso, C., Cosenza, E., 2009. REXEL: computer aided record selection for code-based seismic structural analysis. Bulletin of Earthquake Engineering, 8, 339-362.

[23] Grünthal, G. 1998. Cahiers du Centre Européen de Géodynamique et de Séismologie: Volume 15–European Macroseismic Scale 1998. European Center for Geodynamics and Seismology, Luxembourg.

[24] Del Gaudio C., Ricci, P., Verderame, G.M., 2018. A class-oriented mechanical approach for seismic damage assessment of RC buildings subjected to 2009 L'Aquila earthquake. Bulletin of Earthquake Engineering, 16, 4581-4605.

[25] Morandi P., Hak, S., Magenes, G., 2018. Performance-based interpretation of in-plane cyclic tests on RC frames with strong masonry infills. Engineering Structures 156, 2018.

[26] Del Gaudio C., De Risi, M.T., Ricci, P., Verderame, G.M., 2019. Empirical drift-fragility functions and loss estimation for infills in reinforced concrete frames under seismic loading. Bulletin of Earthquake Engineering, 17, 1285-1330.

[27] Baggio, C., Bernardini, A., Colozza, R., Coppari, S., Corazza, L., Della Bella, M., Di Pasquale, G., Dolce, M., Goretti, A., Martinelli, A., Orsini, G., Papa, F., Zuccaro, G., 2014. Manuale per la compilazione della scheda di 1° livello di rilevamento danno, pronto intervento e agibilità per edifici ordinari nell'emergenza post-sismica (AeDES). Dipartimento della Protezione Civile. Rome, Italy.

COMPDYN 2023
9th ECCOMAS Thematic Conference on
Computational Methods in Structural Dynamics and Earthquake Engineering
M. Papadrakakis, M. Fragiadakis (eds.)
Athens, Greece, 12-14 June 2023

# METRICS FOR EVALUATING THE SEISMIC VULNERABILITY OF TELECOMMUNICATION NETWORKS

**Alessandro Cardoni**[1], **Gian Paolo Cimellaro**[1]

[1] Department of Structural, Geotechnical and Building Engineering, Politecnico di Torino, Corso Duca degli Abruzzi 24, 10129, Turin, Italy
e-mail: {alessandro.cardoni,gianpaolo.cimellaro}@polito.it

## Abstract

*Urban communities have been massively relying on telecommunication infrastructures for everyday activities in the past decade. Their importance is also crucial during emergencies to enable communication among users and first responders. This paper presents a methodology to model and assess the seismic vulnerability of wireless telecommunication networks on the urban scale. The case study is a virtual testbed that is representative of a typical European city. The information to model the infrastructure has been collected from a crowdsourced database and satellite imagery. Since most of the telecommunication network components are located on the roof and inside buildings, the vulnerability of the network has been linked to the damages caused by a given earthquake scenario to the built environment. Different simulations allowed to estimate the failed towers, the available throughput, and the number of users served by each base station after the seismic event. These results have been used to formulate three vulnerability metrics that can be used for detailed resilience analyses.*

**Keywords:** telecommunication infrastructure, seismic vulnerability assessment, wireless mobile network, physical interdependencies, seismic damage simulation.

# 1 INTRODUCTION

Telecommunication networks are among the most critical infrastructures for urban communities as they are essential both to daily activities and in case of emergencies such as earthquakes. The design and seismic performance of telecommunication infrastructure have improved after the investigation of the effects of past earthquakes.

In the literature, few studies tackling the vulnerability of this type of network can be found. In the HAZUS methodology, FEMA proposed seismic fragility curves of telecommunication facilities for different damage states [1]. Following the 2011 Great East Japan earthquake, Nemoto and Hamaguchi [2] discussed strategies to improve the robustness of wireless networks, such as prompt recovery using mobile equipment, an information distribution platform to collect data for decision-making, a mesh network that bridges communication among satellites and unmanned aerial vehicles. Gomes, et al. [3] discussed approaches to improve the robustness and resilience of communication systems against natural disasters. They also pointed out that the number of failures is still high compared to other infrastructures, mainly because of poor design. Overall, methods to quantify the vulnerability and the resilience on a large-scale are still lacking.

This paper proposed a physical-based procedure for a preliminary vulnerability analysis of urban telecommunication networks. The case study is the *Ideal City* virtual environment, which is inspired by the city of Turin, Italy [4]. The network was modeled through a crowdsourced database and satellite imagery inspection. To define the connectivity among the base station controllers (BSCs) a hierarchical three-layer topology was chosen, while base station transceivers (BTSs) were connected to BSCs according to a star scheme.

The performance of the infrastructure was assessed in terms of throughput under a simulated seismic scenario. In this analysis, the dependence relationship with the building portfolio was considered by associating the vulnerability of the network to the collapse of the buildings. Two metrics were proposed to assess the networks' performance. The first one is based on the physical damage to the towers, while the second on the performance in terms of throughput.

# 2 NETWORK MODEL

## 2.1 Data collection

The elements of wireless telecommunication networks are: (i) mobile switching center (MSC), which handles communications at a regional/state level; (ii) base station controller (BSC), which manages urban communications; (iii) base transceiver station (BTS), typically a steel structure where antennas are installed and other devices located within in a structure at the base; (iv) user equipment (UE), i.e., mobile devices.

Most of the information to model the network was obtained through the crowd-sourced website CellMapper, [5]. Since the virtual case study *Ideal City* is based off the city of Turin, Italy, the available data for that city, such as coordinates of antennas, frequency bands, bandwidth, was used. The three largest MNOs were identified, however, for the purpose of this work, only the largest (MNO_1) was analyzed. MNO_1 serves 35.4% of the population, which is about 900,000 people. The information provided by CellMapper was double-checked and integrated using the GIS map of Turin [6] and satellite imagery from Google Maps [7]. The latter operation was also fundamental to distinguish BSCs. It was possible to identify 387 BTSs and 18 BSCs, which is a reasonable number since each BSC usually manages between 10 and 20 BTSs [8]. All the collected information was structured in a database. Examples of database records for each antenna are the following.

- Coordinates: both in geographical and geometrical format.

- Band: either 3 or 20.
- Frequency: 800 MHz for band 3 and 1,800 MHz for band 20.
- Type of cell: 800MHz BTSs serve macro cells, 1,800MHz BTSs serve micro cells.

Figure 1 illustrates the location of BSCs and BTSs and some characteristics of the network.

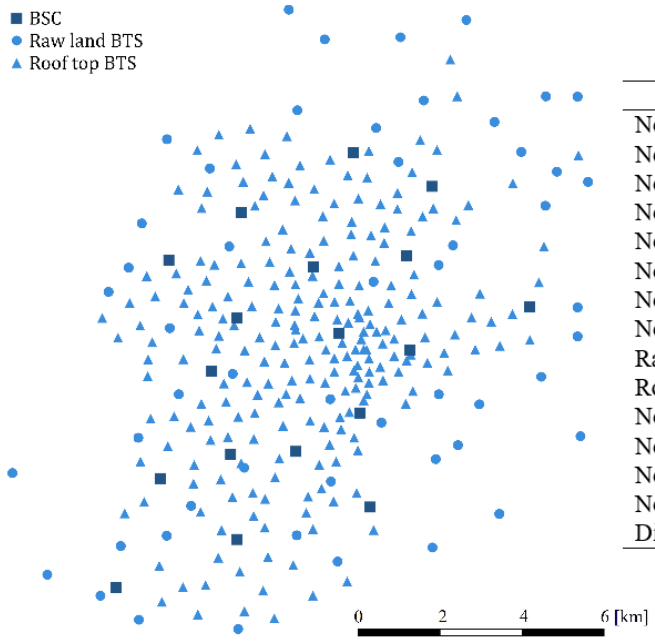


| | MNO_1 |
|---|---|
| No. of BTS | 387 |
| No. of Towers | 304 |
| No. of Raw land towers | 57 |
| No. of Rooftop towers | 247 |
| No. of Raw land macro cells | 33 |
| No. of Raw land micro cells | 50 |
| No. of Rooftop macro cells | 70 |
| No. of Rooftop micro cells | 234 |
| Raw land towers height | 25 – 45m |
| Rooftop towers height | 2.5 – 7m |
| No. of Raw land posts | 35 |
| No. of Raw land masts | 22 |
| No. of Rooftop posts | 186 |
| No. of Rooftop masts | 61 |
| Distribution of customers | 35.4% |

Figure 1: Characteristics of the network.

## 2.2 Topology

A hybrid topology was implemented where BTSs are connected to BSCs through a star topology. The main criterion used for the connections was the shortest distance. It was supposed that all connections are made via underground cables. This topology has many advantages: (i) when a BTS node fails the rest of the network is still functional; (ii) the system can be easily expanded by adding more connections and nodes; (iii) it allows heavy data transfer. However, some negative aspects are that it can be expensive due to the length of the connections and the failure of a BSC causes the failure of all BTSs downstream.

The BSCs were structured in a hierarchy of three layers, namely core, aggregation, and edge, like in a fat tree. The proposed topology consists of two core nodes, both connected to four aggregation nodes. Each of these has six connections to the edge nodes which guarantees that each edge node is connected to two different aggregation nodes.

Based on geographic location and size of the facilities, BSCs were divided into core, aggregation, edge nodes. The most internal BSCs are assumed to be core nodes, then the closest ones were assumed aggregation nodes. The remaining are the edge nodes. Figure 2 shows the topology of the network.

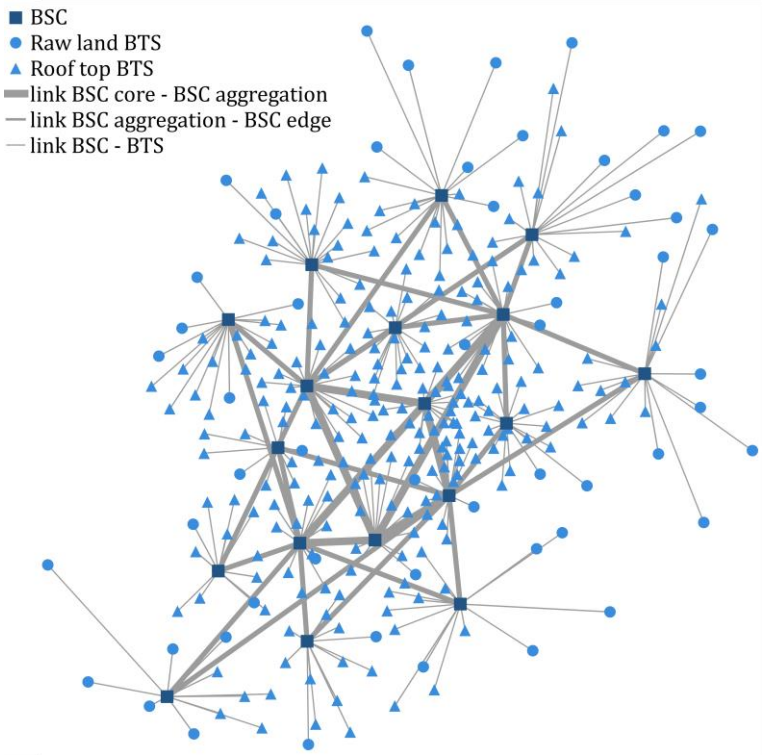


Figure 2: Network topology.

## 3 PERFORMANCE OF THE NETWORK

### 3.1 Signal to interference plus noise ratio (SINR)

The performance of the network was measured in terms of throughput, which is the rate of successfully delivered data per time unit [9]. Obviously, this parameter should be maximized to increase the quality of the service. It can be calculated from the signal to interference plus noise ratio (SINR) through a mapping procedure. The SINR is defined as per Equation 1:

$$SINR = \frac{P}{I + N} \tag{1}$$

where $P$ is the received signal power equal to the difference between the transmission power ($PT$) and the path loss ($PL$); $I$ is the interference; $N$ is the background noise. It was assumed a transmission power $PT$ of 43dBm and 30dBm for macro and micro cells, respectively [10, 11]. The path loss models for macro and micro cells developed by the International Telecom Union were adopted [12].

To calculate the interference, it was assumed that the network has a frequency reuse factor equal to 1. This implies that BTSs can use all the available frequencies, which is a conservative hypothesis. Therefore, the interference can be defined as the difference between the sum of the received power $P$ of all BTSs and the $P$ of the BTS for which the SINR is being calculated. Moreover, since the frequency reuse factor is equal to 1, the interference is so high that including the noise $N$ would not be relevant.

For a faster calculation and better visualization, the population was divided in user clusters corresponding to the occupants in each building. Figure 3 shows an example of the SINR for one user cluster with respect to the macro and micro cells.

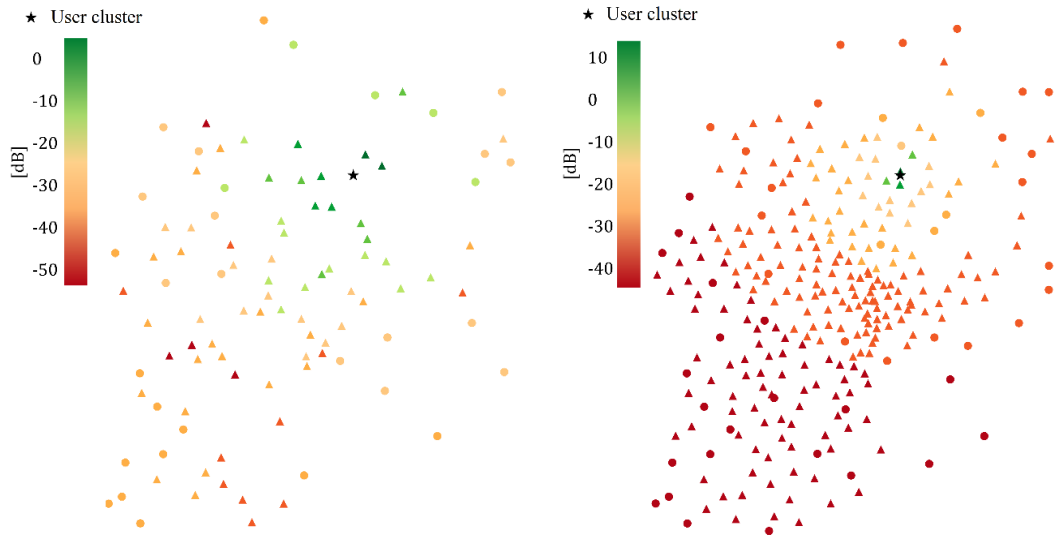


(a) (b)

Figure 3: SINR experienced by a user cluster for (a) macro and (b) micro cells.

Depending on the BTS operating band, different BWs are available. Table 1 summarizes characteristics of bands 3 and 20, those of Ideal City's BTSs. This information was extracted from the "E-UTRA Operating Bands" and "E-UTRA Channel Bandwidth" documentation [13].

| **Band** | **Duplex mode** | **Frequency [MHz]** | **Uplink [MHz]** | **Downlink [MHz]** | **Channel bandwidths [MHz]** |
|---|---|---|---|---|---|
| 3 | FDD | 1,800 | 1,710 - 1,785 | 1,805 - 1,880 | 1.4, 3, 5, 10, 15, 20 |
| 20 | FDD | 800 | 832 - 862 | 791 - 821 | 5, 10, 15, 20 |

Table 1: Characteristics of the selected frequency bands.

Given the lack of data, it was assumed a 10 MHz BW for both bands, which is cautious for modern networks. Therefore, for each BW, 50 resource blocks (RBs) are available. The adopted duplex mode was the frequency division duplex (FDD), which ensures the full BW capacity in uplink and downlink.

After defining the modulation coding scheme (MCS) [14], the BTS selects the transport block size (TBS). Given the TBS and the number of RBs, the number of bits that can be transmitted is calculated [15]. To increase the throughput, a 2x2 multiple-input-multiple-output scheme was adopted [16].

The SINR-throughput relation is modulation specific, as discussed by Olmos, et al. [17]. Mühleisen, et al. [18] mapped the SINR to 13 MCSs for a 20 MHz BW. In this work, a subset of 14 MCSs with a different coding rate for a 10MHz BW defined by the LTE standard was used. The linear envelop curve was then generated from the calculated functions (Figure 4). This represents an ideal situation because users would get the best modulation. However, this is balanced by the fact that using a frequency reuse factor equal to 1 generates large interference that has the effect of lowering the SINR.

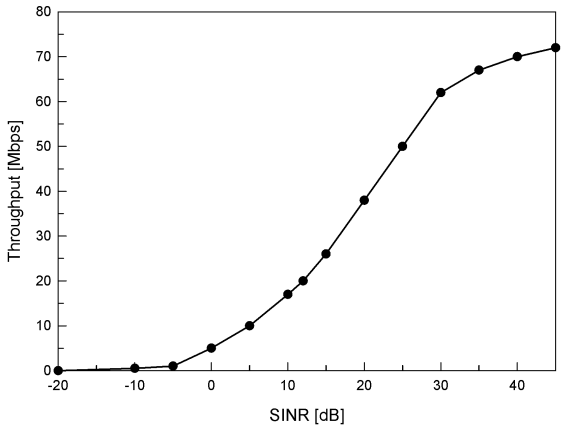


Figure 4: SINR vs. throughput.

### 3.2 Vulnerability of the network

In the literature, few studies can be found related to this endeavor, mainly because networks are privately managed. Masts and monopoles are the most common structures used to install antennas. While FEMA [1] provided fragility curves for telecommunication facilities, few studies can be found on the seismic vulnerability of telecommunication towers, especially at the large-scale network level. Given that these networks are privately managed, and data are confidential, detailed seismic damage simulations cannot be easily performed and many assumptions about section dimensions, types of elements, type of connections should be done. Moreover, even though towers were properly designed and could withstand strong ground motions, cables and other electrical components are likely to be damaged when subjected to large displacements and rotations.

In this preliminary analysis, the vulnerability of the network was related directly to the vulnerability of the built environment. This means that a tower and the corresponding BTS installed in a building would fail if that building collapsed.

### 3.3 Seismic scenario and damage assessment

Details about the methodology developed to estimate the damage to the *Ideal City*'s built environment can be found in [4]. The seismic scenario to evaluate the structural response of the building portfolio is simply defined by epicenter location, moment magnitude, and acceleration time history recorded at the site of the epicenter. At each building location, two horizontal seismic inputs were applied along the principal directions using Ambraseys ground motion model [19]. The damage state of each structure was determined in terms of the maximum inter-story drift thresholds proposed by Ghobarah [20].

### 3.4 Vulnerability metrics

The first metric that is introduced is $R_{TOW}$ which is defined as the ratio between the number of functional towers ($n$) and the total number of towers ($N_T$).

$$R_{TOW} = \frac{n}{N_T} \tag{2}$$

A value close to 1 indicates that the network is robust. Typically, the more redundant the network the higher the probability to obtain a large $R_{TOW}$ value. However, in large-scale networks, if many towers collapse the economic loss might still be substantial and should be considered.

The second proposed metric is $R_{THR}$ which is defined as the ratio between the post- and pre-event mean throughput ($\overline{THR}$).

$$R_{THR} = \frac{\overline{THR}_{post}}{\overline{THR}_{pre}} \tag{3}$$

$\overline{THR}$ is the throughput weighted by the number of users in each cluster as shown in Equation 4:

$$\overline{THR} = \frac{\sum_{i=1}^{k} N_{U,i} \cdot THR_i}{N_U} \tag{4}$$

where: $N_{U,i}$ is the number of users in each cluster, $k$ is the number of clusters, $THR_i$ is the highest throughput for the *i-th* cluster, $N_U$ is the total users. Low values of $R_{THR}$ mean a significant loss in performance, which translates to slow data transfer.

## 4 APPLICATION TO IDEAL CITY

### 4.1 Signal to interference plus noise ratio (SINR)

The proposed procedure was tested on Ideal City under the El Centro (Imperial Valley Irrigation District substation, California, USA) earthquake (Table 2).

| | **El Centro** |
|---|---|
| Date | 5/18/1940 |
| Region | Imperial Valley |
| $M_w$ | 6.9 |
| Depth [km] | 16.00 |
| PGA [g] | 0.35 |

Table 2: Characteristics of the seismic scenario.

BTSs and BSCs were determined from the building damage assessment and the vulnerability model adopted. Figure 5 shows the damage map after the earthquake. The map allows for a preliminary and straightforward understanding of the impact of the event. The number of failed components is reported in Table 3. The collapse of BSCs seemed to be a key factor. Under the applied scenario, the actually collapsed towers were only 31, but since 8 out of 18 BSCs collapsed, the total number of failed towers increased to 141.

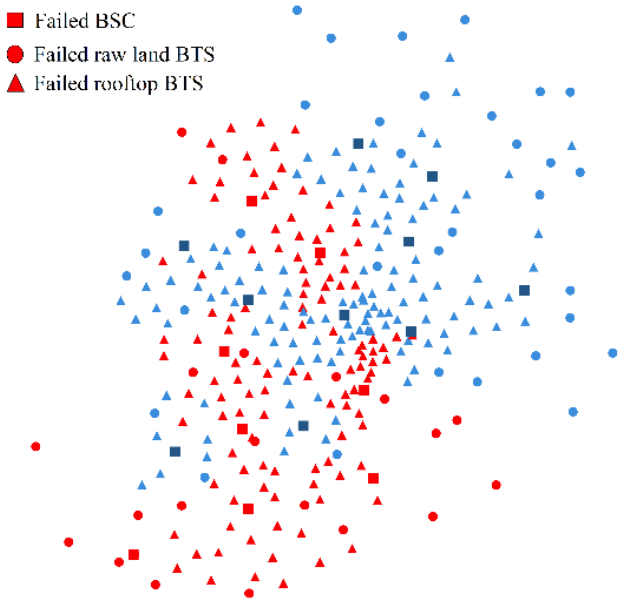


Figure 5: Network damage after the seismic scenario.

| | **El Centro** |
|---|---|
| **No. of collapsed BSCs** | 8 |
| **No. of collapsed towers** | 31 |
| **No. of failed towers** | 141 |
| **$R_{TOW}$** | 0.54 |

Table 3: Number of failed components and RTOW.

Once failed towers were identified and removed from the network model, a post-event throughput was calculated for each cluster. Figure 6 shows part of the throughput map in normal conditions (Figure 6a) and after the El Centro scenario (Figure 6b). As expected, the throughput tends to decrease. However, it was observed that users closer to functional BTSs might experience a better connection because of the reduced interference. The mean weighted throughput in normal conditions was $\overline{THR}_{pre}$ = 19.98 Mbps, while the vulnerability index was $R_{THR}$ = 0.65 indicating a significant performance reduction.

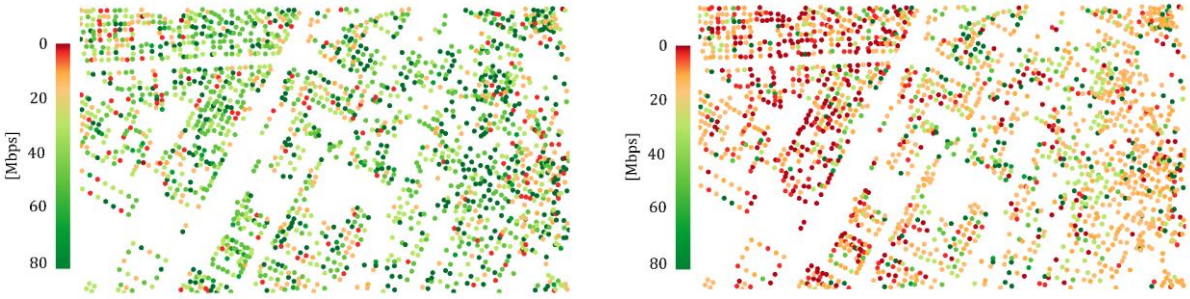


(a) (b)

Figure 6: Throughput in (a) normal conditions and (b) after the seismic scenario.

## 5 CONCLUSIONS

This research focused on the evaluation of the seismic vulnerability of telecommunication networks. The physical infrastructures owned and managed by one of the MNOs was modelled through information collected from a crowdsourced website and satellite imagery. A hybrid topology scheme based on a three-layer hierarchy approach was adopted to define connectivity. Given the limited information available, the vulnerability of the network was related to the vulnerability of the buildings where BSCs and BTSs are located.

Two vulnerability metrics were proposed to evaluate the performance of the network under a simplified seismic scenario. The first metric is representative of the vulnerability of the towers, which could also be interpreted as an economic loss. The second metric is representative of the performance of the network and quality of the service in terms of throughput.

The procedure is intended to be used as a preliminary tool. The obtained results are dependent on the chosen topology and might vary under a different connection scheme. Given the large-scale nature of the problem and the lack of detailed information, simplifications had inevitably to be made, such as attributing the vulnerability of the telecommunication network only to the building vulnerability. However, because telecommunication networks are privately managed, many of the parameters required to perform a complete vulnerability assessment would have to be assumed. In addition, since no information on the actual data traffic was accessible, a hypothesis on the connection of the users to the network had to be made. In this research, it was considered that all the users connect at the same time to the network, which represents the most unfavorable case. Under these conditions, the presented procedure can generate valid results that can be used as a starting point to evaluate the seismic vulnerability of urban telecommunication networks.

## ACKNOWLEDGMENTS

The research leading to these results has received funding from the European Research Council under the Grant Agreement n° ERC_IDEal reSCUE_637842 of the project IDEAL RESCUE— Integrated DEsign and control of Sustainable CommUnities during Emergencies.

## REFERENCES

[1] FEMA, "Multi-hazard loss estimation methodology, earthquake model," *Washington, DC, USA: Federal Emergency Management Agency,* 2003.

[2] Y. Nemoto and K. Hamaguchi, "Resilient ICT research based on lessons learned from the Great East Japan Earthquake," *IEEE Communications Magazine,* vol. 52, pp. 38-43, 2014.

[3] T. Gomes, J. Tapolcai, C. Esposito, D. Hutchison, F. Kuipers, J. Rak, *et al.*, "A survey of strategies for communication networks to protect against large-scale natural disasters," in *2016 8th international workshop on resilient networks design and modeling (RNDM)*, 2016, pp. 11-22.

[4] S. Marasco, A. Cardoni, A. Z. Noori, O. Kammouh, M. Domaneschi, and G. P. Cimellaro, "Integrated platform to assess seismic resilience at the community level," *Sustainable Cities and Society,* p. 102506, 2020.

[5] CellMapper. (2021). *Cellular Coverage and Tower Map*. Available: https://www.cellmapper.net/

[6] Geoportale. (2021). *Geoportale e governo del territorio*. Available: https://geoportale.comune.torino.it/

[7] Google. (2021). *Google Maps*. Available: https://maps.google.com/

[8] S. Giovinazzi, A. Austin, R. Ruiter, C. Foster, M. Nayyerloo, N.-K. Nair, *et al.*, "Resilience and fragility of the telecommunication network to seismic events," *Bulletin of the New Zealand Society for Earthquake Engineering*, vol. 50, pp. 318-328, 2017.

[9] G. Miao, J. Zander, K. W. Sung, and S. B. Slimane, *Fundamentals of mobile data networks*: Cambridge University Press, 2016.

[10] J. Wannstrom, "LTE-advanced," *Third Generation Partnership Project (3GPP)*, 2013.

[11] P. Series, "Propagation data and prediction methods for the planning of short-range outdoor radiocommunication systems and radio local area networks in the frequency range 300 MHz to 100 GHz," *tech. rep., ITU, Tech. Rep. ITU-R*, 2015.

[12] M. Series, "Guidelines for evaluation of radio interface technologies for IMT-Advanced," *Report ITU*, vol. 638, pp. 1-72, 2009.

[13] 3GPP, "Further advancements for E‐UTRA physical layer aspects," *3GPP TR 36.814, Tech. Rep*, 2010.

[14] J. Fan, Q. Yin, G. Y. Li, B. Peng, and X. Zhu, "MCS selection for throughput improvement in downlink LTE systems," in *2011 Proceedings of 20th international conference on computer communications and networks (ICCCN)*, 2011, pp. 1-5.

[15] S. Rathi, N. Malik, N. Chahal, and S. Malik, "Throughput for TDD and FDD 4 G LTE Systems," *International Journal of Innovative Technology and Exploring Engineering (IJITEE), ISSN*, pp. 2278-3075, 2014.

[16] J. Lee, J.-K. Han, and J. Zhang, "MIMO technologies in 3GPP LTE and LTE-advanced," *EURASIP Journal on wireless communications and networking*, vol. 2009, pp. 1-10, 2009.

[17] J. Olmos, S. Ruiz, M. García-Lozano, and D. Martín-Sacristán, "Link abstraction models based on mutual information for LTE downlink," in *COST*, 2010, pp. 1-18.

[18] M. Mühleisen, D. Bültmann, R. Schoenen, and B. Walke, "Analytical evaluation of an IMT-advanced compliant LTE system level simulator," in *17th European Wireless 2011-Sustainable Wireless Technologies*, 2011, pp. 1-5.

[19] N. N. Ambraseys, K. u. Simpson, and J. J. Bommer, "Prediction of horizontal response spectra in Europe," *Earthquake Engineering & Structural Dynamics*, vol. 25, pp. 371-400, 1996.

[20] A. Ghobarah, "On drift limits associated with different damage levels," in *International workshop on performance-based seismic design*, 2004.

COMPDYN 2023
9th ECCOMAS Thematic Conference on
Computational Methods in Structural Dynamics and Earthquake Engineering
M. Papadrakakis, M. Fragiadakis (eds.)
Athens, Greece, 12-14 June 2023

# A CAT BOND-BASED SOLUTION FOR SEISMIC RISK TRANSFER IN ITALY

**Lorenzo Hofer[1*], Mariano Angelo Zanini[1], and Paolo Gardoni[2]**

[1]Department of Civil, Environmental and Architectural Engineering
University of Padova
Padova 35131, Italy
e-mail: lorenzo.hofer@dicea.unipd.it, marianoangelo.zanini@dicea.unipd.it

[2] Department of Civil and Environmental Engineering
University of Illinois at Urbana-Champaign
Urbana, IL 61801-2352, USA
gardoni@illinois.edu

## Abstract

*Natural and man-made disasters are source of significant concern for privates and public authorities worldwide since they commonly imply relevant costs for repairing damaged structures and infrastructure and for a rapid recovery of the involved region's economy. In this context, the Catastrophe Bonds (CAT bonds) are risk-linked securities adopted by insurers to transfer potential high losses to the capital markets. Despite their growing importance, CAT bond pricing formulations and risk-managing solutions based on this financial tool are still limited. For these reasons, this paper wants to propose a general methodology for designing a CAT bond-based loss-coverage scheme for a distributed portfolio, with a pricing formulation able to consider uncertainties deriving from model parameters. The framework is applied to the residential building stock of Italy, proposing an ad-hoc CAT bond-based coverage scheme that consider three different levels of default risk.*

**Keywords:** seismic risk, CAT-bond, risk transfer, structural engineering, earthquake engineering

## 1 INTRODUCTION

Natural and man-made are source of significant concern for privates and public authorities worldwide since they commonly imply relevant costs for repairing damaged structures and infrastructure and for a rapid recovery of the involved region's economy [1]. Every year, floods, earthquakes, tornadoes, and windstorms [2] cause billion dollars losses [3]. Furthermore, losses are expected increasing over time, given the growing urbanization and concentration of population ([4] and [5]). When dealing with natural disasters, losses are strictly spatially and temporally correlated, leading to potential huge losses that are difficult to be covered by insurances or public authorities. For this reason, reinsurance companies, i.e. companies that take on all or part of the risk covered under a policy issued by a first level of insurance companies, that usually have large portfolios, or public governments need to provide coverage of these potential high losses by adopting sophisticated so-called Alternative Risk Transfer products (ART) [6]. One ART solution is represented by the insurance-linked securitization, an alternative way for transforming catastrophe risk into securities (i.e., catastrophe bonds) and selling them to financial entities able to absorb such high levels of losses (i.e., the financial market). CAT bonds offer a significant supply for reinsurance surpassing the capacity of traditional providers and are therefore well suited to provide coverage for substantial losses [7]. So, in case of default, the principal is used to pay the losses of the issuing company, otherwise the capital is returned to the investor at maturity and coupons are also paid as counterweight to the assumed risk. An important aspect in designing an earthquake CAT bond, is the definition of the trigger event. Usually, a common trigger is the exceedance of a loss threshold, that is the one adopted in this study. Recently, [8] proposed a risk-based CAT bond pricing procedure able to consider the propagation of parameter uncertainties on the default probability of a CAT bond and on the pricing, while [9] showed a general methodology for addressing the design of a CAT bond-based coverage for a spatially distributed portfolio. This paper presents the outcomes of [9] in which a CAT bond-based coverage scheme against losses induced by seismic events all over the entire national boarders was priced for the residential building stock in Italy. Further details can be found in [9].

## 2 PROPOSED FRAMEWORK

The design of a possible CAT bond-based coverage scheme, can be subdivided in four main steps, illustrated in Figure 1. The procedure is general and can be easily adapted for designing a CAT bond-based coverage against different hazard by different issuing companies.

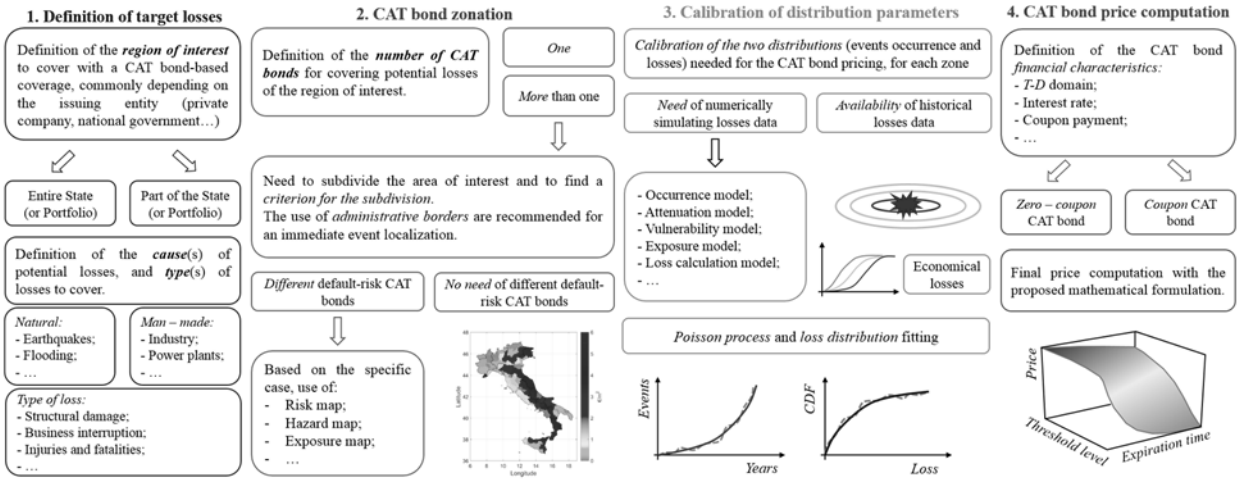

Figure 1: General framework for the designing of a CAT-bond based coverage scheme.

### 2.1 Definition of the target losses

In the first step of the proposed procedure, the issuing company has to identify the spatially distributed portfolio that has to be covered with the CAT bonds. In most of cases, public governments may want to cover the entire national territory, while private company may want to cover the insured portfolio. In many cases, the issuing company can decide to cover only a part of the portfolio, commonly the most exposed at risk. Secondly, the kind of losses to be covered with the CAT bond has to be identified. This decision is very case specific and particularly important, since the trigger event is based on the exceedance of this losses. Commonly, public authorities may consider to cover losses associate to direct structural damage on buildings, while a private issuing company, which offers multi-loss and multi-hazard coverage, has to carefully evaluate the losses to be insured.

### 2.2 Definition of the covered area

When the portfolio is distributed over a wide territory, different risk levels can be identified within the same region. In this context, a common practice is to practice is to tailor CAT bonds associated to different risk levels, in order to meet the needs of different types of investors. An area with many significant events leads to calibrating high-risk CAT bonds with related high gains for risk-seeking investors, while with rare and lowly impacting losses leads to low-risk CAT bonds. If a portfolio is uniformly distributed on a wide area with a quite homogeneous vulnerability and exposure, the subdivision can be guided by the hazard of interest. In this latter case, CAT bond default risk will be strictly connected to the hazard.

### 2.3 Calibration of the distributions' parameters

The third phase consist in the calibration of the distribution's parameters. In particular, the two distributions involved in the price computations are distribution of the expected losses and the Poisson process, representing the occurrence of the events. Regarding the loss distribution, rarely enough historical data of extreme events are available, and thus computer simulations are needed to predict potential losses that can arise for the portfolio of interest. Furthermore, when historical data are available, often they refer to old events for which structural vulnerability and exposure were different from the current ones, highlighting the need of simulations. Based on the specific considered loss, suitable loss models must be adopted.

### 2.4 CAT bond computation

This work adopts stochastic processes for CAT bond pricing. in this case, one common method is to model the credit default probability which follows the way of pricing credit derivatives in finance, and to assume the time to be continuous. The catastrophe process is thus modelled as a compound doubly stochastic Poisson process $M(s)$, where the potentially catastrophic events follow a doubly stochastic Poisson process, and the associated losses $X_i$ are assumed independent and generated from a common cumulative distribution function (CDF). Clearly, this distribution function has to correctly fit the observed claims. The CAT bond's default occurs when the accumulated losses $L(t)$ exceed the money threshold level *D* before the expiration time *T*. Under these assumptions, the price for *zero-coupon* $V_t^{zc}$ (i.e. debt security that does not pay interest but renders profit only at maturity) and coupon $V_t^c$ CAT bond (i.e. debt security that includes attached coupons and pays periodic interest payments during its lifetime and its nominal value at maturity), can be computed as discounted expected value of the future payoff. More formally, the credit default probability can be computed as

$P_f\left(T,D;\boldsymbol{\Theta}\right)=\mathrm{P}\left[L\left(T;\boldsymbol{\Theta}\right)\geq D\right]$, where $\boldsymbol{\Theta}=\left[\boldsymbol{\Theta}_P,\boldsymbol{\Theta}_L\right]$ represents the parameters characterizing the Poisson process $\boldsymbol{\Theta}_P$ and the loss distribution $\boldsymbol{\Theta}_L$. The inclusion of $\boldsymbol{\Theta}$ allows the analyst to take into account in the formulation the uncertainty of the model parameters and thus computing also the $P_f$ and price bounds. Thus, conditioning on the number of events, and considering the independence between the Poisson point process and the incurred losses previous equation becomes $P_f\left(T,D;\boldsymbol{\Theta}\right)=\sum_{n=1}^{\infty}\left[1-F_X^n\left(D;\boldsymbol{\Theta}_L\right)\right]\cdot P\left[M\left(T;\boldsymbol{\Theta}_P\right)=n\right]$, where $F_X^n\left(D;\boldsymbol{\Theta}_L\right)$ is the *n*-fold convolution of the loss distribution evaluated in *D* and represents the CDF of $X_1 + X_2 + \ldots + X_n$ ([10], [11]). This formulation is general and can be applied to every loss distribution type. Fig. 2 shows the procedure for CAT bond pricing based on a fixed accepted level of risk. First, the issuer defines a quantile *q* on the $P_f$ distribution and finds the related CAT bond pricing surface, characterized by a constant risk value for each *T-D* combination. This procedure allows computing the entire $P_f$ and $V_t^{zc-c}$ distribution, or the value corresponding to a specific quantile *q*, for each *T-D* combination.

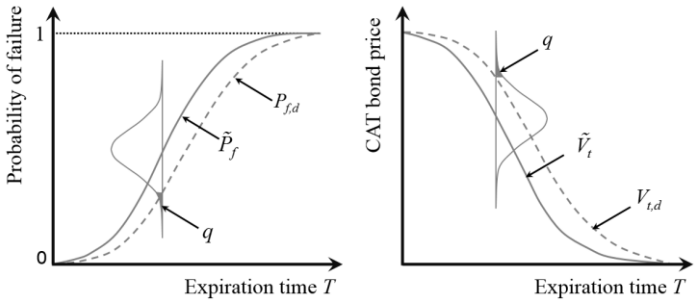


Figure 2: Relationship between $P_f$, $P_{f,d}$ $\tilde{P}_f$ and $V_t$, $V_{t,d}$ given a quantile *q*.

Following [12], the solid line in Fig. 2 represents a predictive $P_f\left(T,D\right)$ or point $P_f\left(T,D\right)$ estimate of $P_f\left(T,D;\boldsymbol{\Theta}\right)$: $P_f\left(T,D\right)$ is computed as expected value of $P_f\left(T,D;\boldsymbol{\Theta}\right)$ over $\boldsymbol{\Theta}$, while $P_f\left(T,D\right)$ is obtained by using a point estimate of $\boldsymbol{\Theta}$ (i.e. $\boldsymbol{\Theta}=\boldsymbol{\Theta}$, where $\boldsymbol{\Theta}$ could be the mean or median). Similarly to $P_f$, $V_t\left(T,D\right)$ (or $V_t\left(T,D\right)$) is a predictive (or point) estimate of the CAT bond price obtained from $P_f\left(T,D\right)$ (or $P_f\left(T,D\right)$). For each *T-D* combination, *q* is the probability that the default probability $P_f$ is smaller than the probability $P_{f,d}$ assumed for the pricing design as the fixed risk, where d in the subscript stands for design value, and represented in Fig. 2 by a dotted line. $P_{f,d}$ is then needed for the calculation of the related CAT bond design price $V_{t,d}$ on the price distribution $V_t$. Assuming a quantile of the $P_f$ distribution implies considering the same probability for the bond to be under-priced. Formally, this condition is given by

$$P\left[P_f < P_{f,d}\right]=P\left[V_t > V_{t,d}\right]=q \tag{1}$$

For computing $P_{f,d}$ for a given quantile *q*, the $P_f$ distribution is thus needed. Since nested reliability calculations are required for the computation of the $P_f\left(T,D;\boldsymbol{\Theta}\right)$ distribution due to

uncertainties in the model parameter, approximated quantiles obtained by first-order analysis can be used [12]. The design default probability $P_{f,d}$ can thus be calculated as

$$P_{f,d}(T,D) = \Phi\left[-\beta(T,d) - k \cdot \sigma_{\beta}(T,D)\right] \tag{2}$$

where $\Phi(\cdot)$ is the standard normal cumulative density function, $\beta(T,d)$ is the reliability index calculated as $\beta(T,d) = \Phi^{-1}\left[1 - P_f(T,D)\right]$ (or similarly $\beta(T,d) = \Phi^{-1}\left[1 - P_f(T,D)\right]$) and $k \cdot \sigma_{\beta}$ represents the quantile of the $\beta$ distribution reflecting the acceptable level of risk. From the assumed quantile *q*, the constant term *k* can be computed as $k = \Phi^{-1}(1-q)$. Following [12]the variance $\sigma_{\beta}(T,D)$ of the reliability index $\beta(T,D;\boldsymbol{\Theta})$ can then be approximated by using a first-order Taylor series expansion around $\mathbf{M}_{\boldsymbol{\Theta}}$, where $\mathbf{M}_{\boldsymbol{\Theta}}$ is the mean vector $\boldsymbol{\Theta}$

$$\sigma_{\beta}^2(T,D) \approx \nabla_{\boldsymbol{\Theta}}\beta(T,D)^T \, \boldsymbol{\Sigma}_{\boldsymbol{\Theta}\boldsymbol{\Theta}} \nabla_{\boldsymbol{\Theta}}\beta(T,D) \tag{3}$$

where $\boldsymbol{\Sigma}_{\boldsymbol{\Theta}\boldsymbol{\Theta}}$ is the covariance matrix of the model parameters and $\nabla_{\boldsymbol{\Theta}}\beta(T,D)$ is the gradient column vector of $\beta(T,D;\boldsymbol{\Theta})$ at $\mathbf{M}_{\boldsymbol{\Theta}}$. The vector $\mathbf{M}_{\boldsymbol{\Theta}}$ can be estimated either with the maximum likelihood estimation method or, more precisely, with the Bayesian updating technique, as the posterior mean vector. As for $\mathbf{M}_{\boldsymbol{\Theta}}$, the covariance matrix can be computed in a simplified way as the negative of the inverse of the Hessian of the log-likelihood function [13] or, again, more precisely with the Bayesian updating technique. The gradient of $\beta$ in Equation (3) is computed applying the chain rule to the definition of reliability index, while the gradient of $P_f$ can be computed numerically using the definition of derivative. Once $P_{f,d}$ is calculated, the corresponding CAT bond price can be computed according to [8] as discounted expected value of the future payoff under the risk-neutral measure (or equivalent martingale measure), considering an arbitrage-free opportunities financial market. For both *zero-coupon* and *coupon* CAT bond, the bond principal is assumed to be completely lost, in case the bond is triggered. Given the threshold *D*, the price of the zero-coupon CAT bond $V_{t,d}^{zc}$ paying the principal Z at maturity time *T* and correspondent to the assumed quantile *q* is

$$V_{t,d}^{zc}(T,D) = E\left[e^{-\int_t^T r(\xi)d\xi|} F_t\right] \cdot Z\left[1 - P_{f,d}(T,D)\right] \tag{4}$$

where $r(\xi)$ represents the stochastic discount factor. Finally, the price of the *coupon* CAT bond $V_{t,d}^{c}(T,D)$ paying the principal value *PV* at maturity, and *coupon* payments *C(s)*, which cease if the bond is triggered, can be obtained as

$$\begin{aligned} V_{t,d}^{c}(T,D) &= E\left[e^{-\int_t^T r(\xi)d\xi} \mid F_t\right] \cdot PV\left[1 - P_{f,d}(T,D)\right] + \\ &+ \int_t^T E\left[e^{-\int_t^T r(\xi)d\xi_t} \mid F_t\right] C(s)\left[1 - P_{f,d}(s,D)\right] ds \end{aligned} \tag{5}$$

Note that when *k* is assumed equal to +/-1, the approximate 15% and 85% percentile bounds of $P_f$ and consequently of $V_t^{zc}$ (or $V_t^c$) containing 70% of the probability, are computed. The complete mathematical derivation of the pricing technique here summarized can be found in [8] and [9].

## 3 CASE STUDY

The exposed framework is applied to design a coverage scheme for the entire residential building asset of Italy considering seismic events as relevant natural hazard. In this application, the Italian Government is taken as the issuing entity, which adopts CAT bonds for a full risk-transfer, considering as lower bound seismic events with magnitude $M_W \geqslant 4.5$. The region of interest is represented by the Italian peninsula, and the target losses are represented by the potential direct costs to be sustained for repairing seismic damage to the Italian residential building stock. First, Italy is divided in three zones based on the seismic risk maps developed by [14]. This zonation (Fig. 3a), based on the seismic risk map and adopting administrative borders, assures an almost constant combination of events frequencies and amount of losses within each zone, and the exact attribution of each event to the corresponding zone. The calibration of the Poisson process and loss distribution parameters is based on the numerical simulation of 100'000 years of seismicity within the national territory, because of the limited number of real losses and claim data. For the generation of 100'000 years of seismic events, the seismogenic source zone model ZS9 of [15] is adopted, together with the seismogenic zone parameters of [16]. The shaking scenario associated to each generated event, is computed in terms of peak ground acceleration with the ground motion prediction equation proposed by [17]. According to [14], the seismic vulnerability of the Italian residential building stock is characterized by setting a building taxonomy consisting in 8 taxonomy classes (TCs): (i) masonry structures built before 1919, (ii) masonry structures built post 1919, (iii) gravity load designed reinforced concrete (RC) structures with 1-2 storeis, (iv) gravity load designed RC structures with 3+ storeis, (v) seismic load designed RC structures with 1-2 storeis, (vi) seismic load designed RC structures with 3+ storeis, (vii) gravity load designed masonry-RC structures, (viii) seismic load designed masonry-RC structures. References and parameters of each class fragility curve can be retrieved in [14]. The exposure model of the national residential building stock is defined at municipality-level granularity and data are retrieved from the 15th census database of the National Institute of Statistics [18]. Fig. 3b and 3c illustrates 100'000 years of simulated seismicity for the seismogenic zone 905. For the calibration of the three sets of distributions parameters, earthquakes occurred inside of each CAT bond zone border were then selected. Fig. 3d shows the selected events for each zone, resulting in 126'414 in Zone 1, 151'245 in Zone 2 and 38'380 in Zone 3. Among the three, Zone 2 has the highest intensity since more events occur in it, in the same time window. Lognormal CDFs were fitted on the cumulative losses to obtain the loss distribution parameters for each zone (Fig. 3e). In the present work, CAT bond price is evaluated at time $t = 0$, assuming a principal equal to 1 €. Two different products were considered for the pricing, a *zero-coupon* and a *coupon* CAT bond, both with a full loss of the principal in case of bond triggering. In the first case, the *zero-coupon* CAT bond is assumed to be priced at 3.5% over LIBOR so that if no trigger event occurs, the total yield is 6%, and consequently $Z = 1.06$ €. For the coupon CAT bond, the yearly coupon payments $C(s) = 0.06$ € and $PV = 1.00$ € are considered. A continuous discount rate r equivalent to LIBOR = 2.5% is assumed constant and equal to $ln(1.025)$ [19]. Expiration time and threshold level are considered respectively ranging between [0.25, 5] years and [0.1, 10] *bn* €, guaranteeing in this way a sufficiently broad *T-D* domain for show-

ing the variation of CAT bond price for a wide range of possible combinations. The bond for a zone is triggered when the accumulated losses caused by earthquakes occurred within the zone are greater than the set threshold before the set expiration time.

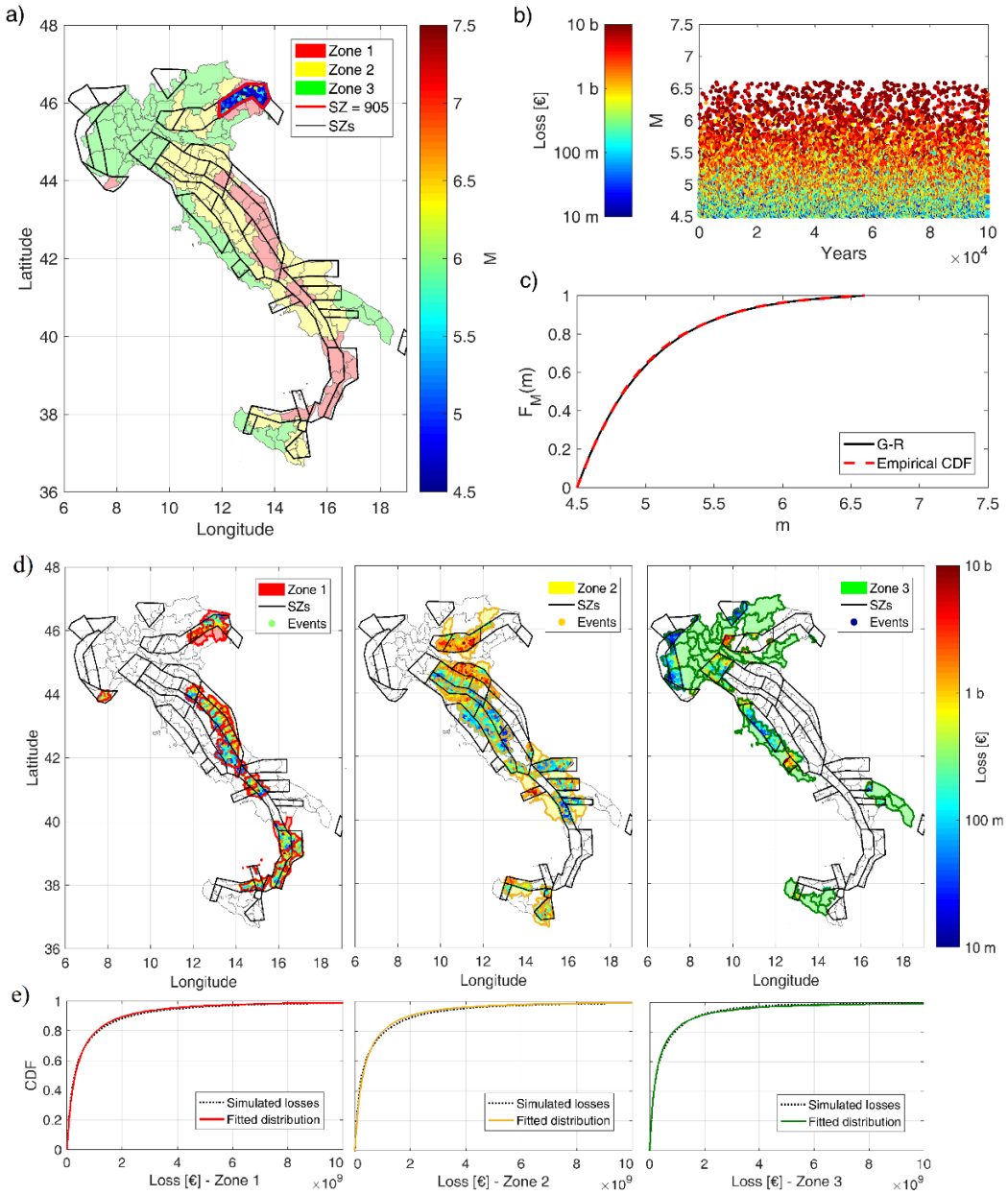


Figure 3: Proposed CAT bond zonation (a), 100'000-years simulated seismicity for SZ #905 (b-c), selected events for each Zone (d) and loss data fitting with lognormal distribution (e) (adapted from [9]).

Fig. 4 shows the probability of failure $P_f$ surfaces for Zones 1, 2 and 3, together with the bounds deriving from considering the parameters uncertainties and containing the 80% of the probability. Two cross sections of the surface are also shown, corresponding to planes with $T$ = 2 years, and $D$ = 3 bn €. As a general behaviour common for all the three zones, for a given expiration time $T$, $P_f$ decreases as the threshold level $D$ increases, whereas for a given threshold level $D$, $P_f$ increases from 0 to 1 over time. $P_f$ of Zone 1 and Zone 2 are comparable

since despite a slightly lower expected loss, Zone 2 has a higher Poisson intensity due to a wider zone area and consequently more events inside. Zone 3 has the lowest $P_f$ due to a combination of lower expected losses and less expected events.

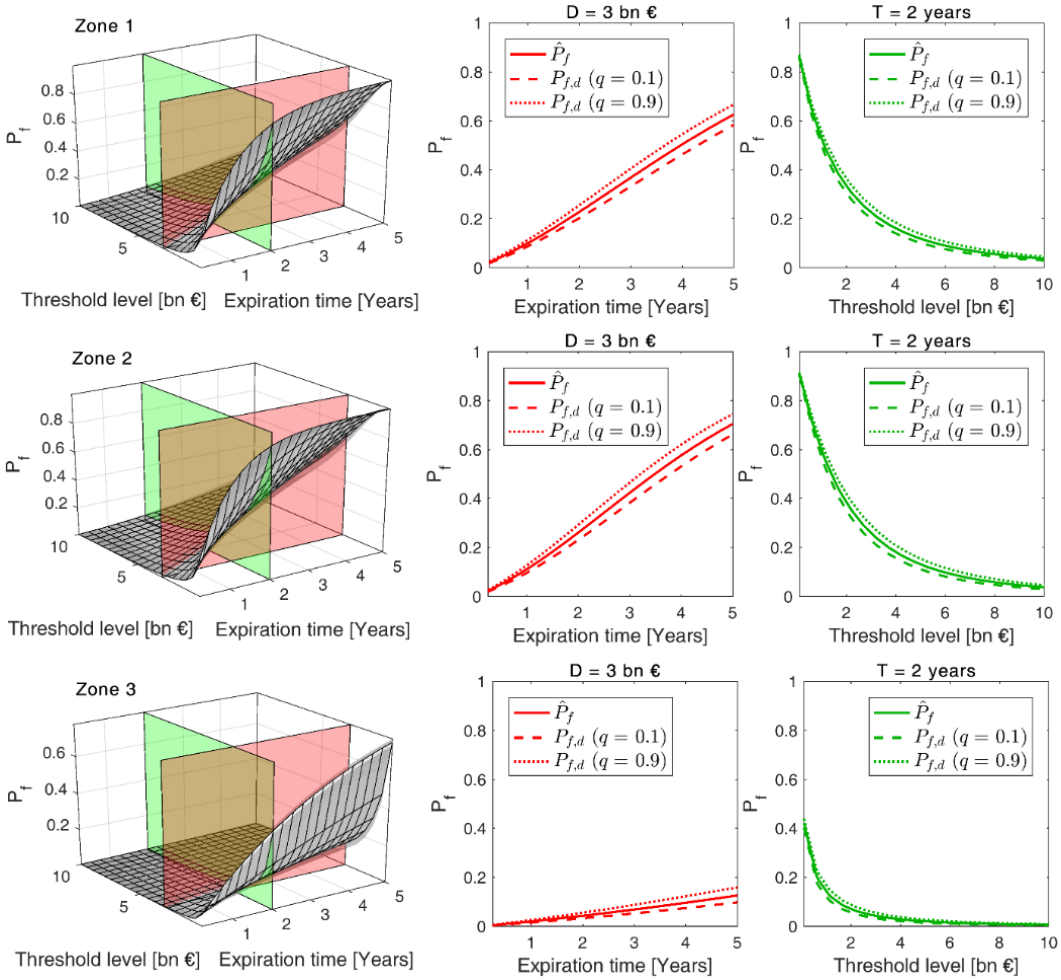


Figure 4. Failure probability surface for the three Zones (adapted from [9]).

Fig. 5a shows the zero-coupon CAT bond pricing surfaces $V^{zc}$ paying $Z = 1.06$ € at maturity, for each Zone. In this case, for a given threshold level *D*, the CAT bond value decreases over time, whereas for a set expiration time *T*, the CAT bond value increases as the threshold level *D* increases. The prices reflect the related failure probabilities: price of Zone 3 is the highest since it is associated with the lowest probability of exceed a given money. Higher gains provided by the bonds are associated to higher failure probabilities. Fig. 5b illustrates the case of the coupon CAT bond, evidencing how the overall trend is similar to the zero-coupon one due to the high ratio intercurrent between the principal and the entity of coupons. Numerical results are the combination of two contributions: as time passes, the chance of receiving more coupon payments is bigger, but at the same time, the possibility of losing the principal increases. Both the zero-coupon CAT bond and the coupon CAT bond price reflect the different seismic risk-levels of the three zones. For a given *T-D* combination, the price for a bond in Zone 1 and Zone 2 is the lowest while the price in Zone 3 is the highest.

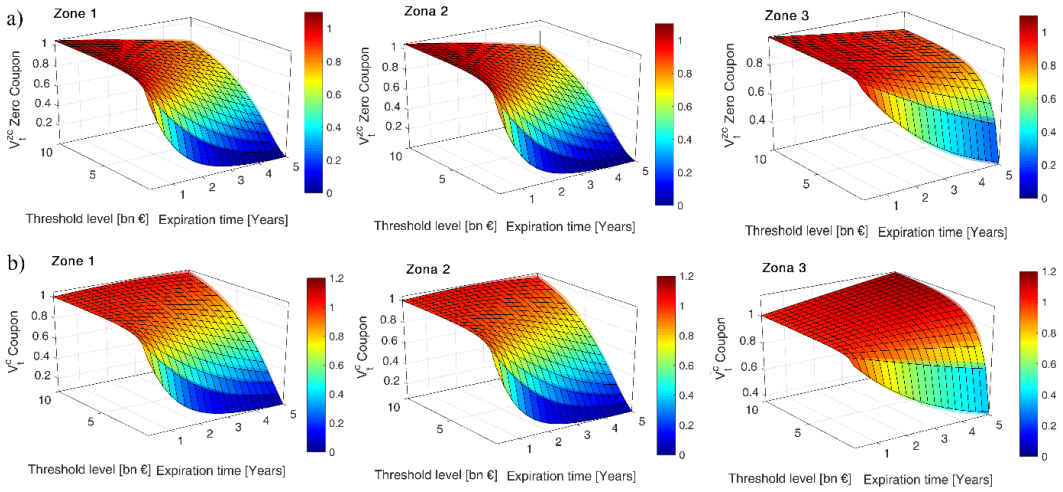


Figure 5. Zero-coupon (a) and coupon (b) CAT bond price for the three Zones (adapted from [9]).

Finally, a sensitivity analysis on the role of the parameters uncertainties on the final variability is performed. In particular, the aim of this analysis is to evaluate the uncertainty of which parameter mostly influences the overall dispersion. The analysis is performed for the *Zero-coupon* CAT bond price of Zone 1, in correspondence of four points of the *T-D* domain:

a) $T$ = 2 years – $D$ = 2 bn €
b) $T$ = 4 years – $D$ = 2 bn €
c) $T$ = 4 years – $D$ = 6 bn €
d) $T$ = 2 years – $D$ = 6 bn €.

In particular, for each *T-D* combination, six covariance matrices have been assumed for testing all the possible combinations of setting equal to zero the variances. AA shows that most of the total variability comes from the uncertainty of the parameter of the lognormal distribution representing losses due to earthquake, and this happens in all the four investigated points of the pricing surface.

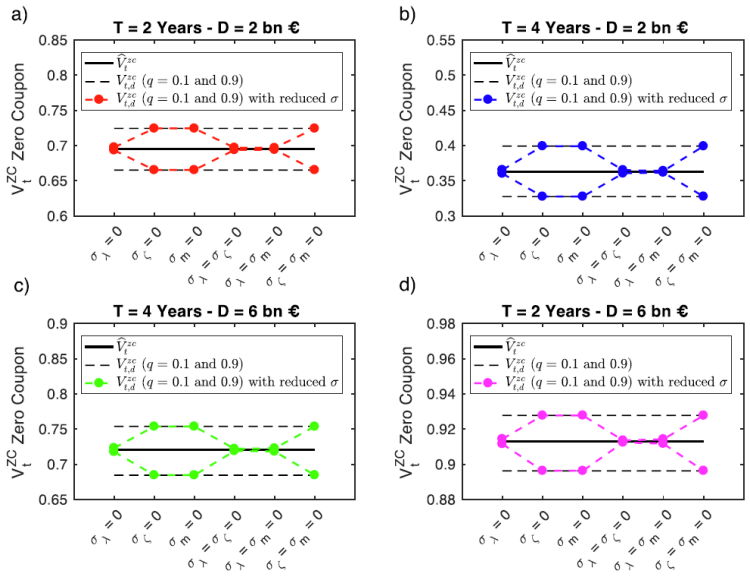


Figure 6. Sensitivity analysis for four points of the T-D domain (adapted from [9]).

## 4 CONCLUSION

This paper presented a general framework for designing a CAT bond coverage system for a distributed portfolio subject to significant losses arising from different possible sources, commonly natural hazards. The flexibility of the proposed methodology allows its adoption by different issuing entities, against various types of losses induced by natural or man-made hazards. For the CAT bond price computation, this paper adopts the mathematical formulation for CAT bond pricing based on a reliability assessment of the $P_f$ underlying the pricing process. In this way, it is possible to obtain a complete knowledge of the default probability and CAT bond price distribution, for a given combination of loss threshold and expiration time. The related CAT bond pricing surface is characterized by a constant reliability for each expiration time *T* - threshold level *D* combination. The general framework is applied to a case-study in which a possible CAT bond-based coverage configuration is designed for the residential building portfolio of Italy against earthquake-induced structural losses. In the application, the Italian territory was subdivided in three zones, based on the Italian seismic risk map, and three different CAT bonds, characterized by different levels of default risk, were priced. The outcomes showed the effect of the CAT bond zonation on the final price computation, and the importance of considering uncertainty in the model parameters in defining a CAT bond pricing. This work can be considered the first original attempt currently retrievable in scientific literature aimed at a rational management of significant losses induced to the Italian residential building stock by seismic events.

## REFERENCES

[1] L. Hofer, M.A. Zanini, F.Faleschini, C. Pellegrino, Profitability Analysis for Assessing the Optimal Seismic Retrofit Strategy of Industrial Productive Processes with Business-Interruption Consequences, *Journal of Structural Engineering*, **144(2)**, 4017205, 2018.

[2] M.A. Zanini, L. Hofer, F. Faleschini, C. Pellegrino, Building damage assessment after the Riviera del Brenta tornado, northeast Italy. *Natural hazards*, **86**, 1247-1273, 2017.

[3] P. Gardoni, J. LaFave, Multi-hazard Approaches to Civil Infrastructure Engineering, Springer, 2016b.

[4] P. Grossi, H. Kunreuther, Catastrophe modeling: a new approach to managing risk, Springer 2005.

[5] C. Murphy, P. Gardoni, R. McKim, Climate change and its impact: risk and inequalities, Springer, 2018.

[6] M.F. Grace, R.W. Klein, P.R. Kleindofer, M.R. Murray, Catastrophe Insurance: Consumer Demand, Markets and Regulation. Boston, MA: Kluwer Academic Publishers; 2003.

[7] H. Kunreuther, M.V. Pauly, Insuring against catastrophes. The known, the unknown, and the unknowable in financial risk management: measurement and theory advancing practice. Princeton University Press; 2001. p. 210–38.

[8] L. Hofer, P. Gardoni, M.A. Zanini, Risk-based CAT bond pricing considering parameter uncertainties, *Sustainable and Resilient Infrastructure*, **6(5)**, 315-329, 2019.

[9] L. Hofer, M.A. Zanini, P. Gardoni, Risk-based catastrophe bond design for a spatially distributed portfolio, *Structural Safety*, **83**: 101908, 2020.

[10] T. Nakagawa, *Stochastic Processes: with Applications to Reliability Theory*. Springer; 2011.

[11] M. Sánchez-Silva, G.A. Klutke, *Reliability and Life-Cycle Analysis of Deteriorating Systems*, Springer; 2016.

[12] P. Gardoni, A. Der Kiureghian, K.M. Mosalam. Probabilistic capacity models and fragility estimates for reinforced concrete columns based on experimental observations. *J Eng Mech*, **128(10)**, 1024-38, 2002.

[13] F.S.G. Richards, A method of maximum likelihood estimation. *The Journal of the Royal Statistical Society*, **23**, 469-75, 1961.

[14] M.A. Zanini, L. Hofer, C. Pellegrino, A framework for assessing the seismic risk map of Italy and developing a sustainable risk reduction program, *International Journal of Disaster Risk Reduction*, **33**, 74-93, 2019.

[15] C. Meletti, F. Galadini, G. Valensise, M. Stucchi, R. Basili, S. Barba, S., et al. A seismic source zone model for the seismic hazard assessment of the Italian territory. *Tectonophysics*, **450**, 85-108, 2008.

[16] S. Barani, D. Spallarossa, P. Bazzurro, Disaggregation of probabilistic ground-motion hazard in Italy. *Bull Seismol Soc Am*, **99(5)**, 2638-61, 2009.

[17] D. Bindi, F. Pacor, L. Luzi, R. Puglia, M. Massa, G. Ameri, et al. Ground motion prediction equations derived from the Italian strong motion database. Bull Earthq Eng, , **9(6)**, 1899-920, 2011.

[18] Istituto Nazionale di Statistica, 15-esimo Censimento Generale della popolazione e delle abitazioni, 2011. Postel Editore, Roma (in Italian), 2011.

[19] K. Burnecki, G. Kukla, D. Taylor, Pricing Catastrophe Bond. In: Cizek P., Härdle W., Weron R., editors. *Statistical Tools for Finance and Insurance*. Berlin: Springer; 2005.

COMPDYN 2023
9th ECCOMAS Thematic Conference on
Computational Methods in Structural Dynamics and Earthquake Engineering
M. Papadrakakis, M. Fragiadakis (eds.)
Athens, Greece, 12-14 June 2023

# SEISMIC RISK ANALISYS OF DISTRIBUTION LINEAR INFRASTRUCTURES

**Mariano Angelo Zanini[1], Chiara Vianello[2], Flora Faleschini[1], Lorenzo Hofer[1*], Carlo Pellegrino[1], Giuseppe Maschio[2]**

[1] Department of Civil, Environmental and Architectural Engineering
University of Padova
Padova 35131, Italy
e-mail: {marianoangelo.zanini, flora.faleschini, lorenzo.hofer, carlo.pellegrino}@dicea.unipd.it

[2] Department of Industrial Engineering
University of Padova
Padova 35131, Italy
{chiara.vianello, giuseppe.maschio}@unipd.it

## Abstract

*Natural Gas distribution networks are fundamental elements for the socio-economical development of region and of an entire country. Their vulnerability with respect to the so-called NaTech events can imply significant consequences both in terms of physical damage in the area surrounding the infrastructure and in terms of service interruption, as documented in past earthquakes occurred worldwide. Therefore, perform the seismic risk analysis of this type of infrastructure is essential and matter of interest for identify the most relevant critical issues and avoid dangerous consequences. In particular, this paper will focus on Natural Gas buried pipelines, aiming to propose a framework for the seismic risk assessment of such infrastructural system. Finally, the procedure is applied to a case study in Italy for highlighting its value and feasibility.*

**Keywords:** Seismic risk analysis, natural gas pipelines, na-tech events, linear infrastructures, pipelines vulnerability.

## 1 INTRODUCTION

The natural gas (NG) distribution network is a key element for the socio-economic development of each country, representing a primary need for both citizens and industrial facilities. Commonly, a NG pipeline is designed for transporting gas among localities situated at large kilometers, with pipes diameters that can reach several hundred centimeters and length that can reach several thousand kilometers. In their spatial development, pipelines can cross different environments, as highly populated and/or industrialized areas, areas exposed to natural hazards as landslides, earthquakes etc. For these characteristics, their possible failure can cause a series of significant consequence, mainly related to two aspects. The first one is mainly related to the physical damage that an explosion following the structural damage of the pipeline may cause in the surrounding area, while the second one is related to the economic effects that the interruption of the NG supply may induce at different levels. Despite the limited number of accidents occurred so far ([1], [2]), some significant events showed the terrible effects on the population and on the surrounding environment. In 2004, in Ghislenghien industrial park (in Ath, close to Brussels, Belgium), there was the explosion of an underground high pressure NG pipelines [3], while another rupture occurred in Kingman (Kansas, USA [4]). Thus, the development of procedures for a quantitative risk assessment for such kind of critical infrastructure is a key step for investigating the potential impact of such events and developing suitable risk reduction programs, as showed by [5].

In some circumstances, pipelines failures can be triggered by natural hazards: in seismic risk prone area, buried pipelines can be subject to permanent ground motions or transitory strong ground shakings which can lead to damages and consequent release of transported substances, causing abrupt service stop or explosions as in the of the 1994 Northridge [6], 1995 Kobe [7] and 1999 Kocaeli [8] earthquakes. Less recently, the 1971 San Fernando earthquake moment magnitude $M_w$ = 6.7 damaged the underground pipelines, while the 1923 Kanto earthquake ($M_w$ = 7.9) caused several breaks in the gas pipelines in the region of Tokio.

In general, pipelines can be subdivided in aboveground and underground pipelines. In the former case suitable supports are adopted for supporting the pipe, while in the latter case pipelines are commonly buried in a range of 1-2 m; less frequently, as for pipelines with very large diameter, pipelines are buried deeper. The advantage of the buried one than respect to the others, is firstly the fact that the landfill protects the pipelines from the above ground damage sources, and secondly the fact that the lateral confinement provided by the surrounding soil reduces possible earthquake-induced damages. As a consequence, pipelines tends to follow the soil deformation and the structural response is strictly related to the geotechnical effects only. According to [9], geotechnical issues for pipelines can be subdivided in two main groups: the first one is related to strong ground shaking, that can cause the deformation of the soil surrounding the pipelines, while the second one is related to the ground failure, e.g., induced by fault movement, landslide liquefaction etc. Of course, this latter case, is strongly dependent on the site where the pipelines is located.

In particular, this work will analyses the risk of seismic-induced explosion of a buried NG pipelines located in North-eastern Italy. First a Probabilistic Seismic Hazard Analysis (PSHA) is performed in order to compute the seismic hazard of the area where the pipeline is located, then a detailed consequences analysis is provided in order to investigate all the possible consequences that the failure of such infrastructures may cause, together with the likely of each possible outcome.

## 2 RISK ANALYSIS

### 2.1 Seismic hazard

The proposed work adopts the classical Probabilistic Seismic Hazard Analysis developed by [10] and [11] for computing the so-called hazard curve, that associates to each level of ground motion intensity measure $im$ the corresponding annual exceedance rate $\lambda_{im}$ at the site of interest. The PSHA integral is given by:

$$\lambda_{im} = \sum_{i=1}^{n_{SZ}} \nu_{m_{\min,i}} \int_{m_{\min,i}}^{m_{\max,i}} \int_{r_{\min,i}}^{r_{\max,i}} P\left[IM > im \mid m,r\right] f_{M_i}(m)\, f_{R_i}(r)\, dmdr \tag{1}$$

where $\nu_{m_{\min,i}}$ is the rate of occurrence of earthquakes greater than a suitable minimum magnitude $m_{\min,i}$ of the $i^{th}$ seismogenic zone (SZ), $f_{M_i}(m)$ and $f_{R_i}(r)$ represent respectively the earthquake magnitude distribution and the source-to-site distance for the $i^{th}$ SZ. Finally $P\left[IM > im \mid m,r\right]$ commonly computed via a Ground Motion Prediction Equation (GMPE), provide the exceedance probability of a given $im$ value conditioned on a seismic event with a specific magnitude $m$ and occurring at a distance $r$. In this specific work, the PSHA is performed on a pipe belonging to the Italian National gas pipeline system [12], focusing on the pipe #048, located in the North-Eastern Italy, in the Friuli Venezia Giulia region. The area is highly prone to seismic hazard and was in the recent past (1976) subject to the $M_w$ 6.4 Friuli earthquake. For the aim of the paper, the pipe has been subdivided in 81 independent sections 1 km spaced (Figure 1).

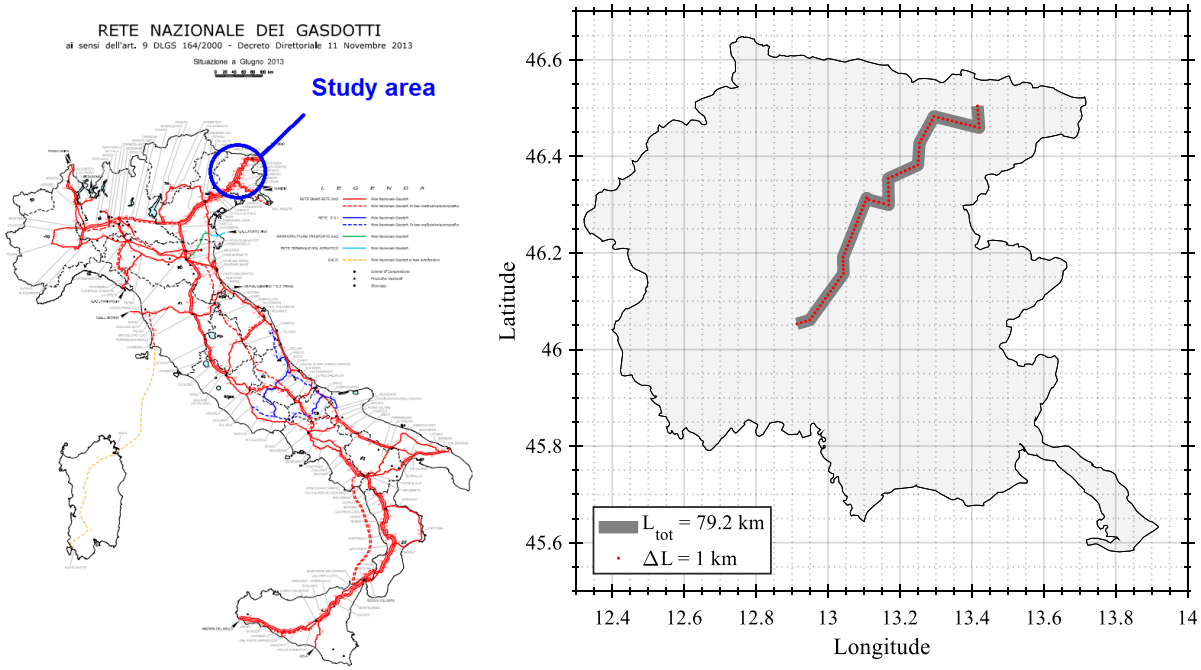


Figure 1: Italian national gas pipeline network (left) and the analyzed Malborghetto-Flaibano pipe #48 (right).

For performing the PSHA, the seismogenic source zone model ZS9 detailed in [13] has been adopted, using Gutenberg-Richter (G-R) recurrence laws for each of the 7 SZs contributing to the seismic hazard (i.e. SZs # 903, # 904, # 905, # 906, # 907, # 912, # 917) within a radius of 200 km from the site of interest (Figure 2). Parameters of the G-R) recurrence laws

for each $i^{th}$ SZ, were retrieved from [14], while the GMPE of [15] were selected as suitable attenuation law. The Peak Ground Velocity (PGV) was adopted as reference intensity measure, mainly for its predictivity than respect to the pipelines damage susceptibility [16]. The soil class of each point is determined from the soil map realized by [17] and it is showed in Figure 3a. Finally, Figure 3b shows the output of the PSHA, in particular the PGV values with an exceedance rate of 0.0021 (return period of 475 years).

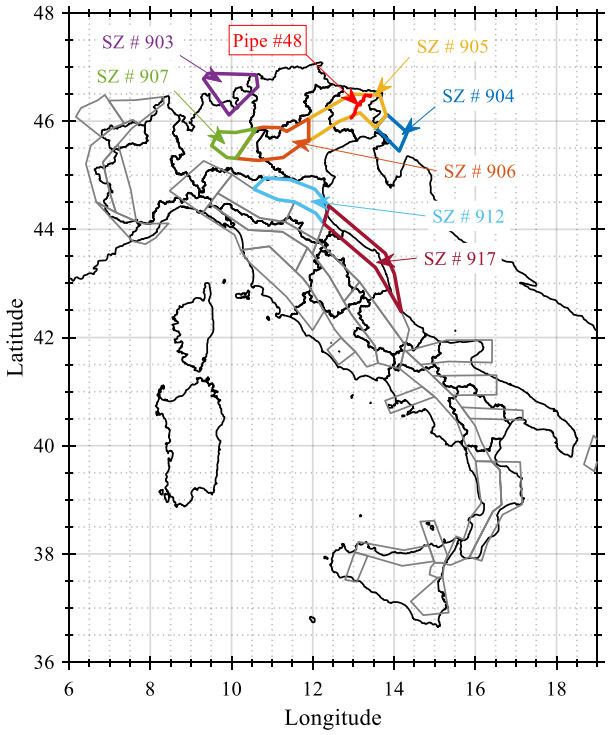


Figure 2: Pipe #48 and adopted seismogenetic source model.

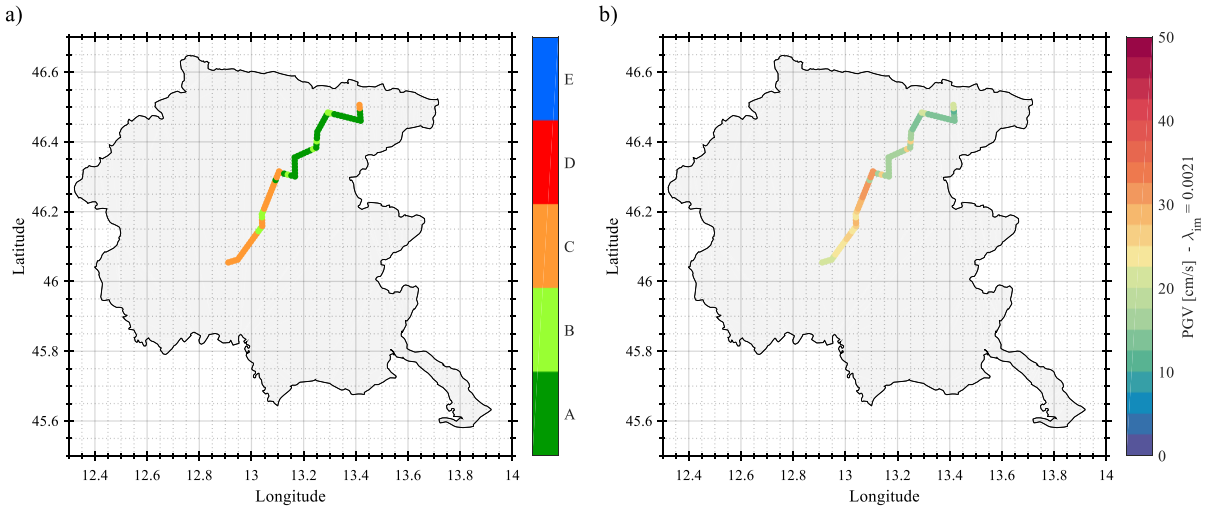


Figure 3: Soil category for each point of Pipe #48 (a) and PGV values for $\lambda_{im}$ = 0.0021 (b)

## 2.2 Seismic fragility

The structural fragility of NG pipelines is defined through fragility curves, that represent the exceedance probability of a set of specific damage thresholds, conditioned on a given value of $im$. Focusing on the loss of hazardous material, structural damage states are converted in terms of release states (*RS*). For pipelines three different RSs are considered according to [16] namely:

- *No damage* (*RS0*), in which the pipe damage does not cause any content loss;
- *Release from hole* (*RS1*), where structural damage causes few content loss, or a time-distributed loss.
- *Catastrophic rupture (RS2)*, where the structural collapse leads to the release of large amounts of fluids in a short time-window.

The characteristics of the analyzed pipeline are listed in Table 1, together with the median values $\mu$ and the shape parameter $\beta$ of the fragility curves retrieved from [16].

| Parameter | Input field | Value |
|---|---|---|
| Material | Discharge material | Methane |
| | Temperature | 20°C |
| Process condition | Pressure | 70 bar |
| | Diameter | 1200 mm |
| | Flow | 294 kg/s |
| Location | Elevation | -1.5 m |

| Risk State RS | $\mu$ (cm/s) | $\beta$ |
|---|---|---|
| *RS1* | 45.22 | 0.39 |
| *RS2* | 71.16 | 0.20 |

Table 1: Main characteristics of Pipe #48 and fragility curves parameters.

## 2.3 Consequences modelling

The last step of the risk assessment procedure deals with the computation of the possible consequences. Given an intensity value at a pipe segment it is possible to calculate using the fragility curves the related *RS* probabilities. A specific event tree is adopted for pipelines components for the assessment of release consequences as shown in Figure 4: each branch of the event tree represents a separate accident sequence, each with the corresponding occurrence probability [5]. In 30% of cases, an immediate ignition can occur, then resulting in a jet fire or fireball. In the remaining 70 % there are no consequences only in the 20% of cases. When there is a delayed ignition, i.e. when released gas finds an ignition source after being dispersed in the atmosphere for several minutes, in 90% of cases it is expected to produce a flash fire (i.e., short-duration fire that spreads by means of a flame front rapidly without the production of damaging pressure) since methane is lighter than air; only in the 10% of cases a vapor cloud explosion (VCE, i.e. the explosion of flammable substance diffused in the surrounding environment) may occur.

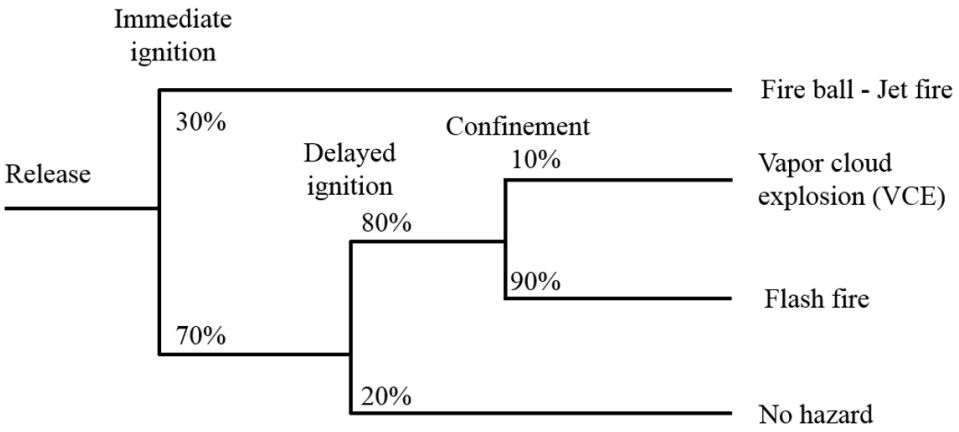


Figure 4: Pipe #48 and adopted seismogenetic source model.

For each specific consequence of Figure 4, it is possible to define a consequence radius which identifies the area affected by each considered outcome, where, for example, consequences can be evaluated in terms of damaged buildings, injured people etc. The consequence radius values are estimated as function of the fluid contained in the pipe and its geometrical characteristics and are reported in Table 2 for each possible damage state.

| Type of release | Jet fire (37.5 KW/m$^2$) | VCE (explosion 0.3 bar) | Flash fire |
|---|---|---|---|
| RS1 - Release from hole | 137 m | 341 m | 1383 m |
| RS2 - Catastrophic rupture | 65 m | 341 m | 1572 m |

Table 2: Consequence radius associated to different possible consequences.

## 3 RESULTS

The consequence radius values of Table 2 were subsequently weighed with probability values retrieved from fragility curves for a specific PGV, and the event tree diagram illustrated in Figure 4 leading to define an average consequence radius adopted as final indicator. In particular, the consequence radius corresponding to PGV values with 8 specific exceedance rates were computed and reported in Figure 5. The reference PGV exceedance rate are: 0.02 (50 years), 0.0139 (72 years), 0.0099 (101 years), 0.0071 (140 years), 0.0050 (201 years), 0.0021 (475 years), 0.0010 (975 years) and 0.0004 (2475 years).

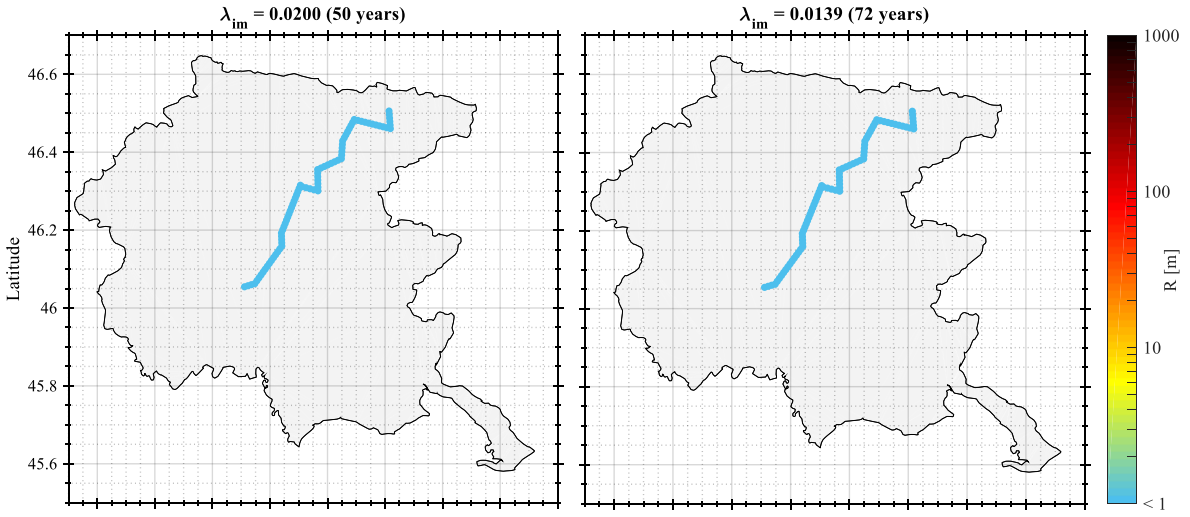

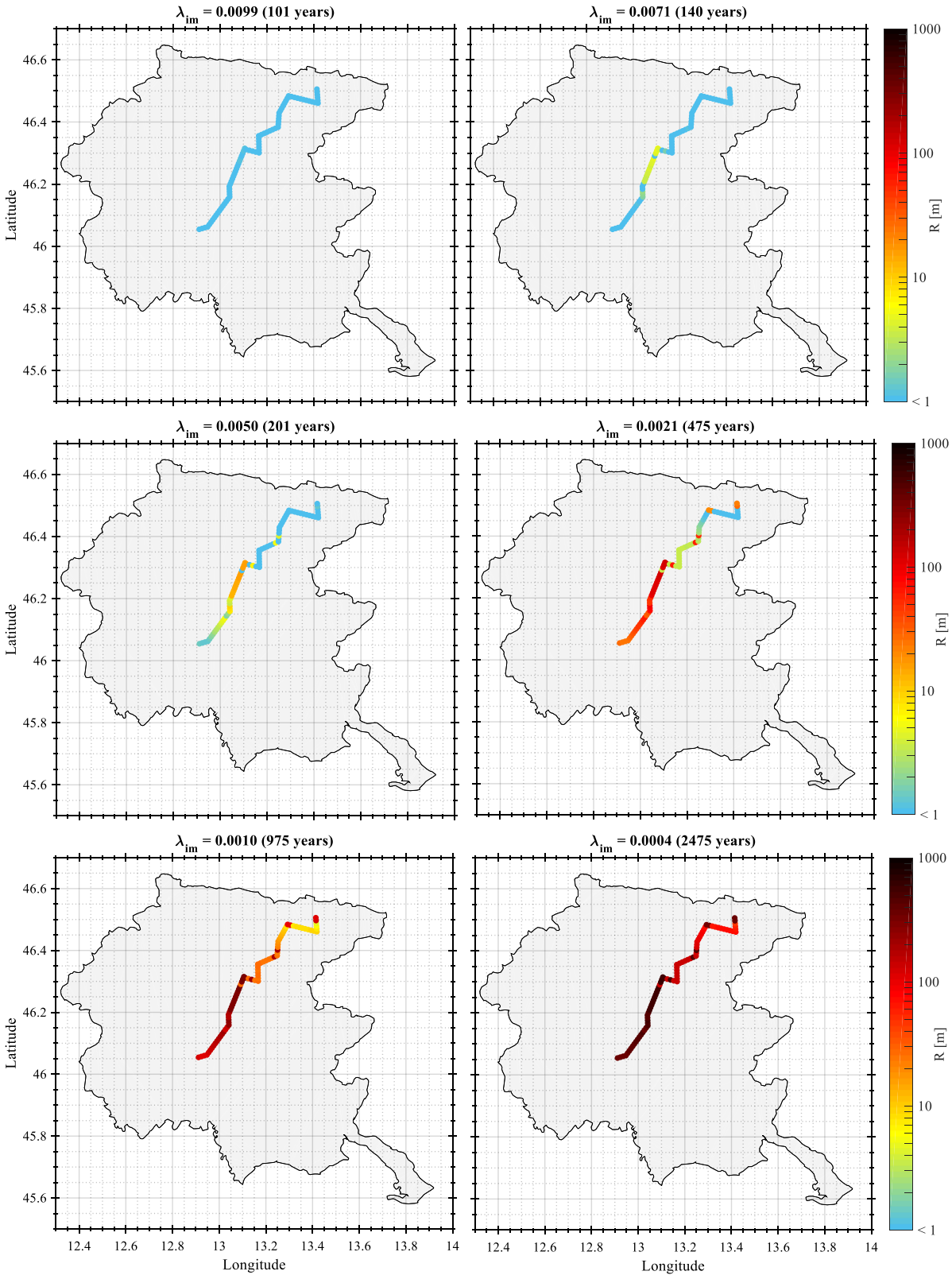


Figure 5: Consequence radius for different PGV exceedance rate.

Results show that for PGV exceedance rate lower than 0.0050 (201 years), i.e. for frequent events of low shaking values, the expected radius is limited for the entire pipe #48, with values lower than 100 m from the pipeline axis. For more rare events, the maximum expected consequence radius significantly increases, still reaching values around 1 km, corresponding to a potential affected area of 3.14 $km^2$.

## 4 CONCLUSIONS

This works presents a framework for computing the possible effects of seismic-induced damage on NG pipelines. Seismic hazard modelling coupled with a quantitative description of pipelines seismic vulnerability in terms of release states lead to estimate potential consequences in terms of expected consequence radius. For each pipe segment release probabilities were assessed through fragility functions, according to a specific level of shaking induced by the quake and corresponding to a given exceedance rate. The proposed framework allows, by using an event tree analysis, to quantify probabilities of occurrence of the different possible consequences of pipe structural failure and then to compute the resultant expected radius. The proposed approach was tested through the simulation of the effects on a pipe belonging to the Italian National gas distribution system located in northeast Italy, showing that for the rarest events, e.g., those characterized by a return period higher than 475 years, the consequence radius can reach values almost close to 1 km, corresponding to a potential affected area of 3.14 $km^2$. Furthermore, the proposed framework can be a useful tool for estimating the area potentially involved in a seismic-induced explosion.

**ACKNOWLEDGEMENT**

This work was funded by the European Commission, Project 2014 – 2020 Interreg V-A | Italy – Croatia CBC Programme: FIRESPILL - Fostering Improved Reaction of crossborder Emergency Services and Prevention Increasing safety Level.

## REFERENCES

[1] Center for Chemical Process Safety, 1995. Guidelines for chemical transportation risk analysis (Center for Chemical Process Safety "Guidelines" series). Wiley-AIChEJ.T.

[2] TNO, 1999. Purple Book – Guidelines for quantitative risk assessment (CPR18E, Ed.). CPR18E.

[3] Hint Dossier, 2005. Gas pipeline explosion at Ghislenghien, Belgium.

[4] National Transportation Safety Board, Pipeline Accident brief (2007) NTSB/PAB-07/02, https://www.ntsb.gov/investigations/AccidentReports/Reports/PAB0702.pdf, January 2023.

[5] C. Vianello, G. Maschio, Quantitative risk assessment of the Italian gas distribution network. *Journal of Loss Prevention in the Process Industries*, **32**, 5-17, 2014.

[6] D.L. Lau, A. Tang, J.R. Pierre, Performance of lifelines during the 1994 Northridge earthquake. *Canadian journal of Civil Engineering*, **22**, 438-451, 1995.

[7] T.D. O'Rourke, F.H. Erdogan, W.U. Savage, L. Val Lund, A. Tang, N. Basoz, et al. Water, gas, electric power and telecommunications performance, special issue on Kocaeli 1999 earthquake, *Earthquake Spectra*, **16-S1**, 377-402, 2000.

[8] S. Girgin, The natech events during the 17 August 1999 Kocaeli earthquake: aftermath and lessons learned, *Natural Hazards Earth System Sciences*, 11, 1129-1140, 2011.

[9] M. O'Rourke, X. Liu, Response of buried pipelines subjected to earthquake effects, MCEER Monograph No. 3, University of New York Buffalo, 1999.

[10] C. Cornell, Engineering seismic risk analysis, *Bulletin of the Seismological Society of America*, **58(5)**, 1583-1606, 1968.

[11] R.K. McGuire, Probabilistic seismic hazard analysis and design earthquakes: closing the loop, *Bulletin of the Seismological Society of America*, **85(5)**:1275-1284, 1995.

[12] SNAM, Rete nazionale dei gasdotti, https://www.snam.it/export/sites/snam-rp/repository-srg/file/Anno_termico_2013x14/Informazioni_utenti/rete-naz-gasdotti/RNG_30GIU2013_ITA.PDF, January 2023.

[13] C. Meletti, F. Galadini, G. Valenzise, A seismic source zone model for the seismic hazard assessment of the Italian territory, *Tectonophysics*, **450**, 85-108, 2008.

[14] S. Barani, D. Spallarossa, P. Bazzurro, Disaggregation of probabilistic ground motion hazard in Italy, *Bulletin of the Seismological Society of America*, **99**, 2638-2661, 2009.

[15] D. Bindi, F. Pacor, L. Luzi, R. Puglia, M. Massa, G. Ameri et al., Ground motion prediction equations derived from the Italian strong motion database, *Bulletin of Earthquake Engineering*, **9(6)**, 1899-1920, 2011.

[16] G. Lanzano, E. Salzano, F. Santucci de Magistris, G. Fabbrocino, Seismic vulnerability of natural gas pipelines, *Reliability Engineering and System Safety*, **117**, 73-890, 2013.

[17] G. Forte, E. Chioccarelli, M. De Falco, P. Cito, A. Santo, I. Iervolino, Seismic soil classification of Italy based on surface geology and shear-wave velocity measurements, *Soil Dynamics and Earthquake Engineering*, **122**, 79-93, 2019.

COMPDYN 2023
9th ECCOMAS Thematic Conference on
Computational Methods in Structural Dynamics and Earthquake Engineering
M. Papadrakakis, M. Fragiadakis (eds.)
Athens, Greece, 12-14 June 2023

# SEISMIC VULNERABILITY ASSESSMENT OF AN URBAN NATURAL GAS NETWORK

**Alessandro Cardoni**[1], **Sebastiano Marasco**[1], **Gian Paolo Cimellaro**[1]

[1] Department of Structural, Geotechnical and Building Engineering, Politecnico di Torino, Corso Duca degli Abruzzi 24, 10129, Turin, Italy
e-mail: {alessandro.cardoni,sebastiano.marasco,gianpaolo.cimellaro}@polito.it

## Abstract

*Natural and man-made hazards have shown that modern societies are heavily dependent on critical infrastructures. The natural gas network plays a key role in a community economy, and seismic events might be detrimental for its safety and wellness. This paper proposes a methodology to assess the seismic vulnerability of urban natural gas networks. A physical-based model of the network of a virtual city has been developed. The modeling and calibration have been executed using a Python simulation tool. The model has then been used to evaluate the damage induced by the ground shaking and permanent soil deformation caused by a given seismic scenario. Network damage has been estimated in terms of gas leaks and pipe breaks. The methodology provides an effective tool to measure vulnerability and identify the critical components of the network. The results of the analysis can be used to assess the resilience of the gas infrastructure and to implement strategies for improving the overall community resilience.*

**Keywords:** gas infrastructure, seismic vulnerability assessment, gas leak model, pipe break model, seismic damage simulation.

## 1 INTRODUCTION

Natural gas networks are one of the most critical infrastructures at the urban level. Man-made and natural hazardous disasters, such as earthquakes, might disrupt this lifeline, causing significant economic and social losses.

Most of the current methodologies to assess the seismic vulnerability of natural gas networks are based on the Performance-Based method adapted to spatially distributed systems [1]. The seismic hazard characterization involves identifying the Intensity Measure (IM) parameters that quantify the hazard intensity within the urban area, typically, the Peak Ground Velocity (PGV) and Peak Ground Displacement (PGD). The first describes the failure mechanism induced by the transient soil deformation caused by the seismic wave [2]. The latter describes ground failure due to the permanent soil movements caused by liquefaction phenomena and uplifts.

A frequently discussed aspect of buried pipeline systems is the vulnerability assessment through seismic fragility functions. Lanzano, et al. [3] adopted an extensive database to define reliable fragility models of buried pipelines. The HAZUS [4] is one of the most widespread fragility relationships database. It uses fragility functions defined by [5] based on the damage due to wave propagation and ground deformation. Several studies have been done using the HAZUS methodology at different scales [6, 7]. Cavalieri [8] integrated the use of the FEMA methodology with the guidelines published by the American Lifeline Alliance [2]. A review of existing fragility curves for buried natural gas pipelines subjected to seismically-induced transient ground deformations was carried out by Tsinidis, et al. [9], who put particular emphasis on evaluating the efficiency of different IMs. Although these research works have focused on the seismic vulnerability assessment of NG networks using fragility functions as empirical relationships, the effects of the physical damage to the NG network behavior has not been deeply investigated.

In this work the damage occurrence through fragility functions is simulated, reproducing the physical damage effects in the NG network components (e.g., pressure losses), and updating the gas balance to evaluate the out-of-service network branches and unserved users.

The gas network modeling and calibration are performed through Pandapipes, a python-based simulation tool [10]. The mean thermodynamics and geometric characteristics of the gas network are defined according to the Italian design requirements and technical practices [11]. The case study is a virtual city consisting of an area of about 120 $km^2$ and 900,000 inhabitants [12]. A simplified seismic scenario was defined to test the capabilities of the proposed computational methodology. The results of the simulation are used to evaluate the reduction of pressure and to estimate the vulnerability of the gas network.

## 2 NETWORK MODEL

In this work, the Italian guidelines were followed to model the natural gas network. The Italian national gas pipeline network is mainly composed of a high-pressure transport network, a regional high-medium pressure network, and a local low-pressure distribution network. The latter consists of small diameter pipes and its role is to supply domestic and commercial utilities. The pipes of the distribution network are classified according to the national code [11] as a function of the Maximum Operating Pressure (MOP), defined as the maximum pressure at which the pipeline can operate under normal conditions (Table 1).

| Pressure Class | MOP [bar] |
|---|---|
| 1 | MOP>24 |
| 2 | 12<MOP<24 |

| | |
|---|---|
| 3 | 5<MOP<12 |
| 4 | 1.5<MOP<5 |
| 5 | 0.5<MOP<1.5 |
| 6 | 0.04<MOP<0.5 |
| 7 | MOP<0.04 |

Table 1: Pressure classes according to [11].

Pipelines belonging to classes 1, 2, and 3 are defined as high pressure, those belonging to classes 4, 5, 6 are medium pressure (MP), while class 7 pipelines are low pressure. The medium pressure pipelines are those considered at the urban level.

## 3 NETWORK VULNERABILITY

### 3.1 Definition of the seismic hazard

The seismic characterization of a given site requires detailed geotechnical data, knowledge on the geology profile, and properties of the seismic sources. Many earthquake-prone areas lack the data needed for a detailed seismic hazard characterization. Therefore, in this work, a simplified seismic scenario was implemented. The seismic scenario is defined in terms of (*i*) seismic source, (*ii*) soil characteristics, (*iii*) geometry of the fault rupture area, and (*iv*) PGV and PGD at the source. The NGA West attenuation law [13] was then used to estimate the PGV and PGD at any node of the network. The seismic source is described by the expected moment magnitude and location of the epicenter.

### 3.2 Pipeline fragility model

The assessment of the NG network damage was performed using empirical fragility functions. Current methodologies provide a correlation between the pipeline repair rate (RR), defined as the ratio between number of pipeline repairs and pipeline length, and the seismic IM. The RR per unit of length can be expressed as a function of seismic wave passage or ground failure. The first is usually less damaging for pipes, whereas extensive damage occurs in case of large displacements caused by ground failure phenomena such as liquefaction and landslides uplifting. Seismic wave failure mechanism is typically linked to PGV while ground failure mechanism to PGD. Several PGV-based empirical relationships of the pipe RR can be found in the literature [14, 15].

In this paper, the ALA formulations [2] have been chosen (Equation 1).

$$\begin{aligned} RR &= 0.002416 \cdot PGV \cdot K_1 \\ RR &= K_2 \cdot 1.06 \cdot PGD^{0.319} \end{aligned} \tag{1}$$

The values of the modification factors $K_1$ , $K_2$ are provided by [2] for different pipe material, diameter, joint type, soil. For the ground failure mechanism, the proposed PGD relationship is based on post-earthquake data where soil liquefaction was the predominant ground failure mechanism. These formulations are independent from the damage state (DS). Instead, the HAZUS methodology [15] considers leakage and failure of pipelines as possible DSs. In case of ground failure, it is assumed that 80% of the pipes breaks and 20% leaks, while in case of ground shaking it is assumed that 20% of the pipes breaks and 80% leaks [15]. The probability to have a total of *n* damages and repairs for a pipeline with length *l* is given by a Poisson distribution (Equation 2).

$$P(DS) = 1 - e^{-RR \cdot l} \tag{2}$$

The expression in Equation 2 can be seen as a binomial term. If the probability value is greater than a predefined percentile, the pipe is considered damaged. The percentile value has been fixed to 50% for both leak and break DSs, which corresponds the median probability of having leak and break on the pipeline. In this research, it was considered that NG components located inside buildings suffering from extensive and complete damage are failed.

## 4 NETWORK MODEL

### 4.1 Simulation approach

To model and simulate the effects of earthquakes on the natural gas network, the Pandapipes Python package was used [10]. It provides pressure values in all network nodes and the flow rates in the pipes. The node balance rule is based on the principle behind Kirchhoff's laws (Equation 3).

$$\begin{aligned} \sum_{b=1}^{N_b} m_b + m_n &= \sum_{b=1}^{N_b} v_b A_b \rho_b + m_n = 0 \\ \sum_{b=1}^{N_b} q_n &= \sum_{b=1}^{N_{b,in}} m_b c_p T_b - \sum_{b=1}^{N_{b,out}} m_b c_p T_n = 0 \end{aligned} \tag{3}$$

where $m_b$ is the mass flow of pipe connected to the analyzed node and $m_n$ is the mass flow, incoming or outcoming; $q_n$ refers to the incoming or outcoming heat flow; $N_b$ is the number of connected branches. The temperature is assumed constant in the branch. The mesh rule states that the sum of the pressure or temperature variation is null. The pressure variation along a pipe section can be defined using Equation 4:

$$dp = -\frac{\rho \cdot v^2}{2} \cdot \left( \frac{\lambda}{d} \cdot dl + \zeta \right) + \rho \cdot g \cdot dh \tag{4}$$

where friction is considered through the Darcy factor $\lambda$, $d$ is the pipe diameter, $\zeta$ is a lumped pressure loss, $\rho$ is the fluid density and $v$ the flow velocity. The second addend is the pressure variation caused by the height difference $dh$.

In Pandapipes, the previous equations are set up in a nonlinear system and the unknown variables are computed through the Newton–Raphson method.

### 4.2 Modeling leaks and breaks

A novel methodology is proposed to update the network in case of leaks and breaks. When there is a leak, this generates a lumped loss of pressure (Equation 5).

$$dp = -\frac{\rho \cdot v^2}{2} \cdot \zeta \tag{5}$$

Pressure, velocity, density and temperature can be considered constant at low pressures. The loss coefficient $\zeta$ is strictly connected to the leak flow rate. In this paper, the flow rate model through a small hole proposed by Hou, et al. [16] was adopted (Figure 1). In their model the soil column height was fixed to 0.6m and the soil weight to 1500 kg/m$^3$ which are common for an urban network. The thermodynamics characteristics of methane were taken from Moran, et al. [17] and reported in Table 2.

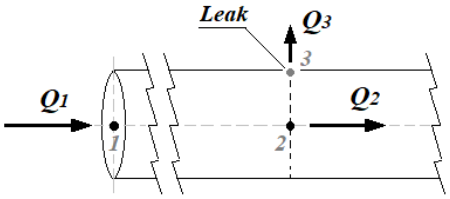


Figure 1: Scheme of the leak model.

| Parameter | Value |
|---|---|
| M [g/mol] | 16.044 |
| ρ [kg/m$^3$] | 0.662 |
| k [-] | 1.31 |
| Z [-] | 1.000 |
| $C_D$ [-] | 1.000 |
| R [J/mol °K] | 8.314 |

Table 2: Thermodynamics characteristics of methane.

For minor leaks the main challenge is estimating the $\zeta$ coefficient. In the proposed method the flow rate is assessed through iteration and the loss coefficient is estimated using Equation 6:

$$\zeta = 7 \cdot 10^{-6} \cdot \frac{d^4}{T^2 \cdot \left(Q_1 - Q_3\right)^2} \cdot P_2^2 \cdot \left(P_1 - P_2\right) \tag{6}$$

where T is the temperature (assumed to be constant) P1 and P2 are the pressures at sections 1 and 2 as indicated in Figure 1, Q1 is the incoming flow rate, Q3 is the leak flow rate. Finally, the lumped loss of pressure in section 3 is computed and the Pandapipes model balance is updated. This iterative procedure is repeated for each pipe. The inlet flow rate for each pipe depends on the cumulated losses due to leaks or breaks. For the $i^{th}$ pipe, the inlet flow can be expressed as shown in Equation 7:

$$Q_{in,p(i)} = Q_{in,p(i-1)} - \sum_{j=1}^{i-1} Q_{leak,p(j)} \tag{7}$$

Pipe breaks are modeled as out of service pipes in Pandapipes, which means that the entire flow rate leaks in that breakage area.

## 5 APPLICATION TO IDEAL CITY

The proposed method was applied to the natural gas network of Ideal City (Sebastiano Marasco et al., 2020). This consists of three MP classes of pipelines as summarized in Table 3.

| | $v_{max}$ [m/s] | $Q_{min,req}$ [kg/s] | $Q_{peak}$ [kg/s] | d [m] | l [km] | P [bar] |
|---|---|---|---|---|---|---|
| MP 4$^{th}$ class | 20 - 25 | 1.70 | 2.40 | 0.32 | 62.40 | 2.50 |
| MP 5$^{th}$ class | 10 - 15 | 0.30 | 0.90 | 0.20 | 16.20 | 1.00 |
| MP 6$^{th}$ class | 10 | 0.10 | 0.30 | 0.15 | 83.70 | 0.20 |

Table 3: Design parameters per class of pipelines.

A simplified seismic scenario based on the 6.9 $M_w$ Northridge earthquake was defined. The epicenter was located 6.5 km away from the downtown. Accordingly, a PGV of 26.30 cm/s and a PGD of 12.20 cm were assumed at the epicenter location. The [13] ground motion model was used to estimate the PGV and PGD in all nodes. The building damage was assessed using the HAZUS methodology [18]. As a result, 14% of the buildings suffered extensive damage and 27% were completely damaged. It was assumed that network components inside buildings which suffered extensive and complete damage failed.

The gas network of *Ideal City* consists of 12 metering and reduction (M/R) stations, 775 final reduction groups (FRGs) for standard and 102 for commercial users, and 33 industrial reduction groups (IRGs). Each IRG serves a given number of users based on the population density. The pipelines are made of steel, and a constant temperature of 278 °K was assumed across the network. The pipe roughness was set to 0.04 mm.

Results in terms of node pressures are shown in Figure 2. Compared to the normal conditions (Figure 2a), the applied seismic scenario caused few pipe breaks in the area closer to the epicenter (Figure 2b). In the same area, the pressure of some MP class 4 pipes also decreased due to leaks.

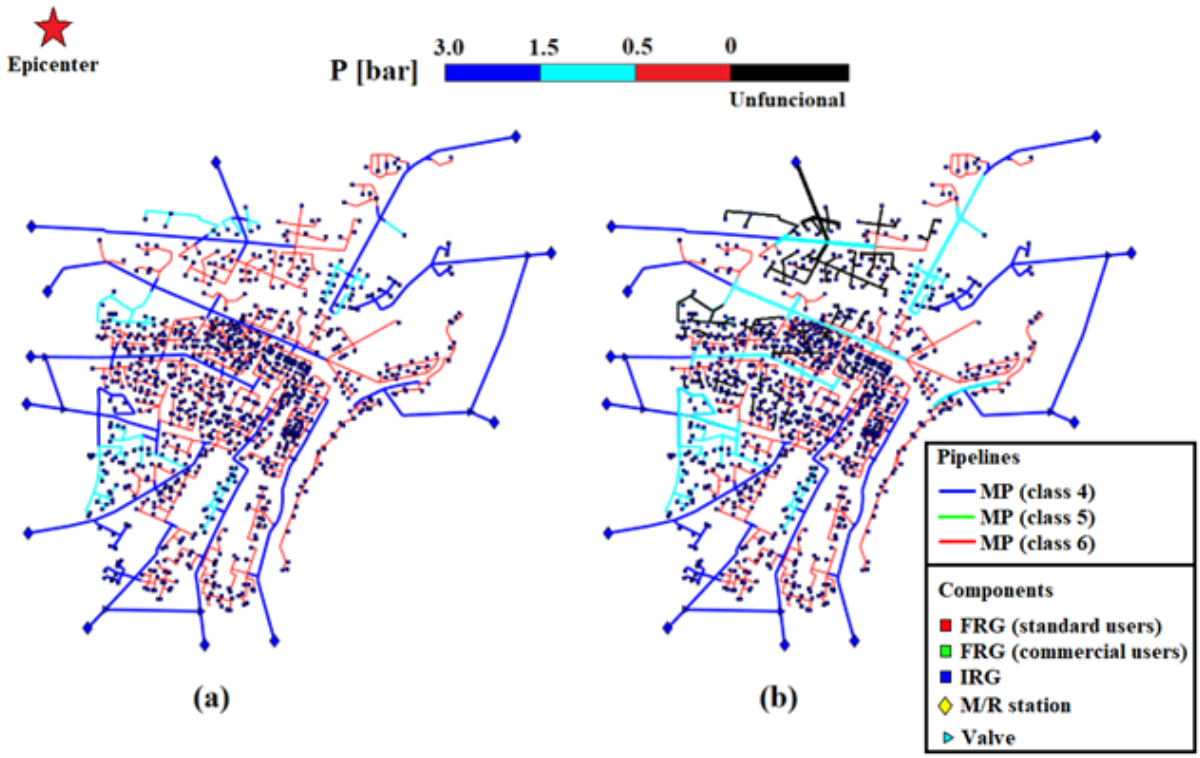


Figure 2: Pipe pressures (a) before and (b) after the seismic event.

A straightforward indicator of the vulnerability of the network $R$ can be defined as the ratio between the number of supplied users ($U_{SUPPL}$) and the total number of users ($U_{TOT}$) as described in Equation 8.

$$R = \frac{U_{SUPLL}}{U_{TOT}} \tag{8}$$

It was found that in this application for standard users $R$ = 0.85, while $R$ = 0.92 for commercial users.

## 6 CONCLUSIONS

This research focused on the evaluation of the seismic vulnerability of natural gas networks at the urban scale. A physical-based methodology was proposed to simulate pipeline damage caused by ground shaking and ground failure. The model and computation were performed using the Pandapipes Python package. The methodology consists of three steps: (i) assessment of leaks and breaks for each pipe; (ii) evaluation of the expected leak and break flow rate through a physical model; (iii) update the network model. The updated Pandapipes model is capable of evaluating the new node balance and flow rate.

The methodology was applied to *Ideal City*, a virtual case study, considering the interdependence between the building damage and the gas network components. This application showed how the physical-based model can simulate the pressure reduction due to leaks and breaks of pipes caused by the seismic input. Finally, a straightforward indicator of the vulnerability of the network was introduced. The presented method could be replicated on different scales, providing an effective tool that can be used to implement strategies aimed at improving the overall community resilience.

## ACKNOWLEDGMENTS

The research leading to these results has received funding from the European Research Council under the Grant Agreement n° ERC_IDEal reSCUE_637842 of the project IDEAL RESCUE— Integrated DEsign and control of Sustainable CommUnities during Emergencies.

## REFERENCES

[1] J. W. Baker, "Issues with applying performance-based engineering to distributed infrastructure systems," in *Eleventh US National Conference on Earthquake Engineering: Integrating Science, Engineering & Policy, Los Angeles, CA, United States*, 2018.

[2] ALA. (2001). *Seismic fragility formulations for water systems*.

[3] G. Lanzano, E. Salzano, F. S. de Magistris, and G. Fabbrocino, "Seismic vulnerability of natural gas pipelines," *Reliability Engineering & System Safety*, vol. 117, pp. 73-80, 2013.

[4] F. NIBS, "Hazus MR4 Multi-Hazard Loss Estimation Methodology," in *Earthquake model*, ed, 2003.

[5] M. J. O'Rourke and X. Liu, *Response of buried pipelines subject to earthquake effects*: Mceer New York, 1999.

[6] P. Vazouras and S. A. Karamanos, "Structural behavior of buried pipe bends and their effect on pipeline response in fault crossing areas," *Bulletin of Earthquake Engineering*, vol. 15, pp. 4999-5024, 2017.

[7] G. C. Sarvanis, S. A. Karamanos, P. Vazouras, E. Mecozzi, A. Lucci, and P. Dakoulas, "Permanent earthquake‐induced actions in buried pipelines: Numerical modeling and experimental verification," *Earthquake Engineering & Structural Dynamics*, vol. 47, pp. 966-987, 2018.

[8] F. Cavalieri, "Seismic risk assessment of natural gas networks with steady-state flow computation," *International Journal of Critical Infrastructure Protection*, vol. 28, p. 100339, 2020.

[9] G. Tsinidis, L. Di Sarno, A. Sextos, and P. Furtner, "A critical review on the vulnerability assessment of natural gas pipelines subjected to seismic wave propagation. Part 1: Fragility relations and implemented seismic intensity measures," *Tunnelling and Underground Space Technology*, vol. 86, pp. 279-296, 2019.

[10] D. Lohmeier, D. Cronbach, S. R. Drauz, M. Braun, and T. M. Kneiske, "Pandapipes: An Open-Source Piping Grid Calculation Package for Multi-Energy Grid Simulations," *Sustainability*, vol. 12, p. 9899, 2020.

[11] *Regola tecnica per la progettazione, costruzione, collaudo, esercizio e sorveglianza delle opere e dei sistemi di distribuzione e di linee dirette del gas naturale con densita' non superiore a 0,8,* Decreto interministeriale 16 aprile 2008, 2008.

[12] S. Marasco, A. Cardoni, A. Z. Noori, O. Kammouh, M. Domaneschi, and G. P. Cimellarof, "Integrated platform to assess seismic resilience at the community level," *Sustainable Cities and Society*, p. 102506, 2020.

[13] K. W. Campbell and Y. Bozorgnia, "NGA ground motion model for the geometric mean horizontal component of PGA, PGV, PGD and 5% damped linear elastic response spectra for periods ranging from 0.01 to 10 s," *Earthquake Spectra*, vol. 24, pp. 139-171, 2008.

[14] M. O'Rourke and G. Ayala, "Pipeline damage due to wave propagation," *Journal of Geotechnical Engineering*, vol. 119, pp. 1490-1498, 1993.

[15] FEMA, "HAZUS-MH flood loss estimation methodology. I: Overview and flood hazard characterization," in *Natural Hazards Review* vol. 7, ed, 2006, pp. 60-71.

[16] Q. Hou, D. Yang, X. Li, G. Xiao, and S. C. M. Ho, "Modified Leakage Rate Calculation Models of Natural Gas Pipelines," *Mathematical Problems in Engineering*, vol. 2020, 2020.

[17] M. J. Moran, H. N. Shapiro, D. D. Boettner, and M. B. Bailey, *Fundamentals of engineering thermodynamics*: John Wiley & Sons, 2010.

[18] C. A. Kircher, R. V. Whitman, and W. T. Holmes, "HAZUS earthquake loss estimation methods," *Natural Hazards Review*, vol. 7, pp. 45-59, 2006.

COMPDYN 2023
9th ECCOMAS Thematic Conference on
Computational Methods in Structural Dynamics and Earthquake Engineering
M. Papadrakakis, M. Fragiadakis (eds.)
Athens, Greece, 12-14 June 2023

# A NEW METHODOLOGY FOR COMBINED SEISMIC AND ENERGY ASSESSMENT OF BUILDINGS

**Sotiria Stefanidou[1], Olga Markogiannaki [1], Anna Karatzetzou[1], Charoula Zaki[1], Anna Diamanti[1]**

[1] SURE Competence Center
Koila Kozanis, Greece
e-mails: sotiria.stefanidou@gmail.com, markogiannaki.olga@gmail.com, akaratze@civil.auth.gr
charoulazk18@gmail.com, anna.diam13@gmail.com

## Abstract

*Due to climate change and the increasing $CO_2$ emissions within the years, the European Union has set up ambitious targets for the decrease of the energy consumption until 2030, promoting funding programs for interventions that increase the energy class of the buildings. In addition, the damage level and the losses after recent earthquake events highlighted the need for pre-earthquake assessment and strengthening of buildings, ensuring life safety and functionality. Several methodologies exist in the literature, proposing seismic classes and a first order prioritization (ranking) system for buildings within an inventory. A second stage assessment is also proposed for the critical buildings of the first ranking, based on risk indexes estimated for selected hazard scenarios and fragility curves. Methodologies and indexes for the combined seismic and energy assessment have also been recently proposed, however, their application is limited to pilot studies and selected inventories. Due to the increased scientific interest on the combined seismic and energy assessment a new methodology has been developed and applied within SURE (Competence Center for Sustainable and Resilient Built Environment). The proposed methodology is based on the fragility curves of buildings and the correlation of seismic hazard with the performance levels (limit states) in order to provide an index indicative of the seismic performance for various levels of earthquake intensity and the relevant damage probability, also proposing weighting factors. The safety index is subsequently combined with an energy efficiency index to provide a holistic approach for the seismic and energy assessment. The energy efficiency index is based on the energy consumption level of buildings and their corresponding classification. The energy-safety bilateral indices provide valuable input to support decision-making systems on renovation strategies of private and public building inventories.*

**Keywords:** seismic assessment, energy assessment, building inventory, performance levels, combined index

## 1 INTRODUCTION

In contemporary society, communities are increasingly exposed to natural disasters, highlighting the necessity of building safety. Nevertheless, the majority of existing buildings lack compliance with modern seismic [1] and energy [2] codes and standards, making them susceptible to significant earthquake damage and energy deficiency. This situation results in substantial economic losses, expressed in terms of human casualties, high damage costs, and excessive energy consumption. To address this, preventive measures and retrofitting solutions seem vital. However, until recently, seismic and energy issues have only been handled independently. Contrary to this practice, adopting an integrated holistic approach that combines seismic and energy considerations would provide a more accurate infrastructure performance assessment and successful risk mitigation. More specifically, implementing energy interventions in buildings significantly impacted by earthquakes seems unfeasible, since seismic damage could undermine the effectiveness and economic viability of energy retrofit investments. A comprehensive approach also extends the building lifespan, aligns with sustainable growth policies, reduces energy demand, and minimizes the need for constructing new buildings. Despite prior research efforts in recent years, there is a need for additional investigation into the current issue. This paper represents a further endeavor, aiming at developing a comprehensive combined seismic and energy performance assessment methodology. To address this purpose, seismic and energy efficiency methods are first reported individually, ultimately leading to combined estimation approaches.

The seismic performance evaluation comprises various methods, mainly focusing on probabilistic seismic performance assessment and risk prioritization. Regarding the first, building-based assessment approach, the initial step involves establishing a classification system, aiming at a comprehensive database development [3]. Subsequently, a structural finite element model is compiled and subjected to a seismic intensity measure (IM), linked to the results of the probabilistic seismic hazard analysis. The response output, Engineering Demand Parameter (EDP), captures inter-storey drifts and enables the estimation of building losses. Depending on the research scope and available resources, researchers choose between two main analysis types, Non-Linear Static analysis (NLS) [4] or Non-Linear Dynamic analysis (NLD) [5]. The NLS, also known as pushover analysis, generates capacity curves, which ultimately identify the thresholds of damage states. Given the capacity of the structure, the model is consequently submitted to multiple earthquake intensities, to evaluate the structural seismic performance. The pushover curve is transformed from Force-Displacement to Acceleration-Displacement-Response Spectra (ADRS), utilizing the acceleration-response spectra acquired from seismic records [6]. On the other hand, NLD analysis requires ground motion records for dynamic analysis on a numerical model employing Incremental Dynamic Analysis (IDA) [7]. Both methods produce fragility curves for the predefined damage states, enabling the generation of vulnerability curves by translating physical damage into monetary losses [8]. Combining vulnerability curves with calculated direct loss functions, functionality curves are derived as a percentage of a structure's functionality over time [9]. Ultimately, the Seismic Resilience Index (SRI) can be calculated as the area under the functionality curve, providing a quantitative measure for assessing seismic performance. In some cases, the robustness index is also estimated, a measure that denotes a system's ability to limit the number of failed components and prevent collapse [5]. The alternative approach to evaluating the seismic resilience of buildings involves estimating a risk ranking index. The methodology entails computing a vulnerability index that identifies high-risk buildings based on increasingly detailed filters [10]. Alternatively, a nominal seismic risk index can be estimated based on visual inspection forms for buildings [11]. By encompassing the sum of all infrastructure information, a total building

score is calculated, to express the seismic risk class or performance assessment of the infrastructure [12] [13].

Regarding the energy performance assessment, a building categorization of energy classes is developed, expressed in terms of primary energy consumption. Specifically, an energy study is carried out, where a reference building with identical geometric attributes (location, orientation, use) to the inspected one is modeled and is by default categorized as energy class B. Respectively the energy classification of the existing inspected building is estimated as the ratio of primary energy consumption between the existing and reference building. To address this, a specialized energy analysis software, compliant with relevant regulations [14] is utilized. This software incorporates a comprehensive set of building data, encompassing geometric parameters, structural and non-structural components, and thermal characteristics. The primary energy consumption is quantified separately for each end use, both in the existing and the reference building. The resulting energy classification indicates the infrastructure energy efficiency, ranging from A+ (highest achievable energy class) to G (lowest energy class). The classification of the inspected building is determined as the ratio of total primary energy (across all end uses) of the existing (inspected) and reference structure.

However, as already mentioned, no real optimization can be achieved, as a good structural solution could correspond to poor environmental performance and vice versa, highlighting the importance of a combined seismic and energy assessment approach. Most of the modern methodologies, propose an integrated seismic and energy efficiency estimation, expressed in terms of economic parameters, namely cost estimation indices prior to or after retrofitting solutions. More specifically, a comprehensive method initially developed by Romano et al. [15] and later refined by Tornaghi et al. [16], comprises structural and environmental aspects of buildings and summarizes them into a single economic parameter. The SSD (Sustainable Structural Design) approach is based on three main evaluation steps, namely, Energy Performance Assessment, Life-Cycle Assessment, and Structural Performance Assessment. The first two procedures determine the energy consumption and equivalent $CO_2$ emissions, respectively, while the third one evaluates the building safety performance with respect to structural costs. The final step involves converting the outcomes of the three procedures into economic terms to establish the Global Assessment Parameter of the SSD methodology. Other researchers [17] aim to determine the economic feasibility of the proposed retrofitting alternatives of existing RC structures, in terms of losses. This involves seismic and thermal analyses before and after retrofitting implementation. Economic feasibility is evaluated using the expected annual loss (EAL) measure, which estimates the potential loss in value of the construction over a given period, such as one year. The EAL value is calculated as the sum of two components: the expected annual energy loss ($EAL_E$), namely the annual energy building consumption multiplied by relative energy cost units, and the expected annual seismic loss ($EAL_S$).

Notwithstanding the available modern research conducted on this subject so far, there remains a further need for future investigation into the development of an integrated framework that encompasses both seismic risk and energy efficiency of buildings. The present paper aims to address this issue, by employing a new comprehensive consistent approach to existing RC buildings.

## 2 METHODOLOGY

The proposed methodology identifies the seismic properties of the buildings of the repository. Based on these properties (i.e. structural system, infills, seismic code, regularities,etc.), the buildings are classified and then, the fragility curves are defined according to the database developed by Stefanidou et al. [18]. For every identified building class, the mean of the fragility curves available in the database is calculated at 5 different limit states, namely $LS_1$: Slight damage, $LS_2$: Minor damage, $LS_3$: Moderate damage, $LS_4$: Major damage, and $LS_5$: Collapse. For each i-th limit state, an $ag_{,50,i}$ is defined as the horizontal ground acceleration that corresponds to a 50% probability of exceedance of each limit state, according to the respective fragility curve. Each limit state is also matched with a different performance level, i.e., $PL_1$: Operationality, $PL_2$: Damage limitation, $PL_3$: Significant damage, $PL_4$: Near collapse, and $PL_5$: Collapse, respectively, which in turn corresponds to a specific return period ($T_p$). A targeted performance level is selected and the ag of each building site that corresponds to this performance level is defined as the $a_{g,LSi}$, expressing the seismic hazard of the examined building site, following the values of Table 1. The ratio of these two $a_g$ values is the safety factor against the i-th limit state:

$$SF_i = \frac{a_{g,50,i}}{a_{g,LSi}} \quad (1)$$

The prioritization criterion, which is the main outcome of this procedure, is the Structural Performance Index, calculated according to Eq. 2:

$$SPI = \sum_{i=1}^{5} SF_i \cdot W_{PLi} \quad (2)$$

where $W_{PL,i}$ is a user-selected weighting factor for every assessed performance level i, indicating the influence of each performance level on the prioritization of the buildings in terms of the necessity to retrofit. The sum of the weighting factors $\sum_{i=1}^{5} W_{PLi}$ should always be equal to 1. For instance, if the user selects $W_{PL,4} = 1$ and $W_{PL,1} = W_{PL,2} = W_{PL,3} = W_{PL,5} = 0$ for an examined building stock, it is implied that the structural prioritization of the buildings within this stock will be based exclusively on the 'Near Collapse' performance level.

| Matching between $LS_i$ (Limit State) / $PL_i$ (Performance Level) and $T_p$ (Return period) | | | | | |
|---|---|---|---|---|---|
| Building Consequence Class (CC) | $T_p$ years | | | | |
| | LS: LS1 (Slight) PL: OP (Operationality) | LS: LS2 (Minor) PL: DL(Damage Limitation) | LS: LS3(Moderate) PL: SD (Significant Damage) | LS: LS4 (Major) PL: NC (Near Collapse) | LS: LS5 (Collapse) PL: C (Collapse) |
| CC1 – Minor importance for public safety | 30 | 50 | 50 | 250 | 800 |
| **CC2- Ordinary** | **40** | **60** | **60** | **475** | **1600** |
| CC3a – Important consequences associated with collapse | 40 | 60 | 60 | 800 | 2500 |

| | | | | | |
|---|---|---|---|---|---|
| CC3b – Vital importance for civil protection | 80 | 100 | 100 | 1600 | 5000 |

Table 1 Matching between $LS_i$ / $PL_i$ and $T_p$

The steps of the proposed methodology are described in the following:

**Step 1**: Identification of the building repository properties.

**Step 2**: Classification of the selected buildings according to their structural properties to the classes of the database.

**Step 3**: Input of the building properties to the fragility curve database.

**Step 4**: Fragility curves of the selected buildings at 5 limit states (LSi, i = [1,2,3,4,5]).

**Step 5**: Matching between LSi (Limit State) with the corresponding performance level (PL) and $T_p$ (return period), based on Table 1.

LS1: slight damage, corresponding to the 'operationality' performance level, LS2: minor damage, corresponding to the 'damage limitation' performance level, LS3: moderate damage, corresponding to the 'significant damage' performance level, LS4: major damage, corresponding to the 'near damage' performance level, LS5: collapse, corresponding to the 'collapse' performance level.

**Step 6**: Calculation of Safety Factor related to every considered i-th limit state: $SF_i = \frac{a_{g,50,i}}{a_{g,LSi}}$

where $\alpha_{g,50,i}$ is the horizontal ground acceleration derived from the fragility curves corresponding to a 50% probability of exceedance of LSi for the examined building, and $\alpha_{g,LSi}$ is the horizontal ground acceleration that expresses the seismic hazard of the examined building site and corresponds to a selected limit state i, according to Table 1.

**Step 7**: Calculation of SPI (Structural Prioritization Index): $SPI = \sum_{i=1}^{5} SF_i \cdot W_{PLi}$

The building energy assessment begins with the identification of the thermophysical properties and geometrical characteristics of the buildings of the repository and then their primary energy consumption is calculated according to the Greek Regulation on the Energy Performance of Buildings (REPB) [19]. Based on this consumption, the buildings are categorized into the 9 building energy classes that are defined by the classification system of the Greek REPB. In this regulation, the categorization of the buildings is based on the ratio of the primary energy consumption of the examined building over the primary energy consumption of the 'reference building' (Table 2), which is a building unit that is similar to the studied building in terms of geometry, location, orientation, use and operation characteristics, but its technical specifications meet the minimum requirements imposed by the REPB for the construction of new buildings. Other systems that adopt raw values of the primary energy consumption as classification criterion can also be adopted, such as the various regional specifications of the Italian building classification (Table 3). In the presented framework, the categories of the selected classification system are matched to an increasing index, starting from 1 for the lowest energy class (i.e., the class that corresponds to the buildings with the highest primary energy consumption). Last, an Energy Prioritization Index (EPI) corresponding to the building energy class is defined. The steps of the proposed methodology are described concisely in the following:

**Step 1**: Identification of the building repository properties

**Step 2**: Calculation of the total primary energy consumption per end use for the selected and reference building

**Step 3**: Classification of the buildings to energy classes according to their primary energy consumption or the Greek EPB Regulation classification system.

**Step 4**: Energy Prioritization Index (EPI), corresponding to the building energy class.

| Energy Class | Energy Performance |
|---|---|
| A+ | EP < 0.3 |
| A | 0.33 < EP < 0.5 |
| B+ | 0.5 < EP < 0.75 |
| B | 0.75 < EP < 1 |
| C | 1 < EP < 1.41 |
| D | 1.41 < EP < 1.82 |
| E | 1.82 < EP < 2.27 |
| F | 2.27 < EP < 2.73 |
| G | 2.73 < EP |

Table 2 Energy classification of buildings depending on the comparison with the reference building [19]

| Energy Class | Primary Energy Consumption (Residential) (kWh/m$^2$) |
|---|---|
| A+ | $EP_{tot} < 25$ |
| A | $25 < EP_{tot} < 40$ |
| B | $40 < EP_{tot} < 60$ |
| C | $60 < EP_{tot} < 90$ |
| D | $90 < EP_{tot} < 130$ |
| E | $130 < EP_{tot} < 170$ |
| F | $170 < EP_{tot} < 210$ |
| G | $EP_{tot} > 210$ |

Table 3 Energy classification of buildings depending on their primary energy consumption (Italian building classification, regional specification for Emilia-Romagna) [20]

Energy classes derived from the energy analysis categorize the building to the energy prioritization index respectively, indicating the priority order for energy upgrade interventions, as illustrated in Table 4.

| Energy Class | Energy Prioritization Index |
|---|---|
| A+ | 1 |
| A | 2 |
| B+ | 3 |
| B | 4 |
| C | 5 |
| D | 6 |
| E | 7 |
| F | 8 |
| G | 9 |

Table 4 Energy class and prioritization index correspondence

Once the seismic and energy prioritization indices are calculated, a comprehensive integrated index is estimated with respect to the priority order required for future seismic and energy retrofit interventions. Three prioritization levels are developed, Low, Medium, and High according to the building seismic and energy assessment respectively. Table 5 and Table 6 depict the corresponding range values for the three levels based on the SPI and EPI index respectively.

| Prioritization Level | SPI |
|---|---|
| Low | >2.5 |
| Medium | 1 - 2.5 |
| High | <1 |

Table 5 Prioritization level – SPI correspondence

| Prioritization Level | EPI |
|---|---|
| Low | 1, 2, 3 |
| Medium | 4, 5, 6 |
| High | 7, 8, 9 |

Table 6 Prioritization level – EPI correspondence

A 4x4 “color cell” matrix is ultimately developed, demonstrating the priority level order for seismic and energy retrofit interventions respectively, as depicted in Table 7.

| | E1 (Low) | E2 (Medium) | E3 (High) |
|---|---|---|---|
| S1 (Low) | | | |
| S2 (Medium) | | | |
| S3 (High) | | | |

Table 7 Prioritization seismic and energy level

# 3 CASE STUDY APPLICATIONS

## 3.1 Description of the buildings

The application of the methodology to selected case studies aims to demonstrate the concept of the herein proposed framework for combined seismic and energy assessment of buildings. For the implementation of the methodology, four distinct RC buildings, located in Greece, are selected, aiming at encompassing a range of structural and energy-related characteristics. The selected buildings differ in terms of their structural system, the year of their construction, the number of storeys, plan, and elevation regularity, and energy classification.

An existing reinforced concrete four-storey apartment building (A) constructed in the Municipality of Kozani in the 1980s, is first considered. It's a moment-resisting frame with plan and elevation regularity. Prior to any energy retrofitting interventions, the total primary energy consumption categorizes the structure as energy class F. The second selected building (B), as illustrated in Fig. 1., is a 1980s two-storey residential building in Kozani respectively, characterized by a moment-resisting frame with shear walls and energy classification G according to energy performance.

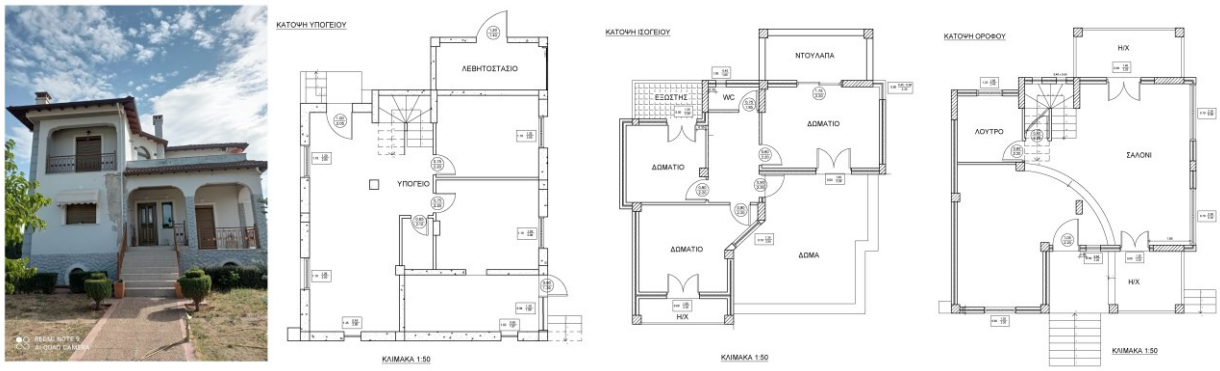


Figure 1 Photograph and plan view of building B in Kozani

The two remaining selected buildings are both located in the Municipality of Thessaloniki, one constructed prior to 1959 while the other in the 1980s respectively. Specifically, a single-storey residential building (C) is studied, plan, and elevation regular with a force-resisting frame as structural system. Based on its primary energy consumption is classified as energy category G. Fig. 2 depicts a 1980s five-storey apartment (D) with pilotis in Thessaloniki respectively. It employs a moment-resisting frame and is categorized as energy class E.

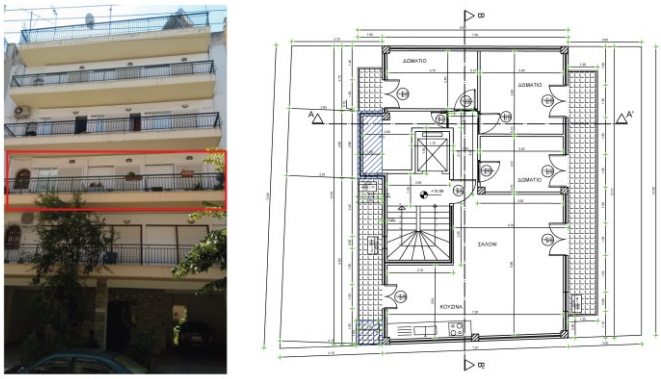


Figure 2: Photograph and plan view of building D in Thessaloniki

Table 8 provides a cumulative overview of the seismic and energy properties of the building classification, required for the application of the proposed methodology.

| Building | Properties | | | | | | | |
|---|---|---|---|---|---|---|---|---|
| | Force Resisting Mechanism | Height Level | Code Level | Intensity Measure | Plan/ Elevation Regularity | Infill | Ductility | Energy class |
| A | Moment-Resisting Frame | Mid Rise (4-7) | Low Code | PGA | Regular/ Regular | Regular Infill | Non-Ductile | F |
| B | Moment-Resisting Frame with shear Walls | Low Rise (1-3) | Non-Code | PGA | Irregular/ Irregular | Regular Infill | Non-Ductile | G |
| C | Moment-Resisting Frame | Low Rise (1-3) | Low Code | PGA | Regular/ Regular | Regular Infill | Non-Ductile | G |
| D | Moment-Resisting Frame | Mid Rise (4-7) | Low Code | PGA | Regular/ Regular | Irregular Infill | Non-Ductile | E |

Table 8 Building Taxonomy

### 3.2 Application of the methodology proposed

Once the building taxonomy is established, the methodology proposes individually estimating the seismic and energy prioritization index. A cloud fragility database [18] is employed, containing the available in literature fragility curves. Fragility curves for five predefined limit states are extracted, by utilizing the structural building properties as search criteria. To estimate the Structural Prioritization Index (SPI), the seismic hazard is to be initially assessed, using the European Seismic Hazard Model 2020 (ESHM20) [21] through the EFEHR web platform, a network aiming at earthquake hazard and risk assessment in the European-Mediterranean region. The hazard curve development includes selecting the location of interest based on the geographical coordinates for each of the four selected buildings. Subsequently, the hazard model for a relevant intensity measure (in the present paper peak ground accelerations are utilized) are determined. Finally, the site class and aggregation type are specified. Fig. 3 illustrates the hazard curve for building C, indicating the probability of exceedance of the selected seismic action over a 50-year period.

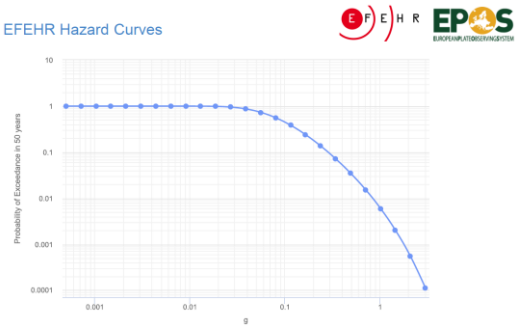


Figure 3 Hazard curve of building C

Table 9 summarizes the horizontal ground acceleration $a_{g,\,LSi}$ estimated from the generated hazard curves of all four buildings, expressing the seismic hazard of the examined building corresponding to the selected limit states.

| Building | $a_{g,LSi}$ (m/s$^2$) | | | | |
|---|---|---|---|---|---|
| | LS1 (Slight) | LS2 (Minor) | LS3 (Moderate) | LS4 (Major) | LS5 (Collapse) |
| | $T_P$ years (CC2) | | | | |
| | 40 | 60 | 60 | 475 | 1600 |
| A | 0.049 | 0.066 | 0.066 | 0.223 | 0.397 |
| B | 0.052 | 0.069 | 0.069 | 0.227 | 0.380 |
| C | 0.058 | 0.078 | 0.078 | 0.279 | 0.511 |
| D | 0.058 | 0.078 | 0.078 | 0.270 | 0.490 |

Table 9 $a_{g,LSi}$ values overview

Aligning with the steps outlined in the methodology section, the horizontal ground acceleration $a_{g,50,i.}$ is derived from the generated mean fragility curves, as depicted in Fig. 4, corresponding to a 50% probability of exceedance for each limit state of the selected buildings. Table 10 provides a comprehensive overview of the horizontal ground acceleration values, a prerequisite measure for the Safety Factor assessment.

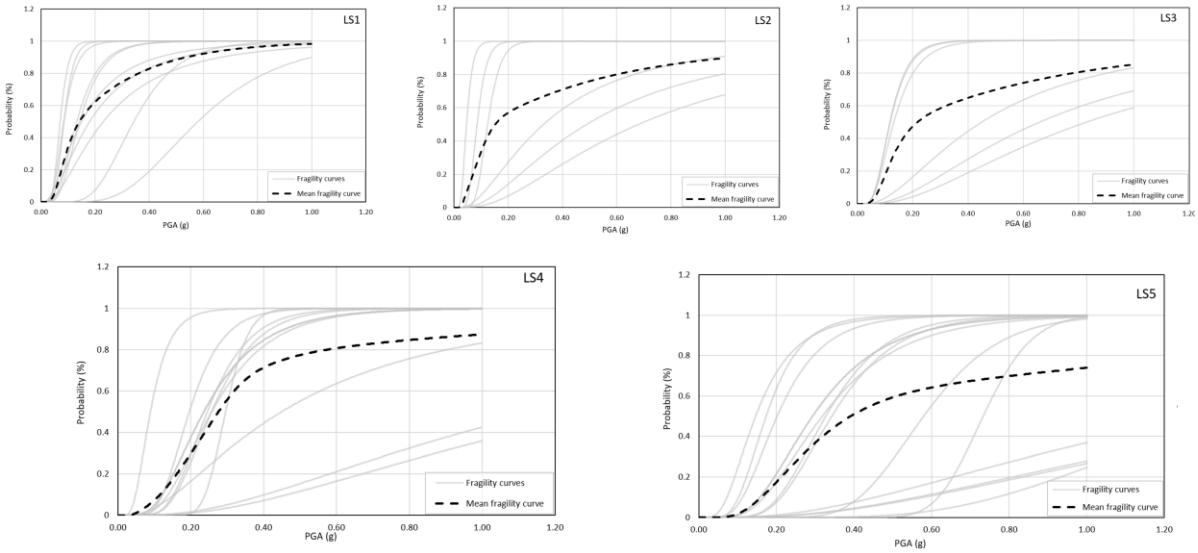


Figure 4 Mean and fragility curves for the five limit states

| Building | $a_{g,50,i}$ (m/s$^2$) | | | | |
|---|---|---|---|---|---|
| | LS1 (Slight) | LS2 (Minor) | LS3 (Moderate) | LS4 (Major) | LS5 (Collapse) |
| A | 0.021 | 0.090 | 0.199 | 0.218 | 0.311 |
| B | 0.070 | 0.280 | 0.464 | 0.618 | 0.850 |
| C | 0.142 | 0.152 | 0.217 | 0.276 | 0.391 |
| D | 0.020 | 0.021 | 0.083 | 0.117 | 0.283 |

Table 10 $a_{g,50,i}$ values overview

The Safety Factor index estimation is ultimately established as the ratio of horizontal ground accelerations $a_{g,50,i}$ and $a_{g,LSi}$, as depicted in Table 11. The Structural Prioritization Index (SPI) is then derived by multiplying the safety factor values for all limit states of the selected buildings with user-selecting weighting factors $W_{LSi}$ for each performance level, highlighting the influence of Limit State 4, representative of design earthquake with a return period of 475 years.

| Building | SFi | | | | | Wi | | | | | SPI |
|---|---|---|---|---|---|---|---|---|---|---|---|
| | LS1 | LS2 | LS3 | LS4 | LS5 | LS1 | LS2 | LS3 | LS4 | LS5 | |
| A | 0.429 | 1.364 | 3.015 | 0.978 | 0.783 | 0.125 | 0.125 | 0.125 | 0.50 | 0.125 | 1.19 |
| B | 1.346 | 4.058 | 6.725 | 2.722 | 2.237 | 0.125 | 0.125 | 0.125 | 0.50 | 0.125 | 3.16 |
| C | 2.448 | 1.949 | 2.782 | 0.989 | 0.765 | 0.125 | 0.125 | 0.125 | 0.50 | 0.125 | 1.49 |
| D | 0.345 | 0.269 | 1.064 | 0.433 | 0.578 | 0.125 | 0.125 | 0.125 | 0.50 | 0.125 | 0.50 |

Table 11 Structural Performance Index assessment

The present framework proposes the Energy Prioritization Index (EPI) assessment as the ratio of the primary energy consumption of the selected, existing building to the reference one. The energy analysis TEE KENAK software [14] was employed to estimate the primary energy consumption per end-use, encompassing all building parameters, namely geometric data, thermophysical properties of structural elements, and technical characteristics of the HVAC systems. Energy classes derived from the energy analysis categorize the building to the energy prioritization index respectively, indicating the priority order for energy upgrade interventions (see Table 4). Table 12 describes the Energy Prioritization Index (EPI) assessment for the four selected buildings, corresponding to the estimated energy classes.

| Building | Inspected building Total primary energy consumption ($kWh/m^2$) | Reference building Total primary energy consumption ($kWh/m^2$) | Energy Class | EPI |
|---|---|---|---|---|
| A | 316.3 | 128.6 | F | 8 |
| B | 491.2 | 177.0 | G | 9 |
| C | 1041.7 | 183.6 | G | 9 |
| D | 335 | 174.3 | E | 7 |

Table 12 Energy Performance Index assessment

The four selected buildings considered in this case study are classified into three different levels (Low, Medium, High) according to their priority order for future seismic and energy interventions. Table 13 presents the prioritization level categorization based on Tables 5 and 6 for the seismic and energy indices respectively, applied for the set of the four buildings, as illustrated in Table 14.

| Building | SPI Level | EPI Level |
|---|---|---|
| A | S2 (Medium) | E3 (High) |
| B | S1 (Low) | E3 (High) |
| C | S2 (Medium) | E3 (High) |
| D | S3 (High) | E3 (High) |

Table 13 Prioritization SPI and EPI levels

| | E1 (Low) | E2 (Medium) | E3 (High) |
|---|---|---|---|
| S1 (Low) | | | Building B |
| S2 (Medium) | | | Building A, C |
| S3 (High) | | | Building D |

Table 14 Prioritization seismic and energy level for the selected buildings

## 4 CONCLUSIONS

The individually studied seismic and energy performance assessment of the existing RC buildings in modern literature, highlights the necessity of a comprehensive, integrated approach development. Despite the recent attempts of a combined seismic and energy efficiency investigation, parameters as performance levels and their weighting factors are usually overlooked in common practice. To address this gap, the present study encompasses five performance levels for a selected seismic hazard parameter, described by user-selected weighting factors with a primary focus on the design earthquake for a return period of 475 years. The applicability of the proposed methodology is examined through its implementation to four existing buildings with a minimal set of required parameters, namely a building classification system, hazard definition, and fragility data repository [18]. A qualitative index of three levels is ultimately developed, indicating the prioritization order for further seismic and energy upgrade and retrofit interventions. However, future research would undoubtedly enhance knowledge about this relatively new subject of integrating building design.

## 5 AKNOWLEDGEMENT

This research is co-financed by Greece and the European Union (European Social Fund- ESF) through the Operational Programme “Competitiveness Enterpreneurship Innovation 2014-2020” in the action «Competence Centers» in the context of the project “Competence Center for a Sustainable and Resilient Built Environment using smart technologies” (MIS 5130744).

## REFERENCES


[1] CEN Eurocode 8 : Design of structures for earthquake resistance, Part 1, EN 1998-1 (2004).

[2] Directive 2010/31/EU of the European Parliament and of the Council of 19 May 2010 on the energy performance of buildings (2010)

[3] D'Ayala, D., Galasso, C., Nassirpour, A., Adhikari, R. K., Yamin, L., Fernandez, R., Lo, D., Garciano, L., & Oreta, A., Resilient communities through safer schools, International Journal of Disaster Risk Reduction, 2020.

[4] Cosenza, E., Del Vecchio, C., Di Ludovico, M., Dolce, M., Moroni, C., Prota, A., & Renzi, E., The Italian guidelines for seismic risk classification of constructions: technical principles and validation, Bulletin of Earthquake Engineering, 2018.

[5] Chee Yin, H., Kassem, M. M., Mohamed Nazri, F., & El Maissi, A. M, Development of seismic resilience index methodology for RC structures via functionality curve, MethodsX, 2022.

[6] Ayala, D. ', Meslem, A., Vamvatsikos, D., Porter, K., Rossetto, T., & Silva, V, GEM GLOBAL EARTHQUAKE MODEL Vulnerability and loss modelling GEM TECHNICAL REPORT 2014-12 V1.0.0 Guidelines for Analytical Vulnerability Assessment-Low/Mid-Rise, 2015.

[7] Rezaei Ranjbar, P., & Naderpour, H, Probabilistic evaluation of seismic resilience for typical vital buildings in terms of vulnerability curves. Structures, 23, 314–323, 2020.

[8] Samadian, D., Ghafory-Ashtiany, M., Naderpour, H., & Eghbali, M., Seismic resilience evaluation based on vulnerability curves for existing and retrofitted typical RC school buildings, Soil Dynamics and Earthquake Engineering, 127, 2019.

[9] Lu, X., Liao, W., Fang, D., Lin, K., Tian, Y., Zhang, C., Zheng, Z., & Zhao, P., Quantification of disaster resilience in civil engineering: A review, Journal of Safety Science and Resilience, 1(1), 19–30, 2020.

[10] Petruzzelli, F., & Iervolino, I., NODE: a large‐scale seismic risk prioritization tool for Italy based on nominal structural performance, Bulletin of Earthquake Engineering, 19(7), 2763–2796, 2021.

[11] FEMA P-154, Rapid Visual Screening of Buildings for Potential Seismic Hazards: A Handbook Third Edition, 2015.

[12] FEK_405_b_2014_dedota, E.P.P.O (Earthquake Planning and Protection Organization), 2014.

[13] New Zealand Society for Earthquake Engineering, Assessment and improvement of the structural performance of buildings in earthquakes: prioritisation, initial evaluation, detailed assessment, improvement measures: recommendations of a NZSEE study group on earthquake risk buildings, 2006.

[14] Technical Chamber of Greece, TEE KENAK 1.29. 1.19: Software Inspection and Certification of Energy Buildings, Study of Energy Efficiency Boiler Inspection/Heating In-

stallations and Facilities Air Conditioning-Manual. Technical Chamber of Greece Publications Athens, Greece, 2012.

[15] Romano, Elvira., Negro, Paolo., Taucer, Fabio., & European Commission, Joint Research Centre. Institute for the Protection and the Security of the Citizen., Seismic performance assessment addressing sustainability and energy efficiency. Publications Office, 2014.

[16] Lamperti Tornaghi, M., Loli, A., & Negro, P., Balanced evaluation of structural and environmental performances in building design, Buildings, 2018.

[17] Gkournelos, P. D., Bournas, D. A., & Triantafillou, T. C., Combined seismic and energy upgrading of existing reinforced concrete buildings using TRM jacketing and thermal insulation, Earthquake and Structures, 2019.

[18] Stefanidou S., Markogiannaki O., Mixios K., Argyroudis S., & Fragiadakis M., Database and comparative evaluation of seismic fragility curves for RC buildings., 2022.

[19] Dascalaki, E. G., Balaras, C. A., Gaglia, A. G., Droutsa, K. G., & Kontoyiannidis, S., Energy performance of buildings-EPBD in Greece. Energy Policy, 45, 469–477, 2012.

[20] Calvi, G. M., Sousa, L., & Ruggeri, C., Energy efficiency and seismic resilience: A common approach. In Multi-Hazard Approaches to Civil Infrastructure Engineering (pp. 165–208). Springer International Publishing, 2016.

[21] Danciu L., Nandan S., Reyes C., Basili R., Weatherill G., Beauval C., Rovida A., Vilanova S., Sesetyan K., Bard P-Y., Cotton F., Wiemer S., Giardini D., The 2020 update of the European Seismic Hazard Model: Model Overview. EFEHR Technical Report 001, v1.0.0, 2021.

COMPDYN 2023
9th ECCOMAS Thematic Conference on
Computational Methods in Structural Dynamics and Earthquake Engineering
M. Papadrakakis, M. Fragiadakis (eds.)
Athens, Greece, 12-14 June 2023

# RELIABILITY ANALYSIS OF EMBEDDED BASE CONNECTIONS

**Pablo Torres-Rodas**[1], **Fernando Gomez**[2]

[1] Universidad San Francisco de Quito USFQ, Colegio de Ciencias e Ingenierías
Diego de Robles
e-mail: patorresr@usfq.edu.ec

[2] Universidad San Francisco de Quito USFQ, Colegio de Ciencias e Ingenierías
Diego de Robles
fgomez@usfq.edu.ec

## Abstract

*Column base connections are critical components of Steel Moment Frames (SMFs) since these connections transfer the loads (e.g., gravity, seismic) from the superstructure to the concrete foundation, being an interface between them. Because of it, these connections have been extensively investigated in the last decade. Notable large-scale experimental programs have been conducted, and numerical and analytical investigations have complemented these programs. Traditionally, column-base connections are divided into exposed base plates and embedded bases. The former type of connection is mainly used for low and mid-rise buildings, while the latter detail is the norm for tall buildings.*

*The behavior of embedded base connections has been studied in recent experimental programs. As a result, design methodologies and models to simulate their hysteretic characteristics have been proposed. However, surprisingly a reliability analysis of these connections has not been conducted so far. Motivated by this issue, this study presents a reliability analysis of the embedded base connections with the aim of providing design recommendations. For this purpose, nonlinear mathematical models of archetype frames are developed and subjected to nonlinear dynamic analysis to obtain the column base connection demands. These results are then used to conduct statistical simulations and recommend preliminary resistance factors for the design of embedded base connections. Limitations of the investigation are discussed, and future lines of investigation are outlined.*

**Keywords:** Embedded Base Connections, Reliability Analysis, Earthquake Engineering, Steel Moment Frames

## 1 INTRODUCTION

In the context of earthquake-resistant design, column-base connections are perhaps the most critical component of Steel Moment Frames (SMFs). These connections transfer the loads (e.g., dead load, live load, or earthquake load) from the superstructure to the concrete foundation, being an interface between them. In relation to US engineering practice, column-base connections are traditionally divided into two groups: exposed base plates (EBPs) and embedded base connections (EBCs). The former detail is used in low and mid-rise buildings, while the second detail is the norm for tall buildings, where the applied loads make the exposed base plate detail impractical. Figure 1 illustrates both types of column base connections.

The importance of column base connections in the seismic performance of SMFs has led to the development of numerous research programs. Early studies on the topic started with experimental programs aimed at identifying modes of failure, understanding the performance, and establishing strength methodologies for EBPs. (e.g., [1–4]). These studies resulted in notable analytical models to predict the strength of EBPs (e.g., [5]). In the US, the Steel Design Guide 1 (DG1) [6] provides a design methodology for EBPs, while the Seismic Design Manual (Example 9 [7]) details practical examples regarding their design procedure. These documents constitute the basis of the modern design of EBPs. Subsequent studies on EBPs included experimental programs to refine the design methodologies described earlier (e.g., [8]). Other studies presented methodologies to estimate their rotational stiffness [9] and models to simulate their hysteretic behavior [10].

In contrast to EBPs, embedded base connections received attention more recently. Grilli and Kanvinde [11] conducted a large-scale experimental program to study the behavior of embedded base connections and suggested a strength method based on the tests. This method assumes an internal stress distribution responsible for counteracting the applied loads (Axial Load and Flexural Moment). This assumption is illustrated in Figure 2. As per this internal stress assumption, the applied loads are resisted by the interactions between the embedded column and the surrounding concrete foundation. Thus, the method postulates that the applied moment is resisted by the force-couple developed by the horizontal and vertical stresses (Figure 2), and the fraction of moment taken by each mechanism is computed with an empirical factor that depends on the embedded length.

Later studies on EBCs focus on methods to estimate their rotational stiffness and simulate their hysteretic behavior. For instance, Torres-Rodas et al. [12] developed a methodology to compute the secant stiffness of these connections by aggregating the deformations within their components (i.e., embedded column, surrounding media). Similarly, Torres-Rodas et al. [13] presented a hysteretic model to simulate the cyclic behavior of EBCs. This phenomenological model consists of a two-parallel springs model. Each spring captures the assumed load-carrying mechanism, i.e., horizontal bearing stresses and vertical bearing stresses. The model includes hysteretic rules appropriate for these connections as well as rules to predict cyclic deterioration observed in the experimental tests.

More recently, efforts have focused on determining appropriate load combinations for their design. Specifically, Torres-Rodas [14] recommended design loads for these connections based on nonlinear time history analyses (NTHA) of archetype steel moment frames (SMFs). Other studies investigated their behavior using sophisticated finite element models (e.g., [15–17]) determining internal stress distributions and patterns of deformation. Apart from that, the influence of the behavior of EBCs on the seismic performance of SMFs has been studied with the use of NTHA conducted on archetype frames [18–21]. These studies conclude that the EBCs pose good hysteretic characteristics that can be incorporated as part of the energy dissipative mechanisms of SMFs.

Although EBCs have been studied extensively in the last decade, reliability analyses of these components are absent in the literature. In contrast to EBCs, reliability analyses have been conducted on exposed base plates [22–24], but at least, to our best knowledge, are absent for EBCs. Motivated by this issue, this paper presents the first approximation to address the reliability analysis problem of EBCs. Specifically, this study presents preliminary strength resistance factors appropriate for the seismic design of these connections. Results from NTHA conducted on an 8-story archetype frame are used as seismic demands.

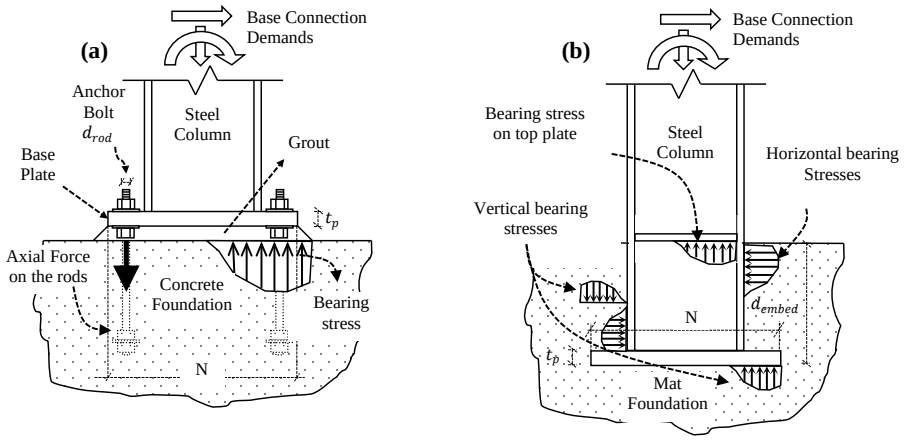


**Figure 1:** a) Exposed Base Plate, b) Embedded Base Connections [14].

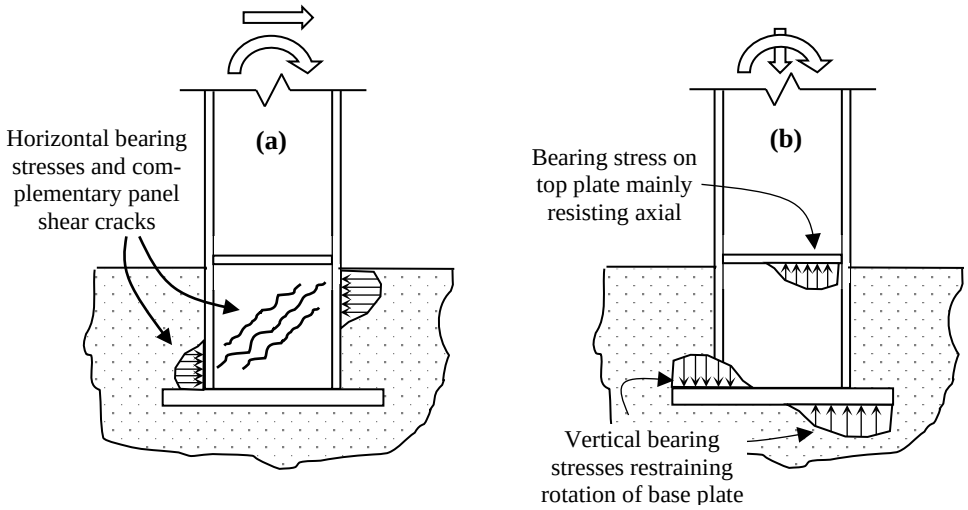


**Figure 2:** a) Horizontal bearing stresses, b) Vertical bearing stresses [12].

## 2 METHODOLOGY

This study conducted a reliability analysis of the design methodology of EBCs developed by Grilli and Kanvinde [11] using a single scenario, including dead, live, and earthquake loads. The earthquake loads are considered from NTHA carried out on an 8-story archetype SMF. Details of the nonlinear models and the ground motions used in the analyses are explained in the following subsections. The reliability analysis is conducted by means of Monte Carlo simulations, in which all the uncertainties are sampled from their respective assumed probability

density functions (PDF) and the number of failure cases is counted to compute the probability of failure.

## 2.1 Archetype Frame

For this study, an archetype SMF is used to conduct NTHA and monitor the demands at the column base connection. Specifically, an 8-story frame representative of US construction practice is used. Fig. 3a illustrates the plan view, while Fig. 3b shows the mathematical model representative of the SMF. As per these figures, the SMF is located at the perimeter of the building, while the other components are part of the gravity framing system. The building was designed as per ASCE 7-16 [25]. Thus, a dead load of 4.78 kN/m$^2$ and an unreduced live load of 2.38 kN/m$^2$ were applied to all floors except the roof, where the live load applied was 0.95 kN/m$^2$. Apart from these loads, a perimeter load of 1.20 kN/m$^2$ was considered to simulate the cladding. For the seismic design of the archetype frame, it was assumed the seismic design category $D_{max}$ and site class "D," which is consistent with the far-field conditions of the Los Angeles basin. The SMF is a three-bay frame with a width of 6.10m and a typical floor height of 3.90m, while the first-story floor is 4.50m.

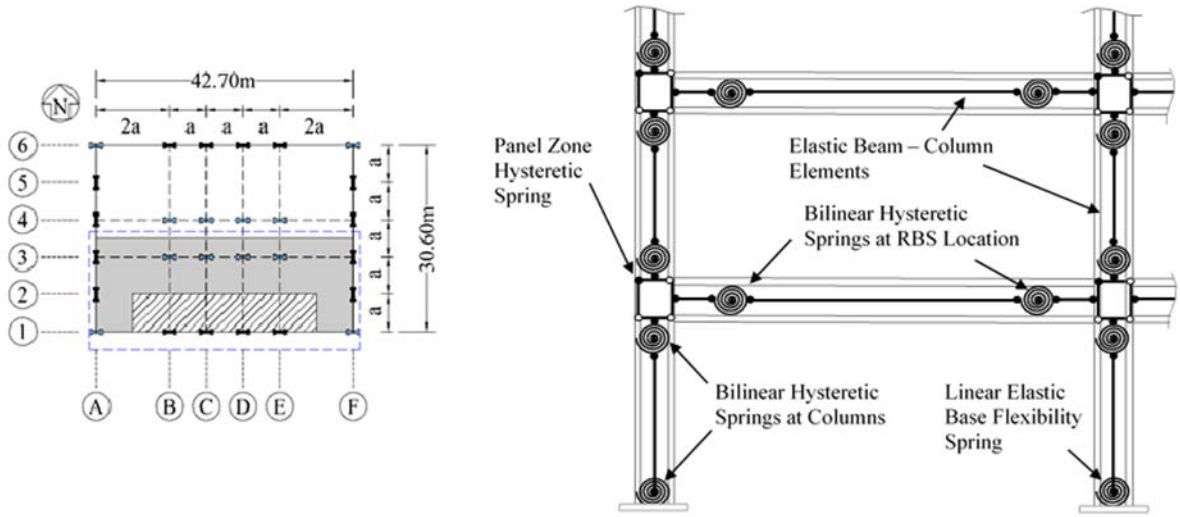


**Figure 3:** a) Typical plan view of all frames, b) Mathematical models of the SMFs

Referring to Figure 3b, concentrated plasticity models are used for the NTHA. This assumption is justified for the purpose of this research since several parametric studies on SMFs in the past have adopted this procedure (e.g., [18,19,21,26–29]). Thus, beams and columns are idealized as linear-elastic elements with nonlinear springs at their ends. These springs are simulated with the well-known IMK bilinear model [30]. This model consists of a trilinear backbone curve with rules to capture cyclic and in-cyclic strength and stiffness deterioration. As with all uniaxial plasticity models, the IMK model cannot capture the interaction between the axial load with the bending moment (P-M). This limitation is important in column members where P-M interaction is present and is addressed in an approximate manner. First, the gravity loads (dead load and live load) are assumed as an average value present during the NTHA. Next, the moment capacity of the columns is reduced with the interactive equations from AISC 360-16 [31], and this reduced moment is used in all the column springs. This procedure has been adopted in the past in several studies on SMFs (e.g., [20,21,29]) and has been validated experimentally in shaking tables [32].

The panel zones are idealized as a hinged parallelogram assembly by rigid elements with one single rotational spring in a corner to simulate shear distortion. A leaning column loaded with gravity loads corresponding to half of the area in the plan-building (Figure 3a) is used to capture the P-Δ effects through large displacement geometric nonlinear. Finally, the column base hysteretic behavior is simulated with the mathematical model developed by Torres-Rodas et al., 2018 [13] for embedded base connections.

### 2.2 Ground Motions

In this paper, the seismic demands in the EBCs are monitored through NTHA. The above-mentioned SMF is subjected to a total of 120 ground motion records. These records are obtained from the NGA-West 2 [33] database and consist of 4 sets of 30 records from different source conditions, including 1) near-fault ground motions from the reverse-fault mechanism, 2) near-fault ground motions from the strike-slipe mechanism, 3) far-fault ground motions from the reverse mechanism, 4) far-fault ground motions from the strike-slipe mechanism. The resulting set of 120 ground motions is scaled to the design basis earthquake intensity level (i.e., return period of 475 years) corresponding to the life safety performance limit state worldwide use for design purposes.

### 2.3 Column Base Connection Design

For the reliability assessment, a column base connection, representative of an 8-story SMF, is designed as per the strength method presented by Grilli and Kanvinde [11]. For this reason, the method is briefly summarized. First, the authors postulated a mechanism for internal force distribution within the connection. This mechanism consists of horizontal bearing stresses developed by the contact between the column flanges and the surrounding media, a concrete panel zone shear, and vertical bearing stresses of the embedded base plate. Thus, an indeterminate system results from this mechanism, which is solved by the use of an empirical coefficient that distributes the applied moment to each bearing mechanism (i.e., horizontal and vertical bearing stresses). This coefficient mainly relies on the embedded depth and is based on the Winkler beam theory on elastic media. Figure 2 idealizes the internal force distribution.

Following this design procedure, the CBCs of the 8-story SMF represented in Figure 3 are designed. For this purpose, a single-load combination scenario is assumed. Specifically, the load combination used herein to compute the axial load, shear, and applied moment is: $1.2D + 0.5L + \Omega_0 E$, which is consistent with published documents on the topic (e.g., [14,20,21]) where $D$ and $L$ are the Dead and Live Loads respectively, and E the earthquake load. The first to loads come from gravity analysis while the latter is computed from a pushover analysis. Table 1 summarizes the dimensions of the CBCs obtained.

| Column type | $d_{emb}$(mm) | $b_f$ (mm) | B (mm) | N (mm) | Mn (kN.m) |
|---|---|---|---|---|---|
| Exterior | 406 | 328 | 558 | 660 | 1167 |
| Interior | 914 | 508 | 762 | 762 | 2309 |

Table 1: Column base connection dimensions.

### 2.4 Reliability Assessment

The reliability analysis is divided into two components. First, from the NTHA, the reactions in the connections are computed as described previously. From each analysis, the envelopes of

the total shear V, axial P, and moment M in the connection are obtained. From these results, it is clear that these quantities are uncertain, and their probability density function (PDFs) needs to be estimated. From the numerical data, a kernel density estimation is computed for each quantity, which is assumed as a good estimation for the reliability analysis.

The second component consists of Monte Carlo simulations to estimate the probability of failure. The uncertain demands are given by V, P, and M in the connection, which is sampled from the estimated PDF in the first component. It is needed the inverse cumulative density function (CDF) for each of the random variables so that the variables are given by the inverse CDF of a random variable sampled uniformly in the interval [0,1]; the CDF is obtained directly, and a simple interpolation is used to obtain other values of the inverse CDF. These random variables are assumed as independent for this preliminary analysis. For the geometry and material properties, the following table provides the summary of the random variables considered, which are based on values in the study by Song et al. [24]. In this study, the dead and live loads are assumed deterministic as their values are small compared to the earthquake load, and the envelopes from the NTHA already include their effect.

| Variable | Bias | CoV (%) | Distribution |
|---|---|---|---|
| Base plate length | 1.0 | 2.5 | Normal |
| Base plate width | 1.0 | 4 | Normal |
| Base plate thickness | 1.0 | 3 | Normal |
| Embedment depth | 1.0 | 4 | Normal |
| Column properties | 1.0 | 2 | Normal |
| Concrete compressive strength | 1.235 | 14.5 | Normal |
| Yield strength of base plate steel | 1.16 | 7 | Normal |

Table 2: Summary of random variables for Geometry and Material properties.

The failure is assumed as demand exceeds capacity, given by the following equation:

$$f = M_n / \phi - M \leq 0 \tag{1}$$

where $M$ is the total demand that comes from the PDF obtained in the first component, $M_n$ is the capacity that is a function of the random variables in Table 2 and the uncertain reactions in the connection, and $\phi$ is a global reduction factor for the EBP. In the previous equation, as only one design is considered, the real capacity is approximated as the ratio of the capacity by the strength reduction factor. The probability of failure is estimated as the total cases where f is smaller than 0 over the total samples. The goal is this study is to obtain a global reduction factor $\phi$ for a target probability of failure.

## 3 ANALYSIS OF RESULTS

From the NHTA of the building with different earthquakes, the envelopes of the total shear V, axial P, and moment M in the connection are obtained. Figure 4 shows the histograms for this data for each quantity and exterior and interior columns. It also shows the kernel density estimates of the PDF for each quantity, which are used for the Monte Carlo simulations.

Next, the Monte Carlo simulations are performed using $10^6$ samples to obtain a global reduction factor $\phi$ for a target reliability index $\beta$ of 3.6, which is standard for connections subjected to gravity and seismic loads [24].

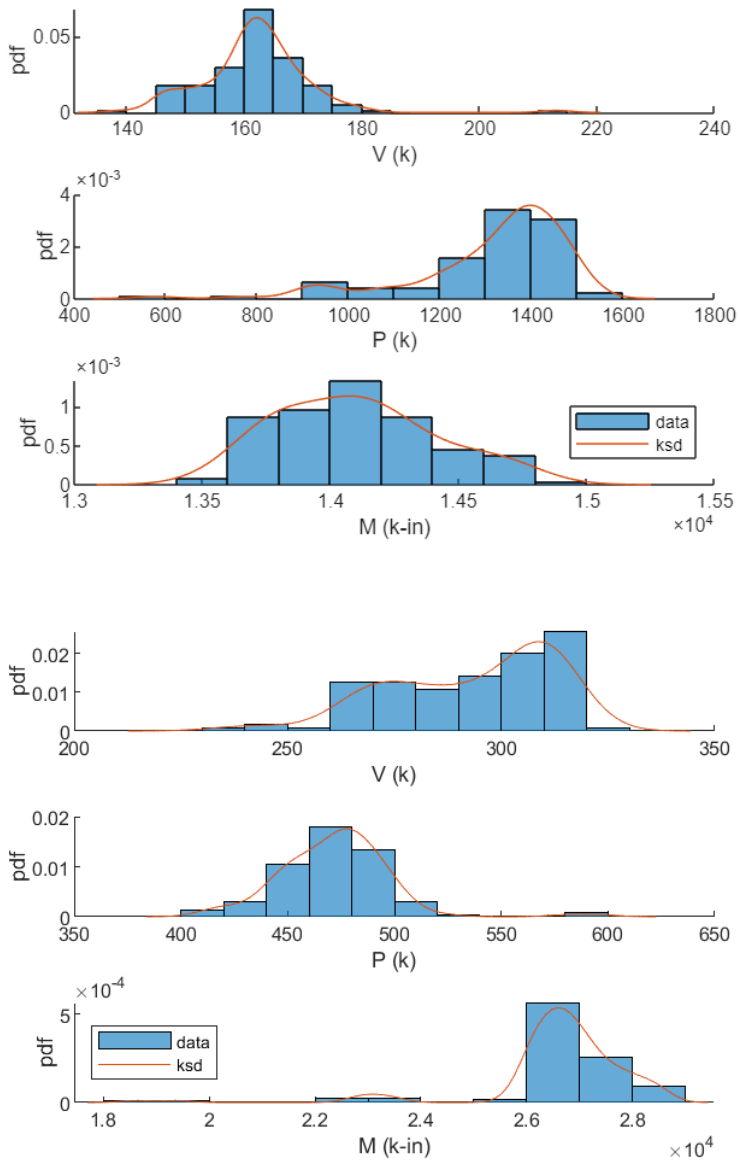


**Figure 4:** Histograms from the envelopes of V, P, and M in the connection from the NTHA and kernel density estimation PDFs for the a) exterior column and b) interior column

Figure 5 shows the curves of the reliability index vs. strength reduction factor for both types of columns. A median value is estimated from both cases, and as a result, a global reduction factor of 0.4 is recommended in this case. Note that obtained reduction factors are somewhat small due to the fact that the nominal capacities shown in Table 1 are smaller than the results obtained in the NTHA shown in Figure 4; consequently, this uncertainty in the connection load reduces the strength reduction factor.

Further studies are required to incorporate other designs as well as other building characteristics. Also, the obtained reduction factor is a global value, and it does not take into account the different types of failures; therefore, further studies are required to obtain a reduction factor for different contributions, as recommended in the study by Song et al. [24].

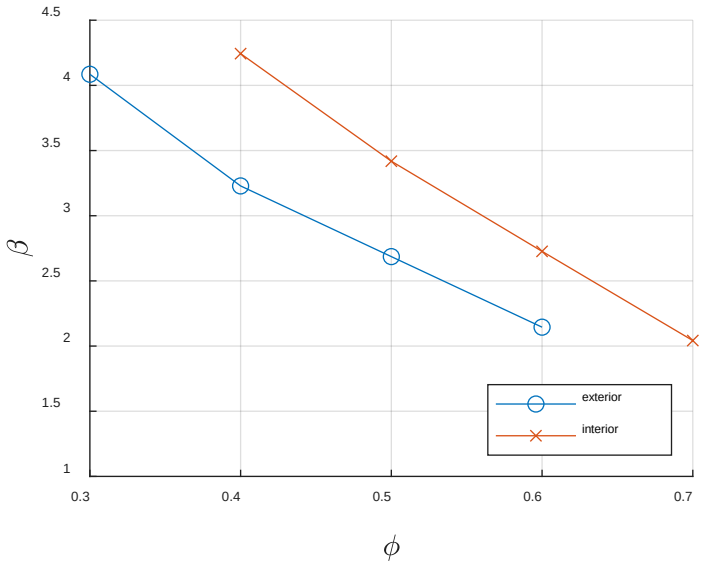


**Figure 5:** Reliability index vs. strength reduction factor

## 4 CONCLUSIONS

Column base connections are critical components of Steel Moment Frames (SMFs) since these connections transfer the loads (e.g., gravity, seismic) from the superstructure to the concrete foundation, being an interface between them. Notable large-scale experimental programs have been conducted, and numerical and analytical investigations have complemented these programs. Traditionally, column-base connections are divided into exposed base plates and embedded bases. The former type of connection is mainly used for low and mid-rise buildings, while the latter detail is the norm for tall buildings.

The behavior of embedded base connections has been studied in recent experimental programs. However, surprisingly a reliability analysis of these connections has not been conducted so far. Motivated by this issue, this study presents a reliability analysis of the embedded base connections with the aim of providing design recommendations. For this purpose, nonlinear mathematical models of archetype frames are developed and subjected to nonlinear dynamic analysis to obtain the column base connection demands. From the results of the NTHA, the probability distribution of the loads in the connection is obtained. Then, a Monte Carlo analysis is performed, including these uncertainties as well as material and geometry uncertainties in the connection. A global reduction factor of 0.4 is recommended to achieve a target reliability of 3.60, which is a typical reliability index worldwide accepted for connections.

This study represents the first approximation of the reliability assessment problem. Thus, it must be interpreted with caution once a designer wants to incorporate its results into a design office. First, in this study, only one building was utilized in the NTHA, which limits its scope. More building configurations need to be considered in a further study. Furthermore, in this preliminary study, a global strength reduction factor was proposed herein. Other studies can explore the effect of using different strength reduction factors for each limit state assumed in the design of the connection.

## REFERENCES


[1] DeWolf J, Sarislay E. Column Base Plates with Axial Loads and Moments. J Struct Div 1980;106:2167–84.

[2] Astaneh A, Bergsma G, Shen JH. Behavior and design of base plates for gravity, wind and seismic loads. Proc. Natl. steel Constr. Conf., AISC Chicago, IL; 1992, p. 209–14.

[3] Burda JJ. Studies of seismic behavior of steel base plates. University of Nevada, Reno; 1999.

[4] Fahmy M, Stojadinovic B, Goel SC. Analytical and experimental studies on the seismic response of steel column bases. Proc. 8th Can. Conf. Earthq. Eng., 1999.

[5] Drake RM, Elkin SJ. Beam-column base plate design-LRFD method. Eng Journal-American Inst Steel Constr 1999;36:29–38.

[6] Fisher; James M. Base Plate and Anchor Rod Design. AISC Des Ser 2006:73.

[7] Grilli DA, Kanvinde AM. Special moment frame base connection: Design example 8. 2012 IBC SEAOC Struct Des Manual, Examples Steel-Frame Build 2013;4:255–80.

[8] Gomez I, Kanvinde A, Deierlein GG. Exposed Column Base Connections Subjected to Axial Compression and Flexure. AISC, Chicago 2010:257.

[9] Kanvinde AM, Grilli DA, Zareian F. Rotational Stiffness of Exposed Column Base Connections: Experiments and Analytical Models. J Struct Eng 2012;138:549–60. https://doi.org/10.1061/(asce)st.1943-541x.0000495.

[10] Rodas PT, Zareian F, Kanvinde A. Hysteretic Model for Exposed Column–Base Connections. J Struct Eng 2016;142:04016137. https://doi.org/10.1061/(asce)st.1943-541x.0001602.

[11] Grilli DA, Kanvinde AM. Embedded column base connections subjected to seismic loads: Strength model. J Constr Steel Res 2017;129:240–9. https://doi.org/10.1016/j.jcsr.2016.11.014.

[12] Rodas PT, Zareian F, Kanvinde A. Rotational Stiffness of Deeply Embedded Column–Base Connections. J Struct Eng 2017;143:04017064. https://doi.org/10.1061/(asce)st.1943-541x.0001789.

[13] Torres-Rodas P, Zareian F, Kanvinde A. A hysteretic model for the rotational response of embedded column base connections. Soil Dyn Earthq Eng 2018;115. https://doi.org/10.1016/j.soildyn.2018.08.015.

[14] Torres-Rodas P, Zareian F, Kanvinde A. Seismic demands in column base connections of steel moment frames. Earthq Spectra 2018;34:1383–403.

[15] Mora-Bowen N, Torres-Rodas P. Nonlinear Finite Element Models for Embedded Base Connections. In: Eccomas Proceedia, editor. 8th ECCOMAS Themat. Conf. Comput. Methods Struct. Dyn. Earthq. Eng., 8th ECCOMAS Thematic Conference on Computational Methods in Structural Dynamics and Earthquake Engineering; 2021, p. 4331–40. https://doi.org/10.7712/120121.8789.18586.

[16] Inamasu H, Kanvinde AM, Lignos DG. Seismic design of non-dissipative embedded column base connections. J Constr Steel Res 2021;177.

https://doi.org/10.1016/j.jcsr.2020.106417.

[17] Inamasu H, Lignos DG. Finite element modeling and behavior of dissipative embedded column base connections under cyclic loading. J Constr Steel Res 2022;189:107063.

[18] Torres-Rodas P, Flores F, Zareian F. Seismic response of steel moment frame considering gravity system and column base flexibility. 11th National Conference Earthquake Engineering 2018, NCEE 2018 Integration Science Engineering Policy 2018;12:7383–93.

[19] Torres-Rodas P, Flores F, Astudillo B, Pozo S. Sensitivity of Special Steel Moment Frames to the influence of column-base hysteretic behavior including gravity framing system. Proc. Int. Conf. Struct. Dyn. EURODYN 2 3629-3642, 2020, p. 3629–42. https://doi.org/10.47964/1120.9298.19279.

[20] Falborski T, Torres-Rodas P, Zareian F, Kanvinde A. Effect of Base-Connection Strength and Ductility on the Seismic Performance of Steel Moment-Resisting Frames. J Struct Eng 2020;146:04020054. https://doi.org/10.1061/(asce)st.1943-541x.0002544.

[21] Torres-Rodas P, Flores F, Pozo S, Astudillo BX. Seismic performance of steel moment frames considering the effects of column-base hysteretic behavior and gravity framing system. Soil Dyn Earthq Eng 2021;144:106654. https://doi.org/10.1016/j.soildyn.2021.106654.

[22] Aviram A, Stojadinovic B, Kiureghian A Der. Performance and reliability of exposed column base plate connections for steel moment-resisting frames 2010:190.

[23] Torres-Rodas P, Fayaz J, Zareian F. Strength resistance factors for seismic design of exposed based plate connections in special steel moment resisting frames. Earthq Spectra 2020;36:537–53. https://doi.org/10.1177/8755293019891714.

[24] Song B, Galasso C, Kanvinde A. Reliability Analysis and Design Considerations for Exposed Column Base Plate Connections Subjected to Flexure and Axial Compression. J Struct Eng 2021;147:04020328. https://doi.org/10.1061/(asce)st.1943-541x.0002903.

[25] American Society of Civil Engineers. Minimum design loads for buildings and other structures, American Society of Civil Engineers (ASCE). Reston, VA. 2016.

[26] Campos, Liseth; Torres-Rodas, Pablo;Quinde, Pablo; Yepez F. Influence of earthquake mechanisms to the seismic response of steel moment frames. In: Proceedings C, editor. 8th Int. Conf. Comput. Methods Struct. Dyn. Earthq. Eng. COMPDYN 2021, Athens: 8th ECCOMAS Thematic Conference on Computational Methods in Structural Dynamics and Earthquake Engineering; 2021. https://doi.org/10.7712/120121.8853.18546.

[27] Miranda, E., Eads, L., Davalos, H., & Lignos D. Assessment of the Probability of Collapse of Structures Under Earthquakes. Proc. 16th World Conf. Earthq. Eng., 2017.

[28] Jalayer F, Cornell CA, Chakroborty S, Roy R, Miranda E, Eads L, et al. Assessment of the probability of collapse of structures during earthquakes. Earthq Eng Struct Dyn 2016;128:122. https://doi.org/10.1115/1.4034725.

[29] Fayaz J, Torres-Rodas P, Medalla M, Naeim F. Assessment of ground motion amplitude scaling using interpretable Gaussian process regression: Application to steel moment frames. Earthq Eng Struct Dyn 2023.

[30] Ibarra LF, Medina RA, Krawinkler H. Hysteretic models that incorporate strength and

stiffness deterioration. Earthq Eng Struct Dyn 2005;34:1489–511. https://doi.org/10.1002/eqe.495.

[31] American Institute of Steel Construction. Specification for Structural Steel Buildings. ANSI/AISC 360-16. Chicago 2016.

[32] Kanvinde AM. Micromechanical simulation of earthquake-induced fracture in steel structures. Stanford University; 2004.

[33] Ancheta TD, Darragh RB, Stewart JP, Seyhan E, Silva WJ, Chiou BS-J, et al. NGA-West2 database. Earthq Spectra 2014;30:989–1005.

**COMPDYN 2023**

**Proceedings of the**
**9th International Conference on**
**Computational Methods in Structural Dynamics and Earthquake Engineering**

M. Papadrakakis, M. Fragiadakis (Eds.)

First Edition, October 2023

ISBN (set): 978-618-5827-01-4
ISBN (vol II): 978-618-5827-00-7



**Institute of Structural Analysis and Antiseismic Research**
**National Technical University of Athens, Greece**